European Community on Computational Methods in Applied Sciences

ECCOMAS Thematic Conference

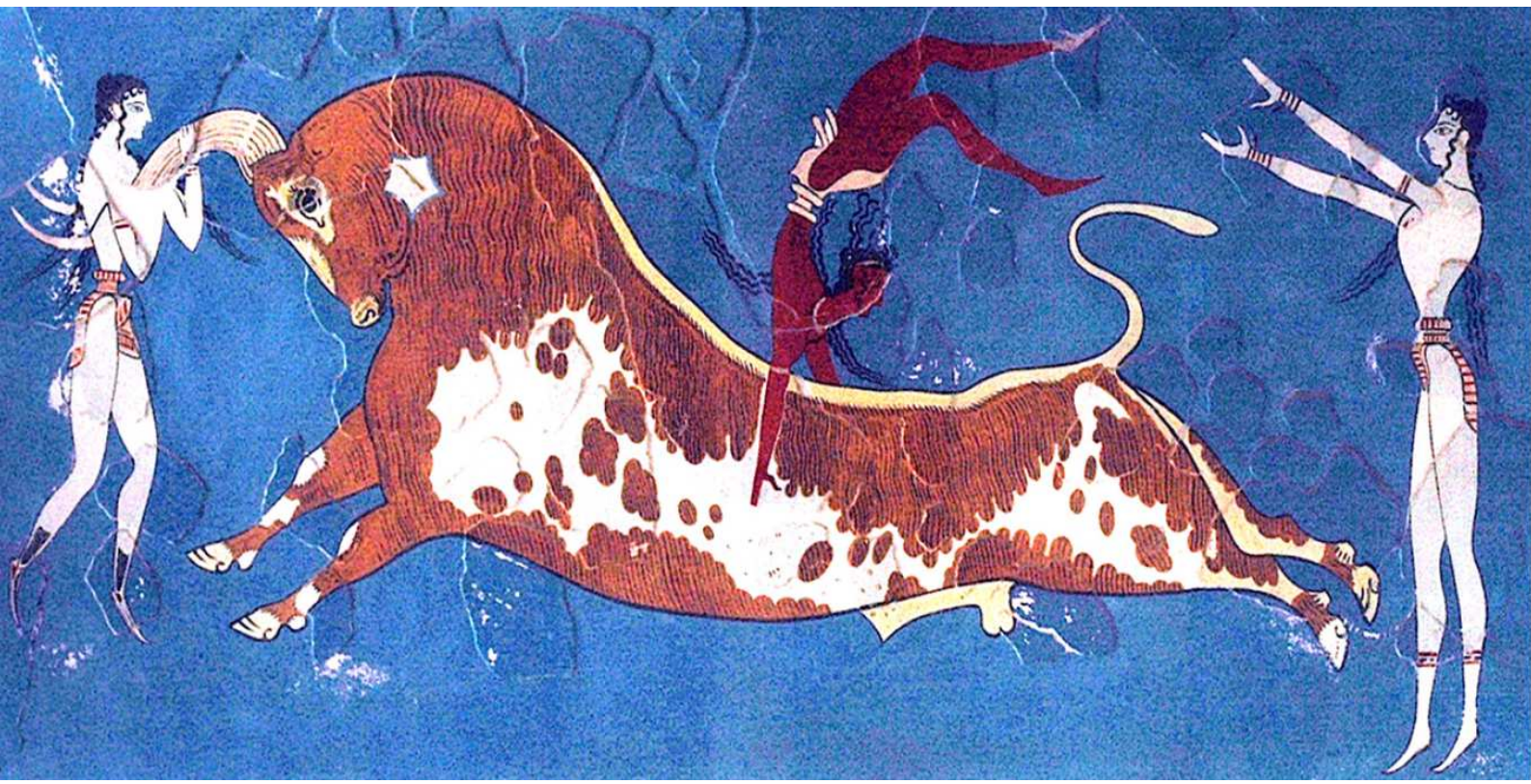
COMPDYN 2015

5th International Conference on
Computational Methods in Structural Dynamics and Earthquake Engineering

PROCEEDINGS

Volume I

M. Papadrakakis, V. Papadopoulos, V. Plevris (Eds)



An IACM Special Interest Conference

COMPDYN 2015

Computational Methods in Structural Dynamics and Earthquake Engineering

Proceedings of the 5th International Conference on Computational
Methods in Structural Dynamics and Earthquake Engineering
Held in Crete, Greece
25-27 May 2015

Edited by:

M. Papadrakakis
National Technical University of Athens, Greece

V. Papadopoulos
National Technical University of Athens, Greece

V. Plevris
School of Pedagogical and Technological Education, Athens, Greece

A publication of:

Institute of Structural Analysis and Antiseismic Research
School of Civil Engineering
National Technical University of Athens (NTUA)
Greece

COMPDYN 2015
Computational Methods in Structural Dynamics and Earthquake Engineering
M. Papadrakakis, V. Papadopoulos, V. Plevris (Eds)

First Edition, September 2015

© The authors

ISBN: **978-960-99994-7-2**

PREFACE

This volume contains the full-length papers presented in the 5th International Conference on Computational Methods in Structural Dynamics and Earthquake Engineering (COMPDYN 2015) that was held on May 25-27, 2015 on the Crete Island, Greece.

COMPDYN 2015, one of the thematic Conferences of the European Community on Computational Methods in Applied Sciences (ECCOMAS), is a Special Interest Conference of the International Association for Computational Mechanics (IACM) and has been promoted by the European Committee on Computational Solid and Structural Mechanics (ECCSM) of ECCOMAS. The purpose of the Conference is to bring together the scientific communities of Computational Mechanics, Structural Dynamics and Earthquake Engineering in an effort to facilitate the exchange of ideas in topics of mutual interests and to serve as a platform for establishing links between research groups with complementary activities. The communities of Structural Dynamics and Earthquake Engineering will benefit from this interaction, acquainting them with advanced computational methods and software tools which can highly assist in tackling complex problems in dynamic/seismic analysis and design, while also giving the Computational Mechanics community the opportunity to become more familiar with very important application areas of great social interest. The COMPDYN 2015 Conference is supported by the National Technical University of Athens (NTUA), the European Association for Structural Dynamics (EASD), the European Association for Earthquake Engineering (EAEE), the Greek Association for Computational Mechanics (GRACM) and the John Argyris Foundation.

The editors of this volume would like to thank all authors for their contributions. Special thanks go to the colleagues who contributed to the organization of the Minisymposia and to the reviewers who, with their work, contributed to the scientific quality of this e-book.

M. Papadrakakis
National Technical University of Athens, Greece

V. Papadopoulos
National Technical University of Athens, Greece

V. Plevris
School of Pedagogical and Technological Education, Athens, Greece

ACKNOWLEDGEMENTS

The conference organizers acknowledge the support towards the organization of the "5th International Conference on Computational Methods in Structural Dynamics and Earthquake Engineering", to the following organizations:

- European Community on Computational Methods in Applied Sciences (ECCOMAS)
- International Association for Computational Mechanics (IACM)
- School of Civil Engineering, National University of Athens (NTUA)
- Greek Association for Computational Mechanics (GRACM)
- European Association for Structural Dynamics (EASD)
- European Association for Earthquake Engineering (EAEE)
- John Argyris Foundation
- Hellenic Republic – Region of Crete

Plenary Speakers and Invited Session Organizers

We would also like to thank the Plenary and Semi-Plenary Speakers and the Minisymposia Organizers for their help in the setting up of a high standard Scientific Programme.

Plenary Speakers: Alain Combescure, C. Farhat, James Ricles, Shinobu Yoshimura

Semi-Plenary Speakers: Domniki Asimaki, Dimitri Beskos, Alexander Idesman, H. A. Jensen, Boris Jeremić, Andreas J. Kappos, Steen Krenk, Daniel Rixen, Y. B. Yang, Yong Yuan

MS Organizers: Pedro Costa Alves, António Arêde, Mitsuteru Asai, Panagiotis Asteris, Alessandro Baratta, Rui Barros, Elsa Caetano, Rui Calcada, Álvaro Cunha, Guido De Roeck, Raimundo Delgado, Pedro Delgado, Raimundo Delgado, Ioannis Dikaros, Dan Givoli, Jose Maria Goicolea, Muneo Hori, Mohammed Hussein, Alexander Idesman, Andreas Kappos, Spyros A. Karamanos, Radek Kolman, Dimitris Lignos, George Manos, Hermann Matthies, Mikayel Melkumyan, Jiri Naprstek, Roger Ohayon, Stavroula Pantazopoulou, Anthoula Panteli, Vissarion Papadopoulos, K-C. Park, Vagelis Plevris, Goran Sandberg, Evangelos Sapountzakis, Geza Seriani, Tasos Sextos, Sergey Sorokin, Aram Soroushian, Constantine Spyrakos, John Tsompanakis, Dimitris Vamvatsikos, Peter Van den Broeck, Katrien Van Nimmen, Ioannis Vayas, Castorina Vieira, Shinobu Yoshimura

SUMMARY

Preface..... iii

Acknowledgements..... iv

Contents..... viii

Volume I

Semi-plenary Lectures 1

Minisymposia

MS 1: Vibrations Induced By Rail And Road Traffic 26
Organized by Pedro Costa Alves and Mohammed Hussein

MS 2: Advances In Computational Structural Vibrations 146
Evangelos Sapountzakis and Ioannis Dikaros

MS 3: Progress And Challenges In Geotechnical Earthquake Engineering 218
Organized by Castorina Vieira and John Tsompanakis

MS 4: Innovative Systems For Seismic Resistant Steel Buildings 299
Organized by Ioannis Vayas

MS 5: Modern Methods In Creation Of Seismic Isolation Systems 349
Organized by Mikayel Melkumyan

MS 6: Numerical Simulation And Experimental Verification On Problems In The Field Of Earthquake Engineering And Structural Dynamics 388
Organized by George Manos

MS 7: Seismic Safety Assessment Of Structures 721
Organized by Raimundo Delgado, António Arêde and Pedro Delgado

MS 8: Periodicity-Induced Effects And Methods In Structural Dynamics 922
Organized by Sergey Sorokin

MS 9: Advances In Modeling Of Wave Propagation And Applications 946
Organized by Dan Givoli and Geza Seriani

MS 10: Control Of Vibrations In Civil Engineering By Passive, Active And Semi-Active Devices 972
Organized by Rui Barros and Alessandro Baratta

MS 11: Software Development In The Field Of Earthquake Engineering And Structural Dynamics 1011
Organized by Tasos Sextos

MS 12: Advances In Numerical Methods For Linear And Non-Linear Dynamics 1054
Organized by Alexander Idesman

MS 13: Renewable Energy Structures (Wind Turbines, Solar Irradiation, Hydropower) 1236
Organized by Álvaro Cunha and Elsa Caetano

MS 15: Reduced-Order Modeling Of Aero, Civil And Mechanical Dynamical Systems 1342
Organized by K-C. Park, Roger Ohayon, Hermann Matthies and Goran Sandberg

MS 16: Loss, Risk, Uncertainty And Modeling For Seismic Performance Assessment Of Structures 1379
Organized by Dimitris Vamvatsikos and Dimitris Lignos

MS 17: Dynamic Effects On Railway Bridges 1637
Organized by Rui Calcada, Raimundo Delgado and Jose Maria Goicolea

MS 18: Seismic Analysis Methods For Existing Bridges Prior To And After Retrofitting 1731
Organized by Andreas Kappos

MS 19: High-Performance Computing For Structural Mechanics And Earthquake / Tsunami Engineering 1824
Organized by Shinobu Yoshimura, Muneo Hori and Mitsuteru Asai

MS 20: New Technologies And Methods For Damage Control And Seismic Retrofit Of Heritage Structures In Earthquakes: Simulation, Devices And Digital Technologies 1838
Organized by Stavroula Pantazopoulou

MS 22: Accuracy And Computational Efficiency Of Structures Dynamic/Seismic Analyses 1899
Organized by Aram Soroushian and Anthoula Panteli

MS 23: Non-Linear Dynamics And Wave Propagation 1941
Organized by Jiri Naprstek, Radek Kolman and K-C. Park

MS 24: Seismic Behavior Of Industrial Facilities And Pipelines 2004
Organized by Spyros A. Karamanos and Vissarion Papadopoulos

MS 25: Modeling And Vulnerability Assessment Of Masonry Structures 2105
Organized by Vagelis Plevris and Panagiotis Asteris

MS 27: Condition Assessment And Intervention On Monuments And Historic Structures 2273
Organized by Constantine Spyrakos

MS 28: Human Induced Vibrations 2440
Organized by Guido De Roeck, Peter Van Den Broeck and Katrien Van Nimmen

Volume II

Regular Sessions

RS 1: Algorithms For Structural Health Monitoring 2536

RS 2: Constitutive Modelling Under Earthquake Loading 2611

RS 3: Dynamics Of Coupled Problems And Micro 2659

RS 4: Geotechnical Earthquake Engineering 2728

RS 5: Impact Dynamics 2865

RS 6: Inverse Problems In Structural Dynamics 2961

RS 7: Structural Dynamics 2995

RS 8: Numerical Simulation Methods For Dynamic Problems 3151

RS 9: Optimum Design In Structural Dynamics And Earthquake Engineering 3274

RS 10: Steel And Composite Structures 3610

RS 11: Performance-Based Earthquake Engineering 3675

RS 12: Repair And Retrofit Of Structures 3861

RS 13: Seismic Isolation 4011

RS 14: Seismic Risk And Reliability Analysis 4114

RS 15: Soft Computing Applications 4223

RS 16: Soil-Structure Interaction 4268

RS 17: Sound And Vibration 4364

RS 18: Concrete Structures 4528

RS 19: Wave Propagation And Soil Dynamics 4584

CONTENTS

Semi-plenary Lectures

THE USE OF MODEL REDUCTION TECHNIQUES IN COMPLEX SIMULATION-BASED PROBLEMS INVOLVING FINITE ELEMENT MODELS……1
H.A. Jensen, A. Muñoz, E. Millas

SEISMIC ANALYSIS OF LONG TUNNEL: SIMPLIFIED OR UNIFIED……16
Yong Yuan, Haitao Yu

Minisymposia

MS 1: VIBRATIONS INDUCED BY RAIL AND ROAD TRAFFIC

RAILWAY-INDUCED GROUND VIBRATIONS IN THE PRESENCE OF LOCAL TRACK IRREGULARITIES AND WHEEL FLATS……26
Georges Kouroussis, Georgios Alexandrou, David Connolly, Konstantinos Vogiatzis, Olivier Verlinden

IMPACT RESPONSES OF PRESTRESSING TENDONS IN RAILWAY CONCRETE SLEEPERS IN HIGH SPEED RAIL ENVIRONMENTS……38
Sakdirat Kaewunruen, Alex Remennikov

EXPERIMENTAL AND NUMERICAL EVALUATION OF THE EFFICIENCY OF A STIFF WAVE BARRIER IN THE SOIL……49
Pieter Coulier, Vicente Cúellar, Geert Degrande, Geert Lombaert

FAST COMPUTATION OF TRAIN-INDUCED VIBRATIONS IN HOMOGENEOUS AND LAYERED SOILS……66
Lutz Auersch

THE INFLUENCE OF DEGRADATION OF SHEAR MODULUS OF SOIL ON PREDICTED RAILWAY VIBRATIONS IN TUNNELS EXCAVATED WITH TBM: A NUMERICAL ANALYSIS……83
J. Fernández Ruiz, P. Alves Costa, P. Lopes, L. Medina Rodríguez

A MIXED SPACE-TIME AND WAVENUMBER DOMAIN MODEL FOR PREDICTING GROUND VIBRATION FROM RAILWAY TRACKS……96
Samuel Koroma, David Thompson, Mohammed Hussein, Evangelos Ntotsios

VIBRATIONS IN BUILDINGS DUE TO RAILWAY TRAFFIC IN TUNNELS: MODELLING STRATEGIES AND INFLUENCE OF SOIL STIFFNESS……108
P. Lopes, P. Alves Costa, R. Calçada, A. Cardoso

THE DYNAMIC INTERACTION OF TWIN TUNNELS EMBEDDED IN A HOMOGENEOUS HALF-SPACE……120
Waleed I. Hamad, Hugh E.M. Hunt, James P. Talbot, Mohammed F.M. Hussein, David J. Thompson

PREDICTIONS OF THE DYNAMIC RESPONSE OF PILED FOUNDATIONS IN A MULTI-LAYERED HALF-SPACE DUE TO INERTIAL AND RAILWAY INDUCED LOADINGS……133
Evangelos Ntotsios, Waleed Hamad, David Thompson, Mohammed Hussein, Hugh Hunt, James Talbot

MS 2: ADVANCES IN COMPUTATIONAL STRUCTURAL VIBRATIONS

MODELLING OF WARPING EIGENVIBRATION BY NON-UNIFORM TORSION……146
Justín Murín, Mehdi Aminbaghai, Juraj Hrabovský, Herbert Mang

GENERALIZED WARPING EFFECT IN THE DYNAMIC ANALYSIS OF BEAMS OF ARBITRARY CROSS SECTION……..165
Ioannis Dikaros, Evangelos Sapountzakis, Amalia Argyridi, Dimitrios Papadopoulos

MODAL AND FREQUENCY DOMAIN BASED TECHNIQUES FOR FINITE ELEMENT MODEL CORRELATION……..191
Judith Mercer, Guglielmo Aglietti, Andrew Kiley

ON THE FORCED VIBRATION TEST BY VIBRODYNE……209
Mariano Modano, Francesco Fabbrocino, Antonio Gesualdo, Giovanni Matrone, Ilenia Farina, Fernando Fraternali

MS 3: PROGRESS AND CHALLENGES IN GEOTECHNICAL EARTHQUAKE ENGINEERING

SOIL STRUCTURE INTERACTION ASSESSMENT WITH ADVANCED NUMERICAL SIMULATIONS……218
Davide Forcellini, Stefania Gobbi

UNDERSTANDING SHEAR WAVE VELOCITIES CORRELATIONS WITH N-SPT AND QC-CPT VALUES……230
Muhsin Elie Rahhal, Farah Harake

NUMERICAL SIMULATIONS OF LIQUEFACTION PHENOMENA AFTER EMILIA ROMAGNA (20 MAY 2012) EARTHQUAKE……242
Davide Forcellini, Laura Tonni, Cristina Osti, Guido Gottardi

SEISMIC EVALUATION OF EMBANKMENT-TYPE STRUCTURES WITH COUPLED HYDRO-MECHANICAL MODEL……251
Ioanna Rapti, Fernando Lopez-Caballero, Arezou Modaressi-Farahmand-Razavi, Alexandre Foucault, Francois Voldoire

SEISMIC RESPONSE ANALYSIS OF A GEOGRID REINFORCED WALL CONSTRUCTED WITH RECYCLED CONSTRUCTION AND DEMOLITION WASTE……262
Castorina Silva Vieira

SEISMIC GROUND RESPONSE AT LOTUNG (TAIWAN)……277
Dimitrios Karofyllakis, Gaetano Elia, Mohamed Rouainia

THREE DIMENSIONAL ANALYSIS OF A CFRD DAM USING THE MATERIAL POINT METHOD……287
F. Zabala, R. D. Rodari, L. O. Oldecop

MS 4: INNOVATIVE SYSTEMS FOR SEISMIC RESISTANT STEEL BUILDINGS

COLLAPSE RISK EVALUATION OF SELF-CENTERING STEEL MRFS WITH VISCOUS DAMPERS IN NEAR-FAULT REGIONS……299
George Kamaris, Angelos Tzimas, Theodore Karavasilis, Carmine Galasso

BEHAVIOR OF HIGH STRENGTH STEEL FUSEIS SEISMIC RESISTANT SYSTEMS……318
Stella Avgerinou, Ioannis Vayas

PERFORMANCE OF MULTI-STOREY COMPOSITE STEEL-CONCRETE FRAMES WITH DISSIPATIVE FUSE DEVICES……334
Alper Kanyilmaz, Carlo Andrea Castiglioni

MS 5: MODERN METHODS IN CREATION OF SEISMIC ISOLATION SYSTEMS

ON THE USE OF MECHANICAL METAMATERIALS FOR INNOVATIVE SEISMIC ISOLATIONS SYSTEMS……349
F. Fraternali, G. Carpentieri, R. Montuori, A. Amendola, G. Benzoni

METHODS OF CREATION OF BASE ISOLATION SYSTEMS FOR RETROFITTING OF EXISTING REINFORCED CONCRETE FRAME BUILDINGS……359
Mikayel Melkumyan

INNOVATIVE TECHNIQUE FOR THE BASE ISOLATION OF EXISTING BUILDINGS……377
Alessandro De Stefano, Paolo Clemente, Stefano Invernizzi, Emiliano Matta, Antonino Quattrone

MS 6: NUMERICAL SIMULATION AND EXPERIMENTAL VERIFICATION ON PROBLEMS IN THE FIELD OF EARTHQUAKE ENGINEERING AND STRUCTURAL

A NOVEL MECHANISM FOR RESTRAINING SEISMIC ACTIONS IN DUCTILE BRIDGES: ANALYTICAL MODELING AND EXPERIMENTAL VERIFICATION……388
Vasileios Pilitsis, Vassilis K. Papanikolaou, Ioannis Tegos, Kosmas-Athanasios Stylianidis

EXPERIMENTAL AND ANALYTICAL INVESTIGATION OF AN UNCONVENTIONAL, ROCKING TYPE RESPONSE MECHANISM FOR EARTHQUAKE-RESISTANT BRIDGES……402
Vasileios Pilitsis, Ioannis Tegos, Vassilis K. Papanikolaou, Kosmas-Athanasios Stylianidis

IN-SITU MEASURED DYNAMIC RESPONSE OF THE BELL TOWER OF AGIOS GERASIMOS IN LIXOURI-KEFALONIA, GREECE AND ITS UTILIZATION IN THE NUMERICAL PREDICTIONS OF ITS EARTHQUAKE RESPONSE……417
G.C. Manos, E. Kozikopoulos

THE DYNAMIC AND EARTHQUAKE RESPONSE OF A TWO STORY OLD R/C BUILDING WITH MASONRY INFILLS IN LIXOURI-KEFALONIA, GREECE INCLUDING SOIL-FOUNDATION DEFORMABILITY……435
George Manos, Dionisios Naxakis, Vasilios Soulis

THE DYNAMIC AND EARTHQUAKE RESPONSE OF BASILICA CHURCHES IN KEFALONIA, GREECE INCLUDING SOIL FOUNDATION DEFORMABILITY AND WALL DETACHMENT……460
George Manos, Evaggelos Kozikopoulos

NUMERICAL SIMULATION OF THE LIMIT NON-LINEAR BEHAVIOUR OF UNREINFORCED STONE MASONRY UNDER IN-PLANE STATE OF STRESS FROM GRAVITATIONAL AND SEISMIC ACTIONS……487
G.C. Manos, L. Kotoulas, V. Soulis, O. Felekidou

EXPERIMENTAL INVESTIGATION AND NUMERICAL SIMULATION OF SHEAR BEHAVIOUR OF RC T-BEAM SPECIMENS WITH OR WITHOUT SFRP-STRIPS UNDER CYCLIC LOADING……505
George Manos, Konstantinos Katakalos, Marios Theofanous

CYCLIC RESPONSE OF A STEEL BEAM-TO-COLUMN CONNECTIONS – AN EXPERIMENTAL AND NUMERICAL STUDY……519
G.C. Manos, A. Nalmpantidou, V. Kourtides, A. Anastasiadis,

THE DYNAMIC RESPONSE OF A MOCK-UP OF THE RESTORED ANCIENT NORTH WALL SCHEME FOR THE MACEDONIAN PALACE AT VERGINA - GREECE……537
George Manos, Konstantinos Katakalos, Lambros Kotoula, Olympia Felekidou

STUDY OF THE LOADING ARRANGEMENT FOR THE STIFFNESS TESTS OF THE COLUMN HEAD ASSEMBLY AND ITS SPRINGS UTILIZED AT THE NIARCHOS CULTURAL CENTER AT ATHENS - GREECE……551
G.C. Manos, V. Kourtides, K. Katakalos, L. Kotoulas, A. Nalmpantidou

ANALYTICAL AND EXPERIMENTAL STUDY ON THE RESPONSE OF A SEISMIC RESTRAINER SYSTEM FOR BRIDGES……568
Olga Markogiannaki, Ioannis Tegos

ANALYTICAL AND EXPERIMENTAL INVESTIGATION ON EXPLOITING PREFABRICATION IN PIER CONSTRUCTION OF PRECAST BRIDGES……583
Nikolaos G. Orologopoulos, Vasileios G. Pilitsis, Konstantinos Katirtzoglou, Ioannis A. Tegos, Kosmas-Athanasios Stylianidis

MODELING AND IDENTIFICATION OF THE DYNAMIC RESPONSE OF AN EXISTING THREE-STORY STEEL STAIRWAY……595
Triantafyllos Makarios, George Manolis, Ioanna Karetsou, Michael Papanicolaou, Vasiliki Terzi

INVESTIGATION OF NOVEL ANCHORING DEVICES FOR OPEN HOOP CFRP STRIPS BONDED ON R/C ELEMENTS UNDER MONOTONIC AND CYCLIC LOADING-UNLOADING CONDITIONS……607
Konstantinos B. Katakalos, George C. Manos

SEISMIC FRAGILITY ASSESSMENT OF MEDICAL COMPONENTS……628
Luigi Di Sarno, Fabio Gustuti, Gennaro Magliulo, Crescenzo Petrone

MULTIPLE SUPPORT EXCITATION OF A BRIDGE BASED ON BEM ANALYSIS OF THE SUBSOIL-STRUCTURE-INTERACTION PHENOMENON……639
Ioanna-Kleoniki Fontara, Magdalini Titirla, Frank Wuttke, Asimina Athanatopoulou, George Manolis, Anastasios Sextos

SLENDER PROFILES FOR MOMENT RESISTING FRAMES IN MODERATE SEISMICITY REGIONS - NUMERICAL AND EXPERIMENTAL INVESTIGATIONS……653
Matthias Wieschollek, Benno Hoffmeister And Markus Feldmann

CONCRETE-TO-CONCRETE INTERFACES UNDER CYCLIC LOADING: FINITE ELEMENT ANALYSIS TOWARDS EXPERIMENTAL VERIFICATION……666
Vassilis Papanikolaou, Georgia Thermou

DEFORMATION CAPACITY OF NON-CONFORMING RC SHEAR WALLS: ANALYTICAL AND NUMERICAL ESTIMATION - TEST VERIFICATION……680
Konstantinos Christidis, Vasiliki Anagnostopoulou, Konstantinos Trezos, Christos Zeris

SEISMIC ANALYSIS OF PRESTRESSED STADIUM ROOF……696
P. Rosko, A. Bekö

THE USE OF ELASTIC OSCILLATIONS OF DIFFERENT WAVELENGTHS TO EVALUATE THE DYNAMIC PARAMETERS OF BUILDINGS AND STRUCTURES AND ASSESS THE STRENGTH OF MATERIALS OF THE BUILDING CONSTRUCTION……706
Sergey Savin, Valerios Tsakalidis

MS 7: SEISMIC SAFETY ASSESSMENT OF STRUCTURES

SEISMIC PERFORMANCE OF HIGH-RISE STEEL MRFS WITH OUTRIGGER AND BELT TRUSSES THROUGH NONLINEAR DYNAMIC FE SIMULATIONS……721
Emanuele Brunesi, Roberto Nascimbene, Gian Andrea Rassati, Lorenzo Casagrande

EFFECT OF OPENINGS ON NONLINEAR DYNAMIC RESPONSES OF MASONRY INFILLED RC FRAMES……736
Y. P. Yuen, J. S. Kuang

A DESIGN PROCEDURE FOR SEISMIC RETROFITTING OF REINFORCED CONCRETE FRAME AND CONCENTRIC BRACED STEEL BUILDINGS WITH DISSIPATIVE BRACINGS……746
Alessandro Vittorio Bergami, Camillo Nuti

ROCKING BEHAVIOUR OF SIMPLE UNREINFORCED LOAD-BEARING MASONRY WALLS INCLUDING SOUNDPROOFING RUBBER LAYERS……759
C. Mordant, V. Denoël, H. Degée

NUMERICAL MODELLING, ANALYSIS AND RETROFIT OF THE HISTORICAL MASONRY BUILDING “LA SAPIENZA”……772
Silvia Caprili, Federico Mangini, Walter Salvatore

INFLUENCE OF MODELLING PARAMETERS ON THE FRAGILITY ASSESSMENT OF PRE-1970 ITALIAN RC STRUCTURES……788
Gerard O'Reilly, Timothy Sullivan

DEVELOPMENT OF A SIMPLIFIED DISPLACEMENT-BASED PROCEDURE FOR THE SEISMIC ASSESSMENT OF RC WALL BUILDINGS……810
Timothy Sullivan, Matthew Fox

STRENGTH AND STABILITY ASSESSMENT OF EXISTING BUILDINGS IN ISRAEL……825
Nicolae Gluck, Rina Farhat, Rami Eid, Uri Tzadka

PROBABILISTIC EVALUATION OF DAM BASE SLIDING……836
Gabriele Fiorentino, Luca Furgani, Simone Magliano, Camillo Nuti

NUMERICAL SEISMIC SAFETY ASSESSMENT OF RC BRIDGES WITH HOLLOW PIERS ……845
Pedro Delgado, António Arêde, Nelson Vila Pouca, Aníbal Costa

EFFICIENCY OF DIFFERENT RETROFITTING TECHNICHS FOR RC COLUMNS UNDER BIAXIAL LOADING: EXPERIMENTAL STUDY……865
H. Rodrigues, A. Furtado, P. Rocha, A. Arêde

A MODEL FOR CARBON AND STAINLESS STEEL REINFORCING BARS INCLUDING INELASTIC BUCKLING FOR EVALUATION OF CAPACITY OF EXISTING STRUCTURES……876
Zhihao Zhou, Davide Lavorato, Camillo Nuti, Giuseppe Carlo Marano

USING DIFFERENT UNCERTAINTY MODELS FOR SEISMIC ASSESSMENT OF RC BRIDGES……887
Ricardo Monteiro, Raimundo Delgado, Rui Pinho

PERFORMANCE BASED EARTHQUAKE ENGINEERING APPROACH APPLIED TO BRIDGES IN A ROAD NETWORK……900
C. Zelaschi, G. De Angelis, F. Giardi, D. Forcellini, R. Monteiro

DEMAND HAZARD ANALYSIS: A TOOL FOR ASSESSING THE ADEQUACY OF CAPACITY DESIGN APPROACH FOR DEFINITION OF THE DESIGN SHEAR FORCES IN THE FRAME BUILDINGS……911
Jure Žižmond, Matjaž Dolšek

MS 8: PERIODICITY-INDUCED EFFECTS AND METHODS IN STRUCTURAL DYNAMICS

USING PERIODICITY TO MITIGATE GROUND VIBRATION……922
Lars Vabbersgaard Andersen

TWO-DIMENSIONAL LINEAR MODEL OF ELASTIC SHELL MADE OF ANISOTROPIC HETEROGENEOUS MATERIAL……933
Petr Tovstik, Tatiana P. Tovstik, Daniil Al'chibaev

MS 9: ADVANCES IN MODELING OF WAVE PROPAGATION AND APPLICATIONS

MULTI-SCALE/MULTI-DATA INVERSION FOR ELASTIC EARTH STRUCTURE - A CONCEPT……946
Andreas Fichtner, Michael Afanasiev, Korbinian Sager, Laura Ermert

A FICTITIOUS DOMAIN APPROACH FOR WAVE PROPAGATION PROBLEMS IN UNBOUNDED DOMAINS……959
Silvia Falletta, Giovanni Monegato

MS 10: CONTROL OF VIBRATIONS IN CIVIL ENGINEERING BY PASSIVE, ACTIVE AND SEMI-ACTIVE DEVICES

EFFECTIVENESS OF TUNED MASS DAMPER IN DAMAGE REDUCTION OF BUILDING UNDER FAR-FIELD GROUND MOTIONS……..…….…….972
Chayut Ngamkhanong, Tospol Pinkaew

NEURO-FUZZY MODELING OF A SPONGE-TYPE MR DAMPER……..……..984
Manuel T. Braz-César, Rui C. Barros

SEISMIC RESPONSE REDUCTION OF BUILDING STRUCTURES USING A SEMI-ACTIVE CONTROL SYSTEM BASED ON A BRAIN EMOTIONAL LEARNING CONTROLLER……..……998
Manuel T. Braz-César, Rui C. Barros

MS 11: SOFTWARE DEVELOPMENT IN THE FIELD OF EARTHQUAKE ENGINEERING AND STRUCTURAL DYNAMICS

AN INTEGRATED FRAMEWORK FOR THE ANALYSIS OF MIXED-TYPE REINFORCED CONCRETE STRUCTURES……..…..1011
Vahid Sadeghian, Oh-Sung Kwon, Frank Vecchio

NUMERICAL SEISMIC ASSESSMENT OF AN EXISTING BRIDGE WITH DIFFERENT SUPPORT CONFIGURATIONS……..……1024
Ciro Del Vecchio, Maria C. Caruso, Luigi Di Sarno, Oh-Sung Kwon, Andrea Prota

OBJECTIVE EVALUATION OF THE Q FACTOR OF IRREGULAR RC BUILDINGS DESIGNED ACCORDING TO EC8 – DESIGN AND ANALYSES PROCEDURES……..1040
Vasiliki Anagnostopoulou, Stratis Volakos, Christos Zeris

MS 12: ADVANCES IN NUMERICAL METHODS FOR LINEAR AND NON-LINEAR DYNAMICS

CRACKING AND FRACTURE OF HSS BRACES UNDER CYCLIC LOADING……..1054
Madhar Haddad, Robert Tremblay, Liang Chen, Lucea Tirca

CALCULATING THE FREQUENCY OF AN ACTUAL STRUCTURE USING THE RAYLEIGH TECHNIQUE……..……1070
Alexandre De M. Wahrhaftig, Reyolando M. L. R. F. Brasil

EFFICIENT NONLINEAR DYNAMIC ANALYSIS OF FRAME STRUCTURES……..1080
Johannes Burtscher

A NEW 3D CO-ROTATIONAL BEAM ELEMENT FOR NONLINEAR DYNAMIC ANALYSIS……..1087
Thanh-Nam Le, Jean-Marc Battini, Mohammed Hjiaj

ENERGY METHOD FOR COUPLING NEWMARK AND ALPHA-SCHEMES TIME INTEGRATORS WITH DIFFERENT TIME STEPS……..1111
Michael Brun, Anthony Gravouil, Alain Combescure

MULTIGRID SOLVER WITH DOMAIN DECOMPOSITION SMOOTHING FOR STEADY-STATE INCOMPRESSIBLE FSI PROBLEMS……..1128
Eugenio Aulisa, Simone Bná, Giorgio Bornia

OPTIMAL DESIGN FOR HIGH RESISTANT ROCKFALL BARRIERS……1145
Juan Escallon, Perry Bartelt, Eleni Chatzi

SMOOTH AND NON-SMOOTH SOLUTIONS FOR GEOMETRICALLY EXACT BEAMS SUBJECTED TO IMPACT……1169
Tien Long Nguyen, Mohammed Hjiaj, Carlo Sansour

A VARIATIONAL FORMULATION OF DISCONTINUOUS-GALERKIN TIME INTEGRATORS……1178
Pablo Mata Almonacid, Yongxing Shen, Vahid Ziaei-Rad

SVD FAMILY FOR ANALYZING CAR CRASH BEHAVIOR……1188
Thi-Thanh-Thuy Vuong, Louis Jezequel, Yves Tourbier

COMPARISON OF INTEGRATION ALGORITHMS FOR REAL-TIME HYBRID SIMULATION USING FREQUENCY DOMAIN-BASED ERROR INDICATORS……1208
Reza Mirza Hessabi, Ali Ashasi-Sorkhabi, Yanhui Liu, Oya Mercan

DE3: YET ANOTHER HIGH-ORDER INTEGRATION SCHEME FOR LINEAR STRUCTURAL DYNAMICS……1216
Alexandre Depouhon, Emmanuel Detournay, Vincent Denoël

A MESHLESS NEURAL NETWORK APPROACH FOR THE DYNAMIC ANALYSIS OF ELASTIC SYSTEMS……1224
Luca Facchini, Michele Betti

MS 13: RENEWABLE ENERGY STRUCTURES (WIND TURBINES, SOLAR IRRADIATION, HYDROPOWER)

GENETIC OPTIMIZATION OF TOWER VIBRATIONS WITH PENDULUM TMD UNDER THE INFLUENCE OF SEVERAL WIND SPECTRUMS……1236
Gino B. Colherinhas, Maura A. M. Shzu, Suzana M. Avila, Marcus V. G. De Morais

SLENDER LARGE-SCALE PARABOLIC TROUGHS USING SHAPE-OPTIMIZED HOLLOW STRUCTURES MADE OF HIGH-STRENGTH CONCRETE……1249
Christoph Kämper, Janna Krummenacker, Patrick Forman, Peter Mark, Jürgen Schnell

PROPABILISTIC FATIGUE ANALYSIS OF OFFSHORE WIND TURBINES……1257
Dimitrios V. Bilionis, Dimitrios Vamvatsikos

ONE YEAR OF CONTINUOUS DYNAMIC MONITORING OF A WIND TURBINE. STRUCTURAL INTEGRITY AND FATIGUE ASSESSMENT……1274
Gustavo Oliveira, Filipe Magalhães, Álvaro Cunha, Elsa Caetano

A CLOSED-FORM APPROACH TO PREDICT GUST INDUCED FATIGUE DAMAGES……1288
Frank H. Kemper

MULTIVARIATE STOCHASTIC METHODS FOR THE STRUCTURAL DESIGN OF WIND TURBINES……1306
Frank H. Kemper, Juan Jose Calle Escribano

SEMI-ACTIVE PENDULUM TO CONTROL OFFSHORE WIND TURBINE VIBRATIONS……1317
Suzana Moreira Avila, Pedro Varella Barca Guimarães

ANALYSIS OF COUPLED SYSTEMS CONSISTING OF SUPPORT STRUCTURE AND HIGH VOLTAGE SUBSTATION EQUIPMENT WITH VERIFICATION VIA FULL-SCALE SHAKING TABLE TESTS……1330
Shakhzod M. Takhirov, Amir S.J. Gilani, Frank Blalock, Cary Ahrano

MS 15: REDUCED-ORDER MODELING OF AERO, CIVIL AND MECHANICAL DYNAMICAL SYSTEMS

STOCHASTIC REDUCED-ORDER MODELS FOR CALCULATING RESPONSE STATISTICS OF STRUCTURAL SYSTEMS SUBJECTED TO RANDOM INPUT……1342
Alin Radu, Mircea Grigoriu

SEMI-ANALYTICAL REDUCED-ORDER MODELS FOR THE UNSTEADY AERODYNAMIC LOADS OF SUBSONIC WINGS……1353
Marco Berci

MS 16: LOSS, RISK, UNCERTAINTY AND MODELING FOR SEISMIC PERFORMANCE ASSESSMENT OF STRUCTURES

VERTICAL ACCELERATION DEMANDS ON NONSTRUCTURAL COMPONENTS IN BUILDINGS……1379
Lukas Moschen, Ricardo A. Medina, Christoph Adam

INFLUENCE OF ROTATED GROUND MOTION COMPONENTS ON THE RESPONSE DISTRIBUTION OF INELASTIC OSCILLATORS……1400
Dimitrios Giannopoulos, Dimitrios Vamvatsikos

A NEXT GENERATION SCALAR INTENSITY MEASURE FOR ANALYTICAL VULNERABILITY STUDIES……1410
Athanasia Kazantzi, Dimitrios Vamvatsikos

NEAR -SOURCE PULSE-LIKE SEISMIC DEMAND FOR MULTI-LINEAR BACKBONE OSCILLATORS……1421
Georgios Baltzopoulos, Dimitrios Vamvatsikos, Iunio Iervolino

SEISMIC RELIABILITY ASSESSMENT OF ROCKING BEHAVIOUR UNDER NEAR-FAULT EXCITATIONS……1435
Elias Dimitrakopoulos, Themelina Paraskeva

POST-EARTHQUAKE RECOVERY OF A COMMUNITY AND ITS ELECTRICAL POWER SUPPLY SYSTEM……1451
Max Didier, Li Sun, Siddhartha Ghosh, Bozidar Stojadinovic

ESTIMATION OF CUMULATIVE SEISMIC DAMAGE TO URM BUILDINGS DURING EARTHQUAKE SEQUENCES……1462
Amaryllis Mouyiannou, Maria Rota, Andrea Penna

RELATIONSHIP BETWEEN THE VARIATION OF SEISMIC CAPACITY AFTER DAMAGING EARTHQUAKES, COLLAPSE PROBABILITY AND REPAIR COSTS: DETAILED EVALUATION FOR A NON-DUCTILE BUILDING……1478
M. Gaetani D'Aragona, M. Polese, A. Prota

EARTHQUAKE LOSS ASSESSMENT OF STEEL FRAME BUILDINGS DESIGNED IN HIGHLY SEISMIC REGIONS……1496
Seong-Hoon Hwang, Ahmed Elkady, Samy Al.Bardaweel, Dimitrios G. Lignos

CATASTROPHE RESILIENCE RELATED TO URBAN NETWORK SHAPE: PRELIMINARY ANALYSIS……1513
Anna Bozza, Domenico Asprone, Alessandro Fiasconaro, Vito Latora, Gaetano Manfredi

APPLICATION OF A DAMAGE STATE METHOD BASED ON PERIOD ELONGATION FOR TIME VARIANT VULNERABILITY OF DEGRADING REINFORCED CONCRETE BUILDINGS……1532
Konstantinos Trevlopoulos, Philippe Guéguen

RECORD-TO-RECORD VARIABILITY IN THE SEISMIC RESPONSE OF RC WALLS BUILDINGS SUBJECTED TO GROUND MOTIONS MATCHED TO THE CONDITIONAL SPECTRUM……1548
Matthew Fox, Timothy Sullivan

INFLUENCE OF JOINT RESPONSE IN THE ASSESSMENT OF SEISMIC PERFORMANCE OF EXISTING REINFORCED CONCRETE FRAMES……1560
Maria Teresa De Risi, Paolo Ricci, Gerardo Mario Verderame

ASSESSMENT OF MULTISTORY RC BUILDINGS SUFFERING INTER-STORY POUNDING……1580
Maria Favvata, Sofia Mochla, Maria Naoum, Chris Karayannis

SEISMIC RETROFIT DECISION-MAKING OF BRIDGES BASED ON LIFE-CYCLE COST CRITERIA……1591
Hossein Ebrahimian, Fatemeh Jalayer, Gaetano Manfredi

RISK-BASED DESIGN CHECK FOR COLLAPSE SAFETY USING FEW GROUND MOTIONS……1628
Marko Brozovič, Matjaž Dolšek

MS 17: DYNAMIC EFFECTS ON RAILWAY BRIDGES

DYNAMIC ANALYSIS OF TRAIN-BRIDGE SYSTEM SUBJECTED TO EARTHQUAKE ACTION CONSIDERING TOPOGRAPHIC EFFECTS……1637
Hong Qiao, He Xia, Xianting Du, Yong Nan

DRIVE-BY STRUCTURAL HEALTH MONITORING OF RAILWAY BRIDGES USING TRAIN-MOUNTED ACCELEROMETERS……1652
Cathal Bowe, Paraic Quirke, Daniel Cantero, Eugene J. Obrien

TEMPERATURE WARPING AND TRAIN-TRACK DYNAMIC ANALYSIS OF CRTS II SLAB BALLASTLESS TRACK……1664
Jingjing Yang, Nan Zhang

PARAMETRIC EVALUATION OF VISCOUS DAMPER RETROFIT FOR HIGH-SPEED RAILWAY BRIDGES……..1672
Sarah Rådeström, Viktor Tell, Mahir Ülker-Kaustell, Raid Karoumi

TRANSVERSAL VIBRATION CONTROL FOR CATENARY POLES ON A HIGH SPEED RAILWAY BRIDGE……..1682
Celine Anicotte, Dominique Botton

SEISMIC RESPONSE OF CABLE-STAYED BRIDGE STEEL TOWER PROVIDED WITH BRACING SYSTEM……..1700
Mohamed Omar

MODAL PROPERTIES OF SIMPLY SUPPORTED RAILWAY BRIDGES DUE TO SOIL-STRUCTURE INTERACTION……..1709
Christoffer Svedholm, Costin Pacoste, Raid Karoumi

SAFETY ASSESSMENT OF A SMALL SPAN HIGH-SPEED RAILWAY BRIDGE USING AN EFFICIENT PROBABILISTIC METHODOLOGY……..1720
João M. Rocha, António A. Henriques, Rui Calçada

MS 18: SEISMIC ANALYSIS METHODS FOR EXISTING BRIDGES PRIOR TO AND AFTER RETROFITTING

OPTIMAL DESIGN AND DYNAMICS OF TRUSS BRIDGES……..1731
G. Carpentieri, M. Modano, F. Fabbrocino, F. Fraternali

SEISMIC RESPONSE ANALYSIS OF A COUPLED VEHICLE- BRIDGE SYSTEM……..1741
Qing Zeng, Elias Dimitrakopoulos, Themelina Paraskeva

A STRUCTURAL HEALTH MONITORING DATA MANAGING SCHEME WITH RESILIENCY TO SEISMIC EVENTS: IMPLEMENTATION ON A ROAD NETWORK BRIDGE……..1757
George Sergiadis, Stelios Hadjidimitriou, Vasileios Charisis, Panagiotis Panetsos, Theodoros Chrysanidis

EVALUATION OF THE STIFFNESS AND DAMPING OF ABUTMENTS TO EXTEND DIRECT DISPLACEMENT-BASED DESIGN TO THE DESIGN OF INTEGRAL BRIDGES……..1767
Stergios Mitoulis, Sotiris Argyroudis, Mervyn Kowalsky

METHODOLOGY FOR THE DEVELOPMENT OF STRUCTURE SPECIFIC FRAGILITY CURVES FOR BRIDGES IN A ROADWAY NETWORK……..1780
Sotiria Stefanidou, Andreas Kappos

SEISMIC RETROFITTING OF R/C BRIDGES WITH THE USE OF UNBONDED TENDONS……..1799
Olga Markogiannaki, Ioannis Tegos

EXPERIMENTAL AND NUMERICAL ANALYSIS ON THE CYCLIC BEHAVIOR OF BRIDGE PIERS WITH AND WITHOUT CFRP RETROFIT……..1812
Pedro Delgado, Frutuoso Sousa, Patrício Rocha, António Arêde, Nelson Vila Pouca, Aníbal Costa, Raimundo Delgado

MS 19: HIGH-PERFORMANCE COMPUTING FOR STRUCTURAL MECHANICS AND EARTHQUAKE / TSUNAMI ENGINEERING

META-MODELING FOR CONSISTENT SEISMIC RESPONSE ANALYSIS……1824
Muneo Hori, Seizo Tanaka, Tsuyoshi Ichimura, W.L.L.Wijerathne, J.A.S.C. Jayasinghe

MS 20: NEW TECHNOLOGIES AND METHODS FOR DAMAGE CONTROL AND SEISMIC RETROFIT OF HERITAGE STRUCTURES IN EARTHQUAKES: SIMULATION, DEVICES AND DIGITAL TECHNOLOGIES

PARAMETRIC NUMERICAL STUDY OF THE SEISMIC RESPONSE OF CLASSICAL COLUMNS……1838
Ioannis Kavvadias, Lazaros Vasiliadis

ASSESSMENT OF SEISMIC VULNERABILITY OF HISTORICAL DEFENSIVE WALLS……1850
Graziano Leoni, Alessandro Zona, Quintilio Piattoni, Alessandra Meschini, Enrica Petrucci, Andrea Dall'Asta, Luigino Dezi

VULNERABILITY OF TORSIONALLY SENSITIVE HISTORICAL BUILDINGS UNDER SEISMIC LOADS……1865
Stylianos Pardalopoulos, Stavroula Pantazopoulou

ASSESSMENT OF STONE MASONRY WALLS WITH DETERIORATION AT THEIR BASE USING NON-LINEAR FINITE ELEMENT ANALYSES……1885
Georgios Papadopoulos, Dimos Charmpis, Rogiros Illampas

MS 22: ACCURACY AND COMPUTATIONAL EFFICIENCY OF STRUCTURES DYNAMIC/SEISMIC ANALYSES

FROM THE NOTIONS OF NONLINEARITY TOLERANCES TOWARDS A DEFICIENCY IN COMMERCIAL TRANSIENT ANALYSIS SOFTWARES AND ITS SOLUTION……1899
Aram Soroushian, Peter Wriggers, Jamshid Farjoodi

ON THE CONVENTIONAL FINITE ELEMENT SIZES IN PSEUDOSTATIC SEISMIC ANALYSES OF 2D FRAMES……1908
Amir Hossein Pariz, Bahram Kordbagh, Kiyanoush Ghazvini, Seyed Mohsen Borghei Razavi, Abbas Ali Jalalabadi

ON THE PERFORMANCE OF A TECHNIQUE TO ACCELERATE TIME INTEGRATION WHEN APPLIED TO SPACE STRUCTURES ANALYSES……1914
Alireza Garakaninezhad, Reza Kamyab Moghadas

USING ENERGY - BASED PUSHOVER METHODS IN SEISMIC EVALUATION OF STEEL BRACING STRUCTURES…..1921
Kaveh Nezamisavojbolaghi

MS 23: NON-LINEAR DYNAMICS AND WAVE PROPAGATION

ANALYSIS OF INFLUENCE OF SHORT MAGNETORHEOLOGICAL DAMPING ELEMENTS ON VIBRATIONS ATTENUATION OF RIGID ROTORS……1941
Jaroslav Zapomel, Petr Ferfecki

DESTRUCTION OF THIN FILMS WITH A DAMAGED SUBSTRATE AS A RESULT OF WAVES LOCALIZATION CAUSED BY PERIODIC IMPACT……1949
Andrei Abramian, Sergey Vakulenko

PRESTRESS TUNING OF THE NONLINEAR DYNAMICS OF TENSEGRITY METAMATERIALS……1960
F. Fraternali, A. Amendola, E. Hernández-Nava, R. Goodall, R.E. Skelton, V.F. Nesterenko

COMPARISON OF NUMERICAL AND SEMI-ANALYTICAL SOLUTION OF A SIMPLE NON-LINEAR SYSTEM IN STATE OF THE STOCHASTIC RESONANCE……1971
Jiří Náprstek, Cyril Fischer, Radomil Král, Stanislav Pospíšil

TIME DOMAIN SIMULATION OF VORTEX-INDUCED VIBRATION OF A CURVED BEAM USING A WAKE OSCILLATOR MODEL……1983
Yang Qu, Andrei Metrikine

PROBLEM OF NON-STATIONARY WAVES IN VISCOELASTIC ORTHOTROPIC STRIP SOLVED USING ANALYTICAL METHOD……1995
Vítězslav Adámek, František Valeš, Jan Červ

MS 24: SEISMIC BEHAVIOR OF INDUSTRIAL FACILITIES AND PIPELINES

PROBABILISTIC ASSESSMENT OF PIPELINE - FAULT CROSSING……2004
Vasileios Melissianos, Dimitrios Vamvatsikos, Charis Gantes

SEISMIC PERFORMANCE OF INDUSTRIAL PRESSURE VESSELS: PARAMETRIC INVESTIGATIONS OF SIMPLIFIED MODELING APPROACHES FOR VULNERABILITY ASSESSMENT……2021
Christos Z. Karakostas, Ioannis F. Moschonas, Vassilios A. Lekidis, Savvas P. Papadopoulos

SEISMIC PERFORMANCE ASSESSMENT OF OIL & GAS PIPING SYSTEMS THROUGH NONLINEAR ANALYSIS……2038
Oreste S. Bursi, Fabrizio Paolacci, Md Shahin Reza

SEISMIC FRAGILITY ANALYSIS OF STEEL STORAGE TANKS……2054
Fabrizio Paolacci, Hoang N. Phan, Daniele Corritore, Silvia Alessandri, Oreste S.Bursi, M. Shahin Reza

SURROGATE MODELLING OF LIQUID STORAGE TANKS FOR SEISMIC PERFORMANCE DESIGN AND ASSESSMENT……2066
Konstantinos Bakalis, Michalis Fragiadakis, Dimitrios Vamvatsikos

BURIED PIPELINES SUBJECTED TO GROUND DEFORMATION CAUSED BY LANDSLIDE TRIGGERING……2081
Angelos Tsatsis, Rallis Kourkoulis, George Gazetas

PERFORMANCE EVALUATION OF BURIED STEEL PIPES SUBJECT TO STRIKE SLIP FAULT OFFSETS……2093
E. Uckan, B. Akbas, F. Cakir, J. Shen, M. O'Rourke, M. Caglar, F. Paolacci

MS 25: MODELING AND VULNERABILITY ASSESSMENT OF MASONRY STRUCTURES

SHEAR STRENGTH AND DEFORMATION MECHANISMS OF COMBINED AND CONFINED MASONRY WALLS SUBJECTED TO CYCLIC LOADING……..2105
Arturo Tena-Colunga, Artemio Juárez-Ángeles, Víctor Hugo Salinas-Vallejo

ASSESSMENT OF THE LATERAL STIFFNESS OF WALLS WITH OPENINGS……..2123
Arturo Tena-Colunga, Germán Rivera-Hernández

DEM & FEM/DEM MODELS FOR LATERALLY LOADED MASONRY WALLS……..2144
Daniele Baraldi, Emanuele Reccia, Antonella Cecchi

3D FE PUSHOVER AND NON-LINEAR DYNAMIC ANALYSES OF A MASONRY CHIMNEY BEFORE AND AFTER SHORTENING……..2158
Elisa Bertolesi, Antonio Del Grosso, Gabriele Milani, Fabio Minghini, Antonio Tralli

SEISMIC PERFORMANCE OF HOLLOW BRICK INTERNAL PARTITIONS……..2167
Crescenzo Petrone, Gennaro Magliulo, Marco Russo, Gaetano Manfredi

DEFINITION OF MECHANICAL PROPERTIES OF EXISTING MASONRY ACCOUNTING FOR EXPERIMENTAL NOWLEDGE BY BAYESIAN UPDATING……..2177
Stefano Bracchi, Maria Rota, Andrea Penna, Guido Magenes

EVALUATION OF SEISMIC VULNERABILITY ASSESSMENT PARAMETERS FOR PORTUGUESE VERNACULAR CONSTRUCTIONS WITH NONLINEAR NUMERICAL ANALYSIS……..2191
Javier Ortega, Graça Vasconcelos, Mariana Correia, Hugo Rodrigues, Paulo B. Lourenço, Humberto Varum

MODELLING OF DIAGONAL COMPRESSION MASONRY WALLETS BY FINITE ELEMENTS WITH EMBEDDED DISCONTINUITIES……..2206
Gelacio Juárez-Luna, Arturo Tena-Colunga

ON THE SEISMIC RISK OF MEDIEVAL ITALIAN MASONRY TOWERS……..2216
Gianni Bartoli, Michele Betti, Silvia Monchetti

SEISMIC VULNERABILITY OF THE PIERO DELLA FRANCESCA'S FRESCO CALLED "RESURRECTION"……..2236
Giulio Castori, Antonio Borri, Romina Sisti, Alessandro De Maria, Marco Corradi

SENSITIVITY ANALYSIS OF THE SEISMIC RESPONSE OF BRITTLE STRUCTURAL ELEMENTS UNDER NEAR-FIELD SEISMIC INPUT EFFECTS……..2248
Paloma Pineda, Jorge D Navarro-Rubio, Miguel Ángel Gil-Martí

ANISOTROPIC FAILURE CRITERION FOR BRITLE MATERIALS USING ARTIFICIAL NEURAL NETWORKS……..2259
Vagelis Plevris, Panagiotis Asteris

MS 27: CONDITION ASSESSMENT AND INTERVENTION ON MONUMENTS AND HISTORIC STRUCTURES

EVALUATION OF THE SEISMIC VULNERABILITY OF THE "ANCIEN HÔPITAL DE SION" USING APPLIED ELEMENT MODELLING (AEM) AND LOCAL MECHANISM ANALYSIS.....2273
Angelo Garofano, Pierino Lestuzzi

NONLINEAR ANALYSIS AND SEISMIC STRENGTHENING OF MASONRY ARCHES: THE BLOCK-JOINT AND BLOCK-BLOCK FEM MODELS.....2287
Francesco Pugi, Alessio Francioso

SEISMIC PROTECTION OF HEAVY NON-STRUCTURAL MONOLITHIC OBJECTS AT THE TOP OF A HISTORICAL MASONRY CONSTRUCTION THROUGH BASE ISOLATION.....2300
Andrea Chiozzi, Michele Simoni, Antonio Tralli

THE COMBINATION OF NDTS FOR THE DIAGNOSTIC STUDY OF HISTORICAL BUILDINGS: THE CASE OF KAISARIANI MONASTERY.....2321
Antonia Moropoulou, Maria Apostolopoulou, Petros Moundoulas, Maria Karoglou, Ekaterini Delegou, Kyriakos Lampropoulos, Margarita Gritsopoulou, Asterios Bakolas

EXPERIMENTAL AND NUMERICAL INVESTIGATIONS FOR THE STRUCTURAL CHARACTERIZATION OF A HISTORIC RC ARCH BRIDGE.....2337
R. Ferrari, D. Froio, E. Chatzi, C. Gentile, F. Pioldi, E. Rizzi

EVALUATION OF THE DYNAMIC RESPONSE FOR A HISTORIC BYZANTINE CROSSED-DOME CHURCH THROUGH BLOCK-JOINT AND KINEMATIC ANALYSIS.....2354
Constantine C. Spyrakos, Francesco Pugi, Charilaos A. Maniatakis, Alessio Francioso

NUMERICAL INVESTIGATION OF THE SEISMIC RESPONSE OF HEPHAESTUS TEMPLE IN ATHENS, GREECE.....2366
Maria-Eleni Dasiou, Ioannis Psycharis

LASER SCANNING, MODELING, AND ANALYSIS FOR DAMAGE ASSESSMENT AND RESTORATION OF HISTORICAL STRUCTURES.....2375
Shakhzod Takhirov, Khalid M. Mosalam, Mohamed A. Moustafa, Liliya Myagkova, Brian Quigley

STRUCTURAL HEALTH MONITORING AND DIAGNOSTIC INVESTIGATIONS OF THE SCROVEGNI CHAPEL, ITALY.....2396
Claudio Modena, Filippo Lorenzoni, Mauro Caldon, Maria Rosa Valluzzi

STRUCTURAL MONITORING OF MONUMENTAL BUILDINGS: THE BASILICA OF SANTA MARIA DEGLI ANGELI IN ASSISI (ITALY).....2410
Nicola Cavalagli, Massimiliano Gioffrè, Vittorio Gusella

SEISMIC RISK OF HISTORIC STRUCTURES AND MONUMENTS: A NEED FOR A UNIFIED POLICY.....2423
Constantine C. Spyrakos

MS 28: HUMAN INDUCED VIBRATIONS

THE IMPACT OF VERTICAL HUMAN-STRUCTURE INTERACTION FOR FOOTBRIDGES.....2440
Katrien Van Nimmen, Kristof Maes, Geert Lombaert, Guido De Roeck, Peter Van Den Broeck

INFLUENCE OF HUMAN INDUCED FLOOR VIBRATIONS ON THE MEASUREMENT PRECISION OF FORCE PLATES IN A BIOMECHANICS LABORATORY.....2457
Horst Werkle, Wolfgang Francke, Andrei Firus

EQUIVALENT SPECTRAL MODEL FOR PEDESTRIAN-INDUCED FORCES ON FOOTBRIDGES: A GENERALIZED FORMULATION.....2469
Alberto Ferrarotti, Federica Tubino

EXPERIMENTAL INVESTIGATINO ON COHERENCY FACTOR OF RHYTHMIC JUNMPING AND ITS APPLICATION FOR SIMULATION OF CROWD JUMPING LOAD.....2484
Ziye Pan, Yonglei Zhao, Jun Chen

DYNAMIC ANALYSES OF A CURVED CABLE-STAYED FOOTBRIDGE UNDER HUMAN INDUCED VIBRATIONS: NUMERICAL MODELS AND EXPERIMENTAL TESTS.....2495
Elisa Bassoli, Paola Gambarelli, Laura Simonini, Loris Vincenzi

ROBUST VIBRATION SERVICEABILITY DESIGN OF A TUNED MASS DAMPER FOR THE PHÉNIX FOOTBRIDGE.....2512
Klaus Lievens, Peter Van Den Broeck, Guido De Roeck, Geert Lombaert

WALKING-INDUCED VIBRATION OF A FOOTBRIDGE.....2525
Eleonora Lai, Maria Gabriella Mulas

Regular Sessions

RS 1 : ALGORITHMS FOR STRUCTURAL HEALTH MONITORING

APPLICATION OF LASER MEASUREMENT TO THE DRIVE-BY INSPECTION OF BRIDGES.....2536
Abdollah Malekjafarian, Eugene J Obrien

UNCERTAINTY OF BRIDGE VIBRATION PROPERTIES AND ITS CONSEQUENCE FOR DAMAGE IDENTIFICATION.....2545
Marian Ralbovsky, Maciej Kwapisz, Alois Vorwagner

VIBRATION MEASUREMENT-BASED SIMPLE TECHNIQUE FOR STRUCTURAL APPRAISAL OF STEEL BRIDGES.....2558
W.A.Indika Priya Wijesooriya, Sudath C. Siriwardane, P.B. Ranjith Dissanayake

STRUCTURAL HEALTH MONITORING USING TIME-DELAY EMBEDDING AND PHASE-SPACE WARPING.....2568
Mohammad H. Alhamaydeh, Kenneth Wong, Ralston Fernandes, Jeongcheol Seok, Eihab M. Abdel-Rahman, Sami El-Borgi

SYSTEM IDENTIFICATION AND DAMAGE DETECTION OF R.C. STRUCTURE.....2576
Prodip K. Paul, Anjan Dutta, Sajal K. Deb

EXPERIMENTAL VERIFICATION OF DAMAGE LOCATION TECHNIQUES FOR FRAME STRUCTURES ASSEMBLED USING BOLTED CONNECTIONS.....2588
Bartlomiej Blachowski, Andrzej Swiercz, Nikos Pnevmatikos

ANALYSIS OF THE VIBRATION LEVELS OF A SLENDER FOOTBRIDGE MEASURED BY A CONTINUOUS DYNAMIC MONITORING SYSTEM.....2600
Carlos Moutinho, Filipe Magalhães, Elsa Caetano

RS 2 : CONSTITUTIVE MODELLING UNDER EARTHQUAKE LOADING

A MULTISCALE APPROACH FOR MODELING OF INFILLED FRAMES.....2611
Andrea Fiore, Francesco Porco

MACRO-MODEL CALIBRATION OF A STRONG CLAY MASONRY INFILL TO IN-PLANE CYCLIC TESTS.....2623
Milad Oliaee, Paolo Morandi, Guido Magenes

SHEAR HYSTERESIS MODEL FOR REINFORCED CONCRETE ELEMENTS INCLUDING THE POST-PEAK RANGE.....2640
Dimitrios K. Zimos, Panagiotis E. Mergos, Andreas J. Kappos

RS 3 : DYNAMICS OF COUPLED PROBLEMS AND MICRO-MACRO SYSTEMS

DYNAMIC ANALYSIS OF GRADIENT ELASTIC BEAMS BY FINITE ELEMENTS.....2659
Ioannis Pegios, Ioannis Dinopoulos, Sofia Papargyri-Beskou

VIBRATIONS OF SPORTS STADIUM GRANDSTAND STRUCTURE DUE TO CROWD-JUMPING LOADS.....2674
Tadeusz Tatara, Bartosz Ptasznik

NATURAL FREQUENCY OF TRAFFIC FLOW-BRIDGE SYSTEM BASED ON CELLULAR AUTOMATON TECHNIQUE.....2690
Mao Ye, Shifan Huang, Baoxing Cao, Min Ren

INFLUENCE OF FLOATER RESPONSE ON WIND TURBINE TOWER MOMENTS IN FLOATING WIND TURBINE SYSTEM.....2700
Muhammad Bilal Waris, Takeshi Ishihara

A NEW APPROACH ON THE CALCULATION OF DYNAMIC LOAD FACTORS OF HUMAN INDUNCED LOAD.....2711
Lu Dai, Na Yang

COMPUTATIONAL MODELING OF MULTI-SCALE FEATURES IN CEMENTITIOUS MATERIALS.....2722
Ram Mohan, Arunachalam Rajendran, Wayne Hodo

RS 4 : GEOTECHNICAL EARTHQUAKE ENGINEERING

SOFT COMPUTING APPLICATION IN SOIL CLASSIFICATION ANALYSIS.....2728
Saman Yaghmaei-Sabegh

NONLINEAR ANALYSIS ON SEISMIC RESPONSE OF A MULTI-GEOMORPHIC COMPOSITE SITE.....2735
Chen Guoxing, Jin Dandan, Gao Hongmei, Zhu Jiao

FINITE ELEMENT ANALYSIS OF AN EARTH DAM SUBJECTED TO BLAST-INDUCED LOADING USING A HIGH STRAIN-RATE BOUNDING SURFACE MODEL.....2743
Tianhua Xu, Limin Zhang

3D FAILURE ENVELOPE OF A SINGLE PILE IN SAND.....2752
Zheng Li, Panagiotis Kotronis, Sandra Escoffier

SOME EXPERIMETNAL EVIDENCES ON DYNAMIC SOIL-STRUCTURE INTERACTION.....2761
Maria Rossella Massimino, Giovanni Biondi

COUPLING BETWEEN STRATIGRAPHIC AND TOPOGRAPHIC EFFECTS ON SLOPES.....2775
S. Rizzitano, E. Cascone, G. Biondi

CLASS A PREDICTION FOR SEISMIC CENTRIFUGE MODELING OF MULTI-BLOCK QUAY-WALL: UNDRAINED (PLAXIS) VERSUS COUPLED (FLAC) EFFECTIVE STRESS ANALYSIS.....2787
Panagiota Tasiopoulou, Nikos Gerolymos, George Gazetas

STATIC AND DYNAMIC ANALYSES OF DAHR EL BAIDAR SLOPE.....2802
T. Matar, F. Hage Chehade, J. Harb, M. Rahhal, D. Youssef Abdel Massih, C. Abdallah, E. Ibrahim, L. Khalaf-Keyrouz, G. Nasr, G. Abou-Jaoude, A. Sursock

A SEISMIC PERFORMANCE-BASED DESIGN APPROACH FOR SLOPE STABILIZING PILES.....2815
Marianna Adinolfi, Raffaele Di Laora, Rosa Maria Stefania Maiorano, Stefano Aversa

THREE-DIMENSIONAL NUMERICAL MODELLING OF CIRCULAR TUNNELS UNDER SEISMIC ACTIONS.....2828
E. Bilotta, R.M.S. Maiorano, A. Viglione, S. Aversa

NONLINEAR DYNAMIC RESPONSE OF HARDENING, SOFTENING AND ELASTOPLASTIC SDOF SYSTEMS USING GENERALIZED SINGLE STEP ALGORITHMS WITH NEWTON-RAPHSON ITERATIONS.....2838
George Papazafeiropoulos, Vagelis Plevris, Manolis Papadrakakis

RS 5 : IMPACT DYNAMICS

CREATION OF A NEW EQUATION OF MOTION TO CALCULATE DISSIPATED ENERGY BETWEEN TWO ADJACENT BUILDINGS.....2865
Hosein Naderpour, Seyed Mohammad Khatami, Rui Carneiro Barros

PRELIMINARY INVESTIGATIONS OF THE LOW-VELOCITY IMPACT RESPONSE OF A SMART TRIMORPH PLATE FOR ACTIVE DAMAGE MITIGATION.....2876
Akuro Big-Alabo, Philip Harrison, Matthew Cartmell

POUNDING BETWEEN BRIDGE DECKS: COMPUTATIONAL DETAILS AND RESULTS……2890
Bharat Mandal, Vincenzo Bianco, Giorgio Monti

NUMERICAL INVESTIGATION OF THE BEHAVIOUR OF RC WIDE BEAMS UNDER IMPACT LOADS……2904
Ali Abbas, Demetris Cotsovos

STRUCTURE RESPONSE UNDER BLAST WAVE LOAD……2915
D. Makovička, D. Makovička, Jr.

PERFORMANCE OF STEEL COLUMNS SUBJECTED TO VEHICLE IMPACT – EXPERIMENTAL AND NUMERICAL STUDIES……2926
J. Korndörfer, B. Hoffmeister, M. Feldmann

VALIDATION OF A NUMERICAL AND ANALYTICAL MODEL OF IMPACTED COLUMNS BY MEANS OF SMALL-SCALE DROP WEIGHT EXPERIMENTS……2937
Carles Colomer Segura, Nils Horbach, Markus Feldmann

VIBRATION ANALYSIS OF HIGH-SPEED RAIL SYSTEM USING THE MOVING ELEMENT METHOD……2951
Reda Mezeh, Marwan Sadek, Fadi Hage Chehade, Dalia Abdelmassih, Nisrinemakhoul, Ahmad Younes

RS 6 : INVERSE PROBLEMS IN STRUCTURAL DYNAMICS

TIME REVERSAL IN ELASTODYNAMICS AND APPLICATIONS TO STRUCTURAL HEALTH MONITORING……2961
Christos Panagiotopoulos, Yiannis Petromichelakis, Chrysoula Tsogka

MODEL-BASED JOINT INPUT-STATE ESTIMATION ON A THIN-WALLED CANTILEVER BEAM……2971
Øyvind W. Petersen, Ole Øiseth, Torodd S. Nord

SENSITIVITY ANALYSIS OF DISCRETE-FORCE IDENTIFICATION ALGORITHMS TO MEASUREMENT NOISE……2983
A. Rezayat, V. Nassiri, K. Maes, G. Lombaert, S. Vanlanduit, P. Guillaume

RS 7 : STRUCTURAL DYNAMICS

ELASTIC INVERTED PENDULUM UNDER HYSTERETIC NONLINEARITY IN SUSPENSION: STABILIZATION AND OPTIMAL CONTROL……2995
Mikhail E. Semenov, Andrey M. Solovyov, Andrey M. Semenov, Vladimir A. Gorlov, Peter A. Meleshenko

SEISMIC ENERGY RESPONSE OF TEN-STORY STEEL ROCKING FRAMES WITH COLUMN MID-HEIGHT UPLIFT AT FIRST STORY……3004
Mitsumasa Midorikawa, Naoto Kotani, Taichiro Okazaki, Tetsuhiro Asari, Tadashi Ishihara, Tatsuya Azuhata

NONLINEARITY DETECTION AND IDENTIFICATION USING DISCRETE-TIME VOLTERRA SERIES: APPLICATION TO A SOLAR ARRAY STRUCTURE……3014
Cristian Hansen, Samuel Da Silva, Emmanuel Foltête, Scott Cogan

FREQUENCY DETUNING EFFECTS FOR PARAMETRICALLY AND DIRECTLY EXCITED ELASTIC STRUCTURES……..3029
Stefan Neumeyer, Matthijs H. M. Van Gastel, Vladislav S. Sorokin, Jon Juel Thomsen

A FAST SEMI-ANALYTICAL METHOD FOR COMPUTING THE RESPONSE OF RAILWAY TRACKS ON NONLINEAR FOUNDATIONS……3036
T. Hoang, D. Duhamel, G. Foret, H. Yin, G. Cumunel, P. Joyez, R. Caby

VALIDITY DOMAIN OF AN ENERGETIC METHOD FOR THE ESTIMATION OF MODAL DAMPING IN THE CASE OF NON LINEAR LOCALIZED DISSIPATION……3048
M. Krifa, N. Bouhaddi, G. Chevallier, And S. Cogan

NONLINEAR DYNAMICS OF A 2D ARRAY OF COUPLED PENDULUMS UNDER PARAMETRIC EXCITATION……3057
Aymen Jallouli, Najib Kacem, Noureddine Bouhaddi

FINITE ELEMENT SIMULATION OF A STEEL BRACED FRAME STRUCTURE DAMAGED BY THE 2011 TOHOKU EARTHQUAKE……3065
Taichiro Okazaki, Yuriko Kato, Naoto Kotani, Mitsumasa Midorikawa, Tetsuhiro Asari

NUMERICAL INVESTIGATION OF THE SEISMIC RESPONSE OF PRECAST BUILDINGS WITH INTEGRATED RC CLADDING WALLS……3072
Ioannis Kalyviotis, Ioannis Psycharis

EVALUATION OF THE APPLICABILITY OF THE LUGRE MODEL FOR MODELLING THE DYNAMIC BEHAVIOUR OF BOLT CONNECTED FRAMES……3084
Sergio Sánchez Gómez, Mihai I.Badila, Andrei Metrikine

NONLINEAR DYNAMICS OF PARAMETRICALLY EXCITED CARBON NANOTUBES FOR MASS SENSING APPLICATIONS……3096
S. Souayeh, N. Kacem, F. Naja, E. Foltête

A COMPUTATIONAL MODEL FOR LARGE-AMPLITUDE NONLINEAR VIBRATION OF CIRCULAR CMUTS UNDER PRIMARY RESONANCE……3107
Aymen Jallouli, Najib Kacem, Patrice Lemoal, Gilles Bourbon, Joseph Lardies

SEISMIC ASSESSMENT OF THE FULL SCALE FOUR STOREY E-DEFENSE ROCKING SHEAR WALL SHAKE TABLE TEST……3117
Giorgio T. Proestos, Hossein Aghabeigi, Paolo M. Calvi

OUT-OF-PLANE BEHAVIOUR OF SINGLE-BODY UNREINFORCED-MASONRY WALL RESTRAINED BY A FLEXIBLE DIAPHRAGM……3127
Sanjeev Prajapati, Omar Alshawa, Luigi Sorrentino

INVESTIGATION OF DYNAMIC RESPONSE OF ROCKING WALL STRUCTURES USING INELASTIC MODAL DECOMPOSITION TECHNIQUE……3139
Irshad M. Qureshi, Pennung Warnitchai, Tahir Mehmood

RS 8 : NUMERICAL SIMULATION METHODS FOR DYNAMIC PROBLEMS

EVALUATION OF THE DYNAMIC AMPLIFICATION FACTOR FOR RAILWAY BRIDGES SUBJECTED TO A SERIES OF MOVING MASS……3151
Mehrdad Bisadi, Quincy Tsun Ming Ma, Sherif Beskhyroun

A MODE SELECTION ALGORITHM FOR THE FLEXIBILITY-BASED COMPONENT MODE SYNTHESIS……3162
Jin-Gyun Kim, Phill-Seung Lee, Kwang-Chun Park

BEHAVIOUR OF REINFORCED CONCRETE KNEE BEAM-COLUMN JOINT IN CASE OF GROUND CORNER COLUMN LOSS-NUMERICAL ANALYSIS……3172
B. Abdelwahed, B. Belkassem, L. Pyl, J. Vantomme

3-D DYNAMIC ANALYSIS OF BRIDGES WITH ROCKING ISOLATION UNDER EXTREME EARTHQUAKES……3184
Tzu-Ying Lee, Kun-Jun Chung, Hung-Yuan Lee

STRUCTURAL INTEGRITY ANALYSIS AND OPTIMIZATION OF AN ELEVATOR FRAME, THROUGH FE MODELING AND EXPERIMENTAL TESTS……3194
Dimitrios Giagopoulos, Iraklis Chatziparasidis, Nikolas Sapidis

SEISMIC ANALYSIS OF COUPLED BUILDINGS WITH MR DAMPER……3205
Fangshu Lin, Xilin Lu

NUMERICAL ASSESSMENT ON THE SEISMIC RESPONSE OF A BASE-ISOLATED BUILDING UNDER BI-DIRECTIONAL MOTION……3216
Marco Furinghetti, Alberto Pavese

DYNAMIC SENSITIVITY OF MULTI-BLOCK STACKS SUBJECTED TO BASE PULSE EXCITATION – EXPERIMENTAL EVIDENCE AND NON SMOOTH CONTACT DYNAMIC SIMULATIONS……3234
Nina Čeh, Antonio Pellegrino, Jean-Francois Camenen, Nik Petrinić, Gordan Jelenić, Tomasz Koziara, Nenad Bićanić

ADAPTIVE CONTROL OF THE ROCKING MOTION OF ART OBJECTS……3248
Rosario Ceravolo, Marica Leonarda Pecorelli, Luca Zanotti Fragonara

REDUCED ORDER MODEL OF CIRCULAR FLANGE-BOLTED CONNECTION AND ITS APPLICATION TO DYNAMIC SUBSTRUCTURING OF TELECOMMUNICATION TOWERS……3262
Bartlomiej D. Blachowski, Witold Gutkowski, Piotr Wisniewski

RS 9 : OPTIMUM DESIGN IN STRUCTURAL DYNAMICS AND EARTHQUAKE ENGINEERING

COMPARATIVE STUDY OF THE WIND AND EARTHQUAKE DYNAMIC RESPONSES OF FIRE EXPOSED STEEL FRAMED BUILDINGS……3274
Fabio Mazza, Marco Fiore

ESTIMATING OF OVERSTRENGTH FACTOR OF CONCENTRICALLY X-BRACED STEEL FRAMES……3288
T. Branci, D. Yahmi

SENSOR PLACEMENT OPTIMIZATION USING ENSEMBLE KALMAN FILTER AND GENETIC ALGORITHM……..3296
Dana Nasr, George Saad

TOPOLOGY OPTIMIZATION OF TWO-DIMENSIONAL WAVE BARRIERS FOR THE REDUCTION OF GROUND VIBRATION TRANSMISSION……..3309
Cédric Van Hoorickx, Ole Sigmund, Mattias Schevenels, Boyan S. Lazarov, Geert Lombaert

MULTI-OBJECTIVE OPTIMIZATION UNDER UNCERTAINTY WITH REAL-TIME INTEGRATED DECISION MAKING APPLIED TO STRUCTURAL ENGINEERING……..3320
Mariapia Marchi, Mauro Munerato, Luca Rizzian, Stefano Costanzo

A CODE COMPATIBLE APPROACH TO JUSTIFY THE SEISMIC DESIGN OF SIMPLIFIED STRUCTURES……..3344
H.F. Karadogan, Y. Durgun, I.E. Bal, S. Z. Yuce, E. Yuksel, C. Soydan

DESIGN OF "DOG-BONE" CONNECTION: THE ROLE OF VERTICAL LOADS……..3368
Rosario Montuori

NON-LINEAR ANALYSES OF SEISMIC RESISTANT CONCRETE FRAME FOR THE VALIDATION OF A FAILURE MODE CONTROL METHODOLOGY……..3388
Roberta Muscati

FEASIBILITY STUDY ON OFFSHORE SOLAR UPDRAFT TOWER POWER PLANT……..3412
Hayami Sato, Yasuo Suzuki, Kunitomo Sugiura

IMPLEMENTATION OF ROBUST CONTROL THEORY IN SMART STRUCTURE DESIGN USING FREQUENCY DOMAIN DATA……..3419
A. J. Moutsopoulou, A. D. Pouliezos, G. E. Stavroulakis

AN ENHANCED COMPONENT BASED MODEL FOR STEEL LINKS IN HYBRID STRUCTURES: DEVELOPMENT, CALIBRATION AND EXPERIMENTAL VALIDATION……..3435
M. Manfredi, F. Morelli, W. Salvatore

ROBUST CONTROL OF SMART STRUCTURES WITH OPTIMALLY PLACED ACTUATORS AND SENSORS……..3451
Amalia Moutsopoulou, Georgia Foutsitzi, Christos Gogos, Georgios Stavroulakis

OPTIMAL DESIGN OF STRUCTURAL INTERFACES BY A POWER FLOW MODE APPROACH……..3461
Thomas Weisser, Noureddine Bouhaddi

CONTROL METHOD FOR ADJACENT BUILDINGS CONSIDERING SOIL-STRUCTURE INTERACTION……..3472
Luis Pérez, Suzana Avila, Graciela Doz

HOW TO ACHIEVE REGULAR SEISMIC BEHAVIOR OF IRREGULAR BRIDGES WITH UNEQUAL HEIGHT PIERS?……..3485
Mena Ishak, Sameh Mehanny

OPTIMIZATION OF QUATROPOD JACKET SUPPORT STRUCTURES FOR OFFSHORE WIND TURBINES SUBJECT TO SEISMIC LOADS USING GENETIC ALGORITHMS……..3505
Mohammad Alhamaydeh, Samer Barakat, Omar Nassif

EVALUATION OF SEISMIC RESPONSE OF BUILDINGS USING DYNAMIC ANALYSIS ON STICK MODELS……..3514
Marco Bovo, Marco Savoia

A PROCEDURE FOR THE DETAILING DESIGN OF SIMPLY SUPPORTED R.C. BRIDGE DECKS SUBJECTED TO IN-PLANE ACTIONS……3530
Fabrizio Palmisano, Angelo Elia

MULTI-OBJECTIVE STRUCTURAL OPTIMIZATION UNDER STRESS CRITERIA BASED ON MIXED PLATE FEM AND GENETIC ALGORITHMS……..3545
Pierre Garambois, Sebastien Besset, Louis Jézéquel

THE STUDY OF X-BRACING ON LIMIT STATE BEHAVIOR OF BUCKLING RESTRAINED BRACE (BRB) IN STEEL FRAMES USING PUSHOVER ANALYSIS……3559
Peyman Shadman Heidari, Ali Golara, Pouya Shadman Heidari, Roohollah Ahmady Jazany

OPTIMIZED RETROFIT OF SEISMICALLY DESIGNED STRUCTURES TO WITHSTAND PROGRESSIVE COLLAPSE……3568
Georgios S. Papavasileiou, Dimos C. Charmpis

ASSESMENT OF OPTIMUM STRENGTHENING DESIGN OF A REINFORCED CONCRETE BUILDING WITH VULNERABILITY CRITERIA……..3580
Evangelia Skoulikari, Vissarion Papadopoulos, Nikos Lagaros

ENERGY BASED OPTIMUM DESIGN OF TUNED MASS DAMPERS……3593
Giuseppe Carlo Marano

A PRELIMINARY ASSESSMENT OF SLENDERNESS AND OVERSTRENGTH HOMOGENEITY CRITERIA USED IN THE DESIGN OF CONCENTRICALLY BRACED STEEL FRAMES IN MODERATE SEISMICITY……3599
Alper Kanyilmaz, C.A Castiglioni, Hervè Degèe, Pierre-Olivier Martin

RS 10 : STEEL AND COMPOSITE STRUCTURES

SIMPLE FORMULAE FOR DAMAGE ESTIMATION OF COMPOSITE STEEL/CONCRETE MOMENT RESISTING FRAMES……3610
George Kamaris, Konstantinos Skalomenos, George Hatzigeorgiou, Dimitri Beskos

RENEWABLE ENERGY TENSEGRITY STRUCTURES……3621
F. Fraternali, E. De Chiara, A. Fortunato, E. Sicignano, R. E. Skelton

SEISMIC PERFORMANCE OF INNOVATIVE STEEL AND CONCRETE HYBRID COUPLED SHEAR WALLS……..3629
Luca Tassotti, Alessandro Zona, Graziano Leoni, Andrea Dall'Asta

DAMAGE DETECTION AND MONITORING OF COMPOSITE STRUCTURES WITH THE USE OF PIEZOELECTRIC SENSORS……..3638
Piotr Kêdziora, Adam Stawiarski, Marek Barski

INFLUENCE OF CONNECTIONS MODELING ON THE SEISMIC BEHAVIOUR OF INDUSTRIAL BUILDINGS……..3652
Luca Tassotti, Mohammed Radi, Fabrizio Gara, Laura Ragni

INELASTIC CYCLIC NUMERICAL ANALYSIS OF STEEL STRUTS USING DISTRIBUTED PLASTICITY APPROACH……3663
Alper Kanyilmaz

RS 11 : PERFORMANCE-BASED EARTHQUAKE ENGINEERING

SIMPLIFIED SEISMIC COLLAPSE ASSESSMENT OF GENERIC FRAME STRUCTURES SUBJECTED TO PDELTA AND MATERIAL DETERIORATION……3675
David Kampenhuber, Christoph Adam

DISTRIBUTED AND CONCENTRATED INELASTICITY BEAM-COLUMN ELEMENTS: APPLICATION TO REINFORCED CONCRETE FRAMES AND VERIFICATION……3694
Armin Gharakhanloo, Amir M. Kaynia, Gergios Tsionis

A GROUPED MAXIMAL CONDITIONED SPECTRAL ORDINATE METHOD (MCSO) FOR GROUND MOTION SELECTION……3704
Ahmad Nicknam, Ehsan Yousefi Dadras, Mohammad Javad Asgari

ADVANCED MODELS FOR THE LIMIT ANALYSIS OF MASONRY STRUCTURES……3716
A. Fortunato, E. De Chiara, F. Fraternali, M. Angelillo

DYNAMIC RESPONSE OF A GOTHIC CATHEDRAL IN CYPRUS……3726
Zehra Cagnan, Christis Chrysostomou, Nicholas Kyriakides, Renos Votsis

APPLICATION OF THE PUSHOVER-BASED PROCEDURE TO PREDICT THE LARGEST PEAK RESPONSE OF ASYMMETRIC BUILDINGS WITH BUCKLING-RESTRAINED BRACES……3739
Kenji Fujii

SEISMIC LOSS OPTIMIZATION OF FRAME BUILDINGS USING VISCOUS DAMPERS……3767
Arun M. Puthanpurayil, Oren Lavan, Rajesh Dhakal

HOW CAN INSURERS GET PREPARED TO CATASTROPHES? ASSESSING EARTHQUAKE EXPECTED LOSSES FROM HISTORICAL CATALOGUE……3778
Anna Bozza, Domenico Asprone, Fatemeh Jalayer, Gaetano Manfredi

APPLICATION OF INCREMENTAL DYNAMIC ANALYSIS TO SEISMIC EVALUATION OF UNDERGROUND STRUCTURE……3793
Tong Liu, Yong Yuan, Zhiyi Chen

GRAPHICAL DYNAMIC TRENDS FOR EARTHQUAKE INCIDENCE RESPONSE OF PLAN-ASYMMETRIC SYSTEMS……3801
M. Faggella, R. Gigliotti, G. Mezzacapo, E. Spacone

SIGNIFICANCE OF EARTHQUAKE INCIDENCE ON RESPONSE OF PLAN-IRREGULAR INFILLED R/C BUILDINGS……3809
M. Faggella, G. Mezzacapo, R. Gigliotti, E. Spacone

BEHAVIOR OF NON-CONFORMING R.C. MEMBERS UNDER COMPRESSIVE AXIAL LOAD AND BIAXIAL BENDING……3816
Marta Del Zoppo, Marco Di Ludovico, Aurelio Ghersi

STIFFNESS MODELING OF RC COLUMNS REINFORCED WITH PLAIN REBARS……3830
Okan Ozcan

CORRELATION BETWEEN THE PROBABILISTIC SEISMIC ASSESSMENT OF FRAME STRUCTURES WITHOUT AND WITH ADDED DAMPERS……3841
Luca Landi, Cristina Vorabbi, Pier Paolo Diotallevi

RS 12 : REPAIR AND RETROFIT OF STRUCTURES

NUMERICAL MODELING OF FRP - RETROFITTED CIRCULAR RC COLUMNS INCLUDING SHEAR……3861
Konstantinos G. Megalooikonomou, Giorgio Monti

SEISMIC VULNERABILITY IN CASE OF FIRE OF EXISTING R.C. FRAMED BUILDINGS: MODELLING AND NONLINEAR DYNAMIC ANALYSIS……3875
Fabio Mazza, Antonio De Luca

THE EFFECT OF STEEL SLIT PANELS IN RETROFITTING WEAK BUILDINGS……3889
Fatemeh Jamshidzadeh, Benyamin Mohebi

REHABILITATION OF AN EDIFIED BUILDING IN A SEISMIC ZONE IN ALGERIA ACCORDING TO THE EUROCODE 8-3……3896
Amar Kassoul, Abdelkader Zerrouk, Imane Djafar Henni

SEISMIC ANALYSIS AND RETROFIT OF A MID-RISE BUILDING……3909
Fernando Saitta, Paolo Clemente, Giacomo Buffarini, Giovanni Bongiovanni

ADVANCED NUMERICAL MODELLING FOR DAMAGE ANALYSIS OF RC STRUCTURES: A CASE STUDY ON BEAM-COLUMN JOINTS……3919
C. Del Vecchio, M. Di Ludovico, A. Prota, G. Manfredi

SEISMIC RETROFITTING EFFECT OF 10-STORY RESIDENTIAL BUILDING RETROFITTED USING PASSIVE SEISMIC CONTROL SYSTEM WITH AMPLIFIER MECHANISM……3934
Y. Takase, T. Ikeda, T. Suzumura

VERIFICATION OF THE TOGGLE DAMPING SYSTEM FOR THE SRC BUILDING DURING THE 2011 OFF THE PACIFIC COAST OF TOHOKU EARTHQUAKE……3946
Takaaki Ikeda, Yuya Takase, Yoshiaki Senoo

SEISMIC RESPONSE VERIFICATION AND RETROFITTING OF RC BUILDING SUBJECTED TO 2014, CEPHALONIA EARTHQUAKES……3953
Ioannis Kavvadias, Ifigeneia Litina, Varvara Kyriakidou, Fani Mamatsopoulou, Lazaros Vasiliadis

DESIGN METHODOLOGY FOR SEISMIC UPGRADING OF TORSIONALLY UNBALANCED EXISTING R.C. BUILDINGS……3972
Georgia Thermou, Manousos Psaltakis

A COMPUTATIONAL INVESTIGATION FOR THE SEISMIC RESPONSE OF RC STRUCTURES STRENGTHENED BY CABLE ELEMENTS……3997
Angelos A. Liolios

RS 13 : SEISMIC ISOLATION

INCREMENTAL DYNAMIC ANALYSIS OF FIRE-EXPOSED BASE-ISOLATED R.C. FRAMED BUILDINGS SUBJECTED TO NEAR-FAULT GROUND MOTIONS……4011
Fabio Mazza, Fabio Alesina

ROLLING-BALL RUBBER-LAYER ISOLATION SYSTEM: STATE OF THE ART, PERFORMANCE AND DESIGN PROCEDURE……4025
Marco Donà, Giovanni Tecchio, Claudio Modena, Alan H. Muhr

THE EFFECT OF MODIFIED LINEAR VISCOELASTIC IMPACT MODELS ON THE POUNDING RESPONSE OF A BASE-ISOLATED BUILDING WITH ADJACENT STRUCTURES……4038
Eftychia A. Mavronicola, Panayiotis C. Polycarpou, Petros Komodromos

ANALYSIS AND EXPERIMENT OF ISOLATED BRIDGES USING POLYNOMIAL ROCKING BEARINGS……4056
Tzu-Ying Lee, Lyan-Ywan Lu, Jing-Hung Tzeng, Kun-Jun Chung

FINITE ELEMENT INVESTIGATION OF A NEW SEISMIC ENERGY ABSORPTION DEVICE THROUGH SIMOULTANEOUSLY YIELD AND FRICTION……4065
Magdalini Titirla, Panikos Papadopoulos

SEISMIC ANALYSIS OF BASE-ISOLATED CYLINDRICAL LIQUID STORAGE TANK USING COUPLED ACOUSTIC-STRUCTURAL INTERACTION……4078
Aruna Rawat, Vasant Matsagar, A.K. Nagpal

OPTIMIZATION OF SEISMIC ISOLATION SYSTEMS WITH VISCOUS FLUID DAMPERS USING GENETIC ALGORITHMS……4086
Samer Barakat, Mohammad Alhamaydeh, Omar Nassif

IN PLAN DISTRIBUTION OF ISOLATORS EFFECTIVE STIFFNESS FOR MINIMIZING THE TORSIONAL RESPONSE OF BASE ISOLATED BUILDINGS……4096
Konstantinos Kostinakis, Asimina Athanatopoulou, Dimitra Arampatzi, Athanasios Atsalos

RS 14 : SEISMIC RISK AND RELIABILITY ANALYSIS

THE EFFECTS OF THE SEISMIC INPUT ON THE SEISMIC RESPONSE OF RC BUILDINGS……4114
Maria Pianigiani, Valentina Mariani, Marco Tanganelli, Stefania Viti

BIDIRECTIONAL ANALYSIS OF A REAL RC BUILDING ACCORDING TO THE ITALIAN CODE PROVISIONS……4126
Stefania Viti, Valentina Mariani, Marco Tanganelli, Mario De Stefano

THE EFFECTS OF THE AXIAL LOAD VARIATION ON THE SEISMIC PERFORMANCE OF EXISTING RC BUILDINGS……..4136
Valentina Mariani, Marco Tanganelli, Stefania Viti, Mario De Stefano

IMPROVED FRAGILITY FUNCTIONS FOR RC BRIDGE POPULATIONS……..4147
C. Zelaschi, R. Monteiro, R. Pinho

SIMPLIFIED CLOSED-FORM SOLUTION FOR THE DETERMINATION OF THE MOMENT-CURVATURE RESPONSE OF A CIRCULAR RC SECTION……..4160
Domenico Raffaele, Roberto Gentile, Mauro Mezzina

ENERGY DISSIPATION CHARACTERISTICS OF SLAB TYPE BUILDINGS WITH SPECIAL CONNECTORS……4171
Erkan Şenol, Ahmet Anıl Dindar, Ercan Yüksel, Faruk Karadoğan

SEISMIC FRAGILITY ANALYSIS OF EXISTING URM BUILDINGS: A STUDY ON KATHMANDU VALLEY……..4182
Sujan Shrestha, Lorenzo Colarusso, Domenico Liberatore, Daniela Addessi

MAPPING HAZARD POTENTIALS IN SEISMIC ZONES BASED ON GEOTECHNICAL DATA FOR DESIGNING TRANSPORTATION NETWORKS INFRASTRUCTURE……..4196
Mohamed Elmasry, Tarek Abdelaziz, Amr Wagdy

RELIABILITY-BASED METHOD FOR ASSESSING LIQUEFACTION POTENTIAL OF SOILS……..4214
M.Naghizaderokni, Dr.A.Janalizade, M.Naghizaderokni

RS 15 : SOFT COMPUTING APPLICATIONS

SEISMIC RESILIENCE OF A BRIDGE BASED ON FUZZY-PROBABILISTIC APPROACH……..4223
J. Andrić And D.G. Lü

NEURAL NETWORKS FOR THE PREDICTION OF MINE-INDUCED VIBRATIONS TRANSMISSION FROM THE GROUND TO BUILDING FOUNDATION……..4235
Krystyna Kuzniar

BAYESIAN IDENTIFICATION OF ELASTIC PARAMETERS IN COMPOSITE LAMINATES APPLYING LAMB WAVES MONITORING……..4246
Marek Slonski

DEVELOPMENT OF A HYBRID SYSTEM FOR IDENTIFICATION OF ELASTIC MATERIAL IN COMPOSITE LAMINA: APPLICATION OF LAMB WAVES AND NEURAL NETWORKS……..4254
Zenon Waszczyszyn, Piotr Nazarko, Pawel Packo, Lukasz Ambrozinski, Tadeusz Uhl

RS 16 : SOIL-STRUCTURE INTERACTION

SIMPLIFIED MODEL FOR COUPLED VIBRATION OF ADJACENT STRIP FOOTINGS……..4268
Jue Wang, Ding Zhou, Weiqing Liu

CALIBRATION AND VALIDATION OF A SIMPLIFIED MODEL OF NONLINEAR SOIL-STRUCTURE INTERACTION FOR SHALLOW FOUNDATIONS……..4277
Simon Lambert, Charisis Chatzigogos, Andrea Godoy

OPTIMIZATION OF WIND TURBINE FOUNDATIONS FOR POOR SOIL……..4292
Wael Mohamed, Per-Erik Austrell

A SSI NUMERICAL MODEL FOR LAYERED SOILS USING A BEM-FEM FORMULATION IN TIME DOMAIN……..4305
A. Romero, P. Galvín

THE ROLE OF SOIL-STRUCTURE INTERACTION IN THE REDISTRIBUTION OF INTERNAL FORCES IN CONCRETE BUILDINGS DUE TO SEISMIC EXCITATION……..4324
Giorgos Mantzaras, Dimitris Karabalis

SOIL-PILE-STRUCTURE-INTERACTION: EXPERIMENTAL RESULTS AND NUMERICAL SIMULATIONS……..4339
Maria Giovanna Durante, Luigi Di Sarno, Colin A Taylor, George Mylonakis, Armando Lucio Simonelli

A NEW SEISMIC DESIGN METHOD FOR DEEPLY EMBEDDED FOUNDATIONS ACCOUNTING FOR SSI EFFECTS……..4350
Nikos Gerolymos, Athanasios Zafeirakos

RS 17 : SOUND AND VIBRATION

DISPERSION ANALYSIS OF ACOUSTIC WAVES IN FLUID MEDIA DISCRETIZED BY ENERGY-ORTHOGONAL FINITE ELEMENTS……..4364
Francisco José Brito Castro

WAVE BASED DESIGN OPTIMISATION OF COMPOSITE STRUCTURES OPERATING IN DYNAMIC ENVIRONMENTS……..4390
Dimitrios Chronopoulos, Manuel Collet, Mohamed Ichchou, Ioannis Antoniadis

NEW REDUCED ORDER FINITE ELEMENT FORMULATIONS FOR VIBRATION ATTENUATION USING PIEZOELECTRIC SHUNT DAMPING……..4409
Walid Larbi, Luciano Pereira Da Silva, Jean-François Deü

SYSTEM IDENTIFICATION AND ACTIVE MODAL CONTROL OF A FLEXIBLE TRUSS STRUCTURE……..4425
Carlos Joventino, Gustavo Abreu, Vicente Lopes Jr.

A 2D WAVE FINITE ELEMENT-BASED SUPERELEMENT FORMULATION FOR ACOUSTIC ANALYSIS OF CAVITIES OF ARBITRARY SHAPES……..4439
Jean-Mathieu Mencik, Denis Duhamel, Marie-Laure Gobert

ON THE IMPLEMENTATION OF BOUNDARY CONDITIONS IN RBF-PS METHOD APPLIED TO VIBRATION ANALYSIS OF KIRCHHOFF PLATES……..4455
Artur Krowiak

MODELLING OF THE VIBRO-ACOUSTIC TRANSMISSION ON MULTI-PLATE PERFORATED PANELS USING TWO-SCALE HOMOGENIZATION……..4468
Eduard Rohan, Vladimír Lukeš

DRY FRICTION INFLUENCE ON STRUCTURE DYNAMICS……..4483
Marco Claudio De Simone, Domenico Guida

ANALYSIS OF VIBRO-ACOUSTIC PROPAGATION IN A MOBILE SCREW COMPRESSOR FOR THE DETERMINATION OF EMITTED ACOUSTIC POWER RADIATED OUTSIDE ITS HOUSING……..4492
Jan Dupal, Jan Vimmr, Vítězslav Adámek, Ondřej Bublík

INTERNAL PARAMETRIC RESONANCE AND AEROELASTIC EFFECTS FOR LONG-SPAN SUSPENSION BRIDGES……..4508
Raffaele Ardito, Antonio Capsoni, Andrea Guerrieri

RS 18 : CONCRETE STRUCTURES

FEM SIMULATION OF THE EXPERIMENTAL RESPONSE OF AAC MASONRY INFILLS IN RC FRAMES……..4528
Riccardo Raimondo Milanesi, Paolo Morandi, Guido Magenes, Baris Binici

DOUBLE-LAYER PLATFORM OF HIGH PERFORMANCE COMPUTING FOR DAMAGE PREDICTION OF RC BUILDINGS SUBJECT TO EARTHQUAKE AND SUBSEQUENT TSUNAMI IN A TARGET AREA……..4548
Panon Latcharote, Yoshiro Kai

DETERMINATION OF THE PERIODS OF COUPLED SHEAR WALLS BY RECURSIVE DIFFERENTIATION METHOD……..4571
Duygu Ozturk, Kanat Burak Bozdogan

SEISMIC BEHAVIOUR OF BRIDGE STRUCTURES MADE OF NATURAL FIBRE REINFORCED POLYMER-CONCRETE COMPOSITE……..4577
Jiaxin Chen, Nawawi Chouw

RS 19 : WAVE PROPAGATION AND SOIL DYNAMICS

FINITE ELEMENT ELASTIC ANALYSIS OF 3-D FLEXIBLE PAVEMENTS UNDER MOVING LOADS……..4584
Niki Beskou, Stefanos Tsinopoulos, Dimitrios Theodorakopoulos

NUMERICAL ANALYSIS OF THE PLANE WAVES SCATTERING BY SEMI-SPHERICAL ALLUVIAL VALLEY……..4596
S L. Chen, X J. Zhu

PLANE WAVE AT THE INTERFACE BETWEEN WATER AND A GASSY POROELASTIC LAYER WITH UNDERLYING ELASTIC SEABED……..4604
Weiyun Chen, Guoxing Chen

A WAVE-BASED REDUCTION TECHNIQUE FOR THE DYNAMIC BEHAVIOR OF PERIODIC STRUCTURES……..4621
Denis Duhamel, Jean-Mathieu Mencik

ANALYSIS OF GROUND MOTION ALONG A TOPOGRAPHIC RELIEF: THE CERRETO DI SPOLETO CASE-HISTORY (CENTRAL ITALY)…….4635
Dario Rinaldis, Salomon Hailemikael, Antonella Paciello, Guido Martini

A PERFECTLY MATCHED LAYER FOR SEISMIC WAVE PROPAGATION IN UNBOUNDED DOMAIN BY USING HETEROGENEOUS MULTI-TIME STEP SUBDOMAIN METHODS…….4645
Eliass Zafati, Michaêl Brun, Irini Djeran-Maigre

LONGITUDINAL SEISMIC VIBRATIONS OF A SEGMENTED PIPELINE CONSIDERED AS THE PERIODICALLY INHOMOGENEOUS ROD…….4663
Mukhady Israilov

EXAMINING THE INITIATION MECHANISMS OF STATIC AND DYNAMIC LIQUEFACTION USING THREE DIMENSIONAL DEM SIMULATIONS…….4672
Zitao Zhang, Yu-Hsing Wang

DAMAGE CHARACTERIZATION IN WAVEGUIDES WITH ULTRASONIC SHEAR WAVES…….4682
Dimitra Achillopoulou, Annamaria Pau, Fabrizio Vestroni

APPLICATION OF NEW DAMAGE INDICATOR-BASED SEQUENTIAL LAW TO ESTIMATE FATIGUE LIFE OF OFFSHORE JACKET STRUCTURES…….4690
Redion Kajolli, Sudath C. Siriwardane, Ove T. Gudmestad

COMPDYN 2015
5th ECCOMAS Thematic Conference on
Computational Methods in Structural Dynamics and Earthquake Engineering
M. Papadrakakis, V. Papadopoulos, V. Plevris (eds.)
Crete Island, Greece, 25–27 May 2015

THE USE OF MODEL REDUCTION TECHNIQUES IN COMPLEX SIMULATION-BASED PROBLEMS INVOLVING FINITE ELEMENT MODELS

H.A. Jensen[1], **A. Muñoz**[1], **and E. Millas**[1]

[1]Department of Civil Engineering, Santa Maria University
Valparaiso, Chile
hector.jensen@usm.cl

Keywords: Bayesian updating, Finite element models, Model reduction techniques, Reliability-based design, Stochastic simulation

Abstract. *This work presents a strategy for integrating a class of model reduction techniques into two types of complex problems: finite element model updating using dynamic response data; and reliability-based design of stochastic finite element models. The solution of this type of problems is computationally very demanding due to the large number of finite element model analyses required. Substructure coupling techniques for dynamic analysis are proposed to reduce the corresponding computational cost involved in these processes. The idea is to carry out the updating and design processes efficiently in a reduced space of generalized coordinates.*

1 INTRODUCTION

Finite element model updating using measured system response has a wide range of applications in areas such as structural response prediction, structural control, structural health monitoring, reliability and risk assessment, etc. [1, 2, 3, 4]. For a proper assessment of the updated model all uncertainties involved in the problem should be considered. The ability to quantify the uncertainties accurately and appropriately is essential for a robust prediction of future responses and reliability of structures [5]. In this context, a fully probabilistic Bayesian model updating approach provides a robust and rigorous framework for model updating due to its ability to characterize modeling uncertainties associated with the underlying structural system [6, 7, 8]. A stochastic simulation approach called transitional Markov chain Monte Carlo method is considered here for identification purposes [9]. Such algorithm requires a large number of finite element re-analyses to be performed over the space of model parameters. Thus, the computational demands depend on the number of re-analyses and the time required for performing each finite element re-analysis.

On the other hand, under uncertain conditions the field of reliability-based optimization provides a realistic and rational framework for structural optimization which explicitly accounts for the uncertainties [10, 11]. Of particular interest in this work is the case of structural design problems involving finite element models under stochastic loading. The design problem is formulated as the minimization of an objective function subject to multiple design requirements including standard and reliability constraints. The solution of this type of problems requires a large number of finite element analyses to be perform during the design process. These analyses correspond to finite element re-analyses over the design space (required by the optimizer), and system responses over the uncertain parameter space (required by the simulation technique for reliability estimation). Consequently, the computational demands depend highly on the number of finite element analyses and the time taken for performing an individual finite element analysis. Thus, the computational demands in solving these reliability-based design problems may be large or even excessive [12, 13, 14, 15].

In this framework, it is the main objective of this work to present a strategy for integrating a class of model reduction techniques into the updating and design processes in order to reduce the computational cost involved in the corresponding dynamic re-analyses of the finite element models. Specifically, a class of model reduction techniques known as substructure coupling for dynamic analysis is considered in the present implementation [16]. Such technique can be used to carry out system analyses in a significantly reduced space of generalized coordinates. A particular parametrization scheme in terms of the model parameters and design variables is implemented in the present work. Such scheme reduces drastically the computational demands involved in the updating and design processes without compromising the solution accuracy.

2 FINITE ELEMENT MODEL UPDATING

2.1 Problem Formulation

In this section the first type of problems to be considered is introduced. It corresponds to finite element model updating using dynamic response data. To this end, consider a finite element model class M of a structural system parameterized by a set of model parameters $\boldsymbol{\theta} \in \Theta \subset R^{n_d}$. The plausibility of each model within a class M based on data D is quantified by the updated joint probability density function $p(\boldsymbol{\theta}|\boldsymbol{M}, \boldsymbol{D})$ (posterior probability density function).

By Bayes' Theorem the posterior probability density function of $\boldsymbol{\theta}$ is given by

$$p(\boldsymbol{\theta}|\boldsymbol{M},\boldsymbol{D}) = \frac{p(\boldsymbol{D}|\boldsymbol{M},\boldsymbol{\theta})\ p(\boldsymbol{\theta}|\boldsymbol{M})}{p(\boldsymbol{D}|\boldsymbol{M})} \tag{1}$$

where $p(\boldsymbol{D}|\boldsymbol{M})$ is the normalizing constant which makes the probability volume under the posterior probability density function equal to unity, $p(\boldsymbol{D}|\boldsymbol{M},\boldsymbol{\theta})$ is the likelihood function based on the predictive probability density function for the response given by model class M, and $p(\boldsymbol{\theta}|\boldsymbol{M})$ is the prior probability density function selected for the model class M which is used to quantify the initial plausibility of each predictive model defined by the value of the parameters $\boldsymbol{\theta}$, allowing in this manner prior information to be incorporated. In what follows, it is assumed that D contains input dynamic data and output responses from measurements on the system. Specifically, let $x_n(t_j,\boldsymbol{\theta})$ denotes the output at time t_j at the n^{th} observed degree of freedom predicted by the proposed structural model, and $x_n^*(t_j)$ denotes the corresponding measured output. The prediction and measurement errors $e_n(t_j,\boldsymbol{\theta}) = x_n^*(t_j) - x_n(t_j,\boldsymbol{\theta})$ for $n = 1,...,N_o$, and $j = 1,...,N_T$, where N_o denotes the number of observed degrees of freedom and N_T denotes the length of the discrete time history data, are modeled as independent and identically distributed Gaussian variables with zero mean [17]. Using the above probability model for the prediction error it can be shown that the likelihood function $p(\boldsymbol{D}|\boldsymbol{M},\boldsymbol{\theta})$ can be expressed in terms of a measure-of-fit function $J(\boldsymbol{\theta}|\boldsymbol{M},\boldsymbol{D})$ between the measured response and the model response at the measured degrees of freedom. Such function is given by [18, 19]

$$J(\boldsymbol{\theta}|\boldsymbol{M},\boldsymbol{D}) = \frac{1}{N_t N_o}\sum_{n=1}^{N_o}\sum_{j=1}^{N_t}[x_n^*(t_j) - x_n(t_j,\boldsymbol{\theta})]^2 \tag{2}$$

2.2 Simulation-Based Approach

An efficient method called transitional Markov chain Monte Carlo is implemented for Bayesian model updating [9]. Validation calculations have shown the effectiveness of this approach in a series of practical Bayesian model updating problems [9, 20, 21]. The method can be applied to a wide range of cases including high-dimensional posterior probability density functions, multimodal distributions, peaked probability density functions, and probability density functions with flat regions. The method iteratively proceeds from the prior to the posterior distribution. It starts with the generation of samples from the prior distribution in order to populate the space in which also the most probable region of the posterior distribution lies. For this purpose a number of non-normalized intermediate distributions $p_j(\boldsymbol{\theta}|\boldsymbol{M},\boldsymbol{D}), j = 1,...,J$, are defined as

$$p_j(\boldsymbol{\theta}|\boldsymbol{M},\boldsymbol{D}) \propto\ p(\boldsymbol{D}|\boldsymbol{M},\boldsymbol{\theta})^{\alpha_j} p(\boldsymbol{\theta}|\boldsymbol{M}) \tag{3}$$

where the parameter α_j increases monotonically with j such that $\alpha_0 = 0$ and $\alpha_J = 1$. The parameter α_j can be interpreted as the percentage of the total information provided by the dynamic data which is incorporated in the j^{th} iteration of the updating procedure. The first step ($j = 0$) corresponds to the prior distribution and in the last stage ($j = J$) the samples are generated from the posterior distribution. The idea is to choose the values of exponents α_j in such a way that the change of the shape between two adjacent intermediate distributions be small. This small change of the shape makes it possible to efficiently obtain samples from $p_{j+1}(\boldsymbol{\theta}|\boldsymbol{M},\boldsymbol{D})$ based on the samples from $p_j(\boldsymbol{\theta}|\boldsymbol{M},\boldsymbol{D})$. The value of the parameter α_{j+1} is chosen such that the coefficient of variation for $\{p(\boldsymbol{D}|\boldsymbol{M},\boldsymbol{\theta}_j^k)^{\alpha_{j+1}-\alpha_j}, k = 1,...,N_j\}$ is equal to some prescribed target value. The upper index $k = 1,...,N_j$ in the previous expression denotes the sample number

in the j^{th} iteration step ($\boldsymbol{\theta}_j^k, k = 1, ..., N_j$). Once the parameter α_{j+1} has been determined, the samples are obtained by generating Markov chains where the lead samples are selected from the distribution $p_j(\boldsymbol{\theta}|M, D)$. Each sample of the current stage is generating by applying the Metropolis-Hastings algorithm [22]. The lead sample of the Markov chain is a sample from the previous step that is selected according to the probability equal to its normalized weight $\bar{w}(\boldsymbol{\theta}_j^k) = w(\boldsymbol{\theta}_j^k)/\sum_{l=1}^{N_j} w(\boldsymbol{\theta}_j^l)$, where $w(\boldsymbol{\theta}_j^k)$ represents the plausibility weight which is given by $w(\boldsymbol{\theta}_j^k) = p(D|M, \boldsymbol{\theta}_j^k)^{\alpha_{j+1}-\alpha_j}$. The proposal probability density function for the Metropolis-Hastings algorithm is a Gaussian distribution centered at the preceding sample of the chain and with a covariance matrix equal to a scaled version of the estimate covariance matrix of the current intermediate distribution $p_j(\boldsymbol{\theta}|M, D)$. The procedure is repeated until the parameter α_j is equal to 1 ($j = J$). At the last stage the samples ($\boldsymbol{\theta}_J^k, k = 1, ..., N_J$) are asymptotically distributed as $p(\boldsymbol{\theta}|M, D)$. For a detailed implementation of the transitional Markov chain Monte Carlo method the reader is referred to [9].

3 RELIABILITY-BASED DESIGN OPTIMIZATION

3.1 Design Problem

The second type of problems to be considered consists in the reliability-based design of finite element models under stochastic excitation. The problem is formulated in terms of the constrained non-linear optimization problem

$$\begin{aligned} \text{Min}_{\boldsymbol{\theta}} \;& c(\boldsymbol{\theta}) \\ \text{s.t.} \;& g_i(\boldsymbol{\theta}) \leq 0 \;\; i = 1, ..., n_c \\ & P_{F_i}(\boldsymbol{\theta}) - P_{F_i}^* \leq 0 \;, i = 1, ..., n_r \\ & \boldsymbol{\theta} \in \Theta \end{aligned} \tag{4}$$

where $\boldsymbol{\theta}, \theta_i, i = 1, ..., n_d$ denotes the vector of design variables with side constraints $\theta_i^l \leq \theta_i \leq \theta_i^u$, $c(\boldsymbol{\theta})$ is the objective function, $g_i(\boldsymbol{\theta}) \leq 0, \; i = 1, ..., n_c$ are standard constraints, and $P_{F_i}(\boldsymbol{\theta}) - P_{F_i}^* \leq 0$ are the reliability constraints which are defined in terms of the failure probability functions $P_{F_i}(\boldsymbol{\theta})$ and target failure probabilities $P_{F_i}^*, \; i = 1, ..., n_r$. It is assumed that the objective and constraint functions are smooth functions of the design variables. For structural systems under stochastic excitation the probability that design conditions are satisfied within a particular reference period T provides a useful reliability measure (first excursion probability). In this context, a failure event F_i can be defined as $F_i(\boldsymbol{\theta}, \mathbf{z}) = d_i(\boldsymbol{\theta}, \mathbf{z}) > 1$, where d_i is the so-called normalized demand function defined as $d_i(\boldsymbol{\theta}, \mathbf{z}) = \text{max}_{j=1,...,l}\text{max}_{t\in[0,T]} \mid r_j^i(t, \boldsymbol{\theta}, \mathbf{z}) \mid /r_j^{i^*}$, where $\mathbf{z} \in \Omega_{\mathbf{z}} \subset R^{n_z}$ is the vector of uncertain variables involved in the problem (characterization of the excitation and system parameters), $r_j^i(t, \boldsymbol{\theta}, \mathbf{z}), j = 1, ..., l$ are the response functions associated with the failure event F_i, and $r_j^{i^*}$ is the acceptable response level for the response r_j^i. The response functions r_j^i are obtained from the solution of the equation of motion that characterizes the structural model. The uncertain variables $\mathbf{z}$ are modeled using a prescribed probability density function $p(\mathbf{z})$. The probability of failure evaluated at the design $\boldsymbol{\theta}$ is formally defined as

$$P_{F_i}(\boldsymbol{\theta}) = P[\text{max}_{j=1,...,l}\text{max}_{t\in[0,T]} \frac{\mid r_j^i(t, \boldsymbol{\theta}, \mathbf{z}) \mid}{r_j^{i^*}} > 1] \tag{5}$$

where $P[\cdot]$ is the probability that the expression in parenthesis is true. Equivalently, the failure

probability function evaluated at the design $\boldsymbol{\theta}$ can be written in terms of the multidimensional probability integral

$$P_{F_i}(\boldsymbol{\theta}) = \int_{d_i(\boldsymbol{\theta},\mathbf{z})>1} p(\mathbf{z})d\mathbf{z} \tag{6}$$

3.2 Reliability Estimation and Optimization Strategy

The reliability constraints of the nonlinear constrained optimization problem (4) are defined in terms of the first excursion probability functions $P_{F_i}(\boldsymbol{\theta}), i = 1, ...n_r$. In general, these reliability measures are given in terms of high-dimensional integrals in the framework of dynamical systems under stochastic excitation. The difficulty in estimating these quantities favors the application of advanced simulation techniques. In particular, a general applicable method named subset simulation is adopted in the present formulation [23]. In this advanced simulation technique the failure probabilities are expressed as a product of conditional probabilities of some chosen intermediate failure events, the evaluation of which only requires simulation of more frequent events. The intermediate failure events are chosen adaptively using information from simulated samples so that they correspond to some specified values of conditional failure probabilities. Therefore, a rare event simulation problem is converted into a sequence of more frequent event simulation problems. The method uses a Markov chain Monte Carlo method based on the Metropolis algorithm for sampling from the conditional probabilities [23, 24]. Validation calculations have shown that subset simulation can be applied efficiently to a wide range of dynamical systems [25, 26, 27]. Regarding the solution of the reliability-based optimization problem, it can be obtained, in principle, by a number of techniques such as standard deterministic optimization schemes or stochastic search algorithms [28, 29, 30, 31]. Of particular importance are interior point algorithms based on descent feasible direction [32, 33]. By construction these algorithms generate a sequence of steadily improved feasible designs. The above schemes have proved to be quite effective for a wide range of applications including stochastic optimization problems [34, 35].

4 MODEL REDUCTION TECHNIQUE

The proposed Bayesian model updating technique is computationally very demanding due to the large number of dynamic finite element analyses required. In fact, the model updating technique based on the transitional Markov chain Monte Carlo method involves drawing a large number of samples (of the order of thousands) for populating the importance region in the uncertain parameter space. Similarly, the solution of the reliability-based optimization problem is also very expensive from a computational point of view. The reliability estimation at each design requires the evaluation of the system response at a large number of samples in the uncertain parameter space (of the order of hundreds or thousands). In addition, the iterative nature of the optimization strategy may impose additional computational demands. Consequently, the computational cost may become excessive when the computational time for performing a dynamic analysis is significant. To cope with this difficulty, a model reduction technique is considered in the present formulation. In particular, a method based on component-mode synthesis is implemented in order to define a reduced-order model for the structural system [16, 36, 37]. The basic equations and relationships involved in the model reduction technique are reviewed in this section.

4.1 Reduced-Order Model

The so-called fixed-interface normal modes and interface constrain modes are considered here to define a reduced-order model [16]. To this end, the following partitioned form of the mass matrix $\mathbf{M}^c \in R^{n^c \times n^c}$ and stiffness matrix $\mathbf{K}^c \in R^{n^c \times n^c}$ of the component $c, c = 1, ..., N_c$ is considered

$$\mathbf{M}^c = \begin{bmatrix} \mathbf{M}^c_{ii} & \mathbf{M}^c_{ib} \\ \mathbf{M}^c_{bi} & \mathbf{M}^c_{bb} \end{bmatrix} \quad , \quad \mathbf{K}^c = \begin{bmatrix} \mathbf{K}^c_{ii} & \mathbf{K}^c_{ib} \\ \mathbf{K}^c_{bi} & \mathbf{K}^c_{bb} \end{bmatrix} \tag{7}$$

where the indices i and b are sets containing the internal and boundary degrees of freedom of the component c, respectively. The internal coordinates are kept in the set $\mathbf{x}^c_i(t) \in R^{n^c_i}$ while all boundary coordinates are kept in the set $\mathbf{x}^c_b(t) \in R^{n^c_b}$. The displacement vector of physical coordinates of the component c is given by $\mathbf{x}^c(t)^T =< \mathbf{x}^c_i(t)^T, \mathbf{x}^c_b(t)^T > \in R^{n^c}$, where $n^c = n^c_i + n^c_b$. The fixed-interface normal modes are obtained by restraining all boundary degrees of freedom and solving the eigenproblem $\mathbf{K}^c_{ii}\mathbf{\Phi}^c_{ii} - \mathbf{M}^c_{ii}\mathbf{\Phi}^c_{ii}\mathbf{\Lambda}^c_{ii} = \mathbf{0}$, where the matrix $\mathbf{\Phi}^c_{ii}$ contains the complete set of n^c_i fixed-interface normal modes, and $\mathbf{\Lambda}^c_{ii}$ is the corresponding matrix containing the eigenvalues. The fixed-interface normal modes are normalized with respect to the mass matrix $\mathbf{M}^c_{ii}$. On the other hand, the interface constraint modes are defined by setting a unit displacement on the boundary coordinates $\mathbf{x}^c_b(t)$ and zero forces in the internal degrees of freedom. From this condition the interior partition of the interface constraint-mode matrix can be written as $\mathbf{\Psi}^c_{ib} = -{\mathbf{K}^c_{ii}}^{-1}\mathbf{K}^c_{ib}$. Based on the previous normal and constraint modes the following displacement transformation matrix is introduced to define a set of generalized coordinates [16, 36]

$$\mathbf{x}^c(t) = \begin{Bmatrix} \mathbf{x}^c_i(t) \\ \mathbf{x}^c_b(t) \end{Bmatrix} = \begin{bmatrix} \mathbf{\Phi}^c_{ik} & \mathbf{\Psi}^c_{ib} \\ \mathbf{0}^c_{bk} & \mathbf{I}^c_{bb} \end{bmatrix} \begin{Bmatrix} \mathbf{v}^c_k(t) \\ \mathbf{v}^c_b(t) \end{Bmatrix} = \mathbf{\Psi}^c \ \ \mathbf{v}^c(t) \ \ , c = 1, ..., N_c \tag{8}$$

where $\mathbf{\Phi}^c_{ik} \in R^{n^c_i \times n^c_k}$ is the interior partition of the matrix $\mathbf{\Phi}^c_{ii}$ of the n^c_k kept fixed-interface normal modes, $\mathbf{v}^c(t)$ represents the component generalized coordinates composed by the modal coordinates $\mathbf{v}^c_k(t)$ of the kept fixed-interface normal modes and the boundary coordinates $\mathbf{v}^c_b(t) = \mathbf{x}^c_b(t)$, $\mathbf{\Psi}^c \in R^{n^c \times \hat{n}^c}$ is a transformation matrix with $\hat{n}^c = n^c_k + n^c_b$, and all other terms have been previously defined. Based on the previous transformation two vectors of generalized coordinates are introduced. First, the vector of generalized coordinates for all the N_c components $\mathbf{v}(t)^T =< \mathbf{v}^1(t)^T, ..., \mathbf{v}^{N_c}(t)^T > \in R^{n_v}$, where $n_v = \sum_{c=1}^{N_c} \hat{n}^c$, and the vector $\mathbf{u}(t)$ that contains the independent generalized coordinates consisting of the fixed-interface modal coordinates $\mathbf{v}^c_k(t)$ for each component and the physical coordinates $\mathbf{v}^l_b(t), l = 1, ..., N_b$ at the N_b interfaces $\mathbf{u}(t)^T =< \mathbf{v}^1_k(t)^T, ..., \mathbf{v}^{N_c}_k(t)^T, \mathbf{v}^1_b(t)^T, ..., \mathbf{v}^{N_b}_b(t)^T > \in R^{n_u}$, where $n_u = \sum_{c=1}^{N_c} n^c_k + \sum_{l=1}^{N_b} n^l_b$, and n^l_b is the number of degrees of freedom at the interface l ($l = 1, ..., N_b$). These two vectors are related by the transformation $\mathbf{v}(t) = \mathbf{T}\mathbf{u}(t)$, where the matrix $\mathbf{T} \in R^{n_v \times n_u}$ is a matrix of zeros and ones that couples the independent generalized coordinates $\mathbf{u}(t)$ of the reduced system with the generalized coordinates of each component. The assembled mass matrix $\hat{\mathbf{M}} \in R^{n_u \times n_u}$ and the stiffness matrix $\hat{\mathbf{K}} \in R^{n_u \times n_u}$ for the independent reduced set $\mathbf{u}(t)$ of generalized coordinates take the form

$$\hat{\mathbf{M}} = \mathbf{T}^T \begin{bmatrix} {\mathbf{\Psi}^1}^T\mathbf{M}^1\mathbf{\Psi}^1 & \mathbf{0} & \mathbf{0} \\ \mathbf{0} & \ddots & \mathbf{0} \\ \mathbf{0} & \mathbf{0} & {\mathbf{\Psi}^{N_c}}^T\mathbf{M}^{N_c}\mathbf{\Psi}^{N_c} \end{bmatrix} \mathbf{T} \ , \tag{9}$$

$$\hat{\mathbf{K}} = \mathbf{T}^T \begin{bmatrix} {\Psi^1}^T \mathbf{K}^1 \Psi^1 & \mathbf{0} & \mathbf{0} \\ \mathbf{0} & \ddots & \mathbf{0} \\ \mathbf{0} & \mathbf{0} & {\Psi^{N_c}}^T \mathbf{K}^{N_c} \Psi^{N_c} \end{bmatrix} \mathbf{T} \tag{10}$$

where all terms have been already defined. Note that the dimension of the reduced-order matrices can be much more smaller than the dimension of the unreduced matrices, e.g. $n_u \ll n^c$.

4.2 Model Parametrization

In what follows, a particular parametrization scheme in terms of the model parameters and design variables is considered. Let C_0 be the set of components that do not depend on the vector of uncertain system parameters $\boldsymbol{\theta}$ (model parameters or design variables). In this case, the component fixed-interface normal modes and interface constraint modes are independent of the system parameter value. Thus, only a single analysis is required to estimate the interface modes for a particular component $c \in C_0$. The modes of these components are computed once during the updating and design processes. On the other hand, let C_j be the set of components that depend on the system parameters. Specifically, it is assumed that the stiffness matrix depends on only one of the system parameters and it takes the form $\mathbf{K}^c = \bar{\mathbf{K}}^c h_K^j(\theta_j)$, where the matrix $\bar{\mathbf{K}}^c$ is independent of θ_j, and $h_K^j(\theta_j)$ is a linear or nonlinear function of θ_j. This parametrization scheme is often encountered in several practical applications of model updating and structural optimization. From Eq. (7) it is clear that the partitions of the stiffness matrix $\mathbf{K}^c$ admits the same parametrization. Then, the eigenvalues and eigenvectors associated with the kept fixed-interface normal modes can be expressed as

$$\boldsymbol{\Lambda}_{kk}^c = \bar{\boldsymbol{\Lambda}}_{kk}^c \; h_K^j(\theta_j) \;\; , \;\; \boldsymbol{\Phi}_{ik}^c = \bar{\boldsymbol{\Phi}}_{ik}^c \tag{11}$$

where the matrices $\bar{\boldsymbol{\Lambda}}_{kk}^c$ and $\bar{\boldsymbol{\Phi}}_{ik}^c$ are the solution of the eigenproblem $\bar{\mathbf{K}}_{ii}^c \bar{\boldsymbol{\Phi}}_{ik}^c = \bar{\mathbf{M}}_{ii}^c \bar{\boldsymbol{\Phi}}_{ik}^c \bar{\boldsymbol{\Lambda}}_{kk}^c$, where the matrices $\bar{\boldsymbol{\Phi}}_{ik}^c$ and $\bar{\boldsymbol{\Lambda}}_{kk}^c$ are independent of θ_j. Furthermore, the interface constraint modes are also independent of θ_j since $\boldsymbol{\Psi}_{ib}^c = -{\bar{\mathbf{K}}_{ii}^c}^{-1} \; {h_K^j}^{-1}(\theta_j) \bar{\mathbf{K}}_{ib}^c \; h_K^j(\theta_j) = -{\bar{\mathbf{K}}_{ii}^c}^{-1} \bar{\mathbf{K}}_{ib}^c = \bar{\boldsymbol{\Psi}}_{ib}^c$. Therefore, a single component analysis is required to provide the exact estimate of the normal and constraint modes for any value of θ_j. This is a very important result since the computationally intensive re-analyses for estimating the fixed-interface constrained modes and the interface constraint modes of each component for different values of θ_j required during the updating and design processes are completely avoided. Based on the previous parametrization, it can be shown that the partitions for the component stiffness matrix $\hat{\mathbf{K}}^c = {\boldsymbol{\Psi}^c}^T \mathbf{K}^c \boldsymbol{\Psi}^c \in R^{\hat{n}^c \times \hat{n}^c}, c \in C_j$ (see Eq. (10)) follows the parametrization

$$\hat{\mathbf{K}}_{kk}^c = \bar{\boldsymbol{\Lambda}}_{kk}^c h_K^j(\theta_j) \;\; , \;\; \hat{\mathbf{K}}_{kb}^c = {\hat{\mathbf{K}}_{bk}^c}^T = \mathbf{0}_{kb}^c \;\; , \;\; \hat{\mathbf{K}}_{bb}^c = (\bar{\mathbf{K}}_{bb}^c + \bar{\mathbf{K}}_{bi}^c \bar{\boldsymbol{\Psi}}_{ib}^c) h_K^j(\theta_j) \tag{12}$$

The previous parametrization allows the stiffness matrix of the reduced-order system to be written as

$$\hat{\mathbf{K}} = \hat{\mathbf{K}}_0 + \sum_{j=1}^{n_d} \hat{\bar{\mathbf{K}}}_{1j} h_K^j(\theta_j) \tag{13}$$

where the matrices $\hat{\mathbf{K}}_0$, and $\hat{\bar{\mathbf{K}}}_{1j}$, $(j = 1, ..., n_d)$ are independent of the values of the vector $\boldsymbol{\theta}$, and n_d is the number of independent model parameters or design variables. These matrices can be obtained directly by replacing the parametrization defined in Eq. (12) into Eq. (10). It

is noted that the previous formulation guarantees that the reduced-order model is based on the exact component modes for all values of the system parameters.

4.3 Implementation Aspects

The dynamic response of the original unreduced finite element model, which is needed for the updating and design processes, is approximated by the modal solution of the reduced-order model. Such approach is quite effective since the dimension of the reduced-order model can be substantially smaller than the dimension of the original model. In other words, dividing the structural system into components and reducing the number of physical coordinates to a much smaller number of generalized coordinates have an important impact in the computational effort of the overall processes. The computational efficiency of the proposed approach can be increased additionally by considering high performance computing techniques at the computer hardware level. In fact, the proposed updating and design processes are very-well suited for parallel implementation in a computer cluster [21]. For example, the Markov chains generated at the different stages during the updating and design processes are independent from each other, which means that the generation of different chains can be performed in parallel. Parallelization techniques can also be used at the model level. In this case the definition of all component matrices in generalized coordinates can be carry out concurrently, reducing the computational time of the proposed implementation even further.

5 EXAMPLE PROBLEM

5.1 Formulation

For illustration purposes the effectiveness of the proposed strategy is demonstrated in the second class of problems, that is, reliability-based design of finite element models under stochastic excitation. Applications of the proposed model reduction technique for updating finite element models can be found in [38]. The structural model to be considered consists of a three-span two dimensional frame structure shown in Figure (1). The structure has a total length of 30.0 m and a constant floor height of 5.0 m, leading to a total height of 40.0 m. The finite element model comprises 160 two dimensional beam and column elements of square cross section with 140 nodes and a total of 408 degrees of freedom. The dimension of the square cross section of the column elements is equal to 0.4 m. The axial deformation of the column elements is assumed to be small and they are neglected in the model. The Young's modulus of the different elements is equal to $E = 2.0 \times 10^{10}$ N/m^2. A 5% of critical damping for the modal damping ratios is introduced in the model. The structural system is excited horizontally by a ground acceleration modeled as a non-stationary stochastic process. In particular, a stochastic point-source model characterized by a series of seismicity parameters such as the moment magnitude and rupture distance is considered in the present implementation [39, 40].

The input for the stochastic excitation model involves a white noise sequence and a series of seismological parameters as previously pointed out. Details of the entire procedure can be found in [39, 41]. The duration of the excitation is equal to $T = 30$ s with a sampling interval equal to $\Delta T = 0.01$ s. Based on the characterization of the point source model, the generation of the stochastic ground motions involves more than 3000 random variables for the duration and sampling interval considered. Thus, the vector of uncertain parameters $\mathbf{z}$ involved in the problem (see Section 3) has more than 3000 components.

The cost represented by the total volume of the column elements is chosen as the objective function for the design problem. The design variables comprise the dimension of the column

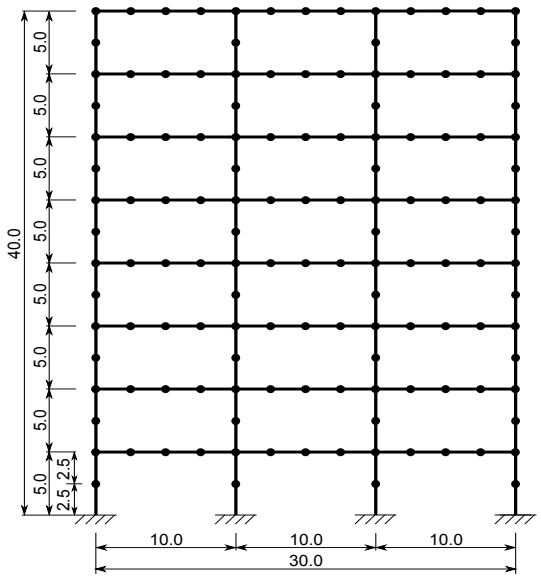


Figure 1: Three-span eight-story structural model

elements square cross section of the different floors. In particular, the dimension of the column elements square cross section are linked into two design variables in this example problem. Design variable number one (θ_1) is related to the dimension of the column elements of floors 1 to 4, while the second design variable (θ_2) controls the dimension of the column elements of floors 5 to 8. To control serviceability, the design criteria are defined in terms of the relative displacements of the first, fifth and eighth floor with respect to the ground. The failure probability functions are defined as

$$P_{F_i}(\boldsymbol{\theta}) = P[\max_{t\in[0,T]} \frac{\mid \delta^i(t,\boldsymbol{\theta},\mathbf{z}) \mid}{\delta^{i*}} > 1] \;\; , \;\; i = 1,2,3 \tag{14}$$

where $\delta^i(t,\boldsymbol{\theta},\mathbf{z}), i = 1,2,3$ are the relative displacements of the first, fifth and eighth floor with respect to the ground, respectively, and $\delta^{i^*}, i = 1,2,3$ are the corresponding critical threshold levels. The threshold levels are defined in terms of a percentage of the total height of the frame structure. The following values are considered: 0.05%; 0.3%; and 0.5% for the threshold levels corresponding to the failure events associated with the first, fifth and eighth floor, respectively. The design problem is formulated as

$$\begin{aligned} \text{Min}_{\boldsymbol{\theta}} \;\; & c(\boldsymbol{\theta}) \\ \text{s.t.} \;\; & P_{F_i}(\boldsymbol{\theta}) \leq 10^{-4} \quad i = 1,2,3 \\ & 0.3\text{m} \leq \theta_i \leq 0.8\text{m} \quad i = 1,2 \end{aligned} \tag{15}$$

Note that the estimation of the probability of failure for a given design $\boldsymbol{\theta}$ represents a high-dimensional reliability problem.

5.2 Reduced-Order Model

The structural model is subdivided into sixteen components as shown in Figure (2). Components 1 to 8 are composed by the column elements of the different floors, while components 9 to 16 correspond to the beam elements of the different floors. Based on this subdivision it

is noted that components 1 to 4 depend on the design variable θ_1, components 5 to 8 depend on the design variable θ_2, while components 9 to 16 are independent of the design variables. In connection with the previous section, the nonlinear functions of the design variables θ_j are given by $h_K^j(\theta_j) = \theta_j^4, j = 1, 2$. For each component it is selected to retain all fixed-interface normal modes that have frequency ω such that $\omega \leq \alpha\omega_c$, with α being a multiplication factor and ω_c is a cut-off frequency which is taken equal to 41.0 rad/s in this case (4^{th} modal frequency of the unreduced model). The multiplication factor is selected to be 10.0 for components 1 to 8, and 2.9 for components 9 to 16. With this selection of parameters only one fixed-interface normal mode is kept for each component. Thus, the reduced-order model comprises a total of 16 generalized coordinates out of the 312 internal degrees of freedom of all components (95% reduction in terms of the internal degrees of freedom). On the other hand, the total number of interface degrees of freedom is equal to 96 in this case. Based on this parametrization, the errors between the modal frequencies using the unreduced reference finite element model and the modal frequencies computed using the reduced-order model are quite small. In fact, the error for the lowest 4 modes fall bellow 0.1%. The comparison with the lowest 4 modes seems to be reasonable since validation calculations show that the contribution of the higher order modes (higher than the 4^{th} mode) in the dynamic response of the model is negligible. It is observed that an important reduction in the number of generalized coordinates is obtained with respect to the number of the degrees of freedom of the original unreduced finite element model. In fact, an almost 75% reduction is obtained in this example problem.

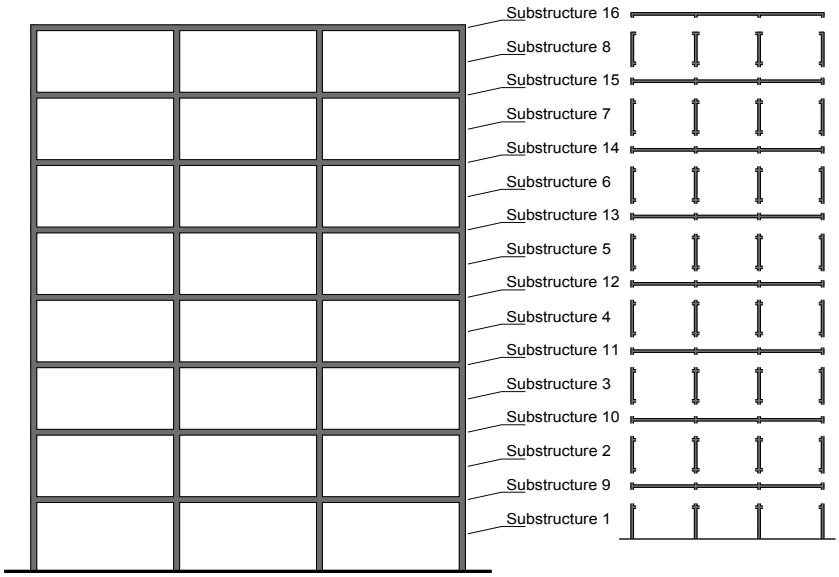


Figure 2: Components (substructures) of the finite element model for design purposes

5.3 Results of the Example Problem

The effectiveness of the model reduction technique in the context of the design problem is shown in Figures (3) and (4). These Figures show some iso-probability curves in the design space constructed by using the original unreduced finite element model and the reduced-order model, respectively. It is observed that the iso-probability curves obtained by the full and reduced-order model are very similar. There is only a slight difference between the iso-probability curves corresponding to low probability events ($\leq 10^{-5}$). The small differences at

low probability levels are due mainly to the advanced simulation scheme used to estimate such probabilities. The previous results imply that the final design for the example at hand can be obtained with high accuracy by using the reduced-order model instead of the full model. On the other hand, the shape and structure of the iso-probability curves associated with the different failure events give a valuable insight into the interaction and effect of the design variables on the reliability of the structural model. For example, the iso-probability curves associated with the relative displacement of the first floor (P_{F_1}) show a weak interaction between the dimension of the column elements square cross section of the lower and upper floors. Contrarily, the iso-probability curves associated with the roof displacement (eighth floor) (P_{F_3}) show a substantial non-linear interaction between the dimension of the column elements square cross section of all floors.

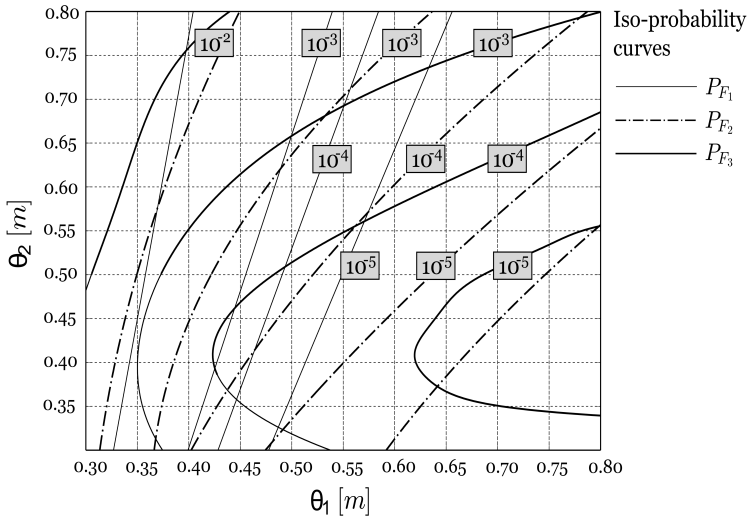


Figure 3: Iso-probability curves associated with the failure events of the first, fifth, and eighth floor (unreduced finite element model)

Figure (4) also shows some normalized objective contours, the feasible domain and the final design. It is observed that the side constraints are inactive at the final design. The reliability constraints related to the relative displacement of the first and eighth floor with respect to the ground are active at the final design. In terms of the computational cost, the number of finite element runs involved during the design process depends mainly on the number of iterations and the number of simulations necessary to estimate the failure probability for the different designs required by the optimizer. Numerical results show that the speedup achieved by the proposed formulation is about 8. In this context, the speedup is defined as the ratio of the execution time of the design process by using the unreduced original model and the execution time of the design process by using the reduced-order model. This reduction in computational effort is achieved without compromising the accuracy of the final design.

6 CONCLUSIONS

A methodology that integrates a model reduction technique into a two types of complex problems, namely, finite element model updating using dynamic response data, and reliability-based design of stochastic finite element models has been presented. In particular, a method based on fixed-interface normal modes and interface constraint modes is considered in this

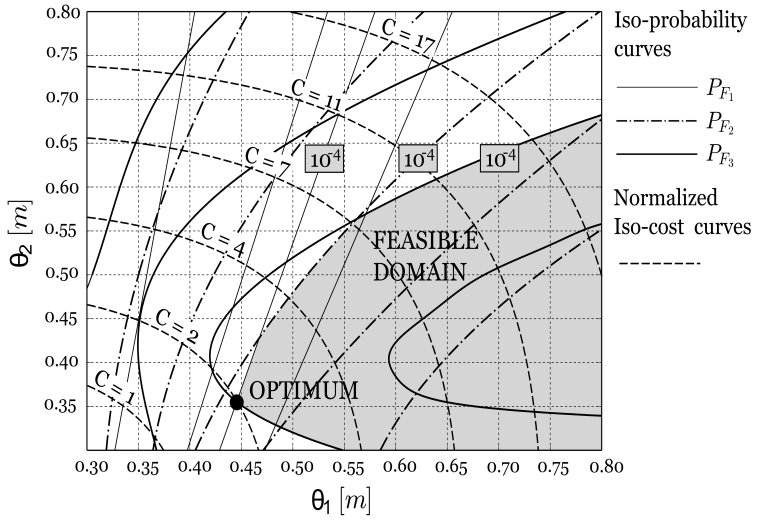


Figure 4: Iso-probability curves associated with the failure events of the first, fifth, and eighth floor (reduced-order model)

work. The method produces highly accurate models with relatively few component modes. It is demonstrated that under certain parametrization schemes, the fixed-interface normal modes and the interface constraint modes of each component are computed once from a reference finite element model. In this manner the re-assembling of the reduced-order system matrices is avoided during the updating and design processes. Results show that the computational effort for updating and designing the reduced-order model is decreased drastically by one or more orders of magnitude with respect to the unreduced model, that is, the full finite element model. Furthermore, the drastic reduction in computational efforts is achieved without compromising the predictive capability of the proposed updating and design processes.

ACKNOWLEDGMENTS

The research reported here was supported in part by CONICYT (National Commission for Scientific and Technological Research) under grant number 1110061, and by the European Union Project PIRSES-GA-2010-269222: Analysis and Design of Earthquake Resistant Structures (ADERS) of the FP7-PEOPLE-2010-IRSES, Marie Curie Actions. This support is gratefully acknowledged by the authors.

REFERENCES

[1] G. Deodatis, H. Asada, S. Ito. Reliability of aircraft structures under nonperiodic inspection- a Bayesian approach. *Journal of Engineering Fracture Mechanics*, 53(5):789–805, 1996.

[2] C. Cremona. Reliability updating of welded joints damaged by fatigue. *International Journal of Fatigue*, 18:567–575, 1996.

[3] H. Shoji, M. Shinozuka, S. Sampath. A Bayesian evaluation of simulation models of multiple-site fatigue crack. *Probabilistic Engineering Mechanics*, 16:355–361, 2001.

[4] P. Beaurepaire, M.A. Valdebenito, G.I. Schuëller, H.A. Jensen. Reliability-based optimization of maintenance scheduling of mechanical components under fatigue. *Computer Methods in Applied Mechanics and Engineering*, 221-222:24–40, 2012.

[5] C. Papadimitriou, J.L. Beck, L. Katafygiotis. Updating robust reliability using structural test data. *Probabilistic Engineering Mechanics*, 16:103–113, 2001.

[6] J.L. Beck. Bayesian system identification based on probability logic. *Structural Control and Health Monitoring*, 17(7):825–847, 2010

[7] S.H. Cheung, J.L. Beck. Bayesian model updating using hybrid Monte Carlo simulation with application to structural dynamic models with many uncertain parameters. *Journal of Engineering Mechanics*, 1135(4):243–255. 2009

[8] K.V. Yuen. *Bayesian methods for structural dynamics and civil engineering*, John Wiley & Sons. 2010.

[9] J. Ching, Y.C. Chen. Transitional Markov chain Monte Carlo method for Bayesian updating, model class selection, and model averaging. *Journal of Engineering Mechanics*, 133:816–832, 2007.

[10] J.O. Royset, A. Der Kiureghian, E. Polak. Reliability-based optimal structural design by the decoupling approach. *Reliability Engineering and System Safety*, 73(3):213-221, 2001.

[11] B.D. Youn, K.K. Choi, Y.H. Park. Hybrid analysis method for reliability-based design optimization. *Journal of Mechanical Design*, 125(2): 221-232, 2003.

[12] H.A. Jensen, M.A. Valdebenito, G.I. Schuëller, D.S. Kusanovic. Reliability-based optimization of stochastic systems using line search. *Computer Methods in Applied Mechanics and Engineering*, 198(49-52):3915–3924, 2009.

[13] M.A. Valdebenito, G.I. Schuëller. Efficient strategies for reliability-based optimization involving non linear, dynamical structures. *Computers and Structures*, 89(19-20):1797–1811, 2001.

[14] G.I. Schuëller, H.A. Jensen. Computational methods in optimization considering uncertainties - An Overview. *Computer Methods in Applied Mechanics and Engineering*, 198(1):2–13, 2008.

[15] J. Wang, L.S. Katafygiotis. Reliability-based optimal design of linear structures subject to stochastic excitations. *Structural Safety*, 47:29–38, 2014

[16] R.R Craig Jr. *Structural Dynamics, An Introduction to Computer Methods*, John Wiley & Sons. New York, 1981.

[17] J.L. Beck, K.V. Yuen. Model selection using response measurements: Bayesian probabilistic approach. *Journal of Engineering Mechanics*, 130(2):192–203, 2004.

[18] J. Beck, L. Katafygiotis. Updating models and their uncertainties. I: Bayesian statistical framework. *Journal of Engineering Mechanics*, 124(4):455–461, 1998.

[19] L. Katafygiotis, J. Beck. Updating models and their uncertainties. II: Model Identifiability. *Journal of Engineering Mechanics*, 124(4):463–467, 1998.

[20] B. Goller, M. Broggi, A. Calvi, G.I. Schuëller. A stochastic model updating technique for complex aerospace structures. *Finite Elements in Analysis and Design*, 47:739–752, 2011

[21] P. Angelikopoulos, C. Papadimitriou, P. Koumoutsakos. Bayesian uncertainty quantification and propagation in molecular dynamics simulations: a high performance computing framework. *The Journal of Chemical Physics*, 137:1441103-1–144103-19, 2012.

[22] W. Hastings. Monte Carlo sampling methods using Markov chains and their applications. *Biometrika*, 57(1):97–109, 1970.

[23] S.K. Au, J.L. Beck. Estimation of small failure probabilities in high dimensions by subset simulation. *Probabilistic Engineering Mechanics*, 16(4):263–277, 2001.

[24] N. Metropolis, S. Ulam. The Monte Carlo method. *Journal of the American Statistical Association*, 44(247):335–341, 1949.

[25] J. Ching, J.L. Beck, S.K. Au. Hybrid subset simulation method for reliability estimation of dynamical systems subject to stochastic excitation. *Probabilistic Engineering Mechanics*, 20(3):199–214, 2005.

[26] H.A. Jensen, M.A. Catalan. On the effects of non-linear elements in the reliability-based optimal design of stochastic dynamical systems. *International Journal of Non-Linear Mechanics*, 42(5):802–816, 2007.

[27] K. M. Zuev, J.L. Beck, S. K. Au, L. Katafygiotis. Bayesian post-processor and other enhancements of Subset Simulation for estimating failure probabilities in high dimensions. *Computers and Structures*, 92-92:283–296, 2012.

[28] J. Arora. *Optimization of Structural and Mechanical Systems*. World Scientific; 2007.

[29] R.T. Haftka, Z. Gürdal. *Elements of Structural Optimization*. Kluwer, 3^{rd} edition; 1992.

[30] A.A. Taflanidis, J.L. Beck. Stochastic subset optimization for optimal reliability problems. *Probabilistic Engineering Mechanics*, 23(2-3):324–338, 2008.

[31] H. Kushner, G. Yin. *Stochastic approximation and recursive algorithms and applications*. Springer, New York; 2003.

[32] J. Nodecal, S.J. Wright. *Numerical optimization*. Springer-Verlag, New York; 1999

[33] J. Herskovits, G. Santos. On the computer implementation of feasible direction interior point algorithms for nonlinear optimization. *Structural Optimization*, 14(2-3):165–172, 1997.

[34] F.J. Baronand, O. Pironneau. Multidisciplinary optimal design of a wing profile. *Proceedings of Structural Optimization 93*. COPPE, p.61-68. Rio de Janeiro, Brazil; 1993.

[35] H.A. Jensen, L. Becerra, M.A. Valdebenito. On the use of a class of interior point algorithms in stochastic structural optimization. *Computers and Structures*, 126:69–85, 2013.

[36] R.R Craig Jr., M.C.C. Bampton. Coupling of substructures for dynamic analysis. *AIAA Journal*, 6(5):678-685, 1965.

[37] C. Papadimitriou, D.Ch. Papadioti. Component mode synthesis techniques for finite element model updating. *Computers and Structures*, 126:15–28, 2013

[38] H.A. Jensen, E. Millas, D. Kusanovic, C. Papadimitriou. Model-reduction techniques for Bayesian finite element model updating using dynamic response data. *Computer Methods in Applied Mechanics and Engineering*, 279:301–324, 2014

[39] D.M. Boore. Simulation of ground motion using the stochastic method. *Pure and Applied Geophysics*, 160(3-4):635–676, 2003.

[40] G.M. Atkinson, W. Silva. Stochastic modeling of California ground motions. *Bulletin of the Seismological Society of America*, 90(2):255–274, 2000.

[41] G.P. Mavroeidis, A.S. Papageorgiou. A mathematical representation of near-fault ground motions. *Bulletin of the Seismological Society of America*, 93(3):1099–1131, 2003.

COMPDYN 2015
5th ECCOMAS Thematic Conference on
Computational Methods in Structural Dynamics and Earthquake Engineering
M. Papadrakakis, V. Papadopoulos, V. Plevris (eds.)
Crete Island, Greece, 25–27 May 2015

SEISMIC ANALYSIS OF LONG TUNNEL: SIMPLIFIED OR UNIFIED

Yong Yuan[1] **and Haitao Yu**[2]

[1] State Key Laboratory of Disaster Reduction in Civil Engineering, Tongji University
1239 Siping Road, Shanghai, China
yuany@tongji.edu.cn

[2] Key Laboratory of Geotechnical and Underground Engineering, Tongji University
1239 Siping Road, Shanghai, China
yuhaitao@tongji.edu.cn

Keywords: Earthquake Engineering, Tunnel Structure, Seismic Analysis, Multi-scale Simulation, Large-scale Computation.

Abstract. *Seismic analysis of long tunnel is important for safety evaluation of tunnel structure under earthquakes. Simplified models of long tunnel are commonly adopted in seismic analysis by structural engineers. Meanwhile, tunnel is usually modelled as a beam continuously supported by ground. Solving of the dynamic system is easy to get an overall response of tunnel structure. However, tunnels are not a tube with uniform cross-section. Road tunnel in mountain areas will be of varying section for emergence parking. Shield tunnel is assembled with segments to form a lining ring. Furthermore, the soil stratum, where a long tunnel is situated, is never at an identical geological condition. All of these would invoke non-uniform excitation if there be an earthquake. Tunnel engineers would like to know what it would be if a long tunnel subjects to earthquake, whether overall or locally, with the help of improved continuous-based or discrete-based dynamic analysis. This paper presents several examples to handle the seismic analysis with unified method, in comparison with simplified method. The proposed method developed a framework, with FDM and DEM, to compute both overall seismic responses of tunnel and damage in particular locations. A multi-domain analysis coupling discrete model and continuum model is proposed to reduce the computational cost and improve the accuracy, and a bridging scale term is introduced such that compatibility of dynamic behavior between the DEM-based and FDM-based models is enforced. To simulate the damage process of lining structure numerical method based on continuous mechanics and failure process by means of discrete method are hired to develop a coupled multi-scale method. Examples demonstrate the applicability.*

1 INTRODUCTION

Tunnels constitute a major part of civil infrastructure and serve as public transportation facilities, sanitation and irrigation utilities and storage places [1]. In seismically active areas, these tunnels are subject to earthquake induced risks. Recent events such as Kobe Earthquake in Japan (1995), Duzce Earthquake in Turkey (1999), Chi-Chi Earthquake in Taiwan (1999), Bam Earthquake in Iran (2003) and the Wenchuan Earthquake in China (2008) showed that tunnels are susceptible to receive irrecoverable damage due to seismic loading [2].

Dynamic behavior of tunnels subjected to seismic loading has been widely studied by a number of researchers [3-5]. There are two basic approaches in present seismic design and analysis of tunnel structures. The first approach is to carry out dynamic, nonlinear soil-structure interaction analysis using finite element methods. The excitation inputs in these analyses are time histories emulating design response spectra, and the excitations are applied to the boundaries of a "soil island" to represent vertically propagating shear waves. The second approach assumes that the seismic ground motions induce a pseudo-static loading condition on the structure. This approach allows the development of analytical relationships to evaluate the magnitude of seismically induced strains in tunnel structures [6-8]. These relationships are based on the premise that tunnel structures under seismic loading tend to deform with the surrounding ground, and thus the structure is designed to accommodate the free-field deformations without loss of its structural integrity.

The objective of this paper is to illustrate the seismic analysis of long tunnels with two different methods, i.e. simplified and unified. In the simplified method, multibody dynamics model and mass-spring-beam model for long tunnels are presented. The focus of the unified method is on the proposed multiscale method coupling both discrete model and continuum model to reduce the computational cost and improve the accuracy of the large soil-tunnel system. Examples are given to demonstrate the applicability of the proposed method.

2 CASES OF LONG TUNNEL

Three typical real-world long tunnels are described in this section, which will be used to demonstrate the simplified and unified methods presented in this study.

2.1 HZM immersed tunnel

HZM (Hong Kong-Zhuhai-Macau linkage) immersed tunnel, located at Lingding Sea, is under construction currently to connect Hong Kong, Zhuhai, and Macau, the cities around the Pear River. The length of the tunnel is more than 5,600 meters with 4-lane for highway, as shown in Figure 1. The immersed tunnel is made up of 33 concrete elements. Each element is 180m long, made up of 8 segments each 22.5 m long. The deep point of the seabed and the foundation level are approximately 30m and 45m below the mean sea level, respectively. The tunnel construction area is located in the seismic activity region, which is designed in accordance with the Chinese standards.

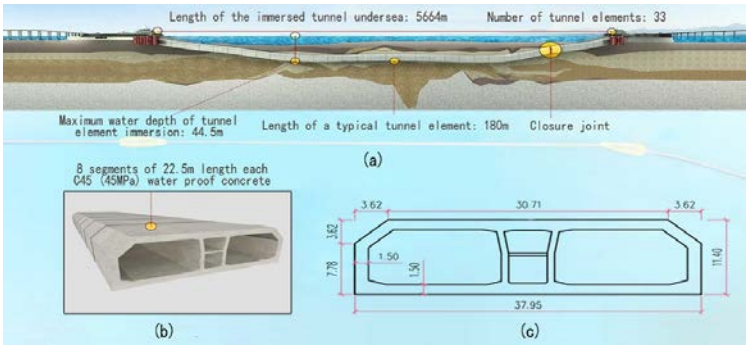


Figure 1: Layout of the HZM immersed tunnel

2.2 Qingcaosha water conveyer tunnel

The Qingcaosha water-conveyance tunnel is a double-line shield tunnel used for water supply in Shanghai, China. The tunnel has a total length of 14 km. Its layout can be divided into three segments: island, cross-river and land. The general layout and location of the shield tunnel are shown in Figure 2. Each ring consists of six segments, each with a length of 1.5 m. A stagger-jointed assembly is adopted between segments.

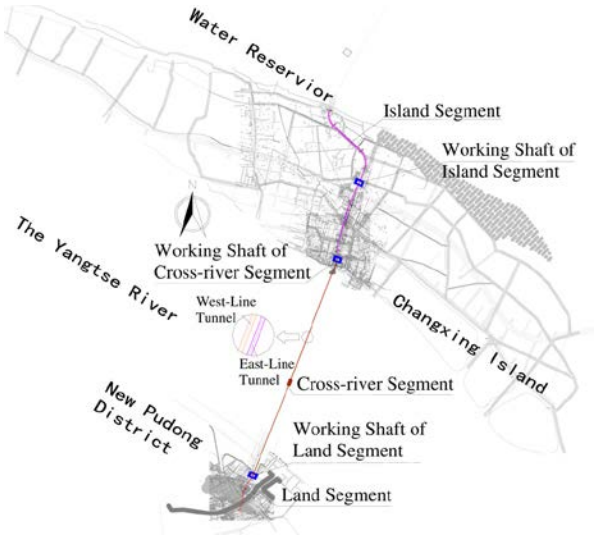


Figure 2: Map of the Qingcaosha tunnel

2.3 Road tunnel damaged during the Wenchuan earthquake

In western areas of China, a number of tunnels have suffered severe damage during the Wenchuan earthquake in 2008. For instance, the Longxi road tunnel, 2 kilometers far away from the epicenter of Wenchuan earthquake and at the faulted zone, suffered significant damage. The total length of the tunnel is 3,658 m, with a cross section composed of two parallel twin tunnels in two directions, 30m separated between axes. There were

a number of cross sections where the liner was observed to be collapsed. Close to the fault the tunnel completely collapsed, as shown in Figure 3.



Figure 3: Collapse of the Longxi tunnel at the crossing of the fault.

3 SIMPLIFIED SEISMIC ANALYSIS OF TUNNEL

Two simplified models, i.e. multibody dynamics and mass-spring-beam, for seismic analysis of long tunnels are presented as follows.

3.1 Rigid model

Based on the modeling theory of MS-DT-TMM (discrete time transfer matrix method for multibody dynamics) and the structural characteristics of long tunnels, a chain of multi-system model for long tunnels is developed as a simplified method due to its high computational efficiency, as shown in Fig. 4. In this approach, a long tunnel is simplified and assumed as two types of components, rigid bodies and joints. Tunnel linings are considered as rigid bodies and the joints connecting each adjacent tunnel linings are assumed as elastic damping hinges. Soil-structure interaction is taken into account by damping joints. The procedure of implementing the multibody dynamics model (Figure 4) is illustrated as follows: all the bodies and joints are digitized as numbers; the mechanical properties of each element are expressed in matrix; then mathematical calculation is conducted for each body and the system, yielding the overall transfer matrices and the equations of the system simultaneously, and finally the dynamic response of the system are acquired according to boundary and initial conditions.

The MS-DT-TMM based method is realized by using modern time integral approach at each discrete time in time domain. Compared with the finite element method, the MS-DT-TMM method is simple, high-efficiency and practical, which provides a powerful tool for dynamic response of long tunnels.

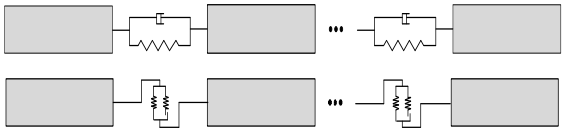


Figure 4: simplified multi-body dynamics model for long tunnels

3.2 Beam model

Another simplified method using mass-spring-beam model, as shown in Fig.5, is widely used in seismic design and analysis of long tunnels, especially for immersed tunnels. In this approach), a beam element is used to simulate tunnel linings or segments; a nonlinear spring element is used to simulate soil-structure or soil-soil interaction and tunnel joints; and a mass element is used for soil. For the immersed tunnel, the spring stiffness for tunnel joints is derived with the assumption that the GINA rubber is assumed as a spring with only the compression behavior.

Based on the equivalence theory, a new method, i.e. one-dimensional multiple-degree-of-freedom (MDOF) system, is developed in this study to represent the one-dimensional layered soil deposit. A series of one-dimensional MDOF system is further connected to constitute a two-dimensional mass-spring model for soil. The equivalent mass-spring model is then used for the longitudinal seismic analysis of long tunnels. The modal equivalent MDOF system has the distinction and advantage that it can characterize the exact properties of one-dimensional ground under shaking, such as natural frequency and hysteretic damping. By comparing the amplification function of the modal equivalent MDOF system with theoretical solution from one-dimensional wave propagation, it is concluded that an equivalent system of few degrees-of-freedom can provide accurate results.

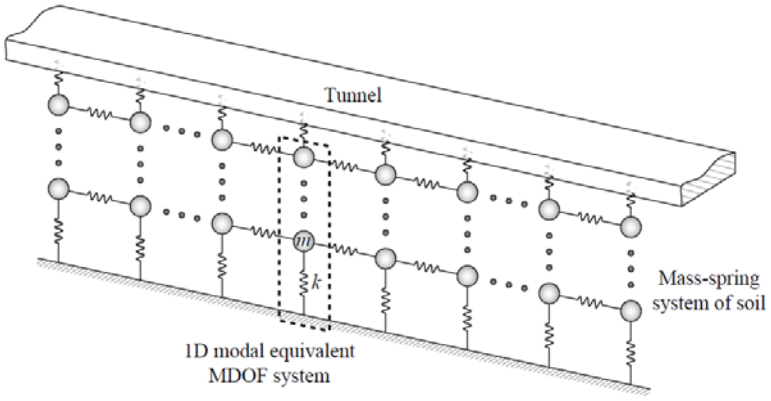


Figure 5: Mass-spring model for longitudinal seismic analysis of long tunnel

4 MULTISCALE MESHES FOR DETAILED SIMULATION

It should be pointed out that simplified seismic analysis may not be able to provide the overall understanding of the dynamic behavior of long tunnels subjected to seismic loadings. A multiscale approach is developed to investigate the dynamic properties of long tunnels described in Section 2.

4.1 Multiscale coupling approach

The multiscale approach combines the discrete element method (DEM) and the finite difference method (FDM). The DEM has been shown to be particularly suitable for capturing physical phenomena at small length scales where continuum mechanics is no

longer applied. Its efficiency, however, is limited because of the computational intensity required. A multidomain analysis coupling DEM and FDM is thus proposed to reduce the computational cost. A bridging scale term is introduced such that the compatibility of dynamic behavior between the DEM-based and FDM-based models is enforced. The proposed method does not result in spurious wave reflections and does not need additional filtering or damping in the overlapping domain between the FDM meshes and the DEM particles. It starts with the discretization of the entire domain with finite difference meshes and discrete particles. The meshes are employed to capture dynamic response characteristics of the system, whereas the particles are used to describe the dynamic response at the mesoscale or microscale. In the overlapping domain as shown in Figure 6, the constraints between mesh and particle subdomains are imposed to the motion equations using Lagrange multipliers, which are developed in a consistent manner from the energy potential. This approach filters the high-frequency components at the interface.

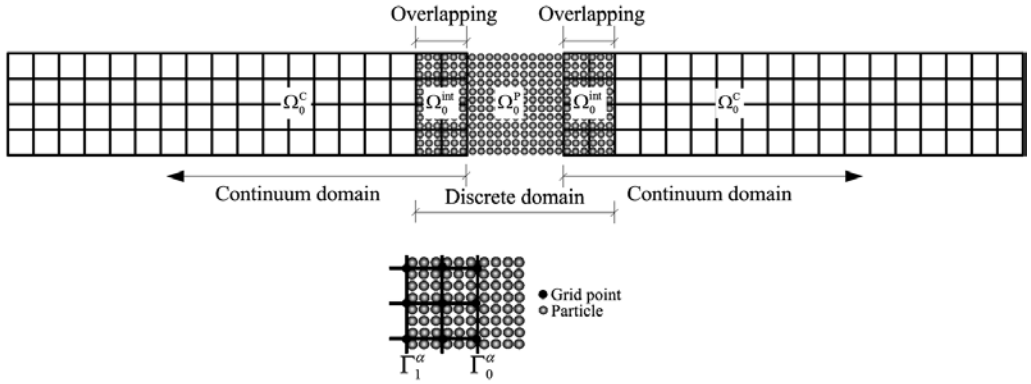


Figure 6: Bridging domain coupling discrete and continuum regions

The equations of motion for the coupling method including Lagrange multipliers are [9]

$$\bar{M}_J \ddot{\mathbf{u}}_J = \mathbf{f}_J^{\text{ext C}} - \mathbf{f}_J^{\text{int C}} - \mathbf{f}_J^{\text{LC}}, \text{ in } \Omega_0^{\text{C}} \tag{1}$$

$$\bar{m}_I \ddot{\mathbf{d}}_I = \mathbf{f}_I^{\text{ext P}} - \mathbf{f}_I^{\text{int P}} - \mathbf{f}_I^{\text{LP}}, \text{ in } \Omega_0^{\text{P}} \tag{2}$$

where $\bar{M}_J$ and $\bar{m}_I$ are the lumped mass of node J and particle I, respectively; $\mathbf{f}_J^{\text{ext C}}$ and $\mathbf{f}_I^{\text{ext P}}$ are the external node force and particle force, respectively; and $\mathbf{f}_J^{\text{int C}}$ and $\mathbf{f}_I^{\text{int P}}$ are the internal node force and particle force, respectively.

The forces $\mathbf{f}_J^{\text{LC}}$ and $\mathbf{f}_I^{\text{LP}}$ are caused by the constraints, enforced by Lagrange multipliers, and given by [9]

$$\mathbf{f}_J^{\text{LC}} = \sum_K \boldsymbol{\lambda}_K \frac{\partial \mathbf{g}_K}{\partial \mathbf{u}_J} = \sum_K \boldsymbol{\lambda}_K \mathbf{G}_{KJ}^C \tag{3}$$

$$\mathbf{f}_I^{\text{LP}} = \sum_K \boldsymbol{\lambda}_K \frac{\partial \mathbf{g}_K}{\partial \mathbf{u}_I} = \sum_K \boldsymbol{\lambda}_K \mathbf{G}_{KI}^{\text{P}} \tag{4}$$

where $\boldsymbol{\lambda}_K$ is a vector of Lagrange multipliers, and $\mathbf{g}_K$ is the representation of the kinematic constraints in the overlapping domain satisfying

$$\mathbf{G}_{KJ}^{\mathrm{C}}=\left[\frac{\partial \mathbf{g}_K}{\partial \mathbf{u}_J}\right]=\left[N_{JK}\mathbf{I}\right],\ \mathbf{G}_{KI}^{\mathrm{P}}=\left[\frac{\partial \mathbf{g}_K}{\partial \mathbf{u}_I}\right]=\left[-\delta_{IK}\mathbf{I}\right] \tag{5}$$

in which $N_{IK}=N_I\left(\mathbf{X}_K\right)$ is the interpolation function.

To solve the coupled dynamic system with the Lagrange multiplier method, an explicit algorithm is developed based on the central difference method. In this approach, displacements and velocities are assumed to be known at time steps n and n+1/2. First, a set of displacements and velocities are initialized by neglecting the constraints. Second, Lagrangian multipliers are obtained to satisfy the constraints. Finally, displacements and velocities are updated.

4.2 Implementation

In the proposed multiscale method, the FDM subdomain is employed to capture seismic response characteristics of the integral system, whereas the DEM subdomain describes in detail the dynamic response in locations with potential damage. This multiscale method couples two 2D commercial packages. The DEM computations are performed using Particle Flow Code (PFC) v4.0 and the FDM computations utilize Fast Lagrangian Analysis of Continua (FLAC) v5.0. Although data exchange at each time step, using different codes, is inconveniency, it should be noted that, both of these two codes are developed by Itasca software firm and share the same dynamic explicit algorithm. They have TCP/IP socket connection ability, which means that data can be exchanged rapidly on the same machine or on separate machines with a network connection. The data transmission between the two codes is invoked by FISH functions that allow large arrays of data to be exchanged with single function call [9].

The proposed multiscale method enforcing velocity continuity at the interface is adopted to handle FDM and DEM. The aim is to enforce the energy compatibility at the interface, and to ensure that energy can propagate through interface without spurious reflection.

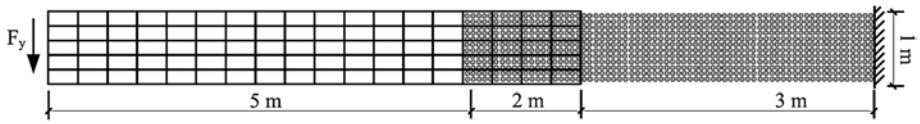
5 UNIFIED SIMULATION OF DAMAGE PROCESS

5.1 Model description

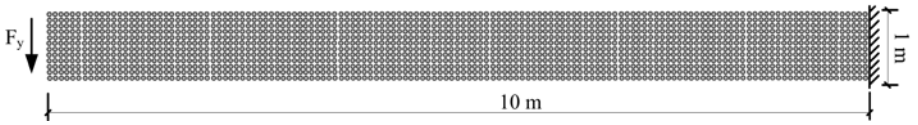
To validate the proposed multiscale coupling method for damage simulation, a 2D beam model, with dimensions of 1 m in height and 10 m in length beams as shown in Figure 7, is simulated by two different approaches, i.e. DEM and the multiscale coupling method. The radius for each particle is 0.09615 m, and the mesh size in both coupling and full continuum models is the same, i.e. 0.25 m×0.5 m. The overlapping zone is 2 m long and composed of 131 particles and 30 grid points. The right end of the model is fixed and the left end is subjected to dynamic bending loads in the vertical direction. The applied dynamic loading is described in Equation (6), where the circular frequency is f=50 Hz.

$$F_y=\begin{cases}5.0e6*\sin(2\pi\, ft) & t\le 0.01s\\ 0.0 & t>0.01s\end{cases}\quad Unit:N \tag{6}$$

The parameters used in the continuum and the discrete model can be found in detail in [9].



(a) Coupling method



(b) DEM

Figure 7: The cantilever beam model subjected to dynamic bending loads

5.2 Results and analysis

Cracks form between bonded particles and each subsequent bond-break event will result in a crack in the tunnel. The geometry and location of each crack are determined by the sizes and current locations of the two parent particles from which the crack originated.

Figure 8 (a) shows particle force chains calculated by DEM at time t=0.028 seconds. It can be observed that the maximum force chain between particles is 1,388 kN, but no crack is observed on the beam at this time. With the time increasing, cracks are observed at the fixed end of the beam and the maximum particle force chain increases to 8,611 kN at time t=0.032 s, as shown in Figure 8 (b). Figure 8 (c) illustrates the results obtained by the multiscale coupling method at the same time t=0.032 s. From the comparison between Figure 8 (b) and (c), it can be observed that cracking is observed at the same location (i.e. at the fixed end of the beam) and the difference of the maximum particle force chain is less than 1.2 percent.

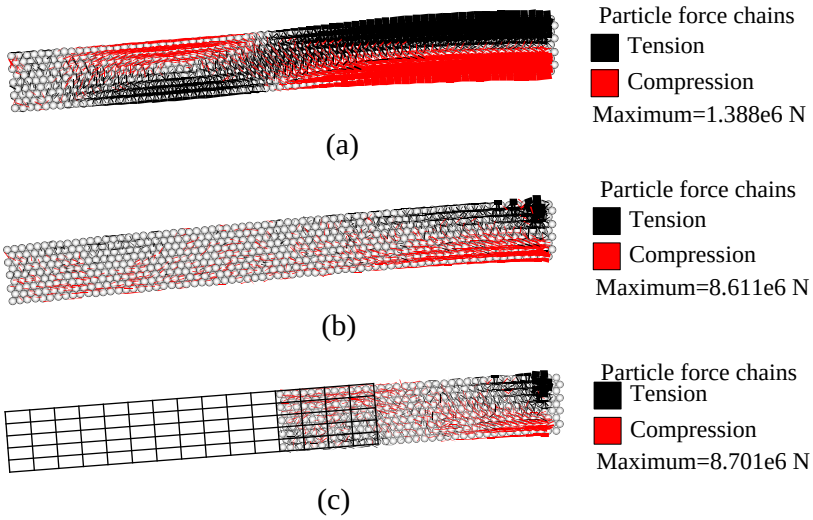


Figure 8: Particle force chains at time: (a) t=0.028 s by DEM, (b) t=0.032 s by DEM, and (c) t=0.032 s by the multiscale coupling method.

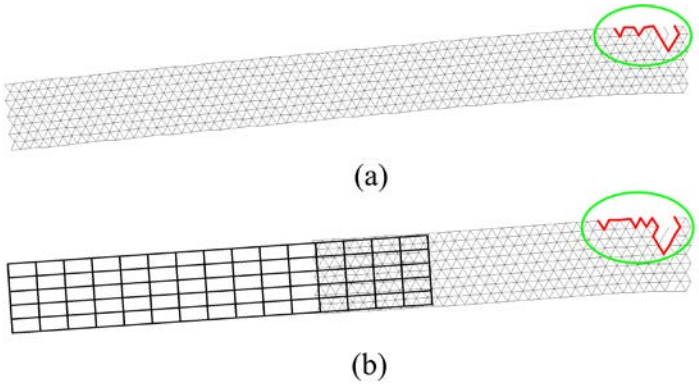


Figure 9: Particle contact bonds at time t=0.032 s. (a) DEM , (b) the multiscale coupling method.

Figure 9 (a) and (b) show the contact bonds of particles calculated by DEM and the multiscale method at time t=0.032 s, respectively. It can be seen from the figures that both the location and shape of the cracks are similar with the two methods.

6 CLOSING REMARKS

Two different methods, simplified method and unified method, are fully introduced to be used in seismic analysis of long tunnels. The simplified method using the rigid model or beam model can be an effective tool for practitioners. They allow readily identification of the variables controlling the magnitude of the distortions and thus provide an insight into the behavior of the structure. However, the simplified method fails to address in detail the structural response and damage process in positions of potential failure due to the simplified assumption of tunnel structure and soil-tunnel interaction.

Thus, a novel and reliable multiscale coupling method is proposed to solve the problem. Two distinguished numerical methods: continuum-based FDM and discrete-based DEM are coupled in the proposed method. An overlapping domain is created between the finite difference meshes and the discrete particles and a bridging scale term is introduced to ensure the compatibility of energy in the overlapping domain. The bridging domain coupling method is implemented to minimize, or at least reduce, spurious wave reflections at the continuum-discrete interface. The multiscale coupling governing equations are derived between the FDM and DEM, and the user-defined subroutines are developed based on two commercial packages, FLAC and PFC. The advantage of the multiscale continuum-discrete coupling approach is that it allows modeling of local physical phenomenon occurring at meso- or micro-scope scales in very large systems. An example is used to validate the proposed multiscale coupling method for damage simulation and hence demonstrate the applicability of the multiscale method in seismic analysis of long tunnels.

Acknowledgement: The authors would like to gratitude financial support from NSFC (Grant No. 51208296 & 51478343) and the Shanghai Committee of Science and Technology (13231200503). The joint supports are also from the Fundamental Research Funds for the Central Universities (2013KJ095), Shanghai Educational Development Foundation (13CG17), and the National Key Technology R&D Program (2012BAK24B04).

REFERENCES

[1] H.T. Yu, Y. Yuan, Z.Z. Qiao, Y. Gu, Z.H. Yang, X.D. Li, Seismic analysis of a long tunnel based on multi-scale method. *Engineering Structures*, **49**, 572-587, 2013.

[2] H.T. Yu, Y. Yuan, X. Liu, Y.W. Li, S.W. Ji, Damages of the Shaohuoping road tunnel near the epicentre. *Structure and Infrastructure Engineering*, **9**, 935-951, 2013.

[3] S.E. Kattis, D.E. Beskos, A.H.D. Cheng, 2D dynamic response of unlined and lined tunnels in poroelastic soil to harmonic body waves. *Earthquake Engineering and Structure Dynamics*, **32**, 97-110, 2003.

[4] S.A.S. Youakim, S.E.E. El-Metewally, W.F. Chen, Nonlinear analysis of tunnels in clayey/sandy soil with a concrete lining. *Engineering Structure*, **22**, 707-722, 2000.

[5] A. Amorosi, D. Boldini, Numerical modeling of the transverse dynamic behavior of circular tunnels in clayey soils. *Soil Dynamics and Earthquake Engineering*, **29**, 1059-1072, 2009.

[6] J. Penzien, C.L. Wu, Stresses in linings of bored tunnels. *Earthquake Engineering and Structure Dynamics*, **27**, 283-300, 1998.

[7] J. Penzien, Seismically induced raking of tunnel linings. *Earthquake Engineering and Structure Dynamic*, **29**, 683-691, 2000.

[8] H. Huo, A. Bobet, G. Ferna´ndez, J. Ramı´rez, Analytical solution for deep rectangular structures subjected to far-field shear stresses. *Tunnelling and Underground Space Technology*, **21**, 613-625, 2006.

[9] M.G. Li, H.T. Yu, J.H. Wang, X.H. Xia, J.J. Chen, A multiscale coupling approach between discrete element method and finite difference method for dynamic analysis. *International Journal for Numerical Methods in Engineering*, **102**, 1-21, 2015.

[10] Itasca. PFC2D-particle flow code. Version 3.0. *Itasca Consulting Group Inc.* 2002.

COMPDYN 2015
5th ECCOMAS Thematic Conference on
Computational Methods in Structural Dynamics and Earthquake Engineering
M. Papadrakakis, V. Papadopoulos, V. Plevris (eds.)
Crete Island, Greece, 25–27 May 2015

RAILWAY-INDUCED GROUND VIBRATIONS IN THE PRESENCE OF LOCAL TRACK IRREGULARITIES AND WHEEL FLATS

G. Kouroussis[1], G. Alexandrou[1], D. P. Connolly[2], K. Vogiatzis[3], and O. Verlinden[1]

[1]University of Mons — UMONS, Faculty of Engineering,
Place du Parc 20, B-7000 Mons, Belgium
e-mail: {georges.kouroussis,georgios.alexandrou,olivier.verlinden}@umons.ac.be

[2] Heriot-Watt University, School of Energy, Geoscience, Infrastructure & Society,
Edinburgh EH14 4AS, United Kingdom
e-mail: d.connolly@hw.ac.uk

[3] University of Thessaly, School of the Civil Engineering,
Pedion Areos, 383 34 Volos, Greece
e-mail: kvogiatz@uth.gr

Keywords: wheel/rail impact, vehicle/track interaction, ground-borne vibration, environmental impact assessment, flat wheel, local track irregularities

Abstract.

Rapid growth in railway infrastructure has led to numerous environmental technical challenges. This includes ground-borne vibration, which is becoming an increasing problem, particularly in urban environments. A common source of this vibration is local defects (e.g. rail joints, switches and crossings) which cause large amplitude excitations at isolated locations. Modelling this type of excitation mechanism using typical linear frequency domain analysis is challenging and therefore non-linear time domain methods are required. Therefore, in this study a validated and comprehensive time domain, three-dimensional ground vibration prediction model is used to investigate the vibrations generated at the wheel/rail contact due to local rail and wheel surface defects. Different types of rail and wheel defect are mathematically modelled, including rail joints, switches, crossings and wheel flats. The track is modelled as a typical ballasted track, using a two-step approach where the vehicle/track dynamics and ground wave propagation are simulated separately. The first step models the effect of railway vehicles (using a multibody approach with many degrees of freedom) on the dynamic excitation of the track and incorporates a non-linear Hertzian contact law at the wheel/rail interface. The second step applies these track-vehicle model forces to a finite/infinite element model to accurately generate vibration time histories for required ground-borne vibration assessment. This work focuses on the AM96 trainset, largely used in the Brussels Region (Belgium). The geometries of a variety of local defect types are analysed and a sensitivity analysis is undertaken based on the defect size and train speed. It is found that defect type and geometry have a significant influence on vibration levels, and that only selected geometry types are effected by train speed.

1 INTRODUCTION

Much research into railway-induced ground vibrations has focused on the effect of high-speed trains on the environment. This is motivated by the so-called "supercritical phenomenon" which appears when the vehicle speed is close to the Rayleigh ground wave speed. The latter depends on the soil flexibility and may be close to that of conventional high-speed lines [1, 2]. Despite the large vibration levels generated by these lines which are underlain by soft soils [3], the distance d between the track and neighbouring structures is relatively high and the vibration attenuates rapidly. In the case of railway traffic, the attenuation is associated with a power law of the form d^{-q}, where q lies between 0.5 and 1.1, depending on the soil configuration [4]. Connolly et al. [5] proved that it is possible to establish relationships between six key railway variables for ground vibration metrics in the case of high-speed lines. The situation is significantly different in the case of urban transit, due to the presence of local defects which induces elevated localised vibrations (dynamic effect).

The latter observation represents the main contribution of dynamic excitation in railway track. The pioneering work of Nielsen and Abrahamsson [6], Zhai et al. [7] and Oscarsson, Andersson and Dahlberg [8, 9] focus on the interaction between the track and the vehicle, in order to establish accurate models. They take into account the different elements of the track/foundation system. Similar work was recently done by Kouroussis et al. [10] to prove that an accurate simulation of track/soil interaction is important in the prediction of ground-borne vibration [11]. These numerical approaches offer the possibility of studying local defect effects on track dynamics. The study of vehicle/track coupling with local defects and the associated degree of dynamic coupling are of growing interest. The influence of vehicle-flexible mode shapes on the ride quality has been investigated [12], including local geometrical imperfections. Zhao et al. [13] employ a three-dimensional finite element model to evaluate the wheel/rail impact forces at local rail surface defects. They also evaluate the resulting dynamic forces at the discrete supports of the rail under different rolling speeds.

The aforementioned studies focus on the track/vehicle whereas few studies have analysed the effect of local defects on ground vibration. Despite this, many ground-borne vibration complaints in urban environments are due to local rail and wheel surface defects (e.g. switches, rail joints, ...). Kouroussis et al. [14] quantify the vibration generated by a tram running on a local rail defect using a numerical model in two successive steps (vehicle/track). Using the same approach, Alexandrou et al. [15] also study the wheel flat effect on ground motion and analyse the influence of wheel flat size. Vogiatzis [16, 17] undertakes a large-scale analysis of ground vibrations generated by underground Athens metro lines by studying wheel flat impact forces as impulses. As the source of vibration results from the wheel/rail contact, it is essential to study vehicle interaction with the track and the soil. Therefore, Costa et al. [18] show the importance of integrating a multibody model of the vehicle in the track/soil simulation and that in the case of a distributed rail's unevenness, sprung masses have minimal effects on the ground vibration motion. Furthermore, Kouroussis et al. [19] conclude that the choice between a simple model or a detailed model for the vehicle depends upon the importance of wheel and rail unevenness.

The purpose of this paper is to show the effect of typical rail and wheel surface defects. The study utilizes a numerical two-step approach, previously validated for this kind of situation. It focuses on the AM96 trainset circulating in Brussels, for which substantial measured data exists [20]. The present work deals with a layered soil based on geophysical tests performed at the same test site. In order to compile a dataset of the main parameters that influence ground vibration levels, different defect geometries are considered for various train speeds and defect

sizes.

2 CLASSIFICATION OF LOCAL DEFECTS

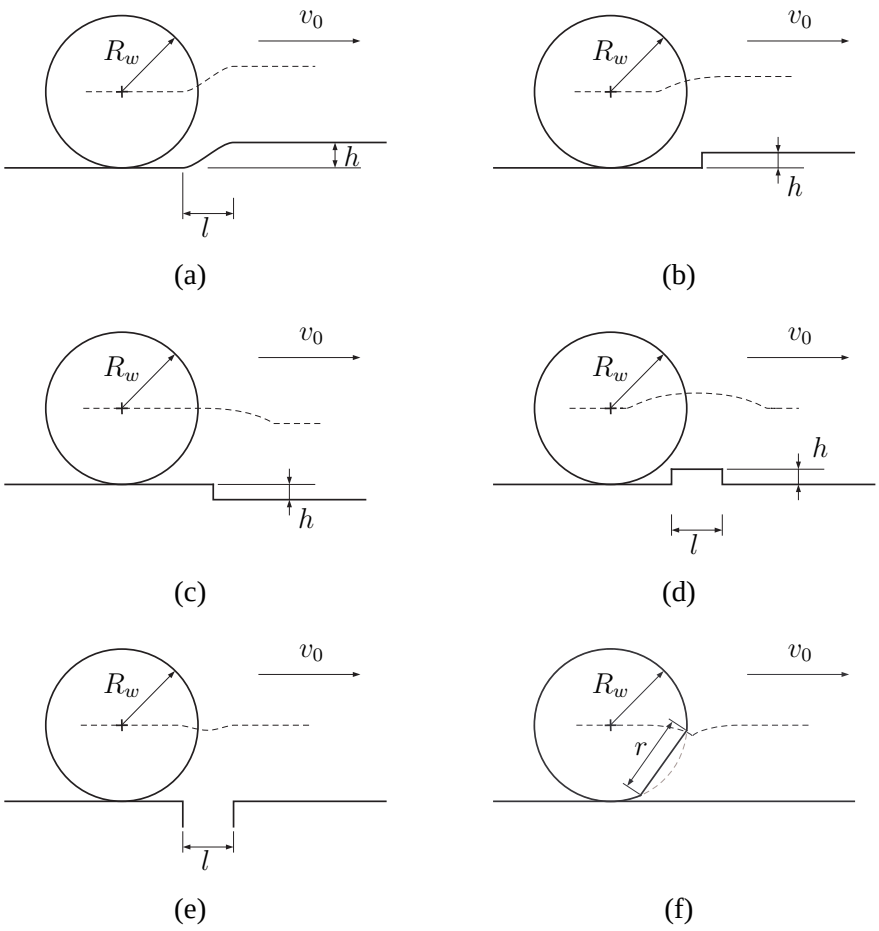


Figure 1: Mathematical modelling of local rail and wheel surface defects: (a) smooth irregularity, (b) step-up joint, (c) step-down joint, (d) stepwise joint (step-up), (e) stepwise joint (step-down) and (f) wheel flat.

Figure 1 presents the mathematical interpretation deduced from defects encoutered in practice. It shows the local discontinuity encountered in urban areas that commonly contribute to ground vibration generation. For each defect, the dimensions are presented (illustrated by the solid line under the wheel in Figure 1), and the shape "seen" by the wheel/rail interface (illustrated by the dotted line in Figure 1) which can be different than the defect shape, taking into account the wheel radius R_w and the vehicle speed v_0.

3 NUMERICAL MODEL

The proposed prediction model is based on two successive calculations [21]. Complexity required the problem to be split. This approach allows the most well-suited modelling approach to be used for each subsystem. First of all, the dynamics of the vehicle/track subsystem is simulated by considering a multibody vehicle model moving at speed v_0 on a flexible track with a rail irregularity (Figure 2). The wheel/rail forces are defined using non-linear Hertz's theory and allows coupling between the vehicle model and the track. The latter is defined as a flexible beam (Young modulus E_r, geometrical moment of inertia I_r, section A_r and density ρ_r) discretely

supported by the sleepers (of mass m and with spacing d), including viscoelastic elements for the ballast (stiffness k_b and damping coefficient d_b) and the railpads (stiffness k_p and damping coefficient d_p). To take into account the dynamic behaviour of the foundation, which plays an important role at low frequencies, a coupled lumped mass (CLM) model is added to the track model, with interconnection elements for the foundation-to-foundation coupling [22]. A C++ object-oriented program was developed, using the in-house EasyDyn library [23]. An application based on a symbolic engine platform generates mathematical kinematic expressions for the vehicle. The generalized coordinates approach is used to obtain a system of pure ordinary differential equations, without constraint equations. The symbolic engine platform creates a C++ code directly compilable against the EasyDyn library. The problem definition is completed by generating applied forces (suspensions, wheel/rail contact) and a link to the track model (which is already established and depends on site parameters only). An implicit scheme is used for the simulation in this first step. The ballast reactions are then saved and used as input forces for the second step.

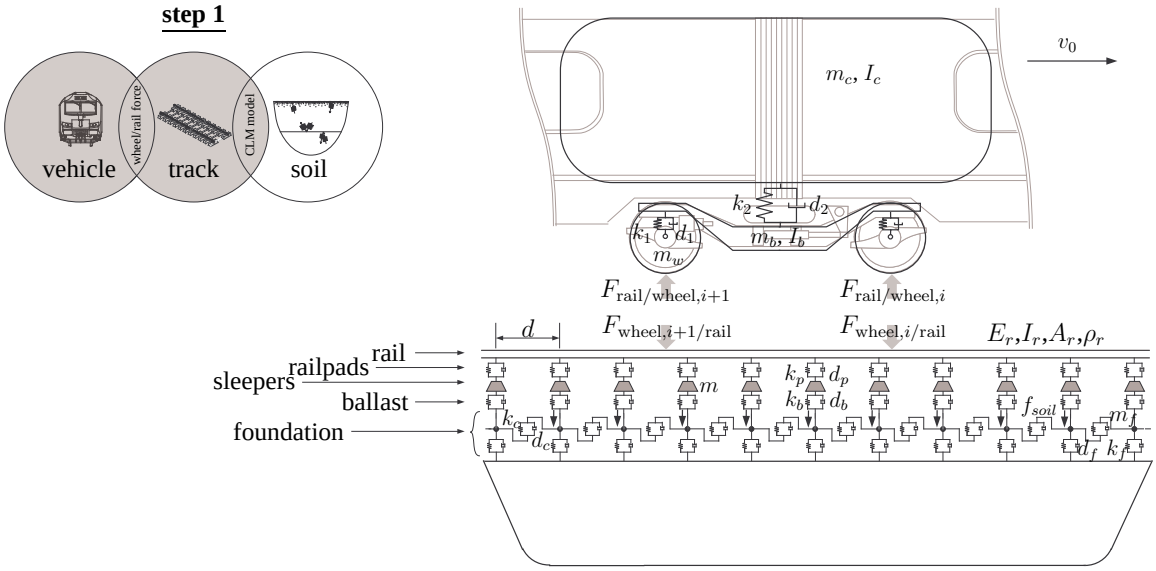


Figure 2: Description of the prediction model: vehicle/track/foundation simulation.

The second step addresses the dynamics of the soil subsystem, with the soil surface forces representing the contribution from the sleepers (Figure 3). The dynamic ground response is calculated using the finite element method, which is well suited for 3D analysis. Some analyses were recently conducted by the authors to improve the performance of their finite element model [24], namely:

- *Complex geometry*. A fully 3D finite element model allows treating complex geometry (track embankment, inclined layer interfaces). Moreover, variability in track profile and high ground vibrations originating in singular rail surface defects can be treated without any difficulty.

- *Non-reflecting boundary conditions*. The combined use of viscous boundaries and infinite elements provides more efficient non-reflecting condition than classical setups (free or fixed boundaries). Here, the small dependence on incident wave angle and dynamic parameters is quantitatively carried out for each solution. A spherical soil border geom-

etry is defined, to which infinite elements are attached. This convex shape configuration insures the condition of non-crossing infinite elements.

- *Reasonable computation time*.The simulation in time domain is an interesting solution to study ground vibrations in a relatively small region of interest. As ground vibrations are inherently a transient phenomenon, the time domain analysis is appropriate to simulate wave propagation and does not impose any condition on the domain size, which would be required in the frequency domain. Moreover, the equations of motion describing the soil dynamics are integrated using explicit central difference integration to reduce the computational burden.

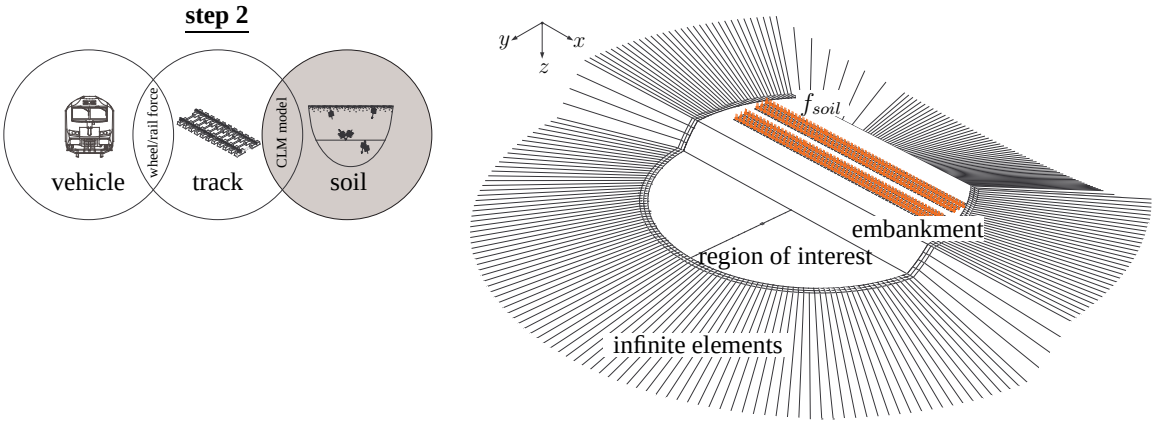


Figure 3: Finite element soil modelling using infinite elements and viscous boundary conditions.

4 NUMERICAL SIMULATIONS AND RESULTS

This study focuses on the InterCity train operating in Brussels (Belgium). The AM96 trainset, largely used by the Belgian Railway Operator, SNCB, is typically used for InterCity and InterRegion connections. This study evaluates the AM96 trainset's generation of elevated ground vibration levels in comparison to other domestic trains [20]. It consists of three carriages, designated HVBX, HVB, and HVADX. The HVBX leading wagon is equipped with motorised bogies, whereas the HVB (middle) and HVADX (end) wagons are trailer carriages. Figure 4 represents the configurations and the positions of each wheelset on the vehicle. A classical multibody approach is used and limits the vehicle dynamics to pitch and bounce motions.

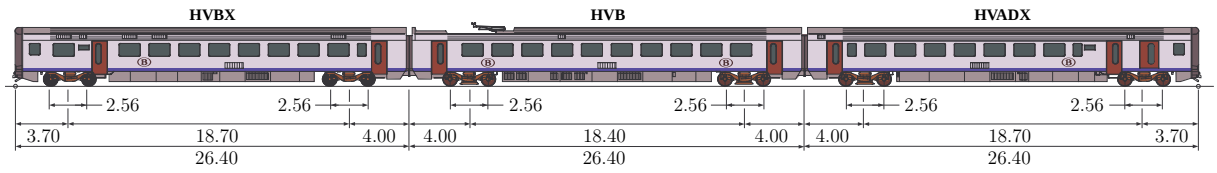


Figure 4: Configuration of the AM96 electric multiple unit.

4.1 Free-field ground vibrations

Figure 5 presents an analysis of the numerical results, considering the cases without defect and with a step-up stepwise joint representing a pulse defect (vertical height $h = 5\,\mathrm{mm}$ and horizontal length $l = 10\,\mathrm{mm}$). The AM96 trainset runs at a speed v_0 of $120\,\mathrm{km/h}$. The comparison

is based on the time history of numerical velocities in the vertical direction (Figure 5(a)) and the corresponding normalized frequency content (Figure 5(b)), both for a distance of $10\,\mathrm{m}$ from the track. A significant difference in levels is observed between the two cases' velocity traces (more than ten times magnification). The passing of each wheelset is more clearly defined in the case where the defect is present. Although the frequency content is spread over a range $[0;100\,\mathrm{Hz}]$, all dominant frequencies are located in the frequency range 0 – $60\,\mathrm{Hz}$.

The frequency spectra present some similarities. For instance, both datasets identify several dominant frequencies due to the fundamental and harmonic carriage frequencies. Moreover, the fundamental axle and bogie passage frequencies imply a double amplitude modulation, as considered in [19]. The effect of distance from the track is also analysed. As presented in Figure 5(c), it shows the far field peak particle velocity, PPV, defined as the maximum absolute amplitude of soil surface velocity in the vertical direction. The investigations are based on a track with an embankment: receivers are placed out the embankment area (in the far field) where ground vibration is most likely problematic.

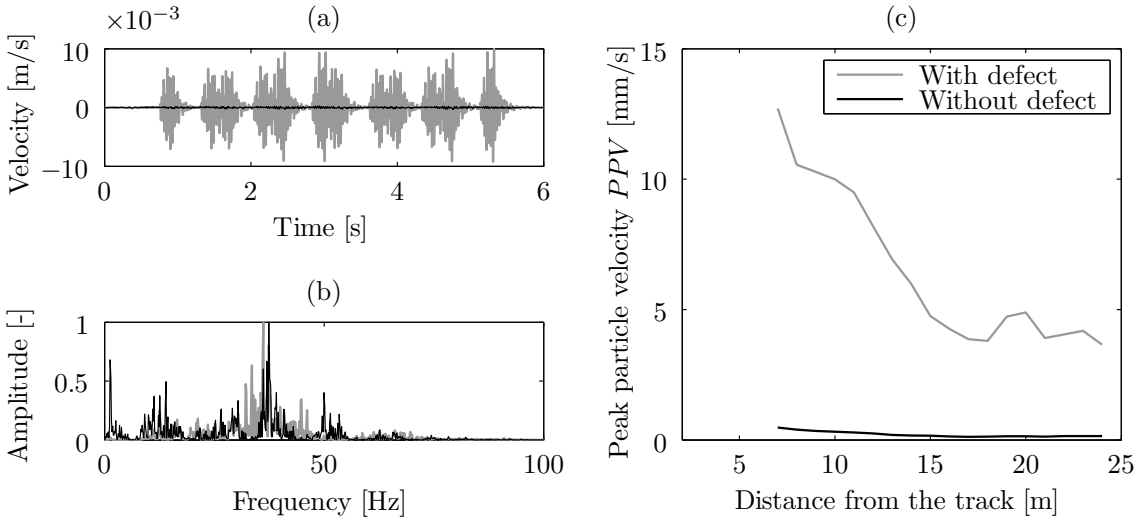


Figure 5: Comparison between numerical data (grey: with $5\,\mathrm{mm}$ height pulse defect; black: without defect) related to the passage of an AM96 trainset (2×3 carriages) at a speed v_0 of $120\,\mathrm{km/h}$, (a) time histories at $10\,\mathrm{m}$ from the track, (b) frequency contents at $10\,\mathrm{m}$ from the track and (c) Peak particle velocity as a function of the distance from the track.

Figure 6 demonstrates the associated ground wave propagation for the same aforementioned defect. It gives a comprehensive view of the free field response on the soil's surface. The selected time histories emphasize the instants when the first bogie crosses the local defect. At times before $t = 0.75\,\mathrm{s}$, the ground wave generation is due to the quasi-static contribution of the vehicle (no contact with the local defect). At times after $t = 0.75\,\mathrm{s}$, the ground wave propagation is amplified by the wheel/defect contact due to the vehicle/track dynamics. This effect is visible until $t = 1\,\mathrm{s}$, showing that the phenomenon is transient and affects each wheel/defect impact.

4.2 Influence of the defect type

The six shapes of discontinuity presented in Figure 1 (representing various defect types such as transition zones, switches, crossings, rail joints, and wheel flats) are analysed in this section. The case of an AM96 trainset running at a constant speed v_0 and separately interacting with

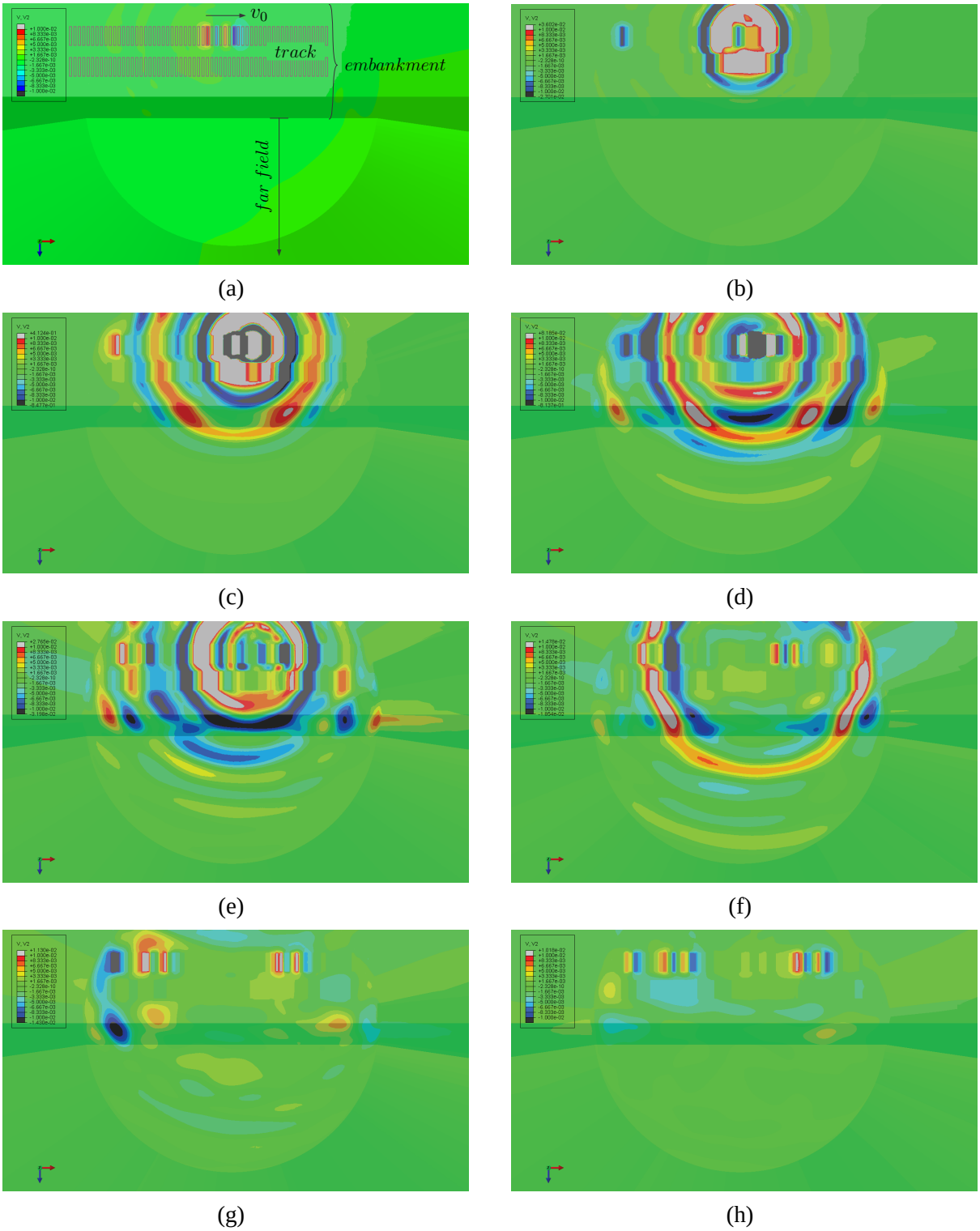


Figure 6: Birdseye view visualisation of the passage of an AM96 trainset at a speed of $120\,\mathrm{km/h}$ on a $5\,\mathrm{mm}$ height pulse defect: free field vertical component of the soil vibration waves (a) at $0.7\,\mathrm{s}$, (a) at $0.75\,\mathrm{s}$, (b) at $0.8\,\mathrm{s}$, (c) at $0.85\,\mathrm{s}$, (d) at $0.9\,\mathrm{s}$, (e) at $0.95\,\mathrm{s}$, (f) at $1.0\,\mathrm{s}$, (g) at $1.05\,\mathrm{s}$.

these defects is studied.

Figure 7 presents the level of surface ground vibration at different distances from the track, in a region outside the embankment. The values of defect length and size were selected according

to those commonly found in practice. For the smooth irregularity (ramp function), the length l is $200\,\mathrm{mm}$ (sufficiently long to replicate a smooth transition zone) with a height $h = 10\,\mathrm{mm}$. For the pulse function (step-up stepwise joint), the length is fixed at $l = 10\,\mathrm{mm}$ with a height $h = 5\,\mathrm{mm}$. For the negative pulse function (step-down stepwise joint), the length is fixed at $l = 20\,\mathrm{mm}$. For the other rail defects, only the height is relevant, and is fixed as $h = 5\,\mathrm{mm}$. The flat spot is selected with a length $r = 30\,\mathrm{mm}$. The results show large discrepancies between ground vibration levels, with very small levels for the step-down stepwise joint and wheel flat, which were close to those obtained without local defects (Figure 5(c)). Specifically, a difference in results between the step-up and step-down joint cases occurs as a result of symmetrically identical geometry. This is due to the non-linear effects at the wheel/rail contact where climbing and dropping do not represent the same dynamic effect. The change in vibration level with the distance from track offset has a general tendency to decrease.

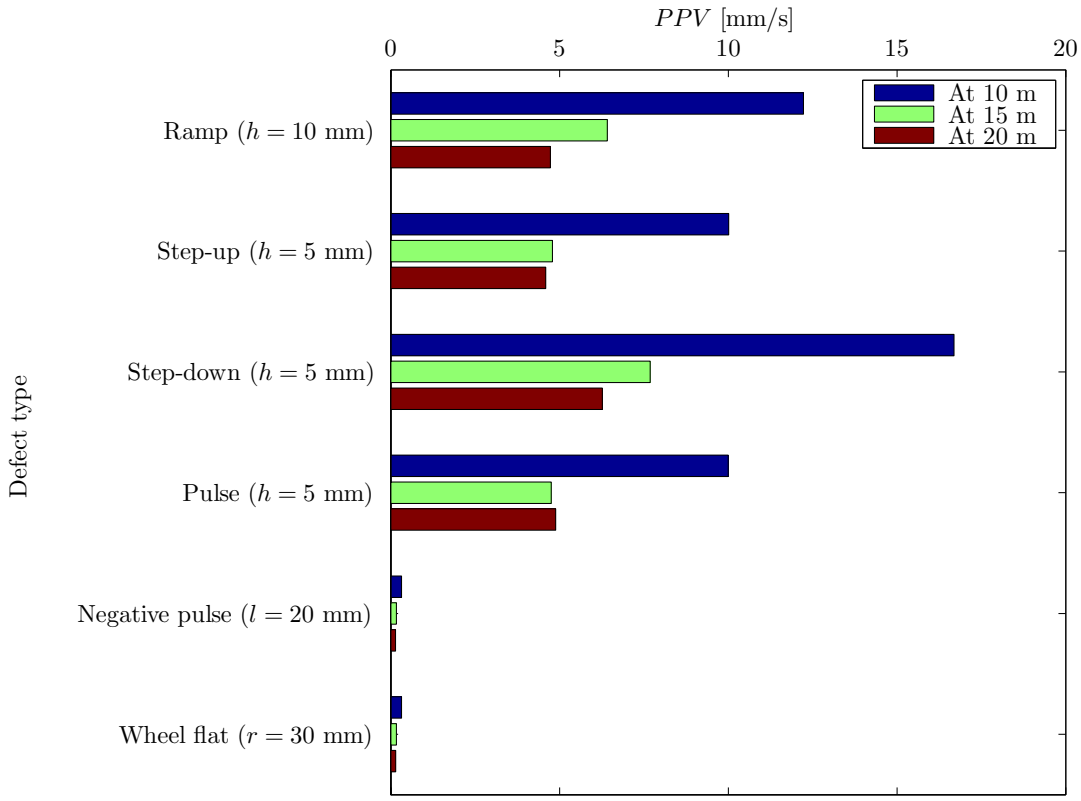


Figure 7: Peak particle velocity as a function of the distance from the source and the defect type for an AM96 trainset running at $120\,\mathrm{km/h}$.

4.3 Influence of the defect size

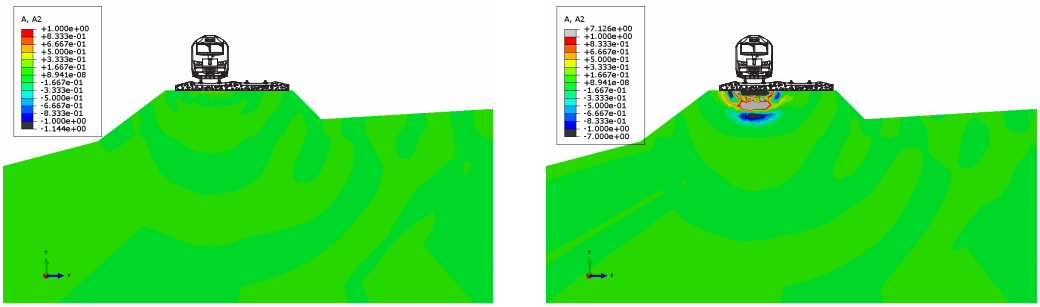
A sensitivity analysis is presented in Table 1 for when the main dimension varies (h for the smooth irregularity, the step-up joint, the step-down joint, step-up stepwise joint; l for the step-down stepwise joint; r for the wheel flat). Generally, there is a positive relationship between the PPV and defect size.

At $120\,\mathrm{km/h}$, the wheel flat and negative pulse have zero effect on ground vibrations. This is due to the vehicle speed shifting the frequency content to a higher range. These high frequencies are are then rapidly dampened by the soil and the track, meaning that at the studied distances,

	$l = 200\,\mathrm{mm}$	$l = 200\,\mathrm{mm}$	$l = 200\,\mathrm{mm}$
	$h = 5\,\mathrm{mm}$	$h = 10\,\mathrm{mm}$	$h = 15\,\mathrm{mm}$
Smooth irregularity	$4.78\,\mathrm{mm/s}$ $(-61\,\%)$	$12.23\,\mathrm{mm/s}$	$20.64\,\mathrm{mm/s}$ $(+69\,\%)$
	$h = 2.5\,\mathrm{mm}$	$h = 5\,\mathrm{mm}$	$h = 7.5\,\mathrm{mm}$
Step-up joint	$4.29\,\mathrm{mm/s}$ $(-57\,\%)$	$10.01\,\mathrm{mm/s}$	$11.43\,\mathrm{mm/s}$ $(+14\,\%)$
	$h = 2.5\,\mathrm{mm}$	$h = 5\,\mathrm{mm}$	$h = 7.5\,\mathrm{mm}$
Step-down joint	$2.13\,\mathrm{mm/s}$ $(-87\,\%)$	$16.69\,\mathrm{mm/s}$	$28.49\,\mathrm{mm/s}$ $(+71\,\%)$
	$l = 10\,\mathrm{mm}$	$l = 10\,\mathrm{mm}$	$l = 10\,\mathrm{mm}$
	$h = 2.5\,\mathrm{mm}$	$h = 5\,\mathrm{mm}$	$h = 7.5\,\mathrm{mm}$
Step-up stepwise joint	$4.06\,\mathrm{mm/s}$ $(-59\,\%)$	$10.00\,\mathrm{mm/s}$	$10.31\,\mathrm{mm/s}$ $(+3\,\%)$
	$l = 10\,\mathrm{mm}$	$l = 20\,\mathrm{mm}$	$l = 30\,\mathrm{mm}$
Step-down stepwise joint	$0.32\,\mathrm{mm/s}$ $(-0.4\,\%)$	$0.32\,\mathrm{mm/s}$	$0.32\,\mathrm{mm/s}$ $(+1\,\%)$
	$r = 20\,\mathrm{mm}$	$r = 30\,\mathrm{mm}$	$r = 40\,\mathrm{mm}$
Wheel flat	$0.32\,\mathrm{mm/s}$ $(+0.5\,\%)$	$0.32\,\mathrm{mm/s}$	$0.32\,\mathrm{mm/s}$ $(+0.5\,\%)$

Table 1: Ground vibration level at $10\,\mathrm{m}$ from the source for an AM96 trainset running at $120\,\mathrm{km/h}$.

their effect is insignificant. Figure 8 illustrates this by comparing the ground wave propagation generated by the train's passing. In Figure 8(a), the reference case without a defect is presented and Figure 8(b) is related to the case with a defect. The same colour scale is used in both results (vertical acceleration is displayed in order to more clearly emphasize the high frequency content), showing the difference between the two cases observed in the near-field's embankment area.



(a) (b)

Figure 8: Numerical visualisation (x-axis planar view) of the passage of an AM96 trainset at a speed of $120\,\mathrm{km/h}$ (a) without defect and (b) with a $40\,\mathrm{mm}$ length negative pulse defect.

4.4 Influence of the vehicle speed

The previous section is devoted to the variation in vehicle speed levels ($v_0 = 100\,\mathrm{km/h}$, $120\,\mathrm{km/h}$ and $140\,\mathrm{km/h}$). Figure 9 presents, for some studied defect, the variation in PPV. Note that the two defects — step-down stepwise joint and wheel flat — present the same characteristics, confirming that these defects are not greatly effected by train speed (in this case, the effect with the speed is associated with the quasi-static contribution of the vehicle only). Despite this, for some defects (e. g. smooth irregularity), the higher the vehicle speed, the greater the ground vibration level. For other defects (e.g. step-down joint), the opposite is true. To understand this difference, a frequency content study of the ground vibration signal is necessary.

Therefore Figure 10 shows the corresponding frequency content in the case of the step-up joint. For each speed, an additional curve representing the amplitude modulation, due to the fundamental axle passage frequency, is added. This illustrates that the frequency content of the initial defect impact content is also modulated by the axle periodicity [19]. The maximum amplitude of vibration generated by the defect impact can be inside the lobes (Figures 10(a) and 10(c)) or between two lobes (Figure 10(b)).

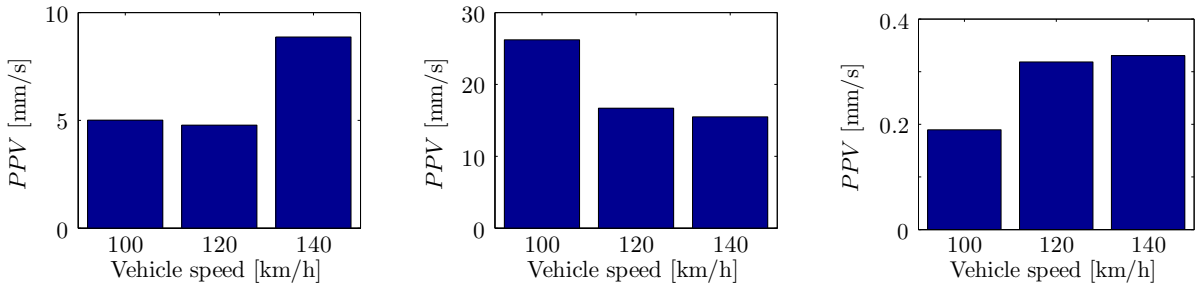


Figure 9: Peak particle velocity as a function of the vehicle speed at $10\,\mathrm{m}$ from the track and for an AM96 trainset running on (a) smooth irregularity ($l = 200\,\mathrm{mm}$, $h = 5\,\mathrm{mm}$), (b) step-down joint ($h = 5\,\mathrm{mm}$) and (c) wheel flat ($r = 50\,\mathrm{mm}$).

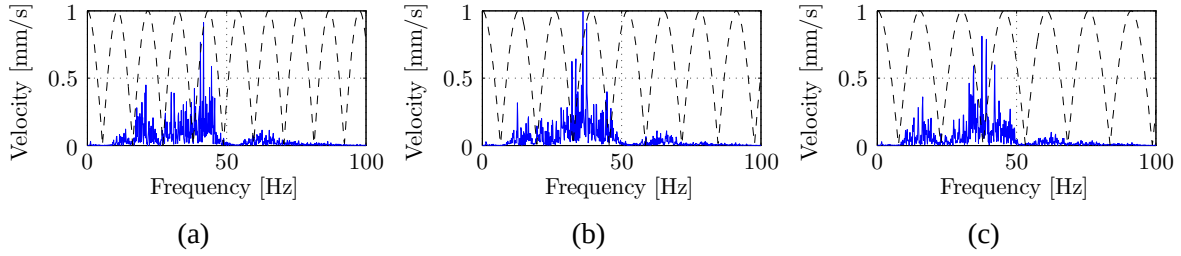


Figure 10: Frequency content of ground vibrations calculated at $10\,\mathrm{m}$ from the track for the step-up joint ($h = 5\,\mathrm{mm}$) and for a speed of (a) $v_0 = 100\,\mathrm{km/h}$, (b) $v_0 = 120\,\mathrm{km/h}$ and (c) $v_0 = 140\,\mathrm{km/h}$ (the dash lines represent the amplitude modulation due to the fundamental axle passage frequency).

5 CONCLUSION

Ground-borne vibration from railway traffic is becoming an increasing problem, particularly in urban environments. A common source of this vibration is individual, localised local defects which generate large amplitude excitations.

This study uses a time domain vibration prediction model is used to investigate the vibrations generated at the wheel/rail contact due to these defects. Different types of rail and wheel defect are mathematically modelled, including rail joints, switches, crossings and wheel flats. The problem was broken into two sub-models: one for the train-track and one for the soil. This work focuses on the AM96 trainset, largely used in the Brussels Region (Belgium). The geometries of a variety of local defect types are analysed and a sensitivity analysis is undertaken based upon the defect size and train speed. It is found that defect type and geometry have a significant influence on vibration levels, and that only selected geometry types are effected by train speed.

ACKNOWLEDGEMENT

The first author would like to acknowledge, Sébastien Mercier and Joseph Tsongo, from the Faculty of Engineering of the University of Mons, for their investigations into the local defect analysis.

REFERENCES

[1] C. Madshus and A. M. Kaynia. High-speed railway lines on soft ground: dynamic behaviour at critical train speed. *Journal of Sound and Vibration*, 231(3):689–701, 2000.

[2] D. P. Connolly, G. Kouroussis, O. Laghrouche, C. Ho, and M. C. Forde. Benchmarking railway vibrations — track, vehicle, ground and building effects. *Construction and Building Materials*, doi: 10.1016/j.conbuildmat.2014.07.042 (in press), 2014.

[3] D. P. Connolly, G. Kouroussis, P. K. Woodward, P. A. Costa, O. Verlinden, and M. C. Forde. Field testing and analysis of high speed rail vibrations. *Soil Dynamics and Earthquake Engineering*, 67:102–118, 2014.

[4] L. Auersch and S. Said. Attenuation of ground vibrations due to different technical sources. *Earthquake Engineering and Engineering Vibration*, 9:337–344, 2010.

[5] D. P. Connolly, G. Kouroussis, P. K. Woodward, O. Verlinden, A. Giannopoulos, and M. C. Forde. Scoping prediction of re-radiated ground-borne noise and vibration near high speed rail lines with variable soils. *Soil Dynamics and Earthquake Engineering*, 66:78–88, 2014.

[6] J. C. O. Nielsen and T. J. S. Abrahamsson. Coupling of physical and modal components for analysis of moving non-linear dynamic systems on general beam structures. *International Journal for Numerical Methods in Engineering*, 33(9):1843–1859, 1992.

[7] W. Zhai and X. Sun. A detailed model for investigating vertical interaction between railway vehicle and track. *Vehicle System Dynamics*, 23(supplement):603–615, 1994.

[8] J. Oscarsson and T. Dahlberg. Dynamic train/track/ballast interaction - computer models and full-scale experiments. *Vehicle System Dynamics*, 29(supplement):73–84, 1998.

[9] C. Andersson and J. Oscarsson. Dynamic train/track interaction including state-dependent track properties and flexible vehicle components. *Vehicle System Dynamics*, 33(supplement):47–58, 1999.

[10] G. Kouroussis, G. Gazetas, I. Anastasopoulos, C. Conti, and O. Verlinden. Discrete modelling of vertical track–soil coupling for vehicle–track dynamics. *Soil Dynamics and Earthquake Engineering*, 31(12):1711–1723, 2011.

[11] G. Kouroussis and O. Verlinden. Prediction of railway ground vibrations: accuracy of a coupled lumped mass model for representing the track/soil interaction. *Soil Dynamics and Earthquake Engineering*, 69:220–226, 2015.

[12] D. Younesian, S. R. Marjani, and E. Esmailzadeh. Importance of flexural mode shapes in dynamic analysis of high-speed trains traveling on bridges. *Journal of Vibration and Control*, 20(10):1565–1583, 2014.

[13] X. Zhao, Z. Li, and J. Liu. Wheel–rail impact and the dynamic forces at discrete supports of rails in the presence of singular rail surface defects. *Journal of Rail and Rapid Transit*, 226(2):124–139, 2012.

[14] G. Kouroussis, O. Verlinden, and C. Conti. Efficiency of resilient wheels on the alleviation of railway ground vibrations. *Journal of Rail and Rapid Transit*, 226(4):381–396, 2012.

[15] G. Alexandrou, G. Kouroussis, and O. Verlinden. A comprehensive prediction model for vehicle/track/soil dynamic response due to wheel flats. *Journal of Rail and Rapid Transit*, doi: 10.1177/0954409715576015 (in press), 2015.

[16] K. Vogiatzis. Noise and vibration theoretical evaluation and monitoring program for the protection of the Ancient "Kapnikarea Church" from Athens metro operation. *International Review of Civil Engineering*, 1:328–333, 2010.

[17] K. Vogiatzis. Protection of the cultural heritage from underground metro vibration and ground-borne noise in Athens centre: The case of the Kerameikos archaeological museum and Gazi cultural centre. *International Journal of Acoustics and Vibration*, 17:59–72, 2012.

[18] P. A. Costa, R. Calçada, and A. S. Cardoso. Influence of train dynamic modelling strategy on the prediction of track–ground vibrations induced by railway traffic. *Journal of Rail and Rapid Transit*, 226(4):434–450, 2012.

[19] G. Kouroussis, D. P. Connolly, and O. Verlinden. Railway induced ground vibrations — a review of vehicle effects. *International Journal of Rail Transportation*, 2(2):69–110, 2014.

[20] G. Kouroussis, C. Conti, and O. Verlinden. Experimental study of ground vibrations induced by Brussels IC/IR trains in their neighbourhood. *Mechanics & Industry*, 14(02):99–105, 2013.

[21] G. Kouroussis, J. Florentin, and O. Verlinden. Ground vibrations induced by intercity/interregion trains: A numerical prediction based on the multibody/finite element modeling approach. *Journal of Vibration and Control*, doi: 10.1177/1077546315573914 (in press), 2015.

[22] G. Kouroussis, L. Van Parys, C. Conti, and O. Verlinden. Prediction of ground vibrations induced by urban railway traffic: an analysis of the coupling assumptions between vehicle, track, soil, and buildings. *International Journal of Acoustics and Vibration*, 18(4):163–172, 2013.

[23] O. Verlinden, L. Ben Fekih, and G. Kouroussis. Symbolic generation of the kinematics of multibody systems in EasyDyn: from MuPAD to Xcas/Giac. *Theoretical & Applied Mechanics Letters*, 3(1):013012, 2013.

[24] G. Kouroussis, L. Van Parys, C. Conti, and O. Verlinden. Using three-dimensional finite element analysis in time domain to model railway–induced ground vibrations. *Advances in Engineering Software*, 70:63–76, 2014.

COMPDYN 2015
5th ECCOMAS Thematic Conference on
Computational Methods in Structural Dynamics and Earthquake Engineering
M. Papadrakakis, V. Papadopoulos, V. Plevris (eds.)
Crete Island, Greece, 25–27 May 2015

IMPACT RESPONSES OF PRESTRESSING TENDONS IN RAILWAY CONCRETE SLEEPERS IN HIGH SPEED RAIL ENVIRONMENTS

Sakdirat Kaewunruen[1] **and Alex M. Remennikov**[2]

[1] Birmingham Centre for Railway Research and Education, School of Civil Engineering
The University of Birmingham, Edgbaston, B15 2TT UK
e-mail: s.kaewunruen@bham.ac.uk

[2] School of Civil, Mining, and Environmental Engineering
University of Wollongong, Northfield Ave, Wollongong, NSW 2522 Australia
e-mail: alexrem@uow.edu.au

Keywords: Railway, Concrete Sleepers, Railroad Ties, Prestressing Tendons/Wires, Impact Analysis, Dynamic Responses, LS-Dyna.

Abstract. *Prestressed concrete sleepers (or railroad ties) are designed in order to carry and transfer the wheel loads from the rails to the ground and are installed as the crosstie beam support in railway track systems. They are subjected to impact loading conditions that are resulted from train operations over wheel or rail abnormalities, such as flat wheels, dipped rails, crossing transfers, rail squats, corrugation, etc. The magnitude of the shock load relies on various factors such as axle load, types of wheel/rail imperfections, speeds of vehicle, track stiffness, etc.*

This paper demonstrates the development of finite element modelling to evaluate the dynamic responses of prestressed tendons or wires embedded in concrete sleepers, particularly under a variety of impact loads. The force prediction under high speed rail environment was conducted using D-TRACK. The 3D finite element model of prestressed concrete sleeper has been developed using a finite element package, LS-Dyna. It has been verified by the experiments carried out using the high capacity drop-weight impact machine at the University of Wollongong, Australia. The experimental results provide very good correlation with numerical simulations. In this paper, the numerical studies are extended to evaluate the dynamic behaviors of high strength steel wires and their responses under different parameters in high speed rail environments. The outcome of this study can potentially lead to the dynamic design guideline for prestressed concrete sleepers under low-cycle fatigues. Future work includes more detailed investigation into the effect of track bed and rail pad degradation subject to higher frequency impacts.

1 INTRODUCTION

For ballasted tracks worldwide, railway sleeper is a major component to redistribute train axle loads from the rails to the underlying ballast supporting system. Typical ballasted railway track and its components can be seen in Figure 1 [1]. It has been chronically believed based on the industry practice that railway concrete sleepers possess reserved strength that are untapped. Accordingly, it is crucial to evaluate the spectrum and amplitudes of forces applied to the railway track, in order to understand more clearly the behaviors in which track components respond to those forces, and to identify the processes whereby concrete sleepers in particular carry those force actions. Recent findings show that the nature of the majority of loading conditions on track structures is of dynamic impact [2]. Those loads are normally of short duration but of very high magnitude. They are ascribed to the wheel/rail interactions associated with irregularities, i.e. wheel burns, wheel flats, corrugations, non-uniform track modulus, and any other out-of-round wheel defects. Structural performance monitoring is an effective way to establish better understanding into the impact behaviors of prestressed concrete sleepers**.**

In addition, cracks in concrete sleepers have been visually observed by many railway organizations. As described in the review [3], the principal cause of cracking is the infrequent but high-magnitude wheel loads produced by a small percentage of "bad" wheels or railhead surface defects. For instance, the typical loading duration produced by wheel flats is about 1-10 msec, while the force magnitude can be over 400 kN per rail seat. Existing structural design concept for prestressed concrete sleepers in Australia is based on permissible stress principle taking into account only the static and quasi-static loads, which are unrealistic to the actual dynamic loads on tracks. However, it is inevitable to avoid those criteria in any consideration of rail track designs since even the standard quality ride of rail vehicles still involves with the low-velocity impact forces. In order to devise a new limit states design concept whereas the extreme loading conditions can be taken into account, the research efforts are required to perform comprehensive studies of the loading conditions, the static behaviour, the dynamic response, and the impact resistance of the prestressed concrete sleepers [4]. A major research task at the University of Wollongong is to evaluate the dynamic responses of concrete sleepers under static and impact loads. There have been only a few studies related to the modelling of prestressed concrete sleepers. Most of them predicted the rail seat flexural behaviour of the concrete sleepers [5-6]. Also, since high-capacity impact tests require significant amount of resources and are time consuming, a suitable way to develop an understanding of the impact behaviour is to use the numerical impact simulations.

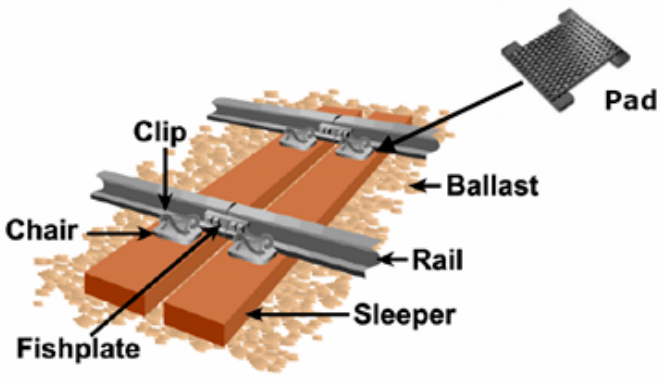


Figure 1 Typical ballasted railway track and its components [1]

Finite element analysis (FEA) provides a tool that can simulate and predict the responses of reinforced and prestressed concrete members. A three-dimensional non-linear finite element model of a railway prestressed concrete sleeper for static analysis was developed using the general purpose finite element analysis package, ANSYS10 [7]. The concrete section was modelled using SOLID65 solid element where the compressive crushing of concrete and the concrete cracking in tension zone can be accommodated. In the current practice, the railway concrete sleeper is designed to resist prestressing force fully throughout the whole cross section as the force/moment redistribution can be seen in Figure 2. This makes the smeared crack analogy unsuitable for the replacement of prestressing tendons in the fully prestressed concrete sleeper. The use of a truss element, LINK8, for discrete reinforcement modelling, is then more practicable. An initial strain real-constant feature in ANSYS appropriately substituted the pre-tensioning forces in the tendon elements. However, it was assumed that perfect bonding between concrete and pre-stressing wires. The static full-scale experiment was conducted to validate this FE model [7]. The experimental details were based on the associated Australian Standards [8, 9].

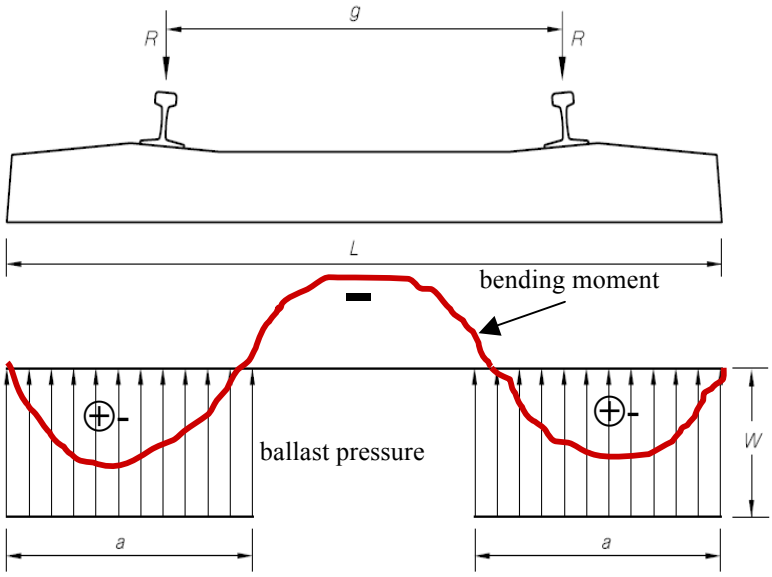


Figure 2 Moment distribution for standard gauge sleepers (8)

The calibrated finite element model has been extended to include ballast support and in situ boundary conditions. The extended model was linked to LS-Dyna [10] for impact analysis and validation against the drop impact tests. This paper investigates the impact responses of pre-stressing tendons in prestressed concrete sleepers and compares such the results with experimental data obtained from the drop impact machine, which are equivalent to the peak dynamic forces ranging from 200-1,700 kN. The highlights in this paper are the better understandings into the influence of track components particularly the ballast support and train speeds, which can be simulated by impulse duration, on the behavior of railway prestressed concrete sleepers.

2 THREE DIMENSIONAL FINITE ELEMENT MODEL

In this study, the concrete part of the sleeper was modelled using a three-dimensional solid element, which has the material model to predict the failure of brittle materials [7]. This ele-

ment is defined with eight nodes – each with three degrees of freedom: translations in nodal x, y, and z directions. To simulate the behaviour of prestressing wires, a truss element, were used to withstand the initial strain attributed to prestressing forces, by assuming perfect bond between these elements and concrete. Note that this truss element cannot resist neither bending moments nor shear forces. Non-linear elastic behaviour of concrete can alternatively be defined by the multi-linear stress-strain relationships. The modulus of elasticity of concrete (E_c) can be found based on AS3600 [11] using the compressive strength of 88 MPa.

For prestressing wires, the bi-linear elasto-plastic material models can be used as well as the multi-linear isotropic model from the manufacturer's data. The 0.2% proof stress is 1,700 MPa and the ultimate stress is 1,930 MPa. The static and dynamic elasticity of moduli of prestressing wire are 190,000 MPa.

The multi-linear isotropic dynamic stress-strain curve for the concrete and prestressing wires can be calculated based on the consideration of the effect of strain rate. Based on the assumption of perfect bond between prestressing wires and concrete, the dynamic material properties of concrete and prestressing wires can be determined as follows [12].

Concrete:

$$\sigma = f'_{c,dyn}\left[2\frac{\varepsilon}{\varepsilon_{c0,dyn}} - \left(\frac{\varepsilon}{\varepsilon_{c0,dyn}}\right)^2\right] \tag{1}$$

$$\frac{f'_{c,dyn}}{f'_{c,st}} = 1.49 + 0.268\log_{10}\dot{\varepsilon} + 0.035\left[\log_{10}\dot{\varepsilon}\right]^2 \tag{2}$$

$$\frac{\varepsilon_{c0,dyn}}{\varepsilon_{c0,st}} = 1.24 + 0.053\log_{10}\dot{\varepsilon} \tag{3}$$

where σ is the dynamic stress, $f'_{c,dyn}$ is the dynamic compressive strength, $f'_{c,st}$ is the static compressive strength of concrete, ε is the dynamic strain, $\varepsilon_{c0,st}$ is the static ultimate strain, and $\dot{\varepsilon}$ is the strain rate in concrete fibre.

Prestressing wires:

$$\frac{f_{y,dyn}}{f_{y,st}} = 10^{0.38\log_{10}\dot{\varepsilon}^{-0.258}} + 0.993 \tag{4}$$

where $f_{y,dyn}$ is the dynamic upper yield point stress, $f'_{c,st}$ is the static upper yield point stress of prestressing wires (about 0.84 times proof stress), and $\dot{\varepsilon}$ is the strain rate in tendon.

A three-dimensional model of a typical railway prestressed concrete sleeper was developed initially in ANSYS [7] as illustrated in Figure 3. The dedicated solid bricks represent the concrete and the embedded three-dimensional spar elements are used as the prestressing wires. The pre-tensioning was modelled using an initial strain in the tendons corresponding to the prestressing forces at final stage (sustained prestressing force after all losses). For impact

simulations, a FE model was extended to include rails, rail pads, ballast bed, and falling mass, as shown is Figure 4. The extended finite element model was calibrated using vibration data [13-16]. The updated finite element model was then transferred to LS-Dyna. The simulation results were achieved by assigning the initial velocity to the drop mass to generate an impact event, similarly to the actual drop tests.

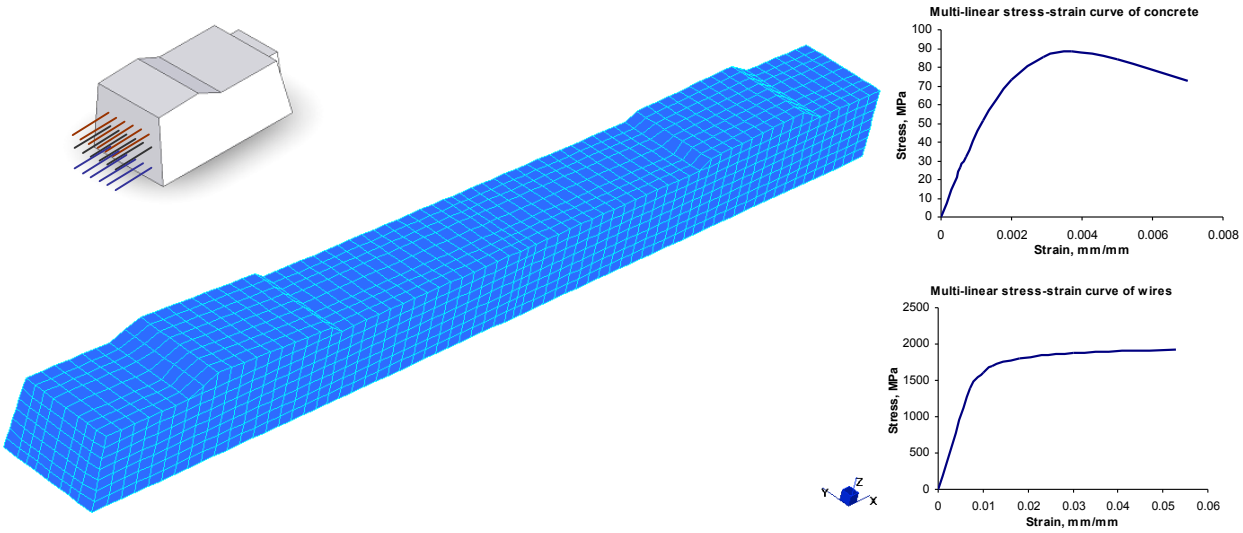


Figure 3 A three-dimensional model of railway sleeper [4]

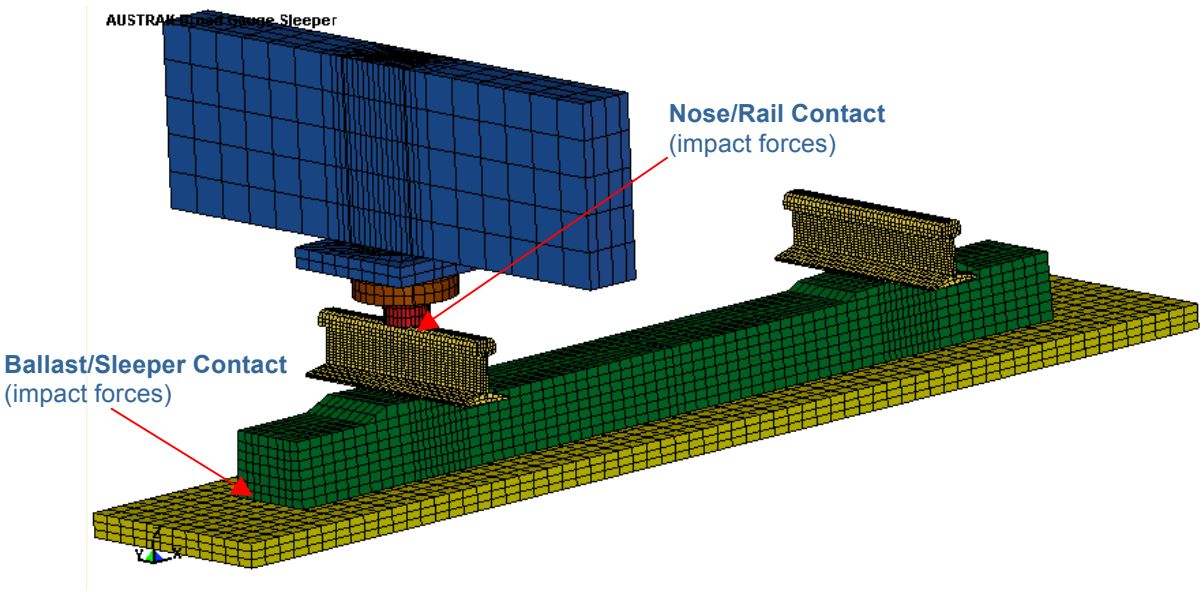
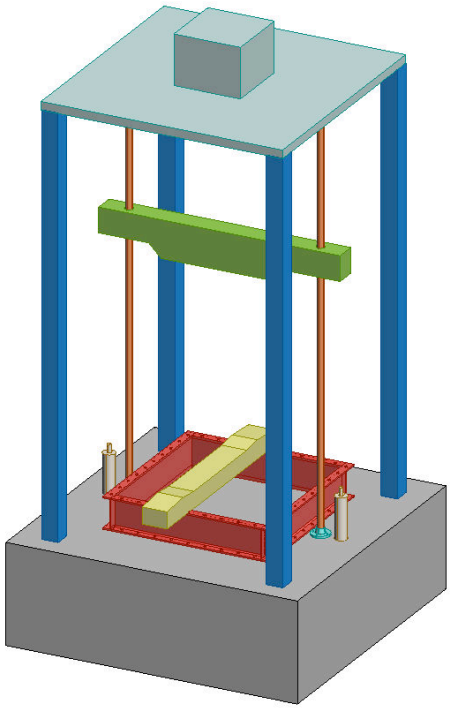


Figure 4 Extended finite element model of railway sleeper [4]

3 EXPERIMENT AND FINITE ELEMENT MODEL VALIDATION

The prestressed concrete sleepers used in this study were kindly supplied by an Australian manufacturer, under a collaborative research project of the Australian Cooperative Research Centre for Railway Engineering and Technologies (Rail CRC). A series of static tests on the concrete sleepers was performed in accordance with the Australian Standards. The details of static responses, rotational capacity, post-failure mechanism, and residual load-carrying capacity of the prestressed concrete sleeper can be found in ref: [17].



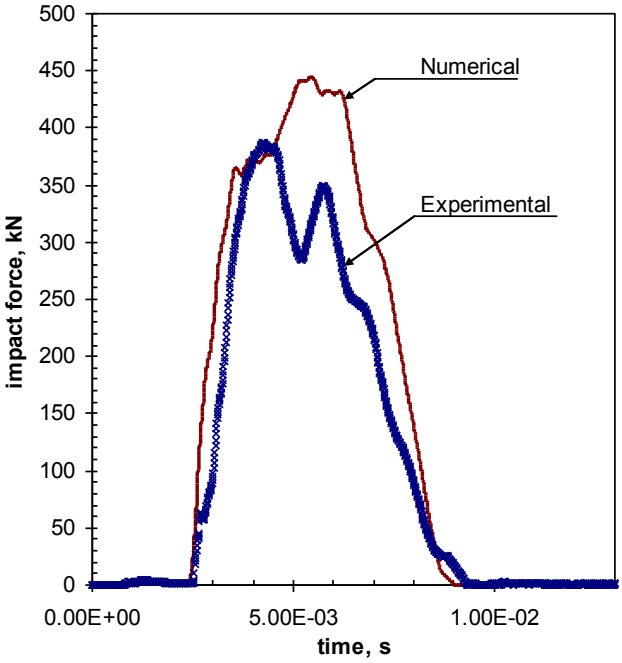
a) sketch of impact machine



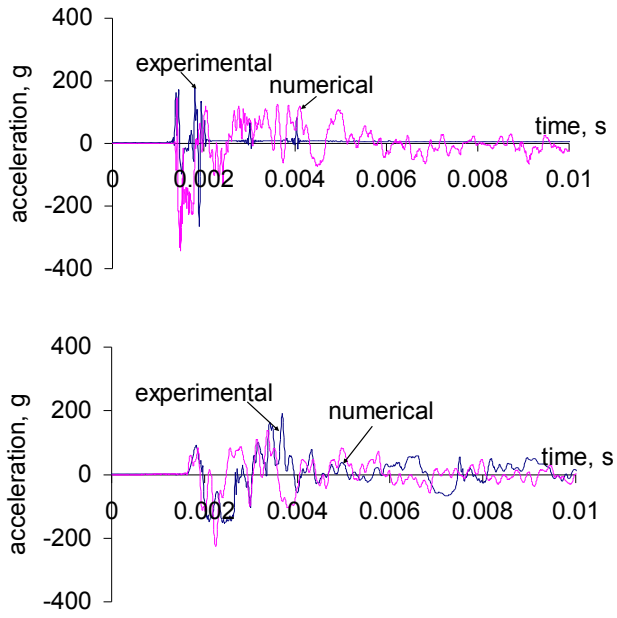
b) impact test setup

Figure 5 Experimental overview

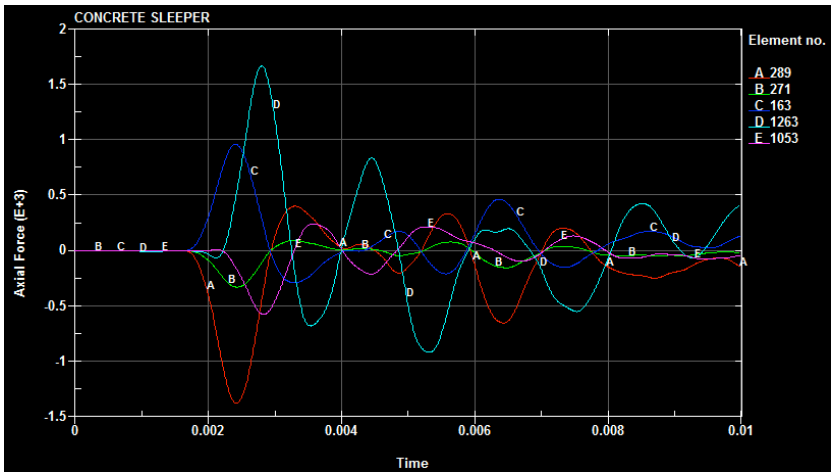
A new high-capacity drop-weight impact testing machine has been developed at the University of Wollongong, as depicted in Figure 5a. The drop mass assembled is 5.81 kN with the varied height from 0 to 6m in total, which provide the maximum capacity of 10m/s drop velocities. Experimental setup and impact tests were arranged in accordance with the Australian Standards, as shown in Figure 5b. The accelerometers have been used to measure the dynamic responses at mid-span and railseat. The contact impact force between impactor and rail was recorded using the dynamic load cell connected to the data acquisition system. For the verification purpose, the drop height used was 0.1m since there was the measurement limitation for the accelerometers employed. The in-situ conditions of railway concrete sleeper were replicated. Attempts to simulate impact loading actually occurred in tracks were succeeded experimentally and numerically. Comparison between numerical and experimental results can be found in Figure 6. It is found that the finite element model is fairly sufficient for use in predicting impact responses of the prestressed concrete sleepers. The trends of peak acceleration responses are quite close to each other, although there is certain phase difference.



a) contact shock load



b) at railseat (top); at mid-span (bottom)



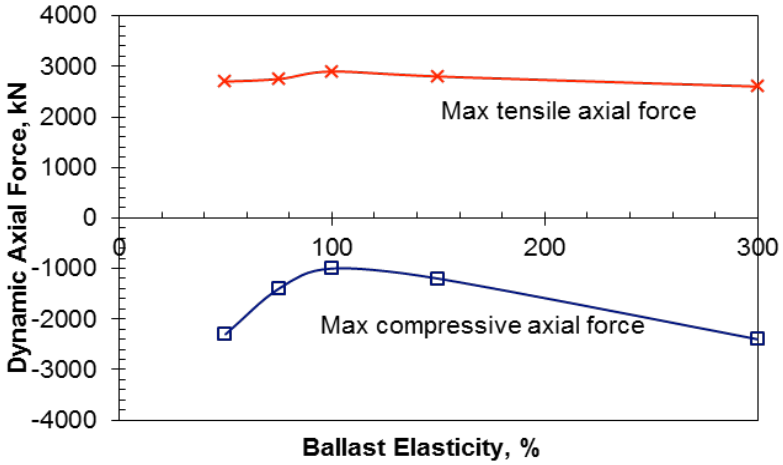
c) an example of prestressing force (at impact velocity 3 m/s)

Figure 6 Comparison of numerical and experimental results

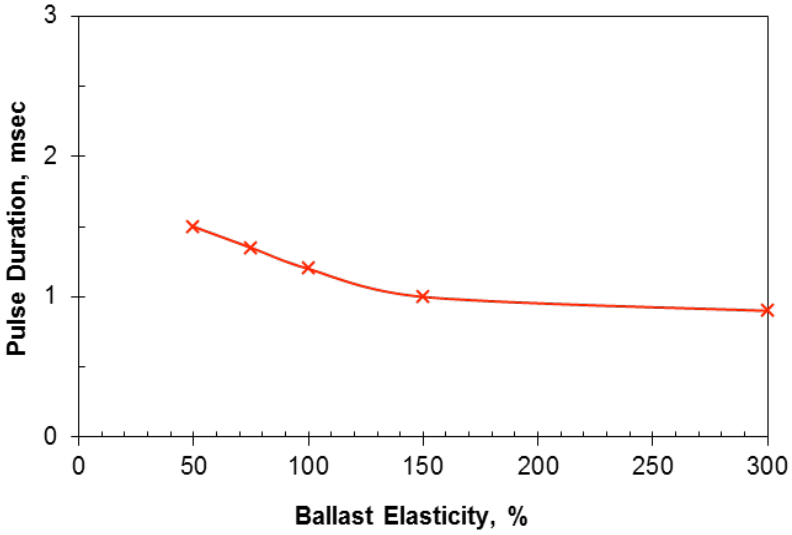
4 EFFECT OF TRACK ENVIRONMENTS

In general, the main track components that require maintenance or renewal apart from the sleeper itself include the ballast bed and rail pads. The ballast bed requires re-packing and tamping every six months or a year depending on the characteristics of gravels used at particular locations. It degrades through the breakage of gravel, resulting in the large settlement of railway tracks [16-20]. Rail pads deteriorate through the age of use. Based on this understanding, the parametric studies have been conducted and highlighted in this paper.

In the impact analysis, the drop velocity is also varied to evaluate the effect of drop heights on the impact force occurring on railway track structures. On the other hand, this analysis provides the insight into the effect of railway track environments on the contact impact forces due to the identical causes and the responses of concrete sleepers to such loading. For example, a wheel, with 10mm wheel flat on a specific vehicle and running at 300 km/hr, generates different contact impact forces on tracks with different environments. However, this study focuses only on ballast and rail pad parameters as they play key role on the interface impact force characteristics and axial responses of pre-stressing tendon as illustrated below.



a) Axial force (ballast stiffness as percentage of original value)

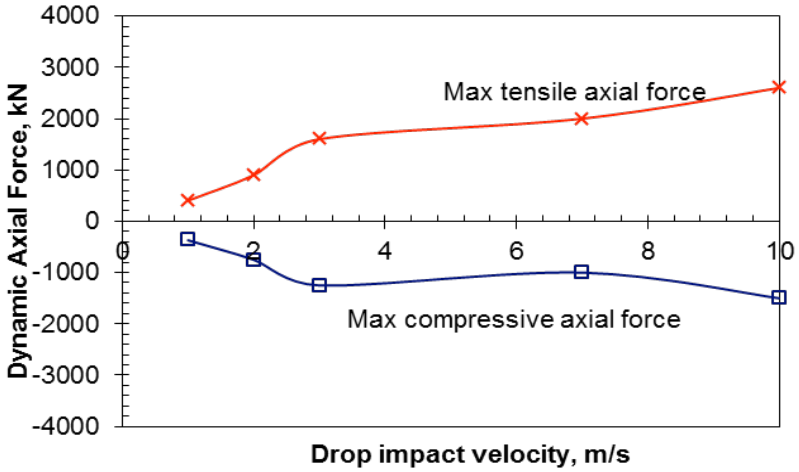


b) Pulse duration

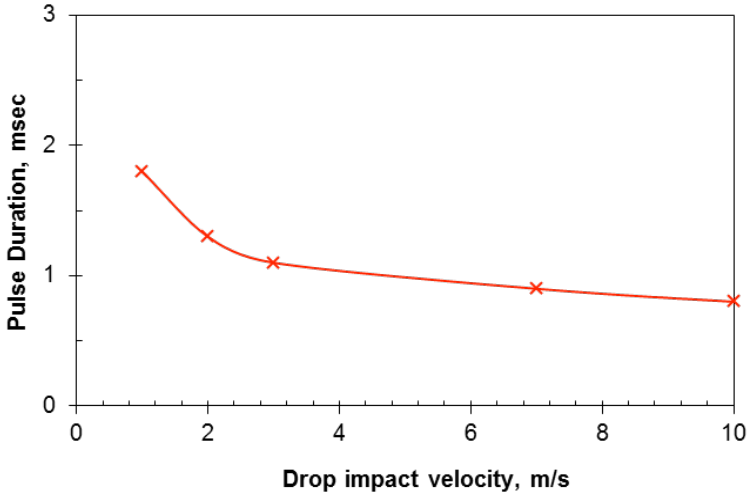
Figure 7 Influence of ballast elasticity on axial forces of prestressing tendons

5 EFFECT OF DROP VELOCITIES (TRAIN SPEEDS)

High speed trains often generate high frequency impact loading when they experience either wheel or rail abnormalities such as out-of-round wheel, wheel flats, rail squats, rail surface defects, rail joints and so on. In general, the high speed trains are designed to have light weights (around 12 to 14ton axle loads) in order to efficiently travel at high speeds. As a result, the magnitude of impact loads is somewhat similar to those in heavy rail operations. However, the effect of high speeds often results in higher-frequency impacts (i.e. shorter duration of impact forces). In this study, the effect of short duration impact (which can be simulated by increasing drop impact velocity in the numerical model) has been investigated. Figure 8 shows some results of the maximum positive and negative axial forces in prestressing tendons. In this study, the weight of impact mass is maintained constant to investigate impulsive effect due to larger magnitude but shorter duration of dynamic forces. In the future, the drop impact mass will be modified to evaluate the parametric study of impulse duration.



a) Axial force



b) Pulse duration

Figure 8 Influence of drop impact velocity on axial forces of prestressing tendons

6 CONCLUSIONS

The experimental and numerical simulations of prestressed concrete sleepers subjected to impact loading have been carried out in this paper. The three-dimensional finite element model have been established for investigate both static and dynamic behaviors of the railway sleepers. It has then been appended the track components to mimic in-situ conditions often found in actual tracks. A commercial finite element package, LS-Dyna, has been employed to extend the model for impact analysis and it has been validated against experimental drop impact tests. Nonlinear material properties under high strain rate effects were used. The emphasis of this study is placed on the dynamic responses of pre-stressing tendons inside the concrete sleeper. The further study on the effect of high train speeds and better nonlinear material models of track component degradation will be presented in the future. However, this paper firstly illustrates the influences of ballast moduli and drop impact velocity (simulating train speed effect) on the impact behavior of the pre-stressing tendons.

It is found that the ballast bed has an influence over the contact impact force characteristics including magnitude and duration. On the other hand, train speeds tend to play a role by generate high flexures of concrete sleepers as observed from the tension and compression.

ACKNOWLEDGEMENT

The first author would like to gratefully acknowledge the University of Birmingham's BRIDGE Grant, which financially supports this work as part of the project "Improving damping and dynamic resistance in concrete through micro- and nano-engineering for sustainable and environmental-friendly applications in railway and other civil construction". This project is part of a collaborative BRIDGE program between the University of Birmingham and the University of Illinois at Urbana Champaign. The pre-stressed concrete sleepers were kindly provided by Austrak Ltd. The authors would also like to thank Alan Grant, Ian Bridge, Bob Roland, and Jason Knurst, for their assistance during the course of the experimental work.

REFERENCES

[1] Kaewunruen, S and Remennikov, AM, Non-destructive testing (NDT): A tool for dynamic health monitoring of railway track structures. *Materials Australia*, 39(6), 14-16 (invited), 2006.

[2] Remennikov, A.M. and Kaewunruen, S., A review on loading conditions for railway track structures due to train and track vertical interaction. *Structural Control and Health Monitoring*, 15, 207-234, 2008.

[3] Murray, M and Cai, Z, Literature review on the design of railway prestressed concrete sleeper. *RSTA Research Report*, Australia, 1998.

[4] Kaewunruen, S and Remennikov, AM, "Experimental and numerical studies of railway prestressed concrete sleepers under static and impact loads." *Civil Computing*, AIT-ACECOMS, inpress, 2007, (invited).

[5] Gustavson, R, "Static and dynamic finite element analyses of concrete sleepers*", Licentiate of Engineering Thesis*, Department of Structural Engineering, Chalmers University of Technology, Sweden, 2000.

[6] Gustavson, R, "Structural behaviour of concrete railway sleepers", *PhD Thesis*, Department of Structural Engineering, Chalmers University of Technology, Sweden, 2002.

[7] Kaewunruen, S and Remennikov, AM, "Nonlinear finite element modelling of railway prestressed concrete sleeper", *Proceedings of the tenth East Asia-Pacific Conference on Structural Engineering & Construction (EASEC-10)*, Bangkok, Thailand, August 3-5, 2006, Vol. 4, pp. 323-328.

[8] Standards Australia, "Railway track material - Part 14: Prestressed concrete sleepers" *Australian Standard: AS1085.14-2003*, 2003a.

[9] Standards Australia, "Railway track material - Part 19: Resilient fastening assemblies" *Australian Standard: AS1085.19-2003*, 2003b.

[10] Livermore Software Technology Corporation, *LS-DYNA theoretical manual*. Livermore Software Technology Corporation, May 1998.

[11] Standards Australia, "Design of concrete structures" *Australian Standard: AS3600-2001*, 2001.

[12] Wakui H and Okuda H, "A study on limit-state design for prestressed concrete sleepers." *Concrete Library of JSCE* 33: pp. 1-25, 1999.

[13] Remennikov, AM and Kaewunruen, S, "Determination of dynamic properties of rail pads using instrumented hammer impact technique." *Acoustics Australia*, 33(2), 63-67, 2005.

[14] Remennikov, AM and Kaewunruen, S, "Experimental investigation on dynamic railway sleeper/ballast interaction." *Experimental Mechanics*, 46(1), 57-66, 2006.

[15] Kaewunruen, S and Remennikov, AM, "Sensitivity analysis of free vibration characteristics of an in-situ railway concrete sleeper to variations of rail pad parameters." *Journal of Sound and Vibration*, 298(1-2), 453-461, 2006.

[16] Kaewunruen, S and Remennikov, AM, "Effect of improper ballast tamping/packing on dynamic behaviors of on-track railway concrete sleeper." *International Journal of Structural Stability and Dynamics*, 7(1), 1-11, 2007.

[17] Kaewunruen, S and Remennikov, AM, "Post-failure mechanism and residual load-carrying capacity of railway prestressed concrete sleeper under hogging moment", *Proceedings of the International Conference on Structural Integrity and Failure (SIF-2006)*, Sydney, Australia, September 27-29, pp. 331-336, 2006.

[18] Remennikov, AM, Kaewunruen, S, and Ikaunieks, K, "Deterioration of dynamic rail pad characteristics." *Proceedings of Conference of Railway Engineering 2006*, Apr 30 - May 3, Melbourne, Australia, pp.173-179, 2006.

[19] Kaewunruen, S and Remennikov, AM, "Monitoring structural degradation of rail bearing pads in laboratory using impact excitation technique." *Proceedings of the 1st International Conference on Structural Condition Assessment, Monitoring, and Improvement*, Dec 12-14, Perth, Australia, pp. 399-405, 2005.

[20] Kaewunruen, S. and Remennikov, A., 2007, "Low-velocity impact analysis of prestressed concrete sleepers." *Concrete Institute of Australia's 23rd Biennial Conference 07*, October 18-20, Adelaide, Australia, [CD Rom].

COMPDYN 2015
5th ECCOMAS Thematic Conference on
Computational Methods in Structural Dynamics and Earthquake Engineering
M. Papadrakakis, V. Papadopoulos, V. Plevris (eds.)
Crete Island, Greece, 25–27 May 2015

EXPERIMENTAL AND NUMERICAL EVALUATION OF THE EFFICIENCY OF A STIFF WAVE BARRIER IN THE SOIL

Pieter Coulier[1], Vicente Cuéllar[2], Geert Degrande[1], and Geert Lombaert[1]

[1]KU Leuven, Department of Civil Engineering
Kasteelpark Arenberg 40, 3001 Leuven, Belgium
e-mail: {pieter.coulier,geert.degrande,geert.lombaert}@bwk.kuleuven.be

[2]CEDEX, Laboratoria de Geotecnia
Alfonso XII 3, 28014 Madrid, Spain
e-mail: vicente.cuellar@cedex.es

Keywords: Railway induced vibrations, stiff wave barrier, in situ experiment, vibration mitigation.

Abstract. *This paper discusses the design, the installation, and the experimental and numerical evaluation of the effectiveness of a stiff wave barrier in the soil as a mitigation measure for railway induced vibrations. A full scale in situ experiment has been conducted at a site in El Realengo (Spain), where a barrier consisting of overlapping jet grout columns has been installed along a railway track. This barrier is stiff compared to the soil and has a depth of* $7.5\,\mathrm{m}$*, a width of* $1\,\mathrm{m}$*, and a length of* $55\,\mathrm{m}$*. Geophysical tests have been performed prior to the installation of the barrier for the determination of the dynamic soil characteristics. Extensive measurements have been carried out before and after installation of the barrier; this paper focuses on free field vibrations during train passages. Measurements have also been performed at a reference section adjacent to the test section in order to verify the effect of changing train, track, and soil conditions over time. The in situ measurements show that the barrier is very effective: during train passages, a reduction of vibration levels by* $5\,\mathrm{dB}$ *is already obtained from* $8\,\mathrm{Hz}$ *upwards, while a peak reduction of about* $12\,\mathrm{dB}$ *is observed near* $30\,\mathrm{Hz}$ *immediately behind the barrier. The performance decreases further away from the jet grouting wall, but remains significant. This in situ test hence serves as a 'proof of concept', demonstrating that stiff wave barriers are capable of significantly reducing vibration levels, provided that they are properly designed.*

1 INTRODUCTION

Railway induced vibrations can lead to annoyance for residents of nearby buildings. During the past decades, a lot of research has been performed to develop efficient and cost–effective vibration countermeasures for reducing excessive levels of building vibration [1, 2, 3]. Measures can either be taken at the source (railway track) [4, 5, 6], on the propagation path between source and receiver [7, 8, 9], or at the receiver (building) [10, 11]. An advantage of interventions on the propagation path is that no modifications to the track are required, while multiple buildings can be protected simultaneously from vibration. Furthermore, this type of measures can relatively easily be implemented along an existing track.

A basic type of a mitigation measure on the propagation path is an open trench in the soil. The latter aims at reflecting the impinging waves and is expected to be effective if its depth is comparable to the penetration depth of the Rayleigh waves in the soil. The effectiveness of open trenches has been investigated numerically by many authors as Woods [12], Segol et al. [13], Beskos et al. [14], and Klein et al. [15]. For stability reasons, the construction of an open trench in the soil is limited to shallow depths. Furthermore, an open trench can easily get inundated due to surface water run–off or groundwater infiltration, posing concerns on effectiveness, durability, and safety. The use of either soft (polystyrene [9], rubber chips [16]) or stiff (concrete, grout) in–fill materials (compared to the original soil) allows reaching larger depths and results in a more sustainable solution. Various numerical approaches have been explored for predicting the effectiveness of open and in–filled trenches, such as the finite element (FE) [17], the boundary element (BE) [18], or coupled FE–BE methods [9]. Other examples of vibration mitigation measures on the propagation path include buried wall barriers [19], wave impeding blocks [20], rows of piles [21], and heavy masses placed along a railway track for scattering the incident surface waves [22, 23].

Although numerical simulations are indispensable for understanding and designing efficient wave barriers, there remains a strong need to validate the outcome of these simulations by means of in situ tests. Early experiments with trenches have been reported by Woods [12], while results from more recent field measurements involving open and filled trenches have been presented by Al–Hussaini et al. [24] and Çelebi et al. [25]. The use of a soft geofoam in–fill material has been assessed experimentally by Alzawi and El Naggar [17]; François et al. [9] describe the design and efficiency of a composite vibration isolation screen near a tramway in Brussels. In most of the aforementioned experiments, the length of the vibration isolation screens was limited to a few meters and only artificial excitation sources such as impact hammers or harmonic shakers were employed for assessing the isolation performance. Examples of longer screens (tens of meters) can be found in Sweden and Germany, where gas–filled cushions have been installed and tested [26, 27]. Apart from in situ experiments, complementary small scale laboratory tests are also valuable. Haupt [28] presents model tests of various types of barriers, while Murillo et al. [29] have investigated the efficiency of expanded polystyrene (EPS) barriers by means of centrifuge tests. A small scale experimental study of a stiff wave barrier in gelatine has been reported in [30].

This paper presents a full scale in situ experiment that has been specifically designed for assessing the performance of stiff wave barriers in the soil. The circumstances in which such barriers are expected to be effective have been analysed in detail in [31] by means of state–of–the–art numerical simulations, highlighting how their performance critically depends on site specific characteristics such as dynamic soil properties. Furthermore, the physical mechanism that results in a reduction of vibration levels for stiff barriers has been identified and was found

to fundamentally differ from that of open trenches or soft barriers. Based on these findings, a field test has been designed and carried out in Spain within the frame of the EU FP7 project RIVAS (Railway Induced Vibration Abatement Solutions) [32], which forms the topic of the present paper. A more elaborate discussion with additional experimental results as well as a comparison with numerical simulations can be found in [33].

The outline of this paper is as follows. Section 2 introduces the test site in Spain and addresses the determination of the dynamic soil characteristics. The design and construction of the stiff wave barrier are also discussed, while the main physical principles affecting the performance of this type of barrier are briefly reviewed. The measured free field response during train passages before and after installation of the barrier is subsequently presented in section 3. Conclusions are drawn in section 4.

2 EXPERIMENTAL SETUP

2.1 Description of the test site

A suitable site for testing a stiff wave barrier was identified in El Realengo (south–east of Spain) along the conventional railway line between Murcia and Alicante. The track at this site is a classical ballasted track with bi–block reinforced concrete sleepers supporting RN 45 rails with Spanish wide gauge ($1.668\,\mathrm{m}$). It is supported by a ballast layer and an embankment, each $0.50\,\mathrm{m}$ high. Geotechnical studies, performed in preparation of the construction of a new high speed railway line next to the conventional line, indicated the presence of soft silty clay soil layers with a thickness of approximately $10\,\mathrm{m}$ on top of stiffer alluvial soil. These are particular circumstances where a stiff wave barrier is expected to be very effective [31]. At the site, a test section as well as a reference section were chosen, as indicated on figure 1. The jet grouting wall is implemented along the test section; the aim of the reference section is to verify the effect of changing track, train, and soil conditions over time. This is important when evaluating the mitigation performance of the wave barrier, as will be discussed in detail in section 3.

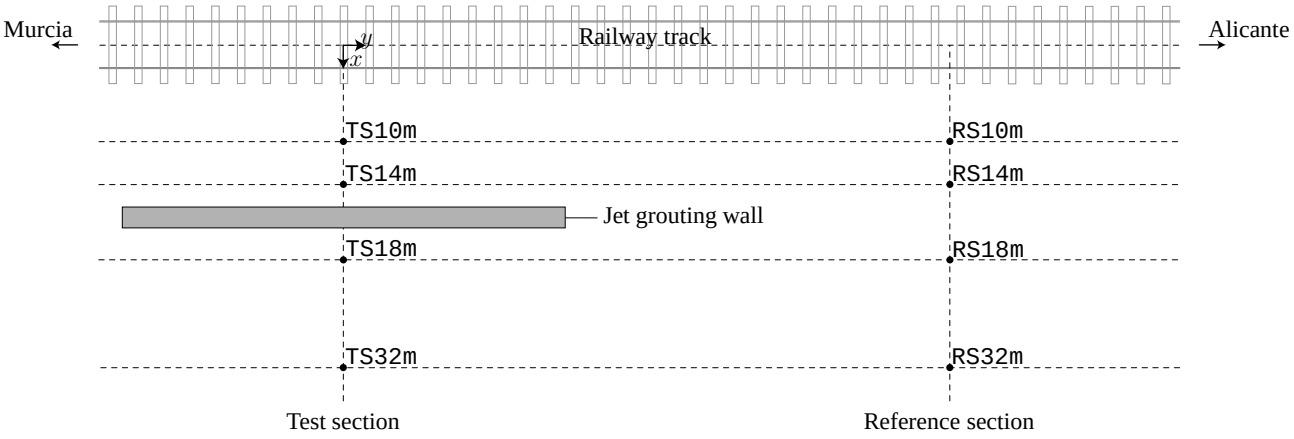


Figure 1: Setup for the measurement of the free field response due to train passages (figure not to scale).

2.2 Determination of the dynamic soil characteristics

As numerical simulations indicate that the vibration mitigation efficiency of a stiff wave barrier strongly depends on the dynamic soil characteristics [31], several geotechnical and geophysical tests were carried out for an accurate determination of these properties. This includes Spec-

tral Analysis of Surface Waves (SASW) tests, seismic piezocone down–hole tests (SCPTU), and seismic refraction tests. These tests have allowed for the identification of a simplified horizontally layered soil model, as summarized in table 1 (layer thickness h, shear wave velocity C_s, dilatational wave velocity C_p, material damping ratios β_s and β_p in both deviatoric and volumetric deformation, density ρ). The soil densities given in the table are those determined from undisturbed samples retrieved from boreholes drilled in preparation of the construction of the new high speed railway line. The identified soil profile confirms the presence of a soft layer of silty clay with a thickness of approximately $10\,\mathrm{m}$ (layers 2 and 3) that overlies hard alluvial soil. The soil is saturated at depths below $1.50\,\mathrm{m}$ due to the presence of the ground water table. This leads to a high dilatational wave velocity C_p for layers 3, 4, and 5.

Layer	h [m]	C_s [m/s]	C_p [m/s]	β_s [-]	β_p [-]	ρ [kg/m^3]
1	0.30	270	560	0.123	0.123	1800
2	1.20	150	470	0.112	0.112	1750
3	8.50	150	1560	0.014	0.014	1750
4	10.00	475	1560	0.010	0.010	1900
5	∞	550	2030	0.010	0.010	1900

Table 1: Dynamic soil characteristics at the site in El Realengo.

The dynamic soil characteristics summarized in table 1 have subsequently been used to calculate free field transfer functions. Figure 2 shows the transfer functions between a vertical point source and the vertical velocity at $8\,\mathrm{m}$ and $16\,\mathrm{m}$ from the source. With increasing distance from the source, the transfer functions show a stronger decrease at higher frequencies due to material damping in the soil. The predictions are compared to the mean value and the 95% confidence interval of the measured transfer functions at the test and reference section. The latter have been determined using the H_1–estimator, which is based on the average cross and auto power spectral densities [34]. A good agreement is found between the predictions and the experimental results, in particular in the frequency range up to $50\,\mathrm{Hz}$. This demonstrates that the dynamic soil properties have been identified with sufficient accuracy for making reliable numerical predictions. The signal–to–noise ratio decreases at higher frequencies which leads to a large confidence interval, however, making it more difficult to assess the accuracy of the predictions. Furthermore, figure 2 shows a significant difference between the transfer functions measured at the test and reference section, hence indicating a spatial variability of the dynamic soil characteristics.

2.3 Design of the stiff wave barrier

Numerical simulations have revealed that a stiff wave barrier in the soil can be a very effective vibration countermeasure, which is due to the interaction between Rayleigh waves in the soil and bending waves in the barrier [31, 35]. The mechanism that leads to a reduction of free field vibrations is concisely summarized in the following paragraphs; the reader is referred to [31, 35] for a detailed discussion.

Figure 3a shows the real part of the vertical displacement $u_z(\mathbf{x}, f)$ in the soil due to a unit harmonic point load at $5\,\mathrm{Hz}$ and $15\,\mathrm{Hz}$ at the surface of the halfspace, if no barrier is present. The railway track is disregarded in order to facilitate physical interpretation. The propagation of Rayleigh waves can clearly be observed. The wavefield in the case of an infinitely long stiff

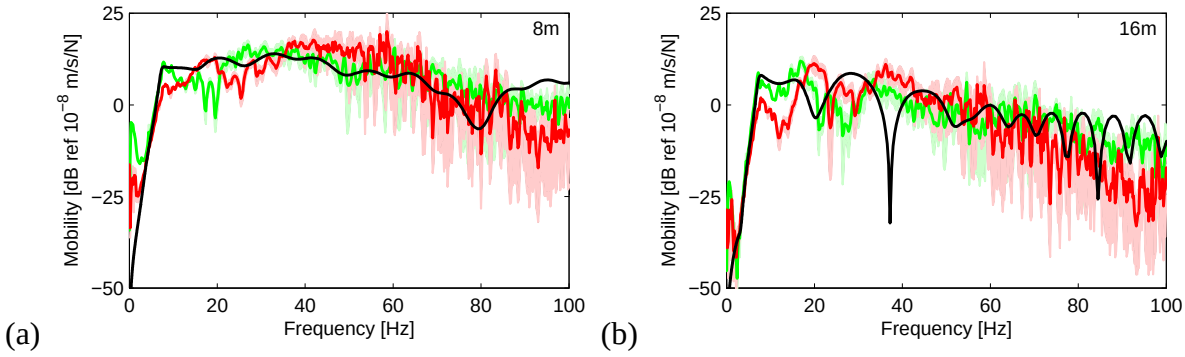


Figure 2: Predicted free field transfer functions (black line) compared to the experimental results at the test (red line) and reference (green line) section at (a) $8\,\mathrm{m}$ and (b) $16\,\mathrm{m}$ from the impact point. The 95% confidence interval of the measurements is indicated as a shaded area.

barrier (with a depth of $7.5\,\mathrm{m}$, a width of $1\,\mathrm{m}$, and dynamic characteristics as listed in table 2) embedded in the soil is shown in figure 3b. The barrier's vibration reduction effectiveness is quantified through the vertical insertion loss $\mathrm{IL}_z(\mathbf{x}, f) = 20\log_{10}\left(|u_z^{\mathrm{ref}}(\mathbf{x}, f)|/|u_z(\mathbf{x}, f)|\right)$ in figure 3c, where positive values of the insertion loss indicate a reduction of the vertical free field vibrations. Figure 3c indicates that the barrier is unable to impede the propagation of Rayleigh waves at $5\,\mathrm{Hz}$, while a significant reduction of vibration levels is achieved at $15\,\mathrm{Hz}$, but only in a limited area behind the barrier.

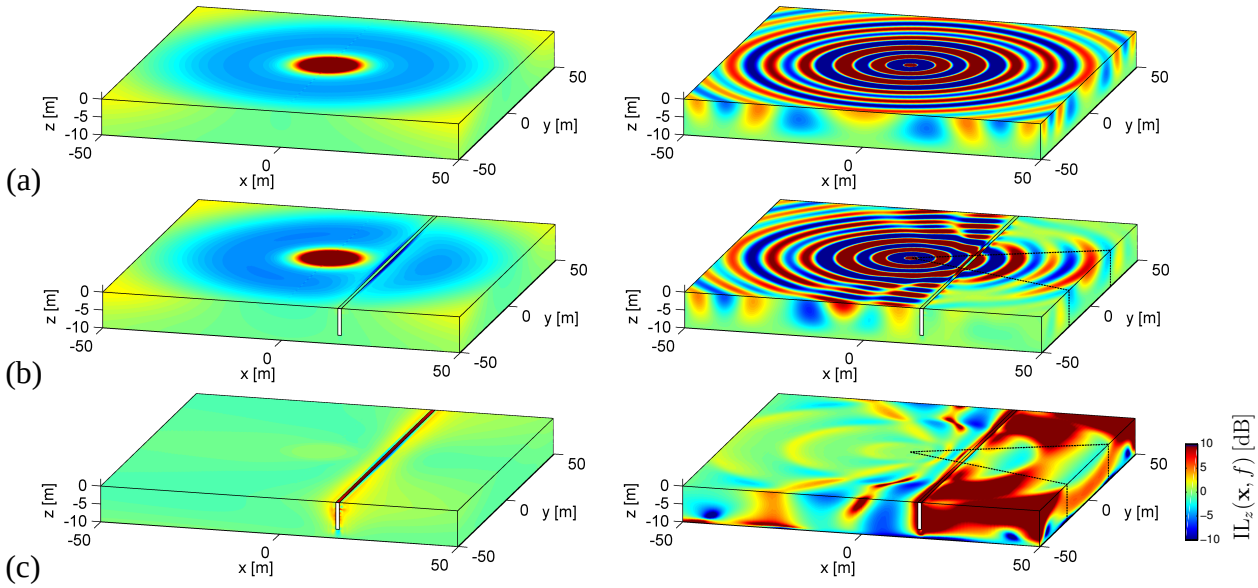


Figure 3: Real part of the vertical displacement $u_z(\mathbf{x}, f)$ due to harmonic excitation at $5\,\mathrm{Hz}$ (left hand side) and $15\,\mathrm{Hz}$ (right hand side) (a) without and (b) with a stiff wave barrier. The corresponding insertion loss $\mathrm{IL}_z(\mathbf{x}, f)$ is shown in (c). The dotted lines in (b) and (c) delimit $2\theta_{\mathrm{c}}(f)$.

The observations in figure 3 can be explained by considering a decomposition of the wavefield into plane waves, satisfying the Rayleigh wave dispersion relation $1/\lambda_x^2 + 1/\lambda_y^2 = 1/\lambda_{\mathrm{R}}^2(f)$ [36]. For propagating plane waves, the trace wavelength λ_y observed by the barrier is situated between $\lambda_y = \infty$ (for plane waves impinging perpendicularly on the barrier) and $\lambda_y = \lambda_{\mathrm{R}}(f) = C_{\mathrm{R}}(f)/f$ (for plane waves travelling along the barrier), where $C_{\mathrm{R}}(f)$ is the frequency depen-

dent velocity of the fundamental Rayleigh wave in the soil. Figure 4 compares $C_{\mathrm{R}}(f)$ to the velocity of a free bending wave in the stiff wave barrier $C_{\mathrm{b}}(f)$. The latter is obtained using Timoshenko beam theory and assuming bending with respect to the barrier's horizontal axis. At low frequencies (i.e. $5\,\mathrm{Hz}$ in figure 3), the Rayleigh wave velocity $C_{\mathrm{R}}(f)$ is larger than the bending wave velocity $C_{\mathrm{b}}(f)$ and all plane waves in the soil have a trace wavelength λ_y larger than the free bending wavelength $\lambda_{\mathrm{b}}(f) = C_{\mathrm{b}}(f)/f$ of the barrier ($\lambda_{\mathrm{b}}(f) < \lambda_{\mathrm{R}}(f) \leq \lambda_y \leq \infty$). These waves propagate unhindered through the barrier, as observed in figure 3. If the velocity $C_{\mathrm{R}}(f)$ matches the velocity $C_{\mathrm{b}}(f)$, a critical frequency f_{c} is attained. From this critical frequency $f_{\mathrm{c}} = 6.5\,\mathrm{Hz}$ upwards, the wavefield contains plane waves in the soil with a trace wavelength λ_y that is smaller than the free bending wavelength $\lambda_{\mathrm{b}}(f)$. The transmission of these plane waves is impeded by the stiff barrier, as the latter's bending stiffness varies proportionally to $(\lambda_{\mathrm{b}}/\lambda_y)^4$ at a given frequency. Waves with a trace wavelength λ_y larger than $\lambda_{\mathrm{b}}(f)$ remain unaffected by the presence of the barrier, however. As a result, a reduction of vibration levels is only achieved in an area delimited by a critical angle $\theta_{\mathrm{c}}(f) = \sin^{-1}\left(C_{\mathrm{R}}(f)/C_{\mathrm{b}}(f)\right)$, which can clearly be distinguished at $15\,\mathrm{Hz}$ on figure 3.

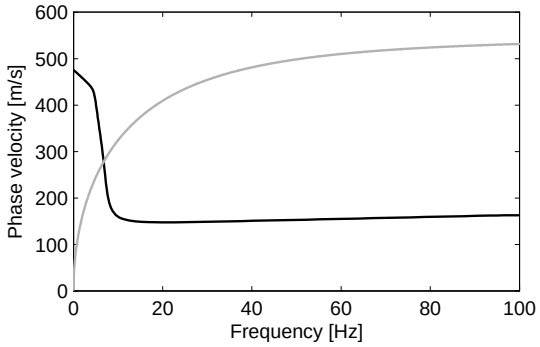


Figure 4: Phase velocity $C_{\mathrm{R}}(f)$ of the fundamental Rayleigh wave in the soil (black line) compared to the phase velocity $C_{\mathrm{b}}(f)$ of bending waves in the stiff barrier (grey line)

If the passage of a train is considered (rather than transfer functions as in figure 3), several dynamic axle loads contribute to the ground vibration at a certain receiver point of interest in the free field. Due to the existence of the critical angle $\theta_{\mathrm{c}}(f)$, the contribution of the axle loads moving towards or away from the receiver will be reduced more effectively than the contribution of the axle loads located near the receiver. The largest reduction is therefore expected to take place at locations close to the track (as the contribution of a larger number of axle loads is mitigated) and, at a particular location, at high frequencies (due to the decreasing critical angle).

2.4 Installation of the jet grouting wall

Several construction techniques are available for creating a stiff wave barrier in the soil, such as deep vibro–compaction, the installation of gravel or cement columns, hydraulic fracture injection with stable cement–bentonite mixtures, and vacuum consolidation. Jet grouting was selected as an appropriate technique for the site in El Realengo due to its versatility and possibility to strengthen a wide range of weak natural soils. Jet grouting is a bottom–up procedure, where grout is injected under high pressure at the design depth in order to initiate the erosion of the soil. A uniform rotation and lifting of the nozzle hence allows for the creation of in situ cemented column formations, while the spoil material is expelled at the top of the borehole. 60

overlapping grout columns with a diameter of $1.5\,\mathrm{m}$ and a centre–to–centre distance of $0.9\,\mathrm{m}$ were installed to create a stiff wave barrier with an overall length of $55\,\mathrm{m}$ and a width of $1\,\mathrm{m}$. This was achieved using a monofluid consisting of $90\,\mathrm{kg}$ of cement per $100\,\mathrm{l}$ of water injected under a pressure of $40,000\,\mathrm{kN/m^2}$, while maintaining a flow rate of $310 - 320\,\mathrm{l/min}$, a nozzle lift speed of $200\,\mathrm{mm/min}$, and a nozzle rotation speed of $20\,\mathrm{rpm}$ during the whole injection procedure. Figure 5a shows the equipment that has been employed for creating the jet grout columns, while the surface of the resulting wave barrier is shown in figure 5b. For safety reasons and due to the presence of a water duct, the barrier could only be constructed at a distance of $16.2\,\mathrm{m}$ from the center of the railway track.

(a)  (b) 

Figure 5: (a) Construction of the jet grout columns and (b) the stiff wave barrier upon completion at the site of El Realengo.

Five test columns were realized prior to the construction of the jet grouting wall. Furthermore, multiple test samples have been taken during the installation of the individual columns to verify their strength and stiffness. Laboratory tests (unconfined compression tests, non–dispersive P—S sonic tests, dispersive bender element tests) have been performed on these samples; the best estimate of the dynamic characteristics (two months after construction) is given in table 2. The lower part of the barrier is saturated, resulting in a higher dilatational wave velocity C_p and density ρ below a depth of $1.50\,\mathrm{m}$.

Layer	h [m]	C_s [m/s]	C_p [m/s]	β_s [-]	β_p [-]	ρ [kg/m^3]
1	1.50	600	1150	0.03*	0.03*	1400
2	6.00	600	1650	0.03*	0.03*	1750

Table 2: Dynamic characteristics of the jet grouting wall. Estimated values are indicated by a star.

3 EXPERIMENTAL EVALUATION OF THE VIBRATION MITIGATION PERFORMANCE

Extensive measurement campaigns have been carried out before and after installation of the stiff wave barrier in El Realengo in order to evaluate its performance. This includes the

measurement of the free field response due to train passages, transfer functions between the track and the free field, and track receptance tests. The experimental results are discussed in the following. Only train passages are discussed in this paper, however; the reader is referred to [33] for a discussion of the additional tests.

Passages of three different train types were recorded at the El Realengo site, before (October 2013) and after (December 2013) construction of the jet grouting wall: S592 commuter trains, S599 medium distance trains, and long distance Talgo VI trains. These are train passages on the classical ballasted track; the new high speed railway line was not in operation yet at the time of the experimental campaigns. In this paper, only results obtained during the passage of S592 commuter trains are discussed, as similar trends are found for the other train types. The S592 commuter train is a short train consisting of three carriages. Each carriage has two bogies, while each bogie is supported by two axles. The train has a total length of $65\,\mathrm{m}$ between the first and last axle. Each axle has an estimated unsprung mass of $2000\,\mathrm{kg}$. As only a single track is present at the site, both train passages from Murcia to Alicante and vice versa are recorded. The train velocities are estimated from strain measurements on the rails at the reference and test section. Ten and eleven passages of S592 trains have been recorded in October and December 2013, respectively, with a train speed varying between $112\,\mathrm{km/h}$ and $122\,\mathrm{km/h}$ (with an average speed of $117\,\mathrm{km/h}$). Free field vertical vibration velocities were measured by means of geophones along a line perpendicular to the track, at $10\,\mathrm{m}$, $14\,\mathrm{m}$, $18\,\mathrm{m}$, and $32\,\mathrm{m}$ from the outer rail, both at the reference and test section (and thus at $10.834\,\mathrm{m}$, $14.834\,\mathrm{m}$, $18.834\,\mathrm{m}$, and $32.834\,\mathrm{m}$ from the center of the track). These locations are referred to as RSxx and TSxx in the following, respectively, where the label xx represents the distance from the outer rail. The receiver locations at $18\,\mathrm{m}$ and $32\,\mathrm{m}$ at the test section are situated behind the jet grouting wall, as indicated on figure 1. Only vertical vibration velocities were recorded in this test, although vibrations in the transversal and longitudinal direction might also be of interest in practical situations [37].

Figure 6 shows the time history and frequency content of the vertical rail velocity at the test and reference section during the passage of a S592 commuter train at a speed of $117\,\mathrm{km/h}$ in December 2013, i.e. after construction of the jet grouting wall. This particular train runs from Murcia to Alicante, implying that it first passes the test section and subsequently the reference section, as can be observed in figure 6. The passage of each individual axle is clearly apparent in the time history, while the quasi–discrete spectrum is mainly situated below $20\,\mathrm{Hz}$. The response at the reference and test section are very similar, indicating that the track conditions at the reference and test section are alike, but also that the presence of the jet grouting wall has little effect on the response of the rail (as expected from numerical simulations [31]).

Figure 7 shows the time history and frequency content of the vertical free field velocity at the reference and test section during the same train passage. As the train approaches, the measured ground velocity increases, is subsequently followed by a nearly stationary part during the passage, and finally decreases when the train moves away. The passage of individual axles can no longer be distinguished as in the case of the rail response, however. The vibration amplitude decreases with increasing distance from the track; the high frequency components are especially attenuated due to material damping in the soil. Peaks are observed in the frequency spectrum near $10\,\mathrm{Hz}$ and $30\,\mathrm{Hz}$. Figures 7a and 7b indicate that the response at $10\,\mathrm{m}$ and $14\,\mathrm{m}$ from the track is slightly larger at the test section than at the reference section. As can be observed in figures 7c and 7d, the vibration levels at $18\,\mathrm{m}$ and $32\,\mathrm{m}$ from the track (i.e. behind the barrier) are significantly lower at the test section than at the reference section, especially from $8\,\mathrm{Hz}$ upwards. This clearly suggests that the jet grouting wall is effectively reducing the vibration levels.

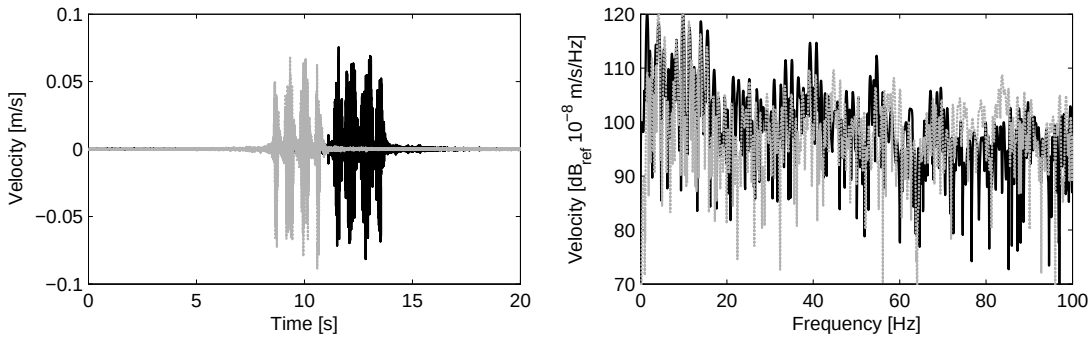


Figure 6: Time history (left) and frequency content (right) of the measured vertical rail velocity during the passage of a S592 commuter train at a speed of $117\,\mathrm{km/h}$ at the reference (solid black line) and test (dotted grey line) section.

Vibrations due to train passages can also be quantified in terms of the vibration velocity level $L_{\mathrm{v}}(f)$, which is defined as the one–third octave band spectrum of the stationary part of the vibration velocity $v_{z\mathrm{RMS}}(f)$:

$$L_{\mathrm{v}}(f) = 20\log_{10}\left(\frac{v_{z\mathrm{RMS}}(f)}{v_0}\right) \tag{1}$$

where $v_{z\mathrm{RMS}}(f)$ is the running Root Mean Square (RMS) value of the velocity, while $v_0 = 10^{-8}\,\mathrm{m/s}$ represents a reference velocity. The stationary part of the measured response during a train passage is selected using the German DIN standard [38]. Figure 8 shows the measured vibration velocity levels $L_{\mathrm{v}}(f)$ during the passages of all S592 commuter trains before and after construction of the jet grouting wall at the reference and test section, respectively. The arithmetically averaged vibration velocity levels $\bar{L}_{\mathrm{v}}(f)$ are also superimposed on figure 8. Although train passages of the same train type at approximately the same speed are considered, a considerable variation is observed in the frequency spectrum. This variability is caused by differences in train properties (train speed, wheel unevenness) and the variation of track characteristics (rail unevenness, ballast stiffness) and soil conditions (water table) in space and time. It is crucial to take the latter into account when evaluating the performance of the jet grouting wall. Despite the large variability between different train passages, it is nevertheless clear from figures 8c and 8d that the installation of the barrier leads to a significant reduction of vibration levels at the test section.

The vibration reduction effectiveness of the jet grouting wall is quantified by means of the vertical insertion loss $\mathrm{IL}_z(f)$. A first straightforward approach for determining $\mathrm{IL}_z(f)$ consists of comparing vibration velocity levels at the test section before and after installation of the barrier:

$$\mathrm{IL}_z(f) = L_{\mathrm{v}}^{\mathrm{test,before}}(f) - L_{\mathrm{v}}^{\mathrm{test,after}}(f) \tag{2}$$

This approach does not account for the changing train, track, and soil conditions in time, however, which might be significant as there was a two month period between the measurements before and after installation of the barrier. Alternatively, the insertion loss is computed by comparing vibration velocity levels at the reference and test section at the same moment (i.e. after installation of the barrier):

$$\mathrm{IL}_z(f) = L_{\mathrm{v}}^{\mathrm{ref,after}}(f) - L_{\mathrm{v}}^{\mathrm{test,after}}(f) \tag{3}$$

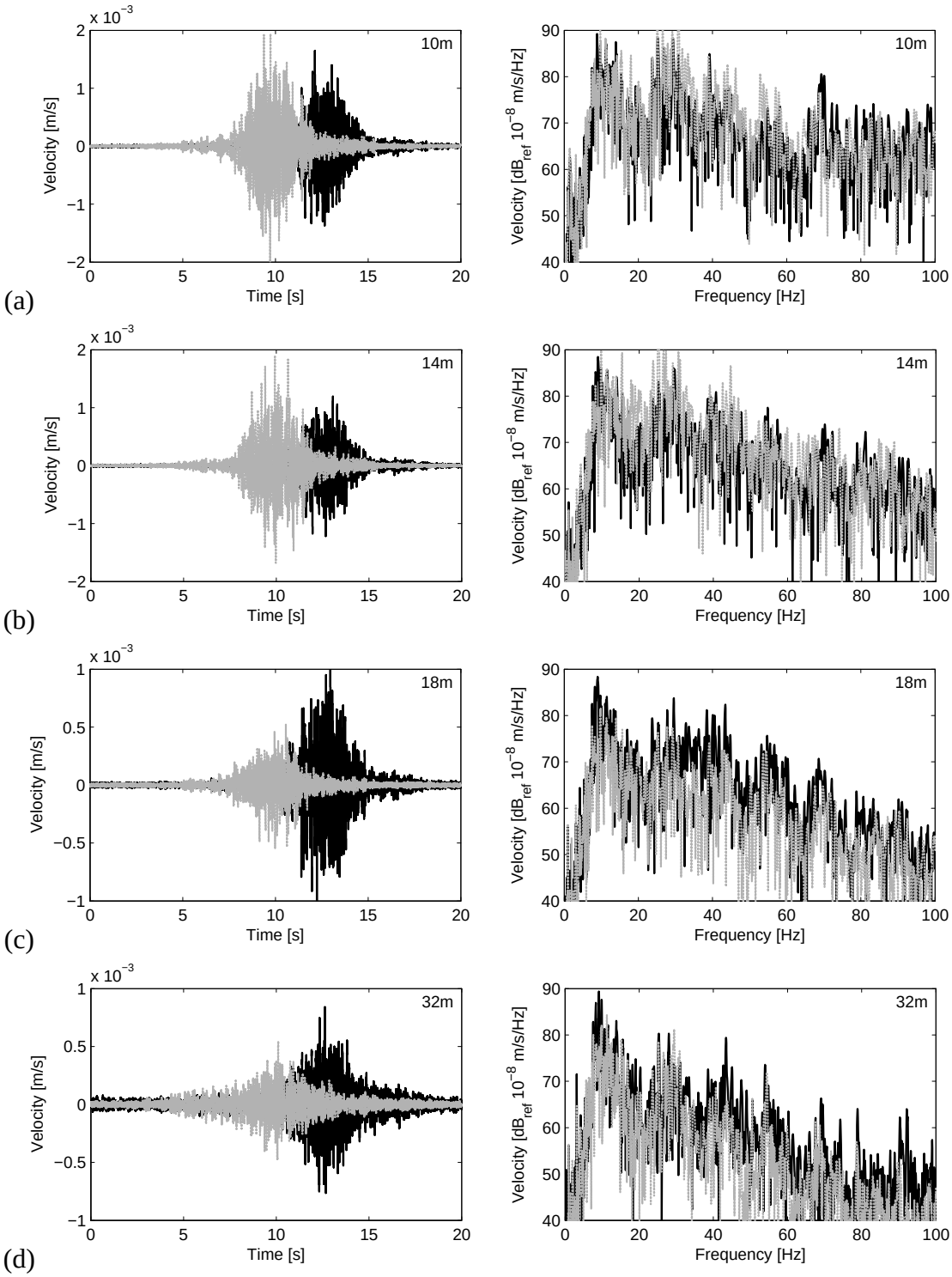


Figure 7: Time history (left) and frequency content (right) of the measured vertical free field vibration during the passage of a S592 commuter train at a speed of $117\,\mathrm{km/h}$ at the reference (solid black line) and test (dotted grey line) section, at (a) $10\,\mathrm{m}$, (b) $14\,\mathrm{m}$, (c) $18\,\mathrm{m}$, and (d) $32\,\mathrm{m}$ from the outer rail.

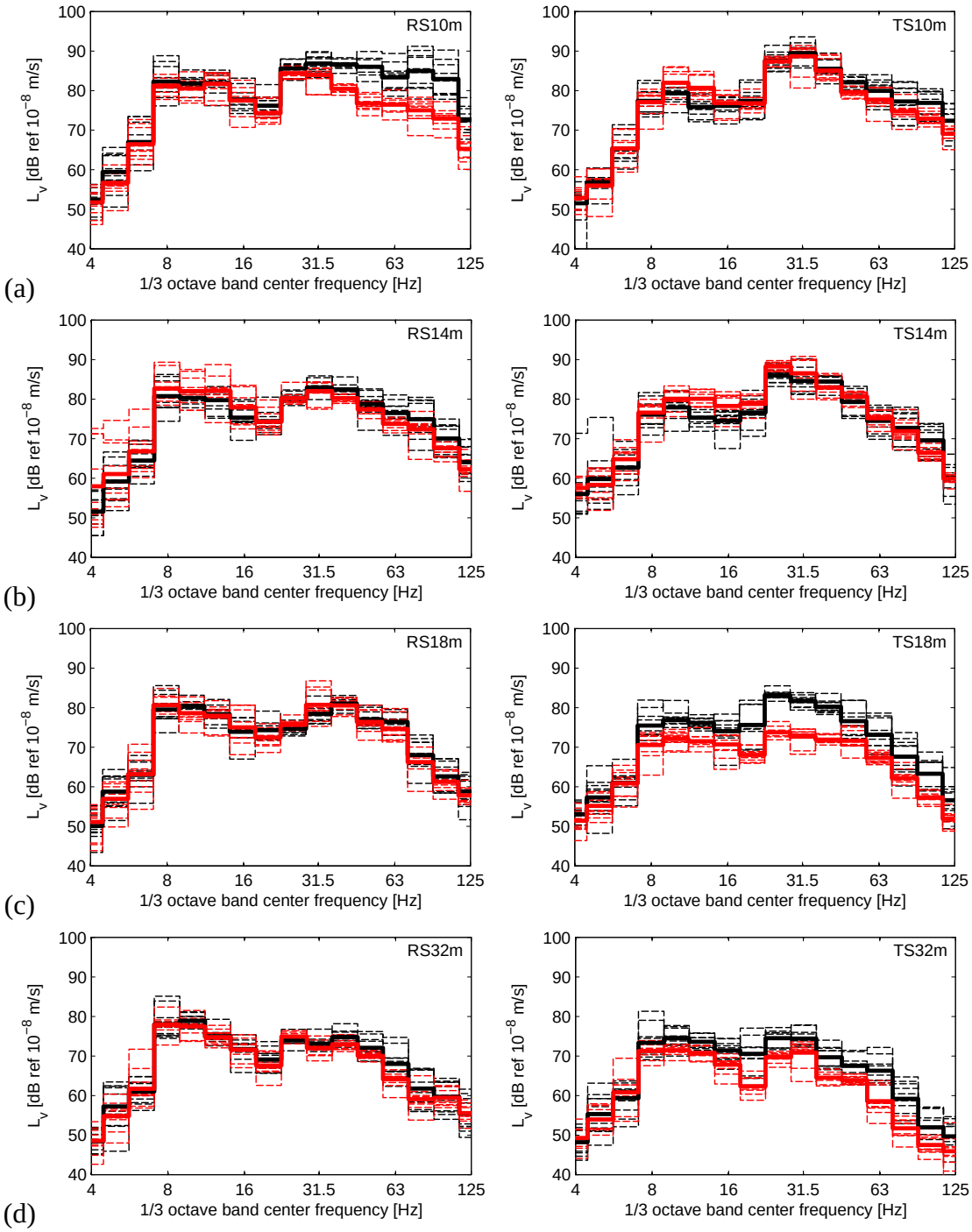


Figure 8: Measured vibration velocity levels $L_{\mathrm{v}}(f)$ in one–third octave bands at the reference (left) and test (right) section during the passage of S592 commuter trains before (dashed black lines) and after (dashed red lines) construction of the jet grouting wall, at (a) $10\,\mathrm{m}$, (b) $14\,\mathrm{m}$, (c) $18\,\mathrm{m}$, and (d) $32\,\mathrm{m}$ from the outer rail. The averaged vibration velocity levels $\bar{L}_{\mathrm{v}}(f)$ are indicated in solid bold lines.

The track and soil conditions at the reference and test section are not exactly the same, however, hampering the use of equation (3). A more rigorous quantification of the vibration mitigation performance is obtained in a combined procedure, in which measurements at the reference and test section before and after installation of the barrier are simultaneously accounted for [39]:

$$\begin{aligned} \mathrm{IL}_z(f) &= \left(L_\mathrm{v}^{\mathrm{test,before}}(f) - L_\mathrm{v}^{\mathrm{test,after}}(f)\right) - \left(L_\mathrm{v}^{\mathrm{ref,before}}(f) - L_\mathrm{v}^{\mathrm{ref,after}}(f)\right) && (4)\\ &= \Delta L_\mathrm{v}^{\mathrm{test}}(f) - \Delta L_\mathrm{v}^{\mathrm{ref}}(f) \\ &= \left(L_\mathrm{v}^{\mathrm{ref,after}}(f) - L_\mathrm{v}^{\mathrm{test,after}}(f)\right) - \left(L_\mathrm{v}^{\mathrm{ref,before}}(f) - L_\mathrm{v}^{\mathrm{test,before}}(f)\right) && (5)\\ &= \Delta L_\mathrm{v}^{\mathrm{after}}(f) - \Delta L_\mathrm{v}^{\mathrm{before}}(f) \end{aligned}$$

The first bracketed term $\Delta L_\mathrm{v}^{\mathrm{test}}(f)$ in equation (4) corresponds to equation (2) and characterizes the reduction of vibration levels at the test section, while the second term $\Delta L_\mathrm{v}^{\mathrm{ref}}(f)$ is a correction for possible variations in time, based on measurements at the reference section. The insertion loss is alternatively rewritten as equation (5), where the vibration levels at the reference and test section are compared as in equation (3), with a correction $\Delta L_\mathrm{v}^{\mathrm{before}}(f)$ for possible spatial variations between the reference and test section. Both expressions yield the same result, but equation (5) is particularly useful for assessing the variability of the insertion loss $\mathrm{IL}_z(f)$. The quantities $\Delta L_\mathrm{v}^{\mathrm{after}}(f)$ and $\Delta L_\mathrm{v}^{\mathrm{before}}(f)$ can be evaluated for each individual train passage before and after installation of the barrier, respectively, and their sample mean and variance can be computed straightforwardly. This allows estimating the sample variance of the insertion loss $\mathrm{IL}_z(f)$ as $\sigma^2_{\mathrm{IL}_z}(f) = \sigma^2_{\Delta L_\mathrm{v}^{\mathrm{after}}}(f) + \sigma^2_{\Delta L_\mathrm{v}^{\mathrm{before}}}(f)$, assuming that $\Delta L_\mathrm{v}^{\mathrm{after}}(f)$ and $\Delta L_\mathrm{v}^{\mathrm{before}}(f)$ are uncorrelated. This is not the case when employing equation (4), as the quantities $\Delta L_\mathrm{v}^{\mathrm{test}}(f)$ and $\Delta L_\mathrm{v}^{\mathrm{ref}}(f)$ can only be evaluated using the mean vibration velocity levels $\bar{L}_\mathrm{v}(f)$ (as they involve a different set of train passages before and after installation of the barrier).

Figure 9 shows the insertion loss $\mathrm{IL}_z(f)$ at $10\,\mathrm{m}$, $14\,\mathrm{m}$, $18\,\mathrm{m}$, and $32\,\mathrm{m}$ from the track, decomposed according to equations (4) and (5). The interval $\mathrm{IL}_z(f) \pm \sigma_{\mathrm{IL}_z}(f)$ is superimposed in the second case, clearly illustrating the variability of the experimental results. Especially at low frequencies, a large scatter up to $10\,\mathrm{dB}$ and more is observed. At $18\,\mathrm{m}$ and $32\,\mathrm{m}$, the mean and the confidence interval estimates of the insertion loss are consistently above $0\,\mathrm{dB}$ from $8\,\mathrm{Hz}$ upwards. The mean value reaches a maximum of about $10\,\mathrm{dB}$ near $25 - 35\,\mathrm{Hz}$ at $18\,\mathrm{m}$, which is also the frequency range where the highest vibration levels are found during train passages. The insertion loss decreases further away from the barrier at $32\,\mathrm{m}$, although it still reaches almost $7\,\mathrm{dB}$ near $20\,\mathrm{Hz}$ (but vibration levels also decrease further away from the barrier). These results clearly demonstrate the vibration reduction effectiveness of the jet grouting wall. The mean value of the insertion loss remains close to $0\,\mathrm{dB}$ in front of the barrier, except above $30\,\mathrm{Hz}$ at $10\,\mathrm{m}$, where significant negative values are obtained (indicating an amplification). It is emphasized, however, that this results from a reduction of vibration levels at the reference section (for unclear reasons) and not at the test section, which leads to a negative insertion loss through the correction term $\Delta L_\mathrm{v}^{\mathrm{ref}}(f)$ in equation (4). No increase of vibration levels is actually observed at the test section, nor at the reference section (cfr. figure 8a). Figure 9 also illustrates that the correction terms $\Delta L_\mathrm{v}^{\mathrm{ref}}(f)$ in equation (4) are significantly smaller than the correction terms $\Delta L_\mathrm{v}^{\mathrm{before}}(f)$ in equation (5) (except at $10\,\mathrm{m}$), indicating that spatial variations between the reference and test section are more important than variations in time. This suggests that, if no combined procedure can be applied for evaluating the mitigation performance (i.e. if no correction terms can be computed), the methodology corresponding to equation (2) should be favoured over the one corresponding to equation (3).

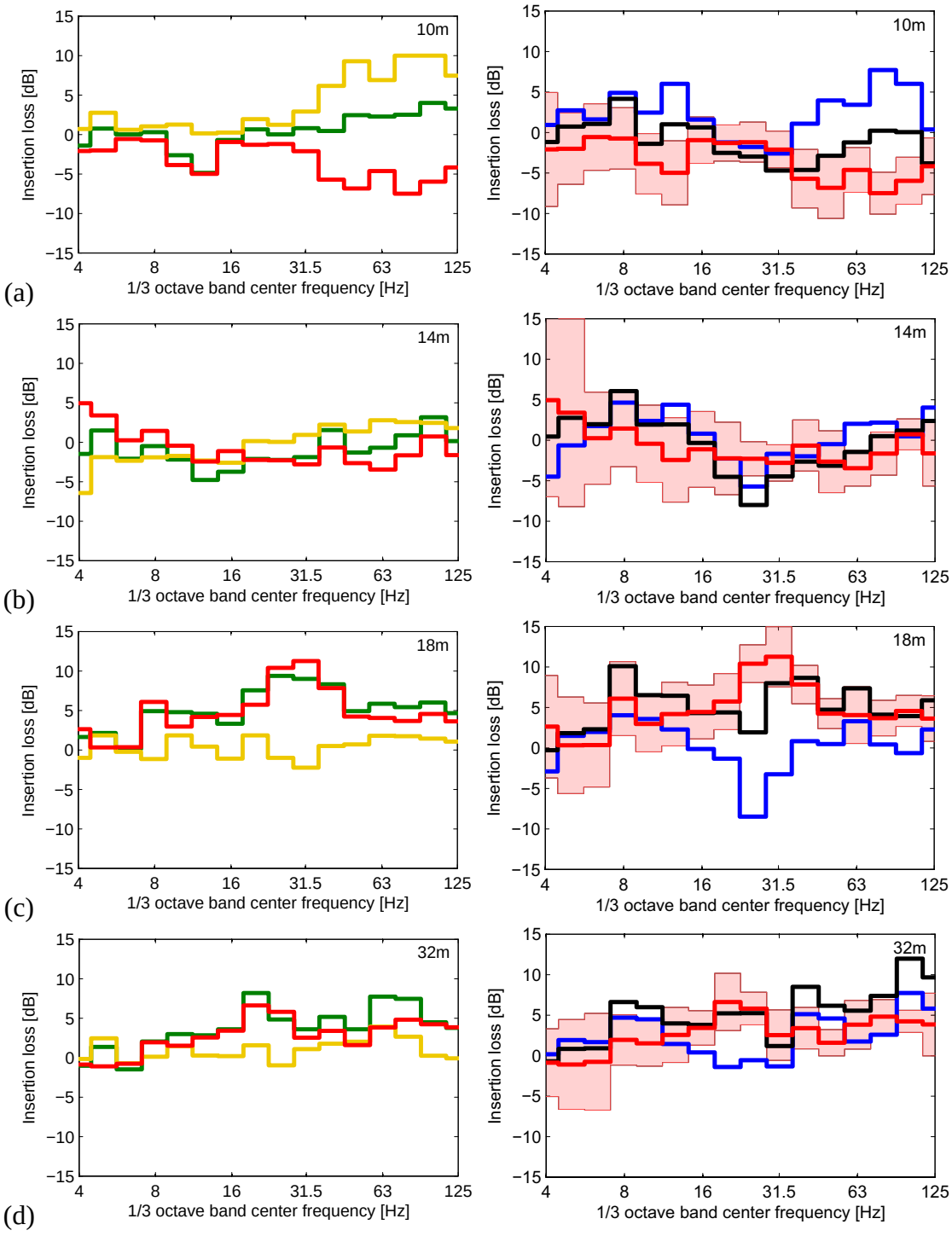


Figure 9: Insertion loss $\mathrm{IL}_z(f)$ in one–third octave bands (red line) during the passage of S592 commuter trains at (a) $10\,\mathrm{m}$, (b) $14\,\mathrm{m}$, (c) $18\,\mathrm{m}$, and (d) $32\,\mathrm{m}$ from the outer rail. The insertion loss is decomposed according to equation (4) (left) into $\Delta L_\mathrm{v}^\mathrm{test}(f)$ (green line) and $\Delta L_\mathrm{v}^\mathrm{ref}(f)$ (yellow line), and according to equation (5) (right) into $\Delta L_\mathrm{v}^\mathrm{after}(f)$ (black line) and $\Delta L_\mathrm{v}^\mathrm{before}(f)$ (blue line). The confidence interval estimates $\mathrm{IL}_z(f) \pm \sigma_{\mathrm{IL}_z}(f)$ of the measurements are indicated as a shaded area for the second decomposition.

The experimental results presented in this subsection clearly demonstrate the effectiveness of the stiff wave barrier for reducing the free field response during train passages. Additional experiments have been performed in order to gain further insight in the dynamic behaviour of the barrier. Furthermore, the measurements have been compared to state-of-the-art numerical simulations; a reasonable agreement was found. The reader is referred to [33] for an elaborate discussion.

4 CONCLUSIONS

In this paper, the experimental and numerical evaluation of the vibration reduction effectiveness of a stiff wave barrier has been discussed. A site with soft soil characteristics was selected at El Realengo and a full scale in situ test was performed. A barrier of $7.5\,\mathrm{m} \times 1\,\mathrm{m} \times 55\,\mathrm{m}$ composed of overlapping jet grout columns was designed and installed near a conventional railway line. Free field vertical vibration velocities were recorded during several train passages at a test and reference section, before and after installation of the barrier. A combined procedure has been adopted for assessing the effectiveness of the jet grouting wall, hence accounting for varying train, track, and soil properties in space and time. The measurements demonstrate that the barrier is very effective, as insertion loss values of $5\,\mathrm{dB}$ are obtained from $8\,\mathrm{Hz}$ upwards, with a peak of almost $12\,\mathrm{dB}$ near $30\,\mathrm{Hz}$, corresponding to the dominant frequency during train passages. The performance decreases further away from the barrier, but remains significant. This in situ test hence serves as a 'proof of concept', demonstrating that stiff wave barriers are capable of significantly reducing vibration levels, provided that they are properly designed.

ACKNOWLEDGEMENTS

The results presented in this paper have been obtained within the frame of the EU FP7 project RIVAS (Railway Induced Vibration Abatement Solutions) [32] under grant agreement No. 265754. The authors would like to thank the project partners involved in the realization of the in situ test at El Realengo (Keller Cimentaciones, ADIF, and CEDEX), and especially Goran Vukotic (Keller Cimentaciones), Álvaro Andrés (ADIF), Miguel Rodríguez (ADIF), and all the members of the geophysical and soil dynamic testing groups of CEDEX's Geotechnical Laboratory.

The first author is a post–doctoral fellow of the Research Foundation Flanders (FWO). The financial support is gratefully acknowledged.

REFERENCES

[1] C.J.C. Jones. Use of numerical models to determine the effectiveness of anti-vibration systems for railways. *Proceedings of the Institution of Civil Engineers-Transport*, 105(1):43–51, 1994.

[2] Y.B. Yang and H.H. Hung. A parametric study of wave barriers for reduction of train-induced vibrations. *International Journal for Numerical Methods in Engineering*, 40(20): 3729–3747, 1997.

[3] A.M. Kaynia, C. Madshus, and P. Zackrisson. Ground vibration from high speed trains: prediction and countermeasure. *Journal of Geotechnical and Geoenvironmental Engineering, Proceedings of the ASCE*, 126(6):531–537, 2000.

[4] G. Lombaert, G. Degrande, B. Vanhauwere, B. Vandeborght, and S. François. The control of ground borne vibrations from railway traffic by means of continuous floating slabs. *Journal of Sound and Vibration*, 297(3-5):946–961, 2006.

[5] H. Loy. Mitigating vibration using under-sleeper pads. *Railway Gazette International*, 168(4):40–43, 2012.

[6] P.A. Costa, R. Calçada, and A.S. Cardoso. Ballast mats for the reduction of railway traffic vibrations. Numerical study. *Soil Dynamics and Earthquake Engineering*, 42:137–150, 2012.

[7] H.H. Hung, Y.B. Yang, and D.W. Chang. Wave barriers for reduction of train-induced vibrations in soils. *Journal of Geotechnical Engineering, Proceedings of the ASCE*, 130(12):1283–1291, 2004.

[8] A. Karlström and A. Boström. Efficiency of trenches along railways for trains moving at sub- or supersonic speeds. *Soil Dynamics and Earthquake Engineering*, 27:625–641, 2007.

[9] S. François, M. Schevenels, B. Thyssen, J. Borgions, and G. Degrande. Design and efficiency of a vibration isolating screen in the soil. *Soil Dynamics and Earthquake Engineering*, 39:113–127, 2012.

[10] D.E. Newland and H.E.M. Hunt. Isolation of buildings from ground vibration: a review of recent progress. *Proceedings of the Institution of Mechanical Engineers, Part C: Journal of Mechanical Engineering Science*, 205:39–52, 1991.

[11] J.P. Talbot and H.E.M. Hunt. A generic model for evaluating the performance of base-isolated buildings. *Journal of Low Frequency Noise, Vibration and Active Control*, 22(3):149–160, 2003.

[12] R.D. Woods. Screening of surface waves in soils. *Journal of the Soil Mechanics and Foundation Division, Proceedings of the ASCE*, 94(SM4):951–979, 1968.

[13] G. Segol, P.C.Y. Lee, and J.F. Abel. Amplitude reduction of surface waves by trenches. *Journal of the Engineering Mechanics Division, Proceedings of the ASCE*, 104(3): 621–641, 1978.

[14] D.E. Beskos, B. Dasgupta, and I.G. Vardoulakis. Vibration isolation using open or filled trenches. Part I: 2-D homogeneous soil. *Computational Mechanics*, 1: 43–63, 1986.

[15] R. Klein, H. Antes, and D. Le Houédec. Efficient 3D modelling of vibration isolation by open trenches. *Computers and Structures*, 64:809–817, 1997.

[16] M. Kim, P. Lee, D. Kim, and H. Kwon. Vibration isolation using flexible rubber chip barriers. In G. Schmid and N. Chouw, editors, *Proceedings of the International Workshop Wave 2000, Wave propagation, Moving load, Vibration reduction*, pages 289–298. A.A Balkema, Amsterdam, 2000.

[17] A. Alzawi and M.H. El Naggar. Full scale experimental study on vibration scattering using open and in-filled (geofoam) wave barriers. *Soil Dynamics and Earthquake Engineering*, 31(3):306–317, 2011.

[18] P.K. Banerjee, S. Ahmad, and K. Chen. Advanced application of BEM to wave barriers in multi-layered three-dimensional soil media. *Earthquake Engineering and Structural Dynamics*, 16: 1041–1060, 1988.

[19] L. Andersen and S.R.K. Nielsen. Reduction of ground vibration by means of barriers or soil improvement along a railway track. *Soil Dynamics and Earthquake Engineering*, 25:701–716, 2005.

[20] X. Sheng, C.J.C. Jones, and D.J. Thompson. Modelling ground vibrations from railways using wavenumber finite- and boundary-element methods. *Proceedings of the Royal Society A - Mathematical, Physical and Engineering Sciences*, 461:2043–2070, 2005.

[21] S.E. Kattis, D. Polyzos, and D.E. Beskos. Vibration isolation by a row of piles using a 3-D frequency domain BEM. *International Journal for Numerical Methods in Engineering*, 46:713–728, 1999.

[22] V.V. Krylov. Scattering of Rayleigh waves by heavy masses as method of protection against traffic-induced ground vibrations. In H. Takemiya, editor, *Environmental vibrations. Prediction, Monitoring, Mitigation and Evaluation*, pages 393–398. Taylor and Francis Group, London, 2005.

[23] A. Dijckmans, P. Coulier, J. Jiang, M.G.R. Toward, D.J. Thompson, G. Degrande, and G. Lombaert. Mitigation of railway induced vibrations by using heavy masses next to the track. In A. Cunha, E. Caetano, P. Ribeiro, and G. Müller, editors, *Proceedings of the 9th International Conference On Structural Dynamics, EURODYN 2014*, pages 751–758, Porto, Portugal, 2014.

[24] T.M. Al-Hussaini, S. Ahmad, and J.M. Baker. Numerical and experimental studies on vibration screening by open and in-filled trench barriers. In G. Schmid and N. Chouw, editors, *Proceedings of the International Workshop Wave 2000, Wave propagation, Moving load, Vibration reduction*, pages 241–250. A.A Balkema, Amsterdam, 2000.

[25] E. Celebi, S. Firat, G. Beyhan, I. Cankaya, I. Vural, and O. Kirtel. Field experiments on wave propagation and vibration isolation by using wave barriers. *Soil Dynamics and Earthquake Engineering*, 29(5):824–833, 2009.

[26] F. De Cock and C. Legrand. Influence of underground gas cushions on the wave propagation of ground vibrations. In *Proceedings of the 4th International Conference on the Application of Stress Wave Theory to Piles*, The Hague, The Netherlands, September 1992.

[27] K.R. Massarsch. Vibration isolation using gas-filled cushions. In *Proceedings of the Geo-Frontiers 2005 Congress*, Austin, Texas, January 2005. American Society of Civil Engineers.

[28] W. Haupt. Model tests on screening of surface waves. In *Proceedings of the 10th International Conference on Soil Mechanics and Foundation Engineering*, volume 3, pages 215–222, 1981.

[29] C. Murillo, L. Thorel, and B. Caicedo. Ground vibration isolation with geofoam barriers: Centrifuge modeling. *Geotextiles and Geomembranes*, 27(6):423–434, 2009.

[30] P. Coulier and H.E.M. Hunt. Experimental study of a stiff wave barrier in gelatine. *Soil Dynamics and Earthquake Engineering*, 66:459–463, 2014.

[31] P. Coulier, S. François, G. Degrande, and G. Lombaert. Subgrade stiffening next to the track as a wave impeding barrier for railway induced vibrations. *Soil Dynamics and Earthquake Engineering*, 48:119–131, 2013.

[32] http://www.rivas-project.eu, 2011.

[33] P. Coulier, V. Cuéllar, G. Degrande, and G. Lombaert. Experimental and numerical evaluation of the effectiveness of a stiff wave barrier in the soil. *Soil Dynamics and Earthquake Engineering*, Accepted with minor revisions.

[34] D.J. Ewins. *Modal testing: theory and practice*. Research Studies Press Ltd., Letchworth, UK, 1984.

[35] P. Coulier, A. Dijckmans, S. François, G. Degrande, and G. Lombaert. A spatial windowing technique to account for finite dimensions in 2.5D dynamic soil–structure interaction problems. *Soil Dynamics and Earthquake Engineering*, 59:51–67, 2014.

[36] A.C. Eringen and E.S. Suhubi. *Elastodynamics, Volume 2, Linear theory*. Academic Press, New York, USA, 1975.

[37] International Organization for Standardization. *ISO 2631-2:1997: Mechanical vibration and shock - Evaluation of human exposure to whole-body vibration - Part 1: General requirements. Second Edition*, 1997.

[38] Deutsches Institut für Normung. *DIN 45672 Teil 2: Schwingungsmessungen in der Umgebung von Schienenverkehrswegen: Auswerteverfahren*, 1995.

[39] D. Stiebel. Protocol for free field measurements of mitigation effects in the project RIVAS for WP 2, 3, 4, 5. RIVAS project SCP0-GA-2010-265754, Deliverable D1.2, Report to the EC, October 2011.

COMPDYN 2015
5th ECCOMAS Thematic Conference on
Computational Methods in Structural Dynamics and Earthquake Engineering
M. Papadrakakis, V. Papadopoulos, V. Plevris (eds.)
Crete Island, Greece, 25–27 May 2015

FAST COMPUTATION OF TRAIN-INDUCED VIBRATIONS IN HOMOGENEOUS AND LAYERED SOILS

Lutz Auersch[1]

[1] BAM Federal Institute of Material Research and Testing, 12200 Berlin, Germany
lutz.auersch-saworski@bam.de

Keywords: Train-induced ground vibration, transfer functions of layered soil, dispersal soil method, frequency-dependant half-space, layer resonance frequency, train speed effects

Abstract. *The computation of the wave propagation in homogeneous and layered soils can be performed by a numerical integration in wavenumber domain. The numerical difficulties of an infinite integral and an integrand with poles can be solved. But if this computation must be repeated for many distances, many frequencies, many loads, or many soil models, it becomes a time consuming task which is not acceptable for a user-friendly prediction tool for railway induced ground vibration. Therefore, an approximate method for the computation of the wave field has been developed. The computation consists of several steps. At first, an approximate dispersion profile is calculated according to rules which have been derived from exact solutions. Secondly, the dispersion is used to achieve the amplitude for a certain frequency and a certain distance by calculating the approximate solution of a corresponding homogeneous half-space. Thirdly, three layer corrections are added which include low-frequency near-field effects, high-frequency far-field effects, and a resonance amplification around the layer frequency. This procedure yields the wave field due to a point load. For a train load, many of these point-load responses have to be summed up, and a frequency-dependant reduction factor has to be multiplied to incorporate the effect of the load distribution along and across the track. - The prediction method is applied to real sites, and the appropriate soil models are identified by approximating the measured transfer functions (frequency-dependant amplitudes) which is presented as an alternative to the approximation of the dispersion (frequency-dependant wave velocities). These examples demonstrate the general behavior of layered soils: the low amplitudes of the stiff half-space at low frequencies, the high amplitudes of the softer layer at high frequencies, the strong increase of amplitudes and a possible resonance amplification at mid frequencies. The material damping of the layer yields a strong attenuation of the amplitudes with the distance for high frequencies. The response depends strongly on the resonance or layer frequency which is shown for different layer depths and velocities always in good agreement with measurements. The layer frequency can be of immense influence if train-speed effects are analysed in a layered soil. The good agreement with many measurements in this contribution as well as in the references [1-4] validates the prediction of ground vibration based on the theory of a layered half-space.*

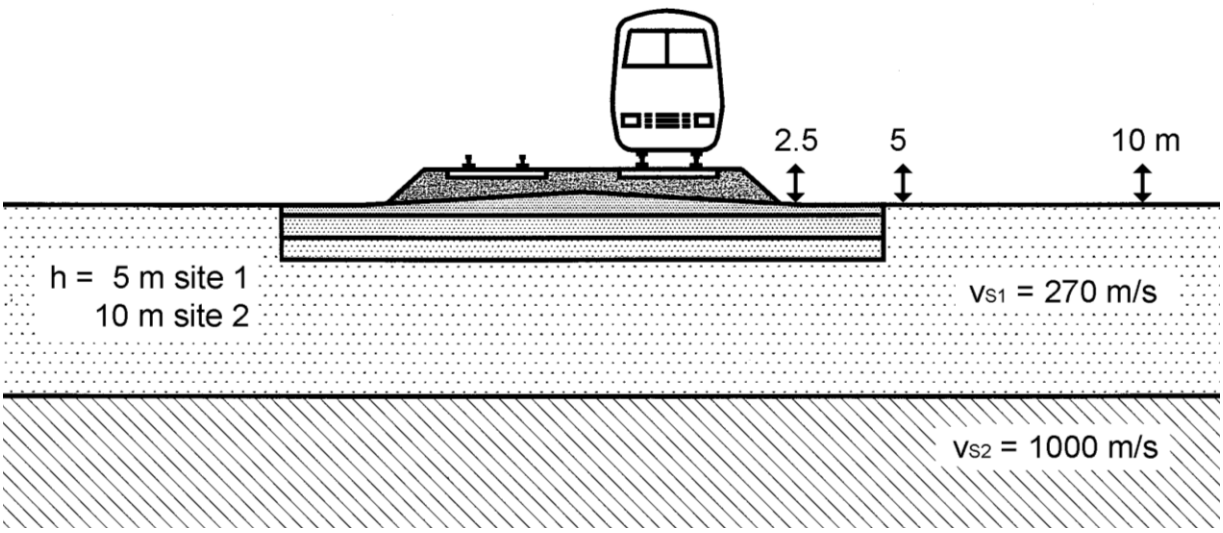


Figure 1: Train induced ground vibration at a layered soil (sites W_1 and W_2 near a German high-speed line)

1 EXACT METHOD FOR THE WAVE FIELD OF LAYERED SOILS

The compliance $N(f, k)$of the layered soil is calculated by matrix methods in frequency-wavenumber domain [1], and the particle velocity response v at a distance r from a point force F with frequency f follows as the infinite wavenumber integral

$$\frac{v}{F}(r, f) = f\int_0^\infty N(f,k)\mathrm{J}_0(kr)kdk = H_P(r, f) \tag{1}$$

with the Bessel function J_0, and the result H_P is also called the transfer (admittance) function. The maxima of the admittance $fN(f,k)$ in frequency-wavenumber domain can also be used to establish the dispersion of the soil model [5].

2 APPROXIMATE METHODS FOR THE PREDICTION OF TRAIN INDUCED GROUND VIBRATION

The approximate prediction of train induced ground vibration [6] consists of four parts.

The first part is the dynamic axle load spectrum $F(f)$ which is approximately 1 kN per third-of octave [7]. The second part is a force reduction function due to the distribution of the load across the track width a

$$\frac{F'}{F}(f) = \begin{cases} \sin a^*/a^* & \text{for} \quad a^* \le \pi/2 \\ 1/a^* & \text{for} \quad a^* > \pi/2 \end{cases} \qquad \text{with} \qquad a^* = \frac{2\pi f a}{v_R} \tag{2}$$

where v_R is the velocity of the Rayleigh wave. The third part is the transfer function of the soil for a train load excitation

$$H_T(x, f) = \sqrt{\sum_{j=1}^{n} {H_P}^2(\sqrt{x^2 + {y_j}^2}, f)} \tag{3}$$

which is calculated as the sum of the contributions of all n axles at positions y_j along the train length L (where n = 40 and L = 250 m are used as standard values), and x is the distance from the track. For each axle, the transfer function of a point load $H_P(r_j, f)$ is used. This transfer

function includes the characteristics of the soil, and its fast approximate calculation is shown in the next section. The prediction of the railway induced ground vibration follows as

$$v(x,f) = H_T(x,f)\frac{F'}{F}(f)F(f) \tag{4}$$

3 APPROXIMATE DISPERSAL SOIL METHOD

A two step procedure to calculate approximately the transfer function of a layered soil has been developed. In the first step, the dispersion of the layered soil is approximated, and in the second step, the transfer function of a dispersal soil is approximated. The approximate method is faster and also yields smoother results than the exact method which can sometimes include strong interferences between different wave types.

3.1 Approximate dispersion

The exact dispersion curves of layered, multi-layered and continuously layered soils have been used to derive an approximate calculation of the Rayleigh wave dispersion $v_R(f)$ from the soil profile $v_S(z)$. It is based on the approximated dispersion of a layer on a stiffer half-space with the wave velocities v_{R1} and v_{R2}

$$v_R(f) = v_{R1} + (v_{R2} - v_{R1})\,0.5\left(1+\cos\frac{\pi}{2}\frac{f}{f_1}\right) \qquad \text{with} \qquad f_1 = \frac{v_{S1}}{3h_1} \tag{5}$$

which is extended to a multi-layered situation. A correction for each layer is added to the wave speed v_{R1} of the top layer

$$v_R(f) = v_{R1} + \sum_{i=1}^{n-1}(v_{Ri+1} - v_{Ri})\,0.5\left(1+\cos\frac{\pi}{2}\frac{f}{f_i}\right) \qquad \text{with} \qquad f_i = \frac{v_{Si}}{3h_i} \tag{6}$$

h_i is the depth where the layer i ends.

3.2 Approximate transfer functions

The amplitudes of a homogeneous soil can be approximated by the asymptotes

$$H_P(r,f) = \frac{v}{F}(r,f) = \frac{f(1-\nu)}{G\,r}\,\mathrm{e}^{-D\kappa r^*}\begin{cases} 1 & \text{for } r^* \le r_0^* \\ \sqrt{r^*/r_0^*} & \text{for } r^* > r_0^* \end{cases} \qquad \text{with} \qquad r^* = \frac{2\pi f r}{v_S} \tag{7}$$

The upper part of equation (6) describes the near-field and the low-frequency response. At $r^* = r_0^*$ starts the lower part of equation (6), the far field which is dominated by the Rayleigh wave, see [4] for more details.

The amplitudes of a homogeneous soil can be used to calculate the wave-field of an inhomogeneous soil. The amplitudes of the inhomogeneous soil with its dispersion $v_R(f)$ are approximated by the amplitudes of a homogeneous half-space, but for each frequency the half-space has a different wave speed – the wave speed $v_R(f)$. This method works very well for a soil with continuously increasing stiffness.

If this method is applied to a clearly layered situation, the following modifications must be included:

A frequency-dependent resonance amplification

$$V = \frac{1}{1 + i2D_R\eta - \eta^2} \tag{8}$$

can be introduced, where

$$\eta = \begin{cases} f/f_0 & \text{for } f \le f_0 \\ 2 - f/f_0 & \text{for } f > f_0 \end{cases} \qquad f_0 = \frac{v_S}{3h} \qquad \text{and} \qquad D_R = \frac{2}{\pi}\frac{\rho_1 v_1}{\rho_2 v_2}$$

are used for the normalized frequency η, the resonance frequency f_0, and the resonance damping D_R is calculated according to the 1-dimensional wave theory.

The effect of soft top layers on the low-frequency near-field and the effect of stiff deeper layers on the high-frequency far-field are included by a general procedure. Normally at a certain frequency f, the half-space amplitudes of the corresponding wave velocity $v_R(f)$ is calculated. Corrections of the transfer functions are made if deeper and stiffer soil material yields greater half-space amplitudes, or softer top layers yield greater "layer amplitudes" which are approximated by $A_L = A_H \exp(-ar/h)$, according to the low frequency behaviour of a layer on a rigid base. The greatest amplitude is always chosen as the correct transfer function.

It has been observed that the method is improved if a modified dispersion, which is shifted one third of octave to the left, and a minimum resonance damping of $D_R = 0.1$ is used.

4 IDENTIFICATION OF THE SOIL MODEL

4.1 Wave method

The dispersion $v_R(f)$ of the soil is derived from the measurements by the frequency-wavenumber transform method in this contribution, but other methods as the spectral analysis of surface waves SASW or the spatial autocorrelation method SPAC are also in use [5].

The corresponding soil model is found by comparing the calculated dispersion $\tilde{v}_R(f)$ for each soil model with the measured dispersion $v_R(f)$. The total error for all frequencies is minimized on a grid of soil parameters yielding the soil model that fits best the measured dispersion (grid search algorithm). Instead of calculating the exact dispersion, the approximate dispersion function (6) can be used to achieve acceptable results in short computation time. In addition to the velocity profile $v_S(z)$ from the dispersion, the damping D of the soil is evaluated from the measured amplitude-distance relations [5].

4.2 Transfer function method

The soil parameters can also be derived from the measured transfer function $H(f, x)$. A high number of transfer functions $\tilde{H}(f, x)$ have to be calculated and compared with the measured transfer function $H(f, x)$. The total error for all distances and frequencies is minimized on a grid of soil parameters yielding the soil model that fits best the measured transfer function (grid search algorithm). This identification procedure yields both, the wave velocities and the damping, and therefore it is more time consuming than the wave method. The simplified calculation of the transfer function can be used to achieve an acceptable computation time.

5 APPLICATION TO HOMOGENEOUS SOILS

At first, two examples of homogeneous soils are presented in Figure 2. Measurements have been performed with an electro-dynamic vibrator and a sensor line from $r = 2$ to 100 m distance. The excitation force is measured by the acceleration of the moving mass of 150 kg. A resonance of the vibrator and base-plate mass of 200 kg is observed by an additional sensor at 50 or 90 Hz. The increased excitation force at and the reduced force above the resonance have been corrected. The smooth transfer functions, the slowly increasing admittances of all distances can be well approximated by a homogeneous soil model. The shear stiffness or shear wave velocity of the soil determines the amplitudes of the wave field. The small

damping has only little effect on the wave amplitudes. The identified soil parameters (v_S = 175 and 250 m/s, D = 1.5 and 2 %) agree well with those determined by the wave methods (see Table 1).

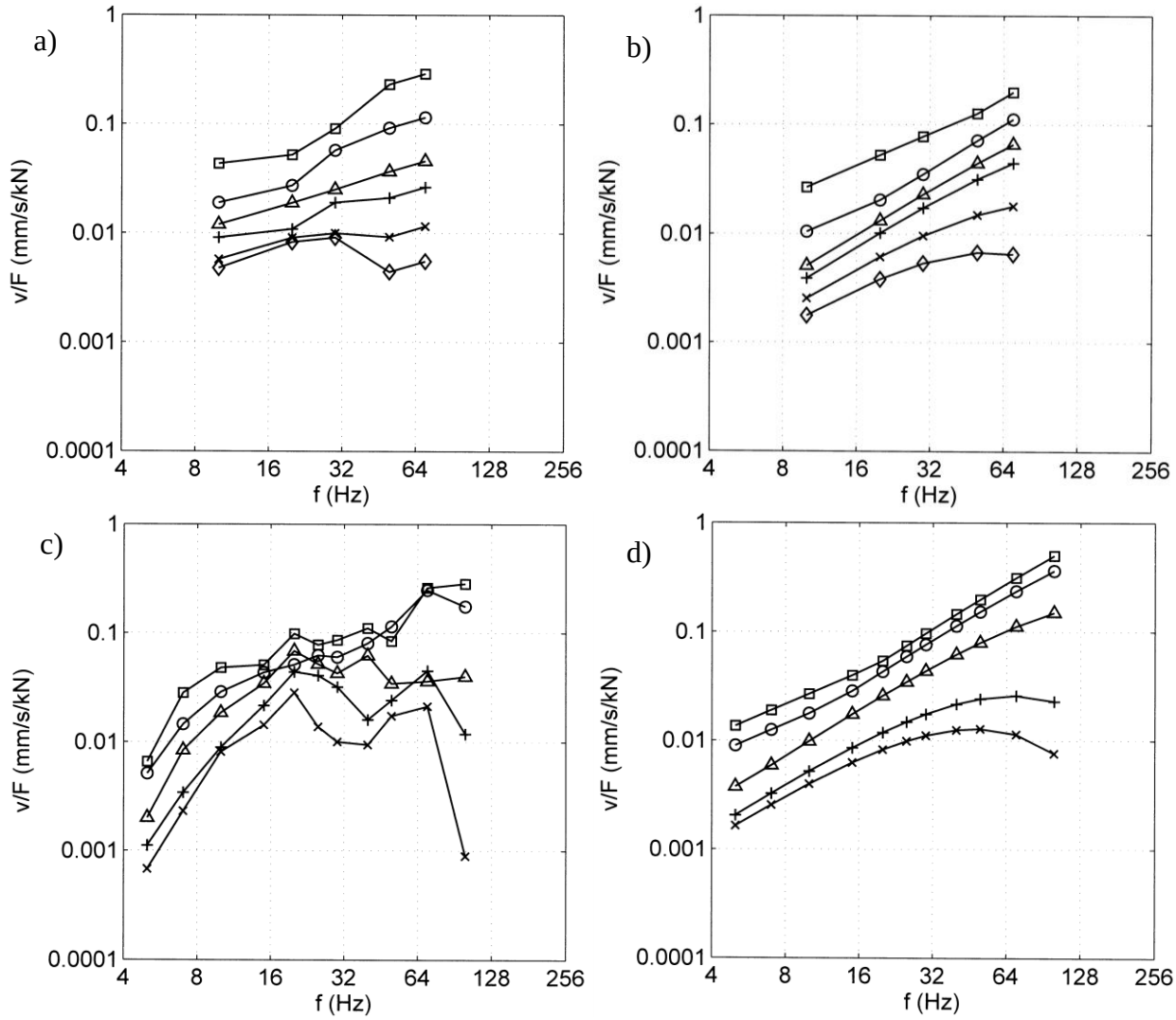


Figure 2: Transfer function measured by vibrator excitation (a,c) and approximated (b,d); homogeneous soil at site M (a,b), r = □ 2, ○ 5, △ 10, + 15, × 30, ◇ 50 m, and at site G (c,d), r = □ 4, ○ 6, △ 14, + 38, × 54 m.

6 APPLICATION TO DIFFERENT LAYERED SOILS

A total of 11 layered soils are presented in the next three sections and four of them are presented in this section by the following detailed results. The measured transfer functions for hammer excitation are shown in Figures 3a to 6a together with the approximating theoretical transfer function (Figs. 3b to 6b) where the approximating parameters can be found in Table 1. The transfer function which is found from the wave measurements is presented in Figures 3c to 6c for the point load and in Figures 3d to 6d for a standard train load. Figures 3e to 6e show specific predictions of train vibrations for each site which are compared with the measured train-induced ground vibrations (Figs. 3f to 6f). The stiffest underlying soil has a velocity of v_{S2} = 1000 m/s, the softest layer has a v_{S1} = 75 m/s. Low layer velocities of v_{S1} = 100 to 125 m/s have also been found at sites X_i A, and V. The damping values in Table 1 are all in the normal range of D = 1 to 5 %. The damping yields a strong attenuation with distance at

the high frequencies, and therefore a strong reduction at the far-field points. This can be clearly observed at Figures 4b and 6b for the sites D and X_1 with the strongest damping of D = 4.5 and 5 %. It should be mentioned that high-frequency amplitudes can be reduced by a stronger damping or by a stiffer soil so that the identification of a soil model is not unique.

Site	v_{S1}(m/s)	v_{S2} (m/s)	h (m)	D (%)	Method	Figure
A	125	350	4	3.5	Transfer	3b
A	150	250	3.5	2	Wave	3c-e
D	150	300	2.5	4.5	Transfer	4b
D	325	850	5	2.5	Wave	4c-e
G	175		homogeneous	1.5	Transfer	2d
G	170		homogeneous	1	Wave	[2]
M	250		homogeneous	2	Transfer	2b
M	250		homogeneous	2	Wave	
O	150	300	1	4	Transfer	5b
O	350	1000	17	1.5	Wave	5c-e
U_1	75	500	2.5	5	Transfer	7f
U_2	300	700	13	3	Wave	8e
V	100	p = 0.25	continuous	4	Transfer	9d
V	115	p = 0.25	continuous	3.8	Wave	[2]
W_1	250	1000	5	4	Transfer	9f
W_1	270	1000	5	5.9	Wave	[2]
W_2	270	1000	10	5	Transfer	[8]
X_1	125	350	2.5	5	Transfer	6e
X_1	200	500	3.5	4	Wave	6c-e
X_1	150	p = 0.25	continuous	4.5	Transfer	9a
X_1	125	p = 0.4	continuous	5	Transfer	9b
X_2	100	250	2	3	Transfer	7b
X_2	150	300	3.5	2.2	Wave	
X_3	125	300	3	4	Transfer	7d
X_3	150	350	3	2.1	Wave	
Y	150	300	2.5	5	Transfer	8b
Y	180	900	3	6	Wave	8c

Table 1: Parameters of the soil models, shear wave velocities v_{S1} and v_{S2}, layer depth h and damping D.

6.1 The characteristics of a layered soil

The transfer functions of a layered soil for example in Figure 3 show a stronger increase at low and mid frequencies compared to the homogeneous soils in Figure 2. The increase is strongest just below the resonance frequency of the layer, where a small resonance amplification can be observed. The resonance or layer frequencies lie between 10 and 64 Hz for all measured sites. The lowest resonance frequency corresponds with a thick layer (h = 17 m, Fig. 5b), whereas the highest resonance frequency has been found for a thin layer (h = 1 m, Fig. 5c). For the same thickness h = 2.5 m of the layer, the softer soil of 75 m/s yields the lower resonance frequency of 16 Hz (site U_1, Fig. 7f compared with site D, Fig. 4b). The resonance amplification can be higher if the velocity contrast of the shear wave is stronger (sites U_1, Fig. 7f and Y, Fig. 8a-d).

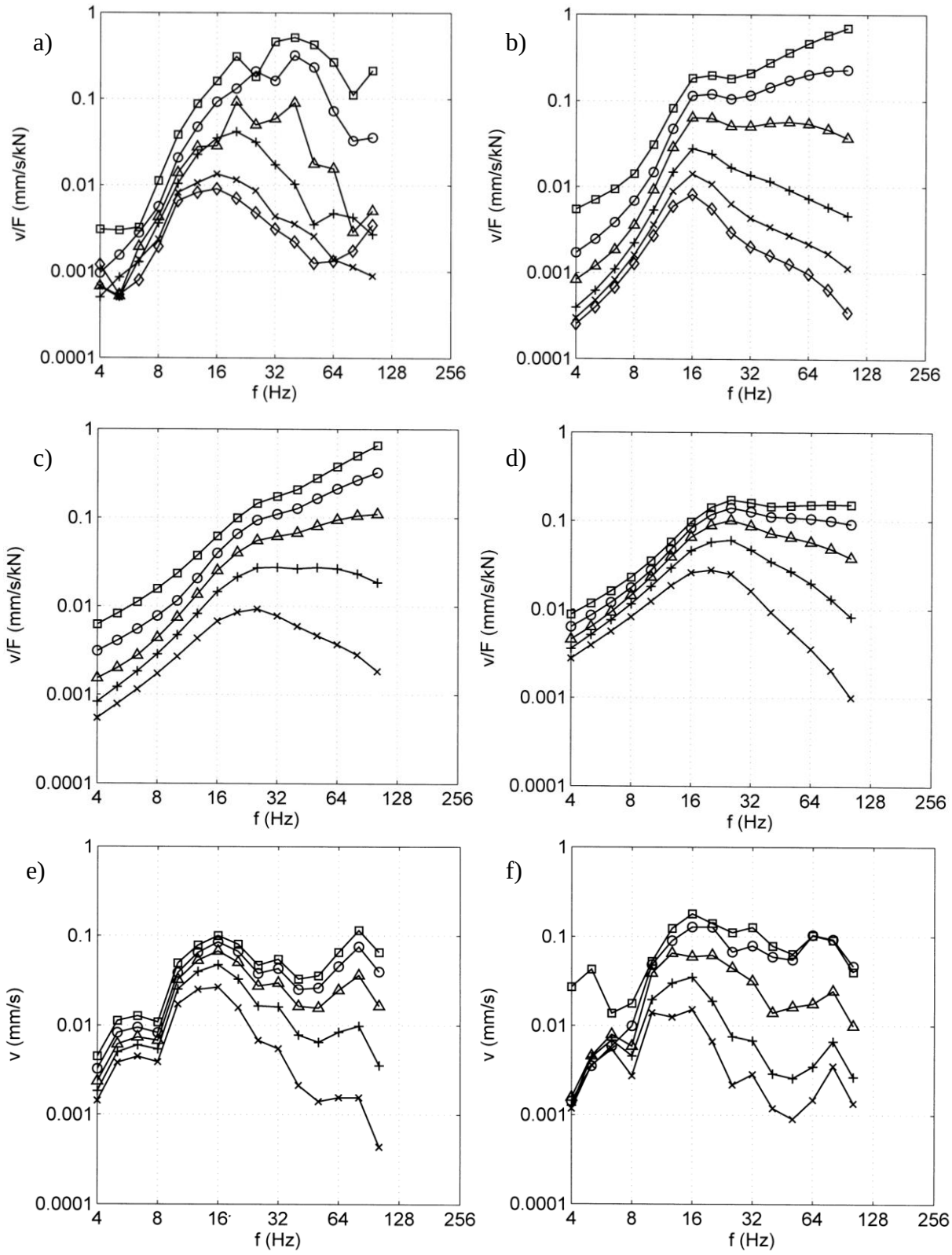


Figure 3: Transfer functions for layered soil at site A, a) measured by hammer excitation, b) approximated, c) for soil model from wave measurements, d) for standard train load; e) specific train prediction and f) measurement of train vibration (r = □ 4, ○ 8, △ 16, + 32, × 48, ◇ 62 m, a-b, r = □ 4, ○ 8, △ 16, + 32, × 64 m, c-f)

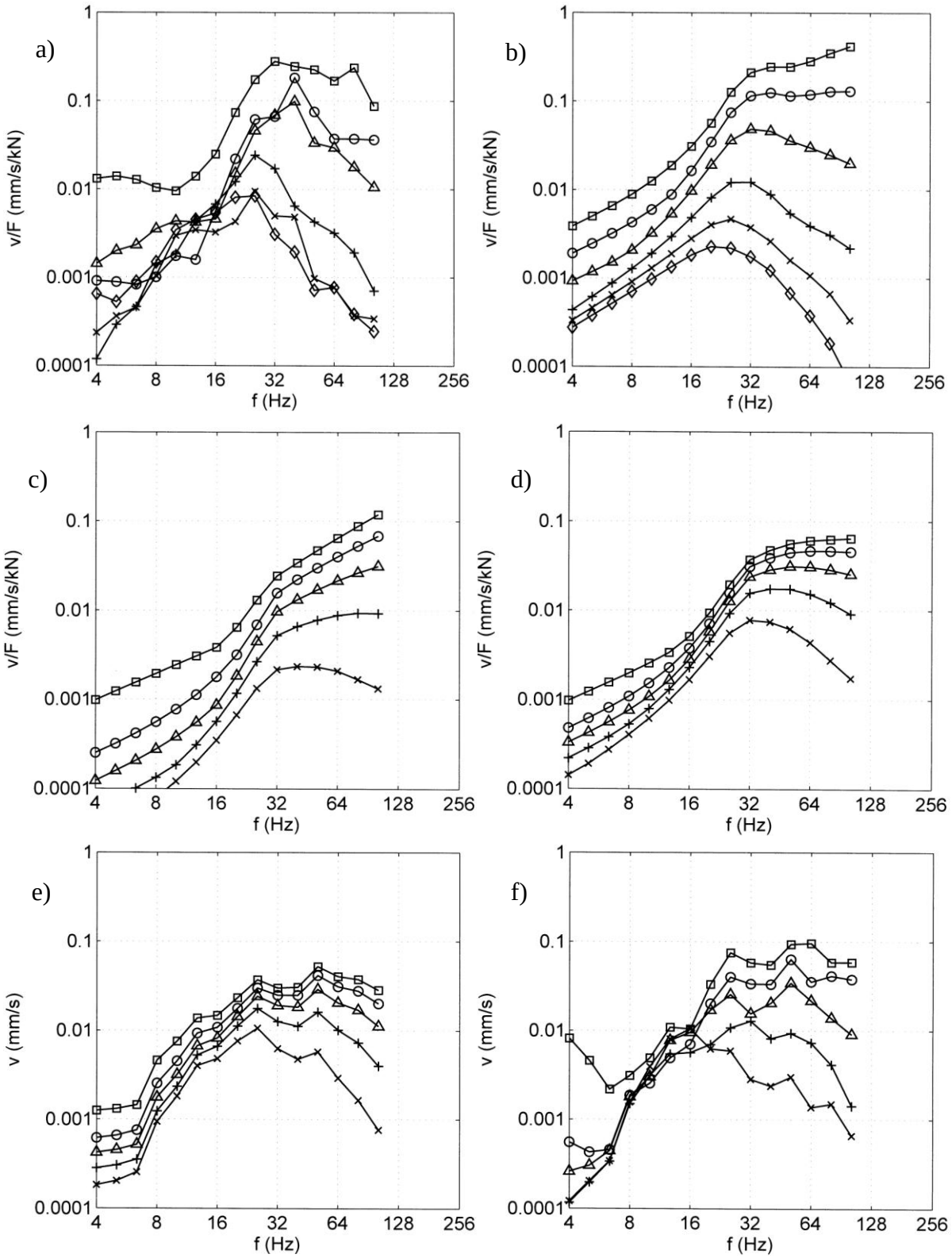


Figure 4: Transfer functions for layered soil at site D, a) measured by hammer excitation, b) approximated, c) for soil model from wave measurements, d) for standard train load; e) specific train prediction and f) measurement of train vibration (r = □ 4, ○ 8, △ 16, + 32, × 48, ◇ 62 m, a-b, r = □ 4, ○ 8, △ 16, + 32, × 64 m, c-f)

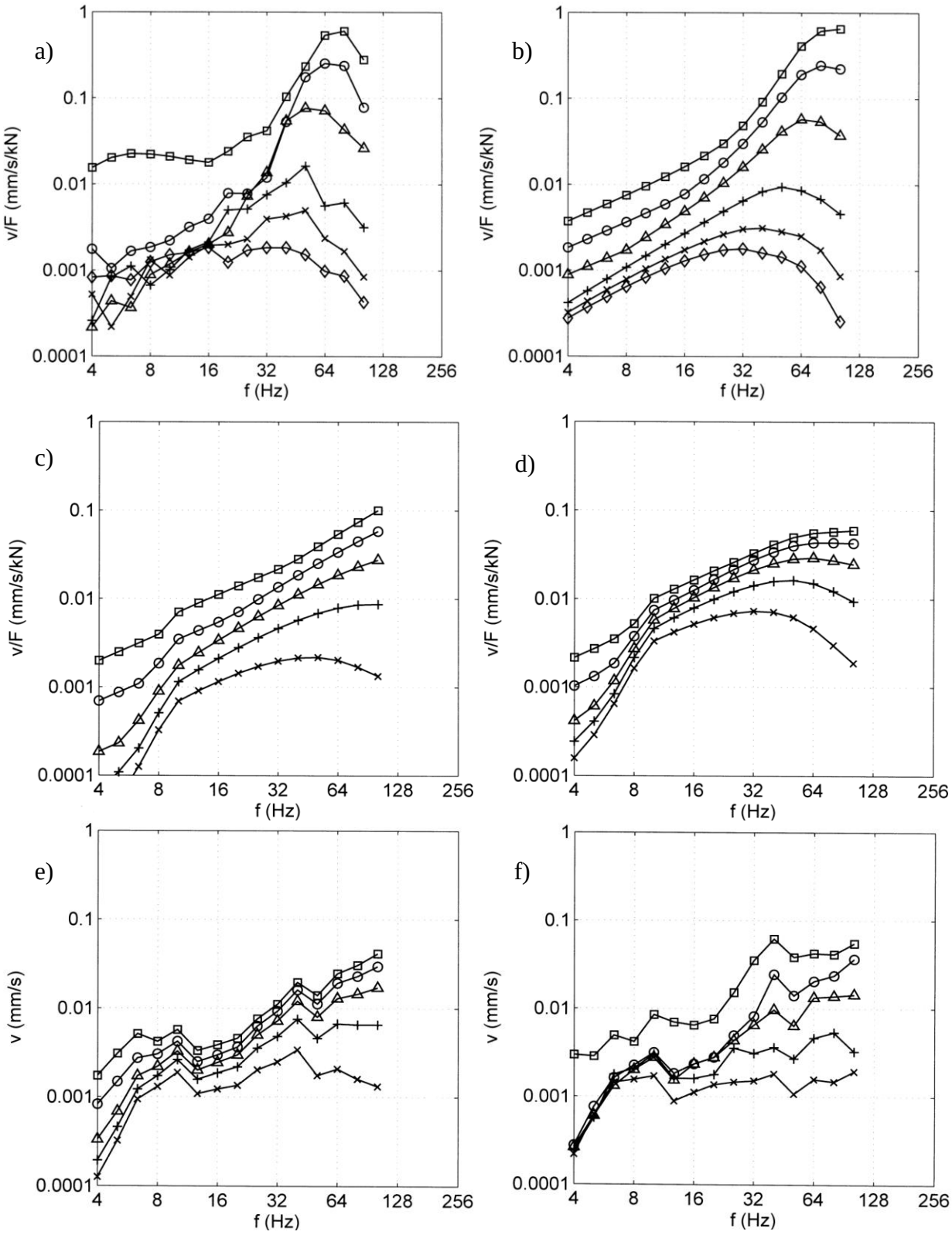


Figure 5: Transfer functions for layered soil at site O, a) measured by hammer excitation, b) approximated, c) for soil model from wave measurements, d) for standard train load; e) specific train prediction and f) measurement of train vibration (r = □ 4, ○ 8, △ 16, + 32, × 48, ◇ 60 m, a-b, r = □ 4, ○ 8, △ 16, + 32, × 64 m, c-f)

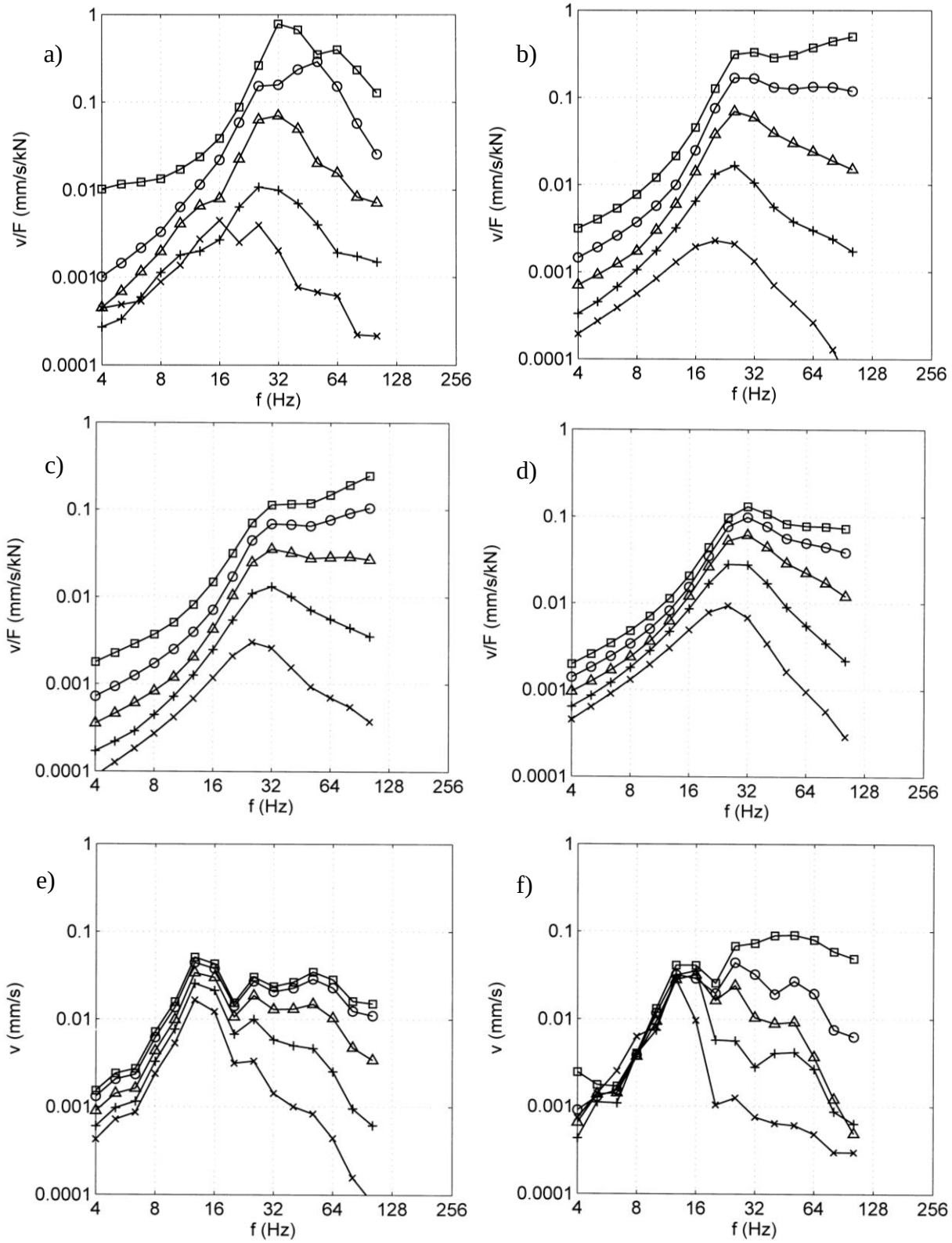


Figure 6: Transfer functions for layered soil at site X_1 a) measured by hammer excitation, b) approximated, c) for soil model from wave measurements, d) for standard train load; e) specific train prediction and f) measurement of train vibration (r = □ 4, ○ 8, △ 16, + 32, × 48, ◇ 62 m, a-b, r = □ 6, ○ 8, △ 16, + 32, × 64 m, c-f).

6.2 Comparison of measurements with the approximate theory

The approximated transfer functions in Figures 3b to 6b agree quite well with the measured transfer functions in Figures 3a to 6a. The approximate transfer functions as well as the attenuation with distance are smoother what is beneficial for a robust prediction of railway vibration. Namely the low-frequency low amplitudes are more regular in the approximate theory and compensate possible measurement errors (environmental noise).

6.3 Comparison of the transfer function for point and train load

The transfer functions for a point load in Figures 3c to 6c show a stronger attenuation with distance than the transfer functions for a train load (Figs. 3d to 6d). This effect is strongest for the low frequencies where only the geometric attenuation occurs. At high frequencies with a strong attenuation due to the damping, the reduction of the geometric attenuation is not so noticeable.

6.4 Comparison of the predicted and measured train vibration

The prediction of the train induced ground vibration is done with the transfer functions for a train load (Figs 3d to 6d) and a specific excitation spectrum suited for the measurements. The specific excitation spectrum is always close to $F(f) = 1$ kN for all thirds of octaves (compare Figures 3e to 6e with Figures 3d to 6d). The predicted train vibration agrees well with the measured train vibration in Figures 3f to 6f. The train spectra are rather smooth spectra with only small peaks. The measured low-frequency amplitudes come close together at some sites, in theory there is always a weak attenuation with distance.

6.5 Comparison of train and hammer excitation

The measured transfer function and train vibration (Figs 3a to 6a and 3f to 6f) generally show a good agreement for all sites (except site X_1 where the maximum train vibration are found below the resonance frequency of the layered soil). The characteristics of the layered soils are very similar for the hammer and train excitation while the attenuation is stronger for the hammer.

6.6 Comparison of the transfer and wave method

The characteristic layer frequencies are very similar for the transfer and wave method (Figs 3b to 6b and 3c to 6c), 20-25 Hz at site A, 25-32 Hz at site X_1, and 32 Hz at site D. At site O (Fig. 5), both methods identify a stiff soil of $v_S = 300$-350 m/s which yields the correct amplitudes in a wide mid-frequency range. A stiffer underlying soil is identified by the wave methods which yields a very low-frequency resonance also observable in the train measurements, whereas the hammer experiments clearly show a high frequency resonance and a softer top layer. Due to environmental noise, the transfer method has some uncertainties at very low frequencies. For site D and particular for site X_1, the transfer functions for both methods are very similar. The amplitudes are a little lower for the wave method, and the high-frequency amplitudes are approximated by a softer layer and a higher damping using the transfer method. The mid-frequency region with the strong increase and the resonance are usually best evaluable in wave and transfer measurements [5]. A generally good agreement at all frequencies has been found for site A.

7 MORE EXAMPLES AND CONTINUOUSLY INCREASING SOIL STIFFNESS

The transfer functions of two more sites X_2 and X_3, which are not far from site X_1, are given in Figure 7 as measurements and theory. In this case, the soil models are very similar,

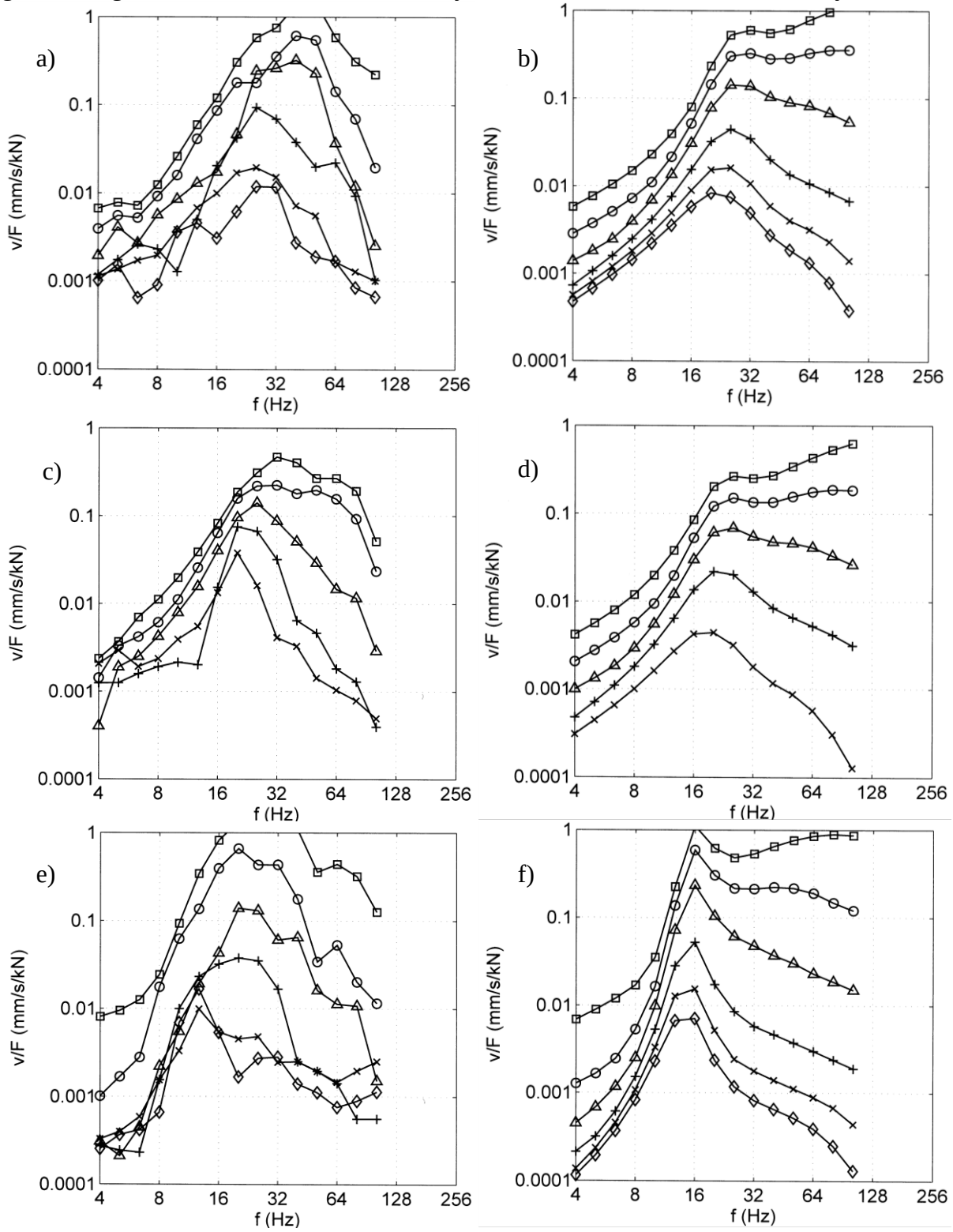


Figure 7: Transfer functions for layered soil at site X_2 (a,b), site X_3 (c,d), and site U_1 (e,f), a,c,e) measured by hammer excitation, b,d,f) approximated, (r = □ 4, ○ 8, △ 16, + 32, × 48, ◇ 62 m).

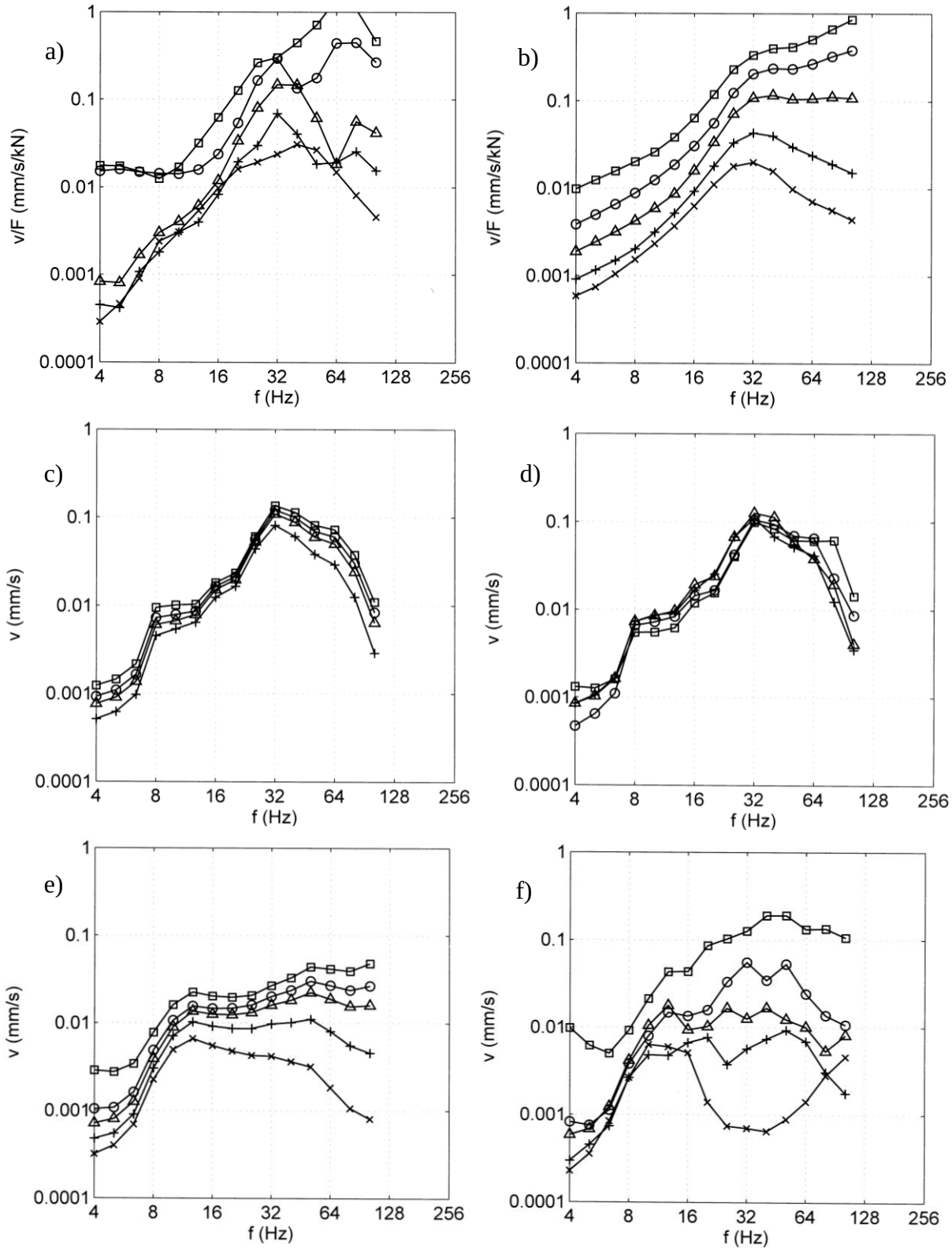


Figure 8: Transfer functions for layered soil at site Y (a-d) and site U_2 (e-f), a) measured by hammer excitation, b) approximated; c,e) specific train prediction and d,f) measurement of train vibration, (r = □ 2, ○ 4, △ 8, + 14, × 24 m, a-b, r = □ 5, ○ 6, △ 8, + 10, × 12m, c-d, r = □ 4, ○ 10, △ 16, + 32, × 64 m, e-f).

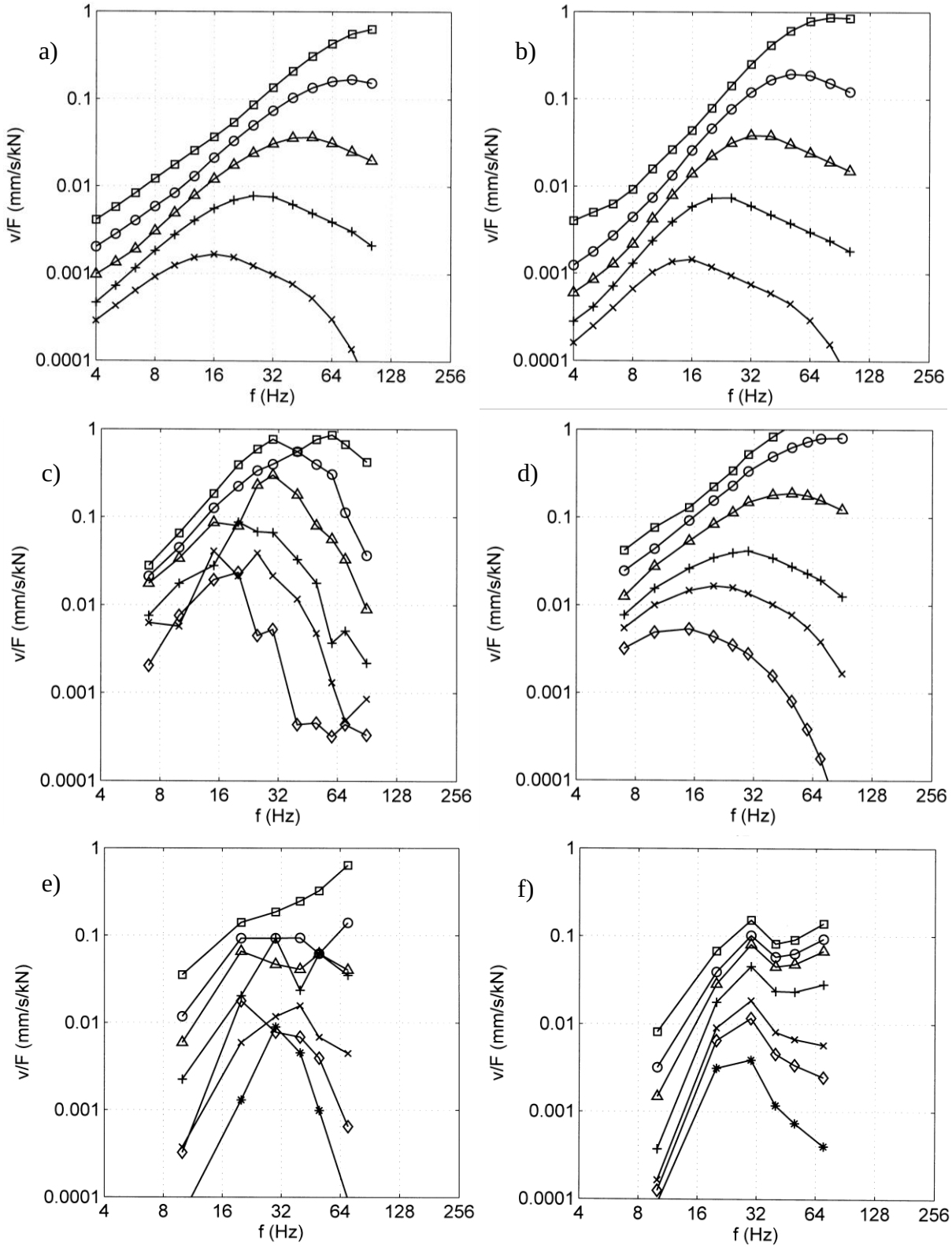


Figure 9: Transfer functions for continuously varying soil at site X_1 (a,b) and site V (c,d) and for layered soil at site W (e,f), approximated by a) $v_S \sim z^{0.25}$, b) $v_S \sim z^{0.40}$ (best fit), c) measured by vibrator excitation, d) approximated by $v_S \sim z^{0.25}$, e) measured by vibrator excitation, f) approximated, (r = □ 4, ○ 8, △ 16, + 32, × 48, ◇ 62 m, a-b, r = □ 3, ○ 5, △ 10, + 20, × 30 , ◇ 50 m, c-d, r = □ 3, ○ 5, △ 7, + 14, × 30, ◇ 40 m, e-f).

but this should always be checked experimentally as will be demonstrated in Section 8. Site X_3 (Fig. 7c) shows a stronger resonance amplification in the far field. A similar observation is made at site U_1 in experiment and theory (Figs. 7e,f) and some sites in [2]. Amplitudes higher than 1 mm/s/kN have been measured at this site which correspond with the softest layer material of $v_{S1} = 75$ m/s x. A soft layer yields a low resonance frequency without a great thickness ($h = 2.5$ m). A soft soil also yields the strongest damping effect, and in addition the damping value $D = 5$ % is also high for site U_1. Therefore a very strong attenuation with distance at high frequencies is observed.

Figure 8 shows measurements and predictions of site Y where all results show a resonance at 32 Hz, for the hammer as well as for the train excitation. The clear resonance is attributed to the strong velocity contrast v_{S1}/v_{S2} between the layer and the underlying half-space. At site U_2, the resonance region is well predicted in Figure 8e, but the measured strong attenuation in the following mid-frequency range (Fig. 8f) cannot be represented by the theory. The medium attenuation at high frequencies, however, is in good agreement with the material damping of $D = 3$ %.

The results at site X_1 (Fig. 6) are rather smooth, so that a soil with continuously increasing stiffness has also been fitted to the measurements. Figure 9a shows the approximation with the theoretical law $v_S(z) = v_{S1}\, z^{0.25}$ and Figure 9b the result with a higher best-fit power $v_{S1}\, z^{0.4}$ which yields a stronger increase with frequency in better agreement with the measurements (Fig. 6a). It can be seen that the layer approximation in Figure 6b is a little better than the continuous approximation.

Figure 9c shows the results of a vibrator testing at site V with a continuously increasing stiffness of the soil. The approximating transfer functions in Figure 9d agree well with the vibrator measurements as well as with the hammer measurements in [1], and the corresponding model agrees well with the model identified from the wave measurements. Due to the very soft top layer, a rather low resonance frequency of the vibrator on the soil has been found at 30 Hz. This has been confirmed and corrected by stress measurements in the soil below the vibrator.

The layered soil of the next section (site W_1) has also been investigated by vibrator excitation (Fig. 9e). The strong increase of the transfer functions up to 25 Hz indicates the layered situation with a corresponding resonance frequency. The vibrator resonance at 50 Hz has been corrected as well as a redistribution of the low amplitudes at 10 Hz to higher harmonics at 20 and 30 Hz. The transfer-based soil models of this section and namely those from the vibrator experiments are in good agreement with the results of the wave method.

8 SPEED DEPENDANCY OF THE AMPLITUDES IN LAYERED SOILS

At the two sites W_1 and W_2 in only 100 m distance, trains with different speeds have been measured. At site W_1 a strong increase of the amplitudes with train speed has been found whereas the amplitudes remain constant at site W_2. The explanation has been identified by the different layering of the soils (Figs 10a,c). Both sites have the same layer and half-space materials, but site W_2 has a deeper layer ($h = 10$ m) compared to site W_1 ($h = 5$ m). This fact yields a lower resonance frequency at 12 Hz compared to 25 Hz at site W_2.

The ground vibration due to the train passage with 200 km/h is shown for both sites in Figure 10b,d. An important component can be seen around 16 Hz (Fig. 10d) which is dominant in the far field. This component is above the resonance frequency and has high amplitudes for site W_2. At site W_1 (Fig. 10b), this component is below the resonance frequency and has smaller amplitudes. The maximum amplitudes are rather at the layer resonance than at the mid-frequency excitation. For the speed variation it can be concluded: High and nearly constant amplitudes are observed for different train speeds if the mid-

frequency range is higher than the resonance frequency. A strong increase of the amplitudes is observed if the mid-frequency component is just in the range of the strong increase before the resonance. These two extreme situations have been met at sites W_1 and W_2 during the high-speed tests [8].

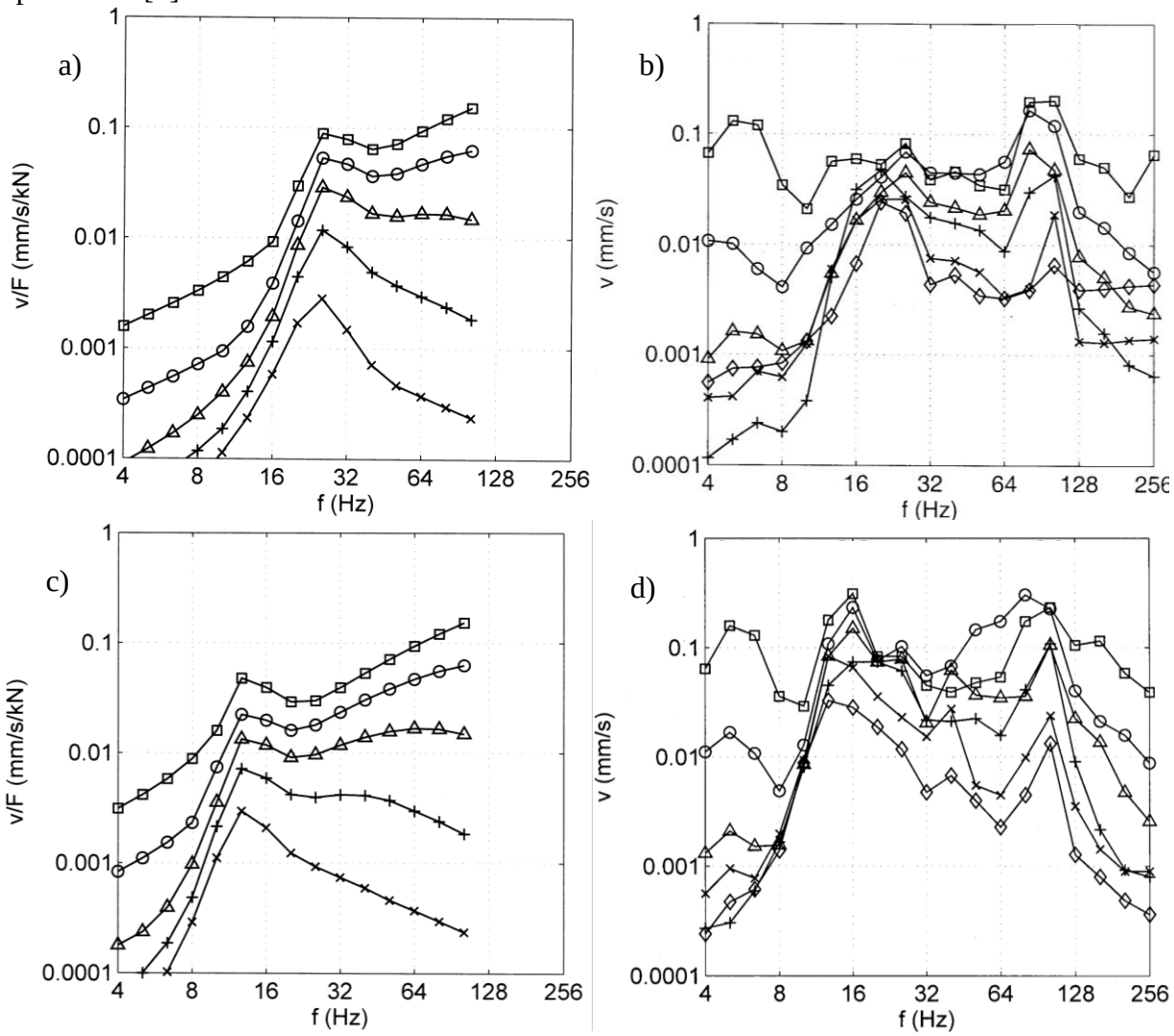


Figure 10: Layered soil at site W_1 (a,b) and W_2 (c,d), a,c) approximated transfer functions, (r = □ 4, ○ 8, △ 16, + 32, × 64 m), b,d) measured train vibration, (r = □ 2.5, ○ 5, △ 10, + 20, × 30, ◇ 50 m).

9 CONCLUSIONS

A fast method has been presented to calculate approximately the transfer functions of a layered soil in good agreement with the exact theory. The approximate method has been beneficially used for the identification of a soil model and for the prediction of train-induced ground vibration at 14 real sites, see Table 1. Whereas two sites consist of an almost homogeneous soil and one site of a soil with continuously increasing stiffness, all other sites clearly demonstrate the typical behaviour of a layered soil. The transfer functions have low low-frequency amplitudes of the stiffer underlying soil and high high-frequency amplitudes of the softer layer. In the mid-frequency range the amplitudes strongly increase and a resonance amplification can occur. The resonance or layer frequency has been found between 10 and 64 Hz for the different sites, depending on the stiffness and depth of the layer. The influence of the soil has been clearly presented for an example of train vibration, but it is generally

stronger for hammer excitation. Many items agree well between predicted and measured transfer functions and train vibrations, and between the transfer- and wave-based soil identification, validating thereby the prediction method. Alternative prediction methods are also available which use directly the measured or the exactly calculated transfer functions [4], or calculated force spectra [7].

ACKNOWLEDGEMENT

The measurements have been performed during the last 30 years. Special thanks to S. Said who participated in almost all measurements and evaluations, to W. Schmid, W. Wuttke, F. Ziegler, M. Manjock, U. Schmidt, and C. Meinhardt for their cooperation in our measurements, and to R. Frenz for his assistance in the soil identification.

REFERENCES

[1] L. Auersch, Wave propagation in layered soil: theoretical solution in wavenumber domain and experimental results of hammer and railway traffic excitation. *Journal of Sound and Vibration*, **173**, 233-264, 1994.

[2] L. Auersch: Technically induced surface wave fields, Part II: Measured and calculated admittance spectra. *Bulletin of the Seismological Society of America*, **100**, 1540-1550, 2010.

[3] L. Auersch, S. Said: The influence of soil properties on the ground vibration due to railway traffic and other sources – the comparability of different sites. *Proc. 6th International Symposium on Environmental Vibration*, Tongji University Press, 175-186, 2013.

[4] L. Auersch: The use and validation of measured, theoretical and approximated point-load solutions for the prediction of train induced vibration in homogeneous and inhomogeneous soils. *International Journal of Acoustics and Vibrations*, **19**, 52-64, 2014.

[5] L. Auersch, S. Said: Comparison of different dispersion evaluation methods and a case history with the inversion to a soil model, related admittance functions, and the prediction of train induced ground vibration. *Journal of Near Surface Geophysics*, (2015, accepted).

[6] L. Auersch, W. Rücker: A user-friendly prediction tool for railway induced ground vibrations: Emission – Transmission – Immission. *Proc. 9th International Workshop on Railway Noise (IWRN9)*, München, 1-9 (CD-ROM), 2007.

[7] L. Auersch: Theoretical and experimental excitation force spectra for railway induced ground vibration – vehicle-track soil interaction, irregularities and soil measurements. *Vehicle System Dynamics*, **48**, 235-261, 2010.

[8] L. Auersch: Train induced ground vibrations: different amplitude-speed relations for two layered soils. *Journal of Rail and Rapid Transit*, **226**, 469-488, 2012.

COMPDYN 2015
5th ECCOMAS Thematic Conference on
Computational Methods in Structural Dynamics and Earthquake Engineering
M. Papadrakakis, V. Papadopoulos, V. Plevris (eds.)
Crete Island, Greece, 25–27 May 2015

THE INFLUENCE OF DEGRADATION OF SHEAR MODULUS OF SOIL ON PREDICTED RAILWAY VIBRATIONS IN TUNNELS EXCAVATED WITH TBM: A NUMERICAL ANALYSIS

J. Fernández Ruiz [1], P. Alves Costa [2], P. Lopes [3], L. Medina Rodríguez[4]

[1] University of La Coruña
Campus de Elviña, 15071 La Coruña (Spain)
e-mail: jesus.fernandez.ruiz@udc.es

[2]University of Porto
Rúa Dr. Roberto Frías, s/n 4200-465 Porto (Portugal)
e-mail: pacosta@fe.up.pt

[3]University of Porto
Rúa Dr. Roberto Frías, s/n 4200-465 Porto (Portugal)
e-mail: cpl@isep.ipp.pt

[4] University of La Coruña
Campus de Elviña, 15071 La Coruña (Spain)
e-mail: lmedina@udc.es

Keywords: Railway vibrations in tunnels, G_s soil degradation due to TBM

Abstract. *In this paper the influence of the stress state within the soil on predicted railway vibrations in tunnels is studied, regarding Gs modulus degradation that occurs when the tunnel is excavated with Tunnel Boring Machine (TBM). The adopted procedure is uncoupled, using a 2D FEM model to simulate the process of tunnelling which incorporates the constitutive model known as Hardening Soil with small strain stiffness (HS-small). The Gs modulus values are then used in a dynamic numerical model based on a 2.5D FEM-PML approach in order to simulate the vibrations induced by railway traffic. Simulations are then performed assuming two different scenarios for the elastic properties of the ground: i) assuming Gs modulus for low strain deformation for whole domain, i.e., neglecting the perturbation of the soil due to the tunnel construction; ii) assuming values of Gs modulus computed taking into account the strains induced by the tunnel construction. The numerical results show a clear influence of tunnelling process, being more relevant at closest distances to the tunnel.*

1. INTRODUCTION

Vibrations induced by railway traffic in tunnels is a special interest and development topic in recent years, mainly in urban areas where nuisance generated can be common if no preventive measures are taken or if the initial design is not right. It is reasonable to affirm that transport infrastructure in the 21st century has much more requirements than previously, since environmental aspects have gained a significant importance. Nowadays, the impact of vibrations on working and living environments is considered as an important problem of modern societies [1]. Moreover, the relevant growth of population around metropolitan areas implies the need for more sustainable underground transport systems. One of the key advances to minimize the impact of railway systems is the development of the numerical models that are capable of predicting correctly the level of vibrations on free-field or on buildings and to help in finding technical solutions for mitigating possible nuisances. For that, in last recent years several models have been developed in order to understand the complex problem of railway vibrations in tunnels. It is worth mentioning semi-analytical models such as those proposed by Hussein and Hunt [2], Kuo et. al [3] and Muller [4], whose main advantage is a high computational efficiency although they could not be rigorously applied in some situations. Complex numerical models have also been developed, such as those presented by Clouteau et al. [5] and Gupta et al. [6, 7], among others.

An interesting approach of the problem has been presented by Hung and Yang [8] and Lopes et al. [9, 10] in which 2.5D models are developed. The former is a 2.5D FEM-IEM model while the latter is a 2.5D FEM-PML model. The 2.5D models can be applied for longitudinally invariant structures, obtaining the 3D solution by numerical discretization of the cross-section combined with the Fourier transformation of the domain along the orthogonal direction. In addition to these three last researches, similar models have also been applied for the study of several railway lines both in surface and in tunnels [11-14].

In the above-mentioned studies the soil behaviour has been considered as linear-elastic as the vibrations induced by railway traffic in tunnels generate very small strains in soils. This approach seems to be clear and reasonably correct. Nevertheless, none of them has considered the possible effect of the tunnel construction on the degradation of the shear modulus of the soil. In fact and to authors' knowledge, there are no studies about railway vibrations in tunnels in which this phenomenon had been taken into account. During tunnelling process the shear modulus of soil does not remain constant and its degradation magnitude depends on multiple factors such as diameter and depth of tunnel, excavation method and soil stiffness, among others. It is not easy to quantify standard values of shear strains during tunnel excavation although they could range between 10^{-4}-10^{-2} [15]. Even though tunnel excavation with TBM is a three dimensional problem, Panet and Guénot [16] demonstrated that 3D ground response can be approximately analysed with a plane strain approach, introducing a stress release coefficient that could be evaluated through 2D and 3D numerical comparisons. However, such comparisons are very limited in the technical literature. Because of underground railway vibrations is the main focus of this paper, a 2D simplified method has been applied for studying G_s degradation during tunnelling process where the tunnel lining grouting has not been considered due to G_s degradation induced by this process is very located in the soil attached to the tunnel lining.

Regarding the complete behaviour of the soil, from very small strains to large strains range, several constitutive models have been developed such as the *Hyperbolic model* [17], the *Equivalent linear model* [18], the *Hardening soil model* [19] and, recently, the *Hardening soil model with small-strain stiffness* [20], among others. The latter is applied in this paper in order to take into account G_s degradation during tunnelling process.

2. NUMERICAL APPROACH

2.1 Generalities

The applied computational scheme is uncoupled, using a 2D FEM static model to simulate the tunnelling process and calculate G_s degradation within soil by using the PLAXIS commercial code. The *Hardening soil model with small-strain stiffness* (HS-small) has been used to take into account the G_s modulus degradation. Once calculated the resulting stress state in soil after tunnel construction, a 2.5D FEM-PML model formulated in the wavenumber/frequency domain is used to obtain the free-field response, assigning on every finite element the resulting soil stiffness from the 2D FEM static model. This stiffness (different for each finite element) remains constant during the computing process with the 2.5D FEM-PML model, since the strains induced by the traffic are very small. The computed results are compared with those obtained without regarding tunnel excavation, i.e. neglecting the perturbation of the soil due to tunnel construction. In the followings sections these numerical models are briefly described.

2.2 2D Numerical simulation of tunnelling with TBM

To simulate tunnel construction with TBM, a 2D FEM model has been used through software PLAXIS. A 2D simplified method is applied in order to calculate the stress state within soil. Some of the 2D available methods are: Core Support Method (α-method), Lining Reduction Method (δ-method) and Stress Reduction Method (β-method), among others [21]. In this research, β-method has been used to simulate the construction process of tunnel, whose main feature is to take into account arching effect that occurs within the soil due to near presence of tunnel face. The basis of this method is schematized in *Fig. 1* and the idea is that the initial stresses p_k that act in the contour of the tunnel are divided into two parts: the first is $(1-\beta)\cdot p_k$ that is applied to the unsupported tunnel and the second is $\beta \cdot p_k$ that is applied to the supported tunnel. In PLAXIS code this approach is performed through three construction phases, controlling in each one the staged construction process (through parameter ∑Mstage), as follows:

1- Phase 1: Generate the initial stress field with K_0-procedure in case of horizontal soil layers
2- Phase 2: Eliminate tunnel clusters applying an ultimate level of ∑Mstage equal a 1-β
3- Phase 3: Activate the lining, allowing a complete staged construction (∑Mstage = 1)

The main uncertainty of this method applied to tunnel excavation is the β value. This parameter can oscillate between 0.2-0.8 depending on excavation method, tunnel diameter, among others factors. In the TBM cases, β value is usually between 0.4-0.8.

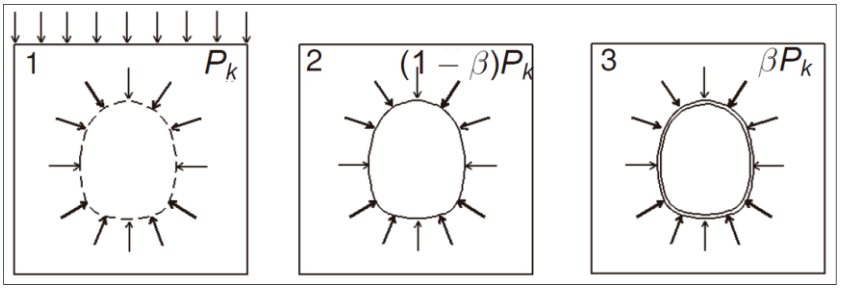


Fig. 1. Schematic representation of the β-method for the analysis of tunnels

2.3 2.5D FEM-PML approach for simulation of traffic vibrations

Contrarily to what happens on the tunnelling operations simulation, where a reasonable solution can be found using a 2D approach, the problem of vibrations induced by railway traffic is fully 3D and, consequently is not compatible at all with a 2D plane strain state approach. However, assuming that the system is invariant and infinitive along the longitudinal direction, the 3D solution can be achieved adopting a 2.5D procedure, i.e., only the cross-section of the problem needs to be discretised into finite elements (in the present case a finite elements approach is considered; alternative approaches using BEM or MFS can be found on [13, 22] since a Fourier transformation is applied regarding the longitudinal coordinate.

For the present case study, the 2.5D FEM approach seems to be advantageous since non-homogeneous cross-sections are considered. However, there is a pitfall when using finite elements approaches on dealing with dynamics of unbounded domains: the demands of limitation of the discretized domain gives rise to the need for treatment of the artificial boundaries in order to prevent the spurious reflexion of waves. In the present approach this requirement is fulfilled using a 2.5D PML's approach along the artificial boundaries.

Due to the length limitation of the paper, the mathematical formalism inherent to the 2.5D FEM-PML approach is not here presented. However, it can be found in other papers of the authors, namely in: [9, 10, 23].

The prediction of vibrations due to railway traffic in tunnels constitutes a challenge by several reasons. One of these particular aspects is the train-track interaction, which is provided by the track irregularities, the out-of-roundness of the wheels or by the non-homogeneous support of the rail. These heterogeneities of the system give rise to inertial forces on the train, i.e., to a train-track interaction force which is variable along time. By that reason, the structural behaviour of the train needs to be also simulated on the prediction model. In the present model, a sub-structured approach is followed, where the train simulated by a multi-body approach and the remaining system by the 2.5D FEM-PML model described above. *Fig. 2* shows a schematic representation of the distinct models considered on the sub-structured approach. The dynamic interaction of the different models is also depicted on the same figure. Once again, the limitation of length of the paper prevents an exhaustive description of the train-track interaction model, but the reader can found a detailed description on previous papers of the authors, namely in: [9, 10, 24]

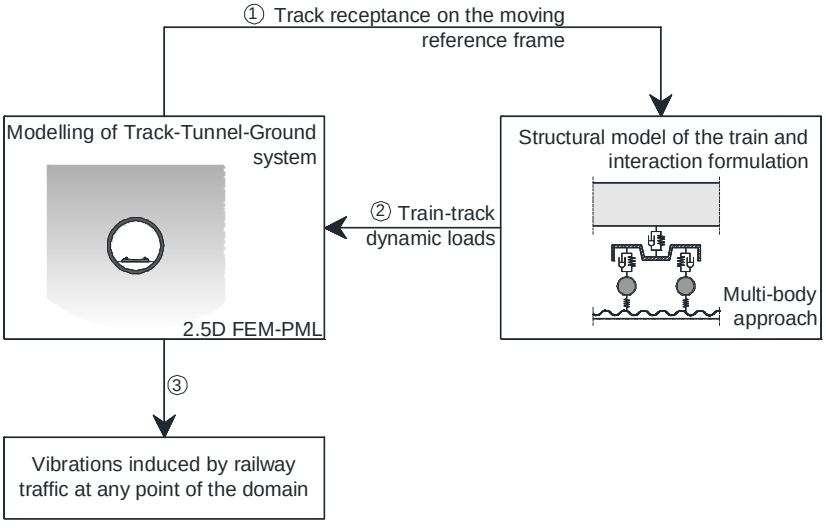


Fig. 2. Schematic representation of the sub-structured model used for prediction of vibration due to railway traffic

Despite the ability of the model for dealing with different sources of excitation of the train, as for instance the out-of-roundness of the wheels, in the present application it is assumed that the only source of dynamic excitation corresponds to the track unevenness.

3. APPLICATION EXAMPLE

3.1. Objectives

As emphasized above, the main objective of this research is to study the influence of G_s degradation that occurs within the soil during the excavation process of tunnel with TBM on predicted railway vibrations in tunnels. For that, an only case has been analysed with a homogeneous soil for the whole domain, where β-value has been considered as 0.5.

3.2. Model description

*Fig. 2*shows the geometry of the finite element mesh used to simulate the tunnel construction with PLAXIS code. Although it usually works with unstructured mesh, in this case it has been structured in order to use a similar mesh to study both tunnel construction and railway vibrations. The size of mesh to analyse the tunnel excavation has been estimated according to Meissner [24]. The depth of tunnel has been chosen in order to consider a realistic geometry in which is possible to build it with TBM method.

Fig. 4. shows the 2.5D FE-PML model to study railway vibrations. The size of finite element in the soil has been estimate regarding 6 elements per wavelength, limiting frequencies up to 80 Hz. The interest domain is limited by PML's in order to avoid the spurious reflexion of the waves that impinges the artificial boundaries.

3.3. Soil and tunnel properties

The soil constitutive model applied is the *HS-small* (only in 2D FEM model for simulating tunnel construction) which is based on the *Hardening soil model* but considering the complete stress-strain curve including the very small strain range. The *Hardening soil model* and the *Hardening soil model with small-strain stiffness* are explained in detail by Schanz et al. [19] and Benz [20] respectively. The soil properties are shown in table 1 according to the *HS-small model.*

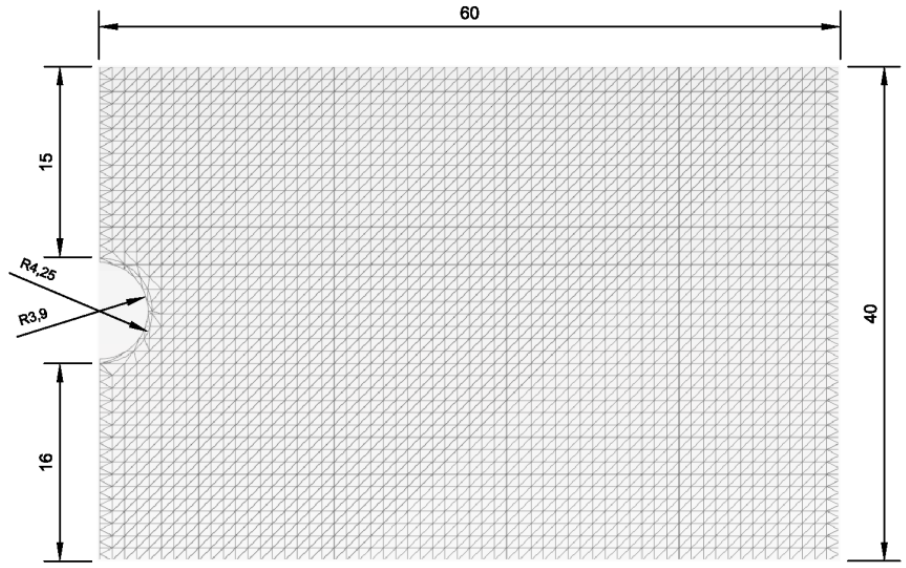


Fig. 3. Finite element mesh (in metres) for tunnelling

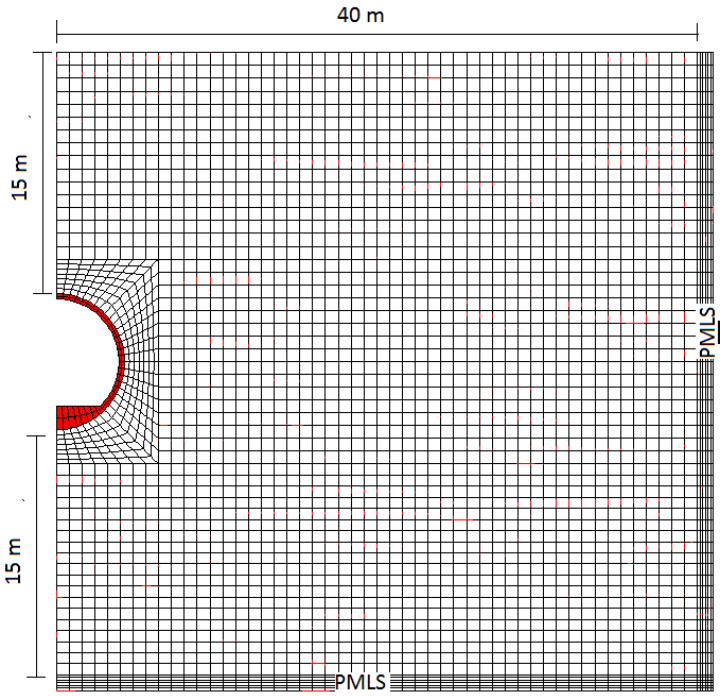


Fig. 4. 2.5D FEM-PML mesh adopted for the analysis of vibrations due to railway traffic

γ_{ap} (kN/m^3)	20
E_{50}^{ref} (kN/m^2)	$200 \cdot 10^3$
E_{oed}^{ref} (kN/m^2)	$200 \cdot 10^3$
E_{ur}^{ref} (kN/m^2)	$400 \cdot 10^3$
m	0.5
c' (kN/m^2)	25
φ'	35º
ψ	5º
ν_{ur}'	0.2
K_o^{nc}	0.4264
$\gamma_{0.7}$	$1.8 \cdot 10^{-4}$
G_0^{ref} (kN/m^2)	$310 \cdot 10^3$
P_{ref} (kN/m^2)	100
R_f	0.9
C_p (m/s)	643
C_s (m/s)	394

Table 1: Soil properties in HS-small model and P and S-waves velocity

The relationship between E_{50}^{ref} and E_{oed}^{ref} has been estimated according to Schanz [25] and the relationship between E_{50}^{ref} and E_{ur}^{ref} is supposed to be equal to 2. G_0^{ref} has been calculated as follows:

$$G_0^{ref} = \frac{E_0^{ref}}{2(1+\upsilon_{ur})} \quad (1)$$

Where E_0^{ref} has been calculated according to Alpan [26]. The relationships given by Alpan between E_0 and E_{ur} are shown in *Fig. 5.*

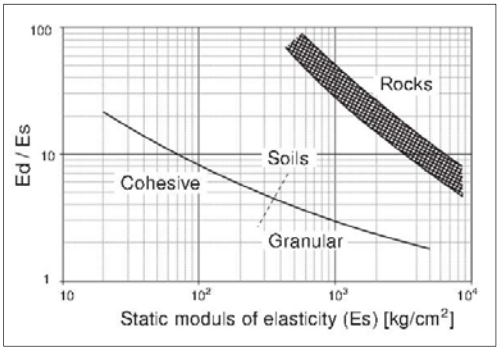


Fig. 5. Relation between dynamic stiffness (E_d=E_0) and static soil stiffness (E_s=E_{ur}) [27]

The "m" exponent has been estimated according to Benz [19]. The soil has been considered as normally consolidated and in this way K_0 has been calculated according to Jaky [27]. Although $\gamma_{0.7}$ is dependent on confining stress, in this case it has been considered to be constant for the whole domain and is obtained as follows [20]:

$$\gamma_{0.7} = \frac{0.385}{4G_0}[2c'(1+\cos(2\varphi')) + \sigma'_1(1+K_o)\sin(2\varphi')] \quad (2)$$

Where σ'_1 is the effective vertical stress in the middle of considered soil layer in the numerical model. *Fig. 6* shows the G_s/G_0-γ_s relationship for the soil in the *HS-small* constitutive model and the tunnel properties are summarized in table 2.

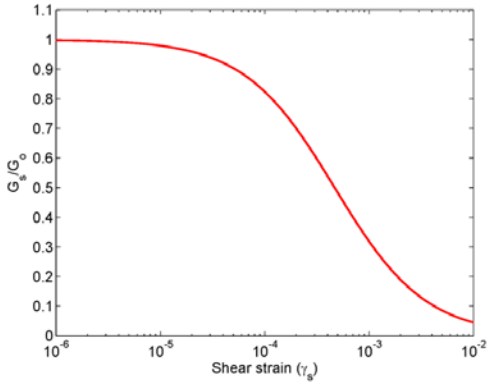


Fig. 6. G_s/G_0-γ_s relationship in HS-small

Thickness (m)	0.35
Inner radius (m)	3.9
Density (kg/m^3)	2500
Elastic modulus (kN/m^2)	$30 \cdot 10^6$
Poisson ratio	0.2

Table 2: Tunnel properties

3.4. Stress state within soil after tunnelling

Fig. 7 shows computed G_s/G_0 and shear strains (γ) contours after numerical simulating of tunnel construction, in which can be seen as G_s degradation is more evident closed to lining, even reaching

the ground surface although the effect of tunnelling process at ground surface is limited until a distance of 25-30 meters from symmetric axis of the model.

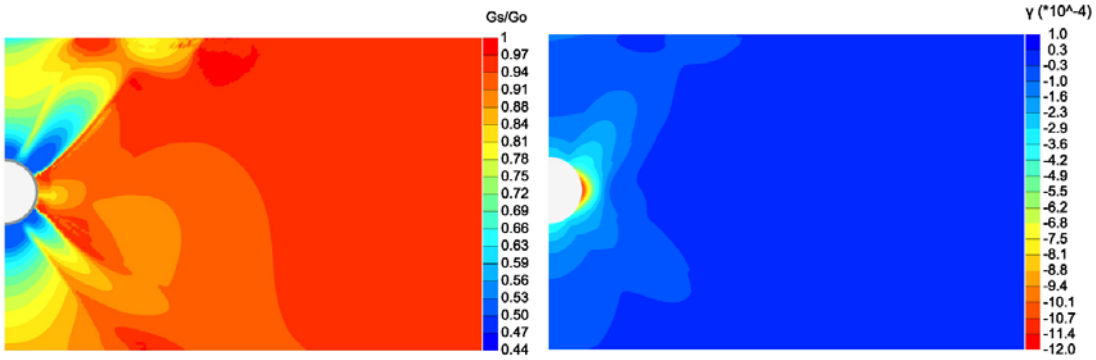


Fig. 7. Computed contours G_s/G_o (left) and shear strains (γ) (right)

3.5. Track and train properties

In what concerns the modelling of vibrations induced by railway traffic, additional description of the model is required. Two distinct computations are performed: i) non disturbed ground; ii) disturbed ground due to tunnel construction operations. In the former case, the shear modulus of the ground is assumed constant with value of G_0 indicated in Table 1. On the other hand, the second computation set corresponds to the disturbed ground, where the distribution of G depicted in *Fig. 7* is adopted. In both situations, the volumetric mass was assumed as 2000 kg/m3; the Poisson ratio equal to 0.2 and a hysteretic damping ratio of 0.04.

The railway track is composed by a continuous concrete slab track 0.3 m thick and 2.5 m wide, with a longitudinal bending stiffness of 1.62×10^8 N/m2 and a mass of 3000 kg per unit of length. The rails, materialized by UIC60 profiles are continuously supported by railpads with a stiffness of 2.5×10^8 N/m2 and a damping coefficient of 6×10^4 Ns/m2. It is assumed a floating slab solution, introducing a resilient mat between the slab and the tunnel invert. The stiffness of the mat is 0.153×10^9 N/m2 per meter in the longitudinal direction and a damping of 5.5×10^4 Ns/m2 is considered.

In what concerns to the rolling stock, it was assumed the passage of the Alfa-Pendular train at a running speed of 40 m/s. The main geometrical and mechanical properties of the train Alfa-Pendular are summarized in *Fig. 8* and in Table 3.

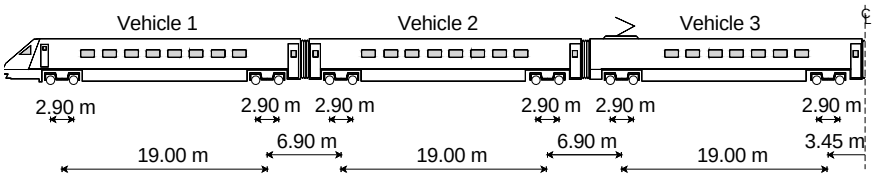


Fig. 8. Alfa-Pendular geometry

Axles	**Mw (kg)**	1538-1884
Primary	**Kp (kN/m)**	3420
suspension	**Cp (kNs/m)**	36
Bogies	**Mb (kg)**	4712-4932
	Jb (kg/m^2)	5000-5150
Car body	**Mc (kg)**	32900-35710

Table 3: Mechanical properties of the train

As mentioned above, the first step of the calculation procedure concerns the solving of the train-track interaction problem. The quasi-static and dynamic excitation mechanisms are uncoupled, being the solution obtained through a superposition procedure.

In the present study, the source of vibration is due to the track unevenness. An artificial unevenness profile was generated taking into account the power spectral density of amplitude of the track unevenness for a range of wavelengths between 28 m and 0.55 m. The following equation was used for address the PSD of the track unevenness:

$$S(k_1) = S(k_{1,0})\left(\frac{k_1}{k_{1,0}}\right)^{-w} \tag{3}$$

where, $k_{1,0}$=1 rad/s, w=3.5 and $S(k_{1,0})$ was assumed equal to $1x10^{-8}$ m^3.

Once the train speed was assumed to be 40 m/s, the unnevess profile considered excitates the train in the frequency range between 1.4 Hz to 72 Hz..

4. RESULTS AND DISCUSSION

4.1. Transfer functions for stand still loads

Firstly, to the study of the impact of construction operations of the tunnel on the vibration levels perceived at the ground surface, a simple analysis is presented where a unitary stand still load is applied at the centre of tunnel invert and the dynamic response is recorded at different positions at the ground surface. This simple analysis allows observing how the shear modulus degradation affects the transfer functions between the tunnel invert and the ground surface. In the present case it is assumed that the load is applied at the cross section defined by x=0 m (x is the longitudinal axle), and the receiver points are located at the same cross-section.

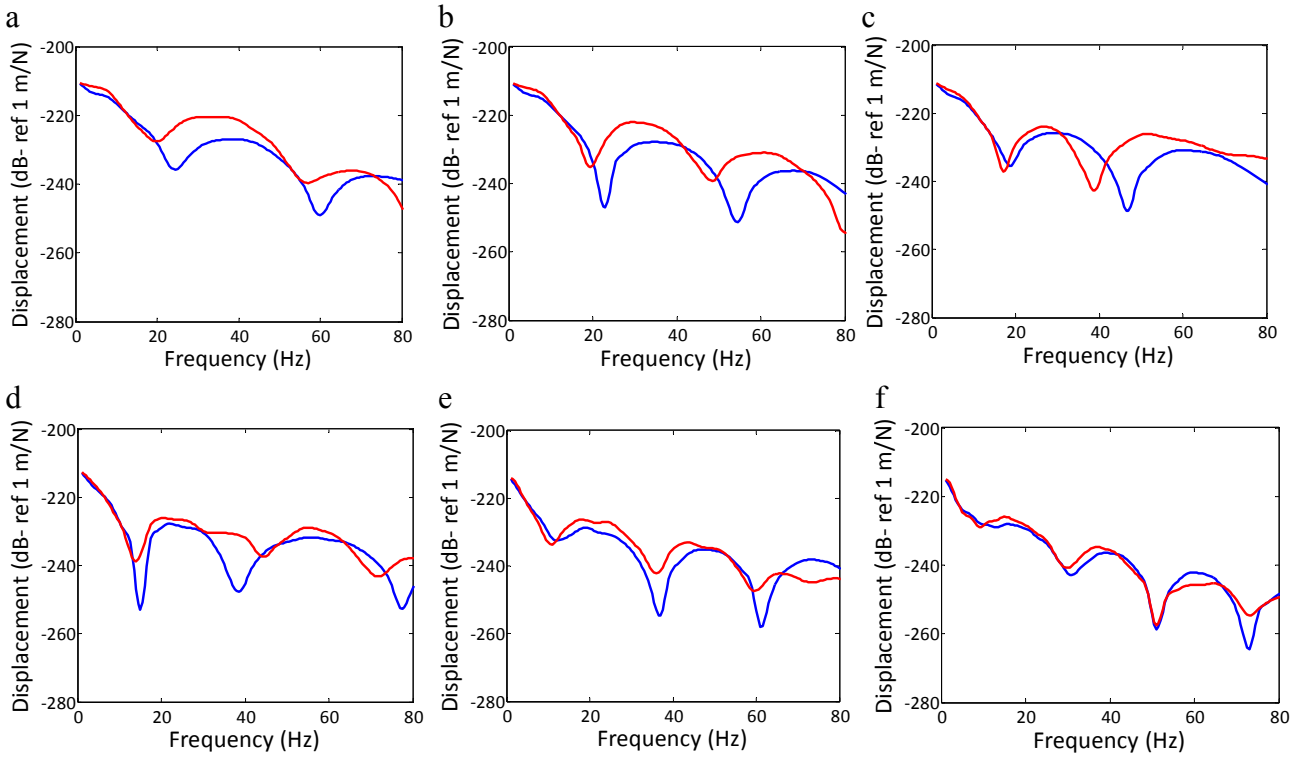


Fig. 9. Vertical displacement transfer functions due to a load applied at the tunnel invert and evaluated at distinct positions of ground surface: a) P1(0,0,0); b) P2 (0,5,0); c) P3 (0,10,0); d) P4 (0,15,0);e) P5 (0,20,0) f) P6 (0,40,0) (blue line – non disturbed soil; red line – disturbed soil)

The analysis of *Fig. 9* allows to see an agreement of the response obtained for both scenarios in the lower frequency range, i.e., up to 15 Hz. Actually, the wavelengths generated in this frequency range are quite large, being not so much affected by point variations of the ground stiffness. On the other hand, for the receiver points located close to the tunnel, and for frequencies above the mentioned limit, a relevant influence of the construction operations on the transfer function is detectable. On *Fig. 9*.a to d, it is possible to see a change of the frequency of the troughs of the transfer function when the stiffness degradation due to the tunnel construction is taken into account. On the other hand, it seems that the difference between the two scenarios evanesces with the increase of the distance between the source and the receiver. This aspect is quite evident in *Fig. 9*f, where, for frequencies up to 50 Hz, there is a good agreement between the results obtained from both scenarios. However, for frequencies above this limit, differences remain, being justified by the fact that the wavelengths generated are short enough to be influenced by local changes on soil stiffness.

4.2. Vibrations due to railway traffic

Figs. 10 and *11* show time record and one-third octave spectrum of vertical velocity due to passage of the Alfa Pendular train respectively. It is worth mentioning that only 4 points at ground surface are shown, located at several distances from symmetric axis of the model: 0, 5, 20 and 40 metres.

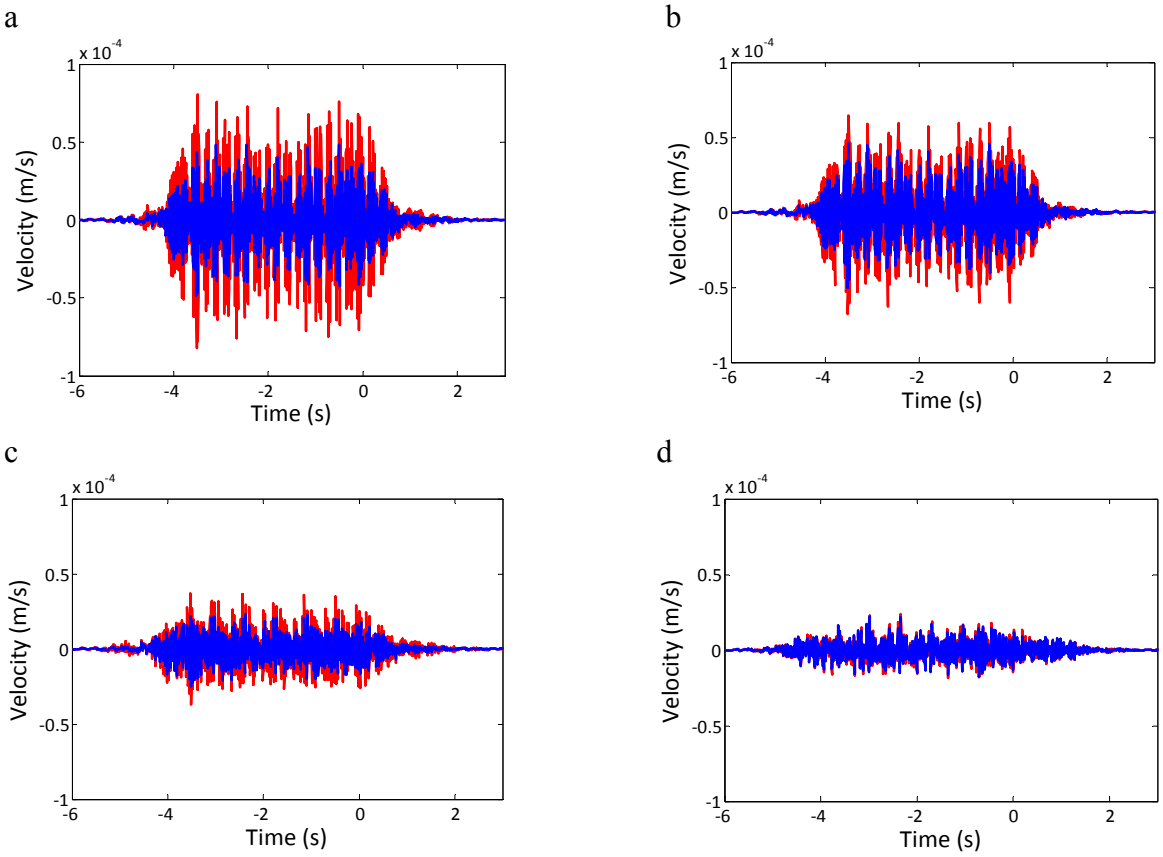


Fig. 10. Time record of vertical velocity at distinct points located at the ground surface: a) P1(0,0,0); b) P2 (0,5,0); c) P5 (0,20,0) d) P6 (0,40,0) (blue line – non disturbed soil; red line – disturbed soil)

Regarding the compared response in the time domain is noteworthy that the effect of taking into account the tunnelling process is more notorious at points located closer to the tunnel, resulting minor differences between the two scenarios with the increase of the distance to the tunnel. In fact, the difference found at a distance of 40 metres is almost negligible. However, at the other points (0,

5 and 20 metres) the differences are noteworthy, being more important for smaller distances to the tunnel.

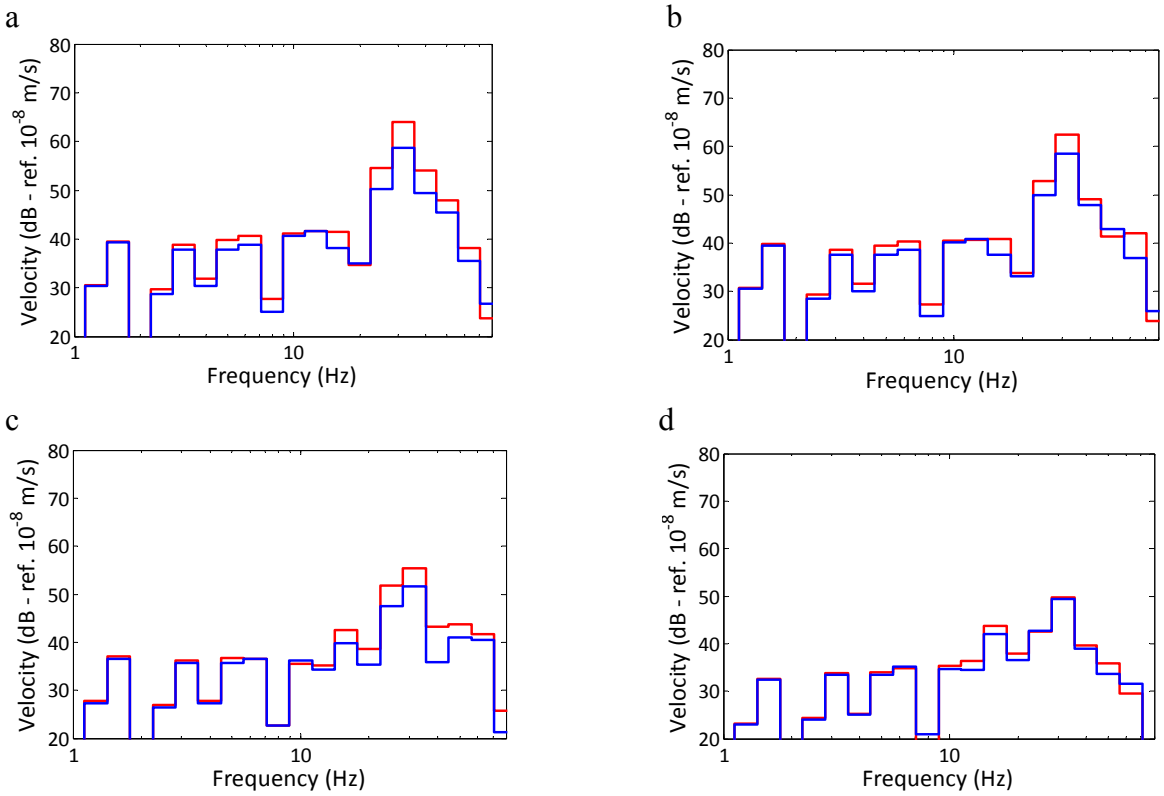


Fig. 11. One-third octave spectrum of vertical velocity at distinct points located at the ground surface: a) P1(0,0,0); b) P2 (0,5,0); c) P5 (0,20,0) d) P6 (0,40,0) (blue line – non disturbed soil; red line – disturbed soil)

A more clear comparison between the two considered scenarios is provided by *Fig. 11*, in which it can seen that the influence of tunnelling process is more evident with the decrease of the distance between the source and the receiver. However, regarding one-third octave spectrum it is also possible to comment that there are more differences in frequencies above 15 Hz than below this value, due to the wavelengths generated below 15 Hz are quite large, being not so much affected by point variations of the ground stiffness. Similar conclusion was also found for the analysis of transfer functions depicted on *Fig. 9*. Comparing the two scenarios in terms of decibels, it is possible to conclude that in frequencies below 15-20 Hz the maximum difference is 3 dB while above 20 Hz is it possible to achieve differences around 7 dB for the points located close to the tunnel. However, the influence of tunnelling process evanesces with the increase of the distance source-receiver. Actually, the differences found on *Fig. 11*d are almost negligible.

5. CONCLUSIONS

In this paper, the influence of the stress state within the soil on predicted railway vibrations in tunnels has been studied, regarding the degradation of shear modulus that occurs when the tunnel is excavated with Tunnel Boring Machine (TBM). In this way, the main conclusions are:

- The influence of the degradation of shear modulus of soil during tunnelling process with TBM on predicted railway vibrations can be relevant, providing a higher level of vibrations at the ground surface when G_s degradation is considered.
- This fact is more notorious at the closest points of the tunnel, being practically negligible at distances greater than 20 metres from the line of centre of the tunnel.

- The influence is more important for frequencies above 15 Hz than below this value. So, the maximum difference above this mentioned limit has been 7 dB while for frequencies up to 15 Hz has been 3 dB.

The numerical results show that the effect of degradation of shear modulus of the soil during tunnelling process on predicted railway vibrations should be taken into account in design process in order to find more accurate results.

The research is on-going and numerical studies will be performed for other geotechnical conditions in order to accomplish more conclusive remarks.

REFERENCES

[1] M.G. Smith, L. Cray, M. Ögren, K. Persson Waye, On the Influence of Freight Trains on Humans: A Laboratory Investigation of the Impact of Nocturnal Low Frequency Vibration and Noise on Sleep and Heart Rate. *PLoS ONE, 2013.* **8**(2): p. e55829.

[2] M. Hussein, H. Hunt, A numerical model for calculating vibration from a railway tunnel embedded in a full-space. *Journal of Sound and Vibration*, 2007. **305**(3): p. 401-431.

[3] K.A. Kuo, H.E.M. Hunt, M.F.M. Hussein, The effect of a twin tunnel on the propagation of ground-borne vibration from an underground railway. *Journal of Sound and Vibration*, 2011. **330**(25): p. 6203-6222.

[4] K. Muller, *Dreidimensionale dynamische Tunnel-Halbraum-Interaktion*, in *Lehrstuhl fur Baumechanik*. 2007, Technische Universitat Munchen: Munchen.

[5] D. Clouteau, M. Arnst, T.M. Al-Hussaini, G. Degrande, Free field vibrations due to dynamic loading on a tunnel embedded in a stratified medium. *Journal of Sound and Vibration*, 2005. **283**(1-2): p. 173-199.

[6] S. Gupta, M.F.M. Hussein, G. Degrande, H.E.M. Hunt, D. Clouteau, A comparison of two numerical models for the prediction of vibrations from underground railway traffic. *Soil Dynamics and Earthquake Engineering*, 2007. **27**(7): p. 608-624.

[7] S. Gupta, Y. Stanus, G. Lombaert, G. Degrande, Influence of tunnel and soil parameters on vibrations from underground railways. *Journal of Sound and Vibration*, 2009. **327**: p. 70-91.

[8] H. Hung, Y. Yang, Analysis of ground vibrations due to underground trains by 2.5D finite/infinite element approach. *Earthquake Engineering and Engineering Vibration*, 2010. **9**(3): p. 327-335.

[9] P. Lopes, P. Alves Costa, M. Ferraz, R. Calçada, A. Silva Cardoso, Numerical modelling of vibrations induced by railway traffic in tunnels: from the source to the nearby buildings. *Soil Dynamics and Earthquake Engineering*, 2014. **61-62**: p. 269-285.

[10] P. Lopes, P. Alves Costa, R. Calçada, A. Silva Cardoso, Influence of soil stiffness on vibrations inside buildings due to railway traffic: numerical study. *Computers & Geotechnics*, 2014. **61**: p. 277-291.

[11] P. Galvín, S. François, M. Schevenels, E. Bongini, G. Degrande, G. Lombaert, A 2.5D coupled FE-BE model for the prediction of railway induced vibrations. *Soil Dynamics and Earthquake Engineering*, 2010. **30**(12): p. 1500-1512.

[12] Y. Yang, H. Hung, Soil Vibrations Caused by Underground Moving Trains. *Journal of Geotechnical and Geoenvironmental Engineering,* 2008. **134**(11): p. 1633-1644.

[13] P. Alves Costa, R. Calçada, A. Silva Cardoso, Track–ground vibrations induced by railway traffic: In-situ measurements and validation of a 2.5D FEM-BEM model. *Soil Dynamics and Earthquake Engineering*, 2012. **32**(1): p. 111-128.

[14] S. François, P. Galvín, M. Schevenels, G. Lombaert, G. Degrande, A 2.5D coupled FE–BE methodology for the dynamic interaction between longitudinally invariant structures and a layered halfspace. *Computer Methods in Applied Mechanics and Engineering*, 2010. **199**(23-24): p. 1536-1548.

[15] R. J. Mair, Developments in geotechnical engineering research: application to tunnels and deep excavations. *Proceedings of Institution of Civil Engineers: Civil Engineering*, 1993. **93**: p. 27-41.
[16] M. Panet, A. Guenot, Analysis of convergence behind face of a tunnel, *in Proc. Tunnelling'82*. 1982. p. 197-203.
[17] J. M. Duncan, C.Y. Chang, Nonlinear analysis of stress and strain in soil. *ASCE Journal of the Soil Mechanics and foundations Division*, 1970. **16**: p. 1629-1653.
[18] J. Lysmer, T. Udaka, C. Tsai, H. Bolton Seed, *FLUSH: a computer program for approximate 3-D analysis of soil-structure interaction problems*, R.E. 75-30, Editor. 1974, University of California: Berkeley.
[19] T. Schanz, P.A. Vermeer, P.G. Bonnier, The hardening soil model: Formulation and verification, in *Beyond 2000 in Computational Geotechnics-10 YEARS of Plaxis*. Rotterdam 1999.
[20] T. Benz, *Small-strain stiffness of soils and its numerical consequences.* 2006, Institut für Geotechnik der Universität Stuttgart.
[21] K. Schikora, T. Fink, Berechnungsmethoden moderner bergmännischer bauweisen beim u-bahn-bau. *Bauingenieur*, 1982. **57**: p. 193-198.
[22] P. Amado Mendes, L. Godinho, P. Alves Costa, 2.5D modeling of soil-structure interaction using a coupled MFS-FEM formulation, in *11th World Congress on Computational Mechanics*, E. Onate, J. Oliver, and A. Huerta, Editors. 2014: Barcelona.
[23] P. Lopes, P. Alves Costa, R. Calçada, A. Silva Cardoso, Numerical Modeling of Vibrations Induced in Tunnels: A 2.5D FEM-PML Approach, in *Traffic Induced Environmental Vibrations and Controls: Theory and Application*, H. Xia and R. Calçada, Editors. 2013, Nova. p. 133-166.
[24] P. Alves Costa, R. Calçada, A. Silva Cardoso, *I*nfluence of train dynamic modelling strategy on the prediction of track-ground vibrations induced by railway traffic. *Proceedings of the Institution of Mechanical Engineers, Part F: Journal of Rail and Rapid Transit* 2012. **226**(4): p. 434-450.
[25] T. Schanz, *Modellierung des Mechanischen Verhaltens von Reibungsmaterialen.*, in Stuttgart Universität. 1998.
[26] I. Alpan, *The geotechnical properties of soils. Earth-Science Reviews* 1970. **6**: p. 5-49.
[27] J. Jaky, Pressure in silos., in *Proc. 2nd International Conference on Soil Mechanics and Foundation Engineering*. 1948: Rotterdam. p. 103-107.

COMPDYN 2015
5th ECCOMAS Thematic Conference on
Computational Methods in Structural Dynamics and Earthquake Engineering
M. Papadrakakis, V. Papadopoulos, V. Plevris (eds.)
Crete Island, Greece, 25–27 May 2015

A MIXED SPACE-TIME AND WAVENUMBER DOMAIN MODEL FOR PREDICTING GROUND VIBRATION FROM RAILWAY TRACKS

Samuel G. Koroma[1], David J. Thompson[1], Mohammed F.M. Hussein[2] and Evangelos Ntotsios[1]

[1] Institute of Sound and Vibration Research, University of Southampton,
Highfield Campus, Southampton, SO17 1BJ, UK
e-mail: {S.G.Koroma,E.Ntotsios}@soton.ac.uk, djt@isvr.soton.ac.uk

[2] Civil and Architectural Engineering Department, Qatar University
P.O. Box 2713, Qatar
e-mail: mhussein@qu.edu.qa

Keywords: Ground Vibration, Finite Element Method, Space-Time Domain, Wavenumber Domain.

Abstract. *In this paper, a mixed model for studying ground vibration generated from surface railway tracks is presented. A ballasted track with nonlinear resilient components is modelled in the time domain using the Finite Element method. The ground is modelled as a linear homogeneous half-space in the wavenumber domain for faster computation. The interaction between the track and the ground is incorporated into the track model through a lumped parameter model representing the vertical dynamic stiffness of the ground. The coefficients of the components of the lumped parameter model are obtained by curve fitting of the transfer function of the half-space for a load applied at its origin.*

The coupled equation of motion for the track/ground system is formulated with excitation from a stationary point load- consisting of static and dynamic parts- acting at the centre of the rail. The coupled equation is solved by numerical integration. The calculated interaction forces at the ballast/ground interface from the space-time domain track model are Fourier transformed to the wavenumber domain and used as excitation to the ground model in order to calculate free-field surface vibration of the ground.

Results are presented for the vertical dynamic stiffness for the ground, and for the track and ground displacement in the vicinity of the track and in the free-field. A comparative study between the mixed formulation with the lumped parameter model for the ground, and a fully coupled wavenumber domain model is conducted for linear parameters. Using the fully coupled model as a benchmark, it is observed that the inclusion of the lumped parameter ground model in the track model gives good estimation of the transmitted forces, and hence ground vibration, both in the near and far fields. Finally, the effect of nonlinear track components is briefly investigated for different levels of static preload.

1 INTRODUCTION

The numerical modelling of ground vibration from surface railways has been the focus of much research over the years. When linear parameters are used for the track and ground, the modelling can be readily done in the frequency-wavenumber domain, e.g. [1, 2]. However, time domain techniques such as Finite Element (FE) and Boundary Elements (BE) are necessary for this problem when nonlinear components and/or complex irregular geometries are to be modelled, e.g. [3]. The use of FE and BE methods can be very costly indeed in terms of the computational hardware and the time required for the simulations. This is mainly due to the large number of elements required to discretise the ground.

An alternative, which is widely used in soil-structure interaction problems, e.g. vibration of machine foundation on a half-space, is to represent the ground as approximate lumped parameter models consisting of spring, dashpot and mass elements. This approach has been applied to ground vibration from surface trains in [4, 5]. The lumped parameter model was formulated based on Lysmer's analogue fitting which, due to its simplicity, is mostly accurate for modelling the asymptotic values of the dynamic stiffness at low and high frequencies, without capturing mid frequency fluctuations. A systematic approach for formulating consistent lumped parameter models with real, frequency independent coefficients, to represent an unbounded soil medium was presented in [6, 7]. In this approach, each dynamic stiffness component in the frequency domain; e.g. the vertical stiffness due to a vertical load, can be represented in discrete form as a rational fraction. This is subsequently decomposed into singular, first- and second-order parts, depending on the nature of the roots of the rational fraction. These models can provide a high degree of accuracy when sufficiently high order of approximating polynomials are used. They also have the advantage of being incorporated in standard FE/BE routines which allows nonlinear parameters to be included in the structure.

In this paper, a mixed space-time and wavenumber-frequency domain approach for predicting ground vibration is presented. In Section 2, a lumped parameter model for a halfspace subjected to a rectangular loading is formulated by fitting the vertical dynamic stiffness calculated in the wavenumber-frequency domain. This model is then used in a time domain nonlinear FE model of a railway track, presented in Section 3, in order to calculate the dynamic track/ground interaction forces. Once these forces are obtained, they can be transformed to the wavenumber domain and used as input for predicting surface ground vibration in the far-field. The procedure for doing this is briefly discussed in Section 4. Results are presented in Section 5 which show the validity of the method and the influence of track nonlinearity on the predicted ground vibration.

2 MODELLING OF THE GROUND

The ground is modelled here as a homogeneous elastic half-space in the wavenumber-frequency domain. The excitation is a harmonic load distributed over a rectangular area and centred about the origin of the half-space. The wavenumber-frequency domain representation of the vertical dynamic stiffness of the ground is presented in Section 2.1. The approximate lumped parameter model for this dynamic stiffness function is formulated in Section 2.2.

2.1 Wavenumber-domain modelling of the ground

Figure 1 shows a 3D model of a half-space that represents the ground. A harmonic rectangular load, centred at the origin, acts on the halfspace with dimensions $2a$ and $2b$ in the x and y directions respectively. The formulation for this problem was presented in [1].

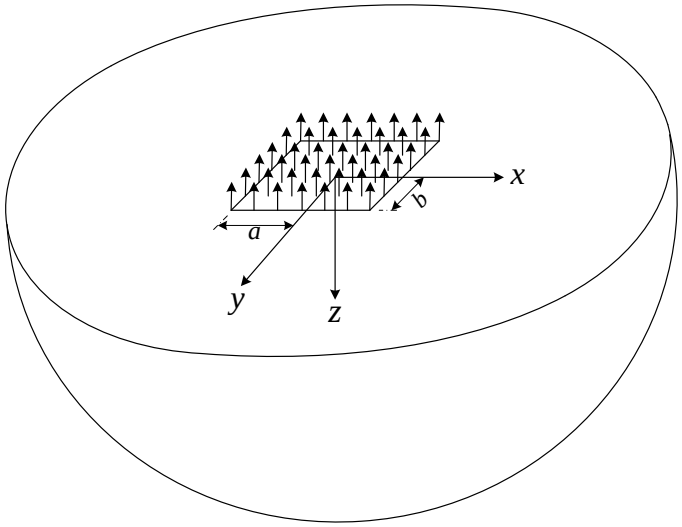


Figure 1: Ground modelled as a 3D half-space and subjected to a rectangular load.

The distributed force on the rectangular area is defined as $F_0(x,y)\mathrm{e}^{\mathrm{i}\omega t}$, where $F_0(x,y)$ is related to the total force, F_g, by

$$F_0(x,y) = \begin{cases} F_g/4ab, & |x| < a \quad \text{and} \quad |y| < b, \\ 0, & \text{elsewhere} \end{cases}. \tag{1}$$

The complex amplitude of the displacement of the ground in the wavenumber domain can be expressed as

$$\tilde{U}_g(\xi,\gamma,\omega) = \tilde{H}_g(\xi,\gamma,\omega)F_g\frac{\sin\xi a\sin\gamma b}{\xi a\gamma b}, \tag{2}$$

where $\tilde{H}_g(\xi,\gamma,\omega)$ is the displacement of the ground at the origin due to the total force, F_g, concentrated at the origin. $\tilde{H}_g(\xi,\gamma,\omega)$ is given by [8]

$$\tilde{H}_g(\xi,\gamma,\omega) = \frac{1}{\mu}\left[\frac{\eta_3\left(\xi^2+\gamma^2-\eta_1^2\right)}{\left(\xi^2+\gamma^2+\eta_1^2\right)^2 - 4\eta_1\eta_3\left(\xi^2+\gamma^2\right)}\right], \tag{3}$$

where $\eta_1 = -\sqrt{\xi^2+\gamma^2-\omega^2/v_s^2}$, $\eta_3 = -\sqrt{\xi^2+\gamma^2-\omega^2/v_p^2}$; for $\Re(\eta_1) \leq 0$ and $\Re(\eta_1) \leq 0$, $v_p^2 = (\lambda+2\mu)/\rho$, $v_s^2 = \mu/\rho$; with v_p and v_s being the compressional and shear wave speeds respectively, λ and μ the Lamé constants and ρ the soil density.

By transforming Eq. (2) from the wavenumber to the space domain using double inverse Fourier transforms, the displacement in the space domain is obtained as

$$u_g(x,y,\omega) = \frac{F_g}{4\pi^2}\int_{-\infty}^{\infty}\int_{-\infty}^{\infty}\tilde{H}_g(\xi,\gamma,\omega)\frac{\sin\xi a\sin\gamma b}{ab\xi\gamma}\mathrm{e}^{\mathrm{i}(\xi x+\gamma y)}\mathrm{d}\xi\mathrm{d}\gamma. \tag{4}$$

The vertical dynamic stiffness $k_g(x,y,\omega)$ is the ratio of the input force to the displacement and can therefore be written as

$$k_g(x,y,\omega) = \frac{4\pi^2}{\int_{-\infty}^{\infty}\int_{-\infty}^{\infty}\tilde{H}_g(\xi,\gamma,\omega)\frac{\sin\xi a\sin\gamma b}{ab\xi\gamma}\mathrm{e}^{\mathrm{i}(\xi x+\gamma y)}\mathrm{d}\xi\mathrm{d}\gamma}. \tag{5}$$

In the next section, the lumped parameter model that approximately models the dynamic stiffness function in Eq. (5) will be formulated.

2.2 Lumped parameter representation of the ground

The objective of this section is to formulate a lumped parameter model with spring and dashpot components having real frequency independent coefficients [6, 7], to approximately model the dynamic stiffness function in Eq. (5). Suppose that Eq. (5) can be represented in discrete form as the sum of its singular part, $\bar{K}_s(\mathrm{i}\omega)$, and the remaining regular part, $\bar{K}_r(\mathrm{i}\omega$. The singular part, $\bar{K}_s(\mathrm{i}\omega) = k_0 + \mathrm{i}\omega c_0$, describes its asymptotic value at high frequencies. The regular part, $\bar{K}_r(\mathrm{i}\omega)$ can be expressed as a rational fraction with numerator having order one less than the denominator. Hence, the discrete dynamic stiffness, $\bar{K}(\mathrm{i}\omega)$ can be summarised as

$$\bar{K}(\mathrm{i}\omega) = \underbrace{k_0 + \mathrm{i}\omega c_0}_{\text{singular part}} + \underbrace{\frac{1 + p_1(\mathrm{i}\omega) + p_2(\mathrm{i}\omega)^2 + \cdots + p_{M-1}(\mathrm{i}\omega)^{M-1}}{1 + q_1(\mathrm{i}\omega) + q_2(\mathrm{i}\omega)^2 + \cdots + q_M(\mathrm{i}\omega)^M}}_{\text{regular part}} \tag{6}$$

where p_i and q_i are the $2M-1$ unknown real coefficients to be determined by numerical curve fitting. The regular part, $\bar{K}_r(\mathrm{i}\omega)$ can be alternatively represented using a partial fraction expansion as

$$\bar{K}_r(\mathrm{i}\omega) = \sum_{l=1}^{M} \frac{A_l}{\mathrm{i}\omega - s_l}, \tag{7}$$

where s_l and A_l are the poles and corresponding residues of $\bar{K}_r(\mathrm{i}\omega)$. Note that for a stable system, each s_l should have a negative real part, and this condition can be achieved by adopting an iterative procedure in the curve fitting routine. The poles of $\bar{K}_r(\mathrm{i}\omega)$ can be all real, all complex conjugate pairs or a combination of these. A real pole results in a first-order approximation term with corresponding real coefficients whereas a pair of complex conjugate poles, when added together, form a second-order term with real coefficients. For J complex conjugate pairs and the remaining $M-2J$ real poles, the dynamic stiffness for the generalised lumped parameter model can be written in parallel form that includes all the sub components as

$$\bar{K}(\mathrm{i}\omega) = k_0 + \mathrm{i}\omega c_0 + \sum_{l=1}^{J} \frac{\beta_{1l}\mathrm{i}\omega + \beta_{0l}}{(\mathrm{i}\omega)^2 + \alpha_{1l}\mathrm{i}\omega + \alpha_{0l}} + \sum_{l=1}^{M-2J} \frac{A_l}{\mathrm{i}\omega - s_l}, \tag{8}$$

The coefficients of the second-order term are as follows

$$\alpha_{0l} = \prod_{i=j}^{j+1} s_i, \quad \alpha_{1l} = -\sum_{i=j}^{j+1} s_i, \quad \beta_{0l} = -(A_j s_{j+1} + A_{j+1} s_j), \quad \beta_{1l} = \sum_{i=j}^{j+1} A_i,$$

where $j \in \{1, 3, \cdots, 2J-1\}$ and $j+1$ form a pair of complex conjugates of poles and of corresponding residues at those poles.

Figure 2 shows the generalised lumped parameter model, with the components marked (I), (II) and (III) being the singular part, first-order terms and second-order terms of the regular part respectively. The coefficients of the first and second order terms are derived in [6] as being related to the poles and residues of $\bar{K}_r(\mathrm{i}\omega)$ as follows

$$k_{1,l} = \frac{A_l}{s_l}, \quad c_{1,l} = -\frac{A_l}{s_l^2}, \quad k_{2,j} = -\frac{\beta_{0l}}{\alpha_{0l}}, \quad c_{2,j} = \frac{\alpha_{0l}\beta_{1l} - \alpha_{1l}\beta_{0l}}{\alpha_{0l}^2},$$
$$k_{2,j+1} = \frac{\beta_{0l}(-\alpha_{0l}\beta_{1l} + \alpha_{1l}\beta_{0l})^2}{\alpha_{0l}^2(\alpha_{0l}\beta_{1l}^2 - \alpha_{1l}\beta_{0l}\beta_{1l} + \beta_{0l}^2)}, \quad c_{2,j+1} = \frac{\beta_{0l}^2(-\alpha_{0l}\beta_{1l} + \alpha_{1l}\beta_{0l})}{\alpha_{0l}^2(\alpha_{0l}\beta_{1l}^2 - \alpha_{1l}\beta_{0l}\beta_{1l} + \beta_{0l}^2)}.$$

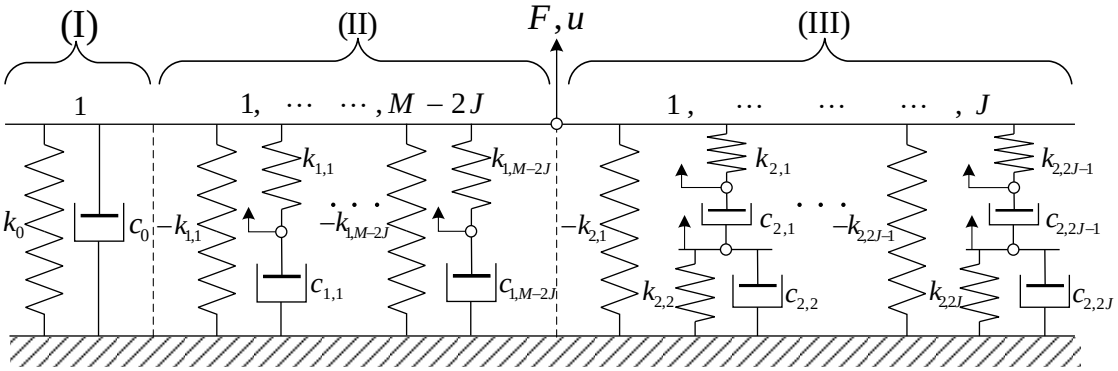


Figure 2: Lumped parameter ground model approximation for a half-space

The force-displacement relationship of the generalised lumped parameter model can be expressed in matrix form as

$$\left\{F_g\right\} = \left[C_g\right]\left\{\dot{U}_g\right\} + \left[K_g\right]\left\{U_g\right\}, \tag{9}$$

where

$$K_g = \begin{bmatrix} k_0 & -k_{1,1} & \cdots & -k_{1,M-2J} & -k_{2,1} & 0 & \cdots & \cdots & -k_{2,2J-1} & 0 \\ -k_{1,1} & k_{1,1} & & & & & & & & \\ \vdots & & \ddots & & & & & & & \\ -k_{1,M-2J} & & & k_{1,M-2J} & & & & & & \\ -k_{2,1} & & & & k_{2,1} & & & & & \\ 0 & & & & & k_{2,2} & & & & \\ \vdots & & & & & & \ddots & & & \\ \vdots & & & & & & & \ddots & & \\ -k_{2,2J-1} & & & & & & & & k_{2,2J-1} & \\ 0 & & & & & & & & & k_{2,2J} \end{bmatrix},$$

$$C_g = \begin{bmatrix} c_0 & & & & & & & & & \\ & c_{1,1} & & & & & & & & \\ & & \ddots & & & & & & & \\ & & & c_{1,M-2J} & & & & & & \\ & & & & c_{2,1} & -c_{2,1} & & & & \\ & & & & -c_{2,1} & c_{2,1}+c_{2,2} & & & & \\ & & & & & & \ddots & \ddots & & \\ & & & & & & \ddots & \ddots & & \\ & & & & & & & & c_{2,2J-1} & -c_{2,2J-1} \\ & & & & & & & & c_{2,2J-1} & c_{2,2J} \end{bmatrix},$$

and $\left\{U_g\right\}^T = \left\{u_0,\ u_1,\ \cdots,\ u_{M-2J},\ u_{M-2J+1}, \cdots\ \cdots\ , u_M\right\}$, with u_0 being the displacement at the ground surface and the remaining variables are internal degrees of freedom. Equation (9) can be directly used in coupling a structure to the ground, as will be described for the case of a railway track in the next section.

3 SPACE-TIME DOMAIN MODELLING OF THE TRACK

3.1 Model description

Figure 3 shows a model of a ballasted railway track. The model consists of rail discretely supported on sleepers via railpads. The sleepers are resting on ballast which is in turn resting on the ground. The rail is modelled as an Euler-Bernoulli beam of mass, m_r, per unit length and

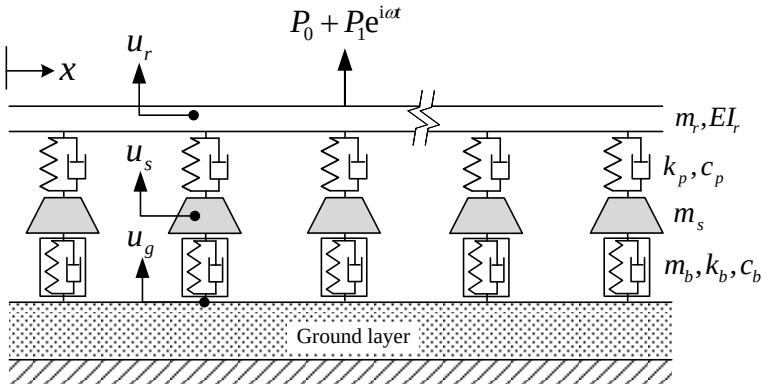


Figure 3: Model of a ballasted railway track on supporting ground layer, excited by a moving vehicle on irregular rail surface

bending stiffness, EI. The railpads are modelled as nonlinear with preload dependent stiffness and damping, k_p and c_p respectively. The sleepers are modelled as lumped masses, m_s, having only vertical translation. At each sleeper position, the ballast is modelled as having a mass, m_b, consistently distributed between the sleeper and ground nodes, stiffness and damping, k_b and c_b respectively. The lumped parameter model formulated in the previous section to represent the ground is coupled to the each sleeper node, with the assumption that there is no coupling through the ground. It should be noted that appropriate scaling of the lumped parameter model needs to be done to correctly account for the sleeper spacing.

3.2 Equation of motion of the track/ground model

The differential equation for the coupled track/ground model is given by

$$\begin{bmatrix} \mathbf{M}_r & \mathbf{0} & \mathbf{0} \\ \mathbf{0} & \mathbf{M}_s + \mathbf{M}_b^{ss} & \mathbf{M}_b^{sg} \\ \mathbf{0} & \mathbf{M}_b^{gs} & \mathbf{M}_b^{gg} \end{bmatrix} \begin{Bmatrix} \ddot{\mathbf{U}}_r \\ \ddot{\mathbf{U}}_s \\ \ddot{\mathbf{U}}_g \end{Bmatrix} + \begin{bmatrix} \mathbf{C}_p^{rr} & \mathbf{C}_p^{rs} & \mathbf{0} \\ \mathbf{C}_p^{sr} & \mathbf{C}_p^{ss} + \mathbf{C}_b^{ss} & \mathbf{C}_b^{sg} \\ \mathbf{0} & \mathbf{C}_b^{gs} & \mathbf{C}_b^{gg} \end{bmatrix} \begin{Bmatrix} \dot{\mathbf{U}}_r \\ \dot{\mathbf{U}}_s \\ \dot{\mathbf{U}}_g \end{Bmatrix} + \begin{bmatrix} \mathbf{K}_r + \mathbf{K}_p^{rr} & \mathbf{K}_p^{rs} & \mathbf{0} \\ \mathbf{K}_p^{sr} & \mathbf{K}_p^{ss} + \mathbf{K}_b^{ss} & \mathbf{K}_b^{sg} \\ \mathbf{0} & \mathbf{K}_b^{gs} & \mathbf{K}_b^{gg} \end{bmatrix} \begin{Bmatrix} \mathbf{U}_r \\ \mathbf{U}_s \\ \mathbf{U}_g \end{Bmatrix} = - \begin{Bmatrix} \mathbf{F}_r \\ \mathbf{0} \\ \mathbf{F}_g \end{Bmatrix}, \tag{10}$$

where $\mathbf{M}_{\{\cdot\}}$, $\mathbf{C}_{\{\cdot\}}$, $\mathbf{K}_{\{\cdot\}}$ and $\mathbf{U}_{\{\cdot\}}$ are the global mass, damping and stiffness matrices and displacement vector of the track components indicated by the subscripts, r, s, b and g, for the rail, sleeper, ballast and ground respectively. The superscripts on the other hand designate cross-coupling between these components. $\mathbf{F}_r$ is the external nodal force vector of the rail due to the excitation force and $\mathbf{F}_g$ is the interaction force vector at the ballast/ground interface. $\mathbf{F}_g$

contains the forces at all the ground nodes, each node represented by Eq. (9). Since the ground displacements are also unknowns, direct substitution of $\mathbf{F}_g$ results in a modification to the global damping and stiffness matrices of the track/ground model.

3.3 Nonlinear railpad and ballast properties

As stated earlier, the railpad and ballast properties are modelled as generally nonlinear with preload dependent stiffness and damping. The static force-displacement behaviour of the railpad and ballast can be approximated by polynomials of degree α and β respectively,

$$f_{ps}(u_{ps}) = k_{p,1}u_{ps} + k_{p,2}u_{ps}^2 + \cdots + k_{p,\alpha}u_{ps}^{\alpha} \tag{11a}$$

$$f_{bs}(u_{bs}) = k_{b,1}u_{bs} + k_{b,2}u_{bs}^2 + \cdots + k_{b,\beta}u_{ps}^{\beta}, \tag{11b}$$

where f_{ps}, u_{ps} and $k_{p,1}\cdots k_{p,\alpha}$ are the static force (in Newton), displacement (in metre) and stiffness coefficients of the railpad respectively. f_{bs}, u_{bs} and $k_{b,1}\cdots k_{b,\beta}$ are the corresponding values for the ballast. For the railpad, the values of the non-zero coefficients are $k_{p,1} = 20.0$ MN/m, $k_{p,3} = 3.94 \times 10^6$ MN/m^3, $k_{p,5} = -1.78 \times 10^{12}$ MN/m^5 and $k_{p,7} = 3.28 \times 10^{18}$ MN/m^7 [9], and for the ballast, $k_{b,1} = 22.75$ MN/m and $k_{b,3} = 2.6 \times 10^8$ MN/m^3 [10]. Note that when the track is fully unloaded, the railpad and ballast possess unloaded stiffnesses of $k_{p,1}$ and $k_{b,1}$ respectively.

3.4 Solution of the coupled equation of motion

Under the action of the static load, the preloads and hence the preloaded stiffness of the railpads and ballast are calculated by solving the nonlinear static equivalent of Eq. (10) using a Newton-Raphson iterative routine. These are then used as input values for the dynamic part of the problem, defined by Eq. (10). The solution for the track and ground displacements and the interaction forces at the ballast/ground interface are obtained by progressive numerical integration.

The calculated interaction forces at the ballast/ground are then used as input to calculate ground vibration in the far-field. This process is described in the next section.

4 FREE-FIELD GROUND VIBRATION CALCULATION

Using the computed displacement and its derivatives, the interaction forces at the ballast/ground interface can also be computed. For this problem, all sleeper and ground nodes vibrate with the same frequency as the load. Therefore it is sufficient to consider only the complex amplitude of the interaction force in the space-time domain. This is given as

$$\mathbf{F}_g(x_s) = |\mathbf{F}_g(x_s, t)| = |\mathbf{C}\dot{\mathbf{U}}_g + \mathbf{K}_p\mathbf{U}_g|. \tag{12}$$

The non-zero forces of $\mathbf{F}_g(x_s)$ occur at the ground nodes that are coupled to the sleepers, with the internal nodes of the lumped parameter model being zeros. These non-zero forces are assembled in a new vector, $\bar{\mathbf{F}}_g(x_s)$, with size $2n_s + 1 \times 1$, where n_s and x_s are the number of sleepers and sleeper positions respectively. It is convenient to convert $\bar{\mathbf{F}}_g(x_s)$ into a piecewise continuous function, $\bar{F}'_g(x)$, using linear interpolation functions.

The spatial Fourier transformation of $\bar{F}'_g(x)$ to the wavenumber domain can be obtained from

$$\hat{\bar{F}}'_g(\xi) = \int_{-\infty}^{\infty} \bar{F}'_g(x)\mathrm{e}^{-\mathrm{i}\xi x}\mathrm{d}x. \tag{13}$$

The complex amplitude of the ground displacement in the wavenumber domain is therefore given by

$$\tilde{U}'_g(\xi,\gamma,\omega) = \tilde{H}_g(\xi,\gamma,\omega)\hat{\tilde{F}}'_g(\xi)\frac{\sin\gamma b}{\gamma b}. \tag{14}$$

Finally, the corresponding displacement in the space-time domain is obtained by applying the double inverse Fourier transformation as follows

$$u'_g(x,y,\omega) = \frac{1}{4\pi^2}\int_{-\infty}^{\infty}\int_{-\infty}^{\infty}\tilde{H}_g(\xi,\gamma,\omega)\hat{\tilde{F}}'_g(\xi)\frac{\sin\gamma b}{\gamma b}\mathrm{e}^{\mathrm{i}(\xi x+\gamma y)}\mathrm{d}\xi\mathrm{d}\gamma. \tag{15}$$

In the next section, numerical results will be presented to show the validity of this approach and to investigate the effect of nonlinear track properties on ground vibration.

5 RESULTS AND DISCUSSION

Section 5.1 presents the result of the lumped parameter model approximation of the ground dynamic stiffness. The lumped parameter model is then used to study nonlinear track dynamics. Results for this application are given in Section 5.2 while free-field ground displacements are presented in Section 5.3.

5.1 Dynamic stiffness of the LPM

The following parameters are used for the ground: $\rho = 1800$ kg/m^3, $v_s = 245$ m/s and $v_p = 750$ m/s and damping ratio of 5%.

The vertical dynamic stiffness from Eq. (5) is computed using $b = 1.35$ m and $a = 0.724$ m. For the lumped parameter model approximation, polynomials of order 6 and 7 for the numerator and denominator respectively are used. This results in one real and three pairs of complex conjugate poles, hence the regular part of the lumped parameter model consists of one first-order and three second-order terms. These are then arranged in parallel with the singular part of the spring, $k_0 = -12.853$ and dashpot, $c_0 = 2.569$. The values of the coefficient of the components of the lumped parameter model are given in Table 1.

Table 1: Coefficients of the components of the lumped parameter model

j	$k_{1,j}$	$c_{1,j}$	$k_{2,j}$	$k_{2,j+1}$	$c_{2,j}$	$c_{2,j+1}$
1	-16.290	-1.142	1.755	-0.381	-0.110	0.077
3			2.524	-0.141	0.108	-0.106
5			1.821	-0.067	-0.118	0.109

Figure 4 shows the real and imaginary parts of the dynamic stiffness, normalised against the static stiffness, K_0. It shows a comparison between the semi-analytical and lumped parameter model representations. A dimensionless frequency has been adopted, $\bar{\omega} = \omega h/v_s$, where $\bar{\omega} = 1$ corresponds to ≈ 54 Hz. h is a characteristic length, taken as the smaller of the rectangular load dimensions a and b. It can be seen that the lumped parameter model is a good representation of the computed dynamic stiffness of the half-space.

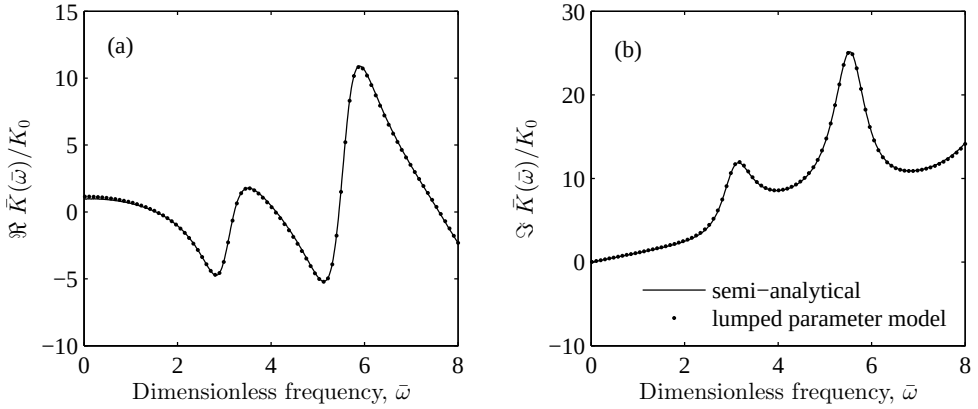


Figure 4: (a) Real and (b) imaginary parts of the dynamic stiffness of a half-space subjected to rectangular harmonic load. Comparison between the semi-analytical and lumped parameter models

5.2 Track and ground vibration

Table 2 contains the track parameters used in the computation of the track dynamic response and, together with the lumped parameter model model, the ground response.

Table 2: Track parameters used in the numerical study

Rail	Railpad	Sleeper	Ballast
m_r = 60.21 kg/m	ζ_p = 0.125	m_s = 250 kg/m	m_b = 870 kg/m
EI_r = 6.4 MN m^2			ζ_b = 0.50

Figure 5 shows the variation of the rail, sleeper and ground displacement amplitude and phase at the driving point with frequency for a unit load at the rail. The results obtained using the lumped parameter model are compared with those of the semi-analytical procedure for linear track parameters. For this calculation, the rail is modelled using 240 elements, each of length 0.3 m, 121 sleepers and therefore same number of ground nodes. Good agreement between the two methods can be observed. At low frequencies, the rail displacement is about 6.1 dB larger than the sleeper and 18.5 dB than the ground displacement. Resonances can be seen to occur for the sleeper/ballast at around 48-60 Hz and for the rail at around 220 Hz. The fluctuations in the ground displacement due to the width of the ballast can also be seen.

Results are now presented to show the effect of track nonlinearity for static loads of 0, 50, 87.5 and 125 kN. The stiffness of the railpad and ballast increases significantly with preload. Figure 6 shows the amplitude and phase of the rail, sleeper and ground displacements at the driving point, plotted against frequency for these preload levels. The effect of increasing stiffness of the railpad and ballast, which is a direct consequence of the preload dependence, is apparent in the figure with lower amplitudes and increased resonance frequencies observed with increase in static load. Also the preload dependence of the railpad and ballast results in higher interaction forces at the ballast/ground interface and consequently leads to larger ground displacements over a wide range of frequencies. Since the ground is linear, however, the peaks in the ground displacement occur at approximately the same frequencies for all preload levels.

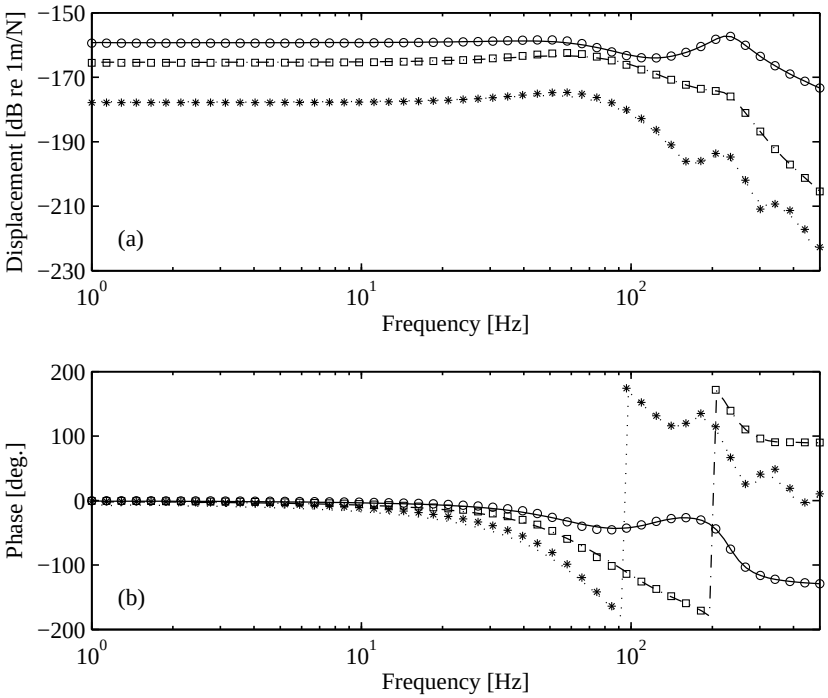


Figure 5: Displacement amplitude and phase of the rail (—,○), sleeper (-··-,□) and ground (· · · ,*), plotted against excitation frequency. Comparison between track on half-space [2] (lines) and on lumped parameter model for the ground (markers).

5.3 Free-field ground vibration

Finally, using the interaction forces at the ballast/ground interface, free-field ground vibration can be calculated in accordance with the procedure in Section 4.

Figure 7 shows the ground displacement amplitude at $x = 0$ plotted against distance away from the track for the preload levels specified above, for a load oscillating at (a) 10 Hz and (b) 120 Hz. For the case in (a), it can be seen that the ground displacement consistently increases with increase in the preload level, as is the case in Fig. 6, with maximum differences of up to 4 dB observed. For the higher frequency case in (b), however, this is not the case. The equivalent nonlinear stiffness of the track foundation affects the load distribution on the halfspace. This results in different levels of excitation of the ground, resulting in differences of up to 2.3 dB between the ground displacements for the linear nonlinear cases.

6 CONCLUSIONS

This paper presents a mixed formulation involving both space-time and wavenumber-frequency domain techniques applied to the study of ground vibration from surface trains. The track is modelled in the time domain in order to include nonlinear track elements, and the ground in the wavenumber domain. For the purpose of calculating the track/ground interaction forces in the space-time domain, the ground is represented by a layer of consistent lumped parameter model consisting of frequency independent stiffness and damping components. The calculated interaction forces are then transformed to the wavenumber domain and used as input to study ground vibration in the far field. For the example case presented, the lumped parameter model shows good comparison with the fully coupled track-ground model. The effect of nonlinearity

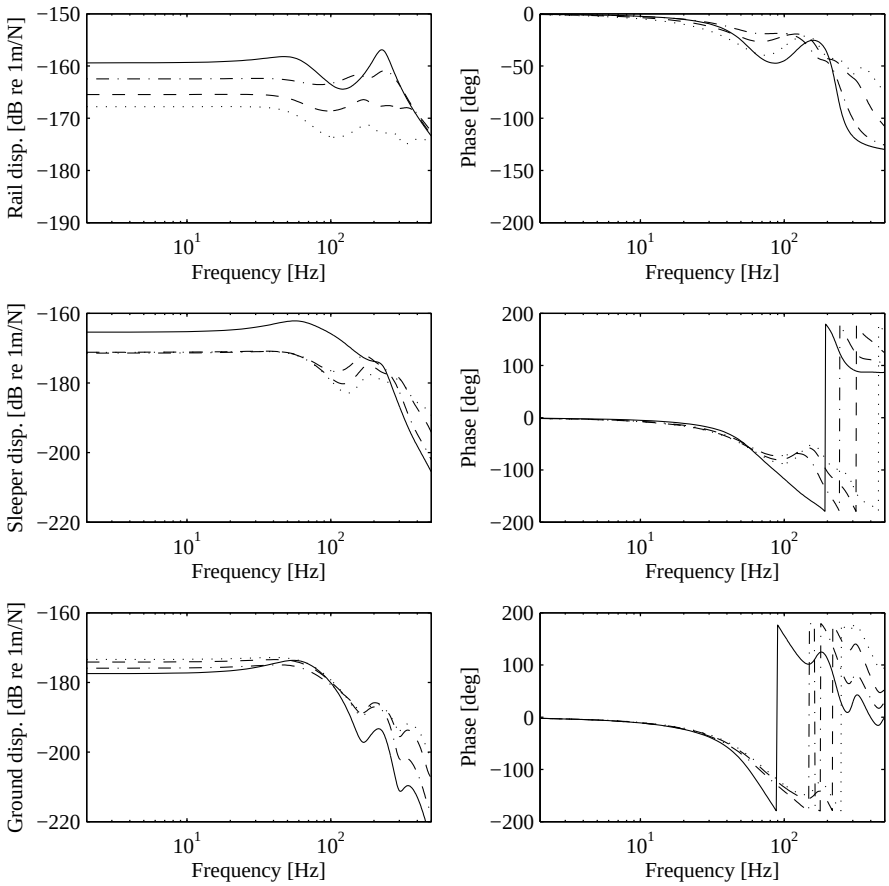


Figure 6: Displacement amplitude and phase of the rail, sleeper and ground, plotted against excitation frequency for preload levels of 0 kN —, 50 kN -·-, 87.5 kN - - -, 125 kN · · · .

on ground vibration has been found to be significant in the vicinity of the track as well as in the far field, with differences of up to 4 dB observed between the linear and the highly nonlinear cases.

ACKNOWLEDGEMENTS

This work is undertaken as part of the MOTIV (Modelling of Train Induced Vibration) project which is funded by the EPSRC under grant EP/K005847/2.

REFERENCES

[1] D.V. Jones, D. Le Houedec, M. Petyt, Ground vibrations due to a rectangular harmonic load. *Journal of Sound and Vibration*, **212**, 67-74, 1998.

[2] X. Sheng, C.J.C. Jones, M. Petyt, Ground vibration generated by a harmonic load acting along a railway track. *Journal of Sound and Vibration*, **225**, 3-28, 1999.

[3] P.A. Costa, R. Calçada, A.S. Cardoso, A. Bodare, Influence of soil non-linearity on the dynamic response of high-speed railway tracks. *Soil Dynamics & Earthquake Engineering*, **30**, 221-235, 2010.

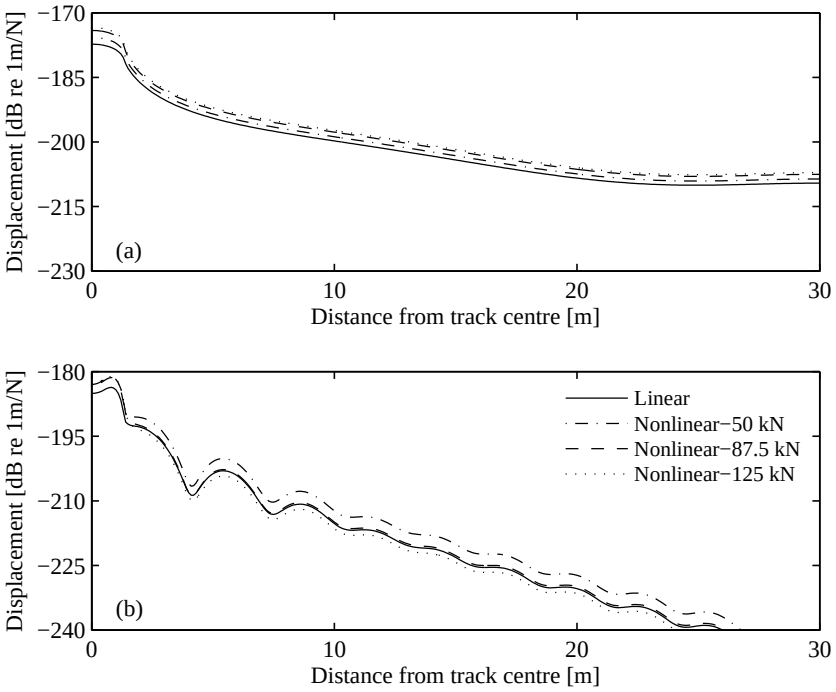


Figure 7: Variation of ground displacement amplitude with distance away from the track for the four preload levels and load frequency of (a) 10 Hz, (b) 120 Hz.

[4] G. Kouroussis, G. Gazetas, I. Anastasopoulos, C. Conti, O. Verlinden, Discrete modelling of vertical track-soil coupling for vehicle-track dynamics. *Soil Dynamics & Earthquake Engineering*, **192**, 1711-1723, 2011.

[5] G. Kouroussis, O. Verlinden, C. Conti, A two-step time simulation of ground vibrations induced by the railway traffic. *Proceedings of the Institution of Mechanical Engineers, Part C: Journal of Mechanical Engineering Science*, **226**, 454-472, 2012.

[6] J.P. Wolf, Consistent lumped-parameter models for unbounded soil: Physical representation. *Soil Dynamics & Earthquake Engineering*, **20**, 11-32, 1991.

[7] J.P. Wolf, Consistent lumped-parameter models for unbounded soil: Frequency-independent stiffness, damping and mass matrices. *Soil Dynamics & Earthquake Engineering*, **20**, 33-41, 1991.

[8] K.F. Graff, *Wave Motion in Elastic Solids*. Dover publications, inc., 1991.

[9] S.G. Koroma, M.F.M. Hussein, J.S. Owen, The effects of railpad nonlinearity on the vibration of railway tracks under harmonic load. Z. Dimitrovová, J.R. de Almeida, R. Gonçalves eds. *11th International Conference on Vibration Problems (ICOVP-2013)*, Lisbon, Portugal, September 9-12, 2013.

[10] T.X. Wu, D.J. Thompson, The effects of track non-linearity on wheel/rail impact. *Proceedings of the Institution of Mechanical Engineers, Part F: Journal of Rail and Rapid Transit*, **218**, 1-15, 2004.

COMPDYN 2015
5th ECCOMAS Thematic Conference on
Computational Methods in Structural Dynamics and Earthquake Engineering
M. Papadrakakis, V. Papadopoulos, V. Plevris (eds.)
Crete Island, Greece, 25–27 May 2015

VIBRATIONS IN BUILDINGS DUE TO RAILWAY TRAFFIC IN TUNNELS: MODELLING STRATEGIES AND INFLUENCE OF SOIL STIFFNESS

P. Lopes[1], P. Alves Costa[2], R. Calçada[3] and A. Cardoso[4]

[1] Department of Civil Engineering, Faculty of Engineering of University of Porto
e-mail: cpl@isep.ipp.pt

[2] Department of Civil Engineering, Faculty of Engineering of University of Porto
pacosta@fe.up.pt

[3] Department of Civil Engineering, Faculty of Engineering of University of Porto
ruiabc@fe.up.pt

[4] Department of Civil Engineering, Faculty of Engineering of University of Porto
scardoso@fe.up.pt

Keywords: Railway vibrations in tunnels, Soil-structure interaction, 2.5D FEM-PML

Abstract. *In this paper a numerical study about the influence of soil stiffness on the assessment of vibrations induced by railway traffic in tunnels is performed. A comprehensive numerical model is used to achieve the lumped objective, where the source of vibration (train-track interaction), the propagation of vibrations (tunnel-ground system) and their reception (building close to the railway infrastructure) are simulated by a sub-structuring approach. It was found that the soil stiffness plays a relevant role on the mechanisms of propagation of vibrations through the ground as well as on the soil-structure interaction. Regarding the last topic, different approaches were attended for the inclusion of the SSI effects, namely a detailed boundary elements formulation and a simplified lumped-parameter model. The study performed revealed that the usage of lumped parameter models can be faced as a good option taking into account the compromise between accuracy of the solution and reduction of the computation effort.*

1. Introduction

The relevance of environmental problems related with vibrations induced by underground railway traffic has increased over the last years. Actually, the influence of vibrations on working and living environments is now considered one of the seven main environmental problems of modern societies [1, 2]. The first step to the minimization of the negative impact induced by vibrations due to railway traffic lies on a better understanding of this complex problem. Therefore, several prediction models have been developed during recent years, ranging from scope models [3] to analytical models [4, 5], without forgetting complex numerical models, as the ones suggested by Clouteau et al [6], Gupta et al. [7, 8] and Hung and Yang [9], among others.

Due to the inherent complexity of the problem, Lai et al [10] suggests that the development of a comprehensive prediction tool for railway-induced ground vibrations should consider three distinct perspectives: i) the source problem associated to train-track dynamic interaction; ii) the propagation problem, comprising the transmission of borne vibrations from the source to the receiver; iii) the structural response problem, regarding to the soil-structure dynamic interaction developed due to the vibration field that impinges buildings surrounding railway facilities.

The source problem has been object of intensive research during the last couple of years, so that it is now possible to state that the excitation source provided by the dynamic interaction mechanism plays the most relevant role in terms of vibrations induced in the ground due to railway traffic [11, 12]. This fact demands for the solving of a dynamic interaction problem where the unsprung mass of the train plays an important role.

However, it should be emphasised that the major research effort is visible on the second part of the problem, i.e., the propagation of vibrations from the tunnel through the surrounding ground. In the present paper, a numerical model based on the 2.5D FEM-PML (perfectly matched layers) concept is used to simulate the propagation of waves induced by railway traffic in tunnels. [13].

In spite of the considerable recent advances in this topic, there is still a lack of studies comprising the complete problem, i.e., from the source to the receiver. The last part of the problem, comprising the dynamic response of the receiver (building close to the tunnel), has only been considered in a very small number of studies [14-17].

The present paper aims to contribute to a better discernment of the comprehensive problem, taking into account not only the generation and propagation of vibrations induced by railway traffic in tunnels, but also its effect inside of buildings close to the tunnel. The soil-structure interaction is taken into account by a detailed formulation based on the sub-structuring approach.

Among several parameters that influence the dynamic response of the system, Gupta et al.[18] concluded that soil stiffness plays an important role on the vertical vibration levels predicted at the ground surface. However, when the presence of the building is taken into account, the stiffness of the ground is also expected to affect the soil-structure interaction mechanism. So, the present paper develops a parametric study in order to assess the influence of soil stiffness not only on the vibration propagation mechanism, but also on the soil-structure (building) mechanism. Regarding this aspect, alternative approaches for dealing with SSI are investigated.

Finally, the paper ends with a summary of the main conclusions of the developed study.

2. Numerical approach

2.1 Generalities

Fig. 1 shows the main parts of the proposed numerical model, as well as the main steps involved in the solution [19]. As can be seen, a substructuring approach is followed, being each part of the problem simulated through distinct suitable approaches.

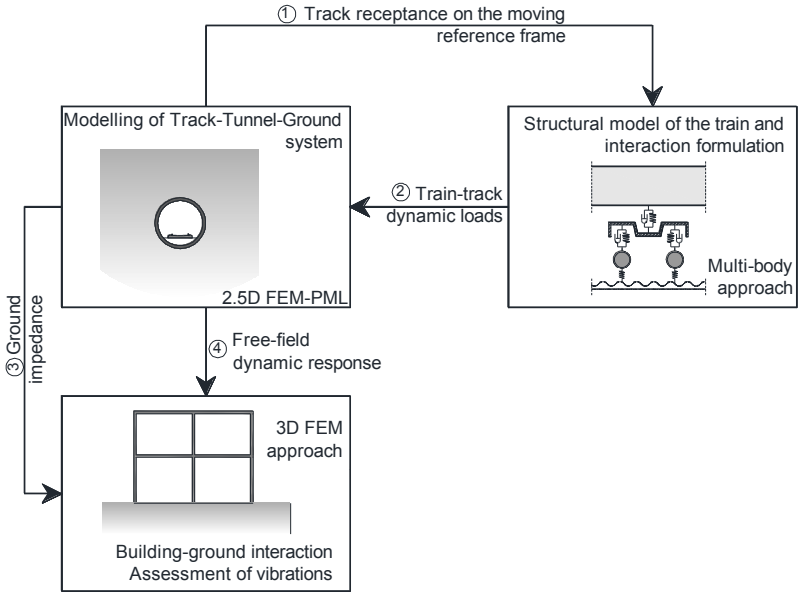


Fig. 1. Numerical modelling strategy.

Since the model depicted in Fig. 1 was previously presented and validated [20] by the authors, a detailed description of the models is omitted. The reader is advised to consult the following documents [11, 15, 19, 20] for a detailed description of the modelling strategy followed to simulate the source and the propagation medium.

Regarding the mathematical formulation followed for the soil-structure interaction, the reader can find a comprehensive description in recent papers of the same authors, namely on Lopes et al. [21]. Nevertheless, it should be referred that in the present paper two distinct methodologies are used for the assessment of the impedance of the building's footings: i) a 3D BEM approach; ii) a lumped parameter approach. Fig. 2 shows both approaches followed.

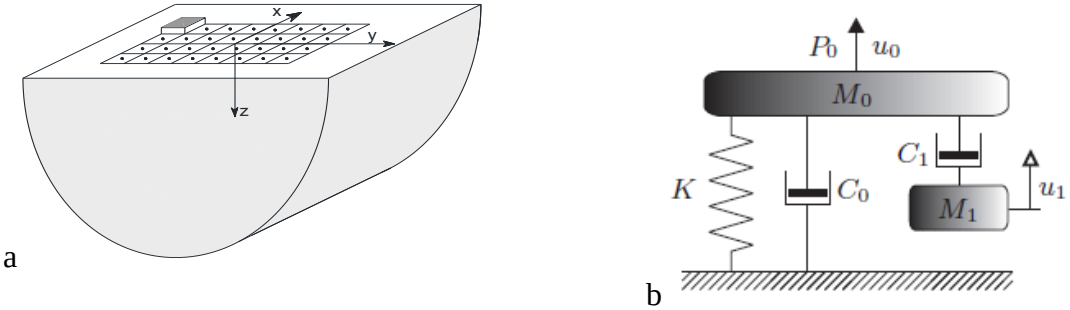


Fig. 2. Assessment of footing impedance: a) 3D BEM; b) lumped parameter model [21].

3. Application example

3.1. Model Description

Fig 3 represents a shallow tunnel embedded in a half-space. The circular geometry tunnel has a 6.0 m diameter and is lined on the inside with a thickness of concrete of 0.3 m (continuous liner, i.e., without joints along the longitudinal direction). The mechanical properties of the tunnel liner and the ground are also indicated in Fig 3.

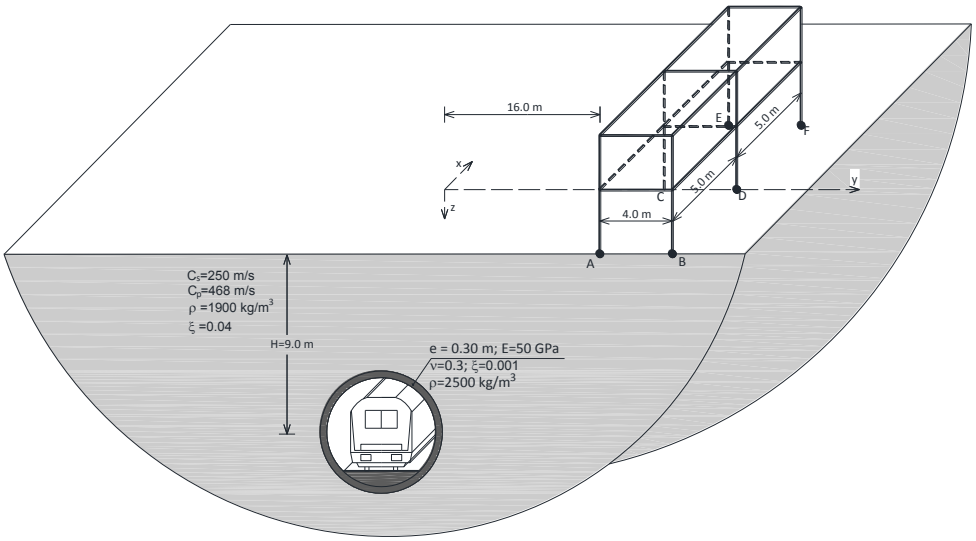


Fig 3. Geometry and properties of the application example.

The railway track is composed by a continuous concrete slab track 0.3 m thick and 2.5 m wide, with a longitudinal bending stiffness of 1.62x108 N/m2 and a mass of 2800 kg per unit of length. The rails, materialized by UIC60 profiles are continuously supported by railpads with a stiffness of 2.5x108 N/m2 and a damping coefficient of 6x104 Ns/m2. It assumed a floating slab solution, introducing a resilient mat between the slab and the tunnel invert. The stiffness of the mat is 0.153x109 N/m2 per meter in the longitudinal direction and a damping of 5.5x104 Ns/m2 is considered.

Regarding soil properties, three distinct scenarios are assumed according to

Table 1:

Table 1 – Properties of ground

Scenario	Cs (m/s)	ν	ρ (kg/m^3)	β
1	150	0.3	1900	0.04
2	250	0.3	1900	0.04
3	410	0.3	1900	0.04

Regarding the building, the presence of a two-story small building in the vicinity of the tunnel was also assumed. The geometry of the building is illustrated in Fig. 4. The footings of the building are squared with an area of 2x2 m2. The most distant column alignment of the building is 20 m away from the plane of symmetry of the cross-section of the tunnel.

Table **2** summarizes the properties of the main elements of the building. Regarding the damping, Rayleigh damping factors were adopted in order to address a damping coefficient of around 2% in the frequency range between 5 Hz and 80 Hz. The coordinates of the centre of the footing are: A(-5;16;0); B(-5;20;0); C(0;16;0); D(0;20;0); E(5;16;0); F(5;20;0).

Additionally, a distributed mass of 300 kg/m2 was considered on the floors, in order to take into account the other permanent masses.

To compute the impedance of the ground, the area of the footing-ground interface was discretized by 144 square elements, corresponding to a maximum length size of 0.167 m. In what concerns to the dimensions of the elements of the 2.5D FEM-PML model, it should be mentioned that the mesh was designed taking into account the recommendations presented by Yang et al.[22] and Alves Costa et al.[23].

Table 2 – Properties of the structural elements of the building

Elements	Properties	Dimensions

	E(GPa),ν,ρ (kg/m^3)	
Slabs	30, 0.2, 2500	Thickness: 0.25 m
Beams	30, 0.2, 2500	0.3 x0.60 m^2
Columns	30, 0.2, 2500	0.30x0.30 m^2

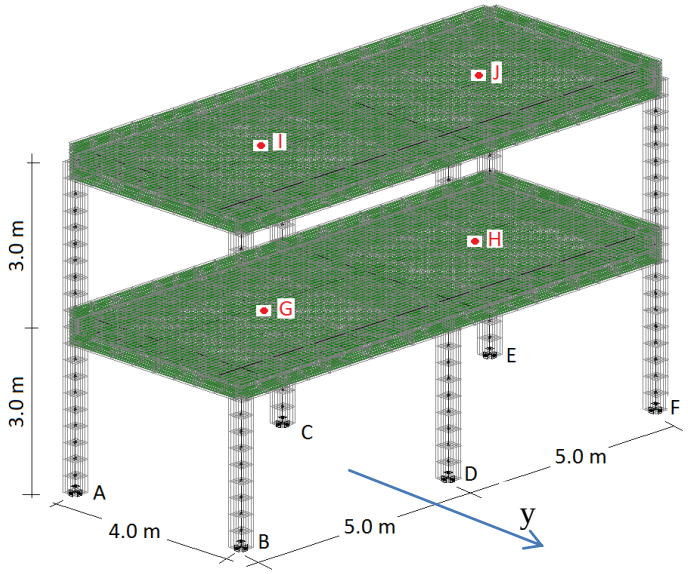


Fig. 4.Geometry of the building.

Regarding the rolling stock, the passage of the Alfa-Pendular train at a running speed of 40 m/s was assumed. The main geometrical and mechanical properties of the Alfa-Pendular train are summarized in Fig. 5 and in **Erro! A origem da referência não foi encontrada.**.

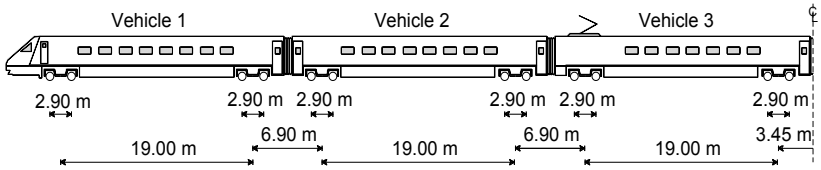


Fig. 5. Alfa-Pendular geometry.

Table 3 – Mechanical properties of the train

Axles	Mw (kg)	1538-1884
Primary suspension	Kp (kN/m) Cp (kNs/m)	3420 36
Bogies	Mb (kg)	4712-4932
	Jb (kg/m^2)	5000-5150
Car body	Mc (kg)	32900-35710

As mentioned before, the train-track interaction is taken into account, so, the dynamic interaction mechanism is given by the unevenness of the track. An artificial unevenness profile was generated taking considering the power spectral density (PSD) of amplitude of the track unevenness for a range of wavelengths between 28 m and 0.55 m. The following equation was used to address the PSD of the track unevenness [12]:

$$S(k_1) = S(k_{1,0})\left(\frac{k_1}{k_{1,0}}\right)^{-w} \quad (1)$$

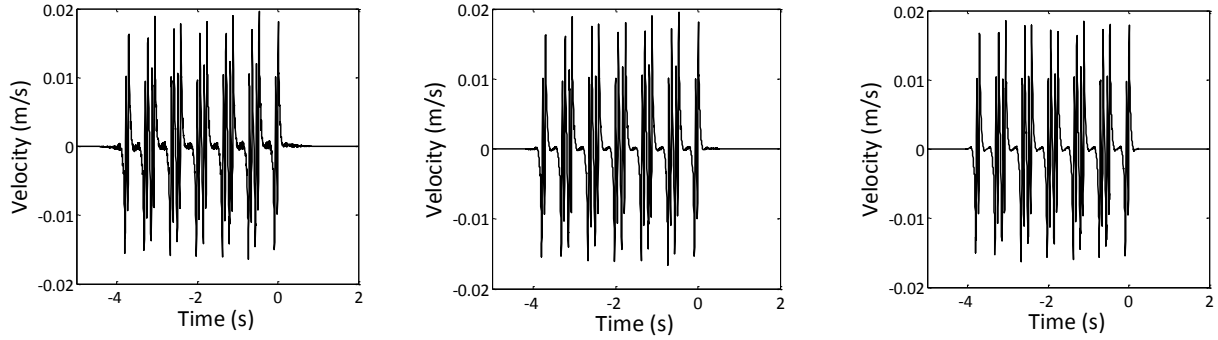
where k1,0=1 rad/s, w=3.5 and S(k1,0) is equal to 1x10-8 m3.

Since the train speed was assumed to be 40 m/s, the adopted unevenness profile excites the train in the frequency range between 1.4 Hz and 72 Hz. This range of frequencies is particularly interest-

ing for the study of vibrations induced by traffic in buildings, since for frequencies above 80 Hz the building structure itself filters the vibration levels.

3.2. Dynamic response of the track

Fig. 6 shows the vertical velocity of the rail, at position x=0 m, during the passage of the train for the different scenarios under study (it is assumed that at t=0 s, the last wheelset of the train is at x=0m). Since almost all the resilience of the track is given by the elastomeric elements (railpads and mats beneath the slab), the track displacements almost aren't affected by the elastic properties of the ground. However, it should be emphasize that outside the track, as for instance at the invert of the tunnel, the ground properties start to gain some relevance.



a b c

Fig. 6. Time history of the vertical velocity of the rail for soil properties: a) Cs=150 m/s; b) Cs=250 m/s; c) Cs=410 m/s.

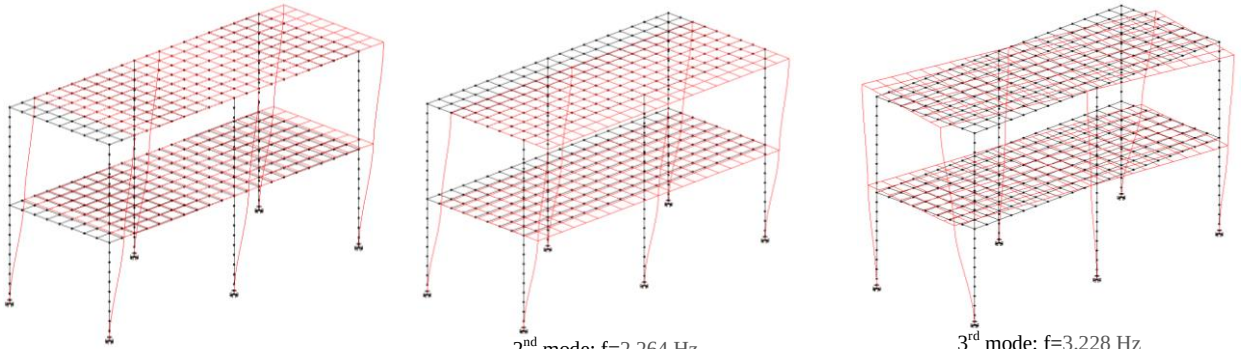
3.3. The dynamic response of the building

The SSI effects are considered by evaluating the footing impedance (or the dynamic stiffness), which can be done using one of the two methodologies previously mentioned. The first methodology, based on a 3D BEM formulation, is more accurate, however the computation effort required is somewhat higher.

In order to obtain a better discernment of the effects involved in the problem, the following sections are organized as follows: i) analysis of the dynamic behavior of the building including SSI effects; ii) detailed approach of the dynamic response of the building due to the train passage.

Dynamic behaviour of the building.

Fig. 7 shows the mode shapes of the building structure associated to the first twelve natural frequencies. The mode shapes herein presented were computed assuming full restriction of the degrees of freedom of the building that connect it to the ground, i.e., discarding the SSI effects.



1st mode: f=2.259 Hz 2nd mode: f=2.264 Hz 3rd mode: f=3.228 Hz

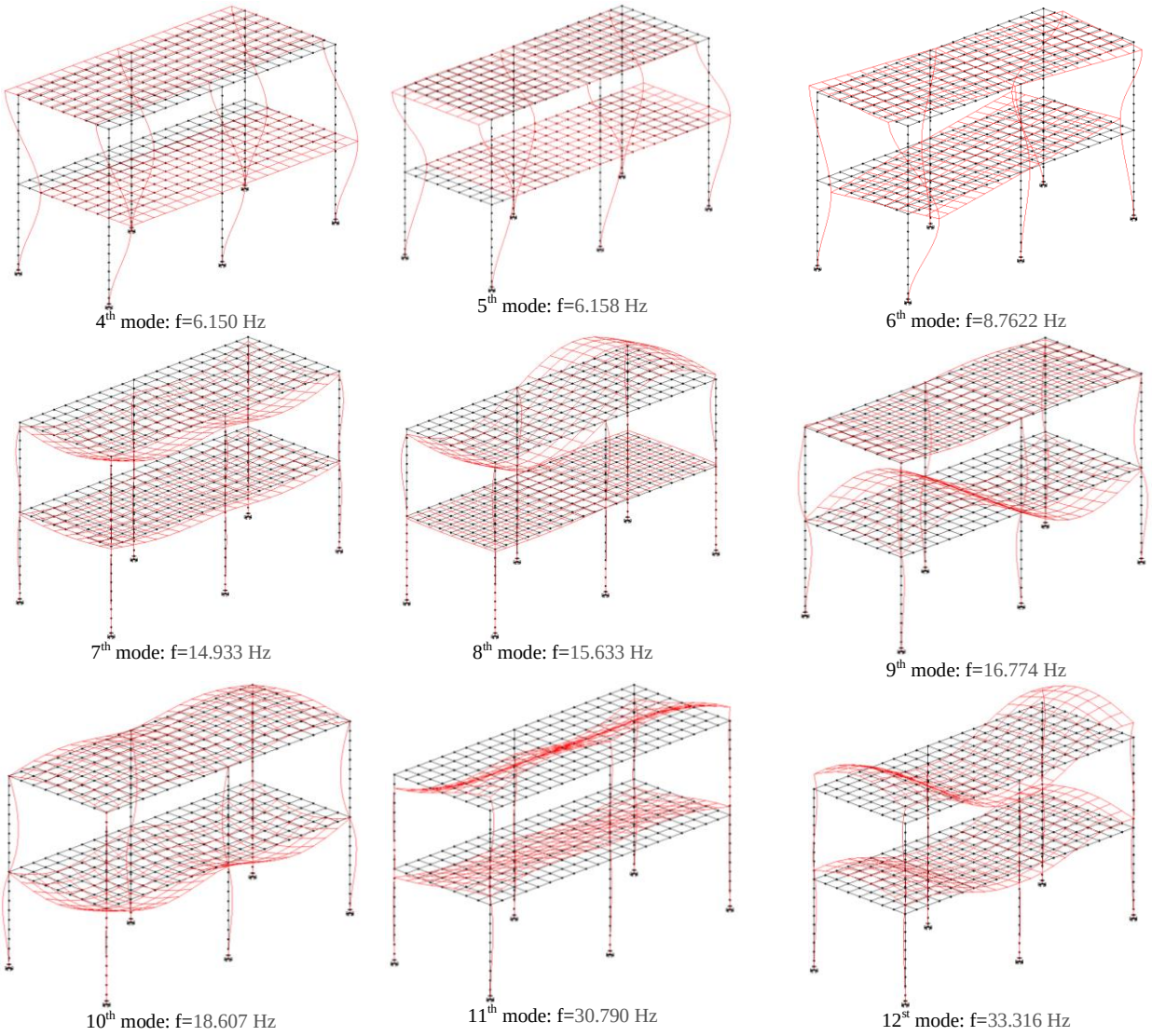


Fig. 7. Mode shapes of the building structure

Observing Fig. 7, it is possible to conclude that the mode shapes related with natural frequencies up to 10 Hz comprise horizontal movement of the building slabs. On the other hand, the vertical movement of the slabs is mainly related to the natural frequencies that occur between 14 Hz and 20 Hz, while the natural frequencies above 30 Hz are related with local mode shapes that also imply bending of the slabs and axial deformation of the columns.

Since the ground is not infinitely stiff, the SSI effect will influence the dynamic behaviour of the building. This influence is seen in the shift of the natural frequencies towards lower values, due to the increase of flexibility of the system, and also in the attenuation of the response amplitude due to the radiation of energy of the footing towards the ground. These effects are clearly observed in Fig. 8, where the FRF (Frequency Response Function) of the vertical displacement of point H (see Fig. 4) caused by a vertical unitary displacement applied at all footings of the building are depicted. In order to better discern the influence of the building-ground coupling, a null value was assumed for the damping of the building structure at Fig. 8a.

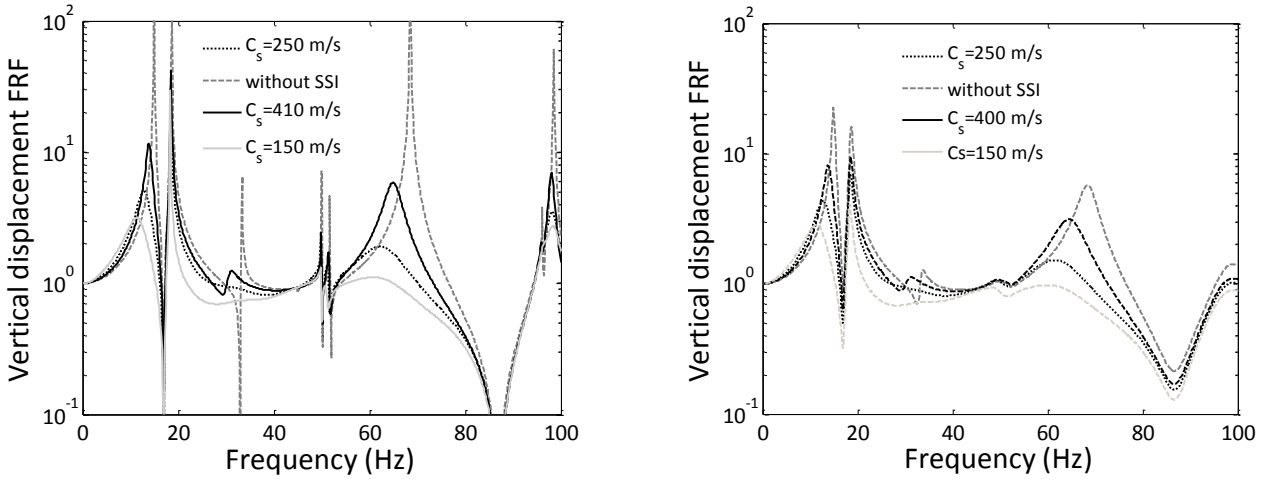


Fig. 8. FRF of the vertical displacement of point H caused by an unitary harmonic vertical displacement applied at the footings structure: a) undamped scenario; b) damped scenario.

As expected, the soil-structure interaction (SSI) has a huge influence on the dynamic behaviour of the building. This influence becomes more pronounced as the ground becomes softer. However, even for the stiffer scenario, it is possible to see a slight shift of the natural frequencies of the system associated with mode shapes where the vertical movement of the footings can be involved.

The dynamic response of the building due to traffic induced vibrations

In what the vertical dynamic response of the slabs of the building is concerned, it is possible to see a clear influence of soil stiffness in the results depicted in Fig. 9.

A first analysis of the results allows concluding that the peak vertical velocity increases as soil stiffness increases. Moreover, damping effect induced by the SSI is quite evident. For the stiffer scenario, it is possible to see a tail of free vibration of the building after the passage of the train, which is not so perceptible for the softer scenario.

Generally, the major concern when dealing with vibrations in buildings due to traffic has to do with the vertical component of the response. However, the properties of the soil also affect the horizontal components, as shown in the one-third octave spectra of the horizontal velocity (y-direction) depicted in Fig. 10. As can be seen, the frequency content of the response is concentrated in a narrow low frequency band, according to the natural frequencies of the building with the 2nd and 4th mode shapes. For the higher frequency range, the structure of the building acts as a "filter" of the incident wave field. However, it is notorious that the velocity increases with the decrease of the soil stiffness, since for this frequency range the system response is only affected by the quasi-static stiffness of the soil.

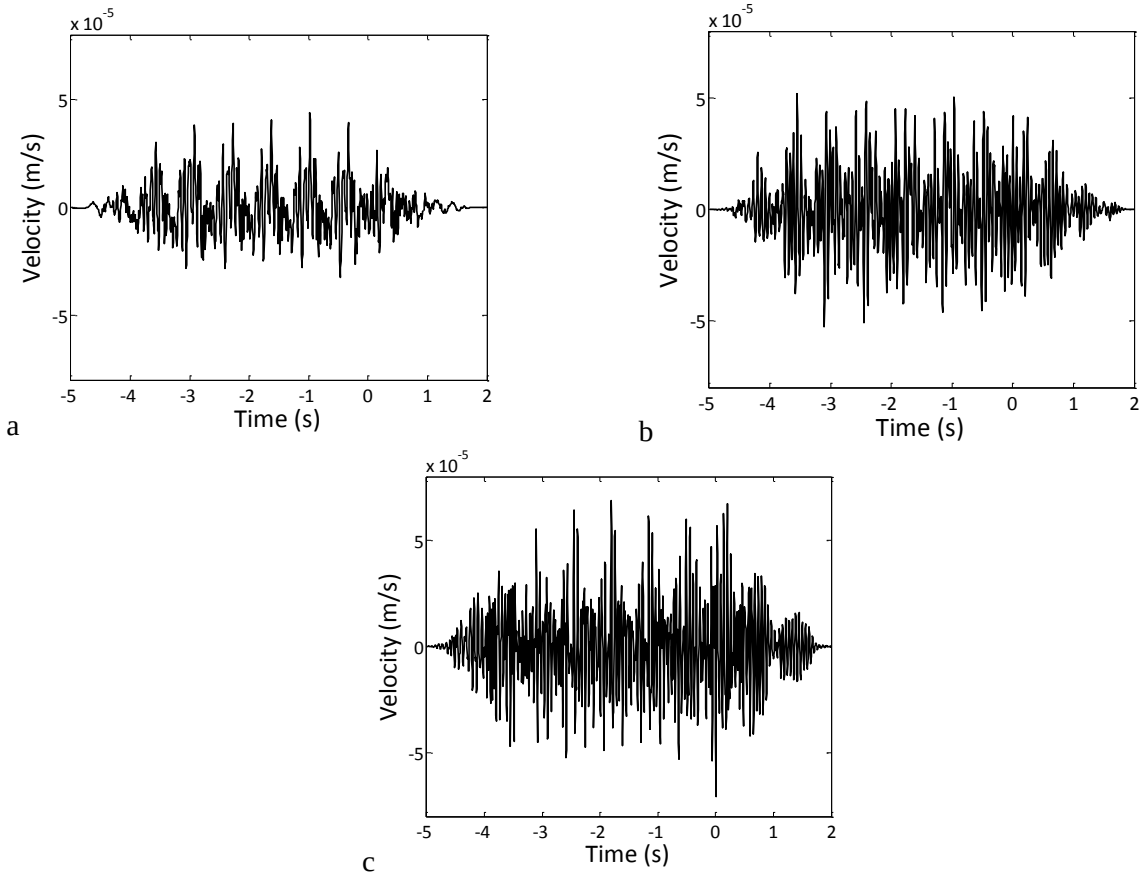


Fig. 9. Time record of the vertical velocity of point H: a) Cs=150 m/s; b) Cs=250 m/s; c) Cs=410 m/s.

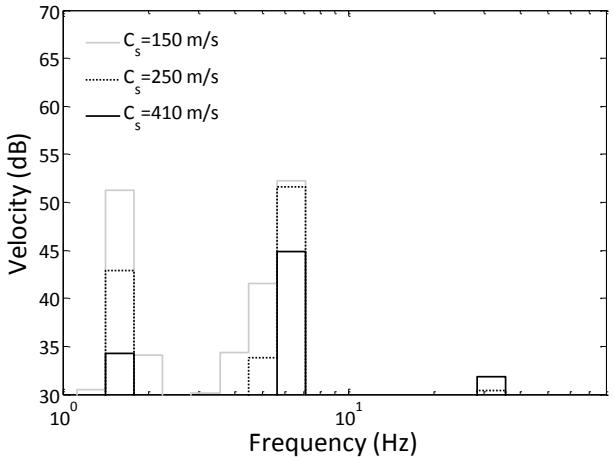


Fig. 10. One-third octave spectra of the horizontal velocity (y direction) of point H for different ground properties.

The relevance of the SSI analysis and alternative approaches

The results presented in the last section were computed assuming a detailed 3D FEM-BEM analysis of the building-ground system. However, alternative approaches, preferably more simple, can also be considered. The simplest way is neglecting the contribution of the ground on the dynamic behaviour of the building, i.e., assuming that the stiffness of the ground is so high that its contribution is not relevant. Taking into account the FRF functions presented before it seems that this option is only acceptable when considering very stiff grounds. However, between that and the detailed

modelling of the ground impedance by a 3D BEM formulation, the reasonability of lumped-parameter models should be checked in more detail.

Fig. 11 compares the vertical velocity time history of point H, computed by the three distinct methods for the softest and stiffest scenarios under analysis.

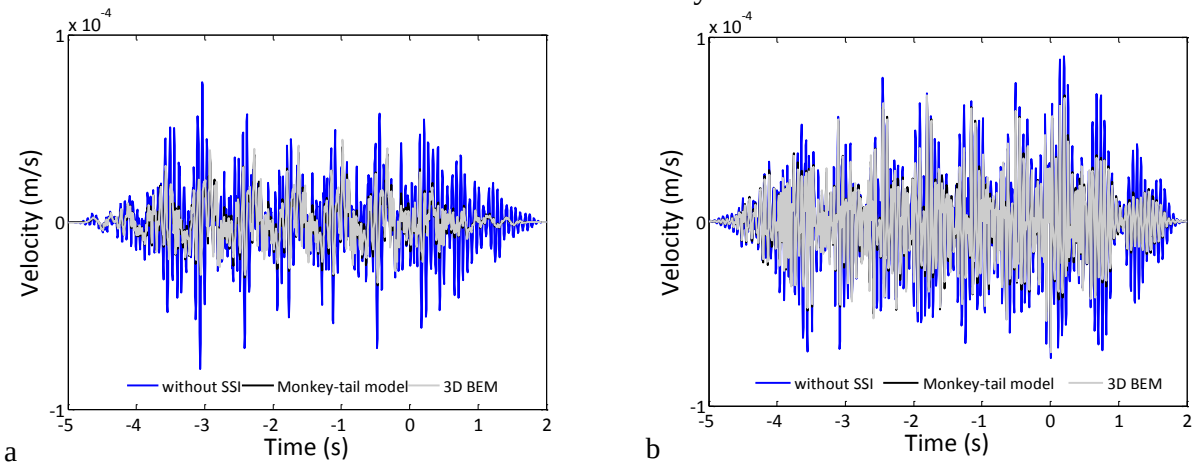


Fig. 11. The influence of SSI on the time record of the vertical velocity of point H: a) Cs=150 m/s; b) Cs=410 m/s.

The results shown here point out two main remarks: i) the consideration of SSI effects is mandatory for an accurate assessment of vibrations inside of buildings due to railway traffic in tunnels; ii) in the present case, the results obtained using the monkey-tail model on the computation of the ground stiffness cope very well with the solution obtained by the 3D FEM approach. The first remark is particularly evident on Fig. 11a, where a strong overestimation of the peak values is achieved when SSI effects are discarded. These remarks gain robustness when analyzing the homologous results on the frequency domain, which can be seen in Fig. 12.

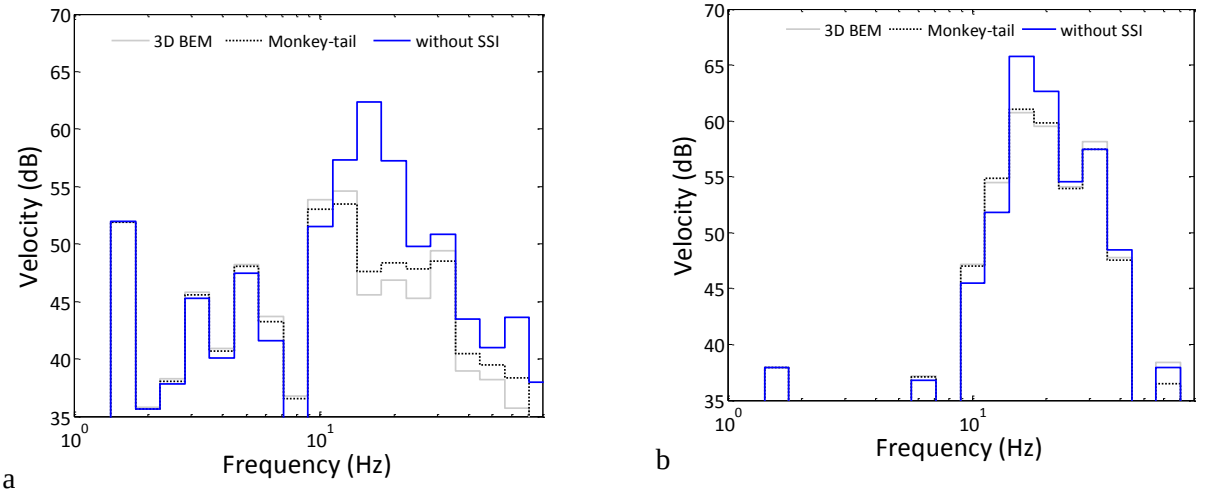


Fig. 12. The influence of SSI on the frequency content of the vertical velocity of point H: a) Cs=150 m/s; b) Cs=410 m/s.

As can be observed, for the softer scenario, the SSI effects negligence can lead to the overestimation of the response up to 15 dB in the frequency range around 20 Hz. This overestimation is minimized for 5 dB when the stiffer scenario is assumed. Despite the differences in the results obtained by the lumped-parameter model when compared with the 3D BEM, a general good agreement is obtained, even when ground stiffness is quite low, which highlights the potentialities of the model.

4. Conclusions

A comprehensive numerical model was used to investigate of the influence of the soil stiffness on the vibrations induced by railway traffic in tunnels. The proposed model includes the simulation of the main aspects of the problem, i.e., the generation of vibrations, the propagation trough the ground and the reception of vibrations inside buildings surrounding the railway infrastructure. Due to the complexity of the problem, a sub-structuring approach was followed, using distinct numerical methods for the simulation of each part of the domain.

Concerning the parametric study developed about the influence of soil stiffness on the dynamic response of the system the following key conclusions were obtained:

i) The dynamic response of the track, as well as of the train, is not particularly affected by soil stiffness. This remark should be made carefully, since it is valid when resilient elements are included on the track. In these cases, almost all the flexibility of the track is given by these resilient elements and the soil stiffness influence is negligible.

ii) The influence of soil stiffness on the dynamic response of the building comprises two main parts: i) the influence of soil-stiffness on the "incident wave field"; ii) the influence of soil-stiffness on the dynamic behaviour of the building. The former aspect depends only on the propagation mechanism, and can be analyzed without the need of ground-structure interaction. As for the latter aspect, it was found that the influence of ground stiffness on the SSI mechanism is quite relevant, mainly when dealing with relatively soft ground.

iii) Since the lower frequency range dominates the response of the building on the horizontal directions, i.e., up to 8 Hz, it is possible to establish the trend of the response to decrease with the increase of soil stiffness. Nevertheless, it should be noticed that this trend relies of the building structural characteristics, so the generalization of this conclusion should be made carefully.

iv) The reasonability of the usage of lumped-parameter models on this kind of problem was checked, and it was found that it constitutes an attractive alternative observing the compromise between accuracy and computational cost.

References

1. INCEJ, *The Regional Environmental Vibrations*. 2001: Tokyo.

2. Smith, M.G., et al., *On the Influence of Freight Trains on Humans: A Laboratory Investigation of the Impact of Nocturnal Low Frequency Vibration and Noise on Sleep and Heart Rate.* PLoS ONE, 2013. **8**(2): p. e55829.

3. Hansen, H.M.M., *High-speed ground transportation. Noise and vibration impact assessment* 2005, Federal Railroad Administration.

4. Hussein, M. and H. Hunt, *A numerical model for calculating vibration from a railway tunnel embedded in a full-space.* Journal of Sound and Vibration, 2007. **305**(3): p. 401-431.

5. Hussein, M. and H. Hunt, *A computationally efficient software application for calculating vibration from underground railways.* Journal of Physics Conference Series, 2009. **181**(1): p. 1-6.

6. Clouteau, D., et al., *Free field vibrations due to dynamic loading on a tunnel embedded in a stratified medium.* Journal of Sound and Vibration, 2005. **283**(1-2): p. 173-199.

7. Gupta, S., et al., *A comparison of two numerical models for the prediction of vibrations from underground railway traffic.* Soil Dynamics and Earthquake Engineering, 2007. **27**(7): p. 608-624.

8. Gupta, S., G. Degrande, and G. Lombaert, *Experimental validation of a numerical model for subway induced vibrations.* Journal of Sound and Vibration, 2009. **321**: p. 786-812.

9. Hung, H. and Y. Yang, *Analysis of ground vibrations due to underground trains by 2.5D finite/infinite element approach.* Earthquake Engineering and Engineering Vibration, 2010. **9**(3): p. 327-335.

10. Lai, C., et al., *Prediction of railway-induced ground vibrations in tunnels* Journal of Vibration and Acoustics, 2005. **127**(5): p. 503-514.

11. Alves Costa, P., R. Calçada, and A. Cardoso, *Influence of train dynamic modelling strategy on the prediction of track-ground vibrations induced by railway traffic.* Proceedings of the Institution of Mechanical Engineers, Part F: Journal of Rail and Rapid Transit 2012. **226**(4): p. 434-450.

12. Lombaert, G. and G. Degrande, *Ground-borne vibration due to static and dynamic axle loads of InterCity and high-speed trains.* Journal of Sound and Vibration, 2009. **319**(3-5): p. 1036-1066.

13. Lopes, P., et al., *Modeling of infinite structures by 2.5D FEM-PML. Application to the simulation of vibrations induced in tunnels*, in *Railways 2012. The First International Conference on Railway Technology: Research, Development and Maintenance*, J. Pombo, Editor. 2012: Tenerife, Canarias.

14. Hussein, M., et al., *The dynamic effect of a piled-foundation building on an incident vibration field from an underground railway tunnel*, in *20th International Congress on Sound and Vibration 2013, ICSV 2013*. 2013: Bangkok, Thailand. p. 1594-1601.

15. Lopes, P., et al., *An efficient numerical model for the simulation of vibrations induced by railway traffic in tunnels*, in *ISEV 2013 - International Symposium on Environmental Vibrations*. 2013: Shangai, China. p. 105-118.

16. Hussein, M., et al., *The use of sub-modelling technique to calculate vibration in buildings from underground railways* Proceedings of the Institution of Mechanical Engineers Part F: Journal of Rail and Rapid Transit, 2013: p. DOI: 10.1177/0954409713511449

17. Lopes, P., et al., *Modelling of vibrations induced by traffic in tunnels: from the source to the receiver*, in *11th International Conference on Vibration Problems*, Z. Dimitrovová, Editor. 2013: Lisbon. p. 1-10.

18. Gupta, S., et al., *Influence of tunnel and soil parameters on vibrations from underground railways.* Journal of Sound and Vibration, 2009. **327**: p. 70-91.

19. Lopes, P., et al., *Numerical modelling of vibrations induced by railway traffic in tunnels: from the source to the nearby buildings.* Soil Dynamics and Earthquake Engineering, 2014. **61-62**: p. 269-285.

20. Lopes, P., et al., *Numerical Modeling of Vibrations Induced in Tunnels: A 2.5D FEM-PML Approach*, in *Traffic Induced Environmental Vibrations and Controls: Theory and Application*, H. Xia and R. Calçada, Editors. 2013, Nova. p. 133-166.

21. Lopes, P., et al., *Influence of soil stiffness on vibrations inside buildings due to railway traffic: numerical study.* Computers & Geotechnics, 2014. **61**: p. 277-291.

22. Yang, Y., S. Kuo, and H. Hung, *Frequency independent infinite elements for analyzing semi-infinite problems.* International Journal for Numerical Methods in Engineering, 1996. **39**: p. 3553-3569.

23. Alves Costa, P., et al., *A 2.5D finite element model for simulation of unbounded domains under dynamic loading*, in *7th European Conference on Numerical Methods in Geotechnical Engineering*, T. Benz and S. Nordal, Editors. 2010: Trondheim. p. 782-790.

COMPDYN 2015
5th ECCOMAS Thematic Conference on
Computational Methods in Structural Dynamics and Earthquake Engineering
M. Papadrakakis, V. Papadopoulos, V. Plevris (eds.)
Crete Island, Greece, 25–27 May 2015

THE DYNAMIC INTERACTION OF TWIN TUNNELS EMBEDDED IN A HOMOGENEOUS HALF-SPACE

Waleed I. Hamad[1], Hugh E.M. Hunt[1], James P. Talbot[1], Mohammed F.M. Hussein[2], and David J. Thompson[3]

[1]Department of Engineering, University of Cambridge
Trumpington Street, Cambridge, CB2 1PZ, UK
e-mail:{wih22, hemh1, jpt1000}@cam.ac.uk

[2]Department of Civil and Architectural Engineering, College of Engineering, Qatar University
Doha, 2713, Qatar
e-mail:mhussein@qu.edu.qa

[3] Institute of Sound and Vibration Research, University of Southampton
Highfield, Southampton, SO17 1BJ, UK
e-mail: djt@isvr.soton.ac.uk

Keywords: Railway, Ground-borne Vibration, Soil-Structure Interaction, Twin Tunnels.

Abstract. *Vibration generated by underground railways can be a major source of disturbance to occupants of nearby buildings. The numerical prediction of ground-borne vibration is a complicated problem that has received extensive research attention in the past decades. However, simplifying assumptions are always required in state-of-the-art numerical models in order to reduce computational effort and resources. A common simplifying assumption is to neglect the presence of a neighbouring tunnel, despite the fact that many underground railway lines around the world consist of two tunnels. This paper investigates the dynamic interaction of two parallel tunnels embedded in a homogeneous half-space. Two different methods are used to tackle the problem. The first is a fully coupled approach, where two cavities are generated in the half-space to which the tunnels are coupled. The second adopts a superposition approach, where two sub-models each consisting of a single tunnel are superposed to calculate the vibration response of the twin tunnels. In both modelling approaches, the tunnel wall is modelled using the thick-shell theory, while the boundary element method is used to simulate the half-space of the ground. The vibration response of the twin-tunnel system on the ground surface due to a harmonic point load at one tunnel invert is studied and compared to that of a single tunnel. The efficacy of the superposition method in modelling the dynamic interaction of the twin tunnels is assessed against the fully coupled approach at different points on the surface. The results reveal the significance of the interaction between the twin tunnels and also demonstrate the accuracy of the superposition method. The feasibility of the superposition method in modelling the dynamic interaction between tunnels and piled-foundations is also highlighted.*

1 INTRODUCTION

Underground railway systems are an environmentally-friendly solution to society's increasing demand for mass transport. A growing issue associated with railways, nevertheless, is ground-borne noise and vibration that can cause significant annoyance within the built environment. Vibration is generated at the wheel-rail interface, due to wheel and track irregularities, and propagates to buildings in close proximity with dominant frequencies in the range from 25Hz to 250Hz. Within this frequency range, both ground-borne vibration and re-radiated noise may be perceived, causing discomfort to people and malfunctioning of sensitive equipment.

In the past decades, the numerical prediction of ground-borne vibration from railways has received extensive research effort. Several numerical models have been developed for scrutinising the propagation of vibration from underground railway tunnels adopting, for example, semi-analytical [1, 2, 3], finite-infinite element [4] and coupled finite element-boundary element (FE-BE) [3, 5, 6, 7] approaches. The required number of parameters, however, to accurately simulate the underground environment makes the formulation of a comprehensive model a challenging task, due mainly to computational resources. For this reason, most researchers have adopted simplifying assumptions in the modelling process such as assuming homogeneous or horizontally layered soil, imposing perfect contact at the soil-structure interface and neglecting the existence of nearby buildings. Recently, some attention have been paid to the influence of these simplifying assumptions, such as inclined layers and inhomogeneities of soil [8, 9, 10], voids at the tunnel-soil interface [11] and source-building interaction [12, 13].

Another common simplifying assumption adopted in the majority of numerical studies of vibration from underground railway tunnels is to neglect the presence of a neighbouring tunnel. Twin tunnels constitute many underground railway lines around the world, such as in London, Bangkok and Washington, DC, where one tunnel is used for the outbound direction and the other is used for the inbound direction [14]. There exist in the literature a number of investigations studying the static effects of excavating twin tunnels. However, with regard to the dynamic interaction of twin tunnels, to date only two models are available in the literature. The first is a wavenumber FE-BE model of twin tunnels embedded in a half-space developed by Sheng *et al.* [15]. This model compares the performance of twin tunnels with that of a single double-track tunnel in terms of vibration response on the ground surface. The second model is a semi-analytical model of twin tunnels buried in a full-space developed by Kuo *et al.* [14]. In this model, which is based on the well-known PiP model [1, 2], the dynamic interaction of twin tunnels is acquired from the solution of a single tunnel model.

This paper presents a model of two parallel tunnels embedded in a homogeneous half-space, in order to investigate the effect of a neighbouring tunnel on the propagation of surface ground-borne vibration. Two different methods are used to tackle the problem. The first is a fully coupled approach, where two cavities are generated in the half-space soil to which the tunnels are coupled. The second is a superposition method, where two sub-models, each consisting of a single tunnel, are superposed together to calculate the vibration response of the twin tunnels. In both modelling approaches, the tunnels are modelled using the cylindrical thick-shell theory, while the half-space soil is simulated using the BE method. The system is assumed invariant in the longitudinal direction allowing for the formulation of the governing equations in the wavenumber-frequency domain and hence implementing a 2.5D approach.

The paper falls into four sections. Section 2 summarises the modelling procedure of the soil and tunnel and describes the superposition method and its governing equations. Section 3 gives the simulation results and comparisons, and finally Section 4 highlights the concluding remarks.

2 MODELLING STRATEGY

The modelling work presented in this paper is aimed at studying the dynamic interaction between twin tunnels in a homogeneous half-space (Fig. 1). Two techniques are adopted: one is a fully coupled approach and the other applies the superposition method. The fully coupled approach is based on generating two cavities in the half-space soil in which the tunnels are inserted, whereas the superposition method produces the response of twin tunnels from the solution of a single tunnel. In both techniques, the soil cavities are modelled using the BE method, while the cylindrical thick-shell theory is used for simulating the tunnel wall. It must be noted that, both the fully coupled approach and superposition method account for the strong coupling between the twin tunnels.

In the analysis, it is assumed that the tunnel is invariant in the longitudinal direction allowing for the use of a 2.5D approach. In this approach, the calculations are performed in the wavenumber domain (ξ_y), thereby representing the full 3D response of the structure and the radiated wave field on a 2D mesh. Hence, a frequency response function (FRF) matrix of a 2D cavity is calculated at the frequency of interest and coupled to the FRF matrix of the tunnel wall. The response in the space domain is obtained by applying the inverse Fourier transform as

$$u(y,\omega) = \frac{1}{2\pi}\int_{-\infty}^{\infty} u(\xi_y,\omega)e^{(i\xi_y y)}d\xi_y, \tag{1}$$

where $u(\xi_y,\omega)$ is the response in the wavenumebr domain. The following sections describe the methods applied in modelling the soil and the tunnel, and present the superposition method.

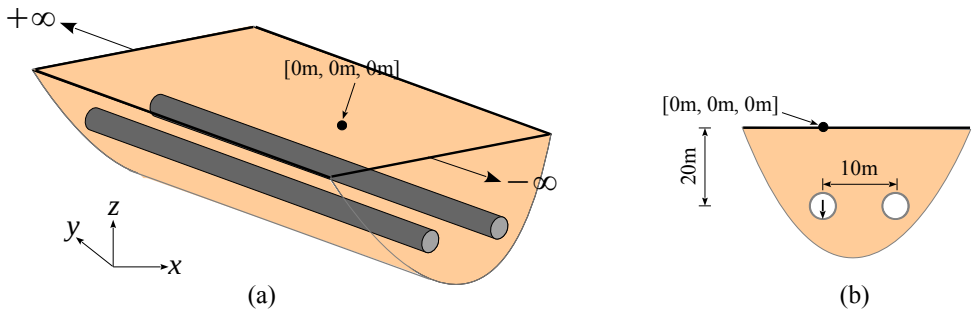


Figure 1: (a) 3D and (b) 2D (invariant section) illustrations of the layout of the model for twin tunnels embedded in a homogeneous half-space.

2.1 The soil model

The soil is modelled using the BE method, based on 2.5D Green's functions for a homogeneous half-space obtained with the aid of the ElastoDynamics Toolbox (EDT) [16]. These fundamental solutions are calculated numerically based on the direct stiffness and thin-layer methods of modelling wave propagation in layered media.

The BE mesh consists of a total of N_s constant nodal-collocated elements, at which tractions and displacements are assumed to be uniform. For each of the N_s nodes of the BE mesh, there are three values of displacements and tractions related by

$$\mathbf{Hu} = \mathbf{Gp}, \tag{2}$$

where $\mathbf{H}$ and $\mathbf{G}$ are $3N_s \times 3N_s$ matrices describing the behaviour of the soil in terms of its Young's modulus (E), density (ρ), Poisson's ratio (ν), damping ratio (η) and frequency of interest (f). The $3N_s \times 1$ vectors $\mathbf{u}$ and $\mathbf{p}$ are assembled from the complex displacement and traction amplitudes of each node as

$$\begin{array}{l} \mathbf{u} = \{u_x^1\ u_y^1\ u_z^1\ u_x^2\ u_y^2\ u_z^2 \cdots u_x^{N_s}\ u_y^{N_s}\ u_z^{N_s}\}^\top \\ \mathbf{p} = \{p_x^1\ p_y^1\ p_z^1\ p_x^2\ p_y^2\ p_z^2 \cdots p_x^{N_s}\ p_y^{N_s}\ p_z^{N_s}\}^\top \end{array}, \tag{3}$$

where $\mathbf{u}^j$ and $\mathbf{p}^j$ are the displacement and traction vectors of node j.

Eq. (2) is rearranged as

$$\begin{array}{l} \mathbf{u} = \mathbf{H}^{-1}\mathbf{G}\mathbf{p} \\ \mathbf{u} = \mathbf{H}_s\mathbf{p} \end{array}, \tag{4}$$

in which $\mathbf{H}_s$ is the FRF matrix relating displacements and tractions at the frequency of interest. Throughout the BE analysis, a minimum of six constant elements are used per wavelength to satisfy the Domínguez recommendations [17] and achieve convergence.

2.2 The tunnel model

The tunnel is simulated by the cylindrical thick-shell theory, in which the equations of motion are formulated in the wavenumber-frequency domain. The tunnel is assumed periodic around the tangential coordinate (θ), and hence any applied force can be represented by a Fourier series of sine and cosine components. If the applied loading comprises harmonic components in space and time, the equations of motion are satisfied by similarly harmonic displacement components. Thus, the modal displacements $\{\tilde{U}_{rn}, \tilde{U}_{\theta n}, \tilde{U}_{zn}\}^\top$ at the mean radius (a) of the cylinder due to applied forces in the radial, tangential and longitudinal directions $\{\tilde{Q}_{rn}, \tilde{Q}_{\theta n}, \tilde{Q}_{zn}\}^\top$ read,

$$\begin{Bmatrix} \tilde{U}_{rn} \\ \tilde{U}_{\theta n} \\ \tilde{U}_{zn} \end{Bmatrix} = [\mathbf{U}]_{r=a}[\mathbf{T}]^{-1}_{r=r_i, r=r_e} \begin{Bmatrix} \tilde{Q}_{rn} \\ \tilde{Q}_{\theta n} \\ \tilde{Q}_{zn} \end{Bmatrix}, \tag{5}$$

where the radial and tangential displacements are associated with $\cos n\theta$, and the tangential is associated with $\sin n\theta$ for the symmetrical loading and vice versa for the anti-symmetrical loading. The top half of matrix $[\mathbf{T}]$ is calculated by substituting the inner radius and the bottom half is obtained by substituting the outer radius. The elements of matrices $[\mathbf{U}]$ and $[\mathbf{T}]$ can be found in [14] for symmetric and antisymmetric cases.

Since the tunnel in this paper is subject to a point harmonic load at its invert, it is necessary to decompose the point load into its space-harmonic components before finding the corresponding displacement. The variation of the load can be written as a linear combination of the ring modes (n) by means of a Fourier series as,

$$\frac{\delta(\theta)}{a} = \frac{1}{2\pi a} + \sum_{n=1}^{\infty} \frac{1}{\pi a} \cos n\theta = \sum_{n=1}^{\infty} b_n \cos n\theta, \tag{6}$$

on the interval $-\pi < \theta \leq \pi$, where $\delta(\theta)$ is the Dirac delta function. Using the representation of the point load in Eq. (6), the input force can be written in a form that suits the formulation in Eq. (5) in order to calculate the response due to symmetric and antisymmetric forces for a given ring mode (n).

The FRF matrix of the tunnel is formulated using the dynamic stiffness approach by dividing the shell into N_t nodes. Each node has three degrees-of-freedom (DoFs) representing the longitudinal, tangential and radial directions (Fig. 2). With the aid of the thick-shell formulation

in Eq. (5) and the representation of the point load in Eq. (6), a FRF matrix $(\mathbf{H}_t)$ relating the response at each DoF to the applied force is assembled.

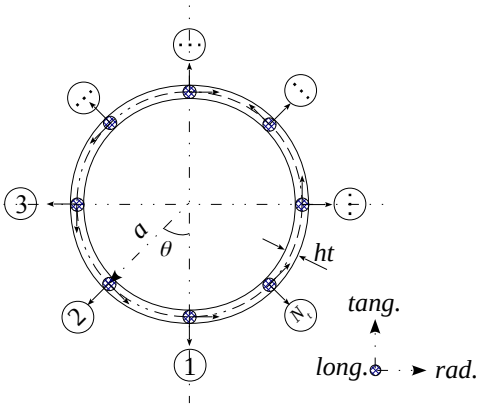


Figure 2: Cross-section a thick-shell divided into N_t nodes.

Before combining, the systems in Eqs. (2) and (5), two transformations are carried out. First, the soil FRF matrix is modified to relate displacements and forces instead of tractions by dividing it by the area of the elements in the BE mesh. Second, the tunnel FRF matrix is modified to relate displacements and forces in the Cartesian coordinates rather than in the cylindrical coordinates as,

$$\mathbf{H}_t^c = \mathbf{T}_r^\top \mathbf{H}_t \mathbf{T}_r, \tag{7}$$

where the size of the transformation matrix $\mathbf{T}_r$ is $3N_t \times 3N_t$.

The tunnel can now be coupled to the soil cavity in the wavenumber domain by applying compatibility of displacements, i.e. soil displacement $(\mathbf{U}_s)$ equals tunnel displacement $(\mathbf{U}_t)$ and equilibrium of forces at the interface as

$$\begin{aligned} \mathbf{U}_s &= \mathbf{H}_s \mathbf{F}_s \\ \mathbf{U}_t &= \mathbf{H}_t^c \left(\mathbf{F}_a - \mathbf{F}_s\right) \\ \mathbf{F}_s &= \left(\mathbf{H}_s + \mathbf{H}_t^c\right)^{-1} \mathbf{H}_t^c \mathbf{F}_a \end{aligned} \quad , \tag{8}$$

in which $\mathbf{F}_a$ is the force applied in the tunnel and $\mathbf{F}_s$ is the resulting force applied in the soil. Knowing $\mathbf{F}_s$, the response at any point in the soil can be calculated.

2.3 The superposition method

The superposition method is used to solve the system in Fig. 1 by breaking it into two sub-models, each representing a single cavity embedded in a homogeneous half-space. As shown in Fig. 3, each sub-model has a horizontal cavity, referred to here as a real cavity, and a virtual cavity at the position of the real cavity in the other sub-model. The method used in this paper is similar to that applied by Kuo *et al.* [14] for modelling twin tunnels embedded in a full-space.

The displacement fields for each sub-model due to forces acting on a single cavity can be calculated at its interface and also at the interface of the virtual cavity. The vibration response of the coupled system can be written as the superposition of the two displacement fields $(\mathbf{U}^r, \mathbf{U}^v)$. One displacement field is the result of forces acting on a single cavity, while the other is the result of the interaction between the two cavities. Likewise, the total forces applied to the

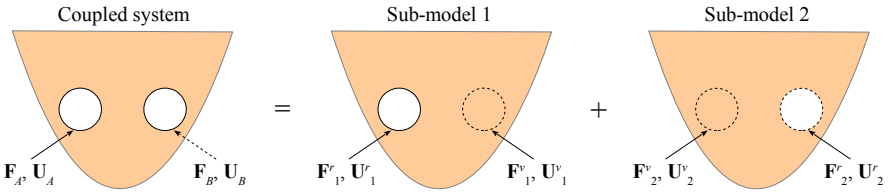


Figure 3: Schematic for the superposition method used for solving the twin tunnels, showing the coupled system and the sub-models. The subscripts A and B refer to the cavity number, and 1 and 2 denote sub-model 1 respectively sub-model 2, whereas the superscripts r and v refer to real and virtual cavity respectively.

coupled system $(\mathbf{F}^r, \mathbf{F}^v)$ are equal to the summation of the forces acting on one cavity with those representing the motion induced by the neighbouring cavity. This is described by the following equations,

$$\begin{aligned} \mathbf{U}_A &= \mathbf{U}_1^r + \mathbf{U}_2^v \\ \mathbf{F}_A &= \mathbf{F}_1^r + \mathbf{F}_2^v \\ \mathbf{U}_B &= \mathbf{U}_1^v + \mathbf{U}_2^r \\ \mathbf{F}_B &= \mathbf{F}_1^v + \mathbf{F}_2^r \end{aligned} , \tag{9}$$

in which the subscripts A and B refer to the cavity number and 1 and 2 refer to the sub-model number, and superscripts r and v denote the real and virtual cavity respectively.

From the sub-model 1 in Fig. 3, relationships between the forces $(\mathbf{F}_1^r)$ on the real cavity and its displacements $(\mathbf{U}_1^r)$ as well as the displacements $(\mathbf{U}_1^v)$ and tractions $(\mathbf{Q}_1^v)$ on the virtual cavity read

$$\begin{aligned} \mathbf{U}_1^r &= \mathbf{H}_1^{rr}\mathbf{F}_1^r \\ \mathbf{U}_1^v &= \mathbf{H}_1^{vr}\mathbf{F}_1^r \\ \mathbf{Q}_1^v &= \mathbf{G}_1^{vr}\mathbf{F}_1^r \end{aligned} , \tag{10}$$

where $\mathbf{H}_1^{rr}$ is the FRF matrix relating the real cavity forces and displacements, and $\mathbf{H}_1^{vr}$ and $\mathbf{G}_1^{vr}$ are the FRF matrices relating the real cavity forces and the virtual cavity displacements and forces respectively. The force vector $(\mathbf{F}_1^v)$ is obtained by integrating the traction vector $(\mathbf{Q}_1^v)$.

Similarly for sub-model 2 in Fig. 3, relationships between the forces on the interface of the real cavity $(\mathbf{F}_2^r)$ and its displacements $(\mathbf{U}_2^r)$ in addition to the virtual cavity displacements $(\mathbf{U}_2^v)$ and tractions $(\mathbf{Q}_2^v)$ yield

$$\begin{aligned} \mathbf{U}_2^r &= \mathbf{H}_2^{rr}\mathbf{F}_2^r \\ \mathbf{U}_2^v &= \mathbf{H}_2^{vr}\mathbf{F}_2^r \\ \mathbf{Q}_2^v &= \mathbf{G}_2^{vr}\mathbf{F}_2^r \end{aligned} , \tag{11}$$

in which $\mathbf{H}_2^{rr}$ is the FRF matrix relating the real cavity forces and displacements, and $\mathbf{H}_2^{vr}$ and $\mathbf{G}_2^{vr}$ are the FRF matrices relating the real cavity forces and the virtual cavity displacements and forces respectively. The force vector $(\mathbf{F}_2^v)$ is obtained by integrating the traction vector $(\mathbf{Q}_2^v)$.

The FRF matrices $(\mathbf{H}_1^{rr},\ \mathbf{H}_1^{vr},\ \mathbf{H}_2^{rr},$ and $\mathbf{H}_2^{vr})$ are obtained by applying a unit force at each DoF of the real cavity $(\mathbf{F}_1^r,\ \mathbf{F}_2^r)$ and calculating the corresponding displacements of the real cavity $(\mathbf{U}_1^r,\ \mathbf{U}_2^r)$ as well as the virtual cavity $(\mathbf{U}_1^v,\ \mathbf{U}_2^v)$. The FRF matrices $(\mathbf{G}_1^{vr},\ \mathbf{G}_2^{vr})$ are acquired from the displacements of the virtual cavity by calculating: (i) strains by differentiating displacements, (ii) stresses from strains using constitutive relationships, and (iii) tractions using Caushy's stress law as

$$\mathbf{Q} = \boldsymbol{\sigma}\mathbf{n}, \tag{12}$$

where $\mathbf{Q}$ is the traction vector, $\boldsymbol{\sigma}$ is the stress tensor and $\mathbf{n}$ is the normal vector.

Now, there are $10 \times 3N_s$ system of equations presented in Eqs. (9) to (11), that can be solved together to give the FRF matrix of the coupled system in Fig. 3. Substituting the displacement vectors of the sub-models in Eqs. (10) and (11) in the displacement vectors of the coupled system in Eq. (9) yields

$$\begin{bmatrix}\mathbf{U}_A\\ \mathbf{U}_B\end{bmatrix} = \begin{bmatrix}\mathbf{U}_1^r\\ \mathbf{U}_1^v\end{bmatrix} + \begin{bmatrix}\mathbf{U}_2^v\\ \mathbf{U}_2^r\end{bmatrix} = \begin{bmatrix}\mathbf{H}_1^{rr} & \mathbf{H}_2^{vr}\\ \mathbf{H}_1^{vr} & \mathbf{H}_2^{rr}\end{bmatrix} \begin{bmatrix}\mathbf{F}_1^r\\ \mathbf{F}_2^r\end{bmatrix}. \tag{13}$$

Likewise, substituting the force vectors of the sub-models in Eqs. (10) and (11) in the force vectors of the coupled system in Eq. (9) gives

$$\begin{bmatrix}\mathbf{F}_A\\ \mathbf{F}_B\end{bmatrix} = \begin{bmatrix}\mathbf{F}_1^r\\ \mathbf{F}_1^v\end{bmatrix} + \begin{bmatrix}\mathbf{F}_2^v\\ \mathbf{F}_2^r\end{bmatrix} = \begin{bmatrix}\mathbf{I}_1\\ \mathbf{G}_1^{vr}\end{bmatrix} \mathbf{F}_1^r + \begin{bmatrix}\mathbf{G}_2^{vr}\\ \mathbf{I}_2\end{bmatrix} \mathbf{F}_2^r = \begin{bmatrix}\mathbf{G}_2^{vr}\\ \mathbf{I}_2\end{bmatrix} \mathbf{F}_2^r = \begin{bmatrix}\mathbf{I}_1 & \mathbf{G}_2^{vr}\\ \mathbf{G}_1^{vr} & \mathbf{I}_2\end{bmatrix} \begin{bmatrix}\mathbf{F}_1^r\\ \mathbf{F}_2^r\end{bmatrix}, \tag{14}$$

where $\mathbf{I}_1$ and $\mathbf{I}_2$ are identity matrices.

Rearranging Eq. (14) and substituting in Eq. (13), the displacement and force vectors of the coupled system are related together as

$$\begin{bmatrix}\mathbf{U}_A\\ \mathbf{U}_B\end{bmatrix} = \begin{bmatrix}\mathbf{H}_1^{rr} & \mathbf{H}_2^{vr}\\ \mathbf{H}_1^{vr} & \mathbf{H}_2^{rr}\end{bmatrix} \begin{bmatrix}\mathbf{I}_1 & \mathbf{G}_2^{vr}\\ \mathbf{G}_1^{vr} & \mathbf{I}_2\end{bmatrix}^{-1} \begin{bmatrix}\mathbf{F}_A\\ \mathbf{F}_B\end{bmatrix}. \tag{15}$$

From Eq. (15), the soil FRF matrix of the coupled system $(\mathbf{H}_s^c)$ in Fig. 3 reads

$$\mathbf{H}_s^c = \begin{bmatrix}\mathbf{H}_1^{rr} & \mathbf{H}_2^{vr}\\ \mathbf{H}_1^{vr} & \mathbf{H}_2^{rr}\end{bmatrix} \begin{bmatrix}\mathbf{I}_1 & \mathbf{G}_2^{vr}\\ \mathbf{G}_1^{vr} & \mathbf{I}_2\end{bmatrix}^{-1}, \tag{16}$$

which is to be coupled to the twin tunnels FRF matrix in the same manner of Eq. (8).

3 SIMULATION PARAMETERS AND RESULTS

The simulation results presented in this paper are intended to serve two purposes. The first is to scrutinise the effect of a neighbouring tunnel on the vibration field from an existing tunnel. The second is to testify the validity of the superposition method for modelling the dynamic interaction of twin tunnels. These purposes are met by simulating twin tunnels embedded at a depth of 20m and separated by a distance of 10m, see Fig. 1. One tunnel is subject to a unit harmonic point load at its invert and the responses on the free-surface are calculated in the frequency range from 1Hz to 80Hz, with a resolution of 1Hz for the fully coupled approach and 5Hz for the superposition method. A coarse frequency resolution is used for the superposition method to reduce computation time. The number of elements in the BE mesh (N_s), which comprises 40 constant elements of equal size, conforms to those in the tunnel model (N_t). Table 1 summarises the parameters used in the simulations.

3.1 Effects of a neighbouring tunnel

The significance of the interaction of twin tunnels is presented here by investigating the displacement fields of single and twin tunnels on the free-surface at example frequencies of 30Hz and 70Hz. Waves generated at the tunnel due to a harmonic point load at the invert propagate through the soil and result in Rayleigh waves at the surface of the half-space. The

Parameter	Tunnel	Soil
Radius, a	2.875m	3m
Thickness, h	0.25m	–
Young's modulus, E	50GPa	550MPa
Density, ρ	2500kg/m^3	2000kg/m^3
Poisson's ratio, ν	0.3	0.44
Damping loss factor, η	0.06	0.06
Shear wave velocity, c_s	–	309m/s
Compression wave velocity, c_p	–	944m/s

Table 1: Tunnel and soil parameters used in the simulations.

results presented in this section are produced by the fully coupled approach. The insertion gain (IG) between the two systems is calculated at both frequencies to quantify the effect of a neighbouring tunnel as

$$\mathrm{IG} = 20\log_{10}\left(\left|\frac{u(y,\omega)_{twin}}{u(y,\omega)_{single}}\right|\right). \tag{17}$$

Fig. 4 depicts the transverse (*x-axis*) displacement field generated by single and twin tunnels due to a harmonic point load at the invert. It can be observed for the single tunnel model that, due to symmetry, there are no displacements on the plane $x = 0$, while the displacements at other symmetry points are equal in magnitude and opposite in direction. The insertion of a second tunnel at a centre-to-centre distance of 10m clearly disrupts this symmetry, causing diffraction of the wavefronts particularly at 70Hz. The net effect of the second tunnel is a change in the displacement field of up to $\pm$10dB at both frequencies, as illustrated in the insertion gain plots.

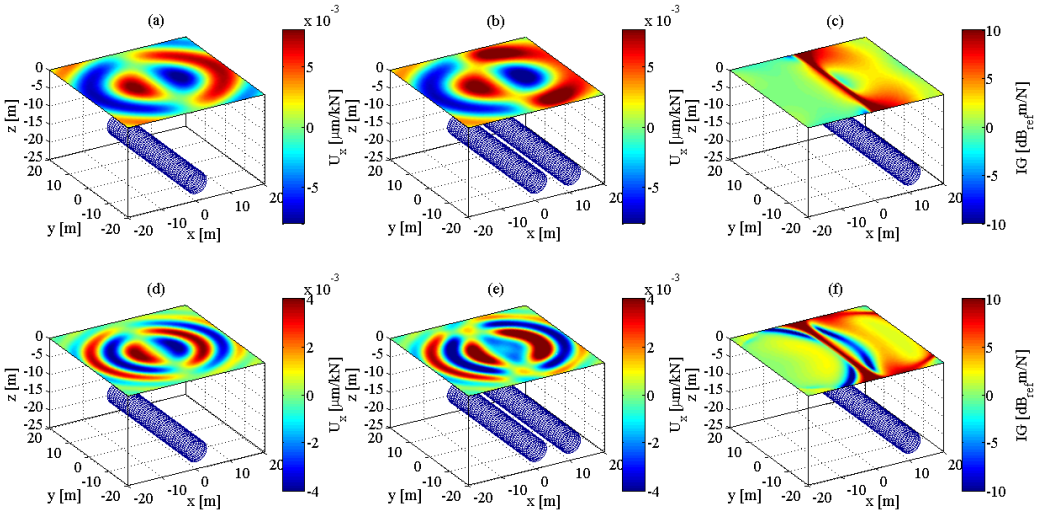


Figure 4: Real part of the transverse (*x-axis*) displacement on the free-surface due to a unit harmonic point load on one tunnel invert at a frequency of (a-c) 30Hz and (d-f) 70Hz for (a), (d) a single tunnel and (b), (e) twin tunnels, and (c), (f) the corresponding insertion gain, as computed by the fully coupled approach.

The longitudinal (*y-axis*) displacement field of the single and twin tunnels due to a harmonic

point load at the invert is shown in Fig. 5. All displacements on the plane $y = 0$ equal zero due to symmetry for both the single and twin tunnels. At other symmetry points, the displacements are equal in magnitude and opposite in direction. Again, the inclusion of a neighbouring tunnel clearly distorts the wavefronts at both frequencies, resulting in an insertion gain of up to $\pm$20dB.

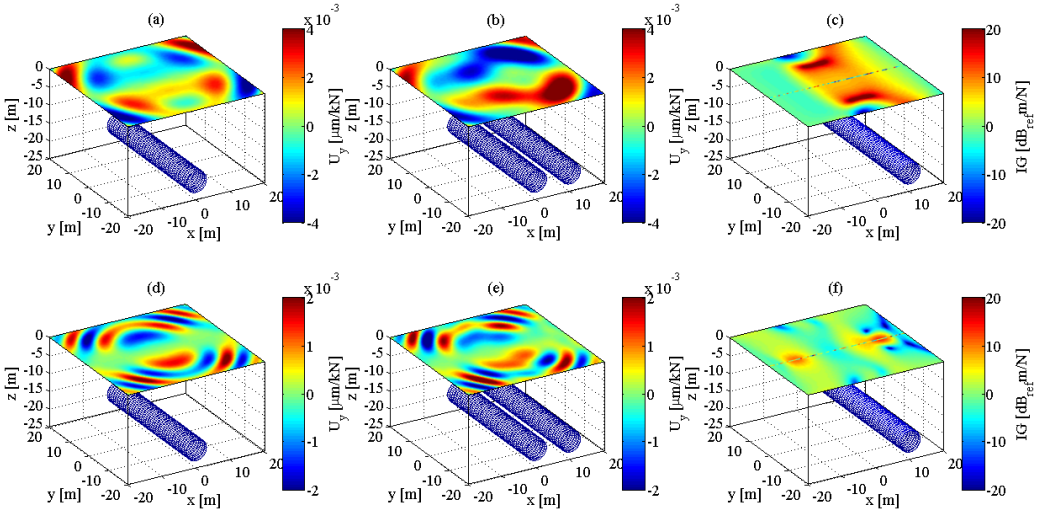


Figure 5: Real part of the longitudinal (*y-axis*) displacement on the free-surface due to a unit harmonic point load on one tunnel invert at a frequency of (a-c) 30Hz and (d-f) 70Hz for (a), (d) a single tunnel and (b), (e) twin tunnels, and (c), (f) the corresponding insertion gain, as computed by the fully coupled approach.

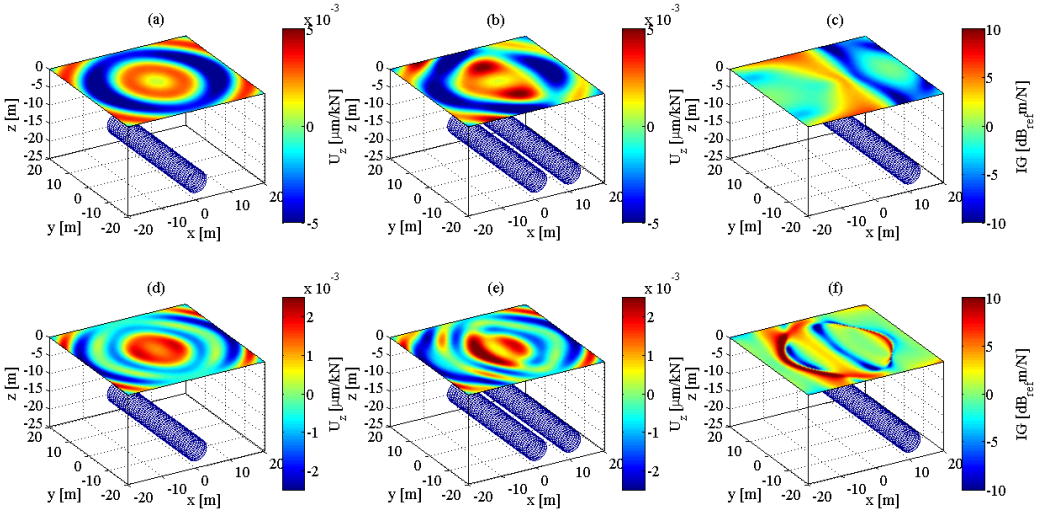


Figure 6: Real part of the vertical (*z-axis*) displacement on the free-surface due to a unit harmonic point load on one tunnel invert at a frequency of (a-c) 30Hz and (d-f) 70Hz for (a), (d) a single tunnel and (b), (e) twin tunnels, and (c), (f) the corresponding insertion gain, as computed by the fully coupled approach.

Fig. 6 illustrates the vertical (*z-axis*) displacement field on the free-surface, which shows that the wavefronts are not cylindrical due to the nature of the source and the dynamic interaction

between the soil and the tunnels. For the single tunnel, the displacements at the symmetry points are equal, yet they are not equal for the twin tunnels. The addition of the second tunnel modifies the displacement field by up to $\pm$10dB. It is also noted that the second tunnel appears to diffract the wavefront more than in the horizontal displacement field in Fig. 4.

Similar observations to those presented in Figs. 4 to 6 have been highlighted in a recent study of dynamic interaction between twin tunnels in a full-space [14]. In this study, it was shown that the presence of a neighbouring tunnel can modify the vibration field of an existing tunnel at times of the order of 20dB.

3.2 Verification of the superposition method

The efficacy of the superposition method in modelling the twin tunnels is now assessed against the fully coupled approach. The free-surface vibration response due to a harmonic point load at one tunnel invert is calculated at points [0m, 0m, 0m], [5m, 0m, 0m], [10m, 0m, 0m], [0m, 10m, 0m], [5m, 10m, 0m] and [10m, 10m, 0m] as shown in Fig. 1. Such predictions might be useful for practising engineers who are often interested in vibration levels on the ground surface for the assessment of train-induced vibration and vibration countermeasures.

Figs. 7 to 9 show the magnitude of the three displacement components $(\mathrm{U}_x,\ \mathrm{U}_y,\ \mathrm{U}_z)$ at the six points on the free-surface as predicted by the fully coupled approach and the superposition method. It is worth noting that the longitudinal displacements at points [0m, 0m, 0m], [5m, 0m, 0m] and [10m, 0m, 0m] are equal to zero due to symmetry. In general, a good agreement between the two techniques is seen for all displacements, with small differences of less than 0.5dB at some frequencies. Such differences are still acceptable for vibration predictions, given their sensitivity to changes in the measurement techniques, environmental conditions and/or material properties.

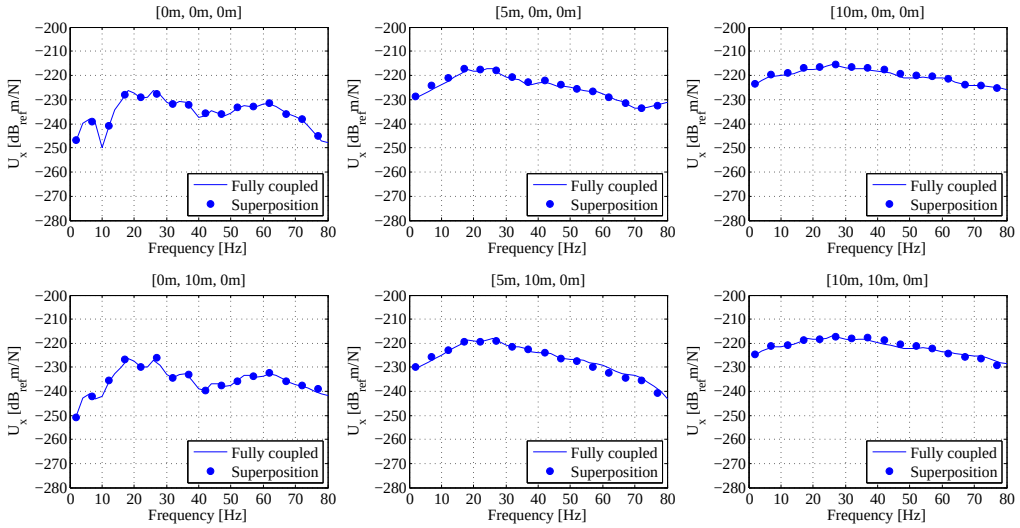


Figure 7: Magnitude of the transverse displacement at points on the free-surface above twin tunnels in a homogeneous half-space due to a unit harmonic point load on one tunnel invert, as computed by the fully coupled and superposition approaches.

Theoretically, the superposition method should give exact results to those of the fully coupled approach since the system in Fig. 1 is linear. The method, however, inevitably involves

computation errors as it approximates the tractions of the virtual cavity numerically. It is therefore believed that the small differences are due to numerical errors resulting from calculating strains by differentiating displacements.

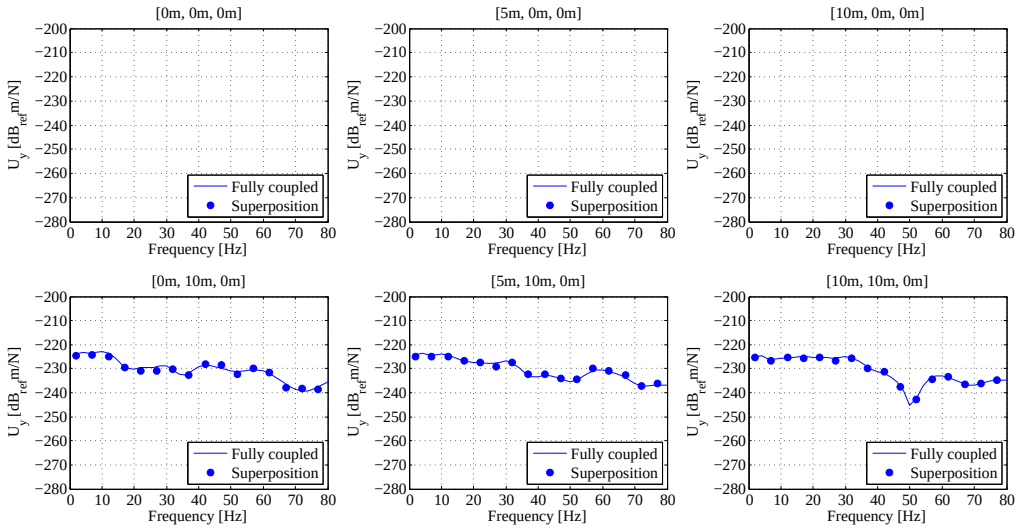


Figure 8: Magnitude of the longitudinal displacement at points on the free-surface above twin tunnels in a homogeneous half-space due to a unit harmonic point load on one tunnel invert, as computed by the fully coupled and superposition approaches.

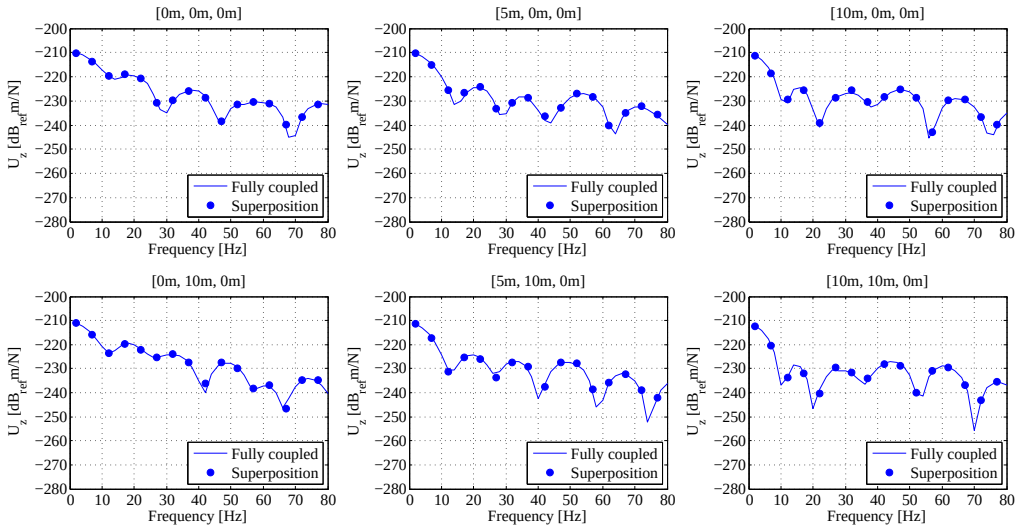


Figure 9: Magnitude of the vertical displacement at points on the free-surface above twin tunnels in a homogeneous half-space due to a unit harmonic point load on one tunnel invert, as computed by the fully coupled and superposition approaches.

The results shown in Figs. 7 to 9 have indicated that the superposition method can robustly model the dynamic interaction between underground neighbouring structures. This is essential

for modelling systems that cannot practically be simulated by the fully coupled approach, due to computational limitations, such as those including both fully coupled piled-foundations and underground tunnels. The superposition method is valuable in such cases because it breaks the problem into two manageable sub-models; one representing the tunnels efficiently in the wavenumber domain (2.5D), and the other representing the full 3D behaviour of the piled-foundations.

4 CONCLUSIONS

There are a number of underground railway lines around the world consisting of twin tunnels, including those in London, Bangkok and Washington, DC. Despite this fact, the majority of previous numerical studies of ground-borne vibration from underground railways consider a single tunnel in the modelling process. This paper has presented two techniques for modelling twin tunnels in a homogeneous half-space, both using the boundary element method for the soil and the cylindrical thick-shell theory for the tunnels. The models have studied the vibration response on the ground surface due to a harmonic point load at one tunnel invert.

It has been demonstrated that the dynamic interaction between twin tunnels is highly significant. At the examined frequencies, the insertion gain of the displacement field on the free-surface between the twin tunnels and the single tunnel reaches up to $\pm$10dB for the transverse and vertical directions, and up to $\pm$20dB for the longitudinal direction.

The accuracy of the superposition method in predicting the dynamic interaction between twin tunnels has been assessed against the fully coupled approach. Small discrepancies between the two techniques are attributed to the inevitable numerical errors associated with calculating the tractions of the virtual cavity in the superposition method. However, these discrepancies are acceptable, and unlike the fully coupled approach, the superposition method is deemed a feasible technique for modelling the interaction between longitudinally invariant structures and finite structures, such as underground tunnels and piled-foundations.

Acknowledgements

The authors would like to acknowledge the EPSRC for funding this research, which is part of the MOTIV project (`www.motivproject.co.uk`), grant numbers (EP/K006665/1, EP/K006002/1, EP/K005847/2). We also thank the contribution of the Katholieke Universiteit Leuven for providing the EDT and some functions of BEMFUN used in the BE models.

REFERENCES

[1] J. A. Forrest, H. E. M. Hunt, A three-dimensional tunnel model for calculation of train-induced ground vibration. *Journal of Sound and Vibration*, **294**, 678-705, 2006.

[2] M. F. M. Hussein, H. E. M. Hunt, A numerical model for calculating vibration from a railway tunnel embedded in a full-space. *Journal of Sound and Vibration*, **305**, 401-431, 2007.

[3] M. F. M. Hussein, S. François, M. Schevenels, H. E. M. Hunt, J. P. Talbot, G. Degrande, The fictitious force method for efficient calculation of vibration from a tunnel embedded in a multi-layered half-space. *Journal of Sound and Vibration*, **333**, 6996-7018, 2014.

[4] Y. B. Yang, H. H. Hung, A 2.5D finite/infinite element approach for modelling visco-elastic bodies subjected to moving loads. *International Journal for Numerical Methods in Engineering*, **51**, 1317-1336, 2001.

[5] L. Andersen, C. J. C. Jones, Coupled boundary and finite element analysis of vibration from railway tunnels − a comparison of two- and three-dimensional models. *Journal of Sound and Vibration*, **293**, 611-625, 2006.

[6] S. Gupta, M. F. M. Hussein, G. Degrande, H. E. M. Hunt, D. Clouteau, A comparison of two numerical models for the prediction of vibrations from underground railway traffic. *Soil Dynamics and Earthquake Engineering*, **27**, 608-624, 2007.

[7] S. François, M. Schevenels, G. Lombaert, P. Galvín, G. Degrande, A 2.5D coupled FE-BE methodology for the dynamic interaction between longitudinally invariant structures and a layered halfspace. *Computer Methods in Applied Mechanics and Engineering*, **199** (23-24), 1536-1548, 2010.

[8] S. Jones, H. Hunt, The effect of inclined soil layers on surface vibration from underground railways using the thin layer method. *ASCE Journal of Engineering Mechanics*, **137** (12), 887-900, 2011.

[9] S. Jones, H. Hunt, Predicting surface vibration from underground railways through inhomogeneous soil. *Journal of Sound and Vibration,* **331** (9), 2055-2069, 2012.

[10] W. Yang, M. F. M. Hussein, A. M. Marshall, Centrifuge and numerical modelling of ground-borne vibration from an underground tunnel. *Soil Dynamics and Earthquake Engineering*, **51**, 23-34, 2013.

[11] S. Jones, H. Hunt, Voids at the tunnel-soil interface for calculation of ground vibration from underground railways, *Journal of Sound and Vibration*, **330** (2), 245270, 2011.

[12] P. Coulier, G. Lombaert, G. Degrande, The influence of source-receiver interaction on the numerical prediction of railway induced vibrations. *Journal of Sound and Vibration*, **333**, 2520-2538, 2014.

[13] P. Lopes, P. A. Costa, M. Ferraz, R. Calçada, A. Cardoso, Numerical modelling of vibrations induced by railway traffic in tunnels: From the source to the nearby buildings. *Soil Dynamics and Earthquake Engineering*, **61**-**62**, 269-285, 2014.

[14] K. Kuo, H. E. M. Hunt, M. F. M. Hussein, The effect of a twin tunnel on the propagation of ground-born vibration from an underground railway. *Journal of Sound and Vibration* **330**, 6203-6222, 2011.

[15] X. Sheng, C. J. C. Jones, D. J. Thompson, Modelling ground vibration from railways using wavenumber finite- and boundary-element methods. *Proceedings of the Royal Society A*, **461**, 2043-2070, 2005.

[16] M. Schevenels, S. François, G. Degrande, EDT: An elastodynamics toolbox for MATLAB. *Computers & Geosciences* **35**(80), 1752-1754, 2009.

[17] J. Domínguez, *Boundary Elements in Dynamics*. Computational Mechanics Publications and Elsevier Applied Science, 1993.

COMPDYN 2015
5th ECCOMAS Thematic Conference on
Computational Methods in Structural Dynamics and Earthquake Engineering
M. Papadrakakis, V. Papadopoulos, V. Plevris (eds.)
Crete Island, Greece, 25–27 May 2015

PREDICTIONS OF THE DYNAMIC RESPONSE OF PILED FOUNDATIONS IN A MULTI-LAYERED HALF-SPACE DUE TO INERTIAL AND RAILWAY INDUCED LOADINGS

Evangelos Ntotsios[1], Waleed I. Hamad[2], David J. Thompson[1], Mohammed F.M. Hussein[3], Hugh E.M. Hunt[2], and James P. Talbot[2]

[1] Institute of Sound and Vibration Research, University of Southampton
Southampton, SO17 1BJ, U.K.
e-mail: e.ntotsios@soton.ac.uk; djt@isvr.soton.ac.uk

[2] Department of Engineering, University of Cambridge
Trumpington Street, Cambridge CB2 1PZ, U.K.
{wih22,hemh1,jpt1000}@cam.ac.uk

[3] Department of Civil and Architectural Engineering, College of Engineering, Qatar University
Doha, 2713, Qatar
mhussein@qu.edu.qa

Keywords: Pile Foundations, Pile-Soil-Pile Interaction, Ground Wave Propagation, Railway Induced Vibration.

Abstract. *In this paper, the dynamic pile-soil-pile interaction (PSPI) in a multi-layered half-space is investigated for the prediction of the response of piled foundations due to railway vibrations. Two methods of modelling piled foundations in a multi-layered half-space are presented. The first is an efficient semi-analytical model that calculates the Green's functions of the multi-layered half-space soil using the thin layer and the dynamic stiffness matrix methods. The second is a fully-coupled model that utilises the boundary element (BE) method to simulate the soil, where the Green's functions are calculated using the ElastoDynamics Toolbox (EDT). The paper aims to investigate the accuracy and the efficiency of the semi-analytical model by comparing the predictions of the two methods. A set of comparisons is performed, including the driving point response of a single pile and the interaction between two piles. The comparisons reveal that, at most frequencies, the semi-analytical model can predict the driving point response and the dynamic interaction with acceptable accuracy and computational efficiency. The model is then used for predicting the response of a pile-group due to the vibration field generated by a railway in varying distance from the piles. The vibration field generated by the railway is modelled as the superposition of the response due to harmonic loadings generated at the wheel-rail interface and the vibration response is examined at different points on the free surface away from the piles. The comparisons highlight the efficiency and accuracy of the semi-analytical model and illustrate its practical application.*

1 INTRODUCTION

Ground-borne vibration generated by sources such as earthquakes, railways, roads and construction activities often causes disturbance to nearby buildings that may lead to significant social and economic impacts. Usually, structural foundations, such as piled foundations, act as a transmission path for ground-borne vibration into buildings. In some cases, however, piled foundations can serve as wave barriers to isolate vibration when arranged in appropriate configurations. As such, over the past four decades the dynamic pile-soil-pile interaction (PSPI) has received extensive research effort. Different techniques of modelling the dynamic PSPI have been formulated, most of them were recently reviewed by Kuo and Hunt [1].

The research interest in the dynamic PSPI was sparked by the pioneering work of Poulos [2, 3] on the static behaviour of pile groups. In his work, Poulos introduced the concept of interaction factors, which express the displacement of a pile group as a function of the motion of the loaded, adjacent pile. A number of researchers have later applied this concept to study the dynamic behaviour of pile groups, which was observed to be a strongly frequency dependent [4, 5]. These findings, along with the increasing interest in soil-structure interaction, have led researchers to develop further analytical methods for modelling the dynamic behaviour of pile groups [6, 7]. However, despite offering considerable reduction in computation time, the analytical models only provide approximate solutions for PSPI as the presence of neighbouring piles is ignored when calculating the interaction between two piles. The existence of neighbouring piles has two effects; the soil-stiffening effect, which dominates at low frequencies (wavelengths are greater than pile spacing), and the wave scattering effect, which dominates at high frequencies (wavelengths are less than the diameter of the piles) [8]. These shortcomings limit the application of such models in studying ground-borne vibration, and hence an efficient, yet rigorous analytical model is still required.

The boundary element (BE) method, on the other hand, is considered to be a reliable approach for modelling the dynamic PSPI. Unlike the finite element method, wave radiation is inherently accounted for, resulting in accurate solutions within the interior of the domain. For instance, Sen et al. [9] presented a BE model of a pile group, in which the piles are modelled as an elastic bar/beam and inserted into a homogeneous half-space with multiple cavities. Talbot and Hunt [8] avoided adding extra cavities in the soil by adopting instead the periodic structure theory to model an infinitely long row of piles embedded in a homogeneous half-space. Maeso et al. [10] developed a pile group model by simulating the piles as continuous elastic solids and the soil as an isotropic homogeneous fluid-filled poroelastic material. More recently, Millán and Domínguez [11] devised a simplified BE model for pile groups in viscoelastic and poroelastic soils. All these previous BE models provide a good solution for PSPI and are capable of considering different types of motion of pile heads. BE models of piles, in general, can serve as a benchmark to scrutinise the effects of simplifying assumptions inherent in the analytical models. However, BE models are computationally inefficient and thus they may not be a suitable tool for design use by practicing engineers. This in turn shows the need for efficient models that account for essential aspects of the dynamic PSPI.

This paper presents two approaches of modelling piled foundations in a multi-layered half-space. The first is an efficient semi-analytical model that simulates the soil as a horizontally layered semi-infinite system. The second is a fully-coupled model that utilises the BE method to model the soil. The pile is modelled, in both approaches, by an elastic bar for axial loading and an Euler-Bernoulli beam for transverse loading. The approaches adopted for modelling the ground are discussed in Section 2. In Section 3 the pile model and the coupling techniques are presented. The simulation parameters and results are presented in Section 4, and finally some findings and conclusions are highlighted in Section 5.

2 GROUND MODELLING

To model the dynamic soil-structure interaction appropriately, it is essential to have an acceptable representation of the soil. Given the low strain amplitudes of ground-borne vibration, it is plausible to assume that the soil behaves in a linear-elastic manner. In the following sections, the two techniques adopted in the current work to model the ground, which both treat the soil as a linear-elastic medium, are described.

2.1 Semi-analytical approach

In the semi-analytical approach, the soil is modelled as a horizontally layered semi-infinite system and the response field is obtained by the use of integral transforms. For this formulation the source fields (displacements and tractions) are transformed to the wavenumber/frequency domain and the layered medium is modelled as an assembly of homogeneous layer and half-space elements. Closed-form solutions can be obtained to the Navier equations, governing wave propagation in a homogeneous layer or a homogeneous half-space, for each frequency and wavenumber. The response fields can be transformed back to the space/time domain by inverse Fourier transformation operations.

From the different available methods based on the wavenumber/frequency domain approach, a hybrid formulation of the Thin Layer Method (TLM) [12, 13] and the Direct Stiffness Matrix Method (DSMM) [12, 14] is used for the calculation of the response field in the soil. In both these methods, which are similar to the finite element method, element stiffness matrices are used to express the relation between displacements and stresses at the soil element boundaries. The difference between the two methods is that the TLM is an approximate method using less computationally demanding polynomial functions whereas in the DSMM transcendental functions are used that are exact solutions for a given wavenumber and frequency. It should be noted that, due to its approximate nature, the TLM requires that the layer elements have a thickness that is small compared with the smallest relevant wavelength. This gives rise to systems of equations with more degrees of freedom than the DSSM. Nevertheless, the coupling between the pile and the soil introduces multiple source tractions in the soil along the length of the pile, so that each soil layer has to be divided to multiple sublayers. Consequently, the TLM is considered to be more suitable since it already offers high density of soil discretization with depth. Below the depth reached by the piles no more traction sources exist, so the soil layers and the homogenous half-space are modelled using DSMM. In addition this is necessary as the TLM is only applicable to media with a finite thickness.

Using the hybrid formulation and dropping for simplicity the dependence on the frequency ω , the response $\mathbf{u}_s(r)$ of the soil (receiver) due to a load vector (source) $\mathbf{g}$ at a distance r is given by

$$\mathbf{u}_s(r) = \mathbf{H}_h(r)\mathbf{g} \tag{1}$$

where $\mathbf{H}_h$ is the frequency response function (FRF) matrix relating displacements and tractions at the frequency of interest for an area or point load $\mathbf{g}$.

It should be noted that the soil with the cavity cannot be modelled using the semi-analytical formulation. This means that effectively the volume of the piles is neglected, the interface between the pile and the soil being reduced to a line and the load delivered from the pile to the soil at each coupling node is distributed over an area. More details about the interaction between the pile and the soil is given in Section 3.

2.2 Boundary element approach

In the second approach, the soil is modelled using the BE method, where three-dimensional Green's functions for a multilayered half-space are obtained with the aid of the ElastoDynamics Toolbox (EDT) [12]. These fundamental solutions are calculated numerically based on the DSMM for wave propagation in layered media. A BE mesh is generated at the soil-structure interface to simulate a vertical cylindrical cavity. The mesh consists of a number of elements with nodal collocation, at which there are three values of displacements and three tractions. These variables are related at each collocation point N_S by

$$\mathbf{Hu} = \mathbf{Gp} \tag{2}$$

where $\mathbf{H}$ and $\mathbf{G}$ are $3N_S \times 3N_S$ matrices describing the behaviour of the soil in terms of its density (ρ), shear modulus (μ), Poisson's ratio (ν), damping ratio (η), shear wave speed (c_S), compressional wave speed (c_P) and frequency of interest (f). The $3N_S \times 1$ vectors $\mathbf{u}$ and $\mathbf{p}$ are assembled from the complex displacement and traction amplitudes of each node as

$$\begin{aligned} \mathbf{u} &= \left[u_x^1 \quad u_y^1 \quad u_z^1 \quad u_x^2 \quad u_y^2 \quad u_z^2 \quad \cdots \quad u_x^{N_S} \quad u_y^{N_S} \quad u_z^{N_S}\right]^T \\ \mathbf{p} &= \left[p_x^1 \quad p_y^1 \quad p_z^1 \quad p_x^2 \quad p_y^2 \quad p_z^2 \quad \cdots \quad p_x^{N_S} \quad p_y^{N_S} \quad p_z^{N_S}\right]^T \end{aligned} \tag{3}$$

where $\mathbf{u}^j$ and $\mathbf{p}^j$ are the displacement and the traction vectors of node j.

Equation (2) is rearranged as,

$$\begin{aligned} \mathbf{u} &= \mathbf{H}^{-1}\mathbf{Gp} \\ \mathbf{u} &= \mathbf{H}_S\mathbf{p} \end{aligned} \tag{4}$$

in which $\mathbf{H}_S$ is the FRF matrix relating displacements and tractions at the frequency of interest. To couple the soil's cavity to the pile, this FRF matrix is modified to relate displacements to forces instead of tractions by dividing it by the area of the corresponding elements in the BE mesh. Throughout the BE analysis, it is ensured that there are more than six elements for each wavelength to satisfy Domínguez recommendations [13] and achieve convergence.

3 PILE MODELLING AND COUPLING

The pile model is identical in both modelling approaches, and it is modelled as an elastic bar for axial loading and an Euler-Bernoulli beam for transverse loading. It is represented by its centroid axis, which has N_l equally spaced nodes, Figure 1. At each node, there are six degrees of freedom (DOF) representing displacements and rotations in the three directions. The pile is assumed to be unconstrained at its ends and any local deformation of the cross-section is neglected. Only the responses due to unit harmonic axial and transverse loads are given in this paper.

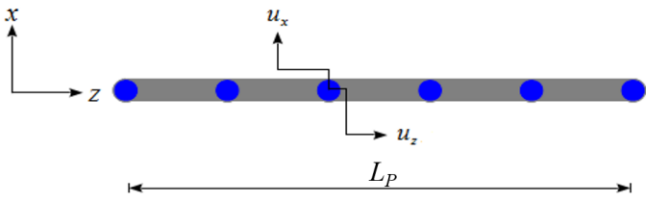


Figure 1: Pile centroid (drawn horizontally) where the circles represent the nodes at which the forces are applied and the responses are calculated. Only the x-z plane is shown.

3.1 Pile response

The response of the pile to a unit harmonic force with angular frequency ω applied in the vertical z direction at node j is calculated as

$$\begin{aligned} u_z^I(z,\omega) &= A^I \cos(\alpha z) + B^I \sin(\alpha z) \text{ for } 0 \le z \le z^j \\ u_z^{II}(z,\omega) &= A^{II} \cos(\alpha z) + B^{II} \sin(\alpha z) \text{ for } z^j \le z \le L_P \end{aligned} \tag{5}$$

where $\alpha = \omega\sqrt{\rho_P / E_P}$ is the wavenumber, the superscripts I and II indicate the sections above and below the excited node j and the coefficients A^I, A^{II}, B^I and B^{II} are calculated from the boundary conditions. L_P is the length, ρ_P is the density and E_P is Young's modulus.

The general response of the pile to a unit harmonic force with angular frequency applied in the transverse directions (x, y) at node j is given by

$$\begin{aligned} u_{x,y}^I(z,\omega) &= A^I \exp(\beta z) + B^I \exp(i\beta z) + C^I \exp(-\beta z) + D^I \exp(-i\beta z) \text{ for } 0 \le z \le z^j \\ u_{x,y}^{II}(z,\omega) &= A^{II} \exp(\beta z) + B^{II} \exp(i\beta z) + C^{II} \exp(-\beta z) + D^{II} \exp(-i\beta z) \text{ for } z^j \le z \le L_P \end{aligned} \tag{6}$$

where $\beta = \left(\rho_P A_P \omega^2 / E_P I_P\right)^{\frac{1}{4}}$ is the wavenumber and the coefficients A^I - D^I and A^{II} - D^{II} are calculated from the boundary conditions. A_P is the cross-section area and I_P is the second moment of inertia.

The FRF matrix of the pile's centroid $\mathbf{H}_l$ is assembled from the general responses in equations (5) and (6) for forces at each node in turn and the response of the pile due to a load vector $\mathbf{p}$ is given by

$$\mathbf{u}_l = \mathbf{H}_l \mathbf{p} \tag{7}$$

This FRF matrix is transformed, for the case of the BE approach, to give the FRF matrix $\mathbf{H}_P$ of the pile's nodes around the circumference as,

$$\mathbf{H}_P = \mathbf{T}_r' \mathbf{H}_l \mathbf{T}_r \tag{8}$$

in which $\mathbf{T}_r$ is the transformation matrix, and the size of $\mathbf{H}_P$ is $3N_S \times 3N_S$.

3.2 Coupling technique

In the semi-analytical approach, two assumptions are adopted to perform the coupling between the soil and the pile. First, compatibility of displacements, i.e. the soil displacement $\mathbf{u}_S(r)$ in is equal to the pile displacement $\mathbf{u}_l$, and equilibrium of forces are assumed at the soil-pile interface. Second, the loads transmitted by the pile to each discretised ground layer are distributed either over a circular area of radius equal to that of the pile or over a circular annulus of width equal to one tenth of the pile radius. It should be noted that the calculation of the FRF due to an annulus loading is achieved by subtracting the FRF due to loading through the inner disc from the FRF due to loading through the outer disc.

Considering these assumptions, the coupling is achieved by combining equation (1) with

$$\mathbf{u}_l = \mathbf{H}_l (\mathbf{f}_a - \mathbf{g}) \tag{9}$$

that derives from equation (7) by substituting $\mathbf{p} = \mathbf{f}_a - \mathbf{g}$. In equation (9), $\mathbf{f}_a$ is the vector of applied forces at the pile centroid, and $\mathbf{g}$ is the vector of reaction forces between the pile and the soil, given by

$$\mathbf{g} = \left[\mathbf{H}_h(0) + \mathbf{H}_l\right)\right]^{-1}\mathbf{H}_l\mathbf{f}_a . \tag{10}$$

Once $\mathbf{g}$ is known, the response at any point in the soil can be calculated using equation (1).

For the case of multiple piles, the soil response is given as a superposition of the displacement fields due to the tractions $\mathbf{g}_i$ of each individual pile i as

$$\mathbf{u}_S = \sum_{i=1}^{N} \mathbf{H}_h(r_i)\mathbf{g}_i . \tag{11}$$

where r_i is the distance between the receiver and i th pile. For known applied forces $\mathbf{f}_{ai}$, the forces on the soil $\mathbf{g}_i$ are given by

$$\mathbf{H}_h(0)\mathbf{g}_i + \mathbf{H}_l\mathbf{g}_i + \sum_{j=1}^{N} \mathbf{H}_h(r_{ij})\mathbf{g}_j(1-\delta_{ij}) = \mathbf{H}_l\mathbf{f}_{ai}. \tag{12}$$

where r_{ij} is the distance between the and i th and j th pile, and δ_{ij} is the Kronecker delta.

In the BE approach, the coupling is again performed by applying at the interface compatibility of displacements and equilibrium of forces. This is obtained by combining the systems in equations (4) and (7) as,

$$\begin{aligned} \mathbf{U}_S &= \mathbf{H}_S\mathbf{F}_\mathbf{S} \\ \mathbf{U}_P &= \mathbf{H}_P\left(\mathbf{F}_\alpha - \mathbf{F}_\mathbf{S}\right) \\ \mathbf{F}_\mathbf{S} &= \left(\mathbf{H}_S + \mathbf{H}_P\right)^{-1}\mathbf{H}_P\mathbf{F}_\alpha \end{aligned} \tag{13}$$

where $\mathbf{F}_\alpha$ is the vector of forces applied to the pile circumference and $\mathbf{F}_S$ is the resulting vector of soil force, from which the response at any point in the soil can be calculated.

4 PILE MODELLING AND COUPLING

To compare the two modelling approaches, three cases are considered as shown in Figure 2. The pile has radius $R_P = 0.5\,\text{m}$, length $L_P = 10\,\text{m}$ and is made of concrete with Young's modulus $E_P = 50\,\text{GPa}$, Poisson's ratio $\nu_P = 0.3$, damping loss factor $\eta_P = 0.01$, and density $\rho_P = 2500\,\text{kg/m}^3$. The soil consists of four layers of increasing stiffness; the top three have thickness $d_1 = 2$ m, $d_2 = 4$ m and $d_3 = 6$ m while the fourth represents the half-space. All layers have density $\rho_S = 2000\,\text{kg/ m}^3$ and damping loss factor $\eta_S = 0.06$ associated with both Lamé constants. The layers have shear wave velocities $\mathrm{c}_1 = [185, 228, 260, 309]$ m/s and compressional wave velocities $\mathrm{c}_2 = [277, 373, 485, 944]$ m/s respectively.

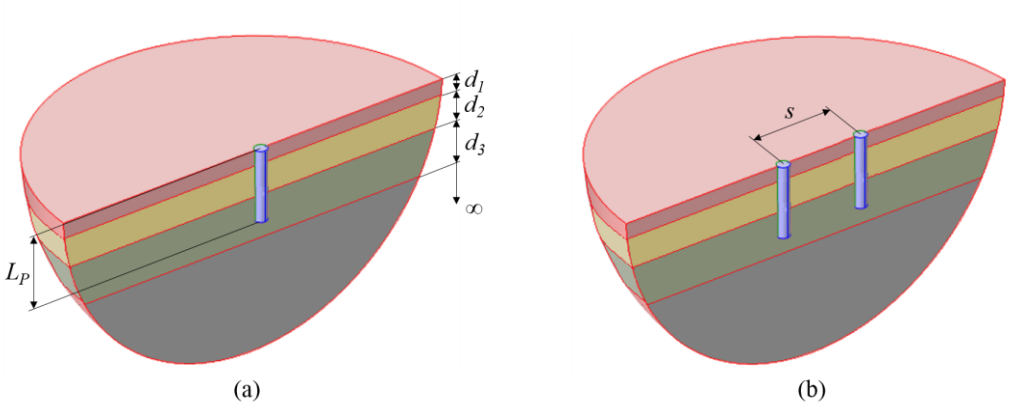


Figure 2: Pile in a multi-layered half-space: (a) single pile, (b) two piles with separation distance s.

4.1 Free-surface displacement field

The first set of results show the predictions of the BE model for the displacement field at the free surface for the cases in Figure 2 when one pile head is subject to a unit harmonic axial or transverse load at a frequency of 50 Hz. In Figure 3(a), the vertical displacement field exhibits concentric circular wavefronts, which is expected when a single pile is subject to axial loading on its head. However, these circular wavefronts diffract when a second pile is inserted at 2 m in Figure 3(c) and at 4 m in Figure 3(e). This diffraction is more apparent in Figure 3(e) as the wavelength of the surface waves (~3.7 m) is of the order of the separation distance. When the pile is subject to transverse load as in Figure 3(b), the horizontal displacement field does not show cylindrical wavefronts due to the nature of the source and the dynamic interaction between the soil and the pile. These wavefronts are not much influenced by the insertion of the pile at a distance 2 m as in Figure 3(d) where they slightly diffract. However, when a second pile is added at a distance 4 m the diffraction is more pronounced as shown in Figure 3(f).

4.2 Comparison between the two models

The comparisons between the models are given in terms of the driving point response of a single pile, and the interaction between two piles. The first is used to ensure that the semi-analytical model is able to simulate the dynamic pile-soil interaction, whereas the other measures are utilised to scrutinise the dynamic PSPI. Since the BE model has been validated in [17] for a single pile, it is used to benchmark the semi-analytical model. For the semi-analytical model both the case where the loads from the pile are transmitted to the ground layers distributed over a circular disc, and the case where they are distributed over an annulus are considered.

Figure 4, presents the driving point response of a single pile predicted by both models for axial and transverse unit harmonic loading. In general, very good agreement is seen between the semi-analytical model and the BE model. When considering the disc loading, the FRF due to axial loading (Figure 4(a)) of both models compares well up to 40 Hz, above which an al most constant difference of less than 1 dB remains. In the FRF due to transverse load (Figure 4(b)), however, this difference begins at very low frequencies and continues to increase until it reaches about 2 dB at frequencies higher than 70 Hz. For the annulus load the comparison of the FRF is much better for both axial and transverse loads. Nevertheless, when comparing the phase of the response between the two models, it is seen that the annulus load shows very good agreement with the BEM for the case of axial loading, but does not give such good agreement for the case of transverse loading.

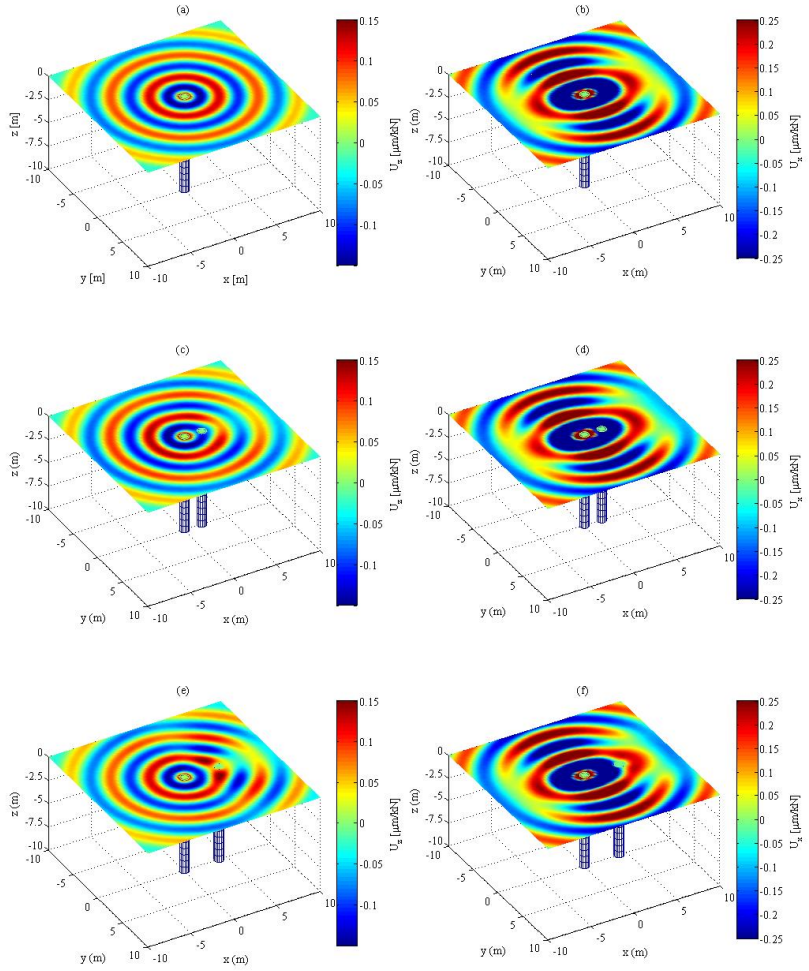


Figure 3: Pile Free-surface displacement field predicted by the BE model due to a unit harmonic load on the pile's head at a frequency 50Hz. (a), (c), (e) vertical response due to axial load and (b), (d), (f) horizontal response due transverse load for (a)-(b) single pile, (c)-(d) two piles with 2 m separation distance, and (e)-(f) two piles with 4 m separation distance.

In Figure 4, in general, it is seen that the FRF of the semi-analytical model is higher than that of the BE model, indicating that the semi-analytical model is softer even though it does not have a cavity as the BE model. This is believed to be due to the way of calculating the soil response in the semi-analytical model by applying circular or annulus load instead of a rigid disc load. The absence of the cavity in the semi-analytical model is believed to be another reason for these differences, which may lead to more inertia effects. This is apparent in the phase plots, where the differences reach about 5º.

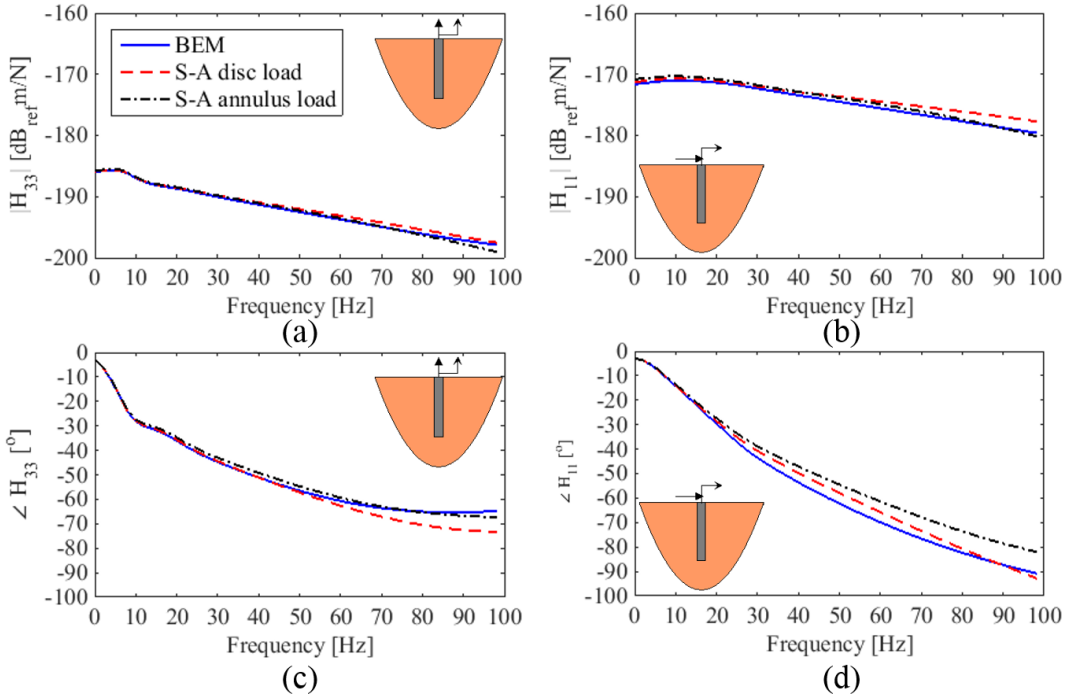


Figure 4: Driving point response of a single pile in a multilayered half-space due to (a)-(c) axial load and (b)-(d) transverse load predicted by the BE model (solid) and the semi-analytical model for disc loading (dashed) and annulus loading (dashed-dotted).

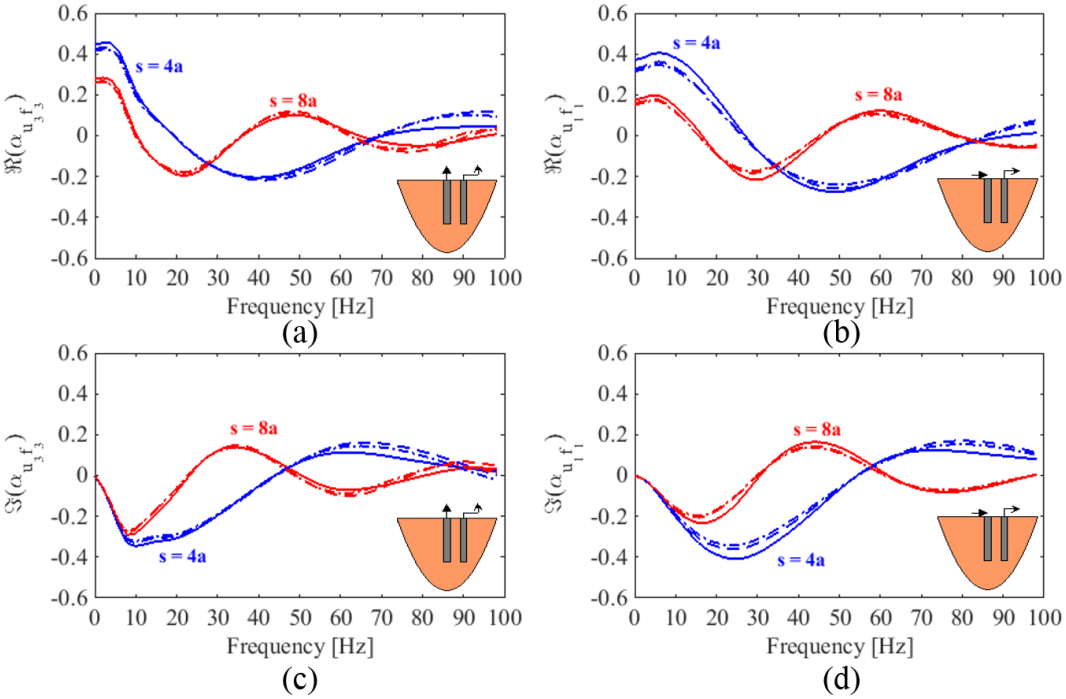


Figure 5: Dynamic interaction between two piles in a multi-layered half-space due to (a)-(c) axial load and (b)-(d) transverse load predicted by BE model (solid) and semi-analytical model for disc loading (dashed) and annulus loading (dashed-dotted). The piles' separation distances are $s = 4a$ and $s = 8a$, where a is the pile radius.

The interaction between two piles, which is calculated at the pile head, is presented by means of the dynamic interaction factor [2]

$$\alpha_{u_i f_i} = \frac{u_{i_b}, f_{i_a}}{u_{i_a}, f_{i_a}} \tag{14}$$

where u_{i_b}, f_{i_a} is the displacement i of pile b due to load i applied on pile a, and u_{i_a}, f_{i_a} is the static displacement i of pile a due to load i applied on pile a.

Figure 5, shows the dynamic interaction factors between two piles at separation distances s of 2 m and 4 m. Both real (top) and imaginary (bottom) parts of the dynamic interaction factors are given for axial and transverse loading. The predictions of the semi-analytical model are generally in good agreement with those of the BE model, in particular when the separation distance is 4 m. For axial loading, discrepancies appear at frequencies higher than 50 Hz, while discrepancies appear at very low frequencies for transverse loading, especially for the real part (Figure 5(b)). The reason for these discrepancies is believed to be twofold; one is due to the absence of the cavity in the analytical model and another is because of the procedure followed in calculating the soil response.

4.3 Free-surface response in the existence of a pile group

The semi-analytical model has shown it is capable of predicting the driving point response of a single pile and the dynamic PSPI with acceptable accuracy. In this section, the response of the free surface, generated by a vertical harmonic point source in the presence of a pile or a pile group is presented using the semi-analytical model. Since the vibration field generated by a railway is modelled as the superposition of the response due to harmonic loadings generated at the wheel-rail interface, the current investigation is the first important step for the developing of a fully coupled railway-soil-pile model using the semi-analytical approach. More effort is needed in order to couple a model of a railway track with the coupled soil-pile model that was developed in the current paper.

The results are presented in terms of the insertion gain (IG) between the displacements for the ground without any pile (free ground) and the displacements calculated with the existence of piles as

$$IG = 20\log_{10}\frac{u_{i,with}}{u_{i,free}} \tag{15}$$

where $u_{i,with}$ is the displacement with the pile and $u_{i,free}$ is the displacement of the free ground due to a point harmonic force.

The response is calculated at a distance of 8 m from the vertical point source and three cases are considered, as shown in Figure 6. In the first case, a single pile is included midway between the source and the receiver (4 m from the source). In the second case, the pile is at 6 m from the receiver and in the third case two piles, one at 4 m and one at 6 m from the source are considered. The soil and pile material properties used are the same as in the previous sections and only the disc loading is considered for the current application.

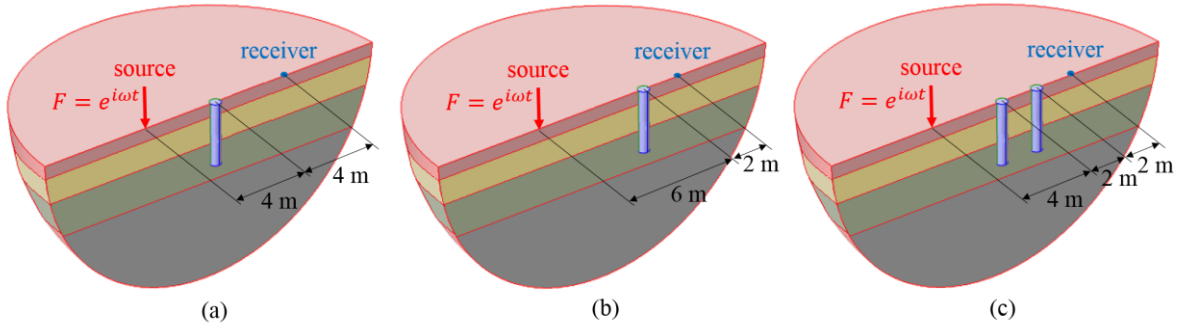


Figure 6: Pile(s) insertion cases between a point harmonic source and a receiver at 8 m: (a) single pile at 4 m, (b) single pile at 6 m, (b) two piles at 4m and 6m.

Figure 7(a) and 7(b), compare the vertical and horizontal displacements respectively, for the three cases considered, with the displacement of the free ground. Figure 7(c) and (d) show the corresponding insertion gains IG. From these plots, it can be seen that the existence of the piles reduces significantly the displacements in both directions and this reduction increases at mid- frequencies where it can be up to 4 dB for the case of the pile inserted at 4 m. The case where a single pile is inserted closer to the receiver (6 m from the source), shows 1 to 2 dB additional reduction compared with the case where the single pile is inserted at the mid-point (4 m). For the third case where two piles are inserted, the IG is, as expected, clearly better leading to an average reduction of about 4.5 dB in the whole frequency range for the vertical and about 7 dB in the range 10 to 60 Hz for the horizontal response.

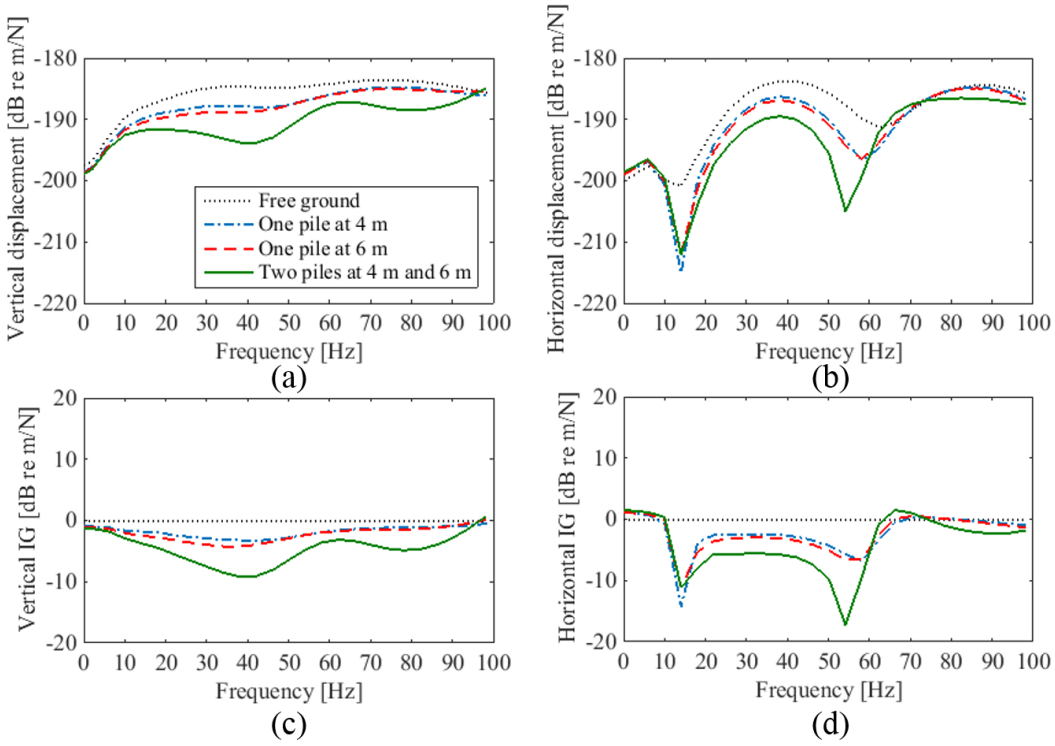


Figure 7: Vertical (a) and horizontal (b) FRF of the receiver at a distance 8 m from the source and IG of the vertical (c) and horizontal (d) displacement of the receiver for the free-ground (dotted), for the existence of a pile at 4 m (dashed-dotted), 6 m (dashed) and two piles at 4 m and 6 m (solid) from the source.

Figure 7 showed that piled foundations can serve as wave barriers to isolate vibration in the far field which for the case of railway ground-borne vibrations can be used for vibration mitigation. It should be noted that for optimizing the performance of such piled wave barriers the piles should be arranged at appropriate distances and in appropriate configurations. Current modelling techniques can provide accurate and computationally efficient tools for the designing of such mitigation measures.

5 CONCLUSIONS

Investigating the dynamic interaction between piled foundations and soil is of great importance for predictions of ground-borne vibration. Such investigation entails comprehensive yet efficient models that consider essential aspects of the problem. This paper has presented an efficient semi-analytical model and a more versatile BE model to simulate the dynamic PSPI in multi-layered half-space. The models are compared together for predictions of the driving point response of a single pile subject to axial and transverse loading and the dynamic interaction between two piles. It has been demonstrated that the semi-analytical model captures the driving point response and the dynamic interaction between piles reasonably well, with some small differences at high frequencies. It is believed that the differences are due to (i) the absence of cavities in the semi-analytical model, which may provoke more inertia effects and (ii) the procedure followed in obtaining the soil response, which may result in a softer system. The semi-analytical model has then been used to predict the response of a pile-group due to the vibration field generated by a vertical load in varying distance from the piles. The example showed that the insertion of the piles in the wave propagation path can significantly reduce the level of vibration at the far field. Understanding and resolving the limitations of the semi-analytical model and coupling it with a detailed railway track model is the subject of ongoing work.

ACKNOWLEDGEMENTS

The authors would like to thank the EPSRC for funding this research, which is part of the MOTIV project (www.motivproject.co.uk) under the research grants EP/K006002/1 and EP/K006665/1. The authors also acknowledge the contribution of the Katholieke Universiteit Leuven in providing the EDT and also for some functions of BEMFUN used in the BE models.

REFERENCES

[1] K.A. Kuo, H.E.M. Hunt, Dynamic models of piled foundations. *Applied Mechanics Reviews*, **65**(3), 031003-1-031003-9, 2013.

[2] H.G. Poulos, Analysis of the settlement of pile groups. *Geotechnique*, **18**(4), 449-471, 1968.

[3] H.G. Poulos, Behaviour of laterally loaded piles: II-pile groups. *ASCE Journal of Geotechnical Engineering Division*, **97**, 733-751, 1971.

[4] T. Nogami, Dynamic group effect of multiple piles under vertical vibration. *Proceedings of the American Society of Civil Engineering Mechanics Division Speciality Conference*, Austin, Texas, USA, 750-754, 1979.

[5] M. Sheta, M. Novak, Vertical vibration of pile groups. *ASCE Journal of Geotechnical Engineering Division*, **108**, 570-590, 1982.

[6] G. Gazetas, N. Makris, Dynamic pile-soil-pile interaction. Part 1: analysis of axial vibration. *Earthquake Engineering and Structural Dynamics*, **20**, 115-132, 1991.

[7] A.M. Kaynia, E. Kausel, Dynamics of piles and pile groups in layered soil media. *Soil Dynamics and Earthquake Engineering*, **10**(8), 386-401, 1991.

[8] J.P. Talbot, H.E.M. Hunt, A computationally efficient piled-foundation model for studying the effects of ground-borne vibration on buildings. *Proc. the Institution of Mechanical Engineers, Part C: Journal of Mechanical Engineering Science*, **217**, 975-989, 2003.

[9] R. Sen, T.G. Davies, P.K. Banerjee, Dynamic analysis of piles and pile groups embedded in homogeneous soils. *Earthquake Engineering and Structural Dynamics*, **13**, 53-65, 1985.

[10] O. Maeso, J.J. Anárez, F. García, Dynamic impedances of piles and pile groups in saturated soils. *Computers and Structures*, **83**, 769-782, 2005.

[11] M.A. Millán, J. Domínguez, Simplified BEM/FEM model for dynamic analysis of structures on piles and pile groups in viscoelastic and poroelastic soils. *Engineering Analysis with Boundary Elements*, **33**, 25-34, 2009.

[12] E. Kausel and J.M. Roësset, Stiffness matrices for layered soils. *Bulletin of the Seismological Society of America*, **71**(6), 1743–1761, 1981.

[13] E. Kausel, R. Peek, Dynamic loads in the interior of a layered stratum: an explicit solution. *Bulletin of the Seismological Society of America*, **72**(5), 1459-1481, 1982.

[14] E. Kausel, *Fundamental solutions in elastodynamics: a compendium*. Cambridge University Press, New York, 2006.

[15] M. Schevenels, S. Françcois, G. Degrande, EDT: An elastodynamics toolbox for MATLAB. *Computers & Geosciences*, **35**(80), 1752-1754, 2009.

[16] J. Domínguez, *Boundary Elements in Dynamics*. Computational Mechanics Publications and Elsevier Applied Science, Southampton, 1993.

[17] W.I. Hamad, H.E.M. Hunt, M.F.M. Hussein, J.P. Talbot, Tunnel-soil-pile interaction in the prediction of vibration from underground railways: validation of the sub-models. *9th International Conference on Structural Dynamics (EURODYN 2014)*, Porto, Portugal, 767-774, June 30-July 2,2014.

COMPDYN 2015
5th ECCOMAS Thematic Conference on
Computational Methods in Structural Dynamics and Earthquake Engineering
M. Papadrakakis, V. Papadopoulos, V. Plevris (eds.)
Crete Island, Greece, 25–27 May 2015

MODELLING OF WARPING EIGENVIBRATION BY NONUNIFORM TORSION

Justín Murín[1*], Mehdi Aminbaghai[2], Juraj Hrabovský[1], Herbert Mang[2,3]

[1] Faculty of Electrical Engineering and Information Technology
Slovak University of Technology, Ilkovičova 3, 812 19 Bratislava, Slovakia
justin.murin@stuba.sk, juraj.hrabovsky@stuba.sk

[2] Institute for Mechanics of Materials and Structures
Vienna University of Technology, Karlsplatz 3, A/1040 Vienna, Austria
mehdi.aminbaghai@tuwien.ac.at, herbert.mang@tuewien.ac.at

[3]National RPGE Chair Professor, Tongji University, Siping Road 1239, Shanghai, China,
herbert.mang@tuewien.ac.at

Keywords: Modal Analysis, Nonuniform Torsion, Warping Eigenfrequencies.

Abstract. *This contribution contains a novel investigation of the influence of warping of the cross-section of twisted beams on their eigenvibrations. The investigation is based on the analogy of the bending beam theory and the non-uniform torsion theory of thin-walled open and closed cross-sections. Based on them, the differential equations for dynamic loads, considered as equivalent static loads, are presented. The effect of the secondary torsion moment deformation is taken into account. A part of the first derivative of the twist angle is taken as a warping degree of freedom. The solution of this differential equation is then used for setting up the transfer matrix. The numerical investigation contains the analysis of the natural frequencies and mode shapes of straight cantilever beams with and without consideration of the influence of warping of the cross-section. Beams with open and closed cross-sections are considered. Obtained results are compared with the ones calculated by standard solid and warping beam finite elements.*

1 INTRODUCTION

Beam structures are often exposed to time-dependent loads. Commercial FEM codes allow performing modal and transient dynamic analysis by 3D beam finite elements with and without consideration of the warping effect. Very often the improved Saint-Venant theory of torsion is used and special mass matrices are proposed. Mostly, the bicurvature is chosen as an additional warping degree of freedom and the secondary torsion moment deformation effect (STMDE) is not considered.

For example in [1], the beam element can be used with a lumped or a consistent mass matrix. The consistent mass matrix includes warping effects but does not include the effect of shear deformation. For the standard beam element, the consistent mass matrix is based on reference [2] with the exception that there are additional terms arising from the warping constant I_ω. For the warping element, lumped masses for the warping degree of freedom (bicurvature) are defined [3]. As stated in [1], for solid and closed thin-walled sections, the standard beam element can be used without significant error. However, for the open thin-walled sections, the warping beam element should be used. In [4], the warping beam finite element is recommended to be used only for open thin walled section beams. In [5], the finite beam element is implemented with unrestrained or restrained warping (BEAM188). In [6], the warping beam finite element can be used only for elastostatic analysis of straight beams. It should be noted that in technical practice as well as in the Eurocodes 3 (EC3) the effect of non-uniform torsion by the steel beams with closed cross-sections is not considered.

In the most recent literature relatively little information can be found that refers to the solution for free and forced torsional vibration of beams with hollow cross-sections that include non-uniform torsion effects. In [7], a boundary element method is developed for the nonuniform torsional vibration problem of doubly symmetric composite bars of arbitrary variable cross-section. Dynamic analysis of 3-D beam elements, restrained at their edges, subjected to arbitrarily distributed dynamic loading, is presented in [8]. In [9], Ref. [7] is extended taking the geometrical nonlinearity into account, and in [10], the effect of rotary and warping inertia is implemented. In [11], the nonlinear torsional vibrations of thin-walled beams exhibiting primary and secondary warping are investigated. In [12], a solution for the vibrations of Timoshenko beams by the isogeometric approach is presented, but warping effects are not considered. In [13], geometrically non-linear free and forced vibrations of beams with non-symmetrical cross sections are investigated by the Saint-Venant theory of torsion. In [14], an axial-torsional vibration of rotating pretwisted thin-walled composite box beams, exhibiting primary and secondary warping, are investigated. In [15], a new formulation of a 3D beam element is presented with a new method of describing the transversal deformation of the beam cross-section and its warping.

As follows from the above overview of research papers on the area of nonuniform torsion and of the papers [16], [17], [18], the effect of warping should be considered also by torsion of closed thin-walled section beams. This fact was yet also experimentally proved by elastostatic torsional loading of hollow section beams [17]. It was also shown that the effect of the secondary torsion moment has to be taken into account especially by closed-section beams. Because the bicurvature cannot be used in the constraint equations, e.g. [1], it is straightforward to consider the part of the first derivative of the angle of twist caused by bimoment as the warping degree of freedom also for modal analysis. The new degree of freedom can be used in the constraint condition (it is e.g. exactly equal to zero at the clamped end of the beam), and it can make modal analysis more accurate as this is the case for nonuniform torsion elastostatic analysis [16 – 18]. That is the motivation for the investigation in the following chapters of the present paper.

In chapter 2, the differential equations of 4th order for nonuniform torsion eigenvibrations are established. The part of the bicurvature caused by the bimoment is taken into account as the warping degree of freedom, and the STMDE is also considered. The general semianalytical solution of the differential equation is presented and the transfer matrix relation is established. In chapter 3, the numerical investigation is performed. The results of modal analysis of open I and rectangular hollow cross-section beams by our method are presented and compared with the ones obtained by commercial FEM codes. The effect of STMDE is studied and evaluated. Final assessment of the proposed method and of the obtained results is listed in the summary and conclusions.

2 EIGENVIBRATIONS DUE TO NONUNIFORM TORSION

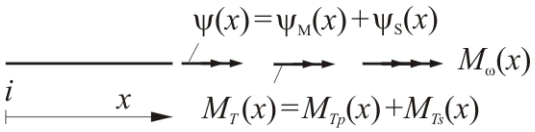


Figure 1: Non-uniform torsion: torsional moments and angles of twist.

Fig. 1 refers to determination of the eigenvibrations due to non-uniform torsion. It shows the torsional moment $M_T(x)$, representing the sum of the primary torsional moment $M_{Tp}(x)$ and the secondary torsional moment $M_{Ts}(x)$, and the bimoment $M_\omega(x)$. Fig. 1 also shows the angle of twist, $\psi(x)$, corresponding to $M_{Tp}(x)$. It represents the sum of the angle of twist, resulting from the primary deformation $\psi'_M(x)$ and the secondary deformation $\psi'_S(x)$. Here and in the following, $' := d/dx$.

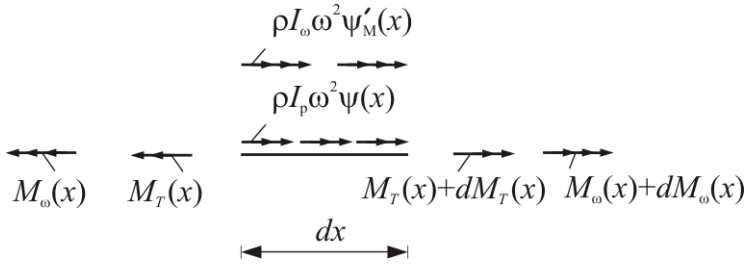


Figure 2: Non-uniform torsion: equivalent static line load and line moment acting on an infinitesimal beam element.

Fig. 2 illustrates an infinitesimal element of the beam. It is loaded by the torsional line moment $\rho I_p \omega^2 \psi(x)$ and the line bimoment $\rho I_\omega \omega^2 \psi'_M(x)$, where I_ω stands for the warping constant. These line moments represent the static equivalent of the respective dynamic action. In the following, the equilibrium equations will be formulated, considering the analogy between non-uniform torsion and second-order beam theory, see Table 1. They are obtained as

$$M'_T(x) = -\rho I_p \omega^2 \psi(x), \tag{1}$$

$$M'_\omega(x) = M_T(x) - M_{Tp}(x) + \rho I_\omega \omega^2 \psi'_M(x) = M_{Ts}(x) + \rho I_\omega \omega^2 \psi'_M(x), \tag{2}$$

where

$$M_T(x) = M_{Tp}(x) + M_{Ts}(x). \tag{3}$$

According to Table 1:

$$\psi''_M(x) = -\frac{M_\omega(x)}{EI_\omega}, \tag{4}$$

and

$$\psi'(x) = \psi'_M(x) + \psi'_S(x) \tag{5}$$

with

$$\psi'(x) = \frac{M_{Tp}(x)}{GI_T} \tag{6}$$

$$\psi'_S(x) = \frac{M_{Ts}(x)}{GI_{Ts}}, \tag{7}$$

where I_{Ts} denotes the secondary torsion constant.

Differentiation of equation (5) with respect to *x* and consideration of the equations (4) and (7) gives

$$\psi''(x) = \psi''_M(x) + \frac{M'_{Ts}(x)}{GI_{Ts}} = -\frac{M_\omega(x)}{EI_\omega} + \frac{M'_{Ts}(x)}{GI_{Ts}}. \tag{8}$$

Making use of the equations (1) and (4) and of the derivative of equation (3) in equation (8) yields

$$\begin{aligned} \psi''(x) &= \psi''_M(x) + \frac{M'_{Ts}(x)}{GI_{Ts}} = -\frac{M_\omega(x)}{EI_\omega} + \frac{M'_T(x) - M'_{Tp}(x)}{GI_{Ts}} = \\ &= -\frac{M_\omega(x)}{EI_\omega} + \frac{-\rho I_p \omega^2 \psi(x) - M'_{Tp}(x)}{GI_{Ts}} = -\frac{M_\omega(x)}{EI_\omega} + \frac{-\rho I_p \omega^2 \psi(x) - GI_T \psi''(x)}{GI_{Ts}}. \end{aligned} \tag{9}$$

Multiplication of equation (9) by EI_ω results in

$$\begin{aligned} &EI_\omega \psi''(x) + M_\omega(x) + \frac{EI_\omega}{GI_{Ts}}\left(\rho I_p \omega^2 \psi(x) + GI_T \psi''(x)\right) = \\ &= EI_\omega \left(1 + \frac{GI_T}{GI_{Ts}}\right)\psi''(x) + M_\omega(x) + \frac{EI_\omega}{GI_{Ts}}\left(\rho I_p \omega^2\right)\psi(x) = 0. \end{aligned} \tag{10}$$

Differentiation of equation (10) with respect to *x* and substitution of equation (3) into the so-obtained relation yields

$$EI_\omega \left(1 + \frac{GI_T}{GI_{Ts}}\right)\psi'''(x) + \frac{EI_\omega}{GI_{Ts}}\left(\rho I_p \omega^2\right)\psi'(x) + M_T(x) - M_{Tp}(x) + \rho I_\omega \omega^2 \psi'_M(x) = 0. \tag{11}$$

Consideration of the equations (5), (6), and (7) in equation (11) yields

$$EI_\omega \left(1 + \frac{GI_T}{GI_{Ts}}\right)\psi'''(x) + \frac{EI_\omega}{GI_{Ts}}\left(\rho I_p \omega^2\right)\psi'(x) + M_T(x) - GI_T \psi'(x) + \rho I_\omega \omega^2 \left(\psi'(x) - \frac{M_{Ts}(x)}{GI_{Ts}}\right) = 0. \tag{12}$$

Differentiation of equation (12) with respect to x and consideration of equation (3) results in

$$EI_\omega\left(1+\frac{GI_T}{GI_{Ts}}\right)\psi''''(x)+\left(\frac{EI_\omega}{GI_{Ts}}\rho I_p\omega^2+\rho I_\omega\omega^2-GI_T\right)\psi''(x)+M_T'(x)-\frac{\rho I_\omega\omega^2}{GI_{Ts}}\left(M_T'(x)-M_{Tp}'(x)\right)=0. \quad (13)$$

Substitution of equation (1) and of the derivative of equation (6) into (13) gives

$$EI_\omega\left(1+\frac{GI_T}{GI_{Ts}}\right)\psi''''(x)+\left(\frac{EI_\omega}{GI_{Ts}}\rho I_p\omega^2+\left(1+\frac{GI_T}{GI_{Ts}}\right)\rho I_\omega\omega^2-GI_T\right)\psi''(x)+\rho I_p\omega^2\left(\frac{\rho I_\omega\omega^2}{GI_{Ts}}-1\right)\psi(x)=0. \quad (14)$$

Equation (14) is a linear homogeneous differential equation of fourth order for the angle of twist. It can be verified by means of the analogy between non-uniform torsion and second-order beam theory (see Table 1).

For free-of-warping cross-sections, for which $I_\omega=0$, equation (14) degenerates to the equation for Saint-Venant torsion.

The general semianalytical solution of the differential equation (14) can be written as follows:

$$\psi(x)=b_0(x)\psi_i+b_1(x)\psi_i'+b_2(x)\psi_i''+b_3(x)\psi_i''', \quad (15)$$

where $b_0(x)$, $b_1(x)$, $b_2(x)$, $b_3(x)$ denote the transfer functions and ψ_i, ψ_i',ψ_i'',ψ_i''' represent the integration constants referring to the starting point i (e.g. $\psi_i=\psi_i(x)$ for $x=0$, etc…).

Equation (15) and its first three derivatives with respect to x are integrated into the following matrix equation:

$$\underbrace{\begin{bmatrix}\psi(x)\\ \psi'(x)\\ \psi''(x)\\ \psi'''(x)\end{bmatrix}}_{\boldsymbol{\psi}(x)}=\underbrace{\begin{bmatrix}b_0(x) & b_1(x) & b_2(x) & b_3(x)\\ b_0'(x) & b_1'(x) & b_2'(x) & b_3'(x)\\ b_0''(x) & b_1''(x) & b_2''(x) & b_3''(x)\\ b_0'''(x) & b_1'''(x) & b_2'''(x) & b_3'''(x)\end{bmatrix}}_{\boldsymbol{B}(x)}\cdot\underbrace{\begin{bmatrix}\psi_i\\ \psi_i'\\ \psi_i''\\ \psi_i'''\end{bmatrix}}_{\boldsymbol{\psi}_i} \quad (16)$$

In equation (16), $\boldsymbol{B}(\mathrm{x})$ is a matrix containing the solution functions and its first three derivatives at x, $\boldsymbol{\psi}(x)$ is a vector containing the angle of twist and its first three derivatives at x, and $\boldsymbol{\psi}_i$ is a vector containing the angle of twist and its first three derivatives at the starting point i. The transformation matrix $\boldsymbol{T}$ in the following matrix equation relates the vector $\boldsymbol{\psi}(x)$ to the "static vector" $\boldsymbol{Z}(x)$, containing $\psi(x)$, $\psi_M'(x)$, $M_\omega(x)$, and $M_T(x)$.

$$\underbrace{\begin{bmatrix}\psi(x)\\ \psi_M'(x)\\ M_\omega(x)\\ M_T(x)\end{bmatrix}}_{\boldsymbol{Z}(x)}=\underbrace{\begin{bmatrix}1 & 0 & 0 & 0\\ 0 & \dfrac{\left(\frac{\omega^4EI_\omega\rho I_p\rho I_\omega}{GI_{Ts}\left(GI_{Ts}-\omega^2\rho I_\omega\right)}+\frac{\omega^4\rho I_\omega^2}{GI_{Ts}-\omega^2\rho I_\omega}\right)}{-\frac{\omega^2GI_{Ts}\rho I_\omega}{GI_{Ts}-\omega^2\rho I_\omega}+\frac{\omega^4\rho I_\omega^2}{GI_{Ts}-\omega^2\rho I_\omega}} & 0 & \dfrac{\omega^2EI_\omega\left(GI_T+GI_{Ts}\right)\rho I_\omega}{GI_{Ts}\left(GI_{Ts}-\omega^2\rho I_\omega\right)\left(-\frac{\omega^2GI_{Ts}\rho I_\omega}{GI_{Ts}-\omega^2\rho I_\omega}+\frac{\omega^4\rho I_\omega^2}{GI_{Ts}-\omega^2\rho I_\omega}\right)}\\ -\frac{EI_\omega}{GI_{Ts}}\rho I_T\omega^2 & 0 & -\frac{EI_\omega\left(GI_T+GI_{Ts}\right)}{GI_{Ts}} & 0\\ 0 & \dfrac{-GI_TGI_{Ts}+\omega^2\left(EI_\omega\rho I_p+\left(GI_{Ts}+GI_T\right)\rho I_\omega\right)}{\left(\rho I_\omega\omega^2-GI_{Ts}\right)} & 0 & \dfrac{EI_\omega\left(GI_T+GI_{Ts}\right)}{\rho I_\omega\omega^2-GI_{Ts}}\end{bmatrix}}_{\boldsymbol{T}}\cdot\underbrace{\begin{bmatrix}\psi(\mathrm{x})\\ \psi'(\mathrm{x})\\ \psi''(\mathrm{x})\\ \psi'''(\mathrm{x})\end{bmatrix}}_{\boldsymbol{\psi}(x)} \quad (17)$$

Details concerning determination of $\boldsymbol{T}$ are given in [20].

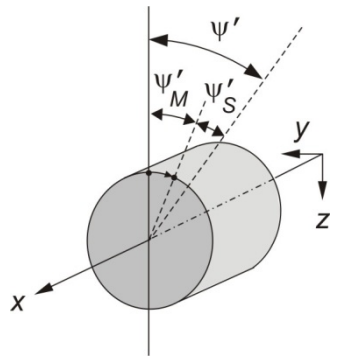
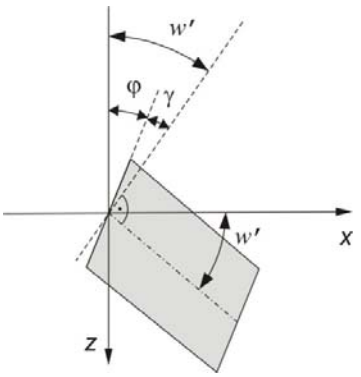
 Non-uniform torsion		 Second-order beam theory	
Angle of twist	$\psi(x)$	$w(x)$	Deflection
Bimoment	$M_\omega(x)$	$M(x)$	Bending moment
Torsional moment	$M_T(x)$	$R(x)$	Transversal force
Primary torsional moment	$M_{Tp}(x)$	$Nw'(x)$	Without a mechanical meaning
Secondary torsional moment	$M_{Ts}(x)$	$V(x)$	Shear force
Derivative of the twist angle with respect to x	$\psi'(x)$	$w'(x)$	Derivative of the deflection with respect to x
Derivative of the twist angle from the primary deformation with respect to x	$\psi'_M(x)$	$\varphi(x)$	Rotation of the cross-section
Derivative of the twist angle from the secondary deformation with respect to x	$\psi'_S(x)$	$\gamma = \frac{V(x)}{GA_s}$	Shear force/Shear stiffness
Torsional stiffness (Saint-Venant)	GI_T	N	Axial force according to second-order beam theory
Secondary torsional stiffness	GI_{Ts}	GA_s	Shear stiffness
Warping stiffness	EI_ω	EI	Bending stiffness
Warping inertia moment	ρI_ω	ρI	Mass inertia moment
Primary torsional inertia moment	ρI_p	ρA	Mass inertia force

Table 1: Analogy between non-uniform torsion and second-order beam theory.

By substitution of equation (16) into (17) the static vector $\boldsymbol{Z}(x)$ at x is obtained as

$$\boldsymbol{Z}(x) = \boldsymbol{F_{xi}}(x) \cdot \boldsymbol{Z}_i, \tag{18}$$

where $\boldsymbol{Z}_i$ is the a static vector at the starting point i and $\boldsymbol{F_{xi}}(x)$ is the transfer matrix, given as

$$\boldsymbol{F}_{xi}(x) = \boldsymbol{T} \cdot \boldsymbol{B}(x) \cdot \boldsymbol{T}^{-1}. \tag{19}$$

Calculation of the warping eigenfrequencies involves the following steps: At first, the equations (16) and (17) and the transfer matrix $\boldsymbol{F}_{xi}(x)$ are specialized for the beam length L. The transfer equation (18) is specialized for the nodes i and k to the transfer matrix $F_{ki}(x = L)$. Taking into account the boundary conditions, the reduced system of two homogeneous algebraic equations is obtained. The circular natural frequencies ω_j, $j = 1, 2, \ldots$, follow from

the zeros of the determinant of the reduced system of equations. An iterative method was used to find the zeros of the determinant. The natural frequencies $f_j = \omega_j / 2\pi$, $\mathrm{j} = 1,2,\ldots$, are determined subsequently.

The above algorithm was implemented into the software MATHEMATICA [21]. The eigenfrequencies were calculated for cantilever beams with thin-walled open and closed cross-sections. In chapter 3, the results of the numerical experiments are presented and compared with the results obtained from the available commercial software.

3 NUMERICAL EXAMPLES

In this chapter, the results of modal analysis concerning the nonuniform torsion eigenmodes of chosen open and closed shaped beams are investigated.

3.1 Cantilever beam with an I cross-section

Saint-Venant and nonuniform torsion eigenfrequencies of the cantilever beam (Fig. 3) with length $L = 2\,\mathrm{m}$ were calculated. The cross-section is the one of a HEA-100 [22]. In Table 2 and Table 3, the cross-sectional parameters and the material properties are listed, respectively.

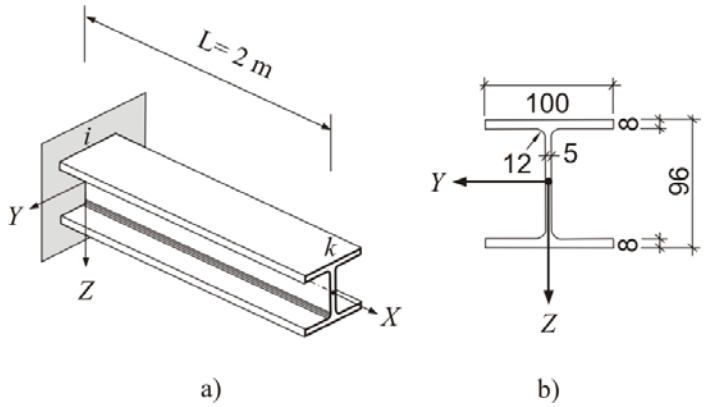


Figure 3: Cantilever beam with an I cross-section a) system, b) cross-section.

Cross-sectional parameters [22]:		
Polar moment of inertia:	$I_p = I_y + I_z = 4830 \cdot 10^{-9}$	m^4
Torsion constant:	$I_T = 52.4 \cdot 10^{-9}$	m^4
Secondary torsion constant:	$I_{Ts} = 2581.3 \cdot 10^{-9}$	m^4
Warping constant:	$I_\omega = 258.1 \cdot 10^{-11}$	m^6

Table 2: Cross-sectional parameters for nonuniform torsion.

Material characteristics:		
Young's modulus:	$E = 21 \cdot 10^7$	$\mathrm{kN/m^2}$
Poisson's ratio:	$\nu = 0.3$	
Shear modulus:	$G = 8.0769 \cdot 10^7$	$\mathrm{kN/m^2}$
Mass density:	$\rho = 7.85$	$\mathrm{t/m^3}$

Table 3: Material properties.

In the torsional modal analysis the following boundary conditions were applied:
a) Saint-Venant torsional vibration:

$$\psi(x)\big|_{x=0} = \psi_i = 0,\ M_T(x)\big|_{x=L} = M_{T,k} = 0. \tag{20}$$

d) Warping vibration (according to chapter 2):

$$\psi(x)\big|_{x=0} = \psi_i = 0, \qquad \psi'_M(x)\big|_{x=0} = \psi'_{M,i} = 0,$$

$$M_\omega(x)\big|_{x=L} = M_{\omega,k} = 0, \qquad M_T(x)\big|_{x=L} = M_{T,k} = 0.$$

Important notice: According to the analogy between non-uniform torsion and second-order beam theory (Table 1), it holds at the clamped beam end:

for the flexural vibration case $\left.\frac{\partial w}{\partial x}\right|_{x=0} = w'_i \neq 0$ but $\varphi\big|_{x=0} = \varphi_i = 0$; and for the warping vibration $\left.\frac{\partial \psi}{\partial x}\right|_{x=0} = \psi'_i \neq 0$ but $\left.\frac{\partial \psi'_M}{\partial x}\right|_{x=0} = \psi'_{M,i} = 0$.

Table 4 contains a comparison of the results for the first three eigenfrequencies with corresponding results obtained by the computer programs RSTAB [6] and ANSYS [5]. All values were obtained by the mentioned computers programs with following number of finite elements:

- 39700 elements of the type SOLID186 and 200 elements of the type BEAM188 – ANSYS [5];
- 50 elements of the type BEAM – RSTAB [6].

Type of eigenvibrations	Eigenfrequencies [Hz]			
	f_j	Proposed method	RSTAB [6]	ANSYS [5] SOLID186/BEAM188
Saint-Venant torsion about the *x*-axis	f_1	41.7	41.7	---/36.3
	f_2	125.2	125.5	---/109.1
	f_3	208.8	209.9	---/181.9
Warping torsion about the *x*-axis including deformations due to the secondary torsional moment	f_1	51.4	---------	50.8/---
	f_2	177.4	---------	172.8/---
	f_3	366.2	---------	356.8/---
Warping torsion about the *x*-axis without deformations due to the secondary torsional moment	f_1	51.6	---------	50.8/46.5
	f_2	178.7	---------	172.8/165.5
	f_3	373.0	---------	356.8/356.7

Table 4: First three eigenfrequencies of a cantilever beam with an I cross-section.

As expected, the difference between the uniform torsional eigenfrequencies (Saint-Venant) and the eigenfrequencies obtained by the proposed method and the commercial programs RSTAB [6] are negligible. But there is a visible deviation from the BEAM188 (warping unrestrained) results. These discrepancies are caused by the fact that in the FEM model based

on BEAM188 element the non-round transition between the web and the flange of I - profile was assumed, which has a small influence on the cross-sectional characteristics.
In nonuniform torsion analysis without STDME by the proposed approach and by the BEAM188 finite element with restrained warping the eigenfrequencies difference has decreased. The both results agree relatively well also with the SOLID186 solution results.
Our nonuniform torsion approaches with and without STMDE produce nearly the same results, what proves the fact, that the secondary torsion moment does not play significant role in torsion of open-section beams. On the other hand, the first three eigenfrequencies calculated with STMDE are closer to the SOLID186 solution results.

The first three torsional modes of the beam are shown in Fig. 4 and 5. They were obtained by means of the SOLID186 finite element [5]. It is seen that the cross-section satisfies the deformation conditions for nonuniform torsion of thin-walled cross-sections, as given by the thin tube theory (TTT). The torsional eigenmodes can be evaluated by means of the transfer relations (17), but the graphical representation is quite cumbersome (as it is also the case for the beam finite elements). This problem will be treated in our future work.

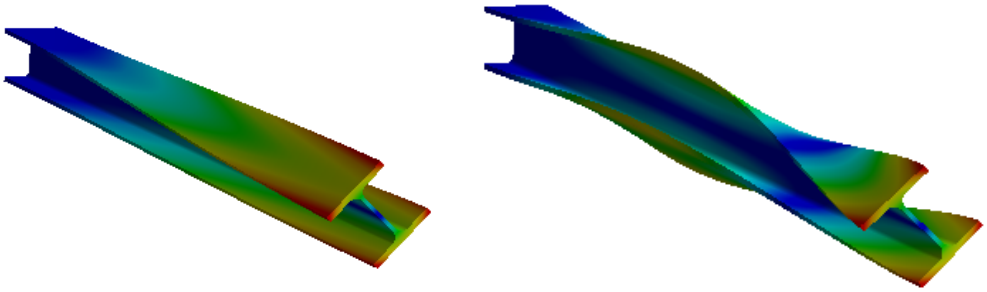


Figure 4: Mode shapes corresponding to the first and the second warping eigenfrequencies [5].

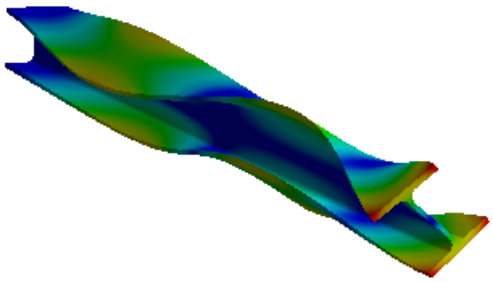


Figure 5: Mode shape corresponding to the third warping eigenfrequency [5].

3.2 Warping eigenfrequencies and mode shapes of a cantilever rectangular hollow section beam with constant ratio of *h/b* = 80/40 and *h/b* = 50/40, and with variable length *L* and wall thickness *t*.

Fig. 6 refers to the investigated cantilever beam. Fig. 6(a) shows the rectangular hollow beam and Fig. 6(b) illustrates the cross-section.

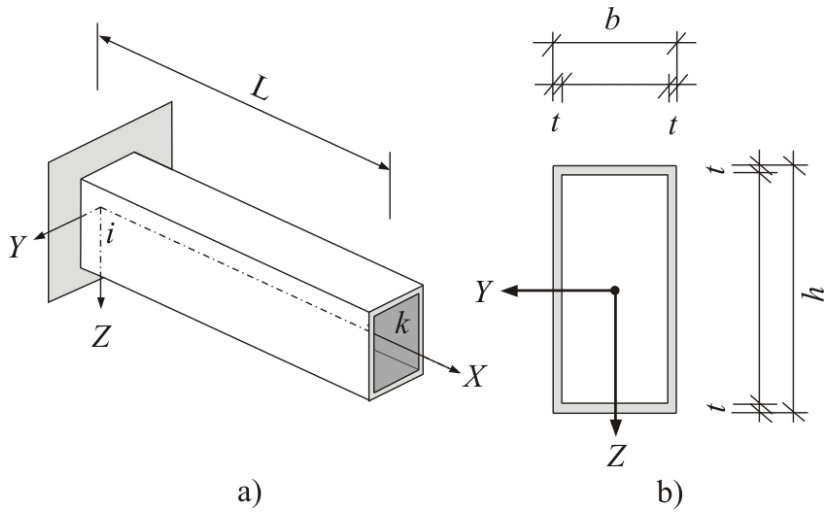
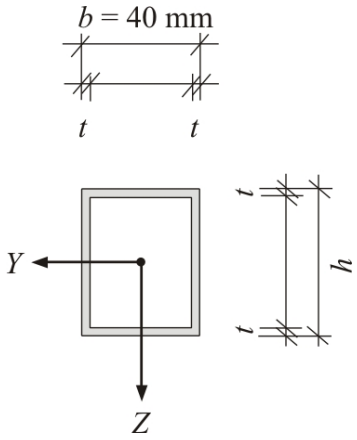


Figure 6: Cantilever beam with a rectangular hollow cross-section: a) system, b) cross-section.

The chosen material characteristics and the cross-sectional parameters are listed in Tables 3 and 5. The boundary conditions are the same as in section 3.1, expressions (20) and (21). In the following, the cross-sectional parameters and the cross-sectional characteristics are calculated by ANSYS [4] and [23] for t = 5 mm and t = 10 mm:

<table>
<tr><td colspan="4">Cross-sectional parameters [5], [23] :

</td></tr>
<tr><td rowspan="10">Cross-sectional area [5]:</td><td>$h/b/t = 40/40/5$
$h/b/t = 40/40/10$</td><td>$A = 7\cdot10^{-4}$
$A = 12\cdot10^{-4}$</td><td rowspan="10">m²</td></tr>
<tr><td>$h/b/t = 50/40/5$
$h/b/t = 50/40/10$</td><td>$A = 8\cdot10^{-4}$
$A = 14\cdot10^{-4}$</td></tr>
<tr><td>$h/b/t = 60/40/5$
$h/b/t = 60/40/10$</td><td>$A = 9\cdot10^{-4}$
$A = 16\cdot10^{-4}$</td></tr>
<tr><td>$h/b/t = 70/40/5$
$h/b/t = 70/40/10$</td><td>$A = 10\cdot10^{-4}$
$A = 18\cdot10^{-4}$</td></tr>
<tr><td>$h/b/t = 80/40/5$
$h/b/t = 80/40/10$</td><td>$A = 11\cdot10^{-4}$
$A = 20\cdot10^{-4}$</td></tr>
</table>

Polar moment of inertia [5, 23]:	$h/b/t = 40/40/5$ $h/b/t = 40/40/10$	$I_p = I_y + I_z = 29.167 \cdot 10^{-8}$ $I_p = I_y + I_z = 40.000 \cdot 10^{-8}$	m^4
	$h/b/t = 50/40/5$ $h/b/t = 50/40/10$	$I_p = I_y + I_z = 43.333 \cdot 10^{-8}$ $I_p = I_y + I_z = 61.833 \cdot 10^{-8}$	
	$h/b/t = 60/40/5$ $h/b/t = 60/40/10$	$I_p = I_y + I_z = 61.500 \cdot 10^{-8}$ $I_p = I_y + I_z = 90.667 \cdot 10^{-8}$	
	$h/b/t = 70/40/5$ $h/b/t = 70/40/10$	$I_p = I_y + I_z = 84.167 \cdot 10^{-8}$ $I_p = I_y + I_z = 127.500 \cdot 10^{-8}$	
	$h/b/t = 80/40/5$ $h/b/t = 80/40/10$	$I_p = I_y + I_z = 111.833 \cdot 10^{-8}$ $I_p = I_y + I_z = 173.333 \cdot 10^{-8}$	
Torsion constant [5]:	$h/b/t = 40/40/5$ $h/b/t = 40/40/10$	$I_T = 23.111 \cdot 10^{-8}$ $I_T = 33.068 \cdot 10^{-8}$	m^4
	$h/b/t = 50/40/5$ $h/b/t = 50/40/10$	$I_T = 33.099 \cdot 10^{-8}$ $I_T = 48.812 \cdot 10^{-8}$	
	$h/b/t = 60/40/5$ $h/b/t = 60/40/10$	$I_T = 43.641 \cdot 10^{-8}$ $I_T = 65.382 \cdot 10^{-8}$	
	$h/b/t = 70/40/5$ $h/b/t = 70/40/10$	$I_T = 54.561 \cdot 10^{-8}$ $I_T = 82.473 \cdot 10^{-8}$	
	$h/b/t = 80/40/5$ $h/b/t = 80/40/10$	$I_T = 65.753 \cdot 10^{-8}$ $I_T = 99.913 \cdot 10^{-8}$	
Secondary torsion constant [23]:	$h/b/t = 40/40/5$ $h/b/t = 40/40/10$	$I_{Ts} = 0.169 \cdot 10^{-8}$ $I_{Ts} = 9.836 \cdot 10^{-9}$	m^4
	$h/b/t = 50/40/5$ $h/b/t = 50/40/10$	$I_{Ts} = 0.374 \cdot 10^{-8}$ $I_{Ts} = 8.040 \cdot 10^{-9}$	
	$h/b/t = 60/40/5$ $h/b/t = 60/40/10$	$I_{Ts} = 2.048 \cdot 10^{-8}$ $I_{Ts} = 28.418 \cdot 10^{-9}$	
	$h/b/t = 70/40/5$ $h/b/t = 70/40/10$	$I_{Ts} = 4.503 \cdot 10^{-8}$ $I_{Ts} = 62.903 \cdot 10^{-9}$	
	$h/b/t = 80/40/5$ $h/b/t = 80/40/10$	$I_{Ts} = 7.910 \cdot 10^{-8}$ $I_{Ts} = 12.754 \cdot 10^{-8}$	

Warping constant [5]:	$h/b/t = 40/40/5$ $h/b/t = 40/40/10$	$I_\omega = 0.160 \cdot 10^{-12}$ $I_\omega = 46.796 \cdot 10^{-14}$	m^6
	$h/b/t = 50/40/5$ $h/b/t = 50/40/10$	$I_\omega = 1.080 \cdot 10^{-12}$ $I_\omega = 23.901 \cdot 10^{-13}$	
	$h/b/t = 60/40/5$ $h/b/t = 60/40/10$	$I_\omega = 4.652 \cdot 10^{-12}$ $I_\omega = 92.648 \cdot 10^{-13}$	
	$h/b/t = 70/40/5$ $h/b/t = 70/40/10$	$I_\omega = 12.371 \cdot 10^{-12}$ $I_\omega = 23.610 \cdot 10^{-12}$	
	$h/b/t = 80/40/5$ $h/b/t = 80/40/10$	$I_\omega = 25.762 \cdot 10^{-12}$ $I_\omega = 47.890 \cdot 10^{-12}$	

Table 5: Cross-sectional parameters [4] and [23] for t = 5 and 10 mm.

The aim of the investigation is the evaluation of the influence of the warping and the STMDE on the eigenfrequencies of the closed-section beam depending on the beam length and the wall thickness.

Tables 6 – 8 contains a comparison of the results for the first three torsional eigenfrequencies obtained by proposed method (Saint-Venant torsion, in lines a) and non-uniform torsion with STMDE, in lines b)) and with corresponding results obtained by the computer programs RSTAB [6] and ANSYS [5] for t = 5 mm and t = 10 mm, respectively. The results of RSTAB [6] are based on number of 50 Saint-Venant torsion beam finite elements (denoted by WW-E). The results of ANSYS [5] solution are based on number of 37 500 of SOLID186 elements (denoted by 3D-E) and on number of 100 of BEAM188 elements (warping unrestrained) denoted by WW-E, and non-uniform torsion (warping restrained without STMDE) denoted by W-E.

	Type of eigen-vibrations	Eigenfrequencies [Hz]				
		f_j	Proposed method	Type of elements	RSTAB [6]	ANSYS [5]
h/b/t = 80/40/5 L = 100 [mm]	a)	f_1	6149.0	WW-E	6149.0	6149.0
		f_2	18446.8	WW-E	18447.3	18449.0
		f_3	30744.7	WW-E	30746.8	30753.0
	b)	f_1	6333.0	W-E	---------	6205.8
				3D-E	---------	7493.8
		f_2	19017.8	W-E	---------	19827.0
				3D-E	---------	22315.0*
		f_3	30530.2	W-E	---------	36090.0
				3D-E	---------	40007.0*
h/b/t = 80/40/5 L = 200 [mm]	a)	f_1	3074.5	WW-E	3074.5	3074.5
		f_2	9223.4	WW-E	9223.5	9224.3
		f_3	15372.4	WW-E	15372.6	15376.0
	b)	f_1	3126.9	W-E	---------	3082.9
				3D-E	---------	4041.8
		f_2	9417.1	W-E	---------	9442.7
				3D-E	---------	10957.0*
		f_3	15825.5	W-E	---------	16322.0
				3D-E	---------	18816.0*

h/b/t = 80/40/5 L = 300 [mm]	a)	f_1	2049.6	WW-E	2049.6	2049.7
		f_2	6148.9	WW-E	6148.9	6149.5
		f_3	10248.2	WW-E	10248.3	10251.0
	b)	f_1	2073.3	W-E	---------	2052.3
				3D-E	---------	3306.8
		f_2	6240.9	W-E	---------	6218.9
				3D-E	---------	7497.3*
		f_3	10463.0	W-E	---------	10562.0
				3D-E	---------	11961.0*
h/b/t = 80/40/5 L = 400 [mm]	a)	f_1	1537.2	WW-E	1537.2	1537.3
		f_2	4611.7	WW-E	4611.7	4612.1
		f_3	7686.2	WW-E	7686.2	7688.2
	b)	f_1	1550.5	W-E	---------	1538.4
				3D-E	---------	1430.8
		f_2	4663.4	W-E	---------	4642.3
				3D-E	---------	5728.0*
		f_3	7807.2	W-E	---------	7825.3
				3D-E	---------	9221.4*
h/b/t = 80/40/5 L = 500 [mm]	a)	f_1	1229.8	WW-E	1229.8	1229.8
		f_2	3689.4	WW-E	3689.4	3689.7
		f_3	6149.0	WW-E	6149.0	6150.5
	b)	f_1	1238.2	W-E	---------	1230.4
				3D-E	---------	1178.8
		f_2	3721.9	W-E	---------	3705.4
				3D-E	---------	4735.5*
		f_3	6224.5	W-E	---------	6222.5
				3D-E	---------	7464.6*

Table 6: Torsional eigenfrequencies of a cantilever beam with a hollow cross-section (Fig. 6) with $h \times b \times t = 80 \times 40 \times 5$ [mm] and varying length L: a) Sant-Venant torsion; b) Warping torsion including deformations due to the secondary torsion moment.

	Type of eigen-vibrations	Eigenfrequencies [Hz]				
		f_j	Proposed method	Type of elements	RSTAB [7]	ANSYS [4]
h/b/t = 80/40/10 L = 100 [mm]	a)	f_1	6088.3	WW-E	6088.4	6088.4
		f_2	18265.0	WW-E	18265.4	18267.0
		f_3	30441.7	WW-E	30443.9	30449.0
	b)	f_1	6291.0.1	W-E	---------	6154.7
				3D-E	---------	9096.3*
		f_2	18885.1	W-E	---------	19856.0
				3D-E	---------	22694.0*
		f_3	38296.1	W-E	---------	36482.0
				3D-E	---------	39558.0*

h/b/t = 80/40/10 L = 200 [mm]	a)	f_1	3044.2	WW-E	3044.2	3044.2
		f_2	9132.5	WW-E	9132.6	9133.3
		f_3	15220.8	WW-E	15221.1	15225.0
	b)	f_1	3102.8	W-E	---------	3054.2
				3D-E	---------	2975.0
		f_2	9346.6	W-E	---------	9392.1
				3D-E	---------	12326.0*
		f_3	15723.6	W-E	---------	16333.0
				3D-E	---------	19293.0*
h/b/t = 80/40/10 L = 300 [mm]	a)	f_1	2029.4	WW-E	2029.4	2029.5
		f_2	6088.3	WW-E	6088.4	6088.9
		f_3	10147.2	WW-E	10147.3	10150.0
	b)	f_1	2056.1	W-E	---------	2032.6
				3D-E	---------	2019.8
		f_2	6191.5	W-E	---------	6171.8
				3D-E	---------	9200.8*
		f_3	10388.3	W-E	---------	10519.0
				3D-E	---------	13346.0*
h/b/t = 80/40/10 L = 400 [mm]	a)	f_1	1522.1	WW-E	1522.1	1522.1
		f_2	4566.3	WW-E	4566.3	4566.7
		f_3	7610.4	WW-E	7610.5	7612.4
	b)	f_1	1537.0	W-E	---------	1523.5
				3D-E	---------	1522,0
		f_2	4624.8	W-E	---------	4602.9
				3D-E	---------	8037.7*
		f_3	7747.5	W-E	---------	7776.4
				3D-E	---------	10592.0*
h/b/t = 80/40/10 L = 500 [mm]	a)	f_1	1217.7	WW-E	1217.7	1217.7
		f_2	3653.0	WW-E	3653.1	3653.3
		f_3	6088.3	WW-E	6088.8	6089.9
	b)	f_1	1227.3	W-E	---------	1218.4
				3D-E	---------	1219.7
		f_2	3689.9	W-E	---------	3672.3
				3D-E	---------	3443.2*
		f_3	6174.5	W-E	---------	6176.2
				3D-E	---------	5061.7*

Table 7: Torsional eigenfrequencies of a cantilever with a rectangular hollow cross-section (Fig. 6) with $h \times b \times t = 80 \times 40 \times 10$ [mm] with varying length L: a) Saint-Venant torsion; b) Warping torsion including deformations due to the secondary torsion moment.

	Type of eigen-vibrations	Eigenfrequencies [Hz]				
		f_j	Proposed method	Type of elements	RSTAB [7]	ANSYS [4]
h/b/t = 50/40/10 L = 100 [mm]	a)	f_1	7124.9	WW-E	7125.0	7125.0
		f_2	21374.8	WW-E	21375.3	21377.0
		f_3	35624.6	WW-E	35627.1	35634.0
	b)	f_1	7154.1	W-E	---------	7135.1
				3D-E	---------	7145.9
		f_2	21461.6	W-E	---------	21643.0
				3D-E	---------	22261.0*
		f_3	35820.6	W-E	---------	36812.0
				3D-E	---------	36583.0*
h/b/t = 50/40/10 L = 200 [mm]	a)	f_1	3562.5	WW-E	3562.5	3562.5
		f_2	10687.4	WW-E	10687.5	10688.0
		f_3	17812.3	WW-E	17812.7	17817.0
	b)	f_1	3570.7	W-E	---------	3563.8
				3D-E	---------	3576.3
		f_2	10716.9	W-E	---------	10724.0
				3D-E	---------	10435.0*
		f_3	17880.4	W-E	---------	17980.0
				3D-E	---------	18632.0*
h/b/t = 50/40/10 L = 300 [mm]	a)	f_1	2375.0	WW-E	2375.0	2375.0
		f_2	7124.9	WW-E	7125.0	7125.6
		f_3	11874.9	WW-E	11875.0	11878.0
	b)	f_1	2378.6	W-E	---------	2375.4
				3D-E	---------	2382.1
		f_2	7138.8	W-E	---------	7136.4
				3D-E	---------	7092.7
		f_3	11906.7	W-E	---------	11928.0
				3D-E	---------	11389.0*
h/b/t = 50/40/10 L = 400 [mm]	a)	f_1	1781.2	WW-E	1781.2	1781.2
		f_2	5343.7	WW-E	5343.7	5344.2
		f_3	8906.1	WW-E	8906.2	8908.4
	b)	f_1	1783.3	W-E	---------	1781.4
				3D-E	---------	1785.6
		f_2	5351.5	W-E	---------	5348.8
				3D-E	---------	5336.7
		f_3	8923.9	W-E	---------	8929.7
				3D-E	---------	8793.5*
h/b/t = 50/40/10 L = 500 [mm]	a)	f_1	1425.0	WW-E	1425.0	1425.0
		f_2	4275.0	WW-E	4275.1	4275.3
		f_3	7125.0	WW-E	7125.4	7126.7
	b)	f_1	1426.3	W-E	---------	1425.1
				3D-E	---------	1427.9
		f_2	4279.9	W-E	---------	4277.7
				3D-E	---------	4273.9
		f_3	7136.1	W-E	---------	7137.7
				3D-E	---------	7081.7

Table 8: Torsional eigenfrequencies of a cantilever beam with a hollow cross-section (Fig. 6) with $h \times b \times t = 50 \times 40 \times 10$ mm and with varying length L: a) Saint-Venant torsion; b) Warping torsion including deformations due to the secondary torsion moment.

The main conclusion drawn from Tables 6 – 8 is that, in contrast to the previous example, the influence of warping and the STMDE on the torsional eigenfrequencies of the beam with a rectangular hollow cross-section is not significant. It could be explained by the fact, that the beam stiffness is influenced by warping very locally only. This local action influences strongly the stress state at the restrained cross-sections of the closed sectional beam through the bimoment and secondary torsion moment, but not the eigenfrequency.
As expected, the influence of the STMDE on the eigenfrequency increases with decreasing beam length L. For very small beam length the system is closer to 3D solid. Thus, the beam theory is not longer suitable. For longer beams the warping and the STMDE influence on the torsional eigenfrequencies is less significant.
The best agreement of results obtained by the solid finite elements (denoted by 3D-E) and the proposed method (as well by the Saint-Venant and the warping beam solutions), achieved for the 1st torsional eigenfrequency. For the higher modes the discrepancy increases. The 2nd and 3rd torsional eigenfrequency (denoted as 3D-E and by "*"in Tables 5 – 7) show buckling of the cross-sectional walls. This effect cannot be considered as by the proposed method as by the beam finite elements with restrained and unrestrained warping. These discrepancies are partly reduced by the beam with larger length with smaller section ratio h/b and by greater wall thickness t.
The mode shapes corresponding to the first three torsional eigenfrequencies (obtained by the SOLID186 finite element) are shown in Figs. 7 – 9 (evaluated for $h \times b \times t = 80 \times 40 \times 10$ and L = 400 [mm]). Except for the first torsional eigenmode, the cross-section walls are buckling. Therefore a comparison of the eigenfrequencies obtained by means of beam theories with eigenfrequencies based on 3-D solid theory is problematic.

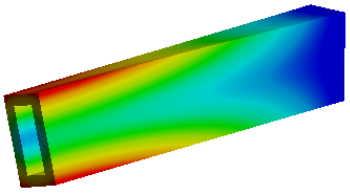


Figure 7: Mode shape corresponding to the 1st torsional eigenfrequency [5].

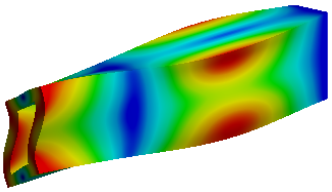


Figure 8: Mode shape corresponding to the 2nd torsional eigenfrequency [5].

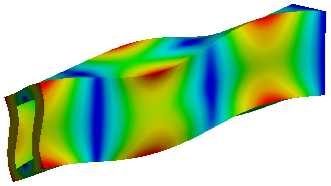


Figure 9: Mode shape corresponding to the 3rd torsional eigenfrequency [5].

4 SUMMARY AND CONCLUSIONS

On the bases of the analogy of the beam theory and the nonuniform torsion theory of thin-walled open and closed cross-sections, the differential equation of 4th order for nonuniform torsion eigenvibration was established. The general semianalytical solution of the differential equation was presented and the transfer matrix relation was established. The results from modal analysis of open I and rectangular hollow section beam by the proposed method were presented and compared with the ones obtained by commercial FEM codes. In the theoretical investigations by the authors, the effect of the secondary torsion moment deformation (STDME) was taken into account. A part of the first derivative of the twist angle was chosen as a warping degree of freedom. Contrary to the bicurvature, this warping degree of freedom can by used for satisfaction of boundary conditions.
The main conclusions that can be drawn from this investigation are as follows:

(1) Eigenvibrations of open I-section beam:

- The results of modal analysis concerning nonuniform and uniform torsion of open section beams show large differences of the eigenfrequencies. This verifies the-well known fact that the warping effect must be taken into account by torsional analysis of open cross-sections in static and in dynamic analysis.
- The proposed approach for calculation of nonuniform torsional eigenvibrations with and without STMDE produces nearly the same results. This proves the fact that the secondary torsion moment does not play a significant role in torsion of open-section beams. On the other side, the torsional eigenfrequencies obtained with STMDE are very close to results obtained by 3D solid finite elements.

(2) Eigenvibrations of rectangular hollow-section beam

- In contrast to the open cross-section, the influence of warping (with or without STMDE) on the nonuniform torsional eigenfrequencies of beams with a rectangular hollow cross-section is not significant. This is explained by the fact, that the beam stiffness is affected by warping only very locally. This has a strong influence on the local stress state at the restrained cross-sections, but not on the eigenfrequency. As expected, the influence of the STMDE on the eigenfrequency increases with decreasing length of the beam. For longer beams the influence of warping and of STMDE on the torsional eigenfrequencies is less significant.
- The best agreement of results obtained by the solid finite elements and the proposed method (as well by the Saint-Venant and the warping beam solutions), achieved for the 1st torsional eigenfrequency. For the higher modes the discrepancy increases. The higher torsional eigenmodes show buckling of the cross-sectional walls. This effect cannot be considered as by the proposed method as by the beam finite elements with restrained and unrestrained warping. These discrepancies are partly reduced by the beam with larger length with smaller section ratio h/b and by greater wall thickness t.
- Because of to the discrepancies between the warping torsion eigenfrequencies of beams with a closed section obtained by the beam theory and the 3D solid theory, an experimental verification of the results is needed.

In future work on the bases of the presented method, a new 3D finite beam element for modal and transient structural analysis will be established, wherein the STMDE and the new warping degree of freedom will be included. It is expected, that for forced torsional vibrations of

closed-section beams, with restrained warping, the effect of warping and of the secondary torsion moment will be stronger than it is in case of modal analysis.

ACKNOWLEDGEMENT

This paper has been supported by the Slovak Grant Agencies APVV-0246-12, VEGA No. 1/0228/14, VEGA No. 1/0453/15 and KEGA No. 007STU-4/2015.

REFERENCES

[1] ADINA R&D, Inc., *Theory and Modelling Guide.Vol. I*: *ADINA.* 2013.

[2] J.S. Przemieniecki, *Theory of matrix structural Analysis.* McGraw-Hill Book Co., 1968.

[3] K.J. Bathe, A. Chaudhary, On the displacement formulation for torsion of shafts with rectangular cross-section. *Num. Methods in Engineering*, **18, 1**565-1568, 1982.

[4] ABAQUS/CAE, Version 6.10-1, Dassault Systems Simulia Corp. Providence, RI, USA.

[5] ANSYS Swanson Analysis System, Inc., 201 Johnson Road, Houston, PA 15342/1300, USA.

[6] RSTAB, Ingenieur – Software Dlubal GmbH, Tiefenbach 2006.

[7] E.J. Sapountzakis, Torsional vibration of composite bars of variable cross-section by BEM. *Comp. Meth. Appl. Mech. Engineering.* **194**, 2127-2145, 2005.

[8] E.J. Sapontzakis, V.G. Mokos, Dynamic analysis of 3-D beam elements including warping and shear deformation effects. *Non-linear Mechanics*. **43**, 6707-6726, 2006.

[9] E.J. Sapontzakis, V.J. Tsipiras, Nonlinear nonuniform torsional vibration. **329**, 1853-1874, 2010.

[10] E.J. Sapountzakis, I.C. Dikaros, Non-linear flexural – torsional dynamic analysis of beams of arbitrary cross section by BEM. *Non-linear mechanics*. **46**. 1853-1874, 2011.

[11] S.A. Sina, H. Haddadpour, Nonlinear free vibration of thin walled beams in torsion.

[12] S.J. Lee, S.B. Park, Vibrations of Timoschenko beams with isogeometric approach. *Applied mathematical Modelling.* **37**, 9174-9190, 2013.

[13] S. Stoykov, P. Ribeiro, Non-linear vibrations of beams with non-symetrical cross sections. *Non-linear Mechanics.* **55**, 153-169, 2013.

[14] S.A. Sina, H. Haddadpour, Axial – torsional vibrations of rotated pretwisted thin walled composite beams. *Mechanical Sciencies.* **80**, 93-101, 2014.

[15] K.F. Ferradi, X.A. Cespedes, A new beam element with transversal and warping eigenmodes. *Computers and Structures.* **131**, 12-33, 2014.

[16] H. Rubin, Wölbkraftorsion gechlossener Querschnitte und ihrer Irrtümer – Grundlagen. 29. *Stahlbauseminar.* **140**, 2007.

[17] J. Murín, M. Aminbaghai, V. Kutiš, V. Kralovič, T. Sedlár, V. Goga, H. Mang, A new 3D Timoshenko finite beam element including non-uniform torsion of open and closed cross sections. *Engineering Structures.* **59**, 153 – 160, 2014.

[18] E.J. Sapountzakis, I.C. Dikaros, Advanced 3D beam element of arbitrary composite cross-section including generalized warping effect. *Numerical Methods in Engineering.* DOI: 10.1002/nme.4849, 2015.

[19] H. Rubin, Wölbkrafttorsion von Durchlaufträgern mit konstantem Querschnitt unter Berücksichtigung sekundärer Schubverformung. *Stahlbau.* **76**, 826 – 842, 2005.

[20] M. Aminbaghai, J. Murín, J. Hrabovský, H. Mang, Torsional warping eigenmodes including secondary torsion moment deformation effect. Paper in preparation. 2015.

[21] Wolfram MATHEMATICA. 9.0.1.0, Wolfran Research, 2013.

[22] M. Schneider-Bürger, *Stahlbau Profile*. Verlag Stahleisen GmbH, Düsseldorf 2001; Volume 23.

[23] DUENO, Version 7.01, Dlubal.

COMPDYN 2015
5th ECCOMAS Thematic Conference on
Computational Methods in Structural Dynamics and Earthquake Engineering
M. Papadrakakis, V. Papadopoulos, V. Plevris (eds.)
Crete Island, Greece, 25–27 May 2015

GENERALIZED WARPING EFFECT IN THE DYNAMIC ANALYSIS OF BEAMS OF ARBITRARY CROSS SECTION

Ioannis C. Dikaros[1], **Evangelos J. Sapountzakis**[2], **Amalia K. Argyridi**[3] **and Dimitris S. Papadopoulos**[4]

[1]School of Civil Engineering, National Technical University of Athens
Zografou Campus, GR–157 80, Athens, Greece
dikarosgiannis@gmail.com.

[2-3]School of Civil Engineering, National Technical University of Athens
Zografou Campus, GR–157 80, Athens, Greece
cvsapoun@central.ntua.gr, a.argyridi@gmail.com.

[4]Engineer Officers Technical School, Corps of Engineers, Hellenic Army General Staff
Papadiamantopoulou 190, GR-115 27, Athens, Greece,
papadopoulosdimitris9@gmail.com.

Keywords: Nonuniform warping; Shear lag; Shear deformation; Dynamic Analysis; Boundary Element Method.

Abstract. *In this paper a general formulation for the nonuniform warping dynamic analysis of beams of arbitrary simply or multiply connected cross section, under arbitrary external loading and general boundary conditions is presented taking into account the effects of rotary and warping inertia. The nonuniform warping distributions are taken into account by employing four independent warping parameters multiplying a shear warping function in each direction and two torsional warping functions, respectively, which are obtained by solving the corresponding boundary value problems, formulated exploiting the longitudinal local equilibrium equation. A shear stress "correction" is also performed in order to improve the stress field arising from the employed kinematical considerations. Ten initial boundary value problems are formulated with respect to the displacement and rotation components as well as to the independent warping parameters and solved using the Analog Equation Method, a Boundary Element Method based technique in combination with an appropriate time integration scheme. The warping functions and the geometric constants including the additional ones due to warping are evaluated employing a pure BEM approach.*

1 INTRODUCTION

In engineering practice, the dynamic analysis of beam-like members under flexure is frequently encountered. Besides, many conditions occurring in engineering practice, such as rotating machinery, wind and traffic loads, blast and earthquake forces, require taking into account inertial effects in the dynamic analysis of beams. The inclusion of such effects, especially through distributed mass models, which are considered to be more reliable, requires a rigorous analysis. In the vast majority of these cases, Euler – Bernoulli beam theory assumptions are adopted, and when shear deformation effect is non-negligible these assumptions are relaxed by using Timoshenko beam theory. However, both theories maintain the assumption that plane cross sections remain plane after deformation. By maintaining this assumption, the formulation remains simple; however, it fails to capture the well-known shear lag phenomenon, which was reported long ago (e.g. [1-3]) and observed in many structural members (e.g., beams of box-shaped cross sections, folded structural members, beams made of materials weak in shear). Shear lag is associated with a significant modification of normal stress distribution, especially near the joint of the various cross-sectional components [4], due to nonuniform distribution of shear warping [Figs. 1(d and e)] [5].

In up-to-date regulations, the significance of shear lag effect in flexure is recognized; however, to simplify the analysis, the effective width concept [6-8] is recommended. This simplifying approach may fail to capture satisfactorily the actual structural behaviour of the member, because the influence of the shear lag phenomenon is not constant along the beam length. Apart from the geometrical configuration of the cross section, it depends also on the type of loading [9]. Therefore, it is necessary to include the effects of nonuniform shear warping distribution in both the static and the dynamic analysis.

Generalizing the shear lag analysis problem, considerations similar to those made for flexure could be also adopted for the problem of torsion. It is well known that when a beam undergoes general twisting loading under general boundary conditions, it is led to nonuniform torsion. This problem has been extensively examined in the literature (e.g. see [10,11]), and its major characteristic is the presence of normal stress due to primary torsional warping [Fig. 1(c)]. In an analogy with Timoshenko beam theory, when shear deformation is of importance, the so-called secondary torsional shear deformation effect (STSDE) [12,13] has to be taken into account as well. Thus, it could be concluded that the additional secondary torsional warping due to STSDE [Fig. 1(f)] can cause effects similar to shear lag in flexure, i.e., a modification of the initial normal stress distribution. It is noted that because of the complicated nature of torsion, simplified concepts such as effective width cannot be applied to take this behavior into account.

Toward investigating shear lag effects, the inclusion of nonuniform warping in beam element formulations based on so-called higher-order beam theories [14] is of increased interest because of their important advantages over more refined approaches (e.g. [15-17]). Beam elements are practical and computationally efficient and offer better insight into the structural phenomena, since they permit their isolation and independent investigation. Furthermore, because of easy parameterization of all necessary data, beam elements are more convenient for parametric analyses than more refined models which, in most cases, require the construction of multiple models.

The dynamic analysis of the generalized nonuniform warping problem has received relatively less attention than the static one. Some researchers have employed the assumptions of TTT (Thin Tube Theory) and the nonuniform torsion theory with an additional degree of freedom for nonuniform warping that is the rate of angle of twist [23-34] or an independent

warping parameter [35-36]. Egidio et al [37] describe the non-linear warping of open cross-section thin-walled beams in terms of the flexural and torsional curvatures. Minghini et al [38] take into account shear strain effects due to both nonuniform bending and torsion in the analysis of thin walled cross sections. Some other researchers have employed the nonuniform torsion theory for beams with arbitrarily shaped cross sections with the rate of the angle of twist as an additional degree of freedom [39-46].Sapountzakis and Tsipiras [47] have taken into account nonouniform torsion in the analysis of beam with arbitrarily shaped doubly symmetric cross sections using a secondary warping function. On the other hand Li et al [48] developed an element that includes the effect of warping using a displacement field that is assumed to be cubic in the axial direction and quadratic in the transverse direction. Moreover, to the authors ' knowledge, a BEM procedure for the dynamic analysis of the general nonuniform warping problem of beams of arbitrary cross sections has never been reported in the literature.

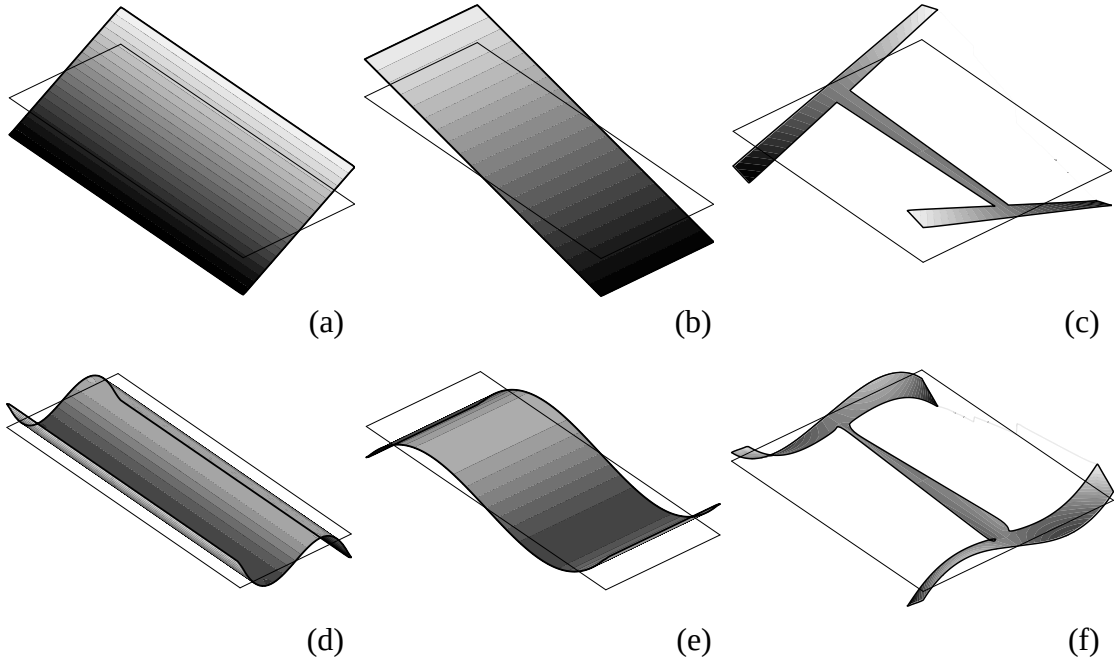


Fig.1. Normal stress distribution due to flexure (a,b), primary torsional warping (c), shear warping (d,e) and secondary torsional warping (f).

In the current study, which is an extension of a previous work of the same authors [49-50] at the dynamic regime, a general boundary element formulation for the dynamic nonuniform warping analysis of beams of arbitrary cross section, taking into account shear lag effects due to both flexure and torsion, is presented. The beam cross section (thin- or thick-walled) is homogeneous and can surround a finite number of inclusions. The beam is subjected to the combined action of arbitrarily distributed or concentrated dynamic axial loading and transverse loading, as well as to bending, twisting, and warping moments. Nonuniform warping distributions are taken into account by using four independent warping parameters multiplying a shear warping function in each direction [49-50] and two torsional warping functions, which are obtained by solving corresponding boundary value problems. It is worth mentioning here that the stress field arising from the preceding kinematical considerations leads to the violation of the longitudinal local equilibrium equation and the corresponding boundary condition [22] due to inaccurate representation of shear stresses. In the current study, to keep the sim-

plicity of the formulation to the highest possible level, the increment of the number of unknowns in global equilibrium is avoided and a correction of the stress field is performed with the aid of the longitudinal local equilibrium equation. Ten initial-boundary value problems are formulated with respect to the displacement and rotation components and the independent warping parameters and solved using the analog equation method (AEM) [52], a BEM-based method in combination with an appropriate time integration scheme (Mean Acceleration Method [56]). The warping functions, the additional geometric constants due to warping, and the elementary ones are evaluated with a pure BEM approach, i.e., only boundary discretization of the cross section is used. After establishment of the kinematical components, the aforementioned boundary discretization can be used to evaluate through BEM the normal and shear stress components at any arbitrary point of each cross section.

The essential features and novel aspects of the present formulation are summarized as follows:

- The cross section is an arbitrarily shaped thin- or thick-walled. The formulation does not stand on the assumption of a thin-walled structure, and therefore the cross section's warping rigidities are evaluated exactly (in a numerical sense).
- An improved stress field is adopted with the aid of the longitudinal local equilibrium equation, leading to a better evaluation of stress components without increasing the global degrees of freedom.
- The beam is subjected to arbitrary external loading and is supported by the most general boundary conditions, including elastic support or restraint.
- The proposed formulation is suitable for the investigation of flexural and torsional shear lag effects in beams of closed or open cross sections.
- The proposed method uses a BEM approach (requiring boundary discretization for the cross-sectional analysis) resulting in line or parabolic elements instead of area elements of the FEM solutions (requiring the whole cross section to be discretized into triangular or quadrilateral area elements), whereas a small number of line elements are required to achieve high accuracy.
- The use of BEM permits the accurate computation of deriveatives of the field functions (e.g., stresses) which is very important in the nonuniform warping analysis of beams.
- The generalized warping theory of beams presented in [49-50] is extended at the dynamic regime.
- The necessity to include warping inertial and generalized warping effects is investigated in both thin- and thick walled open- and closed shaped cross section bars.
- Both free and forced vibrations of bars are investigated obtaining free vibration characteristics and both kinematic and stress results in the time domain, respectively.

2 STATEMENT OF THE PROBLEM

2.1 Displacement, strain and stress components

Consider a prismatic beam of length l, of arbitrary cross section of area A. The homogeneous isotropic and linearly elastic material of the beam's cross section, with modulus of elasticity E, shear modulus G, Poisson's ratio ν and mass density ρ occupies the two dimensional multiply connected region Ω of the yz plane and is bounded by the Γ_j ($j=1,2,...,K$) boundary curves, which are piecewise smooth, i.e. they may have a finite number of corners. In Fig.2 $CXYZ$ is the principal bending coordinate system through the cross section's centroid C, while y_C, z_C are its coordinates with respect to $Sxyz$ reference system of axes through

the cross section's center of twist S. The beam is subjected to the combined action of the arbitrarily distributed or concentrated time-dependent axial loading $p_x = p_x(X,t)$ along X direction, transverse loading $p_y = p_y(x,t)$, $p_z = p_z(x,t)$ along the y, z directions, respectively, twisting moments $m_t = m_t(x,t)$ along x direction, bending moments $m_Y = m_Y(x,t)$, $m_Z = m_Z(x,t)$ along Y, Z directions, respectively, as well as warping moments $m_{\varphi_S^P} = m_{\varphi_S^P}(x,t)$, $m_{\varphi_S^S} = m_{\varphi_S^S}(x,t)$, $m_{\varphi_{CY}^P} = m_{\varphi_{CY}^P}(x,t)$, $m_{\varphi_{CZ}^P} = m_{\varphi_{CZ}^P}(x,t)$ (Fig.2) which will be later defined in section 2.2.

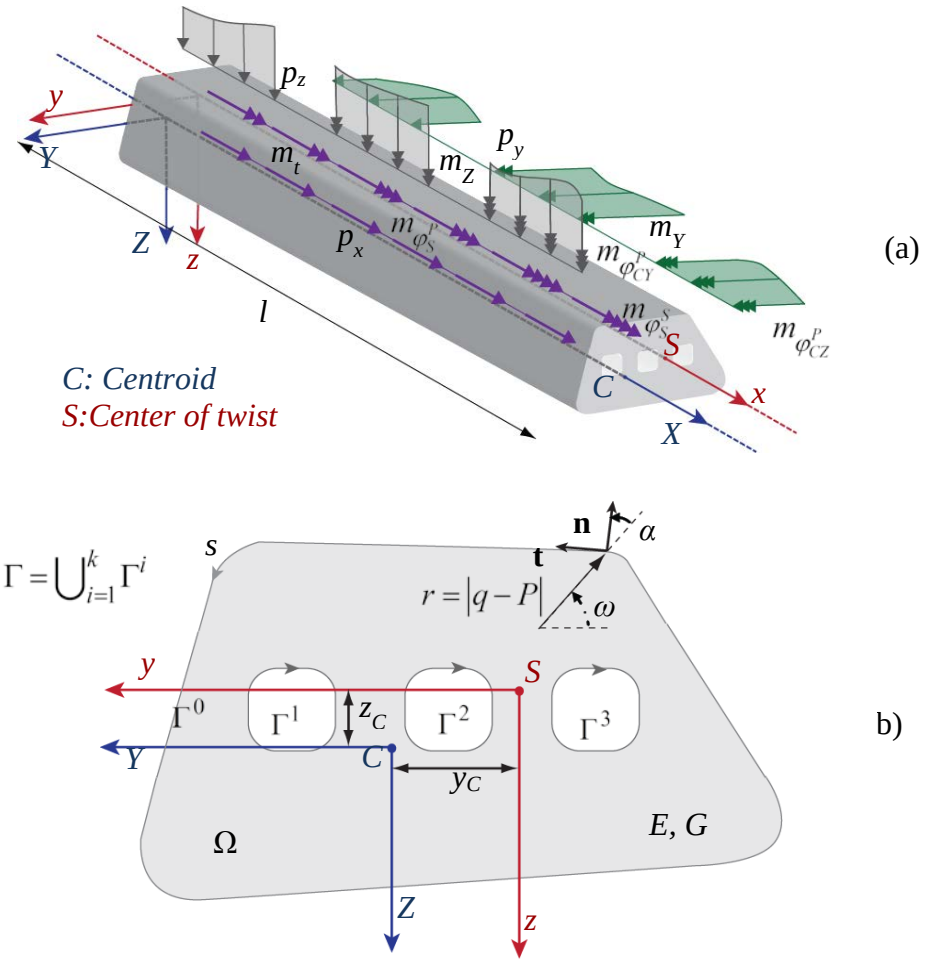


Fig.2. Prismatic beam under axial-flexural-torsional dynamic loading (a) of an arbitrary cross section occupying the two dimensional region Ω (b).

Under the action of the aforementioned general loading and of possible restraints, the beam is leaded to flexural, axial and/or torsional vibrations. In order to take into account nonuniform warping distributions which are responsible for shear lag effects due to both flexure and torsion, four additional time-dependent degrees of freedom (warping parameters), namely $\eta_x(x,t)$, $\eta_Y(x,t)$, $\eta_Z(x,t)$, $\xi_x(x,t)$ multiplying a shear warping function in each direction (η_Y, η_Z) and two torsional warping functions (η_x, ξ_x), respectively, are employed [49, 50]. These additional DOFs describe the "intensities" of the corresponding cross sectional warping along the beam length at any time instant, while these warpings are defined by corresponding

warping functions ($\varphi_{CY}^{P}(y,z)$, $\varphi_{CZ}^{P}(y,z)$, $\varphi_{S}^{P}(y,z)$, $\varphi_{S}^{S}(y,z)$), depending only on the cross sectional configuration. Thus, the "actual" deformed configurations of the cross section due to primary (in each direction) shear and primary, secondary torsional warpings are given as $\eta_Y(x,t)\varphi_{CY}^{P}(y,z)$, $\eta_Z(x,t)\varphi_{CZ}^{P}(y,z)$, $\eta_x(x,t)\varphi_{S}^{P}(y,z)$ and $\xi_x(x,t)\varphi_{S}^{S}(y,z)$ at any position and time instant. It is worth here noting that the shear stresses generated by the above displacement considerations exhibit an inconsistency concerning the non-vanishing of tractions τ_{xn} on the lateral surface of the beam [22, 49, 50]. As shown in previous studies, this inconsistency may be responsible for non-negligible errors in estimated normal stress values. In the present study this inconsistency is removed by performing a suitable shear stress correction, which is discussed in detail in a previous work of the same authors [49, 50]. Within the context of the above considerations, the displacement components of an arbitrary point of the beam at an arbitrary time instant are given as

$$\begin{aligned}\bar{u}(x,y,z,t) &= \bar{u}^{P}(x,y,z,t)+\bar{u}^{S}(x,y,z,t)= \\ &= \underbrace{u(x,t)+\theta_Y(x,t)Z-\theta_Z(x,t)Y+\eta_x(x,t)\phi_S^{P}(y,z)}_{\text{primary}}+ \\ &+\underbrace{\eta_Y(x,t)\phi_{CY}^{P}(y,z)+\eta_Z(x,t)\phi_{CZ}^{P}(y,z)+\xi_x(x,t)\phi_S^{S}(y,z)}_{\text{secondary}}\end{aligned} \tag{1a}$$

$$\bar{v}(x,y,z,t)=v(x,t)-z\theta_x(x,t) \qquad \bar{w}(x,y,z,t)=w(x,t)+y\theta_x(x,t) \tag{1b,c}$$

where $\bar{u}$, $\bar{v}$, $\bar{w}$ are the axial and transverse beam displacement components with respect to the $Sxyz$ system of axes, while $\bar{u}^{P}$, $\bar{u}^{S}$ denote the primary and secondary longitudinal displacements, respectively. Moreover, $v(x,t)$, $w(x,t)$ describe the deflection of the center of twist S, while $u(x,t)$ denotes the "average" axial displacement of the cross section. $\theta_Z(x,t)$, $\theta_Y(x,t)$ are the angles of rotation due to bending about the centroidal Y, Z axes, respectively. $\eta_x(x,t)$, $\xi_x(x,t)$ are the independent warping parameters introduced to describe the nonuniform distribution of primary and secondary torsional warping, while $\eta_Y(x,t)$, $\eta_Z(x,t)$ are the independent warping parameters introduced to describe the nonuniform distribution of primary warping due to shear [49, 50]. $\varphi_{S}^{P}(y,z)$, $\varphi_{S}^{S}(y,z)$ are the primary and secondary torsional warping functions with respect to the center of twist S [13], while $\varphi_{CY}^{P}(y,z)$, $\varphi_{CZ}^{P}(y,z)$ are the primary shear warping functions with respect to the centroid C [49, 50]. Finally, it holds that $Z=z-z_C$, $Y=y-y_C$.

Employing the displacement expressions given from eqns. (1) to the strain-displacement relations of the three-dimensional elasticity for small displacements and the Hooke's stress-strain law, the non-vanishing components of the Cauchy stress tensor are obtained as

$$\sigma_{xx}=\underbrace{E^{*}\left[u_{,x}+\theta_{Y,x}Z-\theta_{Z,x}Y+\eta_{x,x}\varphi_S^{P}\right]}_{\text{primary}}+\underbrace{E^{*}\left[\eta_{Y,x}\varphi_{CY}^{P}+\eta_{Z,x}\varphi_{CZ}^{P}+\xi_{x,x}\varphi_S^{S}\right]}_{\text{secondary}} \tag{2a}$$

$$\mathbf{t} = \underbrace{G\left[\gamma_Z^P \nabla\left(Z+\varphi_{CY}^P\right)+\gamma_Y^P \nabla\left(Y+\varphi_{CZ}^P\right)+\gamma_x^P\left(\mathbf{r}+\nabla\varphi_S^P\right)\right]}_{\text{primary}}+$$
$$+\underbrace{G\left[\gamma_Z^S \nabla\varphi_{CY}^S+\gamma_Y^S \nabla\varphi_{CZ}^S+\gamma_x^S \nabla\left(\varphi_S^P+\varphi_S^S\right)\right]}_{\text{secondary}}+\underbrace{G\left[\gamma_x^T \nabla\varphi_S^S\right]}_{\text{tertiary}} \tag{2b}$$

where $\mathbf{t}=\left[\tau_{xy} \quad \tau_{xz}\right]^T$, $\mathbf{r}=\left[-z \quad y\right]^T$ and $E^* = E(1-\nu)/\left[(1+\nu)(1-2\nu)\right]$. If the plane stress hypothesis is undertaken then $E^* = E/\left(1-\nu^2\right)$ holds [10], while E is frequently considered instead of E^* ($E^* \approx E$) in beam formulations [10]. The first consideration has been followed throughout the paper, while any other reasonable expression of E could also be used without any difficulty. Furthermore, $(\cdot)_{,i}$ denotes differentiation with respect to i, while $\nabla \equiv (\cdot)_{,y}\,\mathbf{i}_y + (\cdot)_{,z}\,\mathbf{i}_z$ is the gradient operator and $\mathbf{i}_y$, $\mathbf{i}_z$ the unit vectors along y, z axes, respectively. $\gamma_x^P = \theta_{x,x}$, $\gamma_x^S = \eta_x - \theta_{x,x}$, $\gamma_x^T = \xi_x - \eta_x + \theta_{x,x}$, $\gamma_Y^P = v_{,x} - \theta_Z$, $\gamma_Y^S = \eta_Y - v_{,x} + \theta_Z$, $\gamma_Z^P = w_{,x} + \theta_Y$ and $\gamma_Z^S = \eta_Z - w_{,x} - \theta_Y$ are "average" shear strain quantities. In eqns. (2b) the primary shear stress terms correspond to the St. Venant shear stresses (τ_{xy}^P, τ_{xz}^P) [14], while the rest of the terms to warping shear stresses (τ_{xy}^S, τ_{xz}^S, τ_{xy}^T, τ_{xz}^T) arising from the use of independent warping parameters. The above stress components (2) could be employed in order to derive the global equations of motion. However, as stated above, attention should be paid to the fact that the terms $\gamma_Y^S \varphi_{CY,i}^P$, $\gamma_Z^S \varphi_{CZ,i}^P$, $\gamma_x^T \varphi_{S,i}^S$ ($i = y, z$) are not capable of representing an acceptable shear stress distribution, leading to violation of the longitudinal local equilibrium equation and the corresponding zero-traction condition on the lateral surface of the beam. This observation reveals an analogy with Timoshenko beam theory and nonuniform torsion theory with STSDE [12,13]. As a consequence, discrepancies in stress components near fixed supports or concentrated loads may arise [12,13,21,49,50]. In the present study, a correction of stress components is performed without increasing the number of global kinematical unknowns, following the analysis presented in [49, 50]. To this end, three additional warping functions $\varphi_{CY}^S(y,z)$, $\varphi_{CZ}^S(y,z)$, $\varphi_S^T(y,z)$ are introduced in expressions (2b), which are modified as

$$\mathbf{t} = \underbrace{G\left[\gamma_Z^P \nabla\Phi_{CY}^P+\gamma_Y^P \nabla\Phi_{CZ}^P+\gamma_x^P\left(\mathbf{r}+\nabla\varphi_S^P\right)\right]}_{\text{primary}}+\underbrace{G\left[\gamma_Z^S \nabla\Phi_{CY}^S+\gamma_Y^S \nabla\Phi_{CZ}^S+\gamma_x^S \nabla\Phi_S^S\right]}_{\text{secondary}}+$$
$$+\underbrace{G\left[\gamma_x^T \nabla\Phi_S^{\mathrm{T}}\right]}_{\text{tertiary}} \tag{3}$$

where

$$\Phi_{CY}^P = Z + \varphi_{CY}^P \qquad \Phi_{CY}^S = \varphi_{CY}^P + \varphi_{CY}^S \tag{4a,b}$$
$$\Phi_{CZ}^P = Y + \varphi_{CZ}^P \qquad \Phi_{CZ}^S = \varphi_{CZ}^P + \varphi_{CZ}^S \tag{4c,d}$$

$$\Phi_S^S = \varphi_S^P + \varphi_S^S \qquad \Phi_S^T = \varphi_S^S + \varphi_S^T \tag{4e,f}$$

Warping functions (4) can be determined by formulating boundary value problems exploiting the longitudinal local equilibrium equation and the associated boundary condition, which will be discussed in next section.

2.2 Global equations of motion

In order to establish the differential equations of motion, the principle of virtual work including virtual work due to inertial forces

$$\delta W_{\text{int}} + \delta W_{\text{mass}} = \delta W_{\text{ext}} \tag{5}$$

is employed, where

$$\delta W_{\text{int}} = \int_V \left(\sigma_{xx}\delta\varepsilon_{xx} + \tau_{xy}\delta\gamma_{xy} + \tau_{xz}\delta\gamma_{xz} \right) \mathrm{d}V \tag{6a}$$

$$\delta W_{\text{mass}} = \int_V \rho \left(\overline{u}_{,tt}\delta\overline{u} + \overline{v}_{,tt}\delta\overline{v} + \overline{w}_{,tt}\delta\overline{w} \right) \mathrm{d}V \tag{6b}$$

$$\delta W_{\text{ext}} = \int_{\text{Lat}} \left(t_x\delta\overline{u} + t_y\delta\overline{v} + t_z\delta\overline{w} \right) \mathrm{d}F \tag{6c}$$

In the above equations, $\delta(\cdot)$ denotes virtual quantities; t_x, t_y, t_z are the components of the traction vector applied on the lateral surface of the beam including the end cross sections, denoted by F and V is the volume of the beam. Moreover, the stress resultants of the beam can be defined as

$$N = \int_\Omega \sigma_{xx}\,\mathrm{d}\Omega \qquad M_Y = \int_\Omega \sigma_{xx} Z\,\mathrm{d}\Omega \qquad M_Z = \int_\Omega \sigma_{xx} Y\,\mathrm{d}\Omega \tag{7a,b,c}$$

$$M_{\varphi_S^P} = \int_\Omega \sigma_{xx}\varphi_S^P\,\mathrm{d}\Omega \qquad M_{\varphi_S^S} = \int_\Omega \sigma_{xx}\varphi_S^S\,\mathrm{d}\Omega \tag{7d,e}$$

$$M_{\varphi_{CY}^P} = \int_\Omega \sigma_{xx}\varphi_{CY}^P\,\mathrm{d}\Omega \qquad M_{\varphi_{CZ}^P} = \int_\Omega \sigma_{xx}\varphi_{CZ}^P\,\mathrm{d}\Omega \tag{7f,g}$$

$$Q_y^P = \int_\Omega \left(\tau_{xy}\Phi_{CY,y}^P + \tau_{xz}\Phi_{CY,z}^P \right) \mathrm{d}\Omega \qquad Q_y^S = -\int_\Omega \left(\tau_{xy}\Phi_{CY,y}^S + \tau_{xz}\Phi_{CY,z}^S \right) \mathrm{d}\Omega \tag{7h,i}$$

$$Q_z^P = \int_\Omega \left(\tau_{xy}\Phi_{CZ,y}^P + \tau_{xz}\Phi_{CZ,z}^P \right) \mathrm{d}\Omega \qquad Q_z^S = -\int_\Omega \left(\tau_{xy}\Phi_{CZ,y}^S + \tau_{xz}\Phi_{CZ,z}^S \right) \mathrm{d}\Omega \tag{7j,k}$$

$$M_t^P = \int_\Omega \left[\tau_{xy}\left(\varphi_{S,y}^P - z \right) + \tau_{xz}\left(\varphi_{S,z}^P + y \right) \right] \mathrm{d}\Omega \tag{7l,m}$$

$$M_t^S = -\int_\Omega \left(\tau_{xy}\Phi_{S,y}^S + \tau_{xz}\Phi_{S,z}^S \right) \mathrm{d}\Omega \qquad M_t^T = \int_\Omega \left(\tau_{xy}\Phi_{S,y}^T + \tau_{xz}\Phi_{S,z}^T \right) \mathrm{d}\Omega \tag{7n,o}$$

where M_i ($i = Y, Z$) are the bending moments and M_i ($i = \varphi_S^P, \varphi_S^S, \varphi_{CY}^P, \varphi_{CZ}^P$) are the warping moments (bimoments). Q_i^j ($i = y, z$ $j = P, S$) are the primary and secondary parts of total shear forces Q_i ($i = y, z$). It is noted that the secondary shear forces are also referred to as bishear stress resultants [5,18] since they equilibrate the corresponding warping moments (bimoments). Similarly, M_t^j ($j = P, S, T$) are the primary, secondary and tertiary parts of total twisting moment M_t. Moreover, the geometric constants of the beam can be obtained by the following definitions [49, 50]

$$A=\int_{\Omega}\mathrm{d}\Omega \qquad S_Y=\int_{\Omega}Z\,\mathrm{d}\Omega \qquad S_Z=\int_{\Omega}Y\,\mathrm{d}\Omega \tag{8a-c}$$

$$I_{YY}=\int_{\Omega}Z^2\,\mathrm{d}\Omega \qquad I_{ZZ}=\int_{\Omega}Y^2\,\mathrm{d}\Omega \qquad I_{YZ}=\int_{\Omega}YZ\,\mathrm{d}\Omega \tag{8d-f}$$

$$S_i=\int_{\Omega}(i)\,\mathrm{d}\Omega,\quad i=\varphi_S^P,\varphi_S^S,\varphi_{CY}^P,\varphi_{CZ}^P \tag{8g}$$

$$I_{ij}=\int_{\Omega}(i)(j)\,\mathrm{d}\Omega,\quad i,j=y,z,\varphi_S^P,\varphi_S^S,\varphi_{CY}^P,\varphi_{CZ}^P \tag{8h}$$

$$D_{ij}=\int_{\Omega}\nabla(i)\cdot\nabla(j)\,\mathrm{d}\Omega,\quad i,j=\Phi_S^S,\Phi_S^{\mathrm{T}},\Phi_{CY}^P,\Phi_{CY}^S,\Phi_{CZ}^P,\Phi_{CZ}^S \tag{8i}$$

$$I_t^P=\int_{\Omega}\left(y^2+z^2-z\varphi_{S,y}^P+y\varphi_{S,z}^P\right)\mathrm{d}\Omega \tag{8j}$$

$$I_p=\int_{\Omega}\left(y^2+z^2\right)\mathrm{d}\Omega \tag{8k}$$

while as analyzed also in [49,50] it holds that

$$A_Y^P\equiv D_{\Phi_Z^P\Phi_Z^P} \qquad A_Y^S\equiv D_{\Phi_Z^S\Phi_Z^S} \tag{11a,b}$$

$$A_Z^P\equiv D_{\Phi_Y^P\Phi_Y^P} \qquad A_Z^S\equiv D_{\Phi_Y^S\Phi_Y^S} \tag{11c,d}$$

$$I_x^S\equiv D_{\Phi_x^S\Phi_x^S} \qquad I_x^T\equiv D_{\Phi_x^T\Phi_x^T} \tag{11e,f}$$

Using the expressions of the strain components, the definitions of the stress resultants (eqns. (7)) and applying the principle of virtual work (eqn. (5)), the differential equations of motion in terms of the kinematical components can be written as

$$-E^*Au_{,xx}+\rho\mathrm{A}u_{,tt}=p_x \tag{12a}$$

$$\begin{aligned}&-G\left(A_Y^P+A_Y^S\right)\left(v_{,xx}-\theta_{Z,x}\right)+GA_Y^S\eta_{Y,x}+G\left(D_{\Phi_{CY}^S\Phi_S^S}-D_{\Phi_{CY}^S\Phi_S^T}\right)\left(\eta_{x,x}-\theta_{x,xx}\right)+\\&\quad+GD_{\Phi_{CY}^S\Phi_S^T}\xi_{x,x}+\rho A\left(v_{,tt}-z_C\theta_{x,tt}\right)=p_y\end{aligned} \tag{12b}$$

$$\begin{aligned}&-G\left(A_Z^P+A_Z^S\right)\left(w_{,xx}+\theta_{Y,x}\right)+GA_Z^S\eta_{Z,x}+G\left(D_{\Phi_{CZ}^S\Phi_S^S}-D_{\Phi_{CZ}^S\Phi_S^T}\right)\left(\eta_{x,x}-\theta_{x,xx}\right)+\\&\quad+GD_{\Phi_{CZ}^S\Phi_S^T}\xi_{x,x}+\rho A\left(w_{,tt}+y_C\theta_{x,tt}\right)=p_z\end{aligned} \tag{12c}$$

$$\begin{aligned}&-E^*I_{ZZ}\theta_{Z,xx}-G\left(A_Y^P+A_Y^S\right)\left(v_{,x}-\theta_Z\right)+GA_Y^S\eta_Y+G\left(D_{\Phi_{CY}^S\Phi_S^S}-D_{\Phi_{CY}^S\Phi_S^T}\right)\left(\eta_x-\theta_{x,x}\right)+\\&\quad+GD_{\Phi_{CY}^S\Phi_S^T}\xi_x+\rho I_{ZZ}\theta_{Z,tt}=m_Z\end{aligned} \tag{12d}$$

$$\begin{aligned}&-E^*I_{YY}\theta_{Y,xx}+G\left(A_Z^P+A_Z^S\right)\left(w_{,x}+\theta_Y\right)-GA_Z^S\eta_Z-G\left(D_{\Phi_{CZ}^S\Phi_S^S}-D_{\Phi_{CZ}^S\Phi_S^T}\right)\left(\eta_x-\theta_{x,x}\right)-\\&\quad-GD_{\Phi_{CZ}^S\Phi_S^T}\xi_x+\rho I_{YY}\theta_{Y,tt}=m_Y\end{aligned} \tag{12e}$$

$$\begin{aligned}&-E^*\left(I_{\varphi_{CY}^P\varphi_S^P}\eta_{x,xx}+I_{\varphi_{CY}^P\varphi_{CY}^P}\eta_{Y,xx}+I_{\varphi_{CY}^P\varphi_S^S}\xi_{x,xx}\right)+GA_Y^S\left(\eta_Y-v_{,x}+\theta_Z\right)+\\&\quad+G\left(D_{\Phi_{CY}^S\Phi_S^S}-D_{\Phi_{CY}^S\Phi_S^T}\right)\left(\eta_x-\theta_{x,x}\right)+GD_{\Phi_{CY}^S\Phi_S^T}\xi_x+\end{aligned}$$

$$+\rho\left(I_{\varphi_{CY}^P\varphi_S^P}\eta_{x,tt}+I_{\varphi_{CY}^P\varphi_S^S}\xi_{x,tt}+I_{\varphi_{CY}^P\varphi_{CY}^P}\eta_{Y,tt}\right)=m_{\varphi_{CY}^P} \tag{12f}$$

$$\begin{aligned}&-E^*\left(I_{\varphi_{CZ}^P\varphi_S^P}\eta_{x,xx}+I_{\varphi_{CZ}^P\varphi_{CZ}^P}\eta_{Z,xx}+I_{\varphi_{CZ}^P\varphi_S^S}\xi_{x,xx}\right)+GA_Z^S\left(\eta_Z-w_{,x}-\theta_Y\right)+\\&\quad+G\left(D_{\Phi_{CZ}^S\Phi_S^S}-D_{\Phi_{CZ}^S\Phi_S^T}\right)\left(\eta_x-\theta_{x,x}\right)+GD_{\Phi_{CZ}^S\Phi_S^T}\xi_x+\\&\quad+\rho\left(I_{\varphi_{CZ}^P\varphi_S^P}\eta_{x,tt}+I_{\varphi_{CZ}^P\varphi_S^S}\xi_{x,tt}+I_{\varphi_{CZ}^P\varphi_{CZ}^P}\eta_{Z,tt}\right)=m_{\varphi_{CZ}^P}\end{aligned} \tag{12g}$$

$$\begin{aligned}&-G\left(I_t^P+I_t^S+I_t^T\right)\theta_{x,xx}+G\left(I_t^S+I_t^T\right)\left(\eta_x-\theta_{x,x}\right)-GI_t^T\xi_{x,x}+\\&\quad+G\left(D_{\Phi_{CY}^S\Phi_S^S}-D_{\Phi_{CY}^S\Phi_S^T}\right)\left(\eta_{Y,x}-v_{,xx}+\theta_{Z,x}\right)+G\left(D_{\Phi_{CZ}^S\Phi_S^S}-D_{\Phi_{CZ}^S\Phi_S^T}\right)\cdot\\&\quad\cdot\left(\eta_{Z,x}-w_{,xx}-\theta_{Y,x}\right)+\rho\left[A\left(-z_C v_{,tt}+y_C w_{,tt}\right)+I_p\theta_{x,tt}\right]=m_t\end{aligned} \tag{12h}$$

$$\begin{aligned}&-E^*\left(I_{\varphi_S^P\varphi_S^P}\eta_{x,xx}+I_{\varphi_{CY}^P\varphi_S^P}\eta_{Y,xx}+I_{\varphi_{CZ}^P\varphi_S^P}\eta_{Z,xx}\right)+G\left(I_t^S+I_t^T\right)\left(\eta_x-\theta_{x,x}\right)-GI_t^T\xi_x+\\&\quad+G\left(D_{\Phi_{CY}^S\Phi_S^S}-D_{\Phi_{CY}^S\Phi_S^T}\right)\left(\eta_Y-v_{,x}+\theta_Z\right)+G\left(D_{\Phi_{CZ}^S\Phi_S^S}-D_{\Phi_{CZ}^S\Phi_S^T}\right)\cdot\\&\quad\cdot\left(\eta_Z-w_{,x}-\theta_Y\right)+\rho\left(I_{\varphi_S^P\varphi_S^P}\eta_{x,tt}+I_{\varphi_{CY}^P\varphi_S^P}\eta_{Y,tt}+I_{\varphi_{CZ}^P\varphi_S^P}\eta_{Z,tt}\right)=m_{\varphi_S^P}\end{aligned} \tag{12i}$$

$$\begin{aligned}&-E^*\left(I_{\varphi_{CY}^P\varphi_S^S}\eta_{Y,xx}+I_{\varphi_{CZ}^P\varphi_S^S}\eta_{Z,xx}+I_{\varphi_S^S\varphi_S^S}\xi_{x,xx}\right)+GI_t^T\left(\xi_x-\eta_x+\theta_{x,x}\right)+\\&\quad+GD_{\Phi_{CY}^S\Phi_S^T}\left(\eta_Y-v_{,x}+\theta_Z\right)+GD_{\Phi_{CZ}^S\Phi_S^T}\left(\eta_Z-w_{,x}-\theta_Y\right)+\\&\quad+\rho\left(I_{\varphi_S^S\varphi_S^S}\xi_{x,tt}+I^{\rho}_{\varphi_{CY}^P\varphi_S^S}\eta_{Y,tt}+I^{\rho}_{\varphi_{CZ}^P\varphi_S^S}\eta_{Z,tt}\right)=m_{\varphi_S^S}\end{aligned} \tag{12j}$$

where the externally applied dynamic loads are related to the components of the traction vector applied on the lateral surface of the beam t_x, t_y, t_z as

$$p_i\left(x,t\right)=\int_\Gamma t_i\,\mathrm{d}s,\quad i=x,y,z \tag{13a}$$

$$m_t\left(x,t\right)=\int_\Gamma t_z y-t_y z\,\mathrm{d}s \tag{13b}$$

$$m_Y\left(x,t\right)=\int_\Gamma t_x Z\,\mathrm{d}s \qquad m_Z\left(x,t\right)=-\int_\Gamma t_x Y\,\mathrm{d}s \tag{13c,d}$$

$$m_i\left(x,t\right)=\int_\Gamma t_x\left(i\right)\mathrm{d}s,\quad i=\varphi_S^P,\varphi_S^S,\varphi_{CY}^P,\varphi_{CZ}^P \tag{13e}$$

The above governing differential equations (eqns. (12)) are also subjected to the initial conditions ($x\in\left(0,l\right)$)

$$u\left(x,0\right)=u_0\left(x\right) \qquad u_{,t}\left(x,0\right)=u_{0,t}\left(x\right) \tag{14a,b}$$

$$v\left(x,0\right)=v_0\left(x\right) \qquad v_{,t}\left(x,0\right)=v_{0,t}\left(x\right) \tag{14c,d}$$

$$\theta_Z\left(x,0\right)=\theta_{Z0}\left(x\right) \qquad \theta_{Z,t}\left(x,0\right)=\theta_{Z0,t}\left(x\right) \tag{14e,f}$$

$$w\left(x,0\right)=w_0\left(x\right) \qquad w_{,t}\left(x,0\right)=w_{0,t}\left(x\right) \tag{14g,h}$$

$$\theta_Y(x,0)=\theta_{Y0}(x) \qquad \theta_{Y,t}(x,0)=\theta_{Y0,t}(x) \qquad (14i,j)$$

$$\theta_x(x,0)=\theta_{x0}(x) \qquad \theta_{x,t}(x,0)=\theta_{x0,t}(x) \qquad (14k,l)$$

$$\eta_x(x,0)=\eta_{x0}(x) \qquad \eta_{x,t}(x,0)=\eta_{x0,t}(x) \qquad (14m,n)$$

$$\xi_x(x,0)=\xi_{x0}(x) \qquad \xi_{x,t}(x,0)=\xi_{x0,t}(x) \qquad (14o,p)$$

together with the corresponding boundary conditions of the problem at hand, which are given as

$$a_1 u+\alpha_2 N_b=\alpha_3 \qquad (15a)$$

$$\beta_1 v+\beta_2 V_{by}=\beta_3 \qquad \gamma_1 w+\gamma_2 V_{bz}=\gamma_3 \qquad (15b,c)$$

$$\overline{\beta}_1\theta_Z+\overline{\beta}_2 M_{bZ}=\overline{\beta}_3 \qquad \overline{\gamma}_1\theta_Y+\overline{\gamma}_2 M_{bY}=\overline{\gamma}_3 \qquad (15d,e)$$

$$\tilde{\beta}_1\eta_Z+\tilde{\beta}_2 M_{b\varphi_{CZ}^P}=\tilde{\beta}_3 \qquad \tilde{\gamma}_1\eta_Y+\tilde{\gamma}_2 M_{b\varphi_{CY}^P}=\tilde{\gamma}_3 \qquad (15f,g)$$

$$\delta_1\theta_x+\delta_2 M_{bt}=\delta_3 \qquad \overline{\delta}_1\eta_x+\overline{\delta}_2 M_{b\varphi_S^P}=\overline{\delta}_3 \qquad \tilde{\delta}_1\xi_x+\tilde{\delta}_2 M_{b\varphi_S^S}=\tilde{\delta}_3 \qquad (15h,i,j)$$

at the beam ends $x=0,l$, where N_b, V_{by}, V_{bz}, M_{bZ}, M_{bY}, $M_{b\varphi_{CY}^P}$, $M_{b\varphi_{CZ}^P}$, M_{bt}, $M_{b\varphi_S^P}$, $M_{b\varphi_S^S}$ are the reaction forces, moments and warping moments respectively.

Finally, α_k, β_k, $\overline{\beta}_k, \tilde{\beta}_k$ γ_k, $\overline{\gamma}_k$, $\tilde{\gamma}_k, \delta_k, \overline{\delta}_k, \tilde{\delta}_k$ $(k=1,2,3)$ are functions specified at the boundaries of the beam ($x=0,l$). The boundary conditions (15) are the most general boundary conditions for the problem at hand, including also the elastic support. It is apparent that all types of the conventional boundary conditions (clamped, simply supported, free or guided edge) can be derived from these equations by specifying appropriately these functions (e.g. for a clamped edge it is $\alpha_1=\beta_1=\overline{\beta}_1=\tilde{\beta}_1=\gamma_1=\overline{\gamma}_1=\tilde{\gamma}_1=\delta_1=\overline{\delta}_1=\tilde{\delta}_1=1$, $\alpha_2=\alpha_3=\beta_2=\beta_3=\overline{\beta}_2=\overline{\beta}_3=\tilde{\beta}_2=$
$=\tilde{\beta}_3=\gamma_2=\overline{\gamma}_3=\tilde{\gamma}_2=\tilde{\gamma}_3=\delta_2=\delta_3=\overline{\delta}_2=\overline{\delta}_3=\tilde{\delta}_2=\tilde{\delta}_3=0$).

2.3 Warping functions due to shear Φ_{CY}^P, Φ_{CZ}^P, Φ_{CY}^S, Φ_{CZ}^S

The analysis described in the previous section presumes that the warping functions Φ_{CY}^P, Φ_{CZ}^P, Φ_{CY}^S, Φ_{CZ}^S with respect to the centroidal principal bending system $CXYZ$ are already established. According to the procedure presented in [49, 50], examining each primary warping function Φ_{Ci}^P $(i=Y,Z)$ separately, a boundary value problem in each direction is formulated as

$$\nabla^2\overline{\Phi}_{CY}^P=Z \qquad \overline{\Phi}_{CY,n}^P=0 \qquad \text{on the boundary} \qquad (17a,b)$$

$$\nabla^2\overline{\Phi}_{CZ}^P=Y \qquad \overline{\Phi}_{Z,n}^P=0 \qquad \text{on the boundary} \qquad (18a,b)$$

where $\overline{\Phi}_{CY}^P=-\left(I_{YY}/A_Z^P\right)\Phi_{CY}^P$, $\overline{\Phi}_{CZ}^P=-\left(I_{ZZ}/A_Y^P\right)\Phi_{CZ}^P$, while $(\cdot)_{,n}$ indicates the derivative with respect to the outward normal vector to the boundary **n** (directional derivative). After establishing $\overline{\Phi}_{Ci}^P$ $(i=Y,Z)$, geometric constants A_i^P $(i=Y,Z)$ can be evaluated employing definition (8i) as

$$A_Y^P = \frac{\left(I_{ZZ}\right)^2}{D_{\bar{\Phi}_Z^P \bar{\Phi}_Z^P}} \qquad A_Z^P = \frac{\left(I_{YY}\right)^2}{D_{\bar{\Phi}_Y^P \bar{\Phi}_Y^P}} \tag{19a,b}$$

Moreover, after evaluating Φ_{Ci}^P $(i = Y, Z)$, warping functions φ_{Ci}^P $(i = Y, Z)$ can be established through eqns. (4c,d).

Subsequently, φ_{Ci}^S $(i = Y, Z)$ employed in order to correct shear stresses are indirectly computed through Φ_{Ci}^S $(i = Y, Z)$ which can be established by formulating the following boundary value problem in each direction

$$\nabla^2 \tilde{\Phi}_{Ci}^S = \varphi_{Ci}^P, \ (i = Y, Z) \qquad \tilde{\Phi}_{Ci,n}^S = 0 \qquad \text{on the boundary} \tag{20a,b}$$

while it holds that $\bar{\Phi}_{CY}^S = \tilde{\Phi}_{CY}^S + Z\left(I_{\varphi_{CY}^P \varphi_{CY}^P} \Big/ A_Z^P\right)$, $\bar{\Phi}_{CZ}^S = \tilde{\Phi}_{CZ}^S + Y\left(I_{\varphi_{CZ}^P \varphi_{CZ}^P} \Big/ A_Y^P\right)$ and $\bar{\Phi}_{CY}^S = -\left(I_{\varphi_{CY}^P \varphi_{CY}^P} \Big/ A_Z^S\right)\Phi_{CY}^S$, $\bar{\Phi}_{CZ}^S = -\left(I_{\varphi_{CZ}^P \varphi_{CZ}^P} \Big/ A_Y^S\right)\Phi_{CZ}^S$. After establishing $\bar{\Phi}_{Ci}^S$, the geometric constants A_i^S $(i = Y, Z)$ can be evaluated employing definition (8i) as

$$A_Y^S = \frac{\left(I_{\varphi_{CZ}^P \varphi_{CZ}^P}\right)^2}{D_{\bar{\Phi}_{CZ}^S \bar{\Phi}_{CZ}^S}} \qquad A_Z^S = \frac{\left(I_{\varphi_{CY}^P \varphi_{CY}^P}\right)^2}{D_{\bar{\Phi}_{CY}^S \bar{\Phi}_{CY}^S}} \tag{21}$$

2.4 Warping functions due to torsion φ_S^P, Φ_S^S, Φ_S^T

Similarly with the previous section, the torsional warping functions are established independently as follows. φ_S^P is given by the following boundary value problem (St. Venant problem of uniform torsion) as

$$\nabla^2 \varphi_S^P = 0 \qquad \varphi_{S,n}^P = z n_y - y n_z \qquad \text{on the boundary} \tag{22a,b}$$

It is noticed that in order for φ_S^P to be the primary torsional warping function, the analysis has to be carried out with respect to the center of twist S, which is initially specified according to the procedure presented in [11]. Following the strategy presented in the previous section, Φ_S^S can be established by formulating the following boundary value problem as

$$\nabla^2 \bar{\Phi}_S^S = \varphi_S^P \qquad \bar{\Phi}_{S,n}^S = 0 \qquad \text{on the boundary} \tag{23a,b}$$

where $\bar{\Phi}_S^S = -\left(I_{\varphi_S^P \varphi_S^P} \Big/ I_t^S\right)\Phi_S^S$. Employing eqn. (8i), I_t^S is evaluated as

$$I_t^S = \frac{\left(I_{\varphi_S^P \varphi_S^P}\right)^2}{D_{\bar{\Phi}_S^S \bar{\Phi}_S^S}} \tag{24}$$

while, after evaluating Φ_S^S, φ_S^S can be established through eqn. (4a). The final boundary value problem for Φ_S^T is constructed as

$$\nabla^2\tilde{\Phi}_S^T = \varphi_S^S \qquad \tilde{\Phi}_{S,n}^T = 0 \qquad \text{on the boundary} \tag{25a,b}$$

while it holds that $\bar{\Phi}_S^T = \tilde{\Phi}_S^T + \varphi_S^P \left(I_{\varphi_S^S \varphi_S^S} \Big/ I_t^S \right)$ and $\bar{\Phi}_S^T = -\left(I_{\varphi_S^S \varphi_S^S} \Big/ I_t^T \right) \Phi_S^T$. Finally, employing definition (10b), I_t^T is evaluated as

$$I_t^T = \frac{\left(I_{\varphi_S^S \varphi_S^S} \right)^2}{D_{\bar{\Phi}_S^T \bar{\Phi}_S^T}} \tag{26}$$

It is remarked that all boundary value problems (17), (18), (20), (22), (23), (25) have solution, since the condition $\int_\Gamma \left(i_{,n} \right) \mathrm{d}s = 0$, ($i = \bar{\Phi}_j^P, \tilde{\Phi}_j^S, \varphi_x^P, \bar{\Phi}_x^S, \tilde{\Phi}_x^T$, $j = Y, Z$, $m, n = 1, ..., M$) [21] is satisfied. It is also worth here noting that, since the problems (17), (18), (20), (22), (23), (25) have Neumann type boundary conditions, each warping function contains an arbitrary integration constant indicating a parallel displacement of the cross section along the beam axis. The evaluation of these constants is performed as presented in [11].

3 NUMERICAL SOLUTION

According to the precedent analysis, the flexural-torsional dynamic analysis of beams of arbitrary composite cross section including generalized warping effects reduces in establishing the components $u(x,t)$, $v(x,t)$, $w(x,t)$, $\theta_X(x,t)$, $\theta_Z(x,t)$, $\theta_Y(x,t)$, $\eta_x(x,t)$, $\eta_Y(x,t)$, $\eta_Z(x,t)$ and $\xi_x(x,t)$ having continuous derivatives up to the second order with respect to x at the interval $(0,l)$ and up to the first order at $x = 0, l$ and up to the second order with respect to t, satisfying the initial-boundary value problem described by the coupled governing differential equations of equilibrium (eqns. (12)) along the beam, the initial conditions (eqns. (14)) and the boundary conditions (eqns. (15)) at the beam ends $x = 0, l$. Eqns. (12), (14), (15) are solved using the Analog Equation Method [52]. Application of the boundary element technique yields a system of linear coupled differential-algebraic equations of motion which can be solved employing any efficient time-integration scheme (e.g. Mean Acceleration Method). The geometric constants defined in eqns. (8) are evaluated by converting the domain integrals into line ones along the boundary using integration by parts, the Gauss theorem and the Green identity. The expressions of these constants are given in the appendix A of [50].

4 NUMERICAL EXAMPLES

On the basis of the analytical and numerical procedures presented in the previous sections, a computer program has been written and representative examples have been studied. A commercial FEM package with solid and beam modeling capabilities [51] is employed to compare and verify the results of the proposed method.

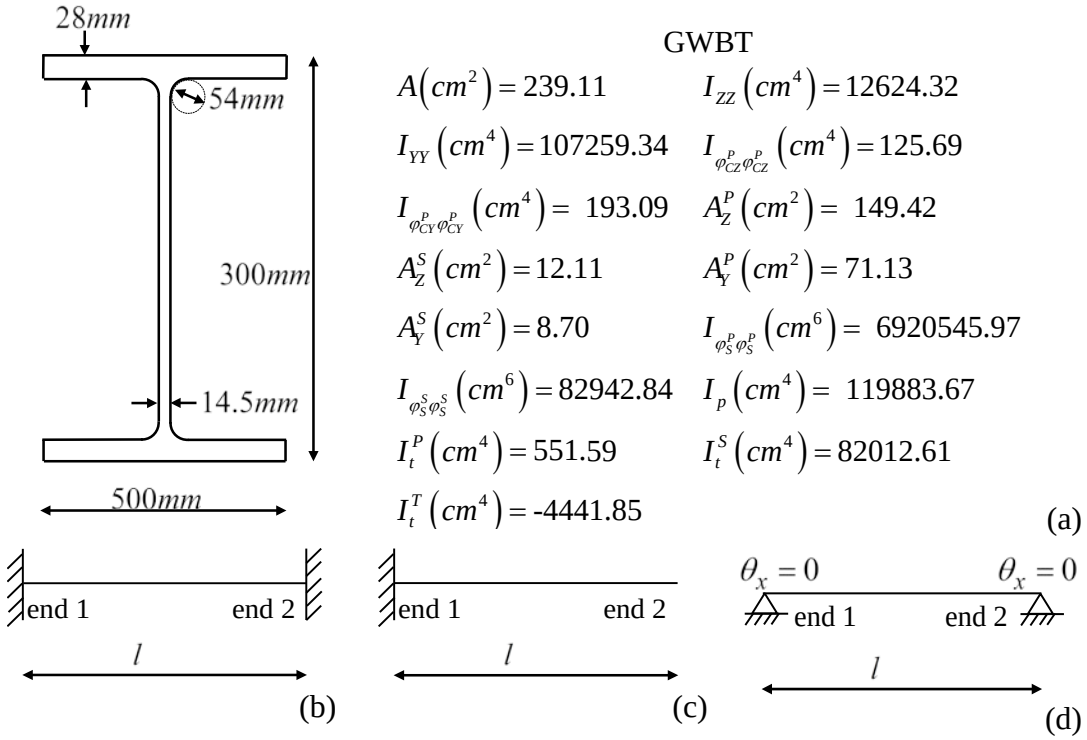


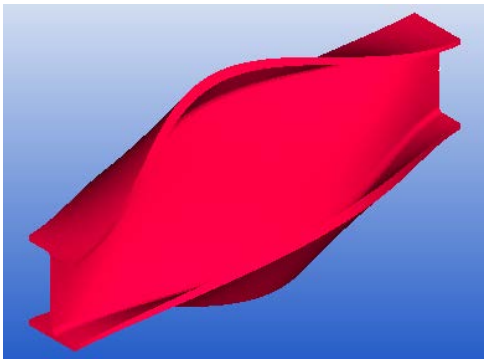
Fig. 3. Cross sections of beams of examples 1 (a) along with three types of boundary conditions (b-d).

Example 1

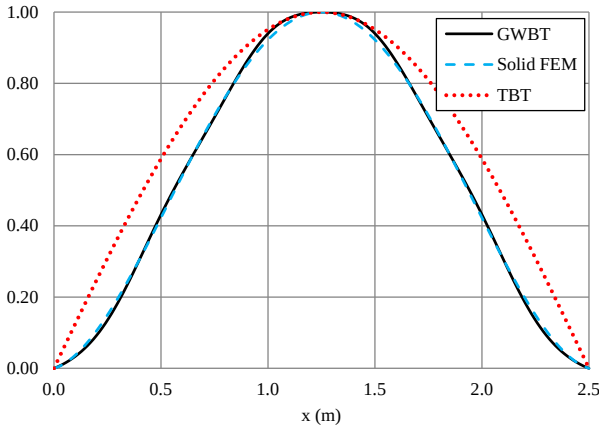
In the first example, the free vibration characteristics of four HEB500 cross section (Fig. 3a) steel ($E = 210GPa$, $G = 80.8GPa$, $\nu = 0.3$, $\rho = 7.85kN\,sec^2/m^4$) beams of lengths $l = 2.5m, 3.5m, 4.5m, 5.5m$ for three types of boundary conditions (clamped at both ends (Fig. 3b), cantilever (Fig. 3c), simply supported with fixed torsional rotation (Fig. 3d)) have been analyzed. More specifically, the generalized eigenvalue problem of eqn(35) has been solved to obtain the natural frequencies for the Generalized Warping Beam Theory (GWBT). For comparison reasons Timoshenko Beam Theory (TBT [51]) and Solid (3-D hexahedral elements extruded by quadrilateral surfaces) FEM (Solid FEM [51]) models have been analyzed. In the Solid models, rigid diaphragms at every set of nodes having the same longitudinal coordinate have been employed, pointing out that the diaphragms are designed so as each set of nodes has the same translation and rotation in the cross section plane, corresponding to the assumption employed in the proposed method that the cross section maintains its shape at the transverse directions during deformation (no distortion). In GWBT solutions 88 elements have been used while in TBT [51] 100 elements per meter of length. The number of Solid FEM [51] elements that have been used is 24300. There are three types of natural frequencies under examination, namely bending natural frequencies with deflections along the y (v natural frequencies) and the z axis (w natural frequencies) and torsional natural frequencies (θ_x natural frequencies).

Table 1. Discrepancies (%) of natural frequencies between GWBT- Solid FEM [51] and TBT [51]- Solid FEM [51] of the clamped beam of example 1 for various lengths.

Natural frequency type	l=2.5m		l=3.5m		l=4.5m		l=5.5m	
	GWBT	TBT	GWBT	TBT	GWBT	TBT	GWBT	TBT
1st v	-0.04	11.46	-0.21	12.48	-0.39	12.96	-0.59	13.23
2nd v	0.07	9.25	-0.14	11.00	-0.34	11.96	-0.56	12.52
3rd v	0.16	7.43	-0.08	9.50	-0.29	10.83	-0.52	11.67
4th v	0.23	6.02	-0.02	8.12	-0.25	9.68	-0.48	10.75
1st w	0.77	4.35	0.44	5.61	0.26	6.99	0.17	8.21
2nd w	1.10	3.36	0.71	3.80	0.48	4.63	0.33	5.59
3rd w	1.16	3.38	0.77	3.36	0.56	3.78	0.41	4.39
4th w	1.24	3.19	0.80	14.34	0.58	3.17	0.44	3.59
1st θ_x	-0.64	54.61	-1.35	54.29	-0.22	52.42	-0.39	49.93
2nd θ_x	0.17	30.71	-0.11	36.00	-0.30	37.73	-0.46	38.03
3rd θ_x	-1.14	12.06	-1.99	22.40	0.14	26.93	-0.38	29.09
4th θ_x	0.49	-5.02	0.10	-39.43	-0.19	17.69	-0.43	21.57



(a)



(b)

Fig. 4. 1st torsional modeshape of the clamped beam of length $l = 2.5m$ of example 1 as obtained from Solid FEM [51] (a) in comparison with those obtained by GWBT and TBT [51] (b).

In Tables 1, 2 and 3the natural frequencies as obtained from GWBT and TBT [51] are compared with Solid FEM [51] solutions for the clamped, cantilever and simply supported boundary condition, respectively. Figs. 4a and 4b illustrate the 1st torsional modeshape of bar of length $l = 2.5m$ of example 1 as obtained from Solid FEM [51] and comparison among those obtained by GWBT and TBT [51] and Solid FEM [51] , respectively. Figs. 5a, 5b and 6c illustrate the first four bending natural frequencies with deflections along the y axis, the z axis and torsional natural frequencies, respectively as obtained from GWBT, TBT [51] and Solid FEM [51] solutions for the clamped boundary condition. Figs. 6a and 6b show the first four torsional natural frequencies for the cantilever boundary condition and the first four bending natural frequencies with deflections along the y axis for the simply supported

boundary condition, respectively, as calculated by GWBT, TBT [51] and Solid FEM [51] solutions.

From the results of Tables 1-3, it is concluded that TBT [51] can not predict the natural frequencies as accurate as GWBT can. In more detail the discrepancies of GWBT with respect to Solid solutions is up to 2.00% (absolute value) for any of the examined boundary condition or length. On the contrast the discrepancies of TBT [51] with respect to Solid FEM [51] solutions is up to 54.61% for Table 1, 52.49% for Table 2 and 16.91% for Table 3 (absolute values).

Table 2. Discrepancies (%) of natural frequencies between GWBT- Solid FEM [51] and TBT [51]- Solid of the cantilever beam of example 1 for various lengths.

Natural frequency type	*l*=2.5m		*l*=3.5m		*l*=4.5m		*l*=5.5m	
	GWBT	TBT	GWBT	TBT	GWBT	TBT	GWBT	TBT
1^{st} v	-0.15	13.39	-0.27	13.58	-0.42	13.66	-0.61	13.70
2^{nd} v	-0.09	11.39	-0.24	12.48	-0.41	12.97	-0.60	13.24
3^{rd} v	-0.02	9.16	-0.20	11.03	-0.38	12.01	-0.58	12.57
4^{th} v	0.05	7.05	-0.15	9.41	-0.34	10.83	-0.56	11.70
1^{st} w	0.13	9.88	0.07	11.46	0.04	12.30	0.02	12.77
2^{nd} w	0.54	2.90	0.29	5.17	0.17	7.04	0.09	8.49
3^{rd} w	0.56	2.09	0.36	3.35	0.24	4.62	0.16	5.82
4^{th} w	0.54	-0.47	0.37	1.68	0.26	2.88	0.18	3.93
1^{st} θ_x	0.13	52.49	0.20	42.86	0.21	36.37	0.29	31.75
2^{nd} θ_x	-0.06	31.13	-0.17	31.13	-0.25	29.58	-0.40	27.62
3^{rd} θ_x	0.00	16.11	-0.16	21.44	-0.27	23.22	-0.35	23.58
4^{th} θ_x	0.21	1.42	-0.12	11.73	-0.33	16.24	-0.55	18.39

Table 3. Discrepancies (%) of natural frequencies between GWBT- Solid FEM [51] and TBT [51]- Solid FEM [51] of the simply supported beam of example 1 for various lengths.

Natural frequency type	*l*=2.5m		*l*=3.5m		*l*=4.5m		*l*=5.5m	
	GWBT	TBT	GWBT	TBT	GWBT	TBT	GWBT	TBT
1^{st} v	-0.14	12.98	-0.27	13.36	-0.43	13.53	-0.62	13.62
2^{nd} v	-0.10	11.04	-0.24	12.25	-0.41	12.83	-0.61	13.14
3^{rd} v	-0.06	8.84	-0.21	10.76	-0.38	11.82	-0.59	12.43
4^{th} v	-0.02	6.94	-0.18	9.21	-0.36	10.65	-0.57	11.56
1^{st} w	-0.01	7.34	0.00	9.53	0.01	10.88	0.00	11.71
2^{nd} w	-0.05	3.19	-0.04	4.97	-0.04	6.63	-0.03	8.01
3^{rd} w	-0.05	2.01	-0.07	2.93	-0.07	4.11	-0.07	5.30
4^{th} w	0.00	1.83	-0.07	2.13	-0.08	2.84	-0.09	3.70
1^{st} θ_x	-0.10	9.81	-0.08	9.64	-0.06	8.79	-0.04	7.79
2^{nd} θ_x	-0.16	4.63	-0.24	8.35	-0.33	9.61	-0.42	9.93
3^{rd} θ_x	-0.15	-4.64	-0.25	3.54	-0.38	7.04	-0.52	8.72
4^{th} θ_x	-0.15	-16.19	-0.24	-3.07	-0.38	2.94	-0.53	6.10

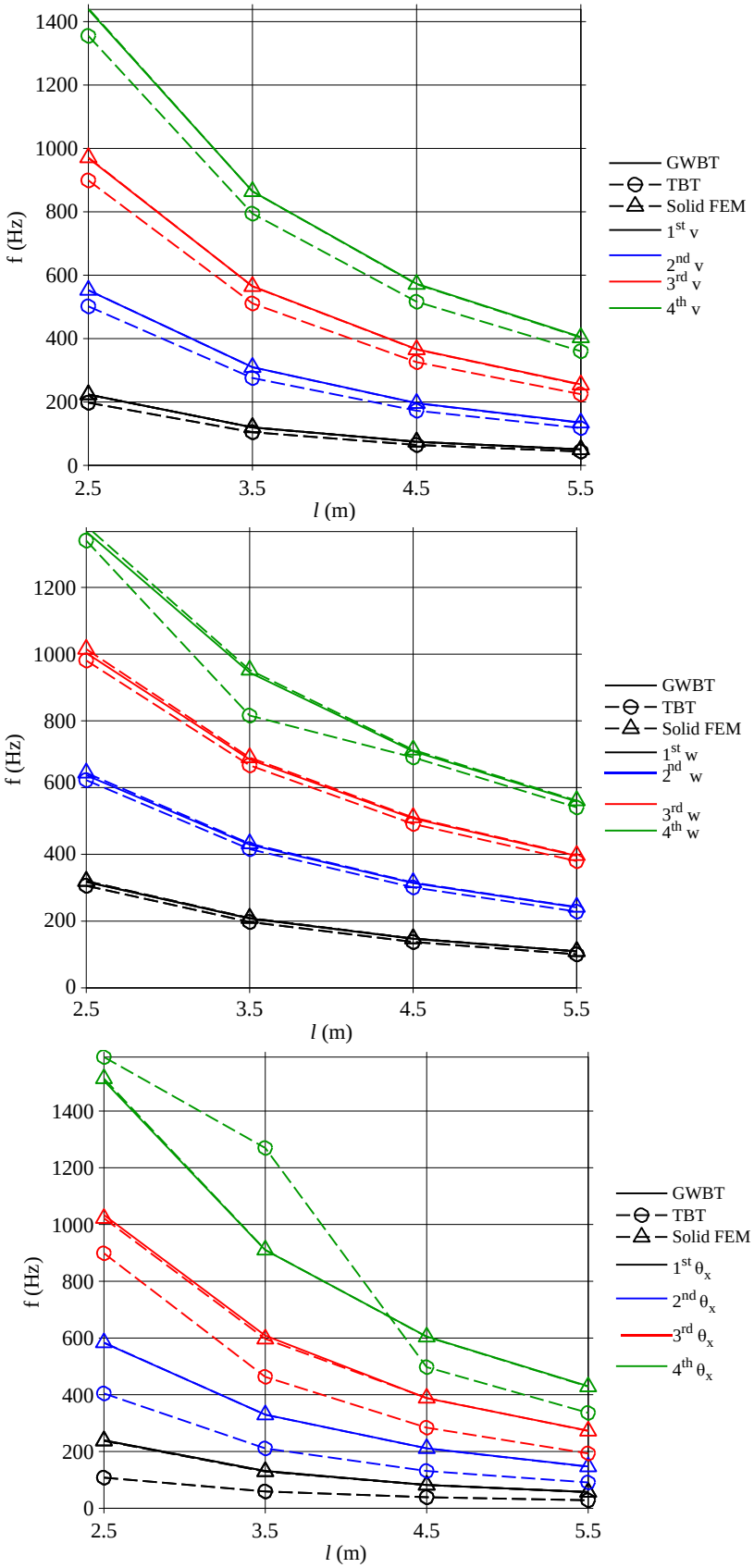


Fig. 5. Comparison of first four bending natural frequencies with deflections along the y axis (a) and the z axis (b) and first four torsional natural frequencies among GWBT, TBT [51] and Solid FEM [51] solutions of clamped beam of example 1 for various lengths.

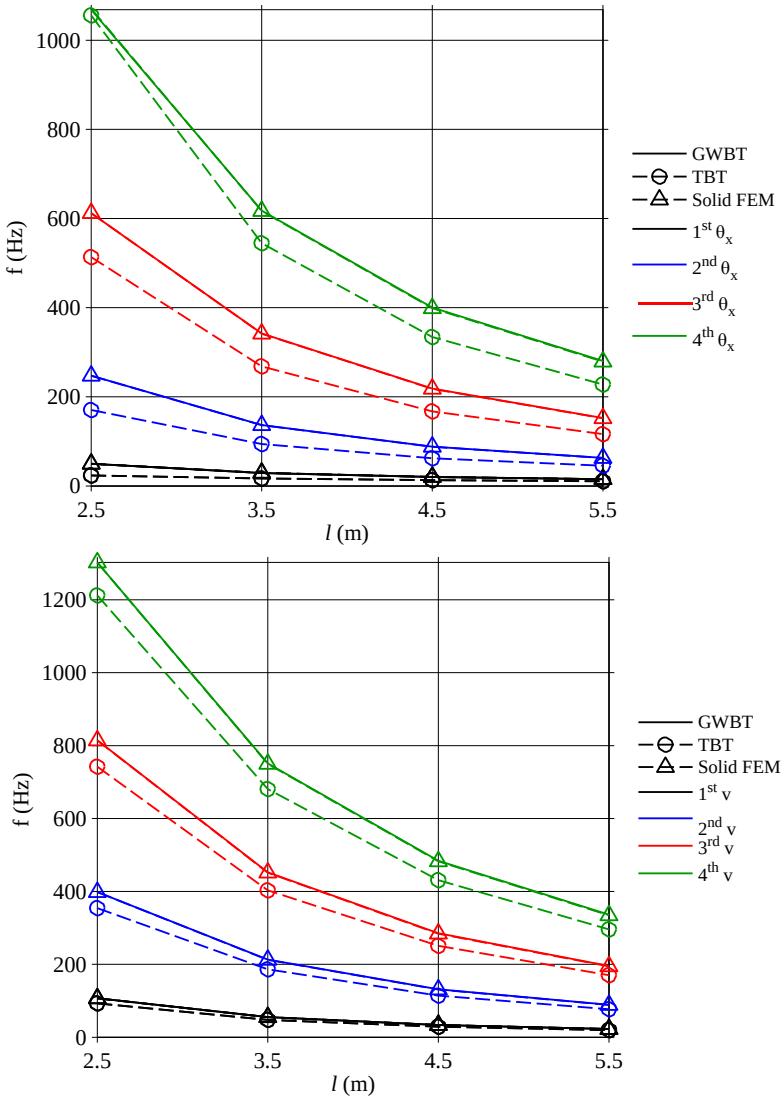


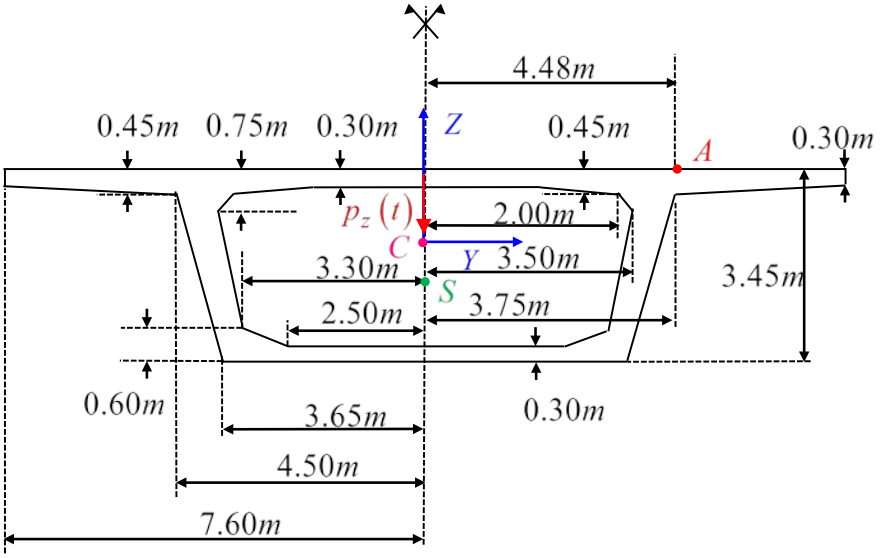
Fig. 6. Comparison of first four torsional natural frequencies of cantilever beam of example 1 (a) and of first four bending natural frequencies with deflections along the y axis of simply supported beam of example 1 for various lengths among GWBT, TBT [51] and Solid FEM [51] solutions.

Example 2

As a final example, the forced vibrations of a box shaped cross section (Fig. 7a) steel ($E = 21\,GPa$, $G = 8.08\,GPa$, $v = 0.3$, $\rho = 2.5\,kN\,sec^2/m^4$) beam of length $l = 30m$, clamped at end 1 and simply supported with fixed torsional rotation at end 2 (Fig 7b), have been examined. The beam is subjected to a uniform distributed dynamic load $p_z(t)$ (Fig 7a, b) along the axis of symmetry Z . Three load cases have been examined (Fig 7c). The time history of loading is constant for load case I and sinusoidal for load cases II and III. The frequency of load case III is $51.48\,rad/\sec$ that is very close to the first natural frequency as calculated by model B ($56.44\,rad/\sec$) while it is not valid for load case II that is $30.00\,rad/\sec$.

More specifically, the initial boundary value problem of eqns(12),(14),(15) has been solved to obtain the response of Generalized Warping Beam Theory (GWBT). For comparison reasons Timoshenko Beam Theory (TBT [51]) and Solid (3-D hexahedral elements extruded by quadrilateral surfaces) FEM [51] models have been analyzed. In the Solid model, rigid dia-

phragms at every set of nodes with the same properties as in the first example have been used. In GWBT solution 62 elements have been employed as in TBT [51]. The number of Solid FEM [51] elements that have been used is 16400.



Model B

$A(m^2) = 11.28$ $I_{ZZ}(m^4) = 169.89$ $I_{YY}(m^4) = 19.07$

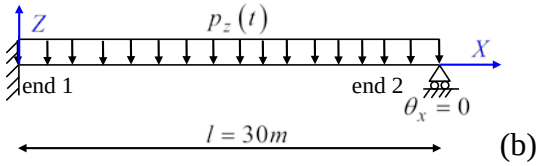
$I_{\varphi^P_{CZ}\varphi^P_{CZ}}(m^4) = 1.20$ $I_{\varphi^P_{CY}\varphi^P_{CY}}(m^4) = 3.36$ $A^P_Z(m^2) = 2.61$

$A^S_Z(m^2) = 29.74$ $A^P_Y(m^2) = 6.76$ $A^S_Y(m^2) = 0.77$

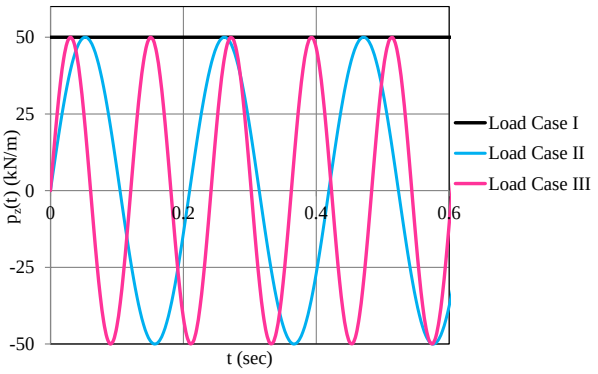
$I_{\varphi^P_S\varphi^P_S}(m^6) = 62.74$ $I_{\varphi^S_S\varphi^S_S}(m^6) = 14.22$ $I_p(m^4) = 192.83$

$I^P_t(m^4) = 42.46$ $I^S_t(m^4) = 27.05$ $I^T_t(m^4) = 1.21$

(a)



(b)



(c)

Fig. 7. Cross section (a), boundary conditions and loading (b), load cases (c) of the beam of example 2.

Figs. 8a, 10a and 11a illustrate the time history of the displacement w at $x = 16.94m$ (position of maximum displacement) for Load Cases I, II and III, respectively.

Figs. 8b, 10b and 11b illustrate the time history of normal stress σ_{xx} at the point A (see Fig. 7a) at $x = 1.5m$ of the beam for Load Cases I, II and III, respectively. From these figures, it is deduced the results of the Solid FEM [51] solution are closer to the proposed methodology (GWBT) than the TBT [51], so the effect of Generalized Warping is pronounced.

Figs. 9a, 9b and 9c show the distribution of normal stresses σ_{xx} at $x = 1.5m$ for Load Case I acording to Solid FEM, GWBT and Timoshenko solutions, respectively, at time instances that appears the maximum stress at point A for each solution. The discrepancies of the distribution and the extreme values of GWBT and TBT [51] with respect to Solid FEM [51] solutions indicates that GWBT is much more appropriate for the analysis than the TBT [51].

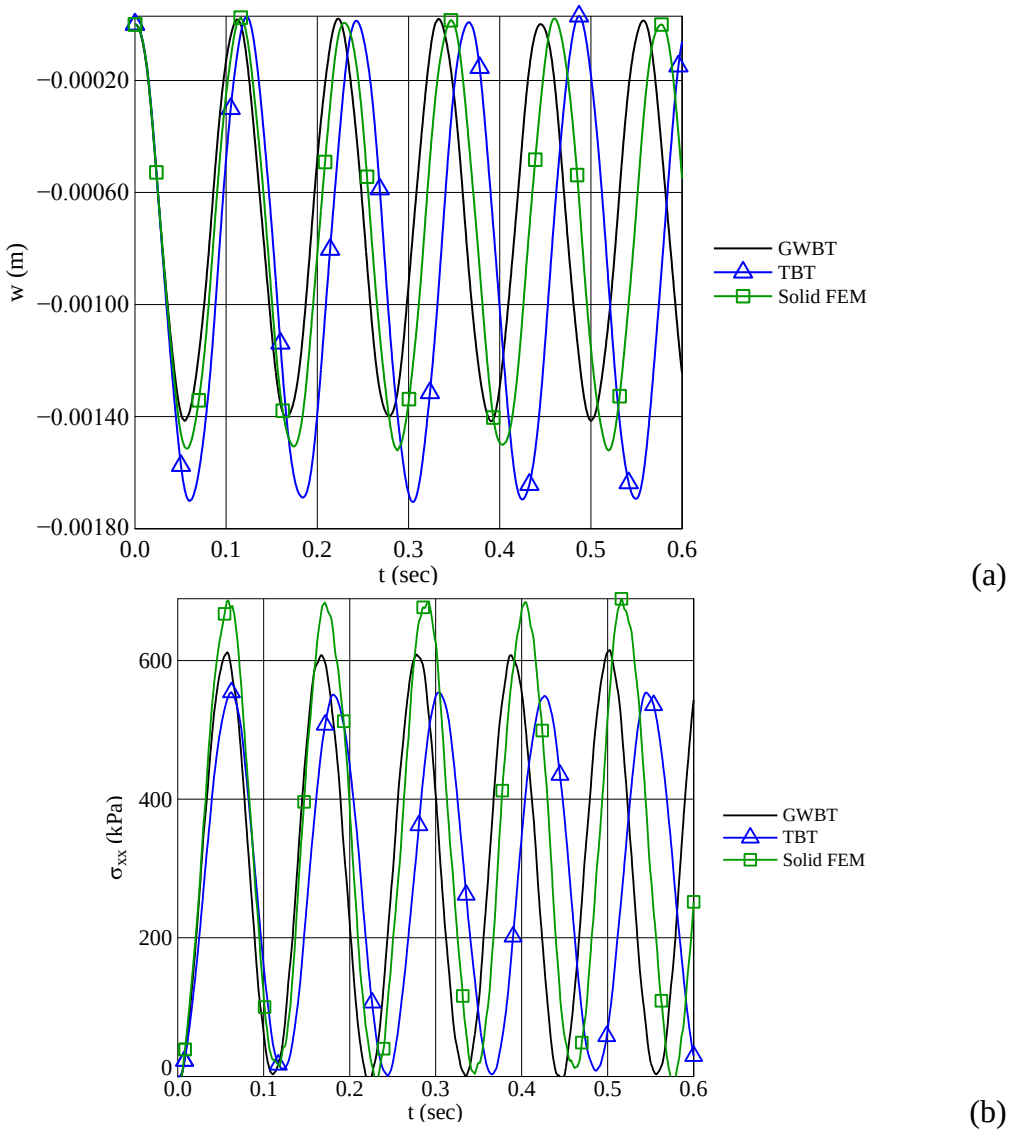


Fig. 8. Time history of the displacement w at $x = 16.94m$ (a) and normal stress σ_{xx} at the point A at $x = 1.5m$ (b) of the beam of example 2 for Load Case I.

5 CONCLUSIONS

In this paper a boundary element solution is developed for the nonuniform warping dynamic analysis of arbitrary cross section beams including shear lag effects due to both flexure and torsion. The beam is subjected to arbitrarily distributed or concentrated external loading, and its ends are supported by the most general boundary conditions. The formulation based on displacements stems from an improved stress field and is capable of yielding more accurate stress component values. The main conclusions that can be drawn from this investigation are

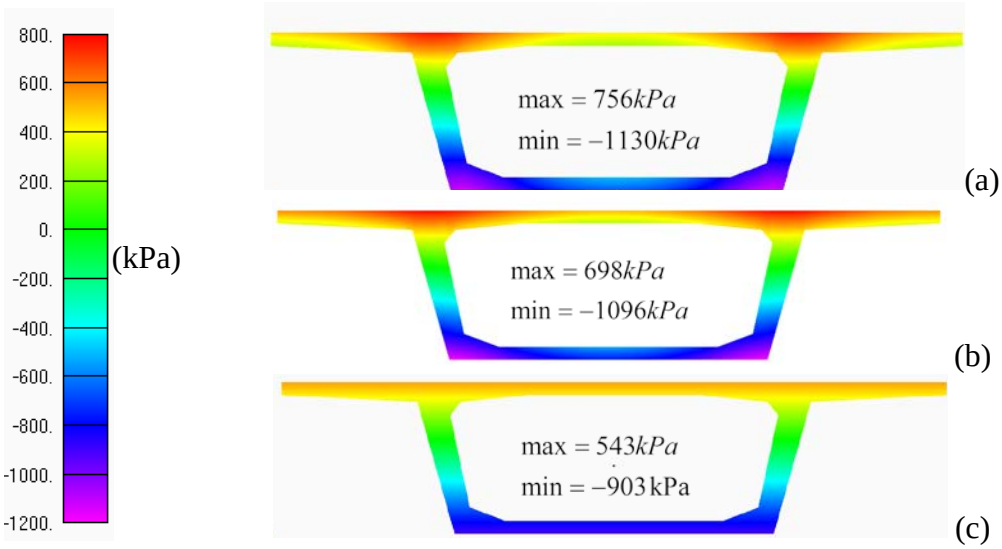


Fig. 9. Distribution of normal stresses σ_{xx} at $x = 1.5m$ for Load Case I of example 2, acording to Solid FEM [51] (a), GWBT (b) and TBT [51] (c) solutions at time instances 0.516sec, 0.5025sec and 0.0624sec, respectively.

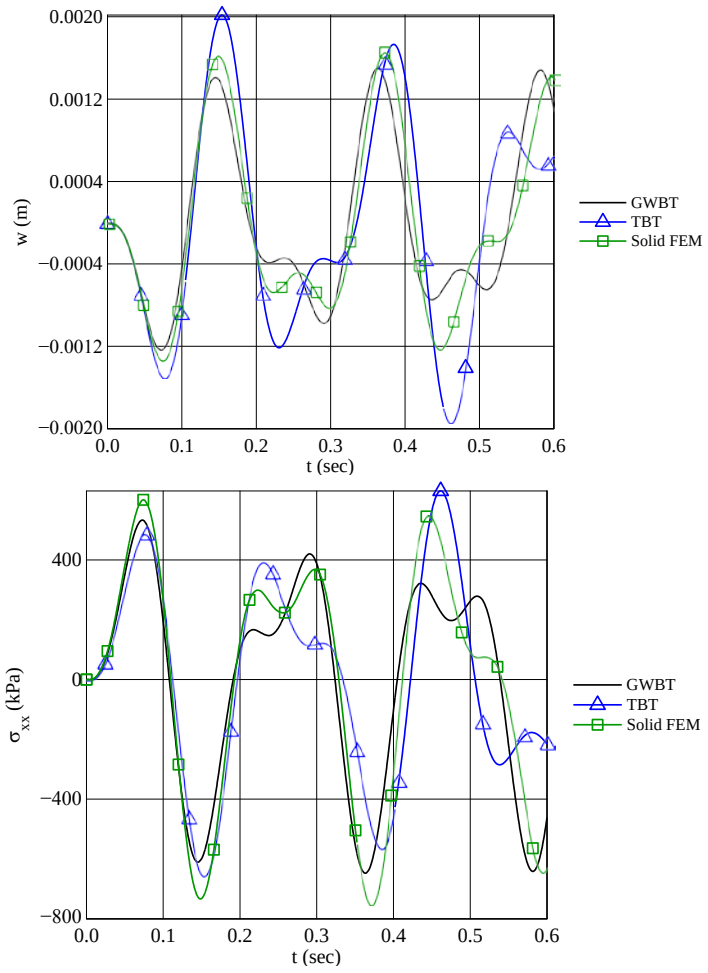


Fig. 10. Time history of the displacement w at $x = 16.94m$ (a) and normal stress σ_{xx} at the point A at $x = 1.5m$ (b) of the beam of example 2 for Load Case II.

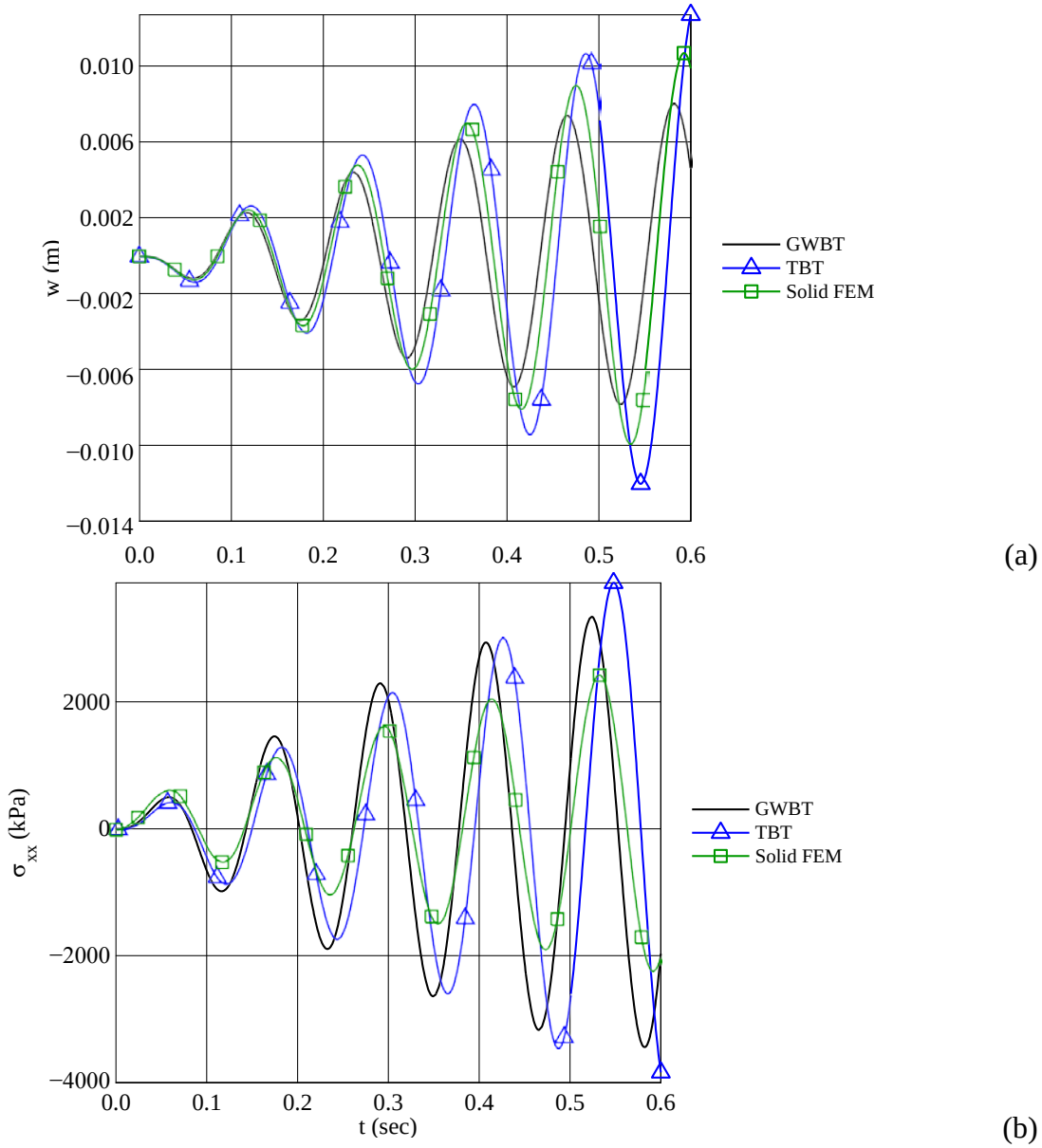


Fig. 11. Time history of the displacement w at $x = 16.94m$ *(a) and normal stress* σ_{xx} *at the point* A *of the end 1 cross section (b) of the beam of example 2 for Load Case III.*

as follows:

- The developed procedure retains most of the advantages of a BEM solution over a FEM approach, although it requires longitudinal domain discretization.
- The accuracy and the validity of the proposed method are noteworthy.
- TBT cannot predict the bending natural frequencies as accurate as GWBT can.
- By GWBT normal stresses are evaluated with high accuracy compared with solid FEM model results.
- The developed formulation is capable of giving accurate results without increasing the number of the involved kinematical unknowns.
- In the treated examples, the influence of flexural and torsional shear lag effects was apparent, modifying significantly the distribution of normal stress.

ACKNOWLEDGEMENTS

The third author would like to express her sincere thanks to the "Onassis Foundation" and the "A.G. Leventis Foundation" for the financial support she was given for her PhD studies during of which she participated in this research work.

REFERENCES

[1] Reissner, E. Analysis of shear lag in box beams by the principle of minimum potential energy. *Q. Appl. Math.*, 1946;41:268-78.

[2] Malcolm, D.J. and Redwood, R.G. Shear lag in stiffened box-girders. *J. Struct. Div. ASCE*, 1970;96(ST7):1403-15.

[3] Moffatt, K.R. and Dowling, P.J. Shear lag in steel box-girder bridges. *Struct. Engineer*, 1975;53:439-48.

[4] Razaqpur, A.G. and Li, H.G. A Finite Element with Exact Shape Functions for Shear Lag Analysis in Multi-Cell Box Girders. Computers & Structures, 1991;39(1):155-163.

[5] Dikaros, I.C. and Sapountzakis, E.J., Nonuniform Shear Warping Analysis of Composite Beams of Arbitrary Cross Section using the Boundary Element Method, Civil-Comp Press, Proceedings of the 14th International Conference on Civil, Structural and Environmental Engineering Computing, 2013.

[6] Eurocode 3: Design of Steel Structures – Part 1.5: Plated Structural Elements, European Committee for Standardization, prEN 1993-1-5: 2004.

[7] Eurocode 4: Design of Composite Steel and Concrete Structures – Part 1.1: General Rules and Rules for Buildings, European Committee for Standardization, prEN 1994-1-1: 2004.

[8] Eurocode 4: Design of Composite Steel and Concrete Structures – Part 2: General Rules and Rules for Bridges, European Committee for Standardization, prEN 1994-2: 2004.

[9] Ie, C.A. and Kosmatka, J.B. On the Analysis of Prismatic Beams Using First-Order Warping Functions. International Journal of Solids and Structures 1992;29(7):879-891.

[10] Vlasov, V., *Thin-walled elastic beams*. Israel Program for Scientific Translations, Jerusalem 1963.

[11] Sapountzakis, E.J. and Mokos, V.G. Warping Shear Stresses in Nonuniform Torsion of Composite Bars by BEM. Computational Methods in Applied Mechanics and Engineering 2003;192:4337-4353.

[12] Mokos, V.G. and Sapountzakis, E.J. Secondary Torsional Moment Deformation Effect by BEM. International Journal of Mechanical Sciences 2011;53, 897-909.

[13] Tsipiras, V.J. and Sapountzakis, E.J. Secondary Torsional Moment Deformation Effect in Inelastic Nonuniform Torsion of Bars of Doubly Symmetric Cross Section by BEM. International Journal of Non-linear Mechanics 2012;47, 68-84.

[14] El Fatmi, R. and Ghazouani, N. Higher Order Composite Beam Theory built on Saint-Venant's Solution. Part-I: Theoretical Developments. Composite Structures 2011;93:557-566.

[15] Tahan, N., Pavlović, M.N. and Kotsovos, M.D. Shear-Lag Revisited: The Use of Single Fourier Series for Determining the Effective Breadth in Plated Structures. Computers & Structures 1997;63(4):759-167.

[16] Katsikadelis, J.T. and Sapountzakis, E.J. A realistic estimation of the effective breadth of ribbed plates. International Journal of Solids and Structures 2002;39:897-910.

[17] Gupta, P.K., Singh, K.K. and Mishra, A. Parametric Study on Behaviour of Box-Girder Bridges Using Finite Element Method, Technical Note. Asian Journal of Civil Engineering (Building and Housing) 2010;11(1):135-148.

[18] Hjelmstad, K.D. Warping Effects in Transverse Bending of Thin-Walled Beams. Journal of Engineering Mechanics 1987;113(6):907-924.

[19] Ghazouani, N. and El Fatmi, R. Extension of the non-uniform warping theory to an orthotropic composite beam. Comptes Rendus Mecanique, 2010;338:704-711.

[20] Ghazouani, N. and El Fatmi, R. Higher Order Composite Beam Theory built on Saint-Venant's Solution. Part-II: Built-in Effects Influence on the Behavior of End-Loaded Cantilever Beams. Composite Structures 2011;93:567-581.

[21] Ferradi, M.K., Cespedes, X. and Arquie, M. A higher Order Beam Finite Element with Warping Eigenmodes. Engineering Structures 2013;46:748-762.

[22] Genoese, A., Genoese, A., Bilotta, A. and Garcea, G. A Mixed Beam Model with Non-Uniform Warpings Derived from the Saint Venànt Rod. Computers and Structures 2013;121:87-98.

[23] Jun, L., Rongying, S., Hongxing, H. and Xianding J. Response of monosymmetric thin-walled Timoshenko beams to random excitations. International Journal of Solids and Structures 2004; 41:6023-6040.

[24] Kim, N.I., Seo, K. J. and Kim, M. Y. Free vibration and spatial stability of non-symmetric thin-walled curved beams with variable curvatures. International Journal of Solids and Structures 2003; 40:3107-3128.

[25] Kim, N.I., Shin, D.K. and Park, Y.S. Dynamic stiffness matrix of thin-walled composite I-beam with symmetric and arbitrary laminations. Journal of Sound and Vibration 2008; 318:364-388.

[26] Kwak, H.G., Kim, D.Y. and Lee, H.W. Effect of warping in geometric nonlinear analysis of spatial beams. Journal of Constructional Steel Research 2001; 57:729-751.

[27] Librescu, L., Qin, Z. and Ambur, D.R. Implications of warping restraint on statics and dynamics of elastically tailored thin-walled composite beams. International Journal of Mechanical Sciences 2003; 45:1247-1267.

[28] Mitra, M., Gopalakrishnan, S. and Bhat, M. S. A new super convergent thin walled composite beam element for analysis of box beam structures. International Journal of Solids and Structures 2004; 41:1491-1518.

[29] Piovan, M.T. and Cortidnez, V.H. Out-of-plane vibrations of shear deformable continuous horizontally curved thin-walled beams 2000; 237(1):101-118.

[30] Piovan, M. T. and Cortınez, V.H. Mechanics of shear deformable thin-walled beams made of composite materials. Thin-Walled Structures 2007; 45:37-6

[31] Senjanovic, I., Catipovic, I., and Tomasevic, S. Coupled flexural and torsional vibrations of ship-like girders. Thin-Walled Structures 2007; 45:1002-1021.

[32] Piovan, M.T. and Cortınez, V.H.. Mechanics of thin-walled curved beams made of composite materials, allowing for shear deformability. Thin-Walled Structures 2007 45:759-789.

[33] A. Prokic. On triply coupled vibrations of thin-walled beams with arbitrary cross-section Journal of Sound and Vibration 2005; 279:723-737.

[34] Shadmehri, F., Haddadpour, H. and Kouchakzadeh M.A. Flexural–torsional behavior of thin-walled composite beams with closed cross-section. Thin-Walled Structures 2007; 45:699-705.

[35] Piovan, M.T., Filipich, C.P. and Cortınez, V.H. Exact solutions for coupled free vibrations of tapered shear-flexible thin-walled composite beams. Journal of Sound and Vibration 2008; 316:298-316.

[36] Le, T.N., Battini, J.M. and Hjiaj, M. Corotational formulation for nonlinear dynamics of beams with arbitrary thin-walled open cross-sections. Computers and Structures 2014; 134:112-127.

[37] Egidio, A.D., Luongo, A. and Vestroni, F. A non-linear model for the dynamics of open cross-section thin-walled beams-Part I: formulation International Journal of Non-Linear Mechanics 2003; 38:1067-1081.

[38] Minghini, F., Tullini, N. and Laudiero, F. Vibration analysis with second-order effects of pultruded FRP frames using locking-free elements Thin-Walled Structures 2009; 47:136-150.

[39] Sapountzakis, E.J. and Mokos, V.G. Vibration analysis of 3-D composite beam elements including warping and shear deformation effects Journal of Sound and Vibration 2007; 306:818-834.

[40] Sapountzakis, E.J. and Tsipiras, V.J. Nonlinear nonuniform torsional vibrations of bars by the boundary element method Journal of Sound and Vibration 2010; 329:1853-1874.

[41] Sapountzakis, E.J. and , Dikaros, I.C. Non-linear flexural–torsional dynamic analysis of beams of arbitrary cross section by BEM International Journal of Non-Linear Mechanics 2011; 46:782-794.

[42] Stoykov, S. and Ribeiro, P. Nonlinear forced vibrations and static deformations of 3D beams with rectangular cross section: The influence of warping, shear deformation and longitudinal displacements International Journal of Mechanical Sciences 2010; 52:1505-1521.

[43] Stoykov, S.and Ribeiro, P. Non-linear vibrations of beams with non-symmetrical cross sections International Journal of Non-Linear Mechanics 2013; 55:153-169.

[44] Voros, G.M. Buckling and free vibration analysis of stiffened panels Thin-Walled Structures 2009; 47:382-390.

[45] Yu, A.M., Yang, C.J., Nie, G.H. Analytical formulation and evaluation for free vibration of naturally curved and twisted beams Journal of Sound and Vibration 2010; 329:1376-1389.

[46] Sapountzakis, E.J. and Mokos, V.G. Dynamic analysis of 3-D beam elements including warping and shear deformation effects International Journal of Solids and Structures 2006; 43:6707-6726.

[47] Sapountzakis, E.J., Tsipiras, V.J. Warping shear stresses in nonlinear nonuniform torsional vibrations of bars by BEM Engineering Structures 2010; 32:741-752.

[48] Li, P., Gantoi, F.M. and Shabana, A.A. Higher order representation of the beam cross section deformation in large displacement finite element analysis Journal of Sound and Vibration 2011; 330:6495-6508.

[49] Dikaros, I.C. and Sapountzakis, E.J. Generalized Warping Analysis of Composite Beams of an Arbitrary Cross Section by BEM. I: Theoretical Considerations and Numerical Implementation. Journal of Engineering Mechanics 2014; 140(9): 04014062.

[50] Dikaros, I.C. and Sapountzakis, E.J. Generalized Warping Analysis of Composite Beams of an Arbitrary Cross Section by BEM. II: Numerical Applications. Journal of Engineering Mechanics 2014; 140(9): 04014063.

[51] Siemens PLM Software Inc., NX Nastran User's Guide; 2008.

[52] Katsikadelis, J.T. The Analog Equation Method. A Boundary – only Integral Equation Method for Nonlinear Static and Dynamic Problems in General Bodies. Theoretical and Applied Mechanics 2002;27:13-38.

[53] Sapountzakis, E.J. and Katsikadelis, J.T. Analysis of plates reinforced with beams. Computational Mechanics 2000;26:66-74.

[54] Katsikadelis, J.T. Boundary Elements: Theory and Applications, Elsevier, Amsterdam-London; 2002.

[55] Beer, G., Smith, I. and Duenser, Ch. The Boundary Element Method with Programming – For Engineers and Scentists, Springer Wien Niew York; 2008.

[56] Chopra, A.K. Dynamics of Structures Theory and Applications to Earthquake Engineering, Prentice Hall, Upper Saddle River, NJ, 1995.

COMPDYN 2015
5th ECCOMAS Thematic Conference on
Computational Methods in Structural Dynamics and Earthquake Engineering
M. Papadrakakis, V. Papadopoulos, V. Plevris (eds.)
Crete Island, Greece, 25–27 May 2015

MODAL AND FREQUENCY DOMAIN BASED TECHNIQUES FOR FINITE ELEMENT MODEL CORRELATION

J.F. Mercer[1], G.S. Aglietti[1], and A.M. Kiley[2]

[1] University of Surrey
Guildford, Surrey, GU2 7XH, United Kingdom
e-mail: {j.mercer,g.aglietti}@surrey.ac.uk

[2] Airbus Defence and Space
Stevenage, Herts., SG1 2AS, United Kingdom
andy.kiley@astrium.eads.net

Keywords: Finite Element Analysis (FEA), Finite Element Model (FEM), FEM validation, FEM correlation, sine sweep test, operating deflected shapes, modal parameter estimation.

Abstract. *It is common for Finite Element Model (FEM) validation activities to be carried out in the modal domain; using finite element modal analysis results and modal parameters extracted from test measured data. In order to obtain the required mode shapes and natural frequencies from the test measured Frequency Response Functions (FRFs), a modal parameter estimation method must be employed. An alternative approach involves correlation based in the frequency domain. In that case the FRFs would be considered directly from the test, without the need to apply advanced modal parameter extraction, and compared to FEM FRFs. In this work, sine sweep test-FEM correlations of two full spacecraft have been considered. A variety of the aforementioned modal parameter estimation methods have been applied and compared in order to establish which approach is most suitable to the considered applications. Findings highlight the issues associated with applying the simple 'peak picking' approach to modal correlation, and as such indicate that more sophisticated parameter estimation techniques often need to be employed in modal correlation. Frequency based methods therefore have potential inherent advantages as the issue of modal parameter extraction, and the associated introduction of further errors, is avoided. Frequency domain method also have several drawbacks, however, including the inflexibility of the FRF based methods to account for a deflected shape being well matched between test and FEM, but occurring at a slightly different frequency.*

1 INTRODUCTION

From a structural perspective, launch is one of the most challenging phases in the mission of a spacecraft. The interaction between the spacecraft and the launch vehicle is an important aspect of this; however for many reasons, not least of which being the size of the launch vehicle, it is not possible to practically test the two systems together. Thus, in order to simulate the launch experience, Coupled Loads Analyses (CLAs) are carried out which couple a Finite Element Model (FEM) of the spacecraft with a model of the launcher to virtually predict flight loads.

If there is to be confidence in the results of the CLA, it is necessary to first validate the spacecraft FEM against test measured data. The analytical and experimental results are compared and the FEM updated where necessary to improve its representation of the behaviour of the real structure at the vibration modes of interest. This correlation and model update process can take a considerable effort and time. Therefore, one means of containing this process is through ensuring that the comparisons made between test and FEM are meaningful and able to accurately quantify the level of correlation.

The focus here is on the ability of the mode shapes extracted from Frequency Response Functions (FRFs) to represent true mode shapes of the structure. This is an important issue to explore as the data collected during the fixed base sine test of the structure is a representation of how the structure behaves when excited at a given frequency; this is known as the Operating Deflected Shape (ODS). When the structure is excited at a resonant frequency, which is well separated and uncoupled from any other modes, the ODS will be essentially the same as the mode shape with the deflection dominated exclusively by that mode. It is, however, often the case that modes are closely spaced and the ODS at a resonant frequency is 'contaminated' by other nearby modes and is not equivalent to the mode shape. This issue has led to the development of many algorithms and software, such as Frequency-Domain Direct Parameter Identification (FDDPI) [1], Least Squares Complex Exponential (LSCE) [2] or PolyMAX [3] methods for estimating and extracting modal parameters and mode shapes from test data. Here comparisons are made between: mode shapes estimated from FRFs obtained through sine-sweep analysis of spacecraft FEMs; and those found through direct modal/eigen- analysis of the same FEMs.

As there will always be some level of 'errors' introduced through the modal parameter estimation process, one alternative approach is to avoid the effort and uncertainty associated with this process by performing correlation comparisons in the frequency/response domain through direct use of the FRFs. As such, this topic is to be the subject of further investigation.

2 CORRELATION CRITERIA

It is essential that the spacecraft FEM provides a realistic representation of the behaviour of the real structure as the mathematical model will subsequently be employed in the CLA to investigate the spacecraft-launcher interactions and thus ensure that the spacecraft does not encounter unacceptable launch loads. The spacecraft FEM correlation exercise is essentially a comparison between the experimental data and the analytical model. The purpose of the correlation is therefore to evaluate how well the FEM replicates the behaviour of the real structure, as depicted in Figure 1, at important modes such that updates to the model can be made where necessary to achieve a final spacecraft FEM which is 'fit for purpose'. In order to perform these correlations it is necessary to define some criteria to quantify and evaluate how well matched the FEM is to the test for a given target mode.

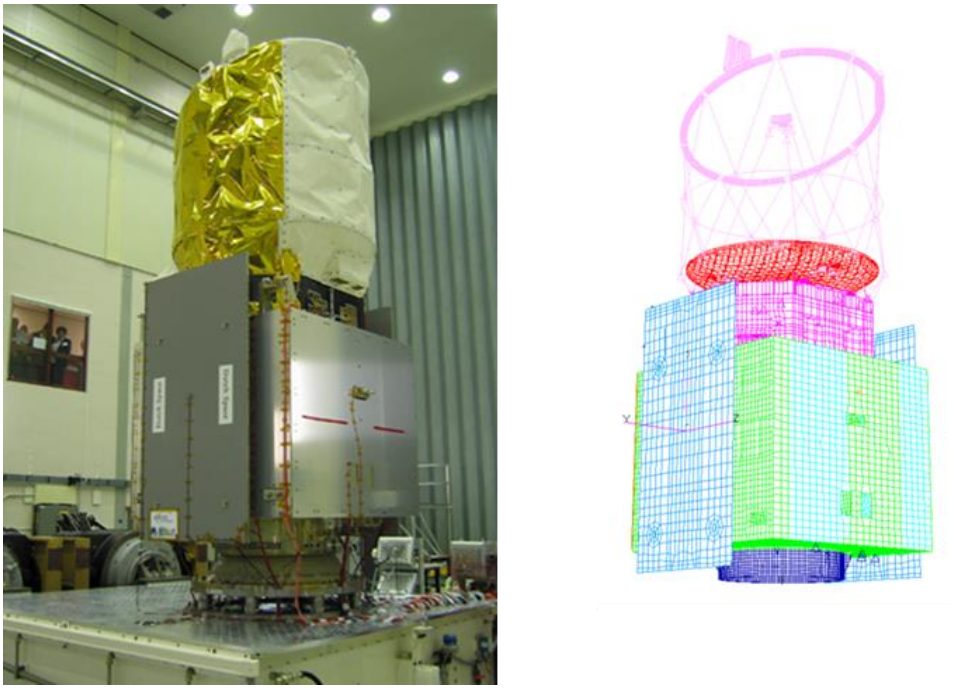


Figure 1. Aeolus STM [4] (left) and Aeolus FEM (right).

There are a wide variety of methods which may be used to perform these comparisons; some of the main methods are outlined in the table below from European Cooperation for Space Standardisation (ECSS) modal survey assessment document ECSS-E-ST-32-11C [5].

Type	Techniques
Vector based techniques	- Modal assurance criterion (MAC) [a] - Orthogonality or cross-orthogonality [a]
DOF based techniques	- Coordinate modal assurance criterion (CoMAC) - Modulus difference [a] - Coordinate orthogonality check
Frequency based techniques	- Frequency difference [a] - Frequency response assurance criterion (FRAC) - Response vector assurance criterion (RVAC)
a Mandatory (see 5.8.1.1b)	

Table 1. ECSS [5] table of commonly used correlation techniques.

2.1 Modal Based Correlation Techniques

At this point one approach to the correlation of spacecraft models is modal analysis and subsequent comparison of FEM eigenvalues and eigenvectors with test derived natural frequencies and mode shapes. Comparisons may be made by using the common vector based techniques: Modal Assurance Criteria (MAC) [6] and Cross-Orthogonality Checks (COC) [7].

Modal Assurance Criteria (MAC)

For MAC, the test mode shapes, ψ, and FEM eigenvectors, φ, are compared, resulting in a value between 0 and 1 which indicates how closely matched the vectors are, with a perfect match yielding a 1.

$$\mathrm{MAC} = \frac{(\psi^{\mathrm{T}}\phi)^2}{(\psi^{\mathrm{T}}\psi)\cdot(\phi^{\mathrm{T}}\phi)} \tag{1}$$

It is generally considered, and indicated in the table below from ECSS-E-ST-32-11C [5], that target modes achieving a MAC of at least 0.9 indicates a good correlation and is the minimum required value for the fundamental bending modes of a spacecraft. It is, however, also clear from Table 2 that the required degree of correlation is dependent on the perceived relative importance of the mode under consideration.

Cross-Orthogonality Check (COC)

The COC is also an ECSS [5] required check, and works similarly to MAC, but with the mass matrix employed to weight the relative importance of the DoFs being considered. This approach takes advantage of the orthogonal relationship between normal modes and the system mass matrix. An ideal result of perfectly matched mode shapes which are orthogonal to the mass matrix will yield a diagonal matrix, and for mass normalised modes this becomes an identity matrix. Again, in Table 2, it is shown that off-diagonal values <0.1 and leading diagonal terms >0.9 are deemed to indicate a good correlation. The typical cross-orthogonality check is given by:

$$\mathrm{COC} = \frac{(\psi^{\mathrm{T}}\mathrm{M}_{\mathrm{TAM}}\phi)}{\sqrt{(\psi^{\mathrm{T}}\mathrm{M}_{\mathrm{TAM}}\psi)}\sqrt{(\phi^{\mathrm{T}}\mathrm{M}_{\mathrm{TAM}}\phi)}} \tag{2}$$

where the Test Analysis Model (TAM), or reduced mass matrix, $\mathrm{M}_{\mathrm{TAM}}$, is generated by application of an appropriate model reduction method. The experimental and analytical mode shapes are again given by ψ and φ respectively.

The introduction of the mass matrix has potential benefits as the mass associated to the modal vectors is accounted for and as such there is a weighting of the DoFs depending on their relative influence, which is not accounted for by the MAC criteria. Although, the practical benefits are potentially reduced in circumstances where the DoF set is pre-selected and the perceived relative importance of selected DoFs is not necessarily directly related solely to mass weighting.

Item	**Quality criterion** [a]	
Fundamental bending modes of a spacecraft	MAC: Eigenfrequency deviation:	> 0,9 < 3 %
Modes with effective masses > 10 % of the total mass	MAC: Eigenfrequency deviation:	> 0,85 < 5 %
For other modes in the relevant frequency range [b]	MAC: Eigenfrequency deviation:	> 0,8 < 10 %
Cross-orthogonality check	Diagonal terms: Off-diagonal terms:	> 0,90 < 0,10
Damping	To take measured values as input for the response analysis. To use realistic test inputs for this purpose.	
Interface force and moment measurements	For modes with effective masses > 10 %: deviations of interface forces and moments < 10 %.	

a The quality criteria given are not normative and are given as examples for achieving a satisfactory test–analysis correlation.

b The relevant frequency range is, in general, determined by the launcher excitation spectrum up to 100 Hz. This frequency range can, however, be extended due to, for example, high frequency launcher dynamic excitations or specific requirements for AOCS control purposes.

Table 2: ECSS [5] required correlation levels.

Co-Ordinate Modal Assurance Criteria (COMAC)

Co-Ordinate Modal Assurance Criteria (COMAC) [8] is similar to MAC, however, it compares the test and FEM responses at a given DoF across all modes, rather than comparing the response at all DoFs for a single mode. This method is therefore useful in situations where the level of correlation for an individual DoF, or set of key DoFs, is of particular interest.

For a given DoF, i, the COMAC is given by:

$$\mathrm{COMAC_i} = \frac{\left(\sum_{n=1}^{N} |\psi_{in}\phi_{in}|\right)^2}{\sum_{n=1}^{N} \psi_{in}^2 \sum_{n=1}^{N} \phi_{in}^2} \tag{3}$$

The experimental and analytical mode shapes are again given by ψ and φ respectively. The subscript n represents the index of the considered mode pair, whilst N denotes the number of mode pairs to be considered.

This method is less commonly applied than the aforementioned MAC and COC checks, and is not considered mandatory by ECSS [5], see Table 1. One drawback of this method is that it requires all of the modes under consideration to be pre-paired, most likely through the use of MAC to match the modes from the test to the correct corresponding FEM mode shape. [9]

2.2 Frequency Based Correlation Techniques

Frequency Difference

Frequency difference is simply the difference between the resonant frequencies identified from the test data and the eigenvalues from the FEM analysis, and is often given in the form of a percentage difference. The equation given below can be used to calculate the frequency difference, where f is the natural frequency in Hz corresponding to the mode being considered.

$$\text{Frequency Difference} = \frac{|f_{FEM} - f_{Test}|}{f_{Test}} \times 100\% \tag{4}$$

Frequency Response and Response Vector Assurance Criteria (FRAC and RVAC)

The frequency based equivalents of MAC and COMAC are Response Vector Assurance Criteria (RVAC) [10] and Frequency Response Assurance Criterion (FRAC) [11], respectively. For the frequency based methods, rather than comparing mode shapes, the FRFs are compared as shown in Figure 2. FRAC compares the FRFs, for a given DoF, across all measured frequencies. RVAC compares Operating Deflected Shapes (ODSs), i.e. the responses of all measured DoFs at a given frequency.

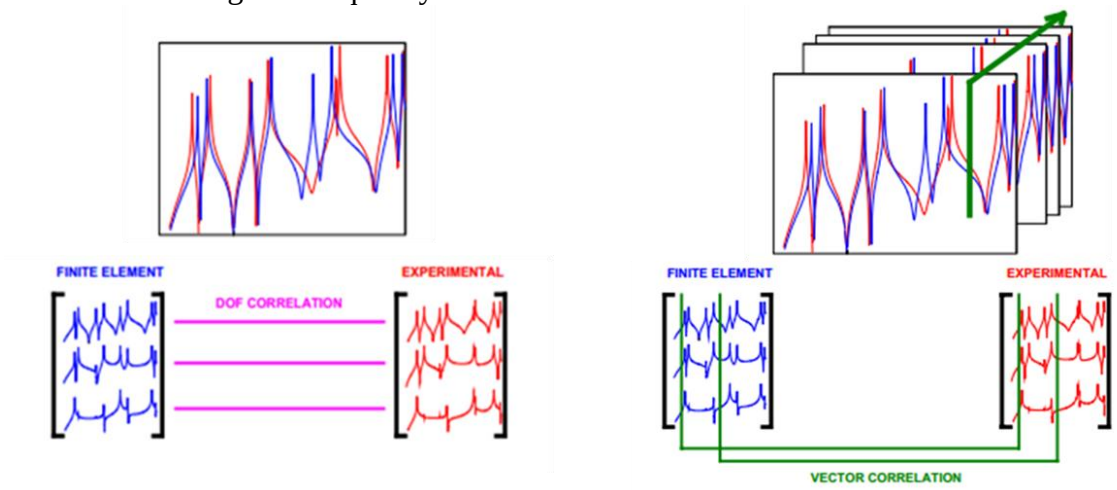


Figure 2. Illustration of FRAC (left) and RVAC (right) FRF Based Correlation Criteria [9]

The equations for FRAC and RVAC are given below. For FRAC, the FRF for a given DoF across the entire frequency range of interest is given by H. RVAC makes use of the ODSs, U, at a given frequency across all DoFs from the MPP.

$$\mathrm{FRAC} = \frac{\left(\{\mathrm{H_{Test}}\}\{\mathrm{H_{FEM}}\}^{\mathrm{T}}\right)^2}{\left(\{\mathrm{H_{Test}}\}\{\mathrm{H_{Test}}\}^{\mathrm{T}}\right)\cdot\left(\{\mathrm{H_{FEM}}\}\{\mathrm{H_{FEM}}\}^{\mathrm{T}}\right)} \tag{5}$$

$$\mathrm{RVAC}(\omega) = \frac{\left(\mathrm{U}(\omega)^{\mathrm{T}}_{\mathrm{Test}}\mathrm{U}(\omega)_{\mathrm{FEM}}\right)^2}{\left(\mathrm{U}(\omega)^{\mathrm{T}}_{\mathrm{Test}}\mathrm{U}(\omega)_{\mathrm{FEM}}\right)\cdot\left(\mathrm{U}(\omega)^{\mathrm{T}}_{\mathrm{Test}}\mathrm{U}(\omega)_{\mathrm{FEM}}\right)} \tag{6}$$

An alternative to RVAC is the Frequency Domain Assurance Criteria (FDAC) [12], which is also based on comparing ODSs. Where RVAC compares the ODSs for test and FEM FRFs at a particular frequency, with FDAC the corresponding resonant frequencies for test and FEM are identified separately and thus $\omega_{\mathrm{Test}} \neq \omega_{\mathrm{FEM}}$. In this manner, the deflected shape can be compared and the issue of differing resonant frequency can be considered separately by considering the frequency difference.

These frequency based methods have the advantage that the FRFs from the test can be used directly in the correlation, without requiring the modal parameter extraction used to compare modal data [13]. This is a benefit in that it not only circumvents the effort required to extract the modal parameters, but also avoids the potential errors introduced to the test data as a result of modal parameter estimation issues.

There are, however, significant drawbacks associated with these frequency base correlation methods. One main issue is that damping, which is neglected in modal analysis, must be accounted for in the FEM in order to produce the FRFs required for frequency based correlation [14]. It is also the case that both FRAC and RVAC can be influenced by the potential for a shift in resonance frequencies between test and FEM, although variations on these techniques have been developed which introduce shift parameters attempt to compensate for this effect. The use of ODS rather than mode shapes also has the drawback that a conventional orthogonality check cannot be applied with frequency domain correlation.

As such, modal based correlation is more common and, as shown by Table 1, is mandated by the ECSS modal survey assessment [5] where the FRF techniques are optional. Due to the more frequent application of modal techniques, the results of MAC and COC checks are more widely understood and values indicating good correlation are well established. The required level of correlation in terms of FRF based methods is less clear [15].

3 MODAL PARAMETER ESTIMATION

It is not possible to directly measure the modal parameters of a structure through physical testing alone; therefore it is important to perform appropriate experimental data processing such that as close a representation as possible to the true mode shapes of the structure is obtained for comparison with the analytical modal analysis results from the FEM. If this is not accomplished, then any subsequent modal data based correlation is undermined, possibly triggering FEM updates which are unnecessary.

3.1 Introduction to Modal Parameter Extraction Methods

The data collected during the base-shake sine-sweep test of the structure is a representation of how the structure behaves when excited at a given frequency; this is known as the Operating Deflected Shape (ODS). In theory, the ODS will be a linear combination of all modes contributing to the response of the structure. In practice, when the structure is excited at a resonant frequency, which is well separated and uncoupled from any other modes, the ODS is likely to closely approximate the corresponding mode shape, with deflections dominated by

that mode pattern having negligible contribution from adjacent modes, as illustrated in Figure 3. It is, however, often the case for complex structures that modes are closely spaced and the ODS at a resonant frequency is 'contaminated' by the influence of other nearby modes, and as such is not equivalent to the mode shape.

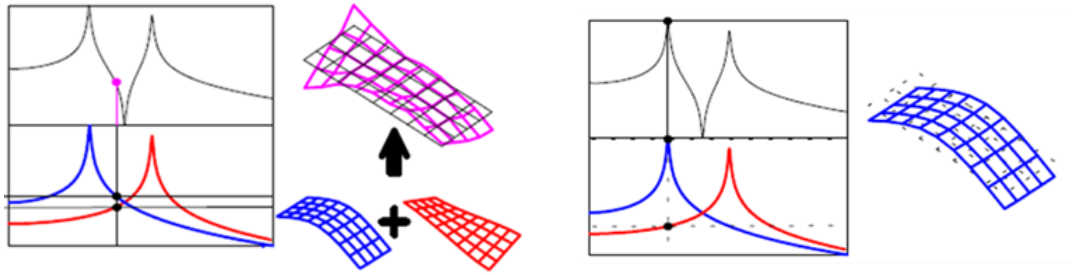


Figure 3. ODS between resonances, left, and ODS at resonant frequency, right. [16]

This issue has led to the development of many algorithms and software packages for estimating and extracting modal parameters from test measured FRF data. The following subsections explore the classifications of these methods and the advantages and disadvantages of each. The method must ideally be selected as appropriate the application under consideration.

Single or Multiple Degrees of Freedom

Single Degree of Freedom (SDoF) methods determine modal parameters for each mode individually. The main benefits of these methods are the ease and speed of application. SDoF approaches work under the assumption that the structure behaves as an SDoF system when excited at resonance, i.e. that the ODS is equivalent to the corresponding pure mode shape with no influence from the other modes of the system. This assumption is only valid under the condition that the system modes are not heavily coupled. When this condition is met, these methods can be appropriate to use and accurate; if, however, this is not the case then Multiple Degree of Freedom (MDoF) methods are required in order to achieve a reasonable approximation of the modal parameters. MDoF methods generate an estimation of modal parameters by analysing data for multiple modes simultaneously. [17, 18]

Local or Global

Local (otherwise referred to as single output) methods are so called as they are applied to one output at a time, such as an individual FRF curve for a particular sensor. As such, any modal parameters estimated will apply to the FRF under consideration and not necessarily to the global system. This has the disadvantage that the outcome is a set of multiple locally estimated values for a single parameter, such as for the natural frequency of a given mode, which may vary slightly between the different FRFs. In such a case, it would be up to the analyst to determine which natural frequency value was most appropriate, or simply apply the average given the results for all of the considered FRFs. [17, 18]

Global (otherwise referred to as multiple output) methods are applied to many output sets, such as the FRFs considered in this work, simultaneously. This allows parameters to be estimated based on all available data on the full system, rather than locally for one sensors data at time. [17, 18]

Single or Multiple Input

Experimental modal analysis can be conducted through the use of single or multiple exciters. Where multiple excitations are applied, it can be advantageous to then employ a modal parameter estimation method which can globally assess the FRFs by taking into account all applied inputs simultaneously. This is possible as the modal parameters are not input dependent, and as such should be consistent regardless of varying applied input location. The main advantage of methods accounting for multiple input scenarios is improved estimation in the occurrence of closely coupled modes and even double poles (two distinct modes occurring at the same excitation frequency). Methods which can accommodate multiple-inputs and multiple-outputs (MIMO) are sometimes referred to as 'polyreference' techniques. [17, 18]

3.2 Single Degree of Freedom Modal Parameter Estimation

SDoF methods are generally very straight forward to implement, computationally efficient and can give sufficiently accurate results under the right circumstances. Where modes are well separated in frequency, see upper plot in Figure 4, these simple SDoF methods are known to be reasonably effective and may therefore be applied without the need to employ more sophisticated techniques for manipulation of the test data. It should be noted, however, that where there is heavy modal coupling, see lower plot in Figure 4, these methods are not sufficient and a method considering the influence of the interactions between multiple modes is required. [19, 20]

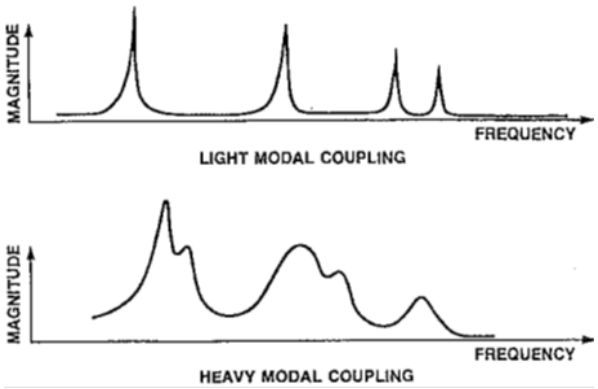


Figure 4. Modes well separated or heavily coupled [20]

'Peak/Mode Picking' Method

One simple SDoF method is to use the peaks in the imaginary part of (acceleration/force) FRFs to identify the resonant frequencies ('peak picking'), and to estimate the mode shapes ('mode picking') as equivalent to the ODSs at those frequencies, as depicted by Figure 5. The validity of this method for some example spacecraft cases has been investigated.

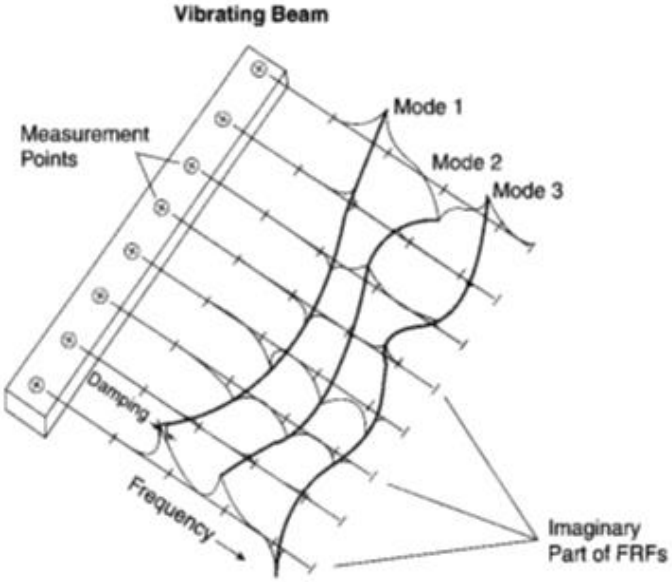


Figure 5. FRF imaginary part 'peak picking' method of SDoF mode approximation [20]

3.3 Multiple Degree of Freedom Modal Parameter Estimation

When modal coupling is such that the simple SDoF methods are not sufficient to provide a sufficiently accurate estimation of the required parameters; more advanced curve fitting methods, which simultaneously consider multiple modes or even an entire set of FRFs, may instead be applied. Various methods have been developed over the years to deal with this important issue in experimental modal analysis.

Maia and Silva [21] observed that the Complex Exponential (CE) [22] method has been one of the most important and influential modal parameter estimation methods. It is a time domain single-input-single-output (SISO) method and appeared in 1970 when proposed by Spitznogle and Quazi [22]. CE was eventually developed further to produce one of the most established methods; the least-squares complex exponential method (LSCE), introduced by Brown et al [2] in 1979. This LSCE method has the advantage of being a global method and has been widely used for processing data from single-input-multiple-output (SIMO) experiments. A frequency domain version of the least squares method, known as Least Squares Complex Frequency (LSCF) was subsequently created [23].

More recent work, such as that of Guillaume et al [24], has overcome some of the limitations of previous techniques by generating a poly-reference version of the LSCF method, capable of handling multiple inputs. There are many important potential benefits to the use of a multi-reference method for the cases to be considered in this work. One of the main benefits from the perspective of this work is that it allows closely coupled modes to be more accurately identified than previous methods [24].

MDoF modal parameter estimation methods often consist of two main procedures: first to determine the global parameters, such as system poles/resonant frequencies; and subsequently to estimate the local parameters, i.e. the modal displacements from which the modal vectors are comprised. Different methods are typically employed to perform each of these key procedures. For the initial phase, Polyreference-LSCFD methods are now the most popularly employed, although Polyreference-LSCE are also still relatively common; whereas for the second phase of the process, Least Squares Frequency Domain (LSFD) techniques are the most commonly implemented. [17]

4 EXAMPLE APPLICATIONS

As described previously, the simple SDoF 'peak picking' method uses the peaks in the imaginary part of the FRFs to identify the resonant frequencies and to extract the ODS at those frequencies. More sophisticated MDoF methods of modal parameter estimation have been developed to account for structures, for which the SDoF method is not sufficient. Poly-reference LSCF methods are currently among the most commonly applied. In order to examine the validity of these method for mode shape estimation in spacecraft applications, a frequency response analysis has been performed on the spacecraft FEMs and the resulting mode shapes estimated from FRFs are compared to the FEM mode shapes obtained directly from modal/eigen- analysis of the same reference spacecraft FEMs.

The studies presented herein focus on two large, unique, scientific spacecraft:

- The ESA/JAXA collaboration spacecraft BepiColombo for the exploration of Mercury which has a stacked configuration comprising of two planetary orbiters and a propulsion module. The spacecraft has a mass of 6446kg and the FEM consist of approximately 1,800,000 DoFs. During base-shake sine-sweep vibration tests, data was collected using accelerometers capturing the response at approximately 400DoFs. The corresponding 400 DoFs from the FEM will be considered in these investigations for the generation of FRFs and mode shape vectors.
- ESA's Atmospheric Dynamics Mission Aeolus spacecraft for global wind-component-profile observation, which aims to improve weather forecasting. This spacecraft has a mass of 1800kg and the FEM consist of approximately 575,000 DoFs. Again, these investigations focus on the 300 DoFs used as measurement points in the sine-sweep vibration test of the spacecraft.

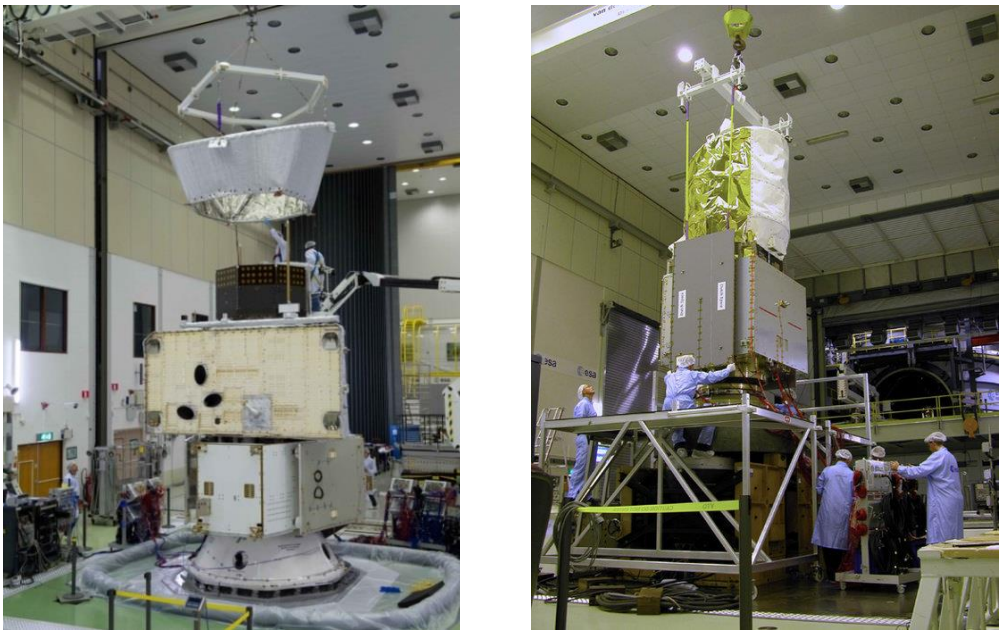


Figure 6. BepiColombo (left) and Aeolus (right) STMs during vibration test preparation [4]

For the purposes of this investigation, the modes of interest have been selected based solely on the modal effective mass of each mode in the translational directions, as shown in Table 3 below. The modal effective mass gives an indication to the level of participation of each mode in the loads analysis and is often used to highlight significant modes for correlation [25].

BepiColombo				Aeolus			
Freq. (Hz)	Effective Modal Mass (%)			Freq. (Hz)	Effective Modal Mass (%)		
	TX	TY	TZ		TX	TY	TZ
12.68	0.66	25.96	0.02	15.96	42.35	0.02	0.00
13.01	25.30	0.73	0.00	16.62	0.02	45.31	0.00
26.50	4.79	0.23	0.00	40.94	0.00	6.89	0.02
27.12	2.40	0.55	0.00	41.30	0.00	3.40	0.02
27.68	1.21	0.00	0.00	48.95	1.50	0.00	0.02
28.43	0.02	8.97	0.07	54.58	2.39	0.14	0.32
32.43	0.11	0.10	1.21	55.63	0.75	0.15	6.76
33.44	0.00	0.12	5.96	56.94	3.65	0.20	0.00
35.82	0.33	1.14	0.08	58.68	0.47	0.58	1.65
37.03	2.91	0.01	2.94	60.00	0.00	0.00	1.84
37.19	0.36	0.19	3.38	61.47	0.00	0.15	1.46
37.55	2.19	0.16	0.05	63.86	0.08	0.00	5.43
37.77	0.50	0.52	13.15	64.35	0.47	0.00	22.90
38.01	0.00	1.13	1.61	64.69	5.45	0.07	2.47
44.07	0.02	0.03	1.32	69.60	0.01	1.04	0.01
44.37	0.16	2.34	0.01	84.64	0.26	0.05	3.65
45.01	0.00	0.00	1.20	85.01	0.02	0.03	1.52
49.10	0.08	0.03	6.95	85.23	0.02	0.01	8.33
49.77	0.00	0.12	1.03				
57.01	1.12	0.00	0.02				
57.17	2.10	0.00	0.02				

Table 3. Modal Effective Masses of Selected Target Modes

Figure 7 shows the MAC comparison of the BepiColombo X-direction target FEM eigenvectors/mode shapes (partitioned to the ≈400 DoFs from the test measurement point plan) compared to their closest matching modes as estimated from the FEM frequency response analysis; with 'peak picking' results on the left and results from a poly-reference LSCF method on the right. From 'peak picking' there is a reasonably good match for the 1st target mode, however higher order modes show some degradation of MAC, as is depicted by the bar charts in Figure 9. Attention should be drawn here that the MAC here is based upon ≈400 DoFs and illustrations here do not present influence of elimination of user identified DoFs to investigate their sensitivity into the MAC. Correlation for example, in this case, for the second order cantilever modes showed the MAC was heavily influenced by certain DoFs which were deemed of low criticality to the mode considered (e.g. high DoF responses on local light structural features within the second order cantilever modes). Once eliminated, via technical justification, such modes were deemed reasonably well correlated.

Figure 8 provides plots of the imaginary part of the FRFs corresponding to selected example DoFs, with vertical lines to indicate the target mode natural frequencies. From these plots, it can be seen that, other than the 1st mode which is well separated, there is heavy coupling between modes and at higher frequencies the curves resemble the lower plot in Figure 4 above. As such, it is to be expected that these 'peak picked' modes/ODSs will not closely match the corresponding mode shapes, and the more sophisticated poly-reference LSCF method will provide a better match, which is consistent with the MAC results given in Figure 7.

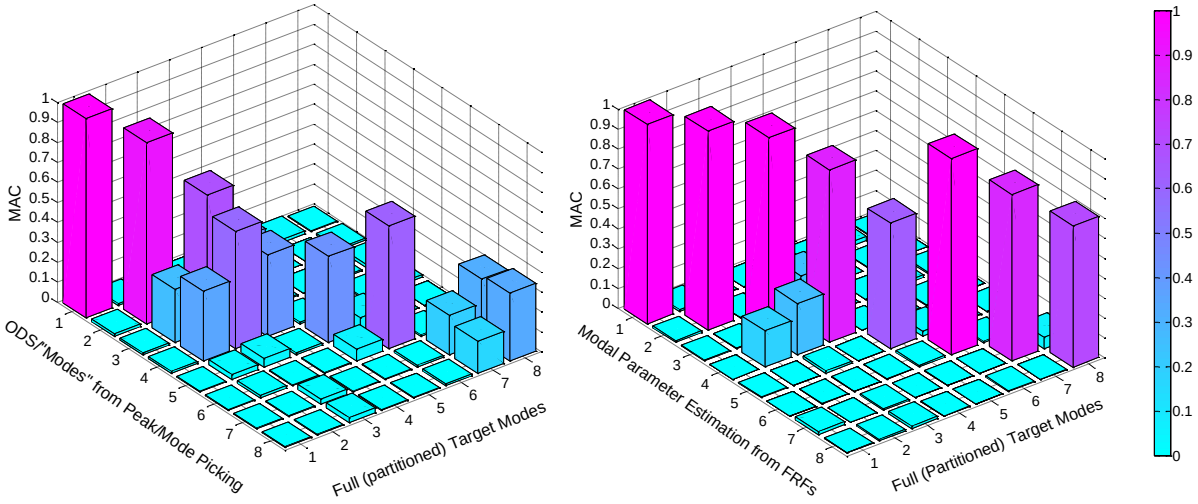


Figure 7. BepiColombo MAC results of FEM X-direction target modes compared with:
Left - FEM ODS/modes from peak picking, Right - FEM modes from modal parameter estimator

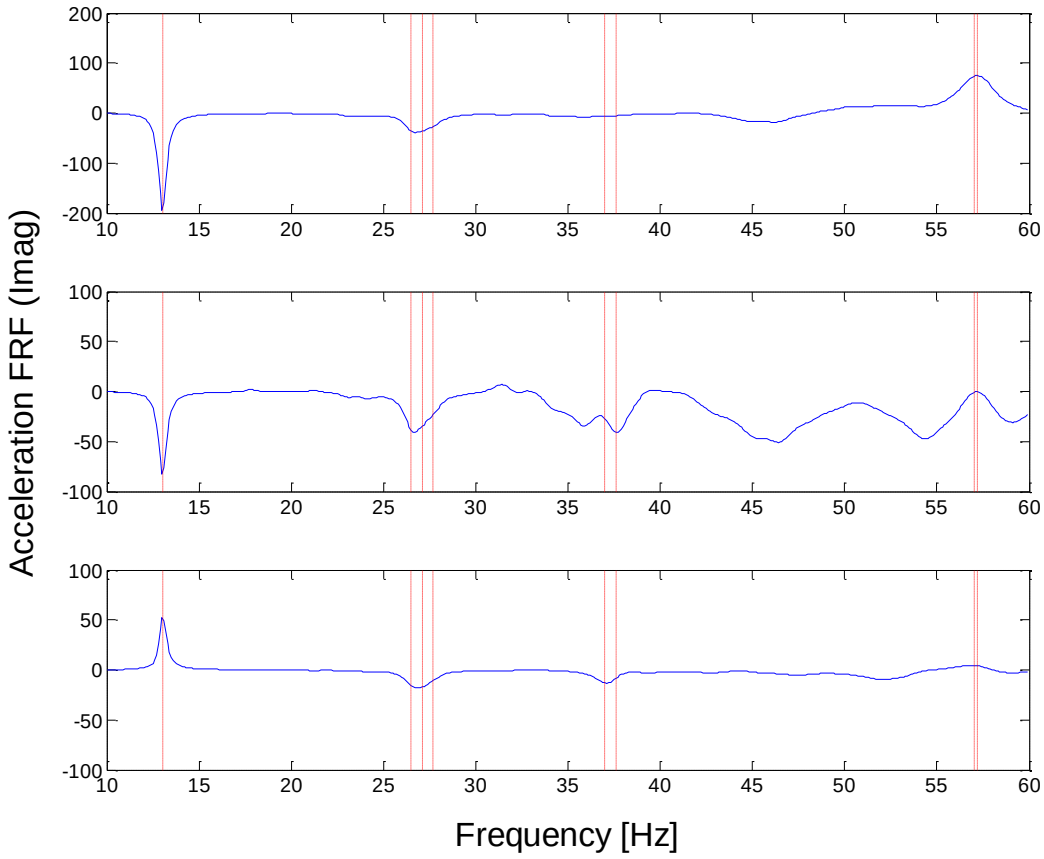


Figure 8. Imaginary part of example FRFs for FEM 'Peak/Mode Picking'

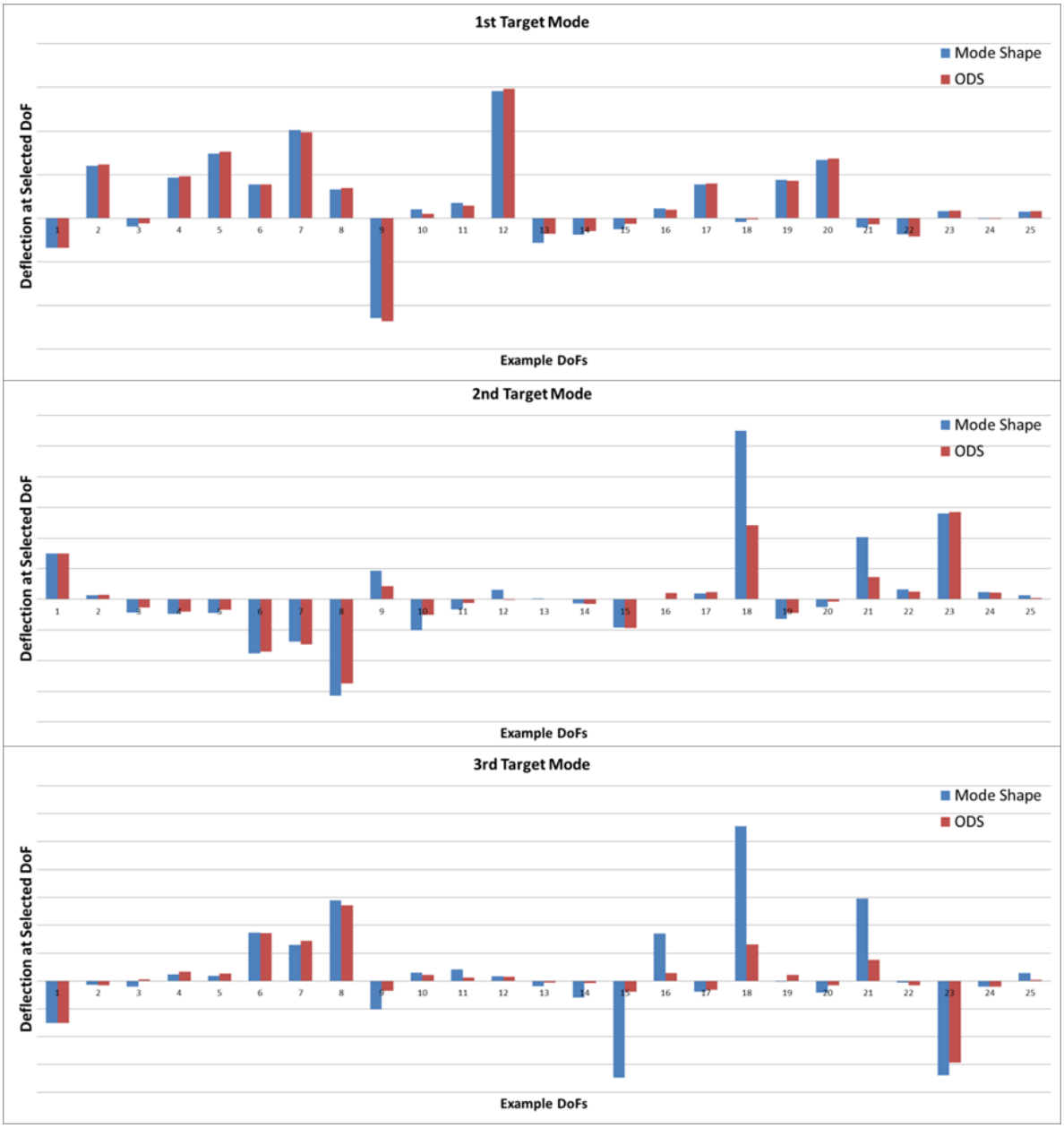


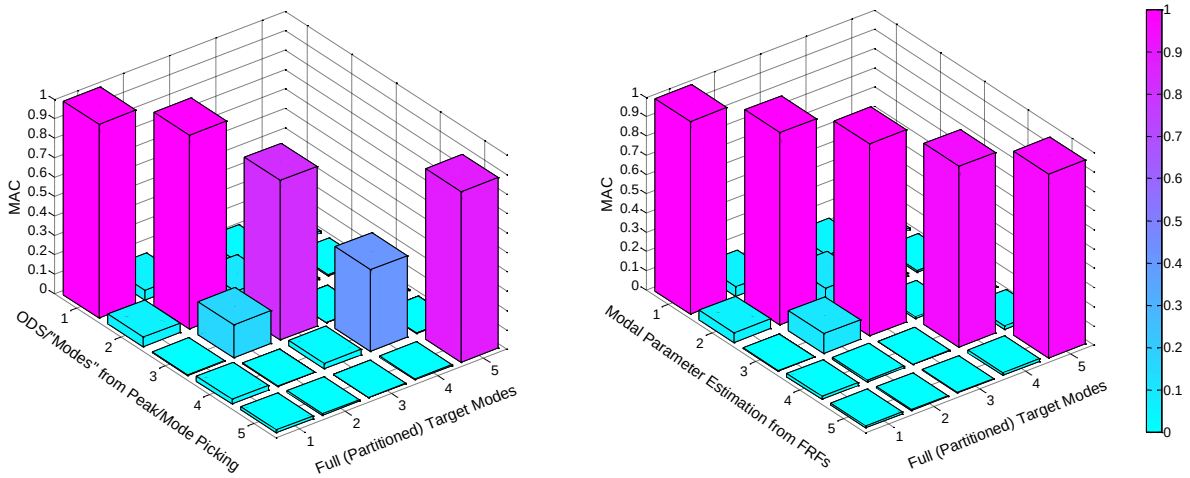
Figure 9. FEM ODS and eigen-mode matches for first 3 x-dominant target modes for 25 example DoFs

Figure 10 shows the MAC comparison of the BepiColombo Y- and Z-direction target FEM mode shapes (directly from FEM normal modal analysis) compared to their closest matching estimates from the FEM frequency response analysis (of the same baseline FEM); again with 'peak picking'/ODS results on the left and result from dedicated modal parameter estimation software, using a poly-reference LSCF method, on the right. Again there is a consistent improvement in the MAC result when the software is used to perform mode shape estimation rather than using simple 'peak picking' of modes equivalent to ODS'.

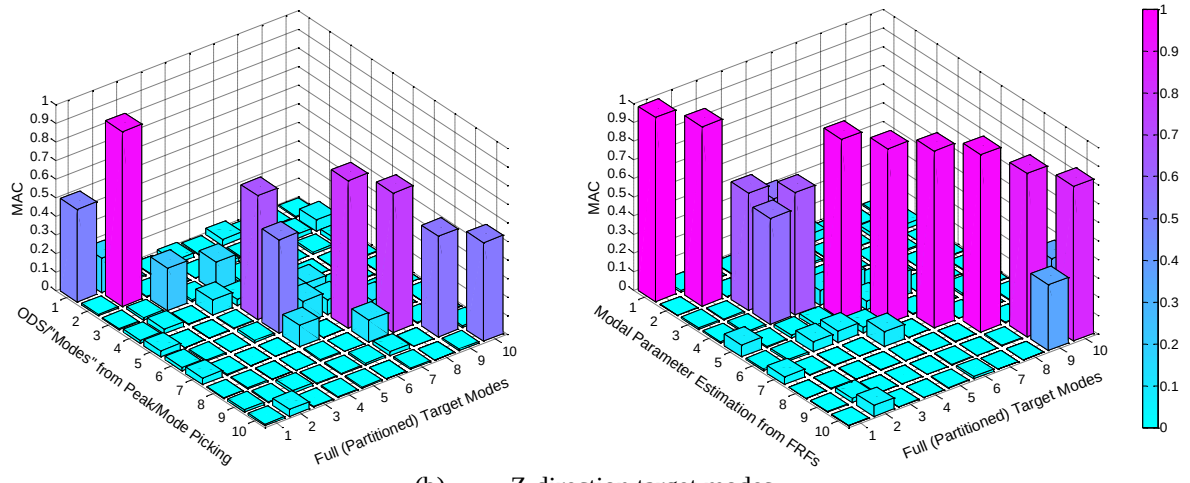
Likewise, Figure 11 shows the MAC comparison of the Aeolus X-, Y- and Z-direction target FEM mode shapes (partitioned to the ≈300 DoFs from the test measurement point plan) compared to their closest matching estimates from the FEM frequency response analysis; again with 'peak picking'/ODS results on the left and result from dedicated modal parameter estimation software on the right. Here the target modes in each direction were reasonably

well separated and so the ‘peak picked’ results appear to give a relatively close match to the target modes. Nevertheless, there is still a notable improvement in the MAC results when the Global MDoF mode shape estimation method is applied.

The actual BepiColombo test data, processed with ‘peak picking’ as described above, was then compared to both the FEM mode shapes (from direct FEA modal analysis) and the FEM ODS/modes (from ‘peak picking’), with the resulting MAC comparisons given in Figure 12. This figure reveals that the test results generally give a better match to the FEM ODS than the FEM mode shapes, confirming that the ODS at resonance frequency is not necessarily representative of the corresponding pure mode shape. This could also be viewed as showing potential for there to be merit in the argument to compare FRF data directly. The right plot in Figure 12 is essentially a comparison of test and FEM ODS; in effect the same as applying the FDAC comparison method.

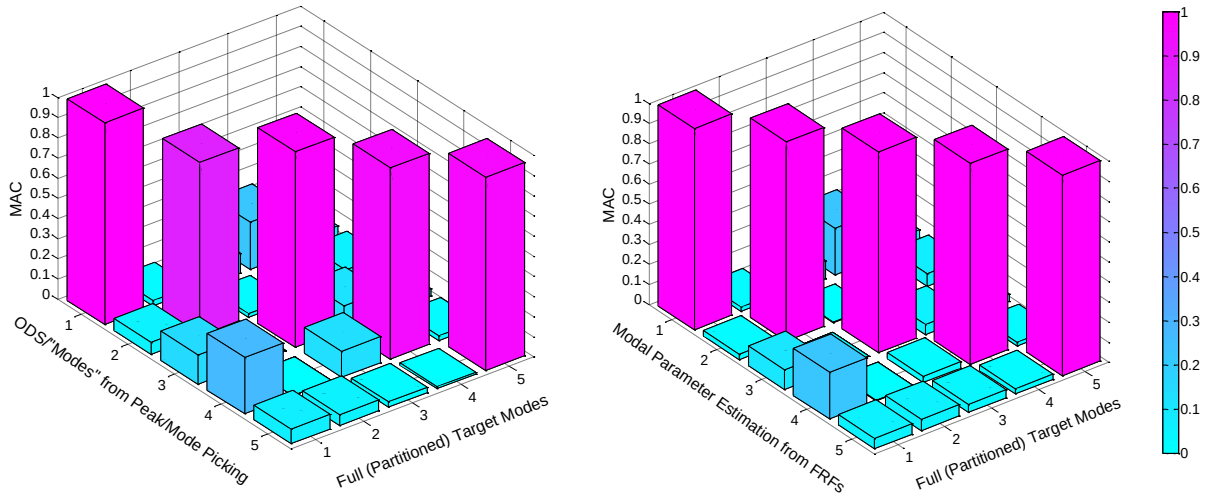


(a) Y-direction target modes

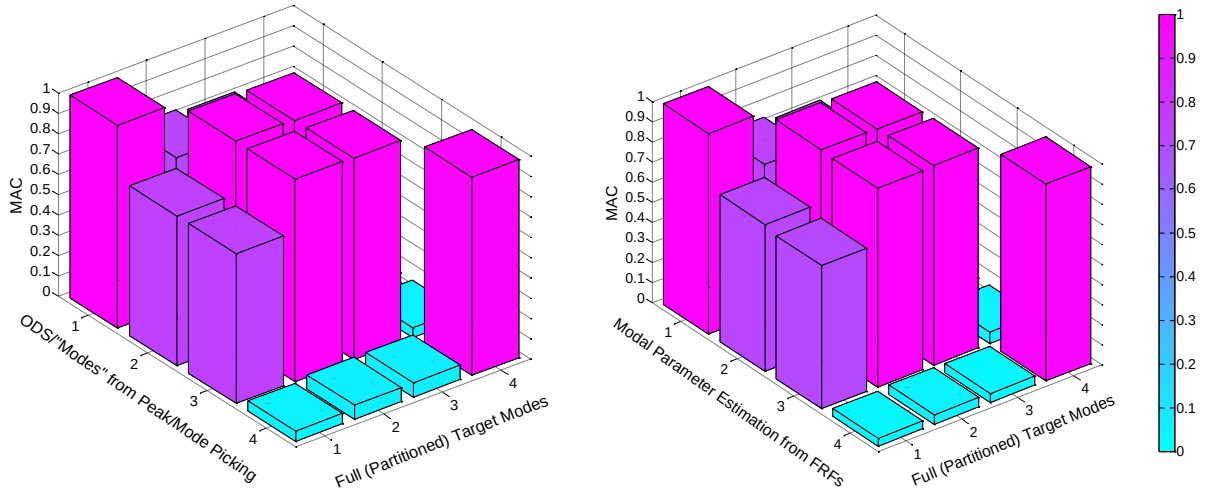


(b) Z-direction target modes

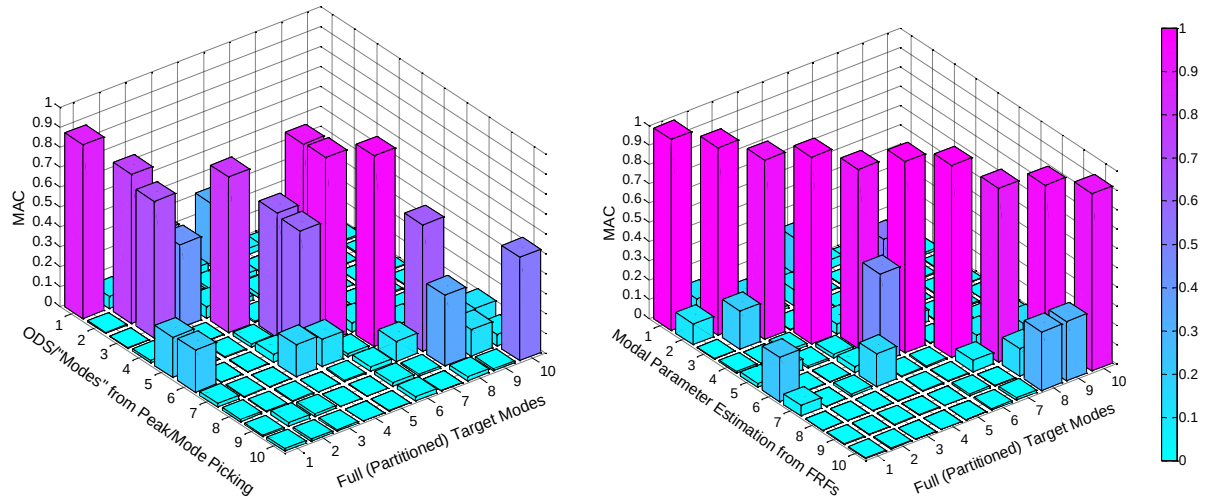
Figure 10. BepiColombo MAC results of FEM normal modes compared with:
Left - FEM ODS/modes from peak picking, Right - FEM modes from modal parameter estimator



(a) X-direction target modes



(b) Y-direction target modes



(c) Z-direction target modes

Figure 11. Aeolus MAC results of FEM X-direction normal modes compared with:
Left - FEM ODS/modes from peak picking, Right - FEM modes from modal parameter estimator

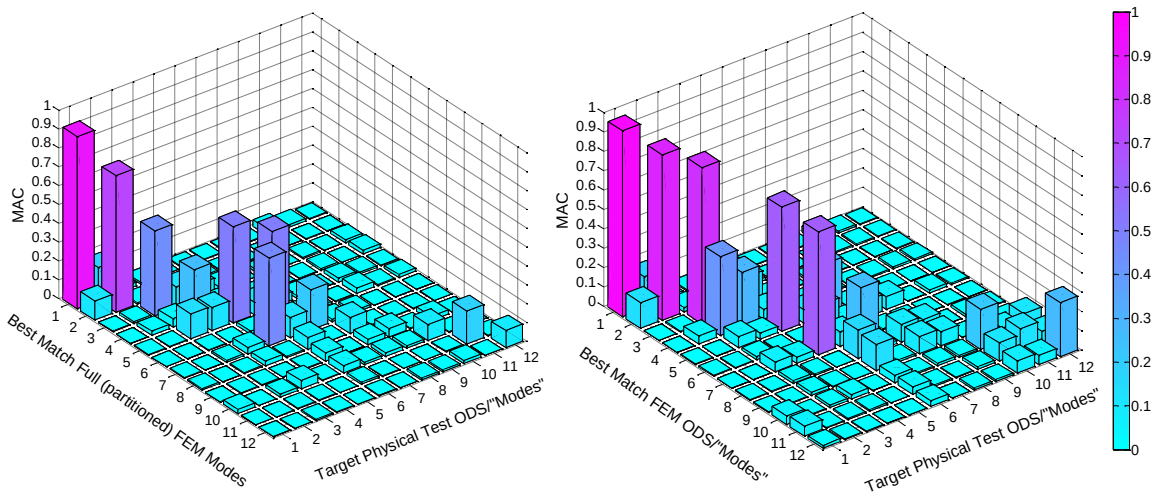


Figure 12. BepiColombo MAC of test ODS vs. FEM modes (left). MAC of test ODS vs. FEM ODS (right)

5 CONCLUSIONS

It has been shown that the modal parameter estimation method must be selected as appropriate to the problem under consideration. Here it has been demonstrated that, although sufficiently accurate under certain conditions, the simple single degree of freedom 'peak picking' method is not appropriate to large, complex spacecraft applications where modes are heavily coupled. Under such circumstances it is observed that more sophisticated methods, such as the poly-reference least squares frequency domain approach, can give a more accurate representation of the mode shapes of the system. This is an important point to note if mode shapes, estimated from test measured imaginary frequency response functions, are used as targets in FEM correlation. If these estimated mode shapes are not an accurate representation of the modes of the system, correlation based on subsequent comparison with analytical mode shapes is undermined.

An alternative which avoids the issue of modal parameter estimation is correlation based directly on frequency response functions. This has been demonstrated by the direct comparison of test ODS with FEM ODS. The potential to avoid both the effort of modal parameter investigation and, more importantly, the introduction of associated errors through the use of frequency domain merits further investigation and has the potential to be the subject of future work.

REFERENCES

[1] F. Lembregts, J. Leuridan, and H. Van Brussel, "Frequency domain direct parameter identification for modal analysis: State space formulation," *Mechanical Systems and Signal Processing*, vol. 4, pp. 65-75, 1990.

[2] D. Brown, R. Allemang, R. Zimmerman, and M. Mergeay, "Parameter estimation techniques for modal analysis," *Training*, vol. 2014, pp. 10-30, 1979.

[3] B. Peeters, G. Lowet, H. Van der Auweraer, and J. Leuridan, "A new procedure for modal parameter estimation," *Sound and Vibration*, vol. 38, pp. 24-29, 2004.

[4] *esa space images*. Available: http://www.esa.int/spaceinimages/Images

[5] ESA-ESTEC, "ECSS-E-ST-32-11 Modal Survey Assessment," ed. Noordwijk, The Netherlands: European Cooperation For Space Standardization, 2008, p. 78.

[6] R. J. Allemang and D. L. Brown, "A correlation coefficient for modal vector analysis," in *Proceedings of the 1st international modal analysis conference*, 1982, pp. 110-116.
[7] J. J. Wijker, *Mechanical vibrations in spacecraft design*: Springer, 2004.
[8] N. Lieven and D. Ewins, "Spatial correlation of mode shapes, the coordinate modal assurance criterion (COMAC)," in *Proceedings of the sixth international modal analysis conference*, 1988, pp. 690-695.
[9] P. Avitabile, "Overview of Analytical and Experimental Modal Model Correlation Techniques," 1998.
[10] H. Van der Auweraer, M. Iadevaia, U. Emborg, M. Gustavsson, U. Tengzelius, and N. Horlin, "Linking test and analysis results in the medium frequency range using principal field shapes," in *Proceedings of the International Seminar on Modal Analysis*, 1999, pp. 823-830.
[11] D. Nefske and S. Sung, "Correlation of a Coarse-Mesh Finite Element Model Using Structural System Identification and a Frequency Response Assurance Criterion," in *Proceedings-SPIE The International Society for Optical Engineering*, 1996, pp. 597-602.
[12] R. Pascual, J.-C. Golinval, and M. Razeto, "A frequency domain correlation technique for model correlation and updating," in *Proceedings SPIE The International Society for Optical Engineering*, 1997, pp. 587-592.
[13] D. Fotsch and D. Ewins, "Application of MAC in the Frequency Domain," *Rolls Royce Plc-Report-RNR*, 2000.
[14] M. Friswell and J. E. Mottershead, *Finite Element Model Updating in Structural Dynamics* vol. 38: Springer, 1995.
[15] W. Heylen and P. Avitabile, "Correlation considerations—Part 5," in *Proceedings of the 16th International Modal Analysis Conference*, 1998, pp. 2-5.
[16] P. Avitabile, "Modal Space-In Our Own Little World," *Experimental Techniques*, vol. 37, pp. 3-5, 2013.
[17] W. Heylen, S. Lammens, and P. Sas, *Modal Analysis Theory and Testing*: Katholieke Universiteit Leuven, Faculty of Engineering, Department of Mechanical Engineering, Division of Production Engineering, Machine Design and Automation, 2013.
[18] D. Ewins, *Modal Testing: theory, practice and application* 2nd Edition ed. Herts, UK: Research Studies Press Ltd., 2000.
[19] R. Allemang, "Vibrations: Experimental Modal Analysis; Structural Dynamics Research Laboratory; University of Cincinnati," University of Cincinnati, Structural Dynamics Research Laboratory1999.
[20] B. J. Schwarz and M. H. Richardson, "Experimental modal analysis," *CSI Reliability Week*, vol. 36, pp. 30-32, 1999.
[21] N. Maia and J. Silva, "Modal analysis identification techniques," *Philosophical Transactions of the Royal Society of London. Series A: Mathematical, Physical and Engineering Sciences*, vol. 359, pp. 29-40, 2001.
[22] F. R. Spitznogle and A. H. Quazi, "Representation and Analysis of Time-Limited Signals Using a Complex Exponential Algorithm," *The Journal of the Acoustical Society of America*, vol. 47, pp. 1150-1155, 1970.
[23] J. Iwaniec and T. Uhl, "The Application of the Nonlinear Least Squares Frequency Domain Method to Estimation of the Modal Model Parameters," *Machine Dynamics Problems*, vol. 27, pp. 37-54, 2003.
[24] P. Guillaume, P. Verboven, S. Vanlanduit, H. Van Der Auweraer, and B. Peeters, "A poly-reference implementation of the least-squares complex frequency-domain estimator," in *Proceedings of IMAC*, 2003, pp. 183-192.

[25] Y. T. Chung and M. L. Sernaker, "Assessment Target Mode Selection Criteria Payload Modal Survey," presented at the 12th International Modal Analysis Conference, 1994.

COMPDYN 2015
5th ECCOMAS Thematic Conference on
Computational Methods in Structural Dynamics and Earthquake Engineering
M. Papadrakakis, V. Papadopoulos, V. Plevris (eds.)
Crete Island, Greece, 25–27 May 2015

ON THE FORCED VIBRATION TEST BY VIBRODYNE

M. Modano[1], F. Fabbrocino[2], A. Gesualdo [1], G. Matrone [1], I. Farina[3], F. Fraternali [4]

[1]Department of Structures for Engineering and Architecture, University of Naples Federico II,
Via Claudio, 21 – 80125 - Naples (NA), Italy
e-mail: M. Modano (modano@unina.it), A.Gesualdo (antonio.gesualdo@unina.it),
G. Matrone (mat_gio@hotmail.it)

[2]Department of Engineering, Pegaso Telematic University
Piazza Trieste e Trento, 48- 80132- Naples (NA), Italy
e-mail: F. Fabbrocino (francesco.fabbrocino@unipegaso.it)

[3]Department of Engineering, University of Naples Parthenope,
Centro Direzionale, Isola C4 - 80143 - Naples (NA), Italy
e-mail: I. Farina (ylenia.farina@gmail.com)

[4] Department of Civil Engineering, University of Salerno
Via Giovanni Paolo II, 132 - 84084 - Fisciano (SA), Italy
e-mail: F. Fraternali (f.fraternali@unisa.it)

Keywords: forced vibrations, experimental modal analysis, model updating, vibrodyne, forcing function

Abstract. *In civil engineering, Experimental Modal Analysis (EMA) dynamic tests are powerful aids to the seismic design of new structures, and useful tools for the structural identification of existing structures. EMA tests require to accurately evaluate the harmonic forcing function that is applied to the structure under testing, in order to correctly apply "model updating" procedures. The present work experimentally investigates on the nature of the forcing function applied by a vibrodyne, and its influence on the results of simulations on the dynamics of a single degree of freedom system . By using wireless accelerometers attached to a vibrodyne, we were able to measure the applied accelerations in the time domain, and the applied forcing function under different frequencies. Such an identification procedure was applied both in presence of 3+3 keyed masses, and in presence of 5+5 keyed masses, considering different angular speeds. In both cases, the forcing function applied by the vibrodyne was accurately determined as a function of time. We found out that the actual forcing function is slightly different from the theoretical sinusoidal profile, featuring marked oscillations.The work is completed by the analysis of the dynamic response a simple degree of freedom system under the action of smooth and oscillating sinusoidal forcing functions. A comparison between the results of the analyzed systems highlights marked mismatches in terms of predicted displacements, velocities, and accelerations. We therefore conclude that an accurate knowledge of the applied forcing function in EMA tests is essential in order to correctly identify the properties of the tested structures.*

1 INTRODUCTION

In civil engineering, dynamic tests can be provided both during the construction phase, as theoretical and technical supports to structural design, and after construction, as useful tools to detect the actual material properties and construction details of existing structures, which have been exposed, e.g., to relevant seismic actions [1-8]. The most frequently employed test procedures involve the application of sinusoidal forcing with variable frequency, providing useful information on a variety of structural properties.

The experimental modal analysis (EMA) consists in exciting a building with harmonic forcing functions at different frequencies, in order to record accelerations, velocities and displacements through applied sensors [6-8]. Numerical simulations are synced to the experimental tests with the aim of simulating the test and identifying target structural properties. Such a procedure requires an accurate knowledge of the real forcing function applied to the tested structure, in order to correctly inform the numerical model of the actual experimental conditions.

The present study deals with an accurate experimental procedure to identify the real forcing function applied by a vibrodyne, and its application to the correct identification of the properties of structural models subject to forced vibrations. Vibration tests were initially introduced in mechanical and aeronautical engineering. Nowadays, such tests are diffusely applied also in civil engineering, since they provide useful results regarding the seismic design of structures.

We tested a real vibrodyne in laboratory, in order to accurately detect the generated force time-history ("experimental forcing function" or EFF). The results of such an identification procedure were compared with the theoretical sinusoidal forcing function ("theoretical forcing function" or TFF), accurately measuring the theory-experiment mismatches. Next, we carried out numerical simulations of the dynamic response of a single degree of freedom oscillator subject to both theoretical and experimental forcing functions applied by the examined vibrodyne. Forcing functions with different frequencies were accounted for, with the aim of investigating the influence of the EFF vs. TFF mismatch on simulation results.

2 VIBRODYNE EXPERIMENTAL SETUP

The vibrodyne is an electro-mechanical excitation machine that is able to generate vibrations, with known frequency and amplitude and is frequently employed in EMA [6-8]. Dynamic identification tests are commonly used to determine natural frequencies, mode shapes and damping ratios of structures [1]. The shaker is able to produce unidirectional harmonic forces, with variable intensity sinusoidal laws, thanks to the movement of lumped masses, which are coupled on disks and are rotated around in opposite directions by an electric motor. Such a system allows to vary with continuity the number of disk laps with moving masses, to modulate the excitation frequency. The counter rotating masses generate centrifugal forces resulting in an unidirectional force. The working principle is based on opposed rotations of the disks. Some cylinder-shaped masses placed on the disks, generate a horizontal force history. The counter-rotating masses generate two centrifugal forces. Their resulting force shows zero axial component, and nonzero component in the normal direction (cf. force R_{tot} in Figure 1).

The theoretical force amplitude is directly proportional to the distance $r \equiv e$ between the rotation axis and the centers of the masses; the square of the angular speed (ω) and the summation (m) of the counter-rotating masses. The theoretical forcing function is sinusoidal in time (t) and it can be written as follows

$$F(t) = \omega^2 \cdot r \cdot m \cdot \sin(\omega t) \quad (1)$$

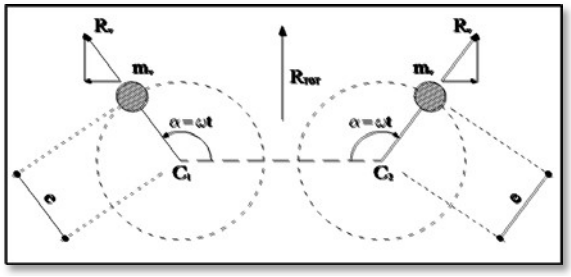


Figure 1: Illustration of the working principle of a vibrodyne.

The maximum force amplitude (in module) is achieved when it results

$$\sin \alpha = \sin(\omega t) = 1 \tag{2}$$

and can be computed as follows

$$Fmax = \omega^2_{max} \cdot m \cdot r \tag{3}$$

The generated force is instead zero when the masses are next to the plane passing through the rotation axis, since the centrifugal actions produced by each disk are opposite in verse in such a configuration. The sinusoidal force function (1) is applied to the tested structure through the connections placed between the vibrodyne support system and the structure.

2.1 Vibrodyne Design

The electric drive motor movement, with programmable and user-adjustable rotational speed, is transferred, by a timing belt kit, to a rotating part; the rotary motion, in turn, is transmitted to the counter-rotating part, through straight cut gears.

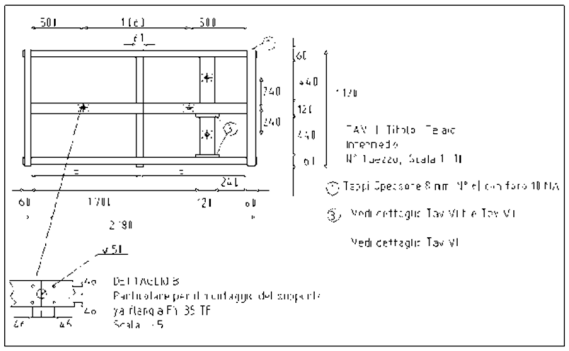


Figure 2: Vibrodyne layout: plan.

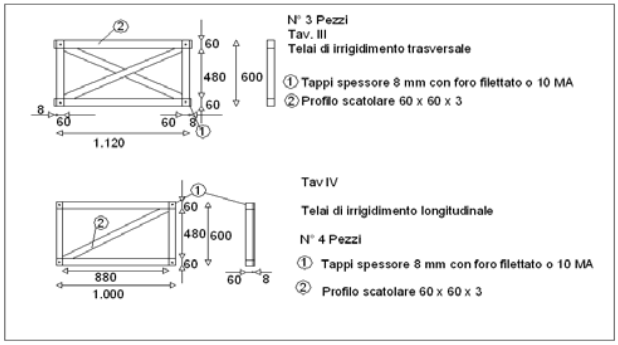


Figure 3: Vibrodyne layout: cross-section.

During the design and the construction of the vibrodyne employed in the present work, a transmission system with timing belt kit on the two belt sides has been adopted, in order to allow the machine to easily work up to a frequency of 50 Hz.

2.2 Test setup

A scrolling system was built to evaluate the forcing function at different frequencies. The scrolling system is composed by rails and rollers put on ball bearings with a very low friction coefficient. Such system permits the vibrodyne to freely scroll according to the force direction. By using wireless accelerometer attached to the vibrodyne, we were able to measure the vibrodyne acceleration in the time domain under different testing frequencies (Figs. 4-6).

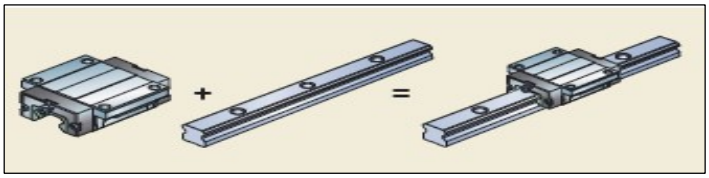


Figure 4: Roller-rail system.

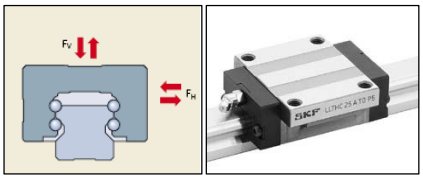


Figure 5: Roller-rail mounting layout.



Figure 6:Vibrodyne on the guides.

2.3 Vibrodyne tests

The system composed by the vibrodyne, the rollers and the guides is secured to two IPE 200 beams through fillet welds (Fig. 7). Such beams are fixed to a steel plate placed on a reinforced concrete slab supported by a pile foundation.



Figure 7: Vibrodyne handling phase.

After fixing the vibrodyne, the eccentric masses were set on the disks. Such operation required an accurate registration of the impellers transmission belt. Tests with 3+3 masses and 5+5 masses were performed. The theoretical forcing parameters generated by the vibrodyne with 5 masses on each disk are shown in Table 1.

2.4 Data acquisition system

A piezoelectric unidirectional accelerometer WiTilt V3 was employed to measure the acceleration produced from rotary motion of the masses. It was attached to the vibrodyne and set in bluetooth connection to a computer for data acquisition and processing. The mass of the overall system was measured by a dynamometer. Upon multiplying the system mass by the measured acceleration, we obtained an accurate recording of the applied forcing function.

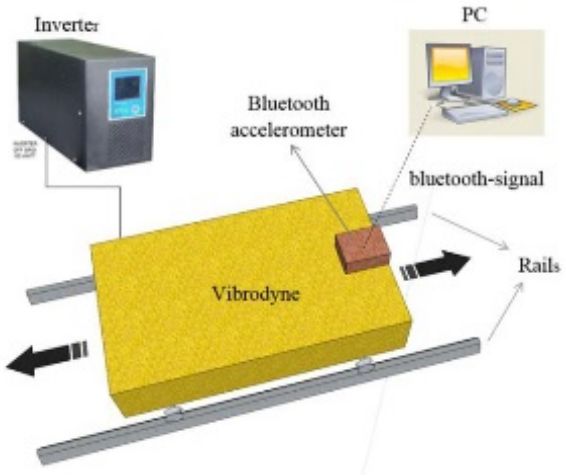


Figure 8: Overall test setup.

rpm	Angular velocity	Angular velocity Ω_{for}	Frequencies f	Period T	Weights on the vibrodyne	Mass	Radius	Forcing F_{max1}	Force generated $F_{max\ tot}$
60	376,99	6,28	1,00	1,00	153,60	15,66	0,40	247,87	495,74
80	502,65	8,38	1,33	0,75	153,60	15,66	0,40	440,66	881,32
100	628,32	10,47	1,67	0,60	153,60	15,66	0,40	688,53	1377,06
120	753,98	12,57	2,00	0,50	153,60	15,66	0,40	626,95	1982,97
140	879,65	14,66	2,33	0,43	153,60	15,66	0,40	1349,52	2699,04
160	1005,31	16,76	2,67	0,38	153,60	15,66	0,40	1762,64	3525,28
180	1130,97	18,85	3,00	0,33	153,60	15,66	0,40	2230,84	4461,68

Table 1: Maximum force values as a function of frequency.

2.5 Main system parameters

The vibrodyne has a weight of 8,60 kN, net of the masses that can be keyed to the discs in rotation. It is 2120 mm long and 1120 mm large. The machine is equipped with two rotors able to guest up to 11 eccentric masses, 6 of which with a weight of 0,33kN, and additional 5 masses with weight of 0,27 kN. The maximum force value that the machine can apply is equal to 220 kN in presence of eleven masses rotating at 275 rpm. We employed a maximum of 5+5 masses for safety reasons and to avoid an excessive pressure on the test apparatus.

3 COMPARISON BETWEEN THEORETICAL AND EXPERIMENTAL FORCING

We compared theoretical and experimental forcing parameters in presence of 3+3 and 5+5 keyed masses at different angular speeds. The comparison between theoretical and experimental (or real) forcing functions was carried out by plotting the corresponding force-time laws for angular frequencies varying in the range 60 ÷ 180 rpm (cf. Figs. 9-12).

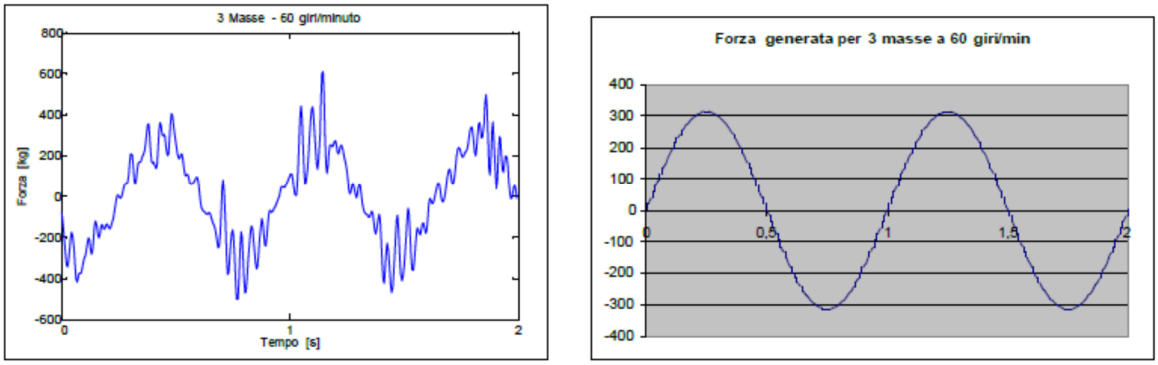


Figure 9: Experimental (left) vs theoretical (right) forcing function with 3+3 masses rotating at 60 rpm.

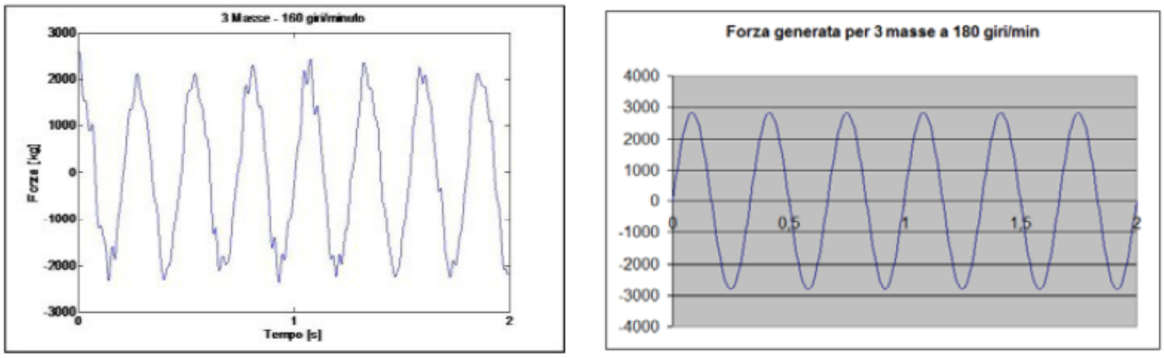


Figure 10: Experimental (left) vs theoretical (right) forcing function with 3+3 masses rotating at 180 rpm.

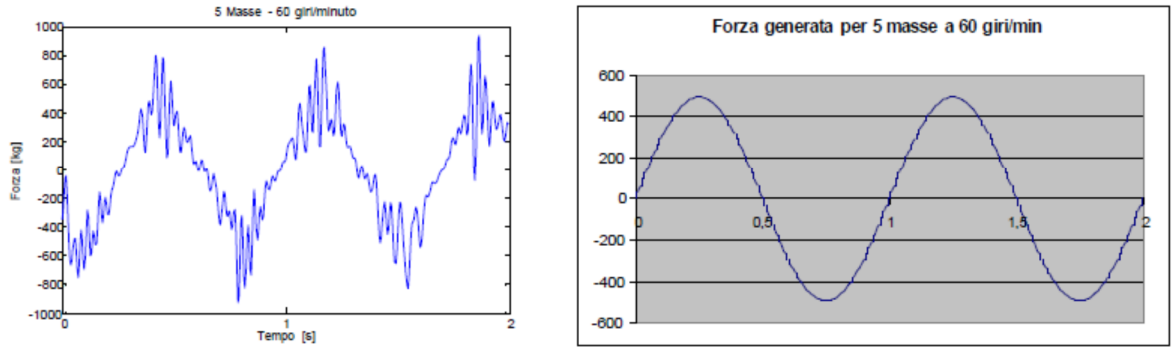


Figure 11: Experimental (left) vs theoretical (right) forcing function with 5+5 masses rotating at 60 rpm.

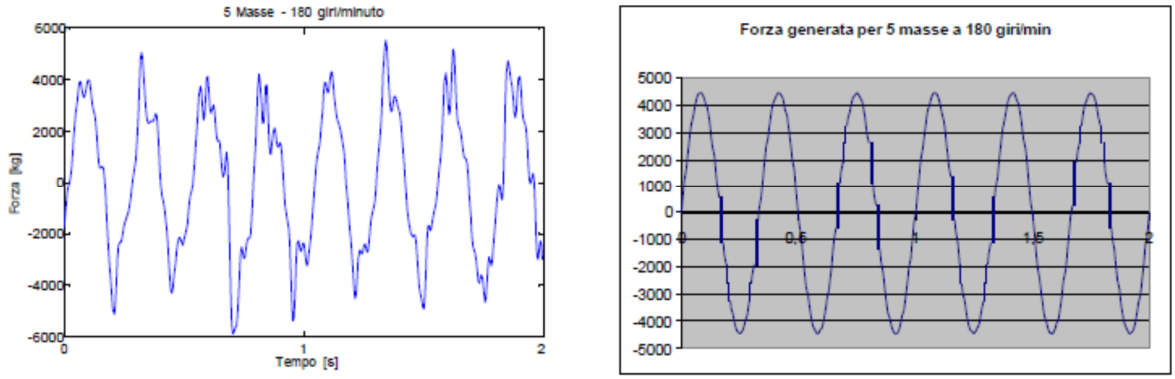


Figure 12: Experimental (left) vs theoretical (right) forcing function with 5+5 masses rotating at 180 rpm.

The results in Figs. 9-12 highlight that the mismatches between theoretical and real forcing functions increase with the angular frequency of the rotating masses, as a consequence of larger friction effects in the high frequency regime. An extensive numerical analysis has shown us that the theory-experiment agreement is satisfactory up to the 160 rpm rotational frequency, and pretty rough for higher rotational frequencies. The results of such an analysis have allowed us to build up a rich numerical database collecting the real forcing functions of the examined vibrodyne over a wide range of test conditions.

4 RESULTS OF DYNAMIC SIMULATIONS UNDER EXPERIMENTAL AND THEORETICAL FORCING FUNCTIONS

The present section aims at investigating the influence of the actual shape of the forcing function applied by a vibrodyne on the results of dynamical simulations of a single degree of freedom (SDOF) system in the elastic regime (Fig. 13). Numerical simulations of the dynamic response of such a system under experimental (real) and theoretical forced functions of the examined vibrodyne were conducted in correspondence with the test setup with 3+3 masses rotating at 180 rpm, on examining a wide range of forcing frequencies. Comparisons between the response of the SDOF system under experimental and theoretical forcing functions are shown in Figs. 14-16 in the frequency domain.

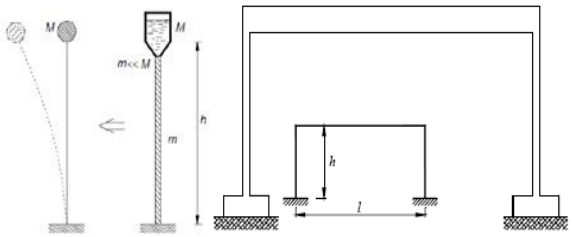


Figure 13: Single degree of freedom system analyzed in dynamical simulations of forced vibrations.

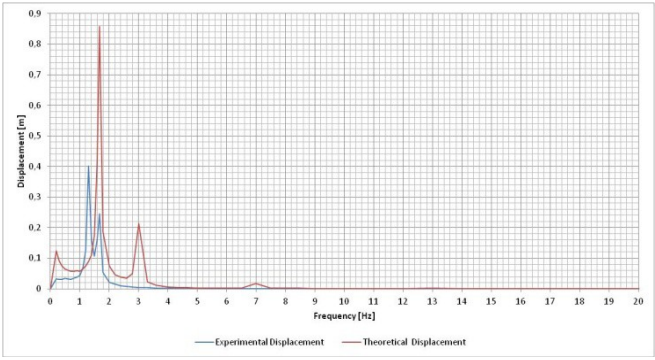


Figure 14: Theoretical (red) vs. experimental (blue) displacement curves in the frequency domain.

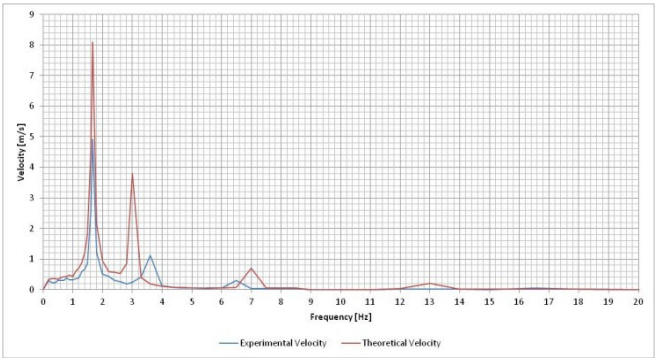


Figure 15: Theoretical (red) vs. experimental (blue) velocity curves in the frequency domain.

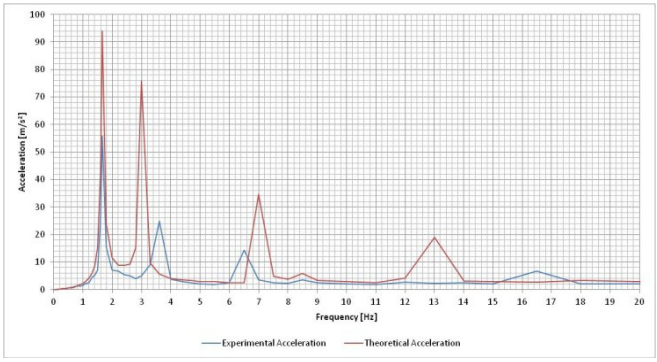


Figure 16: Theoretical (red) vs. experimental (blue) acceleration curves in the frequency domain.

5 CONCLUSIONS

The results shown in Figs. 14-16 of Sect. 4 highlight marked differences in predicted displacements, velocities and accelerations of a SDOF oscillator under real and theoretical forcing functions of a vibrodyne. The study conducted in Sect. 3 showed that such mismatches are particularly significant in correspondence with high angular frequencies of the keyed masses, i.e. for angular frequencies greater than 160 rpm. We are therefore led to conclude that an accurate measurement of the real forcing function applied by a vibrodyne is of fundamental importance when conducting EMA dynamic tests. It appears important to build up a database of the real forcing function applied by such a testing machine over a wide range of operating conditions. Proposed extensions of the present research will deal with accurate vibration tests for diverse structural models, with special focus on the identification of the elastic and damage properties of innovative truss and frame structures [9-15].

REFERENCES

[1] Richardson M. Global frequency and damping estimates from frequency response measurements, *4rd IMAC Conference,* Los Angeles, 1986.

[2] D.J. Ewins. *Modal Testing: Theory, Practice and Applications*, 2nd Edition. Research Study Press, 2000.

[3] Paz M. and Leigh W. *Structural Dynamics: Theory and Computation.* Springer Netherlands, 2003.

[4] Hans, S., Boutin, C., Ibraim, E., Roussillon, P. In Situ experiments and seismic analysis of existing buildings - Part I: Experimental investigations, *Earthquake Engineering and Structural Dynamics*, **34**, n°12, 1513–1529, 2005.

[5] Boutin, C., Hans, S., Ibraim, E., Roussillon, P. In Situ experiments and seismic analysis of existing buildings - Part II: Seismic integrity threshold, *Earthquake Engineering and Structural Dynamics*, **34**, n°12, 1531–1546, 2005.

[6] Rainieri C, Fabbrocino G, Cosenza E, Manfredi G. Implementation of OMA procedures using LabView: Theory and Application, *2nd IOMAC 2007*, Copenhagen, Denmark, 2007.

[7] C. Rainieri, G. Fabbrocino, E. Cosenza. Automated Operational Modal Analysis as structural health monitoring tool: Theoretical and applicative aspects, *Key Engineering Materials*, **347**, 479-484, 2007.

[8] E. Ercan, A. Nuhoglu. Identification of historical veziragasi aqueduct using the operational modal analysis. *The Scientific World Journal*, Volume 2014, Article ID 518608, 2014.

[9] F. Fraternali, L. Senatore, C. Daraio, Solitary waves on tensegrity lattices. *Journal of the Mechanics and Physics of Solids*, **60**, 1137-1144, 2012.

[10] F. Fraternali, G. Carpentieri, A. Amendola, R.E. Skelton, V.F. Nesterenko, Multiscale tunability of solitary wave dynamics in tensegrity metamaterials, *Applied Physics Letters*, **105**, 201903, 2014.

[11] F. Fraternali, C.D Lorenz, G. Marcelli, On the estimation of the curvatures and bending rigidity of membrane networks via a local maximum-entropy approach. *Journal of Computational Physics*, **231**, 528-540, 2012.

[12] B. Schmidt, F. Fraternali, Universal formulae for the limiting elastic energy of membrane networks. *Journal of the Mechanics and Physics of Solids*, **60**, 172-180, 2012.

[13] F. Fraternali, Free Discontinuity Finite element models in two-dimensions for in-plane crack problems. *Theoretical and Applied Fracture Mechanics*, **47,** 274–282, 2007.

[14] G. Gurtner, M. Durand, Stiffest elastic networks, *Proceedings of the Royal Society of London A*, **470**, 20130611, 2014.

[15] F. Fraternali, G. Carpentieri, R. Montuori, A. Amendola, G. Benzoni. On the use of mechanical metamaterials for innovative seismic isolations systems, *CompDyn 2015*, 25-27 May 2015.

COMPDYN 2015
5th ECCOMAS Thematic Conference on
Computational Methods in Structural Dynamics and Earthquake Engineering
M. Papadrakakis, V. Papadopoulos, V. Plevris (eds.)
Crete Island, Greece, 25–27 May 2015

SOIL STRUCTURE INTERACTION ASSESSMENT WITH ADVANCED NUMERICAL SIMULATIONS

D. Forcellini[1], S. Gobbi[1]

1 University of San Marino
Via Salita alla Rocca, 44, 47890, San Marino
davforc@omniway.sm

Keywords: Earthquake Engineering, Soil Structure Interaction, OPENSEES, FE analysis

Abstract. *Soil structure interaction (SSI) plays a significant role during seismic excitations for structures. Therefore many researchers have assessed its importance in emphasizing earthquake response both in buildings and bridge arena. The present study aims at considering a 3D numerical simulation of a soil-structure system that applies nonlinear hysteretic materials with advanced plasticity models. This approach enables to reproduce soil hysteretic elasto-plastic shear response (including permanent deformations) and thus damping foundation impedances. In particular, the paper applies the open-source computational interface OpenSeesPL, implemented within the FE code OpenSees. This framework is capable of performing non linear dynamic analysis and apply user-defined materials to model the soil. It is also powerful in modeling the interface and boundary conditions that are of extreme importance in SSI problems. The aim is to reproduce the seismic response by a parametric study based on mutual behavior of soil and structural deformability in order to assess safety and cost reduction when SSI is considered in design procedures. Therefore, this study can be considered one of the relatively few attempts to assess seismic performances aiming at contributing to new easy-to-use design procedures for engineers all over the world.*

1 BACKGROUND

Soil structure interaction (SSI) takes into account the effects of the ground on the seismic response of a structural system. In particular, free field response can consistently under evaluate effects due to soil structure dynamic interaction. Even if many codes suggest to neglect SSI (for example [1] and [2]) there are some researches where SSI is shown to be non-conservative for safety and cost reduction. In such cases, it is fundamental to take into account SSI in design procedures in order to predict its effects as detailed as possible [3-14].

Unfortunately modelling SSI is a changeling problem for numerical simulations and a few contributions [15-17] have provided insights. Many of them apply SSI simply by introducing springs, dashpots and artificial masses in the interface between the structure and the soil. This could be non-sufficiently detailed in order to model the problem complexity. In this regards, free field response can differ consistently from the soil – structure response because it is straightly connected with the mutual dynamic characteristics (natural frequencies) and thus with structural mass and stiffness, soil shear velocity and layer depth [4]. In particular [5] shows that SSI depends on several dimensionless parameters, such stiffness ratio, slenderness ratio and mass ratio.

Taking into account these relevant contributions, the present study aims overcoming all previous simplifications considering a 3D soil-structure system that applies nonlinear hysteretic materials with plasticity models. This approach enables to reproduce soil hysteretic elasto-plastic shear response (including permanent deformations), damping foundation impedances and realistic boundary conditions at the base of the soils and in correspondence with the interface between the soil and the structure. In particular, the paper applies the open-source computational interface OpenSeesPL, implemented within the FE code OpenSees.

The proposed numerical simulations aim at reproducing the literature background in order to calibrate the model and thus study more detailed insight into soil structure interaction problems in order to obtain numeric results able to provide design and management decision making assessment.

2 COMPUTATIONAL PLATFORM

Numerical simulations proposed in this study aim at reproducing the seismic response of a system structure and soil using the open-source computational interface OpenSeesPL, implemented within the FE code OpenSees [18]. It consists of a framework for saturated soil response as a two-phase material following the *u-p* (where *u* is displacement of the soil skeleton and *p* is pore pressure) formulation.

In the study, the mechanical behavior of the soil has been modeled as a nonlinear hysteretic material, using a Von Mises multi-surface kinematic plasticity approach together with an associate flow rule. This constitutive formulation is able to capture both monotonic and hysteretic elasto-plastic cyclic response of those soils whose shear behavior is assumed insensitive to confining stress. According to this formulation, plasticity is exhibited only in the deviatoric stress-strain response, while volumetric response is linear-elastic. In particular, the study has been divided in two increasing detailed steps.

The first step consists of reproducing one degree of freedom (dof) structural systems with increasing fundamental periods. In particular, two parametric studies have been performed. The height of the structure has been changed in order to consider different number of floor composing the structure. Then, the importance of mass ratio has been investigated. Therefore, representative soil mass (and thus the foundation volume) has been varied and several anal-

yses have been performed considering the same structural configuration. The aim of this first step is to calibrate OpenSees materials and potentialities in reproducing literature results.

The second step consist of considering structural performance when SSI effects are applied. In particular, several structural configurations have been considered in order to assess the influence of stiffness ratio on equivalent system. Displacement have been taken into account as the main parameters in order to assess the system performance. The following sections detail the two steps.

3 CALIBRATION

The first step consists of performing a 3D mesh (Figure 1) aimed at performing tridimensional soil structure interaction analyses, by applying OpenSees PL [19]. Originally the interface has been calibrated for pile analysis. Here it has been modified in order to consider the presence of the system structure – foundation. The study considers two typical concrete shear type structures that can be studied as one single degree of freedom (DOF) models following procedure [20]. In particular dynamic characteristics structural mass (m), stiffness (k) and natural frequency (ω_0) have been calculated and shown in Table 1. The foundation has been considered as a swallow foundation (0.50 m depth) with a rigid element.

The soil has been considered one-layer homogenous cohesive material with a 30 m depth (see table 2). The adopted 3D (20m × 20m x 30m) FE mesh is composed of 2496 brickUP linear isoparametric 8 node elements with 2873 nodes (Figure 1). The model base boundary is set at a depth of 30 m from ground surface. Pore pressure generation effects have been neglected. Opensees is able to simulate real wave propagation adopting realistic boundaries, by assuming that at any special location, symmetry conditions can be adopted and thus, periodic boundaries [21] have been considered. Displacement degrees of freedom of the left and right boundary nodes were tied together both longitudinally and vertically using the penalty method. In this regards, base and lateral boundaries were modelled to be impervious, as to represent a small section of a presumably infinite (or at least very large) soil domain by allowing the seismic energy to be removed from the site itself. For more details, see previous studies [22-25]. Connections between the structure and the soil are built up with Equaldof elements that imposes the displacements to be the same between the structure and the soil nodes [18, 19]. The clay layer has been modelled with the implemented material named Pressure independent Multiyield [19]. It consists of a nonlinear hysteretic material, using a Von Mises multi-surface kinematic plasticity approach together with an associate flow rule. Its constitutive formulation is able to capture both monotonic and hysteretic elasto-plastic cyclic response of those soils whose shear behavior is assumed insensitive to confining stress. According to this formulation, plasticity is exhibited only in the deviatoric stress-strain response, while the volumetric response is linear-elastic. The study has been divided into several steps.

First of all, SSI has been neglected by considering shear velocity values up to 3000 m/s, in order to simulate fixed based conditions and reproducing the fundamental structural periods. In this regards, a eigenvalue analysis has been performed and the fundamental frequencies (3 Hz and 6 Hz) have been confirmed.

Then, soil stiffness has been varied in order to take into account SSI effects. In particular shear wave velocity (Vs) has been varied in order to simulate different soil conditions. Table 2 shows soil characteristics in correspondence of Vs=250 m/s. Following the literature [5, 6], soil-foundation-structure equivalent system dynamic characteristics have been calculated in terms of equivalent system mass (m_e), stiffness (k_e) and natural frequency (ω_e). Figure 2

shows the 3D mesh deformation for Vs equal to 250 m/s and in correspondence with the equivalent system fundamental period.

Therefore, mass ratio value ($\bar{m}$), defined as the ratio between the relative structural mass and the soil mass, has been considered constant and equal to 0.5 for the two structural configurations. Results in terms of stiffness ratio ($\bar{s}$) and ratio of natural frequencies (between the equivalent system and the structure) are represented in Figure 3. Results for both structures show a good agreement with the theoretical approach [5], confirming Opensees potentialities and model assumptions in performing soil structure interaction 3D numerical problems. In particular, results in correspondence with stiff structure (f_0= 6Hz) is shown to be more consistent with the theory (figure 3).

Finally, in order to evaluate the importance of mass ratio, a parametric study has been performed by considering several values ($\bar{m}$=0.5, $\bar{m}$=1.0, $\bar{m}$=3.0). All analyses have been performed considering the stiffest structural configuration (f_0=6 Hz). Figure 4 shows the effects of increasing $\bar{m}$ values (and thus increasing the structural mass in comparison with the soil volume) on the relationship between dynamics characteristics and structural ratio. These results are still consistent with the theory [5].

Structural Parameters	f=6 Hz	f=3 Hz
m [t]	400	400
k [N/m]	$5.60 \cdot 10^8$	$1.40 \cdot 10^8$
h [m]	3.00	4.75
ω_0 [rad/s]	37.40	18.85
T_0 [s]	0.168	0.330

Table 1. structural parameters.

density [t/m^3]	G [kPa]	B [kPa]	ν	C [kPa]	Peak shear strain
1.80	$1.125 \cdot 10^5$	$5.25 \cdot 10^5$	0.4	75.0	3%

Table 2. soil parameters [VS=250 m/s].

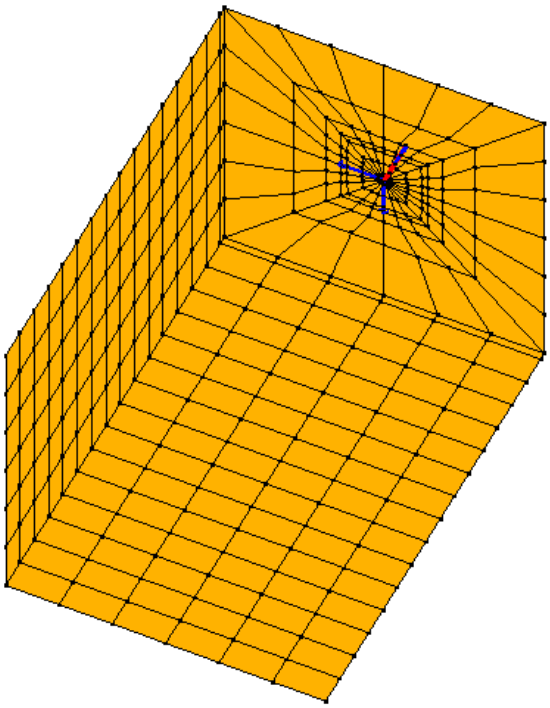


Figure 1. 3D mesh

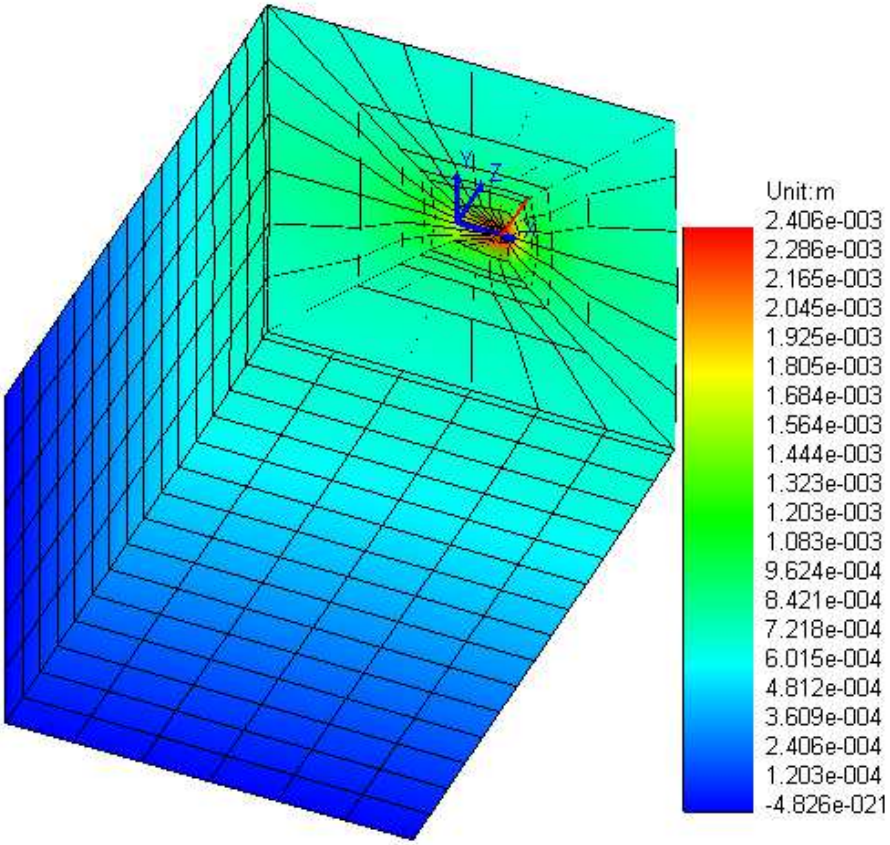


Figure 2. 3D deformed mesh for Vs=250 m/s (scale 1: 1000).

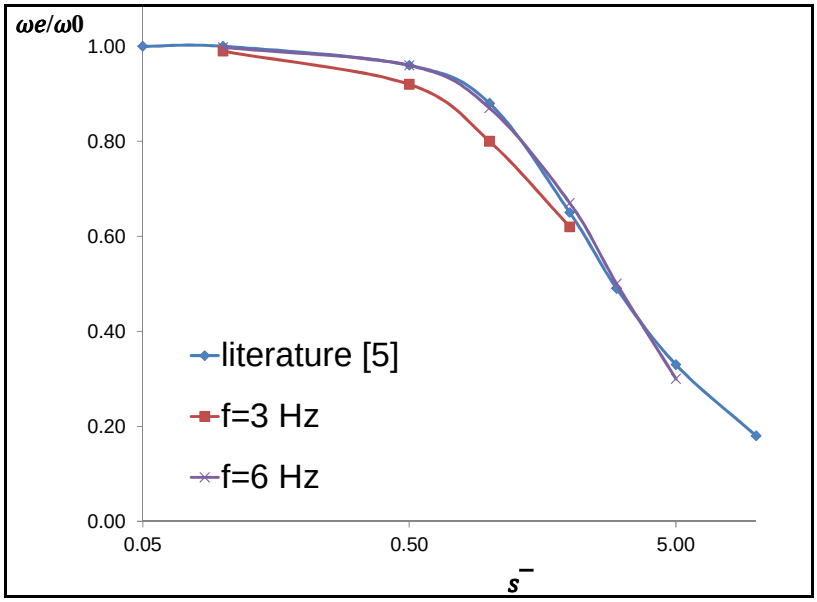


Figure 3. $\bar{m}$=0.5 results. Literature [5] and numerical results.

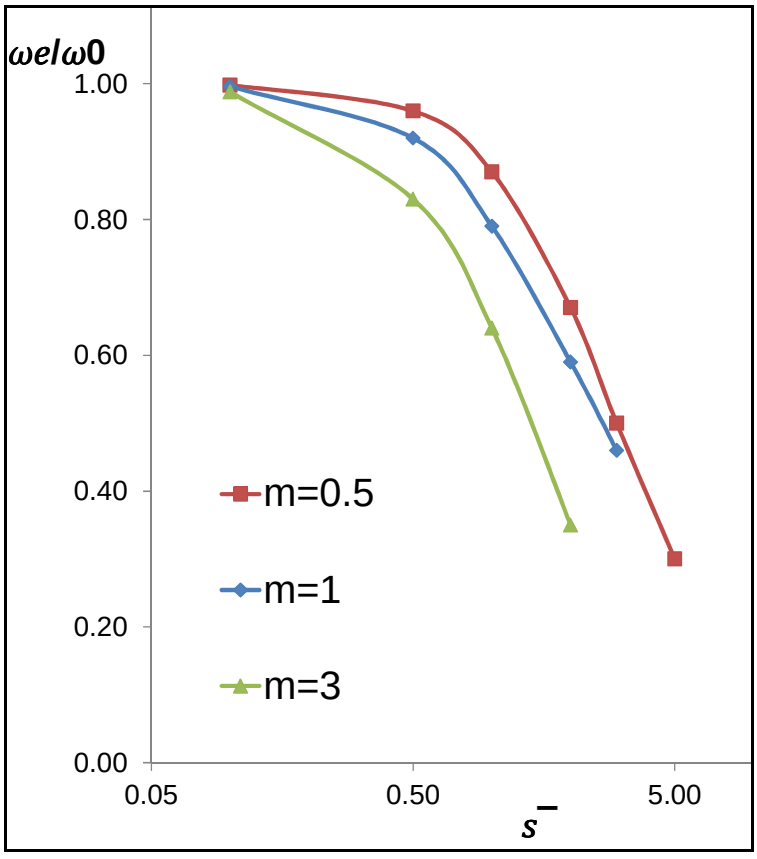


Figure 4. $\bar{m}$=0.5; $\bar{m}$=1; $\bar{m}$=3 numerical results.

4 SSI ASSESSMENT

This section aims at investigating soil structure dynamic interaction significant role during seismic excitations. The study aims at assessing equivalent system seismic performance by referring to displacements. In particular, traditional approaches are based on introduction of linear (translational and rotational) springs and dashpot as to reproduce the stiffness and damping characteristics of the compliant soil-foundation system [5, 6]. On the contrary, the presented approach considers a 3D soil-structure system that applies nonlinear hysteretic materials with advanced plasticity models, without separating the different contributions with artificial elements. In particular, sinusoidal excitations were defined along the base in the longitudinal direction (*x*-axis), with 0.2 g of amplitude and 1 Hz frequency, considering three structural configurations (f_0=3 Hz, f_0=6 Hz and f_0=10 Hz). All the analyses here have been performed considering the same mass ratio ($\bar{m}$=3).

Displacements have been considering at different height of the equivalent system, as shown in Figure 5 that clarifies all the components:

- U_{FF}: free field displacement, calculated without the structure.
- U_s: soil displacement evaluated at the top of the soil layer and caused by the presence of the structure.
- U_{ST}: structural displacement (the sum of the effects of rotation and longitudinal displacement)
- U_{TOP}: top structural displacement: $U_{TOP} = U_{FF} + U_S + U_{ST}$.
- U_{BASE}: displacement relative to free field: $U_{BASE} = U_{FF} + U_S$.

In particular, for each performed case, U_{TOP} and U_{BASE} time histories have been taken into consideration while U_{ST} has been calculated with their difference.

Figure 6 - Figure 8 show the response of equivalent soil-structure system in terms of structural (U_{ST}), top displacements (U_{TOP}) and base displacements (U_{BASE}) respectively, scaled with the maximum displacement reached. SSI effects are shown to increase all the displacements until a particular value of stiffness ratio ($\bar{s}$), where the displacements reach their maximum values. In particular, structural displacement (U_{ST}) is affected by foundation rotations and translations. In this regards, the performed simulations have the advance to overtake the traditional approaches [5, 6] based on introduction of linear (translational and rotational) springs and dashpot reproducing directly stiffness and damping characteristics of the compliant soil-foundation system. Figure 8 shows 3D deformed mesh for f_0=3 Hz, $\bar{s}$=2 case.

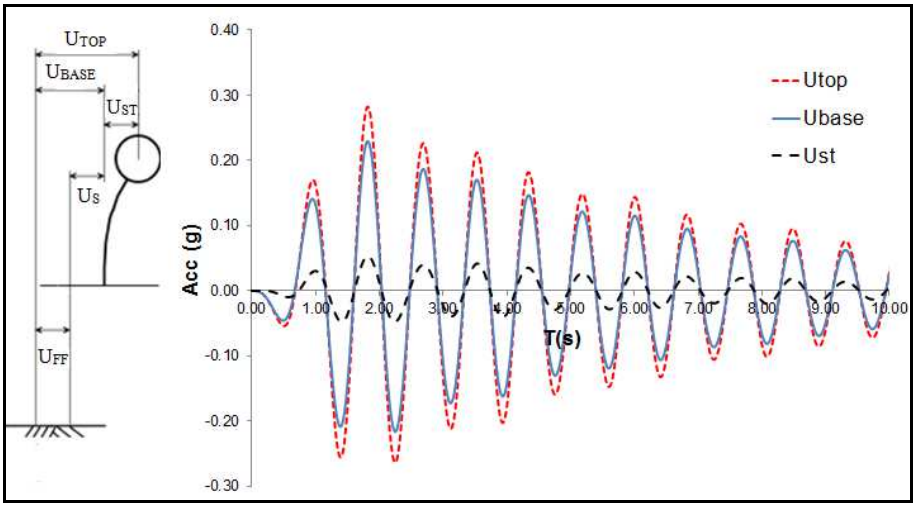


Figure 5. displacements scheme and acceleration.

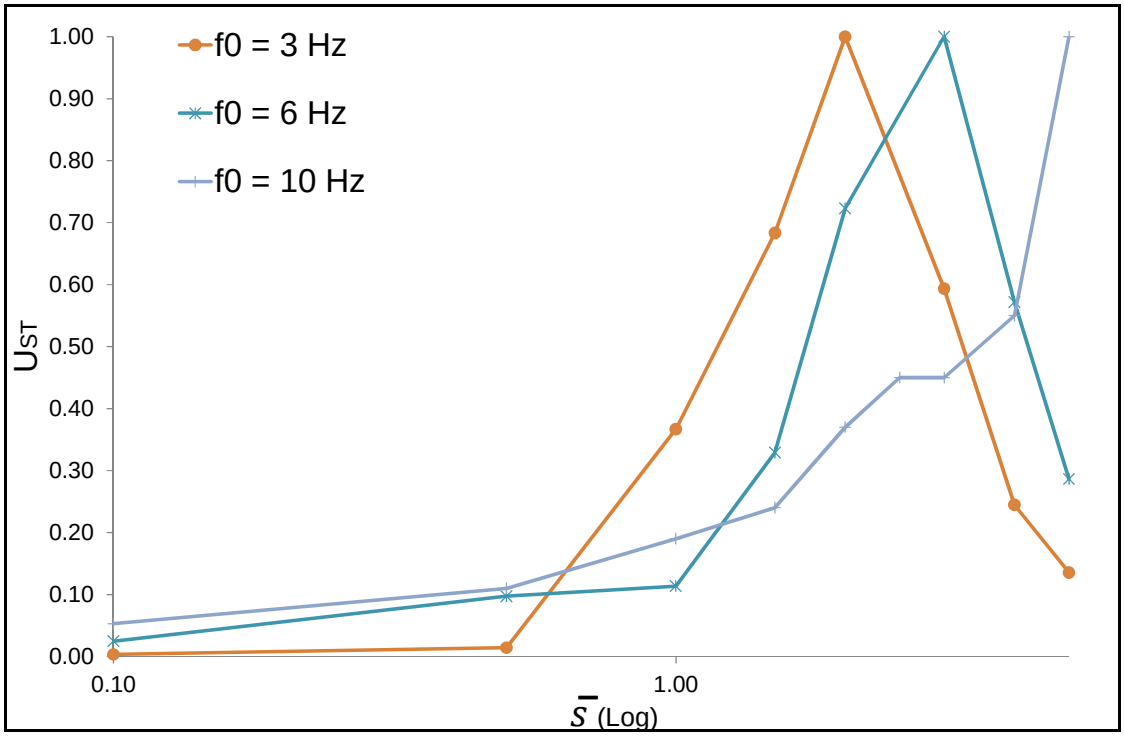


Figure 6. Structural displacement - stiffness ratio ($\bar{m}$=3)

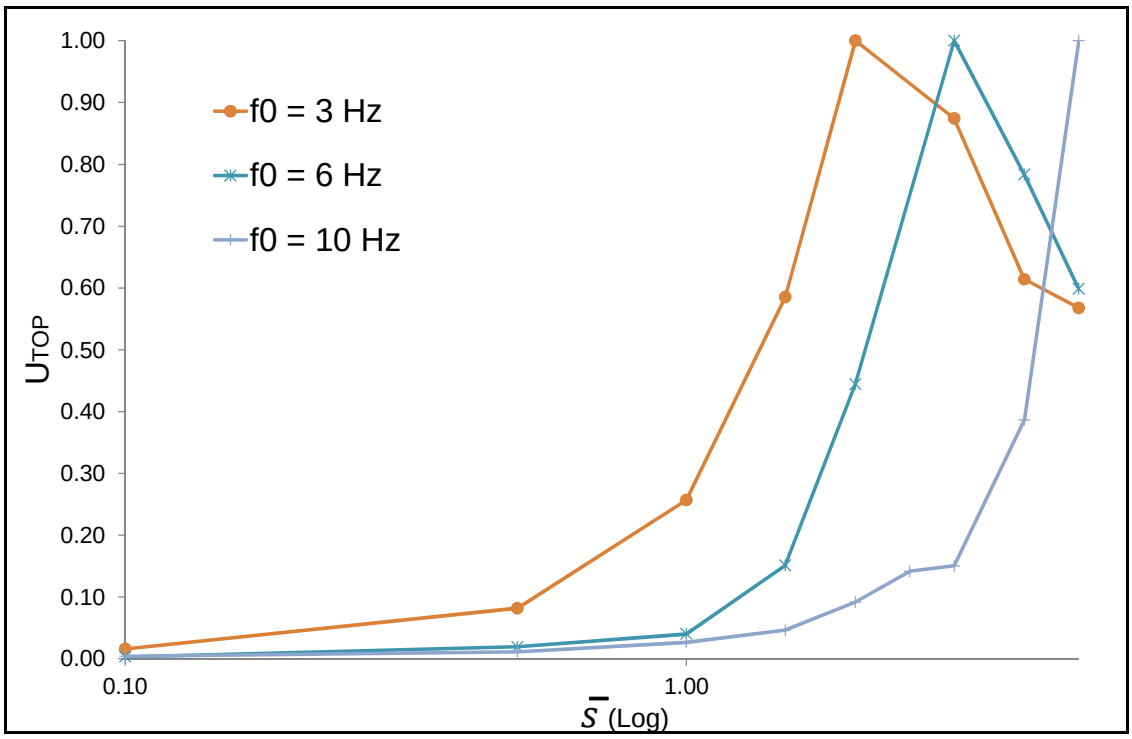


Figure 7 Top displacement - stiffness ratio ($\bar{m}$=3)

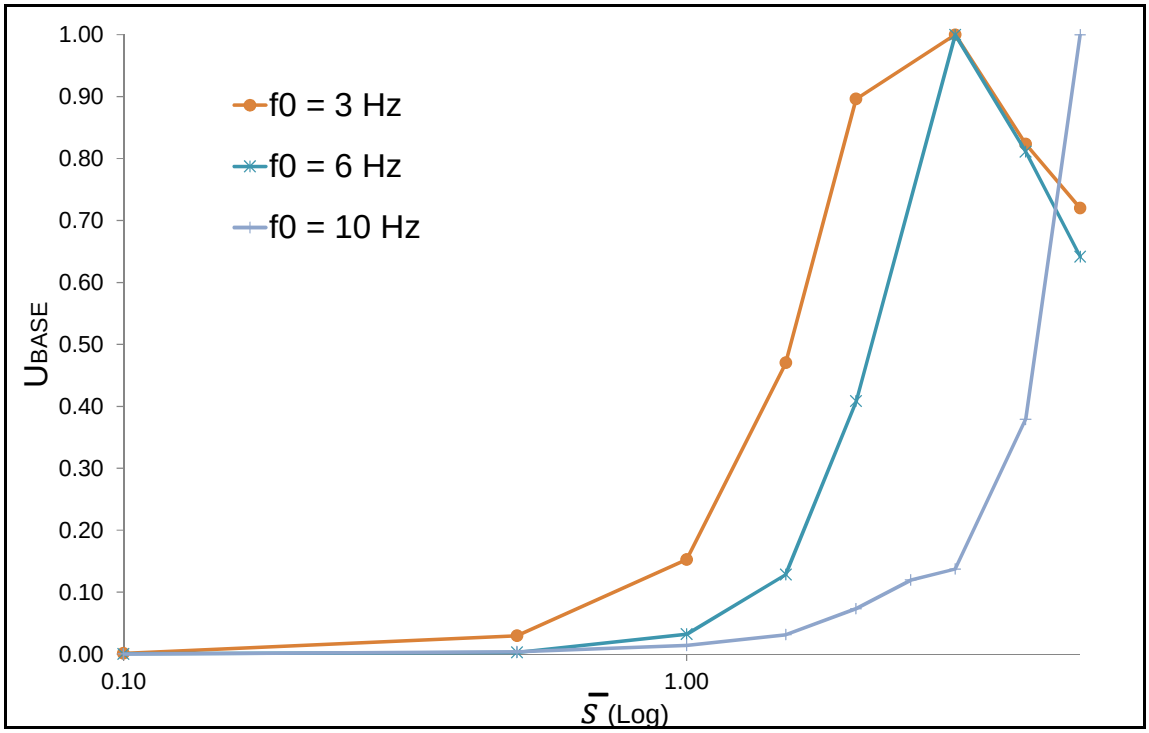


Figure 8 Base displacement - stiffness ratio ($\bar{m}$=3)

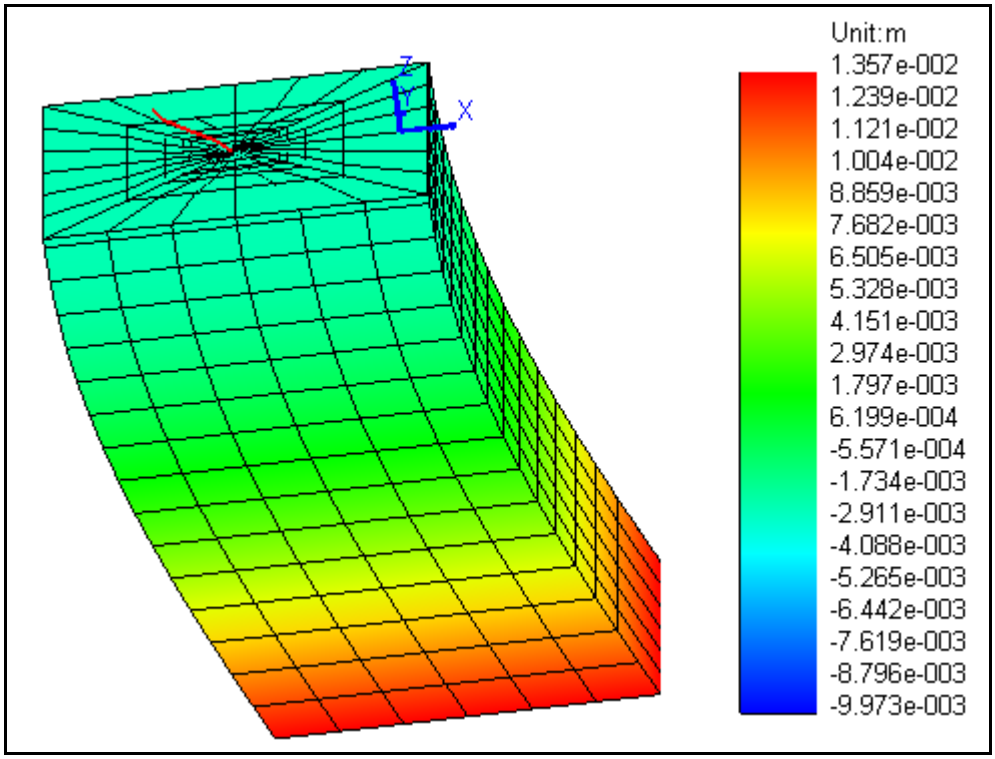


Figure 9. 3D mesh deformations (scale 1:100, f=3 Hz, $\bar{s}$=2 case).

5 CONCLUSIONS

The paper shows a numerical study aimed at investigating soil structure dynamic interaction significant role during seismic excitations. It can be considered a first study able to overcome traditional simplifications adopting a 3D soil-structure system that applies nonlinear hysteretic materials with advanced plasticity models. In particular, the paper applies the open-source computational interface OpenSeesPL, implemented within the FE code OpenSees performing parametric studies based on mutual behavior of soil and structure dynamic characteristics.

Calibration procedures show good agreement with theoretical approaches confirming Opensees potentialities and model assumptions in performing soil structure interaction 3D numerical problems. In particular, two parametric studies have been performed in order to assess the role of structural dynamic characteristics and mass ratio. The paper shows also an assessment study that investigates SSI significant role during seismic excitations assessing seismic performance in terms of displacements. The aim is the safety assessment and cost reduction in design procedures with particular attention to those cases where SSI can become non-conservative.

The study reproduces several one degree of freedom (dof) structural systems with different dynamic characteristics. Further analysis will aim at reproducing more complex systems, such as buildings and bridges.

REFERENCES

[1] ATC-3-06. *Amended tentative provisions for the development of seismic regulations for buildings*. ATC Publication ATC 3-06, NBS Special Publication 510, NSF Publication 78-8, Applied Technology Council. US Government Printing Office: Washington, DC; 1978;

[2] Building seismic safety council, NEHRP. *Recommended provisions for the development of seismic regulations for new buildings (and other structures).*National earthquake hazards reduction programme: Washington, DC; 1985, 1988, 1991, 1994 (1997, 2000);

[3] J. E. Luco, *Linear soil-structure interaction: a review. Earthquake Ground Motionand Its Effects on structures*, 1982;

[4] J. P. Wolf, *Dynamic Soil-Structure Interaction*, Prentice-Hall, Englewood Cliffs, 1985;

[5] S. L. Kramer, *Geotechnical Earthquake Engeneering*, Prentice-Hall, International Series in Civil engineering and engineering Mechanics, William J. Hall Editor, 1996;

[6] National Institute of Standards and Technology, *Seismic soil-structure interactionfor building structure,*Report NIST GCR 12-917-21, 2012.

[7] Mylonakis G, Gazetas G. *Seismic soil-structure interaction: beneficial or detrimental?* Journal of Earthquake Engineering 2000; 4: 277–301;

[8] Veletsos AS, Nair VV. *Seismic interaction of structures on hysteretic foundations*. Journal of Structural Engineering, 101101; 109-129;

[9] Abate G, Massimino MR, Maugeri M, Muir Wood D. *Numerical modelling of a shaking table test for soil-foundation-superstructure interaction by means of a soil constitutive model implemented in a fem code*. Geotechnical and Geological Engineering Journal 2010; 28(1): 37-59;

[10] Saouma V, Miura F, Lebon G, Yagome Y. *A simplifyed 3D model for soil-structure interaction with radiation damping and freefield input*. Bulletin of Earthquake Engineering 2011;9(5):1387–1402;

[11] Barcena A, Esteva L. *Influence of dynamic soil-structure interaction on the nonlinear response and seismic reliability of multistory systems*. Earthquake Engineering and Structural Dynamics 2007; 36: 327–346;

[12] Avilés J, Pérez-Rocha LE. *Evaluation of interaction effects on the system period and the system damping due to foundation embedment and layer depth*. Soil Dynamics and Earthquake Engineering 1996; 15: 11–27;

[13] Mylonakis G, Nikolau S, Gazetas G. *Footing under seismic loading: Analysis and design issues with emphasis on bridge foundations*. Soil Dynamics and Earthquake Engineering 2006; 26: 824–853;

[14] Renzi S, Madiai C., Vannucchi G. *A simplified empirical method for assessing seismic soil-structure interaction effects on ordinary shear-type buildings.* Soil Dynamics and Earthquake Engineering 2013; 55: 100–107;

[15] Paolucci R, Shirato M, Yilmaz T. *Seismic behaviour of shallow foundations: Shaking table experiments vs numerical modelling.* Earthquake Engineering and Structural Dynamics 2008; 37: 577-595;

[16] Rayhani MT, El Naggar MH. *Physical and numerical modeling of seismic soil-structure interaction in layered soils*. Geotechnical and Geological Engineering Journal 2012;30(2):331–342;

[17] Pitilakis D, Dietz M, Wood DM, Clouteau D, Modaressi A. *Numerical simulation of dynamic soil-structure interaction in shaking table testing*. Soil Dynamics and Earthquake Engineering 2008; 28(6): 453–467;

[18] S. Mazzoni, F. McKenna, M. H. Scott, G. L. Fenves, *Open System for Earthquake* Engineering Simulation, User Command-Language Manual, Pacific Earthquake Engineering Research Center, University of California, Berkeley, 2009;

[19] Opensees PL (http://soilquake.net/openseespl/);

[20] Chopra A., *Dynamics of Structures – theory and applications to earthquake engineering.* New Jersey: Prentice Hall, Englewood Cliffs 305-336;

[21] H.K. Law, I.P. Lam, *Application of periodic boundary for large pile group,* Journal of Geotech. Geoenviron. Eng., 127-10, 889–892, 2001;

[22] A. Elgamal, J. Lu, D. Forcellini, *Mitigation of liquefaction-induced lateral deformation in a sloping stratum: three-dimensional numerical simulation,* J. Geotech. Geoenviron. Eng., **135**, 1672–1682, 2009;

[23] D. Forcellini, A.M. Tarantino, *Countermeasures assessment of liquefaction-induced lateral deformation in a slope ground system,* Journal of Engineering, Article ID 183068, 2012;

[24] D. Forcellini, F. della Bartola, and A. M. Tarantino, *Liquefaction-induced lateral deformations computational assessment during Tohoku Earthquake* ISRN Civil Engineering, Article ID 408961, 2013;

[25] D. Forcellini, A.M. Tarantino, Assessment of stone columns as a mitigation technique of liquefaction-induced effects during italian earthquakes (May 2012), Scientific World Journal, Article ID 216278, 201, 2014.

COMPDYN 2015
5th ECCOMAS Thematic Conference on
Computational Methods in Structural Dynamics and Earthquake Engineering
M. Papadrakakis, V. Papadopoulos, V. Plevris (eds.)
Crete Island, Greece, 25–27 May 2015

UNDERSTANDING SHEAR WAVE VELOCITIES CORRELATIONS WITH N-SPT AND QC-CPT VALUES

Muhsin Elie RAHHAL[1], **and Farah HARAKEH**[2]

[1] Saint Joseph University, Faculty of Engineering, ESIB, CLERC
Mar Roukos, Mekalles, BP1514, Beirut, LEBANON
e-mail: muhsin.rahal@usj.edu.lb

[2] Saint Joseph University, Faculty of Engineering, ESIB, CLERC
Mar Roukos, Mekalles, BP1514, Beirut, LEBANON
clerc.esib@usj.edu.lb

Keywords: Shear Wave Velocity, SPT, CPT, Soil Liquefaction.

Abstract. *Prediction of the ground shaking response at soil sites requires knowledge and understanding of soil shear wave velocity Vs, a parameter that is strongly related to small strain shear modulus Gmax. While it is preferable to measure soil parameters in situ, this is often not economically feasible at all locations. For this reason, and in order to improve correlations between geophysical measurements and key geotechnical parameters, this paper attempts to propose new general correlations between shear wave velocity V_s and SPT standard penetration resistance N as well as the CPT cone penetration resistance qc. The studied site is located on the Mediterranean coast, in the North Eastern suburb of Beirut, the capital of Lebanon, where the level of water is present near the ground surface. The variable near surface geological conditions throughout the city results in spatially variable ground shaking characteristics. In order to better understand seismic soil response, geotechnical data comprising both in situ and laboratory tests was gathered. This extensive data allows determining good correlations that may be validated by comparing the calculated shear wave velocity with previously obtained profiles from the inversion parameterization of dispersion estimates in order to derive shear-wave velocities (Vs) within each geological layer. In some relations, the depth factor D or effective stress σ'_v and the corrected SPT-N_{60} were also introduced. The proposed relations are divided into three soil categories: sand, clay and all soils (mixed clay, sand and silt). The equations developed in this study compare very well with most of existing correlations in the literature. The proposed correlations are very important for both Lebanese and other soils, and may be used both in the design of a foundation system as well as in the assessment of soil behavior under earthquake loading conditions (Settlement and liquefaction, soil response...). These correlations should be used with caution in geotechnical earthquake engineering and should be checked against measured V_s.*

1 INTRODUCTION

Geophysical measurements are becoming important and common for geotechnical projects where earthquake loading is anticipated. Older site investigations lack geophysical measurements and mainly provide beside the geologic setting, SPT blow counts or CPT cone tip penetration resistances. Correlations between shear wave velocity, SPT blow counts N and qc cone tip resistance, including geologic setting and site stratigraphy are therefore potentially useful and beneficial at least as a primary screening tool before identifying the necessity for further geophysical testing. Shear wave velocity V_s has become one of the preferred methods for estimating the small strain shear properties and has been incorporated into site classifications systems and ground motion prediction equations. Shear wave velocity (V_s) is an important pointer of the dynamic properties of soil and rock because of its relationship with G_{max}, given by $G_{max} = \rho V^2_s$, where (ρ) is the soil density. Characterization of the stress-strain behavior of soils is a fundamental component of many seismic analyses, including hazard analysis, site response analysis, and soil–structure interaction. The shear modulus (G) of soils is highly reliant upon strain level. The small-strain shear modulus (G_{max}) is typically linked with strains on the order of 10^{-3}% or less [1]. With knowledge of G_{max}, the shear response at various levels of strain can be estimated using modulus reduction (G/G_{max}) curves [2, 3]. The importance of V_s has been widely recognized in ground motion prediction equations by implementation of site factors that modify ground motion based on the difference between a site V_s and a reference V_s or by direct incorporation of a Vs term in the ground motion regression equations. New relations include V_{s30} as a constant required for ground motion prediction, where Vs_{30} is the average shear wave velocity in the upper 30m. Geophysical methods are being increasingly used for analyzing the subsurface, whether for landslides or site effects, because of their mainly non destructive nature and relatively simple execution; nevertheless, the measured geophysical parameters cannot be yet directly used by geotechnical engineers to perform stability or resistance calculations.

In the present study, an overview of some of the existing correlations between shear wave velocity Vs with the SPT blow count number N, or with the cone tip resistance q_c of CPT is given [4, 5, 6, 7]. Afterwards the general setting of the study site is presented with specific emphasis on available geological as well as geotechnical data [8]. And since there are actually no correlations available for Lebanese soil deposits between geophysical measurements such as shear wave velocity and geotechnical measurements such as SPT and CPT in situ tests, the existing correlations in the literature are used to establish specific correlations for the Lebanese context. Finally discussion and recommendations are proposed to help the geotechnical earthquake engineering community make a better assessment of the soil properties as far as liquefaction potential or seismic response are concerned.

2 BACKGROUND AND EXISTING CORRELATIONS

Many researchers have proposed correlations mostly between N-SPT or q_c-CPT and Vs for different soils (sand, silt and clay). There have been attempts to incorporate some additional dependent variables in describing the relationships, among these some researchers tried to include a depth factor or the vertical effective stress in their correlations. The following tables present an overview of the relations that will be the point of departure of the research carried on by the authors. Table 1 presents the correlations with N-SPT and Vs, Table 2 shows correlations involving the depth factor D, and finally Table 3 presents correlations q_c-CPT and Vs. Further discussions on the influence of the parameters as well as propositions of new correlations will be given later in the paper.

Reference	All soils	Sand	Clay
[9]	Vs = 76N^(0.33)		
[10]	-	Vs = 100.5N^(0.29)	-
[11]	-	Vs = 57.4N^(0.49) Vs = 57N^(0.49)	Vs = 114.43N^(0.31) Vs = 114N^(0.31)
[12]	Vs = 51.5N^(0.516)	-	-
[13]	Vs = 22N^(0.85)	-	-
[14]	-	-	Vs = 27N^(0.73)
[15]	-	Vs = 125N^(0.3)	-
[16]	Vs = 107.6N^(0.36)	-	Vs = 76.55N^(0.445)
[17]	Vs = 90N^(0.309)	Vs = 90.82N^(0.319)	Vs = 97.89N^(0.269)

Table 1: Correlations between shear wave velocity Vs and N-SPT.

Reference	All soils
[18]	$V_s = 62.4 \times N_{60}^{0.22} \times D^{0.23}$ $V_s = 72 \times N_{60}^{0.17} \times D^{0.20}$ $V_s = 93.8 \times N_{60}^{0.17} \times D^{0.20}$
[19]	$V_s = 85 \times N_{60}^{0.17} \times D^{0.20}$
[20]	$V_s = 72.3 \times N_{60}^{0.23} \times D^{0.15}$

Table 2: Correlations between shear wave velocity Vs and N_{60}-SPT including depth factor D.

Reference	Type of soil	Correlation
[21]	sand	Vs= 17.48 q_c^(0.13) σ'_v^(0.27)
[22]	sand	Vs= 13.18 q_c^(0.192) σ'_v^(0.179)
[22]	sand	Vs= 12.02 q_c^(0.319) f_s^(-0.0466)
[20]	sand	Vs= 25.3 q_c^(0.163) f_s^(0.029) D^(0.155)
[22]	clay	Vs= 3.18*q_c^(0.549) f_s^(0.025)
[23]	clay	Vs= 1.75 q_c^(0.627)
[20]	clay	Vs= 11.9 q_c^(0.269) f_s^(0.108) D^(0.127)

Table 3: Correlations between shear wave velocity Vs and qc-CPT including depth factor D.

3 GENERAL SETTING OF THE STUDY SITE

Soil investigation was carried out in Antelias, the northern suburb of Beirut, to get an estimate of the physical and mechanical characteristics of the subsurface soil/rock existing beneath the site surface, in order to provide the necessary information for geotechnical aspects relevant to the proposed projects in the area. The site is a relatively flat land. It is bound by Beirut-Tripoli coastal road to the west. A water course passes along the site limits. The site has an irregular surface area of about 10000m^2. The site has an average level of about 3.5mASL. The sea is present at a distance of about 150.0m to the west of the site.

3.1 Field Works

Ten boreholes were drilled down to depths reaching 66.0m from existing ground levels. Some Boreholes were drilled destructively with SPT in the soil formations and using double core barrel in marl and rock formations. Other Boreholes were destructively drilled with pressuremeter Tests at an average interval of 3.0m. A total of seventy nine pressuremeter tests were carried out in these boreholes. Cone penetration test was performed at a few locations. Laboratory tests were performed on selected samples obtained from the borings to help in the classification of the soil and to determine their engineering properties. Undisturbed clay samples were extracted using Shelby Tubes for the purpose of performing Triaxial and Consolidation tests. This amount of data will help in the assessment of sol behavior during the analysis.

3.2 Geology and Subsurface Conditions

According to the geological map of Beirut, the site area is underlain by alluvial sand of the quaternary age followed by in order: 1) a grey fine-bedded limestone and marly limestone of Sanine formation (C4); 2) a brown green marl of Hammana formation (C3); 3) a grey cliff forming limestone of Mdairej formation (C2b); and finally brown green variable units of limestone, marl and sandstone of Abieh formation (C2a). A fault passes at about a distance of 1000m to eastern south direction of the site.

Interpretation of the geotechnical investigation paired with the available field data revealed that the ground formation beneath the site surface consists mainly of a top layer of fill material having a variable thickness ranging between 4.5m and 6.0m, followed by alluvial deposits consisting of interbedding sand, clay, silt and gravels. This alluvial soil is underlain by interbedding marl and marly limestone.

More specifically, the fill material was encountered in all the boreholes in layers ranging in thickness between 4.5m and 6.0m. It generally consisted of beige sand with gravels and cobbles of limestone. The presence of the site close to a water course confirms the presence of alluvial deposits. These deposits encountered beneath the site surface consisted of sand, clay, silt and gravel with thicknesses varying between 21.5m and 54.5m. However, the color of these formations varied between beige, light to grayish brown, red, yellow, and grey.

Finally, the interbedding marl and marly limestone: This formation was encountered beneath the alluviums. The thickness of this layer varied between 12.0m and 33.0m. The marl was generally found to be beige to white sandy gravely marl with cobbles of limestone. The limestone was encountered within the marl in layers having a maximum thickness of 5.0m. These were found to be beige to yellowish cream and interbedded with layers of marl at some locations. Figure 1 shows typical N-SPT results.

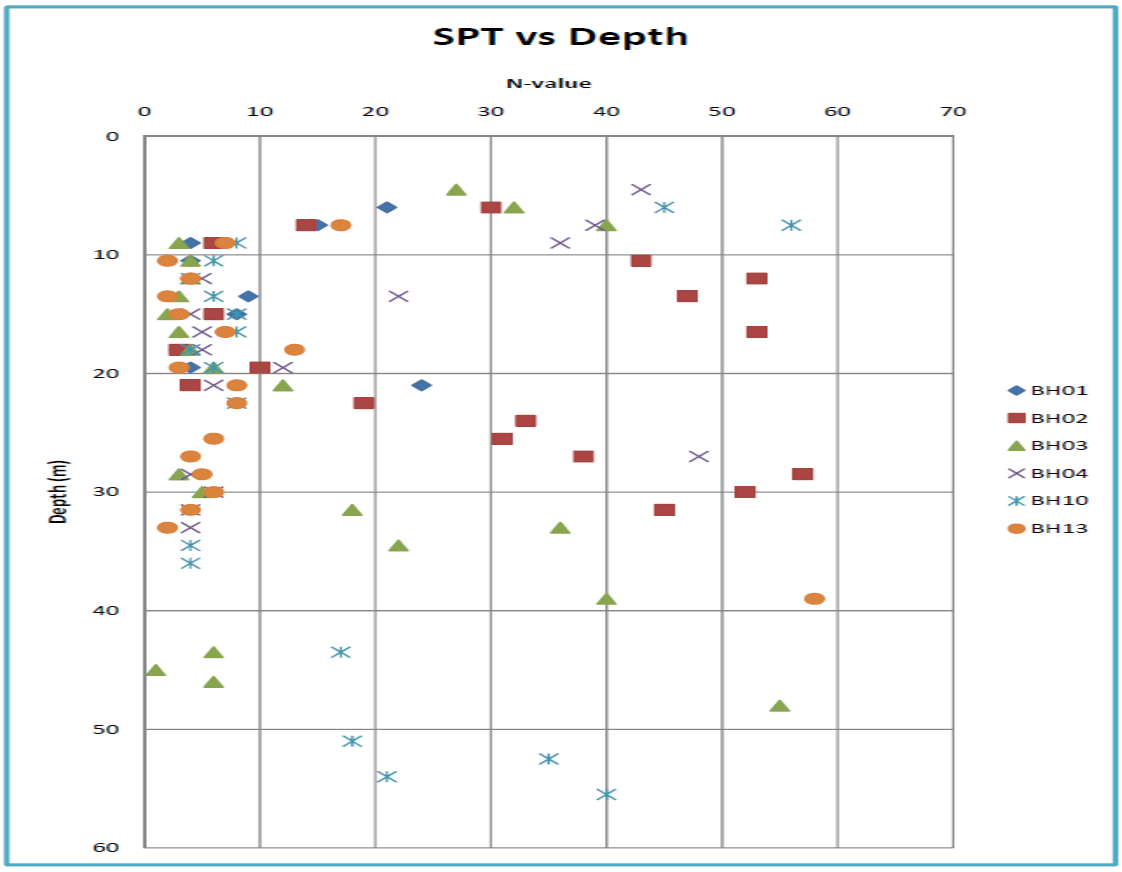


Figure 1 Typical N-SPT results from a series of boreholes.

4 ANALYSIS AND DISCUSSION

In this study, analysis has been carried out for three groups of soils: Sand, Clay and All Soils. In the first phase, values of N as function of depth has been drawn based on all available data. Three envelopes were obtained for each group of soil: an upper limit envelope, a lower limit envelope and an average envelope. Regression analysis was based both on a polynomial third degree approach and a power type approach. For illustration, the polynomial third degree approach is shown in the figures. Figures 2 and 3 show the results of Vs as a function of N for sand. Figures 4 and 5 show the results of Vs as a function of N for clay. Figures 6 and 7 give the results of Vs as a function of N in the case of the group all soils. All the equations used to establish the models for our soils are presented earlier and listed in the references. Of course, all the measured values of Vs are in m/s. Based on the undertaken analysis, the equation for Vs as a function of N for sand based on a polynomial approach is:

$$V_s = 82.878\ N^{0.3763} \tag{1}$$

And if the depth term D is to be included in the case of sands, the following equation to find Vs may be considered using a polynomial approach as a function of N_{60}:

$$V_s = 77.17\ N_{60}^{0.1899}\ D^{0.1960} \tag{2}$$

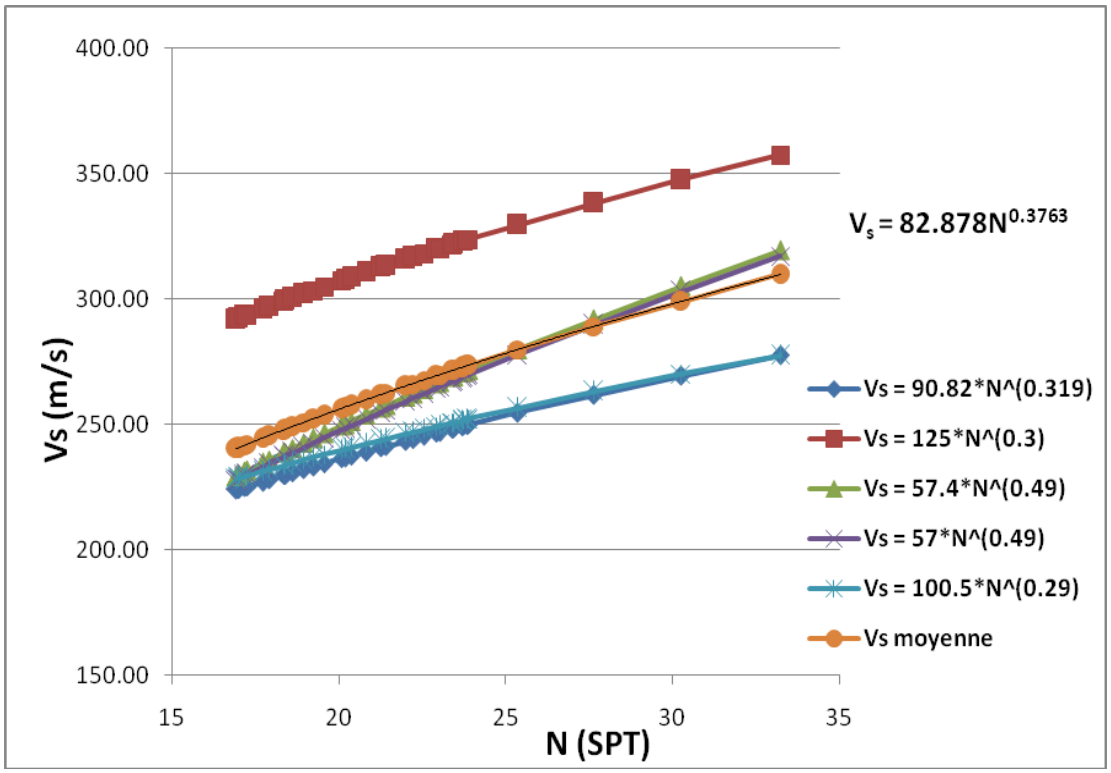


Figure 2 Shear wave velocity Vs as a function of N for Sand

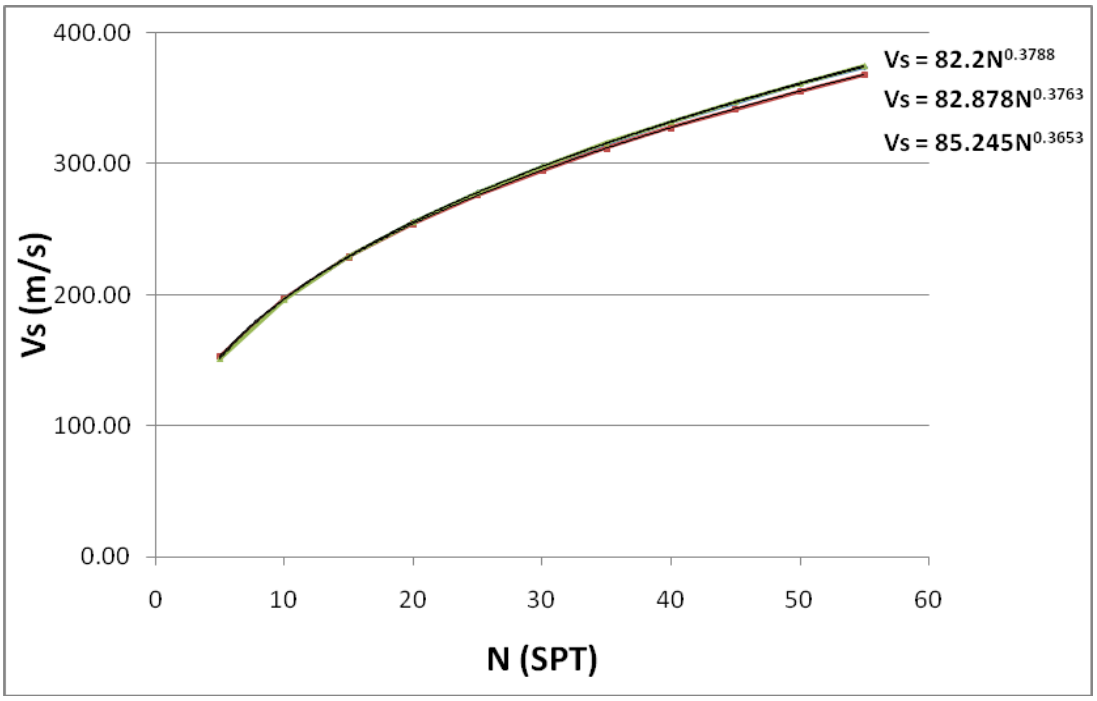


Figure 3 Vs as a function of N for Sand, with upper limit, lower limit and average curves

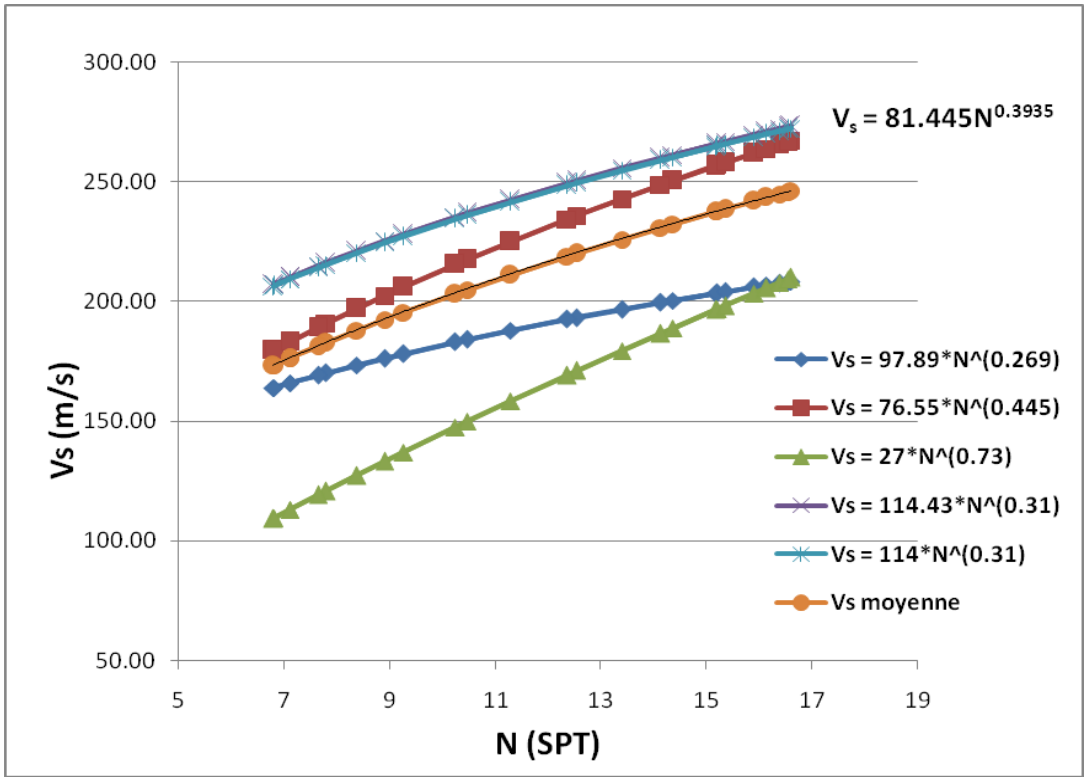


Figure 4 Shear wave velocity Vs as a function of N for Clay

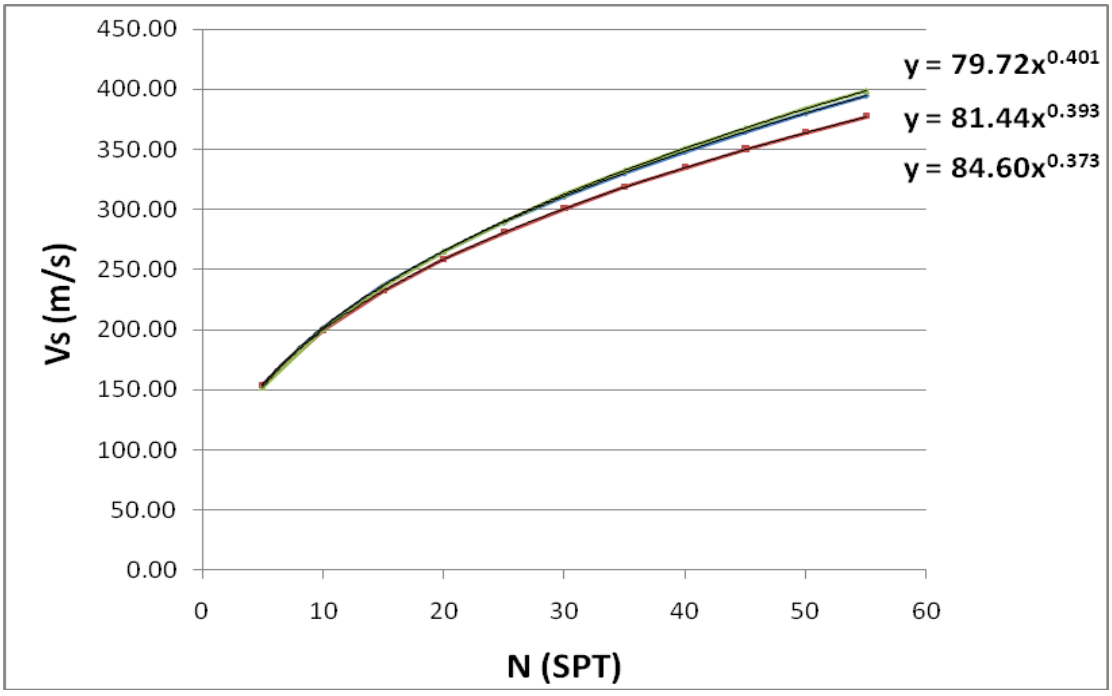


Figure 5 Shear Vs as a function of N for Clay, with upper limit, lower limit and average curves

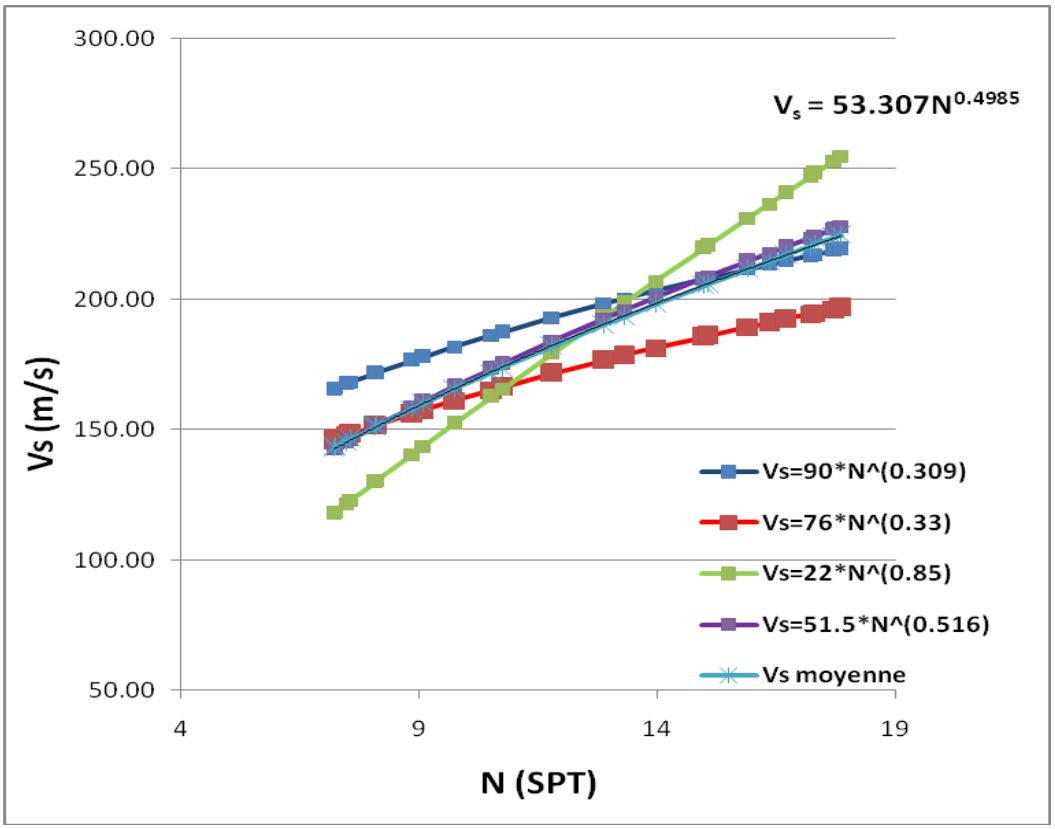


Figure 6 Shear wave velocity Vs as a function of N for All Soils Group

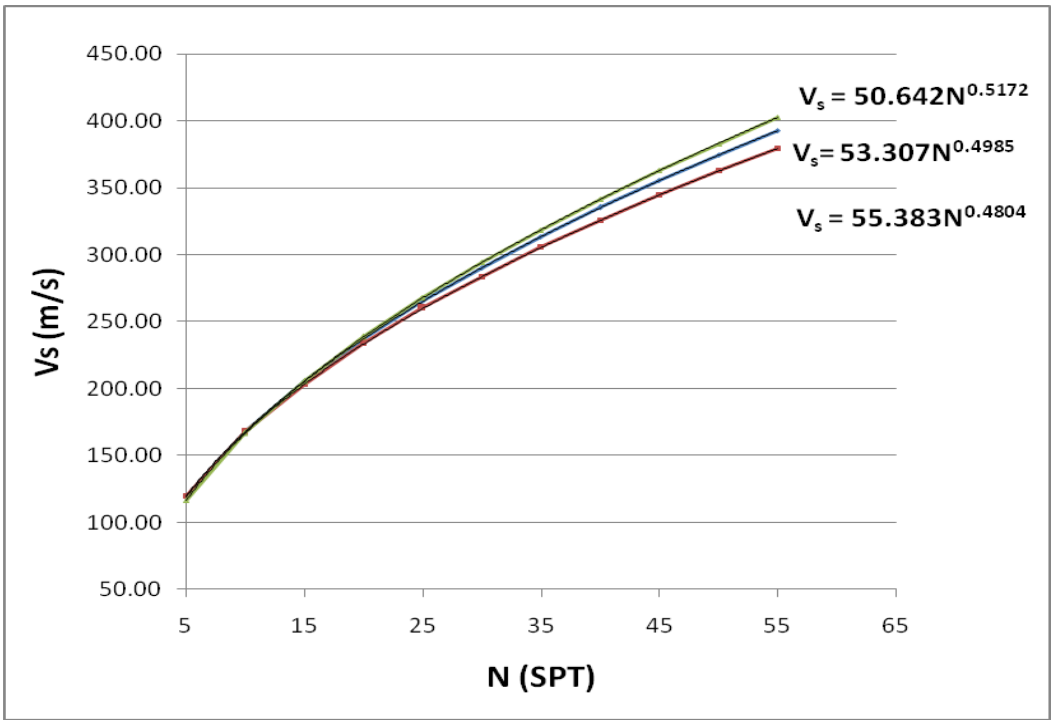


Figure 7 Shear Vs as a function of N for All Soils, with upper limit, lower limit and average curves

For the same data analyzed, the equation to be considered for Vs as a function of N for sand based on a power approach is:

$$V_s = 83.455\ N^{0.3739} \quad (3)$$

And if the depth term D is to be included in the case of sands, the following equation to find Vs may be considered using a power approach, as a function of N_{60}:

$$V_s = 82.03\ N_{60}^{0.1742}\ D^{0.1879} \quad (4)$$

As far as clay is concerned, the equation for Vs as a function of N based on a polynomial approach is:

$$V_s = 81.445\ N^{0.3935} \quad (5)$$

And if the depth term D is to be included in the case of clays, the following equation to find Vs may be considered using a polynomial approach as a function of N_{60}:

$$V_s = 76.39\ N_{60}^{0.1573}\ D^{0.2007} \quad (6)$$

For the same data analyzed, the equation to be considered for Vs as a function of N for clay based on a power approach is:

$$V_s = 82.679\ N^{0.3862} \quad (7)$$

And if the depth term D is to be included in the case of clays, the following equation to find Vs may be considered using a power approach, as a function of N_{60}:

$$V_s = 136.76\ N_{60}^{-0.046}\ D^{0.1204} \quad (8)$$

The third group of soils to be considered is called all soils, which means that correlations found should be applied to all types of soils regardless of their classification. The equation for Vs as a function of N based on a polynomial approach is:

$$V_s = 53.307\ N^{0.4985} \quad (9)$$

And if the depth term D is to be included in the case of all soils, the following equation to find Vs may be considered using a polynomial approach as a function of N_{60}:

$$V_s = 71.22\ N_{60}^{0.2227}\ D^{0.1994} \quad (10)$$

The equation to be considered for Vs as a function of N for all soils based on a power approach is:

$$V_s = 54.308\ N^{0.49} \quad (11)$$

And if the depth term D is to be included in the case of clays, the following equation to find Vs may be considered using a power approach, as a function of N_{60}:

$$V_s = 71.59\ N_{60}^{0.2206}\ D^{0.1990} \quad (12)$$

All the above equations show that results are very close whether considering a polynomial third degree or a power approach. The thing to be noted is that in the case of the group all soils, results are more conservative because all points are considered. Values of Vs found using the equations range from 150 m/s to 400 m/s and these are reasonable values for these types of soils.

In the last part of the discussion of results, CPT based results are considered. Based on the references [20, 21, 22, and 23], the following equations are derived. The correlation to be considered for Vs as a function of q_c and the effective stress σ'_v for sand based on a polynomial approach is:

$$Vs = 225\ q_c^{-0.002}\ \sigma'^{0.0423}_v \quad (13)$$

The correlation to be considered for Vs as a function of q_c and the effective stress σ'_v for sand based on a power approach is:

$$Vs = 234\ q_c^{-0.001}\ \sigma'^{0.0405}_v \quad (14)$$

As far as clay is concerned, the equation for Vs as a function of q_c based on a polynomial approach is:

$$Vs = 156\ q_c^{0.024} \quad (15)$$

For the same data analyzed, the equation to be considered for Vs as a function of q_c for clay based on a power approach is:

$$Vs = 141\ q_c^{0.029} \quad (16)$$

The correlations obtained shall be very helpful for the earthquake geotechnical engineering community. It is very important nowadays to work both with geotechnical as well as geophysical data when available. Not all geotechnical projects include geophysical prospection; this is why the use of correlations might be of interest for a first assessment only. Any soil seismic response analysis requires however a complete geophysical investigation couples of course with the traditional geotechnical investigation. Results obtained in the present study compare very well with an earlier published [24] Vs profile based on inversion parameterization of dispersion estimates obtained in the same area. More geophysical measurements are to be made in the near future.

5 CONCLUSIONS

Geotechnical and geophysical tests are of primary importance and complementary as far as characterizing the soil subsurface. Since geophysical testing is not systematically carried out, the use of existing correlations between in situ geotechnical testing (SPT and CPT) and shear wave velocity for soils is beneficial. In this paper, existing N-SPT and qc-CPT data has been thoroughly analyzed. Correlations between Vs, N-SPT and qc-CPT were established. Some of the proposed correlations include the depth parameter D as well as the effective earth pressure σ'_v. The developed correlations are based on other correlations already available in

the geotechnical literature. The obtained results compare well with previous geophysical measurements conducted at the same site. The proposed correlations should be used with precaution by the earthquake geotechnical engineering community. Further analysis is being conducted in the hope of yielding still more representative correlations. Vs in situ measurements are to be recommended in parallel with the use of the correlations.

REFERENCES

[1] G. Lefebvre, D. Leboeuf, M.E. Rahhal, A. Lacroix, J. Warde, K.H. Stokoe, Laboratory and field determinations of small strain shear modulus for a structured Champlain clay, Canadian Geotechnical Journal, vol. **31**, 61-70,1994.

[2] M.E. Rahhal, G. Lefebvre, Understanding the Cyclic Threshold Strain in Soil Dynamics, Proceedings *11th International Conference on Soil Dynamics and Earthquake Engineering*, and *3rd International Conference on Geotechnical Earthquake Engineering*, University of California, Berkeley, USA, Volume **1**, 453-459, 2004.

[3] M.E. Rahhal, G. Lefebvre, Characterizing Shear Moduli Reduction in Soils Cyclic Behavior, Proceedings *ASCE Geo Congress*, Atlanta, USA. Permalink: http://dx.doi.org/10.1061/40803(187)164, 2006.

[4] R.D. Andrus, P. Piratheepan, B. S. Ellis, J. Zhang, C. H. Juang, Comparing Liquefaction Evaluation Methods using Penetration-Vs relationships, *Soil Dynamics and Earthquake Engineering*, **24**, 713-721, 2004.

[5] R.D. Andrus, N.P. Mohanan, P. Piratheepan, B.S. Ellis, T.L. Holzer, Predicting shear-wave velocity from cone penetration resistance, Proceedings, *4th International Conference on Earthquake Geotechnical. Engineering*, Thessaloniki, Greece, 2007.

[6] U. Dikmen, Statistical correlations of shear wave velocity and penetration resistance for soils, *Journal of Geophysics and Engineering*. **6** (1), 61-72, 2009.

[7] L. Paoletti, Y. Hegazy, S. Monaco, R. Piva, Prediction of shear wave velocity for offshore sands using CPT data – Adriatic sea; *2nd International Symposium on Cone Penetration Testing*, Huntington Beach, CA, USA. Volume **2&3**: Technical Papers, Session 2: Interpretation, Paper No. 29, 2010.

[8] L. Dubertret, Geological Maps of Lebanon, 1/50,000. Ministry of National Defense, Geography Department, Lebanon.

[9] T. Imai, T. and Yoshimura, Y., The relation of mechanical properties of soils to P and S-wave velocities for ground in Japan, *Technical Note*, OYO Corporation (1975).

[10] D.E. Sykora, K.H. Stokoe, Correlations of in-situ measurements in sands of shear wave velocity, *Soil Dynamics and Earthquake Engineering*, **20:**125–36, 1983.

[11] S. H. Lee, Regression models of shear wave velocities, *J. Chin. Inst. Eng.*, **13,** 519–32, 1990.

[12] R. Iyisan, Correlations between shear wave velocity and in situ penetration test results (in Turkish), *Chamber of Civil Engineers of Turkey, Teknik Dergi* **7**(2):1187–1199, 1996.

[13] M.K. Jafari, A. Asghari, I. Rahmani, Empirical correlation between shear wave velocity (VS) and SPT N-value for south of Tehran soils, Proceedings, *4th International Conference on Civil Engineering*, Tehran, Iran, 1997.

[14] M.K. Jafari, A. Shafiee, A Ramzkhah, Dynamic properties of the fine grained soils in south of Tehran, *Journal Seismology and Earthquake Engineering*, **4** (1):25–35, 2002.

[15] T. Okamoto, T. Kokusho, Y. Yoshida, K. Kusuonoki, Comparison of surface versus subsurface wave source for P–S logging in sand layer, *Proceedings 44th Annual Conference. JSCE*, vol. 3, 996–7 (in Japanese), 1989.

[16] G.A. Athanasopoulos, Empirical correlations Vs-NSPT for soils of Greece: a comparative study of reliability, Proceedings. *7th International Conference on Soil Dynamics and Earthquake Engineering (Chania, Crete)* ed. A. S. Cakmak (Southampton: Computational Mechanics), 19–36, 1995.

[17] N. Hasancebi, R. Ulusay, Empirical correlations between shear wave velocity and penetration resistance for ground shaking assessments, *Bulletin Engineering Geology and the Environment*, **66**: 203–213, 2007.

[18] Y. Ohta, N Goto, Empirical shear wave velocity equations in terms of characteristic soil indexes, *Earthquake Engineering Structural. Dynamics*, **6**:167–187, 1978.

[19] H.B. Seed, R.T. Wong, I.M. Idriss, K. Tokimatsu, Moduli and damping factors for dynamic analyses of cohesionless soils, *Journal of Geotechnical Engineering.*, **112**(11):1016–1032, 1986.

[20] P. Piratheepan, *Estimating Shear-Wave Velocity from SPT and CPT Data*. Master of Science Thesis, Clemson University, 2002.

[21] G. R. Baldi, V.N. Bellotti, M. Ghionna, M. Jamiolkowski, D.C.F LoPresti, Modulus of sands from CPTs and DMTs, Proceedings, *12th International Conference. Soil Mechanics and Foundation Engineering*, Vol. **1**, Rio de Janeiro, 165–170, 1989.

[22] Y.A. Hegazy, P.W. Mayne, Statistical correlations between V_S and cone penetration data for different soil types, Proceedings, *International Symposium on Cone Penetration Testing, CPT '95*, Linkoping, Sweden, Vol. **2**, 173–178, 1995.

[23] P.W. Mayne, G.J. Rix, Correlations between shear wave velocity and cone tip resistance in natural clays, *Soils and Foundations*, Vol. **35**, No. 2, 193-194, 1995.

[24] C. Cornou, M. Brax, N. Salloum, M. Rahhal, F. Harakeh, J. Harb, D. Youssef Abdel-Massih, A. Mariscal, C. Voisin, D. Jongmans, P.Y. Bard, Shear-wave velocity structure and correlation with N-SPT values in different geological formations in Beirut, Lebanon, Proceedings, *Second European Conference on Earthquake Engineering and Seismology*, Istanbul, TURKEY, August 25-29, 2014.

COMPDYN 2015
5th ECCOMAS Thematic Conference on
Computational Methods in Structural Dynamics and Earthquake Engineering
M. Papadrakakis, V. Papadopoulos, V. Plevris (eds.)
Crete Island, Greece, 25–27 May 2015

NUMERICAL SIMULATIONS OF LIQUEFACTION PHENOMENA AFTER EMILIA ROMAGNA (20 MAY 2012) EARTHQUAKE

D. Forcellini[1], L. Tonni[2], C. Osti[2] and G. Gottardi[2]

1 University of San Marino
Via Salita alla Rocca, 44, 47890, San Marino
davforc@omniway.sm

2 DICAM, University of Bologna
Viale Risorgimento, 2, 40136 Bologna
laura.tonni@unibo.it

Keywords: Earthquake Engineering, Liquefaction, Emilia Romagna Earthquake (20 May 2012), Numerical simulations, OpenSees PL.

Abstract. *Soil liquefaction has been observed worldwide during earthquakes with induced effects responsible for damage, disruption of function and considerable replacement expenses for structures. The May 20, 2012 M5.9 shock in Emilia Romagna (Italy), is one example of moderate earthquakes yielding extensive liquefaction-related phenomena. The paper provides an attempt to simulate the observed ground effects using a finite element (FE) approach. The study adopts a FE computational interface (OPENSEES PL) implemented in OpenSees and able to analyze the earthquake-induced three-dimensional pore pressure generation. Credited non-linear theories are applied in order to take into account appropriate flow rules as to reproduce the observed strong dilation tendency and resulting increase in cyclic shear stiffness and strength. The interface simplifies the 3D spatial soil domain, boundary conditions and input seismic excitation definition with convenient post-processing and graphical visualization of analysis results including deformed ground response time histories. The possibility to simulate wave propagation adopting realistic boundaries is of particular importance and significance in order to realistically reproduce liquefaction behaviour.*

1 INTRODUCTION

The seismic sequence that in May 2012 struck a large area of the river Po Valley (Emilia-Romagna region, Northern Italy) and led to collapse many industrial buildings, churches, bell towers and more than ten thousand residential constructions [1], also triggered significant fractures and deformations in a number of riverbanks located close to the earthquake epicenter.

Among them, one of the most severely damaged structures turned out to be the banks of an irrigation canal known as *Canale Diversivo di Burana*, flowing through the small village of Scortichino (Municipality of Bondeno), near the historic town of Ferrara (Figure 1). Large, longitudinally-oriented ground cracks were observed along a 3 km bank stretch, causing in turn severe structural damages to a large part of the approximately one hundred houses and productive activities built on the bank crown. At the same time, it was observed that the deformation phenomena did not equally affect the bank over its entire length, being the seismic-induced fracture system particularly evident in the four main areas labelled as A, B, C and D in Figure 1.

This study is based on the large experimental database collected in the context of an extensive study carried out by a number of research groups from various Italian universities in co-operation with technical experts of the Geological, Seismic and Soil Survey Regional Department. The paper provides an attempt to simulate the observed ground effects using a finite element (FE) approach together with an advanced constitutive formulation developed within a multi-surface plasticity framework for modelling of cyclic behavior in saturated sands.

In this regards, FE analysis allows modelling the distribution of effective stress, pore pressure, strain and permanent displacements, thus providing an accurate description of the subsoil response and failure mechanisms. In particular, the study adopts a FE computational interface (OPENSEES PL) implemented in OpenSees [2] based on a three-dimensional formulation as to reproduce the observed strong dilation tendency and resulting increase in cyclic shear stiffness and strength.



Figure 1. Aerial view of the Canale Diversivo di Burana, with location of the investigated areas.

2 GEOTECHNICAL BACKGROUND

Geotechnical characterization of the Canale Diversivo riverbank and the relevant foundation soil was based on a comprehensive experimental program including both in situ and high-quality laboratory tests. Figure 2 shows results from one of the piezocone tests (CPTU) carried out from the top of the bank, in area C, together with the soil stratigraphy detected from an adjacent borehole (S3). Profiles of the corrected cone resistance q_t, sleeve friction f_s and

pore pressure *u* detail a well-defined 9 m thick, rather heterogeneous top layer of alternating sands, silty sands and sandy silts, partly forming the artificial riverbank (*Unit R*, upper 5 m), partly referable to the flood plain environment (lower 5 m, *Unit B*). A fine-grained stratigraphic unit (*C*), mainly composed of clay-silty clay, can be then identified from 9 to 12 m in depth, followed by a medium-coarse sandy layer forming the so-called *Acquifero Padano* (*Unit A*), which was almost continuously detected down to a depth of 50 m. A thin interbedded clayey lens, similar to *Unit C*, was encountered at depths between 29 and 32 m from the top of the embankment. Details on the whole laboratory testing results, including cyclic resistance curves of coarse grained soils and modulus reduction curves *G*-γ, can be found in [3].

Application of some well-known interpretation procedures, based on either piezocone data or dilatometer results, for the cyclic liquefaction susceptibility assessment, showed that a large part of *Unit B* is very likely to have experienced liquefaction phenomena for an earthquake moment-magnitude equal to the May 2012 main event (M_w = 6.1). By contrast, *Unit A* was generally found not susceptible to cyclic liquefaction.

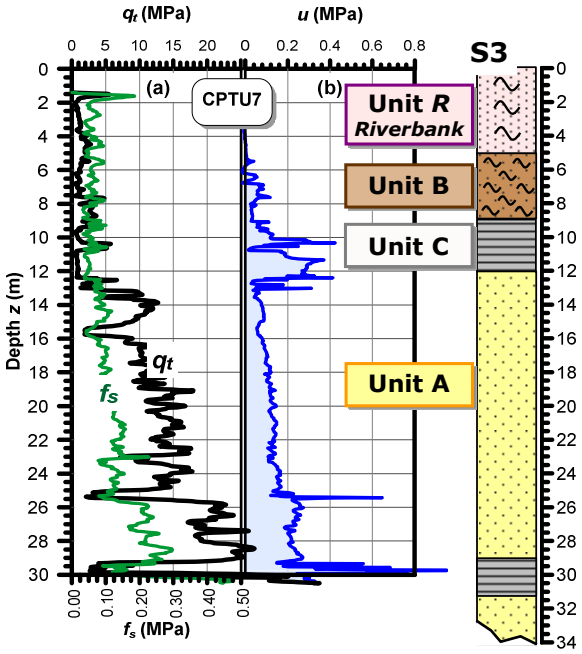


Figure 2. CPTU 7 log profiles compared with the soil column obtained from the nearby borehole S3.

3 COSTITUTIVE FORMULATION

In this study the mechanical behavior of cohesionless soil units *R*, *B* and *A* has been described in terms of an advanced constitutive formulation developed within the framework of multi-yield-surface plasticity for numerical simulations of cyclic liquefaction response and associated accumulation of cyclic shear deformation observed in clean sands and silts. This model [4, 5, 6] is based on a conical yield surface in principal stress space, with the hardening zone defined by a number of similar yield surfaces having a common apex along the hydrostatic axis. The outermost surface is given by the failure locus, related to the shear strength angle ϕ'. Moreover, in order to properly reproduce the phenomenological interaction between shear and volume changes in sands and the associated cyclic mobility mechanisms, the deviatoric component of the flow rule was assumed as associate, non-associativity being solely restricted to the volumetric component. A detailed description of constitutive equations as well as of the parameter calibration can be found in [4, 5, 6]. The model requires the definition of

the soil peak friction angle and the associated shear strain, together with the *G*-γ curve and a set of dilatancy/liquefaction parameters governing the rate of shear-induced volume changes/pore pressure development and the plastic shear strain accumulation.

The clayey Unit C has been treated as a nonlinear hysteretic material, using a Von Mises multi-surface kinematic plasticity approach together with an associate flow rule. This constitutive formulation is able to capture both monotonic and hysteretic elasto-plastic cyclic response of those soils whose shear behavior is assumed insensitive to confining stress. According to this formulation, plasticity is exhibited only in the deviatoric stress-strain response, while the volumetric response is linear-elastic.

4 FINITE ELEMENT MODEL

Numerical model of the riverbank aims at reproducing a more detailed insight into the seismic-induced pore pressure response and displacement development of the silty-sandy sediments, applying a versatile constitutive approach in conjunction with a fully coupled two-phase formulation. In particular, the aim is to reproduce the seismic response of a soil column corresponding to the stratigraphic conditions provided by borehole S3 (Figure 2), applying the open-source computational interface OpenSeesPL, implemented within the FE code OpenSees [2]. This platform consists of a framework for saturated soil response as a two-phase material following the *u-p* (where *u* is displacement of the soil skeleton and *p* is pore pressure) formulation [7, 8]. The 3D soil domain is represented by 20-8 nodes, effective stress fully coupled (solid-fluid) brick elements [2] built up with 20 nodes in order to describe the solid translational degrees of freedom and the eight-corner nodes for the fluid pressure [9]. The interface used in this study, originally calibrated for pile analyses was modified in order to take into account free field response [9].

Figure 3 shows the adopted 3D 40m × 40m x 120m FE mesh, composed of 792 brickUP, linear isoparametric 8 node elements with 1036 nodes. The model base boundary, set at a depth of 120 m from ground surface, corresponds to the top of the bedrock, whose position could be identified from velocity measurements provided by cross-hole tests. Opensees ability to simulate the real wave propagation adopting realistic boundaries is of particular importance in order to realistically reproduce the above scenarios. Assuming that at any special location, symmetry conditions can be adopted, periodic boundaries [10] have been considered. Therefore, displacement degrees of freedom of the left and right boundary nodes were tied together both longitudinally and vertically using the penalty method. In this regards, base and lateral boundaries were modelled to be impervious, as to represent a small section of a presumably infinite (or at least very large) soil domain by allowing the seismic energy to be removed from the site itself (for more details, see previous studies such as [11, 12]).

A seismic excitation was defined along the base in the longitudinal direction (*x*-axis), taking the main shock (M_w = 6.1) occurred on May 20th as reference event. In the absence of any strong motion station located in the area of Scortichino, a number of appropriate input motions were selected from the *Italian Accelerometric Archive* (ITACA, [13]), having moment magnitude M_w 5.50 to 6.50 and epicentral distance in the range 5÷10 km [3]. In this paper, only results of the analyses based on the east-west (E-W) acceleration record from the Cascia site during the 1979 Val Nerina (Italy) earthquake (Figure 4) are discussed.

Table 1 summarizes the values adopted for material parameters, most of these derived from the available experimental data. However, a general difficulty was encountered in defining some of the so-called dilatancy/liquefaction model coefficients, hence values suggested from the literature [9] were preliminary adopted and a sensitive study was carried out in order to

identify the most appropriate set of material parameters. Particular attention was focused on parameters calibration of Unit B, where significant pore pressure build-up and permanent shear strain accumulation presumably gave rise to the observed ground surface effects. Such unit, similarly to the riverbank sediments (R), was modelled as medium-loose coarse soil layer, while the deep unit A was treated as dense sand.

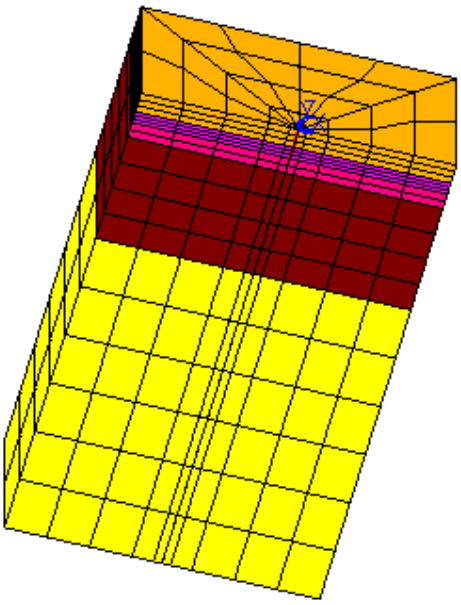


Figure 3. FE model.

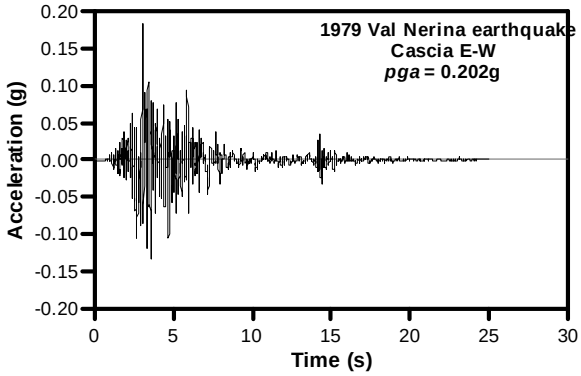


Figure 4. Acceleration time history adopted in the FE analysis.

Soil parameters	Unit R	Unit B	Unit A
ϕ'_{peak} (°)	34	30	34
c_1	0.07	0.15	0.07
d_1	0.4	0.4	0.4
d_2	2	2	2
l_1	10	10	10
l_2	0.01	0.01	0.01
l_3	1	1	1

Table 1. Pressure-dependent multi-yield model parameters.

5 FINITE ELEMENT RESULTS

Figure 5 shows excess pore pressures time histories at relevant depths (5-8 m) in order to study saturated *Unit B* response. The graph clearly shows that significant excess pore pressures develop during seismic excitation and that a maximum constant value is finally attained at each depth. Furthermore, there is no evidence of dissipation phenomena in the 10 seconds after the input motion duration.

The associated R_u values (approximately equal to 0.60 - 0.65) turn out to be in substantial agreement with the estimate of R_u (0.75) obtained from the interpretation of cyclic simple shear tests on the basis of prudential assumptions, i.e. taking into account the combined effect on pore pressure build-up of multiple aftershocks and fully undrained conditions.

Figure 6 shows lateral displacement time history at ground surface and provides immediate evidence of a gradual accumulation of permanent deformations. Time history shows a periodic shape with lateral displacements oscillating around zero. Figure 6 shows in red line that the permanent mean value is equal to 2.6 cm. Such predicted response, computed at the ground surface, is fully consistent with the observed seismic-induced cracks on the riverbank crest. Figure 7 shows that all the lateral spread is concentrated between 5 and 8 m depth (unit B). Therefore, lateral spread does not affect superficial layer (unit R).

The interface allows to show 3D mesh deformation. Figure 8 represents 3D full mesh in correspondence of the maximum longitudinal displacements (t = 7.80 sec). In particular, lateral displacements values are around 5 cm in the deepest layers and 2 cm in the superficial 12 m layers. The corresponding mean deformation result 0.05% and 0.16% respectively. These values show a good agreement with the in situ tests response. Figure 9 details the superficial layers in order to show how they translate rigidly on the lower as a rigid body.

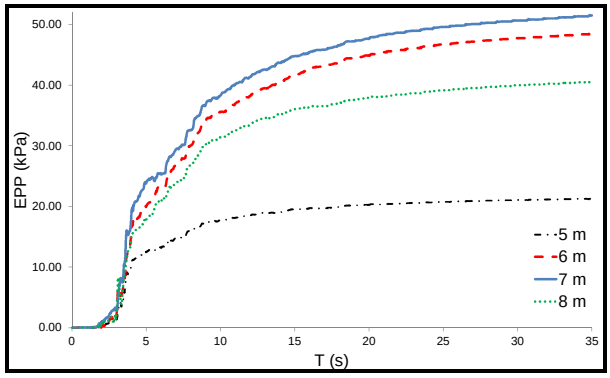


Figure 5. Excess pore pressures time histories at various depths.

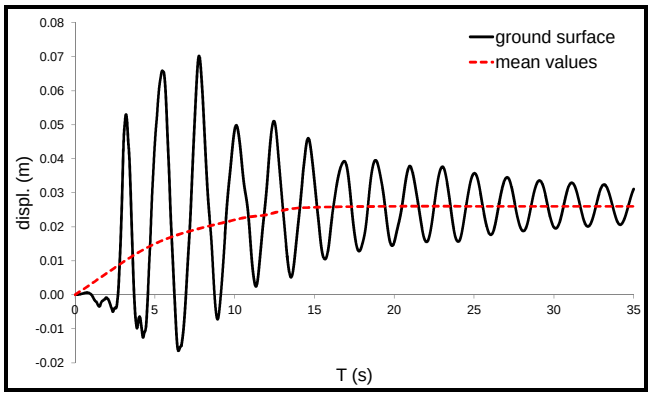


Figure 6. Lateral displacement time histories at ground level.

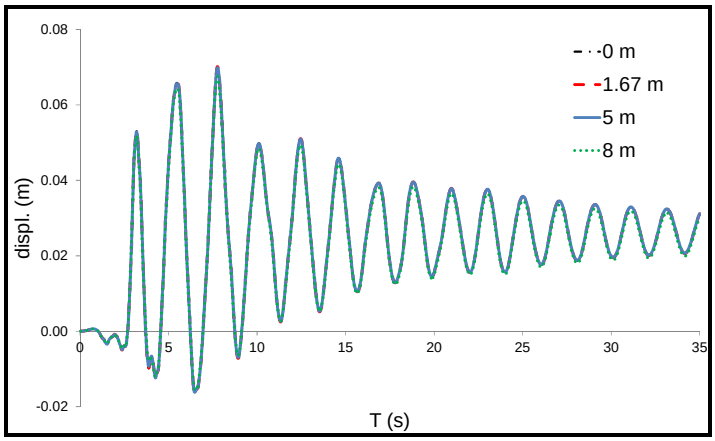


Figure 7. Lateral displacement time histories in the superficial layer (Unit R).

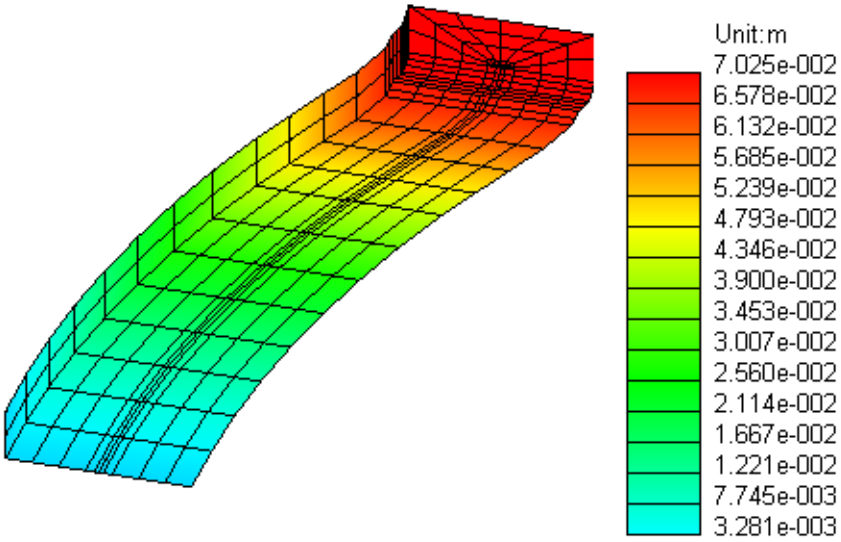


Figure 8. 3D mesh: maximum lateral displacement at 7.80 s (scale: 1:1000).

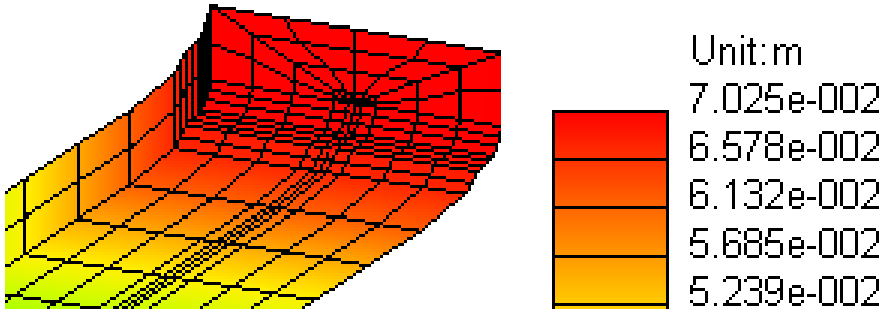


Figure 9. 3D mesh (particular): maximum lateral top displacement at 7.80 s (scale: 1:1000).

6 CONCLUSIONS

The paper shows a numerical study aimed at assessing the seismic response of a riverbank severely damaged by the May 2012 Emilia-Romagna earthquake, adopting OpenSeesPL. The FE computational platform is based on an advanced constitutive formulation specifically intended for describing granular soil behaviour in cyclic loading conditions and thus liquefaction phenomena.

Numerical results have shown that during seismic excitation saturated silty sands of the riverbank subsoil developed significant excess pore pressures and permanent deformations. The proposed FE model confirmed the main observed ground effects at the riverbank surface, consisting in typical lateral spreading phenomena.

According to the presented results, this study may be considered the first step for the development of a detailed FE model of the entire riverbank, accounting for the real topography of the ground structure.

REFERENCES

[1] L. Martelli, G. Marziali, *Terremoto 2012, geologia, rilievi agibilità, analisi dei danni. Geological, Seismic and Soil Survey Regional Department, Emilia-Romagna* (In Italian), 2012.

[2] S. Mazzoni, F. McKenna, M. H. Scott, G. L. Fenves, *Open System for Earthquake Engineering Simulation, User Command-Language Manual,* Pacific Earthquake Engineering Research Center, University of California, Berkeley, 2009.

[3] G. Gottardi, S. Amoroso, R. Bardotti, L. Bonzi, A. Chiaradonna, A. D'onofrio, V. Fioravante, A. Ghinelli, D.Giretti, G. Lanzo, C. Madiai, M. Marchi, L. Martelli, P. Monaco, D. Porcino, R. Razzano, S. Rosselli, P. Severi, F. Silvestri, L. Simeoni, L. Tonni, G. Vannucchi, *Analisi dei fenomeni deformativi indotti dalla sequenza sismica emiliana del 2012 su un tratto di argine del Canale Diversivo di Burana (FE),* Italian Geotechnical J., 2014.

[4] Z. Yang, A. Elgamal, E. Parra, *Computational model for cyclic mobility and associated shear deformation,* J. Geotech. Geoenviron. Eng., 129, 1119–1127, 2003.

[5] A. Elgamal, Z. Yang, E. Parra, A. Ragheb, *Modeling of cyclic mobility in saturated cohesionless soils*, Int. J. of Plasticity 19, 883–905, 2003.

[6] Z. Yang, A. Elgamal, *Influence of permeability on liquefaction induced shear deformation,* J. Eng. Mech., 128, 720–729, 2002.

[7] A. H. C. Chan, *A unified finite element solution to static and dynamic problems in geomechanics,* Ph.D. thesis, Univ. College of Swansea, U.K, 1988.

[8] O.C. Zienkiewicz, A.H.C. Chan, M. Pastor, D.K. Paul, T. Shiomi, *Static and dynamic behavior of soils: A rational approach to quantitative solutions: I. Fully saturated problems.*, Proc. R. Soc. Lond. A 429, 285-309, 1990.

[9] J. Lu, Z. Yang, Z., A. Elgamal, *OpenSees PL, 3D Lateral Pile-Ground Interaction,* Department of Structural Engineering, University of California, San Diego, 2010.

[10] H.K. Law, I.P. Lam, *Application of periodic boundary for large pile group,* Journal of Geotech. Geoenviron. Eng., 127-10, 889–892, 2001.

[11] A. Elgamal, J. Lu, D. Forcellini, *Mitigation of liquefaction-induced lateral deformation in a sloping stratum: three-dimensional numerical simulation*, J. Geotech. Geoenviron. Eng., 135, 1672–1682, 2009.

[12] D. Forcellini, A.M. Tarantino, *Countermeasures assessment of liquefaction-induced lateral deformation in a slope ground system*, Journal of Engineering, Article ID 183068, 2012.

[13] ITACA 1.1, ITalian ACcelerometric Archive (1972-2011) version1.1, http://itaca.mi.ingv.it/ItacaNet/, 2011.

COMPDYN 2015
5th ECCOMAS Thematic Conference on
Computational Methods in Structural Dynamics and Earthquake Engineering
M. Papadrakakis, V. Papadopoulos, V. Plevris (eds.)
Crete Island, Greece, 25–27 May 2015

SEISMIC EVALUATION OF EMBANKMENT-TYPE STRUCTURES WITH COUPLED HYDRO-MECHANICAL MODEL

I. Rapti[1,2], F. Lopez-Caballero[1], A. Modaressi-Farahmand-Razavi[1], A. Foucault[2], F. Voldoire[2]

[1]Laboratoire MSS-Mat CNRS UMR 8579, Ecole Centrale Paris
Grande Voie des Vignes 92295, Châtenay-Malabry Cedex, FRANCE
e-mail: {ioanna.rapti,fernando.lopez-caballero,arezou.modaressi}@ecp.fr

[2]Institut des Sciences de la Mécanique et Applications Industrielles, EDF-CNRS-CEA-ENSTA UMR 9219
1 Avenue du Général de Gaulle, 92140 Clamart, FRANCE
e-mail: {alexandre.foucault,francois.voldoire}@edf.fr

Keywords: Embankment, Dynamic analysis, Coupled hydro-mechanical model, Liquefaction.

Abstract. *The response of geotechnical structures under earthquake loading is highly nonlinear and often leads to problems of slope stability, foundation settlement and soil liquefaction. The prediction of these failure modes is a topic of great interest in geotechnical earthquake engineering, particularly for structural integrity assessment, which requires estimation of structural behavior during and after collapse. In this study, the earthquake response of a road embankment resting on a soil foundation is investigated. Both fully drained and coupled effective stress analysis are performed. Moreover, two different soil types are used for the embankment (loose-to-medium and medium-to-dense sand). In the fully drained case, no failure of the embankment is observed for the medium-to-dense sand and for a certain level of ground motion. However, in the coupled effective stress simulation, for the same material and input motion, liquefaction of the foundation soil can lead to the generation of a thick shear band which produce large settlements and accelerate the failure of the embankment. The response of the loose-to-medium sand is fundamentally different, as several localization zones are generated, at the foundation part and inside the embankment body, as well. In both simulations - fully drained and coupled effective stress analyis - the embankment fail can occur due to shear band generation inside the embankment.*

1 INTRODUCTION

Localization phenomena are observed in most structural failures and can cause huge material and human damage. Localization phenomena have proven particularly challenging to model in conventional finite-element simulations. Several studies have analyzed earthquake triggered landslides and the effect of ground-shaking on dry foundation-structure systems founded near slope crests with a strain-softening soil [1]. The apparition of a shear band extending from toe to crest was identified as failure mode, as soil has reached or exceeded its peak shear strength. The fact that mesh dependency phenomena may appear was also taken into account and explored through a parametric dynamic analysis. After a dynamic parametric analysis of a road embankment subjected to various amplitude ground motions, no significant mesh dependency is observed in dry conditions and the localization zone initiates from the toe, due to the geometric anomaly and produces the failure of the embankment [2].

A road embankment resting on liquefiable soil and subjected to the 2011 Off the Pacific Coast of Tohoku earthquake is simulated by [3]. Their results showed that when the water-saturated region in the embankment liquefies, it leads to large settlements and inclined shear localization zones inside the embankment body.

In this study, the earthquake response of a road embankment resting on a soil foundation is investigated. A plane-strain finite element model is built to analyze the arising failure modes and earthquake induced deformations. Two different materials are used for the embankment, a loose-to-medium and medium-to-dense sand. Moreover, fully drained and coupled effective stress analysis are simulated for both materials. Modeling of advanced soil behavior is achieved using the fully coupled effective stress ECP constitutive model developed at *Ecole Centrale Paris* [4]. Numerical simulations are performed using the open-source FE software Code_Aster, developed by EDF.

In the first section, the numerical model is presented. Thereafter, the dynamic analysis of the road embankment is presented for both materials and simulations. The effect of liquefaction on the foundation of the embankment is evaluated with the coupled hydro-mechanical analysis.

2 NUMERICAL MODEL

2.1 Geometry - Boundary conditions

Two different models are used for the purpose of this study. A thin elastic layer of 0.25m is placed at the top of the embankment, representing a pavement layer. In the first model, the dry road embankment is composed of a medium-to-dense sand (MDS), while in the second one, a loose-to-medium sand (LMS) is used. In both cases, it is placed over a loose-to-medium contractive saturated sand (LMS) substratum and the water table is situated 1m below the embankment. At the lower part of the foundation a dense saturated sand is used. The embankment's slope inclination is equal to 1:2 (vertical:horizontal). The dimensions of the model and its geometry are presented in Fig. 1.

Lateral horizontal displacements are fixed (u_x=0) and the substratum is founded on a rigid base. No flux is possible at the lateral surfaces and at the base. These boundary conditions are equivalent to those of a centrifuge test. The mesh consists of 6-node triangular elements of 0.25m length on average.

The model was constructed in three steps. First, a static analysis was performed in order to proceed to stress initialization. Afterwards, an excavation took place at the right upper part of the embankment. The last step was the dynamic analysis, so as to impose the input seismic signal. In all analyses gravity loading is taken into account.

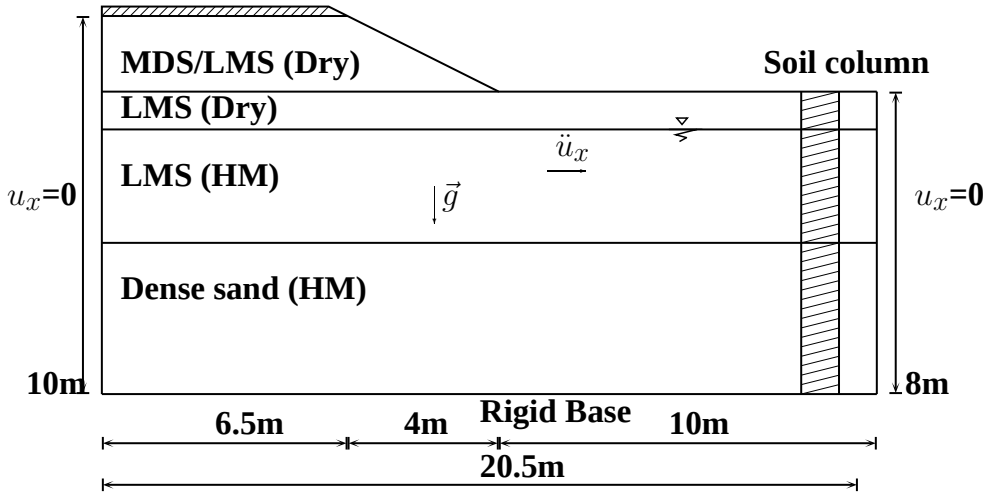


Figure 1: Illustration of numerical model.

The implicit method of Newmark integration is used for the dynamic analysis. Numerical damping equal to ξ = 0.2% is added to the model, as the set of integration parameters used is β = 0.31 and γ = 0.61 [5, 6]. Since, the model is elastoplastic, no damping exists in the elastic domain and numerical damping should be added.

2.2 Mechanical characteristics

The ECP elastoplastic multi-mechanism model [4] is used to represent soil behavior under cyclic loading. This model can take into account soil behavior in a large range of loading paths. The representation of all irreversible phenomena is idealized by four coupled elementary plastic mechanisms: three plane-strain deviatoric plastic deformation mechanisms in three orthogonal planes and an isotropic one. The model uses a Coulomb-type failure criterion and the critical state concept. The evolution of hardening is based on plastic strain (deviatoric and volumetric strain for the deviatoric mechanisms and volumetric strain for the isotropic one). To take into account cyclic behavior both isotropic and kinematical hardenings are used. An implicit integration scheme is used for the equations of the model [7]. The model takes into account non-linear elasticity. Elastic mechanical characteristics E, ν must also be defined.

Adopting the soil mechanics sign convention (compression positive), the deviatoric primary yield surface of the k plane is given by:

$$f_k(\sigma', \varepsilon_v^p, r_k) \quad = \quad q_k - sin\phi'_{pp} \cdot p'_k \cdot F_k \cdot r_k \tag{1}$$

where p'_k and q_k are the effective mean and deviatoric values of stress tensors, ϕ'_{pp} is the friction angle at critical state, the function F_k permits to control the isotropic hardening associated with the plastic volumetric strain, whereas r_k accounts for the isotropic hardening generated by plastic shearing. They represent progressive friction mobilization in the soil and their product reaches unity at perfect plasticity.

In Fig. 2, the curves of deviatoric stress - deviatoric deformation (q-ε_d) are plotted for all materials, after drained and undrained triaxial test simulations. All triaxial tests were carried out at confining pressures corresponding to the average geostatic pressure of each layer, i.e. 17kPa and 45kPa for the dry medium-to-dense and loose-to-medium sand (see Fig.2a), and 60kPa and

90kPa for the saturated loose-to-medium and dense sand (see Fig.2b,2c), respectively. Material parameters can be found in Table 1.

Table 1: ECP model's parameters for the soil.

Parameter	MDS (Embankment)	LMS (Embankment/Foundation)	Dense sand (Foundation)
ρ [kg/m^3]	1755	1755	1755
ν [·]	0.3	0.3	0.4
K_0 [·]	0.5	0.7	0.7
Elasticity			
E [MPa]	571.65	754	1850
n_e [·]	0.4	0.5	0.47
p_{ref} [MPa]	1.0	1.0	1.0
Critical State and Plasticity			
β [·]	43	33	44
b [·]	0.2	0.12	0.8
d [·]	3.5	2.0	5.0
ϕ [^{o}]	31	30	37
p_{c0} [MPa]	1.8	$40{\cdot}10^{-3}$	0.4
Flow Rule and Hardening			
a_{mon} [·]	0.004	0.005	0.0004
a_{cyc} [·]	0.0001	0.0001	0.0002
c_{mon} [·]	0.06	0.004	0.01
c_{cyc} [·]	0.03	0.002	0.005
ψ [^{o}]	31	30	37
α [·]	1.0	1.0	1.0
χ_m [·]	1.0	1.5	1.0
Threshold Domains			
r^d_{ela} [·]	0.005	0.03	0.005
r^{iso}_{ela} [·]	0.001	0.001	0.0001
r^d_{cyc} [·]	0.005	0.03	0.005
r^{iso}_{cyc} [·]	0.001	0.001	0.0001
r_{hys} [·]	0.03	0.04	0.04
r_{mob} [·]	0.8	0.8	0.8

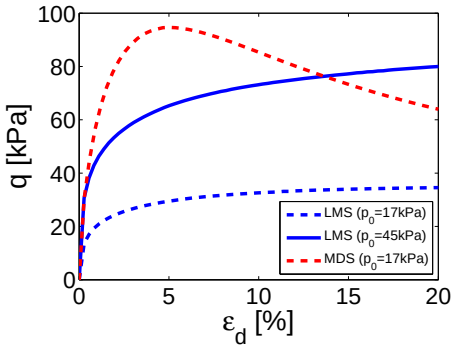
2.3 Hydraulic parameters

Two different simulations are performed, in order to evaluate the effect of the pore water pressure generation, one fully drained and one coupled effective stress analysis [8]. In Table 2, the hydraulic parameters of each material are presented.

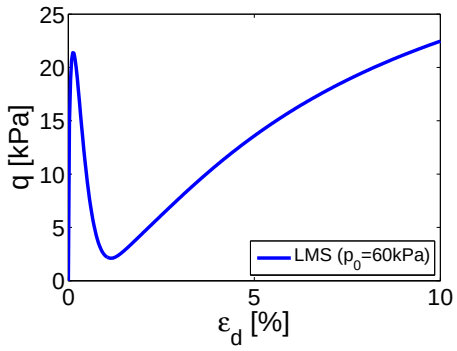
2.4 Input motions

In order to test the dynamic response of the model, a nonlinear soil column with similar material profile was subjected to 6 ground motions chosen from the Pacific Earthquake Engineering Research Center (PEER) database and a coupled effective stress analysis was performed.

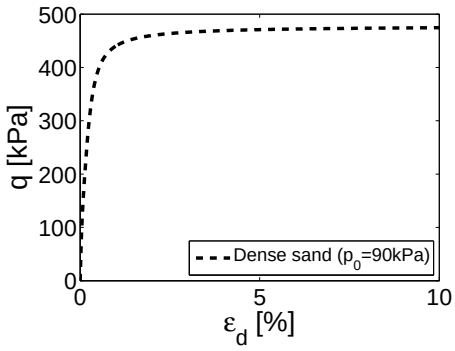
The peak ground acceleration (PGA) in free field was calculated as function of the maximum acceleration of the input signal ($a_{bed,max}$) for all ground motions (Fig. 3). Soil liquefaction was observed for moderate and strong input ground motions with $a_{bed,max}$ >0.2g.



(a) Triaxial drained test (MDS / LMS).



(b) Triaxial undrained test (LMS).



(c) Triaxial undrained test (Dense sand).

Figure 2: Soil response of one material point - ECP constitutive model: q-ε_d.

Table 2: Hydraulic parameters for the soil.

Parameter	**Foundation (LMS)**	**Foundation (Dense sand)**
Fluid mass density, ρ_w [kg/m^3]	1000	1000
Porosity, n [·]	0.35	0.35
Water dynamic viscosity, μ_w [kg/m·s]	0.001	0.001
Permeability, k_s [m/s]	$1{\cdot}10^{-4}$	$1{\cdot}10^{-5}$
Fluid compressibility, H_w [Pa^{-1}]	$3.3{\cdot}10^{-8}$	$3.3{\cdot}10^{-8}$

Consequent to these results and in order to evaluate the response of the embankment due to the liquefiable foundation, a moderate motion ($a_{bed,max}$=0.24g) is used as input signal (see accelerogram and Arias intensity of input motion in Fig.4).

3 DYNAMIC ANALYSIS OF ROAD EMBANKMENT

In this section the results of the dynamic response of the road embankment subjected to the input motion of Fig.4 are presented, for both fully drained and coupled effective stress analysis and for both materials used at the part of the embankment (MDS/LMS). In the first simulation, effective stresses and zero pore water pressure are considered, while in the coupled simulation, the pore water pressure is taken into account [8]. Both simulations start from the same effective stress state at the beginning of the dynamic analysis, as shown in Fig. 5 for the LMS.

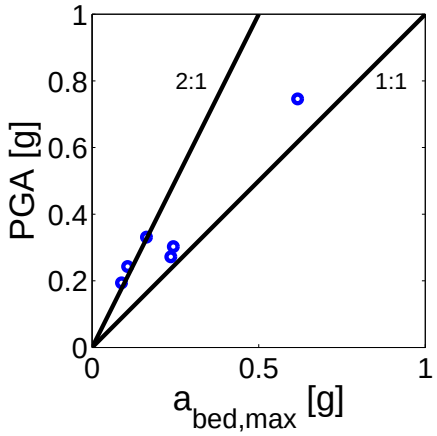
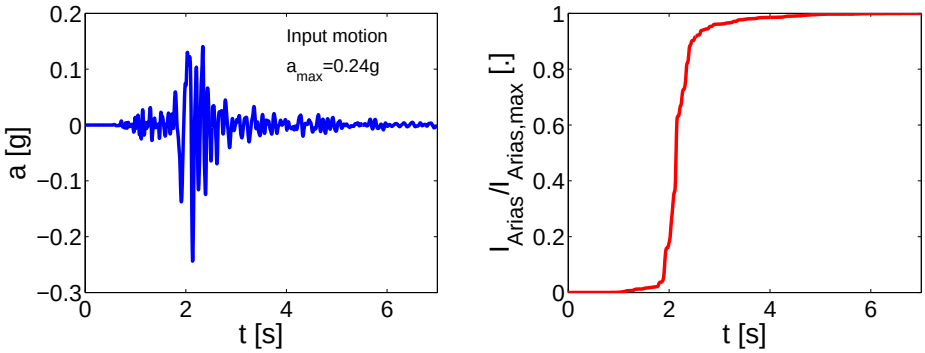
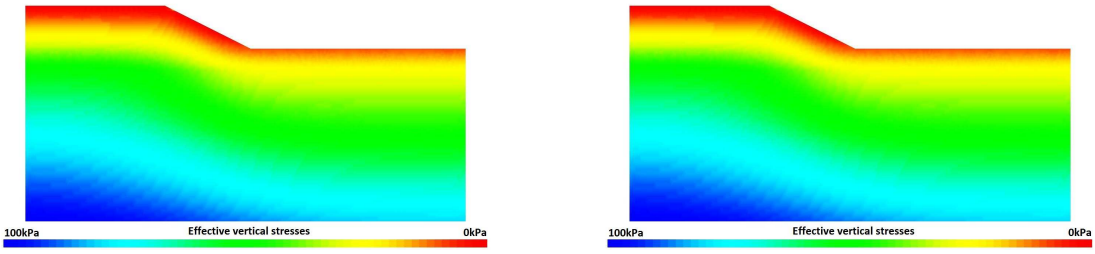


Figure 3: PGA - $a_{bed,max}$ for the soil column.



(a) Accelerogram. (b) I_{Arias} intensity.

Figure 4: Input moderate seismic signal.



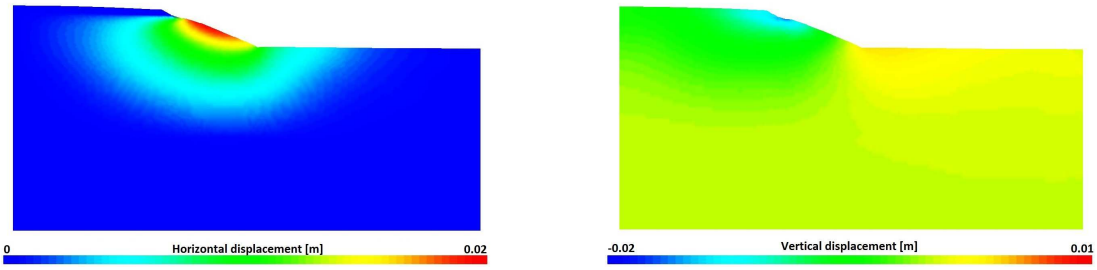
(a) Fully drained effective stress simulation. (b) Coupled effective stress simulation.

Figure 5: Initial vertical effective stresses $\sigma'_{v,0}$ for both simulations (LMS).

3.1 Fully drained effective stress simulation

In the fully drained approach, the embankment with the MDS stays almost unaffected by the ground motion, while in the model with the LMS, greater displacements are observed close to the slope. Particularly, in Fig.6 the deformed shape of horizontal and vertical displacements at the end of the motion are plotted. Horizontal displacement ($\simeq$2cm) is detected close to the slope and settlement at the upper part of the embankment.

Subsequently, the stability of the embankment is tested by calculating the second order work

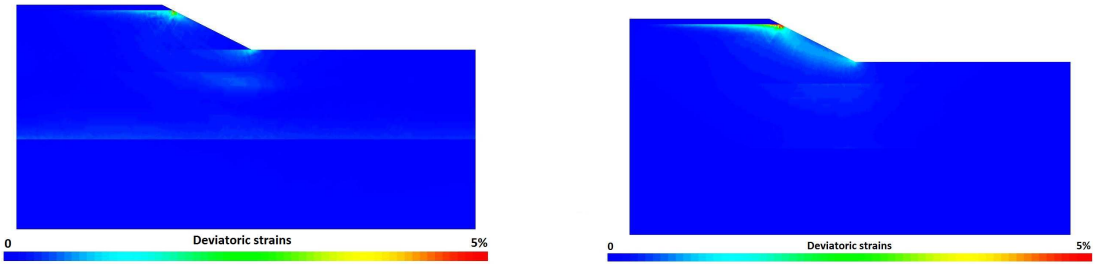


(a) Horizontal displacement. (b) Vertical displacement.

Figure 6: Deformed shape at the end of the ground motion (Fully drained effective stress simulation - LMS).

($d^2W=\dot{\sigma}:\dot{\varepsilon}$) [9, 10]. In this study the second order work is calculated in terms of invariants, i.e. $d^2W=\dot{p}:\dot{\varepsilon_v}+\dot{q}:\dot{\varepsilon_d}$. During the main shock of the ground motion, the embankment - with both materials - remains stable, as $d^2W > 0$ and for the sake of brevity, the figures are omitted as no important information is provided.

In the MDS model, as the embankment is very rigid no remarkable deformations appear. Only the upper part, at the interface with the elastic pavement layer, is affected and generates shear strains (see Fig.7a). However, in the case of LMS, a shear band extending from toe to crest is identified (Fig.7b). A stronger input motion will increase the level of deviatoric strains and the embankment can fail due to this shear band generation.



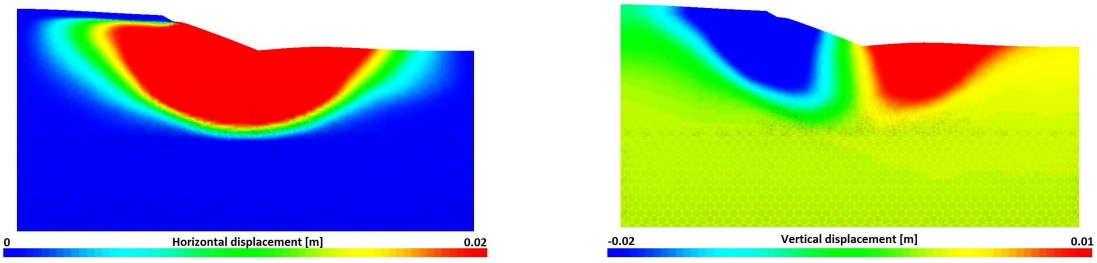
(a) MDS (b) LMS

Figure 7: Deviatoric strains ε_d at the end of the ground motion (Fully drained effective stress simulation).

3.2 Coupled effective stress simulation

In the case of coupled effective stress simulation, the effect of excess pore water pressure in the foundation part is significant for both materials. The liquefied soil at the foundation creates an extended failure zone. In both models (MDS/LMS) almost the whole part of the embankment settles and moves to the right, as a large part of the foundation moves to the right, too, and swells due to the excess pore water pressure. More important displacement and settlement is remarked for the LMS model and its deformed shape at the end of the ground motion is presented in Fig.8. As the embankment is assymetric and it is constrained at the left boundary, it tends always to move to the right.

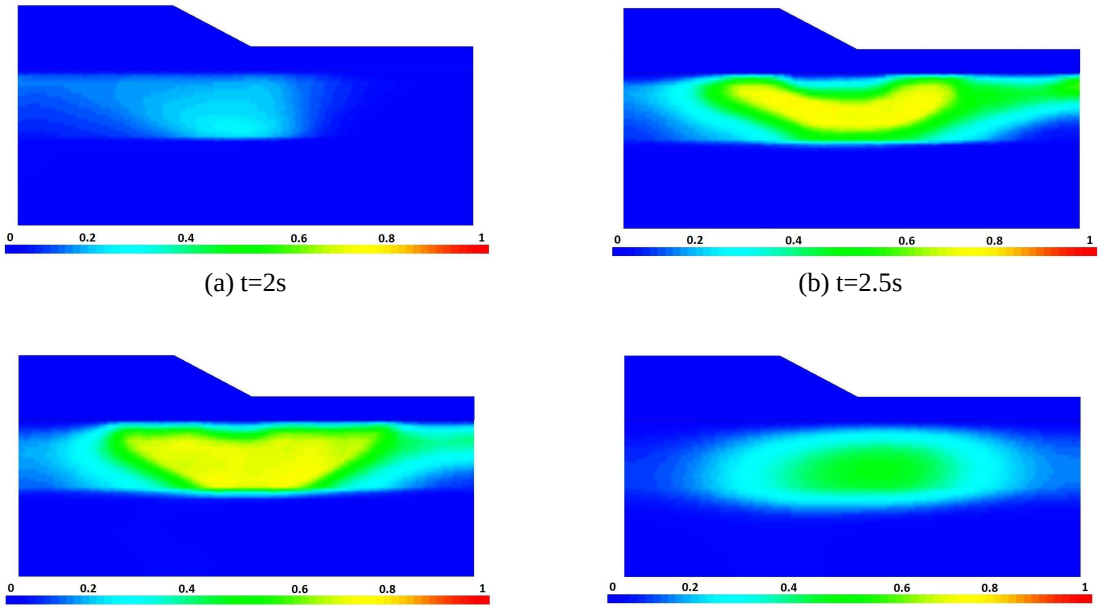
During the main shock (between 2-3s) excess pore water (Δp_w) pressure is observed in the foundation part of LMS. In Fig.9a,9b,9c, the contours of r_u ($\Delta p_w / \sigma'_{v,0}$) are plotted for the LMS



(a) Horizontal displacement. (b) Vertical displacement.

Figure 8: Deformed shape at the end of the motion (Coupled effective stress simulation - LMS).

model at various instants of the ground motion. The soil has almost liquefied in the foundation part of LMS, as $r_u \simeq 0.8$. The evolution of excess pore water pressure can be related to the Arias intensity (Fig.4b), as between t=2-3s the total intensity of the motion has been accumulated. The same response was obtained for the MDS, but the zone of liquefied soil was sligthly thinner. Progressively, the dissipation of pore water pressure starts, as the strength of the ground motion decreases (see Fig.9d for LMS).



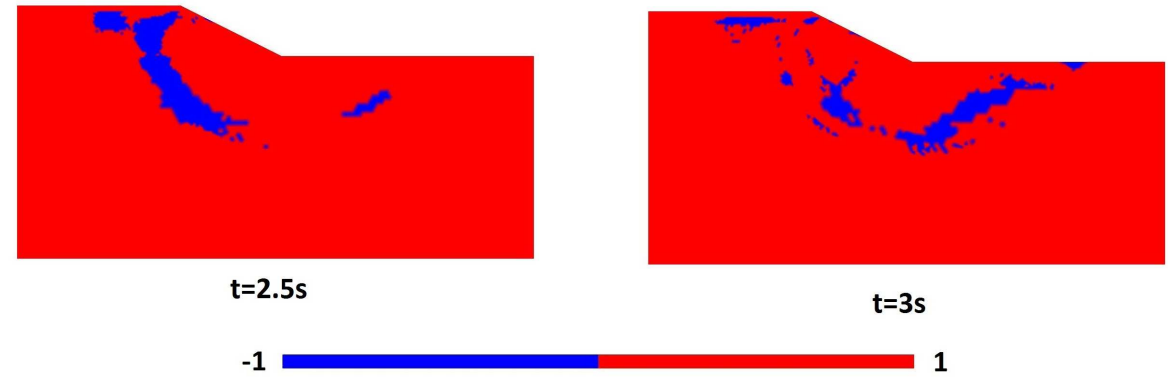
(a) t=2s (b) t=2.5s

(c) t=3s (d) t=7.4s (end)

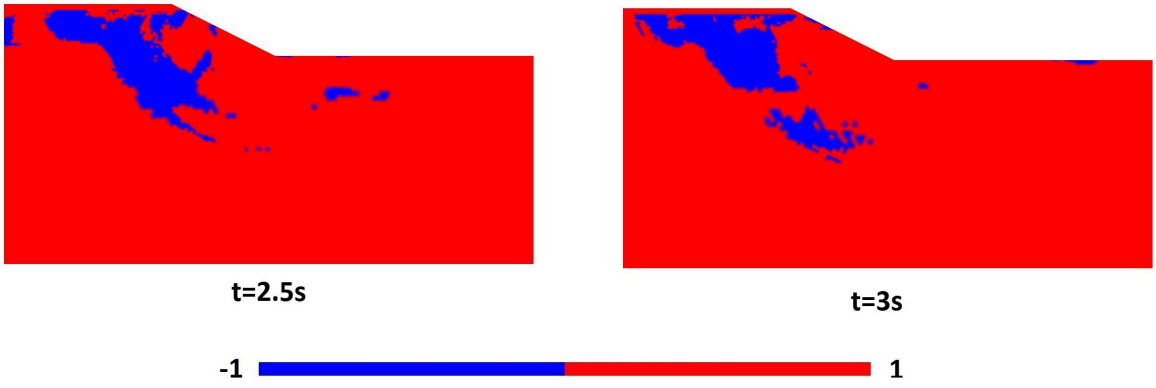
Figure 9: Excess pore water pressure ratio during the motion (r_u) - LMS.

Concerning the stability of the embankment, during the liquefaction phase (2-3s), the embankment becomes unstable ($d^2W < 0$). A circular surface of instability appears in both models (MDS/LMS) which implies the expected failure mode (Fig.10a for MDS, Fig.10b for LMS). Note that the instability becomes more significant in the embankment with the LMS, as almost the whole embankment is unstable.

In the case of MDS model, a localization zone of shear strains is remarked in the foundation part of LMS at the end of the ground motion (see Fig.11a). This shear zone extends through the liquefied soil and leads to the circular failure mode of the foundation. Contrary to the fully



(a) MDS



(b) LMS

Figure 10: Second order work (Coupled effective stress simulation).

drained case, where no shear strain generation is remarked (Fig.7a) and the only deformations observed are those at the interface with the elastic pavement layer.

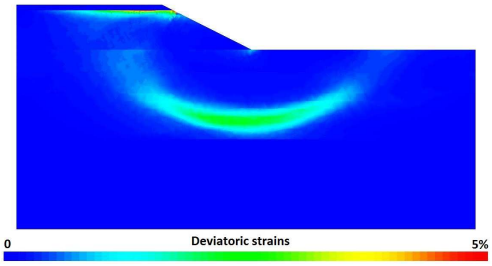
However, in the case of LMS model, two different zones of localization of shear deformations are noticed (Fig.11b). Due to the liquefaction at the foundation part of LMS, a thick and more extended zone of shear strains appears. Moreover, a second shear band is observed inside the embankment body (see zoom of the shear band in Fig.11c), as detected previously in the fully drained approach (Fig.7b). Consequently, it should be highlighted the fact that in the case of coupled simulation with a loose material at the embankment part, two different shear zones are generated and lead to failure.

4 CONCLUSIONS

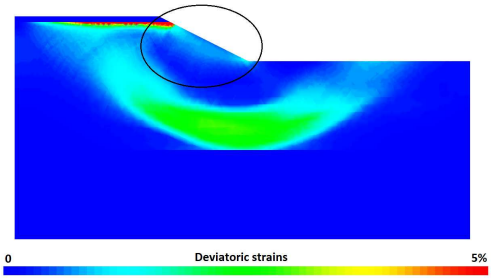
In this study, an analysis of earthquake-induced liquefaction is presented using a fully-coupled hydromechanical model. The effect of a liquefiable foundation on the failure mode of a river embankment is discussed. Two different materials are used for the embankment (MDS/LMS), so as to better investigate the failure mode.

Firstly, a fully drained effective stress approach shows that the embakment consisting of a dense-rigid material is generally unaffected by the moderate motion. Nevertheless, in the case of a loose embankment, a shear band generates from the toe and extends to the crest.

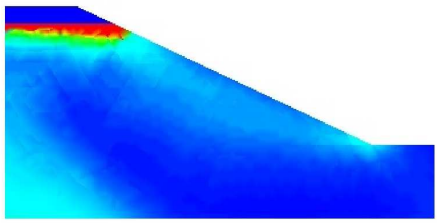
In the coupled effective stress analysis, where the pore water pressure is taken into account,



(a) MDS



(b) LMS



(c) Zoom of shear band (LMS).

Figure 11: Deviatoric strains ε_d at the end of the ground motion (Coupled effective stress simulation).

the embankment with both materials is strongly affected. A liquefied zone at the foundation part leads to noticeable settlement and horizontal displacement. A circular failure mode is produced and a zone of shear deformations at the liquefied foundation part is pointed out at the end of the motion. Furthermore, in the model with the loose sand, a second shear band inside the embankment body amplifies the displacements and leads to an extended failure.

To conclude, the effect of excess pore water pressure is of highly importance, as a stable embankment - in fully drained conditions - becomes unstable in coupled analysis and is leaded to failure due to a liquefiable zone in the foundation. It should also be remarked the double shear band generation in the case of the loose embankment.

In future work, dynamic analyses with stronger seismic motions should be performed, in order to reach flow liquefaction with larger settlements and total collapse. Post-liquefaction effects (settlements) should be also examined. This work can be considered as a first step for dynamic analysis of large scale structures, such as seismic response of earth dams.

REFERENCES

[1] R. Kourkoulis, I. Anastasopoulos, F. Gelagoti, and G. Gazetas, “Interaction of foundation-structure systems with seismically precarious slopes: Numerical analysis with strain softening constitutive model,” *Soil Dynamics and Earthquake Engineering*, vol. 30, pp. 1430–1445, 2010.

[2] I. Rapti, A. Foucault, and E. C. Paris, “Strain localization of a road embankment founded on soil substratum due to seismic loading,” in *9th International Conference on Structural Dynamics, EURODYN 2014. Porto, Portugal, 30 June - 2 July 2014*, vol. 1, pp. 681–688, 2014.

[3] H. Sadeghi, S. Kimoto, F. Oka, and B. Shahbodagh, "Dynamic analysis of river embankments during earthquakes using a finite deformation FE analysis method," in *14th International Conference of the International Association for Computer Methods and Advances in Geomechanics*, no. 2011, (Kyoto, Japan), pp. 637–642, 2014.

[4] J.-C. Hujeux, "Une loi de comportement pour le chargement cyclique des sols," *Presses ENPC*, pp. 278–302, 1985.

[5] S. Kontoe, L. Zdravkovic, and D. Potts, "An assessment of time integration schemes for dynamic geotechnical problems," *Computers and Geotechnics*, pp. 253–264, 2008.

[6] S. Ruiz and G. Saragoni, "Free vibration of soils during large earthquakes," *Soil Dynamics and Earthquake Engineering*, vol. 29, pp. 1–16, 2009.

[7] A. Foucault, "Loi de comportement cyclique de Hujeux pour les sols," *Documentation of Code_Aster [R7.01.23]*, 2009.

[8] S. Montoya-Noguera and F. Lopez-Caballero, "Effect of coupling excess pore pressure and deformation on nonlinear seismic soil response," *Acta Geotechnica*, 2015.

[9] R. Hill, "A general theory of uniqueness and stability in elastic-plastic solids," *Journal of Mechanics and Physics of Solids*, vol. 6, pp. 236–249, 1958.

[10] K. Hamadi, A. . Modaressi-Farahmand Razavi, and F. Darve, "Bifurcation and instability modelling by a multimechanism elasto-plastic model," *International Journal for Numerical and Analytical Methods in Geomechanics*, vol. 32, pp. 461–492, 2008.

COMPDYN 2015
5th ECCOMAS Thematic Conference on
Computational Methods in Structural Dynamics and Earthquake Engineering
M. Papadrakakis, V. Papadopoulos, V. Plevris (eds.)
Crete Island, Greece, 25–27 May 2015

SEISMIC RESPONSE ANALYSIS OF A GEOGRID REINFORCED WALL CONSTRUCTED WITH RECYCLED CONSTRUCTION AND DEMOLITION WASTE

Castorina Silva Vieira[1]

[1] University of Porto – Faculty of Engineering – Civil Engineering Department
R. Dr Roberto Frias, s/n 4200-465 Porto, Portugal
e-mail: cvieira@fe.up.pt

Keywords: Geogrids, Construction and Demolition Wastes, Seismic loading, Shear strength parameters

Abstract. *Over the last years the environmental sustainability has been demanding a progressive increase in the waste valorisation in construction. The valorisation of Construction and Demolition Wastes (C&DW) reduces the use of natural resources (non-renewable) and, simultaneously, avoids congesting landfills with inert wastes coming from buildings and other infrastructures. Although some studies have been carried out on the use of recycled C&DW in construction industry, their valorisation as fill material in geosynthetic reinforced structures is almost an unexplored field. A research project aiming to contribute to the sustainable application of recycled C&DW as backfill material in geosynthetic reinforced structures, is being developed at University of Porto, Portugal. Preliminary results of this research are presented in this paper.*

In this work the two-dimensional finite difference program Fast Lagrangian Analysis of Continua (FLAC) was used to model the behaviour of a geogrid reinforced wall, constructed in Brazil, with recycled C&DW. The wall is 3.6m high and was constructed at an inclination of 1:4.3 (wall batter of 13º from vertical). The backfill was reinforced with six layers of geogrid placed at 0.6 m of vertical spacing and 2.52 m long. The seismic response of a similar wall, hypothetically constructed with recycled C&DW coming from a Portuguese recycling plant, is also evaluated.

An earthquake ground motions artificially generated for the greatest seismicity area of Portugal was considered as seismic input. Two constitutive models were used to model the backfill C&DW material: the Mohr-Coulomb model and a Strain-Softening model. Permanent displacements of the wall face, settlements and reinforcement tensile forces are analysed and discussed. The numerical simulations have shown that the possible decrease of the backfill shear strength during cyclic loading is an important issue to be studied more closely. Notwithstanding it was concluded that a well compacted and drained recycled C&DW can be used as fill material in geosynthetic reinforced structures.

1 INTRODUCTION

The reduction of non-renewable natural resources exploration has been a constant concern relating to the preservation of the environment that, simultaneously, encourages the use of alternative materials. Thus, over the last years the environmental sustainability has been demanding a progressive increase in the waste valorisation in construction.

The Construction and Demolition Wastes (C&DW) are wastes derived from construction, reconstruction, cleaning of the work site and earthworks, demolition and collapse of buildings, maintenance and re-habilitation of existing constructions. The composition of the C&DW is variable depending on the construction type and construction processes that predominate in the area. They include: concrete, bricks, tiles, soils, rocks, vegetation, materials from roads maintenance and a wide variety of other materials.

Although some studies have been carried out on the application of recycled construction and demolition wastes, their purposes are mainly the production of aggregates for use in concrete and in base layers of transportation infrastructures. As regards the application of C&DW in geotechnical works, it has been verified that the valorisation is performed mostly in road construction, particularly in base and sub-base layers of the infrastructures. Outside the scope of road infrastructures, references to C&DW applications in embankments are scarse. The valorisation of Recycled C&DW in geosynthetic reinforced structures is almost an unexplored field.

This paper presents results of a research project under development at University of Porto, aiming to contribute to the sustainable application of recycled C&DW in geosynthetic reinforced structures, proving the good performance of these structures.

A preliminary calibration analysis using instrumentation data of a geogrid reinforced wall constructed with C&DW as backfill material [1] is presented. Based on results of direct shear tests carried out on recycled C&DW and presented by [2], the seismic behaviour of a similar reinforced wall, hypothetically constructed with the characterized C&DW material, is also evaluated. Several numerical analyses were carried out, considering distinct assumptions related to the backfill shear strength parameters.

2 BRIEF DESCRIPTION OF FLAC CODE AND SEISMIC LOADING INPUT

FLAC is an explicit finite difference program that performs a Lagrangian analysis. The finite difference method is perhaps the oldest numerical technique used for the solution of sets of differential equations, given initial values and/or boundary values [3]. For dynamic analyses the full equations of motion are solved using lumped gridpoint masses derived from the real density of surrounding zones (rather than fictitious masses used for static solution). Each triangular sub-zone contributes one-third of its mass (computed from zone density and area) to each of the three associated gridpoints. The final gridpoint mass is then divided by two in the case of a quadrilateral zone that contains two overlays. In finite-element terminology, FLAC uses lumped masses and a diagonal mass matrix [3].

In FLAC, the dynamic input can be applied as an acceleration history, as a velocity history, as a stress (or pressure) history or as a force history. Dynamic input can be applied either in the x or y directions corresponding to the xy axes for the model, or in the normal and shear directions to the model boundary.

In the dynamic analyses presented in this paper, two constitutive models were used: the *Mohr-Coulomb* model and a *Strain-Softening* model.

In the implementation of the *Mohr-Coulomb* model in FLAC, principal stresses σ_1, σ_2, σ_3 are used, being the out-of-plane stress, σ_{zz}, recognized as one of these. With the ordering convention $\sigma_1 \leq \sigma_2 \leq \sigma_3$ (compressive stresses are negative), the failure criterion for this model is represented in the plane (σ_1, σ_3) as illustrated in Figure 3.

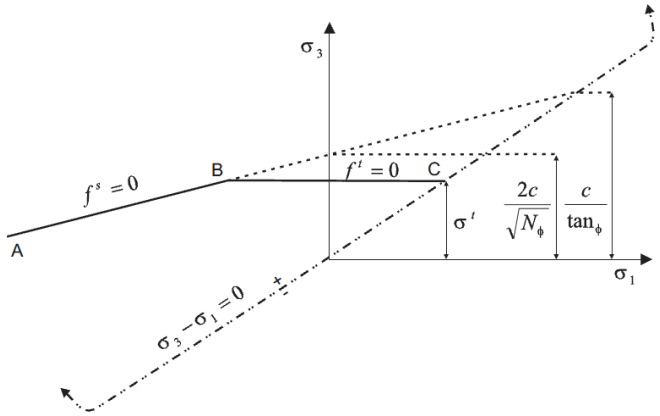


Figure 1: Mohr-Coulomb failure criterion in FLAC [3].

The failure envelope is defined from point A to point B (Figure 3) by the *Mohr-Coulomb* yield function:

$$f^s = \sigma_1 - \sigma_3 N_\phi + 2c\sqrt{N_\phi} \tag{1}$$

and from B to C by a tension yield function of the form:

$$f^t = \sigma^t - \sigma_3 \tag{2}$$

where ϕ is the soil friction angle, c is the cohesion, σ^t is the tensile strength and N_ϕ is defined as:

$$N_\phi = \frac{1+\sin\phi}{1-\sin\phi} \tag{3}$$

The tensile strength of the material, σ^t, cannot exceed the maximum value given by:

$$\sigma^t_{max} = \frac{c}{\tan\phi} \tag{4}$$

The *Strain-Hardening/Softening* model is based on the *Mohr-Coulomb* model with non-associated tension flow rules. The difference lies in the possibility that cohesion, friction, dilatation and tensile strength may harden or soften after the onset plastic yield [3]. The user can define the variation of the cohesion, friction and dilation as a function of the plastic shear strain. The variation of the tensile strength can also be prescribed in terms of plastic tensile strength. The code measures the total plastic shear and tensile strains at each timestep and causes the model properties to conform to the user-defined functions.

An earthquake ground motion artificially generated [4], according to Portuguese National Annexes (PNA) of Eurocode 8, for the greatest seismicity area of Portugal, considering seismic action type 2 (earthquake with moderate magnitude and small focal distance – close

earthquake) and ground type B (deposits of very dense sand, gravel or very stiff clay), was considered as seismic input. According to the PNA of Eurocode 8 for the greatest seismicity area, the peak ground acceleration on type B ground is 2.7m/s^2 for a close earthquake (Figure 2). The duration of the stationary part of the accelerograms is equal to 10 seconds. The Fourier spectrum for the accelerogram presented in Figure 2(a) is plotted in Figure 2(b). This graph indicates that the highest frequency is lower than approximately 20 Hz. Before applying the seismic input motion, it was filtered to remove frequencies above the maximum frequency that can be modelled accurately.

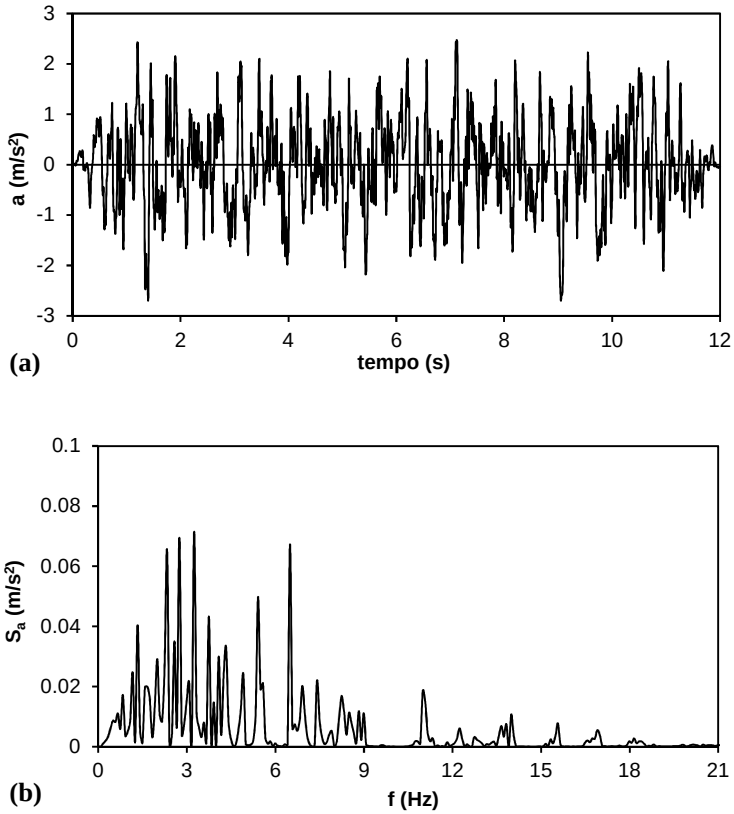


Figure 2: Seismic input motion: a) artificial accelerogram; b) Fourier spectrum

3 CALIBRATION STRUCTURE FOR STATIC LOADING

Before running any dynamic analysis, a preliminary calibration analysis was carried out using instrumentation data of a geogrid reinforced wall constructed with C&DW as backfill material. Santos et al [1] report the performance of an instrumented 3.6 m high wrapped face geogrid reinforced wall constructed with C&DW. The foundation of the test wall is a naturally collapsible soil that is common in Brazil (Figure 2). The wall was constructed in a reinforced masonry block container and the wrapped-face was constructed at an inclination of 1:4.3 (horizontal:vertical). The backfill was reinforced with six layers of geogrid placed at 0.6 m vertical spacing and 2.52 m long [1]. Based on the results presented by [1] an axial tensile stiffness of 200 kN/m was assumed for the geogrids .

The wall was instrumented with topographic markers, vertical and horizontal stress cells and strain gauges in the reinforcements. An inclinometer was also installed close to the wall toe to monitor the displacements of the foundation (Figure 3).

The wall was constructed in the Foundation and Field Investigation Site of the University of Brasilia. Based on field investigations, the foundation soil (porous collapsible soil) was divided in three layers [1, 5]. The main parameters considered for the foundation layers and for the C&D material are presented in Table 1. Following the description presented by [5], layer 1 (immediately bellow the wall) was considered 2 m high and layers 2 and 3 with thickness of 3 m and 2 m, respectively. A rigid layer 1m high was also considered at the base of the model.

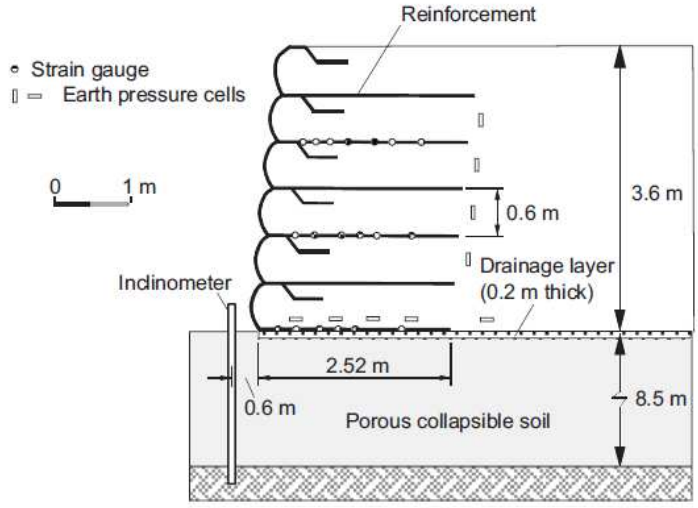


Figure 3: Cross section of the experimental geogrid reinforced wall presented by Santos et al. [1].

Soil	γ (kN/m^3)	c' (kPa)	ϕ' (º)	E (MPa)	ν
Foundation – layer 1	16.7	30	26	50	0.3
Foundation – layer 2	17.3	19	30	50	0.3
Foundation – layer 3	18.3	37	26	60	0.3
Backfill – C&D	19.5	2	35.7	30	0.3

Table 1. Foundation and backfill parameters considered in the calibration model.

The geometry of the model and the numerical grid is illustrated in Figure 4. The reinforcement layers were modelled using linear elasto-plastic cable elements with negligible compressive strength. The tensile yield strength was taken equal to 20 kN/m.

The interface between the reinforcement and the soil was modelled by a grout material. The interface shear strength was considered dependent of the backfill shear strength. A coefficient of interaction of 0.7 was admitted.

Figure 5 compares the horizontal displacements recorded in the foundation inclinometer (Figure 3) at the end of the wall construction with those achieved in the numerical analysis. The trend of the displacements was captured by the numerical model, even if the maximum horizontal displacement was 20% lower than that recorded at the end of construction.

According to Santos et al [1] the negative horizontal displacements close to the ground surface are a consequence of the influence of the superficial stiffer soil crust, which restrains horizontal displacements in that region. This phenomenon was not modelled.

The horizontal displacements of the wall face at the end of construction are illustrated in Figure 6. The results are compared to the values recorded by [1] at the topographic marks located at the wall face.

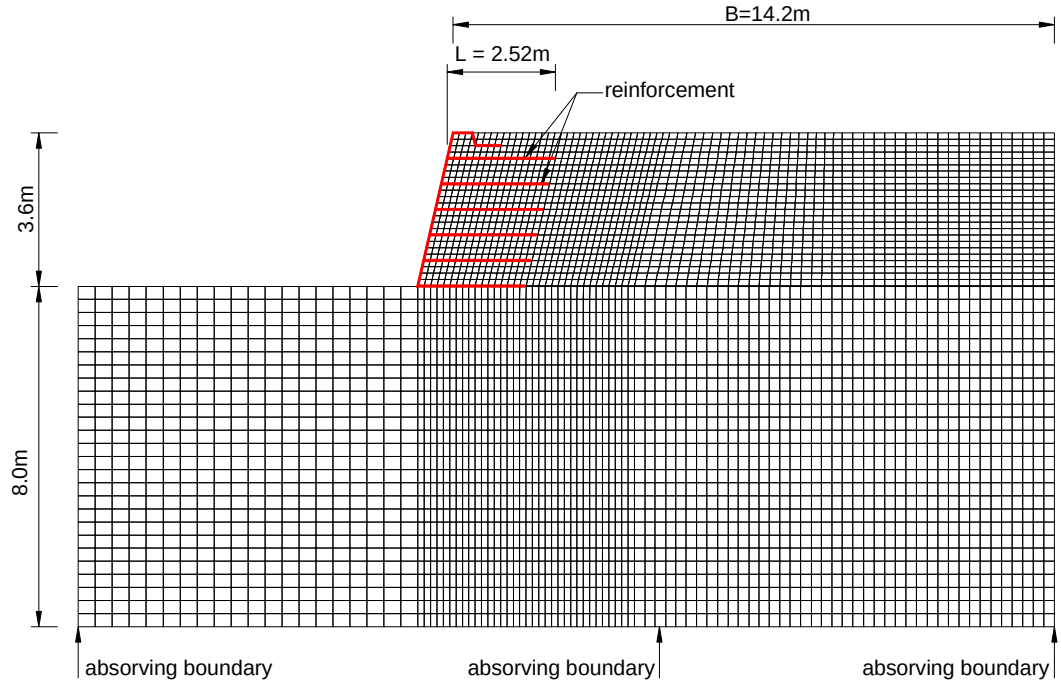


Figure 4: Geometrical properties and numerical grid.

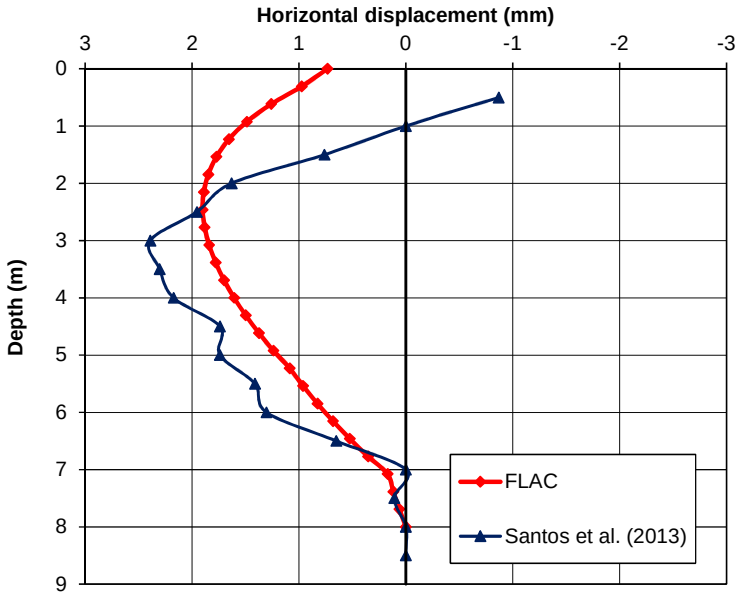


Figure 5: Comparison of horizontal displacements recorded at the foundation inclinometer.

At the end of construction, a maximum outward horizontal displacement of 51 mm at an elevation of approximately 3 m was recorded [1]. Close to the crest of the wall a negative horizontal displacement of 107 mm was measured. This pattern of horizontal displacement was justified by the authors as a consequence of non-uniform deformation of the foundation soil.

The numerical model followed the horizontal displacements of the wall face near the bottom, notwithstanding the pattern of the curve is quite different. The numerical analysis underestimated the horizontal displacements of the wall face. It should be noted, however, that the maximum value of horizontal displacement measured at the end of construction is significant-

ly greater than the values usually found for structures on strong foundation soils [1]. Local bulging at the face was also observed.

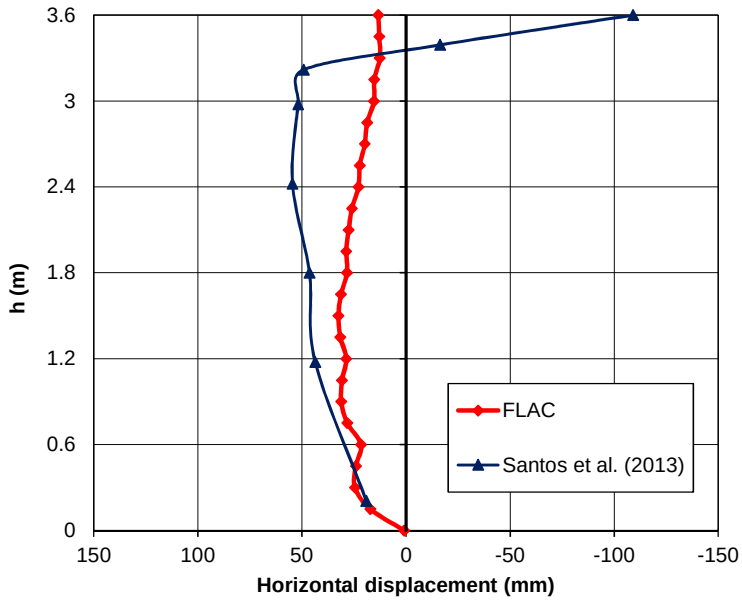


Figure 6: Horizontal displacements of the wall face.

4 DYNAMIC ANALYSES

4.1 General aspects

The shear strength parameters of the C&DW reported by [1] are quite distinct from those that are being estimated in a research project under development at University of Porto, Portugal, studying the use of recycled C&DW as backfill material in geosynthetic reinforced structures.

Results of direct shear tests carried out on fine grain recycled C&D waste materials were presented by [2]. These authors concluded that C&DW, properly selected and compacted, could exhibit similar shear strength (even greater) to the backfill materials commonly used in the construction of geosynthetic reinforced structures. The material studied by [2] have shown a peak friction angle of 44.1° and cohesion value of 17.3kPa. The large displacement shear strength was characterized by a friction angle of 41.2º and a cohesion of 2.8kPa. The large reduction of the cohesive term for large shear displacements was pointed out as an important aspect to be considered in the design of of geosynthetic reinforced structures constructed with C&DW as backfill material.

On this basis, it was decided that dynamic analyses should be carried out considering the shear strength parameters estimated for the recycled C&DW coming from a Portuguese recycling plant.

4.2 Boundary conditions

The modelling of geomechanic problems involves media which are better represented as unbounded. Numerical methods are based on the discretization of a finite region, so the appropriate conditions should be enforced at the artificial numerical boundaries. In static analyses, fixed boundaries can be realistically placed at some distance from the region of interest. In dynamic problems, however, such boundary conditions cause the reflection of outward

propagating waves back into the model and do not allow the necessary energy radiation. The use of a larger model can minimize the problem, however this solution leads to a large computational burden. The alternative is to use absorbing (or quiet) boundaries.

The viscous boundary developed by Lysmer and Kuhlemeyer [6] is used in FLAC. It is based on the use of independent dashpots in the normal and shear directions at the model boundaries. The method is almost completely effective at absorbing body waves approaching the boundary at angles of incidence greater than 30◦. For lower angles of incidence, or for surface waves, there is still energy absorption, but it is not perfect. However, the scheme has the advantage that it operates in the time domain [3]. More efficient energy absorption requires the use of frequency-dependent elements, which can only be used in frequency-domain analyses.

The boundary conditions at the sides of the model must account for the free-field motion. These boundaries should be placed at sufficient distances to minimize wave reflections and achieve free-field conditions. For soils with high material damping, this condition can be obtained with a relatively small distance. However, when the material damping is low, the required distance may lead to an impractical model [3]. FLAC has implemented an alternative procedure in which the free-field motion is "enforced". With these boundaries, *called free-field boundaries*, outward waves originating from the structure are properly absorbed.

The base horizontal boundary also causes the reflection of the waves back into the model. To avoid this reflection FLAC allows the introduction of absorbing boundaries called *quiet boundaries*.

In order to apply quiet boundaries along the same boundary as the dynamic input, the input motion must be applied as a stress history, because otherwise the effect of the quiet boundary will be nullified [3]. It is suggested the following formula to convert a velocity wave into a shear stress wave:

$$\tau_s = a(\rho C_s)v_s \tag{5}$$

where a = adimensional factor (being suggested a value of 2), τ_s = applied shear stress, ρ = mass density, C_s = speed of S-wave propagation and v_s = input velocity. The factor of 2 accounts for the fact that the applied stress must be double that observed in an infinite medium, since half the input energy is absorbed by the viscous boundary [3]. However, if the model is shallow, the free surface can cause an increase in the base velocity and an adjustment is necessary to produce the intended input velocity, that is to say, it is necessary to find the value of the factor "a", which gives a velocity record that corresponds to the input velocity.

Figure 7 illustrates the horizontal displacement and velocity records at the base of the model for "a" equal to 1.0 and 2.0, as well as, the curves achieved by integration of the acceleration record (goal). It can be observed that a = 2.0 gives displacements and velocities greater than those that are supposed to be introduced in the model (goal). On the other hand, for a = 1.0 a good adjustment is achieved.

Prevost [7] demonstrate that at a "silent" boundary (x = h), the shear stress $\tau(h,t)$ can be expressed as:

$$\tau(h,t) = -\rho C v(h,t) \tag{6}$$

where ρ is the mass density, C is the speed of wave propagation and v(h,t) is the velocity at x = h for the instant t. Comparing equations (5) and (6), the factor "a" equal to 1.0 is justified and seems suitable for this model.

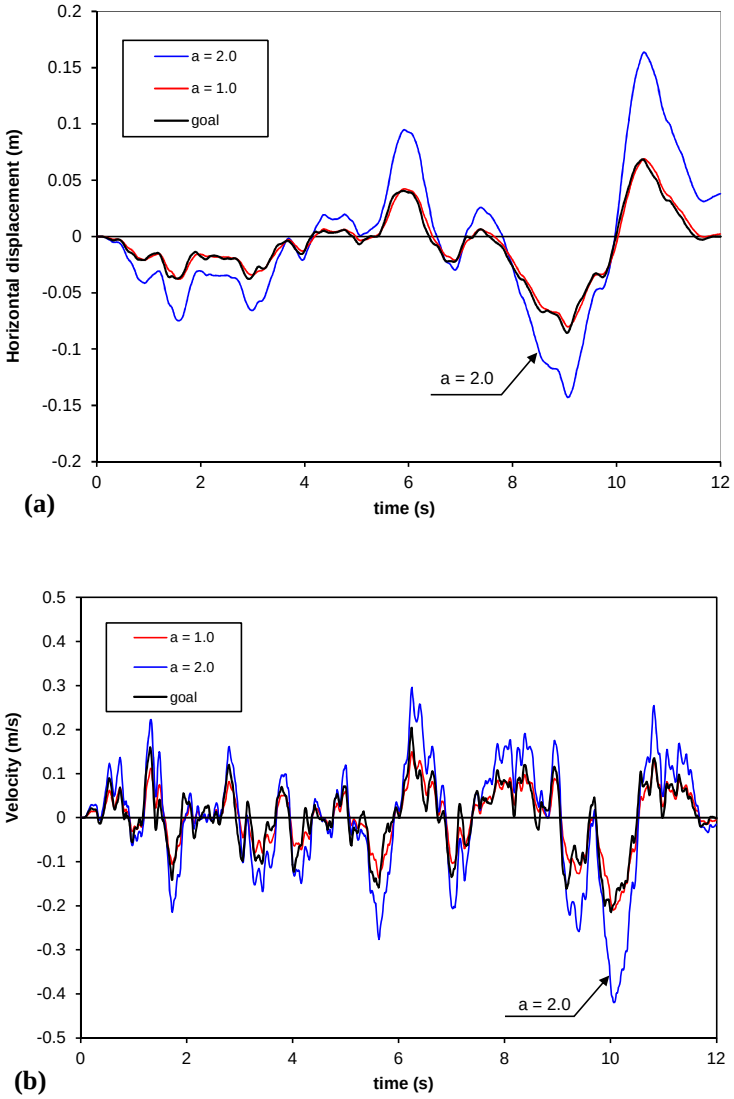


Figure 7: Adjustment to convert a velocity wave into a shear stress wave: a) displacements at the base of the model; b) velocities at the base of the model.

4.3 Effect of the backfill shear strength properties

Most of the guidelines indicate explicitly the use of the peak shear strength parameters instead of the residual shear strength parameters in the design of geosynthetic reinforced soil structures. Notwithstanding this approach is not consensual. Jewell [8] suggests the selection a design value for the soil shearing resistance equal to the critical state shear resistance and Leshchinsky [9] proposes a hybrid approach where the critical slip surface is determined based on peak shear strength and the required long-term reinforcement strength is estimated using the residual shear strength parameters.

Regarding the cohesion of the fill material, earlier versions of some guidelines have precluded the cohesive component of the shear strength, but recent editions [10, 11] allow the use of cohesive fills.

As mentioned in 4.1, Vieira et al. [2] have concluded that the shear strength of the recycled C&DW is frankly encouraging but the cohesion should be used in design with great caution due to the significant reduction for large strain conditions. Based on this evidence, the effect of the values assumed for the backfill shear strength properties was studied in this work. Three numerical analyses were carried out, considering: i) the peak shear strength parameters (*Peak values*); ii) the peak friction angle and neglecting the cohesion (*Peak friction angle*); iii) the large displacement shear strength parameters (*Residual values*).

Figure 8 presents the horizontal displacements of the wall face and the vertical settlements along the wall top at the end of the seismic motion. If the peak shear strength parameters were considered in the numerical analysis, the deformations at the end of the seismic loading would be very small. Nevertheless, if the cohesion is neglected, the backfill deformation will be have some relevance. Local bulging at the wall face, typical of wrapped face structures, is particularly noteworthy (Figure 9). The maximum horizontal displacement of the wall face take place at the crest and it is 8.7% of the wall height. The maximum settlement at the surface occurs, as expected, near the wall face and it is about 5.7% of the wall height. Figure 9 illustrates the contours of the horizontal displacements at the end of the earthquake loading for the *Peak friction angle* analysis, being noticed the large displacements at the crest of the wall.

If the residual shear strength parameters were considered in the analysis, the pattern of the wall deformation is distinct. The local bulging at the wall face is minimized, particularly at the top of the wall, and the surface settlements are also reduced (1.1% of the wall height). This evidence is quite interesting since the difference between the peak friction angle (44.1º) and the residual friction angle (41.2º) is only 2.9º, which demonstrates the importance of the cohesive term of the shear strength. A cohesion of 2.8 kPa makes a significant difference. Based on this finding, the *Peak friction angle* analysis was repeated changing the null cohesion by a cohesion of 1 kPa. This value has not any physical significance but means, due to the removal of numerical instability, smaller deformations in the retaining backfill (Figure 10).

This numerical change leads to the decrease of 64% and 69% on the maximum horizontal displacement at the wall face and maximum settlement, respectively. The differences to the results achieved in the *Residual values* analysis, obviously, are also diminished.

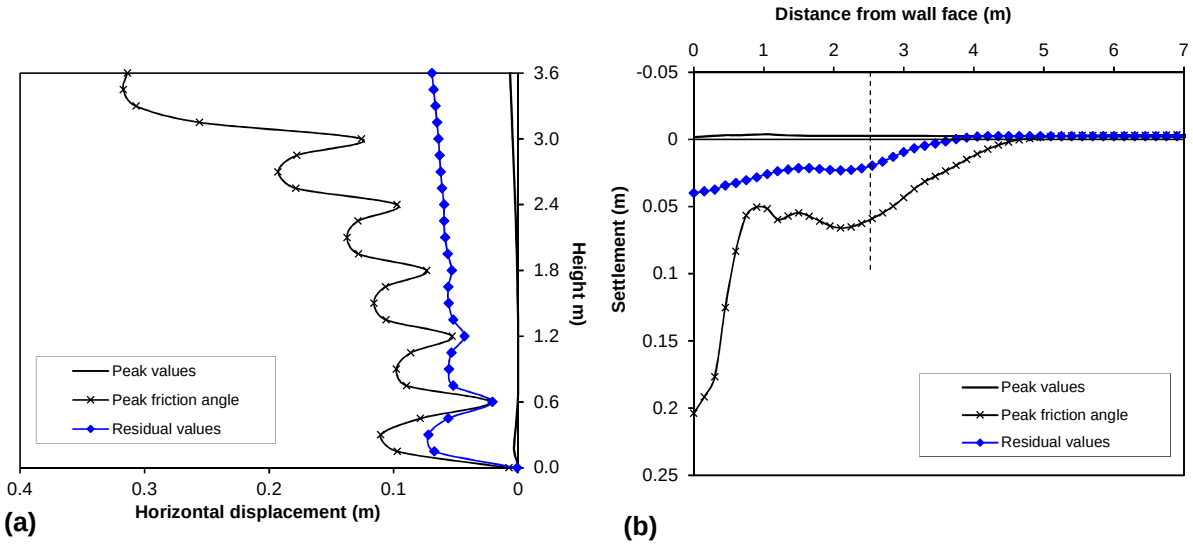


Figure 8: Effect of the backfill shear strength parameters on: a) horizontal displacements of the slope face; b) settlements at the surface.

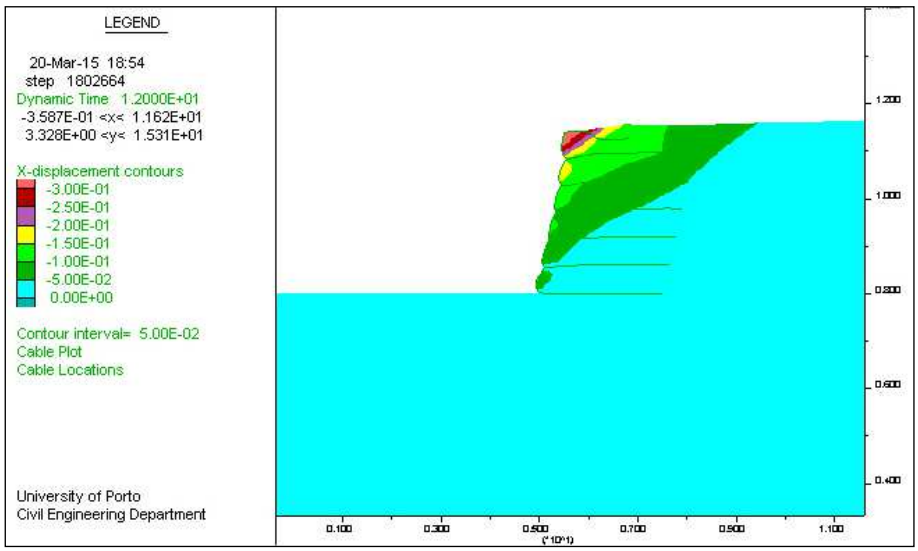


Figure 9: Contours of the seismic horizontal displacements at the end of the earthquake loading (*Peak friction angle*).

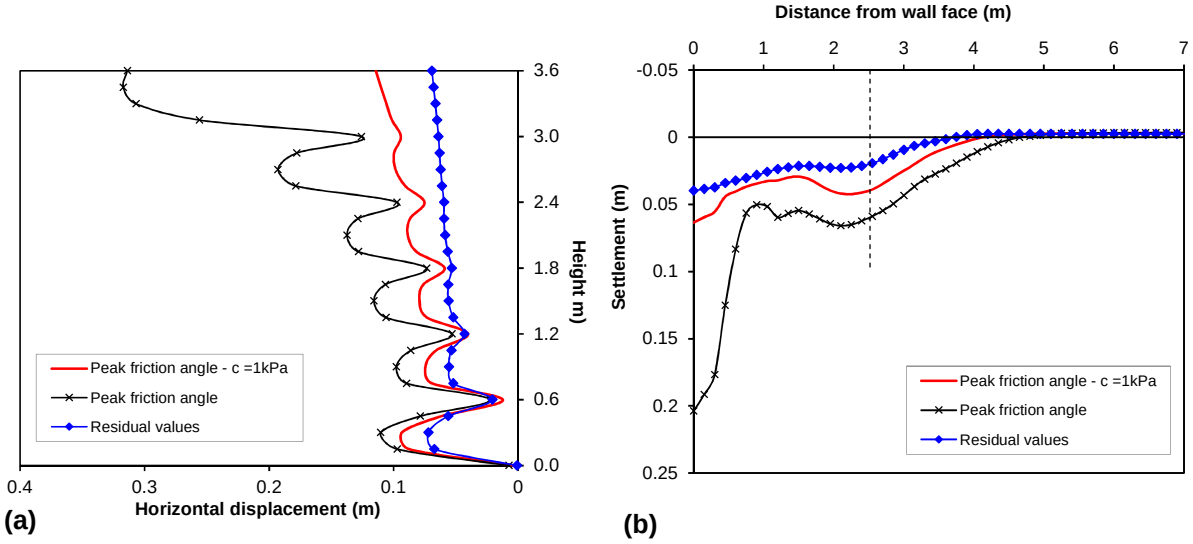


Figure 10: Effect of non-zero value of cohesion on: a) horizontal displacements of the slope face; b) settlements at the surface.

To analyze, mainly, the importance of the backfill cohesion in the seismic behaviour of the reinforced wall, a numerical analysis considering the *Strain-Softening* model for the backfill material was carried out [12]. It was admitted, in the *Strain-Softening* model, the decrease of the friction angle and cohesion from their peak values to the residual values for shear plastic strains higher than 0.5%.

Figure 11 compares the horizontal displacements of the wall face and the maximum tensile load at the reinforcement layers at the end of the seismic loading for the analyses carried out with *Strain-Softening* model and with the residual shear strength parameters. As expected, the analysis with the large displacement shear strength parameters during all the numerical simulation, ie, independent of the shear strain, provides greater horizontal displacements. With the *Strain-Softening* model the bulging effect only occurs at the base of the wall. The maximum horizontal displacement estimated with the *Strain-Softening* model is 14% lower than that ob-

tained with the large displacement shear strength parameters. The difference is maximum at height of 0.9 m and is about 55%.

The tensile load distribution through the wall height estimated in these analyses is also distinct (Figure 11b). The maximum tensile reinforcement load is quite similar but it is recorded at different geogrid layers.

With regard to the increase of the tensile load during seismic loading, an interesting conclusion was also achieved. Figure 12 illustrates the time histories of the normalized maximum tensile load recorded at the 6th reinforcement layer. The tensile load recorded during the seismic motion was normalized by the tensile load at the end of wall construction (T_0). With the *Strain-Softening* model the maximum tensile load recorded at the 6th geogrid layer increased 140 times when compared to the value supported at the end of construction. This finding is justified by the extremely low value supported by this reinforcement layer at the end of construction (note that in this analysis the peak shear strength parameters were considered until 0.5% of shear plastic strain).

The sudden increase observed in the normalized tensile load at 3.2 seconds after the beginning of the motion (Figure 12b) is probably due the increase of the shear plastic strain, visible near the top of the wall, where the potential failure surface rise the top surface.

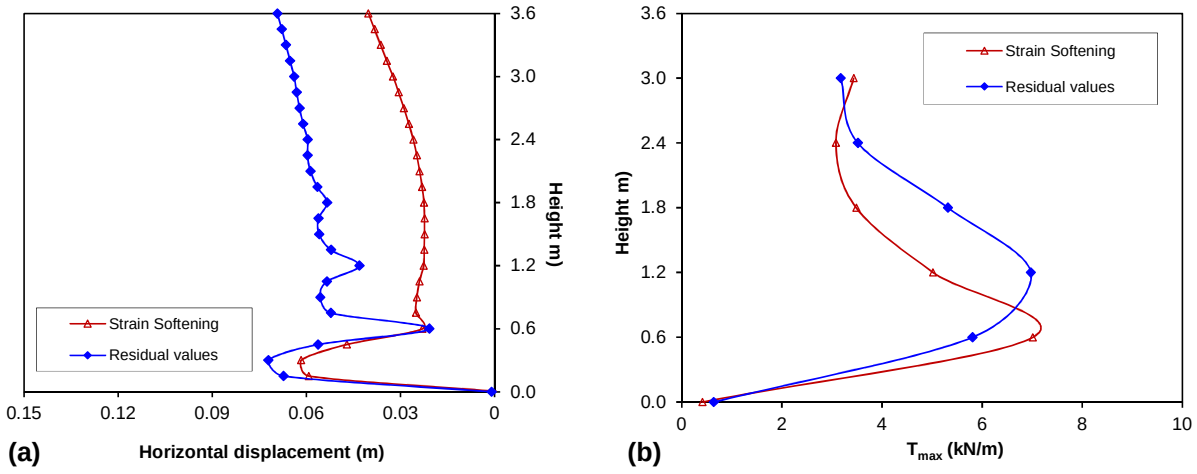


Figure 11: Effect of the backfill constitutive model on: (a) horizontal displacements of the slope face; (b) maximum reinforcement tensile loads.

4.4 Effect of the foundation soil properties

In order to investigate the influence of the foundation soil deformability on the seismic performance of the structure, an additional numerical analyses considering a stiff foundation was carried out. Figure 13 compares the horizontal displacements of the wall face considering the large displacement shear strength parameters (*Residual values)* with those obtained if the geogrid reinforced wall had been constructed over a stiff foundation.

As expected, a stiff foundation induces smaller deformations being the highest differences observed near the wall base (22%). One of the main reasons for this evidence is the occurrence of acceleration amplification for a non-rigid foundation. As shown in Figure 14 when the foundation is deformable an amplification factor greater than 1.5 is recorded at the base of the reinforced wall.

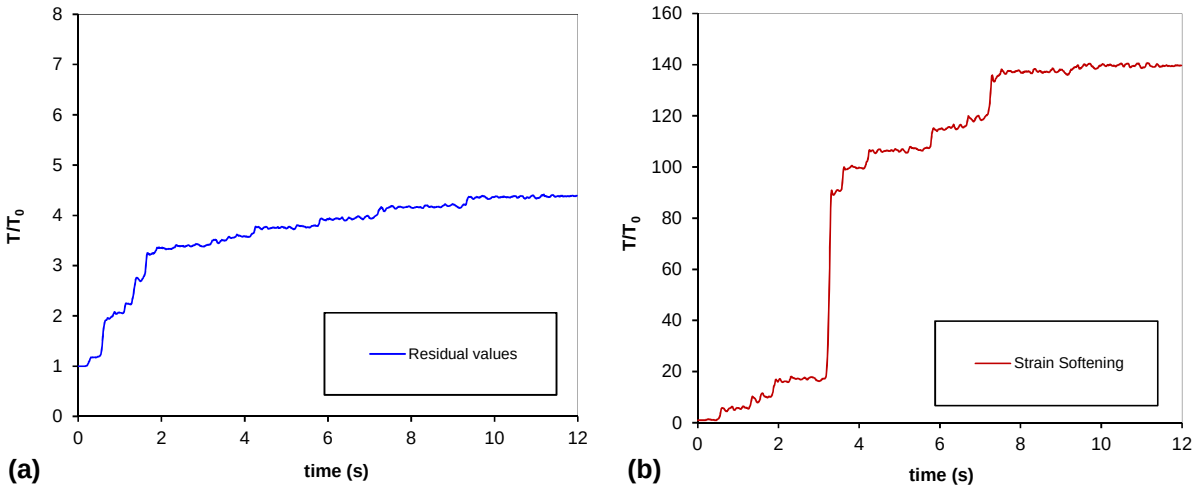


Figure 12: Evolution of the normalized maximum tensile load for the 6th reinforcement layer: (a) analysis with the residual values; (b) analysis with *Strain Softening* model.

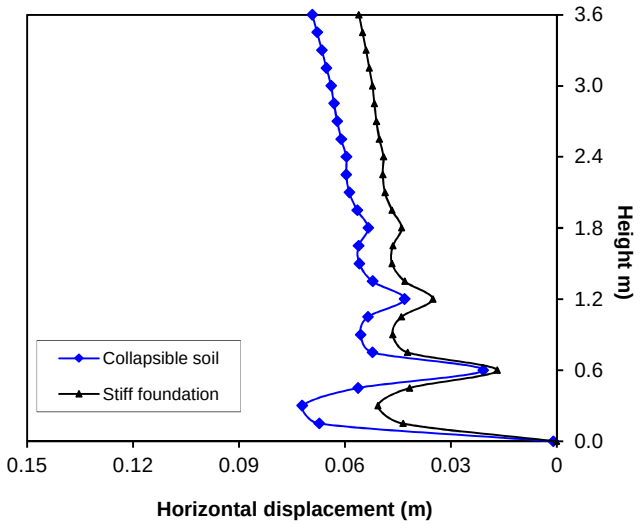


Figure 13: Influence of the foundation stiffness on horizontal displacements of the wall face (*Residual values*).

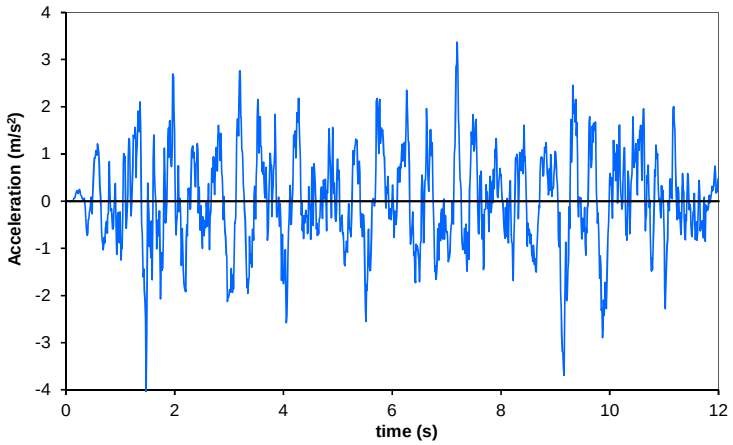


Figure 14: Acceleration record at the wall base for the collapsible soil foundation (*Residual values* analysis).

5 CONCLUSIONS

The use of recycled Construction and Demolition Wastes as backfill material reduces the use of natural resources and, simultaneously, avoids congesting landfills with inert wastes coming from buildings and other infrastructures. Therefore it is important to study the behaviour of geosynthetic reinforced structures constructed with C&D materials.

The numerical study herein presented allows to draw the following main conclusions:

- The introduction of quiet boundaries at the base of the model in FLAC implies the conversion of a velocity wave into a shear stress wave, which means that several analyses should be made to achieve the adjustment of the velocity records at the base to the input velocity;
- The use of the large displacements shear strength parameters seems to be the most appropriate approach to model the seismic behavior of geosynthetic reinforced structures constructed with C&DW as backfill material;
- When neglecting the cohesive term of the backfill shear strength, a null cohesion should be avoided. Due to the numerical instability resulting from zero cohesion, the backfill deformations seems to be overestimated.
- This hypothetical geogrid reinforced wall, constructed with recycled C&DW, showed a good performance when submitted to an earthquake with moderate magnitude and small focal distance, artificially generated for the greatest seismicity area of Portugal.

ACKNOWLEDGMENTS

The author would like to thank the financial support of Portuguese Science and Technology Foundation (FCT) and FEDER, through the Research Project: FCOMP-01-0124-FEDER-028842, RCD-VALOR – Sustainable application of Recycled Construction and Demolition Wastes (C&DW) in geosynthetic reinforced structures (PTDC/ECM-GEO/0622/2012).

REFERENCES

[1] Santos, E.C.G., Palmeira, E.M., and Bathurst, R.J., Behaviour of a geogrid reinforced wall built with recycled construction and demolition waste backfill on a collapsible foundation. Geotextiles and Geomembranes, **39,** 9-19, 2013

[2] Vieira, C.S., Pereira, P.P., and Lopes, M.L., Behaviour of geogrid-recycled Construction and Demolition Waste interfaces in direct shear mode. Proceedings of the 10th International Conference on Geosynthetics, ICG 2014; ESTREL Convention Center Berlin; Germany; 21- 25 September 2014.

[3] Itasca, FLAC - Fast Lagrangian Analysis of Continua, in Version 5.00, Itasca Consulting Group, Inc., USA, 2005

[4] Gasparini, D. and Vanmarcke, E., SIMQKE - A computer program for artificial motion generation, in User's Manual and Documentation, Department of Civil Engineering, Massachussets Institute of Technology, 1976.

[5] Fonseca, E.C.A., Palmeira, E.M., and Santos, E.C.G., Numerical analysis of a geogrid reinforced wall built with no-conventional backfill material, Proceedings of the 10th In-

ternational Conference on Geosynthetics, ICG 2014; ESTREL Convention Center Berlin; Germany; 21- 25 September 2014.

[6] Lysmer, J. and Kuhlemeyer, R.L., Finite Dynamic Model for Infinite Media. J. Eng. Mech., **95**(EM4), 859–877, 1969.

[7] Prevost, J.H., DYNA1D - A computer program for nonlinear seismic site response analysis. Technical Documentation, in Technical Report NCEER-89-0025, Princeton University, 1989.

[8] Jewell, R.A., Soil reinforcement with geotextiles. London: Special Publication 123 CIRIA, Thomas Telford. 332p, 1996.

[9] [9] Leshchinsky, D., Design dilemma: use peak or residual strength of soil. Geotextiles and Geomembranes, **19**, 111-125, 2001.

[10] AASHTO, LRFD Bridge Design Specifications, 3rd Edition: Washington DC, 2012.

[11] BS 8006, Code of practice for strengthened/reinforced soils and other fills, British Standard Institution, 2010.

[12] Vieira, C.S. and Lopes, M.L., Behaviour of a geosynthetic reinforced steep slope constructed with cohesive backfill under earthquake loading, in ECCOMAS Thematic Conference - COMPDYN 2013: 4th International Conference on Computational Methods in Structural Dynamics and Earthquake Engineering, Proceedings - An IACM Special Interest Conference: Kos Island; Greece; 12 June 2013 through 14 June 2013, 2708-2721.

COMPDYN 2015
5th ECCOMAS Thematic Conference on
Computational Methods in Structural Dynamics and Earthquake Engineering
M. Papadrakakis, V. Papadopoulos, V. Plevris (eds.)
Crete Island, Greece, 25–27 May 2015

SEISMIC GROUND RESPONSE AT LOTUNG (TAIWAN)

Dimitrios Karofyllakis[1], Gaetano Elia[2] and Mohamed Rouainia[3]

[1] Newcastle University
School of Civil Engineering and Geosciences
d.karofyllakis@ncl.ac.uk

[2] Newcastle University
School of Civil Engineering and Geosciences
gaetano.elia@ncl.ac.uk

[3] Newcastle University
School of Civil Engineering and Geosciences
mohamed.rouainia@ncl.ac.uk

Keywords: Seismic ground response analysis, Lotung experiment site, Constitutive models, Visco-elastic approach, Non-linear time-domain analysis.

Abstract. *In this paper the ground response of the Lotung experiment site during the strong-motion LSST7 occurred on May 1986 is simulated using two different numerical schemes: a simple equivalent-linear visco-elastic and a fully-coupled non-linear approach. The fully-coupled includes an advanced elasto-plastic soil model which has been calibrated against resonant column data and in-situ cross-hole measurements. The two horizontal components of the input motion are applied separately at bedrock level. The results of the simple and advanced numerical simulations are compared with the down-hole motions recorded in-situ during the investigated seismic event in terms of acceleration time histories and response spectra. The comparison between predicted results and in-situ measurements highlights the limitations of the frequency-domain approach and demonstrates the good performance of the advanced numerical scheme. Further investigation is needed to improve the numerical predictions of the observed ground response, in particular the peak ground acceleration in the N-S direction.*

1 INTRODUCTION

Experience from historical and recent strong earthquakes has demonstrated the significance of local soil conditions on the seismic ground response. The changes in amplitude, frequency content and duration of the seismic motion during its propagation in soil deposits, commonly referred to as site effects, have a crucial impact on the response of buildings and infrastructures during earthquakes [e.g. 1].

Site response analysis methods allow geotechnical engineers to quantify the effects of soil deposits on the propagation of waves from bedrock to ground surface. These methods can be divided into frequency-domain schemes (using equivalent-linear methods) and time-domain schemes (usually performed with finite element procedures). The equivalent visco-elastic approach has been widely adopted in engineering practice during the past thirty years, although its limitations have been highlighted in the literature [e.g. 2, 3]. Alternatively, time-domain finite element (FE) schemes are nowadays available to solve the ground response more accurate accounting for the solid-fluid interaction by means of a coupled effective stress formulation [e.g. 4]. In these schemes, the behaviour of soil can be described by non-linear constitutive models with different level of complexity. From the validation point of view, the performance of the different numerical approaches to simulate the complex wave propagation process has been tested over the last decades using real vertical array data and/or laboratory data obtained from centrifuge models [e.g. 5-8].

This paper presents a validation study of the Lotung Large-Scale Seismic Test (LSST) site in Taiwan using the recordings from accelerometer arrays. In particular, the prediction of the free-field response at Lotung during the event recorded in May 1986 is investigated using a simple equivalent-linear visco-elastic and a fully-coupled non-linear approach.

In the first part of the paper the geological and geotechnical properties of the LSST site are briefly described. Then, the numerical models adopted for the frequency-domain and the time-domain dynamic simulations are summarised along with the calibration against in-situ and laboratory data of the soil constitutive model used in the advanced analyses. Finally, the direct comparison between predicted and recorded motions at different depths within the soil deposit is presented. The predictions obtained with the advanced non-linear approach are particularly successful, although further improvements are still necessary to better capture the observed free-field response.

2 THE LARGE-SCALE SEISMIC TEST AT LOTUNG

The Large-Scale Seismic Test (LSST) is located in one of the most seismically active region in the North-East of Taiwan, and has been originally established in the 80's to study the dynamic behaviour of two scaled-down nuclear plant containment structures [9]. The site response has been monitored by a number of surface and down-hole accelerometer arrays, together with pore pressure transducers. The down-hole accelerometers have been installed at depths of 0, 6, 11, 17 and 47 m, oriented in N-S, E-W and vertical directions. Figure 1 shows the elevation and plan views of the instrumentation. Of particular interest here is the vertical array named DHB in Figure1(a) which has been considered as representative of the free-field response at Lotung.

The site geology consists of recent alluvium and Pleistocene materials over a Miocene basement. The upper alluvial layer, 30 to 40 m thick, consists mainly of clayey-silts and silty-clays [10]. The water table is located approximately at a depth of 1 m. The local geological profile shows a first layer of grey silty-sand and sandy-silt about 20 m thick underlain by about 10 m of more gravelly layer resting on a thick deposit of silty clay, as indicated by the SPT log profile reported in Figure 2(a).

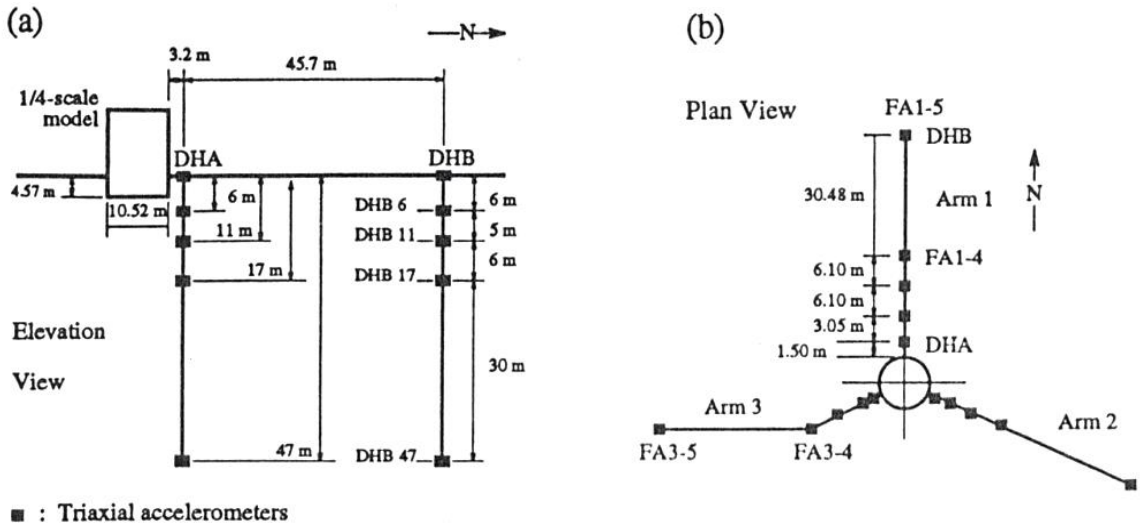


Figure 1: Instrumentation at the LSST site: (a) down-hole arrays; (b) surface arrays [11].

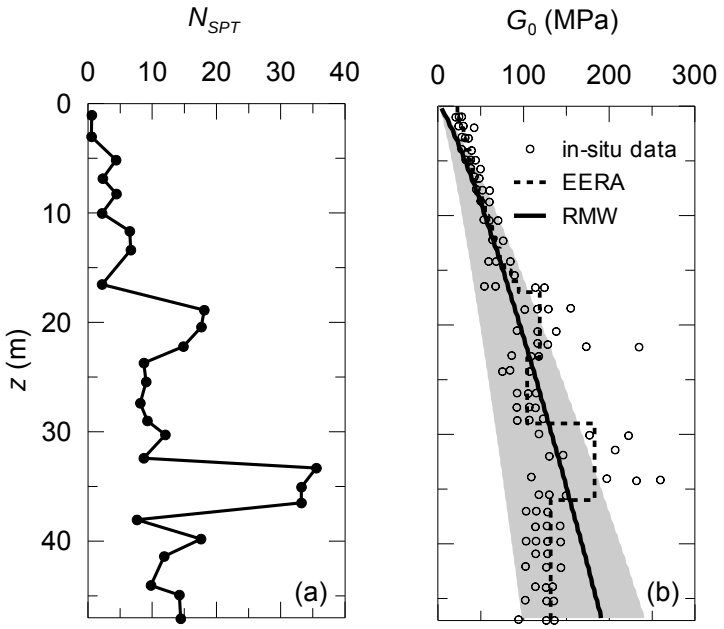


Figure 2: Local soil profile at the LSST site: (a) SPT log; (b) elastic shear modulus.

A series of geophysical seismic tests have been performed to measure shear and compression wave velocities at the LSST site. Figure 2(b) shows the elastic shear modulus data obtained from seismic cross-hole tests [12]. The bedrock formation can be assumed to be at a depth of 47 m. Shear modulus and damping ratio curves have been measured through resonant column and cyclic torsion tests on undisturbed specimens [12, 13]. Alternatively, Zeghal *et al*. [14] have proposed to back-figure the in-situ moduli ratio curves for Lotung soil based directly on its seismic response recorded along the down-hole arrays during 18 earthquakes which occurred between 1985 and 1986. In particular, different sets of G/G_0 and D-γ curves have been developed for the depths of 0-6, 6-11 and 11-17 m, producing for each depth a least-square best fit (SF) as well as an upper (UB) and a lower bound (LB) curve indicative of the possible variations in the material dynamic properties (Figure 3). The shear modulus and damping ratio curves of the soil between 17 and 47 m have been assumed to be the same as those from 11 to 17 m.

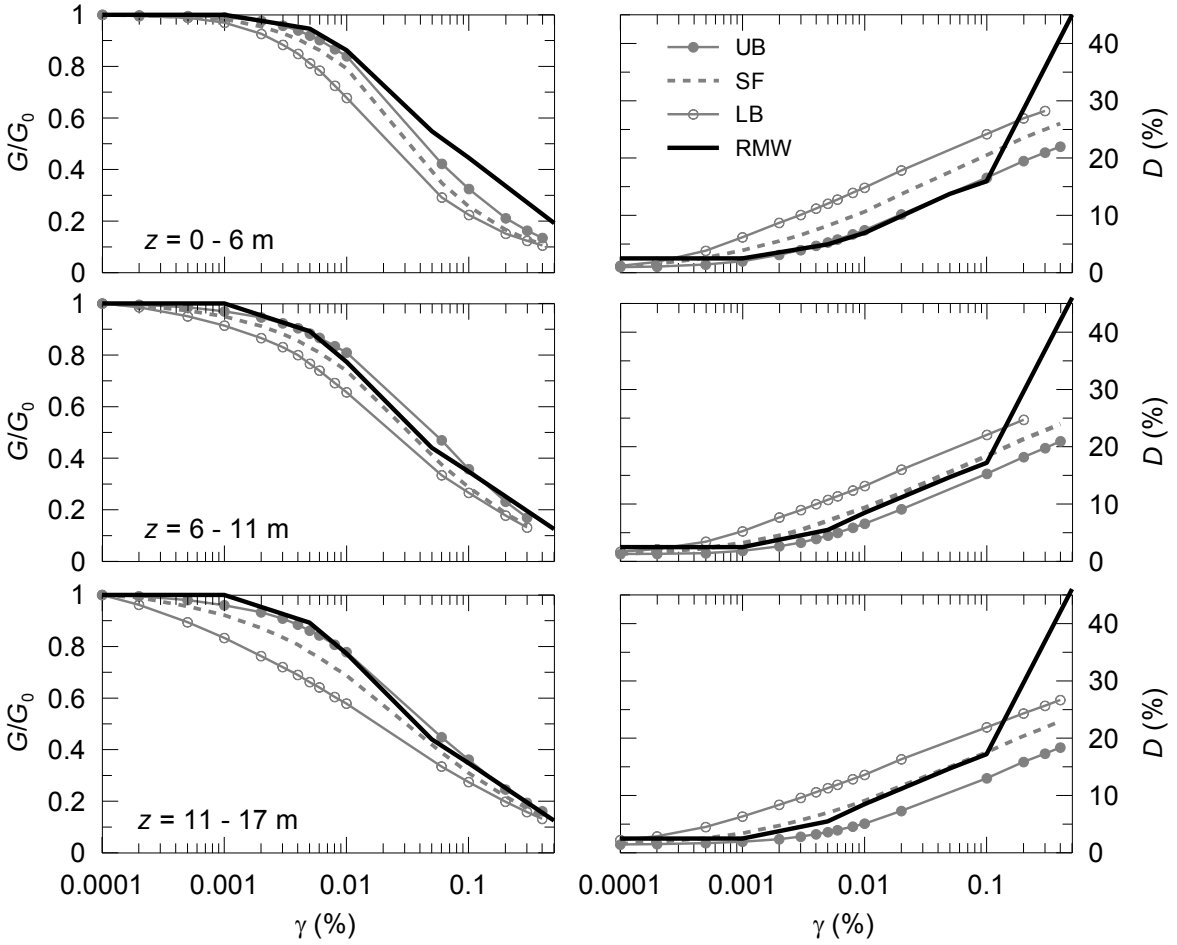


Figure 3: Shear modulus and damping curves developed by Zeghal *et al.* [14] and RMW predictions.

3 NUMERICAL MODEL

The ground response analyses of the Lotung site during the LSST7 event occurred on May 1986 have been performed using the equivalent-linear visco-elastic code EERA [15] and the FE code SWANDYNE II [16]. The earthquake, characterised by maximum accelerations of 0.16 g and 0.21 g respectively in the E-W and N-S direction, has been selected due to its strong-motion characteristics. The two horizontal components of the seismic event have been applied separately as input motions at the bedrock level (i.e. at 47 m).

3.1 Equivalent-linear visco-elastic model

The code EERA is based on the assumption of equivalent-linear visco-elastic soil behaviour. The approach makes use of the exact continuum solution of wave propagation in horizontally layered visco-elastic materials subjected to vertically propagating transient motions [e.g. 17]. The non-linear variation of soil shear modulus, *G*, and damping, *D*, with shear strain is accounted for through a sequence of linear analyses with iterative update of stiffness and damping parameters. For a given soil layer, *G* and *D* are assumed to be constant with time during the shaking. Therefore, an iterative procedure is needed to ensure that the properties used in the linear dynamic analyses are consistent with the level of strain induced by the input motion in each layer.

In the presented EERA analyses, the profile of small-strain stiffness shown in Figure 2(b) with a dashed black line has been discretised by constant stiffness sub-strata of 1 m thickness.

The statistical fit (SF) curves reported in Figure 3 have been adopted in the visco-elastic simulations for the top layers (i.e. between 0 and 17 m). From 17 to 47 m the same curves as those relevant to the depth between 11 and 17 m have been considered.

3.2 Non-linear finite element model

The ground response analysis of the Lotung experiment site has been also undertaken using the two-dimensional fully-coupled finite element code SWANDYNE II. The code allows to perform linear and non-linear dynamic analyses, using the Generalised Newmark method [18] for time integration. In particular, the values of the Newmark parameters selected in all the FE analyses illustrated in this note are $\beta_1 = 0.600$ and $\beta_2 = 0.605$ for the solid phase and $\beta_1^* = 0.600$ for the fluid phase. These values ensure that the algorithm is unconditionally stable, while being dissipative mainly for the high frequency modes [e.g. 4]. A 5 m wide, 47 m high FE mesh composed by 235 isoparametric quadrilateral finite elements with 8 solid nodes and 4 fluid nodes has been used in the dynamic simulations. The base of the mesh has been assumed to be rigid, while equal displacements have been imposed to the nodes along the vertical sides (i.e. tied-nodes lateral boundary conditions). Base and lateral hydraulic boundaries have been assumed as impervious, while drained conditions have been imposed at the top of the mesh. A small amount of viscous damping, equal to 3%, has been introduced into the model through a standard Rayleigh formulation [e.g. 19] to reduce the high frequency spurious spikes.

In order to investigate the effects of soil non-linearity on the wave propagation process, plasticity has been implemented in the FE simulations through the advanced elasto-plastic model (RMW) developed by Rouainia and Muir Wood [20]. The RMW model allows to reproduce some of the key features of the cyclic behaviour of natural soils as the decay of the shear stiffness with strain amplitude, the corresponding increase of hysteretic damping and the related accumulation of excess pore water pressure under undrained conditions. The model has been implemented in SWANDYNE II with an explicit stress integration algorithm adopting a constant strain sub-stepping scheme. RMW has been successfully employed to simulate both static [21, 22] and dynamic geotechnical problems [23, 24]. For more details on its formulation and implementation the reader is referred to Rouainia and Muir Wood [20] and Zhao *et al*. [25].

In previous versions of the model a classical hypoelastic formulation was employed for the determination of the bulk and shear moduli, K and G_0. In this work, the well-known equation proposed by Viggiani and Atkinson [26] for the small-strain shear modulus has been implemented to reproduce the dependency of G_0 on the mean effective stress (p) and the overconsolidation ratio (OCR):

$$\frac{G_0}{p_r} = A\left(\frac{p}{p_r}\right)^n OCR^m \tag{1}$$

where p_r is the reference pressure (equal to 1 kPa). The non-dimensional parameters A, m and n depend on the properties of the soil and can be determined as function of the plasticity index. In the initialisation of the FE model, a higher overconsolidation ratio has been assumed for the upper part of the FE column (from 0 to a depth of 6 m), with an average OCR equal to 4, while a constant OCR of 2 has been imposed for the remaining part of the model. The assumed variation of OCR with depth is deemed to be realistic in accordance with the G_0 data shown in Figure 2(b), where a non zero elastic shear modulus of about 25 MPa can be observed near the ground surface (corresponding to a measured shear wave velocity of about 100 m/s). Once the FE model has been initialised, a range of possible elastic shear modulus

profiles, reported in Figure 2(b) with the shaded area, have been investigated and the final G_0 profile adopted in the FE dynamic simulations is shown in the same figure with a solid black line.

Numerical simulations of undrained cyclic simple shear tests have been carried out with RMW in order to produce normalized shear modulus and damping curves. The secant shear modulus and the damping ratio for each shear strain amplitude have been assessed after 500 load cycles, a number sufficient to reach steady-state condition. The results of the single element tests performed with the RMW model are reported in Figure 3 with a solid black line for each depth and compared with the corresponding curves presented by Zeghal *et al*. [14]. Table 1 summarises the RMW model parameters adopted for the different soil layers.

Depth	λ^*	κ^*	M	R	B	ψ	r_0
0-17 m	0.03	0.0015	0.922	0.08	0.60	1.0	1.0
17-23 m	0.03	0.0015	1.096	0.08	0.60	1.0	1.0
23-29 m	0.03	0.0015	0.814	0.08	0.60	1.0	1.0
29-37 m	0.03	0.0015	0.941	0.08	0.60	1.0	1.0
37-47 m	0.03	0.0015	0.730	0.08	0.60	1.0	1.0

Table 1: Material parameters for the RMW model.

4 RESULTS AND DISCUSSION

The results of the EERA simulations are shown in Figure 4 with a dashed black line in terms of acceleration time histories recorded at depths 0 and 11 m. The corresponding downhole motions recorded in-situ during the earthquake along the DHB array [27], named FA1-5 and DHB-11, are reported in the same figure. The comparison shows that EERA is able to predict the E-W motion very well, particularly at the depth of 11 m both in terms of peak acceleration and zero crossing. The peak acceleration at ground surface in the E-W direction is slightly over-estimated. On the contrary, a poorer prediction can be obtained by applying the N-S component at bedrock level: the equivalent-linear analysis under-predicts the peak acceleration significantly both at ground surface and at the depth of 11 m. Moreover, a time shift in the acceleration peak between the recorded and predicted motions can be observed at surface. A similar performance of the equivalent-linear visco-elastic approach has been observed by Borja *et al*. [5] and Amorosi *et al*. [8].

In addition to the EERA results, Figure 4 also shows the predictions obtained with the FE non-linear approach. The time-domain analyses, undertaken within the SWANDYNE II finite element code along with the RMW constitutive model, are in good agreement with the recorded data, especially at the depth of 11 m from surface, for both the E-W and N-S component. The predicted peak acceleration of the E-W motion at ground surface agrees well with the observed array data, while a slight under-estimation of the PGA can be seen in the N-S direction. A very good agreement with the array data is obtained in terms of zero crossing.

The response spectra (for 5% damping) of the acceleration time histories recorded during the EERA and SWANDYNE II simulations at ground surface and 11 m depth are presented in Figure 5. While the agreement with the array data obtained by both the visco-elastic and FE non-linear schemes is evident for the E-W component of the input motion, EERA is not able to correctly capture the frequency content of the N-S component both at 0 and 11 m depth. On the contrary, a significant improvement in the frequency prediction of recorded data is obtained by the advanced numerical approach. It should be noted that the wave signal arrives at the depth of 11 m already significantly damped from the deeper soil layers, for which a proper

geotechnical characterization in terms of reduction in shear modulus and damping is not available.

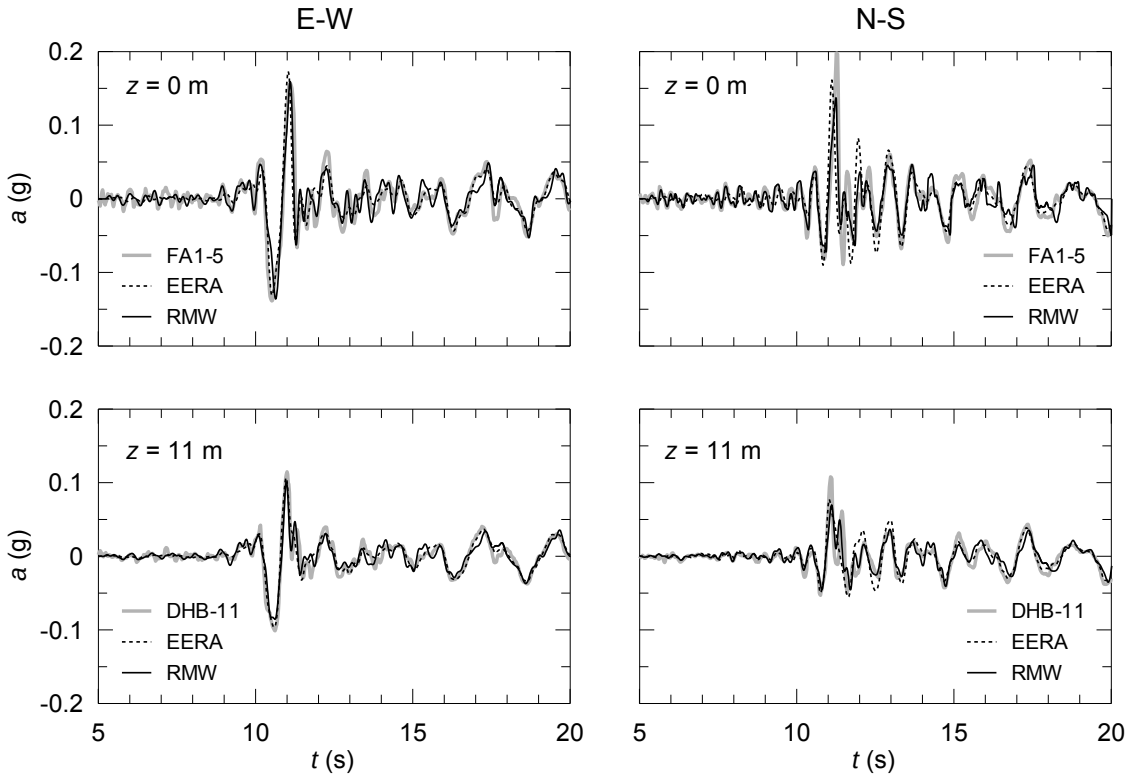


Figure 4: Comparison between predicted acceleration time histories and array data.

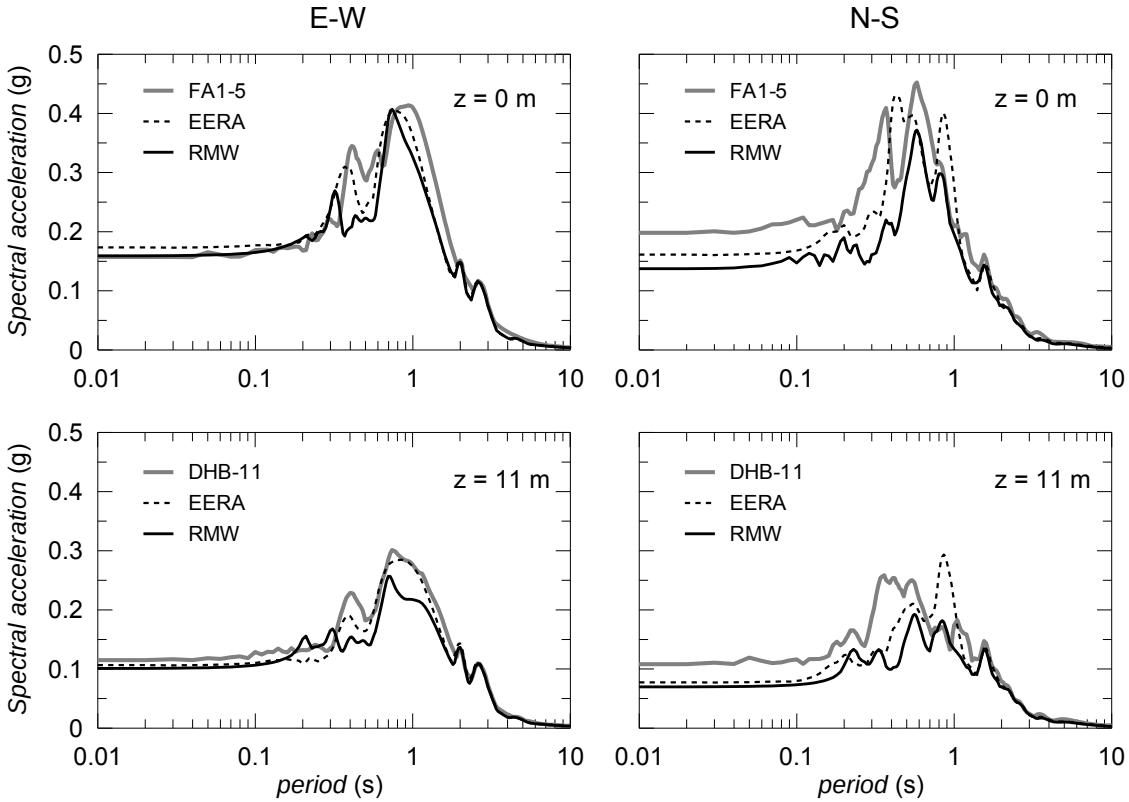


Figure 5: Comparison between predicted response spectra and array data.

5 CONCLUSIONS

The ground response analysis of the Large-Scale Seismic Test site in Lotung has been studied in this work using the simple equivalent-linear visco-elastic method and a fully-coupled non-linear FE approach The incorporation of plasticity through an advanced elasto-plastic model, which has been calibrated against laboratory and in-situ data, has allowed the effects of soil non-linearity on the wave propagation to be investigated. The comparison with recorded array data has enabled to assess the performance of the two numerical schemes, highlighting the limitations of the visco-elastic method and the advantages of the advanced approach. In particular, the results have shown how the frequency-domain approach is unable to capture the frequency content of the observed acceleration in the N-S direction at all investigated depths. In contrast, the fully-coupled simulations are in good agreement with the array data in terms of frequency, although a small under-estimation of the peak ground acceleration in the N-S direction has been observed. Further improvements are still necessary to better simulate the observed free-field response.

REFERENCES

[1] J.E. Daniell and A. Vervaeck, *Damaging Earthquakes Database 2012 – The Year in Review*, CEDIM Research Report 2013-01, Center for Disaster Management and Risk Reduction Technology, Potsdam, Germany, 2013.

[2] A.O.L. Kwok, J.P. Stewart, Y.M.A. Hashash, N. Matasovic, R. Pyke, Z. Wang, Z. Yang, Use of exact solutions of wave propagation problems to guide implementation of nonlinear seismic ground response analysis procedures, *Journal of Geotechnical and Geoenvironmental Engineering*, 133(11):1385-1398, 2007.

[3] A. Amorosi, D. Boldini, G. Elia, Parametric study on seismic ground response by finite element modelling, *Computers & Geotechnics*, 37(4):515-528, 2010.

[4] O.C. Zienkiewicz, A.H.C. Chan, M. Pastor, B.A. Schrefler, T. Shiomi, *Computational Geomechanics (with special reference to earthquake engineering)*, Wiley & Sons, Chichester, 1999.

[5] R.I. Borja, H.Y. Chao, F.J. Montáns, C.H. Lin, Nonlinear ground response at Lotung LSST site, *Journal of Geotechnical and Geoenvironmental Engineering*, 125(3):187-197, 1999.

[6] A.W. Elgamal, Z. Yang, E. Parra, Computational modelling of cyclic mobility and post-liquefaction site response, *Soil Dynamics and Earthquake Engineering*, 22:259-271, 2002.

[7] C. Phillips and Y.M.A. Hashash, Damping formulation for nonlinear 1D site response analyses, *Soil Dynamics and Earthquake Engineering*, 29:1143-1158, 2009

[8] A. Amorosi, G. Elia, D. Boldini, F. Schiavone, Seismic ground response analysis: comparison between numerical simulations and observed array data, *Proc. 5th Int. Conf. on Earthquake Geotechnical Engineering*, Santiago, Chile, 10-13 January, 2011.

[9] H.T. Tang, Y.K. Tang, J.C. Stepp, Lotung large-scale seismic experiment and soil-structure interaction method validation, *Nuclear Engineering and Design*, 123:197-412, 1990.

[10] D.G. Anderson, *Geotechnical synthesis for the Lotung large-scale seismic experiment*, Tech. Rep. No. 102362, Electric Power Research Institute, Palo Alto, California, 1993.

[11] A.W. Elgamal, M. Zeghal, H.T. Tang, J.C. Stepp, Lotung downhole array. I: Evaluation of site dynamic properties, *Journal of Geotechnical Engineering*, 121(4):350-362, 1995.

[12] D.G. Anderson and Y.K. Tang, Summary of soil characterization program for the Lotung large-scale seismic experiment, *Proc. EPRI/NRC/TPC Workshop on Seismic soil-struct. interaction anal. techniques using data from Lotung*, Taiwan, EPRI NP-6154, Electric Power Research Institute, Palo Alto, California, 1, 4.1-4.20, 1989.

[13] EPRI, *Guidelines for determining design basis ground motions – Vol. 1: Method and guidelines for estimating earthquake ground motion in Eastern North America*, Rep. No. TR-102293, Electric Power Research Institute, Palo Alto, California, 1993.

[14] M. Zeghal, A.W. Elgamal, H.T. Tang, J.C. Stepp, Lotung downhole array. II: Evaluation of soil nonlinear properties, *Journal of Geotechnical Engineering*, 121(4):363-378, 1995.

[15] J.P. Bardet, K. Ichi, G.H. Lin, *EERA: A computer program for Equivalent-linear Earthquake site Response Analyses of layered soil deposits*, Department of Civil Engineering, University of Southern California, Los Angeles, California, 2000.

[16] A.H.C. Chan, *User Manual for DIANA-SWANDYNE II*, School of Engineering, University of Birmingham, UK, 1995.

[17] J.M. Roesset, Soil amplification of earthquakes. Desai and Christian eds. *Numerical Methods in Geotechnical Engineering*, McGraw-Hill, New York, pp. 639-682, 1977.

[18] M.G. Katona and O.C. Zienkiewicz, A unified set of single step algorithms Part 3: the Beta-m method, a generalisation of the Newmark scheme, *International Journal of Numerical Methods in Engineering*, 21:1345-1359, 1985.

[19] R.W. Clough and J. Penzien, *Dynamics of Structures, 2nd Edition*, McGraw-Hill, New York, 1993.

[20] M. Rouainia and D. Muir Wood, A kinematic hardening constitutive model for natural clays with loss of structure, *Géotechnique*, 50:153-164, 2000.

[21] N.A. Gonzáles, M. Rouainia, M. Arroyo, A. Gens, Analysis of tunnel excavation in London Clay incorporating soil structure, *Géotechnique*, 62(12):1095-1109, 2012.

[22] S. Panayides, M. Rouainia, D. Muir Wood, Influence of degradation of structure on the behaviour of a full-scale embankment, *Canadian Geotechnical Journal*, 49:344-356, 2012.

[23] G. Elia and M. Rouainia, Seismic performance of earth embankment using simple and advanced numerical approaches, *Journal of Geotechnical and Geoenvironmental Engineering*, 139(7):1115-1129, 2013 .

[24] G. Elia and M. Rouainia, Performance evaluation of a shallow foundation built on structured clays under seismic loading, *Bulletin of Earthquake Engineering*, 12(4):1537-1561, 2014.

[25] J. Zhao, D. Sheng, M. Rouainia, S.W. Sloan, Explicit stress integration of complex soil models, *International Journal of Numerical and Analytical Methods in Geomechanics*, 29(12):1209-1229, 2005.

[26] G. Viggiani and J.H. Atkinson, Stiffness of fine-grained soil at very small strains, *Géotechnique*, 45(2):249-265, 1995.

[27] H.T. Tang, *Large-scale soil structure interaction*, Rep. No. NP-5513-SR, Electric Power Research Institute, Palo Alto, California, 1987.

COMPDYN 2015
5th ECCOMAS Thematic Conference on
Computational Methods in Structural Dynamics and Earthquake Engineering
M. Papadrakakis, V. Papadopoulos, V. Plevris (eds.)
Crete Island, Greece, 25–27 May 2015

THREE DIMENSIONAL ANALYSIS OF A CFRD DAM USING THE MATERIAL POINT METHOD

F. Zabala[1], R. D. Rodari [2], and L. O. Oldecop [2]

[1] Earthquake Engineering Research Institute, National University of San Juan. Argentina

fzabala@unsj.edu.ar

[2] Earthquake Engineering Research Institute, National University of San Juan. Argentina

rodari@unsj.edu.ar, oldecop@unsj.edu.ar

Keywords: Material Point Method, plastic strain localization, earth dams

Abstract. Seismic safety of earth or rockfill dams and embankments is strongly conditioned by permanent displacements caused by earthquakes. For a severe earthquake, the permanent displacement pattern results from the combination of displacements generated by volumetric and shear plastic strains distributed within the structure, and those caused by sliding of the soil mass along one or more failure surfaces. Numerical procedures commonly used in practice do not consider the strain localization phenomena at failure surfaces and the associated mesh dependence of the solution. Typically, nonlinear finite element or finite difference codes yield an estimate of distributed deformations and dynamic response, without accounting for the plastic strain localization problem. In addition, some of the numerical approaches used in practice do not consider the change of configuration caused by large displacements. The material point method or MPM is a lagrangian "particle-mesh" numerical method. It has been previously used in modeling dynamic problems with large displacements and strain localization. With MPM, a body is discretized into a collection of lagrangian particles, which carry all the data needed to define the body's state. Interaction between particles takes place in a background fixed mesh, similar to those used in the finite element method. The MPM is applied in this paper to model the three dimensional dynamic response of Punta Negra dam, a concrete faced gravel dam which is being built in San Juan Province, Argentina..

1 INTRODUCTION

The geomorphologic and climatic features of the central-west part of Argentina cause most of the population to concentrate in oases served by artificial irrigation. Water supply to these oases, both for irrigation and for human consumption, and the need of power generation have encouraged the construction of large dams in all rivers with permanent flow regimes. All these dams are located upstream of important population centers and crop fields. Collapse of one of these works would threat human lives, properties and lifelines, like water provision systems for human consumption and for irrigation. In addition, this region is the one with the greatest seismic activity in the country. Considering the magnitude of past earthquakes it is clear that the region of Precordillera in west Argentina has a seismic hazard level comparable to that of the most seismically active areas in the world.

During the 90's decade of the twentieth century, the knowledge about the seismic motion in epicentral areas was substantially improved. This was due to the increase in extension and density of strong motion seismographs networks, which were installed in many countries across the world since the 80's. The major increase in the amount of field data and the possibility of obtaining measurements of the motion within the epicentral area (less than 20 km from the seismic source), have led to the identification of new features of seismic motions that were previously unknown.

Several conclusions can be drawn from the strong motion information that was obtained. First, instrumental information shows that peak ground accelerations occurring in epicentral areas are substantially larger than the limits assumed as physically possible before the 90's decade. In rock sites, the largest ground acceleration for any earthquake magnitude was supposed to be less than 0.8g. This limit has been largely exceeded in many epicentral records obtained during recent earthquakes. Also it has been noted that many epicentral records contain large velocity pulses, reaching values significantly larger than the ones thought as reasonable before the 90's decade. These velocity pulses are known to be caused by directivity (Somerville [1]) and fling effects (Steward [2]). Such features were detected in various earthquakes as Loma Prieta (USA, 1989), Landers (USA, 1993), Kocaeli (Turkey, 1999), Chi-Chi (Taiwan, 1999) and Ducze (Turkey, 1999). These velocity pulses imply the content of long period components in the acceleration record. These long period components particularly affect large earth dams, which have typical natural periods (in the inelastic range) between 0.5 and 2 seconds.

On the other hand, advances in seismic source characterization techniques, fundamentally neotectonic and paleoseismology, have led to a re-evaluation of seismic threat in dams sites, allowing detection of cases in which this threat had been underestimated at the time of dam design.

It is important to emphasize the main role that paleoseismicity research plays in the seismic characterization of a region. This research is of main concern for the seismic design of dams, since seismic motions usually specified for the design of these structures have return periods between 5000 and 10000 years, whereas historical seismic activity in the midwest region of Argentina has been observed and recorded just for little more than 200 years. Paleoseismicity research allows the extension of the observation window to the whole Quaternary (1.6 million years), bringing great enhancement to our ability to understand and characterize a region's seismic activity.

2 CRITERIA FOR SEISMIC VERIFICATION OF DAMS

According to international practice, dams should be verified under two scenarios: normal operation earthquake and safety earthquake. Under the normal operation earthquake, the dam is expected to sustain seismic action with minor damage that not implies interruption in operation. For the safety earthquake, the structure is expected neither to collapse nor reach a situation of uncontrolled water release, although it is acceptable the occurrence of important damage leading to the need of stopping the operation or even to empty the reservoir in order to carry out reparations.

From a methodological point of view and considering the available tools, analysis of the behavior of a dam sustaining normal operation earthquake does not pose great difficulty in most cases. The design process normally involves stability check, permanent deformation and displacements estimation and stress check in concrete structures. In contrast, when considering the safety earthquake, dams located in areas of high seismic hazard are expected to sustain major damage, taking the structure to a near-collapse stage. In fact, evaluation of safety should include analysis of all possible collapse mechanisms for the structure, in order to study the structure's safety margin with respect to each of these mechanisms. An earthquake can induce over earth dams (Seed [3]) different natures of damage such as: settlement (loss of freeboard), embankments sliding, sliding of dam over foundation and cracking of watertight members and uncontrolled water leaks.

Safety evaluation at high damage stages such as those expected to be produced by the safety earthquake may require sophisticated analysis tools. From a mechanical and hydraulic point of view, the analysis should take into account a series of complex phenomena. In earth dams, such phenomena may include the occurrence of plastic strains, liquefaction or cyclic mobility of saturated granular materials, strain localization in sliding surfaces, cracking, large displacements problems and water seepage with particle erosion.

In general, the kind of analysis tools that would be required to perform a complete analysis of the dam behavior under the action of the safety earthquake are still under development, some of them being used for research purposes, but they are not of common use in engineering practice. The main obstacle to achieve the spreading of sophisticated analysis tools to practice is that they are not yet conveniently tested against measurements and observations of real cases, being an additional difficulty the low number of dams that had sustained intense, epicentral area seismic motion.

3 ANALYSIS TOOLS FOR EVALUATION OF DAMS SEISMIC BEHAVIOR.

The level of seismic excitation currently considered for safety assessment of dams takes the analyses into behavior stages that were not considered previously, changing in many cases the scope and methodology of verification.

As an example, in the case of earth dams with central clay core, years ago the goal of verification was to ensure that, within the body and the foundation of the dam, the water pressure built-up due to earthquake action is limited to moderate values. This was the logical design criterion following the Terzaghi's effective stress principle, since if the pore pressure increase becomes equal to the existing effective stress, the material's strength would drop to zero and such a dangerous situation should be avoided. This situation does not really imply the structure to be at risk of collapse. Since dense granular materials tend to dilate when subjected to shear strains, the pore pressure would drop immediately if any minor sliding takes place. The undrained residual strength of dense granular materials is high, and therefore the stability of

many structures is ensured even if the earthquake does cause high pore pressures. In fact, the dilatant material can reach cyclic mobility during the seismic motion, which implies a momentary loss of stiffness without loss of strength. If this were the case, it would be necessary to estimate permanent deformations caused by the earthquake, and to check that these deformations do not represent a risk to the structure (overtopping risk, for example).

Traditional tools used to perform safety analysis of dams subjected to seismic action are stability evaluation by limit equilibrium methods, dynamic response analysis by means of elastic or linear equivalent finite element models and estimation of permanent displacements using Newmark [4] method. Table 1 shows some features of the evolution of analysis methods, from the linear equivalent model used in the 80´s to nonlinear coupled effective stress analysis.

Particle models can deal with large displacement without the mesh distortion that arises with finite element method. Mesh preparation and 3d models are simpler to develop.

	Dynamic analysis with linear equivalent finite element model	**Nonlinear coupled effective stress analysis. Finite elements**	**Nonlinear coupled effective stress analysis. Finite elements and Particle methods**
Model Results	Final pore pressure distribution. Acceleration response.	Step by step pore pressure buildup and dissipation. Acceleration response. Permanent deformations.	Step by step pore pressure buildup and dissipation. Acceleration response. Permanent deformations. Localized deformation zones. Collapse mechanism arises from the model.
Safety checks	Post-earthquake stability analysis with effective stresses. Deformation potential. Newmark displacement analysis using acceleration response.	Post-earthquake stability analysis with materials residual strength. Newmark displacement analysis. Final freeboard loss.	Final displacements. Final freeboard loss.
Model features	Dynamic response errors. No estimation of plastic deformation.	Poor definition of localized zones, yield surfaces and cracks. Mesh dependence of localized deformation zones.	Need of regularization techniques for softening materials. Large displacement without mesh distortion.

Table 1. Evolution of models for safety assessment of earthdams

Seismic safety of earth and rockfill dams is strongly dependent on the magnitude of the final displacements of the dam's body and its foundation after a destructive earthquake. Permanent displacements are caused by volumetric and shear plastic strains distributed within the structure combined with displacements caused by sliding along several failure surfaces. The numerical procedures used in current practice usually do not consider the strain localization in these failure surfaces nor the dependence of the solution upon the size of the finite element or finite difference mesh. Most of the nonlinear dynamic codes currently used, yield only an estimate of the strains distribution and dynamic response, without adequately considering the localization of plastic deformations. In addition, some of the numerical procedures used in practice do not consider the changes in the configuration of the dam caused by large displacements.

In the dynamic analysis of finite element models of earth dams, it does not seem practical to solve the numerical problems arising from the strain localization phenomenon by using adaptive meshes coupled with some regularization procedure or discrete sliding surfaces or cracks that propagate within the dam model. This is because external loads change at every moment along the base acceleration history, imposing variable conditions of strain localization to the soil mass. In other words, during the movement a number of failure surfaces may appear in downstream or upstream slopes. These surfaces may be active or not, depending on the evolution of accelerations imposed by the earthquake. On the other hand the width of the zone of localized plastic strains, or failure surface, is in the order of a few nominal diameters of soil particles, while a reasonable computation time for the calculations requires a minimum size of the mesh in the order of 1 to 2 m. Therefore the practical possibilities to solve this problem are reduced to the use of constitutive equations that render the softening strain response as dependent on the size of the element or to introduce discontinuities in the displacement field combined with discrete stress-displacement constitutive equations. Non-local constitutive equations or constitutive equations that take into account the strain gradient are unable to capture the failure surface, with the mesh sizes used in practice, but can provide mesh independence of the solution.

It is worth noting that the behavior of each type of earthdam structure is different. In zoned dams, upstream displacements of the upstream shell are expected due to the phenomenon of cyclic mobility taking place in the saturated materials. On the contrary, in concrete faced dams, larger permanent displacements are expected to occur in the downstream slope when the reservoir is full. The upstream portion of the dam is under high confinement stresses due to the action of water loads over the concrete face and hence this portion is much stiffer than the rest.

High accelerations are to be expected at the crest of dams, due to dynamic amplification effects. These accelerations may induce sliding failures in the crest area. Other failure surfaces may occur by the presence of weak zones. In these cases, unless special techniques are applied, usual finite element codes cannot satisfactorily reproduce this kind of failure involving strain localization.

4 MATERIAL POINT METHOD

The method was initially described by Sulsky et al. ([5], [6]) and by Sulsky and Schreyer [7]. The material point method represents the material contained in a region as a collection of unconnected material points or lagrangian “particles”. An initial mass is assigned to each particle. Particle masses remain fixed throughout the calculation process, thus insuring global mass conservation. Other initial quantities, such as velocities, strains and stresses, are also assigned to the material points.

The discrete motion equations are not solved at the material points. Instead a support mesh, built to cover the domain of the problem, is used (Figure 1). This mesh is composed of elements of the same type as those used in the finite element method. For the sake of simplicity, it is common to use bilinear regular quadrilateral elements. The variables required to solve the motion equations in the mesh at any step of the analysis are transferred from the particles to the nodes of the mesh by using mapping functions. These are the typical shape functions used in the finite element method. The boundary conditions are imposed at the mesh nodes and the motion equations are solved by using an incremental scheme. Then the quantities carried by the material points are updated through the interpolation of the mesh results, using the same shape functions. The information associated to the mesh is not required for the next step of the analysis; therefore it can be discarded provided that the boundary conditions that may have

been established are preserved. This avoids mesh distortion for large displacements and convection errors. The method is well suited for dynamic problems with large displacements and incorporates in a natural way a non-slip contact algorithm. MPM is similar to the finite element method because the weighting functions which are used in the mesh are of the same type as those used in FEM, and the "particles" could be considered in some cases, as integration points that are not necessarily located at the coordinates of the Gaussian integration points used in FEM. Implementation of the MPM is easy because several of its fundamental assumptions and mathematical technologies are similar to those that support the widely extended finite element method.

MPM is now being used in geotechnical engineering and some interesting applications have been developed. It was applied to the modelling of anchors placed in soil [8], to excavator bucket filling [9], to problems of granular flow in a silo [10], to the simulation of experiments related to fault induced ground deformations [11], to run-out analysis of earthquake-induced soil flows [12] and to geomembrane response to settlement in landfills [13]. Also, a quasi-static version of MPM has been developed for large deformations in geomechanics [14].

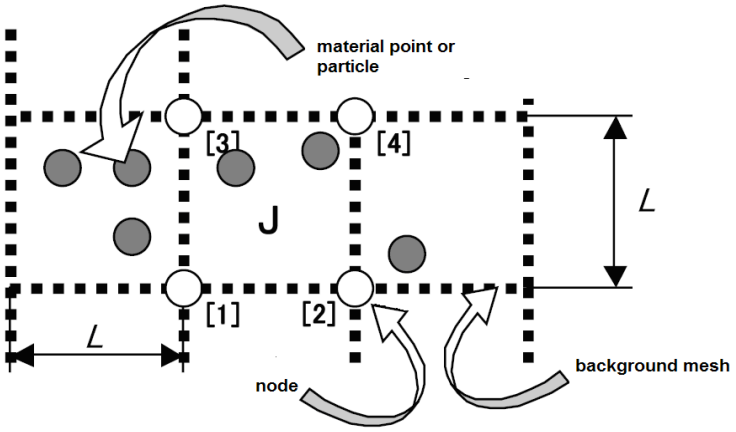


Figure 1: Components of a material point method model

5 PUNTA NEGRA DAM SEISMIC HAZARD

Punta Negra is a concrete faced gravel dam under construction near San Juan city in Argentina. Figure 2 shows the Uniform Hazard Spectrum for a return period of 10000 years as a result of a probabilistic seismic hazard analysis (PSHA) for the site of Punta Negra Dam [15]. Figure 2 also shows the response spectra obtained from three horizontal strong motion records used for the dam seismic assessment.

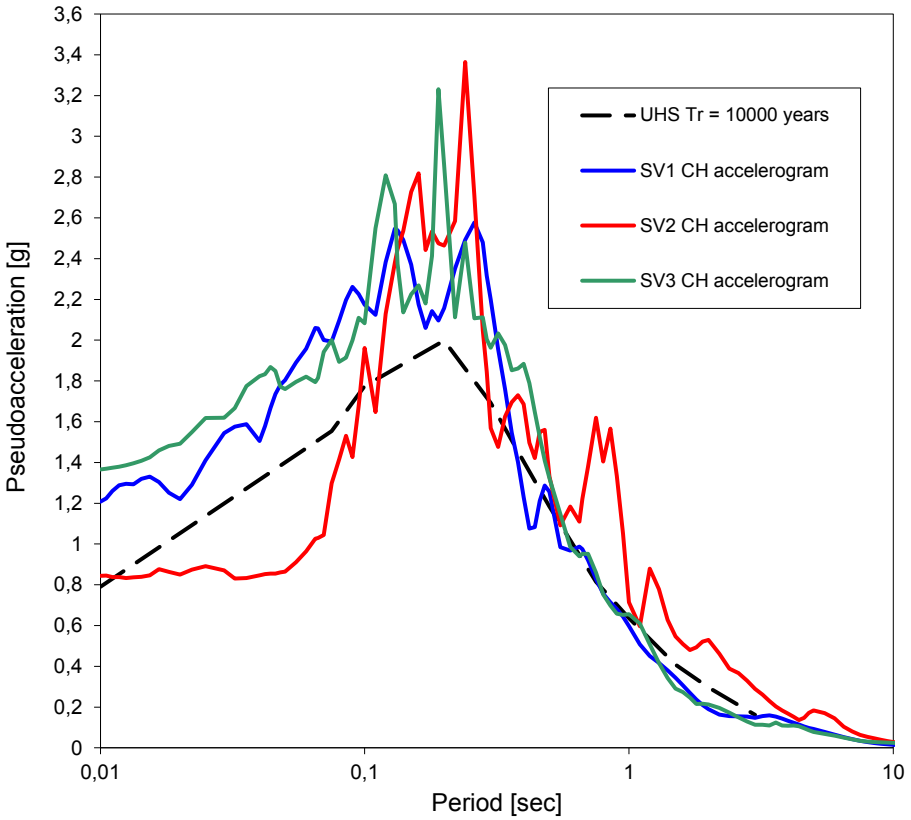


Figure 2. Uniform Hazard Spectra for Punta Negra dam

6 ANALYSIS OF PUNTA NEGRA DAM

Figure 3 shows a simplified three-dimensional particle MPM model of Punta Negra dam. The initial downstream slope is 1:1.65 (vertical: horizontal) and the upstream slope is 1:1.5. With the aim of exploring the capabilities of MPM in dam analysis a first coarse model was made with 56250 particles, and a supporting grid of 5m x 5m cell size with 1 particle per cell in the initial configuration. A solid obtained from a 3d Delaunay triangulation of the initial particles position using Paraview [16] is shown in Figure 4.

The results presented here were computed using a modified version of Pastor–Zienkiewicz constitutive model [17] which is described in the appendix.

Figure 5 shows the dam body clipped by a symmetry plane (upstream-downstream). In this figure particle colors refer to vertical effective stresses due to self-weight and reservoir water pressure applied on the concrete face (left side of figure). As can be seen there is a zone below the concrete face highly compressed due to water pressure. These pressures confine the material, increasing both the stiffness and the strength of the soil, so it is less likely that plastic strains will develop in that area. The downstream slope is far less confined and therefore it is reasonable to expect larger deformations there.

Shear equivalent plastic strains (equation 1) are shown in Figure 6 for a step during the model dynamical analysis with SV2 accelerogram and empty reservoir. Figure 7 shows a 2D cross-section derived from these results. In this case the larger shear strains are developed in the more stepped upstream slope.

$$\dot{\varepsilon}_{eq}^{p} = \sqrt{\frac{2}{3}\dot{e}_{ij}^{p}\dot{e}_{ij}^{p}} \tag{1}$$

$\dot{\varepsilon}_{eq}^{p}$: equivalent plastic shear strain increment,

$\dot{e}^{p}$: deviatoric plastic strain

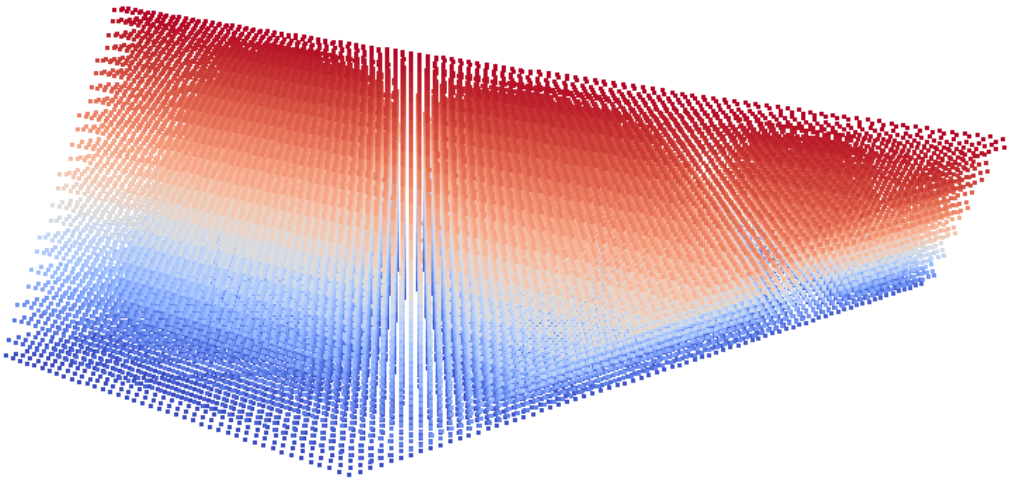


Figure 3. CFRD tridimensional particle model. Initial particle position

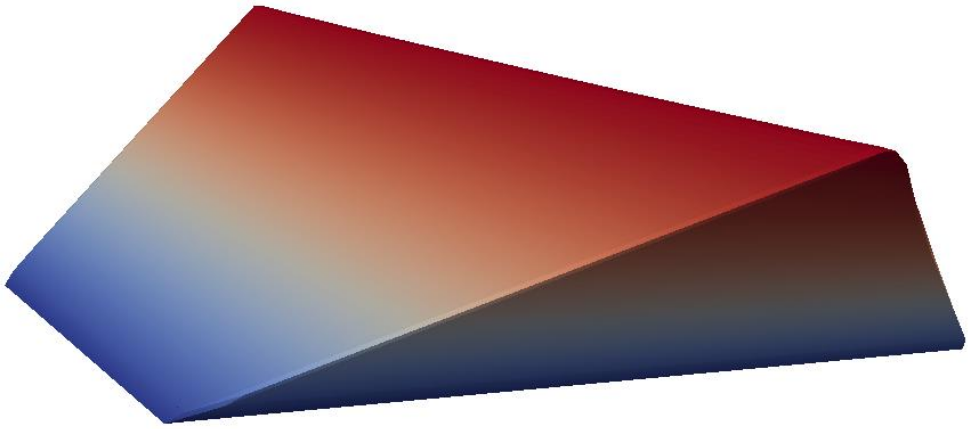


Figure 4. 3D Delaunay triangulation of the initial particles position

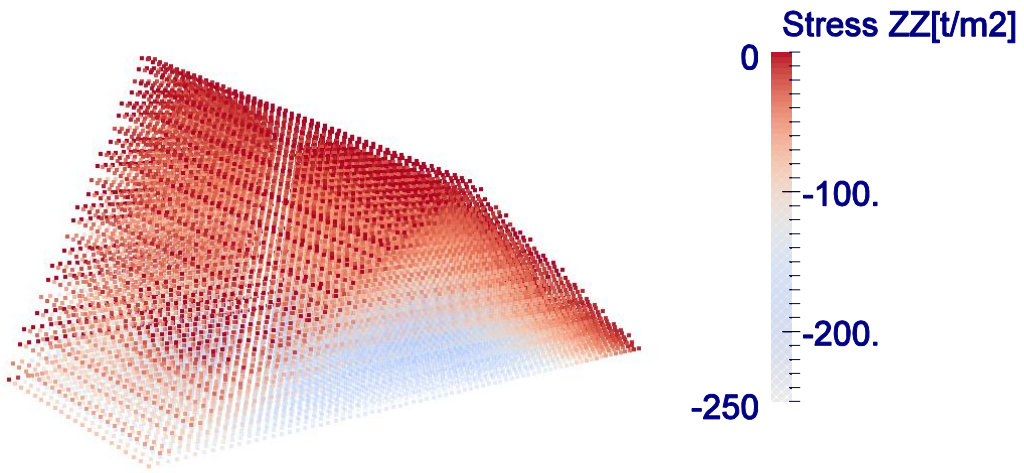


Figure 5. Particle model central cross section. Vertical stresses

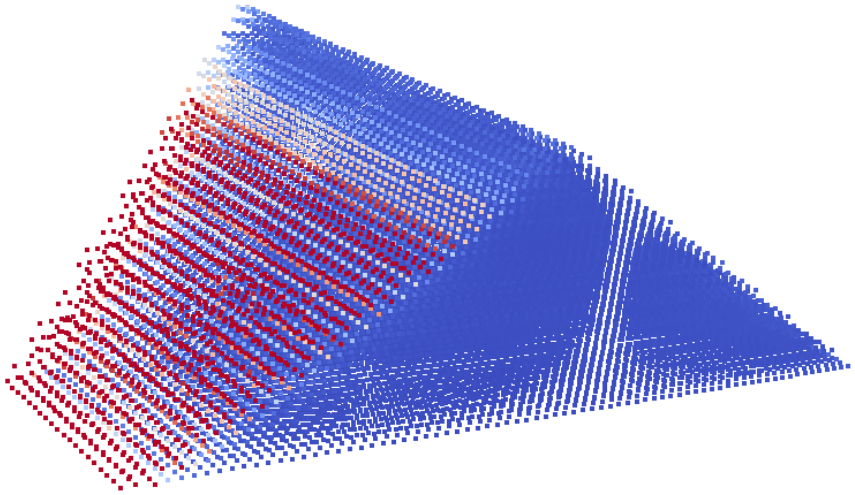


Figure 6. Particle model central cross section. Equivalent plastic shear strain

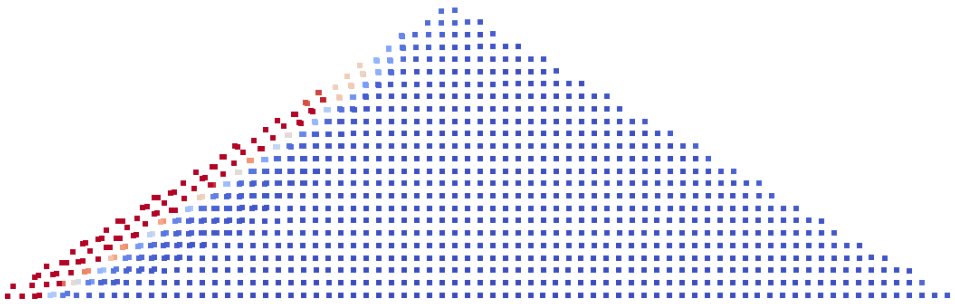


Figure 7. Dam central cross section of particle model. Equivalent plastic shear strain

6.1 Strain localization

In order to take account of strain localization the concept of smeared crack or sliding surface in the cell has been applied, i.e. plastic strain concentrated on a sliding surface is distributed throughout the cell. To obtain an objective response (non dependent on the size of cells) in strain softening we follow the approach described in reference [18]. The volume averaged total strain rate of particles can be expressed as:

$$\dot{\boldsymbol{\varepsilon}} = f\dot{\boldsymbol{\varepsilon}}_i + (1-f)\dot{\boldsymbol{\varepsilon}}_o \qquad (2)$$

where subscripts ‘‘i’’ and ‘‘o’’ are used for the strain inside and outside the localisation region, respectively and f = h/H is the volume fraction of the locatization band to the total particle volume.

7 CONCLUSIONS

The Material Point Method can help to improve the dynamic analysis of geotechnical structures taking into account in a simple manner many of the issues related. The model presented in this paper captures the principal features of the expected dam behavior and can deal with large displacements without mesh distortion.

8 APPENDIX. GENERALISED PLASTICITY CONSTITUTIVE MODEL

Pastor – Zienkiewicz model [17] for sands was used for the analysis. This model is formulated in the frame of generalised plasticity. Constitutive matrix is defined as:

$$D^{ep} = D^e - \frac{D^e n_g n_f{}^T D^e}{n_g D^e n_f + H_{L/U}}$$

The plastic modulus $H_{L/U}$ is a hardening parameter that is a function of effective stress ratio, effective pressure and accumulated strain. The model is formulated in terms of the three invariant: effective mean pressure p’, deviatoric stress q, and Lode angle. The flow direction is a function of dilatance d, for loading and unloading.

$$n_g = (n_v, n_s, n_\theta) \qquad \mathrm{d} = (1+\alpha)(\mathrm{Mg} - \eta)$$

η =q/p' : stress ratio

α = material constant

M_g = slope of the critical state line

$$n_v = \frac{d}{\sqrt{(1+d^2)}} \qquad n_s = \frac{1}{\sqrt{(1+d^2)}}$$

.

The loading direction vector is defined in a similar form:

$$n_{L/U} = (n_p, n_q, n_\theta) \qquad \mathrm{d_f} = (1+\alpha)(\mathrm{Mf} - \eta)$$

$$n_q = \frac{1}{\sqrt{(1+d_f^2)}} \qquad n_p = \frac{d_f}{\sqrt{(1+d_f^2)}}$$

and the plastic modulus H for loading is:

$$H_L = H_0 p'(H_v + H_s) H_f H_{DM}$$

The details of the model formulation can be found in [17].

8.1 Modification of P-Z model.

The model was modified due to the difficulties founded on selecting appropriate parameters that can represent accurately the material steady state strength, using a plastic modulus for loading:

$$H_L = H_0 p'(H_v + H_s H_{ff}) H_f H_{DM}$$

$$H_{ff} = 1 - \frac{\eta}{\eta_{CS}}$$

$$\eta_{CS} = \eta_f \left[1 - \left(\frac{p'}{p_{cr}} \right)^{\alpha} \left(1 - \frac{M_g}{\eta_f} \right) \right]$$

$$\eta_f = (1 + 1/\alpha)\, M_f$$

η_{CS} : limit stress ratio that causes H_f =0 for p´=p´cr and $\eta = M_g = \eta_{CS}$

p`cr is the effective pressure which the material reach under steady state conditions and depends on the void ratio.

REFERENCES

[1] Somerville, P.G., N.F. Smith, R.W. Graves, and N.A. Abrahamson. Modification of empirical strong ground motion attenuation relations to include the amplitude and duration effects of rupture directivity, Seismological Research Letters 68, 199-222,1997.

[2] Steward, J.P., S.J. Chiou, J.D. Bray, R.W. Graves, P.G. Somerville y N.A. Abrahamson. Ground Motion Evaluation Procedures for Performance-Based Design. PEER Report 2001/9. Pacific Earthquake Engineering Research Center, Berkeley, 2001.

[3] Seed HB. "Earthquake-resistant design of earth dams", International Conference on Recent Advances in Geotechnical Earthquake Engineering and Soil Dynamics 1981, Vol III, St. Louis, Missouri

[4] Newmark N. “Effects of earthquakes on dams and embankments”. Geotechnique 1965; 15(2): 139-160.

[5] Sulsky, D., Z. Chen, & H. L. Schreyer. A Particle Method for History-Dependent Materials. Computer Methods in Applied Mechanics and Engineering. Vol. 118(1), pp 179-96,1994.

[6] Sulsky D, Schreyer HL, Zhou S-J, “Application of a particle-in-cell method to solid mechanics”, Computer Physics Communications 1995; 87: 236-252.

[7] Sulsky, D. & H. L. Schreyer. Axisymmetric Form of the Material Point Method with Applications to Upsetting and Taylor Impact Problems. Computer Methods in Applied Mechanics and Engineering. 139(1), 409-29, 1996.

[8] Coetzee, C. J., Vermeer, P. A & Basson A. H. The Modelling of Anchors using the Material Point Method. International Journal for Numerical and Analytical Methods in Geomechanics. 29(9), 879-895,2005.

[9] Coetzee, C. J., Basson A. H., &. Vermeer P. A. Discrete and Continuum Modelling of Excavator Bucket Filling. Journal of Terramechanics. 44(2), 177-186, 2007.

[10] Więckowski Z., Youn S.K., Yeon Y.H. A particle-in-cell solution to the silo discharging problem. Int. J. Numer. Meth. Engng., 45, 1203-1225,1999

[11] Johansson, J. & K. Konagai. Fault Induced Permanent Ground Deformations: Experimental Verification of Wet and Dry Soil, Numerical Findings' Relation to Field Observations of Tunnel Damage and Implications for Design. Soil Dynamics and Earthquake Engineering. 27(10), 938-956, 2007

[12] Konagai, K., Johansson J. & Itoh H. Pseudo-three dimensional lagrangian particle finite difference method for modeling earthquake induced soil flows, 13th World Conference on Earthquake Engineering. No 547, 2004.

[13] Zhou, S., Stormont J. & Chen Z. Simulation of Geomembrane Response to Settlement in Landfills by using the Material Point Method. International Journal for Numerical and Analytical Methods in Geomechanics. 23(15), 1977-1994,1999

[14] Vermeer P. A.,Beuth L. & Benz T. A. Quasi-Static Method for Large Deformation Problems in Geomechanics The 12th International Conference of International Association for Computer Methods and Advances in Geomechanics (IACMAG) Goa, India, 2008

[15] Oldecop L & Zabala F. Evaluación de la amenaza sísmica para el proyecto hidroeléctrico Punta Negra. Instituto de Investigaciones Antisísmicas. Universidad Nacional de San Juan, 2009

[16] The ParaView Guide: A Parallel Visualization Application by Utkarsh Ayachit. Published by Kitware Inc. in, Clifton Park, NY,2015.

[17] Pastor M. Zienckiewics,O.C. and Chan A.H. "Generalized plasticity and the modelling of soil behavior". International Journal for numerical and analytical methods in geomechanics" vol 14. Ed.John Wiley and Sons,1990

[18] Nguyen G.D., Korsunsky A,M and Einav I...A constitutive modelling framework featuring two scales of behaviour: Fundamentals and applications to quasi-brittle failure. Engineering Fracture Mechanics 115 221–240, 2014.

COMPDYN 2015
5th ECCOMAS Thematic Conference on
Computational Methods in Structural Dynamics and Earthquake Engineering
M. Papadrakakis, V. Papadopoulos, V. Plevris (eds.)
Crete Island, Greece, 25–27 May 2015

COLLAPSE RISK EVALUATION OF SELF-CENTERING STEEL MRFS WITH VISCOUS DAMPERS IN NEAR-FAULT REGIONS

George S. Kamaris[1], Angelos S. Tzimas[1], Theodore L. Karavasilis[1], and Carmine Galasso[2]

[1] School of Engineering, University of Warwick
Coventry CV4 7AL, United Kingdom
{G.Kamaris,A.Tzimas,T.Karavasilis}@warwick.ac.uk

[2] Department of Civil, Environmental and Geomatic Engineering and Institute for Risk and Disaster Reduction, University College London (UCL)
London WC1E 6BT, United Kingdom
c.galasso@ucl.ac.uk

Keywords: Self-centering, Steel frames, Dampers, Collapse Risk, Near-fault, Hazard analysis.

Abstract. *This paper presents an evaluation of the seismic collapse risk of self-centering moment-resisting frames (SC-MRFs) with viscous dampers located in near-fault regions. This evaluation is based on the comparison of different designs of a prototype steel building using four lateral load resisting frames: 1) conventional moment-resisting frames (MRFs), 2) MRFs with viscous dampers,* 3) *SC-MRFs and 4) steel SC-MRFs with viscous dampers. The frames are modeled in OpenSees where material and geometrical nonlinearities are taken into account as well as cyclic strength and stiffness degradation. A database of 91 near-fault, pulse-like ground motions with varying pulse periods is employed for the nonlinear dynamic analyses. Collapse resistance of the frames is evaluated through incremental dynamic analysis (IDA). The results of the IDA are combined with probabilistic seismic hazard analysis models that account for near-fault directivity to assess collapse risk of the structures. Results show that the predicted collapse capacity is affected by the pulse period of the near-fault ground motions and highlight that self-centering connections can significantly improve the collapse resistance of conventional MRFs. Finally, it is shown that supplemental damping provides superior collapse resistance for all frames.*

1 INTRODUCTION

A distinct velocity pulse with a long period often characterizes near-fault earthquake ground motions. Such pulse is typically observed at the beginning of the fault-normal (FN) ground velocity time-history and has a probability of occurrence that depends on the site-to-source geometry, earthquake magnitude and other parameters [1-2]. Starting from the pioneer studies of Veletsos and Newmark [3] and Bertero et al. [4], the response of yielding single-degree-of-freedom systems subjected to near-fault earthquake ground motions has been extensively studied by many researchers [5-6 and references therein]. Other studies focused on yielding frames and showed the potential of near-fault ground motions to induce large story drifts [7-9 and reference therein].

The destructive potential of near-fault ground motions was evident after many earthquakes such as the Northridge, California (1994); Kobe, Japan (1995); Chi-Chi, Taiwan (1999); and L'Aquila, Italy (2009). The economic losses caused by these earthquakes at near-fault sites highlighted the limitations of conventional seismic-resistant systems, which experience significant inelastic deformations (i.e. damage) in main structural members and appreciable residual story drifts.

Modern codes in the USA have adopted risk-targeted seismic design maps, which define design spectral acceleration values that are intended to ensure that newly designed buildings have a uniform probability of collapse of 1% in 50 years [10]. However, in their current form, they do not explicitly account for the higher potential collapse risk for buildings located in the near-fault region. A recent study highlighted the need to account for such higher collapse risk by showing that the probability of collapse in 50 years for reinforced concrete buildings at a representative near-fault site is approximately 6%, i.e. significantly higher than the 1% limit [11].

The issue of large residual story drifts and higher collapse risk in the near-fault region could be possibly addressed by employing modern resilient structures instead of the conventional yielding structures, which are promoted by current seismic codes such as the Eurocode 8 (EC8) [12]. Steel self-centering moment-resisting frames (SC-MRFs) using post-tensioned (PT) beam-column connections are a promising class of resilient structures. SC-MRFs exhibit softening force-drift behavior and eliminate beam inelastic deformations and residual drifts (RDs) as the result of gap opening developed in beam-column interfaces and elastic PT bars which clamp beams to the columns and provide self-centering capability. PT connections use yielding-based [13-19] or friction-based [20-23] energy dissipation devices, which are activated when gaps open and can be easily replaced if damaged. Seismic design procedures for SC-MRFs have been proposed in [24-25]. Steel moment-resisting frames (MRFs) equipped with passive dampers are another class of resilient structures. Previous analytical and experimental research showed that steel MRFs with passive dampers can be designed to be lighter and perform better than conventional steel MRFs under the design basis earthquake (DBE) and the maximum considered earthquake (MCE) [26-27]. A study shows that supplemental viscous damping does not always ensure adequate reduction of RDs [26-28]. A recent work evaluates the seismic collapse resistance of steel MRFs with linear viscous dampers and shows that supplemental viscous damping does not always guarantee a better seismic collapse resistance when the strength of the steel MRF with dampers is lower or equal to 75% of the strength of a conventional steel MRF [29].

Recent studies investigated the effectiveness of a seismic design strategy that combines self-centering systems with viscous dampers. The use of viscous dampers in parallel to self-centering precast concrete base rocking walls has been proposed as an effective way to control peak story drifts [30]. The parallel combination of hysteretic and viscous energy dissipa-

tion along with a friction slip mechanism in series connected to the viscous energy dissipation mechanism were found to achieve high levels of seismic performance for self-centering systems [31]. Tzimas et al. [32] also proposed a new seismic design procedure for SC-MRFs equipped with viscous dampers in the framework of EC8 [12].

Although the response of resilient structures has been thoroughly investigated up to the MCE, research on their behavior near collapse is still missing. In addition, their collapse risk in the near-source has not been studied. In this paper, the seismic collapse risk of SC-MRFs with viscous dampers subjected to near-fault ground motions is evaluated and compared to that of ordinary MRFs. The recently developed PT connection with web hourglass shape pins (WHPs) [15,18] is utilized for the SC-MRFs. A prototype building is designed as a SC-MRF with or without viscous dampers. Different design approaches for the SC-MRF with viscous dampers are considered to investigate all possible scenarios. The structures are modeled in OpenSees [33] where material and geometrical nonlinearities are taken into account as well as cyclic strength and stiffness degradation. A database of 91 near-fault, pulse-like ground motions with varying pulse periods is employed for the nonlinear dynamic analyses of this study. The concept of incremental dynamic analysis (IDA) [34] is used for the prediction of collapse, in which each ground motion is scaled appropriately, using as intensity measure the first-mode spectral acceleration, $S_a(T_1)$, until dynamic instability occurs. The probability of collapse is then calculated as a function of ground motion characteristics i.e. the ground motion intensity and the period of the velocity pulse. Finally, the results of the IDA are combined with probabilistic seismic hazard analysis models that account for near-fault directivity to assess collapse risk of the structures.

2 SC-MRFS WITH VISCOUS DAMPERS

2.1 *SC-MRFs using PT connections with WHPs*

Figure 1(a) shows a SC-MRF using PT connections with WHPs and Figure 1(b) shows an exterior PT connection with WHPs. The PT connection with WHPs has been experimentally and numerically evaluated by Vasdravellis et al. [15,18]. Two high strength steel bars located at the mid depth of the beam, one at each side of the beam web, pass through holes drilled on the column flanges. The bars are post-tensioned and anchored to the exterior columns. WHPs are inserted in aligned holes on the beam web and on supporting plates welded to the column flanges. Energy is dissipated through inelastic bending of the WHPs that have an optimized hourglass shape (Figure 1(c)) with enhanced fracture capacity. The beam web and flanges are reinforced with steel plates. The panel zone is strengthened with doubler and continuity plates. A fin plate welded on the column flange and bolted on the beam web is used for easy erection and resistance against gravity loads before post-tensioning. Slotted holes on the beam web ensure negligible influence of the fin plate on the PT connection hysteretic behavior.

The connection behavior is characterized by gap opening and closing in the beam-column interface as a result of the re-centering force in the PT bars. Figure 2(a) shows the free body diagram of an external PT connection where d_{1u} and d_{1l} are the distances of the upper and lower WHPs from the center of rotation that is assumed to be at the inner edge of the beam flange reinforcing plates; d_2 is the distance of the PT bars from the center of rotation; T is the total force in both PT bars; $F_{WHP,u}$ and $F_{WHP,l}$ are the forces in the upper and lower WHPs; C_F is the compressive force in the beam-column interface; V_{C1u} and V_{C1l} are the shear forces in the upper and lower column, M is the PT connection moment, V is the beam shear force; and N is the horizontal clamping force that is transferred to the beam-column interface through the slab diaphragm and the beam. Figure 2(b) shows the SC-MRF expansion due to rotations θ in the PT connections.

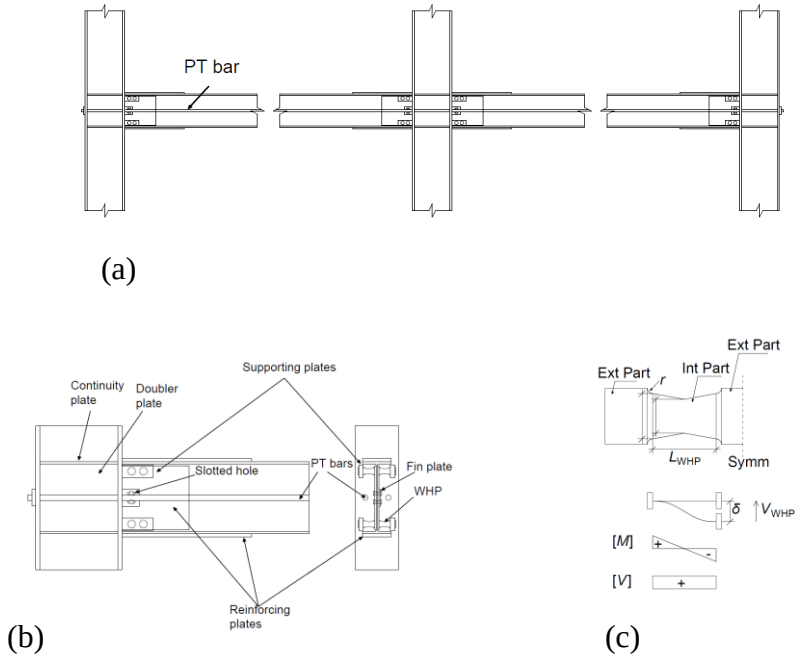


Figure 1: (a) SC-MRF; (b) exterior PT connection with WHPs; and (c) WHP geometry and assumed static system.

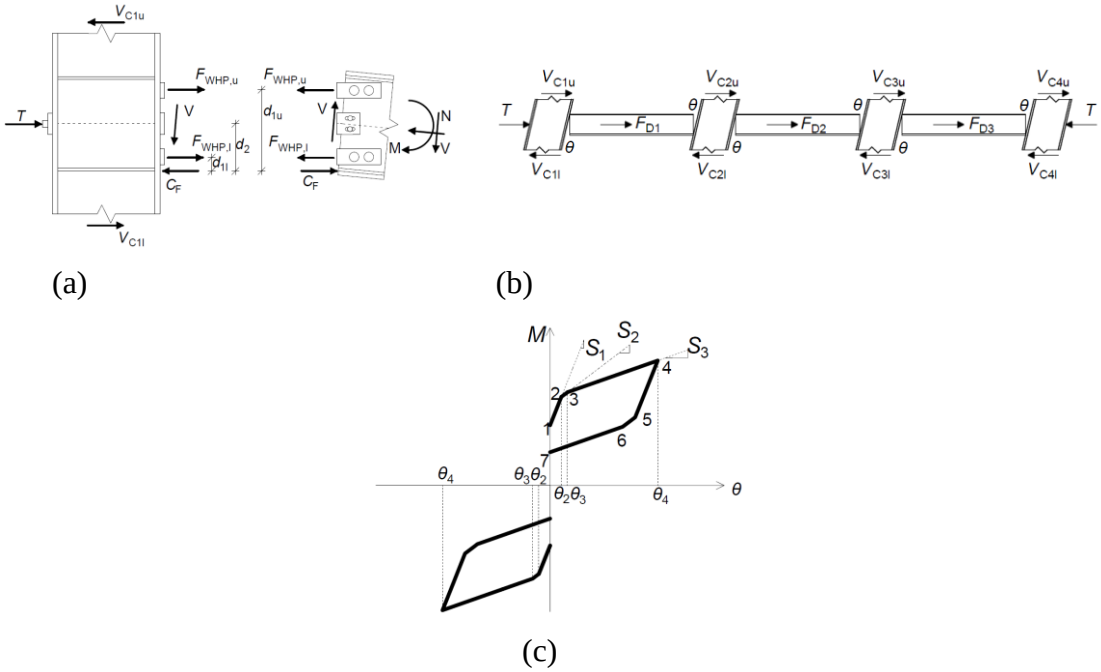


Figure 2: (a) Free body diagram of an external PT connection; (b) SC-MRF expansion and horizontal forces equilibrium; and (c) theoretical cyclic behaviour of the PT connections with WHPs.

Figure 2(c) shows the theoretical cyclic moment-rotation (M-θ) behavior of the PT connection with WHPs, which has been verified by the large-scale experiments conducted by Vasdravellis et al. [15]. After decompression of the PT connection (Point 1 in Figure 2(c)), gap opens and the behavior becomes nonlinear elastic with rotational stiffness S_1. At point 2, the upper WHPs yield and M continues to increase with slope S_2. At point 3, the lower WHPs

yield and M continues to increase with slope S_3. When loading is reversed, the connection begins to unload until the gap closes. More details about the connection behavior can be found in [32].

2.2 *Prototype building*

Figure 3(a) shows the plan view of a 5-storey, 5-bay by 3-bay prototype building having two identical lateral resisting frames (MRFs or SC-MRFs) in the x plan direction. Braced frames are located in the y plan direction. Viscous dampers are inserted in the interior gravity frames, with pinned connections, that are coupled with the perimeter lateral resisting frames through the floor diaphragm as shown in Figure 3(b). Due to the symmetry of the building, this paper focuses on one perimeter lateral resisting frame. The building has ductile non-structural elements, and thus, maximum interstory drift ratio $\theta_{s,max}$, should be lower than 0.75% under the under the frequently occurred earthquake (FOE) according to EC8 [12]. The DBE is expressed by the Type 1 elastic response spectrum of EC8 [12] with peak ground acceleration equal to 0.35g and ground type B. The FOE has intensity of 40% the intensity of the DBE. The model used for the design is based on the centerline dimensions of the lateral resisting frame without accounting for the finite panel zone dimensions. A "lean-on" column is included in the model to account for the P-Δ effects of the vertical loads acting on the gravity columns in the tributary plan area (half of the total plan area) assigned to the lateral resisting frame. The steel yield strength is equal to 355 MPa for the columns, 275 MPa for the beams, 930 MPa for PT bars, 235 MPa for the WHPs, 275 MPa for the beam reinforcing plates and 235 MPa for the fuse. The beam and column sections have different steel grades to achieve the capacity design rules of EC8 [12]. Nonlinear viscous dampers are designed with a horizontal configuration and a velocity exponent a equal to 0.5. The inherent damping ratio of the SC-MRF is equal to 3%.

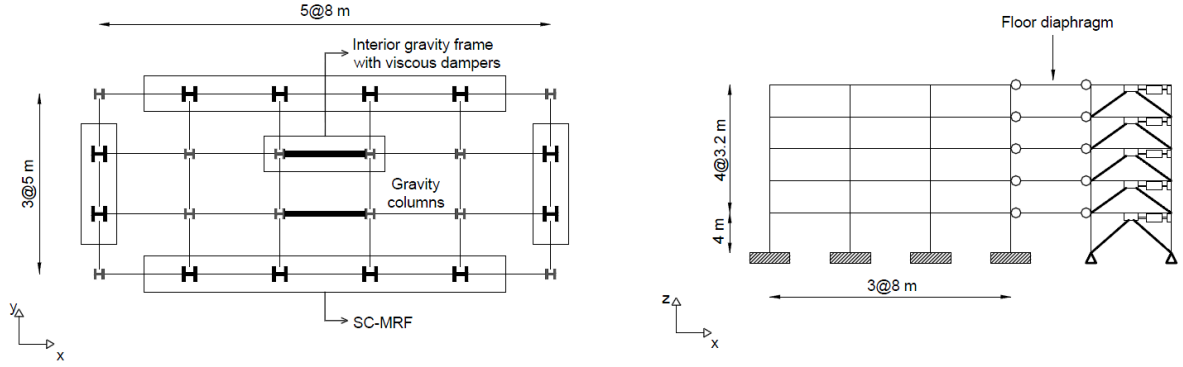


Figure 3: (a) Plan and (b) side views of the prototype building.

2.3 *Design cases*

Four frames were designed as SC-MRFs with and without viscous dampers and conventional MRFs with and without viscous dampers. All the frames have the same cross sections, but different structural performance under strong earthquakes. Table 1 provides the steel weight, fundamental period T_1, damping ratio ξ_t and interstory drift ratio, $\theta_{s,max}$, under the FOE and DBE of the frames discussed below:

CP3D (SC-MRF or MRF): Conventional performance frame without viscous dampers (ξ_t =3%).

HP20D (SC-MRF or MRF): High performance frame with viscous dampers (ξ_t =20%). Its target performance led to the same cross sections and PT connections details with those of *CP3D* frame. It demonstrates the design scenario where viscous dampers are used to achieve $\theta_{s,max}$ significantly lower than the EC8 [12] limit. It also demonstrates the design scenario where strict design criteria for the PT connections along with a low $\theta_{s,max}$ target value are enforced to genuinely achieve seismic resilience.

Table 2 provides the beams and columns cross-sections and the damping coefficient of the dampers, c, of the frames. The PT bar diameter, d_{PT}, the total initial post-tensioning force, T_0, the length, L_{rp}, the area, A_{rp}, of the beam flange reinforcing plate, the length of half a WHP, L_{WHP} (Figure 1(c)), the external, D_e, and internal, D_i, diameters of the WHPs of the SC-MRFs are also listed in this table.

FRAME	Steel weight* (kN)	T (s)	ξ_t (%)	$\theta_{s,max}$ FOE (%)	$\theta_{s,max}$ DBE (%)
CP3D SC-MRF	268	1.27	3.00	0.72	1.80
HP20 SC-MRF	268	1.27	20.0	0.48	1.20
CP3D MRF	268	1.27	3.00	0.72	1.80
HP20D MRF	268	1.27	20.0	0.48	1.20

*Beams and columns

Table 1: Data and design criteria for the frames with and without viscous dampers.

Storey	Cross sections			PT bars		WHPs			Reinforcing plates		Viscous dampers c (kN·(s./m)$^{0.5}$)	
	Beams	Columns	Gravity columns	T_0 (kN)	d_{PT} (mm)	D_e (mm)	D_i (mm)	L_{WHP} (mm)	L_{rp} (mm)	A_{rp} (mm)	CP3D	HP20D
1	IPE550	HEB650	HEB240	1087	50	43	33	70	1392	7350	-	2139
2	IPE600	HEB650	HEB240	1256	60	46	36	70	1660	10120	-	1641
3	IPE550	HEB650	HEB240	1087	48	43	33	70	1416	7350	-	1416
4	IPE500	HEB600	HEB220	941	38	41	30	70	1092	5200	-	1102
5	IPE500	HEB600	HEB220	941	36	39	28	70	743	4400	-	810

Table 2: Design details for the CP3D and the HP20D frames.

3 NONLINEAR MODELS

Models for the SC-MRFs are developed in OpenSees [33]. The columns and the reinforced lengths of the beams are modeled as nonlinear force-based beam-column fiber elements. Fibers have bilinear elastoplastic stress-strain behavior (Steel01 [33]) with post-yield stiffness ratio equal to 0.003.

Beam local buckling is expected after the end of the reinforcing plates, and so, the unreinforced lengths of the beams are modeled as elastic elements with zero length nonlinear fiber hinges at their ends that exhibit strength and stiffness deterioration [35]. The fiber hinge sections are composed of the *Bilin* material [33] that simulates the modified Ibarra–Krawinkler [35] deterioration model. The hinges are calibrated individually in order to exhibit the same behavior as the multi-linear deteriorating concentrated hysteresis model [36].

For the PT connection, a simplified model is adopted [37] where the M-θ behavior of the PT connection is simulated by inserting 2 rotational springs in parallel at the beams ends. The

first spring corresponds to the PT bars behavior, while the second one corresponds to the behavior of the WHPs. The PT bars behavior is modeled using a bilinear elastic model, while for the modeling of the WHPs, a smooth bilinear elastoplastic model is used.

Panel zones are modeled using the Krawinkler model [38] which consists of four rigid links connected at the corners by rotational springs. The springs at the lower left and upper right corners have no stiffness, and thereby act as true hinges. The spring at the upper left is used to represent panel zone shear resistance, and the spring at the lower right is used to represent column flange bending resistance.

To account for P-Δ effects, the gravity columns associated with one of the two lateral resisting frames of the plan in Figure 3(a) are modeled as 3 lean-on columns, i.e. one for each bay of the frame. Diaphragm action is modeled with truss elements connecting the lean-on columns nodes to nodes defined along the length of the beams at the points where secondary beams are placed. These trusses have stiffness of 100 times the axial beam stiffness.

Nonlinear viscous dampers are modeled with zero length elements (Viscous material [33]), while their supporting braces are modeled with elastic braces as they are strong enough to avoid buckling. In the analytical model, the damper limit states caused by their stroke limit are not considered, i.e. it is assumed that dampers will be manufactured with enough stroke to avoid reaching their limit states even under very large storey drifts.

The connections of the conventional MRFs are assumed to be rigid and have full strength, while beams are modeled as elastic elements with zero length rotational springs at their ends that exhibit strength and stiffness deterioration [35]. Columns and panel zones are modeled as described above for the SC-MRFs.

The OpenSees models for the SC-MRFs and the conventional MRFs include the effect of the panel zone stiffness, and so, result in T value shorter than 1.27 s that is based on the centerline models used for design. T from the OpenSees [35] models is 0.94 s for *CP3D* and *HP20D* SC-MRFs and 1.18 s for *CP3D* and *HP20D* MRFs.

4 GROUND MOTIONS CONSIDERED

A set of 91 pulse-like ground motions is used in 2D nonlinear dynamic time history analyses of the abovementioned SC-MRFs and MRFs. These ground motions were selected by Baker [39] from the PEER NGA [40] database by implementing wavelet analysis for the detection of pulses. A wavelets-based algorithm was used, which assigns a score, a real number between 0 and 1, to each record and determines the pulse period, T_p. The larger the score the more likely the record is to show a pulse. Only the FN ground motions having a pulse score equal or larger than 0.85 and a minimum peak ground velocity of 30cm/s were, arbitrarily, counted as pulse-type records.

Ground motions were recorded from earthquakes with moment magnitudes, M, varying from 5.0 to 7.6 and include pulse periods that vary between 0.4 and 12.9 s. Although all of the records exhibit velocity pulses, site-to-source distances were not considered in the selection criteria and range from 0.10 to 102 km. Thus, some of the observed pulses were probably caused by other geological mechanisms, such as basins. Nevertheless, all pulse-like records are taken as representative of near-fault ground motions, assuming that large velocity pulses will produce similar structural response regardless of their geological characteristics. All of the records in the database have been rotated to the fault-normal direction. A complete list of the pulse-like ground motions used in this study can be found in [39].

In this study, the collapse seismic risk of the structures depends on the probability of occurrence or not of a pulse-like ground motion, which is calculated through the theorem of total probability. For this reason, a second set of far-field records is needed for the determination of collapse probability for sites that are not influenced by forward directivity

effects. Similarly to [11], the set of far-field ground motions used in this study is based on the FEMA P695 [41] far-field ground motion set, which includes 22 record pairs, each with two horizontal components for a total of 44 ground motions. Those ground motions are recorded at sites located greater than or equal to 10 km from fault rupture; event magnitudes range from *M* 6.5 to *M* 7.6 with an average magnitude of *M* 7.0. According to the NEHRP Site Class, 16 sites are classified as Site Class D (stiff soil sites) and the remaining are classified as Site Class C (very stiff soil sites). The wavelet classification algorithm developed by Baker [40] indicates that nine of these ground motion records have pulses in the velocity history [11]; these pulse-like record were then removed from the far-field database. It is worth noting that the ground motion records were selected without consideration of spectral shape. In fact, the FEMA P695 [41] far-field ground motion set consists of records that are structure type and site hazard independent, i.e., records do not depend on period, or other building-specific properties of the structure, as well as on hazard disaggregation, or other site- or hazard- dependent properties.

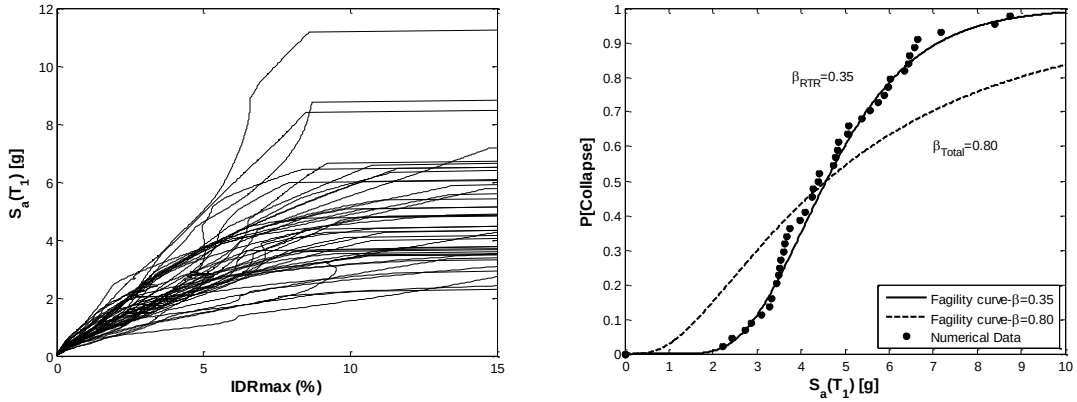
5 COLLAPSE EVALUATION

The collapse seismic intensity of each frame is assessed through IDA [34]. According to this methodology, the frame model is subjected to a specific ground motion scaled to multiple levels of intensity, until collapse occurs, as indicated by the dynamic instability of the structural system. For each intensity level a response parameter of the structure (e.g., story displacements, floor accelerations, etc.) is monitored to produce an IDA curve. This process is repeated for all earthquake records and for each frame. In this work, the spectral acceleration at the fundamental period T_1 of each building, $S_a(T_1)$, is used as intensity measure and the interstory drift ratio is the response parameter that is monitored. To determine the limit of total loss of lateral resistance, the incremental slopes are calculated by drawing straight lines between the consecutive data points in the IDA curve. The lowest S_a value corresponding to the i^{th} data point with the slope between the i^{th} and $i+1^{th}$ points being less than 10% of the initial slope on the IDA curve is defined as the collapse capacity of the frames in this study, where the initial slope is determined from the straight line from the origin of axis to the first data point of the IDA curve. The IDA curves for the *HP20D* SC-MRF, obtained for the ensemble of the far-fault ground motions, are shown in Figure 4(a).

The collapse capacities obtained from the IDA curves are used for the construction of a fragility curve for each frame. Fragility curves express the probability of collapse due to earthquakes as a function of ground motion intensity. They are usually assumed to have the form of a lognormal cumulative distribution function with a median value, θ, and logarithmic standard deviation, β, of the ground motion intensities at which collapse occurs in IDA. The fragility curve resulted for the *HP20D* SC-MRF is shown in Figure 4(b) with a solid line together with the results from the numerical analyses.

The parameter β influences the shape of the fragility curve and reflects the level of uncertainty in the analysis results. Figure 4(b) shows two fragility curves corresponding to two different values of β. The solid curve has a value of β_{RTR}=0.35 and the dashed curve reflects a β_{Total}=0.80. As indicated in this figure, larger values of β have the effect of "flattering" the curve. Two sources of uncertainty in quantifying the collapse capacity of structural systems are considered herein: aleatory sources and epistemic. The aleatory or record-to-record uncertainty, reflects the variability in the response of the structures due to the random nature of ground motions. The epistemic or modeling uncertainty is mainly due to lack of knowledge about the building's real model and real element properties. It is associated with nonlinear modeling, based on the evaluation of the accuracy and robustness of the nonlinear models

used and their ability to represent the true physical properties and the seismic response of structures.



(a) (b)

Figure 4: (a) IDA curves for the *HP20D* SC-MRF (b) Corresponding fragility curve.

In order to combine the contributions of aleatory and epistemic uncertainties, the mean estimates approach is used herein [42]. When the record-to-record uncertainties are only considered, the structural response is well-described by a lognormal distribution, with a median, θ, and standard deviation, β_{RTR}. In addition, it is assumed that the epistemic uncertainty is also lognormally distributed with a median, θ, and standard deviation, $\beta_{modeling}$, and that the random variables associated with these two uncertainties are statistically independent. Consequently, when these two distributions are combined the resulting distribution is also lognormal with a median, θ, and a standard deviation given by the following equation:

$$\beta_{Total} = \sqrt{\beta_{RTR}^2 + \beta_{\mathrm{mod}eling}^2} \tag{1}$$

Thus, when the mean estimates approach is used, the median is unchanged when modeling uncertainties are incorporated, but the standard deviation increases. Values of β_{Total} are taken as 0.80, β_{RTR} is calculated based on the IDA results and the $\beta_{modeling}$ is derived though Equation (1). This value of β_{Total} has been adopted by other researchers [11] and seems to be logical for the risk assessment of frame systems. Note that the fragility curves, as shown in Figure 4(b), have not yet been adjusted to account for the distinct spectral shape of rare ground motions, characterized by the parameter ε [43]. To do so, the methodology proposed by Haselton et al. [44] was employed.

The risk assessment procedure of the frames, when subjected to near fault ground motions, is modified properly to take into account the effect of the pulse period of the record, T_p, and is based on the approach proposed by Champion and Liel [11]. This methodology is described in the following sections.

6 EFFECT OF PULSE PERIOD IN COLLAPSE ASSESSMENT

The pulse period, T_p, of the near-field ground motions strongly affects seismic collapse capacity of structures. To show this effect in the frames studied herein, the collapse capacities of the *HP20D* SC-MRF obtained from IDA curves are plotted versus the ratio T_p/T_1 and are shown in Figure 5 as individual points.

In addition, the moving average of the numerical data is computed by averaging the point of interest with the five previous and subsequent data points. This is done to fit the data points with a trend-line in order to investigate the behavior of collapse capacity. The shape of the

moving average curve illustrates the influence of the pulse period to collapse capacity. The maximum values of collapse capacities are obtained in the region of the moving average curve where the fundamental period of the frame is approximately equal to the T_p of the record, i.e. $T_p/T_1 \approx 1$. This result is not consistent with the response of structures in the elastic range, since the largest displacement demand of these systems is observed when the period of the excitation is very close to T_1. In contrary, collapse of structures is a very nonlinear phenomenon, which is characterized by large inelastic deformations due to severe damage induced to the structure. For this reason, the stiffness of the structure decreases, resulting in a significant elongation of its effective period. Therefore, collapse capacity is larger in this region, because it is influenced by the real elongated period of the building which is different than the elastic one. In addition, ground motions with longer pulse period are the most damaging, giving very low collapse resistances. This is attributed to the effective lengthened period of the structure which tends to coincide with the pulse period of the excitation. In the region of $T_p < T_1$ the collapse capacity of the frame tends to decrease, and this is probably due to high spectral velocities exhibiting in the shortest pulse period records.

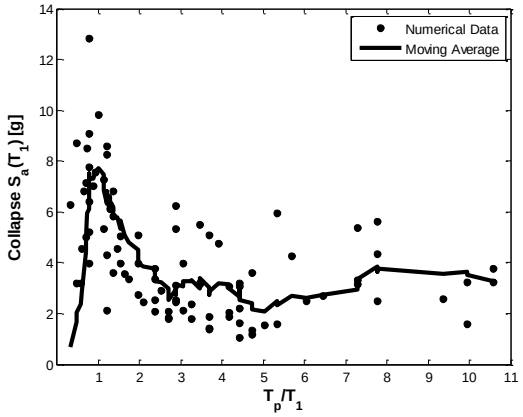


Figure 5: Collapse capacities of the *HP20D* SC-MRF versus the T_p/T_1 ratio together with the generated moving average curve.

7 COLLAPSE FRAGILITY FUNCTIONS INCLUDING NEAR-FAULT DIRECTIVITY

Near-fault directivity has an impact in collapse capacity of the structures, so it should be taken into account in their risk assessment. Collapse of structures depends not only on $S_a(T_1)$, but also whether a ground motion record exhibits a velocity pulse and the corresponding pulse period (see Figure 5). To incorporate this effect in the collapse fragility functions, the theorem of total probability is utilized to calculate the probability of collapse, $P[Col|S_a = x]$, given a specific value of $S_a(T_1)$, i.e. the fragility function of each frame [11]:

$$P[Col \mid S_a = x] = P[Col \mid S_a = x, Pulse] \cdot P[Pulse \mid S_a = x] + P[Col \mid S_a = x, NoPulse] \cdot P[NoPulse \mid S_a = x] \quad (2)$$

where $P[Col|S_a = x, Pulse]$, $P[Col|S_a = x, No\ Pulse]$, $P[Pulse|S_a = x]$ and $P[No\ Pulse|S_a = x]$ are the probability of collapse for pulse like ground motions, the probability of collapse for far-fault ground motions, the probability that a ground motion record exhibits a velocity pulse and the probability that a ground motion record does not exhibit a velocity pulse, respectively.

The term $P[Col|S_a = x, No\ Pulse]$ is determined from the fragility curves, obtained from the IDA results for the far-fault ground motions. The collapse probability when a pulse occurs, $P[Col|S_a = x, Pulse]$, depends on the pulse period and the likelihood of different pulse periods occurring, $P[T_p = t_i|S_a = x, Pulse]$:

$$P[Col \mid S_a = x, Pulse] = \sum_{i=1}^{All\ T_p} P[Col \mid T_p = t_i, S_a = x, Pulse] \cdot P[T_p = t_i \mid S_a = x, Pulse] \quad (3)$$

The probability of collapse for a given pulse period T_p value, $P[Col|T_p=t_i, S_a=x, Pulse]$, is computed through the moving average curve constructed for each frame. The moving average represents the median collapse capacity as a function of T_p. For any value of T_p and $S_a(T_1)$, the probability of collapse is computed by assuming a lognormal distribution with a median equal to the value of $S_a(T_1)$ of the moving average curve for a given T_p and a standard deviation $\beta_{Total} = 0.8$.

The remaining parts of Equations (2) and (3) are computed with the aid of probabilistic seismic hazard analysis (PSHA), which provides the mean annual frequency, λ, of exceeding an IM level, x. Conventional far-field PSHA gives λ according to the following equation:

$$\lambda_{IM>x} = \sum_{i=1}^{N} \nu_i \int_m \int_r P[IM > x \mid m, r] f_{M,R}(m, r) dm dr \quad (4)$$

where ν_i is the mean annual rate of earthquakes occurrence on a nearby fault i, N is the total number of faults, M is the moment magnitude, R is the source-to-site distance and $f_{M,R}$ is the joint probability density function of M and R. The expression $P[IM > x|m, r]$ is the probability that the ground motion intensity exceeds a specific value, x, given an earthquake of magnitude m at distance r, which can be obtained from ground motion prediction equations (GMPEs). Different IM are used in these equations (in this work $S_a(T_1)$ is adopted).

PSHA has been recently modified to account for near source conditions, i.e., Near-source Probabilistic Seismic Hazard Analysis (NS-PSHA); more details, including implementation and applications, can be found in [2,45-49]. According to this methodology, Equation (4) is adjusted to account for potential near-source directivity by an additional term, Z, which defines the site-to-source geometry:

$$\lambda_{IM>x} = \sum_{i=1}^{N} \nu_i \int_m \int_r \int_z P[IM > x \mid m, r, z] f_{M,R,Z}(m, r, z) dm dr dz \quad (5)$$

In this case the probability that a specific ground motion intensity value is exceeded, $P[IM > x|m, r, z]$, depends on the probability of occurrence of a pulse, the distribution of possible pulse periods and the peculiar spectral shape induced by the pulse. The probability of a pulse occurring is a function of site-to-source geometry and decreases with distance from the fault and for shorter fault rupture lengths [2,46]. The pulse period distribution is a function of earthquake magnitude, with larger magnitude events usually causing longer pulse periods [46,50].

When the NS-PSHA has been conducted for a given IM level, the probability that a pulse occurs, $P[Pulse|S_a = x]$, can be calculated by the following equation:

$$P[Pulse \mid S_a = x] = \frac{\lambda_{S_a=x,Pulse}}{\lambda_{S_a=x,Total}} \quad (6)$$

where $\lambda_{Sa=x,Pulse}$ is the mean annual frequency of $S_a = x$ when only pulse-like ground motions are considered and $\lambda_{Sa=x,Total}$ is the mean annual frequency of $S_a = x$ when both pulse-like and far-fault ground motions occur. Note that NS-PSHA is computed here as $\lambda_{Sa=x}$ rather than $\lambda_{Sa>x}$ to allow for combination with the collapse fragility curves. The hazard disaggregation of Eq. (6) is required for each spectral acceleration level of interest (from the collapse fragility); a similar disaggregation process can also be used to identify the contribution of each pulse

period, t_i, to each spectral value, i.e., $P[T_p = t_1|S_a = x, Pulse]$. Finally, the term $P[No\ Pulse|S_a = x]$ is derived through the following equation:

$$P[NoPulse \mid S_a = x] = 1 - P[Pulse \mid S_a = x] \tag{7}$$

As an example, a fixed (characteristic) M 7 strike-slip (SS) fault is considered here to compare the seismic performances of the structural systems introduced earlier. The single fault is 42km long based on the median Wells and Coppersmith magnitude-scaling relation [51] and is assumed to have a recurrence rate of 0.05 earthquakes per year. The location of earthquake epicenters is uniformly distributed along the fault while six sites with site-to-source distances equal to 5, 10 and 15 km at the end ("End-of-Fault" sites) and midpoint ("Midfault" sites) of the fault line are considered in this study (Figure 6(a)).

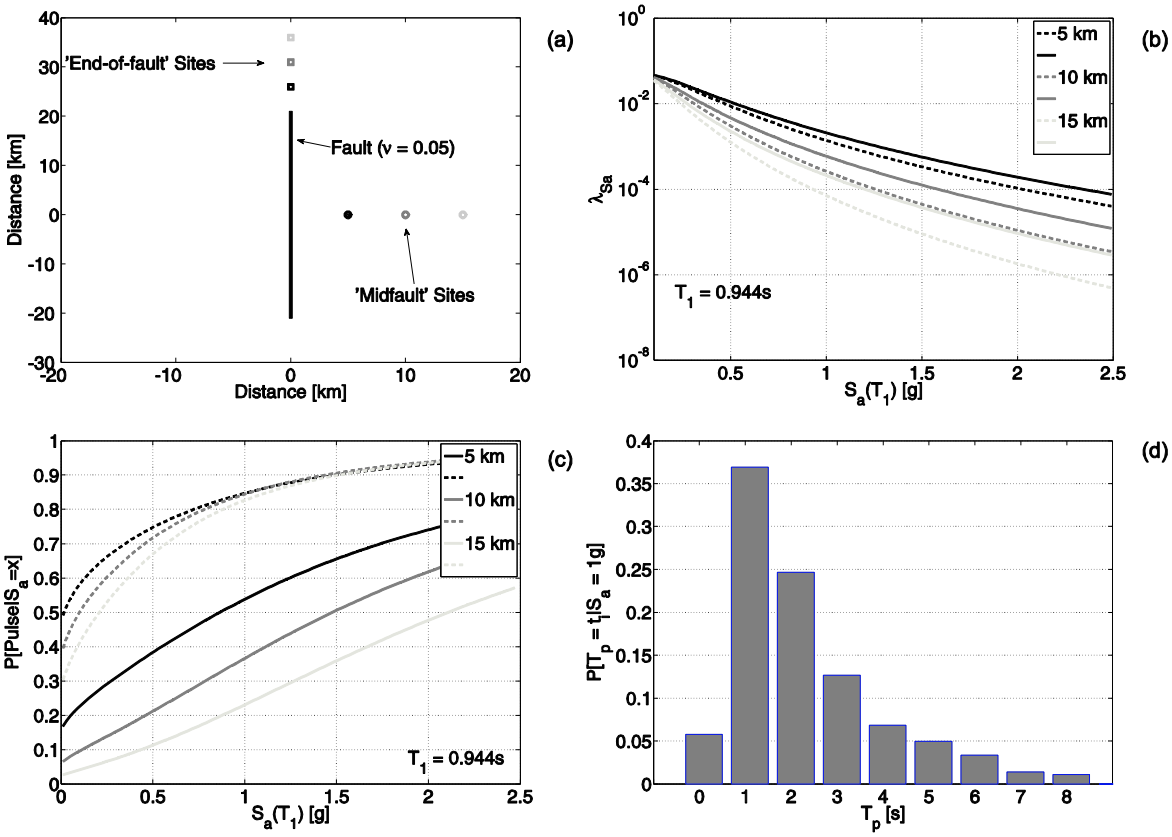


Figure 6: Representative near-field sites considered in this study, showing (a) site location and (b) seismic hazard curves for the midfault (dashed lines) and end-of-fault (solid lines) sites with varying site-to-source distances. Hazard disaggregation results show (c) the probability of pulse occurrence for the different sites at $S_a(T_1 = 0.944$ s) and (d) a typical pulse period distribution for one hazard level, $S_a(T_1) = 1$ g, at the 5 km midfault site.

The probability of a pulse occurring is computed by using the model in [2] and depends, in the case of a SS rupture, on rupture-to-site distance, R, the distance from the epicenter to the site measured along the rupture direction, s, and angle between the fault strike and the path from the epicenter to the site, θ (a similar model is introduced in [46]). As noted in [49], a deterministic relationship between these parameters and rupture length, position of the rupture on the fault and epicenter location exist, allowing to easily simulate the uncertainty involved for the hazard computations. However, while rupture length and rupture position are, in principle, random variables, the application here is implemented in the simplifying hypothesis of fixed rupture and position, similarly to the applications in [49]. Such a hypothesis appears to be acceptable if a single magnitude can be generated by the considered fault, as assumed in

this study where the main focus is to compare the seismic performances of different structural systems rather than to investigate NS-PSHA.

Finally, the pulse period prediction is based on the empirical model in [47], although others are available (e.g., [46]). More details for the NS-PSHA calculation used here, including the GMPE modification to account for the 'bump' of spectral ordinates around the pulse period, can be found in [48].

NS-PSHA results are illustrated in Figure 6(b) for T_1 = 0.944 *s*. Figures 6(c) and (d) provide disaggregated hazard results in terms of $P[Pulse|S_a = x]$ and $P[T_p = t_i|S_a = x, Pulse]$ respectively (the latter refer to S_a = 1 g as an example).

8 SEISMIC COLLAPSE RISK ASSESSMENT IN THE NEAR-SOURCE

Using the methodology of the previous section, the collapse fragility curves of all frames at the midfault sites for a distance 15 km away from the fault, are constructed and depicted in Figure 7(a). The fragility curves of the frames suggest that the least susceptible structures to collapse are the frames equipped with viscous dampers, with the *HP20D* SC-MRF exhibiting the lowest probabilities of collapse. Figure 7(b) shows the fragility curves obtained for the *HP20D* SC-MRF located at the midfault sites for site-to-source distances equal to 5, 10 and 15 km. It observed that the probability of collapse is reduced with distance from the fault, because the likelihood that a pulse occurs, $P[Pulse|S_a = x]$, decreases with distance and that affects the first part of Equation (2).

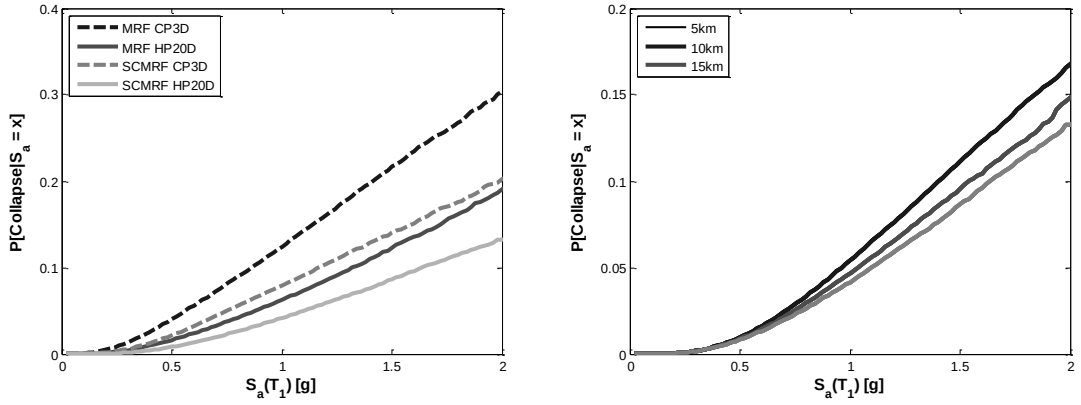
In addition, the probability of collapse in 50 years of the four frames is calculated at the midfault and end-of-fault sites, for site-to-source distances equal to 5, 10 and 15 km. To do so, a Poisson distribution of the earthquake occurrences is utilized, which is given by the following equation:

$$P[Collapse\ in\ 50\ \ years] = 1 - e^{-\nu t} \tag{8}$$

where t is the time in years and ν is the mean annual frequency of collapse, computed by integrating the collapse probability distribution, i.e. the fragility curve of each frame, with the rate of exceedance for each spectral acceleration and site of interest. The results of this calculation are listed in Table 3.

A trend showing reduced seismic collapse risk with distance from the fault is obvious from the results of Table 3. When the site-to-source distance is decreased from 15 to 10 km the probability of the frames collapsing in 50 years is increased by a factor varying from 1.8 to 1.9 at both the midfault and end-of-fault sites. In addition, collapse risk of the frames located 5 km away from the fault, is 4.0 to 5.0 and 4.7 to 5.0 larger than that when they are located 15 km from the fault, at the midfault and end-of-fault sites, respectively. The aforementioned observations suggest a very large increase in the collapse risk of the structures due to near-fault directivity, even in the case of site-to-source distances of 10 km. In general, modern seismic design codes, such as EC8 [12], use spectra derived from far-field ground motions, the majority of them are recorded at sites with distances from the nearest fault greater than 15 km. Therefore, structures designed based on EC8 [12], which does not take into account near-fault directivity, are more susceptible to collapse, when located at sites close to the fault, since their collapse risk is much larger in this region. Thus, there is a need of introducing in EC8 [12] more strict criteria for the design of structures situated in the near-source.

When comparing the collapse risk at each of midfault and end-of-fault sites for a particular frame, it is observed that the seismic risk is not as largely affected by the relative position of the site to the fault axis as it is by the distance to the fault. However, slightly larger values of the probability of collapse of the frames are found at the end-of-fault sites.



(a) (b)

Figure 7: Collapse fragility functions for (a) all the frames of the study when located at midfault sites for site-to-source distance equal to 15 km (b) the *HP20D* SC-MRF at three different midfault sites.

The efficiency of the SC-MRFs with and without viscous dampers to reduce seismic collapse risk should be evaluated in comparison to the corresponding conventional MRFs. The probability of collapse in 50 years of the *HP20D* SC-MRF is approximately 0.7 times the one of the *HP20D* MRF, for all site-to-source distances and type of sites. A similar trend is observed for the *CP3D* SC-MRF and the *CP3D* MRF. These results indicate that self-centering connections can significantly improve the collapse resistance of the frames. Moreover, self-centering connections are very effective in reducing the collapse risk of the frames to which they were inserted, since an approximately 30% decrease in the collapse risk was observed.

	P[Collapse in 50 yrs]					
	Midfault sites			End-of-fault sites		
Frame	5km	10km	15km	5km	10km	15km
HP20D MRF	3.49%	1.40%	0.73%	3.59%	1.46%	0.77%
CP3D MRF	7.36%	3.30%	1.83%	7.55%	3.42%	1.92%
HP20D SC-MRF	2.40%	0.93%	0.47%	2.52%	0.99%	0.51%
CP3D SC-MRF	4.98%	2.14%	1.16%	5.21%	2.28%	1.25%

Table 3: Probability of collapse in 50 years for the frames of this study.

Finally, the effectiveness of providing supplemental damping in the frames examined herein, is investigated. The *HP20D* MRF exhibits 0.5, 0.4 and 0.4 times the probability of collapse in 50 years of the *CP3D* MRF for site-to-source distances equal to 5, 10 and 15 km, respectively, at the midfault sites. Similarly, the *HP20D* SC-MRF has 0.5, 0.4 and 0.4 times the collapse risk of the *CP3D* SC-MRF for site-to-source distances equal to 5, 10 and 15 km, respectively, at the midfault sites. Similar results were obtained at the end-of-fault sites. This suggests that the frames with viscous dampers have superior collapse resistance compared to the frames without viscous dampers. In addition, it can be concluded that supplemental damping reduced the collapse risk of the frames up to 60%, and its effectiveness was increased for larger distances from the fault.

9 CONCLUSIONS

In this paper, the collapse risk of self-centering steel MRFs with viscous dampers subjected to near-fault ground motions was evaluated. The evaluation was based on the comparison of four different designs of a prototype steel building using as lateral load resisting frames: 1) conventional steel MRFs, 2) steel MRFs with viscous dampers, 3) steel SC-MRFs and 4) steel SC-MRFs with viscous dampers. Collapse capacity of these frames was predicted based on the concept of IDA. Results of IDA were combined with NS-PSHA to construct fragility curves for the probability of collapse of the frames and to compute the corresponding probabilities in 50 years. On the basis of the developments presented in this paper, the following conclusions can be drawn:

- The collapse capacity of all the frames strongly depends on the pulse period, T_p, of the excitation and it takes its larger value when the fundamental period of the frames is approximately equal to T_p.
- Collapse risk of the frames is reduced with distance from the fault, indicating that structures designed based on EC8 can be very vulnerable when located in the near source.
- Self-centering connections can significantly improve the collapse resistance of the frames. Moreover, they are very effective in reducing the probability of collapse of the frames to which they were inserted, since an approximately 30% decrease in the collapse risk of all SC-MRFs was observed.
- The frames with viscous dampers have superior collapse resistance compared to the frames without viscous dampers. Supplemental damping is very efficient in reducing the collapse risk of the frames, since an up to 60% decrease was observed, and its effectiveness was increased for larger distances from the fault.

10 ACKNOWLEDGEMENTS

This research has been supported by a Marie Curie Intra European Fellowship within the 7th European Community Framework Programme and by the Engineering and Physical Sciences Research Council of the United Kingdom (Grant Ref: EP/K006118/1). The authors acknowledge Professor Abbie Liel and Dr Eugenio Chioccarelli for providing explanations on their published research work.

REFERENCES

[1] P.G. Somerville, N.F. Smith, R.W. Graves, N.A. Abrahamson, Modification of Empirical Strong Ground Motion Attenuation Relations to Include the Amplitude and Duration Effects of Rupture Directivity. *Seismological Research Letters*, **68**, 199–222, 1997.

[2] I. Iervolino, C.A. Cornell, Probability of Occurrence of Velocity Pulses in Near-Source Ground Motions. *Bulletin of the Seismological Society of America*, **98**, 2262–2277, 2008.

[3] A. Veletsos, N.M. Newmark, Effect of inelastic behaviour on response of simple systems to earthquake motions. *Proc., 2nd World Conf. on Earthquake Engineering Vol. II*, Tokyo, 895–912, 1960.

[4] V.V. Bertero, S.A. Mahin, R.A. Herrera, Aseismic design implications of near-fault San Fernando earthquake records. *Earthquake Engineering and Structural Dynamics*, **6**, 31–42, 1978.

[5] A.K. Chopra, C. Chintanapakdee, Comparing response of SDF systems to near-fault and far-fault earthquake motions in the context of spectral regions. *Earthquake Engineering and Structural Dynamics*, **30**, 1769–1789, 2003.

[6] G.P. Mavroeidis, G. Dong, A.S. Papageorgiou, Near-fault ground motions and the response of elastic and inelastic, single-degree-of-freedom (SDOF) systems. *Earthquake Engineering and Structural Dynamics*, **33**, 1023–1049, 2004.

[7] B. Alavi, H. Krawinkler, Behavior of moment-resisting frame structures subjected to near-fault ground motions. *Earthquake Engineering and Structural Dynamics*, **33**, 687–706, 2004.

[8] N. Makris, T. Psychogios, Dimensional response analysis of yielding structures with first-mode dominated response. *Earthquake Engineering and Structural Dynamics*, **35**, 1202–1224, 2006.

[9] T.L. Karavasilis, N. Makris, N. Bazeos, D.E. Beskos, Dimensional response analysis of multistory regular steel MRF subjected to pulselike earthquake ground motions. *Journal of Structural Engineering*, **136**, 921–932, 2010.

[10] N. Luco, B.R. Ellingwood, R.O. Hamburger, *Risk-Targeted versus Current Seismic Design Maps for the Conterminous United States*, SEAOC 2007 Convention Proceedings, 2007.

[11] C. Champion, A. Liel, The effect of near-fault directivity on building seismic collapse risk. *Earthquake Engineering and Structural Dynamics*, **41**, 1391–1409, 2012.

[12] EC8. *Eurocode 8. Design of structures for earthquake resistance*, 2013.

[13] J.M. Ricles, R. Sause, M.M. Garlock, C. Zhao, Postensioned seismic-resistant connections for steel frames. *ASCE Journal of Structural Engineering*, **127**, 113–121, 2001.

[14] C. Christopoulos, A. Filiatrault, C-M. Uang, Post-tensioned energy dissipating connections for moment resisting steel frames. *ASCE Journal of Structural Engineering*, **128**, 1111–1120, 2002.

[15] G. Vasdravellis, T.L. Karavasilis, B. Uy, Large-scale experimental validation of steel post-tensioned connections with web hourglass pins. *Journal of Structural Engineering* (ASCE), **139**,1033-1042, 2013.

[16] C.C. Chou, Y.J. Lai, Post-tensioned self-centering moment connections with beam bottom flange energy dissipators. *Journal of Constructional Steel Research*, **65**,1931-1941, 2009.

[17] C-C. Chou, K-C. Tsai, W-C. Yang, Self-centering steel connections with steel bars and a discontinuous composite slab. *Earthquake Engineering and Structural Dynamics*, **38**, 403-422, 2009.

[18] G. Vasdravellis, T.L. Karavasilis, B. Uy, Finite element models and cyclic behaviour of self-centering post-tensioned connections with web hourglass pins. *Engineering Structures*, **52**, 1-16, 2013.

[19] A. Dimopoulos, T.L. Karavasilis, G. Vasdravellis, B. Uy, Seismic design, modelling and assessment of self-centering steel frames using post-tensioned connections with web hourglass shape pins. *Bulletin of Earthquake Engineering*, **11**, 1797-1816, 2013.

[20] P. Rojas, J.M. Ricles, R. Sause, Seismic performance of post-tensioned steel moment resisting frames with friction devices. *Journal of Structural Engineering*, **131**, 529-540, 2004.

[21] H.J. Kim, C. Christopoulos, Friction damped posttensioned self-centering steel moment-resisting frames. *Journal of Structural Engineering*, **134**, 1768-1779, 2008.

[22] K.C. Tsai, C.C. Chou, C.L. Lin, P.C. Chen, S.J. Jhang, Seismic self-centering steel beam-to-column moment connections using bolted friction devices. *Earthquake Engineering and Structural Dynamics*, **37**, 627-645, 2008.

[23] M. Wolski, J.M. Ricles, R. Sause, Experimental study of a self-centering beam-column connection with bottom flange friction device. *Journal of Structural Engineering*, **135**,479-488, 2009.

[24] M. Garlock, R. Sause, J.M. Ricles, Behavior and design of posttensioned steel frame systems. *Journal of Structural Engineering*, **133**, 389-399, 2007.

[25] H.J. Kim, C. Christopoulos, Seismic design procedure and seismic response of post-tensioned self-centering steel frames. *Earthquake Engineering and Structural Dynamics*, **38**, 355-376, 2008.

[26] T.L. Karavasilis, R. Sause, J.M. Ricles, Seismic design and evaluation of steel MRFs with compressed elastomer dampers. *Earthquake Engineering and Structural Dynamics*, **41**, 411-429, 2012.

[27] T.L. Karavasilis, J.M. Ricles, R. Sause, C. Chen, Experimental evaluation of the seismic performance of steel MRFs with compressed elastomer dampers using large-scale real-time hybrid simulation. *Engineering Structures*, **33**, 1859-1869, 2011.

[28] T.L. Karavasilis, C-Y. Seo, Seismic structural and non-structural performance evaluation of highly damped self-centering and conventional systems. *Engineering Structures*, **33**, 2248-2258, 2011.

[29] C-Y. Seo, T.L. Karavasilis, J.M. Ricles, R. Sause, Seismic performance and probabilistic collapse resistance assessment of steel moment resisting frames with fluid viscous dampers. *Earthquake Engineering and Structural Dynamics*, **43**, 2135-2144, 2014.

[30] Y.C. Kurama, Seismic design of unbonded post-tensioned precast concrete walls with supplementary viscous damping. *ACI Structural Journal*, **97**, 648–658, 2000.

[31] W.Y. Kam, S. Pampanin, A. Palermo, AJ. Car, Self-centering structural systems with combination of hysteretic and viscous energy dissipations. *Earthquake Engineering and Structural Dynamics*, **39**, 1083-1108, 2010.

[32] A.S. Tzimas, A.I. Dimopoulos, T.L. Karavasilis, EC8-based seismic design and assessment of self-centering steel frames with viscous dampers. *Journal of Constructional Steel Research*, **105**, 60-73, 2015.

[33] S. Mazzoni, F. McKenna, M. Scott, G. Fenves, *Open system for earthquake engineering simulation (OpenSees). User Command Language Manual*, Pacific Earthquake Engineering Research Center, University of California, Berkeley, 2006.

[34] D. Vamvatsikos, C.A. Cornell, Incremental dynamic analysis. *Earthquake Engineering Structural Dynamics*, **31**, 491-514,2002.

[35] D.G. Lignos, H. Krawinkler. Deterioration Modeling of Steel Components in Support of Collapse Prediction of Steel Moment Frames under Earthquake Loading. *Journal of Structural Engineering*, **137**, 1291-1302, 2011.

[36] M. Hamidia, A. Filiatrault, A. Aref, Simplified seismic sidesway collapse analysis of frame buildings. *Earthquake Engineering and Structural Dynamics*, **43**, 429–448, 2014.

[37] T.L. Karavasilis, A.I. Dimopoulos, A.S. Tzimas, George S. Kamaris, D. Vamvatsikos, estimation of economic losses in seismic-resistant post-tensioned steel frames with viscous dampers, *8th International Conference on Advances in Steel Structures (ICASS 2015)*, Lisbon, Portugal, July 22-24, 2015.

[38] H. Krawinkler, Shear Design of Steel Frame Joints. *Engineering Journal*, AISC, **15**, 82-91, 1978.

[39] J.W. Baker, Quantitative Classification of Near-Fault Ground Motions Using Wavelet Analysis. *Bulletin of the Seismological Society of America*, **97**, 1486–1501, 2007.

[40] Pacific Earthquake Engineering Research Center (PEER), NGA Database. http://peer.berkeley.edu/nga/.

[41] FEMA P695, *Quantification of building seismic performance factors*. ATC-63 Project. Applied Technology Council. CA. USA; 2008.

[42] A.B. Liel, C.B. Haselton, G.G. Deierlein, J.W. Baker, Incorporating Modeling Uncertainties in the Assessment of Seismic Collapse Risk of Buildings. *Structural Safety*, **31**, 197–211, 2009.

[43] J.W. Baker, C.A. Cornell, Spectral shape, epsilon and record selection. *Earthquake Engineering and Structural Dynamics*, **35**, 1077–1095, 2006.

[44] C.B. Haselton, J.W. Baker, A.B. Liel, G.G. Deierlein, Accounting for Ground Motion Spectral Shape Characteristics in Structural Collapse Assessment Through an Adjustment for Epsilon. *Journal of Structural Engineering*, **137**, 332–344, 2011.

[45] P. Tothong, C.A. Cornell, J.W. Baker, Explicit Directivity-Pulse Inclusion in Probabilistic Seismic Hazard Analysis. *Earthquake Spectra*, **23**, 867–891, 2007.

[46] S.K. Shahi, J.W. Baker, An Empirically Calibrated Framework for Including the Effects of Near Fault Directivity in Probabilistic Seismic Hazard Analysis. *Bulletin of the Seismological Society of America*, **101**, 742–755, 2011.

[47] E. Chioccarelli, I. Iervolino, Near-Source Seismic Demand and Pulse-Like Records: a Discussion for L'Aquila Earthquake. *Earthquake Engineering and Structural Dynamics*, **39**, 1039–1062, 2010.

[48] E. Chioccarelli, I. Iervolino, Near-source seismic hazard and design scenarios. *Earthquake Engineering and Structural Dynamics*, **42**, 603-622, 2013.

[49] E. Chioccarelli, I. Iervolino, Sensitivity analysis of directivity effects on PSHA. *Bollettino di Geofisica Teorica e Applicata*, **55**, 41-53,2014.

[50] PG. Somerville, Magnitude Scaling of the Near Fault Rupture Directivity Pulse. *Physics of the Earth and Planetary Interiors*, **137**, 201–212, 2003.

[51] D.L. Wells, K.J. Coppersmith, New empirical relationships among magnitude, rupture length, rupture width, rupture area, and surface displacement. *Bulletin of the Seismological Society of America*, **84**, 974-1002,1994.

COMPDYN 2015
5th ECCOMAS Thematic Conference on
Computational Methods in Structural Dynamics and Earthquake Engineering
M. Papadrakakis, V. Papadopoulos, V. Plevris (eds.)
Crete Island, Greece, 25–27 May 2015

BEHAVIOR OF HIGH STRENGTH STEEL FUSEIS SEISMIC RESISTANT SYSTEMS

Stella Avgerinou[1], **Ioannis Vayas**[1]

[1] Institute of Steel Structures, National Technical University of Athens, Greece
e-mail: avgerinoustella@gmail.com, vastahl@central.ntua.gr

Keywords: High strength steel, Fuseis seismic resistant systems, RBS, Full scale tests

Abstract. *FUSEIS is an innovative seismic resistant system consisting of two closely spaced strong columns rigidly connected through multiple beams. The system resists lateral loads as a vertical Vierendeel beam. The dissipative elements are the FUSEIS beams and they usually have reduced beam sections (RBS) towards beam ends in order for the plastic hinge formation to be shifted away from the connections. In this paper, the behavior of a FUSEIS system with SHS and CHS beams made of high strength steel S700 is evaluated. The results of two full scale experimental investigations with different loading protocols are presented, together with corresponding numerical simulation. The tests were conducted in NTUA. Furthermore an application of the system in a four-storey building case study is presented along with the assessment of its behavior factor based on non-linear static and dynamic analyses.*

1 INTRODUCTION

Seismic resistant systems are those which provide lateral stability and hence seismic safety to a structure. The most common seismic resistant systems in steel structures are currently: moment resisting frames, concentric braced frames, eccentric braced frames and steel or composite vertical walls. Despite the structural efficiency of these conventional systems, their reparability after a strong earthquake is not equally advantageous. The FUSEIS on the other hand, is an innovative seismic resistant system with increased reparability while comparable to the conventional systems in terms of stiffness and ductility. The system was introduced and studied in the framework of a recent European Research Program named "FUSEIS" [8]. It is now further investigated with respect to its material properties in another European Research Program named "MATCH".

The system is composed by two strong columns rigidly connected by multiple beams. The beams run continuously from column to column or are cut in the middle and connected by short pins. The system resists lateral loads as a vertical Vierendeel beam mainly by combined bending and shear of the beams and axial forces of the columns. Considering a typical floor height of 3.4 m, four or five beams may be placed per storey. The seismic resistance of a building with Fuseis systems may be provided either by the systems alone or by a combination of their action with a moment resisting frame action. That depends on whether the beam-to-column connections of the structure are simple or rigid/semi-rigid. In order to prevent the transfer of moments to the foundations, the system's columns supports are formed as simple and also a fuse beam just above foundation level is used.

Modern seismic codes allow for the development of inelastic deformations in a structure's dissipative zones during the design earthquake. In case of a strong seismic event, the dissipative elements of the FUSEIS that can undergo damage up to a certain extent are the beams (or the pins) that thus constitute easily reparable fuses. In order for the plastic hinge formation to be shifted away from the beam-to-column joints the beams have reduced beam sections (RBS) towards their ends. The fuses-to-column connections must be designed with sufficient overstrength to achieve energy absorption only in the fuses and with bolted end-plates in order to enable the replacement of the fuses beams if needed. The fuses beam sections may be hollow or open and they also may vary between the floors of a multi-story structure following the increase of story shear or even vary within a story, leading to sequential plasticization of the fuses.

This study presents the results of two full scale tests on FUSEIS frames with hollow section beams. The beams material is high strength steel with nominal yield stress S700. The tests results are used for the development and calibration of simple FE models. Furthermore an example of the application of the system in a four-story structure is presented using fuses sections similar to those tested. The response of this case study is evaluated, using non-linear static and dynamic analyses.

2 DESCRIPTION OF TESTS

In total, eight FUSEIS full scale tests will be performed in the Institute of Steel Structures of the National Technical University of Athens in the context of the "MATCH" research program, in addition to the tests that were performed in the previous "Fuseis" research program [9],[10]. The parameters differentiating the various experimental investigations are the cross sections of the fuses, their materials and the loading protocols applied. In this paper the results of two tests with identical fuses beam specimens but different loading protocol are presented.

The experimental setup includes a rigid frame test rig available in NTUA's Laboratory, a computer controlled hydraulic cylinder and the test frame. The dimensions of the test frame

correspond to a real building frame: its height is 3.4m and the axial distance of the strong columns is 1.50m. The strong columns are rigidly connected by five fuses beams (Figure 3). The beam specimens were provided by RUUKKI-SSAB, a steel producer that focuses on high strength steel and also a participant in the research project. The beams have different cross sections along the height of the frame in order to achieve a sequential yielding of the specimens. All beam specimens have the same length and consist of hollow sections welded with identical plates at both ends. Bolted connections are used between the plates and the flanges of the strong columns in order to facilitate the replacement of the fuses after tests (Figure 1). Mounting of the test configuration is carried out with a crane due to the size and weight of the various parts. Aiming to shift the plastic hinge formation away from the beam-column connections, most of the specimens have reduced beam sections (RBS) towards their ends. The general properties of the fuses beams are summarized in Table 1. The steel grade of all beam specimens is S700 while the material of the end plates is S500. The yield stress of the material of the beams was provided by the steel producer and was specified as 790 MPa.

Cross section	Steel	Length (mm)	RBS
SHS 100*4	S700	722	yes
SHS 80*4	S700	722	yes
SHS 60*3	S700	722	no
CHS 76.1*3.2	S700	722	yes
CHS 60.3*4	S700	722	yes

Table 1: Summary of beam specimens



Figure 1: Fuses beam specimens

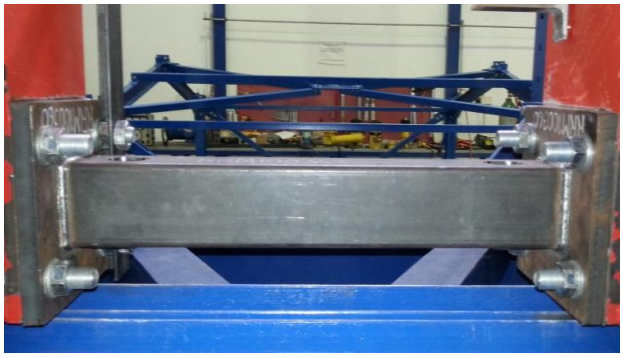


Figure 2: Bolted fuse beam

The columns of the test frame are connected to the rigid test rig by pin connections. At the bottom of the columns two UPN horizontal beams are connected at each side of the frame with pins in order to simulate the floor diaphragm at this level and assure equal displacements of the columns during the tests. In order to avoid displacements of the test frame in its out-of-plane direction, steel plates/leaders are used. The above details are depicted in Figure 3 and Figure 4.

Cyclic loading was applied through a hydraulic actuator positioned horizontally between the bottom of the columns and a base via two hinges. The actuator is computer controlled and its capacity is 500kN and 250mm back and forth. Both testing procedures are displacement controlled. The maximum drift of the frame reached in Test 1 is 4.8% while the (constant) maximum drift applied for Test 2 is 3.0%.

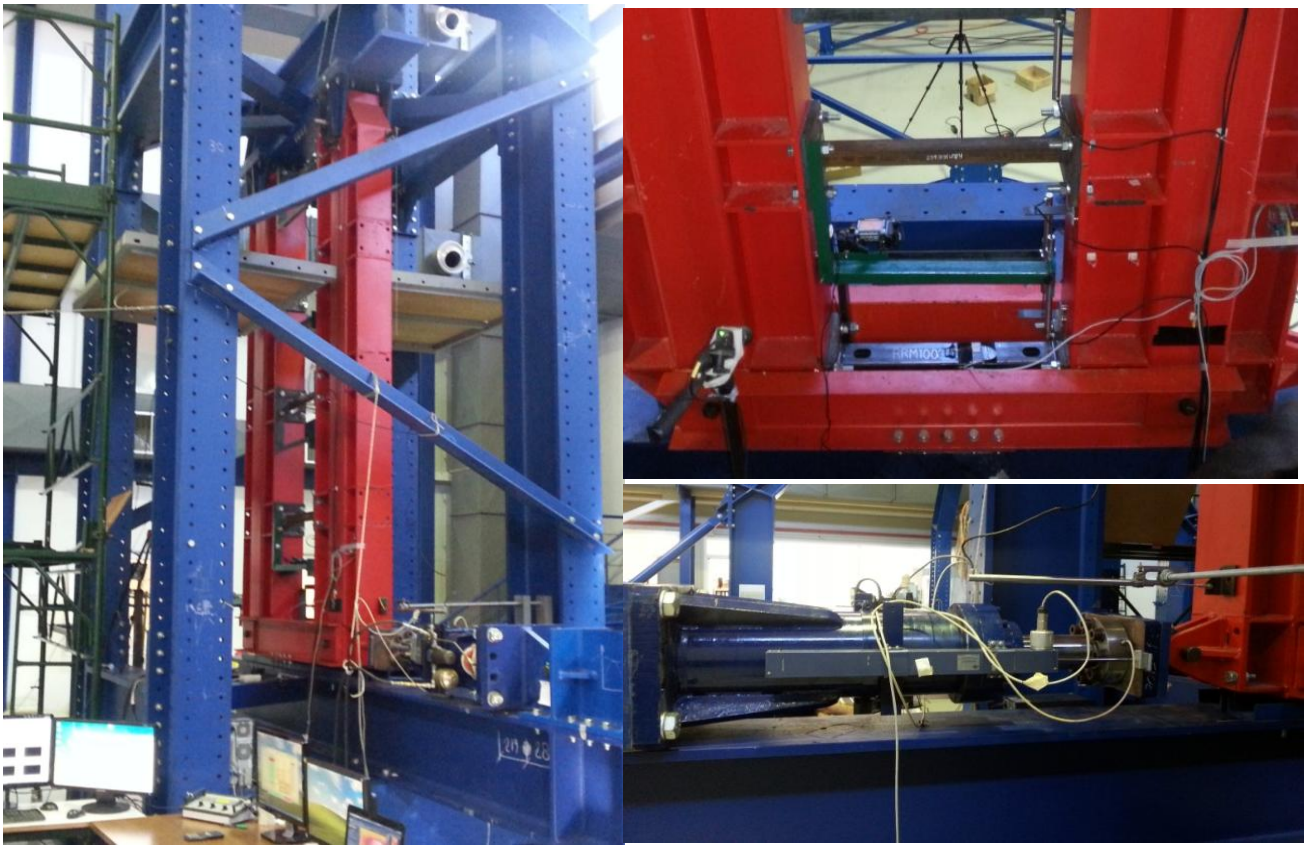


Figure 3: Experimental setup, test frame, “diaphragm” simulation and actuator



Figure 4: Pinned supports of columns steel leaders to avoid out-of-plane displacements

As far as the energy dissipation zones are concerned, the reduction of the fuses beam flanges at a certain distance from the connection areas was designed taking into account the EC8 and FEMA 350 recommendations [5],[16]. The selected reduced beam section properties are summarized in Table 2. The location and dimensions of the RBS are decided based on the following checks:

$$M_{cf,Ed} = (0.85 \div 1.00) * M_{pl,Rd,b} \quad (1)$$

$$V_{Ed,max} / V_{pl,rd} \leq 1.00 \quad (2)$$

where $M_{cf,Ed}$ is the capacity design bending moment that develops at the column face when a plastic hinge forms at the centre of the RBS, $M_{pl,Rd,b}$ is the beam plastic moment resistance away from the RBS, $V_{Ed,max}$ is the capacity design shear force and $V_{pl,rd}$ is the beam's shear force resistance.

	Distance a (mm)	RBS length (mm)	Flange reduction
FEMA 350	$0.5 \div 0.75 * b_f$	$0.65 \div 0.85 * h_b$	$<0.50 * b_f$
EC 8	$0.6 * b_f$	$0.75 * h_b$	$<0.50 * b_f$
SHS 100*4	50	60	$0.44 * b_f$
SHS 80*4	50	60	$0.40 * b_f$
SHS 60*3	-	-	-
CHS 76.1*3.2	50	50	-
CHS 60.3*4	50	50	-

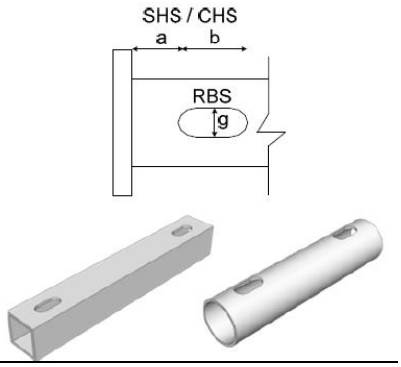


Table 2: Reduced beam sections

2.1 Loading procedures and data measurements

As mentioned above, the only difference between the two tests is the applied load protocol: in the first test the loading procedure has increasing amplitude and is based on the relevant ECCS recommendation [14] while in the second test a constant amplitude load protocol is applied. Both loading procedures are presented in Figure 5 andFigure **6** and Table 3. The required displacements are applied by the computer controlled hydraulic actuator with constant velocity 1.5mm/s. Short pauses are input between each cycle while longer pauses are input between cycles with increasing amplitude. The duration of each test was approximately 1.5 hours.

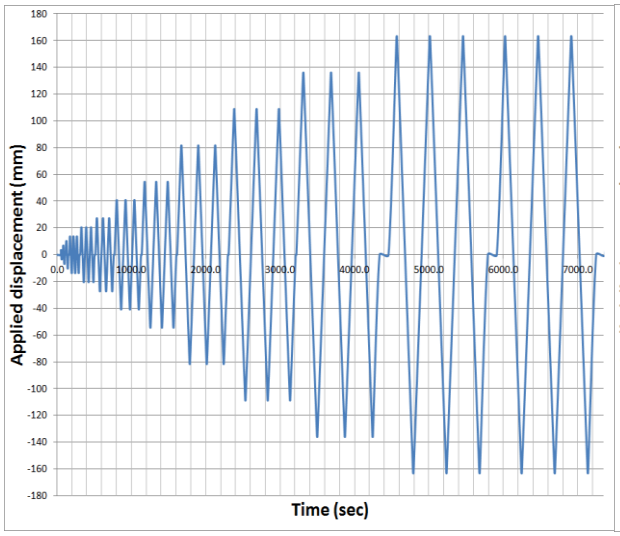


Figure 5: Load protocol for Test 1

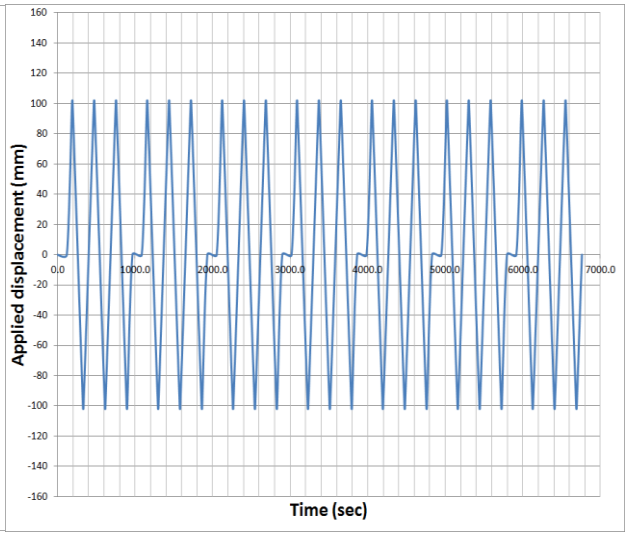


Figure 6: Load protocol for Test 2.

During the tests the following data were measured:

- Displacement of the actuator (controlled)
- Hydraulic load applied by the cylinder piston
- Differential displacement of beam ends in the direction vertical to the beams

- Displacement of the column connected with the actuator

Furthermore, a thermal camera was constantly recording one of the beam specimens.

Cycles	Test 1		Test 2	
	Displacement (mm)	Interstorey drift (%)	Displacement (mm)	Interstorey drift (%)
1	±3.4	±0.1	-	-
1	±6.8	±0.2	-	-
1	±10.2	±0.3	-	-
3	±13.6	±0.4	±102.0	±3.0
3	±20.4	±0.6	±102.0	±3.0
3	±27.2	±0.8	±102.0	±3.0
3	±40.8	±1.2	±102.0	±3.0
3	±54.4	±1.6	±102.0	±3.0
3	±81.6	±2.4	±102.0	±3.0
3	±108.8	±3.2	-	-
3	±136.0	±4.0	-	-
3	±163.2	±4.8	-	-

Table 3: Loading procedures of tests

2.2 Test results

In the following figures the test frame response curves (in terms of actuator force vs. frame drift) of the Fuseis systems are presented. As it can be noticed both tests were carried out until the frame strength dropped to less than 50% of its peak resistance. Load degradation occurred due to crack formation and opening and also due to local buckling. Plastic deformations took place within the fuses devices only.

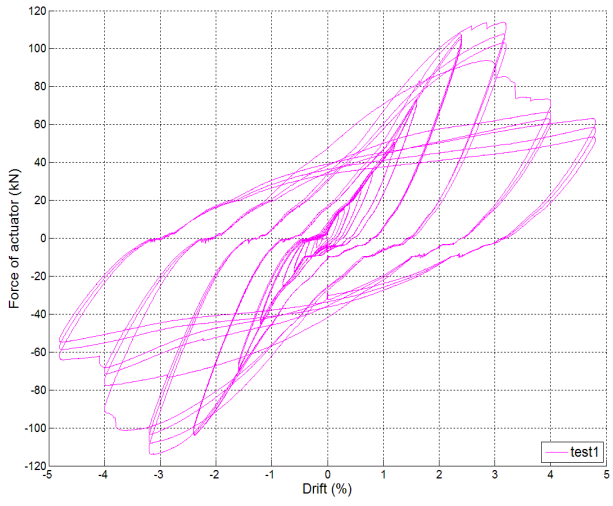


Figure 7: Frame response for Test 1

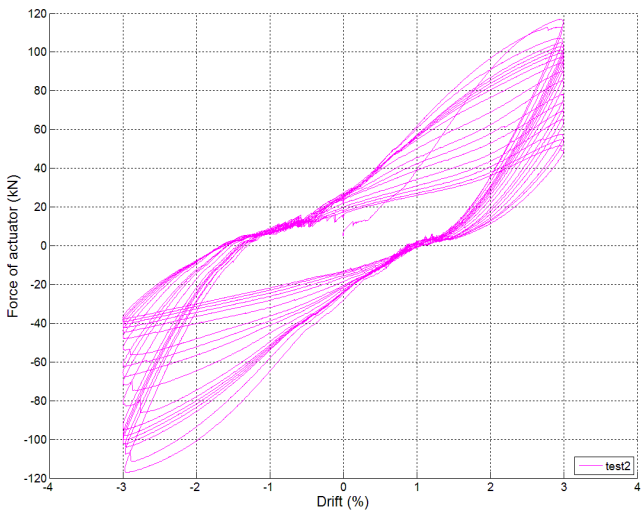


Figure 8: Frame response for Test 2.

Yielding of most specimens started at the reduced beams sections (RBS) area where eventually ductile fractures were observed. In the following figures the deformations as well as the failure of some specimens are presented indicatively.



Figure 9: (a) Cracks at RBS of a SHS beam and (b) at welds of a beam without RBS



Figure 10: (a) Cracks and (b) local buckling of CHS beam

The process of hinge formation in the reduced beam section area is shown in Figure 11 with snapshots of the thermal camera during the second (constant amplitude) test. The increase of temperature in the area of the RBS can be easily observed.

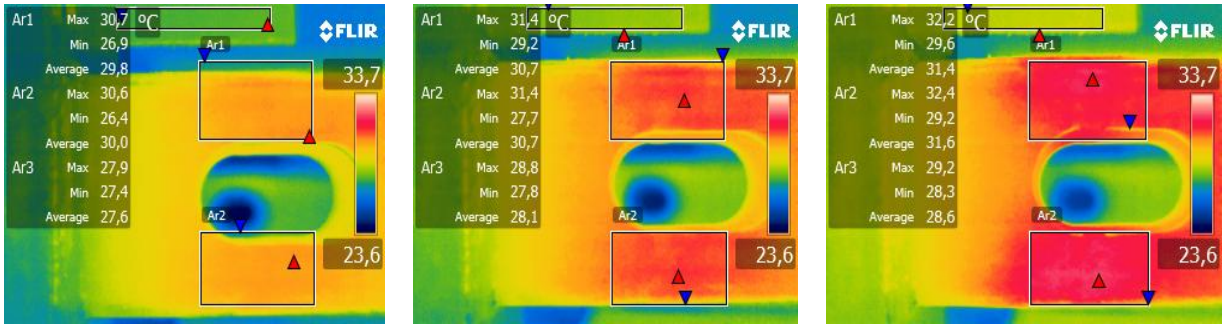


Figure 11: Thermal camera snapshots of a SHS during Test 2 in cycles 5,9 and 14 respectively.

The experimental investigations verified that the system behaves like a Vierendeel beam, resisting lateral loads by combined bending of the fuses and axial forces of the columns. Assuming that the hinges are formed in the midpoints of the reduced beam sections (and in case there are no RBS, they are formed at the beam end points), Figure 12 shows the theoretical static model of the frame and the forces equilibrium. The maximum theoretical story resistance (F_{theor}) can be calculated as following:

$$F_{theor} = (2\sum M_{pl,Rd,RBS} / l_{RBS}) * (L/h_{story}) \quad (3)$$

where L is the axial distance of the fuses columns and l_{RBS} is the distance of the midpoints of the reduced beam sections.

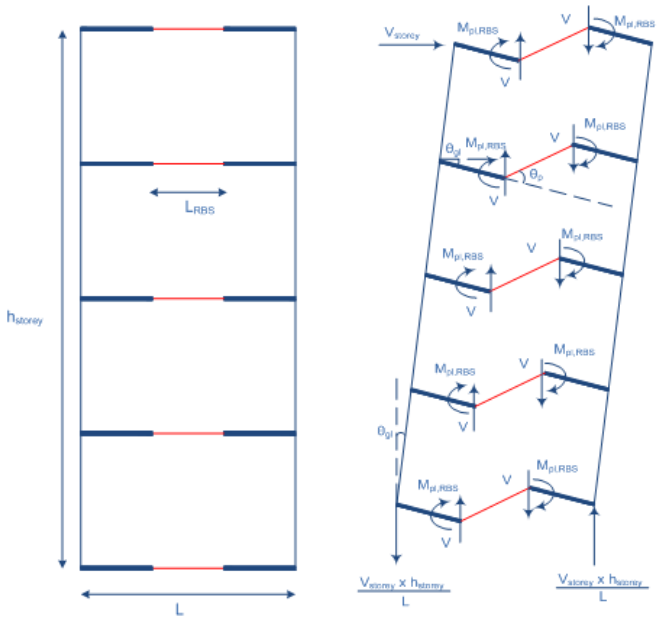


Figure 12: Static system and force/moments equilibrium

Table 4 shows the theoretical force as derived from eq. (3), together with the maximum forces achieved by the tests. The good relation indicates that the Vierendeel model describes well the ultimum capacity of the system. The table shows also the ultimate rotations and number of cycles achieved during the two tests. Two values of this rotation are given that correspond to different failure criteria: The first criterion represents the 20% reduction of the maximum strength and/or initial stiffness and the second criterion relates to 80% of the theoretical value F_{theor}. While for the first test -which was performed with increasing displacements- the failure criterion is stated in terms of drifts, in the second test -which had constant amplitude- failure is presented in terms of cycles (Table 4).

Test	Load Prot.	F_{max} (kN)	F_{theor} (kN)	F_{max}/F_{theor}	crit.1	crit.2
T1	ECCS	113	113	1.00	θ=0.034	θ=0.034
T2	const.ampl.	117	113	1.04	N=8	N=10

Table 4: Comparison between maximum frame resistance and theoretical force

2.3 Calibration of simple test model in SAP

The relatively common software SAP2000 is selected in order to form a simple model that approaches the behaviour of the Fuseis test frames. The fuses beams are simulated with appropriate beam finite elements. Their net length is subdivided to five zones representing the full sections and the reduced beam sections (RBS). Rigid zones are assigned from column centres to column faces. Aiming to match the initial stiffness of the model frame with its experimental elastic stiffness, rotational links were used in the position of the bolted end plates of the fuses beams and stiff translational springs are used (Figure 13).

The response of the model frame under lateral loading is evaluated using non-linear incremental static analysis. The pushover's target displacement corresponds to the maximum displacement applied by the actuator on the test frames. Having located the energy dissipation zones on the fuses during the experimental investigations, hinges were assigned respectively. More specifically regarding the RBS elements, plastic hinges were located in their middle.

The moments and rotations required to describe the non-linear behaviour of each fuse were calculated using the following equations:

$$M_{pl,RBS} = W_{pl,RBS} * f_y \text{ and } M_{y,RBS} = M_{pl,RBS} / a_{pl} \quad (4)$$

$$\theta_y = M_y * l_b / (6 * E * I_y) \quad (5)$$

The definition of the moment-rotation hinge properties was approached through comparison with the experimental data but remain to be verified with additional numerical and experimental investigations.

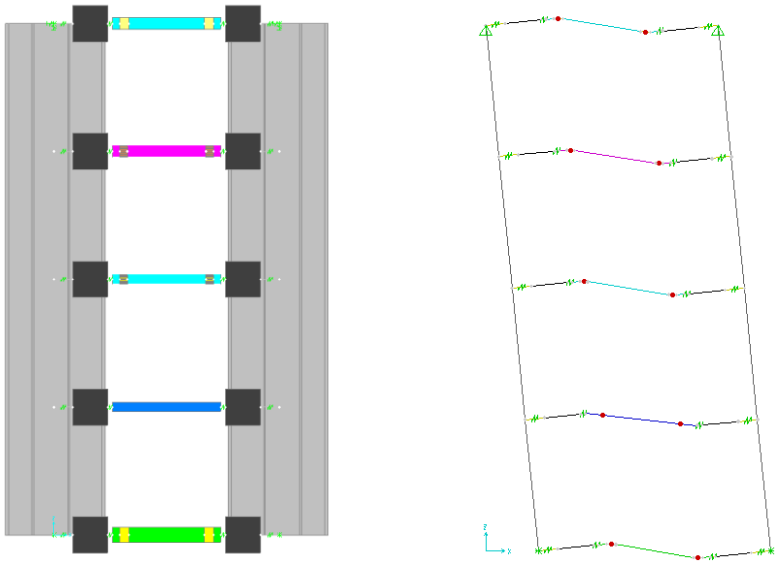


Figure 13: SAP model, pushover deformation and plastic hinge formation

The pushover curve of the model is compared with the positive and negative skeleton curves derived from Test 1 (Figure 14).

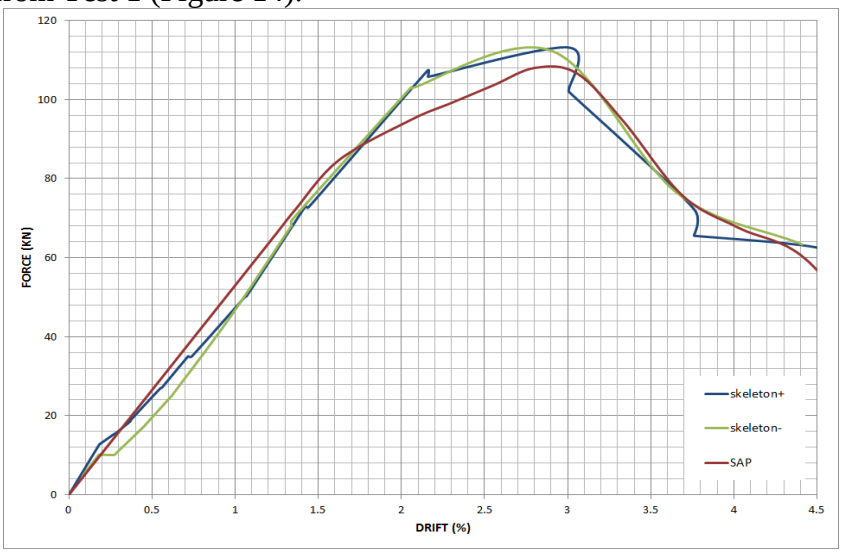


Figure 14: Comparison of pushover with skeleton curve for test calibration

3 DESIGN OF A MULTI-STORY BUILDING FRAME WITH FUSEIS

Based on the feedback from the experimental investigations, a four-storey building with Fuseis systems was designed using the SAP2000 software. The dimensions of the 2D frame are typical: the storey height is 3.4m and the span length is 7.0m. The axial distance of the

Fuseis strong columns is 1.50m (Figure 15). The loads applied are representative for office or residential buildings according to EC1 [1] while the effective width for the loads in the transverse direction of the frame is assumed 6.0m. Composite action is taken into account, assuming composite decks consisting of profiled steel sheeting. The effective widths as well as the equivalent lengths of the composite beams were calculated according to EC4 [3]. Composite beam sections are simulated by adversely taking into account only the participation of the concrete above the profiled sheeting. The general assumptions for the design of the buildings in terms of materials, vertical loads and seismic parameters are displayed in Table 5.

Materials	
Steel members	S355
Fuses beams	S700
Vertical loads	
Dead (slabs)	2.2 kN/m^2
Additional dead	2.0 kN/m^2
Imposed loads	3.0 kN/m^2
Seismic parameters	
Type of spectrum	EC8, Type 1
PGA	0.25g
Importance class	II, γ=1.00
Ground /Soil	Type B, S=1.2
Behaviour factor q_{des}	5.00
Factors φ (EC8,p.1, 4.2.4)	φ = 1.00 (roof) φ = 0.80

Table 5: General assumptions for the design of the case study

The design of the building was according to the provisions of EC3, EC4 and EC8 [1],[2],[3],[4],[5]. Additional rules given in the FUSEIS Design Guide [7] were applied to ensure that yielding, takes place in the FUSEIS beams prior to any yielding or failure elsewhere. The sections of the fuses beams used in the design were chosen amongst the types tested. However, the specific sections chosen as well as the required number of the FUSEIS systems was mainly determined by the limitations of inter-storey drifts (*dr*v < 0.0075*H*, for buildings with ductile non-structural members) and second order effects.

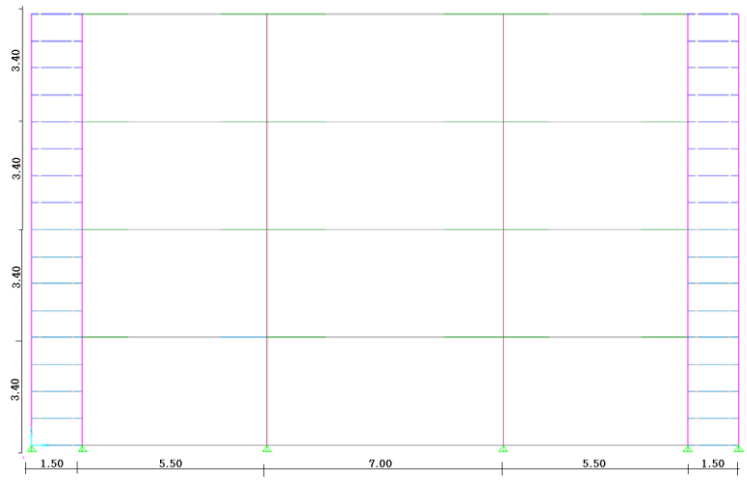


Figure 15: model of the 4story frame in SAP

As far as the beam-to-column connections are concerned, in this case they were chosen to be semi rigid which means that the Fuseis systems are combined with the overall moment resisting frame to provide the seismic resistance of the building.

Regarding the modal analysis, the period of the first mode of vibration is 1.3sec and the mass participation ratio exceeds 88%. One more mode is needed for the activation of 97% of the mass while the respective percentage required by codes is 90%.

4 NON-LINEAR STATIC ANALYSIS AND EVALUATION OF THE BEHAVIOUR FACTOR

For further investigation of the case study's seismic behaviour, non-linear static analysis was performed. The scope was to quantify the structure's maximum base shear capacity and the ultimate displacement and eventually calculate the behaviour, ductility and overstrength factors. The analysis was performed under displacement control and the maximum displacement applied on the top floor translated to an average building drift equal to 6%. Two types of vertical distribution of the lateral load were used: one with uniform pattern and another proportionate to the fundamental modal shape (inverted triangle).These two types in a way represent an upper and a lower limit for the structure's response (Figure 17). While the lateral loads increased monotonically, the gravity loads remained constant (1.0*G+0.3*φ* Q). Second order effects were taken into account.

In order to simulate material non-linearity, potential plastic hinges were assigned in all areas prone to exhibiting very large deformations or inelastic behaviour. More specifically plastic hinges were located in the middle of the fuses reduced beam sections (RBS), at the beams close to the beam-to-column connections and at selected areas of the columns. While the columns were assigned with automatic hinges taking into account the interaction between axial forces and bending moments, the beams and the fuses RBS were assigned with user defined moment-rotation hinges. The simulation of the behaviour of the fuses hinges was based on the results of the test's calibration presented above.

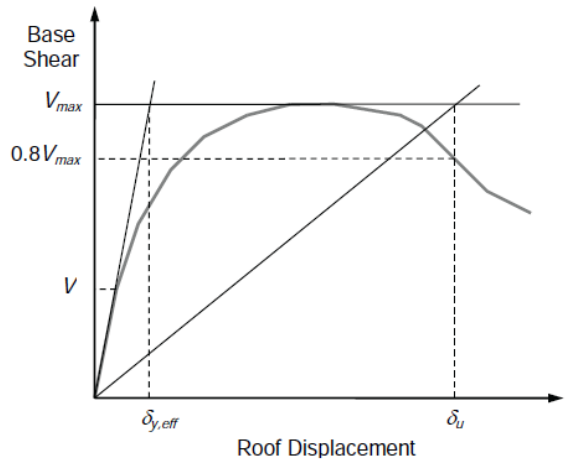


Figure 16: Idealized pushover curve (FEMA695)

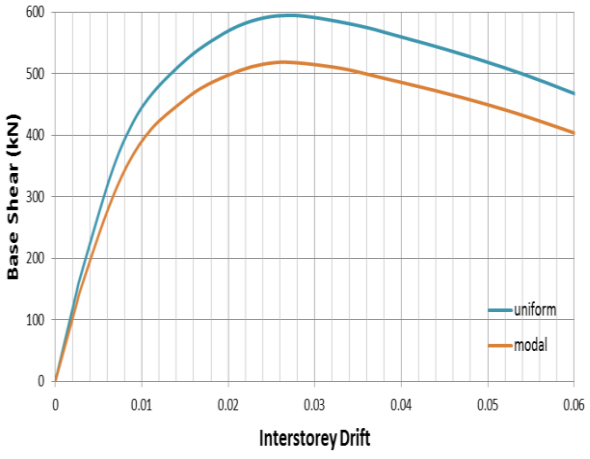


Figure 17: Pushover curves for "uniform" and "modal shape" lateral load distribution

In order to evaluate the structure's behaviour factor the product of overstrength and ductility must be calculated. The overstrength of the structure is defined as the ratio of the maximum base shear resistance on the pushover curve over the base shear at first (fuse) yield ($\Omega = V_{max}/V_1$). Ductility is defined as the ratio of the ultimate roof displacement over the effective yield displacement ($\mu=\delta_u/d_{yeff}$) (Figure 16). The ultimate roof displacement may be assumed to represent either the point of 20% strength loss (δ_u) or a point at which another non-

simulated failure mode occurs such as for example, the failure mode indicated by the experimental investigations (δ_{uexp}) (Figure 18)[6]. In Table 6 the results of the pushover analysis are summarized. Calculations were based on the pushover analysis with uniform lateral load distribution. The performance point is also presented according to ATC-40 provisions [15]. It should be noted that the values of the factors presented need further recalculation to take better into account the additional future experimental results and respective numerical simulations.

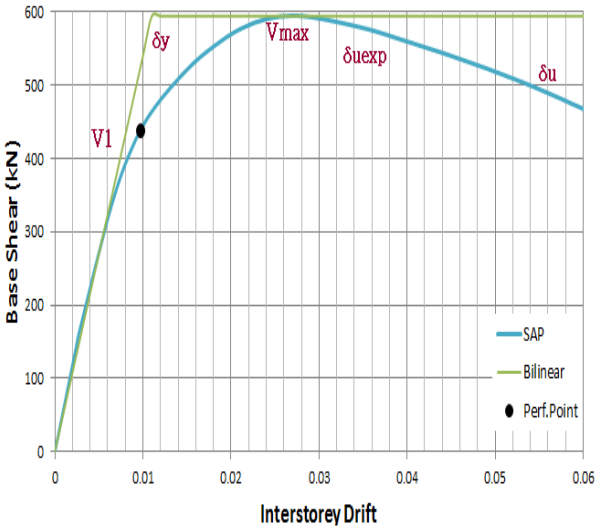


Figure 18: Pushover curve and bilinear approach

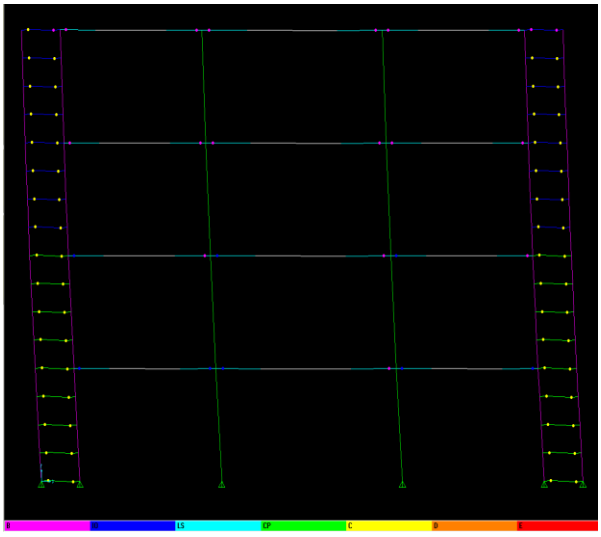


Figure 19: Deformed frame at δu and hinge formation

$\mu=\delta_u/\delta_y$	$\mu_{exp}=\delta_{uexp}/\delta_y$	$\Omega=V_{max}/V_1$	$q=\mu*\Omega$	$q_{exp}=\mu_{exp}*\Omega$
5.1	3.1	1.4	7.3	4.4

Table 6: Calculation of μ,Ω and q factors

5 NON-LINEAR DYNAMIC ANALYSIS AND PERFORMANCE ASSESSMENT

Non-linear dynamic analysis was performed on the four-story case study using the Far-Field Real Accelerograms set suggested by FEMA provisions [6]. This set includes 22 records (44 individual components) taken from 14 strong seismic events that have occurred around the world during the last decades (events with average magnitude of M7.0 and average site-source distance 16.4km).The analysis was performed using OpenSees software.

The scaling factors used for Incremental Dynamic Analysis (IDA) were obtained by dividing the desirable level of acceleration over the first mode spectral acceleration for each accelerograms input ($Sa(_{T1})$). In this case, 20 scaling factors were used ranging from 0.1g up to 2.0g, aiming to cover the range from elastic behaviour to collapse. In order to describe the scaling of each ground motion record and the structural response, an intensity measure (IM) and a damage measure (DM) were introduced respectively. For each ground motion record and every iteration the overall maximum (absolute) inter-story drift was selected and thus the IDA curve was produced.

Generally, the IDA study is accelerogram and structural model specific, therefore the differences between the various IDA curves represent the differences of the structure's response when subjected to earthquakes with different frequency characteristics [11],[12]. As it can be seen in Figure 20, all curves exhibit a distinct elastic linear region that ends when the first nonlinearity occurs. IDA curves terminate at different levels of acceleration with a final sof-

tening segment ("flatline") which indicates increasingly high accumulation of DM and signals dynamic instability.

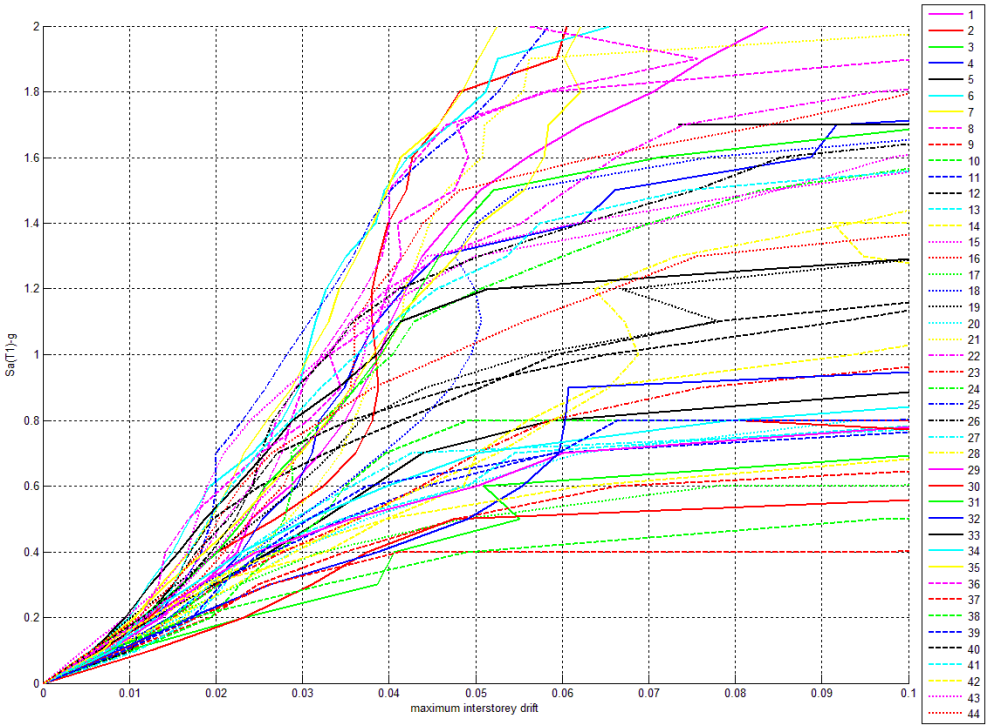


Figure 20: 44 IDA curves (FEMA Far-Field Record Set)

For a better evaluation of the IDA results, the 16%, 50% and 84% fractile curves were calculated. The flatline of the 50% fractile (median curve) represents the median collapse intensity S_{CT}. The Collapse Margin Ratio (CMR) is used to characterize the collapse safety of the structure and is calculated as the ratio of the median collapse capacity S_{CT} over the intensity of the maximum considered earthquake $S_{MT.}$ [12][13]

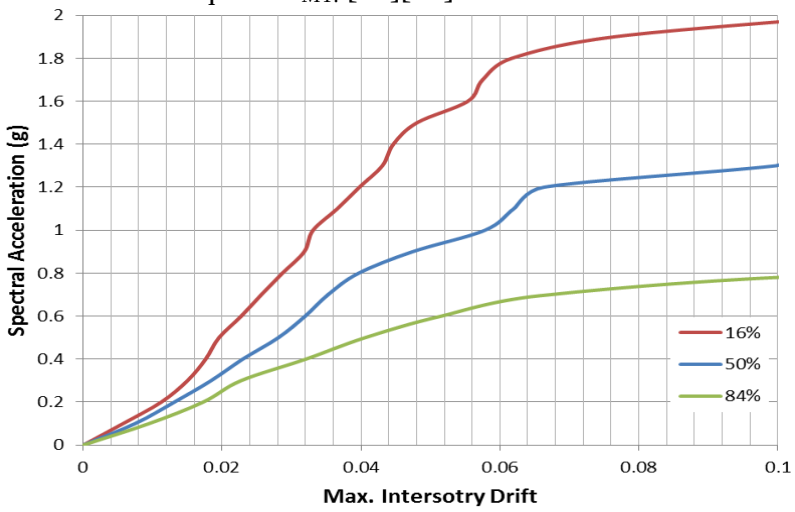


Figure 21: IDA fractiles (16%, 50% and 84%)

Collapse for a ground motion is judged to occur either directly from dynamic analysis (existence of "flatlines") or assessed indirectly through non-simulated component limit state criteria. The results of the IDA can be then summarized using a fragility function which describes probability of the defined collapse as a function of an earthquake's intensity (accel-

eration level) [6]. In this case, fragility curves are drawn by assuming two types of failure: (a) collapse due to excessive lateral displacements (flatlines) and (b) a non-simulated collapse due to exceedance of the drift representing a selected Limit State (Figure 22). More specifically, non-simulated collapse is assumed to occur at drifts beyond 3.4% which corresponds to 20% strength loss of the Fuseis system as indicated by the experimental investigations. Both collapse fragility curves were defined by a cumulative lognormal distribution function and were fitted to the points representing the aforementioned failure criteria. The parameters required for the definition of these functions were the median collapse intensity S_{CT} and a factor β representing dispersion in results due to uncertainties, for each case.

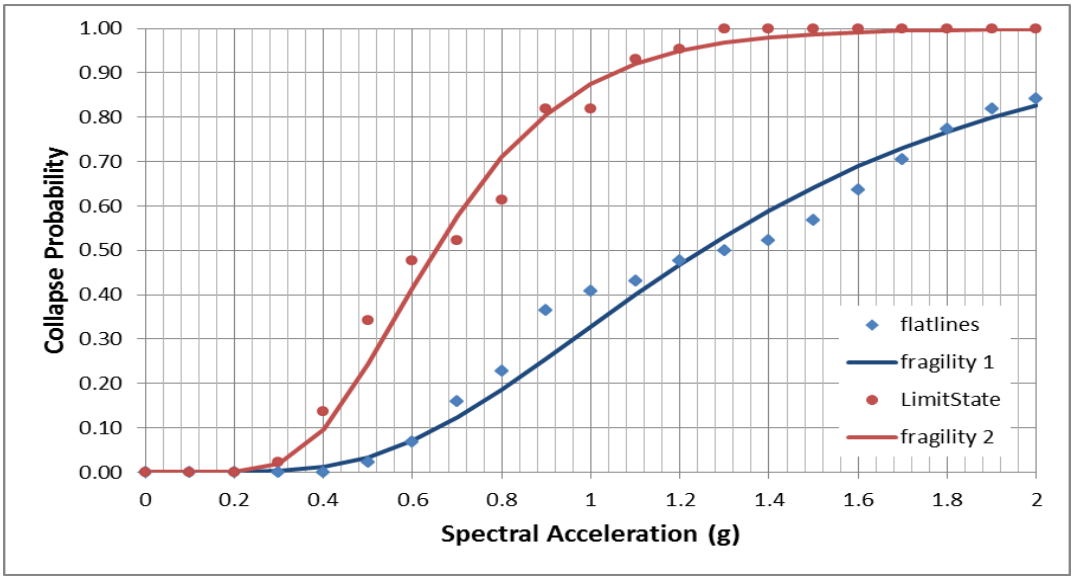


Figure 22: Fragility curves for simulated and non-simulated failure modes

As far as performance evaluation is concerned, the methodology suggested by FEMA 695 is followed (Table 7) [6]. First, CMR is subjected to spectral shape adjustment by means of the SSF (spectral shape factor) which is a function of the fundamental period T and the structures ductility μ (*ACMR=CMR*CCF*). This adjustment is to assure that the peaked spectral shapes of the rare ground motions used in IDA are not less damaging than a standard design spectrum. Then acceptability is measured by comparing the ACMR to the acceptable values of $ACMR_{10\%}$ that depend on the systems uncertainties (β).

Collapse type	S_{CT}	CMR	ACMR	$ACMR_{10\%}$
Sidesway (flatline)	1.25	2.90	3.87	1.90
Non-simulated	0.65	1.50	2.01	1.62

Table 7: Assessment of collapse performance according to FEMA695

As it can be observed in Figure 22 and Table 7, in case collapse is defined by non-simulated limit state criteria, the probability of collapse for a certain level of acceleration is significantly increased while the Collapse Margin Ratio (CMR) is reduced likewise. However in both cases, the acceptance criterion was satisfied.

6 CONCLUSIONS

- Innovative fuses systems may be applied to multi-storey steel buildings as an alternative to conventional seismic resistant systems. They combine ductility, architectural versatility, stiffness and reparability.
- The system is composed of two closely spaced columns rigidly connected with multiple short beams that are its dissipative elements.
- As an extension to previous research, experimental and analytical/numerical investigations have been carried out where the dissipative beams are of high strength steel S 700.
- Results indicate that the system with high strength beams still shows ductility, together with strength and stiffness and could be used in seismic regions.

7 ACKNOWLEDGEMENTS

The research presented is made in the framework of the European Research Project RFSR-CT-2013-00024: "Material Choice for Seismic Resistant Structures (MATCH)". The financial contribution of the Research Fund for Coal and Steel of the European Community is greatly acknowledged. The other partners of the project are: RWTH Aachen (coordinator), University of Pisa, University of Thessaly, RUUKKI-SSAB metals Oy and ILVA Spa.

REFERENCES

[1] Eurocode 1: Actions on structures - Part 1-1: General actions - Densities, self-weight, imposed loads for buildings; EN 1991-1-1:2002

[2] Eurocode 3: Design of steel structures - Part 1-1: General rules and rules for buildings; EN 1993-1-1:2005

[3] Eurocode 4: Design of composite steel and concrete structures - Part 1-1: General rules and rules for buildings; EN 1994-1-1:2004

[4] Eurocode 8: Design of structures for earthquake resistance - Part 1: General rules, seismic actions and rules for buildings; EN 1998

[5] Eurocode 8: Design of structures for earthquake resistance - Part 3: Assessment and Retrofitting of buildings; EN 1998-3:2004

[6] FEMA P695: Quantification of building seismic performance factors, 2009.

[7] Vayas, Ph. Karydakis, D. Dimakogianni, G. Dougka, C.A. Castiglioni, A. Kanyilmaz, B. Hoffmeister, T. Rauert, et al, "Dissipative devices for seismic resistant steel frames – The FUSEIS project, Design guide". Research Programme of the Research Fund for Coal and Steel, 2012.

[8] Vayas, Ph. Karydakis, D. Dimakogianni, G. Dougka, C.A. Castiglioni, A. Kanyilmaz, B. Hoffmeister, T. Rauert, et al, "Dissipative devices for seismic resistant steel frames – The FUSEIS project, Final Report". Research Programme of the Research Fund for Coal and Steel, 2012.

[9] Dougka, G., Dimakogianni, D., Vayas,(in press) I. Innovative energy dissipation systems (FUSEIS 1-1) - Experimental analysis. Journal of Constructional Steel Research, Vol. 96 (5), pp 69-80, 2014

[10] Dimakogianni, D., Dougka, G., Vayas, I. Innovative seismic-resistant steel frames (FUSEIS 1-2) experimental analysis. Steel Construction Design and Research, Vol. 5 (4), pp. 212-221, 2012.

[11] Vamvatsikos D.,Cornell C.A, 2002, "Incremental Dynamic Analysis", Earthquake Engineering & Structural Dynamics, John Wiley & Sons, Ltd.

[12] Vamvatsikos D.,Cornell C.A, 2005, "Seismic Performance, capacity and reliability of structures as seen through Incremental Dynamic Analysis", The John A. Blume Earthquake Engineering Center, Stanford University

[13] ASCE Standard 7-05: Minimum Design Loads for Buildings and Other Structures, American Society of Civil Engineers, 2006

[14] ECCS: Recommended testing procedure for assessing the behaviour of structural steel elements under cyclic loads. Technical committee 1: structural safety and loadings, technical working group 1.3: seismic design, 1986

[15] ATC 40: Seismic evaluation and retrofit of concrete buildings, Applied Technology Council, California Seismic Safety Commission, 1996

[16] FEMA 350: Recommended seismic design criteria for new steel moment frame buildings, 2000.

COMPDYN 2015
5th ECCOMAS Thematic Conference on
Computational Methods in Structural Dynamics and Earthquake Engineering
M. Papadrakakis, V. Papadopoulos, V. Plevris (eds.)
Crete Island, Greece, 25–27 May 2015

PERFORMANCE OF MULTI-STOREY COMPOSITE STEEL-CONCRETE FRAMES WITH DISSIPATIVE FUSE DEVICES

Alper Kanyilmaz[1], Carlo A. Castiglioni[2]
[1,2] Department of Architecture, Built Environment and Construction Engineering
Politecnico di Milano
Via Ponzio 31, 20133 Milano, Italy
alper.kanyilmaz@polimi.it, carlo.castiglioni@polimi.it

Keywords: Dissipative devices, replaceable fuses, seismic resilience, composite steel-concrete

Abstract. *Repair work of conventional steel-concrete composite frames can be very expensive, sometimes impossible due to practical problems. EU-funded research project FUSEIS (RFCS-CT-2008-00032) has introduced two innovative types of seismic resistant steel-concrete composite frame types with dissipative fuses, which are cost-effective and robust alternatives to conventional frame types. In these frames, damage concentrates mainly in the fuses, which are easily and inexpensively replaceable after strong seismic events. In this study, performance of the type-2 fuse device from FUSEIS project have been assessed inside a multi-level 2D steel-concrete composite frame, by means of nonlinear time history analysis. Performance of a benchmark building with and without fuse devices has been compared in terms of damage, floor displacements and drifts.*

1 INTRODUCTION

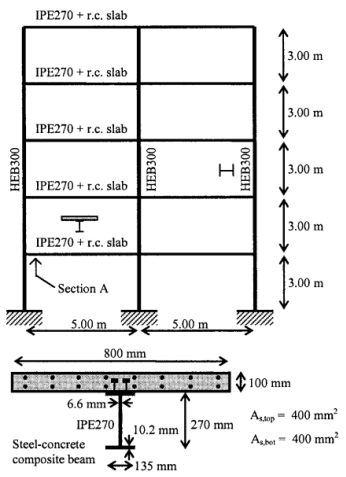
In general, it can be stated that the behavior of steel buildings during devastating earthquakes of the last three decades was quite satisfactory, if they were designed according to the modern seismic codes [1]. However, in most of the cases, despite not causing global collapse, main structural elements (steel beams, columns and concrete slabs) suffered costly damages. Repair work in these cases was most of the time not feasible, if not too expensive.

In order to enhance the seismic performance of steel-concrete composite frames, and facilitate the repair work after strong seismic events, two innovative dissipative devices were developed within European research program FUSEIS (Dissipative devices for seismic resistant steel frames) [2]. The first device type (fuseis 1) is used as a dissipative "shear wall" [3], whereas the second device type (fuseis 2) resembles "replaceable plastic hinges" for moment resisting frames [4]. Both systems aim at controlling and concentrating inelastic deformations in the "fuse devices", without imposing significant damage in the rest of the structure (steel columns and beams, concrete slab). In this way, after the seismic event, the damaged fuse devices can be replaced with the new ones, instead of the costly operation of repairing major structural beams and columns. Therefore, the building with new fuses can turn back to service with a relatively minor repair cost.

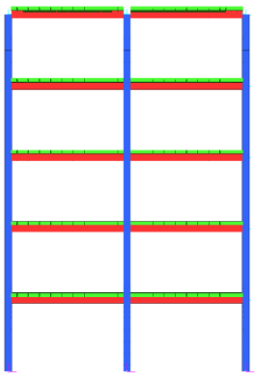
Behaviour of these fuse devices was studied numerically and experimentally during the FUSEIS research project, and the results have been published in several articles [2-8].

This article presents the performance of a benchmark building, with and without fuse devices (figure 1b, 1c), in terms of damage, floor displacements and drifts, by means of nonlinear transient dynamic analysis. Post processing of the results of this study is still underway, with which the authors aim to provide the energy dissipation characteristics of the building with fuses, based on the criteria suggested by Castiglioni et. al [9], and Ballio et. al. [10]

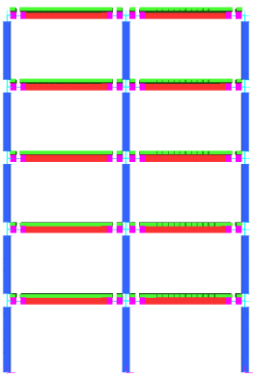
The benchmark building is a five-storey and two-bay steel-concrete composite frame, which was studied numerically by Zona et.al [11]. Each bay has a span of 5.00 m and story height of 3.00 m. The steel columns are made of European HEB300 wide flange beams, while the composite beams are made of steel European IPE270 I-beams connected by means of stud connectors to a 100-mm-thick concrete slab with an effective width estimated at 800 mm, top and bottom reinforcements of 400 mm^2 and a concrete cover of 30 mm (figure 1). Yield stress of column and beam steel is 275 MPa, reinforcement steel is 430 MPa, and compressive strength of concrete is 33 MPa.



a. Benchmark steel-concrete composite frame [11]



b. Numerical model of building without fuse (NOFUSE)



c. Numerical model of building with fuse (FUSE)

Figure 1 Benchmark frame and its representation with and without fuse devices

2 NUMERICAL SIMULATION

Parametric analysis of the fuse devices were performed with refined numerical models at Politecnico di Milano, which can only be used for specific research applications. In order to study the performance of whole building structures, a simplified model has been proposed hereafter and validated against experimental results from previous studies.

Numerical models of this study have been developed with the commercial software package Straus7 [12]. Nonlinear transient dynamic analyses have been performed, considering material and geometrical nonlinearities, using inelastic fiber-based cross sections for the beam and column elements, and plastic links for fuse elements.

Fiber based modeling distributes plasticity by numerical integrations through the member cross sections and along the member length, and with a "plane sections remain plane" assumption [13]. Uniaxial material models are used to capture the nonlinear hysteretic axial stress-strain characteristics in the element cross sections. Fibers are numerically integrated over the cross section to monitor the axial force and moments, incremental moment-curvature and axial force-strain relations (figure 2). The cross section parameters are numerically integrated at several sections along the member length, using displacement or force interpolation functions. This approach allows performing nonlinear analysis considering both geometric and material nonlinearity, within a time much more limited than a 3D continuum finite element analysis. However, using this approach local behaviour such as degradation due to local buckling is difficult to capture without sophisticated models. Fiber-based modeling approach with distributed plasticity (DPE) offers a good compromise in terms of accuracy and computational time to model hysteresis behavior of steel struts. Kanyilmaz [14] has demonstrated the accuracy and efficiency of this modeling approach for steel beam-column elements.

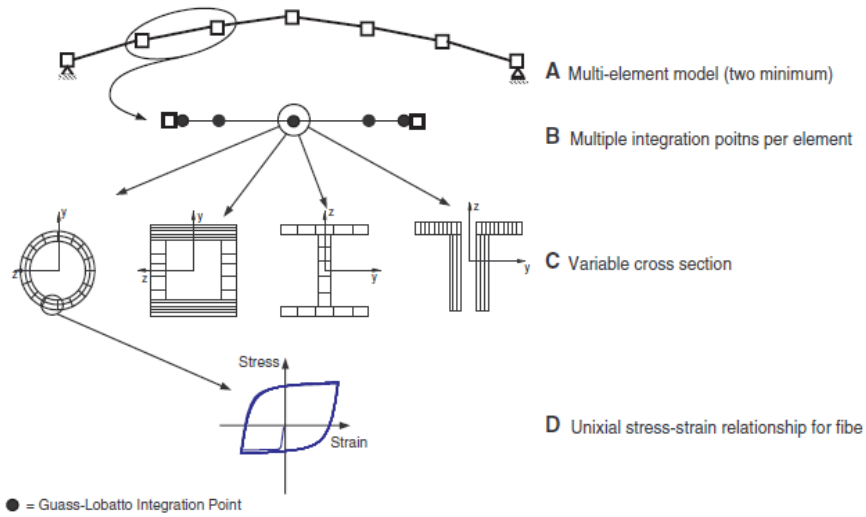


Figure 2 Fiber based distributed plasticity approach [15]

In order to investigate the effect of using fuse devices in building structures, two buildings have been analyzed:

Model 1: Benchmark building with conventional moment-resisting steel-concrete composite frame (NOFUSE)

Model 2: Benchmark building with Fuse devices that are placed close to the end of composite beams (FUSE).

Since the sliding between steel beam and concrete slab has a negligible influence on the global response of the building, a simplified procedure has been used to model the composite

steel beam. The concrete slab has been modeled as a beam element accounting for its effective width and height. An additional beam element has been used to simulate the two rows of steel reinforcement, placed at the centroid of concrete slab. The distance between the centroids of concrete and steel beam is taken into account applying an offset to the concrete slab element (figure 3).

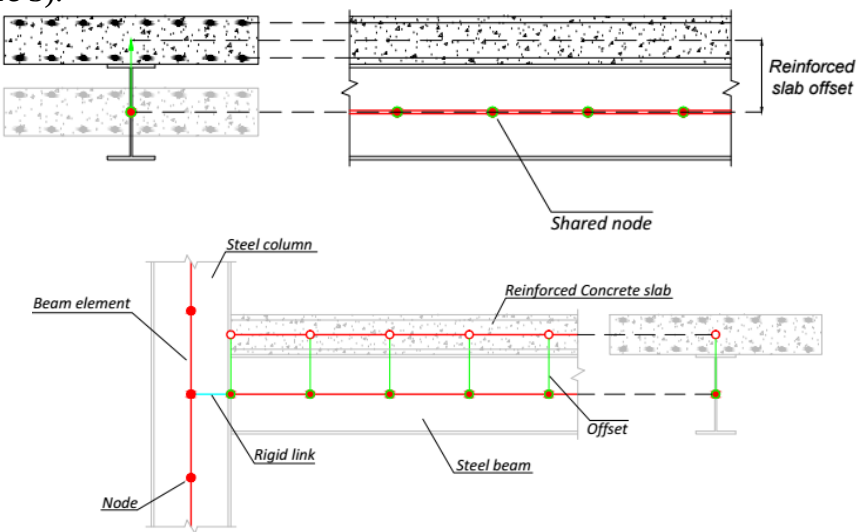


Figure 3 Numerical modeling of composite steel-concrete beam

Elasto-plastic material has been used for all structural elements in the model, with kinematic hardening. This approach will give an insight on the distribution of plasticity in the structure under nonlinear time history analysis. Figure 4 presents the constitutive models of the material properties used for steel profiles, concrete slab, and steel reinforcement bars. The exact values of each material property are shown in the reference articles.

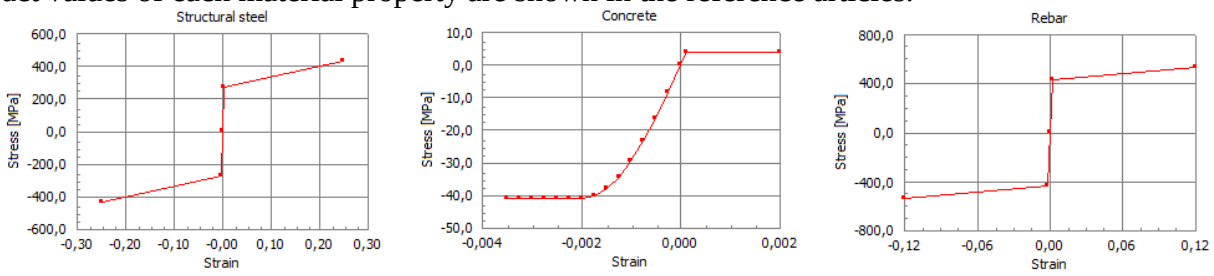


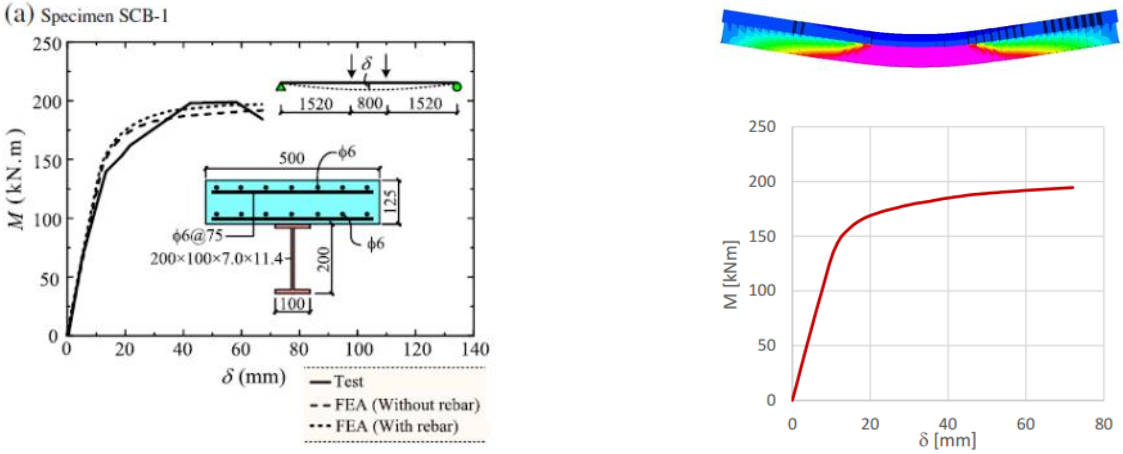
Figure 4 Material properties used in the models

This numerical modeling procedure has been validated with reference to the previous experimental studies [16-18]. A summary of the validation process is given in the following sub-chapters.

2.1 Validation of Steel-Concrete Composite Frame Models

The proposed modeling procedure has been validated with the experimental results of tests performed with simply supported beams (i) [16], continuous beams (ii) [17], and plane frames (iii) [18].

i) The nonlinear static behaviour of a simple composite steel-concrete beam has been simulated under monotonic loading, and the numerical results have been compared with the experimental results. Figure 5 shows the test specimen, experimental and numerical results of the original study, and numerical results of this study. Initial stiffness and moment capacity behaviour of the test specimen have been captured adequately.

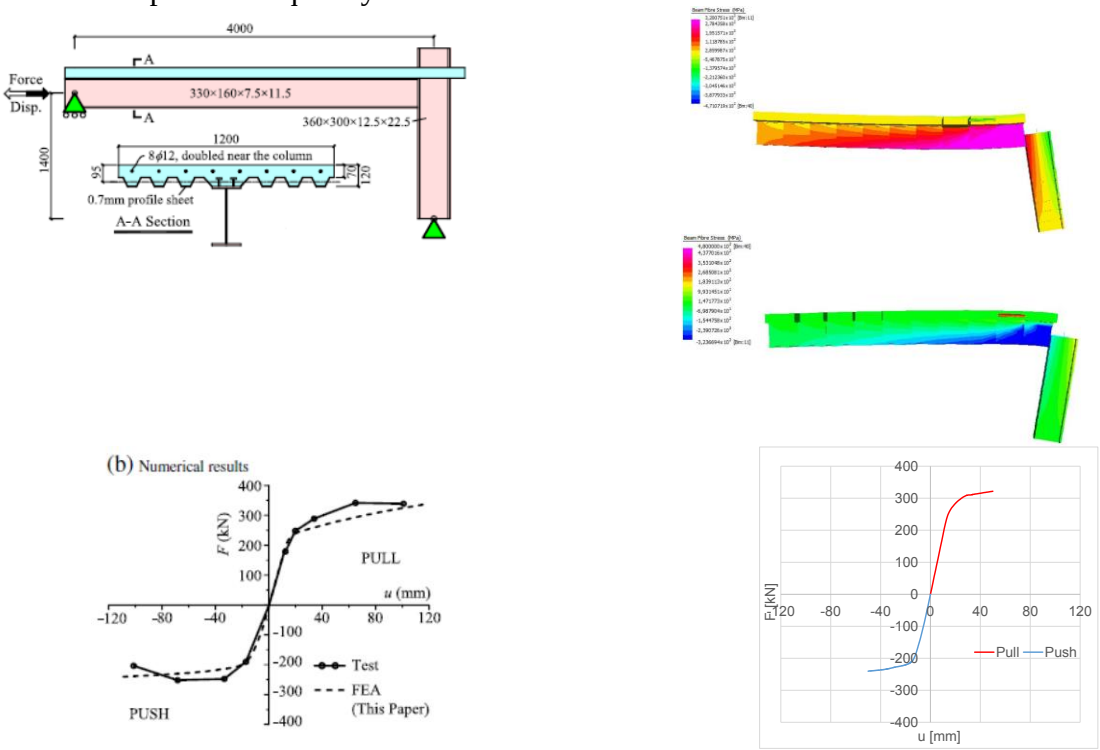


a. Experimental and numerical results of the original study [16]

b. Numerical results of this study

Figure 5 Numerical validation of composite simple beam element

ii) The nonlinear behaviour of a composite steel-concrete joint has been simulated under cyclic loading, and the numerical results have been compared with the experimental results. Figure 6 shows the test specimen, experimental and numerical results of the original study, and numerical results of this study. Initial stiffness and moment capacity behaviour of the test specimen under sagging and hogging have been interpreted adequately.



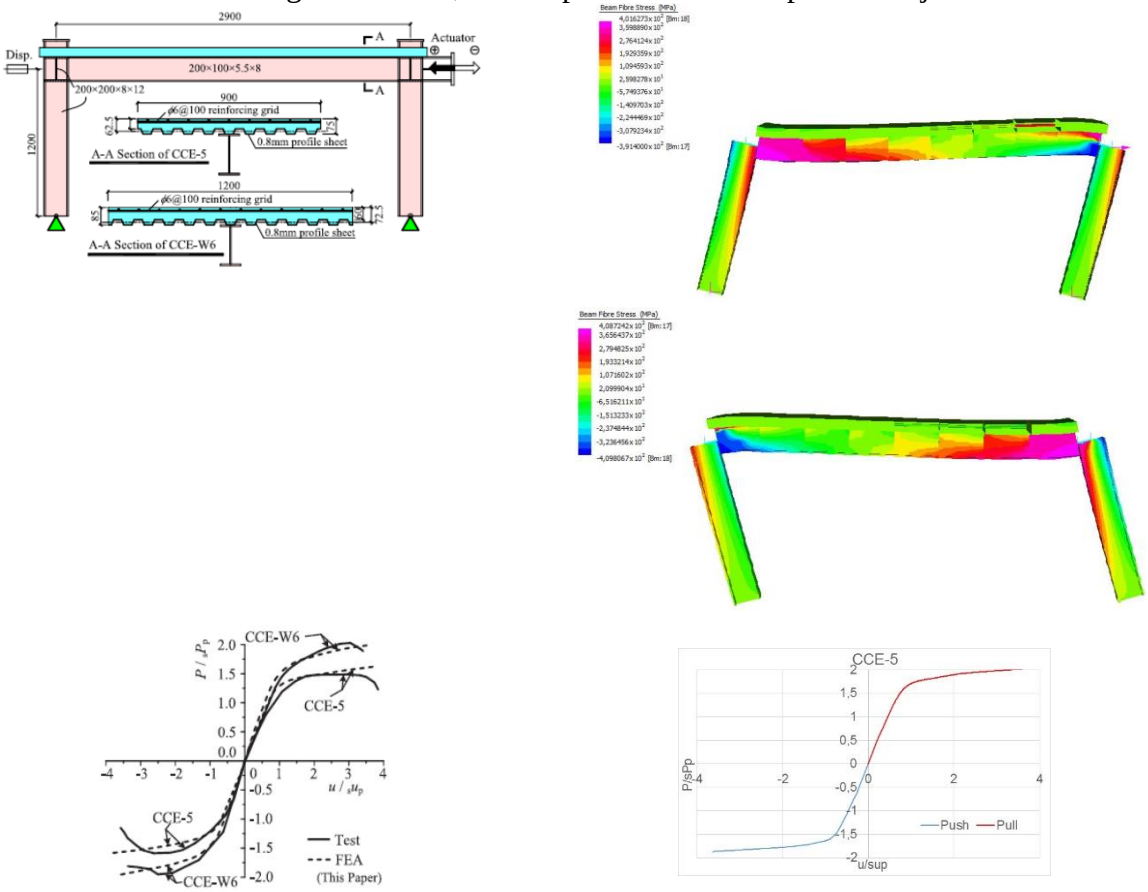
c. Experimental and numerical results of the original study [17]

d. Numerical results of this study

Figure 6 Numerical validation of composite joint

iii) The nonlinear static behaviour of a 2D planar composite steel-concrete frame has been simulated under cyclic loading, and the numerical results have been compared with the

experimental results. Figure 7 shows the test specimen, experimental and numerical results of the original study, and numerical results of this study. Numerical models overestimate the moment capacity of the specimen, yet the results are quite reasonable to be used in a global model, for the performance comparison objective.



a. Experimental and numerical results of Nie et. al [18]

b. Numerical results

Figure 7 Numerical validation of planar frame

2.2 Validation of Numerical Models of Composite Steel-Concrete Frames with Fuse Devices

A numerical model has been developed, which simulates the nonlinear cyclic behavior of the full-scale specimen tested during the FUSEIS project. The specimen is a two dimensional portion of a storey of a composite steel multistory building, the configuration of which can be seen in figure 8. The frame consists of four HEB240 steel columns, two IPE300 steel beams, and a 150 mm thick reinforced concrete slab. The slab is supported by IPE160 transverse beams placed every 1.4 meters, in addition to a pair of transverse beams that are placed at each beam-column connection. Full shear connection is provided between the slab and the steel beam by means of IPE100 sections welded on top of the beam flange, acting as shear studs. To connect the steel plates to the beams in the fuse parts, high strength friction grip (HSFG) bolts are used.

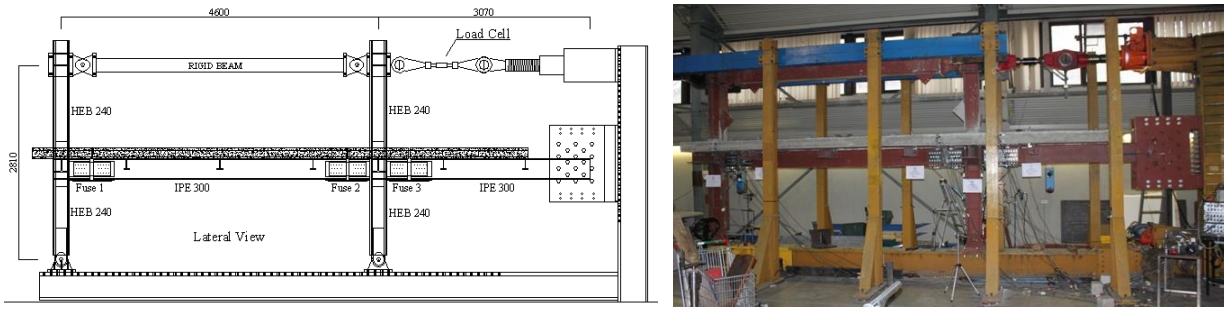
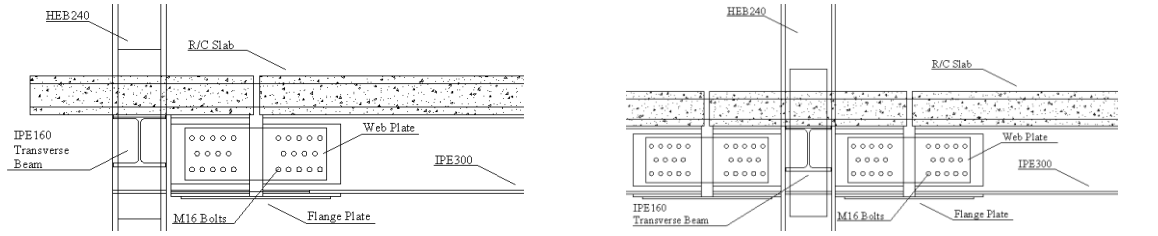


Figure 8 Full scale test specimen of FUSEIS project [1]

The column bases are restrained against horizontal and vertical displacement through pin connections. The beam-to-column connections are welded off site and can be considered as rigid connections. The IPE300 beam connected to the right column by fuse device n.3 is restrained only against the vertical displacement, but free to slide in horizontal direction. The out of plane stability of the frame is provided with transversal elements providing a pinned joint free to slide longitudinally on the reaction frame of the laboratory (Figure 8).

The fuse devices are obtained by means of plates bolted to the web and the lower flange of the beam. They are installed within the distance of a beam depth to the beam-to-column connection. The part of the beam near the connection is reinforced with steel plates welded to the web and to the flanges. These plates are positioned in order to avoid yielding of the beam due to bearing. Their thicknesses are chosen in order to provide, in that section, a total thickness two times the one of the web and the lower flange of the main beam respectively. In this way no plasticization is expected to occur in the beam but only in the replaceable part where the failure is expected to take place. Also the part of the column near to the connection is reinforced in order to obtain a rigid joint and hence concentrate all the damage on the fuse device. The interior and exterior fuse connection details are shown in figure 9. Thanks to this connection arrangement, the center of rotation at the fuse device is shifted above, and it stays in between the two reinforcement layers. As a result, the steel plates in the fuse devices can be easily deformed and buckled, causing energy dissipation without damaging the whole structure. At the same time the reinforced concrete slab does not get a significant damage due to large story drifts which cause large rotations in the fuse devices.



a. Exterior Beam-Column Joint Detail b. Interior Beam-Column Joint Detail

Figure 9 Details of fuse devices

To avoid cracking of the concrete in the fuse section due to flexural deformation, a gap of 50 mm is left in the concrete slab in the section of the fuse. The steel reinforcement is not interrupted in the gap section. The scope of this gap is to allow concentrated rotational deformation to occur in the gap section, avoiding both crushing of the concrete as well as damage to the floor finishes (like tiles, or other). For this reason, the gap is conceived to exist anywhere there is a need to accommodate concentrated rotational deformation according to the global deformed shape of the building under seismic action, provided that diaphragm action is ensured.

Columns, steel beams, concrete slab, and reinforcement steel are modelled with fiber-based inelastic beam elements. Reinforced parts of the structure (beam-column joints, and segment of beams close to the fuse device) are modeled with rigid links, and the beam element representing the concrete slab has been introduced with an offset. Fuse elements are simulated as a "connection element" (figure 10).

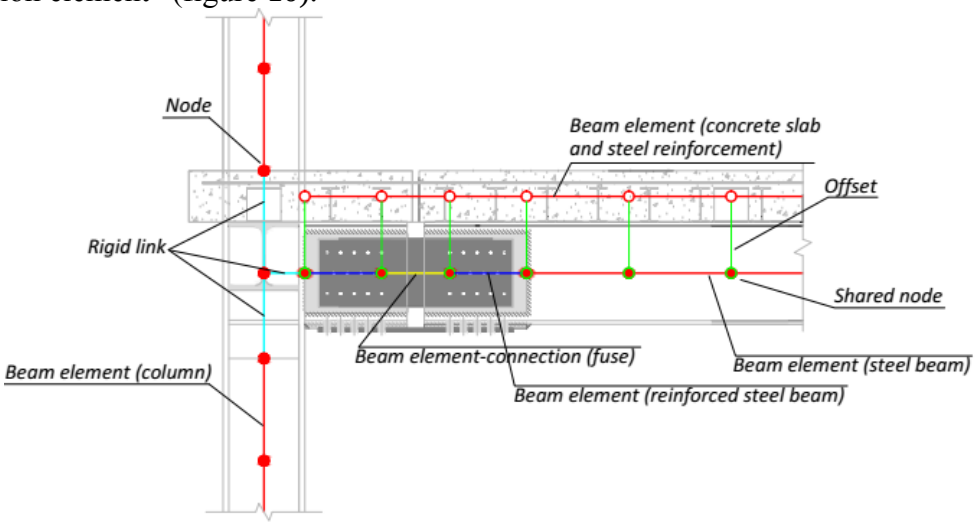


Figure 10 Numerical modeling of composite steel-concrete beam joints with fuse devices

Elasto-plastic material has been used for all structural elements in the model, with kinematic hardening. This approach will give an insight on the distribution of plasticity in the structure under nonlinear time history analysis. Figure 11 presents the material properties used for steel profiles, concrete slab, and steel reinforcement bars.

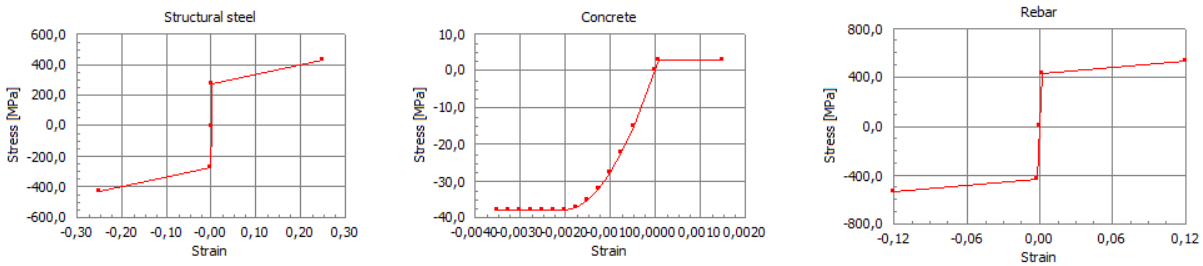


Figure 11 Material properties used in the numerical model

Connection elements have multilinear plastic moment-rotation input, which are calculated analytically according to design guide of fuse-2 device [19], and calibrated according to the results of the component tests performed during FUSEIS project [20] (figure 12).

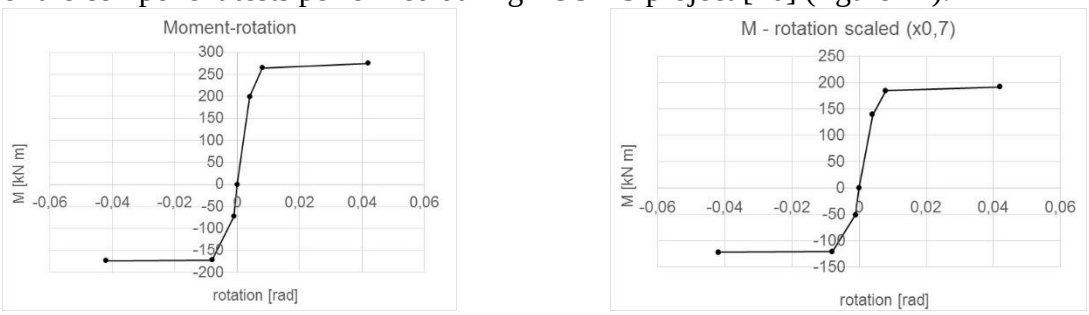


Figure 12 Moment rotation input for fuse devices

The conformity of numerical and experimental results in terms of global force-displacement behavior is shown in figure 13. The differences in the initial stiffness and amplitude of the hysteresis plots are due to pinching phenomena occurred in the connections between the fuse devices, which were not accounted for in the numerical model.

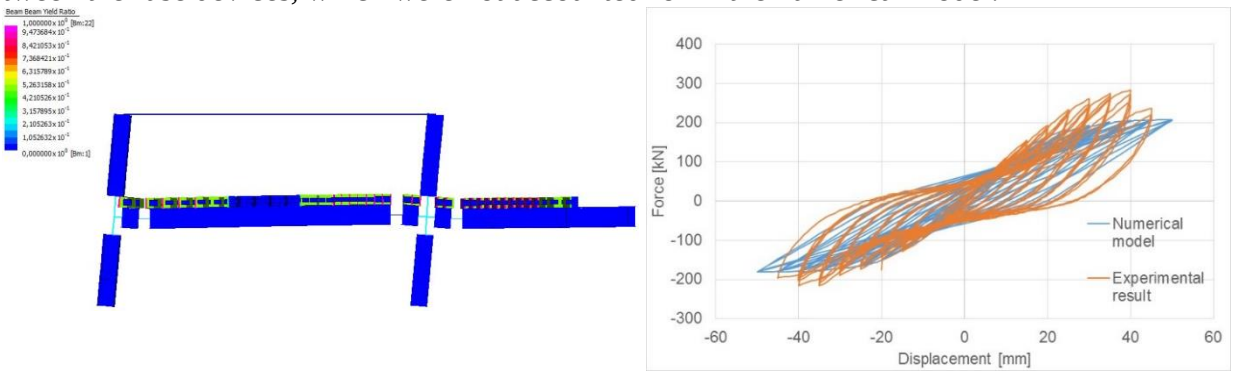


Figure 13 Numerical validation of FUSEIS test specimen

The results of these simple models validate the modeling procedures used in this study, which can be used to study the nonlinear dynamic behavior of multi-story steel-concrete composite frames.

3. BUILDING MODELS

To evaluate the performance innovative multi-story building frames with fuse devices under seismic actions, nonlinear dynamic analyses have been performed for the two building models:

1) Benchmark building with conventional moment-resisting steel-concrete composite frame (NOFUSE)
2) Benchmark building with Fuse devices that are placed close to the end of composite beams (FUSE). Fuse device is the same, the validation of which is shown in chapter 2.

All the elements in both models are inelastic beams with fiber-based formulation, so that the differences between two models in terms of "plasticity" index can be seen. Figure 14 shows the input material properties.

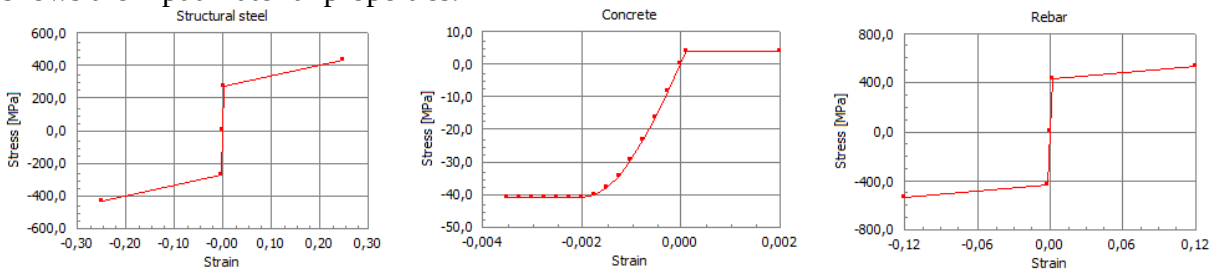


Figure 14 Material properties used in the building models

The analyses have been performed under artificial accelerograms produced according to the design criteria of the benchmark building previously studied by Zona et.al. [11]. This building was designed according to Eurocode 4 to resist the static loads (composite cross section self-weight=2.36 kN/m, permanent load G=16 kN/m, and live load Q=8 kN/m, uniformly distributed along the composite beams), and seismic forces were evaluated using response spectrum analysis with peak ground acceleration=0.35 g, Type 1 spectrum of Eurocode 8, modal damping ratio=0.05, and soil class B. Accelerograms have been produced with Gosca software [21]. Response spectra can be seen in figure 15.

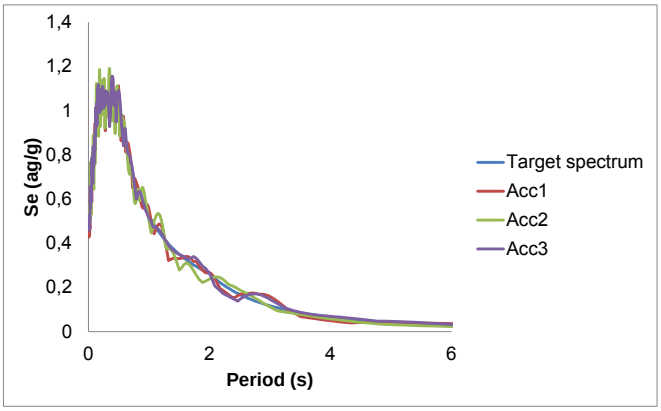


Figure 15 Response spectra for 0.35g, Type 1, Soil type B, Damping ratio 5%.

Each accelerogram has the last 5 seconds with zero accelerations, which will help to observe the residual displacements and drifts in the buildings, after the seismic event (figure 16).

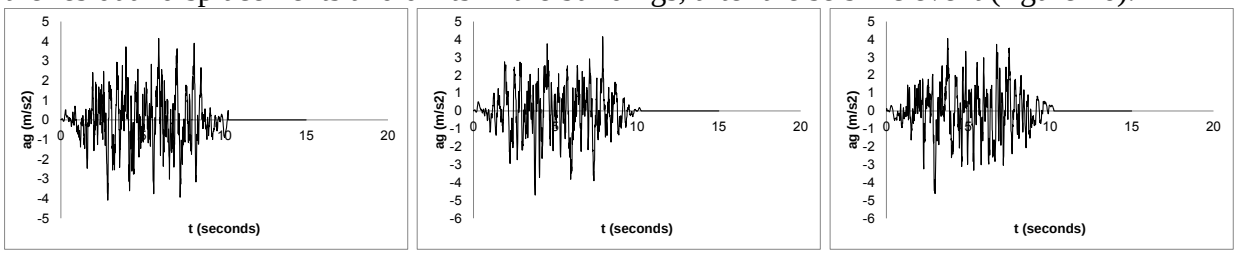
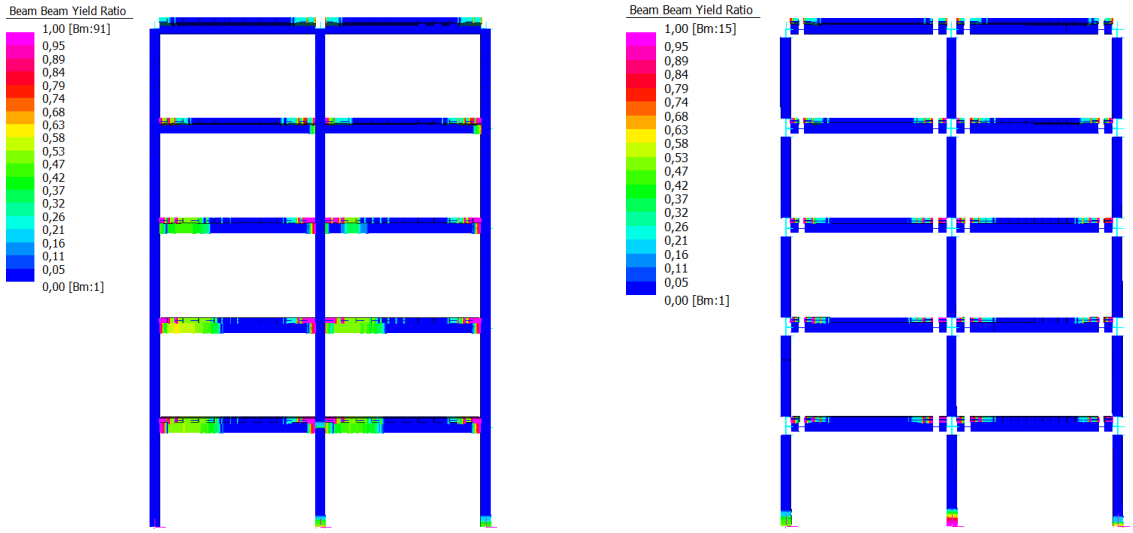


Figure 16 Three artificial accelerograms

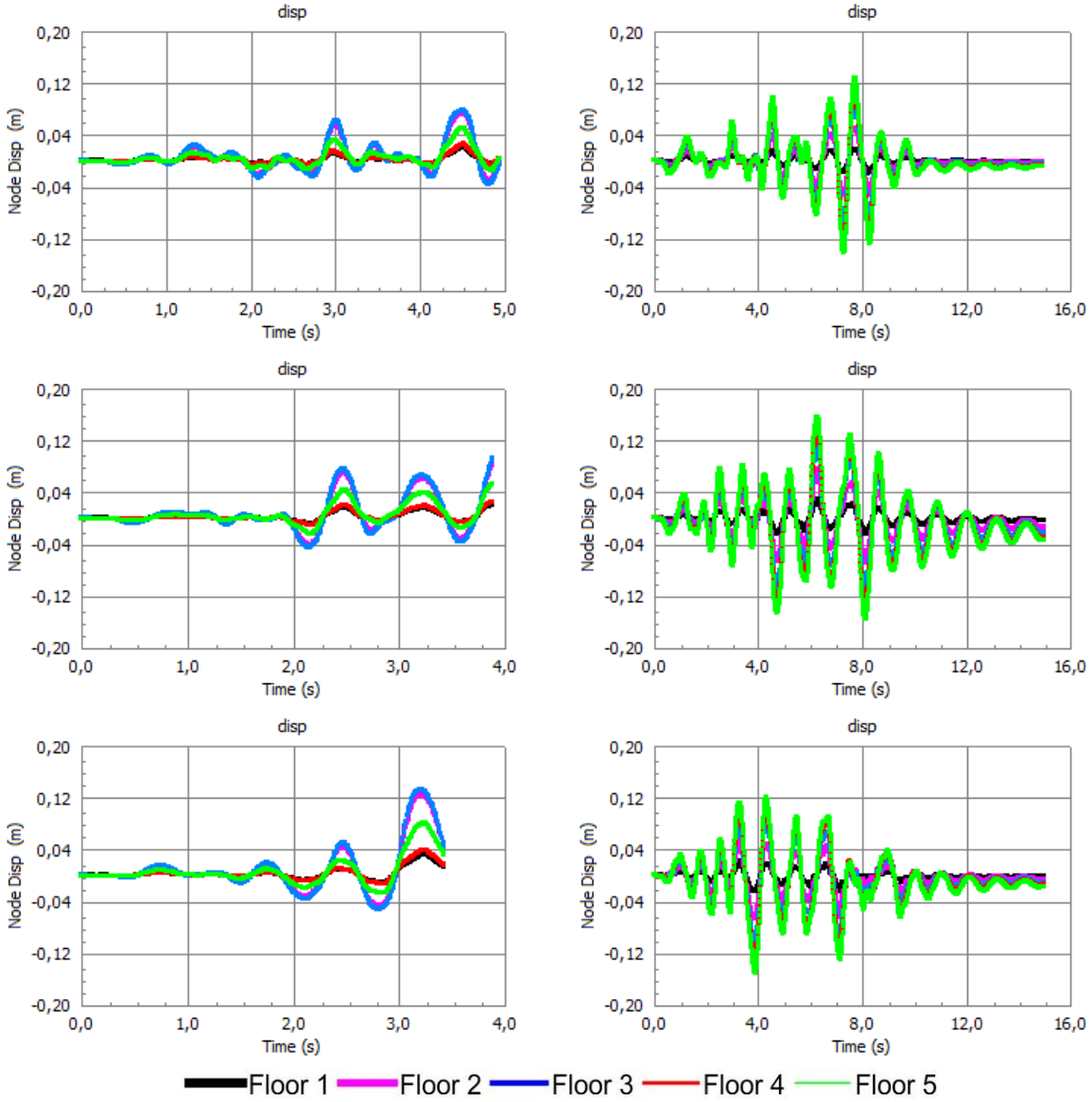
Results show the capability of innovative frame (FUSE) in controlling and concentrating the plasticity in the fuse devices. Figure 17 shows the yield index obtained at the end of the seismic event (acc2), for both frames. While in the NOFUSE frame, main steel beams and concrete slabs are significantly damaged, in FUSE frame, the damage is mainly concentrated in the "connection elements" that represent the fuse devices. Indeed, numerical convergence problems occurred in the former case, which probably indicates a "collapse" or very large damage in the structural elements. All three analyses of FUSE frame were finalized without convergence problems. Plasticity observed in the concrete slab of FUSE model are due to tension cracks.



a. NOFUSE frame b. FUSE frame

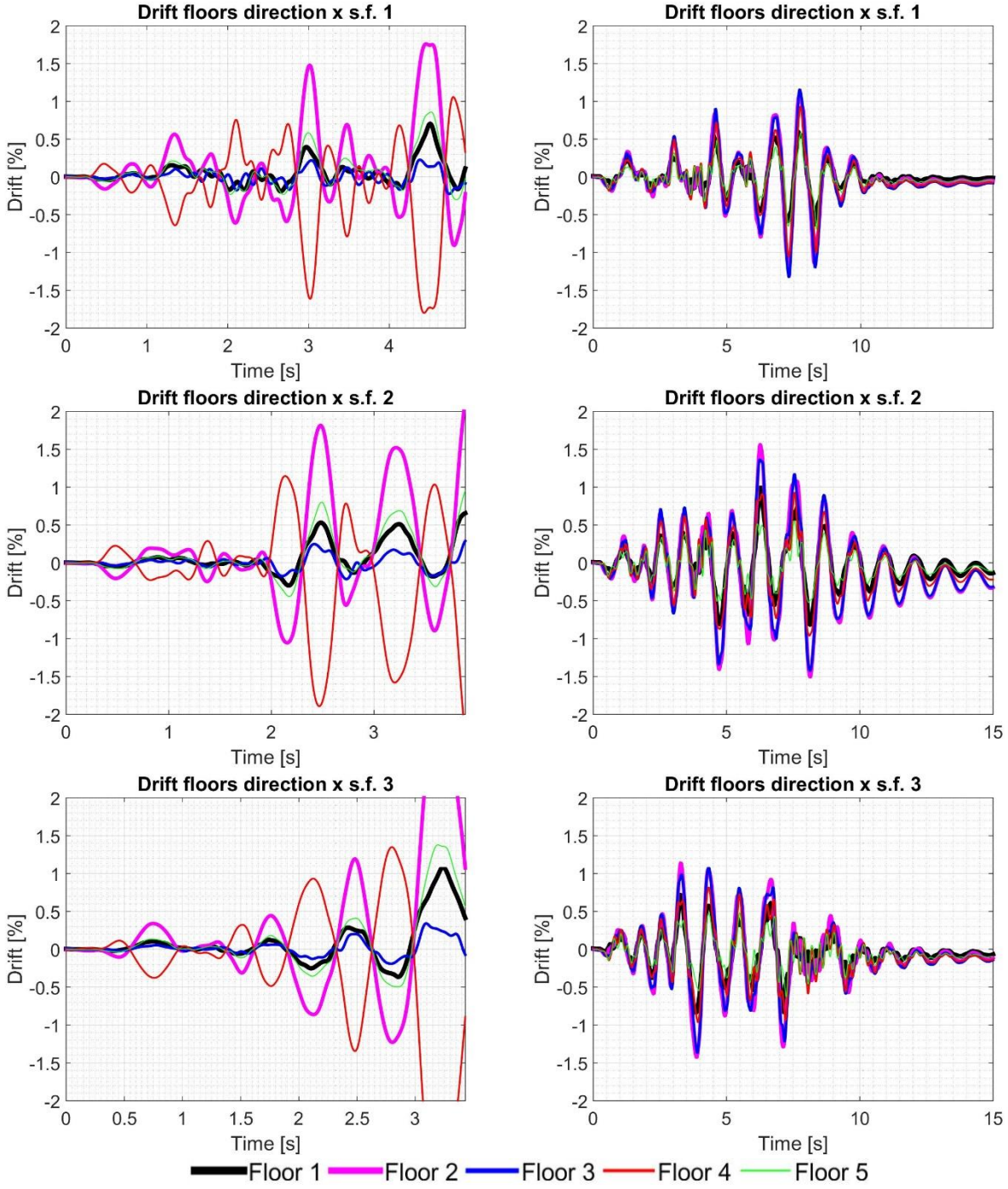
Figure 17 Comparison of cumulative ratios between two building models

Figure 18 and 19 show comparisons in terms of floor displacements and drift ratios between two cases. It is seen that the structure with fuse devices reaches the end of the seismic event with limited displacements and drifts, whereas original building suffers from non-homogenuous distribution of floor displacements and drifts (which can indicate a soft-storey behaviour). It is also interesting to see that after the seismic event, the residual floor drifts in the FUSE frame remain insignificant. In practice, this means that the repair work should be easy, which would not be the case for the NOFUSE frame.



a. NOFUSE frame b. FUSE frame

Figure 18 Comparison of floor displacements



a. NOFUSE frame b. FUSE frame

Figure 19 Comparison of floor drift ratios

4. CONCLUSIONS

This article compared the yield index, and floor displacements and drifts of a benchmark composite steel-concrete frame by means of nonlinear transient analysis, with and without fuse devices that were developed in FUSEIS project [19].

First, the proposed modeling procedure has been validated with the results of previously performed experiments. Then a numerical model has been developed, which successfully simulates the nonlinear cyclic behavior of the full-scale specimen tested during the FUSEIS project. Based on the results of these numerical validations, multi-story steel-concrete composite frames have been modeled with and without fuse devices. Nonlinear transient dynamic analyses have been performed to study the seismic performance of these building frames.
In the FUSE frame, damage was mainly concentrated in the fuse devices, the rest of the structure remaining mostly elastic. In this case, only concrete slabs had tension cracks, and column bases had some plasticity. Whereas conventional frame without fuse devices suffered from highly yielding beams and crushed concrete slabs which resulted in excessive story drifts.

These results show that, using fuse devices, inelastic deformations can be controlled and concentrated in "replaceable fuses", without damaging the main structural elements of a composite steel-concrete frame. Authors suggest to investigate the problem of column base yielding, which can again be solved through an innovative replaceable technology. Further analyses, which investigate the behavior of 3D buildings, are underway, and will be published soon.

5. ACKNOWLEDGMENT

The contribution of MSc thesis student Federica Spitaleri, in performing the numerical analysis shown in this paper is deeply acknowledged.

REFERENCES

[1] C. A. Castiglioni, A. Zambrano, Determination of the behaviour factor of steel moment resisting (MR) frames by a damage accumulation approach, *Journal of constructional steel research,* **66**, 723-735, 2010

[2] D. Dimakogianni, G. Dougka, I. Vayas, Innovative seismic-resistant steel frames (FUSEIS 1-2) - Experimental analysis, *Steel Construction Design and Research*, **5**, 212-221, 2012

[3] G. Dougka, D. Dimakogianni, I. Vayas, Innovative energy dissipation systems (FUSEIS 1-1) Experimental Analysis, *Journal of Constructional Steel Research*, **96**, 69-80, 2014

[4] C.A. Castiglioni, A. Kanyilmaz, L. Calado, Experimental analysis of seismic resistant composite steel frames with dissipative devices, *Journal of constructional steel research*, **76**, 1-12, 2012

[5] G. Dougka, D. Dimakogianni, I. Vayas, Seismic behavior of frames with Innovative Energy Dissipation Systems (FUSEIS1-1), *Earthquakes and Structures*, **6**, 561-580, 2014.

[6] C. A. Castiglioni, A. Drei, A. Kanyilmaz, , L. Calado, I. Vayas, B. Hoffmeister, R. Gonçalves, Numerical and Experimental Results of Project FUSEIS (Seismic Resistant Composite Steel Frames), 15 WCEE, Lisbon, 2012

[7] C. A. Castiglioni, A. Drei, A. Kanyilmaz, , L. Calado, I. Vayas, B. Hoffmeister, R. Gonçalves, Seismic Resistant Composite Steel Frames with Dissipative Devices, STESSA 2012, Chile, 2012

[8] A. Kanyilmaz, C.A Castiglioni, A. Drei, I. Vayas, L. Calado, T. Rauert, Nonlinear dynamic response of dissipative devices for seismic resistant steel frames: Experimental behaviour and numerical simulation, *ECCOMAS Thematic Conference - COMPDYN 2011: 3rd International Conference on Computational Methods in Structural Dynamics and Earthquake Engineering: An IACM Special Interest Conference*

[9] C. A. Castiglioni, R. Pucinotti, Failure criteria and cumulative damage models for steel components under cyclic loading, *Journal of constructional steel research,* **65**, 751-765, 2009

[10] Ballio, G. and Castiglioni C. A. (1995). "A Unified Approach for the Design of Steel Structures under Low and/or High Cycle Fatigue", Journal of Constructional Steel Research (34), 75-101.

[11] A. Zona, M. Barbato, J.P. Conte, Nonlinear Seismic Response Analysis of Steel–Concrete Composite Frames, *Journal of structural engineering*, **134**, 986 -997, 2008

[12] *G+D Computing Pty Limited*, Straus7. Theoretical Manual. Sydney (Australia), 2004.

[13] R. Sabelli, Research on Improving the design and analysis of earthquake resistant steel braced frames, *The 2000 NEHRP Professional Fellowship Report*, 2001

[14] A. Kanyilmaz, Inelastic cyclic numerical analysis of steel struts using distributed plasticity approach, *COMPDYN 2015, 5th ECCOMAS Thematic Conference on Computational Methods in Structural Dynamics and Earthquake Engineering, Crete Island, Greece, 2015*

[15] P. Uriz, S.A Mahin, Toward Earthquake-Resistant Design of Concentrically Braced Steel Frame Structures. *PEER Report 2008/08.* Pacific Earthquake Engineering Research Center, University of Berkeley, 2008

[16] J. G. Nie, C.S. Cai, Steel–concrete composite beams considering shear slip effects. *Journal of Structural Engineering*, ASCE 2003, 1 29(4):495– 506.

[17] K. Udagawa, H. Mimura, Behavior of composite beam frame by pseudodynamic testing, *Journal of Structural Engineering*, ASCE 1991, 117(5):1317– 35.

[18] O.S. Bursi, G. Gramola G, Behavior of composite substructures with full and partial shear connection under quasi-static cyclic and pseudo-dynamic displacements. Materials and Structures, Paris 2000, 33:154–63.

[19] I. Vayas, P. Karydakis., D. Dimakogianni, G. Dougka, C. A. Castiglioni,. A. Kanyilmaz, L. Calado, J. Proença, M. Espinha, B. Hoffmeister, T. Rauert, D. Kalteziotis: Dissipative Devices for Seismic Resistant Steel Frames, Fuseis project, final report research programme of the research fund for coal and steel

[20] L. Calado, J.M. Proenca, M. Espinha, C.A. Castiglioni, Hysteretic behaviour of dissipative bolted fuses for earthquake resistant steel frames, *Journal of constructional steel research,* **85,** 151 -162, 2013

[21] V. Denoel, Generation of Spectrum Compatible Accelerograms, GOSCA, 2001

COMPDYN 2015
5th ECCOMAS Thematic Conference on
Computational Methods in Structural Dynamics and Earthquake Engineering
M. Papadrakakis, V. Papadopoulos, V. Plevris (eds.)
Crete Island, Greece, 25–27 May 2015

ON THE USE OF MECHANICAL METAMATERIALS FOR INNOVATIVE SEISMIC ISOLATIONS SYSTEMS

F. Fraternali[1], G. Carpentieri[1], R. Montuori[1], A. Amendola[1], and G. Benzoni[2]

[1] Department of Civil Engineering, University of Salerno
Via Giovanni Paolo II, 132 - 84084 - Fisciano (SA), Italy
e-mail: F. Fraternali (f.fraternali@unisa.it), G. Carpentieri (gcarpentieri@unisa.it), R. Montuori (r.montuori@unisa.it); A. Amendola (adaamendola1@unisa.it)

[2] Department of Structural Engineering, University of California San Diego
9500 Gilman Dr., La Jolla, CA 92093, United States
gbenzoni@ucsd.edu

Keywords: Metamaterials, Periodic Lattices, Pentamode Materials, Seismic Isolation

Abstract. *We design novel versions of pentamode materials whose bulk and shear moduli are controlled by adjusting the dimensions of the struts and nodal junctions, and the material properties. We show that layers of such metamaterials can be effectively employed as deformable pads of novel base isolation systems. Benchmark examples highlight that a commercial rubber bearing can be effectively replaced by innovative isolators formed by pentamode pads confined between steel plates. Future research lines concerned with seismic applications of tunable pentamode materials are presented and discussed.*

1 INTRODUCTION

The nascent, rapidly growing field of mechanical and acoustic metamaterials is attracting increased attention from many research sectors, due to the great technological potential of unconventional materials with properties mainly derived by their geometrical structure, rather than their chemical composition (refer, e.g., to review papers [1,2]). Mechanical and acoustic metamaterials exhibit a variety of unusual behaviors that are not found in natural materials. These may include: exceptional strength- and stiffness-to-weight ratios; excellent strain recoverability; very soft and/or very stiff deformation modes; auxetic behavior; phononic bandgaps; sound control ability; negative effective mass density; negative effective stiffness; negative effective refraction index; superlens behavior; and/or localized confined waves, to name some examples (cf. [1-14] and references therein). The category of "extremal materials" has been introduced in [3] to define materials that simultaneously show very soft and very stiff deformation modes (unimode, bimode, trimode, quadramode and pentamode materials, depending on the number of soft modes). This definition applies to a special class of mechanical metamaterials – composite materials, structural foams, cellular materials, etc. – which feature special mechanical properties. Rapid prototyping techniques for the manufacture of materials with near-pentamode behavior have been recently presented in [8] (macroscale) and [9] (microscale). Pentamode materials have been proposed for transformation acoustics and elasto-mechanical cloak (refer, e.g., to the recent paper [10] and the references therein), but their potential in different engineering fields is still only partially explored.

The present study with the use of pentamode lattices as tunable seismic isolation devices, making profit from the control of the soft modes of such materials through the tuning of the bending moduli of members and junctions [8-11]. An illustrative numerical example shows a practical implementation of a pentamode lattice as a base isolation device, establishing a comparison of the elastic moduli and the force-displacement response of such a system with those exhibited by a conventional rubber bearing.

2 ELASTIC MODULI OF LATTICE MATERIALS

A recent study by A. N. Norris [11] presents a discrete-to-continuum approach to the elastic moduli of different periodic structures, including pentamode, simple cubic, BCC, FCC octet truss and tetrakaidecahedral lattices. We hereafter summarize the main results of such a study, with reference to the unit cell of a *d*-dimensional lattice that is composed of a number *Z* of elastic members (rods) and occupies a volume *V*.

With reference to the unit cells examined in [11], it is easily shown that the elastic stiffness tensor that characterize the lattice response at the mesoscopic scale shows cubic symmetry with independent stiffness coefficients C_{11}, C_{12} and C_{44} (Voigt notation). Let us introduce the following notations

$$M_i = \int_0^{R_i} \frac{dx}{E_i A_i}, \; N_i = \int_0^{R_i} \frac{x^2 dx}{E_i I_i} \tag{1}$$

for the axial and bending compliances of the lattice members, where x is an axial coordinate with origin at the junction of the rods; while R_i, E_i, A_i and I_i respectively indicate the reference length, the Young modulus of the material, the cross-sectional area and the moment of inertia of the cross-section of *i*-th rod, assuming polar-symmetry of such a cross-section ($i = 1, \ldots, Z$). By discarding the member forces induced by the node compliances, we obtain the results presented in Table 1, where $K = \left(C_{11} + 2C_{12}\right)/3$ denotes the bulk modulus of the lat-

tice; $G = \mu_1 = C_{44}$ denotes the shear modulus; and we set: $\mu_2 = (C_{11} - C_{12})/2$. All the lattices examined in Table 1, with exception to the case $Z = 14$ (*tetrakaidecahedral lattice*), are characterized by members with equal values of R_i, M_i, and N_i (respectively denoted by R, M, and N). The tetrakaidecahedral unit cell can be regarded as the summation of the simple cubic unite cell ($Z = 6$) and a scaled version of the BCC cell ($Z = 8$). It is obtained by truncating the BCC members with an octahedron featuring 14 faces and 36 edges of equal length a. In this case, the members of the parent simple cubic cell have equal length $R_1 = \sqrt{2}a$ and equal compliances M_1 and N_1; while the members of the parent BCC cell have equal length $R_2 = \sqrt{\frac{3}{2}}a$ and equal compliances M_2 and N_2. It is worth noting that, in the stretch-dominated limit ($N_i \to \infty$), the pentamode unit cell ($Z = 4$) has zero shear moduli: ($G = \mu_2 = 0$) and nonzero bulk modulus K. This means that such a lattice material can be regarded as a "solid water" [3,8,9], which is well suited for the manufacturing of next generation seismic isolation devices.

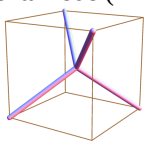
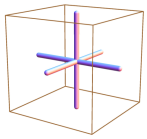
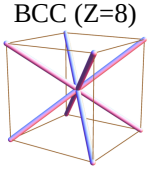
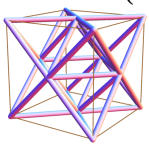
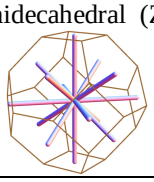
unit cell	K	G/K	μ_2/K	V
pentamode (Z=4) 	$\frac{4R^2}{9MV}$	$\frac{9M}{4M+2N}$	$\frac{3M}{2N}$	$\frac{64}{3\sqrt{3}}R^3$
simple cubic (Z=6) 	$\frac{2R^2}{3MV}$	$\frac{3M}{2N}$	3/2	$8R^3$
BCC (Z=8) 	$\frac{8R^2}{9MV}$	$1+\frac{M}{2N}$	$\frac{3M}{2N}$	$\frac{32}{3\sqrt{3}}R^3$
FCC octet truss (Z=12) 	$\frac{4R^2}{3MV}$	$\frac{3}{4}+\frac{3M}{4N}$	$\frac{3}{8}+\frac{9M}{8N}$	$4\sqrt{2}R^3$
tetrakaidecahedral (Z=14) 	$\frac{1}{9V}\left[\frac{6R_1^2}{M_1}+\frac{8R_2^2}{M_2}\right]$	$\frac{3}{2}\frac{1/M_1+1/N_2}{1/M_1+1/M_2}$	$\frac{1/N_2+2/M_2+3/N_1}{2(1/M_1+1/M_2)}$	$8\sqrt{2}a^3$

Table 1: Unit cells and elastic properties of three-dimensional lattice materials [11].

3 USE OF PENTAMODE LATTICES FOR BASE ISOLATION DEVICES

Let us refer to the representative pentamode element shown in Fig. 1, which is composed of four unit cells endowed with rods composed of two truncated bi-cones. The latter show a

small-size diameter d at the extremities of the rods, and a larger diameter D at the mid-span of the rods. The lattice constant a is related to the rod length R through

$$a = \frac{4R}{\sqrt{3}} \tag{2}$$

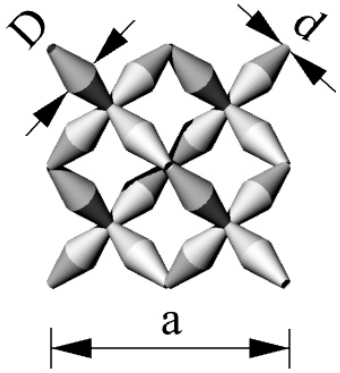


Figure 1: Geometry of a pentamode module formed by four unit cells.

The law of variation the generic rod radius r with the abscissa x is written as

$$r\left(x\right) = r_{\min} + \left(\frac{r_{\max} - r_{\min}}{R/2}\right)x, \quad 0 \le x < \frac{R}{2} \tag{3}$$

$$r\left(x\right) = r_{\max} - \left(\frac{r_{\max} - r_{\min}}{R/2}\right)\left(x - \frac{R}{2}\right), \quad \frac{R}{2} \le x \le R \tag{4}$$

where $r_{\min} = d/2$ and $r_{\max} = D/2$. On using the above relationships, and taking into account that the cross-section area and the moment of inertia of the rods are respectively given by $A\left(x\right) = \pi\left[r\left(x\right)\right]^2$ and $I\left(x\right) = \pi\frac{\left[r\left(x\right)\right]^4}{4}$, we finally obtain the following expressions of the axial and bending compliances of the generic rod

$$M = \frac{R}{\pi E\, r_{\max} r_{\min}}, \quad N = \frac{R^3\left(2r_{\max}^2 + r_{\max}r_{\min} + r_{\min}^2\right)}{3\pi E\, r_{\max}^3 r_{\min}^3} \tag{5}$$

where E denotes the Young modulus of the rod material. Making use of Eqns. (5) into the expressions of K and G/K ratio given in Tab. 1 ($Z = 4$), we finally obtain

$$K = \frac{4R^2}{9VM} = \frac{\pi EdD}{64\sqrt{3}R^2}, \quad G = \frac{9\sqrt{3}\pi\left(dD\right)^3 E}{768\left(dDR\right)^2 + 512\left(d^2 + 2D^2 + dD\right)R^4} \tag{6}$$

$$\frac{G}{K} = \left[\frac{4}{9} + \frac{8\left(2D + dD + d^2\right)R^2}{27d^2D^2}\right]^{-1} \tag{7}$$

It is worth comparing the analytic prediction of the G/K ratio provided by Eqn. (7), with the numerical estimate of the same ratio given in Kadic et al. [9], which has been obtained by fitting the results of finite element simulations of pentamode lattices under hydrostatic pressure and simple-shear loading

$$\frac{G}{K}=\left[\left(\frac{R}{d}\right)^2\sqrt{\frac{R}{D}}\right]^{-1} \tag{8}$$

Fig. 2 compares the predictions of Eqns. (7) and (8) for the G/K ratio, assuming the lattice constant $a=15$ mm ($R=6.5$ mm), different D/a ratios ($D/a=0.174, 0.087, 0.044$), and letting the d/D ratio vary from zero to one. The limiting cases with $d/D=0$ and $d/D=1$ respectively correspond to a stretch-dominated pentamode lattice (no bending effects), and a pentamode lattice showing rods with constant cross-section (cylindrical rods).

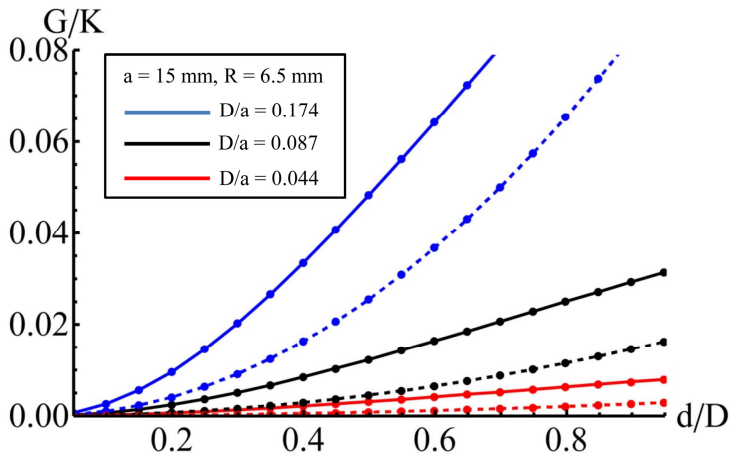


Figure 2 Curves plotting the G/K ratio of pentamode lattices against the d/D ratio, for $a=15$ mm and different values of the D/a ratio. The solid curves correspond to the analytic predictions of Eqn. (7) [11], while the dashed curves correspond to the numerical estimates of Eqn. (8) [9].

The mismatches between the analytic and numerical predictions of the G/K ratio in Fig. 1 are explained by the fact that the analytic formula (7) is based on a beam model for the rods (1D theory), while the numerical estimate (8) accounts for a 3D elastic response of such elements (through fine meshes of tetrahedral finite elements [9]). Both predictions highlight that the shear modulus of pentamode lattices can be finely tuned by properly designing the diameters d and D of the struts [8,9]. The following section illustrates practical implementations of pentamode lattices for the construction of innovative seismic isolation devices.

3.1 Practical examples

Let us compare the mechanical response of pentamode lattices with that of a commercial rubber bearing with diameter $\varnothing 33.5"\,(0.8509\,m)$ and height $13.85"\,(0.3518\,m)$, which is composed of 29 rubber layers of $7\,mm$ each; 28 steel shims (spacers) of $3.04\,mm$ each; two terminal rubber layers of $31.8\,mm$ each and covers, without lead plug (isolator Type E [RB-800] produced by Dynamic Isolation Systems, Inc, McCarran, NV, USA). Figs. 3 and 4 illustrate the hysteretic (low-damping) response of such an isolator in terms of cyclic shear stress (τ) vs. shear strain (γ) curves, and normal stress (σ) vs. axial strain (ε) curves (with preload

of $\sigma = 0.31 MPa$) at constant velocity (courtesy of Caltrans Testing Facility, University of California, San Diego). Such experimental results provide an average shear modulus $\bar{G} = 0.791 MPa$, and an average compression modulus of the rubber-steel composite $\bar{E}_c = 330\, MPa$ [15].

Table 2 illustrates the geometrical properties of different pentamode pads, which can be confined between steel plates to form innovative pentamode bearings (PMBs). Such pads are obtained by replicating the pentamode module shown in Fig. 1 $n_a \times n_a$ times in the plane of the pad, and one single time along the thickness ($n_v = 1$), implying pad thickness $t \equiv a$. The lattice struts are made of steel (SPMB1 and SPMB2: $E = 206 GPa$) or the "FullCure850 VeroGray" polymeric material supported by Stratasys® 3D printers (PPMB1 and PPMB2: $E = 1.4 GPa$ [8]), and show different values of the geometric variables a , D and d . Making use of Eqn. (6) for the shear modulus of the pentamode pad, and the following formula for the composite, steel-pentamode compression modulus [15]

$$E_c = 6.73 G S_1^2 \tag{9}$$

where $S_1 = \frac{L}{4t} = \frac{n_a}{4n_v}$, we predict $G = \bar{G} = 0.791 MPa$, $E_c = 341 MPa$ for all the PMBs based on the pads described in Table 2, i.e., shear and compression moduli almost equal to those of the comparative rubber bearing. Figures 3 and 4 provide comparisons between the experimental stress-strain curves of the analyzed rubber bearing and the linear stress-strain responses of the PMBs in Table 2 (assuming absence of dissipation in the latter, to a first, simplifying, approximation).

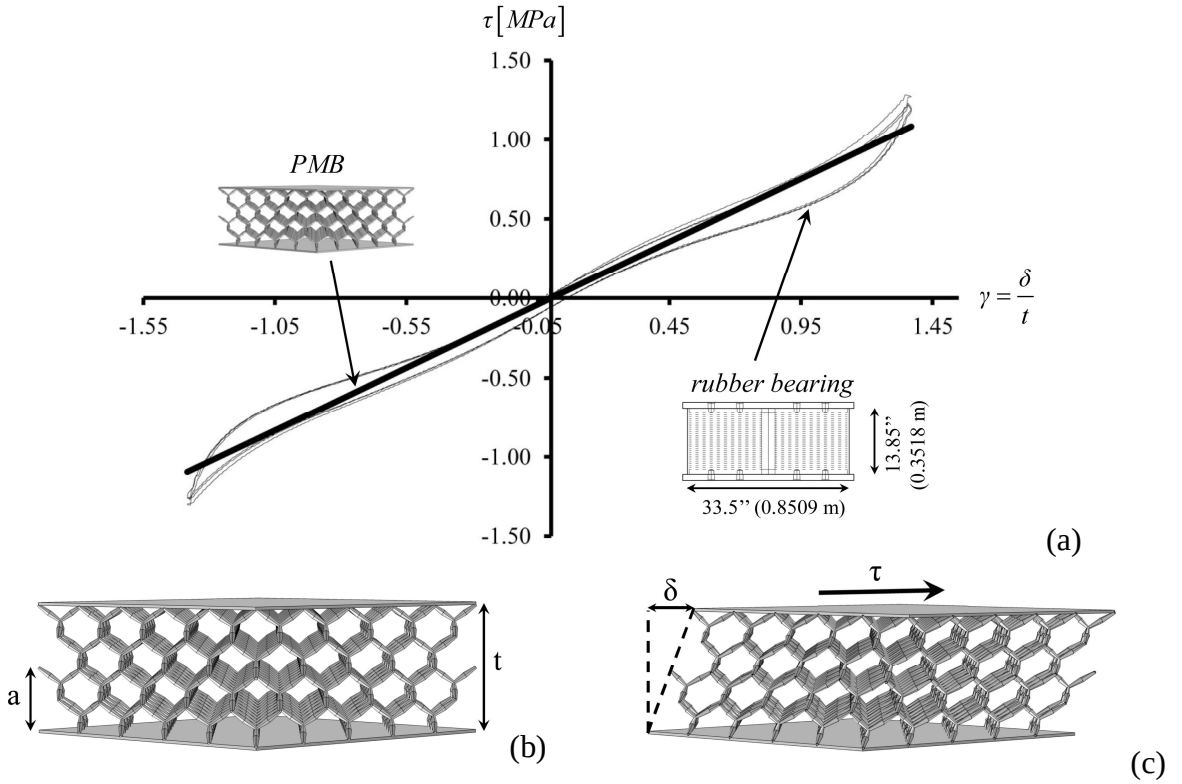


Figure 3: (a) Comparison between the shear stress vs. shear strain responses of the pentamode bearings (PMBs) in Table 2 and a low-damping rubber bearing; (b-c) undeformed and deformed configurations of a PMB.

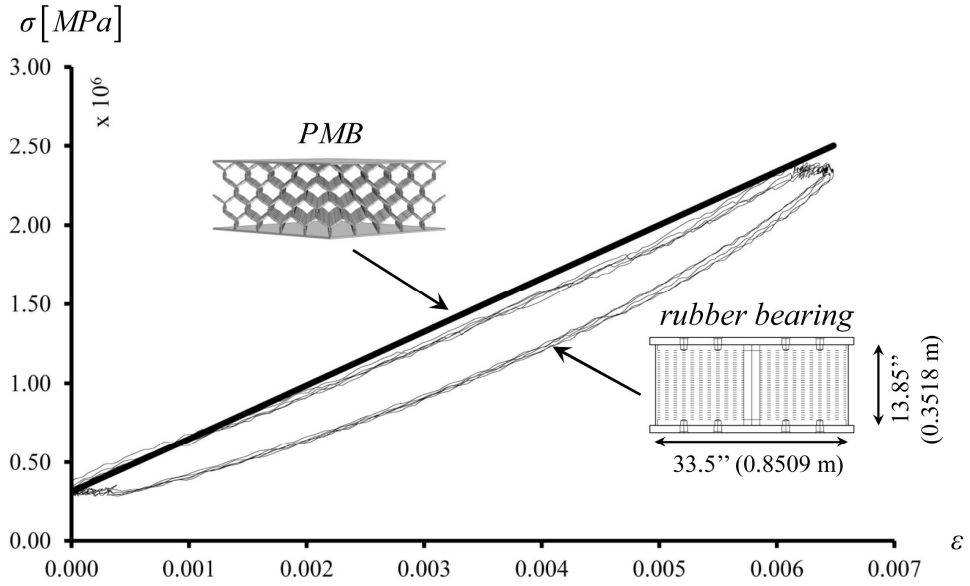


Figure 4 Comparison between the axial stress vs. axial strain responses of the pentamode bearings (PMBs) in Table 2 and a low-damping rubber bearing.

Case	$t \equiv a[mm]$	$R[mm]$	n_a	$L = n_a\, a[m]$	$d = \frac{D}{2}[mm]$
SPMB1	5	2.17	32	0.16	0.19
SPMB2	10	4.33	32	0.32	0.37
PPMB1	5	2.17	32	0.16	0.66
PPMB2	10	4.33	32	0.32	1.32

Table 2: Geometric properties of pentamode pads to be employed to form seismic isolators.

4 CONCLUSIONS

We have presented novel versions of pentamode materials: artificial structural crystals showing shear moduli markedly smaller than the bulk modulus [3,8,9]. Innovative seismic isolators based on pentamode lattices confined between steel plates have been designed. The soft modes of such materials have been controlled by tuning of the bending moduli and the geometry of members and junctions. We have shown that such novel isolators can exhibit mechanical response similar to that of conventional rubber bearings, provided that the material and the geometry of the lattice are suitably designed.

We may conclude that the main advantages of pentamode bearings over traditional structural bearings [16-18] are the following:

- the mechanical properties of the soft layers forming such devices mainly depend on the geometry of the pentamode lattices, more than on the chemical nature of the employed materials (metallic, ceramic, polymeric, etc.);

- it is easy to adjust the mechanical properties of pentamode bearings to those of the structure to be isolated, by playing with the lattice geometry and the nature of the material (see Eqn. (6) and Table 2), as opposed to rubber bearings, where instead the achievement of very low shear moduli implies marked reductions of the vertical load carrying capacity, making such devices not particularly convenient in the case of structures with very high fundamental periods of vibrations (such as, e.g., very tall buildings; highly compliant structures; very soft soils; etc.) [16-18];
- the dissipation of pentamode bearings can be conveniently designed through an accurate choice of the material to be used for the pentamode lattices, and inserting, - when necessary, an additional dissipative element within the device (such as, e.g., a lead core);
- the possibility to design and fabricate laminated composite bearings showing layers with different materials, geometries and properties: such a design approach is instead much less effective in the state-of-the-art laminated rubber bearings, where the only lamination variable consists of the type of rubber to be employed for the soft pads (natural rubber or synthetic rubber);
- the freedom in the choice of the materials of the pentamode lattices, by keeping the elastic properties of the device essentially unchanged, allows the designer to adapt the energy dissipation capacity and the life span (i.e., the durability) of the device to the actual use conditions [17-18];
- the possibility to replace the fluid components of the structural bearings and energy absorbing devices currently available on the market (such as, e.g., viscous fluid dampers and tuned mass dampers) with pentamode lattices: such a replacement would lead to significantly reduce the technical issues related to fluid leaking and frequent maintenance, which currently affect the state-of-the-art devices involving fluid materials [17-18];
- the mechanical properties of pentamode bearings can be dynamically adjusted and measured, by equipping selected struts of the pentamode lattices with sensors and/or actuators;
- pentamode bearings directly manufactured from computer-aided design data outputted by a computational material design phase, employing advanced and fast additive manufacturing techniques at different scales and single or multiple materials (metals, polymers, etc.).

Several aspects of the present work pave the way to relevant further investigations and generalizations that we address to future work. First, mechanical models for composite rubber-steel bearings [15] need to be generalized to pentamode-steel bearings, accounting for the peculiar deformation models of such systems. Second, physical models of pentamode isolators need to be constructed, employing, e.g., additive manufacturing techniques [8,9], and laboratory tested as seismic base-isolation devices [19], in order to experimentally asses their isolation and dissipation capabilities arising, e.g., from inelastic response and/or material fracture [20]. Another relevant generalization of the present research regards the design of dynamically tunable systems based on the insertion of prestressed cables and/or curved rods within pentamode lattices, with the aim of designing novel metamaterials and bio-inspired lattices tunable by local and global prestress [12-14, 21-28]. Future studies will also address the experimentation of pentamode materials as components of new-generation seismic dampers.

REFERENCES

[1] M.H. Lu, L. Feng, Y.F. Chen, Phononic crystals and acoustic metamaterials. *Materials Today*, **12**, 34-42, 2009.

[2] M. Maldovan, Sound and heat revolution in phononics. *Nature*, **503**, 209-217, 2013.

[3] G.W. Milton, A.V. Cherkaev, Which Elasticity Tensors are Realizable? *Journal of Engineering Materials and Technology,* **117**, 4, 483-493, 1995.

[4] C. Daraio, D. Ngo, V.F. Nesterenko, F. Fraternali, Highly nonlinear pulse splitting and recombination in a two dimensional granular network. *Physical Review E*, **82**, 036603, 2010.

[5] F. Fraternali, L. Senatore, C. Daraio, Solitary waves on tensegrity lattices. *Journal of the Mechanics and Physics of Solids*, **60**, 1137-1144, 2012.

[6] L.R. Meza, S. Das, J.R. Greer, Strong, lightweight, and recoverable three-dimensional ceramic nanolattices. *Science*, **345**, 1322-1326, 2014.

[7] X. Zheng, H. Lee, T.H.Weisgraber, M. Shusteff, J. Deotte, E.B. Duoss, J.D. Kuntz, M. M. Biener, Q. Ge, J.A. Jackson, S.O. Kucheyev, N.X. Fang, C.M. Spadaccini, Ultralight, ultrastiff mechanical metamaterials. *Science*, **344**, 6190, 2014.

[8] M. Schittny, T. Bückmann, M. Kadic, M. Wegener, Elastic measurements on macroscopic three-dimensional pentamode metamaterials. *Applied Physics Letters*, **103**, 231905, 2013.

[9] M. Kadic, T. Bückmann, N. Stenger, M. Thiel, M. Wegener, On the practicability of pentamode mechanical metamaterials. *Applied Physics Letters*, **100**, 191901, 2012.

[10] T. Bückmann, M. Thiel, M. Kadic, R. Schittny, M. Wegener, An elastomechanical unfeelability cloak made of pentamode metamaterials. *Nature Communications*, **5**, 4130, 2014.

[11] A.N. Norris, Mechanics of elastic networks. *Proceedings of the Royal Society of London A*, **470**, 20140522, 2014.

[12] A. Amendola, G. Carpentieri, M. de Oliveira, R.E. Skelton, F. Fraternali, Experimental investigation of the softening stiffening response of tensegrity prisms under compressive loading. *Composite Structures*, **117**, 234–243, 2014.

[13] F. Fraternali, G. Carpentieri, A. Amendola, On the mechanical modeling of the extreme softening/stiffening response of axially loaded tensegrity prisms. *Journal of the Mechanics and Physics of Solids*, **74**, 136–157, 2015.

[14] F. Fraternali, G. Carpentieri, A. Amendola, R.E. Skelton, V.F. Nesterenko, Multiscale tunability of solitary wave dynamics in tensegrity metamaterials, *Applied Physics Letters*, **105**, 201903, 2014.

[15] J.M. Kelly, J.-W Lai, The use of tests on high-shape-factor bearings to estimate the bulk modulus of natural rubber. *Seismic Isolation and Protective Systems*, **2**, 1, 21-33, 2011.

[16] M. Higashino, H. Hamaguchi, S. Minewaki, S. Aizawa. Basic characteristics and durability of low-friction sliding bearings for base isolation, *Earthquake Engineering and Engineering Seismology*, **4**(1), 95-105, 2003.

[17] J.C. Monaldo-Mercaldo, Passive and Active Control of Structures, MSc Thesis in Civil and Environmental Engineering, Massachusetts Institute of Technology, USA, 1995.

[18] F. Adebowale Oladimeji, Bridge Bearings - Merits, Demerits, Practical Merits, Demerits, Practical Issues, Maintenance and Extensive Surveys on Bridge Bearings, PhD Thesis, MSc Thesis , Royal Institute of Technology (KTH), Department of Civil and Architectural Engineering, Division of Structural Engineering and Bridges, Stockholm, Sweden, 2012.

[19] M. Modano, F. Fabbrocino, A. Gesualdo, G. Matrone, I. Farina, F. Fraternali, On the forced vibration test by vibrodyne, *CompDyn 2015*, 25-27 May 2015.

[20] F. Fraternali, Free Discontinuity Finite element models in two-dimensions for in-plane crack problems. *Theoretical and Applied Fracture Mechanics*, **47,** 274–282, 2007.

[21] G. Gurtner, M. Durand, Stiffest elastic networks, *Proceedings of the Royal Society of London A*, **470**, 20130611, 2014.

[22] L. Ascione, F. Fraternali, A penalty model for the analysis of composite curved beams, *Computers & Structures*, **45**, 985-999, 1992.

[23] F. Fraternali, G. Bilotti, Non-linear elastic stress analysis in curved composite beams, *Computers & Structures*, **62**, 837-869, 1997.

[24] F. Fraternali, S. Spadea, L. Ascione, Buckling behavior of curved composite beams with different elastic response in tension and compression, *Composite Structures*, **100**, 280-289, 2013.

[25] F. Fraternali, C.D Lorenz, G. Marcelli, On the estimation of the curvatures and bending rigidity of membrane networks via a local maximum-entropy approach. Journal of *Computational Physics*, **231**, 528-540, 2012.

[26] F. Fraternali, G.Marcelli, A multiscale approach to the elastic moduli of biomembrane networks. *Biomechanics and Modeling in Mechanobiology*, **11** (7), 1097-1108,2012

[27] B. Schmidt, F. Fraternali, Universal formulae for the limiting elastic energy of membrane networks. *Journal of the Mechanics and Physics of Solids*, **60**, 172-180, 2012.

[28] F. Fraternali, I. Farina, G. Carpentieri. A discrete-to-continuum approach to the curvatures of membrane networks and parametric surfaces. *Mechanics Research Communications*, **56**, 18-15, 2014.

COMPDYN 2015
5th ECCOMAS Thematic Conference on
Computational Methods in Structural Dynamics and Earthquake Engineering
M. Papadrakakis, V. Papadopoulos, V. Plevris (eds.)
Crete Island, Greece, 25–27 May 2015

METHODS OF CREATION OF BASE ISOLATION SYSTEMS FOR RETROFITTING OF EXISTING REINFORCED CONCRETE FRAME BUILDINGS

Mikayel G. Melkumyan

Armenian Association for Earthquake Engineering
1, Charents str., 0025, Yerevan Armenia
e-mail: mmelkumi@yahoo.com

Keywords: Existing Buildings, Retrofitting, Base Isolation, Structural Concepts, Seismic Code Analysis, Time History Analysis.

Abstract. *Isolation of structures from horizontal ground motions is gradually becoming a more common method of providing protection from earthquake damage. By reducing the seismic forces transmitted, isolation protects the contents and secondary structural features as well as the main structure. Methods of retrofitting by base isolation of existing frame buildings were developed by the author of this paper and they are described for two buildings: 4-story Armenian-American Wellness Center (AAWC) and 8-story Hematology Center Hospital Building (HCHB). These buildings were constructed about 40-50 years ago in Yerevan, the capital of Armenia. The bearing structure of AAWC existing building represents the moment resisting reinforced concrete (R/C) frames in both longitudinal and transverse directions. There are also stone bearing walls in some parts at the level of basement and the first floor. In the development of the structural concept of retrofitting of this building the objective was pursued to equip it with base isolation at the level of basement without interruption of the Center's operations. There was also a task to increase the number of floors from 4 to 6 with creation of a conference hall in the top two floors. The bearing structure of HCHB, however, represents the R/C frames with shear walls in longitudinal direction and the moment resisting frames in transverse direction. For this building the objective was to create a base isolation system again at the level of basement and to carry out reconstruction/ renovation works in superstructure simultaneously. Paper describes in detail the new structural concepts of retrofitting by base isolation and the results of analyses of these buildings in accordance with the provisions of Armenian Seismic Code and also time history analyses. The created solutions are proposed for the first time and envisage gradual cutting the structural elements and placing simultaneously the seismic isolators. Operations are designed to be performed in several stages for the columns and for the shear walls.*

1 INTRODUCTION

The retrofitting technique using base isolation has great potential for rehabilitation of ordinary civil structures such as apartment blocks and critical facilities such as schools, hospitals. It is well known that in this case the first dynamic mode of the isolated building involves deformation only in the isolation system, the building above being to all intents and purposes rigid. The higher modes do not participate in the motion so that the high energy in the ground motion at these higher frequencies cannot be transmitted into the building [1].

Several remarkable projects on retrofitting by base isolation were developed and implemented using technologies created by the author of this paper. One of them is retrofitting of a 5-story stone apartment building in the city of Vanadzor (Armenia). The operation was made without resettlements of the occupants. World practice provides no similar precedent in retrofitting of apartment buildings. The project was implemented in 1996 [2].

Then by the end of nineties, another project on retrofitting of about 100 years old 3-story stone bank building was implemented in the city of Irkutsk (Russia) with increasing of the number of stories up to 4 [3]. For retrofitting of this building by base isolation the author of this paper provided to Russian and Chinese colleagues all the needed drawings, photos, video film related to the retrofitting works carried out in Armenia.

The other project is retrofitting of the 60 years old non-engineered 3-story stone school building which has historical meaning as well as a great architectural value. Unique operations were carried out in order to install the isolation system within the basement of this building and to preserve its architectural appearance. The project was implemented in Vanadzor (Armenia) in 2002 [4].

Experience accumulated in Armenia in retrofitting of existing buildings including those of historical and architectural value created a good basis for participation in the international competition announced by the Government of Romania for development of the design on retrofitting of about 180 years old 3-story historical building of the Iasi City Hall by base isolation. The structural concept, including the new approach on installation of seismic isolation rubber bearings was developed and the design of retrofitting was accomplished in cooperation with the Romanian company MIHUL S.R.L. The design was finally approved by the Technical Committee for Seismic Risk Reduction (a body especially created by the Government of Romania) on June 1, 2009 [5].

By given above the brief description of several projects an objective is pursued to demonstrate experience accumulated in Armenia in the field of retrofitting by base isolation of existing buildings with stone bearing walls. Later on the author of this paper has developed and proposed principally new structural approaches for seismic isolation of the existing buildings with R/C moment resisting frames, as well as with R/C frames which include the shear walls. One of them is a new structural concept on seismic isolation of the 4-story industrial R/C frame building located in the city of Yerevan (Armenia) and its simultaneous reconstruction into a 6-story hotel building [6].

The other new structural concepts are described in this paper for two buildings: 4-story Armenian-American Wellness Center (AAWC) [7] and 8-story Hematology Center Hospital Building (HCHB) [8] both constructed in Yerevan about 40-50 years ago. The seismic isolation of the buildings in these projects is planned to implement at the basement level. Seismic isolation laminated rubber-steel bearings (SILRSBs) with medium damping of about 10% were used. Their sizes and physical/mechanical parameters together with the detailed description of all phases for cutting the columns and shear walls and placing the seismic isolators are given in the paper. Results of analysis of these retrofitted buildings by the Armenian Seismic Code and the time histories are also given and discussed.

2 BASE ISOLATION RETROFITTING DESIGN FOR AN EXISTING 4-STORY R/C ARMENIAN-AMERICAN WELLNESS CENTER FRAME BUILDING

Retrofitting technology using seismic isolation rubber bearings was developed for the existing R/C frame building of the AAWC [9]. It is a 4-story building with a bearing structure mainly in the form of R/C frames, as well as with stone bearing walls in some parts on the level of basement and the first floor. In the development of the structural concept the objective was pursued to equip this building with base isolation without interruption of the use of AAWC. There was also a task to increase the number of floors from 4 to 6 with creation of a conference hall on the top two floors. The design view of the retrofitted AAWC building with already increased number of floors and its vertical elevation are shown in Figure 1.

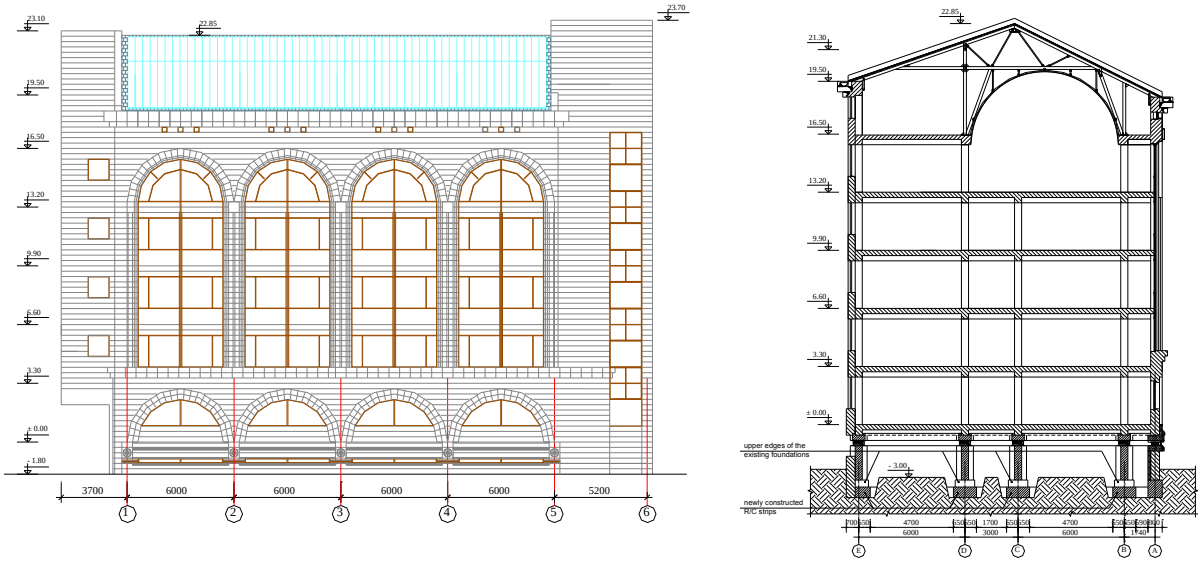


Figure 1: Design view of the retrofitted AAWC and its vertical elevation.

2.1 Structural concept of retrofitting by base isolation of the R/C frame building

The medium damping rubber bearings (MDRBs) from neoprene for seismic isolation of AAWC building were designed to provide for a horizontal displacement of 170 mm. Analysis of the isolation system for the design level earthquake was carried out based on spectral curves of Armenian Seismic Code and Spitak earthquake accelerogram recorded at Ashotsk station in 1988, scaled to 0.4g and digitized at the laboratory of Prof. Okada and Nakano of the Institute of Industrial Science, University of Tokyo [10], as well as accelerograms of Imperial Valley earthquake recorded at El Centro station (0.448g) and those of Northridge earthquake recorded at Arleta, Nordhoff Ave. fire station (0.444g).

Two types of seismic isolators were proposed for this project. The first one, with a diameter of 580 mm and height of 300 mm, was designed for placing in the columns of the basement, simultaneously with their strengthening. The second type, with a diameter of 380 mm and height of 202 mm, was envisaged for placing in the basement's bearing walls. This type of smaller size isolators with horizontal stiffness equal to 0.81 kN/mm was designed earlier [11] and widely used for retrofitting of existing and construction of new buildings in Armenia.

Seismic isolation method for an existing building with R/C bearing frames is illustrated by Figure 2. Before starting the works on strengthening the existing columns, their surfaces should be cleaned from plaster and thoroughly washed. This is needed to ensure a good contact between the fresh concrete of the jackets and the concrete surfaces of the existing col-

umns. The R/C jackets around the existing columns, which have cross-sections of 400×400 mm, are constructed using angles of 100×100×16 mm and steel plates of 10×100 mm, as well as reinforcing steel bars with diameter of 28 mm. Then immediately below the beams the parts of the columns with the height of about 200 mm are cleaned from the concrete cover layers and the steel plates of 20×200 mm are welded to the existing reinforcing bars of the columns. Created by these operations, the steel boxes right under the existing beams have four angles of 100×100×16 mm with short steel bars of 84×84 mm welded to them, which, in their turn, have bolts screwed into their body. The lower parts of these bolts are spherical and they rest on the spherical surfaces in the similar short steel bars of 84×84 mm welded to the angles of the jackets. Cross-section of the strengthened columns in the basement is 950×950 mm.

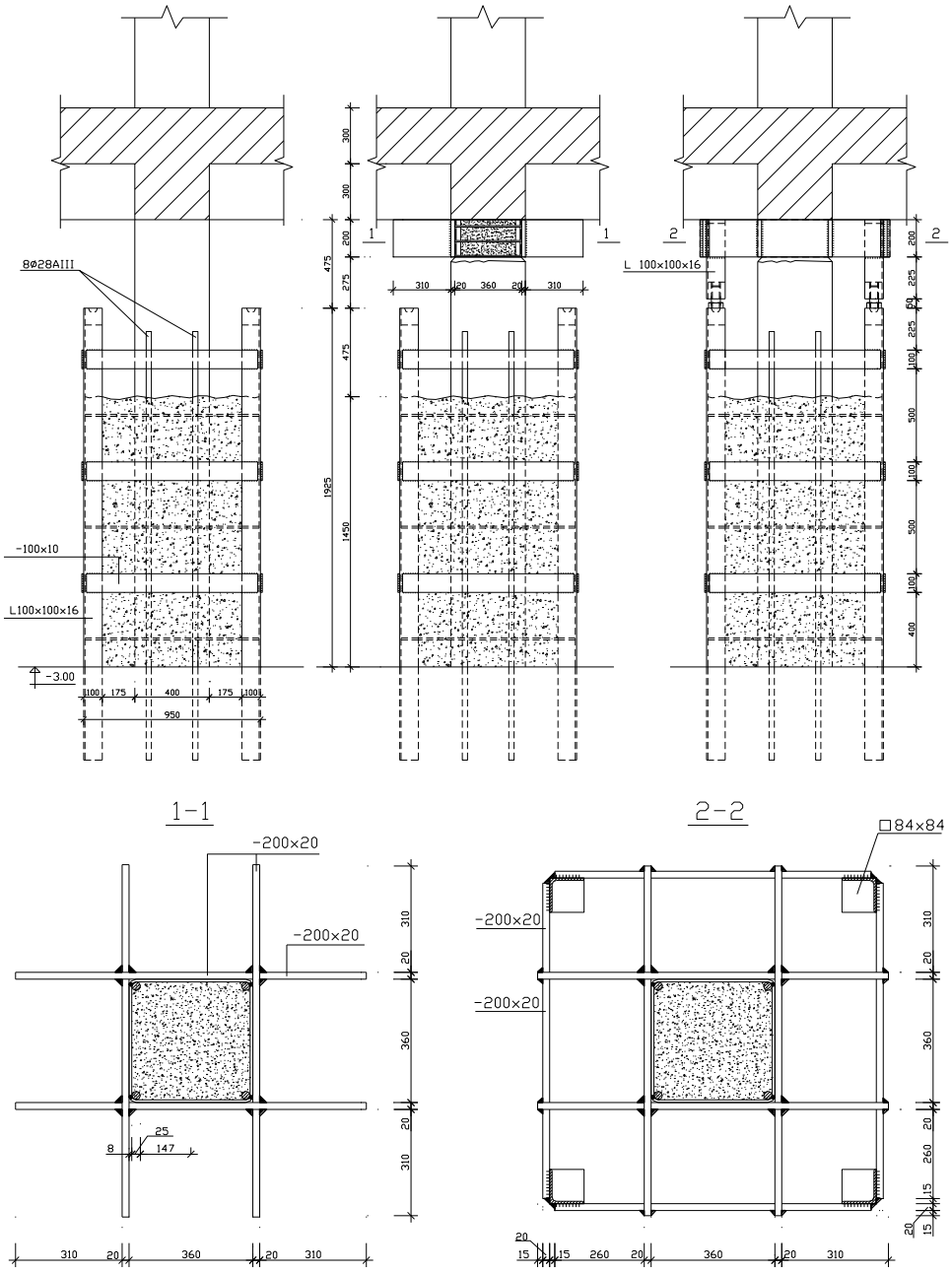


Figure 2: Sequence of placing the large size rubber bearings in the columns of the existing R/C frame building of the AAWC.

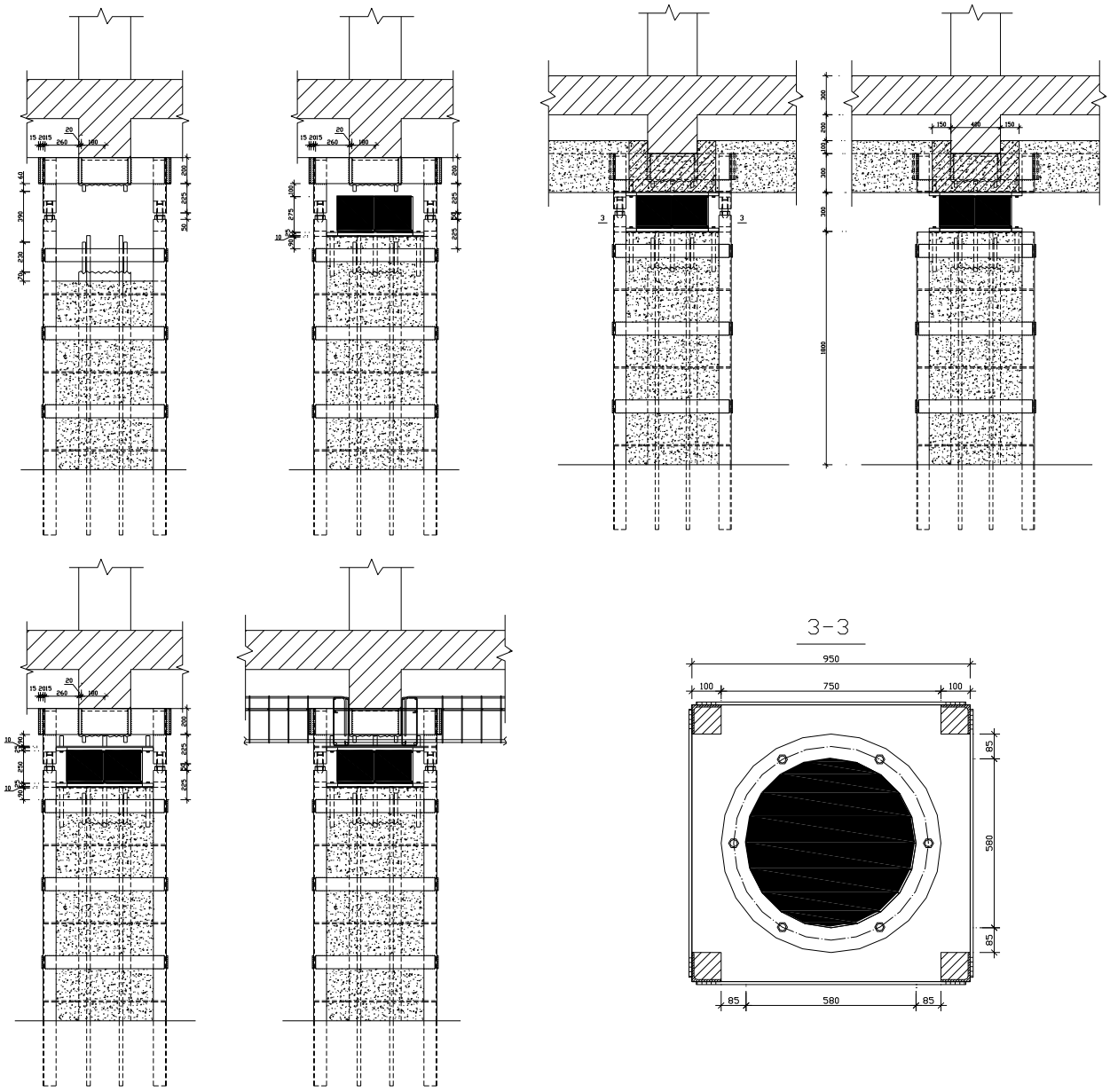


Figure 2: Sequence of placing the large size rubber bearings in the columns of the existing R/C frame building of the AAWC (continued).

In the next step the bolts should be unscrewed to a certain extent so that after cutting the existing columns the vertical loads could be reliably passed to the jackets without causing any damage to the existing beams. Operations of cutting of the columns should be performed in a special order stipulated in the design, and columns located next to each other should not be cut simultaneously. When any column is cut then immediately the following operations have to be implemented: placement of the isolator lower socket; placement of the isolator itself and its upper socket. The next step is the installation of the reinforcement frames above the isolators. These reinforcement frames are needed in order to strengthen the existing beams, creating a strong base for the whole superstructure. Actually, these frames serve as jackets for existing beams and when the concrete placed in the jackets gets to 70% of its design strength, the bolts are loosened. This operation should be done very carefully, slowly and gradually un-

til all bolts get out from the spherical surfaces of the lower jackets and the building is settled on rubber bearings.

2.2 Design of the large-size isolator for retrofitting of the R/C frame building

For the AAWC building the frequency of the first mode of oscillations was chosen equal to 0.48 Hz. The total weight of the building W=37800 kN. Maximum vertical load on a single isolator w=2268 kN. Consequently, the total horizontal stiffness of isolation system is equal to:

$$K_{ht} = \frac{4\pi^2 m}{T^2} = \frac{4 \times 3.14^2 \times 37800}{2.08^2 \times 9.81} = 35125 \, kN/m \tag{1}$$

The plan of the seismic isolators' location is shown in Figure 3, which demonstrates that 20 isolators of a larger size are intended for placing in the columns and 8 isolators of a smaller size – for placing in the load bearing walls. The total horizontal stiffness of the 8 small-size isolators with a diameter of 380 mm is equal to:

$$K_{hs} = 0.81 \times 8 = 6.48 \, kN/mm = 6480 \, kN/m, \tag{2}$$

and the total horizontal stiffness of the 20 large-size isolators is equal to:

$$K_{hb} = 35125 - 6480 = 28645 \, kN/m \tag{3}$$

Using the value of total design displacement D_t = 170 mm and taking into account that the shear strain of rubber for this application was assumed γ = 1.5, the total thickness of the rubber t_r was defined from the expression $D_t = \gamma t_r$.

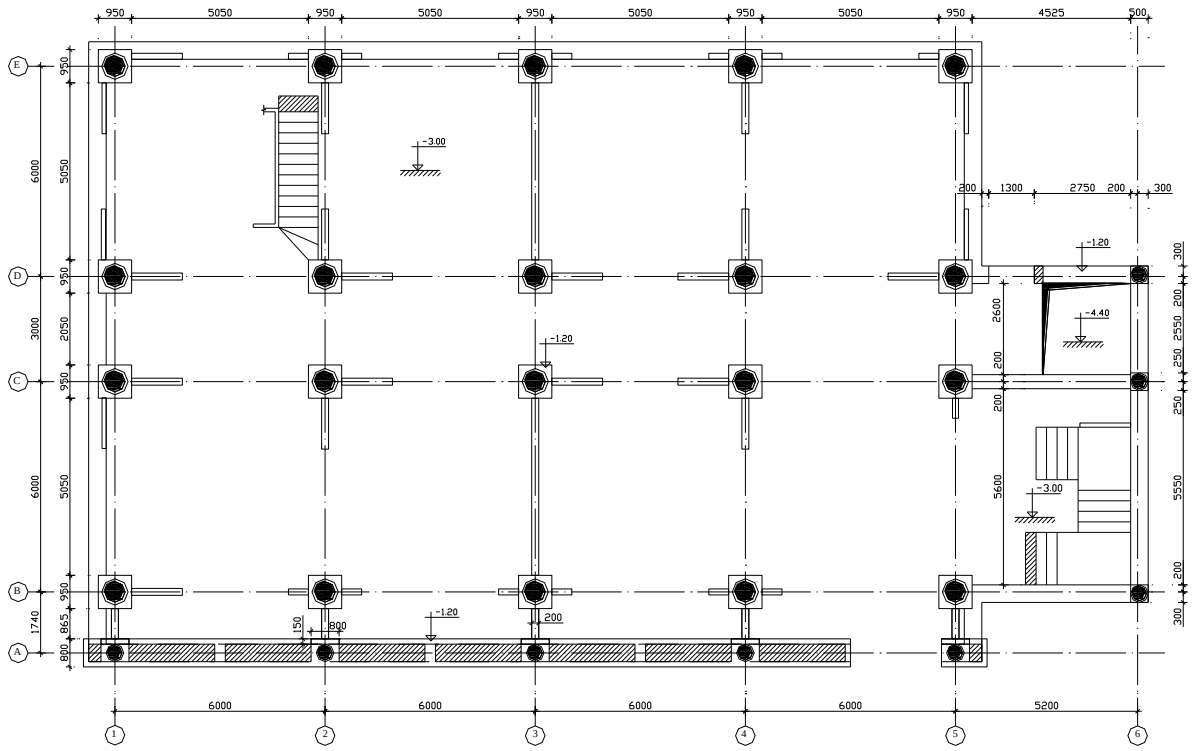


Figure 3: Plan of the seismic isolation MDRBs' location in the basement of the AAWC building.

Thus, the total thickness of the rubber is t_r=17.0:1.5=11.3 cm. The full cross-sectional area of the large-size rubber bearing was calculated by the formula:

$$A = \frac{K_{hb}}{20} \times \frac{t_r}{G} = \frac{28645}{20} \times \frac{0.113}{1000} = 0.1618 m^2, \quad (4)$$

where G is the shear modulus of rubber.

In this case the diameter of large-size isolator Φ is equal to 0.454 m. The shape factor S is taken equal to 10 and the thickness of a single rubber layer is equal to:

$$t = \frac{\Phi}{4S} = \frac{0.454}{4 \times 10} = 0.0144 m = 11.4 mm. \quad (5)$$

This means the number of the rubber layers is $n_r = t_r/t$=113÷11.4≈10. Let us assume the thickness of a single steel sheet equal to 3 mm, the thickness of the steel end-plates equal to 25 mm and the thickness of the end cover layer equal to 2.5 mm. Then the total height of the bearing comes to h_t=2×25+10×11+9×3+2.5×2=192 mm (h=137mm). The safety factor SF against buckling, which is defined by the expression SF= P_{crit}/w has to be checked. For most types of bearings where S≥5, the Euler buckling load P_E is much higher than the shear stiffness per unit length P_S, and the critical load can be approximated as follows [1, 7]:

$$P_{crit} = \sqrt{P_S \times P_E}, \quad (6)$$

where $P_S = GA\frac{h}{t_r}$ and $P_E = \frac{\pi^2}{h^2}\frac{1}{3}E_c I \frac{h}{t_r}$, E_c=507 MPa, I≅0.05×0.4544=0.0021 m^4.

Consequently, the shear stiffness per unit length is equal to:

$$P_S = 1000 \times 0.1618 \times \frac{0.137}{0.113} \cong 196 kN, \quad (7)$$

and the Euler buckling load is equal to:

$$P_E = \frac{3.14^2 \times 507000 \times 0.0021}{0.137 \times 3 \times 0.113} \cong 226030 kN. \quad (8)$$

Thus, the critical load is P_{crit}=6656 kN and the safety factor is SF=6656/2268=2.93<3. From this it follows that the size of bearings should be reconsidered. The static compressive stress in the above designed bearing is about 14 MPa. Now let us assume this value is not more than 9 MPa, as it was taken for the small-size isolator. In this case the full cross-sectional area and diameter of the large-size bearing will increase:

$$A = \frac{226800}{90} = 2520 cm^2, \quad \Phi = 56.65 cm. \quad (9)$$

Let us finally accept Φ=58 cm and A=2641 cm^2. Then the total thickness of the rubber will be equal to t_r=18.4 cm, the thickness of a single rubber layer t=15 mm and the number of the rubber layers n_r=184÷15≅13.

Assuming the thickness of the end cover layer equal to 2.5 mm and the thickness of the steel end-plates equal to 32 mm, the total height of the bearing will comprise h_t=32×2+15×13+3×12+2.5×2=300 mm (h=231 mm). With these new recalculated values the shear stiffness per unit length is equal to:

$$P_S = 1000 \times 0.2641 \times \frac{0.231}{0.195} \cong 313 kN. \quad (10)$$

Taking into account that for the accepted diameter of the bearing I≅0.05×0.584=0.0057 m^4, the Euler buckling load is equal to:

$$P_E = \frac{3.14^2 \times 507000 \times 0.0057}{0.231 \times 3 \times 0.195} \cong 210850kN, \tag{11}$$

and the critical load and the safety factor are respectively equal to:

$$P_{crit} = \sqrt{210850 \times 313} \cong 8124\,kN, \text{ and } SF = \frac{8124}{2268} = 3.58 > 3. \tag{12}$$

This means the designed bearing is acceptable and satisfies the requirement related to the safety factor. Its geometrical dimensions are shown in Figure 4 where the picture of the manufactured large-size bearing is given as well.

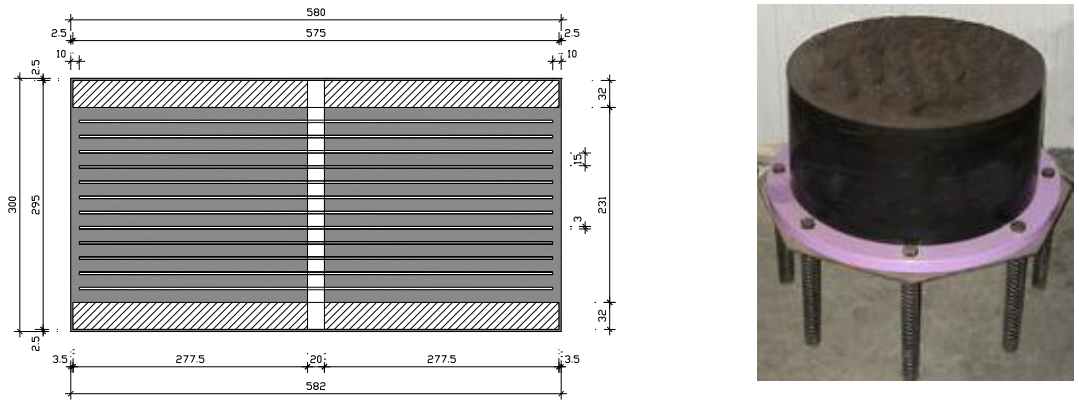


Figure 4: Geometrical dimensions and the view of the manufactured large-size bearing (seismic isolator) designed for retrofitting of the AAWC building.

3 BASE ISOLATION RETROFITTING DESIGN FOR AN EXISTING 8-STORY R/C HEMATOLOGY CENTER HOSPITAL FRAME BUILDING WITH SHEAR WALLS

Implementation of the project of seismic isolation and reconstruction of the 8-story (plus a basement) HCHB (Fig. 5) has started in 2014.

a. b.

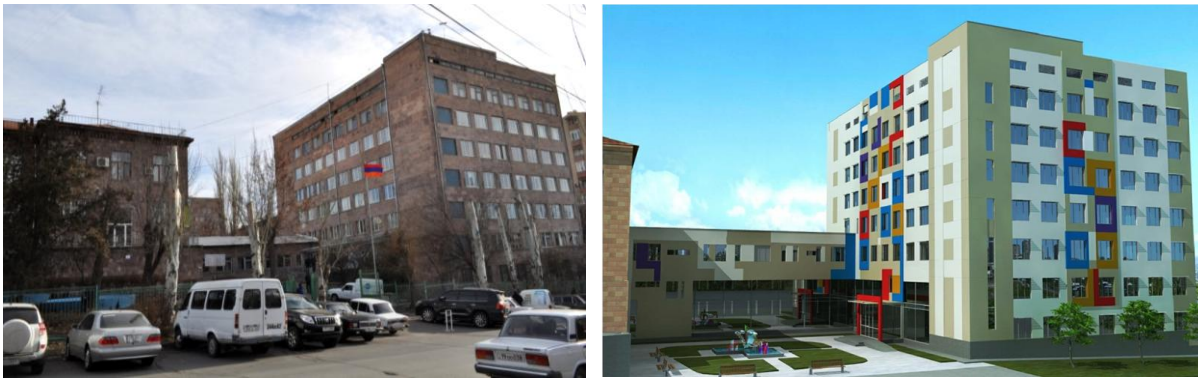


Figure 5: View of the existing HCHB before (a) and its design view after renovation and retrofitting by base isolation (b)

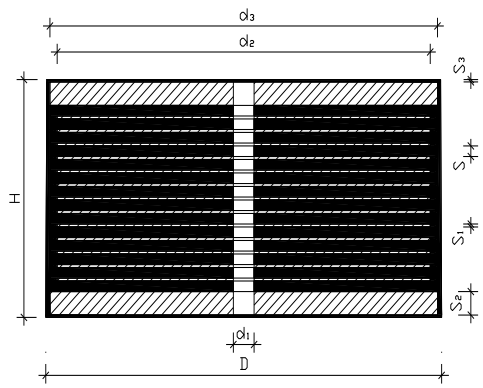
During the development of the project design, principally new structural approaches have been proposed by the author of this paper for seismic isolation of the building's R/C bearing

frames and shear walls. The existing building has rectangular plan with dimensions of 36.4×24.4 m, six spans of 6 m each in longitudinal direction and four spans of 6 m each in transverse direction. The bearing (moment resisting) frames with strong beams of cross section 400x520(h) mm are located in transverse direction, while in longitudinal direction, there are frames with the interior weak beams of cross section 1200x250(h) mm and exterior weak beams of cross section 800x250(h) mm and with shear walls of the thickness equal to 140 mm. Cross section of all the columns is equal to 400x400 mm. The height of floors from 1-st to 7-th is equal to 3.3 m, of 8-th (technical) floor – 2.5 m.

3.1 The set objectives and parameters of the used SILRSBs

The seismic isolation of the building in this project is planned to be implemented at the basement level. The main objective is to implement the proposed structural solution for seismic isolation of the existing building in parallel with its full renovation. This is one of the advantages of retrofitting by base isolation when superstructure can be renovated immediately with the implementation of the works on retrofitting. Obviously, this will significantly shorten the whole construction process. Such an approach becomes possible as due to application of base isolation to this existing building there is no need to strengthen the structural elements of the superstructure. Along with providing the high reliability to the building, seismic isolation also allows considerable savings in construction cost. The experience in seismic isolation of existing buildings in Armenia has shown that compared to other methods for improving the earthquake resistance of the buildings, seismic isolation is several times less expensive [5].

Seismic isolators of same type and sizes were used to make the seismic isolation system. Total 117 SILRSBs were used with aggregate horizontal stiffness of 94,770 kN/m. These were manufactured according to the Republic of Armenia Standard HST 261-2007 with the sizes and physical/mechanical parameters given in Figure 6.



External diameter of the bearing (D): (380 ± 2.0) mm;
Diameter of the bearing's central hole (d_1): (19 ± 1.0) mm;
Height of the bearing (H): (202.5 ± 2.5) mm;
Thickness of the rubber layers (S): (9 ± 0.1) mm;
Diameter of the steel shim plates (d_2): (360 ± 0.5) mm;
Thickness of the steel shim plates (S_1): (2.5 ± 0.1) mm;
Diameter of the upper and lower flanges (d_3): (376 ± 0.5) mm;
Thickness of the upper and lower flanges (S_2): (20 ± 0.2) mm;
Thickness of this flanges' protective layer (S_3): (2 ± 0.1) mm;
Mass of the bearing: (77.5 ± 2.5) kg;
The bearing must withstand a maximum (design) permissible vertical loading of 1500 kN;
Shear modulus of the bearing's rubber: (0.97 ± 0.15) MPa;
Vertical stiffness of the bearing: no less than 300 kN/mm;
Horizontal stiffness of the bearing: (0.81± 0.1) mm;
The bearing must withstand a maximum (design) permissible horizontal displacement of 280 mm, without causing cracks greater than 3 mm deep and 6 cm long;
Shore A hardness of the bearing: 70 ± 5 points;
Damping coefficient of the bearing: 13-15%.

Figure 6: Dimensions and physical/mechanical parameters of SILRSB

At the same time, an objective is set to determine the dynamic characteristics of the building after completing the seismic isolation and reconstruction works, and to compare displacements during micro-oscillations for the superstructure and part of the building below the seismic isolation plane level. It is decided to thoroughly follow/record all activities in all phases of seismic isolation system construction by photo and video cameras, to archive the obtained materials, as well as to place seismic sensors with identical specifications at all lev-

els of the building, including the basement floor, in order to record accelerations, displacements and dynamic characteristics during seismic impacts in mutually perpendicular directions.

3.2 Proposed structural solution of retrofitting by base isolation of the R/C frame building with shear walls

The seismic isolation system is constructed at the basement floor level, between marks -0.9 and -1.1. The seismic isolators are placed under all columns of the superstructure, grouped in two or three isolators. They are placed also within the limits of shear walls. The given structural solution developed for cutting the columns and shear walls and placing the seismic isolators is proposed for the first time ever and it is performed in 11 stages for the columns (Fig. 7), and 12 stages for shear walls (Fig. 8).

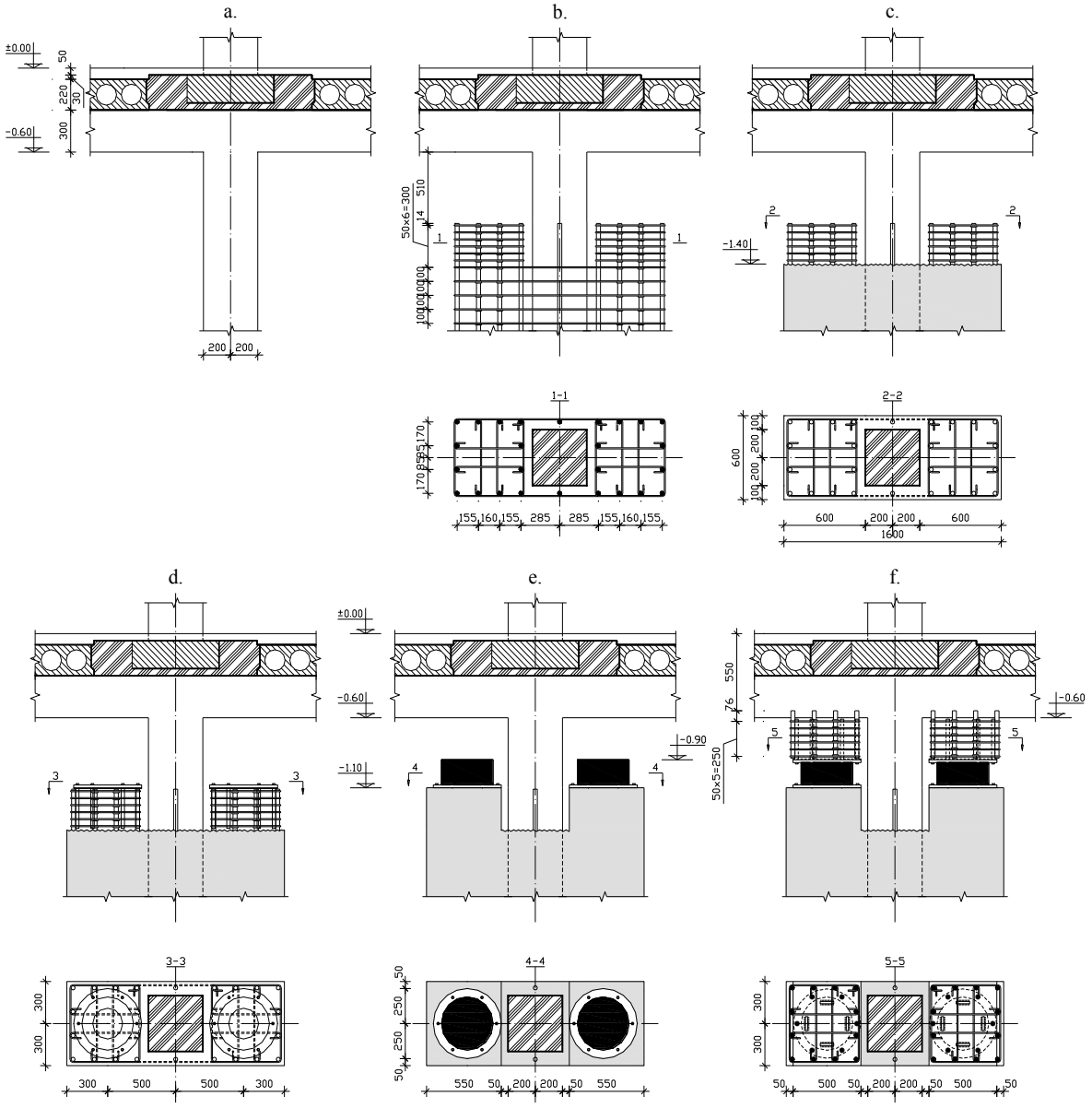


Figure 7: Stages of installation of the seismic isolation rubber bearings under the existing interior columns of HCHB

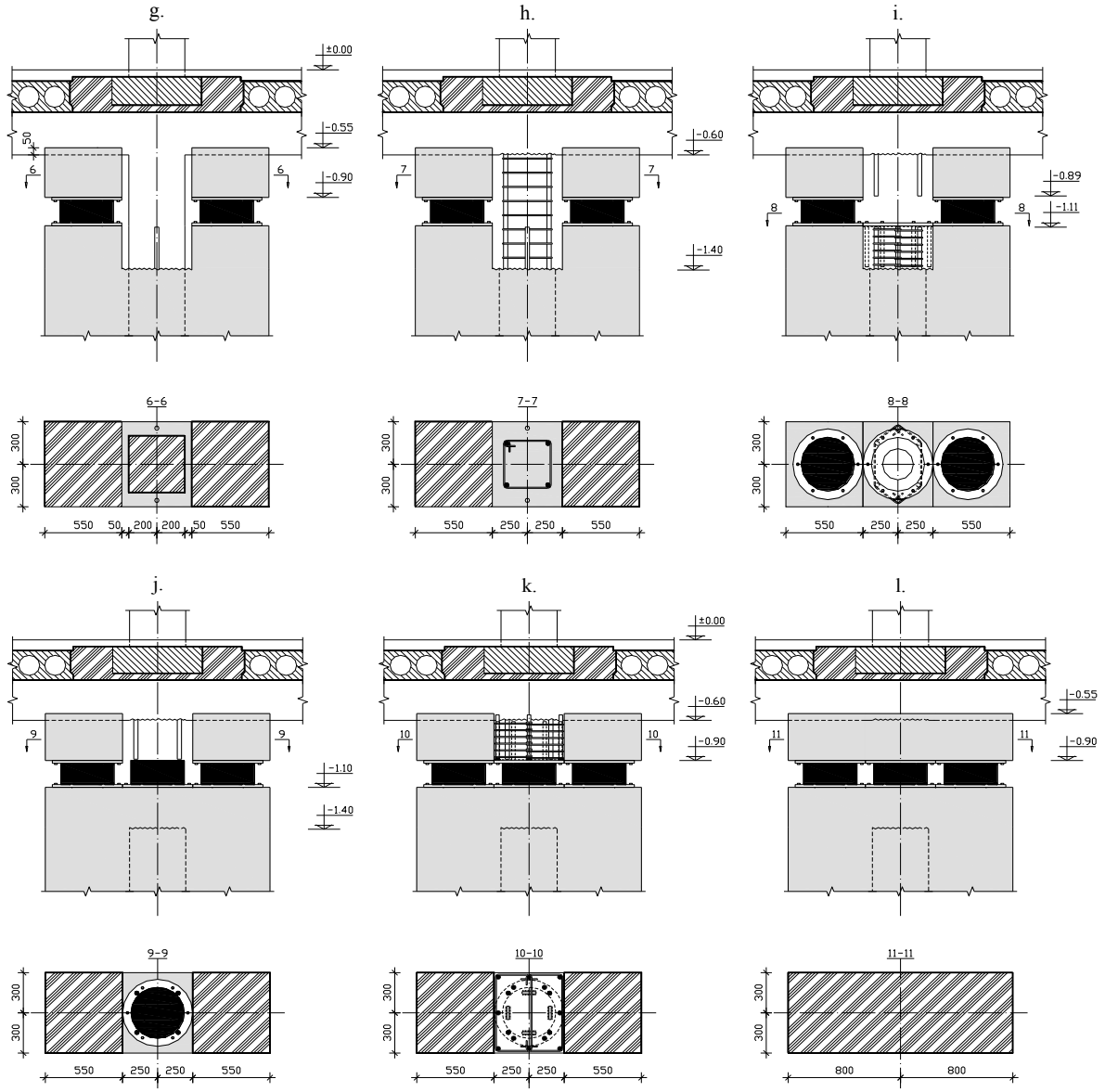


Figure 7: Stages of installation (Continued)

Additional reinforcement around existing columns of the basement is anchored both to the existing spread footings and newly designed beams that connect the spread footings to each other. The mentioned additional parts increase cross-sections of the columns and ensure their required stiffness. Only after placing the reinforcement cages for these parts, concrete can be cast to make the designed mutually perpendicular strap beams that will connect the existing spread footings.

As concrete is casted on the parts containing additional reinforcement around basement columns, it is necessary to follow that the lower sockets of seismic isolators are in strictly horizontal position. The same applies to concreting of the lower pedestals in sheer walls of the basement. All operations related to cutting the columns till the stage 6 can be performed simultaneously. However, after cutting a first column, all remaining stages up to stage 11 inclusive have to be performed for it, by concreting the part above the seismic isolator. Afterwards, the next column can be dealt with and so on.

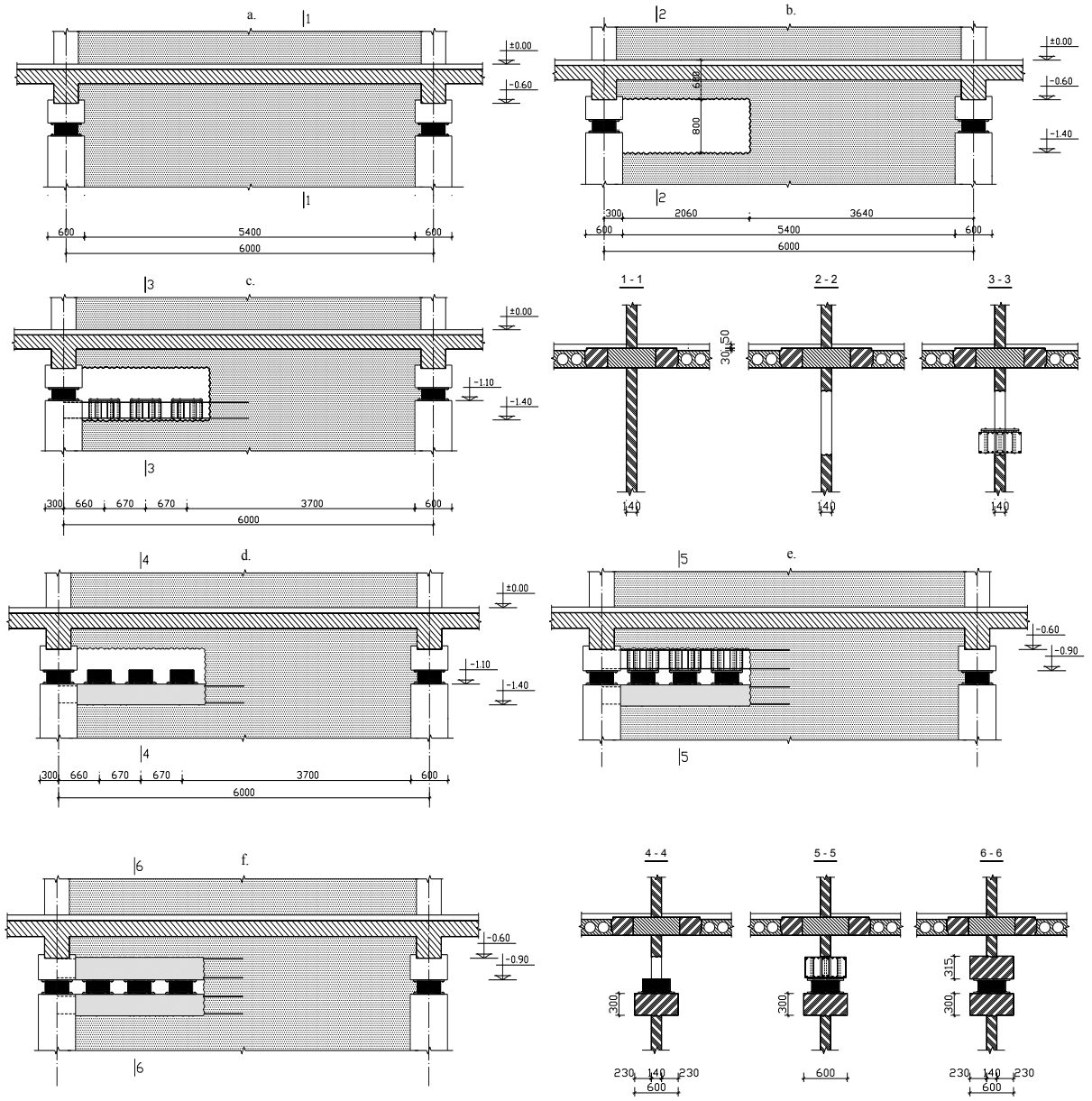


Figure 8: Stages of installation of the seismic isolation rubber bearings within the limits of the existing shear walls of HCHB

In parallel to the above-mentioned operations, the shear wall cutting can be performed up to the stage 5 inclusive. It is not allowed to make openings in the shear walls next to each other simultaneously. Special attention needs to be paid to the stairs to be built near the building's back entrance and those leading to the basement. All these structures have gaps between them and superstructure. These gaps ensure unhindered movement of the superstructure and displacement of the seismic isolation system during design earthquakes. In the basement floor limits, the elevator shafts have metallic carcasses, which are hung on new beams designed at the mark ±0.00. There are 100 mm gaps between the lower parts of the mentioned metallic shafts and bottoms of the elevator pits. The sizes of pits are chosen in such way that during design earthquakes they allow free movement of elevator shafts, without touching the pit walls.

Placing all isolators of the seismic isolation system brings in separating of the building's superstructure from its base (Fig. 9). Consequently, the mass of the building and horizontal

seismic loads are passed to vertical structures and footings of the basement floor only through seismic isolators.

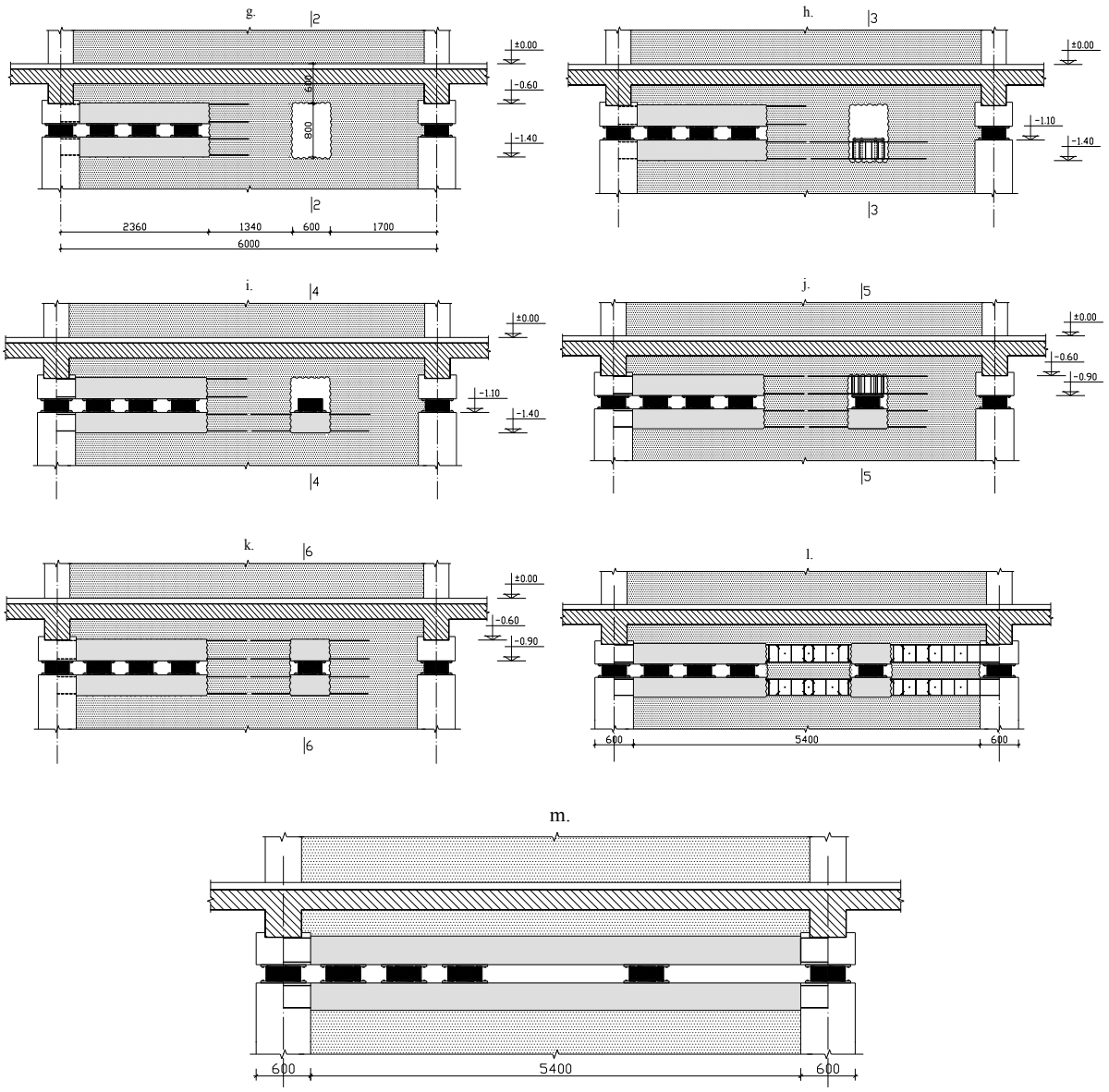


Figure 8: Stages of installation (Continued)

The seismic isolation works around the perimeter of the building are performed in a specific sequence. First, earthworks are implemented. According to the design, trenches are dug along the outer perimeter of the building. Then, the self-supporting walls at the first floor level and part of the walls encasing the basement down to the mark -1.10 are dismantled, and all façade beams along the outer perimeter of the building are constructed. Afterwards, around the basement's outer perimeter retaining walls are built, which are covered by cantilever slabs, in order to protect the formed gap from precipitation and avoid possible accumulation of trash. However, the main purpose of this gap is to ensure effective action of the seismic isolation system during a seismic impact.

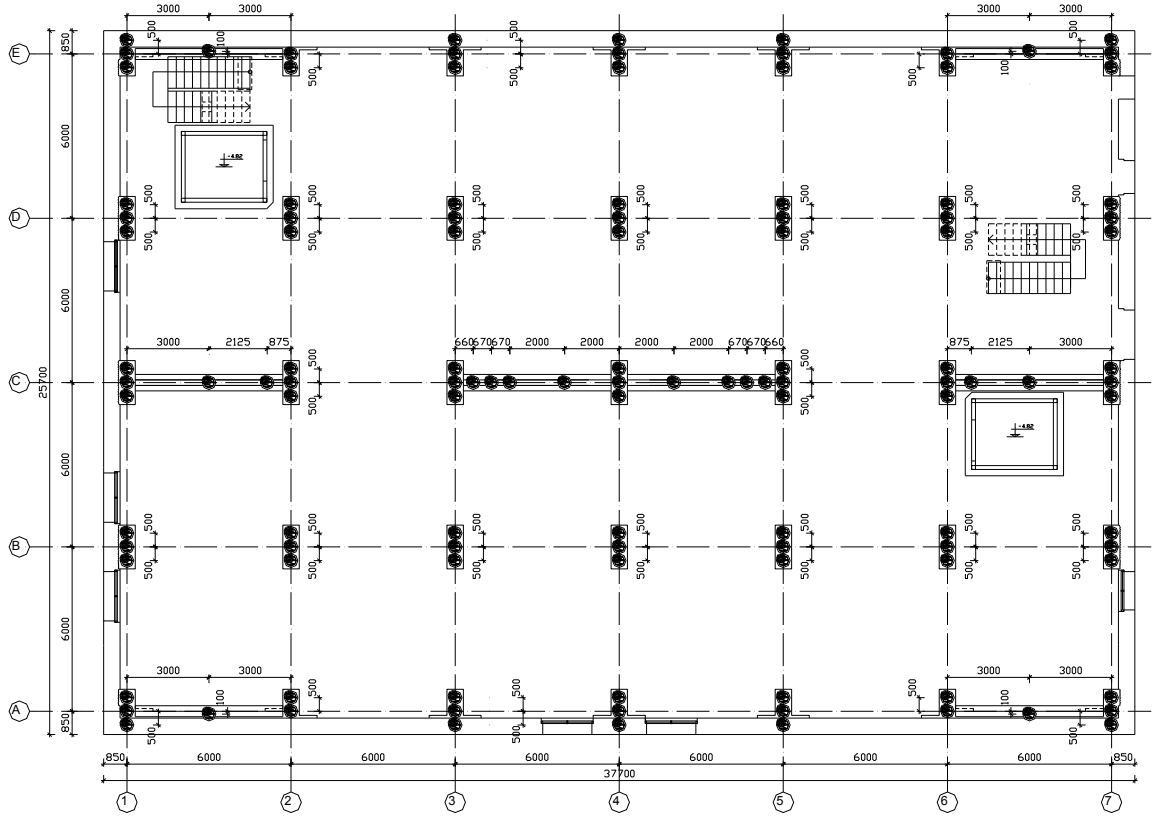


Figure 9: Plan of location of seismic isolators on the level of the existing basement of HCHB

Once the seismic isolation system is completed, all partitions of the basement have to be built, with gaps ensuring unhindered movement of bearing structures above and below the seismic isolation plane relative to each other. The sizes of the gaps are determined by displacement values obtained by calculations. The design involves constructing 50 mm thick R/C layers on all inter-storey floor slabs of the building. For this purpose, top surfaces of all prefab floor slabs and connecting cross-beams have to be bared, whereas the joints between these structural elements have to be cleaned from debris. Before making the R/C layers, all surfaces and joints must be thoroughly washed. After that, 300 mm long rebars with diameter of 8 mm have to be placed in joints with a spacing of 900 mm and concrete has to be cast. The rebars are necessary for creating reliable connection between reinforcement meshes of R/C layers and existing prefab slabs. Given the extremely low quality of connection between existing sheer walls and columns, it is also planned to strengthen these joints with R/C coatings. The areas to be coated must be cleaned beforehand from plaster and washed.

3.3 Analysis of the seismic isolated existing HCHB on the basis of the Armenian Building Code and acceleration time histories

According to a geological report, the site of the building is located in the Seismic Zone 3, and the site Soil Category is II corresponding to the Republic of Armenia Building Code (RABC II-6.02-2006). The report suggests an expected peak ground acceleration value of 0.4g. Vertical loading and seismic impact analysis of the seismic isolation system and the whole structure was performed in accordance with RABC II-6.02-2006 and by the acceleration time histories, using LIRA-SAPR2013 R2 software. The 3D design model (Fig. 10) was developed using bar frame finite elements, as well as membrane finite elements, with due consideration of the structural solution of the superstructure (i.e. part of the building above the seismic isolation plane).

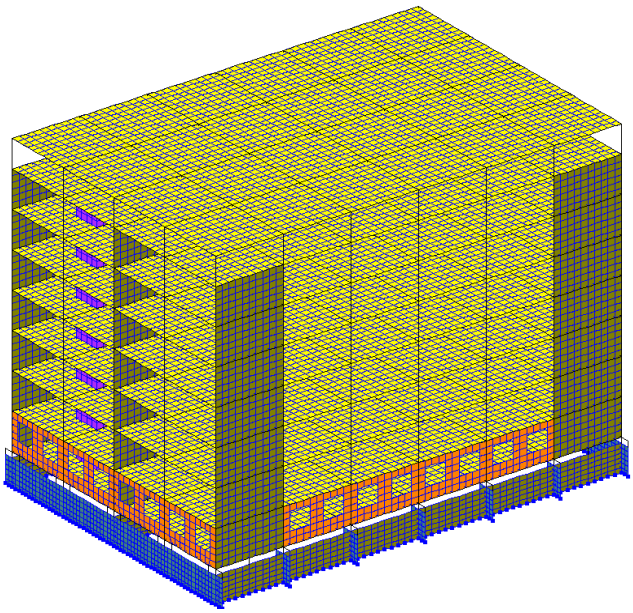


Figure 10: The 3D design model of the seismic isolated existing HCHB

According to the RABC II-6.02-2006, the following parameters were assumed for analysis:
- soil category II;
-soil conditions coefficient is K_0=1.0 and the site prevailing period of vibrations 0.3≤T0≤0.6 sec;
-permissible damage coefficient for determining displacements – K_1=0.8;
-permissible damage coefficient for analysis of seismic isolation system and reinforced concrete structures below it – K_{1z}=0.8;
-permissible damage coefficient for analysis of the superstructure – K_1=0.4;
-importance coefficient of the building – K_2=1.3;
-coefficient of seismicity – A=0.4.

The following 8 acceleration time histories given in Table 1 were selected for calculations and acceleration amplitude was scaled to 0.52g (0.4g×1.3) taking into account the importance of the building. The oscillations periods obtained for the building for the first oscillation mode were equal to T_{1long}=1.9 sec in longitudinal and T_{1trans}=2.0 sec in transverse directions. Maximum design displacements were equal to $D_{max,long}$=146 mm and $D_{max,trans}$=126 mm, respectively. As an example, Table 2 presents some results of calculations related to the middle axes of the building in mutually perpendicular directions. Here the shear forces impacting the seismic isolation system, horizontal displacements and accelerations of the seismic isolation system and all floors and maximum drifts of superstructure's floors, according to calculations by RABC II-6.02-2006 and respective average values by the time histories analysis are given.

The obtained results prove high effectiveness of the seismic isolation system, thanks to which the superstructure of the Hematology Center building practically will not deform during an earthquake and will act as a rigid body. This will ensure high reliability of the building, which will suffer no damage under seismic impacts, since the structural elements below and above the seismic isolation plane will work only in the elastic phase. Indeed, according to the RABC II-6.02-2006, the permissible drift in longitudinal direction (for braced frames) is equal to 1/300 of the floor height, which comprises 8.3 mm for the technical floor and 11.0 mm for the other floors. These values are about 4.5 times in average bigger than the calculated drifts. Also in transverse direction (for moment resisting frames) permissible drift is equal to 1/200 of the floor height, which comprises 12.5 mm for the technical floor and 16.5 mm for the other floors and these values are about 1.8 times in average bigger than the calculated drifts. An input acceleration of 0.52g at the foundation bed gets damped in average up to

3.3 times in the superstructure, and accelerations induced at the first and last floor slabs of the structure differ only by around 28% in average.

Earthquake and record component	Date	Predominant period, sec	Duration, Sec
Hollister (USA)	09.03.49	0.30	9
Eureka (USA) in horizontal NE direction	20.12.54	0.44	26
Bar (former Yugoslavia) in horizontal EW direction	15.04.79	0.55	15
Chiba (Japan) in horizontal NS direction	17.12.87	0.35	39
Spitak (Armenia) in horizontal EW direction	07.12.88	0.43	18
Spitak (Armenia) in horizontal NS direction	07.12.88	0.47	18
Loma Prieta (USA) in horizontal EW direction	17.10.89	0.34	10
Manjil (Iran) in horizontal NE direction	20.06.90	0.49	20

Ttable 1: Acceleration time histories selected for earthquake response analysis of the seismic isolated HCHB

Calculated values		As per RABC II-6.02-2006		Average by the time histories	
		longitudinal direction along middle axis “C”	transverse direction along middle axis “4”	longitudinal direction along middle axis “C”	transverse direction along middle axis “4”
$S_{i.s.}$, kN		13050	12100	11200	9900
$D_{i.s.}$, mm		119.9	122.6	109.1	105.5
$A_{i.s.}$ in portion of “g”		0.137	0.119	0.125	0.103
D_n, mm/A_n in portion of “g”	1	121.0/0.138	128.5/0.125	110.0/0.126	110.6/0.108
	2	123.5/0.142	137.9/0.134	112.4/0.129	118.7/0.116
	3	125.8/0.144	147.7/0.144	114.5/0.131	127.1/0.124
	4	128.2/0.146	157.3/0.153	116.6/0.133	135.4/0.132
	5	130.6/0.150	166.7/0.162	118.8/0.136	143.4/0.140
	6	133.0/0.152	175.4/0.171	121.0/0.138	151.0/0.147
	7	135.5/0.155	183.1/0.178	123.2/0.141	157.6/0.153
	8	137.4/0.157	185.6/0.181	125.0/0.143	159.7/0.154
Δ, mm		2.5	9.8	2.4	8.4

$S_{i.s.}$ – Shear forces at the level of the seismic isolation system
$D_{i.s.}$ – Displacements of the seismic isolation system
$A_{i.s.}$ – Accelerations above the seismic isolation system
D_n – Displacements of the n^{th} floor of superstructure
A_n – Accelerations of the n^{th} floor of superstructure
Δ – Maximum drifts of the floors of superstructure

Ttable 2: Some results obtained by calculations in accordance with Armenian Building Code and average by the time histories for seismic isolated HCHB

The obtained results also show that vertical loads on seismic isolators do not exceed the stipulated value of 1500 kN, which is achieved through satisfying the requirements set in paragraphs 10.5.4 and 10.5.7 of the RABC II-6.02-2006. Consequently, there is practically no eccentricity between the horizontal stiffness center of the seismic isolation system and projec-

tion of the structure's mass center on SILRSBs' plane. This is proven and also can be well observed in analysis by the time histories during the oscillations of the building.

4 CONCLUSIONS

- Paper briefly describes seismic isolation technologies developed by the author for retrofitting of the different types of existing buildings. Five projects, where base isolation is applied, are mentioned, demonstrating retrofitting experience accumulated in Armenia.
- Paper dedicated to the further developments on retrofitting of existing buildings and is mainly focused on: (i) retrofitting by base isolation of the 4-story R/C frame building of Armenian-American Wellness Center with simultaneous increasing of the number of floors from 4 to 6, and (ii) retrofitting by base isolation of the 8-story R/C frame building of Hematology Center Hospital Building constructed 40-50 years ago.
- Methods of creation of base isolation systems in both existing buildings at the level of their basements with application of the newly developed different types of large-size (Φ=580 mm, h_t=300 mm) and small-size (Φ=380 mm, h_t=202.5 mm) seismic isolators are described.
- Details of the new and original structural concepts for retrofitting of the R/C frame hospital buildings are presented in the paper by stages of installation of the seismic isolation rubber bearings under the existing columns and within the limits of the existing shear walls.
- Retrofitting by base isolation of the existing 8-story Hematology Center Hospital Building is the most recent application in the city of Yerevan and the retrofitting process is currently going on in the mentioned building. Results of analysis of this building by the Armenian Seismic Code and the time histories have shown that the structural elements below and above the seismic isolation plane will work only in the elastic phase. The permissible floor drifts are about 2-4 times bigger than the calculated values. An input acceleration of 0.52g at the foundation bed gets damped in average up to 3.3 times in the superstructure.

REFERENCES

[1] F. Naeim, J. Kelly, *Design of seismic isolated structures. From theory to practice*, John Wiley & Sons Inc., 1999.

[2] M. Melkumyan, The use of high damping rubber isolators to upgrade earthquake resistance of existing buildings in Armenia. *International Post-SMiRT Conference Seminar on Seismic Isolation, Passive Energy Dissipation and Active Control of Seismic Vibrations of Structures*, Taormina, Sicily, Italy, 861-867, 1997.

[3] V. Smirnov, J. Eisenberg, F. Zhou, Y. Chung, A. Nikitin, Seismoisolation for upgrading of an existing historical building in Irkutsk-City, Siberia-Russia. *12th World Conference on Earthquake Engineering*, Auckland, New Zealand, Paper No. 0962, 2000.

[4] M. Melkumyan, G. Käppeli, R. Khalatyan, H. Hovivyan, Application of seismic isolation for retrofitting of existing 3-story stone building of the school #4 in the city of Vanadzor, Armenia, *8th World Seminar on Seismic Isolation, Energy Dissipation and Active Vibration Control of Structures*, Yerevan, Armenia, 557-565, 2003.

[5] M. Melkumyan, V. Mihul, E. Gevorgyan, Retrofitting by base isolation of existing buildings in Armenia and in Romania an comparative analysis of innovative vs. conventional retrofitting, *3rd International Conference on Computational Methods in Structural Dynamics and EarthqukeEngineering*, Corfu Island, Greece, Paper No. 121, 2011.

[6] M. Melkumyan, New structural concept for an existing 4-story reinforced concrete industrial frame building to be retrofitted by base isolation and simultaneously reconstructed into a 6-story hotel building. *Engineering and Technology*, *Vol. 1*, *No. 1*, 1-12, 2014.

[7] M. Melkumyan, *New solutions in seismic isolation*, Yerevan, LUSABATS, 2011.

[8] M. Melkumyan, Seismic isolation retrofitting experience in Armenia and new structural concept for an existing 8-story reinforced concrete hospital building to be retrofitted by base isolation, *Study of Civil Engineering and Architecture*, *Vol. 3*, 78-92, 2014.

[9] M. Melkumyan, Base and Roof Isolation for Earthquake Retrofitting and Protection of Existing Buildings in Armenia, *International Symposium on Seismic Risk Reduction (the JICA Cooperation Project in Romania),* Bucharest, Romanian, 593-600, 2007.

[10] T. Inoue, M. Melkumyan, F. Kumazawa, Y. Nakano, T. Okada, Earthquake response analyses of precast reinforced concrete buildings damaged due to Armenia Spitak earthquake, *Bulletin of Earthquake Resistant Structures Research Center, Institute of Industrial Science, University of Tokyo, No. 24*, 57-64, 1991.

[11] K. Fuller, C. Lim, S. Loo, M. Melkumyan, K. Muniandy, Design and testing of high damping rubber earthquake bearings for retrofit project in Armenia, *Earthquake Hazard and Seismic Risk Reduction*. S. Balassanian, A. Cisternas, M. Melkumyan eds. Kluwer Academic Publishers. The Netherlands, 379-385, 2000.

COMPDYN 2015
5th ECCOMAS Thematic Conference on
Computational Methods in Structural Dynamics and Earthquake Engineering
M. Papadrakakis, V. Papadopoulos, V. Plevris (eds.)
Crete Island, Greece, 25–27 May 2015

INNOVATIVE TECHNIQUE FOR THE BASE ISOLATION OF EXISTING BUILDINGS

Alessandro De Stefano[1], Paolo Clemente[2], Stefano Invernizzi[3], Emiliano Matta[3], Antonino Quattrone[3]

[1] Politecnico di Torino, C.so Duca degli Abruzzi 24, 10129, Turin, Italy
alessandro.destefano@polito.it
[2] ENEA, Via Anguillarese 301, 00123 Rome, Italy
paolo.clemente@enea.it
[3] Politecnico di Torino, C.so Duca degli Abruzzi 24, 10129, Turin, Italy
stefano.invernizzi@polito.it, emiliano.matta@polito.it, antonino.quattrone@polito.it

Keywords: Monitoring; closely-spaced micro-tunnels; damage assessment; soil-structure interaction; base-isolation.

Abstract. *An innovative base isolation system has been recently proposed for the retrofitting of existing buildings, in which the isolation layer is inserted under the building foundations so that the building, along with its foundations, is isolated from the surrounding soil. The isolation layer resides in closely-spaced micro-tunnels, constructed under the entire width of the building. These micro-tunnels, along with the trenches around the building, isolate the structure from the surrounding soil. The execution of these micro-tunnels is the most critical construction stage, because it may result in settlements which can damage the structure. In this paper, the behaviour of an existing structure, consisting of a masonry wall subjected to tunnelling-induced ground subsidence, is analysed. A parametric study is conducted using 2-D nonlinear finite element analyses to understand the role of key factors such as strength and stiffness of soil and masonry, roughness of soil-structure interface, excavation sequence of tunnels, wall dimensions and openings configuration. The study identifies the design variables which influence the most the risk of structural damage and suggests the most effective damage symptoms to be monitored during construction.*

1 INTRODUCTION

The usual base isolation design to improve the seismic resistance of existing buildings leads to extensive and intrusive manipulations of the construction body that severely alter the original structural configuration, thus resulting generally inapplicable to historical constructions or whenever existing architectural features are of economic importance.

An innovative way of isolating buildings from seismic actions has been proposed by Clemente and De Stefano [1][2], which, unlike conventional methods, does not involve any modification of the existing structure. The method calls for isolation of the building along with its foundation soil from the rest of the ground and consists in executing a series of closely-spaced micro-tunnels under the building and in placing isolators within the thickness of the tunnels lining. The execution of micro-tunnels is the most critical construction stage of the proposed intervention, because it may result in settlements, and therefore can induce structural or non-structural damage into the building. In order to keep damage below the desired thresholds, it is of paramount importance to develop adequate analytical, numerical and empirical tools, which can accurately and reliably predict the effect of excavations, and execution procedures capable to minimize the expected damage. Furthermore, it is important to properly track, during construction, possible deviations between the expected and the actual response of the soil-structure system, so as to identify the necessary corrections, if needed, to the execution process (soil consolidation, modification of the tunnelling sequence, etc.).

Surface and subsurface ground subsidence accompanying tunnelling operation, as well as the effect of the tunnel-related ground subsidence on the structures on surface, have received attention in the form of empirical, numerical and analytical studies [3][4][5][6][7][8][9]. These studies refer to single tunnels only, and were subsequently extended to the case of multiple tunnels [10][11][12]. Researchers, such as Boscardian & Cording [13] and Burland & Wroth [6], identified damage indicators for structures undergoing tunnel-induced settlements and used them to establish several levels of damage-thresholds; they used average horizontal strain, angular distortion/strain and deflection ratio in their studies. Various case studies have been done in the past where the tunnelling-induced damage was anticipated in terms of damage-indicators; damage-thresholds were determined for them and building was monitored during tunnel construction, keeping those damage-thresholds in mind. Those studies involved cases where deformation caused by one tunnel was the main source of damage on the existing structure. No studies are reported, to the best of the authors' knowledge, regarding closely-spaced multiple tunnels like the one discussed in the present application and the correlated structural damage.

The present paper aims to investigate how closely-spaced micro-tunnelling can adversely affect the structural state of existing masonry buildings and how monitoring during construction can help to reduce the risk of unpredicted damage. To this purpose, accurate 2-D nonlinear analyses are performed, simulating the coupled soil-structure interaction problem during sequential micro-tunnelling execution. The influence of different design variables on the onset and development of structural damage (crack opening) is first studied, and design recommendations are formulated regarding the best procedures to adopt in executing closely-spaced micro-tunnels so as to minimize damage. Correlations are then searched for between the extent of damage and different damage-indicators, and recommendations are finally inferred as to which indicators should be observed during monitoring of tunnel-construction.

2 THE INNOVATIVE ISOLATION SYSTEM

The new solution proposed consists in the realization of an isolated platform under the foundations of the building, without touching the building itself. A discontinuity between the foundations and the soil is created by means of the insertion of horizontal pipes and the positioning of isolation devices at the horizontal diametric plane. Then the building is separated from the surrounding soil in order to allow the horizontal displacements required by the isolation system. So the structure is seismically isolated but not interested by interventions that could modify its architectural characteristics, which is very important for historical buildings but also for large structures such as industrial plants [14][15].

Even underground level are not modified but can be part of the seismically protected building. In more details the construction phases are the following:

- a trench is first excavated of at one side of the building and pipes are inserted by means of auger boring or micro-tunnelling technique; the diameter of pipes should be ≥ 2 m, in order to allow the inspection of the isolation system; the pieces of pipe should have a particular shape and are composed by two portions, the lower and the upper sectors, respectively, which are connected by means of removable elements.
- the connection elements placed in correspondence of the isolation devices are removed and each pipe is joined with the two adjacent ones, for example by means of a reinforced concrete elements;
- the isolation devices are positioned and the upper adjacent sectors are connected in correspondence of the isolators;
- successively also the other connection elements are removed, so the lower and upper sectors are definitely separated;
- finally vertical walls are built along the four sides of the building.

The construction phases could be preceded by a stiffening of the soil by using jet grouting technique or others. This allows avoiding collapses during the works and is absolutely due when the distance from close structures is low. The system allows also the realization of a tunnel for pedestrian or vehicles. The size of the pipes must guarantee the accessibility and the possibility to substitute the devices.

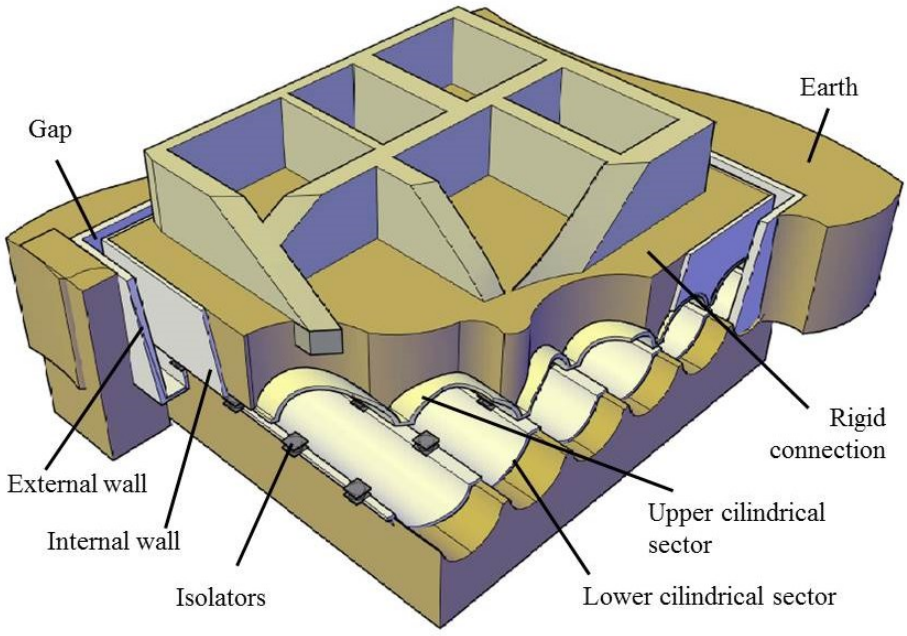


Figure 1 : The proposed method for seismic isolation

During the response to the earthquake the ground mass, added to the isolated structure as part of the mechanical system in relative motion with respect to the supporting ground, can play a positive role thanks to a more regular mass distribution and reduction of the overturning moment. It makes easy to obtain a very long fundamental period and, consequently, a large acceleration reduction. The trench surrounding the isolated structure, if necessary, can be used to install supplementary damping devices to keep under control the relative displacements.

The following chapter is devoted to the numerical settlement prediction during the construction of the micro-tunnels. A specific case study is explored in detail as a simulated experiment. Results are not fully extendable to every possible application, with different soil conditions, different building configurations and bore depth. In specific cases a previous mechanical improvement of the ground can be required. Anyway the numerical simulation can suggest some general conclusions

3 THE NUMERICAL MODEL

3.1 The baseline model

The 2-D numerical model used in the parametric study has been built using the commercial finite-element-method (FEM) software DIANA [16]. A general view of the model is reported in Figure 2, where two different opening configurations are exemplified, either with or without crack pattern and mesh discretization. Soil is modelled as a homogeneous, isotropic, linear-elastic perfectly-plastic material with Mohr-Coulomb yield surface and zero-tension cut-off. The soil is represented with 8-nodes quadrilateral plane-strain elements; few soil elements, inside and around excavation, are modelled as 6-nodes triangular plane-stress elements [17].

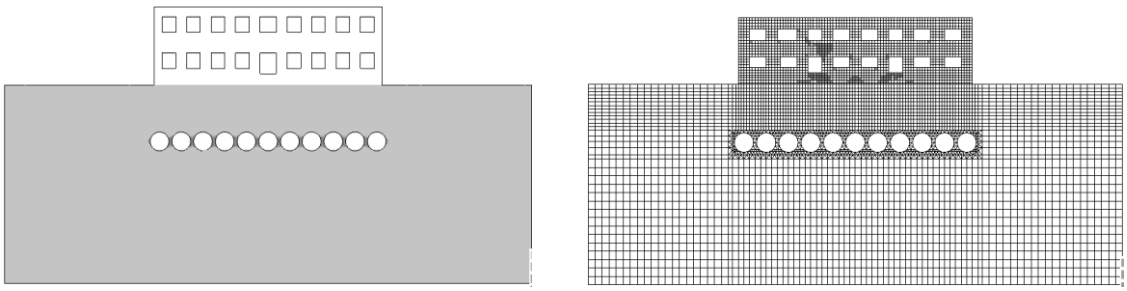


Figure 2 : The two different opening configurations for the 24.2 m long wall (1-Door on the left, 2-Door on the right), either with or without showing the final crack pattern and mesh discretization

Masonry is modelled as a homogeneous and isotropic material. A linear response is assumed for masonry in the elastic regime, while a smeared crack approach with strain decomposition is used to simulate its behaviour in cracking. A fixed-crack model with linear tension softening and constant tension cut-off criteria is used to simulate crack initiation and propagation (Figure 3). Masonry wall is modelled with 8-nodes quadrilateral plane-stress elements.

The interaction between soil and masonry is modelled through interface elements, relating normal and shear forces to normal and shear relative displacements across the interface. The values of interface stiffness are chosen such that the interface allows slip (tangential movement) between soil and masonry at very low shear stress. Interface is represented as 6-nodes line-interface elements.

The lining and the lintel are modelled as a linear-elastic, isotropic and homogeneous material; lining is represented as 3-nodes curved shell elements and lintel with 3-nodes 2-D beam elements. The bottom and lateral boundaries of soil are constrained in perpendicular direction;

top boundary is free to move in both directions. The model is loaded with gravity and superimposed loads, including dead and live loads acting on floors. In order to simplify the problem, dampers are not included in the model.

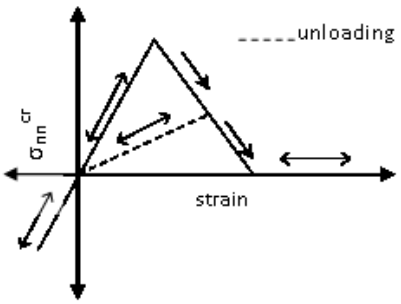


Figure 3 : Masonry constitutive law adopted in simulations

3.2 Modelling excavation process

Simulation of sequential tunneling obeys the following procedure. Initial soil stresses are established first, which are based on unit weight of soil and coefficient of earth pressure at rest; displacements are suppressed in this phase. Next step involves activation of masonry elements along with their self-weight and superimposed load. Then the excavation process modelled. Namely:

- Soil elements, corresponding to the first tunnel, are removed, and the model is allowed to establish equilibrium under gravity and superimposed loads. No internal pressure is applied on the periphery of excavation. DIANA's 'phased analysis' is used for this purpose.
- Soil elements, corresponding to the second tunnel, are then removed; lining elements are added around the first tunnel and the model is allowed to establish equilibrium under gravity and superimposed loads. No internal pressure is applied on the periphery of the excavation.
- The previous step is repeated for the remaining tunnels.

In the above steps, it is assumed that the "annular space" or the "gap" (i.e. the space between soil and lining) is the main source of volume loss, owing to the relatively stiffer soil conditions and small size of tunnel. Volume loss is simulated by allowing the tunnel to undergo instantaneous settlement, with no pressure applied on the excavated boundary, before the installation of lining elements. Since the introduction of the lining elements into the model prevents further closure of the gap, the model is meant to be representative of a real tunnelling process in which the gap must be completely filled with grout after installation of lining.

3.3 Wall configurations and excavation sequences in the parametric study

The parametric study has been conducted assuming three different values of the length of the masonry wall (24.2 m, 15.5 m, and 12.6 m) while keeping constant the height of the wall and the diameter (D) of the tunnels. Consequently, the number of tunnels required to cover each wall length are: 11 tunnels for the 24.2 m wall; 7 tunnels for the 15.5 m; and 6 tunnels for the 12.6 m wall.

Two types of opening configurations are considered for the 24.2 m wall, either 1-Door or 2-Door (Figure 2), while other walls are analysed with one type of opening configuration only. Three construction sequences are considered for the 11-tunnel assembly, three for the 7-tunnel assembly, one for the 6-tunnel assembly. The adopted sequences are shown in Figures 4 to 6. For all the models, soil bottom boundary is kept at 8D from the centre of tunnels, the side

boundary is kept at 8*D* from the centre of the outermost tunnels, and the depth of the centre of tunnels is chosen as 6 m for all models.

3.4 Geometric and material properties

Material properties adopted for soil and masonry are shown in Tables 1 and 2, where E is the elastic modulus, c is the cohesion, γ is the unit weight, ν is the Poisson's ratio, Ψ is the dilatancy angle, ϕ is the friction angle and K_o is the coefficient of lateral earth pressure at rest. Material parameters adopted for lining are: γ = 24.5 kN/m^3, E = 21 GPa, ν = 0.15. For lintel, the same γ and ν are adopted as for lining, but E is reduced to 15 GPa. The normal stiffness of the interface elements is selected as 4x10^8 N/m^3, while its tangential stiffness is 5 N/m^3, as suggested by literature.

In all the models, the height and the thickness of the wall are kept at, respectively, 6.75 m and 0.22 m; the thickness of lining at 0.1 m; the cross-section of the lintel at 0.22 x 0.16 m; the diameter of the tunnels at 2 m; and the distance between their centre at 2.2 m.

Tunnel assembly	E (MPa)	c (kPa)	γ (kN/m^3)	ν (-)	Ψ (°)	ϕ (°)	K_o (-)
11	200	80	17.5	0.3	0	13	0.47
7	150	70	17.5	0.3	0	13	0.47
6	50	70	17.5	0.3	0	13	0.47

Table 1 : Material properties for soil

Tunnel assembly	Shear retention factor	E (GPa)	F_t (kPa)	G_f (N/m)	γ (kN/m^3)	ν (-)
11	0.01	9	400	50	20.5	0.2
7	0.01	5	275	45	20.5	0.2
6	0.01	4.5	200	45	20.5	0.2

Table 2 : Material properties for masonry wall

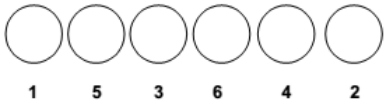


Figure 4 : Sequence of excavation for the 6-tunnel assembly

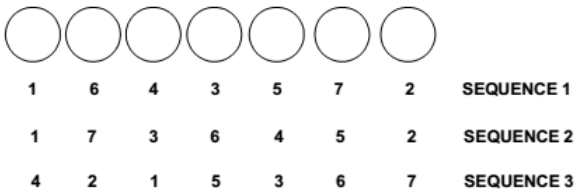


Figure 5 : Sequences of excavation for the 7-tunnel assembly

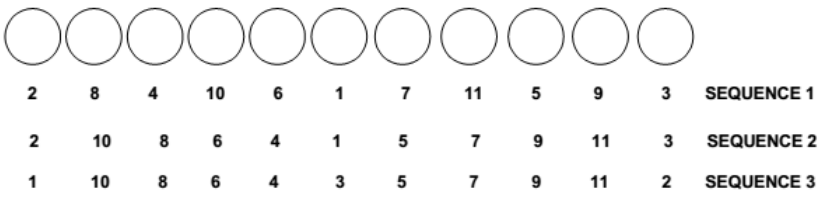


Figure 6 : Sequences of excavation for the 11-tunnel assembly

4 RESULTS

Results from different cases are looked at in terms of, on the one hand, the extent of damage, and, on the other hand, a set of different possible damage indicators or symptoms, observed in their respective evolution during the excavation process. The extent of damage is expressed by a measure of crack opening, either in mean or in maximum terms.

Many different observation variables are alternatively considered as possible damage indicators or symptoms, including: maximum angular strain, deflection ratio, maximum average horizontal strain, maximum differential settlement, tilt and maximum change in slope. Deflection ratio, maximum average horizontal strain and maximum angular strain have already been extensively used as damage indicators in the literature [13][6], whilst a correlation between the maximum change of slope and damage has not been presented yet to the best of the authors' knowledge. In the present work, no apparent correlation with damage has been found for tilt and maximum differential settlement, so results will be presented in terms of the following quantities only:

- Maximum average horizontal strain (ε_h), defined as the maximum change in length of wall at the foundation level over a distance of 1m;
- Maximum change in slope ($\Delta\theta$), defined as the maximum of the second derivative of the vertical settlement profile;
- Angular strain (β) and deflection ratio (DR), defined as explained in Figure 7;
- Maximum crack width (crack max) and mean crack width (crack mean).

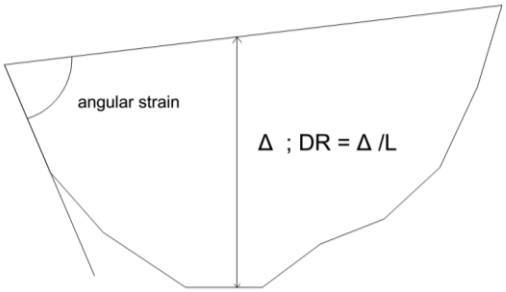


Figure 7 : Angular strain (β) and deflection ratio (DR)

Analyses were carried out for the 6-, 7-, 11-tunnel assemblies. Only the 11-tunnels assembly is shown here, with two different opening configurations (one door and two doors) and different excavation sequence. Two different excavation sequences were considered for the case of opening configuration with one door. Results are reported in Figures 8-19. Figures in dotted lines depict the evolution of damage (in terms of maximum crack width) with the progression of excavation stages; figures in continuous lines present the damage-symptom correlation at each excavation stage. Unlike the previous cases, tunnel-related damage started from the first excavation in this case. This is due to the fact that the excavation process started from the central portion for both excavation sequences (see again Figure 6).

The last excavation stage inflicted much more damage than the other stages in excavation sequence 1, while the sixth excavation stage proved to be the one inducing most damage in excavation sequence 2. Overall, excavation sequence 2 inflicted much more damage than the excavation sequence 1.

The behaviour of wall is very different for the two excavation sequences. The only symptom showing a satisfactory correlation with damage for both sequences is $\Delta\theta$.

In the case of opening configuration with two doors, three different excavation sequences were considered in this case. Results are reported in Figures 20-31. The tunnel-related damage

started from the first excavation for sequence 1 and 2, while it started from the third excavation for sequence 3; excavation commenced from the outermost tunnels for sequence 3 (Figure 6).

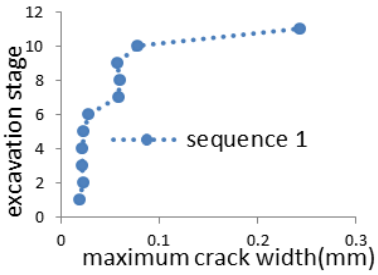


Figure 8 : Crack max evolution

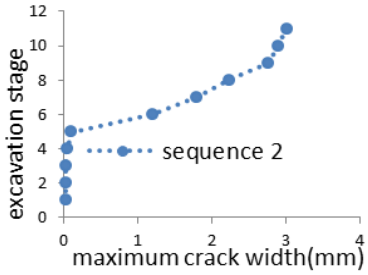


Figure 9 : Crack max evolution

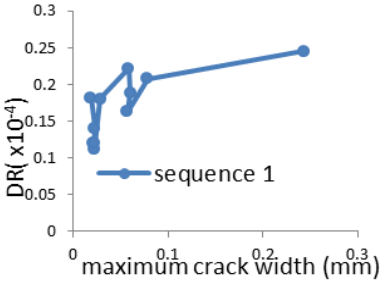


Figure 10 : DR vs. crack max

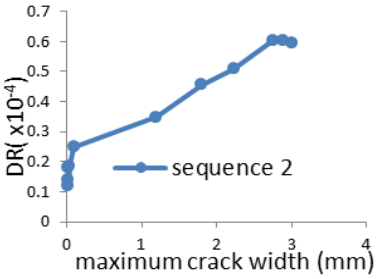


Figure 11 : DR vs. crack max

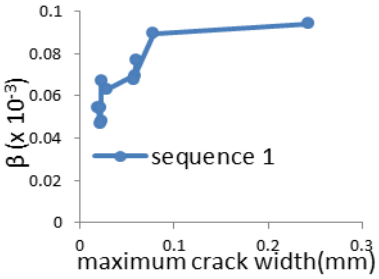


Figure 12 : β vs. crack max

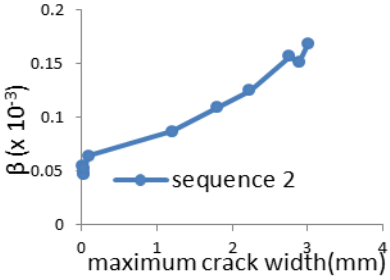


Figure 13 : β vs. crack max

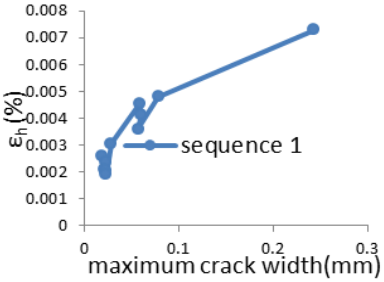


Figure 14 : ε_h vs. crack max

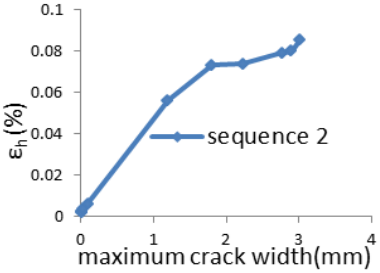


Figure 15 : ε_h vs. crack max

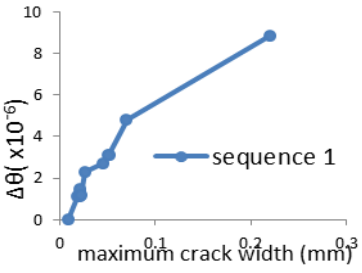


Figure 16 : Δθ vs. crack max

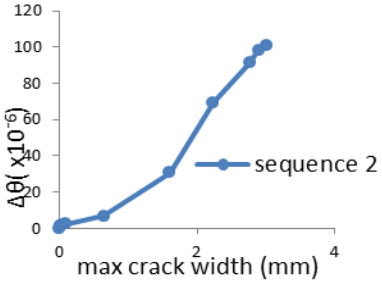


Figure 17 : Δθ vs. crack max

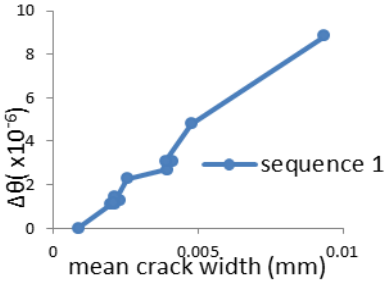


Figure 18 : Δθ vs. crack mean

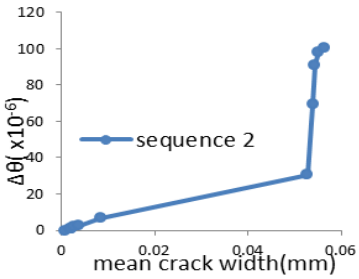


Figure 19 : Δθ vs. crack mean

The sequence 2 inflicted much more damage than the other two sequences. Excavation sequence 3 can be adopted for this case along with β as damage-indicator. Excavation sequences 1 and 3 gave highly nonlinear and chaotic correlation between DR/ε_h and maximum crack width; excavation sequence 2 resulted in regular nonlinear relationship between DR and ε_h,

and fairly linear relationship between average horizontal strain and maximum crack width. The correlation between β and maximum crack width is almost similar for all three sequences.

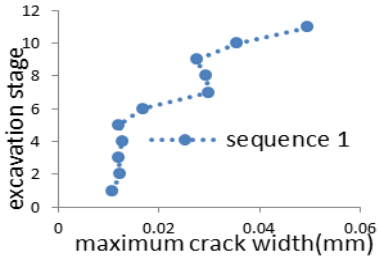


Figure 20 : Crack max evolution

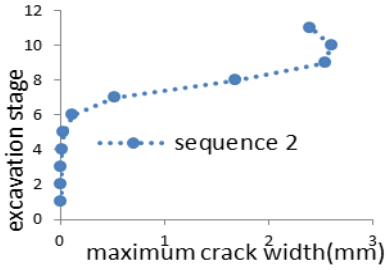


Figure 21 : Crack max evolution

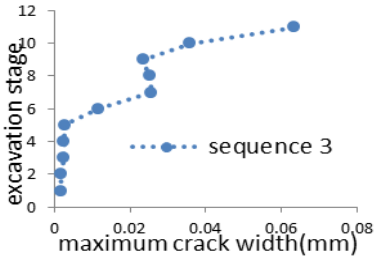


Figure 22 : Crack max evolution

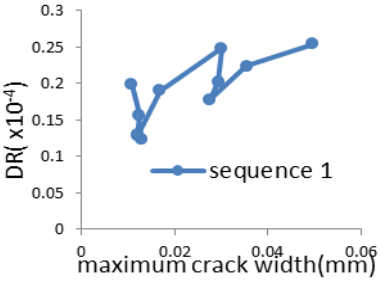


Figure 23 : DR vs. crack max

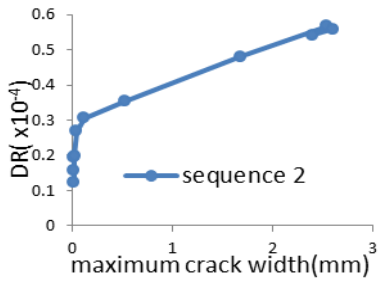


Figure 24 : DR vs. crack max

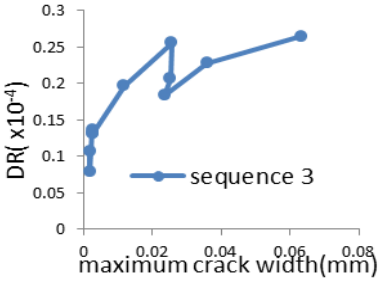


Figure 25 : DR vs. crack max

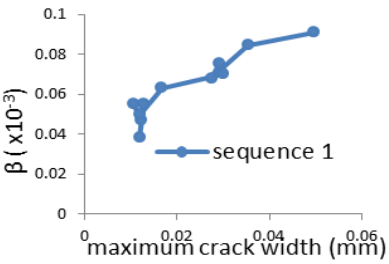


Figure 26 : β vs. crack max

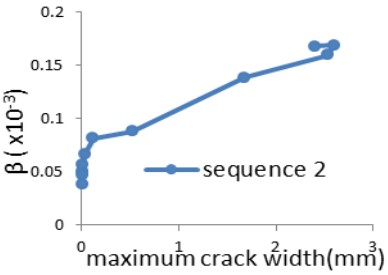


Figure 27 : β vs. crack max

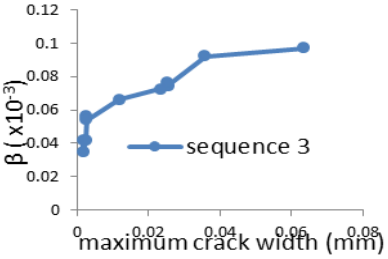


Figure 28 : β vs. crack max

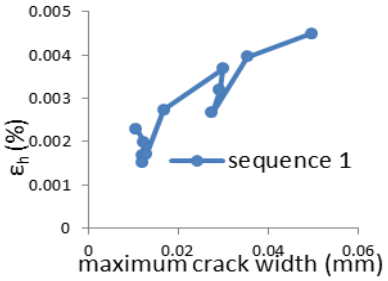


Figure 29 : ε_h vs. crack max

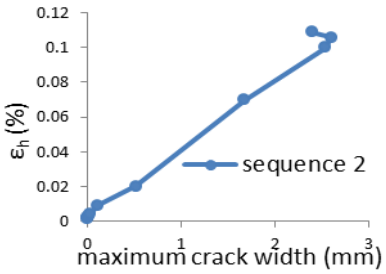


Figure 30 : ε_h vs. crack max

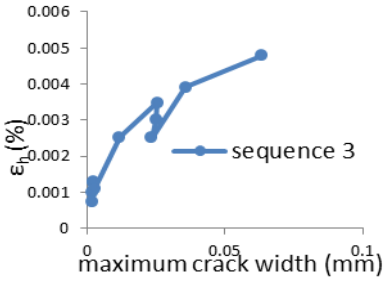


Figure 31 : ε_h vs. crack max

5 CONCLUSIONS AND RECOMMENDATIONS

The present paper aimed at investigating how closely-spaced micro-tunnelling can inflict damage onto existing masonry buildings and how monitoring during construction can help to reduce the risk of damage. In the light of the results discussed above, the following conclusions can be drawn:

- For any given wall configuration/geometry, the extent of damage at the completion of the entire excavation process strongly depends on the excavation sequence. Damage is much less when excavation starts from outermost tunnels.
- In all simulated cases, if the proper excavation sequence is adopted in design, the maximum crack experienced during excavation is limited to values ranging from 0.05 to 0.35 mm depending on the case at hand; this can be regarded as a "very slight" damage according to the literature. This result is acknowledged to be strongly dependent on the geometric and mechanical parameters of the structure and the soil as well as on the design of micro-tunnels. In order to generalize this result, however, simulations need to be extended to include a wider range of mechanical/geometrical properties of soil and masonry. These preliminary results suggest the feasibility of the proposed, innovative base isolation system.
- Different possible damage indicators or symptoms have been monitored during simulations, some taken from the literature and others newly proposed. In general no simple correlation can be identified between damage and any particular symptom. No symptom appears to neatly prevail over the others in all explored simulation cases. On average, the best damage indicators, capable of well tracking damage evolution during construction, appear to be the maximum average horizontal strain, ε_h, and the maximum change in slope, $\Delta\theta$, which provide a nearly linear relationship with the maximum or the mean crack width in several cases. The worst damage indicators appear to be the tilt and the maximum differential settlement. These results suggest that "global" indicators based on the knowledge of few settlement values along the structure, which are typically monitored in common practice, are generally insufficient to reliably track the evolution of damage in a problem of closely-spaced multiple tunnels. "Local" indicators, unfortunately requiring a larger number of measurement points from closely-spaced sensors, appear much more representative of the actual damage extent in the present application. Image acquisition and processing monitoring systems (e.g. laser-scanner) or distributed fibre optic sensoring technologies seem the most indicated to this purpose.

ACKNOWLEDGEMENTS

The Authors thank very much Dr. Badar Zeeshan for his very helpful contribution to this study.

REFERENCES

[1] Clemente P., De Stefano A. (2011). "Application of seismic isolation in the retrofit of historical buildings". In Brebbia C.A.& Maugeri M. (eds) Earthquake Resistant Engineering Structures, 41-52, WIT Transactions on The Built Environment, Vol. 120, ISSN 1743-3509 (on line).

[2] Clemente P., De Stefano A., Renna S. (2011). "Isolation system for existing buildings". Proc., 12th World Conf. on Seismic Isolation, Energy Dissipation and Active Control of Structures - 12WCSI (Sept. 20-23, Sochi, Russia).

[3] Peck, R. D. (1969). "Deep excavations and tunneling in soft ground", *Proceeding 7th International conference on soil mechanics and foundation engineering*, (pp. 225-290).

[4] O' Reilly, M. P. and New, B. M. (1982). "Settlements above tunnels in United Kingdom: their magnitude and prediction", *Proceeding of Tunneling* (pp. 55-64). Institue of Mining and Metallurgy, London.

[5] Sagaseta, C. (1987). "Analysis of undrained soil deformation due to ground deformation", *Géotechnique, 37*, pp. 301-320.

[6] Burland, J. B. and Wroth, C. P. (1974). "Settlement of buildings and associated damage", *Settlement of stuctures*, (pp. 611-654). Cambridge.

[7] Rots, J. (1991). Numerical simulation of cracking in structural masonry. *HERON, 36*(2), pp. 49-63.

[8] Rots, J. G. and Invernizzi, S. (2004). "Regularized sequentially linear saw-tooth softening model", *International Journal for Numerical and Analytical methods in Geomechanics, 28*, pp. 821-856.

[9] Franzius, J. N., Potts, D. M. and Burland, J. B. (2006). "The response of structures to tunnel construction", *ICE- Journal of Geotechnical Engineering, 159*(1), 3-17.

[10] Addenbrooke, T. I. and Potts, D. M. (2001). "Twin tunnel interaction-surface and subsurface effects", *International Journal of Geomechanics, 1*, pp. 249-271.

[11] Sagaseta, C., Lopez, A., Gomez, J. and Pina, R. (1999). "Soil deformation due to the excavation of two parallel caverns", In F. B. Barends, J. Lindenberg and H. Luger (Ed.), 12th European Conference on Soil Mechanics and Geotechnical Engineering , (pp. 2125-2131). Amsterdam.

[12] Chapman, D. N., Ahn, S. K., Hunt, D. and Chan, A. (2006). "The use of model test to investigate the ground displacements associated with multiple tunnel construction in soil", *Tunnelling and Undergound Space Technology, 21*(3-4), pp. 413-413.

[13] Boscardian, M. and Cording, E. J. (1989). "Building response to excavation-induced settlement", *ASCE-Journal of Geotechnical Engineering, 115*(1), 1-21.

[14] Clemente, P., Bontempi, F. and De Stefano, A. (2012). "Application of seismic isolation in masonry buildings", *5th Europeon conference on structural control*, (p. paper no. 117). Genoa, Italy.

[15] Clemente, P., De Stefano, A. and Zago, R. (2012). "Seismic isolation in existing complex structures", *15th World Conference on Earthquake Engineering, paper No 712.* Lisbon.

[16] DIANA Finite Element Analysis (2012). *User's Manual, Release 9.4.4.* TNO Building Construction & Reseacrch.

[17] Zeeshan B.A., De Stefano A., Matta E. and Quattrone A. (2013). Monitoring of existing masonry buildings during construction of an ainnovative base-isolation system. Proc. 6th International Conference on Structural Health Monitoring of Intelligent Infrastructure, Hong Kong, 9-11 December 2013.

COMPDYN 2015
5th ECCOMAS Thematic Conference on
Computational Methods in Structural Dynamics and Earthquake Engineering
M. Papadrakakis, V. Papadopoulos, V. Plevris (eds.)
Crete Island, Greece, 25–27 May 2015

A NOVEL MECHANISM FOR RESTRAINING SEISMIC ACTIONS IN DUCTILE BRIDGES: ANALYTICAL MODELING AND EXPERIMENTAL VERIFICATION

Vasileios G. Pilitsis, Vassilis K. Papanikolaou, Ioannis A. Tegos and Kosmas-Athanasios Stylianidis

Aristotle University of Thessaloniki
Faculty of Engineering
School of Civil Engineering
Laboratory of Reinforced Concrete and Masonry
vpilitsi@civil.auth.gr
billy@civil.auth.gr
itegos@civil.auth.gr
kcstyl@civil.auth.gr

Keywords: Integral bridges, abutment, serviceability, experimental, seismic.

Abstract. *In the present study, a mechanism for restraining seismic actions on ductile bridges is suggested and verified analytically and experimentally. The mechanism consists of the wall abutment which is monolithically connected to the end of the deck and is rested either on elastomeric bearings on the pile cap or on the abutment foundation as a stopper of adequate width, based on the serviceability demands due to the deck length variation. Using the suggested mechanism, the restraining of seismic deformations is attained on both bridge directions, without any complications during serviceability states, also alleviating stresses in the end-spans due to a more favorable moment distribution. There are Code provisions which permit the computational analytical modeling of the system, however it was considered appropriate to further examine of the proposed mechanism experimentally. For this purpose, eight 1:3 scale specimens of the suggested mechanism were prepared. Four of them were designed for normal (large) shear ratios, while the other four were designed for small shear ratios. The specimens were subjected in cyclic loading and interesting results were observed regarding the three response indexes, namely, strength, stiffness and ductility.*

1 INTRODUCTION

Integral abutment and integral pier bridges are jointless bridge structures whose deck is rigidly connected to the abutment and piers. They improve aesthetics and earthquake resistance compared to traditional systems with expansion joints, bearings and other structural releases which permit expansion/contraction due to thermal actions, creep and shrinkage. The design of bridges has to accommodate both serviceability and earthquake resistance, which are conflicting components of the same problem and they impose opposite design requirements [1].

A novel mechanism for restraining seismic actions in ductile bridges while accommodating serviceability demands has been already suggested as an adjustment on the abutments [2], [3], [4]. The wall-web of the conventional abutment is suggested to be rigidly connected to the end-parts of the deck and the sliding bearings of the abutment are placed on the footing of the abutment wall, which is contained inside a gap (Fig. 1). The gap width depends on the total length of the bridge and is relevant to the expansion/contraction of the deck due to thermal actions and creep/shrinkage. The longitudinal restraining of the approach embankment is secured by the existence of a second wall and its lateral restraining by the wing-walls.

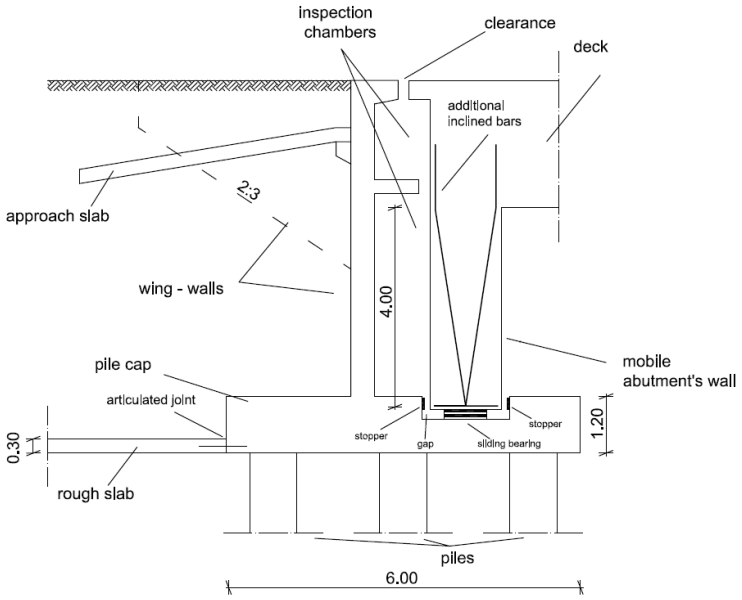


Figure 1: Longitudinal section cut of the novel mechanism.

An experimental investigation of the mechanical behavior of this novel mechanism for restraining seismic actions in ductile bridges is attempted in this study. In particular three response indexes are examined, namely strength, stiffness and ductility. Furthermore, the influence of the gap is examined in terms of energy dissipation capacity and durability of the abutment walls during cyclic loading.

2 SPECIMEN GEOMETRY

Eight cantilever specimens were prepared in 1:3 scale corresponding to the dimensions of two typical cases of wall-web for the suggested type of abutment: (a) a flexible wall-web with a height of 4.50 m and a thickness of 50 cm and (b) a stiffer wall-web with a height of 1.50 m and a thickness of 50 cm. Since it is difficult to achieve full fixity conditions in the laboratory, the eight cantilever specimens were formed as four beams, simply supported in both ends. Two of the beams had a length of 3.20 m while the other two of 1.20 m. Each beam consists

of two cantilevers of net length of 0.375 m for case (a) and 1.375 m for the case (b) (Fig. 2, Fig. 3). The width of the beams was equal to 36 cm for proper mounting of the loading device (actuator) to the beams. In the midspan of each beam, a stiff zone was formed with a thickness of 35 cm and a length of 25 cm, in which the external load is imposed and by which full fixity of each cantilever is achieved. The diagrams of internal forces and the deformed shape of a simply supported beam with a concentrated force in the midspan is equivalent to the composition of two mirrored cantilevers with a concentrated load at one end part, equal to the half of the simply supported beam force (Fig. 4). The hinge supports were placed at 10 cm from the edges of each beam.

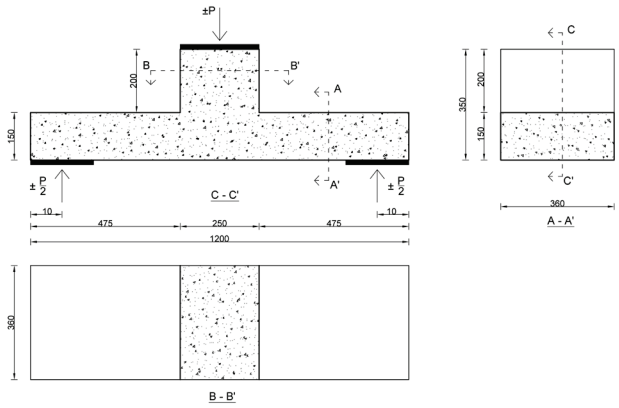


Figure 2: Geometry of the short span specimens.

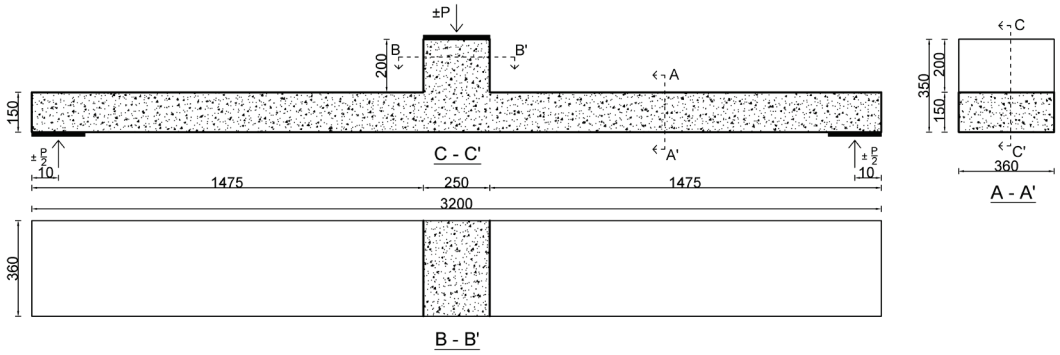


Figure 3: Geometry of the long span specimens.

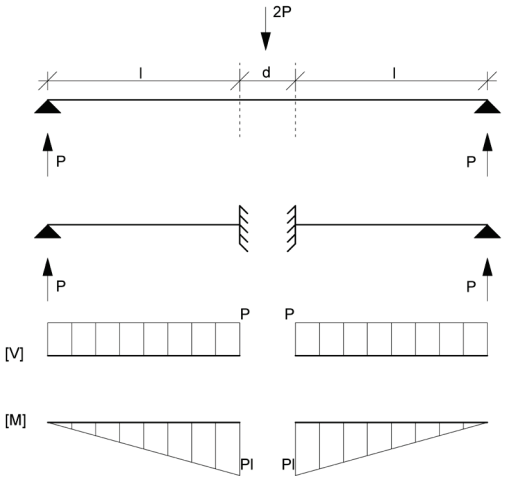


Figure 4: Static system, shear and moment diagrams of the specimens.

3 REINFORCEMENT DETAILING AND MATERIAL PROPERTIES

The longitudinal reinforcement of each specimen consists of ten Ø10 bars, arranged as shown in Fig. 5 and Fig. 6. This corresponds to a longitudinal reinforcement ratio of ρ_l = 1.45 %. The transverse reinforcement selected in both types of specimens guarantee that the specimens will experience flexural failure. The concrete cover was equal to 1.0 cm in both cases.

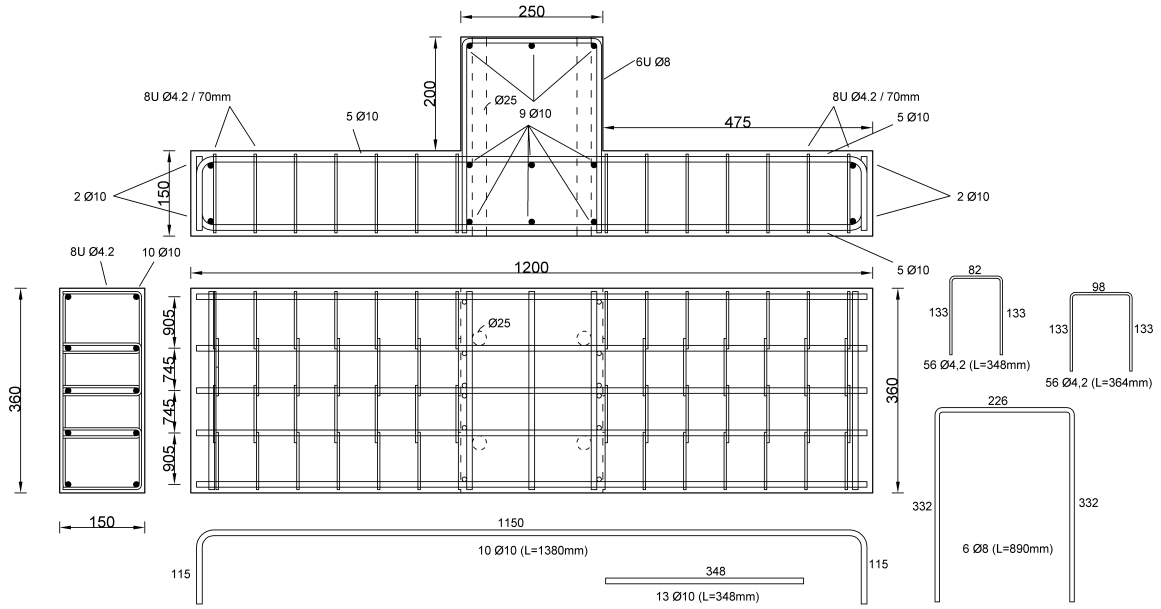


Figure 5: Reinforcement of the short span specimens.

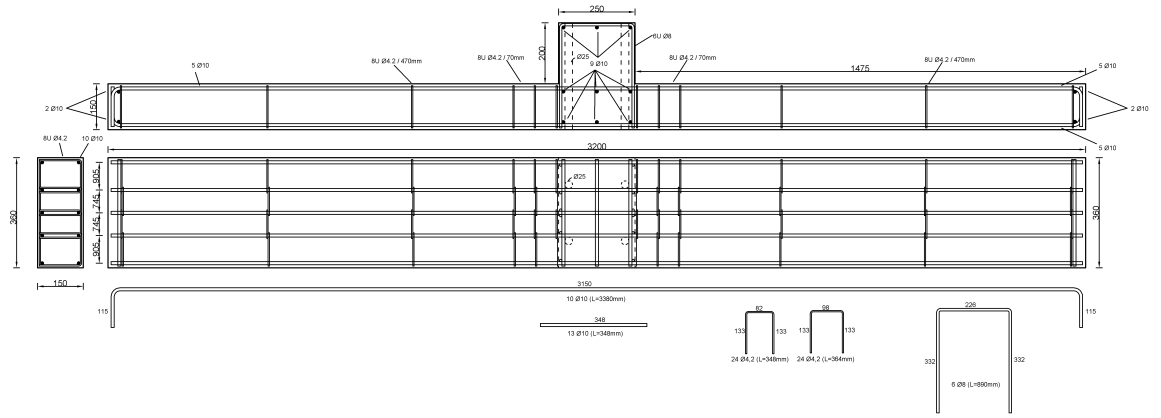


Figure 6: Reinforcement of the long span specimens.

The steel class used for longitudinal reinforcement corresponds to B500A [5]. Yield strength was equal to 586 MPa, the maximum strength equal to 700 MPa, the strain at yielding was ε_y = 2.94 ‰ and the ultimate strain is equal to ε_u = 3.41 %. These values were the mean values of ten specimens of steel rebar used for the longitudinal reinforcement. Similarly, the yield strength of the transverse reinforcement was measured equal to 680 MPa.

The properties of the used concrete were estimated by testing three cubic concrete specimens in uniaxial compression for the case of the short beams (low shear span ratio) and six cubic concrete specimens in the case of the two long beams (high shear span ratio). The

strength class of concrete in the first case was estimated as C25/30 and in the second case as C30/37.

Four through holes with a diameter of 25 mm were formed during casting of the specimens using PVC pipes. The mounting of the loading device (actuator) was achieved by using threaded rods passing through the holes.

The hinge supports at the beam ends were implemented by two steel supports as shown in Fig. 7. The cylindrical rod of each support was inserted in the laboratory floor slab holes (77 mm diameter). The rectangular opening of the steel supports where the beams (15 cm width) are inserted was equal to 16 cm. One short beam and one long beam were firmly mounted in the steel supports steel plates in order to suppress the 1 cm gap, while the other two beams were placed in the opening without closing the gap (i.e. free movement). However, by examining the resulting hysteresis loops of the specimens, the first two beams were not totally fixed in the supports, but a ±2 mm lash was measured. The other two beams had a measured lash of ±3.5 mm (instead of the nominal ±5 mm). The above information is summarized in Table 1.

	Span Length (m)	Concrete Class	Gap Width (mm)
S-4	1.0	C30/37	4
S-7	1.0	C30/37	7
L-4	3.0	C25/30	4
L-7	3.0	C25/30	7

Table 1: Specimen labeling and characteristics.

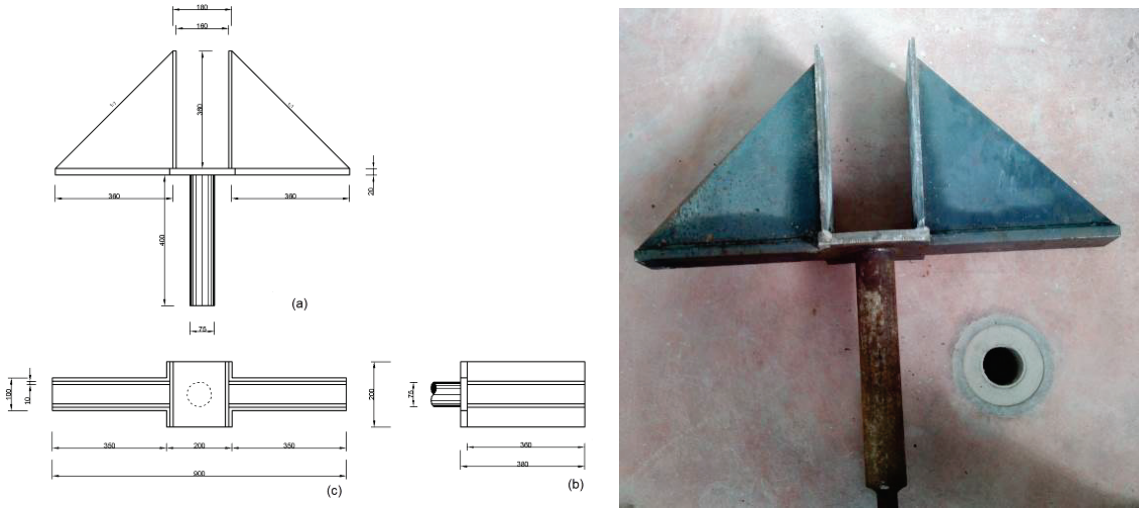


Figure 7: (left) Plans of the steel supports, (right) steel support.

4 EXPERIMENTAL SETUP

The four beams were subjected to cyclic displacement using a hydraulic actuator [6]. The time-history of the imposed displacements for specimens S-4 and S-7 is shown in Fig. 8 (left) and in Fig. 8 (right) for specimens L-4 and L-7. Each time-history is consisted of eighteen cycles divided into groups of three, of equal maximum displacement. Each cycle has duration of two minutes and the total running time is 36 mins.

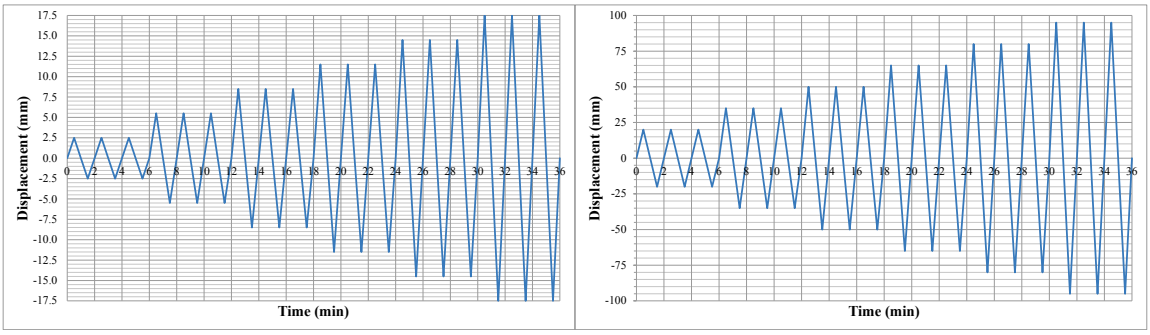


Figure 8: Imposed displacement time-histories of S-4 and S-7 (left) and of L-4 and L-7 (right).

In Fig. 9 a sketch of the experimental setup is shown, for the case of short beams. The cyclic displacement is imposed in the midspan of the beams, where the hydraulic actuator is attached to the rigid zone of the beams through a QHS 140x140x4 mm steel hollow beam of 460 mm length.

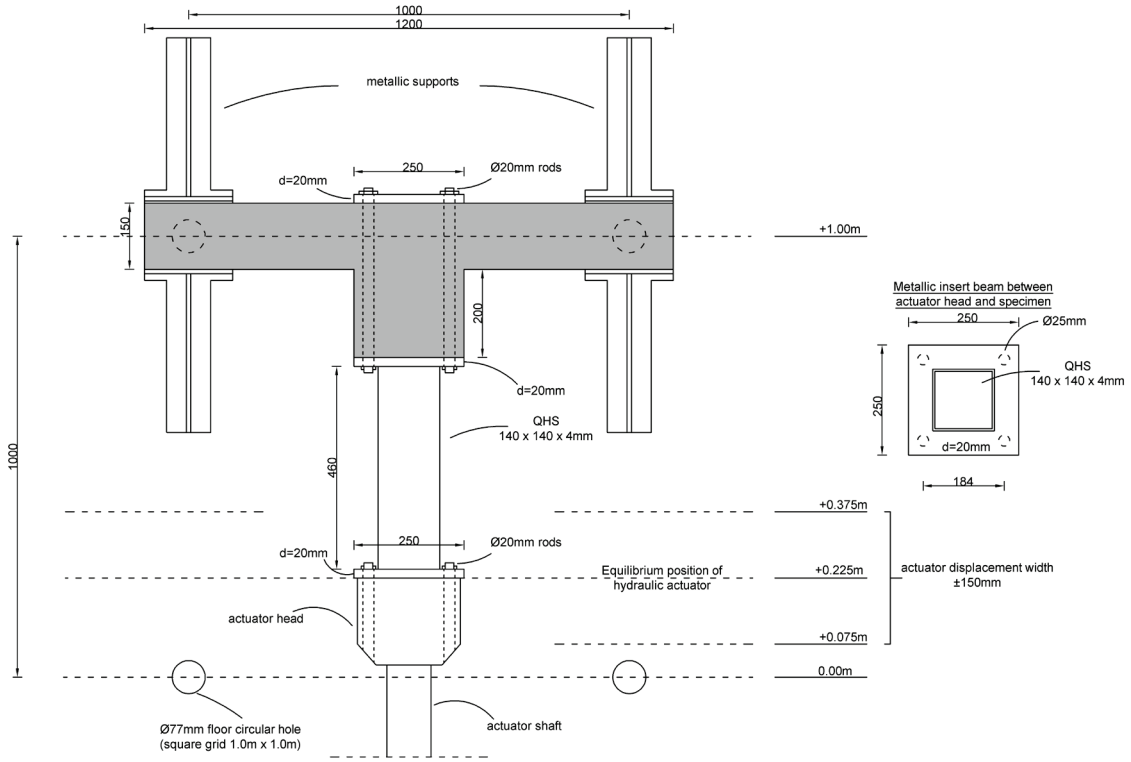


Figure 9: S-specimens position relative to the hydraulic actuator.

The displacement load history was imposed by a double acting hydraulic actuator in the Laboratory of Reinforced Concrete and Masonry Structures, Department of Civil Engineering, Aristotle University of Thessaloniki. Its load capacity is ±250 kN and its full stroke is ±150 mm. The actuator is equipped with a build-in LVDT device for measuring the imposed displacements. However, as shown in Fig. 10, the actuator was mounted on a horizontal support steel beam which is naturally susceptible to (elastic) bending during specimen loading. As a result, additional displacements due to this bending could be picked up by the actuator internal LVDT, resulting to considerable differences between the desired (target) displacement load history and the measured displacement of the internal LVDT. For this reason, the actuator closed-loop control was not based on this internal LVDT (default setting) but was rather

transferred to an external measurement system, specifically an external ±75 mm LVDT for the short beams and a ±112.5 mm draw wire sensor for the long beams, attached to the specimen midspan. This decision was eventually justified by the comparative results shown in Fig. 11, where the blue line shows the actuator internal LVDT measurement for the ±5.5 mm cycle, unfavorably deviating for about 2.5 mm from this target value. On the contrary, the closed-loop reference external LVDT yields the desired target displacement (red line), while the green line shows the support beam midspan displacement (maximum 2 mm, measured using an auxiliary LVDT). The remaining 0.5 mm difference between the internal and external LVDTs can be attributed to mechanical lash of the various mounting bolts.

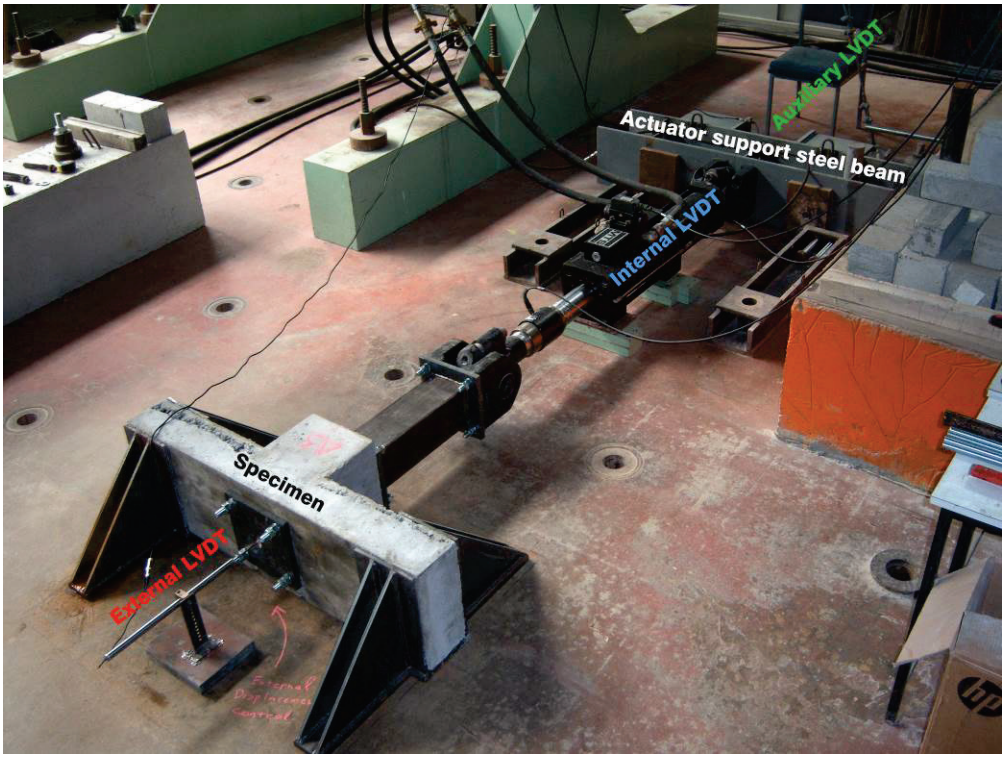


Figure 10: Experimental setup - measurement points.

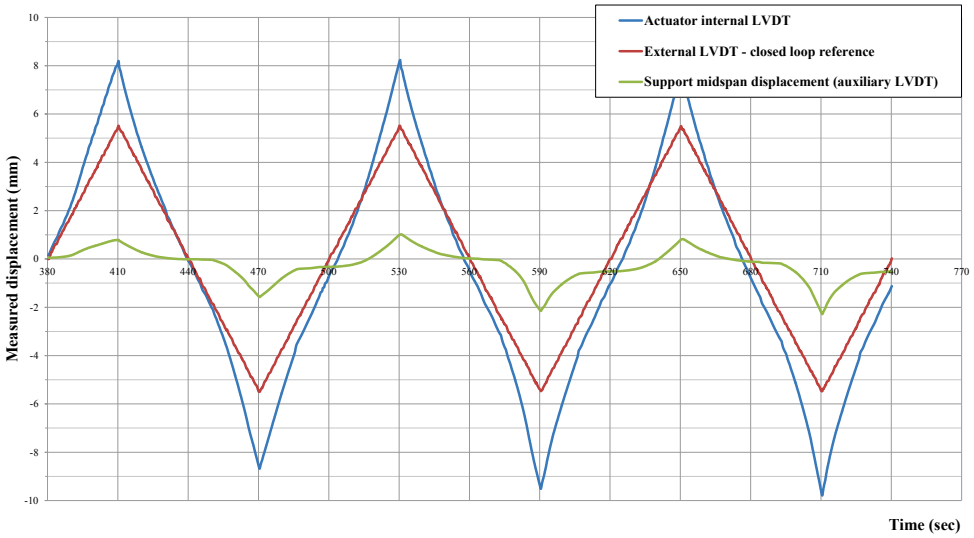


Figure 11: Measurement comparison between internal (actuator) and external closed-loop reference LVDTs.

5 ANALYTICAL CALCULATION OF THE SPECIMEN PROPERTIES

The analytical calculation of the specimen properties regarding deformation and strength is based on Fig. 4 and the results of the section analysis (Fig. 13). These analyses were performed using AnySection v.4.0.4 software [7]. The stress-strain law considered for the concrete behavior was the parabolic-rectangular diagram of EC2-Part 1 [5]. Regarding reinforcement steel, its stress-strain law was initially considered as bilinear without hardening. The analytical results did not approximate well the experimental results and thus a stress-strain diagram according to Park & Sampson [8] was considered, which offered a better approximation (Fig. 12).

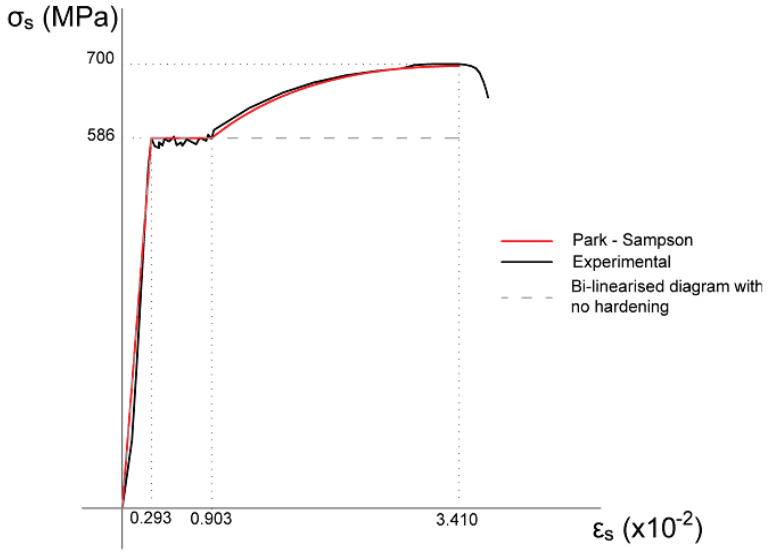


Figure 12: Stress-deformation diagramm of longitudinal reinforcement steel.

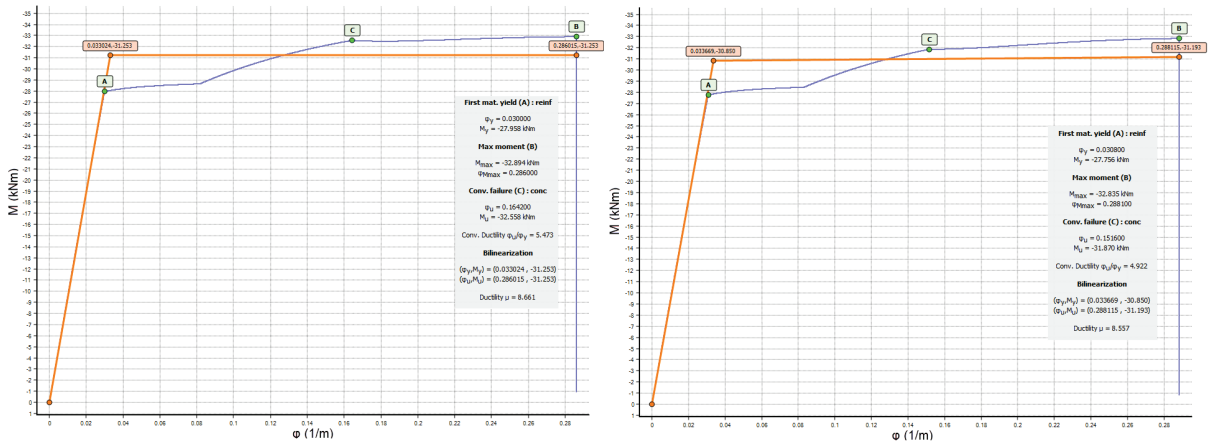


Figure 13: Moment-curvature diagrams of the S-specimens (left) and L-specimens (right).

The calculation of the effective stiffness of the specimens was based on the method described in section C.3 of EC8-Part 2 [9]. The calculation of the deformation ductility is based on the equations given in Fig. 14 for a cantilever beam. The length of the plastic hinge was calculated as proposed in EC8-Part 2. The results are given in Table 2 considering no gap in the supports for the S-specimens and in Table 3 for the L-specimens.

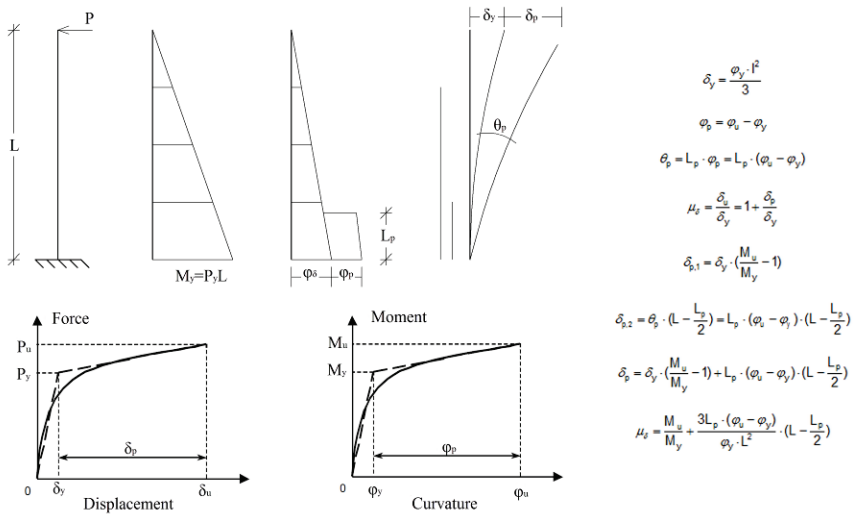


Figure 14: Elastic-plstic behaviour of a cantilever beam.

M_y (kNm)	P_y (kN)	EJ_{eff} / EJ_{un} (%)	φ_y (1/m)	φ_u (1/m)	L_p (mm)	δ_y (mm)	δ_u (mm)	μ_δ
31.25	166.7	33.99	0.033	0.286	114.5	1.5	10.8	6.94

Table 2: Analytical results for the S-specimens.

M_y (kNm)	P_y (kN)	EJ_{eff} / EJ_{un} (%)	φ_y (1/m)	φ_u (1/m)	L_p (mm)	δ_y (mm)	δ_u (mm)	μ_δ
30.85	44.9	35.03	0.034	0.288	225.4	21.2	93.6	4.41

Table 3: Analytical results for the L-specimens.

6 EXPERIMENTAL RESULTS

Interesting results were observed during the experimental procedure regarding the three response indexes, namely, strength, stiffness and ductility. Regarding the L-specimens, flexural cracks were observed in the area around the stiff zone of the beams, which increased along the increase of the imposed deflection and the progressive formation of plastic hinge. Crosswise cracks occurred in S-specimens, which indicated the intense presence of shear effect (Fig. 15). However these specimens managed to deplete their flexural strength as show by the experimental results.



Figure 15: Crack formation in S-4 (left) and L-7 (right).

By processing the specimen hysteresis loops (Fig. 16 and Fig. 17), the results given in Table 4 and Table 5 were obtained. Table 4 summarizes the results considering no gap in the supports while in Table 5 test results are presented by taking into account the existence of the gap. It should be noted that the values of these tables are average values for both directions of cyclic loading. Equation (1) was used for the calculation of the experimental effective stiffness of the cantilevers:

$$P_y \cdot \delta_y = \int_0^L \frac{M^2_{(x)}}{EJ_{eff}} dx + \int_0^L \frac{V^2_{(x)}}{GA_s} dx \quad (1)$$

where $M_{(x)}$ and $V_{(x)}$ are the moment and shear values of the cantilevers, respectively, P_y is the half of the yield load of the beam, δ_y is the yield displacement of the beam, G is the shear modulus considering cracked concrete and A_s is the cantilever section shear area.

	P_y (kN)	δ_y (mm)	δ_u (mm)	EJ_{eff} / EJ_{un} (%)	μ_δ
S-4	172.4	3.4	13.2	13.5	3.91
S-7	174.1	3.6	13.0	12.9	3.61
L-4	44.3	19.9	>93.0	30.8	>4.67
L-7	44.8	20.3	91.5	30.5	4.51

Table 4: Experimental results disregarding the existence of the gap in the supports.

	P_y (kN)	δ_y (mm)	δ_u (mm)	EJ_{eff} / EJ_{un} (%)	μ_δ
S-4	172.4	5.4	15.2	8.5	2.82
S-7	174.1	7.1	16.5	7.1	2.32
L-4	44.3	21.9	>95.0	28.0	>4.36
L-7	44.8	23.8	95	26.0	3.99

Table 5: Experimental results taking into account the existence of the gap in the supports.

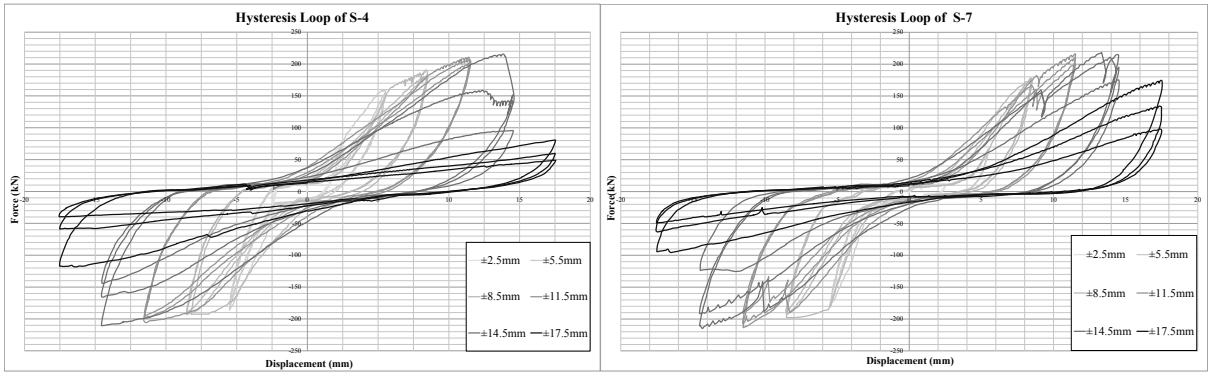


Figure 16: Hysteresis loops of the S-specimens

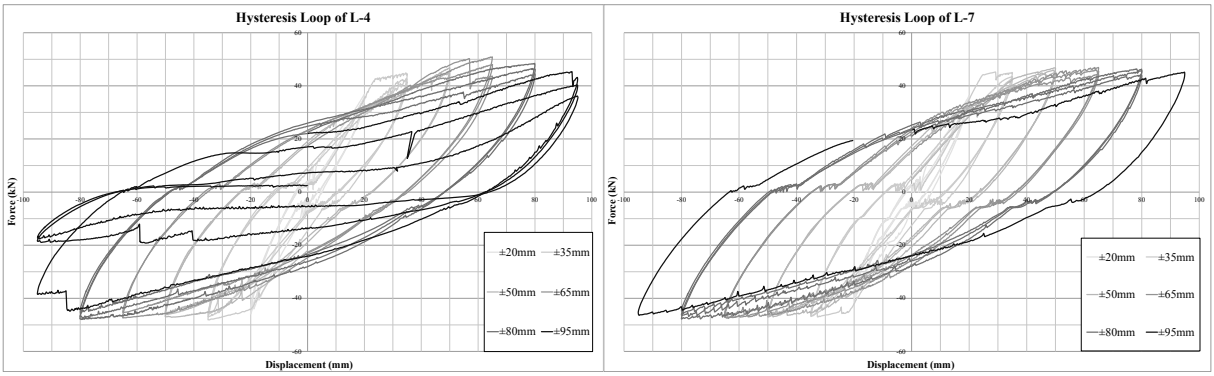


Figure 17: Hysteresis loops of the L-specimens.

By comparing Table 3 to Table 5, regarding the L-specimens, the analytical and experimental results are almost identical. The existence of the gaps at the supports causes no change in the response indexes of the specimens. Regarding the S-specimens and the difference observed between the analytical and experimental results in tables in Table 2 and Table 4 respectively, the following is stated:

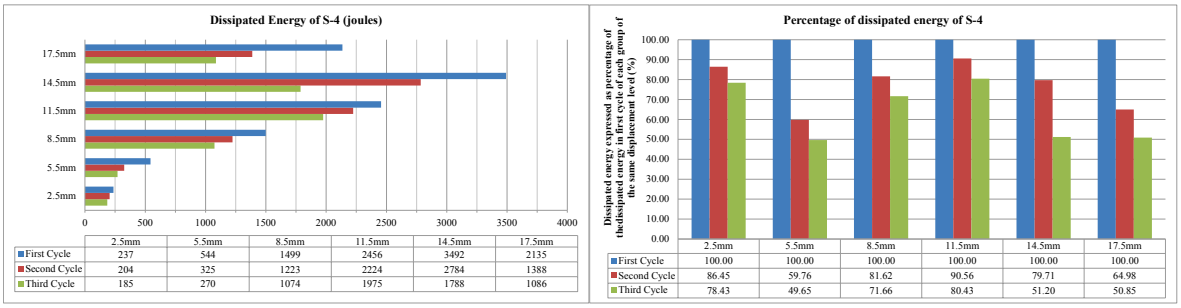
- Perhaps the main reason of the results deviation is the non-regularity of these specimens regarding the shear span ratio. In this case the shear span ratio the difference observed between the analytical and experimental results is equal to as=0.375/0.15=2.5 and the shear deformation influences significantly the longitudinal stresses of the specimens.
- Due to the high stiffness of the cantilevers with length of 0.375 m, the consideration of the full fixity of the cantilevers isn't achieved in the side of the rigid zone but inside it near the midlength of the beams.

Regarding the effective stiffness of the L-specimens, where the experimental results can be comparable to the analytical estimation, the experimental values are slightly lower. This is due to the provision of the EC8-Part 2 factor n = 1.20 which is a correction factor representing the effect of the stiffness of the non-cracked part of the cross section. The method presented in the Code concerns the calculation of the effective stiffness at bridge piers where normally the absolute value of the normalized axial force is greater than 0.10, while in this case there was no axial load. The analytical calculation of the effective stiffness omitting the n-factor gives results which are almost identical to the experimental.

Comparing the values of Table 4, it is observed that the existence of gaps in the supports degrades the effective stiffness of the specimens. This effect is more intense in the case of the S-specimens whose yield displacement is comparable to the gap width.

Regarding the available displacement ductility, it is observed that the existence of gaps in the supports affects it meiotically. This decrease is more profound in S-specimens, which are stiffer and have a yield displacement comparable to the gap width. In the case of the L-specimens, whose yield displacement is greater, the effect in the available displacement ductility is minimal. It should be noted that the failure of the specimens was defined as the point at which specimens lose 20% of their strength.

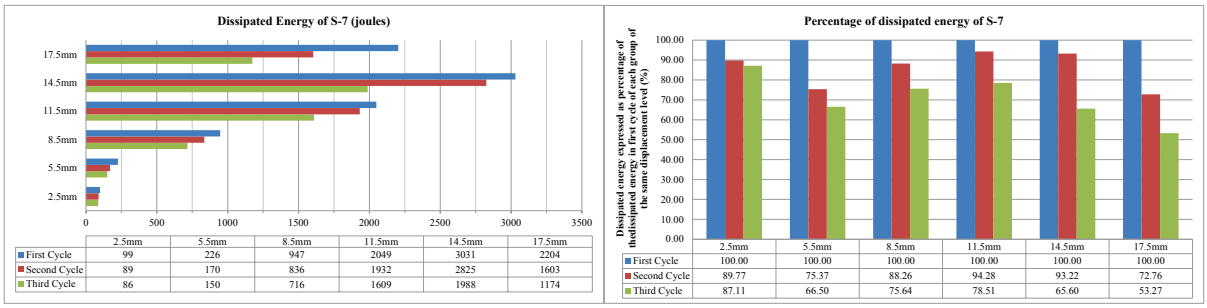
The absolute values of dissipated energy and the dissipated energy per cycle (as a percentage of the dissipated energy of the first cycle of each group of the same displacement level) are presented in Figures 18 to 21. A general increase of the dissipated energy is observed as the deformation increases. The percentage of the dissipated energy of the second and the third cycle compared to the first of each displacement level group increases as the imposed displacements increase and the plastic hinge progressively forms, except of the last two displacement level groups in which the specimens are close to their failure.



	2.5mm	5.5mm	8.5mm	11.5mm	14.5mm	17.5mm
First Cycle	237	544	1499	2456	3492	2135
Second Cycle	204	325	1223	2224	2784	1388
Third Cycle	185	270	1074	1975	1788	1086

	2.5mm	5.5mm	8.5mm	11.5mm	14.5mm	17.5mm
First Cycle	100.00	100.00	100.00	100.00	100.00	100.00
Second Cycle	86.45	59.76	81.62	90.56	79.71	64.98
Third Cycle	78.43	49.65	71.66	80.43	51.20	50.85

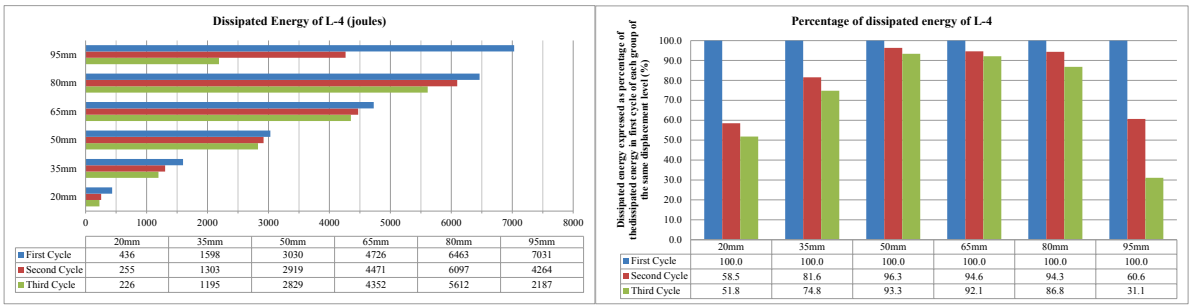
Figure 18: Energy dissipation of specimen S-4.



	2.5mm	5.5mm	8.5mm	11.5mm	14.5mm	17.5mm
First Cycle	99	226	947	2049	3031	2204
Second Cycle	89	170	836	1932	2825	1603
Third Cycle	86	150	716	1609	1988	1174

	2.5mm	5.5mm	8.5mm	11.5mm	14.5mm	17.5mm
First Cycle	100.00	100.00	100.00	100.00	100.00	100.00
Second Cycle	89.77	75.37	88.26	94.28	93.22	72.76
Third Cycle	87.11	66.50	75.64	78.51	65.60	53.27

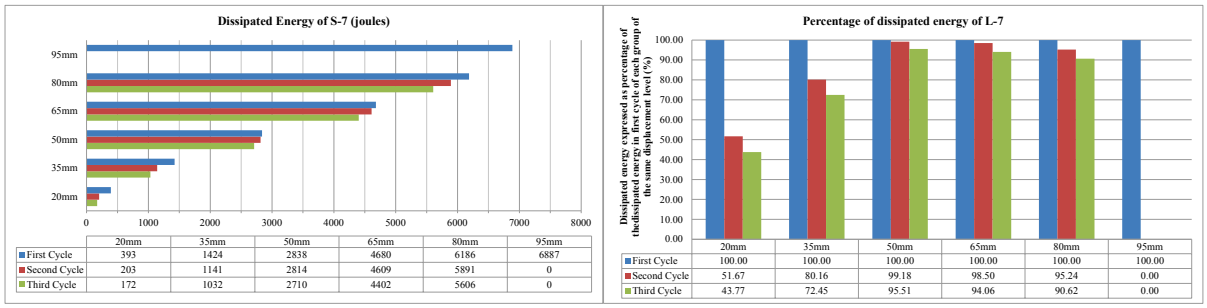
Figure 19: Energy dissipation of specimen S-7.



	20mm	35mm	50mm	65mm	80mm	95mm
First Cycle	436	1598	3030	4726	6463	7031
Second Cycle	255	1303	2919	4471	6097	4264
Third Cycle	226	1195	2829	4352	5612	2187

	20mm	35mm	50mm	65mm	80mm	95mm
First Cycle	100.0	100.0	100.0	100.0	100.0	100.0
Second Cycle	58.5	81.6	96.3	94.6	94.3	60.6
Third Cycle	51.8	74.8	93.3	92.1	86.8	31.1

Figure 20: Energy dissipation of specimen L-4.



	20mm	35mm	50mm	65mm	80mm	95mm
First Cycle	393	1424	2838	4680	6186	6887
Second Cycle	203	1141	2814	4609	5891	0
Third Cycle	172	1032	2710	4402	5606	0

	20mm	35mm	50mm	65mm	80mm	95mm
First Cycle	100.00	100.00	100.00	100.00	100.00	100.00
Second Cycle	51.67	80.16	99.18	98.50	95.24	0.00
Third Cycle	43.77	72.45	95.51	94.06	90.62	0.00

Figure 21: Energy dissipation of specimen L-7.

The damage factor of the specimens regarding the stiffness loss in each cycle [10] is given in Figures 22 and 23. It is observed that the damage factor is constant and low, around 3 % to 5 %, except of the groups of same displacement level cycles that are near to the failure of the specimens. It is noted that specimen L-7 failed completely during the first cycle of the 95mm imposed displacement.

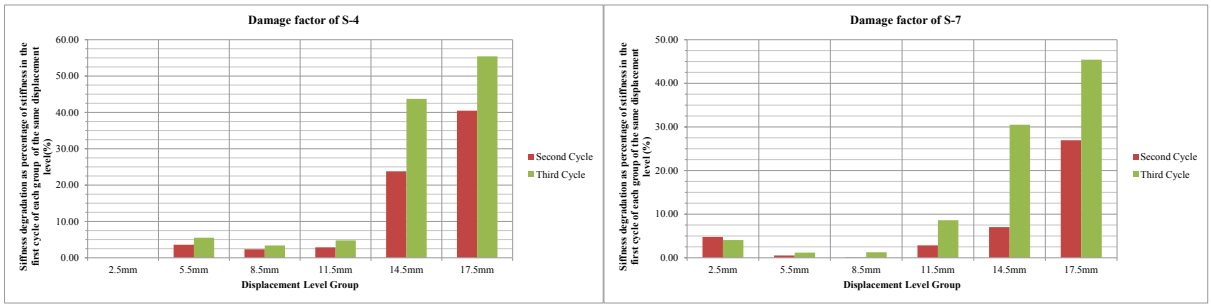


Figure 22: Damage factor (stiffness degradation) of the S-specimens.

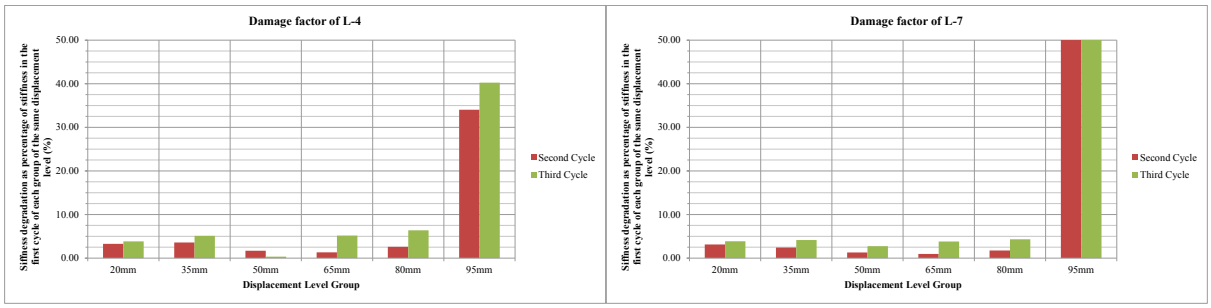


Figure 23: Damage factor (stiffness degradation) of the L-specimens.

7 CONCLUSIONS

The experimental study of the mechanical behavior of a novel mechanism for restraining seismic actions in ductile bridges was presented in this study. In particular, three response indexes were examined namely strength, stiffness and ductility. The importance of the experimental investigation of this mechanism is intensified by the nonlinear behaviour of the mechanism during a seismic event due to the existence of the gap in the support of the abutment wall. Furthermore, the influence of the existence of the gap on energy dissipation capacity and durability of the abutment walls during cyclic loading was examined.

The following conclusions are stated:

- The strength and deformation of the examined specimens with high shear span ratio (long) were similar to the analytically calculated. The same conclusion applies on the available displacement ductility as well. This implies that the existence of the gap in the supports did not affect the mechanical properties of these specimens.
- In the case of specimens with low shear span ratio (short), the analytically calculated strength had no significant difference from the experimentally derived. On the contrary, the experimentally measured specimen deformation and available displacement ductility, disregarding the existence of the gap at the supports, differed from the calculated values. This difference is due to the low shear span ratio of the specimens and their diversion from the pure bending case.
- The existence of the gaps in the supports degrades the specimen stiffness. This decrease is more profound in the stiffer specimens and in the case of wider gaps. This observation confirms the ability of the mechanism to reduce the developing stresses in the serviceability state.

- The gaps in the supports cause the reduction of available displacement ductility. The reduction is higher in the cases of the wider gaps and in stiffer specimens, in which the yield displacement is comparable to the width of the gaps.
- The examined specimens had good behaviour regarding the energy dissipation capacity, regardless of the gap width and shear span ratio. It is observed that in the case of the wider gap, the specimens are activated in higher imposed displacements and this also confirms the ability of the mechanism to reduce the developing stresses in the serviceability state.
- The performance of the examined specimens is considered stable, regardless of the gap width and shear span ratio.

REFERENCES

[1] S. Mitoulis, I. Tegos, *An Unconventional Retraining System for Limiting the Seismic Movements of Isolated Bridges.* Engineering Structures, Elsevier Ltd., **32**: 1100-1112, 2010.

[2] V. Pilitsis, M. Skordeli, I. Tegos, A Suggestion for Adjustment of the Load-Bearing Structure of Bridges with Antiseismic, Economic and Aesthetic Benefits. *2013 FIB International Symposium,* Tel-Aviv, Israel, April 22-24, 2013.

[3] V. Piltisis, I. Tegos, Employment of Abutments and Approach Embankments for Seismic Protection of Bridges. *2013 International Van Earthquake Symposium,* Van, Turkey, October 23-27, 2013.

[4] D. Anastasopoulos, Z. Kopelia, V. Piltisis, I Tegos, Conventional and Alternative Design of Highway Bridge in Egnatia Motorway Including many Innovative Solutions. *International Conference IBSBI 2014, "Innovations on Bridges and Soil-Bridge Interaction",* Athens, Greece, October 16-18, 2014.

[5] CEN [Comité Européen de Normalisation], EN 1992-1-1: Eurocode 2: Design of Concrete Structures - Part 1-1: General Rules and Rules for Buildings, 2004.

[6] K.-A. Stylianidis, K.V. Papanikolaou, C. Ignatakis, T. Salonikios, The Novel Cycle-Loading System of The Laboratory of Reinforced Concrete and Masonry of A.U.Th. - Potential and First Applications (Greek). *11th Greek Conference on Reinforced Concrete,* Corfu, Greece, May 18-20, 1994.

[7] V. K. Papanikolaou, *Analysis of arbitrary composite sections in biaxial bending and axial load.* Computers & Structures **98-99**, 33-54, 2012.

[8] R. Park, R.A. Sampson, *Ductility of Reinforced Concrete Column Sections in Seismic Design,* Journal of the ACI, **69-9**: 543-551, 1972.

[9] CEN [Comité Européen de Normalisation], EN 1998-2: Eurocode 8: Design of Structures for Earthquake Resistance - Part 2: Bridges, 2005.

[10] S.K. Kunnath, C. Jenne, Seismic Damage Assessment of Inelastic RC Structures, *5th U.S. National Conference on Earthquake Engineering*, Chicago, U.S.A., July 10-14, 1994.

COMPDYN 2015
5th ECCOMAS Thematic Conference on
Computational Methods in Structural Dynamics and Earthquake Engineering
M. Papadrakakis, V. Papadopoulos, V. Plevris (eds.)
Crete Island, Greece, 25–27 May 2015

EXPERIMENTAL AND ANALYTICAL INVESTIGATION OF AN UNCONVENTIONAL, ROCKING TYPE RESPONSE MECHANISM FOR EARTHQUAKE-RESISTANT BRIDGES

Vasileios G. Pilitsis, Ioannis A. Tegos, Vassilis K. Papanikolaou and Kosmas-Athanasios Stylianidis

Aristotle University of Thessaloniki
Faculty of Engineering
School of Civil Engineering
Laboratory of Reinforced Concrete and Masonry
vpilitsi@civil.auth.gr
itegos@civil.auth.gr
billy@civil.auth.gr
kcstyl@civil.auth.gr

Keywords: Integral bridges, reinforcement bond, rocking, experimental, seismic.

Abstract. *In the present study a new technique is investigated, which takes advantage of the rocking principle for the treatment of the two ambivalent demands in bridge designing, i.e. due to seismic and serviceability actions. The idea is based on the formation of cracks only in two positions on each bridge pier, which are the pier cross-sections in contact with the deck and the pile cap respectively, excluding the possibility of cracking in the mid-length of the piers. The possibility of flexural crack formation in one of these cross-sections was examined experimentally in order to reach the above objective. This was achieved through partial suppression of the longitudinal reinforcement bond with the surrounding concrete. In order to confirm the feasibility of the above objective and to verify the influence of the bond suppression on all three response indexes, namely strength, stiffness and ductility, eight experimental specimens in the form of cantilevers, representing ductile bridge piers, were prepared. The varying parameter was the shear span ratio. Useful results were observed regarding the three response indexes and interesting conclusions were obtained.*

1 INTRODUCTION

The basic objective of a seismic isolation system is to increase the fundamental period of the structure and reduce the design seismic acceleration. This phenomenon is known in the literature as "period shift effect" [1]. Increasing the fundamental period may be achieved by using seismic isolation devices, such as elastomeric bearings. A new technique for precast concrete bridges is the use of rocking as seismic isolation. Pure precast elements are connected though unbonded post-tensioning techniques; the inelastic demand is accommodated within the connection where a "controlled rocking" motion occurs with opening and closing of existing gap [2], [3], [4].

An alternative to the rocking technique method is the canceling of total bond (i.e. adhesive, friction and mechanical interlock) between steel rebar and the surrounding concrete in the connection joint of the deck-pier and its pier-pile cap. This adjustment aims at the improvement of the response, compared to with the corresponding monolithic connection, regarding the serviceability and seismic requirements, while reducing cost. The innovation consists in the way of anchoring the longitudinal reinforcement underlying pile-cap and the overlying deck of the bridge (Fig. 1). According to Fig. 1, longitudinal reinforcement is overlapped with awaiting rebars which are anchored to the pile cap in a way where a part of reinforcement length, nearest to the web of the pier, is not integrated into the surrounding concrete. Similarly, the outbound awaiting rebars on the head of the pier are not anchored in their full length to the deck, but only in their upper part. The construction joint in the footing of the pier is inserted in the pile cap for 15 cm, while the joint at the heading of the pier is inserted for 15 cm in the deck. These measures aim to prevent drifts at the interface of construction joints. The measures taken in order to prevent full fixity of the longitudinal reinforcement in the areas of anchorages, lead to the partial release regarding the rotations of the end-part sections of the piers. Via these rotations, the stiffness of the piers can be dramatically reduced for the benefit of serviceability requirements which are associated with alleviating stresses arising from the constraints caused by the expansion/contraction of the deck. By this generated high degree of flexibility, a satisfactory degree of seismic isolation is also achieved, since it leads to the significant increase of the fundamental period [5].

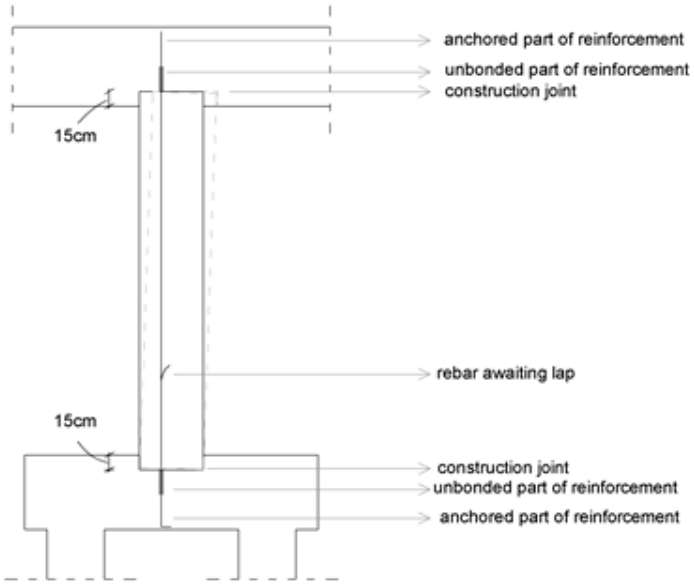


Figure 1: Anchorage conditions of typical reinforcement.

An experimental evaluation of the mechanical behavior of this novel type of joint connection is attempted in this study. In particular, three response indexes are examined namely strength, stiffness and ductility. Furthermore, the influence of reinforcement to concrete bond suppression is examined on energy dissipation capacity and constant performance of the piers during cyclic loading.

2 SPECIMEN GEOMETRY

Eight cantilever specimens were prepared in 1:3 scale corresponding to the dimensions of two typical cases of a wall-web of an abutment with pinned base: (a) a flexible wall-web with height of 4.50 m and thickness of 50 cm and (b) a stiffer wall-web with height of 1.50 m and thickness of 50 cm. Since it is difficult to achieve full fixity conditions in laboratory, the eight cantilever specimens were formed as four beams simply supported in both ends. Two of the beams had length of 3.20 m and while the other two had length of 1.20 m respectively to the represented cases. Each beam consists of two cantilevers of net length of 0.375 m for case (a) and 1.375 m for the case (b) (Fig. 2, Fig. 3). The width of the beams was chosen 36 cm for proper mounting of the loading device (actuator) to the beams. In the midspan of each beam, a stiff zone is formed with thickness of 35 cm and length of 25 cm, in which the external load is imposed and by which the full fixity of each cantilever is achieved. The diagrams of internal forces and the elastic line of a simply supported beam with a concentrated load in the midspan is equivalent to the composition of two cantilevers diametrically opposed with concentrated load at one end-part and equal to the half of the simply supported beam's load. The hinge supports were implemented at 10 cm from the edges of each beam.

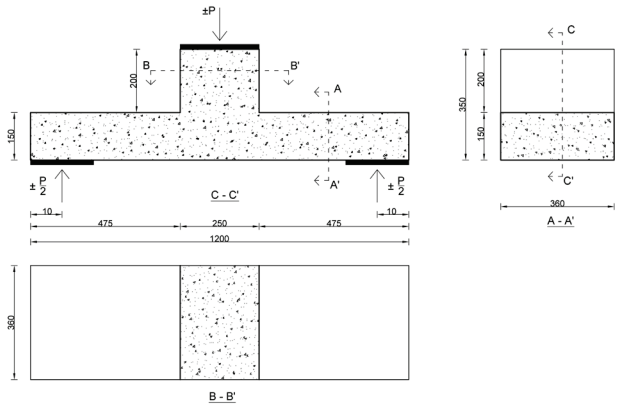


Figure 2: Geometry of the short span specimens.

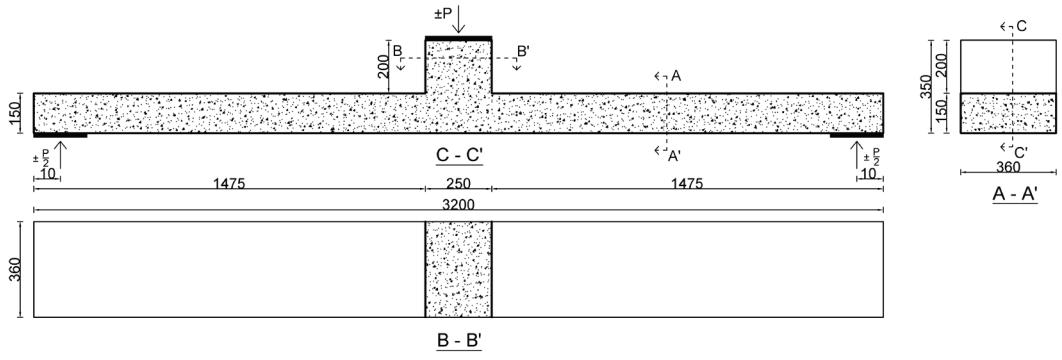


Figure 3: Geometry of the long span specimens.

3 REINFORCEMENT DETAILING AND MATERIAL PROPERTIES

Longitudinal reinforcement of each specimen consists of ten Ø10. That corresponds to a longitudinal reinforcement ratio of ρ_l=1.45 %. The transverse reinforcement used in both types of specimens accrued so that to ensure that the specimens will experience flexural failure. The concrete cover was equal to 1.0 cm in both cases.

Two of the specimens, namely one short specimen (low shear span ratio) and one long specimen (high shear span ratio), were reinforced without suppressing bond between concrete and reinforcement. In the other two specimens, the total bond of longitudinal reinforcement with the surrounding concrete was suppressed in specific regions. In the short specimen the suppression took place in length of 65mm symmetrically extended to the mid-length of the beam (Fig. 4). In the long specimen the suppression took place in length of 205 cm also symmetrically extended to the mid-length of the beam (Fig. 5). The reinforcement to concrete bond suppression was achieved by meticulous wrapping of the reinforcement rebar with polyethylene sheets (Fig. 6).

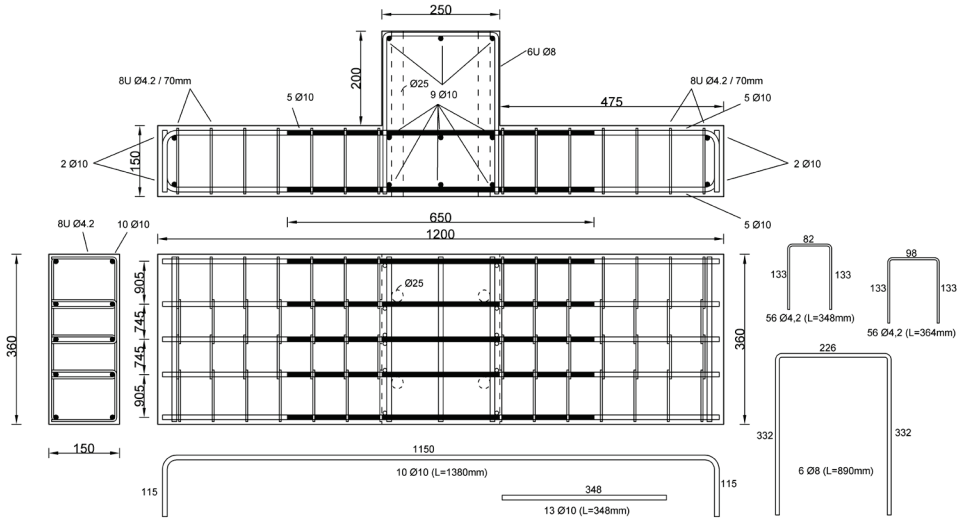


Figure 4: Unbonded reinforcement of the short span specimen.

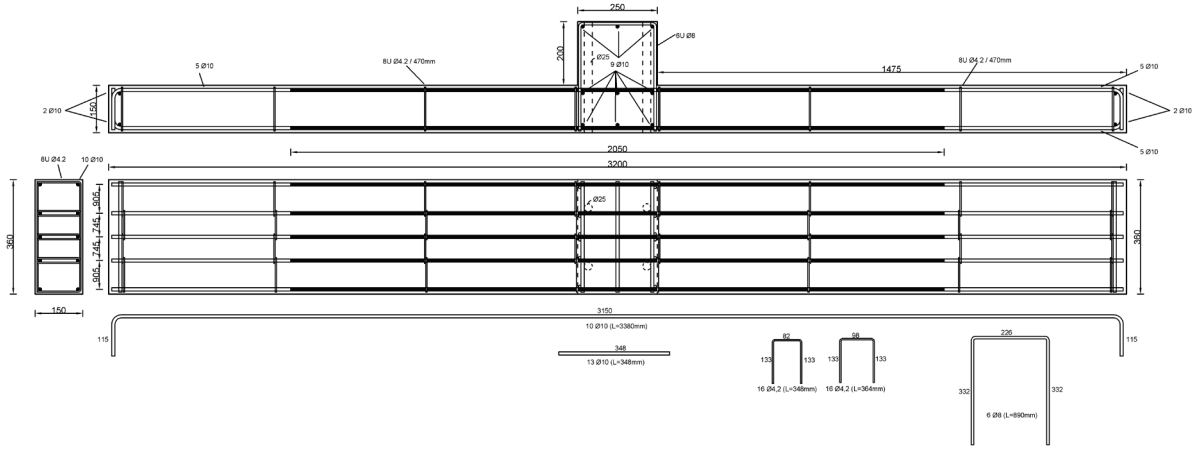


Figure 5: Unbonded reinforcement of the long span specimen.



Figure 6: Unbonded reinforcement in specimen SU-4.

The steel class used for the longitudinal reinforcement corresponds to B500A [6]. Yield strength was equal to 586 MPa, the maximum strength equal to 700 MPa, the strain at yielding point was ε_y=2.94 ‰ and the ultimate strain was equal to ε_u=3.41 %. These values were the mean values of ten specimens of steel rebar used for the longitudinal reinforcement. Similarly, the yield strength of the transverse reinforcement was calculated equal to 680 MPa.

The concrete properties were estimated by testing three cubic concrete specimens in uniaxial compression for the case of the two short beams and six cubic concrete specimens in the case of the two long beams. The strength class of concrete in the first case was estimated as C30/37 and in the second case as C25/30.

Four through holes with diameter of 25 mm were formed during casting of the specimens by using PVC pipes. The mounting of the loading device (actuator) was achieved by using threaded rods passing through the holes.

The hinge supports at the end-parts of the beams were implemented as in the case of reference [7]. After examining the hysteresis loops, a lash of 4 mm was measured in the supports of all specimens. The above mentioned information is summarized in Table 1.

	Span Length (m)	Concrete Class	Unbondment Length (cm)
S-4	1.0	C30/37	0
SU-4	1.0	C30/37	65
L-4	3.0	C25/30	0
LU-4	3.0	C25/30	205

Table 1: Specimen labeling and characteristics.

4 EXPERIMENTAL SETUP

The four beams were subjected in cyclic displacement with the use of a hydraulic piston [8]. The time-history of the imposed displacements for specimens S-4 and SU-4 is presented in Fig. 7(left) and for specimens L-4 and LU-4 is presented in Fig. 7(right). Each time-history is consisted of eighteen cycles divided into groups of three, of equal displacement. Each cycle has duration of two minutes and the total running time is 36 mins.

In Fig. 8 a sketch of the experimental setup is shown, for the case of the short beams. The cyclic displacement is imposed in the midspan of the beams, where the hydraulic actuator is attached to the rigid zone of the beams through a QHS 140x140x4 mm steel hollow beam of 460 mm length.

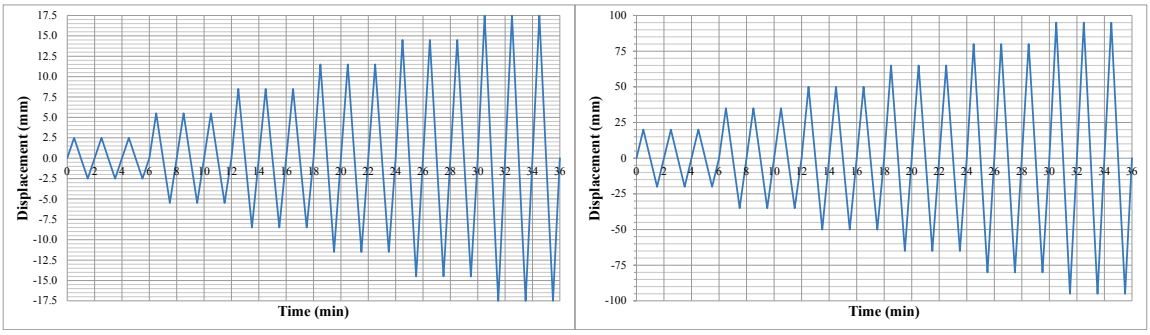


Figure 7: Imposed displacement time – histories of S-4 and SU-4 (left) and of L-4 and LU-4 (right).

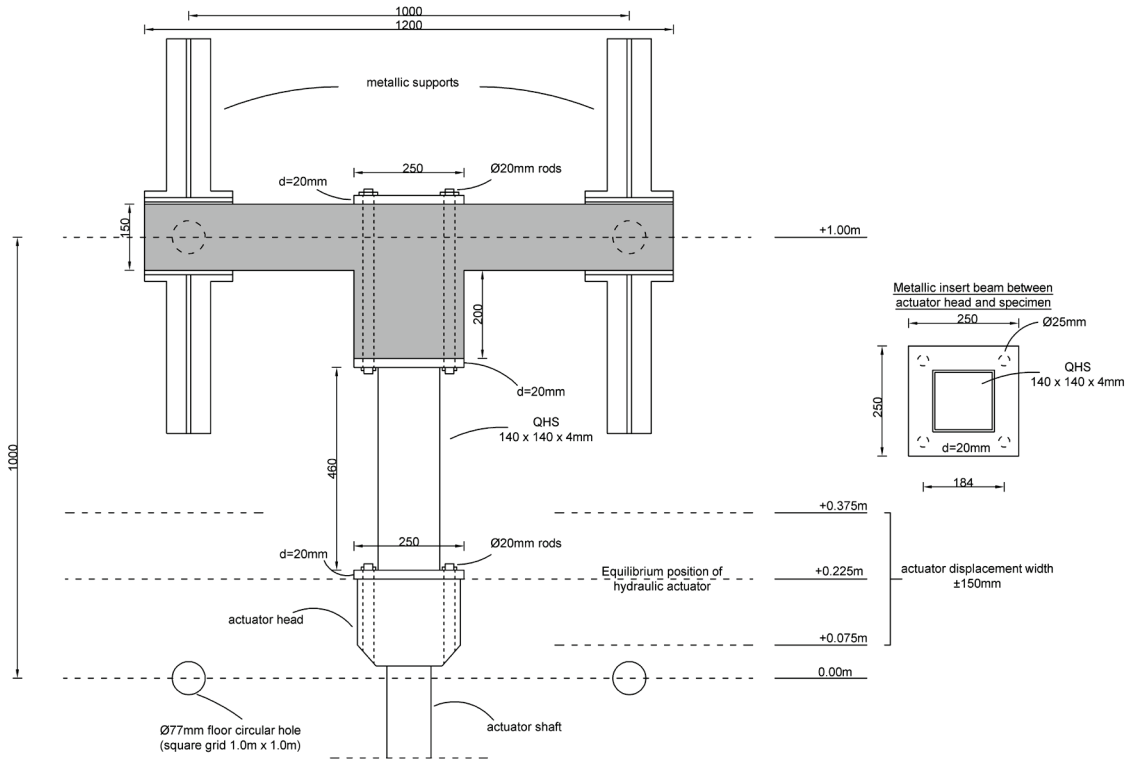


Figure 8: S-specimen position relative to the hydraulic piston.

The displacement load history was imposed by a double acting hydraulic actuator in the Laboratory of Reinforced Concrete and Masonry Structures, Department of Civil Engineering, Aristotle University of Thessaloniki. Full details of the experimental setup can be found in [7].

5 ANALYTICAL ESTIMATION OF THE SPECIMEN PROPERTIES

The analytical calculation of the specimens S-4 and L-4 properties regarding deformation and strength is presented on reference [7]. These analyses were performed using AnySection v.4.0.4 software [9]. The stress-strain law considered for the concrete behavior was the parabolic-rectangular diagram of EC2-Part 1 [6]. Regarding reinforcement steel, its stress-strain law was considered according to Park & Sampson [10]. The calculation of the effective stiffness of the specimens was based on the method described in section C.3 of EC8-Part 2 [11]. The calculation of the deformation ductility is based on the elastic-plastic behavior of a cantilever beam [7]. The results of the analytical estimation of the S-4 and L-4 specimens are presented in Table 2 and Table 3.

The yield moment of specimens SU-4 and LU-4 (and consequently their yield load and displacement) cannot be calculated in the same way due to the partial suppression of the reinforcement to concrete bond. In this case, at global (specimen) yielding, reinforcement stress remains constant in the area of the unbondment and is equal to the reinforcement yield stress. As a result, the moment in the fixed end of the cantilevers will be the yield moment. It is noted that due to reinforcement unbondment, one single crack will be formed in the point of the maximum moment, which is the fixed end of each cantilever. The width of the crack is determined by the deformation of the rebar (Fig. 9).

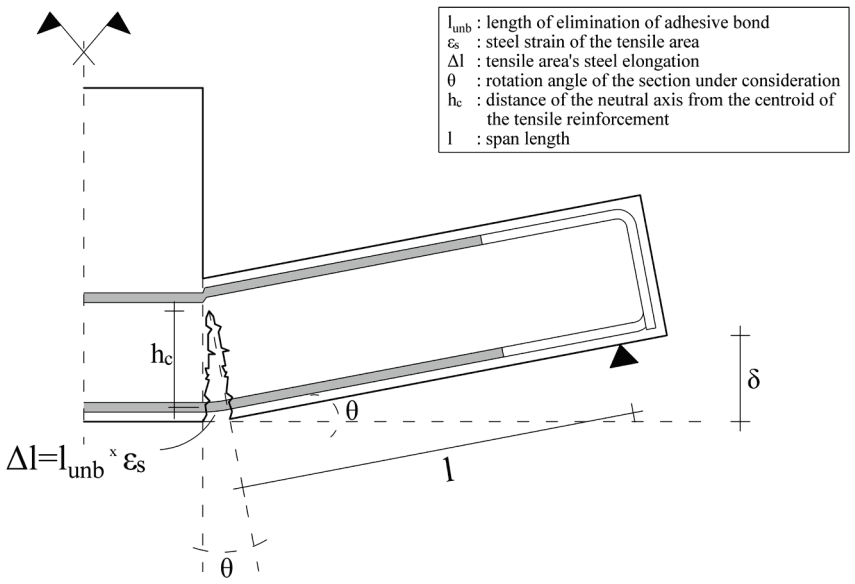


Figure 9: Schematic representation of the crack formation in the side of the rigid zone.

The crack width in each cantilever can be calculated with the following equation:

$$\Delta l = \frac{l_{unb,tot}}{2} \cdot \varepsilon_s \tag{1}$$

where $l_{unb,tot}$ is the total unbondment length. Considering that the deformation of the specimen is negligible in bonded reinforcement regions, the displacement of each specimen is calculated according to:

$$\delta = l \cdot \tan\theta \tag{2}$$

where θ is the rotation angle, equal to $\Delta l / h_c$.

The distance of the neutral axis from the centroid of the tensile reinforcement (h_c) and consequently the rotation angle (θ) were determined by modeling the section under consideration in SAP2000 [12]. More specifically, a totally rigid frame (according to the Bernoulli–Euler assumption, i.e. plane sections remain plane and perpendicular to the axis of the element) with a length of 15 cm was meshed in segments of 1 cm. In each node a non-linear spring was assigned representing the rebar or the concrete of the section (Fig. 11). The force-displacement law defined for the springs representing the concrete of the section is the parabolic-rectangular stress-deformation law of the EC2-Part 1 multiplied by the tributary area, namely 1 cm x 36 cm (Fig. 10-left). The force-displacement law defined for the springs representing the rebar of the section is the stress-deformation law according to Park & Sampson multiplied

by the area reinforcement of each spring (5Ø10), considering deformation on yielding and failure that correspond to the length of the unbonded part of reinforcement (Fig. 10-right).

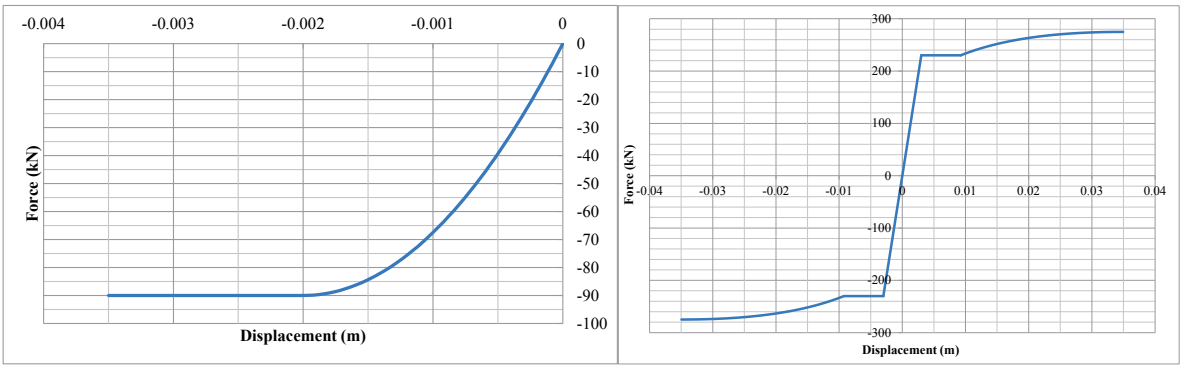


Figure 10: (Left) Sping stiffness diagram for concrete in the case of LU-4, (Right) Spring stiffness diagram for rebar in the case of LU-4

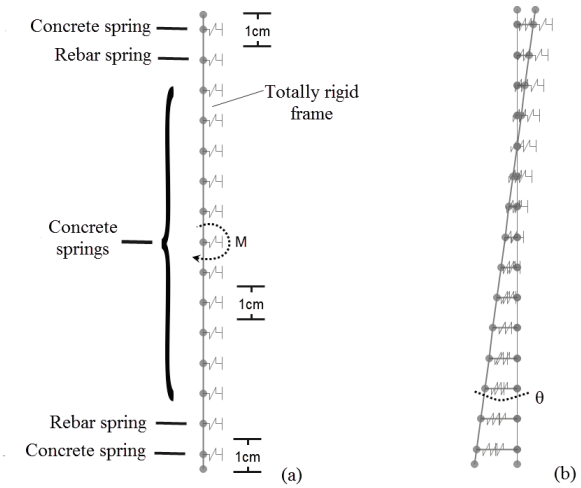


Figure 11: Finite element modelling of the section under consideration.

The type of the analysis conducted was static non-linear by gradual increase of the moment applied in the rigid frame. In both cases failure caused due to the failure of the tensile reinforcement. The moment-rotation diagrams and their bilinearization as calculated with BILIN software [13] are presented in Fig.12.

The yield load can be calculated according Fig. 12 and the yield displacement is calculated according to the equation (2). The effective stiffness can be calculated from the following equation:

$$EJ_{eff} = \frac{M_y \cdot l^2}{3\delta_y} \tag{3}$$

where l is the length of the cantilever from the side of the rigid zone to the support.

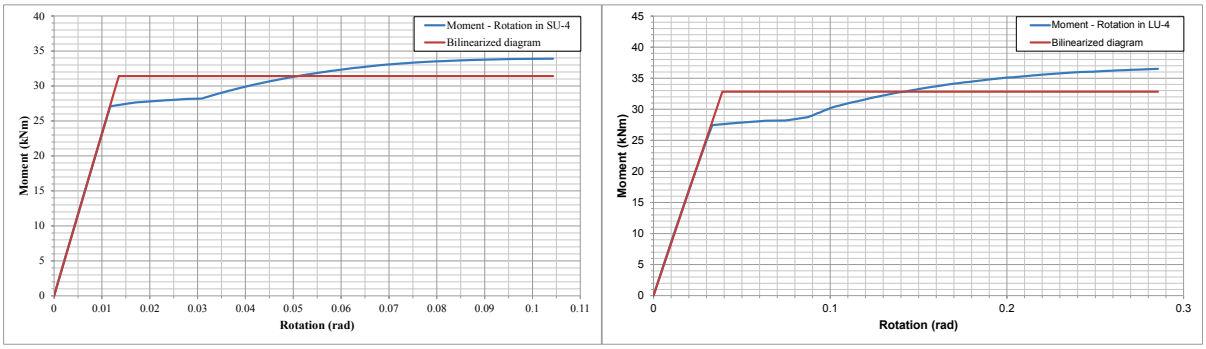


Figure 12: Moment-rotation diagrams of the critical section of SU-4 and LU-4.

The analytically calculated properties of the specimens with the unbounded parts of reinforcement are presented in Table 4 and Table 5.

M_y (kNm)	P_y (kN)	EJ_{eff} / EJ_{un} (%)	φ_y (1/m)	φ_u (1/m)	L_p (mm)	δ_y (mm)	δ_u (mm)	μ_δ
31.25	166.7	33.99	0.033	0.286	114.5	1.5	10.8	6.94

Table 2: Analytical results for the specimen S-4.

M_y (kNm)	P_y (kN)	EJ_{eff} / EJ_{un} (%)	φ_y (1/m)	φ_u (1/m)	L_p (mm)	δ_y (mm)	δ_u (mm)	μ_δ
30.85	44.9	35.03	0.034	0.288	225.4	21.2	93.6	4.41

Table 3: Analytical results for the specimen L-4.

θ_y (rad)	θ_u (rad)	M_y (kNm)	P_y (kN)	EJ_{eff} / EJ_{un} (%)	δ_y (mm)	δ_u (mm)	μ_δ
0.014	0.104	31.41	167.5	8.69	5.1	39.3	7.71

Table 4: Analytical results for the specimen SU-4.

θ_y (rad)	θ_u (rad)	M_y (kNm)	P_y (kN)	EJ_{eff} / EJ_{un} (%)	δ_y (mm)	δ_u (mm)	μ_δ
0.039	0.286	32.83	47.8	17.77	53.5	403.6	7.54

Table 5: Analytical results for the specimen LU-4.

6 EXPERIMENTAL RESULTS

Interesting results were observed during the experimental procedure regarding the three response indexes, namely, strength, stiffness and ductility. Regarding L-4, flexural cracks were observed in the area around the stiff zone of the beam, which increased along the increase of the imposed deflection and the progressive formation of plastic hinge. Crosswise cracks oc-

curred in S-4, which indicated the intense presence of shear effect (Fig. 13). However these specimens managed to deplete their flexural strength as show by the experimental results.

Regarding specimens SU-4 and LU-4 the failure mode was different from the initially supposed. In low level displacements the cracks were formed at the side of the rigid zone, like it was initially supposed (Fig. 14). Along the increase of the imposed displacements, cracks showed up in the section around the end-part of the unbonded reinforcement. This happened because stress in the unbonded part of reinforcement was of constant value. The form of the cracks in the last load cycles, during high level of imposed displacements, is presented in Fig. 15. The width of the initially supposed single crack at the side of the rigid zone was distributed into two cracks, one at the side of the rigid zone and one at the section of the end-part of the unbonded rebar. Especially, the absence of transverse reinforcement in the end-part of the unbonded rebar led to the delamination of the concrete coating and to intensive disrupt of the section concrete core (Fig. 15-right).

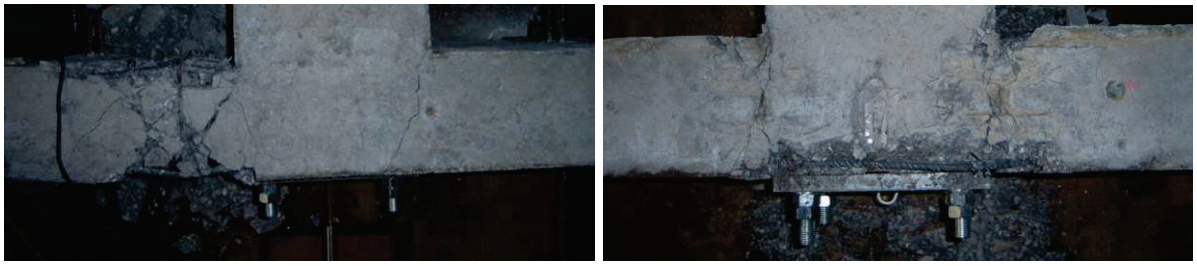


Figure 13: Crack formation in S-4 (left) and L-4 (right).



Figure 14: Crack formation at the side of the rigid zone in LU-4.



Figure 15: (Left) Crack final form in SU-4, (Right) Concrete disrupt in LU-4.

By processing the specimen hysteresis loops (Fig. 16 and Fig. 17), the results given in Table 6 were obtained. The 4 mm gap in the supports of the specimens was omitted from the

calculations and the specimens were considered as firmly mounted in the supports. It should be noted that the values of these tables are average values of both the directions of cyclic loading. Equation (4) was used for the determination of the experimental effective stiffness of the cantilevers:

$$P_y \cdot \delta_y = \int_0^L \frac{M^2_{(x)}}{EJ_{eff}} dx + \int_0^L \frac{V^2_{(x)}}{GA_s} dx \quad (4)$$

where $M_{(x)}$ and $Q_{(x)}$ are the moment and shear values of the cantilevers respectively, P_y is the half of the yield load of the beam, δ_y is the yield displacement of the beam, G is the shear modulus considering cracked concrete and A_s is the cantilevers section shear area.

	P_y (kN)	δ_y (mm)	δ_u (mm)	EJ_{eff} / EJ_{un} (%)	μ_δ
S-4	172.4	3.4	13.2	13.5	3.91
SU-4	167.8	5.7	>15.5	7.8	>2.81
L-4	44.3	19.9	>93.0	30.8	>4.67
LU-4	42.1	29.8	89.6	19.5	3.01

Table 6: Experimental results disregarding the existence of the 4 mm gap in the supports.

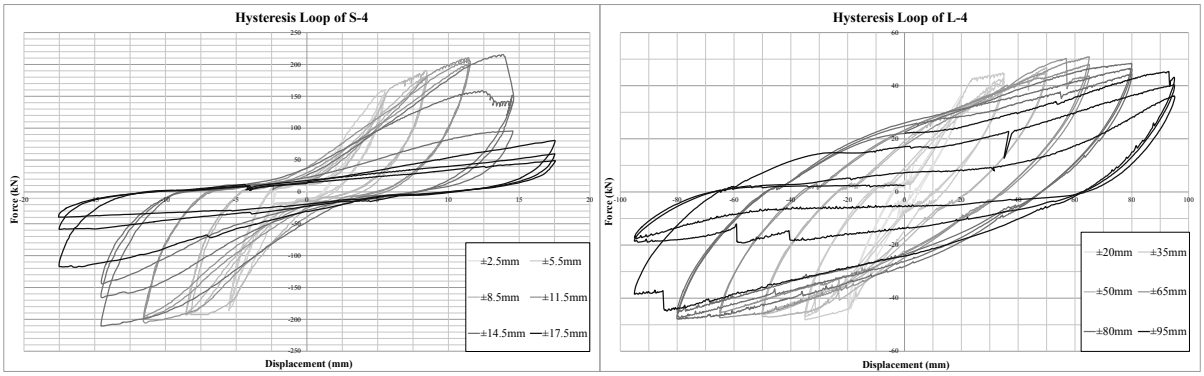


Figure 16: Hysteresis loops of the specimens S-4 and L-4.

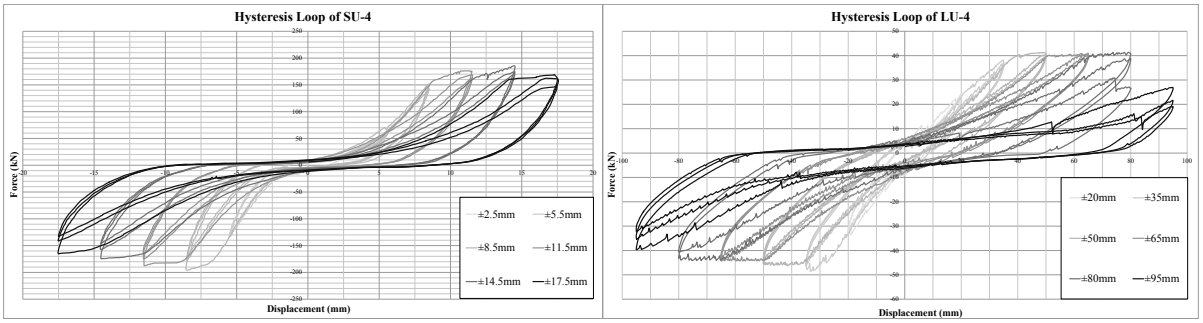


Figure 17: Hysteresis loops of the specimens SU-4 and LU-4.

By comparing the analytically calculated specimen properties with the experimental results of Table 6, regarding specimen S-4, the difference observed between the analytical and experimental results is due to the low shear span ratio of the specimen and the influence of shear stresses. Regarding L-4, the analytical results are close to the experimental. The same denotation applies for specimen SU-4. It is noted that SU-4 in contrast to LU-4 did not fail in the last

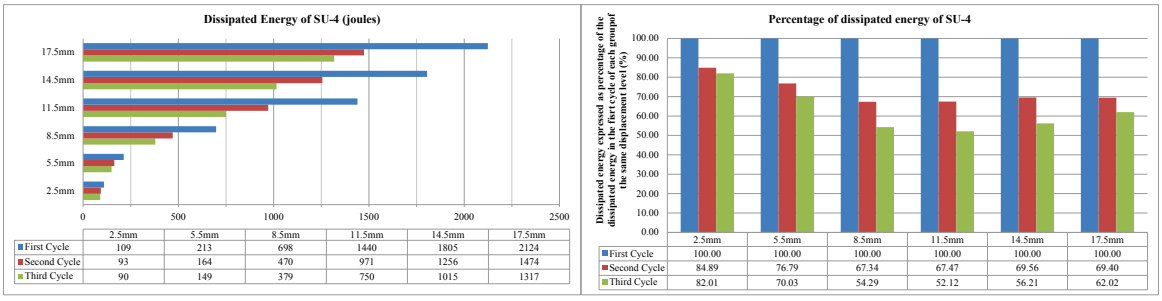
displacement level group of ±17.5 mm (by losing 20% of its strength). On the contrary, regarding specimen LU-4, the analytical results of displacements and the available displacement ductility are different from the experimentally obtained. This is due to the different mode of deformation and crack formation the specimen experienced. Initially, for the analytical calculation of its properties, the assumption of a single crack formation (at the side of the rigid zone) was made. During the experiment it was observed that a second crack formatted at the area of the end-part of the unbonded rebar. A part of the total deformation due to the rebar elongation was concentrated in that area. In addition, the absence of transverse reinforcement in that area led to the premature disrupt of the concrete. As a result of this were the lower than the expected displacements and available displacement ductility.

Comparing the results of the four specimens the following can be stated:

- The bond suppression in SU-4 and LU-4 did not seem to affect their strength, regardless of shear span ratio.
- The specimens with the unbonded reinforcement yield in larger deformations than the specimens S-4 and L-4. Therefore, their effective stiffness is significantly lower compared to the stiffness of S-4 and L-4.
- Specimen SU-4 did not reach failure. Comparing its analytically calculated available displacement ductility with the one of S-4, the first mentioned has slightly greater value. Specimen LU-4, although it was analytically expected to have almost twice the available displacement ductility of L-4, experimentally presented lower displacement ductility due to the formation of a second crack in the area of the end-part of the unbonded rebar.

The absolute values of dissipated energy and the dissipated energy per cycle (as a percentage of the dissipated energy of the first cycle of each group of the same displacement level) of specimens SU-4 and LU-4 are presented in Figures 18 and 19. The corresponding diagrams of S-4 and L-4 are presented in reference [7]. An increase of the dissipated energy is observed when imposed displacement is increasing in both cases. The percentage of the dissipated energy of the second and third cycle compared to the corresponding of the first cycle of each displacement group increases in both cases along with the increase of the imposed displacement. In the case of SU-4 this increase is not as obvious as in the case of the other specimens because this specimen was far from its failure according to Table 4 and Table 6. Specimen LU-4 corresponding dissipated energy percentage is descending in the last group of imposed displacements because of its premature failure.

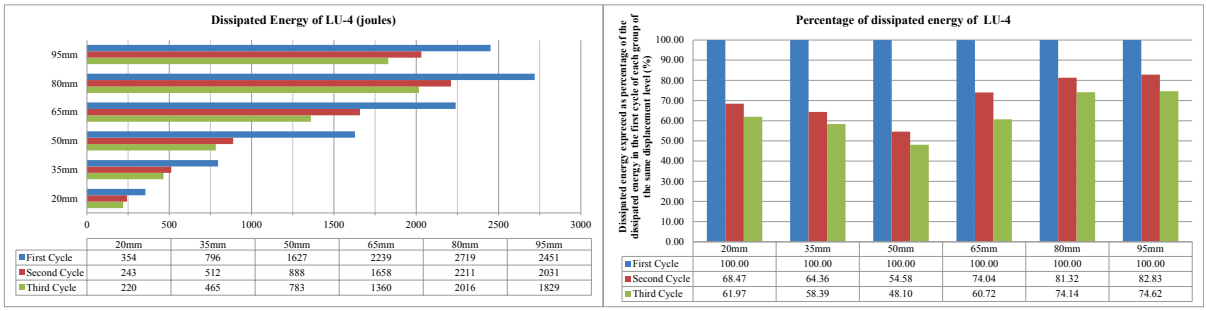
Comparing the dissipated energies of SU-4 and LU-4 with the corresponding of S-4 and L-4 we observe that for the same extend of imposed displacements the second two specimens present in average 2.5 times larger amount of dissipated energy than the specimens with the unbonded reinforcement. It can be seen that specimens SU-4 and LU-4 appear to be activated in larger imposed displacements than specimens S-4 and L-4.



	2.5mm	5.5mm	8.5mm	11.5mm	14.5mm	17.5mm
First Cycle	109	213	698	1440	1805	2124
Second Cycle	93	164	470	971	1256	1474
Third Cycle	90	149	379	750	1015	1317

	2.5mm	5.5mm	8.5mm	11.5mm	14.5mm	17.5mm
First Cycle	100.00	100.00	100.00	100.00	100.00	100.00
Second Cycle	84.89	76.79	67.34	67.47	69.56	69.40
Third Cycle	82.01	70.03	54.29	52.12	56.21	62.02

Figure 18: Energy dissipation of specimen SU-4.



	20mm	35mm	50mm	65mm	80mm	95mm
First Cycle	354	796	1627	2239	2719	2451
Second Cycle	243	512	888	1658	2211	2031
Third Cycle	220	465	783	1360	2016	1829

	20mm	35mm	50mm	65mm	80mm	95mm
First Cycle	100.00	100.00	100.00	100.00	100.00	100.00
Second Cycle	68.47	64.36	54.58	74.04	81.32	82.83
Third Cycle	61.97	58.39	48.10	60.72	74.14	74.62

Figure 19: Energy dissipation of specimen LU-4.

The damage factor of the specimens SU-4 and LU-4 regarding the stiffness loss in each cycle [14] is given in Figure 20 and the corresponding diagrams of S-4 and L-4 are given in reference [7]. Regarding specimens S-4 and L-4, it is noted that the damage factor is constant and low, around 3 % to 5 %, except of the groups of displacement cycles that are near to the failure of the specimens. Specimen SU-4 exhibits stable performance during the consecutive cyclic imposing of displacement. On the contrary, specimen LU-4, which depletes its available displacement ductility in imposed displacement below the maximum imposed during the experiment, presents sudden loss of stiffness in the second and third cycle in displacement groups of ±14.5 mm and ±17.5 mm.

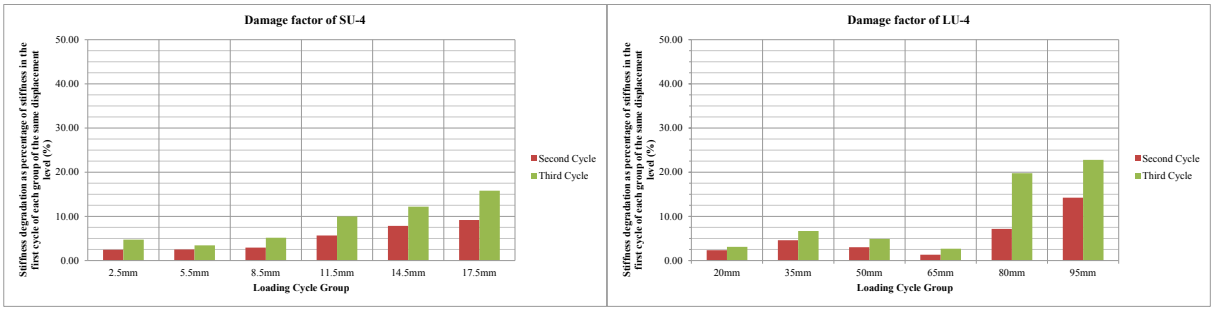


Figure 20: Damage factor (stiffness degradation) of SU-4 and LU-4.

7 CONCLUSIONS

The experimental study on the mechanical behavior of a novel type of joint connection between pier and deck or between pier and pile cap was presented in this study. In particular, three response indexes were examined namely strength, stiffness and ductility. Furthermore, the influence of longitudinal reinforcement unbonding on energy dissipation capacity and constant performance of the pier during cyclic loading was examined.

The main conclusions are as follows:

- The specimen strength, where the reinforcement to concrete bond had partially been suppressed, was slightly reduced - by 5 % - compared to the specimens without bond suppression. Therefore, it can be stated that the reinforcement partial bond suppression does not seem to significantly affect strength.
- The analytically calculated and the experimental values of the specimen effective stiffness with unbonded reinforcement were significantly degraded compared to those with regular reinforcement. In the stiff (short) and flexible (long) specimens the degradation was 42 % and 37 %, respectively. This means that reinforcement partial bond suppres-

sion renders piers more flexible and capable to withstand serviceability loads without developing major stress.

- The available displacement ductility of the short specimen (low shear span ratio) did not depleted during the maximum imposed displacement. The analytically calculated value was increased by 11 % compared to the regularly reinforced specimen. Regarding the long specimen (high shear span ratio), its available displacement ductility depleted and accrued significantly lower to the analytically calculated. A safe conclusion cannot be obtained because the failure mechanism was not the same in the two cases.
- The fact of plastic hinge formation in the area of the end-part of the unbondment leads to the conclusion that the bond suppression must not take place in the web of the piers but inside the connection joint of deck and pier or pile cap and pier.
- The amounts of dissipated energy in the case of the specimens with unbonded reinforcement are significantly lower than in the case of their ordinary counterparts, for a given size of imposed displacement. Comparing the percentage of the dissipated energy in the two cases, it is concluded that the specimens with unbonded reinforcement are activated in a higher level of imposed displacements compared to ordinary reinforcement.
- Stiffness loss in the case of specimens with unbonded reinforcement during the consecutive imposed displacement cycles is similar to the loss of specimens with ordinary reinforcement.

REFERENCES

[1] M.J.N. Priestley, F. Seible, G.M. Calvi, *Seismic Design and Retrofit of Bridges*. John Wiley & Sons Inc., 1996.

[2] M.J.N. Priestley, The PRESSS Program-Current Status and Proposed Plans for Phase III. *PCI Journal,* **41-6**, 22-40, 1996.

[3] M.J.N. Priestley, S. Sritharan, J.R. Conley, S. Pampanin, Preliminary Results and Conclusions from the PRESSS Five-story Precast Concrete Test-Building. *PCI Journal,* **44-6**, 42-67, 1999.

[4] A. Palermo, S. Pampanin, G.M. Calvi, The Use of "Controlled Rocking" in Seismic Design of Bridges. *13th World Conference on Earthquake Engineering*, Vancouver, Canada, August 1-6, 2004.

[5] I. Tegos, V. Piltisis, Th. Chrysanidis, A Proposal for the Use of a New Type of Pier Connections with Deck and Pile Cap with Financial, Functional and Seismic Advantages. *International Conference IBSBI 2014, "Innovations on Bridges and Soil-Bridge Interaction",* Athens, Greece, October 16-18, 2014.

[6] CEN [Comité Européen de Normalisation], EN 1992-1-1: Eurocode 2: Design of Concrete Structures - Part 1-1: General Rules and Rules for Buildings, 2004.

[7] V. G. Pilitsis, V.K. Papanikolaou, I.A. Tegos, K.-A. Stylianidis, A Novel Mechanism for restraining Seismic Actions in Ductile Bridges: Analytical Modeling and Experimental Verification. *5th International Conference on Computational Methods in Structural Dynamics and Earthquake Engineering,* Crete Island, Greece, May 25-27, 2015.

[8] K.-A. Stylianidis, K.V. Papanikolaou, C. Ignatakis, T. Salonikios, The Novel Cycle-Loading System of The Laboratory of Reinforced Concrete and Masonry of A.U.Th. - Potential and First Applications (Greek). *11th Greek Conference on Reinforced Concrete,* Corfu, Greece, May 18-20, 1994.

[9] V. K. Papanikolaou, *Analysis of arbitrary composite sections in biaxial bending and axial load.* Computers & Structures **98-99**, 33-54, 2012.

[10] R. Park, R.A. Sampson, *Ductility of Reinforced Concrete Column Sections in Seismic Design,* Journal of the ACI, **69-9**, 543-551, 1972.

[11] CEN [Comité Européen de Normalisation], EN 1998-2: Eurocode 8: Design of Structures for Earthquake Resistance - Part 2: Bridges, 2005.

[12] Computers and Structures Inc., *SAP2000 Nonlinear ver.11.0.3 - User's Reference Manual,* 2007.

[13] G. Panagopoulos, A.J. Kappos, Bilinear Approximations of Force - Displacement Curves. *16th Greek Conference on Reinforced Concrete,* Paphos, Cyprus, October 21-23, 2009.

[14] S.K. Kunnath, C. Jenne, Seismic Damage Assessment of Inelastic RC Structures, *5th U.S. National Conference on Earthquake Engineering*, Chicago, U.S.A., July 10-14, 1994.

COMPDYN 2015
5th ECCOMAS Thematic Conference on
Computational Methods in Structural Dynamics and Earthquake Engineering
M. Papadrakakis, V. Papadopoulos, V. Plevris (eds.)
Crete Island, Greece, 25–27 May 2015

IN-SITU MEASURED DYNAMIC RESPONSE OF THE BELL TOWER OF AGIOS GERASIMOS IN LIXOURI-KEFALONIA, GREECE AND ITS UTILIZATION IN THE NUMERICAL PREDICTIONS OF ITS EARTHQUAKE RESPONSE

G.C. Manos[1] **and E. Kozikopoulos**[2]

[1] Professor and Director of the Lab. of Strength of Materials and Structures, Aristotle University
e-mail: gcmanos@civil.auth.gr

[2] Postgraduate student, Lab. of Strength of Materials and Structures, Aristotle University
e-mail: {vago_kozi@outlook.com.gr}, {dnaxakis@civil.auth.gr}

Keywords: Bell tower, In-situ Dynamic Measurements, Numerical Simulation, Earthquake Response, Soil-structure Interaction.

Abstract. *The dynamic and earthquake response of the bell tower of Agios Gerasimos, located at the city center of Lixouri in the island of Kefalonia, Greece is examined here. This structure was subjected during the winter of 2014 in an intensive earthquake sequence. The dynamic characteristics of this bell tower were measured in-situ through a series of free vibration tests that were performed following the earthquake sequence. Subsequently the dynamic and earthquake response of the bell tower was numerically simulated employing a 3-D elastic numerical simulation shell elements. The foundation was included in the numerical model assumed to be a mass-less concrete block that is formed by mass-less horizontal slabs and vertical slabs. A number of linear horizontal and vertical links are also employed aimed at representing the resistance of the soil surrounding the foundation block in the x-x (N-S), y-y (E-W) and vertical (z-z) directions. The numerical simulation examines the value of the stiffness of these vertical or horizontal links in a parametric way. First, the axial stiffness for all the vertical and horizontal links attains the value of 10000000KN/m that represents a non-deformable soil. Next, the vertical and horizontal links are given a value for their axial stiffness in such a way that the resulting 1st translational E-W (y-y) eigen-frequency is approximately equal to the corresponding value that was measured during the free vibration tests. Then a third case is also examined whereby the stiffness of these links becomes even lower. The obtained numerical results of all these examined cases are presented and discussed. It is demonstrated that the soil – foundation – structure interaction influences the dynamic and earthquake response predictions for this structure quite significantly. It also demonstrates the usefulness of such in-situ testing towards formulating realistic numerical models in order to yield realistic predictions of the dynamic and earthquake response of the examined structures.*

1 INTRODUCTION

The objective of this paper is to study the dynamic and earthquake response of a bell tower. This bell tower belongs to the church of Agios Gerasimos which is located at the city center of Lixouri in the island of Kefalonia, Greece. The whole locality was subjected during the winter of 2014 in an intensive earthquake sequence and this gave the opportunity to focus on the earthquake response of this bell tower which remained unscathed, despite the intensity of the seismic ground motion and the damage to neighboring structures. In figure 1 the location of the Agios Gerasimos bell tower is shown together with the location of the city hall of Lixouri at a distance of 0.35km from the bell tower.



Figure 1. View of the center of Lixouri



Figure 2. The two-story R/C building that housed the City Hall of Lixouri prior to the seismic event of 3rd February 2015. Because of the developed structural damage is not occupied at present.

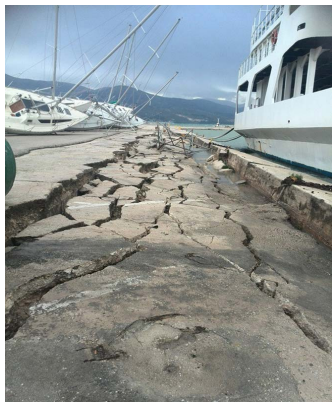


Figure 3. The earth fill embankment at the harbor immediately after the seismic event of 3rd February 2015

The Lixouri City Hall is also shown in figure 2, a two-story reinforced concrete building, developed light structural damage during the 3rd of February 2014 strong seismic ground motion. Similarly, the columns of another two-story reinforced concrete building were also damaged, namely hotel Palatino shown at the left side of figure 1. It is interesting to note that the

intensity of shaking during this damaging 3rd of February 2014 seismic event was recorded by a strong motion accelerograph located at the ground floor of the city hall building [1]. Moreover, spectacular damage was observed at the earth fill embankment [1] that forms the harbor of Lixouri (shown at the bottom of figure 1) as well as the overturning of boats that were free standing at the sea front of this harbor (figure 3).

Bell towers are structures that are of particular interest regarding their dynamic and earthquake response, which has been the subject of research in the past. A large number of bell towers with dimensions much larger than the one examined here are located in numerous cities in Italy and elsewhere. The largest percentage of these bell towers is built by stone or brick masonry. One of the well known cases of a bell tower collapse is that of the St. Marcus bell tower in Venice in July 1902 depicted in figures 4. The Campanile of St. Mark's Church, ninety-eight meters high, collapsed at 10:41 o'clock Monday morning and fell with a great, crash into the piazza. The Campanile, which was entirely detached from the cathedral, collapsed where it stood in a heap of ruins (figure 5). This collapse was not due to an earthquake excitation.



Figure 4-5. The Collapse of St. Mark’s Bell Tower in Venice in 1902.



Figure 6-7. Torre dei Modenesi, Emilia-Romagna earthquake, May 2012

However, in many other cases earthquake activity constitutes the major cause of serious damage for bell towers that many times leads to partial or total collapse. These structures are characterized with considerable height, relatively to their narrow foundation, and considerable masses along their height; these facts together with the added weight from heavy bells at high elevations lead to large overturning moments and shear forces at their base. There are numer-

ous examples of bell towers that were heavily damaged or collapsed due to earthquake activity. Relatively recently, a 6.0 magnitude earthquake in the region of Emilia-Romagna of Italy caused the collapse of an old tower in the town of Finale Emilia on May 20, 2012. Torre dei Modenesi, a 13th century clock tower was destroyed during this earthquake (figure 6-7). An extensive effort was made by volunteers from all across the country to help salvage, collect and catalogue fragments of the 32-meter high tower in an effort to eventually restore it. On October 16th 2013, a 7.2 magnitude earthquake shook Bohol province in the central Philippines. The Basilica Minore del Santo Niño established in the 1500s and rebuilt in its present form in 1737. The earthquake caused the collapse of its bell tower and portions of its main building. the bell tower of the Church of San Pedro Apostol in Loboc, Bohol that collapsed during the same earthquake.

.





Figure 8-9 . The Basilica Minore del Santo Niño



Figure 10. The bell tower of the Church of San Pedro Apostol.

Consequently, there is a major international concern for the stability of numerous bell towers. This resulted to significant international research effort that includes in-situ monitoring of the response of bell towers on a temporary basis, like the one attempted here, or more sophisticated and on a permanent basis ([4, 6, 7, 8, 9, 12, 13, 14, 15, 16, 17, 18, 20]). Foundation problems for bell towers are evident in many case the most celebrated being Pisa's grand bell tower in Italy (figure 11) that is quoted as a major medieval engineering error. The two leaning bell towers in Bolognia in Italy Another represent another example (figure 12). Therefore, the soil flexibility is also an area of research interest for these structures especially when their dynamic and earthquake response is under investigation [5, 16, 17, 18, 20].



Figure 11. Pisa's grand bell tower



Figure 12. Two leaning bell towers in Bolognia



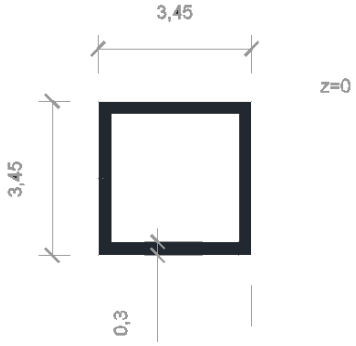
East view of the bell tower



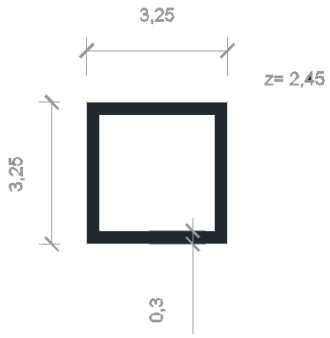
West view of the bell tower

Figure 13-14. Pictorial view of the Agios Gerasimos bell tower (September 2014)

The bell tower that is studied here is depicted in figures 13-14. The height of this bell tower is approximately 20m and it is made of reinforced concrete with a hollow cross-section that has dimensions 3.45m by 3.45m at the ground level and it keeps being reduced along the height, as shown in figures 15-16.



Cross section and dimensions in meters of the bell tower at ground level



Cross section and dimensions in meters of the bell tower at a height of 2.45m from ground level

Figure 15-16. Horizontal cross sections of the bell tower at two different elevations

The walls of the bell tower are made of reinforced concrete with a thickness equal to 300mm. This bell tower was constructed during 1963, almost ten years after the damaging earthquake sequence of 1953 that hit this region [2]. Its foundation consists of a reinforced concrete foundation block that extends at a depth of at least 3.0 meters below ground level. Initially, summary results are presented in section 2 based on measurements of the dynamic response of this bell tower obtained during an in-situ experimental campaign conducted for this purpose on September 2014. Next, the dynamic response of this bell tower is also predicted through a 3-D numerical simulation. From the comparison between the measured and the numerically predicted dynamic response the influence of the soil-foundation interaction is studied and is presented in section 3. Based on the outcome of this comparison the numerical simulation that yield the best predictions is next being utilized to predict the earthquake re-

sponse of this structure during the main event of February 3rd, 2015 [1]. The relevant results are presented in a summary form section 4 together with the final conclusions.

2 IN-SITU MEASUREMENT OF THE DYNAMIC RESPONSE OF THE BELL TOWER

The dynamic characteristics of this bell tower were measured in-situ through a series of free vibration tests that were performed following the damaging earthquake sequence 3rd of February 2014 seismic. A set of two tri-axial accelerometers were utilized together with a digital data acquisition system. These accelerometers were fixed at two locations along the height of the bell tower. The first accelerometer was fixed on a horizontal reinforced concrete (R/C) slabs which was built internally on this bell tower and was connected in a monolithic way with all four peripheral R/C walls. This R/C slab was immediately below the bells and could be reached through a R/C staircase which was also built internally and was also connected in a monolithic way with the peripheral R/C walls. This R/C slab was located at 15.4m from the ground level, which is named here "High Measuring Point (up)" and the accelerometer fixed at this level is depicted in figures 17-18. The second tri-axial accelerometer was also fixed internally on the West R/C wall at a location 11.5m from ground level, which is named here "Low Measuring Point (down)". This instrumentation arrangement is also shown in figure 19 where it can be seen that both instruments were located at an axis of symmetry of this structure named y-y in figure 19 (East-West).



Figure 17-18. Accelerometer fixed at "High Measuring Point (up)".

The bell tower was excited by a pull-out free vibration test sequence ([4, 6, 7, 8, 9, 12, 13, 14, 15, 16, 17, 18, 20]) utilizing a sudden rupture of a high strength wire that was previously stretched being attached at on end at the bell tower just above the "High measuring point" level at the other end on a reaction point at the street level that passed near the South side of the bell tower and was accessible for this purpose. This is depicted schematically in figures 20 and 21. As can be seen in figure 21 the excitation axis was at an angle of 14.7 degrees with the East-West axis of symmetry (y-y). As a result, and despite the structural symmetry, it was expected that the dynamic acceleration response of the bell tower for this excitation would be developed both in the y-y as well as in the x-x (North-South) direction.

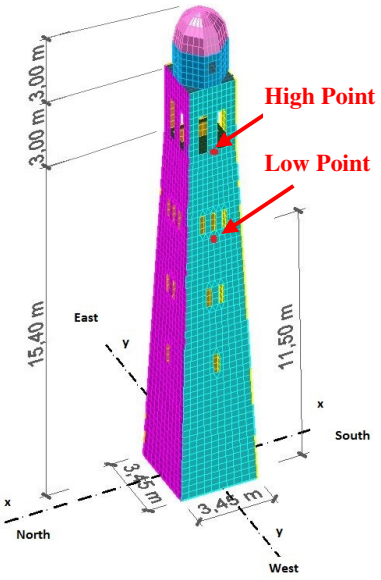


Figure 19. Used instrumentation



Figure 20. Pull-out free vibration test sequence

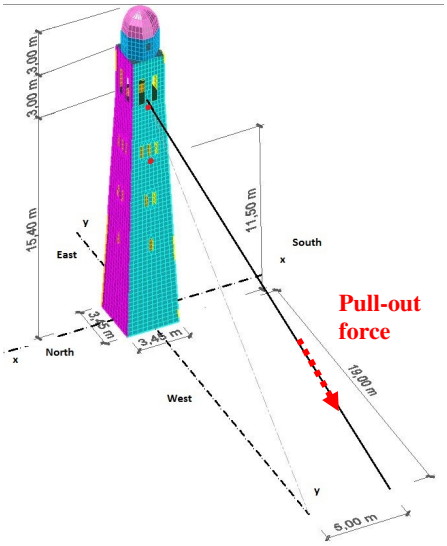
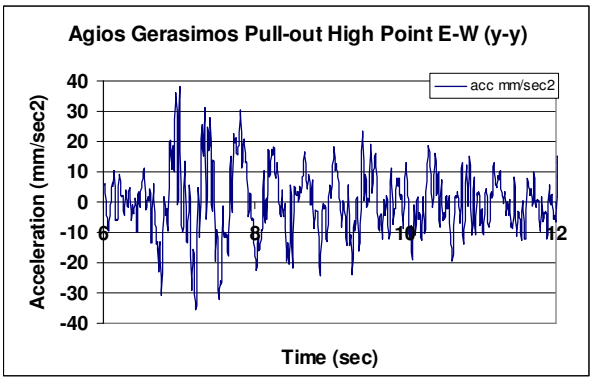


Figure 21. Used pull-out excitation



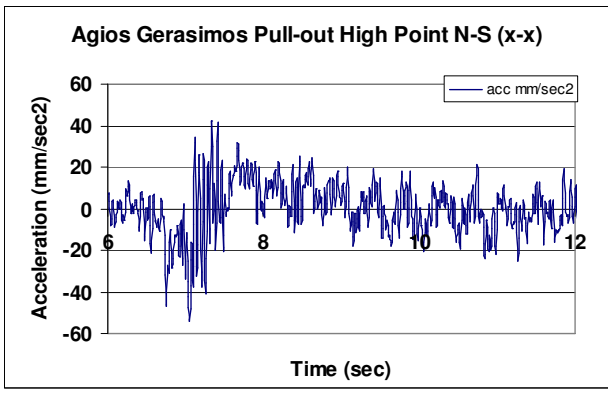
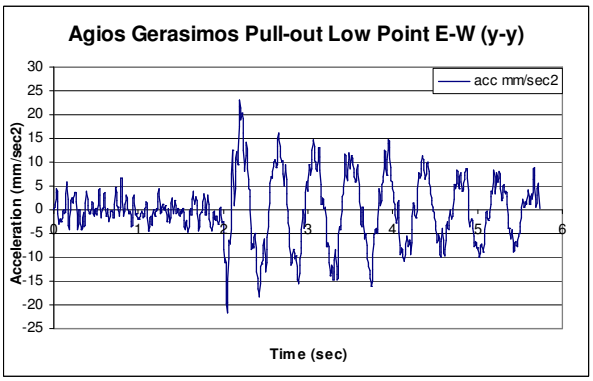


Figure 22-23. Free vibration horizontal acceleration response at the "High measuring point" of the bell tower



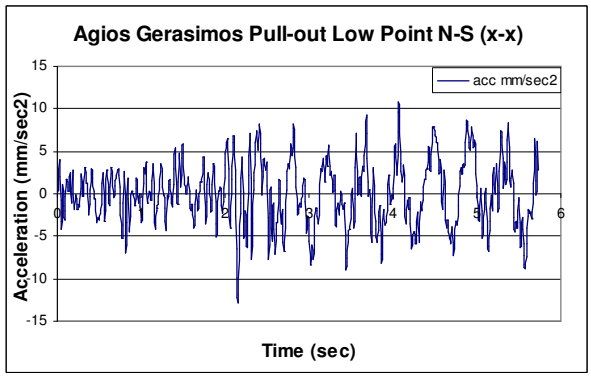


Figure 24-25. Free vibration horizontal acceleration response at the "Low measuring point" of the bell tower

Because the used instruments were tri-axial the response in these two horizontal directions x-x and y-y could be recorded simultaneously and are depicted in figures 22-23 and 24-25 for the "High and Low measuring points", respectively. As can be seen, the presense of a quite dominant frequency is quite clear in all these free vibartion dynamic acceleration responses. This dominant response frequency was extracted from transforming the obtained

measurements in the frequency domain through a fast fourier transform (FFT) algorithm. The following table 1 lists the results of this FFT frequency analysis of the obtained measurements.

Table 1. Peak values from FFT frequency analysis of the East-West (y-y) free vibration acceleration response of the bell tower

	Frequency (Hz)	Period (sec)	FFT amplitude	FFT Phase (rad)	FFT phase adjusted (rad)	Phase Difference Up-down (deg) FFTup/FFTdown
	Agios Gerasimos High measuring point Test 006 (pass filter 0.1Hz-25Hz)					
High Point	2.344	0.427	30.32(up)	-1.411	1.365	0 / 1.789
	Agios Gerasimos Low measuring point (down) Test 006 (pass filter 0.1Hz-25Hz)					
Low point	2.342	0.427	19.627	1.365	1.365	0

The peak FFT values of the East-West free vibration acceleration response of the bell tower are listed in this table together with the measured in this way dominant frequency which is equal to 2.343Hz (0.427 sec. period). Moreover, it can be seen in this table that the peak acceleration response at this dominant vibration frequency is at phase for the two "High and Low measiring points"

3 NUMERICAL SIMULATION OF THE FREE VIBRATION RESPONSE OF THE BELL TOWER

The dynamic response of the bell tower was numerically simulated employing a linear elastic dynamic analysis utilizing shell elements assumed to be of reinforced concrete as an isotropic material with a Young's Modulus equal to E=10000MPa and typical to reinforced concrete. The bells were assumed to weight 500kg. They were simulated with a steel beam that was placed at the right location and height where the actual steel beam supporting the bells is located. A mass and weight multiplier was used for this beam to account for the extra mass and weight of the bells.

The foundation was assumed to be a mass-less concrete block that was numerically formed by the following parts:

- Two mass-less and stiff horizontal slabs with a thickness 0.15m were located one at the ground level and the other at a depth of 3.0m from the ground level. These slabs represent the upper and lower horizontal planes of the foundation concrete block. In addition, four mass-less and stiff vertical slabs having a thickness 0.789m were also added. Two of these slabs were placed at the x-z plane and the other two at the y-z plane of the numerical model. These vertical slabs represent the peripheral vertical planes of the foundation block facing the East-West (x-z plane) and the North-South (y-z plane) directions. In this way the foundation block was formed (figure 26). All the stiffness properties of the finite elements representing these slabs were numerically increased by a multiplier equal to 1000.
- Next, four mass-less and weightless stiff vertical slabs were also formed parallel to the previously described vertical slabs. These later vertical slabs were placed in a way surrounding externally the foundation block. They were located at a distance of 50mm externally surrounding the vertical slabs representing the foundation block. An additional mass-less and

weightless stiff horizontal slab was also added placed 50mm below the horizontal slab that represents the bottom of the foundation block (-3.0m from the ground level). All these slabs, both vertical and horizontal are presumed to represent the non-deformable support medium for the foundation block of the bell tower, and for this purpose they were considered to be practically non-deformable as well as they were constrained at all their nodes in the x-y-z direction.

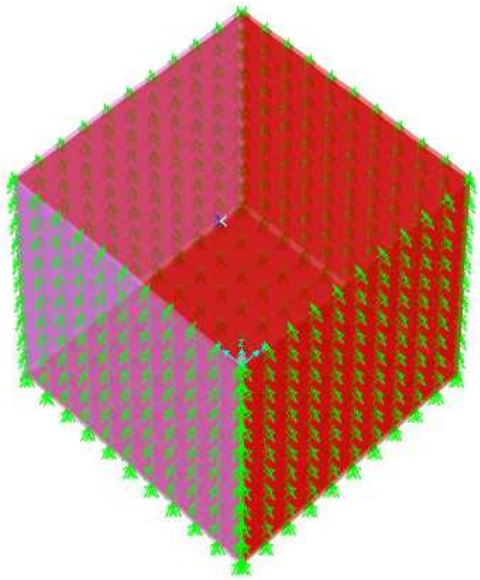


Figure 26. Numerical simulation of the foundation block

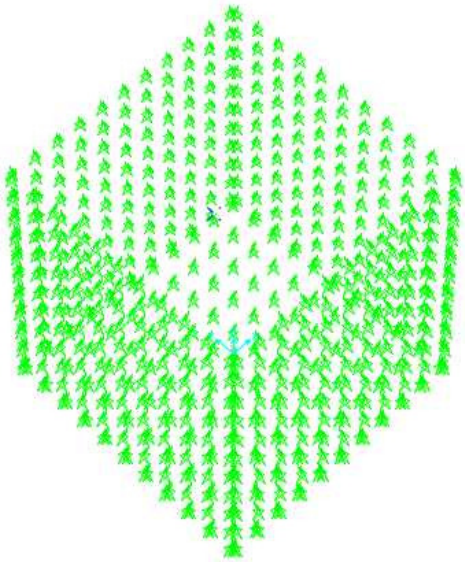
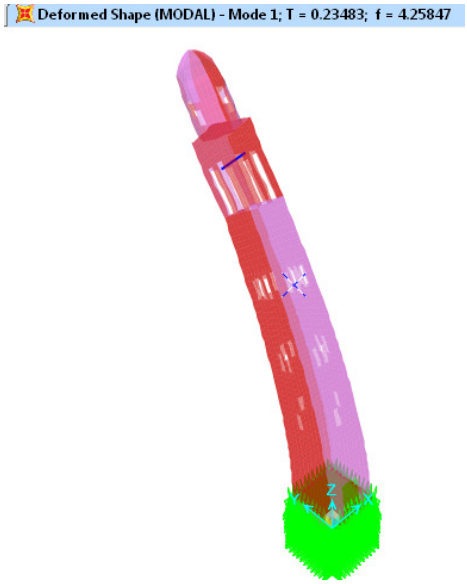


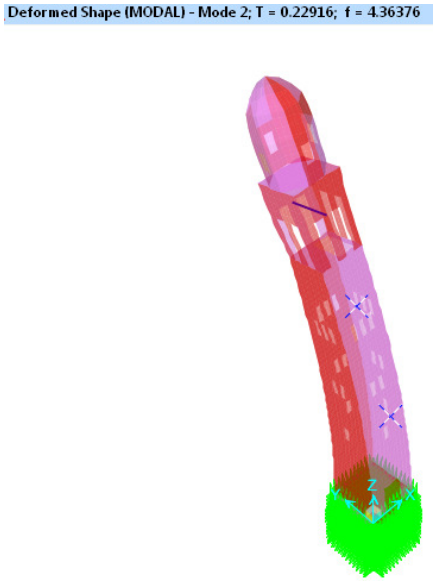
Figure 27. Numerical simulation of the soil-foundation interaction with links

- In order to account for the soil deformability the rigid slabs representing the non-deformable supports of the foundation block were connected to the corresponding vertical and horizontal slabs representing all the sides of the foundation block in contact with the surrounding soil with two-node links (figure 27). These two-node links were placed within the space that was left in the numerical model between the non-deformable support slabs and the non-deformable foundation slabs. In this way, all the foundation soil interaction that could arise from the soil deformability was concentrated locally on these two-node links at the 50mm space left for this purpose surrounding the numerical model of the foundation block from all its sides.

- Three cases were considered regarding the value of the stiffness of these vertical or horizontal links. In the first case the axial stiffness for all the vertical and horizontal links attains the value of 10000000KN/m. That represents a non-deformable soil. In the second case all the vertical and horizontal links are given a value for their axial stiffness in such a way that the resulting 1st translational E-W (y-y) eigen-frequency of the bell tower is approximately equal to the corresponding value that was measured during the free vibration tests. The axial stiffness value for all the links in this case was found to be equal to 21000KN/m. This was assumed to represent medium stiffness conditions for the soil.



Translational mode E-W (y-y)
T=0.235 sec., f=4.258Hz (rigid soil)

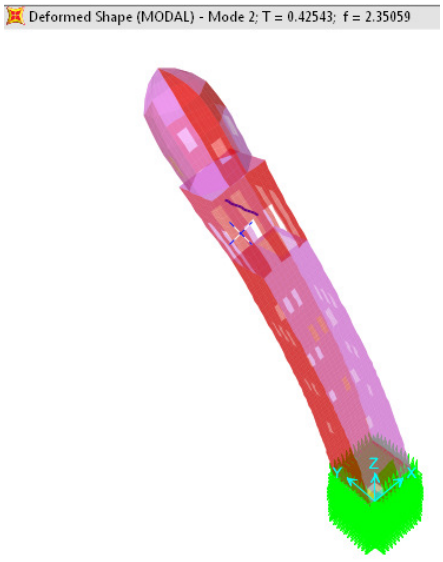


Translational mode N-S (x-x)
T=0.229, f=4.364Hz (rigid soil)

Figure 28-29. Predicted translational mode for the first examined soil condition (rigid soil) Axial link stiffness 10000000KN/m



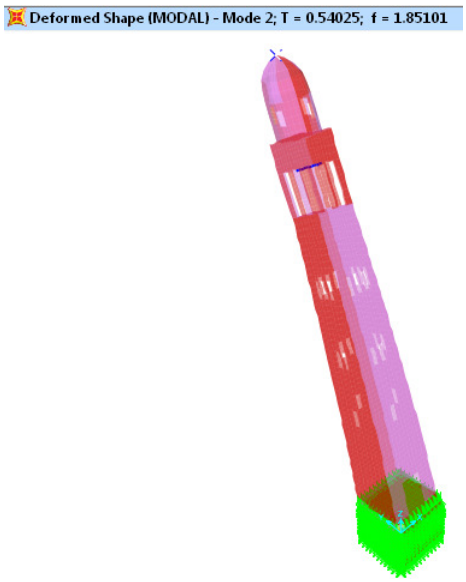
Translational mode E-W (y-y)
T=0.4267sec., f=2.343Hz, (medium soil)



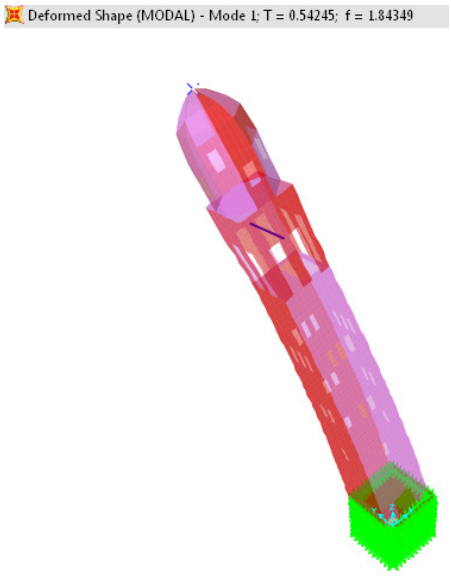
Translational mode N-S (x-x)
T=0.4254, f=2.351Hz, (medium soil)

Figure 30-31. Predicted translational mode for the first examined soil condition (medium soil). Axial link stiffness 21000KN/m

The excitation introduced by the free vibration tests that were performed in-situ should be considered as a rather low intensity excitation. Therefore, the soil surrounding the foundation is presumed to have stiffness properties that may be reduced when subjected to an intense excitation during a prototype earthquake ground motion like the one experienced during the damaging 3rd of February 2014 seismic event at Lixouri. For this purpose, a third case of axial link stiffness was also considered. In this third case the axial stiffness value for all the links was set equal to 10000KN/m. The values of the predicted eigen-frequencies / eigen-periods for the dominant translational modes for the examined three soil conditions of the Agios Gerasimos bell tower are shown in figures 32 to 33 and listed in table 2.



Translational mode E-W (y-y)
T=0.540sec., f=1.851Hz, (flexible soil).



Translational mode N-S (x-x)
T=0.542, f=1.843Hz, (flexible soil).

Figure 32-33. Predicted translational mode for the first examined soil condition (flexible soil). Axial link stiffness 10000KN/m

Table 2. predicted eigen-frequencies / eigen-periods for the dominant translational modes for the examined three soil conditions of the Agios Gerasimos bell tower

Soil Foundation deformability	Predicted East-West translational mode eigen-frequency (Hz) / eigen-period (sec)	Predicted North-South translational mode eigen-frequency (Hz) / eigen-period (sec)
1st case Rigid Soil Axial stiffness for links 10000000KN/m	4.258Hz / 0.235sec.	4.364Hz / 0.229sec.
2nd case Medium Soil Axial stiffness for links 21000KN/m	2.343Hz / 0.4267sec.	2.351Hz / 0.4254sec.
3rd case Flexible Soil Axial stiffness for links 10000KN/m	1.851Hz / 0.540sec.	1.843Hz / 0.542sec.

As already mentioned, the objective of this parametric study of soil-deformability was to be able to investigate the sensitivity of the fundamental dynamic properties of this bell-tower that arises from the deformability of the soil-foundation [5, 10, 16, 17, 18, 20]. In the table that follows the values of the measured eigen-frequencies / eigen-period that were obtained from the in-situ free vibration dynamic measurements are compared with the corresponding predicted values for the three soil-foundation conditions.

As can be seen from the eigen-frequency / eigen-period values listed in table 3, the predictions obtained through the bell tower numerical simulation employing deformable linear links at the interface between the foundation and the soil, as was described in this section, demonstrate very good agreement with the measured values for the 2nd case representing a medium flexibility soil which is approximated in the numerical simulation through an axial stiffness value for the links equal to 21000KN/m.

Table 3. predicted eigen-frequencies / eigen-periods for the dominant translational modes for the examined three soil conditions of the Agios Gerasimos bell tower

Soil Foundation deformability	**Predicted** 1st case Rigid Soil	**Predicted** 2nd case Medium Soil	**Predicted** 3rd case Flexible Soil	**Measured** values
Axial stiffness for links	10000000KN/m	21000KN/m	10000KN/m	--
East-West translational mode eigen-frequency (Hz)/ eigen-period (sec)	4.258Hz / 0.235sec.	2.343Hz / 0.4267sec.	1.851Hz / 0.540sec.	2.343Hz / 0.4268sec.
North-South translational mode eigen-frequency (Hz) / eigen-period (sec)	4.364Hz / 0.229sec.	2.351Hz / 0.4254sec.	1.843Hz / 0.542sec.	2.344Hz / 0.4266sec.

4 EARTHQUAKE RESPONSE OF THE AGIOS GERASIMOS BELL TOWER

Next, the numerical simulation of the earthquake response of the Agios Gerasimos bell tower for the previously presented three cases of soil-foundation deformability was examined. In this investigation the following load case combinations were considered in an effort to approximate the seismic forces that this structure was subjected to during the 3rd of February 2015 actual earthquake excitation.

1. The gravity loads is signified as DEAD. It represents all the vertical gravity forces that are generated from the weights of all the structural and the non-structural components of the bell tower including the bells themselves. All the inclined R/C walls of the tower were considered to have a thickness of 0.3m. The 3-D shell F.E. representation follows the middle plane of these walls. From the level upwards from the upper slab (below the bells) the wall are vertical till the level of the upper dome. The top of the dome rises 21.4m from the ground level. All the window and door openings are replicated in the F.E. model.
2. The horizontal seismic loads in the y-y (E-W) direction are applied in a static way. They are approximated as being 50% of the vertical gravity forces acting horizontally in the x-x direction. These loads are denoted as 0.5 Ey (E-W) static and together with the vertical gravity forces (DEAD) represent combination 1. Thus COMBI-1 = DEAD + 0.5 Ey (E-W). In a similar way, the horizontal seismic loads in the x-x (N-S) direction are also applied in a static way. They are approximated as being 50% of the vertical gravity forces acting horizontally in the x-x direction. These loads are denoted as 0.5 Ex (N-S) static and together with the vertical gravity forces (DEAD) represent load-combination 2. Thus COMBI-2 = DEAD + 0.5 Ex (N-S)
3. Alternatively, The horizontal seismic loads in the y-y (E-W) direction are applied through the Lixouri E-W elastic acceleration response spectral curve for 5% damping ratio as it was derived from the E-W component of the acceleration record that was recorded during the strong aftershock of 3-2-2014 ([1]). This was recorded by an instrument located at the ground floor slab of a R/C two-story building (Dimarchion) located at a distance of 350m from the bell tower, as indicated in figure 1. This response spectrum values are scaled to ac-

count for a response modification factor with a value equal to 2.5. This value must be considered as rather high value based on the fact that the bell tower is a cantilever and there were no visible signs that the reinforced concrete sections with their reinforcing bars were stressed to post-yield levels. Due to these reasons it is expected that the response of the bell tower predicted by dividing the response spectra curve by μ=2.5 will be rather low than what this bell tower could possibly have experienced during the actual seismic event according to the recorded ground acceleration. These seismic loads are denoted as E-W response spectrum and together with the vertical gravity forces (DEAD) represent load-combination 3. Thus COMBI-3 = DEAD + E-W Response spectrum.

As already mentioned, figure 34 depicts the East-West constant ductility acceleration response spectral curve, for damping ratio equal to 5% of critical and for ductility factor μ=2.5, together with the Euro-code 8 design spectral curves (Type 1 and Type 2) for soil category D (flexible soil) for design ground acceleration equal to 0.36g (g the acceleration of gravity), for importance factor γ=1, and for response modification factor q=3 [21]. In the same figure the acceleration spectral values corresponding to the measured and predicted eigen-periods values listed in table 3 for the three examined soil conditions are also indicated. The acceleration spectral value indicated in this figure as L.P.T. corresponds to the lowest eigen-period value of the bell tower for the 1st case of rigid soil conditions. The acceleration spectral value indicated in this figure as "measured" corresponds to eigen-period value of the bell tower for the 2nd case of medium soil conditions that also coincides with the measured value during the in-situ tests described before. Finally, the acceleration spectral value indicated in this figure as H.P.T. corresponds to the highest eigen-period value of the bell tower for the 3rd case of flexible soil conditions.

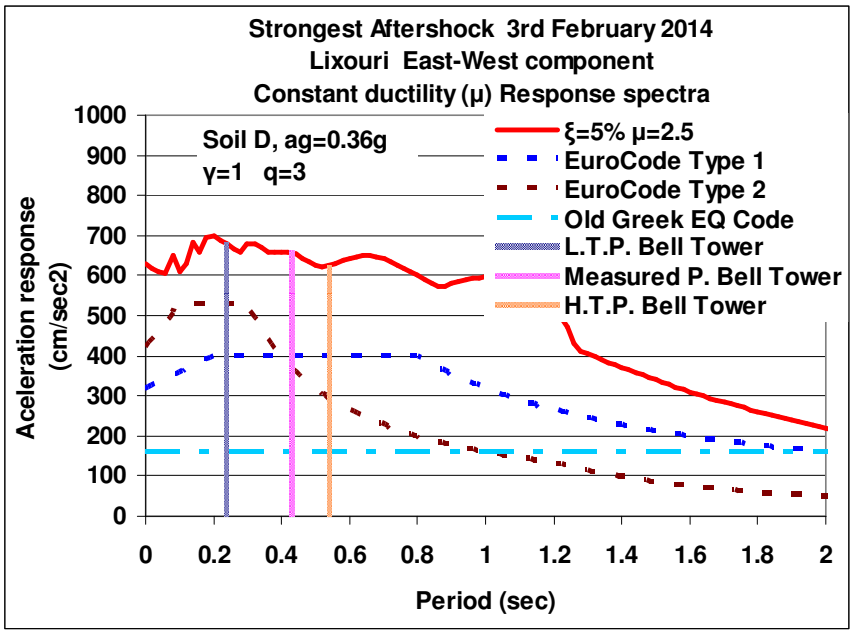


Figure 34. East-West acceleration spectral values for the examined cases of soil conditions for the bell tower

4. The horizontal seismic loads in the x-x (N-S) direction are approximated in a similar way as the one described below utilizing the Lixouri N-S elastic acceleration response spectral curve for 5% damping ratio as it was derived from the N-S component of the acceleration record that was recorded during the strong aftershock of 3-2-2014 [1]. These loads are denoted as N-S response spectrum and together with the vertical gravity forces (DEAD) represent loadcombination 4. Thus COMBI-4 = DEAD + N-S Response spectrum.

Figure 35 depicts the North-South constant ductility acceleration response spectral curve, for damping ratio equal to 5% of critical and for ductility factor μ=2.5, together with the Euro-code 8 design spectral curves (Type 1 and Type 2) for soil category D (flexible soil) for design ground acceleration equal to 0.36g (g the acceleration of gravity), for importance factor γ=1, and for response modification factor q=3 [21]. In the same figure the acceleration spectral values corresponding to the eigen-period values of table 3 are plotted again here with the same symbols.

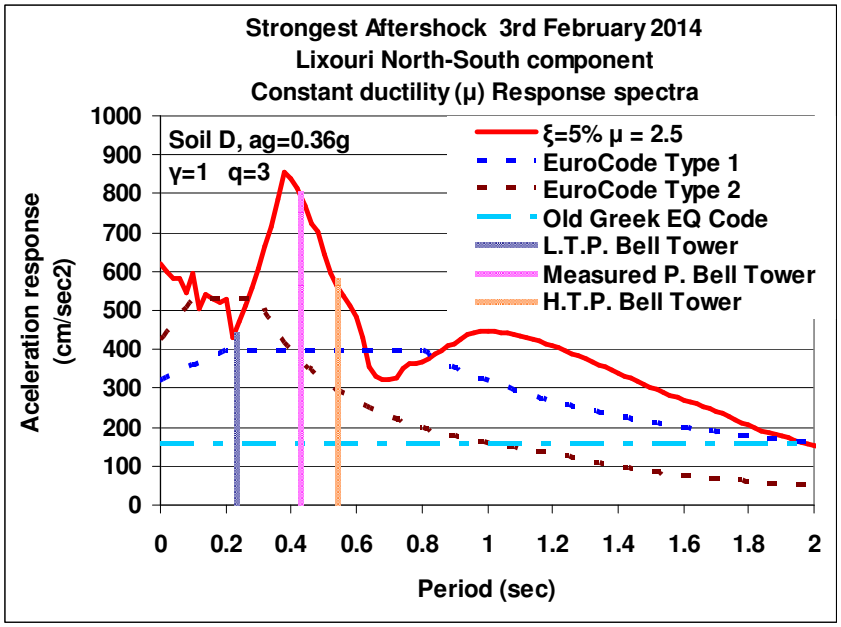


Figure 35. North-South Acceleration spectral values for the examined cases of soil conditions for the bell tower

5. Finally, the horizontal seismic loads in the y-y (E-W) direction are applied through the the E-W component of the acceleration record that was recorded during the strong aftershock of 3-2-2014. This is denoted as E-W time history. Similarly, the horizontal seismic loads in the x-x (N-S) direction are applied through the N-S component of the acceleration record that was recorded during the strong aftershock of 3-2-2014. This is denoted as N-S time history. Both these forcing actions together with the vertical gravity forces (DEAD) represent combination 5. Thus COMBI-5 = DEAD + E-W time history + N-S time history. For all these acceleration forcing actions no scaling was introduced as was done for the horizontal forces based on the response spectral curves that were applied in the way explained before. The step-by-step direct integration method was used for these time history dynamic analyses. For the case of flexible soil damping was introduced at all the vertical and horizontal links with the value of 10% of critical. This increase in the damping ratio value was introduced in order to mitigate the resulting earthquake response for this loading case and to account up to a point the radiation damping that would be introduced in this case from the soil-foundation interaction.

The following observations can be deduced from figures 34 and 35.

a) For almost all the examined soil conditions the acceleration spectral values of the bell tower are considerably higher than the corresponding values of the Euro-code [21] (either type 1 or 2). The only exception is the spectral acceleration value for the rigid soil condition and for the type 2 Euro-code design spectral curve. This means that in

almost all cases the actual seismic loads that this structure experienced during this particular earthquake are larger than the design seismic loads even if this bell tower was designed with the current earthquake loads, as these are specified by Euro-code 8.

b) The previous remark becomes even more outstanding if one uses for comparison the level of design seismic loads that was specified by the old Greek seismic code design acceleration levels which are also indicated in figures 34 and 35 [11]. It must be pointed out here that during the period that this structure was designed and constructed the seismic loads generally considered were those indicated in figures 34 and 35 as "Old Greek EQ Code' [11].

Table 4. Maximum base shear and horizontal displacement at the top of the bell tower

Load Combination	1st case Rigid soil		2nd case Medium soil		3rd case Flexible soil	
	Base Shear (KN)	Top Displ. (mm)	Base Shear (KN)	Top Displ. (mm)	Base Shear (KN)	Top Displ. (mm)
Combination 1 D + static (E-W)	Qy=633	Uy=11.7	Qy=633	Uy=38.8	Qy=633	Uy=61.2
Combination 2 D + static (N-S)	Qx=633	Ux=12.4	Qx=633	Ux=38.7	Qx=633	Ux=62.2
Combination 3 D + R. Spectrum (E-W)	Qy=344	Uy=12.4	Qy=511	Uy=36.6	Qy=380	Uy=52.8
Combination 4 D + R. Spectrum (N-S)	Qx=278	Ux=9.1	Qx=438	Ux=37.6	Qx=324	Ux=44.7
Combination 5 D + Time history (N-S) +Time history (E-W)	Qx=754 Qy=1096	Ux=18.8 Uy=25.2	Qx=1246 Qy=1249	Ux=102.5 Uy=88.3	Qx=839 Qy=1218	Ux=107.8 Uy=139.2

Table 4 lists the maximum (minimum) values of the earthquake response of the bell tower for all five examined load combinations as they were previously described. The listed values correspond to the base shear and to the horizontal displacements (Ux / Uy) at the top of the bell tower at a height equal to 21.4m from ground level. From the values listed in this table the following remarks can be made:

a1) As can be seen from the values listed in table 4 the most demanding load combination for all three cases of soil flexibility is load combination 5 where the dead load is combined with the two horizontal acceleration time histories of the ground motion in the East-West and North-South direction recorded at the top surface of the foundation slab of the 2-story City Hall R/C building located 350m away from the bell tower. This increase in the earthquake response of the bell tower when load combination 5 is employed becomes significantly enlarged for medium and flexible soil conditions.

b1) For load combinations 3, 4 and 5 that take into account the dynamics of the studied structure the flexibility of the soil resulted in larger response in terms of base shear. This increase in the value of the base shear must be attributes to the variation of the fundamental period of the structure with the soil flexibility combined with the characteristics of this earthquake ground motion, which can also be seen in the shape of the spectral curves depicted in figure 34 and 35.

c1) The very noticeable increase in the amplitude of the horizontal displacement at the top of the bell tower when the soil conditions become relatively flexible is partly due to the corresponding increase of the horizontal seismic forces resulting from the variation of the soil deformability, as discussed in b1 before, as well as to a component of the horizontal

displacement at the top of the bell tower resulting from the rocking of the foundation block. Obviously, this rocking tends to increase when the flexibility of the foundation becomes larger [20].

d1) This investigation is under process in order to examine further the implications of the structure-foundation-soil interaction as well as the structural performance of the bell tower. For the later task a more detailed investigation is needed in order to ascertain important structural details of this bell tower.

5 CONCLUSIONS

- It was demonstrated by the in-situ measurements of the dynamic response of the Agios Gerasimos bell tower that the foundation deformability is a significant parameter that must be taken into account in order for the numerical response predictions to have any realism.
- It was also demonstrated that for these measured fundamental eigen-period values the bell tower has been subjected to seismic loads higher than the ones specified by the current Euro-code 8 provisions.
- Furthermore, it was shown that for these measured fundamental eigen-period values the bell tower has been subjected to seismic loads considerably higher than the ones specified by the "Old Greek Seismic Code" provisions that were valid at the tine of its design and construction.
- From the numerical prediction of the earthquake response of this bell tower based on the actual the earthquake ground motion recorded at a very close distance it was shown that the soil flexibility results in both an increase of the seismic loads as well as in a considerable increase of the resulting horizontal displacements that apart from the increase in the seismic loads bear also the outcome of the rocking response of the foundation block.
- In situ measurements like the ones presented here are very important to be able to identify sources that may significantly influence the dynamic and earthquake response of civil engineering structures. They may also serve the purpose to help formulate a realistic numerical model by properly incorporating such influences in order to yield realistic predictions of the dynamic and earthquake response of the examined structure.

ACKNOWLEDGEMENTS

The authors would like to thank Civil Engineer D. Naxakis for his assistance during the in-situ measurements. Moreover, we would like to thank the priest of the church of Agios Gerasimos at Lixouri, Kefalonia-Greece, father Athanasios Likoudis, for all the information he has provided.

REFERENCES

[1] GEER - EERI - ATC - Cephalonia GREECE *Earthquake Reconnaissance January 26th/ February 2nd 2014 Version 1: June 6 2014*

[2] Papazachos, B. and Papazachou, K., 1989, 1997, 2003. The earthquakes of Greece, *Zitis Publ.,Thessaloniki, 356 pp., 304 pp., 286 pp. (in Greek).*

[3] L. de Stefani, R. Scotta, M. Lazzari, A. Saetta. Seismic improvement of Slender Bell Tower and Minarets. – *PROHITECH, Antalya, Turkey, 2014*

[4] R. M. Azzara, L. Zaccarelli, A. Morelli, T. Trombetti. Seismic Monitoring of the Asinelli and Garisenda Medieval Towers in Bologna (Italy), an Instrumental Contribution to the Engineering Modeling Directed to their Protection. - *PROHITECH, Antalya, Turkey, 2014*

[5] Casolo Siro, Uva Giuseppina. Non-Linear dynamic analysis of masonry towers under natural accelerograms accounting for soil-structure interaction. – *COMPDYN 2013 - Kos Island, Greece, June 12-14, 2013*

[6] A. Saisi, C. Gentile, L. Cantini. Post – Earthquake assessment of a masonry tower by on – site inspection and operational modal testing. – *COMPDYN 2013 - Kos Island, Greece, June 12-14, 2013*

[7] D. Colapieto, A.Fiore, A. Netti, F. Fatiguso, G Marano, M. de Fino D. Cascella, A. Antocona. Dynamic identification and evaluation of the seismic safety of a masonry bell tower in the south Italy. – *COMPDYN 2013 - Kos Island, Greece, June 12-14, 2013*

[8] R. Guidorzi, R. Diversi, L.Vincenzi, C. Mazzotti, V. Simioli. Structural monitoring of the Tower of the Faculty of Engineering in Bologna using MEMS –based sensing. – *EURODYN 2011 – Leuven, Belgium, 4-6 July 2011*

[9] C. Blasi M. Carfagni, S. Carfagni. The use of impulsive actions for the structural identification of Slender monumental buildings- *STREMAH-1991 - Seville, Spain, 14-16 May 1991*

[10] S. Dumorier, W.P. De Wilde. Finite element study of the Tower of Brussels City Hall – *STREMAH 1995 – Chania, Crete, Greece, 1995.*

[11] G.C. Manos, Seismic Code of Greece, Chapter 17, International Handbook of Earthquake Engineering: "Codes, Programs and Examples", *edited by Mario Paz, by Chapman and Hall,* ISBN 0-412-98211-0, 1994.

[12] G.C. Manos, et al. (1996) "Predictions of the dynamic characteristics of a 5-story R.C. building at the Volvi Euro-SeisTest Site, utilizing low-intensity vibrations", *3rd European Conference on Structural Dynamics, Eurodyn 1996, Florence, II, 877–884.*

[13] G. C. Manos, (1998). "The Dynamic Response of a 5-story Structure at the European Test site at Volvi-Greece." *6th U.S. National Earthquake Engineering Conference, May 31 - June 4, Seattle, Washington, U.S.*

[14] G. C., Manos, et al.. (2004). "Dynamic and Earthquake Response of Model Structures at the Volvi – Greece European Test Site." *13th World Conference on Earthquake Engineering, Vancouver, Canada.*

[15] G. C., Manos, V. Kourtides, V.J. Soulis, A.G. Sextos, A. G., and P. Renault, (2006). "Study of the dynamic response of a bridge pier model structure at the Volvi - Greece European

Test Site." *8th National Conference on Earthquake Engineering, April 18-22, San Fransisco, U.S.A.*

[16] G.C. Manos, V. Kourtides, A. Sextos, P. Renault, S. Chiras "Study of the dynamic soil-structure interaction of a bridge pier model based on structure and soil measurements" *9th Canadian Conf. on Eartquake Engineering, Ottawa, Ontario, Canada, 26-29 June 2007.*

[17] G.C. Manos, V. Kourtides, A. Sextos, S. Chiras "Soil-Foundation-Bridge Pier Interaction at the Euro-Seis Test Site", *4th Int. Conference on Geotechnical Engineering, Thessaloniki, 24-28 June, 2007.*

[18] G.C. Manos, V. Kourtides, A. Sextos, "Model Bridge Pier Foundation- Soil Interaction implementing, in-situ / shear stack testing and numerical simulation", *14WCEE, Beijing, CHINA, 2008.*

[19] Manos George, "Consequences on the urban environment in Greece related to the recent intense earthquake activity", *Int. Journal of Civil Engineering and Architecture, Dec. 2011, Volume 5, No. 12 (Serial No. 49), pp. 1065–1090.*

[20] G. C. Manos , K.D. Pitilakis, A.G. Sextos, V. Kourtides, V. Soulis, J. Thauampteh, "Field experiments for monitoring the dynamic soil-structure-foundation response of model structures at a Test Site" *Journal of Structural Engineering, American Society of Civil Engineers, Special Issue "Field Testing of Bridges and Buildings, D4014012, Vol. 141, Issue 1, January 2015.*

[21] Eurocode 8: Design of structures for earthquake resistance - Part 1: General rules, seismic actions and rules for buildings, *FINAL DRAFT prEN 1998-1, December 2003.*

COMPDYN 2015
5th ECCOMAS Thematic Conference on
Computational Methods in Structural Dynamics and Earthquake Engineering
M. Papadrakakis, V. Papadopoulos, V. Plevris (eds.)
Crete Island, Greece, 25–27 May 2015

THE DYNAMIC AND EARTHQUAKE RESPONSE OF A TWO STORY OLD R/C BUILDING WITH MASONRY INFILLS IN LIXOURI-KEFALONIA, GREECE INCLUDING SOIL-FOUNDATION DEFORMABILITY.

G.C. Manos[1], D. Naxakis[2], V. Soulis[3]

[1] Professor and Director of the Lab. of Strength of Materials and Structures, Aristotle University
e-mail: {gcmanos@civil.auth.gr}

[2] Postgraduate student, Lab. of Strength of Materials and Structures, Aristotle University
e-mail: {dnaxakis@civil.auth.gr}

[3] Dr. Civil Engineer, Lab. of Strength of Materials and Structures, Aristotle University
e-mail: {soulis@yahoo.com.gr}

Keywords: Masonry infills, In-situ observations, Numerical Simulation, Soil-structure Interaction, Earthquake Response Predictions

Abstract. *The dynamic and earthquake behaviour of a two-story reinforced concrete(R/C) frame building with masonry infills located in Lixouri-Kefalonia-Greece is examined. This building was constructed according to old seismic code provisions and was subjected to intense earthquake ground motion during the recent 2014 earthquake activity in the island. Despite the intensity of the seismic action this structure developed light to moderate damage that is confined mainly to the masonry infills and to the spalling of the unconfined concrete cover of the columns. The numerical simulation includes influences arising from the masonry infulls that are within the R/C frames as well from the R/C foundation mat that is resting on relatively flexible soil. Use is made in the numerical simulation of the deformability of the foundation based on the results obtained from a specific investigation that dealt in measuring the dynamic characteristics of a bell tower located at a close distance from the examined building. The response of the masonry infills is also included employing a methodology that takes into account various non-linear mechanisms that develop during the infill-R/C frame interaction when this type of structural system is subjected to horizontal seismic forces. In addition, the possibility of the development of plastic hinges at predetermined locations of the reinforced concrete elements is also included in the numerical investigation. Through the study of the obtained numerical predictions an effort is made to understand the observed performance of this building. The obtained numerical predictions of its earthquake response demonstrate that the minimum observed structural damage in this case may be attributed to the favourable influence of the well built masonry infills as well as of the continuous foundation mat interaction with the flexible soil without adverse effects.*

1 INTRODUCTION

The objective of this paper is to study the dynamic and earthquake response of a two-story reinforced concrete(R/C) structure that houses the City Hall of the city of Lixouri in the island of Kefalonia, Greece. This structure has two particular points of interest. The first point is that its ground floor R/C foundation mat hosted an instrument which recorded the acceleration of the damaging earthquake of 3rd February, 2014. The second point is that this structure is at a 350m distance from the bell tower of Agios Gerasimos (figures 1 and 2).



Figure 1. View of the center of Lixouri



Figure 2. The two-story R/C building that housed the City Hall of Lixouri prior to the seismic event of 3rd February 2015. Because of the developed structural damage is not occupied at present.

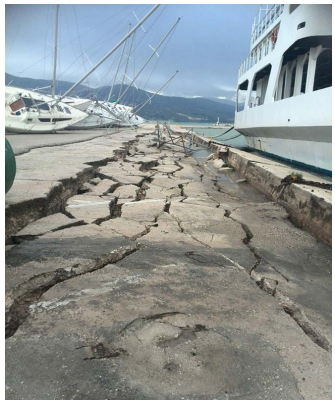


Figure 3. The earthfill embankement at the harbor immediately after the seismic event of 3rd February 2015

This bell tower has been the subject of in-situ dynamic measurements in order to quantify the influence of the soil-foundation deformability at this site[14]. Moreover, spectacular damage was observed at the earth fill embankment that forms the harbor of Lixouri (shown at the bottom of figure 1) as well as the overturning of boats that were free standing at the promenade that was at a relatively close distance from the City Hall building (figure 3). The in-situ

study of the effects of strong earthquake ground motion gives the basis to check the validity of methods of analysis as the one attempted here [1, 2, 8, 13]. Use is made in this study of the measured acceleration of this particular strong ground earthquake motion.

The island of Kefalonia has been subjected to intense earthquake activity for a long time [2]. The whole region near Lixouri was subjected during the winter of 2014 in an intensive earthquake sequence and this gave the opportunity to focus, among other structures, on the earthquake response of the City Hall building as well as this bell tower which remained unscathed, despite the intensity of the seismic ground motion and the damage of neighboring structures [14]. In figure 1 the location of the City Hall of Lixouri is shown together with the bell tower of Agios Gerasimos at a distance of 0.35km where in-situ tests for measuring its dynamic characteristics were performed ([14]). It is interesting to note that the intensity of shaking during this damaging 3rd of February 2014 seismic event was recorded by a strong motion accelerograph located at the ground floor of the City Hall building (figures 4 to 6).



Figure 4. Ground floor location of accelerograph

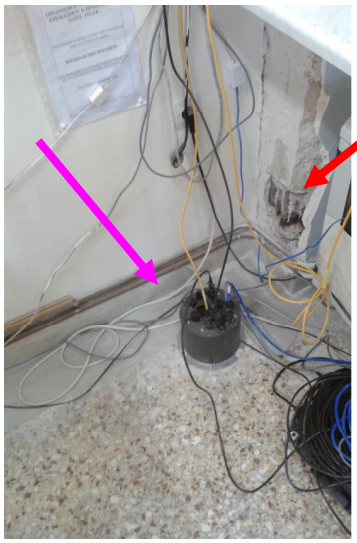


Figure 5. Ground floor location of accelerograph

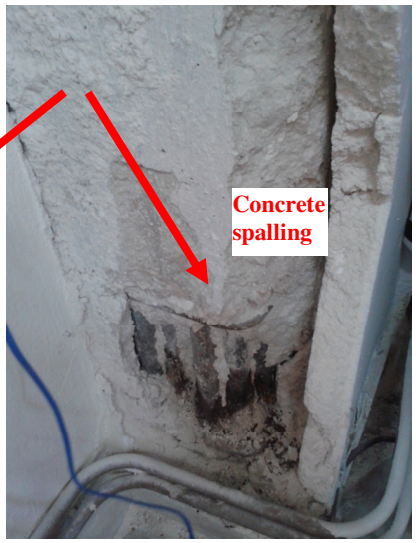


Figure 6. Signs of distress at the toe of nearby R/C column

Figure 7 depicts the plan of the ground floor and the 1st story of the City Hall at Lixouri. The total length in the longitudinal North-South (x-x) direction is equal to 24.3m whereas the total length in the transverse East-West (y-y) direction at the North side is equal to 16.54m and at the South side 11.07m. The mid-plane of the R/C slab that serves as the ground floor ceiling is located at 4.24m from the ground floor level (top surface of the foundation slab) whereas the mid-plane of the R/C slab that serves as the 1st story ceiling is located at 9.19m from this ground floor level. The structural system in the longitudinal North-South (x-x) direction is characterized by relatively short length R/C beams, approximately 4m long, that are joined monolithically with the adjacent columns. On the contrary, in the transverse East-West (y-y) direction the structural system is formed by a number of single bay two-story R/C frames. The bays of these frames have a clear span of approximately 8.40m from the mid-axes of their columns. Moreover, as can be seen in figure 7 the columns of these two-story R/C frames are 300mm x 500m and the relevant beams are 300mm wide and 700mm deep. Most of these frames in the upper 1st story are without any masonry infills in the transverse East-West (y-y) direction, thus creating a considerable clear space which was utilized for the City Hall meetings (figure 8). On the contrary, brick masonry infills occupy most of the bays of these R/C frames at the ground floor, thus creating various separations to be utilized as office space.

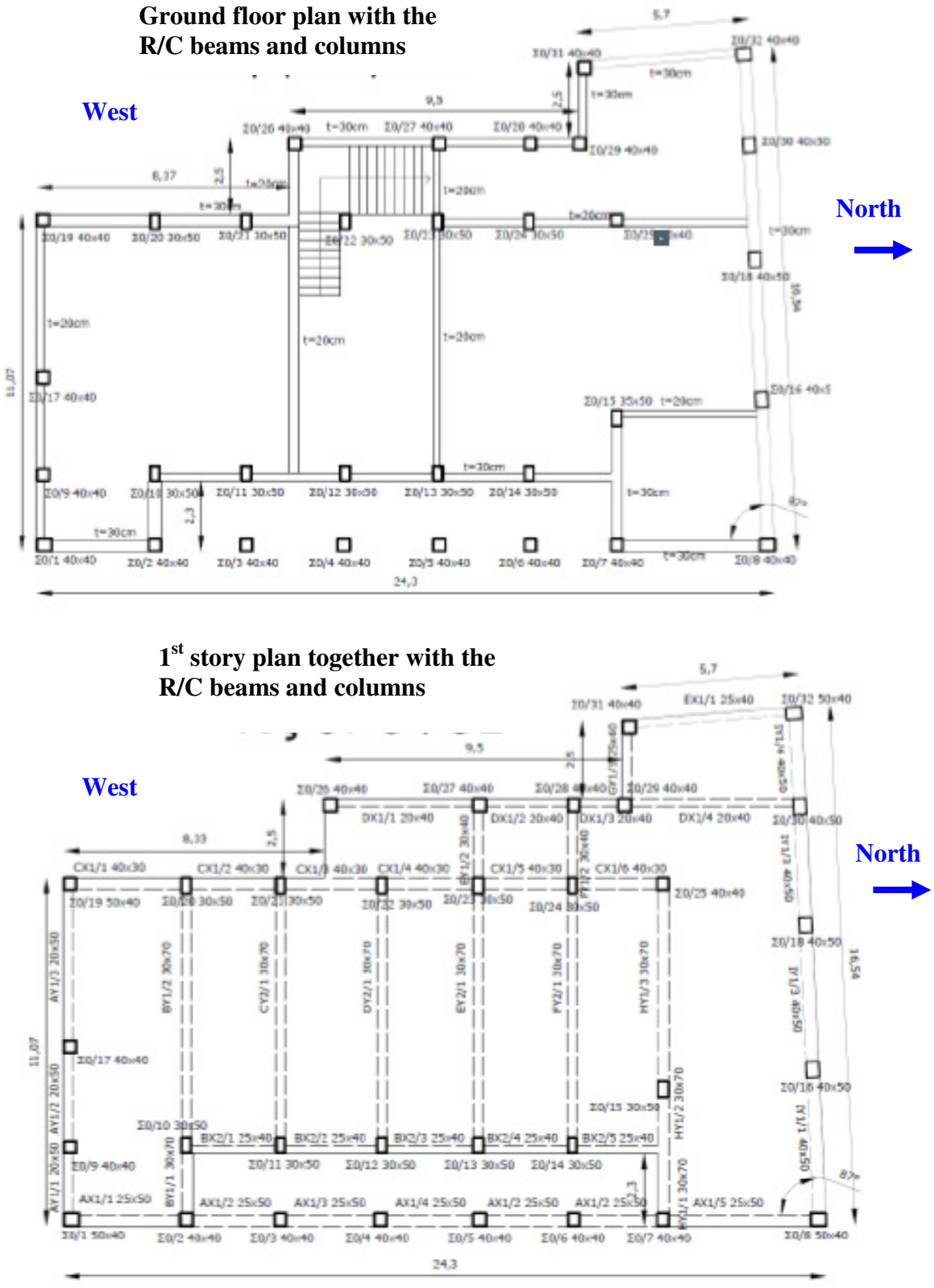


Figure 7. Plan of the ground floor and the 1st story of the City Hall at Lixouri



Figure 8. Reinforced concrete frames in the upper 1st story at the East-West y-y direction. The clear space was utilized for the City Hall meetings. Visible signs of masonry infill R/C frame interaction. Exterior wall.

Masonry infills occupy a large number of bays of the R/C frames that are created at all the external sides of this structure. These sides facing East, West and North (figure 7) have door and window openings whereas the side facing South is fully built with masonry infills as it is almost in contact with the adjacent building.

The most visible damage of the City Hall due to the 3rd of February 2014 strong seismic ground motion was in the interior and exterior masonry infills (figures 8, 9 and 10). Signs of distress at the toe of certain interior and exterior R/C columns at the ground floor level could also be observed (figures 6 and 11, respectively).



Figure 9. Visible signs of masonry infill R/C frame interaction. Interior wall .



Figure 10. Visible signs of masonry infill R/C frame interaction. Exterior walls .



Figure 11 Signs of distress at the toe of an exterior R/C column

As can be concluded from the material presented here one point that is worth being investigated is the influence of the presence of masonry infills in the dynamic and seismic response of this building. Significant research effort has been devoted in the past in the study of the interaction between masonry infills and the surrounding R/C frames during earthquake excitations [4, 5, 6, 7, 9, 10, 11, 12]. These studies have investigated this problem experimentally as well as numerically in trying to understand the most significant response mechanisms. The experimental results were utilized to validate analytical and numerical tools capable of predicting the response of R/C structures with frames hosting relatively strong of masonry infilled frames [9, 10, 12]. Such tools will be employed also in this present work as will be explained in the following sections. The second point of interest is investigating the influence of the foundation deformability. As already mentioned, from various observation in the Lixouri area it becomes apparent that the soil foundation deformability may have exerted certain influence in the observed dynamic and seismic response. This became evident from the in-situ measurements of the dynamic response of the Agios Gerasimos bell tower ([]). Therefore, it was decided to study this soil-foundation deformability in a parametric way as will be explained in the following sections.

.Finally, the presence of a R/C staircase that leads from the ground floor to the 1st story it is a third point of interest, which is also investigated. In summary the following parameters are studied:

a1. The soil-foundation deformability, **a2.** The presence of the masonry infills, **a3.** The presence of the staircase.

2 SOIL – FOUNDATION DEFORMABILITY

The foundation of this building is a R/C continuous slab with a thickness approximately equal to 0.5m. It is already mentioned that in-situ studies were performed with the Agios Gerasimos bell tower in order to research influences on the dynamic and earthquake response arising from soil-foundation deformability [14]. In order to study numerically the soil-foundation deformability the following process was utilized.

First, a numerical model of the R/C foundation slab was formed as shown in figure 12. Together with the foundation slab, which was modeled with shell elements having linear elastic properties based on the Young's modulus of concrete, the soil layers underneath this slab were also modeled being in full contact with the R/C slab. These soil layers extended to a depth of 4m and were formed with linear elastic solid brick elements.

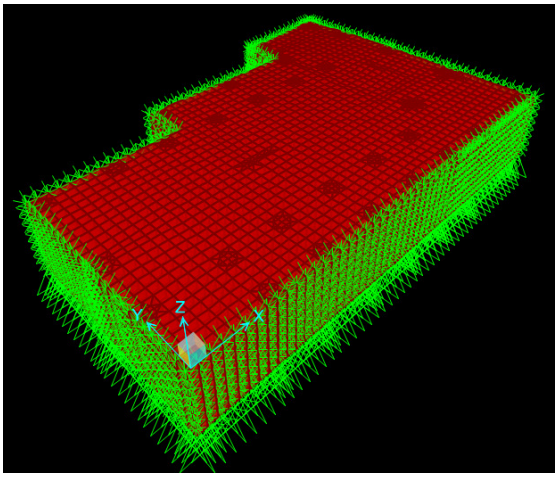


Figure 12. Numerical model of the foundation slab and the underlying soil.

Because it was not possible to find reliable geotechnical data in the vicinity of the studied structure the investigation of the soil-foundation deformability was attempted in a parametric way as will be explained below in order to define the elastic properties of the soil elements.

1st case. A shear wave velocity equal to 450m/sec was assumed for the underlying soil. This value, together with a soil density equal to 20KN/m3 leads to a shear modulus equal to 416.7MPa. This value together with a Poisson's ratio value equal to 0.2 leads to a Young's modulus value for the soil equal to 1000MPa. This represents a rather hard soil.

2nd case. Following the same rational but this time assuming a shear wave velocity value equal to 200m/sec leads to a the Young's modulus value for the soil equal to 196MPa. This represents a medium stiffness soil and is comparable with the corresponding value found from the Agios Gerasimos in-situ measurements.

3rd case. This time the shear wave velocity value was set equal to 150m/sec that represents a rather flexible soil that leads to a Young's modulus value for the soil equal to 110MPa.

Next, the top surface of the foundation slab was loaded in the vertical direction with a uniformly distributed pressure equal to -1.0MPa, with the positive vertical axis being upwards (figure 12). The bottom surface of the bottom layer of the soil volume was constrained to have zero displacements in all three directions. The side boundaries of the soil volume were constrained only in the two horizontal directions. In this way the foundation slab was displaced almost uniformly in the vertical direction being compressed in this way. The following table 1 lists the resulting vertical deformation of the slab for the three cases of soil deformability being considered.

Table 1. Vertical deflections of the soil-foundation simulation

Soil deformability	1st case Vs=450m/sec	2nd case Vs=200m/sec	3rd case Vs=150m/sec
Vertical slab deflection (mm)	3.6mm	18mm	33mm

In order to simplify the final numerical model of the City Hall structure including the soil-foundation deformability the following approximation was made. An alternative numerical model of the foundation slab was formed. This model retained the R/C foundation slab simulated with shell elements. However, the soil layers being simulated before with solid brick elements were replaced with two-node 3-D link elements having one node fully restrained in the all three directions as the support to the earth and the other node in full contact with each node of the foundation slab. Moreover, these two-node links were given such an axial stiffness that when the foundation slab was compressed with the same surface pressure as before (1.0MPa) the resulting vertical deflection of the foundation slab remained the same as before. Moreover, in certain cases a non-linearity was introduced in the axial direction of these two-node link elements resulting in their inability to sustain any tension. Following this rational the axial stiffness of these two-node link elements is listed in the following table 2.

Table 2. Axial stiffness of the equivalent two-node links

Soil deformability	1st case Vs=450m/sec	2nd case Vs=200m/sec	3rd case Vs=150m/sec
Axial Stiffness of the vertical two-node links (KN/mm)	55	10.5	5.9

3 THE PRESENCE OF THE MASONRY INFILLS

Use is made here of an equivalent post-elastic "pushover" type of analysis that draws information on the stiffness and strength variation from one-bay, one-story R/C masonry infilled unit frames that compose a given multistory structural formation [9, 10, 11, 12]. This numerical simulation is based on the well known substitution of the masonry infills with equivalent multi-linear diagonal struts. However, in order for this substitution to be realistic the following procedure is adopted, as is briefly described below.

a1) The multi-story structural formation is decomposed to a number of individual single-story masonry infilled frame units that are grouped according to their common geometric and mechanical characteristics of the R/C elements and their masonry infills, in order to minimize in this way the number of different units to be analyzed in the next steps (steps b1 to e1).

b1) For each one of these single-story masonry infilled R/C frame units a fully non-linear simulation is performed in order to obtain through a "pushover" type of analysis the full non-linear response for each individual single-story masonry infilled R/C frame composing the multi-story structural formation. This simulation, which is described in detail in [10] and [12] includes:

- The numerical simulation of the masonry infill utilizing non-linear plane stress finite elements.
- The numerical simulation of the surrounding R/C frame with linear elastic beam and column members together with predetermined locations of possible plastic hinge formation at the ends of each element.
- The numerical simulation of the interface between the R/C frame and the masonry infill with 2-D non-linear joint elements in the axial and transverse direction.

c1) For each one of these single-story masonry infilled R/C frame units a "pushover" type A analysis is performed and the horizontal load (H) versus horizontal displacement (δ) or shear strain (γ) response curve is obtained.

d1) For each one of these single-story masonry infilled R/C frame units a number of alternative numerical simulations are next prepared. Each one of these alternative simulations assumes that the R/C members of the surrounding frame retain their capability of developing plastic hinges at their ends as in b1) above whereas the masonry infill is replaced with an equivalent multi-linear diagonal strut member with properties as explained in e1) below.

e1) The alternative numerical analysis is now performed for the same single-story units of step d1; the objective here is to obtain horizontal load (H) versus horizontal displacement (δ) or shear strain (γ) response for a number of inter-story drift values corresponding to a number of pre-selected shear-strain levels for the masonry infill (e.g. 0.1%, 0.15%, 0.2%, 0.25%, 0.3%, etc.). The alternative analysis response results should be in reasonable agreement with the response values obtained through the fully non-linear simulation for the same infill masonry single-story frame unit. This is achieved through a trial and error approach by adjusting properly in the alternative analysis the multi-linear properties of the diagonal strut that replaces the masonry infill for each one of the single-story masonry infill R/C frame units obtained initially by n the fully non-linear simulation in step c1.

f1) Next, all the masonry infills in the numerical simulation of the multi-story structural formation are replaced with such multi-liner equivalent struts

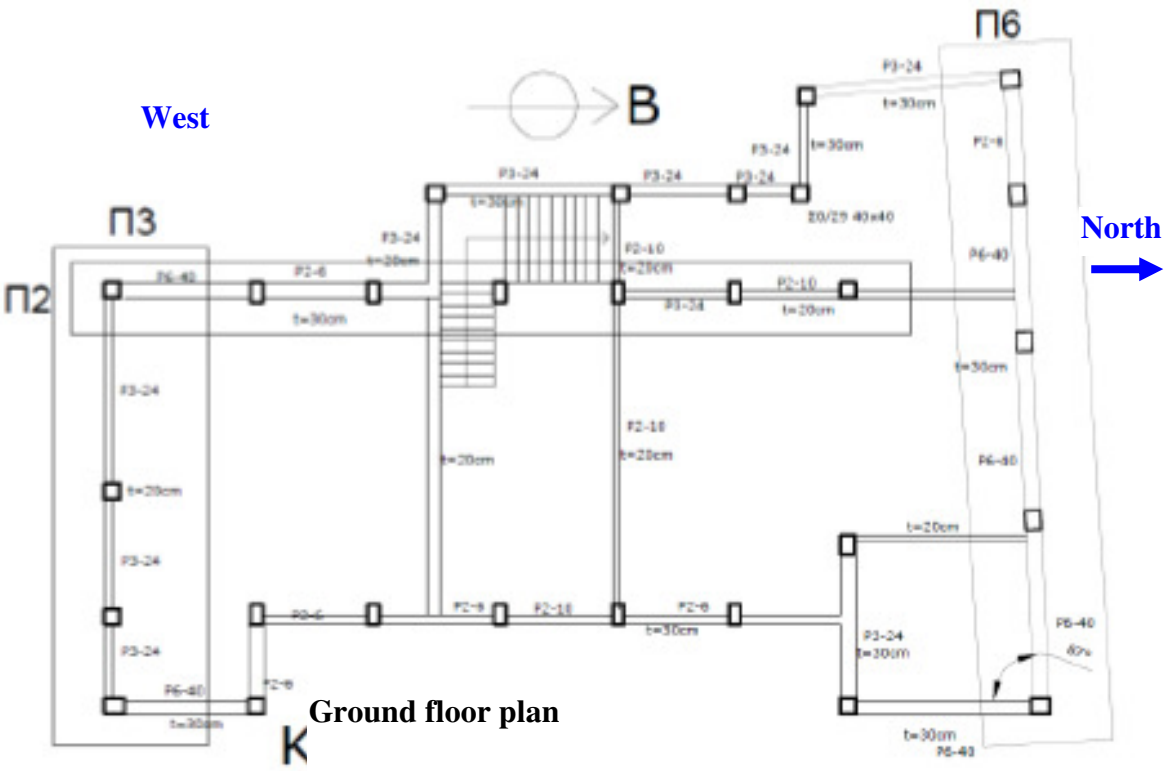


Figure 13 Ground floor plan with the indications of the masonry infilled "unit" frames designated with their code names: P2-10, P2-6, P3-24, P6-40

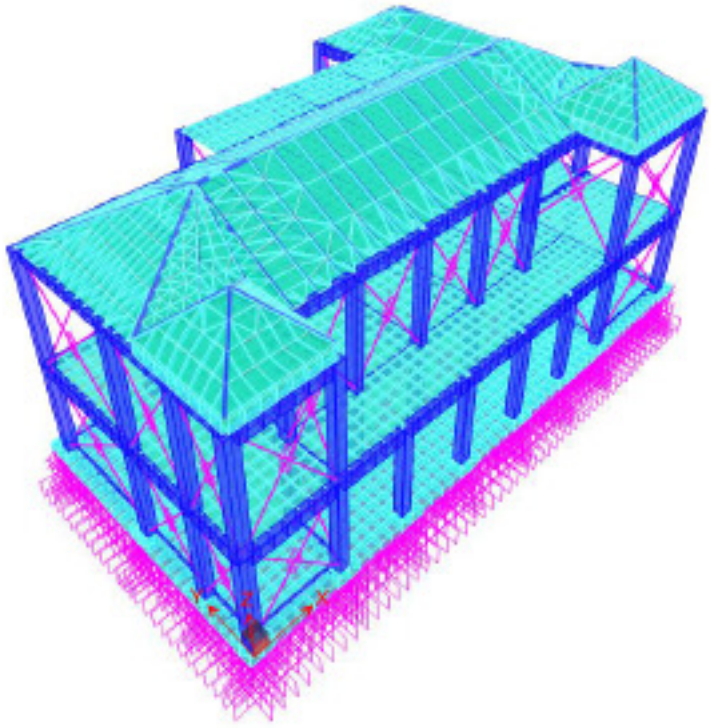


Figure 14 3-D representation of the City Hall building with the diagonal struts representing the masonry infills in place for the ground floor as well as for the 1st story.

Figure 13 depicts the ground floor plan where the various single-story one-bay infilled frames are denoted with a code name such as P3-24 for the infilled of the South side and most of the West side, P6-40 for the infilled frames of the North side and some of the East side, P2-6 the remaining infilled frames of the East side and P2-10 an infilled frame of the interior in the East-West direction and some remaining infilled frames at the exterior of the City Hall R/C building. The same process is followed for the infilled frames of the first story (figure 14). These single-story one-bay infilled R/C frames represent the "unit" infilled frames that this multi-story building is decomposed to. Following the numerical process described before the properties of multi-linear equivalent diagonal struts are found for each one of these the "unit" infilled frames. These diagonal struts are represented in the numerical simulation with two-node links having axial stiffness properties found in the way described before (steps a1 to f1).

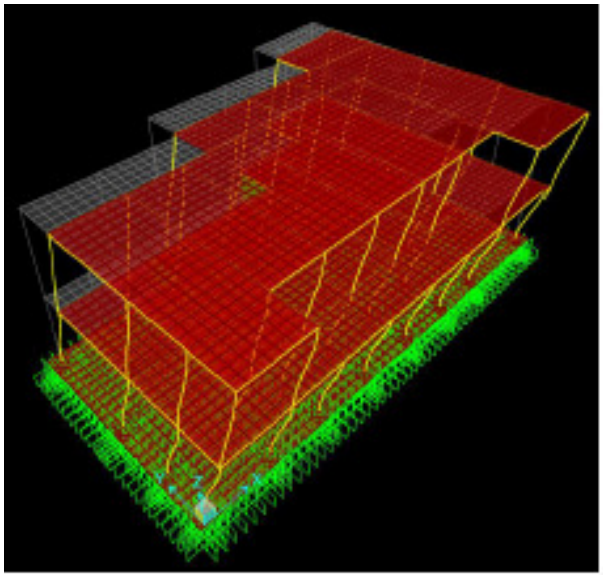


Figure 15. Numerical model of the City Hall building without masonry infills

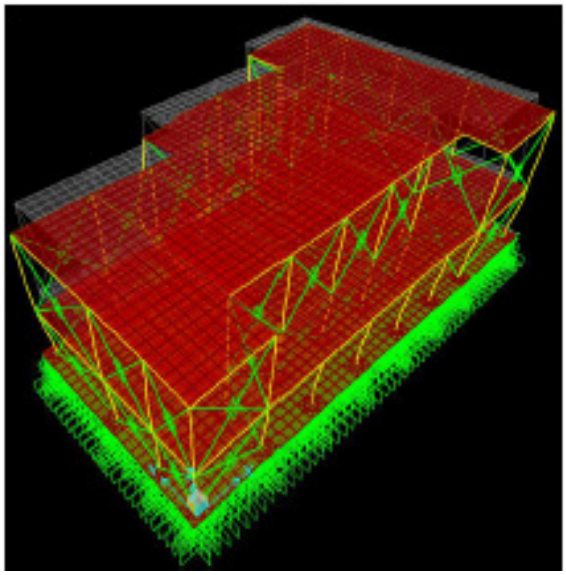


Figure 16. Numerical model of the City Hall building without masonry infills

For the linear elastic analyses the masonry infill in each bay was represented by two diagonal struts (figure 16) having 50% of the stiffness of the single "equivalent" diagonal strut defined in the way described before (steps a1 to f1). In figure 15, the numerical simulation of the City Hall R/C building without masonry infills is also shown. The following table 3 lists (2nd row) the stiffness value of the first branch of these equivalents struts that is valid for the linear numerical analyses.

Table 3. Axial stiffness value for the employed diagonal struts

	Code Name of "Unit" infilled frame and Used initial stiffness values KN/mm			
	P2-10	P2-6	P3-24	P6-40
Linear case 50% of or the single "equivalent" diagonal strut. Two struts per bay	85.2	19.6	60.9	79.0
Non-linear case 100% of or the single "equivalent" diagonal strut. One strut per bay	170.3	39.2	121.8	158.0

For the non-linear push-over type of analyses these multi-linear links were defined in a way to be able to sustain only compression and no tension with initial stiffness equal to the full 100% of the value found for the single equivalent" diagonal struts (Table 3 3rd row). Moreover, only a single two-node link was provided per "unit" frame joined diagonally with the surrounding frame nodes in a way as to develop compression with the given stiffness value up to a level of inter-story drift beyond which each link was assumed to yield as shown in the following figures .

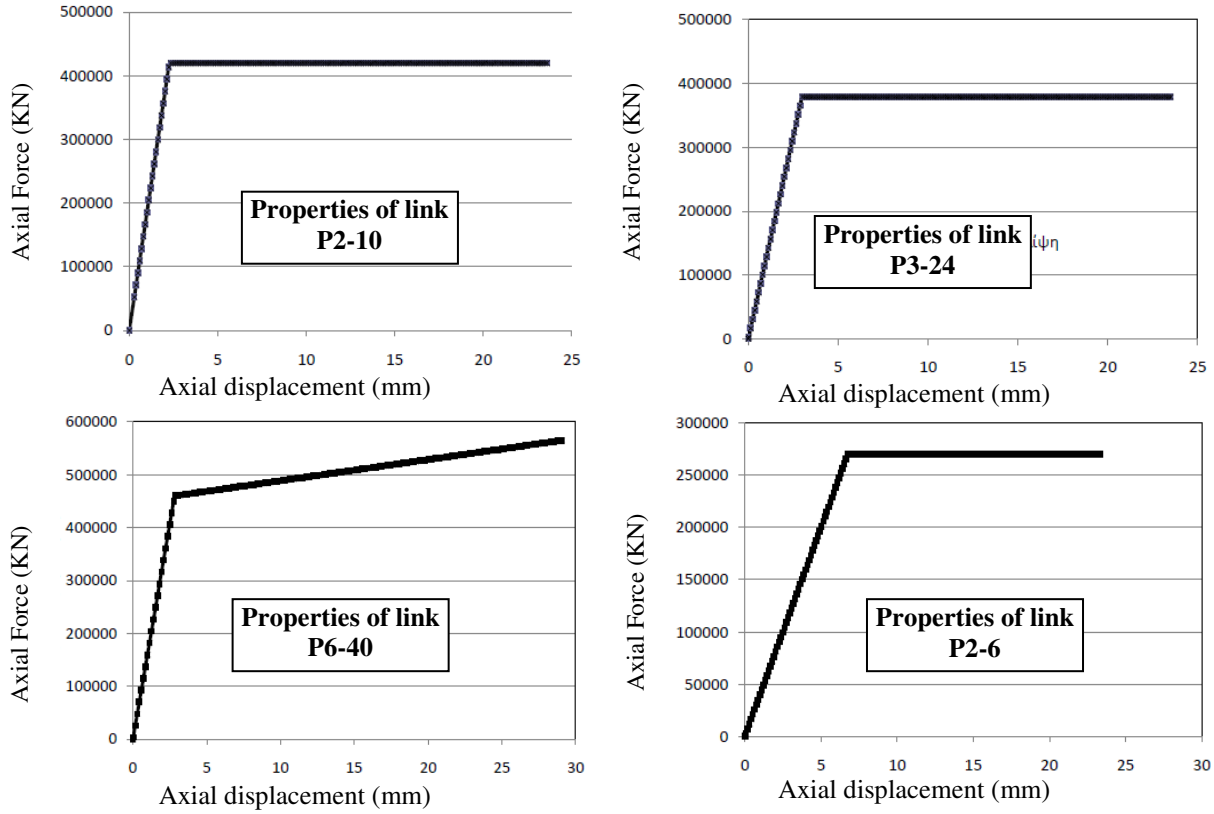


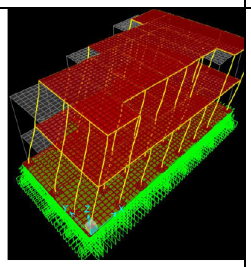
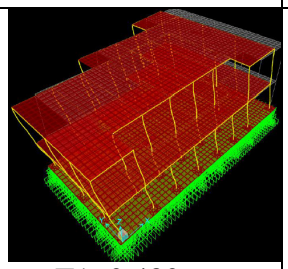
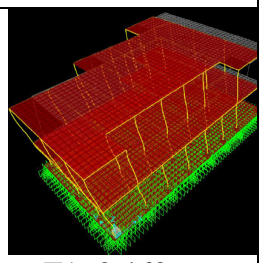
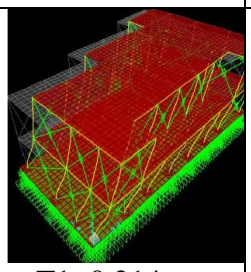
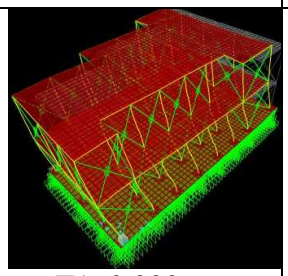
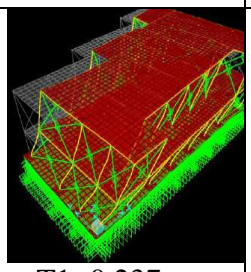
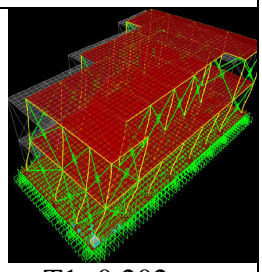
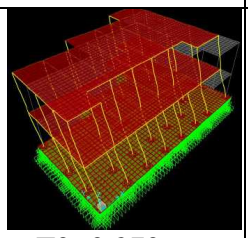
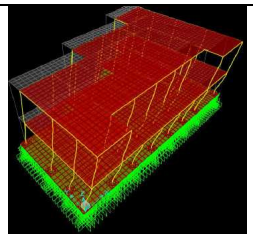
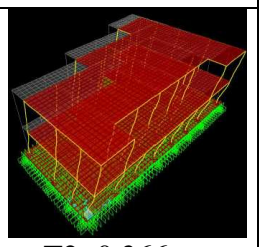
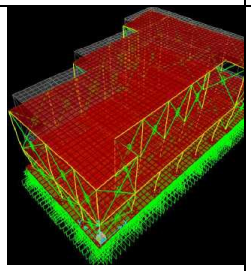
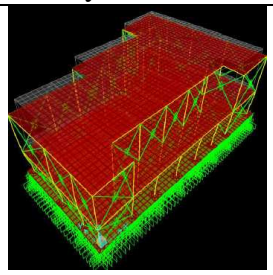
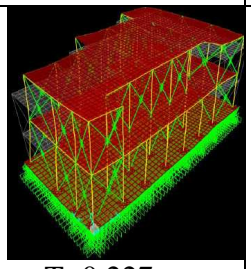
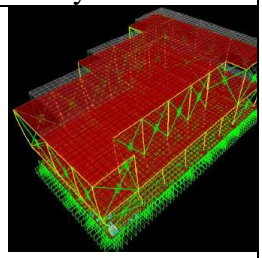
Figure 17. Axial load – axial displacement properties of the nultilinear two-node links representing the equivalent diagonal struts as a numerical approximation of the maonry infills.

4 THE LINEAR DYNAMIC RESPONSE OF THE CITY HALL BUILDING

The eigen-modes and eigen-periods of the City Hall building are investigated next in a parametric way, assuming linear elastic behaviour of all the elements, including the diagonal struts and the foundation links. The following parameters are varied:

a2) The superstructure is considered either with the diagonal struts representing the masonry infills or without these struts, thus numerically simulating the "bare" superstructure only with the reinforced concrete structural elements (slabs, beams and columns). These structural elements are the same in the numerical simulation without and with masonry infills when the diagonal struts are added with properties as outlined in section 3 (figures 15 and 16)
b2) The soil-foundation deformability is approximated in the way described in section 2. That is a 1st case is examined having vertical two-node links at the soil-foundation slab interface with axial stiffness equal to 55KN/mm, representing relatively hard soil conditions. Then, a 2nd case is examined having vertical two-node links at the soil-foundation slab interface with

axial stiffness equal to 10.5KN/mm, representing a soil of medium deformability. Next, a 3rd case is examined having vertical two-node links at the soil-foundation slab interface with axial stiffness equal to 5.9KN/mm, representing a rather flexible soil. Finally, a 4th case is examined whereby the foundation slab is presumed to be rigidly attached to the soil-foundation interface.

Figure 18	Soil-Foundation deformability 1st eigen-period T1			
	1st case hard soil	2nd case medium soil	3rd case Flexible soil	Non-deformable Soil
Bare superstructure without masonry infills North-South (x-x)	 T1=0.474sec mx = 83.8%	 T1=0.480sec mx = 83.8%	----	 T1=0.462sec mx = 87.6%
Superstructure with masonry infills (two diagonal struts per bay) North-South (x-x) East-West (y-y)	 T1=0.214sec mx = 53.9% my = 31.6%	 T1=0.229sec mx = 45.0% my = 39.2%	 T1=0.237sec mx = 34.1% my = 48.9%	 T1=0.202sec mx = 23.8% my = 64.8%
	Soil-Foundation deformability 2nd eigen-period T2			
	1st case hard soil	2nd case medium soil	3rd case Flexible soil	Non-deformable Soil
Bare superstructure without masonry infills North-South (x-x)	 T2=0.379sec my = 86.5%	 T2=0.386sec my = 86.2%	----	 T2=0.366sec my = 89.8%
Superstructure with masonry infills (two diagonal struts per bay) North-South (x-x) East-West (y-y)	 T2=0.209sec mx = 35.8% my = 52.3%	 T2=0.220sec mx = 43.7% my = 44.0%	 T=0.227sec mx = 53.9% my = 33.7%	 T2=0.20sec mx = 71.6% my = 23.6%

The variation of the two structural formations (with and without masonry infills) and the four soil-foundation deformability conditions results in (8) different numerical models of the City Hall building. In figure 18 the 1st and 2nd eigen-modes are depicted together with the corresponding eigen-periods and the mass participation ratios mx and my. The following remarks can be made on the basis of the results presented in figure 8.

1) As was expected, the addition of masonry infills increases drastically the stiffness of the structural system, and therefore reduces considerably the corresponding eigen-period values, despite the mass increase that accompanies these masonry infills. It is well known that up to the point these masonry infills remain undamaged, and thus active in terms of in-plane stiffness, the resulting structural formation is considerably stiffer than the corresponding structure that either it was not being built with such masonry infills or the infills become eventually inactive by being damaged during the earthquake sequence.
2) An additional influence that becomes apparent from the eigen-periods values listed in figure 18 together with the corresponding mass participation ratio values is the fact that the structural system of the City Hall building, when it is considered as "bare" that is without the masonry infills, vibrates in its two fundamental eigen-modes in a mainly translational way, either in the North-South or in the East-West direction. The addition of masonry infills results in the two fundamental eigen-modes becoming coupled in the North-South and East-West direction. This must be attributed to the fact that the location and the stiffness of these masonry infills in the City Hall building is not symmetric thus resulting in this coupled dynamic response.
3) The influence of the soil-foundation deformability is less drastic. Again, as was expected, the more flexible soil-foundation condition results in a modest increase in the fundamental eigen-periods values.
4) The increase in the soil-foundation deformability does not have a noticeable influence on the mass participation ratio values for the two fundamental eigen-modes when the structural system is without masonry infills ("bare" structure). The addition of the masonry infills apart from resulting in a coupled translational response in the North-South and East-West direction also has a noticeable influence on the corresponding mass participation ratio values.

5 PREDICTIONS OF THE EARTHQUAKE RESPONSE FOR THE CITY HALL BUILDING

Next, numerical simulations of the earthquake response of the City Hall building are presented. The numerical analyses that were performed towards obtaining earthquake response predictions of the City Hall building fall in the following two main categories.

5.1 Static numerical analyses with non-linear mechanisms for the two-node links at the foundation-soil interface and for the diagonal struts

In the first category a non-linear step-wise analysis is followed. For this type of numerical analyses the first step represents the application of the vertical loads; these loads result from the load combination D+0.3Q, where D represents the permanent vertical loads and Q represents the variable vertical loads. The horizontal seismic loads are next applied stepwise at the levels of the slabs of the 1st story floor and the 1st story ceiling either in the North-South (x-x) or in the East-West (y-y) direction. The ratio of the amplitude of these horizontal forces is

kept constant in all steps and is set equal to the ratio of the corresponding horizontal displacements that resulted from the modal analysis at the story mass centers in the horizontal direction (either x-x or y-y) being considered. These are obtained for each particular structural formation, resulting from the combination of the superstructure with or without masonry infills and of the soil-foundation deformability variations, from the modal dynamic analyses presented in section 4. Two types of non-linearity are introduced in this first category of numerical seismic analyses; the first is the one described in section 2 for the two-node links representing the soil-foundation deformability; that is that these links are unable to sustain any tension. The second type of non-linearity is the one related to the behaviour of the diagonal struts representing the masonry infills, as described in section 3; this time these diagonal struts are assumed to yield at a certain level of axial deformation (figure 17). For this 1st category of numerical seismic analyses the R/C members are considered not to yield. The maximum seismic load that is applied in each case is defined according to the following rational.

It is presumed that the seismic loads could be defined according to the acceleration response spectral values derived from the acceleration measurements at the top surface of the foundation slab of this building. These are depicted in figures 19 and 20 for the North-South (x-x) and East-West (y-y) directions, respectively.

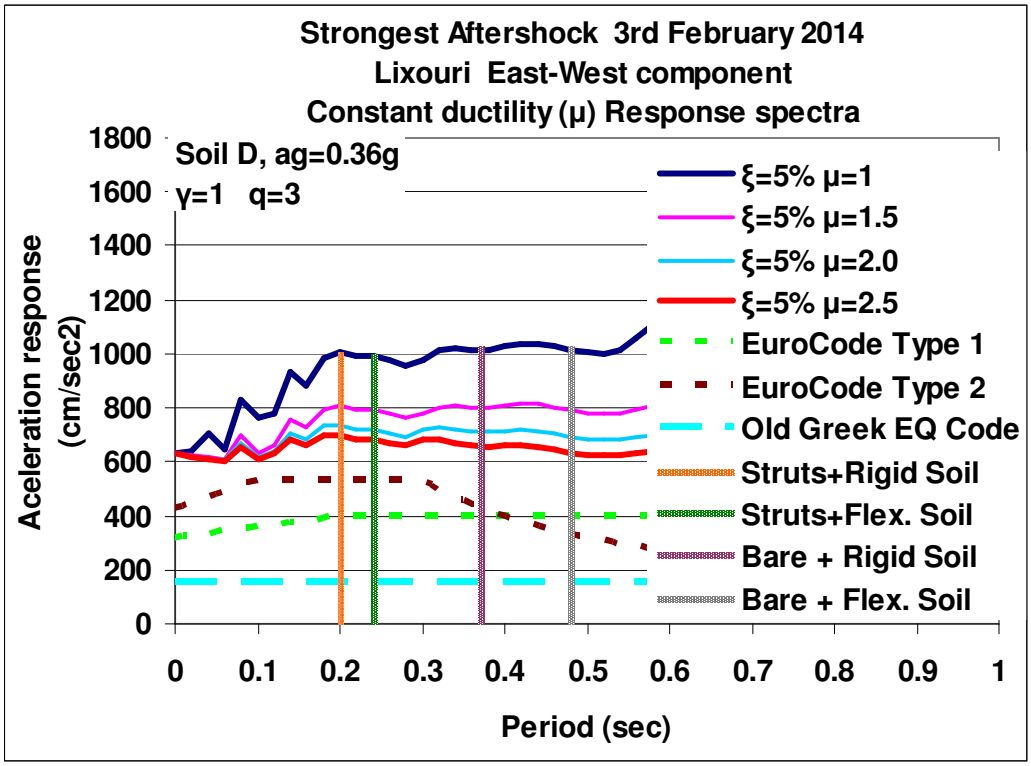


Figure 19. Definition of East-West (y-y) seismic loads through the recorded ground motion

The horizontal seismic loads in the y-y (E-W) direction are applied through the Lixouri East-West elastic acceleration response spectral curve for 5% damping ratio (figure 19, q=1) as it was derived from the E-W component of the acceleration record that was recorded during the strong aftershock of 3-2-2014 ([1]). This was recorded by an instrument located at the ground floor slab of a R/C two-story building (City Hall) located at a distance of 350m from the bell tower, as indicated in figure 1 (se also figures 4 to 6).

The response spectrum values have not being scaled to account for a response modification factor. The reason for this is the fact that, apart from the visible damage of the masonry infills, that has been described in the introduction (figures 7 to 9), the main R/C structural elements

are with relatively limited signs of distress at the toe of few interior and exterior R/C columns at the ground floor level (figures 6 and 11). As can be seen, the acceleration spectral values for 5% damping and response modification value (q) equal to 1 are quite high at the level of the acceleration of gravity (g=981cm/sec2). In comparison, the "Old Greek Seismic Code" level of seismic forces that one presumes that this building was designed for are approximately 5 times less than these acceleration spectral values [3]. If this building would have been designed today according to the Euro-code 8 [15] design specrtra (either type 1 or 2) and for a response modification factor value equal to q=3 (typical for this type of R/C frame building) the corresponding force levels would be one half (1/2) of the force levels resulting from the recorded ground motion response spectra values shown in figure 19. Under these considerations, it is rather surprising that the structural damage of this building is at so minimal levels. This issue will be further discussed on the basis of the numerical predictions. It is interesting to underline here that the various eigen-periods, as they resulted from the eigen-mode study that was presented in section 4, correspond to almost the same acceleration spectral value for 5% damping and q=1 for all the various structural configurations considered in this study (with or without diagonal struts and rigid or flexible soil conditions).

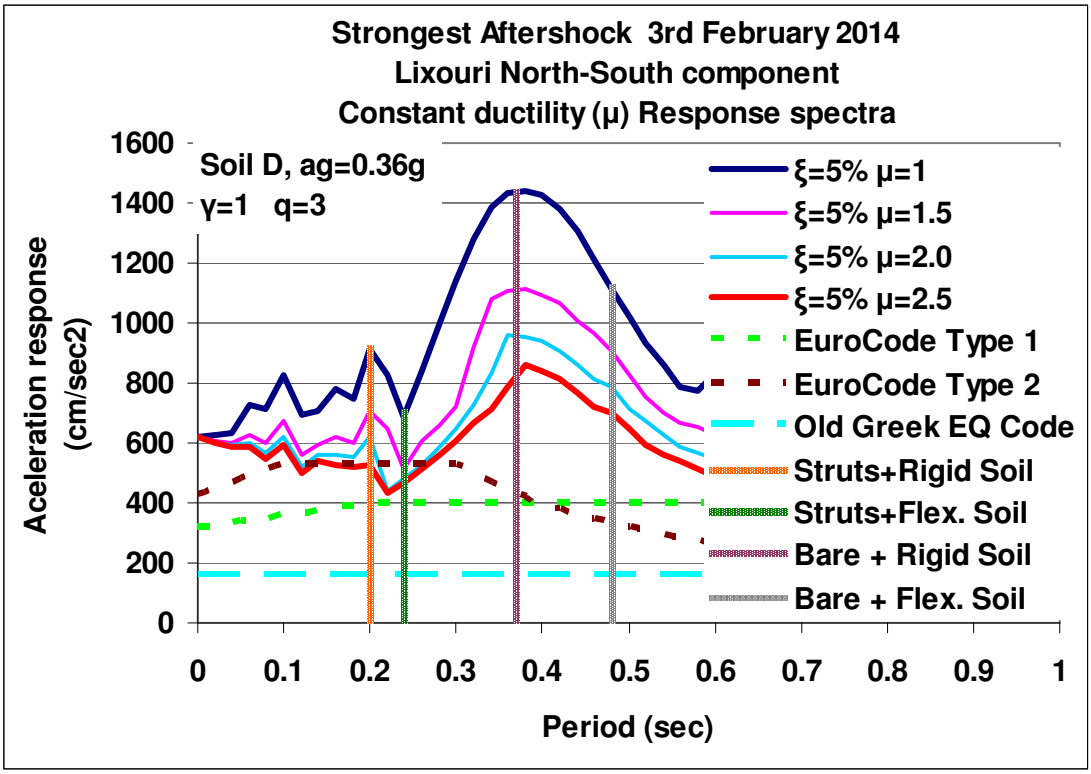


Figure 20. Definition of North-South (x-x) seismic loads through the recorded ground motion

As explained before, the horizontal seismic loads in the x-x (N-S) direction are applied through the Lixouri North-South elastic acceleration response spectral curve for 5% damping ratio (figure 20, q=1) as it was derived from the N-S component of the acceleration record that was recorded during the strong aftershock of 3-2-2014, [1] (figure 1).

The response spectrum values have not being scaled to account for a response modification factor, as explained before. As can be seen the acceleration spectral values for 5% damping and response modification value (q) equal to 1 are very high, reaching 1.3 times the acceleration of gravity (g=981cm/sec2) in case the masonry infills were not present or approximately 80% of the acceleration of gravity with the masonry infills present and before serious damage

could render them inactive. In comparison, the "Old Greek Seismic Code" level of seismic forces, that one presumes that this building was designed for, are approximately 6 to 4 times less than these acceleration spectral values [3]. If this building would have been designed today according to the Euro-code 8 [15] design specrtra (either type 1 or 2) and for a response modification factor value equal to q=3 (typical for this type of R/C frame building) the corresponding force levels would be 70% of the force levels resulting from the recorded ground motion response spectra values shown in figure 20. Under these considerations, it is again rather surprising that the structural damage of this building is at so minimal levels. This issue will be further discussed on the basis of the numerical predictions. It is interesting to underline here that the various eigen-periods, as they resulted from the eigen-mode study that was presented in section 4, correspond to much larger spectral acceleration values for the N-S recorded ground motion when the structural system is considered without masonry infills ("bare" structure) than when the masonry infills are present and not yet inactive by being damaged.

The following table lists the base shear values (at the top surface of the foundation slab) as they resulted from a linear elastic dynamic spectral analyses utilizing the East-West or North-South acceleration response spectral curves for 5% damping and q=1 derived from the recorded ground acceleration (figures 19 and 20).

	Base shear Values (KN)			
	"Bare" structure without masonry infills and Medium soil	Structure with masonry infills and Rigid foundation	Structure with masonry infills and Medium soil (2^{nd} case)	Structure with masonry infills and Flexible soil (3^{rd} case)
North-South (x-x) direction	7180	6179	5209	4844
East-West (y-y) direction	6756	6448	6036	6046

5.2 Push-over numerical analyses with non-linear mechanisms for the two-node links at the foundation-soil interface, for the diagonal struts and all the R/C members

In the 2^{nd} category of numerical seismic analyses the non-linear behaviour of all the R/C members is also considered on top of the non-linearity of the two-node soil-deformability links and of the non-linearity described for the diagonal struts representing masonry infills. Thus, an additional set of non-linearity is introduced at all the ends of the R/C elements (representing either R/C beams or R/C columns) in an effort to simulate numerically the development of flexural plastic hinges at these locations when the flexural demand rises beyond certain amplitude. This type of numerical seismic analysis was performed considering the seismic loads and response only in the East-West (y-y) direction. This time the numerical analysis has again a first step when the vertical loads from the load combination D+0.3Q are introduced. Next, a "push over" type of horizontal loads are introduced at the 1^{st} story floor and the 1^{st} story ceiling levels. These horizontal seismic loads are applied at the center of mass of these slabs and result from the product of the corresponding story masses with the same acceleration amplitude that is gradually being increased at each subsequent step. The seismic horizontal displacement attained at each step is checked at the center of mass of the 1^{st} story ceiling.

6 NUMERICAL PREDICTIONS OF THE SEISMIC RESPONSE

6.1 Results from the static numerical analyses with non-linear mechanisms for the two-node links at the foundation-soil interface and for the diagonal struts

In order to present the obtained results in a summary form the following process is followed. First, the flexural demands in terms of maximum/minimum bending moment values, as they are obtained from the 1st category of numerical analyses are found at the top and foot of all the columns as well as at the ends of all beams. This is done for all the studied numerical simulations of the structure with or without masonry infills and for the four cases of soil-foundation deformability. In what follows, earthquake response predictions from the structure with diagonal struts (presence of masonry infills) and for three soil-foundation deformability (rigid, medium and flexible soil) are presented. Moreover, the seismic loads are applied both in the North-South / South-North (±x-x) and East-West / West-East (±y-y) directions.

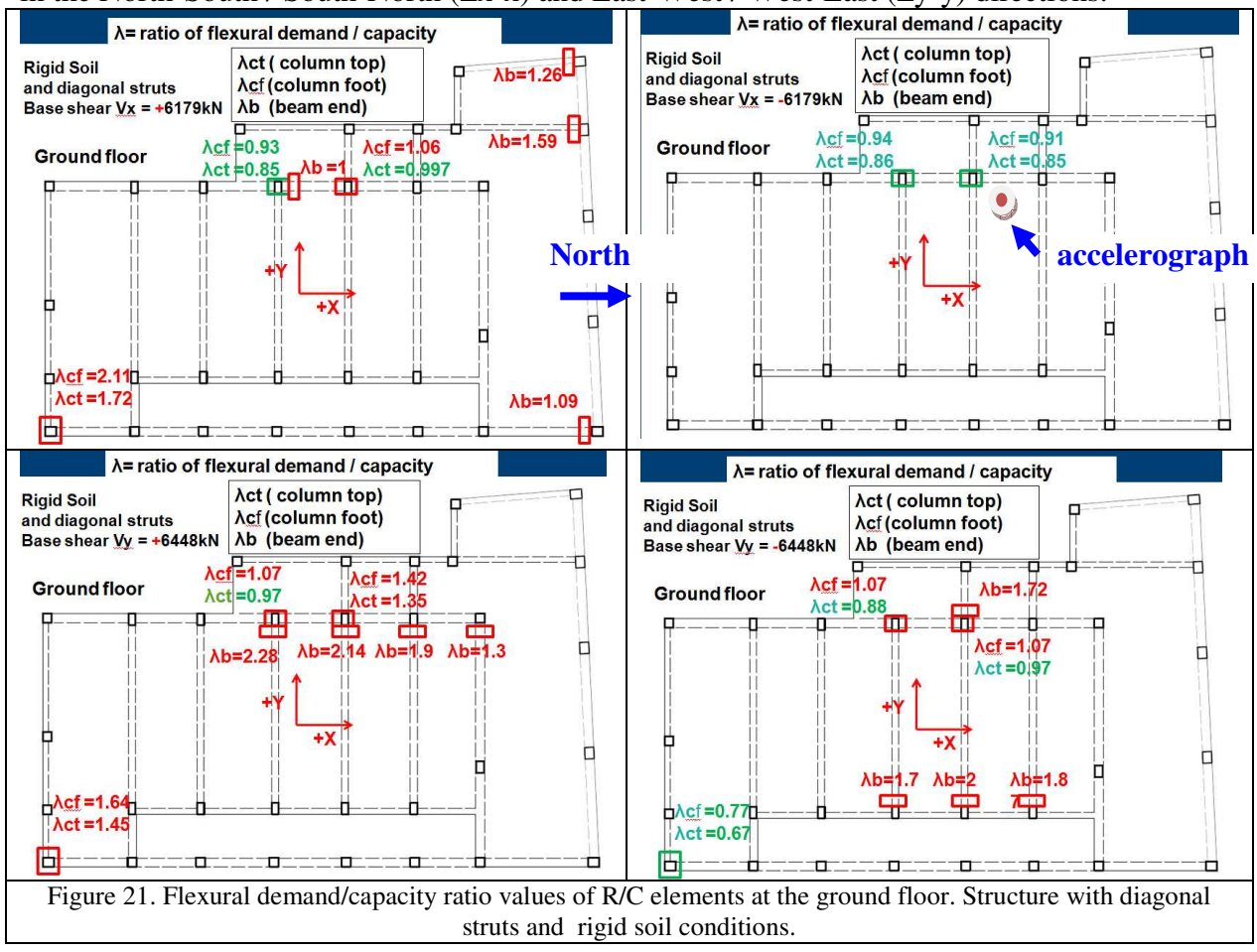


Figure 21. Flexural demand/capacity ratio values of R/C elements at the ground floor. Structure with diagonal struts and rigid soil conditions.

These results are presented in figures 21, 22 and 23 for the soil-foundation deformability cases that correspond to rigid, medium and flexible soil conditions, respectively. Instead of presenting the flexural demands by themselves these demands are compared with the corresponding flexural capacities at the same location and the ratio values (λ) of flexural demand / capacity are finally plotted in figures 21 to 23. The flexural capacity of the cross-sections was found by employing RCCOLA.NETv0.972 assuming the concrete strength equal to 20MPa

and the steel yield stress equal to 385MPa. Apart from checking the various R/C members in flexure the shear capacity was also checked but is not reported here.

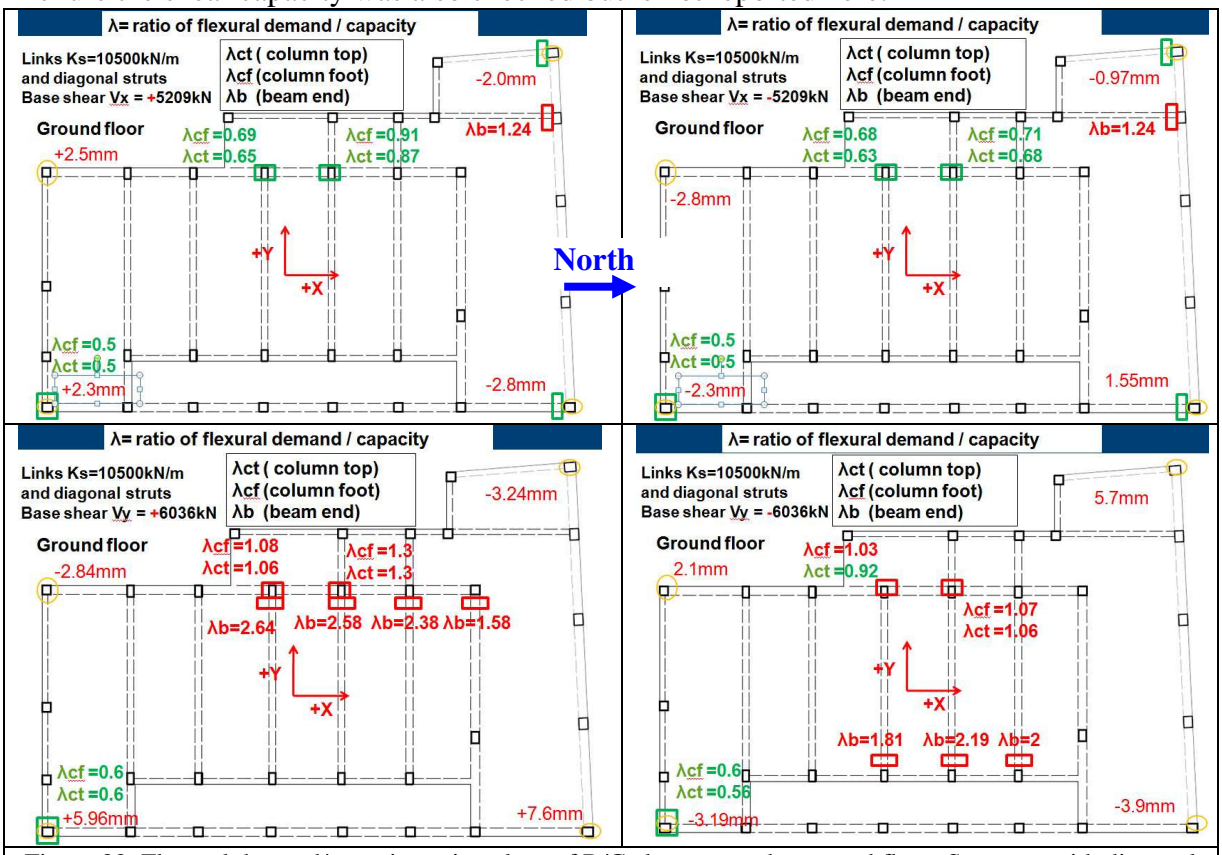
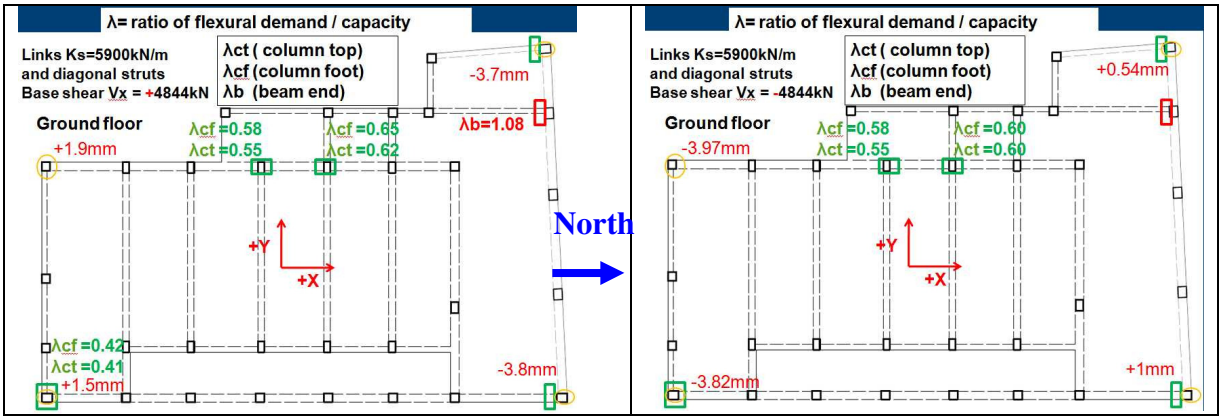


Figure 22. Flexural demand/capacity ratio values of R/C elements at the ground floor. Structure with diagonal struts and medium soil conditions.



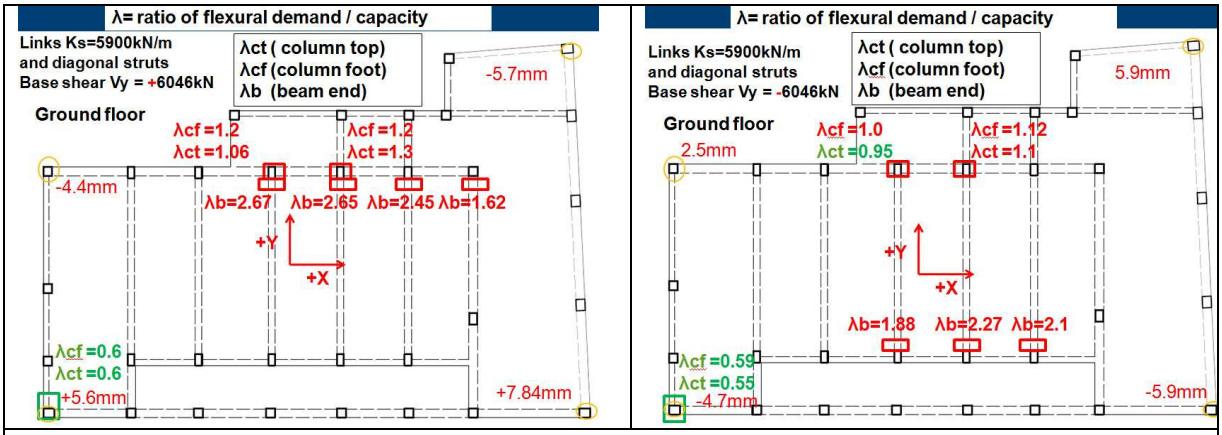


Figure 23. Flexural demand/capacity ratio values of R/C elements at the ground floor. Structure with diagonal struts and flexible soil conditions.

These **λ** ratio values are further detailed as **λb** when this ratio value refers to the end of a beam; when the ratio value refers to the top of a column is designated as **λct** or **λcf** when it refers to the foot of the column. When these ratios attain values larger than one (**λ > 1**, e.g. the predicted demand is larger than the capacity) then structural damage is expected to develop at this location. When this is the case the relevant value is plotted with the red color in figures 21, 22 and 23 otherwise is plotted with the green color when these ratio values are smaller than one (**λ < 1**), indicating that no structural damage is expected. Selected results are presented in the plots of figures 21, 22 and 23 for the columns of the ground floor and for the beams of the ground floor ceiling. Apart from these **λ** ratio values, the displacement demands at the four corners of the ground floor ceiling are also indicated in each plot of figures 21 to 23. The following remarks can be made on the basis of these results.

1. The largest **λct** or **λcf** (demand/capacity) ratio values are observed for the columns of the ground floor in the case of rigid soil conditions. The corresponding values for the medium or flexible soil conditions are smaller in comparison and many times become smaller than 1. This indicates that whereby structural damage is predicted in the columns for the rigid soil the presence of flexible soil results in most cases that these columns remain undamaged. The above observation can be explained by the value of the corresponding level of seismic forces used in each case in terms of base shear amplitude.
2. For approximately the same level of base shear amplitude in either the ±North-South (x-x) or ±East-West (y-y) direction the predicted performance of the ground floor columns demonstrates that the studied structure is more vulnerable when the seismic forces are applied in ±the East-West (y-y) direction than when applied in the ±North-South direction. This must be partly explained by the difference in the presence of the masonry infills as well as by the fact that the structural system in the ±the East-West (y-y) direction is composed by a series of two-column two-story R/C one-bay frames that, as already mention, have a clear span of 8.40m and develop high flexural demands.
3. For the same reasons, the beams of these frames are predicted to have large flexural demands that exceed in many cases the corresponding capacities (**λb > 1**), thus predicting structural damage in many end of these beam locations when the seismic forces are applied in the ±the East-West (y-y) direction.
4. The largest value of the **λcf** ratio (demand/capacity at the foot of the ground floor columns) is predicted for the column at the South-East corner at the ground floor of the City Hall building for the case of the rigid soil (**λcf** =2.12, figure 21). This occurs when the seismic forces are applied towards the North. The same column is predicted to be in

distress for the same soil conditions when the direction of the seismic forces is towards the West. This prediction agrees, up to a point, with the in-situ observations as this column exhibited signs of distress (figures 24 to 26).

5. Another location that the numerical analysis results predict column structural damage is the one at the west foot of the 4th from the left long y-y R/C frame with a clear span of 8.40. The value of the **λcf** ratio (demand/capacity at the foot of the ground floor columns) attains its largest value for rigid soil and seismic forces applied towards the West (**λcf** =1.42, figure 21). Structural damage is also predicted for this column for the same direction of seismic forces even for medium and flexible soil conditions; this time, however, the value of this ration is lower than the value for rigid soil (**λcf** =1.30 for medium soil figure 22 and **λcf** =1.20 for flexible soil figure 23). It should be pointed out here that this is also a location that is quite close to the accelerograph (figure 21) that recorded the seismic ground motion which was made use extensively here (see also figures 4 to 6). This prediction also agrees, up to a point, with in-situ observations as this column exhibited signs of distress (figures 4 to 6).
6. Structural damage is also predicted at the ends of the ground floor beams that belong to the long y-y R/C frame with a clear span of 8.40.This is predicted for all soil conditions when the seismic forces are applied in the East-West (y-y) direction. The largest **λb** ratio value (flexural demand/capacity for the beams) is obtained for the case of the rigid soil and the seismic forces applied towards the West (**λb**=2.28, figure 21). In-situ observations could not confirm obvious structural damage and distress at these locations. This is partly due to the fact that heavy plaster covered these locations which were at a considerable height from ground level as not to be easily accessible.



Figure 24. Spalling of concrete all along the height of this column



Figure 25. The exposed corroded longitudinal reinforcement at the foot of this column.



Figure 26. Measuring in-situ the distance between the stirrups of this column

6.2 Results from the Push-over numerical analyses with non-linear mechanisms for the two-node links at the foundation-soil interface, for the diagonal struts and all the R/C members

As already mentioned, in this 2nd category of numerical seismic analyses, the non-linear behaviour of all the R/C members is also considered here. A considerable number of numerical simulations were performed. Here only summary results are presented in figure 27.

The base shear (Q) versus horizontal displacement (δ) at the center of mass of the 1st story ceiling response is depicted in this figure. At the same time for certain levels of the base shear amplitude the numerically predicted non-linear mechanisms that develop at this stage are also indicated in this figure as follows:

a) At the level of a base shear approximately equal to 7000KN the formation of plastic hinges is predicted for the foot of the ground floor columns together with the yielding of the masonry infills at the South side.

b) At the level of a base shear approximately equal to 9500KN the yielding of the North side masonry infills is predicted. This is followed by the yielding of the interior masonry infills at the level of base shear approximately equal to 14000KN. The later occurs for levels of horizontal displacements at the center of mass of the 1st story ceiling of the order of 50mm.

c) Further increase in this horizontal displacement level leads to relatively modest increase in the resistance of the structure in this East-West direction, in terms of base shear levels, with plastic hinges developing at the top and foot of all the columns of the ground floor together with large horizontal displacement amplitudes at the 1st story ceiling (120mm, ground floor collapse mechanism).

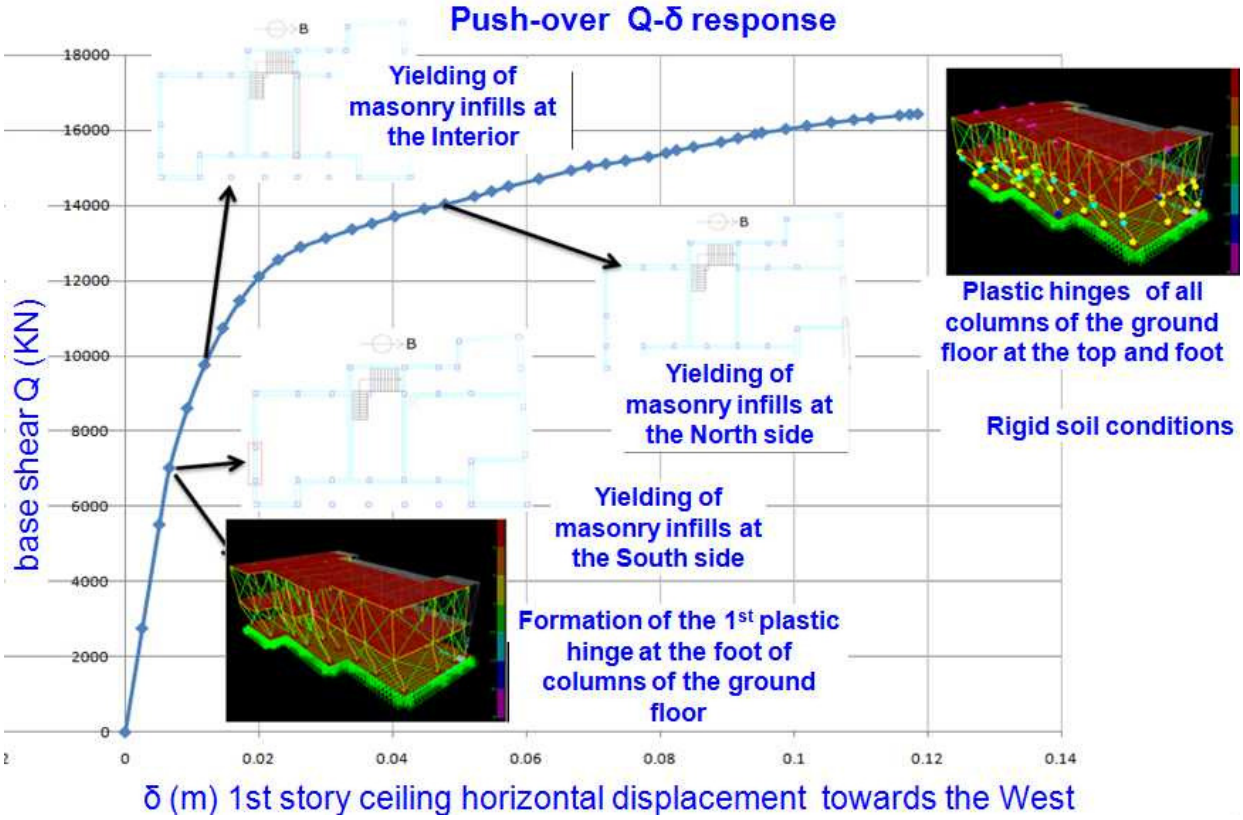


Figure 27. Push-over response of the City Hall structure with rigid soil conditions being forced towards the West.

As can be seen from the results of this analysis, the seismic force levels required to result in serious structural damage are above the forcing levels that were applied in the 1st category of numerical analyses presented previously.

One observation that becomes apparent from this comparison rises from the fact that both the 1st and 2nd category of the numerical analyses followed here do no incorporate the loss of bearing capacity of the masonry infills after a certain inter-story drift limit. This limitation can be tackled in a valid way by applying the full non-linear methodology described in [10]. Therefore, although these 2nd category numerical predictions can be accepted in describing reasonably well in a qualitative way all the incorporated various non-linear mechanisms, such as masonry infills, flexural plastic hinges of the R/C members, tension cut-off for the soil-foundation interface, the predicted seismic resistance in terms of base shear levels can be considered as rather non-conservative. In any case, the results of this category of numerical analyses demonstrate once more the contribution of well built masonry infills to resisting the seismic forces up to the point of their failure. This is more likely to occur when the earthquake excitation is of relatively short duration, as was the case of the strongest aftershock of 3rd of February, 2015 of the Kefalonia earthquake sequence that is studied here.

7 CONCLUSIONS

- It was demonstrated that masonry infills, as is already known, can significantly influence the seismic response of an R/C framed structural system by increasing its stiffness.

- It was also demonstrated that in certain cases these masonry infills can also increase the seismic capacity of such structural systems, when adverse effects of short columns or soft stories are avoided in these structural systems.
- The numerical predictions of the 1st category of analyses, apart from the above conclusion, can be considered as rather realistic, as these predictions are in reasonably good agreement with corresponding signs of distress of the ground floor columns of the Lixouri City Hall observed after this earthquake.
- The 2nd category of analyses result in base shear versus horizontal displacement numerical predictions that describe reasonably well the various non-linear mechanisms in a qualitative way. The results of this category also underline the favourable contribution of well built masonry infills of the Lixouri City Hall in resisting the seismic forces up to the point of their failure. This is likely to occur when the earthquake excitation is of relatively short duration, as was the case of the strongest aftershock of 3rd of February, 2015 of the Kefalonia earthquake sequence that is studied here.
- One observation that became apparent from the comparison of the numerical results with the actual performance rises from the fact that both the 1st and 2nd category of the numerical analyses followed here do no incorporate the loss of bearing capacity of the masonry infills after a certain inter-story drift limit. This limitation can be tackled in a valid way by applying the full non-linear methodology that is presented in [10].
- It was shown, that the seismic force levels which were assumed to have acted on the City Hall building are well beyond those that were valid at the time of the design and construction of this building. It was also shown that the seismic force levels that this structure as well as many neighboring structures experienced during the 3rd of February earthquake are higher than the force levels defined by the current provisions of Eurocode part 8.
- Factors that may have contributed to the relatively limited structural damage for these high seismic force levels, apart from the contribution of well built masonry infills, is the influence of the soil deformability that through the effects of the radiation damping may have had favourable effects in cases like the one examined here with a continuous foundation slab that prohibited the development of destructive differential foundation displacements and settlements during this earthquake excitation.

ACKNOWLEDGEMENTS

We would like to thank the personnel of the City Hall of Lixouri, Kefalonia-Greece for all the information and assistance they have provided.

REFERENCES

[1] GEER - EERI - ATC - Cephalonia GREECE *Earthquake Reconnaissance January 26th/ February 2nd 2014 Version 1: June 6 2014*

[2] Papazachos, B. and Papazachou, K., 1989, 1997, 2003. The earthquakes of Greece, *Zitis Publ.,Thessaloniki, 356 pp., 304 pp., 286 pp. (in Greek).*

[3] G.C. Manos, Seismic Code of Greece, Chapter 17, International Handbook of Earthquake Engineering: "Codes, Programs and Examples", *edited by Mario Paz, by Chapman and Hall,* ISBN 0-412-98211-0, 1994.

[4] G.C. Manos, et al. (1996) "Predictions of the dynamic characteristics of a 5-story R.C. building at the Volvi Euro-SeisTest Site, utilizing low-intensity vibrations", *3rd European Conference on Structural Dynamics, Eurodyn 1996, Florence, II, 877–884.*

[5] G. C. Manos, (1998). "The Dynamic Response of a 5-story Structure at the European Test site at Volvi-Greece." *6th U.S. National Earthquake Engineering Conference, May 31 - June 4, Seattle, Washington, U.S.*

[6] G. C., Manos, et al.. (2004). "Dynamic and Earthquake Response of Model Structures at the Volvi – Greece European Test Site." *13th World Conference on Earthquake Engineering, Vancouver, Canada.*

[7] G.C. Manos, V.J. Soulis, J. Thauampteh, "Evaluation of the numerical simulation of masonry-infilled RC frames under cyclic loading" , 7th International Masonry Conference, London, Oct. 30 – Nov. 1, 2006.

[8] Manos George, "Consequences on the urban environment in Greece related to the recent intense earthquake activity", *Int. Journal of Civil Engineering and Architecture, Dec. 2011, Volume 5, No. 12 (Serial No. 49), pp. 1065–1090.*

[9] G.C. Manos, V.J. Soulis, J. Thauampteh, "The behavior of masonry assemblages and masonry-infilled R/C frames subjected to combined vertical and cyclic horizontal seismic-type loading" I. J. Advances in Engineering Software 45 (2012) 213–231.

[10] G.C. Manos, V.J. Soulis, J. Thauampteh, "A nonlinear numerical model and its utilization in simulating the in-plane behaviour of multi-story R/C frames with masonry infills", The Open Construction and Building Technology Journal, 2012, 6, (Suppl 1-M16) 254-277.

[11] G. C. Manos & E. Papanaoum, "Assessment of the earthquake behavior of Hotel Ermionio in Kozani, Greece constructed in 1933 before and after its recent retrofit ", Earthquake Engineering Retrofitting of Heritage Structures, Design and evaluation of strengthening techniques, pp. 25-40, Edited By: S. Syngellakis, Wessex Institute of Technology, UK, ISBN: 978-1-84564-754-4, eISBN: 978-1-84564-755-1, 2013.

[12] G.C. Manos, V. Soulis, J. Thauampteh, " In-plane behaviour of masonry infills within multi-storey R/C frames subjected to seismic type loads and utilization in retrofitting", 4th ECOMASS Thematic Conference on Computational Methods in Structural Dynamics and Earthquake Engineering – COMPDYN 2013, 12-14 June 2013, Kos Island, Greece.

[13] G. C. Manos , K.D. Pitilakis, A.G. Sextos, V. Kourtides, V. Soulis, J. Thauampteh, "Field experiments for monitoring the dynamic soil-structure-foundation response of model structures at a Test Site" *Journal of Structural Engineering, American Society of Civil Engineers, Special Issue "Field Testing of Bridges and Buildings, D4014012, Vol. 141, Issue 1, January 2015.*

[14] G.C. Manos and E. Kozikopoulos, "In-situ measured dynamic response of the bell tower of Agios Gerasimos in Lixouri-Kefalonia, Greece and its utilization in the numerical predictions of its earthquake response", *CompDyn 2015 to be published.*

[15] Eurocode 8: Design of structures for earthquake resistance - Part 1: General rules, seismic actions and rules for buildings, *FINAL DRAFT prEN 1998-1, December 2003.*

COMPDYN 2015
5th ECCOMAS Thematic Conference on
Computational Methods in Structural Dynamics and Earthquake Engineering
M. Papadrakakis, V. Papadopoulos, V. Plevris (eds.)
Crete Island, Greece, 25–27 May 2015

THE DYNAMIC AND EARTHQUAKE RESPONSE OF BASILICA CHURCHES IN KEFALONIA, GREECE INCLUDING SOIL-FOUNDATION DEFORMABILITY AND WALL DETACHMENT.

G.C. Manos[1], **E. Kozikopoulos**[2]

[1] Professor and Director of the Lab. of Strength of Materials and Structures, Aristotle University
e-mail: {gcmanos@civil.auth.gr}

[2] Postgraduate student, Lab. of Strength of Materials and Structures, Aristotle University
e-mail: {vago_kozi@outlook.com.gr}

Keywords: Christian churches, Numerical simulation, Dynamic and seismic response, Soil-foundation deformability, detachment of walls, push-over non-linear analyses

Abstract. *The dynamic and earthquake behaviour of structural systems representing Post-Byzantine Christian churches located in Kefalonia-Greece is examined. All these churches are made of stone masonry. They developed damage to their masonry elements due to the amplitude of the gravitational forces acting together with the seismic forces that were generated by the recent 2014earthquake activity, combined with the deformability of the foundation. The numerical results together with assumed strength values are utilized to predict the behaviour of the various masonry parts of these churches in in-plane, shear, and normal stress as well as out-of-plane flexure. Use is made in the numerical simulation of the deformability of the foundation of the results obtained from a specific investigation that dealt in measuring the dynamic characteristics of a bell tower located in Lixouri-Kefalonia-Greece. It is shown that the foundation deformability partly explains the appearance of structural damage. When comparing the numerically predicted regions that reach limit state conditions with actual damage patterns a reasonably good agreement in a qualitative sense can be observed. In addition, the numerical simulation focused in reproducing numerically certain non-linear mechanisms that are typical for this type of structural systems. The numerically predicted non-linear response mechanisms at the corners of the masonry walls as well as at the roof to masonry wall level seem to reproduce in a realistic way the observed damage patterns in these regions.*

1 INTRODUCTION

The objective of this paper is to study the dynamic and earthquake behavior of Christian churches of the Basilica typology in the island of Kefalonia, Greece (figure 1). The recent devastating earthquake activity in the island during the period from 26th of January till the 3rd of February 2014 caused extensive damage to the masonry walls of many of these structures. The worst hit region lies at the West part of the island of Kefalonia with the peninsula of Paliki claiming the biggest share of damaged churches. This region is marked in figure 1 with the dotted circle. The most damaging seismic event for this region was the ground motion during the major aftershock of this earthquake sequence that occurred during the 3rd of February, 2014 [1, 2, 3, 4]. This is depicted in figures 2 and 3. Figure 2 shows the location of the epicenters of the aftershocks of the earthquake sequence of January-February 2015 for the island of Kefalonia, including the epicenter of the strongest aftershock of 3rd February, 2015 [2]. Figure 3 marks the location of some of the various churches in the Paliki peninsula that were shaken by this strongest aftershock, leading to considerable damage and to certain cases to spectacular partial collapse (figures 4 and 5).

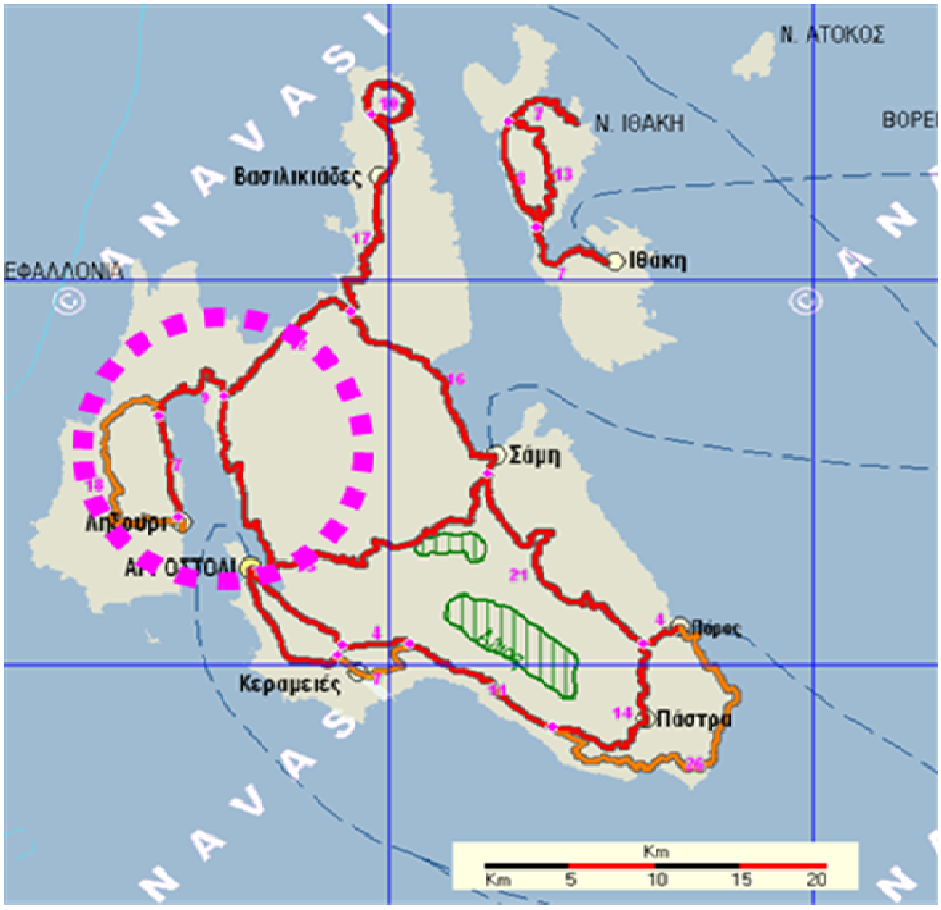


Figure 1. View of the island of Kefalonia, Greece together with the peninsula of Paliki

The main event of this earthquake sequence occurred on the Sunday, 26th of January 2015, 13:55 local time [1]. Fortunately, this event was not so damaging for the churches and despite the fact that it occurred Sunday the Christian services were already completed by that time. The damaging aftershock occurred on the Monday of 3rd February 2015, local time 05:09. The fact that at this time the churches were empty companied with the warning of the

preceded main event are factors that helped to have no loss of life from the structural damage and partial collapse that was observed in certain churches as well as to a number of other structures and facilities ([1, 2, 3]).

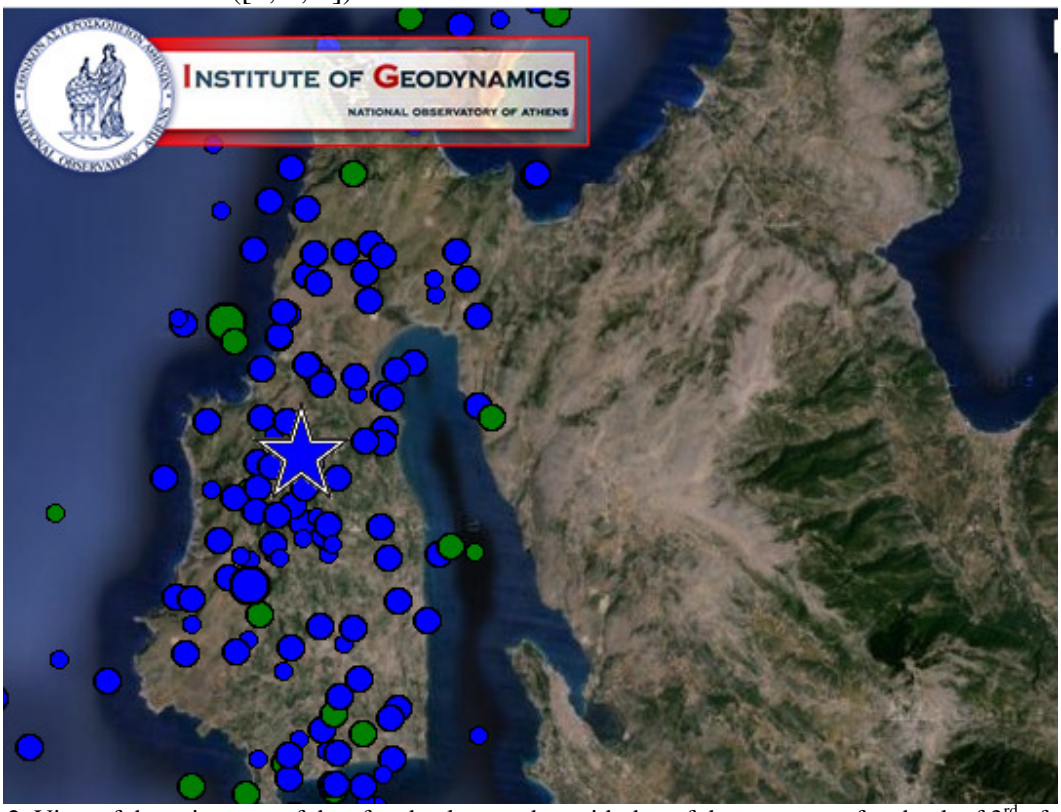


Figure 2. View of the epicenters of the aftershocks together with that of the strongest aftershock of 3rd of February, 2015 (blue star) as they were recorded by the Institute of Geodynamics of the National Observatory of Athens, Greece.



Figure 3. View of peninsula of Paliki together with the location of some of the churches that developed structural damage during the strongest aftershock of 3rd February, 2015.



Figure 4. Virgin Mary of Roggoi



Figure 5. St. Marina Soullaroi

During the Frankish and Venetian periods in Kefalonia many churches of this typology were rebuilt in Kefalonia. Indicatively, around the late 18th century there were 350-400 churches in this beautiful island of the Ionian sea with the very active geological seismic background. Numerous churches in this island have the structural form the single aisle basilica (Ionian) with an elongated rectangular shape. The value of the ratio of their longitudinal length over the transverse length varies from 1: 1.5 for relatively small churches to 1: 5 for the largest structures. This relatively simple structural system for these churches is formed by load-bearing stone-masonry peripheral walls that are connected with well built corners as well as by the presence of a soft system of trusses that form the lightweight roof. Table 1 lists a number of churches that were affected by this earthquake sequence together with the century of their construction as well as the century of their damage repair due to a previous earthquake activity [3]. The island of Kefalonia belongs to a high seismic hazard region, as this is depicted by the map of seismic zones of Greece in figure 6. This seismic zonation is included in the current seismic code of Greece[26]; it can be seen in this figure that the island of Kefalonia belongs to the seismic zone having seismic design ground acceleration value equal to 0.36g (g the acceleration of gravity equal to 9.81m/sec. However, it must be pointed out that this is a relatively recent regulation that does not apply to the construction methods of the 17th century.

Table 1. The name of the studied churches and the century of construction and repair.

A/A	name of church	Century of Construction / Repair
1	Kechrionos Monastery	17th / 20th
2	Virgin Mary Kontogennada	18th / 20th
3	St. Thekla	17th / 20th
4	Virgin Mary Damoulianouta	19th / 20th
5	**Virgin Mary of Roggoi**	**17th**
6	Virgin Mary Dematora	19th / 20th
7	St. Blaise Dematora	18th
8	St. Dimitrios Kalata	18th / 20th
9	Birth of the Virgin Mary Kalata	18th
10	12 Apostles -Chavdata	19th
11	Birth of the Virgin Mary Havriata	17th / 20th
12	**St. Marina in Soullaroi**	**17th**

* The repair for the 20th century refers to interventions introduced after the damaging 1953 earthquake sequence

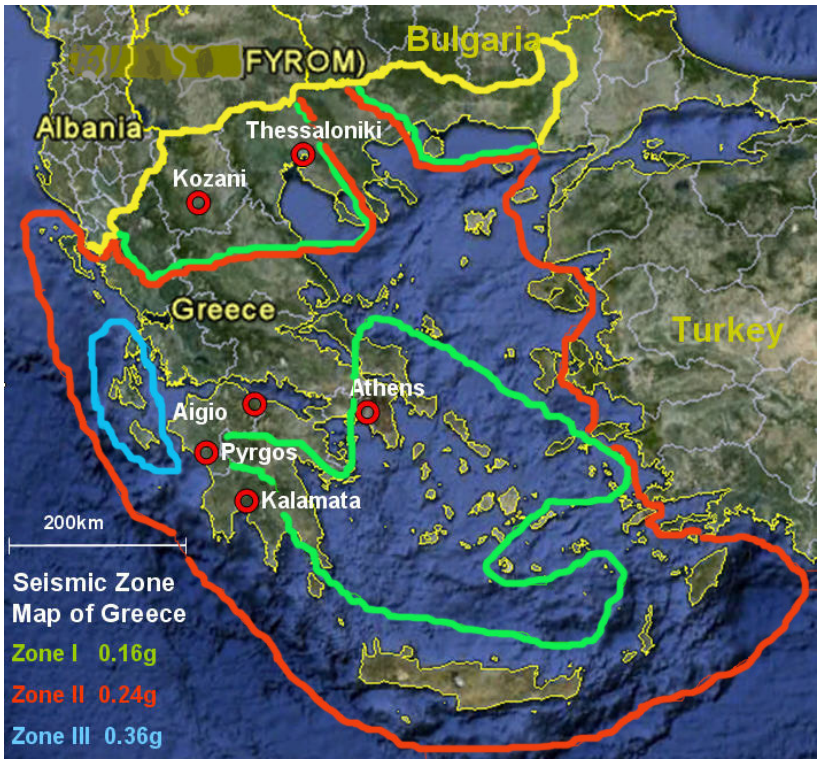


Figure 6. The location of the six most damaged urban areas of Greece form the earthquake activity during the last thirty years together with the seismic zoning map (see also Tables 1 and 5).

Damage to Christian churches from earthquake activity in Greece is quite frequent [6 to 21]. This must be attributed to the intense earthquake activity and the accumulation of damage as well as to the fact that such structures made of weak masonry are quite vulnerable as their heavy walls and heavy elements in their superstructure results in large amplitude earthquake demands that cannot be met by the resistance offered by relatively weak stone masonry structural elements [6]. This is also the case in the damaged churches of Kefalonia that will be investigated in the following sections.



Figure 7. Peninsula of Paliki with the location of the two churches being examined here

It should be underlined here that neither the long history of intense seismic activity in the island nor the attempted damage repair from previous earthquake activity (see table 1) were able to create effective interventions that would protect these structures from future seismic

events. As can be seen in table 1 most of the repair efforts are dated on the 18th century. The objective of this paper is to present currently available scientific tools that can help understand the earthquake behaviour of this type of structures and therefore serve the objective of their protection in a possible more effective way than the experience of the current earthquake damage indicates. As indicated in table, the 20th century repair effort refers to interventions introduced to these churches after the damaging 1953 earthquake sequence. In general, typical interventions in these churches included the construction of a reinforced concrete beam at the top of the masonry wall to connect the wooden roof at this level. However, as the full details of these interventions were not available their effectiveness in the observed performance is so far non-conclusive.

This investigation presents the evaluation of two Christian Basilica churches that are indicated with relatively large letters in Table 1. The first is the church of Virgin Mary of Roggoi (No 5 in Table 1) and the second is church of St. Marina in Soullaroi (No 12 in Table 1 and figure 4). Both these churches are structure that did not experienced any interventions after the 1953 earthquake sequence. The first church of Virgin Mary of Roggoi has dimensions in plan 7.5m by 15.8m and a height of 9.3m (No 5 in Table 1) and the second church of St. Marina in Soullaroi has dimensions in plan 9.5m by 22.3m and a height of 9.6m, a somewhat larger structure. The investigation being conducted here includes the effects of foundation deformability [21]. It has been demonstrated in the past [17, 19, 22, 23] as well as in two companion works that are presented in this conference [22, 23], that the foundation deformability is a significant parameter in the effort to understanding the earthquake behaviour of these structures. The location of these two churches in the Paliki peninsula is shown in figure 7 together with the location of the accelerographs that recorded the seismic ground motion during the strongest aftershock of 3rd of February, 2015. Use of this recorded ground motion will be made in the framework of the current investigation.

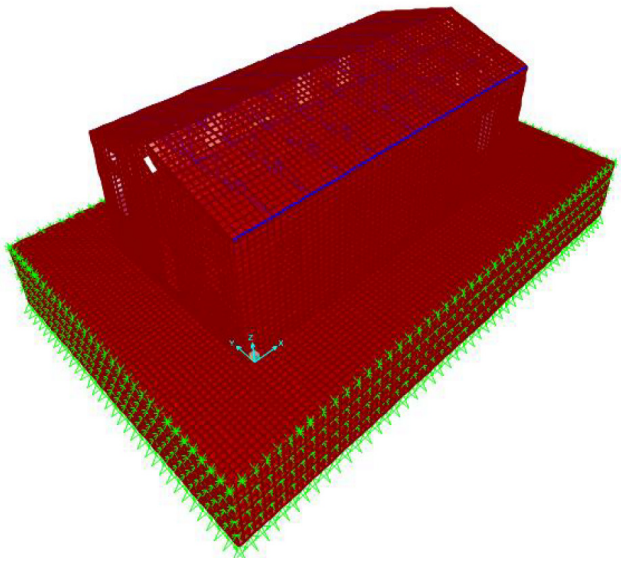


Figure 8. Numerical model of the foundation slab and the underlying soil.

2 SOIL – FOUNDATION DEFORMABILITY

The foundation of both churches is considered to be formed by a peripheral masonry strip that is an extension of the masonry walls in the sub-soil at a depth of 0.5 m. In-situ studies that were performed with the Agios Gerasimos bell tower have demonstrated that certain in-

fluences can arise on the dynamic and earthquake response from soil-foundation deformability [22, 23] that should be investigated. In order to study numerically the soil-foundation deformability of these two churches the following process was utilized.

First, a numerical model of the structure and the masonry foundation strip was formed as shown in figure 8. Together with the foundation masonry strip, which was modeled with shell elements having linear elastic properties based on the Young's modulus of masonry, the soil layers underneath were also modeled being in full contact with the masonry foundation. These soil layers were formed with solid "brick" type finite elements with linear elastic properties that extended to a depth of 4m below the foundation – soil interface.

Because it was not possible to find reliable geotechnical data in the vicinity of the studied structures the investigation of the soil-foundation deformability was attempted in a parametric way as will be explained below in order to define the elastic properties of the soil elements.

1st case. A shear wave velocity equal to 419m/sec was assumed for these underlying soil layers. This value, together with a soil density equal to 20KN/m3 leads to a shear modulus equal to 354MPa. This value together with a Poisson's ratio value equal to 0.2 leads to a Young's modulus value for the soil equal to 1000MPa. This represents a rather hard soil.

2nd case. Following the same rational but this time assuming a shear wave velocity value equal to 200m/sec leads for the same value of soil density as in the 1st case to a the Young's modulus value for the soil equal to 230MPa. This represents a medium stiffness soil and is comparable with the corresponding value found from the Agios Gerasimos in-situ measurements [22].

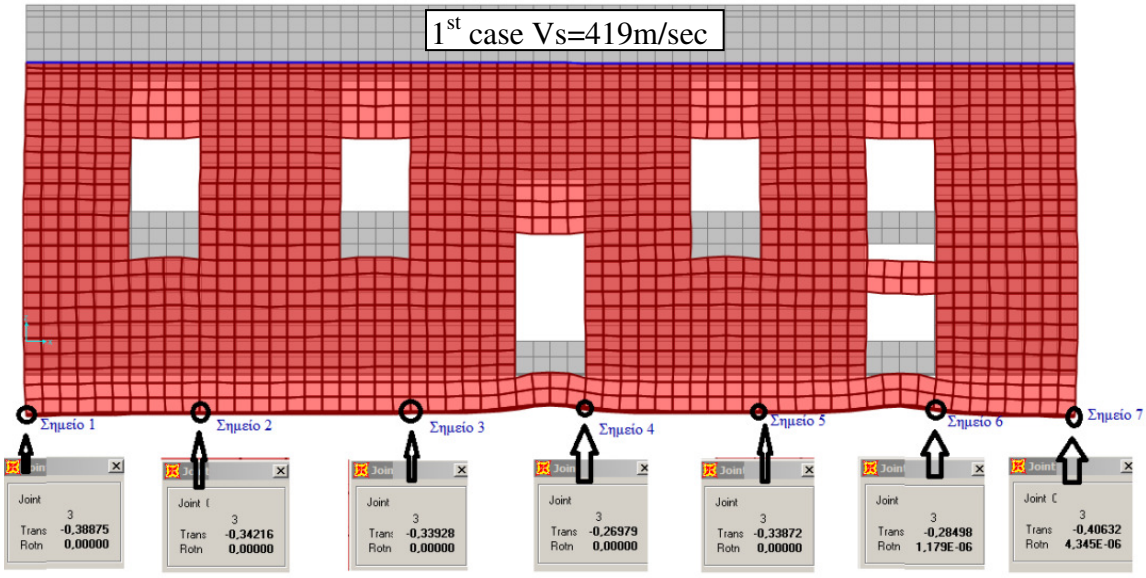


Figure 9. Vertical deflections of the soil-foundation simulation, for 1st case Vs=419m/sec

Next, this numerical simulation that included the superstructure, the foundation masonry strip and the soil layers, as described before, was subjected to the dead weight. The bottom surface of the bottom layer of the soil volume was constrained to have zero displacements in all three directions. The side boundaries of the soil volume were constrained only in the two horizontal directions. In this way the foundation was displaced almost uniformly downwards in the vertical direction being compressed in this way. Figures 9 and 10 depict the resulting vertical deformation patterns of the foundation-soil interface for the 1st (Vs=419m/sec) and 2nd (Vs=200m/sec) case of soil deformability, respectively.

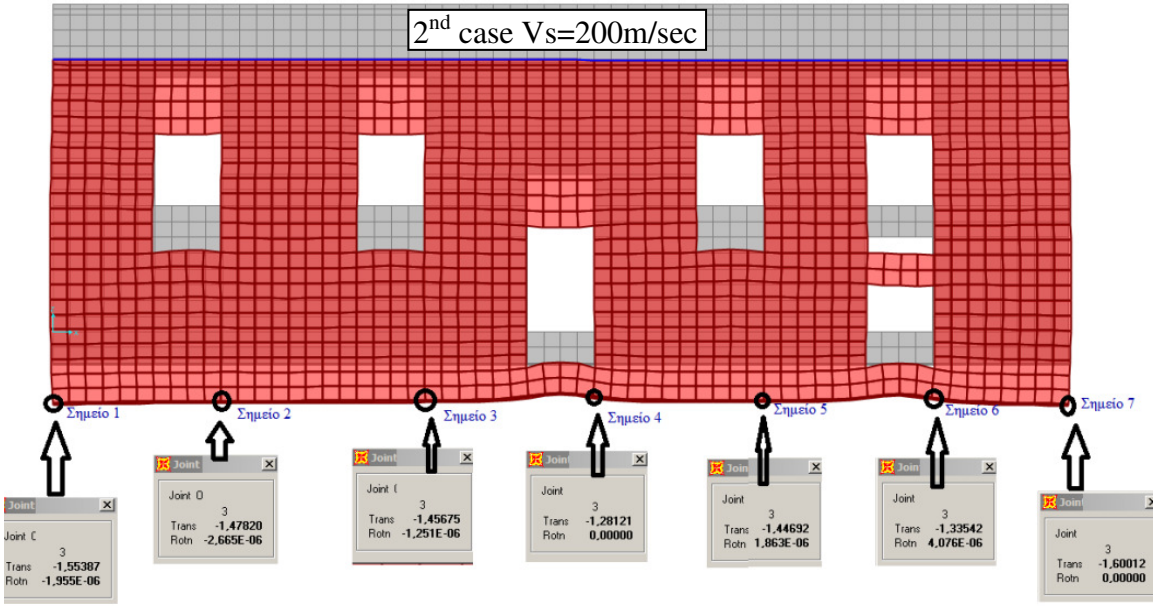


Figure 10. Vertical deflections of the soil-foundation simulation, for 2nd case Vs=200m/sec

In order to simplify the final numerical model of the examined churches including the soil-foundation deformability the following approximation was made. An alternative numerical model of the foundation masonry strip – soil interface was formed. This model retained all the aspects of the superstructure and the foundation masonry strip. However, this time the soil layers being simulated before with solid brick elements were replaced with two-node 3-D link elements having one node fully restrained in the all three directions as the support to the earth and the other node in full contact with each node of the shell elements which simulate the bottom surface of foundation masonry strip. Moreover, these two-node links were given such an axial stiffness that when the same load was applied as before (Dead load) the resulting vertical deflection of the bottom surface of the foundation – soil interface was as close as possible to the values indicated before in figures 8 and 10. Moreover, for certain types of numerical analyses a non-linearity was introduced in the axial direction of these two-node link elements resulting in their inability to sustain any tension. Following this rational the axial stiffness of these two-node link elements, utilized for case 1 and 2 of soil-foundation deformability, is listed in the following table 2.

Table 2. Axial stiffness of the equivalent two-node links

Soil deformability	1st case Vs=419m/sec	2nd case Vs=200m/sec
Axial Stiffness of the vertical two-node links (KN/mm)	109	24.5

3 THE LINEAR DYNAMIC RESPONSE OF THE CHURCHES

The eigen-modes and eigen-periods of the two temples are investigated next in a parametric way, assuming linear elastic behaviour of all the elements of the superstructure as well as the foundation links [21]. The following parameters are varied:

a1) The church of the **Panagia (Virgin Mary) of Roggoi**. It is one of the oldest -along with Ag. Marina in Soullaroi- Christian churches that developed severe damage during the recent earthquake. It is a relatively small church with heavy structural damage in the façade (West side) and wide shear cracks in the longitudinal North (figure 12) and South walls.



Figure 11: West side



Figure 12 North side

a2) The church of **Agia Marina** is located in **Soullaroi** and was built in the 17th century, without being repaired in 1953. It has old type double stone masonry walls, which sustained heavy damage. There is almost partial collapse of the East (figure 5) and West side (figure 13) and a wide detachment of the longitudinal and transverse walls (figure 14). very crosswise shear cracks in columns. There is also global failure of the east pediment and intense horizontal cracks appear at the base of the west.



Figure 13: West side



Figure 14 South-East corner

In all these linear elastic simulations of the dynamic response the soil-foundation deformability was approximated in the way described in section 2. That is a 1st case is examined having vertical two-node links at the soil-foundation slab interface with axial stiffness equal to 109KN/mm, representing relatively hard soil conditions. Then, a 2nd case is examined having vertical two-node links at the soil-foundation slab interface with axial stiffness equal to 24.5KN/mm, representing a soil of medium deformability. Moreover, in all cases the vertical walls were connected at the corners with two-node 3-D links in an effort to control the rigidity of these connections as well as to approximate the structural behaviour when the examined structures exhibited heavy damage in these locations.

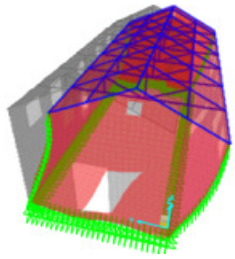
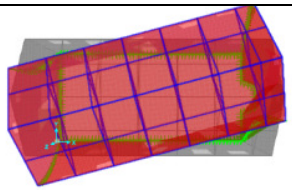
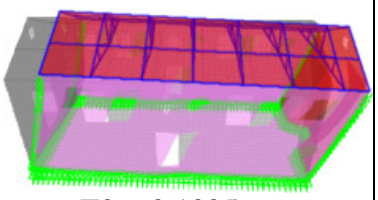
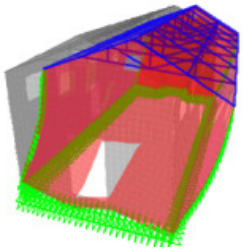
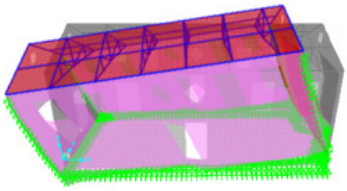
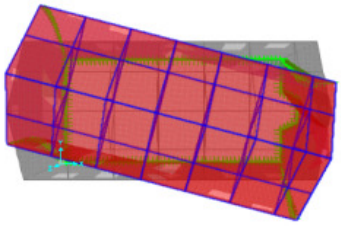
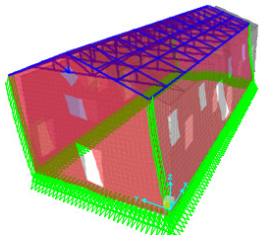
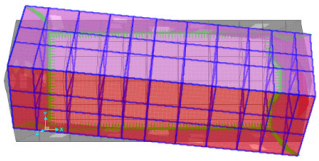
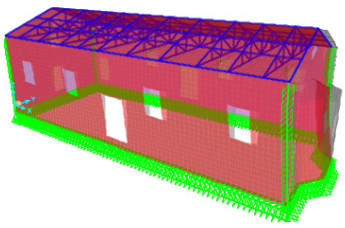
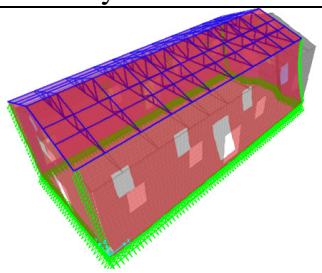
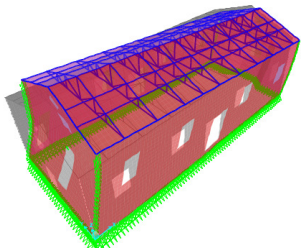
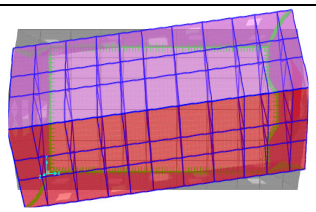
Figure 15	Panagia (Virgin Mary) of Roggoi Soil-Foundation deformability eigen-period T		
	T_1	T_2	T_3
1st case hard soil	 T1y=0.1773sec mx = 0.0% my = 77.9%	 T2=0.1051sec mx = 0.4% my = 79.3%	 T3x=0.1025sec mx = 72.8% my = 79.3%
2nd case Soft soil	 T1y=0.2014sec mx = 0.0% my = 75.3%	 T2x=0.1196sec mx = 60.6% my = 75.3%	 T3=0.1086sec mx = 60.6% my = 76.0%

Figure 16	Agia Marina in Soullaroi - Soil-Foundation deformability 2nd eigen-period T2		
	T_1	T_2	T_3
1st case hard soil	 T1y=0.1786sec mx = 0.0% my = 80.3%	 T2=0.1109sec mx = 6.8% my = 80.4%	 T3x=0.1088sec mx = 74.2% my = 80.4%
2nd case Soft soil	 T1y=0.1975sec mx = 0.0% my = 77.4%	 T2x=0.1206sec mx = 64.6% my = 77.4%	 T3=0.1133sec mx = 65.2% my = 77.5%

The results of this dynamic analyses in terms of eigen-modes, eigen-period values and values of the corresponding mass participation ratios are included in figures 15 and 16 for the church of Panagia of Roggoi and Agia Marina of Soularroi, respectively ([7 to 21]).

The following remarks can be made on the basis of the results presented in these figures.

1) The first dominant eigen-mode for both churches and for both cases of foundation-soil flexibility is the translational mode in the North-South direction (y-y). The eigen-period for this mode varies from approximately 0.18sec (hard soil) to 0.20sec. (medium soil) for both churches. This eigen-mode mobilizes in all cases approximately 75% to 80% of the total mass.

2) The second dominant mode in the case of hard soil conditions is a torsional mode. The eigen-period for this mode is approximately 0.11sec for both churches. However, this mode mobilizes very little mass.

3) The third dominant mode in the case of hard soil is the translational mode in the East-West direction (x-x). The eigen-period for this mode is approximately 0.10sec. for both churches. This eigen-mode mobilizes for both churches approximately 70% of the total mass.

4) The second dominant mode in the case of medium soil conditions is the translational mode in the East-West direction (x-x). The eigen-period for this mode is approximately 0.12sec. for both churches. This eigen-mode mobilizes for both churches approximately 60% of the total mass. In the case of medium soil the third dominant mode is a torsional mode. The eigen-period for this mode is approximately 0.11sec for both churches. However, this mode mobilizes again very little mass.

From the above remarks it can be concluded that the assumed variation of the soil-foundation deformability results, as expected, in a modest increase in the fundamental eigen-period values. Moreover, the increased soil-foundation deformability results in the two translational North-South (x-x) and East-West (y-y) eigen modes becoming the dominant eigen-modes of the structural response for these churches mobilizing 75% and 60% of the total mass, respectively.

4 PREDICTIONS OF THE EARTHQUAKE RESPONSE FOR THE POST-BYZANTINE CHRISTIAN CHURCHES

Next, numerical simulations of the earthquake response of these two churches are presented. The numerical analyses that were performed towards obtaining earthquake response predictions of such Christian Basilica churches fall in the following two main categories.

4.1 Static numerical analyses with linear mechanisms for the two-node links at the foundation-soil interface as well as at the corner of masonry wall interconnections.

In these dynamic numerical analysis use will be made of the ground acceleration that was recorded at two stations during the 3rd of February strongest aftershock [1, 3]. As can be seen in figure 7, the location of one station is the center of the town of Lixouri (City Hall building) whereas the location of the 2nd station in the old school of the village of Chavriata. As could be observed in figure 7 the church of Agia Marina at Sullaroi is at a distance of approximately 2km from either the Lixouri or the Chavriata station located between these two locations. The church of Panagia of Roggoi is at a distance of approximately 5km North from Chavriata and North-West from Lixouri. In order to obtain an estimate of the horizontal seismic forces that these two churches were subjected to during the damaging aftershock of 3rd of February 2015 the constant ductility (μ=1.5) response spectra in the East-West and North-South direction were derived from those recordings of the ground motion. The corresponding response spectral curves are depicted in figures 17 and 18 for the Lixouri recording and in figures 19 and 20

for the Chavriata recording in the East-West and North-South horizontal directions, respectively.

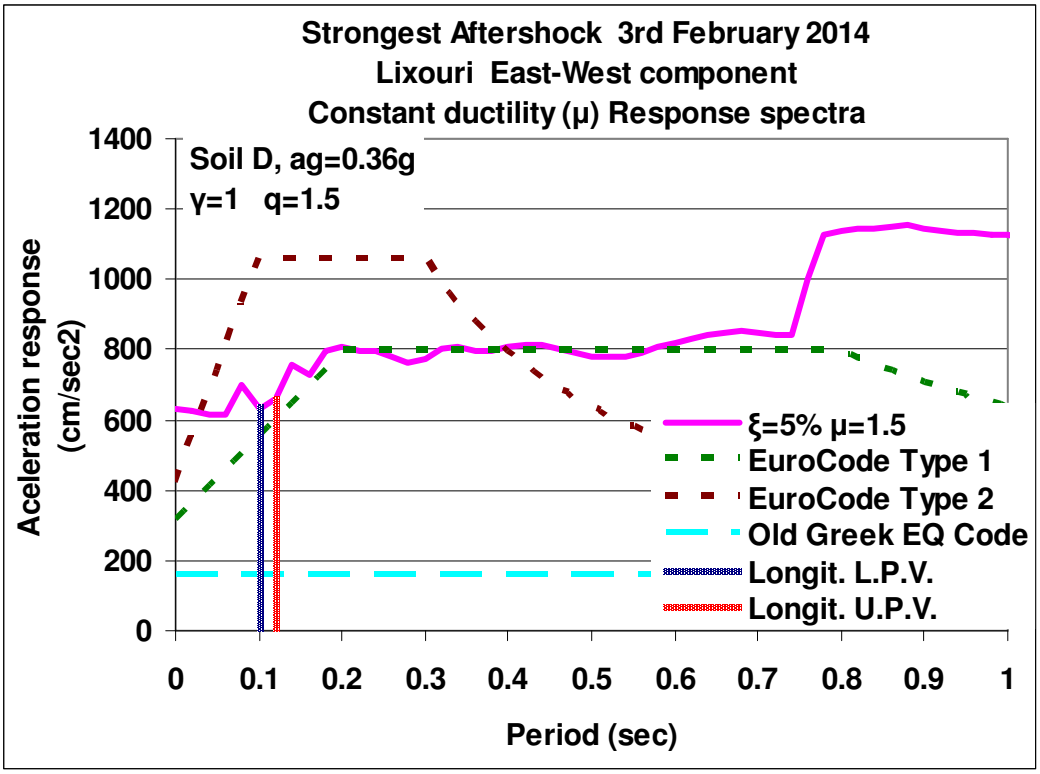


Figure 17. Definition of East-West (y-y) seismic loads through the recorded ground motion at Lixouri during the 3rd of February strongest aftershock

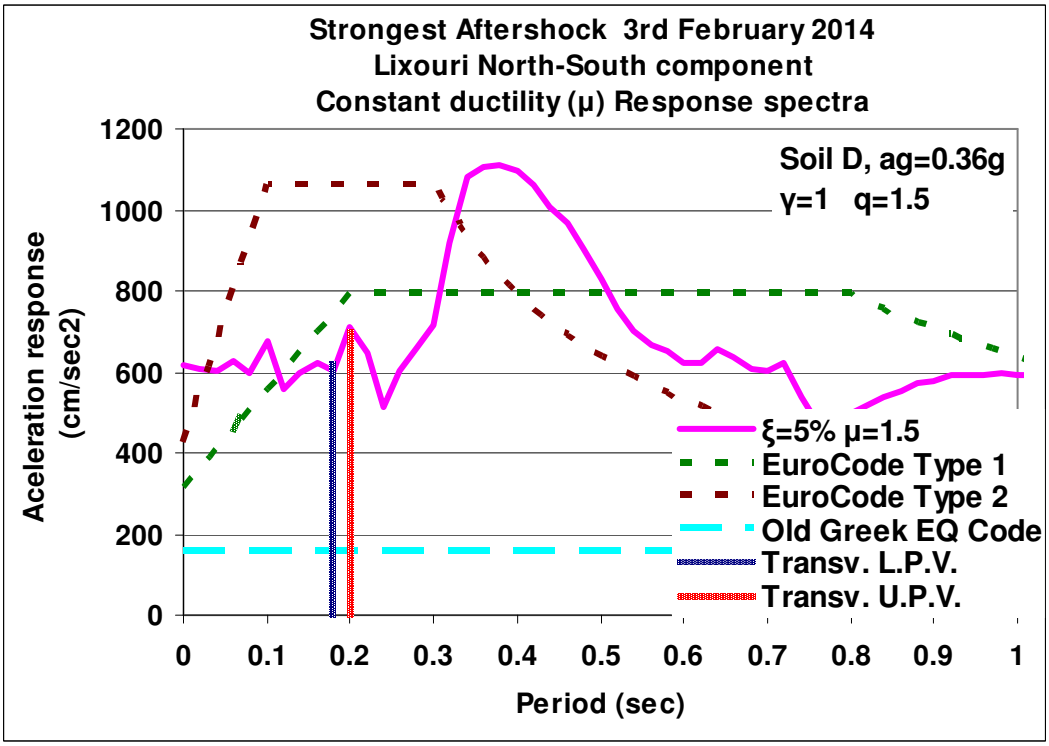


Figure 18. Definition of North-South (x-x) seismic loads through the recorded ground motion at Lixouri during the 3rd of February strongest aftershock

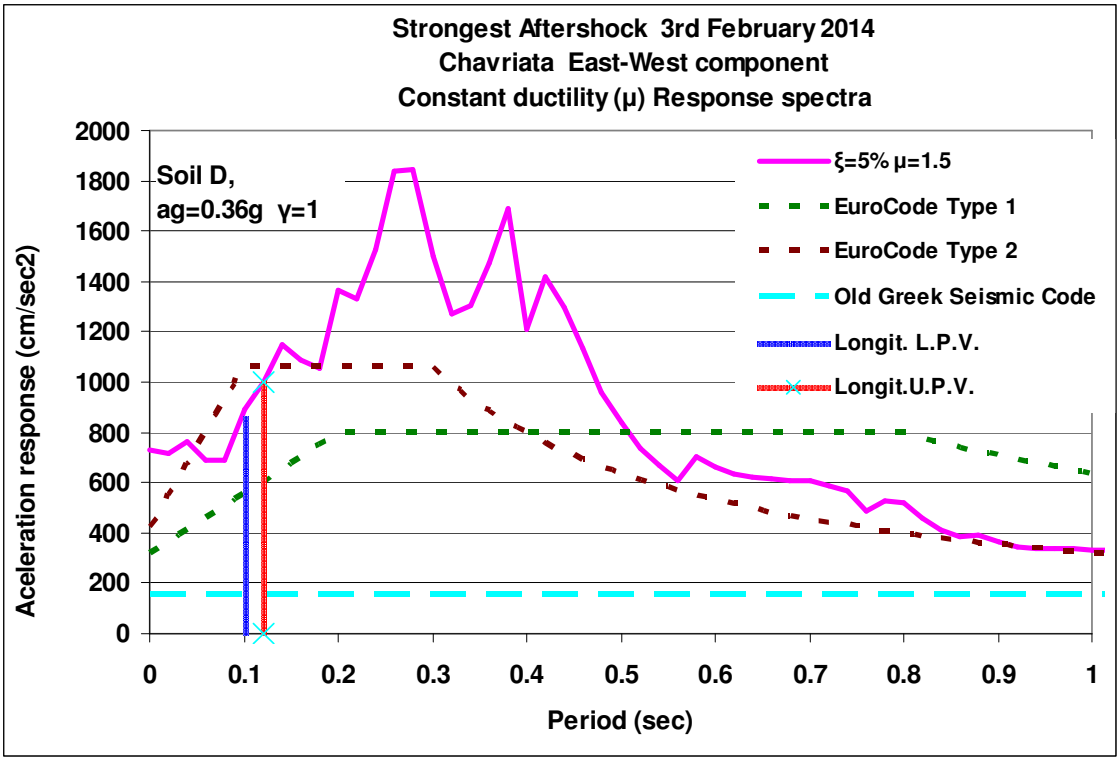


Figure 19. Definition of East-West (y-y) seismic loads through the recorded ground motion at Chavriata during the 3rd of February strongest aftershock

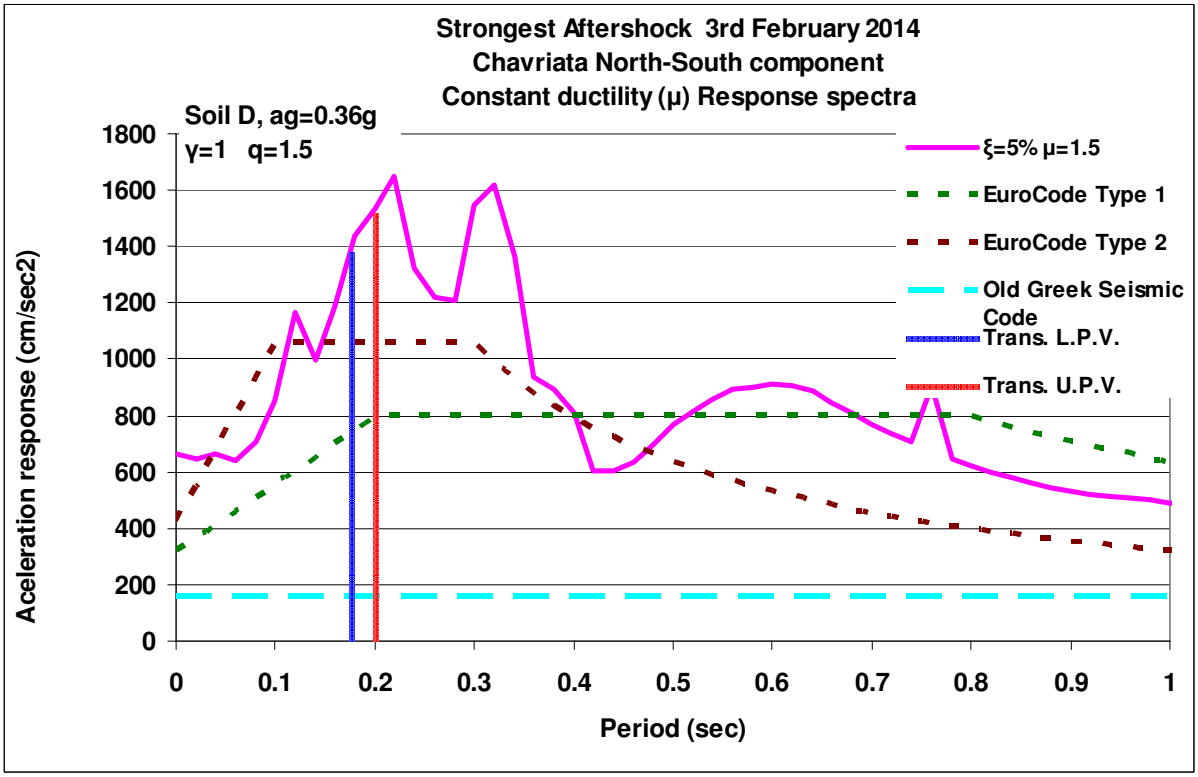


Figure 20. Definition of North-South (x-x) seismic loads through the recorded ground motion at Lixouri during the 3rd of February strongest aftershock

The ductility factor value μ=1.5 is presumed to be a good approximation for these type of relatively brittle unreinforced masonry construction. In the same figures the design spectral

acceleration curves are also plotted for type 1 and type 2 earthquake, as these design spectral values are defined by EuroCode part 8 [24] assuming again a response modification factor value q=1.5 Soil category D (flexible soil) importance factor 1 and design peak ground acceleration equal to 0.36g (g the acceleration of gravity) as defined by the current Greek seismic code for Kefalonia [25]. In comparison, the "Old Greek Seismic Code" level of seismic forces that were introduced in 1959 are also indicated in this figure as "Old Greek Seismic Code" [5]. Moreover, the values of the eigen-periods found from the dynamic analyses of these two churches, as they were presented in figures 15 and 16 are also plotted in figures 17 to 20. These values are designated as Longit. L.P.V or U.P.V., which correspond to the eigen-periods in the longitudinal East-West (x-x) direction for either the hard soil (Lower Period Value) or the medium soil (Upper Period Value). The same hold for the transverse North-South (y-y) direction which are designated as Trans. L.P.V or U.P.V., for the hard soil (Lower Period Value) or the medium soil (Upper Period Value), respectively. The following remarks can be made on the basis of figures 17 to 20.

1) For the period range from 0.1sec. to 0.4sec the Chavriata spectral acceleration curve would result in more demanding seismic forces for the corresponding structures, like the studied churches, than the Lixouri spectral acceleration curve for both the North-South and the East-West directions.
2) Structural systems that would be more flexible than the ones examined here, either because of more flexible soil-foundation conditions than the medium soil of this study or for more flexible structures themselves than the structures considered here, they would have been subjected to larger horizontal seismic forces than the ones to be considered for the studied here churches. This remark is valid for the Chavriata record for both the North-South and East-West direction and for the East-West direction for the Lixouri record.
3) The Chavriata spectral acceleration curves (for μ=1.5 either E-W or N-S) for the period range from 0.1sec. to 0.4sec would result in more demanding seismic forces for the corresponding structures, like the churches studied here, than the EuroCode 8 design spectral curves for q=1.5.
4) The Lixouri spectral acceleration curve (for μ=1.5 either N-S or E-W) for the period range from 0.1sec. to 0.4sec would result in less demanding seismic forces for the corresponding structures, like the churches studied here, than the Type 1 EuroCode 8 design spectral curves for q=1.5. The difference is not very significant for the type 2 EuroCode 8 design spectral curves for q=1.5. The
5) Seismic force levels for the period range from 0.1sec. to 0.4sec according to the old Greek seismic code are approximately 3 to 4 times smaller than the corresponding levels obtained on the basis of the Lixouri spectral curves (for μ=1.5 either E-W or N-S) or the type 2 EuroCode 8 design spectral curves for q=1.5.
6) Seismic force levels for the period range from 0.1sec. to 0.4sec according to the old Greek seismic code are approximately 5 to 6 times smaller than the corresponding levels obtained on the basis of the Chavriata spectral curves (for μ=1.5 either E-W or N-S) or the type 2 EuroCode 8 design spectral curves for q=1.5.
7) All the previous points underline the severity of seismic forces levels the examined churches had to withstand. One favourable parameter for the structural performance was the short duration of this intense shaking. However, the preceding discussion on the severity of the seismic forces ignored the unfavourable effect of the vertical component of the ground motion, which is usually present in localities close to the epicen-

ter like the ones examined here. This unfavourable influence of the vertical component of the ground motion is ignored throughout this study.

The seismic forces that are used in this type of numerical analyses are obtained in the following way.

a) First, employing either the Lixouri or the Chavriata spectral curves for μ=1.5 and the linear elastic numerical simulation of the examined structural system the base shear values in the North-South or the East-West direction are obtained. This is done through a dynamic spectral analysis utilizing the first four (4) eigen-modes and the relevant North-South or East-West spectral curves, respectively. Alternatively, a response spectrum can be used resulting from the elastic response spectral curve for 5% damping divided by a response modification factor equal to 1.5 for unreinforced masonry. In the subsequent analysis the later process was adopted.

b) An amplification factor is also utilized to compensate for the fact that these first four (4) eigen-modes, which correspond to realistic structural responses for this type of structures, do not sum up to 90% of the total mass of the structure.

c) The horizontal seismic forces are finally applied either in the x-x East-West longitudinal direction (Ex) or the y-y North-South transverse direction (Ey) as static forces resulting from constant acceleration along the height of the examined structures as shown in figure 21. This constant acceleration has such a value that results in the same base shear value found from the dynamic spectral analysis of steps a and b described before. These equivalent seismic forces Ex or Ey are combined with the permanent loads (D) to form the load combinations 0.9D ± Ex or 0.9D ± Ey.

d) This is done because it is much easier to obtain in this way the demands of the various masonry structural elements from the seismic forces described in step c. Thus, the evaluation of the seismic performance of these structural elements can be done.

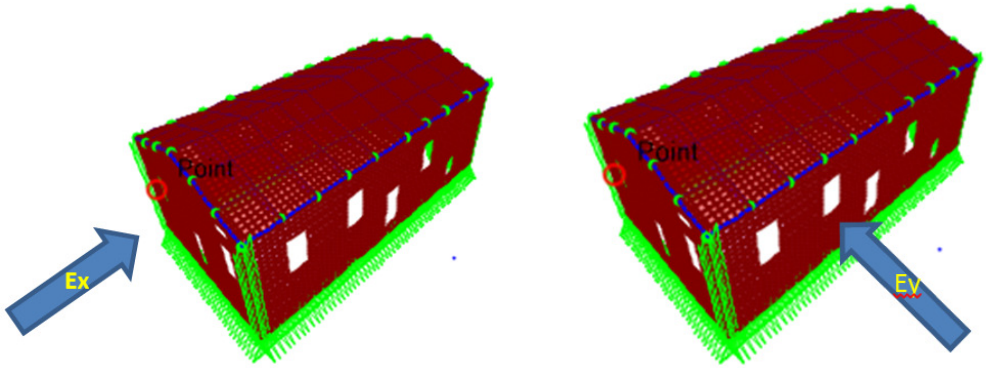


Figure 21: Equivalent static loads.

Table 3	***Base shear Values (KN) based on the Chavriata response spectra***			
	Virgin Mary of Roggoi Hard Soil	Virgin Mary of Roggoi Soft Soil	Ag. Marina Soullaroi Hard Soil	Ag. Marina Soullaroi Soft Soil
North-South (x-x) direction	2465	2498	5229	5803
East-West (y-y) direction	2367	2874	8397	8828

Table 3 lists the base shear values, as they resulted from the linear elastic dynamic spectral analyses utilizing the East-West or North-South acceleration response spectral curves for 5% damping and q=1.5 derived from the recorded ground acceleration (figures 17 to 20). As explained above, these values coincide with the equivalent seismic forces Ex or Ey.

4.2 Push-over numerical analyses with non-linear mechanisms for the two-node links at the foundation-soil interface and the link elements which connect the vertical walls in the corners and the top face of the wall with the roof.

In the 2nd category of numerical seismic analyses the non-linear behaviour of the examined structures is considered by introducing the following non-linear mechanisms.

a1) First, the two-node 3-D links at the soil-foundation interface introduced to account for the soil-foundation deformability are provided with tension a cut-off limit so they can sustain only compression in their axial direction and no tension.

b1) Similarly, two-node 3-D non-linear link elements are also utilized in connecting the vertical walls at their corners with a tension cut-off limit in a way to transfer compression between the intersecting walls at the corner but limit transfer of tension.

c1) A similar connection is used between the wooden elements of the roof and the tympana of the masonry walls at the East and West sides or at the top of the North or South longitudinal masonry walls.

Thus, through the proper use of these non-linear 3-D two-node link elements these non-linear mechanisms are introduced in an effort to simulate numerically the capability of the uplifting of the structure at the soil-foundation interface, the possibility of detachment between the wooden elements of the roof and the masonry walls or between the vertical walls themselves at the corners.

These numerical analyses were a push-over step-by-step type of analyses [6] with the first step being the application of the permanent vertical loads (D). Next, the horizontal seismic loads are introduced at each shell element (each mass) as a gravity load at direction either in the North-South (y-y) or East-West (x-x) directions. This is done gradually by increasing the level of the applied seismic forces by a small amount at each subsequent step. The seismic horizontal displacement attained at each step is checked certainly at the top point of East wall for the East-West (x-x) push-over analyses or at the top of the middle of the North wall for the push-over analyses direction in the North-South (y-y) direction.

5 ASSUMED FAILURE CRITERIA USED IN THE VALUATION OF THE OBSERVED PERFORMANCE

Table 4 lists the assumed mechanical characteristics for the stone masonry elements of both churches [5]. Moreover, a Mohr-Coulomb failure envelope was adopted for the in-plane shear limit state of the stone masonry, when a on normal stress is acting simultaneously, that is defined through the relationship (1) ([6], [21], [26]).

$$fvk = fvko + 0.4\ \sigma_n \qquad (1)$$

where: fvko is the shear strength of the stone masonry when the normal stress is zero; fvko was assumed to be equal to 0.160 N/mm2. σ_n is the compressive axial stress acting on the bed joint .

Table 4 lists the assumed mechanical characteristics for the stone masonry in terms of Young's modulus and Poisson's ratio as well as compressive and tensile strength values. The values listed in table 4 were assumed to be valid for both churches based on relevant strength values employed in similar studies [6 to 21]. However, the necessity to quantify such limit value through tests based on in-situ samples must once more be underlined.

Table 4. Assumed Mechanical Characteristics of the Stone Masonry

	Young's Modulus (N/mm^2)	Poisson's Ratio	Compressive Strength (N/mm^2)	Tensile Strength normal /parallel bed-joint (N/mm^2)	shear strength f_{vko} (N/mm^2)
Limit values	1000	0.2	3.50	0.15 / 0.60	0.16

The above strength values will be used to evaluate the seismic performance of the various masonry structural elements in the most critical locations that the demands, obtained through the numerical analyses results, have maximum values. This will be done in comparing the various demands S_{Ed} with the corresponding strengths S_{Rd} through the following inequality (2):

$$S_{Ed} < S_{Rd} \quad \text{indicates safe structural performance.} \tag{2}$$

The above inequality can also have the form of a S_{Rd} / S_{Ed} in inequality (3).

$$S_{Rd} / S_{Ed} > 1 \quad \text{indicates safe structural performance.} \tag{3}$$

This inequality in ratio terms is further detailed through the following ratios. For the in-plane or the out of plane demands the following demands are checked (inequalities 4 to 6):

a2) The in-plane shear demand in terms of shear stress for various bed-joint locations where shear and normal stresses are acting. This is done through the value of the following ratio $\mathbf{R_\tau}$

$\mathbf{R_\tau}$ = shear strength / shear stress demand. **< 1** signifies shear failure (in-plane) (4)

b2) The in-plane compression stress demand for various bed-joint locations where compressive stresses are acting normal to bed-joints. This is done through the value of the following ratio $\mathbf{R_\varsigma}$.

$\mathbf{R_\varsigma}$ = compressive strength / compressive stress demand **< 1** signifies compression failure (in-plane) (5)

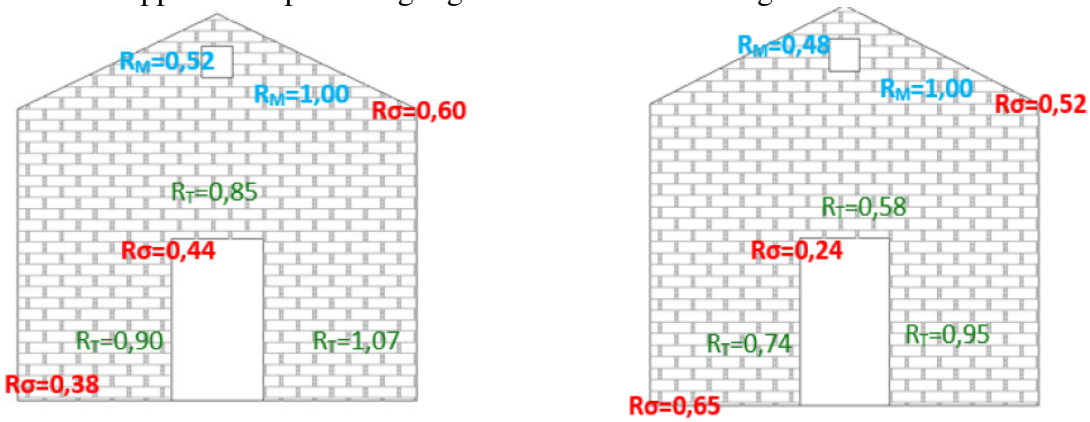
c2) The in-plane tensile stress demand for various bed-joint locations where tensile stresses are acting normal to bed-joints. This is done through the value of the following ratio $\mathbf{R\sigma}$.

$\mathbf{R\sigma}$ = tensile strength (fxk1) / tensile stress demand **< 1** signifies tensile failure normal to bed joint (in-plane) (6)

d2) The out-of-plane tensile stress demand for various bed-joint locations where tensile stresses are acting normal to bed-joints. This is done through the value of the following ratio $\mathbf{R_M}$

$\mathbf{R_M}$= tensile strength / tensile stress demand from out-of-plane flexure $\mathbf{< 1}$ signifies out-of-plane tensile failure normal to bed joint at the extreme fiber (out of plane) (7)

All the masonry parts of the studied structures were examined in terms of in-plane and out-of-plane stress demands posed by the considered load combinations against the corresponding capacities, as these capacities were obtained by applying the Mohr-Coulomb criterion of equation 1 or the stone masonry compressive and tensile strength limits listed in Table 4. Ratio values smaller than one ($\mathbf{R\tau, R\varsigma, R\sigma, R_M < 1}$) predict a corresponding limit state condition. As can be seen, the followed methodology is based on combining numerical stress demands resulting from elastic analyses with limit-state strength values. A different approach is to incorporate these limit-state strength values in a non-linear push-over type of analysis (see Manos et al. [1]). It was shown that the methodology applied here correlates quite well with the non-linear approach in predicting regions of structural damage.



a. Hard Soil b. Medium Soil

Figure 22. Predicted performance of the West side wall of the church of Panagia of Roggoi

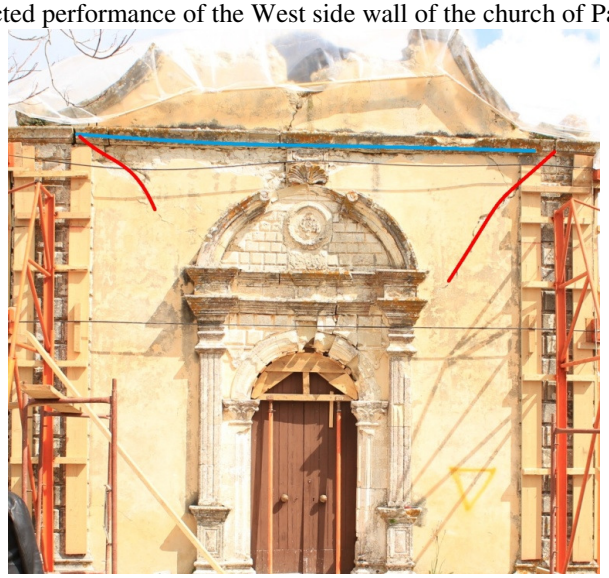


Figure 23. Observed damage of the West side of the church Panagia of Roggoi

6 THE RESULTS OF THE NUMERICAL ANALYSES

Next, selected results from the numerical simulations of the earthquake response of these two churches are presented. The numerical analyses results obtained following the linear static approach, described in sub-section 4.1, are presented first in sub-section 6.1. This is done by showing the predicted performance of the various masonry elements utilizing the obtained demands with the corresponding strength values through the process outlined in section 5. Selected results obtained through the push-over type of numerical analyses, described in subsection 4.2, are next presented in a summary form in sub-section 6.2.

6.1 Static numerical analyses with linear mechanisms for the two-node links at the foundation-soil interface as well as at the corner of masonry wall interconnections.

Figures 22a and 22b depict **Rτ, Rσ, R_M** ratio values for the in-plane and out-of-plane performance of the West side of the Panagia of Roggoi church for either hard or medium soil, respectively. As can be seen in these figures the demands exceed by far the corresponding strengths either in shear or tension (in-plane) at the lower part of this masonry wall or the out-of-plane tension at its upper part. The presence of medium soil signifies that these ratio values become in general even smaller. Thus, it is demonstrated that the presence of medium soil conditions increases the possibility of damage in this case. Good agreement can be seen by comparing the predicted (figures 22) with the observed (figure 23) performance for this wall.

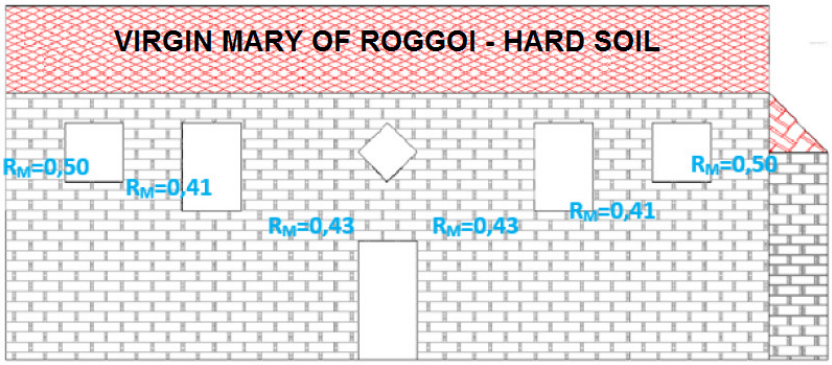


Figure 24a. Predicted out-of-plane performance, South wall, hard soil, church Panagia of Roggoi

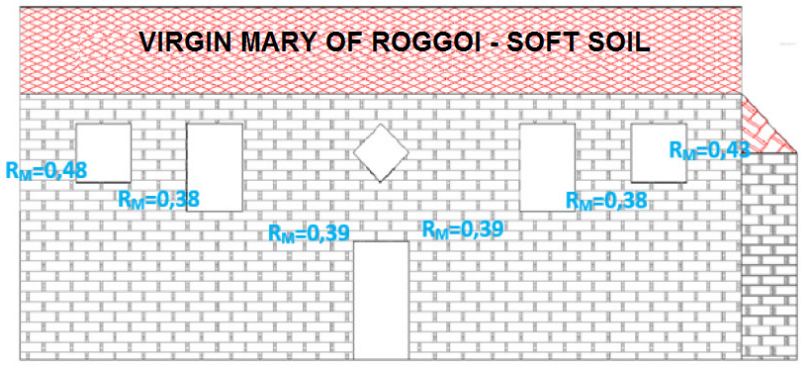


Figure 24b. Predicted out-of-plane performance, South wall, medium soil, church Panagia of Roggoi

Figures 24a and 24b depict **R_M** ratio values for out-of-plane predicted performance of the South side of the Panagia of Roggoi church for either hard or medium soil, respectively. As can be seen in these figures the demands exceed by far the corresponding strengths in tension (out-of-plane) at the upper part of this masonry wall between the door and window openings.

Again, the presence of medium soil signifies that these ratio values become in general even smaller. Thus, it is demonstrated that the presence of medium soil conditions increases the possibility of damage in this case. Good agreement can be seen again by comparing the predicted (figures 24) with the observed (figure 25) performance for this wall.

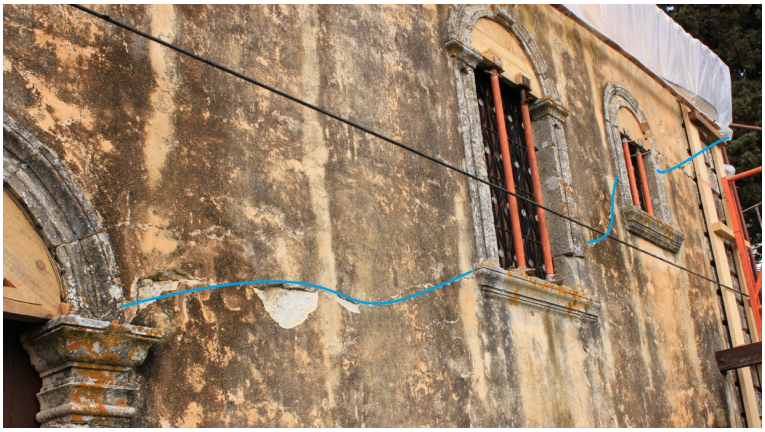
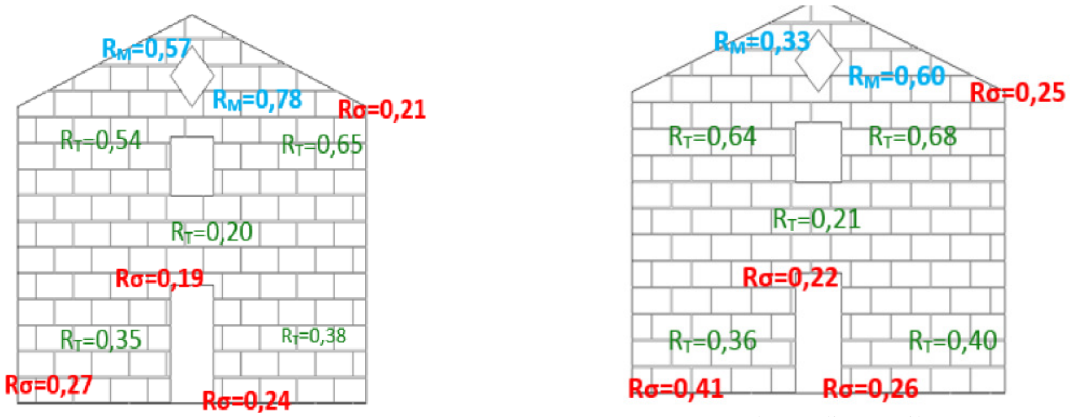


Figure 25. Observed out-of-plane performance, South wall, church Panagia of Roggoi



a. Hard Soil b. Medium Soil

Figure 26. Predicted performance of the West side wall of the church of Agia Marina



Figure 27. Observed damage of the West side of the church of Agia Marina

Figures 26a and 26b depict **Rτ, Rσ, R_M** ratio values for the in-plane and out-of-plane performance of the West side of the Agia Marina church for either hard or medium soil, respectively. As can be seen in these figures the demands exceed by far the corresponding strengths either in shear or tension (in-plane) at the lower part of this masonry wall or the out-of-plane tension at its upper part. The presence of medium soil signifies that these ratio values become in general even smaller. Thus, it is demonstrated that the presence of medium soil conditions increases the possibility of damage in this case. Good agreement can be seen by comparing the predicted (figures 26) with the observed (figure 27) performance for this wall.

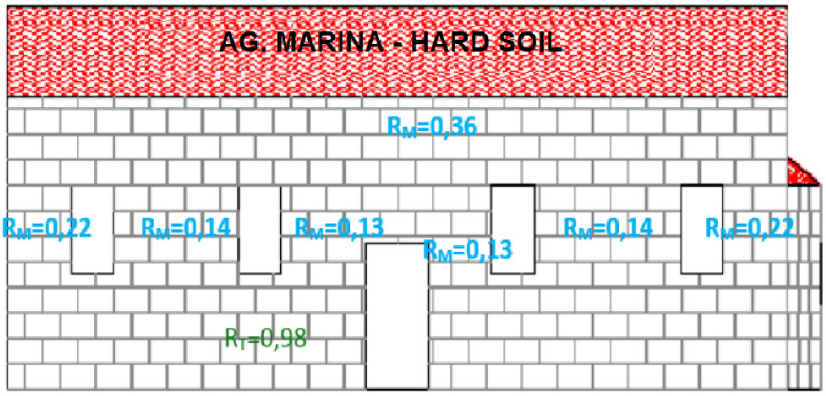
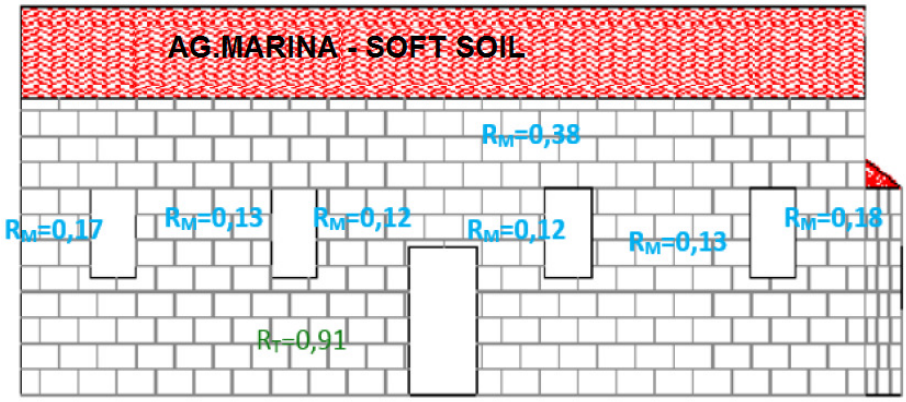


Figure 28a. Predicted out-of-plane performance, South wall, hard soil, church Agia Marina



28b. Predicted out-of-plane performance, South wall, medium soil, church Agia Marina



Figure 29. Observed out-of-plane performance, South wall, church Agia Marina

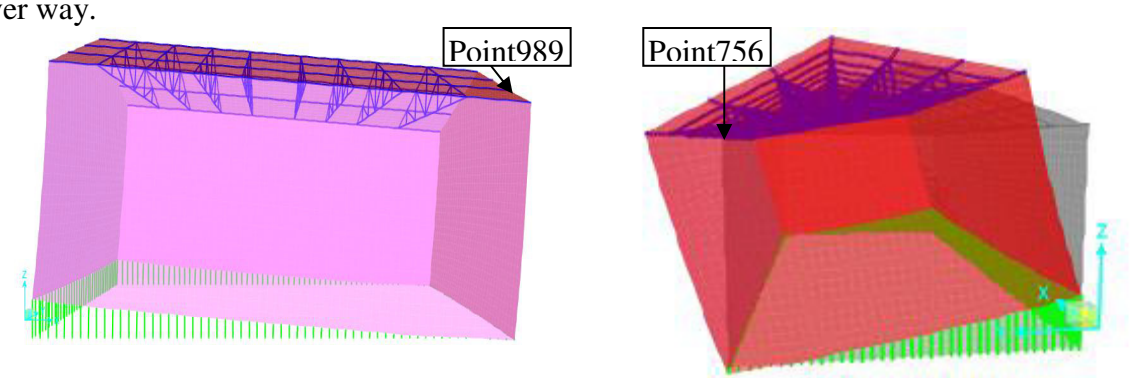
Figures 28a and 28b depict $\mathbf{R_M}$ ratio values for out-of-plane predicted performance of the South side of the Agia Marina church for either hard or medium soil, respectively. As can be seen in these figures the demands exceed by far the corresponding strengths in tension (out-of-plane) at the upper part of this masonry wall between the door and window openings. Again, the presence of medium soil signifies that these ratio values become in general even smaller. Thus, it is demonstrated that the presence of medium soil conditions increases the possibility of damage in this case. Good agreement can be seen again by comparing the predicted (figures 28) with the observed (figure 29) performance for this wall.

7 RESULTS FROM THE PUSH-OVER NUMERICAL ANALYSES

Next, selected results from the push-over numerical simulations of the earthquake response of this type of churches are presented.

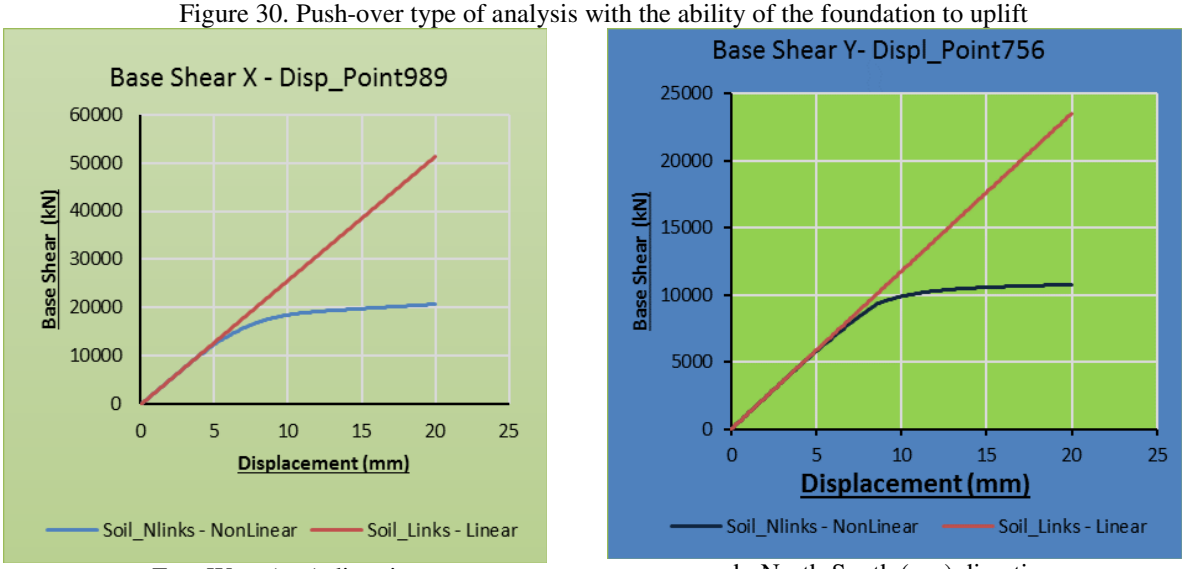
7.1 The uplifting of the foundation.

Figures 30a and 30b depict the push-over displacement response as predicted from the numerical simulations that included the 1st non-linear mechanism, that of the ability of the foundation to uplift from the foundation-soil interface, when the loads combinations 0.9D + Ex or 0.9D + Ey, with the seismic forces Ex (East-West) or Ey (North-South), are applied in a push-over way.



a. East-West (x-x) direction b. North-South (y-y) direction

Figure 30. Push-over type of analysis with the ability of the foundation to uplift



a. East-West (x-x) direction b. North-South (y-y) direction

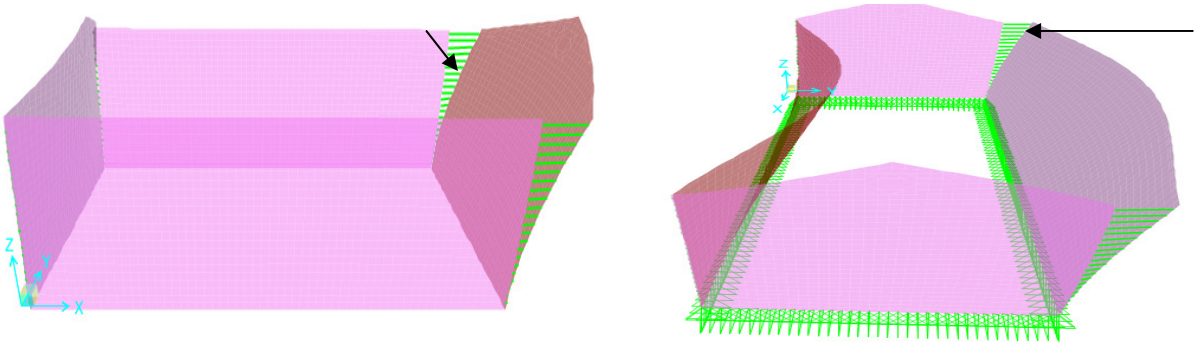
Figure 31. Base-shear versus top horizontal displacement Push-over response with foundation uplift

The obtained base shear – horizontal displacement response from these push-over numerical analyses are depicted in figures 31a (0.9D + Ex) and 31b (0.9D + Ey) for the East-West and North-South directions, respectively.

As can be seen in figures 31a and 31b the uplifting of the foundation limits the base shear levels in the East-West direction to approximately 12000KN and in the North-South direction approximately 9000KN. If the above values are compared with the corresponding values, listed in Table 3, which were obtained from the dynamic spectral analyses that employed the recorded ground motion response spectra (Chavriata record), it can be concluded that for these force levels the uplifting of the foundation is unlikely.

7.2 The detachment of the walls at the corners.

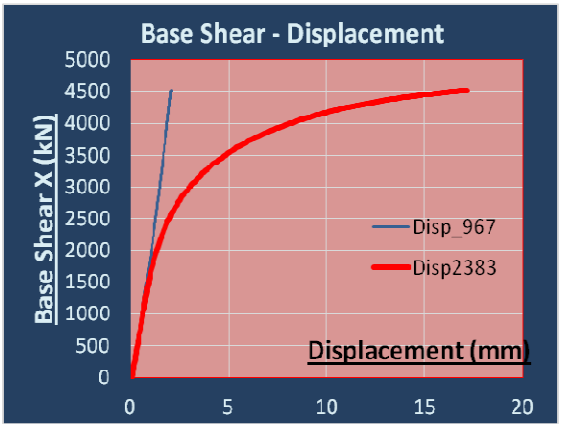
Figures 32a and 32b depict the push-over displacement response as predicted from the numerical simulations that included the 2nd non-linear mechanism, that of the ability of the walls to be detached at the corners where these vertical walls are interconnected. This is simulated when the load combinations 0.9D + Ex or 0.9D + Ey, with the seismic forces Ex (East-West) or Ey (North-South) are applied in a push-over way.



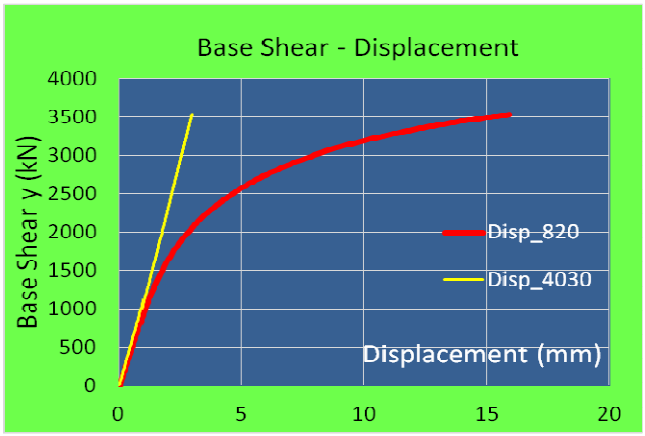
a. East-West (x-x) direction – detachment of East wall from the North wall

b. North-South (y-y) direction – detachment of North wall from West wall

Figure 32. Push-over type of analysis with the ability of the foundation to uplift



a. East-West (x-x) direction – detachment of the East wall from the North wall



b. North-South (y-y) direction – detachment of the North wall from the West wall

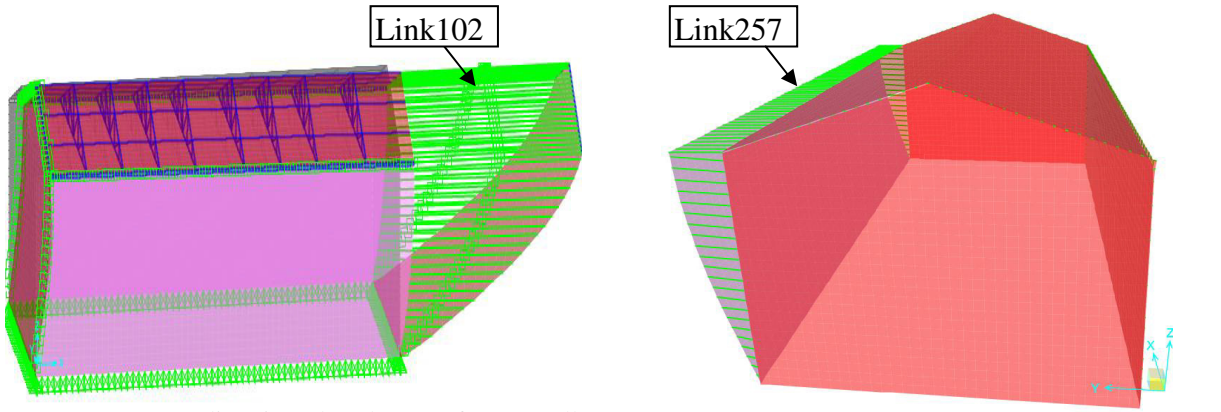
Figure 33. Base-shear versus top horizontal displacement Push-over response with the ability of the vertical walls to be detached at the corners

The obtained base shear – horizontal displacement response from these push-over numerical analyses are depicted in figures 33a (0.9D + Ex) and 33b (0.9D + Ey) for the East-West

and North-South directions, respectively. As can be seen in figures 32a and 33a the detachment of the East wall from the North wall, when the seismic forces act in the East-West direction, limits the base shear levels in the East-West direction to approximately 4000KN. Similarly, the detachment of the North wall from the West wall (figures 32b and 33b), when the seismic forces act in the North-South direction, limits the base shear at the level of approximately 3500KN. If the above values are compared with the corresponding values, listed in Table 3, which were obtained from the dynamic spectral analyses that employed the recorded ground motion response spectra (Chavriata record), it can be concluded that for these force levels the detachment of these walls at the corners is very likely.

7.3 The detachment of the walls at the corners as well as at the roof level.

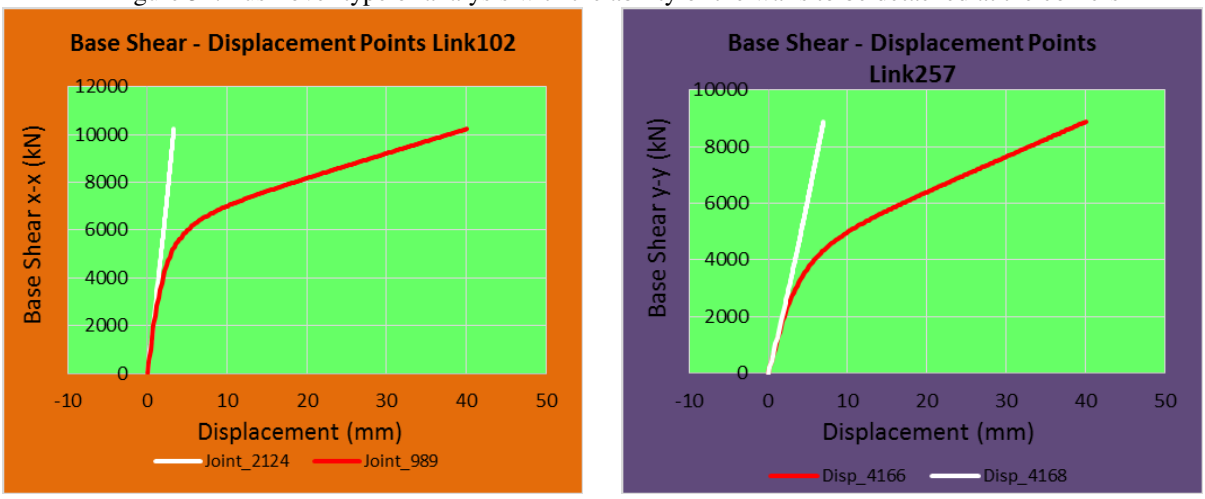
Figures 34a and 34b depict the push-over displacement response as predicted from the numerical simulations that included the 2nd and the 3rd non-linear mechanisms; that is the ability of the walls to be detached at the corners where these vertical walls are interconnected as well as at the roof level. This is simulated when the load combinations 0.9D + Ex or 0.9D + Ey, with the seismic forces Ex (East-West) or Ey (North-South) are applied in a push-over way.



a. East-West (x-x) direction- detachment of West wall

b. North-South (y-y) direction-detachment of North wall

Figure 34. Push-over type of analysis with the ability of the walls to be detached at the corners



a. East-West (x-x) direction – detachment of the West wall

b. North-South (y-y) direction – detachment of the North wall

Figure 35. Base-shear versus top horizontal displacement Push-over response with foundation uplift

The obtained base shear – horizontal displacement response from these push-over numerical analyses are depicted in figures 35a (0.9D + Ex) and 35b (0.9D + Ey) for the East-West and North-South directions, respectively. As can be seen in figures 33a and 33b the detachment of the West wall limits the base shear levels in the East-West direction to approximately 6000KN and in the North-South direction approximately 5000KN. If the above values are compared with the corresponding values, listed in Table 3, which were obtained from the dynamic spectral analyses that employed the recorded ground motion response spectra (Chavriata record), it can be concluded that for these force levels the detachment of these walls at the corners is very likely. These are in agreement with the observed performance (see figures 13 and 14).

8 CONCLUSIONS

- Through the systematic study of the characteristics of the ground motion records and the dynamic properties of the structural systems, representing the examined Christian churches damaged in Kefalonia by the 3rd of February 2015 strongest aftershock, the levels of the seismic forces land their severity that these churches had to withstand was established. One favourable parameter for the structural performance was the short duration of this intense shaking. However, this study ignored the unfavourable effect of the vertical component of the ground motion, which is usually present in localities close to the epicenter like the ones examined here.
- The predicted performance of the examined Christian churches, employing demands from a linear analysis that utilizes these horizontal seismic force levels and assumed strength values for stone masonry, yield good agreement with the observed performance.
- The predicted performance is approximated through a detailed process that makes use of strength / demand ratio values ($\mathbf{R\tau}$, $\mathbf{R\varsigma}$, $\mathbf{R\sigma}$, $\mathbf{R_M}$) in order to approximate the ability of the masonry structural elements to withstand or not the posed demands in in-plane shear, in-plane compression/tension and out-of-plane tension.
- The push-over non-linear numerical analyses that were next performed including the ability of foundation uplift and the ability of the walls to be detached from their interconnections at the corners or at their connection with the roof seems to yield realistic estimates of the observed performance.

REFERENCES

[1] GEER - EERI - ATC - Cephalonia GREECE *Earthquake Reconnaissance January 26th/ February 2nd 2014 Version 1: June 6 2014*

[2] Institute of Geodynamics-National Observatory of Athens-Greece, "The earthquake sequence of January-February 2014 in Kefalonia-Greece", Draft report of , Athens 20th February, 2014.

[3] Ch. Papaioannou et al. "Strong ground motion of the 3rd February 2014, (M=6.0) Kefalonia Earthquake", Institute of Earthquake Engineering and Engineering Seismology Report, February, 2014.

[4] Papazachos, B. and Papazachou, K., 1989, 1997, 2003. The earthquakes of Greece, *Zitis Publ.,Thessaloniki, 356 pp., 304 pp., 286 pp. (in Greek).*

[5] G.C. Manos, Seismic Code of Greece, Chapter 17, International Handbook of Earthquake Engineering: "Codes, Programs and Examples", *edited by Mario Paz, by Chapman and Hall,* ISBN 0-412-98211-0, 1994.

[6] G.C. Manos, V.J. Soulis, A. Diagouma, "Numerical Investigation of the behaviour of the church of Agia Triada, Drakotrypa, Greece", Advances in Engineering Software, Vol. 39/4, pp 284-300, 2007.

[7] G.C. Manos, V.J. Soulis, O. Felekidou, "The dynamic and Earthquake Behavior of Greek Post-Byzantine Churches", 14WCEE, Beijing, CHINA, 2008.

[8] G. C. Manos, V. J. Soulis, O. Felekidou, A. Koutsianou, P. Lipiridou, «The dynamic and earthquake response of Greek Byzantine and Post-Byzantine Basilicas", COMDYN 2009, Rhodes, Greece.

[9] G.C Manos, V. Soulis, N. Karamitsios, O. Felekidou, Numerical Simulation of the Dynamic and Earthquake Behaviour of Greek Post-Byzantine Churches with and without Base Isolation", PROHITECH 2009, 21 to 24 June 2009, Rome, Italy..

[10] Manos George, Soulis V., Felekidou O., Karamitsios N., Kotoulas L., "Dynamic and Seismic Behavior of Greek Post-Byzantine Churches with or without Base Isolation", 8th International Masonry Conference, 2010, Dresden, Germany.

[11] Manos George, Soulis V., Felekidou O., "Numerical Study of the Dynamic and Earthquake Behavior of Byzantine and Post-Byzantine Basilicas", 8th International Masonry Conference, 2010, Dresden, Germany.

[12] Manos George, Soulis V., Felekidou O., Matsou V. "A Numerical Investigation of the Dynamic and Earthquake Behavior of Byzantine and Post-Byzantine Basilicas", 9th U.S. National and 10th Canadian Earthquake Engineering Conference, 2010, Toronto, Canada.

[13] G. C. Manos, V. Soulis, O. Felekidou, N. Karamitsios, L. Kotoulas, "Numerical Study of the Dynamic and Earthquake Response of Greek Post-Byzantine Churches with or without Base Isolation", 3rd International Workshop on Conservation of Heritage Structures Using FRM and SHM, 2010, Ottawa, Canada.

[14] Manos George, Soulis V., Felekidou O., Matsou V. "A Numerical Investigation of the Dynamic and Earthquake Behavior of Byzantine and Post-Byzantine Basilicas", 3rd International Workshop on Conservation of Heritage Structures Using FRM and SHM, 2010, Ottawa, Canada.

[15] G.C. Manos, N. Karamitsios, " Numerical Simulation of the Dynamic and Earthquake Behavior of Greek Post-Byzantine Churches with and without Base Isolation", COMPDYN 2011, Corfu, Greece, 26–28 May 2011.

[16] G.C. Manos, N. Karamitsios, "Study of the Dynamic and Earthquake Response of Greek Post-Byzantine Churches with and without Base Isolation" EURODYN 2011, Leuven, Belgium, 4-6 July, 2011.

[17] G. C. Manos and N. Karamitsios, "Earthquake Numerical Simulation of the Dynamic and Earthquake Behaviour of Greek Post-Byzantine Churches with and without Base Isolation", STREMAH-2011, Chianciano, Italy, Sep. 2011.

[18] Manos George, "Consequences on the urban environment in Greece related to the recent intense earthquake activity", Int. Journal of Civil Engineering and Architecture, Dec. 2011, Volume 5, No. 12 (Serial No. 49), pp. 1065–1090.

[19] G. C. Manos, V. J. Soulis & N. Karamitsios, "The Performance of Post-Byzantine churches during the Kozani-1995 Earthquake – Numerical Investigation of their Dynamic and Earthquake Behavior", 15WCEE, (2012) Portugal.

[20] G. C. Manos & N. Karamitsios , "Numerical simulation of the dynamic and earthquake behavior of Greek post-Byzantine churches with and without base isolation", Earthquake Engineering Retrofitting of Heritage Structures, Design and evaluation of strengthening techniques, pp. 171-186, Edited By: S. Syngellakis, Wessex Institute of Technology, UK, ISBN: 978-1-84564-754-4, eISBN: 978-1-84564-755-1, 2013.

[21] G.C. Manos, L. Kotoulas, V. Matsou, O. Felekidou, "Dynamic behaviour of Greek Post-Byzantine churches with foundation deformability and evaluation of their earthquake performance", 4th ECOMASS Thematic Conference on Computational Methods in Structural Dynamics and Earthquake Engineering – COMPDYN 2013, 12-14 June 2013, Kos Island, Greece.

[22] G.C. Manos and E. Kozikopoulos, "In-situ measured dynamic response of the bell tower of Agios Gerasimos in Lixouri-Kefalonia, Greece and its utilization in the numerical predictions of its earthquake response", *CompDyn 2015 to be published.*

[23] G.C. Manos, D. Naxakis, V. Soulis, "The Dynamic and earthquake response of a two-story old R/C building with masonry infills in Lixouri-Kefalonia Greece, including soil-foundation deformability", *CompDyn 2015 to be published.*

[24] Eurocode 8: Design of structures for earthquake resistance - Part 1: General rules, seismic actions and rules for buildings, *FINAL DRAFT prEN 1998-1, December 2003.*

[25] Provisions of Greek Seismic Code 2000 , EPPO, Earthquake Planning and Protection Organization Athens, Greece, December 1999.

[26] Eurocode 6 part 1: Design of structures for earthquake resistance - Part 1: General rules, seismic actions and rules for buildings, *FINAL DRAFT prEN 1998-1, December 2003.*

COMPDYN 2015
5th ECCOMAS Thematic Conference on
Computational Methods in Structural Dynamics and Earthquake Engineering
M. Papadrakakis, V. Papadopoulos, V. Plevris (eds.)
Crete Island, Greece, 25–27 May 2015

NUMERICAL SIMULATION OF THE LIMIT NON-LINEAR BEHAVIOUR OF UNREINFORCED STONE MASONRY UNDER IN-PLANE STATE OF STRESS FROM GRAVITATIONAL AND SEISMIC ACTIONS

G.C. Manos[1], L. Kotoulas[2] , V. Soulis[3], O. Felekidou[2]

[1] Professor and Director of the Lab. of Strength of Materials and Structures, Aristotle University
e-mail: {gcmanos@civil.auth.gr}

[2] Postgraduate student, Lab. of Strength of Materials and Structures, Aristotle University
e-mail: Κωτούλας Λάμπρος {kotoulaslambros@gmail.com}, {felekidou23@yahoo.gr}

[3] Dr. Civil Engineer, Lab. of Strength of Materials and Structures, Aristotle University
e-mail: {soulis@yahoo.com.gr}

Keywords: Stone masonry, In-plane behavior, Gravitational forces, Seismic actions, Limit non-linear behaviour, In-plane behaviour

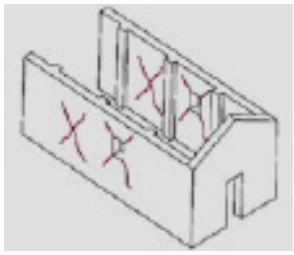
Abstract. *Unreinforced masonry made of stone and low strength mortar has been used for centuries in forming the structural system of old type buildings as well as monumental structures (such as churches etc.) The behaviour of this type of structural systems that survive today, when subjected to the combined gravitational loads and seismic actions, is still of interest. In this framework, the present work tries to evaluate the limit-state in-plane behavior of stone masonry vertical structural elements. Initially, the basic aspects of a methodology are presented whereby the performance of vertical structural elements under seismic actions can be examined through a decomposition process whereby the demands at critical locations of individual piers, that the whole structural system is decomposed to, are compared with the corresponding bearing capacities in either in-plane shear/flexure or in out-of-plane flexure. Next, this methodology is applied to predicting with a reasonably good agreement the performance of stone masonry piers of two churches damaged by the recent Kefalonia-Greece 2014 earthquake. The possibilities offered by non-linear inelastic numerical analyses as alternative means for examining the performance of unreinforced stone masonry vertical structural elements is briefly presented. In addition, numerical simulation results are also presented making use of such non-linear inelastic numerical analyses. The predictions obtained through such non-linear inelastic numerical analyses toward predicting the measured behaviour of stone masonry specimens that were subjected in the laboratory to simultaneous compression and shear or diagonal compression had a reasonable level of success.*

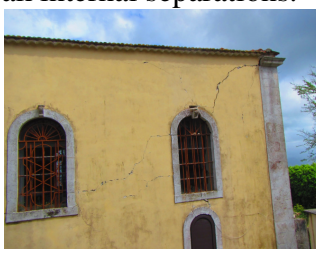
1 INTRODUCTION

During the last thirty years various parts of Greece have been subjected to a number of damaging earthquakes ranging from Ms=5.2 to Ms=7.2 on the Richter scale. Some of these events, not necessarily the most intense, occurred near urban areas (Manos [7] and [10]). One of the most demanding tasks for counteracting the consequences of all these seismic events was the effort to ensure the structural integrity of old churches, that were built in periods ranging from 400 A.D. till today; in many cases they sustained considerable damage. Selected results and summary observations of the seismic behavior of a specific type of structural system are presented by Manos et al. [5, 6, 8]. This system is utilized in many churches belonging to the so called Basilicas. This structural system is one of the oldest structural forms and it is frequently utilized for Greek Christian Churches with a number of variations in plan and height. The "Basilica" structural system is of rectangular shape, formed by the peripheral walls; a semi-cylindrical apse is usually part of the East wall, whereas the interior is divided in a number of naves by longitudinal colonnades of various dimensions and shapes, as shown in figure 1a. The roofing system is mainly in the longitudinal direction; this roofing system at the central nave usually rises at a higher level than that of the side-naves; in this sense, it can be seen as an elevated extension of the interior colonnades. On the contrary, the roofing system that covers the side naves is partially supported on the peripheral walls and is usually lower than the roof of the central nave (figure 1b). In some instances this structural type takes the simplest form of one nave with no internal separations. This is also the form of rectangular old age masonry buildings with strong peripheral walls and weak internal separations.



Patras-Greece Earthquake 2008



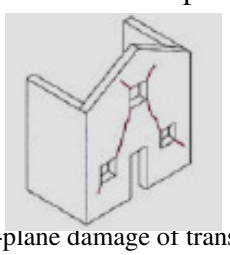


Kefalonia-Greece Earthquake 2014

Figure 1. Typical damage patterns of longitudinal walls

2 TYPICAL DAMAGE PATTERNS

When such structural formations are subjected to horizontal earthquake forces the longitudinal and transverse walls represent the main structural elements that resist these forces ([3]). Despite the fact that the total structural dynamic response is quite complex it is convenient to simplify this response for each one of these main resisting structural elements by decoupling it to in-plane and out-of-plane response that leads to a corresponding state of stress which acts together with the state of stress due to the gravitational forces. When the state of stress due the earthquake forces keeps increasing certain in-plane and out of plane limit strength values are reached that lead to corresponding modes of failure (figures 1, 2 and 3).



Typical in-plane damage of transverse walls



Kefalonia-Greece Earthquake 2014

Figure 2. Typical in-plane damage patterns for transverse walls

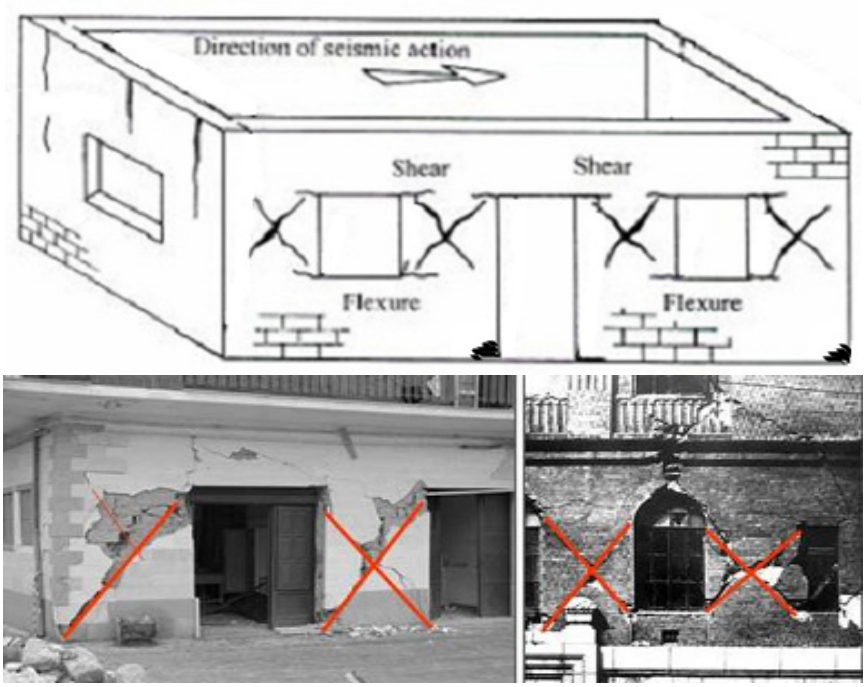


Figure 3. Typical in-plane damage patterns

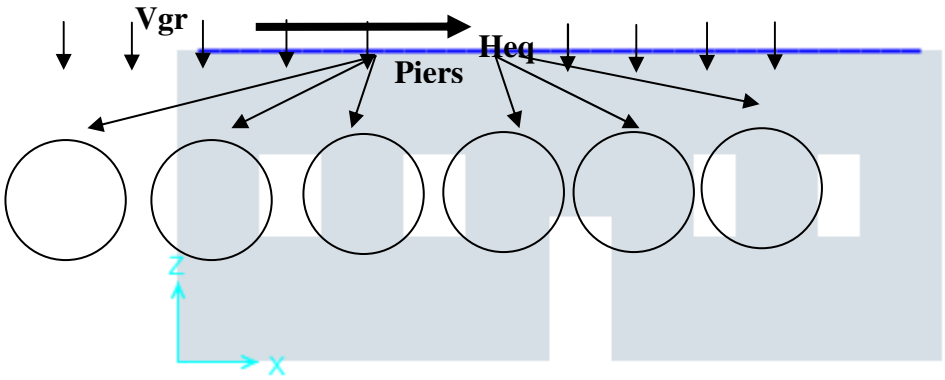


Figure 4. Decomposition of a masonry wall to piers between openings

3 THE STATE OF STRESS OF PIERS BETWEEN OPENINGS IN MASONRY WALLS

Figures 1, 2 and 3 depict such typical in-plane damage patterns for longitudinal and transverse masonry walls. Each one of the in-plane damage patterns that develops in either the longitudinal or the transverse walls arises from the fact that at a certain location the state of stress resulting from combination of the gravitational loads (Vgr) and the earthquake forces (Heq), as shown in figure 4, leads to a demand that exceeds the capacity at this location.

3.1 The decomposition of a masonry wall in a number of masonry piers

One way to deal with this problem is to be able to continuously reaching realistic estimates of the demands at each location and compare these demands with the corresponding capacities and in this way at every forcing level Heq have a continuous adjustment of the contribution of

each part of the wall in the total stiffness and strength and note all the important changes as well as the location where a certain strength limit is reached. This requires a non-linear analysis. For earthquake loads this non-linear analysis is usually performed by applying the horizontal earthquake forces in a step-by-step push-over way. This has been applied with reasonable success by Manos and Soulis for the church of Metamorphosi toy Sotiros in Zaborda, Kozani, Greece.

Alternatively, one can see each vertical wall as being composed by a number of masonry piers that are formed by door or window openings that are usually present, as indicated in figure . These piers usually form the weakest part of the structure. As was shown previously by figures 1 to 3, these piers are the locations where the most severe structural damage usually concentrates.

The demands that arise at each location can be found by various simple or complex methods of numerical approximations and is not part of the current study. In any case these demands can be seen as arising at the top of each individual pier that a vertical wall can be envisaged as being formed of. Thus, in this way each longitudinal and transverse wall is on its own by being composed of various vertical parts (piers) that together with the openings form each wall as a whole (figures 1 and 3). Following this decomposition of a wall to a sum of piers between openings it is on the conservative side to ignore the connections between the longitudinal and the transverse walls at the corner. Consequently each individual pier can be seen as a simple rectangular vertical structural element that is forced by the relevant stress resultants at its upper horizontal boundary and is supported in its lower horizontal boundary in a way capable to transfer axial forces as well as in-plane shear forces and bending moments at depending on the shear and flexural capacity of this lower boundary of the masonry wall, located at a distance equal to ***h*** form the upper boundary.

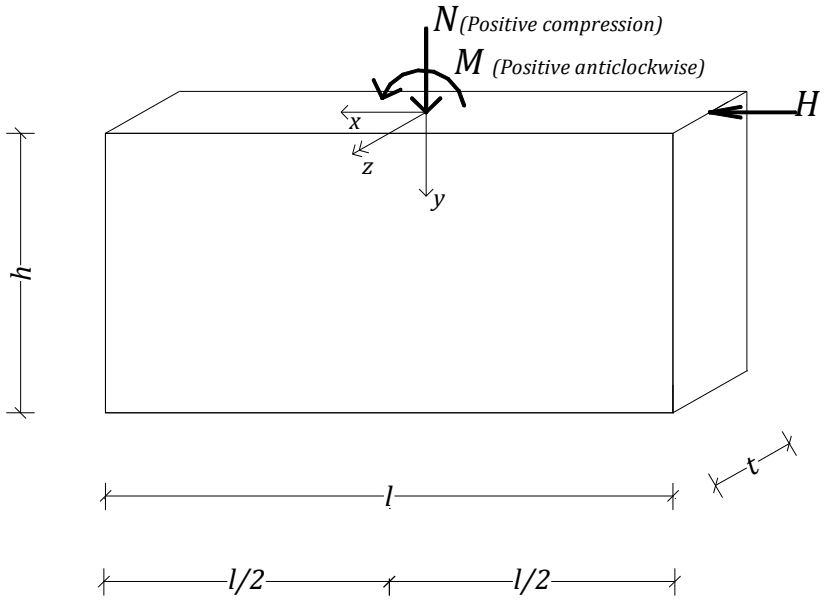


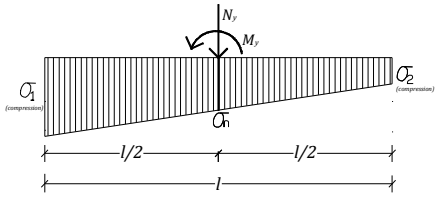
Figure 5. Single masonry pier being stresses in its upper boundary

Consequently, each one of the piers is considered as being stressed in-plane mainly in their upper horizontal boundary and is being supported at their lower horizontal boundary as shown in figure 5. Figure 5 depicts the geometry of such a masonry pier together with the in-plane loads (***N, H, M***) acting on its upper boundary. The stress resultants N_y, Q_y, M_y at an horizontal cross section located at a distance ***y*** from the top horizontal boundary of the pier are given below:

$$M_y = M + H\,y \quad , \quad N_y = M + lt\rho\, y \quad , \quad Q_y = H \tag{1}$$

Where ρ is the specific gravity of the wall, l and t are the geometrical dimension of the pier as shown in figure 5. The calculation of the normal stress at this horizontal cross section is carried out as follows:

Having obtained the demands in every horizontal cross section of the pier in this way the performance of this pier can be evaluated next by comparing these demands with the corresponding shear and flexural capacities. Towards this objective it is essential to be able to approximate the state stress in any horizontal cross-section in terms distribution of axial stresses normal to this cross section and shear stresses parallel to the same cross-section. One particular complication for obtaining such realistic axial and shear stress distributions springs from the fact that masonry and especially old type stone masonry is constructed with mortar that is relatively much weaker in tension and shear than in compression. Moreover, the mortar is also much weaker in tension and shear than the masonry units that can be either man-made or formed from natural stone.

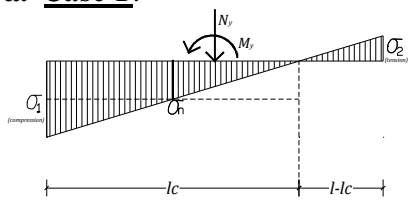


a. *Case 1*:

The normal stress distribution is compressive along all the length of the pier:

$$\sigma_1 \geq 0 \quad and\, \sigma_2 \geq 0$$

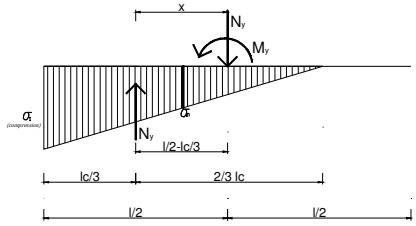
The largest normal stress value must be smaller than the masonry compressive strength f_{kd}



b. *Case 2*:

There is tension at the right zone of the cross section with stress σ_2 lower than the tensile limit stress f_{xk1d} ; consequently, the tensile zone is assumed being active:

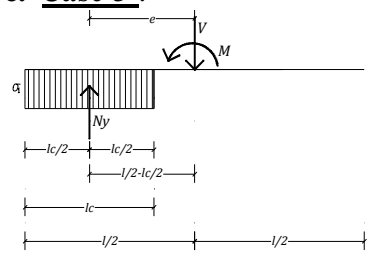
$$\sigma_1 > 0\,; \sigma_2 < 0;\ |\sigma_2| \leq f_{xk1d}\ and\ \sigma_1 < f_{kd}$$



c. *Case 3*:

There is tension at the right fiber of the cross section, larger than the tensile limit stress f_{xk1d} ; consequently, the tensile zone is assumed being inactive:

$$\sigma_1 > 0\,; \sigma_2 < 0;\ |\sigma_2| > f_{xk1d}\ and\ \sigma_1 < f_{kd}$$



d. *Case 4*:

The tensile zone remains inactive but the compressive zone becomes narrower than before (towards developing flexural mode of failure):

$$\sigma_1 > 0\,; \sigma_2 < 0;\ |\sigma_2| \geq f_{xk1d}$$

and

$$e = \frac{M_y}{N_y l} \geq 0{,}45$$

Figure 6. Normal to the bed-joint axial stress distribution patterns

3.2 Predicting the shear bearing capacity of a pier against sliding

For this purpose use could be made of the provisions of Eurocode 6 [1]. For the masonry pier which is studied here the shear strength of the masonry (f_{vk}) is the minimum value of the following:

$$f_{vk} = f_{vk0} + 0.4\ \sigma_n \tag{2}$$

where σ_n is the value of the average normal stress, f_{vk0} the shear strength of the masonry for zero normal stress that is specified by the provisions of Eurocode 6 [1].

$$f_{vk} < 0.065\, f_b \tag{3}$$

where f_b is the compressive strength of the masonry unit.

$$f_{vk} < f_{vklim} \tag{4}$$

where f_{vklim} is the upper shear strength of the masonry, as it is specified by the national appendix of each member state.

The distribution of axial stress (σ_n) normal to a bed joint with thickness equal to the pier thickness that develops at this horizontal section is assumed to be one of the following four simple cases depicted in figures 6a to 6d, which are incorporated in many design provisions. In order to obtain the shear capacity against sliding one should properly chooses which of these four cases of normal stress distribution develops based on the geometry, the stress resultants (N_y, Q_y, M_y) and the masonry compressive and tensile strength values, f_{kd} and f_{xk1d} respectively. These strength values as well as the checks being performed are based on the provisions of Eurocode 6 [1]; however, provisions from other codes can be easily incorporated. Together with the normal stress distribution, the length of the compressive zone (l_c) is also calculated as well as the value of the average normal stress (σ_n), which is assumed to act in this compressive zone as depicted in figures 6a to 6d. Use is made of both the compressive zone length and the average normal stress value for calculating next the masonry shear strength (see equations 2 to 4).

3.3 Predicting the shear bearing capacity of a masonry pier against diagonal tension

` This is done based on the following formula (Eq. 5) given by Turnsek and Cacovic [8, 9, 10]. It is assumed that the tensile strength of the masonry $\sigma_t = f_{xk1}$ depends on the maximum average shear stress τ_{max} of a horizontal section of the masonry pier and on the average compressive stress $\sigma_d = \frac{N}{A}$ that develops on the same location where A the area of this section and N the compressive load.

$$\sigma_t = f_{xk1} = \sqrt{(\sigma_d/2)^2 + (b\,\tau_{max})^2} - \sigma_d/2 \tag{5}$$

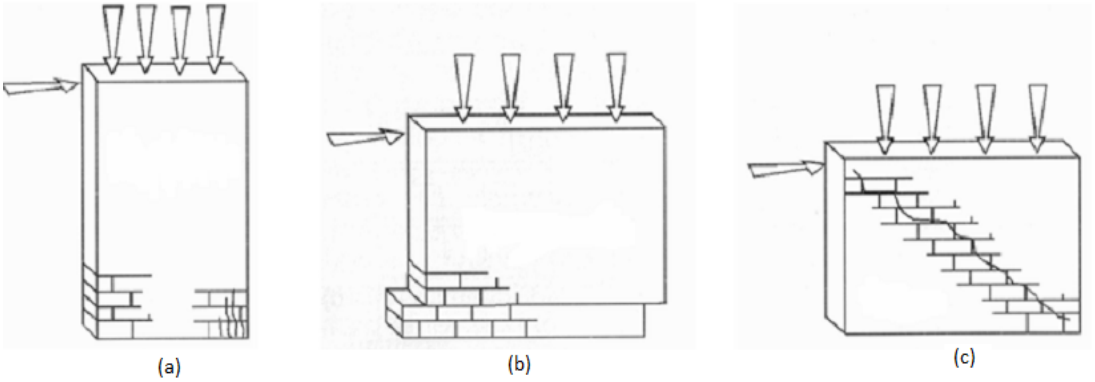
Where b represents the shear stress distribution factor, which is related to the stress distribution on the section and the slenderness ratio of the wall. It can be assumed that $b = \frac{h}{l}$, where h is the height and l is the length of the pier. In this case $b = 1.5$ is the upper limit value and b

= 1 is the lower limit value. From the above relationship the value of τ_{max} can be obtained based on the values of $\sigma_t = f_{xk1}$ and σ_d:

$$\tau_{max} = \frac{f_{xk1}}{b}\sqrt{f_{xk1} + \sigma_d} \tag{6}$$

4 EVALUATING THE PERFORMANCE OF MASONRY WALLS WITH OPENINGS

Based on the above described procedures from predicting the bearing capacity of a masonry pier either against sliding or against diagonal tension the following steps can be followed in order to predict the expected performance of a given unreinforced masonry pier in terms of shear bearing capacity and expected mode of failure. The basis of such a prediction is to include in the expert system the most common modes of failure that such a structural element can develop under the in-plane loads shown in figures 7. Because the focus of this study are the modes of failure that are due mainly to the seismic actions the first checks try to identify the development of the following modes of failure:



a) Flexural b) shear/sliding c) shear / diagonal tension

Figure 7. Typical in-plane failure modes, considered by the expert system, for individual piers subjected to gravitational forces and in-plane seismic actions.

a) The flexural mode of failure (figure 7a). This is done by assessing the distribution of the normal stress at a horizontal cross section, as explained before (figures 6a to 6d). At the same time the maximum compressive stress is also checked which must attain values below the limit compressive strength of the masonry (f_{kd}). If not, flexural failure is predicted.

b) The sliding mode of failure of a horizontal cross-section located either at the bottom or at mid-height of the pier (figure 7b). In doing so the simple Mohr-Coulomb friction is assumed as it is expressed by the provisions of Eurocode 6 (Eq. 2, [7]), for unreinforced masonry, as presented before. The shear/sliding capacity in this case is found based on the masonry sliding shear strength, presented before, and on the compressive zone length (l_c) (see figures 6a to 6d).

c) The shear/diagonal mode of failure (figure 7c); this is calculated from the combined state of stress for the pier, as outlined before. The objective here is to predict this shear/diagonal tension capacity based on the procedure that calculates the maximum shear/diagonal tension stress (Eq. 6).

Both procedures, which were described in 3.2 and 3.3, are incorporated in an expert system that can predict through steps a), b) and c) the bearing capacity of a given pier and the expected mode of failure [ ]. This is applied in the following cases that were selected from vertical masonry walls of two churches damaged during the recent 2014 Kefalonia-Greece earthquake sequence [ ].

These Basilica churches are Panagia at Chavriata and Agia Marina at Soullaroi. Both churches sustained heavy structural damage depicted in figures 8a and 8b, respectively. The dimensions in meters are also indicated in these figures. The examined by the expert system piers are the ones at the West transverse wall (façade) between the door at and the North and South walls (see figures 8a and 8b). The base shear forces for the two churches were obtained through a dynamic spectral analysis with an acceleration spectrum the one derived from the ground acceleration recorded by an accelerograph located at the floor of an old school at Chavriata. The distance between the Agia Marina at Soullaroi and Chavriata is less than two kilometers. Consequently, the same input response spectrum (q=1.5) was used for both churches (4 and 5 first eigen-modes for Ag. Marina and Panagia, respectively). Two types of soil were examined by introducing two-node links at the soil-foundation interface; hard soil conditions were assumed with link axial stiffness equal to 109KN/mm and soft soil conditions when this link axial stiffness value was equal to 24.5KN/mm

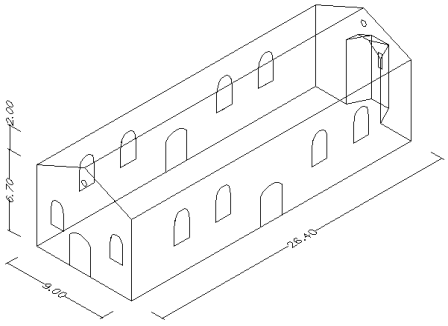


Figure 8a. Church of Panagia at Chavriata

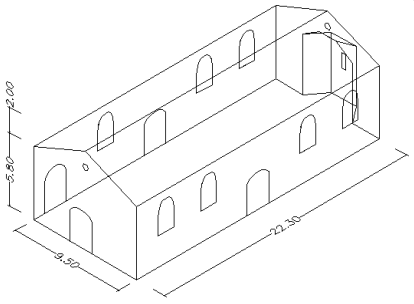


Figure 8b. Church of Agia Marina at Soullaroi

The shear demands when the seismic forces act in the transverse (y-y) North-South direction and thus subject the relatively short East or West masonry walls of these churches to in-plane seismic actions are listed in table 1. The listed values are the base shear demands in this direction for the whole church as well as the shear demand (Q) for the examined here masonry piers.

Table 1	***Shear demands based on the Chavriata response spectra in the East-West (y-y) transverse direction***	
Name of church	Base Shear (KN) for the whole Church, Hard Soil	Shear Q (KN) for the studied pier (l, t), Soft Soil
Agia Marina, Soullaroi	8828	1351 (4156mm x 750mm)
Panagia, Chavriata	16308	2330 (3600mm x 750mm)

Table 2	Compressive strength f_k (MPa)	Shear Strength f_{vko} (MPa)	Axial tensile strength normal/parallel to bed-joint f_{xk1}/f_{xk2} (MPa)
Limit values	3,50	0,16	0,15/0,6

Table 2 lists the assumed mechanical characteristics for the stone masonry in terms of compressive, shear and tensile strength values. f_{vko} is the shear strength of the stone masonry when the normal stress is zero; fvko was assumed to be equal to 0.160 N/mm2. The values listed in table 4 were assumed to be valid for both churches based on relevant strength values employed in similar studies [1, 3, 4, 5, 11, 12, 15, 16, 17]. However, the necessity to quantify such limit value through tests based on in-situ samples must once more be underlined (see section 5).

Table 3	***Shear demands based on the Chavriata response spectra in the East-West (y-y) transverse direction***	
Name of church	**Demands** on the Pier N_y (KN) / M_y (KNm) / and Q_y (KN)	**Shear Capacity** Q_{sl} (KN) / against sliding Q_{dg} (KN) against diagonal failure
Agia Marina, Soul-laroi	560 / 325 / **1351**	864 / **694** (KN)
Panagia, Chavriata	1059 / 475 / **2330**	725 / **779** (KN)

Next, the expert system [18] will be utilised in order to evaluate the performance of the piers of the West walls for both churches that are formed from the door openning. Table 3 lists the more severe demands for these piers in terms of stress resultants N_y, M_y, and Q_y, as these demands resulted from the numerical analyses with horizontal seismic forces equal to the base shear values listed in table 1. Together with these demands the shear capacity values of the examined piers are also listed in this table, against sliding and against diagonal failure, as they were found by applying the developed expert system. As can be seen for the piers of both churches the diagonal failure is predicted. Moreover, it can also be seen that the values of the shear capacity / demand ratio based on the values of table 3 are equal to 0.51<1 for the church of Agia Marina at Soullaroi, and 0.33<1 for the church of Panagia at Chavriata. Again, through this process of evaluating the performance of the examined piers the shear damage predictions are in agreement with the observed performance.

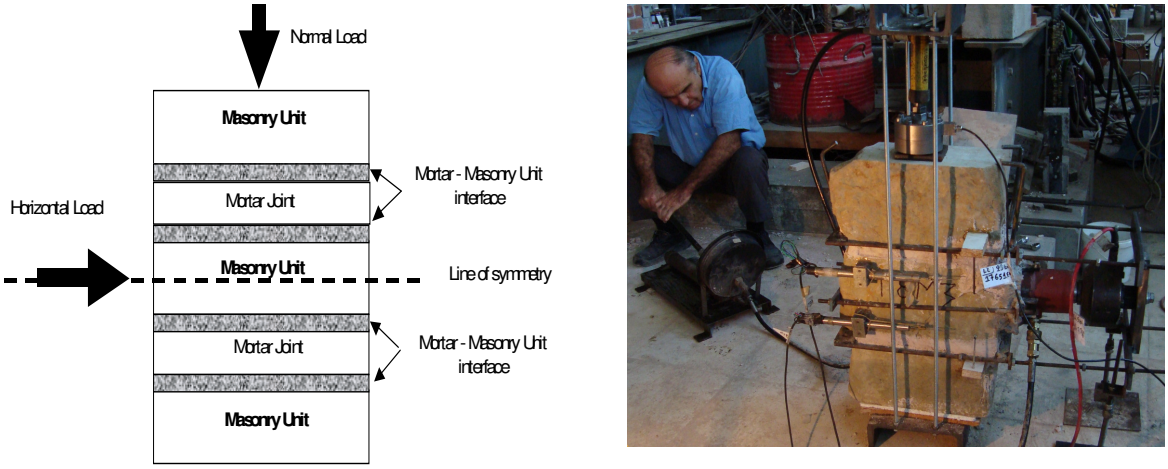


Figure 9. Test arrangement for a triplet test

5 SIMPLE TESTS FOR OBTAINING THE SHEAR STENGTH OF STONE MASONRY PIERS

5.1 The triplet test

This a relatively simple and well known tests whereby two mortar joints are subjected to axial normal stress (σ_n) that remains at a constant amplitude throughout all the duration of the test. The horizontal load is applied in a way as to produce the desired sliding failure between the stones and the mortar joints as it is indicated in figure 9. The objective of such tests is to be able to quantify the parameters included in the Mohr-Coulomb criterion as expressed by equation 2.

Mohr Coulomb failure criterion fv = fvo + 0.45 σ
fvo = 0.12 Mpa

	Normal Stress σ (Mpa)	Predicted fv = fvo + 0.45 σ (Mpa)	Measured value fv (Mpa)	Ratio Measured fv / Predicted fv
Sample 1	0.53	0.359	0.396	1.103
Sample 2	0.61	0.395	0.41	1.038
Sample 3	0.46	0.327	0.305	0.933
Sample 4α	0.30	0.255	0.20	0.784
Sample 4β	0.54	0.363	0.375	1.033

Figure 10a. Verification of the Mohr-Coulomb criterion

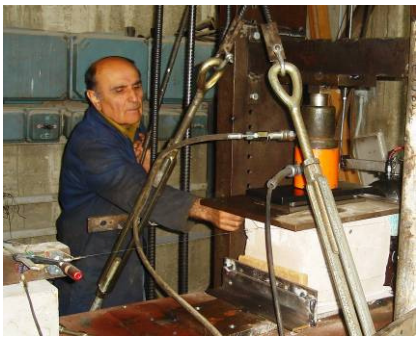


Figure 10b. Experimental set-up



Figure 9c. Sliding mode of failure



Figure 9d. Sliding mode of failure

A more complex extension of the above triplet test is the one shown in figures 10 to 10d where a short stone masonry pier with dimensions in plan somewhat larger than its height ia again subjected simultaneously to constant axial normal stress *(σ_n)* whereas at the same time a continuously increasing horizontal load tries to produce a shear mode of failure for this short pier. A number of short stone masonry specimens were built at the laboratory of Strength of Materials and Structures of Aristotle University using lime mortar and natural stones. The lime mortar had such a composition as to be representative of old relatively weak mortars commonly used in the past. A series of such samples were tested accompanied by constant compression with variable shear as shown in figure 10b. This set-up was designed in an effort to record the shear force at a limit state which represented the failure of the mortar bed-joint as depicted in figures 10c,d. Based on these experimental results, the Mohr-Coulomb limit state criterion (figure 10a, equation 2) can be approximately quantified.

Following these initial samples, another sequence of tests will be performed aimed at quantifying the Mohr-Coulomb failure envelope representing old stone masonry that was injected in the framework of a mild retrofitting scheme. The injected mortar should be of such a

composition as: a) to be compatible with the existing materials b) to be able to fill the existing voids and c) to result in higher strength values.

5.2 Diagonal tension of masonry piers.

This type of tests is shown in figure 11 for a brick masonry pier. In the usual test set-up such masonry piers having equal length and height are placed in a diagonal orientation and the compressed in order to produce in this way the diagonal tension mode of failure, which was described in section 3.2. This testing arrangement is relatively difficult to be applied at stone masonry piers (figure 12). For such piers testing arrangement described in the next section is usually adopted.



Figure 11. Brick masonry pier being subjected to diagonal compression/tension at the laboratory.



Figure 12. Stone masonry pier being subjected to diagonal compression/tension in-situ.

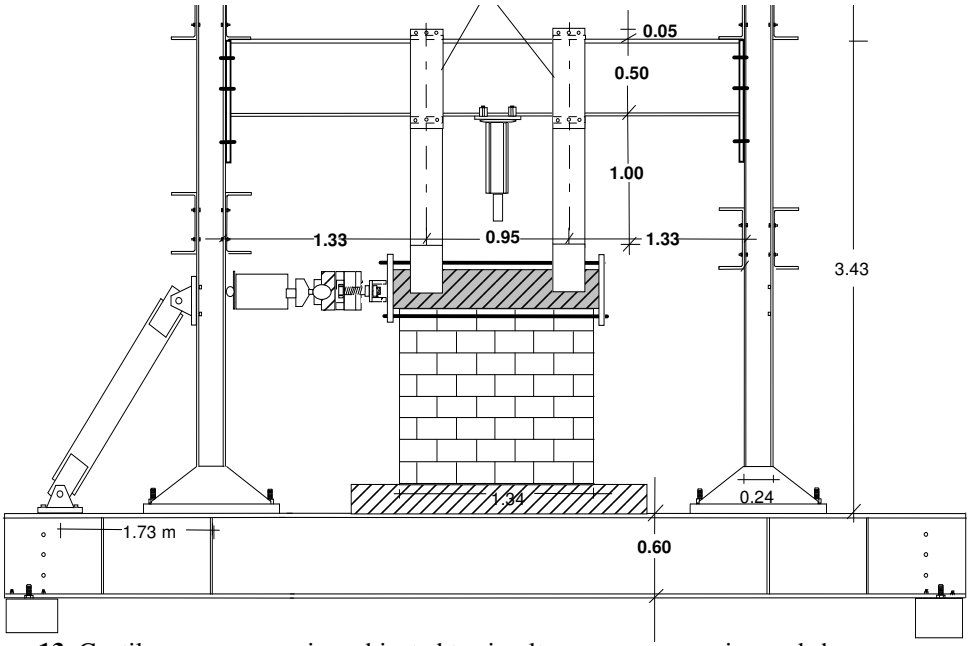


Figure 13. Cantilever masonry pier subjected to simultaneous compression and shear

5.3 Cantilever masonry piers being subjected to simultaneous compression and shear.

This type of tests is shown in figure 13. This loading arrangement reproduces under controlled laboratory conditions the state of stress described by equation 1 and shown by figure 6.

The vertical load is applied at a desired level and kept constant throughout the test whereby the horizontal load is progressively increased. More advanced tests of this type include the variation of the horizontal load in a cyclic way thus simulating a seismic type of loading. The objective of this type of test is to be able through all the measured response parameters to identify the state of stress distribution for this pier and to be able to account for its mode of failure validating in this way one of the failure criteria presented in sections 3.2. and 3.3.

6 NUMERICAL SIMULATIONS

There is a variety of numerical simulations that can be performed in order to predict in a realistic way the performance of structures built with stone masonry. Elastic dynamic spectral numerical analyses try to obtain the demands in the various masonry components for a simple or complex structural system and then evaluate their performance by applying well established failure criteria or code provisions as was presented in section 3. Alternatively, non-linear inelastic "push-over" type of numerical analyses were also performed whereby a masonry structure is subjected first to the permanent vertical loads and then the seismic horizontal forces are applied through a realistic form of horizontal displacement pattern in order to obtain the bearing capacity of the structure under such a horizontal seismic-type loading [12].

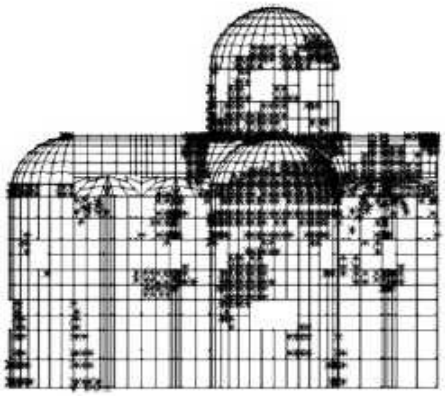


Figure 14. Predicted limit state locations

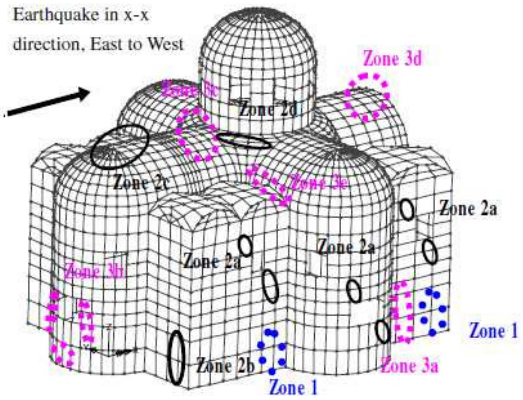


Figure 15. Predicted modes of failure

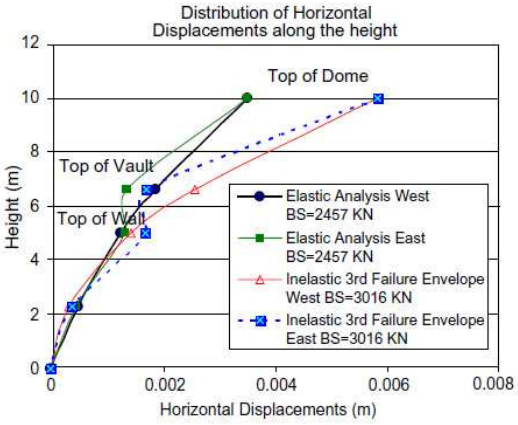


Figure 16. Displacement patterns along the height

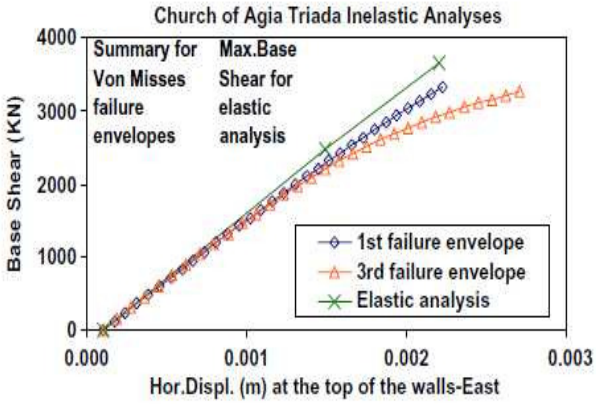


Figure 17. Top displacement versus base shear response

Summary results are shown in figures 14 to 17 from such an inelastic "push-over" type of numerical analysis. In figures 14, the location where the limit state conditions are predicted is shown whereas in figure 15 the predicted modes of failure for the peripheral walls of a Post-

Byzantine church are depicted as they resulted from this push-over non-linear inelastic type of analysis. These predictions are based on realistic parameters of the incorporated in these non-linear numerical analyses of the Modified Von-Misses failure criteria for the various masonry components [12]. Zones of tensile failure (3a, 3b, 3c, 3d), zones of compression/tension failure (2a, 2b, 2c, 2d) and zones compression/compression failure (zones 1) are predicted from these analyses and are shown in figure 15. In figure 16 the distribution of the horizontal displacement along the height of this church as it results from an elastic and non-linear inelastic numerical analysis. Finally, the response of the examined structural system in terms of horizontal displacement at the top of the roof of this church against the base shear is depicted in figure 17 as it resulted either from the elastic or the inelastic numerical analyses.

6.1 Numerical simulation of the triplet test for short stone masonry piers.

In figures 18 to 21 the numerical simulation of the behaviour of the short pier and its loading conditions, described in sub-section 5.1, is depicted utilizing the ABAQUS commercial software package [13]. The numerical prediction of the bearing capacity of this pier in terms of shear stress is shown in figure 20 and it compares quite well with the measured maximum shear capacity that was observed during the cyclic test for this short pier (figure 21). Similarly, in figure 22 predicted by the non-linear inelastic analyses plastic strains are shown and can be compared with the observed damage pattern for the short pier that is shown in figure 23. As can be seen good agreement can be observed. Finally, figure 24 depicts the distribution of the principal tensile stresses that compares well both with the plastic strain distribution and the observed damage

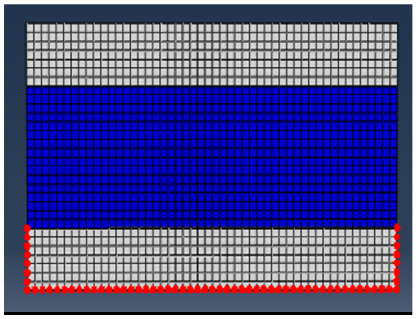


Figure 18. Fixing the low part of the short pier numerical simulation in the same way that the actual test specimen was supported.

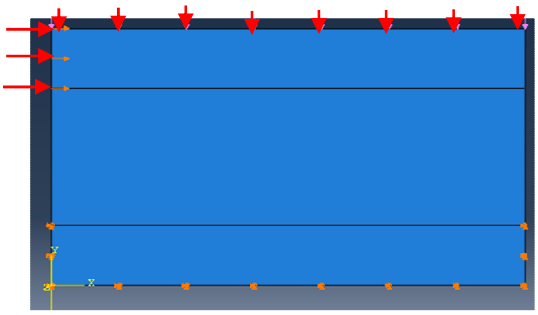


Figure 19. Fixing of the low part of the numerical simulation of the short pier in the same way that the actual test specimen was supported together with the application of uniform compression at the upper boundary equal to 0.16MPa.

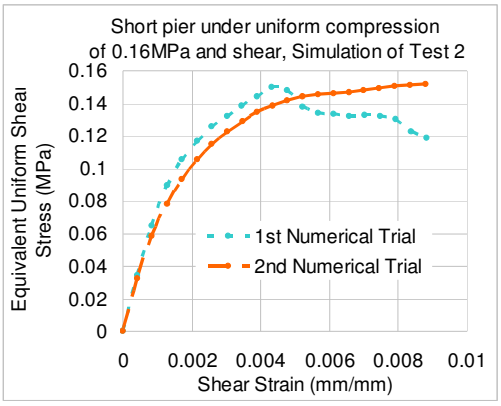


Figure 20. Numerical prediction of the monotonic response of the short pier in terms of shear stress (τ) /shear strain (γ) with simultaneous normal compressive stress 0.16MPa

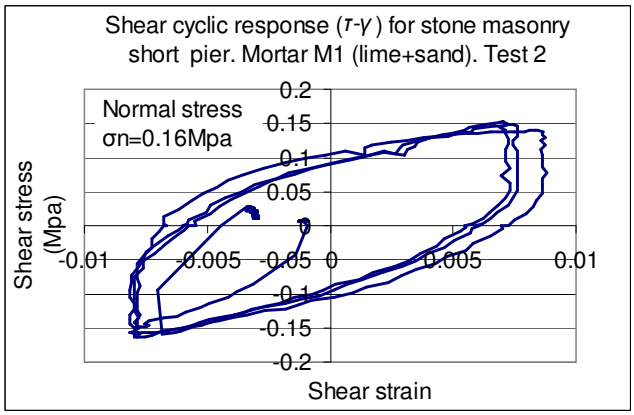


Figure 21. Measured cyclic response of the short pier in terms of shear stress and shear strain when it is simultaneously compressed with a normal stress equal to 0.16MPa

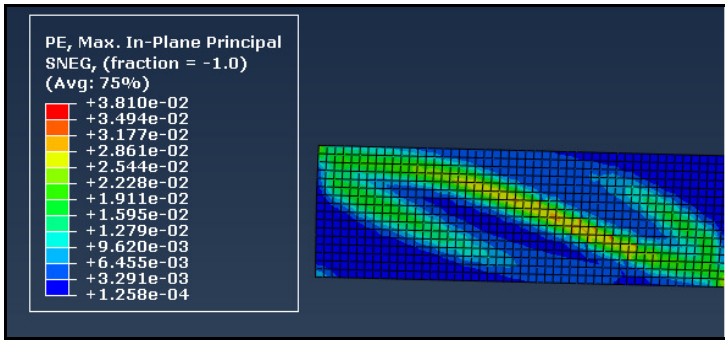


Figure 22. Distribution of predicted plastic strains



Figure 23. Observed damage patterns of the short pier

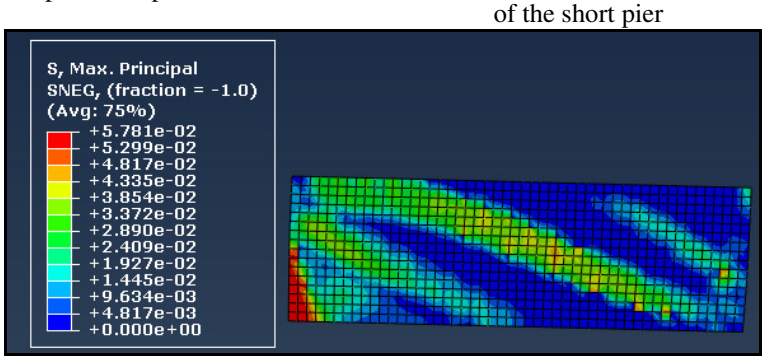


Figure 24. Distribution of tensile principal stresses at maximum load

6.2 Numerical simulation of a stone masonry pier subjected to diagonal compression

An unreinforced masonry wallette made of low quality three-leaf stone masonry with a length of 0.70 m a height of 0.90 m and a thickness 0.50 m was compressed diagonally as shown in figure 24. This is a numerical simulation of specimen 4 from an experimental sequence described in detail by Vintzileou [14] that tested 8 stone masonry specimens; three of those were in axial compression and 5 in diagonal compression. All the information provided in [14] was utilized in this numerical simulation. The ABAQUS [13] commercial software package was employed for these numerical analyses.

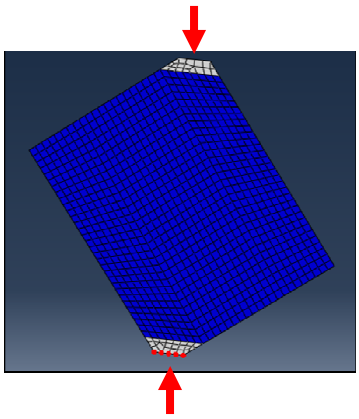


Figure 24. Diagonal compression

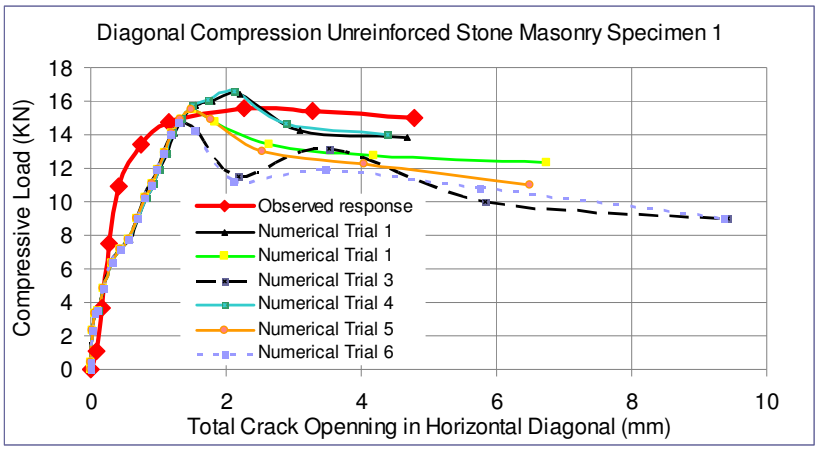


Figure 25. Comparison of numerical predictions with test results for the diagonal compression test

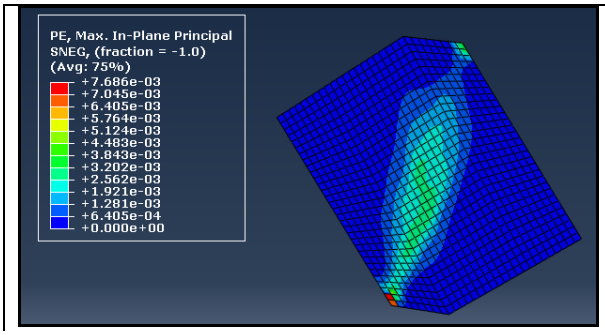


Figure 26. Distribution of predicted plastic strains

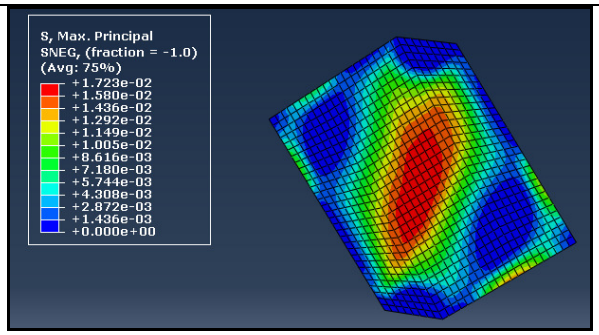


Figure 27. Distribution of tensile principal stresses at maximum load

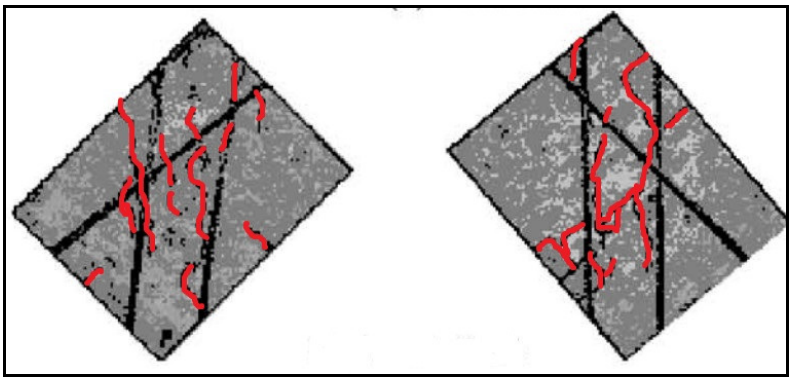


Figure 28. Observed cracking patterns of the diagonal compression specimen [14]

6.3 Numerical simulation of a cantilever pier with simultaneous compression and horizontal load.

A stone masonry pier is examined here with a length equal to ***l***=1500 mm height ***h***=1400 mm and thickness ***t***= 500 mm. This pier is subjected to its upper boundary with a uniform compressive pressure equal to 0.1MPa. The special gravity of this masonry wall is considered equal to 2.20 tn/m3. Because this pier is assumed to be constructed by a relatively weak masonry therefore the Young's modulus for the horizontal load is presumed to be equal to 200 MPa. The horizontal load results from the imposed horizontal displacement at the upper boundary that reaches at the final stages of this numerical study to have a value equal to 30mm. The material properties listed in table 2 were considered together with the Mohr-Coulomb criterion given in equation (1), e.g. $f_{vk} = f_{vk0} + 0.4\ \sigma_n$

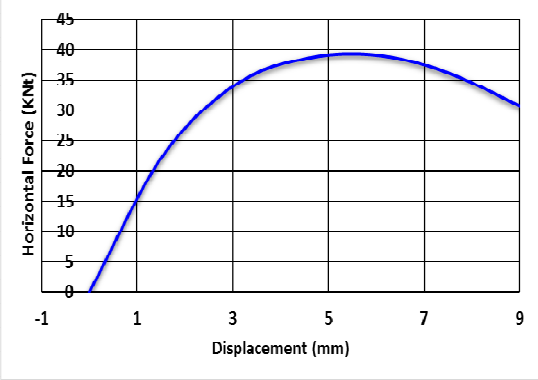


Figure 29. Horizontal load versus horizontal displacement of the studied cantilever pier.

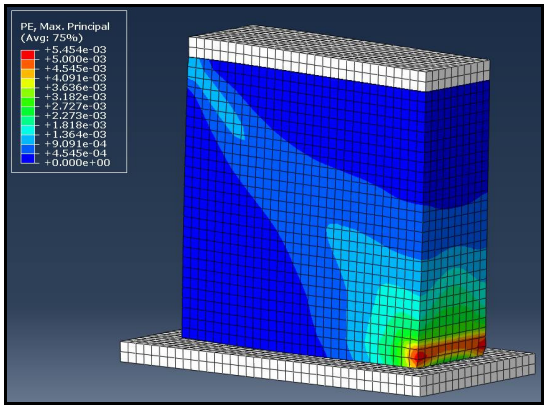


Figure 30. Plastic strains during the response of the pier beyond the maximum load.

Figure 29 depicts the horizontal load versus horizontal displacement response at the top of studied pier whereas figure 30 depicts the plastic strains that develop at the right bottom toe of the pier when it reaches horizontal displacement levels at the top beyond the maximum load. Moreover, figures 31 the overall horizontal and vertical uplift displacement patterns of this pier at maximum load. Finally, figures 32 and 33 depict the distribution of the axial stresses normal to the bed joint and the principal tensile stresses, respectively,

.

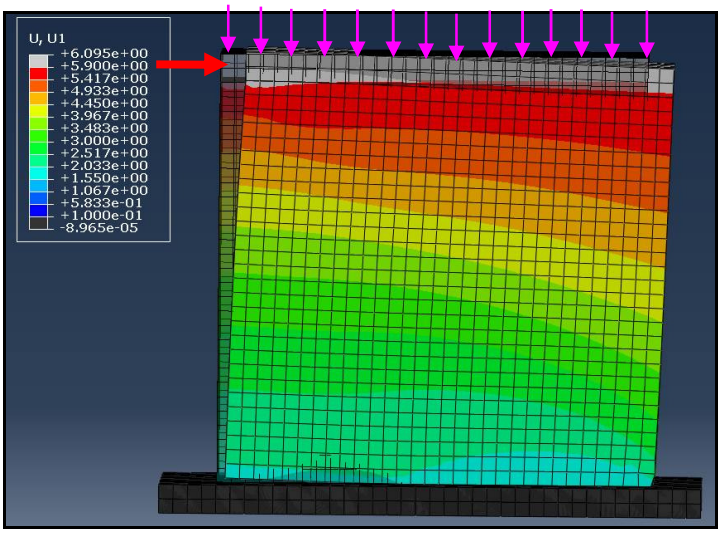


Figure 31. Horizontal sliding displacements at maximum load together with partial vertical uplift

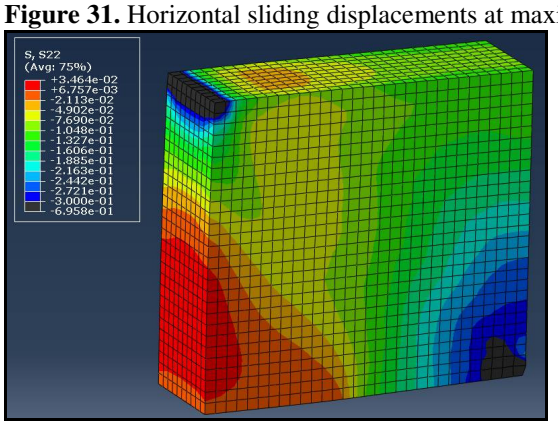


Figure 32. Distribution of axial stresses normal to the bed joints

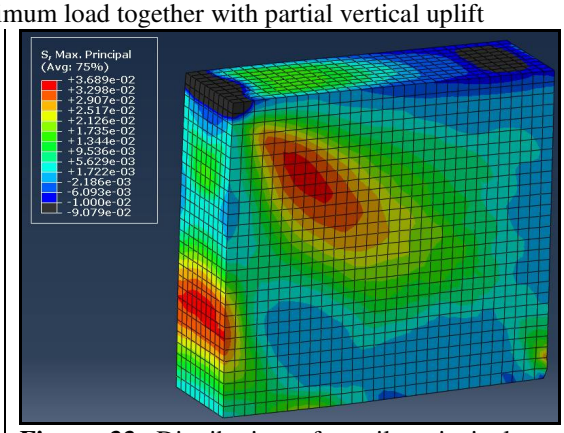


Figure 33. Distribution of tensile principal stresses at maximum load

As can be seen from these figure, the numerical simulation of the behaviour of this pier, under the simultaneous action of the constant vertical compression and the horizontal force at the top of the pier (figure 31), results in the complex state of stress described in sections 3.1. and 3.2. The resulting pattern of the horizontal and vertical uplift displacements are compatible with the assumed limit-state tensile and shear strength values. The shear capacity of this pear is governed by the sliding response rather than the diagonal tensile bearing capacity, despite the fact that figure 33 shows the initiation of such a diagonal tensile crack pattern.

7 CONCLUSIONS

- The performance of masonry structures under seismic actions can be examined through a decomposition process whereby the demands of critical locations of individual piers that the whole structural system is decomposed to are compared with the corresponding bear-

ing capacities in either in-plane shear/flexure or in out-of-plane flexure. The relevant methodology is outlined that forms the basis of an expert system which was developed for this purpose.

- When this methodology is applied for predicting the performance of stone masonry piers of two churches damaged by the recent Kefalonia-Greece 2014 earthquake, good agreement could be found between shear damage predictions and the observed performance.
- The importance of employing realistic limit-state criteria to be utilized in assessing the bearing capacities of unreinforced stone masonry structural elements is then out-lined together with a summary presentation of relatively simple laboratory testing that can be employed for this purpose.
- The possibilities offered by non-linear inelastic numerical analyses as alternative means for examining the performance of unreinforced stone masonry structural elements is briefly presented. In addition, numerical simulation results are also presented making use of such non-linear inelastic numerical analyses. The objective here is to numerically simulate the performance of masonry specimens that were subjected to relatively simple laboratory testing. Successful predictions of the observed performance are means to increase the confidence in these numerical tools before employing them in more complex structural formations.
- The predictions obtained through such non-linear inelastic numerical analyses toward predicting the measured behaviour of stone masonry specimens that were subjected to simultaneous compression and shear or diagonal compression can be considered that had a reasonable level of success.

ACKNOWLEDGEMENTS

The authors would like to thank Civil Engineer N. Parcharidis for his assistance during the numerical simulations.

REFERENCES

[1] Manos G. C., (2011) “Consequences on the urban environment in Greece related to the recent intense earthquake activity”, Int. Journal of Civil Engineering and Architecture, Volume 5, No. 12 (Serial No. 49), pp. 1065–1090.

[2] Provisions of Greek Seismic Code with revisions of seismic zonation”, Government Gazette, Δ17α /115/9/ΦΝ275, No. 1154, Athens, 12 Aug. 2003.

[3] Manos G., Soulis V., Felekidou O., Matsou V. (2010) “A Numerical Investigation of the Dynamic and Earthquake Behaviour of Byzantine and Post-Byzantine Basilicas”, 9th U.S. and 10th Canadian Earthq. Eng. Conf., Canada.

[4] Manos, G.C, Kotoulas, L., Matsou, V., Felekidou, O. “Dynamic behaviour of Greek Post-Byzantine churches with foundation deformability and evaluation of their earthquake performance”, CompDyn2013, 12-14 June 2013, Greece.

[5] Manos G.C., Soulis V., Karamitsios N. (2012) "The Performance of Post-Byzantine churches during the Kozani-1995 Earthquake – Numerical Investigation of their Dynamic and Earthquake Behavior", 15WCEE, Portugal.

[6] Gulkan P., Clough R.W., Manos G.C. and Mayes R.L., (1990), "Seismic Testing of Single-story Masonry Houses : Parts 1&2", Journal of Str. Eng. ASCE, Vol. 116, No 1, January 1990, pp. 235-274.

[7] European Committee for Standardization, Euro-code 6 (2005); "Design of Masonry Structures, Part 1-1:General Rules for Building. Rules for Reinforced and Un-reinforced Masonry", EN 1996-1-1:2005.

[8] Turnsek V, Cacovic F (1971) Some experimental results on the strength of brick masonry walls. In: Proceedings of the 2nd international brick-masonry conference. British Ceramic Society, Stoke-on-Trent, pp 149–156

[9] Bernardini A, Modena C, Turnsek V, Vescovi U (1980) A comparison of three laboratory test methods used to determine the shear resistance of masonry walls" Proc. 7th WCEE, vol 7, IAEE, Istanbul, pp 181–184.

[10] Tomaževič M., 2009 "Shear resistance of masonry walls and Eurocode 6: shear versus tensile strength of masonry", Materials and Structures, August 2009, Volume 42, Issue 7, pp 889-907

[11] Manos G.C. & Kozikopoulos E. , (2015) "The dynamic and earthquake response of Basilica Churches in Kefalonia-Greece including soil-foundation deformability and wall detachment", CompDyn2015, Krete-Greece, 2015.

[12] Manos G.C., Soulis V., Diagouma A. (2008) "Numerical Investigation of the behaviour of the church of Agia Triada, Drakotrypa, Greece", Journal in Advances in Engineering Software 39, 284-300.

[13] Hibbitt, Karlsson, Sorensen. Inc. ABAQUS user's manual volumes I–V and ABAQUS CAE manual. Version 6.10.1. Pawtucket, USA; 2010.

[14] Vintzileou, E. "Effect of Timber Ties on the Behavior of Historic Masonry", American Society of Civil Engineers, Journal of Structural Engineering, Vol. 134, No. 6, June 1, 2008. ©ASCE, DOI: 10.1061/ (ASCE) 0733-9445 (2008) 134:6(961)

[15] G.C Manos, V. Soulis, N. Karamitsios, O. Felekidou, Numerical Simulation of the Dynamic and Earthquake Behaviour of Greek Post-Byzantine Churches with and without Base Isolation", PROHITECH 2009, 21 to 24 June 2009, Rome, Italy.

[16] G. C. Manos & N. Karamitsios , "Numerical simulation of the dynamic and earthquake behavior of Greek post-Byzantine churches with and without base isolation", Earthquake Engineering Retrofitting of Heritage Structures, Design and evaluation of strengthening techniques, pp. 171-186, Edited By: S. Syngellakis, Wessex Institute of Technology, UK, ISBN: 978-1-84564-754-4, eISBN: 978-1-84564-755-1, 2013.

[17] George C. Manos and Lampros Kotoulas "Earthquake Performance of Greek Post-Byzantine Churches with Foundation Deformability " Proc. 2nd Int. Conf. on Protection of Historical Constructions, pp. 297-303, 2014, ISBN 978-975-518-361-9.

[18] G. C. Manos, L. Kotoulas, O. Felekidou, S. Vaccaro and E. Kozikopoulos, "Earthquake damage to Christian Basilica Churches – Application of an expert system for the preliminary in-plane design of stone masonry piers", Int. Conf. STREMAH 2015.

COMPDYN 2015
5th ECCOMAS Thematic Conference on
Computational Methods in Structural Dynamics and Earthquake Engineering
M. Papadrakakis, V. Papadopoulos, V. Plevris (eds.)
Crete Island, Greece, 25–27 May 2015

EXPERIMENTAL INVESTIGATION AND NUMERICAL SIMULATION OF SHEAR BEHAVIOUR OF RC T-BEAM SPECIMENS WITH OR WITHOUT SFRP-STRIPS UNDER CYCLIC LOADING

George C. Manos[1], Konstantinos B. Katakalos[1] and Marios Theofanous[2]

[1,2] Aristotle University of Thessaloniki
School of Engineering, Egnatia street, University Campus, Thessaloniki, Greece
e-mail: kkatakal@auth.gr, gcmanos@civil.auth.gr

[2] University of Birmingham
School of Engineering, Edgbaston, Birmingham, UK, B15 2TT
m.theofanous@bham.ac.uk

Keywords: Shear strengthening, Reinforced concrete T-beams, FRPs, Experimental investigation, Numerical simulation FRP strip anchoring instructions.

Abstract. *The successful validation of a numerical model is presented that can realistically approximate the shear behavior of reinforced concrete (RC) T-section beams strengthened against shear with externally applied open hoop steel fiber reinforcing polymer (SFRP) strips. For this purpose, the measured load-deformation response of three (3) full-scale R/C beam specimens is utilized. These specimens were imposed in a cyclic loading sequence up to failure. Open hoop steel FRP strip shear reinforcement was applied externally to upgrade the shear capacity of two (2) RC beam specimens. For the first specimen the SFRP strips were applied without anchorage, whereas for the other strengthened specimen the SFRP strips were attached together with a novel anchoring device. The successful numerical simulation predicts with a very good degree of approximation the observed load-deformation behavior and the ultimate shear capacity of all these specimens as well as the observed modes of failure including diagonal concrete cracking, debonding of the CFRP strips in the case of no anchoring, or the plastification of parts of the anchoring devices plus the adjacent crushing of the concrete.*

1 INTRODUCTION

Reinforced Concrete (R/C) structures represent a substantial portion of the current infrastructure and building stock in most countries worldwide. A large percentage of these were built several decades ago and in some cases require retrofitting or structural upgrading in order to conform to more stringent design regulations, to accommodate additional live loads due to possible changes in the building's function or to make up for the loss of strength brought about by environmental parameters that speed up structural deterioration. Moreover, the rapid evolution of seismic codes over the past two decades, which utilizes the knowledge gained following devastating earthquakes, necessitates the structural upgrading of most concrete structures that were built according to older design regulations, following a different design philosophy, in which the role of ductility was not central to the design process. On the contrary, all current seismic design codes pay particular attention to enforce ductile behavior on the various R/C structural elements, which is accomplished by prohibiting shear types of failure and favoring instead flexural types of failure with sufficient ductility [1-4, 10-18]. This ductile behavior is also desirable when one is faced with the task of designing a retrofitting scheme that aims at upgrading the seismic performance of R/C structures designed by older design codes [19]. This paper deals with the objective of upgrading the shear capacity of R/C T-beams, that are poorly reinforced against shear, as part of such a retrofitting scheme [5,17,18,20].

Among several upgrading techniques available, the utilization of FRP sheets or plates that can be attached externally to existing structural components with the aid of resin has attracted considerable attention from both academics and practicing engineers [2,6,15,28]. Various researchers have derived models for the prediction of the bond-slip response and required anchor lengths of FRP sheets attached to concrete [22,24-26,29]. Depending on the application, fibre reinforcing polymer (FRP) sheets can be employed to increase the flexural strength, the shear strength, the ductility and the serviceability performance of R/C structures, utilizing these FRP sheets as additional external reinforcement.

FRP sheets possess very high strength in the orientation of their fibres; however only a small part of the available strength can be exploited in practice, due to the onset of debonding at relatively small strains, which can initiate either at the ends of the FRP sheets, due to insufficient anchoring or within the mid-parts of the FRP sheets, when anchoring is provided at the FRP-strip ends, following the formation of cracks in the concrete [5-12,27]. Therefore, the development of innovative means for effective anchorage of the FRP sheets/plates in the concrete volume, which ensures the satisfactory transfer of forces from the FRP sheet to the concrete part of the structural member and allows for a more efficient utilization of the FRP strength, is warranted [24–28].

In the present paper, a novel anchorage device [13] for FRP sheets employed as external shear reinforcement, which was recently developed at the Laboratory of Strength of Materials and Structures of Aristotle University of Thessaloniki is studied numerically. Its effectiveness has been experimentally verified. [18,25,26] The aim of the present study is to replicate numerically the experimentally obtained results and to identify the key parameters controlling the structural response of reinforced concrete T-beams strengthened against shear by external FRP reinforcement, that will allow the optimization of the anchorage device and hence the more effective utilization of the FRP sheets, thus leading to more efficient design. Finally the R/C concrete T-beams are imposed to a cyclic loading sequence.

2 EXPERIMENTAL SETUP

Several theoretical and experimental studies [4,9,15] have been carried out to analyze the phenomenon of the shear failure of reinforced concrete (RC) beams. Russo et al. [22] presents a comprehensive review of various proposed methods for predicting the shear behavior of reinforced concrete beams without any transverse reinforcement. In the design of R/C beams, this is usually considered as an initial condition that is supplemented by the strength provided by the transverse reinforcement in order to predict the total shear capacity of such a structural element. Following this rationale a comprehensive experimental program has been designed and carried out at the Laboratory of Experimental Structural Mechanics at the Aristotle University of Thessaloniki aimed to assess the structural efficiency and effectiveness of shear strength provided to R/C beams by externally attached open hoop FRP transverse shear reinforcement. Initially, one R/C T-beam specimens with only longitudinal reinforcement was tested. Two identical R/C T-beam specimens were then tested which were provided with open hoop FRP strips external shear reinforcement in order to study in this way the additional shear strength that can be attained by such a strengthening scheme. This open hoop FRP strip shear reinforcement was examined in two distinct forms. First, these open hoop FRP strips were simply attached on the external surface of the R/C specimens. The prevailing mode of failure for this specimen is the debonding of the FRP strips, which renders this type of shear reinforcement ineffective. This is because the FRP strips' debonding occurs long before the tensile strength capacity of such FRP strips is reached. In order to prohibit such a premature debonding type of failure a novel anchorage device [24–27] is introduced together with the open hoop FRP strips that can be attached relatively easily at R/C T-beams, which is the primary practical application. The second T-beams was strengthened utilizing this technique.

2.1 T-section beam tests

Three cantilever reinforced concrete beams with a T-section were fabricated and tested under cycling loading conditions at the Laboratory of Strength of Materials and Structures of Aristotle University of Thessaloniki. The reinforcing details are depicted in figure 1. The setup consists of a T-beam with dimensions 120 by 360 mm with a slab width of 360mm and a rectangular column with cross sectional dimensions 400 by 500 mm. The part of the specimen that resembles the column was securely fastened to a rigid wall using two steel I-beams. The free end of the beam was attached via a hinge to a 2500 kN capacity hydraulic actuator which was used to apply the cycling load. The load was controlled with a 1000 kN capacity load cell under deflection control, driven by a personal computer. After applying three cycles in elastic region, loading cycles were increased gradually up to failure. Same loading methodology was applied to all specimens. The beam's free end deflection and moment curvature at the maximum moment region were measured using LVDT's. LVDT's were also positioned vertical to the longitudinal axis of the beam to ensure that the beam did not deflect out of plain. LVDT's were also placed at an angle of 45^{o}. SFRP strains were measured with strain gauges. Strain gauges were attached on 8 consecutive SFRP tapes starting from the second from the fixed end. A strain gauge was attached to the mid-height of each SFRP tape along the fiber direction. Finally the time history of the loading sequence is presented in figure 2.

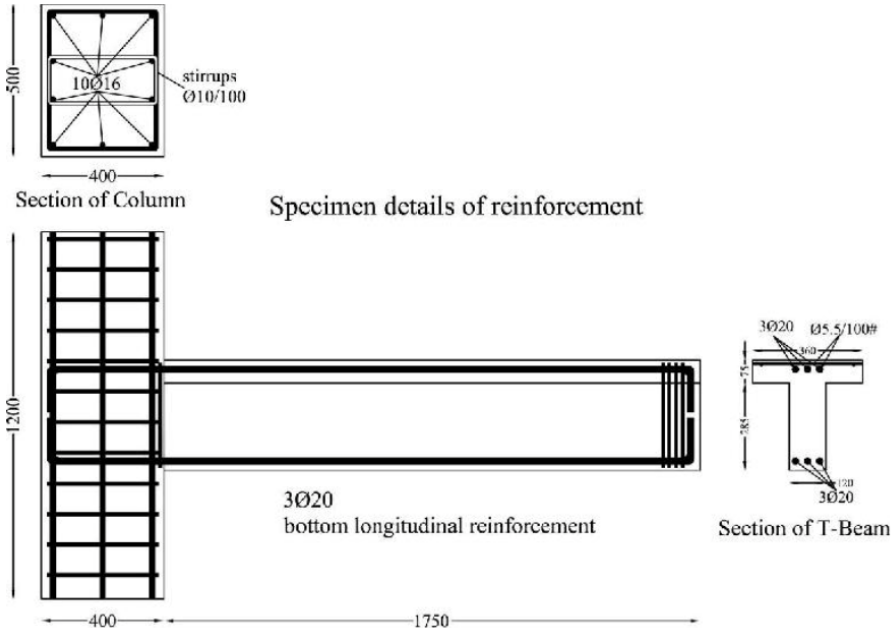


Figure 1. Specimen Details and Reinforcement

Initially, one concrete T-beam specimen both without any SFRP, namely CTB was tested to obtain the basic structural response. This test was utilized in the present numerical study to calibrate the material parameters of the concrete material model. Subsequently, two more specimens without any steel stirrups were reinforced against shear by externally attaching U-shape open-hoop SFRP strips with and without an anchorage scheme. (named TB150 and TB150a) The spacing of SFRP strips was considered equal to 150 mm. The anchorage was provided by the novel anchorage device [24] depicted in some detail in figures 3a and 3b. In this anchoring device a steel rod is used to wrap around it the FRP strip; this steel rod is secured by a steel plate of equal length which is bolted by two anchor bolts as shown in figure 3b.

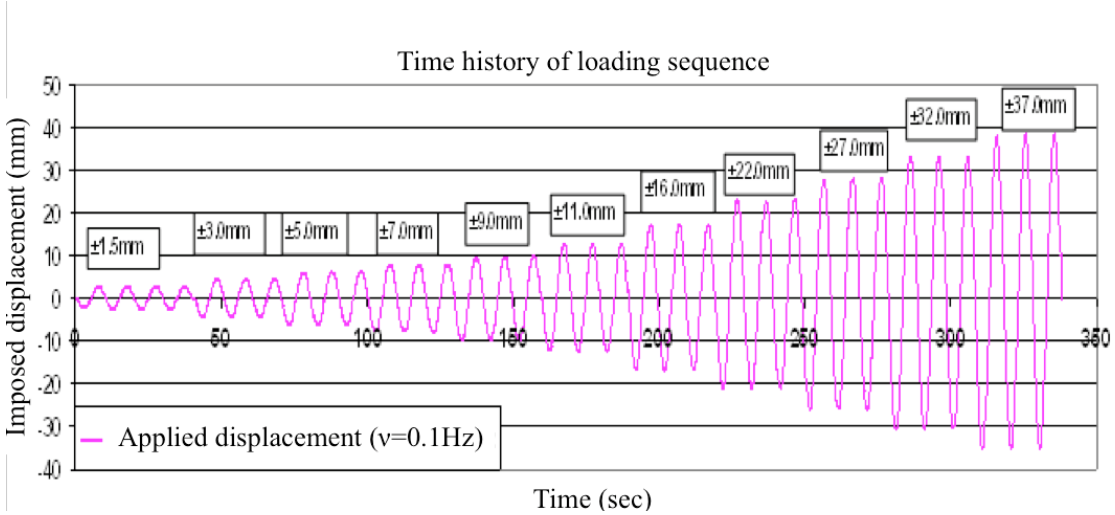
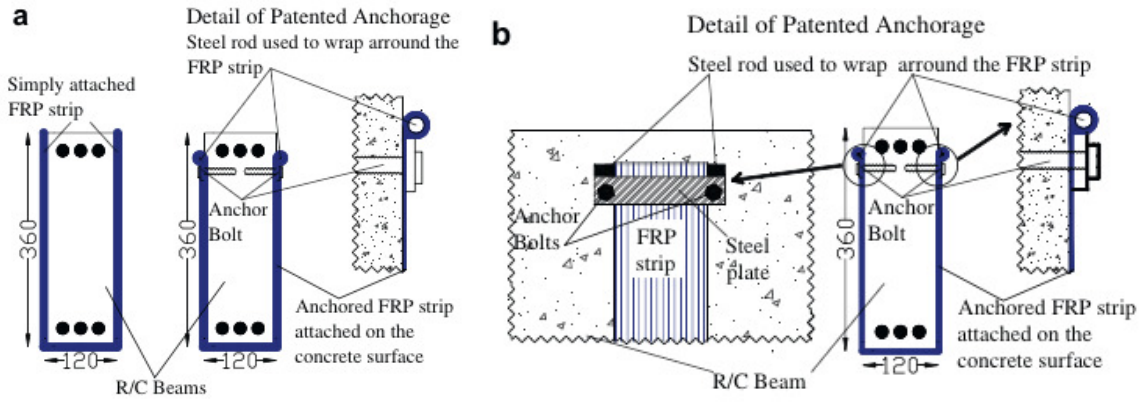


Figure 2. Time history of loading sequence



Figures 3a and 3b. Cross section of the tested specimens with the reinforcement details and the proposed anchoring device (dimensions in mm).

Table 1 lists all the particular aspects that characterize each one of these three specimens.

Table1. Summary of beam tests.

Designation	Shear reinforcement	Mean concrete cylindrical strength (Mpa)	Width of SFRP strip (mm)	Spacing of SFRP strip (mm)	Anchorage	Measured ultimate shear capacity $^{exp}V_{max}$ (kN)	Mode of failure
CTB	No	22.40	100	150	N/A	37.25	Diagonal crack
TB150	SFRP (1layer)				No	73.20	Debonding
TB150a	SFRP (1layer)				Yes	182.40	Anchorage failure

2.2 Material tests

A series of standard tests have been carried out in order to establish the basic material properties for these beam specimens; e.g. basic material properties for the concrete, the reinforcing bars, the SFRP strips as well as the steel plates and steel bolts employed in the anchoring device. These experimentally derived material properties were utilized in the subsequent numerical study. The measured mean concrete cylindrical strength for each specimen is listed in column 3 of Table 1 and is equal to 22.4Mpa. The longitudinal and transverse reinforcement were grade S500, whilst the steel plates were grade S235. The bolts utilized in the anchoring device were manufactured by HILTI and are designated as HILTI HUS herein. The full stress-strain response of all steel parts was experimentally determined and utilized in the numerical studies. The experimentally determined Young's modulus E, yield strength f_y and ultimate strength f_u are reported in Table 2.

Finally, unidirectional tension tests were conducted on resin rich SFRP sheets up to failure to obtain the Young's modulus (E_1) and strength (fu_1) in their fibre orientation and the Poisson's ratio ($\nu_{12} = (E1/E2)\nu_{21}$). The remaining two material properties pertaining to the orthotropic nature of the material under the plane stress assumption, namely the transverse Young's

modulus E_2 and the shear modulus G_{12}, were derived by applying the conventional rule of mixture for composites [17], taking into account the manufacturer's specifications for the resin and the FRP sheets (see acknowledgements) and the experimentally determined volume fraction of resin and FRP sheets.

Both the experimentally and the analytically determined material properties are reported in Table 3. It should be noted that the analytical values obtained by applying the rule of mixture for E_1 and v_{12} compare very well (discrepancy within 5%) with the experimental ones.

Table 2. Material properties of employed steel plates, rebars and bolts.

Material property	Longitudinal rebars of d = 20 mm diameter	Steel plates of anchoring device	Anchor bolts Hilti HUS
E (MPa)	202,700	210,000	210,000
f_y (MPa)	527	255	800
f_u (MPa)	645	390	917

Table 3. Material properties of SFRP.

Material property	E_1 (Mpa)	V_{12}	F_{u1} (Mpa)	E_2 (Mpa)	G_{12} (Mpa)
SFRP	36,350	0.312	330	4,400	1,900

2.3 Summary of observed behavior – modes of failure

The key findings of all beam tests are summarized in Table 1, where the ultimate shear force ($^{exp}V_{max}$) resisted by these specimens is listed in column 7 of this table. As can be seen, the shear strength of the control rectangular beam (CTB) without any stirrups SFRP strips was recorded equal to 37.25 kN. From the results shown in Table 1, it is evident that the maximum recorded shear capacity for the two strengthened T-beams with SFRP strips was significantly greater than the shear capacity of CTB specimen. The observed mode of failure is listed in column 8 of Table 1. As can be seen, when SFRP strips are without anchors the debonding mode of failure of the FRP strips prevails. This debonding mode of failure limits the observed shear capacity increase to 96.5% (nearly 2 times larger than the initial value of 37.25 kN), when the shear capacity of the strengthened specimen is compared to that of specimen CTB (without any shear reinforcement). When the novel anchoring device was utilized for prohibiting this debonding mode of failure it resulted in shear capacity increase of up to 390% (4.9 times larger than the initial value of 37.25 kN). It should be noted that CTB has no internal shear reinforcement. The beneficial effect of anchoring the U-shape open-hoop SFRP strips in order to inhibit the debonding mode of failure is thus demonstrated. The subsequent numerical study will focus on these important features of the observed behavior, that is the prevailing mode of failure and the measured ultimate shear capacity ($^{exp}V_{max}$).

3 NUMERICAL ANALYSIS

The general purpose FE software ABAQUS [9] was employed to generate FE models to simulate numerically the structural response of the previously described concrete beams strengthened with externally attached FRP sheets. The generated models were validated against all respective experimental results. The aim of this part of the study is to generate reliable FE models that can be utilized to enhance the understanding of the fundamental struc-

tural response of the FRP shear strengthening scheme of R/C T-beams with and without anchorage devices, under cyclic loadings and hence optimize the anchorage device design.

3.1 Modeling assumptions

The mean measured specimen geometries were utilized to simulate the test specimens. The full 3D geometry of the concrete volume and the steel plates employed for the anchorage of the SFRP was modeled with 3-D brick-type F.E. elements, whilst the FRP sheets were idealized as planar F.E. elements and their actual thickness (0.75 mm) was utilized as a section property. The bolts were assumed cylindrical with a diameter equal to the equivalent diameter corresponding to the net bolt area (i.e. the threaded part of the bolts was not explicitly modeled). A further idealization pertinent to the bolt assembly simulation is the assumption that the bolt-hole diameter of the steel plate is equal to the assumed bolt diameter (i.e. the clearance has not been accounted for).

In order to reduce the computational cost, the symmetry of the structure with respect to the x–y mid-plane was exploited, by numerically simulating one quarter of the physical model and applying the appropriate boundary conditions at each of the two planes of symmetry as shown in figure 4. The load was applied incrementally as prescribed displacement on a steel plate (SP1) at the point of load application, which was applied iteratively utilizing a smooth amplitude curve available in ABAQUS. Restraint of the structure in the direction of the prescribed displacement was provided by fixing all degrees of freedom of nodes at the supporting element. The sum of the reaction forces in all nodes of the supporting element yields the total reaction that is exerted to the model structure and will be compared with $^{exp}V_{max}$ of Table 1.

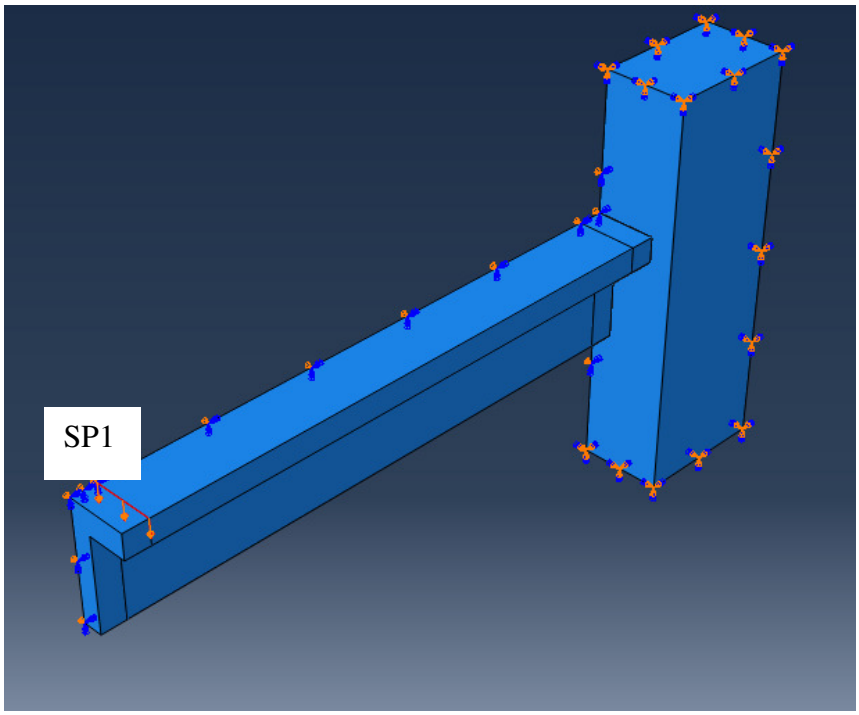


Figure 4. Modeled geometry and applied boundary conditions.

The contact between the various parts of the model (steel bolts, steel plates and concrete volume) was explicitly modeled and a friction coefficient equal to 0.3 was assumed for tangential contact behavior. Variation of the friction coefficient applied to the bolt-concrete inter-

face between the idealized frictionless and rough contact extreme cases was attempted, but no significant effect on the overall solution was observed. Moreover, in order to reduce computational cost, the actual detail of the cylindrical rod of the anchoring device through which load is transferred from the FRP strips to the concrete beam through the steel plate was somewhat simplified (see figures 3b and 5); towards this end, the displacements of the SFRP's edge were constrained to be equal to the respective displacements of the steel plate's mid plane for the numerical representation of the anchoring device. The interface between the SFRP strip and the concrete was simulated as a cohesive zone endowed with a suitable traction separation response, the properties of which are discussed below.

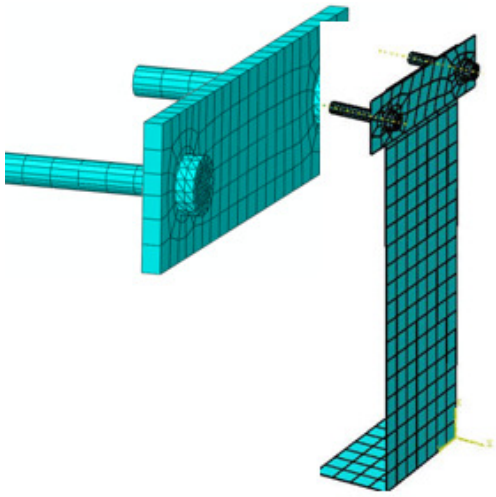


Figure 5. Finite element discretization of the anchoring device

3.2 Material modeling

The auxiliary test results reported previously were utilized herein to define the material response. The SFRP sheets were assumed orthotropic under plane stress conditions and the material properties reported in Table 3 were adopted. The tensile failure in the principal direction was considered and the ultimate stress reported in Table 3 was adopted, whilst other failure modes were considered irrelevant to the present study. A fracture energy equal to 0.01 was assumed to simulate damage evolution, which was rapid, due to the severe stress concentration following the onset of failure. Steel plates, longitudinal reinforcing bars, steel stirrups and steel bolts and plates were assumed elastic-isotropic hardening and the experimentally obtained stress–strain curves for the steel used for these parts were converted into the true stress-logarithmic plastic strain format according to Eqs. (1) and (2) and utilized to define the material response.

$$\sigma_{true} = \sigma_{nom}(1 + \varepsilon_{nom}) \quad \text{eq.1,} \qquad \varepsilon_{\ln}^{pl} = \ln(1 + \varepsilon_{nom}) - \frac{\sigma_{true}}{E} \quad \text{eq.2}$$

The damaged plasticity model for concrete available in the ABAQUS material library was adopted to model concrete response, since it has been shown to perform satisfactorily in similar applications [23]. All material parameters were initially calibrated to accurately simulate the response of the control T-beam specimen CTB. The values adopted for the relevant material parameters, namely the angle of dilation h, the eccentricity, the ratio of equibiaxial to uni-

axial compressive stress fb0/fc0, the ratio of the second stress invariant on the tensile meridian to that on the compressive meridian at initial yield Kc and the viscosity parameter were 40, 0.1, 1.16, 0.666 and 0 respectively and were all within the range encountered in literature [23]. In accordance with similar studies [18], the stress strain response of concrete in compression was derived according to Saenz [23], whilst the tension stiffening response was defined in terms of tensile stress and axial deformation according to Cornelissen et al. [12], assuming a fracture energy equal to 0.06. The Young's modulus E and tensile strength f_{ct} were determined according to ACI [1] as a function of the compressive cylindrical strength, whilst Poisson's ratio was assumed equal to 0.2. The comparison between this assumed in the numerical simulation stress–strain concrete behavior and the one measured by testing concrete cylindrical specimens taken during the construction of the beam specimens is depicted in figure 6. It must be borne in mind that these specimens were simply loaded in compression in such a way that the descending branch of the stress–strain curve could not be obtained.

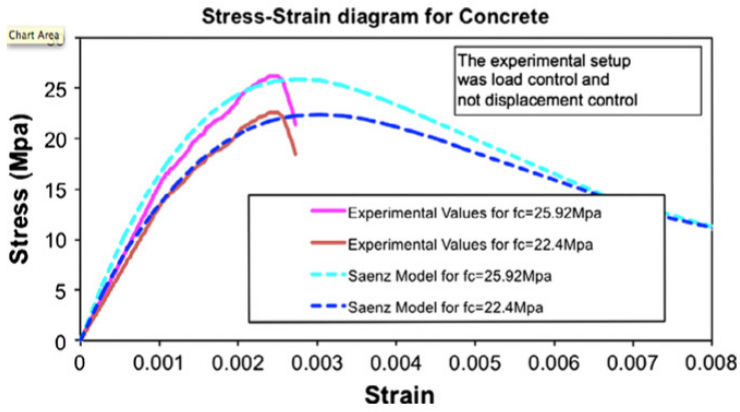


Figure 6. Measured and assumed concrete stress-strain behavior in unconfined uniaxial compression.

The resin rich layer, within which the debonding of the FRP strip from the concrete volume occurs, was modeled as a cohesive zone [3] endowed with a traction-separation response. The initial elastic stiffness for all three modes of debonding was set equal to 106 N/ mm2, which is within the range of values proposed by Turon et al. [28]. The quadratic stress-based damage initiation criterion available in ABAQUS was adopted, with the stress limit in all three principal directions being equal to the respective tensile concrete strength. Damage evolution was defined in terms of fracture energy with linear softening, whilst mixed mode behavior was accounted for according to the model proposed by Benzeggagh and Kenane [8], with a power coefficient equal to 1.45, in accordance with the proposals of Obaidat et al. [29]. Best results were obtained for a fracture energy in both shearing and peeling modes equal to 0.25 (GII = GIII = 0.25 N/mm2), whilst the fracture energy GI associated with the opening mode was set equal to 0.025. It should be noted that overall response is relatively insensitive to the assumed elastic stiffness and limiting stress adopted, but these properties have a significant effect on the numerical cohesive zone length [16,28], which defines the minimum required mesh size.

3.3 Non-linear analysis and discretization

Linear 8-noded brick elements were adopted for the discretization of the concrete beam, steel bolts, steel plates and loading plates, whilst the longitudinal reinforcing bars and the steel stirrups were discretized with linear truss elements embedded in the concrete region (i.e.

no relative displacement between reinforcement and concrete was allowed for). Linear 4-noded shell elements were used to discretize the SFRP sheets, the degrees of freedom (DOF) of which were tied to the respective DOFs of the underlying 8-noded 3D cohesive elements. The mesh size was dictated by the attempt to minimize computational time whilst maintaining accuracy and, upon extensive mesh convergence studies, a uniform mesh size of 15 mm was adopted for the concrete beam, cohesive zone and FRP sheets, whilst smaller mesh sizes were adopted for the steel plates, bolts and concrete regions surrounding the bolts. Due to severe convergence problems typically associated with strongly nonlinear response and with materials exhibiting non-monotonic stress–strain response [13], such as concrete and cohesive elements, the explicit dynamics solver ABAQUS/EXPLICIT was employed to perform the nonlinear analyses. Quasi-static response was achieved by specifying a slow displacement rate and checking that the kinetic energy was smaller than 2% of the internal energy for the greatest part of the analysis.

4 RESULTS AND DISCUSSION

The F.E. numerical predictions regarding the ultimate shear capacity ($^{num}V_{max}$) and failure modes with the ones observed during testing (see Table 1) are summarized in Table 4.

The ratio of numerically predicted over measured ultimate shear capacity is listed in column 3 of Table 4 with values very close to 1.0, which signifies a very good agreement of the numerically predicted ultimate shear capacity values with the respective experimental ones included in Table 1.

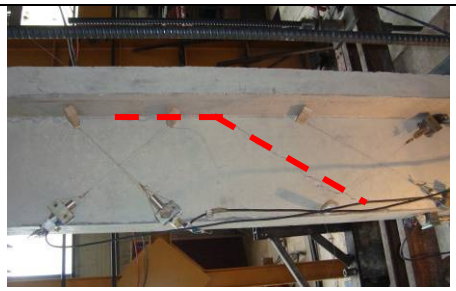
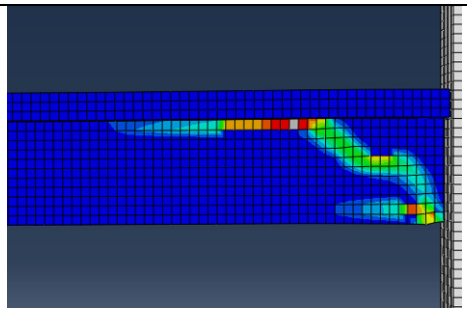
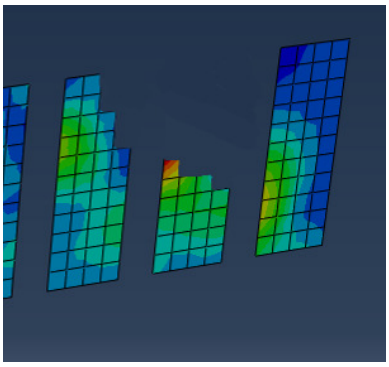
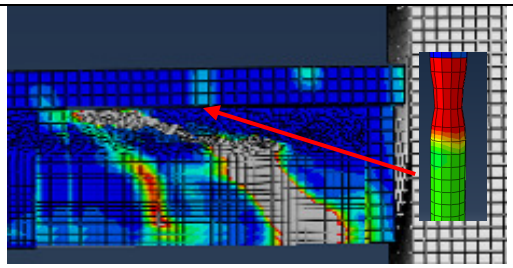
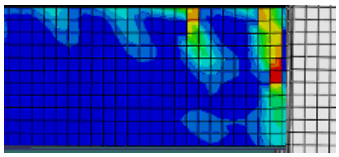
Table 4. Summary of Numerical results and comparison with experimental values.

Designation	Numerical ultimate shear capacity $^{num}V_{max}$ (kN)	$^{num}V_{max}$ / $^{exp}V_{max}$	Numerical failure mode	Experimental failure mode
CTB	37.43	1.00	Diagonal crack	Diagonal crack
TB150	63.63	0.87	Debonding	Debonding
TB150a	187.43	1.03	Anchorage failure	Anchorage failure

Moreover, the numerically predicted modes of failure are also in very good agreement with the ones observed during testing. Detailed discussion for each of the three T-beams considered in the present study follows.

4.1 CTB specimen (non-strengthened)

The observed behavior of the control T-beam specimen, which was tested to obtain the basic structural response of the reinforced concrete beam specimen without the added complexity of the attached SFRP sheets, was, in general, well-predicted by the FE numerical models, as can be seen in Table 5 (1st line), where the experimental and numerical modes of failure are depicted. The experimental failure mode, in the form of the dominant shear crack, and the numerical failure mode of specimen CTB are compared. It should be noted that in all these figures depicting numerical failure modes, the maximum principal plastic strain of concrete is depicted as a means to visualize concrete cracking since no discrete cracks form during the adopted numerical analysis.

Specimen	Experimental failure mode	Numerical failure mode
CTB	 Shear crack	 Shear crack
TB150	 SFRP debonding	 SFRP debonding
TB150a	 Failure of novel anchorage	 Failure of anchorage (yielding of bolt)  Some flexural cracks

4.2 TB150 (strengthened with SFRP without anchorage)

The debonding occurred within a thin resin rich layer of concrete, the properties of which were assumed to be incorporated in the cohesive zone material properties. The crack pattern at ultimate load is shown in Table 5 (2nd line). The numerical failure mode is compared with the corresponding experimental one for specimen TB150; as can be seen, an excellent agreement between the experimental and the numerical results is achieved. The beam specimen behaved elastically prior to the formation of the initial flexural cracks, whereupon the flexural reinforcement prevented the opening of the cracks. Subsequently, a diagonal crack started to form beneath the point of application of the load, which was interrupted by the presence of the FRP

sheets, which were stressed and prevented the opening of the diagonal crack. Finally, the debonding of the FRP sheets commenced and propagated rapidly, leading to the formation of critical diagonal cracks and thus to failure. This observed behavior was also accurately reproduced by the previously described numerical simulations.

4.3 TB150a (strengthened with SFRP with novel anchorage)

As described in section 4.2 the SFRP-strengthened specimen to which no additional anchorage was provided failed abruptly, due to debonding of the SFRP strips. The provision of additional anchorage by means of the device shown in figures 3a and 3b allows for additional forces to be carried by the SFRPs once debonding has occurred; these forces are transferred by the anchoring device finally through the bolts into the concrete thus resulting in an increased ultimate shear capacity and thus in a more efficient utilization of the FRP material. The anchorage zone is stressed from the onset of loading but deformations and stresses remain small as long as the resin remains effective. Upon debonding, the anchorage zone experiences high localized stresses. The failure is no longer due to FRP debonding but rather localized above the anchorage zone, due to the high stresses transmitted by the bolts in the vicinity of the bolt holes. The failure mode is complex and involves a combination of local concrete cracking and yielding of the anchor bolts. The generated complex FE models was in general able to capture the aforementioned failure mode. Table 5 (3rd line) depicts the experimental and numerical failure modes for TB150a with a very good agreement.

5 CONCLUSIONS

- The successful numerical simulation of the application of a novel anchoring device together with open hoop SFRP strips, which enhances the efficiency of these FRP sheets applied as shear reinforcement for reinforced concrete T-section beams, was demonstrated by this study.
- The validation of the numerical simulation is based on the measured behavior of a full-scale reinforced concrete T-beams without nominal shear reinforcement as well as with two (2) full-scale reinforced concrete T-beams that employed open hoop SFRP strips, with or without a novel anchoring device, as a means of upgrading their shear capacity. □
- The success of the deployed numerical simulation is fully demonstrated by comparing first the observed and numerically predicted ultimate shear capacity for all three specimens. The achieved accuracy of the predicted ultimate shear capacity is very good. □
- The success of the deployed numerical simulation is fully demonstrated by then comparing the observed and numerically predicted mode of failure for each one of the three (3) tested specimens. It is shown that the deployed numerical simulations have been articulated with all the significant features, to be able to portray in a very realistic manner complex non-linear mechanisms such as the cracking and crushing of concrete, the debonding and fracture of the SFRP strips and the yielding and fracture of the steel parts of the novel anchoring device. □
- From the above, it must be seen that the accurate numerical prediction of a relatively complex behavior is the result of all these intelligent features that were built into the numerical model together with the accurate representation of all the individual material fea-

tures, which were established by careful testing prior to the numerical simulation. The successful FE models, accurately capturing the basic structural response in terms of ultimate load and failure modes, have been developed and discussed.

- Based on the validated FE numerical models presented here, further research is underway to identify the key features affecting overall structural response and thus to optimize the structural arrangement of the proposed novel anchoring device in terms of strength and ductility.
- A further goal is to derive a generic strengthening technique and associated design guidelines, which allow for a more efficient utilization of the FRPs' strength and significantly enhance the structural performance of existing structures, strengthened with FRP sheets for both static and seismic type loads.

6 ACKNOWLEDGEMENTS

The steel fibres are not commercially available and were provided for the present study by Bekaert Industries. The epoxy resins were provided by Sika Hellas. Partial financial support for this investigation was provided by the Hellenic Earthquake Planning and Protection Organization (EPPO). The anchoring device employed in this study, is patented under Patent No. WO2011073696, which is managed by the Research Committee of Aristotle University.

REFERENCES

[1] ACI. Committee 318. Building code requirements for structural concrete and commentary (ACI 318-99). Detroit (MI): American Concrete Institute; 1999.

[2] ACI. Guide for the design and construction of externally bonded FRP systems for strengthening concrete structures (ACI 440.2R-08). In: ACI 440.2R-08. American Concrete Institute: Farmington Hills; 2008. p. 45.

[3] Bakis et al. Fiber-reinforced polymer composites for construction – state of the art review. J Compos Constr 2002 (May).

[4] Casadei P, Nanni A, Alkhrdaji T, Thomas J. Performance of double-T prestressed concrete beams strengthened with steel reinforcement polymer. Adv Struct Eng 2005;8(4):41.

[5] Chen JF, Teng JG. Shear capacity of fiber-reinforced polymer-strengthened reinforced concrete beams: fiber reinforced polymer rupture. J Struct Eng 2003;129(5):615–25 [May 1, ASCE, 5].

[6] Harper PW, Hallett SR. Cohesive zone length in numerical simulations of composite delamination. Eng Fract Mech 2008;75(16):4774–92.

[7] Hashin Z. Failure criteria for unidirectional fiber composites. J Appl Mech 1980;47(2):329–34.

[8] Hashin Z. Analysis of composite materials – a survey. J Appl Mech, Trans ASME 1983;50(3):481–505.

[9] Hibbitt, Karlsson, Sorensen. Inc. ABAQUS user's manual volumes I–V and ABAQUS CAE manual. Version 6.10.1. Pawtucket, USA; 2010.

[10] Kalfat R, Al-Mahaidi R. Investigation into bond of a new CFRP anchorage system for concrete utilizing mechanically strengthened substrate. Compos Struct 2010;92(11):2738–46.

[11] Katakalos K, Papakonstantinou CG, Manos GC. Comparison between carbon and steel fiber reinforced polymer with or without anchorage. In: 6th CICE, Rome; 2012. □

[12] Lu XZ, Teng JG, Yea LP, Jiang JJ. Bond–slip models for FRP sheets/plates bonded to concrete. Eng Struct 2005;27:920–37. □

[13] Manos GC, Katakalos K, Kourtides V. Construction structure with strengthening device and method. European Patent Office, Patent Number WO2011073696 (A1); 2011 (23.06.11). □

[14] Manos GC, Katakalos K, Papakonstantinou CG. Enhanced repair and strengthening of reinforced concrete (R/C) T-beams utilizing external reinforcement of fiber polymer sheets and novel anchoring devices. 15WCEE, Lisboa; 2012. □

[15] Manos GC, Katakalos K, Koidis G, Papakonstantinou CG. Shear strengthening of R/C beams with FRP strips and novel anchoring. J Civ Eng Res 2012;2(6):73–83. http://dx.doi.org/10.5923/j.jce.20120206.04. □

[16] Manos GC, Katakalos K, Kourtides V. Cyclic behaviour of a hybrid anchoring device enhancing the flexural capacity and ductility of an R/C bridge-type pier strengthened with CFRP sheets. J Civ Eng Res 2012. □

[17] Manos GC, Katakalos K. The use of fiber reinforced plastic for the repair and strenghtening of existing reinforced concrete structural elements damaged by earthquakes. In: Masuelli Martin Alberto, editor. Published in the book, Fiber Reinforced Polymers – The Technology Applied for Concrete Repair; January 23, 2013, ISBN: 978-953-51-0938-9 [ch.3]

[18] Manos GC, Katakalos K, Papakonstantinou CG. Shear behavior of rectangular beams strengthened with either carbon or steel fiber reinforced polymers, Applied Mechanics and Materials, 2011

[19] EPPO. Hellenic earthquake planning and protection organization. Athens: Guidelines for Retrofitting in Reinforced Concrete Buildings; 2011.

[20] Papakonstantinou CG, Katakalos K, Manos GC. Reinforced concrete T-beams strengthened in shear with steel fiber reinforced polymers. In: 6th CICE, Rome; 2012.

[21] Papakonstantinou CG, Katakalos K. Flexural behavior of reinforced concrete beams strengthened with a hybrid inorganic matrix-Steel fiber retrofit system, Structural Engineering and Mechanics, 2009

[22] Paz, Mario. International handbook of earthquake engineering: codes, programs and examples. In: Greece by G.C. Manos, editor. Chapman and Hall; 1994. [chapter 17].

[23] Saenz LP. Discussion of ‘‘equation for the Stress–strain curve for concrete’’ by Desayi P, Krishnan S. ACI J 1964;61:1229–35.

[24] Smith ST, Teng JG. FRP-strengthened RC beams. I: Review of debonding strength models. Eng Struct 2002;24(4):385–95.

[25] Täljsten B. Defining anchor lengths of steel and CFRP plates bonded to concrete. Int J Adhes Adhes 1997;17(4):319–27.

[26] Täljsten B, Elfgren L. Strengthening concrete beams for shear using CFRP materials: evaluation of different application methods. Compos Part B: Eng 2003;31(2):87–96.

[27] Teng JG, Smith ST, Yao J, Chen JF. Intermediate crack-induced debonding in RC beams and slabs. Constr Build Mater 2003;17(6–7):447–62.

[28] Turon A, Dávila CG, Camanho PP, Costa J. An engineering solution for mesh size effects in the simulation of delamination using cohesive zone models. Eng Fract Mech 2007;74(10):1665–82.

[29] Wu Y, Zhou Z, Yang Q, Chen W. On shear bond strength of FRP-concrete structures. Eng Struct 2010;32:897–905.

[30] Zsutty TC. Beam shear strength prediction by analysis of existing data’’. ACI J 1968;65(11):943–51.

COMPDYN 2015
5th ECCOMAS Thematic Conference on
Computational Methods in Structural Dynamics and Earthquake Engineering
M. Papadrakakis, V. Papadopoulos, V. Plevris (eds.)
Crete Island, Greece, 25–27 May 2015

CYCLIC RESPONSE OF A STEEL BEAM-TO-COLUMN CONNECTIONS – AN EXPERIMENTAL AND NUMERICAL STUDY

G.C. Manos[1], A. Nalmpantidou[2], V. Kourtides[3], A. Anastasiadis[3]

[1] Professor and Director of the Lab. of Strength of Materials and Structures, Aristotle University
e-mail: gcmanos@civil.auth.gr

[2] Postgraduate student, Lab. of Strength of Materials and Structures, Aristotle University
e-mail: a.nalbantidou@gmx.de

[3] Dr. Civil Engineer, Research Ass., Lab. of Strength of Materials and Structures, Aristotle University
e-mail: anastasiadisa@hol.gr

Keywords: Steel beams, steel beam-to-column connection, cyclic response, plastic hinge, low-fatigue tests, strain rate effects, earthquake performance of steel connection

Abstract. *The cyclic response of steel beam-to-column connections under a cyclic sinusoidal loading history was studied. The experimental investigation included two full-scale specimens having a cross section of IPE240 and a height of 1.0m. This part of the specimen was rigidly connected to a much stiffer steel beam thus representing a steel beam-to-column connection under investigation. These specimens were tested to failure being subjected to a cyclic sinusoidal point load of continuously increasing amplitude that produced a similarly varying bending moment at the steel beam-to-column connection. Instrumentation was provided to record both the applied moment as well as the deformation of the specimen in the region of the connection in terms of plastic hinge rotation. Each specimen experienced yielding and plastic rotation in this region that resulted initially in a plastic stable response till the final damage, which occurred either in the form of local instability of the flanges or fracture. The response of this beam-to-column connection was numerically simulated employing commercial software that tried to reproduce all the stages of the observed non-linear response. By comparing the numerical predictions with the measured response the success of the employed numerical simulation could be examined. The employed numerical simulation could yield realistic predictions of the limit state local buckling of the flanges of the used IPE 240 cross section as well as good agreement with the observed measured response, in terms of flexural capacity, energy dissipation and deterioration characteristics, provided that the material model in this numerical simulation was equipped with the "proper" parameters.*

1 INTRODUCTION

Steel frame structures are commonly used in seismic areas because of their excellence on seismic resistance. This type of structures are usually composed of moment resistant frames whereby the performance of beam-to-column connections are of particular importance especially when these structures are subjected to strong earthquake ground motions [1, 2, 5]. Usually these connections undergo large moment reversals during the earthquake excitation, thus it is important to exhibit stable plastic flexural response in order to provide dissipative capability, without the development of undesired damage patterns, and in this way prevent any kind of local or global instability. However, two recent earthquakes, in Northridge, California 1994 and Kobe Japan 1995, revealed the vulnerability of this type of construction. Premature cracks were observed at welded connections of steel beam-to-column joints leading to brittle failure without prior warning (obvious yielding) at the area around the weld. Such a failure mode or the development of local buckling when beam-to-column connections undergo low-cycle fatigue seismic-type of loading is of particular research interest [3, 4, 9, 14].

The fatigue life of steel beam-to-column joints depends on the amplitude of the imposed loading cycles and the hysteretic behavior of the constituent material that is linked with the amplitude and rate of the developing plastic strains. In order to investigate the fatigue life of steel beam-to-column joints several fatigue testing investigations have been proposed leading to tests that can be categorized in two groups. Testing regimes in which the elastic strain amplitude is higher than the plastic strain amplitude and testing regimes in which the plastic strain dominates. The first type of tests is generally referred as high cycle fatigue (HCF); these tests typically involve more than 10^6 cycles to cause failure. The second type of tests is named low cycle fatigue (LCF) test and the number of cycles to failure generally ranges from 10^2 to 10^4 cycles and this is usually employed for testing the seismic performance of steel beam-to-column joints [6, 8, 11, 12, 15].

The current work studies the performance of steel beam-to-column joints first by examining steel beam-to-column welded joint specimens at the laboratory subjecting them to cyclic seismic-type low-cycle fatigue loading as is explained in section 2. Next, the performance of the same specimens is simulated numerically. Similar studies have been performed in the past by other researchers. Despite the fact that many similar experiments have been performed in the past [6, 8], the current experimental investigation was considered as necessary in order to provide at first hand all the information required for the numerical analyses. That is, the exact geometric and material characteristics of the specimens as well as specific information on the type of loading conditions and on the measured response. The numerical simulation is performed utilizing a commercial software package that is thought to be suitable to simulate the observed response and the non-linearities that developed and included large plastic strains and local instabilities.

2 MATERIALS AND EXPERIMENTAL SETUP

2.1 Tested specimens

Two full-scale specimens have been constructed with prototype steel cross sections in order to form a beam-to-column joint. Both specimens were of the same geometry and used as the beam part a IPE 240 steel section and as the column part a HEA 300 steel section. These two parts were welded together, as shown in figures 1 and 2, to form the beam-to-column connection to be tested.

In order to confine the damaged region, where large strains were expected to develop thus making this part unusable, it was decided to weld the IPE 240 beam to a steel base plate having a thickness of 20mm. This steel plate in turn was bolted to the HEA 300 column (figure 1). Thus, after the end of the test sequence, the IPE 240 part with the steel base plate could be unbolted and removed from the HEA 300 column, which could be used again. Furthermore, in order to avoid the brittle type of failure at the welds joining the IPE 240 beam part with the base steel plate two 20mm thick steel stiffeners of triangular shape (with a height of 160mm and width of 170mm) were welded at either side of the IPE 240 section connecting its flanges with the base plate as shown in figures 1 and 2. In this way, the region of the IPE 240 beam to be plastified was removed from the welded region to the region above these stiffeners, thus providing a controlled beam-to-column connection to be investigated. The height of the IPE 240 beam part was 1200mm allowing on one hand to construct the beam-to-column connection in the described way and on the other hand to connect its upper part with the forcing fixtures that were provided by a double acting hydraulic actuator. This actuator was controlled by a servo-hydraulic digital electronic controller providing the desired imposed cyclic horizontal displacement amplitude at a distance of 1000mm from the base plate (see figure 2).

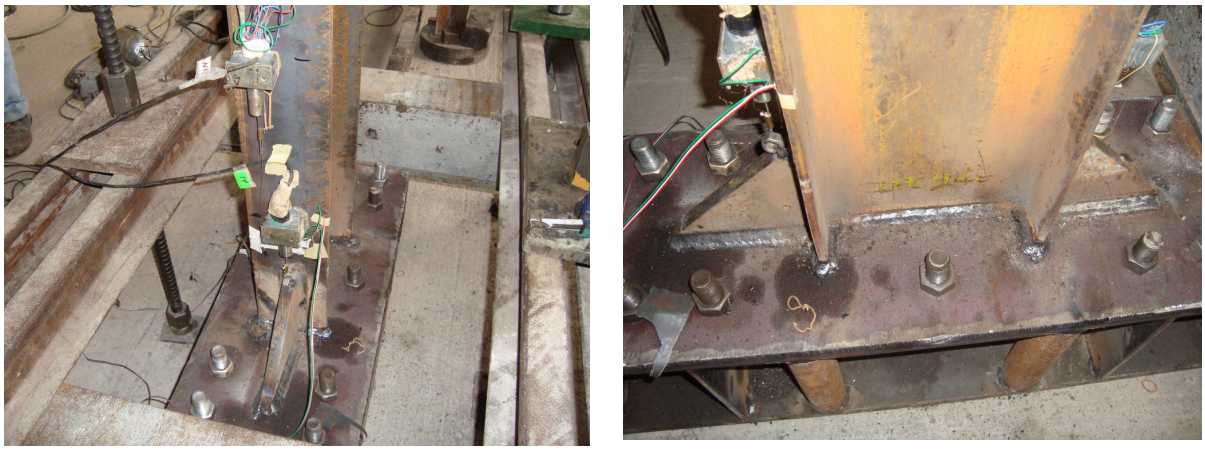


Figure 1. Details of the tested beam-to-column joint specimens

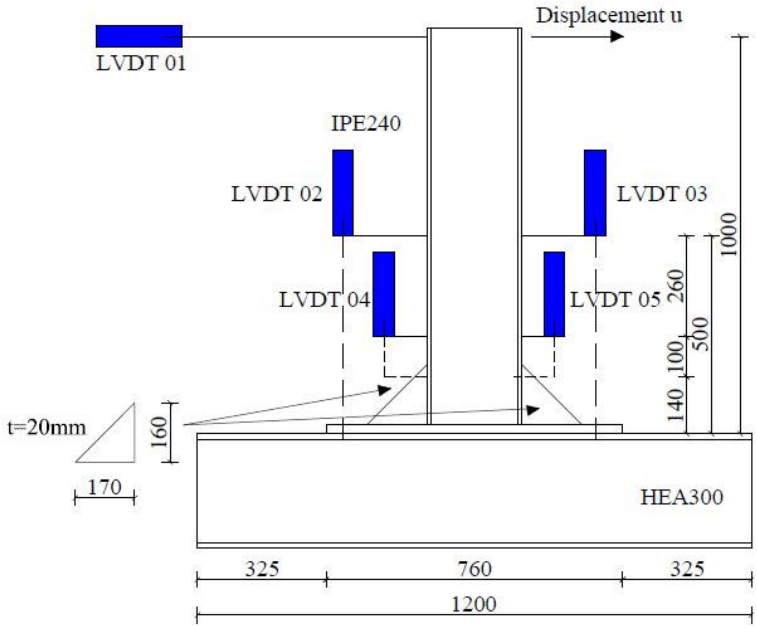


Figure 2. Experimental set-up with the geometry of the specimens, the instrumentation and loading

Two IPE 240 beam-to-column connection specimens, namely Tbeam-2 and Tbeam-4, were tested as shown in figures 2 and 3. Both specimens were of the same overall geometry having webs with thickness equal to 6.5mm. The flange thickness varied from 9.16mm to 9.36mm and from 9.5mm to 9.7mm for specimens Tbeam-2 and Tbeam-4, respectively.

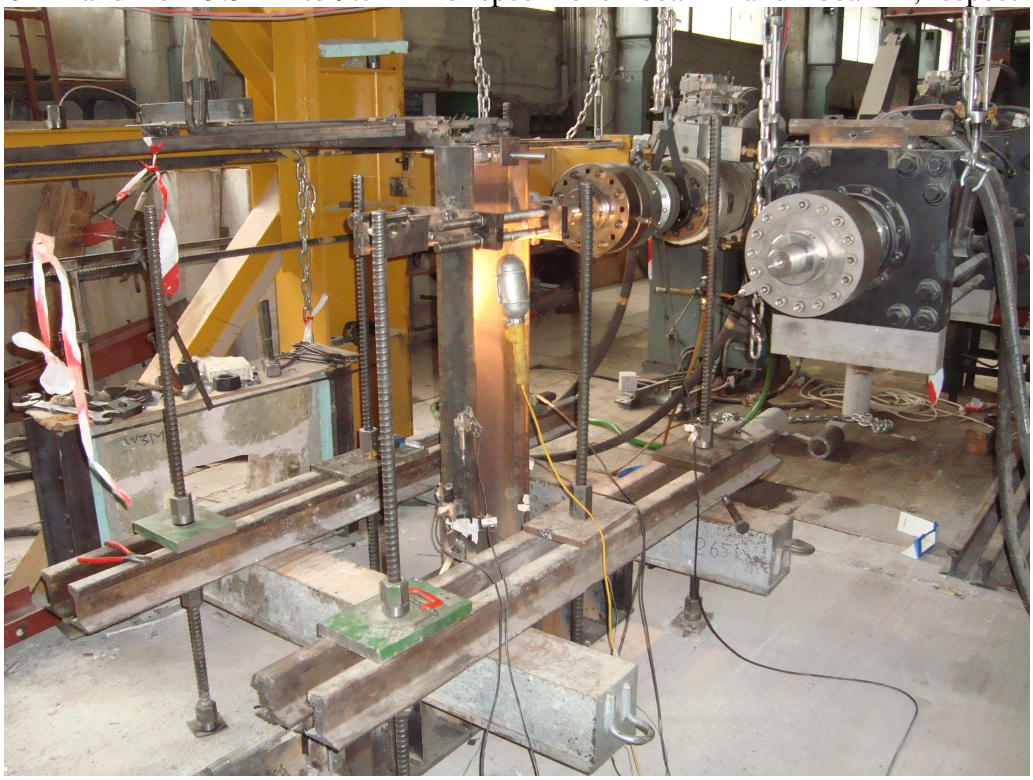


Figure 3: Experimental setup with the specimen being rigidly attached on the strong floor of the Laboratory of Strength of Materials and Structures of Aristotle University.

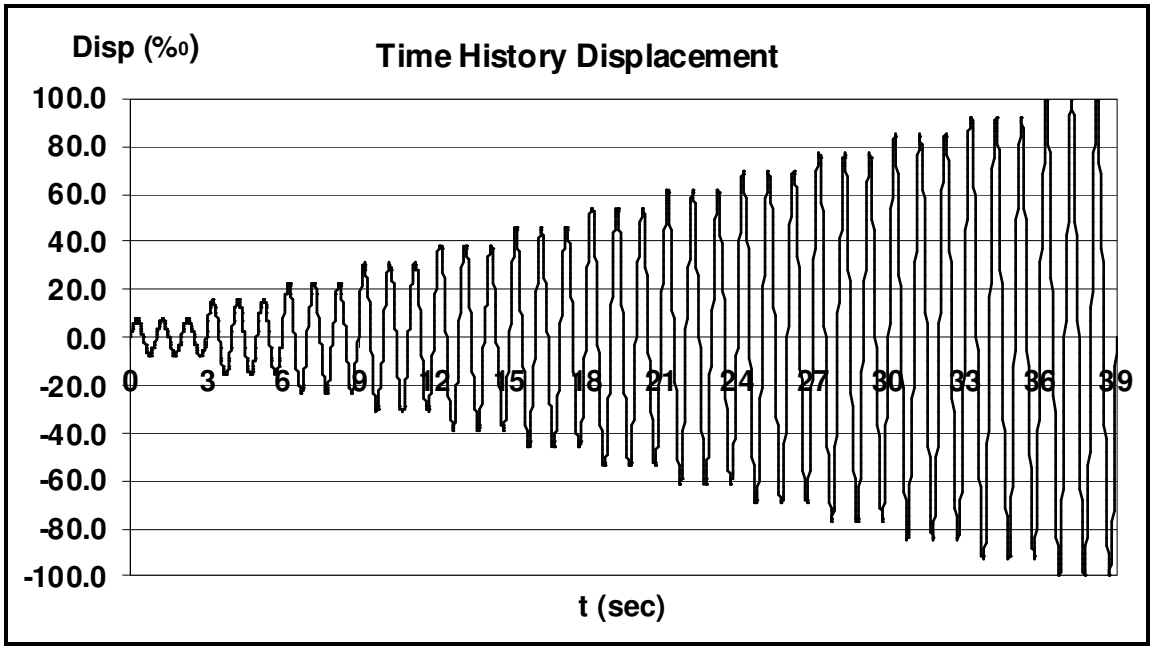


Figure 4. Typical cyclic seismic-type imposed displacement protocol for low fatigue loading

2.2 Loading arrangement

The tested specimens were subjected to a cyclic seismic-type loading arrangement. An extensive discussion on the loading protocols was presented by Krawinkler [11]. This is a very important and difficult issue as on one hand it is believed that it influences the resulting performance and on the other hand it poses demands on the capabilities of the experimental facility [6, 7, 8, 11, 12, 15]. As this work at its present stage aims to produce results that will be utilized for validating the numerical capabilities of existing software rather than checking the validity of code provisions the used loading protocol does not comply exactly with ones suggested by Krawinkler and other researchers [6, 7, 11, 15]. Instead, a series of sinusoidal horizontal cyclic displacements were used and were imposed on the top of the IPE 240 beam part, as shown in figures 2 and 3. Both specimens were rigidly attached on the strong floor of the Laboratory of Strength of Materials and Structures of Aristotle University. The hydraulic actuator was attached on the strong metal frame which together with the strong floor forms this experimental facility. The imposed horizontal displacement and the resulting horizontal load leads to the development of a bending moment at the beam-to-column connection which, if of sufficient amplitude, is expected to bring this part of the beam-to-column connection to a certain limit state condition, as will be explained in section 3. The imposed horizontal displacement in amplitude and frequency content is controlled by the electronic servo-controller. A relatively simple imposed displacement protocol is depicted in figure 4. It consists of thirteen (13) groups of 3 full sinusoidal cycles. In each group the imposed maximum displacement amplitude remains constant and keeps gradually increasing from one group to the next in a prescribed manner, as a percentage of the maximum target displacement. The difficulty in imposing this protocol accurately lies on the fact that the target displacement is known at best through predictions that may differ considerably from the actual target displacement that, when imposed, will produced the desired phenomena. The protocol depicted in this figure was adopted in the current study in a general sense. That is, the amplitude of the imposed horizontal displacement kept increasing from one group to the next till the plastification of the tested specimens led to some type of failure, as will be described in section 3. One distinct difference in the followed loading protocol for the specimen Tbeam-2 is the fact that the frequency content was relatively high (0.1Hz – 1.0Hz) as to allow this test to be characterized as a dynamic test accompanied with medium level of strain rate. On the contrary, the loading protocol for Tbeam-4 specimen was relatively low (0.003Hz to 0.03Hz) that is characterized as cyclic test of relatively low level strain rate.

2.3 Instrumentation

Instrumentation was provided capable to record the dynamic response of the specimen at the top in terms of imposed horizontal displacement (LVDT 01, figure 2) and horizontal force. In addition, four displacement transducers (LVDT 02, LVDT 03, LVDT 04 and LVDT 05) were attached to the specimen in order to record the relative vertical displacement of two sets of horizontal cross sections of each specimen near the plastification zone (figures 1, 2 and 3). The first set of horizontal cross sections was that at the base, where the IPE 240 part was welded at the base steel plate) and the one 500mm higher. Utilizing LVDT 02 and LVDT 03 the relative elongation or shortening between these two cross sections of the specimen was measured at the flanges of both sides of the IPE 240 section. The second set of horizontal cross sections was that at 160mm from the base, where the triangular stiffeners ended, and the one 100mm higher. Utilizing LVDT 03 and LVDT 04 the relative elongation or shortening between these two cross sections of the specimen was measured at the flanges of both sides of

the IPE 240 section. In this way, it became possible to deduce from the measured response the rotation between the first and the second set of these horizontal cross sections. The second set of horizontal cross sections is of particular importance as the highly plastified region (plastic hinge), which was expected to develop during the experimental sequence, lies between the horizontal cross-sections of the second set. Indeed, the used instrumentation was able to capture the plastification of this region from the initial stages of yielding till the final stages of local instability. In addition, a set of strain gauges was also provided in order to control in a different way the initiation and development of plastification in this zone.

Figures 5 and 6 depict the instrumentation of this zone near the beam-to-column joint. The used hydraulic actuator can also be seen in figure 5 whereas in figure 6 the vertical displacement transducer utilized to measure the relative elongation or shortening between two horizontal cross sections above the stiffener having a distance between them equal to 100mm can also be seen (second set of horizontal cross sections).



Figure 5. Instruments located near the beam-to-column joint.

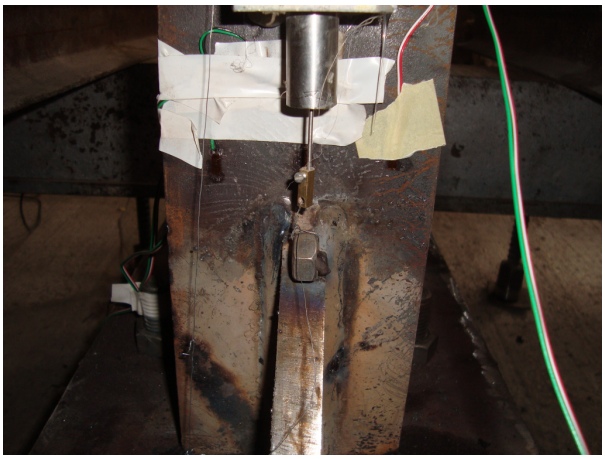


Figure 6. Measuring the relative elongation/shortening between two horizontal cross sections above the stiffener

2.4 Steel tensile properties

In order to input the proper information related to the steel characteristic in the finite element program monotonic tensile tests were performed with coupons taken from both specimens. These coupons were taken from the flanges of the specimens after the completion of the relevant test sequence. In order to measure the material properties of the virgin steel prior to any plastification and permanent straining these coupons were taken from the upper part of the IPE 240 beam sections near the section where the imposed displacement was applied The corresponding results are shown in figures 7 and 8.

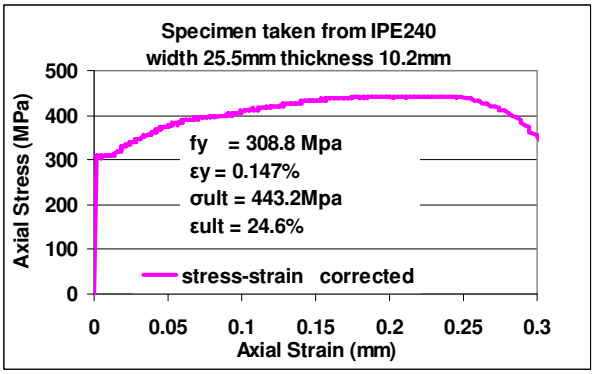


Figure 7. Tensile properties sample 1

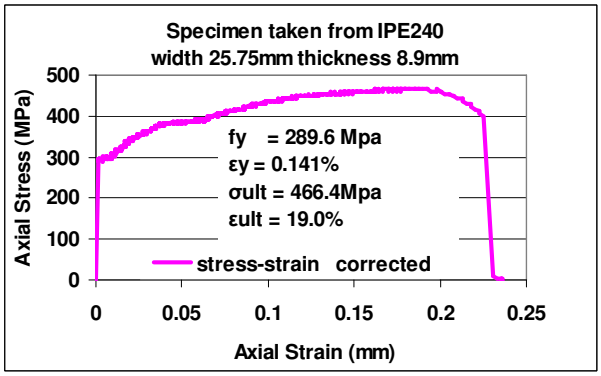


Figure 8. Tensile properties sample 2

3 OBSERVED PERFORMANCE AND CORRESPONDING MEASUREMENTS.

3.1 Observed over-all performance and actual damage

Each specimen experienced plastic rotation above the stiffeners that was captured by the employed instrumentation. Despite the fixity of the attachment of the specimens on the strong floor part of the imposed horizontal displacement was consumed by the rotation of the specimen at its fixed base as well as of the elastic response along the height apart from the plastic rotation that developed at the desired location above the stiffeners. Fortunately, despite the limitations of the capabilities of the experimental facility it was possible to attain the plastic limit state for both studied specimens and produce the expected form of damage. This is depicted in figures 9 and 10 for specimen TBeam-2 and figure 11 for specimen Tbeam-4.

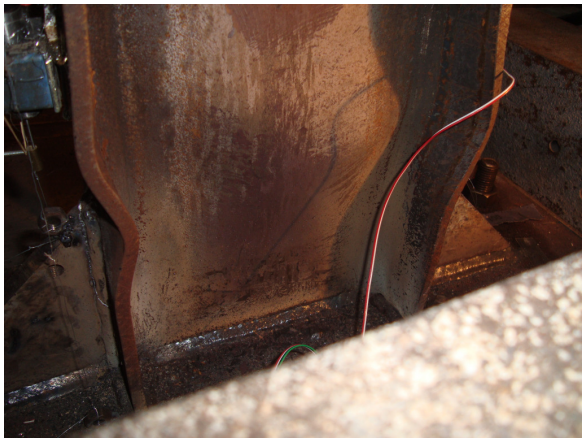


Figure 9. Plastification of specimen TBeam-2 at the end of Test-12

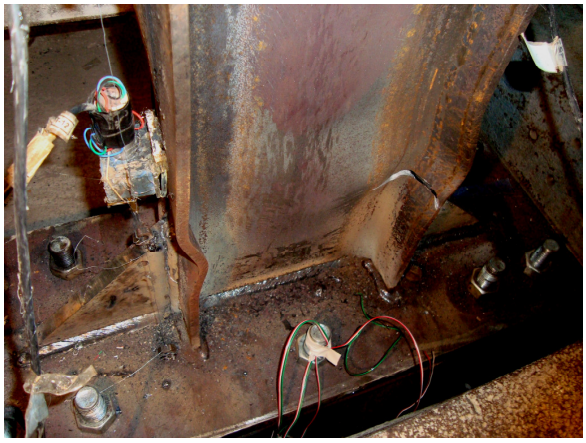


Figure 10. Plastification of specimen TBeam-2 and fracture of the section above the stiffeners after Test-12



Figure 11. Plastification of specimen TBeam-4 after test – 7.

3.2 Measured response in terms of plastic rotations at the plastic hinge.

Figure 12, depicts the full loading sequence in terms of horizontal displacement at the top of the specimen that could be deduced from the employed instrumentation as directly linked with the elastic/plastic rotation at the zone of the specimen extending at a length of 100mm above the stiffeners of the IPE 240 beam (see section 2.3 and figures 2 and 6). The corresponding development of the plastic rotation with time in this plastic hinge region is shown in figure 13. The imposed loading history in terms of plastic hinge rotation and the corresponding horizontal displacement at the top of specimen Tbeam-4 is shown in figure 15 and 14.

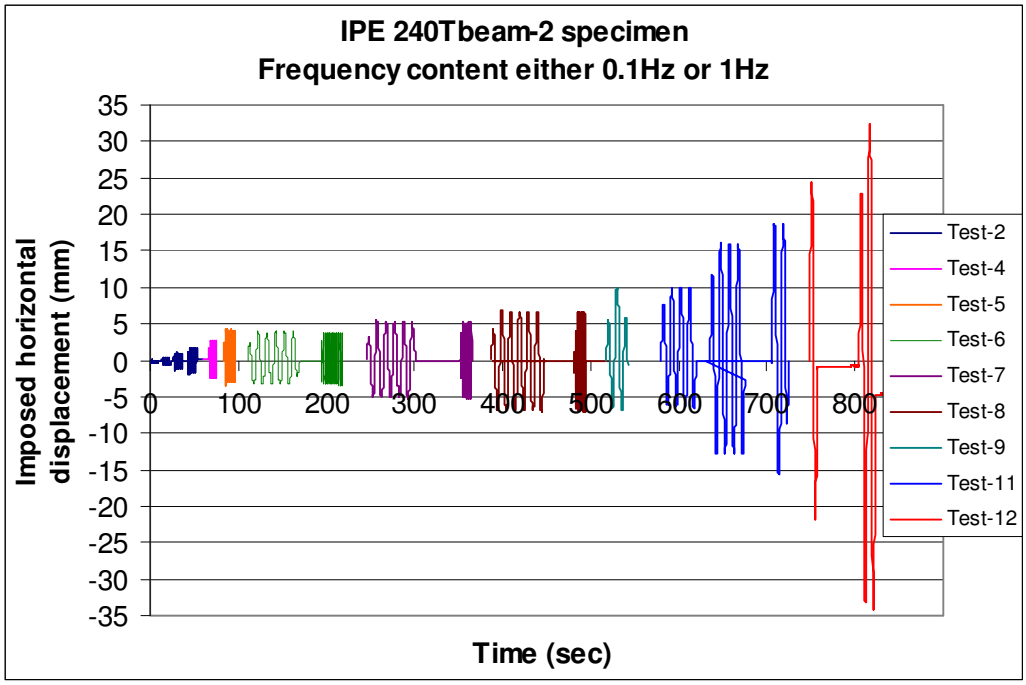


Figure 12: Horizontal displacement at the top of specimen Tbeam-2 due to the plastic rotation at the plastic hinge region.

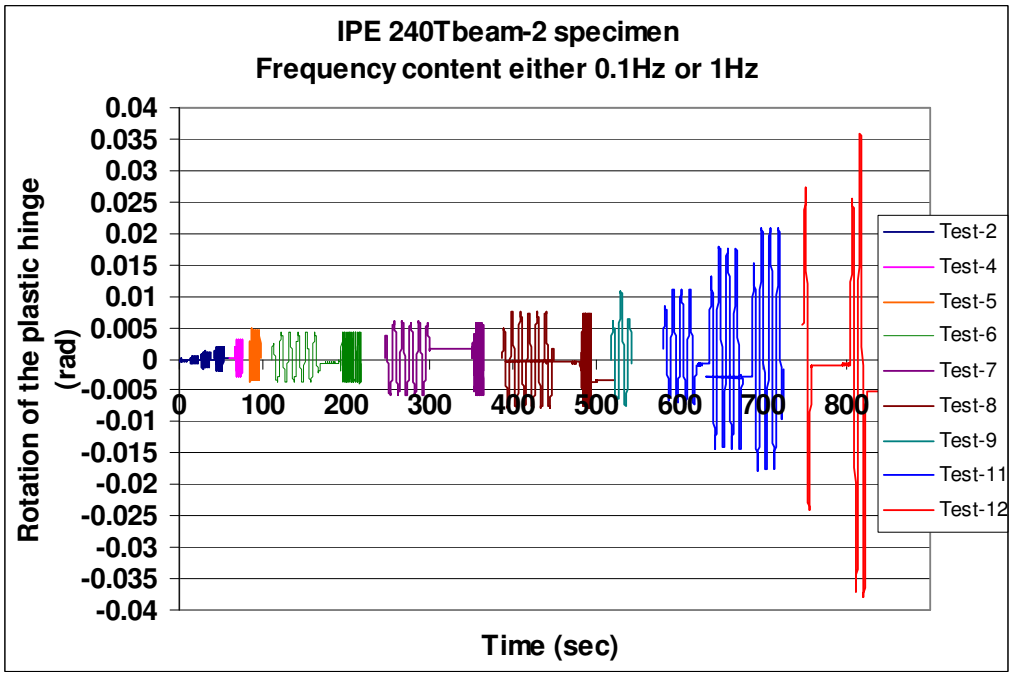


Figure 13: Plastic rotation at the plastic hinge region due to horizontal displacement at the top of specimen Tbeam-2.

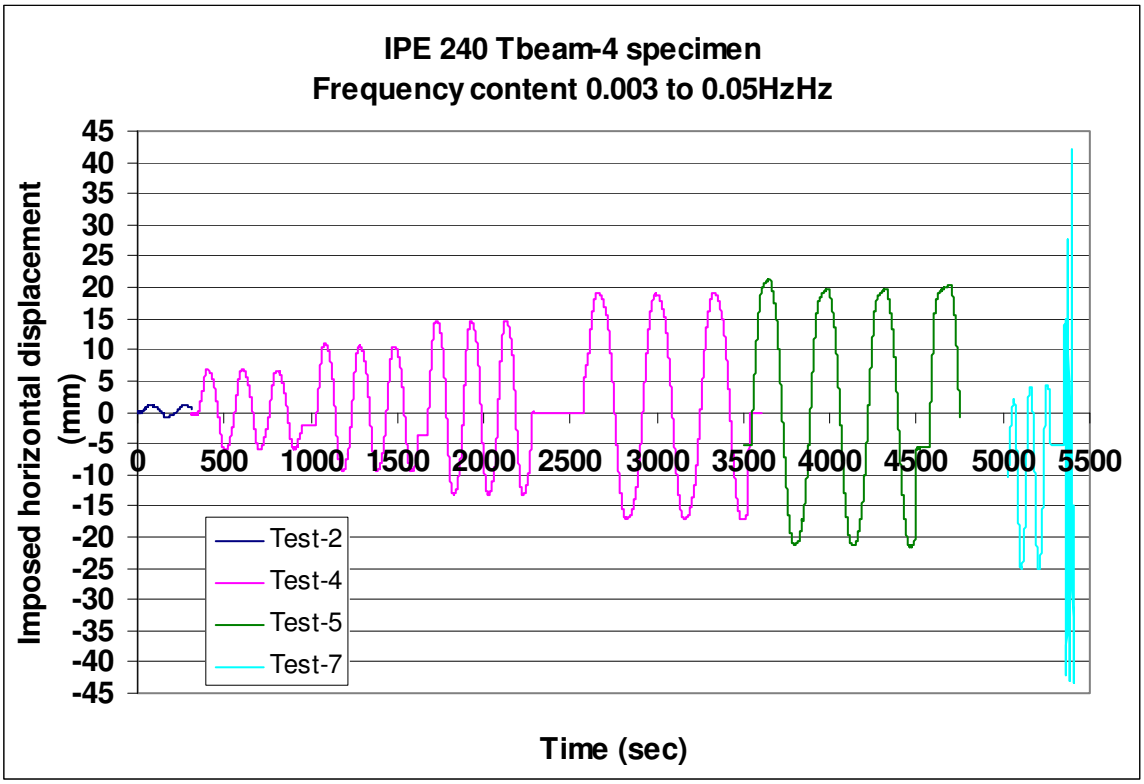


Figure 14: Horizontal displacement at the top of specimen Tbeam-4 due to the plastic rotation at the plastic hinge region.

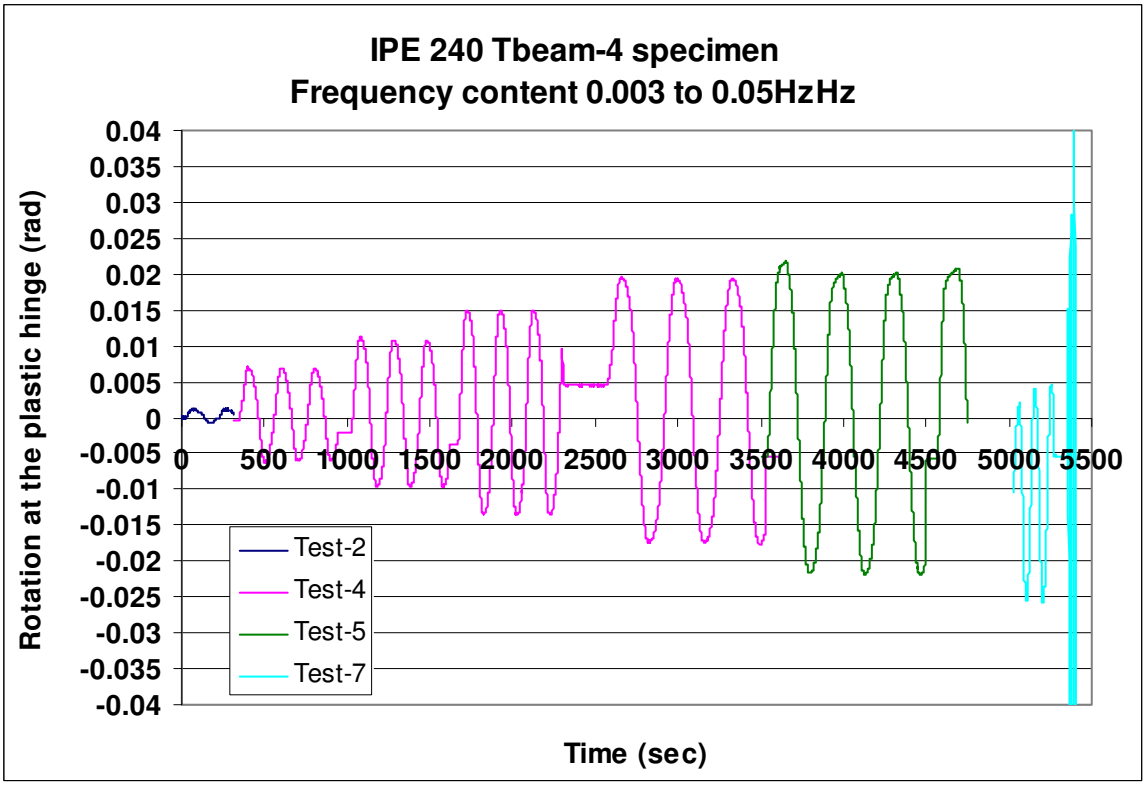


Figure 15: Plastic rotation at the plastic hinge region due to horizontal displacement at the top of specimen Tbeam-4.

As can be seen in figures 13 and 15 both specimens reach their flexural plastic limit for plastic hinge rotations of the order of 0.023 radians, which represents a value approximately equal to $5\Theta_{pl}$ [13], having undergone a considerable number of low-fatigue cycles [10, 13, 14]. Moreover, both specimens failed by developing local instability at the plastic region in the form of flange local buckling and eventually fracture. Figures 16 and 17 portray the observed cyclic response in terms of bending moment and plastic hinge rotation, for specimens Tbeam-2 and Tbeam-4, respectively. The bending moment values were deduced at a section above the stiffeners from the measured horizontal load.

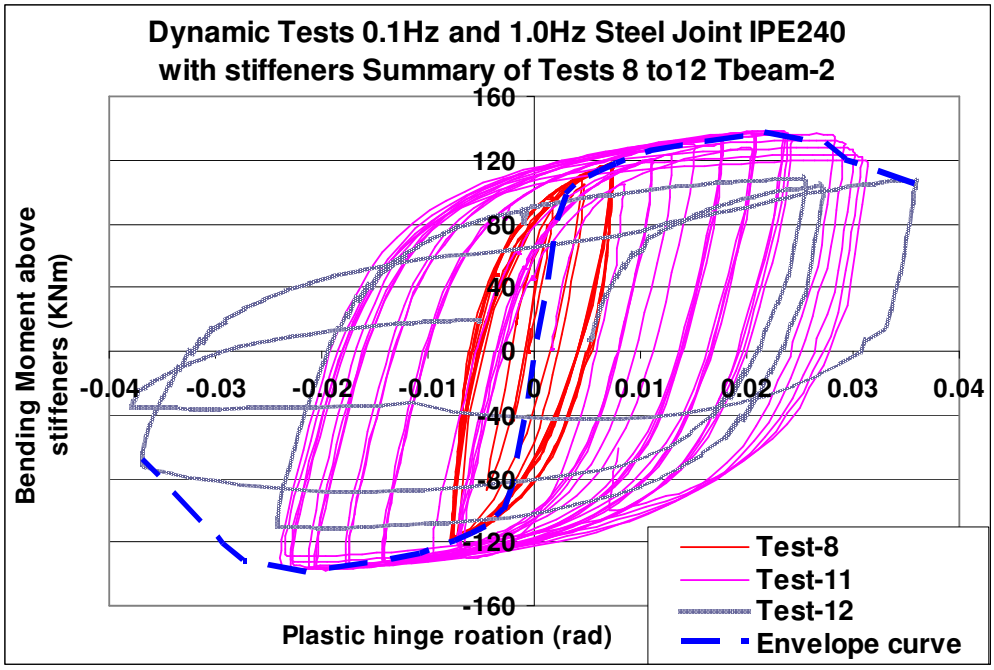


Figure 16: Measured cyclic response of the plastic hinge for specimen Tbeam-2.

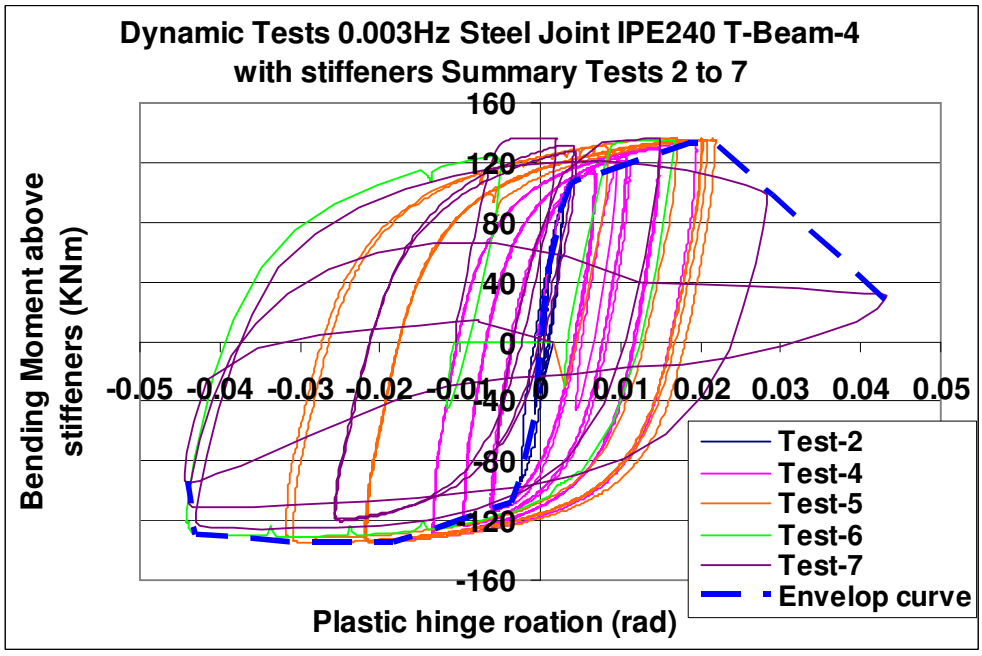


Figure 17: Measured cyclic response of the plastic hinge for specimen Tbeam-4.

In both figures 16 and 17 a corresponding envelop curve is also plotted with a dashed blue line. As can be seen, both specimens developed large cycles of stable plastic response before reaching their failure mode thus dissipating considerable energy in terms of hysteretic damping. Figure 18 depicts this hysteretic cyclic response through the corresponding envelop curves. As can be seen from the comparison of these two envelop curves in figure 18, both specimens performed in a quite similar way in terms of initial stiffness, maximum flexural bearing capacity and plastic hinge rotation corresponding to that flexural capacity. The measured flexural capacity is of the order of 138KNm and 134KNm for specimens Tbeam-2 and Tbeam-4, respectively. Similarly, the plastic hinge rotation values corresponding to these flexural capacity values are in the range approximately 0.020 to 0.025 radians for both specimens. Consequently, it can be concluded that the variation in the frequency content that was employed in the loading sequence for specimen Tbeam-2, which was somehow different from the loading sequence of specimen Tbeam-4 (see figures 13 and 15), did not have any major influence on the observed cyclic response and limit state performance for the two studied specimens.

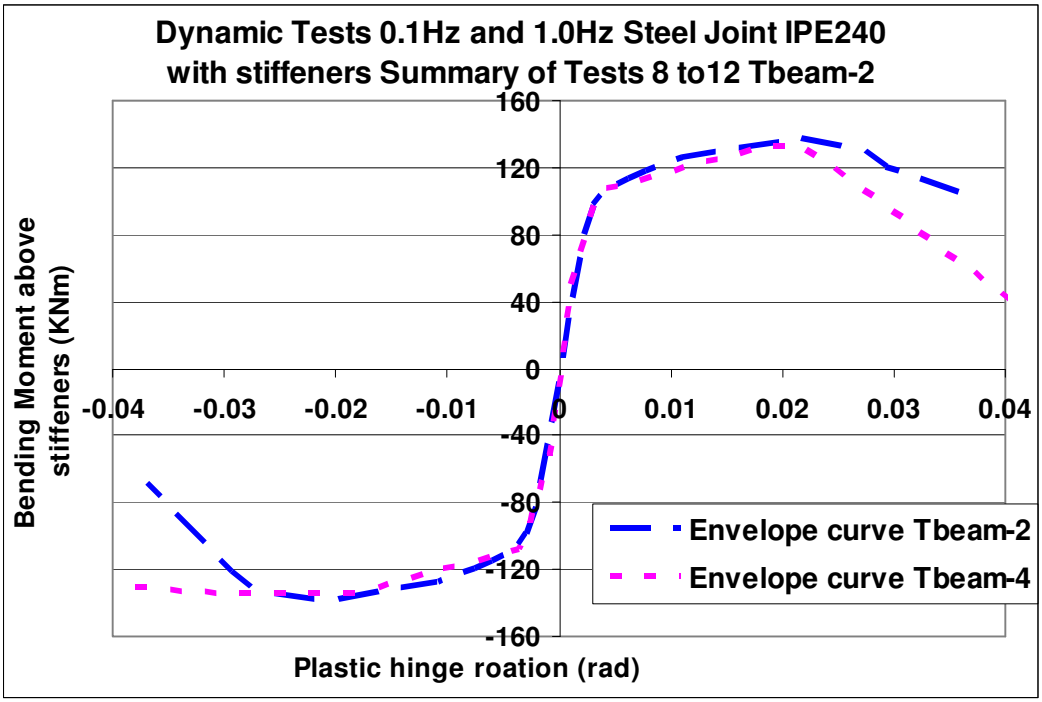


Figure 18: Measured cyclic response of the plastic hinge in terms of envelop curves for both specimens Tbeam-2 and Tbeam-4.

4 NUMERICAL SIMULATION OF THE OBSERVED CYCLIC RESPONSE AND PERFORMANCE

4.1 Numerical modeling.

The commercial software ABAQUS [16] was utilized in this numerical simulation effort. In doing so, the IPE 240 beam part of the experimental sequence was reproduced through the finite element representation as accurately as possible. This is shown in figure 19 whereby it can be seen that the numerical simulation extended all the way from the top section where the horizontal load was imposed to the bottom horizontal section where the IPE 240 beam was welded to the base plate. Moreover, the triangular stiffeners with their actual thickness and

geometry were also included in this numerical simulation. The whole surface of the IPE 240 and the stiffeners at the bottom level where the specimens were welded to the base plate was considered to be represented with absolute fixity conditions in the numerical simulation. Moreover, in one set of numerical simulation the specimen was free to displace horizontally in the out-of-the loading plane direction whereas in another set of numerical analyses this possibility of out-of the loading plane horizontal displacement was constrained. The discretization scheme that was adopted was considerably fine in an effort to be able to catch numerically the observed local modes of buckling of the flanges in the plastic hinge region.

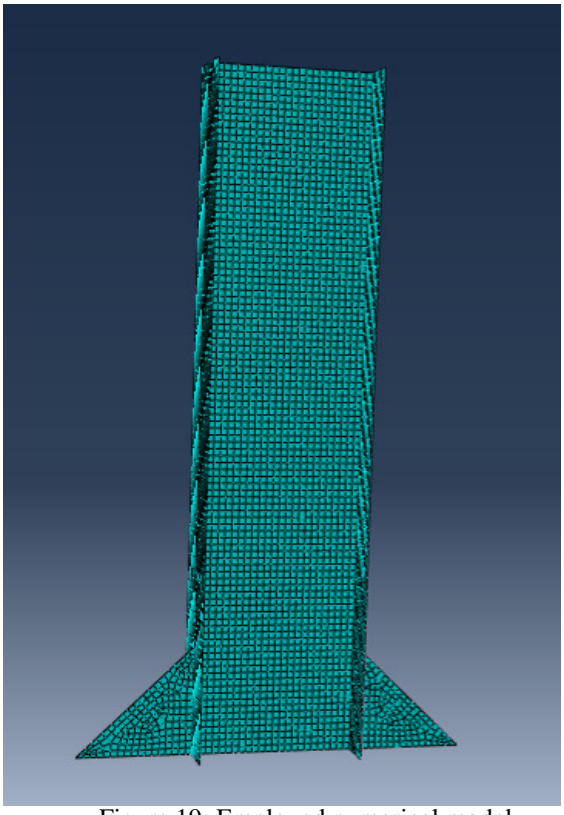


Figure 19: Employed numerical model.

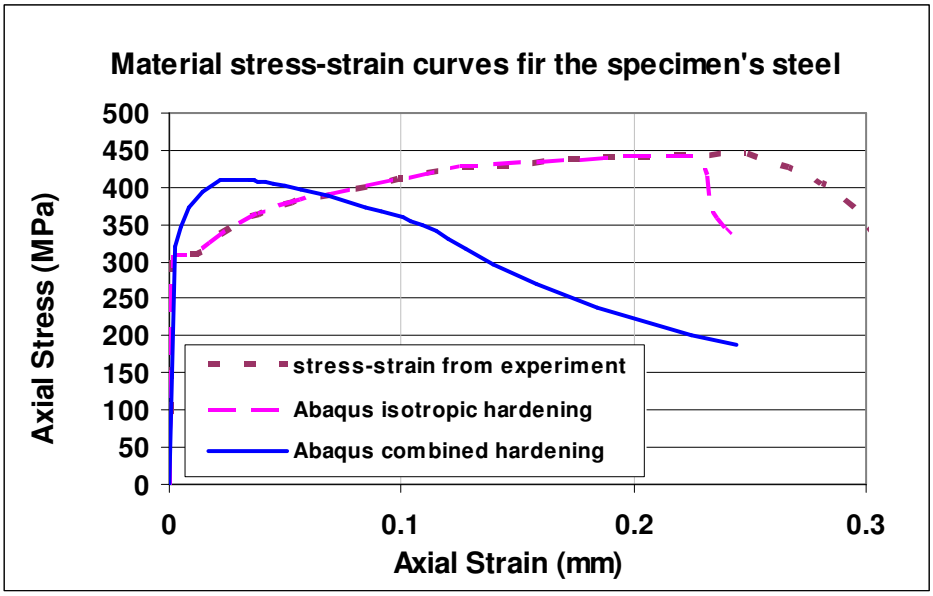


Figure 20: Employed material stress-strain curves

4.2 Material modeling

In the framework of the numerical investigation a parametric study was conducted that focused on the way the steel material properties were introduced in the numerical simulation. Two different approaches were tried. According to the first approach the measured tensile steel properties (see section 2.4) were introduced in the numerical simulation through the Abaqus isotropic hardening parameters whereas in the second approach the measured properties were modified accordingly in order to be introduced in the numerical simulation through the ABAQUS combined hardening material model [16]. This is depicted in figure 20. The measured small differences in the thicknesses and tensile stress-strain behaviour between the first specimen (specimen 1, e.g.Tbeam-2) and the second specimen (specimen 2, e.g. Tbeam-4) were also included in this parametric study. In what follows selected results will be presented.

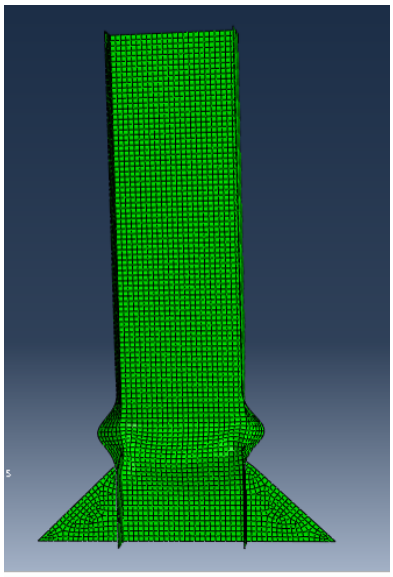


Figure 21: Failure mode of specimen 1 predicted by ABAQUS (see also figures 9 and 10)

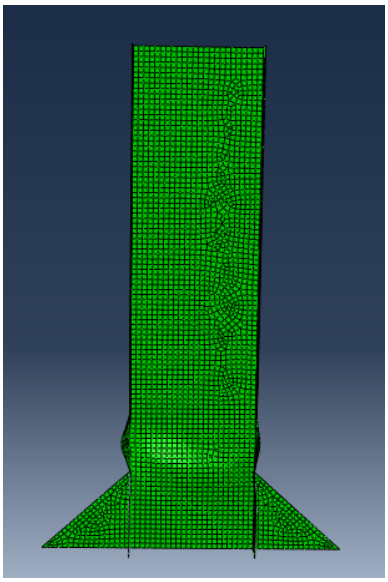


Figure 22 : Failure mode of specimen 2 predicted by ABAQUS (see also figure 11)

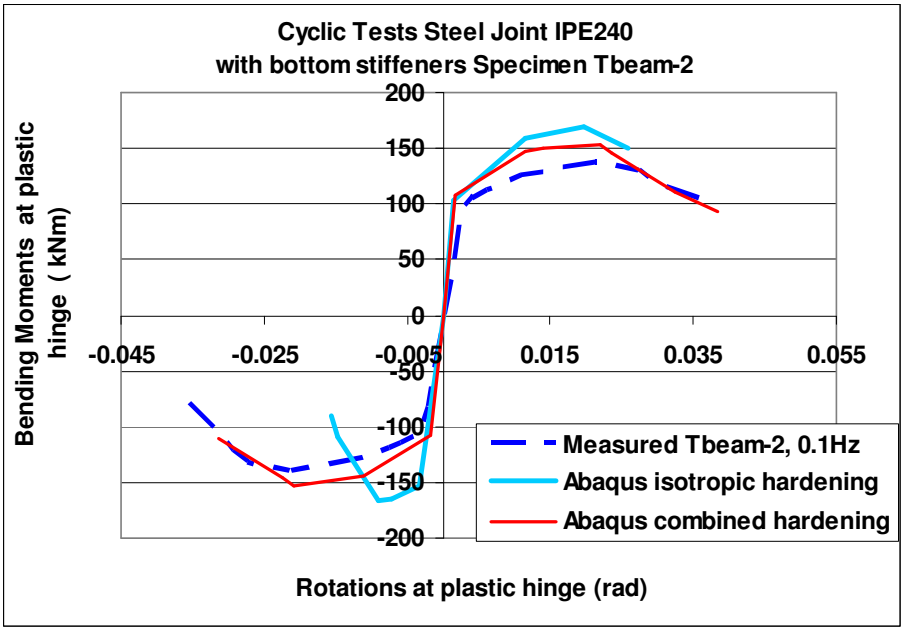


Figure 23: Predicted cyclic response of the plastic hinge in terms of envelop curve for specimen Tbeam-2 together with the measured response.

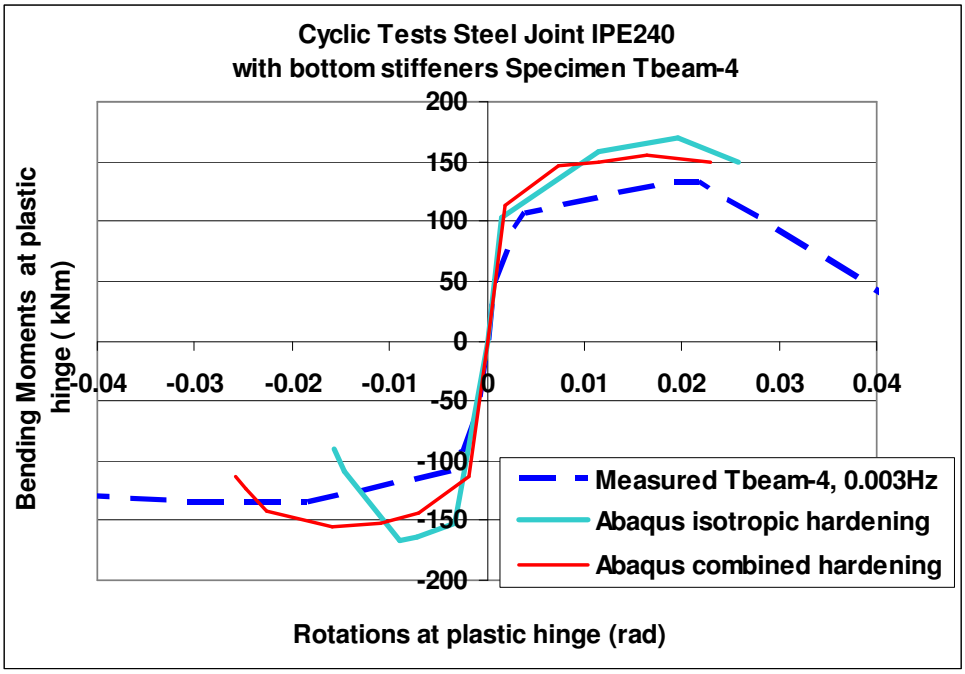


Figure 24: Predicted cyclic response of the plastic hinge in terms of envelop curve for specimen Tbeam-4 together with the measured response.

4.3 Numerical results from the parametric study

Figures 21 and 22 depict the predicted failure mode of specimen 1 and specimen 2, respectively, as predicted by the described numerical simulation (ABAQUS [16], see also figures 9 and 10 and 11). These predicted modes of local buckling of the IPE 240 flanges near the beam-to-column joint are in good agreement with the corresponding performance of the tested specimens. Figures 23 and 24 compare the envelop curves predicted by the numerical simulation for specimens Tbeam-2 and Tbeam-4, respectively, with the corresponding envelop curves of the measured cyclic response for the same specimens. The predicted response was obtained by using either the isotropic or the combined hardening material model. As can be seen from figures 23 and 24 the introduction of the combined hardening material model yields a better agreement with the measured response than the isotropic hardening material model.

The next stage in the numerical study was to systematically vary the various parameters that define the combined hardening material model. As could be seen, the variation of these parameters influences important aspects of the cyclic response such as the predicted flexural capacity as well as the plastic rotation range that the cyclic response remains stable in terms of bending moment and the plastic rotation range that the response deteriorates in terms of bending moment and the rate of this deterioration.

This is depicted in figure 25 with the described numerical simulation applied for representing the cyclic response of specimen Tbeam-2. This resulted from an additional parametric study whereby the characteristic parameters that define the combined hardening model were varied within realistic limits in order to study the sensitivity of the obtained cyclic response to the values of these parameters. These parameters are $\boldsymbol{\sigma}_0$ (yield stress at zero equivalent plastic strain), $\boldsymbol{C}$ and $\boldsymbol{\gamma}$ (material constants) Nip et al. [17] followed a certain experimental process whereby these parameters were defined in an explicit way through measurements obtained from tests of steel samples. The values that were found by Nip et al. [17] were utilized in the parametric study that was performed in the present work. Selective results from this paramet-

ric study are presented in figure 25 whereby the value of parameter $\boldsymbol{\sigma}_0$ (yield stress at zero equivalent plastic strain) is in one case 250MPa and in the other case 308MPa whereas the values of the material constants $\boldsymbol{C}$ and $\boldsymbol{\gamma}$ remain the same for both cases. These two cases were selected from a considerable number of other trial cases. This selection was based on the fact that the resulting response exhibited the best possible comparison with the measured response of specimen Tbeam-2 as shown in figure 26.

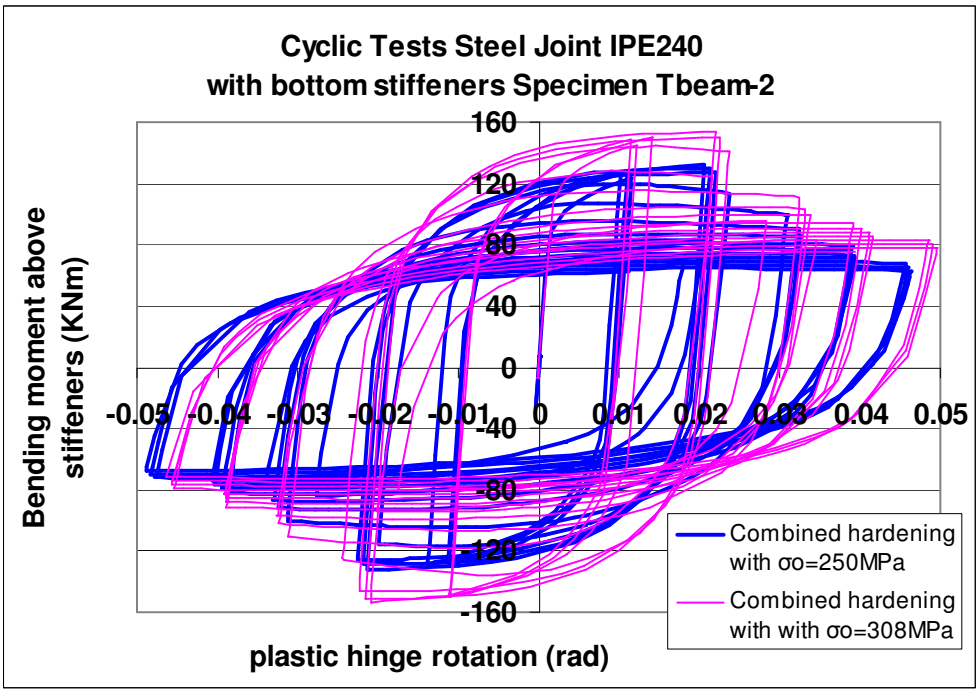


Figure 25: Predicted cyclic response of the plastic hinge in terms of bending moment versus plastic hinge rotation for specimen Tbeam-2 employing two variations of the combined hardening material model.

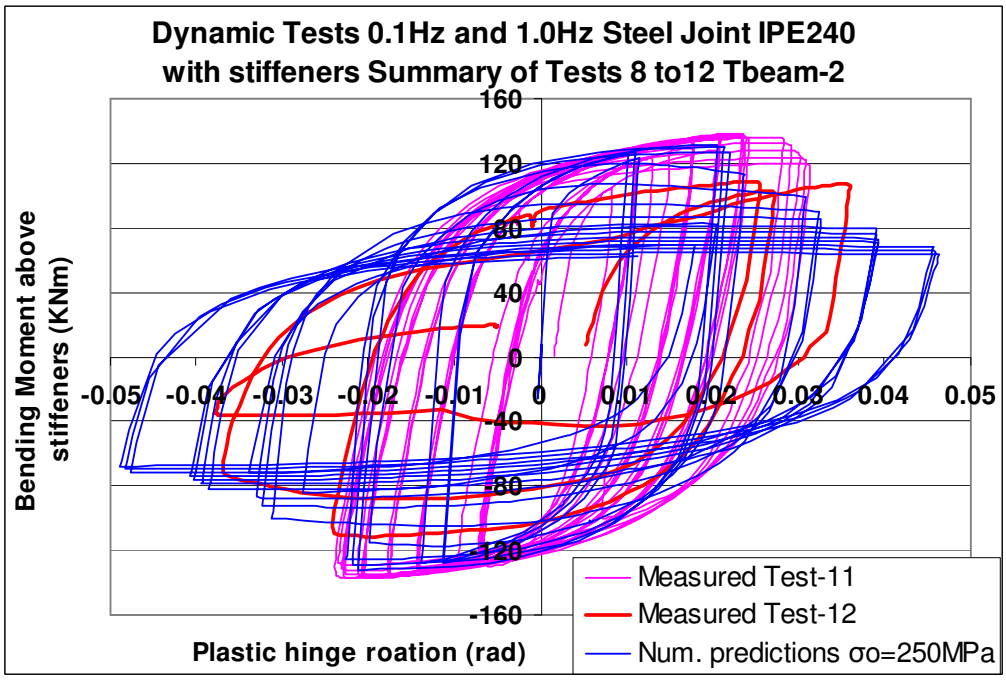


Figure 26: Measured cyclic response of the plastic hinge in terms of bending moment versus plastic hinge rotation for specimen Tbeam-2 and comparison with the best fitted numerical predictions employing the combined hardening material model. .

As can be seen in figure 25, the variation of the value of the parameter σ_0 (yield stress at zero equivalent plastic strain) from 250 to 308 resulted in considerable variation of the predicted maximum value of the bending moment. In addition, as can be seen in figure 26, a reasonably good agreement could be obtained between the measured in specimen Tbeam-2 and the predicted cyclic response in terms of maximum flexural capacity, dissipation characteristics and deterioration of the flexural capacity for plastic hinge rotation values larger than 0.023 radians, when the value of the parameter σ_0 (yield stress at zero equivalent plastic strain) is set equal to 250MPa.

5 CONCLUSIONS

- The seismic performance of a steel beam-to-column connection was studied by subjecting two specimens of such steel beam-to-column connection specimens to imposed cyclic displacements with a variety of low to medium range strain rates. The tested specimens were constructed with prototype steel sections welded in a typical fashion.
- Both these specimens performed in a quite similar way in terms of initial stiffness, maximum flexural bearing capacity and plastic hinge rotation corresponding to that flexural capacity. Both specimens developed local flange buckling modes of failure for plastic hinge rotation values approximately equal 0.023 radians, which represents a value approximately equal to $5\Theta_{pl}$. For values of plastic hinge rotation higher than 0.023 radians the deterioration of the flexural capacity became substantial for both specimens as the local flange buckling mode of failure prevailed.
- The consequence of the previous observation is that the employed strain rate variation in the used loading sequence of specimen Tbeam-2 from that of the loading sequence of specimen Tbeam-4 did not have any major influence on the observed cyclic response and limit state performance between these two studied specimens. However, this is a partial conclusions based on rather limited data. Therefore more research is needed to further investigate the strain rate influence on the beam-to-column connections earthquake performance.
- The numerical simulation of the tested specimens utilizing the capabilities of a commercial software package yielded reasonable good agreement between both the measured and predicted cyclic response in terms of maximum flexural capacity, dissipation characteristics and deterioration of the flexural capacity for plastic hinge rotation values larger than 0.023 radians. Moreover, the numerical simulation also yielded realistic predictions of the limit state local buckling of the flanges of the used IPE 240 cross section thus exhibiting good agreement with the observed performance. However, it is of utmost importance to have realistic estimates of the values of the parameters are σ_0 (yield stress at zero equivalent plastic strain), C and γ (material constants) which define the steel combined hardening material behaviour.

ACKNOWLEDGEMENTS

The authors would like to acknowledge the assistance of M. Theofanous, Dr. Civil Engineer, Lecturer at the Department of Civil Engineering of the University of Birmingham, for all his valuable advice related to the numerical simulation. The technical assistance of T. Koukouftopoulos in preparing the experimental arrangement is also gratefully acknowledged.

REFERENCES

[1] Akiyama H. Earthquake-Resistant Limit-State Design for Buildings. University of Tokyo Press: Tokyo, 1985.

[2] Anastasiadis A., Mosoarca M., Gioncu V., Mazzolani F. M., "Some thoughts for the prediction of the local inelastic capacity of MRF subjected to seismic actions", 8th STESSA Conf. on the Behavior of Steel Structures in Seismic Areas, Tongji Univ., Songhai China, July 2015.

[3] Anastasiadis A, Gioncu V, Mazzolani FM. "New trends in the evaluation of available ductility of steel members." Behavior of Steel Structures in Seismic Areas STESSA 2000; 3-26.

[4] Anderson, James C., Nastar Navid, Rojas Fabian, "Low-Cycle Fatigue Effects on Steel Moment Frames", Safety, Reliability and Risk of Structures, Infrastructures and Engineering Systems – Furuta, Frangopol & Shinozuka (eds)© 2010 Taylor & Francis Group, London, ISBN 978-0-415-47557-0

[5] Ballio Giulio &. Castiglioni, Carlo A, "Seismic Behaviour of Steel Sections", J. Construct. Steel Research 29 (1994) 21-54

[6] Castiglioni Carlo A., Mouzakis Harris P.,. Carydis Panayotis Gr. (2007): "Constant and Variable Amplitude Cyclic Behavior of Welded Steel Beam-to-Column Connections", Journal of Earthquake Engineering, 11:876–902, 2007, 11:6, 876-902, doi.org/10.1080/13632460601188027.

[7] Clark P, Frank K, Krawinkler H, Shaw R. Protocol for fabrication, inspection, testing, and documentation of beam-column connection tests and other experimental specimens. SAC Steel Project Background Document, Report No. SAC/BD-97/02, 1997.

[8] El Hassouni A, Plumier A., Cherrabi A. "Experimental and numerical analysis of the strain-rate effect on fully welded connections", Journal of Constructional Steel Research (2010), doi 10.1016/j.jcsr.2010.09.02

[9] Federal Emergency Management Agency. Interim testing protocols for determining seismic performance characteristics of structural and nonstructural components. FEMA 461 Draft Document, Applied Technology Council, Redwood City, CA, 2007.

[10] Gioncu V, Petcu D. "Available rotation capacity of wide-flange beam and beam-columns part 1, 2.", Journal of Constructional Steel Research 1997; 43: 161-244.

[11] Krawinkler H. Loading histories for cyclic tests in support of performance assessment of structural components. The 3rd International Conference on Advances in Experimental Structural Engineering, San Francisco, 2009.

[12] Lamarche Charles-Philippe and Tremblay Robert, "Seismically induced cyclic buckling of steel columns including residual-stress and strain-rate effects", Journal of Constructional Steel Research 67 (2011) 1401–1410, doi:10.1016/j.jcsr.2010.10.008

[13] Lee Kyungkoo and Stojadinovic Bozidar, "Low-cycle fatigue limit on seismic rotation capacity for US steel moment connections", 13th World Conference on Earthquake Engineering, Vancouver, B.C., Canada, August 1-6, 2004, Paper No. 90.

[14] Vayas I. "Investigation of the cyclic behavior of steel beams by application of low-cycle fatigue criteria." Behavior of Steel Structures in Seismic Areas STESSA 1997; 350-357.

[15] Yu Jiao, Satoshi Yamada, Shoichi Kishiki and Yuko Shimada, "Evaluation of plastic energy dissipation capacity of steel beams suffering ductile fracture under various loading histories" Earthquake Engng Struct. Dyn. 2011; 40:1553–1570.

[16] Hibbitt, Karlsson, Sorensen. Inc. ABAQUS user's manual volumes I–V and ABAQUS CAE manual. Version 6.10.1. Pawtucket, USA; 2010.

[17] Nip, K.H., Gardner L., Davies C.M., Elghazouli A.Y., "Extremely low cycle fatigue tests on structural carbon steel and stainless steel", Journal of Constructional Steel Research 66 (2010) 96-110, doi:10.1016/j.jcsr.2009.08.004

COMPDYN 2015
5th ECCOMAS Thematic Conference on
Computational Methods in Structural Dynamics and Earthquake Engineering
M. Papadrakakis, V. Papadopoulos, V. Plevris (eds.)
Crete Island, Greece, 25–27 May 2015

THE DYNAMIC RESPONSE OF A MOCK-UP OF THE RESTORED ANCIENT NORTH WALL SCHEME FOR THE MACEDONIAN PALACE AT VERGINA - GREECE.

G.C. Manos[1], K. Katakalos[2], L. Kotoulas [2], and O. Felekidou[2]

[1] Professor and Director of the Lab. of Strength of Materials and Structures, Aristotle University
e-mail: gcmanos@civil.auth.gr

[2] Postgraduate student, Lab. of Strength of Materials and Structures, Aristotle University
e-mail: {kkatakal@civil.auth.gr}, {kotoulaslambros@gmail.com}, felekidou23@yahoo.gr

Keywords: Ancient wall, Macedonian Palace, Soil-structure Interaction, Vergina

Abstract. *This paper presents summary results from a numerical study that examined the dynamic behaviour of a mock-up of the proposed retaining wall scheme aimed at supporting the North ancient wall of the Macedonian Palace at Vergina, Greece. Part of this retaining wall scheme represents the ruined ancient wall that will be restored. This wall will have at its base those monoliths of the ancient that survive in good condition so that can be used again. For the rest of the wall new monoliths will be used which will be constructed in-situ for this purpose. The restored wall will be partly supported by an additional wall to be built at its back which will also support the ruins of the Macedonian palace. The restored ancient defense wall will be connected at its back with special ties to the rest of the retaining wall scheme. The stability of the restored ancient wall is examined through a mock-up that simulates the geometric non-linearities from the sliding and rocking of the monoliths as well as those from the special ties. The friction characteristics between the new prototype monoliths were investigated experimentally at the laboratory.*

1 INTRODUCTION

Ancient Greek and Roman walls are usually composed of large heavy members (monoliths) that simply lie on top of each other in an almost perfect-fit construction without the use of connecting mortar (figures 1 and 2). In this way they are distinctly different from other types of fortifications that use connecting mortar and different type of masonry construction. This type of dry stone masonry is also used as part of the typical structural form of ancient Greek or Roman temples of the peripteral form. The columns and the dry stone masonry are connected at the top with the epistyle (entablature), also composed of monolithic orthogonal marble blocks, spanning the distance the columns and the stone masonry wall (figure 3). The earthquake response of free standing columns has been researched by the first author ([5 to 18]) in the past as well as by other researchers ([1 to 4] and [19 to 27]). This paper focuses on the response of square monoliths that lie on top of each other without connecting mortar at their contact horizontal surfaces, as it is typical in the mentioned before dry stone masonry construction.



Figure 1. Greek ancient walls at the ancient Palace of Tyrins, Greece.



Figure 2a. Mycenae, Greece, Outer wall



Figure 2b. Part of the Hadrian wall, North of England



Figure 3. The Erectheum, at the Acropolis of Athens.

The seismic response mechanisms that develop on this solid block structural system during strong ground motions can include sliding and rocking of the various monoliths, thus dissipating the seismic energy in a different way from that of other forms of masonry. This paper presents results and conclusions from an experimental study that examines the dynamic response of such prismatic stone formations. Towards this objective the dynamic response of a simple dry stone masonry assembly that is composed by five (5) stones is studied. This stone dry-masonry assembly is simply supported on the bottom of the first block (figure 4). It is then subjected to various types of horizontal base motions (including sinusoidal as well as earthquake base motions), reproduced by the Earthquake Simulator Facility of Aristotle University, as will be described in section 3.

This study is partially linked with the North ancient walls of the Macedonian Palace of Vergina, Greece. At present, these walls are in a state of ruin; however, the restoration of these walls in their original formation is planned together with similar repair and restoration works for the Macedonian Palace itself. The restoration of the walls will utilize only those original monoliths that are in sound condition (figure 4). However, because such ancient

monoliths are in small numbers the construction of new monoliths, having the same dimensions as the ancient ones is planned.



a) View along the base of the North wall at the Vergina Macedonian Palace with the few remaining monoliths



Figure 4. The remains of the stone monoliths of the ancient North wall of the Macedonian Palace at Vergina Greece.



Figure 5a. Detail of the horizontal contact surface of the new monoliths



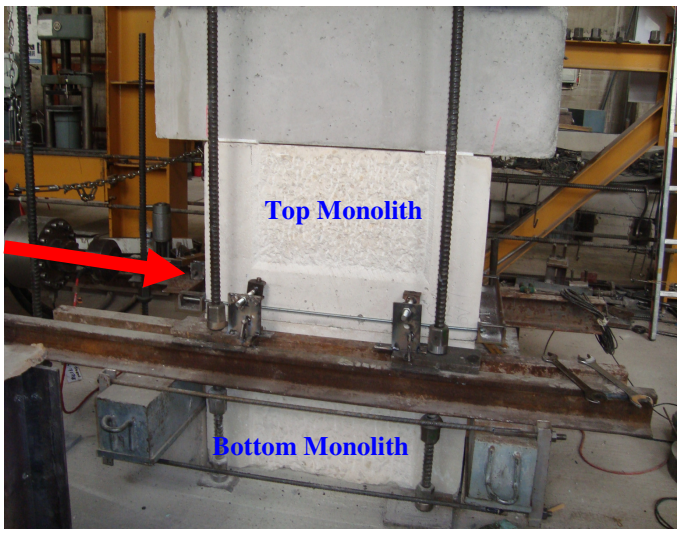
Figure 5b. Arranging two monoliths on top of each other at the laboratory of Strength of Materials and Structure at Aristotle University

Such monoliths are shown in figures 5a and 5b as part of an experimental investigation that was conducted at the laboratory of Strength of Materials and structures of Aristotle University having as an objective to determine the coefficient of friction between these monoliths, as is reported in the next section. These monoliths were constructed in-situ at the archaeological site of Vergina-Greece and were transported at the premises of the laboratory at Aristotle University. Prior to this, an experimental investigation was also conducted in order to deter-

mine the compressive strength of the ancient monoliths as well as the new monoliths in comparison. However, these results are not reported here.

2 STUDY OF FRICTION BETWEEN THE NEW MONOLITHS

In this section summary results are presented as obtained from the study that was performed in order to determine the coefficient of friction between the new monoliths that will be part of the restored ancient North wall of the Macedonian Palace at Vergina, Greece.



a) Friction-sliding testing arrangement



b) Added dead load on top of the tested monoliths

Figure 6. Friction of the new monoliths at the laboratory

The loading arrangement for these tests is shown in figure 6. One monolith (bottom monolith, figure 6a) is attached on the strong reaction floor of the testing rig in a way that it cannot slide whereas the other monolith (top monolith, figure 6a) is simply supported on the bottom monolith in a way that it can slide on this contact surface when a horizontal force is applied very close to this contact surface. In order to permit the sliding displacement between the two monoliths only in the direction of the applied horizontal force and prohibit any other rigid motion between the monoliths a set of two roller sliders were placed at either side of the top monolith as shown in figure 6b. Moreover, in order to study the influence of the amplitude of the dead load acting at a normal direction to the horizontal contact surface a number of concrete and steel blocks were placed above the top monolith for this purpose, as shown in figure 6b. Instrumentation was provided to measure the applied horizontal force as well as the horizontal displacement that would develop at the contact interface between these two monoliths. Two displacement transducers were placed at either side of the monoliths in order to measure the sliding displacement at the interface. Moreover, apart from the load cell measuring the horizontal displacement the normal stress acting on the contact interface was obtained by dividing the weight of all the objects (top monolith as well as the concrete and steel blocks) placed above the top monolith by the area of the contact surface. This weight was varied in such a manner that it results in normal to the contact surface stress amplitudes varying in the following way:

$\boldsymbol{\sigma}_n$ = 0.0126MPa, 0.0265MPa, 0.047MPa, 0.0686MPa and 0.0831Mpa

The sliding displacement was imposed gradually in the following way, shown in figure 7. For a given dead weight (in this case 35.32KN) the horizontal force was applied gradually that initially caused no sliding displacement. Next the horizontal force was increased and a sliding displacement of small amplitude was observed. The load/displacement was imposed in a cyclic seismic-type manner, as shown in figure 7 with a frequency of 0.10Hz. Next, the imposed sliding displacement was further increased in amplitude.

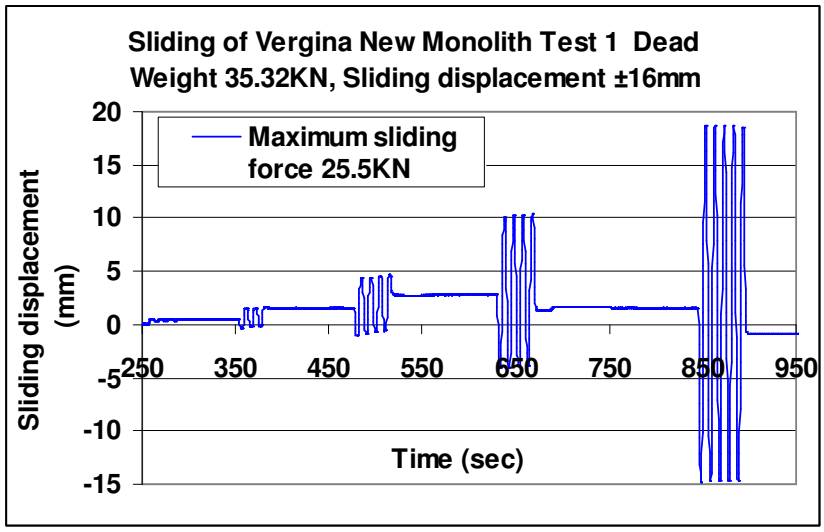


Figure 7. Time history of imposed load/sliding displacement

The last group of imposed load/displacement cycles reached an average maximum sliding displacement amplitude of ±16mm, as shown in figure 7. The obtained sliding response in terms of imposed horizontal load and resulting sliding displacement is depicted in figure 8.

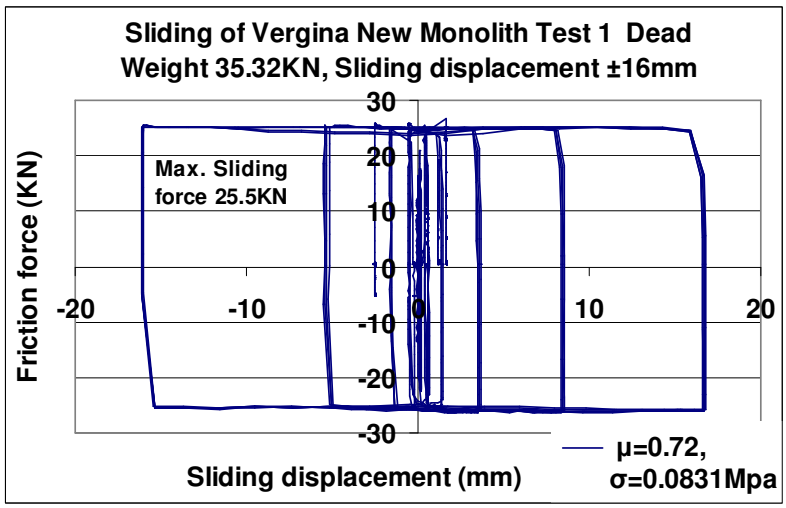


Figure 8. Cyclic friction load / sliding displacement cyclic response obtained for the Vergina new monoliths.

As can be seen in figure 8, the cyclic sliding response of the two monoliths is stable resulting in a dynamic coefficient of friction equal to μ= 0.72. This value of the friction coefficient remained almost constant for all the range of normal stress amplitudes that were tried during this experimental sequence, as already mentioned before.

3 PERFORMANCE OF THE STONE DRY-MASONRY ASSEMBLY UNDER HORIZONTAL BASE MOTIONS

In what follows, summary results from the dynamic performance of the dry-masonry five-stone assembly, mentioned in the introduction, will be presented. Two basic configurations are examined here; the first is that these stones are free to rock and slide till they become geometrically unstable and collapse. In the second configuration a practically non-deformable structure (steel beam) is built at the back of the stone formation that extends to the same height as the stone assembly. Whereas in the first structural formation the stone assembly and the steel beam are not connected in the second structural formation the upper three stones are connected with the steel beam with a system of flexible ties that can develop tensile and compressive forces of certain limited amplitude.

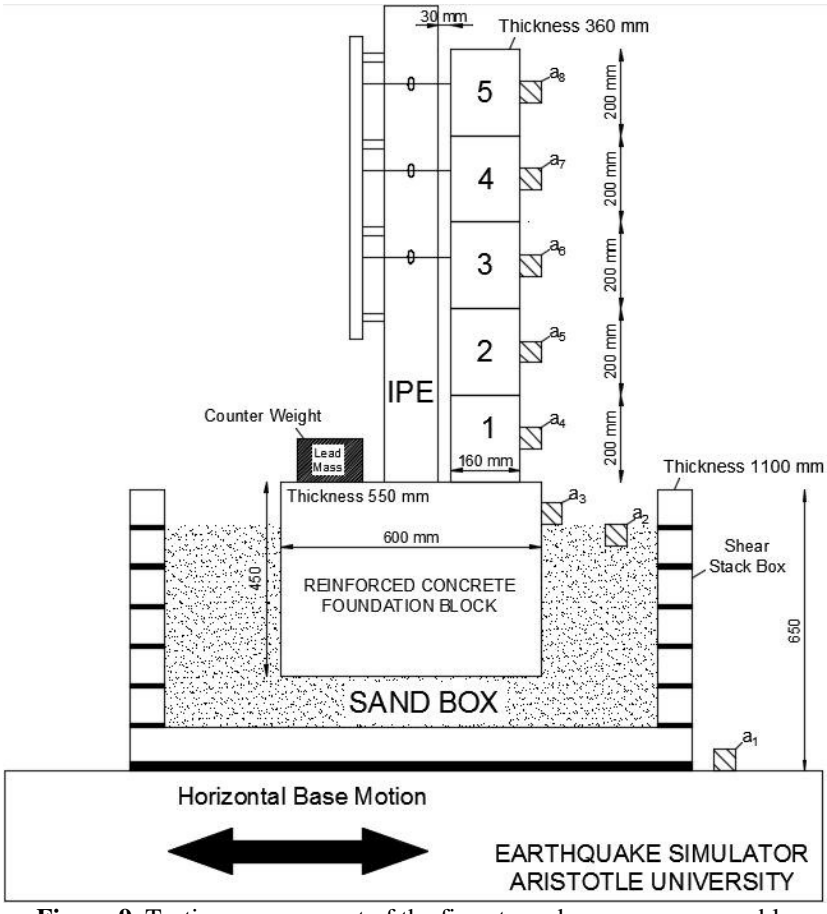


Figure 9. Testing arrangement of the five stone dry-masonry assembly

The used testing arrangement is depicted in figure 9. A shear stack aluminum box filled with dry sand was rigidly secured on top of the earthquake simulator steel platform (shaking table). This box was hosted the foundation block of the five-stone dry masonry assembly as shown in figure 9. This foundation block was partially embedded within the sand and also carried, apart from the five-stone assembly, a counter weight lead mass rigidly fixed on the foundation block as well as a steel beam to be used to partially support the five-stone assembly with horizontal links, as indicated in this figure. This is also shown in figure 10. This testing arrangement was utilized in order to portray up to a point foundation conditions for the five-stone assembly that could be claimed to represent more realistically the in-situ soil-foundation conditions of the ancient wall monoliths. A number of acceleration sensors were

rigidly attached on each of the five stones as well as on the foundation block. Moreover, additional acceleration sensors were also placed near the surface of the sand box as well as on the steel platform of the shaking table. These sensors are indicated in figure 9 from a1 to a8 and are also depicted in figure 10.



Figure 10. Testing arrangement of the five stone dry-masonry assembly

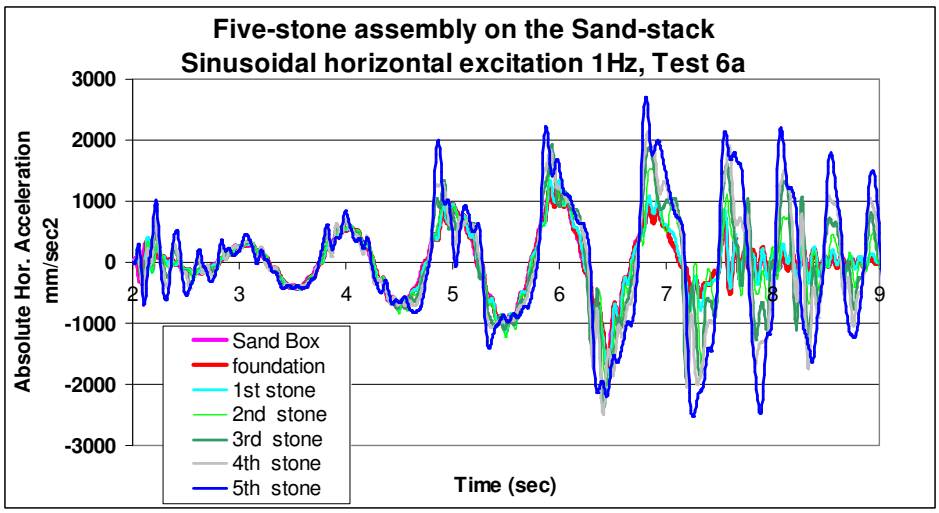


Figure 11. Acceleration response along the height of the unattached five-stone assembly 0.165g, Test 6a.

3.1 Obtained results from sinusoidal tests with the unattached five-stone assembly

In what follows, summary results will be presented from the dynamic tests of the five-stone assembly when it was excited with sinusoidal horizontal base motions being unattached from the steel beam. A number of such dynamic tests were carried out keeping the frequency of the excitation constant (1.0Hz) and gradually increasing the amplitude of the base motion from test to test. Results from two tests will be shown here. Small rocking could be measured when the maximum horizontal base acceleration reached during a test the value of 0.15g, where g the acceleration of gravity. During the next test (Test 6a), despite the observed relative large amplitude of the base motion, the five-stone assembly did not develop any form of large rocking or sliding displacements leading to instability. The acceleration response along

the height of the five-stone assembly is depicted in figure 11. As can be seen in this figure, for a peak base acceleration equal to 0.165g the fifth (top) stone develops a peak acceleration of approximately 0.27g

During the next test (Test 7a) with larger base excitation than Test 6a (0.173g), the five-stone assembly developed large rocking displacement response as shown in figure 12. In addition, sliding between the various stones at their contact interface became also noticeable as depicted in figure 13.



Figure 12. Large rocking displacement response of the unattached five stone dry-masonry assembly, being unattached from the steel beam



Figure 13. Sliding between stone-blocks at the contact interface of the unattached five-stone assembly

The acceleration response along the height of the five-stone assembly for Test 7a is depicted in figure 14. As can be seen in this figure, for a peak base acceleration equal to 0.173g the fifth (top) stone develops a peak acceleration of approximately 0.68g. It was observed in the past during the experimental sequences with columns having drums that for a given frequency of excitation there is a boundary between the stable rocking response and the overturning. This boundary has relatively high values of non-dimensional excitation amplitude for

high frequency values and relatively low values of non-dimensional excitation amplitude for low frequency values.

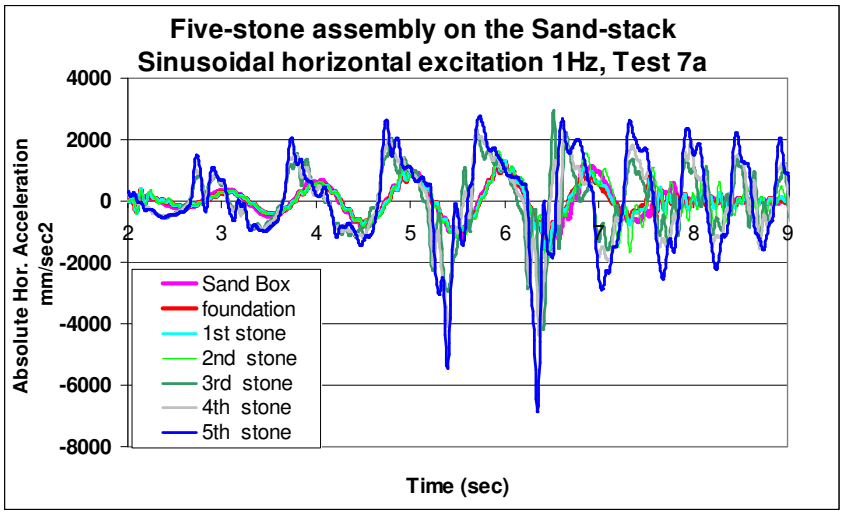


Figure 14. Acceleration response along the height of the unattached five-stone assembly (peak base horizontal acceleration 0.173g, Test 7a)

3.2 Obtained results from sinusoidal tests with the attached five-stone assembly

Again, summary results will be presented from the dynamic tests of the five-stone assembly when it was excited with sinusoidal horizontal base motions. However, the vive-stone assembly is being now attached from the steel beam with relatively weak steel wires. A number of such dynamic tests were carried out keeping again the frequency of the excitation constant (equal to 2.0Hz) and gradually increasing the amplitude of the base motion from test to test. Results from two tests will be shown here. Small rocking could be measured when the maximum horizontal base acceleration reached during a test the value of 0.2g, where g the acceleration of gravity.

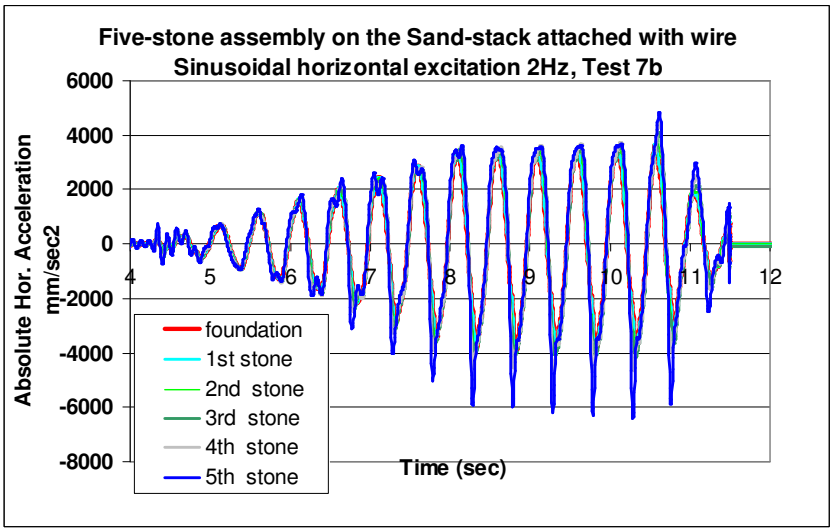


Figure 15. Acceleration response along the height of the attached five-stone assembly (peak base horizontal acceleration 0.4g, Test 7b)

During the next tests, despite the observed relative large amplitude of the base motion, the five-stone assembly did not develop any form of unstable rocking or excessive sliding displacements leading to instability. The acceleration response along the height of the five-stone

assembly is depicted in figure 15 for test 7b. As can be seen in this figure, for a peak base acceleration equal to 0.4g the fifth (top) stone develops a peak acceleration of approximately 0.64g, responding in a stable rocking mode. However, during the next test (Test 8b) the five-stone assembly developed unstable rocking response that was accompanied with the fracture of the wire links as is depicted in figure 16. The maximum acceleration measured at the top stone was in excess of 0.7g, as can be seen in figure 17 where the acceleration response along the height of the five-stone assembly is depicted.



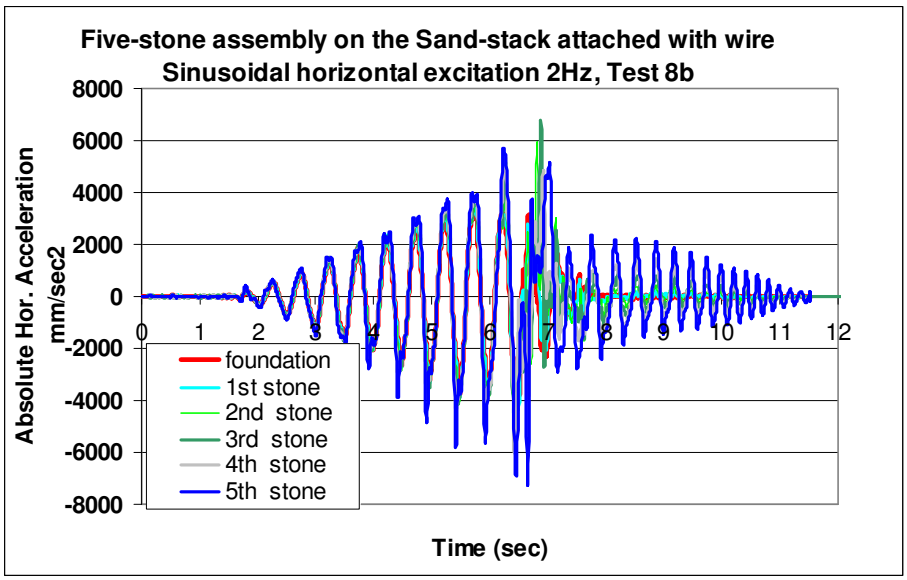


Figure 17. Acceleration response along the height of the attached five-stone assembly (peak base horizontal acceleration 0.4g, Test 8b)

As can be seen by comparing the measured acceleration response in figures 11 and 14 for the unattached mock-up five-stone assembly with the measured acceleration response of the same mock-up being this time attached with steel wire links with a supporting structure (fig-

ure 15 and 17), the stability of the rocking response was retained for much larger base acceleration amplitudes when the steel links were present.

4 CONCLUSIONS

- The value of 0.72 was found as friction coefficient for the new monoliths to be used for the restoration of the North wall of the Macedonian Palace at Vergina, Greece.
- The mock-up of a five stone dry masonry assembly developed stable rocking and unstable rocking dynamic response that was combined with sliding at the contact interfaces.
- This stable-unstable rocking response of the mock-up of a five stone dry masonry assembly resembles similar behaviour that was observed for the response of mock-ups of ancient free standing columns with drums.
- Steel wire links with limited tensile capacity can have, up to a point, beneficial influence on this stable-unstable rocking response of such type stone dry masonry. The stability of the rocking response was retained for much larger base acceleration amplitudes when the steel links were present than when the used mock-up of the five-stone assembly was unattached.
- In this case a supporting structure must also be properly designed to be used as support system for such links.

ACKNOWLEDGEMENTS

The authors would like to thank Ms. A. Kottaridi, the Director of the archaeological studies and restoration works at the Vergina Macedonian Palace and the Head of the 17th Prehistoric and Classical Archaeological Sites Agency of Greece

REFERENCES

[1] Ambraseys, N. and Psycharis, I. N. (2011) "Earthquake stability of columns and statues", Journal of Earthquake Engineering, Vol. 15, pp. 685-710.

[2] Aslam , M.M., et.all. 1978. Rocking and Overturning response of rigid bodies to earthquake motions, Report No. LBL-7539, L. B. Lab. Univ. Of California, Berkeley.

[3] Demosthenous M, 1994. Experimental and numerical study of the dynamic response of solid or sliced rigid bodies, Ph. D. Thesis, Dep. Civil Eng., Aristotle University.

[4] Koh, A.S. and Mustafa G. 1990. Free rocking of cylindrical structures, J. of Eng. Mechanics, Vol. 116, N0 1, pp.35-54.

[5] Manos, G. C. and Demosthenous, M., 1990. The behavior of solid or sliced rigid bodies when subjected to horizontal base motion. Proc. 4th U.S. Nat. Confer. Earth. Eng, Vol. 3, pp. 41-50.

[6] Manos G.C. and Demosthenous M. " Study of the dynamic response of models of ancient columns or colonnades subjected to horizontal base motions", 11WCEE, Session 6.3.3. of Abstract Volume Analysis of Masonry Structures, Acapulco, Mexico, 1996.

[7] Manos G.C. and Demosthenous M. "Models of ancient columns or colonnades subjected to horizontal base motions - study of their dynamic and earthquake behavior", STREMA97, pp. 289-298, San Sebastian Spain.

[8] Manos G.C., "The dynamic performance of models of ancient columns and colonnades with and without the insertion of wires made of shape memory alloy", STREMAH 99, pp. 281-290, Dresden, Germany, 1999.

[9] Manos, G.C., Demosthenous M., Hatzigeorgiou A., Manou-Evison J., "Study of the dynamic and earthquake behavior of models of ancient columns and colonnades with and without the inclusion of wires with energy dissipation characteristics", 12th WCEE, Auckland, New Zealand, 2000.

[10] Manos, G.C., Demosthenous M., Kourtides, V., Hatzigeorgiou A., "The Dynamic and Earthquake Behavior of Ancient Columns and Colonnades with and without Shape Memory Alloy Devices", STREMAH 2001, Florence, Italy, 2001.

[11] Manos G.C. et.al "Study of the Dynamic and Earthquake Behavior of Rigid Bodies with or without the Inclusion of Shape Memory Alloy Devices" , 16SMIRT, Washington D.C. 2001.

[12] Manos, G.C., Demosthenous M., Kourtides V., Hatzigeorgiou A, "Study of the dynamic and earthquake behavior of models of ancient columns and colonnades with and without the inclusion of wires with energy dissipation characteristics", 9th Canadian Conference on Masonry Structures, Univ. New Braunswick, Canada, 2001.

[13] Manos, G.C., Demosthenous M., Kourtides V., "The Response of Models of Ancient Columns and Colonnades under Horizontal Forces with or without SMAD's" 2o Int. Conf. "Studies in Ancient Structures" Constantinoupol, Turkey, 2001.

[14] Manos, G.C., Demosthenous M., Kourtides V., "The Dynamic and Earthquake Response of Models of Ancient Columns and Colonnades with and without Energy Dissipation Devices", 12th European Earthquake Engineering Conference, London, England, 2002.

[15] Manos G.C., Koidis, George and Demosthenous Milton, "Investigation of the Sliding Response of a Rigid Body System to Uni-Direction Horizontal Dynamic and Earthquake Excitations", COMPDYN 2011, Corfu, Greece, 26–28 May 2011.

[16] Manos G. C, Koidis G., Demosthenous M., "The Sliding Response of a Rigid Body System Subjected to Uni-Directional Horizontal Dynamic and Earthquake Excitations" EURODYN 2011, Leuven, Belgium, 4-6 July, 2011.

[17] Manos G. C, Koidis G., Demosthenous M., "The response of a two-degree-of-freedom dynamic sliding system subjected to uni-direction horizontal dynamic and seismic excitations", Int. J. of Computational Methods and Experimental Measurements, Vol. 1, No. 3, pp.221-237, 2013.

[18] Manos G.C., Petalas A., Demosthenous M. "Numerical and experimental study of the rocking response of unachored body to horizontal base excitation", 4th ECOMASS Thematic Conference on Computational Methods in Structural Dynamics and Earthquake Engineering – COMPDYN 2013, 12-14 June 2013, Kos Island, Greece.

[19] Mouzakis, H., Psycharis, I. N., Papastamatiou, D. Y., Carydis, P. G., Papantonopoulos, C. and Zambas, C. (2002) "Experimental investigation of the earthquake response of a

model of a marble classical column", Earthquake Engineering and Structural Dynamics, Vol. 31, pp. 1681-1698.

[20] Mouzakis, H., Psycharis, I. N., Papastamatiou, D. Y., Carydis, P. G., Papantonopoulos, C. and Zambas, C. (2002) "Experimental investigation of the earthquake response of a model of a marble classical column", Earthquake Engineering and Structural Dynamics, Vol. 31, pp. 1681-1698.

[21] Psycharis Ioannis N. (2007) A Probe into the Seismic History of Athens, Greece from the Current State of a Classical Monument. Earthquake Spectra: May 2007, Vol. 23, No. 2, pp. 393-415

[22] Papantonopulos, C., Psycharis, I. N., Papastamatiou, D. Y., Lemos, J. V. and Mouzakis, H. (2002) "Numerical Prediction of the Earthquake Response of Classical Columns Using the Distinct Element Method", Earthquake Engineering and Structural Dynamics, Vol. 31, pp. 1699-1717.

[23] Ambraseys Nicholas, Psycharis Ioannis N., “Assessment of the long-term seismicity of Athens from two classical columns” Bulletin of Earthquake Engineering, December 2012, Volume 10, Issue 6, pp 1635-1666, Date: 13 Oct 2012

[24] Psycharis I. N., "Dynamic Behaviour of Rocking Two-Block Assemblies" (1990) Earthquake Engineering and Structural Dynamics, Vol. 19, pp. 555-575.

[25] Psycharis, I. N., Papastamatiou, D. Y. and Alexandris, A. (2000) "Parametric Investigation of the Stability of Classical Columns under Harmonic and Earthquake Excitations", Earthquake Engineering and Structural Dynamics, Vol. 29, pp. 1093-1109.

[26] Psycharis, I. N., Lemos, J. V., Papastamatiou, D. Y., Zambas, C. and Papantonopoulos, C. (2003) "Numerical Study of the Seismic Behaviour of a Part of the Parthenon Pronaos", Earthquake Engineering and Structural Dynamics, Vol.32, pp. 2063-2084.

[27] Spanos, P.D. and Koh A.S., 1984. Rocking of rigid blocks due to harmonic shaking. J. of Engin. Mech., ASCE 110 (11), pp. 1627-1642.

COMPDYN 2015
5th ECCOMAS Thematic Conference on
Computational Methods in Structural Dynamics and Earthquake Engineering
M. Papadrakakis, V. Papadopoulos, V. Plevris (eds.)
Crete Island, Greece, 25–27 May 2015

STUDY OF THE LOADING ARRANGEMENT FOR THE STIFFNESS TESTS OF THE COLUMN HEAD ASSEMBLY AND ITS SPRINGS UTILIZED AT THE NIARCHOS CULTURAL CENTER AT ATHENS - GREECE.

G.C. Manos[1], V. Kourtides[2], K. Katakalos[2], L. Kotoulas [3], Nalmpantidou[3]

[1] Professor and Director of the Lab. of Strength of Materials and Structures, Aristotle University
e-mail: gcmanos@civil.auth.gr

[2] Dr. Civil Engineer, Research Ass., Lab. of Strength of Materials and Structures, Aristotle University

[2] Postgraduate student, Lab. of Strength of Materials and Structures, Aristotle University

Keywords: Suspension Roof, Stiffness tests, Axial tension tests, Niarchos Cultural Center, Numerical Analyses.

Abstract. *This paper presents the loading arrangements that were conceived and constructed in order to tests in prototype scale the performance of the suspension devices (Column Head Assembly specimens) that are part of the total suspension system of the roof deck that will be constructed at the top of the Stavros Niarchos Foundation Cultural Center that is currently constructed at Athens, Greece. Each suspension device utilizes 4 springs with a tensile capacity of two hundred tons and a corresponding extension of 300mm and two dampers with a maximum damping force of the order of 10tons. These springs and dampers form together with a stiff steel reaction frame and a sliding billet the column head assembly (suspension device) with overall dimension approximately 4.4m x 4.4m in plan and 2.5m height. The billet can slide vertically within the core of the column head assembly approximately 250mm and withstand a vertical force of the order of 300tons. In order to test the performance of these column head assemblies at the laboratory prior to their being used in-situ a special loading arrangement was manufactured at the laboratory of Strength of Materials and Structures of Aristotle University. The basic loading functions of the suspension system of the roof deck that is to be constructed at the Stavros Niarchos Foundation Cultural Center is briefly described as well as how this was simulated at the laboratory of Strength of Materials and Structures of Aristotle University in order to measure the performance of prototype suspension device specimens prior to being installed in-situ. A special loading rig was designed and finally constructed to be utilized in the prototype testing of the performance of the springs. A series of linear and non-linear numerical simulations were employed towards securing the safe performance of this loading rig during the testing of the said springs.*

1 INTRODUCTION

This paper presents a summary of experimental procedures that were utilized to measure at the laboratory environment the basic components of a suspension system that is designed to be utilized in the suspended roof that will be built at the top of the building complex of the "Stavros Niarchos Foundation Cultural Center" that is currently constructed in Athens, that will be designated in the following as NCC. The drawing image of the NCC complex is depicted in figure 1a where it can be seen that the aerodynamically shaped hollow concrete roof deck is supported by a series of slender steel columns [1]. This hollow roof deck is formed by joining in-situ pieces of double relatively thin-skin cross-sections stiffened with vertical webs that are pre-constructed by fero-cement and specially formed steel reinforcement, as shown in figure 1b. The system that this roof is suspended from will not be visible as it will be built within the space left by the top and bottom thin skin faces of the hollow roof deck.

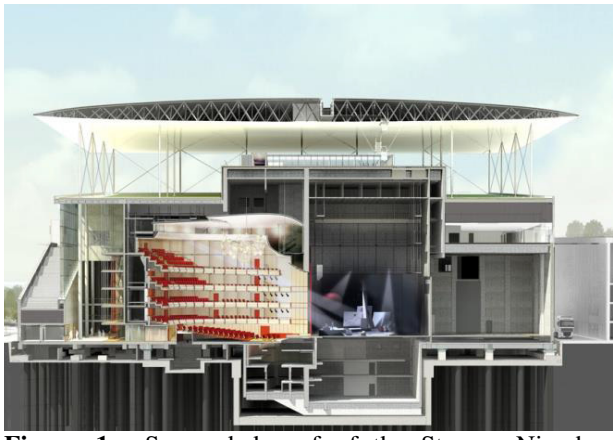


Figure 1a. Suspended roof of the Stavros Niarchos Foundation Cultural Center



Figure 1b. Parts of the suspended roof made of fero-cement and steel reinforcement

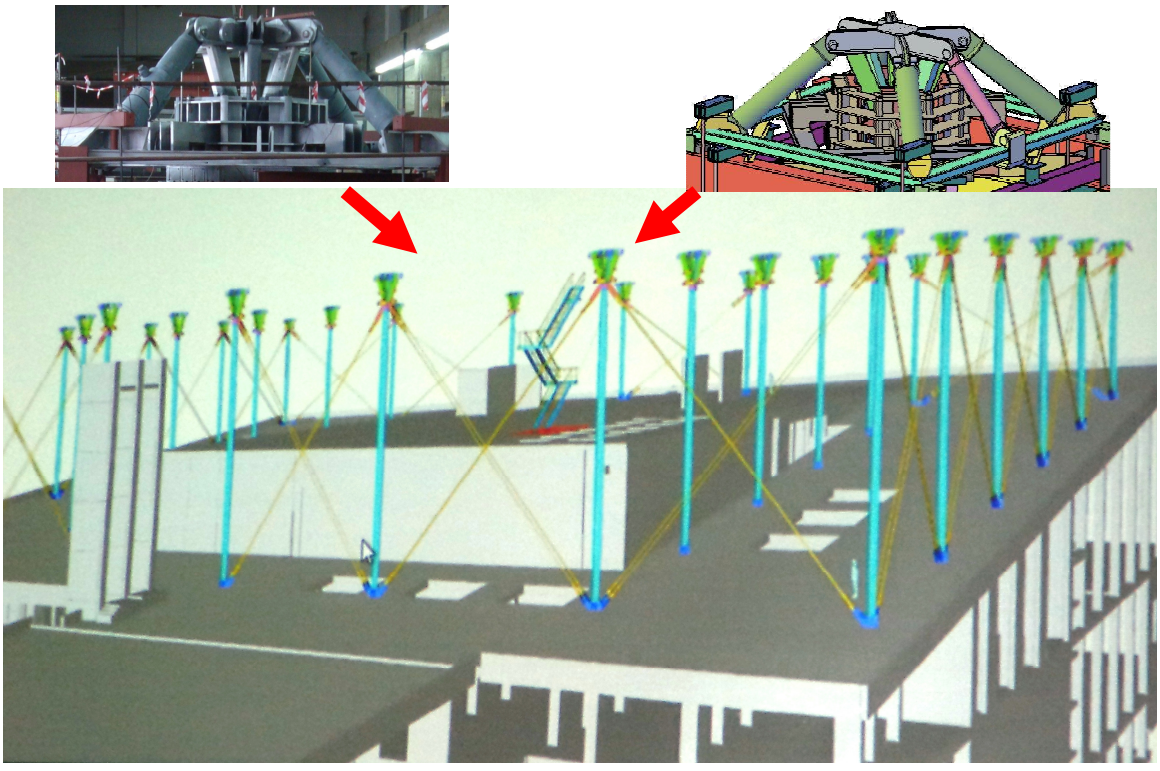


Figure 2. The supporting columns with the suspension devices shown schematically without the roof deck

The concept of this suspension system is shown schematically in figure 2. On top of every column a suspension device is constructed. These suspension devices are all the same for all columns that are named Column Head Assembly Type-4 (designated as CHA Type-4) except the four corner columns that are named Column Head Assembly Type-1 (designated as CHA Type-1). Each suspension device is formed by the following components:



Figure 3. The horizontal strong square steel frame with the hollow cylinder at the center

a) A horizontal strong square steel frame shown in figure 3 that is constructed with four corners where this frame is joined to the concrete deck and at the same time provides the bottom hinged support of the four springs that form the suspensions system. At the center of this strong frame a strong hollow cylinder is formed with a number of polygonal webs from the outside and four identical vertical cylindrical surfaces from the inside that are constructed with special sliding material.
b) A steel sliding core "billet" which is shown in figure 4 in its temporary supports. This sliding core (billet) of the suspension system is shown in figure 5 as it is lowered in a inside the hollow cylinder of the strong steel frame. This billet provided at its top hinged support for the springs of the suspension system.



Figure 4. The sliding core "billet" temporary supported outside of its host-steel frame

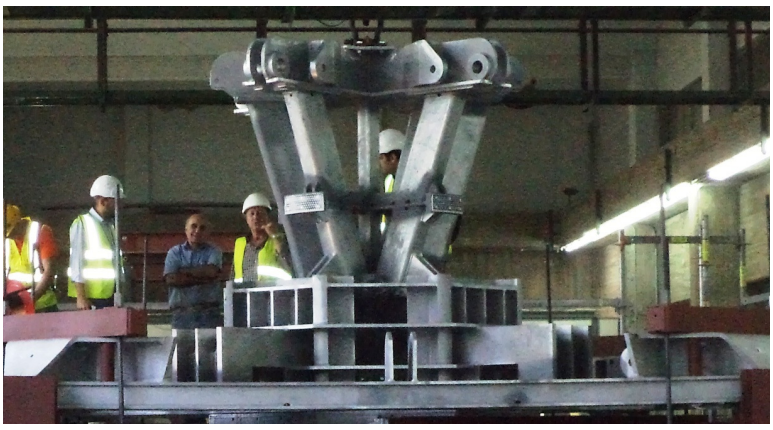


Figure 5. The sliding core "billet" being lowered in position within its host-steel frame

c) Four identical springs having the required stiffness properties that join at their bottom end the four corners of the strong steel frame with the four hinges of the billet at their top end. This is depicted in figure 6. When the four corners of the steel frame do not bear any load the billet is at its lowest possible position and the springs are in their contracted length. At this condition, the only load that is transferred at the bottom of the billet being supported at the top of the steel columns is the dead load of the components of this suspension system that is of the order of 50KN. When the four corners of the strong steel frame are forced downwards with extra vertical load the this results in an extension of the spring by such a length that is required to equilibrate this vertical load. There are two types of springs. The ones depicted in figures 6 and 7 that belong to the CHA Type-4 specimen and are longer than the springs for the CHA Type-1 specimen that is depicted in figure 8.

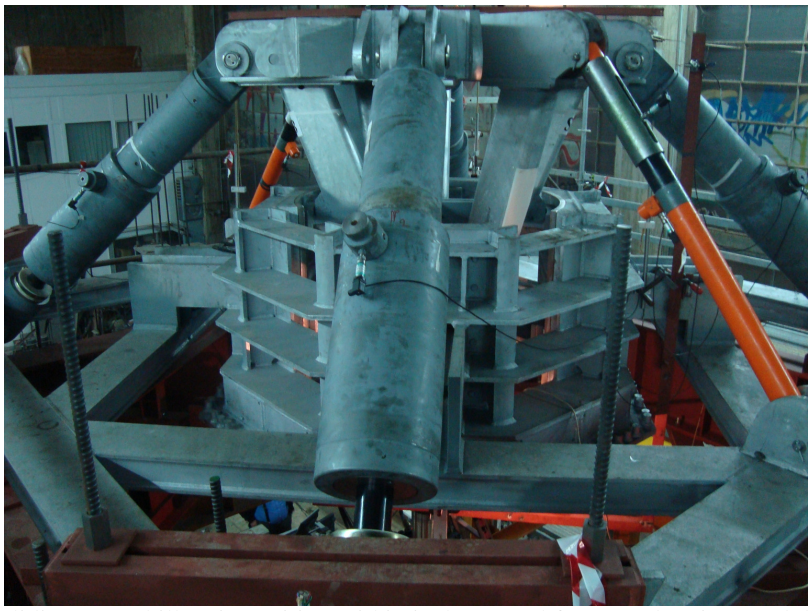


Figure 6. The sliding core "billet" in position within its host-steel frame and springs and dampers

d) Two dampers (new dampers type-4 with the orange colour), that also join the top of the billet with the strong steel frame as shown in figure 6. Similarly, there are two types of dampers; first, the ones that belong to the CHA Type-4 specimen (figures 6 and 7) that are longer than the ones that belong to the CHA Type-1 specimen (figures 8 and 9)



Figure 7. Springs and old dampers for CHA Type-4



Figure 8. Springs for CHA Type-1

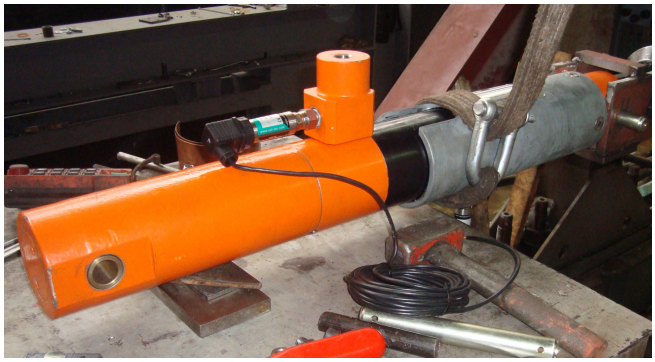


Figure 9. Springs for CHA Type-1

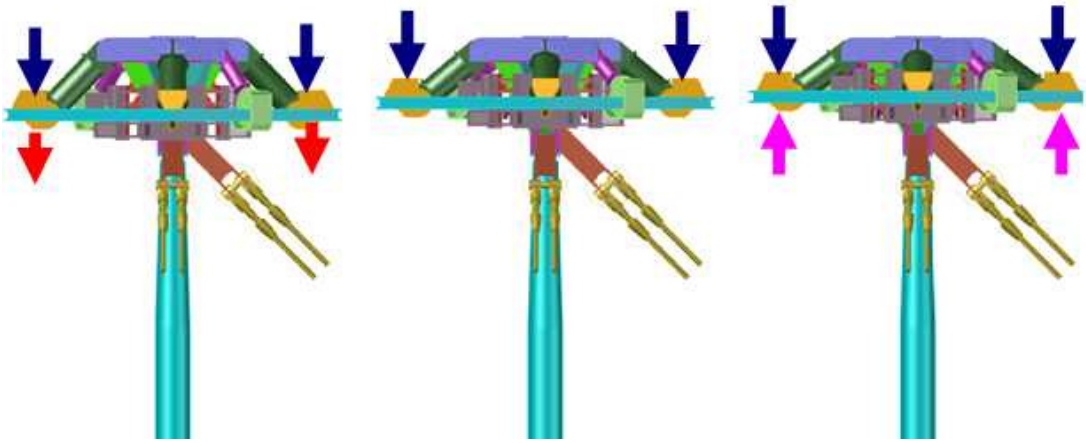


Figure 10. Loading function of the suspension device

2 BASIC LOADING FUNCTIONS OF THE SUSPENSION DEVICE AND EXPERIMENTAL SIMULATION

2.1 Basic loading function of the suspension device.

Figure 10 depicts the basic loading function of the suspension devise. The sketch in the middle of this figure depicts the suspension device carrying the dead weight of the roof deck (blue arrows). To perform this function, the following steps are necessary.

a) The springs are initially extended, without internal forces, at a certain pre-determined length that corresponds to a relative zero condition. This initial extension of the springs corresponds to a vertical upward displacement of their upper length relatively to their bottom end which means that at this initial zero condition the billet has also being moved upwards by sliding into the hollow cylinder at the appropriate location which represents for the billet the initial zero condition. At this initial zero condition the lower corners of the springs and the corresponding corners of the horizontal steel frame are secured being in contact with the corresponding host steel brackets embodied in the low thin-skin of the roof deck. At this stage the suspension devices are not carrying any of the roof deck load, as it is still supported by the temporary shoring.

b) Then, by applying the appropriate external pressure in the four springs simultaneously, the springs are developing internal tensile forces that step-by-step pick-up some portion of the dead weight of the roof deck.
c) This operation is performed in turn gradually for all the suspension devices until the sum of the tensile forces that are exercised by the four springs of each suspension device to the roof deck equilibrate its total dead load. At this point, the roof deck is suspended from the suspension system being freed from the temporary shoring which can thus be removed.
d) With the suspension system at this Dead-Load condition when extra vertical load is applied downwards on the roof (snow, wind, seismic etc.) then the springs will be further extended in length to equilibrate this extra vertical load (red arrows, figure 10 left). This is possible, by an additional upward vertical displacement of the ends of the springs being hinged to the billet, which in turn slides upwards within the central hollow cylinder. The system at this condition has the springs extended to their maximum allowable length developing at the same time the maximum internal tensile forces that through the sliding "billet" core are transferred as maximum compressive vertical reactions on top of the steel column supports.
e) With the suspension system at this Dead-Load condition when extra vertical load is applied upwards on the roof (wind, seismic etc.) then the springs will be shortened in length appropriately to equilibrate this extra vertical load (pink arrows, figure 10 right). This is possible, by a downward vertical displacement of the ends of the springs being hinged to the billet, which in turn slides downwards within the central hollow cylinder. The system at this condition has the springs contracted to their minimum allowable length developing at the same time the minimum internal tensile forces that through the sliding "billet" core are transferred as minimum compressive vertical reactions on top of the steel column supports.
f) The above steps d and e can also be seen in combination as being able to have each suspension devise being displaced from the condition where the springs have their minimum length and very little tensile force (zero load and zero vertical displacement condition for the billet being at its lowest level) to the condition where the springs have their maximum length and their maximum internal tensile force (maximum load and maximum vertical condition for the billet being at its highest level). This rational will be made use of during the experimental process.

2.2 Experimental simulation of the basic loading function of the suspension device.

In order to study the performance of prototype suspension device specimens at the laboratory the rational stated in section 2.1. (step f) above was utilized [2]. That is a prototype suspension device with all its parts being the prototype components was secured at the laboratory environment at a condition representing the minimum length of the springs condition section 2.1. (step e). At this geometry of the suspension device the corners of the horizontal steel frame were secured on the strong reaction steel frame of the laboratory of Strength of Materials and Structures as it is shown in figure 11. This was achieved by a system of pre-stressing steel rods. Moreover, with the suspension device fixed in this geometry the point where the sliding billet is supported on the prototype steel columns in-situ was secured here by supporting it to the rod of a hydraulic jack. This rod could be displaced upwards by a control system exercising in this way an upward force to the billet which by being equilibrated by the four springs would result to the springs being extended by the appropriate amount whereas at the same time the "billet" will also slide upwards by the corresponding amount of vertical dis-

placement. This operation could be applied on a continuous manner till the suspension device reached the conditions with the four springs being extended at their maximum limit length which would correspond to the maximum upward vertical sliding displacement of the billet within the hollow steel cylinder. This condition corresponds to step d) above and obviously requires from the hydraulic jack to be able to apply a vertical force and a vertical displacement that corresponds to the maximum level of forces the suspension device would develop during step d). This was approximately of the order of V=3000KN and δ_v = 250mm. This is depicted in figures 11 and 12.

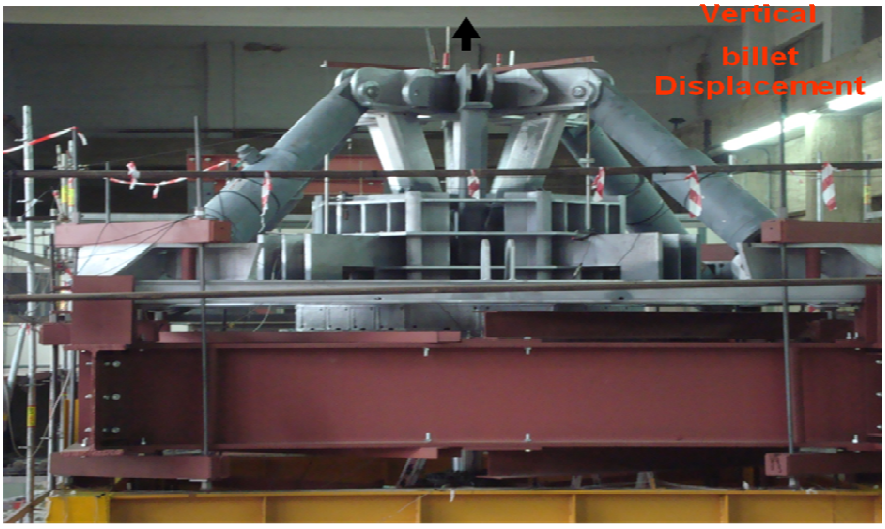


Figure 11. The suspension device CHA Type-4 being supported at the strong reaction frame

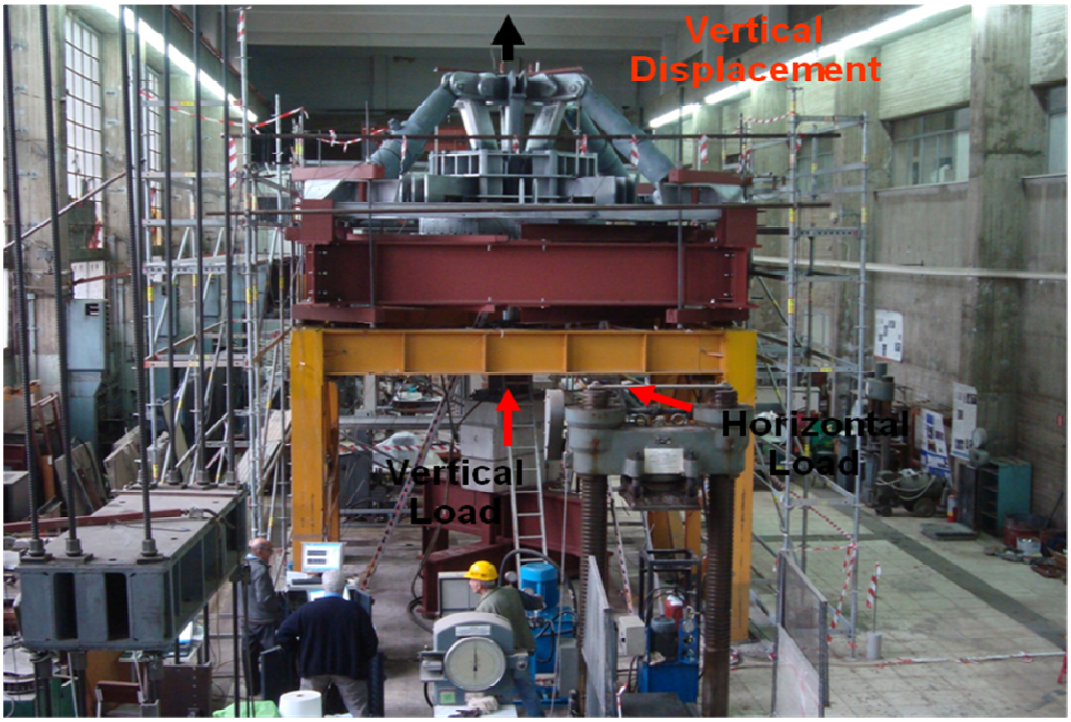


Figure 12. The suspension device CHA Type-4 being supported at the strong reaction frame (brown and yellow colour) together with the hydraulic jack installed in a way to apply the required vertical load at the center of the billet

With this laboratory loading arrangement (figures 11 and 12) the basic loading functions of the prototype suspension device in-situ (section 2.1) was simulated in laboratory con-

ditions. Two suspension devices were tried; the first on that was designated as CHA Type-4 and the 2nd one that was designated as CHA Type-1 (see introduction). A considerable number of tests were performed for each suspension device varying the following parameters:

a1) The inclusion during testing in the device of the relevant two dampers. Thus the same tests were repeated with and without the two dampers.

b1) The simultaneous application at the low part of the billet a certain level of horizontal load, as shown in figure 12, in order to check the performance of the device when apart from the upward and downward displacement each device was subjected to a certain level of bending moment with a tendency to create a rotation φ1 of the billet relative to the surrounding hollow steel cylinder, as is shown in figure 13. This horizontal load was applied through an additional horizontal hydraulic jack at the lowest part of the billet, as shown in figure 13. For each tests the level of horizontal load was kept constant whereas the level of vertical load and vertical displacement of the billet varied from the minimum to the maximum levels (section 2.1. steps d and e). For every vertical load variation two different levels of horizontal load (H) was checked, either horizontal load equal to zero (H=0) or horizontal load equal to H=400KN for CHA Type-4 or H=280KN for CHA Type-2., This combination of vertical and horizontal forces have been applied for all structural formations (with or without dampers).

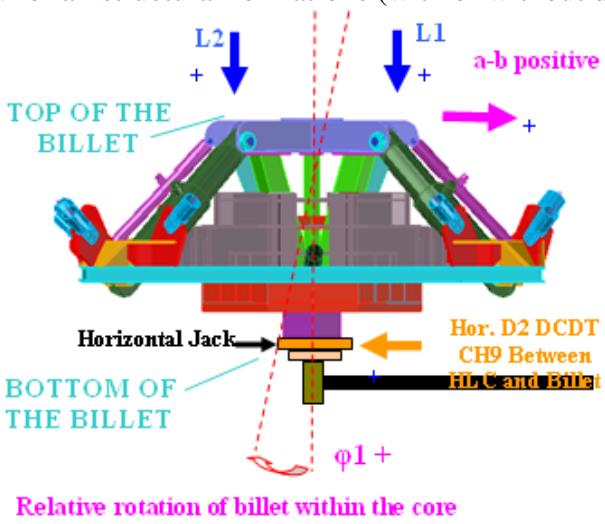


Figure 13. Imposed rotation of the billet relative to the hollow steel cylinder of the horizontal frame through the application of the appropriate horizontal load.

c1) The vertical load (V) / vertical billet (δ_v) displacement that was applied through the vertical hydraulic jack was applied in two different ways. First, this vertical displacement was applied in a continuous non-stop manner from the minimum to the maximum level and then after a brief stop back to the minimum level. Secondly, the vertical load (V) / vertical billet (δ_v) displacement was applied in 20mm vertical displacement intervals from the minimum to the maximum level and then after a brief stop back to the minimum level again in 20mm vertical displacement intervals.

The above parametric variation in the way the vertical load (V) / vertical billet (δ_v) displacement was applied was tried in combination with the variation of the previous two parameters; that is with or without the two dampers and with or without the horizontal H. This parametric variation was done together with the requirement to check the repeatability of the observed performance for each combination by performing at least three identical tests for

each combination. This resulted in a large number of tests and in a similar large number of corresponding measurements.

2.3 Instrumentation scheme

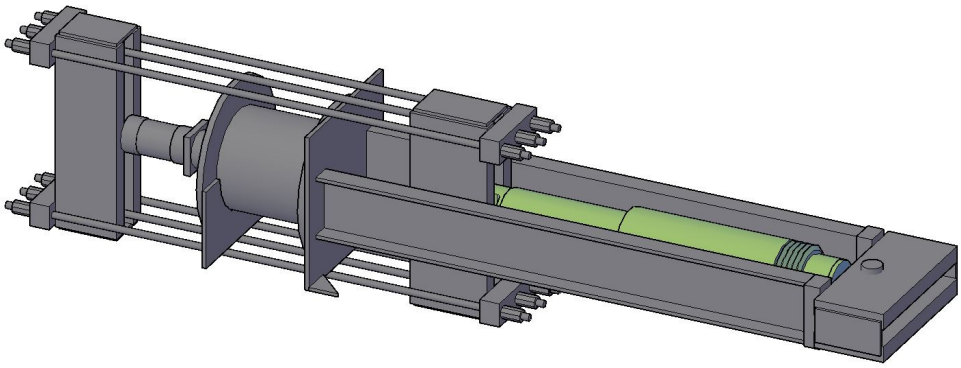
In order to measure the response of the various parts of the tested prototype suspension device specimens at the laboratory a number of load and displacement sensors were attached on the specimens that were continuously recording during testing. The vertical and the horizontal load were measured at the location where they were applied at the bottom of the billet level (figure 13). Moreover, the vertical displacement of the sliding billet relatively to the surrounding hollow cylinder (and the horizontal steel frame) was measured with three vertical displacement sensors that were fixed at the upper billet level (figure 3). The rotation of the billet relatively to the hollow steel cylinder was measured in two independent ways. First, by the differences recorded in the measurement of the vertical displacement of the billet relatively to the surrounding hollow steel cylinder as these vertical displacement sensors were fixed in three different places at the periphery of the billet's upper level. Secondly, by installing horizontal displacement transducers that measured the horizontal displacement of the billet relative to the hollow steel cylinder in two perpendicular directions at both the bottom billet level as well as at the top billet level. Apart from this instrumentation that is very essential to understand and describe the important behavioral characteristics of the performance of the CHA specimens additional instrumentation was also provided in order to che proper operation of the experimental facility especially that of the supporting reaction frame. For this purpose, additional displacement transducers were installed in order to ensure that the CHA specimens were practically fixed at their four supports; in addition, strain gauges were also installed on the pre-stressing bars in order to get the proper warning in the case of an accidental overstress of these pre-stressing rods in transferring the forces that developed on the suspension device during testing.

3 DESIGN AND CONSTRUCTION OF A LOADING RIG FOR TESTING THE INDIVIDUAL SPRINGS.

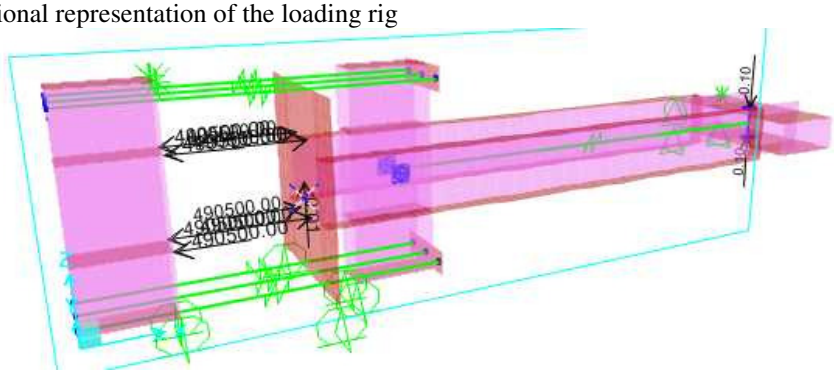
The tests of the full Column Head Assembly units (suspension devices), either Type-4 or Type-1, were complemented by a sequence of tests of every individual spring and damper that formed these CHA specimens. More than one hundred spring of the same type will be employed in the suspended roof of the Stavros Niarchos Cultural Center. In order to test the performance of these springs at the laboratory prior to their being used in-situ a special loading arrangement was manufactured at the laboratory of Strength of Materials and Structures of Aristotle University. A numerical simulation of this loading arrangement was built prior to the actual manufacturing in order to check its design and its expected performance. In what follows the basic steps of the design of the loading rig for these springs are briefly described together with the numerical simulations that were employed as part of this design process that led finally to the construction of this loading rig in the laboratory.

These springs have a maximum tensile capacity of two hundred tons and a corresponding extension in their length of 300mm. Their initial length is approximately 2.0m and their cylindrical part has a diameter of approximately 200mm. This paper presents the most interesting parts of this simulation together with the actual capabilities of this loading arrangement during the stiffness testing of the described springs. The numerical simulation of this loading rig is depicted in figure 14. It is formed of two basic parts. The first is formed by two horizontal UPN320 steel sections that are joined together at the right end by a stiff horizontal steel

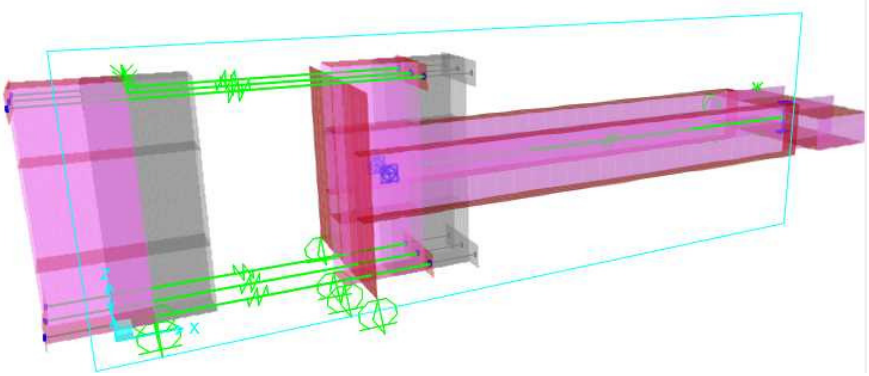
block whereas they are joined together in the front with a vertical steel plate that also forms the basis of hydraulic jack (figure 14a). To the left of the hydraulic jack in figure 14a the load cell measuring the applied load is located. Through this loading cell the far left end vertical steel rigid block is forced horizontally towards the left. This steel block is connected with pre-stressing rods with a similar rigid steel block that is placed at the middle of the loading rig between the UNP320 steel sections. The spring to be tested in axial extension is hinged in this steel block (green colour) as well as in the steel block at the far right of the loading rig. When the hydraulic jack is extended horizontally outwards from right to left it also forces the far left rigid steel block and through the pre-stressing rods the middle steel block. Thus, the spring that is secured between the middle and the far right steel blocks is appropriately extended by a similar amount of horizontal displacement. The force that is required for this horizontal extension of the spring depends upon the stiffness properties of the tested spring and it is provided by the hydraulic jack because the vertical rigid blocks are sliding horizontally in unison providing almost zero horizontal resistance.



a) Conceptional representation of the loading rig



b) The transfer of the horizontal forces from the hydraulic jack to the hinged spring

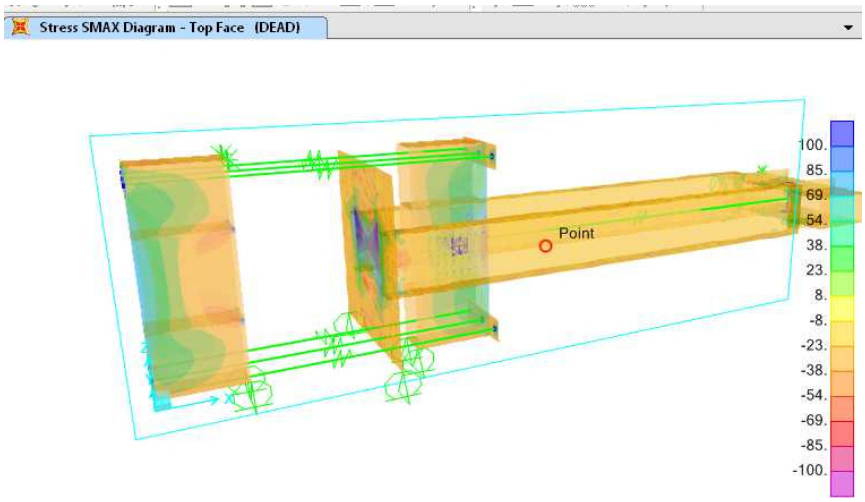


c) The main horizontal deformation mode of the loading rig.

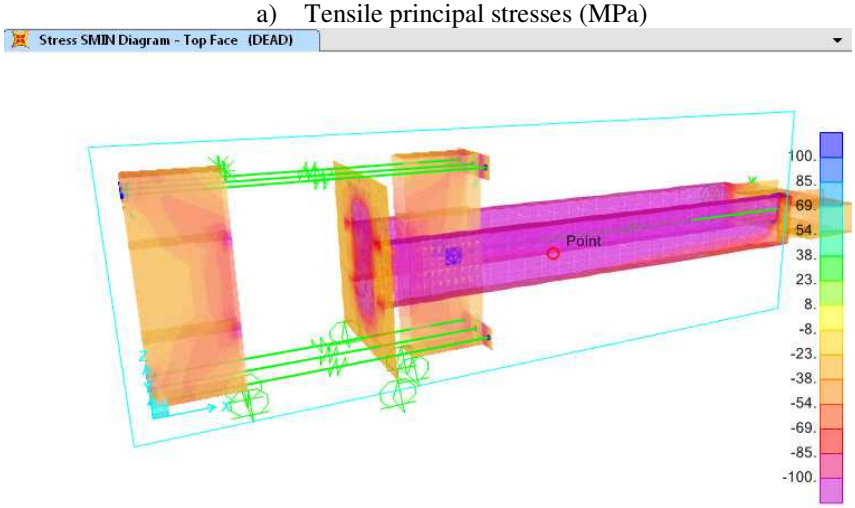
Figure 14. The concept of the loading rig and its numerical simulation

3.1 Static numerical analysis results

The numerical analyses results helped to identify the level of stresses that developed at the various parts of this loading rig and facilitate in this way its design and construction. Typical results are shown in figures 15a and 15b that depict the maximum (tensile) and minimum (compressive) axial stresses in MPa, respectively, that develop in the various steel parts of the loading rig for the maximum applied horizontal load of 2000KN (figure 14b). From the numerical analyses it could be seen that the most stressed parts are the two UPN320 steel sections in compression.



a) Tensile principal stresses (MPa)

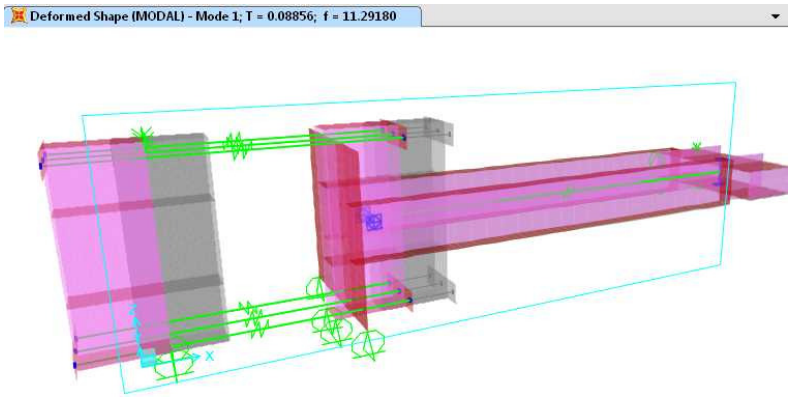


b) Compressive principal stresses (MPa)

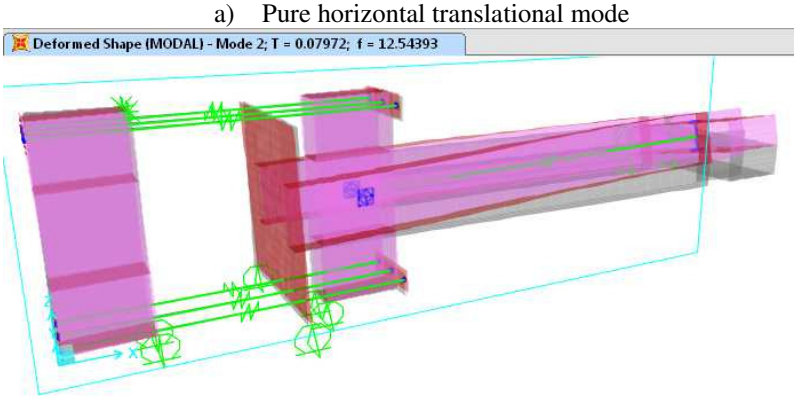
Figure 15. Axial stress distribution for the maximum horizontal load condition of 2000KN

3.2 Modal dynamic numerical analysis results

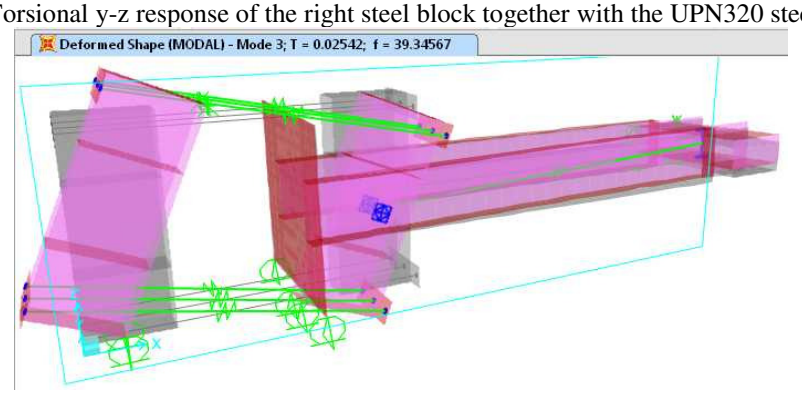
In this section the modal analysis results will be briefly presented and discussed. As part of the testing sequence was to test the spring in dynamic loading with a frequency of 0.75Hz the modal dynamic numerical analyses were aimed to understand the fundamental modes of vibration of this loading rig.



a) Pure horizontal translational mode



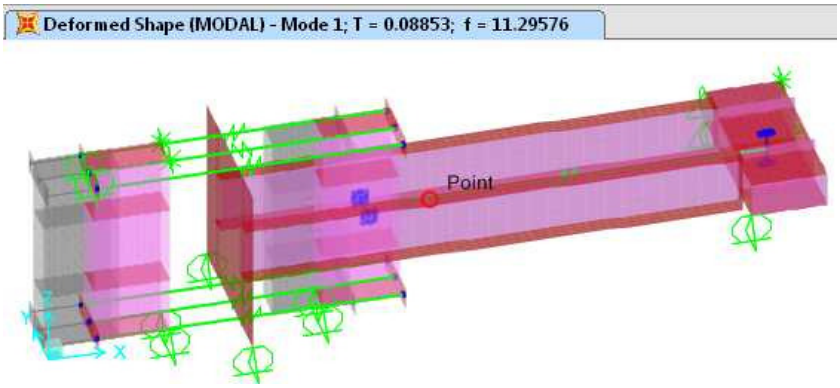
b) Torsional y-z response of the right steel block together with the UPN320 steel sections



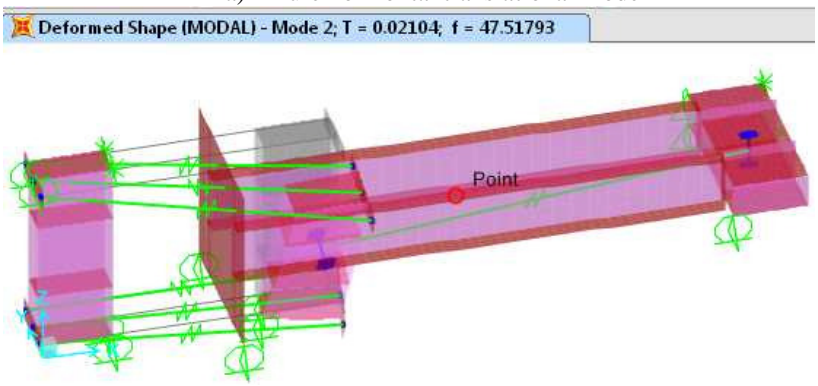
c) Rotational x-z response of the far left and middle steel blocks joined with the pre-stressing rods.

Figure 16. First three modes of vibration of the loading rig.

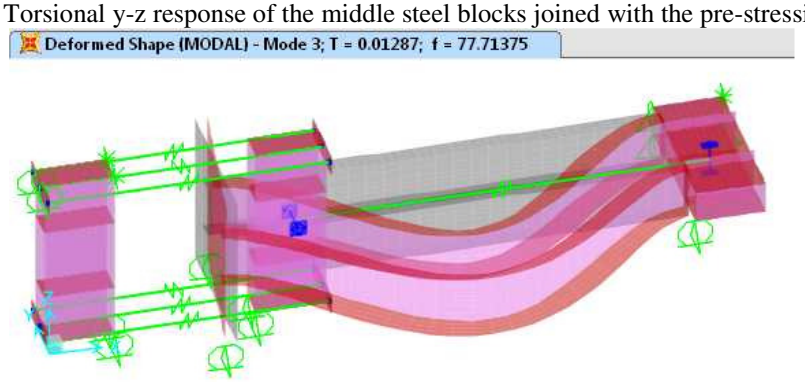
The first fundamental modes of vibration are depicted in figure 16a, b and c. It can be seen that the fundamental mode of vibration that is the pure horizontal translational mode, which coincides with the main displacement pattern that this loading rig is designed to be utilized during testing, is for an eigen-frequency equal to 11.292Hz which is a much higher value than the excitation of 0.75Hz that is the dynamic testing frequency. Moreover, the next two modes of vibration although at high frequencies demonstrate a tendency of the loading ring to deform in torsional and rigid body rotational modes that can be considered as undesired for the main testing objectives of this loading rig. An effort was made to prohibit these undesired modes of vibration by adding a minimum number of support restrains. These restrains were also materialized in the construction stage of this loading rig. Initially, a support was added at the far right steel block (see figures 16a and 17a) in order to prohibit the previously observed torsional response (figure 16b). Next, additional supports were added at the far left block prohibiting its x-z rotational response.



a) Pure horizontal translational mode



b) Torsional y-z response of the middle steel blocks joined with the pre-stressing rods.

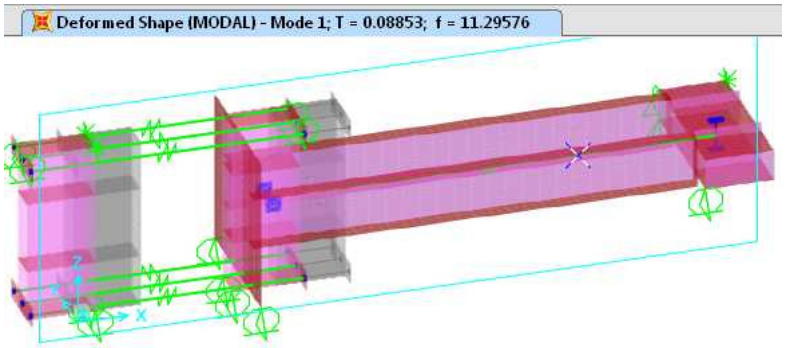


c) Non-symmetric buckling mode of the UPN320 steel sections

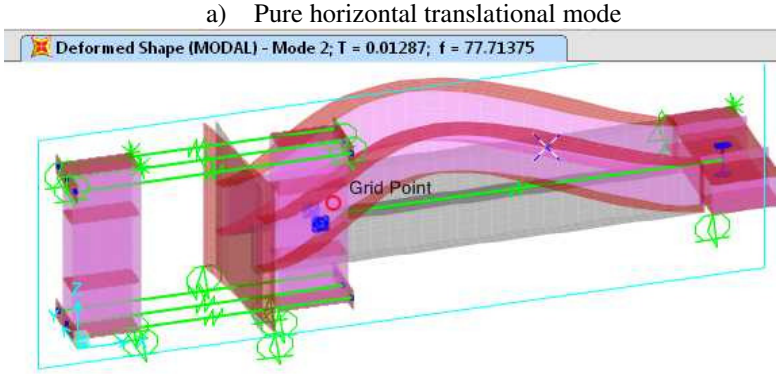
Figure 17. First three modes of vibration of the loading rig.

The first fundamental modes of vibration this time are depicted in figure 17a, b and c. It can be seen that the fundamental mode of vibration that is the pure horizontal translational mode, which coincides with the main displacement pattern that this loading rig is designed to be utilized during testing, remains almost unchanged with an eigen-frequency equal to 11.296Hz which again is a much higher value than the excitation of 0.75Hz that is the dynamic testing frequency. The next mode is a y-z rotational response of the middle steel block whereas the third mode is a buckling flexural mode for the double UPN320 steel sections. These later eigen-modes have relatively very high eigen-frequency values (47Hz and 77Hz).

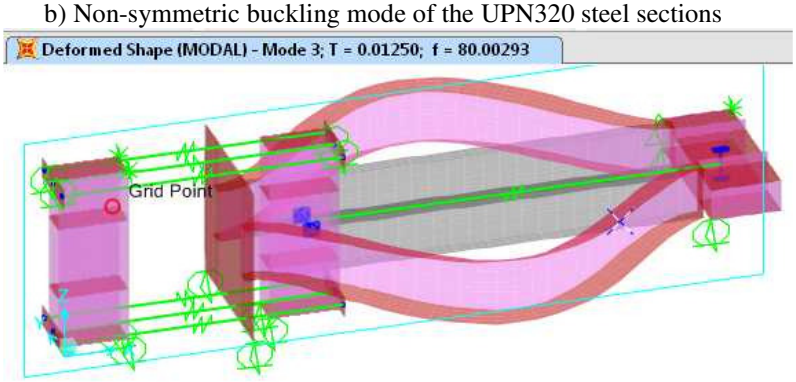
Again, an additional effort was made to prohibit the second mode of vibration by adding again some extra restrains in the middle steel block. The corresponding modal analysis results are depicted in figures 18a, b and c.



a) Pure horizontal translational mode



b) Non-symmetric buckling mode of the UPN320 steel sections



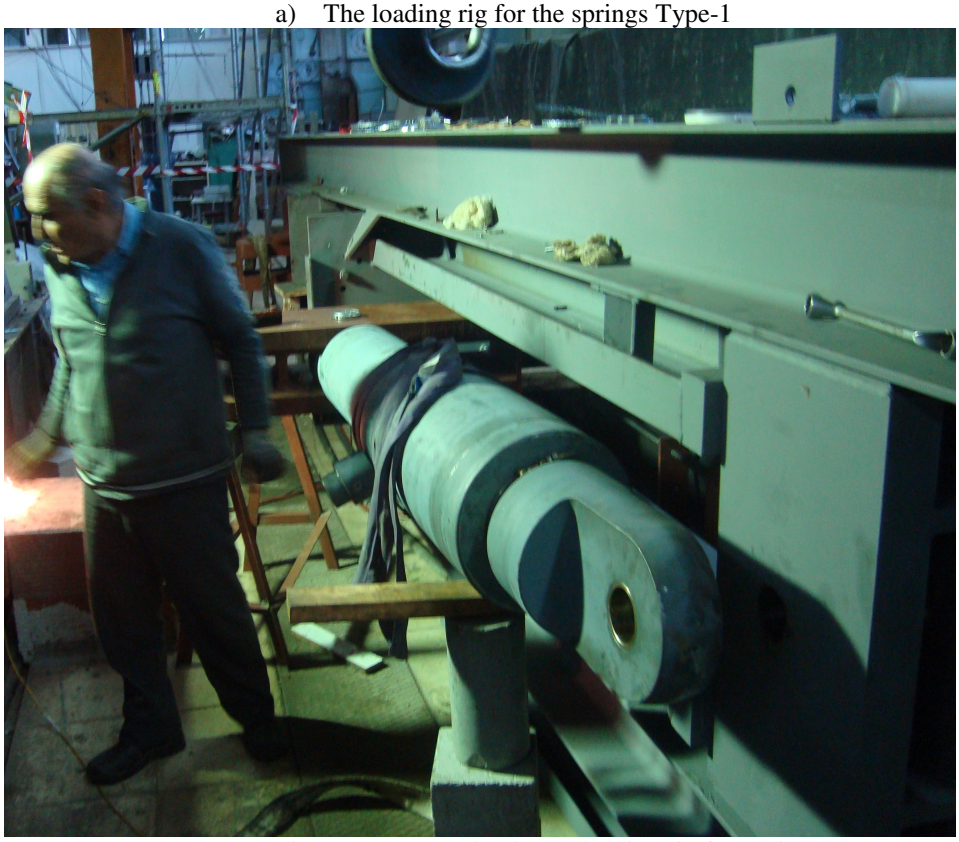
c) Symmetric buckling mode of the UPN320 steel sections

Figure 18. First three modes of vibration of the loading rig.

It can be seen that the fundamental mode of vibration that is the pure horizontal translational mode, which coincides with the main displacement pattern that this loading rig is designed to be utilized during testing, remains almost unchanged with an eigen-frequency equal to 11.296Hz which again is a much higher value than the excitation of 0.75Hz that is the dynamic testing frequency. The rigid body rotational modes are prohibited. Instead, the next two eigen-modes of vibration are the non-symmetric and the symmetric buckling flexural modes of the double UPN320 steel sections. These later eigen-modes have relatively very high eigen-frequency values (77Hz and 80Hz). As already mentioned before, certain measured were taken in the construction process to insure that these undesired modes of torsion or rigid body rotation were prohibited. The finished loading rig is depicted in figure 19.



a) The loading rig for the springs Type-1



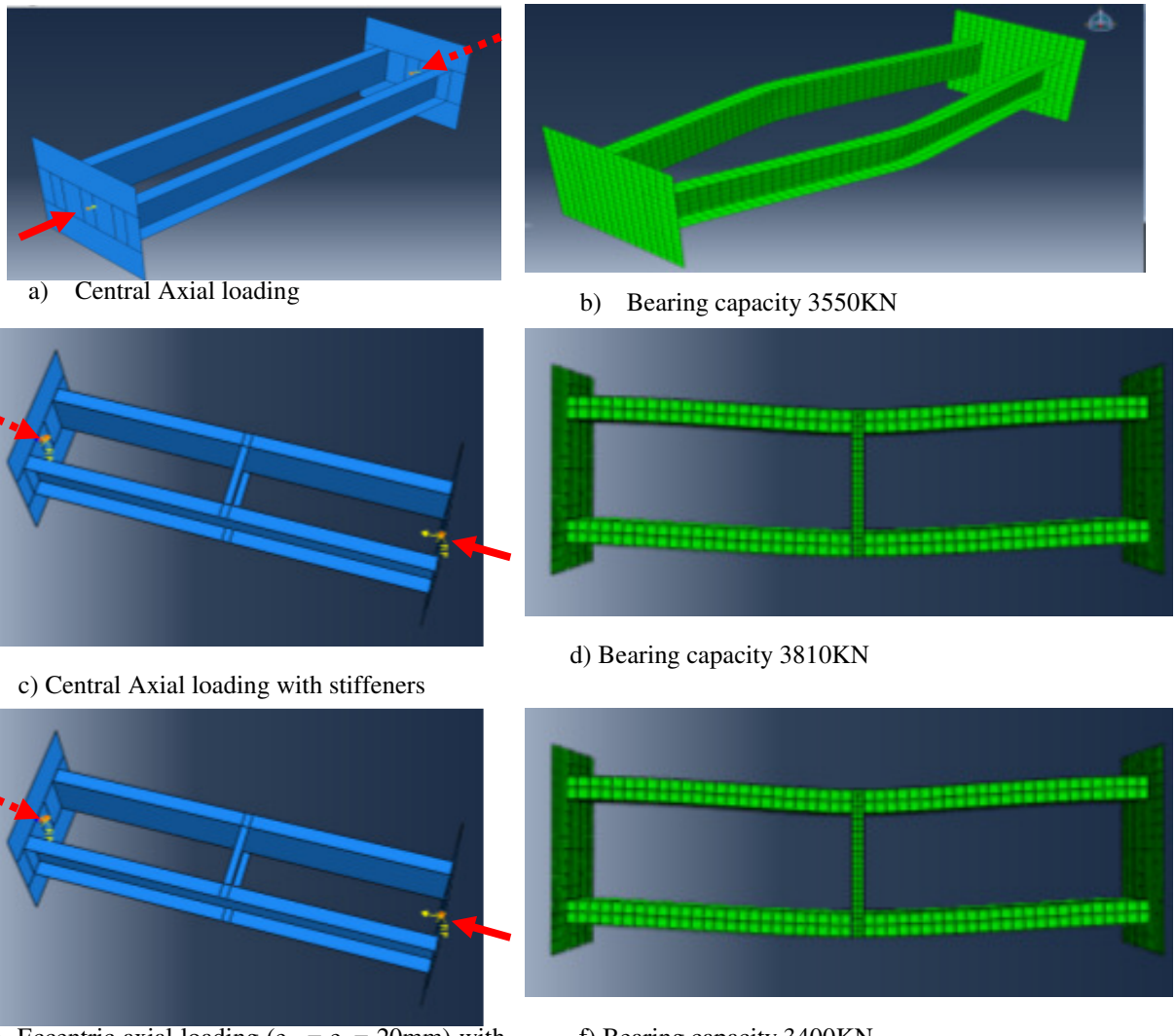
b) Placing a Type-4 spring in the loading rig for testing

Figure 19. The loading ring for the springs during testing

3.3 Static non-linear analysis to identify the bearing capacity of the UPN320 steel cross-sections.

As shown in sections 3.1. and 3.2. the UPN320 steel cross-sections develop considerable compressive stresses for the maximum test load that are of the order of 140MPa. In addition, the modal analysis results demonstrated that the non-symmetric and the symmetric modes of vibration are the two modes expected to develop in the system after the pure horizontal translational mode, when the torsional and rotational modes are prohibited with the proper restraining. In order to investigate the bearing capacity of the loading rig against this type of buckling an additional numerical simulation was performed. In all these numerical simulations the actual dimensions and mechanical properties of the steel cross-sections were employed. Moreover, both end supports were considered to be hinged. Initially, the two UPN320 sections

were joined together only at their ends. Next these two steel cross sections are joined at mid-span with two steel stiffening steel plates with dimensions 600mm x 50mm and 5mm thick, that were placed at either side as shown in figure. The non-linear numerical analyses were performed utilizing the capabilities of the ABAQUS commercial software package ([3], [4]). As can be seen in figures 20b and 20d the buckling bearing capacity is equal to 3550KN in the case without the stiffeners and increases to 3810KN when the described stiffeners are put in place. When these buckling bearing capacity values are compared with the target axial load of 1900KN a safety factor value is found equal to 1.868 and 2.005 for the case without and with the stiffeners, respectively



a) Central Axial loading

b) Bearing capacity 3550KN

c) Central Axial loading with stiffeners

d) Bearing capacity 3810KN

e) Eccentric axial loading ($e_x = e_y = 20$mm) with stiffeners

f) Bearing capacity 3400KN

Figure 20. Numerical simulation results of the buckling bearing capacity

Finally, the last case with the stiffeners is numerically simulated again; this time, however, the axial load is applied with an accidental eccentricity in both the x and y direction equal to $e_x = e_y = 20$mm. The bearing buckling capacity this time is found equal to 3400KN that corresponds to a safety factor value equal to 1.789.

All these safety factor values ensure the safe performance of the described testing rig. This designed loading rid was constructed and was successfully utilized for all the

4 CONCLUSIONS

- The basic loading functions of the suspension system of the roof deck that is to be constructed at the Stavros Niarchos Foundation Cultural Center is briefly described as well as how this was simulated at the laboratory of Strength of Materials and Structures of Aristotle University in order to measure the performance of prototype suspension device specimens prior to being installed in-situ.
- Each one of these suspension devices (Column Head Assemblies) is composed of a steel rigid frame that has in its center a hollow steel cylinder that hosts a sliding billet. In addition there are four springs and two dampers that are hinged at their bottom end to the rigid steel frame and at their top to the sliding billet. Apart from testing the performance of the Column Head Assembly specimens the performance of the prototype springs and dampers that form these suspension devices were also tested in the laboratory.
- A special loading rig was designed and finally constructed to be utilized in the prototype testing of the performance of the springs.
- A series of linear and non-linear numerical simulations were employed towards securing the safe performance of this loading rig during the testing of the said springs.

ACKNOWLEDGEMENTS

The authors would like to acknowledge the relevant information provided by MAGEBA SA, 8180 Bülach – Switzerland, by PENELIS COSNULTING ENGINEERS SA, Thessaloniki-Greece, and by Dr. Civil Engineer K. Antoniadis, Steel Structure Works Manager, Joint Venture Impregilo Terna. The technical assistance of T. Koukouftopoulos in preparing the experimental arrangement is also gratefully acknowledged.

REFERENCES

[1] G.C. Manos, “Progress reports on the testing of the column head assembly specimens and the springs”,

[2] G.C. Manos “Draft report on the visit of the Stavros Niarchos Foundation Cultural Center and presentation of the relevant testing sequence at Aristotle University”, February, 2015.

[3] Hibbitt, Karlsson, Sorensen. Inc. ABAQUS user’s manual volumes I–V and ABAQUS CAE manual. Version 6.10.1. Pawtucket, USA; 2010.

[4] G.C. Manos, A. Nalmpantidou, V. Kourtides, A. Anastasiadis, “Cyclic response of a steel beam-to-column connections – An experimental and numerical study”, Comp-Dyn2015, Krete-Greece, 2015.

COMPDYN 2015
5th ECCOMAS Thematic Conference on
Computational Methods in Structural Dynamics and Earthquake Engineering
M. Papadrakakis, V. Papadopoulos, V. Plevris (eds.)
Crete Island, Greece, 25–27 May 2015

ANALYTICAL AND EXPERIMENTAL STUDY ON THE RESPONSE OF A SEISMIC RESTRAINER SYSTEM FOR BRIDGES

Olga G. Markogiannaki[1], **Ioannis S. Tegos**[2]

[1] Aristotle University of Thessaloniki
Thessaloniki
e-mail: markogiannaki.olga@gmail.com

[2] Professor, Aristotle University of Thessaloniki
Thessaloniki
itegos@civil.auth.gr

Keywords: Seismic Restrainer, Concrete Bridge, Compression Test, Longitudinal Seismic Movements

Abstract. *The present study focuses on the description and the application of a seismic restrainer system on a large scale bridge of Egnatia Highway for limiting the longitudinal bridge seismic movements. The investigated mechanism is considered as an alternative solution to the use of dampers that limit the longitudinal movements, as well. The restrainer system consists of a group of struts - ties that are anchored at the one end in the outer span of the bridge and at the other end in the abutments in a manner that the abutments are activated along with their embankment under seismic loading and the piers develop lower seismic forces. The cross section of the struts –ties consists of a group of common steel rebars of medium diameter that are placed in a cold formed tube inside the bridge sidewalks. Regarding the experimental study and, generally, the evaluation of the efficacy of the restrainer system, especially regarding the behavior of the system under compression loading, a series of experimental sets were conducted. The experimental procedure aimed on identifying the mechanical response of the steel rebar-tube system against buckling. After the completion of the experiments, the experimental results were used in the analytical modeling of the bridge with the restraining mechanism. Nonlinear seismic analysis was performed on the benchmark and the modified bridge systems for the evaluation of the effects of the presence of the restrainer system on the bridge response. The results from the analysis showed remarkable changes in the bridge seismic behavior and significant conclusion for the efficiency of the restraining system could be drawn.*

1 INTRODUCTION

In the last decades, there have been several research efforts for developing innovative methods[1] for the seismic design of bridges. In general, seismic isolation [2] which involves devices, such as bearings (i.e. elastomeric, lead) or dampers (i.e. hydraulic, viscous), is the design method that has been used at most. Another common design practice is the design of bridges as ductile structures[3] that aim on the contribution of the post-elastic behavior of the structural components of the bridge, i.e. more often the piers. Except from the contribution of piers, international seismic design codes, i.e. Eurocode [4] and researchers [5] suggest the participation in the seismic resistance of other structural members of bridges such as the abutments. The ongoing research has shown that except the traditional seismic links that transfer forces to the abutments there are further effective systems that can activate their participation. The activation of the abutments can be achieved with link slabs [6], [7], friction slabs[8] and other examples that include the design of the approach slab for the connection of bridges with the abutments [9], the design of integral abutments with transversely directed R/C walls [10] and the design of sidewalks connected with the abutments as restrainers [11] that can participate in the seismic resistance of bridges. In addition, improved seismic response of bridges especially against increased seismic longitudinal movements can be achieved with the use of steel or cable restrainers [12]. It is common in practice the cable restrainers to be used in retrofit solutions of existing bridges for limiting the relative longitudinal movements between the abutments and the deck of the bridge and between intermediate joint spans and joints in simply supported bridges while they can be used in bridge design, as well.. A lot of researchers have focused on studying the design of this seismic restraining system [12]–[14] and the seismic response of bridges with steel restrainers [15], [16] or restrainers with enhanced materials like shape memory alloys [16]–[18].Although, the restrainers are considered effective in limiting longitudinal displacements, there are issues related to their response since a) they present the limitation of developing unilateral response, because they are activated only under tension loading, b) they are designed with a slack which can result in their late activation under seismic excitation and c) as it is stated in Caltrans[19] an effective design method hasn't been proposed yet. As a result there are cases were steel restrainers failed under strong earthquakes such as in Loma Prieta 1989 and Northridge 1994.

In the frame of developing alternative methods for anti-seismic design, which are effective and with minor cost, the authors have presented in previous research work, [20] [21][22], a restraining system with bundles of steel rebars, which are installed on R/C bridges between deck and the abutments and can increase the contribution of the abutments to the bridge seismic resistance and limit the longitudinal bridge seismic movements aiming at the decrease of the seismic forces on the main structural members, the piers. Although, the proposed mechanism has some common characteristics with the steel restrainers, it has distinguishing differences regarding the actual response of the system and the goal of the application of this method which is the alteration and improved response of the whole bridge system and not the local limitation of bridge movements. The key part of the behavior of the steel bundles is that they can be activated under tension and compression loading, acting as a struts-ties system. It is noted that the restraining system of struts-ties can be applied with some modifications, regarding its installation, in the superstructure of the bridge for the seismic retrofit of concrete bridges, as well [23]. The aim of the present study is to accommodate mechanic response issues that arise regarding the response of the proposed mechanism under compression loading. The steel bundles are placed inside ducts that prevent the transverse deformation of the steel bundles that could be developed due to buckling. An experimental study was conducted for justifying the effective response of the steel bundles. The density, which is the level of filling

of the duct with steel bundles, is considered as the main parameter of the experimental investigation. The specimens tested in the experiment included duct cross sections that had variable densities, filling levels. After the completion of the experiment, the experiment results were used for evaluating the seismic response of a three span R/C bridge with the proposed mechanism.

2 LONGITUDINAL STRUTS - TIES SYSTEM

The restraining system can be described as a mechanism that reduces bridge seismic displacements through the activation of its components that act in tension and compression, (struts-ties), as well. The mechanism can be applied in different bridge classes. In the present study the mechanism is investigated for its response regarding the application on a bridge wih the piers monolithically connected to the deck. A schematic representation is shown in Fig. 1. The restraining system involves the installation of four bundles of steel bars in the sidewalks of the deck of the bridge. The steel bundles are installed along the longitudinal direction of the bridge and each two bundles are placed in the outer spans of the bridge extending through the abutments' wing walls. The steel rebars are placed in ducts in order to avoid bonding between the steel bars and the concrete of the bridge. The steel bars are only bonded with the concrete at their ends to ensure sufficient anchorages. Each of the four bundles consists of groups of steel bars inside the ducts. The steel bars have common steel strength (i.e. S500) and medium diameters of 14mm or 16mm.

The proposed system under seismic excitation receives seismic forces and limits the longitudinal seismic displacements. The steel bundles transfer part of the seismic action to the abutments and the piers receive the rest. In this manner, the abutments that are usually designed not to contribute to the seismic response participate in the seismic resistance, while the piers continue to have the major role in the seismic response as the main structural members. It shall be noted that balance between the contribution of the piers and the abutments is necessary for ensuring an effective bridge seismic behavior with the creation of plastic hinges at the piers and the capacity of the abutments , [22]. Furthermore, the proposed mechanism is activated by in service loading, as well. The steel bundles are in tension during deck contraction and are compressed during deck expansion. Regarding the design of the system the elastic response of the steel rebars under in-service loading is considered as a prerequisite, [22].

Regarding the aforementioned seismic and in-service response, it is assumed that the bundles of the steel bars are not only activated as tension members but also as members that receive compression. This assumption is based on the fact that the installation of the steel bars inside the bridge concrete protects them from any buckling issues. However, the area at the outer joint is the most sensitive regarding the response of the steel bars under compression because of the gap between the decks ad abutments concrete and may induce concerns regarding buckling failures. The following experimental study was conducted in order to eliminate any concerns regarding the development of an effective response without any bucking occurring.

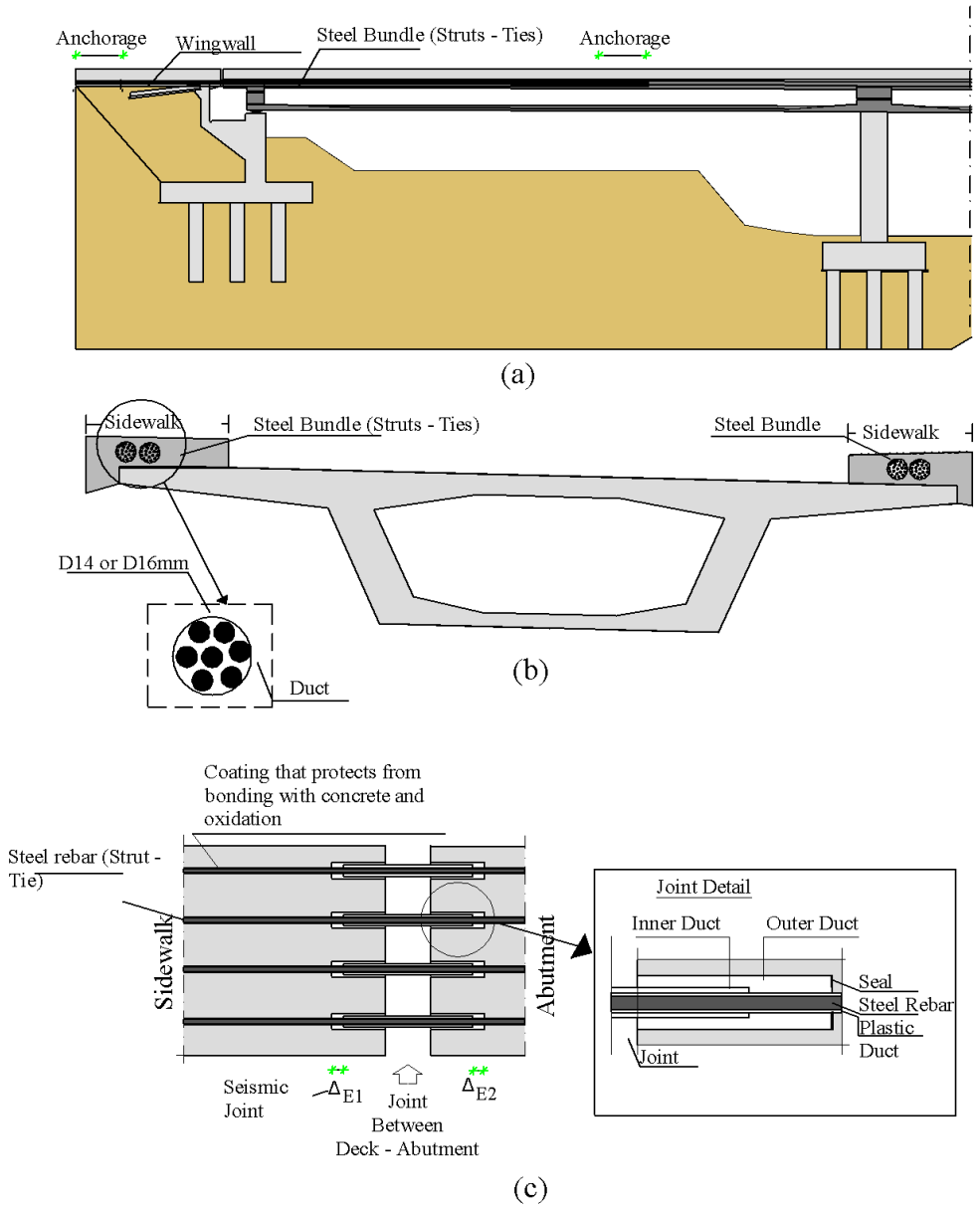


Figure 1: Restraining System. a. Longitudinal view of the bridge, b. Detail 1: cross section of the deck of the bridge, c. Detail at the Expansion Joint between Deck and Abutment

3 EXPERIMENTAL STUDY

3.1 Aim of the study

The target of the experimental investigation is to study the mechanical behaviour of the steel bundles under compression loading. For this purpose several steel bundle specimens were tested. By evaluating the experimental results the goal is to indicate whether the use of the steel bundles in plastic ducts as struts is can be assumed, in other words if the reception of compression loading without buckling is feasible. In addition to the compression tests, a tension loading test on a steel rebar was conducted for identifying the expected stress-strain response of the steel rebars.

3.2 Parameters

The proposed mechanism suggests that the steel bundles are placed inside ducts that prevent the transverse deformation of the steel bundles that could be developed due to buckling. The parameters that were studied are the following:

- One main parameter is the presence or not of concrete around the steel bundles. The presence of concrete corresponds to the position of the steel bundles inside the bridge concrete and the absence of concrete corresponds to the area of the expansion joint where the steel bundles are exposed to the environment.
- Another significant parameter of the experimental investigation is the level of filling of the duct with steel rebars. The specimens tested in the experiment included duct cross sections that had variable filling levels.

3.3 Specimens

In Table 1 the specimens that were used in the experimental tests are presented. The specimen scale is 1:2. The *Table 2* includes the name of each specimen, the characteristics, rebar diameter, number of rebars and surrounded by concrete or not, and the filling level. A total number of 10 specimens were studied. Common steel rebars were used for the research with a diameter of 8mm. The filling level of 76% is the highest feasible for the available diameters. The two large classes of specimens are steel bundles that are inside concrete and bare steel ducts. The ducts used were steel type, 30cm log and had 30mm outer diameter (26mm inner + 4mm wall thickness). High strength concrete (emaco) with spiral 4mm transverse reinforcement was used in order to simulate the presence of the massive bridge concrete. A square steel plate with a steel dowel welded on it was used to all specimens for accommodating the requirement for a smooth surface in order to transfer the compression loading to the steel bars inside the ducts uniformly. The two arrangements are shown in Fig. 2 and Photo 1.

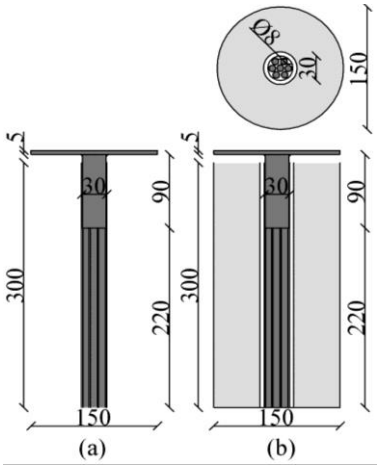


Figure 2:. a) Specimen S-NC b) Specim. S-C

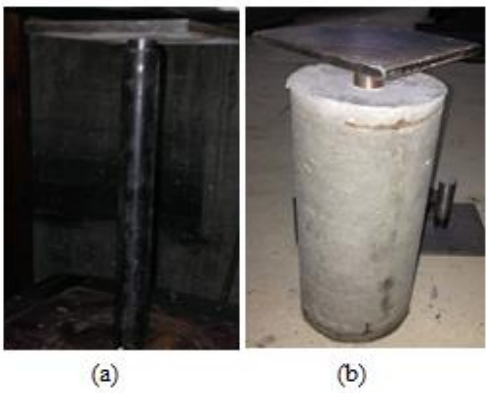


Photo 1:. a) Specimen S-NC b) Specimen S-C

Concrete			No Concrete		
Name	Characteristics	Density (%)	Name	Characteristics	Density (%)
S-C-1	4D8mm	38%	S-NC-1	4D8mm	38%
S-C-2	5D8mm	47%	S-NC-2	5D8mm	47%
S-C-3	6D8mm	57%	S-NC-3	6D8mm	57%
S-C-4	7D8mm	66%	S-NC-4	7D8mm	66%

S-C-5	8D8mm	76%	S-NC-5	8D8mm	76%

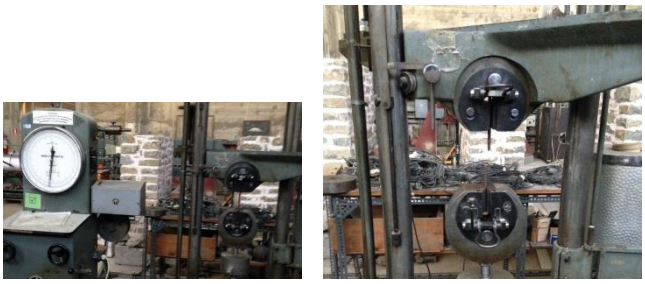
Table 1 :Specimen Properties

3.4 Test Set-up and Results

The experiment was conducted in Aristotle University of Thessaloniki. The preparation of the specimens took place at the Laboratory of Masonry and Concrete Structures and the tests were performed with the Compression Machine at the Laboratory of Experimental Strength of Materials and Structures in Aristotle University of Thessaloniki. The specimens were centred on the table of the machine and the steel smooth plates were placed at the top of the specimens so that the loading part of the machine could rest on them. The target of the process was to induce clear compression loading to the steel bars without any bending or lateral additional forces.



Photo 2: Test set-up



(α) (b)

Photo 3: a) Tension Test, b) Rebar Failure

Photo 2 shows the test set up for the compression of the specimens. The deformation of the specimens was measured during the experiments, as well. The machine used for these tests had a capacity of 20 tonnes in the vertical direction and only static loading could be applied. The compression tests were performed until the failure of the steel bars and returned the machine back to zero loading. After the completion of the compression tests, a tension loading test was performed on a single steel bar, Photo 3.

As it has been described in the previous sections the purpose of the experimental study was to determine whether or not buckling occurs. Regarding buckling the critical buckling load is calculated from the well-known Euler Equation, where E is the Modulus of Elasticity, I is the

Moment of Inertia, L is the Length and K is the effective length coefficient depending on the support conditions. Figure 3 presents the K factor values depending on the support conditions.

$$P_{cr} = \frac{\pi^2 * E * I}{(K * L)^2} \quad (1)$$

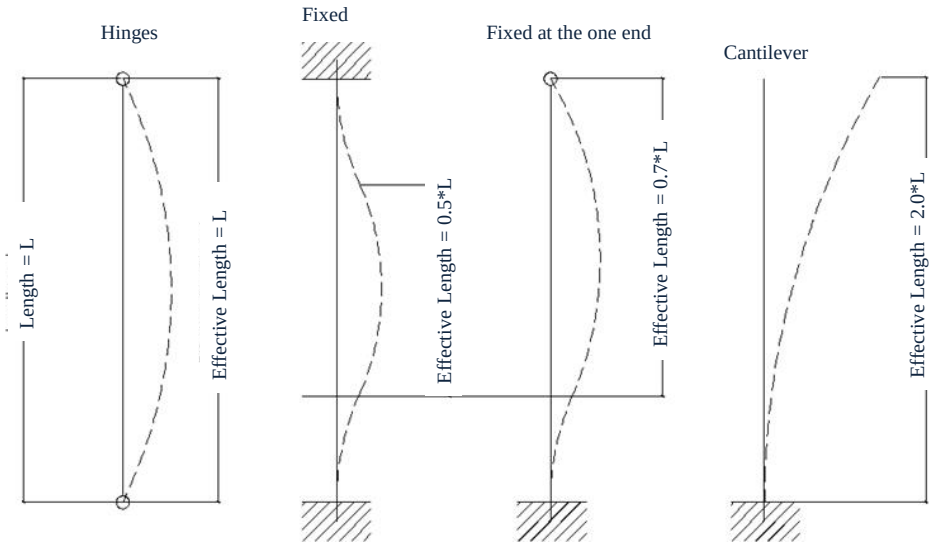


Figure 3 :. Buckling modes and k effective length coefficient

In Table 2, the critical load and stress due to Euler buckling is presented for all different support conditions.

Δοκίμιο		$P_{euler\ (hinges)}$ [kN]	σ_{euler} (hinges) [MPa]	$P_{euler\ (fixed\ at\ one\ end)}$ [kN]	σ_{euler} (fixed at one end) [MPa]	$P_{euler\ (fixed)}$ [kN]	σ_{euler} (fixed) [MPa]
S-C-1	S-NC-1	65.6	326.26	66.94	332.93	131.20	652.54
S-C-2	S-NC-2	82.	326.26	83.67	332.93	164.00	652.54
S-C-3	S-NC-3	98.4	326.26	100.41	332.93	196.80	652.54
S-C-4	S-NC-4	114.8	326.26	117.14	332.93	229.60	652.54
S-C-5	S-NC-5	131.2	326.26	133.88	332.93	262.40	652.54

Table 2 : Specimen critical buckling loading

Photo 4 shows the specimens after the completion of the compression tests. The force-displacement and stress-strain curves derived from the experimental study are shown in Fig. 4 and 5 respectively. Regarding the S-C specimens, that are surrounded by concrete, the observation of the experimental results and the comparison of the results to the buckling loading shows that the specimens failed without any buckling occurring before their failure. In fact, the stress-strain curves follow the stress-strain curve that was derived by the tension test. Regarding the N-SC specimens, the response is differentiated depending on the filling level of the ducts. There are cases where buckling occurs before yielding. Characteristic examples of such failures are specimens S-NC-1 and S-NC-2. From the experimental results, it can be concluded that the sparse (<50%) application of steel bars in a duct has negative effects on their response under compression loading. In the case of high densities the performance is

gradually improved and is similar to that of the tension loading behavior. Especially, in the case of the highest filling level the walls of the steel duct were engaged in the response of the steel bundle due to the development of friction forces resulting in higher forces than the failure of the steel bars.



(a) (b)

(c) (d)

Photo 4 : (a) Specimen Failure S-NC-1, (b) Specimen Failure S-NC-2, (c) S-NC Specimens, (d) Spesimen S-C after test completion

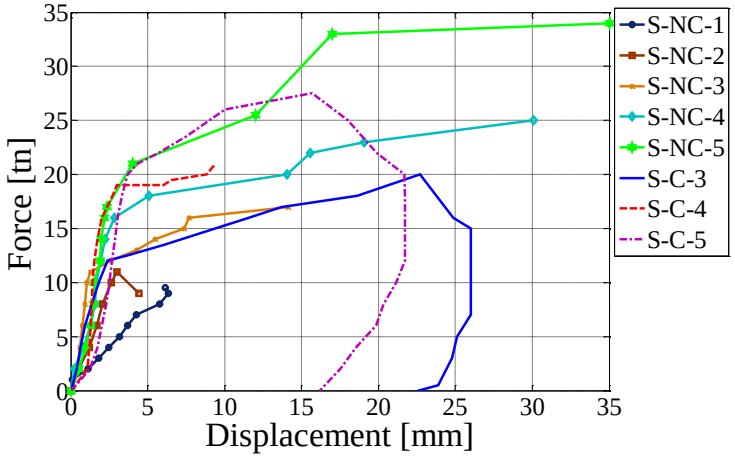


Figure 4 : Force - Displacement Curves

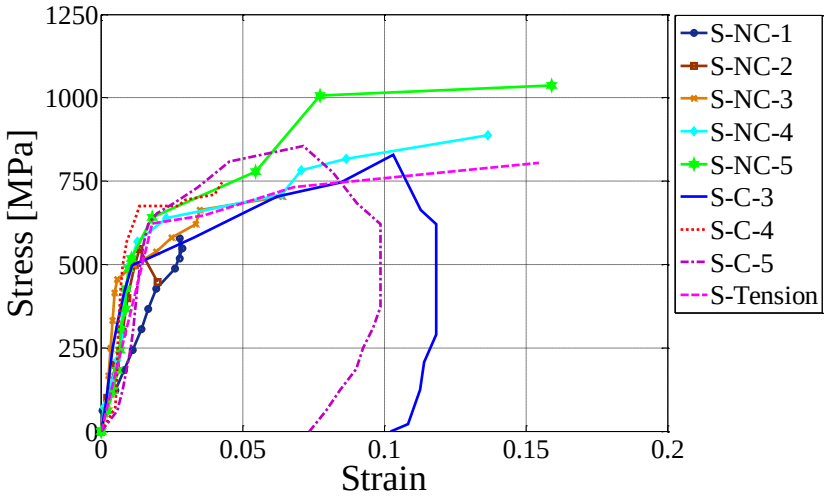


Figure 5 : Stress - Strain Curves

The high activation of the proposed system has two side effects. The one refers to the fact the friction forces that appear between the steel rebars and walls of the steel duct lead to the early damage of the steel duct, which is not a preferable response for the system. In addition, the amount of forces that would be transferred by the mechanism to the abutment would be higher than the expected and could induce capacity issues to the abutments. As a result a level of 67-72% of filling or in other words 7 bars in a duct is a solution that shall be acquired for the analytical investigation of the effectiveness of the proposed mechanism.

4 ANALYTICAL STUDY

The results from the experimental study were used in an analytical case study that evaluates the effectiveness of the proposed mechanism on the seismic response of bridges.

4.1 Description of the Reference Bridge

The Reference Bridge that was used foe the analytical study is a monolithic three span prestressed R/C bridge. The end spans are 45.10m, the middle is 45.60m and the total length is 135.80m. The deck is a concrete box section, connected to the piers monolithically, and is supported on the abutments by low friction sliding bearings. The piers are circular and are founded on 3x3 pile groups. The bridge's abutments are seat-type and have transverse seismic links-stoppers. The bridge is founded on ground type B and the area is in seismic zone I, [24]. A 3-D finite element bridge model, Fig. 6, was generated in the analysis software OpenSees, [25], accounting for abutment-embankment interaction.

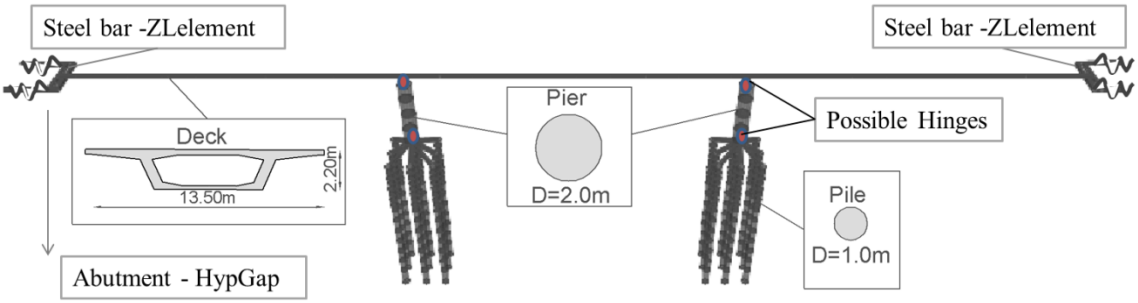
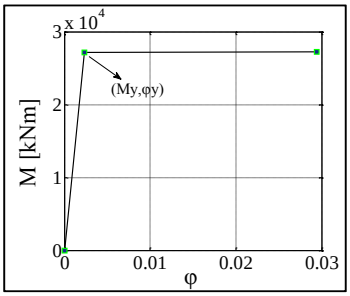


Figure 6 : 3-D Reference Model

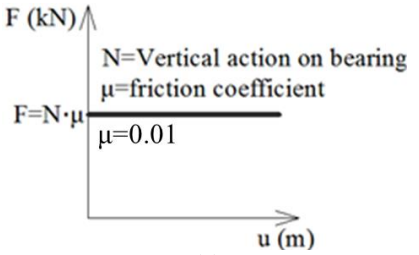


(a)

$$F_{(x)} = \frac{x}{\frac{1}{K_{max}} + R_f \frac{x}{F_{ult}}}$$

Kmax [Kn/m]	81000
Rf	0.7
Fult [kN]	-2739
Gap [m]	-0.07

(b)



(c)

Figure 7 : a)M-φ curve, b) Abutment P-Y curve, c) Sliding Bearing

Bridge members are modeled with frame elements with material nonlinearities. The section analysis, Fig 7(a), for the assignment of concentrated plasticity (hinges) at the top and bottom of piers was performed with AnySection v4.0.6,[26]. The foundation springs were provided by the geotechnical report. The passive resistance of the abutments due to embankment mobilization was simulated according to Shamsabadi guidelines [12],[13] and the HyperbolicGap compression material was used in OpenSees, Fig 7(b). The sliding Bearing were modeled as shown in Fig 7(c).

The proposed mechanism is modeled as nonlinear springs as shown in Fig. 6. The nonlinear response of the steel bars was derived from the stress-strain experimental results. The stress – strain curves for tension and compression were bi-linearized. Respectively to the experiment 7 rebars of a 16mm diameter were used in a steel duct of 52mm inner diameter, as the initial size of the mechanism. In the parametric investigation there were used 1-7 steel ducts in each steel bundle. The bi-linearization of the two stress-strain curves showed almost symmetrical response under tension and compression which is the initial assumption for the proposed mechanism. In the finite element model the response of the mechanism is modeled as a force-displacement response including the cross section of one steel bundle based on the stress - strain curves. The steel bundle yielding force and yielding displacement is calculated by equation (2), where σ_y is the yielding stress, A the cross section of the steel bundle, L is the length of the steel rebars without accounting for the anchorage lengths and ε_y is the yielding strain. The resulting curves are shown in Fig. 8.

$$F_y = \sigma_y * \mathrm{A}, \quad \delta_y = \varepsilon_y * \mathrm{L} \tag{2}$$

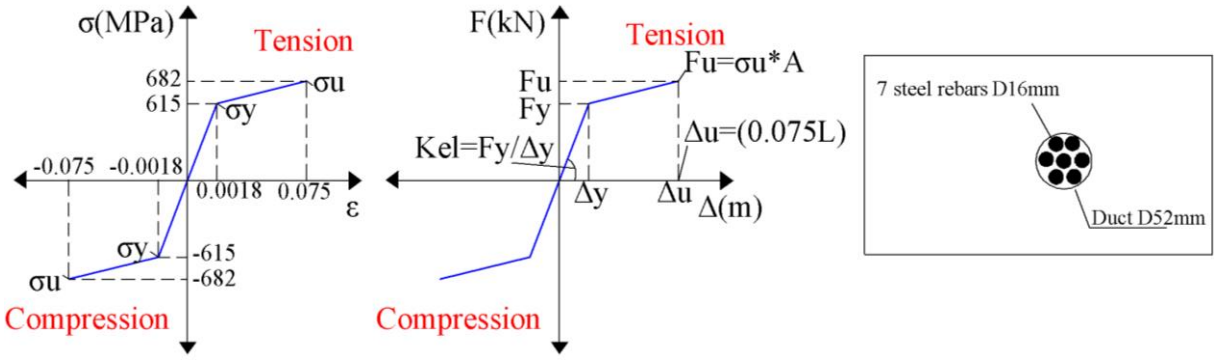


Figure 8 : Steel bundle nonlinear spring response

The proposed mechanism was studied for various characteristics regarding the cross section and length of the steel bundles, in order to indicate the efficiency of the system in limiting seismic movements and seismic actions on the piers. The properties of the system used for the analytical study are presented in Table 3 sorted by initial stiffness. The minimum length of

the longitudinal bars is determined based on the condition that the steel bars remain elastic under serviceability loading,[23]. The seismic analyses were conducted using five artificial accelerograms complying with seismic design zone I. Table 4 shows the analysis results for the Reference Bridge. In Figure 9 the displacement, shear and moment reductions and the response of the steel bundles are shown for the two earthquake intensities respectively.

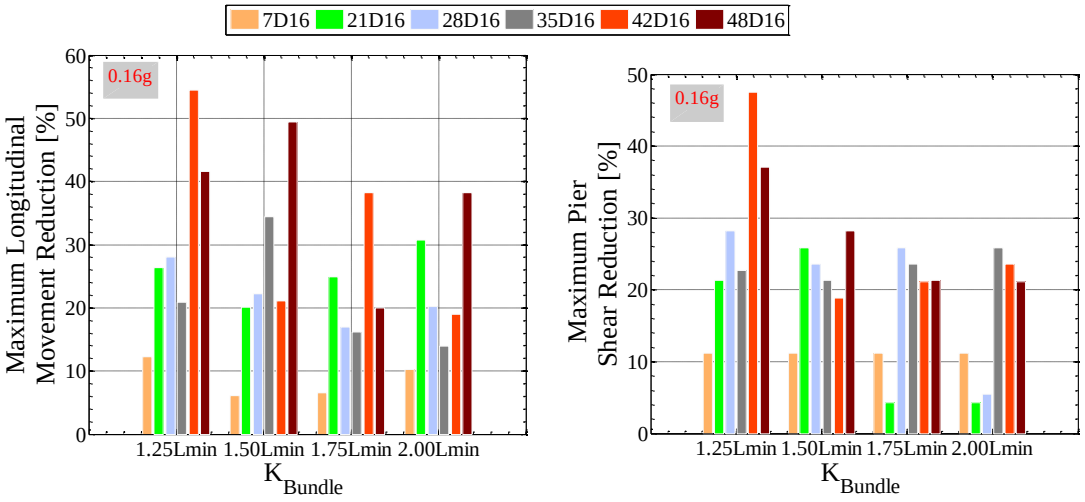
Steel Bundle		K_{el} [kN/m], L_{min}=17.7m			
Steel Duct (D52mm)	No. of Bars	L=1.25L_{min}	L=1.5L_{min}	L=1.75L_{min}	L=2.0L_{min}
1	7D16	12722.56	10602.14	9087.545	7951.602
2	14D16	25445.13	21204.27	18175.09	15903.2
3	21D16	38167.69	31806.41	27262.63	23854.81
4	28D16	50890.25	42408.54	36350.18	31806.41
5	35D16	63612.81	53010.68	45437.72	39758.01
6	42D16	76335.38	63612.81	54525.27	47709.61
7	49D16	87240.43	72700.36	62314.59	54525.27

Table 3 : Steel Bundle Properties

0.16g	max U1 [m]	max V2 [KN]	max M3[KNm]
	0.08	4826	18968

Table 4 : Reference Bridge Analysis Results

The analyses results indicate remarkable reduction, up to 50% in the longitudinal bridge movements and moment and shear force at the piers, as well, especially when large steel bundle cross sections and small steel bar lengths are used. The efficiency of the mechanism is reduced when the length of the steel bundles is increased or the cross section of the steel bundles is low. Regarding the steel bundles, they have inelastic response for small steel bar lengths and a length increase leads to less stresses on the steel bars.



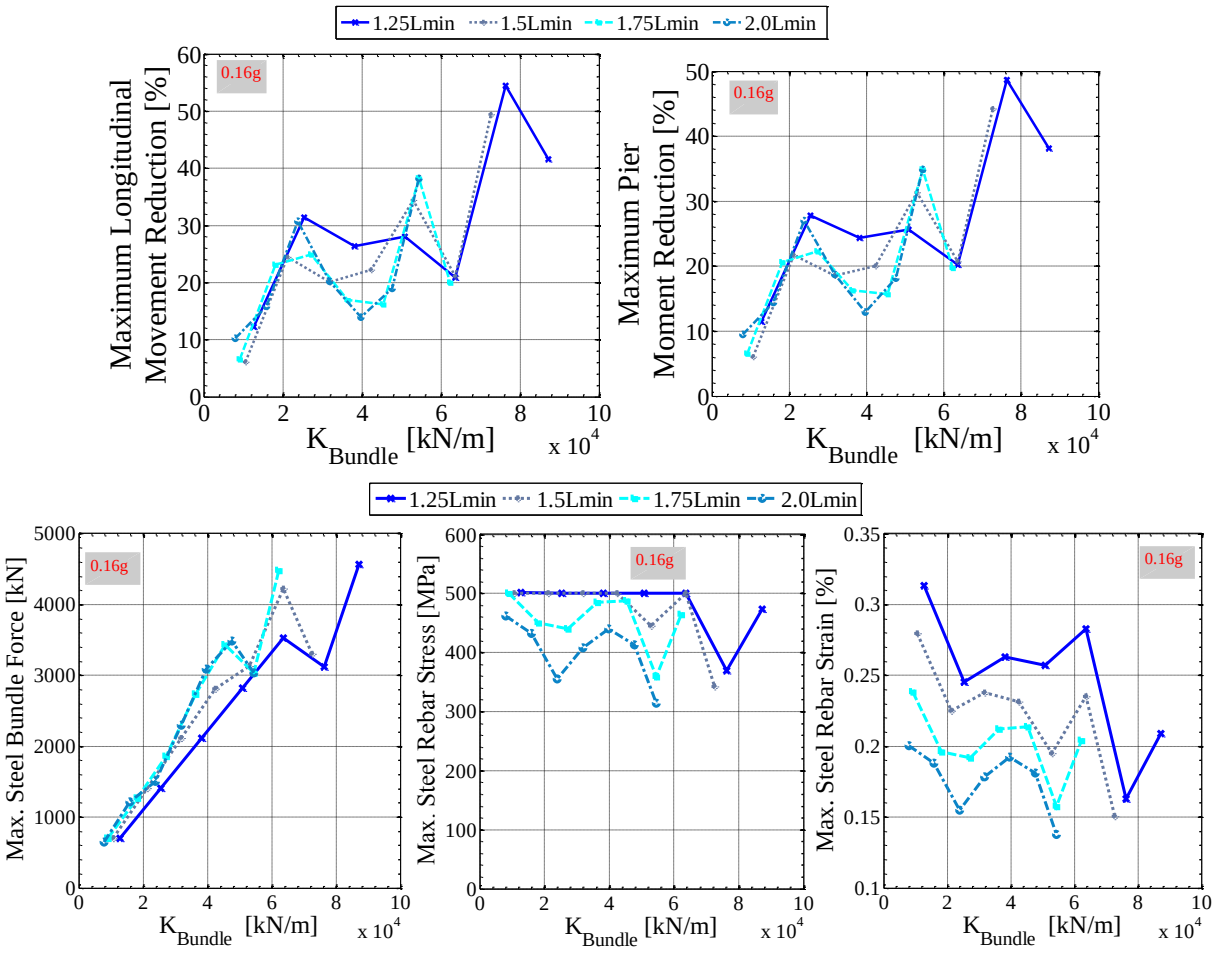


Figure 9 : Analysis Results, 0.16g

The forces that are developed at the proposed mechanism are transferred to the abutments. It is noted that the level of the aforementioned forces is acceptable for the capacity of the abutments, which indicates another aspect of the efficiency and applicability of the proposed system.

5 CONCLUSIONS

The present study focuses on the experimental study of a proposed seismic restrainer system and the use of the experimental results for evaluating the efficiency of the proposed system with an analytical study on an R/C bridge of Egnatia Highway. The following conclusions were derived:

- The experimental results have shown that the cross section of the steel bundles shall be in accordance with the cross section of the steel duct used. A medium to high filling lower than to 76% is preferable for the proposed mechanism. In fact, in the analytical study 7 steel bars of 16mm were used inside a D52mm duct.
- An extremely sparse installation of steel bars in the steel duct indicated that it will cause side effects on the response of the bars as struts, under compression loading. Extreme high filling level of the steel ducts can develop side effects, as well. The side effects developed for the highest density achieved are related to the fact that friction forces are developed and activated which increase the efficiency of the struts. Howev-

er, wear phenomena of the walls of the steel ducts and premature degradation arise that are not acceptable for the use of the ducts as part of the restraining system.

- It has to be noted that as tension members, ties, the steel bars are not affected by the more or less density of the filling level of the steel bars in the steel duct.
- The analytical study that took into account the experimental results for the proposed mechanism response showed high efficiency of the system in limiting longitudinal bridge movements, moment and shear force at the piers.

ACKNOWLEDGMENTS

The authors would like to acknowledge the assistance of the Laboratory of Experimental Strength of Materials and Structures.

REFERENCES

[1] E. W. Chen and L. Duan, *Bridge Engineering Handbook*. CRC Press LLC, Boca Raton, 2000.

[2] F. Naeim and J. M. Kelly, *Design of Seismic Isolated Structures—from Theory to Practice*, vol. 125, no. 10. 1999, pp. 1–296.

[3] B. Kolias, S. A. Denco, K. Ave, and I. Summary, EUROCODE 8 – PART 2 . SEISMIC DESIGN OF BRIDGES, no. see 6, pp. 1–20, 2008.

[4] CEN[Comité Européen de Normalisation], *Eurocode 8: Design of structures for earthquake resistance - Part 2: Bridges*. 2003.

[5] R. V. Nutt and R. L. Mayes, Comparison of Typical Bridge Columns Seismically Designed With and Without Abutment Participation Using AASHTO Division I-A and Proposed AASHTO LRFD Provisions, 2000.

[6] G. Sevgili, A. Caner, and M. Asce, Improved Seismic Response of Multisimple-Span Skewed Bridges Retrofitted with Link Slabs, *J. Bridg. Eng.*, no. December, pp. 452–459, 2009.

[7] A. Caner, E. Dogan, and P. Zia, Seismic Performance of Multisimple-Span Bridges Retrofitted with Link Slabs, *J. Bridg. Eng.*, no. March/April, pp. 85–93, 2002.

[8] Η. Παπαδόπουλος, Αναλυτική και Πειραματική Έρευνα επί ενός Καινοτόμου Μηχανισμού Τριβής για την Ανάσχεση των Σεισμικών Δράσεων, Αριστοτέλειο Πανεπιστήμιο Θεσσαλονίκης, 2015.

[9] S. A. Mitoulis and I. A. Tegos, Connection of Bridges with Neighborhooding Tunnels, *J. Earthq. Eng.*, vol. 14, no. 3, pp. 331–350, Mar. 2010.

[10] S. D. Tegou, S. a. Mitoulis, and I. a. Tegos, An unconventional earthquake resistant abutment with transversely directed R/C walls, *Eng. Struct.*, vol. 32, no. 11, pp. 3801–3816, Nov. 2010.

[11] I. A. Tegos, M. A. Tsitotas, S. D. Tegou, and S. A. Mitoulis, Reduction in seismic actions of bridges by utilizing the sidewalks as restrainers, in *16th Greek Concrete Conference*, 2009.

[12] R. DesRoches and G. L. Fenves, Simplified Restrainer Design Procedure for Multiple-Frame Bridges, *Earthq. Spectra*, vol. 17, no. 4, pp. 551–567, Nov. 2001.

[13] B. M. Saiidi, M. Randall, E. Maragakis, and T. Isakovic, Seismic Restrainer Design Methods for Simply Supported Bridges, *J. Bridg. Eng.*, no. 9, pp. 307–315, 2001.

[14] P. Trochalakis, M. O. Eberhard, and J. F. Stanton, Design of Seismic Restrainers for In-Span Hinges, *J. Struct. Eng.*, no. April, pp. 469–478, 1997.

[15] R. Desroches and S. Muthukumar, Effect of Pounding and Restrainers on Seismic Response of Multiple - Frame Bridges, *J. Struct. Eng.*, no. July, pp. 860–869, 2002.

[16] E. Choi, J. Park, S.-J. Yoon, D.-H. Choi, and C. Park, Comparison of Seismic Performance of Three Restrainers for Multiple-Span Bridges Using Fragility Analysis, *Nonlinear Dyn.*, vol. 61, no. 1–2, pp. 83–99, Dec. 2009.

[17] R. DesRoches and M. Delemont, Seismic retrofit of simply supported bridges using shape memory alloys, *Eng. Struct.*, vol. 24, no. 3, pp. 325–332, Mar. 2002.

[18] R. Desroches and J. E. Padgett, Experimental Evaluation of a new Bridge Retrofit Device : Shape Memory Alloy, in *1st US - Italy Seismic Bridge Workshop*, 2006.

[19] Caltrans, SEISMIC DESIGN CRITERIA VERSION 1 . 6, no. November, 2010.

[20] I. Tegos and O. Markogiannaki, A Seismic Restraining System for Bridges Analytical Study of a Strut-Ties Mechanism, in *IBSBI*, 2011.

[21] O. Markogiannaki and I. Tegos, A smart and costless solution for upgrading the seismic resistance of bridges Description of the proposed struts-ties system, in *IABSE Conference*, 2012.

[22] O. G. Markogiannaki and I. A. Tegos, Parametric Investigation for the Optimization of a Longitudinal Seismic Restraining System Consisting of Struts-Ties for Concrete Bridges, in *COMPDYN 2013 4th ECCOMAS*, 2013, no. June.

[23] O. Markogiannaki and I. Tegos, Seismic retrofit of bridges through the external installation of a new type restraining system, in *15WCEE*, 2012.

[24] CEN[Comité Européen de Normalisation], Eurocode 8 : Design of structures for earthquake resistance — Part 1: General rules, seismic actions and rules for buildings, 2003.

[25] M. C. Constantinou, T. T. Soong, and G. F. Dargush, Passive Energy Dissipation Systems For Structural Design and Retrofit, 1998.

[26] V. K. Papanikolaou, AnySection : Software for the analysis of arbitrary composite sections in biaxial bending and axial load. Aristotle University of Thessaloniki, Greece, 2015.

[27] A. Shamsabadi, K. M. Rollins, and M. Kapuskar, Nonlinear Soil – Abutment – Bridge Structure Interaction for Seismic Performance-Based Design, *J. Geotech. Geoenvironmental Eng.*, no. June, pp. 707–720, 2007.

[28] J. P. Stewart, E. Taciroglu, J. W. Wallace, A. Lemnitzer, C. Hilson, A. Nojoumi, S. Keowan, R. Nigbor, and A. Salamanca, Nonlinear Load-Deflection Behavior of Abutment Backwalls with Varying Height and Soil Density, 2011.

COMPDYN 2015
5th ECCOMAS Thematic Conference on
Computational Methods in Structural Dynamics and Earthquake Engineering
M. Papadrakakis, V. Papadopoulos, V. Plevris (eds.)
Crete Island, Greece, 25–27 May 2015

ANALYTICAL AND EXPERIMENTAL INVESTIGATION ON EXPLOITING PREFABRICATION IN PIER CONSTRUCTION OF PRECAST BRIDGES

Nikolaos G. Orologopoulos, Vasileios G. Pilitsis, Konstantinos Katirtzoglou, Ioannis A. Tegos and Kosmas-Athanasios Stylianidis

Aristotle University of Thessaloniki
Faculty of Engineering
School of Civil Engineering
Laboratory of Reinforced Concrete and Masonry Structures
n.orolog@hotmail.com
vpilitsi@civil.auth.gr
kostaskatir@gmail.com
itegos@civil.auth.gr
kcstyl@civil.auth.gr

Keywords: Prefabrication, refabricated pier, prefabricated crosshead, abutment, experimental.

Abstract. *In the present study, the potential of expanding the use of prefabrication on bridge piers construction is investigated, as so far its use is limited on a portion of the bridge deck, namely the prefabricated girders and the deck panels. Stimuli for this study are the advantages of prefabrication, such as rapidity and convenience in construction and economy as well. The investigation regards any side effects of the suggested construction method concerning safety, serviceability and durability aspects of the final product. Safety concerns flexural and shear resistance, which should particularly be controlled in the construction joints. The critical section of a partially prefabricated pier is undoubtedly located at the bottom of the pier. The response of this section was investigated experimentally. In order to study the response of this type of piers, two specimens were prepared, one representing a conventionally constructed pier and another pier constructed with the suggested method. An analytical investigation of a prefabricated bridge on the main Greek North-South Highway (P.A.Th.E.) was conducted. Specifically, the bridge was studied in two configurations, one with piers constructed with the conventional method and one with piers constructed as suggested. Useful results were obtained by the comparison of the two configurations. Undoubtedly, the conclusions can be regarded as encouraging.*

1 INTRODUCTION

It is commonly known that the most appropriate classification regarding the existing types of concrete bridges is the one that is based on the currently existing construction methods. These methods are five: a) the traditional cast in-situ case, b) the method combining cast in-situ case with prefabrication, c) the incremental launching method, d) the balanced cantilever method and e) the self-advancing formwork system for bridge construction with cast in-situ method. The first two construction methods are the most frequently used, while the other three are special cases and are applied when the use of the first two is not applicable.

The criteria for selecting the most appropriate construction method are mainly technical, economical and time-depended. Technical criteria mainly concern the possibility of using scaffolding placed on the ground, which means that the height of the bridge must not exceed 10 m in order the use of scaffolding to be feasible. When the height is greater than 10 m, the use of prefabrication method is required. The economic criteria mainly concern the construction costs and the time-dependent criteria concern the rapidity of construction offered by the selected method.

Prefabrication, as a bridge construction method, adequately meets the above criteria. The implementation of this method began after World War II and catered for the infrastructure construction of that period. At first implementations, prefabricated bridges consisted of statically independent (in the longitudinal direction of the bridge), simply supported parts of the deck, which caused problems related with functionality and durability, due to the existence of many construction joints. Later implementations of prefabrication included the casting in-situ of a continuous deck slab, the use of which dealt with the two mentioned disadvantages and the seismic requirements. Regarding the piers of this bridge type in past years, hollow rectangular cross-sections were used in cases of large heights, but nowadays hollow circular cross-sections are preferred due to their ability to have similar mechanical behavior regardless direction. On the other hand, regardless of the construction method, abutments are isolated from the deck by the use of bearings for alleviating seismic stresses.

Further on to this review, describing the evolution of prefabricated bridges through time, it can be said that till today prefabrication is very limited regarding the entire bridge structural system. This is not an exaggeration because prefabrication concerns only the beams of the deck and the precast deck panels. The other members, such as the cast in-situ slab of the deck, the piers and their crossheads are casted in-situ. It must be said that the casting in-situ in some cases, i.e. in the case of piers, is a very costly and time consuming construction practice.

In the present study, the implementation of prefabrication in the entire bridge structural system is suggested. Being fully aware that the suggestion of a radical reformation requires appropriate documentation, the authors submit within the present study a documentation including experimental and analytical part.

2 MECHANIZED METHODS OF PIER CONSTRUCTION

The mechanized methods of pier construction are used when the height of bridge is greater than 15 to 20 m. In this case, due to the impossibility of direct concreting, construction of piers is done segmentally. These methods have the characteristic of elevating the formwork from a manufacturing level to the next. There are essentially two different techniques for elevation of the formwork: a) Sliding formwork method and b) Climbing formwork method.

In the method of the sliding formwork, the pier construction proceeds with small but continuous steps and the parts of formwork are lifted by using an elevation system consisting of: hydraulic jacks, lifting rods and a suspension frame. The other parts of the elevating system

are: the formwork (of height circa 1.20 m), a working platform, ramps for inspection and safety barriers. Construction is carried out continuously, on a 24-hour basis.

In the method of climbing formwork, casting of each segment is done within pre-assembled, fixed parts of formwork with suitable height (i.e. 3.0 to 6.0 m). After hardening of the concrete, the formwork parts are released and elevated to the next level, re-assembled and prepared for the next phase of casting. The elevation of the formwork in this case is significantly discontinuous (in contrast to the sliding formwork method) and the elevating is done by construction cranes or specific devices attached to the system (self-climbing). With the evolution of self-climbing systems, the use of this method became insensitive to the height constraints and crane lifting capacity and competes the method of the sliding formwork regardless of pier height and practically tends to replace it [1].

The existing mechanized pier construction methods are not effortlessly implemented and time consuming processes. Operation is performed on a 24-hour per day and depends on weather conditions and the landscape where the project is founded (access). They require constant concrete production rate and a significant amount of special equipment, which increases the manufacturing cost. Besides that, there are construction issues which make these methods difficult to apply. Such problems are the friction development between concrete and formwork, the pressure of freshly casted concrete on the formwork and the casting progress rate dependence on concrete composition and concrete production rate.

3 SUGGESTION OF PIER CONSTRUCTION WITH THE METHOD OF PREFABRICATION

The following sections describe the suggested construction method of piers with exploitation of prefabrication.

3.1 Description of pier construction methodology

In the present study the use of prefabrication in piers of prefabricated bridges is suggested. The suggested methodology and the construction method concerns piers of hollow circular cross-section, which as mentioned above, is the most commonly used cross-section as its moment of inertia is the same regardless of direction. The cross-section of the prefabricated pier consists of two hollow circular prefabricated columns, one contained within the other. Between these two columns a void ring is created, which contains the longitudinal reinforcement of the pier and it is casted in-situ (Fig. 1). Figure 1 presents the implementation of the suggested way of pier construction as an alternative method in the case of prefabricated bridges, which is elaborated in the next paragraph. The transverse reinforcement of the cross-section is placed on both prefabricated columns, which are surrounding the cast in-situ segment. The need of facilitating the transfer of prefabricated elements on the project site and their constructability impose the pier to be composed of segments with ideal height of 5-10 m (Fig. 2), taking into account the overall height of each pier. The short length of each segment facilitates the transportation needs of these elements, in contrast to a greater length which incommodes both transportation and construction.

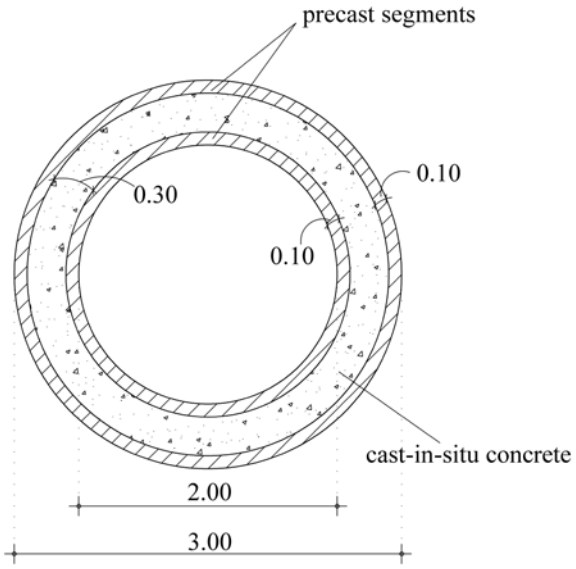


Figure 1: Pier cross-section geometry.

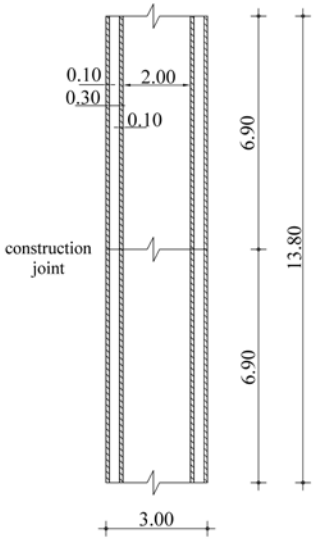


Figure 2: Pier section.

The assembly of individual segments is based on the exploitation of the void between the two precast columns. Initially, at the pile cap (which is casted in-situ), outbound extending rebars with sufficient length are arranged, in order to fit with the geometry of the void between the two prefabricated hollow-circular columns. After placing the first part of the two prefabricated hollow-circular sections, longitudinal reinforcement rebars will be set in the void running the entire height of the first pier part, having a sufficient outbound extending length on the upper part. Subsequently, the void is casted in-situ and the second part of the pier is mounted on the first by repeating the reinforcement and casting in-situ process. This procedure is repeated until the complete assembly of all pier parts, resulting at the end in an integral pier web.

Regarding reinforcement of the hollow-circular columns, it consists of skin and transverse reinforcement against shear, while the longitudinal reinforcement, which is placed in the void, will be the main reinforcement of the cross-section. Indicatively, the length of the outbound extending rebars is 1.75 m, which is based on EC2 provision for rebar diameter Ø25 mm (a commonly used diameter in bridge piers and also in the present case) and a minimum class of concrete C30/37. In this case, reinforcing lap length is calculated by the formula $L = 70Ø = 70 \cdot 0.025 = 1.75$ m [1].

The interaction between the prefabricated segments and the casted in-situ concrete can be improved by embossing the surfaces of the columns in contact with the cast in-situ concrete. In addition, stirrups on the interacting sides of columns (as used for improving the interaction between cast in-situ concrete and prefabricated panels during the construction phase of the deck) can significantly increase the interaction of the prefabricated columns with the cast in-situ concrete.

3.2 Description of the pier crosshead construction methodology

An example of implementation of the suggested methodology is presented in the present study. The segmentation of the pier crosshead into to symmetrically prefabricated parts is preferable for reasons of crane lifting capacity. The two parts are symmetrical along the long side with dimension 14.20 m. The generated vertical joint does not affect the flexural shear resistance of the crosshead.

Through holes are formed in each symmetrical part in order to assemble the pier with the prefabricated crosshead. The holes are geometrically located above the casted in-situ void between the two hollow circular columns of the pier.

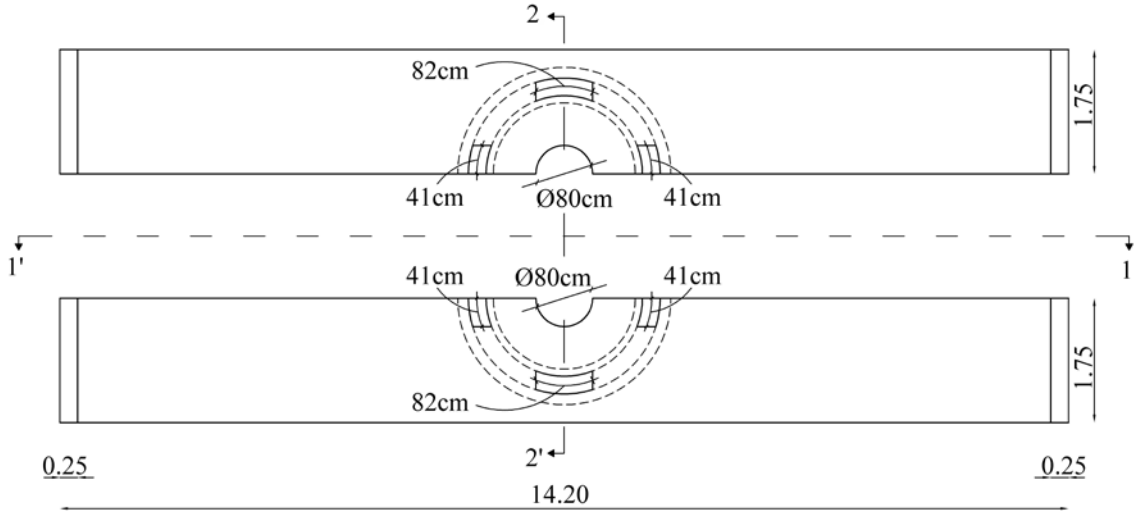


Figure 3: Plan view of prefabricated pier crosshead parts.

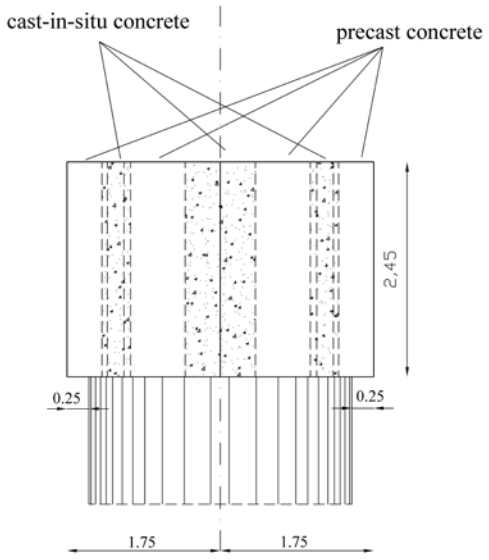


Figure 4: Section 2-2′of the assembled pier crosshead.

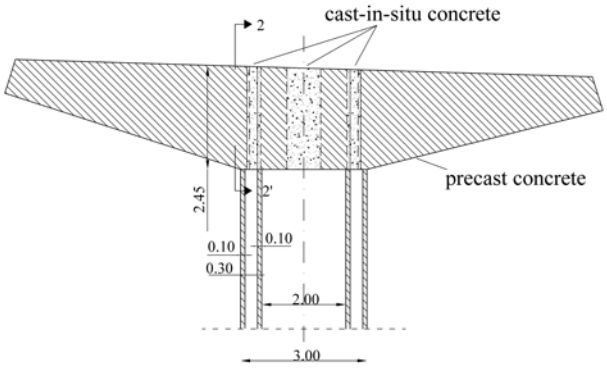


Figure 5: Section 1-1′ of the assembled pier crosshead.

As it is shown in Figures 3 to 5, each prefabricated part has three through holes and an 80 cm diameter semi-circular through hole which serves pier inspection needs. The two holes, which are mirrored to the center of the semi-circular hole, have an arc length dimension of 0.41 m. The arc length dimension of the third hole is 0.82 m.

Once the pier is assembled, the two parts of the pier crosshead are placed onto the pier. The interaction of the two crosshead parts with the pier is achieved by outbound extending

rebars in the upper pier part, suitable to fit with the geometry of the crosshead through holes. Concrete is casted in the through holes, in order the connection joint between pier and the crosshead to gain integrity.

It must be emphasized that the concreting of the peripheral through holes accommodates only the improvement of the pier-crosshead interaction and does not restore integrity between the two prefabricated crosshead parts, the segmentation of which does not affect the its flexural and shear resistance, as mentioned above.

4 EXPERIMENTAL INVESTIGATION OF THE SUGGESTED PIER MECHANICAL PROPERTIES

The purpose of the experimental investigation is to prepare specimens, the testing of which will provide important conclusions regarding the outcome reliability of the suggested construction method. The point at which the experimental research focused is the binding position of the pier prefabricated parts, as this is considered to be the critical cross-section regarding the mechanical behavior during an earthquake.

For this purpose two specimens were prepared: a) a specimen representing a pier constructed segmentally and according to the suggested construction method (Spec1) and b) a specimen representing a pier constructed according to the current pier construction method (Spec2).

Specimen Spec1 consists of two parts. Each part consists of two hollow circular columns having thickness of 5 cm. The inner column has a diameter of 30 cm and the outer column 60 cm. Each part has a height of 1.75 m. The generated void between the two columns is casted in-situ and has a thickness of 5cm. Specimen Spec2 has a height of 3.5 m and the thickness of its hollow cross-section is equal to 15 cm. The longitudinal reinforcement of Spec1 is presented in Fig. 6. The reinforcement of Spec2 is placed at the same position as in case of Spec1 but its length is equal to 3.5 m, in contrary with Spec1, in which the longitudinal reinforcement consists of 1.50 m rebars as shown in Fig. 6. The transverse reinforcement in both cases consists of two coils, an internal coil of Ø8/60 mm and an external coil of Ø8/50 mm. The transverse reinforcement is designed based on a 50% greater shear force than the corresponding to the flexural strength of the specimens (Fig. 9). The yield stress of steel used for longitudinal reinforcement was considered equal to 600MPa in the analytical calculation of their flexural resistance. Accordingly, the class of the concrete was C30/37, and therefore the strength of the concrete was considered to be 30 MPa.

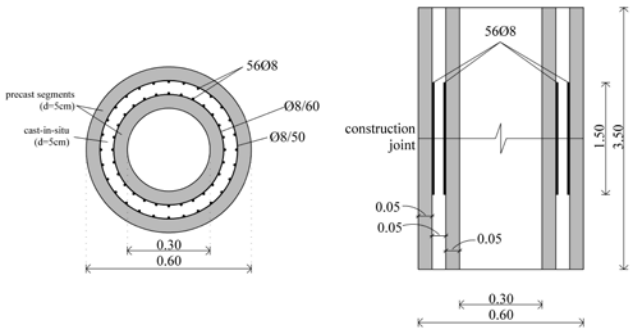


Figure 6: Reinforcement of specimem Spec1.

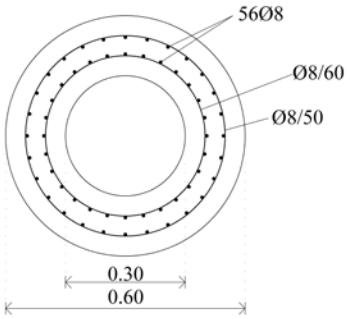


Figure 7: Reinforcement of specimen Spec2.

Each specimen was subjected twice to an incrementally applied point load was applied, in two diametrically opposed points in their mid-length (Fig. 8) until their yield point, which was

circa 500 - 600 kN, as the ultimate load capacity had been calculated previously at about 50tn. Displacement at mid-length of the specimens was recorded by the use of an analog displacement sensor. The static model is presented in Figure 9. The experiment was held in the Laboratory of Experimental Strength of Materials and Structures, Department of Civil Engineering, Aristotle University of Thessaloniki.



Figure 8: Loading of specimen Spec1 in Laboratory.

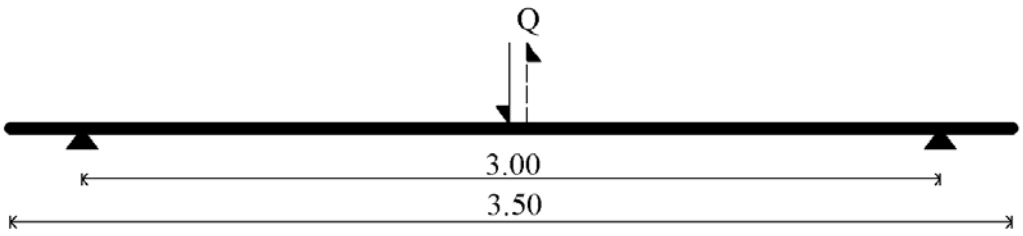


Figure 9: Static model of loading

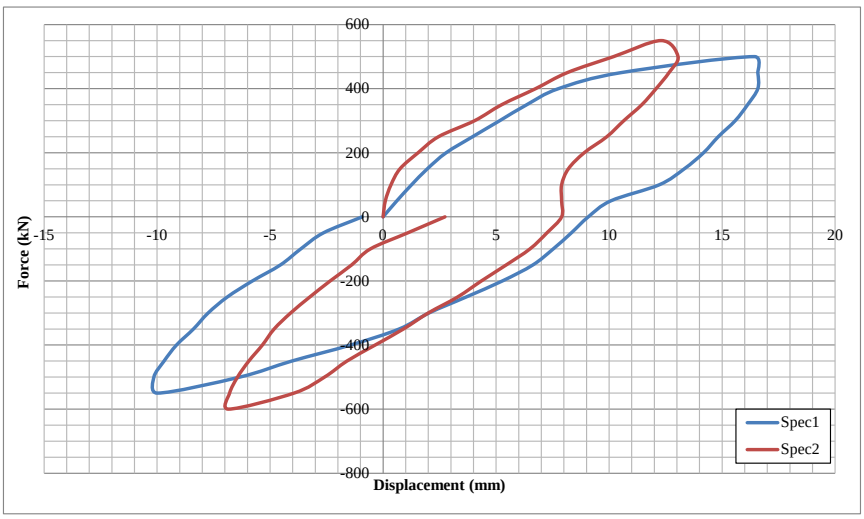


Figure 10: Force – Displacement Diagram for the two specimens.

As it is shown in Figure 10, the diagram slopes at the state of Stage II (cracked section) are similar. That means that the two specimens have similar flexural stiffness. A comparison regarding the specimen displacement is considered not safe due to imponderables during their preparation.

Regarding the spotted cracks, it must be mentioned that the specimen which represents the prefabricated case (Spec1) did not exhibit external cracks, whereas the specimen which represents the conventional case (Spec2) did exhibit cracks. In particular, this specimen during the first load input, exhibited four vertical cracks at its bottom with length 50 cm at a load of 500 kN (Fig. 11-left). During the second load input (at the point diametrically opposed to the first), two vertical cracks with length of 25 cm emerged at a load level of 450 kN (Fig. 11-right). Two cracks that were formed during the first load input extended through the entire circumference of the section and jointed the two cracks that were formed in the second load input.

The absence of cracks in the segmentally constructed specimen can be credited to its construction procedure. After an earthquake event the problem of sealing the cracks (to prevent the corrosion of the rebars) will not exist.



Figure 11: Cracks of specimen Spec2.

5 IMPLEMENTATION OF PRECAST PIERS AS ALTERNATIVE PROPOSAL

The proposed piers were applied as an alternative design to an existing precast bridge in P.A.Th.E. motorway in Greece. The longitudinal axis of the bridge (with total length of 177.5 m) is on a 3000 m radius circular arc. The bridge has five spans. The first and the last span have a length of 34.75 m while the other spans have a length of 36.0 m (Fig. 11). Each span consists of six prestressed-precast beams and a cast in-situ deck slab of 25 cm thickness (Fig. 12-a). The piers are single-column of hollow circular cross-section with diameter of 3.0 m. The thickness of the hollow cross-section is 50 cm (Fig. 12-b). The piers have the form of hammer head with a crosshead of 3.5 m width. The pier heights range from 9.20 m to 13.80 m. The deck is supported on piers and abutments through circular elastomeric bearings with diameter of 450 mm, total height of 211 mm and elastomeric thickness of 99 mm (9 layers of 11mm). The abutments have the typical form of seat-type abutments.

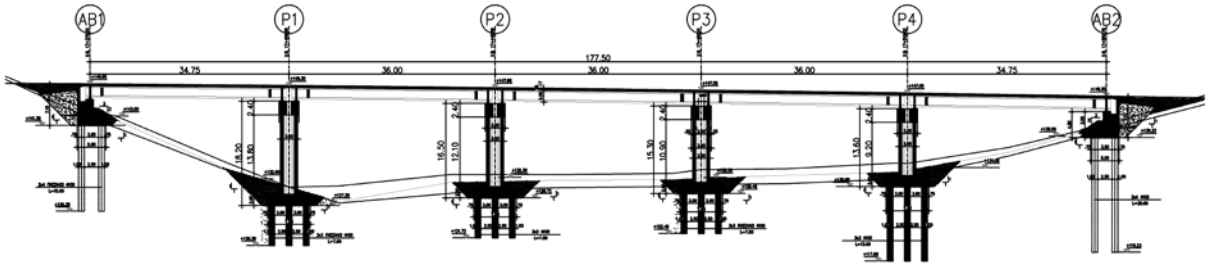


Figure 11: Longitudinal section-cut of the bridge.

The class of the used reinforcing steel is B500C. The class of the prestressing steel is St 1570/1770. The class of the concrete for deck and piers is C30/37 and for abutments C20/25 according to EC2-Part 1 [2] .

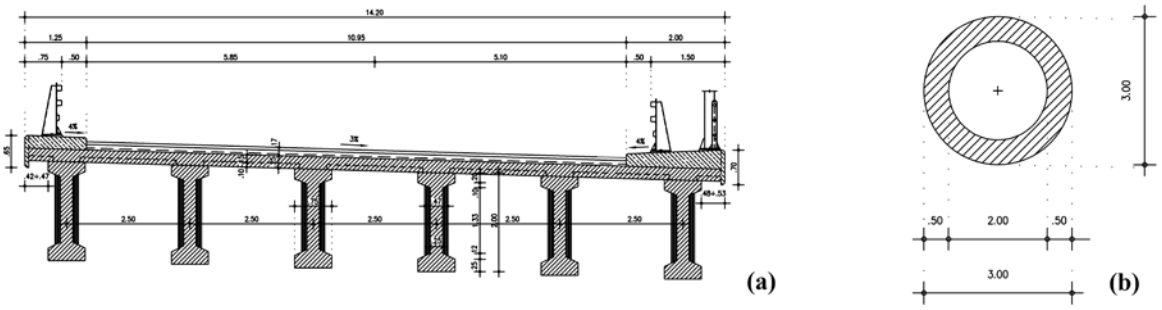


Figure 12: (a) Deck cross-section at midspan, (b) Pier section cross-section.

The bridge is founded on ground type B according to EC8-Part 1 [3] while the seismic design ground acceleration is equal to 0.24g. The importance factor is consedered equal to γ_I=1.0. The sugested type of precast piers is applied in the re-designed case of the bridge. Software SAP2000 v.11.0.4 was used for the dynamic spectrum analysis. The design spectra used for the two horizontal directions of the bridge was calculated based on a behavior factor equal to 1.0 due to the presence of elastomeric bearings [4]. A behavior factor equal to 1.0 was considered for the vertical direction as well.

Each pier is composed of two parts (as described in paragraph 3.1) of equal length. Each part consists of two columns with hollow circular cross-sections of 10 cm thickness. The 30 cm thick void between the two columns is casted in-situ with self-consolidating concrete and it is containing the longitudinal reinforcement of the cross-section arranged in three circular layers. The reinforcing coil (reinforcement against shear) is placed in the outer prefabricated part. The required longitudinal and transverse pier reinforcement is presented in Tables 1 and 2 respectively. The reinforcement of piers P1 and P2 at bottom and top is presented in Figure 13-a. In the re-designed bridge, the longitudinal and transverse reinforcement of the inner ring is considered secondary. The transverse reinforcement of the prefabricated outer ring receives the total amount of shear force, contrary to the conventional case, in which the inner coil receives part of the developing shear force.

Regarding the effective stiffness of the suggested pier cross-section, it accrued similar to the effective stiffness of the conventional case piers (Fig.13-b). Specifically, the effective stiffness in the re-designed case was equal to 45% of the uncracked cross-section stiffness,

while in the existing bridge the effective stiffness was 50%. Therefore the dynamic characteristics and the seismic displacement ($d_{ed,\,x}$ = 20 cm) of the bridge were not different in the two cases.

Position	Reinforcement	Reinforcement Ratio (%)
P1 - bottom	77Φ25	2.89
P1 - top	52Φ25	1.95
P2 - bottom	77Φ25	2.89
P2 - top	52Φ25	1.95
P3 - bottom	52Φ25	1.95
P3 - top	52Φ25	1.95
P4 - bottom	52Φ25	1.95
P4 - top	52Φ25	1.95

Table 1: Longitudinal reinforcement of piers of the re-designed bridge.

Pier	Transverse Reinforcement
P1	2Φ14/135
P2	2Φ14/135
P3	2Φ14/135
P4	2Φ14/160

Table 2: Transverse reinforcement of piers of the re-designed.

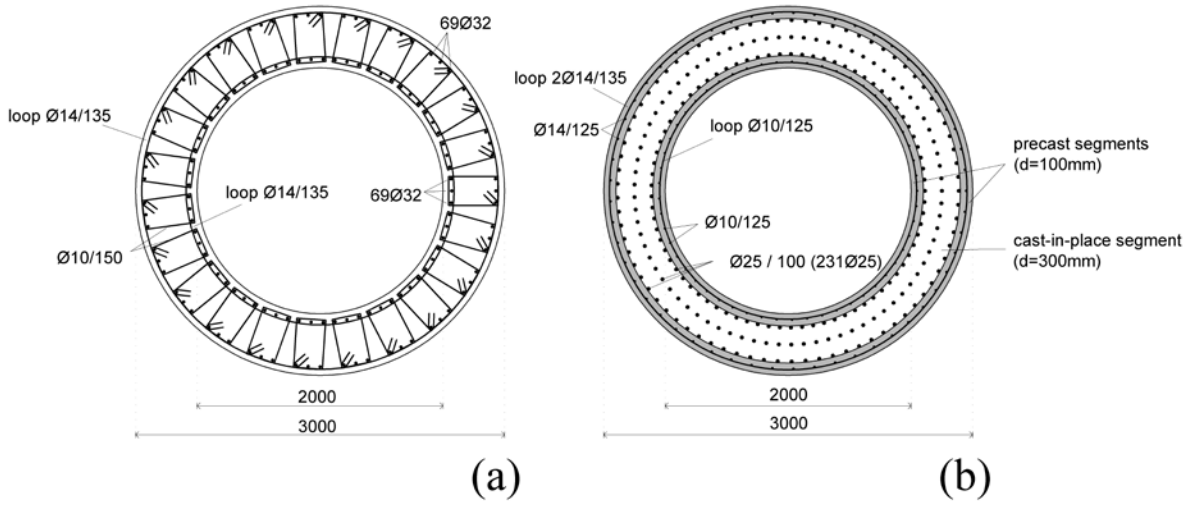


Figure 13: (a) Reinforcement of piers P1(bottom) and P2(bottom) of the reference bridge
(b) Reinforcement of piers P1(bottom) and P2(bottom) of the re-designed bridge.

6 EXPANSION OF PREFABRICATION AT THE ABUTMENTS

Prefabrication can be also exploited in the area of abutments. This implementation contributes to a further increase of the construction speed and to the full standardization of bridges made with the method of prefabrication. In this paragraph, indicative plans of a prefabricated abutment are given, tailored to the case of the examined reference bridge. The prefabricated abutment, due to its size and its geometric complexity, consists of four different kinds of prefabricated products, each in a different quantity. It is assembled in 4 phases. It consists of four parts forming the wall-web of the abutment, four parts forming the back wall, two parts forming the wing-walls (type B) and 2 parts of wing-walls (type A). These parts are assembled in the order they were mentioned (Fig. 14).

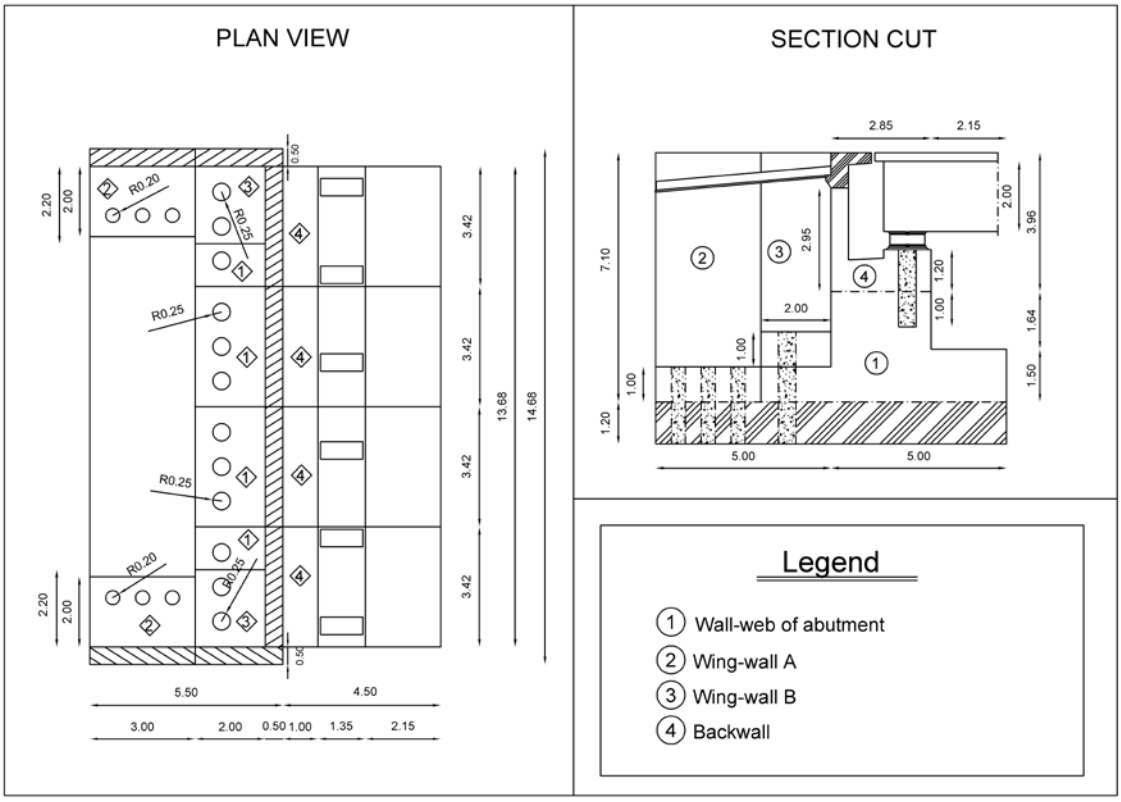


Figure 14: Indicative precast pier assembly drawings.

7 CONCLUSIONS

In the present study a method of exploiting prefabrication at piers and abutments of precast bridges is presented. The applicability of the method and the benefits, gained by its application, were examined analytically and experimentally. The main conclusions of the research are the following:

- The segmentation of the piers in parts of equal length and their crossheads in two symmetrical halves provides a manageable outcome in terms of geometry and transferring them in site.
- Similarly, the segmentation of an abutment, which consists of two main parts (the wall-web and the two wing-walls), complies with the above mentioned criteria.

- Regarding the effects of segmental construction on the mechanical properties of the pier webs, which are the main recipients of seismic action, the presented coarse research concluded that the segmentation resulted in no observable deviation in strength and stiffness from the conventionally constructed piers. Regarding ductility, it is obvious that it does not concern this case because precast bridges reside in non-ductile structures.

8 ACKNOWLEDGEMENTS

The authors wish express their gratitude to the precast factory ARMOS S.A. for preparing the specimens necessary for the experimental section of the study and to METE SYSM S.A. for providing the original study of the bridge for the purposes of the present study.

REFERENCES

[1] F. Leonhardt, *Vorlesungen uebermassivbau-Sechster Teil,* Springer-Verlag, 1978.

[2] CEN [Comité Européen de Normalisation], EN 1992-1-1: Eurocode 2: Design of Concrete Structures - Part 1-1: General Rules and Rules for Buildings, 2004.

[3] CEN [Comité Européen de Normalisation], EN 1998-2: Eurocode 8: Design of Structures for Earthquake Resistance - Part 2: General Rules, Seismic Actions and Rules for Buildings, 2004.

[4] CEN [Comité Européen de Normalisation], EN 1998-2: Eurocode 8: Design of Structures for Earthquake Resistance - Part 2: Bridges, 2005.

COMPDYN 2015
5th ECCOMAS Thematic Conference on
Computational Methods in Structural Dynamics and Earthquake Engineering
M. Papadrakakis, V. Papadopoulos, V. Plevris (eds.)
Crete Island, Greece, 25–27 May 2015

MODELING AND IDENTIFICATION OF THE DYNAMIC RESPONSE OF AN EXISTING THREE-STORY STEEL STAIRWAY

Triantafyllos K. Makarios[1], George D. Manolis[2], Ioanna Karetsou[3], Michael Papanikolaou[3] and Vasiliki Terzi[4]

[1] Assistant Professor
Institute of Static and Dynamic of Structures, Department of Civil Engineering, Aristotle University, Thessaloniki GR-54124, Greece
e-mail: makariostr@civil.auth.gr

[2] Professor
Institute of Static and Dynamic of Structures, Department of Civil Engineering, Aristotle University, Thessaloniki GR-54124, Greece
gdm@civil.auth.gr

[3] Dipl. Eng., MSc Civil Engineer
Institute of Static and Dynamic of Structures, Department of Civil Engineering, Aristotle University, Thessaloniki GR-54124, Greece
joykaretsou@hotmail.com , mipapani@civil.auth.gr

[4] PhD & Staff Member (E.D.I.P.)
Institute of Static and Dynamic of Structures, Department of Civil Engineering, Aristotle University, Thessaloniki GR-54124, Greece
terziv@civil.auth.gr

Keywords: Identification, mode shapes, modal response, acceleration time histories

Abstract. *In this work, we present a modal shape identification technique for an existing steel stairway located within the building complex comprising the Civil Engineering department of Aristotle University in Thessaloniki, Greece. The aforementioned flexible steel stairway was instrumented using a local multi-channel network of accelerometers in September 2014. We installed on the stairway two 12 bit-nominal resolution, digital uniaxial accelerometers of the type KUOWA-PCD-30A, connected by cables and with 'common time' and 'common start' characteristics. The dominant modes of vibration of the stairway were computed by the 'modal response acceleration time history' methodology. In parallel, a detailed finite element method model of the stairway was formed and calibrated according to the ambient vibration results. We note that the identification procedure used for the dynamic characteristics of spatial structures yields results that can be used to develop a family of numerical models for the stairway ranging from the simple single-degree-of-freedom system to highly detailed finite element method models, while some useful information on the theoretical procedure for the identification of modal shapes is included herein.*

1 INTRODUCTION

In the last few years, issues such as "monitoring" and "structural integrity" of structures is being developed rather vigorously by employing suitable, multi-channel networks for measuring acceleration response time-histories, followed by appropriate data processing techniques. If the structural response remains within the linear elastic range, then the recorded acceleration response time-histories contain the structure's modal response. It is well known that a clear deterministic relationship does not exist between ambient vibration loading or ground excitations as input and the ensuing structural response as output. Furthermore, the methodologies used to identify the dynamic characteristics (i.e., natural frequencies, mode shapes and modal damping ratios) of a structure must take into account the instrumentation configuration that is used on that structure. Thus, many methodologies are adapted to investigate dynamic structural response on a case-by-case basis (buildings, bridges, towers, dams, and also other categories of structures such as aircraft frames). Nevertheless, the main objective in all cases is to identify the dynamic characteristics of the structure through an analytic processing of the measured response. In the past, various deterministic and stochastic methods have been proposed (see Basseville *et al*, 2001; Brincker *et al*, 2001; Peeters & De Roeck, 2001; Wenzel & Pichler, 2005; Overschee & De Moor, 1996; Makarios, 2012 & 2013; Manolis *et al* 2014). However, the engineering community has yet to agree on a unique, well-documented procedure for identifying the dynamic characteristics of any structures or structural system through a detailed investigation of their measured response. The present paper identifies the dynamic characteristics of a specialized type of steel stairway with continuous mass distribution and stiffness. These stairways serve as escape routes from high-rise buildings, are placed externally to the building and can be classified as being very flexible structures. The analysis procedure presented in this work is adapted to the particular instrumentation configuration used on the steel stairway, supplemented by the method of "modal time-histories". More specifically, the work is based on material drawn from the MSc diploma thesis of the authors, see Karetsou (2014) and Papanikolaou (2014), where ambient vibrations induced by ordinary, daily use of the stairway by pedestrians were used as the source of excitation to measure the stairway response. Within this framework, a parallel finite element modeling procedure (SAP 2000) was developed and the results obtained were calibrated against the experimental evidence. These finite element models were then reconfigured and used to reproduce details in the dynamic response of the stairway. This way, the numerical models help extend the results of the experimental effort and can be used to trace ageing and deterioration during the useful service life of the stairway.

2 THE STEEL STAIRWAY AND ITS MATHEMATICAL MODEL

The steel stairway under study is located in the courtyard behind the main building of the Civil Engineering Department at the Polytechnic School of Aristotle University in Thessaloniki, Greece, see Fig.1. The stairway was constructed in 1982 and consists of three spans which terminate respectively in three landing levels of a low rise annex building housing laboratories.



Fig.1: The steel stairway with side (left) and front (right) views

The second span is supported by two beams (IPN140 cross section), while the beams supporting the other spans as well as the landings are IPN100 cross sections. The columns supporting the beams at the second landing, as well as the main column of the third landing, are IPN140 cross section. The remaining columns of the structure are IPN100 cross sections. As illustrated in Fig.1, the IPN140 columns are connected by cross diagonal bars with RHS 60x40 cross section. The cross bars reinforce the later stiffness of the stairway and reduced the buckling length of the columns. The vertical stiffness of the landing is reinforced by the contribution of T50 beams on the first landing and IPN beams on the other two. Finally, the landings, the treads and the risers are made of sheet metal plates of 3mm thickness. The same material is used as protective sideway cover for the beams. Next, the instrumentation scheme used during a two week time period comprised three uniaxial accelerometers, as illustrated in Fig. (2).

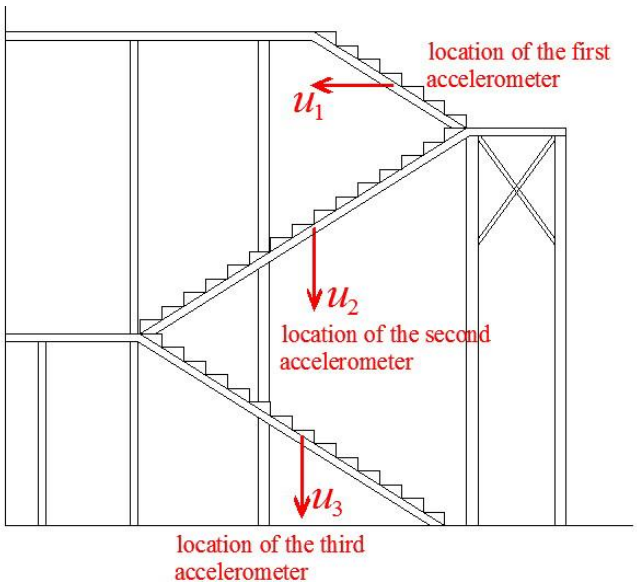


Fig.2: Location of accelerometers at important degrees of freedom of the structure

We note that the stairway under study cannot be modeled as a lumped mass system since there is no detectable concentration of mass at any level. Therefore, the structural system is strongly continuous with both continuous mass and stiffness distributions, and this causes difficulties in the identification of the eigen-modes. In accordance to the accelerometer placement scheme, the vector **u** corresponds to three basic degrees of freedom, and the generalized matrices for the mass **M**, the stiffness **K** and the damping **C** of the steel stairway attain the following form:

$$\mathbf{u} = \begin{bmatrix} u_1 \\ u_2 \\ u_3 \end{bmatrix}, \quad \mathbf{M} = \begin{bmatrix} m_{11} & m_{12} & m_{13} \\ m_{21} & m_{22} & m_{23} \\ m_{31} & m_{32} & m_{33} \end{bmatrix}, \quad \mathbf{K} = \begin{bmatrix} k_{11} & k_{12} & k_{13} \\ k_{21} & k_{22} & k_{23} \\ k_{31} & k_{32} & k_{33} \end{bmatrix}, \mathbf{C} = \begin{bmatrix} c_{11} & c_{12} & c_{13} \\ c_{21} & c_{22} & c_{23} \\ c_{31} & c_{32} & c_{33} \end{bmatrix}$$

Therefore, the equation of motion of the steel stairway subjected to environmentally-induced dynamic loads is the following:

$$\mathbf{M}\,\ddot{\mathbf{u}}(t) + \mathbf{C}\,\dot{\mathbf{u}}(t) + \mathbf{K}\,\mathbf{u}(t) = \mathbf{W}(t) \tag{1}$$

In the above, $\mathbf{W}(t)$ is the load vector encompassing the unknown ambient vibration loading on the specified degrees of freedom.
For this case, the solution of eq.(1) is of the following form:

$$\mathbf{u}(t) = \boldsymbol{\varphi}_1 q_1(t) + \boldsymbol{\varphi}_2 q_2(t) + \boldsymbol{\varphi}_3 q_3(t) = [\boldsymbol{\varphi}_1 \quad \boldsymbol{\varphi}_2 \quad \boldsymbol{\varphi}_3] \begin{bmatrix} q_1(t) \\ q_2(t) \\ q_3(t) \end{bmatrix} = \boldsymbol{\Phi}\,\mathbf{q}(t) \tag{2}$$

where,

$$\boldsymbol{\Phi} = [\boldsymbol{\varphi}_1 \quad \boldsymbol{\varphi}_2 \quad \boldsymbol{\varphi}_3] = \begin{bmatrix} \varphi_{11} & \varphi_{12} & \varphi_{13} \\ \varphi_{21} & \varphi_{22} & \varphi_{23} \\ \varphi_{31} & \varphi_{32} & \varphi_{33} \end{bmatrix}, \qquad \mathbf{q}(t) = \begin{bmatrix} q_1(t) \\ q_2(t) \\ q_3(t) \end{bmatrix}$$

More specifically, $\boldsymbol{\varphi}_1$, $\boldsymbol{\varphi}_2$, $\boldsymbol{\varphi}_3$ are the corresponding three eigen-modes, $\boldsymbol{\Phi}$ is the modal matrix of the steel stairway and $q_i(t), i = 1, 2, 3$ are the corresponding time functions (i.e., generalized coordinates) of each eigen-mode
It can been proved that the system of eq. (1), which is particular to the placement scheme of the three accelerometers, is equivalent to a single degree of freedom vibrator response for each eigne-mode *i* and is described by eq. (3) below (see Makarios 2012 & 2013):

$$\ddot{q}_i(t) + 2\xi\omega_i\dot{q}_i(t) + \omega_i^2 q_i(t) = \frac{\boldsymbol{\varphi}_i^T\,\mathbf{W}(t)}{\boldsymbol{\varphi}_i^T\mathbf{M}\,\boldsymbol{\varphi}_i} \tag{3}$$

Equation (3) shows that the exact solution for the calculation of the time varying modal functions $q_i(t)$ requires knowledge of the environmentally-induced dynamic loading vector $\mathbf{W}(t)$, which is of course impossible to estimate a priori. However, by observing eq. (3), it is clear that the exact solution is a superposition of the solution $q_{o,i}(t)$ to the homogenous equation and of the particular solution $q_{w,i}(t)$, which depends on the dynamic loading $\mathbf{W}(t)$:

$$q_i(t) = q_{o,i}(t) + q_{w,i}(t) \tag{4}$$

However, it is already known that in the free vibration case, the exact solution $q_{o,i}(t)$ for the homogenous equation of the structure coincides with the final, sought after solution. Consequently, suppose a theoretical situation where the structure vibrates, then the action of the dynamic loading $\mathbf{W}(t)$ ceases and its free vibration response is now being recorded. In this case,

the condition that the solution $q_{o,i}(t)$ of the homogenous equation constitutes the final quested solution of the problem is fulfilled, namely:

$$q_i(t) = q_{o,i}(t) \tag{5}$$

More specifically, each term in the summation of eq.(2) represents the modal response movements $\mathbf{u}_i(t)$ for each *i*=1,2,3 eigen-mode:

$$\mathbf{u}_i(t) = \boldsymbol{\varphi}_i\, q_i(t) \quad \Rightarrow \quad \begin{bmatrix} u_{1i}(t) \\ u_{2i}(t) \\ u_{3i}(t) \end{bmatrix} = \begin{bmatrix} \varphi_{1i}\, q_i(t) \\ \varphi_{2i}\, q_i(t) \\ \varphi_{3i}\, q_i(t) \end{bmatrix} \tag{6}$$

From a combination of eq.(5) and eq. (6), the following conclusion is drawn: *If the dissociation of the modal responses* $\boldsymbol{\varphi}_i\, q_i(t)$ *for each degree of freedom of the system was feasible, then the direct estimation of the components of each one of the eigen-modes by the elimination of the time function* $q_i(t)$*, which is common for all the degrees of freedom of the same eigen-mode, would also be feasible*. Indeed, referring at the instant of the simultaneous extreme widths of vibration (*a, b, c)* for the of degrees of freedom (u_1 , u_2, u_3) as shown in Fig. 3, the components of the *i*-eigen-mode are directly described by eq.(7) below:

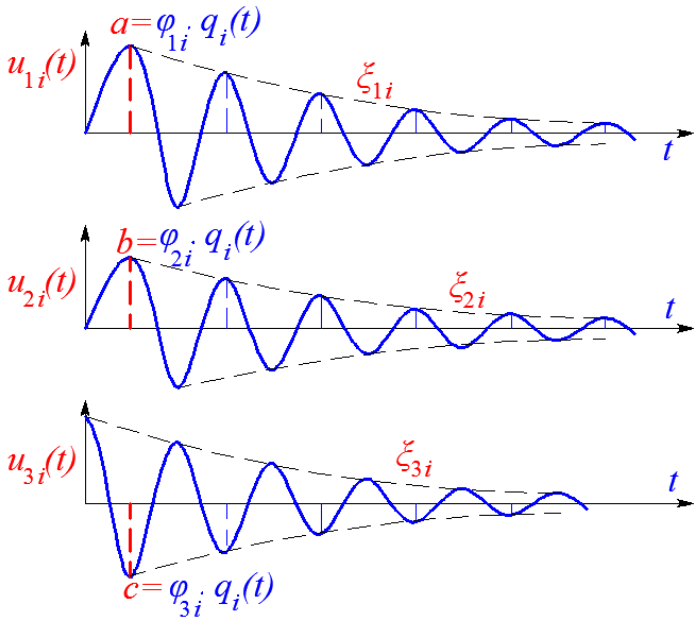


Fig.3: Modal time-histories for a three degree-of-freedom structural system

$$\begin{bmatrix} a \\ b \\ c \end{bmatrix} \Rightarrow \begin{bmatrix} a/a \\ b/a \\ c/a \end{bmatrix} = \begin{bmatrix} \varphi_{1i} \\ \varphi_{2i} \\ \varphi_{3i} \end{bmatrix} = \begin{bmatrix} 1 \\ \varphi_{2i} \\ \varphi_{3i} \end{bmatrix} \tag{7}$$

The dissociation (or uncoupling) of the modal responses is achieved numerically by truncation of the harmonic having a frequency equal to the *i*-eigen-frequency of the structure. This truncation is achieved by the use of an appropriate digital filter applied to the initial recordings. This digital filter must permit only the transition of one specific frequency, which equals to the eigen-frequency of the structure, so long as the latter is already known. The eigen-frequency of the structure can be determined by the combination of the "peak-picking" technique applied to the Fast Fourier Transform diagrams of the recordings, followed by an exam-

ination of the phase difference between the extreme response values. This last point must take into account that a phase difference of 0 or π (rad) between different recordings corresponds to an eigen-mode. The aforementioned method is known as the "modal time-history method" and has been recently developed in Makarios (2012 & 2013). Thus, in the present work, the method is applied to the steel stairway, which is a system with infinite degrees of freedom having a continuous mass and stiffness distribution. This makes the identification of the important eigen-frequencies quite difficult.

3 INSTRUMENTATION PROCEDURE FOR THE STEEL STAIRWAY

The stairway was instrumented by a system of two 12 bit-nominal resolution, digital uniaxial accelerometers of the type KUOWA-PCD-30A. One sensor (ch.1) was used for the recording of the vertical accelerations, while the second sensor (ch. 2) was used for the recording of the horizontal accelerations, see Fig. 4. The fastening of the sensors on the lower surface of the treads was achieved by the use of silicon adhesives. The sensor recording the horizontal accelerations (reference accelerometer) was installed in the middle of the third span, while the sensor recording the vertical accelerations was alternately installed in the middle of the first and second spans, see Fig.2.



Fig.4: Installed accelerometers on the stairway underside during September 2014



Fig.5: Recorded unit of accelerometer network

The ambient vibration loading was realized during regular use, with people ascending and descending the steel stairway. A sufficient number of response recordings was made, and durations of two (2), five (5) and fifteen (15) minutes were considered, including the free vibration part of the response as well. The two accelerometers were connected to a logging unit for receiving data. The latter was connected to a laptop computer (see Fig.5). Using the appropriate software, visualization and calibration of the recordings took place. By selecting a range of 10000 μm/m and a calibration factor of 0.000829, the accelerometer in the vertical vibration direction was capable of recording the acceleration of gravity g=9.81m/s^2 under calm conditions. The software used offers the ability of exporting data in the .xls format. Therefore, the recordings were easily imported and processed in a spreadsheet (MS Excel program).

4 SIGNAL PROCESSING TECHNIQUE

During the processing of the recordings, multiple time windows were examined. The part of the forced vibration was truncated and only the part of the free vibration was taken into consideration. The noise was removed from the free vibration recordings by the use of appropriate filters (see Makarios 2012 & 2013). Finally, the Fast Fourier Transform of each degree of freedom was calculated. The main observation concerning the FFT diagrams refers to the lack of the usual "spikes" for certain eigen-frequencies due to the fact that the steel stairway does not respond as a discrete system, since it does not contain any sizeable lumped masses (see Figs.6 & 7).

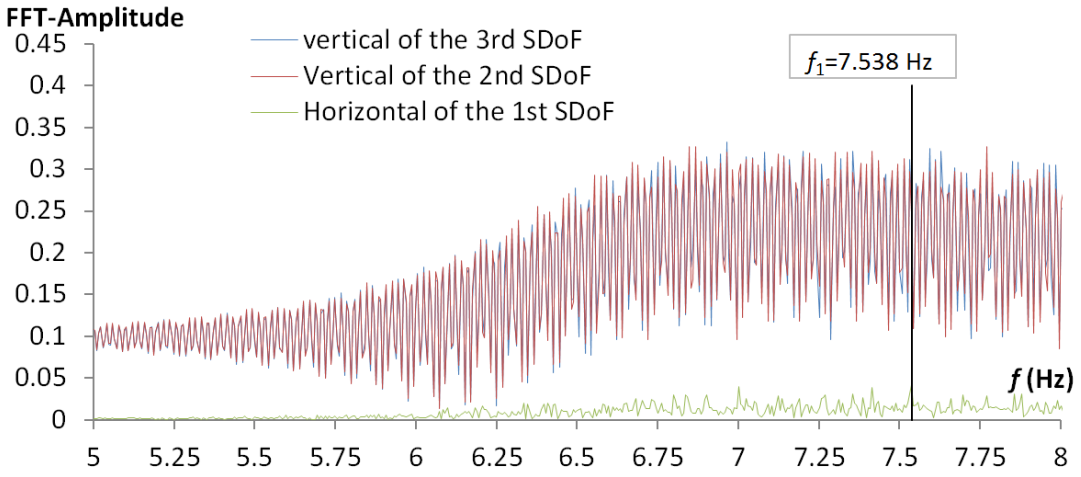


Fig.6: FFT of the three response components in the 5 - 8 Hz frequency range

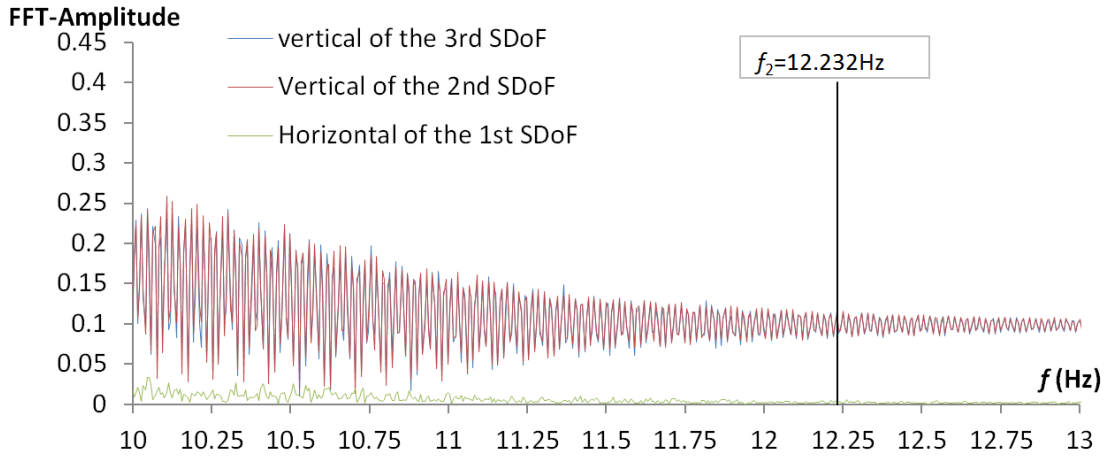


Fig.7: FFT of the three response components in the 10 - 13 Hz frequency range

On the contrary, the FFT displacement amplitudes presented a rather smooth uniformity, due to the fact that that the structure performs as a system with continuous mass and stiffness distribution. Combining the "peak-picking" technique with an estimation of the phase difference between the modal response histories, it is possible to detect whether or not the peaks observed refer to the modal response of the structure or simply stem from the external dynamic loading $\mathbf{W}(t)$. In this way, the peaks in the entire frequency range of FFT diagrams were sequentially examined. As a result, two frequencies, f_1=7.538Hz and f_2=12.232Hz, were estimated as being the eigen-frequencies of the structure. Indeed, the time histories corresponding to these two frequencies, present a phase difference of 0 and π rad respectively, as illustrated in Figs. 8 & 9. According to Fig.(3) and eq. (7), the modal components of the two eigenmodes of the stairway were computed by the SeismoSignal (2012) program and the following values were recovered:

$$\boldsymbol{\varphi}_1 = \begin{bmatrix} \varphi_{11} \\ \varphi_{21} \\ \varphi_{31} \end{bmatrix} = \begin{bmatrix} 1 \\ 41.405 \\ 47.50 \end{bmatrix}, \qquad \boldsymbol{\varphi}_2 = \begin{bmatrix} \varphi_{12} \\ \varphi_{22} \\ \varphi_{32} \end{bmatrix} = \begin{bmatrix} -1 \\ 51.16 \\ 44.00 \end{bmatrix}$$

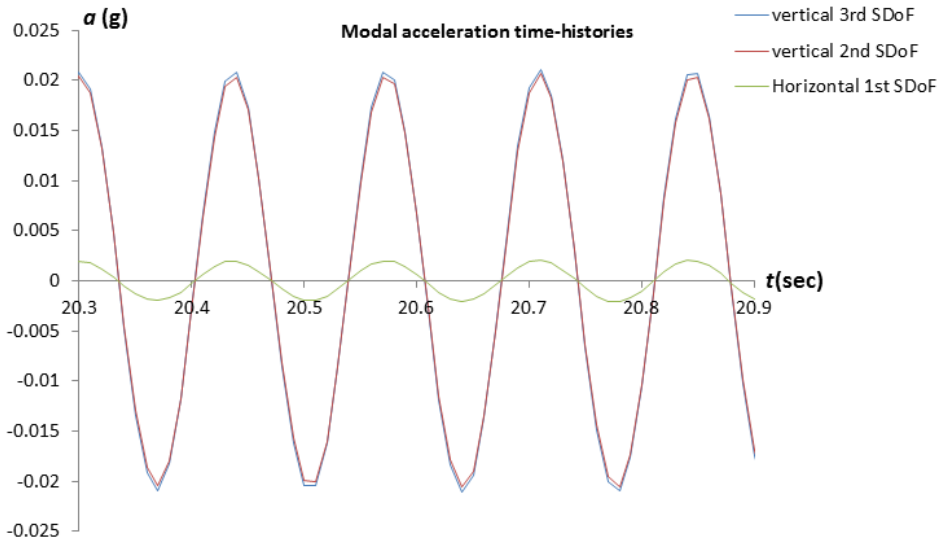


Fig.8: Modal acceleration time-histories for the first frequency f_1=7.538Hz, where the phase difference between the three components is zero

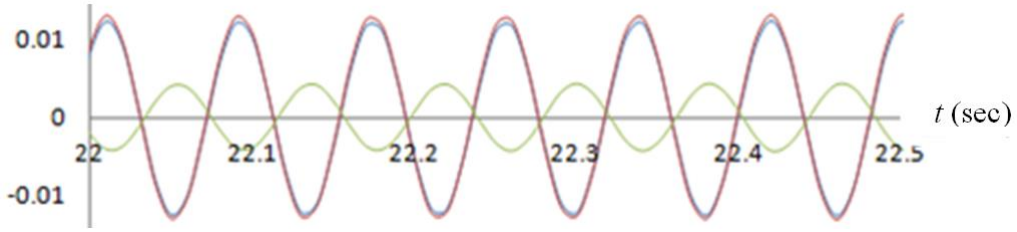


Fig.9: Modal acceleration time-histories for the second frequency f_2=12.232Hz, where the phase between the first component and the other two is equal to π.

Finally, the part of the free vibration of the modal time histories components was used in order to calculate the equivalent modal damping ratios, applying the equation of the logarithmic decrement in each one of the three modal components, see Table 1. The final average equivalent modal damping corresponds to the mean value of the aforementioned equivalent modal damping ratios.

First Eigen-frequency f_1=7.354 Hz	Equivalent viscous damping ratio of modal component	Mean equivalent viscous damping ratio ξ_1.
1st Degree of Freedom	0.0037	0.0045
2nd Degree of Freedom	0.0048	
3rd Degree of Freedom	0.0049	
Second Eigen-frequency f_2=12.232 Hz	Equivalent viscous damping ratio of modal component	Mean equivalent viscous damping ratio ξ_2.
1st Degree of Freedom	0.0073	0.0070
2nd Degree of Freedom	0.0065	
3rd Degree of Freedom	0.0071	

Table 1: Equivalent viscous damping ratios for the steel stairway

5 FINITE ELEMENT MODEL OF THE STEEL STAIRWAY

The finite element program SAP2000 was used for the numerical modeling of the steel stairway, see Fig. 10. Some of the most important features of this simulation are the following:

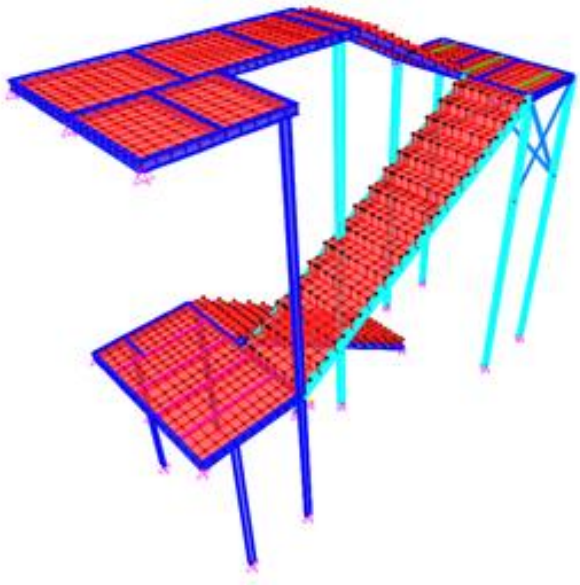


Fig.10: Model of the steel stairway using SAP2000

1. Beam elements were used to model the beams of the columns of the stairway.
2. Isotropic shell elements were used to model the surface elements of the stairway, such as the risers, the treads and the landings, which were made of sheet metal.
3. The total mass of the canopy was taken into account as lumped masses at the common nodes with the stairway beams.
4. The stiffness of the supporting beams was appropriately modified into order to take into account the stiffness of the railways. Furthermore, the mass and the weight of the railways were also taken into account.
5. The welded connections between all of the parts of the stairway were considered to be fully continuous connections.

In order to investigate the effect of the mass change at the landings due to live loads and the effect of the boundary conditions as well on the dynamic characteristics of the stairway, various parametric analyses were carried out. The values of the ten first eigen-frequencies of the optimized finite element model are presented in Table 2. The eigen-frequencies calculated by the use of the program SAP2000 yielded values close to 10Hz (or greater). The aforementioned results support the fact that the range of the real possible eigen-frequencies approaches or even includes the values of the eigen-frequencies estimated by the analytical-experimental results (i.e., frequency values f_1=7.538Hz and f_2=12.232Hz).

6 DISCUSSION AND CONCLUSIONS

In the present work, we present a method for the identification of the dynamic characteristics of a flexible metal structure which responds as a continuous (in terms of mass and stiffness distribution) dynamic system to environmentally-induced loads. This is a rather difficult problem in structural dynamics, since there is a spread of adjacently grouped eigen-frequencies with equivalent response amplitudes, and in the absence of any dominant frequency that would be detectable in terms of a bell or nail shaped bump in the FFT plots. In order to pro-

duce reliable results, the method of modal acceleration time histories was applied, which calculates the phase differences between the recorded degrees of freedoms in the total time history response. Moreover, it is noted that the set up of a finite element model for the steel stairway is equivalent to the development of a "discrete" model. Irrespective of how detailed this model is (in terms of use of large numbers degrees-of-freedom), it will always produce results that deviate from the real response. This means that for flexible and asymmetric types of structures, the dynamic characteristics according to the finite element modeling will not always correspond to reality. Nevertheless, the numerical model is capable of determining an acceptable range of eigen-frequencies, but without the possibility of convergence in terms of better accuracy. The on-site simultaneous recordings from the multichannel system of accelerometers, under the appropriate analytic processing, can produce a very good estimation of the real values of eigen-frequencies and eigen-modes, even in the case of continuous systems. It is of course acknowledged that the use of finite element models contributes to the identification of the eigen-frequency range, narrowing the search for the true eigen-frequencies during the processing of the experimental recordings. However, the development of a numerical modal is not absolutely necessary for the identification of the dynamic characteristics of the flexible structure, since the method of the modal time history accelerations method is autonomous. The true value of finite element models in our case lies elsewhere: Once calibrated, they can be used in conjunction with non-periodic dynamic response recordings to establish the structural decay over time as the stairway remains under continuous use.

Output Case	StepType	Step Num	Period	Frequency	Circ. Freq	Eigenvalue
Text	Text		(sec)	(cyc/sec)	(rad/sec)	$(rad/sec)^2$
MODAL	Mode	1	0.098988	10.102	63.474	4029
MODAL	Mode	2	0.084927	11.775	73.983	5473.5
MODAL	Mode	3	0.078137	12.798	80.413	6466.2
MODAL	Mode	4	0.074687	13.389	84.126	7077.2
MODAL	Mode	5	0.072954	13.707	86.126	7417.6
MODAL	Mode	6	0.067339	14.85	93.306	8706
MODAL	Mode	7	0.057517	17.386	109.24	11934
MODAL	Mode	8	0.049105	20.365	127.95	16372
MODAL	Mode	9	0.045839	21.815	137.07	18788
MODAL	Mode	10	0.044003	22.726	142.79	20389

Table 2: Modal Periods and frequencies by FEM program SAP2000

REFERENCES

[1] M. Basseville, A. Benveniste, M. Goursat, L. Hermans, L. Mevel & H. Auweraer. Output-only subspace based structural identification: from theory to industrial testing practice. *Journal of Dynamic Systems, Measurement and Control, Transactions of the ASME: Special Issue on Identification of Mechanical Systems*; vol. 123, no. 4 pp. 68–76, 2001.

[2] R. Brincker, L. Zhang & P. Andersen. Modal identification of output-only systems using frequency domain decomposition. *Smart Materials and Structures Journal;* vol. 10: pp. 441–45, 2001.

[3] B. Peeters & G. De Roeck. Stochastic system identification for operational modal analysis: a review. *Journal of Dynamic Systems, Measurement and Control, Transactions of*

the ASME: Special Issue on Identification of Mechanical Systems; vol. 123, no. 4, pp. 659–67, 2001.

[4] H. Wenzel & D. Pichler. *Ambient Vibration Monitoring*. John Wiley & Sons, Chichester, England, 2005.

[5] P. Overschee & B. De Moor. *Subspace Identification for Linear Systems*. Kluwer Academic Publishers, Dordrecht, 1996.

[6] T. Makarios. Identification of the mode shapes of spatial tall multi-storey buildings due to earthquakes. The new modal time histories method. *Journal of the Structural Design of Tall and Special Buildings*. vol. 21, pp. 621–641, 2012.

[7] T. Makarios. Identification of building dynamic characteristics by using the modal response acceleration time-histories in the seismic excitation and the wind dynamic loading cases. Chapter 4 in *Accelerometers: Principles, Structure and Applications*, edited by P.S. de Brito Andre & H. Varum, Nova Science Publishers, New York, pp. 7-113, 2013.

[8] G.D. Manolis, A. Athanatopoulou-Kyriakou, K.D. Dragos, A. Arabatzis, A. Lavdas & C.Z. Karakostas. Identification of pedestrian bridge dynamic response trough field measurements and numerical modeling: Case Studies. *Journal of Theoretical and Applied Mechanics*, vol. 44, no. 2, pp. 3-24, 2014.

[9] I. Karetsou, *Instrumentation of steel stairway and identification of its dynamic characteristics: Model of analysis*. MSc Diploma Thesis, Postgraduate Program on Earthquake Engineering and Seismic Design of Structures, Civil Engineering Department, Aristotle University, Thessaloniki, Greece, November 2014 (in Greek).

[10] M. Papanikolaou, *Identification of dynamic characteristics of steel stairway using recordings and development of suitable model*, MSc Diploma Thesis, Postgraduate Program on Earthquake Engineering and Seismic Design of Structures, Civil Engineering Department, Aristotle University, Thessaloniki, Greece, November 2014 (in Greek).

[11] *SeismoSignal, Version 5.1.0*. Seismosoft Ltd, Pavia, Italy, 2012.

[12] *SAP 2000 Nonlinear Version 11.03, User's Reference Manual*, Computer and Structures Inc., Berkley, California, 2007.

COMPDYN 2015
5th ECCOMAS Thematic Conference on
Computational Methods in Structural Dynamics and Earthquake Engineering
M. Papadrakakis, V. Papadopoulos, V. Plevris (eds.)
Crete Island, Greece, 25–27 May 2015

INVESTIGATION OF NOVEL ANCHORING DEVICES FOR OPEN HOOP CFRP STRIPS BONDED ON R/C ELEMENTS UNDER MONOTONIC AND CYCLIC LOADING-UNLOADING CONDITIONS

Konstantinos B. Katakalos[2] and George C. Manos[1]

[1,2] Aristotle University of Thessaloniki
School of Engineering, Egnatia street, University Campus, Thessaloniki, Greece
e-mail: kkatakal@auth.gr, gcmanos@civil.auth.gr

Keywords: Strengthening schemes, R/C elements and CFRP sheets, Novel anchoring devices, load-unload cyclic sequence.

Abstract. *Results obtained from research conducted in the framework of an initiative introduced by the Hellenic Earthquake Planning and Protection Organization aiming to support relevant provisions of the Greek Code for the repair and strengthening of R/C structures are presented and discussed. When trying to utilize fiber polymer sheets, as external reinforcement attached on R/C elements, their potential of high tensile strength is prevented by the FRP sheets' debonding mode of failure thus limiting the exploitation of the material. In order to confront this limitation the effectiveness of two novel types of anchoring devices that can be incorporated together with such FRP strips was studied. For this purpose special unit beam concrete specimens were fabricated and were used to attach the open hoop carbon strips (CFRP). The novel loading arrangement developed at Laboratory of Strength of Materials and Structures was utilized to apply the necessary forces to these unit beam specimens together with instrumentation capable of capturing the behavior of these specimens up to failure. Studying in this way the transfer of forces from the open hoop FRP strips it could be demonstrated that when this type of retrofitting was accompanied with a properly designed anchoring device, a significant increase in the bearing capacity of the tested specimens was observed. The present investigation incorporates also the influence of number of cycles, in a loading-unloading way, on the overall behavior of the strengthening scheme, in terms of ultimate strength and observed mode of failure. Finally, this paper includes the most important findings of a supplementary numerical investigation, using the FEA software ABAQUS, aimed to study the behaviour of the novel anchoring device which is patented in Europe under the patent number WO2011073696.*

1 INTRODUCTION

Many reinforced concrete (R/C) structural members need strengthening either because they were built according to old code provisions and do not meet the current design requirements, or because they are damaged after extreme events such as a strong earthquake sequence and they are in need of repair and strengthening. [1,2] When such a strengthening scheme uses externally bonded FRP layers one of the basic problems is the effectiveness of the anchorage of these polymer sheets to the concrete parts. This is necessary, in order to transfer successfully the desired level of tensile forces that develop on these layers and to exploit their high tensile capacity. Thus the satisfactory behavior of such an anchorage scheme, without premature failure, becomes critical in order to utilize successfully the high levels of tensile forces that these FRP layers can withstand and thus meet the strengthening design requirements for the structural members under consideration.

There is a real necessity to develop reliable anchoring details that can accompany repair and strengthening schemes of Reinforced Concrete elements employing FRP layers in such a way that the FRP parts together with their anchoring detail can provide a feasible and safe solution for such an application.

When fiber reinforced polymer sheets are bonded to the face of an R/C member with the use of a structural epoxy resin, the most common type of failure is the debonding of the FRP sheets from the structural member. Numerous researchers [1-6] have conducted experiments to study this debonding type of failure (figure 1) and to investigate means for improvement. It was shown that the desired capacity of such a R/C member strengthened with the use of FRP's could be reached easier when this debonding type of failure of the FRP sheets is delayed. It was also demonstrated that the surface preparation can be of importance for delaying this debonding type of failure. Apart from the good bonding an alternative way is to use appropriate anchoring devices. It was also shown [7-11] that utilizing mechanical anchors one can rely less on the bond which is provided to the FRP-concrete interface by the use commercially available epoxy resins.

The work reported here is an extension of the research performed by Manos and Katakalos [16] on effective anchoring devices of externally bonded FRP strips. Such devices can uphold the premature FRP strip debonding mode of failure and instead direct the mode of failure to the fracture of the FRP strip, thus resulting in a substantial increase of the ultimate bearing capacity of the strengthening scheme.

2 NOVEL ANCHORING SCHEMES UNDER MONOTONIC LOADINGS NUMRICAL AND EXPERIMENTAL INVESTIGATIONS

2.1 Experimental Setup

The present research aims to investigate the effectiveness of a specific FRP anchoring device (SWFX) combined with a typical FRP strip, by applying them to a number of small concrete prismatic specimens, which can house such strengthening systems with sufficient width and length. Totally 12 specimens were investigated utilizing the novel experimental setup developed on the Laboratory of Strength of Materials and Structures (LSMS) [7, 16] which is presented in figure 1. The details of all specimens are presented in the following Table 1.

Two specimens were utilized as reference specimens having the CFRP strips fully wrapped around the concrete T-section prisms, as depicted in figure1. (Ref-1 and Ref-2) Three speci-

mens were utilized to investigate the behavior of the FRP anchoring scheme it self. (SWFX-1 to SWFX-3) Three specimens were tested having one layer of CFRP strip combined with one anchor; whereas four last specimens were investigated utilizing one layer of CFRP strip combined with two anchors. The materials were provided by SIKA Hellas, which is greatly acknowledged.

All concrete prisms were fabricated using the same concrete mix and the same internal reinforcement, which was used to prohibit any accidental failure. The measured cylinder strength of the concrete was equal to 22 MPa.

Table 1. Details of experimental investigation

Specimen's name	CFRP strip	Anchoring Scheme	No. of tests	Remarks
Ref	1 CFRP strip	No	2	Full Wrapped
SW600C/2	1 CFRP strip	2 X Anchors	4	System Lay Up: Anchor Spread / Fabric / Anchor Spread
SW600C/1	1 CFRP strip	1 X Anchor	3	System Lay Up: Anchor Spread / Fabric
SWFX	No strip	ONLY Anchor	3	Full Wrapping

The main goal of the experimental study is to investigate the combined behavior of the strengthening scheme (anchor + CFRP strip) and to demonstrate any limitations that may arise by the use of such anchoring schemes. For this specific investigation the experimental setup developed in the Laboratory of Strength of Materials and Structures of A.U.Th. (fig. 1) was utilized. [1, 7, 16]

The loading arrangement is also depicted in figure 1, whereby the tensile force is directly applied in the axis of symmetry at the concrete prism; two sides of the FRP strip are bonded in a symmetric way on the top and bottom side of the concrete prism, as shown in this figure.

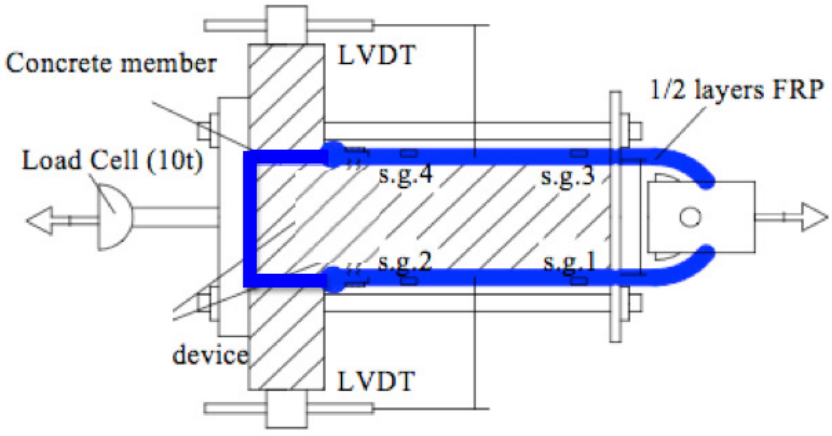


Figure 1. Novel experimental setup developped at LSMS premises [7].

Despite the symmetry of this test set-up, instrumentation was provided that is able to record symmetric as well as asymmetric response of the specimen, especially during the initiation and propagation of the debonding process. During testing, the applied load is measured together with the longitudinal (axial) strains at two different locations of the external surface of the FRP strip, as indicated in figure 1. (s.g.1 and s.g.3) The strains are measured in order to acquire an indication of the developed stresses locally at these specific locations.

The tested specimens with their details are listed in table 1 together with their reference names.

2.2 Experimental results and discussion – monotonic conditions

The summary of the experimental results is listed in Table 2. In this table, the observed failure mechanism is listed together with the corresponding value of the ultimate measured load at each CFRP strip. Moreover, the average maximum strain values measured by the strain gauges at locations 1 and 3 on the CFRP strip surface are also presented.

Table 2. Summary of the obtained results

Specimen's name	Load at each FRP strip (kN)	Average Load (kN)	Average strain from both sides	Average Strain (mm/mm)	Mode of failure
Ref-1	49.33	42.81	0.0066	0.0058	Fracture of FRP strip
Ref-2	36.30		0.0051		Fracture of FRP strip
SW600C/2 -1	39.73	43.06	0.0052	0.0053	Fracture of FRP strip
SW600C/2 -2	48.59		0.0064		Fracture of FRP strip
SW600C/2 -3	30.93		0.0042		Fracture of FRP strip first a width of 8mm
SW600C/2 -4	52.99		0.0053		Fracture of FRP strip
SW600C/1 -1	30.44	33.06	0.0039	0.0042	Fracture of anchor at upper corner
SW600C/1 -2	34.38		0.0044		Delamination of FRP strips form anchor
SW600C/1 -3	34.36		0.0044		Fracture of anchor at upper corner
SWFX -1	34.54	34.89	-		Fracture of anchor
SWFX -2	36.29		-		Fracture of anchor
SWFX -3	33.85		-		Fracture of anchor

CFRP strips of specimens Ref-1 and Ref-2 were fully wrapped around the concrete prisms and are utilized as reference specimens. The average ultimate load was recorded equal to 42.81kN. The mode of failure for both reference specimens was observed at the fracture of the strips. The mode of failure for all specimens is presented in figures 2a to 2e. The performance of the FRP anchoring scheme was separately investigated before its application with CFRP strips. Specimens SWFX-1 to SWFX-3 were tested for this purpose monotonically to failure. The average ultimate load for these three specimens was equal to 34.89kN. The mode of failure was observed at the fracture of the anchoring scheme. (see figure 2d and figure 2e)

The anchoring scheme together with one layer of CFRP strip was applied to strengthen specimens SW600C/1-1 to SW600C/1-3. The average load for all three specimens was recorded equal to 33.06kN, whereas the mode of failure was observed to the fracture of the



Figure 2a. Ref-1 and Ref-2



Figure 2b. SW600C/2-2



Figure 2c. SW600C/1 -1



Figure 2c. SW600C/1 -2



Figure 2d. SWFX -1



Figure 2e. SWFX -2

anchoring scheme. As observed both SW600C/1 and SWFX exhibit similar average ultimate load and similar mode of failure. The premature failure of the anchor, before the fracture of the strip results in decreasing the exploitation of CFRP strips. The fact that the ultimate strength of both SW600C/1 and SWFX is similar, enhance the validity of the experimental investigation.

In order to avoid the premature failure of the anchoring scheme, specimens SW600C/2 were fabricated combining 2 anchors with one CFRP strip. The average load for the three specimens is equal to 43.06kN whereas the mode of failure was observed at the fracture of the CFRP strip. Following the previous rational when applying two anchors the CFRP strip is fully exploited since the mode of failure is located at the fracture of the strip itself.

The measured strains are also demonstrating the same observation. More specifically the average strain of specimens SW600C/2 is equal to 0.0053 (mm/mm) very similar with the measured strains of specimens ref-1 and ref-2. (0.0058 mm/mm) By comparing the average strains of SW600C/1 specimens with SW600C/2 specimens it could be said that the exploitation of the strips increased almost 30%. Summarizing, the use of two anchors combined with one CFRP strip (width=100mm) ensures the full nominal exploitation of the strip, drives the mode of failure to the fracture of the strip it self and avoids the fracture of the anchorage scheme.

When a properly designed anchoring device is employed the mode of failure is driven to the fracture of the FRP strip, resulting to an increase of the ultimate bearing capacity of the strengthening scheme and an increase of the exploitation of the material. The uncertainties imposed by this type of FRP anchor, such as the complete impregnation of the epoxy into the fibers of the anchor, the percentage of the fibers that are fractured during installation, the stress concentration at the edges of the anchoring scheme, are leading the writers to investigate another anchoring device made of steel components which has been patented in Europe under the patent number WO2011073696 [15]. The following paragraph deals with the numerical development of such a novel anchoring setup utilizing the numerical simulation software ABAQUS.

2.3 Numerical development of the novel patented anchoring scheme

At this preliminary design stage, the novel patented anchoring scheme was initially developed through a parametric numerical simulation, which is eventually supplemented by specific tests with pilot anchor specimens. It should be noted that the developed numerical models are rather crude since they aim to extract the basic structural response of the proposed novel anchoring scheme, which are further studied experimentally. Figure 3 depicts the main outline of the device. It consists of two vertical steel bolts that support a horizontal cylindrical steel rod. The largest portion of the vertical steel bolts below the horizontal rod has sufficient length and shape to be effectively embedded within the volume of the R/C foundation. The horizontal steel rod is utilized to facilitate the wrapping of FRP layers around it. Both wings of these FRP layers wrapped around the steel rod become one sheet that is next attached, with the use of epoxy resin and anchor bolts, on to the side of the R/C pier specimen to a sufficient length.

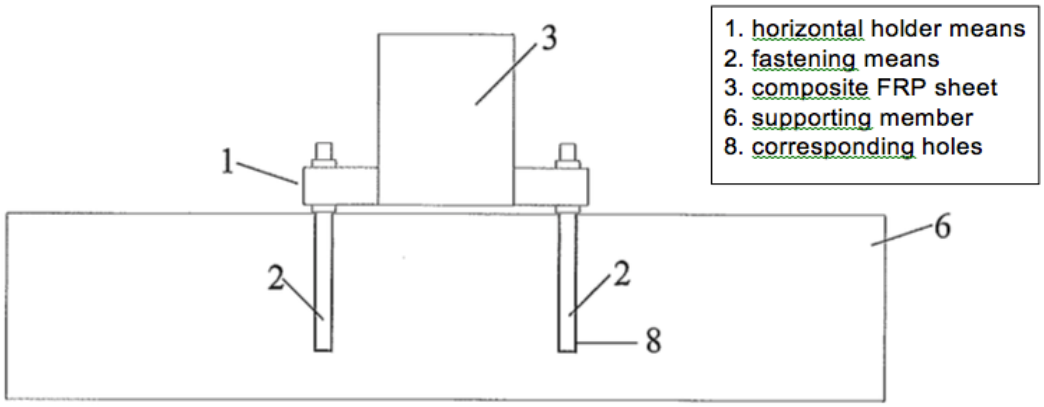


Figure 3. Novel patented anchoring device (WO2011073696 [15])

The limit state that concerns the debonding of FRP layers from the side of the pier specimen is experimentally controlled through this specific attachment technique and the attachment length; as a result it is not investigated further in this section. Furthermore the vertical steel bolts are assumed to have sufficient embedment details as to provide the required resistance against the limit state that leads to the pull-out of these bolts from the concrete foundation. Thus, excluding the debonding of the FRP layers from the side of the specimen and the pulling out of the embedded vertical steel bolts, the remaining failure modes that are considered in the parametric investigation are threefold. The first mode is the yielding and eventual fracture of the vertical steel bolts at the portion that lies between the foundation and the horizontal rod. Any other type of failure of the connection between the vertical bolts and the steel rod is excluded. The second mode of failure is the yielding of the steel horizontal rod and the third and last mode of failure is the fracture of the FRP sheet, which is wrapped around the horizontal rod.

A FEA commercial program, ABAQUS, is used for the parametric numerical simulation utilizing 3D finite elements. The horizontal rod is assumed to be made of mild steel with yield stress equal to 360Mpa, whereas the vertical bolts are assumed to be made of high yield point steel (550Mpa). In any case the same type of investigation can be easily repeated with alternative material properties.

Thus the parametric investigation focuses on the following specific parameters that are directly connected with the novel anchoring scheme. These are:

a) the width and thickness of the FRP layers that are wrapped around the horizontal steel rod
b) the span and the diameter of the horizontal rod
c) the length and the diameter of the portion of the vertical bolts that lies between the foundation and the horizontal rod.

All the parameters mentioned in the a), b), c) above are varied within certain practical limits in order to investigate the sensitivity of the behavior of the novel and patented anchoring scheme to their variation. Of the outmost interest is how the variation of these parameters (a,b,c above) influences the post-elastic behavior and the prevailing mode of failure.

A tri-linear constitutive material low is assumed for the mild steel and the high yield strength steel whereas the FRP layers are assumed to be made of carbon and to behave elastically till a fracture limit stress. The corresponding values for the constitutive laws of each one of these three materials, which were assigned in this particular software, are listed (Table 3).

Table 3. Material properties of the novel, patented anchoring device

Part of HAD	Modulus of Elasticity (Mpa)	Yield stress (Mpa)	Ultimate stress (Mpa)
Horizontal Steel Rod	200000	360	396
Vertical Steel Bolts	200000	550	650
CFRP Sheet	500000	-	5500

Figure 4 shows a typical geometry of the device with a horizontal rod having a total length equal to 280mm and a diameter of 40mm. The vertical steel bolts have a diameter of 18mm. As mentioned before, this is an initial geometry with certain parameters varied through the parametric numerical investigation.

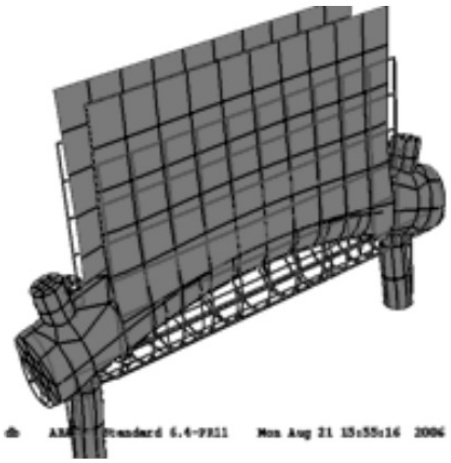


Figure 4. A typical geometry of the novel, patented anchoring device

The numerical investigation assumed, as well, that the bottom ends of the vertical steel bolts are fully fixed. Moreover, the connection between the horizontal rod and the vertical steel bolts was assumed to be monolithic. The loading was imposed as a prescribed uniform vertical displacement pattern at the full length of the upper part of the CFRP sheet. As a result, the CFRP is subjected to tension whereas the horizontal rod undergoes flexure. The contact surface between the CFRP sheet and the horizontal rod is considered as frictionless; thus the CFRP sheet can slip or move independently from the rod.

A large number of parametric numerical simulations have been conducted. Tables 4 and 5 present the most important numerical models that were employed to study the novel, patented anchor's behavior. They are categorized according to the investigated variable, which is listed in the rows of the first column. For the numerical simulations that correspond to each one of the main rows of Tables 4 and 5, the values of the corresponding variable are changed as listed, whereas the values of all the other parameters remain constant (with italics in the 1st column of Table 4) as defined in the initial geometry; that is a horizontal rod with a length of 280mm (235mm from the supports), and a CFRP layer of thickness 0.7mm (4 layers) with a length of 180mm. The typical geometry of the vertical steel bolts is of 18mm diameter and 70mm length. A typical deformed shape of the numerical model of the anchor under the imposed displacement pattern is depicted in Figure 4.

In the first row of Table 4 the variable parameter is the diameter of the horizontal rod from 40mm to 20mm. Figures 5a, b, c depict the axial stress distribution for the CFRP sheet wrapped around the horizontal steel rod. As expected, the bigger the diameter of the horizontal rod the smaller the curvatures it develops along its axis leading to a more uniform axial stress distribution for the CFRP sheet, as shown by the white line diagram that represents the axial stress distribution on a cross section 40mm from the axis of the rod. It was assumed that a strain of 1.1% resulted in the failure of the CFRP sheet.

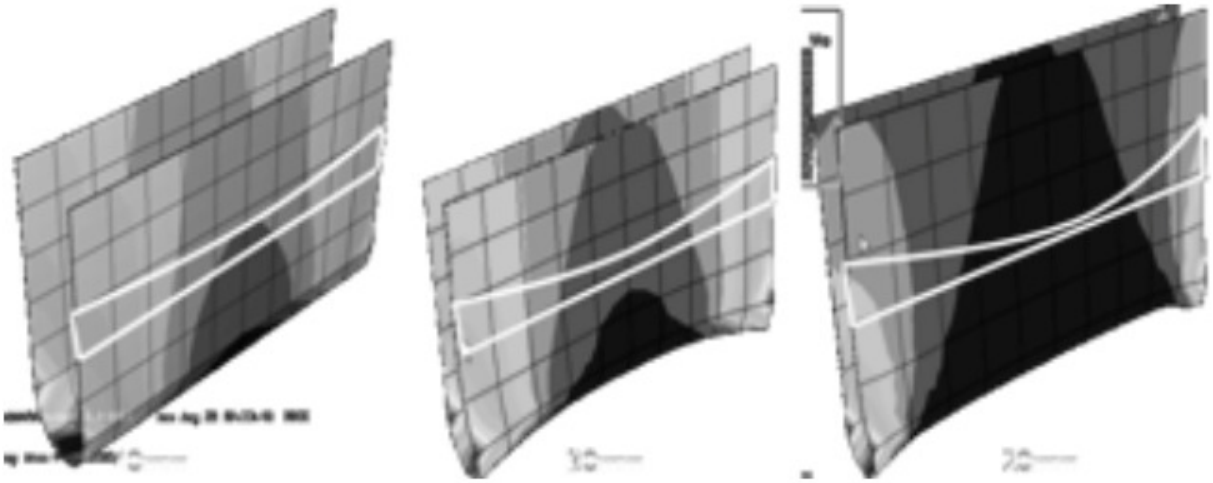


Figure 5. Distribution of axial membrane stresses

Table 4. HAD with uniform diameter of the horizontal steel rod

Studied variable	Value of variable parameter	Applied Total Axial Load (kN)	No. CFRP layer	Limit Displacement (mm) Leading to failure	Mode of failure
(1)	(2)	(3)	(4)	(5)	(6)
rod's diameter *(rod's span 280mm) (CFRP's width 200mm)*	40mm	168	4	1.2	CFRP rupture
	30mm	119	4	1.0	CFRP rupture
	20mm	55	4	0.87	CFRP rupture
rod's span / CFRP's width *(rod's diameter 40mm)*	380mm / 200mm	131	4	2.5	CFRP rupture
	380mm / 300mm	180	4	1.5	CFRP rupture
	200mm / 120mm	217	4	2.5	CFRP rupture
rod's diameter *(rod's span 280mm) (CFRP's width 200mm)*	40mm / 30mm / 20mm	622 / 368 / 158	15 / 9 / 5	30 / 20 / 20	Rod yielding

In the second row of Table 4 the variable parameters is the ratio of the CFRP sheet width over the length of the horizontal steel rod. As can be seen, when this ratio is increased from an initial value corresponding to the typical geometry, this leads to a less uniform axial stress distribution and consequently to a relatively premature fracture of the CFRP sheet. This is again due to the fact that a relatively flexible rod develops larger curvatures along its axis thus influencing the corresponding axial stress distribution of the CFRP sheet. From the above observations it can be further concluded that it is not desirable to have a steel rod, either of relatively small diameter or large span, which develops large curvatures at the part where the CFRP sheet is wrapped around it. At the same time, horizontal rods with relatively large diameter and small span perform in elastic state of stress leading the HAD to develop either fracture of the CFRP, which also remains almost elastic up to its fracture, or leading to the yielding of the vertical steel bolts; the latter present a possible plastic mode of failure as will be discussed next. The resulting non-uniform distribution of the axial stress for the CFRP sheet for relatively large curvatures of the horizontal rod was accompanied by a decrease in the bearing capacity of the device in terms of limit imposed displacement (column 6 of Table 4) and applied total axial load (column 3 Table 4).

At this point it should be mentioned that for the current investigation the longitudinal shear strains were relatively small ($\approx 1.2 \cdot 10^{-4}$), which led to the adoption of a rather simplified failure criterion based on the longitudinal strains. For other more complex applications a more sophisticated failure criterion could be included in the future, which will not neglect the possibility of shear splitting failure.

In the third row of Table 4, the thickness of the CFRP sheet was increased to 2.63mm (15 layers) in order to lead the novel anchoring device into the yielding mode of the horizontal steel rod. As was expected, the smaller diameter rod resulted in much smaller yielding load of the device; however, in all these cases with the yielding of the horizontal rod, the limit total axial load (column 3 of Table 4) attained values larger than the corresponding values for all the previously investigated cases (rows 1 and 2) where the mode of failure developed due to the fracture of the CFRP sheet. Moreover, the obtained load-displacement behaviour of the patented anchoring scheme with the yielding rod, exhibited post-elastic trends that represent a desirable feature of its performance. Consequently, from all these findings of the numerical investigation it became obvious that the numerical performance of the device with a variable diameter, as shown in Figure 6, should be examined next.

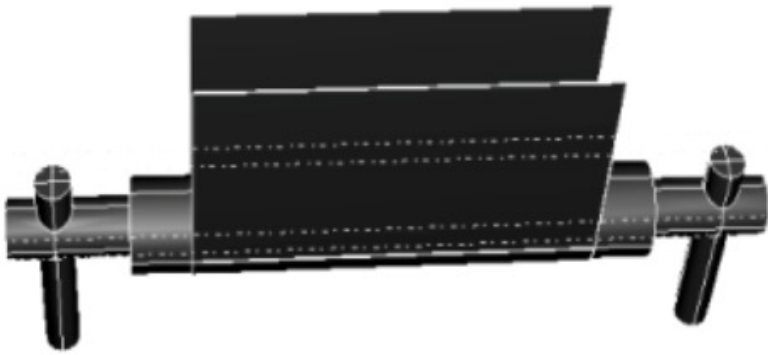


Figure 6. Patented anchoring device with variable diameter

Table 5. HAD with variable diameter of the horizontal steel rod

Studied variable	Value	Applied Load (kN)	No. CFRP layer	Limit Displ. Leading to failure (mm)	Mode of failure
(1)	(2)	(3)	(4)	(5)	(6)
rod with variable diameter	Max diameter: 40mm (span 200mm) Small diameter:20mm (40mm each side)	180.5	4	5.7	Plastic region yielding
Vertical bolt diameter @ length	18mm @ 100mm / 18mm @ 70mm	278 / 300	6 / 6	12 / 10	Vertical Bolt yielding
	20mm @ 100mm / 20mm @ 70mm	310 / 340	6 / 6	10 / 7.5	
Tested HAD	D_{rod} = 40mm L_{rod} = 340 mm L_{CFRP} = 120 mm	48	4	2.35	CFRP rupture

This novel anchoring device model had a horizontal rod with two specific regions; the region near the vertical steel bolts was made with a diameter smaller than the diameter of the central region. The values of these parameters are listed in the first row of Table 5. The reduction of the diameter of the horizontal rod was aimed at developing the large curvatures from flexure leading to the yielding of these two regions, whereas the central region with the relatively large diameter, used for the wrapping of the CFRP sheet, developed much smaller curvatures and thus prohibited the premature fracture of the CFRP. In Figure 7 the obtained load-displacement behavior of the patented scheme with variable diameter is compared with the corresponding behaviour of two model device's with constant diameter. There is no plasticification of the steel rod for the first model with constant diameter value the same as that of the central region of the variable-diameter-scheme (large diameter). On the contrary, plasticification of the steel rod is evident for the second model with constant diameter value equal to the small diameter of the variable-diameter. Similar plasticification is evident for the variable di-

ameter patented device, which develops the desired performance in terms of ductile behavior. Moreover, because of the non-plastification of the central region, which is accompanied with relatively small curvatures, the undesirable premature fracture of the CFRP is avoided.

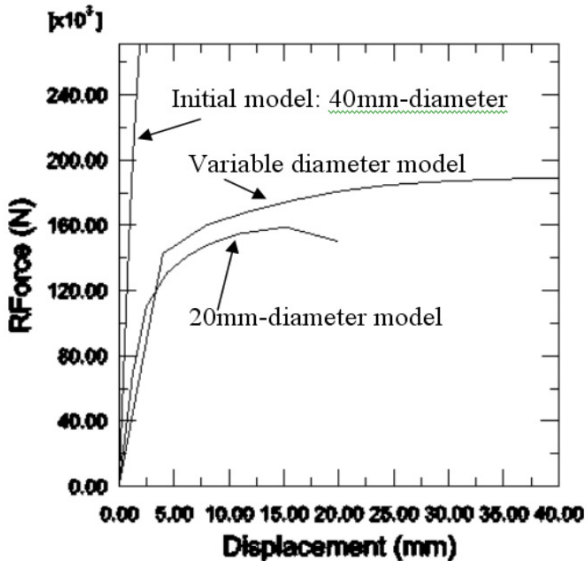


Figure 7. Load-Deflection diagram for the three models

The parameters that are varied in the second row of Table 5 are the diameter and length of the vertical steel bolts. In the corresponding numerical simulations the thickness of the CFRP sheet was increased to 1.05mm (6 layers) in order to lead the HAD into the yielding mode of the vertical steel bolts. The diameter of these bolts was varied from18mm to 20mm whereas the clear length was varied from 70mm to 100mm. In the initial modeling of the yielding behavior of the vertical steel bolts, the horizontal rod was artificially assumed to remain elastic. After this behavior was verified the next numerical model of the variable-diameter model was purposely formed to be capable of capturing the yielding mode of failure either of the vertical steel bolts or of the small diameter portion of the horizontal rod. As expected, relatively small-diameter, long vertical bolts will eventually lead the yielding mode of failure to these bolts rather than the horizontal rod, if so desired. As a result, varying the basic parameters of the device, e.g. the small diameter of the rod, the diameter of the vertical bolt and the number of CFRP layers (with their width and thickness), the desired performance of the patented device in terms of ductile bearing capacity and mode of failure can be obtained by the proposed numerical investigation as a preliminary design of this novel patented anchoring scheme. From the preceding investigation, the ductile performance can be obtained by either the yielding of the small diameter portion of the rod or by the yielding of the vertical bolts, or if the parameters are adjusted properly by the yielding of both parts. However, it is believed that the yielding of the small diameter portion of the horizontal steel rod is preferable as the device can be manufactured in such a way that the ductile behavior of this part is reversible. It is believed that the vertical bolts should have a capacity large enough (with sufficient embedment within the concrete foundation) to exclude the possibility of any pull-out failure mode. Finally, the deformed horizontal rod can be replaced more easily compared to the replacement of the vertical bolts.

The last row of Table 5 lists the parameters of a final numerical model, which was eventually manufactured and tested experimentally as will be explained in the following.

This final numerical device model, depicted in Figure 8, had a horizontal rod with two specific regions called regions of plastic hinges, which were of a diameter smaller than the di-

ameter of the horizontal rod away from these regions. This numerical model incorporated all the capabilities of the previously performed investigation in terms of non-linear behavior. Thus, the rod had sufficient diameter at both of its edges as to be able to incorporate relatively large diameter vertical bolts and confine the yielding of the device at specific regions named "plastic hinges". This final numerical model, with the two plastic hinge regions, developed, as expected, a more uniform distribution of the axial tensile stresses for the CFRP without significant stress concentration that may potentially lead to premature tensile fracture of the CFRP unlike the model with constant diameter. Finally, considerable plastic strains developed at the plastic hinges thus providing this model with the desired ductile behavior for a target axial load bearing capacity (Figure 9).

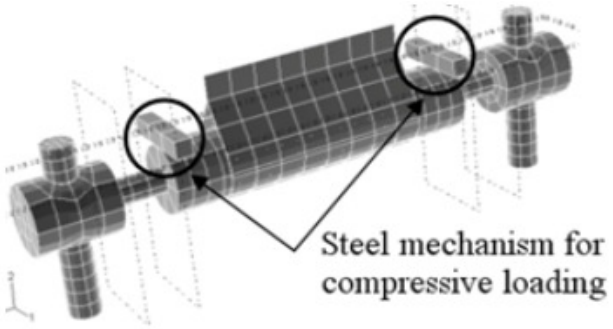


Figure 8. Novel patented anchoring scheme model with plastic hinges (zones)

3 EXPERIMENTAL INVESTIGATION OF THE NOVEL DUCTILE ANCHORING DEVICE UNDER LOAD-UNLOAD SEQUENCE – NUMERICAL VALIDATION

3.1 Experimental setup – cyclic loading sequence

Different anchoring schemes of FRP strips, under monotonic loading conditions, have been studied in the past by several researchers. [12-19] On the other hand experimental investigations under cyclic loading – unloading sequence are rare in the literature. The present study is moreover, focusing on experimentally investigating under cyclic loading conditions, the novel anchoring device developed by the Laboratory of Strength of Materials and Structures of Aristotle University of Thessaloniki in Greece, which is patented with patent number EP 09386037.7 [8,15].

Totally 3 specimens were tested under cyclic loading – unloading conditions. The idea of investigating experimentally the novel and patented anchoring scheme with combining FRP strips is further examined in this section. There are small differences in the shapes of the anchoring device in order to investigate the developed ductility on the anchoring scheme. The first type is an anchoring scheme with plastic zones. The second type is identical with the first type with a small change, which is located in the plastic zones that have smoother corners. Finally the third type is an anchor device without any plastic zone. Figures 9a to 9c present the different types of the novel anchoring device.

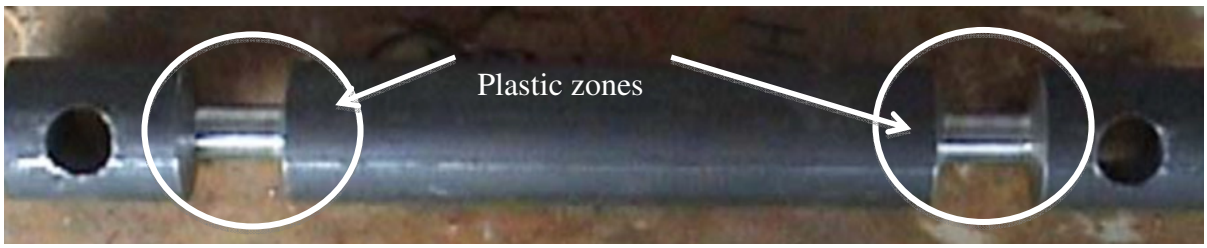


Figure 9a. First type of anchoring scheme

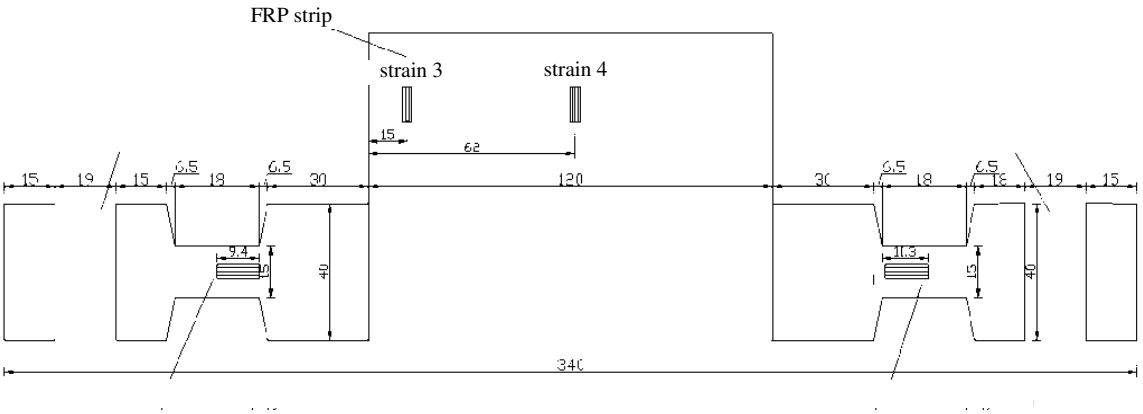


Figure 9b. Second type of anchoring scheme

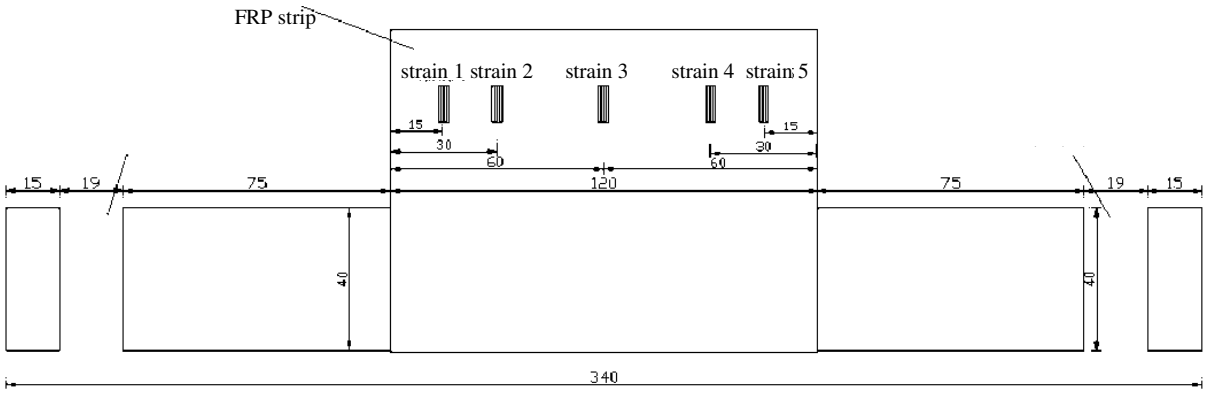
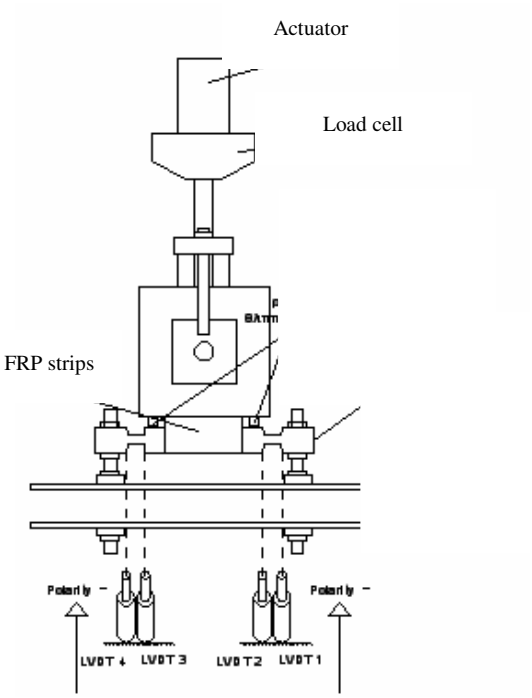


Figure 9c. Third type of anchoring scheme

The experimental setup is depicted in the following figures 10a and 10b. The cyclic loading unloading displacement is imposed utilizing a hydraulic actuator. The imposed load is monitored with a 100kN dynamic load cell.





Figures 10a and 10b. Experimental setup and instrumentation

At the same time four LVDTs are place at the edges of the plastic zones (see figure 11) to monitor their relevant deformations. Finally strain gages were placed to several positions in order to measure accurately the developed strains and stresses both on the anchoring device and on the FRP strips.

The imposed displacement protocol is depicted in the following figure 12. The target displacement was imposed for three cycles and was increased up to failure. For the first and second type of the anchoring scheme, a metallic prismatic element was utilized to enable the ability of the anchoring scheme to withstand negative forces during the unloading sequence.

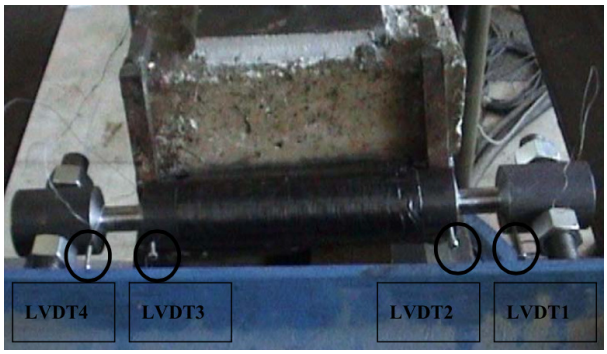


Figure 11. Position of LVDTs at plastic zones

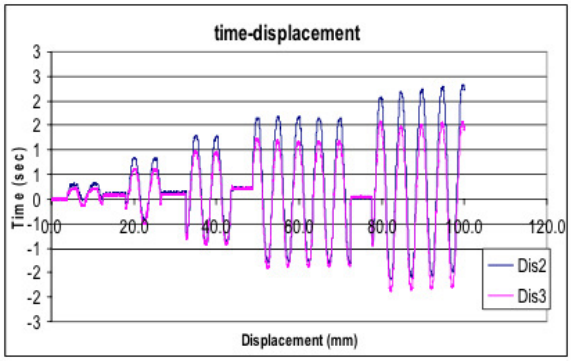


Figure 12. Imposed displacement protocol

3.2 Experimental results – cyclic loading sequence

The cyclic loading – unloading sequence was performed to all three types of the novel patented anchoring scheme that is combined with FRP strips. Figures 13a to 13e present the load - displacement graphs for the three types of the anchoring scheme.

Table 3. Load – displacement graphs for the three types of the novel anchoring scheme

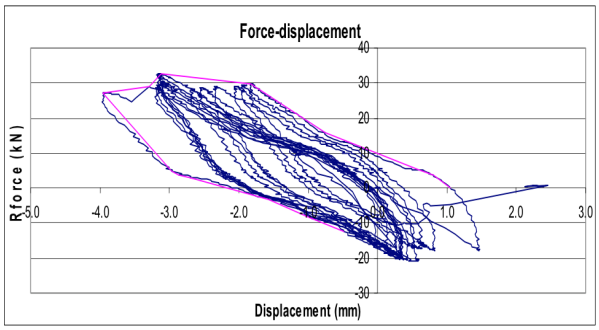


Figure13a.Total force – Displacement of type_1 anchor

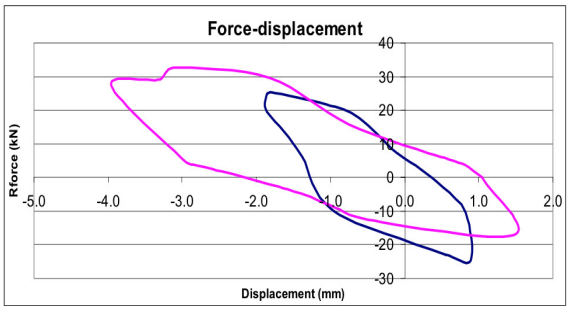


Figure13b. Envelope curves of type_1 anchor

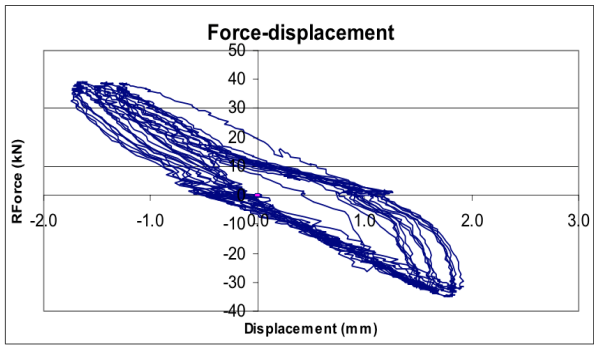


Figure13c.Total force – Displacement of type_2 anchor

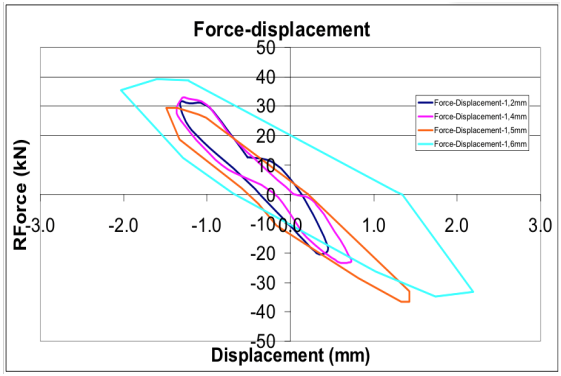


Figure13d. Envelope curves of type_2 anchor

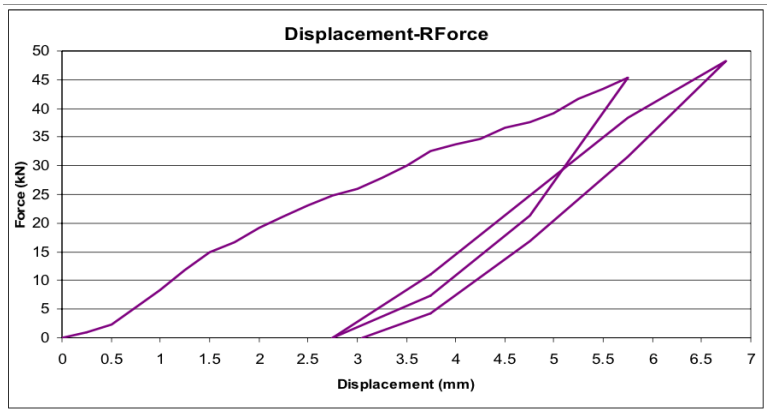


Figure13e. Total force – Displacement of type_3 anchor (two cycles of loading – unloading)

Taking under consideration the graphs depicted above, it could be said that the overall behavior of the strengthening system FRP strip – Anchoring device exhibit a relative ductile behavior. Anchoring schemes with plastic zones exhibit a more ductile behavior than the anchoring zone without the plastic zone (3rd type). The number of cycles does not affect significantly the behavior of the strengthening system. The potential influence of the number of

cycles could arise because of the type of the material, since the components of the anchoring device are made of steel. This parameter is not investigated in the present study.

The novel anchoring device for FRP strips was tested under cyclic loading – unloading sequence. All three types of the novel anchoring device behaved in-elastically. The use of the anchoring system results in transmitting the linear developed stresses of the FRP strip, to the concrete elements in a ductile manner through this patented anchoring device. It is obvious that when the plastic zones exist, the ductile behavior is more pronounced.

The following figure 14 presents four load-stress graphs. The blue and brown curves depict the strains in the middle and at the corner of the width of the FRP strip that is wrapped around the anchoring device with the plastic zones. The yellow and pink curves present the equivalent strains on the FRP strip when it is combined with the anchoring device without the plastic zones.

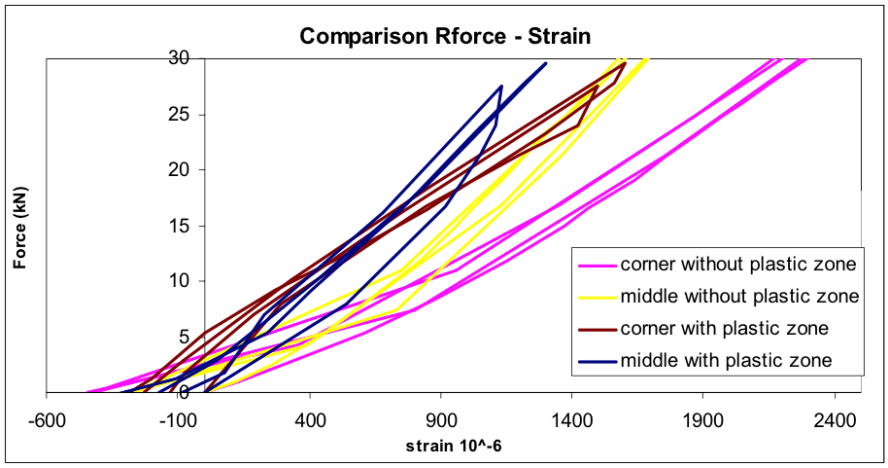
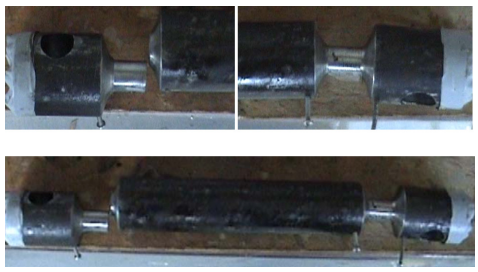


Figure 14. Comparison total load – developed strain graph with and without plastic zones

Table 6. Modes of failure for all three types of the novel anchoring device



Yielding and fracture of plastic zone (type_1 anchor)



Yielding and fracture of plastic zone (type_2 anchor)



Fracture of FRP strip (type_3 anchor)

It is evident that the stress distribution on the FRP strip with the plastic zones is more uni-

form than the equivalent one without the plastic zones. In this point of view and based on the results of the monotonic loading sequence, when the novel anchoring device has the plastic zones, the FRP strip could be exploited more efficiently.

The modes of failure are depicted in table 6. The yielding of plastic zones was followed by their fracture. On the other hand type 3 anchoring scheme, without plastic zones, drove the mode of failure to the fracture of the FRP strip, a much less ductile mode of failure.

3.3 Numerical validation – cyclic loading sequence

The experimental behavior of the novel, patented anchoring scheme is compared with the numerical results of the aforementioned investigation. The mechanical properties of the materials forming the pilot device specimens were obtained by specific tensile experiments that resulted in mechanical values the same as the ones used in the numerical simulation. One pilot novel anchoring device specimen was made with a horizontal steel rod of constant diameter whereas the other had a variable diameter with the aforementioned plastic hinge zones at specific locations, as shown in Figure 8.

Apart from this difference all the rest of the geometric and material properties were the same for all specimens. The depicted geometry is the same as the one assumed as being "typical" for the performed parametric numerical investigation; that is, a horizontal rod with a length of 340mm (290mm from the supports), an initial diameter of 40mm (and a diameter at the plastic hinge regions of 15mm) and a CFRP layer of thickness 0,7mm (formed by 4 CFRP layers) with a length of 120mm. Each plastic hinge region had a length of 20mm and each vertical steel bolt was of 18mm diameter and 70mm length. These two pilot novel anchoring specimens, including the CFRP layers wrapped around their horizontal steel rod, were placed in a reaction frame, which included a dynamic actuator (Figure 10), as mentioned before.

The strains measured at the CFRP sheets are compared with the values predicted from the corresponding numerical simulation. Next, to compare the measured overall load-displacement response of the pilot HAD specimens with that predicted numerically. Finally, to compare the observed mode of failure for both pilot HAD specimens with the relevant limit states predicted by the numerical simulation.

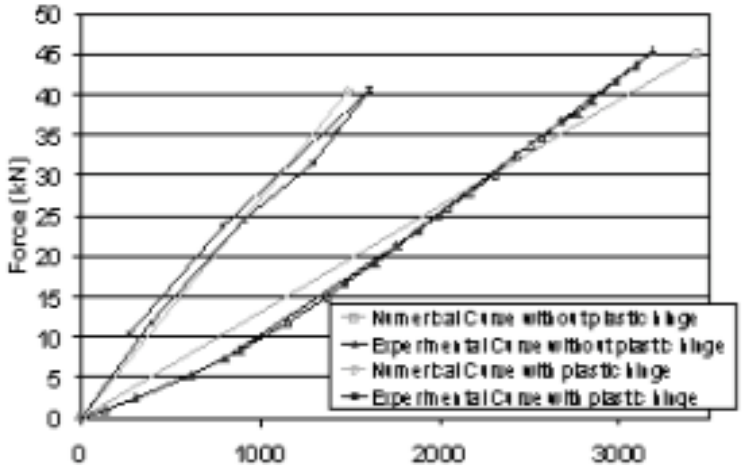


Figure 15. Numerical vs Experimental load-strain variation for the novel anchoring scheme with and without plastic zones (CFRP strains at edge of the CFRP layers)

The term axial strain indicates that the axis of the strains measured by the strain gauges coincide with the axis of the applied load and the axis of the carbon fibers forming the CFRP strips. The variation of the predicted and measured axial strains against the applied load are plotted in Figure 15. This is done for all novel, patented anchoribg schemes with or without plastic zones. For given amplitude of applied load the strains measured near the edge of the CFRP sheet are considerably larger than the corresponding strains measured at the middle of this CFRP sheet, validating a similar finding of the numerical investigation (Figures 5 and 14). As has been already pointed out, this is an undesirable state of stress, which can lead to premature tensile failure of the CFRP sheets. In contrast, the measured strains at the CFRP wrapped around the horizontal rod of the variable-diameter-HAD with the plastic hinge regions remain almost constant along the width of this CFRP sheet, a fact that also verifies the numerical investigation findings. On the basis of this evidence, it can be concluded that the proper location of the "plastic zone" regions along the span of the horizontal rod of the novel anchoring scheme, results in the mitigation of an undesirable non-uniform tensile stress field for the wrapped around this rod CFRP strips.

Figure 16 depicts the measured and numerically predicted applied load – displacement response for the device specimen with the plastic hinges. As can be seen in this figure, the predicted load level that corresponds to the development of large deformations (due to the material yielding of the plastic regions) agrees well with the corresponding measured value.

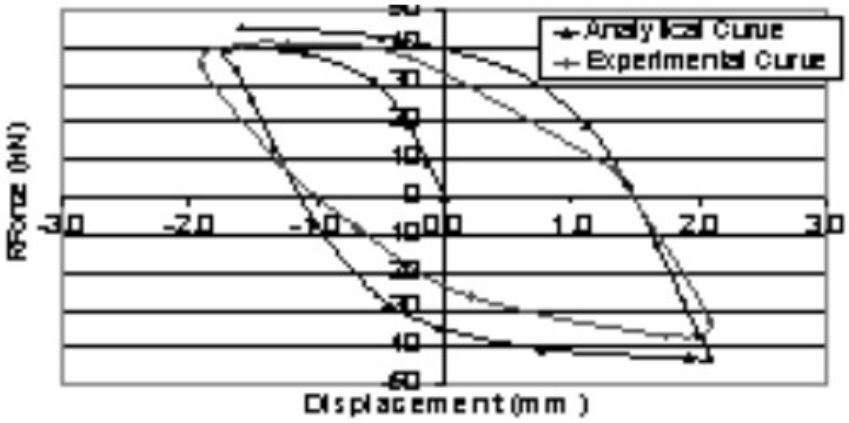


Figure 16. Load-deflection numerical and experimental behavior

The measured initial stiffness is smaller than the numerically predicted value, a fact that must be attributed to the deformability of the vertical steel bolts connecting the experimental anchoring scheme specimen to the reaction frame. This observation can also be made when comparing the predicted and measured load-deflection response of the scheme without the plastic hinge regions. For an applied load of 40.4 kN the measured strain values are compared with the corresponding numerical strains for both the CFRP sheet (left part of Figure 17) and the plastic hinge zone of the horizontal rod of the variable-diameter anchor specimen (right part of Figure 17, $\varepsilon = 1.13\%$). Reasonably good agreement can be seen in this comparison.

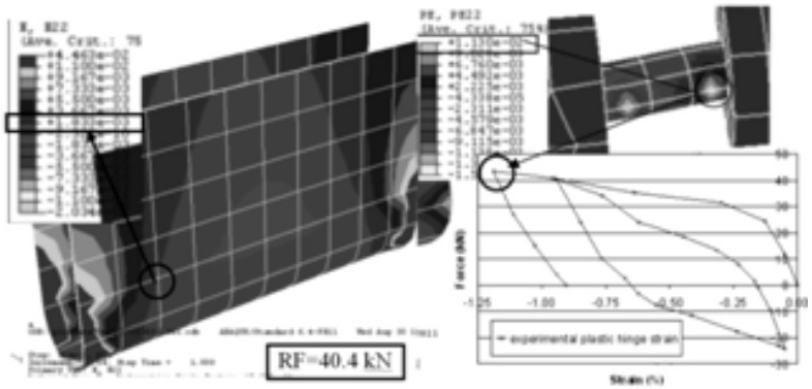


Figure 17. Developed strains on CFRP and on plastic zone

Finally, as discussed in the previous section, the brittle fracture of the CFRP sheet occurred, as expected, for the novel patented anchoring scheme without the plastic hinge zones. In contrast, the patented anchoring scheme with the plastic zones exhibited, as predicted, reasonably good ductile behavior, due to the yielding of the steel at the plastic zones; this led eventually to the fracture of the left plastic hinge, after a considerable number of load reversals that exceeded the measuring capacity of the strain gauges (Table 6). On the basis of all these observations it can be concluded that the behavior of the novel, patented anchoring device can be predicted numerically with sufficient accuracy employing the previously prescribed modeling procedure.

4 CONCLUSIONS

- In order to transfer effectively the tensile forces developed on FRP strips that are bonded externally towards upgrading the flexural or shear capacity of reinforced concrete members a properly designed anchoring device should be employed. In this way, the premature FRP strip debonding mode of failure can be prohibited and instead direct the mode of failure to either the fracture of the FRP strip or the yielding of the anchoring scheme, thus resulting in a substantial increase of the ultimate bearing capacity of the strengthening scheme.
- Such an anchoring device, designated as SWFX, was examined in the framework of the present study under monotonic load conditions. It utilizes one or two FRP anchors with one CFRP strip. This anchoring scheme ensures up to a certain level of load the safe transfer of forces from the strip to the R/C prism. However, the final mode of failure is the fracture of the FRP anchor.
- The alternative patented anchoring device, which is designated as anchoring device with European Patent, utilizes two steel anchor bolts and a steel rod. When properly designed it can withstand one or more FRP strips with the final mode of failure directed either to the fracture of the FRP strips or to the plastic zones of the device itself. In this way a very substantial increase of the targeted bearing capacity could be reached. Moreover, an effective exploitation of the FRP material can also be achieved.

- The anchoring device with the EU patent can also be detailed in a way that can include a zone that can be plastified at certain level of force to be transferred. The stress distribution on FRP strip with such plastic zones is more uniform than the equivalent one without the plastic zones. In this way the FRP strip is protected from premature fracture, which is a common undesired mode of failure that occurs in such FRP location of stress concentration.
- Such an anchoring device with plastification zones was examined under cyclic seismic-type loading. It is demonstrated that this anchoring device was able to withstand a considerable number of cyclic load reversals performing in a stable way and dissipating plastic energy through the zones of the steel rod that this anchoring device was detailed for.
- As already stressed, it is of the utmost importance the design and the detailing of such an effective anchoring device. Towards this objective, results from series of numerical simulations were compared with the corresponding experimental measurements in order to establish the validity of such a numerical simulation as a design tool for such an effective anchoring device.

5 ACKNOWLEDGEMENTS

- Carbon fibers, anchors and epoxy resins were provided by Sika Hellas.
- One of the employed in this study anchoring devices (cyclic investigation) is patented under the no. EP09386037.7
- PartialfinancialsupportforthisinvestigationwasprovidedbytheHellenicEarthquakePlanning and Protection Organization (EPPO)

REFERENCES

[1] C. E. Bakis, L. C. Bank, V. L. Brown, E. Cosenza, J. F. Davalos, J. J. Lesko, A. Machida, S. H. Rizkalla, T. C. Triantafillou. In: Journal of Composites of Construction, ASCE, May 2002.

[2] Manos G.C., Theofanous M., Katakalos K. “Numerical simulation of the shear behaviour of reinforced concrete rectangular beam specimens with or without FRP-strip shear reinforcement”, Advances in Engineering Software, 2014Mich. Fardis, M. N., and Khalili, H. ~1981in: ACI J., 78~6, 440–446.

[3] K Katakalos, CG Papakonstantinou, “Fatigue of reinforced concrete beams strengthened with steel-reinforced inorganic polymers”, Journal of Composites for Construction 13 (2), 103-112C.

[4] CG Papakonstantinou, K Katakalos, “Flexural behavior of reinforced concrete beams strengthened with a hybrid inorganic matrix-Steel fiber retrofit system”, Structural Engineering and Mechanics 31 (5), 567-585

[5] GC Manos, K Katakalos, CG Papakonstantinou, “Shear behavior of rectangular beams strengthened with either carbon or steel fiber reinforced polymers”, Applied Mechanics and Materials 82, 571-576

[6] J. H. Lee, M. M. Lopez, C. E. Bakis. “Flexural Behavior of reinforced concrete beams

strengthened with mechanically fastened FRP strip." FRPRCS-8, World Conference, University of Patras, July, 2007.

[7] GC Manos, K Katakalos, V Kourtides, "The influence of concrete surface preparation when fiber reinforced polymers with different anchoring devices are being applied for strengthening R/C structural members", Applied Mechanics and Materials 82, 600-605

[8] GC Manos, KV Katakalos, "The Use of Fiber Reinforced Plastic for The Repair and Strengthening of Existing Reinforced Concrete Structural Elements Damaged by Earthquakes", Fiber Reinforced Polymers - The Technology Applied for Concrete Repair

[9] Katakalos K, Papakonstantinou CG, Manos GC. Comparison between carbon and steel fiber reinforced polymer with or without anchorage. In: 6th CICE, Rome; 2012. □

[10] Lu XZ, Teng JG, Yea LP, Jiang JJ. Bond–slip models for FRP sheets/plates bonded to concrete. Eng Struct 2005;27:920–37. □

[11] Manos GC, Katakalos KV, "The Use of Fiber Reinforced Plastic for The Repair and Strengthening of Existing Reinforced Concrete Structural Elements Damaged by Earthquakes", Chapter 3, Fiber Reinforced Polymers - The Technology Applied for Concrete Repair

[12] Manos GC, Katakalos KB, Theofanous M., "Experimental Investigation and Numerical Simulation of Shear Behaviour of RC T-Beam Specimens with or without SFRP-strips under Cyclic Loading", Computational Dynamics, Conference, Krete-Greece, 2015

[13] Manos GC, Katakalos, KV "Investigation of the Force Transfer Mechanisms for Open Hoop FRP Strips Bonded on R/C Beams with or without Anchoring Devices", Open Journal of Civil Engineering, 143-153

[14] Manos GC, Katakalos K., "Enhanced Repair and Strengthening of Reinforced Concrete Beams Utilizing External Fiber Reinforced Polymer Sheets and Novel Anchoring Devices", 15th World Conference of Earthquake Engineering

[15] Manos GC, Katakalos K, Kourtides V. Construction structure with strengthening device and method. European Patent Office, Patent Number WO2011073696 (A1); 2011 (23.06.11). □

[16] Manos GC, Katakalos K, Kourtides V. Cyclic behaviour of a hybrid anchoring device enhancing the flexural capacity and ductility of an R/C bridge-type pier strengthened with CFRP sheets. J Civ Eng Res 2012.

[17] Manos GC, Katakalos K. The use of fiber reinforced plastic for the repair and strengthening of existing reinforced concrete structural elements damaged by earthquakes. In: Masuelli Martin Alberto, editor. Published in the book, Fiber Reinforced Polymers – The Technology Applied for Concrete Repair; January 23, 2013, ISBN: 978-953-51-0938-9 [ch.3]

[18] Paz, Mario. International handbook of earthquake engineering: codes, programs and examples. In: Greece by G.C. Manos, editor. Chapman and Hall; 1994. [chapter 17].

[19] Wu Y, Zhou Z, Yang Q, Chen W. On shear bond strength of FRP-concrete structures. Eng Struct 2010;32:897–905.

COMPDYN 2015
5th ECCOMAS Thematic Conference on
Computational Methods in Structural Dynamics and Earthquake Engineering
M. Papadrakakis, V. Papadopoulos, V. Plevris (eds.)
Crete Island, Greece, 25–27 May 2015

SEISMIC FRAGILITY ASSESSMENT OF MEDICAL COMPONENTS

Luigi Di Sarno[1,2], Fabio Gustuti[2], Gennaro Magliulo[2], and Crescenzo Petrone[2]

[1] University of Sannio, Department of Engineering
Piazza Roma 21, 82100 Benevento, Italy
e-mail: ldisarno@unisannio.it

[2] University of Naples Federico II, Department of Structures for Engineering and Architecture
via Claudio 21, 80125 Naples, Italy
{disarno,gmagliul,crescenzo.petrone}@unina.it, fabio.gustuti@gmail.com

Keywords: Nonstructural components, Hospital building, Shake table, Seismic performance, Fragility.

Abstract. *Shake table tests on a full scale three-dimensional model of a consultation room has been carried out at the University of Naples, Federico II ,Italy . The sample room contains a number of typical medical components, which are either directly connected to the panel boards of the perimeter walls or are simple free-standing elements. System identification was firstly carried out in order to identify the modal properties of the tested components. Selected ground motion records were scaled to detect different limit states for the medical devices. Fragility analysis has also been carried out; in so doing, the fragility curves have been evaluated according to a systemic approach. Simplified yet reliable finite element models of the experimentally tested sample components are defined upon the laboratory outcomes through the computer platform routinely used for practical applications. The implemented numerical model is capable to simulate the variations of natural frequency as provided by the experimental tests, in case the component is shaken along the two horizontal directions. The main finding of the present analytical study is therefore that simple models are able to adequately simulate the dynamic properties of the tested cabinets.*

1 INTRODUCTION

Surveys carried out in the aftermath of recent major earthquakes world-wide [1-3], e.g. the 2008 Sichuan (China), the 2009 L'Aquila (Italy), the 2010-2011 Darfield-Christchurch (New Zealand), the 2011 Van (Turkey) and the 2012 Emilia-Romagna (Italy) earthquakes, have emphasized the poor performance of existing hospital buildings.

As a result, in the last decades, numerous governmental actions, aiming at ensuring the life safety and collapse prevention of acute healthcare facilities, have been promoted worldwide. For example, in California, in addition to safety standards, over time, it is enforced that, by 2030, hospitals should also meet performance levels meant to ensure that they are capable of providing services to public after an earthquake or any other disaster. Several initiatives have also been promoted by the World Health Organization (WHO) and the United Nation International Strategy for Disaster Reduction (UNISDR), e.g. the global campaign "Hospital Safe From Disasters" [4]. However, designing for resilient hospitals still remains a challenging task; it needs an interdisciplinary approach encompassing the physical, namely structure, non-structural components and building contents, and non-physical components, i.e. procedures and organization, of a hospital system [5].

Recently, few studies have been initiated to analyze the seismic performance of a variety of furniture items, medical appliances and service utilities of typical hospital buildings and pharmacies [6]. Full scale shake table tests were carried out on a base-isolated four story RC hospital structure [7, 8].

The need to maintain the functionality of health care facilities is essential in the aftermath of earthquake strong motions. The health care facilities are, indeed, classified as critical buildings and the limits on the structural and nonstructural components, as well as building contents, are highly stringent. The hospitals may show several damage when they are struck by an earthquake, especially those that were designed primarily for gravity loads or do not employ base isolation. Due to the scarcity of analytical and theoretical studies on the earthquake response of building contents, there is a urgent need to evaluate the capacity of such contents. Actually, the building contents are not protected by the existing design standards that especially affect the hospital buildings.

The present paper focuses on an ongoing experimental and theoretical research study that was funded by the Consortium Reluis at the University of Naples Federico II. The study is aimed at evaluating the seismic performance of freestanding cabinets, which are typically included in health care rooms.

A shake table test on a full scale three-dimensional consultation room has been carried out in the laboratory of the University of Naples, Federico II. Such room contains a number of typical medical components, which are either directly connected to the panel boards of the perimeter walls or are simple free-standing elements. From the experimental standpoint, the system identification was firstly carried out in order to identify the modal properties of the sample components. The records were scaled up to the onset of different limit states for the building contents. The fragility curves were evaluated according to a systemic approach.

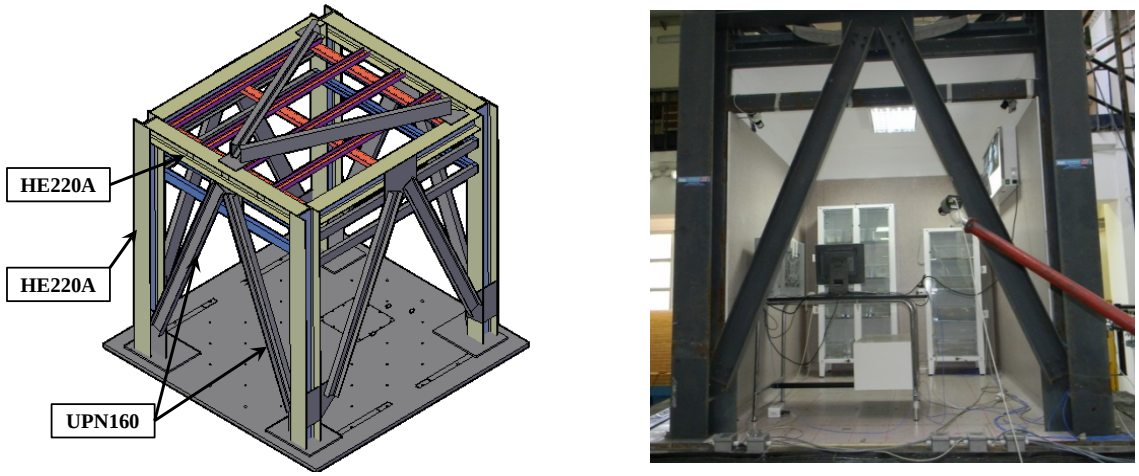
Simplified finite element models of the experimentally tested sample components are defined upon the laboratory outcomes through the computer platform routinely used for practical applications. Their dynamic response is compared to the experimental results, in order to validate such an approach.

2 EXPERIMENTAL TESTS

2.1 Test setup, specimen and testing protocol

A steel single-story framed system was designed (Figure 1a) with the purpose of simulating the seismic effects on the medical contents of a typical hospital room. The seismic tests on hospital building contents are carried out by the earthquake simulator system available at the laboratory of Structures for Engineering and Architecture Department of University of Naples Federico II, Italy. To simulate the effects of the earthquake at different floors on a hospital building, the geometry of the test frame was designed to prevent the onset of the resonance. As a result, the steel frame possesses a large lateral stiffness. Further details on the steel test setup are included in [9, 10]. The total weight of the sample structure is 19.2 kN.

A realistic hospital ambulatory room background is reproduced within the sample steel frame. Plasterboard partitions and ceilings are mounted; linoleum sheets are also installed to cover both the floor and a large portion of the internal partitions. An overhead light and a ray film viewer are also installed in the room (Figure 1b).



(a) (b)

Figure 1: Global perspective of the test setup (a); photo of the hospital ambulatory room contents (b).

The building contents used for the ambulatory room include: (a) a hospital medicine cabinet made of cold formed sheet with dimension 80x60x165 cm, having double moving glass doors with locker and five mobile glass shelves; (b) a hospital medicine cabinet made of cold formed sheet with dimension 53x36x144 cm, having single moving glass door with locker and four mobile glass shelves; (c) a desktop computer (monitor, case, keyboard and mouse); (d) a desk made of a steel pipes frame and a wooden desktop and having two drawers with locker. Cabinet contents with different slenderness such as glass bottles, flasks and test tubes, are placed in the cabinets to simulate the actual conditions of a typical hospital room. Different mass distributions are also selected to distribute such contents in the single- and double-window cabinets.

High quality digital accelerometers are used to monitor the response of the hospital building contents. They are characterized by a measurement range equal to ±10 g and by a frequency range from 0.5 Hz to 3000 Hz. Four accelerometers are placed at the base, i.e. at the lowest shelf level, and at the top of the front side of each cabinet; one accelerometer is positioned at the top of the desk and at the top of the monitor; one accelerometer records the acceleration at the shake table level.

To investigate the seismic behavior of the hospital room, a suite of accelerograms, used as input for the unidirectional horizontal shakings, are adequately selected to match a target re-

sponse spectrum, provided by the ICBO-AC156 code "Acceptance criteria for seismic qualification testing of nonstructural components" [11]. Additional information on testing input and testing protocol is provided in [12, 13].

The definition of a realistic condition for the sample cabinets is a crucial issue of the research study. Different variables, related to the arrangement of the contents on the different shelves, are considered. A few variables are investigated in the six test groups of the undertaken test campaign. Test group 100 assesses the behavior of the cabinet with an equivalent mass, i.e. sand inserted in boxes, at each shelf of the cabinets. 6 kg mass and 4 kg mass is added for each shelf of the double-window cabinet and single-window cabinet, respectively; the mass is representative of the mass of typical contents inserted in such a cabinet. The use of the equivalent mass is required in order to investigate the behavior of the cabinets with different contents on their shelves; the contents are simulated through the use of sand boxes in order to avoid damaging and replacing the contents after each shaking. Test group 200 investigates the behavior of the cabinets with a decreasing mass distribution along the height. From the base to the top, on the four shelves of the double-window cabinet, 6 kg, 4 kg, 4 kg and 2 kg masses are placed. Instead, on the four shelves of the single-window cabinet 4 kg, 2 kg, 2 kg and 0 kg masses are placed. The aim is to investigate the behavior of cabinets in which, as typically suggested, the heaviest contents are placed at the lowest shelves. Typical glass contents are tested in test group 300. The contents are equally placed on the different shelves of each cabinet. They are filled with colored sand, that simulates the presence of water. In this test group the behavior of real contents is also investigated.

In Figure 2a the plan configuration of the different components in test groups 100, 200 and 300 is shown. A different plan configuration is defined in test groups 400, 500 and 600 (Figure 2b). The different components are arranged in such a way that the different components are shaken along the orthogonal direction, given the unidirectional input motion. In test groups 400, 500 and 600 the same content mass configurations of test groups 100, 200 and 300, respectively, are chosen.

Random vibration inputs are also applied in order to dynamically identify the sample components, before executing the shake table tests. In particular, random tests 1000 are performed before the test group 100, random tests 2000 before test group 200, and so on.

For the whole test campaign it is chosen to lock the cabinet windows and do not restrain the cabinet to the wall behind, which is representative of the typical conditions in European hospitals. Each test group provides a set of shakings with increasing intensity. A total number of 63 shakings are performed during the whole test campaign. After each shaking the different components are relocated in their original condition.

2.2 Results and discussion

A damage scheme is defined in order to correlate the visual damage to the achievement of a given damage state. Three damage states are defined, i.e. Damage State 1 (DS1), Damage State 2 (DS2) and Damage State 3 (DS3). The damage state definitions are strictly related to the loss that a given damage state would cause [14]. The level of damage required to reach a limit state is defined for each damage typology of each system component (i.e. cabinet, desk and contents). If possible, the damage type is defined quantitatively. The damage state achieved by the whole specimen is the maximum damage state recorded among the different components.

In Table 1 and Table 2 the peak shake table acceleration (or peak floor acceleration, PFA) that causes the rocking mechanism initiation and the overturning, respectively, in both the cabinets is reported. The video recordings confirm the results of the "visual" damage detection. As expected, in test groups 400 – 500 – 600, in which the cabinets are shaken along their

longitudinal direction, a larger peak floor acceleration is required in order to let the rocking mechanism develop in the single-window cabinet; the double-windows cabinet, instead, does not exhibit the rocking behavior at all, exhibiting a sliding-dominated motion in the same test groups. Moreover, the overturning of the cabinet is recorded only in case the cabinets are shaken along their transversal direction.

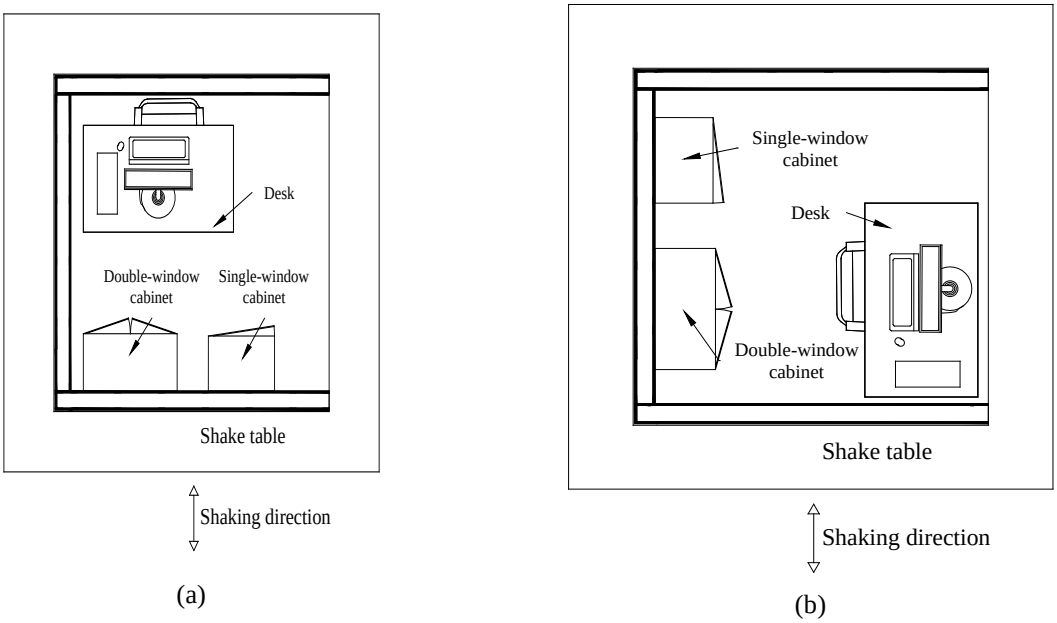


Figure 2: Plan view of the test setup: (a) configuration 1, adopted in test groups 100, 200 and 300 and (b) configuration 2, adopted in test groups 400, 500 and 600.

Table 1. Peak floor acceleration (PFA) that causes the rocking mechanism initiation for the different test groups and for the two tested cabinets.

Rocking	*single-window cabinet*	*double-windows cabinet*
Test group	PFA [g]	PFA [g]
100	0.37	0.48
200	0.49	0.49
300	0.49	0.61
400	0.74	
500	0.95	
600	0.84	

Table 2. Peak floor acceleration (PFA) that causes the cabinet overturning for the different test groups and for the two tested cabinets.

Overturning	*single-window cabinet*	*double-windows cabinet*
Test group	PFA [g]	PFA [g]
100	1.10	1.24
200	1.24	0.97
300	1.10	
400		
500		
600		

The input motion is unidirectional. In order to correlate the chosen engineering demand parameter, i.e. peak floor acceleration (PFA), to the three defined damage states, the results of

the test groups 100, 200 and 300 are combined with the results of the test groups 400, 500 and 600. For instance, the PFA that causes the DS1 threshold is the minimum between the PFA that induces DS1 in test groups 100 and the PFA that induces DS1 in test groups 400. It is assumed that the simultaneous combined effects of the two orthogonal motions are neglected.

Given this assumption the PFA values that trigger the different damage states for the different test groups are reported. It should be noted that DS2 PFA values are omitted. This is due to the fact that DS2 is recorded only in tests 300-600 for the overturning of some contents that are inserted in the cabinets, corresponding to a PFA equal to 0.486 g. In tests 100-400 and 200-500, in which sand equivalent masses are inserted in the cabinets, damage state 2 is not recorded at all, i.e. the specimen directly moves from DS1 to DS3. Hence, experimental data are not sufficient to evaluate the DS2 fragility curve.

Based upon the data in Table 3, the fragility curve for the damage states 1 and 3 are evaluated according to Porter et al. [15, 16] (Figure 3)

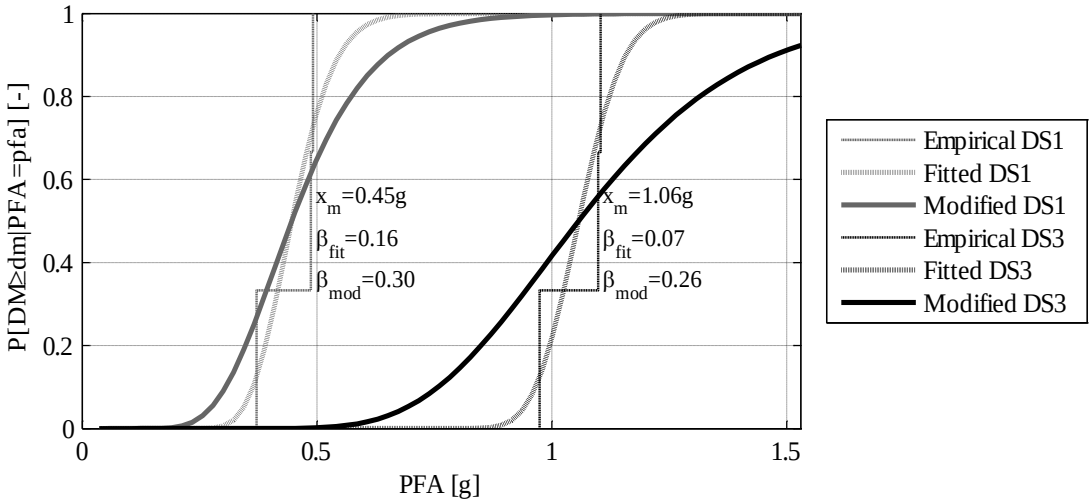


Figure 3: Fragility curves for the damage states 1 and 3 considering mass variability.

3 NUMERICAL MODEL

The tested components are also simulated numerically through the Sap 2000 program [17]. The results of the finite element models are compared to the experimental data measured during the full-scale shaking table tests. The comparison is limited to the linear dynamic response of the tested contents. An accurate survey of the different components is required in order to increase the accuracy of the numerical models.

The cabinets are composed of four steel vertical columns connected each other by steel elements. The global dimensions of both the investigated cabinets are summarized in Table 3.

	height [cm]	width [cm]	depth [cm]
Double-window cabinet	165	74.5	38
Single-window cabinet	139	53	36

Table 3: Dimensions of the investigated cabinets.

The vertical steel elements are characterized by an angular 55 cm x 50 cm “L” section with 0.1 cm thickness, with the 55 mm wide flange parallel to the transversal side of the cabinet. They are connected by two steel horizontal plates with side stiffeners and bolted connections, at the top of the cabinet and at 17 cm height (Figure 4). The steel plates and their stiffeners are characterized by 1 mm thickness, whereas the stiffeners are 3.0 cm high. Three of the four

vertical bays are infilled with 1 mm thick steel plates, whereas glass windows are installed in the fourth bay. The double-window cabinet is also characterized by a 5 cm x 0.1 cm rectangular vertical steel element that separates the two glass windows.



(a) (b)

Figure 4: Global view of the sample cabinets.

3.1 Single-window cabinet

The vertical steel columns are modelled according to their actual geometry. The presence of the steel horizontal plates is modelled through four horizontal steel elements characterized by a 0.1 cm (width) x 3 cm (height) rectangular cross section both at the top and at 17 cm height of the cabinet. These horizontal elements are characterized by a large out-of-plane stiffness, i.e. large moment of inertia about the vertical axis, to simulate the presence of the steel horizontal plate element. Furthermore, two diaphragm constraints are imposed between the 4 points at the top and the 4 points at 17 cm height. The vertical panels are not included in the model, since they are connected so as not to increase the lateral stiffness of the cabinet. The glass window is modelled with a properly meshed shell element, assuming a 80000 N/mm^2 elastic modulus. Hence, the adopted model is able to capture both the global modes in the two horizontal directions, which involve the whole cabinet, and the local ones, which involve a portion of the cabinet. Rigid elements in the out-of-plane direction are included between the steel elements and the glass window in order to model the restraint given by their connection, whereas the glass window does not contribute to the in-plane stiffness; indeed, the glass window is connected to the cabinet only along one of the two vertical sides. A rigid element in the out of plane direction is also included to model the lock of the glass window.

The single-window cabinet mass is 15 kg, excluding the window mass; for the sake of simplicity, the mass is equally divided between the top and the base of the cabinet. The steel elements are characterized by no mass, whereas the mass is included in the glass window in order to correctly estimate the local vibrational modes of the glass window. Different mass amounts are inserted at the shelf levels, according to the actual mass adopted in the experimental phase for the different test groups. The first and the second vibrational modes in test group 1000 are characterized by 6.18 Hz and 7.38 Hz natural frequencies (Figure 5). A local mode that involves the glass window, characterized by a larger natural frequency (23.12 Hz), is also identified.



(a) (b) (c)

Figure 5: Single-window cabinet modal shapes in tests 1000 and 4000: (a) I vibration mode (6.18 Hz), (b) II vibration mode (7.38 Hz), (c) III vibration mode (23.12 Hz).

FEM results match very well the experimental results, evaluated through the use of the transfer curve method [18, 19]. The peak represented in the transfer curve that occurs at 26 Hz is compatible with the frequency of the local mode in the FEM model. The comparison between the numerical and the experimental natural frequencies for the different test groups is summarized in Table 4.

Test group	FEM model	Experiment	Δ [%]
1000	7.38 Hz	7.03 Hz	+5.0
2000	8.84Hz	6.64 Hz	+33.1
3000	6.88 Hz	7.03 Hz	-2.1
4000	6.18 Hz	7.03 Hz	-12.1
5000	7.64 Hz	8.20 Hz	-6.8
6000	5.92Hz	7.81 Hz	-24.2

Table 4: Comparison between the fundamental frequency results from the FEM analysis and the transfer curve.

The numerical and the experimental frequencies of the tested cabinet are close. Considering the low level of accuracy of the model with respect to the complexity of the geometry and the mechanical connections between the elements, the outcomes of the numerical analyses give a good approximation of the experimental ones. It is therefore demonstrated that simple models are able to capture the dynamic properties of the tested cabinet.

3.2 Double-window cabinet

The modelling approach of the double-window cabinet is very similar to the one provided for the single-window cabinet. However, the dimension and the mass, i.e. 20 kg, are slightly different than the corresponding values in the single-window cabinet. The vertical steel element between the two windows is properly modelled according to its own geometry; such an element is hinged to the cabinet, in order to model the single-bolted connection. The connection between the cabinet and glass window is modelled by rigid elements in the out of plane direction, similarly to the single-window cabinet. The rigid elements simulate the actual restraints given to the glass window by a steel connector. The different mass amounts corre-

sponding to the different performed test groups are inserted at the shelf levels. The first two modes involve the whole cabinet, the third one is a local mode that involves the vertical element between the two glass windows and the fourth mode involves the glass windows.

The FEM outcomes (Figure 6) match very well the results of the experimental transfer curves. The three peaks represented in the transfer curves, which occur at about 6 Hz, 11 Hz and 25 Hz, respectively, are compatible with the frequencies of the first, third and fourth modes in the FEM model. In particular, the numerical model allows justifying the differences in the transfer curves among the single- and the double-window cabinets. Indeed, the double-window transfer curve denotes three different peaks, whereas the single-window one exhibits only two peaks. The comparison between the numerical and the experimental natural frequencies for the different test groups is summarized in Table 5.

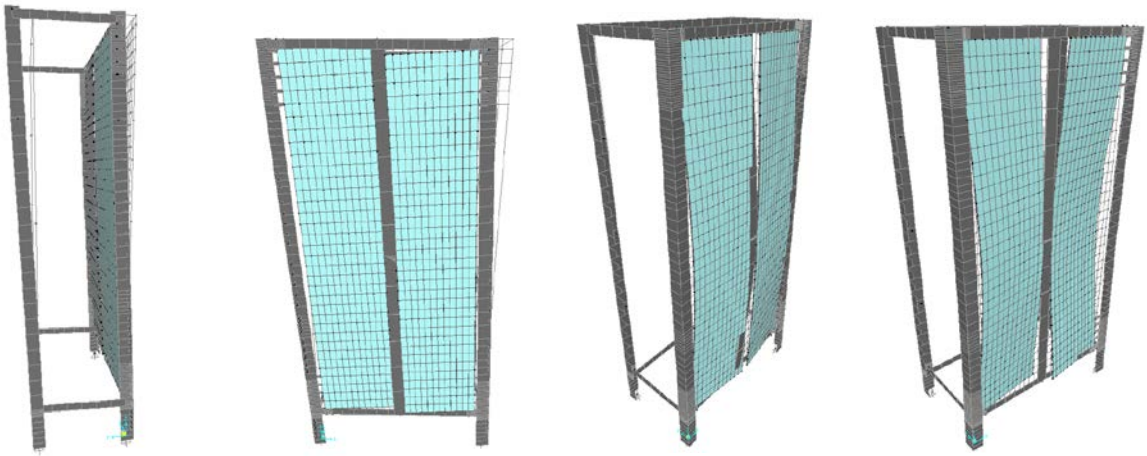


Figure 6: Double-window cabinet modal shapes in tests 1000 and 4000: (a) I vibration mode (4.74 Hz), (b) II vibration mode (5.08 Hz), (c) III vibration mode (10.35 Hz), (d) IV vibration mode (19.90 Hz).

Test group	FEM model	Experiment	Δ [%]
1000	5.08 Hz	6.25 Hz	-18.7
2000	5.57 Hz	5.08 Hz	+9.6
3000	5.30 Hz	6.25 Hz	-15.2
4000	4.74 Hz	4.68 Hz	+1.3
5000	5.40 Hz	5.08 Hz	+6.3
6000	5.04 Hz	4.30 Hz	+17.2

Table 5: Comparison between the frequency results from the FEM analysis and the transfer curve.

Also for the double-window cabinet, the numerical and the experimental frequencies of the tested cabinet are in similar ranges. It can be concluded that simple models are able to simulate reliably the dynamic properties of the cabinets.

Experimental-to-numerical comparison of both mode shapes and transfer curves [18], omitted here for the sake of brevity, confirms the good agreement.

4 CONCLUSIONS

An examination (out patients consultation) room is selected as representative layout for the experimental seismic performance assessment of the core units of hospital buildings. The

building contents utilized for the examination room include two cabinets, a desktop computer and a desk; different glass contents are also included in the cabinets in some tests. Different mass distributions are selected to distribute such contents in the single- and double-window cabinets. 63 shakings are performed during the whole test campaign.

The peak shake table acceleration (PFA) that causes the rocking mechanism initiation and the overturning, respectively, in both the cabinets are analyzed. In particular, the rocking mechanism in the two tested specimen initiates for a PFA that ranges between 0.37 g and 0.61 g; instead the overturning of the cabinets occurs for PFA slightly larger than 1.00 g.

A damage scheme is defined in order to correlate the visual damage to the onset of the selected three-stage damage states in the hospital ambulatory room. Such fragility are derived based on a systemic approach, i.e. encompassing the performance levels of the components within the sample ambulatory rooms. Different groups of specimen are considered in the evaluation of the fragility curves in order to investigate the mass variability.

Simplified yet reliable finite element models of the experimentally tested sample components are defined upon the laboratory outcomes through the computer platform routinely used for practical applications. The implemented numerical model is capable to simulate the variations of natural frequency as provided by the experimental tests, in case the component is shaken along the two horizontal directions. The natural modes of the two tested cabinets are adequately simulated by the numerical model. The multiple peaks observed in the transfer curves are associated to a mode shape. The dynamic response of the defined models is assessed through the numerical-to-experimental comparison of the transfer curves. Considering the low level of accuracy of the model with respect to the complexity of the components, the outcomes of the numerical analyses provide a close approximation of the experimental ones. The main finding of the present analytical study is therefore that simple models are able to adequately simulate the dynamic properties of the tested cabinets.

Finally, it is emphasized that the outcomes related to the developed models is limited to freestanding components which do not exhibit any rocking mechanism, i.e. they are rigidly connected at their base to the floor.

REFERENCES

[1] N. Achour, M. Miyajima, M. Kitaura, A. Price, Earthquake-Induced Structural and Nonstructural Damage in Hospitals. *Earthquake Spectra*, **27**, 617-634, 2011.

[2] L. Di Sarno, C. Yenidogan, M. Erdik, Field evidence and numerical investigation of the Mw= 7.1 October 23 Van, Tabanlı and the Mw> 5.7 November earthquakes of 2011. *Bulletin of Earthquake Engineering*, **11**, 313-346, 2013.

[3] J.K. McIntosh, C. Jacques, J. Mitrani-Reiser, T.D. Kirsch, S. Giovinazzi, T.M. Wilson, The Impact of the 22nd February 2011 Earthquake on Christchurch Hospital. New Zealand Society for Earthquake Engineering conference. 13-15 April 2012, Christchurch, New Zealand, 2012.

[4] World Health Organization (WHO), WHO/UNISDR World Disaster Reduction Campaign. http://www.safehospitals.info/. 2008.

[5] M. Bruneau, S.E. Chang, R.T. Eguchi, G.C. Lee, T.D. O'Rourke, A.M. Reinhorn, M. Shinozuka, K. Tierney, W.A. Wallace, D. von Winterfeldt, A framework to quantitatively assess and enhance the seismic resilience of communities. *Earthquake Spectra*, **19**, 733-752, 2003.

[6] G. Magliulo, C. Petrone, V. Capozzi, G. Maddaloni, P. Lopez, G. Manfredi, Seismic performance evaluation of plasterboard partitions via shake table tests. *Bulletin of Earthquake Engineering*, **12**, 1657-1677, 2014.

[7] G. Magliulo, C. Petrone, V. Capozzi, G. Maddaloni, P. Lopez, R. Talamonti, G. Manfredi, Shake Table Tests on Infill Plasterboard Partitions. *The Open Construction and Building Technology Journal*, **6**, 155-163, 2012.

[8] International Conference of Building Officials (ICBO), AC 156 Acceptance Criteria for the Seismic Qualification of Nonstructural Components. ICBO Evaluation Service, Inc., Whittier, California, USA, 2000.

[9] G. Magliulo, V. Pentangelo, G. Maddaloni, V. Capozzi, C. Petrone, P. Lopez, R. Talamonti, G. Manfredi, Shake table tests for seismic assessment of suspended continuous ceilings. *Bulletin of Earthquake Engineering*, **10**, 1819-1832, 2012.

[10] C. Petrone, G. Magliulo, G. Manfredi, Shake table tests for the seismic assessment of hollow brick internal partitions. *Engineering Structures*, **72**, 203-214, 2014.

[11] E. Cosenza, L. Di Sarno, G. Maddaloni, G. Magliulo, C. Petrone, A. Prota, Shake table tests for the seismic fragility evaluation of hospital rooms. *Earthquake Engineering and Structural Dynamics*, **44**, 23-40, 2014.

[12] K. Porter, R. Kennedy, R. Bachman, Developing Fragility Functions for Building Components for ATC-58. A Report to ATC-58. Applied Technology Council, Redwood City, CA, US, 2006.

[13] K. Porter, R. Kennedy, R. Bachman, Creating Fragility Functions for Performance-Based Earthquake Engineering. *Earthquake Spectra*, **23**, 471-489, 2007.

[14] CSI Computer & Structures Inc., SAP2000. Linear and Nonlinear Static and Dynamic Analysis of Three-Dimensional Structures, Computer & Structures, Inc. Berkeley, California, 2004.

[15] L. Di Sarno, C. Petrone, G. Magliulo, G. Manfredi, Dynamic response analysis of typical consultation room medical components. *Engineering Structures*, **(under review)**, 2015.

[16] L. Di Sarno, C. Petrone, G. Magliulo, G. Maddaloni, A. Prota, Shake table tests to evaluate the seismic demand, capacity and dynamic properties of hospital contents. Second European Conference on Earthquake Engineering and Seismology. Instanbul, 24-29 August 2014, 2014.

COMPDYN 2015
5th ECCOMAS Thematic Conference on
Computational Methods in Structural Dynamics and Earthquake Engineering
M. Papadrakakis, V. Papadopoulos, V. Plevris (eds.)
Crete Island, Greece, 25–27 May 2015

MULTIPLE SUPPORT EXCITATION OF A BRIDGE BASED ON BEM ANALYSIS OF THE SUBSOIL-STRUCTURE-INTERACTION PHENOMENON

Ioanna-Kleoniki M. Fontara[1], Magdalini D. Titirla[2], Frank Wuttke[1], Asimina M. Athanatopoulou[2], George D. Manolis[2] and Anastasios G. Sextos[2]

[1] Institute of Applied Geoscience
Christian-Albrechts University of Kiel, Germany
e-mail: {fontara, fw}@gpi.uni-kiel.de

[2] Department of Civil Engineering
Aristotle University of Thessaloniki, Greece
e-mail: {mtitirla, minak, gdm, asextos}@civil.auth.gr

Keywords: bridge seismic response, spatial variability of earthquake ground motion, site effects, canyon topography, Soil-Structure Interaction, Boundary Element Method.

Abstract. *This study presents a numerical investigation of the influence of spatial variability of earthquake ground motion, site effects and Soil-Structure Interaction (SSI) phenomena on the inelastic dynamic analysis of bridge structures, considering a 2D analysis of the soil profile via Boundary Element Method (BEM). First, seismic waves propagating through complex geological profiles are modeled, so as to recover ground motion records that account for local site conditions. To that purpose, the BEM is employed for computing time-history records for four different geological profiles considering (a) canyon topography, (b) soil layering and (c) material gradient effect. Then bridge support-dependent ground motions and equivalent dynamic impedance matrices at the soil-foundation interface are generated for each support point of a bridge along the canyon. More specifically, a reinforced concrete, straight bridge with monolithic pier-deck connections is adopted as a case study. Next, a series of time history analyses considering local nonlinearities is conducted for the bridge using the Finite Element Method (FEM) taking into account subsoil-structure-interaction phenomena. To emphasize the relative importance of the topographic effects and the asynchronous motion, bridge response is determined under both synchronous and asynchronous earthquake input. In sum, the numerical results of this study show that the effect of spatially variable earthquake ground motion on the seismic response of the bridge studied depends on the interplay between the dynamic characteristics of the structure, the variability in space of soil and the properties of the incoming wavefield itself. It is also demonstrated that the detrimental or beneficial effect of spatially variable earthquake input is primarily dependent on the interplay of all the above mentioned key parameters.*

1 INTRODUCTION

During an earthquake, seismic waves radiate from a fault and travel through the earth's crust. As seismic waves travel through bedrock and soil deposits, the various complex geological profiles produce local distortions in the incoming wave field which lead to large amplifications as well as strong spatial variations in frequency, amplitude and phase along the surface in the seismic motions. For elongated structures such as bridges, pipelines, communication and power transmission grids, dams etc., the effects of local site conditions become especially important because spatial variations of ground motion would lead to multiple support excitation of the structure. The structure would respond differently to a variety of input motions due to its dynamic characteristics that tend to be triggered differently under uniform and non-uniform earthquake excitation patterns. This relative difference between the motions of the soil and the structure is further pronounced by the fact that soil-structure-interaction phenomenon at each pier foundation-soil interface is strongly frequency-dependent, hence, inherently sensitive to the variations of seismic input along the bridge length.

So far, seismic codes for bridge design do not prescribe explicit procedures to simultaneously account for spatial variability, site effects and SSI phenomena maybe with the exception of some sporadic provisions to generate asynchronous ground motions (i.e., Eurocode 8 – Part 2) and some rough guidelines to account for soil compliance in the above code Annex.

Several previous studies have emphasized the significance of this complex problem for the seismic response of bridge structures. Among them, we mention Sextos et al (2003a;b), who developed a general methodology for deriving appropriate modified time histories that account for spatial variability, site effects and soil structure interaction phenomena. Parametric analyses were conducted and demonstrated that the presence of site effects, spatial variability and soil-foundation superstructure interaction strongly influences the input seismic motion and the ensuing dynamic response of the bridge. Jeremic et al. (2009) proposed a numerical simulation methodology and conducted numerical investigations of seismic SSI for a bridge structure on non-uniform soil. It was then stated that the dynamic characteristics of earthquakes, soil and structure all play a crucial role in determining the seismic behavior of an extended construction. Bi et al (2011) studied the simultaneous effect of SSI and ground motion spatial variation on bridge response and estimated the required separation distance that modular expansion joints must provide in order to avoid seismic pounding. Soyluk and Sicacik (2011) further investigated the effects of SSI and multiple support excitation on the seismic response of a cable-stayed bridge, though the latter type of bridges has been recently found to be a rather favorably affected by asynchronous excitations due to the relatively low contribution of the quasi-static component.

However, in all the above mentioned studies the influence of local site conditions is evaluated using models based on a uni-dimensional description of the local soil profile as a soil column and similarly for the seismic wave propagation path. Limited papers can be found which deal with the effects of local site conditions on bridge response considering 2D analysis of the soil profile. Esquivel and Sanchez-Sesma (1980) studied the influence of a semi-circular cylindrical canyon on the dynamic soil-bridge interaction for the case of incident harmonic plane SH waves. Analytical scattered and free-field solutions are used to determine the driving forces and impedance stiffness matrix for the bridge foundation, while the bridge is modelled as a shear beam and solved analytically. Zhou et al. (2010) investigated canyon topography effects on the linear response of continuous, rigid frame bridges under obliquely incident SV waves. The seismic response of the canyon was analyzed using the FEM, while the response of the bridge was computed by the "large mass" method. It was shown that the distribution of ground motions is affected by canyon topographic features and the incident

angle of the waves. In case of vertical incident SV waves, the peak ground accelerations increase greatly at the upper edges of the canyon and decrease at its bottom lateral boundaries. Note here that these studies are restricted to either very simple geometry of the topographic effects (so that can be solved analytically) or to a simple frame-like bridge model which typically neglects salient features of a real bridge.

Along these lines, the main objective of the present work is to investigate the effects of (a) spatial variability of earthquake ground motion, (b) local site conditions and (c) SSI on the dynamic response of reinforced concrete bridges, considering 2D analysis of the soil profile via BEM. Briefly, the procedure consists of the following steps: (i) Time history records are considered as an input at the seismic bed of complex geological profiles with canyon topography, soil layering and material gradient effect; (ii) site dependent ground motions and soil spring coefficients are generated at the surface using the BEM; (iii) the generated ground motions are used as input to a three dimensional, model of a monolithic, straight in plan R/C, bridge; (iv) the bridge is assessed using the FEM under the support-dependent acceleration earthquake input and the dynamic impedance considerations at the pier-foundation-soil and the abutment-embankment interface (vi) the dynamic response of the bridge is then assessed parametrically to identify the relative impact of each one phenomenon studied.

2 WAVE PROPAGATION IN COMPLEX GEOLOGICAL PROFILES: METHODOLOGY

There is a lack of high-performance computational tools able to simulate 2D and possibly 3D complex geological profiles. The BEM is nowadays recognized as a valuable numerical technique to solve wave propagation problems, due to its many advantages with respect to domain techniques such as the FEM. It is briefly mentioned herein that it is possible to deal with semi-infinite media in terms of high accuracy and minimal modeling effort.

In the present study, the BEM is used to model the seismic wave propagation through complex geological profiles so as to recover ground motion records that account for local site conditions. In particular, consider 2D wave propagation in viscoelastic, isotropic and inhomogeneous half-plane consisting of N parallel or non-parallel inhomogeneous layers Ω_n (n=0, 1, 2, …N) with a free surface and sub-surface relief of arbitrary shape. The dynamic disturbance is provided by either an incident SH wave or by waves radiating from an embedded seismic source, see Fig.1. For this problem, a non-conventional BEM is applied which is based on a special class of analytically derived fundamental solution for continuously inhomogeneous media with variable wave velocity profiles (Manolis and Shaw, 1996a, 1996b). The employed here BEM was recently developed and validated in Fontara et al. (2015).

More specifically, the material inhomogeneity is expressed by a spatially variable shear modulus and density of arbitrary variation in terms of depth coordinate. We define the inhomogeneity parameter as $c_n=C^{\text{bottom }(\Lambda n-1)/}\ C^{\text{top }(\Lambda n)}$ namely the ratio of the wave velocity at the bottom to that at the top of any given layer. This model is also able to account for wave dispersion phenomena due to viscoelastic material behaviour and to position-dependent material properties.

Next, for the formulation of the boundary integral equation we use the well-known boundary integral representation formula and insert as kernels the fundamental solutions for geological media with a velocity gradient (Manolis and Shaw, 1996a;b):

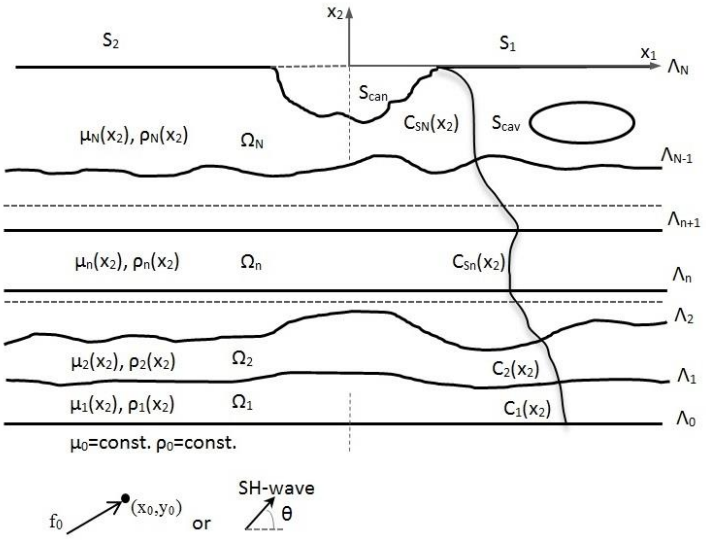


Figure 1: Geometry of the problem treated by BEM: A multi-layered, continuously inhomogeneous geological medium with surface topography and buried inclusions.

$$c\mathbf{u}_3^{(i)}(\mathbf{x},\omega) = \int_\Gamma \mathbf{U}_3^{*(i)}(\mathbf{x},\mathbf{y},\omega)\mathbf{t}_3^{(i)}(\mathbf{y},\omega)d\Gamma - \int_\Gamma \mathbf{P}_3^{*(i)}(\mathbf{x},\mathbf{y},\omega)\mathbf{u}_3^{(i)}(\mathbf{y},\omega)d\Gamma \tag{1}$$

$$\mathbf{x} \in \Gamma = \Omega_i \cup \boldsymbol{S}_{can} \cup \boldsymbol{S}_{cav}$$

In Eqn. 1, ***x, y*** are source and field points, respectively, *c* is the jump term, U^*_3 is the fundamental solution for geological media with variable velocity profile, and $P^*_3(\mathbf{x},\mathbf{y},\omega) = \mu(x_2)U^*_3(\mathbf{x},\mathbf{y},\omega)\, n_i(\mathbf{x})$ is the corresponding traction fundamental solution, where $i=1, 2\ldots N$ is the number of layers. The above equation is written in terms of total wave field and expresses the case of incident SH waves. We note that by using this closed form fundamental solution in the BEM technique, only the layer interfaces, as well as the free and sub-surface relief need be discretized.

After discretization of all boundaries with constant (i.e., single node) boundary elements, the matrix equation system is formed below and displacements along the free surface can be computed:

$$[\boldsymbol{G}]\{\boldsymbol{t}\} - [\boldsymbol{H}]\{\boldsymbol{u}\} = \{\boldsymbol{0}\} \tag{2}$$

The above system matrices ***G*** and ***H*** result from numerical integration using Gaussian quadrature of all surface integrals containing the products of fundamental solutions times interpolation functions used for representing the field variables. They are fully populated matrices of size MxM, where M is the total number of nodes used in the discretization of all surfaces and interfaces, while vectors ***u*** and ***t*** now contain the nodal values of displacements and tractions at all boundaries.

Finally, the generation of transient signals from the hitherto derived time-harmonic displacements is achieved through inverse Fourier transformation. Note here that both negative and positive values in the frequency, as well as in the time domain, are considered and both real and imaginary values for the response parameter are employed. The aforementioned BEM numerical implementation and production of the final seismic signal is programmed using the Matlab (2008) software package.

3 GEOLOGICAL PROFILES

The methodology described in the previous section is now applied to four different hypothetical geological profiles of increasing complexity, on which the R/C bridge in question is considered to be located, see Fig.2 below, in order to examine the influence of the following key parameters: (i) canyon topography; (ii) layering; (iii) material gradient. In particular, the site is represented by the following geological profiles: (A) a homogeneous layer with flat-free surface producing a uniform excitation at all support points of the bridge; (B) a homogeneous layer with a valley in which the bridge is located; (C) a two-layer deposit as a damped soil column with a valley at the surface; (D) a two-layer damped soil column with the bridge valley at the surface, in which the top layer is continuously inhomogeneous with inhomogeneity parameter c=1.2 expressing an otherwise arbitrary variation in the wave speed depth profile. The bottom layer is homogeneous and the interface between the first and the second layers is irregular. All geological profiles are overlying bedrock. The soil material properties of these subsoil geological configurations are shown in Table 1 and Fig.2.

Next, a suite of seven earthquake excitations given in Table 2 are recorded at outcropping rock on a class A site according to FEMA classification and are drawn from the PEER (2003) strong motion database. These records are considered as an input at the seismic bed level for all geological profiles. Note here that the selected ground motion sample is not necessarily unbiased.

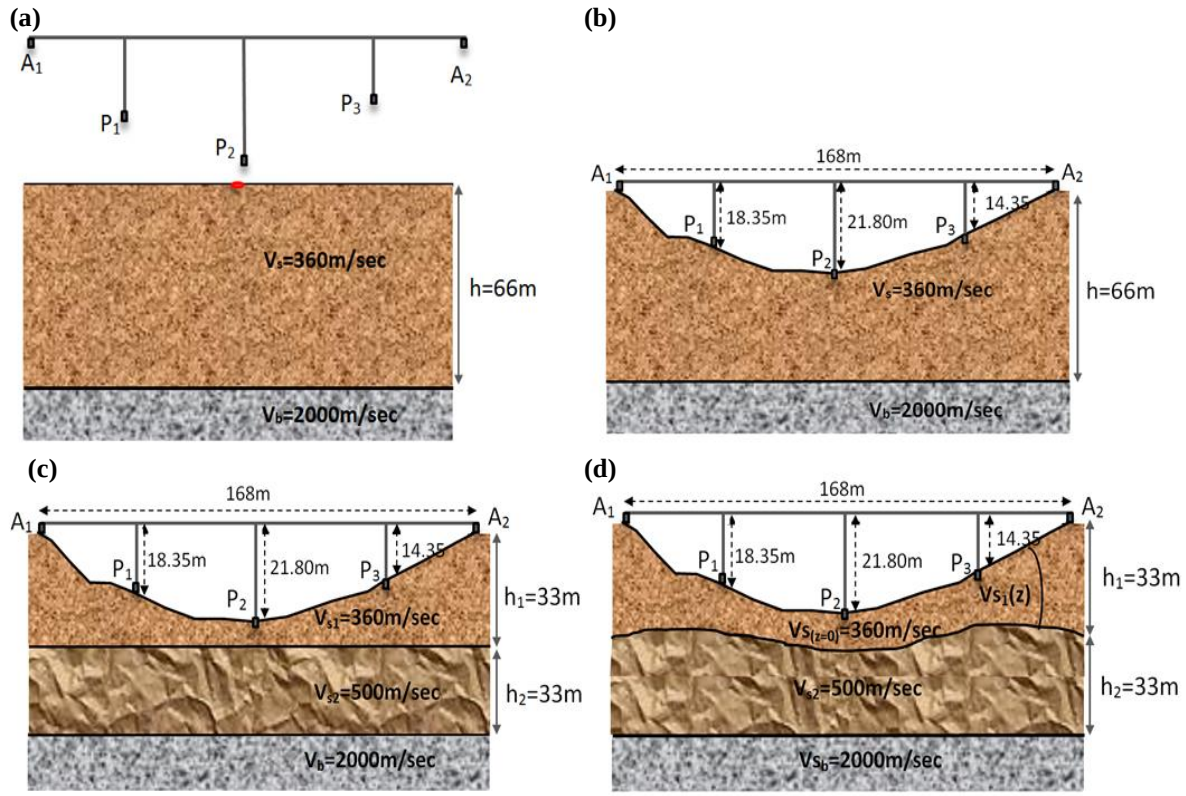


Figure 2: Four geological profiles, namely Types A-D, on which the R/C bridge is assumed to be located.

4 GROUND MOTIONS

We next investigate the influence of canyon topography, layering and material gradient on ground motions recorded along the free surface and start with the first geological profile com-

	Vs (m/sec)	μ (Pa)	ρ (N/m^2)
Layer 1	360	$233.28 \cdot 10^6$	1800
Layer 2	500	$450 \cdot 10^6$	1800
Bedrock	2000	$800 \cdot 10^7$	2000

Table 1: Material properties of the basic geological structure.

prising a single layer with a horizontal free surface that produces a uniform excitation pattern ridge as a reference case. Fig.3 plots the acceleration response spectra recorded at the surface of (a) Type B, (b) Type C and (c) Type D geological profile at the support points of the bridge at the canyon and for Northridge 2 ground motion (listed in Table 2). The shape of the recorded seismic signal is modified as the geological profile becomes more complex. This is also evident from the 3D time history generated along the surface of (a) Type B, (b) Type C and (c) Type D geological profile shown in Fig.5. From Fig.3 we observe that spectral values at the bridge support points are not the same and furthermore, they differ significantly at certain period values from those produced for the reference case of uniform excitation. An expected shifting to the right (higher periods) due to the layering effect is clearly depicted in Fig.3(b) and Fig.3(c). In case of Type D geological profile, the additional presence of material gradient increases the material stiffness gradually and the soil becomes stiffer. Moreover, the continuous variation of the wave speed with depth at the top layer reduces significantly the wave speed contrast between the first and the second layer (see Fig.4) thus, decreasing the amplification levels. As a result the spectral acceleration values are de-amplified across the entire range of periods examined herein.

No	Date	Earthquake name	Magnitude (M)	Station name	Closest distance (Km)	Component (deg)	PGA (g)
1	22.03.1922	San Francisco	5.3	Golden Gate Park	-	100	0.112
2	17.01.1994	Northridge 1	6.7	Mt Wilson CIT	26.8	000	0.234
3	17.01.1994	Northridge 2	6.7	Littlerock Brainard Can	46.9	090	0.072
4	17.01.1994	Northridge 3	6.7	Lake Hughes #9	28.9	090	0.217
5	18.10.1989	Loma Prieta	6.9	Monterey City hall	44.8	000	0.073
6	10.01.1987	Whittier Narrows	6	Mt Wilson CIT	21.2	000	0.158
7	12.09.1900	Lytle Creek	5.4	Cedar Springs, Allen Ranch	20.6 (Hypocentral)	095	0.071

Table 2: Ground motion records from the PEER (2003) strong motion database as recorded on a Class A site.

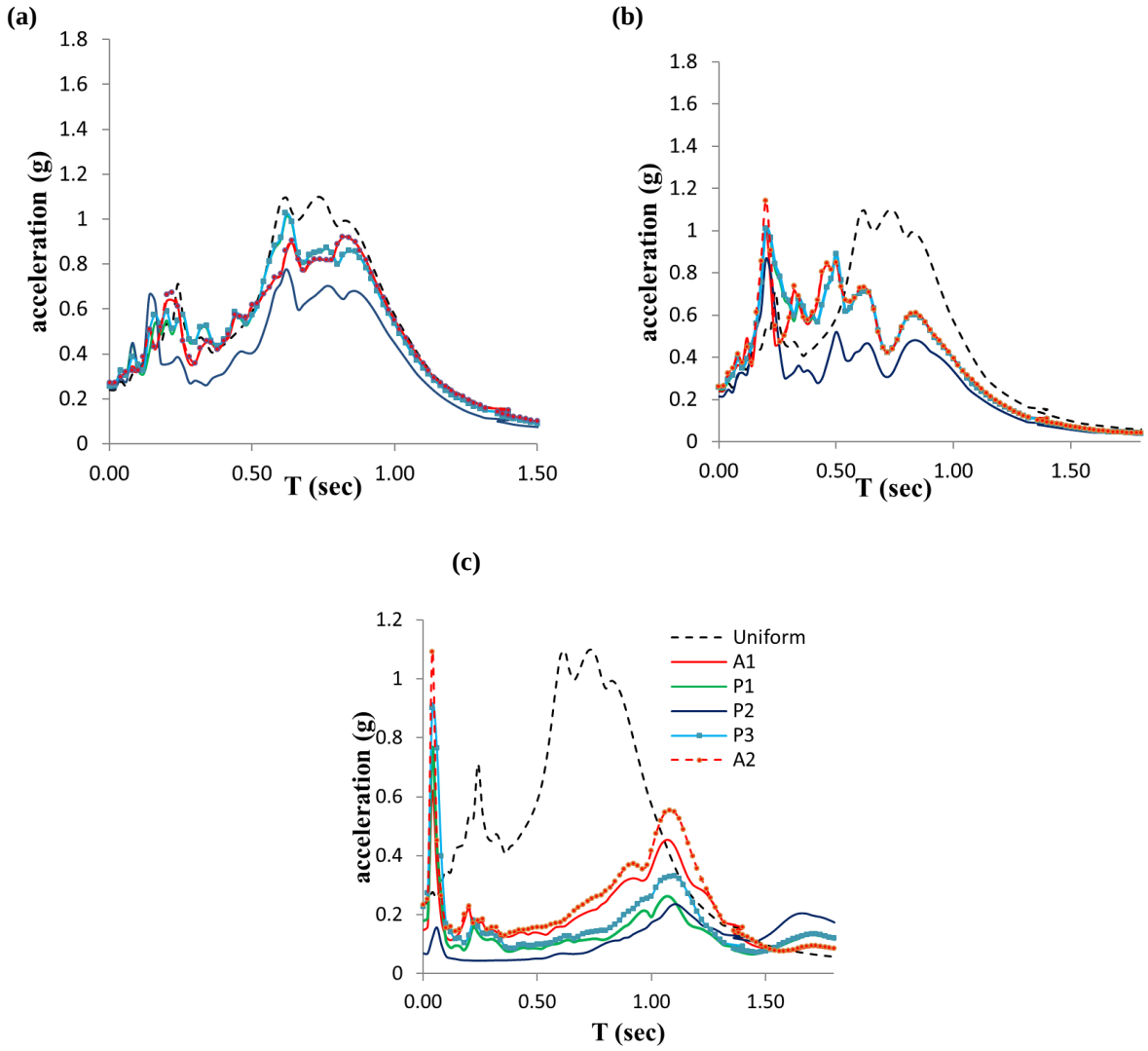


Figure 3: Acceleration response spectra of Northridge No2 ground motion recorded at the free surface of (a) Type B, (b) Type C and (c) Type D geological profile vs Uniform excitation (Type A).

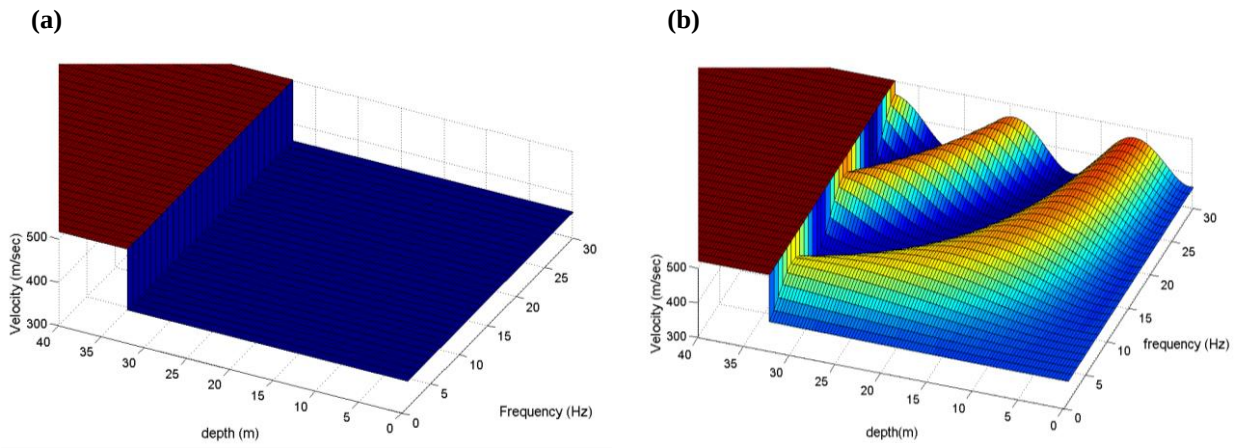


Figure 4: Velocity distribution of the subsoil structure: (a) Type C and (b) Type D geological profile.

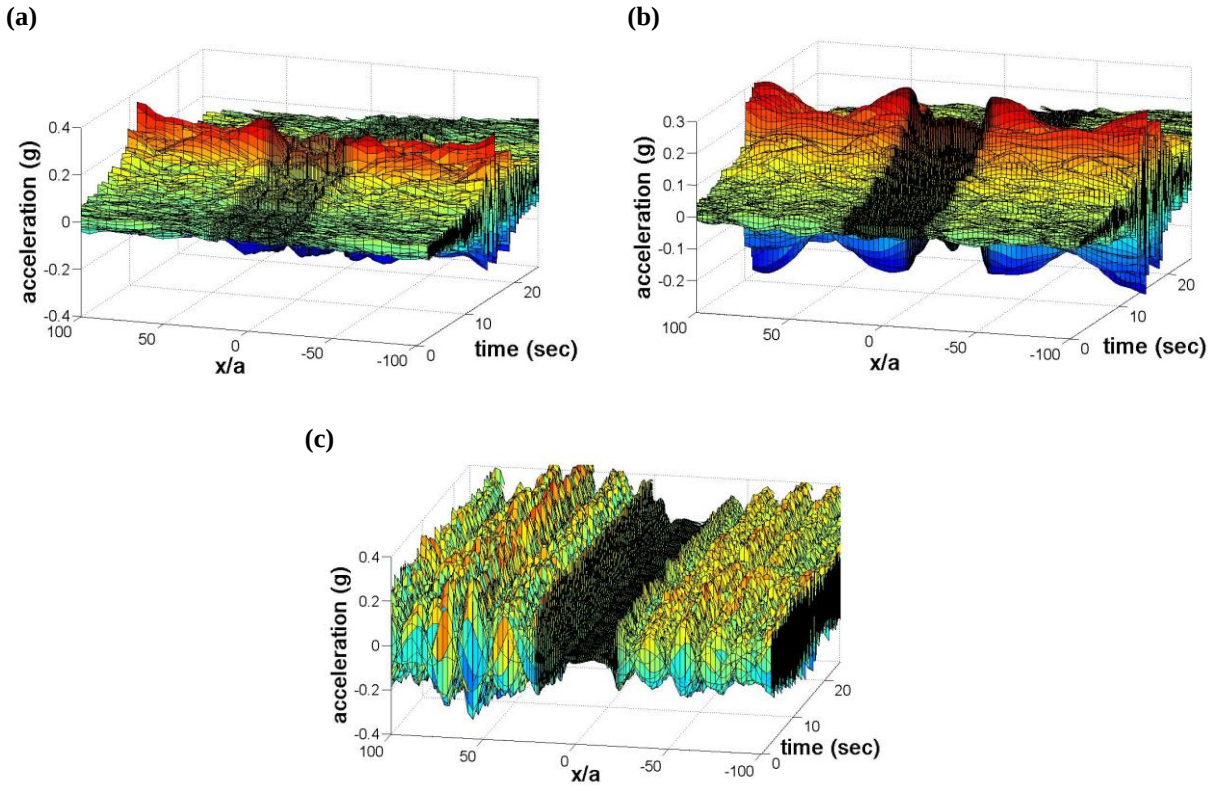


Figure 5: 3D acceleration time history of Northridge No2 ground motion recorded at the free surface of (a) Type B, (b) Type C and (c) Type D geological profile.

5 DESCRIRTION OF BRIDGE AND MODELING

We now focus on the nonlinear response of a theoretical monolithic, reinforced concrete, straight bridge with earthquake resistant abutments proposed by Mitoulis (et al., 2014). The total length of the bridge is equal to168m, supported on rectangular hollow piers of unequal height that varies from 14.35 to 21.8m, as shown in Fig.6.

In terms of some additional details, the two end spans are 39m long, while the two intermediate spans have span lengths of 45m each. The concrete deck is a hollow box girder with a constant cross section along the length. For the design of the expansion joints, 40% of the seismic movements of the deck are considered according to Eurocode 8, Part 2 (2003), as well as serviceability-induced constrained movements of creep, shrinkage, pressing and 50% of the thermal movements of the deck. The cracked flexural stiffness of the piers is estimated as equal to 65% of the original cross-section.

The bridge is modeled using the FEM commercial program SAP2000, ver14 (CSI, 2007). For modeling the bearings, a number of nonlinear-link elements, with bilinear equation, are used in order to reproduce the translational and rotational stiffness of the bearings. Piers and deck are modeled by frame elements. Gap elements are used to model the 25mm opening at the expansion joints, which separate the backwall from the deck. Note here that the nonlinear response of the bridge is localized and considered only by the geometrical non-linearities of the gap elements as both the deck and the piers are designed to remain elastic under the design earthquake.

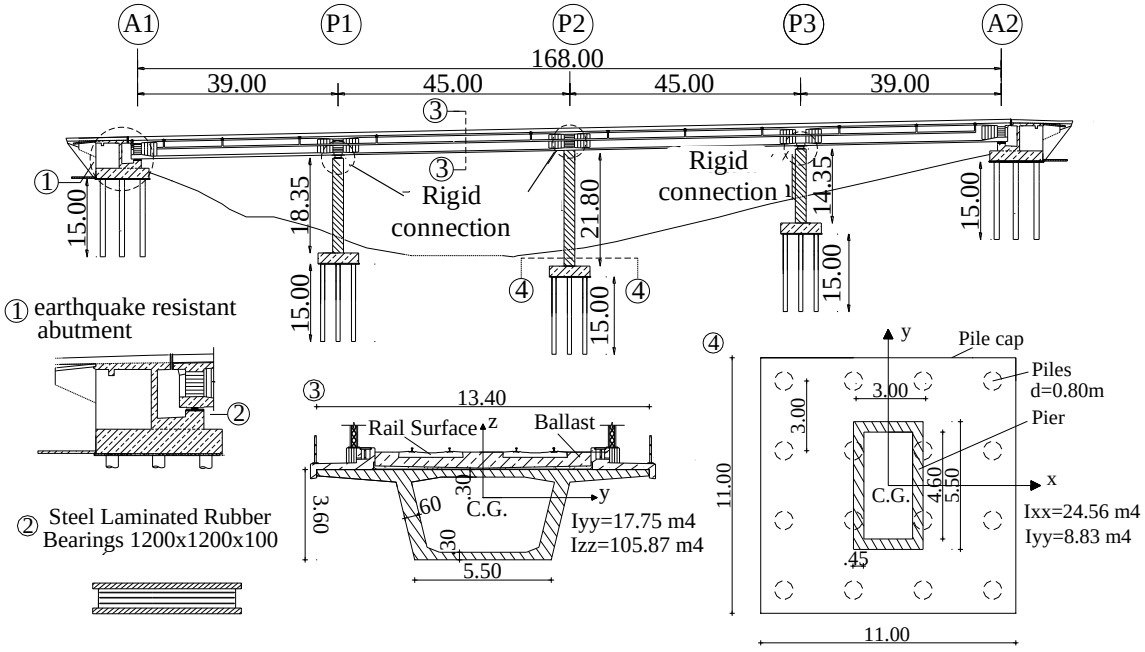


Fig. 6: Section details along the bridge span: (1) Bridge abutment; (2) steel laminated rubber bearings; (3) deck cross-section; (4) plan view of the pier and its foundation.

The interaction of the foundation with the subsoil-structure and the bridge is considered by assigning six spring elements at the contact points, namely three translational and three rotational. For all support points of the bridge and for four different geological profiles, site dependent spring coefficients are computed from closed form equations. For the present case of pile group foundation, equations referring to a single pile (Pender, 1993; Kavadas and Gazetas, 1993) are modified in order to account for the waves that are emitted from the piles and propagate towards the other members of the group. To that purpose, complex dynamic interaction factors α_{ij} are calculated from closed-form equations existing in the literature (Gazetas et al., 1990). Soil-Structure-Interaction is strongly frequency dependent. Nevertheless, it is assumed that the dynamic impedance matrix is calculated based on the predominant frequency of the input motion. This assumption is rather common in the literature but it may not be accurate under certain conditions (Makris and Gazetas, 1992). Hence a range of values between the predominant spectral period and the smoothed spectral predominant period of excitation is considered in the present study

Next, a series of Nonlinear Time History Analyses (NRHA) are conducted under the suite of seven ground motions for the following two cases: (i) the same seismic record is applied to all support points of the bridge(uniform case) and (ii) site dependent ground motions (i.e. the records are different for each support point of the bridge). These ground motions and the corresponding spring coefficients account for (a) canyon topography effect; (b) canyon plus soil layering effect and (c) canyon topography, layering with irregular interfaces and a material gradient effect.

In order to estimate the relative importance of the topographic effects and the subsequent multiple support excitation of the bridge two parametric sets of analyses are carried out.

Namely, the following cases are considered: (1) "uniform" spring values where spring coefficients have the same values for all support points of the bridge for each ground motion and (2) "multiple" spring values where spring coefficients have different values for each support point of the bridge and for each ground motion based on 2D analysis of the subsoil structure.

Fig.6 shows the mean value of piers' dynamic lateral stiffness due to ground motions recorded at the surface of the Types A-D geological profiles that account for i) uniform excitation, ii) canyon effect, iii) canyon and layering effect and iv) canyon, layering and material gradient effect. As can be seen, in terms of the foundation dynamic impedance matrix the presence of local site conditions has a beneficial effect to the bridge foundation stiffness for all here examined ground motions.

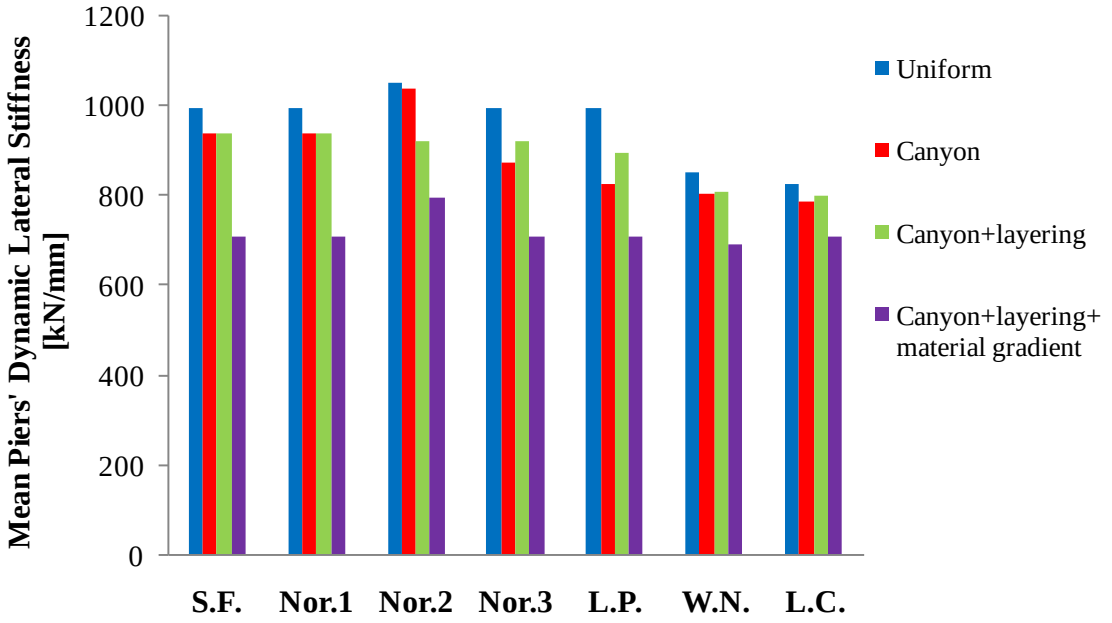


Fig. 7: Mean value of piers' dynamic lateral stiffness due to ground motions recorded at the surface of the Types A-D geological profiles.

6 DYNAMIC RESPONSE OF THE R/C BRIDGE

The influence of (a) site effects, (b) spatial variability in terms of 2D analysis of wave propagation and (c) SSI on structural response of the R/C bridge is demonstrated in Figs.8-10. More specifically, maximum displacements of the bridge deck are shown in Fig.8 for the middle point of the first deck-span (joint A1-P1) and for the second deck-span (joint P1-P2) for the examined case of study. We observe that the presence of local site conditions can modify the kinematic response of the bridge either beneficially or detrimentally. For some ground motions, local site conditions have a significant effect on the response of the deck, while for other ground motions local site conditions produce a minor small difference in the displacement of the deck as compared with the reference type A soil deposit. The pronounce response of the bridge under excitation Northridge 2 and Whittier Narrows for the case of the uniform excitation compared to the other cases that account for site effects is reminiscent of dynamic resonance. In particular, the presence of a complex subsoil structure modifies the frequency of the propagating wave as well as the dynamic characteristics of the bridge through the change in the spring coefficients and the subsequent fundamental period of the structure.

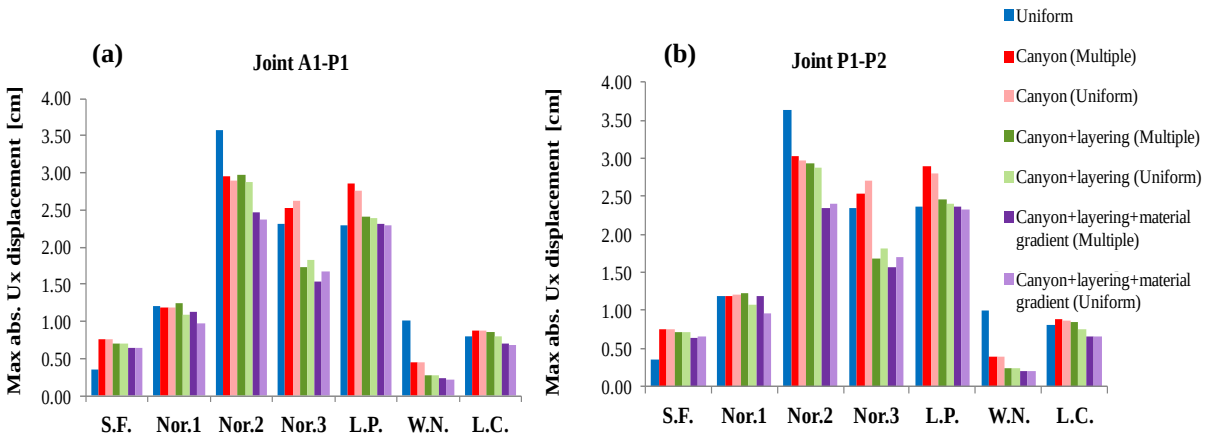


Fig. 8: Maximum absolute deck displacements at joints (a) A1-P1; (b) P1-P2, due to ground motions recorded at the surface of the types A-D geological profiles for (i) uniform spring values and (ii) multiple spring values.

Furthermore, we can see that the effect of multiple spring values for the support points of the bridge produces minor small difference in the deck displacements comparing with the uniform spring values for all support points for each ground motion. Next, maximum absolute displacements at piers P1 and P3 are shown in Fig.10, where we observe that both piers respond similarly to all examined here cases. Ignoring site effects may introduce difference up to 50% in the bridge response in terms of the displacements for the considered here case of study.

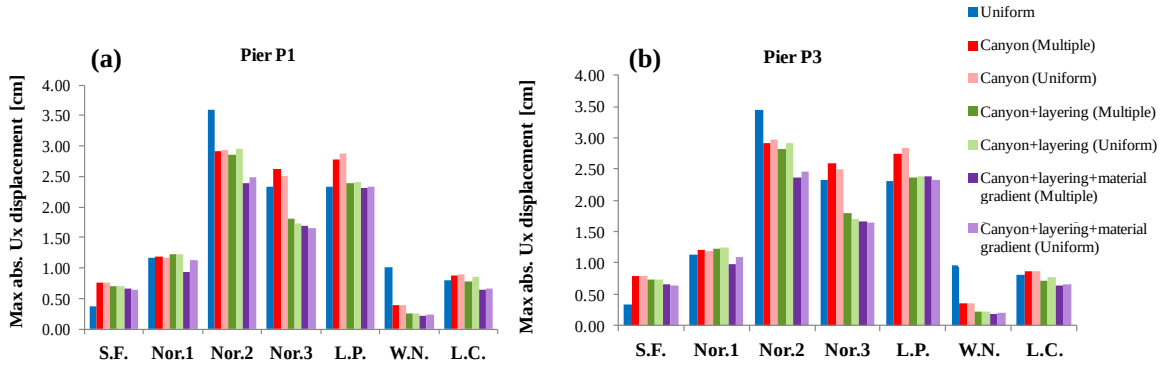


Fig. 9: Maximum absolute pier displacements at joints(a) P1; (b) P3, due to ground motions recorded at the surface of the types a-d geological profiles for (i) uniform spring values and (ii) multiple spring values.

Displacement time history of the bridge deck, and in particular of the middle point of the first span, is presented in Fig.10 for Northridge Nr3 ground motion (listed in Table 2) due to uniform excitation case and to the ground motions that account for canyon, soil layering and material inhomogeneity for uniform or multiple values of spring coefficients. It is observed that canyon topography effect may amplify or de-amplify slightly the displacement time history of the deck (the former holds for the present case). When the canyon effect is combined with soil layering, the effect produces strong de-amplification, due to the increase in stiffness of the soil system, plus an obvious shifting of the peaks. The presence of material gradient additionally to canyon and layering effect does not change the shape of overall time history picture. However in case of multiple spring coefficient values the additional effect of the material gradient produce a small decrease in the amplification levels.

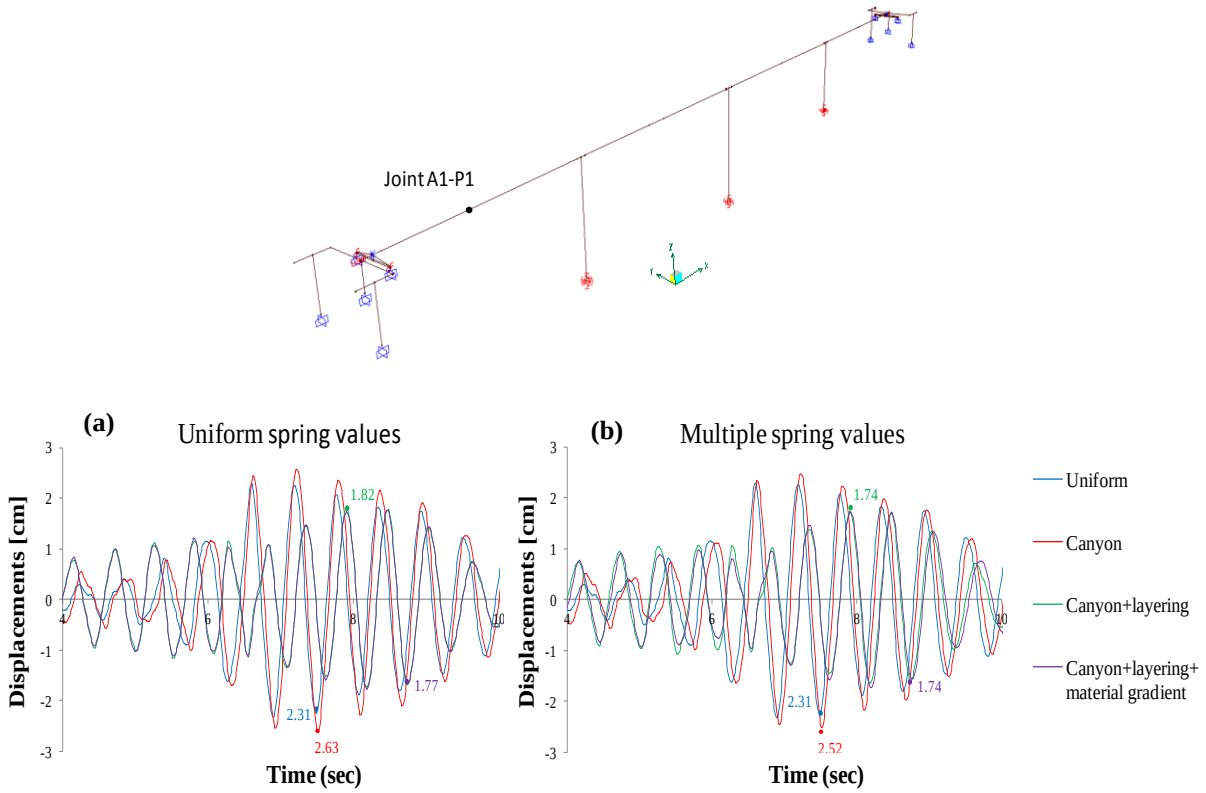


Fig. 10: Displacement time history recorded at point A1-P1 on the deck due to ground motions recorded at the surface of the types A-D geological profiles for (a) uniform spring values and (b) multiple spring values.

7 CONCLUSIONS

In the present study, the influence of local site conditions, spatial variability and Soil-Structure-Interaction on the inelastic dynamic response of a monolithic reinforced concrete bridge are all investigated using a 2D analysis of the subsoil configuration via BEM. Site-dependent time history records and equivalent soil spring coefficients are recovered at the surface of complex geological profiles that account for the following combinations: (i) uniform excitation; (ii) canyon effect; (c) canyon and layering effect; (iv) canyon layering and material gradient effect. Then, a series of dynamic analyses of the bridge, accounting for local nonlinearities, are conducted under site dependent ground motions provided by the previous development, which considers multiple support excitation. From the numerical simulation results, the following conclusions can be drawn:

- Site dependent ground motions are generated by a new-developed BEM that can represent wave propagation in complex geological media with variable velocity profile, nonparallel layers, surface relief and buried cavities and tunnels.

- The site dependent ground motions and the subsequent soil spring coefficients are strongly affected by the canyon topography, layering and material gradient effect and this effect is frequency-dependent.

- The combination of local site conditions, spatial variability and SSI effects influence significantly the nonlinear dynamic response of bridges. These effects cannot be neglected and should be modeled and implemented in as much as possible.

- SSI effect is beneficial in terms of foundation dynamic impedance matrices regardless of the presence of site effects. However, in terms of structural response the combination of SSI, spatial variability and site effects can be detrimental, at least for the bridge examined here.

- Ignoring site effects via 2D analysis of the soil profile may introduce an error around 50% in terms of the kinematic field for the case examined herein.

ACKNOWLEDGEMENTS

The authors would acknowledge support provided by DAAD (through the DeGrieLab project, 2014-2016) and by DFG (through grant Wu 496/5-1).

REFERENCES

[1] Eurocode 8 (2003) *Design of Structures for Earthquake Resistance, Part 1: General Rules, Seismic Actions and Rules for Buildings, Part 2: Bridges,* European Committee for Standardization, Brussels.

[2] A. Sextos, K. Pitilakis, A. Kappos. Inelastic dynamic analysis of RC bridges accounting for spatial variability of ground motion, site effects and soil-structure interaction phenomena. Part 1: Methodology and analytical tools. *Earthquake Engineering and Structural Dynamics* **32**:607-627, 2003a.

[3] A. Sextos, K. Pitilakis, A. Kappos. Inelastic dynamic analysis of RC bridges accounting for spatial variability of ground motion, site effects and soil-structure interaction phenomena. Part 2: Parametric study. *Earthquake Engineering and Structural Dynamics* **32**:629-652, 2003b.

[4] B. Jeremic, G. Jie, M. Preisig, N. Tafazzoli, Time domain simulation of soil-foundation-structure interaction in non-uniform soils. *Earthquake Engineering and Structural Dynamics* **38(5):**699-718, 2009.

[5] K. Bi., H. Hao. and N. Chouw, Influence of ground motion spatial variation, site condition and SSI on the required separation distances of bridge structures to avoid seismic pounding. *Earthquake Engineering and Structural Dynamics,* **40(9)**: 1027–1043, 2011.

[6] K. Soyluk and E. A. Sicacik. Soil-structure interaction analysis of cable-stayed bridges for multiple-support excitations. 8th International Conference on Structural Dynamics, EURODYN, Leuven, Belgium, 4-6 July, MS03-499, pp. 547-554, 2011.

[7] J. A. Esquivel and F. J. Sanchez-Sesma. "Effects of canyon topography on dynamic soil-bridge interaction for incident plane SH waves." Proceedings7th World Conference on Earthquake Engineering, Istanbul, Turkey, pp. 153-160, 1980.

[8] G. Zhou, X. Li and X. Qi. Seismic response analysis of continuous rigid frame bridge considering canyon topography effects under incident SV waves," *Earthquake Science,* **23**:53-61, 2010.

[9] G.D. Manolis, R. Shaw. Harmonic wave propagation through viscoelastic heterogeneous media exhibiting mild stochasticity-I. Fundamental solutions. *Soil Dynamic and Earthquake Engineering* **15**:119-127, 1996a.

[10] G.D. Manolis, R. Shaw. Harmonic wave propagation through viscoelastic heterogeneous media exhibiting mild stochasticity-II. Applications. *Soil Dynamic and Earthquake Engineering* **15**:129-139, 1996b.

[11] I.-K. Fontara, P. Dineva, G. Manolis, S. Parvanova. and F. Wuttke, Seismic wave fields in continuously inhomogeneous media with variable wave velocity profiles. *Archive of Applied Mechanics*, 2015 (under review).

[12] MATLAB. *The Language of Technical Computing*, *Version 7.7*. The Math-Works, Inc., Natick, Massachusetts, 2008.

[13] PEER. Pacific Earthquake Engineering Research Center, *Strong Motion Database*, available at http://peer.berkeley.edu/smcat/, 2003.

[14] S.A. Mitoulis, M.D. Titirla and I.A. Tegos. Design of bridges utilizing a novel earthquake resistant abutment with high capacity wing walls. *Engineering Structures* **66**:35-44, 2014.

[15] *SAP 2000 Nonlinear Version 14, User's Reference Manual*, Computer and Structures Inc., Berkley, California, 2007.

[16] MJ. Pender. Aseismic pile foundation design analysis. *Bulletin of the New Zealand National Society on Earthquake Engineering*; **26** (1):49-161, 1993.

[17] M. Kavadas and G. Gazetas. Kinematic seismic response and bending of free-head piles in layered soil. *Geotechnique*; **43**:207-222, 1993.

[18] G. Gazetas, K. Fan, A. Kaynia, E. Kausel. Dynamic interaction factors for floating pile groups, vol. 1, *NCEER-90-0021*. National Center for Earthquake Engineering Research: Buffalo, NY, 1990.

[19] N. Makris and G. Gazetas. Dynamic pile-soil-pile interaction. Part II: lateral and seismic response. Earthquake Engineering and Structural Dynamics; 21 (2):145-162, 1992.

COMPDYN 2015
5th ECCOMAS Thematic Conference on
Computational Methods in Structural Dynamics and Earthquake Engineering
M. Papadrakakis, V. Papadopoulos, V. Plevris (eds.)
Crete Island, Greece, 25–27 May 2015

SLENDER PROFILES FOR MOMENT RESISTING FRAMES IN MODERATE SEISMICITY REGIONS - NUMERICAL AND EXPERIMENTAL INVESTIGATIONS -

Matthias Wieschollek[1], Benno Hoffmeister[1] and Markus Feldmann[1]

[1] RWTH Aachen University
Institute of Steel Construction
52074 Aachen, Germany
wieschollek@stb.rwth-aachen.de

Keywords: Earthquake Engineering, Moment Resisting Frames, Welded and bolted Connections, Cyclic Behaviour of Slender Profiles, Seismic Design, Behaviour factor.

Abstract. *Moment resisting steel frames offer an excellent ductility and energy dissipation and can be designed using high behaviour factors. The condition however is, that compact cross-sections are used allowing for large rotations in the plastic hinges. Portal frames, as commonly designed and built for storage or industrial applications, are usually aiming at light weight solutions in order to be competitive to prefabricated concrete halls. Class 3 or 4 profiles are preferably used, this prevents however the application of any significant behavior factor. In particular in low and moderate seismicity regions a behaviour factor in the range of 2-3 would be fully sufficient in order to achieve an economically optimum design.*

The aim of the investigations presented in this paper is the determination of the cyclic performance of knee joints made of slender steel-sections. Four different slender joint types are investigated numerically and experimentally and compared to the performance of a compact-section joint. The definition of the test setup and testing procedure is done using a "virtual-push-over" FE-analysis. This analysis is used to define the amplitudes of test cycles as well as the expected forces and deformations. By applying expected material properties also the cyclic tests are predicted allowing for an assessment of the expected damage and an optimum placement of measuring devices. Using the actual, measured dimensions and material properties of the test specimens a more refined calculation of the expected performance is obtained. The experimental tests are performed under cyclic loading only as the static push-over results are available from the numerical simulations. The cyclic tests provide the measured data of global and local deformations and strains, which are essential for the verification of the local buckling phenomena in slender cross-sections under cyclic actions. These results are used for a fine-tuning of the numerical models regarding imperfections and material properties. Knowing the influence and the range of parameter obtained from tests it is possible to extend the numerical simulations to other geometries and to complete frames under realistic seismic actions.

1 INTRODUCTION

As part of the European Research Project MEAKADO "Design of steel and composite structures with limited ductility requirements for optimized performances in moderate earthquake areas" the cyclic behaviour of slender profiles for moment resting frames (MRF) in moderate seismicity regions are currently being researched. The experimental and numerical investigations are described in detail within the Deliverables D2.1a [1] and D2.2 [2]. By analogy with [3] this paper summarize the results for the investigated frame corners made of slender steel cross sections. The motivation for this research was particularly the fact that according to the current version of Eurocode 8 [4] only cross-sectional classes 1 or 2 are permitted for steel or composite structures when a considerable behaviour factor is intended to be taken into account. Within MRF's almost all members are affected by this limitation:

- Single-bay – single-storey steel frames: Such structures are part of a highly competitive marked requiring a strong optimisation in terms of material requirement and ease of construction. Light weight steel frames are an optimum solution so far, with the exception of seismic regions where the above mentioned restrictions strongly limit their applicability despite their low masses.
- Multi-bay – multi-storey composite buildings: Due to the high position of neutral axis of composite cross-sections in negative bending the web of steel profiles is very often to be classified as class 3 or 4 section, although almost all rolled steel profiles may be classified as class 1 or 2 cross-sections.

The above mentioned aspects are of particular importance in countries with moderate seismicity regions, where a special adoption of the otherwise common types of structures presents a great obstacle for the small and medium size companies active in this market. Hence an extension of the applicability of the afore mentioned structural types to moderate seismic regions would largely enhance their competitiveness. This leads to the following objectives:

- Extension of the applicability of class 3 or 4 steel cross sections within single-bay – single-storey frames to moderate seismic actions by means of characterization of class 4 cross sections in terms of rotational behaviour and energy dissipation.
- Extension of the applicability of class 3 (web) composite sections to moderate seismic actions by means of characterization of class 3 composite cross section in terms of rotational behaviour and energy dissipation.
- Identification and definition of b/t values rather than cross-sectional classes to be limited depending on the targeted energy dissipation and the corresponding deformations by means of numerical analyses.

2 EXPERIMENTAL TEST ON FRAME CORNERS

2.1 Generals

The test program considered typical welded profiles typically used for light weight frames of small industrial or storage halls. In total 6 cyclic tests on frame corners with welded and bolted connections as well as haunched and constant depth girders were carried out. The test specimens were designed such that for constant depth girders the plastic hinges developed in the beams whereas for the haunched girders the plastic hinges developed in the top of the column. The tests were performed according to the ECCS testing procedure [5] with increasing amplitudes of deformation cycles and were executed until collapse (e.g. rupture due to low cycle fatigue or extensive local buckling). The measurements were evaluated with regard to the development of the hysteretic behaviour with particular emphasis on the degradation.

2.2 Description of test specimens

The 6 specimens have been manufactured in collaboration with the company OCAM in Italy. Each type of material used for the test specimens has been taken from a single steel charge, whereby plates with equal plate thicknesses were made of the same production batch. In order to have accurate material characteristics for the numerical simulations of the tests and especially for the determination of the test procedure for cyclic loading, some small scale specimens were taken from the material of the specimens. These small scale specimens were tested under monotonic loading. Table 1 summarizes the test results and Figure 1 shows the stress-true strain curves obtained from the tests together with the stress-strain curves extrapolated according to Hollomon [6] which were applied for the monotonic simulations.

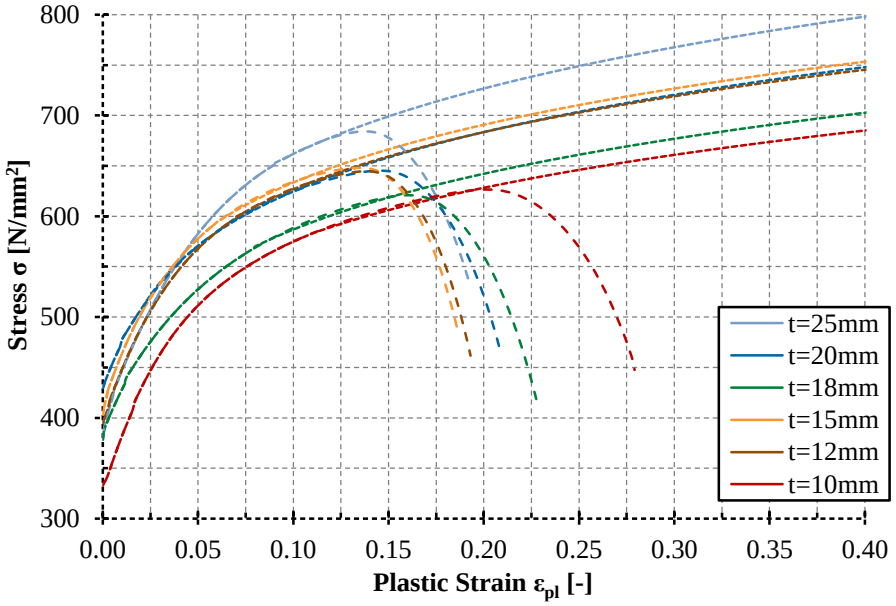


Figure 1: True and extrapolated stress-strain curves

Plate thickness t [mm]	**25.0**	**20.0**	**18.0**	**15.0**	**12.0**	**10.0**
Steel grade	S355J2+N	S355J2+N	S355J2+N	S355J2+N	S355J2+N	S355J2+N
f_y [MPa]	376	420	372	385	389	331
f_u [MPa]	595	553	527	562	562	521
f_y / f_u [-]	0.63	0.76	0.71	0.68	0.69	0.64
ε_u [%]	24.6	30.0	31.2	31.0	31.5	35.7

Table 1: Material characteristics obtained from small scale tests

Different examples for MRF's have been compiled from literature as well as from direct dialogue with manufacturers to mirror the state-of-the-art. Following these examples the geometries, plate thicknesses and joint details have been assigned. Furthermore it has been decided to test only frame corners as subsystems of a complete MRF and due to the test setup the length of the beams and columns were limited. All specimens were made as class 3 cross sections and in order to reach plastic hinges in the beams and columns the panel zones were reinforced, whereby one additional test on a frame corner without a reinforcement and one additional test on a frame corner made of class 1 cross sections with comparable monotonic resistance and stiffness were carried out. The 6 different specimens that was decided on were:

- S1 - Welded frame corner with constant girder
- S2 - Bolted frame corner with constant girder
- S3 - Welded frame corner with haunched girder
- S4 - Bolted frame corner with haunched girder
- S5 - Welded frame corner with constant girder - class 1
- S6 - Welded frame corner with constant girder - unreinforced panel zone

Figure 2 shows the above mentioned specimens or types of frame corners respectively, while Figure 3 illustrates the principle geometry of the test specimens. The main dimensions (e.g. length of column and beam, cross-sectional height and width) were equal for all specimens. After delivery all test specimens have been investigated with regard to tolerances that may influence the test results. Table 2 gives the results of the measured dimensions that have been taken according to the measurement scheme as shown in Figure 3.

The final step to prepare the specimens for the tests was the application of strain gauges at the (numerically predicted) critical positions, but also on undisturbed areas of the beams and columns. These strain gauge applications on the one hand allowed to detect a damage initiation during the tests as well as on the other hand enabled to calibrate and verify the numerical finite element models.

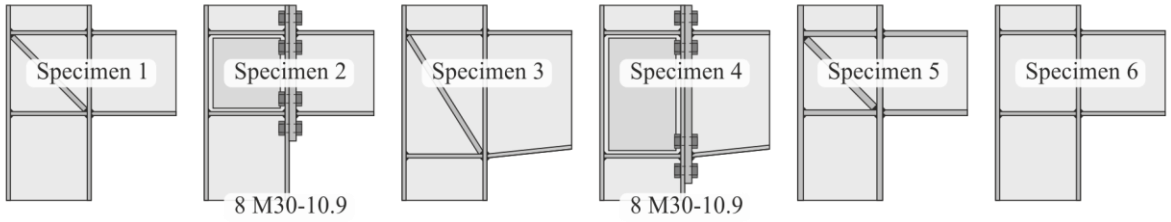


Figure 2: Overview of the specimens - types of frame corners

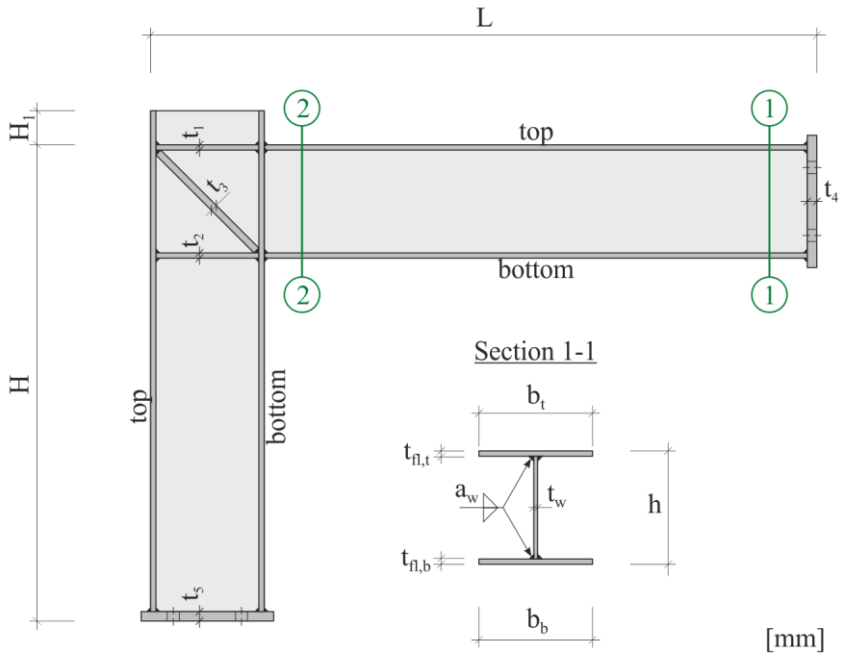


Figure 3: Overview of specimen dimensions using specimen S1

Specimen		L	h_1	h_2	b	t_{fl}	t_w	a_w	Web		Flange	
					[mm]				c/t	Class	c/t	Class
S1	Girder	1772	296	296	300	15.3	10.0	6.0	24.9	1	9.0	3
S2		1760	296	296	300	15.5	10.0	6.0	24.8	1	8.8	3
S3		1760	303	442	300	15.4	10.0	6.0	39.4	1	8.9	3
S4		1760	304	446	300	15.5	10.0	6.0	39.8	1	8.8	3
S5		1760	298	298	250	18.6	10.0	6.0	24.4	1	6.0	1
S6		1760	299	299	300	15.5	10.0	6.0	25.1	1	8.8	3
		H	H_1	h	b	t_{fl}	t_w	a_w	c/t	Class	c/t	Class
S1	Column	1268	90	300	300	15.3	12.0	7.0	20.8	1	8.8	3
S2		1260	90	297	300	15.2	12.0	7.0	20.6	1	8.8	3
S3		1260	90	300	300	15.4	12.0	7.0	20.8	1	8.7	3
S4		1260	88	300	300	15.3	12.1	7.0	20.6	1	8.8	3
S5		1260	90	299	250	18.8	12.1	7.0	20.0	1	5.8	1
S6		1260	90	300	300	15.5	12.0	7.0	20.8	1	8.7	3

		t_1	t_2	t_3	t_4	t_5
S1	Plates	15.2	15.0	18.8	25.2	25.2
S2		15.4	15.4	2x12.0	25.0	25.0
S3		15.3	15.4	18.7	25.1	25.2
S4		15.3	15.3	2x12.0	25.0	25.1
S5		18.7	18.6	21.2	25.2	25.2
S6		15.1	15.3	-	25.3	25.2

Table 2: Actual measured values of the specimen dimensions

2.3 Description of test setup

The boundary conditions of the test setup have been particularly focused on a best possible representation of the real load-deformation behaviour of a complete MRF. The test setup is shown schematically in Figure 4, whereas the final realization with a test specimen can be seen in Figure 5.

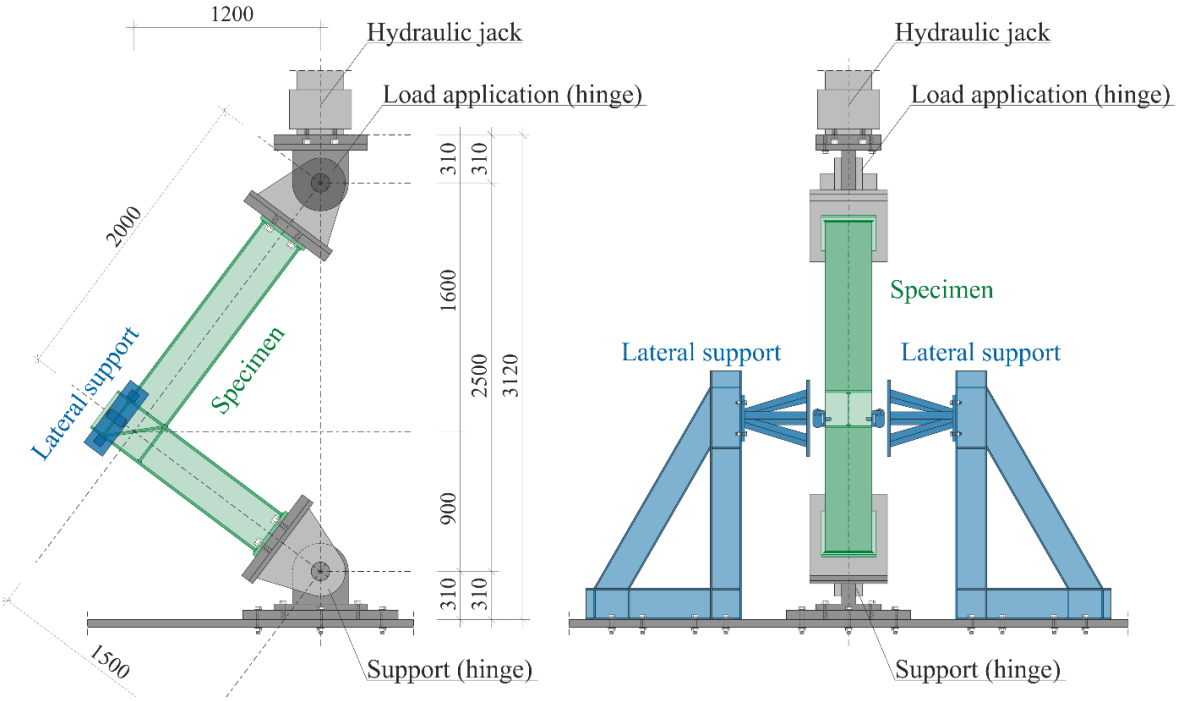


Figure 4: Schematic representation of the test setup



Figure 5: Test setup with test specimen S2

2.4 Test procedure for cyclic loading

According to the ECCS testing procedure [5] monotonic tests are required to define the test procedure for cyclic testing. Instead of these monotonic tests, here numerical simulations were used. Since the displacement e_y corresponding to the yield load *Fy* were similar for tension and compression range, the average values were taken for the cyclic tests (Table 4). The loading history was applied as given schematically in Figure 6 and Table 3. Thereby the loading history was modified such that by refined gradation of the displacement amplitudes e_i until failure the resolution of cyclic results has been increased.

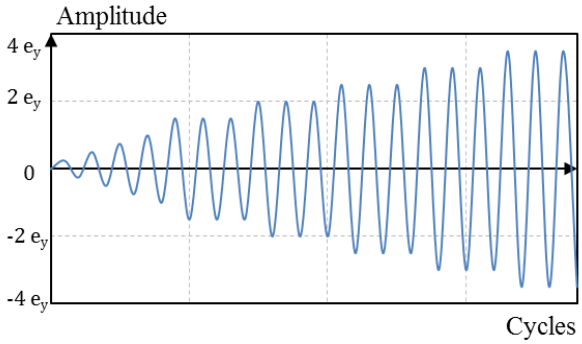


Figure 6: Schematic representation of the modified loading history according to ECCS [5]

Cycle	**1**	**2**	**3**	**4**	**5-7**	**8-10**	**11-13**	**…**
e_i [mm]	$0.25e_y$	$0.5e_y$	$0.75e_y$	e_y	$1.5e_y$	$2.0e_y$	$2.5e_y$	…

Table 3: Amplitudes of displacement for cyclic loading

Specimen	**S1**	**S2**	**S3**	**S4**	**S5**	**S6**
e_y [mm]	24.0	24.0	20.0	20.0	24.0	16.0

Table 4: Reference amplitudes of displacement for cyclic loading

2.5 Test results for cyclic loading

The test results in terms of cyclic load-displacement curves referring to the point of load application and pictures of the specimens at the end of the loading history showing the different failure modes of each specimen are shown in Figure 7 to Figure 12.

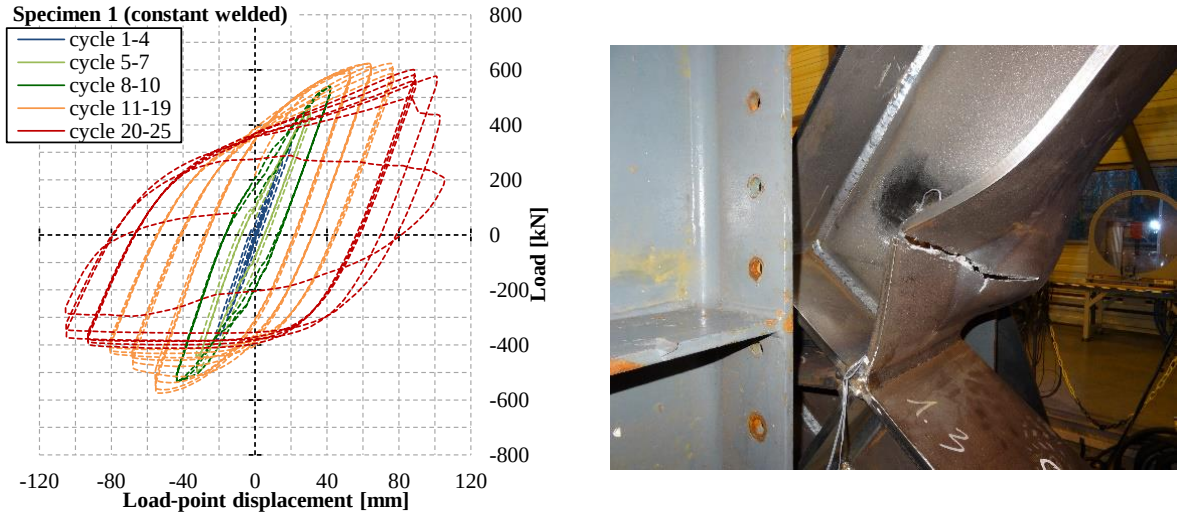


Figure 7: S1 – Cyclic load-displacement curve and failure mode

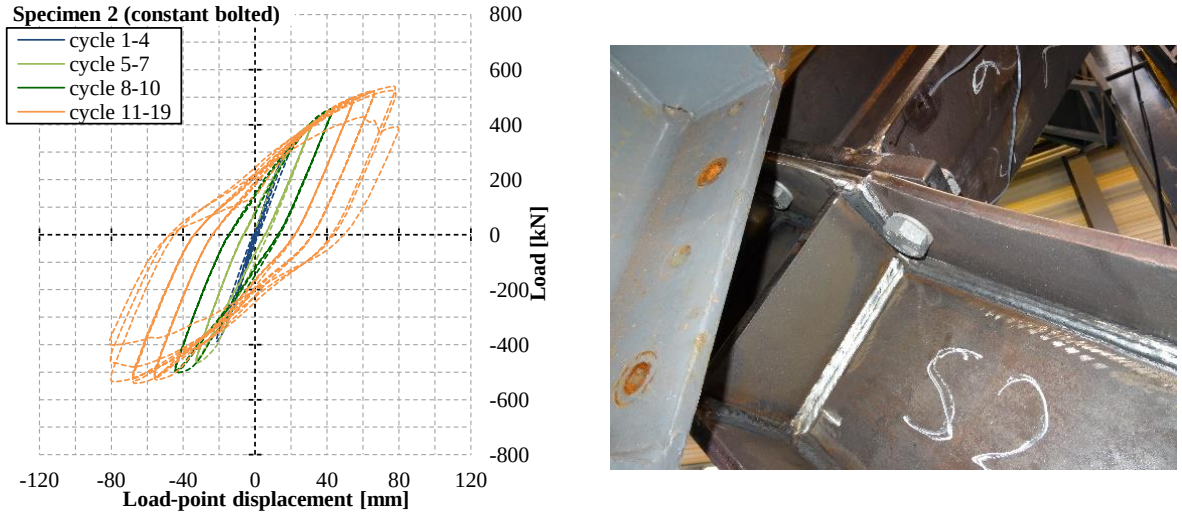


Figure 8: S2 – Cyclic load-displacement curve and failure mode

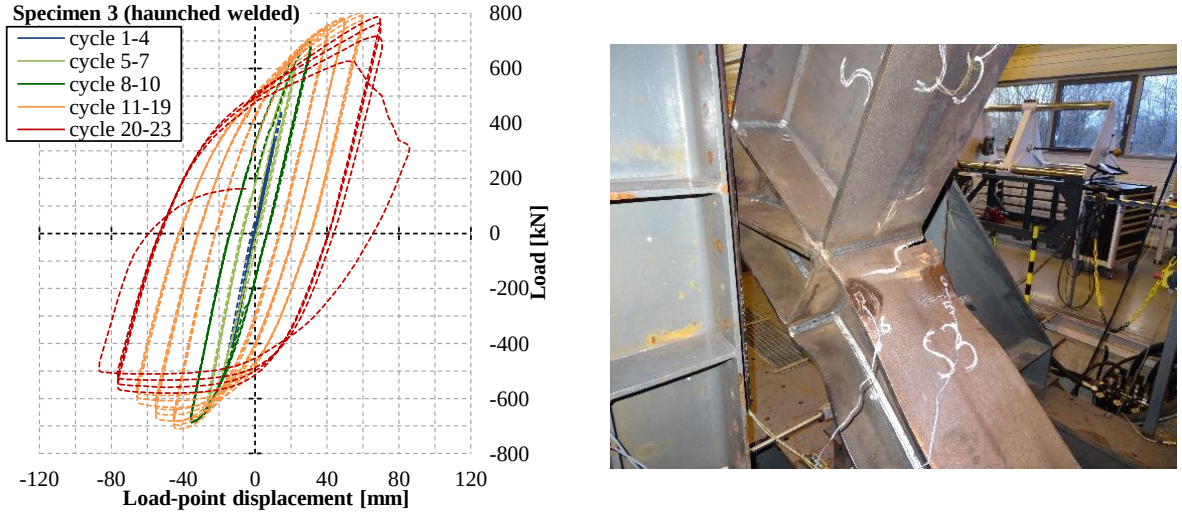


Figure 9: S3 – Cyclic load-displacement curve and failure mode

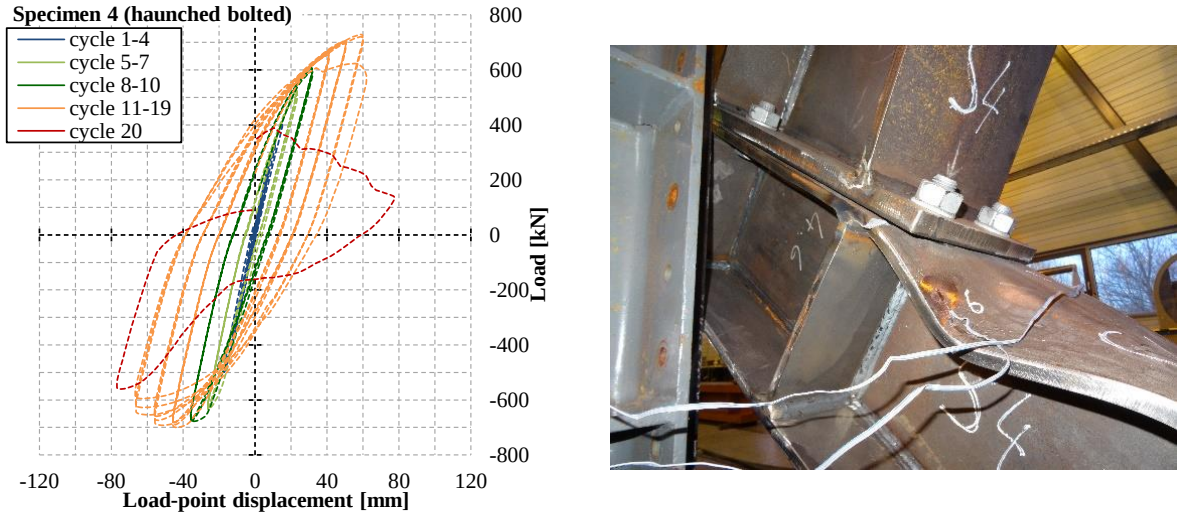


Figure 10: S4 – Cyclic load-displacement curve and failure mode

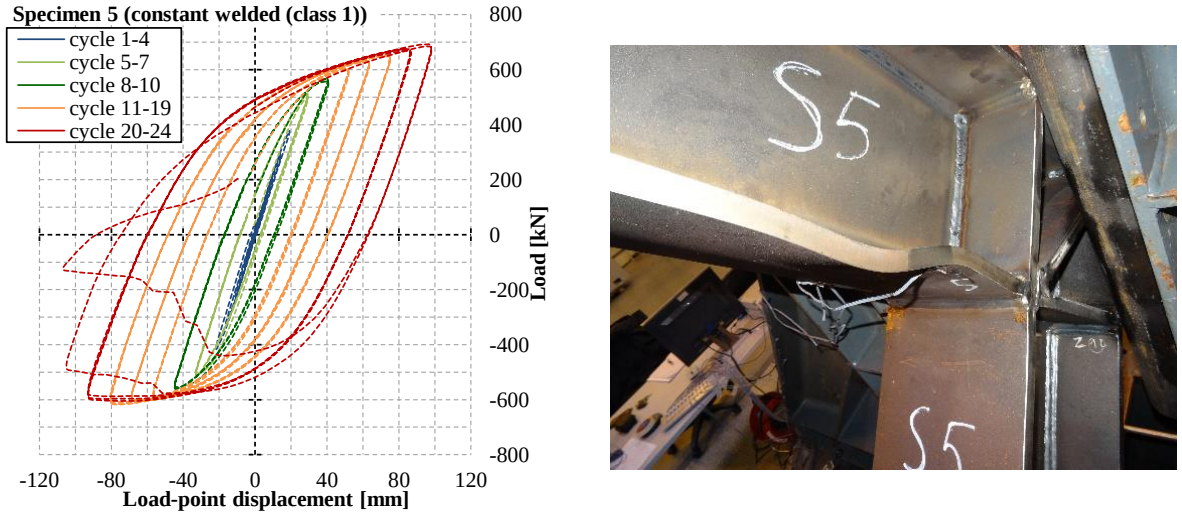


Figure 11: S5 – Cyclic load-displacement curve and failure mode

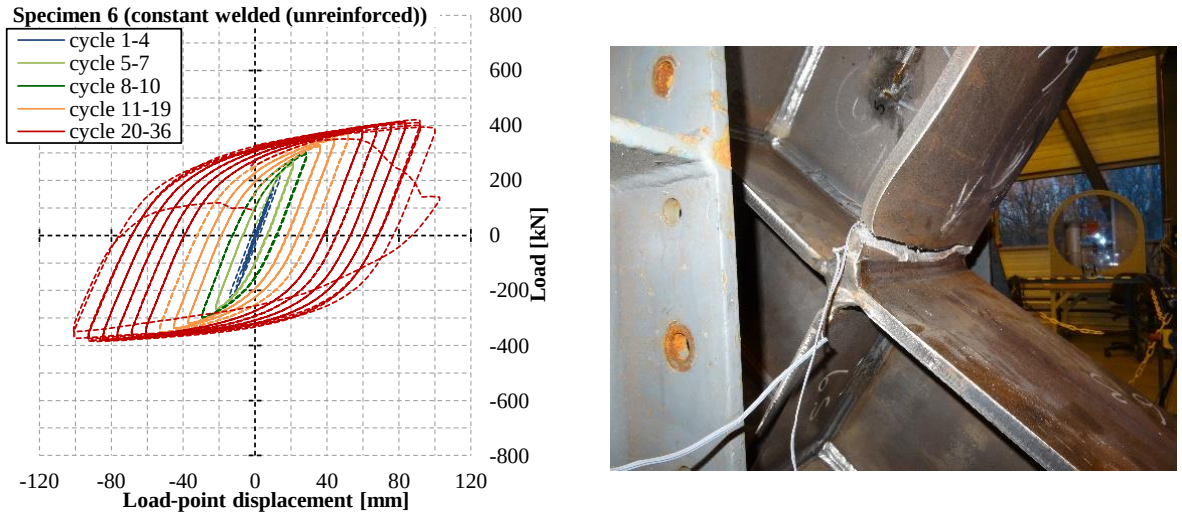


Figure 12: S6 – Cyclic load-displacement curve and failure mode

Due to slippage in the hinges of the test setup the test specimens were loaded with slightly smaller displacements than indicated by the true movement of the jack. The measured values of displacement as well as the number of cycles until failure N_f occurred are shown in Table 5.

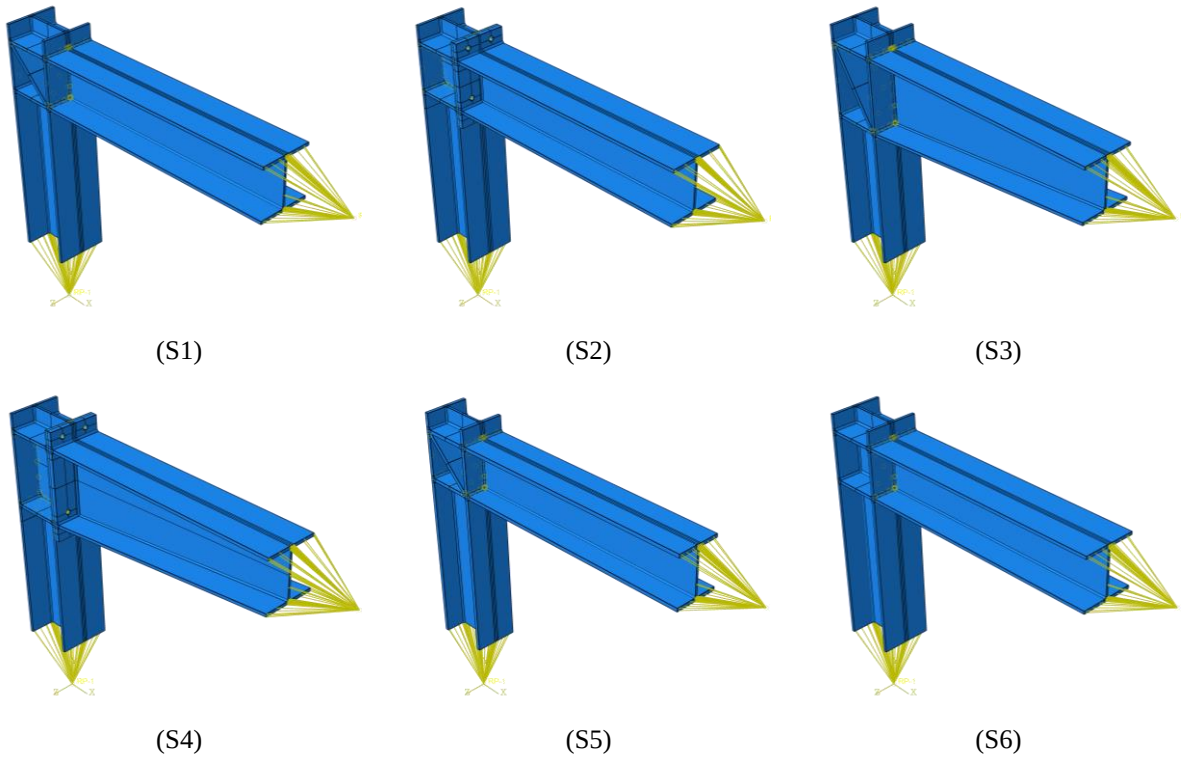
Specimen	e_i in [mm] for cycle												N_f
	4	5-7	8-10	11-13	14-16	17-19	20-22	23-25	26-28	29-31	32-34	35-36	[-]
S1	20.7	31.4	42.7	54.1	66.3	78.6	91.0	104.1	-	-	-	-	23.3
S2	20.8	31.9	43.5	55.1	67.0	79.6	-	-	-	-	-	-	18.3
S3	15.9	24.2	33.2	42.7	52.5	62.6	73.2	86.3	-	-	-	-	22.3
S4	16.1	24.8	33.8	43.4	53.1	63.5	77.2	-	-	-	-	-	18.3
S5	20.4	31.1	42.6	54.2	66.0	77.6	89.6	101.9	-	-	-	-	22.8
S6	13.9	21.4	28.9	36.7	44.5	52.3	60.2	68.1	76.1	84.0	92.2	67.4	35.3

Table 5: Measured values of displacement and number of cycles until failure

3 NUMERICAL SIMULATIONS OF TESTS

3.1 Description of numerical simulations

Subject of these simulations was the numerical recalculation and verification of the above described tests. The geometries of the FE-models were chosen equal to the measured dimensions of the test specimens, Figure 13.



(S1) (S2) (S3)

(S4) (S5) (S6)

Figure 13: Overview FE-models

The FE-program ABAQUS was used and the FE-models were created using 8-node reduced-integration solid elements (type C3D8R). Both geometric and physical non-linearities were considered and moreover the FE-mesh as well as the FE-mesh refinements around the critical points were calibrated to get stable and adequate results.

For monotonic loading conditions, in order to determine the test procedure for cyclic loading, non-linear isotropic hardening was considered using the extrapolated true stress-strain curves shown in Figure 1, whereas for cyclic loading conditions linear isotropic and non-linear kinematic hardening according to Lemaitre Chaboche [7] were considered. The required parameters were determined analytically and were verified using numerical simulations; they are summarized in Table 6.

f_y [N/mm^2]	C [-]	γ [-]	Q [-]	b [-]
320	26000	120	-	-

Table 6: Material parameter for cyclic loading conditions according to Lemaitre Chaboche [7]

The boundary conditions of the test setup were considered using 2 reference points in conjunction with “coupling” definitions at both ends of the specimens (see Figure 14). The lateral support of the frame corner was incorporated by adequate boundary conditions. The simulations were run displacement-controlled with the measured loading history of the tests.

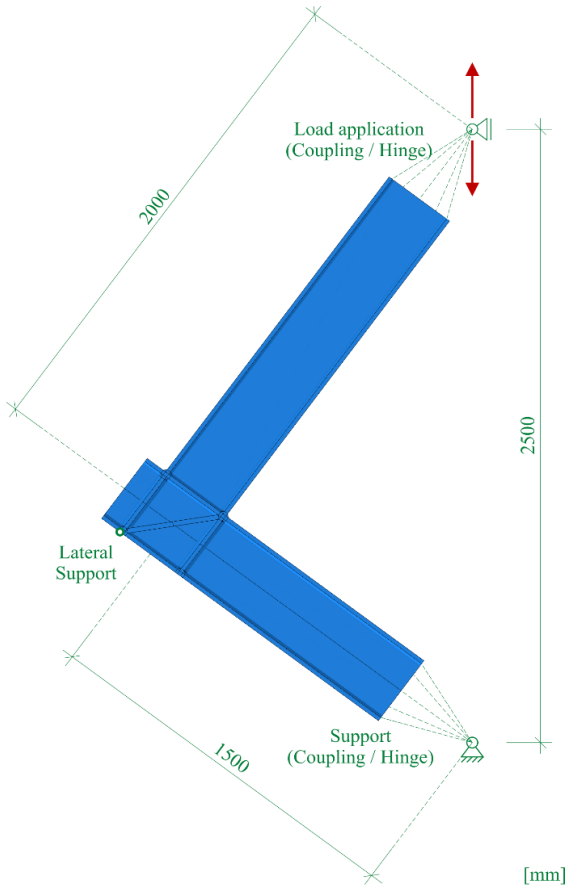


Figure 14: Load application and boundary conditions

3.2 Numerical results for cyclic loading

The numerical results in terms of cyclic load-displacement curves referring to the point of load application as well as deformed shapes showing the accumulated plastic strains at the end of the loading history are given in Figure 15 to Figure 20.

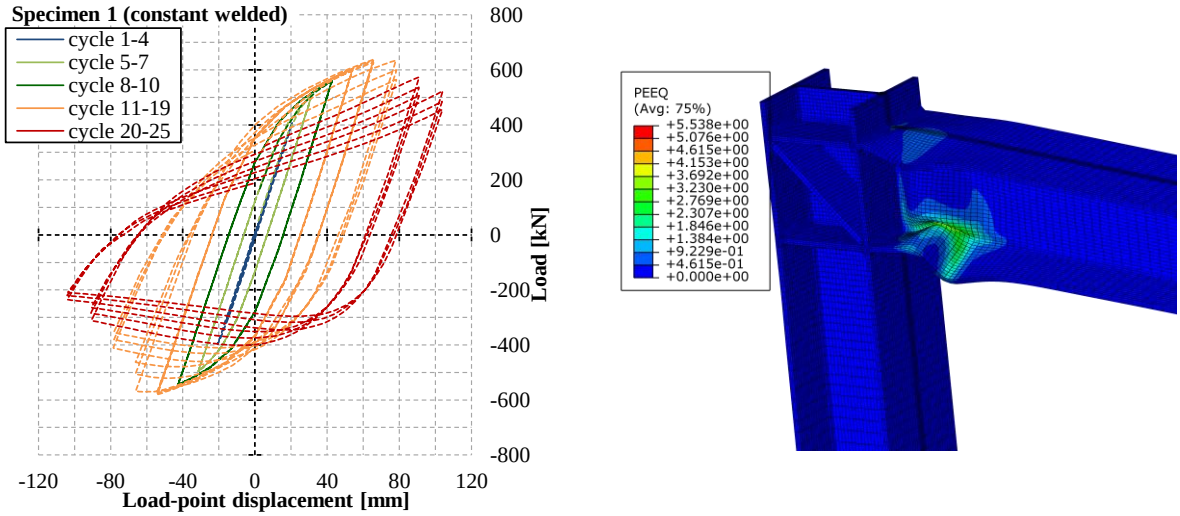


Figure 15: S1 – Cyclic load-displacement curve and failure mode

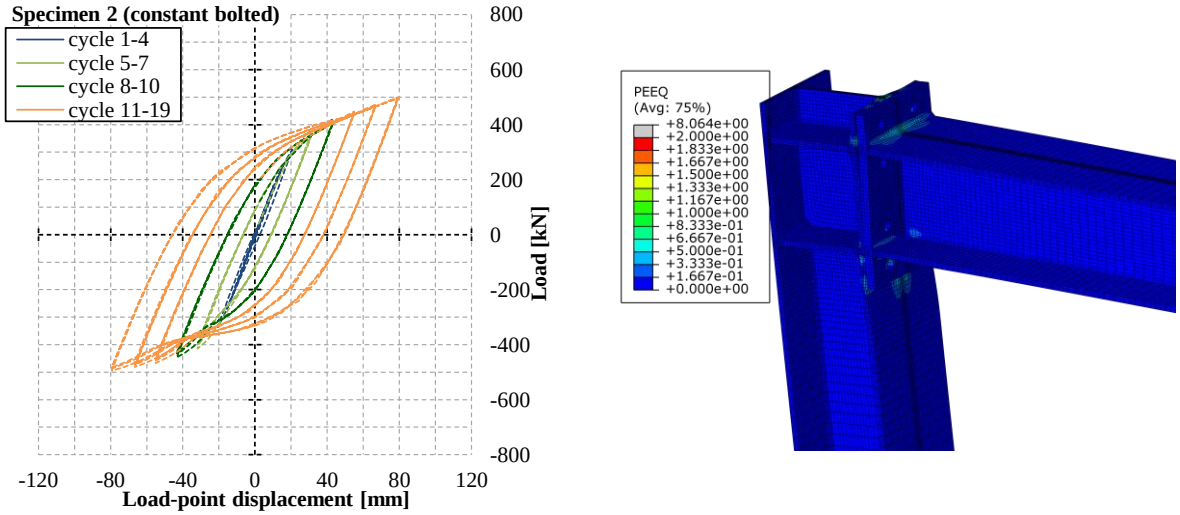


Figure 16: S2 – Cyclic load-displacement curve and failure mode

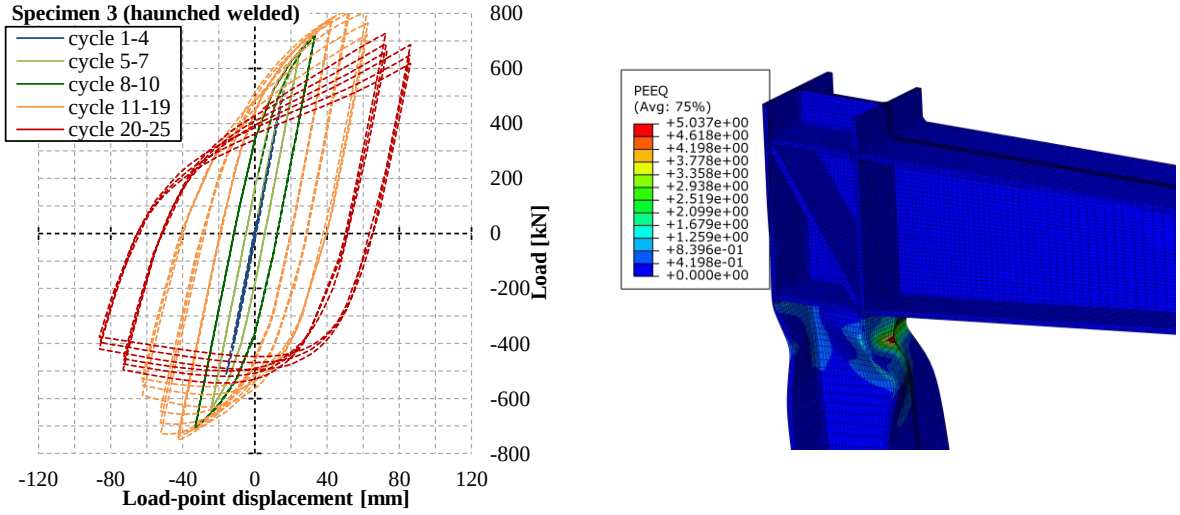


Figure 17: S3 – Cyclic load-displacement curve and failure mode

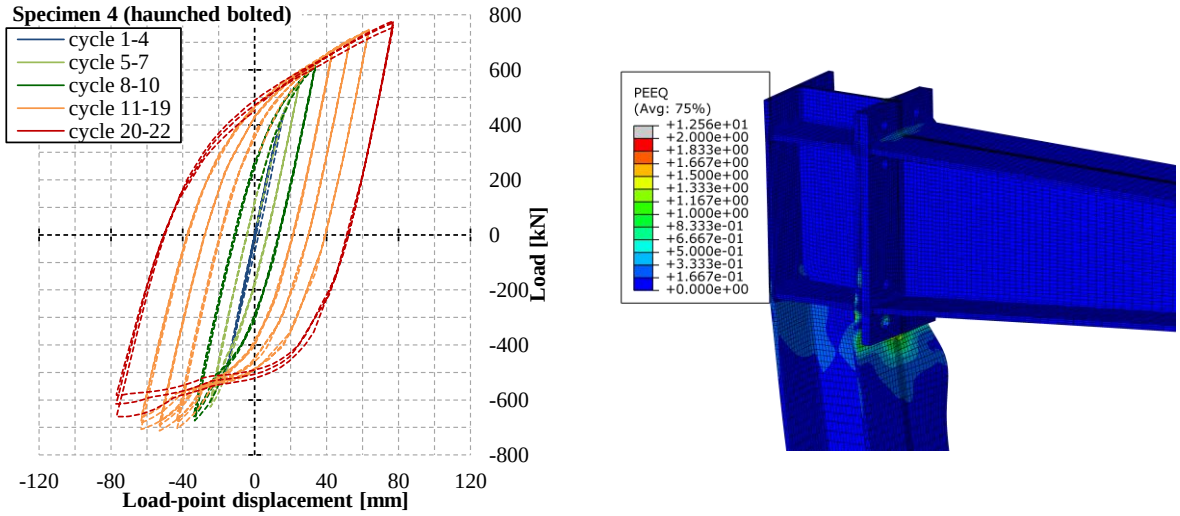


Figure 18: S4 – Cyclic load-displacement curve and failure mode

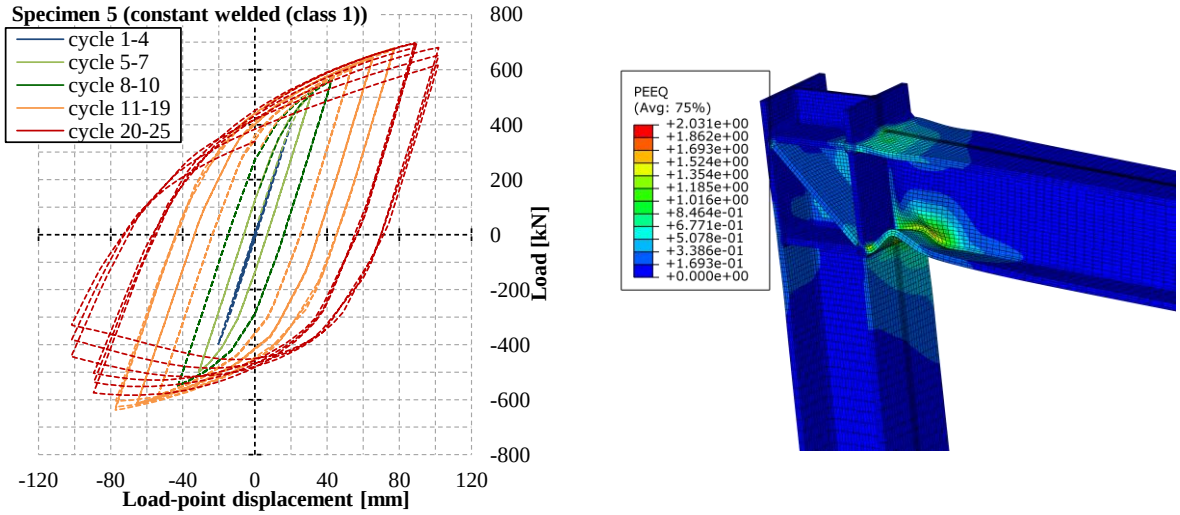


Figure 19: S5 – Cyclic load-displacement curve and failure mode

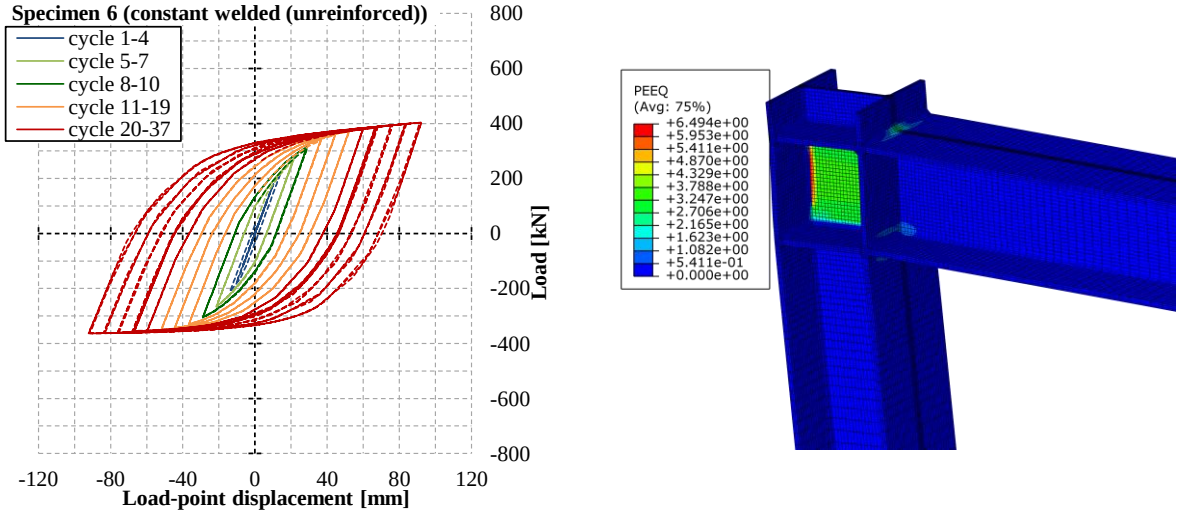


Figure 20: S6 – Cyclic load-displacement curve and failure mode

4 OBSERVATIONS AND CONCLUSIONS

The numerical verification of the tests was aiming at two main aspects, the validation of the numerical model with regard to its accordance with the experimental behaviour and thus its applicability for parametric studies as well as the identification of damage and formulation of a equivalent damage criterion transferrable from damages observed in the tests to the numerical model.

The experimental and numerical load-displacement curves show a very good agreement confirming the capability of the FE-models to represent the overall performance of the investigated frame corners. For the identification of failure modes (cracks) in the numerical FE-models an approach has been selected, in which the accumulated plastic strains $\bar{\varepsilon}_p$ were compared to a limit value $\bar{\varepsilon}_{p,limit}$. The limiting values have been calibrated by the test results such that for each tested specimen respectively its FE-models the location and the accumulated plastic strains have been determined from the simulations at the cyclic deformation stage of the tested specimen corresponding to the first visually detected crack. From this evaluation the number of cycles until failure and the location (point of failure) can be obtained.

On the basis on the findings from the tests as well as from the simulated recalculation of the tests the next step will be a parametric numerical study. The main aim of this study will be the assessment of the influences of the different components on the cyclic behaviour of MRF's as well as the development of pre-normative design rules.

5 ACKNOWLEDGMENTS

This work was carried out with a financial grant from the Research Fund for Coal and Steel of the European Commission, within MEAKADO project: "Design of steel and composite structures with limited ductility requirements for optimized performances in moderate earthquake areas", Grant No. RFSR-CT-2013-00022.

REFERENCES

[1] Deliverable D2.1a:" Experimental testing on class 3 and 4 steel cross-sections", RFCS project MEAKDO, Grant No. RFSR-CT-2013-00022

[2] Deliverable D2.2:" Development of numerical models of class-3 and 4 steel and composite cross-sections", RFCS project MEAKDO, Grant No. RFSR-CT-2013-00022

[3] Wieschollek, M., Hoffmeister, B. and Feldmann, M.: Experimental and numerical investigations on nozzle reinforcements, Proceedings of the ASME 2013 Pressure Vessels & Piping Division Conference PVP2013, Paris 2013, France

[4] EN 1998 1:2010 12: "Design of structures for earthquake resistance – Part 1: General rules, seismic actions and rules for buildings", European Committee for Standardization, Brussels 2010, Belgium

[5] ECCS Recommended Testing Procedure for Assessing the Behaviour of Structural Steel Elements under Cyclic Loading, ECCS - Technical Committee 1 - Structural Safety and Loadings, Technical Working Group 1.3 - Seismic Design, Brussels 1986, Belgium

[6] Hollomon, J.H.: Tensile Deformation. Transactions of the Metallurgical Society of AIME, pp. 268-290, 1962

[7] Lemaitre, J. and Chaboche, J-L.: "Mechanics of Solid Materials", Cambridge University Press, 1990

COMPDYN 2015
5th ECCOMAS Thematic Conference on
Computational Methods in Structural Dynamics and Earthquake Engineering
M. Papadrakakis, V. Papadopoulos, V. Plevris (eds.)
Crete Island, Greece, 25–27 May 2015

CONCRETE-TO-CONCRETE INTERFACES UNDER CYCLIC LOADING: FINITE ELEMENT ANALYSIS TOWARDS EXPERIMENTAL VERIFICATION

Vassilis K. Papanikolaou[1] and Georgia E. Thermou[2]

[1] Aristotle University of Thessaloniki
Civil Engineering Department
e-mail: billy@civil.auth.gr

[2] Aristotle University of Thessaloniki
Civil Engineering Department
gthermou@civil.auth.gr

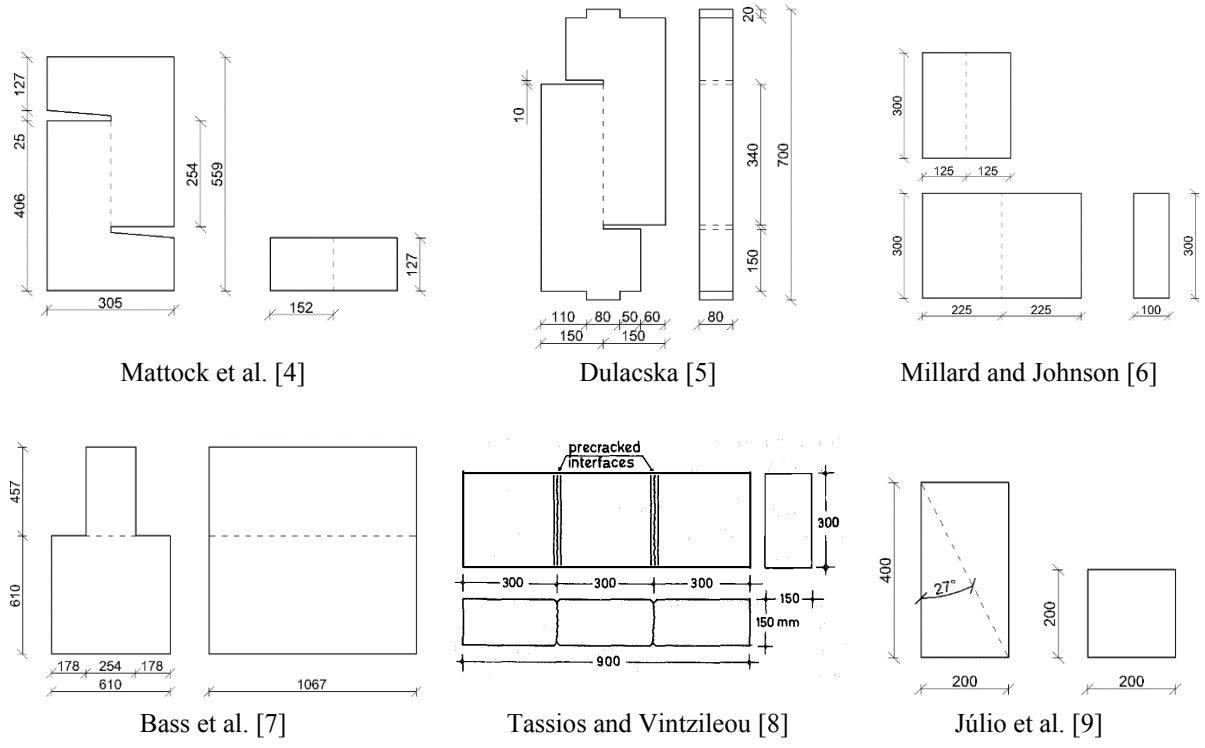
Keywords: Concrete, Shear Transfer, Interface, Experiment, Finite elements

Abstract. *The objective of this paper is to describe a novel experimental setup for testing the concrete-to-concrete interface behavior under cyclic loading. Within the suggested configuration, various investigation parameters can be facilitated, such as the variation of concrete properties, interface roughness and number of transverse dowels. The specimen consists of three distinct concrete blocks in contact, as to create symmetric double interfaces. The middle concrete block has different concrete compressive strength, which suggests interfaces cast in different times. For the specimen preparation, elaborate computer-aided manufacturing (CAM) methods such as 3D design, laser-cutting and CNC-milling have been utilized. Moreover, an ad-hoc numerical analysis is performed, in the form of a blind-test procedure against its forthcoming experimental counterpart. The analysis is based on a three-dimensional nonlinear finite element model, accurately describing the physical specimen properties and loading setup. The analytical results are presented in a form of interface shear stress vs. slip, stress variation contours along the interface area and dowel tensile stress. A comparison with Code-based recommendations is performed and various interesting points are highlighted.*

1 INTRODUCTION

Concrete-to-concrete interfaces are formed in crack planes, construction joints, between concrete elements cast at different times and in prefabrication. Adding a new concrete layer (e.g. flexural strengthening of beams) or a new R/C member in various retrofit techniques (e.g. jacketing, infill walls) entails issues related to the connection between existing and newly cast concrete [1-3]. The response of the composite member, and subsequently of the whole structure, depends largely on the response characteristics of the interface, since shear transfer occurs.

Shear transfer along concrete interfaces is an ongoing subject of research. Many experimental test configurations have been suggested and used for studying the mechanisms that resist sliding along concrete interfaces with different characteristics (e.g. [4- 9], Fig. 1). Moreover, numerous empirical and analytical expressions have been derived for estimating the ultimate shear stress as a resultant of the various shear resistance mechanisms. A significant effort has been also made in deriving expressions describing the response of concrete-to-concrete interfaces under cyclic loading (e.g. [10, 11]). The phenomenon has also been studied numerically by finite element modeling (e.g. [12]).



Mattock et al. [4] Dulacska [5] Millard and Johnson [6]

Bass et al. [7] Tassios and Vintzileou [8] Júlio et al. [9]

Figure 1: Different types of specimens for studying the response of concrete-to-concrete interfaces. Dimensions are given in mm [4-9].

Although the research conducted on the response of concrete-to-concrete interfaces under monotonic loading is extensive, studies referring to cyclic loading are limited. Moreover, regarding surface roughness characterization in most of the experimental studies, qualitative description relying on visual inspection is employed. This implies that the influence of roughness on the overall shear resistance is not explicitly estimated since roughness is not assessed following a quantitative procedure, as for instance the sand patch method suggested by Model Code 2010 [13]. The objective of current research is to study the shear resistance of concrete-to-concrete interfaces under cyclic loading with explicit characterization of the interface roughness. Other parameters of the experimental investigation are the concrete compressive strength

and the number of dowels perpendicularly crossing the interface. Each specimen consists of three distinct concrete blocks in contact, as to create symmetric double interfaces. The middle concrete block has different concrete compressive strength which suggests interfaces cast in different times. Before experimental testing, a finite element model of the test specimen was developed. The analytical results are presented herein in the form of interface shear stress vs slip, shear stress variation contours along the interface area and dowel tensile stresses. This analytical study is preceding, as a blind-test procedure, a consistent experimental verification, which is under preparation.

2 ESTIMATION OF SHEAR RESISTANCE ACCORDING TO CODES

Shear transfer along interfaces plays a crucial role in the response of composite members. Describing in detail the mechanisms mobilized along interfaces due to slip and their interaction is a rather complex mechanical issue, especially under cyclic loading conditions where degradation should also be accounted for. The main contributions to the overall shear resistance are described in [13]:

- Mechanical interlocking and adhesive bonding
- Friction due to external compression forces perpendicular to the interface and clamping action due to reinforcement
- Dowel action of reinforcement crossing the interface

In the following paragraphs, the expressions providing the ultimate shear resistance from codes are presented. The expressions are utilized for estimating the ultimate shear resistance of the test specimens.

Eurocode 2 [14] suggests the following expression for estimating the ultimate shear resistance at the interface between concrete cast at different times:

$$\tau_{Rd} = \underbrace{c \cdot f_{ct}}_{\text{cohesion}} + \underbrace{\mu \cdot \left(\sigma_n + \rho \cdot f_y \right)}_{\text{friction resistance}} \leq 0.5 \cdot \nu \cdot f_c \tag{1}$$

where:

- factor c depends on the roughness classification of the interface (very smooth: c=0.25, smooth: c=0.35, rough: c=0.45, indented: c=0.50).
- μ is the shear friction coefficient (very smooth: μ=0.5, smooth: μ=0.6, rough: μ=0.7, indented: μ=0.9).
- σ_n is the normal stress acting on the interface.
- f_{ct} is the concrete tensile stress.
- $\rho = A_s/A_c$ is the dowel reinforcement ratio.
- f_y is the steel yield stress.
- $\nu = 0.55 \cdot (30/f_c)^{1/3} < 0.55$ is the strength reduction factor.

Eurocode 2 [14], as it is evident from Eq. (1), does not explicitly account for the dowel action.

In Model Code 2010 [13], the shear stress developed at the interface between concrete cast at different times for interfaces intersected by dowels or reinforcement is:

$$\tau_{Rd} = \underbrace{c_r \cdot f_c^{1/3}}_{\text{cohesion}} + \underbrace{\mu \cdot \left(\sigma_n + \kappa_1 \cdot \rho \cdot f_y \right)}_{\text{friction resistance}} + \underbrace{\kappa_2 \cdot \rho \cdot \sqrt{f_y \cdot f_c}}_{\text{dowel resistance}} \leq \beta_c \cdot \nu \cdot f_c \tag{2}$$

The first term corresponds to the aggregate interlock and adhesive bonding where parameter c_r is modified according to the roughness of the interface [13]. The second and third term correspond to the friction and dowel resistance, respectively. Friction is related to any external compression forces normal to the interface and/or clamping forces due to reinforcement crossing the interface. In the problem examined herein, the compressive stress resulting from a normal force acting on the interface is zero ($\sigma_n = 0$). Moreover:

- ρ is the reinforcement area ratio of the reinforcing steel crossing the interface.
- f_c is the concrete compressive strength of the weakest concrete.
- f_y is the yield strength of the reinforcing bars crossing the interface
- μ is shear friction coefficient of the interface.
- κ_1 and κ_2 are interaction coefficients for tensile force activated in the reinforcement and for flexural resistance, respectively.
- β_c is the coefficient for the strength of the compression strut.
- $\nu = 0.55 \cdot (30/f_c)^{1/3} < 0.55$) is the strength reduction factor.

Model Code 2010 [13] relates the roughness of the interface with parameter R_t which is derived from the sand patch method. Coefficients c_r, κ_1, κ_2, β_c and μ receive the values presented in Table 7.3-2 of Model Code 2010 [13]. For the needs of the present study, the selected values of the coefficients c_r, $\kappa 1$, $\kappa 2$, βc and μ are presented in Table 1.

Roughness	$\mathbf{c_r}$	$\boldsymbol{\kappa_1}$	$\boldsymbol{\kappa_2}$	$\boldsymbol{\beta_c}$	$\boldsymbol{\mu}$
Very smooth, $R_t = 0.0$	0	0	1.5	0.3	0.5
Rough, $R_t = 2.5$	0.1	0.5	0.9	0.5	0.7
Very rough, $R_t = 5.0$	0.2	0.5	0.9	0.5	1.0

Table 1: Coefficients for different interface roughness employed in the present study.

The ultimate shear stress of smooth interfaces according to the Greek Code for Interventions [15] is:

$$\tau_{Rd} = \underbrace{\beta_F \cdot \mu \cdot \sigma_o}_{\text{friction resistance}} + \underbrace{\beta_D \cdot \rho \cdot \sqrt{f_y \cdot f_c}}_{\text{dowel resistance}} \le 0.3 \cdot f_c \tag{3}$$

Apart from the friction and dowel resistance, the code refers additionally to the cohesion resistance (a value equal to $0.25 \cdot f_{ct}$ is suggested for smooth interfaces, where f_{ct} is the tensile stress of the weakest concrete) and states that it should be ignored in the presence of clamping action of reinforcing bars crossing the interface. Moreover, it is mentioned that in case of smooth interfaces the contribution of the clamping action is low and could be ignored. From the above, the dowel resistance is considered the only mechanism that resists sliding at the interface. The terms β_F and β_D are participation factors of the friction and dowel resistance, respectively, taken both equal to 0.5. In case of rough interfaces, Eq. (2) is further modified to:

$$\tau_{Rd} = \underbrace{\beta_F \cdot \mu \cdot \left[f_c^2 \left(\sigma_c + \rho \cdot f_y \right) \right]^{1/3}}_{\text{friction resistance}} + \underbrace{\beta_D \cdot \rho \cdot \sqrt{f_y \cdot f_c}}_{\text{dowel resistance}} \le 0.3 \cdot f_c \tag{4}$$

The first term of Eq. (4) represents the contribution of concrete as it depends on the frictional resistance of the interface planes.

The shear strength of an interface where reinforcement is placed perpendicular to the shear plane is estimated according to ACI 318-14 [16]:

$$\tau_{Rd} = \mu \cdot \rho \cdot f_y \tag{5}$$

where $\rho = A_s/A_c$ is the area ratio of the shear-friction reinforcement, f_y is the yield strength of reinforcing bars and μ is the friction coefficient, which for normal weight concrete may range between 0.6 for concrete placed against hardened concrete that is clean and not intentionally roughened and 1.4 for concrete placed monolithically. ACI-318-14 [16] provides upper limits on shear friction strength. In case of normal weight concrete placed monolithically or placed against hardened concrete intentionally roughened the maximum shear strength is calculated as:

$$\tau_{Rd} = \min\left(0.2f_c, 3.3 + 0.2f_c, 11\right) \text{ in MPa} \tag{6}$$

For all the above cases (Eqs. 1-6), the ultimate shear force transferred along the interface is estimated by:

$$V_{Rd} = \tau_{Rd} \cdot A_c \tag{7}$$

where A_c is the area of the interface.

3 DESIGN OF EXPERIMENTAL SETUP

The main concept behind the suggested experimental setup is to test concrete-to-concrete interfaces under pure shear, minimizing any adverse normal-to-interface actions caused by loading or geometric, first or second-order eccentricities (see Fig. 2). These normal actions could considerably affect the interface response, since they may induce additional friction stresses ($\mu \cdot \sigma$) along the interface plane. Consequently, a symmetric double-interface solution was followed (as in [8]), as depicted in Fig. 2.

Specifically, the specimen is consisted of three adjacent 250×250×400 mm concrete blocks, with the central one representing concrete cast at an earlier time (old) and the other two at present (new), allowing different old/new concrete strength configurations, as per the ordinary repair/strengthening practice (e.g. R/C jacketing). Between old and new concrete, two symmetrically arranged interfaces are formed, which effective area is deliberately reduced to 150×300 mm by applying a 50 mm wide, thin insulating material on the perimeter (e.g. clear tape), before casting new concrete. The purpose of the above reduction is twofold, i.e. to localize failure on the interface by avoiding possible edge splitting cracks and to reduce the interface shear resistance to manageable levels. Both interfaces are crossed by a configurable number (2, 4, 6, 8 or 10) of 8 mm diameter (Ø8), 500 mm length dowels. These dowels are arranged on a 60×50 mm, five-row by two-column grid and they are anchored at a length of 125 mm inside the new concrete block, complying with minimum Code requirements [15]. Cyclic loading is vertically applied on the middle block by fixing the two adjacent ones, creating symmetric stress flow to the two centerline-equidistant interface planes. For mounting purposes, four plastic tubes are longitudinally inserted in each block (Ø32 and Ø20 for old and new, respectively), allowing the insertion of threaded rods after casting, which will be subsequently anchored to the testing apparatus (described later). Finally, four Ø8 closed hoops are also inserted in each block, providing a minimum level of confinement.

In order to realize the above elaborate specimen configuration, a special steel mold was designed and manufactured with the aid of 3D software. The main requirements for the design were the ability to facilitate different casting phases (old and new concrete), different dowel configurations and interface roughness, while providing a convenient and fast assembly/disassembly process. Fig. 3 (left) shows the various parts of the steel mold that were laser-cut from a 5 mm thick steel plate. It is based on a modular male-to-female connection concept, assisted by interlocking side bars. Various circular openings can accommodate precise dowel and tube

positioning as well as necessary uplifting handles. The molds were manufactured and assembled in the Laboratory of R/C and Masonry Structures, Civil Engineering Dept., Aristotle Univ. of Thessaloniki, Greece.

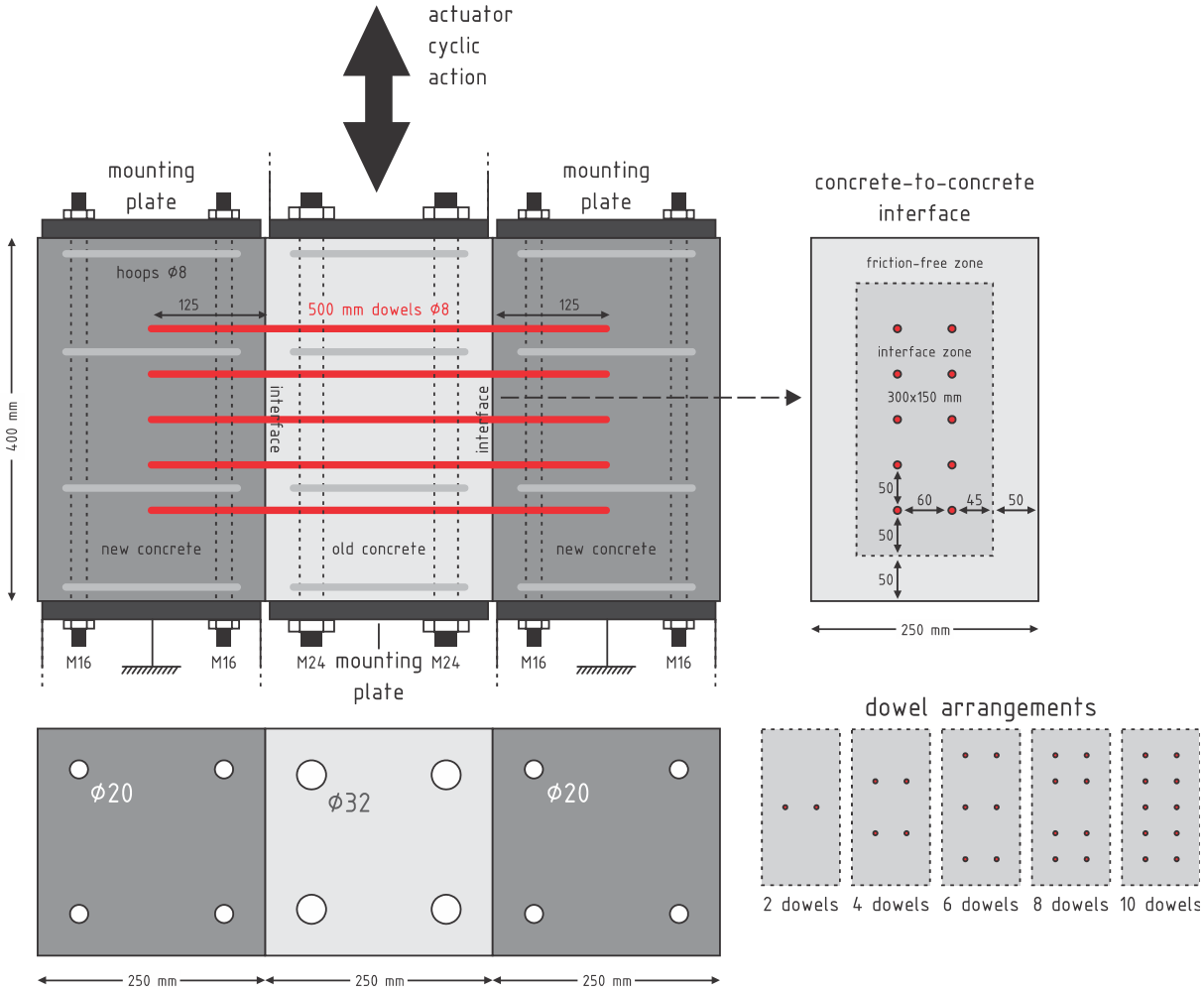


Figure 2: Specimen design concept.

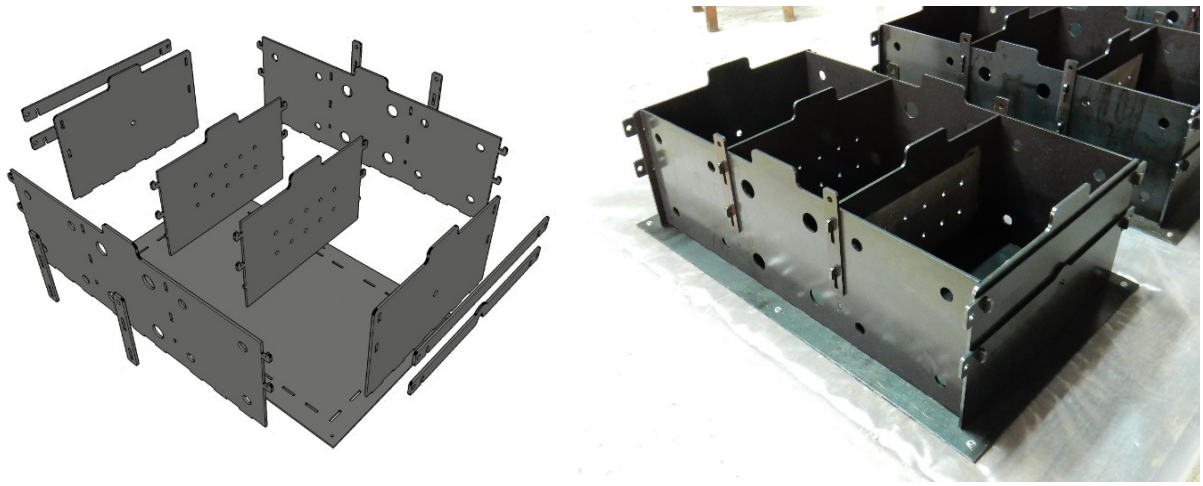


Figure 3: Casting mold design and assembly.

The two middle panels which separate the old from new concrete blocks are removable and can be positioned with either face against the central block. When removed (after casting and curing of the central block), they naturally form a very smooth, effectively zero-roughness surface. However, for investigating the effect of different interface roughness, three middle panel pairs were subsequently machined (on one face), in order to 'stamp' a pattern of prescribed roughness against the central block. These patterns were produced by precise CNC cross-routing using a 90° included angle bit, covering the aforementioned 150×300 interface zone (Fig. 4). The milling depth (h) and spacing (s) were calculated for yielding exact values of the roughness parameter (R_t), according to the sand patch method [13] (Eq. 8, Table 2). Three different roughness values, R_t = 2.5, 5.0 and 10.0 were selected, corresponding to rough, very rough and extremely rough conditions (for the rest smooth panel faces, it is assumed that R_t = 0.0).

$$R_t = \frac{40 \cdot V_{sand}}{\pi \cdot d^2} = \frac{40 \cdot \frac{V_{pyramid}}{V_{parallelogram}} \cdot V_{cylinder}}{\pi \cdot d^2} = \frac{40 \cdot \frac{V_{pyramid}}{V_{parallelogram}} \cdot \frac{\pi \cdot d^2}{4} \cdot h}{\pi \cdot d^2} = 10 \cdot \frac{V_{pyramid}}{V_{parallelogram}} \cdot h \quad (8)$$

R - Rough		VR - Very rough		ER - Extremely rough	
h (mm)	0.5	h (mm)	1.0	h (mm)	2.0
s (mm)	1.6	s (mm)	3.2	s (mm)	6.4
b (mm)	0.6	b (mm)	1.2	b (mm)	2.4
$V_{pyr.} / V_{par.}$	0.505	$V_{pyr.} / V_{par.}$	0.505	$V_{pyr.} / V_{par.}$	0.505
R_t	**2.53**	R_t	**5.05**	R_t	**10.10**

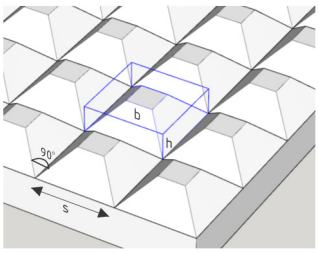


Table 2: Calculation of prescribed roughness.

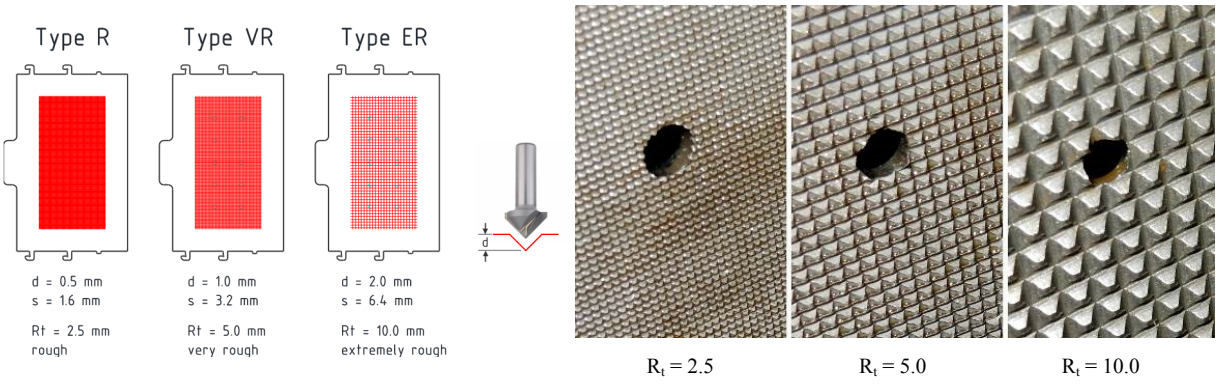


Figure 4: Prescribed roughness configurations.

The specimen preparation using the above steel mold can be easily accommodated in nine steps, as follows (Fig. 5):

Step 1: Assemble the central chamber by positioning both middle panel faces according to the required interface roughness (R_t = 0.0, 2.5, 5.0 or 10.0). Lock middle panels.
Step 2: Insert the four Ø32 tubes and the four Ø8 hoops in the central chamber.
Step 3: Insert the required number of dowels (2, 4, 6, 8, or 10), taping the rest of the holes (if any).
Step 4: Cast the central concrete block (old).
Step 5: After curing of the central block, unlock and remove the two middle panels.

Step 6: Insert and lock the two end panels, insert Ø20 tubes and hoops in the empty chambers and position the two lifting bars (Ø12).
Step 7: Cast the new concrete.
Step 8: After curing, disassemble mold completely.
Step 9: Cut tubes flush, lift and rotate specimen for mounting on the loading apparatus.

The finalized specimen is positioned and mounted on the loading apparatus, as depicted in Fig. 6. The two end blocks are firmly mounted on the two vertical pedestals using eight M16 threaded rods and two 20 mm thick steel plates, placed on the top of the blocks. The middle block is mounted on a hydraulic actuator via a swivel appendage (extender), four M24 threaded rods and a 20 mm thick steel plate, placed on the bottom of the block. This configuration allows the actuator to transfer a prescribed cyclic action to the middle block by applying concentric compressive pressure only, either directly (downward movement) or through the bottom plate, by tensioning the four embedded rods (upward movement). The apparatus base is secured via two M36 threaded rods on the laboratory floor, featuring a 1.0×1.0 m grid of 80 mm diameter holes. The critical loading capacity of the apparatus is determined by the yielding strength of the eight M16 rods (722 kN, considering 8.8 material grade and 10% pre-tension), after providing a large safety margin against welding failure.

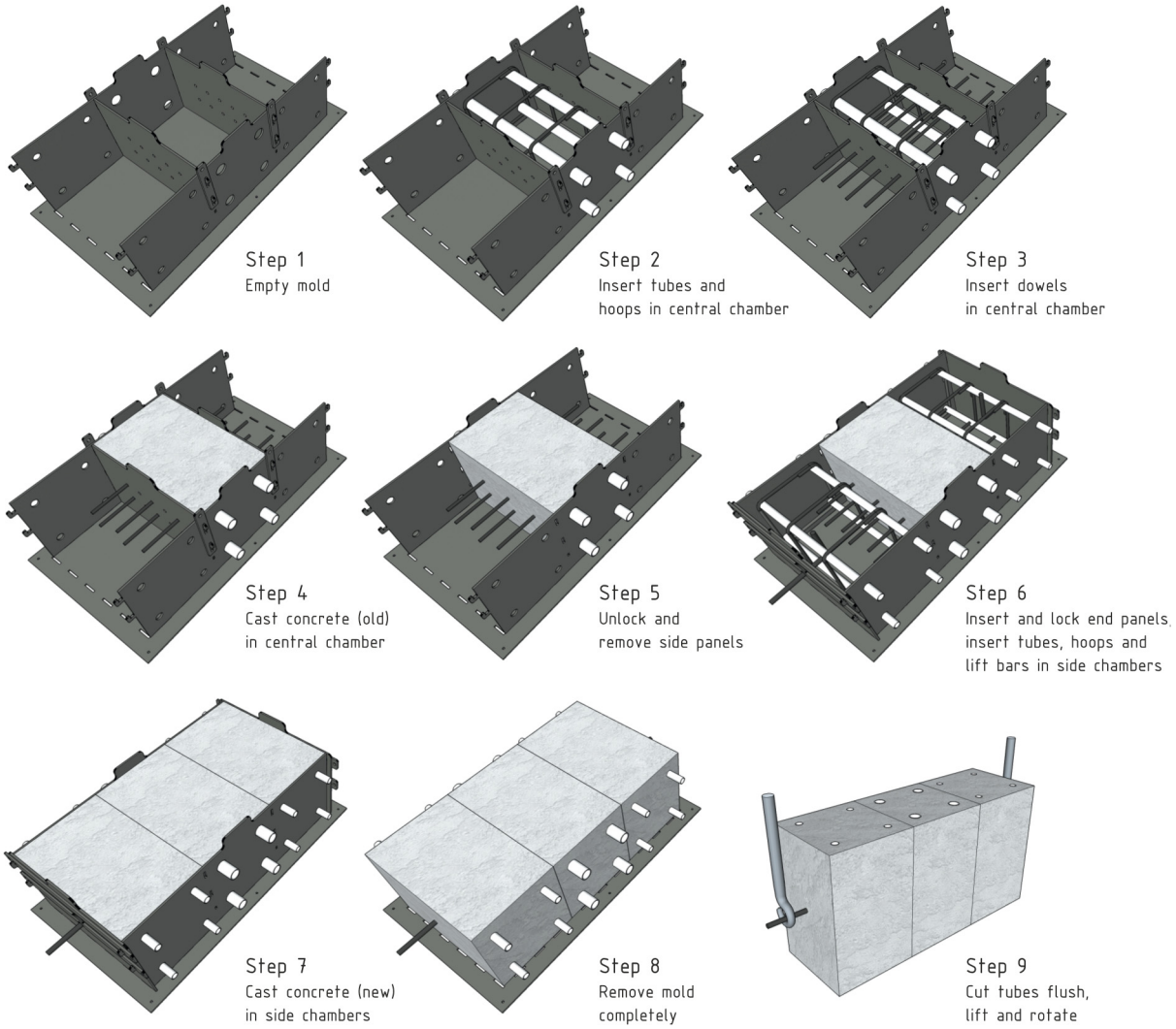


Figure 5: Specimen casting procedure.

A prescribed displacement cyclic load history will be imposed by a single-ended hydraulic actuator (MTS 243.60) mounted on a steel loading frame, with a load capacity of 1013 kN (compression) / 648 kN (tension) and a full stroke of ±250 mm. The actuator is equipped with a build-in LVDT device for measuring the imposed displacements. However, since both the loading frame and the apparatus is naturally susceptible to (elastic) bending during specimen loading (especially for large loads), additional displacements could be picked up by the actuator internal LVDT, resulting to a discrepancy between the desired (target) displacement load history and the measured displacement of the internal LVDT. This adverse effect may become critical in the present setup, since the applied displacements will be in the order of a few millimeters. For this reason, the actuator closed-loop control will be transferred from the default actuator internal LVDT to an external measurement system, based on a draw-wire sensor (or alternatively a short-stroke LVDT), mounted on the transverse beam between two vertical pedestals and connected to the bottom face of the mounting plate (Fig. 6). The above experimental setup is currently under preparation and will be utilized shortly.

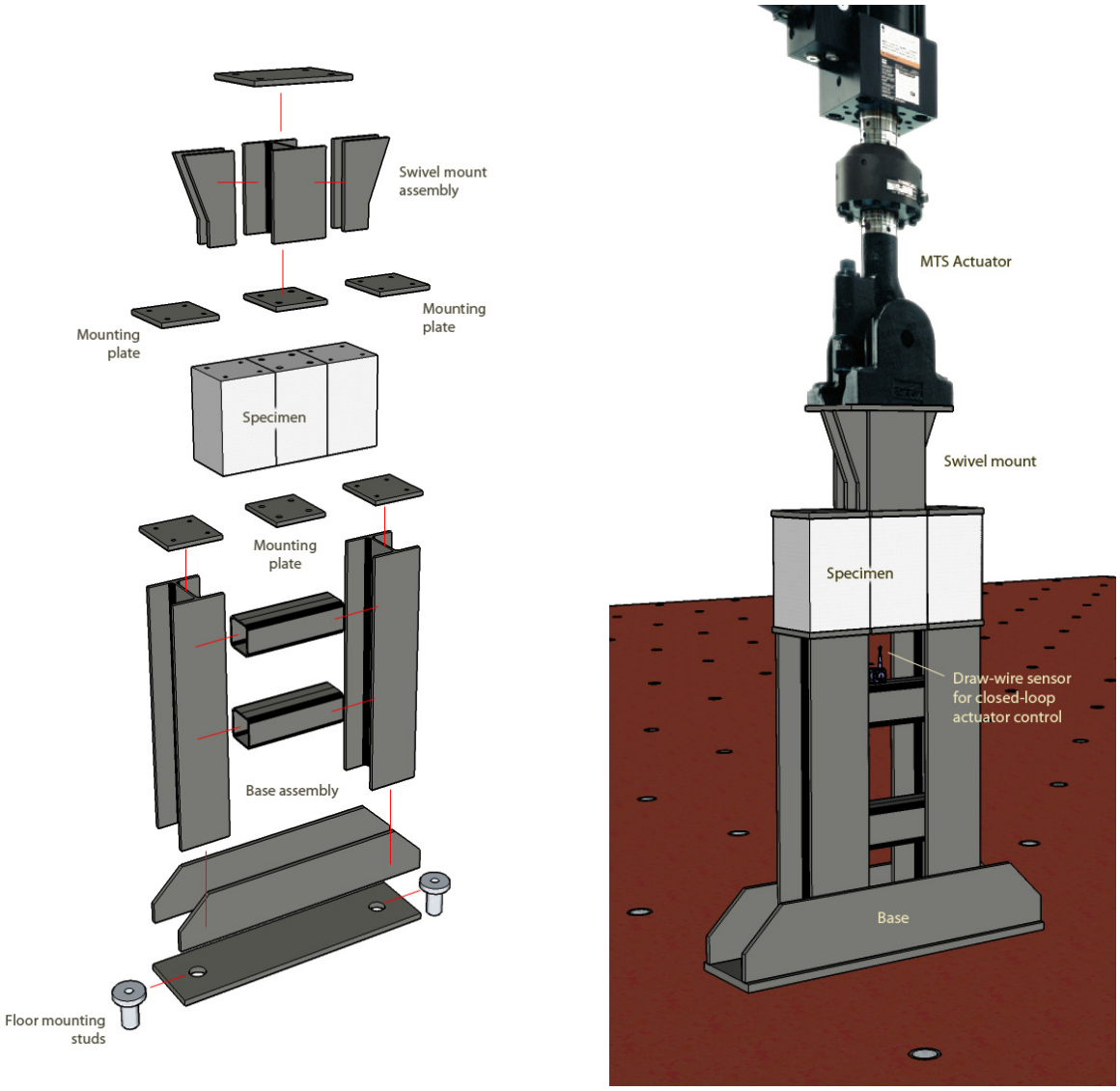


Figure 6: Testing apparatus design, assembly and configuration.

4 NUMERICAL ANALYSIS AND RESULTS

Before conducting experimental testing, an ad-hoc numerical analysis has been performed, serving as a blind-test prediction against its forthcoming experimental counterpart. The analysis is based on a three-dimensional nonlinear finite element model using the ATENA software [17], accurately describing the physical specimen properties and loading setup, as depicted in Fig. 7. For the old and new concrete blocks, the mean compressive and tensile strength properties of C12 and C20 concrete classes were employed, respectively [13, 14], assigned to a nonlinear fracture-plastic concrete constitutive model. Loading was applied in the form of prescribed displacement, via a rigid loading block on the top of the middle concrete block, as per the experimental setup. The top and bottom sides of the two adjacent blocks were fixed. The common planes (contacts) between old and new concrete were divided to the inner interface zone and the friction-free zone (see Fig. 2), assigned to a Mohr-Coulomb interface model and a no-contact formulation, respectively. The dowel reinforcement was modeled using a batch of eight reinforcement fibers for each Ø8 bar (each having an equivalent area of 50.3/8 mm^2 and a yield strength of f_y = 500 MPa). This technique was preferred instead of the standard reinforcement representation using a single axial-only truss element, so that the bending action is modeled as well. The dowel bond-slip behavior was also accounted for, using a Code based constitutive model for pullout action and good bond conditions [13]. The global mesh size was fixed to 2.5×2.5 cm, however, for increased accuracy, the mesh density was increased to 0.5 cm, in both normal directions to each interface zone, for a length of 5 cm. The model parameters analyzed were the number of dowels (2, 4 and 6) as well as the interface roughness, corresponding to smooth, rough and very rough conditions (Rt = 0.0, 2.5, 5.0). The corresponding friction (μ) and cohesion (c) values for the employed Mohr-Coulomb model were taken equal to μ = 0.5, 0.7, 1.0 and $c = c_r \cdot f_c^{1/3}$ = 0.0, 0.27, 0.54 MPa, respectively (Table 1, [13]).

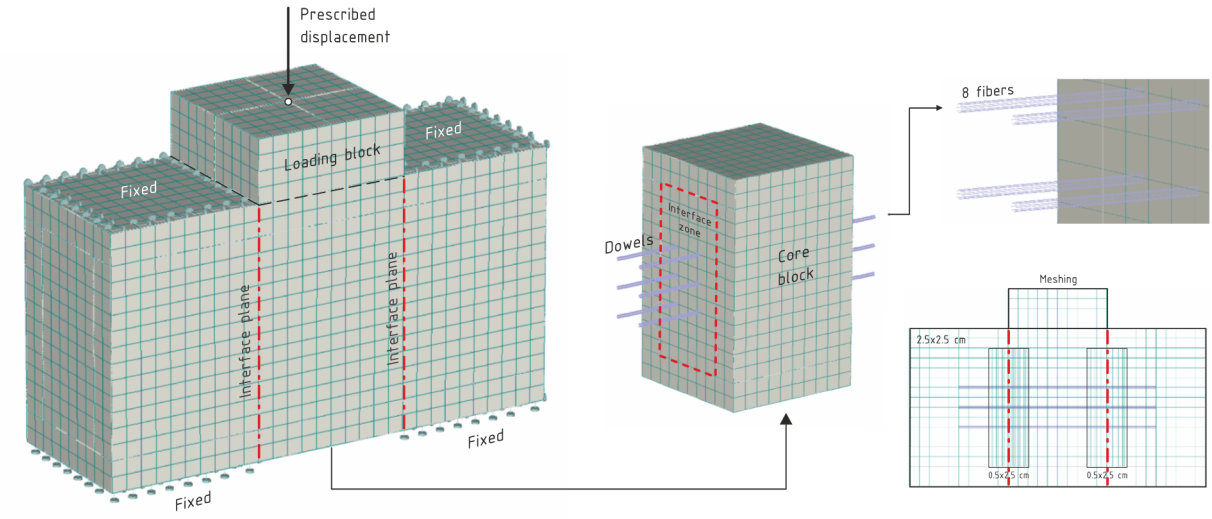


Figure 7: Finite element model details.

The analysis results in terms of total shear force (reaction at the point of prescribed displacement) vs interface slip are shown in Fig. 8. It is observed that the interface shear resistance is clearly increased for an increasing number of transverse dowels, as expected. A similar increase in shear resistance for rougher interfaces is not evident, however, increased roughness yields lower values of interface slip at maximum shear, indicating a stiffer interface response. Moreover, it is observed by comparing against a perfect-bond analysis that the effect of dowel bond-slip plays a predominant role in determining the interface stiffness, leading to a considerably

stiffer response if neglected. By comparing the shear resistance of the various interface configurations between the present analysis and the various code recommendations (Eqs. 1-6, Fig. 9), a large dispersion in the results is observed, especially for different interface roughness levels. This implies that the friction contribution on the interface resistance is an issue that needs further investigation especially in cyclic loading conditions.

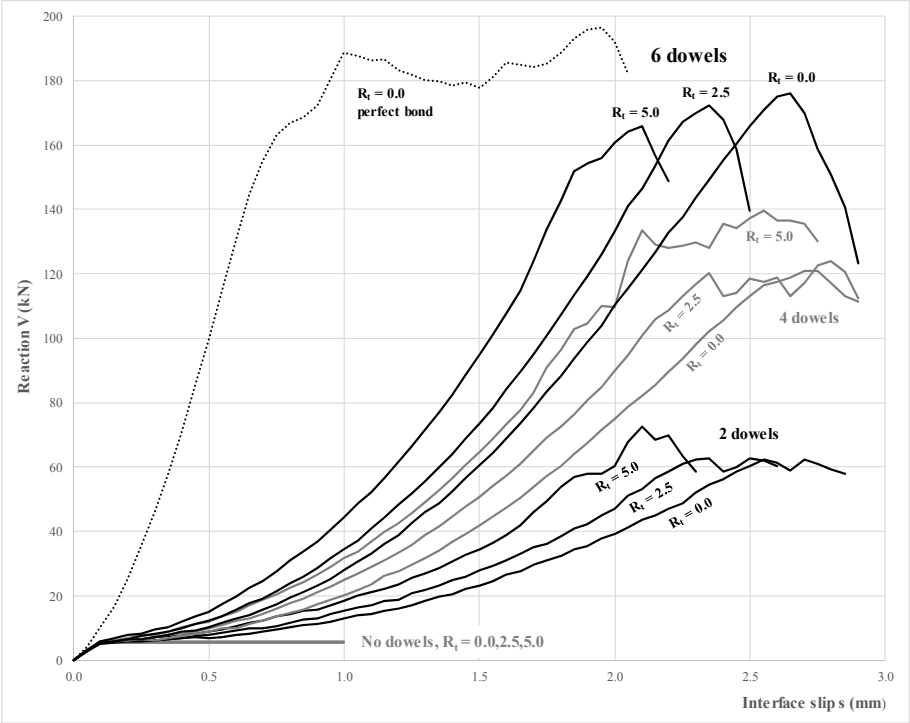


Figure 8: Interface response from finite element analysis.

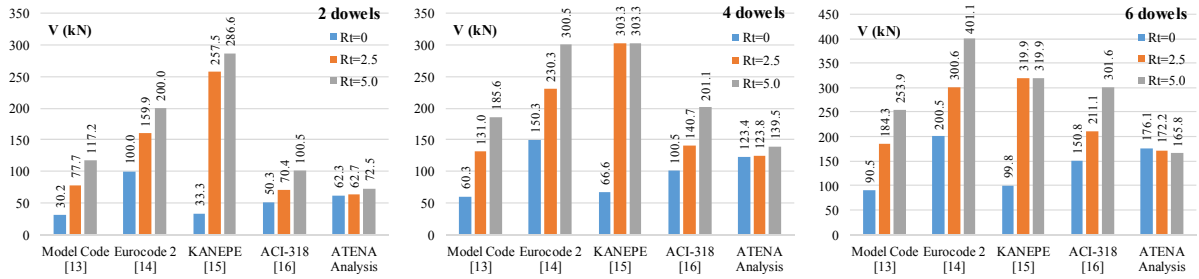


Figure 9: Comparison between analysis and various Code recommendations.

As far as the above friction contribution issue is concerned, all Code recommendations suggest that the total shear stress, which includes a significant friction component (depending on the stress normal to the interface), is uniform throughout the whole interface area (Eq. 7). However, from the analysis stress contours at maximum force (Fig. 10), it is observed that the normal stress produced by the dowel clamping action that creates friction (σ_{xx}) is operating only on a limited ellipsoidal boundary around dowels, while the remaining interface area is practically unstressed (red color), hence inducing no friction resistance. This is also visible in the stress distribution parallel to the interface (σ_{zz}), where unstressed regions are greatly influential. Pending experimental verification, this question is herein raised for further discussion.

In Fig. 11, the dowel deformed shape (10× magnification) and the tensile stress contours at maximum shear force are depicted. It is observed that dowel yielding ($\sigma_c = f_y = 500$ MPa) occurs

at the vicinity of the interface planes as expected, and that a gradual stress degradation is formed along the dowel length (reaching zero at both ends) due to the consideration of the bond-slip effect. Finally, the fiber division technique applied for dowel bars successfully captured their bending action, i.e. stress non-uniformity across the dowel section depth.

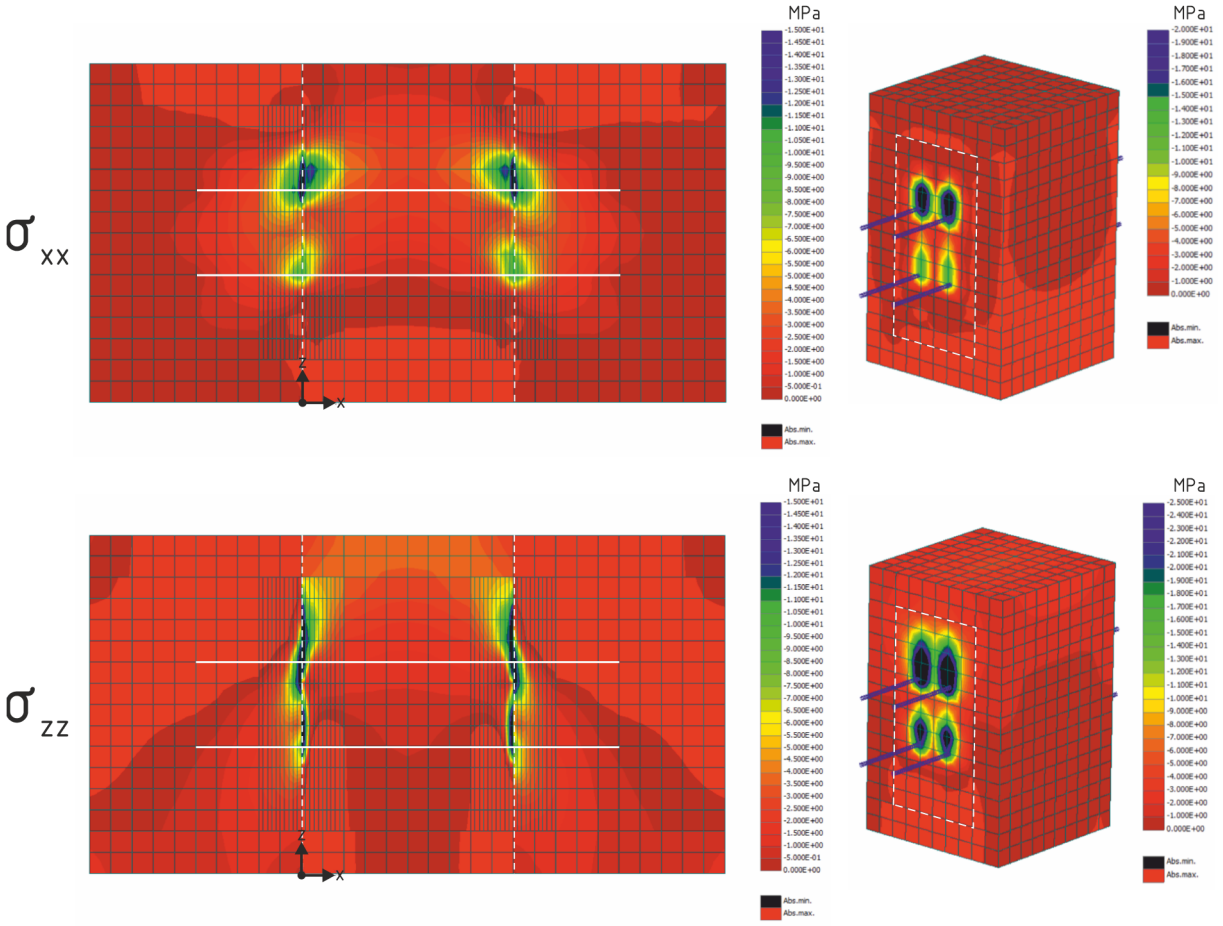


Figure 10: Cross-interface longitudinal and transverse stress contours at max shear force (4 dowels, $R_t = 5.0$)

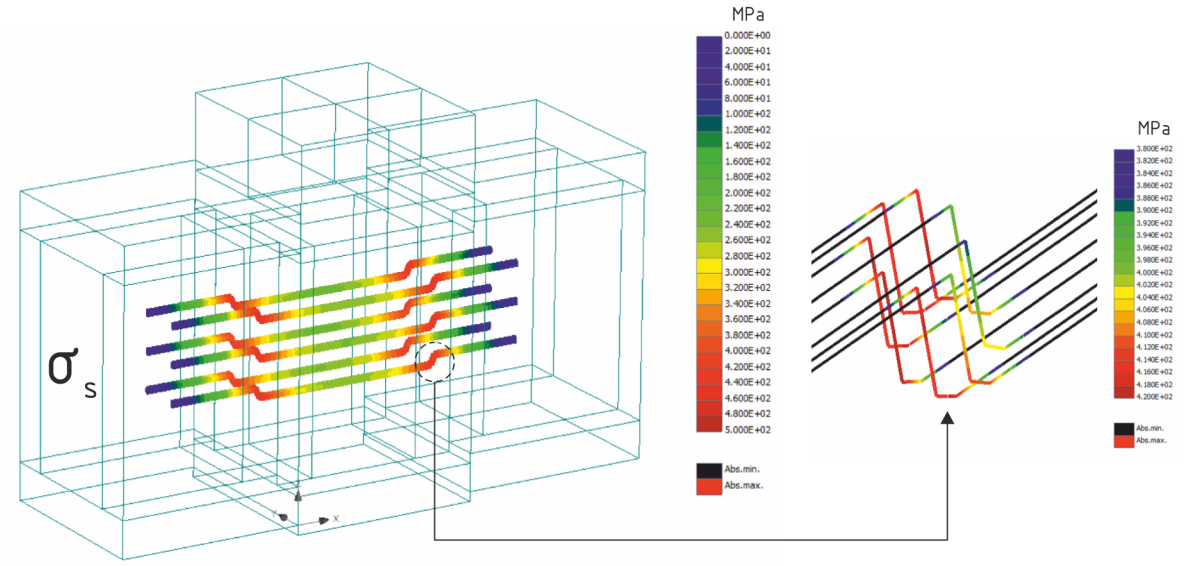


Figure 11: Dowel stresses and deformations at max shear force (6 dowels, $R_t = 0.0$)

5 CONCLUSIONS

In this paper, a novel experimental setup for testing the concrete-to-concrete interface behavior in various configurations under cyclic loading was described. The main concept was to create interfaces under pure shear which resulted in a symmetric double-interface solution, thus minimizing any adverse normal actions due to eccentricities. The parameters to be investigated is the number of transverse dowels and interface roughness, which for the first time is prescribed using elaborate CAM methods. While the suggested setup is under preparation, an ad-hoc nonlinear finite element analysis was performed, serving as a preceding blind test procedure to be compared with forthcoming experimental results. The analysis results showed acceptable correlation in terms of interface shear resistance compared to various Code recommendations, which however show a significant scatter, especially for larger interface roughness levels. This may be accounted to the fact that under pure shear, friction is mobilized on a limited boundary around dowel positions. Moreover, the complete force vs slip curves provided by the finite element model gives a clearer view in terms of interface stiffness, where both roughness and dowel bond-slip play a significant role. Notwithstanding, the actual experimental testing is expected to further clarify the above issues and provide better overall insight on the present complex research topic.

ACKNOWLEDGEMENTS

The present research is funded by the program “Supporting new researchers in lecturer position”, Research Committee, Aristotle University of Thessaloniki, Greece. The first author would also like to thank D. Orfanidis, MSc and TECHNOMETAL for the technological support.

REFERENCES

[1] G.E. Thermou, S.J. Pantazopoulou, A.S. Elnashai, Flexural behavior of brittle R/C members rehabilitated with concrete jacketing. *Journal of Structural Engineering*, ASCE, **133(10)**, 1373-1384, 2007.

[2] G.E. Thermou, V.K. Papanikolaou, A.J. Kappos, Flexural behaviour of reinforced concrete jacketed columns under reversed cyclic loading. *Engineering Structures*, **76**, 270-282, 2014.

[3] G.E. Thermou, Strengthened Structural Members and Structures: Analytical Assessment, *Encyclopedia of Earthquake Engineering*, edited by Michael Beer, Edoardo Patelli, Ioannis Kougioumtzoglou and Ivan Siu-Kui Au, www.SpringerReference.com (invited article), 2014.

[4] A. Mattock, W. Li, T. Wang, Shear transfer in lightweight reinforced concrete. *PCI Journal*, **21(1)**, 20-39, 1976.

[5] H. Dulacska, Dowel action of reinforcement crossing cracks in concrete. *ACI Journal*, **69**, 754-757, 1972.

[6] S.G. Millard, R.P. Johnson, Shear transfer across cracks in reinforced concrete due to aggregate interlock and to dowel action. *Magazine of Concrete Research*, **36(126)**, 9-21, 1984.

[7] R.A. Bass, R.L. Carasquillo, J.O. Jirsa, Shear transfer across new and existing reinforced concrete. *ACI Structural Journal*, **86(4)**, 383-393, 1989.

[8] T.P. Tassios, E.N. Vintzileou, Concrete-to-concrete friction, *ASCE Journal of Structural Engineering*, **113(4)**, 832-849, 1987.

[9] E.N.B. Júlio, F.A. Branco, V.D. Silva, Concrete-to-concrete bond strength. Influence of the roughness of the substrate surface. *Construction and Building Materials*, **18(9)**, 675-681, 2004.

[10] I. Vassilopoulou, T.P. Tassios, Shear transfer capacity along a R/C crack under cyclic sliding. *Proceedings of the fib Symposium*, **271**, Technical Chamber of Greece, Athens, Greece, 2003.

[11] V. Palieraki, E. Vintzileou, C. Zeris, Behaviour of interfaces in repaired/strengthened R/C elements subjected to cyclic actions: Experiments and Modelling. *3rd International Symposium on life-cycle and sustainability of civil infrastructure systems (IALCCE'12)*, Vienna, Austria, 2012.

[12] D. Dias-da-Costa, J. Alfaiate, E.N.B. Júlio, FE modeling of the interfacial behaviour of composite concrete members, *Construction and Building Materials*, **26(1)**, 233-243, 2012.

[13] fib [Fédération Internationale du Béton], Model Code 2010 Vol. 1 & 2, Bulletin No. 65 & 66, 2013.

[14] CEN [European Committee for Standardization], Eurocode 2. Design of concrete structures – Part 1–1: General rules and rules for buildings (EN 1992-1-1). Brussels, 2004.

[15] EPPO [Earthquake Planning and Protection Organization], Greek Code for Interventions (KANEPE), Athens, 2013.

[16] ACI Committee 318 318-14, Building Code Requirements for Structural Concrete (ACI318-02) and Commentary ACI 318 R-02. Detroit, 2014.

[17] V. Červenka, L. Jendele, J. Červenka, ATENA Program Documentation. Part 1: Theory, Červenka Consulting, Prague, Czech Republic, 2015.

COMPDYN 2015
5th ECCOMAS Thematic Conference on
Computational Methods in Structural Dynamics and Earthquake Engineering
M. Papadrakakis, V. Papadopoulos, V. Plevris (eds.)
Crete Island, Greece, 25–27 May 2015

DEFORMATION CAPACITY OF NON-COMFORMING RC SHEAR WALLS: ANALYTICAL AND NUMERICAL ESTIMATION - TEST VERIFICATION

Christidis K.I.[1], Anagnostopoulou V.V.[1], Trezos K.G. [1], and Zeris C.A.[1]

[1] Laboratory of Reinforced Concrete, School of Civil Engineering
National Technical University of Athens (N.T.U.A.)
5, Iroon Polythechniou, Zografou, 15773, Athens, Greece
e-mail: {christidis, vantua, ctrezos, zeris}@central.ntua.gr

Keywords: RC shear walls, EC8-3, numerical analysis, OpenSees, deformation capacity, experimental verification.

Abstract. *An approach for the analytical prediction of the deformation capacity of reinforced concrete (RC) shear walls in existing buildings, designed with past non conforming seismic regulations is presented. Most modern seismic assessment and redesign provisions include models for the prediction of the capacity of existing RC members. Specifically, Eurocode 8-Part 3 provides semi-empirical and analytical expressions which focus on the estimation of yield and ultimate chord rotation. For this purpose, cross section analyses were carried out using OpenSees platform in order to predict the Moment-Curvature diagram (M-φ) which is thereafter transformed, by analytical expressions, into the final Load-Displacement (P-δ) capacity curve of such members. In addition, numerical simulations were carried out using two alternative element models, available in OpenSees library, in order to directly predict the overall Load-Displacement (P-δ) curve of a shear wall. Both analytical and numerical results were compared with test results from a series of experiments of isolated non conforming RC shear wall elements, which were tested as cantilevers under statically reversed lateral loading in the RC Laboratory of the National Technical University of Athens.*

1 INTRODUCTION

Reinforced concrete (RC) shear walls play an important role in modern seismic design, as they constitute a bracing member capable of contributing to the lateral seismic resistance of the structure. Most modern seismic codes give great attention to the seismic detailing of RC shear walls, trying to secure the flexural behaviour of the member and to reach adequate ductility levels. This is mainly achieved by the configuration of confined boundary elements, which increase the ultimate concrete strain and, therefore, the ductility values, and by a capacity design procedure which leads to high ratios of shear reinforcement, in order to prevent a shear brittle failure.

However, in a lot of countries with high seismic exposure, there is a significant number of existing RC buildings designed according to past seismic regulations, which include shear walls which are non-compliant to modern seismic design and detailing provisions. These non conforming shear walls do not include confined boundary elements and they are characterized by relatively thinner web dimension and low ratios of horizontal or vertical shear reinforcement.

2 LITERATURE REVIEW

An extensive experimental investigation of the behaviour of RC shear walls started taking place in the early 1970s. However, in most cases, the studies were made towards the revision of the applicable regulations at that time, so the conclusions and models arising from this research, which was adopted in the revisions that were effected from these, referred to improved design provisions rather than assessment procedures.

In the next decades, the study of the behavior of RC members began to focus not only on the design but also on the assessment and redesign of existing members. Several models have been developed trying to predict the deformation capacity and the degradation of the shear / flexural strength with inelastic cyclic displacements of existing RC members. Some of these models have been adopted, with some modifications, in modern seismic regulations.

2.1 Analytical assessment models – Plastic hinge analysis

The deformation capacity of reinforced concrete members is commonly defined in currently enforced assessment regulations in terms of the chord rotation (or drift ratio), θ, i.e. the angle between the tangent to the axis at the yielding (assumed fixed) end and the chord connecting that end with the end of the shear span; fixed end effects may also be included in this form of deformation, attributed to effects due to bond deterioration in the region of fixity. Plastic hinge analysis of these rotations relates to the Moment-curvature, M-φ (or Force-deformation, P-δ) envelope of the cyclic response of an RC member.

The ultimate chord rotation at failure, θ_u, can be expressed as the sum of two separated terms: the chord rotation at yielding, θ_y, and the plastic part of the chord rotation, θ_{pl}. Assuming a pure flexural behavior, which means neglecting shear and bond slip effects within the member, the ultimate chord rotation can be expressed as:

$$\theta_u=\theta_y+\theta_{pl}=\varphi_y\frac{L_V}{3}+\left(\varphi_u-\varphi_y\right)L_{pl}\left(1-\frac{L_{pl}}{L_V}\right) \quad (1)$$

where

φ_y is the section curvature at yielding

φ_u is the ultimate curvature at failure

L_V is the length of the shear span (L_V=M/V=moment/shear at the end section)

L_{pl} is the plastic hinge length

In the literature, in most cases, the length of the plastic hinge is expressed by empirical or semi-empirical expressions. One of the first is the one of Paulay and Priestley [1]:

$$L_{pl}=0.08L_V+0.022d_bf_y \tag{2}$$

where the second term is the contribution of slippage of the longitudinal rebars expressed by the product of the diameter d_b and the yield stress, f_y, of the longitudinal tension reinforcement.

Along the same premise Panagiotakos and Fardis [2] proposed a modified expression for plastic hinge length, L_{pl}, (Eq.(3)), trying to fit Eq.(1) to the results from a large experimental database. Panagiotakos and Fardis [2] distinguished the cases of monotonic and cycling loading, noting that the shear, bond slip and tension stiffening effects should be taken into account via the plastic hinge length expressions:

For monotonic loading

$$L_{pl}=0.18L_V+0.021a_{sl}d_bf_y \tag{3a}$$

For cyclic loading

$$L_{pl}=0.12L_V+0.014a_{sl}d_bf_y \tag{3b}$$

where a_{sl} equals 1 or 0 depending on whether slippage of the longitudinal steel is possible or not.

Based on an extended experimental database, Biskinis [3], proposed a new parametric expression for calculating the plastic hinge length, L_{pl}, as a function of geometrical characteristics only, taking into account shear and bond slip effects within the expression of ultimate chord rotation. This empirical model gradually evolved to its final form in Biskinis and Fardis [4]-[5], Grammatikou [6] and Grammatikou et al. [7] as:

$$\theta_u=\theta_y+a_{sl}\Delta\theta_{u,slip}+\left(\varphi_u-\varphi_y\right)L_{pl}\left(1-\frac{0.5L_{pl}}{L_V}\right) \tag{4}$$

In Eq.(4) θ_y is the chord rotation at yielding and $\Delta\theta_{u,slip}$ is the rotation due to slippage from yielding until failure, calculated from Eq.(5) and Eq.(6a, 6b), respectively:

$$\theta_y=\varphi_y\frac{L_V+\alpha_V z}{3}+0.0006\left(1+\frac{7}{6}\frac{h}{L_V}\right)+a_{sl}\varphi_y\frac{d_bf_y}{8\sqrt{f_c}} \tag{5}$$

where

$\alpha_V z$ is the tension shift of the bending moment diagram due to shear

z is the length of the internal flexural lever arm, taken equal to $0.8h$ in walls with rectangular section (h is the cross-section depth),

α_V=1 if shear cracking is expected to precede flexural yielding at the end section (i.e. if $M_y>L_VV_{R,c}$); otherwise α_V=0, where $V_{R,c}$ is the shear resistance of the member considered without shear reinforcement according to Eurocode 2 - Part 1-1 [8]

f_c is the concrete compressive strength

According to the model, $\Delta\theta_{u,slip}$ can be calculated as:

For monotonic loading

$$\Delta\theta_{u,slip}=9.5d_b\varphi_u \tag{6a}$$

For cyclic loading

$$\Delta\theta_{u,slip}=5.5d_b\varphi_u \tag{6b}$$

and L_{pl} can be calculated as:

For monotonic loading with or without conforming seismic detailing

$$L_{pl}=h\left[1.1+0.04min(9;\frac{L_V}{h})\right] \tag{7a}$$

For cyclic loading with conforming seismic detailing

$$L_{pl}=0.3h\left[1.0+\frac{1}{6}min(9;\frac{L_V}{h})\right] \tag{7b}$$

Note that there is a direct interaction between L_{pl} and φ_u. Thus, each expression for calculating L_{pl} matches to a specific model for calculating the concrete compressive strength and the corresponding ultimate concrete strain. The model of Eq.(4) to Eq. (7) is based on the Newman and Newman [9] model for the confined concrete, according to which the compressive strength of the confined concrete, f_{cc}, is calculated as:

$$f_{cc}=f_c\left[1+3.7\left(\frac{a\rho_{sx}f_{yw}}{f_c}\right)^{0.86}\right] \tag{8}$$

where

$\rho_{sx}=A_{sx}/bs_h$ is the ratio of transverse steel parallel to the direction x of loading (A_{sx} is the stirrup reinforcement area and s_h is the stirrup spacing),

f_{yw} is the stirrup yield strength (MPa) and

α is the confinement effectiveness factor.

The strain at maximum strength, e_{cc0}, can be calculated as (Fardis [10]):

$$\varepsilon_{cc0}=\varepsilon_{c0}\left[1+5\left(\frac{f_{cc}}{f_c}-1\right)\right] \tag{9}$$

The ultimate concrete strain, ε_{ccu}, is taken as (Biskinis and Fardis [5]):

For monotonic loading

$$\varepsilon_{ccu}=0.0035+\left(\frac{10}{h_0}\right)^2+0.57\frac{a\rho_s f_{yw}}{f_{cc}} \tag{10a}$$

For cyclic loading

$$\varepsilon_{ccu}=0.0035+\left(\frac{10}{h_0}\right)^2+0.40\frac{a\rho_s f_{yw}}{f_{cc}} \tag{10b}$$

where

h_o is the confined core height (in mm): In case the element does not include a confining detailing configuration, the value h_o is replaced by the cross-section height, h, and the third term of Eq.(10) is set equal to zero.

2.2 Eurocode 8 - Part 3 provisions

Eurocode 8 - Part 3 (EC8-3) [11], [12] in Annex A proposes models for the performance assessment of reinforced concrete members that refer to their deformation capacity, in chord rotation terms, and their shear strength. EC8-3 defines three different limit states, indicating the state of damage of the concrete member – Damage Limitation (DL), Significant Damage (SD) and Near Collapse (NC).

The value of the chord rotation, θ_y, in the DL limit state for rectangular walls is given in Eq.(11) and it corresponds to the yielding moment capacity, M_y.

$$\theta_y=\varphi_y\frac{L_V+\alpha_V z}{3}+0.0013+\varphi_y\frac{d_b f_y}{8\sqrt{f_c}} \tag{11}$$

The value of the ultimate (total) chord rotation, θ_u, in the NC limit state is given in Eq.(12) and it corresponds to the ultimate moment capacity, M_u.

$$\theta_u=\frac{1}{\gamma_{el}}0.016(0.3^{\nu})\left[\frac{max(0.01;\omega')}{max(0.01;\omega)}f_c\right]^{0.225}\left(min\left(9;\frac{L_V}{h}\right)\right)^{0.35}25^{\left(\alpha\rho_{sx}\frac{f_{yw}}{f_c}\right)}(1.25^{100\rho_d}) \tag{12}$$

where:

γ_{el} is equal to 1.50 for primary seismic elements and to 1.00 for secondary seismic elements,

$\nu=N/bhf_c$ (b is the width of compression zone, N is the axial force positive for compression),

ω, ω' are the mechanical reinforcement ratios of the tension (including the web reinforcement) and compression, respectively, longitudinal reinforcement,

ρ_d is the steel ratio of diagonal reinforcement (if any), in each diagonal direction.

Note that for shear walls the above value must be multiplied by 0.58, while, specifically for members without seismic detailing, it must be also divided by 1.2. The intermediate value of the chord rotation, θ_{SD}, in the SD limit state may be taken as the $0.75\theta_u$.

Alternatively, EC8-3 proposes an analytical expression for calculating the ultimate chord rotation (Eq.(13)). Note that the specific expression is applicable only for the assessment of existing members with seismic detailing; no proposal for members with poor seismic detailing is made.

$$\theta_u=\theta_y+\left(\varphi_u-\varphi_y\right)L_{pl}\left(1-\frac{0.5L_{pl}}{L_V}\right) \tag{13}$$

where the plastic hinge length, L_{pl}, depends on the constitutive model for confined concrete:

For the confinement model included in Eurocode 2 - Part 1-1 [8]

$$L_{pl}=0.1L_V+0.17h+0.24\frac{d_b f_y}{\sqrt{f_c}} \tag{14a}$$

For a confinement model proposed in EC8-3 (based on Newman and Newman model [9])

$$L_{pl}=\frac{L_V}{30}+0.20h+0.11\frac{d_b f_y}{\sqrt{f_c}} \tag{14b}$$

The above confinement model of EC8-3 adopts Eq.(8) and (9) for f_{cc} and ε_{cc0}, respectively, and proposes that the ultimate concrete strain ε_{ccu} can be calculated as:

$$\varepsilon_{ccu}=0.004+0.5\frac{a\rho_s f_{yw}}{f_{cc}} \tag{15}$$

From the literature review, a main conclusion could be derived: Each empirical expression for predicting the plastic hinge length can be applied only in accordance with a certain model for calculating the ultimate curvature. The fact that the database, on which the above models were calibrated, comprises primarily members with seismic detailing, leads to the result that these expressions have application mainly (or only) to members with seismic detailing (e.g. EC8-3).

2.3 Numerical methods

Apart from the analytical models previously described, efforts have been made towards the development of reliable numerical methods for simulating the monotonic and cyclic behavior of RC members. In most cases these methods are based on Finite Element Methods (FEM).

An alternative numerical model which specially focuses on the simulation of RC shear walls is the one proposed in Massone et al. [13]. The base of the above model is a macroscopic fiber-based model, referred as Multiple-Vertical-Line-Element-Model (MVLEM), proposed by Vulcano et al. [14]. According to this approach an RC shear wall is modeled as a stack of Multiple-Vertical-Line-Elements (MVLEs), placed one upon the other. Each MVLE is simulated by a series of uniaxial elements connected to rigid beams, in order to capture the flexural component, and by a horizontal spring in order to capture the shear behavior. However, this simulation does not take into account the shear-flexure interaction.

In view of this limitation, Massone et al. [13] and Orakcal et al. [15] suggested an improved model, by assigning a shear spring for each uniaxial element, achieving a RC membrane behavior for each element.

3 EXPERIMENTAL PROCEDURE

In order to evaluate both analytical and numerical models presented within this paper, as well as the aforementioned code provisions, a comparison of analytical predictions with experimental results was carried out. The experimental process included the testing of a series of four RC shear walls. This testing forms part of a general experimental program, which is taking place in the RC Laboratory of the National Technical University of Athens (NTUA), whose scope is the assessment and strengthening of existing non-conforming RC shear walls. Two of the specimens (W_9 and W_{11}) were previously presented in Christidis et al. [16], while the other two (W_7 and W_{13}) are described herein.

3.1 Specimens characteristics

Walls W_7 and W_{13} represent a typical modern RC shear wall designed according to Eurocode provisions and a typical existing non-conforming RC shear wall, respectively. Specimens W_9 and W_{11} also represent non-conforming walls but, in addition, a configuration of open stirrups was added in order to prevent the buckling of compressive reinforcement, found often to reduce the bearing capacity of the wall prematurely; in this way the influence of shear reinforcement can be evaluated directly. The dimensions and the reinforcement configuration of all specimens are shown in Fig.1 and they are summarized in Table 1.

	Concrete compression strength f_c (MPa)	Reinforcement yield/failure f_y/f_u (MPa)		Longitudinal reinforcement ratio ρ_{tot} (‰)	Transverse (shear) reinforcement ratio ρ_w (‰)
		Longitudinal Reinforcement	Stirrups		
Wall W_7	32.12	D10:604/705 –D8:588/681	588/681	14.33	6.69
Wall W_9	31.12	580/670	588/681	12.06	2.01
Wall W_{11}	31.12	580/670	568/654	12.06	1.13
Wall W_{13}	25.37	580/670	568/654	12.06	1.13

ρ_{tot}=Area sum of longitudinal reinforcement/cross section area=$\Sigma A_{s,L}/(b_w*h)$

ρ_w=Area sum of stirrup/(wall width*stirrups distance)=$\Sigma A_{s,w}/(b_w*s)$

Table 1: Reinforcement ratios and material properties of the specimens considered.

It should be noted at this point that the flexural inelastic deformations, presented in detail in Section 2 (especially the ultimate values) can be attained provided that the structural

member has not previously reached its shear strength capacity, whose value can be calculated according to EC8-3 provisions. Walls W_{11} and W_{13} include such a shear reinforcement ratio that intentionally leads to a reduced value of shear capacity, typical of existing wall elements, so that the flexural behavior of the wall cannot be attained (see also Christidis et al. [16]). However, the expected brittle-shear behavior of the specimens was not verified by the test results (as also explained later), since all the specimens exhibited their flexural capacity and significant higher values of corresponding lateral displacement, not affected by the different reinforcement ratios. Thus, the evaluation of displacement capacity of Walls W_{11} and W_{13} was conducted in flexural terms: the investigation of the reliability of proposed models for calculating the shear strength capacity is beyond the scope of this paper.

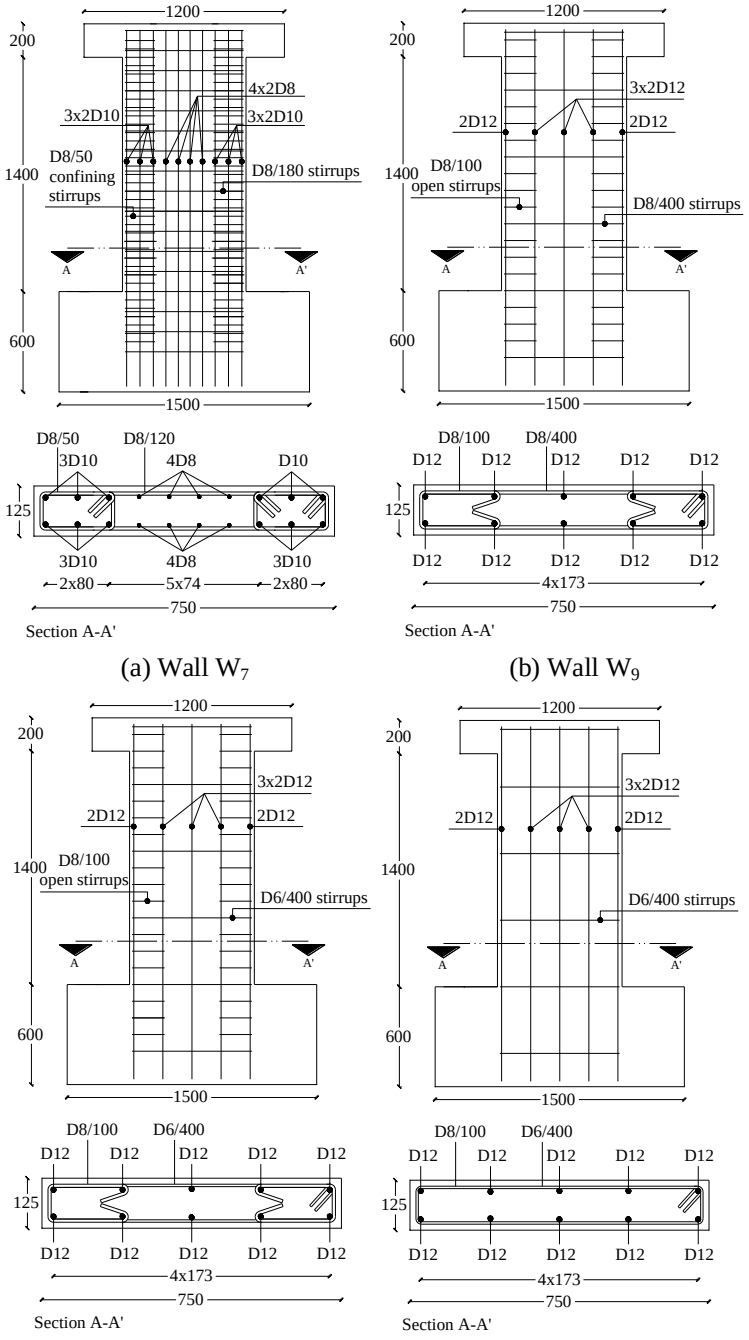


Figure 1: Reinforcement configuration of specimens (in mm).

3.2 Experimental procedure

The specimens were tested as cantilevers under static cyclic loading. During the testing procedure, a displacement control method was adopted, including an initial displacement of ±10 mm with steps of 10 mm until failure. Three cycles of each displacement group were applied: the time history of the loading is shown in Fig.2.

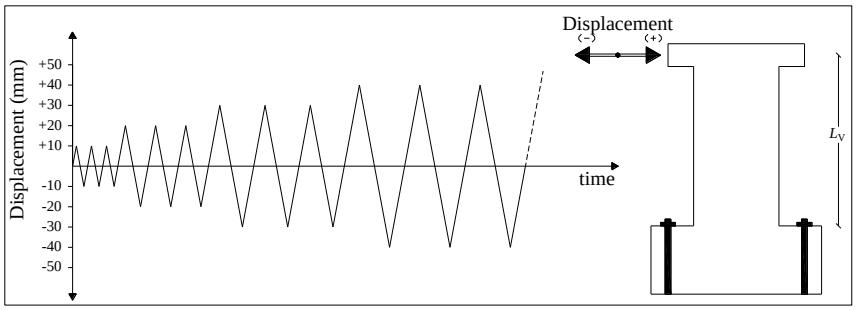


Figure 2: Time history of loading of specimens.

3.3 Experimental results – failure modes

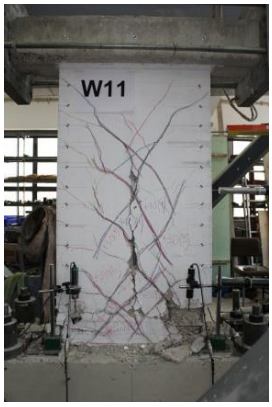
The experimental results are presented in Fig.12 (together with analytical and numerical predictions) in the form of the Load-displacement diagram, *P-δ*, where *δ* refers to the displacement at the top of each specimen. In Fig.3, the cracking pattern is shown at the end of the experimental procedure.



(a) Wall W_7



(b) Wall W_9



(c) Wall W_{11}



(d) Wall W_{13}

Figure 3: Cracks at the end of the experiment (at displacement 0.00mm).

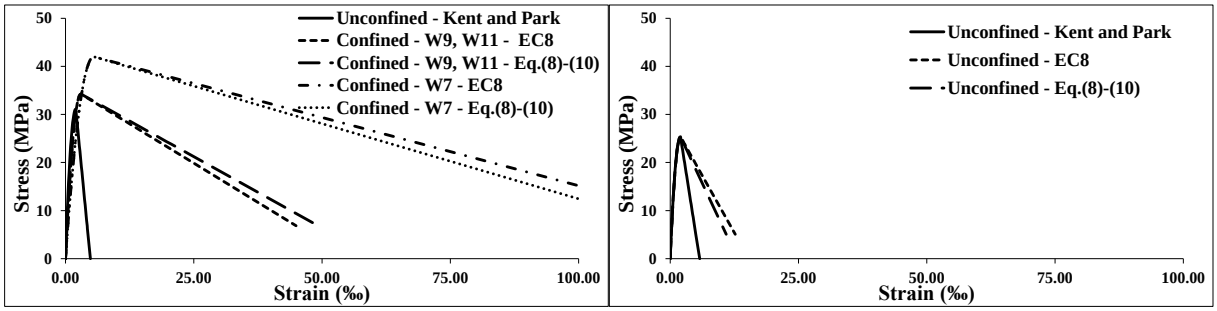
As concluded from the experimental results, low ratios of shear reinforcement seem to affect neither the bearing capacity nor the top displacement capacity of walls. All four specimens reached approximately their flexural bearing capacity, while in most cases they exhibited a flexural post-yield behavior followed by significant values of ductility, except of Wall W_{13} which exhibited a descending post-yield branch, which, however, is attributed to the premature buckling of the compressive longitudinal reinforcement. Contrariwise, low ratios of shear reinforcement seem to determine the crack mode of walls, as in cases of walls W_{11} and W_{13} with low ratios of shear reinforcement the formation of significant inclined X cracks was observed.

4 ANALYTICAL AND NUMERICAL ESTIMATION

EC8-3 provisions (both empirical and analytical) and Eq.(4) to Eq.(10) model (for cyclic loading) were applied for all the four specimens and compared with the experimental results. In order to apply the analytical or empirical models cross-section analyses (CS) were preceded in OpenSees platform [17]. In addition to the analytical predictions of section response, numerical simulations were also carried out at the element level, again using the OpenSees platform [17], which were also compared with experimental results.

4.1 Materials

As previously described, each one of the analytical models can be applied only in accordance with a specific concrete constitutive law. Thus, Eq.(8), (9) and (15) were applied to describe the confined concrete, in order to evaluate the EC8-3 ([11], [12]) provisions while Eq.(8), (9) and (10) were applied in order to evaluate the model of Eq.(4) to Eq.(10). For the numerical analysis at the element level the EC8-3 confined concrete model was applied. Especially in Wall W_{13}, where only unconfined concrete was used across the cross-section, the two previous models were used with a=0 for the unconfined core concrete. Note that in both models the value of strain at failure ε_{ccu} (or e_{cu}) corresponds to a concrete strength equal to $0.85f_{cc}$ (or $0.85f_c$). Finally, the Kent and Park model [18] was used to describe the unconfined cover concrete constitutive law in all cases (Fig.4).

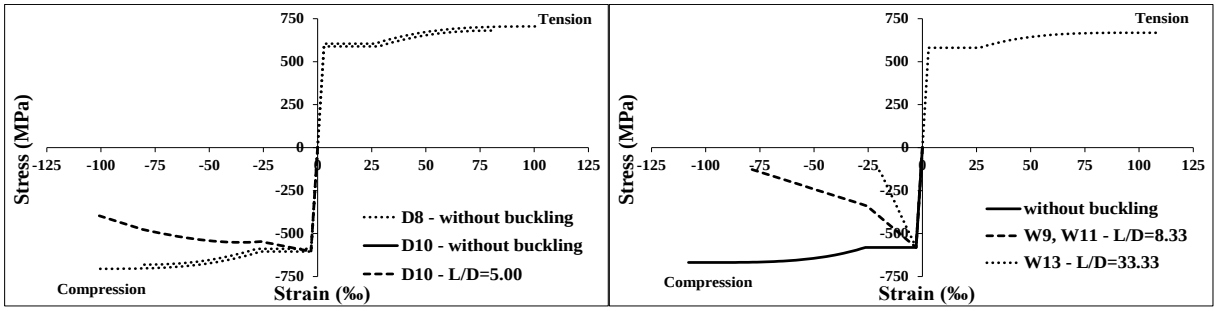


(a) Concrete f_c=31.12MPa (Walls W_7, W_9, W_{11}) (b) Concrete f_c=25.37MPa (Wall W_{13})

Figure 4: Concrete stress-strain (σ-ε) curves in compression.

In all cases (cross-section and element level) the analyses were carried out ignoring the tension strength of concrete, so a *Concrete_01-Zero Tensile Strength* material was used in OpenSees for the concrete. Chang and Mander [19] model was used to describe the reinforcing steel constitutive law including the buckling of compressive bars according to Dhakal and Maekawa [20] model (OpenSees: *Reinforcing Steel Material*) (Fig.5). The buckling of compressive steel depends mainly on the ratio *L/D*, where *L* is the unsupported bar length and *D* is the diameter of the reinforcing bar. The influence of buckling to the

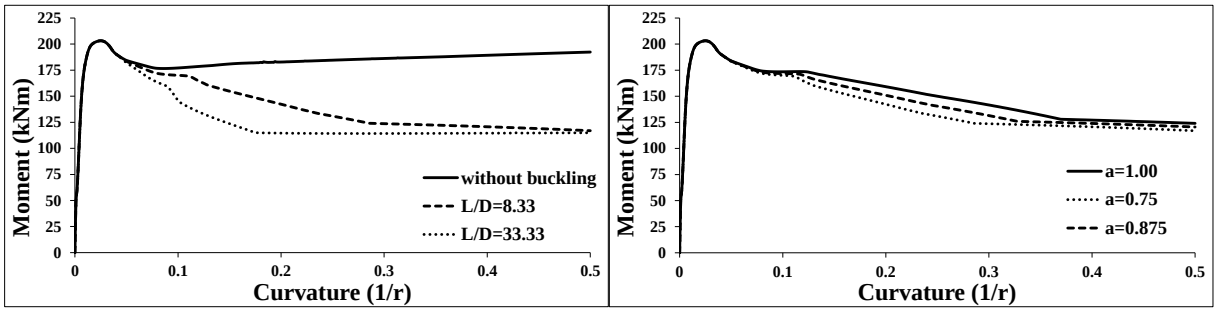
Moment - Curvature diagram is shown indicatively in Fig.6a, where the Moment-Curvature diagram of wall W_{13} is derived from a cross-section analysis for three different cases, namely without buckling and with buckling, for L/D = 8.33 and L/D = 33.33.



(a) Reinforcing bars D10 and D8 in Wall W_7 (b) Reinforcing bar D12 in Walls W_9, W_{11} and W_{13}

Figure 5: Reinforcing bars stress-strain (σ-ε) curves.

Another parameter which influences the reduction of steel stress due to buckling is the parameter *a* (Dhakal and Maekawa [20]). As Dhakal and Maekawa [20] state, the value of *a* is found to be 0.75 for elastic–perfectly plastic bars and 1.0 for bars with continuous linear hardening. Thus, for bars with a limited hardening range, *a* should be chosen between 0.75 and 1. Dhakal and Maekawa [21] recommend a system of equations for calculating the parameter *a*. In the case of reinforcing bars *D*10 and *D*12 of the wall models herein, the above equations lead to values 0.777 and 0.767, respectively, so the lower bound of 0.75 was adopted. Besides, the value of parameter *a* does not seem to have a significant influence on the overall Moment-Curvature of the cross-section, as also shown in Fig.6b.

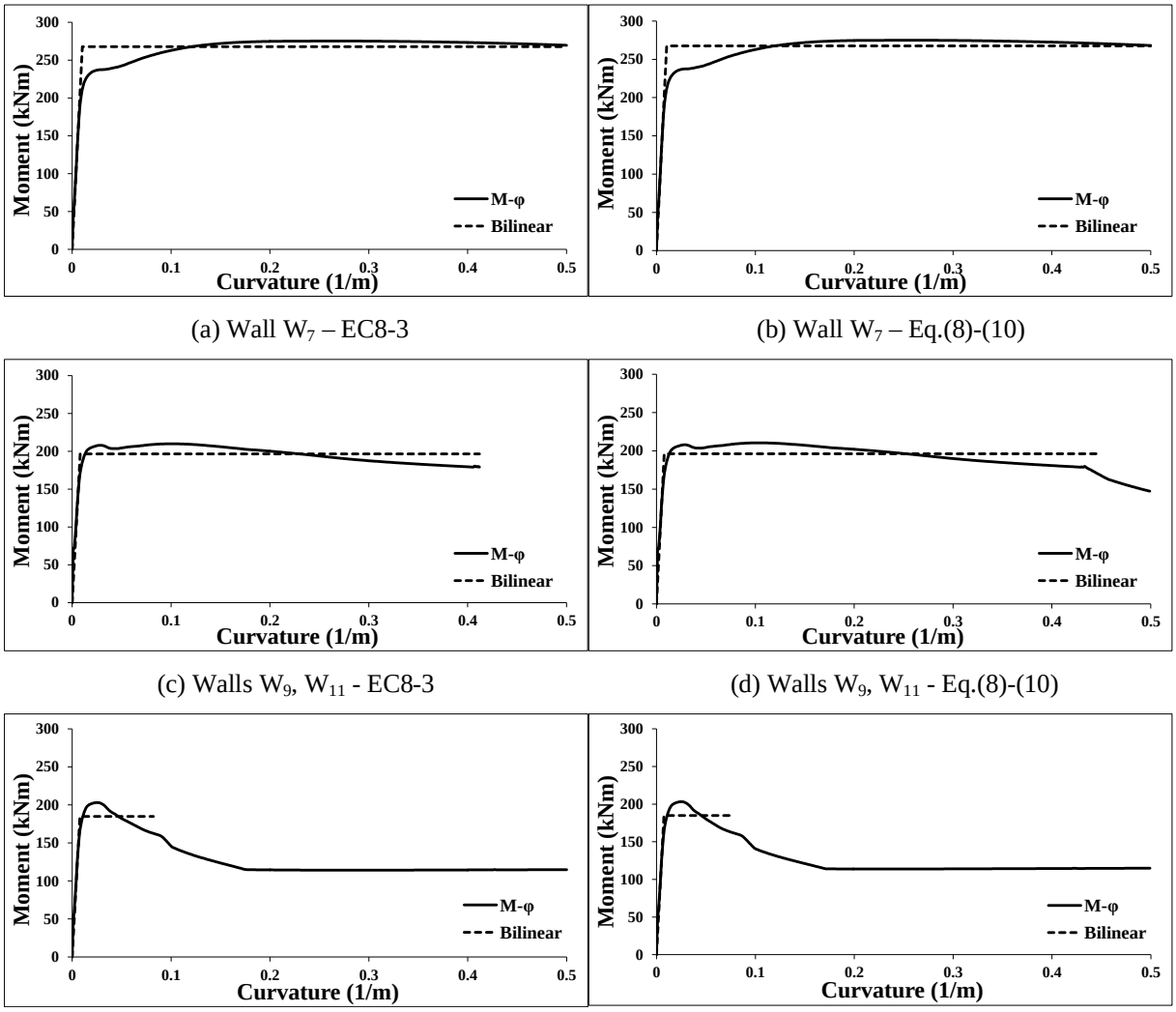


(a) Influence of L/D for constant a=0.75 (b) Influence of a for constant L/D=8.33

Figure 6: Influence of buckling parameters L/D and a to the Moment Curvature diagrams of Wall W_{13}.

4.2 Analytical estimation

In order to apply the analytical equations a conventional yielding point was used, obtained from the bilinearization of the Moment-Curvature diagram, M-φ, using an equivalent bilinear curve (elastic-perfectly plastic), where the initial elastic stiffness is defined from the first yield point (M_{y1}, φ_{y1}). The conventional yield point (M_y, φ_y) was derived by equating the area (energy) of the two curves. Note that the ultimate curvature, φ_u, is taken as the one corresponding to a percentage 20% loss of the bearing capacity. The Moment-curvature diagrams derived from the cross-section analysis in OpenSees and their equivalent bilinear counterparts are summarized in Fig.7; the Load-displacement (P-δ) curves derived from the application of the analytical expressions above, using the M-φ curves are discussed later on, in comparison with numerical and experimental results (see also Fig.12).



(a) Wall W_7 – EC8-3

(b) Wall W_7 – Eq.(8)-(10)

(c) Walls W_9, W_{11} - EC8-3

(d) Walls W_9, W_{11} - Eq.(8)-(10)

(e) Wall W_{13} – EC8-3

(f) Wall W_{13} – Eq.(8)-(10)

Figure 7: Moment curvature diagrams (M-φ).

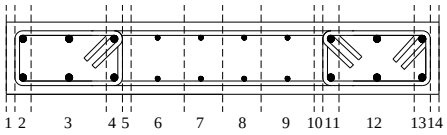
4.3 Numerical analysis

In addition to the previous analytical approach, numerical simulations were carried out using OpenSees platform to predict the experimental response. The simulation of the RC shear wall was held in two alternative ways. The first one was by using the Displacement-Based Beam-Column Element, which considers the spread of plasticity along the element height. This element is a flexural element model based on internal interpolation of deformations, while relying only on the flexural characteristics of the cross-section (i.e. geometry, longitudinal reinforcement, material laws) for the response evaluation; therefore, it does not take into account the shear component neither in the evaluation of the total strength nor the total displacement (also, fixed end effects were not included at the base end). Thus, via this model, it is possible to evaluate the differences in the total P-δ behavior of the wall only due to flexural changes in the cross section, i.e. the influence of the confinement and the influence of the buckling of the compressive longitudinal bars, but not the influence that different shear reinforcement ratios have.

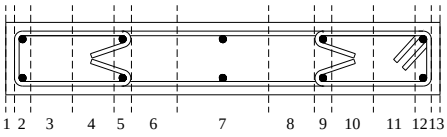
On the other hand, the influence of the shear reinforcement can be simulated by using the Flexure-Shear Interaction Displacement-Based Beam-Column Element available in OpenSees that takes into account the interaction between flexure and shear components, based on

Massone et al. [13] work. The specific model is sensitive to three modelling factors: the discretization of the cross-section in *n* strips, the number of subelements, *m*, along the wall height and the value of the parameter *c*, which is the center of rotation (or the center of gravity of the curvature distribution) in each subelement.

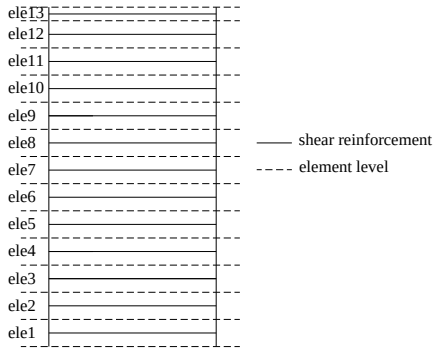
The discretization of the cross section in *n* strips for each element was performed in order to achieve the best simulation of the actual test cross-section configuration, i.e. the exact place of the rebars and the transitions between confined and unconfined concrete (Fig.8a,b).



(a) Discretization in *n* strips - Wall W_7



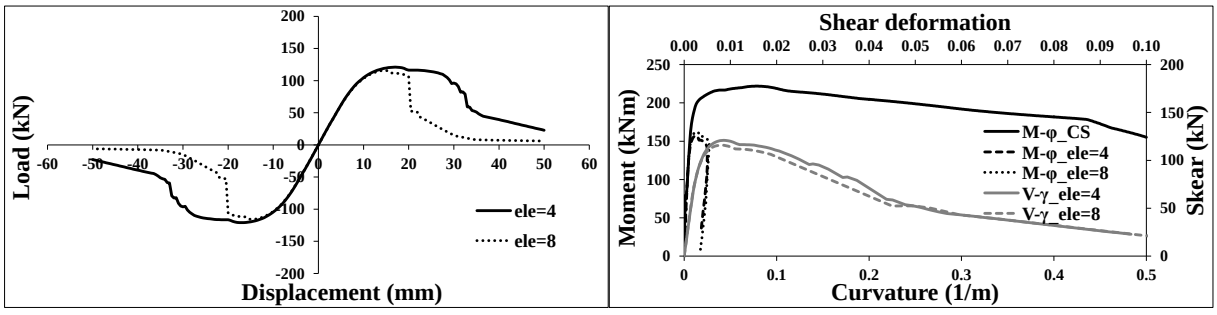
(b) Discretization in *n* strips - Walls W_9, W_{11}, W_{13}



(c) Discretization in *m* subelements - Wall W_7

Figure 8: Modelling of walls in OpenSees.

As far as the number of subelements, *m*, along the wall height (see indicatively Fig.8c), it was decided to divide the total height according to the distance of the horizontal shear reinforcement. Thus, Wall W_7 was divided in m=13 element (at 0.12m) while Walls W_9, W_{11} and W_{13} were divided in m=4 elements (at 0.40m). Each of these elements contains a constant area of shear reinforcement which, divided by the height of each m_i element and the wall width, *b*, gives the actual shear reinforcement ratio, ρ_w, of each shear wall (see also Table 1). As Orakcal et al. [15] state, "*increasing the number of uniaxial elements or the number of MVLEs along wall height does not change significantly the prediction of the global P-δ response*". On the other hand, "*use of more MVLEs along wall height is valuable in terms of obtaining more detailed information on responses at a given location*". So from this point of view, using only m=4 elements for walls W_9, W_{11} and W_{13} was considered as inadequate. However, it was observed that, increasing the number of MVLEs while trying to keep the shear reinforcement ratio constant and equal to the actual so as not to deviate from the actual wall model, led to the use of subelements with less or even no shear reinforcement. In both cases the *P-δ* analysis results were poor, as shown in Fig.9a, without significantly influencing the local behavior *(*flexural *M-φ* or shear *V-γ)*, so the number m=4 elements was adopted herein.

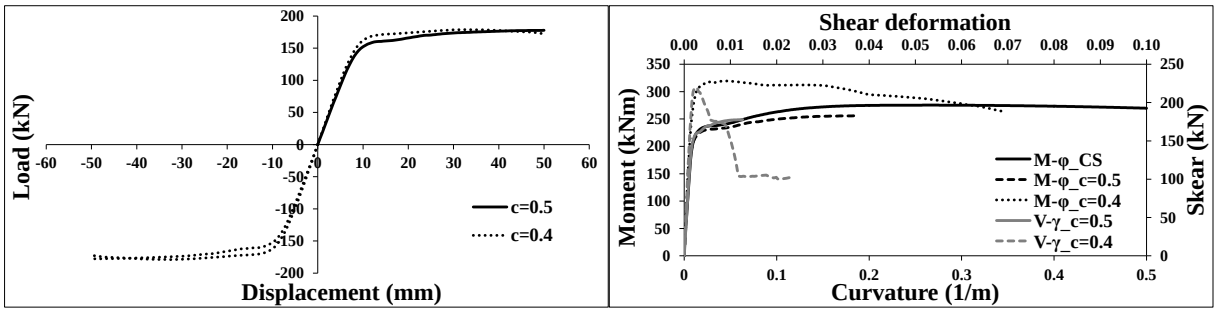


(a) *P-δ* curves

(b) *M-φ* and *V-γ* curves

Figure 9: Comparison of different element number for Wall W_{11}.

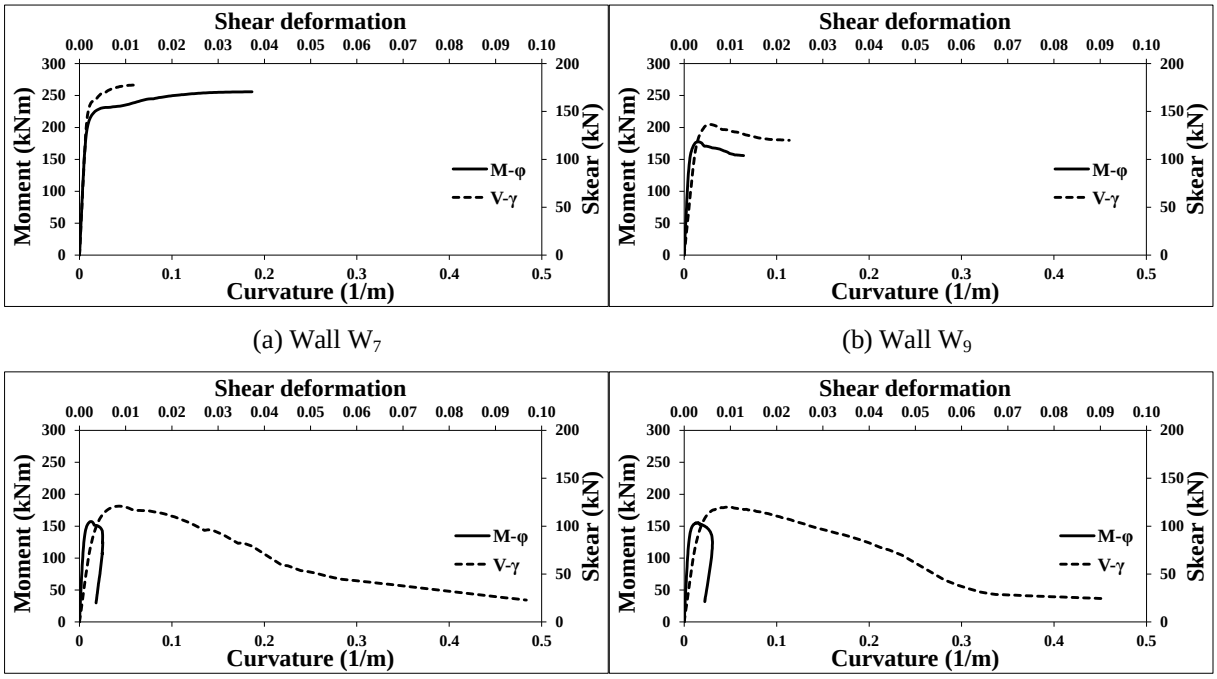
Finally, regarding the location of the center of rotation, a value c=0.4 was recommended by Vulcano et al. [14], however, using a large number of MVLEs along wall height, diminishes the influence of this parameter on the predicted response (Orakcal et al. [15]). However, applying the value c=0.4 in wall W_7, although it did not affect significantly the overall P-δ response (Fig.10a), led to an overestimated M-φ diagram compared to the one obtained from a cross section analysis (Fig.10b). Thus, a value of c=0.5 was adopted in this study, which led to a M-φ curve closer to the one of the cross-section analysis.



(a) P-δ curves (b) M-φ and V-γ curves at the bottom element

Figure 10: Comparison of c=0.4 and c=0.5 for Wall W_7.

All the flexural (curvature φ) and shear (γ) deformations are summarized in Fig.11.



(a) Wall W_7 (b) Wall W_9

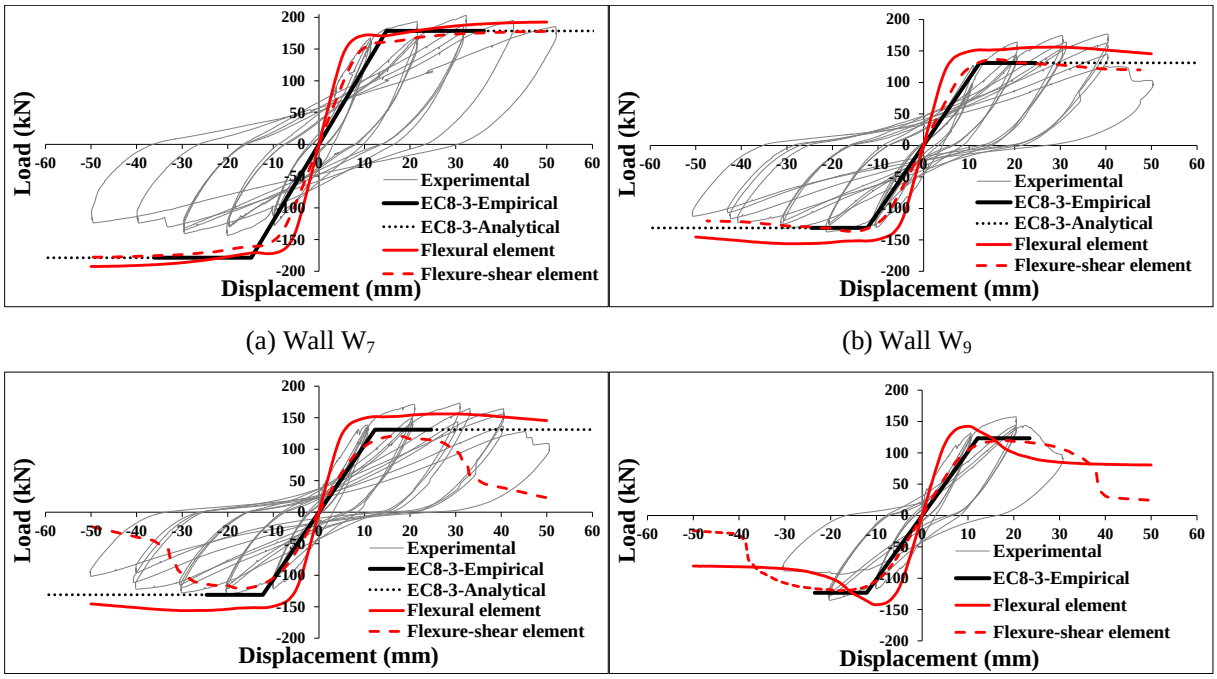
(c) Wall W_{11} (d) Wall W_{13}

Figure 11: Flexural (M-φ) and shear (V-γ) deformations for Flexural-shear analysis (c=0.5) at the bottom element.

As shown in Fig.11 the total deformation, δ, is attributed to the interaction between flexural and shear deformations. As a result shear deformation determines the overall displacement capacity of the walls (W_{11} and W_{13}) with low shear reinforcement ratio.

5 EXPERIMENTAL VERIFICATION

The analytical and numerical models presented within this paper are compared with the experimental results, in the form of comparisons of the corresponding *P-δ* diagrams (Fig.12), where *δ* refers to the lateral displacement of the top (at 1.5m) of the wall.



(a) Wall W_7 (b) Wall W_9

(c) Wall W_{11} (d) Wall W_{13}

Figure 12: Load-displacement, *P-δ*, curves of specimens (analytical, numerical and experimental results).

All methods (analytical and empirical) were considered in wall W_7 which represents a conforming shear wall designed according to modern seismic provisions. On the contrary, in Wall W_{13} only the empirical EC8-3 method was considered, as the specific specimen represents a typical non conforming wall without seismic detailing, where analytical models have no application. As far as specimens W_9 and W_{11} are concerned, which constitute an intermediate case, analytical methods were considered for both walls, but the factor 1.2 for non conforming shear walls was conservatively used within the calculations using the empirical methods. Note that in Fig.12 above, the Eq.(4) to Eq.(10) analytical model is not superimposed, since it yields results very similar to the one of EC8-3(analytical). Both analytical methods seem to estimate with high accuracy the deformation capacity of the test shear walls, as they lead to high ductility levels. On the contrary, the empirical method of EC8-3 seems to underestimate the deformation capacity in most test cases.

As shown in Fig.12, the Flexural element seems to estimate with quite good accuracy the overall *P-δ* response of the walls. As mentioned before, the specific model cannot take into account the shear component, consequently, it is not affected by the negative influence of inadequate shear reinforcement in cases of Walls W_{11} and W_{13}; theoretically, for these walls a premature shear failure is expected. However, such a shear failure is not verified by the experimental results, something which is consistent with the results of the displacement based flexural model prediction.

On the other hand, the theoretically more accurate Flexure-shear interaction element seems to underestimate the behavior of the lightly reinforced (in shear) walls W_{11} and W_{13}, as the numerical analysis leads to significantly lower values, both in load and top displacement

terms. However, it is noted that the Flexure-shear interaction element analysis led to stiffness values, until approximately the yielding point, closer to the experimental ones, something which was expected, as the shear component is added to the total displacement value.

6 CONCLUSIONS

Four reinforced concrete shear walls were tested under static cyclic loading. As concluded from the experimental results, low ratios of shear reinforcement seem to affect neither the bearing capacity nor the deformation capacity of these walls. All the specimens reached a maximum load close to their flexural capacity, while in most cases they exhibited a flexural post yield behavior, followed by significant values of ductility. The low ratios of shear reinforcement seem to influence the cracking pattern of the walls, which was characterized by the formation of significant inclined cracks, which, however did not lead to a loss of bearing capacity. The effect of buckling of the compressive longitudinal reinforcement appears intensely in Wall W_{13} which exhibited a descending post-ultimate branch.

The experimental results were compared with the provisions provided in EC8-3, and with the Eq.(4) to Eq.(10) model proposed in the literature. Both analytical models seem to estimate with accuracy the behavior of RC shear walls, while the empirical method of EC8-3 underestimates the ultimate deformation capacity and leads to lower displacement values than the experimental ones, being however on the safe side. Note that within this paper the equations for estimating the shear strength, which often indicate prior brittle failure and, therefore, poor deformation capacity, were not evaluated. As the experimental behavior seems not to be significantly affected by the presence of low shear reinforcement, the comparisons was conducted in flexural terms.

Finally, the experimental results were compared with numerical analyses conducted with two alternative methods – by using a flexural displacement element type and by using a flexural-shear interaction displacement element type. Between the two types of elements the flexural one seems to estimate more accurately the overall *P-δ* behavior of the walls, while the flexural-shear interaction element estimates better the initial stiffness until yielding. However, the latter element predicts a prior brittle shear failure in the case of the two lightly reinforced walls W_{11} and W_{13}, something which was not confirmed by the experimental results.

REFERENCES

[1] T. Paulay, M.J.N. Priestley, *Seismic design of reinforced concrete and masonry buildings*. John Wiley & Sons, Inc. 1992.

[2] T.B. Panagiotakos, M.N. Fardis, Deformations of reinforced concrete members at yielding and ultimate. *ACI Structural Journal*, **98**, 135–148, 2001.

[3] D. Biskinis, *Strength and deformation capacity of reinforced concrete members with or without strengthening.* PhD Dissertation, University of Patras, 2007 (in Greek).

[4] D. Biskinis, M.N. Fardis, Deformations at flexural yielding of members with continuous or lap-spliced bars. *Structural Concrete*, **11**,127-138, 2010.

[5] D. Biskinis and M.N. Fardis, Flexure-controlled ultimate deformations of members with continuous or lap-spliced bars. *Structural Concrete*, **11**,93-108, 2010.

[6] S. Grammatikou, *Strength, deformation capacity and failure modes of reinforced concrete shear walls under seismic loading.* MSc Dissertation, University of Patras, 2013 (in Greek).

[7] S. Grammatikou, D. Biskinis, M.N. Fardis, Strength, deformation capacity and failure mode of RC walls in cyclic loading. *4th International fib Congress and Exhibition*, Mumbai, India, February 10-13, 2014.

[8] CEN Eurocode 2: *Design of concrete structures - Part 1-1: General rules and rules for buildings (EN 1992-1-1)*. European Committee for Standardization, Brussels, Belgium, 2004.

[9] K. Newman, J. B. Newman, Failure Theories and Design Criteria for Plain Concrete. *Proc., Int. Civil Engrg. Mat. Conference on Structure, Solid Mech. and Engrg. Des. Wiley Interscience*, New York, NY, pp. 936-995, 1971.

[10] M.N. Fardis, *Seismic Design, Assessment and Retrofitting of Concrete Buildings Based on EN-Eurocode8*. Springer Dordrecht Heidelberg, 2009.

[11] CEN Eurocode 8: *Design of Structures for Earthquake Resistance - Part 3: Assessment and Retrofitting of Buildings (EN 1998-3)*. European Committee for Standardization, Brussels, Belgium, 2005.

[12] CEN Eurocode 8: *Design of Structures for Earthquake Resistance - Part 3: Assessment and Retrofitting of Buildings (EN 1998-3:2005/AC).* European Committee for Standardization, Brussels, Belgium, 2010.

[13] L.M. Massone, K. Orakcal, J.W. Wallace, Shear-Flexure Interaction for Structural Walls, *ACI Special Publication*, ***236***, 127- 150, 2006.

[14] A. Vulcano, V.V Bertero, V. Colotti, Analytical Modelling of R/C Structural Walls. *9th World Conference on Earthquake Engineering*, Kyoto – Tokyo, Japan, August 2-9, 1988.

[15] K. Orakcal, L.M. Massone, J.W. Wallace, *Analytical Modeling of Reinforced Concrete Walls for Predicting Flexural and Coupled– Shear-Flexural Responses*. PEER Report 2006/2007, Pacific Earthquake Engineering Research Center, College of Engineering, University of California, Berkeley, 2006.

[16] K. Christidis, E. Vougioukas, K.G. Trezos, Deformation capacity of older RC shear walls: Experimental assessment and comparison with Eurocode 8 – Part 3 Provisions, M.A. Ansal and M. Nurlu eds. *2nd European Conference on Earthquake Engineering and Seismology*, Istanbul, Turkey, August 25-29, 2014.

[17] F. McKenna, G.L. Fenves, B. Jeremic, M.H. Scott, *OpenSees Command Language Manual*, 2007. http://opensees.berkeley.edu.

[18] D.C. Kent, R. Park, Flexural members with confined concrete. *Journal of the Structural Division, Proc. of the American Society of Civil Engineers,* **97(ST7),** 1971.

[19] G.A. Chang, J.B. Mander, *Seismic Energy Basic Fatigue Damage Analysis of Bridge Columns: Part I – Evaluation of Seismic Capacity*. Technical Report NCEER-94-0006, State University of New York at Buffalo, 1994.

[20] R.P. Dhakal, K. Maekawa, Modeling for Post-yield Buckling of reinforcement. *ASCE Journal of Structural Engineering,* **128**, 1139-1147, 2002.

[21] R. Dhakal, K. Maekawa, Path-dependent cyclic stress–strain relationship of reinforcing bar including buckling. *Engineering Structures* **24,** 1383–1396, 2002.

COMPDYN 2015
5th ECCOMAS Thematic Conference on
Computational Methods in Structural Dynamics and Earthquake Engineering
M. Papadrakakis, V. Papadopoulos, V. Plevris (eds.)
Crete Island, Greece, 25–27 May 2015

SEISMIC ANALYSIS OF PRESTRESSED STADIUM ROOF

P. Rosko[1] **and A. Bekö**[2]

[1] Vienna University of Technology
Karlsplatz 13/E2063, Vienna, Austria
peter.rosko@tuwien.ac.at

[2] Vienna Consulting Engineers
Hadikgasse 60, Vienna, Austria
beko@vce.at

Keywords: Earthquake Engineering, Seismic Analysis, Structural Dynamics, Prestressed Large Structure.

Abstract. *The paper deals with seismic analysis of Austria largest stadium roof. Detailed finite element model is updated on the base of experimental modal analysis. The model enables to analyze the seismic behavior of the roof. The real stress in the natural prestressed structure plays an important role and has influence on the dynamic behavior. Natural frequencies and modes of numerical models with and without prestress are compared. The paper presents the time history analysis results using earthquake records from strong motion database.*

1 INTRODUCTION

Stadiums are civil engineering structures which reflect the mastership and building art of particular place and time they are built in. Structures of stadiums surround large spaces with a free view of the field. That results in large spans of the roof structures. The structural design uses not only the advanced material technologies but also geometry, which allows the load transmission into reduced number of supports in the inner space. Places where many people gather demand the fulfillment of rigorous safety requirements. This is the reason why stadium structures are very interesting from civil engineering point of view. Ernst Happel Stadium in Vienna is the largest stadium in Austria. The comprehensive analysis of the stadium was done after 25 year lifetime since last rebuilding. The paper presents some interesting results obtained in dynamic analyses of the stadium roof.



Figure 1: Ernst Happel Stadium.

2 STRUCTURE

The geometry of the roof structure is defined by outer and inner elliptical ring in the plan view. The stadium roof is supported on the outer ring only. The inner ring withstanding tension stabilizes the roof. The shape of the stadium roof meets the minimum of the potential energy. For that reason is the height of the roof variable.

The structure consists of steel beams and steel-concrete composite joints.

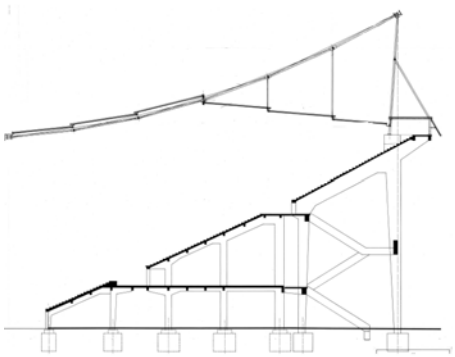


Figure 2: Radial cross-section of the structure.



Figure 3: Steel structure.

3 FINITE ELEMENT MODEL IDENTIFICATION

The finite element model of the stadium roof bearing structure was prepared in ANSYS environment.

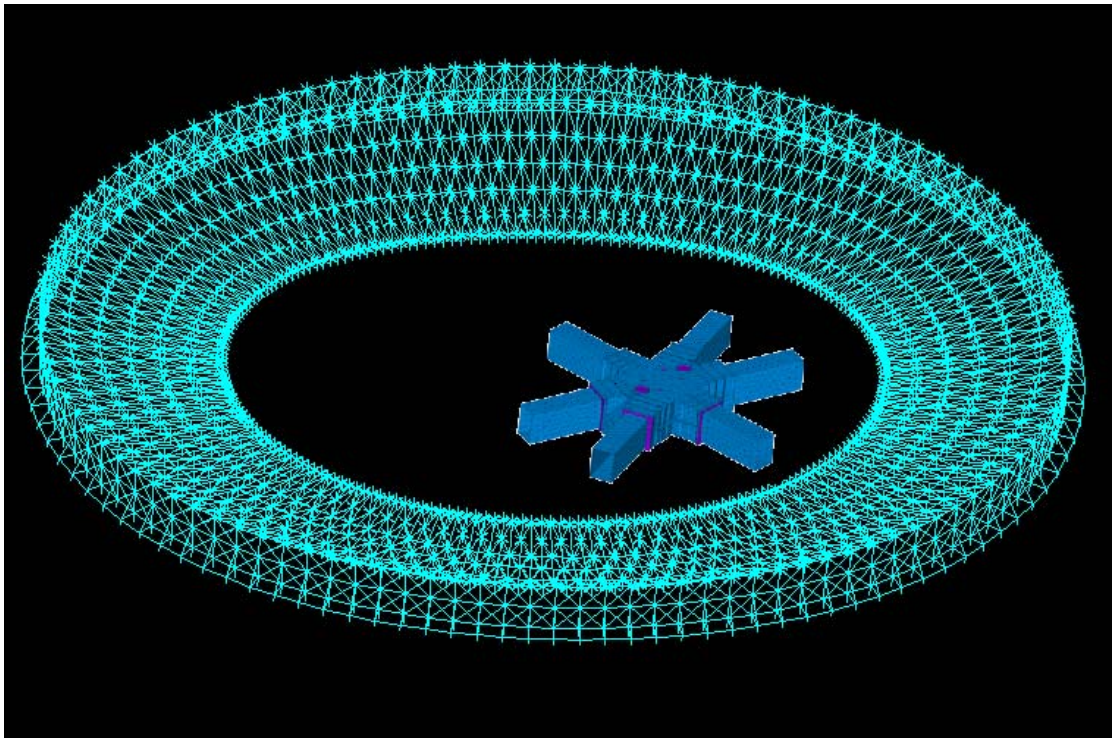


Figure 4: Finite element model of the whole roof bearing structure and join in detail.

The initial state (geometry, stress) of the structure - model without external loading was compared with results of experimental testing. In the modeling the identification process of the model required to follow the process of the real structure erection: in the first phase the roof structure was supported over whole area and in the second phase the preliminary supports were removed. The removal of the preliminary supports resulted in the new roof shape formation and prestress generation.

The simplified join model fulfilled the error minimization criteria of identification procedure.

3.1 Modal analysis

The modal analysis is still the most frequently used method within the frame of structural model identification methods. The numerical modal analysis was carried out by block Lanczos method.

The basic problem of the identification was to define the prestress in the model. The solution of this problem is explained above. Table 1 shows the natural frequencies considering the prestress caused during building and the case without prestress. Figures 5-7 compare the first 10 modes of prestressed roof structure and 10 modes of roof structure without prestress.

Frequency	1	2	3	4	5	6	7	8	9	10
Prestress	0.392	0.392	0.479	0.480	0.645	0.647	0.766	0.789	0.826	0.833
No prestress	0.224	0.225	0.258	0.263	0.338	0.339	0.472	0.474	0.630	0.631

Table 1: Natural frequencies [Hz] for prestressed model and model without prestress.

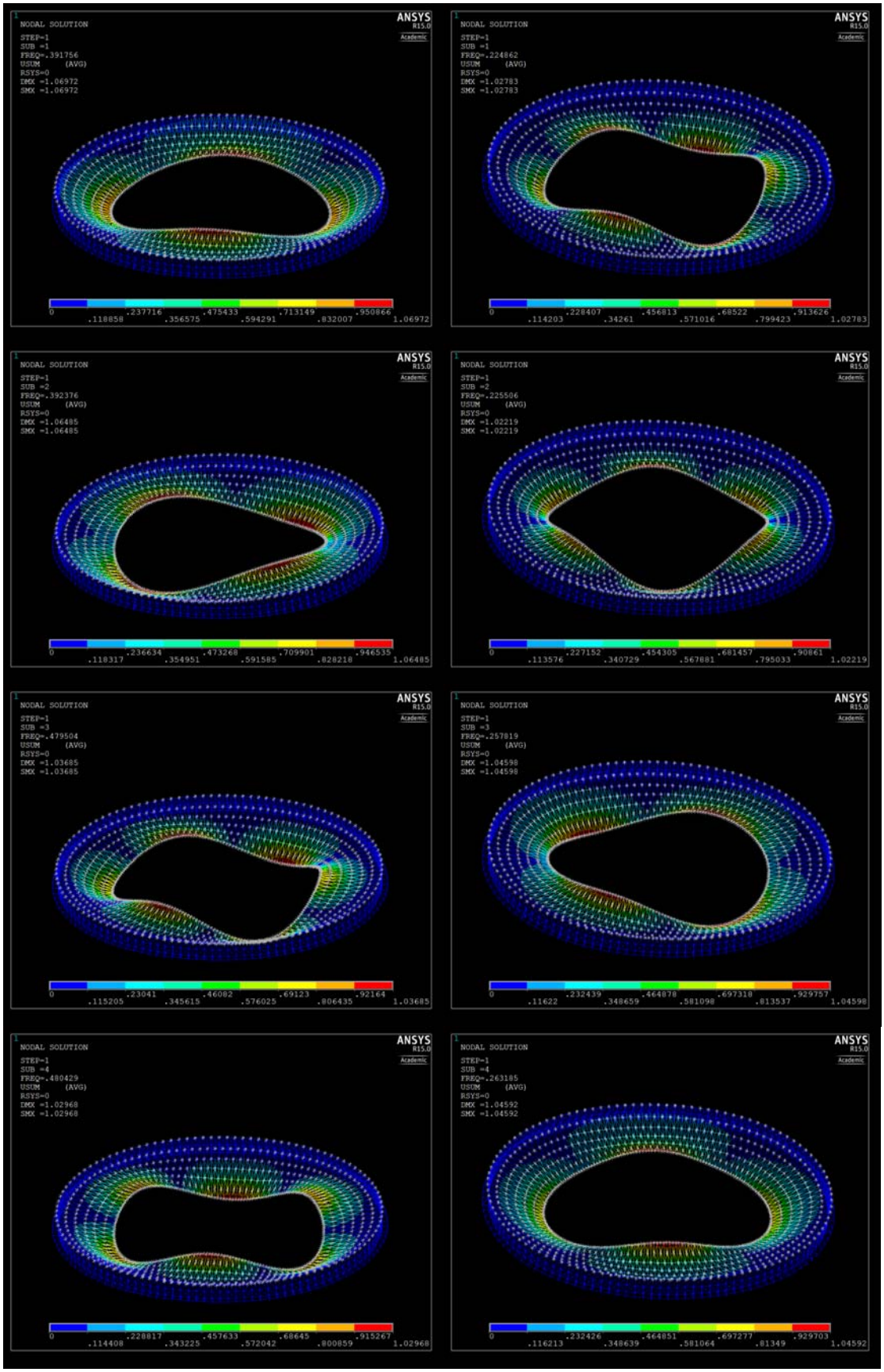


Figure 5: First 4 modes, left: prestressed, right: not prestressed.

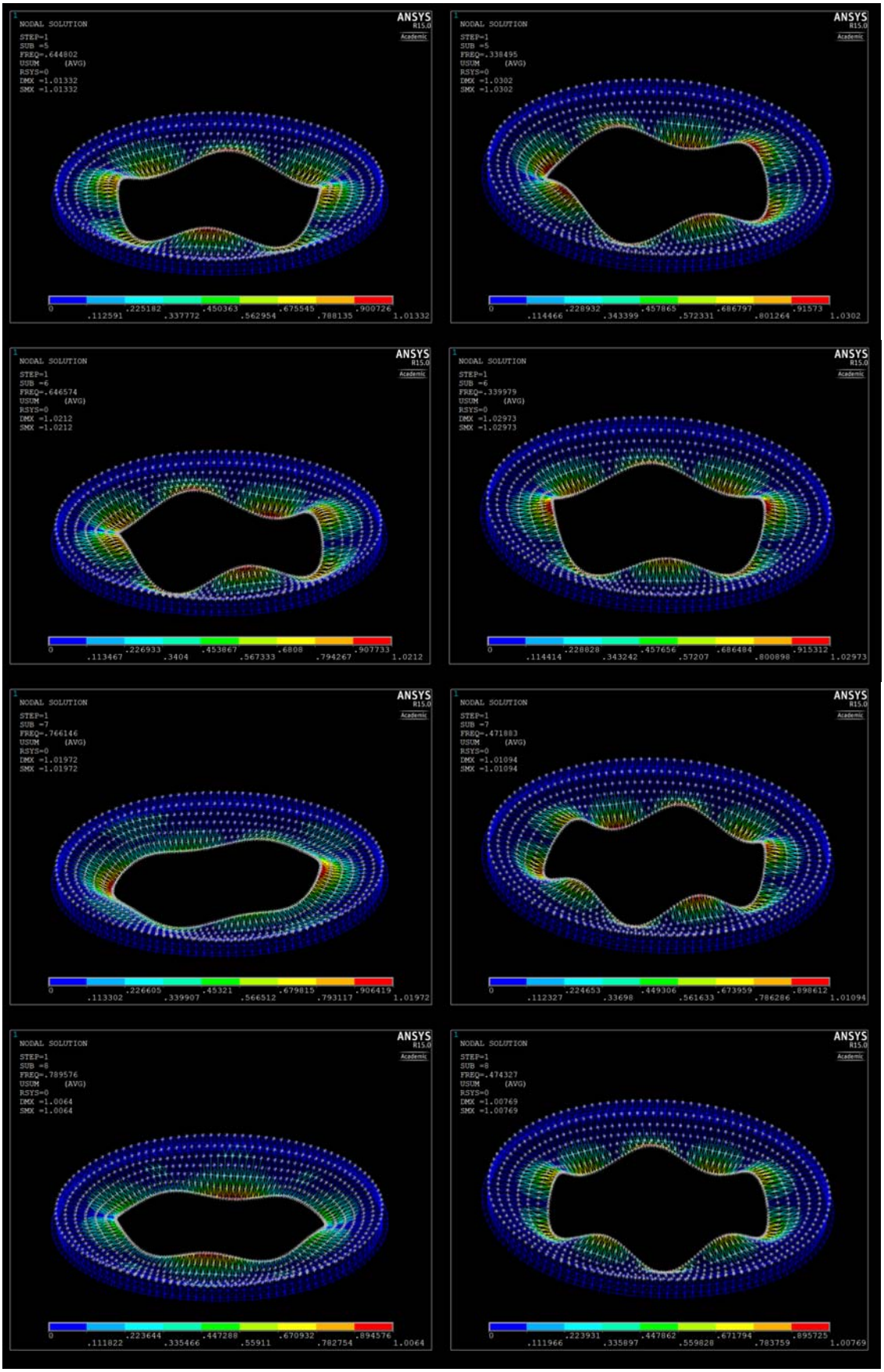


Figure 5: First 4 modes, left: prestressed, right: not prestressed.

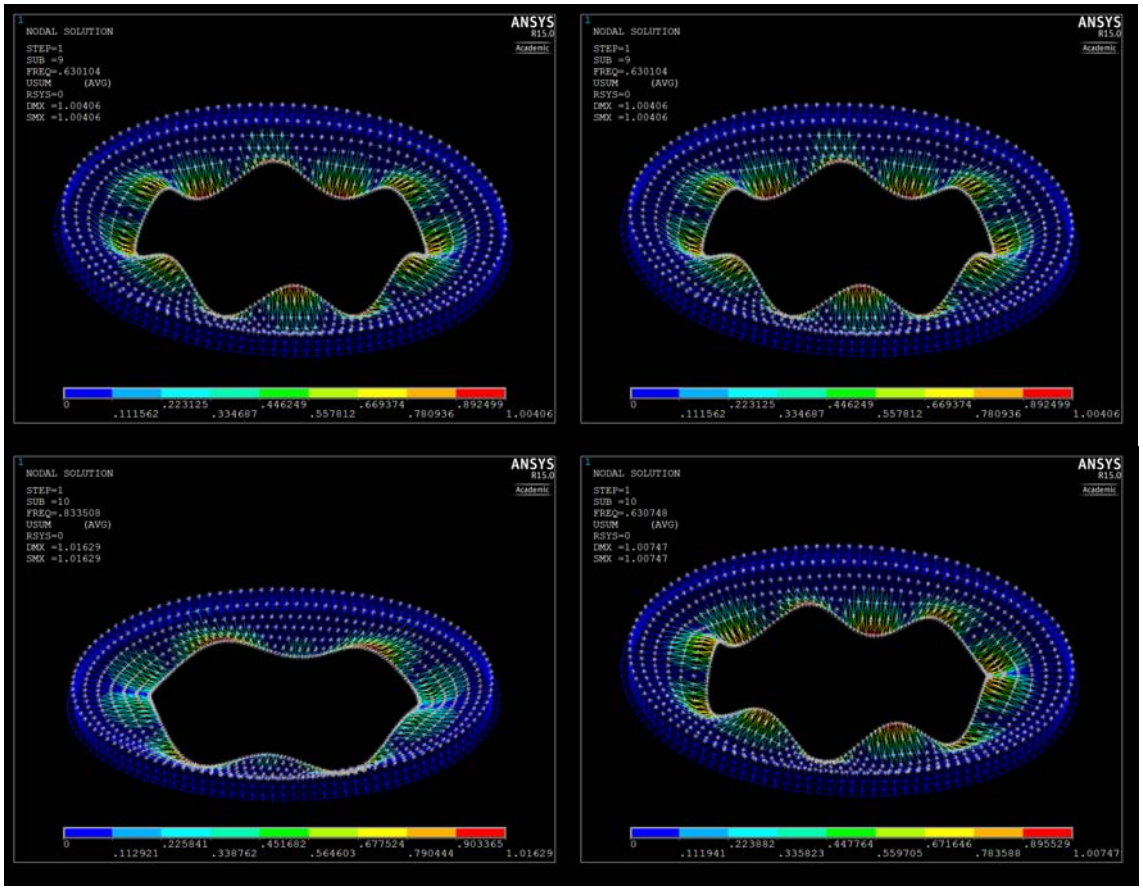
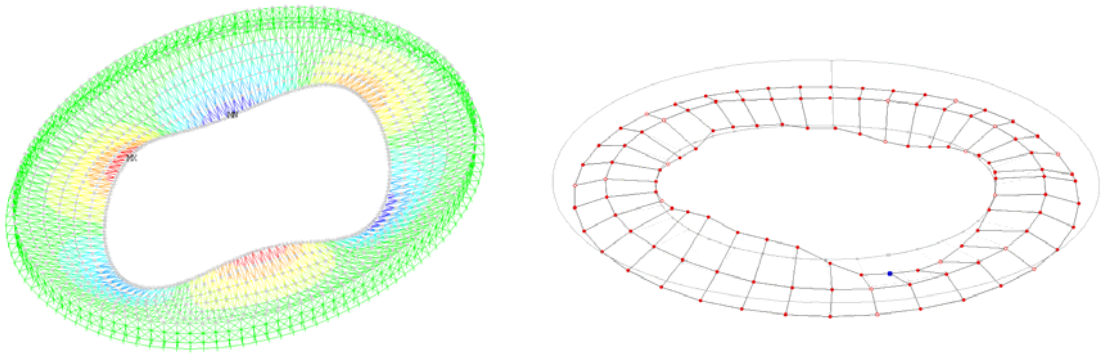


Figure 7: Modes 9-10, left: prestressed right: not prestressed.

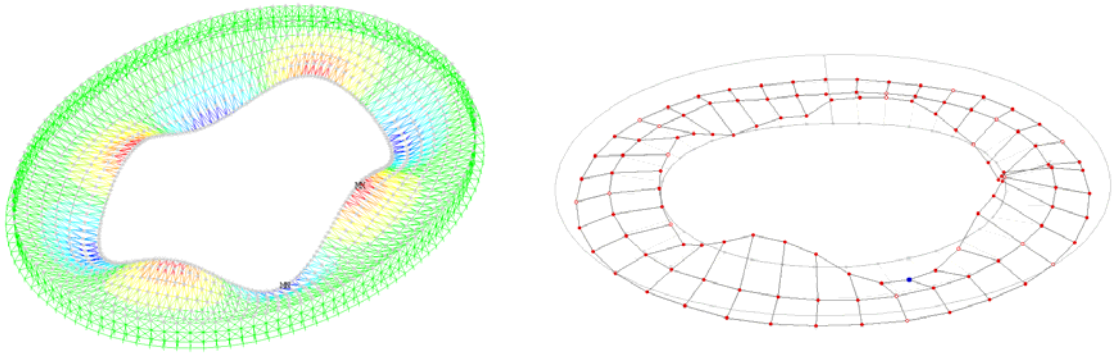
3.2 Model update

The experimental testing of the stadium roof structure was realized by Vienna Consulting Engineers with BRIMOS System. Ambient vibration was analyzed. The Ibrahim random decrement technique enables the modal identification of the structure. Natural frequencies and modes obtained from testing and numerical model were compared. The finite element model update was proceeded until the error of the natural frequencies was < 2%. The Figure 8 shows identified modes.

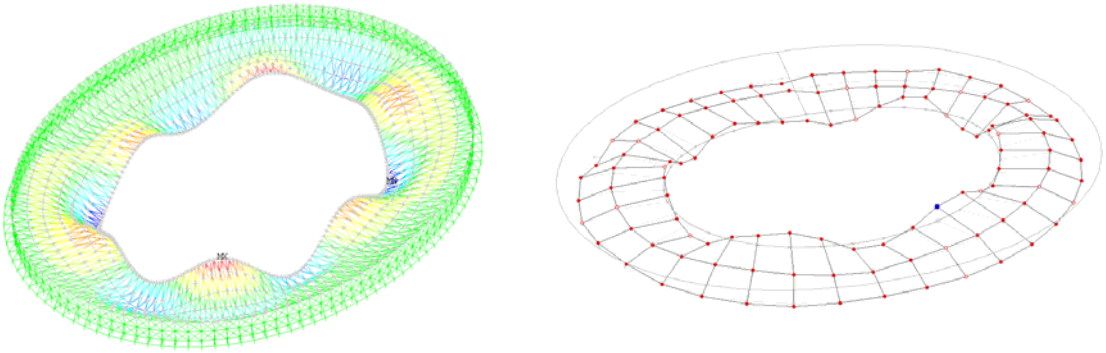


$f_{1i} = 0{,}48\text{Hz}$

Figure 8: Comparison of numerical and experimental obtained modes. (continue)



f_{2i} = 0,65Hz



f_{3i} = 1,0Hz

Figure 8: Comparison of numerical and experimental obtained modes.

3.3 Time history analysis

Comprehensive analysis of the Ernst Happel Stadium structure according Eurocodes [2] was carried out by Vienna Consulting Engineers. Load cases including static and dynamic forces caused by dead load, wind, snow and earthquake in prescribed combinations were analyzed in the report [1].

The presented paper focuses analysis of the response of the structure excited by strong motion signal in time domain. Appropriate accelerogram from earthquake strong motion database is used in time history analyses. Because of the roof geometry not only horizontal components of the seismic acceleration were required, but also the vertical component of the seismic acceleration was needed. Generally, the appropriate accelerogram must have the same frequency content as it is prescribed in EC8 for the soil and for the location of the structure. Inertia forces were calculated from seismic excitation (mass x seismic acceleration) in three directions (x, y, z). Results show that the geometry of the stadium roof had a decisive influence on the dynamics and the vertical displacements (uz) were dominant.

The accelerograms from COSMOS database were applied.

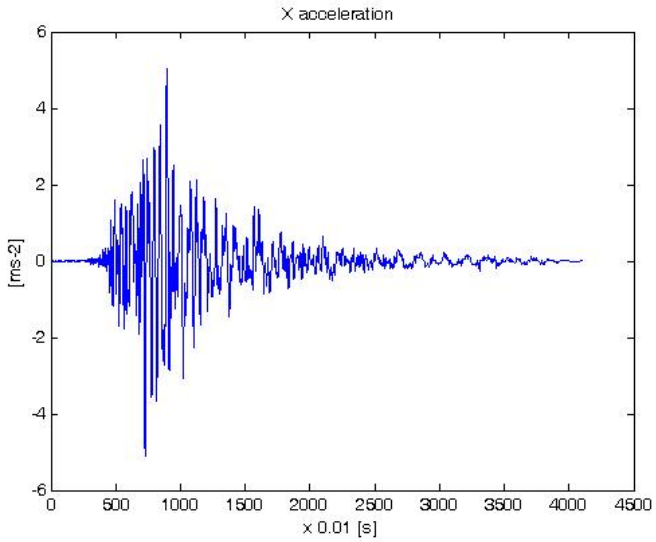


Figure 9: Seismic excitation: X acceleration.

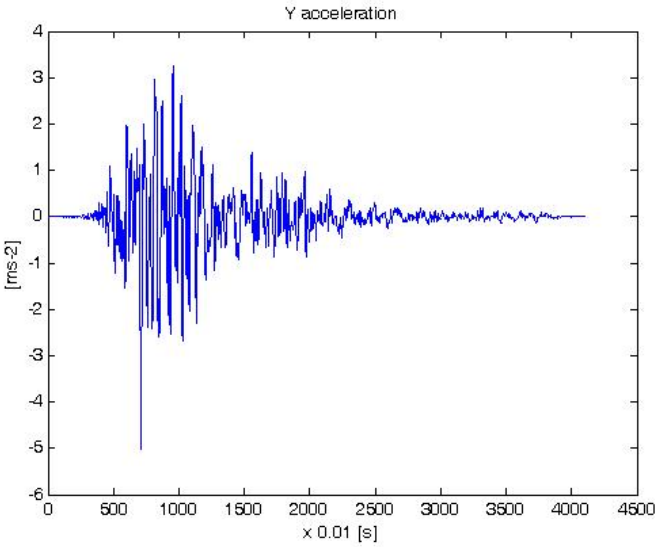


Figure 10: Seismic excitation: Y acceleration.

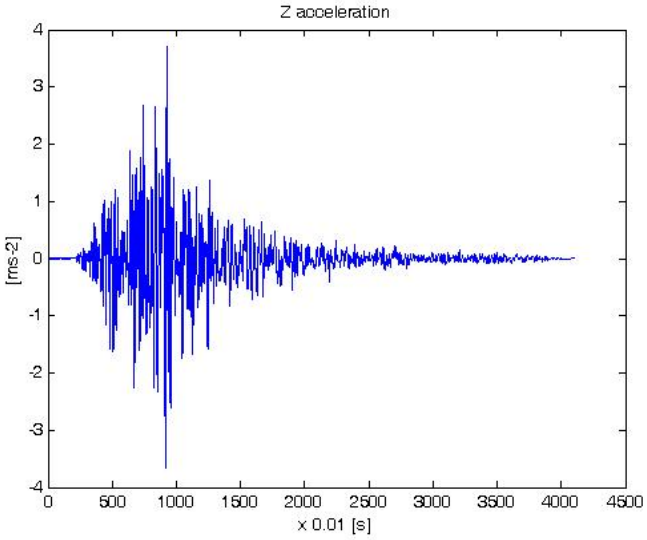


Figure 11: Seismic excitation: Z acceleration.

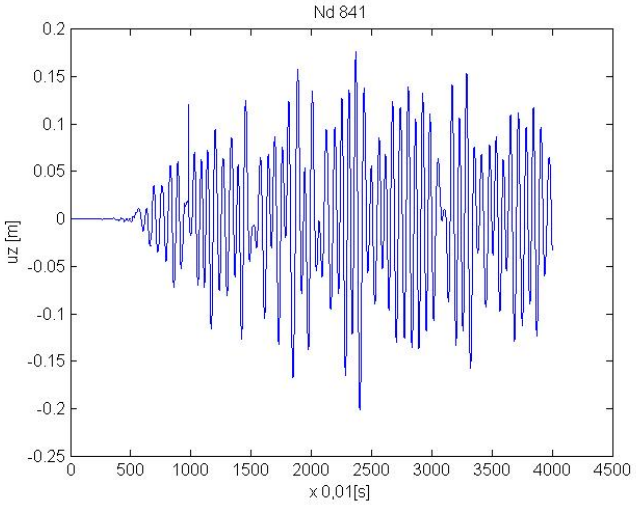


Figure 12: Vertical displacement Nd 841 - major axis.

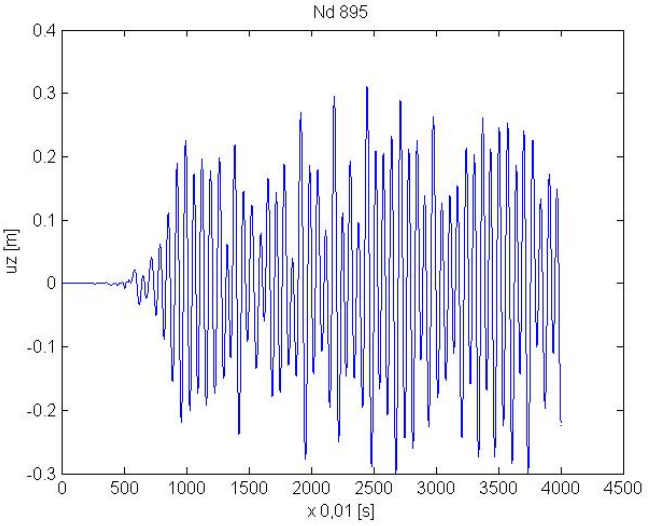


Figure 13: Vertical displacement Nd 895 - minor axis.

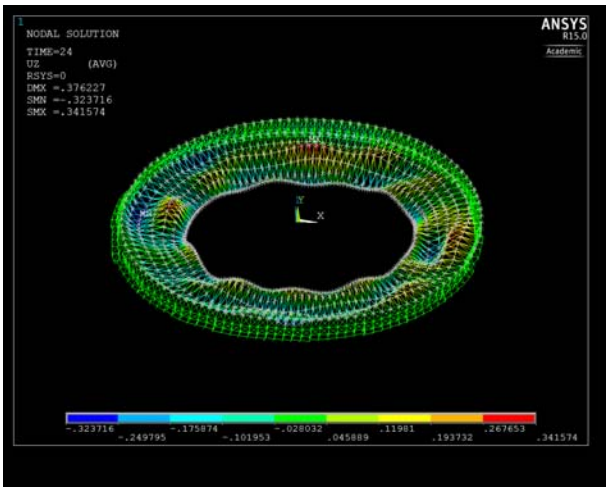


Figure 14: Vertical displacement t = 24s.

4 SUMMARY

Detailed finite element model of Austria largest stadium roof was created. The model was updated on the base of experimental testing. The model was verified using comparison of natural frequencies and modes obtained from numerical analysis and experimental testing. It was shown that the real prestressing in the structure plays an important role. The real prestress in the model was achieved by simulation of the building process. The obtained model was used for seismic analysis in time domain. The 3D excitation was chosen from strong motion database. The results showed the dominancy of vertical displacement according the geometry of the stadium roof.

REFERENCES

[1] VCE (Vienna Consulting Engineers) *Tragsicherheitsbeurteilung des Stadiondaches des Ernst Happel Stadions*, Report, 2011.
[2] Eurocode 8: Design of structures for earthquake resistance, 1998.
[3] A.K. Chopra, Dynamics of structures, 3rd Edition, Prentice Hall, 2007.
[4] http://www.cosmos-eq.org/

COMPDYN 2015
5th ECCOMAS Thematic Conference on
Computational Methods in Structural Dynamics and Earthquake Engineering
M. Papadrakakis, V. Papadopoulos, V. Plevris (eds.)
Crete Island, Greece, 25–27 May 2015

THE USE OF ELASTIC OSCILLATIONS OF DIFFERENT WAVELENGTHS TO EVALUATE THE DYNAMIC PARAMETERS OF BUILDINGS AND STRUCTURES AND ASSESS THE STRENGTH OF MATERIALS OF THE BUILDING CONSTRUCTION

Sergey Savin[1*], **Valerios Tsakalidis**[2]

[1] Professor, Technosphere Safety Department, Saint-Petersburg State University of Architecture and Civil Engineering (SPSUACE),
Saint-Petersburg, Russia
e-mail: savinsn@gmail.com

[2] PhD student, Department of Timber and Plastic Structures, Saint-Petersburg State University of Architecture and Civil Engineering (SPSUACE),
Saint-Petersburg, Russia
e-mail: tsakalidis88@yahoo.com

Keywords: Dynamic parameters, elastic oscillations (vibrations), earthquake resistance, velocity sections, nondestructive testing, compressive strength.

Abstract. *The presented work discusses the potential use of elastic oscillations of different wavelengths to determine the dynamic parameters of the investigated buildings and structures. Furthermore, the use of acoustic methods is examined as nondestructive testing methods to assess the strength and composition of the building construction. Finally, the results of the research are presented, for example, to evaluate the earthquake resistance of buildings, the velocity sections of constructions and soils, as well as the options and measuring systems for research. The presented methods in this work are used in the survey of reinforced concrete, brick and wood structures.*

The monitoring of the building structures state presents on the example of The Naval Cathedral of Saint Nicholas in Kronstadt during the period between 2005 and 2010.

Data on the surface waves velocities is obtained in the soil along the length of the tunnel during the survey behind the subway oblique course linear space.

Data presented on the creation and adaptation of precast concrete structures finite element models with large spans of their actual dynamic parameters. Calculation of carrying capacity using the model is confirmed by the analysis of the initial design decisions of the investigated structures.

The pass-through sensing method is used for the survey, as a rule, of large-scale structures with access to a variety of surfaces, such as foundations of buildings and structures, as well as arrays between underground excavations. The method was also used for cross-borehole sensing.

1 INTRODUCTION

The main objectives of the existing buildings and structures structural design under seismic actions taking into account the survey results are:

- identification of the reserves (or deficit) of the buildings or structures earthquake resistance generally and of its structural elements taking into account the data on their real state which was obtained by results of survey abiding the requirements of the applicable regulatory documents;
- identification of the causes which led to the appearance of building and structural elements' defects and damages, detected in the survey;
- based on the results calculation analysis of earthquake resistance of the buildings or structures, taking into account the survey results to develop proposals for engineering and technical measures that must be performed on an object to restore and maintain its functional stability, as under operational loads and as seismic action at a given intensity, and their design feasibility.

2 DYNAMIC TESTING OF BUILDINGS WITH DIFFERENT STRUCTURAL SYSTEMS EXPOITING THE METHOD OF FREE OSCILLATIONS

The earthquake resistance evaluation requires the use of test methods and means to obtain objective information about the main properties of materials, as well as building and structural elements.

The amount and type of information received by the requirements of the synthesis and identification of the design models.

The initial data for the design models identification uses the following structures and buildings dynamic characteristics, obtained in the free oscillations analysis recorded during the tests:

- Periods and forms of oscillations;
- Logarithmic decrement of oscillations.

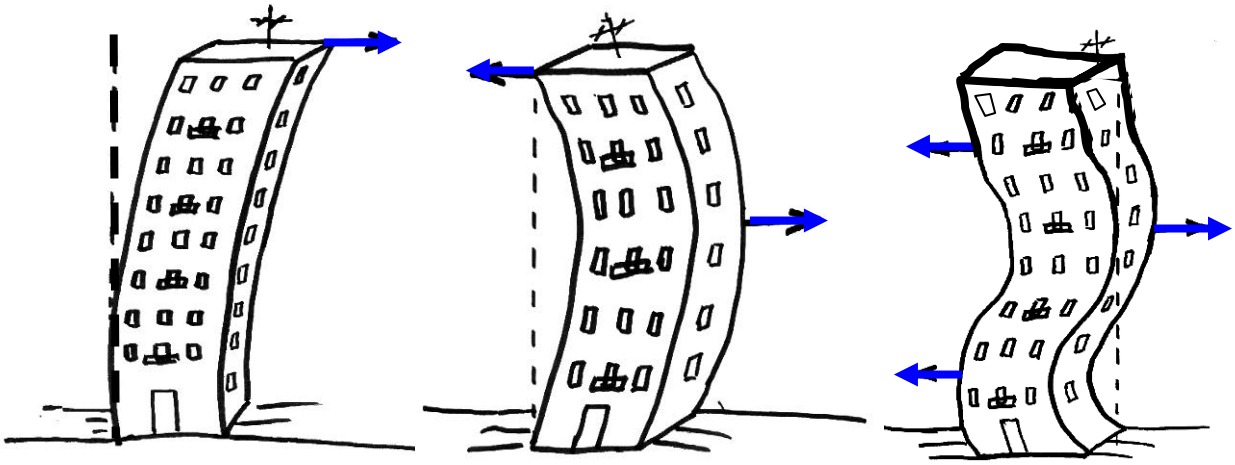
The main free oscillations forms of buildings and structures are presented in figure 1.

For buildings with complex structural system with unevenly distributed weight or stiffness characteristics can exist at different frequencies of higher tones which bending With oscillations height, and sometimes of the first tone, for different parts of the building. In this case, for these forms of oscillations build also diagrams along the length of the building.

In this case the foundation of the building may remain stationary or to some extent involve in oscillations.

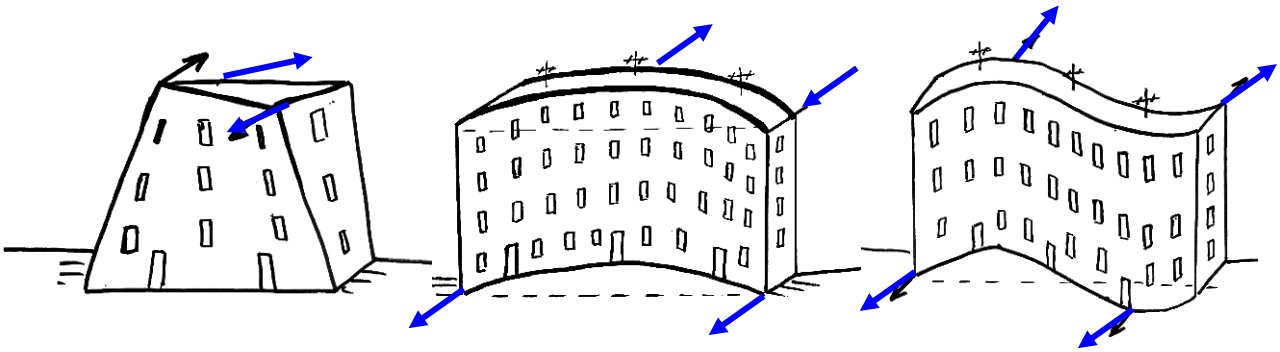
Method of the construction dynamic characteristics' determination according to their free oscillations [1-2] excited by shock impulse load, includes the following steps:

- excitation and recording of oscillations;
- calculation of their Fourier spectra;
- analysis of the Fourier spectra aiming to allocate the resonance peaks corresponding to the various forms of free oscillations;
- obtain the allocated resonance peaks impulse implementation for each form of free oscillations performing the inverse Fourier transform;
- diagram creation of various forms of free oscillations.



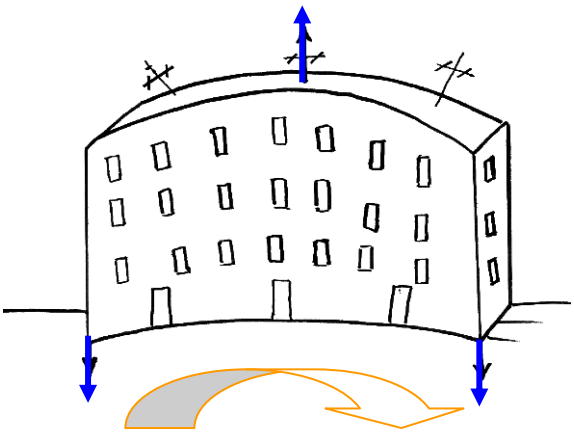
First form building oscillation *Second form building oscillation* *Third form building oscillation*

1a. Bending oscillation about the vertical axis of the building



Building torsional oscillation *Building second form torsional oscillation* *Building third form torsional oscillation*

1b. Bending oscillation about the horizontal axis of the building



1c. Bending oscillation on soil foundation

Figure 1. Main forms of oscillations of rectangular buildings

To register oscillations recommend the use of equipment, technical characteristics of which is given in Table 1.

№	Name	Technical Characteristics
1.	Accelerometer	Sensitivity 300 mV / m / s^2, frequency range 1-300 Hz.
2.	Accelerometer	Sensitivity 10 mV / m / s^2, resonant frequency 15 kHz.
3.	Amplifier	Measurement modes: acceleration, velocity, displacement; amplification from 1 to 10000 with a step increments of 10 dB; frequency range from 1 Hz to 20 kHz; number of measuring channels not less than 8; power supply 220 V or direct current battery.
4.	Analog to digital converter, ADC	Number of channels – not less than 8, resolution – not less than 12 bits, ranges of measured signals – ± 5.12 V, 2.56 V, 1.024 V, conversion maximum frequency – 300 kHz /channel.
5.	Personal Computer, PC	Must be equipped with the measurement information input and processing software. Parallel port availability.
6	Mean for excitation of oscillations, container filled with bulk material, tamper, hammer	Container (sack) weight up to 50 kg, equipped with cushion liner ; Tamper weight up to 12 kg, equipped with cushion liner; Hummer weight up to 2 kg, equipped with cushion liner and threaded hole for fixing an accelerometer

Table 1. Technical characteristics of equipment included in the measurement system

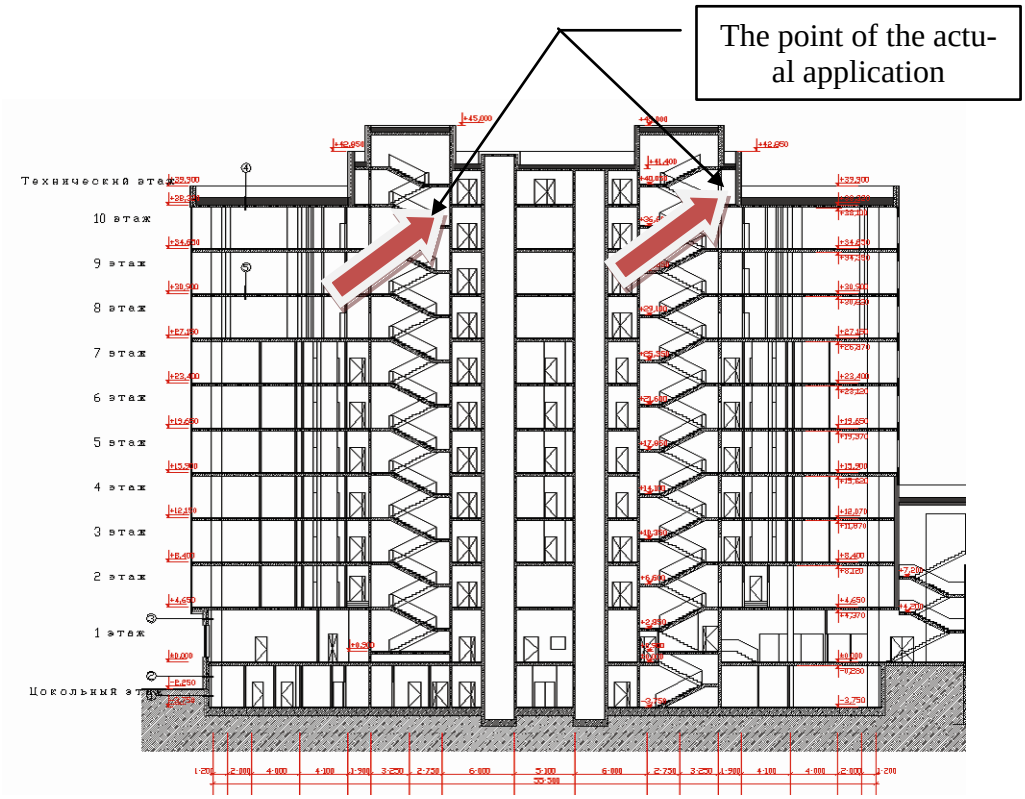
To improve the frequency detection accuracy and for diagram generation of higher forms oscillations from initial implementations which recorded under applied load at different points, use the ***superposition principle***.

The use the superposition principle applied to the impulse method of free oscillations building construction excitation lies in:

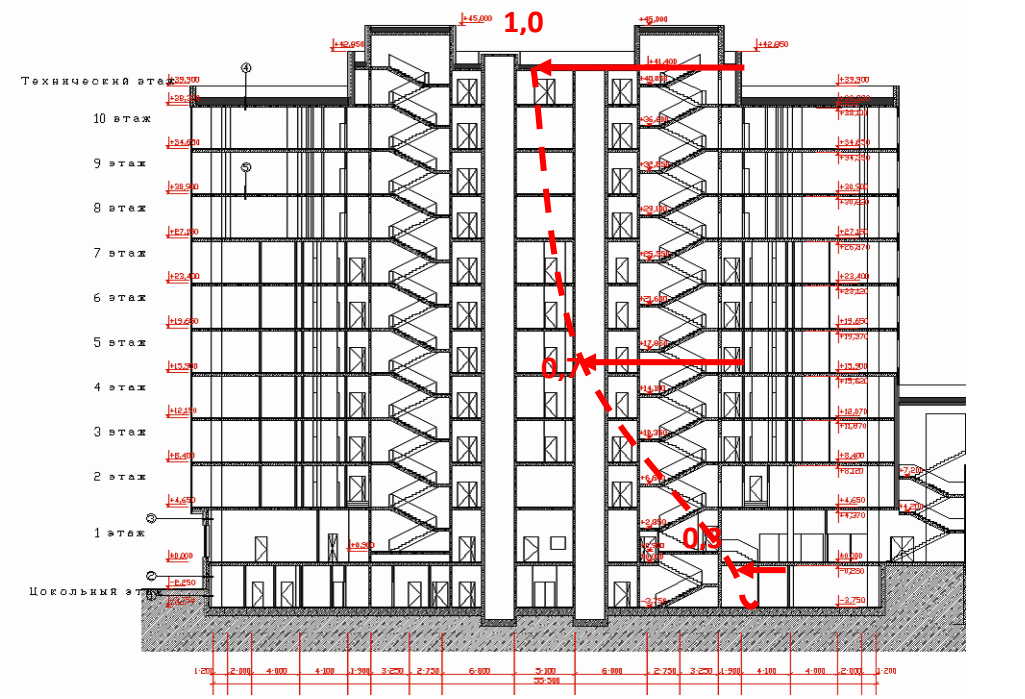
- excitation and recording of oscillations under action of impulse point load application at different points of the structure;
- addition (taking into account the action of the load) of oscillations recorded under applied load at different points of the structure (simulating the simultaneous application of the load in several points).

Processing of the obtained oscillations from the result of addition ***(combined implementations)*** in order to determine the resonance peaks corresponding to the analysed forms of oscillations is performed for each measurement point by adding or subtracting implementations obtained by separate crashes. The inclusion of the implementation in the combination with minus sign means that by the preparation of the combination modelled the action in the opposite direction. Implementations included in the combination, and the corresponding sign are selected in such a way as to amplify the oscillations in the direction of the applied load.

The following are examples of creating combined implementations for the horizontal alignment measurements according to the scheme of sensors arrangement (figure 2).



2a. Scheme of load application



2b. Scheme of sensors arrangement and form of oscillations

Figure 2. Creating combined implementations for the horizontal alignment measurements

The obtained combined implementation treated the same way as any initial implementation. Diagrams of torsional oscillations and bending oscillations along the front of the building showed in figure 3 and 4, respectively.

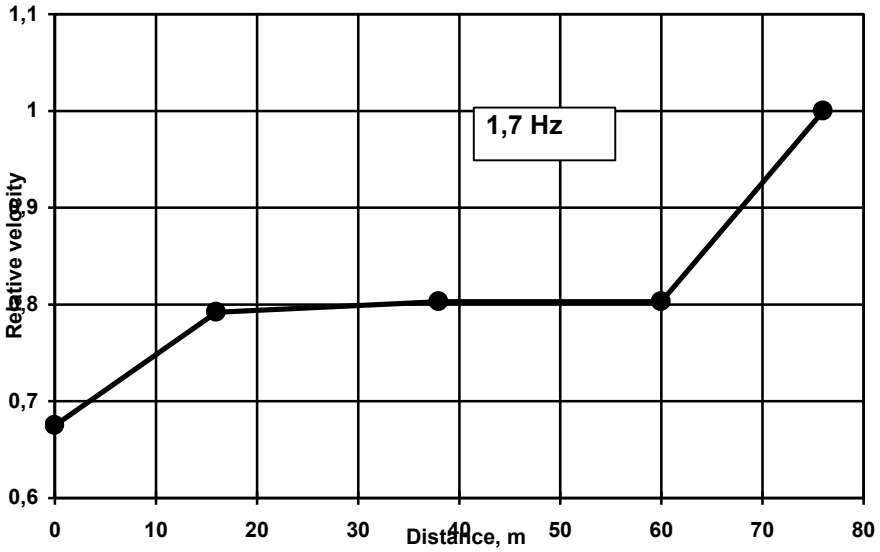


Figure 3. The diagram of oscillations (horizontal alignment, transverse direction, first tone)

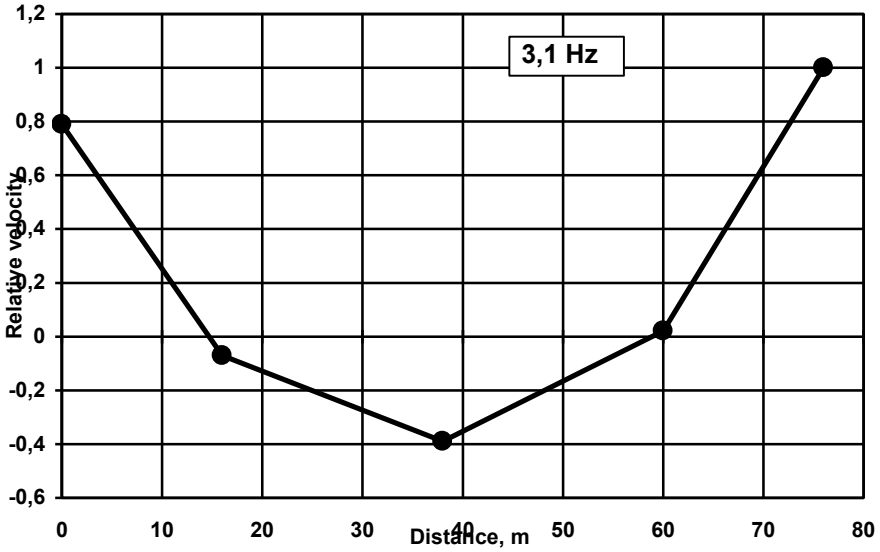


Figure 4. Diagrams of oscillations (horizontal alignment, bending along the front, first tone)

3 MATERIALS INTEGRATED CHARACTERISTICS EVALUATION WITH THE USE OF ELASTIC WAVES

For the evaluation of physic-mechanical material characteristics, the surface elastic waves method use is recommended.

The method of using elastic wave of acoustic frequency range [2] is intended to assess the state of materials of plane multilayer structures, which allow the installation of the measuring sensor on one of the surfaces. The length of the available structure surface for the surveys must be at least three depths of its sensing.

The material characteristics evaluation is executed in three stages:
- At the first stage the building construction surface reaction on the shock impulse action is determined;
- At the second stage the multilayer structures' reaction is theoretically modelled on the shock impulse action;
- At the third stage the measurement processing and results modelling as well as the comparative analysis of experimental and calculated dispersion curves (dependence of wave velocity on its length) of the surface waves and the adaptation of the acoustic model parameters to match criteria of the dispersion curves using the iteration method is performed.

By correlational dependence between the structure's material acoustic characteristics (usually the velocity of longitudinal waves) and its strength the actual strength characteristics of the structure materials and their compliance with the design values are assessed.

3.1 First stage – the surface waves measurement

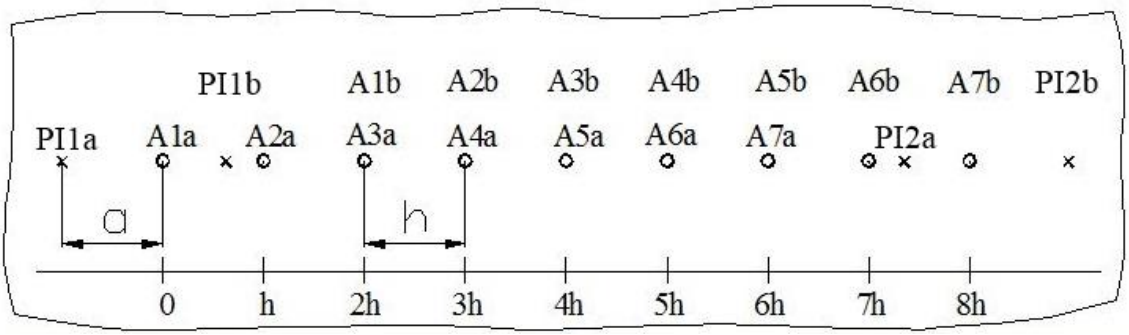
Building structure material acoustic characteristics are determined by oscillations, initiated by shock impulse load which is applied to the structure surface.

For the surface waves the velocity of spread at different wavelengths as well as the damping intensity and the presence of reflections are determined.

The absolute values of the elastic characteristics of the building construction material (elastic or shear modulus) or its different layers (for multilayer structures) are determined using the velocities values of longitudinal or transverse waves for the theoretical model, provided that the maximum coincidence is actually received and calculated dispersion curves of surface waves.

The strength of the structure's material or its individual layers is determined by the correlational dependence between the strength and velocity of longitudinal waves spread in it.

Typical measurement scheme is shown in figure 5.



A1-A7 – the points of installation of accelerometers
PI1, PI2 – the points of load application

Figure 5. The scheme of the surface wave measurements of the velocity in the structure

For generating the dispersion curves separate measuring rays are selected in different parts across structure surface and to build velocity hodograph measuring alignments are selected formed by several measurement rays (arrangement with the letters «a» and «b» in figure 5). In this case measuring rays are arranged in a straight line and shifted relative to each other along the measuring alignment by constant step.

The accelerometers installation locations surface is prepared for the installation of the sensors by cleaning the dust, loose paint, etc., if necessary, dried and coated with a thin layer of plasticine or special mastics.

The measuring layout represents a series connection of transducers (accelerometers), amplifiers, multi-channel analog-to-digital converter (ADC) and a personal computer (PC). One of the measuring channels is allocated to accelerometers installed on the shock loads to measure application moment and impulse value of shock load, and on structure surface.

To excite oscillations tamper (hammer) is prepared, on which the piezoaccelerometer is fitted. The duration of the shock impulse is regulated by cushion liner, which fixed to tamper.

Tamper is a wooden beam weighting of 10-12 kg, one of its end has hemispherical shape or is equipped with an elastic material spherical tip. The accelerometer for measuring the load is fitted to the second end of tamper. For excitation of low-frequency waves it is recommended to use a heavier tamper with soft tip (porolon, cellular rubber).

3.2 Second stage – the mathematical modeling

For cases where the investigated structure can be considered as a homogeneous half-space or homogeneous plate, the acoustic characteristics of the structure material are defined as follows:

- the surface wave velocity for the half-space is equal to the velocity of Rayleigh waves;
- the dispersion curve of the surface (bending) waves in the plate at a predetermined velocity of the Rayleigh wave in its material V_R and thickness of the plate is built by solving the analytical equation of the form:

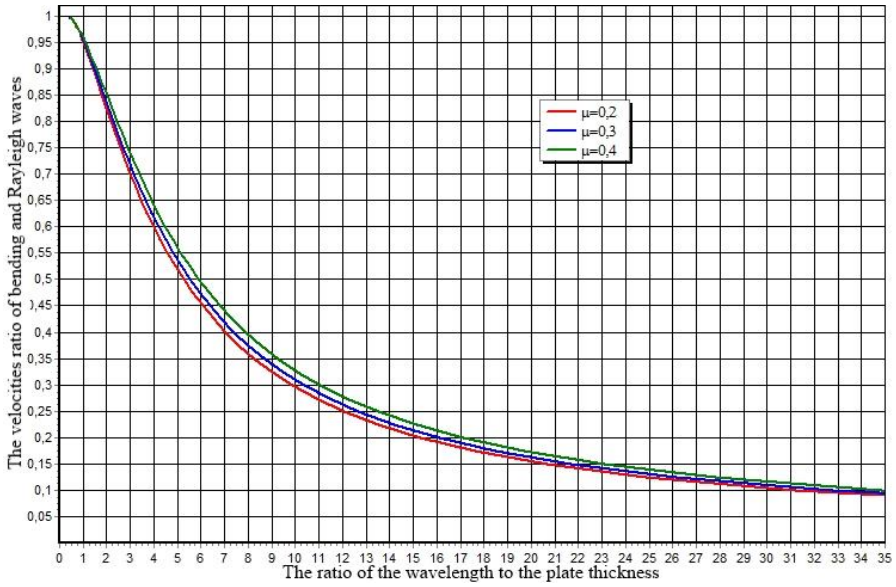
$$\frac{\sqrt{1-\frac{V_u^2(0.87+1.12\mu)^2}{V_R^2(1+\mu)^2}}\sqrt{1-\frac{V_u^2(0.87+1.12\mu)^2(1-2\mu)}{2V_R^2(1+\mu)^2(1-\mu)}}}{\left(1-\frac{V_u^2(0.87+1.12\mu)^2}{2V_R^2(1+\mu)^2}\right)^2} = \frac{th\left(\frac{H}{\lambda}\cdot\pi\sqrt{1-\frac{V_u^2(0.87+1.12\mu)^2(1-2\mu)}{2V_R^2(1+\mu)^2(1-\mu)}}\right)}{th\left(\frac{H}{\lambda}\cdot\pi\sqrt{1-\frac{V_u^2(0.87+1.12\mu)^2}{V_R^2(1+\mu)^2}}\right)} \quad (1)$$

where: H – thickness of the plate;
λ – bending wavelength;
μ – Poisson ratio;
V_u – phase velocity of the bending waves.

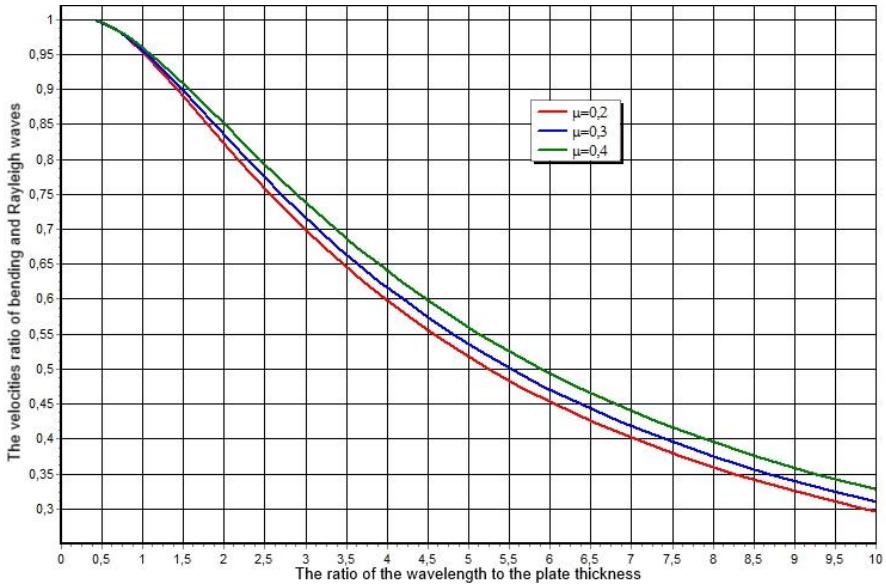
Mathematical modeling of multilayer structure reaction on the shock impulse action is based on the integration of the equations system with using numerical methods in the plane statement.

The transcendental equation solution results using the iteration method yielded text files containing the value λ / H in first column, in second - – V_U / V_R for values of Poisson's ratio of

0.1 to 0.5 through 0,1, which are used for the theoretical calculation of the dispersion curves for given values V_R, H и μ. Dispersion curves diagrams of homogeneous plate for different values of Poisson's ratio shown figure 6 (a – section λ / H from 0 to 30, b – to 10).



6a



6b

Figure 6. Graphics of dispersion curves for different values of Poisson's ratio

3.3 Third stage – the processing of tests measurement

The initial realisations of wave processes are divided into monochromatic beams with a group of band-pass filters. For the selected monochromatic wave beams the time of wave spread successively for all measurement points are determined. The time is determined by the wave peaks or by intersection of the oscillations curve with the zero line.

For each monochromatic wave beam spread time instance ***the phase velocity of the wave spread*** (equation 2) and ***the length of its wave*** (equation 3) are determined:

$$V = L/t, \ (m/sec) \tag{2}$$

where: L – the length of the interval between the measuring points, on which the velocity is determined, m;
t – run time of the surface wave on this interval, sec.

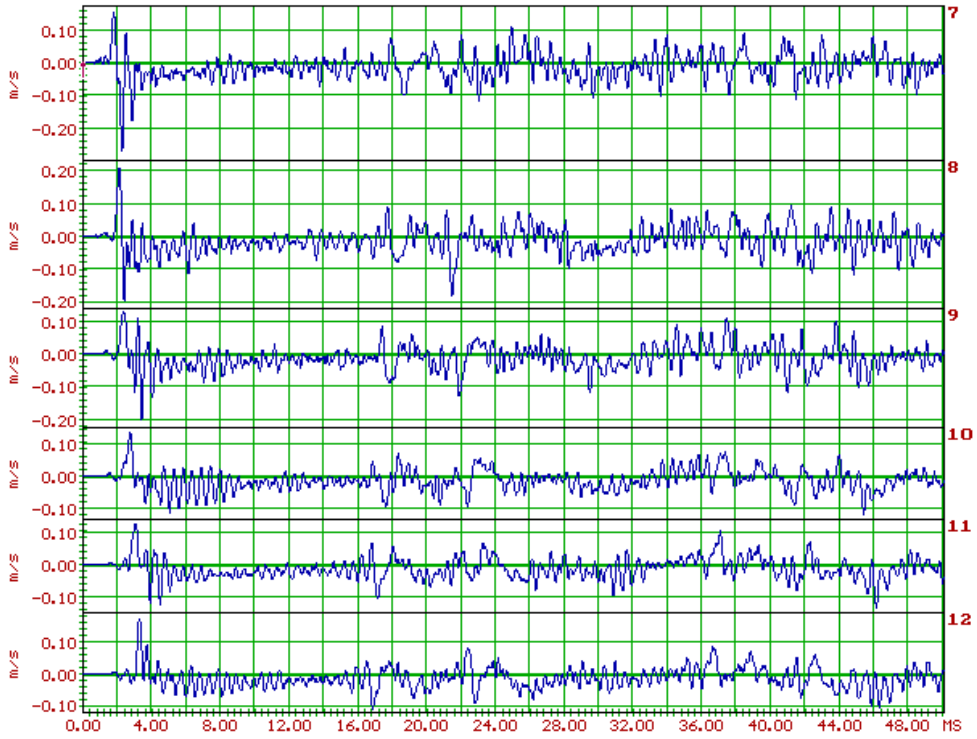
$$\lambda = T \bullet V, \ (m) \tag{3}$$

where: T – period of oscillations in the beam of monochromatic waves, sec.

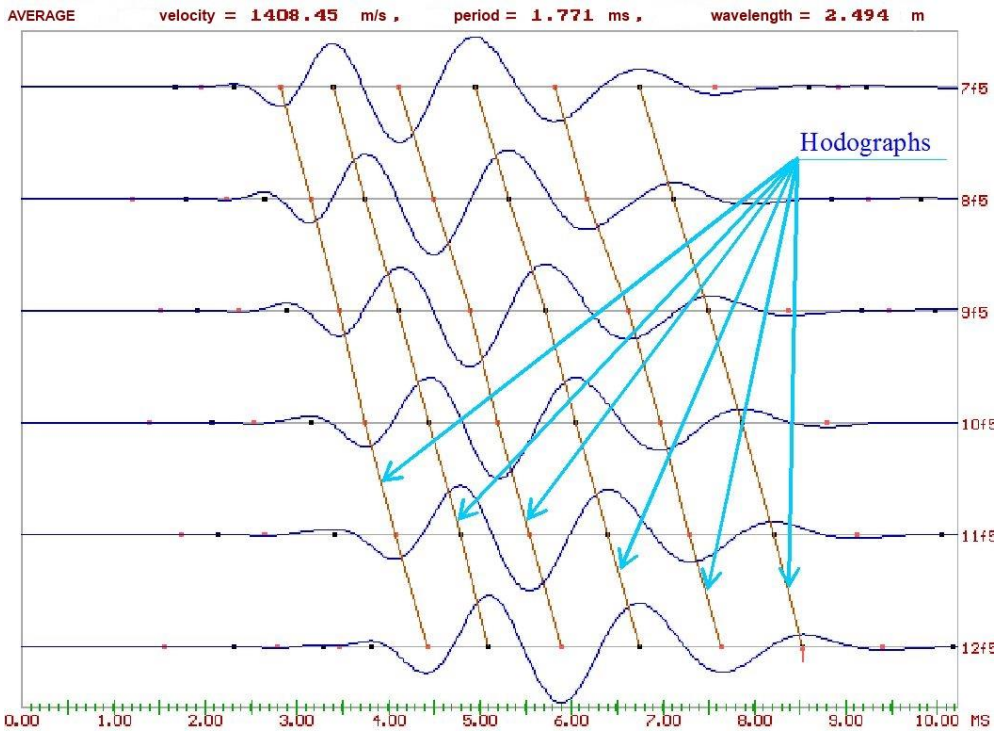
For the dispersion curves generation along the section of the measuring ray by length not less than 4 steps accelerometers placement, each monochromatic beam of wave are processed to yield several instances of wave run time from the beginning to the end of the section. Then, in each case the velocity and the wavelength is calculated. Thus the obtained data "speed - wavelength" is filtered to obtain a smooth dispersion curve.

The velocity section along the length of the measuring alignment is determined by the average run time of the distance between each pair of measurement points in the measurement ray for all placements in both directions of wave spread, which enables the calculation of the wave velocity and its length. The entire range of obtained wavelengths is divided into 2-3 sections where the average velocity of the wave is calculated and the produced graph of wave velocity changes along the length of the alignment.

Figure 7 shows an example of the initial implementation and the selected beam of monochromatic waves with applied lines of wave run time hodograph.



7a



7b

Figure 7. Example of the initial implementation (a) and of selected monochromatic wave beam (b)

Manipulation results of wave processes of structural response by shock impulse action used to determine the acoustic characteristics of building construction materials by comparing the dispersion curves of surface waves, which obtained from the experimental and calculated theoretical responses to the shock impulse action.

The parameters (geometrical and acoustic) of multilayer building construction model selected by the iteration method and taking into account the results of the survey by other methods to achieve the best agreement between the theoretical and the experimental dispersion curves.

Elastic characteristics of the building structure materials are determined by the acoustic characteristics of its different layers obtained in the mathematical model as a result of its adaptation taking into account information about the properties of the structure material (density, Poisson's ratio, etc.) by the equations:

$$\mathbf{V_S} = \mathbf{V_R} \cdot \frac{\mu_d + 1}{0.87 + 1.12 \cdot \mu_d} \tag{4}$$

$$\mathbf{V_P} = \mathbf{V_S} \cdot \sqrt{\frac{2 \cdot \left(1 - \mu_d\right)}{1 - 2 \cdot \mu_d}} = \mathbf{V_R} \cdot \sqrt{\frac{2\left(1 - \mu_d\right)}{1 - 2\mu_d}} \cdot \frac{\mu_d + 1}{0.87 + 1.12\mu_d} \tag{5}$$

$$\mathbf{E_d} = \rho \cdot \mathbf{V_P^2} \cdot \frac{\left(1 + \mu_d\right) \cdot \left(1 - 2\mu_d\right)}{1 - \mu_d} \tag{6}$$

$$\mathbf{G_d} = \rho \cdot \mathbf{V_S^2} = \rho \mathbf{V_P} \sqrt{\frac{1-2\mu_d}{2\left(1-\mu_d\right)}} \tag{7}$$

where: V_S, V_R , V_P – the velocities of transverse, Rayleigh and longitudinal waves, m/sec;
E_d – elastic modulus of material, Pa;
G_d – shear modulus of material, Pa;
ρ – density of the concrete, kg/m^3;
μ_d – dynamic Poisson's ratio.

The strength of the structure material is determined by correlational dependence among the strength of the material and velocity spread of longitudinal elastic waves in it.

According to the test results using surface waves it is recommended to use the following data:

- the surface wave velocity hodograph of different types;
- the dispersion curves of waves on the most characteristic measuring rays;
- the main acoustic characteristics of the structure material:
  - the velocity of longitudinal and transverse waves in different sections of the structure surface;
  - respective to them elastic and shear modulus of the material;
  - the strength of the structure material in different sections of its surface.

To determine the concrete strength is recommended to use the calibration curve which shown in figure 8, and to determine the strength of brick masonry use data of Table 2 from [1].

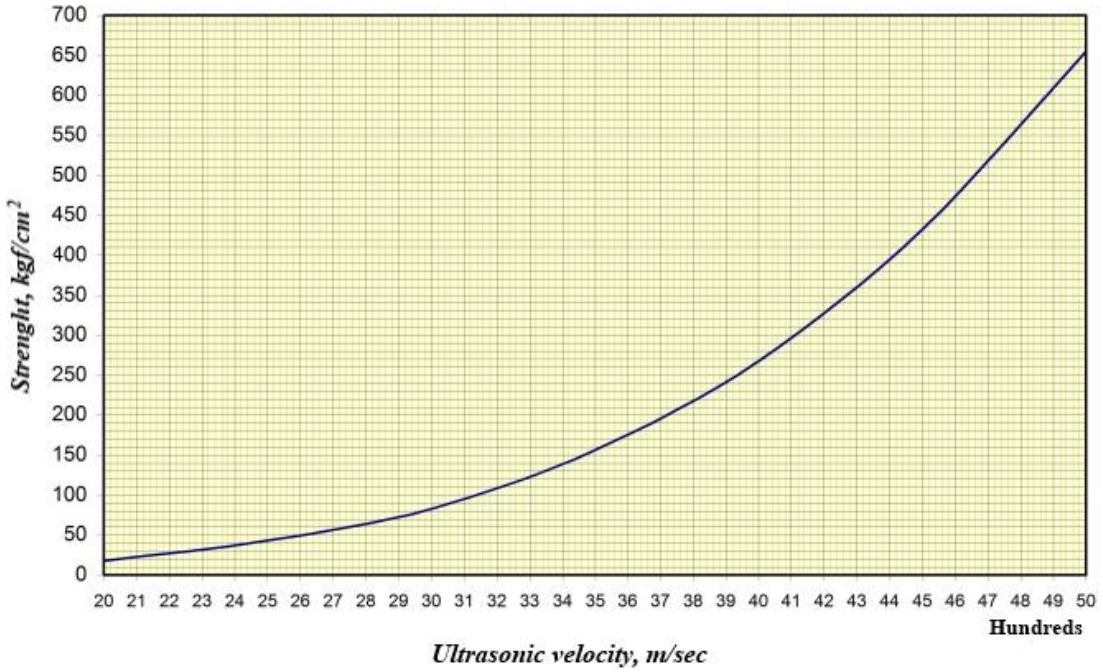


Figure 8. The calibration curve to evaluate the concrete strength

Characteristics of masonry	Rn, MPa	Vp, m/sec
High strength	4 ÷ 4.5	> 3000
Strength	3 ÷ 4	2000 ÷ 3000
Reduced strength	2 ÷ 3	1500 ÷ 2000
Low strength	1.5 ÷ 2	1000 ÷ 1500
Weak strength	1 ÷ 1.5	500 ÷ 1000
Very weak strength	0.5 ÷ 1	~ 500

$\boldsymbol{R_n}$ - the normative masonry compressive strength;
$\boldsymbol{V_p}$ - the longitudinal wave velocity of seismic-acoustic frequency range.

Table 2. Qualitative classification of brick masonry strength by velocity of seismic-acoustic range

For rigid cement masonry the given in the table Rm values, are multiplied by a factor 0,85.

4 DEFECTIVE AREAS DETECTION IN BUILDING CONSTRUCTION MATERIAL USING THE METHOD OF ENSOUNDING

For the defective areas detection in building construction material the use of ***method of ensounding*** is recommended, which is based on measuring of the acoustic waves spread velocity in the material: longitudinal or transverse. Determination of these velocities values in different points of the structure allows to reveal the defective areas and to evaluate the elastic characteristics of structure.

For the wave spread velocity field generation in the building construction the ***tomographic measurement results processing*** of wave run time between its sources and receivers is used.

For the structure's velocity section a ***database*** is determined, which represents a group of tables containing source and receiver of wave coordinates and wave run time between them.

The excitation and detection of longitudinal and transverse elastic waves can be performed using any means allowing a reasonable precision to fix run time of wave:

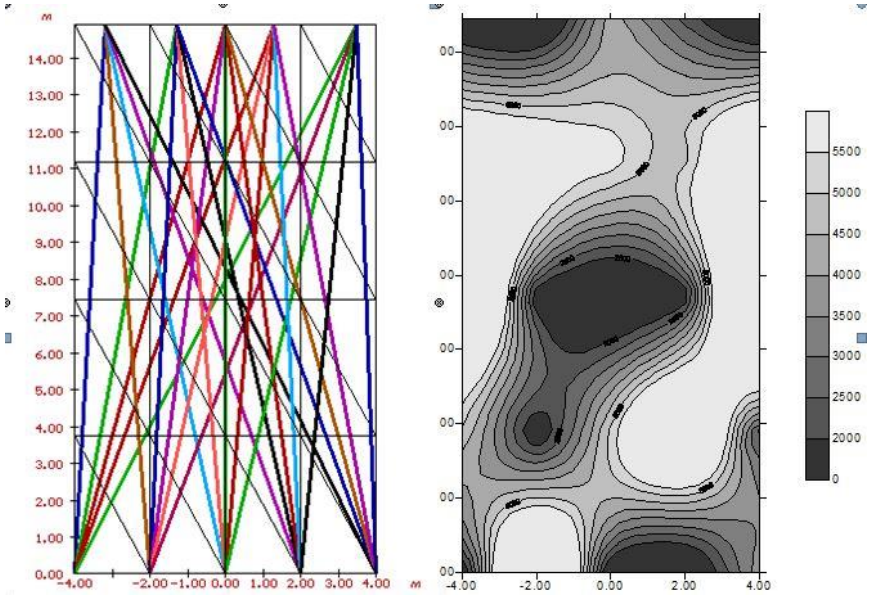
- source should provide a short wave front (up to 1 msec);
- receivers (sensors) must be wideband (1 - 3000 Hz) to measure this wave without dynamic distortion.

Algorithm for calculating the velocity sections of structure is recommended to organize as follows:

- introduce the table of wave run times between all sources and receivers;
- introduce the initial model of structure in the form of layered medium: the relative thicknesses of the layers, the relative velocity at the boundaries of the layers and inclination angle of the layers plane to the coordinate axes, in this case the velocity along the left edge of the first layer V_o is taken equal to 1;
- calculate the run times of waves on all the specified rays for a given structure model at the wave velocity equal to the specified relative velocities;
- calculate the velocity Vo as the ratio of sum run time of wave on all rays;
- calculate the mean square deviation of the experimental and calculated run times of waves;
- calculate the velocity section of structure determined by iteration method, in which the mean square deviation of the experimental and run times of the wave reaches minimum value;

- for ***"optimal velocity section"*** calculate the absolute values of the velocities at the layer boundaries and build the graph in the coordinates "distance (along the axis perpendicular to the plane of the layers) - the velocity of wave spread ";
- calculate the ray paths and build situational plan, on which the ray paths and isolines of wave spread velocity are applied.

Figures 9 and 10 show an example of generation the structure velocity section made of concrete and brick masonry.



9a 9b

Figure 9. The measurement ray paths (a) and velocity section (b) of concrete column

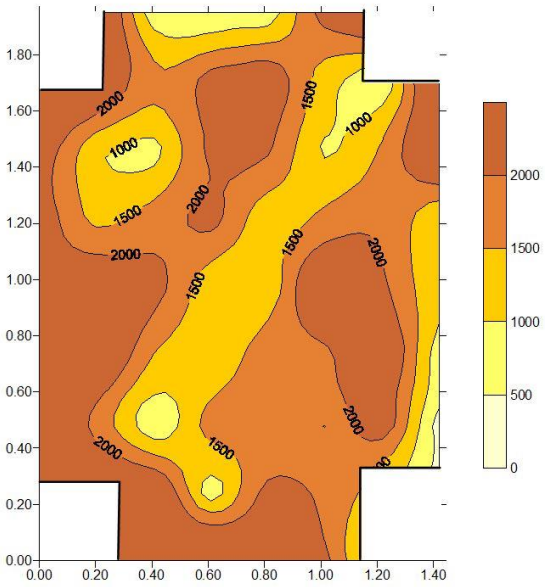


Figure10. The results of tomographic processing data of brick column by through ensounding

5 CONCLUSIONS

The presented methods above of nondestructive testing based on the use of free oscillations of buildings and building construction, as well waves of the acoustic frequency range initial data needed to determine the earthquake resistance and evaluation of technical condition of existing buildings and structures.

The results obtained during long-term practical research allow to recommend these methods to:

- evaluate the actual earthquake resistance of buildings and structures;
- determine of integral strength characteristics of building structures materials;
- evaluate the multilayer structures materials including the one-way access to its surface;
- evaluate the "structural strength" of building structure elements.

The proposed approach has been repeatedly used for mass surveys and certification of buildings and structure, monitoring the technical condition of particularly important objects, for research and practical purposes.

REFERENCES

[1] Savin, S.N., I.V. Sitnikov, A.F. Shnitkovskij and V.A. Zarenkov, 2001. “On evaluation of safety of engineering units of buildings and structures”. Proceedings of 6 International conference on environment and development in Northwest Russia. Saint Petersburg, RU, pp: 261-265.

[2] Aleshin, N.A., 1982. “Electroseismoacoustic methods of structural survey”. Moscow, RU: Strojizdat, pp: 158.

COMPDYN 2015
5th ECCOMAS Thematic Conference on
Computational Methods in Structural Dynamics and Earthquake Engineering
M. Papadrakakis, V. Papadopoulos, V. Plevris (eds.)
Crete Island, Greece, 25–27 May 2015

SEISMIC PERFORMANCE OF HIGH-RISE STEEL MRFs WITH OUTRIGGER AND BELT TRUSSES THROUGH NONLINEAR DYNAMIC FE SIMULATIONS

Emanuele Brunesi[1], Roberto Nascimbene[1], Gian Andrea Rassati[2], Lorenzo Casagrande[3]

[1] EUCENTRE, European Centre for Training and Research in Earthquake Engineering
Via Ferrata 1, 27100 Pavia, Italy
{emanuele.brunesi, roberto.nascimbene}@eucentre.it

[2] Dept. of Civil and Architectural Engineering, University of Cincinnati
765 Baldwin Hall, Cincinnati, OH 45221-0071 USA
Gian.Rassati@uc.edu

[3] EUCENTRE, European Centre for Training and Research in Earthquake Engineering
Via Ferrata 1, 27100 Pavia, Italy
lorenzo.casagrande01@gmail.com

Keywords: high-rise buildings; steel MRFs; outrigger; belt trusses; FE models; nonlinear dynamic analysis.

Abstract. *The work reported herein summarizes the results of a series of nonlinear dynamic FE analyses devoted to assess the main criticalities in the seismic response of high-rise steel MRFs with outrigger and belt trusses. Thirty- and sixty-storey planar frames, extracted from reference three-dimensional structures composed of an internal one-way braced core, are designed in accordance with European rules. The core consists of a CBF system, while outriggers are placed every fifteen stories to limit inter-storey drifts and second order effects. FE models able to account for material and geometric nonlinearities have been developed within an open source FE code, using inelastic force-based fiber elements to model structural members and equivalent nonlinear links to reproduce the behaviour of bolted beam-column joints and welded gusset-plate connections. Out-of-plane imperfections are explicitly included in the braces to allow for potential buckling mechanisms in both braces and gusset plates. NLTHAs have been performed, in comparison with response spectrum analysis, aiming to quantify the potential of such systems, when included in the lateral-force resisting system of modern high-rise steel MRFs. Global and local performance have been investigated in terms of inter-storey drift and acceleration peak profiles and axial force-displacement curves and static-to-seismic load ratios in critical braces at different floor levels. Sensitivity to the structure height has been explored by comparing the response of the two prototype MRFs. Trends are discussed to show that, if accurately designed and detailed, these structural systems provide an optimum combination of stiffness and strength.*

1 INTRODUCTION

Super-tall buildings have become increasingly popular and have large impact on economy and society [1-3]. Such buildings have a complicated structural system consisting of hundreds of different components, including those with complex features and large dimensions. When compared to medium- and low-rise buildings, tall moment resisting frame (MRF) structural systems present several distinctive characteristics in their behavior and peculiar aspects in their design, such as long periods and higher mode effects [1-11]. To ensure safe and economic design, construction and operation under various extreme loading conditions in particular earthquake events, detailed studies are required to predict their response, being the majority of current seismic Standards often unsuitable for them [12-14]. Scaled shaking table tests [15, 16] are at the moment promising analysis techniques for research applications but they are not so easily applicable for design office use. Therefore, high-definition or simplified finite element (FE) idealizations still represent an attractive tool to explore the seismic performance of these complex structural systems, as proposed by a number of research efforts available in literature on that subject [1-11]. If early studies [5-11] introduced simplifications in either FE representation or analysis technique, significant improvements have been more recently achieved [1-4].

In light of this scenario, the present paper details a modeling procedure for large scale nonlinear dynamic simulation of mega-frame systems composed of a concentrically braced frame (CBF) core and belt trusses which are combined to resist vertical and earthquake-induced lateral loads. First, two reference prototypes, the geometric characteristics of which are summarized in the following, have been designed according to current European prescriptions [17], using response spectrum analysis (RSA), and then fiber-based models have been prepared to examine their nonlinear dynamic response using a set of natural ground motions scaled to obtain displacement spectrum compatibility in accordance with EC8 requirements [18, 19].

Hence, global inter-storey drift and acceleration peak profiles, as well as shear and bending moment demands, are collected and their average is compared with the results determined by RSA to highlight design criticalities in current seismic Code provisions [17]. Finally, the local response of these two case-study buildings is discussed in terms of hysteretic behaviour of the braces and peak compressive loads experienced by the outriggers during nonlinear time history analyses (NLTHAs).

2 NONLINEAR DYNAMIC FE ANALYSES

Even though detailed brick- or shell-based FE models, commonly used in seismic analysis of steel and reinforced concrete structural systems and components [20-27], give more insight than equivalent mechanical idealizations, being able to reproduce their local response in terms of stress/strain concentrations, the computational time increases tremendously, requiring necessarily to take advantage of parallel processing on multiprocessor computers. Additionally, a detailed approach is currently almost unfeasible if the response of an entire mega-frame system has to be investigated. By contrast, the complex contribution of bolted [22-25, 28-30] and welded [20, 21, 31, 32] joints can be easily incorporated into classical fiber-based FE models, able to represent the interaction among connection components in an equivalent manner. Thus, mechanical representations have been assumed in this research to include global response and potential failure mechanisms of these systems, as discussed later on. In particular, the prevailing assumptions concerning modeling approach and simulation techniques will be given in the following, after a brief description of the main geometric characteristics and mechanical properties of the thirty- and sixty-storey planar frames examined here. Finally, details of the seismic input selected to perform the series of NLTHAs and RSAs shown in the following section will be provided.

2.1 Description of case-study super-tall buildings

The two prototype thirty- and sixty-storey MRF buildings investigated in this work, namely HR-01 and HR-02, were extracted from reference three-dimensional structures designed for high seismicity (i.e. PGA = 0.40g) in accordance with the current European seismic code [17]. Soil class C (180 m/s < V_s < 360 m/s) was assumed to perform the design by a series of RSAs on three-dimensional models, including vertical seismic component, second order effects and accidental eccentricity of the seismic masses. As depicted in Fig. 1, where a schematic of plan and elevation is provided, the lateral-force resisting system (LFRS) of each high-rise building consisted of an internal one-way CBF core, with outriggers placed every fifteen stories to limit inter-storey drifts and second order effects.

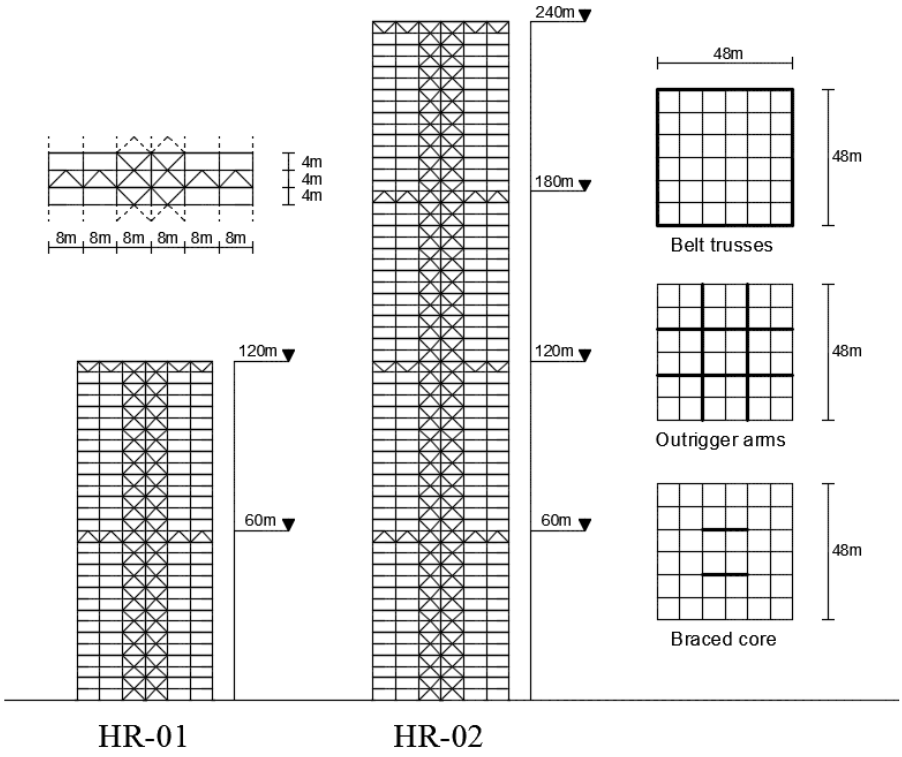


Figure 1: Geometric characteristics of the reference 30- and 60-storey planar frames studied.

The two structural layouts analyzed in this study consisted of a 6x6-bay building; the beam span for all bays was set at 8 m both for transversal and longitudinal direction, while the columns were assumed to have a constant inter-storey height of 4 m, thus implying a total building height of 120 m and 240 m for HR-01 and HR-02, respectively. Dead and live loads were assumed to be 2 kN/m^2 and 4 kN/m^2, respectively. Table 1 summarizes member sizes and mechanical properties adopted for beams, outriggers, columns and braces at different floor levels, while Fig. 2 shows an example of welded gusset-plate and bolted beam-to-column connection systems used to detail the joints of the two structures.

In detail, IPE400 beams were used at all floors for both prototypes, while HD 400x634 and HD 400x1200 tapered profiles were used for the first five columns of HR-01 and HR-02, respectively. Similarly, HD 400x314 profiles were assumed as the outriggers of both structures, while HSS 300x20 and HSS 400x20 braces were chosen in the first five stories for HR-01 and HR-02, respectively. Both brace and column sizes were assumed to decrease along the height of the structure, as presented in Table 1. According to [33], steel grade S-275, S450 and S700 were used for beams, columns and braces, respectively.

	30-storey frames			*60-storey frames*		
	Floor	*Profile*	*Grade*	*Floor*	*Profile*	*Grade*
Columns	1-5	HD 400x634	S450	1-20	HD 400x1200	S450
	6-10	HD 400x509	S450	21-30	HD 400x900	S450
	11-15	HD 400x421	S450	31-40	HD 400x634	S450
	16-20	HD 400x421	S450	41-50	HD 400x509	S450
	21-30	HD 400x237	S450	51-60	HD 400x314	S450
Beams	1-30	IPE400	S275	1-60	IPE400	S275
Outriggers	15/30	HD 400x314	S700	15/30/45/60	HD 400x314	S700
Braces	1-5	HSS 300x20	S700	1-10	HSS 400x20	S700
	6-15	HSS 250x16	S700	11-20	HSS 350x16	S700
	16-20	HSS 200x16	S700	21-30	HSS 300x16	S700
	21-30	HSS 200x16	S700	31-60	HSS 250x16	S700

Table 1: Member sizes and mechanical properties in key structural components for HR-01 and HR-02.

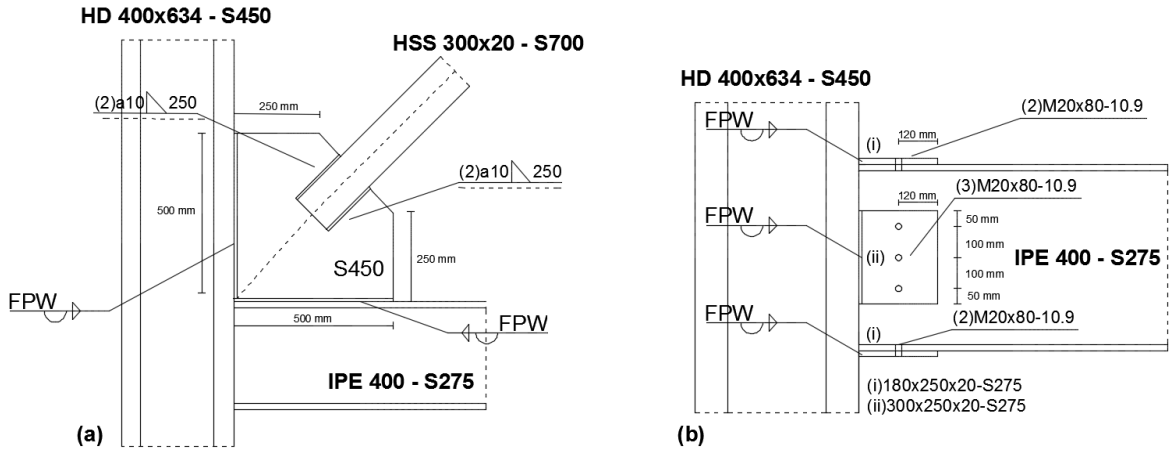


Figure 2: Details of (a) gusset-plate and (b) beam-to-column connections. Note: HR-01 – first floor.

As previously mentioned, Fig. 2 sketches an example of the connection systems used to detail the joints of the two high-rise braced frames. In particular, Fig. 2(a) presents the geometry of the gusset plate used to connect the beam/column and the rectangular hollow section shape brace; fillet welds were provided between the web of the gusset plate and the rectangular HSS brace, while full penetration welds (FPW) were chosen to connect the edge of the gusset plate and the flanges of beam and column. In addition, Fig. 2(b) shows the layout of a bolted beam-to-column connection used in the first floor of HR-01. Three M20x80 – 10.9 bolts were used to bolt the shear tab to the web of the beam and two M20x80 – 10.9 bolts were provided between a 180x250x20 mm plate, welded by FPW to the flange of the column, and the flange of the beam, in accordance with the prescriptions of [34].

2.2 Modeling approach and seismic input

To investigate the seismic response of these two case-study buildings, a series of NLTHAs were carried out, using the open source platform OpenSees [35] to construct their fiber-based idealizations able to account for material and geometrical nonlinearities through classical con-

stitutive law and co-rotational transformation [36]. As suggested in [36], inelastic force-based fiber elements, with five integration points, were used to model structural members, assuming a bi-linear stress-strain relationship with isotropic strain hardening to reproduce the permanent deformations exhibited by plastic materials during the loading-unloading history. The tangent stiffness-proportional Rayleigh damping calibrated on the first period of the two mega-frames was employed to perform the series of nonlinear dynamic analyses, as done in [37, 36]. Finally, the Krylov subspace algorithm was used to iteratively equilibrate loads, since it has a larger radius of convergence and requires fewer matrix factorizations than Newton-Raphson [38, 36].

Fig. 3 shows a schematic of the modeling approach used for brace and gusset-plate connections [20, 21, 31, 32]. The model consists of two inelastic force-based beam-column elements, each of which having five integration points and a discretized fiber section. In order to capture the effects of gusset end restraint [20, 21, 31, 32], the present paper takes advantage of an additional inelastic force-based beam-column element of length $2t$ – where t is the thickness of the gusset plate – at each end of the brace. A set of rigid elements is included to represent the confined portions of beam, column and gusset plate, as shown by [20, 21, 31, 32]. To account for potential buckling mechanisms in both braces and gusset plates, an out-of-plane imperfection equal to 0.1% of the entire brace length is applied, while the nodes of both beam and columns are constrained to deform in-plane only. Similarly, an equivalent idealization developed along the lines of classical mechanical/component approach [22-25] is used to incorporate the cyclic behaviour of bolted joints.

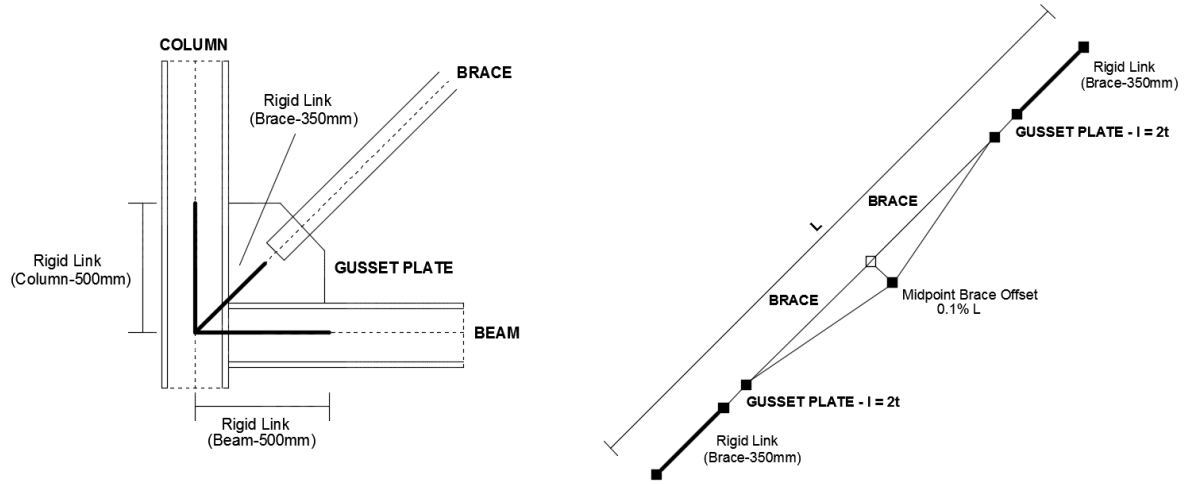


Figure 3: Schematic of the modeling approach used for gusset-plate connections.

A classical displacement/rotation-based convergence criterion, with a threshold set equal to 10^{-3} was adopted for the series of NLTHAs performed by assuming an auto-update integration time-step of the order of one-tenth of the time sampling of the ground motions considered [18, 19]. In particular, a set of ten natural records scaled to obtain displacement spectrum compatibility according to EC8 requirements [17] was selected herein; type 1 spectrum with a PGA of 0.4g and soil type C with T_D equal to 8s were the prevailing criteria for this suite. Further and more comprehensive information may be found in [18, 19].

3 RESULTS AND DISCUSSION

In the following discussion, the main results obtained from the series of numerical analyses carried out (i.e. RSAs and NLTHAs) will be summarized. In particular, the responses of these

two high-rise mega-frame structures will be compared and used to describe the global and local behaviour of their LFRSs, when subjected to severe earthquake-induced demands. A general overview of their main characteristics is given herein, and specific aspects are referenced when needed to explain key points. Particular care is paid to the response of braces and joints, showing their influence on the global structural performance.

3.1 Global performance of mega-frame systems

The global responses of the two super-tall buildings studied are provided in Fig. 4, in terms of inter-storey drift and acceleration peak profiles from NLTHAs and RSAs. In addition, peak displacements obtained at each floor are collected in Fig. 5 for both structures.

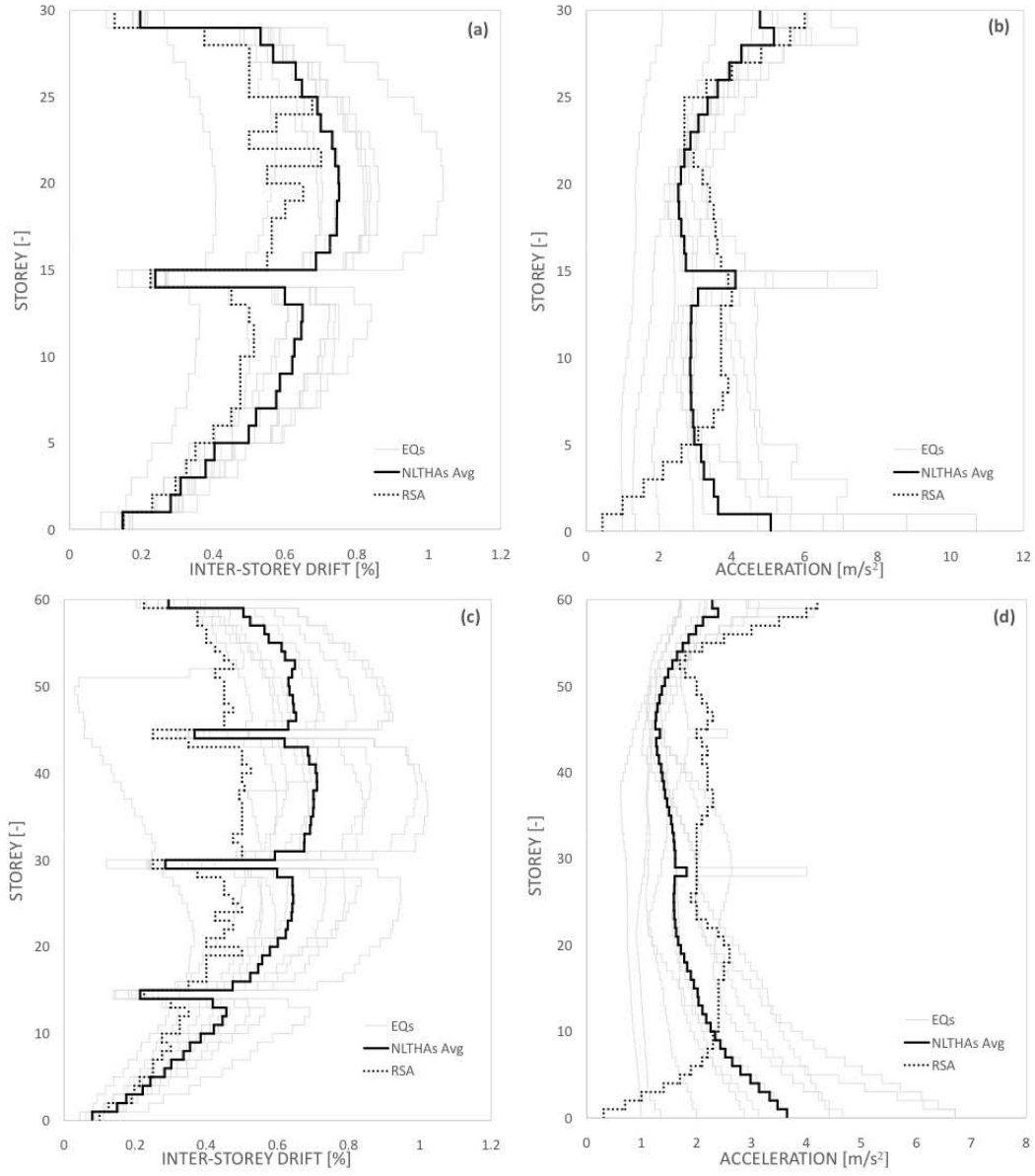


Figure 4: Inter-storey drift and acceleration peak profiles in HR-01 and HR-02 from NLTHAs and RSAs.

Peak roof displacements of up to 0.77 m and 1.83 m were observed for HR-01 and HR-02, in the case of the most severe record, while values of about 0.61 m and 1.17 m were computed in average, thus showing peaks 20% and 36% lower for HR-01 and HR-02, respectively. RSA

deviates from the average of the ten NLTHAs at approximately mid-height, reaching a discrepancy of about 10% and 20% at the top storey of the thirty- and sixty-storey buildings. A fairly cantilevered shape, with discontinuities in correspondence to the outriggers, were predicted for both structures. This trend is even more visible in terms of inter-storey drifts and accelerations, as shown in Fig. 4. In detail, peak inter-storey drifts of approximately 0.75% and 1.00% were shown to occur at two-thirds of the total structural height for both HR-01 and HR-02, in average and in case of the worst event, respectively. The stiffening effect provided by the outriggers was proven to be significant for both structural systems, as evidenced by a pronounced reduction in terms of peak inter-storey drifts experienced by dynamic simulations. By contrast, these members caused a significant acceleration and shear force demand in correspondence to them, as discussed later on.

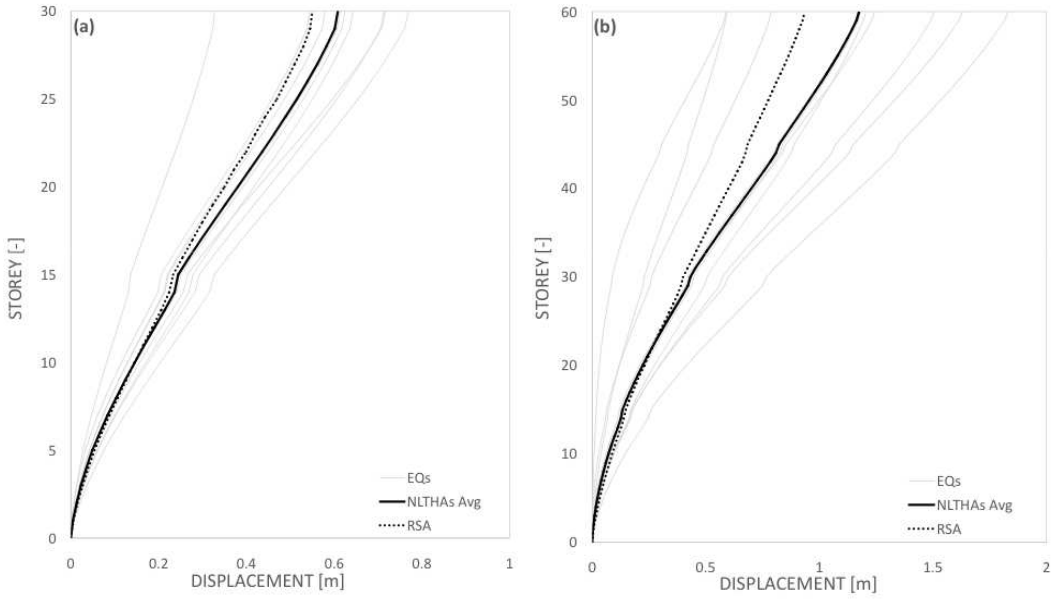


Figure 5: Peak displacement profiles for (a) HR-01 and (b) HR-02.

This trend is particularly evident for the stiffest of the two structures – HR-01 – which has a fundamental period more than halved in comparison with HR-02 (i.e. 2.73 s vs. 6.17 s). The peaks in terms of floor acceleration were approximately 0.53g and 0.37g in HR-01 and HR-02, respectively. If the most severe ground motion is taken as reference, peaks of up to 1.09g and 0.68g were undergone during NLTHAs. Finally, the higher modes contribution is pronounced, particularly in the upper stories of the tallest building, as a consequence of a higher flexibility.

Hence, the series of nonlinear dynamic simulations conducted have confirmed that, if accurately designed, these structural systems provide an optimum combination of overall stiffness and strength for super-tall mega-framed buildings, inducing a good balance between drift and acceleration demands.

3.2 Local response of key structural components

Once the global responses of the two high-rise structures were quantified, the local performance of key components, such as columns, braces and outriggers, will be discussed in detail. Axial load, bending moment and shear force peak profiles in different columns will be shown, as well as the hysteretic response of critical braces in terms of axial force-displacement curves. In addition, the peak profiles of the static-to-seismic axial load ratios will be computed in two reference columns for both structures.

To evidence the effects caused by the in-plane rotation of the outriggers, Fig. 6 collects the set of earthquake-induced compressive loads experienced by the leftmost and central columns of HR-01 and HR-02 in comparison with those obtained in static conditions (i.e. dead and live loads in seismic combination).

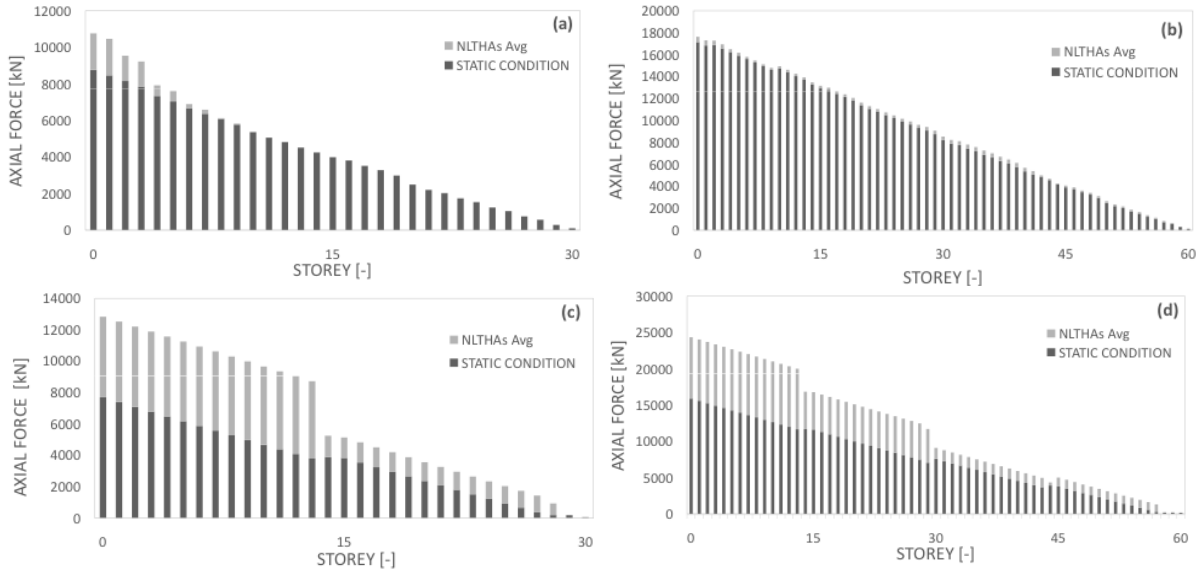


Figure 6: Peak profiles of static-to-seismic axial load ratios in the central column of (a) HR-01 and (b) HR-02 and in the leftmost column of (c) HR01 and (d) HR02, respectively.

As expected, the central column of both building are shown to remain almost unaffected by the dynamic excitation, since negligibly small extra-loads were observed, particularly for HR-02. By contrast, the contribution to lateral resistance ensured by the outriggers caused significant compressive overloads to be transferred to the lateral columns. In detail, an approximately 40% and 30% increase was computed at the base of HR-01 and HR-02, respectively; as the height of the structure increases, this effect tends to decrease, approximately showing a linear piecewise slope with the structure height. Pronounced discontinuities were again predicted in correspondence to the outriggers.

Therefore, only the results collected for the leftmost column of both structures will be presented hereafter. In particular, the bending moment and shear force peak profiles predicted by NLTHAs and RSA for HR-01 and HR-02 are shown in Fig. 7 and Fig. 8. High concentrations are again obtained in correspondence to the outriggers, as a consequence of those highlighted in terms of floor acceleration (see Fig. 4). As previously mentioned, RSA tends to visibly underestimate bending moment and shear force demands from NLTHAs. In some cases, values more than halved were determined.

An example of the axial force-displacement capacity curves predicted in a brace at the first floor is presented, in Fig. 9, to characterize the hysteretic behaviour of such a critical member. A pseudoelastic cyclic response governed by strength rather than ductility can be observed for both HR-01 and HR-02. The narrow hysteresis loops were shown to be too unstable to develop a well-established dissipative mechanism. Compressive peak forces of up to 5000 kN and 7000 kN were obtained, in this case, for the thirty- and sixty-storey CBF structure, respectively. As shown in Fig. 10, where the compressive force peak profiles constructed for HR-01 and HR-02 are provided, a similar demand was predicted in average in the upper stories where the outriggers are placed. RSA is confirmed to underestimate NLTHAs, particularly in the bottom and intermediate floor levels.

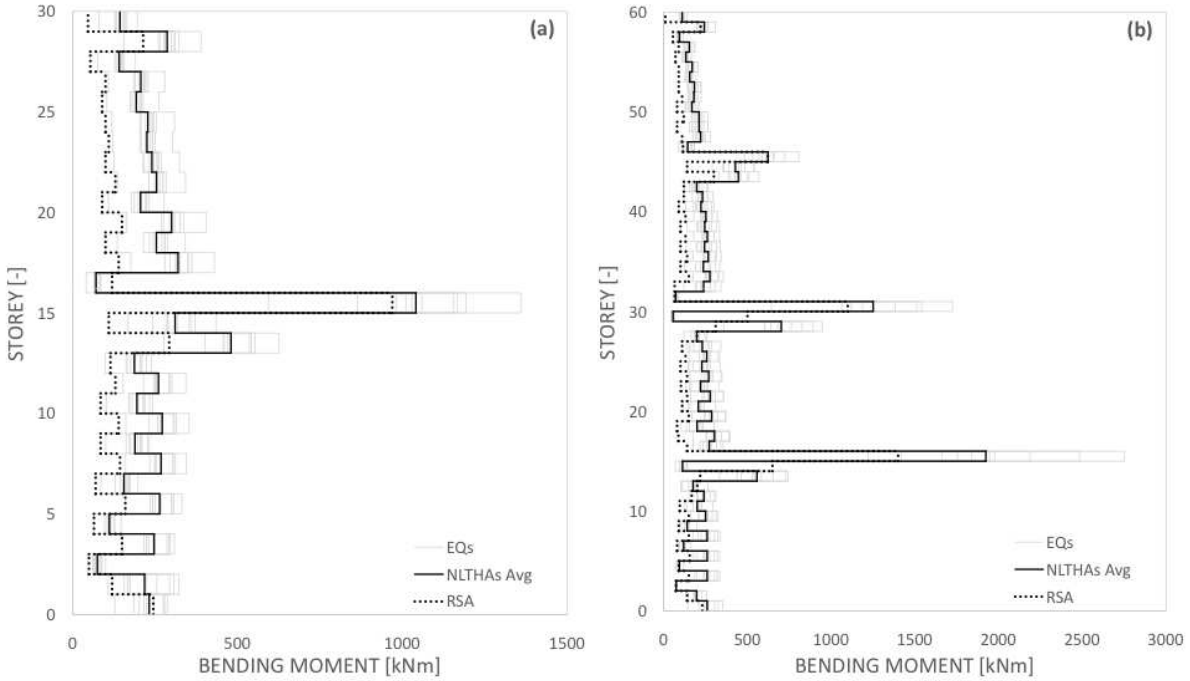


Figure 7: Bending moment peak profiles in the leftmost column of (a) HR-01 and (b) HR-02, respectively.

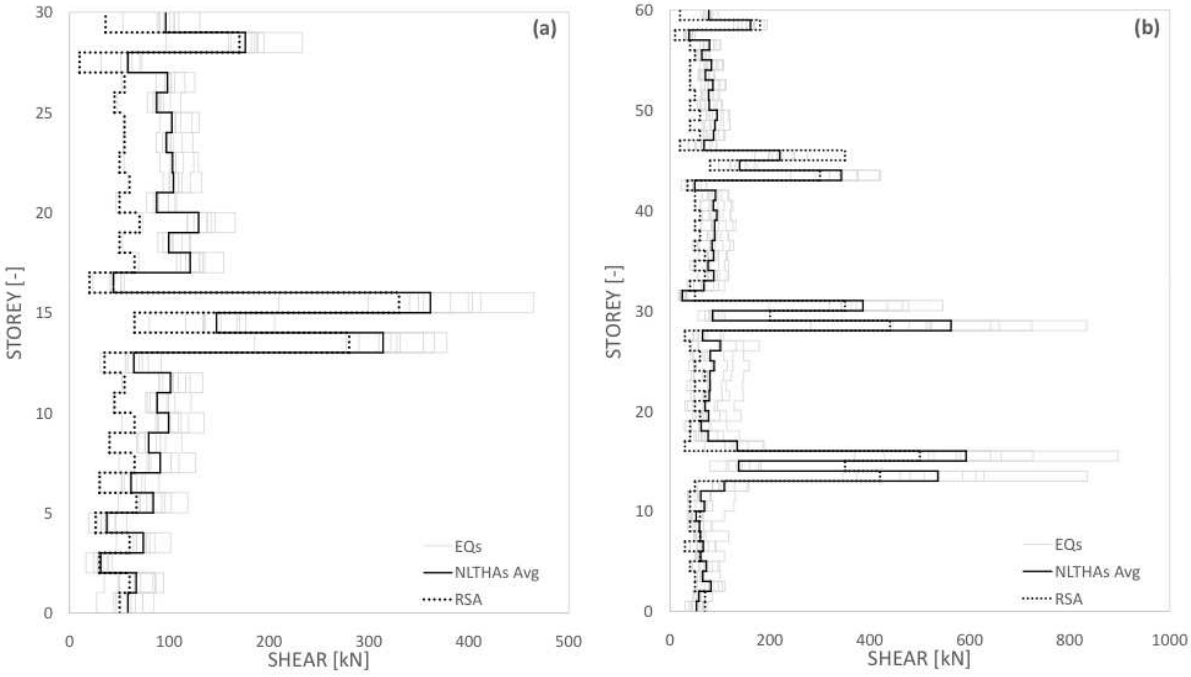


Figure 8: Shear force peak profiles in the leftmost column of (a) HR-01 and (b) HR-02, respectively.

In detail, a discrepancy of about 40% was predicted for both structures, if RSA and the average from NLTHAs are compared.

In Fig. 11, a comparison is provided between the compressive peak loads determined under seismic excitation and static conditions, in the most critical brace, for both high-rise buildings. Dynamic effects much more pronounced than those evidenced in the columns can be observed. Furthermore, Fig. 12 collects the series of NLTHA-to-RSA axial force ratios (R) computed in leftmost and rightmost braces of the core.

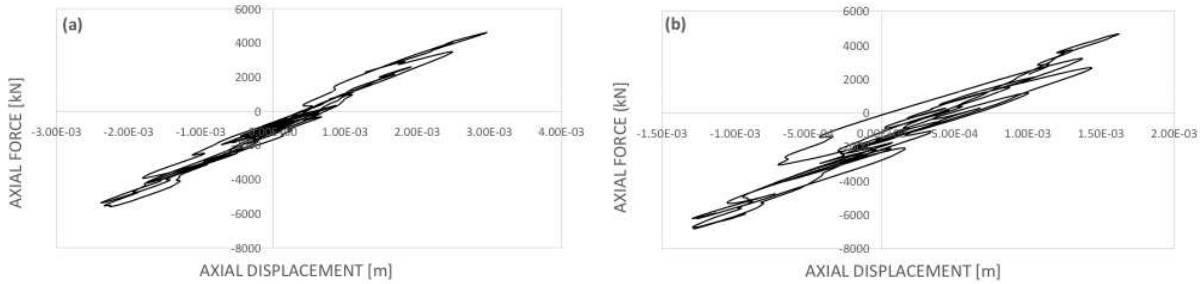


Figure 9: Hysteretic behaviour of a critical brace at the first floor for (a) HR-01 and (b) HR-02.

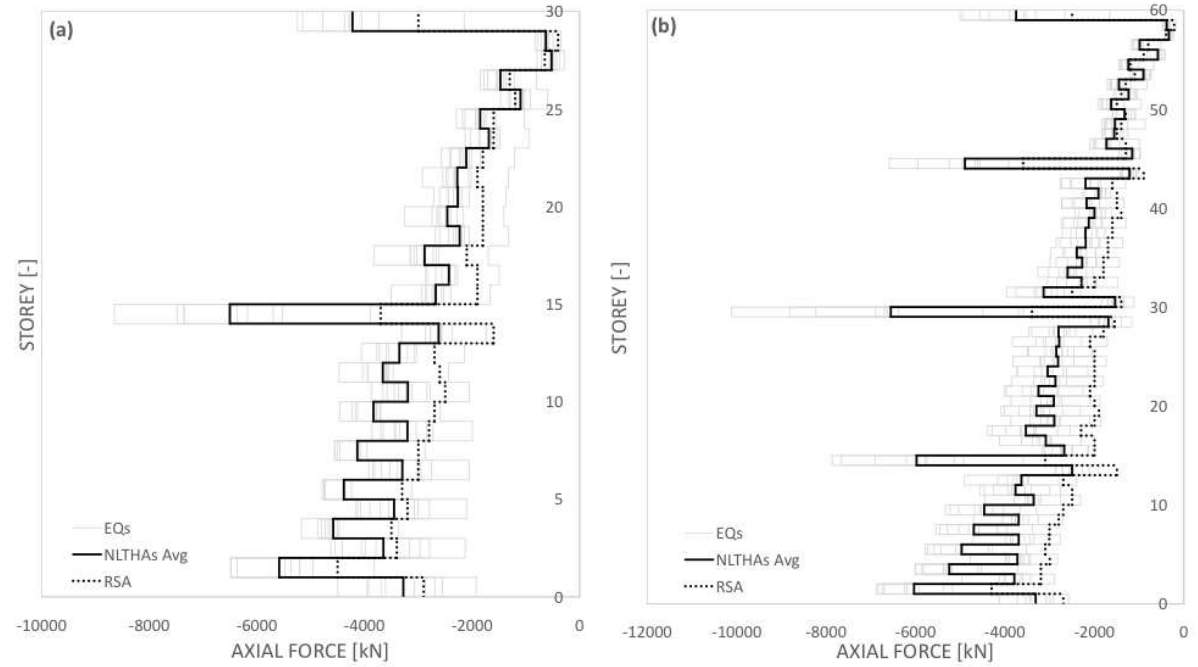


Figure 10: Compressive force peak profiles in a critical brace of the core for (a) HR-01 and (b) HR-02.

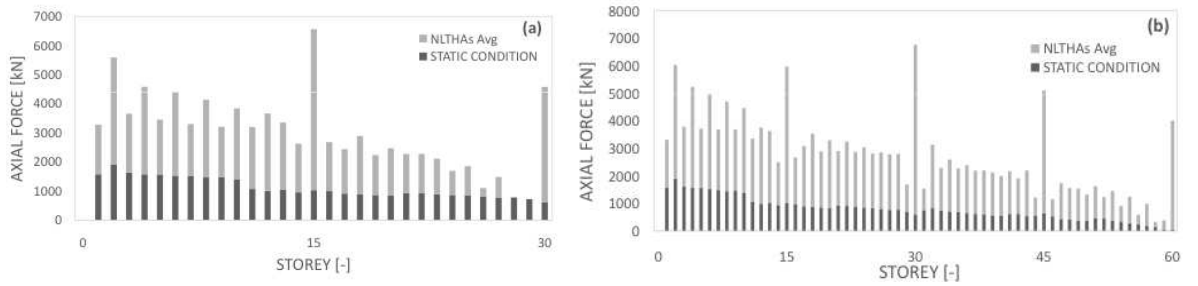


Figure 11: Static-to-seismic axial load ratios in a critical brace of (a) HR-01 and (b) HR-02, respectively.

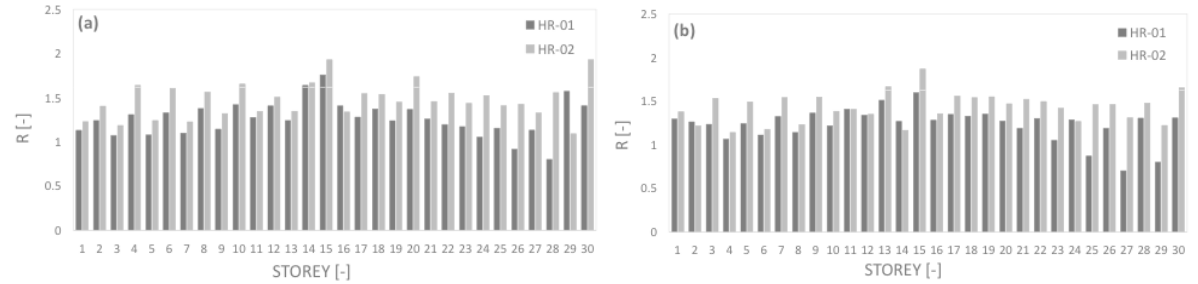


Figure 12: NLTHA-to-RSA axial load ratios in the (a) leftmost and (b) rightmost brace of the core.

Being the mismatch between RSA and NLTHAs in the braces higher than that observed in other members, particular care has to be paid to the earthquake-induced demand considered to design the related joints. In particular, EC8 recommends the following equation to be used for this purpose:

$$R_d = 1.1 \gamma_{ov} R_{fy} \tag{1}$$

where R_d is the axial resistance of the connection, γ_{ov} is the material overstrength factor and R_{fy} is the plastic resistance of the connected dissipative member.

Fig. 13 provides a comparison between the axial force peak profiles obtained by this EC8-based approach and the average from NLTHAs, showing the former to lead to unconservative demands, particularly in correspondence to the outriggers.

Finally, Fig. 14 presents a comparison between the peak axial forces predicted by RSA and NLTHAs in the outriggers placed at the 30th storey of both structures.

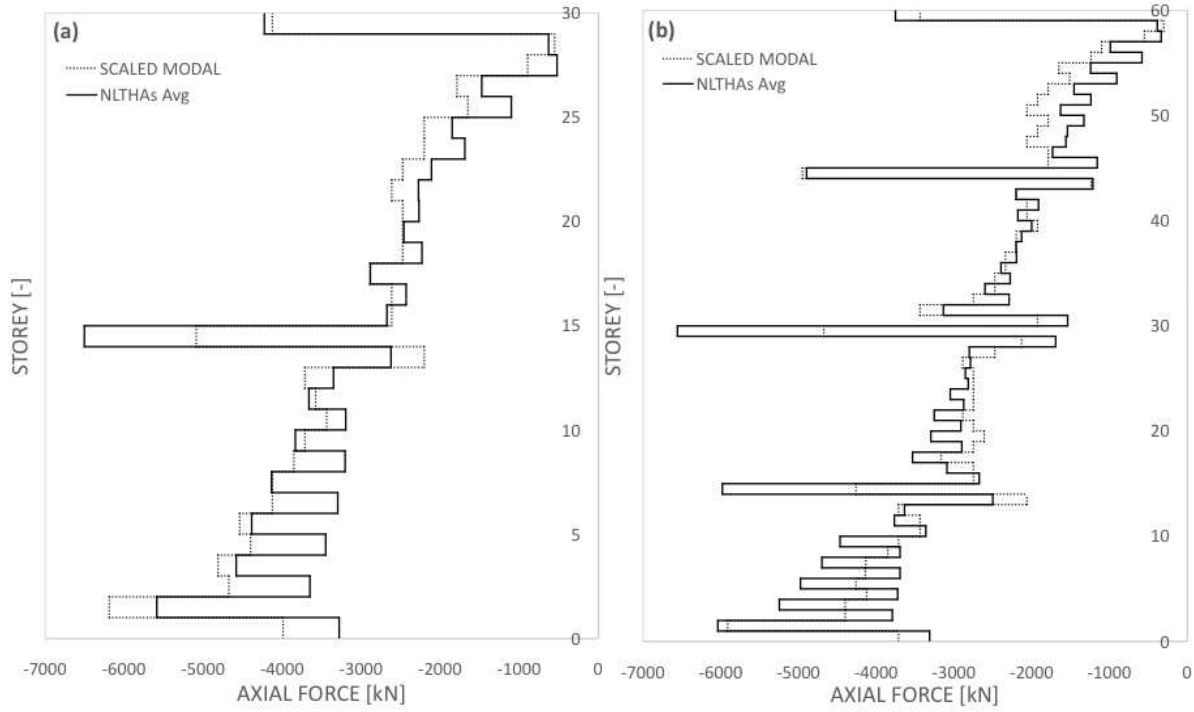


Figure 13: NLTHAs vs. EC8-based demand – axial load peak profiles in a brace of (a) HR01 and (b) HR-02.

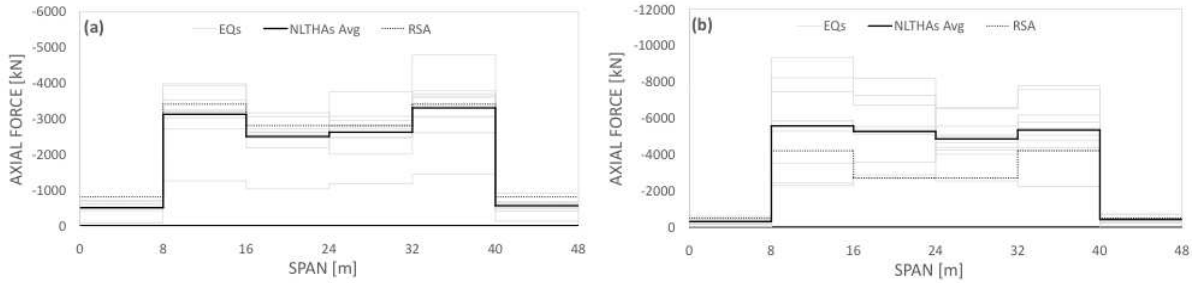


Figure 14: Axial forces in the outriggers at the 30th storey in (a) HR-01 and (b) HR-02, respectively.

Even though a negligibly small differences can be observed between RSA and the average from NLTHAs for HR-01, a larger discrepancy was evidenced in the outriggers at mid-height of the sixty-storey structure.

4 CONCLUSIONS

This paper focuses on the seismic response of super-tall mega-braced frame structures, including outriggers and belt trusses in their LFRS. In detail, thirty- and sixty-storey planar prototype frames, extracted from three-dimensional reference buildings, were designed according to European prescriptions and analyzed, in nonlinear dynamic fashion, to examine both global and local behaviour of structural system and key components. Inelastic force-based fiber elements and mechanical fiber-based idealizations were used to represent structural members and connections in an equivalent manner. NLTHAs were performed in comparison with RSA, using a set of ten natural displacement spectrum compatible records selected from past works as a severe seismic input. The prevailing observations and conclusions drawn from the numerical simulations carried out can be summarized as follows:

- A pseudoelastic response governed by strength rather than ductility was obtained for both structures, thus showing CBFs and outriggers to be effective in limiting inter-storey drifts and second order effects. In particular, peak inter-storey drifts of up to 0.75% and 1.00% were predicted to occur at two-thirds of the total structural height, whether the average of the NLTHAs and the most severe event are considered, respectively.
- Visible discontinuities in displacement, inter-storey drift and floor acceleration peak profiles were shown in correspondence to the outriggers, as a consequence of the significant stiffening effect provided by them, which in turn caused a large increase in bending moment and shear force demands in columns, braces and gusset-plate connections.
- The effects caused by the in-plane rotation of the outriggers were proven to be negligibly small in the central column of both prototypes, while high extra-loads of up to 40% were transferred to the lateral columns. In particular, the compressive force peak profiles were characterized by an approximately linear piecewise decaying slope, with pronounced discontinuities in correspondence to the outriggers.
- RSA tends to largely underestimate NLTHAs and in some cases values more than halved were determined, in terms of local demands on key structural components; a similar consideration can be drawn for peak displacements and inter-storey drifts. Therefore, the use of NLTHAs as a post-design check is reaffirmed to be a crucial aspect for these high-rise systems, the response of which is significantly affected by higher mode effects.
- Sensitivity to the structure height was investigated by comparing the responses of the two prototypes, thus showing current European seismic rules to impose a similar performance point for both HR-01 and HR-02, in terms of global and local behaviour. When accurately designed and detailed, CBFs and outriggers were demonstrated to provide an optimum combination of stiffness and strength for these super-tall buildings, inducing a good balance between drift and acceleration demands.

REFERENCES

[1] H. Fan, Q.S. Li, A.Y. Tuan, L. Xu, Seismic analysis of the world's tallest building. *Journal of Constructional Steel Research*, **65**, 1206-1215, 2009.

[2] X. Lu, X. Lu, H. Guan, W. Zhang, L. Ye, Earthquake-induced collapse simulation of a super-tall mega-braced frame-core tube building. *Journal of Constructional Steel Research*, **82**, 59-71, 2013.

[3] X. Lu, X. Lu, H. Sezen, L. Ye, Development of a simplified model and seismic energy dissipation in a super-tall building. *Engineering Structures*, **67**, 109-122, 2014.

[4] I. Takewaki, S. Murakami, K. Fujita, S. Yoshitomi, M. Tsuji, The 2011 off the Pacific coast of Tohoku earthquake and response of high-rise buildings under long-period ground motions. *Soil Dynamics and Earthquake Engineering*, **31**, 1511-1528, 2011.

[5] M. Poursha, F. Khoshnoudian, A.S. Moghadam, A consecutive modal pushover procedure for estimating the seismic demands of tall buildings. *Engineering Structures*, **31**, 591-599, 2009.

[6] Q.S. Li, Y.H. Zhang, J.R. Wu, J.H. Lin, Seismic random vibration analysis of tall buildings. *Engineering Structures*, **26**, 1767-1778, 2004.

[7] S.A. Meftah, A. Tounsi, A.B. El Abbas, A simplified approach for seismic calculation of a tall building braced by shear walls and thin-walled open section structures. *Engineering Structures*, **29**, 2576-2585, 2007.

[8] J. Ji, A.S. Elnashai, D.A. Kuchma, An analytical framework for seismic fragility analysis of RC high-rise buildings. *Engineering Structures*, **29**, 3197-3209, 2007.

[9] F. Khoshnoudian, M.M.B. Kashani, Assessment of modified consecutive modal pushover analysis for estimating the seismic demands of tall buildings with dual system considering steel concentrically braced frames, *Journal of Constructional Steel Research*, **72**, 155-167, 2012.

[10] M. Poursha, F. Khoshnoudian, A.S. Moghadam, A consecutive modal pushover procedure for nonlinear static analysis of one-way unsymmetric-plan tall building structures. *Engineering Structures*, **33**, 2417-2434, 2011.

[11] T.S. Jan, M.W. Liu, Y.C. Kao, An upper-bound pushover analysis procedure for estimating the seismic demands of high-rise buildings. *Engineering Structures*, **26**, 117-128, 2004.

[12] G. Searer, Poorly worded, ill-conceived, and unnecessary code provisions. *The structural Design of Tall and Special Buildings*, **15**, 533-546, 2006.

[13] R. Englekirk, The impact of prescriptive provisions on the design of high-rise buildings. *The Structural Design of Tall and Special Buildings*, **14**, 455-464, 2005.

[14] J. Moehle, Y. Bozorgnia, T. Yang, The tall buildings initiative. In *Proceedings of the 2007 Convention of the Structural Engineers Association of California*, pp. 26-29, 2007.

[15] C.S. Li, S.S.E. Lam, M.Z. Zhang, Y.L. Wong. Shaking table test of a 1:20 scale high-rise building with a transfer plate system. *Journal of Structural Engineering ASCE*, **132**, 1732-1744, 2006.

[16] X.L. Lu, Y. Zou, W.S. Lu, B. Zhao. Shaking table model test on Shanghai world financial center tower. *Earthquake Engineering & Structural Dynamics*, **36**, 439-457, 2007.

[17] Eurocode 8. Design of structures for earthquake resistance – Part 1: General rules, seismic actions and rules for buildings, EN 1998-1-1. Brussels, Belgium, 2005.

[18] T.J. Sullivan, Direct displacement-based seismic design of steel eccentrically braced frame structures. *Bulletin of Earthquake Engineering*, **11**, 2197-2231, 2013.

[19] T.J. Maley, R. Roldán, A. Lago, T.J. Sullivan, *Effects of response spectrum shape on the response of steel frame and frame-wall structures*. IUSS Press, Pavia, Italy, 2012.

[20] R. Nascimbene, G.A. Rassati, K.K. Wijesundara, Numerical simulation of gusset-plate connections with rectangular hollow section shape brace under quasi-static cyclic loading. *Journal of Constructional Steel Research*, **70**, 177-189, 2011.

[21] S. Santagati, D. Bolognini, R. Nascimbene, Strain life analysis at low-cycle fatigue on concentrically braced steel structures with RHS shape braces. *Journal of Earthquake Engineering*, **16**, 107-137, 2012.

[22] E. Brunesi, R. Nascimbene, G.A. Rassati, Response of partially-restrained bolted beam-to-column connections under cyclic loads. *Journal of Constructional Steel Research*, **97**, 24-38, 2014.

[23] E. Brunesi, R. Nascimbene, G.A. Rassati, Evaluation of the response of partially restrained bolted beam-to-column connection subjected to cyclic pseudo-static loads. *Structures Congress 2013*, pp. 2310-21. Pittsburgh, Pennsylvania, May 2-4, 2013.

[24] E. Brunesi, R. Nascimbene, G.A. Rassati, Seismic response of MRFs with partially-restrained bolted beam-to-column connections through FE analyses. *Journal of Constructional Steel Research*, **107**, 37-49, 2015.

[25] E. Brunesi, R. Nascimbene, GA. Rassati, Seismic performance of steel MRF with partially-restrained bolted beam-to-column connections through FE simulations. *Structures Congress 2014*, pp. 2640-51. Boston, Massachusetts, April 3-5, 2014.

[26] E. Brunesi, D. Bolognini, R. Nascimbene, Evaluation of the shear capacity of precast-prestressed hollow core slabs: numerical and experimental comparisons. *Materials and Structures*, 2014; DOI: 10.1617/s11527-014-0250-6.

[27] E. Brunesi, R. Nascimbene, M. Pagani, D. Beilic. Seismic performance of storage steel tanks during the May 2012 Emilia, Italy, earthquakes. *Journal of Performance of Constructed Facilities ASCE*, 2014; DOI: 10.1061/(ASCE)CF.1943-5509.0000628.

[28] G.A. Rassati, R.T. Leon, S. Noè. Component modeling of partially restrained composite joints under cyclic and dynamic loading. *Journal of Structural Engineering ASCE*, **130**, 343-351, 2004.

[29] A. Braconi, W. Salvatore, R. Tremblay, O.S. Bursi. Behaviour and modelling of partial-strength beam-to-column composite joints for seismic applications. *Earthquake Engineering & Structural Dynamics*, **36**, 142-161, 2007.

[30] M. Latour, V. Piluso, G. Rizzano. Cyclic modeling of bolted beam-to-column connections: component approach. *Journal of Earthquake Engineering*, **15**, 537-563, 2011.

[31] K.K. Wijesundara, R. Nascimbene, T.J. Sullivan, Equivalent viscous damping for steel concentrically braced frame structures. *Bulletin of Earthquake Engineering*, **9**, 1535-1558, 2011.

[32] K.K. Wijesundara, R. Nascimbene, G.A. Rassati, Modeling of different bracing configurations in multi-storey concentrically braced frames using a fiber-beam based approach. *Journal of Constructional Steel Research*, **101**, 426-436, 2014.

[33] EN 10025-2. Hot rolled products of structural steels – Part 2: Technical delivery conditions for non-alloy structural steels. Brussels, Belgium, 2004.

[34] UNI EN 14399-1. High strength structural bolting assemblies or preloading – Part 1: General Requirements. Brussels, Belgium, 2005.

[35] OpenSees. Open system for earthquake engineering simulation. Pacific Earthquake Engineering Research Center, University of California, Berkeley, CA.

[36] E. Brunesi, R. Nascimbene, Extreme response of reinforced concrete buildings through fiber force-based finite element analysis. *Engineering Structures*, **69**, 206-215, 2014.

[37] M.J.N. Priestley, D.N. Grant, Viscous damping in seismic design and analysis. *Journal of Earthquake Engineering*, **9**, 229-255, 2005.

[38] M.H. Scott, G.L. Fenves. Krylov subspace accelerated Newton algorithm: application to dynamic progressive collapse simulation of frames. *Journal of Structural Engineering ASCE*, **136**, 473-480, 2010.

COMPDYN 2015
5th ECCOMAS Thematic Conference on
Computational Methods in Structural Dynamics and Earthquake Engineering
M. Papadrakakis, V. Papadopoulos, V. Plevris (eds.)
Crete Island, Greece, 25–27 May 2015

EFFECT OF OPENINGS ON NONLINEAR DYNAMIC RESPONSES OF MASONRY INFILLED RC FRAMES

Y.P. Yuen[1]**, and J.S. Kuang**[2]

[1] Department of Civil Engineering, Bursa Orhangazi Üniversitesi
Bursa, Turkey
e-mail: terry.yuen@bou.edu.tr

[2] Department of Civil and Environmental Engineering, Hong Kong University of Science and Technology
Clear Water Bay, Kowloon, Hong Kong
cejkuang@ust.hk

Keywords: Infilled frame; Nonlinear seismic response analysis; Discrete finite element; Unreinforced masonry wall

Abstract. *Due to the architectural efficiency of masonry-infilled reinforced concrete frames, the frames are highly common structural forms for buildings. Research on responses of fully infilled RC frames under seismic effects has been active over the last few decades. Nevertheless, the effect of openings in the infills on the nonlinear dynamic responses has seldom been studied. This paper presents a numerical study on the global nonlinear seismic responses of RC frames containing infill walls with three types of openings, namely two-third storey height infills, window-opening infills and door-opening infills. On the basis of the analysis results, it is found that infilled frames with window or door openings exhibit ratchetting phenomena in hysteretic behaviour leading to asymmetric damage and lateral force transfer mechanisms. Furthermore, serious short column phenomenon occurs in the 2/3-storey-height infilled frame structures, in where the central short columns experience serious localised damage resulting significant pinching phenomenon in the hysteretic loops.*

1 INTRODUCTION

Masonry infills are widely applied in partition of reinforced concrete frames. Yet, throughout many worldwide devastating earthquakes [1-4], grave damage and catastrophic collapse of the infilled structures occurred time and again on account of altered structural responses of the RC frames containing infill walls. It is well recognized that he structural behaviour of infilled frames and bare frames may differ because the presence of infills, particularly irregularly arranged infills, can significantly alter local stress distributions in the frame members surrounding the infill walls and vary the overall structural dynamic behaviour. Furthermore, the brittle nature of masonry infill materials often lead to severe degradation of the structural hysteretic behaviour and causes localised damage in the adjacent infill wall-braced structural members under reversed cyclic loading. These modifications of structural action can be detrimental to the seismic performance of buildings, resulting in non-reparable damage of the adjacent structural members, jeopardising human lives and property [5].

Over the last few decades, awareness of the deficiency in current design and analysis methods for infilled frames prompted active research on responses of fully infilled RC frames under seismic effects over the last few decades [6-8], while significant progress in understanding their seismic behaviour has been achieved. Nevertheless, the seismic behaviour of RC frame structures containing infill walls with openings has seldom been studied. It has been reported that under seismic excitations the geometrically symmetric RC frame structures containing infill walls with openings can have significant asymmetric damage patterns [9]. Obviously, this asymmetric damage arising from asymmetric loading transfer mechanisms can have implications for the typical capacity design approach.

To understand the effect of openings in the infill walls on the nonlinear dynamic responses, hysteretic behaviour and force transfer mechanisms of infilled frame structures. This paper presents a numerical study on the global nonlinear dynamic responses of masonry infilled RC frames with different type of openings in infills under seismic. Nonlinear response history analyses of the masonry-infilled RC frames under realistic ground motion records are performed to investigate their seismic behaviour. The prototype used in this study is based on a 2-storey RC building frame designed to resist earthquakes with PGA of 0.15g. Four types of masonry-infills configurations: (1) full infills, (2) 2/3-storey-height infills, (3) infills with window openings and (4) infills with door openings are considered. The prototype structures are modelled with advanced discrete-finite element methods.

2 PROTOTYPE STRUCTURES

The prototype structure is a two-storey RC building frame designed to resist earthquakes with a PGA of 0.15g. Confining transverse reinforcement is provided in the frame members, which are detailed to obtain an expected displacement ductility factor of 2 to 4 [10]. The uniaxial strengths of the concrete and longitudinal and transverse reinforcements are 20.1 MPa, 400 MPa and 235 MPa, respectively. The full height 125-mm-thick infill panels are composed of 600×300×125-mm masonry units (compressive strength = 15 MPa) and 10-mm-thick mortar joints (compressive strength = 5 MPa). The reinforcement details and elevation view of the prototype frame is shown in Figure 1. In addition to the full height infills, three typical types of masonry-infill arrangement containing openings are considered in this study: (1) 2/3-storey-height infills, (2) infills with window openings and (3) infills with door openings. The window size is 900 mm square, with two windows in each wall. The windows are located at 2/3 height (from bottom to top) of the wall and 1/3 width (from left to right) of the wall. The door size is 900×2100 mm, with one door in each wall. The door is located in the middle-bottom of the wall.

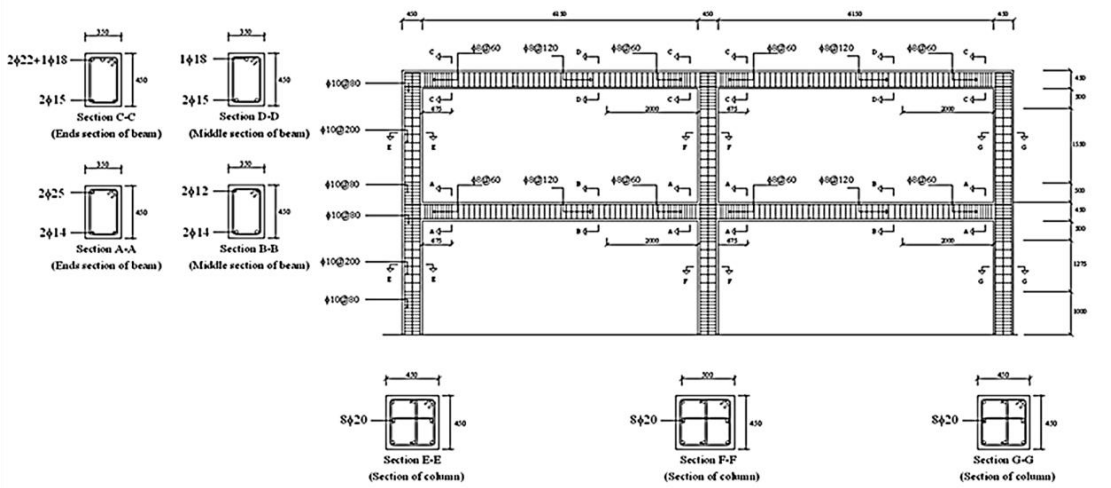


Figure 1: Prototype frame structure.

3 DISCRETE FINITE ELEMENT MODELS

To adequately capture the local infill-frame interacting behaviour, detailed modelling and discretisation of the frame and infill components are required. The prototype structures are modelled with advanced discrete-finite element methods are constructed with ABAQUS [11] and the mechanical behaviour of concrete and steel-reinforcement elements are modelled with the smeared isotropic damage-plasticity model [12] and Modified Menegotto-Pinto model [13] respectively. Furthermore, to simulate the pre- and post-fracture behaviour of the mortar joints in the infills, damage-based cohesive interactions [14] are enforced on the contact surfaces of the masonry units. The formulation of the interfacial constitutive model for the mortar joints is briefly outlined below.

As the strength of mortar joints is often much weaker than that of masonry units in infill walls, damage and cracks will likely propagate along the joints. In computational modelling, inelastic deformation will thus be concentrated in the mortar joints with severe distortion of the elements that may impair the accuracy of the simulation. In view of this, the contact formulation is a more effective tool to simulate extended crack opening and propagation behaviour as well as component disintegration in infills. The incremental form of the traction-separation law for cohesive cracks considering the mixed-mode fracture behaviour of the mortar joints is given by

$$\begin{Bmatrix} \Delta t_n \\ \Delta t_s \\ \Delta t_t \end{Bmatrix} = \begin{bmatrix} k_{nn}(1-D\cdot H(t_n)) & 0 & 0 \\ 0 & k_s(1-D) & 0 \\ 0 & 0 & k_t(1-D)) \end{bmatrix} \begin{Bmatrix} \Delta u_n \\ \Delta u_s \\ \Delta u_t \end{Bmatrix} \tag{1}$$

where $\mathrm{t} = \{t_n, t_s, t_t\}$ and $[\mathrm{u}] = \{u_n, u_s, u_t\}$ are the traction and displacement jump vector between two masonry unit surfaces, respectively, and $\mathbf{k_e}$ is an initial isotropic elastic stiffness tensor. The damage variable D is a scalar parameter of value within [0,1], and normal stiffness is assumed to be completely recovered under the compressive normal traction to account for the unilateral effect. $H(t_n)$ is a step function: $H(a)=1$ if $a \geq 0$, otherwise $H(a)=0$, which is used to characterise the unilateral effect or stiffness recovery effect. Due to the ma-

sonry units' restraint, the macroscopic cracks, which inflict macroscopic stiffness degradation, in mortar joints are eventually aligned with the bed planes regardless of fracture modes. By considering the major macroscopic damage mechanism and typical structural actions experienced by infills, it is sufficient to use a damage variable to model the stiffness degradation effect due to the formation of cracks in mortar joints. The criterion of damage initiation is defined as

$$t_n^2 + \beta_s^2 t_s^2 + \beta_t^2 t_t^2 - f_{nt}^2 = 0 \qquad (t_n \geq 0) \tag{2}$$

$$\beta_s^2 (|t_s| + t_n \tan\phi_s)^2 + \beta_t^2 (|t_t| + t_n \tan\phi_t)^2 - f_{nt}^2 = 0 \qquad (t_n < 0) \tag{3}$$

where f_{nt} is the tensile strength of the mortar joints; β_s and β_t are the ratios of the tensile strength to the mode II shear cohesion strength c_s and mode III tear cohesion strength c_t, respectively; and ϕ_s and ϕ_t are the friction angles under mode II and mode III deformation, respectively. The crack-driving force G_T is defined as

$$\Delta G_T = \{t_n\}\Delta\tau[u_n] + (|t_s| - \{-t_n\}\tan\phi_s)\Delta[u_s] + (|t_t| - \{-t_n\}\tan\phi_t)\Delta[u_t] \tag{4}$$

where $\{\bullet\}$ denotes the Macaulay bracket: $\{a\} = a$ if $a \geq 0$, otherwise $\{a\} = 0$.

It is assumed that the critical strain-energy release rate G_c under mixed-mode fracture is represented [15] as

$$\Delta G_C = -m(G_{IIC} + G_{IIIC} - G_{IC})\left(\frac{G_{IIC} + G_{IIIC}}{G_T}\right)^m G_T \Delta G_T \tag{5}$$

where G_{IC}, G_{IIC}, and G_{IIIC} are critical strain-energy release rates under pure mode I, pure mode II, and mode III fracture, respectively; m is an exponent that depends on the brittleness of the material; and G_0 is the strain-energy release rate at damage initiation. The mixed-mode fraction criterion BK law was developed and verified for ductile and brittle polymer materials, which have amorphous and polycrystalline solid structures, respectively. Hence, the fraction criterion is suitable for a wide range of materials with different molecular or grain structures. The evolution of damage is presented in the form of

$$\Delta D = \max\left(\frac{\Delta G_T}{G_C - G_0} - \frac{G_T \Delta G_C}{(G_C - G_0)^2}, 0\right) \tag{6}$$

When the contact surfaces are under compression, the joints behave similarly to Mohr-Coulomb materials, and crack propagation is governed by mode II fracture. However, when the surfaces are subjected to interacting tension and shear, a mixed-mode fracture criterion of the BK form would control the crack propagation. Once the mortar joints are fractured, $D = 1$, and the post-cracking interaction property of the two contact surfaces follows Coulomb's friction law; thus the slip criterion is defined as

$$f = (|t_s| - \{-t_n\}\tan\phi_s)^2 + (|t_t| - \{-t_n\}\tan\phi_t)^2 = 0 \tag{7}$$

The friction force is treated as constant, i.e., the change is zero at each time increment under the explicit Euler integration scheme, and the possible change in friction force is accounted at the end of integration. The model II or mode III fracture energy presented here is the macroscopically averaged energy, minus the frictional dissipation under normal compression, required for shearing masonry composites to failure or fracture states. Thus frictions are sub-

tracted from the total shear tractions in Eq. 6, and when a certain part of the strain energy is completely released due to fracture $D = 1$, the frictional dissipation dictated by Coulomb's law (Eq. 7) can continue. Hence, a smooth transition from the traction-separation law to Coulomb's law is attained.

The model is implemented in ABAQUS through the user-subroutine VUINTERACTION for traction-separation behaviour in general contact simulations. The integration scheme used for the implementation of the model is based on a standard modified explicit Euler scheme with substepping [16]. To illustrate the numerical algorithms of the model implementation, the solution steps for the mortar joints stressed from the elastic state to the damaged state, which are similar for other states, are outlined in Figure 2.

1. At a integration point on a contact surface, start with $\mathbf{t}^n$, $[\mathbf{u}^n]$, D^n, $G_c{}^n$, $G_T{}^n$, $\mathbf{k_e}$ and $\Delta[\mathbf{u}^{n+1}]$.
2. Check if the mortar joints fractured ($D^n = 1$)? If fractured, go subroutine to integrate the Columb friction problem.
3. Check if the mortar joints damaged ($D^n > 0$)? If damaged, go to step 8 with $\tau = 0$ and $\Delta\tau = 1$, $G_T^0 = G_T^n$, $G_c^0 = G_c^n$ and $\Delta[\mathbf{u}]_d = \Delta[\mathbf{u}^{n+1}]$.
4. Calculate elastic predictor: $\mathbf{t_e} = \mathbf{t}^n + \mathbf{k_e}\Delta[\mathbf{u}^{n+1}]$ and

$$F = \left\langle t_n^{n+1} \right\rangle^2 + \beta_s^2 \left\langle t_s^{n+1} \right\rangle^2 + \beta_t^2 \left\langle t_t^{n+1} \right\rangle^2 - f_{nt}^2 \qquad (t_n^{n+1} \geq 0)$$

$$F = \beta_s^2 \left\langle t_s^{n+1} \right| + t_n^{n+1} \tan\phi_s \left\rangle^2 + \beta_t^2 \left\langle \right| t_s^{n+1} \left| + t_n^{n+1} \tan\phi_s \right\rangle^2 - f_{nt}^2 \qquad (t_n^{n+1} < 0)$$

5. If $F \leq 0$, then $\mathbf{t}^{n+1} = \mathbf{t_e}$ and exit
6. If $F > 0$, calculate portion of $\Delta[\mathbf{u}^{n+1}]$ that cause purely elastic deformation, α, using the modified regula-falsi intersection scheme. Set $\mathbf{t}^0 = \mathbf{t}^n + \mathbf{k_e}\,\alpha\,\Delta[\mathbf{u}^{n+1}]$ and

$$G_0 = G_T^n + \left\{ t_n^{(n+1)/2} \right\} \alpha\Delta\left[u_n^{n+1}\right] + \left(\left| t_s^{(n+1)/2} \right| - \left\{ t_n^{(n+1)/2} \right\} \tan\phi_s \right) \alpha\Delta\left[u_s^{n+1}\right] + \left(\left| t_t^{(n+1)/2} \right| - \left\{ t_n^{(n+1)/2} \right\} \tan\phi_s \right) \alpha\Delta\left[u_t^{n+1}\right]$$

where $\mathbf{t}^{(n+1)/2} = (\mathbf{t_0} + \mathbf{t}^n)/2$

7. Set $\tau = 0$ and $\Delta\tau = 1$, $G_T^0 = G_0$, $G_C^0 = G_C^n$ and $\Delta[\mathbf{u}]_d = (1-\alpha)\,\Delta[\mathbf{u}^{n+1}]$
8. While $\tau < 0$, do steps 9 to 14
9. For $i = 1,2$, calculate

$$\Delta t^i = (\mathbf{I} - D^i \mathbf{S})\mathbf{k}_e \Delta\tau \Delta[\mathbf{u}]_d$$

$$\Delta G_T^i = \left\{ t_n^i \right\} \Delta\tau \left[u_n\right]_d + \left(\left| t_s^i \right| - \left\{ t_n^i \right\} \tan\phi_s \right) \Delta\tau \left[u_s\right]_d + \left(\left| t_t^i \right| - \left\{ t_n^i \right\} \tan\phi_s \right) \Delta\tau \left[u_t\right]_d$$

$$\Delta G_C^i = -m(G_{IIC} + G_{IIIC} - G_{IC}) \left(\frac{G_{IIC} + G_{IIIC}}{G_T^i} \right)^m G_T^i \Delta G_T^i \qquad \Delta D^i = \max\left(\frac{\Delta G_T^i}{G_C^i - G_0} - \frac{G_T^i \Delta G_C^i}{(G_C^i - G_0)^2}, 0 \right)$$

where $S = \begin{bmatrix} H(t_n^i) & 0 & 0 \\ 0 & 1 & 0 \\ 0 & 0 & 1 \end{bmatrix}$ is matrix used to characterise unilateral effect and

$t^1 = t^\tau$, $D^1 = D^\tau$, $G_T^1 = G_T^\tau$, $G_C^1 = G_C^\tau$

$t^2 = t^\tau + \Delta t^1$, $D^2 = D^\tau + \Delta D^1$, $G_T^2 = G_T^\tau + \Delta G_T^1$, $G_C^2 = G_C^\tau + \Delta G_C^1$

10. Compute the new traction vector, damage variable and strain energy releases rates as

$$\Delta t^{\tau+\Delta\tau} = t^\tau + \frac{1}{2}\left(\Delta t^1 + \Delta t^2\right) \qquad , \qquad \Delta D^{\tau+\Delta\tau} = D^\tau + \frac{1}{2}\left(\Delta D^1 + \Delta D^2\right)$$

$$\Delta G_T^{\tau+\Delta\tau} = G_T^\tau + \frac{1}{2}\left(\Delta G_T^1 + \Delta G_T^2\right), \quad \Delta G_C^{\tau+\Delta\tau} = G_C^\tau + \frac{1}{2}\left(\Delta G_C^1 + \Delta G_C^2\right)$$

11. Determine the relative error as

$$R^{\tau+\Delta\tau} = \max_i \left\{ \frac{\left\| \Delta\xi_i^2 - \Delta\xi_i^1 \right\|}{\left\| \Delta\xi_i^{\tau+\Delta\tau} \right\|} \right\}$$ where ξ is a set of all calculated state variables from the previous step.

12. If $R^{\tau+\Delta\tau} \geq TOL$ then go to step 9 with a smaller pseudo-time increment

$$\Delta\tau = \max(0.9\sqrt{TOL / R^{\tau+\Delta\tau}}\,\Delta\tau, 0.1\Delta\tau, \Delta\tau_{\min})$$

13. If $R^{\tau+\Delta\tau} < TOL$ (solution tolerance)

$$t^{\tau+\Delta\tau} = t^\tau + \Delta t^{\tau+1} \qquad , \qquad D^{\tau+\Delta\tau} = D^\tau + \Delta D^{\tau+\Delta\tau} \qquad G_T^{\tau+\Delta\tau} = G_T^\tau + \Delta G_T^{\tau+\Delta\tau} \qquad ,$$

$$G_C^{\tau+\Delta\tau} = G_C^\tau + \Delta G_C^{\tau+\Delta\tau}$$

14. Extrapolate to obtain the pseudo-time increment of the next sub-step by

$$\Delta\tau = \min(0.9\sqrt{TOL / R^{\tau+\Delta\tau}}\,\Delta\tau, \Delta\tau, 1-\Delta\tau) \qquad \tau = \tau + \Delta\tau$$

15. When $\tau = 1$, exit with

$$t^{n+1} = t^1, \quad D^{n+1} = D^1, \quad G_T^{n+1} = G_T^1, \quad G_C^{n+1} = G_C^1$$

Figure 2: Solution steps for the mortar joints stressed from elastic state to damaged state.

4 SEISMIC FAILURE MODES AND FORCE TRANSFER MECHANISMS

Each of the infilled frame structures are subjected to four real earthquake ground motions: (1) 1979 El Centro 1140-component at USGS-station 5056 (PGA = 0.14g), (2) 1987 Superstition Hills 225-component at USGS-station 5051 (PGA = 0.46g), (3) 1995 Kobe 000-component at station Takatori (PGA = 0.61g) and (4) 1999 Chi-Chi EW-component at station CHY080 (PGA = 0.96g). The elastic response spectra of the four ground motions are shown in Figure 3.

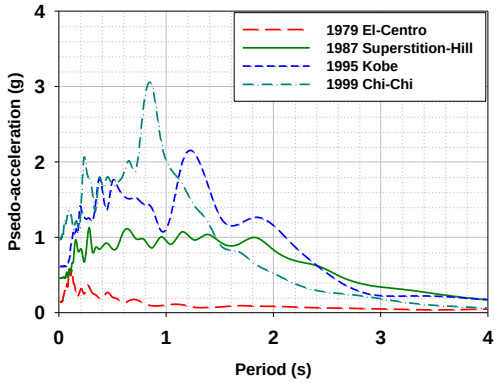


Figure 3: Elastic response spectra of the ground motions.

Under the four ground excitations, the resulted hysteresis loops of the prototype structures are plotted in Figure 4. Comparing with the frames with full-height solid infills, the introduction of openings in the infill panels significantly reduces the incurred bracing action against the bounding frame. The maximum base shears experienced by the infilled frames with window openings are reduced to approximately two-thirds to as much as one-half of that experienced by the fully infilled frames; surprisingly, the damage to the bounding RC frame and the infill panel is the most severe amongst the four infilled structures, as shown in Figure 5. Yet, the structure is still able to attain higher lateral stability than the frame with captive columns, as shown in Figure 4.

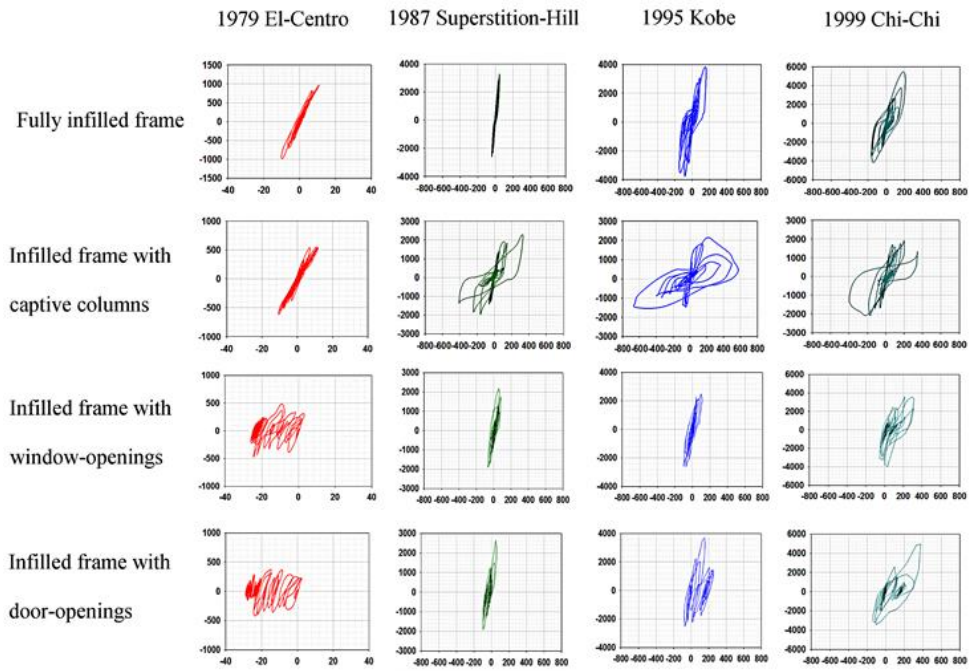


Figure 4: Hysteresis behaviour of infilled frames

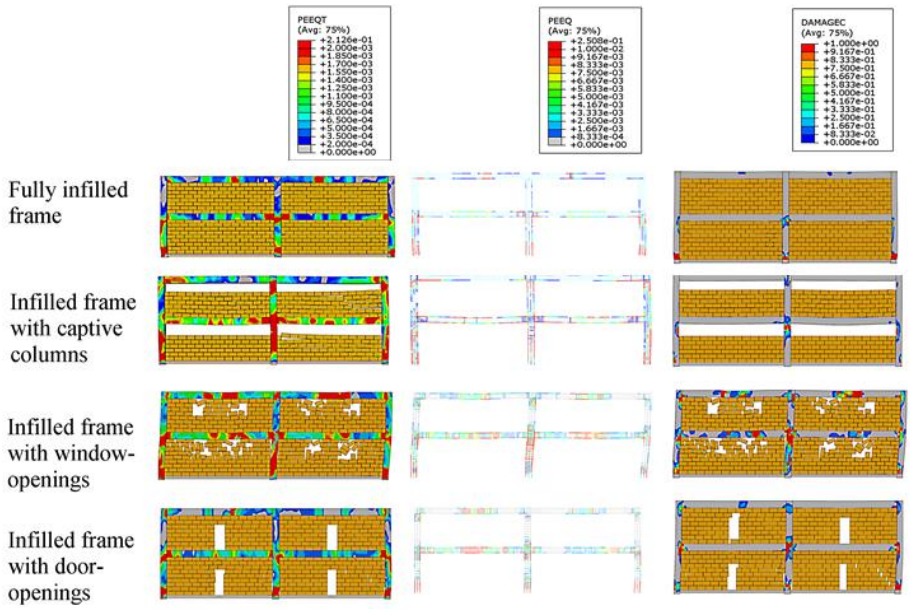


Figure 5: Damage pattern of infilled frames.

Although the incurred seismic forces are quite significantly reduced by the introduction of openings, very serious damage that is much more severe than that inflicted upon the fully infilled frames subjected to higher seismic forces is inflicted on the bounding RC frame under seismic loading. This apparently abnormal behaviour is due to the partial collapse of the holed infill panels, as shown in Figure 5. Stored strain energy in the collapsing infill components is suddenly released, resulting in severe, localised damage to the infill. In other words, following the toppling of infills, most of the seismic vibration energy is absorbed by the bounding frames rather than the infills in infilled frame structures with window openings, in contrast to the fully infilled frames, in which most of the vibration energy is apparently absorbed by the non-toppled infills.

Nevertheless, the infilled frames with window openings can attain quite reasonable post-damage lateral stability, although the structures suffer more extensive damage than other infilled frames. Again, the vertical and lateral bracing actions provided by the full-height infill panels contribute this stability to the structure. This result demonstrates the importance of the continuity of the infill distribution in a bounding frame to the global stability of the structure. A discontinuous infill distribution, such as the infilled frames with captive columns, tends to have lower post-damage lateral stability because any force-flow discontinuity can prohibit the development of other force transfer mechanisms, decreasing the potential for force redistribution. Therefore, even with such severe damage being inflicted on the structure, the continuous non-toppled infills in the infilled frames with window openings are still able to transmit the lateral and vertical forces through multiple strut bracing mechanisms, as shown in Figure 6.

By contrast, while other frames behave elastically under the 1979 El Centro earthquake, the infilled frames with openings exhibit a ratchetting phenomenon in which the irrecoverable inelastic drift develops progressively with each loading cyclic, as shown in Figure 4, quite similar to the fatigue effect. This phenomenon occurs because the cracking strength of the infill panels with openings is lower than that of solid infills due to stress concentration in the corners, as shown in Figure 6. As a result, sliding cracks are initiated at those corners and progressively propagate along the bed joints under cyclic loadings, and the inelastically deformed infill panels restrain the undamaged bounding frame from deflecting back to the original configuration, resulting in the development of residual drift.

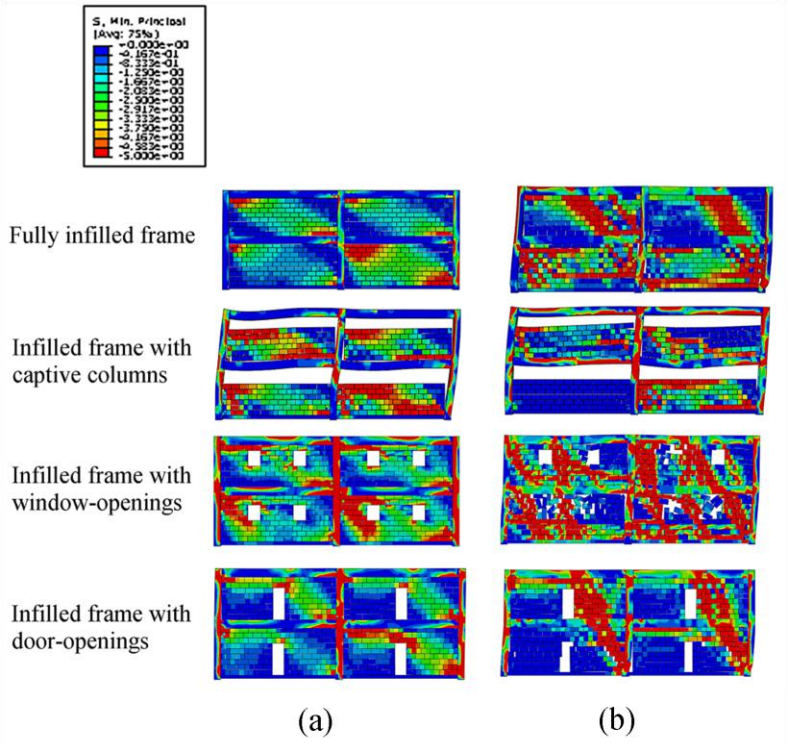


Figure 6: Force transfer mechanisms: plots of the principal compressive stress distribution of infilled frames (a) before major cracking and (b) after major cracking.

Similar to window openings, door openings weaken the bracing action of infills to the bounding frame. The incurred base shear is reduced to approximately 80%, as much as 50% of that experienced by the fully infilled frames. As shown in Figure 5, the structures exhibit rather asymmetrical damage patterns; the rightmost columns suffer more severe damage than the leftmost columns, while opposite damage distributions are evident in the beams, which more damage is inflicted in the left beams. Although the infilled frames with door openings exhibit lower initial stiffness and thus experience less seismic forces than the structures with window openings under the excitation of the El Centro earthquake, the post-damage stiffness and base shear of the former structures become considerably larger than that of the later structures under the other three strong earthquake excitations. This increase can be understood by observing the initial and post-damaged force transfer mechanisms, as shown in Figure 6.

The "door" structures have weaker initial bracing action than the "window" structures, but after the infills suffer severe damage with the formation of major cracks or even partially collapse, the post-damaged lateral bracing mechanisms, as characterised by the inclined compressive struts, of the "door" structures are much stronger and more robust than the "window" structures. As a result, the incurred base shears of the "door" structures are larger in the post-damage states and can reach magnitudes as high as 80% of that experienced by the fully infilled frames. The structural damage of the frames with door openings is less than that incurred on the frames with window openings due to reduced disintegration of infill components.

However, the damage is apparently more severe than that to the fully infilled frames, or more precisely speaking, the damage distribution is considerably asymmetric, as indicated previously. This increase in severity occurs because the initially symmetric lateral force transfer mechanisms are destroyed by the ratchetting effect. In contrast to the "window" structures, the infills founded on the floors in the "door" structures are not horizontally continuous

due to the introduction of the door openings, which results in unrestrained sliding of the infill panels. Sliding of the infill panels leads to strong variation of the lateral force transfer mechanisms, as well as the resulting drifts and hysteresis loops, of the structures under loading acting in two opposite directions. Although the lateral stability remains quite satisfactory for the prototype structure with door openings adopted in this study, if the structures were taller, the stability would decrease because a significant P-Δ effect would be triggered under large vertical loading and lateral drift.

5 CONCLUSIONS

On the basis of the analysis results, the following conclusions are drawn:

- Non-toppled full infills panels can enhance the overall stability and energy dissipation, though the structures suffer much larger seismic forces.
- Infilled frames with window or door openings exhibit, respectively, shakedown or ratchetting phenomena in hysteretic behaviour due to the propagation of sliding cracks initiated from the corners of the openings.
- Unrestrained ratchetting deformation in the infilled frames with door openings incur serious asymmetric damage patterns and lateral force transfer mechanisms.
- Serious short column phenomenon occurs in the 2/3-storey-height infilled frame structures, in where the central short columns experience serious localised damage and this leads to significant pinching phenomenon in the hysteretic loops.

ACKNOWLEDGMENT

The support of Hong Kong Research Grant Council under grant No. 614011 and Scientific and Technological Research Council of Turkey (TÜBİTAK) under project number 214M236 are gratefully acknowledged.

REFERENCES

[1] H. Sezen, A. S. Whittaker, K. J. Elwood, K. M. Mosalam. Performance of reinforced concrete buildings during the August 17, 1999 Kocaeli, Turkey earthquake, and seismic design and construction practise in Turkey. *Engineering Structures*, **25**, 103-114, 2003.

[2] Earthquake Engineering Field Investigation Team (EEFIT). *The 2007 August 15 magnitude 7.9 earthquake near the coast of Central Peru*. The Institution of Structural Engineers, UK, 2007.

[3] Earthquake Engineering Field Investigation Team (EEFIT). *The Wenchuan, China earthquake of 12 May 2008*. The Institution of Structural Engineers, UK, 2008.

[4] M. Manfredi, A. Prota, G. M. Verderame, F. De Luca, P. Ricci. 2012 Emilia earthquake, Italy: reinforced concrete buildings responses. *Bulletin of Earthquake Engineering*, **12**, 2275-2298, 2014.

[5] T. Paulay, M. J. N. Priestley. *Seismic design of reinforced concrete and masonry buildings*. Wiley, New York, 1992.

[6] A. B. Mehrabi, P. B. Shing. Behaviour and analysis of masonry-infilled frames. *Progress in Structural Engineering and Materials*, **4**(3), 320-331, 2002.

[7] P. Ricci, M. T. De Risi, G. M. Verderame, G. Manfredi. Influence of infill distribution and design typology on seismic performance of low- and mid-rise RC buildings. *Bulletin of Earthquake Engineering*, **11**, 1585-1616, 2013.

[8] F. De Luca, G. M. Verderame, F. Gómez-Martínez, A. Pérez-García. The structural role played by masonry infills on RC building performances after the 2011 Lorca, Spain, earthquake. *Bulletin of Earthquake Engineering*, **12**, 1999-2026, 2014.

[9] D. J. Kakaletsis, C. G. Karayannis. Influence of masonry strength and openings on infilled R/C frames under cycling loading. *Journal of Earthquake Engineering*, **12**(2), 197-221, 2008.

[10] SAC. *Code for seismic design of buildings: GB 50011-2001*. China Architecture & Building Press, Beijing, 2001.

[11] ABAQUS, Inc. *ABAQUS theory manual*, 2010.

[12] J. Lubliner, J. Oliver, S. Oller, E. Oñate, A plastic-damage model for concrete. *International Journal of Solids and Structures*, **25**, 229–326, 1989.

[13] J. Sakai, K. Kawashima, Modification of the Giuffre, Menegotto and Pinto Model for unloading and reloading paths with small strain variations. *Journal of Structural Mechanics and Earthquake Engineering*, **738/I-64**, 159–169, 2003.

[14] J. S. Kuang, Y. P. Yuen, Simulations of masonry-infilled RC frames failure. *Engineering and Computational Mechanics, ICE*, **166**, 179-193, 2013.

[15] M. L. Benzeggagh, M. Kenanem. Measurement of mixed-mode delamination fracture toughness of unidirectional glass/epoxy composites with mixed-mode bending apparatus. *Composites Science and Technology*, **56**(4), 439–44 9, 1996.

[16] S. W. Sloan, A. J. Abbo, D. Sheng. Refined explicit integration of elastoplastic models with automatic error control. *Engineering Computations*, **18**(1/2), 121-154, 2001.

COMPDYN 2015
5th ECCOMAS Thematic Conference on
Computational Methods in Structural Dynamics and Earthquake Engineering
M. Papadrakakis, V. Papadopoulos, V. Plevris (eds.)
Crete Island, Greece, 25–27 May 2015

A DESIGN PROCEDURE FOR SEISMIC RETROFITTING OF REINFORCED CONCRETE FRAME AND CONCENTRIC BRACED STEEL BUILDINGS WITH DISSIPATIVE BRACINGS

A.V. Bergami[1*], **C. Nuti**[2]
[1] Research fellow-University of Roma Tre – Department of Architecture
Via C. Segre, 6 - 00146 Rome (Italy)
alessandro.bergami@uniroma3.it
[3] Full Professor-University of Roma Tre – Department of Architecture
Via C. Segre, 6 - 00146 Rome (Italy)
camillo.nuti@uniroma3.it

Keywords: Dissipative braces, earthquake engineering, energy dissipation, seismic retrofitting.

Abstract. *The research presented in this paper deals with the seismic retrofitting of existing frame structures by means of passive energy dissipation. An iterative displacement-based procedure, based on capacity spectrum is described and some applications are discussed. The general procedure has also been discussed referring to the case of existing steel concentric braced frame structures (CBF). The procedure can be used with any typology of dissipative device and for different performance targets. In this work the procedure has been applied, with both traditional pushover (load profile proportional to first mode) and multimodal pushover, to an existing r.c. frame building. In the application presented the buckling restrained braces have been used in order to prevent damages to both the structure and non structural elements. The use of multimodal pushover proves to be more effective than pushover based on single mode in case of medium rise r.c. frame building (higher than 30 metres) but, once this building is retrofitted, and therefore regularized, with a bracing system, the difference between using monomodal or multimodal pushover becomes not significant.*

1 INTRODUCTION

The use of dissipative bracings, though it seems conceptually clear and simple, requires a more complex design procedure than other retrofitting methods like base isolation. This greater complexity derives from the non linear behaviour of the dissipative devices and therefore of the final retrofitted structure. Despite that, during the last years, many design procedure has been published and, between those, the most useful for practical use seem to be those that are based on the capacity spectrum method. In fact with this approach non linear dynamic analyses can be skipped in favor of static non linear analyses that are simpler to be managed. Otherwise, also within those procedures, many have a theoretical approach that can be difficulty associated with a widespread professional use. In fact, frequently, the characteristics of an existing building (e.g. non regular distribution of masses and stiffness, presence of a soft story) can compromise the effectiveness of procedures that impose a predefined loading pattern during pushover analyses. As discussed in Bergami & Nuti (2013), the design of dissipative devices have two main goals: improve dissipation and regularize strength end stiffness distribution (this can be done adopting an adequate criteria to distribute the braces along the elevation and inside the plan of the building). Moreover, in case of medium rise building (quite widespread in Italy), it is a matter of fact that the relevance of higher modes depends not only on their level of irregularity but it is also related to the quite high number of stories. To check such hypothesis the design procedure, that is detailed in is general form and specialized to the case of steel braced frames, has been tested on a medium rise irregular existing r.c. building. The necessity of using a multi modal pushover (Goel & Chopra, 2004) instead of the standard single mode pushover procedure has been investigated performing multimodal pushover and non linear dynamic analysis on both the existing and retrofitted building.

2 DISSIPATIVE BRACINGS POSITIONING: STRUCTURAL EFFECTS

The insertion of dissipative braces into the structural frame involves significant effects that can be grouped in two categories: effects on structural response and effects on the architecture of the building. Concerning the former the braces increase both stiffness and strength and consequently, as usually happens, both modal shapes and the capacity curve of the structure are modified. Moreover, for a given top displacement, these improve damping and, therefore, reduce demand. In this respect stiffness increase could render less efficient, or even useless, the increase of dissipation. Therefore a careful mix of stiffness and dissipation is requested: this subject is discussed in the following.

The bracing system has to be compatible with the architecture of the building: therefore spatial distribution of the braces descents from a compromise between the optimization of the dissipative system and the functionality of the building.

Although braces distribution should be analyzed case by case some general considerations can be made: braces should reduce or eliminate eventual translation-rotation coupling effects, induce constant interstorey drifts, exclude soft storey behavior and maximize damping for a given top displacement.

Different criteria to distribute the additional stiffness are proposed in scientific literature: constant at each story, proportional to story shear, proportional to interstorey drifts of the original structure. In this work the latter is assumed and therefore, given the interstorey drift δ_j, the stiffness $K'_{b,j}$ corresponding to each storey of the bracing system is:

$$K'_{b,j} = K_{global} c_{b,j} \tag{1}$$

where:

$$c_{bj} = \frac{\delta_j}{\max_j \{\delta_j\}} \tag{2}$$

Each brace is a composite element realized coupling an elastic element (usually a steel profile) with a dissipative device in series. The latter will determines the desired yielding force whereas the former will be designed to assure the desired stiffness of the series.

3 EVALUATION OF THE EQUIVALENT VISCOUS DAMPING

A specific energy dissipated by the structure and the braces corresponds to each deformation reached by the structure, be it with or without dissipative braces; the dissipated energy can be expressed in terms of equivalent viscous damping. Referring to the formula proposed by A.K. Chopra (2001), the equivalent viscous damping of the structure $\nu_{eq,S}$ at the generic displacement *D* can be expressed as follows:

$$\nu_{eq,S} = \frac{1}{4\pi}\frac{E_{D,S}}{E_{S,S}} \tag{3}$$

All the parameters of the Eq. (3) can be easily determined from the capacity curve: $E_{D,S}$ is the energy dissipated in a single cycle of amplitude *D* and $E_{S,S}$ is the elastic strain energy corresponding to the displacement *D*. Referring to an equivalent bilinear capacity curve (it can be determined from the capacity curve using one of the methods available in literature) terms of Eq. (3), considering an ideal elasto-plastic hysteretic cycle, can be determined as follow:

$$E_{D,S}^{bilinear} = 4\left(F_{sy}D - D_{sy}F_s(D)\right) \tag{4}$$

$$E_{S,S} = \frac{1}{2}DF_s(D) \tag{5}$$

with:

D	the displacement reached from the structure
$F_s(D)$	the force corresponding to D (the force is the base shear)
D_{sy}	displacement at yielding
F_{sy}	the yielding force (base shear at yielding)

It is well known that the hysteretic cycle of a real structure differs from the ideal cycle, therefore this difference can be taken into account adopting a corrective coefficient χ_S for the structure and χ_B for the braces (χ =1 for the ideal elasto-plastic behaviour). Therefore:

$$E_{D,S} = \chi_S E_{D,S}^{bilinear} \tag{6}$$

$$E_{D,B} = \chi_B E_{D,B}^{bilinear} \tag{7}$$

with $E_{D,B}^{bilinear}$ the energy dissipated by the ideal hysteretic cycle of the dissipative brace.

For the applications discussed in this paper the parameter χ_S has been determined referring to the provisions of *ATC40 [1996]*. For the braces the assumption of $\chi_B \approx 1$ has been considered reasonable: in fact, according to *AISC/SEAOC – Recommended Provisions for Buckling-Restrained Braced Frames [2005]*, the force-displacement relationship of a *BRB* can be ideal-

ized as a bilinear curve. However different values can be adopted, if the case, with no difference in the procedure. Authors have assumed a bilinear curve characterized by a yielding force equal to the yielding traction force (the maximum compressive strength of *BRBs* is slightly larger than the maximum tensile strength due to the confining effect of the external tube): the hysteretic cycle obtained is elasto-plastic but precautionary smaller than the real one. Than the evaluation of the equivalent viscous damping of the braced structure $\nu_{eq,S+B}$, to be added to the inherent damping ν_I (usually ν_I=5% for r.c. structures and ν_I=2% for steel ones), can be obtained using the following expression:

$$\nu_{eq,S+B} = \frac{1}{4\pi}\frac{E_{D,S+B}}{E_{S,S+B}} = \frac{1}{4\pi}\left[\frac{\chi_S E_{D,S}^{bilinear}}{E_{S,S+B}} + \frac{\chi_B \sum_j E_{D,B,j}^{bilinear}}{E_{S,S+B}}\right] \tag{8}$$

$$\nu_{eq,S} = \chi_S \frac{1}{4\pi}\frac{E_{D,S}^{bilinear}}{E_{S,S+B}}; \nu_{eq,B} = \chi_B \frac{1}{4\pi}\frac{\sum_j E_{D,B,j}^{bilinear}}{E_{S,S+B}} \tag{9}$$

where $E_{D,B,j}^{bilinear}$ is the energy dissipated by the dissipative braces placed at level *j*.

Eq. (8) can be generalized assuming that $E_{D,B,j}^{bilinear} = \sum_i E_{D,B,i}^{bilinear}$ with $E_{D,B,i}^{bilinear}$ the energy dissipated by the *i* braces placed at level *j*. Note that $\nu_{eq,S}$ and $\nu_{eq,B}$ are obtained dividing the dissipated energy, determined from the capacity curve of *S* or *B* respectively, by the elastic strain energy of the braced structure, determined from the curve of *S*+*B*.

4 THE DESIGN PROCEDURE: GENERAL FORMULATION MAIN STEPS

The design procedure can be applied using every typology of pushover because it requires the only definition of capacity curve and interstorey drift distribution. Therefore the use of the multimodal procedure doesn't modify the proposed procedure that can be summarized in the following steps:

1. **Define the seismic action**: the seismic action is defined in terms of elastic response acceleration spectrum (T-S_a).
2. **Select the target displacement**: the target displacement is selected (for example the top displacement D_t^*) according to the performance desired (limit state).
3. **Define the capacity curve**: the capacity curve of the braced structure *S*+*B*, in terms of top displacement and base shear (D_t-V_b), is determined via pushover analysis. The pushover analysis can be easily performed using a software for structural analysis: many different force distributions can be adopted selecting the best option for the specific case (*e.g.* modal shape load profile).

If a modal shape load profile has been selected it is important to underline that the modal shape is influenced by the bracing system and consequently, at each iteration, the load profile has to be updated to the modal shape of the current braced structure.

Notice that, at the first iteration, the structure without braces is considered and therefore the capacity curve obtained will be fundamental for the evaluation of the contribution offered by the existing structure to the braced structure of the subsequent iterations.

4. Define **the equivalent bilinear capacity curve**: the capacity curve is approximated by a simpler bilinear curve D_t-F_{s+b} that is completely defined by the yielding point ($D_{s+b,y}$, $F_{s+b,y}$) and the hardening ratio β_{s+b} (at the first iteration the parameters correspond to $D_{s,y}$, $F_{s,y}$, β_s of the existing building).

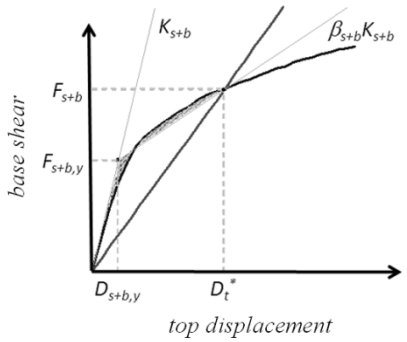


Figure 1: Evaluation of the equivalent bilinear capacity curve

5. **Define equivalent single degree of freedom**: MDOF system is converted in a SDOF system by transforming the capacity curve into the capacity spectrum (S_{dt}-S_{ab})

$$S_{dt} = \frac{D_t}{\Gamma\phi_t}; S_a = \frac{F_{S+B}}{\Gamma \cdot L} \tag{10}$$

where Γ is the participation factor of the modal shape ϕ ($\Gamma=(\phi^T MI)/(\phi^T M\phi)$) and $L=\phi^T MI$. The modal characteristics of the braced structure may change at every iteration due to new brace characteristics. Therefore ϕ, Γ and L have to be updated with the current configuration

6. **Evaluate the required equivalent viscous damping**: the equivalent viscous damping $\nu^*_{eq,S+B}$ of the braced structure to meet the displacement of the equivalent SDOF system and the target spectral displacement $S_{dt}{}^*=D_t{}^*/(\Gamma\phi^T)$ is determined.

According to the Capacity Spectrum Method the demand spectrum is obtained reducing the 5% damping response spectrum by multiplying for the damping correction factor η that is function of ν_{tot}

$$\eta = \sqrt{\frac{10}{5+\nu_{tot}\cdot 100}} = \frac{S_{\nu_{eff}}}{S_{5\%}} \tag{11}$$

From Eq. (11) one obtain ν^*_{tot} the damping needed to reduce displacement up to the target $S_{dt}{}^*$.

$$\nu^*_{tot} = 0.1\left(\frac{S_{5\%}}{S^*_{dt}}\right)^2 - 0.05 \tag{12}$$

7. **Evaluate the equivalent viscous damping contribution due to the naked structure**: the contribute to damping of the structure $\nu^*_{eq,S}(D^*_t)$ can be determined from Eq. (3.12) being $D_t{}^*$ the top displacement corresponding to $E^{bilinear}_{D,S}$ and $E_{S,S+B}$ that are the energy dissipated by S and the elastic strain energy of $S+B$ ($E^{bilinear}_{D,S}$ and $E_{S,S+B}$ are determined from the capacity curve of S and $S+B$ respectively).

8. **Evaluate the additional equivalent viscous damping contribution due to braces**: given ν^*_{tot} from Eq. (12) the equivalent viscous damping needed to be supplied by the braces $\nu^*_{eq,B}(D^*_t)$ is evaluated from Eq. (3.11) and Eq. (4.1) as follows:

$$\nu^*_{eq,B}(D^*_t) = \nu^*_{tot}(D^*_t) - \nu^*_{eq,S}(D^*_t) - \nu_I \tag{13}$$

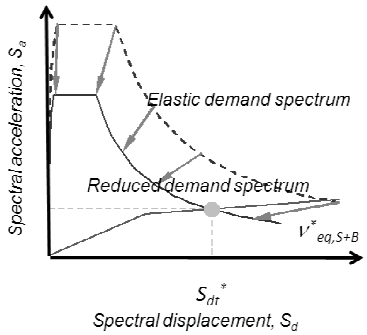


Figure 2: Evaluation of the equivalent viscous damping needed to achieve the target performance point

9. **Dimensioning of the braces**: once the required equivalent viscous damping $\nu^*_{eq,B}(D_t^*)$ has been evaluated from Eq. (13), axial stiffness and yielding strength required to achieve the desired additional damping can be determined with the same procedure previously adopted for the structure (step 7).
The energy dissipated by the braces inserted at each j_{th} level can be expressed as:

$$E_{D,B}^{bilinear} = \sum_{j=1}^{n} 4\left(F_{by}^{'}\delta_j^{'} - \delta_{y,j}^{'}F_{b,j}^{'}(\delta_j^{'})\right) \tag{14}$$

being δ'_j the component of the interstory drift δ_j at j_{th} of the n floors along the axe of the brace ($\delta'_{y,j}$ is the axial displacement corresponding to yielding of the device).

The axial displacement of the damping brace at the j_{th}-floor δ'_{bj} can be determined from its inclination angle $\theta_{b,j}$ and interstorey drift $\delta_j=D_j-D_{j-1}$: therefore $\delta'_{b,j}=\delta_j \cos\theta_{bj}$.

The dissipative brace is usually constituted by a dissipative device (*e.g.* the *BRB*) assembled in series with an extension element (*e.g.* realized with a steel profile) in order to connect the opposite corners of a frame (Fig. 3).

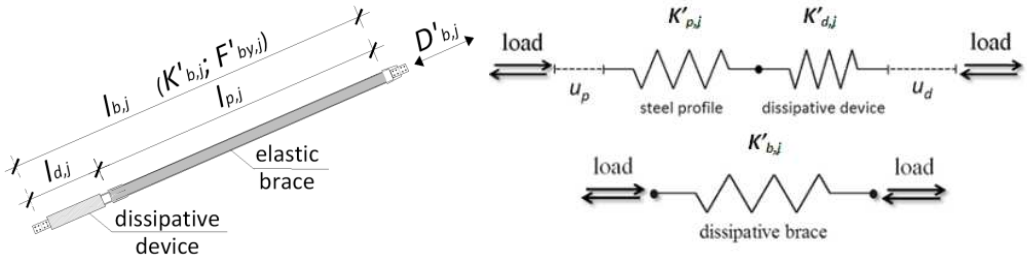


Figure 2: Dissipative device "j" assembled in series with an extension element (e.g. a steel profile): equivalent model of springs in series ($K'_{d,j}$; $K'_{p,j}$) and equivalent single spring model ($K'_{b,j}$)

Therefore, being $K'_{b,j}$ and $K'_{by,j}$ the equivalent stiffness of the spring series in the elastic and plastic range respectively, $\alpha = K_{p,j}^{'}/K_{d,j}^{'}$ the ratio between elastic stiffness of the steel profile and of the device and $\beta_{d,j}$ the ratio between stiffness after and before yielding of the dissipative device, the following expression can be derived:

$$K_{b,j}^{'} = \frac{K_{d,j}^{'}}{\frac{1}{\alpha_j}+1};\ K_{by,j}^{'} = \frac{\beta_{b,j}K_{d,j}^{'}}{\frac{\beta_{b,j}}{\alpha_j}+1};\ \alpha_j = \frac{K_{p,j}^{'}}{K_{d,j}^{'}} \tag{15}$$

Therefore:

$$F'_{b,j} = F'_{by,j} + (\delta'_j - \delta'_{y,j}) \frac{\beta_{b,j} K'_{d,j}}{\frac{\beta_{b,j}}{\alpha_j} + 1} \tag{16}$$

$$\delta'_{y,j} = \frac{F'_{by,j}}{K'_{b,j}} = \frac{F'_{by,j}}{K'_{d,j}} (\frac{1}{\alpha_j} + 1) \tag{17}$$

Consequently, if there is one brace per direction and per floor, substituting Eq. (16) into Eq. (14), $v^*_{eq,B}(D_t^*)$ can be expressed in the following way:

$$v^*_{eq,B}(D_t^*) = \chi_B \frac{2}{\pi} \frac{\sum_{j=1}^{n} \left\{ F'_{by,j} \delta'_j - \delta'_{y,j} \cdot \left[F'_{by,j} + (\delta'_j - \delta'_{y,j}) \frac{\beta_{d,j} K'_{d,j}}{\frac{\beta_{d,j}}{\alpha_j} + 1} \right] \right\}}{F_{S,S+B}(D_t^*) \cdot D^*_{S,S+B}} \tag{18}$$

δ'_j are determined from the pushover analysis for the top displacement D_t and $\delta'_{y,j}$, that is the yielding displacement of devices, can be reasonable assumed as $\delta'_{y,j} \le \delta'_j / 4$.

$F'_{y,j}$ is, for each direction, the yielding force of the floor brace: once $\delta'_{y,j}$ has been defined $F'_{y,j}$ is consequently determined Eq. (17). Thus, according to Eq. (15), $K'_{d,j}$ can be expressed as follows:

$$K'_{d,j} = K_{global} \cdot c_{b,j} \cdot (\frac{1}{\alpha_j} + 1) \tag{19}$$

Therefore substituting Eq. (19) into Eq. (18), K_{global} can be determined as follows:

$$K_{global} = \frac{\pi \cdot v^*_{eq,B}(D_t^*) \cdot F_{S,S+B}(D_t^*) \cdot D^*_{S,S+B}}{2 \cdot \chi_B \cdot C_1} \tag{20}$$

with:

$$C_1 = \sum_{j=1}^{n} c_{b,j} \left\{ \delta'_{y,j} \cdot \delta'_j - \delta'_{y,j} \left[\delta'_{y,j} + (\delta'_j - \delta'_{y,j}) \frac{\beta_{b,j} (\frac{1}{\alpha_j} + 1)}{\frac{\beta_{b,j}}{\alpha_j} + 1} \right] \right\} \tag{21}$$

A value of $\alpha_j > 3$ is usual in applications, therefore $K'_{b,j} > 3/4 K'_{d,j}$, while the steel profile must be stronger (neither yielding nor buckling) than the device: for a given interstorey drift the larger is α_j the larger are device displacements and hysteretic cycles. At this point all terms of Eq. (20) are known so, from Eq. (19) and Eq. (15) , the floor brace stiffnesses $K'_{b,j}$ can be defined (the yielding force $F'_{by,j}$ can be directly derived since the stiffness $K'_{b,j}$ and the yielding displacement $\delta'_{y,j}$ have been defined). Though in this paper the procedure is discussed referring to Eq. (18) it is important to underline that, in a general case, one can have *m* different braces for each level *j*. In fact, at the same level, each brace *i* can be characterized by its specific properties as a consequence, for example, of the geometry of the bays of the structur-

al frame. Consequently Eq. (18) can be generalized as follows.

$$v^*_{eq,B}(D_t^*) = \frac{2}{\pi} \frac{\sum_{j=1}^{n}\sum_{i=1}^{m} \chi_{B,i} \left\{ F'_{by,j,i}\delta'_j - \delta'_{y,j,i} \cdot \left[F'_{by,j,i} + (\delta'_j - \delta'_{y,j,i}) \frac{\beta_{d,j,i} K'_{d,j,i}}{\frac{\beta_{d,j,i}}{\alpha_{j,i}} + 1} \right] \right\}}{F_{S,S+B}(D_t^*) \cdot D^*_{S,S+B}} \tag{22}$$

10. **Check convergence**: one must repeat steps from 3 to 9 until the performance point of the braced structure converges to the target displacement with adequate accuracy.

4.1 Application to steel concentric braced frames (CBF)

Recent studies and experimental courses have pointed out that the seismic capacity of steel concentric braced frames (CBF) is limited by diagonal yielding while buckling of compressed diagonals can be tolerated if they remain in the elastic range. The contribution of compressed diagonals is disregarded in design, though it can affect seismic response, reducing the period of vibration of the structure, while increasing the absorbed energy.

The retrofit procedure previously presented has been specialized also to the case of CBFs, and is presented in this paragraph. The structural elements: beams and columns usually act as pendulum, hinged at their ends, though this assumption can be removed without any modification to the presented procedure.

The procedure allows to design a dissipative bracing system that can guarantee the upgrade of the existing CBF avoiding yielding in tension of the existing diagonals, or even, in some cases, to prevent compressed original diagonal from elastic buckling. In the latter case the pushover analysis can be easily performed using a software for structural analysis in fact, this typologies of structures (CBF) after the retrofitting should remain linear elastic even under seismic action (in some cases, as a rare seismic event, a limited plastic excursion of the diagonals could be accepted to guarantee to survive the event) and therefore the nonlinearity can be concentrated only in the dissipative devices. In case one accept elastic buckling of the compressed original braces, one should consider the nonlinear elastic behavior of these elements, unless it is proved that their contribution to total stiffness is negligible, and disregarded in the analysis.
The specialized procedure can be summarized by modifying steps 2 and 3 as follows:
2. **Select the target displacement**: the target displacement is selected (for example the top displacement D_t^*) according to the performance desired (limit state). Usually, working with steel buildings, deformation limits are relevant for the dimensioning. For CBF (concentric braced frame) the target can be selected as the inter story drift that corresponds to the stability limit of the existing braces in compression. When this latter is too small to be considered than one should accept elastic buckling and displacement corresponding to yielding in tension of the existing diagonals should be the maximum admissible state at least for life safety. Larger target displacement are usually of small practical interest.
3. **Define the capacity curve**:. Given the target CBF displacement, the analysis can be reduced to the evaluation of the top displacement that corresponds to the achievement yielding in tensile original bracings or at most, the prevention of buckling in compressed original braces. This latter seems an excessive request as buckling in the elastic range has small consequences on structural damage and should usually be accepted. However if one prevent

buckling than the capacity curve of the existing CBF (that is the S of the procedure) will be linear elastic, otherwise it will be non linear elastic due to compressed buckled braces. When their contribution to structural stiffnes is negligible, less than 15%, they can certainly be disregarded.

If we disregard compressed diagonals or assume the stability limit of compressed diagonals as performance point, we shall design an additional bracing system that yields well before the performance point (reduction of the interstorey drift to the critical deformation that corresponds to diagonal yielding or buckling: ultimate limite state that corresponds to the ultimate top displacement *Du*). The retrofitted system *S+B* would be elasto-plastic with a post yielding hardening (elastic before reaching $D_{b+s,y}$ and hardening in $D_{b,y}$-D_u). The CBF (S) is in its elastic range (Figure 4), and the structure yields when the dissipative braces yields $D_{b,y}=D_{b+s,y}$.

In case we admit elastic buckling in compressed original braces and we cannot disregard their contribution to structural stiffness, than the pushover curve of the original struscture: S will be non linear elastic, we shall add the elasto plastic curve of the new braces to the original curve. In this case one should note that for the same displacement, the original structure has a larger response with respect to the case of disregarded compressed diagonal, and the equivalent damping is smaller adding the same BRB due to the larger elastic energy at the denominator of expr. 9).

During the design phase it is important to evaluate if, inside the range of displacement that allow to dissipate enough energy to obtain the performance target required, the existing diagonals remain elastic (*e.g.* according to code requirements). If this condition is verified the dissipative braces will be inserted inside the structure without modifying the CBF configuration.

In the opposite case the designer can decide, for example, to remove the existing diagonals and realize a completely new system of diagonals with the dissipative braces.

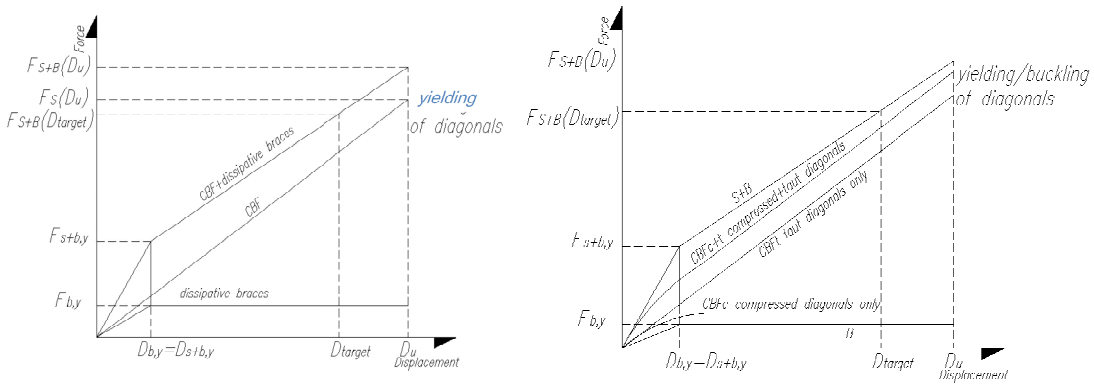


Figure 4: Force-Deformation of the existing structure (CBF) and of the retrofitted structure (CBF+dissipative braces). D_{target} is the target of the retrofitting design: diagonals must remain elastic and $D_{target}<D_u$. Left: original compressed braces neglected. Right: original compressed braces considered. B is the bracing systems (the BRBs) and S is the existing structure (CBF=CBFc+CBFt).

In the following Figures the deformed shape before and after retrofitting are illustrated.

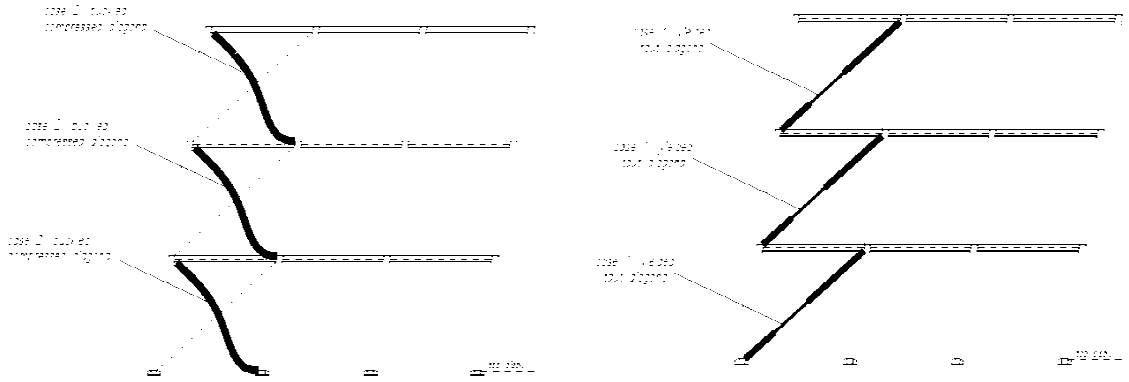


Figure 5: existing structure (CBF) under seismic action. The taut diagonals yielded (case 1 on the right), the compressed diagonals buckled (case 2 on the left) when the top displacement $D_{top}=D_u$

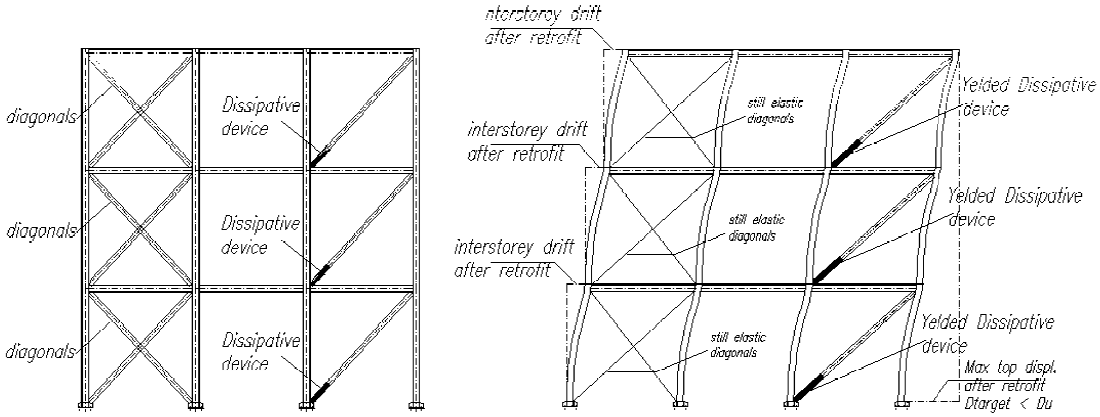


Figure 6: Retrofitted structure (CBF+dissipative braces) before and during seismic action. The diagonals are still elastic and the dissipative braces are yielded D_{top} after retrotting is limited in order to obtain the retrofitting of the structure: $D_{top}=D_{target}>D_u$

5 APPLICATION ON AN EXISTING R.C. STRATEGIC BUILDING

It is well known that results from a non linear static analysis are influenced by: pushover loading profile, characteristics of the numerical models. The loading profile determines loads distribution and deformed shape of the building and, consequently, the plastic distribution of forces and displacements (interstorey drift can be strongly influenced). The most common loading profiles are: proportional to masses, proportional to first mode shape (monomodal), proportional to acceleration, multimodal. The procedure presented in the previous chapter is generally applied using a "standard" monomodal pushover where the structure is subjected to monotonically increasing lateral forces, with an invariant spatial distribution (fundamental mode based), until collapse displacement is reached. This fundamental mode based force distribution doesn't account for higher mode contribution, which can be relevant, and therefore this limits the applicability of this approach to cases where the fundamental mode is dominant. Anyway it has to be highlighted that braces, if well designed, regularize the structure that can become strongly fundamental mode dependent. As discussed in the following has been analyzed, with a specific case study, if the use of the simple monomodal approach can be considered efficient. Therefore the proposed design procedure has been applied to retrofit an existing r.c. frame structure (Fig. 7-8) designed to resist vertical loads only: it is a strategic

building, situated in a seismic area of Italy, that has been designed and built in the 1970*s* without seismic details.

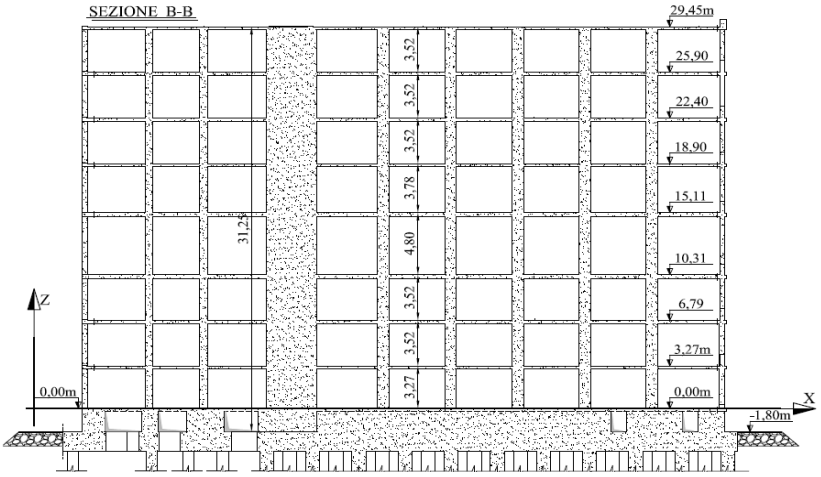


Figure 7: Longitudinal sections of the building

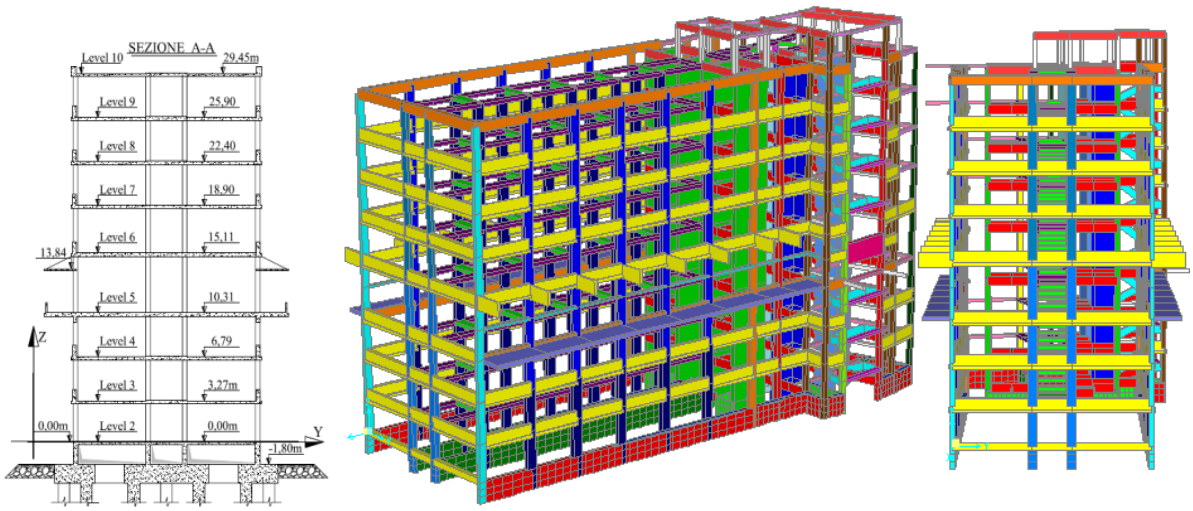


Figure 8: Transverse section of the building and 3D view of the numerical model

For brevity, in this paper, only results from longitudinal analysis are described: the design process has been performed considering the real 3D structure. The procedure has been applied in order to retrofit the building referring to a seismic action evaluated using the technical code currently in force in Italy (*p.g.a.* 0.25g; return period 949 years). The capacity curve has been derived considering a loading profile proportional to the first mode shape. In addition both the existing structure and the retrofitted structure have been studied using the multimodal push-over (Chopra & Goel, 2002) in order to evaluate the effectiveness of the ”standard” procedure and therefore the advantages on using the monomodal pushover for such a building: in this case the effectiveness of the procedure has been confirmed and, comparing results from monomodal and multimodal pushover applied on the retrofitted structure, the use of multimodal pushover can be considered not substantial for the design process applied on this typology of building. The performance point of the existing structure in terms of base shear and top displacement is V_S =9908 kN and $D_{t,S}$=133 mm. Then, the selected performance objective was to reduce displacement in order to avoid damage on both r.c. elements and masonry panels.

Therefore the target displacement has been selected adopting the following parameters: reducing the top displacement of about 50% ($D_{t,S,targ}$=66 mm) and limiting the interstorey drift to 2‰ at whichever level. Convergence to the desired values has been obtained with three iterations and the final result (performance point, iter 3) is the base shear V_{S+B}=12105 kN, with a 19% increase with respect to the original building, and the top displacement $D_{t,S+B}$=61 mm (practically coincident with the target, see Fig. 9).

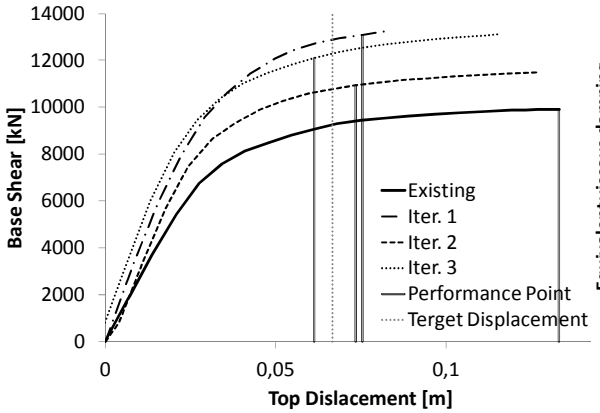


Figure 9: Capacity curves from pushover analysis along the longitudinal direction (Existing structure and braced structure at each iter from 1 to 3)

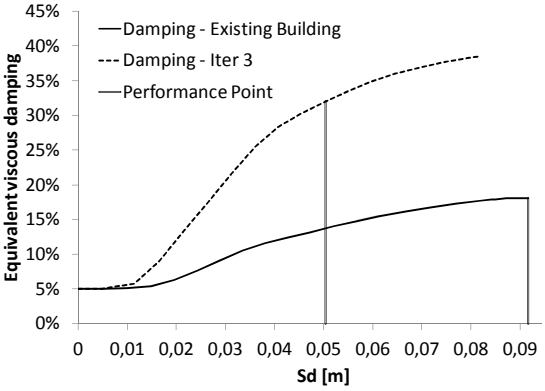


Figure 10: Variation of the total equivalent viscous damping with the spectral displacement S_d. At the p.p. $\nu_{eq,S+B}$=32% for the retrofitted structure and $\nu_{eq,S}$=14% for the existing building.

The contribution to dissipation offered by the dissipative system is ν_{eqB}=20% (ν_{eqS}=12%, ν_I=5%): Figure 10. In the final configuration the interstorey drift of each level has been significantly reduced to values lower than 2‰ and all the dissipative braces are in their plastic range (Fig. 11). The braced structure, if the distribution of interstorey drift is analyzed, is strongly characterized by a dominat first mode and consequently the multimodal analysis can be considered unnecessary: the two approaches differ of less than 1.5% (Fig. 12).

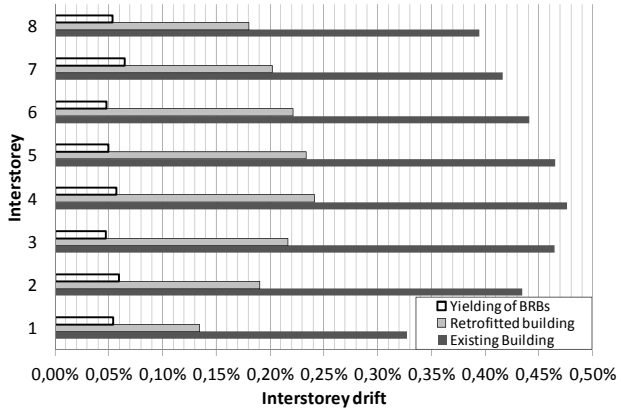


Figure 11: Interstorey drift (longitudinal) distribution for the existing building and the retrofitted building (longitudinal direction). In the graph is also indicated the drift corresponding to the yielding of the BRBs

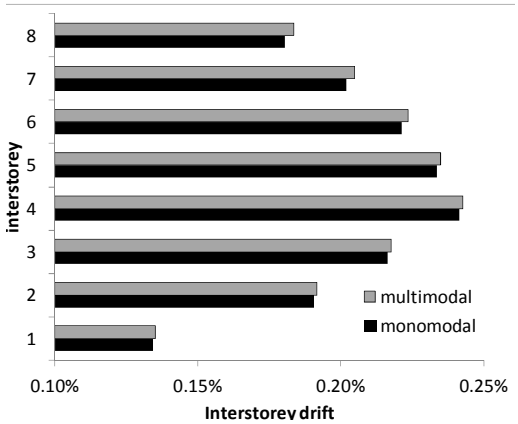


Figure 12: Interstorey drift (longitudinal) distribution in the retrofitted building obtained using the monomodal and the multimodal pushover. Differences are lower than 1,5%

6 CONCLUSIONS

A procedure for design of retrofitting of building structures using dissipative braces has been presented and the specific case of r.c. frame structures and CBFs have been detailed. The pro-

cedure, that in previous works has been applied to retrofit building up to four stories (Bergami & Nuti, 2012), has been updated with the use of the multimodal pushover and successfully applied to a structure having eight floors (30 m height). The target displacement has been determined, both in longitudinal and transverse direction, in order to limit both interstory drifts and ductility demand on existing structural elements. The final configuration obtained (the building braced along both the directions) has been tested performing pushover analyses proportional to the most relevant mode shapes (along both the longitudinal and transverse direction) of the building fully braced. Afterwards, results obtained from the application of monomodal pushover have been compared with results from multimodal pushover: the effectiveness of the procedure has been proved. Moreover, from this comparison, has been observed that, in terms of drifts and displacements, the multimodal pushover can be considered not relevant for the design procedure for dissipative braces proposed by Bergami and Nuti (2012) if it is applied on structures such as the one analyzed (midrise r.c. frame building).

REFERENCES

[1] Applied Technology Council. (1996). Seismic evaluation and retrofit of concrete buildings. Report ATC-40, Redwood City, California.

[2] Bergami A.V., Nuti C. (2013). A design procedure of dissipative braces for seismic upgrating structures. *Earthquakes and Structures,* Vol. **4**, No. 1, 85-108.

[3] Bergami A.V., Nuti C. (2011). Seismic retrofit of r.c. structures with dissipative braces, design and sustainability. fib Symposium 2011, Prague, Czech Republic.

[4] FEMA-274, (1997). "NEHRP Commentary on the Guidelines for the Seismic Rehabilitation of Buildings". Federal Emergency Management Agency Publication, U.S.A., 274.

[5] FEMA – ASCE 356 (2000). "Prestandard and Commentary for the Seismic Rehabilitation of Buildings". Washington, DC, 2000.

[6] Chopra, A. K., and Goel, R. K., 2002. Modal pushover analysis procedure for estimating seismic demands for buildings, Earthquake Eng. Struct. Dyn. 31 (3), 561–582.

[7] Black RG, Wenger WAB, Popov EP. Inelastic buckling of steel struts under cyclic load reversals. In: Rep. No. UCB/EERC-80/40. Berkeley, California; 1980.

[8] Goel SC. Earthquake resistant design of ductile braced steel structures. In: Stability and ductility of steel structures under cyclic loading. 1992; CRC Press. p. 297–308.

[9] Tremblay R. Inelastic seismic response of steel bracing members. J Constr Steel Res 2002;58:665–701

COMPDYN 2015
5th ECCOMAS Thematic Conference on
Computational Methods in Structural Dynamics and Earthquake Engineering
M. Papadrakakis, V. Papadopoulos, V. Plevris (eds.)
Crete Island, Greece, 25–27 May 2015

ROCKING BEHAVIOUR OF SIMPLE UNREINFORCED LOAD-BEARING MASONRY WALLS INCLUDING SOUNDPROOFING RUBBER LAYERS

C. Mordant[1], V. Denoël[1] and H. Degée[2]

[1] University of Liège
Chemin des Chevreuils, 1 – 4000 – Liège (Belgium)
e-mail: cmordant@ulg.ac.be/v.denoel@ulg.ac.be

[2] University of Hasselt
Agoralaan Gebouw H – 3590 – Diepenbeek (Belgium)
herve.degee@uhasselt.be

Keywords: Unreinforced Masonry, Rocking Behaviour, Stacked Blocks, Rubber.

Abstract. *This paper compares experimental measurements with predictions of different rocking models. These comparisons are carried out on the base of recent experimental results obtained by shake-table tests of four simple unreinforced load-bearing clay masonry walls that have exhibited a significant rocking behaviour for the highest acceleration inputs. In a first stage, the simple model proposed by Housner is used after slight modifications needed to properly consider the actual mass distribution. Two parameters are identified as governing the model response, namely the criterion defining the initiation of motion and the restitution coefficient. Then, a two stacked blocks model is developed and solved by an event-driven strategy. This two-block model is intended to allow a better description of the behaviour of tested specimens through a more precise modelling of the additional mass. Finally, the presence of rubber layers positioned at the top and bottom of two of the tested walls with the purpose of improving their acoustic behaviour required the development of an updated rocking model with viscous and flexible interfaces at the base of the wall and between the two stacked blocks. The properties of these interfaces are deduced from experimental data and their significant influence on the response is evidenced.*

1 INTRODUCTION

Rocking has been originally studied by Housner in 1963 [1] with the aim of explaining the survival of tall slender structures during earthquakes. To this purpose, the equation describing the rocking motion of a rigid block resting on a rigid base has been developed under the assumption of neither sliding between the block and its foundation nor bouncing. Numerous studies and scientific contributions resulted from this original "inverted pendulum" model and the interest in this topic is still relevant today.

Some authors have used the simple model of Housner to investigate analytically and numerically the rocking response of rigid blocks subjected to a seismic action as well as their stability [2, 3, 4, 5], while others have defined a new formulation to unify the piecewise equation describing the rocking motion [6] or developed numerical tools based on the Discrete Element Method (DEM) to model the rigid block [7].

Extensions of the simple model have been carried out on various aspects. First, the assumption of a rigid support has been discussed. Psycharis and Jennings [8] introduced an elastic foundation with damping in the problem and compared two possible solutions, namely the Winkler model and a simplified unilateral two-spring model. They concluded that both solutions were equivalent, allowing the use of the simple one. The former solution was also studied in [9], whilst the latter was used in [10, 11]. ElGawady et al. [12] investigated the influence of the material constituting the interface through experimental tests and Vassilou and Makris [13] examined the benefits of different types of isolated base thanks to numerical simulations. A main outcome of this research showed that ancient classical columns of Greek temples are more stable without any isolation. Then, the consideration of sliding and bouncing has been included. Shenton III and Jones established criteria for the transition between the possible modes of response (sliding, rocking, etc.) and derived the corresponding governing equations [14]. A particular attention is given to the effects of the friction coefficients in [15]. Finally, the deformability of the block has been taken into account. Psycharis carried out a parametric analysis on a SDOF oscillator with a harmonic excitation and outlined the importance of the ratio of the natural period of the structure to the period of excitation [16]. Oliveto et al. enhanced previous models with a novel set of coordinates and transition conditions [17] and Acikgos and DeJong were focused on the interaction between elasticity and rocking [18].

All these contributions have extended the range of application defined by the simple model developed by Housner. Nevertheless, these studies were limited to a single symmetric block and horizontal bases. Plaut et al. studied the consequences of an asymmetric geometry and tilted foundations on the rocking behaviour of blocks [19]. They conclude that, in the case of asymmetric bodies, the initial direction of the excitation can significantly affect the response. Two other studies on non-symmetric rigid bodies dealt with the overturning criteria [20] and the assessment of the advantages of base isolation for such blocks [21]. The literature review has also pointed out some attempts to translate the research work into design procedures. To this purpose, Priestley et al. [22] represented the rocking block as an equivalent SDOF oscillator with damping. This analogy was however shown as unsubstantiated and oversimplified [23]. More recently, Kelly presented a design method aiming at substituting for special study required by the latest version of New Zealand code, NZS 1170.5 [24].

Besides the rocking behaviour of single block, a few researchers have been interested in the dynamic behaviour of stacked blocks although related experimental investigations are rather limited. The analytical formulation of the equations translating the rocking motion of two blocks with no sliding was developed by Psycharis [25]. Such structures can behave according to eight different configurations, as illustrated in Figure 1. Spanos et al. [26] improved

these developments by adding different contributions to the transition criteria from one configuration to another and proposed an alternative method for the linearization of the nonlinear piecewise equations. Kounadis et al. assessed the minimum amplitude ground excitation leading to the overturning instability [27]. In order to consider these structures in design procedures, DeJong and Dimitrakopoulos proposed a methodology to derive approximate equivalence between rocking blocks and SDOF structures [28]. An experimental campaign has also been performed at the National Laboratory of Civil Engineering (LNEC) and where single blocks were tested, as well as multi-block structures lying on a rigid support [29]. This campaign allowed a better understanding of the rocking mechanisms and a comparison of measurements with model predictions.

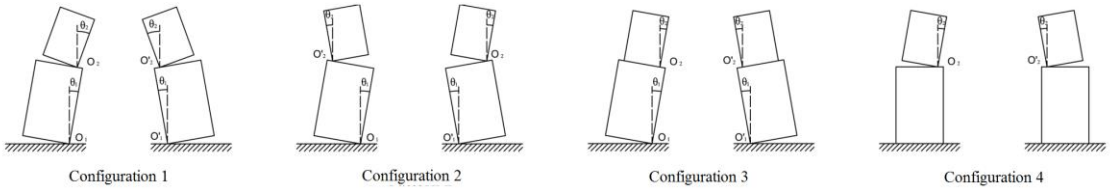


Figure 1: Rocking configurations for two-block assemblies

The present contribution takes place in the general context of experimental shaking table tests carried out at the EQUALS Laboratory in the framework of the SERIES project. The tested specimens are four simple unreinforced load-bearing masonry walls. The walls have two different aspect ratios, namely 1.1 (long walls) and 0.4 (short walls), and are loaded with an additional 5-ton steel mass lying on their top. They are made of thin-bed layered clay masonry with empty vertical joints. One wall of each aspect ratio includes soundproofing rubber layers located at the wall bottom and top for acoustic reasons. Pictures of the walls are given in Figure 2. The objectives of this campaign are to enhance the understanding of the dynamic behaviour of unreinforced masonry and to investigate the influence of the rubber layers. The preliminary assessment based on equivalent static procedure predicted a shear collapse. The observed behaviour of the walls was actually characterized by a significant rocking effect, at least for the highest acceleration inputs. The importance of this rocking effect has also proved to be strongly dependent on the aspect ratio and the presence of acoustic devices. Details of this experimental campaign are given in [30].



Figure 2: Tested specimens

The present paper is focused on the use of rocking models in view of comparing their predictive capacities with experimental measurements. On the one hand, the results obtained for walls without acoustic elements are assumed to be predictable by the simple model of Hous-

ner. Several adjustments of the original theory are however needed in order to take into account the upper steel mass lying on the top of the wall. Two main parameters governing the model response are identified, namely the criterion of motion initiation and the restitution coefficient. A two-block model is then used to better describe the tested specimens by properly considering the upper mass, a priori likely to rock with respect to the underlying wall. On the other hand, a new rocking model is derived for the specimens with rubber devices. It aims at modelling two-block structures with viscous and flexible interfaces between the blocks as well as between the bottom block and the foundation. The properties of these interfaces are deduced from experimental data and highly influence the model response**.**

2 ROCKING MODELS FOR WALLS WITHOUT RUBBER LAYERS

A previous contribution of the same authors [31] already tried to reproduce the hereby considered experimental measurements with a model based on the theory developed by Housner. This model was chosen for its simplicity, but some modifications have been performed to fit with the experimental configurations and to consider the additional mass placed on the wall top especially. The results and conclusions of this work are summarized in the first part of this section. The second part is dedicated to the more complex two-block model. This one matches better the experimental reality as the masonry wall and the upper mass are both represented by a specific block. It is however time-consuming in comparison to the simple model (from 2 to 5 times more).

2.1 Comparison with modified Housner's theory

Figure 3 illustrates the studied rigid block assuming that the additional steel mass can be considered as a point mass, drawn in red. The mass of the block is assumed to be negligible compared to the top mass. In comparison to the developments of Housner, the consideration of the upper mass involves differences for the parameters R and α, representing the radial distance from the centre of rotation O to the gravity centre and the angle between this distance and the vertical axis respectively.

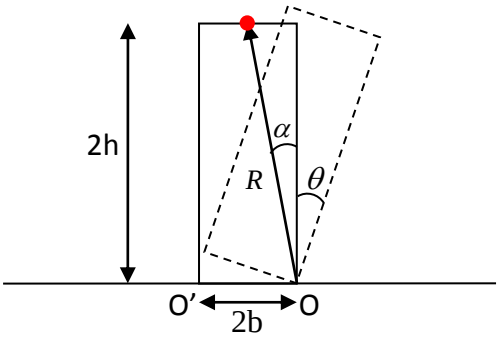


Figure 3: Modified model for simple rigid block

Rocking motion of a single rigid block resting on a rigid foundation and subjected to a horizontal acceleration $\ddot{x}_g$ is characterized by its rotation around one of its bottom corners, measured with the positive clockwise variable θ. The following equation describes this motion

$$I_O\ddot{\theta} + MR\ddot{x}_g \cos\left(\alpha\ sign\,\theta - \theta\right) + MgR\sin\left(\alpha\ sign\,\theta - \theta\right) = 0 \tag{1}$$

where $\ddot{\theta}$ [s^{-2}] is the second time derivative of θ [-], I_O [kgm^2] is the moment of inertia, M [kg] is the mass and g [ms^{-2}] is the gravitational acceleration.

Rocking is initiated if the overturning moment becomes larger than the restoring one, see eq. (2). The block and the support being rigid, energy dissipation only occurs when the block impacts on the base. This is practically translated by an instantaneous reduction of the angular velocity. Considering no bouncing, the angular momentum around the corner is conserved and allows the quantification of this reduction according to eq. (3).

$$2hM\ddot{x}_g \geq bMg \tag{2}$$

$$e = 1 - 2\frac{MR^2}{I_O}\sin^2\alpha \tag{3}$$

The equation of motion has been solved using a standard Newmark integration scheme under the assumption of a constant acceleration. The comparisons of numerical predictions with measurements are given in Figure 4 (left) for the short wall and in Figure 4 (right) for the long wall respectively. The results correspond to the last shaking table test with the highest acceleration input, characterized by a PGA of 0.234g and 0.688g for the short and the long wall respectively.

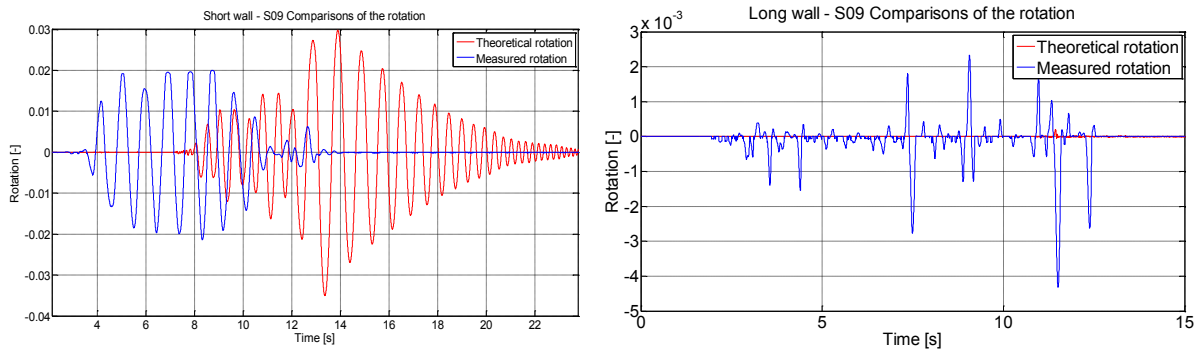


Figure 4: Comparison of the numerical predictions with experimental measurements for the short (left) and long (right) walls without rubber under the assumption of a rigid body

Figure 4 highlights differences between theoretical predictions and experimental measurements. Two issues are identified. First, the initially chosen criterion for defining the initiation of the rocking motion is felt as not appropriate, since the predictions do not capture the moment when rocking starts during the shaking table test on the short wall. This is observed as well for the long wall or for tests with a lower acceleration level for which the numerical simulations do not predict any motion, contrary to the observations. Moreover, the restitution coefficient seems also not to be appropriate. The rotation is indeed getting damped at a slower rate in the model than in reality. Modifications are proposed in [31] and principally consist in discussing the description of the rigid body motion, leading to the choice of a global rotation around an arbitrary point rather than a rotation around the external bottom corners. It results in a change in the parameters R and α as well as in the criterion of motion initiation and restitution coefficient. This latter also integrates a dependence on the square of the aspect ratio and on the ratio of the overall maximum rotation to the one reached during the oscillation before the considered impact. The consequences of these changes on the model predictions are illustrated in Figure 5 for the short wall.

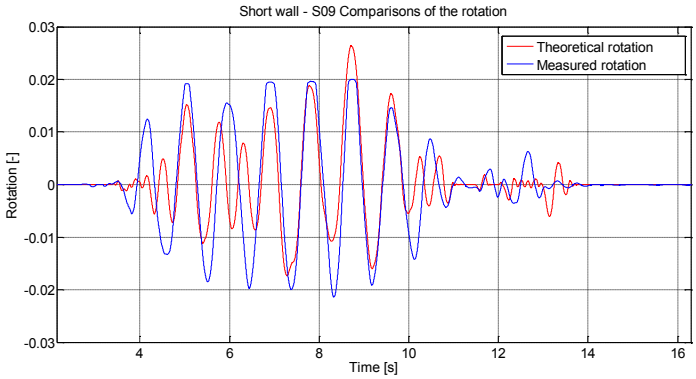


Figure 5: Comparison of the numerical predictions with experimental measurements for the short

The modifications proposed in [31] improve significantly the model predictions. The starting of the rocking motion is better captured and the damping issues at the end of the signal have vanished, albeit some differences remain present. In the case of the long wall, the model is able to predict the occurrence of rotation peak but overestimate their magnitude. Therefore, it can be concluded that such a simple model is not suitable for the present masonry walls. The modelling of the additional mass with a material point located at the block top is identified as a possible reason. A proper consideration of this body should thus enhance the results, which constitutes the topic of the second part of this paper. Another reason for the discrepancies is certainly the need for an educated-guess involved by relaxing the rigid body assumption. Indeed, several possibilities do exist regarding the position of the rotation point. Moreover, the formulation of the restitution coefficient is questionable since the contact between the block and its base is no longer a point.

2.2 Comparison with a two stacked blocks model

With regard to the specimen's configuration and to the results presented in the previous section, the two stacked blocks model seems to be more adapted. In this model, the masonry wall and the upper steel mass are indeed each more consistently represented by a block. The equations of motion implemented in the present model are based on the developments of Spanos et al. [26]. Nevertheless, another linearization of these equations is applied and the adopted numerical scheme resorts to an event-driven strategy which principles are detailed in [32] and summarized as follows. The resolution method consists in the integration of the linearized equations of motion corresponding to the current configuration of the system. Once the system configuration changes, the integration is stopped and the event-driven strategy is activated for the handling of the transition. An event localization function is first applied in the perspective of detecting accurately the moment of the transition. The update of the system variables is then operated. The equations of motion corresponding to the new configuration are chosen and the integration restarts. The activation of the event-driven strategy is controlled by “gap” functions defining the conditions to fulfil to change of configurations. In the present case, these “gap” functions are given by the equations translating the transition between configurations with or without impact.

Using the two-block model with the short wall geometry and the acceleration signal as inputs provides the results given in Figure 6.

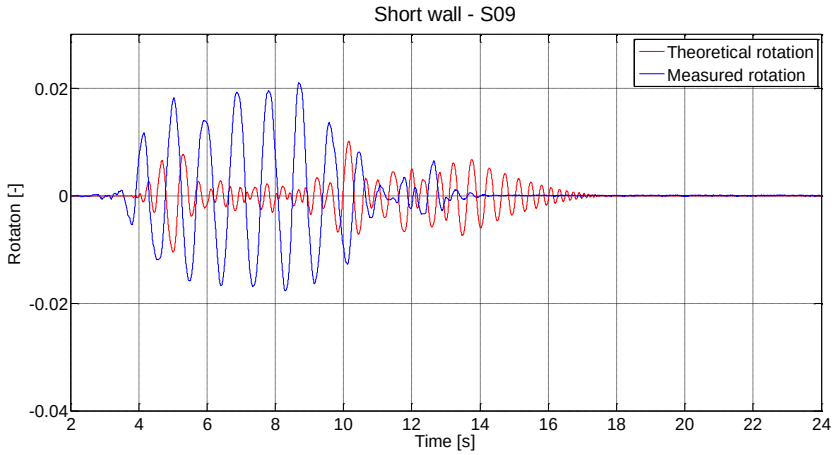


Figure 6: Predictions of the two-stacked-block model for the short wall

As it was observed with the simple model in the previous section (Figure 4), the two-stacked-block model cannot reproduce the specimen response. Nonetheless, the prediction of the initiation of the rocking motion is better, as is the energy dissipation. The assumption of a rigid block to model the masonry wall is also questionable. Similar modifications are made to consider a block rotating around another point than its corner, except for the energy dissipation. This leads to the results presented in Figure 7.

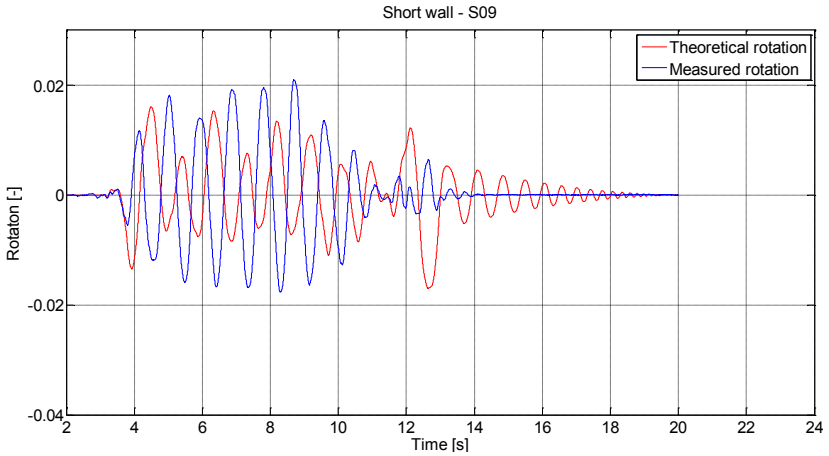


Figure 7: Predictions of the modified two-stacked-block model for the short wall

The initiation of the rocking is now properly captured, but the magnitude of the first theoretical rotation peak is overestimated and occurs too late. This result is possibly due to inadequate account for the energy dissipation. Additional modifications are therefore required. Different attempts have been performed to improve the dissipation of energy at the impacts with a formulation based on the conservation of the angular momentum. These attempts allow a better approximation for the magnitude of the first peak, but the overall response remains remote from the measurements.

As a conclusion, the two stacked blocks model gives better results than the simple model, when based on a similar set of assumptions. Improvements are however required and the assumption of a rigid block for representing the masonry wall seems to be inappropriate. According to the authors, the main reason is the presence of empty vertical joints. Relaxing this assumption to allow rotation around a point to be determined leads to a better prediction of the rocking motion initiation, but makes questionable the quantification of the energy dissipa-

tion by means of the principle of conservation of the angular momentum. This last point will be the topic of forthcoming investigations.

3 ROCKING MODEL FOR WALLS WITH RUBBER LAYERS

Literature review has highlighted a huge interest in the rocking behaviour of single block. Different assumptions have been made on the block, its foundation and the possible behaviours. Besides this, a few research works were focused on the rocking behaviour of two or more stacked blocks. These latter are however limited to rigid blocks standing on a rigid support. This section aims at developing a new rocking model for two-stacked rigid blocks with viscous and flexible interfaces between the support and the bottom block, like blocks standing on a flexible foundation, as well as between the blocks. This model will be then used to compare theoretical predictions with measurements recorded during the shaking table tests on the unreinforced masonry walls including rubber devices.

3.1 Development of the new rocking model

The geometry of the modelled blocks is given in Figure 8 (left). The blocks are symmetric and have bases $2b_i$, heights $2h_i$, masses m_i and centroid moments of inertia I_{Gi} (i is equal to 1 for the base block and 2 for the top block). The centroid of the block is denoted by G_i. The interfaces have heights e_b and e_t respectively and are characterized by a stiffness (k_b or k_t) and a damping ratio (c_b or c_t). Rocking motion of rigid blocks including viscous and flexible interfaces can be described with four variables, namely the rotation of the blocks, θ_1 or θ_2, and the vertical displacement of the interfaces, $z_{b,1}$ and $z_{b,2}$, as denoted in Figure 8 (right). The friction is supposed to be large enough to avoid sliding.

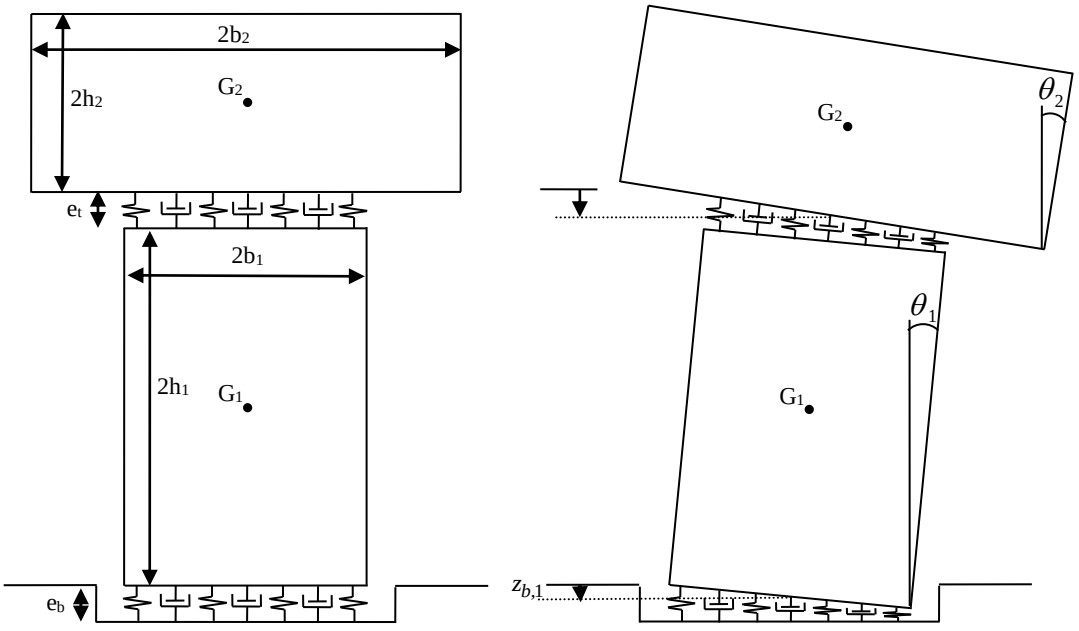


Figure 8: Two-stacked blocks model with viscous and flexible interfaces

It is assumed that the interfaces have no tensile strength. Therefore, uplift occurs when the upward displacement of a part of the base is larger than the deflection due to gravity load. Four different configurations can thus be observed, namely (i) no uplift, (ii) uplift at the base interface, (iii) uplift at the top interface and (iv) uplift at both interfaces. Two parameters g_b and g_t are defined in order to define the configuration. They are equal to the unit if there is no

uplift and become zero in the contrary. The conditions to define the value of the parameters are given by (4) and (5).

$$g_b = \begin{cases} 0 & if\ |z_{b1}| > b_1 \sin\theta_1 \\ 1 & if\ |z_{b1}| \le b_1 \sin\theta_1 \end{cases} \tag{4}$$

$$g_t = \begin{cases} 0 & if\ |z_{b2}| > b_2 \sin\theta_2 \\ 1 & if\ |z_{b2}| \le b_2 \sin\theta_2 \end{cases} \tag{5}$$

The equations of motion for the possible configurations are obtained by the Lagrange's method. Details of these equations will be provided in an upcoming contribution. A linearization is then performed and Eq. (6) presents the result in matrix form when the blocks are subjected to seismic horizontal $\ddot{x}_g$ and vertical $\dot{z}_g$ accelerations.

These linearized equations are implemented in a numerical procedure and is combined with an event-driven strategy for the handling of the transition between configurations. The corresponding "gap" functions are defined by the equations translating the change of value for the two parameters g_b and g_t.

$$\begin{bmatrix} I_{G1}+m_1h_1^2+m_2(2h_1+e_t)^2 & m_2h_2(2h_1+e_t) & 0 & 0 \\ m_2h_2(2h_1+e_t) & I_{G2}+m_2h_2^2 & 0 & 0 \\ 0 & 0 & m_1+m_2 & m_2 \\ 0 & 0 & m_2 & m_2 \end{bmatrix} \begin{pmatrix} \ddot{\theta}_1 \\ \ddot{\theta}_2 \\ \ddot{z}_{b,1} \\ \ddot{z}_{b,2} \end{pmatrix}$$

$$+ \begin{bmatrix} -\frac{(1+g_b)}{3}c_bb_1^3+\frac{(1+g_t)}{3}c_tb_1^3 & -\frac{(1+g_t)}{3}c_tb_1^3 & -\frac{(1-g_b)}{2}c_bb_1^2 & \frac{(1-g_t)}{2}c_tb_1^2 \\ -\frac{(1+g_t)}{3}c_tb_1^3 & \frac{(1+g_t)}{3}c_tb_1^3 & 0 & -\frac{(1-g_t)}{2}c_tb_1^2 \\ -\frac{(1-g_b)}{2}c_bb_1^2 & 0 & (1+g_b)c_bb_1 & 0 \\ \frac{(1-g_t)}{2}c_tb_1^2 & -\frac{(1-g_t)}{2}c_tb_1^2 & 0 & (1+g_t)c_tb_1 \end{bmatrix} \begin{pmatrix} \dot{\theta}_1 \\ \dot{\theta}_2 \\ \dot{z}_{b,1} \\ \dot{z}_{b,2} \end{pmatrix}$$

$$+ \begin{bmatrix} -m_1gh_1-m_2g(2h_1+e_t) & & & \\ +\frac{(1+g_b)}{3}k_bb_1^3+\frac{(1+g_t)}{3}k_tb_1^3 & -\frac{(1+g_t)}{3}k_tb_1^3 & -\frac{(1-g_b)}{2}k_bb_1^2 & \frac{(1-g_t)}{2}k_tb_1^2 \\ -\frac{(1+g_t)}{3}k_tb_1^3 & -m_2gh_2+\frac{(1+g_t)}{3}k_tb_1^3 & 0 & -\frac{(1-g_t)}{2}k_tb_1^2 \\ -\frac{(1-g_b)}{2}k_bb_1^2 & 0 & (1+g_b)c_bb_1 & 0 \\ \frac{(1-g_t)}{2}k_tb_1^2 & -\frac{(1-g_t)}{2}k_tb_1^2 & 0 & (1+g_t)k_tb_1 \end{bmatrix} \begin{pmatrix} \theta_1 \\ \theta_2 \\ z_{b,1} \\ z_{b,2} \end{pmatrix}$$

$$= \begin{pmatrix} -\ddot{x}_g\left[m_1h_1+m_2(2h_1+e_t)\right] \\ -\ddot{x}_gm_2h_2 \\ -(\ddot{z}_g+g)(m_1+m_2) \\ -(\ddot{z}_g+g)m_2 \end{pmatrix} \tag{6}$$

The energy dissipation in this model is a continuous process. The viscous and flexible interfaces indeed dissipate energy through damping in the dash-pots.

3.2 Comparison of the new model with experimental results

The application of the model requires the calibration of the mechanical properties of the interfaces representing the rubber layers. This is one topic of [33] and is based on seismic tests at a low-to-moderate acceleration level. During these tests, the specimens remained in contact with the support. Deteriorated properties have however been chosen as tests at lower acceleration levels probably damage the rubber devices. Tests at the highest seismic input have been therefore performed on damaged specimens. The interfaces are supposed to behave linearly and elastically. The others model inputs are the blocks geometry and the acceleration signals. The chosen acceleration signals have a PGA of 0.171g for the short wall and of 0.457g for the long wall. The results in terms of top and bottom rotations are presented in Figure 9 and Figure 10 for the short and the long walls with rubber respectively.

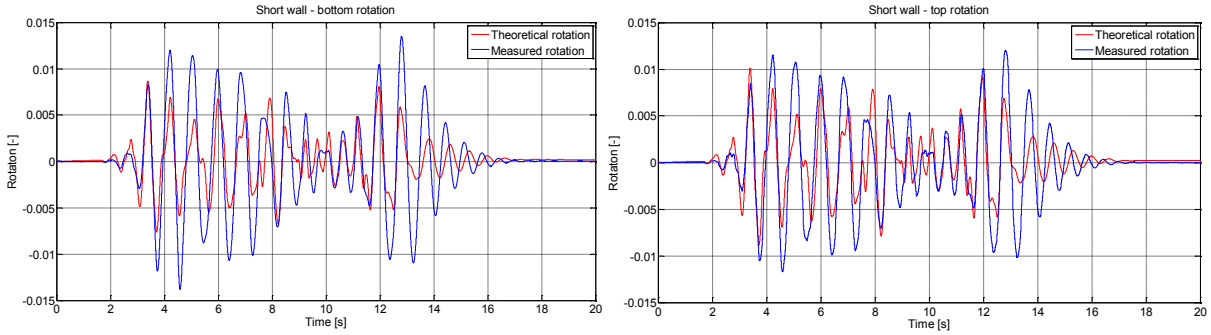


Figure 9: Comparison between model predictions and experimental measurements (short wall)

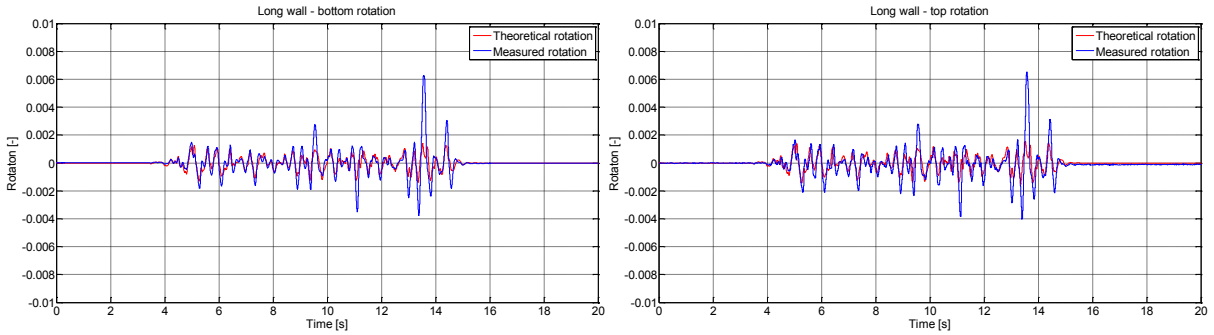


Figure 10: Comparison between model predictions and experimental measurements (long wall)

The mechanical properties used are 4.95 (3.85) MPa for the elastic modulus and 5.44 (1.67) % for the damping ratio in the case of the short (long) wall. The model predictions are in good agreements with the experimental measurements. The beginning of the rocking motion is well approximated without any further modifications. The assumptions of rigid blocks can indeed be felt here as realistic when referring the rigidity of the block to the one of the joints, which was of course not the case without rubber joints since, in that configuration, the rigidity of the blocks had to be referred to an infinitely rigid foundation. Nevertheless, some differences are observed, especially concerning the peak magnitudes. Consequently, further investigations are required. A larger parameter study is planned to highlight the most relevant properties to be tuned at the level of the interfaces. The possible influence of choosing another type of material law for the rubber layers has also to be studied, these interfaces being the main issue of the model.

4 CONCLUSIONS

This paper deals with the rocking behaviour of masonry structures subjected to seismic loading. The main motivation of this paper is the observation during shake-table tests that a significant rocking motion was experienced by the structures when the tested unreinforced load-bearing clay masonry walls including or not soundproofing rubber layers are shaken at a sufficient acceleration level.

On the one hand, the paper is focused on the rocking behaviour of walls without rubber. A first model is developed, based on the simple theory of Housner and modified to consider the additional mass placed on the walls top. The comparisons of the model predictions with the experimental measurements highlight the need in modelling the additional mass properly and the inconveniency of the assumption of a rigid block for the masonry walls. A second model of two-stacked blocks is therefore implemented with the developments of Spanos et al. This is accompanied with an event-driven strategy for the handling of the transition between configurations. Additional investigations are however still required to allow the masonry walls not to be considered as rigid anymore. The energy dissipation is a main issue since the blocks do not rotate around their corners and, thus, the use of the principle of conservation of the angular momentum is not valid.

On the other hand, a new two-stacked blocks model is developed for the walls with rubber. The main innovation is the consideration of a viscous and flexible interface between the blocks. A good agreement between model prediction and experimental data is found, even if some differences are outlined. In this case, the masonry walls can be assumed as rigid in comparison to the rubber interfaces. The comparison leads to a quite good agreement between theoretical results and experimental measurements. In order to improve the results, further developments are however still in progress, especially regarding the mechanical properties of the interfaces to be used in the model. Details of the new model will be the topic of an upcoming contribution.

ACKNOWLEDGEMENTS

The research leading to these results has received funding from the European Union Seventh Framework Programme (FP7/2007-2013) under grant agreement n° 227887, SERIES. C. Mordant also acknowledges the F.R.S - FNRS (Belgian fund for research) for the support of his PhD.

REFERENCES

[1] G. W. Housner, Behaviour of inverted pendulum structures during earthquakes. *Bulletin of the Seismological Society of America*, **53**(2):403–417, 1963.

[2] C-S. Yim, A.L. Chopra, J. Penzien, Rocking response of rigid blocks to earthquakes, *Earthquake engineering and structural dynamics*, **8**:565–587, 1980.

[3] P. D. Spanos, A-S. Koh, Rocking of Rigid Blocks Due to Harmonic Shaking, *Journal of Engineering Mechanics*, **110**(11):1627–1642, 1984.

[4] J. Zhang, N. Makris, Rocking Response of Free-Standing Blocks Under Cycloidal Pulses, *Journal of Engineering Mechanics*, **127**(5):473–483, 2001.

[5] A. N. Kounadis, On the Overturning Instability of a Rectangular Rigid Block Under Ground Excitation, *The Open Mechanics Journal*, **4**:43-57, 2010.

[6] F. Prieto, P.B. Lourenço, On the Rocking Behaviour of Rigid Objects, *Meccanica*, **40**:121-133, 2005.

[7] F. Prieto, F. Peña, P.B Lourenço, J. V. Lemos, Numerical Simulation of Rigid Blocks Subjected to Rocking Motion, *5th conference on Structural Analysis of Historic Constructions*, New Delhi, India, November, 2006.

[8] I. N. Psycharis, P. C. Jennings, ROcking of Slender Rigid Bodies Allowed to Uplift, *Earthquake Engineering and Structural Dynamics*, **11**:57-76, 1983.

[9] A-S. Koh, P. D. Spanos, J. M. Roesset, Harmonic Rocking of Rigid Block on Flexible Foundation, *Journal of Engineering Mechanics*, **112**(11):1165-1180, 1986.

[10] A. Palmeri, N. Makris, Response analysis of rigid structures rocking on viscoelastic foundation, *Earthquake Engineering and Structural Dynamics*, **37**:1039-1063, 2008.

[11] Q. T. Ma, J. W. Butterworth, Simplified Expressions for Modelling Rigid Rocking Structures on Two-spring Foundations, *Annual Technical Conference of NZ Society for Earthquake Engineering*, Wellington, New-Zealand, 26-28 March, 2010.

[12] M. A. ElGawady, Q. T. Ma, J. W. Butterworth, J. Ingham, Effects of interface material on the performance of free rocking blocks, *Earthquake Engineering and Structural Dynamics*, **40**:375-392, 2011.

[13] M. F. Vassiliou, N. Makris, Analysis of the rocking response of rigid blocks standing free on a seismically isolated base, *Earthquake Engineering and Structural Dynamics*, **41**:177 -196, 2011.

[14] H. W. Shenton III, N. P. Jones, Base Excitation of Rigid Bodies. I: Formulation, *Journal of Engineering Mechanics*, **117**(11):2286-2306, 1991.

[15] M-Y. Jeong I-Y. Yang, Characterization on the Rocking Vibration of Rigid Blocks under Horizontal Harmonic Excitations, *International Journal of Precision Engineering and Manufacturing*, **13**(2):229-236, 2012.

[16] I. N. Psycharis, Effect of Base Uplift on Dynamic Response of SDOF Structures, *Journal of Engineering Mechanics*, **117**(3):733-754, 1991.

[17] G. Oliveto, I. Caliò, A. Greco, Large displacement behaviour of a structural model with foundation uplift under impulsive and earthquake excitations, *Earthquake Engineering and Structural Dynamics*, **32**:369 -393, 2003.

[18] S. Acikgoz, M. J. DeJong, The interaction of elasticity and rocking in flexible structures allowed to uplift, *Earthquake Engineering and Structural Dynamics*, **41**:2177-2194, 2012.

[19] R. H. Plaut, W. T. Fielder, L. N. Virgin, Fractal Behaviour of an Asymmetric Rigid Block Overturning Due to Harmonic Motion of a Tilted Foundation, *Choas, Solitons & Fractals*, **7**(2):177-196, 1996.

[20] R. I. Borosheck, D. Romo, Overturning criteria for non-anchored non-symmetric rigid bodies, *13tg World Conference on Earthquake Engineering*, Vancouver, Canada, 1-6 August, 2004.

[21] A. Contento, A. Di Egidio, Investigations into the benefits of base isolation for non-symmetric rigid blocks, *Earthquake Engineering and Structural Dynamics*, **38**:849 -866, 2009.

[22] M. J. N. Priestley, R. J. Evison, A. J. Carr, Seismic response of structures free to rock on their foundations, *Bulletin of the New Zealand National Society for Earthquake Engineering*, **11**(3):141-150, 1978.

[23] N. Makris, D. Konstantinidis, The rocking spectrum and the limitations of practical design methodologies, *Earthquake Engineering and Structural Dynamics*, **32**:265-289, 2003.

[24] T. E. Kelly, Tentative seismic design guidelines for rocking structures, *Bulletin of the New Zealand National Society for Earthquake Engineering*, **42**(4):239-274, 2009.

[25] I. N. Psycharis, Dynamic behaviour of rocking two-block assemblies, *Earthquake Engineering and Structural Dynamics*, **19**:555-575, 1990.

[26] P. D. Spanos, P. C. Roussis, N. P. A. Politis, Dynamic analysis of stacked rigid blocks, *Soil Dynamics and Earthquake Engineering*, **21**:559-578, 2001.

[27] A. N. Kounadis, G. J. Papadopoulos, D. M. Costovos, Overturning instability of a two-rigid block system under ground excitation, *Journal of Applied Mathematics and Mechanics*, **92**(7):536-557, 2012.

[28] M. J. DeJong, E. G. Dimitakopoulos, Dynamically equivalent rocking structures, *Earthquake Engineering and Structural Dynamics*, **43**:1543-1563, 2014.

[29] F. Peña, F. Prieto, P. B. Lourenço, A. C. Costa, Experimental dynamic behavior of free standing multi-block structures under seismic loadings, *Journal of Earthquake Engineering*, **12**:953-979, 2008.

[30] C. Mordant, M. Dietz, H. Degée, *Seismic behaviour of thin-bed layered unreinforced clay masonry shear walls including soundproofing elements*, In: Alper Ilki and Michael N. Fardis (eds), Proc SERIES Workshop. Geotechnical, Geological and Earthquake Engineering series (chapter 6).

[31] C. Mordant, M. Dietz, H. Degée, *Shaking table tests on unreinforced load-bearing masonry walls - comparison with simple rocking models* (Paper n°1238), In: Proc. 4th ECCOMAS Thematic Conference on Computational Methods in Structural Dynamics and Earthquake Engineering (COMPDYN 2013), eds. M. Papadrakakis, V. Papadopoulos & V. Plevris, Kos Island, Greece, 12-14 June 2013

[32] A. Depouhon, E. Detournay, V. Denoël, Event-driven integration of linear structural dynamics models under unilateral elastic constraints, *Computer Method in Applied Mechanics and Engineering*, **276**:312-340, 2014.

[33] C. Mordant, C. Taylor, M. Dietz, L. Vasseur, H. Degée, Shaking table tests on unreinforced load-bearing masonry structures, *9th International Masonry Conference*, Guimarães, Portugal, 7-9 July, 2014.

COMPDYN 2015
5th ECCOMAS Thematic Conference on
Computational Methods in Structural Dynamics and Earthquake Engineering
M. Papadrakakis, V. Papadopoulos, V. Plevris (eds.)
Crete Island, Greece, 25–27 May 2015

NUMERICAL MODELLING, ANALYSIS AND RETROFIT OF THE HISTORICAL MASONRY BUILDING "LA SAPIENZA"

S. Caprili[1], F. Mangini[1] and W. Salvatore[1]

[1] Department of Civil and Industrial Engineering, University of Pisa
Largo L. Lazzarino 1, 56122 Pisa, Italy

silvia.caprili@ing.unipi.it, f.mangini@ing.unipi.it, walter@ing.unipi.it

Keywords: Cultural heritage, masonry building, vulnerability assessment, structural safety

Abstract. *The evaluation of the structural safety and seismic vulnerability of historical masonry buildings represents one of the most important problems affecting countries, like Italy, characterized by a wide cultural heritage whose original configuration shall be preserved against unexpected seismic events or insufficient maintenance. Recent earthquakes in the Italian regions (Umbria-Marche 1997, Molise 2002, L'Aquila 2009 and Emilia-Romagna 2012) evidenced the high vulnerability of historical masonry buildings, severely damaged in both their structural and not-structural components (i.e. walls, vaults, domes, arches, ornaments and others) and the following significant economic effort required for the execution of retrofit interventions. According to the actual Italian Standard for Constructions (D.M. 14/01/2008) and to the Guidelines provided by the Italian Ministry for Infrastructures for the evaluation and reduction of seismic risk on historical heritage (2010), a multi-level approach is generally adopted for the assessment of the structural safety and seismic vulnerability of ancient masonry buildings and for the design of retrofit interventions. In the present work, the above mentioned multi-level approach is applied to "La Sapienza" Palace in Pisa (Italy). The building, ancient seat of the University of Pisa, was subjected to a wide in situ structural survey and to experimental testing campaigns (including geotechnical analyses, mechanical characterization of materials, structural monitoring and other) allowing the elaboration of a reliable FEM model used for the execution of structural verifications and for the individuation of the main retrofit techniques able to preserve its original nature providing, at the same time, a sufficient margin of structural safety.*

1 INTRODUCTION

The evaluation of the static safety and seismic vulnerability of existing buildings represents one of the most important topics in Italy, country characterized by a wide architectural heritage made up of buildings realized without the adoption of suitable measures against horizontal actions, following different and overlapping construction techniques and frequently characterized by the lack of adequate maintenance. Recent seismic events (such as L'Aquila 2009, Umbria-Marche 1997 and Emilia-Romagna 2012) evidenced the high vulnerability of the existing masonry heritage, as well as the need to define suitable strategies for modifying, improving or locally reinforcing structures (or portions of them), without altering their original architectural characteristics but providing, at the same time, a sufficient margin of structural safety.

During the centuries, historical masonry buildings often underwent severe modifications, expansions, enlargements and super-elevations that transformed their original configuration of "*single buildings*" into "*structural aggregates*", made up of different parts connected together without specific devices and not necessarily working in a global way, with the possible following activation of local mechanisms especially in presence of dynamic actions, such as overturning of facades, tilting of corners and others. As a consequence of what above presented, there is a clear and pressing need to execute extensive static safety and seismic vulnerability evaluations, with particular attention to buildings of historical-architectural importance, in order to organize suitable retrofit operations.

Current Italian and international standards for constructions [1, 2, 3] provide a codified procedure for the vulnerability analysis and the planning of readjustment/improvement operations for existing buildings. Such procedure is based on the definition of a "*Level of Knowledge*" of the structure, achieved through structural and geometrical surveys, critical historical analyses and determinations of the material mechanical properties. According to this level, a specific degree of uncertainty is attributed to the execution of safety checks and to the organization of the retrofit proposals. The aforesaid approach, commonly adopted for 'ordinary' structures (both masonry or r.c. ones), can be extended to historical-monumental buildings by accounting for their greater complexity and the following need of a very deep level of knowledge.

A number of examples of evaluations of the seismic behaviour of monumental buildings are presented in the current scientific literature [4, 5, 6]. Within the framework of the European project "Perpetuate" [7, 8, 9], a displacement-based approach for the vulnerability analysis of existing monumental buildings was provided. Wide-scale analyses of historical villages (or portion thereof), to be executed in parallel with the adoption of macroseismic intensity maps in order to assess the behaviour of buildings, to define vulnerability curves and to finally identify the most vulnerable constructions for which the organization of retrofit interventions can be considered a priority, were also proposed [10, 11].

Oliveira [12] strongly discussed the problem of the numerical modelling of complex buildings, evidencing the possibility to adopt many different possible approaches (linear and nonlinear one-dimensional models for individual elements, 2-D and 3-D models for entire building complexes, etc.), as well as the difficulty of determining the most appropriate methodology for each specific case. Despite the ever-more refined and accurate numerical models made possible by modern calculation software, significant uncertainties remain regarding the correct representation of the materials' mechanical properties and the dynamic behaviour of the entire building or portions thereof.

In this context, Italian Technical Regulations for Constructions [1], together with the "Guidelines of the Ministry of Culture and Heritage" [13], underlines the necessity to analyze,

in parallel to the global behaviour of such structural aggregates, the possible activation of local collapse mechanisms of significant structural portions, identified on the base of the critical points and of the cracking scenario revealed during the in situ survey. According to the proposed approach, different evaluation levels of seismic safety, associated to different degrees of investigation/knowledge of the building, can be related to different safety checks, ranging from large-scale evaluations, to the formulation of macroelement models for structurally independent portions of the complex under study and to the execution of safety checks on specific global models of the individual buildings.

In the present paper the methodology developed and refined for assessing the static safety and seismic vulnerability of the Pisa "*Palazzo della Sapienza*", historical site of the University since the 14th century, is presented. Moreover, some general proposals for the retrofit interventions are provided. The verification of the structural safety of a building as complex as the one considered cannot be performed simply based on traditional approaches based on global numerical modelling: methods specifically developed for the particular construction, based on an extensive knowledge of the structure's current state acquired through a multidisciplinary approach that combines historical studies of the building's evolution, morphological-structural-geotechnical surveys, experimental determinations of materials' properties and structural monitoring, are then needed. More in detail, accurate critical historical studies and detailed architectural surveys through both direct and indirect techniques allows the determination of the structural units and of their connections in the whole building. The information obtained through the morphological-structural surveys allow the elaboration of reliable numerical models (both at local and global level) for evaluating the static and seismic behaviour of the entire building and portions thereof, and the following determination of the suitable retrofit techniques to be used for the whole building, for its portion of it or for single structural elements. Figure 1 shows the general scheme adopted for the assessment and retrofit of Palazzo La Sapienza in Pisa.

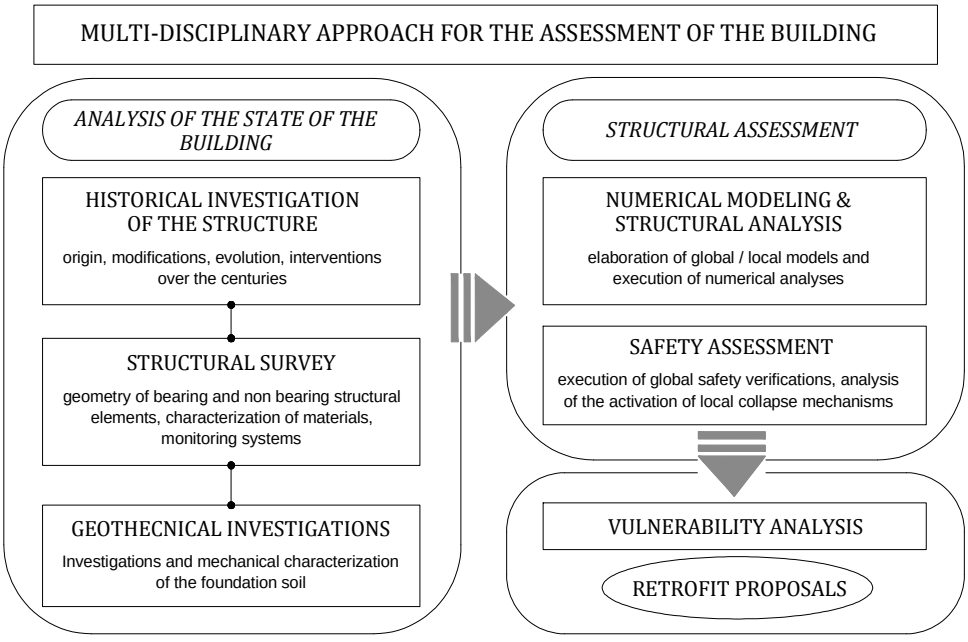


Figure 1: Scheme of the adopted methodology − integrated approach.

2 PALAZZO LA SAPIENZA: ORIGIN AND STATE OF ART

The building, originated from the medieval structures of *Piazza del Grano* and of *Dogana del Sale* adsorbing the adjacent single masonry units and ancient tower houses, was progressively extended, during the XV century, to house the seat of the University of Pisa and all the connected services. A significant modification in the original structure of the Palace was applied at the beginning of the XIX century, with the necessity to increase the available place for the books owned by the University Library (about 30.000 volumes). The works necessary for the enlargement of the building, including the demolition of many internal bearing walls, the super-elevation of the west part of the building of about 3.0 m, the modification of shape and dimensions of doors and windows, the realization of new storey slabs and others, started in 1819 and continued for about three years, immediately leading to structural diseases in several parts of the building: a wide cracking scenario was revealed in correspondence of the north and south-eastern parts of the building. The progressive deterioration of the building, as widely described in the ancient literature, was the direct consequence of the executed structural interventions, that neglected the original configuration of the Palace and its incapability to sustain higher loads respect to the design ones.

Nevertheless, and also despite singular interventions executed during the XIX century (i.e. the application of steel ties to reduce the horizontal thrusts due to vaults, arches and to avoid overturning mechanisms of single and multiple walls), the enlargement of the building, with the following increase of vertical loads, continued during the XX century, once again due to the increase of the University Library. Between 1928 and 1929, the western part of the building was raised up reaching the height of the adjacent parts: this intervention finally transformed the original Renaissance structure of the Palace, made up of a relative small volume of two storeys into the actual massive three storey building (Figure 2). Several additional modifications (for example the reconstruction of the vault of the new Aula Magna) were then executed as a consequence of the damages of the second world war. The detailed description of the morphological development of the building is presented in [14].

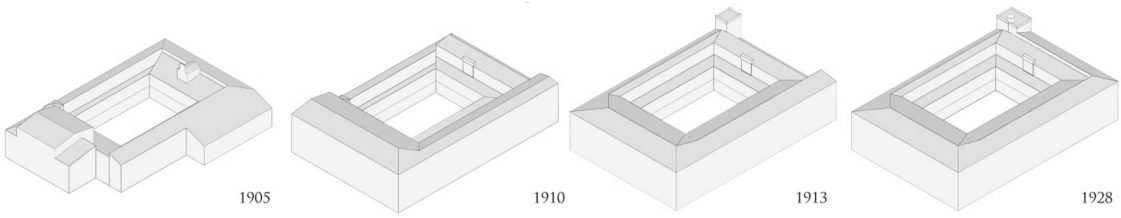
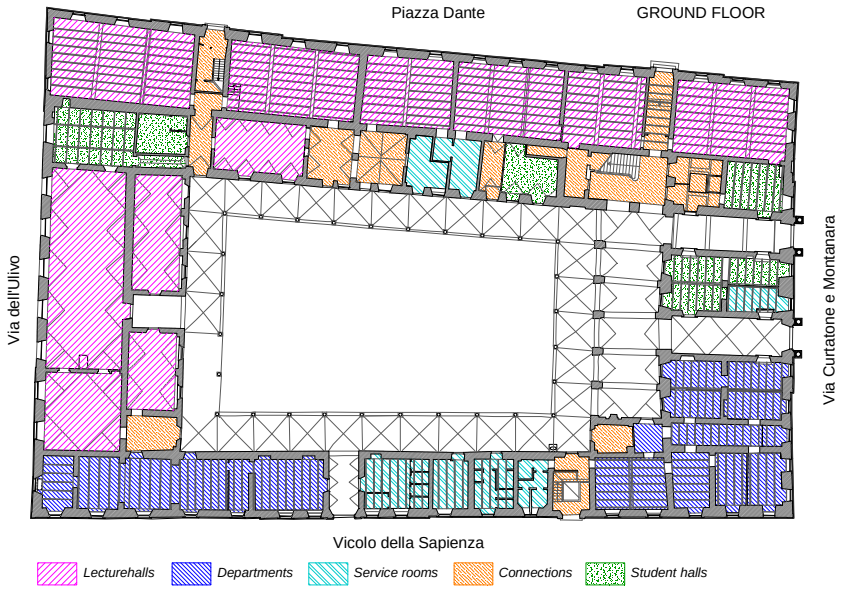


Figure 2: Structural modification of Palazzo La Sapienza during the first two decades of XIX century.

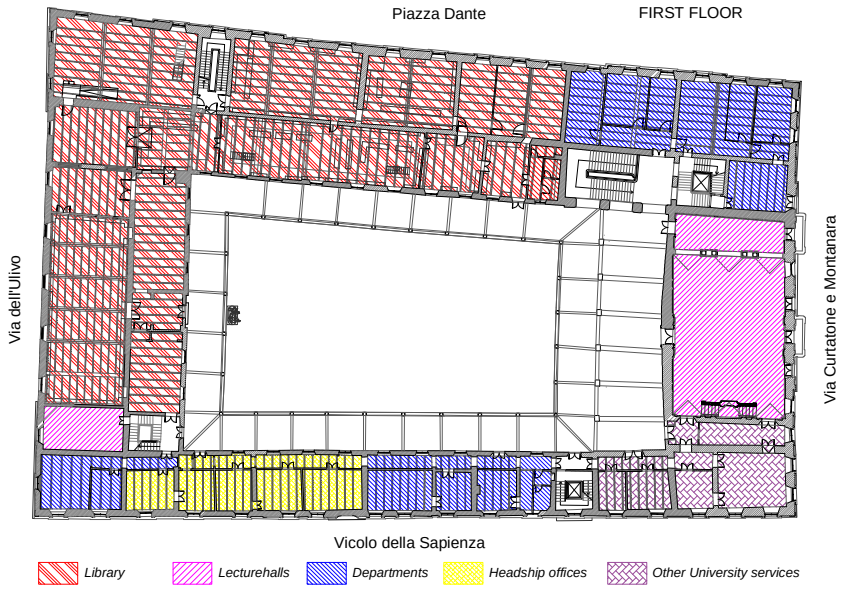
Nowadays, the building presents a trapezoidal plan with three floors above ground, with a gable roof whose garret accessible only for inspection and maintenance. The plan dimensions are 80.0 m by 53.7 m, while the central courtyard, surrounded by a ground-level colonnade and a first-floor arcade running parallel to the ground floor sides, has maximum dimensions of 35.5 m by 21.2 m. Different vaulted surfaces (i.e. cross and cloister vaults, some of them with lunettes) and various types of floor slabs (steel elements with different profiles) are present; the useful height of the ground floor varies from 4.30 m to 5.50 m. The situations are similar on the first and second floors, where the maximum heights attained are respectively equal to 5.60 m and 5.20 m, as measured during the in situ surveys.

The ground floor of the building actually houses several university classrooms, university department offices and the historical “Aula Magna”. The first floor, besides more department offices and the double volume of the “Aula Magna Nuova” (not aligned with the one at

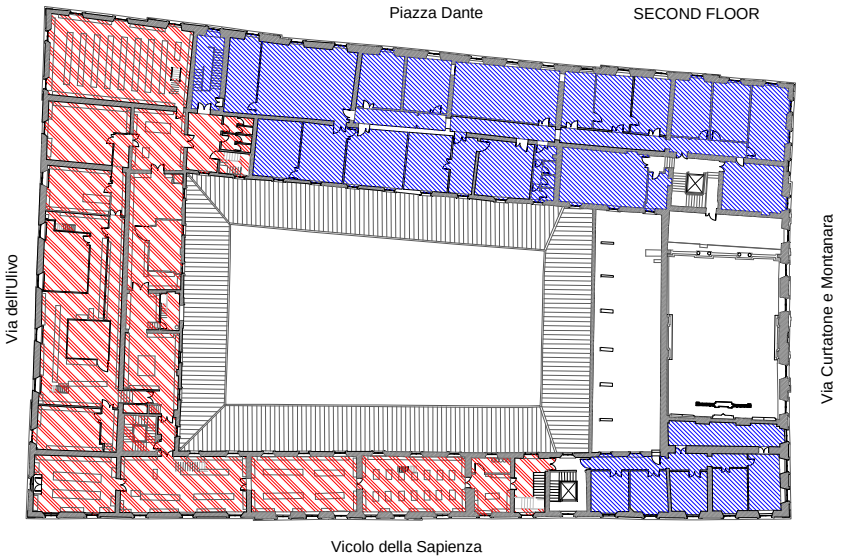
ground floor), houses the University Library, which takes up the entire surface area of two sides of the building (along Piazza Dante square and Vicolo dell'Ulivo). The University Library also covers nearly the entire second floor, in part overlying the first floor sections, in part along the opposite side (along Via della Sapienza). Mezzanine floors and loft structures are, moreover, present in correspondence of the first and second floor of the library. The general plans of the building, with the indication of the different activities carried out, are presented in the Figure 3.



a)



b)



c)

Figure 3: Plans of a) ground floor, b) first and c) second floor with indication of the activities housed.

3 MORPHOLOGICAL-STRUCTURAL SURVEY OF THE BUILDING

The historical analysis of the building evidenced a series of critical structural issues affecting Palazzo della Sapienza, mainly due to the changes and transformations to which the building was subjected during the centuries, nowadays visible through widespread cracks in different portions of the construction. An extensive in situ survey campaign was executed, in order to deeply investigate the current structural condition of the building, with attention to the masonry patterns, horizontal storeys and vaults, roofing system, foundations, mechanical properties of materials and geotechnical properties of the soil.

The masonry patterns were investigated by removing 50x50 cm plaster surface with following endoscopic examinations (Figure 4), necessary to determine the presence of air spaces or adjacent facings of different thickness and type. The studies revealed the presence of 5 different types of masonry patterns (i.e. full brick, full brick and split stone, stone with brick courses, etc.) and the absence of suitable connections between perpendicular walls. The distribution of the different masonry typologies present in the building's various floors was reconstructed bearing in mind the results of the historical analysis (Figure 5). In general, the different types of masonry corresponded to the different historical stages of the building's construction and modification; for example, the area at the corner between Via Curtatone e Montanara and Via della Sapienza, originated from the building's medieval walls and tower-houses, revealed greater complexity and heterogeneity, as well as already evidenced during the historical analysis. Three experimental flat jacks tests were then executed on three different masonry typologies to determine the compressive strength of the material and to estimate the effective actual stress state on vertical elements.

Similar investigations (removal of plaster and endoscopic analyses) were also executed on vaulted surfaces, in order to define the masonry typology, the disposition of blocks and the total thickness of the filling materials. The direct in situ survey of horizontal storeys allowed the determination of the steel profiles' dimensions and of the thickness of the slabs and flooring, necessary to estimate of the effective dead load (Figure 6).

The roofing structure, consisting of trusses of different types and materials on which the secondary elements (longitudinal beams and joists) are placed to support the roof covering, is also the result of the modifications undergone by the building over the years. Steel Polonceau

trusses, wooden trusses of different sizes and shapes, all presenting various degrees of deterioration in their elements are present in the different portions of the building. The poor state of maintenance, the manner in which supports between the various elements were fashioned, the presence of small full-brick walls to support the bearing elements, as well as the accumulations of construction debris and other factors evidenced the strong vulnerability of the roofing system.



Figure 4: Execution of in situ investigations on masonry walls.

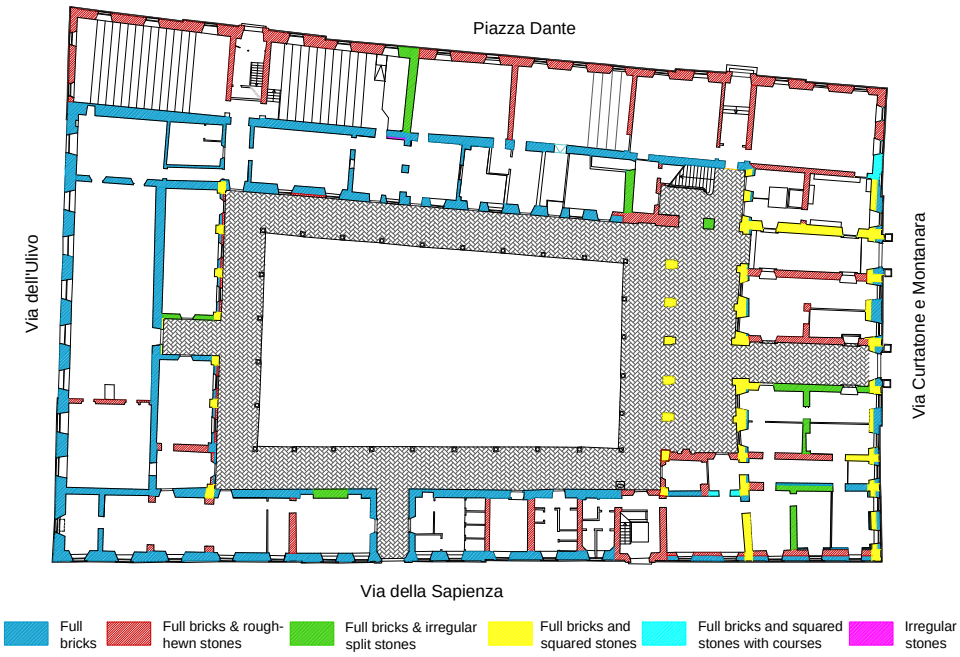


Figure 5: Plan of ground floor with indications of the various types of masonry



Figure 6: Execution of in situ investigations on horizontal floors with steel elements.

The historical analysis of the building evidenced, moreover, the instability and the non-homogeneity of the foundation soil; the continuous growth of the building highlighted the inadequacy of the foundation system in sustaining the increasing loads due to the progressive enlargements of the structure, visible through a well defined cracking scenario. In order to better analyze the state of art of the foundation system, a series of core samplings at different angles in the proximity of the masonry walls, at locations planned according to the evolutionary reconstruction of the building, were executed: different types of foundations, in terms of both size and depth, corresponded to the different stages of the building's construction. The investigations performed in correspondence to the interior colonnade revealed the absence of connections between columns, characterized by an isolated square foundation set at a depth of about 1.9 m from ground level, lower than that of the portico pillars, laid at a depth of 1.75 m below ground level. The foundation of the portico's interior walls reached different depths (ranging from 1.0 m and 1.5 m below ground level), with width varying between 1.50 and 2.40 m. The two investigations performed on the foundation structure on Vicolo dell'Ulivo provided analogous results, with foundation depths of 2.75 and 2.10 m, and widths of 1.75 and 1.60 m, respectively, while the Piazza Dante side foundation reached a depth of about 1.50 m below ground level, with a width of 0.90 m.

Based on the careful survey of the cracking scenario of both vertical walls and horizontal floors/vaults, two monitoring systems − periodic and continuous – were organized and installed in order to determine the possible evolution of the ongoing subsidence and disruptions (Figure 7). The periodic monitoring system involved fixed metal reference gauges straddling the cracks to enable measuring any further widening or narrowing of the cracks at time intervals of about 2 months. The continuous monitoring system, on the other hand, made up of electronic displacement transducers, provided a measurement for each considered point every 5 minutes, allowing the processing of collected data in graph form and the continuous checking of the ongoing cracking process. The analysis of the monitoring results enabled the identification of the areas characterized by differential displacements, such as, for instance, in correspondence to the vaults of the ground floor colonnade and first-floor arcade.

a)  b) 

Figure 7: a) Periodic monitoring system, fixed metal reference; b) Continuous monitoring system.

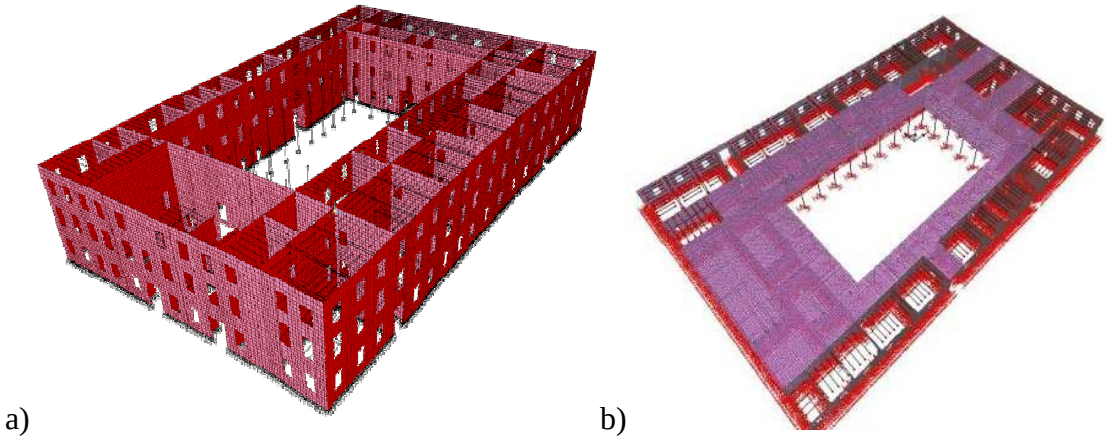
4 NUMERICAL MODELLING AND ANALYSIS

4.1 Elaboration of FEM numerical model

A numerical three-dimensional model of the structure was realized in order to develop numerical analyses according to what prescribed by [1]. Such a complex building shall be considered more similar to a *"structural aggregate"* than to a single building, made up of different parts connected together during the centuries; the difficulty to model material

discontinuities, disconnections between perpendicular walls, and other factors allowed the elaboration of a global numerical model that is representative of an "improved condition" of the structural system. The linear three-dimensional FEM model of the building (**Errore. L'origine riferimento non è stata trovata.**Figure 8) was realized using SAP 2000, with two-dimensional "shell" elements for the walls and one-dimensional "frame" elements for the profiles of the floor slabs, the roofing and the university library mezzanines. The vaulted surfaces were modelled with equivalent two-dimensional plane. The mechanical characteristics of the masonry material were selected according to the results of in situ flat-jack tests and to the indications contained in the Ministerial Memorandum Circ. 617/2009 [15], for the different types of masonry pattern (Table 1). The presence of cracking phenomena was conventionally taken into consideration through the reduction of the stiffness of the masonry walls [1, 16].

The interaction between the superstructure and the ground soil was represented through the Winkler model, with elastic three-directional springs calibrated according to the results of the geotechnical investigations. The horizontal stiffness (both in x and y directions) was assumed equal to the 25% of the vertical one. The stiffness of the Winkler springs was evaluated considering the effective dimension of the foundation structures and a spacing equal to 0.50 m, more or less corresponding to the discretization adopted in the model of masonry elements. The values of effective vertical stiffness (k_v) are presented in the Table 2 for the different portions of the building, being B the average width of the foundation, i the springs' spacing in the model and A the footprint of the foundation area for columns and pillars.



a) b)

Figure 8: a) Global model, b) vaulted surfaces and frame elements of the storeys.

Masonry		σ [MPa]	E [MPa]	Notes
1	Full bricks	2.25 (*)	1500	* flat jack tests (mean values)
2	Irregular split stones	1.40	870	
3	Full bricks and rough-hewn stones	2.20 (*)	1500	* from flat jack tests
4	Full bricks and irregular split stones	2.20 (*)	1500	* type similar to (3)
5	Full bricks and squared stones	2.20 (*)	2150	* type similar to (3)
5	Full bricks and squared stones with courses	2.64 (*)	1500	* (3) improved by courses

Table 1: Resistance and elastic moduli values adopted for the various types of masonry patterns

Foundation type	K [kPa/m]	i [m]	B [M]	A [m^2]	k [N/mm]
Colonnade	32560	-	-	1.21	39398
Portico pillars	25300	-	-	1.80	45540
Via Curtatone Montanara/della Sapienza	3200	0.5	2.4	-	3840
Piazza Dante/Via Curtatone e Montanara	7600	0.5	0.9	-	3420
Other	4500	0.5	1.6	-	3600

Table 2: Rigidity values of the springs modelling the ground-to-structure interactions.

Vertical loads were determined in relation to D.M. 14.01.2008; an accurate estimation of the effective weight of the books of the libraries was also executed in order to obtain more reliable evaluations and safety checks. For what concerns the evaluation of seismic action, due to the complexity of the building, a *local seismic response analysis* under free-field conditions (i.e. neglecting the presence of the building), aiming to evaluate the response spectrum to be used for the safety checks was executed. The definition of the seismic input was performed selecting seven spectrum-compatible accelerograms, scaled according to the site's reference design acceleration [17], and applying them directly to the representative model of the subsoil of the site on which the building rests. The subsoil model employed, made up of a finite number of parallel plane layers with infinite horizontal extension, was represented by an equivalent elastic medium set on a viscous-elastic half-space representing the bedrock. Each layer, assumed to be homogeneous and isotropic, was characterized by thickness h, density ρ, a transverse rigidity modulus G and damping factor D (Table 2). Applying this subsoil model to the seismic input to the bedrock enabled the determination of the specific response spectrum for the considered site. Analysis of the local seismic response was then conducted by calculating the average effects, in terms of acceleration over time at the depth of the foundation plane, of each of the seven accelerograms selected. Figure 9 shows the elastic response spectrum for the site under examination (soil type C) in comparison to the standard spectrum for return period T_R equal to 712 years. Linear dynamic analysis was then finally performed on the Palazzo della Sapienza using the response spectrum resulting from the foregoing determinations. A behaviour factor equal to 2.25 was adopted [15], minimum value allowable for masonry structures with irregular height, quite conservative respect to the value proposed by the Guidelines for cultural heritage [13], which specify a maximum value of 2.80.

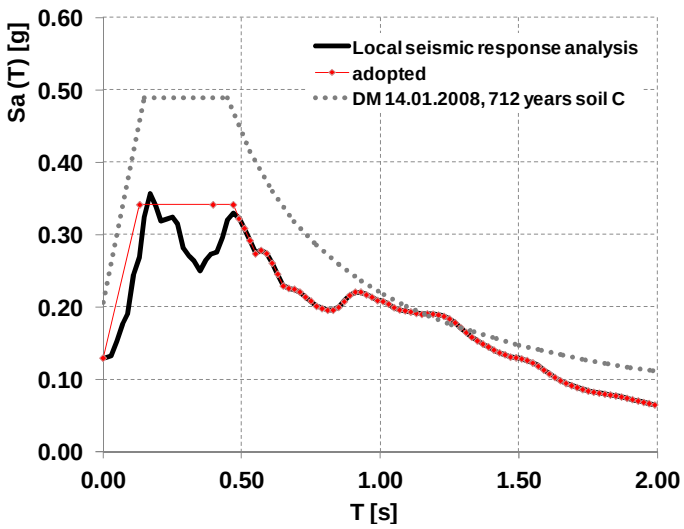


Figure 9: Elastic response spectrum results for the site in comparison to regulatory indications for type C soils.

4.2 Safety checks and evaluation of critical issues

Safety assessment was executed according to the indications provided by [1, 15]. The values of the design actions used to carry out the checks were derived from the global numerical model, which as stated, obviously cannot account for situations such as the lack of connections between perpendicular walls, discontinuities between adjacent walls or between walls and overlying vaults, the presence of air spaces, walled-off openings etc. The obtained results are therefore representative of an "enhanced" condition in comparison to the actual current state. The results of the global checks on the building are however indicative of the effective state of maintenance of the vertical walls, floors, vaults, and roofing and foundation structures.

The obtained results were combined with the ones coming from the investigations of the most significant local collapse mechanisms, allowing the attainment of a general overview of the state of art of the construction.

The global checks on masonry walls evidenced that the building essentially satisfies the safety requirements with regard to both static and seismic combinations, with the exception of extremely small-sized, slender elements characterized by a considerable heterogeneity in shape and materials and by extensive cracking due to the progressive structural layering and modifications made to the building. Relatively critical conditions were encountered in the area of the historical Aula Magna, where two of the original spaces of the colonnade were closed-up, and in the proximity of the double volume of the new Aula Magna.

Problems of out-of-plane overturning were found in correspondence to the interior wall of the 1st floor towards the arcade parallel to Piazza Dante, where the perpendicular masonry restraints were removed without taking into account their structural effects, as well as in correspondence to the wall of the double volume of the new Aula Magna.

The horizontal structures (floors), with the exception of one under-dimensioned slab on the building's second floor, did not evidence significant structural deficiencies in terms of either resistance or deformability, probably because they were realized relatively recently (during the post-war restructuring of the building). Analogous considerations can be executed for the vaulted structures, which, though presenting widespread cracking, especially in the colonnade area and in the proximity of the original Aula Magna, were able to sustain a load equal to 350 daN/m^3, as demonstrated by the in situ load tests executed.

The wooden roofing structures presented signs of widespread degradation due insect and mold damage, with consequent reduction of the resistant section of the bearing elements, with the following not satisfaction of the prescribed safety requirements. Other critical issues were linked to the presence of curtain walls supporting trusses, supports of varying shapes and types, and to the accumulation of construction debris in various areas of the garret.

Analysis and safety checks of the foundation structures, characterized by considerable geometric heterogeneity as previously presented (i.e., foundation depth and the width of the supporting base), revealed the substantial heterogeneity of the overall mechanical behaviour of the foundations, variable stiffness of the ground-foundation assemblage and different limit load values, minimal for ribbon foundations and higher in the case of isolated foundations. The unit load-subsidence diagrams for the foundation-ground assemblage for the various analyzed sections (Figure 10a) highlight the different responses of the various foundation elements as a function of the geometry, especially for unit load values below 1.0 MPa. A substantial difference in the behaviour was visible between the building's perimeter and its interior part (i.e. colonnade and pillars of the interior courtyard, Figure 10b); in the presence of either static or seismic loads, these local differences can expose the building to

considerable damage in those areas with significant differences in rigidity characteristics or those subject to more heterogeneous loads.

Apart from these structural issues, many other intrinsic critical situations were identified as a consequence of the building's morphological conformation itself. Such problems were frequently aggravated by the modifications executed over the centuries in relation to the architectural and functional needs.

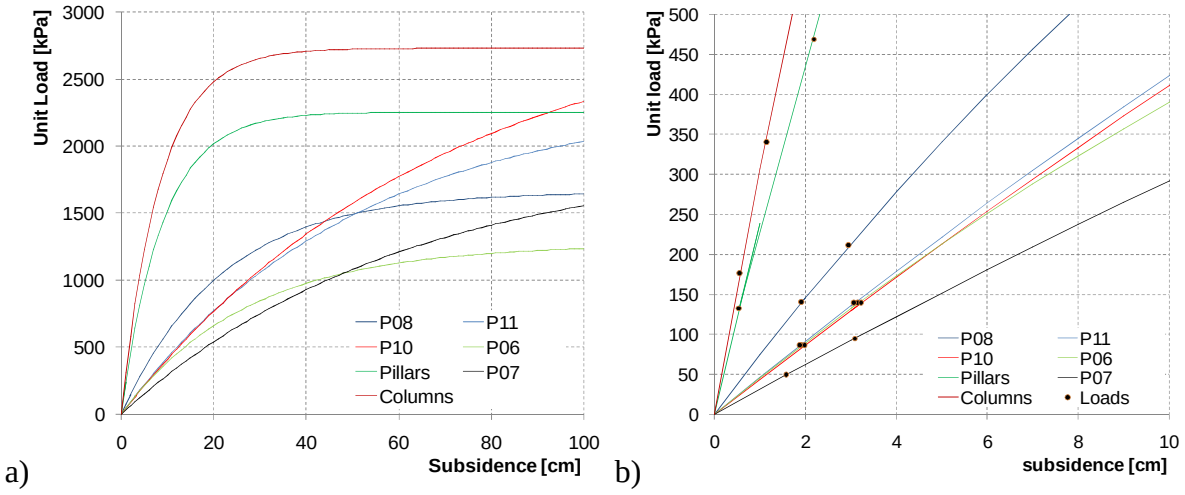


Figure 10: a) Unit load-subsidence curves for the different sections investigated, b) estimates of the subsidence of different building zones.

5 RETROFIT INTERVENTIONS

The organization of retrofit interventions on complex structural aggregates, such as the one presented in the previous paragraphs and, more generally, in the case of historical masonry structures, represents a very difficult engineering topic. The "traditional approach" proposed by current Italian standards [1, 13], that individuates the three possibilities of *global retrofit* (i.e. to make the existing building able to fully satisfy the safety requirements according to current standards), *partial retrofit* (i.e. to obtain a global increment of the structural safety of the building without the complete satisfaction of standards' requirements) and *local intervention* (i.e. strengthening or consolidation of single structural elements), cannot be easily applied to the cultural heritage. This is due to the fact that such historical buildings shall be, above all, preserved towards significant modifications of their original nature, maintaining their historical aspect and providing, at the same time, a considerable margin of structural safety.

As a consequence of what presented, and often in presence of localized static problems due to morphological and intrinsic features of the building, the "global" retrofit intervention on cultural heritage is the final amount of many "local" interventions regarding single elements or different portions of the building (for example masonry walls with significant cracks to be repaired, strengthening of horizontal storey through the introduction of additional elements, replacement of wooden elements of the roof and others). Figures 11, 12 and 13 show some examples of localized interventions regarding, respectively, horizontal floors, masonry walls, and wooden structure of the internal court roof.

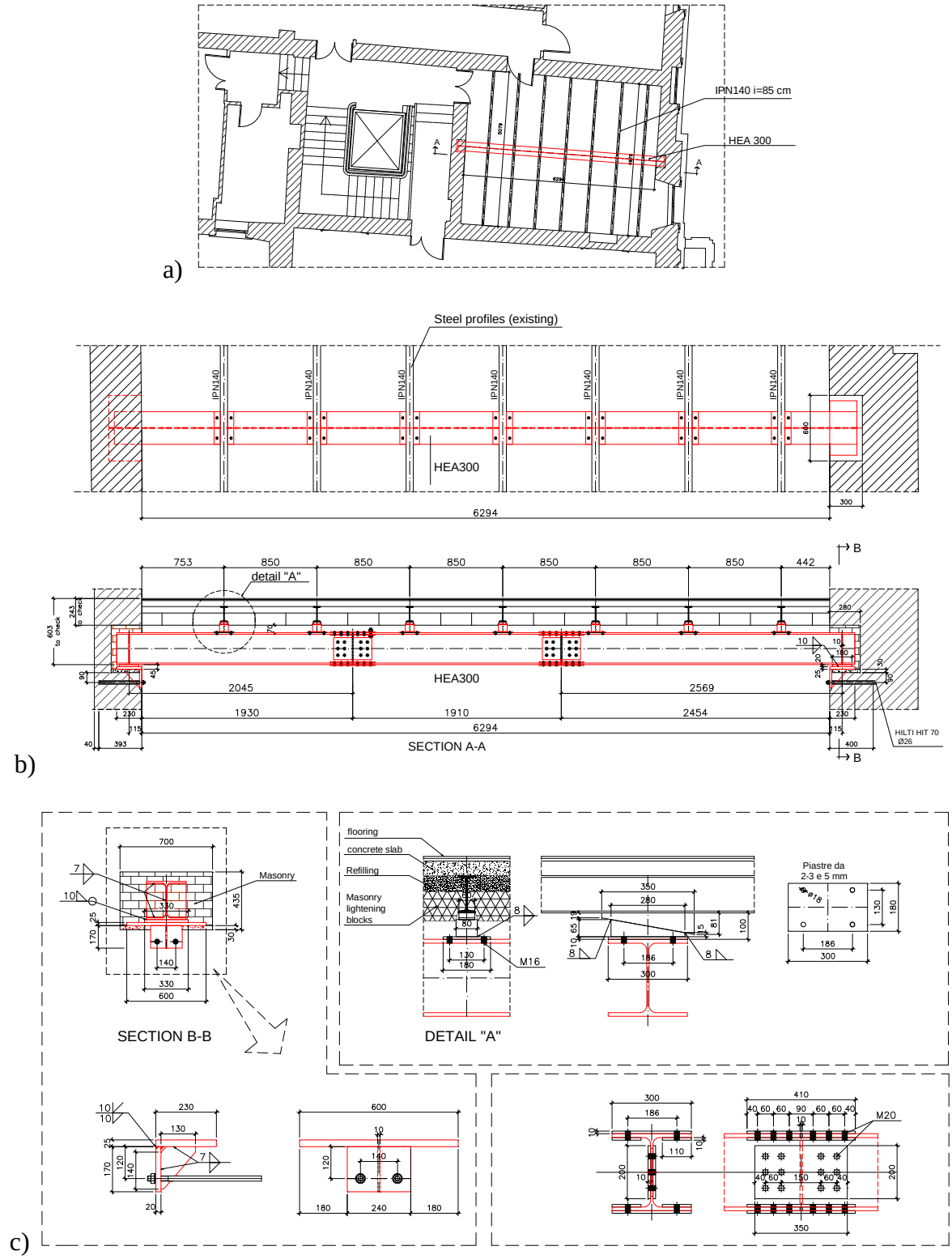


Figure 11: Local strengthening of horizontal floor: a, b) general scheme and sections, c) executive drawings.

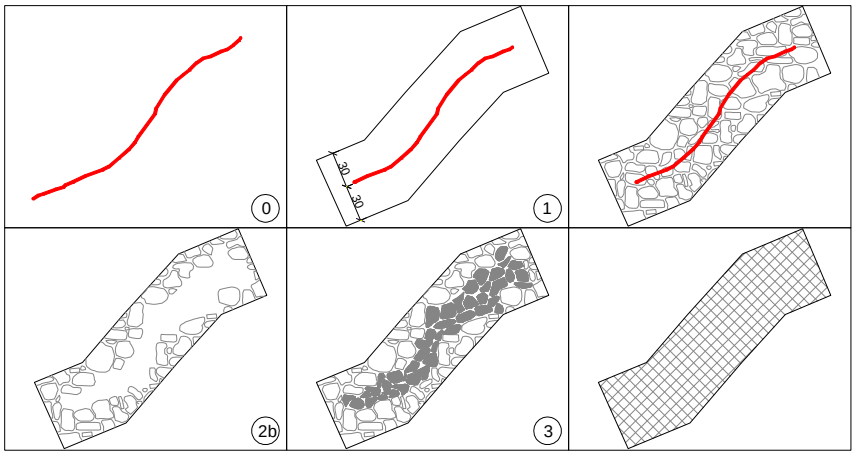


Figure 12: Example of local retrofit intervention of significant cracks on masonry walls.

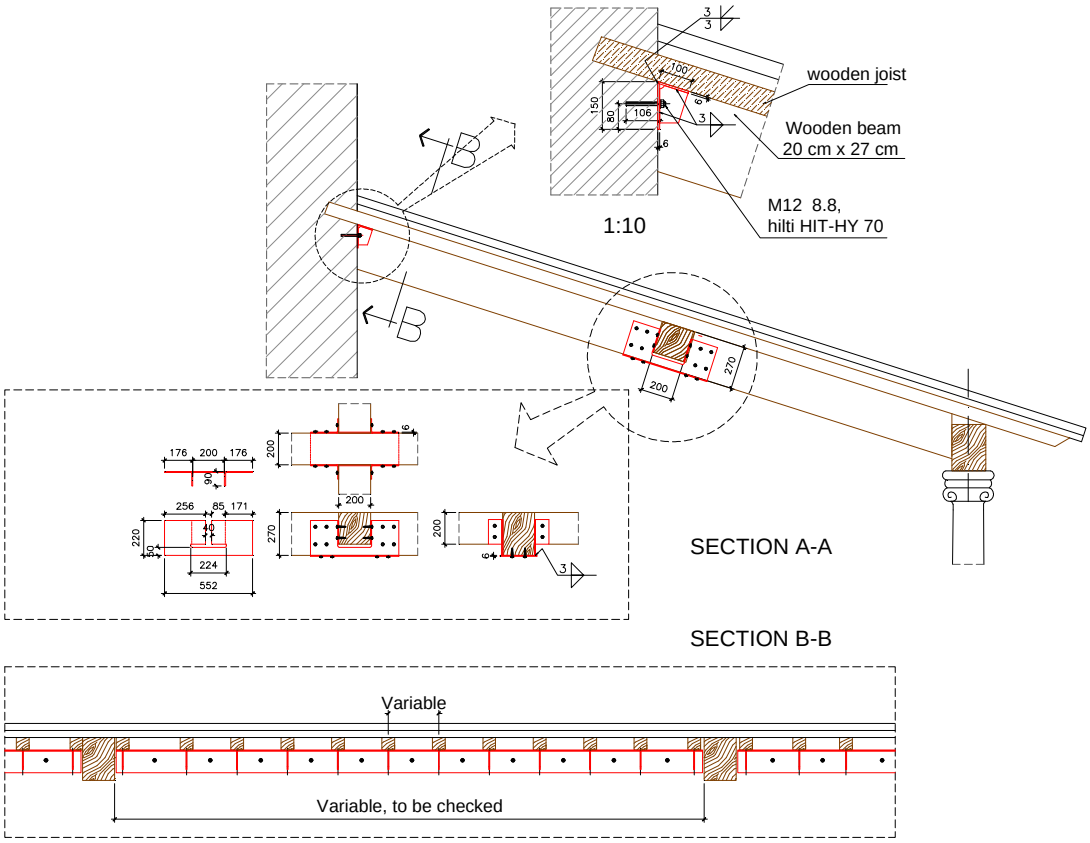


Figure 13: Example of retrofit of wooden elements of the internal court.

6 CONCLUSIONS

According to what presented in the previous paragraphs, the analysis of complex historical buildings such as Palazzo La Sapienza in Pisa shall be executed considering the construction not a single unit but a "structural aggregate", made up of different parts interconnected to each other in various ways and often realized at different times and using different techniques. Such complexities and structural heterogeneity usually result in widely disparate responses of different parts of the building to external actions, with widespread cracking phenomena and possible structural problems and failures similar to the ones occurred over the centuries and

sometimes repaired with singular/local interventions. Moreover, the strong variation in the stiffness of the building's different existing foundation structures (Figure 10) led to differential settlements, with consequent load concentrations, making even worse the already existing instability.

The aforementioned complexity and structural heterogeneity translate into differences in the structural response and performance, consequently requiring detailed analyses of every single portion of the building and of its conditions of use, management and functional aspects. The structural analysis of La Sapienza building was therefore performed, considering the global behaviour of the structure (bearing in mind the simplifications necessarily to perform the numerical modelling for safety checks), and, at the same time, the behaviour of particularly significant sub-portions of building, subjected to the possible activation of local collapse mechanisms (for example out-of-plane tilting and overturning of façades or corners, horizontal thrusts due to vaults and roofing structures, presence of intermediary mezzanines with mechanisms of simple bending, etc.). A critical evaluation of the building's safety, together with a clear, deep understanding and knowledge of the structure itself, constitute the basis to define the objective of any structural interventions, carefully designed to achieve appropriate safety levels, durability of relevant portions of the building and, at the same time, produce the least impact possible on this important living example of Italy's historical heritage.

REFERENCES

[1] NTC2008. D. M. Infrastrutture Trasporti 14 gennaio 2008, Norme Tecniche per le Costruzioni, (In Italian), 2008.

[2] European standard EN1998-3. Eurocode 8: design provisions for earthquake resistance of structures - Part 3: assessment and retrofitting of buildings. European Committee for Standardization, Brussels, 2005.

[3] FEMA 547. Techniques for the Seismic Rehabilitation of Existing Buildings. Federal Emergency Management Agency, Washington DC, 2006.

[4] G. Barbieri, L. Biolzi, M. Bocciarelli, L. Fregonese, A. Frigeri, A. Assessing the seismic vulnerability of a historical building. *Engineering Structures,* **57**, 523–535, 2013.

[5] V. Mallardo, R. Malvezzi, E. Milani, G. Milani. Seismic vulnerability of historical masonry buildings: a case study in Ferrara. *Engineering Structures*, **30**, 2223–2241, 2008.

[6] G. Chellini, L. Nardini, B. Pucci, W. Salvatore, R. Tognaccini. Evaluation of seismic vulnerability of Santa Maria del Mar in Barcelona by an integrated approach based on terrestrial laser scanner and finite element modelling. *International Journal Architectural Heritage*, **8(6)**, 795-819, 2014.

[7] S. Lagomarsino, S. Cattari. PERPETUATE guidelines for seismic performance-based assessment of cultural heritage masonry structures. *Bulletin of Earthquake Engineering,* **13**,13-47, 2015.

[8] D. D'Ayala, S. Lagomarsino. Performance-based assessment of cultural heritage assets: outcomes of the European FP7 PERPETUATE project. *Bulletin of Earthquake Engineering,* **13**, 5-12, 2015.

[9] M. Kržan, S. Gostîc, S. Cattari, V. Bosiljkov. Acquiring reference parameters of masonry for the structural performance analysis of historical buildings. *Bulletin of Earthquake Engineering*, **13**, 206-236, 2015.

[10] S. Lagomarsino. On the vulnerability assessment of monumental buildings. B *Bulletin of Earthquake Engineering*, **4**, 445-463, 2006.

[11] A. Bernardini, S. Lagomarsino. The seismic vulnerability of architectural heritage. In *Proceedings of the Institution of Civil Engineers – Structures & Buildings*, 161 (SB4): 171–181.

[12] C.S. Oliveira. Seismic Vulnerability of Historical Constructions: A Contribution. *Bulletin of Earthquake Engineering*, **1**, 37-82, 2003.

[13] Linee Guida per la valutazione e riduzione del rischio sismico del patrimonio culturale allineate alle nuove Norme Tecniche per le Costruzioni (D.M. 14/01/2008), 2010.

[14] W. Salvatore, P. Iannelli. Verifica della sicurezza statica ed analisi della vulnerabilità sismica dell'edificio La Sapienza di Pisa, Report University of Pisa and MiBACT, 2013.

[15] Ministerial Memorandum Circ. n°617/2009 "Istruzioni per l'applicazione delle "Norme tecniche per le costruzioni" di cui al D.M. 14 gennaio 2008" (in Italian), 2009.

[16] T. Paulay, M.J.N. Priestley. *Seismic design of reinforced concrete and masonry buildings*. John Wiley and sons, INC. New York, U.S.A, 1991.

[17] I. Iervolino, C. Galasso, E. Cosenza. REXEL: computer aided record selection for code-based seismic structural analysis. *Bulletin of Earthquake Engineering*, **8:2**, 339-362, 2010.

COMPDYN 2015
5th ECCOMAS Thematic Conference on
Computational Methods in Structural Dynamics and Earthquake Engineering
M. Papadrakakis, V. Papadopoulos, V. Plevris (eds.)
Crete Island, Greece, 25–27 May 2015

INFLUENCE OF MODELLING PARAMETERS ON THE FRAGILITY ASSESSMENT OF PRE-1970 ITALIAN RC STRUCTURES

Gerard J. O'Reilly[1] and Timothy J. Sullivan[2]

[1] ROSE Programme, UME School, IUSS Pavia
Pavia, Italy
e-mail: gerard.oreilly@iusspavia.it

[2] Department of Civil Engineering and Architecture, Università degli Studi di Pavia
Pavia, Italy
e-mail: timothy.sullivan@unipv.it

Keywords: Modelling, RC Frames, Joint Behaviour, Sensitivity, Assessment.

Abstract. *This paper investigates the importance of numerical modelling decisions on the seismic assessment of reinforced concrete (RC) structures typical of construction practice in Italy prior to the introduction of seismic design codes in the 1970's. In particular, means of accounting for the formation of a shear hinge in the beam-columns, longitudinal reinforcement slippage due to the use of smooth bars with end-hooks, and the strength and stiffness degradation associated with the lapping of longitudinal reinforcement in beam and column member end zones are discussed. A numerical model is validated by developing existing models in the literature capable of representing such behaviour and comparing with results obtained from quasi-static cyclic testing of a three storey RC frame. A case study structure designed using design provisions employed in Italy prior to the 1970's is then analysed via a series of dynamic analyses using ground motions representative of seismic hazard in Italy. An assessment of the structures is conducted at different return periods to determine the median storey drift and peak floor accelerations, as these demand parameters are typically used for refined performance assessment studies. For the considered structure, a number of cases are considered, where various modelling parameters are included or excluded to highlight the influence of each of these on the overall response of the structure. From this study, the importance of different numerical modelling decisions on the seismic assessment of pre-1970s' RC construction in Italy is highlighted and recommendations are provided for the modelling of phenomena critical to the seismic performance assessment process.*

1 INTRODUCTION

Much focus has been placed on developing methods of assessing a structure's performance to a given seismic hazard. These range from simplified pushover analyses to more rigorous numerical analysis methods. The most comprehensive existing approach for the seismic assessment of structures is what is termed the PEER PBEE methodology [1], illustrated in Figure 1, where a convolution integral of site hazard, structural response, damage and loss analysis give a rigorous approach to the seismic assessment of structures. The drawback of such a methodology is the level of numerical analysis required to determine the desired decision variables. As such, more simplified methods of analysis have been developed for RC structures [2] in order to provide the same information, but at a fraction of the computational effort and within an acceptable tolerance, which can then assist designers in quickly establishing effective retrofit solutions for structures, as demonstrated by [3].

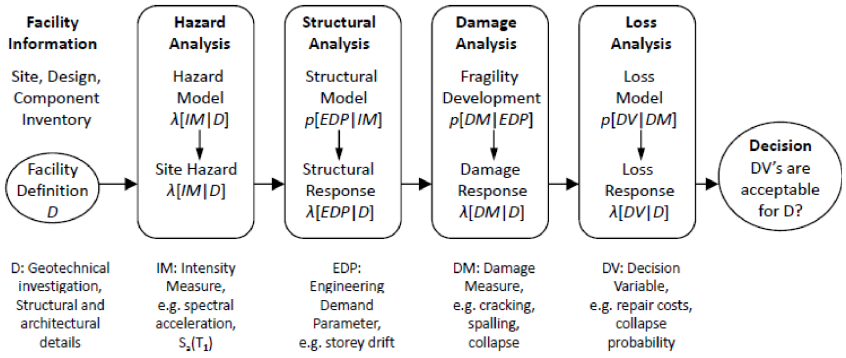


Figure 1: Overview of the PEER PBEE methodology (after [1]**).**

While more simplified approaches to seismic assessment represent an obvious advantage from a practice point of view, there appears to be limited guidance for the use of approaches for the assessment of structures designed prior the introduction of seismic design codes in the 1970's. A number of inherent assumptions regarding the structural response and strength hierarchy in modern structures do not apply to older gravity-only designed structures. In order to develop more simplified methods of seismic assessment for older RC structures, the identification of the relative importance of different possible mechanisms associated with older RC structures in Italy is of concern. As such, this paper discusses the principle behaviour of gravity load designed RC frame structures constructed in Italy prior to the introduction of seismic codes in the 1970's. Numerical modelling of such behaviour is discussed followed by identification of different considerations in relation to the modelling of various parameters. A 3-storey gravity load designed case study structure is then assessed for different levels of seismic hazard and assessed in terms of its roof drift and peak floor accelerations, which are typical demand parameters used in damage analysis step of Figure 1, to establish the relative importance of the various modelling considerations. As a result, this work highlights the importance of accounting for the numerical modelling of different behaviour mechanisms of older Italian RC frame structures.

2 RELEVANCE OF MODELLING IN SEISMIC ASSESSMENT OF RC STRUCTURES

The influence of joint behaviour on the seismic response of frame structures has been the subject of much discussion, and concerns have been raised about the cases where no flexibility or nonlinear behaviour of the joint is considered in numerical modelling. It has

been long recognised that such an assumption of rigid joint behaviour is grossly inadequate, with Paulay & Priestley [4] noting that as much as 20% of the interstorey deflection results from the deformation in the joints alone. As such, numerical modelling has moved to consider this behaviour in analyses with various joint models being proposed, such as that by [5]. However, models from such studies tend to typically consider a joint that has been well detailed with deformed reinforcing bars according to modern design codes. Pampanin et al. [6] noted that RC structures constructed in Italy prior to the introduction of seismic design codes resulted in the absence of shear reinforcement in the joint region, which resulted in a shear hinge mechanism forming in the joint. Accounting for this kind of behaviour specific to Italian construction has been the focus of much work recently, with Sharma et al. [7] providing a review into existing approaches for accounting for joint behaviour. In addition, Shafaei et al. [8] conducted a study on the modelling pre-1970 Iranian RC structures where it was shown that the consideration of joint behaviour considerably affects the lateral response of the structure, in addition to similar work by Jeon et al. [9] for older RC structures in the US where Jeon et al. [9] reported similar findings regarding the importance for proper joint modelling. Therefore, it is imperative that such considerations be developed for older Italian RC construction so that seismic assessments may be carried out using numerical models that are representative in terms of the additional deformability and nonlinear behaviour characteristic of older RC frames.

In addition to consideration of the joint behaviour in older structures, the behaviour of the frame members is also of utmost importance. Experimental testing on members detailed with plain reinforcing bars and inadequate core confinement has shown that the hysteretic behaviour of these members differs quite a lot compared to well detailed ductile members, where the presence of plain bars tends to lead to a lot of hysteretic pinching between inelastic cycles [10–12]. In addition, inadequate confinement of the core concrete and large spacing of the stirrups limits the ductility capacity of older RC members. Studies on the influence of frame member behaviour by [13,14] showed the influence of considering ductile and non-ductile detailing of members to be quite significant on the collapse capacity of RC structures in the US. In addition to affecting the hysteretic properties of frame members, the presence of plain bars can result in a reduction of flexural capacity of the members, where Calvi et al. [15] demonstrates that this reduction can typically be of the order of 20%, depending on the axial loading and bond conditions of the reinforcement. Hence, such a reduction in flexural capacity particular to older Italian RC frame should be taken into consideration when conducting seismic assessments.

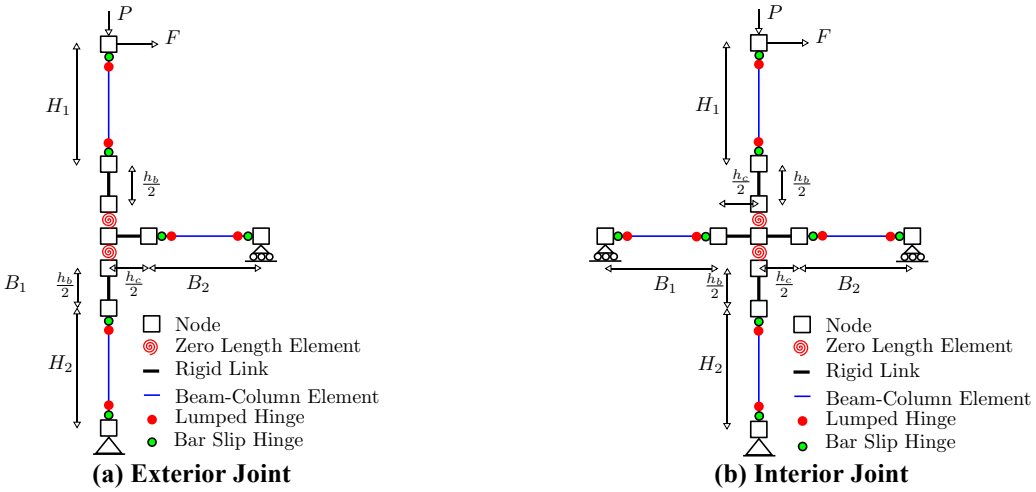
Welch et al. [16] investigated the impacts of some modelling decisions on the loss assessment of ductile RC frames. Between different considerations of initial stiffness calculation, post yield hardening ratio and elastic damping, the parameter that was shown to most heavily influence the loss assessment results was the consideration of elastic damping. Hence, the quantification of such an affect in relation to other modelling parameters considered in this study and those done by others is warranted. In addition to the response of RC frame members, the consideration of masonry infill contribution to the behaviour of RC frames is an important consideration, with [17] (amongst others) noting that the presence of masonry infills considerably modifies the strength and stiffness of the frames and ought to be considered in the numerical modelling of such structures for seismic assessment.

3 NUMERICAL MODELLING OF PRE-1970'S RC STRUCTURES

The numerical modelling of structures examined here is carried out using the OpenSees framework [18]. The model consists of a number of parameters that ought to be considered for the modelling of pre-1970's Italian RC frames such as the aforementioned joint behaviour, frame members and the masonry infills. The numerical model considers both material and geometrical nonlinearity and models the cyclic degradation of both the joint and frame elements. The following sections discuss the particular details regarding each of the modelling parameters, followed by the comparison of the numerical model with the experimental test results of a three storey gravity load designed RC frame.

3.1 Beam-Column Joint Modelling

The joint modelling of RC frames is based on previous efforts by [19,20], where the joint is modelled via a number of rigid links in the joint along with rotational springs to represent the shear response of the joint. Figure 2 shows the layout of both the interior and exterior joints, where the layout of rigid links is illustrated along with the location of the rotational springs. The properties of these springs are determined based on the consideration of the principle tensile stresses developed in the joint during shear deformation, as discussed by [19]. The upper and lower rotational springs are then slaved together in rotation and linked in the vertical direction by an axial spring with the same axial stiffness as the column section. The layout of the nodes and elements in the joint model are as per previous models, such as [20], although the hysteretic materials have been modified. The Hysteretic material rule available in OpenSees has been adopted to represent the shear behaviour of the connections, where the hysteretic parameters have been matched based on existing experimental results. For the case of exterior joints, experimental testing results from [6,21–23] were used, whereas for interior joints testing by [6,22–28] were considered. Using this database of test results, hysteretic parameters that govern the pinching behaviour and stiffness degradation of the joint have been established. In addition, the cyclic degradation parameters of the joint have also been matched to those observed in testing to give a joint model that not only represents the strength and stiffness of the joint, but also represents the hysteretic behaviour and cyclic degradation.



(a) Exterior Joint (b) Interior Joint

Figure 2: Joint Modelling.

3.2 Beam-Column Member Modelling

For the modelling of the frame members, a lumped plasticity beam column element is employed via the beamWithHinges element available in OpenSees. This allows the definition

of the hysteretic behaviour of the member end zones with a specified plastic hinge length and an internal elastic section with cracked section properties, as shown in Figure 2. The hysteretic model used for the plastic hinges is the Pinching4 material model available in OpenSees, which allows for the specification of a number of parameters to define the pinching behaviour of the multi-linear backbone curve. These parameters are determined from comparison with experimental test data provided in [10–12,29,30] members with plain reinforcing bars and poor core confinement. The backbone of the hysteresis rule is determined from consideration of the section flexural capacity with a reduction to account for the bar slippage due to plain bars, as outlined by [15]. The yield rotation specified in the hinge region is determined based on flexural deformations, where the additional flexibility due to the slippage of the longitudinal bars is modelled separately and is discussed further in Section 3.3.

The plastic hinge length of the member end zones is determined as per the empirical expression given in [4]. However, [31] noted that this expression for plastic hinge length was developed based on testing of well detailed ductile members that can distribute plasticity along member ends, whereas testing on members with plain bars and poor core confinement has shown that these plain bar members tend to concentrate the inelasticity in the member ends. However, of the available test information of older RC members, none of the test campaigns appear to report an observed plastic hinge length with the exception of [32], where comparing the observed plastic hinge length of an RC beam with plain bars with the Park and Priestley expression is quite good and is therefore used here. However, experimental evidence suggests that this may not always be the case and is hence recommended for future work.

In addition to modelling the behaviour of poorly detailed RC frame members, this study considers the possibility that the numerical model is developed using hysteretic parameters proposed for well-detailed ductile members. The ductile RC beam column member used in this study is from the calibration study by [33]. This considers a wide range of tests to propose a set of recommended parameters for the hysteretic behaviour of the beam column element using the modified Ibarra Medina Krawinkler material model available in OpenSees.

3.3 Bar Slippage

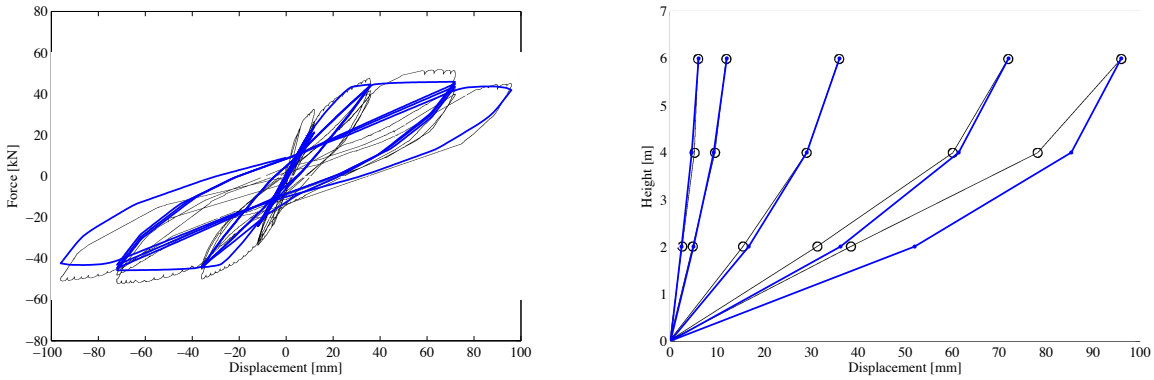
The slippage of the longitudinal bars affects the beam and column member hysteretic response in two ways. First, the slippage of the bars at the member ends results in an additional end-flexibility, therefore increasing the member's yield rotation. Metelli et al. [34] proposed a set of guidelines to determine the additional flexibility of the member ends in old RC frames considering the poor bond conditions of the plain reinforcing bars and this was incorporated into the model considered here via an additional spring at the member ends. This approach is adopted here, where the behaviour due to the slippage of the bars is added to the member ends, as illustrated in Figure 2.

In addition to the increase in member end-flexibility, the presence of plain bars with poor bond conditions can also affect the flexural capacity of the member sections. Calvi et al. [15] discuss how the flexural capacity can be reduced if the lack of a perfect bond between the bars and the joint concrete introduces a state of tension in bars that would ideally act as the compression reinforcement, therefore reducing the flexural capacity as a result of the rebalancing of the section forces. This reduction in flexural capacity was noted [15] to be a function of both axial load ratio and bond conditions, where typical reductions can be between 20 and 30% for column members. In order to consider the affect of the bar slip on the beam and column flexural capacities, the charts provided by [15] are used as a guide here

considering the expected axial load ratio for the case study structure presented in Figure 4, where a reduction of 20% for columns and 5% for beams is used here, the difference between the relative reductions stems from the presence of axial load in the member. This reduction in strength is approximated from the charts provided by [15], but future work should consider a more detailed approach to quantifying this reduction. Since the purpose of this study is to determine the relative influence of modelling parameters, this approximation is deemed sufficient for the case study presented herein.

3.4 Validation of Numerical Model for pre-1970 Italian RC Structures

The above modelling parameters are combined to compare the response of the numerical model to that of an experimental test on a 2/3 scale RC frame designed for gravity loads only and detailed as per pre-1970's Italian concrete construction practice. Calvi et al. [35] outline the testing of a 3-storey RC frame and report the response to quasi-static pushover cycles of increasing amplitude. Figure 3(a) shows the quasi-static cyclic response of the frame along with that obtained from cyclic pushover analyses using the numerical model developed in this study. It is apparent that the numerical model and experimental results match very well. This is especially seen through the initial stiffness and lateral capacity of the model. In addition, the hysteretic behaviour of the numerical model matches that of the test results very well also. In addition, the displaced shape shown in Figure 3(b) is matched reasonably well with that reported in the tests, where the shear mechanism in the joint at the first floor is captured by the model. This represents an improvement of the simplified modelling of pre-1970's Italian RC frames when compared to previous efforts such as [20], where lateral capacity and hysteretic comparisons were reasonable.



(a) Cyclic Pushover Curve **(b) Displaced Shape**

Figure 3: Comparison of numerical model with 3-storey RC frame tested by [35].

3.5 Masonry Infill Modelling

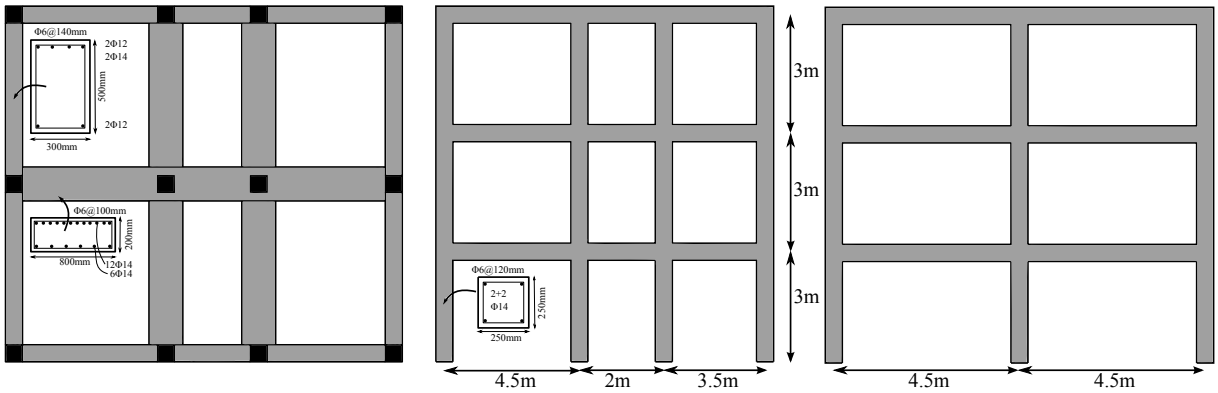
Masonry infills in the case study structure are modelled using the equivalent strut model initially proposed by [36], which consists of modelling the infill through a series of rigid offsets and a single symmetrical hysteretic behaviour. This model was then further developed and incorporated into OpenSees by [37] where calibrations were performed using experimental test data provided in [38,39]. In order to calculate the equivalent strut's hysteretic parameters, expression for first cracking, yield and ultimate lateral force of the infill wall given in [17] are used. The parameters governing the reloading and pinching behaviour of the equivalent strut model are calibrated based on experimental test observations, but agree well with previous parameters identified in [40]. To account for openings such as door and windows in the masonry infill, [37] proposes the force capacity reduction parameters outlined

in [17] and comparisons with testing [39] on a number of specimens with openings showed good agreement. The advantage of using such a simple macro element model such as the one employed here is its simplicity and computational efficiency. In addition, the degradation of the lateral resistance of the infill is no longer uncoupled in either direction, where other diagonal strut models possess a single compression-only strut for each direction. This approach means that one strut may have exhausted its capacity resulting in infill collapse, whereas the other strut will not recognise this loss of strength and continue to provide resistance in the other direction. Crisafulli et al. [41] provides a review into different approaches to modelling masonry infills; where modelling is varied in complexity from a detailed finite element modelling approach down to a single strut model, such as that just outlined. It was concluded that while simple strut models were not so accurate in the distribution of loads at the corners to the surrounding frames, the overall model captures the principle behaviour of the masonry quite well. This conclusion is also mentioned by [17], where the global response of the structure is captured by such models and thus is considered reasonable for studies considered here.

4 CASE STUDY STRUCTURE

The building typology used in this study is taken from a previous study by [42]. The structure consists of a 3-storey RC frame designed for gravity only loading as per Regio Decreto 2229/39 [43], which was typical of Italian construction prior to the introduction of seismic design code provisions in the 1970's. The basic layout of the structure is shown in Figure 4 where the structure possesses three bays in the longitudinal direction and two in the transverse. The structure contains two different types of beam section sizes; exterior beams with 500mm deep sections and shallow interior beams adopted at the time to avoid impeding on ceiling space. Seismic assessment and retrofit of a similar 6-storey version of the building has also recently been reported in [44].

Construction materials at the time of construction were somewhat different to those used in modern ductile seismic design where the cylindrical compressive strength of concrete was prescribed to be at least 12MPa at 28 days and allowable stress equal to one third of the characteristic value was used in design. Reinforcement consisted of plain smooth reinforcement with hook-ended anchorage terminated in exterior joints. The shear reinforcement consisted of stirrups at a minimum spacing and closed at 90°. Since a stirrup closing of 135° is typically required for effective confining of the concrete core, the cores of the beams and columns are considered effectively unconfined. Since the structure is designed for gravity loading only, the beam members are the same section size at each level, where the reinforcement for both beam types is shown in Figure 4(a). Despite the column design forces increasing down the height of the structure, the same section size and detailing are used throughout the entire building, which was typical of construction practice and these column section details are shown in Figure 4(b). Although not shown in Figure 4, the masonry infill considered in this structure consists of a 100mm weak clay masonry infill, which has a diagonal cracking strength of 0.55MPa.



(a) Plan Layout **(b) Front Elevation** **(c) Side View**

Figure 4: Case study structure (after [42]).

5 VARIATIONS IN MODELLING APPROACH

Using the various modelling parameters outlined in Section 3, a number of variations in the structural model are considered for the sensitivity study conducted in Section 7. These can be divided into two main groups of structures - those containing masonry infills and those not. The rationale behind modelling structures without infills is two-fold. Firstly, the structures are modelled as bare RC frames as this is was the anticipated structural configuration at the time of design, where masonry infills were considered a non-structural element that did not contribute to the strength of the system. Although this is now widely known in the field to be wholly untrue, its implications on RC frame response relative to other permutations are highlighted here considering that there may cases where infills are not present. Secondly, the purpose of this study is to demonstrate the influence of the modelling decisions on the response of the RC frame. The combination of stiffening infills and relatively low seismicity results in a limited amount of ductility in the infill structure and therefore, the affects of these modelling decisions are not observed so easily at lower intensity levels.

Considering the two principle variations in structural modelling, a number of parameters are then varied in order to establish their influence on the response of the case study structure. These are chosen in reference to the discussion presented in Section 2 and are listed as follows:

- Reference Model - This consists of the modelling of both the bare and infilled frame with all of the expected response characteristics outlined in Section 3 fully modelled.
- Ductile Members - This changes the beam-column member modelling approach, which has been calibrated for non-seismically detailed RC frame members and replaces it with an equivalent seismically detailed element as per the parameters outlined in [33]. This comparison is intended to highlight the effect of having beam-column members with ductile detailing as opposed to older member with plain reinforcement and unclosed stirrups. In addition the effects of bond slippage on the flexural strength are not modelled in the ductile member.
- No Bar Slip - In this variation, the additional beam and column end flexibility due to slippage of the plain bars is omitted in addition to the negligence of the apparent reduction of flexural strength of the members. This is intended to highlight the importance of properly addressing the influence of plain reinforcing bars with poor bond condition compared to those with a perfect bond and no slippage.

- No Joint Detail - This modelling deficiency consists of removing the rigid offsets and shear hinges at the joint centreline to the beam and columns faces, meaning that any joint flexibility is only provided via the apparent lengthening of the beam and column elements. Omitting the modelling of the shear joint behaviour is of particular interest here, since it is considered an important characteristic behaviour of RC joints susceptible to forming a shear mechanism, such as those constructed in Italy and elsewhere prior to the 1970's.
- Elastic Damping - The variation of the elastic damping is performed as this has been previously shown to significantly affect the loss assessment in ductile RC frames by [16]. Hence, this is an important parameter that ought to be properly justified and its significance to the response of older RC frames is investigated here.

Considering the above comments on the parameters to be modelled and omitted in the various case study permutations, a total of eight structures are therefore analysed. For each of these case study structures, the modelling parameters outlined in Section 3 are utilised to create the numerical models used for the analysis. From each of these models, the first three periods of vibration in the longitudinal direction are reported in Table 1. From these first mode periods, it can seen already that the small changes in modelling have had a noticeable affect on the initial period of the structure for the vase of the bare frame, whereas the infilled frame remains relatively unchanged between variations. These initial periods are then used to determine a suitable set of conditional mean spectrum ground motions in order to carry out the sensitivity study.

Table 1: Periods of case study structures.

	Bare Frame				Infill Frame			
Mode	Full	Ductile Members	No Bar Slip	No Joint	Full	Ductile Members	No Bar Slip	No Joint
1	1.49	1.36	1.34	1.66	0.23	0.23	0.23	0.23
2	0.52	0.47	0.46	0.58	0.08	0.08	0.08	0.08
3	0.32	0.29	0.28	0.38	0.05	0.05	0.05	0.06

6 GROUND MOTIONS

The seismic hazard considered in this study was that of a site in Napoli, using a catalogue of ground motions chosen for the site by [45]. The soil type considered in the hazard information used in [45] was hard rock. Using the disaggregation information available for the site shown in Figure 5, [45] proposed a set of conditional mean spectra for a range of return periods (T_R) and conditioning periods (T*). For each return period considered, a set of 30 earthquake ground motion components were selected to match the conditional mean spectrum in terms of their mean component and corresponding epsilon value [46].

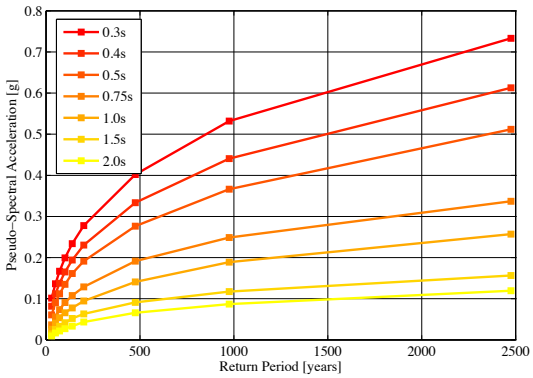
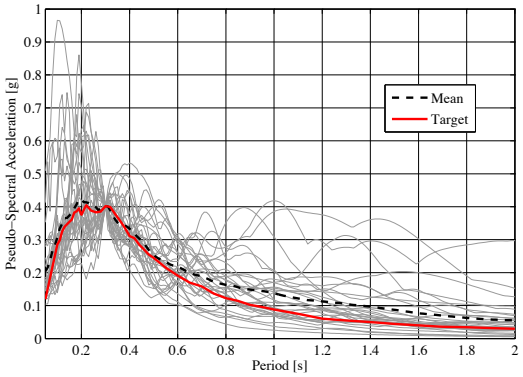
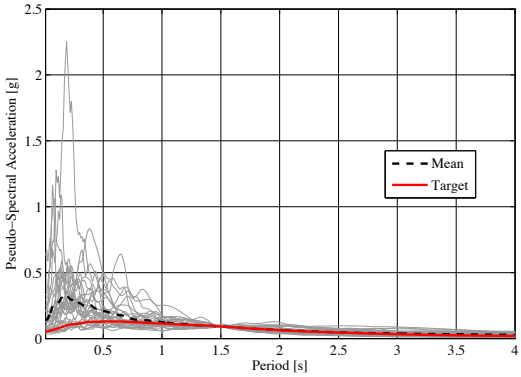


Figure 5: Seismic hazard information for Napoli site (after [45]**).**

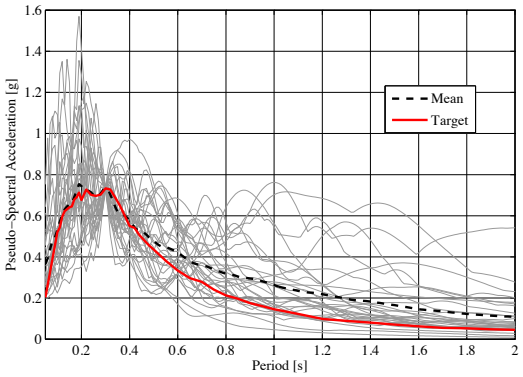
Considering the results of the modal analyses of the case study structure variations shown in Table 1, two sets of conditional mean spectra are selected for the current study; those conditioned to T*=1.5s for the bare frame cases and those conditioned to T*=0.3s for the infilled frame cases. The resulting ground motion sets for the 475 and 2475 year return periods are shown in Figure 6 along with the mean value of both the selected ground motions and the available site hazard information. Since none of the structures in Table 1 have a fundamental period that matches the conditioning period of the available ground motion sets, a degree of dispersion is to be expected in all cases as a result, regardless of nonlinear behaviour of the actual structure.



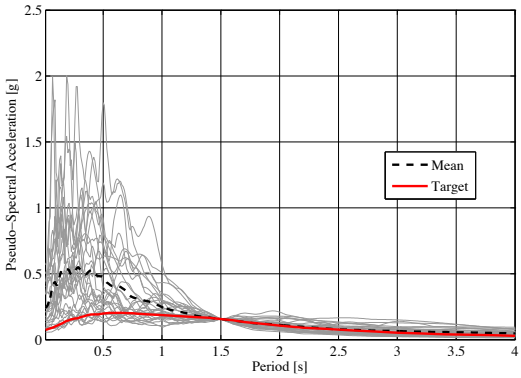
(a) 475 year return period with T*=0.3s



(b) 475 year return period with T*=1.5s



(c) 2475 year return period with T*=0.3s



(d) 2475 year return period with T*=1.5s

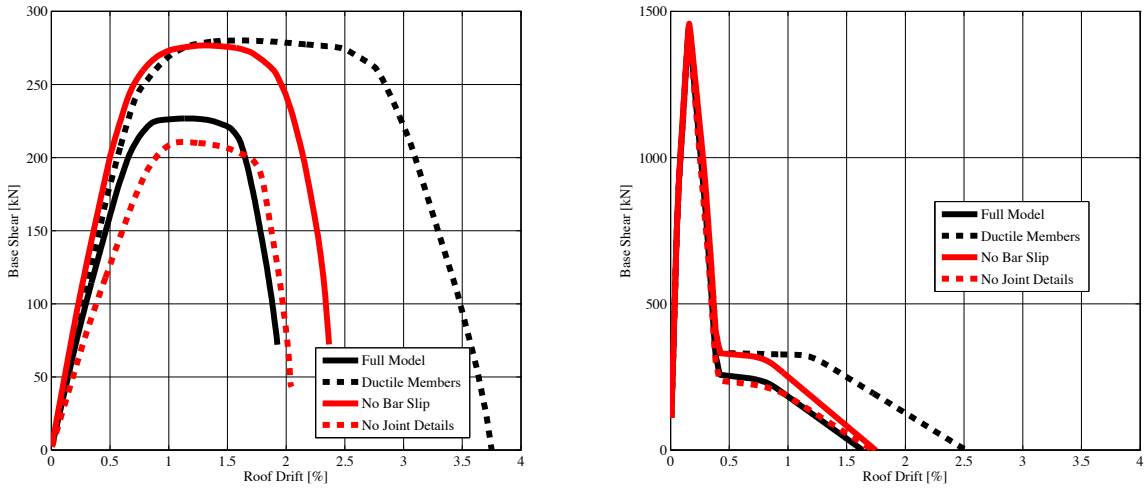
Figure 6: Selected ground motion record sets (after [45]**).**

7 ANALYSIS RESULTS

For each of the variations in the numerical model for the case study structure outlined in Section 5, each of the ground motion sets at both return periods are run using the numerical model to determine the median response parameters and hence examine the sensitivity of the modelling variations of demand parameters of principle interest, namely the storey drifts and peak floor accelerations observed. A pushover analysis is first conducted for each of the structures to illustrate the difference in backbone curve response between model variations, followed by a small discussion into the assumptions for the modelling of the structure for dynamic response and the various assumptions made. The results of the sensitivity study are then presented for each of the modelling variations for both return periods considered.

7.1 Pushover Analysis

Using the modelling outlined in Section 3, a displacement-controlled pushover is performed on each of the configurations of the case study structure using a linear lateral load distribution. Figure 7 shows the pushovers of both the bare and infilled frame with the various modelling approaches. Considering the bare frame in Figure 7(a), the affects of excluding the joint modelling are immediately obvious as the flexibility increases suggesting the joints are stiffer than the equivalent beam elements in addition to a small drop in lateral capacity due t the increase in the span of the beam and column elements. The absence of the bar slip force reduction results in an expected increase in both lateral capacity and stiffness, in addition to the consideration of ductile frame members. The use of ductile frame members also has the anticipated effect of increasing the ductility capacity of the frame by almost double that of the fully modelled frame. Regarding the infilled frame, it is immediately obvious from Figure 7(b) that the presence of masonry infills results in a large increase in lateral capacity compared to that of the corresponding bare frame configuration. Figure 7(b) also shows how the presence of the masonry infill is dominating the initial stiffness, which was already seen through the observed initial periods in Table 1, and the difference between model configurations is not noticeable until the lateral capacity of the infill has been exhausted resulting in the remaining resistance being provided by the bare frame.



(a) Bare frame **(b) Infill Frame**

Figure 7: Pushover analysis.

7.2 Dynamic Analysis Modelling

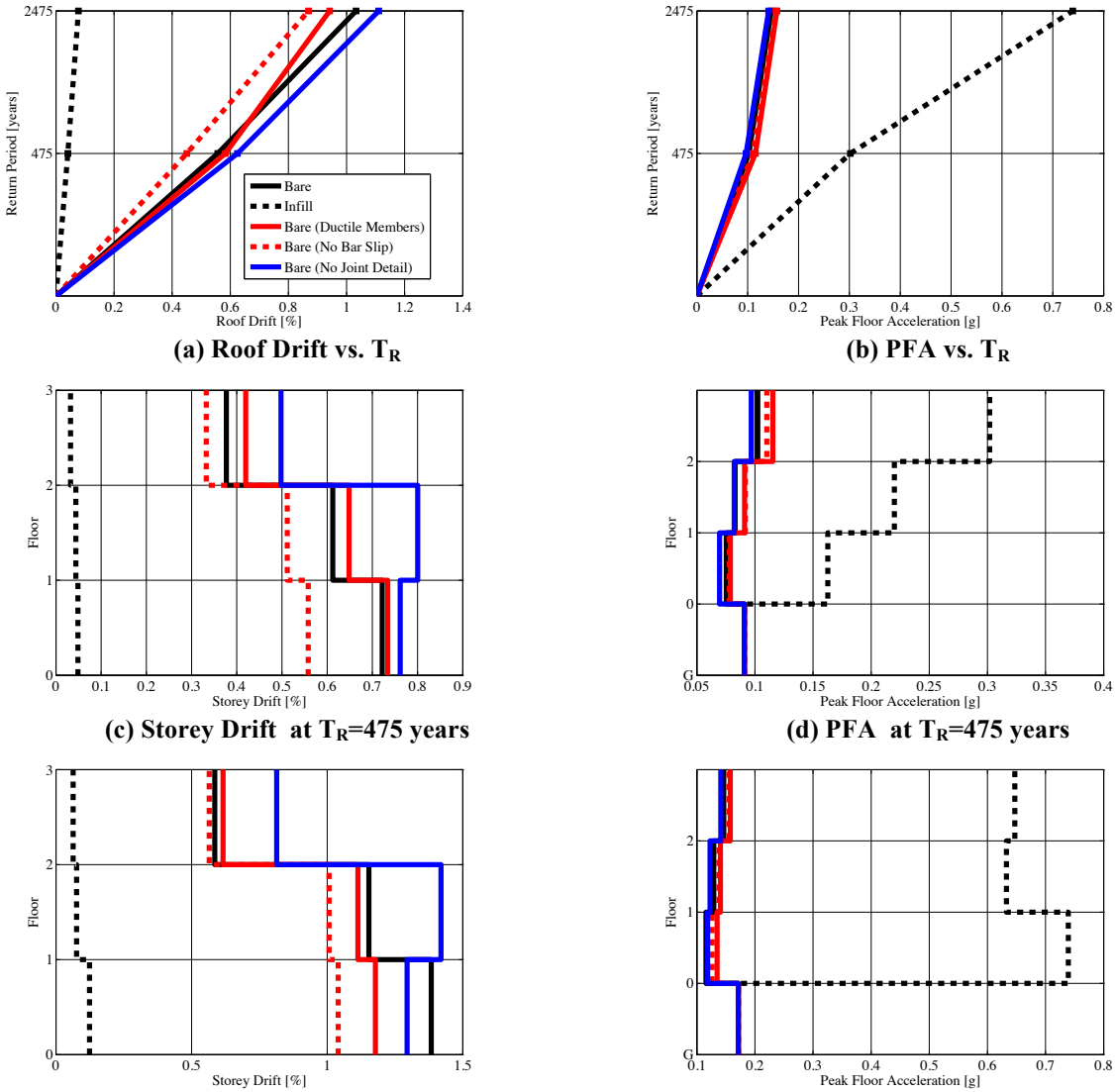
For dynamic analysis, the tributary mass was modelled as a lumped mass at each column centreline node and the corresponding gravity load applied also. A gravity analysis was carried out before each record, whereby the vertical loads were applied and maintained throughout the dynamic analysis to capture second order effects. For the dynamic analysis, an initial time-step of 0.005s was used with a Newmark average acceleration method integrator along with an Energy Increment test tolerance of 1e-8. If the analysis failed to converge after 100 iterations, a sequence of time-step reductions are used for that point of the analysis, where the tolerance is reduced to a minimum of 1e-6 with 500 iterations. Further details on these parameters can be found at [18]. The analysis was carried out in the longitudinal direction and no transverse excitation was applied. For the reference case study structure, 5% tangent stiffness proportional Rayleigh damping was applied to the first and third modes of longitudinal response of the structure, as per recommendations by [47].

7.3 Dynamic Analysis Results

Figure 8 to Figure 11 show the median response values for each of the 30 ground motions of the two considered return periods for each numerical model variation. The first comparison is between the bare frame model, which used the record set at T*=1.5s, whereas the infilled frame was carried out using the T*=0.3s set. In addition, the affects of the elastic damping are shown for both the infilled and bare frames in Section 7.3.3.

7.3.1. Bare Frame Structure

Figure 8 shows the plots of the median storey drifts and peak floor accelerations (PFA) for each of the numerical model variations at both seismic intensity levels. In order to obtain a meaningful comparison between the infilled and bare frame structure, the infilled frame model was also run using the T*=1.5s records and its response included with the bare frame results. From Figure 8 it can be seen that the lack of any joint modelling details results in larger storey and roof at both intensity levels. Although the PFA appears to have reduced slightly with the lack of joint modelling, compared to the increase in PFA caused by the presence of masonry infills it is seen to be relatively small. The addition of the masonry infills is by fare the most influential parameter, with a significant decrease in storey drift and increase in PFA with respect to the bare frame case. This is seen through the amplification of the PFA throughout the height of the structure compared to the relative little amplification of PFA in the bare frame cases. This highlights the fact that the modelling of masonry infills is essential in the seismic assessment of structures and the influence of global structural response is significant, as opposed to considering the infill damage to be solely as a function of the bare frame storey drifts.



(a) Roof Drift vs. T_R

(b) PFA vs. T_R

(c) Storey Drift at T_R=475 years

(d) PFA at T_R=475 years

(d) Storey Drift at T_R=2475 years

(e) PFA at T_R=2475 years

Figure 8: Bare frame structure response.

Comparing the observed median roof drift at the T_R=2475 year intensity with the pushover curve in Figure 7 indicates that the majority of bare frame models have just yielded and exhibit a relatively low ductility. This is more apparent for the case of the infilled frame, where a predominantly elastic response is observed at both intensity levels. Examining the response of the models which considered the ductile members and neglected bar slip with the reference model it can be seen that the use of ductile members does not represent a significant change in response compared to that if the model lacking any bar slip consideration, where the increased flexural capacity of the members results in a noticeable difference in the response. This highlights the importance of the proper consideration of the effects of bar slippage on both the increased member flexibility and the reduction of frame member capacity.

Overall, the difference between some of the results is not particularly large, especially comparing the case of ductile beam and columns with non-ductile member modelling. This is because the principle difference in the two modelling approaches was in the ductility capacity of the structures, with the ductile members model having a much larger ductility capacity.

Since the ductility demand on these structures is relatively low, this difference is not so apparent in the plots of Figure 8. However, if the seismic intensity was incrementally increased (i.e. incremental dynamic analysis [48]), this difference in behaviour would be more apparent in a study such as collapse fragility, where the median collapse drift would be expected to be much higher than that of the non-ductile member model.

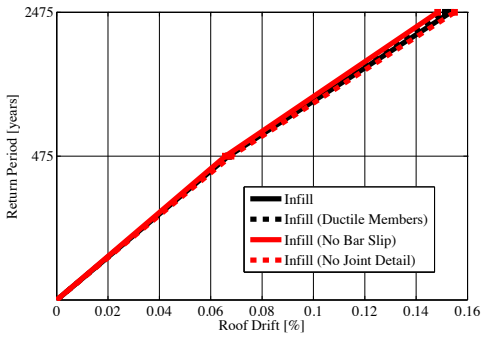
7.3.2. Masonry Infill Structure

Figure 9 shows the response of the various model variations for the case of the infilled frame structures. As it obvious from Figure 9, the presence of the infill results in quite similar median response values for each model variation and the median roof drift value not exceeding the drift a peak force observed in a pushover analysis. This is mainly due to the dominance of the infill frame on the initial stiffness response of the structure. Hence, the combination of low seismicity with limited ductility results in a linear elastic response at both intensities, which from Figure 7 can be seen that the initial stiffness's are quite similar, whereas the post peak behaviour when the infill has failed is quite different. As before with the ductile vs. non-ductile member comparison, this difference would be highlighted more in the collapse fragility of the structure through an incremental dynamic analysis study, where the ductility capacity is fully utilised. Dolsek and Fajfar [17] also noted this behaviour where it was reported that unless the masonry infill exceeds the drift at maximum capacity, the infill would tend to dominate the response of the structure, as can be seen in Figure 9. This is because unless the masonry elements lose significant resistance, the structure essentially becomes a braced frame system with the masonry infill acting as the diagonal bracing members.

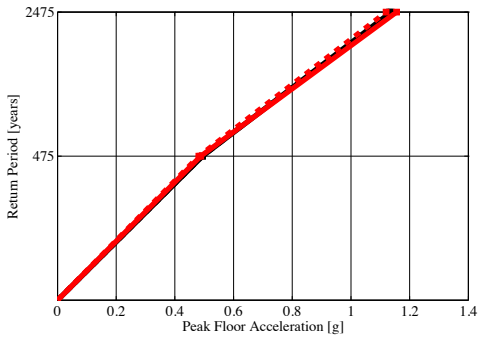
7.3.3. Elastic Damping

Figure 10 and Figure 11 show the response of the bare and infilled reference frames for different levels of elastic damping, respectively. It is seen how the changes in damping result in a noticeable change in the median response ordinates of the structure. This agrees with the finding by [16], where the elastic damping term was shown to heavily influence the results of loss assessment for ductile RC frames compared to other parameters such as initial stiffness and post yield stiffness ratio. It is therefore shown that relative to the other parameters discussed in previous sections for both bare and infilled frames, the level of elastic damping assumed is an important parameter is seismic assessment.

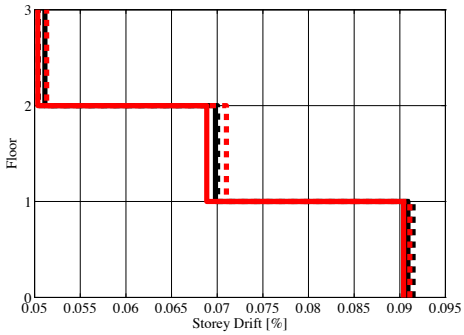
Since the elastic damping parameter is intended to represent the response of all the other elements not modelled, its inclusion is justified. However, should many of the non-structural elements such as cladding and internal partitions be modelled, their response is accounted for and the elastic damping should be reduced accordingly, which has been shown by [16] and also here to be an important parameter which should be properly justifies and not assumed using rules of thumb. Some guidance on the level of elastic damping to be expected from various structural may be obtained from [49].



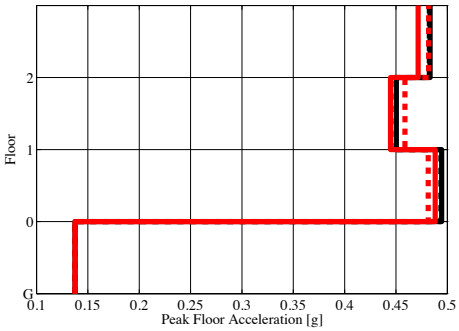
(a) Roof Drift vs. T_R



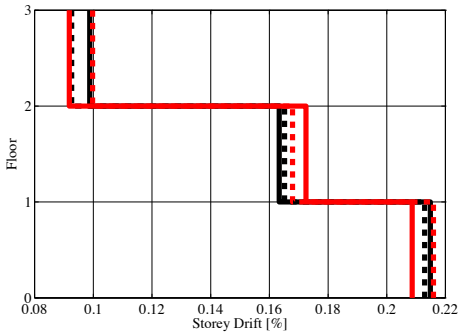
(b) PFA vs. T_R



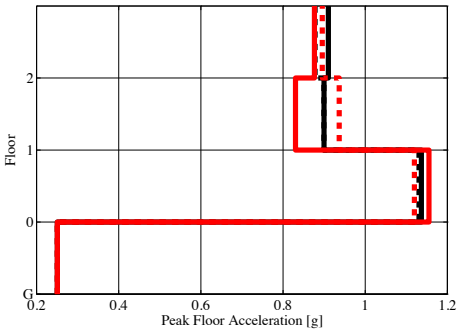
(c) Storey Drift at T_R=475 years



(d) PFA at T_R=475 years



(d) Storey Drift at T_R=2475 years

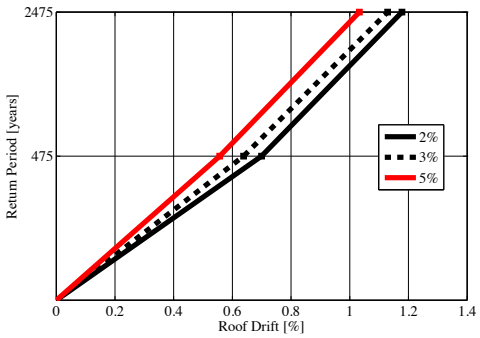


(e) PFA at T_R=2475 years

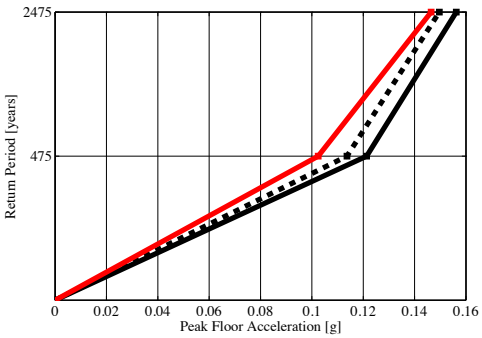
Figure 9: Infill frame structure response.

8 CONCLUSIONS

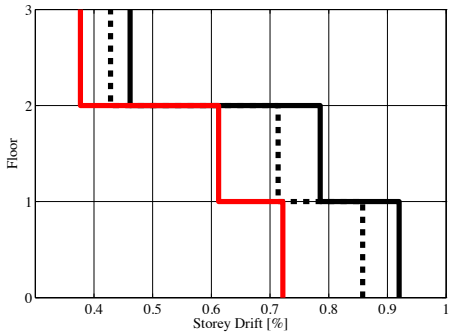
- The numerical modelling of Italian RC frames constructed prior to the introduction of seismic design codes in the 1970's has been discussed. The modelling of the behaviour associated with the joint and beam and column members constructed with plain reinforcing bars and poor seismic detailing was outlined and the behaviour attributed to such characteristics accounted for in a numerical model developed in OpenSees based on available experimental test data. The effects of the bar slippage on both the member flexibility and flexural capacity was discussed and incorporated into the determination of the modelling parameters.



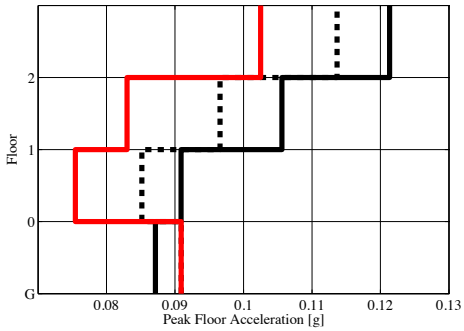
(a) Roof Drift vs. T_R



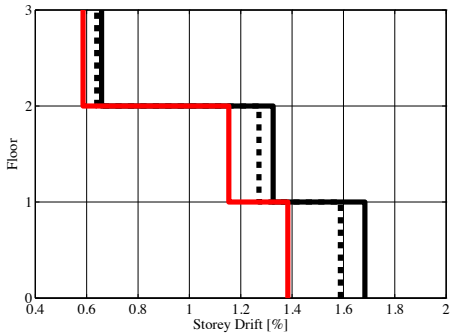
(b) PFA vs. T_R



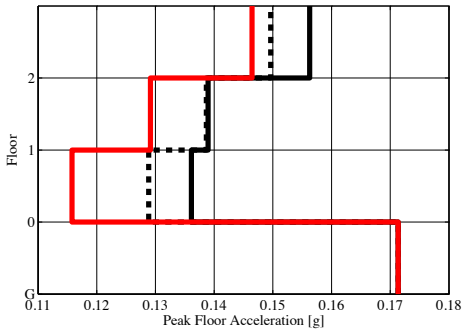
(c) Storey Drift at T_R=475 years



(d) PFA at T_R=475 years



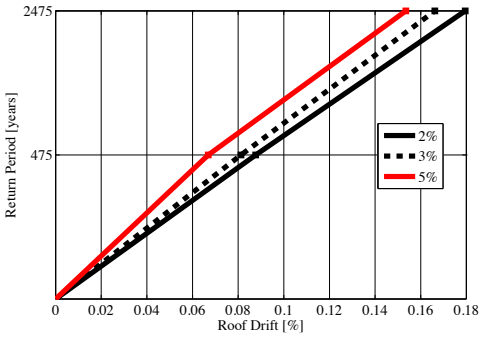
(d) Storey Drift at T_R=2475 years



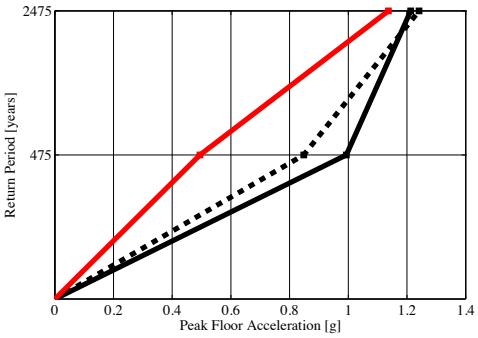
(e) PFA at T_R=2475 years

Figure 10: Influence of elastic damping on bare frame response.

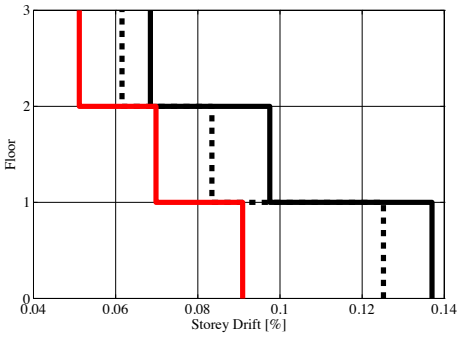
- The aforementioned numerical model was then compared experimental test results of quasi-static cyclic testing carried out on a two-thirds scale three-storey RC frame designed for gravity loads only. The comparison showed the numerical model represents the behaviour very well in terms of strength and stiffness in addition to the hysteretic behaviour and stiffness transitions between reverse cycles.
- A number of variations in modelling of a case study RC frame designed using provisions used in Italy prior to the 1970's were discussed and their expected influence on the seismic response of gravity load designed RC frames considered. As such, a number of numerical model variations were established for an assessment at two different return periods using the proposed numerical model to establish the relative importance of each of these modelling considerations on the response of the structure, which was evaluated in terms of storey drift and peak floor accelerations.



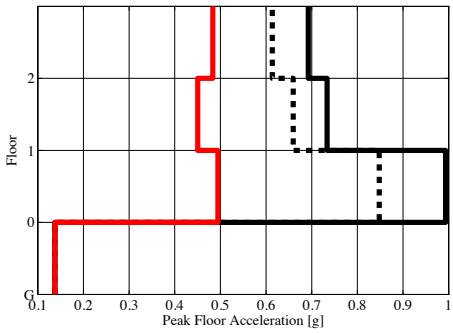
(a) Roof Drift vs. T_R



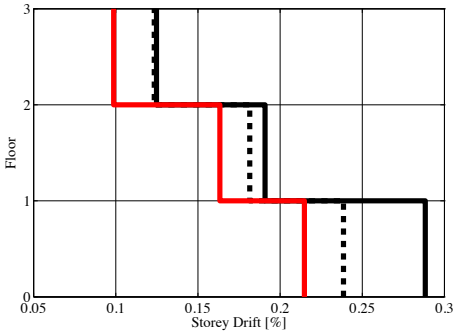
(b) PFA vs. T_R



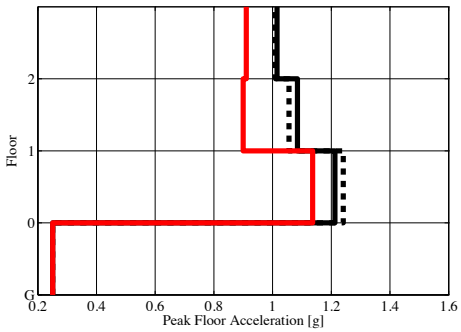
(c) Storey Drift at T_R=475 years



(d) PFA at T_R=475 years



(d) Storey Drift at T_R=2475 years



(e) PFA at T_R=2475 years

Figure 11: Influence of elastic damping on infill frame response.

- The sensitivity study showed that for the bare frame, the modelling of the joint behaviour particular to older RC frames is an influential parameter that should be considered. For the infilled frames, it was shown how the presence of masonry infills resulted in the diagonal strut behaviour dominated the behaviour and resulted in other parameters becoming less relevant at lower storey drifts where the drift at maximum capacity of the infills had not yet been exceeded.
- The variation in elastic damping was shown to be an influential parameter in terms of the storey drift and peak floor accelerations for both the bare frame and infilled frame cases, demonstrating that the amount of elastic damping assumed in seismic assessment needs to be considered carefully with reference to the additional damping provided by elements such as non-structural components.

- While this study has shown that joint modelling and consideration of bar slip can be important parameters in seismic assessment, other parameters such as the use of ductile detailed members did not appear to significantly affect results. This is due to the relatively low level of demand relative to the actual lateral capacity of the frames resulting in relatively low ductility demands, especially in the case of infilled frames. It is therefore recommended for future work that a study such as that presented here be extended to consider the collapse fragility of the structures such that the influence of the entire hysteretic backbone curve will be evident, instead of a small ductility range, where strengths and capacities remain relatively similar for some cases.

9 ACKNOWLEDGEMENTS

The authors would like to acknowledge that part of the work leading to this paper received funding provided by the RELUIS consortium. In addition, the first author would like to acknowledge the funding provided through the IUSS Pavia doctoral programme.

REFERENCES

[1] Porter KA. An Overview of PEER's Performance-Based Earthquake Engineering Methodology. Proc. Ninth Int. Conf. Appl. Probab. Stat. Eng., vol. 8, San Francisco, CA: 2003.

[2] Welch DP, Sullivan TJ, Calvi GM. Developing Direct Displacement-Based Procedures for Simplified Loss Assessment in Performance-Based Earthquake Engineering. J Earthq Eng 2014;18:290–322. doi:10.1080/13632469.2013.851046.

[3] Sullivan TJ, Welch DP, Calvi GM. Simplified seismic performance assessment and implications for seismic design. Earthq Eng Eng Vib 2014;13:95–122. doi:10.1007/s11803-014-0242-0.

[4] Paulay T, Priestley MJN. Seismic Design of Reinforced Concrete and Masonry Buildings. John Wiley & Sons, Ltd.; 1992.

[5] Lowes LN, Mitra N, Altoonash A. A Beam-Column Joint Model for Simulating the Earthquake Response of Reinforced Concrete Frames. Berkeley, California: 2003.

[6] Pampanin S, Calvi GM, Moratti M. Seismic Behaviour of RC Beam-Column Joints Designed for Gravity Loads. 12th Eur. Conf. Earthq. Eng., vol. 726, London, UK: 2002.

[7] Sharma A, Eligehausen R, Reddy GR. A new model to simulate joint shear behavior of poorly detailed beam–column connections in RC structures under seismic loads, Part I: Exterior joints. Eng Struct 2011;33:1034–51. doi:10.1016/j.engstruct.2010.12.026.

[8] Shafaei J, Zareian MS, Hosseini A, Marefat MS. Effects of joint flexibility on lateral response of reinforced concrete frames. Eng Struct 2014;81:412–31. doi:10.1016/j.engstruct.2014.09.046.

[9] Jeon J, Lowes LN, DesRoches R, Brilakis I. Fragility curves for non-ductile reinforced concrete frames that exhibit different component response mechanisms. Eng Struct 2015;85:127–43. doi:10.1016/j.engstruct.2014.12.009.

[10] Di Ludovico M, Verderame GM, Prota A, Manfredi G, Cosenza E. Cyclic Behavior of Nonconforming Full-Scale RC Columns. J Struct Eng 2013;140.

[11] Verderame GM, Fabbrocino G, Manfredi G. Seismic response of r.c. columns with smooth reinforcement. Part I: Monotonic tests. Eng Struct 2008;30:2277–88. doi:10.1016/j.engstruct.2008.01.025.

[12] Verderame GM, Fabbrocino G, Manfredi G. Seismic response of r.c. columns with smooth reinforcement. Part II: Cyclic tests. Eng Struct 2008;30:2289–300. doi:10.1016/j.engstruct.2008.01.024.

[13] Liel AB, Haselton CB, Deierlein GG. Seismic Collapse Safety of Reinforced Concrete Buildings - II : Comparative Assessment of Nonductile and Ductile Moment Frames. J Struct Eng 2011;137:492–502. doi:10.1061/(ASCE)ST.1943-541X.

[14] Haselton CB, Liel AB, Deierlein GG, Dean BS, Chou JH. Seismic Collapse Safety of Reinforced Concrete Buildings - I : Assessment of Ductile Moment Frames. J Struct Eng 2011;137:481–91. doi:10.1061/(ASCE)ST.1943-541X.0000318.

[15] Calvi GM, Magenes G, Pampanin S. Relevance of Beam-Column Joint Damage and Collapse in RC Frame Assessment. J Earthq Eng 2002;6:75–100. doi:10.1080/13632460209350433.

[16] Welch DP, Sullivan TJ. Influence of Structural and Fragility Modelling Decisions in the Loss Assessment of RC Frame Buildings. COMPDYN 2013 - 4th ECCOMAS Themat. Conf. Comput. Methods Struct. Dyn. Earthq. Eng., Kos Island, Greece: 2013.

[17] Dolšek M, Fajfar P. The effect of masonry infills on the seismic response of a four-storey reinforced concrete frame — a deterministic assessment. Eng Struct 2008;30:1991–2001. doi:10.1016/j.engstruct.2008.01.001.

[18] McKenna F, Fenves G, Filippou FC, Mazzoni S. Open System for Earthquake Engineering Simulation (OpenSees) 2000. http://opensees.berkeley.edu/wiki/index.php/Main_Page.

[19] Pampanin S, Magenes G, Carr AJ. Modelling of Shear Hinge Mechanism in Poorly Detailed RC Beam-Column Joints. Concr. Struct. Seism. Reg., Athens, Greece: 2003.

[20] Galli M. Evaluation of the Seismic Response of Existing RC Frame Buildings with Masonry Infills. IUSS Pavia, 2006.

[21] Akguzel U. Seismic Performance of FRP Retrofitted Exterior RC Beam-Column Joints under Varying Axial and Bidirectional Loading. University of Canterbury, 2011.

[22] Melo J, Varum H, Rossetto T, Costa A. Cyclic response of RC beam-column joints reinforced with plain bars : An experimental testing campaign. 15th World Conf. Earthq. Eng., 2012.

[23] Braga F, Gigliotti R, Laterza M. R/C Existing Structures with Smooth Reinforcing Bars: Experimental Behaviour of Beam-Column Joints Subject to Cyclic Lateral Loads. Open Constr Build Technol J 2009;3:52–67. doi:10.2174/1874836800903010052.

[24] Melo J, Varum H, Rossetto T. Cyclic behaviour of interior beam-column joints reinforced with plain bars. Earthq Eng Struct Dyn 2014. doi:10.1002/eqe.2521.

[25] Fernandes C, Melo J, Varum H, Costa A. Experimental and Numerical Analysis of the Cyclic Behaviour of RC Beam-Column Connections with Plain Reinforcing Bars. 15th World Conf. Earthq. Eng., Lisbon, Portugal: 2012.

[26] Genesio G. Seismic Assessment of RC Exterior Beam- Column Joints and Retrofit with Haunches Using Post-Installed Anchors. Universitat Stuttgart, 2012.

[27] Hertanto E. Seismic Assessment of pre1970s Reinforced Concrete Structure. University of Canterbury, 2005.

[28] Bedirhanoglu I, Ilki A, Pujol S, Kumbasar N. Behavior of Deficient Joints with Plain Bars and Low-Strength Concrete. ACI Struct J 2010;107:300–12.

[29] Melo J, Varum H, Rossetto T, Costa A. Experimental response of RC columns built with plain bars under unidirectional cyclic loading. 15th World Conf. Earthq. Eng., 2012.

[30] Melo J, Varum H, Rossetto T. Experimental cyclic behaviour of RC columns with plain bars and proposal for Eurocode 8 formula improvement. Eng Struct 2015;88:22–36. doi:10.1016/j.engstruct.2015.01.033.

[31] Verderame GM, Ricci P, Manfredi G, Cosenza E. Ultimate chord rotation of RC columns with smooth bars: some considerations about EC8 prescriptions. Bull Earthq Eng 2010;8:1351–73. doi:10.1007/s10518-010-9190-x.

[32] Melo J, Fernandes C, Varum H, Rodrigues H, Costa A, Arêde A. Numerical modelling of the cyclic behaviour of RC elements built with plain reinforcing bars. Eng Struct 2011;33:273–86. doi:10.1016/j.engstruct.2010.11.005.

[33] Haselton CB, Liel AB, Taylor Lange S, Deierlein GG. Beam-Column Element Model Calibrated for Predicting Flexural Response Leading to Global Collapse of RC Frame Buildings. Berkeley, California: 2008.

[34] Metelli G, Messali F, Beschi C, Riva P. A model for beam–column corner joints of existing RC frame subjected to cyclic loading. Eng Struct 2015;89:79–92. doi:10.1016/j.engstruct.2015.01.038.

[35] Calvi GM, Magenes G, Pampanin S. Experimental Test on a Three Storey RC Frame Designed for Gravity Only. 12th Eur. Conf. Earthq. Eng., vol. 727, London, UK: 2002.

[36] Rodrigues H, Varum H, Costa A. Simplified Macro-Model for Infill Masonry Panels. J Earthq Eng 2010;14:390–416. doi:10.1080/13632460903086044.

[37] Furtado A, Rodrigues H, Arêde A. Numerical Modelling of Masonry Infill Walls Participation in the Seismic Behaviour of RC Buildings. OpenSees Days Port. 2014, Porto, Portugal: 2014, p. 3–6.

[38] Calvi GM, Bolognini D. Seismic Response of Reinforced Concrete Frames Infilled with Weakly Reinforced Masonry Panels. J Earthq Eng 2001;5:153–85. doi:10.1080/13632460109350390.

[39] Kakaletsis DJ, Karayannis CG. Influence of Masonry Strength and Openings on Infilled RC Frames Under Cycling Loading. J Earthq Eng 2008;12:197–221. doi:10.1080/13632460701299138.

[40] Panagiotakos M, Fardis MN. Seismic Response of Infilled RC Frame Structures. 11th World Conf. Earthq. Eng., Mexico City, Mexico: 1996.

[41] Crisafulli FJ, Carr AJ, Park R. Analytical Modelling of Infilled Frame Structures - A General Review. Bull New Zeal Soc Earthq Eng 2000;33.

[42] Piazza A. Development of a Simpified Displacement-Based Procedure for the Seismic Design and Assessment of RC Frame Structures. Istituto Universitario di Studi Superiori di Pavia, 2013.

[43] Regio Decreto. Norme per la l'esecuzione delle opere conglomerato cementizio semplice od armato. Italy: 1939.

[44] Beigi HA, Christopoulos C, Sullivan TJ, Calvi GM. Gapped-Inclined Braces for Seismic Retrofit of Soft-Story Buildings. J Struct Eng 2014;140. doi:http:/10.1061/(ASCE)ST.1943-541X.0001006.

[45] Ay BO, Fox MJ, Sullivan TJ. Impact of ground-motion selection criteria on the probabilistic seismic performance assessment of RC wall structures. J Earthq Eng 2015;Submitted.

[46] Baker JW, Allin Cornell C. A vector-valued ground motion intensity measure consisting of spectral acceleration and epsilon. Earthq Eng Struct Dyn 2005;34:1193–217. doi:10.1002/eqe.474.

[47] Priestley MJN, Calvi GM, Kowalsky MJ. Displacement Based Seismic Design of Structures. Pavia, Italy: IUSS Press; 2007.

[48] Vamvatsikos D, Allin Cornell C. Incremental dynamic analysis. Earthq Eng Struct Dyn 2002;31:491–514. doi:10.1002/eqe.141.

[49] Welch DP, Sullivan TJ, Filiatrault A. Equivalent Structural Damping of Drift-Sensitive Nonstructural Building Components. 10th US Natl. Conf. Earthq. Eng., Anchorage, Alaska: 2014.

COMPDYN 2015
5th ECCOMAS Thematic Conference on
Computational Methods in Structural Dynamics and Earthquake Engineering
M. Papadrakakis, V. Papadopoulos, V. Plevris (eds.)
Crete Island, Greece, 25–27 May 2015

DEVELOPMENT OF A SIMPLIFIED DISPLACEMENT-BASED PROCEDURE FOR THE SEISMIC ASSESSMENT OF RC WALL BUILDINGS

Timothy J. Sullivan[1,2] **and Matthew J. Fox**[3]

[1] University of Pavia, Department of Civil Engineering and Architecture
Via Ferrata 1, Pavia 27100, Italy
tim.sullivan@unipv.it

[2] EUCENTRE
Via Ferrata 1, Pavia 27100, Italy

[3] ROSE Programme, UME School, IUSS Pavia
Via Ferrata 1, Pavia 27100, Italy
e-mail: matthew.fox@umeschool.it

Keywords: Simplified assessment, RC walls, low-moderate seismicity, displacement-based assessment

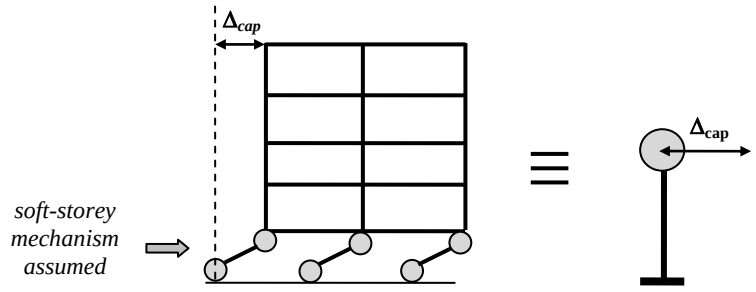
Abstract. *In regions of low or moderate seismicity there may be cases in which a rapid, simplified and conservative seismic assessment may be sufficient to demonstrate that a building satisfies certain seismic risk requirements. In recognition of this, a simplified displacement-based seismic assessment procedure, initially formulated for RC frame structures, is formulated to permit the rapid seismic assessment of reinforced concrete (RC) wall buildings. The key aspect of the procedure is the simplified evaluation of the displacement demand as the maximum spectral displacement across all periods. The displacement capacity, shear capacity and shear demand are also estimated simply, using newly developed equations that are a function of wall geometry and material properties. By adopting such formulations for the displacement and shear, the need to evaluate the period of vibration, stiffness and flexural strength of the walls is eliminated. The proposed approach is evaluated through the design and assessment of several case study buildings. Although the procedure is likely to be conservative in most cases, it is foreseen that it would be used in an initial screening process whereby a pass would require no further assessment and a fail would trigger a more detailed investigation.*

1 INTRODUCTION

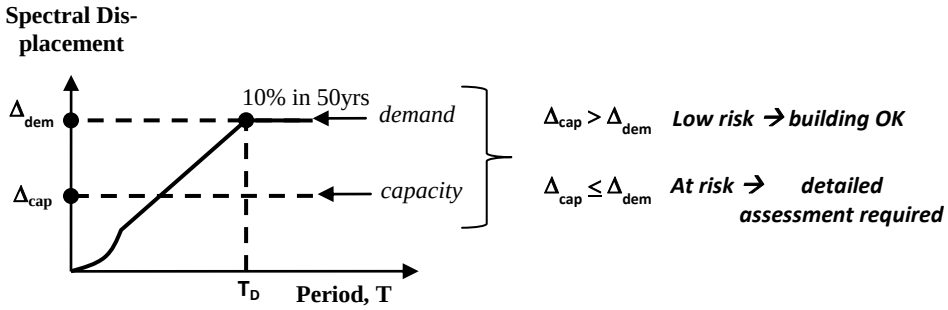
Seismic assessment of a building is traditionally aimed at establishing whether the building satisfies a minimum level of acceptable risk, which is often measured by considering whether code-specified levels of seismic intensity can be sustained. Rigorous seismic assessment requires identification of the structural system, estimation of material properties, and examination of a range of possible failure mechanisms, with an engineer undertaking careful analyses and calculations to quantify the likely capacity and compare this with expected demands. To this extent, a number of guidelines and proposals are available in the literature [1, 2, 3] for the detailed seismic assessment of buildings. In regions of low or moderate seismicity, however, there may be cases in which a rapid, simplified and conservative seismic assessment may be sufficient to demonstrate that a building satisfies minimum seismic risk requirements. In addition, regional building authorities may be interested to assess, with limited resources, groups of buildings in order to identify cases that should be subject to more rigorous seismic assessment and possibly retrofit. In recognition of this, a simplified displacement-based seismic assessment (DBA) procedure has been proposed by Pinho *et al.* [4] and recently developed by Piazza and Sullivan [5] to permit the rapid seismic assessment of RC frame buildings.

Figure 1 illustrates the basis of the simplified procedure proposed by Pinho *et al.* [5]. The approach compares a conservative estimate of the displacement demand, taken equal to the peak spectral displacement demand as shown in Figure 1a, with a conservative estimate of displacement capacity, estimated assuming a column-sway mechanism in the case of RC frame buildings. By assuming a column-sway mechanism the approach intends to achieve a conservative estimate of displacement capacity, and if this capacity is greater that the peak spectral displacement demand, the seismic risk is deemed to be acceptably low. Inputs required to apply the approach are limited to the geometry of the building (member dimensions and the number of storeys) and an estimate of material properties. Note that estimates of the mass and stiffness are not required owing to the fact that the procedure conservatively takes the peak spectral displacement demand, independent of the building period, and nor are estimates of strength required since performance is gauged solely via deformation considerations. The approach has been tested by Piazza and Sullivan [5] for a range of RC frame buildings and was found to perform reasonably well. As such, the objective of this paper is to extend the approach to permit the simplified displacement-based seismic assessment of RC wall buildings. To achieve this, a number of simplified equations, useful for the estimation of displacement capacity, shear capacity and shear demand will first be derived. Subsequently, the approach will be applied to a series of case study wall buildings and results compared with those obtained from more rigorous assessment procedures.

In order to extend the simplified DBA procedure to the case of RC wall buildings, it will be assumed in this work that (i) walls are continuous, with limited openings over the full height of the building; (ii) walls possess aspect ratios (wall height divided by length) greater than 2.5; (iii) walls are at least 200mm thick (this is intended to provide some protection against the likelihood of wall buckling, even though it is recognized [6] that the wall thickness alone is not sufficient to ensure this); (iv) the building possesses stiff, strong foundations, (v) the building is relatively regular in-plan and elevation, and (vi) the building is no more than 20 storeys high and is in reasonable condition (e.g. no signs of concrete cover spalling due to reinforcement corrosion). The guidelines developed in the subsequent sections are not considered applicable to cases where these conditions are not met.



(a) Assessment of displacement capacity for an assumed mechanism (left) & transformation into an equivalent SDOF system displacement capacity (right)



(b) Demand-capacity ratio identified from displacement spectrum

Figure 1. Overview of the displacement-based assessment procedure of Pinho *et al.* [4].

2 SIMPLIFIED EXPRESSIONS FOR THE DISPLACEMENT CAPACITY OF RC WALL SYSTEMS

Slender RC walls can typically be expected to yield in flexure, with a plastic deformation component that will be a function of available confinement reinforcement and the tensile strain capacity of the longitudinal reinforcement. This section develops a simplified approach to estimating the plastic deformation capacity of RC walls, which can then be added to the yield displacement to get the total displacement capacity. It should be kept in mind though that lessons learnt from recent earthquakes have demonstrated [6] that there are a range of other phenomena that can affect the failure mechanism in RC wall structures and this underlines that there will always be considerable uncertainty in any simplified estimate of displacement capacity.

2.1 Simplified estimation of the deformation capacity of RC walls yielding in flexure

The flexural displacement capacity, Δ_{cap}, of a RC wall can be estimated [7] as the sum of the displacement at yield, Δ_y, with a plastic displacement component, Δ_p, as shown in Figure 2 and in Equation 1:

$$\Delta_{cap} = \Delta_y + \Delta_p = \Delta_y + \theta_p f_h H_n \tag{1}$$

The right side of above equation also proposes that the plastic displacement component can be computed as the plastic rotation capacity, θ_p, of a plastic hinge at the base of the wall, multiplied by the total height of the building, H_n, and an effective height factor, f_h, used to relate the total height to an equivalent SDOF system height, noting that the displacement capacity provided by Equation 1 corresponds to an equivalent SDOF system representation of the wall

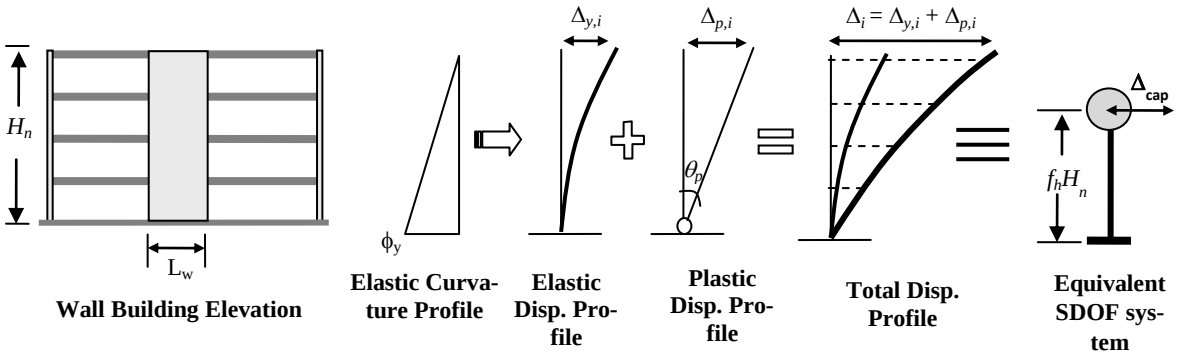


Figure 2. Displacement profile of a cantilever RC wall responding with a flexural plastic hinge (adapted from [8]).

system. In line with the recommendations of [8], the effective height factor can be approximated well by the following expression:

$$f_h = 0.7 + \frac{\sqrt{n} - 0.7}{n^2} \tag{2}$$

where n is the number of storeys in the building.

Subsequently, the flexural yield displacement of a RC wall can be computed using the following expression (adapted from the work of Priestley *et al.* [7]):

$$\Delta_y = \frac{\phi_y (f_h H_n)^2}{2}\left(1 - \frac{f_h}{3}\right) \tag{3}$$

where ϕ_y is the nominal yield curvature for the wall, obtained using the following expression for rectangular wall sections (similar expressions are provided for U-shaped walls by Beyer *et al*. [9] and T-shaped walls by Smyrou *et al.* [10]):

$$\phi_y = 2.0\frac{\varepsilon_y}{L_w} \tag{4}$$

where ε_y is the yield strain of the wall's longitudinal reinforcement, obtained by dividing an estimated reinforcement yield strength, f_y, by the Young's modulus for steel, E_s, and where L_w is the length of the wall (also shown in Figure 2).

For what regards the plastic deformation capacity, part 3 of Eurocode 8 (EC8) [11] states that the plastic rotation capacity of an existing RC wall can be estimated using the following expression:

$$\theta_p = \frac{0.6}{\gamma_{el}} 0.0145 \cdot (0.25^{v}) \left[\frac{\max(0.01;\omega')}{\max(0.01;\omega)}\right]^{0.3} f_c^{0.2} \cdot \left(\frac{L_v}{L_w}\right)^{0.35} 25^{\left(\alpha\rho_{sx}\frac{f_{yw}}{f_c}\right)} (1.275^{100\rho_d}) \tag{5}$$

where γ_{el} is equal to 1.8, v is the axial load ratio, ω' and ω are, respectively, the mechanical reinforcement ratios of the compression and tension longitudinal reinforcement, L_v is the shear span (approximated as the base moment divided by the base shear according to EC8 part

3), L_w is the length of the wall, f'_c and f_y are the mean concrete compressive strength (MPa) and the stirrup yield strength (MPa), respectively, ρ_{sx} is the transverse reinforcement ratio parallel to the direction x of loading, ρ_d is the diagonal reinforcement ratio (if present) and α is the confinement effectiveness factor.

In order to apply the expression it is evident that a considerable amount of information is required; information that is not likely to be available to someone interested in a rapid seismic assessment. As such, in order to obtain a simplified estimate of the plastic rotation capacity, a number of values are assumed for various parameters in order to provide what is considered a reasonable, albeit conservative, estimate of the plastic deformation capacity. In particular, it is assumed that f'_c=25MPa, ω'/ω = 1.0, ν = 0.25, α =0.0, ρ_d =0, and that the shear span can be computed as the effective eight which leads to the following expression:

$$\theta_p = 0.006\left(\frac{f_h H_n}{L_w}\right)^{0.35} \tag{6}$$

where all the symbols have been defined earlier.

At this point, it is clear that one can obtain a quick estimate of the flexural deformation capacity of a RC wall by summing the yield displacement from Equation 3 with a plastic displacement component obtained by multiplying the plastic rotation capacity of Equation 6 by the effective height ($f_h H_n$).

In order to gauge the performance of this simplified approach, displacement capacity estimates obtained using the equations above have been compared with experimental values of the displacement capacity of walls, as reported in the literature. Table 1 lists the experimental test specimens examined together the with reference details from which additional information on the experimental testing could be obtained. Note that while some of the wall specimens listed in in Table 1 actually failed in shear, their displacement capacity values are still of interest here and as such, Figure 3 shows the ratio of the experimentally observed to predicted values of displacement capacity for all specimens.

From the results seen in Figure 3 it is apparent that the new expressions perform reasonably well. In some cases the expressions appear very conservative, and this was expected for walls with good confinement. There are four cases in which the observed displacement capacity is less than the estimated value, but considering the simplicity of the approach and the fact that it is for the large majority of cases conservative, the results above are deemed acceptable.

2.2 Accounting for *P*-Δ effects

In cases where the displacement demand is high and the ratio of strength to system weight is low, *P*-Δ effects may play a significant role in seismic response. To account for *P*-Δ effects it is proposed that an upper limit is placed on Δ_{cap}, based on an allowable stability index of 0.3.

As localised stability is unlikely to be an issue in an RC wall system it is assumed that the stability index can calculated based on an equivalent single-degree-of-freedom (SDOF) system as per Equation 7:

$$\theta_{P-\Delta} = \frac{m_e g}{V_{base}} \frac{\Delta}{H_e} \tag{7}$$

where m_e and H_e are respectively the effective mass and effective height of an equivalent SDOF system, and V_{base} is the base shear strength of the system. Assuming now that the base

shear strength is 10% of the effective weight and taking H_e as equal to $f_h H_n$, an upper limit for the displacement capacity is obtained:

$$\Delta_{cap} < 0.03 f_h H_n \tag{8}$$

TEST NUMBER	SPECIMEN	REFERENCE
1	R1	Oesterle, R.G., *et al*, (1976). "Earthquake Resistant Structural Walls-Tests of Isolated Walls"
2	R2	Oesterle, R.G., *et al*, (1976). "Earthquake Resistant Structural Walls-Tests of Isolated Walls"
3	B1	Oesterle, R.G., *et al*, (1976). "Earthquake Resistant Structural Walls-Tests of Isolated Walls"
4	B3	Oesterle, R.G., *et al*, (1976). "Earthquake Resistant Structural Walls-Tests of Isolated Walls"
5	B2	Oesterle, R.G., *et al*, (1976). "Earthquake Resistant Structural Walls-Tests of Isolated Walls"
6	B5	Oesterle, R.G., *et al*, (1976). "Earthquake Resistant Structural Walls-Tests of Isolated Walls"
7	B6	Oesterle, R.G., *et al*, (1979). "Earthquake Resistant Structural Walls-Tests of isolated Walls-Phase II"
8	B7	Oesterle, R.G., *et al*, (1979). "Earthquake Resistant Structural Walls-Tests of isolated Walls-Phase II"
9	B8	Oesterle, R.G., *et al*, (1979). "Earthquake Resistant Structural Walls-Tests of isolated Walls-Phase II"
10	B9	Oesterle, R.G., *et al*, (1979). "Earthquake Resistant Structural Walls-Tests of isolated Walls-Phase II"
11	B10	Oesterle, R.G., *et al*, (1979). "Earthquake Resistant Structural Walls-Tests of isolated Walls-Phase II"
12	W1	Su, R.K.L., Wong, S.M., (2007). "Seismic behavior of slender reinforced concrete shear walls under high axial load ratio"
13	W2	Su, R.K.L., Wong, S.M., (2007). "Seismic behavior of slender reinforced concrete shear walls under high axial load ratio"
14	W3	Su, R.K.L., Wong, S.M., (2007). "Seismic behavior of slender reinforced concrete shear walls under high axial load ratio"
15	RW-A20-P10-S63	Tran, T.A, Wallace, J.W., (2012). "Experimental Study of Nonlinear Flexural and Shear Deformation of Reinforced Concrete Structural Walls",
16	SHW1	Tasnimi, A.A., (2000). "Strength and deformation of mid-rise shear walls under load reversal"
17	SHW2	Tasnimi, A.A., (2000). "Strength and deformation of mid-rise shear walls under load reversal"
18	SHW3	Tasnimi, A.A., (2000). "Strength and deformation of mid-rise shear walls under load reversal"
19	SHW4	Tasnimi, A.A., (2000). "Strength and deformation of mid-rise shear walls under load reversal"
20	SW1-1	Zhang, H., (2008). "Database on Static Tests of Structural Members and Joint Assemblies"
21	SW1-3	Zhang, H., (2008). "Database on Static Tests of Structural Members and Joint Assemblies"
22	SW1-4	Zhang, H., (2008). "Database on Static Tests of Structural Members and Joint Assemblies"
23	SW2-3	Zhang, H., (2008). "Database on Static Tests of Structural Members and Joint Assemblies"
24	SW4-1	Zhang, H., (2008). "Database on Static Tests of Structural Members and Joint Assemblies"
25	SW4-2	Zhang, H., (2008). "Database on Static Tests of Structural Members and Joint Assemblies"
26	SW4-3	Zhang, H., (2008). "Database on Static Tests of Structural Members and Joint Assemblies"
27	SW5-1	Zhang, H., (2008). "Database on Static Tests of Structural Members and Joint Assemblies"

Table 1. List of RC wall test specimens used to compare experimental and analytical values of displacement capacity.

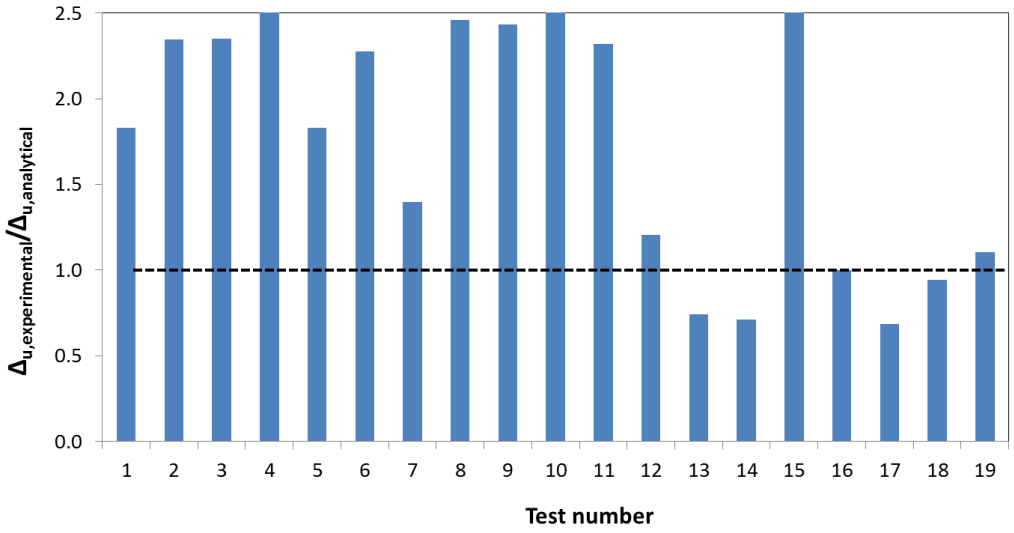


Figure 3. Ratio of the experimentally observed ultimate displacement capacity to the displacement capacity estimated using the simplified analytical approach.

3 SIMPLIFIED EXPRESSIONS FOR SHEAR CAPACITY AND DEMAND

Even if a RC wall building is evaluated and shown to have sufficient displacement capacity there is still the possibility the other failure modes may occur. The most likely of these is shear failure and therefore an additional check is required. The following section develops simplified expressions for estimating both shear capacity and shear demand. It is assumed that the critical region is most likely to be at the base of the wall and therefore the check of shear capacity versus demand is conducted for this location only.

3.1 Simplified estimation of the shear capacity of RC walls

In order to estimate the likelihood of shear failure in RC walls, a simplified estimate is first required of the likely shear resistance. The shear capacity of a RC wall, V_{cap}, is typically estimated in seismic codes by summing a shear contribution, V_c, associated with the concrete tensile strength, together with a contribution, V_s, offered by transverse reinforcing steel, as shown below in Equation 9. Priestley *et al.* [7] explain that the shear resistance of a wall (or column) will also tend to be increased by the axial compression force, but this component is conservatively ignored in formulating a simplified assessment procedure.

$$V_{cap} = V_c + V_s \tag{9}$$

Priestley *et al.* [7] point out that the concrete component of shear resistance tends to degrade as curvature ductility demands increase, in accordance with the modified UCSD shear resistance model. In this work, the concrete shear resistance component of RC walls as predicted by the modified UCSD model is simplified to Equation 10. These simplifications, aimed at avoiding the need for knowledge of reinforcement quantities or material properties, have assumed a concrete compressive strength, f'_c, of 25MPa, and a longitudinal reinforcement content of 0.5% (chosen to be conservatively low). It has further been assumed that the aspect ratio of the critical walls is greater than or equal to 2.0. To avoid the need to calculate the curvature ductility of the wall, it is assumed that the value of γ in the UCSD model is equal to 0.25. This assumption assumes a moderate curvature ductility and therefore will result in overly conservative estimates of shear capacity for walls responding elastically.

$$V_c = 700 L_w t_w \tag{10}$$

where V_c is in units of kilonewtons when the wall length, L_w, and the wall thickness, t_w, have units of meters.

In order to arrive at a simplified estimate of the shear resistance offered by the presence of transverse reinforcement, it is assumed that a typical RC wall section will have at least two transverse reinforcing bars of 10mm diameter every 300mm. In addition, a reinforcement yield strength of f_y=300MPa, a concrete compression zone of approximately 0.2 times the wall length and an inclined strut angle of 30° are assumed appropriate for simplified assessment purposes. Using these values, the traditional expression for transverse reinforcement component of resistance, V_s, simplifies down to:

$$V_s = 220 L_w \tag{11}$$

where V_s is in kilonewtons when the wall length has units of meters.

By making the above simplifications, it is evident that the combination of Equations 10 and 11 permit the total shear resistance of a wall to be estimated with knowledge only of the wall section dimensions, as shown:

$$V_{cap} = 700 L_w t_w + 220 L_w \tag{12}$$

where V_{cap} is in kilonewtons when the wall length and the wall thickness have units of meters.

3.2 Simplified estimation of the shear demands on RC walls

Having obtained an estimate of shear capacity, it is then necessary to obtain an estimate of shear demand. Shear demands in RC walls are likely to be a function of the seismic intensity, the flexural strength of the wall (for cases in which the earthquake intensity is sufficient to make the walls yield in flexure), the periods of vibration of the wall (recognizing that higher modes will contribute significantly to shear demands in multi-storey RC wall buildings) and the ductility demand (or better, the spectral intensity and spectral shape) as explained by Priestley *et al.* [7], Sullivan *et al.* [12] and Sullivan [13] amongst others, who also demonstrated that good estimates of peak shear demands can be obtained using modified modal analysis approaches. Building on the proposal of Pennucci *et al.* [14], Fox *et al.* [15] recently demonstrated that for coupled RC wall buildings, simplified closed-form solutions for total shear demands could be obtained by using a uniform cantilever beam analogy for the walls together with conservative assumptions regarding where the higher mode periods lie in relation to the spectral acceleration plateau. Adapting this approach for simplified assessment purposes here, the total shear demand at the base of a wall can be estimated as:

$$V_d = \sqrt{\left(\frac{3000 \cdot t_w L_w^2}{f_h H_n}\right)^2 + 40\left(H_n A_{f,total} \cdot \frac{t_w L_w}{\sum_{i=1}^{N} A_{w,i}} \frac{\Delta_{dem}}{T_D}\right)^2} \tag{13}$$

where $A_{w,i}$ is the sectional area of wall i and N represents the total number of walls at the ground floor level, t_w is the thickness and L_w the length of the longest wall in the direction of loading under consideration and $A_{f,total}$ the total floor area in the building (such that $H_n A_{f,total}$ gives the building volume), Δ_{dem} is the spectral displacement demand at the corner period, T_D, (which is also taken as the displacement demand, see Figure 1) and the other parameters have been defined earlier. This equation has been formulated assuming that first mode shear demands can be related to the wall flexural strength (which has been approximated using the wall dimensions together with estimated values of reinforcement content and axial load ratio) and that higher mode shear demands can be obtained as described above with reference to the work of Fox *et al.* [15].

3.3 Summary of proposed simplified assessment procedure for RC walls

The previous sections have laid out the ingredients for a simplified displacement-based assessment of RC wall structures. The final recommended procedure is shown in Figure 4. The first step is to obtain information on the building location (to establish seismic hazard information), geometry (building height, number of storeys, total floor area, wall section dimensions) and any other pertinent information that may impact the seismic performance. Secondly, the effective height factor should be found from Equation 2, the flexural yield displacement for the longest walls should be obtained using Equation 3 and the plastic rotation capacity

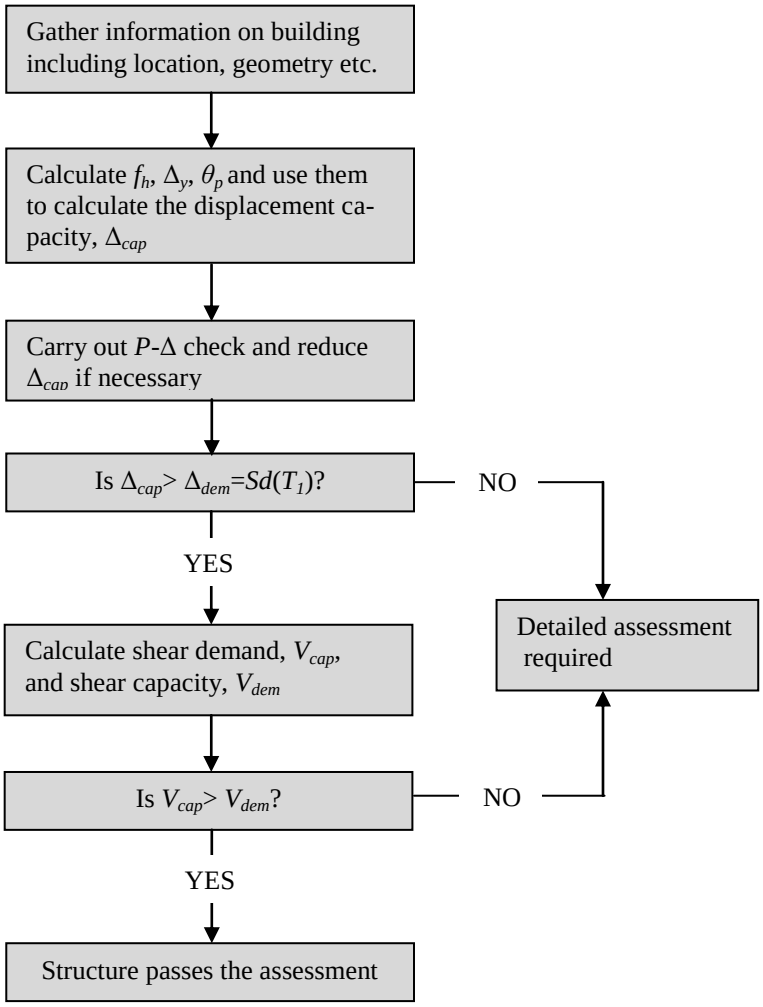


Figure 4. Flowchart of simplified assessment procedure.

from Equation 6. These values are then used in Equation 1 to estimate the displacement capacity, Δ_{cap}. Next the influence of P-Δ should be accounted for by reducing the displacement capacity in accordance with Equation 8 if necessary. The displacement capacity is then evaluated against displacement demand. If the demand is larger than the capacity this indicates the need for a detailed assessment, if not, then the procedure continues to the next step, which is to evaluate the shear capacity and shear demand using Equations 12 and 13 respectively. If the shear demand is greater than the shear capacity then detailed assessment is required, if not, then the structure has passed the assessment and is assumed to be of acceptably low seismic risk.

4 APPLICATION TO CASE STUDY WALL BUILDINGS

4.1 Case study buildings

This work examines various eight storey RC wall buildings all possessing the same generic layout indicated in Figure 5 (from Fox *et al.* [16]) and assumed to lie on rigid foundations. A total of 20 cases for the building are examined, with differences in wall length, reinforcement contents and confinement factors, as shown in Table 2. The buildings are assumed to lie in

one of four different regions of seismicity: two regions of low seismicity, *a* and *b*, in which it is assumed that the reference ground acceleration (a_g) associated with a 475 year return period event is 0.10g but with spectral displacement corner periods of T_D=2s and 4s for sites *a* and *b* respectively, and two regions of moderate seismicity, *c* and *d*, in which the 475 year event a_g is taken as 0.20g and with spectral displacement corner periods of T_D= 2s and 4s for sites *c* and *d* respectively. The corner period spectral displacement demands, $Sd(T_D)$, for each of the four sites are also indicated in Table 2. Note that in all case study buildings the walls are given a thickness of 0.25m and walls 5 and 6 were assumed to possess lengths of 6.5m.

		L_w (m)				ρ_v (%)										
Case	Configuration description	W1	W2	W3	W4	W1	W2	W3	W4	C*	Mass (t)	T_1 (s)	Site	T_D (s)	a_g (g)	$Sd(T_D)$ (m)
1	Simple cantilever	5	5	5	5	0.73	0.73	0.73	0.73	1.13	588	2.47	a	2	0.1	0.086
2	Simple cantilever	5	5	5	5	0.73	0.73	0.73	0.73	1.13	588	2.47	b	4	0.1	0.172
3	Simple cantilever	5	5	5	5	0.73	0.73	0.73	0.73	1.13	588	2.47	c	2	0.2	0.172
4	Simple cantilever	5	5	5	5	0.73	0.73	0.73	0.73	1.13	588	2.47	d	4	0.2	0.342
5	Heavy cantilever	5	5	5	5	0.73	0.73	0.73	0.73	1.13	1176	2.47	a	2	0.1	0.086
6	Heavy cantilever	5	5	5	5	0.73	0.73	0.73	0.73	1.13	1176	2.47	b	4	0.1	0.172
7	Heavy cantilever	5	5	5	5	0.73	0.73	0.73	0.73	1.13	1176	2.47	c	2	0.2	0.172
8	Heavy cantilever	5	5	5	5	0.73	0.73	0.73	0.73	1.13	1176	2.47	d	4	0.2	0.342
9	Large ρ_v cantilever	5	5	5	5	1.5	1.5	1.5	1.5	1.22	588	2.03	a	2	0.1	0.086
10	Large ρ_v cantilever	5	5	5	5	1.5	1.5	1.5	1.5	1.22	588	2.03	b	4	0.1	0.172
11	Large ρ_v cantilever	5	5	5	5	1.5	1.5	1.5	1.5	1.22	588	2.03	c	2	0.2	0.172
12	Large ρ_v cantilever	5	5	5	5	1.5	1.5	1.5	1.5	1.22	588	2.03	d	4	0.2	0.342
13	Unequal lengths	6	3	6	3	0.72	0.96	0.72	0.96	1.2	588	2.76	a	2	0.1	0.086
14	Unequal lengths	6	3	6	3	0.72	0.96	0.72	0.96	1.2	588	2.76	b	4	0.1	0.172
15	Unequal lengths	6	3	6	3	0.72	0.96	0.72	0.96	1.2	588	2.76	c	2	0.2	0.172
16	Unequal lengths	6	3	6	3	0.72	0.96	0.72	0.96	1.2	588	2.76	d	4	0.2	0.342
17	Torsional	6.5	6.5	3.5	3.5	0.59	0.59	0.68	0.68	1.2	588	2.62	a	2	0.1	0.086
18	Torsional	6.5	6.5	3.5	3.5	0.59	0.59	0.68	0.68	1.2	588	2.62	b	4	0.1	0.172
19	Torsional	6.5	6.5	3.5	3.5	0.59	0.59	0.68	0.68	1.2	588	2.62	c	2	0.2	0.172
20	Torsional	6.5	6.5	3.5	3.5	0.59	0.59	0.68	0.68	1.2	588	2.62	d	4	0.2	0.342

Table 2. Properties of case study building configurations.

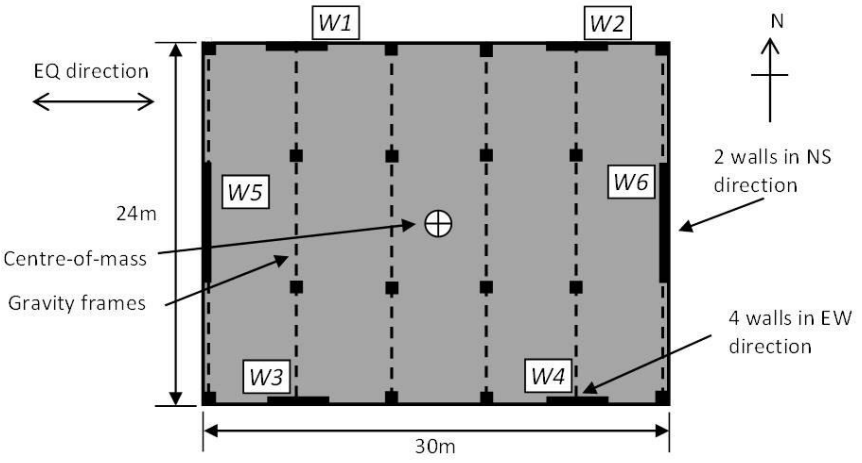


Figure 5. Plan view of case study building (from [17]).

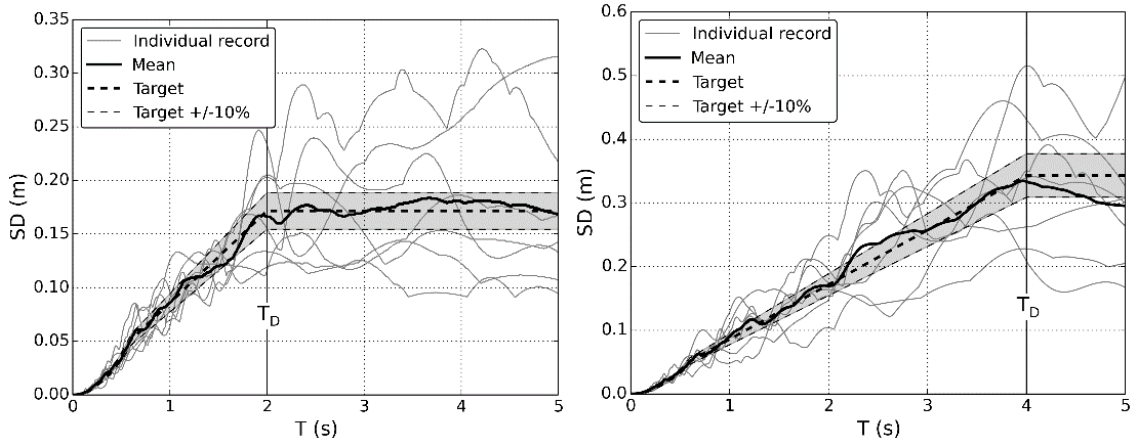


Figure 6. Displacement response spectra of ground motions used in NLRHA (a) Site *a*, and (b) Site *b* (from [17]).

4.2 Modelling and analysis

To rigorously evaluate the performance of the case study buildings they are analysed using nonlinear response-history analyses (NLRHA). All buildings are modelled using a lumped plasticity approach with the finite element program Ruaumoko3D [17]. The frame elements (one per wall per storey) used to model the walls are all linear elastic above level one. Between level one and the foundation Giberson one component frame elements are used, which allow inelastic deformations over a pre-defined plastic hinge length, L_p, which is calculated in accordance with [7]. The 'Takeda thin' hysteresis rule (i.e. a Takeda hysteresis with parameters α=0.5 and β=0.0. Refer Carr [19]) is used to model the hysteretic behaviour in the plastic hinge region. To include *P*-Δ a 'large displacement' analysis regime is used and additional gravity loads not supported by the walls are applied to a 'dummy column'. All walls are connected by rigid diaphragms.

Two sets of seven ground motions were used for the NLRHAs one. Both sets of ground motions (when appropriately scaled) are compatible with the type 1 spectrum from EC8 [11] for ground-type C; however, the first set is selected to be compatible with a spectral displacement corner period of T_D= 2s while the latter is for T_D= 4s. The target spectra and displacement response spectra of the selected ground motions are shown in Figure 6. Further information on the specific ground motions can be found in [16].

4.3 Results

The performance of the proposed assessment procedure is evaluated through comparison of results against those found using equivalent rigorous approaches. In the first instance the demands evaluated using the simplified procedure are compared to the demands obtained from NLRHA. This is shown in Figure 7 for both displacement and shear, and is expressed as a ratio of simplified demand to NLRHA demand, thus making results larger than one conservative. In general the demand predictions using the simplified method are very good. For shear, all values fall between one and 1.8. For displacement the majority of results are between one (or very close to one) and two. There are two exceptions for this in the torsional building, which are due to displacement demands being estimated at the centre-of-mass in the simplified method while NLRHA is able to capture the larger demands at the flexible edge of the building.

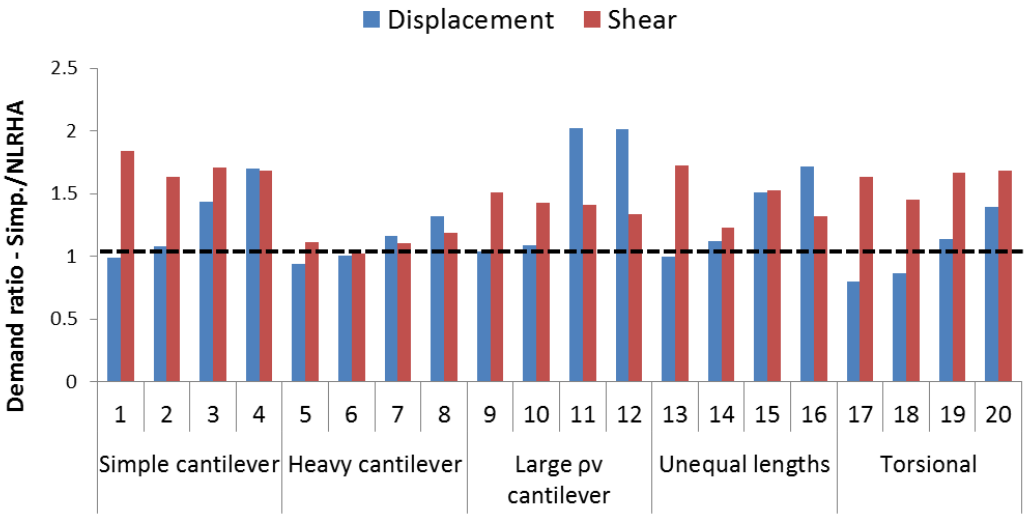


Figure 7. Ratios of demands obtained using the simplified procedure and from NLRHA.

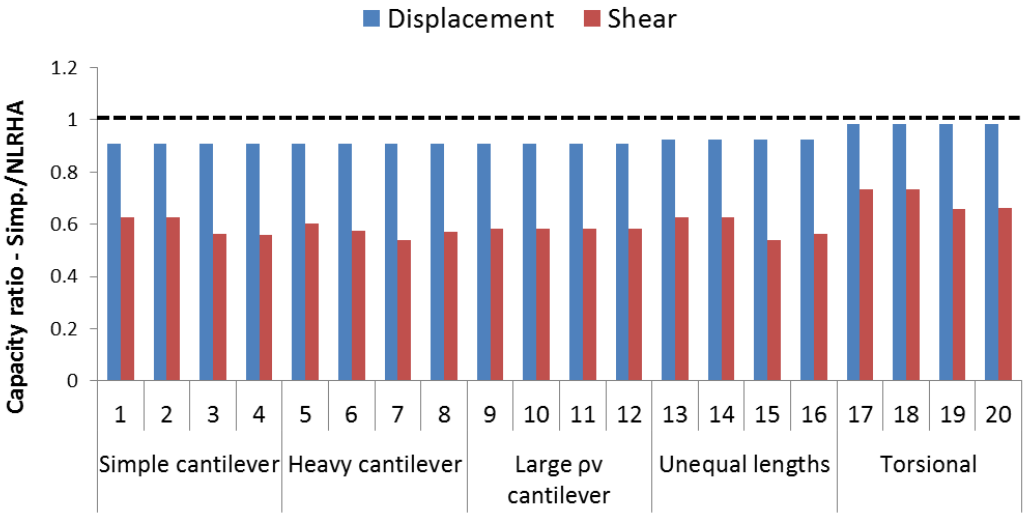


Figure 8. Ratios of capacities obtained using the simplified procedure and equivalent detailed procedures.

Figure 8 shows the same ratios as Figure 7 but this time for capacity. In this case a value less than one is conservative. It can be seen that for both displacement and shear all ratios are less than one. Displacement ratios tend to average around 0.9, while for shear the simplified approach is more conservative giving predictions equal to around 60% of those obtained using the UCSD shear model in full.

Figure 9 shows ratios of demand to capacity calculated using the simplified assessment procedure and using a detailed assessment procedure (with detailed capacity calculations and demand estimates obtained from NLRHA). In each case the ratio is the larger of those obtained from considering displacements or shear. From the detailed assessment results it can be seen that all configurations of the case study building achieve an acceptable level of performance. In fact they tend to have a fairly large reserve capacity against the limits for which they are being assessed. It can be seen that for all cases the simplified procedure produces more conservative demand/capacity ratios (in most cases significantly more conservative). In 10 out of the 20 cases the demand/capacity ratios are large than one, which would invoke the need for a detailed assessment.

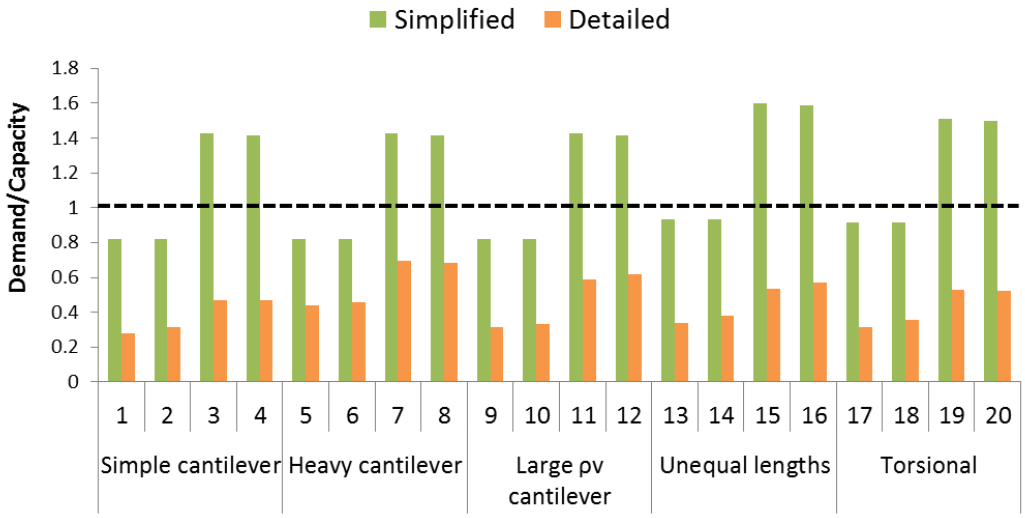


Figure 9. Demand to capacity ratios obtained using the simplified procedure and detailed assessment.

4.4 Discussion

The examination of the case study buildings has shown that the proposed assessment procedure works reasonably well. Predications of demand/capacity ratios are in most cases very conservative; however, this is in-line with the philosophy of the procedure, which is that conservative assumptions can be made and in doing so accuracy is sacrificed for expediency. For the cases considered, 50% would require no further seismic assessment. This reflects the fact that in general the buildings perform very well, as they are in regions of only low and moderate seismicity. Of the two sides of the demand versus capacity equation it appears that the simplified procedure is better at estimating demands, and future work in simplified capacity predictions appears to be the best approach to approving the procedure over all. The results presented in Figure 9 do have to be interpreted with some caution as in all cases shear was critical. It therefore seems prudent that more rigorous evaluations be undertaken on a wider range of case study buildings with widely varying properties.

5 CONCLUSIONS

A simplified procedure has been presented for the seismic assessment of RC wall buildings. The procedure is based on the idea that a number of conservative assumptions can be made and thus the procedure simplified significantly. This has included the development of simplified equations for estimating displacement capacity, shear capacity and shear demand. Also of particular note is the assumption that displacement demand can be approximated by spectral displacement at the corner period of the displacement spectrum (*i.e.* $Sd(T_D)$).

Through a number of case study applications it was shown that the procedure performs reasonable well. As expected it give predictions of demand to capacity that are always more conservative than those obtained using a more detailed assessment with nonlinear response-history analyses. To improve the procedure it was identified that future works should focus on improved shear capacity predictions and the procedure should be tested on a more diverse set of case study buildings.

ACKNOWLEDGEMENTS

The authors gratefully acknowledge that part of the work leading to this research received funding from the Italian Department of Civil Protection (DPC) as part of the EUCENTRE-DPC 2014-2015 agreement.

REFERENCES

[1] M.J.N. Priestley, Displacement-based seismic assessment of reinforced concrete buildings. *Journal of Earthquake Engineering*, **1**, 157-192, 1997.

[2] D.P. Welch, T.J. Sullivan, G.M. Calvi, Development of direct displacement-based procedures for simplified loss assessment in performance-based earthquake engineering. *Journal of Earthquake Engineering*, **18**, 290-322, 2014.

[3] T.J. Sullivan, D.P. Welch, G.M. Calvi, Simplified seismic performance assessment and implications for seismic design. *Earthquake Engineering and Engineering Vibration*, **13**(Supp. 1), 95-122, 2014.

[4] R. Pinho, H. Crowley, M. Faravelli, Studio preliminare per identificare le soglie inferiori significative dello spettro di spostamento (in Italian), *Progetto S5, Deliverable 7, Task 2*, for the Italian Department of Civil Protection, 2007

[5] A. Piazza, T.J. Sullivan, Development of a simplified displacement-based procedure for the seismic design and assessment of RC frame structures. *Proceedings of the Second European Conference on Earthquake Engineering*, Istanbul, Turkey, 2014

[6] S. Sritharan, K. Beyer, R.S. Henry, Y.H. Chai, M.J. Kowalsky, D. Bull, Understanding poor seismic performance of concrete walls and design implications. *Earthquake Spectra*, **30**, 307-334, 2014.

[7] M.J.N. Priestley, G.M. Calvi, M.J. Kowalsky. *Displacement-Based Seismic Design of Structures*. IUSS Press, Pavia, Italy, 2007.

[8] T.J. Sullivan, An energy factor method for the displacement-based seismic design of RC wall structures. *Journal of Earthquake Engineering*, **7**, 1083-1116, 2011.

[9] K. Beyer, A. Dazio, M.J.N. Priestley, *Seismic Design of Torsionally Eccentric Buildings with U-shaped RC Walls*, Research Report Rose 2008/03, IUSS Press, Pavia, Italy, 2008.

[10] E. Smyrou, T.J. Sullivan, M.J.N. Priestley, G.M. Calvi, Sectional Response of T-Shaped RC walls, *Bulletin of Earthquake Engineering*, **11**, 999-1019, 2013.

[11] Comité Européen de Normalisation, Eurocode 8, Design of structures for earthquake resistance – Part 3: Assessment and retrofitting of buildings, EN 1998-3. CEN, Brussels, Belgium, 2005.

[12] T.J. Sullivan, M.J.N. Priestley, G.M. Calvi, Estimating the Higher Mode Response of Ductile Structures. *Journal of Earthquake Engineering*, **12**, 456–472, 2008.

[13] T.J. Sullivan, Capacity Design Considerations for RC Frame-Wall Structures. *Earthquakes and Structures*, **1**, 391-410, 2010

[14] D. Pennucci, T.J. Sullivan, G.M. Calvi, Inelastic higher-mode response in reinforced concrete wall structures. *Earthquake Spectra* in-press, doi: http://dx.doi.org/10.1193/051213EQS123M, 2014.

[15] M.J. Fox, T.J. Sullivan, K. Beyer, Capacity design of coupled RC walls. *Journal of Earthquake Engineering*, **18**, 735-758, 2014.

[16] M.J. Fox, T.J. Sullivan, K. Beyer. Evaluation of seismic assessment procedures for determining deformation demands in RC wall buildings. Submitted to *Earthquakes and Structures*, 2015.

[17] A.J. Carr, *Ruaumoko Manual – Volume 3: User manual for the 3-dimensional version Ruaumoko3D*, Department of Civil Engineering, University of Canterbury, 2012.

[18] A.J. Carr, *Ruaumoko Manual - Volume 5: Appendices*, Department of Civil Engineering, University of Canterbury, 2008.

COMPDYN 2015
5th ECCOMAS Thematic Conference on
Computational Methods in Structural Dynamics and Earthquake Engineering
M. Papadrakakis, V. Papadopoulos, V. Plevris (eds.)
Crete Island, Greece, 25–27 May 2015

STRENGTH AND STABILITY ASSESSMENT OF EXISTING BUILDINGS IN ISRAEL (COMPDYN 2015)

N. Gluck[1], R. Farhat[1], R. Eid[1], U. Tzadka[1]

[1] Sami Shamoon College of Engineering, Dept. of Civil Engineering

Reh. Bialic 56

84100 Beer Sheva, P.B. 45

mikig@sce.ac.il

Keywords: reinforced concrete structures, retrofitting of existent structure, assessment levels nonlinear analysis models, monitoring of existent structures.

Abstract. The Middle East is prone to frequent seismic tremors which affect buildings and civil engineering facilities. New demands of economical nature lead to achievement of larger structures with increased openings and augmented loads. This process affects both the existent and new structures with significant masses which contribute to the development of inertial loads endangering the structure loaded by dynamic effects (earthquake, wind, oscillations, blasts etc.).

The structural safety assessment must take into account the age of the existent building and the future demands previewed by development of the socio-economic conditions. Most of the existent buildings have been erected during the former century. The age of these buildings is close to the life limitation according to the codes. The strength and robustness of the buildings is affected by ageing, corrosion, fatigue etc., so that special attention must be accorded to these buildings to enable them to stand under the loads which might occur. The main goal of the assessment is to avoid occurrence of human or economic losses due to partial or full collapse.

The present work is devoted to the assessment of the strength and the stability of the reinforced concrete buildings according to different levels of assessment enabling the building with nonlinear abilities to stand the previewed seismic and wind excitations, as well as the influence of changes of the temperature.

1 INTRODUCTION

Civil engineering went under significant changes during the last decades. Many improvements have been done concerning the analysis, the structure, materials and the risk definition which endangers the structure. The elements for the modern facilities and commodities lead to new strategies of achievement or to the need to retrofit the existent buildings. The activity to upgrade the buildings and ensuring their stability affects their shape and the structural ability to stand increased loads.

This paper deals with the existent structures and the assessment of their ability to stand the increased loads of the actual demand. The existent structures are the ones built during the last decades and they are residential, cultural, commercial, administrative, communication, industrial, etc. facilities. Since these buildings were designed and erected the demands changed, the codes were improved, new materials are used and new technologies have been provided. But significant money have been invested into these establishments and they must be kept stable for the future. Most of the documentation of these buildings has been lost so that the possibilty to achieve the structural identification of these buildings is almost impossible. Meanwhile the building materials have been changed together with the environmental factors which produce the decay of the materials which did not corrode, calcified or deteriorate a long period during their structural life.

New strategies of ductility provision into new buildings lead to improved abilities of standing the loads which may occur. Reinforced concrete elements have been provided by increased ductility by confining them in specific zones to enable the dissipation of the energy induced by loads of dynamic nature.

The assessment of the structural ability to stand the environmental and physical loads is made according a series of criteria. Among the most common criterion is the age of the structure which involves the codes used at a certain period, the designer which provided the project and the builder which erected the building. Non-destructive tests enable to verify the strength and the stability of a certain structure. The data provided by a series of investigations lead to model the structure and check the structural behavior of the building.

Due to the demands of the structures prone to increased load due to the actual technologies and the dynamic effects due the earthquakes, which might occur, an intense trend of retrofitting the actual structures to increase their strength and stability capacity to the level provided by the actual codes.

2 THE STRUCTURAL ASSESSMENT

Engineers, designers and researchers devote large amount of time to study the causes leading to structural decay. The aim of this activity is to preserve the existing structures and to ensure their stability under the occurring loads. This activity is motivated by economical demands due to the necessity to provide residence and work opportunity for an increasing population with more demands and providing housing for modern technology.

Modern building industry [1] is based on updated codes which enable increased residential areas by achieving higher, more storied buildings with abilities to stand strong winds, temperature effects and other outstanding loads, among them earthquakes. All the mentioned effects may damage both the existent and the newly achieved buildings. The codes have been updated to provide improved materials, better methods of analysis and dissipative solution to diminish the energy penetrating into the structures.

Among the modern solutions which decrease the deformation effects of the structure [2] the piled-raft solution has been developed aiming the diminishing of the settlements of structures resting on clayey and sandy soils. These soils exhibit rheological behavior for clays and are prone to liquefaction under intense vibrations. The provided piled-raft solution ensures stability under the moisture sensitive soils and provides stability in case of liquefaction phenomena.

Reinforced concrete structures [3] must be enabled to stand against chain failure. The design must be accomplished in a manner to avoid the failure of a structural element sustaining more elements to cease to stand under the loads. Avoidance of the structural progressive failure is very important to ensure the stability of the structure which has to be robust and save the life of its occupants.

One of the ways to improve the structural stability is the use of FRP sheet to provide the confining of the sensitive zones in the structural elements increasing the ductility of the entire structure [4]. Increased ductility means the ability to dissipate more energy from the load acting upon the structure. The strengthened structure will absorb the energy of the load and save the retrofitted structure.

One of the most dangerous loads which might occur during the service of a building must be cnsidered the explosion of the gas used by the inhabitants to warm or to cook [5]. Since the danger of such an explosion to provoke a progressive failure is real it must be taken into account the way to ensure the desired robustness and to enable quick repair in case of the accident.

The ability of the structure to stand under the loads which might occur is judged by means of the assessment of the existent structure [5, 7, 8, 9, 10]. A large variety of scenarios have been provided to check both the existent and new buildings. Assessment can be done according several strategies ranging between the simplest to the most intricate way to obtain the robustness of the structure. The structural model built according the information obtained by various investigative procedures may be analyzed by simple methods or numeric software based on linear to nonlinear means [11]. More accurate results may obtained by monitoring of the structural response of the building under dynamic excitations which can be based on provoked loads or simply using the micro seismic movements occurring in the area. The changes of the registered structural frequencies indicate changes of the structural strengthening or decay with time.

The present work presents the expected decay of a wall due to horizontal loads, temperature changes, creep, corrosion, etc. In the same time there is presented a way to use structural monitoring to judge the structural changes.

3. NUMERICAL EXPERIMENTS

3.1 Causes of structural deterioration

The process of structural deterioration continues during the entire life of the structure. The environmental effects lead to loads which affect the properties of the materials the structure is made from.

The reinforced concrete structures are affected from their cast stage from the creep of the concrete and the relaxation or the reinforcement. These effects enable the formation of cracks and initial stresses which reduce the structural stiffness and contribute to further deterioration of the structure. The cracks enable the penetration of the moisture and Cl ions which affect the concrete and cause the corrosion of the reinforcement.

Temperature changes between seasons and day – night produce stress changes in the structure causing ageing effects leading to fractures in the structural system. Microseisms produce

fatigue phenomena affecting the structure. More severe damages are produced by wind, earthquake, traffic and daily loading and unloading.

The phenomena which are exemplified further use the analysis by means the finite elements (ADINA), and the data acquisition by means of the CX1 Network Accelerometer & Inclinometer (SENSR).

3.2 The Dynamic Effects

To exemplify the effect of the horizontal loads on a reinforced concrete wall the ADINA routine was used. The nonlinear behavior was used to follow the deformation, stress - strain behavior and crack development. The structure represents a wall provided by a door opening. The wall was achieved from concrete B30 reinforced by steel F400. The horizontal load was increased gradually till the collapse was achieved. Fig. 1 visualizes the deformation of the wall in x direction (on the left side) and the stresses in z direction (on the right side)

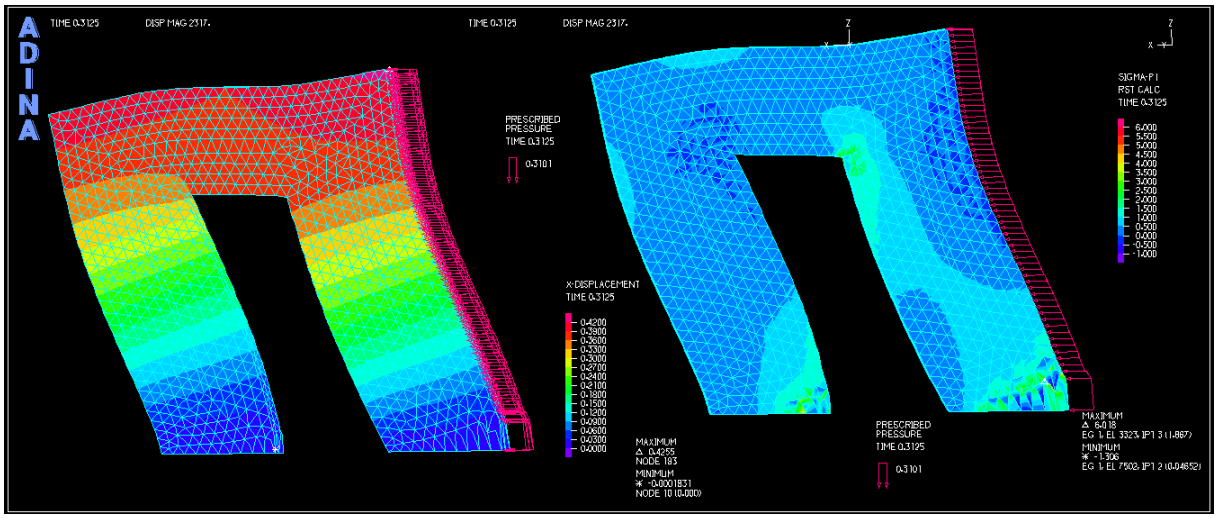


Figure 1 Deformations in direction x and stresses in direction z

Fig. 2 presents graphically the stresses in z direction along the bottom of the column of the concrete of the wall. Since the concrete of the wall exhibits its tension limit for 2 MPa it means that in the analyzed section cracks occur. The cracked area will permit the penetration of moisture and Cl ions enabling the calcification of the concrete and the corrosion of the reinforcement bars. As a demand to avoid development of the cracks on the face of the columns it is compulsory to provide bars with increased areas or to put the bars closer along the vertical direction. Another way to avoid these cracks is by providing steel profiles along the edges of the wall. Since this supplementary steel may corrode and endanger the wall, FPR sheets can be glued along the edges to avoid crack and to improve the ductility of the wall.

Fig. 3 visualizes the force and the stresses in the vertical and horizontal bars in the net which was provided as reinforcement of the wall. Due to modeling intricacy the horizontal bars continue through the opening. This shortcoming does not influence the results of the analysis. For better modeling the areas of the vertical bars at the edges of the wall have to be greater or placed closer.

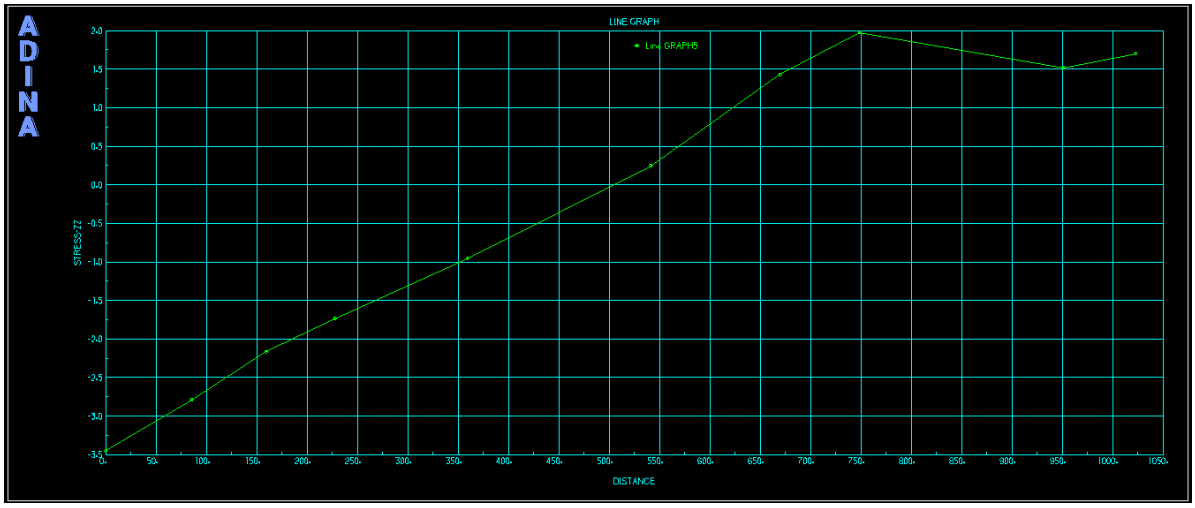


Figure 2 ZZ stress in the wall.

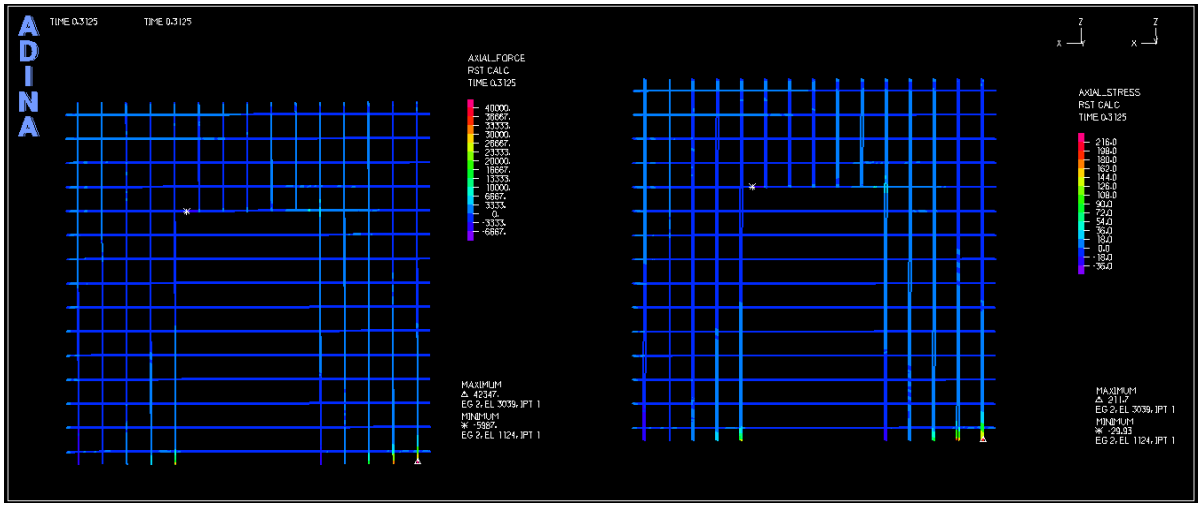


Figure 3 Axial forces and stresses in the reinforcement bars

Fig. 4 presents a graph of the displacement of the upper part of the wall loaded by the horizontal load. This graph visualizes the deformation of the base to the next story where more severe crack might occur in the lintels. This explains the crack which develop at the middle of the beams and their role in diminishing the stiffness of the entire structure. According to design provisions the development of cracks in the beams diminish the stiffness to 60% of the initial calculated stiffness. This kind of cracks may diminish the initial stiffness in a more severe manner and retrofitting is compulsory.

Fig. 5 indicates the zones in the wall where cracks develop. By means of the ADINA software the minimum and maximum amount of cracks are indicated. Taking into account that the dynamic loads act in a cyclic manner the analysis must be achieved in a hysterically. The analysis becomes more intricate and scaled models with similitude procedures can lead to the best assessment analysis.

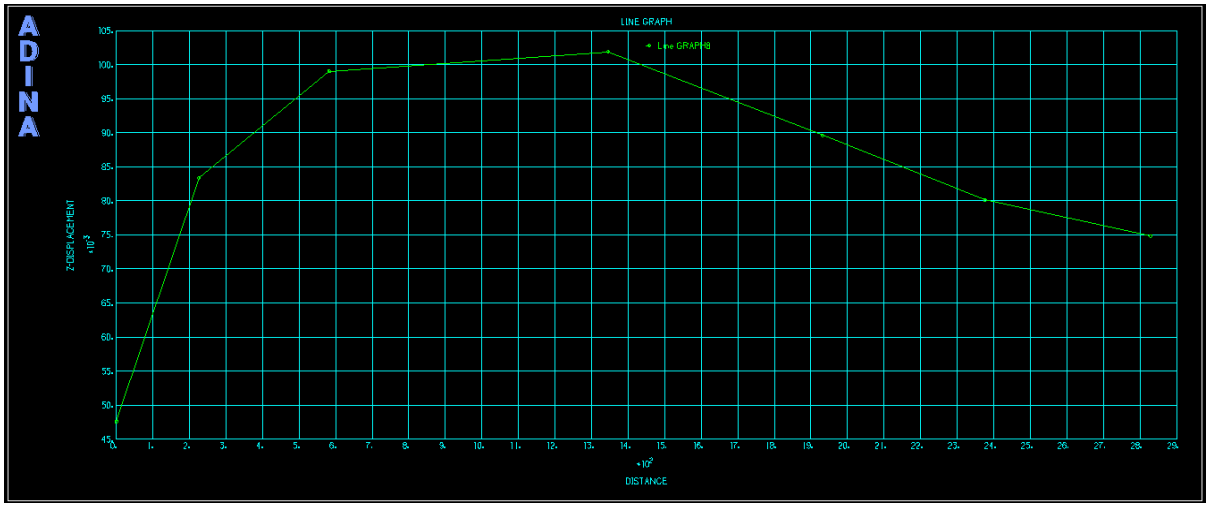


Figure 4. The vertical displacement at the top of the wall

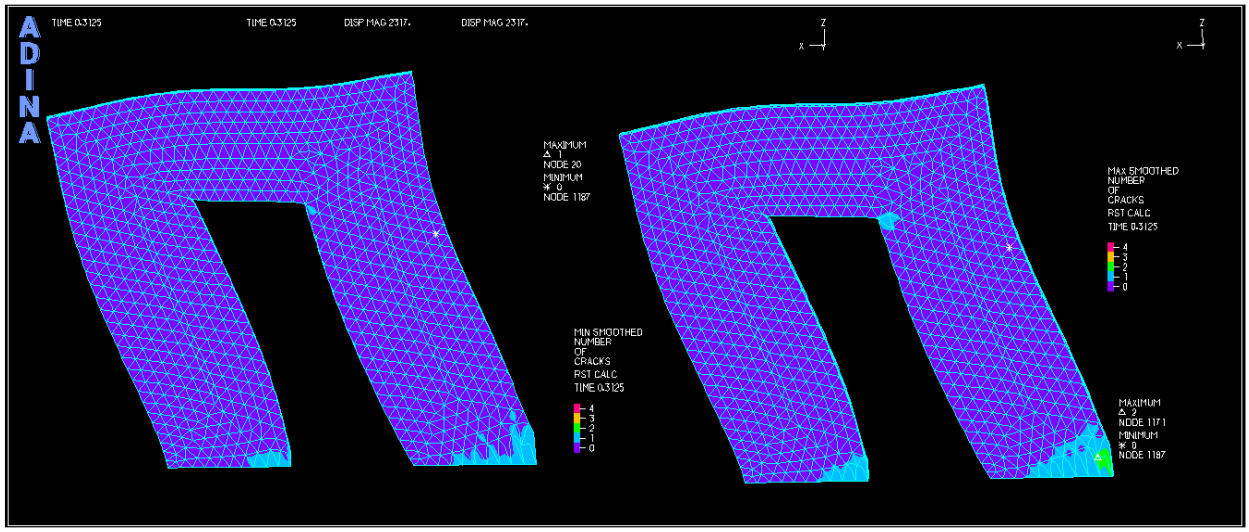


Figure 5 Minimal and maximal cracks in the wall

3.3 Temperature effects

The change of temperature during seasons or day and night affects the structure by inducing stresses into the elements. The design provisions underline the limitation of the dimensions of the buildings to avoid development of stresses due to lengthening or stretching under temperature changes. Taking into account the fact that the wall former presented is fixed at the base hence the dilatation or contraction is prevented at its base and stresses will develop in the structure. Fig. 6 presents the sections along them the stresses were visualized. From the left the first section is done perpendicular to the axe of the beam at its middle. The stresses in x direction are presented in Fig. 7. The section along the base of the columns enables the stresses along the x direction to be represented in the graph from Fig. 8. The last section was made at the middle of the columns while the stresses are presented in Fig.9.

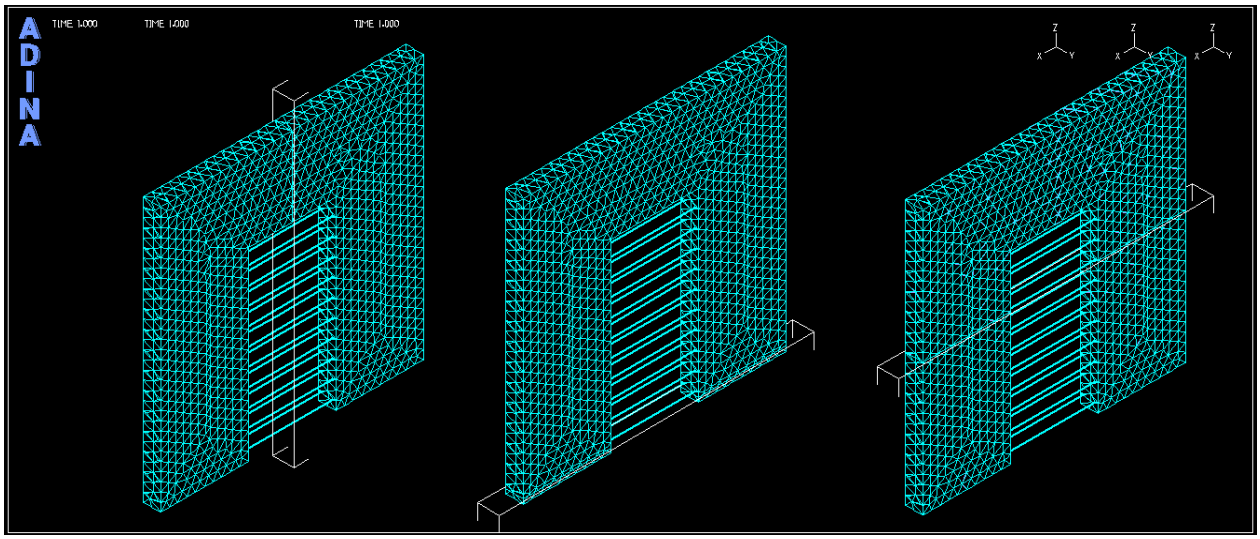


Figure 6 Sections through the wall

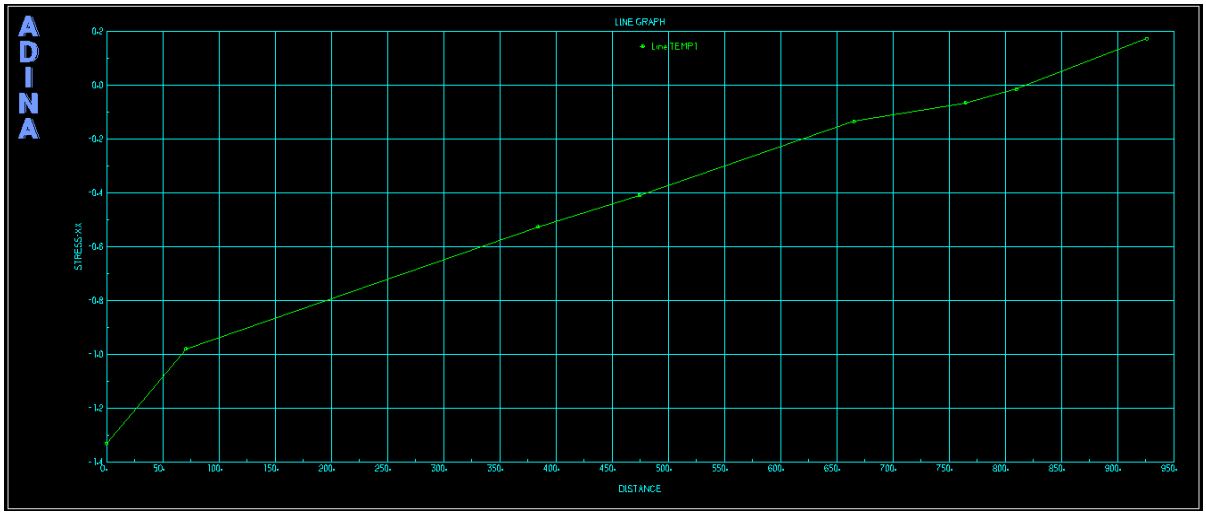


Figure 7 Stresses in the beam

The temperature was augmented by 10 °C a modest difference for most of the cases. The results show the stresses that develop as consequence the difference of temperature. Usually the stresses indicate compression for increasing the temperature. It means that in case of temperature decrease the effect is inverse the elements get tension which produces cracks in the elements.

According Fig. 7 the stress at the middle of the beam varies from -1.4 MPa to 0.2 MPa. This means that this temperature increment does not lead to cracking of the beam. Higher increment or decrement will produce the cracks with the consequence in stiffness diminution and corrosive factor penetration. The most dangerous section is placed at the bottom of the columns (Fig. 8) where for the former change of temperature the stresses vary between -2.35 to -3.45 MPa. It means that for similar contraction the entire section will be cracked. At the middle height of the columns the stresses will be less leaving the structure intact.

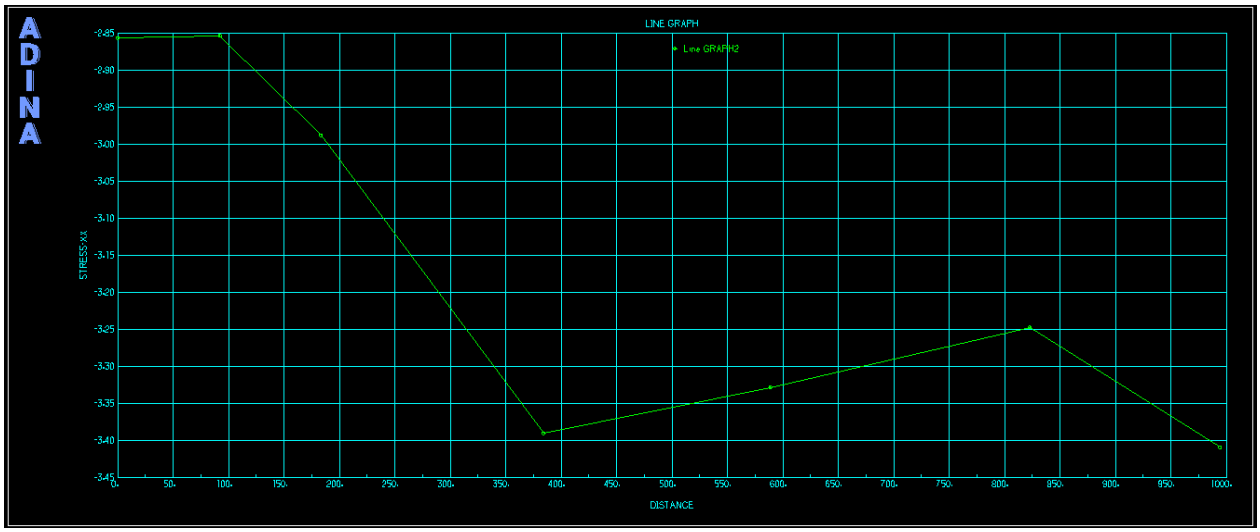


Figure 8 Stresses along the bottom of the columns

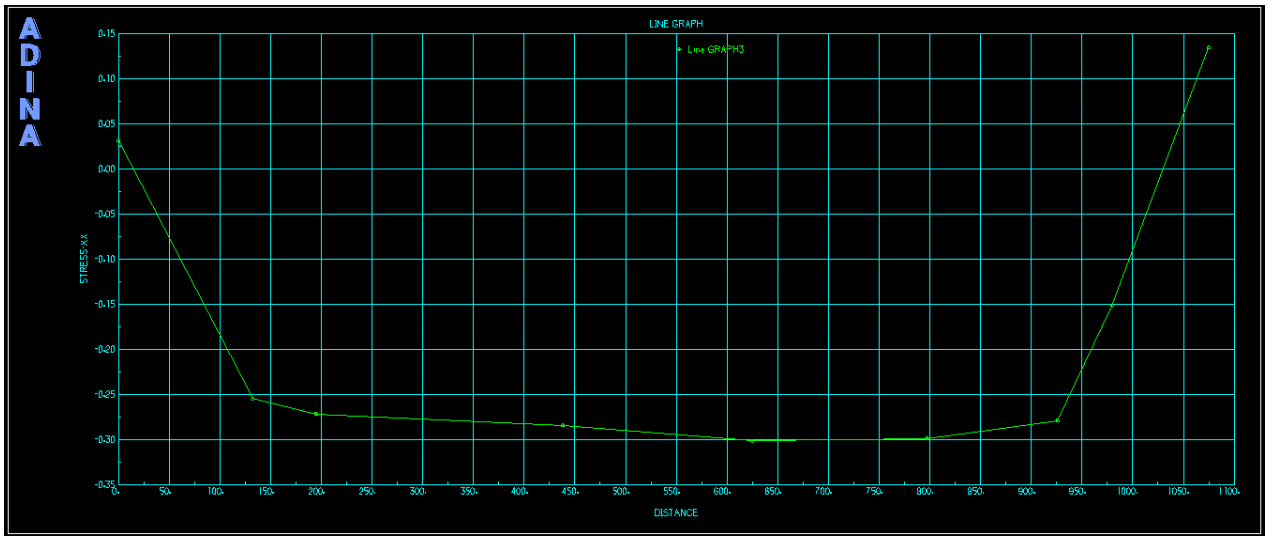


Figure 9 Stresses at the middle of the columns

3.4 Effect of seismic and micro-seismic movements

ADINA enables the dynamic identification of the wall previously analyzed. According the modal analysis in Fig. 10 three eigenvectors where represented for the structure. Following the modal analysis the seismic response can be determined. According the seismic map of the given area the seismic analysis can indicate the expected deformations and stresses in the structure. The expected behavior of the structure can be visualized indicating the damages to develop in the structure.

The dynamic identification of an actual structure can be found by means of a sensitive accelerometer (Fig. 11). The presented device is the CX1 Accelerometer and Inclinometer which can record (monitor) the oscillations of a structure prone to micro – seismic or induced dynamic movements (13). The device can record the vibrations in 3 directions and find the spectral response of the structure showing the eigenvalues of the actual structure. If as conse-

quence of severe loads the eigenvalues change a new seismic analysis may be done and the repairs or structural control can be implemented.

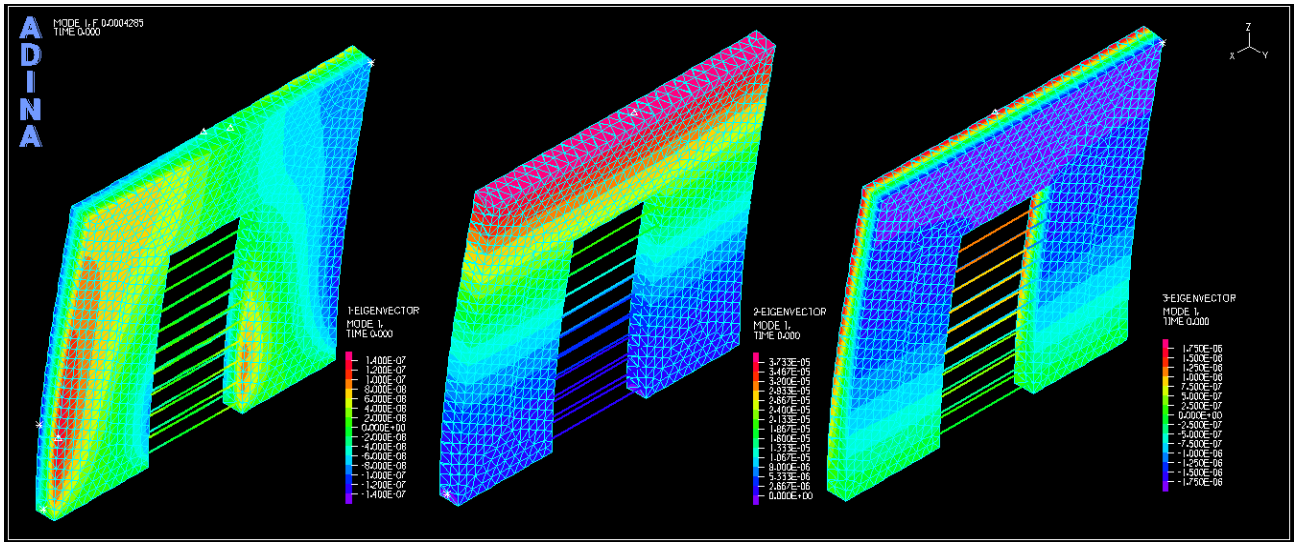


Figure 10 Eigen vectors of the wall



Figure 11 The device for data acquisition

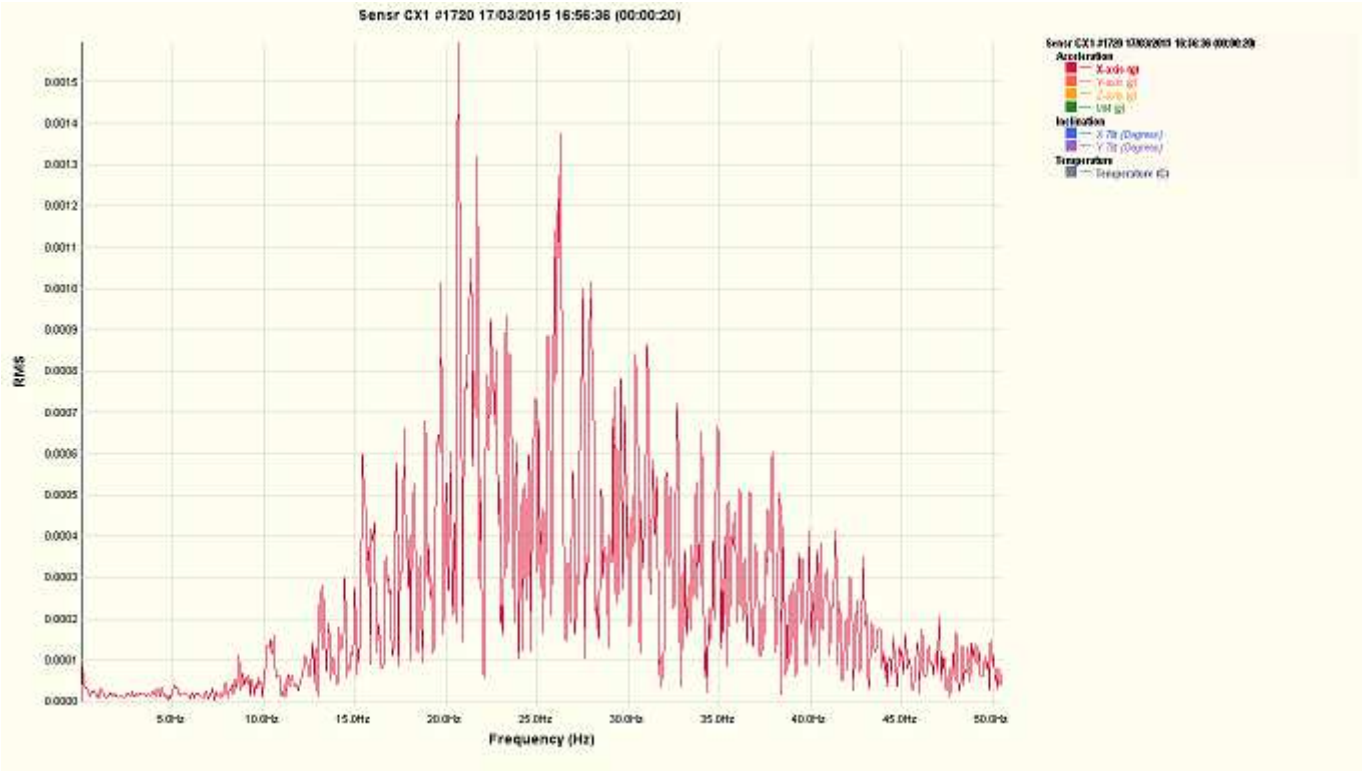


Figure 12 Power Spectrum

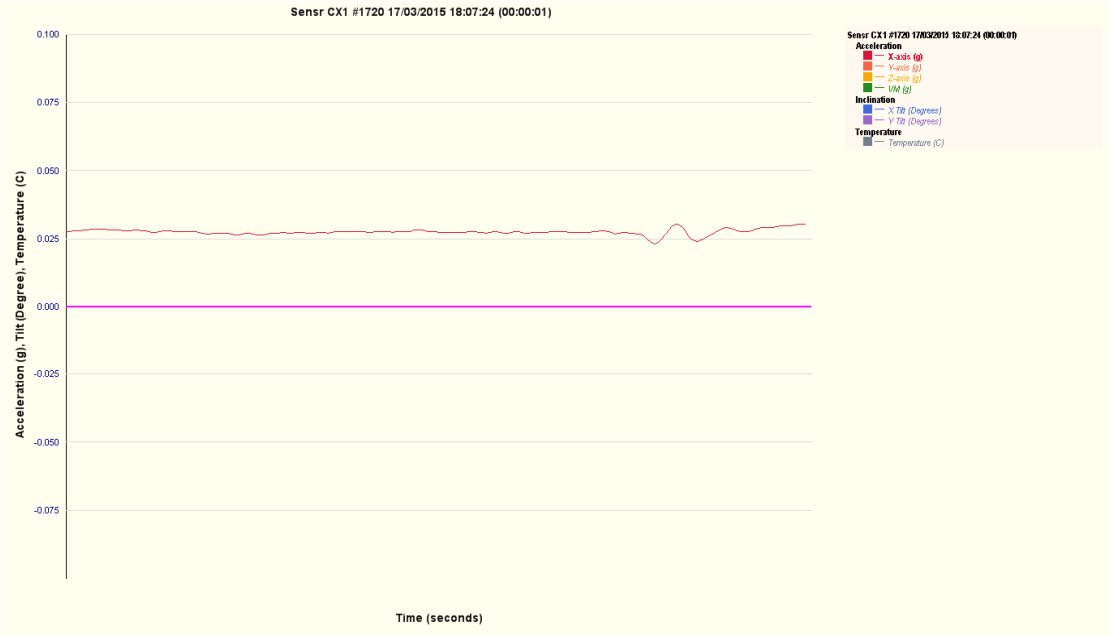


Figure 13 Data acquired for x direction

4 CONCLUSIONS

- In case of reinforced concrete walls the lateral reinforcement must be provided

- Walls may be strengthened by means of steel profiles.
- FRP sheets can be uses to strengthen the structural elements
- It must be taken into account the cyclic nature of most dynamic loads.
- Temperature changes can lead to crack development.
- The structure must be protected by materials which avoid the penetration of corrosive factors.

REFERENCES

[1] N. Gluck, R. Farhat, R. Eid, U. Tzadka, Heuristic approach in structural strength evaluation and retrofitting of existent buildings in seismic areas, COMPDYN 2013, Kos Island, Greece, 12 – 14 June 3013.

[2] N. Gluck, R. Farhat, R. Eid, U. Tzadka, Numerical analysis on the interaction of combined piled-raft foundations on liquefaction prone soils, 11th World Conference on Computational Mechanics.

[3] R. Farhat, N. Gluck, R. Eid, U. Tzadka, On detailing of reinforced concrete frame structures for robustness and for earthquake resistance, 15WCEE, Lisboa 2012.

[4] R. Eid, N. Gluck, On the confinement mechanism in FRP- strengthened reinforced concrete columns, The 7th International Conference on FRP Composites in Civil Engineering, Vancouver, Canada, August 20-22, 2014

[5] C. Bob, Evaluation and rehabilitation of a building affected by a gas explosion, Prog. Struct. Engng Mater. , 2004; 6: 137-146.

[6] FEMA 445, Appendix B, Example Application of Seismic Performance Assessment Using Numerical Integration Techniques.

[7] M.B. Shoraka, T. Y. Yang and K.J. Elwood, Seismic loss estimation of non-ductile reinforced concrete buildings. EARTHQUAKE ENGINEERING & STRUCTURAL DYNAMICS, Earthquake Engng Struct. Dyn. 2013: 42:297-310.

[8] S. Sankararaman and S. Mahadevan, Bayesian methodology for diagnosis uncertainty quantification and health monitoring, STRUCTURAL CONTROL and HEALTH MONITORING, Struct. Control Health Monit, 2013; 19:88-106

[9] W. Rucker, F. Hille, R. Rohrmann, SAMCO Final Report 2006, F08a Guideline for the Assessment of Existing Structures.

[10] D. Ireland, R. Koerth, Structural Engineering Assessments of Existing Buildings, Engineering Dimensions November/December 2012.

[11] ADNA, Automatic Dynamic Incremental Nonlinear Analysis, Theory and Modeling Guide, ADINA R&D, Inc. Watertown, MA 02472 USA.

[12] SENSR, Intelligent technology. Measurement results, CX1 Network Accelerometer User Guide, February 8, 2010.

COMPDYN 2015
5th ECCOMAS Thematic Conference on
Computational Methods in Structural Dynamics and Earthquake Engineering
M. Papadrakakis, V. Papadopoulos, V. Plevris (eds.)
Crete Island, Greece, 25–27 May 2015

PROBABILISTIC EVALUATION OF DAM BASE SLIDING

Gabriele Fiorentino[1], **Luca Furgani**[1], **Simone Magliano**[1], **Camillo Nuti**[1]

[1] Department of Architecture, University of Roma Tre
Largo Giovanni Marzi 10, Rome, Italy
e-mail: gabriele.fiorentino@uniroma3.it

Keywords: Concrete gravity dams, Monte Carlo Analysis, Dam base sliding evaluation, seismic analysis.

Abstract. *Concrete gravity dams represent a relevant part of the 500 large dams existing in Italy. Most of them were built following obsolete seismic design criteria, so they need to be verified with modern seismic analyses according to the new Italian Code on Dams (2014). Many of the parameters utilized in this evaluation are affected by large uncertainties. In the paper we present a procedure based on Monte Carlo simulation which evaluates the probability of exceedance of the sliding equilibrium of the dam obtained via static or response spectrum analysis in case of seismic action, as well as the probability of exceedance of different sliding displacements via nonlinear dynamic analyses. The application to four seismic sites (of different seismic hazard) and to three dams with different heights is presented.*

1 INTRODUCTION

The seismic risk connected to the collapse of a large dam is very high and it has to be assessed with appropriate methods of analysis. According to the new Italian Code on Dams (2014) concrete gravity dams need to be verified using response spectra with 1950 years return period for existing dams and 2500 years return period for new dams.

The evaluation of seismic safety of large concrete gravity dams is nowadays a challenging topic specially in country as Italy where great part of the existing 500 dams have to be reassessed. Modern codes require to take into account all the uncertainties using characteristic values and safety factors. To high risk and strategic structures as dams it could be useful to solve this problem using a full probabilistic approach. In the following the Monte Carlo method is used to take into account the parameters uncertainty.

Programs as CADAM [1] already permit to compute the probability that the SSF is smaller than 1, however CADAM doesn't perform dynamic analyses and it's not possible to obtain the actual value of the residual slip.

Considering the definitions of the modern limit states associated to the collapse and the loss of service it is fundamental to estimate the damage produced by the earthquake. To obtain these information dynamic nonlinear analysis are requested.

Some studies stated that the base sliding is the most probable failure mechanism which can produce the collapse in a concrete gravity dam [2] The aim of this work was to develop a program capable to evaluate the probability to have a sliding at the base of a concrete gravity dam, to compute the probability of having a base displacement and to evaluate if this could lead to damage or collapse of the dam.

The program was developed using an increasing degree of complexity of analysis, starting from equivalent static analyses to understand which combinations of values of the input variables could lead to a Sliding Safety Factor SSF<1. Then these combinations were assigned to a simplified SDOF system to perform nonlinear dynamic analyses using acceleration time histories. Knowing the evolution of the base displacement it is possible to understand if there could be failure of some part of the dam due to the base sliding.

2 INPUT DATA

2.1 Random variables

The variables considered in Monte Carlo simulation analysis are the water level, friction angle and the Young modulus of elasticity of the concrete. All variables have a lognormal distribution.

The water level governs the design of the dams. During an earthquake the level of the impounded water plays an important role acting with an additional hydrodynamic pressure, changing the modal periods of the structure and, as consequence of this, the seismic actions. Considering that the maximum flood has a little probability to occur together with the earthquake, it’s useful to take into account the probability associated to the water level.

In the present study, on the base of some water level registrations, reporting the daily variation in a 5 years of observation, it is assumed that the maximum level is equal to the total height of the dam and the minimum level is 75% of the total height. The friction angle variation was chosen after an evaluation of the experimental values documented in literature [3]. The average value chosen was 40° with a minimum of 35° and a maximum of 45°. The associated standard deviation was 1,5°. The contribution given by cohesion was neglected.

For the Young modulus, referring to real data observed on existing dams, the average value chosen was $24{,}7 \times 10^6$ kN/m^2, the minimum value $18{,}78 \times 10^6$ kN/m^2 and the maximum $29{,}08 \times 10^6$ kN/m^2. Standard deviation was chosen as $1{,}5 \times 10^6$ kN/m^2.

2.2 Seismic input

In seismic areas where PGA > 0,15g for a 475 years return period, the Code requests a specific seismo-tectonic study in order to evaluate the response spectra.

In this work four Italian dam sites (Table 1) requiring seismic hazard assessment and with different seismicity from 1 site to 4 site were chosen, and the seismic input for a return period of 1950 years was evaluated.

Site	Location (Region)	PGA for Tr=475 yrs	PGA for Tr=1950 yrs
1	Calabria	0,27g	0,46g
2	Abruzzo	0,26g	0,42g
3	Toscana	0,22g	0,35g
4	Piemonte	0,15g	0,25g

Table 1: Dam sites considered for seismic input evaluation

To evaluate response spectra a hybrid method combining both PSHA and DSHA was used, referring to the works of Bommer [4] and Ordaz [5]. The entire procedure is fully described in a previous work [6].

The target response spectra is evaluated with the Ground Motion Predictive Equation ITA10 [7]. A value of 1,5 standard deviation is added to the median value after a comparison with the Italian Code and the probabilistic response spectrum.

3 EQUIVALENT STATIC ANALYSIS

3.1 Monte Carlo method

In the Monte Carlo method a distribution of probability which characterizes the epistemic uncertainty and the variability of the parameter in space and time is associated to each random variable. The output of the analysis is than computed n times through the random extraction of input variables obtaining n values of the response of the system. Given a large number n it is possible to obtain the probability distribution of the output variable, and to calculate the statistic moments of the distribution.

According to the law of large numbers as the number of experiments or simulations increases the average of the results should be closer to the expected value. It is therefore necessary to define a minimum number of analyses to perform in order to obtain a stable solution. In this work a criteria suggested by Melchers [1] is used, so a minimum of 20.000 analyses is adopted.

Latin Hypercube sampling method was used to exclude values with no physical meaning (e.g. height of impounded water bigger than the height of the dam) limiting the sample within a specific interval of the probability distribution.

3.2 Sliding Safety Factors

The aim of the simplified static analysis is to rapidly identify the input data combinations which could be critical for the structure. The Sliding Safety Factor (SSF) is a parameter which can be useful to evaluate the probability of the base sliding of the structure. The SSF is de-

fined as the ratio between the sum of the stabilizing forces and the sum of the destabilizing forces. There is a possibility of sliding when SSF<1. In this work three different SSF were considered:

1. Static SSF: is the most simple SSF because depends only on static forces, easy to evaluate. Remembering that cohesion was neglected, it is possible to write:

$$SSF_{st} = \frac{(W - U_P) \cdot tg\varphi}{P_W} \tag{1}$$

Where W is the weight of the dam, Up is the uplift pressure, tgφ is the tangent of the friction angle. Pw is the hydrostatic pressure on the upstream wall of the dam.

2. Dynamic SSF - 1° vibration mode: this SSF considers the dynamic contribution of the first mode of vibration, as proposed by Fenves and Chopra [8].

$$SSF_{dyn1} = \frac{(W - U_P) \cdot tg\varphi}{P_W + f_1(y)} \tag{2}$$

Where f1(y) is the seismic force acting on the dynamic system formed by the dam and the impounded water, for the first vibration mode.

3. Dynamic SSF - 1° vibration mode and higher modes: this SSF considers the dynamic contribution of the first mode of vibration and the contribution of the higher modes.

$$SSF_{dyn2} = \frac{(W - U_P) \cdot tg\varphi}{P_W + f_1(y) + f_d(y)} \tag{3}$$

This factor was considered to obtain the failure set to be analyzed in the second part of the program.

For each value of SSF the failure probability of exceedance has been obtained.

3.3 Static analyses output

In Figure 1, considering a dam with 100 m height and for site 1 seismic input the probability density functions of the random variables defined as input are displayed. From left to right the friction angle, water level and Young Modulus PDF are showed.

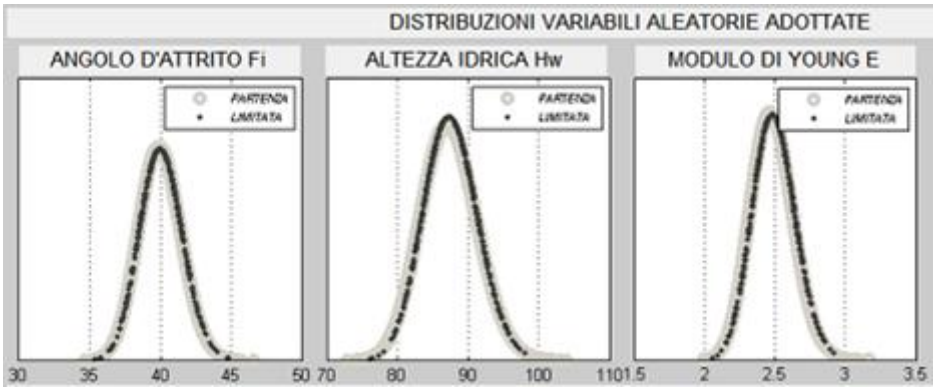


Figure 1: Results of the static equivalent analysis

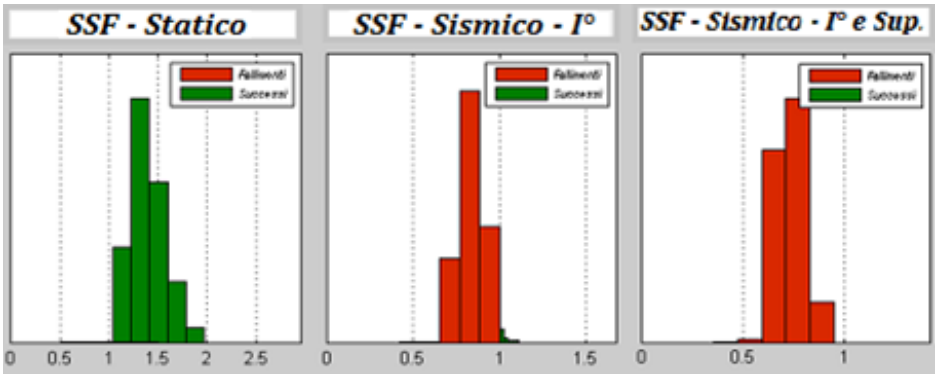


Figure 2: Relative frequencies of SSF

Figure 2 shows the results of the Monte Carlo analysis for the three SSF obtained on the base of a static analysis. For each SSF the histogram represents the values of SSF obtained with all the analyses. The values are displayed in green when the SSF>1, whereas the values for SSF<1 are displayed in red. A table reporting the number of failures for each SSF factor and the probability that each SSF could be minor than 1 is given.

4 DYNAMIC ANALYSES

4.1 Dynamic analyses

The dam is modeled as an equivalent SDOF system defined by the Nuti-Basili method [9] which includes fluid-foundation- structure interaction. According to this, the mass is increased to take into account reservoir contribution, the stiffness is modified to reproduce the effects of the interaction with the foundation and the damping is increased to consider both the contribution of fluid and soil. To evaluate the residual displacement produced during the earthquake, a nonlinear roller was introduced at the base of the system. A frictional sliding resistance was used for this scope.

The system depicted in Figure 3 is analyzed using the open source program "Opensees" using a set of 20 accelerograms scaled in order to match the response spectra chosen as target. In static analyses there is a base sliding only if SSF<1, but when dynamic analyses are performed it could be possible to have base sliding also for SSF major than 1. For this reason for dynamic analyses all SSF minor than 1,1 were considered. The second output includes all the statistical parameters of the analysis with the purpose to correlate the SSF values with the base sliding values.

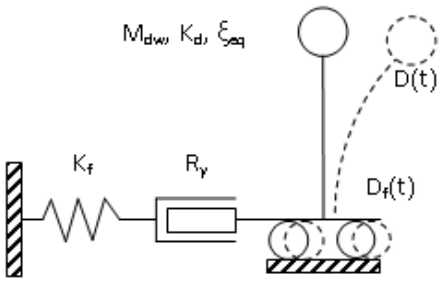


Figure 3: SDOF system

It is possible to perform the dynamic analyses considering different initial values. There are three options:

1. Only values of the basic variables that lead to SSFmin, SSFmax, SSFav (average SSF).
2. All the initial values that brought to a base sliding are considered.
3. All the initial values are considered.

4.2 Dynamic analyses output

Let us first show the case of the response to a single accelerogram obtained for site 1, where PGA=0,46g. The response spectrum of the acceleration time history is given in Figure 4 compared with the target response spectrum. Figure 5 shows the comparison between the linear and nonlinear displacement at the top of the 100 m dam, while Figure 6 displays the sliding response at the base .

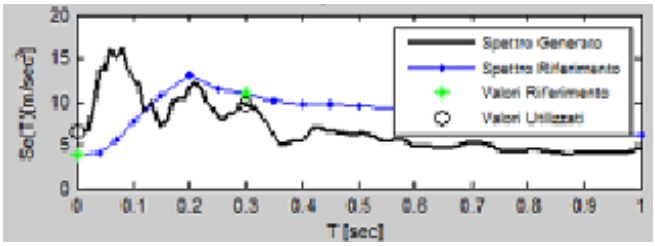


Figure 4: Comparison between single accelerogram (blue) and target response spectra (black) for site 1- H=100 m

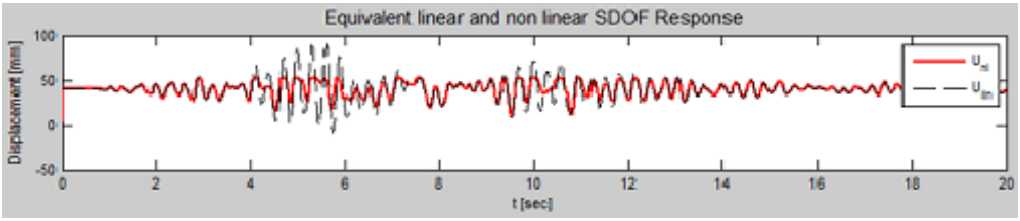


Figure 5: Equivalent linear and nonlinear SDOF response for site 1 - H=100 m

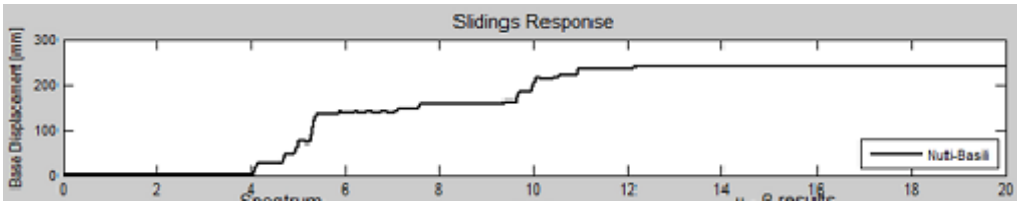


Figure 6: Sliding displacement at the base of the dam for site 1 - H=100 m

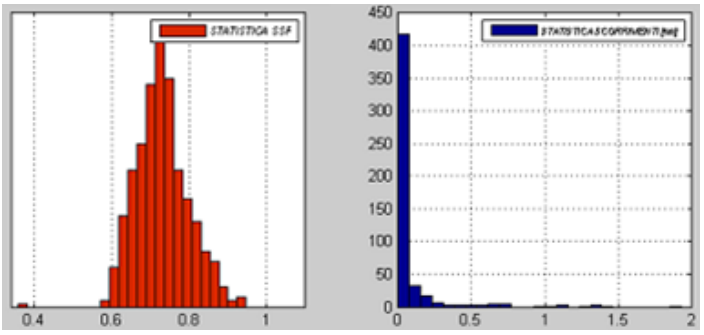


Figure 7: a) SSF statistic b) Base sliding statistic

In Figure 7 are displayed two histograms showing the outcomes of the SSF minor than 1,1 and of the base sliding. Probabilities to assume a value of base sliding displacement included in a certain interval are also reported. In Figure 8 the most critical values of acceleration (i.e. structural period) are reported.

5 APPLICATION

5.1 Case studies and results

The two stage procedure is applied to three concrete gravity dams with different height: 100 m, 75 m and 50 m using the seismic input of the 4 sites studied defined above. The failure probability of the three structures is computed taking into account the results of simplified static analyses and the dynamic nonlinear analyses.

The probability of exceedance of SSF=1 has been obtained with static analysis and the probability of exceedance of displacement δ>0, 0,10 and 1 meter has been obtained by dynamic analysis. For the four sites these results are shown in figure 8. From a sensitivity analysis it seems that the most influent parameter is the water level hw. The larger the water level the larger is the probability of failure also in case of seismic action. The effect of the water level changes for different dam heights and region (i.e. seismic hazard).

The probability rapidly decreases in the dynamic case if the probability to have a base sliding capable to trigger the collapse of the structure (δ>1 m). In fact the probability to have base sliding is 100%, the probability to have a sliding major than 10 cm is 64,4% and the probability to have a sliding major than 1 m is only 13,4%.

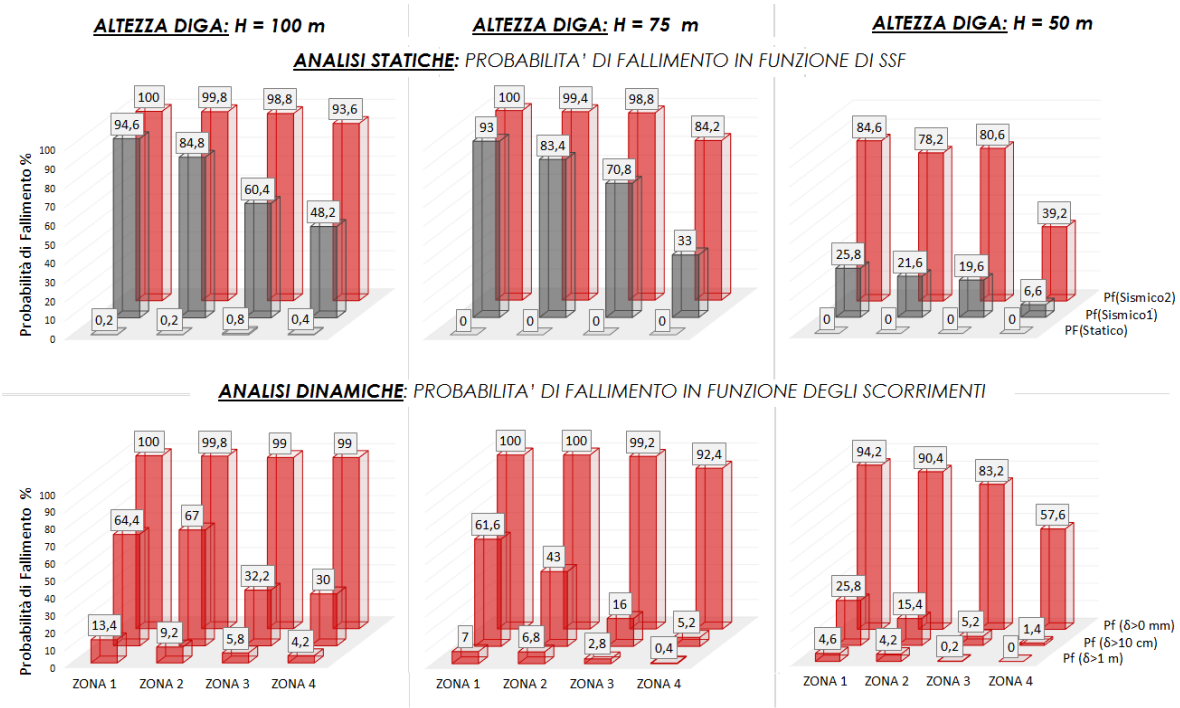


Figure 8: Probabilities of failure for dams with height H=50, 75, 100 m and for sites 1,2,3,4

Comparing the static case $P_{fsismico}1$ or 2 with the dynamic case one notes that the latter is slightly larger. The static cases in which higher modes are included are very similar to the dynamic for δ>0.

If one accept to have δ=0,10 m as a failure the dynamic values are smaller than the static even with a single mode ($P_{fsismico}1$). Higher modes give a substantial contribution for all cases, especially when the probability of sliding is smaller: see for example site 4, dam H=75 m and site 1, dam H=50 m.

6 CONCLUSIONS

Great part of the Italian concrete gravity dams have been built following obsolete design criteria and now need to be verified against seismic action with a modern approach as that proposed in the new Italian Code concerning Dams Safety (2014). Several studies show that base sliding should be the first mechanism leading this type of structure to collapse. In this work a procedure to study the base sliding taking into account the uncertainty of the input parameters is presented. As preliminary check the Sliding Safety Factor (SSF) of static or response spectrum analysis is evaluated using a Monte Carlo simulation procedure. If the SSF<1 it is necessary to carry out nonlinear dynamic analyses to evaluate the residual slip after the earthquake. In this work the base sliding is obtained using the Nuti-Basili simplified method [9] which evaluates it by means of nonlinear dynamic analysis of an equivalent SDOF system that takes into account the interaction of the structure with the foundation and with the impounded water. The two stage assessment procedure was implemented in a Matlab software and applied to four dams with different heights considering four levels of seismic hazard.

The results obtained demonstrate the effectiveness of the method and the useful information given to rapidly estimate the risk connected to the sliding of a concrete gravity dam, considering the main parameters at hand and their dispersion. It represent a powerful tool for a preliminary but meaningful analysis of concrete gravity dams.

REFERENCES

[1] M. Leclerc, P. Léger, R. Tinawi. "Computer aided stability analysis of gravity dams—CADAM." *Advances in Engineering Software* 34.7 (2003): 403-420.

[2] A.K. Chopra, L. Zhang. "Earthquake-induced base sliding of concrete gravity dams." *Journal of structural Engineering* 117.12 (1991): 3698-3719.

[3] ITCOLD, Italian Commission on Large Dams, Risk analysis - Applied researches and possible applications of risk analysis methods to Italian situation, 2004.

[4] J.J. Bommer: Deterministic Vs. Probabilistic Seismic Hazard Assessment: An Exaggerated And Obstructive Dichotomy, *Journal of Earthquake Engineering*, 6:S1, 43-73, 2002.

[5] M. Ordaz, A. Aguilar, J. Arboleda: CRISIS2007 – A Program for computing Seismic Hazard, 2007.

[6] G. Fiorentino G., L. Furgani, C. Nuti, F. Sabetta, *Seismic Hazard and use of strong motion time histories for dam seismic analyses*, 2ECEES, Istanbul, 24-29 august 2014.

[7] D. Bindi, F. Pacor, L. Luzi, R. Puglia, M. Massa, G. Ameri, R. Paolucci: Ground Motion Prediction Equations Derived from the Italian Strong Motion Database, Bulletin of Earthquake Engeenering 9:1899–1920, 2011.

[8] G. Fenves, A.K. Chopra. Simplified analysis for earthquake resistant design of concrete gravity dam. Berkley California : University of California- Earthquake Engineering Research Center, 1986.

[9] C. Nuti, M. Basili, Seismic simulation and base sliding of concrete gravity dams, *Computational Method in Earthquake Engineering*, 21:427-454, 2009.

COMPDYN 2015
5th ECCOMAS Thematic Conference on
Computational Methods in Structural Dynamics and Earthquake Engineering
M. Papadrakakis, V. Papadopoulos, V. Plevris (eds.)
Crete Island, Greece, 25–27 May 2015

NUMERICAL SEISMIC SAFETY ASSESSMENT OF RC BRIDGES WITH HOLLOW PIERS

Pedro Delgado[1], António Arêde[2], Nelson Vila Pouca[2], and Aníbal Costa[3]

[1] Instituto Politécnico de Viana do Castelo
Apartado 574, 4901-908 Viana do Castelo, Portugal
pdelgado@estg.ipvc.pt

[2] Universidade do Porto - Faculdade de Engenharia
R. Dr. Roberto Frias, s/n 4200-465 Porto, Portugal
aarede@fe.up.pt, nelsonvp@fe.up.pt

[3] Universidade de Aveiro
Campus Universitário de Santiago, 3810-193 Aveiro, Portugal
acosta@civil.ua.pt

Keywords: RC Bridges; Structural Modeling; Safety Assessment; Non-linear behavior.

Abstract. *The seismic damages of reinforced concrete bridges in recent events show that many of them have an inadequate behavior and safety. Therefore, is important to accurately define bridge safety assessment and hence evaluate the accuracy of the analytical methodologies for seismic response of bridges. The main objective of this paper is to present several options for structural simulation with different complexities in order to assess the seismic response of bridges and then use the results for the safety assessment with probabilistic approaches. The numerical simulations are carried out using three different methodologies: (i) plastic hinge model, (ii) fiber model and (iii) damage model. Seismic response of bridges is based on a simplified plane model, with easy practical application and involving reduced calculation efforts while maintaining adequate accuracy. The evaluation of seismic vulnerability is carried out through the failure probability quantification involving a non-linear transformation of the seismic action in its structural effects. The applicability of the proposed methodologies is then illustrated in the seismic analysis of two reinforced concrete bridges, involving a series of experimental tests and numerical analysis, providing an excellent set of results for comparison and global calibration.*

1 INTRODUCTION

In the evaluation of the seismic vulnerability of bridges, considering their non-linear behavior (a necessary consideration when a realistic analysis of the seismic response is intended) could involve enormous computing resources and corresponding calculation efforts. On the other hand, the development of research studies in this field has enabled a better understanding of their behavior, and the availability of numerical and experimental results allows the possibility of the calibration of simplified procedures.

However very high refined models could be adopted, involving a 3D space modelling and the spread of the plasticity along the member length as well as across the section area, in this work a substantial more simplified model (without losing accuracy) is also explored. This simplicity is evidenced by a much lower number of parameters involved and an enormous lesser computing time – about 50 times less when compared with a more refined model. Therefore, the adoption of such simplified model shows the great advantage, from the practical use point of view, when a large number of analysis is needed, as is the case of vulnerability analysis.

Several examples of numerical modeling can be mentioned, in particular, the fiber model [1-3], the continuous damage model developed by Faria *et al.* [4], the model of compression field theory modified [5], plastic hinge type models Takeda [6] and models based on distributed flexibility [7]. Some other numerical studies focusing on pier finite element modelling can also be found in the literature [8-10], which addressed the simulation of 3D pier behavior by considering several models ranging from elasto-plastic to microplane formulations for solid section piers. An approach based on a fracture-plastic model was also proposed and used for 3D numerical modelling of hollow piers in a more recent work [11,12], which discusses issues related with concrete confinement.

2 METHODOLOGIES FOR NON-LINEAR ANALYSIS

For the numerical simulations of bridge elements three main different methodologies were used. The plastic hinge model have adopted a simplified structural modelling with 2D characteristics and the non-linear behavior lumped in the elements extremities (plastic hinges). The fiber model considered a finite element mesh with non-linear behavior spread along the elements and cross sections. The more complex and detailed numerical model used in this work is the damage model, which is based on refined finite element meshes and the non-linear behavior considered in the constitutive laws defined for both concrete and steel materials.

2.1 Plastic Hinge Model

In order to obtain moderate calculation efforts, a structural modelling with plane bar elements could be adopted, where the elastic or inelastic behavior is carried out through an elastic central zone and two extreme zones with plastic characteristics. Thus, the non-linear material behavior of the bar elements are concentrated on its extremities, since those are the critical zones where cracking occurs, being developed in a short extension, generally not exceeding the cross section height.

For the dynamic analysis of the bridge in the perpendicular direction of the deck axis (transverse direction), a simplified structural model is proposed. Such a model accurately simulates tri-dimensional behavior through a bi-dimensional analysis [13], when the bridge is nearly straight, as is the case. Taking into account that the main behavior of the bridge, for transverse direction actions, is dictated by bending moments on the deck and axial forces and bending moments on the piers, and that there is no significant interaction between torsional

effects on the deck and bending moments on piers, it could be concluded that, for obtaining the bridge response for transverse actions, the coupling between deck and piers could be made only by imposing the same transverse displacement at the points where the deck and the piers are linked. Therefore, with the model illustrated in Figure 1 it is possible to simulate, in a 2-D domain, the links between piers and deck through ties that insure compatibility of displacements, allowing independent rotations. The piers are oriented to have their larger dimension in the plane direction and an axial load equal to the vertical action of the deck must be considered. This plane model is extremely economic in terms of calculation effort, especially when non-linear effects must be considered, but it allows the main aspects of the structural behavior of the bridge for horizontal actions in the transverse direction of the deck axis to be captured in an accurate way. As mentioned above, only the eventual torsion stiffness of the deck mobilized with the rotation of the top extremity of the piers is not included.

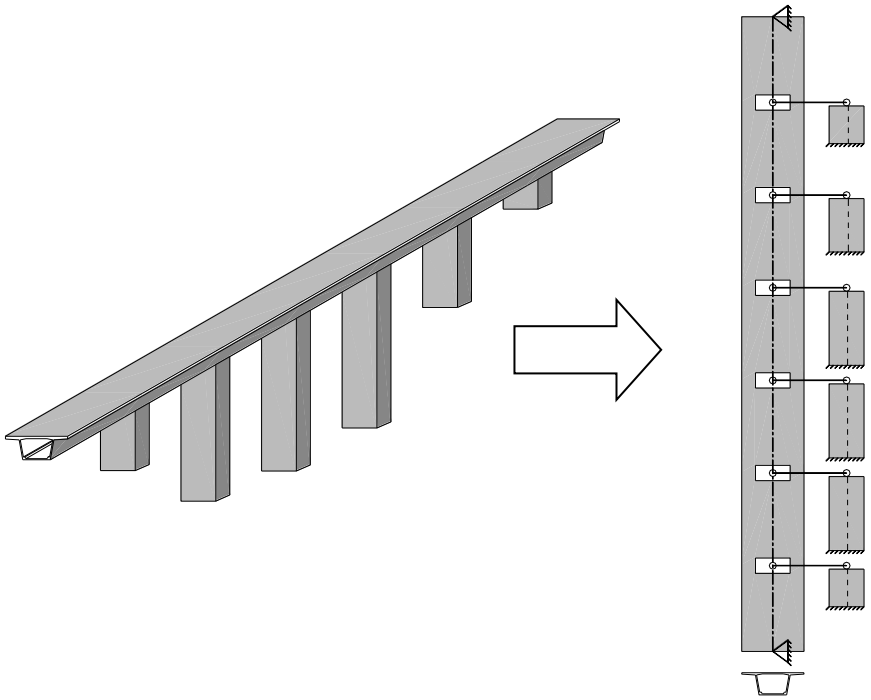


Figure 1: Bridge structural modelling.

To characterize the plastic hinges behavior, a global non-linear model for the sections must be considered. Thus, the moment-curvature loops used in the idealization of the reinforced concrete are obtained by a modified Takeda model [6, 14, 15]. The characterization of these moment-curvature relationships is based on the initial cracking of the concrete and the yielding of the reinforcement that could be obtained from the monotonic material behavior of the reinforced concrete element. Therefore, the laws of monotonic material behavior cloud be numerically established through a procedure based on a cross section fiber model [16], knowing the geometric characteristics of the piers sections, reinforcement dimensions and location, and material characteristics. For the materials behavior several models are available for concrete and steel. An example of possible model that could be adopted for concrete is the

Kent-Park [17], which have in consideration the confined and unconfined properties for monotonic and cyclic behavior. This cross section fiber model also allows the separation of confined and unconfined concrete regions. As for the steel model, the widely used Giuffrè-Menegotto-Pinto model [18] could be adopted, where the Bauschinger effect is considered in the cyclic behavior. The definition of the cyclic stress-strain response can be evaluated through the monotonic stress-strain curve of the structural element, associated with adequate rules that control the response evolution, in load-unload cycles, load inversion and the pinching effect, [6, 15]. The moment-curvature curve (m-ρ), obtained with this procedure, is used to simulate the non-linear behavior and the hysteretic dissipation of energy for the structural seismic response analysis, including the stiffness degradation in the unload case and the pinching effect in the load inversion, essential aspects in the seismic behavior of structures.

2.2 Fiber Model

Fibers models are usually supported by a finite element discretization and based on a modeling section fibers (for concrete and steel fibers), where the non-linear behavior is distributed along the element length and cross-sectional area. Several models have been developed and suggested in the past [2, 3, 16]. Such type of numerical models are carried out with a three-dimensional structural modeling based on finite elements, where the structure is divided into 3D bar elements which are then divided into longitudinal fibers. Therefore, these fibers constitute a mesh at the level of their cross-sections, with no forces interaction between the fibers, i.e. each fiber mobilizes only the force corresponding to the cross section position and material properties. For the distribution of the nonlinearity along the length of the structural elements, a formulation based on its global deformations is performed. The numerical integration of this formulation is carried out at the level of Gauss points of each element. Thus, the behavior of spatial structures subject to static or dynamic loads can be carried out through analyzes that consider the local (beam-column effect) and global (effect of large displacements / rotations) geometric non linearity, as well as the material plasticity.

2.3 Damage Model

This numerical tool is supported on refined finite element (FE) meshes, with high complexity and detail levels in the constitutive laws defined for both concrete and steel. The concrete is simulated with a continuum damage model which is briefly described further on. As for the steel, it could be modelled by applying the well-known and widely used Giuffrè-Menegotto-Pinto model. The continuum damage model used in these applications was initially developed by Faria [4, 19] to characterize the non-linear behavior of large-scale concrete mass structures and has proven to be a powerful tool [20, 21]. Essentially, this model is based on continuum damage mechanics applied to determine a given point stress tensor σ relying on two independent scalar damage variables which account for the non-linearity associated with continuous and irreversible concrete degradation. Such a stress tensor is defined by:

$$\sigma = \left(1 - d^{+}\right)\overline{\sigma}^{+} + \left(1 - d^{-}\right)\overline{\sigma}^{-} \tag{1}$$

where d^{+} and d^{-} are, respectively, the tensile and compressive scalar damage variables, whereas $\overline{\sigma}^{+}$ and $\overline{\sigma}^{-}$ are the corresponding principal tensile and compressive effective stress tensors as defined in Faria and Oliver [19]. The damage variables are controlled by evolution

laws related to material properties r_0^+ and r_0^- (whose initial values are associated with uniaxial tensile and compressive concrete strengths which can be experimentally obtained) and expressed as follows:

$$d^+ = 1 - \frac{r_0^+}{\bar{\tau}^+} \cdot e^{A^+\left(1-\frac{\bar{\tau}^+}{r_0^+}\right)} \quad \text{, for } \bar{\tau}^+ \geq r_0^+ \qquad (2)$$

$$d^- = 1 - \frac{r_0^-}{\bar{\tau}^-} \cdot \left(1 - A^-\right) - A^- \cdot e^{B^-\cdot\left(1-\frac{\bar{\tau}^-}{r_0^-}\right)} \quad \text{, for } \bar{\tau}^- \geq r_0^- \qquad (3)$$

where $\bar{\tau}^+$ and $\bar{\tau}^-$ are equivalent stress quantities derived from the components of tensors $\bar{\sigma}^+$ and $\bar{\sigma}^-$, respectively. The A+, A- and B- parameters must be finely adjusted so that the expected uniaxial tensile and compressive responses can be suitably simulated by the model. The numerical analyses in this work were based on 3D solid FE modelling which, in particular, aimed to realistically simulate the main phenomena associated with shear, with special emphasis on the well-known shear lag effect that is characteristic of I or T shape sections as well as hollow-section elements. Even so, this 3D modelling strategy does not make it possible to directly and totally simulate the confining effects provided by stirrups, particularly concerning the effect of the increased concrete deformation capacity. As such, a complementary strategy was adopted, which consists on conveying these confining effects on the uniaxial compressive curve that is used for defining the A+, A- and B parameters. In this work, both the "confined" and "unconfined" compressive characterization curves are defined according to the proposal by Kent and Park [17], later modified by Park [22]. This strategy is essentially the same as the one used in previous works [20, 21, 23], which was found to yield good results in similar simulation studies.

3 SEISMIC SAFETY ASSESSMENT

Nowadays, several methodologies to assess the seismic safety of structures have being used, since the more complex and general to the more simples and easy to apply. These last ones involve usually more assumptions and simplifications in opposition with the more general methodologies that tries to reproduce the reality as close as possible.

One safety assessment methodology wherein proposed, that correspond to a quite general procedure, can be used for any probability distribution of the seismic action and correspondent vulnerability functions with the desired polynomial approximation (including high order polynomial functions), as well as any probability distribution of the capacity. Although the origins of this methodology go back to the beginning of the 1980s [15, 24, 25], it continues to be developed and used for the calculation of seismic risk for a chosen confidence level. In addition, results obtained by this method may provide an excellent support for calibration of other methods involving simplifying assumptions. The fact that this methodology represents a more general approach for seismic risk assessment may imply a larger number of structural analyses.

In order to evaluate the structural safety with the proposed methodology, it is necessary to calculate the probability of collapse, given by the convolution of the probability distribution of demand with the probability distribution of capacity, [15]. To obtain the demand probability distribution it is necessary to know the probability distribution of the seismic

action and define the so called vulnerability curve, a non-linear function that relates the seismic action with the action effect. Therefore, to establish the vulnerability curve, a seismic response of the bridge for increasing seismic intensities must be computed and, for each intensity level, the maximum response value obtained. This curve relates the seismic magnitude with the maximum value of the parameter chosen for describing the structural response, for example, the maximum ductility demand on the pier base. These values could be adopted as the control parameters for the safety evaluation, bearing in mind that in these structural elements the higher strains and the greater non-linear incursions are developed specially in the zones close to the foundation, which significantly influence the bridge behavior.

Several accelerograms, in order to take into account the stochastic characteristic of earthquakes, should be synthesized, by a random manner, matching the response spectra that characterize the earthquake ground motion. With these accelerograms, the average values of the ductility demanded for each magnitude of seismic action are obtained and polynomial functions can be adjusted through this series of points, thus obtaining the vulnerability functions of each pier, and, consequently, of the bridge, illustrated with the curve number 3 in Figure 2. The intensity of an earthquake could be defined by the peak acceleration value in the horizontal direction, a. To a given region, these intensities should be estimated by combining i) seismological information expressed by: generation models, distribution of location, magnitude and intensity of a past earthquake in the region and ii) geological and geotechnical data [24]. The maximum annual values of peak acceleration can be computed using generation models based on the magnitude values and source locations observed from past earthquakes; magnitudes being transformed into bedrock accelerations by means of attenuation formula. The characteristic value of the distribution of peak acceleration, a_k, to 50 years of the structure life time, is equal to the 0.95 fractile (975 years of return period) of the annual extreme distribution, a_{975}, as stated by Eq(4).

$$F(a_k) = \left(1 - \frac{1}{975}\right)^{50} = 0.95 \tag{4}$$

The most important part of the distribution of maximum peak accelerations in 975 years can be identified as an extreme type I probability distribution [26, 27]. Thus, the seismic action, represented as curve number 1 in Figure 2, can be characterized by the following equation, Eq (5):

$$f(a) = \alpha . \exp\left(y - \exp(y)\right) \tag{5}$$

with $y = -\alpha(a - u)$ and where α and u are the parameters that characterize the extreme distribution. The information that allows the estimation of the variation coefficient of the probability distribution of maximum peak acceleration in 975 years is scarce. The value of 0.5 can be adopted, taking in consideration the research made by Borges and Castanheta [24], to the Portuguese territory. In this case, considering the characteristic value of the peak acceleration predicted to Lisbon, a_k = 219,4cm/s^2, that corresponds to a medium seismicity zone, the parameters of the extreme distribution α = 22,5E-3 and u = 87.4cm/s^2 are obtained.

A transformation of this action through the vulnerability function is carried out, and the action effect in the bridge obtained, more precisely in each of its piers, once the vulnerability function for each pier can be defined through the bridge response (curve 3 in Figure 2). Thus the probability density function of the action effect, f_{EA}, expressed in demanded ductilities is

obtained (curve 4 in Figure 2) and the corresponding probability distribution of maximum ductility demand, F_{EA}, is achieved.

For the capacity characterisation of pier sections - in this case their available ductility - a probability density function, f_R , was considered (curve 2 in Figure 2). This function could be defined through the mean ductility, μ_d, and its variation coefficient, VC, by means of a simulation method, the Latin Hypercubic Sampling, as employed by Delgado *et al.* [28].

Finally, the collapse probability of the bridge is evaluated through the integration of the convolution function, Eq (6) and curve number 5 in Figure 2, defined through the probability distribution function of the action effect, F_{EA} - expressed in maximum ductilities demanded in the bridge - and the capacity probability density function, f_R - expressed in available ductilities, [24, 25].

$$C(\mu) = (1 - F_{EA}) \cdot f_R \tag{6}$$

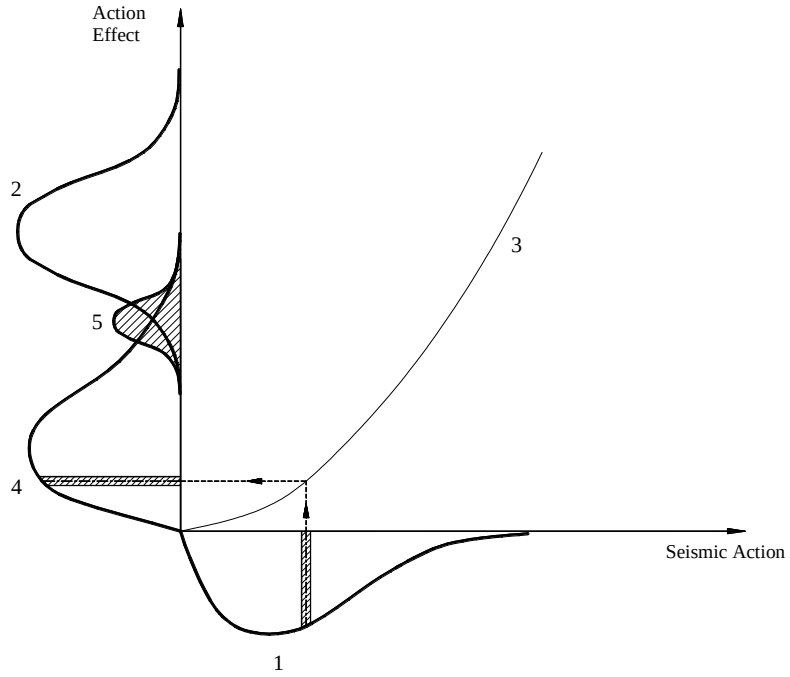
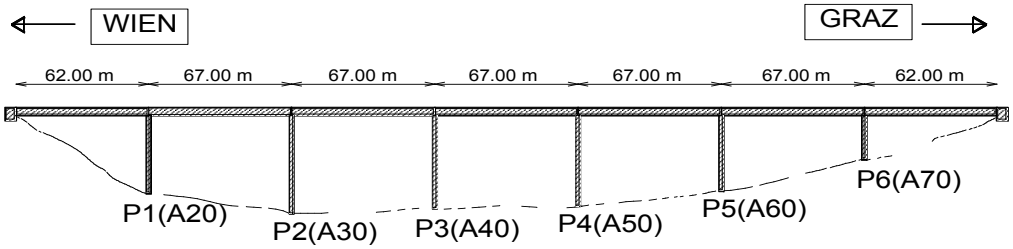


Figure 2: Graphic representation of safety assessment procedure.

4 APPLICATION TO THE TALÜBERGANG WARTH'S BRIDGE

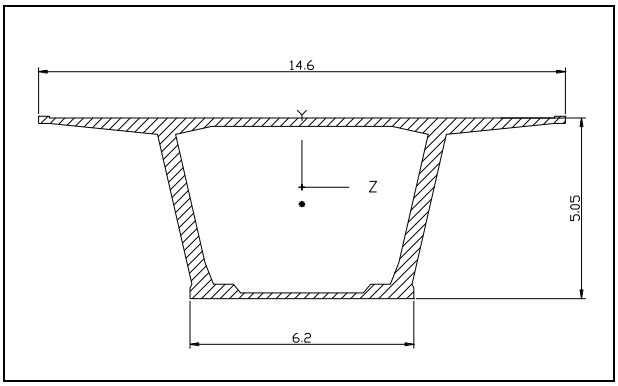
The first application, corresponds to the Talübergang Warth's bridge, built in the seventies in Vienna and designed for a low seismic level, where the comparison and calibration of the numerical simulations were carried out. For this purpose, static analysis were performed to the bridge piers with imposed displacements on the pier top end. This bridge was the main study purpose on the scope of a European project, Vulnerability Assessment of Motorway Bridges (VAB). The reinforced concrete Talübergang Warth bridge is located approximately 63 km to south of Vienna and it is constituted by a continuous deck, with five central spans of 67m and two extreme spans of 62m, supported by piers with rectangular hollow section, pinned in their connection to the deck and fully-fixed in the base, where is concentrated the largest seismic effects. This bridge is constituted by six piers with heights between 16.9 and 38.9 meters and identical rectangular hollow sections in concrete, being the external dimensions of 2.5x6.8m2

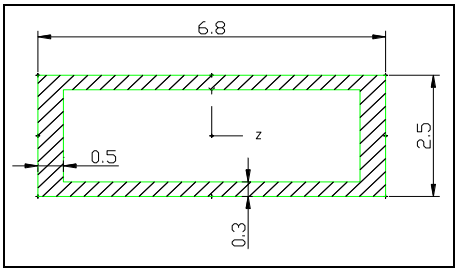
with the largest dimension in the transverse direction of the deck axis, and with a walls thickness of 0.3m along the largest dimension of the section of the pier and 0.5m along the smallest. In Figure 3 the geometry of the bridge is illustrated, with the further on adopted designation for the piers, and in Table 1 the piers height are presented, measured from the top of the foundation to the deck base.



Deck section properties:

Area : 10.02062 m^2
Prin. moment of inertia Y : 124.3786 m^4
Prin. moment of inertia Z : 34.77017 m^4
Torsional constant : 52.84362 m^4





Pier section properties:

Area : 5.98 m^2
Prin. moment of inertia Y : 34.61394 m^4
Prin. moment of inertia Z : 5.538984 m^4
Shear ratio Y : 3.40178
Shear ratio Z : 1.736134
Torsional constant : 15.12595 m^4

Figure 3: Warth Bridge Geometry.

Pier	P1 (A20)	P2 (A30)	P3 (A40)	P4 (A50)	P5 (A60)	P6 (A70)
L (m)	29.8	38.9	37.8	36.0	30.0	16.9

Table 1: Piers height.

4.1 Non-linear material behavior of the piers sections

All the piers have the same transverse hollow section in concrete, with the external dimensions of 2.5x6.8m^2 and the interiors, corresponding to the hollow interior zone, of 1.9x5.8m^2. The piers longitudinal reinforcement is suppressed along its height in three regions, but it is distributed evenly in the transverse section. For all the piers the transverse reinforcement spacing is 20 cm, constituted by a single rectangular stirrup in each of the four walls of the hollow section, with an 8 mm diameter rebar for the current section and a 12 mm diameter rebar in a zone of 1m close to the basis of each pier. For all the piers, a 4cm thick cover concrete was used.

The concrete of the piers bridge is the B400, with a maximum compression tension of 43.0 MPa and a Young modulus of 33.5 GPa. The concrete confinement depends on the efficiency of the stirrups. In this case, very small values are adopted, due to the much reduced confinement obtained with the transverse reinforcement, since only the four corners of the piers are really confined. The steel is the type TR50 according to the supplied design project, and a bilinear curve was adopted, defined through a Young modulus of 200 GPa and a yielding tension of 545.0 MPa, being considered that no hardening exists, therefore with a horizontal yielding.

The axial force resulting from the deck and the piers weights are the following: 26460kN for the pier P1, 28633kN for the pier P2, 28473kN for the pier P3, 28218kN for the pier P4, 27353kN for the pier P5 and 24610kN for the pier P6.

In Figure 4 the moment-curvature curves computed at the base of piers P3 and P6 are illustrated, with several structural models.

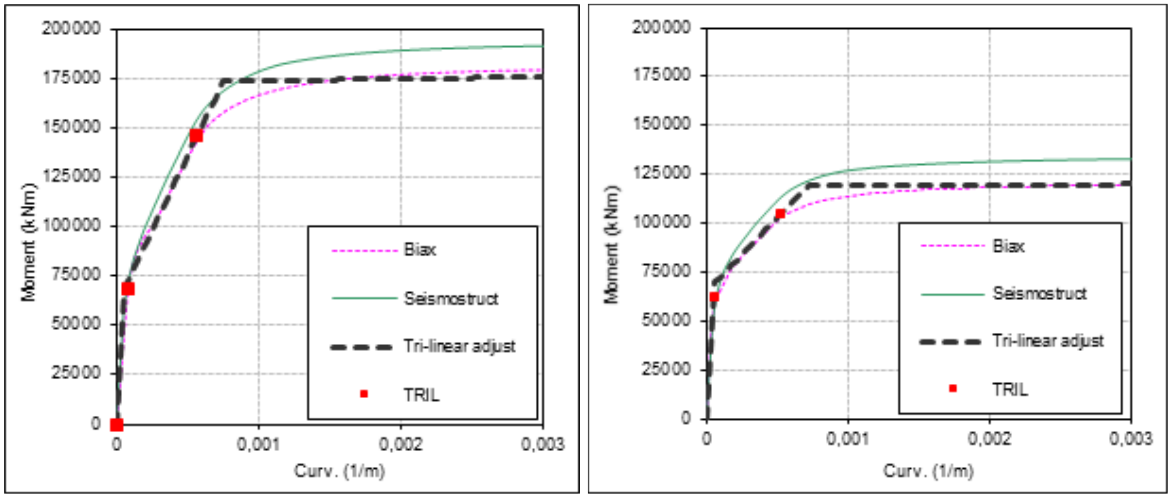


Figure 4: Moment-curvature curves at the base of piers P3 (left) e P6 (right).

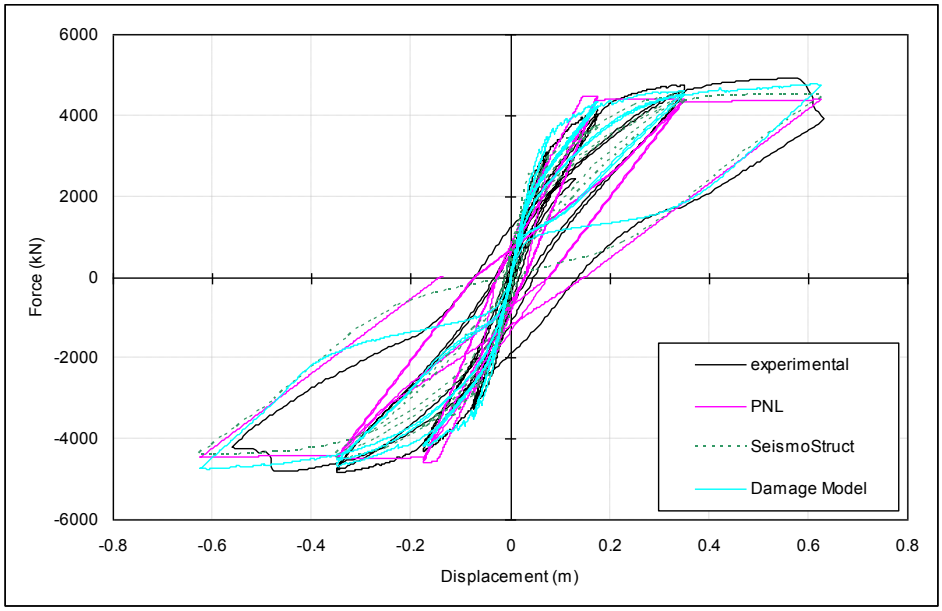
Using the cross section fiber model, Biax [16, 29] the moment-curvature curves with dot line were obtained, computing the section moment for a given curvature and axial force applied to the pier. Based on this curves, tri-linear laws were adjusted for the monotonic loading, ruling the piers non-linear behavior in the plastic hinge model (the PNL program). For this application the fiber model adopted was the Seismostruct program, where the moment-curvature monotonic curve (solid line) at the piers base was obtained through a pushover analysis. The concrete first crack and the steel first yielding in the cross section at the piers base were also computed with the analytical equations programmed (TRIL), developed by Arêde [30] and illustrated (in Figure 4) with square points.

As it can be seen, the curves obtained with the cross section fiber model (Biax) and with the fiber model (Seismostruct) are reasonably close, but the ultimate moment value is higher in the Seismostruct program. For the plastic hinges model (PNL), these monotonic laws are the basis for the characterization of the piers cyclic behavior, involving alterations to their initial characteristics, caused by the cyclic loads, simulating the strength and stiffness degradation, as well as the pinching effect.

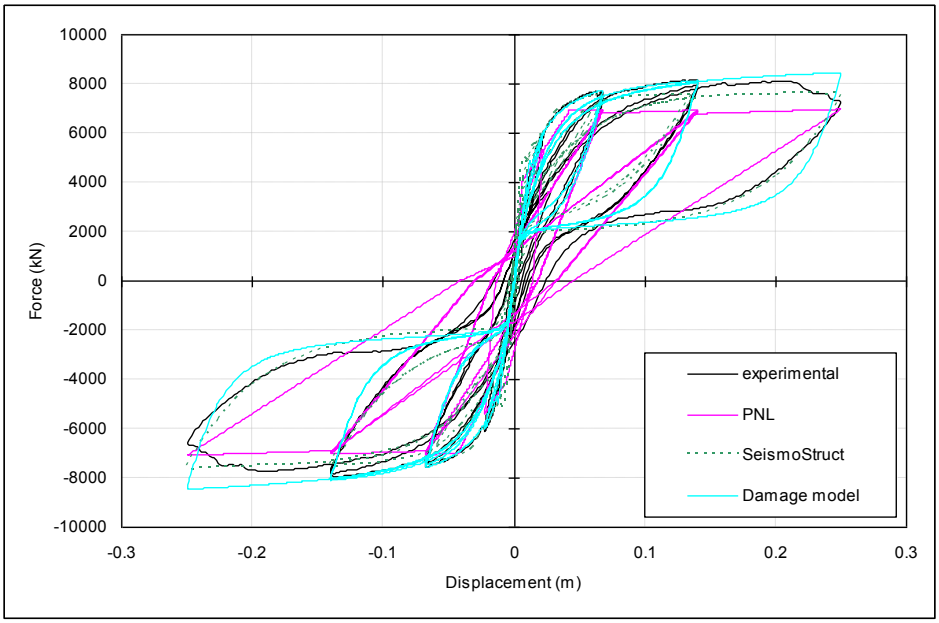
4.2 Pier response to imposed top displacements

The analysis of the piers for cyclic loads is presented, corresponding to a horizontal displacement law applied to their top extremities, and considering an independent operation in each of them. The displacement is applied in the free extremity of the pier (P3 e P6) and in the largest transverse direction, therefore, in the perpendicular direction of the deck axis. The displacement time history imposed on the piers, corresponds to the application of twelve semi-cycles with 4 levels of growing intensity. For pier P3, the intensity levels correspond to 0.08m, 0.18m, 0.35m and 0.62 and, for pier P6, the intensity levels correspond to 0.02m, 0.07m, 0.14m and 0.25.

These experimental cyclic tests were carried out at Ispra laboratory, Italy, giving a good basis for comparing the results obtained by the different numerical models. It was also possible to compare the results with a damage model carried out by Vila Pouca [20], as referred before one much more refined (and accurate) methodology based on finite elements. Figure 5 illustrated the force-displacement relationships obtained experimentally and numerically (PNL, Seismostruct and Damage Model) on the top of the piers, due to the displacement time history imposed on the piers. The force values and the dissipated energy of these numerical results are very close to the experimental results of Ispra [31, 32], showing the good performance of the numerical model used for simulating the inelastic behavior of the piers under cyclic loads.



a) Pier P3



b) Pier P6

Figure 5: Force-displacement curves.

5 APPLICATION TO THE PREC8 BRIDGE

This second application, corresponds to one reinforced concrete bridge experimentally studied at the Joint Research Centre, in Ispra, in the scope of the PREC8 (Prenormative Research in support of EuroCode 8), on which several studies are known. The methodologies for numerical simulation of bridges were applied in order to study its possibilities and the ability to assess the seismic behavior of reinforced concrete structures. In addition, the bridge seismic risk assessment, involving a larger number of structural analyses, was also performed.

This bridge is a reinforced concrete bridge experimentally studied at the Joint Research Centre, in Ispra, in the scope of the PREC8 (Prenormative Research in support of EuroCode 8), subjected to experimental and numerical studies, which constitutes an excellent basis for the calibration of the proposed models for the seismic safety assessment of bridges.

Many methods of analysis were used to this bridge but as it is stated in the report n.º 4, November 1996, ECOEST/PREC8 (G.M Calvi and P. E. Pinto) there is an acute need of analytical tools for non-linear dynamics analysis which are simple and economical to use and provide answers of acceptable levels of accuracy. Therefore, this application is an effort to contribute for the development of analytical tools.

The experimental studies [2] were accomplished on a reduced scale model of this bridge, represented in Figure 6, whose geometric characteristics correspond to a deck with four spans of 20m each and three piers of hollow section, 5.6, 2.8 and 8.4m in height, fully-fixed in the base and pinned in their connection to the deck.

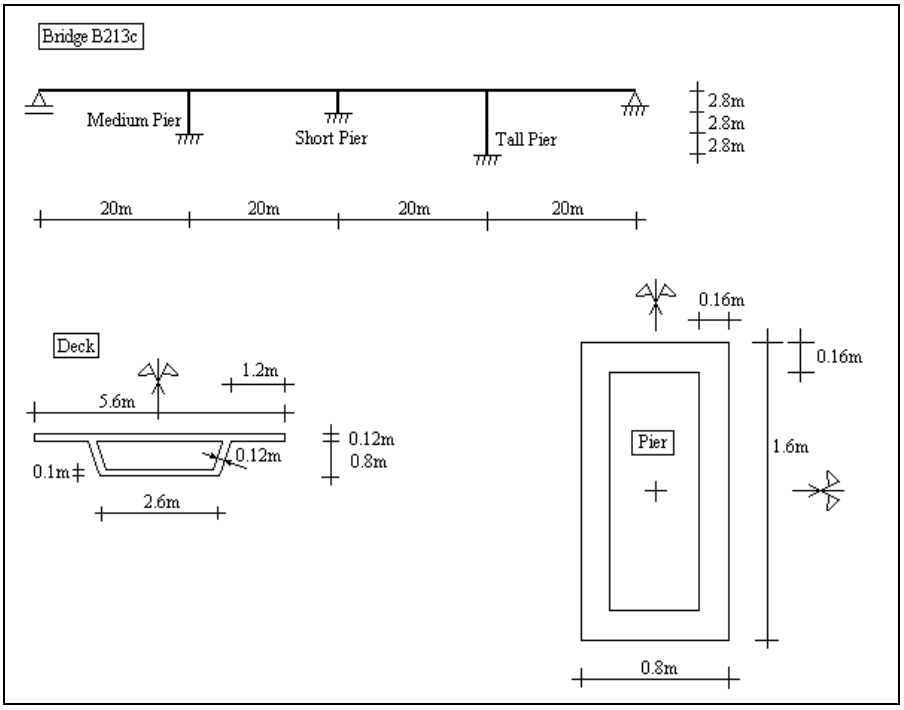


Figure 6: Scaled bridge geometry.

5.1 Non-linear material behavior of the piers sections

The bridge was designed for a peak ground acceleration of 0.35g (343cm/s^2) in medium soil condition (soil type B) and applying the EC8 provisions. The longitudinal reinforcement of the tall and medium piers is 7680mm^2 (1.15%) and of the short pier, 3330mm^2 (0.5%), being the current spacing of the transverse reinforcement of 80mm. In the first 1.5m next to the pier base, the confinement is better, once the spacing between stirrups is smaller, being 60mm to the tall and medium piers and 50mm to the short pier. In the model the same reinforcement cover of 8mm was used for all the piers. Figure 7 illustrates the localization and the section diameters of the longitudinal reinforcement, as well as the transverse reinforcement details, with close stirrups assembling steel bars alternatively.

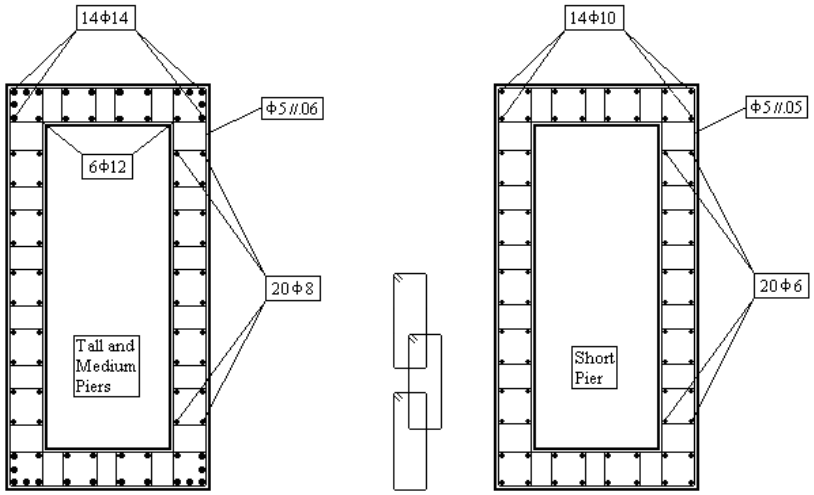


Figure 7: Piers reinforcement.

In agreement with the supplied project details, the bridge piers concrete presents a maximum stress compression of 39.0 MPa and a Young modulus of 25 GPa. The confinement depends on the efficiency of the stirrups in the concrete jacketing, adopting for this case a confinement coefficient corresponding to a transverse reinforcement rate of ρ_v = 0.00555 [33].

For the steel a bilinear curve was adopted, defined through a Young modulus of 206 GPa and a yielding tension of 500.0 MPa, considering that no hardening exists, therefore with a horizontal yielding.

The moment-curvature curves were obtained by using the abovementioned cross section fiber model and, for a given curvature and the axial strain of the piers, the corresponding moment was evaluated. The axial strain in the piers was considered equal to 1700kN. Based on these curves, tri-linear laws were adjusted for a monotonic loading that simulates the non-linear behavior of the piers. These laws are the basis for the cyclic behavior definition of the piers, involving alterations to their initial characteristics, caused by the cyclic loads, simulating the strength and stiffness degradation, as well as the pinching effect [6].

5.2 Pier response to imposed top displacements

The analysis of the piers for cyclic loads is presented, corresponding to a horizontal displacement law applied to their top extremities, and considering an independent operation in each of them. The displacement application was accomplished in the free extremity of the pier and in the largest transverse direction, therefore, in the perpendicular direction of the deck axis.

In order to simulate the isolated behavior of each pier, the structural modelling was carried out only considering a vertical bar, composed by a central zone with linear and elastic behavior, and two zones in the bar extremities with inelastic behavior - the plastic hinges, where the non-linear behavior of the pier is concentrated. It was considered 0.8m for the length of the plastic hinge (*lp*), about half of the cross section height of the pier [33].

The displacement time history imposed on the piers top corresponds to the application of twelve semi-cycles of growing intensity.

Figure 8 represents the force-displacement relationships obtained numerically on the top of the tall and short piers, due to the displacement time history imposed on the piers. The force values and the dissipated energy of these numerical results are very close to the experimental results of Ispra [2], showing the good performance of the numerical model used for simulating the inelastic behavior of the piers under cyclic loads.

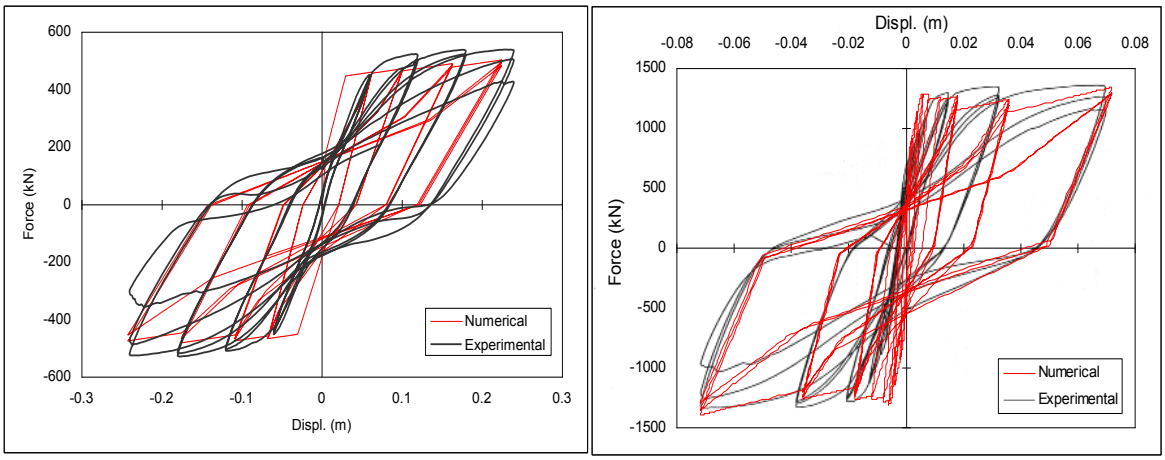


Figure 8: Force-displacement curves for the tall pier (left) and short pier (right).

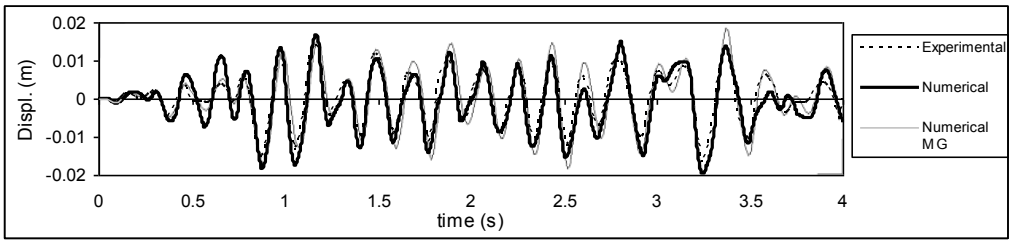
5.3 Seismic response

For the dynamic and non-linear analysis of the bridge several accelerograms should be used to take into account the stochastic characteristic of earthquakes, but in this application only the generated artificial accelerogram compatible with the response spectrum of the EC8, and used in Ispra [2], was considered. The numerical analysis was performed on the reduced scale model of the bridge (Figure 6), with a scale factor of 2.5, and so the peak acceleration and duration of the accelerogram were, respectively, multiplied and divided by this factor, obtaining 0.875g and 4s.

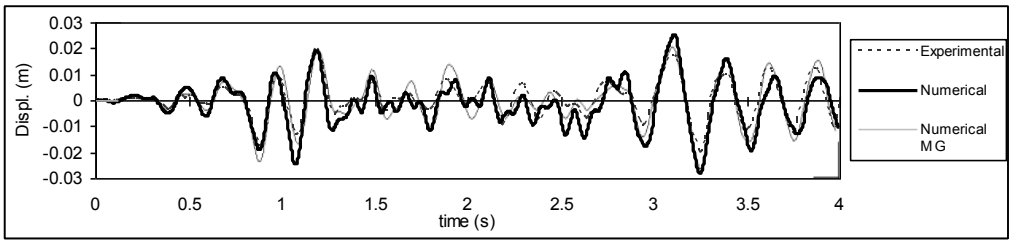
The discretization of the structure was made with 22 elements, the deck comprising 16 elements and the connecting ties and piers six elements. The deck bars and the connecting ties have elastic linear behavior, while the piers are made up of bars with plastic hinges, 0.8m long, at their extremities. Hence, the non-linear behavior of the structure is concentrated on the piers, more precisely at their plastic hinges close to the foundation, an acceptable assumption, since those will be the zones of the structure with greater strength during seismic action.

Due to the hysteretic material behavior when subjected to cyclic loadings, the hinges carry the main responsibility for energy dissipation in the structure, so a null structural damping was considered, only bearing in mind the hysteretic mechanism with regard to energy dissipation.

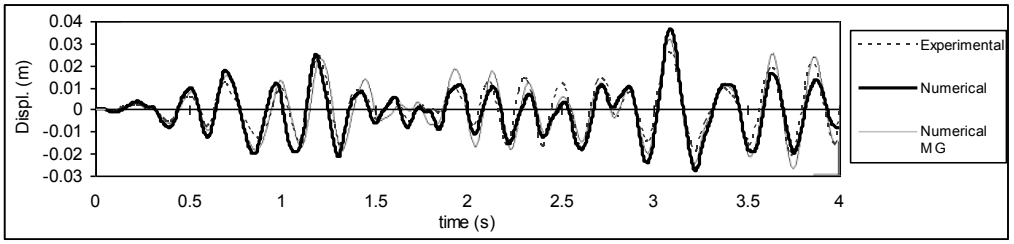
Figure 9 illustrates the comparison of the medium, short and tall piers top displacement response obtained numerically with the plastic hinge model (black curve) with the ones obtained in Ispra, by Guedes [2], which corresponds to the numerical analyses with a fiber model (grey curve with the label: Numerical MG) and the experimental results (black dashed curve).



a) Medium pier



b) Short pier



c) Tall pier

Figure 9: Seismic response of the piers.

The seismic response obtained for the three piers is reasonably close with the experimental results, as much in frequency as in maximum values, thus demonstrating a satisfactory behavior. As it could also be seen, the solution obtained with the plastic hinge numerical approach has, in general, values a little bit lower than the experimental ones meanwhile the solution obtained by Guedes (referred as Numerical MG) has values a little bit greater. This illustrates the sensibility of the numerical non-linear dynamic analysis to the material parameters used when comparative analysis with experimental tests is made. In this application the problem is even greater because the boundary conditions could cause lower displacements in the numerical analysis, once in laboratory testing it is not possible to completely restrict the displacements at the piers base, especially the base rotation, as it was done in the present analysis where zero displacements were prescribed.

Furthermore, during the experimental campaign a local deformation on the foundation connection with the pier was observed (Report EUR 16358 by Guedes and Pinto [34]). The numerical analysis carried out by Guedes has considered an additional elastic element between the pier and the foundation (with a support hinge at top of this element) to simulate the rotational deformation (without horizontal displacement) and accurately reproduce the experimental tests. The same strategy was performed in the plastic hinge model, using elastic characteristics for the additional elements in a way that the elastic stiffness of the piers become similar to the experimental conditions. The length of these additional elements was

0.025m and the Young modulus was: 0.13 GPa for medium pier, 0.04 GPa for short pier and 0.10 GPa for tall pier.

As expected, the short pier has the more significant non-linear behavior and, conversely, the tall one has the lesser non-linear behavior, being the closest to the experimental result.

5.4 Safety assessment

In the Portuguese code, to obtain the design value of the peak acceleration the characteristic value must be multiplied by a safety factor of 1.5, therefore the design earthquake and the extreme probability distribution of the action are referred to the same acceleration, about 0.35g, once the safety analysis was carried out in the full scale bridge (prototype).

In order to obtain the vulnerability curves of the piers, different intensities of the referred earthquake were increasingly applied to the bridge. Therefore, from each peak acceleration value the corresponding moment-curvature result was obtained, allowing the evaluation of the maximum ductility demanded at the piers base, the values adopted as the control parameters to evaluate the safety assessment of the piers.

Using the least-squares method, polynomial functions of 2nd order were adjusted through a series of points of the demanded ductilities for each level of seismic action, obtaining relationships between action and action effects that characterize the vulnerability functions of each pier, as represented in Figure 10.

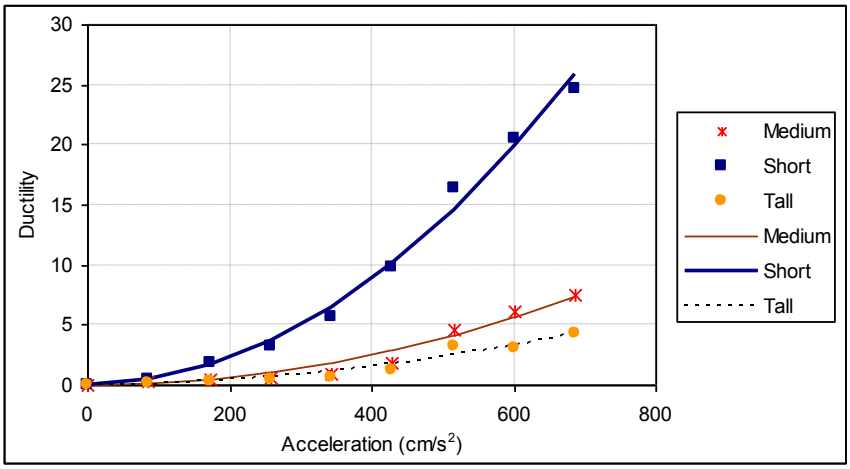


Figure 10: Vulnerability functions of the piers.

To quantify the collapse probability of the bridge, a sensitive analysis was carried out with different values for the characterization of the piers strength function - referred before in Figure 2 as curve number 2. In Table 2 the collapse probability values for each pier are referred to, given that the strength density function is defined by a normal distribution function with mean ductility values of 4, 8 and 12, and variation coefficient values of 0.05 and 0.20.

Pier	VC = 0.05			VC = 0.20		
	$\mu_{d=4}$	$\mu_{d=8}$	$\mu_{d=12}$	$\mu_{d=4}$	$\mu_{d=8}$	$\mu_{d=12}$
Short	0.0002689	0.0000462	0.0000093	0.0060939	0.0015345	0.0004698
Medium	0.0000003	0.0000000	0.0000000	0.0000213	0.0000023	0.0000016
Tall	0.0000000	0.0000000	0.0000000	0.0000011	0.0000005	0.0000006

Table 2: Collapse Probabilities.

As expected, observing at Table 2, the greater collapse probabilities occur consistently in the short pier (which correspond the more severe vulnerability functions), for any pair of mean ductility and variation coefficient values, being the one that controls the safety of the bridge. It is also possible to verify that the collapse probability increase for lower values of mean ductility and greater values of variation coefficient. The safety evaluation therefore shows that only for large available ductility and low variation coefficients values the bridge presents a collapse probability close to a reasonable limit ($\approx 10^{-5}$).

These values of collapse probability were computed considering that a flexural failure mechanism has occurred before the shear strength reaches the capacity value and, therefore, no brittle failure in shear was achieved in any pier. The experimental tests at Ispra have showed that the collapse mechanism was achieved with a horizontal crack at the base of the short pier, with the failure of the reinforcement bar in tension. To prove that, the shear capacity in the plastic hinges of the piers was computed, using the equations of Priestley *et al.* [35] and assuming high ductility: Medium pier – 1185kN; Short pier – 1375kN and Tall pier – 1115kN. These values were not achieved in the piers base (plastic hinge) when the plastic moment capacity was reached.

6 CONCLUSIONS

In this work several numerical models were suggested for the cyclic and seismic responses of RC bridges, involving different approaches for the consideration of the structural modeling (plane or tri-dimensional behavior of the bridge) and for the simulation of the non-linear behavior. One methodology for seismic safety assessment of bridges, involving the evaluation of its failure probability, was also presented.

Two applications were carried out with the proposed methodologies, which shows good accuracy for the structural assessment analyses of bridges subjected to cyclic and seismic loading confirmed by the excellent comparison of the obtained results with experimental responses. For calibration of the methodologies, the first application was mainly focus on the bridge piers static and cyclic analysis, of which several experimental and numerical results are known, allowing the comparison of results and evidencing the potentiality of the numerical models. The comparison of different approaches for the monotonic response of the cross section moment-curvature was performed, with quite good comparison of results. For cyclic response of the piers, with imposed top displacements, several numerical model simulations were carried out, allowing to conclude that all responses were satisfactorily close to the experimental tests.

An irregular bridge was used for seismic analysis, with numerical simulations performed with plastic hinge model and fiber model. The numerical responses obtained compares quite well with the experimental results, both in the maximum displacement values and the frequencies. This models also allows the seismic response of the bridge to be obtained in a

realistic way, with reduced calculation efforts and a reasonable simplicity, which is a necessary condition for studies of risk assessment where a great number of analyses are required. Taking pier ductility as the control parameter, the seismic vulnerability of the bridge was evaluated, for different values of mean ductilities and variation coefficient of the strength distribution function. The safety evaluation performed provided the conclusion that the bridge only presents a collapse probability below an acceptable level for μd = 12 and VC = 0.05, demonstrating the total inability of this irregular bridge in dealing with earthquake loadings.

REFERENCES

[1] Taucer, F., Spacone, E., & Filippou, F.C. A Fiber Beam-Column Element for Seismic Response Analysis of R/C Structures, *Report EERC 91-17, Earthquake Engineering Research Center*. University of California. Berkeley, 1991.

[2] Guedes, J. Seismic Behaviour of Reinforced Concrete Bridges – Modelling, Numerical Analysis and Experimental Assessment. *PhD Thesis*, FEUP, Porto, 1997.

[3] SeismoSoft. SeismoStruct - A computer program for static and dynamic nonlinear analysis of framed structures [online], 2004. Available from URL: http://www.seismosoft.com.

[4] Faria, R., Oliver, J. and Cervera, M. A strain based plastic viscous damage model for massive concrete structures, *International Journal of Solids and Structures* 35(14), 1533-1558, 1998.

[5] Vecchio, F.J., & Collins, M.P. Predicting the response of reinforced concrete beams subjected to shear using modified compression field theory. *ACI structural journal* – technical paper, 258-268, American Concrete Institute, 1988.

[6] Costa & Costa hysteretic model. RC Frames Under Earthquake Loading. *CEB; Comité Euro-International du Béton*, Bulletin nº231, 1996.

[7] Arêde, A. Seismic Assessment of Reinforced Concrete Frame Structures with a New Flexibility Based Element, *PhD Thesis*, FEUP, Porto, 1997.

[8] Kang, H.D., Willam K., Shing, B. and Spacone E. Failure analysis of R/C columns using a triaxial concrete model, *Computers and Structures* 77, 423-440, 2000.

[9] Liu, J. and Foster S.J. A three-dimensional finite element model for confined concrete structures, *Computers and Structures* 77, 441-451, 2000.

[10] Kwon, M. and Spacone E. Three-dimensional finite element analyses of reinforced concrete columns, *Computers and Structures* 80, 199-212, 2002.

[11] Papanikolaou, V.K. and Kappos A.J. Numerical study of confinement effectiveness in solid and hollow reinforced concrete bridge piers: Methodology, *Computers and Structures* 87, 1427-1439, 2009.

[12] Papanikolaou, V.K. and Kappos A.J. Numerical study of confinement effectiveness in solid and hollow reinforced concrete bridge piers: Analysis results and discussion, *Computers and Structures* 87, 1440-1450, 2009.

[13] Delgado, P., Costa, A., & Delgado, R. A Simple Methodology for Seismic Safety Assessment of Bridges. *12ECEE - The Twelfth European Conference on Earthquake Engineering*, London, UK, 9-13 September, 2002.

[14] Takeda, T., Sozen, M.A., & Nielsen, N.N. Reinforced concrete response to simulated earthquakes. *Journal of the Structural Mechanics Division of the ASCE*, ST12, 96, 1970.

[15] Duarte, R.T., Oliveira, C.S., Costa, A.C., & Costa, A.G. A Non-linear Model for Seismic Analysis, Design and Safety Assessment of Reinforced Concrete Buildings. *Earthquake Damage Evaluation & Vulnerability Analysis of Building Structures*, edited by A.Koridze, OMEGA Scientific, 1990.

[16] Vaz, C. T. Comportamento Sísmico de Pontes com Pilares de Betão Armado, *PhD Thesis*, FEUP/LNEC, 1992. (in Portuguese)

[17] Kent, D. & Park, R. Flexural Members with Confined Concrete, *Journal of Structural Division* 97(7), 1969-1990, ASCE, 1971.

[18] Menegotto, M., & Pinto, P.E. Method of Analysis for Cyclically Loaded R.C. Plane Frames Including Changes in Geometry and Non-Elastic Behavior of Elements Under Combined Normal Force and Bending. *Symposium on Resistance and Ultimate Deformability of Structures Acted On by Well Defined Repeated Loads*, IABS Reports Vol. 13, Lisbon, 1973.

[19] Faria, R. and Oliver, J. A rate dependent plastic-damage constitutive model for large scale computations in concrete structures, *CIMNE Monograph* 17, Barcelona, 1993.

[20] Vila Pouca, N. Simulação Numérica da Resposta Sísmica de Elementos Laminares em Betão Armado, *PhD Thesis*, FEUP, Porto, 2001 (in Portuguese).

[21] Faria, R., Vila Pouca, N. and Delgado, R. Simulation of the cyclic behaviour of R/C rectangular hollow section bridge piers via a detailed numerical model, *Journal of Earthquake Engineering* 8(5), 725-748, 2004 (DOI:10.1142/S1363246904001547).

[22] Park, R., Priestley, M. and Gill, W. Ductility of Square-Confined Concrete Columns, *Journal of Structural Division* 108(4), 929-950, ASCE, 1982.

[23] Faria, R., Vila Pouca, N. and Delgado, R. Seismic behaviour of an R/C wall: Numerical simulation and experimental validation, *Journal of Earthquake Engineering* 6(4), 473-498, 2002.

[24] Borges, J. F., & Castanheta, M. *Structural Safety*; Curso 101, 3ª Edition, LNEC, Lisbon, 1982.

[25] Costa, A. G. Seismic Analysis of Irregular Structures. *PhD Thesis*, FEUP, Porto, 1989. (in Portuguese)

[26] Oliveira, C. S., Sousa, M. L., & Costa, A. C. Definition of Seismic Action in the Context of EC-8. Topics for Discussion, *12th World Conference on Earthquake Engineering*, Auckland, New Zealand, 1999.

[27] Costa, A. C. A Acção dos Sismos e o Comportamento das Estruturas. *PhD Thesis*, FEUP, Porto, 1993. (in Portuguese)

[28] Delgado, J. M., Azeredo, M., & Delgado R. M. Probability of failure estimation of current reinforced structures using the Latin Hypercube Sampling. *RISK ANALYSIS II*, pp. 105-114, Editor C.A. Brebbia, Wit Press, Southampton, Boston, 2000.

[29] Varum, H. Modelos Numéricos para a Análise Sísmica de Pórticos Planos de Betão Armado, *MSc Thesis*, FEUP, Porto, 1996. (in Portuguese)

[30] Arêde, A. Seismic Assessment of Reinforced Concrete Frame Structures with a New Flexibility Based Element, *PhD Thesis*, FEUP, Porto, 1997.

[31] Pinto, A.; Pegon P.; Magonette G.; Molina J.; Buchet P.;Tsionis G. Pseudodynamic Tests on a Large-Scale Model of na Existing RC Bridge Using Non-linear Substructuring and Asynchronous Motion, *EUR 20525 EN, Joint Research Centre*, Ispra, Italy, 2002.

[32] Gago, A.; Varum, H.; Pinto, A.V. Preliminary Non-linear Analyses of a Reinforced Concrete Bridge, *VAB Project, Joint Research Centre*, Ispra, 1999.

[33] Delgado, P. (2009). Avaliação da Segurança Sísmica de Pontes. *Ph.D. thesis*, FEUP (in Portuguese), (http://ncrep.fe.up.pt/web/artigos/PDelgado_PhD_Thesis.pdf).

[34] Guedes, J., & Pinto, A. V. Numerical Simulation of the ELSA PSD Tests of R/C Bridges, *Report EUR 16358 EN*, EC, JRC, Ispra, Italy, 1996.

[35] Priestley, M.J.N., Seible, F., & Calvi, G.M. *Seismic Design and Retrofit of Bridges*. New York, 1996.

COMPDYN 2015
5th ECCOMAS Thematic Conference on
Computational Methods in Structural Dynamics and Earthquake Engineering
M. Papadrakakis, V. Papadopoulos, V. Plevris (eds.)
Crete Island, Greece, 25–27 May 2015

EFFICIENCY OF DIFFERENT RETROFITTING TECHNICHS FOR RC COLUMNS UNDER BIAXIAL LOADING: EXPERIMENTAL STUDY

H. Rodrigues[1], A. Furtado[2A], P. Rocha[3] and A. Arêde[2B]

[1] School of Technology and Management, Polytechnic Institute of Leiria
Portugal
hugo.f.rodrigues@ipleiria.pt

[2] Faculty of Engineer of Oporto University
Portugal
e-mail A: afurtado@fe.up.pt and email B: aarede@fe.up.pt

[3] Superior School of Technology and Management, Polytechnic Institute of Viana do Castelo
Portugal
procha@estg.ipvc.pt

Keywords: RC column, biaxial cyclic behaviour, RC column retrofitting, stiffness degradation, energy dissipation

Abstract. *The main purposes of this work it to present an experimental campaign of different strengthening strategies of RC columns, and evaluating benefits concerning their structural behaviour cyclic loading. 9 RC columns were tested, two of them original and the rest composed by strengthened columns by CFRP and steel plates jacketing. The aim is, therefore, to contribute for developing and calibration a procedure that enables the evaluation of the efficiency of the strengthening strategies, their possibilities and application. It was also an objective of this work to explore the possibility of use this techniques on the improvement of existing buildings performance*

1 INTRODUCTION

The seismic behaviour of RC structures is a widely studied theme in the last decades, however the experimental response of RC elements under biaxial cyclic bending still very limited [1, 2]. Rodrigues et al. [3-7] tested 17 RC specimens with four types of full-scale rectangular building columns tested for different loading histories. The horizontal loading patterns considered were: cruciform; diamond; expanding quadrangular; and circular. In this study the comparison of the biaxial results is performed with similar columns under uniaxial load. Based on the obtained results, it was verified that: i) The initial column stiffness in both directions it is not significantly affected by the biaxial load path; ii) when comparing the maximum strength in one specific direction of the columns, for each biaxial test against the corresponding uniaxial test, lower values were obtained for all biaxial tests than uniaxial ones (the biaxial loading induces a 20-30% reduction of the columns maximum strength in their weak direction, while reductions from 8-15% for the stronger direction); iii) the ultimate ductility is significantly reduced in columns subjected to biaxial load paths; iv) the strength degradation is practically zero, in the first loading cycles, increasing after displacement ductility demands of about 3. (from the strength degradation analysis, more pronounced strength degradation was observed for biaxial tests when compared with corresponding uniaxial tests; v) the biaxial loading can introduce higher energy dissipation (circular, rhombus and cruciform load paths) than uniaxial loading, as previously recognized by other authors; vi) the viscous damping highly depends on the biaxial load path (however the repetition of cycles, for the same maximum displacement level, has practically no influence on the equivalent damping).

The available experimental and numerical information allows us to recognize that RC elements under biaxial proved that the effect of biaxial cyclic bending moment is recognized as a very important topic for building structures in earthquake prone regions. Is also recognize the needs to strengthening of existing buildings. The experimental research work in this field is currently very limited and much behind the present knowledge about 1D bending.

It is known that many buildings, designed with older codes, can be more susceptible to serious damage when submitted to earthquake. Older buildings have been design, according to at the time the codes, for much lower seismic actions. RC column jacketing is a very effective strength technique [8] to increase the strength capacity. To increase the shear strength can be added jackets (in steel, concrete, or other types) across the column length. A variety of techniques have been subjected to experimental studies [9, 10] in order to evaluate their performances. From the analysis of the available experimental work, it was possible to verify that all the strengthening techniques improves the bending strength, the stiffness, the ductility and the shear capacity.

To analyze and assess the efficiency of different strategies for the seismic strengthening of RC columns, an experimental campaign was performed by the investigation group of Laboratory of Earthquake and Structural Engineering (LESE). The experimental campaign and the solutions were based on the previous experience of the research team in the retrofitting of columns under uniaxial bending [11]. Full-scale RC columns were tested, in the original undamaged state and original undamaged with strengthening interventions according to different techniques. This paper presents the results of nine tested specimens, two “as built” columns and seven strengthened columns with steel plates and with Carbon Fibre Reinforced Polymers (CFRP) plates jacketing.

2 EXPERIMENTAL CAMPAIGN

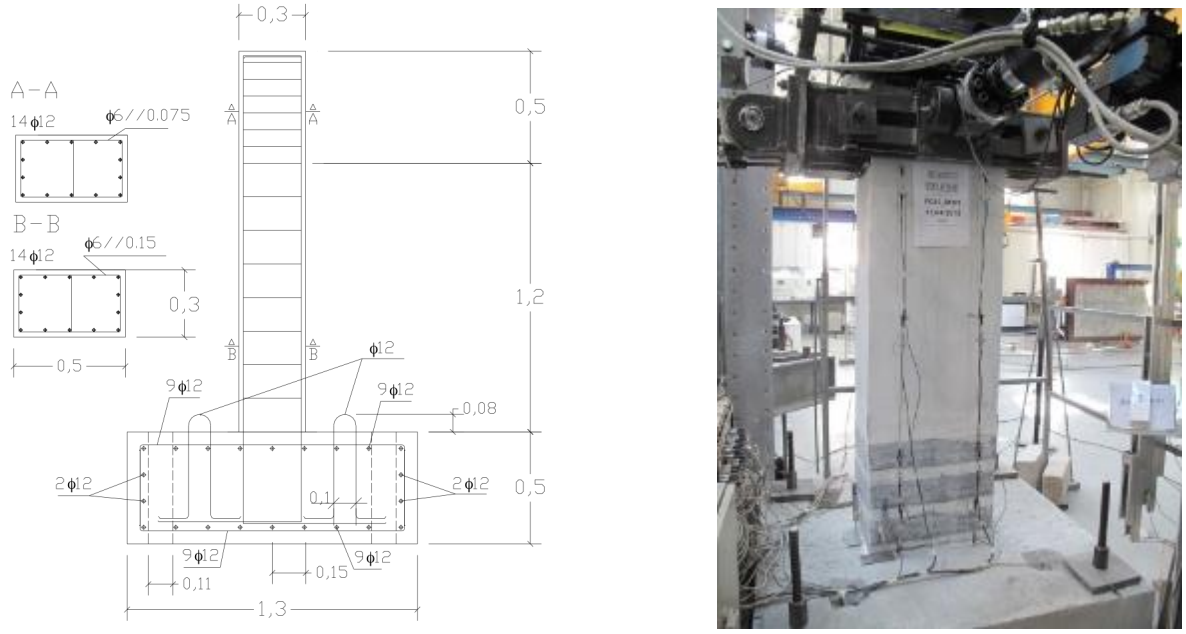
2.1 Specimens' description and experimental setup

Nine rectangular RC columns were constructed with the same geometric characteristic and reinforcement detailing, and were cyclically tested for two different loading histories. The columns and cross-section reinforcement detailing are presented in Figure 1. The specimens have 1.70m height, and are cast in strong concrete foundation blocks (1.30 x 1.30 x 0.50 m^3). The foundation block has four holes near the corners to fix the specimen to the laboratory strong floor.

With this kind of cantilever model it is assumed that the inflection point of a 3.0m height column is located at its mid-height (1.5 m). The same behaviour, special at the base, can be found in a column of a typical building when subjected to lateral demands induced by earthquakes. An extra 0.20 m height is added for attaching the actuator devices.

Details of the reinforcement and material properties are summarized and shown in Fig. 1a and Table 1.

The test setup is illustrated in Fig. 1b. The system includes two independent horizontal actuators to apply the lateral loads on the column specimens and one vertical actuator to apply the axial load. But, because the axial load actuator must remain in the same vertical during the test while the column specimen laterally deflects, a sliding device is used (placed between the top-column and the actuator), which was built to minimize spurious friction effects.



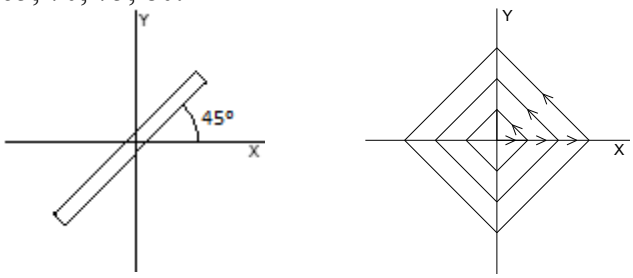
a) b)

Figure 1: a) RC column specimen dimensions and reinforcement detailing b) General view of the experimental test setup.

2.2 Loading condition

In order to characterize the response of the strengthened column specimens, several loading conditions were considered. Cyclic lateral displacements were imposed at the top of the column with steadily increasing displacement levels. The adopted load paths are summarized in Figure

2 and for each lateral deformation demand level, three cycles were repeated. The following nominal peak displacement levels (in mm) were considered: 3, 5, 10, 4, 12, 15, 7, 20, 25, 30, 35, 40, 45, 50, 55, 60, 65, 70, 75, 80.



Diagonal - 45º Diamond

Figure 2: Horizontal displacement paths types.

For the two "As built" specimens and the rest of the specimens, strengthened with different strategies as described next, were adopted to biaxial load the paths indicated in Table 1.

Table 1: Specimens' specifications and loading characteristics.

Specimen	Geometry [cm x cm]	f_{cm} [MPa]	f_{yk} [MPa]	Axial Load [kN]	Horizontal Displace-ment path type	Strengthening Technique
PC12-N13	30 x 50	14.8	575.6	300	Diagonal – 45º	As Built
PC12-N14					Diamond	
PC12-N10S		8.4	573.7		Diamond	CFRP plates jacketing
PC12-N11S						Steel plates jacketing bonded with epoxy resin
PC12-N12S						CFRP plates jacketing
PC12-N15S		14.8	575.6		Diagonal – 45º	Steel plates jacketing bonded with epoxy resin
PC12-N16S					Diamond	Steel plates jacketing bonded with epoxy resin
PC12-N17S					Diagonal – 45º	CFRP plates jacketing
PC12-N18S					Diamond	CFRP plates jacketing

2.3 Retrofit Techniques

Seven specimens were strengthened with two different techniques: CFRP plate's jacket; and steel plates (see Table 1) The design and retrofit procedure is based on previous research work [12-14].After the construction of all specimens, seven of them were submitted to two different strengthening techniques: CFRP plates jacketing and steel plates jacketing.

2.3.1. CFRP plates jacketing

The total thickness of CFRP jacketing t_j = 0.342 mm was obtained for the total repaired zone height (500 mm). The total area value along this height (0.342 x 500 = 171 mm^2) was divided

by 3 CFRP plates with 80 mm wide, spaced at 70mm (40mm between the footing and the first plate), each one with 6 layers of CFRP sheet thickness of 0.117mm. Figure shows a general schematic view of the CFRP plates jacketing for specimens strengthened with this technique (Table 1).

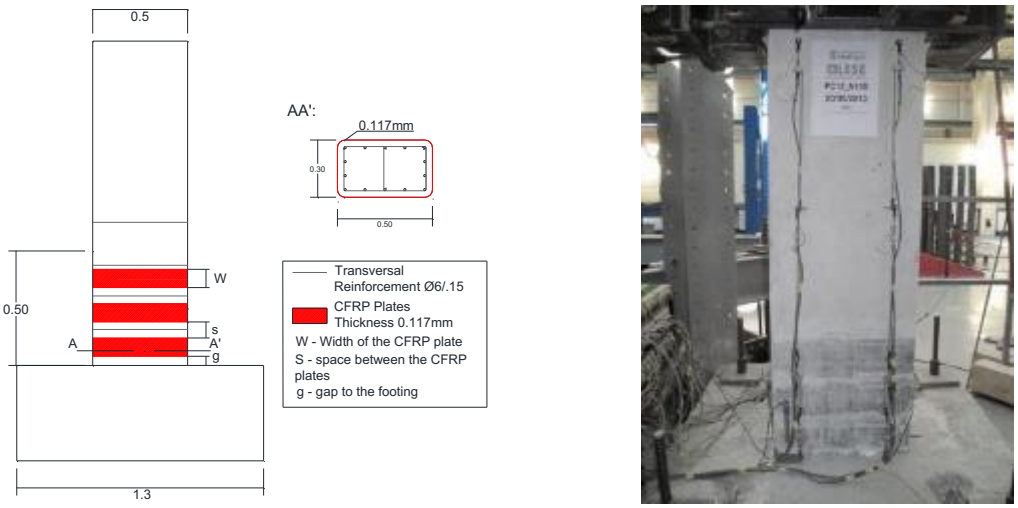


Figure 3 - Strengthened column specimen with CFRP plates jacketing.

2.3.2. Steel plates jacketing

The plates were placed in four previously defined levels at different distances from the footing (125 mm, 225 mm, 325mm and 425 mm). After welding the steel bars in place, the voids between the plates and the concrete were filled with injection of two component epoxy resin in order to ensure full contact and early efficiency of the external strengthening. Figure 4 shows the general schematic view of the specimen strengthened with steel plates jacketing.

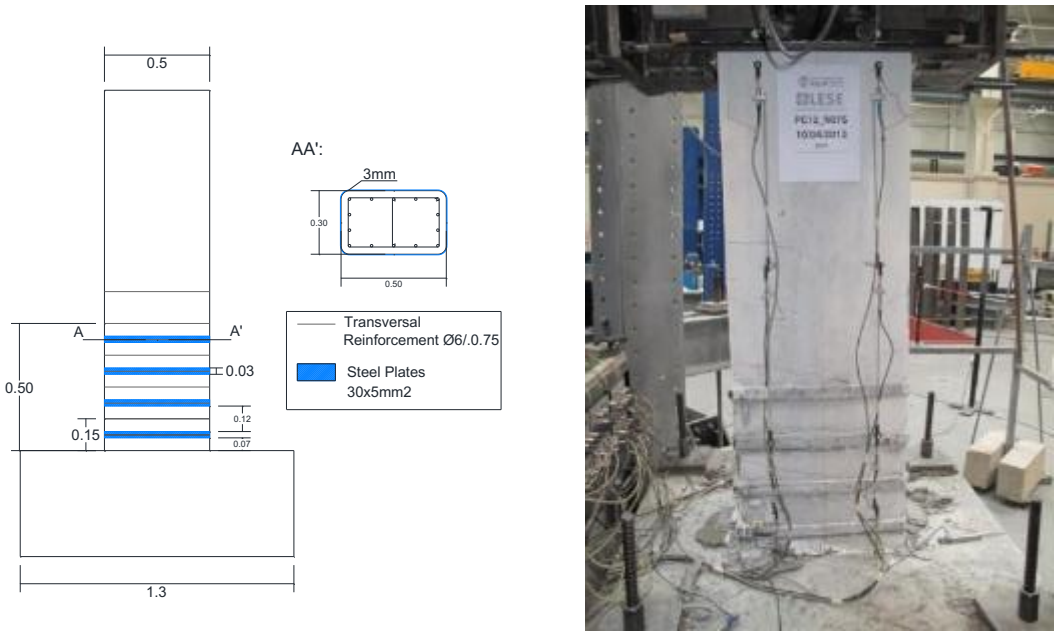


Figure 4 - Strengthened column specimen with steel plates jacketing.

The different strengthening techniques and details are described in Table 2.

Table 2 - Specimen's strengthening techniques and details.

Specimen	Strengthening technique	Solution details
PC12-N10S	CFRP plates jacketing	3 CRFP plates, 8cm wide spaced at 7cm, with 4cm of gap to the footing and 3 CFRP layers per plate
P12-CN11S	Steel plates jacketing bonded with epoxy resin	Steel plates (3x0.5 cm^2), simply bonded with epoxy resin, spaced at 12cm with 7 cm of gap to the footing
PC12-N12S	CFRP plates jacketing	3 CRFP plates, 8cm wide spaced at 7cm, with 4cm of gap to the footing and 3 CFRP layers per plate
PC12-N15S	Steel plates jacketing bonded with epoxy resin	Steel plates (3x0.5 cm^2), simply bonded with epoxy resin, spaced at 12cm with 7 cm of gap to the footing
PC12-N16S	Steel plates jacketing bonded with epoxy resin	Steel plates (3x0.5 cm^2), simply bonded with epoxy resin, spaced at 12cm with 7 cm of gap to the footing
PC12-N17S	CFRP plates jacketing	3 CRFP plates, 8cm wide spaced at 7cm, with 4cm of gap to the footing and 3 CFRP layers per plate
PC12-N18S	CFRP plates jacketing	3 CRFP plates, 8cm wide spaced at 7cm, with 4cm of gap to the footing and 3 CFRP layers per plate

3 EXPERIMENTAL RESULTS

For the study of the efficiency of the strengthening technics applied in the behaviour of RC columns, the measured displacement and shear force paths (along the X and Y directions) are analyzed: Figure 5 shows the shear-drift results for the “As built” specimens; and in Figure 6 and 7 the shear-drift diagrams for the columns strengthened with CFRP plates jacketing; and steel plates jacketing strengthened columns respectively. In order to help the understanding of each strengthening technic increments, the enveloping obtained in the tested ‘as built’ column with the same biaxial load path was also included, and a picture

The analysis of the obtained results can be summarized as follows:

- In their enveloping curves the post-yield hardening zone is larger and the softening phase tends to start for higher drift demands in strength columns with both technics. This tendency is more evident in the tests with the diamond biaxial load path.
- The initial column stiffness, in both directions, it is not significantly affected by the strengthening technic.
- When comparing the maximum strength in one specific direction of the columns, for each strengthening technic against the corresponding ‘as built’ column test, higher values were obtained for all tests with the diamond load path (increase around 12%). In the tests with the diagonal load path the maximum strength is similar in “as built” and strength columns.

As pointed by Rodrigues *et al* [15], the columns under biaxial load the post yielding plateau tends to be shorter and the softening is more pronounced. With the tested strengthening technics was enhanced the behavior of the columns mostly given by the; delaying of the strength degradation beginning of, keeping the initial stiffness and, small increasing of the maximum strength of the elements.

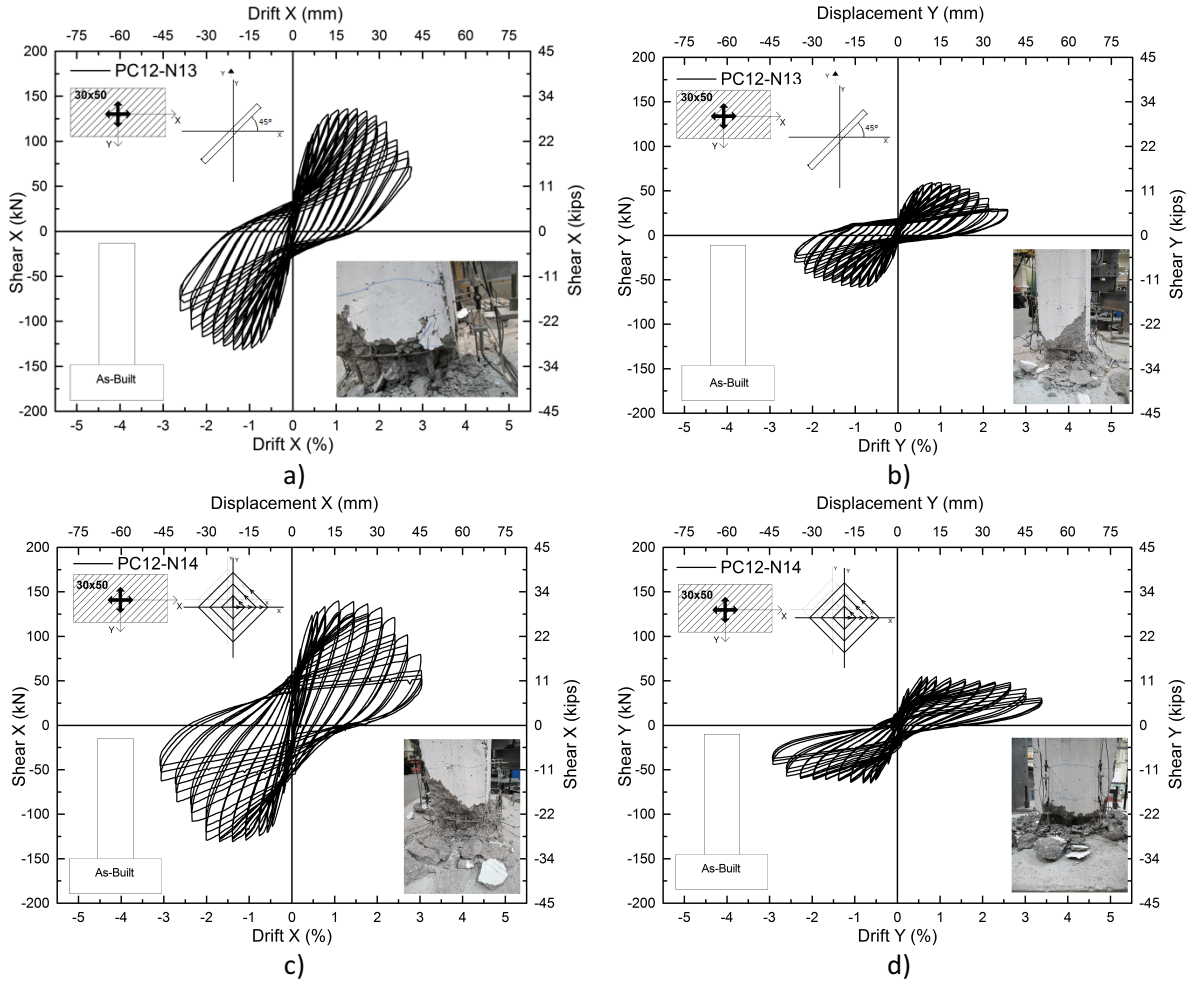
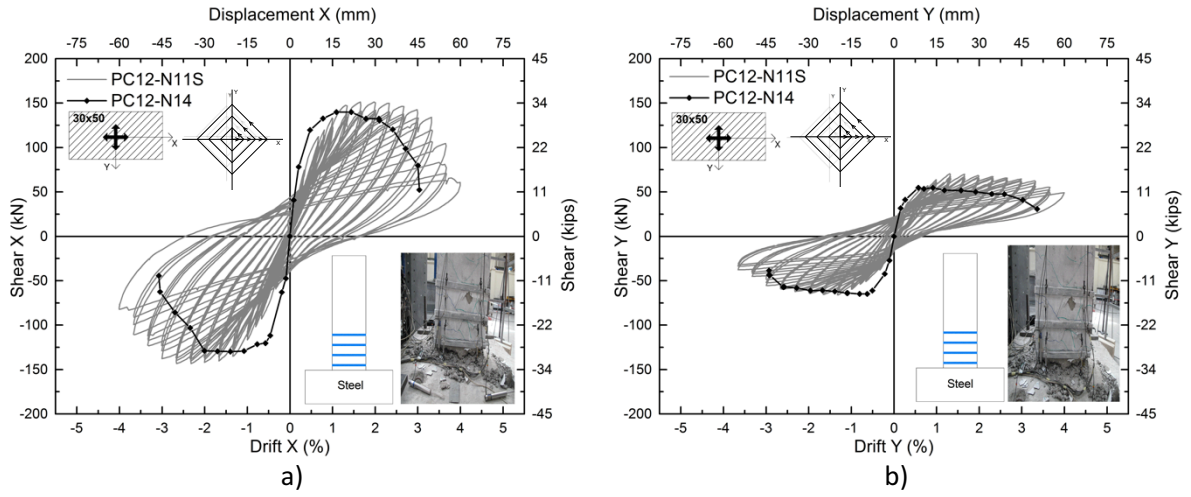


Figure 5: Shear-drift diagrams for "As built" columns under biaxial load path a) and b) PC12-N13 and c) and d) PC12-N14.



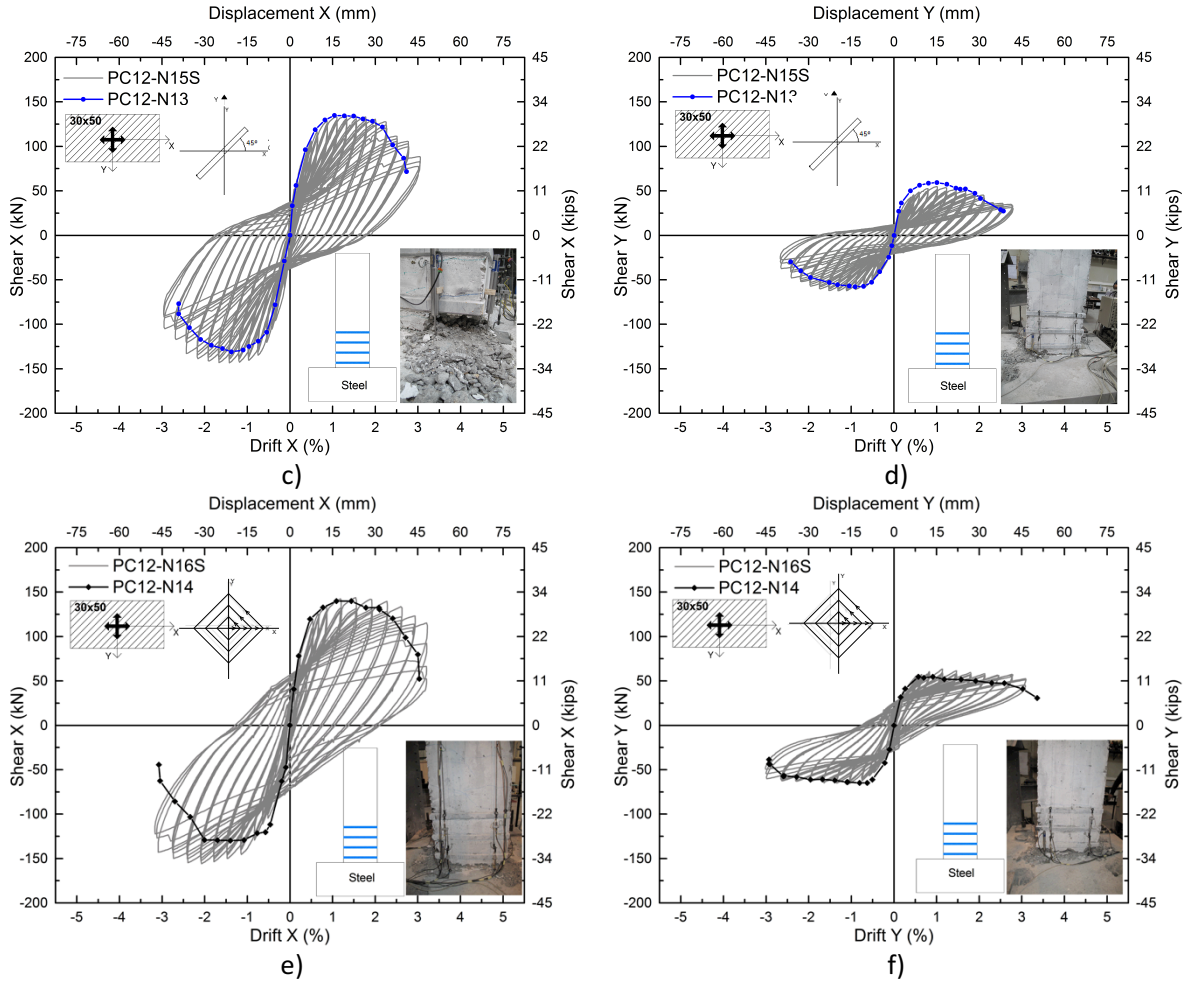
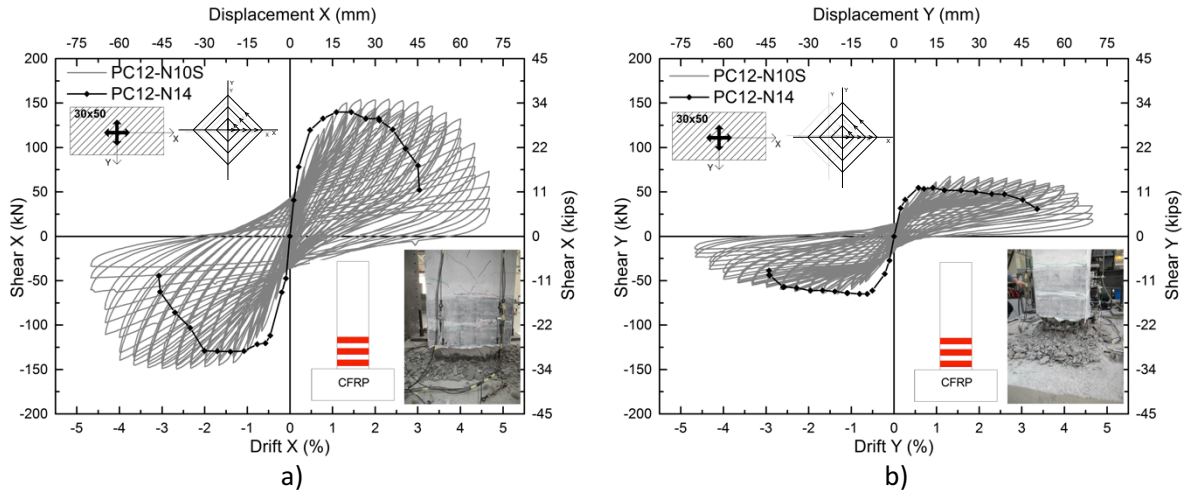


Figure 6: Shear-drift diagrams for strengthened columns with steel plates jacketing a) and b) PC12-N11S and c) and d) PC12-N15S and e) and f) PC12-N16.



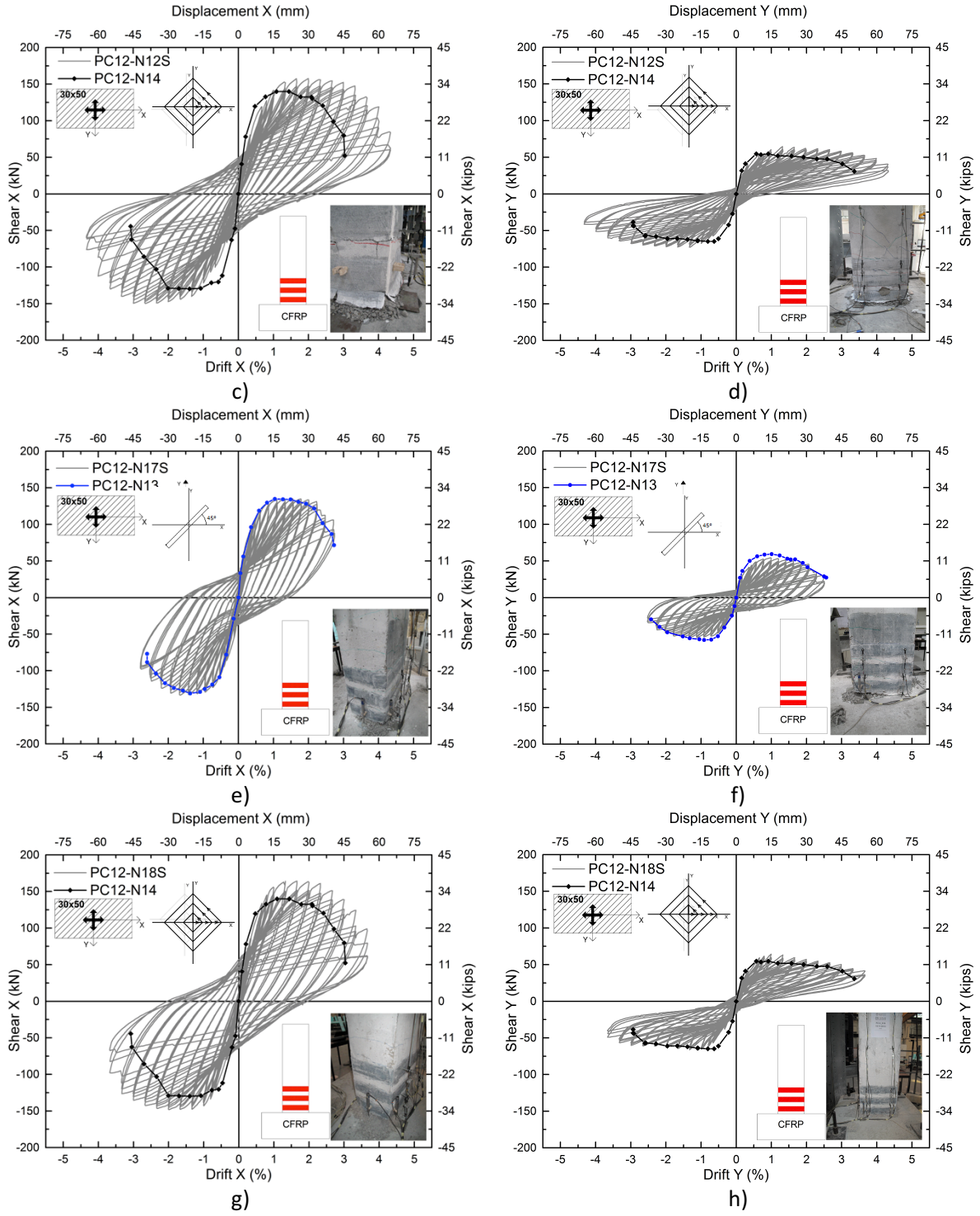


Figure 7: Shear-drift diagrams for strengthened columns with CFRP plates jacketing a) and b) PC12-N10S and c) and d) PC12-N12S and e) and f) PC12-N17S and g) and h) PC12-N18S.

CONCLUSIONS

An experimental campaign was carried out on 9 RC columns with: same geometries and reinforcement; subjected to similar biaxial horizontal displacement paths; and with equal constant

axial load. The study was focus on the influence of different strengthening strategies on the behavior of columns under certain load conditions.

In different strengthening strategies studied and in both directions the initial stiffness it is not significantly affected. However, the strengthened columns present higher maximum strength capacity of about 12% (in particular in columns under diamond biaxial horizontal load path). The strength degradation in the strengthened columns starts for higher levels of drift demand. This improvement that different strategies caused on strength degradation is clear and more significant for the diamond path.

The stiffness degradation is significantly reduced in the strengthened columns when compared with the original columns tested. Any of the proposed strengthening strategies leads to strong concentration of deformation and the concrete degradation at the critical section (base) of the specimens reducing significantly the plastic hinge length.

A large number of questions are still open concerning the influence strengthening technics and the influence of the biaxial behavior of RC columns. In the present work, an exploratory work is presented giving a preliminary step towards this goal. Even so, the research work reported is expected to contribute towards a better understanding of the biaxial response of RC columns and for the calibration of suitable numerical models for the response representation of reinforced concrete strengthened columns under biaxial lateral cyclic loading reversals.

ACKNOWLEDGMENTS

This paper reports research developed under financial support provided by “FCT - Fundação para a Ciência e Tecnologia”, Portugal, namely through the research project PTDC/ECM/102221/2008References

REFERENCES

[1] V. Bertero, "Lessons Learned from Recent Earthquakes and Research and Implications for Earthquake-Resistente Design of Building Structures in the United States," *Earthquake Spectra,* vol. 2, p. 34, 1986.

[2] X. Romão, A.A.Costa, E. Paupério, H. Rodrigues, R. Vicente, H. Varum*, et al.*, "Field observations and interpretation of the structural performance of constructions after the 11 May 2011 Lorca earthquake," *Engineering Failure Analysis,* vol. 34, pp. 670-692, 2013.

[3] H. Rodrigues, "Biaxial seismic behaviour of reinforced concrete columns," PhD Thesis, Departamento de Engenharia, University of Aveiro, Aveiro, 2012.

[4] H. Rodrigues, A. Arêde, H. Varum, and A. Costa, "Behaviour of RC building columns under cyclic loading: experimental study," *Journal of Earthquake and Tsunami, JET, World Scientific Publishing* vol. 6, 2012.

[5] H. Rodrigues, A. Arêde, H. Varum, and A. Costa, "Damage evolution in reinforced concrete columns subjected to biaxial loading " *Earthquake Engineering and Structural Vibration,* vol. 42, pp. 239-259, 2013.

[6] H. Rodrigues, A. Arêde, H. Varum, and A. G. Costa, "Experimental study on the biaxial bending cyclic behaviour of RC columns," presented at the 14th European Conference on Earthquake Engineering Ohrid, Republic of Macedonia, 2010.

[7] H. Rodrigues, A. Arêde, H. Varum, and A. G. Costa, "Experimental evaluation of rectangular reinforced concrete column behaviour under biaxial cyclic loading," *Earthquake Engineering Structural Dynamics,* 2012.

[8] H. Varum, "Seismic assessment, strengthening and repair of existing buildings," Departamento de Engenharia Civil, Universidade de Aveiro, Aveiro, 2003.

[9] M. Priestley, F. Seible, and M. Calvi, "Seismic design and retrofit of bridges," Wiley, New York, 1996.

[10] P. Rocha, "Reforço e reparação de pilares de edifícios de betão armado em zonas sísmicas," Departamento de Engenharia Civil da Faculdade de Engenharia Universidade do Porto, Porto, 2011.

[11] P. Rocha, P. Delgado, N. Pouca, A. Arêde, A. Costa, and R. Delgado, "Retrofit techniques for cyclic behavior improvement of rc columns," presented at the The 14th World Conference on Earthquake Engineering, Beijing, China, 2008.

[12] Y. Chai, M. Priestley, and F. Seible, "Seismic retrofit of circular bridge columns for enhanced flexural performance," *ACI Structural Journal,* vol. 88, pp. 572-584, 1991.

[13] G. Monti, N. Nisticó, and S. Santini, "Design of FRP jackets for upgrade of circular bridge piers," *J. Compos. Constr.,* vol. 5, pp. 94-101, 2001.

[14] M. D. Saiidi, M. Asce, and Z. Cheng, "Effectiveness of composites in earthquake damage repair of reinforced concrete flared columns," *Journal of Composites for Construction,* vol. 8, p. 306, 2004.

[15] H. Rodrigues, A. Arêde, H. Varum, and A. Costa, "Experimental evaluation of rectangular reinforced concrete column behaviour under biaxial cyclic loading," *Earthquake Engineering and Structural Dynamics,* vol. 43, pp. 239-259, 2013.

COMPDYN 2015
5th ECCOMAS Thematic Conference on
Computational Methods in Structural Dynamics and Earthquake Engineering
M. Papadrakakis, V. Papadopoulos, V. Plevris (eds.)
Crete Island, Greece, 25–27 May 2015

A MODEL FOR CARBON AND STAINLESS STEEL REINFORCING BARS INCLUDING INELASTIC BUCKLING FOR EVALUATION OF CAPACITY OF EXISTING STRUCTURES

Zhihao ZHOU[1], Davide LAVORATO[2], Camillo NUTI[3], and Giuseppe Carlo MARANO[4]

[1] Department of Architecture, Rome Tre University
10 Largo Giovanni Battista Marzi, Rome, Italy
e-mail: zhihaozhou0@gmail.com

[2] Department of Architecture, Rome Tre University
10 Largo Giovanni Battista Marzi, Rome, 00153, Italy
e-mail: davide.lavorato@uniroma3.it

[3] Department of Architecture, Rome Tre University
10 Largo Giovanni Battista Marzi, Rome, 00153, Italy
e-mail: camillo.nuti@uniroma3.it

[4] Department of Civil Engineering and Architecture, Technical University of Bari
4 Via Orabona, Bari, Italy
e-mail: giuseppecarlo.marano@poliba.it

Keywords: Steel model, inelastic buckling, modified Monti-Nuti Model, parameter identification, anisotropy.

Abstract. *Proper steel model for reinforcing bar incorporating inelastic buckling is essential for precise seismic analysis of reinforced concrete structures. Steel model without considering inelastic buckling will obviously overestimate the corresponding stress if the rebar is under cyclic loading and the inelastic buckling emerges in compressive loading. In this paper, a modified version of the Monti-Nuti steel model that includes the inelastic buckling for reinforcing bar is proposed. This modified model considers the effect of the yielding stress on the critical slenderness and the behavioral anisotropy in tension and compression of some type of stainless steel rebars. A parameter identification is carried out to calibrate the main parameters of the modified model. The identified parameters are robust. The effectiveness of the modified model is verified comparing the numerical stress-strain curves of carbon steel and stainless steel rebar with the experimental ones.*

1 INTRODUCTION

There are plenty of existing reinforced concrete (r.c.) structures built more than thirty years ago when the effects of the seismic actions on the r.c. structures were not sufficiently considered. The stirrup spacing in the column of those existing structures exceeds the maximum stirrup spacing limit in current seismic design codes. According to the investigations on damaged r.c. structures during the severe earthquake, the longitudinal rebars in the column showed lateral deformations due to the unsufficient confinement of the transversal rebar, and this phenomenon is called as inelastic buckling. In order to estimate the seismic performance of existing r.c. structures, proper steel rebar model is essential. All the models could be divided into three classes: the implicit algebraic model, the explicit algebraic model and the differential model, and among which the algebraic models are widely used in the numerical analysis with the Finite Element Method (FEM). In the implicit model, stress is the independent variable, and strain is the corresponding dependent variable. (i.e. Ramberg-Osgood [1]). On the contrary, in the explicit model, the strain is the independent variable and the stress is the corresponding dependent variable. Different explicit models were proposed to describe the behavior of the steel rebars. Menegotto and Pinto [2] built up a widely applied model to describe the cyclic stress-strain relationship. Filippou, Bertero and Popov [3] put forward one model including the isotropic hardening base on the Menegotto-Pinto Model. Monti and Nuti [4] proposed the first model which could consider the buckling of the reinforcement based on a series of experimental tests on carbon steel rebar. Gomes and Appleton [5] built up one model describing the monotonic compressive skeleton curve based on the equilibrium of plastic mechanism of a buckled rebar. Dhakal and Maekawa [6] suggested the monotonic skeleton curves of reinforcement in tension and compression respectively. Also they presented formulas to update the tangent modulus at the reversal points in tension and compression, respectively. Then the parameter b (hardening ratio) in the Menegetto-Pinto model is modified and the skeleton curves are applied to describe the stress-strain relationship when the strain exceeds the attained maximum or minimum strain of previous half cycles. The Gomes-Appleton model and Dhakal-Maekawa model have been adopted in OpenSees which was developed by Kunnath [7]. Zong [8] proposed the "beam on spring" model which considers the stiffness of the confinement from the transverse stirrups. In this paper, the modified Monti-Nuti model incorporating the inelastic buckling for steel rebar with or without anisotropy is proposed. Through comparing with the experimental stress-strain curves, the effectiveness of this model is validated.

2 ORIGINAL MONTI-NUTI MODEL FOR CARBON STEEL REBAR

Consisting of four hardening rules, named as kinematic rule, isotropic rule, memory rule and saturation rule, the Monti-Nuti steel model was based on a series of experimental observations. Different rebars specimens (old steel Italian type FeB44k) with yield stress of 450 MPa, diameter D=16, 20, 24 mm, were tested by monotonic tensile, monotonic compressive and cyclic tests applying different deformations histories.

It is shown that the slenderness ratio L/D (L is the length between two subsequent transversal rebars and D is the rebar diameter) determines the stress-strain relationship. When the slenderness ratio L/D=5, the monotonic compressive curve coincides with the monotonic tensile curve. While the monotonic compressive curve diverges from the tensile ones as soon as it reaches the yield point when the slenderness ratio value is L/D=11. When the slenderness ratio L/D varies between 5 and 11, the compressive curve coincides with the tensile one until a given deformation value and then the compressive curve diverges from the tensile one. The rules to update the model parameters are described below.

2.1 In absence of buckling

In absence of buckling, the yielding stress is updated by Eq. (1):

$$\sigma_y^{n+1} = \sigma_y^1 sign\left(-\xi_p^n\right) + P\Delta\sigma_K^n + \left(1-P\right)\Delta\sigma_{IM}^n \tag{1}$$

Where $\Delta\sigma_K^n$ is the Kinematic Rule, $\Delta\sigma_{IM}^n$ is the Isotropic Rule mixed with Memory Rule.

The branch after yielding could be defined by the hardening ratio *b*. Moreover, it is found that *b* varies according to the summation of plastic excursions of previous branches. *b* is defined by Eq. (2) named as Saturation Rule.

$$b^{n+1} = b_0 e^{b_0 E\sum\gamma/\left(\sigma_y-\sigma_\infty\right)} \tag{2}$$

2.2 In presence of buckling

In case of buckling of reinforcement, the yielding stress is updated by Eq. (3).

$$\sigma_y^{n+1} = \sigma_y^1 sign\left(-\xi_p^n\right) + P\Delta\sigma_{KM,b}^n + \left(1-P\right)\Delta\sigma_I^n \tag{3}$$

Where $\Delta\sigma_{KM,b}^n$ is the Kinematic Rule combined with Memory Rule, $\Delta\sigma_I^n$ is the Isotropic Rule.

Concerning the tensile branch, *b* is defined by Eq. (2), while *b* is defined by Eq. (4) in compressive branch, named as Saturation Rule.

$$b^- = \begin{cases} b_0^+ e^{b_0^+ E\sum\gamma/\left(\sigma_y-\sigma_\infty\right)}, & \sum\gamma \le \gamma_s \\ b_0^- e^{b_0^- E\sum\gamma\left(\sigma_y-\sigma_\infty\right)}, & \sum\gamma > \gamma_s \end{cases} \tag{4}$$

3 IMPROVEMENT OF ORIGINAL MONTI-NUTI MODEL

The original Monti-Nuti steel model is updated by the authors to consider the effects of the yield stress value on the critical slenderness ratio and the anisotropic behavior of some stainless steel types in tension and compression.

3.1 Effect of yielding stress on critical slenderness

According to the experiments on the carbon steel rebars with yield stress equal to 450 MPa, Monti and Nuti suggested that the critical slenderness ratio (the length between two subsequent transversal rebars divided by diameter of the reinforcing bar) is 5. Dhakal [6] demonstrated that both the yield strength and the slenderness have effect on the critical slenderness and proved that the combined parameter $\mathrm{L}/D\sqrt{f_y}$ determines the cyclic behaviors. Through a series of numerical experiments, it is illustrated that the rebars with different slenderness ratio L/D and different yield strengths could generate the identical cyclic stress-strain curves if the combined parameter $\mathrm{L}/D\sqrt{f_y}$ is equal. This conclusion is verified by Zong [8] who built three dimensional finite element model of individual reinforcing bar and verified that identical stress-strain curves could be obtained for the same value of the combined parameter $\sqrt{f_y/420}(\mathrm{L}/D)$ where 420 representing the average yield stress of commonly used steel rebar in structure and the unit is MPa.

Based on the experimental data of Monti and Nuti [4], the slenderness ratio of longitudinal rebar should be redefined as $\sqrt{f_y/450}(\mathrm{L}/D)$. If $\sqrt{f_y/450}(\mathrm{L}/D)$ exceeds 5, the buckling of longitu-

dinal rebar will emerge. It could be concluded that the greater the yield strength, the smaller the critical slenderness ratio L/D when the buckling turns up.

3.2 Anisotropy of rebar

For the stainless steel reinforcing bar produced according to earlier production specifications, the yield stresses in tension and in compression are different, and this phenomenon is named as anisotropy of stainless steel. Tests on the stainless steel rebar specimens AISI304 or 1.4301 [9] provided by Valbruna Italy, with slenderness ratio equaling 5 and 11, the monotonic tensile and compressive curves are shown in Fig. 1. It could be observed that the yield stress in tension is around 800 MPa, but the yield stress in compression is 700 MPa.

In order to improve the versatility of the model for reinforcing bar with different yield stresses in tension and in compression which is different from the original carbon steel rebar, three parameters were named as anisotropy coefficient α, critical slenderness coefficient β and yield stress strengthening coefficient γ, defined in Eq. (5).

$$\alpha = f_{yt} / f_{yc}\ ,\ \beta = f_{yc} / f_Y\ ,\ \gamma = f_{yt} / f_Y \tag{5}$$

where f_Y is the yield strength of the carbon steel rebar FeB44k tested by Monti and Nuti [4], f_{yt} is the yield strength of stainless steel rebar in tension, f_{yc} is the yield strength in compression.

For the stainless steel with different yield stresses in tension and in compression, the critical slenderness should depend on the yield stress in compression because the buckling of reinforcement emerges under compressive load. Thus, the combined parameter should be modified as $L/D\sqrt{f_{yc}}$, where f_{yc} is the yield stress of the reinforcement in compression.

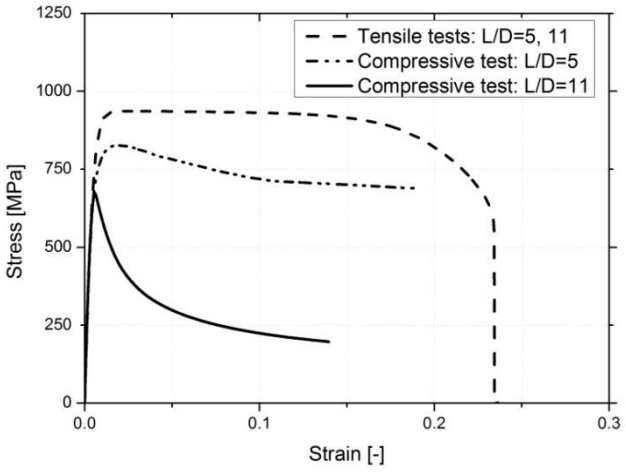


Fig. 1 Monotonic tests on stainless steel rebar

4 PARAMETER IDENTIFICATION

In order to do the parameter identification [10], the fitness function, as generally defined in Eq. (6), has the form:

$$f = \frac{\Delta Y}{Y} \tag{6}$$

Where ΔY represents the difference between the numerical curve and the experimental curve and is defined as: $\Delta Y = \sum_{i=1}^{n} y_{E,i}^2 - y_{N,i}^2$, and $y_{E,i}$ and $y_{N,i}$ are the stress on the experimental curve and numerical curve corresponding to the same x value; Y is the sum of the square of the experimental stresses, and is defined as: $Y = \sum_{i=1}^{n} y_{\mathrm{E},i}^2$.

If there are more than one experimental test, define the weight coefficient w_k to decide the contribution of each test, thus the fitness function could be defined as:

$$f = \sum_{k=1}^{\mathrm{m}} w_k f_k \tag{7}$$

$$f_k = \frac{\Delta Y_k}{Y_k} \tag{8}$$

4.1 Framework of parameter identification

The general flowchart of the parameter identification method is shown in Fig. 2. It summarizes the main steps of the method used in this study by means of a MATLAB script that is not described here.

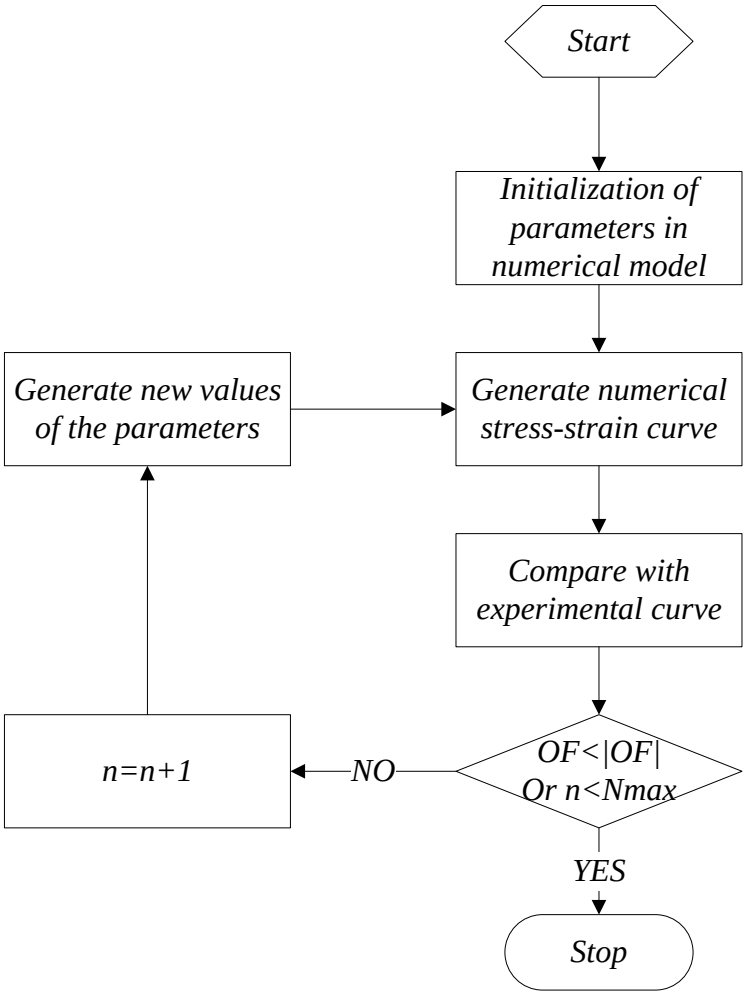


Fig. 2 General flowchart of parameter identification method

4.2 Proposed formulas to improve Monti-Nuti model

The anisotropy of the reinforcing bar results in different curve transitions in tension and in compression and then different parameters definitions to describe tensile and compressive curve branches. The parameters in the formula related to R were redefined in Eq. (9). The values of parameters R_0, A_1 and A_2 are defined by Eqs. (10-14), considering the effects of anisotropy and the yield value. The anisotropy is considered by three parameters: anisotropy coefficient α, critical slenderness coefficient β and yield stress strengthening coefficient γ.

The formula for R in the original model is modified:

$$R=\begin{cases} R_0-\dfrac{A_1^t\xi_{max}}{A_2^t+\xi_{max}}, & \textit{in tensile branch} \\ R_0-\dfrac{A_1^c\xi_{max}}{A_2^c+\xi_{max}}, & \textit{in compressive branch} \end{cases} \tag{9}$$

where R_0 is the initial value of R, defined in Eq. (10); A_1^t, A_2^t are the coefficients under tensile loading defined in Eq. (11) and A_1^c, A_2^c are the coefficients under compressive loading defined in Eq. (12), which are related to the mechanical properties of reinforcing bar; in presence of buckling R_1^b is the lower bound, thus $R \geq R_1^b$, is defined in Eq. (13).

$$R_0=\begin{cases} r_t R_0^1 \ \ (\textit{in tension}) \\ r_c R_0^1 \ \ (\textit{in compression}) \end{cases} \tag{10}$$

where r_t and r_c are the coefficients to calculate the initial value of R_0 for the tensile curve and compressive curve respectively.

$$A_1^t=\frac{1}{100}\left[\lambda_c\gamma^2\left(\lambda-\lambda_c\right)\right]+\alpha,\ A_2^t=-\frac{8\gamma}{10^4}\left(\lambda-4\lambda_c\right) \tag{11}$$

$$A_1^c=\alpha A_1^t,\ A_2^c=\frac{6\beta}{10^3}\left(\lambda-2\beta\right) \tag{12}$$

$$R_1^b=10\left[L/D-\lambda_C\right]b^+,\ \lambda_C=5/\sqrt{\beta} \tag{13}$$

$$r_t=\frac{\gamma}{2},\ r_c=\frac{r_t}{\alpha}=\frac{\gamma}{2\alpha} \tag{14}$$

4.3 Robustness of Parameter Identification Method

The bounds of the parameters and the identified values for the experimental tests are shown in table 1 and table 2.

	XA1	XA2	XA3	XA	Mean	Standard Deviation	Difference (%) Standard Deviation/ Mean
A_1^t	2.524	2.765	2.473	2.759	2.587	0.127	4.9
A_2^t	0.007	0.020	0.004	0.010	0.010	0.007	67.2
A_1^c	2.949	2.254	2.911	2.403	2.705	0.319	11.8
A_2^c	0.002	0.001	0.012	0.001	0.005	0.005	99.3

Note: XA means the optimized values for XA1, XA2 and XA3, with L/D=5.

Table 1: Results of parameter identification for different experimental tests on rebar with L/D=5

	XC1	XC2	XC3	XC	Mean	Standard Deviation	Difference (%) Standard Deviation/ Mean
A_1^t	2.584	2.858	2.985	2.842	2.809	0.167	6.0
A_2^t	0.004	0.003	0.002	0.002	0.003	0.001	27.2
A_1^c	2.509	2.004	2.688	2.429	2.400	0.290	12.1
A_2^c	0.004	0.002	0.009	0.002	0.005	0.003	58.9
Note: XC means the optimized values for XC1, XC2 and XC3, with L/D=11.							

Table 2: Results of parameter identification for different experimental tests on rebar with L/D=11

The robustness of the optimized could be observed from table 1 and table 2. A_1^t and A_1^c are sensitive to the numerical model, and the identified values of the parameters vary in a little range. But A_2^t and A_2^c are not sensitive to the model, thus the derivation of values have little effect on the numerical results. The column diagram of A_1^t and A_1^c is shown in Fig. 3, the variations of the parameter A_1^t and A_1^c for the stainless steel rebar with different slenderness in different loading cases are small.

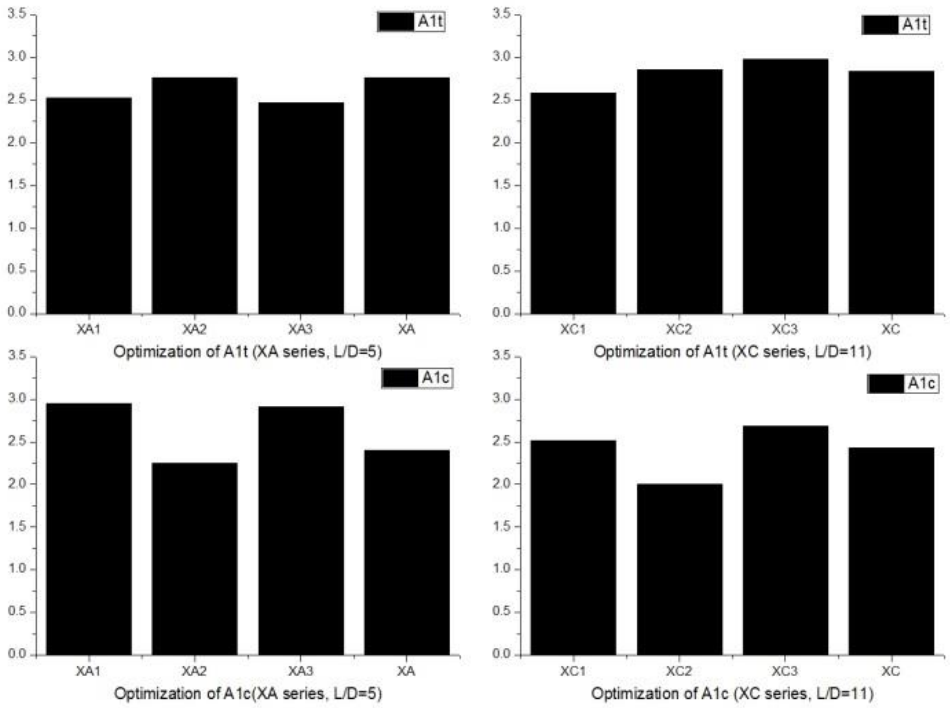


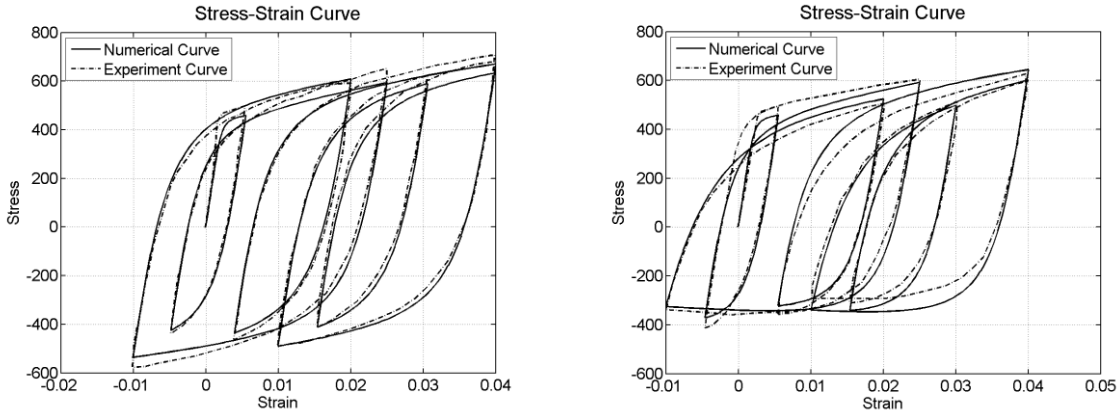
Fig. 3 Results of the optimization of the steel model parameters A1t and A1c for rebar with L/D=5 or rebar with L/D=11

5 VALIDATION OF THE MODIFIES MONTI-NUTI MODEL

The proposed modified Monti-Nuti model was calibrated and validated by comparisons with experimental tests on carbon steel rebars and stainless steel rebars.

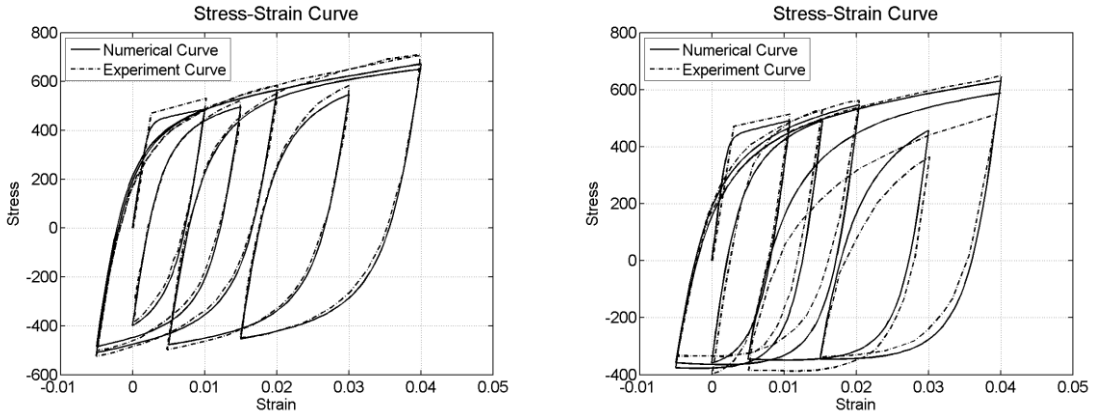
5.1 Steel Model for Carbon steel rebar

For the carbon steel rebar, the specimen steel type is FeB44k (old Italian steel type), with yield stress equaling 450 MPa, diameter 12mm, 16mm and 20mm. For loading cases A1, A2 and A3, the slenderness L/D=5, which means no buckling occurs during test; while C1, C2 and C3 with slenderness L/D=11, and the buckling emerges during test.



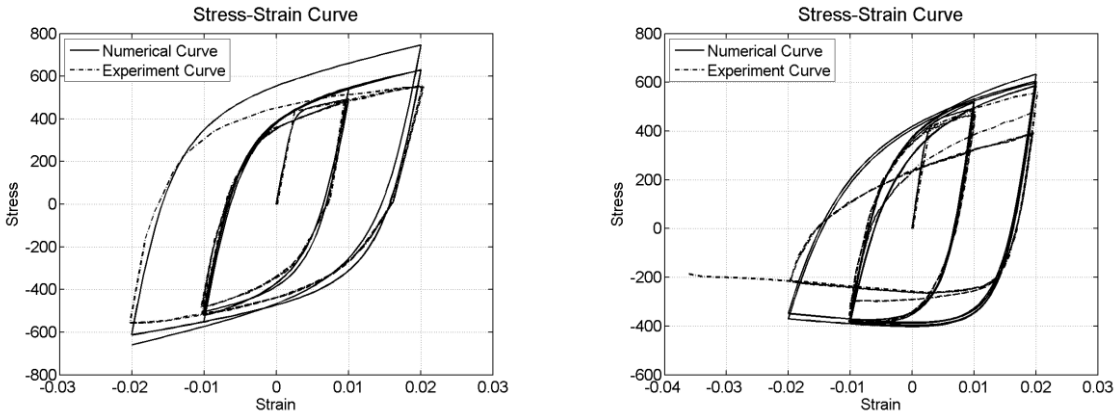
(a) in absence of buckling-A1 (L/D=5) (b) in presence of buckling-C1 (L/D=11)

Fig. 4 Comparison between numerical and experimental curves for carbon steel rebars with different slenderness and the same deformation history



(a) in absence of buckling-A2 (L/D=5) (b) in presence of buckling-C2 (L/D=11)

Fig. 5 Comparison between numerical and experimental curves for carbon steel rebars with different slenderness and the same deformation history



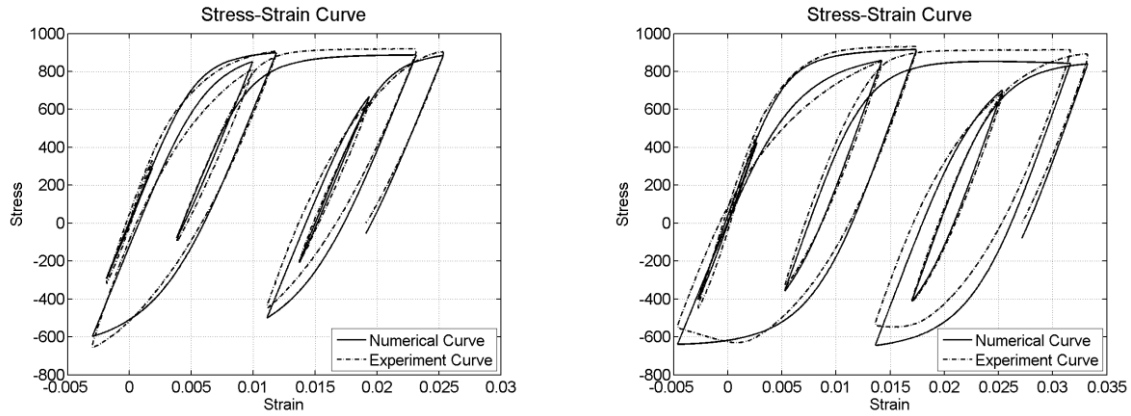
(a) in absence of buckling-A3 (L/D=5) (b) in presence of buckling-C3 (L/D=11)

Fig. 6 Comparison between numerical and experimental curves for carbon steel rebars with different slenderness and the same deformation history

From the above comparison in Figs.4, 5 and 6, it is shown that the numerical curves could coincide with the experimental curves very well. There are some disagreements if the absolute compressive strain exceeds 0.01. However, the real absolute compressive strain of the rebar in r.c. structures could not exceed 0.01 due to the confinement of concrete, thus this model is still capable to simulate well the cyclic behaviors of rebar.

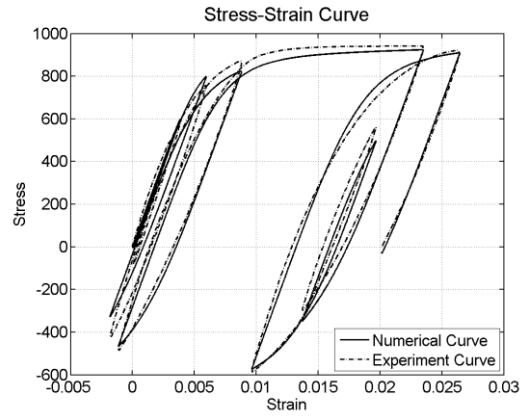
5.2 Steel Model for Stainless steel rebar

The specimen of the stainless steel rebar is AISI304 or 1.4301. The yield stress is equal to 780Mpa in tension while it is equal to 680 MPa in compression. As for the loading cases XA1, XA2 and XA3, the slenderness L/D=5, and the diameter D=12 mm; while for XC1, XC2 and XC3, the slenderness L/D=11, and the diameter D=12 mm.

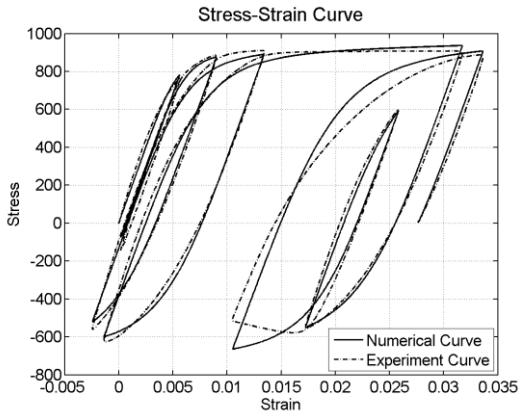


(a) in presence of buckling-XA1 (L/D=5) (b) in presence of buckling-XC1 (L/D=11)

Fig. 7 Comparison of numerical curves and experimental ones for stainless steel rebars with different slenderness

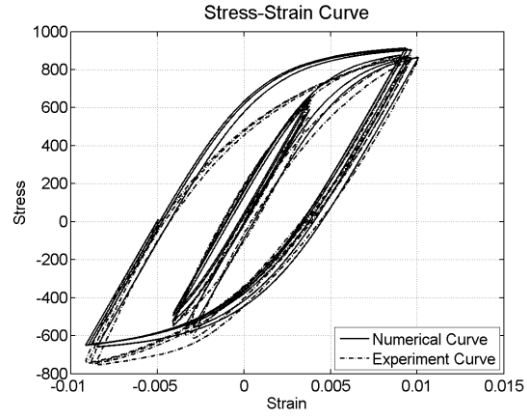


(a) in presence of buckling-XA2 (L/D=5)

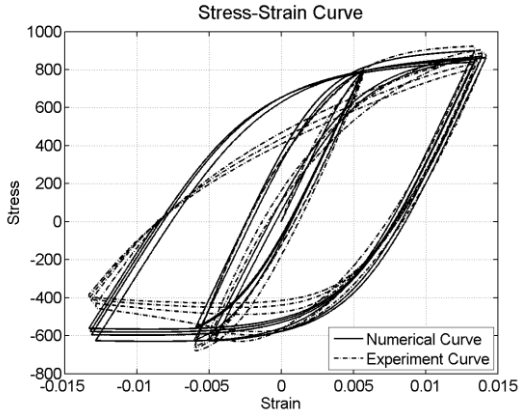


(b) in presence of buckling-XC2 (L/D=11)

Fig. 8 Comparison of numerical curves and experimental ones for stainless steel rebars with different slenderness



(a) in presence of buckling-XA3 (L/D=5)



(b) in presence of buckling-XC3 (L/D=11)

Fig. 9 Comparison of numerical curves and experimental ones for stainless steel rebars with different slenderness

From the comparisons in Figs. 7, 8 and 9, the effectiveness of the modified model could be verified.

6 CONCLUSIONS

This paper proposes a modified Monti-Nuti cyclic model including the inelastic buckling for the reinforcing bar. The inelastic buckling of the steel rebars has important effects on the seismic behavior of the existing r.c. structures with poor seismic details and drop of resistance and ductility are observed. Following conclusions are obtained:

- The inelastic buckling occurs when rebar slenderness is greater than the critical one. It is important to define the correct value of the critical slenderness. The yield strength has effects on the critical slenderness value. The proposed modified version of the steel model simulates properly the inelastic buckling including a correct estimation of the critical slenderness considering also the yield strength of the rebar.
- Some stainless steel rebar types show an anisotropic behavior in tension and compression (i.e. different yielding strength). This behavior is described well in the proposed modified

version of the steel model including different parameters for tension and compression model branches description in case of cyclic deformation history.

- The parameter identification method is adopted in this paper to identify properly the main parameters of the steel model equations for a better description of the cyclic behavior of the steel on the base of different experimental curves.
- Through comparing with the experimental stress-strain curves of carbon steel rebars and stainless steel rebars, the effectiveness of the modified Monti-Nuti is verified.

ACKNOWLEDGEMENTS

The authors thank Acciaierie Valbruna and SISMIC who provided stainless steel reinforcement for the present study. This research is partially funded by the CSC (China Scholarship Council) and by Italian Civil Protection Department RELUIS Project 2010-2013 AT-1 TASK 1.1.2 and RELUIS Project 2014 Reinforced concrete TASK 4.1. local reinforcement intervention.

REFERENCES

[1] Ramberg, W., and Osgood, W.R. (1943). Description of stress-strain curves by three parameters.

[2] MENEGOTTO, M. (1973). Method of analysis for cyclically loaded RC plane frames including changes in geometry and non-elastic behavior of elements under combined normal force and bending. Paper presented at: Proc of IABSE Symposium on Resistance and Ultimate Deformability of Structures Acted on by Well Defined Repeated Loads.

[3] Filippou, F.C., Popov, E.P., and Bertero, V.V. (1983). Effects of bond deterioration on hysteretic behavior of reinforced concrete joints.

[4] Monti, G., and Nuti, C. (1992). Nonlinear cyclic behavior of reinforcing bars including buckling. Journal of Structural Engineering 118, 3268-3284.

[5] Gomes, A., and Appleton, J. (1997). Nonlinear cyclic stress-strain relationship of reinforcing bars including buckling. Engineering Structures 19, 822-826.

[6] Dhakal, R.P., and Maekawa, K. (2002). Modeling for post yield buckling of reinforcement. Journal of Structural Engineering 128, 1139-1147.

[7] Kunnath, S., Heo, Y., and Mohle, J. (2009). Nonlinear Uniaxial Material Model for Reinforcing Steel Bars. Journal of Structural Engineering 135, 335-343.

[8] Zong, Z. (2010). Uniaxial material model incorporating buckling for reinforcing bars in concrete structures subjected to seismic loads, Vol 71.

[9] Albanesi, T., Lavorato, D., and Nuti, C. (2006). Prove sperimentali monotone e cicliche su barre di acciaio inox. Sperimentazione su materiali e strutture, Convegno nazionale, 357-366.

[10] Marano G.C., Quaranta G., Monti G. (2009). "Genetic Algorithms in Mechanical Systems Identification: State-of-the-art Review", in Soft Computing in Civil and Structural Engineering (Chapter 2), B.H.V. Topping and Y. Tsompanakis, Eds., Stirlingshire (Scotland): Saxe-Coburg Publications.

COMPDYN 2015
5th ECCOMAS Thematic Conference on
Computational Methods in Structural Dynamics and Earthquake Engineering
M. Papadrakakis, V. Papadopoulos, V. Plevris (eds.)
Crete Island, Greece, 25–27 May 2015

USING DIFFERENT UNCERTAINTY MODELS FOR SEISMIC ASSESSMENT OF RC BRIDGES

R. Monteiro[1,2], R. Delgado[2], and R. Pinho[3]

[1] Institute for Advanced Study of Pavia
Palazzo del Broletto, Piazza della Vittoria n. 15, 27100 Pavia (Italy)
e-mail: ricardo.monteiro@iusspavia.it

[2] Faculty of Engineering, University of Porto
Rua Dr. Roberto Frias, s/n Porto (Portugal)
e-mail: rdelgado@fe.up.pt mailto:rui.pinho@unipv.it

[3] University of Pavia, Department of Civil Engineering and Architecture
Via Ferrata n. 1, 27100 Pavia (Italy)
e-mail: rui.pinho@unipv.it

Keywords: Seismic Assessment, RC Bridges, Failure Probability, Latin Hypercube Sampling, Uncertainty Models, Nonlinear Demand Prediction

Abstract. *The seismic assessment of structures depends on a large number of aleatory and epistemic uncertainties, which are majorly associated to the estimation of the structural demand and capacity, both usually featuring considerable dispersion levels, particularly when reinforced concrete structures are being assessed. When focusing on bridges, additional complexity may be introduced by the irregular behaviour in the transverse direction. Several procedures may be used for the assessment of the seismic safety of bridges, deterministic or probabilistic, and all rely on an accurate prediction of the demand, obtained via linear or nonlinear static or dynamic analysis. This work employs both static and dynamic analysis methods for demand estimation within a relatively straightforward framework to compute the failure probability of existing bridges. Different variables typically considered in a seismic assessment procedure (geometry, material properties, earthquake records, intensity level) are statistically characterized, catering for a global simulation process, where each iteration step is associated to an independent structural nonlinear static or dynamic analysis. Failure probability is then obtained through different uncertainty models, corresponding to the convolution of capacity and demand distributions or the probabilistic analysis of a safety indicator, defined as the difference between capacity and demand at each random simulation realisation. A case study of seven bridge configurations, with different (ir)regularity levels, is considered together with a relatively large set of real earthquake records. The simulation process is carried out using Latin Hypercube sampling, expected to considerably reduce the number of realizations with no reliability loss. Conclusions have allowed the identification of vulnerable configurations and shown the differences in considering different uncertainty models.*

1 INTRODUCTION

A typical seismic safety assessment procedure involves a set of relevant elements that need to be properly defined, until the seismic safety itself is assessed. Such ultimate step may, similarly to all the other safety problem components, feature different approaching scenarios, even though it will essentially consist in the comparison of the demand, estimated based on a properly selected seismic ground motion input, with the capacity of the structural elements to accommodate it, characterised according to the geometry, material properties, nonlinear behaviour models, among others. Even though the deterministic approaches are most likely the ones that practitioners are most familiarised with, given that it certainly goes along with the traditional design practice or structural safety verifications, the research trend of the past decades is mostly addressing the employment of probabilistic approaches, which tend to gain weight, as rationally more consistent, e.g. [1-3]. However, the employment of probabilistic procedures for seismic assessment by practitioners is far from being straightforward, which gives room to the proposal of relatively simple methodologies that do not require deep mathematical formulations but still provide accurate results. Even if simple, any probabilistic procedure requires a substantial amount of statistical information, in comparison with the deterministic ones, to characterise the uncertainty in the structural safety problem. Such information includes the probabilistic characterisation of seismic hazard, as well as the capacity and structural demand.

For what concerns the seismic demand prediction, even if obviously depending on the structural characteristics and on the seismic hazard itself, the main differences tend to be associated to the nature of the employed analysis approach, either static or dynamic, each comprising different concepts and procedures. It is commonly recognised that nonlinear dynamic analysis (NDA), which reproduces directly the real phenomenon, will produce more accurate results. Nevertheless, several drawbacks may be pointed out when considering dynamic analysis, particularly related to the employment of ground motion records, to the structural modelling (including the reproduction of damping phenomena, the post-elastic behaviour and corresponding energy dissipation, during loading and unloading periods), amongst others. In addition, attention must also be paid to computational onus, which is well known to be significant in dynamic analysis. The commonly employed alternative to NDA is nonlinear static analysis, based on pushover analysis, which typically has the goal of somewhat enveloping all, or at least a considerable part, of the possible dynamic analysis results at each intensity level. This kind of outcome is accomplished through the application of an increasing lateral force or displacement vector to the structure. Even if inherently limited with respect to its dynamic counterpart, nonlinear static analysis constitutes nonetheless a very valuable tool within the framework of performance-based seismic assessment of structures, since it readily provides important insight into the main characteristics of the response of the latter when subjected to horizontal excitation. Consequently, in the last decade or so considerable effort has been placed in the development of credible, yet relatively simple, pushover-based methodologies, an effort that lead to the introduction of the so-called Nonlinear Static Procedures (NSP) in a number of guideline documents, such as ATC-40 [4, 5] and FEMA-273 [6], or design codes, such as Eurocode 8 [7, 8]. The main drawback of the pushover-based approaches is noticeably the level of simplification, given that one assumes that the structural behaviour obtained from horizontal pseudo-static loading is somehow equivalent to its dynamic counterpart. Although these have focused mainly on the application to seismic assessment of buildings, rather than bridges, recent studies, listed in the subsequent Section, have been made to explicitly verify the application of NSPs to individual and populations of bridge structures. However, these studies have been directed mainly at the direct validation of the nonlinear static procedures in

predicting the seismic demand and hence there is still a need for assessing the performance of such procedures within the scope of probabilistic safety assessment.

In light of the above, this paper presents two different methodologies for the seismic safety assessment of structures, applied to bridges, which foresee the computation of the failure probability, through a relatively straightforward process, which can be used in current practice for seismic design or assessment purposes, without significant onus. In order to accomplish so, as well as to duly incorporate the uncertainty associated to all the considered variables of the safety problem, both capacity and demand are statistically characterised by means of assumed and/or adjusted distributions. Such statistical definition is carried out by obtaining, when necessary, random samples making use of the Latin Hypercube sampling (LHS) technique. Roughly, the safety assessment of a single structural system could be carried out through the statistical characterisation of a safety indictor, given by multiple, aleatory deterministic differences between the capacity and the demand, or a failure probability obtained from the independent statistical characterisation of the variables that are part of the process. Therefore, essentially, the difference between the two proposed methodologies lies on the way of dealing with the uncertainty of the different variables, which yield distinct failure probabilities. The distinction is established between accounting for uncertainty locally or globally. Both approaches are tested for a case study of seven bridge configurations, featuring different deck lengths and regularity levels. A companion paper addresses the relative accuracy of different nonlinear analyses (static and dynamic) in estimating the seismic demand within probabilistic framework, such as the ones herein proposed. This study also addresses the performance of a commonly employed nonlinear static procedure, within such probabilistic framework, with respect to the nonlinear dynamic counterpart, including the use of different versions of the static analysis, corresponding to different types of pushover load distributions. The parametric comparison of the static and dynamic approaches is then carried out.

2 SAFETY ASSESSMENT

The safety assessment herein carried out for RC bridges consists essentially of the probabilistic *comparison* between the demand, properly characterized through the probability density function of the structural effects, with the structural capacity, statistically defined in terms of parameters such as the geometry of the sections, properties and models of nonlinear behaviour of materials, among others. The statistical models of demand and capacity are then combined to obtain the failure probability according to two different models – local and global uncertainty – described ahead.

2.1 Nonlinear Static Demand

Nonlinear Static Procedures (NSP) are nowadays extensively spread within the earthquake engineering community to rapidly estimate the nonlinear demand, mainly due to its simplicity and potentially easy application when assessing a large number of structures. Although these methods were initially thought having the application to buildings in mind, some very recent endeavours have dealt with the application to bridges of this kind of procedures (e.g. [9-13]). These methods are essentially based on the computation of the pushover curve, a representation of the nonlinear force-deformation behaviour of the structure and with the use of appropriate transformation relationships, the capacity curve of the single-degree-of-freedom (SDOF) system equivalent to the original multi-degree-of-freedom (MDOF) structure may be obtained. At this point the main differences between the proposed methods arise, such as the contemplation or not and choice for a reference node, the way of reducing the demand spectrum so as to

account for the hysteretic energy dissipation, the consideration of higher modes of vibration, on the way to determine the displacement demand for a given ground motion.

There are many available procedures to carry out nonlinear static analysis, ranging from truly simplified methods, based on coefficients, to others, more complex, including nonlinear and modal effects. A first group of proposed NSPs corresponds to the earliest attempts to propose a static method that would quickly lead to accurate results and includes the pioneering Capacity Spectrum Method (CSM), introduced by Freeman [14] and implemented in ATC-40 guidelines, and N2 method [15] included in the recommended simplified procedures of the European Design Code [8]. Recently, an improved version of the CSM has been presented in FEMA-440 guidelines [5], mainly consisting of the update of the prescribed empirical relations to determine both the equivalent viscous damping and spectral reduction factor. Later, the Displacement Coefficient Method [6] has been proposed within the NEHRP Guidelines for the Seismic Rehabilitation of Buildings. An additional group of procedures includes more recent approaches to nonlinear static analysis, such as the Modal Pushover Analysis (MPA) [16, 17], the Adaptive Modal combination Procedure (AMCP), by Kalkan and Kunnath [18] and later adapted to bridges by Shakeri et al. [19], or the Adaptive Capacity Spectrum Method (ACSM), developed by Casarotti and Pinho [20] and optimized by Monteiro et al. [21] also for building frames. All of them come up with improvements, mainly the inclusion of higher modes contribution or, as in the ACSM, an alternative way of addressing the reference node issue.

Recent studies [11, 22] have addressed the validation of different NSPs in estimating the seismic response of single or populations of bridges and the conclusions tend to point out to N2 and ACSM or modified MPA as the most accurate nonlinear static procedures. Moreover, the increased accurateness when using improved methods (ACSM, MPA) did not seem particularly advantageous when compared to the employment of N2, numerically less onerous. Similar findings were observed for RC building frames in a study by Pinho et al. [23]. Based on such, the N2 method was selected herein to test the use of nonlinear static analysis in the probabilistic seismic safety assessment of bridges. In addition, adaptive pushover analysis, which does not require the definition of a reference node, was included in the comparison.

2.2 N2 Method

The N2 method was proposed by Fajfar and Fischinger [15], and features the use of pushover analysis of a MDOF model combined with the inelastic response spectrum analysis of its equivalent SDOF system. Its implementation in the bridges chapter of Eurocode 8 foresees the computation of at least two pushover curves; one derived with a loading vector shape factor that is uniform along the deck and another where the first mode proportional shape is used instead. Two different loading possibilities have been considered in the application of the N2 method: uniform load distribution and first mode load distribution. Because of the method's reference node dependency, each of these modalities was carried out considering the reference node as both the deck's centre of mass or the maximum modal displacement.

2.3 Latin Hypercube sampling

Safety assessment based on reliability calculations will involve repetitive simulation of several variables representing structural modelling parameters, which may become, for complex finite element models, quite time-consuming and demanding in terms of computational onus. In order to overcome such drawback, advanced simulation techniques have been proposed on the basis of relatively simple integrated modifications in the existing general procedures. The Latin Hypercube sampling (LHS) simulation scheme [24, 25] is one of such

examples and can be seen as a particular case of the standard Monte Carlo (SMC) numerical simulation, requiring a smaller number of runs, tens to hundreds, to achieve an accurate random distribution. Such key features are accomplished by means of the stratification of the theoretical probability distribution function of input random variables. The method is not restricted to the estimation of statistical parameters of structural response but offers a quite broad usage domain that goes from sensitivity analysis to Bayesian updating, among other possibilities. The use of LHS as a valid sampling technique and is becoming widely employed in structural analysis of bridges [26-30].

2.4 Failure probability

The probabilistic methodologies considered herein are described in detail in a study by Monteiro et al. [31, 32] whereas a brief summary is provided next.

2.4.1. Local uncertainty model

This is considered the traditional approach, originally developed and applied in the work by Costa [33], which is focused on the definition of the probability density function of the seismic demand, which will be convolved with the capacity one. In order to do so, there is the need for a relationship between an intensity measure (herein considered as the peak ground acceleration) and a proper engineering demand parameter, measured from nonlinear static or dynamic analysis of the structure for that specific ground motion level. That relation is herein named vulnerability function and is essentially a mapping function, establishing the correlation between the seismic intensity, its probability and the actual structural demand, to be "compared" with the capacity to obtain the final collapse probability. For a predefined number of intensity levels, corresponding to different return periods and probabilities of occurrence, different real ground motion records or corresponding response spectra, scaled to match the corresponding PGA, are considered. Nonlinear static or dynamic analysis is carried out using each of the scaled accelerograms or spectra, yielding a sample of the seismic demand that accounts for record-to-record variability. For each ground motion intensity, and corresponding PGA, a statistical value, defined by the mean (or median) response measure, is computed and a polynomial function is adjusted to those points, to define the aforementioned vulnerability function, curve 3 in Figure 1 (*left*). Once the vulnerability function is defined, the statistical distribution of the seismic demand can be easily obtained through a numerical procedure based on equal areas under the probability density function, i.e. probability of occurrence, along with the changing of the variable from intensity measure to the selected engineering demand parameter. The entire procedure corresponding to the traditional approach is schematically depicted in Figure 1 (*left*). The seismic intensity is characterised by its probability density function, the curve 1. Analogously, for every intensity measure level for which curve 1 is defined, the seismic demand is obtained, in terms of a chosen parameter (for instance, ductility). The so-called vulnerability function, curve 3, is therefore defined, representing the structural demand with increasing intensity. The latter function is fundamental to 'intersect' with the seismic action probability density function and define the statistical distribution of the seismic demand, curve 4. In other words, by putting together the probability density associated to an intensity measure level with the corresponding structural demand, one can obtain the probability density of such demand to be verified.

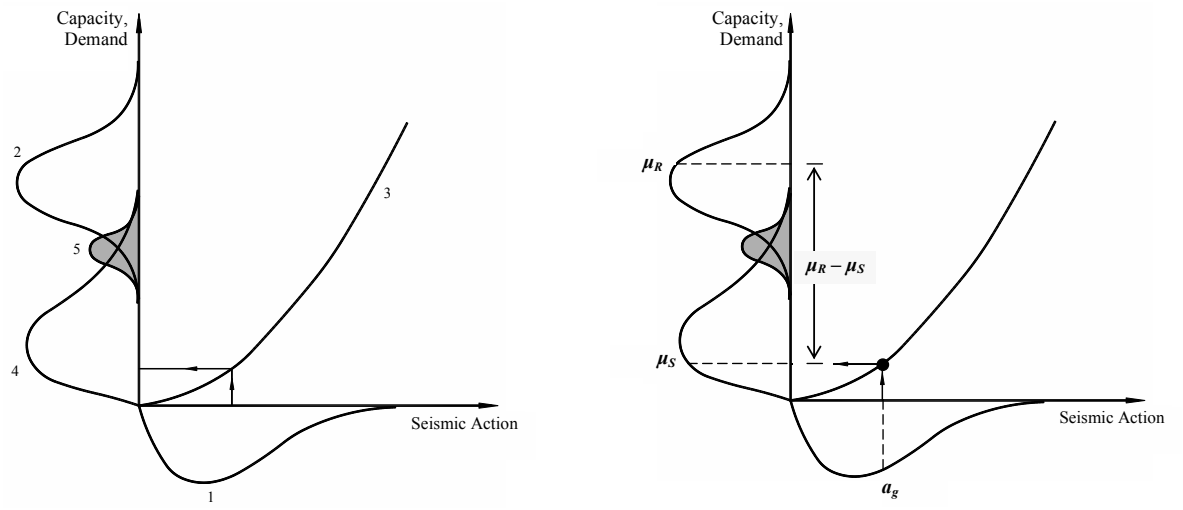


Figure 1: Failure probability computation with: (*left*) local uncertainty, (*right*) global uncertainty.

At the same time, the distribution of the capacity, curve 2, in terms of the engineering demand parameter used to define curves 3 and 4 (curvature ductility) needs to be defined. This step is typically carried out using random simulation procedures (herein Latin Hypercube sampling [24, 25, 34, 35] was adopted), based on the statistical distributions of the variables with a relevant role, usually cross section material properties. Finally, the convolution of capacity with the demand yields the intended failure probability.

2.4.2. Global uncertainty model

An alternative approach to the local uncertainty based failure probability computation consists in considering the uncertainty associated to the different variables in a global manner, i.e. simultaneously rather than independently, within a global procedure carried out fully at each iteration step. It is recalled that in the procedure previously described the uncertainty has been taken into account independently, i.e. each relevant variable of the problem identified in Figure 1 (*left*) was defined by a statistical distribution, based on independent sets of random sampling. On the other hand, the approach herein presented uses the statistical distributions of the different variables differently, as illustrated in Figure 1 (*right*). First, the distributions are defined, characterising each input variable (e.g. material properties), the seismic hazard and the capacity. Once that initial step is completed, the assessment procedure is carried out completely, but individually, making use of those distributions. Using a global random simulation technique, the Latin Hypercube, each variable with known uncertainty, seismic intensity level, type of record and material properties, is randomly simulated; a nonlinear dynamic analysis is carried out on the bridge modelled with such parameters; the structural demand and capacity are determined; and the difference between those two figures, usually referring to ductility or displacement, is calculated. A statistical distribution is then adjusted to the variable given by such difference, which will enable the computation of the failure probability as the ordinate of the corresponding cumulative density function for the null abscissa. The difference (μ_R - μ_S), eventually non-positive, will represent the non-failure interval. The concept behind this procedure is that the entire process, up to the definition of such interval, can be repeated N times in order to fit a statistical distribution to that variable and the knowledge of such distribution will enable the calculation of the failure probability as the area under the corresponding probability density function, $f_{R\text{-}S}$, for (μ_R - μ_S) < 0. The global uncertainty model for the calculation of the failure probability has not been employed with nonlinear static analysis, for the sake of

computational onus. However, given that it has yielded conservative results with respect to the local uncertainty model, it has been include in this comparison study for completeness.

3 CASE STUDY

The comparison of the use of different approaches for seismic demand estimate, within different safety assessment uncertainty models has been carried out using the a set of seven bridge configurations, corresponding to two bridge lengths (viaducts with four and eight 50 m spans), with regular, irregular and semi-regular layout of the piers' height and continuous deck-abutment connections supported on piles, with bilinear behaviour. The bridges are depicted, in Figure 2, where the label numbers 1, 2 and 3 stand for pier heights of 7, 14 and 21 metres, respectively.

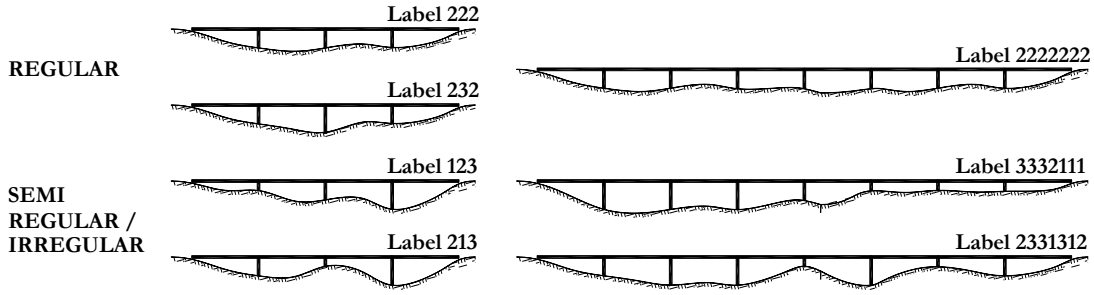


Figure 2: Case study bridge configurations.

The employed set of seismic excitations is defined by an ensemble of ten records selected from a suite of historical earthquakes [36] scaled to match the 10% exceeding probability in 50 years (475 years return period) uniform hazard spectrum for Los Angeles, which corresponds, in the current endeavour, to the intensity level 1.0. Figure 3 illustrates the pseudo-acceleration and displacement spectra for the selected earthquake records, with damping ratio of 5%, together with the median spectrum. The ground motions were obtained from California earthquakes with a magnitude range of 6-7.3 recorded on firm ground at distances of 13-30 km; their significant duration [37] ranges from 5 to 25 seconds, whilst the PGA (for intensity level 1.0) varies from 0.23 to 0.99g.

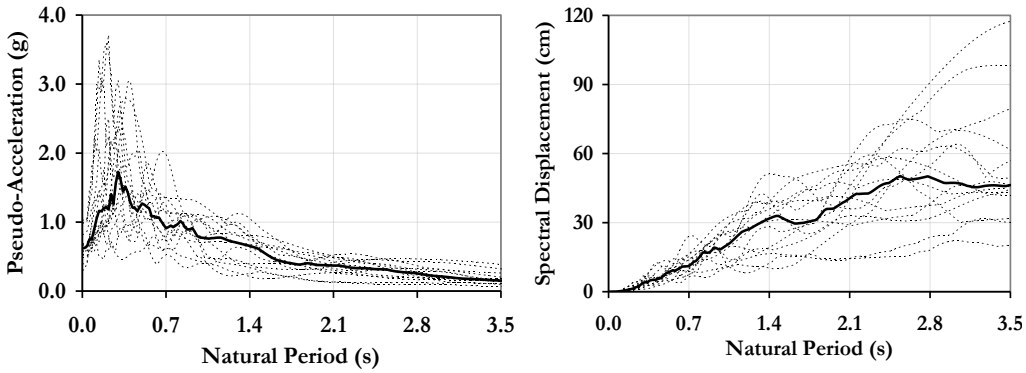


Figure 3: Elastic pseudo-acceleration and displacement spectra.

4 SAFETY ASSESSMENT – COMPARATIVE STUDY

Two different procedures for the failure probability computation have thus been considered (traditional numerical safety assessment with local uncertainty and numerical safety assess-

ment based on global uncertainty simulation with Latin Hypercube sampling) together with nonlinear static or dynamic analysis for the estimate of the seismic demand. The suitability of the nonlinear static predictions has been scrutinised by direct comparison with the failure probability obtained with nonlinear dynamic analysis (NDA).

4.1 Nonlinear dynamic based failure probability – local uncertainty model

The collapse probability for the several bridge configurations, obtained with nonlinear dynamic analysis and applying the local uncertainty model is summarised in Figure 4. For the sake of simplicity and interpretation of the results in the same plot, only the failure probability of the critical pier of each bridge is presented. The results have been sorted by increasing failure probability with drift limitation. The capacity has been defined as drift-limited or not, which can result in important changes on the available ductility and consequent safety evaluation. When drift limitation was considered, a threshold of 5% drift was preliminarily assumed for the piers, after which it is considered, particularly for the 21m piers, that the top displacement is too high to ensure the stability of the deck.

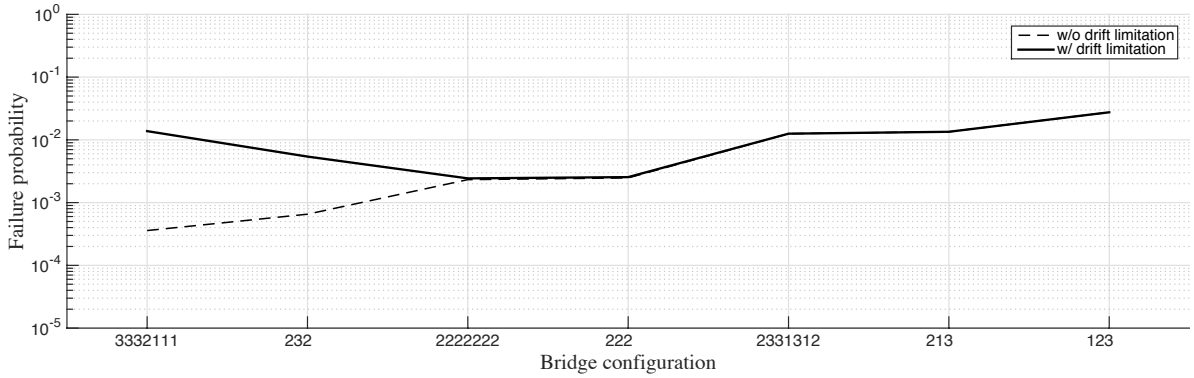


Figure 4: Failure probability per bridge configuration – local uncertainty approach.

Globally, there is agreement between considering the top deformation of the piers limitation or not, given that the trend of results is similar. The exception occurs when a type 3 pier becomes the most vulnerable, such as in configurations 232 and 3332111. Moreover, the distinction between regular/semi-regular and irregular configurations is immediate from Figure 4, the latter being more vulnerable of about one order of magnitude, all in the right side of the plot. The record-to-record variability of the seismic input plays a very important part and the failure probability, traditionally computed using mean ductility demand, will indeed vary considerably. The magnitude of the effect caused by such variability will depend on the bridge configuration or the pier characteristics.

4.2 Nonlinear dynamic based failure probability – global uncertainty model

The collapse probability obtained with nonlinear dynamic analysis and applying the global uncertainty model is summarised in Figure 5. Similarly to the safety assessment procedure using a local uncertainty model, which considers the variability of each component separately, there is a fair match of the collapse probability across the different configurations, whether drift limitation takes place or not.

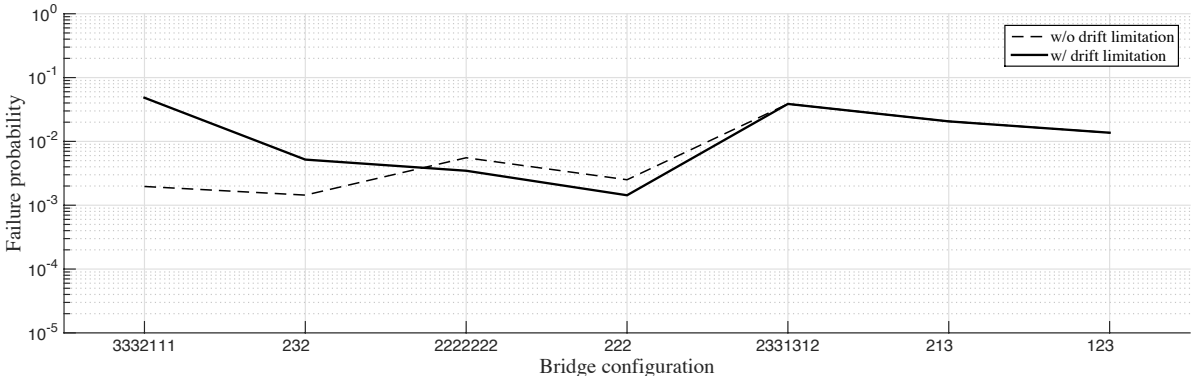


Figure 5: Failure probability according to bridge configuration – global uncertainty approach.

Major differences occur for the configurations where the critical pier is a type 3 one, 21 meters high, the one that is most affected by the capacity reduction. Again the distinction between regular and irregular bridges is very noticeable (the former are safer) together with the trend for the short configurations to be also less vulnerable.

4.3 Nonlinear static based failure probability

The failure probability of the different bridge piers, obtained with the employment of static and dynamic vulnerability functions (local uncertainty) are compared and illustrated in Figure 6. Again, for the sake of simplicity, the probability of failure is assumed as the highest among the different piers. Conventional and adaptive (*adapt*) pushover analysis have been used. According to the recommendations on the application of the N2 method, two loading distributions, uniform and 1st mode proportional (*mod* and *uni*), have also been tested. Additionally, two reference nodes have been considered: centre of mass of the deck and maximum modal displacement (*centr* and *max*), leading to a total of four versions using conventional pushover and one corresponding to the adaptive pushover, which skips the need for a reference node or load pattern.

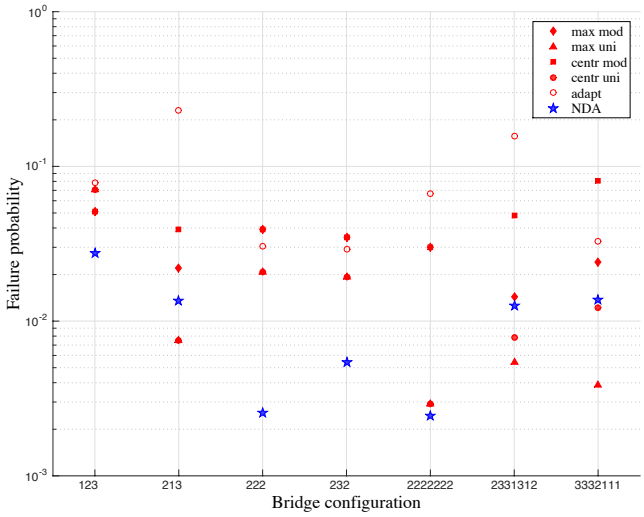


Figure 6: Critical pier failure probability, per bridge configuration.

The observation of the plot indicates that regular configurations feature lower collapse probabilities, particularly through nonlinear dynamic analysis, even though associated to larger variability in terms of different pushover approaches. Regarding the type of pushover to

use, if a simple static analysis is intended, modal load pattern does not introduce significant advantage when compared to the uniform one, which, in addition, is easier to apply. Adaptive pushover, generally overpredicting, becomes relevant for highly irregular configurations, even if not necessarily for the critical piers. No important differences are found concerning the length of the configuration: short bridges are slightly less safe than the long ones together with a little less dispersion within different versions.

4.4 Overall comparison of approaches

Finally, Figure 7 illustrates the comparison of the static failure probabilities with the dynamic ones, obtained with local and global uncertainty models. For the sake of simplicity, and based on the conclusions drawn from Figure 6, only static failure probabilities based on conventional pushover, with uniform load pattern and central reference node, and adaptive pushover versions are presented.

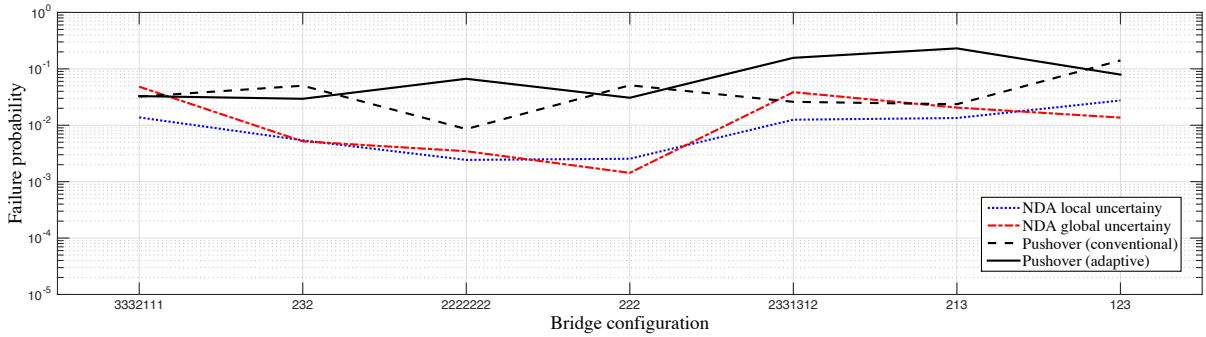


Figure 7: Failure probability, according to bridge configuration, for static and dynamic analysis based versions.

The general observation is that pushover-based estimation of seismic demand leads, in most of the cases, to higher failure probability, especially when using adaptive analysis, which is frequently associated to a failure probability of one order of magnitude above. When compared to the global uncertainty dynamic failure probabilities, which were observed to play on the safe side, the static based approaches still play an enveloping role. These results reinforce the important supporting role played by nonlinear static analysis in the use of probabilistic methods, when compared to dynamic counterpart.

5 CONCLUSIONS

The analysis of different approaches to carry out seismic safety assessment of reinforce concrete bridges constituted the main objective of this manuscript. Alternative procedures have been proposed, corresponding to uncertainty models that account for the variability of the different variables: material properties, type of record and intensity level. An innovative statistical sampling method has been used to characterise capacity as well as to compute the failure probability within a global simulation procedure, using nonlinear dynamic analysis as seismic demand prediction technique.

The parametric study concerning the aforementioned components of the safety assessment procedure, the observation of the performance of the alternative methodologies and the final comparison of results validated both of the uncertainty models in a range of seven bridges and ten real accelerograms, with good matching throughout the different configurations. The employed simulation method, Latin Hypercube, proved itself equally effective in simplifying the procedures by requiring a smaller number of realisations without accuracy loss.

In terms of nonlinear demand prediction, the observation of the results has indicated a tendency for the static analysis approaches to be conservative, even when applied with conventional uniform loading shape. The adaptive pushover is more suitable for the prediction of the behaviour of irregular configurations whereas conventional pushover, with uniform load pattern, is enough to get rather acceptable estimates for regular configurations. Within methodologies such as the probabilistic ones, in which the seismic demand needs to be estimated through a large number of nonlinear analyses, this feature constitutes an important asset, at least for a preliminary analysis.

The final results also confirmed that the seismic hazard and record-to-record variability are critical in for the evaluation of the structural vulnerability, as their consideration as a probabilistic variable within the global uncertainty model led to higher probabilities of failure.

6 ACKNOWLEDGMENTS

Financial support to the first author was provided by the Portuguese Science and Technology Foundation (FCT – Fundação para a Ciência e a Tecnologia).

REFERENCES

[1] A.C. Cornell, F. Jalayer, R.O. Hamburger, Probabilistic Basis for 2000 SAC Federal Emergency Management Agency Steel Moment Frame Guidelines. *Journal of Structural Engineering*, **128**, 526-532, 2002.

[2] K. Mackie, B. Stojadinovic, Probabilistic Seismic Demand Model for California Bridges. *Journal of Bridge Engineering*, **6**, 468-480, 2001.

[3] C. Zelaschi, G. De Angelis, F. Giardi, D. Forcellini, R. Monteiro, Performance based earthquake engineering approach applied to bridges in a road network. M. Papadrakakis, V. Papadopoulos, V. Plevris eds. *5th ECCOMAS Thematic Conference on Computational Methods in Structural Dynamics and Earthquake Engineering (COMPDYN 2015)*, Crete Island, Greece, 25–27 May, 2015.

[4] Applied Technology Council, *Seismic Evaluation and Retrofit of Concrete Buildings*, ATC-40 Report. Volumes 1 and 2, ATC, California, USA, 1996.

[5] Applied Technology Council, *Improvement of nonlinear static seismic analysis procedures*, Rep. No. FEMA-440, Washington, DC, USA, 2005.

[6] Applied Technology Council, *NEHRP Guidelines for the Seismic Rehabilitation of Buildings*, Rep. No. FEMA-273, Washington, DC, USA, 1997.

[7] CEN, *Eurocode 8: Design of Structures for Earthquake Resistance - Part 1: General rules, seismic actions and rules for buildings*. EN 1998-2, Comité Européen de Normalisation, Brussels, Belgium, 2005.

[8] CEN, *Eurocode 8: Design of Structures for Earthquake Resistance - Part 2: Bridges*. EN 1998-2, Comité Européen de Normalisation, Brussels, Belgium, 2005.

[9] T. Isakovic, M. Fischinger, Higher modes in simplified inelastic seismic analysis of single column bent viaducts. *Earthquake Engineering and Structural Dynamics*, **35**, 95-114, 2006

[10] T.S. Paraskeva, A.J. Kappos, A.G. Sextos, Extension of modal pushover analysis to seismic assessment of bridges. *Earthquake engineering and Structural dynamics*, **35**, 1269-1293, 2006.

[11] R. Pinho, R. Monteiro, C. Casarotti and R. Delgado, Assessment of Continuous Span Bridges through Nonlinear Static Procedures. *Earthquake Spectra*, **25**, 143-159, 2009.

[12] C. Casarotti, R. Monteiro, R. Pinho, Verification of spectral reduction factors for seismic assessment of bridges. *Bulletin of the New Zealand Society for Earthquake Engineering*, **42**, 111-121, 2009.

[13] M. Kohrangi, R. Bento, M. Lopes, Seismic performance of irregular bridges–comparison of different nonlinear static procedures. *Structure and Infrastructure Engineering*, 1-19, 2014.

[14] S.A. Freeman, Development and use of capacity spectrum method. *Proceedings of the Sixth U.S. National Conference on Earthquake Engineering*, Seattle, Oakland, USA, 1998.

[15] P. Fajfar, M. Fischinger, N2 – A method for non-linear seismic analysis of regular buildings. *Proceedings of the Ninth World Conference in Earthquake Engineering*, Tokyo-Kyoto, Japan, 5, 111-116, 1988.

[16] A.K. Chopra, R.K. Goel, A modal pushover analysis procedure for estimating seismic demands for buildings. *Earthquake Engineering and Structural Dynamics*, **31**, 561-582, 2002.

[17] A.K. Chopra, R.K. Goel, C. Chintanpakdee, Evaluation of a Modified MPA Procedure Assuming Higher Modes as Elastic to Estimate Seismic Demands. *Earthquake Spectra*, **20**, 757-778, 2004.

[18] E. Kalkan, S.K. Kunnath, Adaptive modal combination procedure for nonlinear static analysis of building structures. *Journal of Structural Engineering*, **132**, 1721-1731, 2006.

[19] K. Shakeri, K. Tarbali, M. Mohebbi, Modified adaptive modal combination procedure for nonlinear static analysis of bridges. *Journal of Earthquake Engineering*, 17, 918-935, 2013.

[20] C. Casarotti, R. Pinho, An Adaptive Capacity Spectrum Method for assessment of bridges subjected to earthquake action. *Bulletin of Earthquake Engineering*, **5**, 377-390, 2007.

[21] R. Monteiro, M. Marques, G. Adhikari, C. Casarotti, R. Pinho, Spectral reduction factors evaluation for seismic assessment of frame buildings. *Engineering Structures*, **77**, 129-142, 2014.

[22] R. Monteiro, X. Zhang, R. Pinho, Different approaches to derive analytical fragility functions of bridges. *Proceedings of the Second European Conference on Earthquake Engineering and Seismology*, Istanbul, Turkey, 2014.

[23] R. Pinho, M. Marques, R. Monteiro, C. Casarotti, R. Delgado, Evaluation of nonlinear static procedures in the assessment of building frames. *Earthquake Spectra*, **29**, 1459-1476, 2013.

[24] A. Olsson, G. Sandberg, Latin Hypercube Sampling for Stochastic Finite Element Analysis. Journal of Engineering Mechanics, **128**, 121-125, 2002.

[25] A. Olsson, G. Sandberg, O. Dahlblom, On Latin hypercube sampling for structural reliability analysis. *Structural Safety*, **25**, 47-68, 2013.

[26] J.E. Padgett, R. DesRoches, Retrofitted bridge fragility analysis for typical classes of multispan bridges. *Earthquake Spectra*, **25**, 117-141, 2009.

[27] C. Zelaschi, R. Monteiro M. Marques, R. Pinho, Comparative analysis of intensity measures for seismic assessment of RC bridges. *Proceedings of the Second European Conference on Earthquake Engineering and Seismology*, Istanbul, Turkey, 2014.

[28] C. Zelaschi, R. Monteiro, R. Pinho, Parametric characterization of reinforced concrete Italian bridges for seismic assessment purposes. *Structure and Infrastructure Engineering* (submitted for publication), 2015.

[29] C. Zelaschi, R. Monteiro, R. Pinho, Improved fragility functions for RC bridge populations. M. Papadrakakis, V. Papadopoulos, V. Plevris eds. *5th ECCOMAS Thematic Conference on Computational Methods in Structural Dynamics and Earthquake Engineering (COMPDYN 2015)*, Crete Island, Greece, 25–27 May, 2015.

[30] R. Monteiro, Using Latin Hypercube sampling for seismic assessment of continuous span RC bridges. *Computers and Structures* (submitted for publication), 2015.

[31] R. Monteiro, R. Delgado, R. Pinho, Probabilistic seismic assessment of RC bridges: Part I – Uncertainty models. *Structures* (submitted for publication), 2015.

[32] R. Monteiro, R. Delgado, R. Pinho, Probabilistic seismic assessment of RC bridges: Part II – Nonlinear static prediction. *Structures* (submitted for publication), 2015.

[33] A.G. Costa, *Análise sísmica de estruturas irregulares*. Ph.D. Thesis, University of Porto, Porto, Portugal (in Portuguese), 1989.

[34] B.M. Ayyub, K.L. Lai, Structural reliability assessment using latin hypercube sampling. *Proceedings of the ICOSSAR'89*, San Francisco, USA, 1989.

[35] D. Novák, B. Teplý, Z. Keršner, The Role of Latin Hypercube Sampling Method in Reliability Engineering. *Proceedings of the ICOSSAR'97*, Kyoto, Japan, 1997.

[36] SAC, *Develop Suites of Time Histories*. Project Task 5.4.1 Draft Report, SAC Joint Venture, Sacramento, CA, 1997.

[37] J.J. Bommer, A. Martínez-Pereira, The effective duration of earthquake strong motion. *Journal of Earthquake Engineering*, **3**, 127-172, 1999.

COMPDYN 2015
5th ECCOMAS Thematic Conference on
Computational Methods in Structural Dynamics and Earthquake Engineering
M. Papadrakakis, V. Papadopoulos, V. Plevris (eds.)
Crete Island, Greece, 25–27 May 2015

PERFORMANCE BASED EARTHQUAKE ENGINEERING APPROACH APPLIED TO BRIDGES IN A ROAD NETWORK

C. Zelaschi[1], G. De Angelis[2], F. Giardi[2], D. Forcellini[2], R. Monteiro[1]

[1] Institute for Advanced Study of Pavia
Palazzo del Broletto, Piazza della Vittoria n. 15, 27100 Pavia (Italy)
e-mail: ricardo.monteiro@iusspavia.it

[2] University of San Marino
Via Salita alla Rocca, 44, 47890, Republic of San Marino
e-mail: davforc@omniway.sm

Keywords: Performance based earthquake engineering, RC Bridges, Infrastructure, Networks.

Abstract. *The most recent developments in earthquake engineering design are based on the concept of prescribed performance levels, rather than the traditional prescriptive approaches. A relatively well-known software tool for conducting PBEE studies for bridge-ground systems (BridgePBEE), which is based on three-dimensional (3D) finite element model analyses carried out in OpenSees, considering a simplified soil-structure interaction macro element, has been recently applied to a limited number of individual bridge structures. This study aims to apply a Performance-Based Earthquake Engineering (PBEE) methodology to the seismic assessment of an existing road network, in which the nodes correspond to bridges, rather than to a single structural configuration, using BridgePBEE to study the response of different real bridges. Such versatile Finite-Element (FE) environment provided the possibility of processing detailed information on effective damage, safety and economic assessment. In addition, by definition of PBEE, informed decisions of the evolution of seismic losses in terms of cost and time repair quantities were derived at different Peak Ground Acceleration (PGA) levels. Nonlinear dynamic analyses were then run by using properly selected seismic records as input, by means of the conditional spectrum method applied to the seismic hazard outputs for the considered target site, using peak ground acceleration as reference intensity measure. The conclusions provide performance considerations of the investigated population of bridges in terms of repair costs and time, deriving relevant considerations for design procedures.*

1 INTRODUCTION

Performance-Based Earthquake Engineering (PBEE) is a recent methodology developed by the Pacific Earthquake Engineering Research (PEER) Center based on the concept of design for prescribed performance as opposed to more conventional prescriptive approaches. The contributions of PEER to theoretical development, applications in academia and industry and the inclusion of precepts into building/design codes have also been applied to bridges: Mackie et al. [1] used the numerical PEER platform OpenSees [2] with the inclusion of ground-foundation interaction and the definition of a list of performance groups (PGs), on the basis of the commonly used repair methods and aggregation of decision data of typical prestressed, single-column bent, multi-span, box girder bridges in California. In addition, damage to these PGs was tied to explicit repair procedures and repair quantities allowing the cost estimation of repair efforts necessary to bring back the bridge to the pre- seismic event functionality level. Simultaneously, Elgamal et al. [3] developed a graphical user interface for three-dimensional (3D) ground-foundation systems, OpenSeesPL [4], which uses OpenSees as the finite element (FE) analysis engine, adding pre- and post-processing capabilities, which include material properties, boundary conditions and mesh characterization together with the possibility of performing pushover or seismic response analyses of single piles or group of piles.

The aforementioned tools for the application of PBEE methodologies to bridge structures on one side and for the evaluation of the soil-structure interaction effects on the other, resulted in the development of bridge PBEE user interface [1, 3] to evaluate effective damage, safety and economic assessment either when nonlinear static analysis or nonlinear dynamic response of bridge structures are considered, following the trend of many other studies focusing on the nonlinear behaviour of bridge and building structures [5, 6, 7 ,8, 9].

Past studies were carried out in order to scrutinize such framework [10, 11] however, in all of them, the pre-defined seismic input and individual bridge structures with certain properties were considered. On the other hand, the present paper considers the employment of such analysis framework to classes of existing bridges of a road network located in Italy, made up of structures with homogeneous and similar elements.

Nonlinear dynamic analyses were run using properly selected seismic records [12] as input, compatible with the seismic hazard of the target site for 2% probability of exceedance in 50 years. The response of the bridge class was then assessed in terms of repair cost, time quantities such as Crew Working Days (CWD), and the ratio between the cost of repair and the cost of the new construction as function of PGA. The selection of PGA as reference intensity measure was motived by the findings of recent studies [4, 5], which place PGA among the optimal intensity measures to predict reliable seismic response of populations of bridges.

2 PBEE METHODOLOGY

The PBEE methodology aims to assess structural performance in terms of the probability of exceeding threshold values of socio-economic decision variables (DVs) in a seismic hazard environment. The PEER PBEE framework is essentially based on the application of the total probability theorem to disaggregate the problem into several intermediate probabilistic models that involve intermediate variables, such as repair items or quantities (Qs), damage measures (DMs), engineering demand parameters (EDPs), and seismic hazard intensity measures (IMs) [1, 3].

The definition of Performance Groups (PGs) representing a collection of structural and non-structural components, used as indicator of global structural performance for decision-making strategies, in which the decision variables in terms of repair cost ratio (RCR) and re-

pair time (RT) are based on the most common repair methods, is a crucial phase of the PBEE methodology. The notion of a PG allows grouping several bridge components according to the associated repair work and, as such, PGs are not necessarily the same as the individual load-resisting structural components.

The interface is built with 11 PGs [3] and 29 Quantities (Qs), representative of typical Californian bridge schemes, which in the present study are applied to a class of Italian bridges. Event though the US-based PGs were not updated to the Italian context, due to lack of information for the present case study, such limitation is expected to be overcome in future work with additional investigations. The total repair cost was generated through a unit cost function based on the considered Quantities and for each Quantity an estimate of the repair effort was obtained through a production rate. More information regarding the derivation of the default DSs, Qs, unit costs, and production rates and numerical implementations inside the interface can be found in previous studies [1, 3].

3 CASE STUDY

The PBEE methodology is herein applied to the seismic assessment of a group of bridges of similar characteristics, which are part of an existing road network and can be represented by a single structural configuration. More specifically, the present study focuses on a set of 13 bridges (Figure 1) located in one of the major north-south connections in Italy, the A14 Italian freeway (16.9 km total length), which connects Bologna to Taranto. General information for each bridge in terms of geographical position and connection functionality is provided in Table 1.

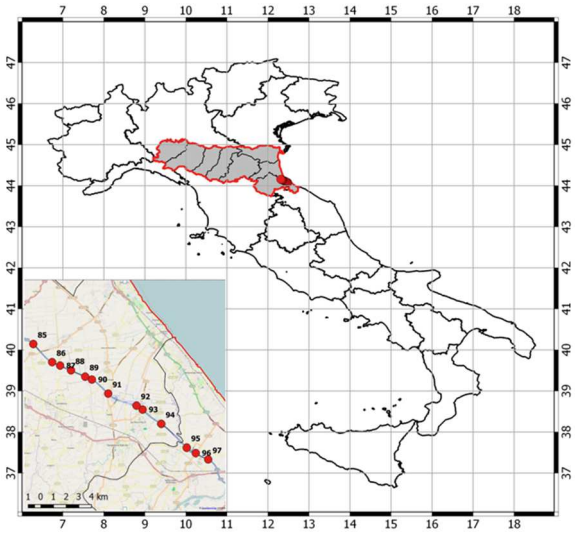


Figure 1: Selected bridges in a road network.

A functionality level (FL) has been defined considering a scale of values, in which “3” means that the connected network is a primary way of connection, such as the entrance to the cities nearby; “1” means a very small way such as connections to the countryside; and “2” is an average connection between the previous two (Table 1). Such piece of information might be particularly useful when priorities need to be established for the allocation of funds for retrofitting operations in in the immediate aftermath of an earthquake.

In order to apply the PBEE methodology to a set of bridges, due to some practical limitations of such software package, either in terms of bridge geometry or computational onus, some simplified assumptions were made. BridgePBEE is capable of performing different

types of analyses in bridges with two spans only and solid reinforced concrete pier sections hence the selection of typical Italian overpass bridges was carried out to match such features. Consequently, the set of selected bridges can thus constitute a bridge class and be represented by a single configuration.

Bridge ID	Location		Latitude	Longitude	FL
97	via Variano	Rimini	44° 4'42.63"N	12°29'0.06"E	1
96	via Tolemaide	Rimini	44° 4'58.52"N	12°28'15.83"E	2
95	via orsoleto	S.Vito	44° 5'11.59"N	12°27'43.92"E	3
94	sp13bis	S.M. Pascoli	44° 6'10.59"N	12°26'13.38"E	3
93	sp10	S. M. Pascoli	44° 6'46.34"N	12°25'6.87"E	3
92	via del lavoro	S.M. Pascoli	44° 6'56.31"N	12°24'45.19"E	2
91	Sp33	Gatteo	44° 7'26.32"N	12°23'4.50"E	3
90	sp97	Cesenatico	44° 8'1.38"N	12°22'6.65"E	3
89	via vicinale Sala	Bulgarnò	44° 8'8.73"N	12°21'42.78"E	1
88	via Pavirana	Pavirana	44° 8'24.48"N	12°20'52.30"E	1
87	via Capannaguzzo	Bulgarnò	44° 8'36.32"N	12°20'13.68"E	1
86	SP123	Cesena	44° 8'45.00"N	12°19'45.30"E	3
85	via Sant'Agà	Cesena	44° 9'30.22"N	12°18'38.30"E	1

Table 1: Bridge database

The considered bridges have similar geometry, characterized by 38m long, 2-span deck (Figure 2), supported on rectangular columns (8m x 1m) 6m tall (Figure 3). The steel-concrete deck is 12m wide and 1.80m deep and exhibits a self-weight of 140 kN/m. The connections to the abutments consist of elastomeric bearings (represented in Figure 4) and each abutment is 10m long with 10000 kN as total weight.



Figure 2: Typical characteristics of the considered bridge class

4 FINITE ELEMENT MODEL

The seismic response of the representative bridge was assessed through the nonlinear dynamic analyses of the numerical model obtained with the open-source computational interface BridgePBEE, implemented within the FE code OpenSees [13]. A 3D soil model soil is represented by 208 nodes, effective stress fully coupled (solid-fluid) brick elements built up with 20 nodes in order to investigate soil structure interaction behaviour (Figure 3).

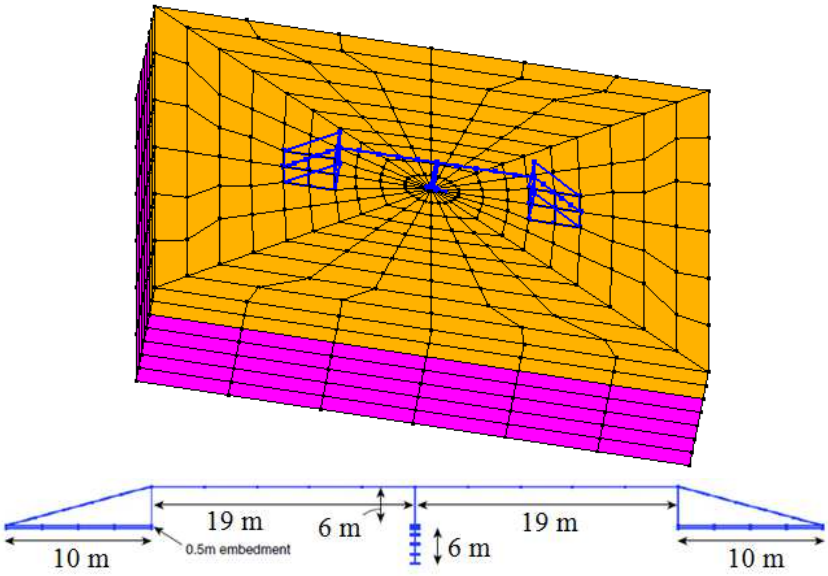


Figure 3: Benchmark bridge model.

In a preliminary stage of the study, a very stiff soil was considered. The ability of Opensees to simulate the real wave propagation adopting realistic boundaries is of particular importance in order to realistically reproduce the above seismic input scenarios. Assuming that at any special location, symmetry conditions can be adopted, periodic boundaries [14] have been considered therefore displacement degrees of freedom of the left and right boundary nodes were tied together both longitudinally and vertically using the penalty method. To this extent, base and lateral boundaries were modelled to be impervious, as to represent a small section of a presumably infinite (or at least very large) soil domain by allowing the seismic energy to be removed from the site itself (more details can be found in [15]).

The reinforced concrete column of the adopted bridge model adopted (Figure 3) is modelled with nonlinear beam-column elements and fibre cross section, whilst the deck is modelled with five separate elastic beam-column (BC) elements considering the equivalent characteristic of a homogenous material (Table 2). As far as abutments properties are concerned, no additional resistance of the soil (at large relative bridge-abutment displacement) is considered and simple roller link connections between the deck and the abutments have been used. The approach ramps make the connection with the longitudinal boundaries. Each abutment has been embedded 0.5m, 10m long and with 10000 kN as total weight.

Deck property	Crossing
Young modulus [kPa]	$1.03 \cdot 10^7$
Shear modulus [kPa]	$6.22 \cdot 10^6$
Cross Section Area [m^2]	5.40
Moment of inertia (trasverse) [m^4]	0.81
Weight per unit length [kN/m]	140

Table 2: Deck properties.

The dynamic characteristics of the bridge have been assessed by comparison with a 3D model performed in SAP2000 (Figure 4) and simple hand calculation considerations. The comparison between the calculated longitudinal period of vibration, the SAP 2000 output

(Figure 5) and the BridgePBEE result (Table 3) denotes a fair agreement, confirming BridgePBEE potentialities and the assumptions done in performing 3D model.

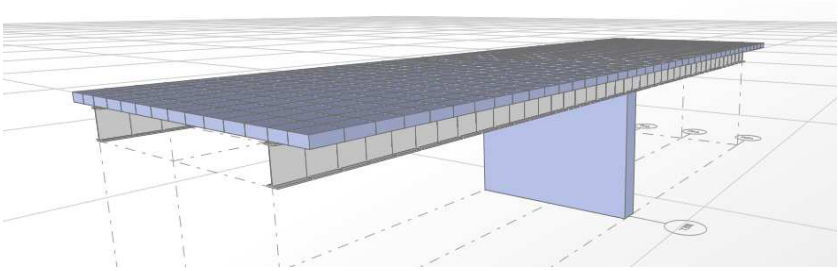


Figure 4: 3D Model (SAP 2000).

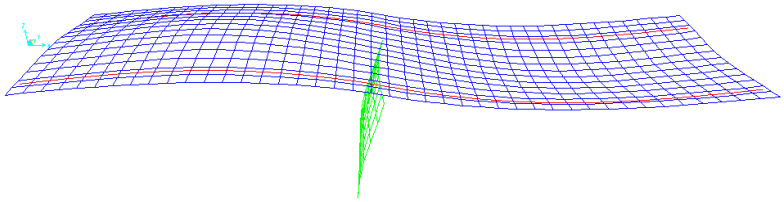


Figure 5: Fundamental shape mode, scale 40:1(T_1= 0.459 s, SAP 2000).

Model	T [s]
Manual	0.473
SAP2000 (3D)	0.459
PBEE (3D)	0.460

Table 3: Fundamental period comparison

5 SEISMIC HAZARD

The considered set of bridges are located in a central region of Italy, close to Rimini, and a full hazard characterization was carried out in order to properly select a suite of records as input for the nonlinear dynamic analyses performed through BridgePBEE. For such purpose, Openquake [16] was used for seismic hazard and disaggregation computations in order to coherently establish the connection between seismic hazard and structural assumptions. The stochastic seismic hazard analysis was undertaken using the seismic hazard harmonization in Europe (SHARE) model for Italy [17], available in Openquake, which.was used to evaluate the hazard corresponding to 2% probability of exceedance in 50 years, considering a circular area of 250 km around the target location (Longitude: 12.483, Latitude: 44.079). “Very stiff soil” site condition (class B) was assumed, according to Eurocode 8 ground type classification, assuming 600 m/s as vs_{30} value. Such simplified assumption, particularly when dealing with road networks that can refer to broad areas, can be nonetheless seen as reasonable considering the soil modelling assumptions described in Section 4. The obtained hazard curve for the site is illustrated in Figure 6.

Future developments can consider the effect of the variation in the soil type when different nodes of the network are considered.

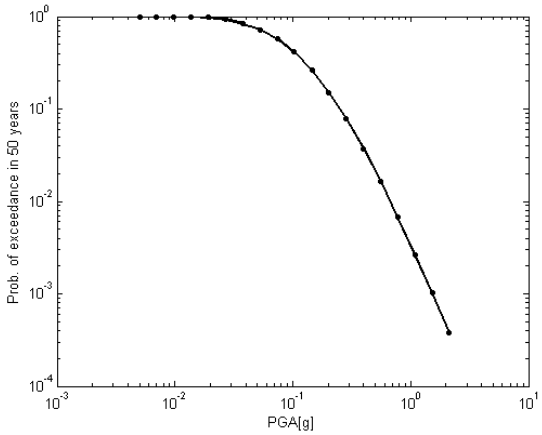


Figure 6: Hazard curve for the target site.

6 RECORD SELECTION AND SEISMIC ANALYSES

The main source of uncertainty associated with seismic excitation is record-to-record variability [18], which has led researchers to investigate innovative record selection and scaling strategies for the reduction of such variability. In the present work the conditional spectrum method [12], a recently proposed selection and scaling procedure, recently employed with success in bridge assessment studies [19], has been employed for the selection of nine records, considered with the two horizontal and vertical components, as seismic input. To accomplish so, disaggregation results conditioned at the spectral acceleration of the target site at the fundamental period of 0.40s was considered in terms of mean values of magnitude, distance and epsilon, which for the target site were evaluated as 6, 14.5 and 1.5 respectively. The main characteristics of the selected records are summarized in Table 4 whereas the corresponding scaled response spectra are shown in Figure 7.

Record ID	Scaling factor	Horizontal component (longitudinal) PGA [g]	Horizontal component (transversal) PGA [g]	Vertical component PGA [g]
CHICHI/NST	2.42	0.748	0.939	0.2625
DUZCE/MDR	2.99	0.360	0.169	0.178
CHICHI04/CHY035	2.22	0.262	0.298	0.104
LOMAP/G	0.67	0.275	0.3170	0.140
CHICHI05/HWA2	2.52	0.253	0.322	0.062
LOMAP/SFO	1.29	0.305	0.425	0.084
WHITTIER/A-EJS	1.16	0.494	0.514	0.239
LOMAP/GMR	1.50	0.338	0.484	0.173
NORTH392/E-RRS	0.82	0.534	0.353	0.491

Table 4: Ground motion records.

In the present study, only PGA was taken as intensity measure with which draw the functions of the main findings whereas the consideration of alternative intensity measures is envisaged in future developments.

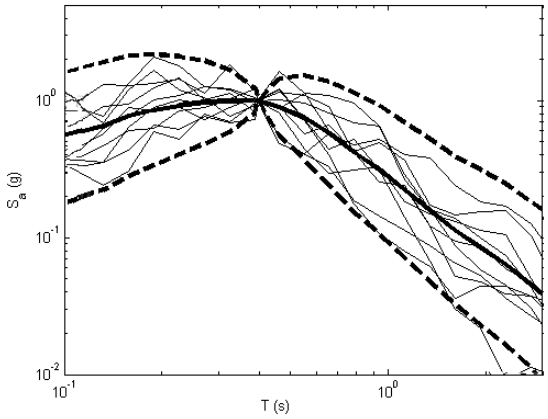


Figure 7: Response spectra of the ten selected ground motion records for Sa(T1=0.40s).

7 RESULTS

Due to the assembly-based (vector) nature of the applied method and according to the total probability theorem, it is possible to disaggregate the results (repair costs and time) into individual contributions. Nine performance groups have been taken into consideration (Table 5).

Performance group (PG) #	Performance group names
1	Max column drift ratio
2	Residual column drift ratio
3	Max relative deck-end/abutment displacement (left)
4	Max relative deck-end/abutment displacement (right)
5	Max bridge-abutment bearing displacement (left)
6	Max bridge-abutment bearing displacement (right)
7	Approach residual vertical displacement (left)
8	Approach residual vertical displacement (right)
9	Abutment residual pile cap displacement (left)
10	Abutment residual pile cap displacement (right)
11	Column residual pile displacement at ground surface

Table 5: Performance Groups.

The results in terms of costs for each performance group, total repair cost ratio (%) and total repair time in crew working days (CWD) are illustrated in Figures 8 to 11. In particular, the main contribution to the Total Repair Cost and Time is shown to be the longitudinal residual drift ratio (PG2), representing column damage (Figure 9). The abutments seem to provide longitudinal and transverse resistance to the bridge deck displacement, not affecting the seismic demand on the bridge. Figures 10 and 11 show that damage (and thus costs and time) is activated only at high PGA levels (approximately 0.95g), for which the bridge will be under severe conditions hence in need for re-design or retrofitting to avoid collapse.

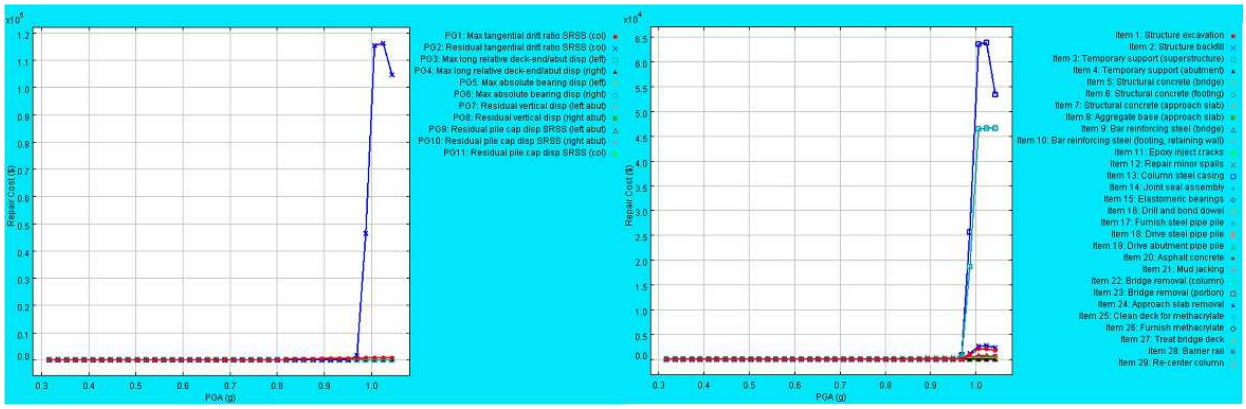


Figure 8. Contribution to expected repair cost ($) from each performance group (left) and from each repair quantity (right)

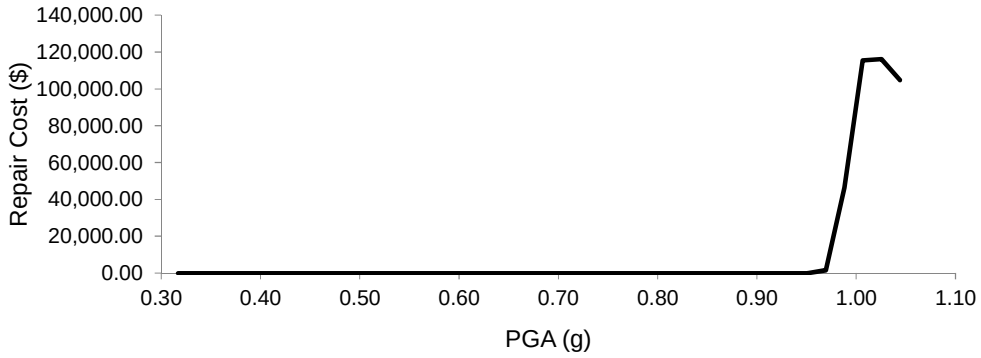


Figure 9. Costs ($) for column damage (PG2).

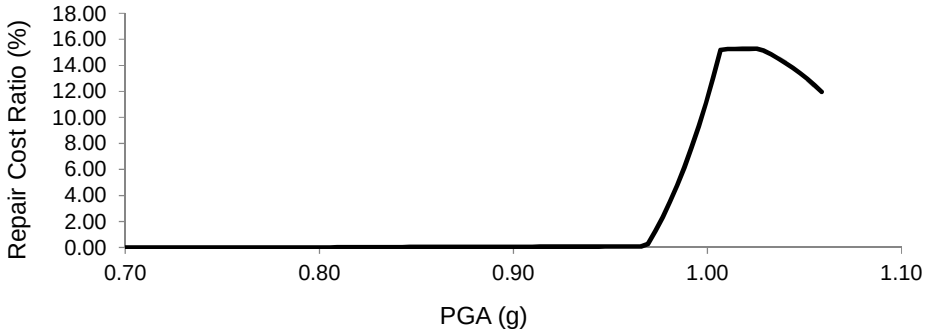


Figure 10. Total Repair cost ratio (%).

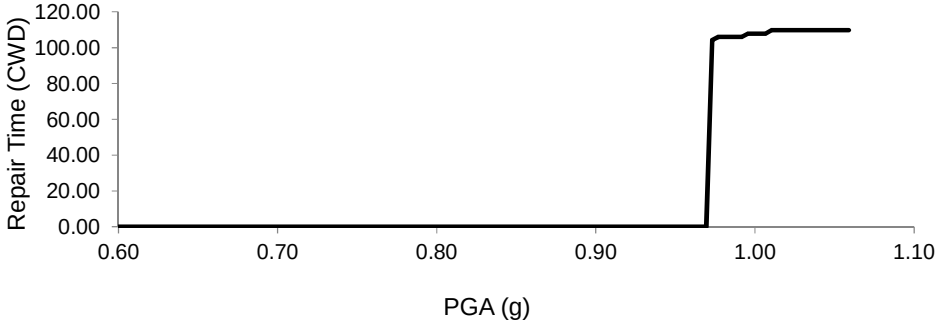


Figure 11. Total Repair Time (CWD).

8 CONCLUSIONS

This study presents a probabilistic based earthquake engineering based tool that enables a comprehensive analysis of single-column bridge-abutment models, applying the overall PBEE analysis framework. The utilization of such software tool allows for the expedite assessment of individual bridges that can represent a wider class of bridges with similar characteristics. The outputs in terms of expected damage ratios, losses and vulnerable elements represent an important information asset for different stakeholders involved with seismic risk analysis. In particular, a single benchmark bridge, representative of those overpassing one of the Italian freeway named A14, connecting Bologna to Taranto, was herein studied as the first step towards a full seismic assessment of the involving network. The results have shown that the damage is essentially concentrated on the pier but only for relatively high values of PGA. The abutments seem to provide longitudinal and transverse resistance to the bridge deck displacement, improving the seismic demand on the bridge. Further analysis will aim to consider more realistic configurations, especially for what concerns bridge connections, in order to properly assess the structural performance. The model for soil structure interaction also requires improvement in order to reproduce more realistically the abutments influence on the entire bridge-soil system.

REFERENCES

[1] K. Mackie, J. Lu, A. Elgamal, Performance-based earthquake Performance-based earthquake assessment of bridge systems including ground-foundation interaction. *Soil dynamic and earthquake engineering*, **2**, 184–196, 2012.

[2] OpenSees, *Open System for Earthquake Engineering simulation*, Pacific Earthquake Engineering Research Center, US, available from http://opensees.berkeley.edu/.

[3] K. Mackie, J. Lu, A. Elgamal, User interface for performance-based earthquake engineering: a single bent bridge pilot investigation. *9th US National and 10th Canadian Conference on Earthquake Engineering: Reaching Beyond Borders*. Toronto, Canada, July 25-29, 2010b.

[4] OpenSeesPL, available from http://soilquake.net/openseespl/.

[5] C. Casarotti, R. Monteiro, R. Pinho, Verification of spectral reduction factors for seismic assessment of bridges. *Bulletin of the New Zealand Society for Earthquake Engineering*, **42**, 111-121, 2009.

[6] R. Pinho, R. Monteiro, C. Casarotti, R. Delgado, Assessment of continuous span bridges through nonlinear static procedures. *Earthquake Spectra*, **25**, 143-159, 2009.

[7] R. Pinho, M. Marques, R. Monteiro, C. Casarotti, R. Delgado, Evaluation of nonlinear static procedures in the assessment of building frames. *Earthquake Spectra*, **29**, 1459-1476, 2013.

[8] R. Monteiro, M. Marques, G. Adhikari, C. Casarotti, R. Pinho, Spectral reduction factors evaluation for seismic assessment of frame buildings. *Engineering Structures*, **77**, 129-142, 2014.

[9] R. Monteiro, R. Delgado, R. Pinho, Using different uncertainty models for seismic assessment of RC bridges. M. Papadrakakis, V. Papadopoulos, V. Plevris eds. *5th ECCOMAS Thematic Conference on Computational Methods in Structural Dynamics*

and Earthquake Engineering (COMPDYN 2015), Crete Island, Greece, 25–27 May, 2015.

[10] D. Forcellini, A.M. Tarantino, A. Elgamal, J. Lu, K.Mackie, Seismic Assessment of Isolated Bridge configurations on deformable soils adopting a PBEE methodology. *Proceedings of the 15th World Conference on Earthquake Engineering*, Lisbon, Portugal, September 24-28, 2012.

[11] D. Forcellini, M. Banfi, Case studies on several isolated bridge configurations adopting a performance based design approach, *Durability of Bridge Structures*. CRC Press, ISBN 978-1-13-800112-1: 185-194, 2013.

[12] N. Jayaram, T. Ling, M.EERI, J.W. Baker, A computationally Efficient Ground-Motion Selection algorithm for Matching a Target Response Spectrum Mean and Variance. *Earthquake Spectra*, **27**, 797-815, 2011.

[13] S. Mazzoni, F. McKenna, M. H. Scott, G.L. Fenves, Open System for Earthquake Engineering Simulation, User Command-Language Manual, Pacific Earthquake Engineering Research Center, University of California, Berkeley, 2009.

[14] H.K. Law, I.P. Lam, Application of periodic boundary for large pile group, *Journal of Geotechnical and Geoenvironmental Engineering*, **127**, 889-892, 2001.

[15] A. Elgamal, J. Lu, D. Forcellini, Mitigation of liquefaction-induced lateral deformation in a sloping stratum: three-dimensional numerical simulation, *Journal of Geotechnical and Geoenvironmental Engineering*, **135**, 1672-1682, 2009.

[16] D. Monelli, M. Pagani, G. Weatherill, V. Silva, H. Crowley, The hazard component of OpenQuake: the calculation engine of the Global Earthquake Model. *Proceedings of the 15th World Conference on Earthquake Engineering*, Lisbon, Portugal, September 24-28, 2012.

[17] J. Woessner, D. Giardini, the SHARE Consortium, Seismic hazard estimates for the Euro-Mediterranean region: a community-based probabilistic seismic hazard assessment. *Proceedings of the 15th World Conference on Earthquake Engineering*, Lisbon, Portugal, September 24-28, 2012.

[18] N. Shome, C.A. Cornell, Probabilistic seismic demand analysis of nonlinear structures. *Technical Report RMS-35*, RMS Program: Stanford CA, 1999.

[19] C. Zelaschi, R. Monteiro, R. Pinho, Improved fragility functions for RC bridge populations. M. Papadrakakis, V. Papadopoulos, V. Plevris eds. *5th ECCOMAS Thematic Conference on Computational Methods in Structural Dynamics and Earthquake Engineering (COMPDYN 2015)*, Crete Island, Greece, 25–27 May, 2015.

COMPDYN 2015
5th ECCOMAS Thematic Conference on
Computational Methods in Structural Dynamics and Earthquake Engineering
M. Papadrakakis, V. Papadopoulos, V. Plevris (eds.)
Crete Island, Greece, 25–27 May 2015

DEMAND HAZARD ANALYSIS: A TOOL FOR ASSESSING THE ADEQUACY OF CAPACITY DESIGN APPROACH FOR DEFINITION OF THE DESIGN SHEAR FORCES IN THE FRAME BUILDINGS

Jure Žižmond[1], **Matjaž Dolšek**[2]

[1] University of Ljubljana, Faculty of Civil and Geodetic Engineering
Jamova 2, 1000 Ljubljana, Slovenia
jzizmond@fgg.uni-lj.si

[2] University of Ljubljana, Faculty of Civil and Geodetic Engineering
Jamova 2, 1000 Ljubljana, Slovenia
mdolsek@fgg.uni-lj.si

Keywords: Demand Hazard Analysis, Capacity Design, Eurocode 8, Design Shear Force, Incremental Dynamic Analysis

Abstract. *The risk-based design of buildings using nonlinear analysis is a challenging task. A question how to design components for non-simulated failure still remains unsolved. The simplified possibility is to use the capacity design which prevents shear failure of the components according to deterministic approach. In this paper an attempt has been made to obtain additional insight regarding this issue. For this purpose, the demand hazard analysis was performed for an example of an eight-storey reinforced concrete building. The ground motions were selected to match different target spectra. In addition to the uniform hazard spectrum, the conditional spectra conditioned to the first, second and third vibration periods were used. It was found that the return period of the design shear force according to capacity design vary significantly depending on location of the column as well as on the set of ground motions. However, for the investigated building it can be concluded that conditional spectrum with consideration of the first period of structure can be sufficient for determination of design shear forces.*

1 INTRODUCTION

No-collapse requirement is a fundamental performance objective of current standards for earthquake-resistant design of ordinary buildings which has to be met with an adequate reliability. Although the significant damage is allowed in the case of this fundamental performance objective, a structure is almost always designed by the linear elastic response analysis. Consequently the dissipation of energy due to damage of a structure is only implicitly accounted in the design. Several assumptions have to be introduced when a structure is designed by utilizing linear elastic response analysis. For example, the global plastic mechanism is assumed on the basis of capacity design approach, which, in the case of frame buildings, involves the concept of strong column – weak beam. Additionally, the objective of the capacity design is to prevent shear failure of the columns and beams. However, it is well known that many different global plastic mechanisms can occur in frame buildings due to earthquakes although they are designed according to the capacity design approach. Some of them can be similar to that considered by the capacity design, whereas some other can be significantly different. Therefore it can be argued that the capacity design does not always guaranty global plastic mechanism which is considered in design. To overcome this issue the alternative methods of designing the structures can be used. For example, Lazar Sinković et. all [1] and Lazar and Dolšek [2] recently proposed an iterative design procedure which makes it possible to use different type of analyses (including non-linear), and to control the adjustment of structure during an iterative design. The iterative procedure is currently used for checking the adequacy of collapse risk, whereas other performance objectives are considered according to building codes. Although the proposed procedure solves a wide range of issues (e.g. incompleteness of capacity design procedure, the design of structure to target collapse risk), the problem of design against shear failure is still unsolved if the non-linear model is not capable of simulation of shear failure of the structural components.

The aim of the study presented in this paper was to investigate if the design shear forces in the columns, which are obtained by capacity design, can be justified in terms of uniformity of mean annual frequency of exceedance. For this purpose demand hazard analysis [3–5] was performed for an example of an 8-storey building, which was analyzed for one direction of seismic action. Different sets of ground motions were selected using conditional spectrum (CS) approach [6] in order to study whether the conditioning period has an impact on the return period of shear forces. The three conditioning periods corresponded to the first three periods of the investigated 8-storey building. For comparison, the uniform hazard spectrum was also used as a target spectrum for the selection of a set of ground motions. The results are presented in terms of so-called demand hazard curves for the shear forces in selected columns. A discussion regarding the variability of return periods corresponding to design shear forces in the columns as well as the discussion about the relationship between so-called maximum credible design shear force and design shear force based on capacity design is also given. Finally the impact of the conditioning period of CS on the demand hazard curves for shear forces in the columns is presented.

2 THE SEISMIC DEMAND HAZARD

A conventional risk integral can be used to determine the so-called seismic demand hazard, which provides relationship between mean annual frequency of exceedance of certain engineering demand parameter:

$$\lambda_{EDP}\left(edp\right)=\int_{0}^{\infty}P\left[EDP>edp\mid IM=im\right]\left|\frac{d\lambda_{IM}\left(im\right)}{dIM}\right|dIM \tag{1}$$

where $P\left[EDP > edp \mid IM = im\right]$ is the probability that *EDP* is greater than *edp* with given *IM*=*im*, and the $\lambda_{IM}\left(im\right)$ is the seismic hazard curve which provides the rate of exceedance of *IM*>*im*. Integrating the equation for intensities [0, ∞) mean annual frequency of exceedance is computed for only one *edp*. The entire seismic demand hazard curve is therefore obtained by evaluated the Eq. (1) for entire range of *edp*. More details about demand hazard and the corresponding limitations are given elsewhere (e.g. [7,8]).

The demand hazard curve is obtained by numerical integration of the Eq.(1). In the case if it is assumed that the probability P_i, which represent the probability that *EDP* is greater than *edp* at given intensity $IM=im_i$, is constant in the range $[im_i-\Delta im/2 \;\; im_i+\Delta im/2]$ and the trapezoidal rule on integration of derivate of hazard function is used, the Eq.(1) can be rewritten as follows:

$$\lambda_{EDP}\left(edp\right) \approx \sum_{i=1}^{n} P_i\left[EDP > edp \mid IM = im_i\right] \cdot \left| \frac{\lambda_{IM}\left(im_i + \Delta im\right) - \lambda_{IM}\left(im_i - \Delta im\right)}{2} \right| \tag{2}$$

The Δim is defined as difference between intensities im_{i+1} and im_i. The probability P_i could be calculated directly from complementary cumulative distribution function obtained on the basis of results of dynamic analysis. In such a case the type of distribution (usually lognormal) has to be assumed and the distribution parameters μ and σ which are obtained from *EDP*s at intensity $IM=im_i$ has to be calculated. However, in case of this study the probability P_i was estimated as the fraction of ground motions for which it was observed that at given intensity $IM=im_i$ the *EDP*>*edp*. For example, if 30 ground motions were used for calculation of *EDP*s and 4 of it exceed *edp*, then the probability P_i was equal to 4/30.

In this study, the engineering demand parameter (*EDP*) is the shear force in columns *Q*, which is presented as a function of the return period ($T_R = 1/\lambda_Q$) and not as a function of mean annual frequency of exceedance of shear force.

3 DESCRIPTION OF THE INVESTIGATED STRUCTURE

The geometry of the 8-storey building is presented in Figure 1. The building was designed according to provisions of Eurocode 8 [9] for ductility class M, peak ground acceleration at rock outcrop equal to 0.25 g (Ljubljana, Slovenia) and soil type C (soil factor 1.15). The behavior factor was assumed 3.9, the quality of reinforcing steel was prescribed S500B whereas the concrete C30/37 was used. The slab depth was 20 cm. The total mass of structure amounted to 2338 t. The first three periods in X direction were, respectively, 1.23 s, 0.40 s and 0.23 s. The ratio between the design base shear and the weight was estimated to 7.6% and 7.3% for X and Y direction, respectively. The typical reinforcement of columns and beams are presented in Figure 1.

Dimension of plan and elevation view are in [m]

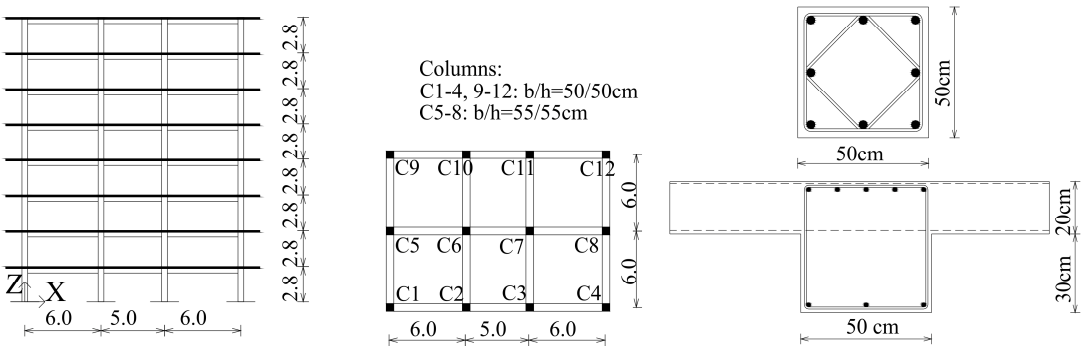


Figure 1: The elevation, plan view and reinforcement in typical columns and beams of 8-storey building

4 SEISMIC HAZARD AND THE SETS OF GROUND MOTIONS FOR DYNAMIC ANALYSIS

The seismic hazard curves for spectral acceleration at the first three vibration periods of the investigating building when analysed only in X direction (Figure 2) were obtained on the basis of probabilistic seismic hazard analysis (PSHA) which was performed for the purpose of seismic hazard maps used in Slovenia [10,11]. The PSHA based on so-called distributed (background) seismicity since the seismicity could not be assigned to specific geologic structures due to inaccurate and insufficient seismologic and geologic data. Five different seismicity models which were appropriately weighted were considered in the analysis in order to adequately take into account distribution of hypocentres and energy released during earthquakes.

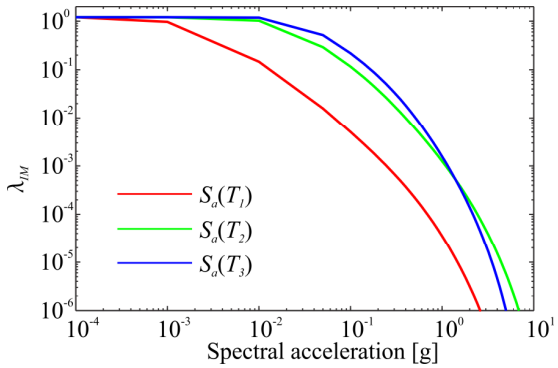


Figure 2: The hazard curves for Ljubljana for the spectral acceleration corresponding to the first, second and third period of the investigated building.

The relationship between engineering demand parameters and seismic intensity, which is needed to calculate seismic demand hazard, was simulated by incremental dynamical analysis [12]. Four sets of 30 ground motions (Figure 3) were selected from PEER Next Generation Attenuation (NGA) strong-motion database [13,14]. Ground motions of the first three sets were selected according to conditional spectrum approach [6]. The conditioning periods corresponded to the first three periods (hereinafter referred as set CS T_1, CS T_2 and CS T_3). For comparison, the fourth set of ground motions was also selected. It is consistent with the uniform hazard spectrum (hereinafter referred as set UHS). In this case the spectral acceleration corresponding to the first vibration period was selected for the intensity measure. All target spectra corresponded to return period of 475 years which defined in Eurocode 8 for design of ordinary buildings. The target conditional mean spectra were defined using Sabetta and Pugliese [15] attenuation relationship which was also used in the PSHA. The mean magnitude (M), mean distance (R) and the epsilon (ε) are presented in Table 1. All selected ground motions were recorded on soil type C (Eurocode 8, shear-wave velocity in the upper 30 m from 180 to 360 m/s), and corresponded to events with magnitudes between 4.0 and 7 and source-to-site distances in the range from 4.5 to 50 km.

	CS T_1	*CS* T_2	*CS* T_3
R [km]	10.2	8.4	6.9
M	6.0	5.8	5.6
ε	0.78	0.89	0.94

Table 1: The mean distance, mean magnitude and epsilon used for definition of conditional spectra.

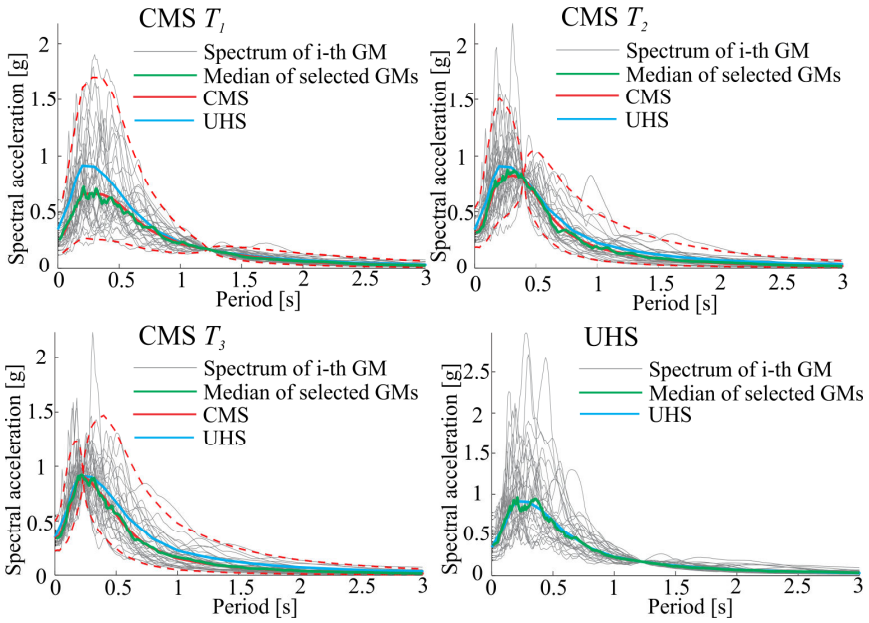


Figure 3: Spectra of selected ground motions (GM) corresponding median spectrum and the of target spectrum for the four sets of ground motions.

5 STRUCTURAL MODEL

The structural model for nonlinear analysis is based on the Eurocode 8 requirements as discussed elsewhere [16]. The beam and column flexural behavior is therefore modelled by one-component lumped plasticity elements, composed of an elastic beam and two inelastic rotational hinges (defined by a moment-rotation relationship). The element formulation is based on the assumption of an inflexion point at the midpoint of the element. The gravity load is represented by the uniformly distributed load on the beams, and by the concentrated loads at the top of the columns. For the beams, the plastic hinge is used for major axis bending only. For the columns, two independent plastic hinges for bending about the two principal axes are used. The moment-rotation relationship before strength deterioration is modelled by a bi-linear relationship. A linear negative post-capping stiffness is assumed after the maximum moment has been achieved. The axial force due to gravity loads is taken into account when determining the moment-rotation relationship for the columns, while in the case of the beams zero axial force and the T cross-sections were assumed. The ultimate rotation Θ_u in the columns and beams at the near collapse (NC) limit state, which corresponds to a 20% reduction in the maximum moment, is estimated by means the EC8-3 formulas [17]. The parameter γ_{el} was assumed to be equal to 1.0, since mean values of near collapse rotation were used. Mean (actual) concrete (38 MPa) and steel (570 MPa) strength were assumed. Post-capping negative stiffness is calculated by assuming the ratio between the rotation at zero strength and the rotation corresponding to the maximum moment equal to 3.5.

All the analyses were performed with OpenSees [18], using the PBEE toolbox [16], which is a simple yet effective tool for the seismic performance assessment of reinforced concrete.

6 THE DEMAND HAZARD CURVES AND SHEAR DEMAND IN COLUMN ACCORDING TO CAPACITY DESIGN

The return period of design shear forces (Q_{CD}) in columns, which were estimated according to capacity design, are presented on the basis of demand hazard analysis for four sets of ground motion (Table 2). Furthermore the influence of different target spectrum on the de-

mand hazard curves for the shear forces in the columns are also presented. For simplicity, the results are presented only for columns C5 and C6 (Figure 4 and 5).

In the most cases the lowest return periods for Q_{CD} corresponded to the ground motions consistent with the UHS, follows the set CS T_1, CS T_2 and CS T_3. It is interesting to note, that the return periods for inner column C6 are greater than that observed for the column C5, which is positioned in the peripheral frame. The exception is the first storey. The return periods for Q_{CD} are the lowest in the 6-th and 7-th storey (271-480 years and 363-834 years, respectively, in the case of columns C5 and C6) and the greatest in last 8-th storey (3310-10100 years in case of column C5 and 4910-24400 for column C6). Note also, that the return period for Q_{CD} in storey one is greater than the return period for Q_{CD} in storey two in case of both columns.

			T_R [years]			
	Storey	Q_{CD} [kN]	*CS* T_1	*CS* T_2	*CS* T_3	*UHS*
C5	1	371	3600	5430	8410	2120
	2	237	532	605	512	396
	3	247	1060	983	1130	804
	4	236	885	898	856	782
	5	216	609	585	667	442
	6	206	426	375	338	271
	7	193	480	371	336	271
	8	234	6900	8240	10100	3110
C6	1	451	1240	1410	1560	681
	2	369	987	1390	1460	624
	3	379	1910	2330	2450	1300
	4	327	1230	1220	1200	849
	5	307	1,020	832	1,390	797
	6	299	718	763	834	431
	7	268	602	546	537	363
	8	293	9110	10100	24400	4910

Table 2: The return periods for the design shear forces in columns C5 and C6 over stories for different sets of ground motions.

However, it was realized that it may be misleading to judge the adequacy of the design shear forces on the basis of uniform return period of demand. For example, let's compare the results for column C6 in 3-th and 6-th storey. The return period of design shear force in 3-rd storey amounted from 1300 to 2450 years whereas in the 6-th storey the corresponding return periods are around three times lower (431-834 years). Although the design shear force is more frequent in the 6-th storey it cannot be concluded that the column in the 6-th storey is more sensitive to shear failure than the column in the 3-rd storey.

The return period of the design forces in the columns may not be sufficient parameter in order to decide whether the occurrence rate of shear failure of the columns is acceptable or not. Several other issues may affect the decision. Firstly, the return period presented in Table 2 corresponds to the design shear forces which are significantly smaller in comparison to the median shear resistance. Thus the return period of shear resistance of the columns is certainly significantly larger. Secondly, the return period is very sensitive to the variation of the shear force and the shape of demand hazard curve is slightly different for each column. Therefore, the ratio between actual shear strength and design shear force can be different in comparison to the ratio between the corresponding return periods. It is also worth to note that the nonline-

ar model, which is used in dynamic analysis, is based on the median strength of the material, whereas the design shear forces are used to estimate the amount of shear reinforcement taking into account the design value of the material strength. Consequently the decision regarding an acceptable occurrence rate of shear failure cannot be solely based on the occurrence rate of design forces.

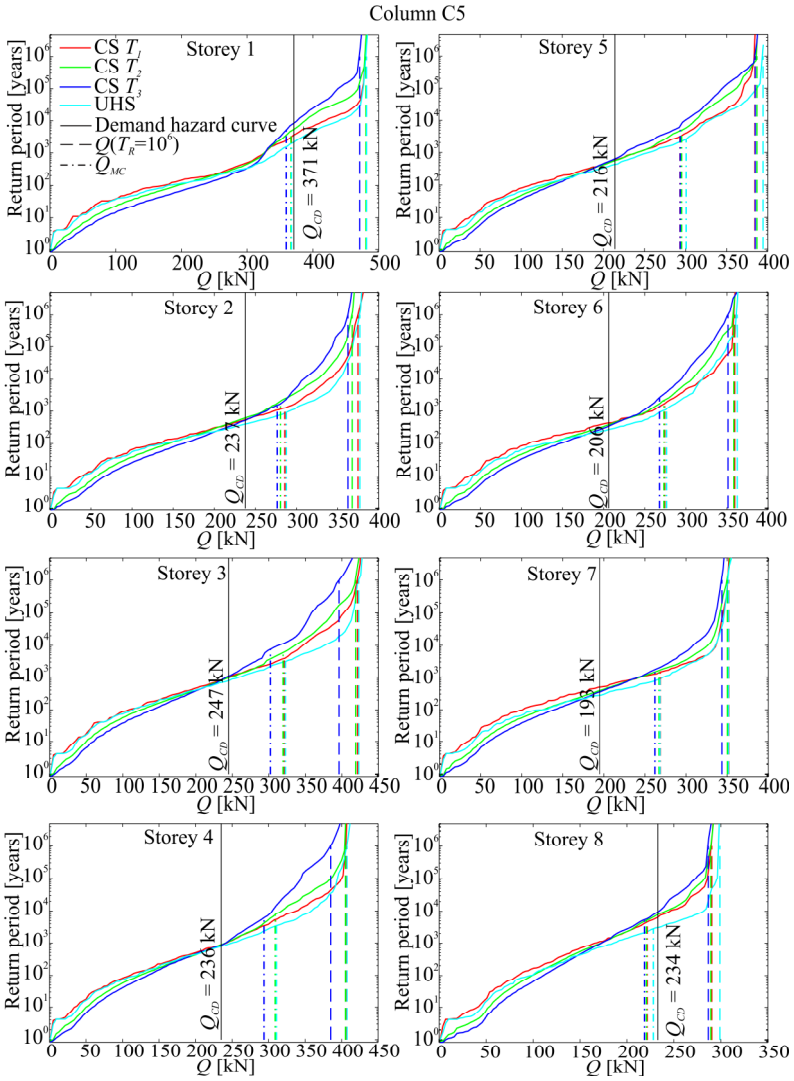


Figure 4: The demand hazard curves for column C5

In order to provide more insight into the adequacy of design shear forces in structural components it is quite reasonable to estimate the so-called maximum credible design shear force (Q_{MC}). Different definitions can be used for Q_{MC}. In this study it was simply assumed that Q_{MC} (Figures 4 and 5) is the shear force in the component which has very long return period, e.g. $Q(T_R=10^6)$, divided by the overstrength factor, which takes into account the difference between the median value of shear capacity and design value of shear capacity of a structural component. If it is assumed that the contribution of the shear reinforcement is a dominant part to the shear resistance of the structural components (e.g. Eurocode 2), then the overstrength factor depends on the material safety factor used for the strength of steel (γ_S=1.15) and the ratio between median strength and the characteristic strength of steel, which was estimate from experiments (1.14). The total overstrength factor was thus estimated to 1.31 (1.14·1.15). The actual overstrength is even higher since the contribution of concrete and

diagonal strut to the shear strength, was neglected. The minimum requirement of standards Eurocode 2 and 8 [17,19] can additionally increase the overstrength. The Q_{MC} was then estimates as $Q(T_R=10^6)/1.31$. In this procedure, it is assumed that when Q_{MC} is based on $Q(T_R=10^6)$ the shear failure of the components, if simulated in the nonlinear model, do not have an impact on the probability of the failure of the system. Note that such an assumption may be even too conservative since the $Q(T_R=10^6)$ is almost always close to the maximum possible shear force observed from dynamic analysis. However, such hypothesis still has to be proven.

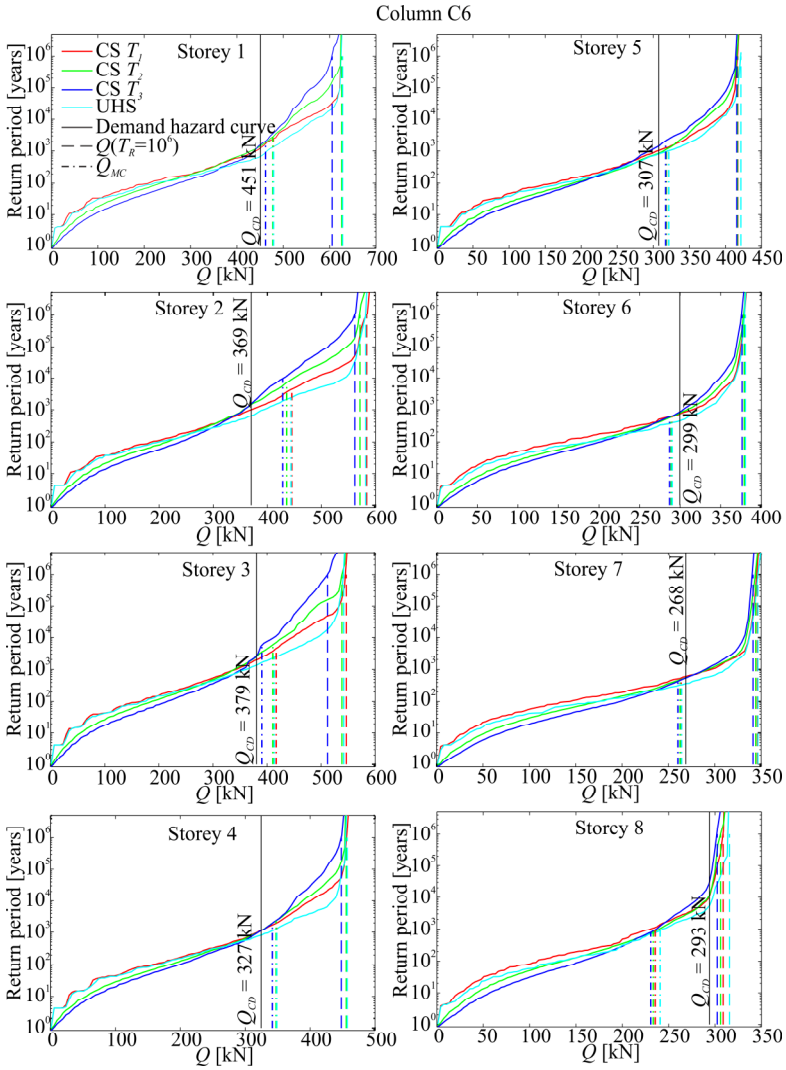


Figure 5: The demand hazard curves for column C6

The maximum credible design shear forces (Q_{MC}) were then compared to the design shear forces according to Eurocode 8 (Q_{CD}) (see Figure 4 and 5). Firstly, it can be observed that Q_{MC} does not vary significantly depending on the shape of the target spectrum. The smallest (3 kN) and the greatest (27 kN) difference are observed for column C6 respectively in 6-th and 3-th storey. Note that this is only 1-5% of total mean $Q(T_R=10^6)$. However, the variation between Q_{MC} and Q_{CD} is quite significant. For column C6 the Q_{MC} and Q_{CD} were quite similar for most of stories, but for the top storey it was observed that $Q_{CD} > Q_{MC}$. This means that the design shear force Q_{CD} is overestimated in the case of the column C6 at the top. The opposite conclusion can be made for the exterior column C5, where $Q_{CD} < Q_{MC}$ in most of the stories.

In the worst case the Q_{CD} is only around 70% of maximum credible design shear force. Additional studies are needed in order to provide more insight regarding such observations.

An interesting results of the study presented in this papers are the demand hazard curves for the shear forces in the columns, which were estimated using different sets of ground motions. Several trends can be observed. If someone would be interested to estimate the maximum shear force for given the return period it can be concluded that this cannot be achieved by a single set of ground motions. For example, if the long return periods are of the interest, then the maximum shear forces are obtained on the basis of the UHS spectrum using $S_a(T_1)$ for the intensity measure. However, this is not the case for the shear forces having high occurrence rate (short return period). In this case the shear forces are underestimated if assessed on the basis of UHS spectrum.

If it is assumed that the UHS spectrum is not appropriate target spectrum for dynamic analysis, then it can be concluded that shear forces estimated on the basis of CS conditioned to the first vibration period can be considered appropriate to use in design since in the case of long return periods so-determined shear forces are the greatest. However, this statement may not be general since it is based on the results obtained only for the investigated building. For this particular example, the envelope of the demand hazard curve is obtained by using CSs conditioned to the first and third vibration period.

7 CONCLUSIONS

In the presented study the return periods of capacity design shear forces in the columns of 8-storey building were calculated for different sets of ground motions. It was found that the return period of the design shear force depends on position, storey and set of ground motion. The smallest return periods of Q_{CD} were observed for the exterior column (except in the top storey) when the demand was estimated on the basis of the ground motions consistent with target UHS.

The adequacy of the design shear force in the columns according to capacity design was estimated by the ratio between Q_{CD} and the maximum credible design shear force. The results of the demand hazard analysis point to the following conclusions: (i) it is expected that the safety in design using capacity design procedure is greater for inner columns and (ii) the sets of ground motions do not have great impact on maximum credible design shear force.

It was also observed that if the long return periods are of the interest, then the maximum shear forces for given return period are obtained on the basis of the UHS spectrum using $S_a(T_1)$ for the intensity measure, whereas in case of short return period, the maximum shear force are obtained for CS conditioned to the third vibration period (CS T_3).

Since only one example was used for this study, it is important to note that the conclusions are not general. Several issues have to be addressed in future research in order to develop guidelines for design of shear forces using demand hazard analysis.

8 ACKNOWLEDGMENTS

The results presented in this paper are based on work supported by the Slovenian Research Agency. This support is gratefully acknowledged.

REFERENCES

[1] N. Lazar Sinković, M. Brozovič, M. Dolšek, Risk-based seismic design for collapse safety. *Earthquake Engineering and Structural Dynamics* 2015;in review.

[2] N. Lazar, M. Dolšek, Risk-based seismic design – An alternative to current standards for earthquake-resistant design of buildings. *Proceedings of 15h World Conference of Earthquake Engineering*, Lisboa, Portugal: 2012, p. 1–10.

[3] B.A. Bradley, The seismic demand hazard and importance of the conditioning intensity measure. *Earthquake Engineering and Structural Dynamics,* **41**(11), 1417–1437, 2012. doi:10.1002/eqe.2221.

[4] N. Shome, *Probabilistic seismic demand analysis of nonlinear structure*. Doctoral dissertation. Stanford University, Department of Civil and Environmental Engineering, 1999.

[5] V. K. Victorsson, *The reliability of capacity-designed components in seismic resistant systems*. Doctoral dissertation. Stanford University, Department of Civil and Environmental Engineering, 2011.

[6] J. W. Baker, Conditional mean spectrum: Tool for ground-motion selection. *Journal of Structural Engineering,* **137**(3), 322–331, 2011. doi:10.1061/(ASCE)ST.1943-541X.0000215.

[7] B. A. Bradley, Practice-oriented estimation of the seismic demand hazard using ground motions at few intensity levels. *Earthquake Engineering and Structural Dynamics,* **42**(14), 2167–2185, 2013. doi:10.1002/eqe.2319.

[8] B. A. Bradley. A comparison of intensity-based demand distributions and the seismic demand hazard for seismic performance assessment. *Earthquake Engineering and Structural Dynamics*, **42**(15), 2235–2253, 2013. doi:10.1002/eqe.2322.

[9] CEN. EN 1998-1:2004. Eurocode 8: Design of structures for earthquake resistance - Part 1: General rules, seismic actions and rules for buildings. Brussels: European Committee for Standardisation.

[10] B. Zabukovec, OHAZ: A computer program for spatially smoothed seismicity approach. *Proceedings of the Workshop Seismicity Modeling in Seismic Hazard Mapping*, Poljče, Slovenija: 2000, p. 135–40.

[11] J. Lapajne, B. Šket Motnikar, P. Zupančič, Probabilistic seismic hazard assessment methodology for distributed seismicity. *Bulletin of the Seismological Society of America*, **93**(6), 2502–2515, 2003. doi:10.1785/0120020182.

[12] D. Vamvatsikos, C. A. Cornell, Incremental dynamic analysis. *Earthquake Engineering and Structural Dynamics*, **31**(3), 491–514, 2002.

[13] B. S-J. Chiou, R. R. Youngs, An NGA Model for the average horizontal component of peak ground motion and response spectra. *Earthquake Spectra*, **24**(1), 173–215, 2008. doi:10.1193/1.2894832.

[14] N. Jayaram, T. Lin, J. W. Baker, A computationally efficient ground-motion selection algorithm for matching a target response spectrum mean and variance. *Earthquake Spectra*, **27**(3), 797–815, 2011. doi:http://dx.doi.org/10.1193/1.3608002.

[15] F. Sabetta, A. Pugliese. Estimation of response spectra and simulation of nonstationary earthquake ground motions. *Bulletin of the Seismological Society of America*, **86**(3), 337–352, 1996.

[16] Dolsek M. Development of computing environment for the seismic performance assessment of reinforced concrete frames by using simplified nonlinear models. *Bulletin of Earthquake Engineering*, **8**(6), 1309–1329, 2010. doi:10.1007/s10518-010-9184-8.

[17] CEN. EN 1998-3:2005. Eurocode 8: Design of structures for earthquake resistance - Part 3: Assessment and retrofitting of buildings. Brussels: European Committee for Standardisation.

[18] McKenna F, Fenves GL. Open System for Earthquake Engineering Simulation (OpenSees)Pacific Earthquake Engineering Research Center; 2010. http://opensees.berkeley.edu.

[19] CEN. EN 1992-1-1:2004. Eurocode 2: Design of concrete structures - Part 1-1: General rules and rules for buildings. Brussels: European Committee for Standardisation.

COMPDYN 2015
5th ECCOMAS Thematic Conference on
Computational Methods in Structural Dynamics and Earthquake Engineering
M. Papadrakakis, V. Papadopoulos, V. Plevris (eds.)
Crete Island, Greece, 25–27 May 2015

USING PERIODICITY TO MITIGATE GROUND VIBRATION

Lars Vabbersgaard Andersen

Aalborg University, Department of Civil Engineering
Sofiendalsvej 9–11, DK-9200 Aalborg SV, Denmark
e-mail: la@civil.aau.dk

Keywords: Wave mitigation, wave impeding block, WIB, finite element analysis, FEA.

Abstract. *Introduction of trenches, barriers and wave impeding blocks on the transmission path between a source and receiver can be used for mitigation of ground vibration. However, to be effective a barrier must have a depth of about one wavelength of the waves to be mitigated. Hence, while great reductions of energy transmission can be obtained within the medium and high frequency ranges, barriers are a poor solution at low frequencies.*

As an alternative, a periodic change in the properties of the soil can be introduced—to the geometry and/or to the material. Periodic structures are known to act as filters for wave propagation, effectively reducing the transmission of energy in certain frequency bands known as stop bands or band gaps, thus only allowing propagation in the so-called pass bands.

In this paper, a stratified ground with two soil layers is considered and two types of periodicity is analysed: A soil with periodic stiffening (ground improvement) and a ground with periodic changes in the surface elevation obtained by artificial landscaping. By means of a two-dimensional finite-element model, the stiffness and mass matrices are determined for a single cell of the ground with horizonal periodicity. Floquet analysis is then performed in order to quantify the number of propagating wave modes as well as modes with low degrees of attenuation. As a conclusion of the analysis, effective mitigation in the low frequency range can be established. The position of stop bands can be manipulated by engineering the soil with periodic changes to the geometry and material.

1 INTRODUCTION

Ground vibration from traffic or unbalanced machinery is a nuisance to people living and working next to railways, roads or production facilitiesespecially in cases with poor sub grades where waves can propagate over long distances. Further, sensitive equipment in laboratories and hospitals may malfunction due to even small vibration levels. Different methods for mitigation of ground vibration have been studied and tested, ranging from ground improvement and use of trenches or barriers [1] to application of damping or isolation devices.

This paper proposes a different approach, namely the use of periodic shaping of the landscape, inspired by the curvy hills and valleys formed around the Max IV laboratory near Lund, Sweden. Originally intended by the architects as an aesthetic improvement of the environment, Persson [2] found in his licentiate work that the modification of the terrain is able to provide ground vibration mitigation.

The idea of using periodic structures for mitigation of vibrations is not new. In the classical work by Mead [3], wave propagation in a periodic one-dimensional waveguide was studied, and many others have followed the same idea. Simple problems can be analysed analytically by means of Floquet analysis, and combining this approach with, for example, the finite-element method, periodic two and three-dimensional structures of complex geometries can be studied regarding their wave propagation properties. Such models have been used, for example, by Manconi and Mace [4] to study curved panels, and by Domadiya *et al.* [5] to study wave propagation in beams with periodically placed masses or changes to the cross section. The combination of Floquet theory and finite-elements has also be used for analysis of railways [6], mainly to allow studying long structures with low computational cost. For a similar reason, Bian et al. [7] used a so-called 2.5D model to study ground vibrations from a train running on a track with irregular surface.

In the present work, the wave propagation in a soil layer is analysed by combining the finite-element method with Floquet theory. A reference cell, *i.e.* one period of the periodic ground geometry, is modeled using the commercial finite-element analysis software Abaqus 6.14 [8]. The stiffness and mass matrices are then extracted, and an in-house code is utilized for Floquet analysis. The wave characteristics of the soil including periodicity are discussed in terms of propagating, attenuating and evanescent modes, and pass and stop bands for vibration transmission are identified. Two different types of ground are examined. Firstly, a layer with periodically changing material properties is considered, corresponding to a case with jet grouting or another type of ground improvement implemented with equidistant spacing. Secondly, inspired by the Max IV laboratory, a ground with periodic changes in the surface geometry is concerned.

2 COMPUTATIONAL MODEL

2.1 Finite-element formulation for soil with periodic geometry

Wave propagation in the layered soil is analysed by a two-dimensional finite-element model assuming plane strain and linear elastic response. The geometry is periodic in the direction along the ground surface—*i.e.* a reference "cell" is repeated infinitely many times in the x direction as illustrated in Figure 1. In the absence of damping, the equation of motion for the finite-element model of the cell can be written in the time domain as

$$\mathbf{M}\ddot{\mathbf{u}}(t) + \mathbf{K}\mathbf{u}(t) = \mathbf{f}(t), \tag{1}$$

where $\mathbf{M}$ and $\mathbf{K}$ are the mass and stiffness matrices, respectively, whereas $\ddot{\mathbf{u}}(t)$ and $\mathbf{u}(t)$ are the nodal acceleration and displacement vectors, respectively, and $\mathbf{f}(t)$ is the vector of external

nodal forces. After Fourier transformation with respect to time, t, Eq. (1) may be written in frequency domain:

$$\left(\mathbf{K} + (\mathrm{i}\omega)^2\mathbf{M}\right)\mathbf{U}(\omega) = \mathbf{D}(\omega)\mathbf{U}(\omega) = \mathbf{F}(\omega), \qquad \mathbf{D}(\omega) = \mathbf{K} - \omega^2\mathbf{M}, \tag{2}$$

where $\mathrm{i} = \sqrt{-1}$ is the imaginary unit and ω signifies the angular frequency, whereas $\mathbf{U}(\omega)$ and $\mathbf{F}(\omega)$ are the complex-valued Fourier coefficients of the displacement and external force vectors, respectively. Finally, $\mathbf{D}(\omega)$ is introduced as the complex-valued dynamic stiffness matrix.

In what follows, all calculations are expressed in the frequency domain and for convenience the dependence of the angular frequency ω is assumed implicit. For example, $\mathbf{U}(\omega) = \mathbf{U}$. The next step is to split the dynamic stiffness matrix as well as the displacement and force vectors into components associated with internal degrees of freedom and components associated with degrees of freedom at the boundary where periodicity constraints are to be applied. Introducing subscripts i and b to identify degrees of freedom for internal nodes and periodicity boundary nodes, respectively, sub-matrices and sub-vectors are defined as:

$$\mathbf{D} = \begin{bmatrix} \mathbf{D}_{bb} & \mathbf{D}_{bi} \\ \mathbf{D}_{ib} & \mathbf{D}_{ii} \end{bmatrix}, \qquad \mathbf{U} = \begin{Bmatrix} \mathbf{U}_b \\ \mathbf{U}_i \end{Bmatrix}, \qquad \mathbf{F} = \begin{Bmatrix} \mathbf{F}_b \\ \mathbf{F}_i \end{Bmatrix}. \tag{3}$$

It is noted that the internal degrees of freedom include those at nodes on parts of the boundary that are not subject to periodicity conditions. Inserting Eq. (3) into Eq. (2) and assuming that no external forces are applied to the interior degrees of freedom provides:

$$\begin{bmatrix} \mathbf{D}_{bb} & \mathbf{D}_{bi} \\ \mathbf{D}_{ib} & \mathbf{D}_{ii} \end{bmatrix} \begin{Bmatrix} \mathbf{U}_b \\ \mathbf{U}_i \end{Bmatrix} = \begin{Bmatrix} \mathbf{F}_b \\ \mathbf{F}_i \end{Bmatrix} = \begin{Bmatrix} \mathbf{F}_b \\ \mathbf{0}_i \end{Bmatrix}. \tag{4}$$

Here $\mathbf{0}_i$ is the null vector with the same dimensions as $\mathbf{F}_i$.

By condensation of the internal degrees of freedom it follows that

$$\tilde{\mathbf{D}}\mathbf{U}_b = \mathbf{F}_b, \qquad \tilde{\mathbf{D}}_{bb} = \mathbf{D}_{bb} - \mathbf{D}_{bi}\mathbf{D}_{ii}^{-1}\mathbf{D}_{ib}, \tag{5}$$

where $\tilde{\mathbf{D}}$ is a dynamic stiffness matrix for the cell, expressed in terms of boundary degrees of freedom only. For the present problem, $\tilde{\mathbf{D}}$ is much smaller than the original dynamic stiffness matrix for the cell, $\mathbf{D}$, given a small number of boundary nodes compared to internal nodes.

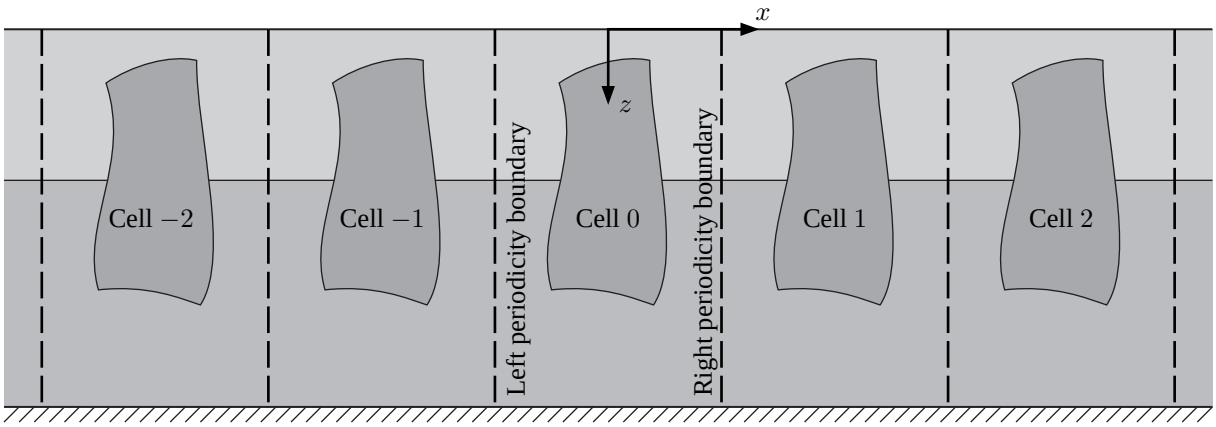


Figure 1: Periodic ground with two layers over bedrock and repeated inclusion of an object.

With reference to Figure 1, the boundary nodes are divided into those belonging to the *left* periodicity boundary and those belonging to the *right* periodicity boundary, using the subscripts L and R, respectively. Equation (5) can then be expressed into the form

$$\left[\begin{array}{cc} \tilde{\mathbf{D}}_{LL} & \tilde{\mathbf{D}}_{LR} \\ \tilde{\mathbf{D}}_{RL} & \tilde{\mathbf{D}}_{RR} \end{array} \right] \left\{ \begin{array}{c} \mathbf{U}_L \\ \mathbf{U}_R \end{array} \right\} = \left\{ \begin{array}{c} \mathbf{F}_L \\ \mathbf{F}_R \end{array} \right\}, \tag{6}$$

where the sub-matrices $\tilde{\mathbf{D}}_{LL}$, $\tilde{\mathbf{D}}_{LR}$, $\tilde{\mathbf{D}}_{RL}$ and $\tilde{\mathbf{D}}_{RR}$ are all square matrices since the number of nodes and degrees of freedom must be the same at the left and right boundaries of the cell. Likewise, $\mathbf{U}_L$, $\mathbf{U}_R$, $\mathbf{F}_L$ and $\mathbf{F}_R$ are column vectors of the same length. Otherwise, periodicity constraints cannot be applied.

The next step is to apply periodicity conditions. Based on Floquet theory, the following continuity and equilibrium condiotions must hold for the displacements and forces, respectively, at the left and right periodicity boundaries:

$$\mathbf{U}_R = \exp\left(-\mathrm{i}k\Delta\right)\mathbf{U}_L = \lambda\mathbf{U}_L, \qquad \exp\left(-\mathrm{i}k\Delta\right)\mathbf{F}_L + \mathbf{F}_R = \lambda\mathbf{F}_L + \mathbf{F}_R = \mathbf{0}_L. \tag{7}$$

Here $\mathbf{0}_L$ is the null vector having the same length as $\mathbf{F}_L$ and $\mathbf{F}_R$. Further, k is the complex-valued wavenumber related to a given mode of vibration or propagation, Δ is the length of the cell, *i.e.* the distance between the left and right boundaries, and $\lambda = -\mathrm{i}k\Delta$. Propagating modes without attenuation are characterised by real-valued wavenumbers and $|\lambda| = 1$.

Equation (7) can be reformulated into the form

$$\mathbf{U}_b = \left\{ \begin{array}{c} \mathbf{U}_L \\ \mathbf{U}_R \end{array} \right\} = \left[\begin{array}{c} \mathbf{I} \\ \lambda\mathbf{I} \end{array} \right] \mathbf{U}_L = \mathbf{\Lambda}_R\mathbf{U}_L, \qquad \mathbf{\Lambda}_R = \left[\begin{array}{c} \mathbf{I} \\ \lambda\mathbf{I} \end{array} \right], \tag{8a}$$

$$\left[\begin{array}{cc} \lambda\mathbf{I} & \mathbf{I} \end{array} \right] \left\{ \begin{array}{c} \mathbf{F}_L \\ \mathbf{F}_R \end{array} \right\} = \mathbf{\Lambda}_L\mathbf{F}_b = \mathbf{0}_L, \qquad \mathbf{\Lambda}_L = \left[\begin{array}{cc} \lambda\mathbf{I} & \mathbf{I} \end{array} \right], \tag{8b}$$

where $\mathbf{I}$ is the identity matrix with the same dimensions as $\tilde{\mathbf{D}}_{LL}$. Pre-multiplying Eq. (5) by $\mathbf{\Lambda}_L$ and making use of the results obtained in Eq. (8) lead to an equation in the form

$$\mathbf{\Lambda}_L\tilde{\mathbf{D}}\mathbf{\Lambda}_R\mathbf{U}_L = \mathbf{\Lambda}_L\mathbf{F}_b = \mathbf{0} \quad \Rightarrow \quad \left[\begin{array}{cc} \lambda\mathbf{I} & \mathbf{I} \end{array} \right] \left[\begin{array}{cc} \tilde{\mathbf{D}}_{LL} & \tilde{\mathbf{D}}_{LR} \\ \tilde{\mathbf{D}}_{RL} & \tilde{\mathbf{D}}_{RR} \end{array} \right] \left[\begin{array}{c} \mathbf{I} \\ \lambda\mathbf{I} \end{array} \right] \mathbf{U}_L = \mathbf{0}_L \tag{9}$$

which can be expressed as a non-linear eigenvalue problem in terms of the eigenvalues λ and the eigenvectors $\mathbf{U}_L$:

$$\left(\lambda^2\tilde{\mathbf{D}}_{LR} + \lambda\left(\tilde{\mathbf{D}}_{LL} + \tilde{\mathbf{D}}_{RR}\right) + \tilde{\mathbf{D}}_{RL}\right)\mathbf{U}_L = \mathbf{0}_L. \tag{10}$$

This may conveniently be reformulated into a generalized linear eigenvalue problem of the doubled dimensions,

$$\left(\left[\begin{array}{cc} \mathbf{0}_{LL} & \tilde{\mathbf{D}}_{LL} + \tilde{\mathbf{D}}_{RR} \\ \tilde{\mathbf{D}}_{LR} & \tilde{\mathbf{D}}_{LL} + \tilde{\mathbf{D}}_{RR} \end{array} \right] - \lambda \left[\begin{array}{cc} \tilde{\mathbf{D}}_{LL} + \tilde{\mathbf{D}}_{RR} & \mathbf{0}_{LL} \\ \mathbf{0}_{LL} & -\tilde{\mathbf{D}}_{LR} \end{array} \right] \right) \left\{ \begin{array}{c} \mathbf{U}_L \\ \mathbf{U}_R \end{array} \right\} = \left\{ \begin{array}{c} \mathbf{0}_L \\ \mathbf{0}_L \end{array} \right\}, \tag{11}$$

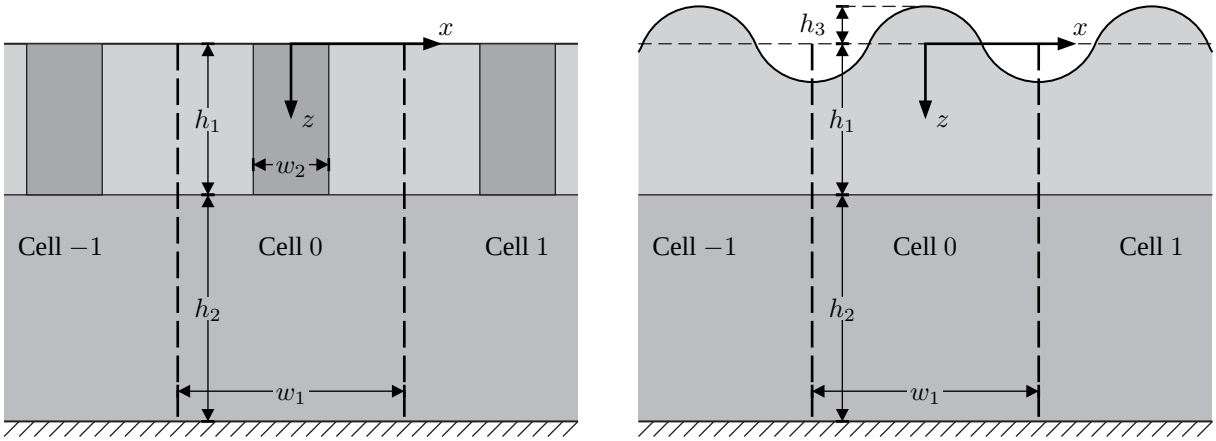
where $\mathbf{0}_{LL}$ is the null matrix with the same dimensions as $\tilde{\mathbf{D}}_{LL}$. It is observed that the eigenvector corresponds to the boundary displacement vector $\mathbf{U}_b$. Once the eigenvalue problem (11) has been solved, *i.e.* λ and $\mathbf{U}_b$ have been determined for a given angular frequency ω, the internal degrees of freedom are determined as $\mathbf{U}_i = -\mathbf{D}_{ii}^{-1}\mathbf{D}_{ib}\mathbf{U}_b$, which follows directly from Eq. (4).

2.2 Geometry and material properties for the models

Two different periodic soil geometries are considered: a top layer with periodically changing material properties (Model I), and a top layer with periodically changing position of the ground surface (Model II). The overall geometry of the reference cells for the two cases are illustrated in Figure 2. The first case may be considered as periodic ground improvement or wave impeding blocks (WIBs) obtained by, for example, jet grouting. The second case can be obtained by artificial landscaping. The curved ground surface is a combination of circular arcs. The concave and convex parts each constitute one half of the cell length with the convex arc being placed at the centre and the two concave parts constituting one quarter each in the left and right sides, respectively. As shown in Figure 2, a second layer is present below the topsoil in either case, separated from the upper layer by a horizontal interface. Further, it is noted that both cells are symmetrical around the z axis.

Models I and II are characterized by the following parameters: width of the cell, w_1; width of the WIB, w_2 (only Model I); depth of the top layer, h_1; depth of the bottom layer, h_2; amplitude of the surface elevation, h_3 (only Model II). Each material is defined by Young's modulus, E, Poisson's ratio, ν, and mass density, ρ. In the present analysis, the properties listed in Table 1 have been utilized. The properties correspond to a top layer of medium stiff clay, a bottom layer of till, and a WIB made of weak concrete. At the bottom layer is fixed in the x and z directions at its base. This corresponds to a stratified soil over bedrock.

For the finite-element analysis of the master cell, the commercial code Abaqus/Standard [8] has been employed, using Python scripting to allow parametric studies. Quadrilateral elements with eight nodes, quadratic interpolation of the displacement and full integration are applied in all models. A structured mesh is utilized with a global mesh size of 1.0 m, employing the intrinsic mesh generator in Abaqus.



(a) Changing material properties (b) Changing ground surface elevation

Figure 2: Geometry of the two cell configurations considered in the analysis.

Table 1: Material properties.

Material	Young's modulus E [MPa]	Poisson's ratio ν [$-$]	Mass density ρ [kg/m^3]
Top layer soil	50	0.48	2000
Bottom layer soil	500	0.45	2200
Stiff WIB material	5000	0.20	2400
Soft WIB material	5	0.20	1200

3 ANALYSES AND DISCUSSION

In the following, results are presented and discussed for the two cases presented as Models I and II in the previous section.

3.1 Model I: Periodic inclusions (wave impeding blocks)

Figure 3 shows the results for Model I with different cell lengths and wave impeding blocks made of stiff material as defined in Table 1. The figure indicates the number of propagating modes (in one direction only) that exist at frequencies in the range 0–20 Hz. Further, the numbers of attenuating and evanescent modes (decaying in one direction only) have been plotted. Modes with absolute values of the imaginary parts of the wavenumber higher than 1.0 m^{-1}, corresponding to high degrees of attenuation, have been filtered out. Hence, only propagating

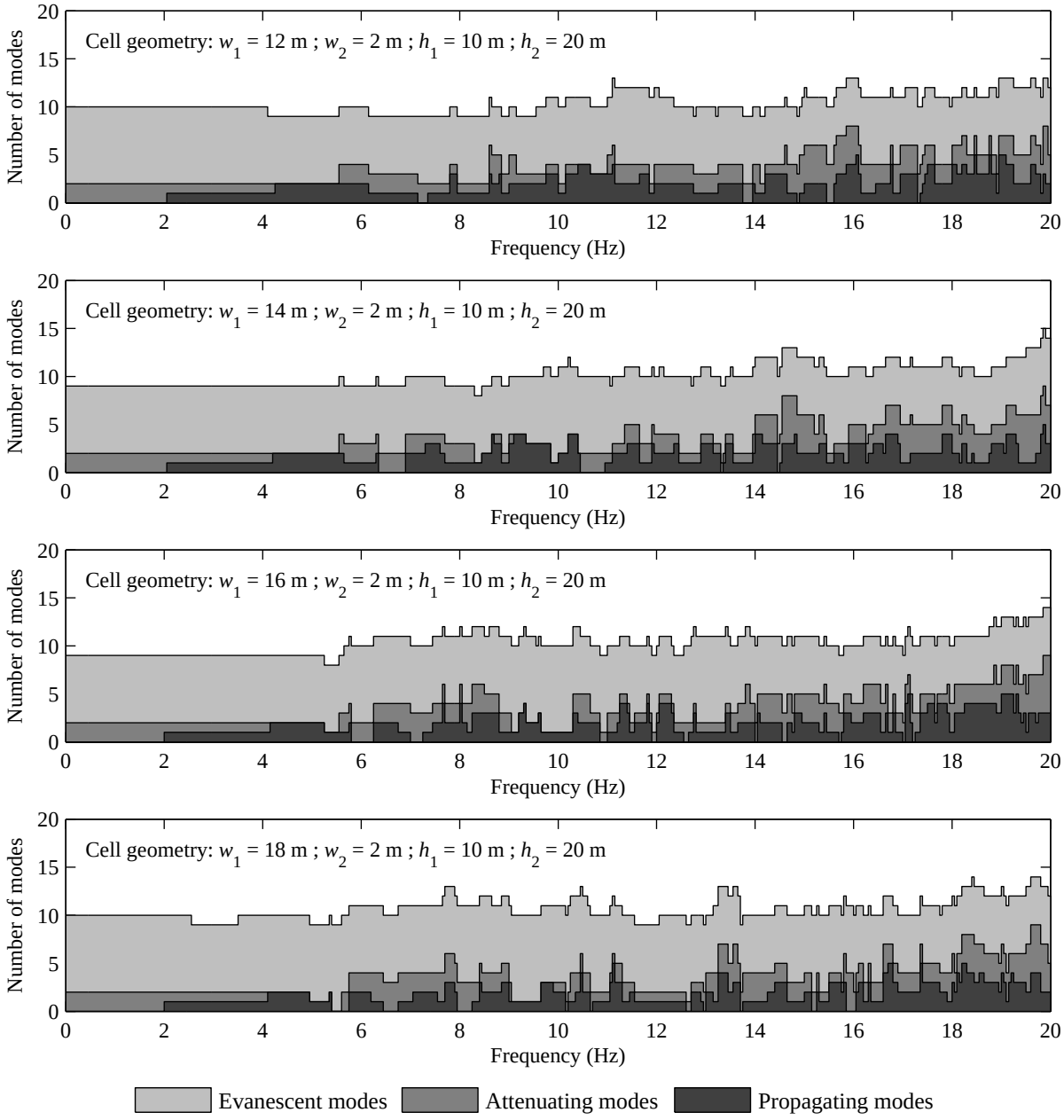


Figure 3: Skyline plots for Model I with different geometries: Stiff WIB material.

modes and evanescent or attenuating modes with low damping are included in the plots which have been given the name “skyline plots” due to their visual appearance.

For all values of w_1 included in the study, a number of stop bands are present in the frequency range 0–20 Hz, though most of the stop bands are narrow. Among the tested configurations, the cell width of 14 m provides the better solution in terms of wave mitigation. Here, relatively wide band gaps are present around 6.5 Hz and 10.5 Hz. Figuratively, these band gaps can be considered “parks” where the “noise of the city” diminishes.

Results of Model I with soft WIB material are plotted in Figure 4. Evidently, the soft WIBs provide an overall better solution in terms of mitigation. Especially it is noticed that a marked band gap occurs at frequencies of around 7 to 8 Hz, depending on the width of the cell and only for $w_1 = 14$ to 18 m. This stop band has the interesting feature that not only propagating modes but also attenuating modes disappear, leading to absolute tranquility at these frequencies.

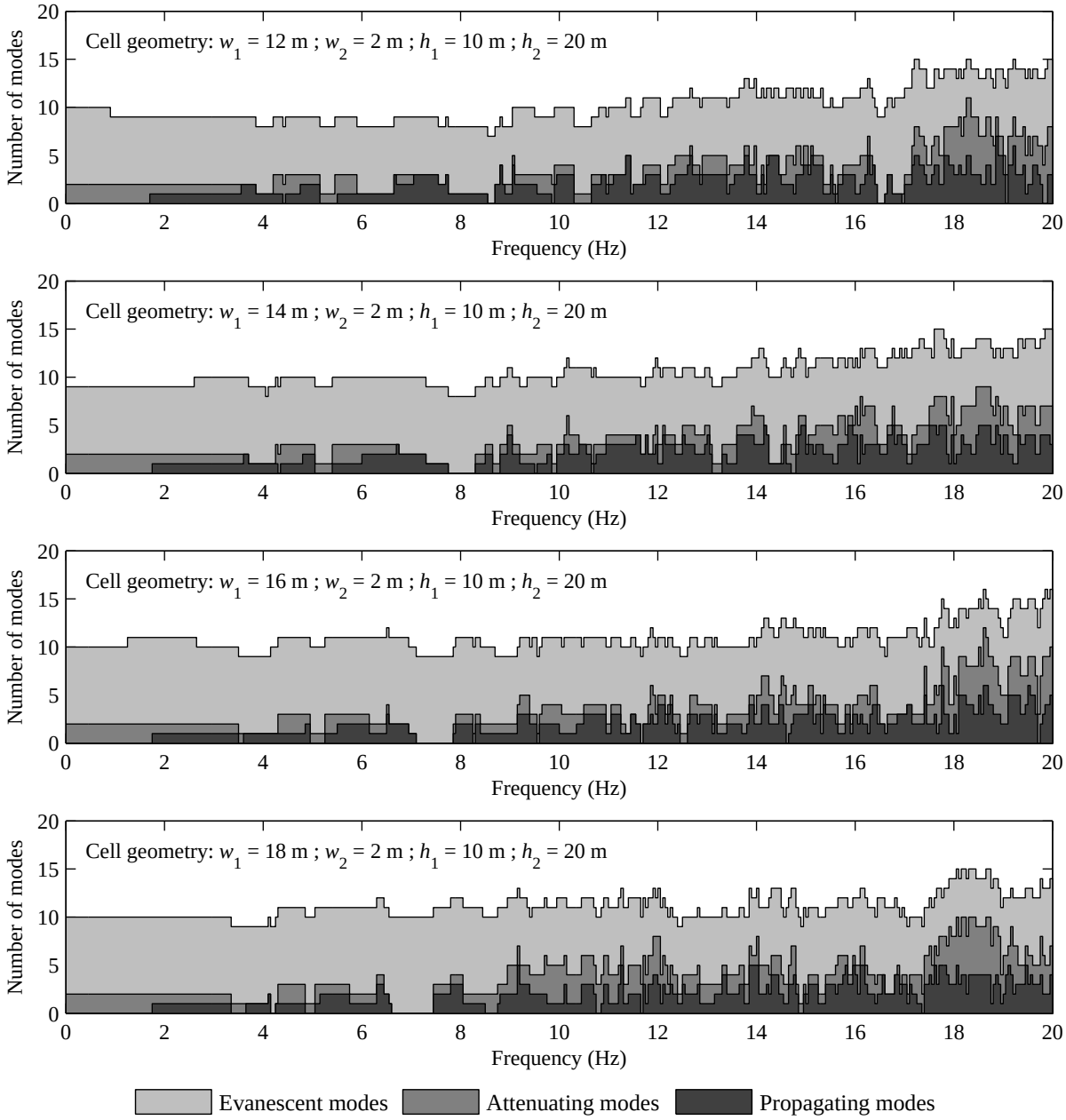


Figure 4: Skyline plots for Model I with different geometries: Soft WIB material.

3.2 Model II: Curved landscape

Figures 5 and 6 contain results of Model II with two different surface elevations, *i.e.* $h_3 = 1$ m and $h_3 = 2$ m. Again, modes with absolute values of the imaginary parts of the wavenumber higher than 1.0 m^{-1} are disregarded. Cell lengths smaller than about 8 m have been found to be ineffective for mitigation purposes. However, the cell length should neither be too large as this will make it difficult to obtain a sufficient number of repetitions to provide the required near-periodicity. Due to these reasons, cell lengths of 8, 10, 12 and 14 m have been analysed, and as in Model I it is observed that a number of stop bands occur.

Based on the results presented in Figure 5, the cells with $w_1 = 10$, 12 or 14 m perform almost equally well for the surface elevation $h_3 = 1$ m, but the band gaps occur at different frequencies. This should be taken into consideration when the ground surface is engineering

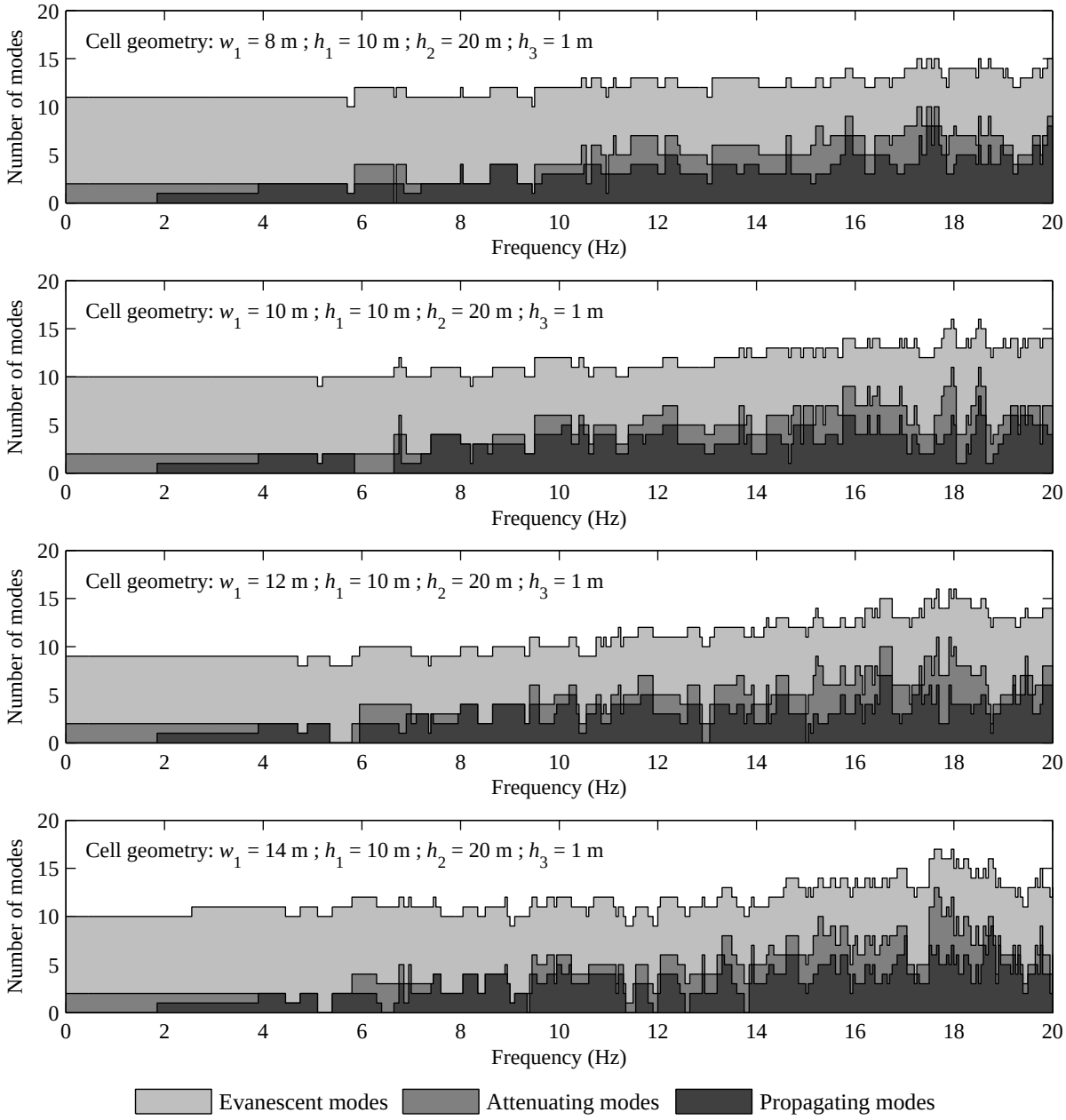


Figure 5: Skyline plots for Model II with different geometries: Surface elevation $h_3 = 1$ m.

to prevent wave propagation a certain frequencies. On the other hand, when $h_3 = 2$ m (cf. Figure 6) the cells with $w_1 = 12$ and 14 m have a superior performance. Here, a relatively wide range of frequencies is covered by two closely space band gaps around 5 and 6.5 Hz.

4 Discussion

The skyline plots presented in Figures 3–6 provide an intuitive approach to understanding how many propagating, attenuating and evanescent modes exist at a given frequency. The target of vibration mitigation is to reduce the height of the "buildings" in the plot, especially the front row which quantifies the number of propagating modes. It must be mentioned that the number of propagating modes should not be influenced by the discretization of the finite-element model of the cell, given that the solution has converged. Similarly, the number of lightly damped

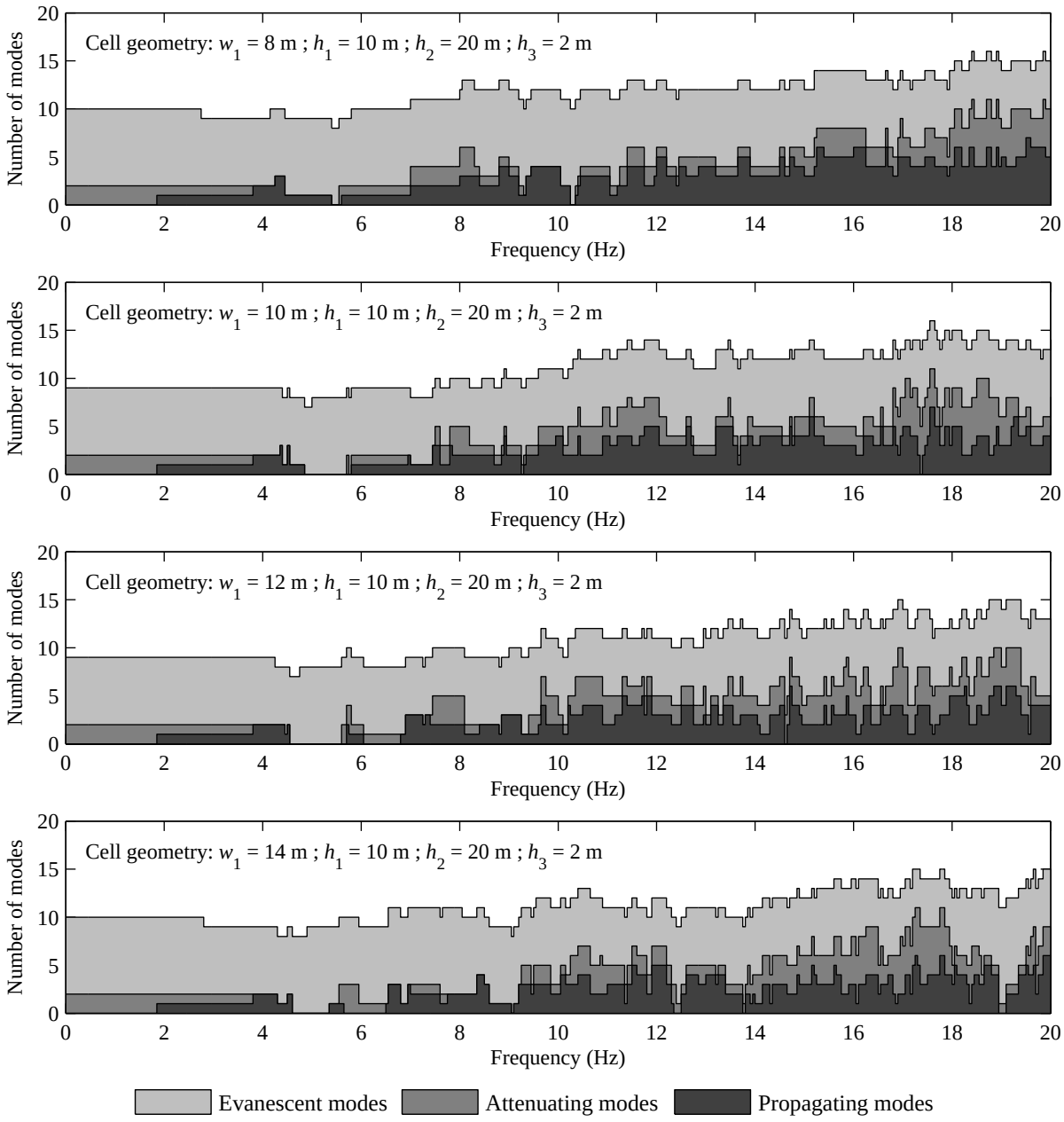


Figure 6: Skyline plots for Model II with different geometries: Surface elevation $h_3 = 2$ m.

attenuating and evanescent modes will not be influenced, *i.e.* only the number of highly damped modes will increase as a result of mesh refinement.

Comparing the results of Models I and II, it is observed that stop bands of similar width can be achieved by either concept of periodicity for the layered soil considered in the present examples. A cell length of 14–18 m has the higher efficiency for Model I, whereas a cell length of about 10–12 m is optimal for Model II. It must be noticed that this conclusion is only valid for the stratification considered in the present case, *i.e.* with the material properties listed in Table 1 and with the layer depths $h_1 = 10$ m and $h_2 = 20$ m.

From an installation point of view, the main advantage of Model I is that the ground surface does not need to be changed, *i.e.* it can remain plane. The main disadvantage is that new material (stiff or soft WIB material) needs to be put into the top layer by grouting or another technique. For Model II it is the opposite. No new material is needed—it is simply a relocation of material from one place to another—but the ground surface elevation is changed by the artificial landscaping. Thus, Model II is interesting for sites where no buildings, roads or other structures are going to be placed directly on the ground as, for example, the site surrounding the Max IV facility near Lund in Sweden [2].

Regarding the frequency range that can effectively be influenced by the periodic inclusions of wave impeding blocks or artificial landscaping, the present analyses indicate that mitigation can be achieved at frequencies well below 10 Hz. Here the wavelength of shear waves in the topsoil is more than 9 m and typically, single barriers with depths less than one Rayleigh wavelength are ineffective. Finally, it should be emphasized that the first modes of resonance in buildings typically occur at frequencies around 4–6 Hz, and modes of individual floors may occur at frequencies below 10–15 Hz. Consequently, the method of wave mitigation presented in this paper can be attractive—especially for facilities with sensitive equipment or people (*e.g.* hospitals and laboratories) in the vicinity of railways or heavily trafficked roads.

5 CONCLUSIONS

Mitigation of wave propagation in layered soil can effectively be achieved by periodic inclusion of stiff or soft wave impeding blocks (WIBs) or by altering the ground surface in a periodic manner. Based on the combined finite-element and Floquet analysis presented in this paper, the following conclusions can be made:

- Stop bands for wave propagation can be obtained at frequencies as low as 5 Hz;
- To obtain an efficient solution, the cell length must be about 10–12 m for a solution with periodic changes in the ground surface elevation, whereas for the WIB-based solution a slightly longer cell (14–18 m in length) has been found optimal in the considered case;
- A “skyline plot” has been suggested as an intuitive way of illustrating the modal density related to propagating, attenuating and evanescent modes in strata.

It should be noted that real soil layers are not perfectly homogeneous and horizontal. Hence, the performance of a periodic change to the top layer of natural soils is subject to great uncertainty. But if the entire top layer is engineered, which may be the case at sites like the Max IV facility, mitigation of low-frequency ground vibration can be achieved.

Finally, the conclusions drawn in the present paper are only valid for the considered strata which consists of a 10 m deep top layer of soft clayey soil on a 20 m deep bottom layer of till over bedrock. Future investigations should include other stratifications, and expansion to a three-dimensional model should is relevant to study the efficiency regarding point sources.

REFERENCES

[1] L. Andersen and S.R.K. Nielsen, Reduction of ground vibration by means of barriers or soil improvement along a railway track. *Soil Dynamics and Earthquake Engineering*, **25** (7–10), 701–716.

[2] P. Persson, *Reduction in ground vibrations by the use of wave obstacles*. Licentiate Dissertation, Department of Construction Sciences, Lund University, Sweden, 2013.

[3] D.J. Mead, Free wave propagation in periodically supported, infinite beams. *Journal of Sound and Vibration*, **11**, 181–197, 1970.

[4] E. Manconi and B.R. Mace, Wave characterization of cylindrical and curved panels using a finite element method. *Journal of Acoustical Society of America*, **125** (1), 154–163, 2009.

[5] P.G. Domadiya, E. Manconi, M. Vanali, L.V. Andersen, and Andrea Ricci, Numerical and experimental investigation of stop-bands in finite and infinite periodic one-dimensional structures. *Journal of Vibration and Control*, Published online before print June 25, 2014, doi: 10.1177/1077546314537863.

[6] G. Degrande, D. Clouteau, R. Othman, M. Arnst, H. Chebli, R. Klein, P. Chatterjee, and B. Janssens, A numerical model for ground-borne vibrations from underground railway traffic based on a periodic finite elementboundary element formulation. *Journal of Sound and Vibration*, **293** (3–5), 645–666, 2006.

[7] X. Bian, C. Chao, W. Jin, and Y. Chen, A 2.5D finite element approach for predicting ground vibrations generated by vertical track irregularities. *Journal of Zhejiang University SCIENCE A*, **12**(12), 885–894, 2011.

[8] Abaqus 6.14. Dassault Systèmes Simulia Corp., Providence, RI, USA.

COMPDYN 2015
5th ECCOMAS Thematic Conference on
Computational Methods in Structural Dynamics and Earthquake Engineering
M. Papadrakakis, V. Papadopoulos, V. Plevris (eds.)
Crete Island, Greece, 25–27 May 2015

TWO-DIMENSIONAL LINEAR MODEL OF ELASTIC SHELL MADE OF ANISONROPIC HETEROGENEOUS MATERIAL

Petr E. Tovstik[1], **Tatiana P. Tovstik**[2], **and Daniil Alchibaev**[3]

[1]St.Petersburg State University, Professor
198504, St.Petersburg, Universitetsky str., 22, Russia
e-mail: peter.tovstik@mail.ru

[2] Institute for Problems in Mechanical Engeneering of RAS, Senior scientist
199178, St.Petersburg, Bolshoy pr., 61, Russia
e-mail: tovstik_t@mail.ru

[3]St.Petersburg State University, Post-graduate student
198504, St.Petersburg, Universitetsky pr., 22, Russia
e-mail: peter.tovstik@mail.ru

Keywords: Thin Shell, Linear Two-dimensional model, General Anisotropy, Asymptotical Expansions.

Abstract. *A thin linearly elastic shell made of heterogeneous anisotropic material is studied. The general anisotropy described by 21 elastic moduli is examined. The material may be functionally graduated or multi-layered. The asymptotic expansions in powers of the relative shell thickness of the three-dimensional elasticity equations are used to deliver the two-dimensional shell model. In the zeroth-order approximation the model of 8th differential order is obtained. The asymptotic precision of this model is the same as the precision of the classic Kirchhoff–Love model for isotropic shell. Influence of the elastic moduli variation in the thickness direction is examined. As an example the Donnell system for shallow shells is presented, and this system is used to discuss the free transversal shell vibrations spectrum.*

1 INTRODUCTION

Numerous studies are devoted to derive the two-dimensional (2D) models of plates and shells from the three-dimensional (3D) equations of the theory of elasticity. The main used methods are the following: the method of hypotheses about distributions of unknown functions in the thickness direction z [1-4], the methods of expansions in the series of the Legendre polynomials in z [5,6], and the asymptotic expansions in series in the small parameter h_* which is equal to the dimensionless thickness [7-11].

An anisotropy of the material introduces additional difficulties. Some 2D models including a transverse shear for a transversely isotropic material are proposed in [12]. The Timoshenko–Reissner hypotheses are used and the resulting system of the 10th order is obtained.

In the present paper we study the case of the general anisotropy with 21 elastic moduli. It is shown [13,14] that for plates with the general anisotropy (in contrast to isotropic or orthotropic materials) the 2D models based on the Kirchhoff–Love (KL) or on the Timoshenko–Reissner (TR) hypotheses are inconsistent in the principal terms with respect to h_*. It is illustrated by comparison with the asymptotic 3D solutions for the test problems. To obtain the correct 2D plate model the generalized TR hypotheses are suggested [13,14]. The same hypotheses are used to deliver the 2D shell model in the case of the general anisotropy [10,11]. The system of 10th differential order is obtained. The main defect of this system consists in its high order and as a result in the presence of boundary layers among its solutions. The main principle of the correct 2D shell model is that the length of tangential waves is much longer than the shell thickness [15]. The boundary layers do not satisfy this principle.

In the present paper it is assumed that all elastic moduli are of the identical orders, we expect that in this case the KL model is better. But in connection with the generalized TR hypotheses we have the TR model. In the studied case the TR model gives asymptotically the same results as the more simple KL model. That is why it is desirable to exclude the boundary layers from the TR model and to decrease the differential order of system to 8. This simplification of model is partly made in [10], but some difficulties appear.

On the other hand if the transversal elastic moduli are relatively small the TR model gives the essentially better results than the KL model [16,17].

In this paper the asymptotic expansions in powers of the relative shell thickness of the 3D elasticity equations are used to deliver the 2D shell model. In the zeroth-order approximation the model of 8th differential order is obtained. The asymptotic precision of this model is of the order h_*, and is the same as the precision of the classic KL for isotropic shell. The accepted way allows us to avoid any hypotheses and to obtain the desired model. Additionally this model is acceptable for multi-layered (sandwich) and functionally graduated shells. For plates with the general anisotropy the similar model is proposed in [18], and for transversely isotropic material it is given in [19,20].

2 THE MAIN ASSUMPTIONS, 3D EQUATIONS AND ELASTICITY RELATIONS

Consider a thin shell of the constant thickness h with smooth mid-surface. We introduce curvilinear co-ordinates x_1, x_2 in the mid-surface coinciding with lines of curvature. The third co-ordinate $x_3 = z$ ($|z| \le h/2$) coincides with the mid-surface normal (Fig. 1). The Lame coefficients of a shell body are $H_i = A_i(1 + k_i z),\ i = 1, 2,\ H_3 = 1$, where A_i, k_i are the Lame coefficients of the mid-surface and its main curvatures. Further with the error of order h_* we put approximately $H_i \simeq A_i$, but $\partial H_i/\partial z = A_i k_i$.

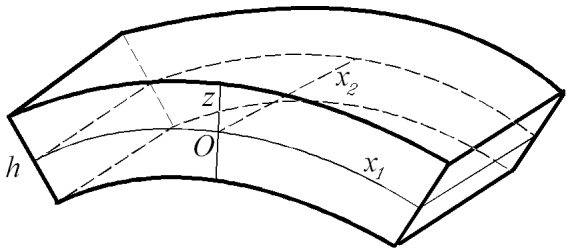


Figure 1: The shell.

In these co-ordinates the equilibrium equations are [21]

$$\begin{aligned}
&\frac{\partial(A_2\sigma_{11})}{A_2\partial y_1}+\frac{\partial(A_1\sigma_{12})}{A_1\partial y_2}+\frac{\partial A_1}{A_1\partial y_2}\sigma_{12}-\frac{\partial A_2}{A_2\partial y_1}\sigma_{22}+\frac{\partial\sigma_{13}}{\partial z}+k_1\sigma_{13}+f_1=0, \quad (1\leftrightarrow 2),\\
&\frac{\partial(A_2\sigma_{13})}{A_2\partial y_1}+\frac{\partial(A_1\sigma_{23})}{A_1\partial y_2}+\frac{\partial\sigma_{33}}{\partial z}-k_1\sigma_{13}-k_2\sigma_{23}+f_3=0,\\
&\partial y_1=A_1\partial x_1, \quad \partial y_2=A_2\partial x_2,
\end{aligned} \tag{1}$$

where σ_{ij} are stresses, $f_i(x_1, x_2, z, t)$ are the components of the external body forces densities.

Consider the material with general anisotropy containing 21 elastic moduli. To describe the elasticity relations it is more convenient to use the matrix designations instead of the 4th rank tensor. We divide stresses σ_{ij} and strains ε_{ij} into groups of tangential $\boldsymbol{\sigma}_t,\ \boldsymbol{\varepsilon}_t$ and non-tangential $\boldsymbol{\sigma}_n,\ \boldsymbol{\varepsilon}_n$ stresses and strains,

$$\begin{aligned}
&\boldsymbol{\sigma}_t=(\sigma_{11},\,\sigma_{12},\,\sigma_{22})^T, && \boldsymbol{\sigma}_n=(\sigma_{13},\,\sigma_{23},\,\sigma_{33})^T,\\
&\boldsymbol{\varepsilon}_t=(\varepsilon_{11},\,\varepsilon_{12},\,\varepsilon_{22})^T, && \boldsymbol{\varepsilon}_n=(\varepsilon_{13},\,\varepsilon_{23},\,\varepsilon_{33})^T;
\end{aligned} \tag{2}$$

the superscript ^{T} designates a transposition. Then the relations between stresses and strains are written in the matrix form

$$\boldsymbol{\sigma}_t=\mathbf{A}\cdot\boldsymbol{\varepsilon}_t+\mathbf{B}\cdot\boldsymbol{\varepsilon}_n, \quad \boldsymbol{\sigma}_n=\mathbf{B}^T\cdot\boldsymbol{\varepsilon}_t+\mathbf{C}\cdot\boldsymbol{\varepsilon}_n, \tag{3}$$

where $\mathbf{A}=\{A_{ij}\},\ \mathbf{B}=\{B_{ij}\},\ \mathbf{C}=\{C_{ij}\}$ are the matrices of the elastic moduli, the matrices $\mathbf{A}$ and $\mathbf{C}$ being symmetric. The relations (3) contain 21 elastic moduli. It is assumed that the matrix of 6th order

$$\begin{pmatrix} \mathbf{A} & \mathbf{B} \\ \mathbf{B}^T & \mathbf{C} \end{pmatrix} \tag{4}$$

is positively definite.

The strains ε_{ij} (in assumption that $H_i=A_i$) are

$$\begin{aligned}
&\varepsilon_{11}=\varepsilon_{11}(u_1,u_2,w)=\frac{\partial u_1}{\partial y_1}+\frac{\partial A_2}{A_1\partial y_2}u_2+k_1w, \quad (1\leftrightarrow 2);\\
&\varepsilon_{12}=\varepsilon_{12}(u_1,u_2,w)=A_1\frac{\partial}{\partial y_2}\left(\frac{u_1}{A_1}\right)+A_2\frac{\partial}{\partial y_1}\left(\frac{u_2}{A_2}\right),\\
&\varepsilon_{13}=\frac{\partial w}{\partial y_1}+\frac{\partial u_1}{\partial z}-k_1u_1, \ \ (1\leftrightarrow 2), \qquad \varepsilon_{33}=\frac{\partial w}{\partial z},
\end{aligned} \tag{5}$$

where $u_i,\ i=1,2$ and w are the tangential and normal displacements respectively. With an error of order h_* the terms k_iu_i may be neglected.

Assume that the upper and lower shell surfaces $z = \pm h/2$ are free from external forces,

$$\sigma_{13} = \sigma_{23} = \sigma_{33} = 0, \quad z = \pm h/2. \tag{6}$$

If the surface external forces are presented, we assume that the conditions (6) are fulfilled and these forces are included into the body external forces.

3 ASYMPTOTIC SIMPLIFICATION OF THE EQUILIBRIUM EQUATIONS

Relations (1–6) contain the full 3D description of the problem. To obtain the approximate 2D model we use the asymptotic expansions in powers of the relative shell thickness h_*. Introduce the dimensionless variables (with the sign $\hat{}$).

$$\begin{aligned} &\{x_i, u_i, w\} = l\{\hat{x}_i, \hat{u}_i, \hat{w}\}, \quad i = 1, 2, \quad x_3 = hz, \quad h_* = \frac{h}{l}, \\ &\{A_{ij}, B_{ij}, C_{ij}, \sigma_{ij}\} = E\{\hat{A}_{ij}, \hat{B}_{ij}, \hat{C}_{ij}, \hat{\sigma}_{ij}\}, \quad \{f_i\} = (E/l)\{\hat{f}_i\}, \quad i, j = 1, 2, 3, \end{aligned} \tag{7}$$

where l is the typical length of shell, E is the typical value of the elastic moduli, h_* is the small parameter. Further the sign $\hat{}$ is omitted.

As a result we get the system with small parameter h_* on the right sides

$$\frac{\partial w}{\partial z} = h_* \varepsilon_{33}; \tag{8.1}$$

$$\frac{\partial u_i}{\partial z} = h_* \left(\varepsilon_{i3} - \frac{\partial w}{\partial y_i} + k_i u_i \right), \quad i = 1, 2, \tag{8.2}$$

$$\frac{\partial \sigma_{i3}}{\partial z} = -h_* \hat{L}_i, \quad \hat{L}_i = L_i(\boldsymbol{\sigma}_t) + k_i \sigma_{i3} + f_i, \quad i = 1, 2, \tag{8.3}$$

$$\frac{\partial \sigma_{33}}{\partial z} = -h_* \hat{L}_3, \quad \hat{L}_3 = L_3(\boldsymbol{\sigma}_n) - k_1 \sigma_{11} - k_2 \sigma_{22} + f_3, \tag{8.4}$$

where

$$\begin{aligned} &L_1 = L_1(\boldsymbol{\sigma}_t) = \frac{\partial (A_2 \sigma_{11})}{A_2 \partial y_1} + \frac{\partial (A_1 \sigma_{12})}{A_1 \partial y_2} + \frac{\partial A_1}{A_1 \partial y_2} \sigma_{12} - \frac{\partial A_2}{A_2 \partial y_1} \sigma_{22}, \quad (1 \leftrightarrow 2), \\ &L_3 = L_3(\sigma_{13}, \sigma_{23}) = \frac{\partial (A_2 \sigma_{13})}{A_2 \partial y_1} + \frac{\partial (A_1 \sigma_{23})}{A_1 \partial y_2}. \end{aligned} \tag{9}$$

The main unknowns in the system (8) are $u_1, u_2, w, \sigma_{13}, \sigma_{23}, \sigma_{33}$. For deriving the right sides we use the relations (see(3))

$$\boldsymbol{\varepsilon}_n = \boldsymbol{C}^{-1} \cdot \boldsymbol{\sigma}_n - \boldsymbol{C}^{-1} \cdot \mathrm{B}^T \cdot \boldsymbol{\varepsilon}_t, \qquad \boldsymbol{\sigma}_t = \boldsymbol{A}^* \cdot \boldsymbol{\varepsilon}_t + \boldsymbol{B} \cdot \boldsymbol{C}^{-1} \cdot \boldsymbol{\sigma}_n, \quad \boldsymbol{A}^* = \boldsymbol{A} - \boldsymbol{B} \cdot \boldsymbol{C}^{-1} \cdot \boldsymbol{B}^T. \tag{10}$$

We seek the solution of the system (8) that satisfies conditions (6)

$$\sigma_{i3} = 0, \quad i = 1, 2, 3, \quad z = \pm 1/2 \tag{11}$$

in assumption that all elastic moduli are of the identical orders.

Let $\sigma_t,\ \sigma_s,\ \sigma_n$ be the typical values of the tangential stresses, $\sigma_{11}, \sigma_{12}, \sigma_{22}$, of the transversal shear stresses, σ_{13}, σ_{23}, and of the normal stresses, σ_{33}, respectively. From equations (8.3) and (8.4) the asymptotic estimates follow

$$\sigma_s \sim h_* \sigma_t, \quad \sigma_n \sim h_* \sigma_s \sim h_*^2 \sigma. \tag{12}$$

Accepting $\sigma_s = \sigma_n = 0$ we get the classic Kirchhoff–Love model. If we hold the stresses σ_s, then we obtain the Timoshenko–Reissner model.

4 ASYMPTOTIC SOLUTION OF THE SYSTEM (8)

As in [19,20], to find the approximate solution we use the method of iteration consisting in the successive solution. The equations (8). After integration at z equations (8.1) (8.2) the arbitrary functions $w^0(x_1,x_2)$ and $u_i^0(x_1,x_2)$ are introduced. Then these functions may be found from the compatibility conditions of equations (8.3), (8.4) and boundary conditions (11), which consist in the equality to zero of the average values of the right sides of equations (8.3), (8.4)

$$\left\langle \hat{L}_i \right\rangle = 0, \quad i=1,2,3, \qquad \langle Z\rangle \equiv \int_{-1/2}^{1/2} Z dz. \tag{13}$$

In zeroth-order approximations equations (8.1) and (8.2) give

$$w = w^0(x_1,x_2), \qquad u_i = u_i^0(x_1,x_2) - h_* z\varphi_i, \quad \varphi_i = \frac{\partial w^0}{\partial y_i}, \quad i=1,2. \tag{14}$$

From relation (10) omitting the small summand with $\boldsymbol{\sigma}_n$ we get

$$\begin{aligned} &\boldsymbol{\sigma}_t^0 = (\sigma_{11}^0, \sigma_{12}^0, \sigma_{22}^0)^T = \boldsymbol{A}^*\cdot(\boldsymbol{\varepsilon}_t^0 - h_* z\boldsymbol{\varepsilon}_t^{\varphi}),\\ &\boldsymbol{\varepsilon}_t^0 = (\varepsilon_{11}(u_1^0,u_2^0,w^0),\ \varepsilon_{12}(u_1^0,u_2^0,w^0),\ \varepsilon_{22}(u_1^0,u_2^0,w^0))^T,\\ &\boldsymbol{\varepsilon}_t^{\varphi} = (\varepsilon_{11}(\varphi_1,\varphi_2,0),\ \varepsilon_{12}(\varphi_1,\varphi_2,0),\ \varepsilon_{22}(\varphi_1,\varphi_2,0))^T. \end{aligned} \tag{15}$$

The compatibility conditions (13) with $i=1,2$ give two equations for the unknown functions $u_i^0(x_1,x_2)$, $w^0(x_1,x_2)$

$$\begin{aligned} &L_i(\boldsymbol{a}^{(0)}\cdot\boldsymbol{\varepsilon}_t^0) - h_* L_i(\boldsymbol{a}^{(1)}\cdot\boldsymbol{\varepsilon}_t^{\varphi}) + k_i\sigma_{i3} + F_i = 0, \quad i=1,2,\\ &\boldsymbol{a}^{(k)} = \left\langle z^k \boldsymbol{A}^* \right\rangle, \quad k=0,1,2, \qquad F_i = \langle f_i\rangle. \end{aligned} \tag{16}$$

The term $k_i\sigma_{i3}$ is small and it may be omitted.

Here we study the general case in which the elastic moduli in matrix $\boldsymbol{A}^*$ depend on z. Therefore the multi-layered shells and functionally graduated shells are not excluded from consideration. If matrix $\boldsymbol{A}^*$ is constant in z or it is symmetric, $\boldsymbol{A}^*(-z) = \boldsymbol{A}^*(z)$, then $\boldsymbol{a}^{(1)} = \boldsymbol{0}$ (further we refer to this case as to symmetric one, the opposite case is asymmetric).

Now we find stresses σ_{13}^0 and σ_{23}^0 in zeroth-order approximation

$$\begin{aligned} &\sigma_{i3}^0(x_1,x_2,z) = -h_*\left(L_i(\tilde{\boldsymbol{a}}^{(0)}\cdot\boldsymbol{\varepsilon}_t^0) - h_* L_i(\tilde{\boldsymbol{a}}^{(1)}\cdot\boldsymbol{\varepsilon}_t^{\varphi}) + \tilde{F}_i\right), \quad i=1,2,\\ &\tilde{\boldsymbol{a}}^{(k)}(z) = \textstyle\int_{-1/2}^{z} z^k \boldsymbol{A}^* dz, \quad \tilde{F}_i(z) = \int_{-1/2}^{z} f_i dz. \end{aligned} \tag{17}$$

Lastly the compatibility condition for equation (8.4) gives the third equation for functions $u_i^0(x_1,x_2)$, $w^0(x_1,x_2)$

$$\begin{aligned} &h_* L_3\left(L_1(\boldsymbol{a}^{(0)}\cdot\boldsymbol{\varepsilon}_t^0)), L_2(\boldsymbol{a}^{(0)}\cdot\boldsymbol{\varepsilon}_t^0))\right) - h_*^2 L_3\left(L_1(\boldsymbol{a}^{(1)}\cdot\boldsymbol{\varepsilon}_t^{\varphi})), L_2(\boldsymbol{a}^{(1)}\cdot\boldsymbol{\varepsilon}_t^{\varphi}))\right) +\\ &+h_* L_3(\langle zF_1\rangle, \langle zF_2\rangle) - k_1\sigma_{11}^0 - k_2\sigma_{22}^0 + F_3 = 0. \end{aligned} \tag{18}$$

Three equations (16) and (18) give the system from which the unknown functions $u_i^0(x_1,x_2)$, $w^0(x_1,x_2)$ are to be found. The differential order of this system is 8 as in the Kirchhoff–Love model.

5 COMPARISON WITH THE KIRCHHOFF–LOVE MODEL

We introduce the tangential stress-resultants, $\hat{\boldsymbol{T}}$, the stress-couples, $\hat{\boldsymbol{M}}$, and the shear stress-resultants, $\hat{\boldsymbol{Q}}$, by relations

$$\begin{aligned}
&\hat{\boldsymbol{T}} = (\hat{T}_{11}, \hat{T}_{12}, \hat{T}_{22})^T = \langle \boldsymbol{\sigma}_t \rangle = \boldsymbol{T} + \boldsymbol{N}^{\varphi}, \quad \boldsymbol{T} = \boldsymbol{a}^{(0)} \cdot \boldsymbol{\varepsilon}_t^0, \quad \boldsymbol{N}^{\varphi} = -h_* \boldsymbol{a}^{(1)} \cdot \boldsymbol{\varepsilon}_t^{\varphi}, \\
&\hat{\boldsymbol{M}} = (\hat{M}_{11}, \hat{M}_{12}, \hat{M}_{22})^T = \langle z \boldsymbol{\sigma}_t \rangle = \boldsymbol{M} + \boldsymbol{N}^t, \quad \boldsymbol{M} = -h_*^2 \boldsymbol{a}^{(2)} \cdot \boldsymbol{\varepsilon}_t^{\varphi}, \quad \boldsymbol{N}^t = h_* \boldsymbol{a}^{(1)} \cdot \boldsymbol{\varepsilon}_t^0, \\
&\boldsymbol{Q} = (Q_1, Q_2)^T = (\langle \sigma_{13} \rangle, \langle \sigma_{23} \rangle)^T.
\end{aligned} \tag{19}$$

From (8.3), (11), (17) it follows

$$Q_i = \langle \sigma_{i3} \rangle = -\left\langle z \frac{\partial \sigma_{13}}{\partial z} \right\rangle = h_* \left\langle z (L_i(\boldsymbol{\sigma}_t^0) + f_i) \right\rangle = L_i(\hat{\boldsymbol{M}}) + h_* \langle z f_i \rangle \tag{20}$$

Therefore equations (16) and (18) coincide with the corresponding Kirchhoff–Love equations, respectively

$$\begin{aligned}
&L_i(\hat{\boldsymbol{T}}) + F_i = 0, \quad i = 1, 2, \\
&\frac{\partial (A_2 Q_1)}{A_2 \partial y_1} + \frac{\partial (A_1 Q_2)}{A_1 \partial y_2} - k_1 \hat{T}_{11} - k_2 \hat{T}_{22} + F_3 = 0.
\end{aligned} \tag{21}$$

In the non-symmetric case equations (21) are complex enough. In the symmetric case $\boldsymbol{a}^{(1)} = \boldsymbol{0}$ and $\boldsymbol{N}^t = \boldsymbol{N}^{\varphi} = \boldsymbol{0}$, $\hat{\boldsymbol{T}} = \boldsymbol{T}$, $\hat{\boldsymbol{M}} = \boldsymbol{M}$, and the equations (21) accept the ordinary form of the Kirchhoff–Love equations.

The surface potential energy density is

$$U = \frac{1}{2} \sum_{i,j=1}^{3} \langle \sigma_{ij} \varepsilon_{ij} \rangle \tag{22}$$

and after the accepted simplifications we get approximately

$$U \approx U^0 = \frac{1}{2} \left\langle (\boldsymbol{\varepsilon}_t^0 - h_* z \boldsymbol{\varepsilon}_t^{\varphi})^T \cdot \boldsymbol{A}^* \cdot (\boldsymbol{\varepsilon}_t^0 - h_* z \boldsymbol{\varepsilon}_t^{\varphi}) \right\rangle. \tag{23}$$

The variation of the full potential energy $\Pi = \int\int_S U^0 \, dS$ (here S is the shell mid-surface) with respect to functions $u_1^0(x_1, x_2)$, $u_2^0(x_1, x_2)$, $w^0(x_1, x_2)$ gives the equations (16), (18) or the equations (21) and the boundary conditions.

6 THE DONNELL TYPE SIMPLIFICATION

The more complex system (than the system (21)) of 10th differential order of the Timoshenko–Reissner type is obtained in [10,11], and the main stress-strain states (SSS) are described. After excluding the boundary layer the order of this system is decreased to 8, the obtained system coincides with the system (21) in the symmetric case.

Here we study the system (21) in the asymmetric case in assumptions which lead to the Donnell system. We suppose that the Lame coefficients, A_1, A_2, the curvatures, k_1, k_2, of the mid-surface, and the matrices of elasticity, $\boldsymbol{a}^{(0)}, \boldsymbol{a}^{(1)}, \boldsymbol{a}^{(2)}$, $(\boldsymbol{a}^{(1)} \neq \boldsymbol{0})$ are constant, the external forces $f_1 = f_2 = 0$. These assumptions are valid for the shallow shell, for the cylindrical shell,

and for the SSS with the large variability (see [7] and the relation (33) below). Under these assumptions the governing relations are

$$\begin{aligned}&\boldsymbol{\varepsilon}_t^0 = (p_1u_1 + k_1w,\, p_1u_2 + p_2u_1,\, p_2u_2 + k_2w)^T,\\ &\boldsymbol{\varepsilon}_t^\varphi = (p_1^2w,\, 2p_1p_2w,\, p_2^2w)^T,\end{aligned}\qquad p_1 = \frac{\partial}{\partial y_1},\quad p_2 = \frac{\partial}{\partial y_2}. \tag{24}$$

$$\begin{aligned}&p_1\hat{T}_{11} + p_2\hat{T}_{12} = 0,\quad p_1\hat{T}_{12} + p_2\hat{T}_{22} = 0,\\ &\hat{\boldsymbol{T}} = (\hat{T}_{11}, \hat{T}_{12}, \hat{T}_{22})^T = \boldsymbol{a}^{(0)}\cdot\boldsymbol{\varepsilon}_t^0 - h_*\boldsymbol{a}^{(1)}\cdot\boldsymbol{\varepsilon}_t^\varphi.\end{aligned} \tag{25}$$

$$\begin{aligned}&p_1Q_1 + p_2Q_2 - k_1\hat{T}_{11} - k_2\hat{T}_{22} + F_3 = 0,\\ &Q_1 = p_1\hat{M}_{11} + p_2\hat{M}_{12},\quad Q_2 = p_1\hat{M}_{12} + p_2\hat{M}_{22} = 0,\\ &\hat{\boldsymbol{M}} = (\hat{M}_{11}, \hat{M}_{12}, \hat{M}_{22})^T = h_*\boldsymbol{a}^{(1)}\cdot\boldsymbol{\varepsilon}_t^0 - h_*^2\boldsymbol{a}^{(2)}\cdot\boldsymbol{\varepsilon}_t^\varphi.\end{aligned} \tag{26}$$

The system (24)–(26) may be reduced to the system with two unknown functions, $w(x_1, x_2)$,$\Phi(x_1, x_2)$,

$$\begin{aligned}&L_4(p_1, p_2)\Phi - (k_1p_2^2 + k_2p_1^2)w + h_*\hat{L}_4(p_1, p_2)w = 0,\\ &h_*\hat{N}_4(p_1, p_2)\Phi - (k_1p_2^2 + k_2p_1^2)\Phi - h_*^2N_4(p_1, p_2)w + F_3 = 0,\end{aligned} \tag{27}$$

where differential operators $L_4, \hat{L}_4, N_4, \hat{N}_4$ of forth order are

$$\begin{aligned}&L_4 = \boldsymbol{P}_1^T\cdot\boldsymbol{b}\cdot\boldsymbol{P}_1,\quad \hat{L}_4 = \boldsymbol{P}_1^T\cdot\boldsymbol{c}\cdot\boldsymbol{P}_2,\qquad \boldsymbol{b} = \left(\boldsymbol{a}^{(0)}\right)^{-1},\quad \boldsymbol{c} = \boldsymbol{b}\cdot\boldsymbol{a}^{(1)}\\ &N_4 = \boldsymbol{P}_2^T\cdot\hat{\boldsymbol{a}}^{(2)}\boldsymbol{P}_2,\quad \hat{N}_4 = \boldsymbol{P}_2^T\cdot\boldsymbol{c}^T\cdot\boldsymbol{P}_1 = \hat{L}_4,\\ &\hat{\boldsymbol{a}}^{(2)} = \boldsymbol{a}^{(2)} - \boldsymbol{a}^{(1)}\cdot\boldsymbol{b}\cdot\boldsymbol{a}^{(1)},\qquad \boldsymbol{P}_1 = (p_2^2,\, -p_1p_2,\, p_1^2)^T,\quad \boldsymbol{P}_2 = (p_1^2,\, 2p_1p_2,\, p_2^2)^T.\end{aligned} \tag{28}$$

Function Φ is the stress-function connected with the stress-resultants by relations

$$\hat{T}_{11} = p_2^2\Phi,\quad \hat{T}_{12} = -p_1p_2\Phi,\quad \hat{T}_{22} = p_1^2\Phi. \tag{29}$$

The first equation (27) (the so called compatibility equation) is obtained after excluding u_1 and u_2 from the relations (25). The second equation (27) is the equilibrium equation (26) after simplifications.

In the symmetric case

$$\boldsymbol{a}^{(1)} = 0,\quad \hat{L}_4 = \hat{N}_4 = 0,\quad \hat{\boldsymbol{a}}^{(2)} = \boldsymbol{a}^{(2)} \tag{30}$$

and the system (27) coincides with the earlier obtained Donnell system [22-24].

7 THE SHORT ASYMPTOTIC ANALYSIS OF THE DONNELL SYSTEM (27)

In the symmetric case the analysis of the Donnell system for anisotropic shells is carried out in [10]. Here we pay attention to the difference between the symmetric and the asymmetric cases.

Firstly, we estimate the possible values of the stiffness matrices. Assume that all elements of the matrix $\boldsymbol{A}^*(z)$ depend of z as

$$\boldsymbol{A}^*(z) = f(z)\boldsymbol{A}_0^*,\quad \langle f(z)\rangle = 1. \tag{31}$$

If the function $f(z)$ is linear then the most difference between the linear and the non-linear cases has place for $f(z) = 1 - 2z$. For this $f(z)$ we get

$$\begin{aligned} &\boldsymbol{a}^{(0)} = \boldsymbol{A}_0^*, \quad \boldsymbol{a}^{(1)} = -\frac{1}{6}\boldsymbol{a}^{(0)}, \quad \boldsymbol{b}\cdot\boldsymbol{a}^{(1)} = -\frac{1}{6}\boldsymbol{E}, \\ &\boldsymbol{a}^{(2)} = \frac{1}{12}\boldsymbol{a}^{(0)}, \quad \hat{\boldsymbol{a}}^{(2)} = \frac{1}{18}\boldsymbol{a}^{(0)} = \frac{2}{3}\boldsymbol{a}^{(2)}, \end{aligned} \tag{32}$$

where $\boldsymbol{E}$ is the unit matrix of the third order. Therefore, for a functionally graduated material with $f(z) = 1 - 2z$ the bending stiffness matrix $\hat{\boldsymbol{a}}^{(2)}$ is 2/3 times of the matrix $\boldsymbol{a}^{(2)}$ for an isotropic material.

To fulfill the asymptotic analysis of the system (27) or of the system (24–(26), and to describe the asymptotic behavior of functions at $h_* \to 0$ let us introduce partial variability indices t_1, t_2 of the state (SSS) by the relations

$$\frac{\partial Z}{\partial x_1} \sim h_*^{-t_1} Z, \quad \frac{\partial Z}{\partial x_2} \sim h_*^{-t_2} Z, \tag{33}$$

where Z is any unknown function. We refer to $t = \max(t_1, t_2)$ as to a common variability indix. From (24) it follows that

$$p_1 \sim h_*^{-t_1}, \quad p_2 \sim h_*^{-t_2}. \tag{34}$$

The asymptotic approach allows us simply to estimate the orders of the unknown variables and to construct the approximate equations and their solutions (see also ([7,10,11,25]).

For the momentless (membrane) SSS the variability of unknowns is small ($t = 0$) and with the error of the order h_* the system (27) accepts the form

$$L_4(p_1, p_2)\Phi - (k_1 p_2^2 + k_2 p_1^2)w = 0, \quad (k_1 p_2^2 + k_2 p_1^2)\Phi = F_3. \tag{35}$$

As it is clear the effects of the asymmetry are not contained in (35). Also the equations (35) may be approximately used to describe the SSS with $t < 1/2$, but the error is larger and it is of the order h_*^{1-2t}.

The differential order of the system (35) is not enough to satisfy all 4 boundary conditions at the shell edges, and it is necessary to construct the additional SSS, namely the edge effect solutions. Let us study the edge effect near the edge $x_1 = 0$, for which the variability indices are $t_1 = 1/2,\ t_2 = 0$. In this case with the error of the order $h_*^{(1/2)}$ the edge effect satisfies to the equation

$$h_*^2(b_{33}\hat{a}_{11}^{(2)} + c_{13}^2)\frac{\partial^4 w}{\partial y^4} - 2h_* k_2 c_{13}\frac{\partial^2 w}{\partial y^2} + k_2^2 w = 0, \tag{36}$$

where we hold only the largest elements of operators (28) and

$$\boldsymbol{b} = \{b_{ij}\}, \quad \boldsymbol{c} = \{c_{ij}\}, \quad \hat{\boldsymbol{a}}^{(2)} = \{\hat{a}_{ij}^{(2)}\}. \tag{37}$$

According to (36) the asymmetry influence on the edge effect is essential.

If $t_1 = t_2 = 1/2$ then all terms in the system (27) are of the identical order and the asymmetry influence is also essential.

For plates $k_1 = k_2 = 0$, and the equations (27) are

$$L_4(p_1, p_2)\Phi + h_*\hat{L}_4(p_1, p_2)w = 0, \qquad h_*\hat{N}_4(p_1, p_2)\Phi - h_*^2 N_4(p_1, p_2)w + F_3 = 0. \tag{38}$$

In the symmetric case (with $\hat{L}_4 = \hat{N}_4 = 0$) the equations (38) may be solved separately, but in the general (asymmetric) case these equations are connected.

8 FREE VIBRATIONS OF A SHALLOW SHELL

As an example of the Donnell equations applications we study the free transversal vibrations of a shallow shell. According to the assumptions, in which the Donnell equations are acceptable, we hold only the normal inertia forces. In equation (27) we put

$$F_3 = \Lambda w, \quad \Lambda = \langle\rho\rangle\, l^2\omega^2 E, \tag{39}$$

where Λ is the unknown dimensionless frequency parameter, ω is the natural frequency, $\langle\rho\rangle$ is the average mass density.

We seek the solution of system (27) in the form

$$w(x_1,x_2) = w_0 \exp\{i(q_1y_1+q_2y_2)\}, \quad \Phi(x_1,x_2) = \Phi_0 \exp\{i(q_1y_1+q_2y_2)\}, \quad i=\sqrt{-1}. \tag{40}$$

Then equations (27) give

$$\Lambda = h_*^2 N_4(q_1,q_2) + \frac{\Big(k_1q_2^2 + k_2q_1^2 + h_*\hat{L}_4(q_1,q_2)\Big)^2}{L_4(q_1,q_2)}. \tag{41}$$

This expression (through the term $\hat{L}_4$) indicates influence the asymmetry of elastic properties on the natural frequencies. To use the expression (41) for calculations it is necessary to know the wave numbers q_1 and q_2. They may be found satisfying the boundary conditions at the shell edges. In the general case it is a very complex problem. For the rectangular shallow shell ($0 \le x_1 \le l_1,\ 0 \le x_2 \le l_2$) this problem is solved in [26] by adding to the form (40) solutions of the so-called dynamic edge effects decreasing away from the shell edges.

The expression (41) allows us to get a lot of qualitative conclusions about the dependence of natural frequencies on the shell curvatures k_1 and k_2, and on the variability indices t_1 and t_2 of the form (40) ($q_i \sim h_*^{-t_i}$).

For the circular cylindrical shell we take $q_2 = m$ (m is integer).

The equations (27) and the expression (41) do not describe the tangential vibrations, and frequencies of these vibrations are of the order $\Lambda \sim 1$. That is why we discuss the lowest part of the shell spectrum containing frequencies with $\Lambda << 1$.

The functions $L_4(q_1,q_2)$ and $N_4(q_1,q_2)$ are positively defined. Taking into account that all elements of matrices $\hat{\boldsymbol{a}}^{(2)}$, $\boldsymbol{b}$, $\boldsymbol{c}$ are of the order of 1 we deliver from the expression (41) the following estimate

$$\Lambda \sim h_*^{2-4t} + \big((k_1h_*^{-2t_2} + k_2h_*^{-2t_1})h_*^{2t} + j_ch_*\big)^2, \qquad t=\max(t_1,t_2), \quad t_1\ge 0,\ t_2\ge 0, \tag{42}$$

where $j_c = 0$ in the symmetric case and $j = 1$ in the asymmetric case.

From (42) it follows that

— inequality $\Lambda \ll 1$ is fulfilled only if $t < 1/2$,

— for the cylindrical shell (with $k_1 = 0$) $\min\Lambda \sim h_*k_2$ at $t_1 = 0,\ t_2 = 1/4$,

— for the shell with negative Gaussian curvature (with $k_1k_2 < 0$) $\min\Lambda \sim h_*^{2/3}$ at $t_1 = t_2 = 1/3$,

— for the convex shell (with $k_1k_2 < 0$) inequality $\Lambda \ll 1$ is possible only if $k_1^2 + k_2^2 \ll 1$.

For shells made of isotropic homogeneous material the similar conclusions are obtained in [27]. In the accepted assumptions the anisotropy and the asymmetry of material effects on the value of Λ, but its asymptotic order at $h_* \to 0$ remains the same.

9 BUCKLING OF THE CIRCULAR CYLINDRICAL SHELL

The same method may be applied in study of the buckling of shallow shell. Consider for example the circular cylindrical shell under normal pressure. For this case, we put in equation (27)

$$F_3 = \Lambda p_2^2 w, \tag{43}$$

where Λ is the unknown loading parameter.

For the cylindrical shell the curvilinear coordinates x_1, x_2 coincide with the arc lengths in the longitudinal and circumferential directions, $0 \le x_2 \le 2\pi$ and $k_1 = 0, k_2 = 1$. For the cylindrical shell the SSS is described with the variability indices $t_1 = 0,\ t_2 = 1/4$ (semi-momentless SSS).

We seek the solution of system (27) in the form

$$w(x_1, x_2) = w(y_1)\exp\{imy_2\}, \quad \Phi(x_1, x_2) = \Phi(y_1)\exp\{imy_2\}, \quad i = \sqrt{-1}. \tag{44}$$

where m is integer.

Since $t_2 = 1/4$, we will seek the solutions $w(y_1), \Phi(y_1)$ and Λ as an asymptotic series of a small parameter $\mu = h_*^{1/4}$.

Let us assume, for example, that the boundary conditions are of clamped edge

$$w = u_1 = u_2 = \gamma = 0, \tag{45}$$

where γ is average angle of the normal fibers rotation.

In zeroth-order approximation, equations (27) give

$$p_1^4 w_0 - r^4 w_0 = 0, \quad r^4 = m^4 b_{11}\left(m^2\Lambda_0 - m^4 h_*^2 \hat{a}_{33}^{(2)}\right), \tag{46}$$

with boundary conditions

$$w_0 = p_1 w_0 = 0, \quad y_1 = \pm 1/2. \tag{47}$$

For $r^* \approx 4.73$ equation (46) with boundary conditions (47) has a non-zero solution

$$w_0(y_1) = \frac{\cos(ry_1)}{\cos(0.5r)} - \frac{\cosh(ry_1)}{\cosh(0.5r)}. \tag{48}$$

Opposed to the free vibrations case, we are interested in only finding minimal loading parameter. The expression for Λ_0 and minimal m can be derived from (46):

$$\Lambda_0 = \min_m \frac{1}{m^6}\left(\frac{r^4}{b_{11}} + m^4 h_*^2 \hat{a}_{33}^{(2)}\right).$$

As it was said earlier, the solution of equation (46) might not satisfy all 4 boundary conditions because the differential order of equation (46) is less than order of the system (27). Nonetheless, solution (48) satisfies the particular boundary conditions (45).

The equation in first approximation is

$$p_1^4 w_1 - r^4 w_1 = \Lambda_1 m^2 b_{11} w_0 + 2irm^7\left(\hat{a}_{23}^{(2)} b_{11} - \hat{a}_{33}^{(2)} b_{12} + \frac{\Lambda_0}{m^5} b_{12}\right) p_1 w_0 \tag{49}$$

with following boundary conditions

$$w_1 = 0, \quad p_1 w_1 = i\frac{b_{12}}{m^3 b_{11}} p_1^2 w_0, \quad y_1 = \pm 1/2.$$

Here, for equation (49) to have a solution, Λ_1 should satisfy the compatibility condition:

$$\int_{-1/2}^{1/2}\left(\Lambda_1 m^2 b_{11} w_0 + 2irm^7\left(\hat{a}_{23}^{(2)} b_{11} - \hat{a}_{33}^{(2)} b_{12} + \frac{\Lambda_0}{m^5} b_{12}\right) p_1 w_0\right) w_0 dy_1 = 0. \tag{50}$$

It is easy to see that $\Lambda_1 = 0$.

The solution $w_1(y_1)$ can be written in form

$$w_1 = i\left(\frac{\alpha_1 y_1}{4r^4} p_1^2 w_0 + \alpha_2 p_1 w_0 + \alpha_3 p_1^3 w_0\right), \tag{51}$$

where

$$\alpha_1 = 2rm^7\left(\hat{a}_{23}^{(2)} b_{11} - \hat{a}_{33}^{(2)} b_{12} + \frac{\Lambda_0}{m^5} b_{12}\right),$$

$$\alpha_2 = \frac{\alpha_1\left(16r^4 - 4 + r\tan(r/2) - r\tanh(r/2)\right)}{16r^4}, \alpha_3 = \frac{\alpha_1}{4r^5\left(\tan(r/2) - \tanh(r/2)\right)}.$$

Let us examine the material with elastic moduli of symmetric case discussed in [10] with the following matrix A_0^*:

$$A_0^* = \begin{pmatrix} 1.0577 & 0.0185 & 0.3056 \\ 0.0185 & 0.3903 & -0.0103 \\ 0.3056 & -0.0103 & 1.0482 \end{pmatrix}. \tag{52}$$

For the cylindrical shell of the relative thickness $h_* = 0.01$ we will have the loading parameter $\Lambda \approx 4.388 \times 10^{-4}$ with number of half-waves in circumferential direction $m = 8$.

On figure 2 the buckling form of first-order approximation is presented. Unlike the isotropic case, the buckling form has an incline on circumferential direction.

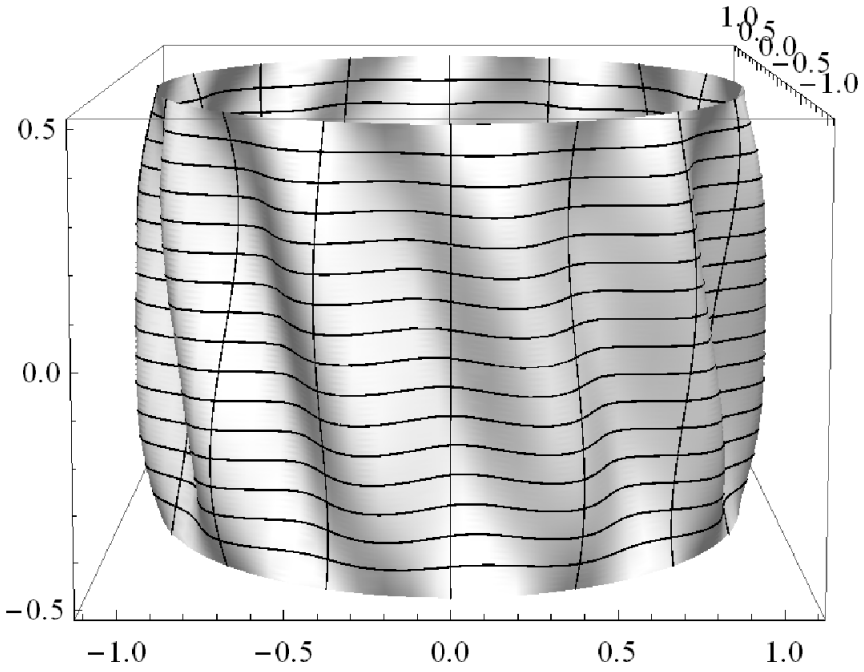


Figure 2: The buckling form of the cylindrical shell.

10 CONCLUSIONS

- For thin anisotropic heterogeneous in the thickness direction shell the 2D model is built. To deliver this model the asymptotic expansions of the 3D equations of elasticity in powers of the relative shell thickness h_* are used. As a result in zeroth-order approximation the system of the 8th differential order is obtained. This approximation is based on the approximate elasticity relations $\boldsymbol{\sigma}_t = \boldsymbol{A}_* \cdot \boldsymbol{\varepsilon}_t$ which establish the dependence between the tangential stresses $\boldsymbol{\sigma}_t$ and strains $\boldsymbol{\varepsilon}_t$. These relations contain 6 effective elastic moduli while the initial elasticity relations contain 21 elastic moduli.

- The same governing system may be obtained also by two alternative ways. One of them consists of the direct using of the KL hypotheses in combination with the mentioned approximate elasticity relation, and then of the averaging the result in the thickness direction z. In the other way we introduce the approximate elastic energy density $\boldsymbol{\sigma}_t(z) \cdot \boldsymbol{\varepsilon}_t(z)/2$ based on the approximate elasticity relation. After calculating the variation of energy in u_1, u_2, w and after averaging in z we get the equilibrium equations and the boundary conditions.

10.1 Acknowledgements

Financial support by Russian Foundation for Basic Research, grants 12.01.92000.HHC-a, 13.01.00523-a, 15-01-05903-a and the Program by Division of Mechanics by Russian Academy of Sciences is acknowledged.

REFERENCES

[1] G. Kirchhoff, *Vorlesungen uber Matematische Physik. Mechanik*. Leipzig, 1876.

[2] A.E.H. Love, *The Mathematical Theory of Elasticity*. Cambridge Univ. Press, 1934.

[3] S.P. Timoshenko, *Strength of Materials*. Van Vistrand, New York, 1956.

[4] E. Reissner, *The effect of transverse shear deformation on the bending of elastic plates*. Trans. ASME, J. Appl. Mech. **1**2, 69-77.

[5] I.N. Vekua, *Some General Methods of construction of the Various Models of Shell Theories*. Nauka. Moscow. 1982. (in Russian)

[6] V.A. Rodionova, B.F. Titaev, K.F. Chernykh, *Applied theory of anisotropic plates and shells*. St.Petersburg Univ. Press. 1996. (in Russian)

[7] A.L. Goldenveizer, *Theory of Elastic Thin Shells*. Nauka, Moscow. 1976. (in Russian)

[8] L.A. Agalovyan, *Asymptotic theory of anisotropic plates and shells*. Nauka, Moscow 1997. (in Russian)

[9] Y. Vetyukov, A. Kuzin, M. Krommer, Asymptotic splitting in the three-dimensional problem of elasticity for non-homogeneous piezoelectric plates. *Int. J. Solids & Structures*. **48**, 12-23. 2011.

[10] P.E. Tovstik, T.P. Tovstik, Two-dimensional models of shells made of an anisotropic material. *Acta mechanica*. V.225(3), 647-661. 2014.

[11] P.E. Tovstik, T.P. Tovstik, Two-dimensional linear model of anisotropic shells. *SSTA. 2013.* Gdansk. V.3, 153-156. 2013.

[12] S.A. Ambartsumyan, *General theory of anisotropic shells*. Nauka, Moscow 1974.(in Russian)

[13] P.E. Tovstik, T.P. Tovstik, Two-dimensional models of plates made of an anisotropic material. *In "Computer methods in mechanics of continuous media". Issue 3.* St. Petersburg Univ. Press. 4-16. 2008.

[14] P.E. Tovstik, Two-dimensional models of plates made of an anisotropic material. *Doklady Physics*. **5**4. No 4, 205-209. 2009.

[15] V.V. Novozhilov, *Theory of Thin Shells*. Sudpromgiz. Leningrad 1962. (in Russian)

[16] P.E. Tovstik, On the asymptotic character of approximate models of beams, plates and shells. *Vestnik St.Petersburg Univ. Math. Allerton Press. No 3,* 49-54. 2007. (in Russian)

[17] P.Ye. Tovstik, Vibrations and stability of a prestressed plate on an elastic foundation. *J. Appl. Math. & Mech.* **7**3. 77-87. 2009.

[18] P.E. Tovstik, T.P. Tovstik, Two-dimensional model of plate made of anisotropic inhomogeneous material. *ICNAAM 2014.* AIP Conference Proceedings, 2014.

[19] P.E. Tovstik, T.P. Tovstik, On the 2D models of plates and shells including the shear. *ZAMM*. **8**7. No 2, 160–171. 2007.

[20] P.E. Tovstik, T.P. Tovstik, A thin-plate bending equation of second-order accuracy. *Doklady Physics.* Volume 59, Issue 8, 389-392. 2014.

[21] V.V. Novozhilov, *Theory of elasticity*. Sudpromgiz. Leningrad 1958. (in Russian)

[22] V.Z. Vlasov, *General Series of Shells and its Applications in Technique*. Gostexizdat, Moscow. 1949. (in Russian)

[23] L.H. Donnell, *Beams, Plates and Shells*. McGraw-Hill, Inc. 1976.

[24] H.M. Mushtari, K.Z. Galimov, *Nonlinear Theory of Elastic Shells*. Tatknigoizdat, Kazan. 1957. (in Russian)

[25] P.E. Tovstik, A.L. Smirnov, *Asymptotic methods in the buckling theory of thin shells*. World scientific. Singapore, New Jersey, London, Hong Kong 2002.

[26] V.V. Bolotin, Edge effect at vibrations of elastic shells. *Appl. Math. Mekh.* V. 24. No 5. 1960.

[27] A.L. Goldenweizer, V.B. Lidsky, P.E. Tovstik, *Free vibrations of thin elastic shells*. Nauka, Moscow. 1979. (in Russian)

COMPDYN 2015
5th ECCOMAS Thematic Conference on
Computational Methods in Structural Dynamics and Earthquake Engineering
M. Papadrakakis, V. Papadopoulos, V. Plevris (eds.)
Crete Island, Greece, 25–27 May 2015

MULTI-SCALE/MULTI-DATA INVERSION FOR ELASTIC EARTH STRUCTURE - A CONCEPT

Andreas Fichtner[1], Michael Afanasiev[1], Korbinian Sager[1] and Laura Ermert[1]

[1]Department of Earth Sciences, ETH Zurich
Sonneggstrasse 5, 8092 Zurich, Switzerland
e-mail: andreas.fichtner@erdw.ethz.ch

Keywords: Seismic tomography, computational seismology, seismic wave propagation, inverse theory

Abstract. *Complex interactions of small- and large-scale processes are characteristic for the physics of the Earth, and their proper quantification is key to the integration of interdependent geophysical systems that are today mostly treated as isolated.*

Inferring Earth structure over a wide range of scales is the long-standing goal of seismic tomography. While much progress has been made in recent years, tomographic resolution remains limited by our inability to model and invert seismic wave propagation across the complete observable frequency band with the currently available computational resources.

Here we propose a new concept for multi-scale seismic tomography intended to resolve Earth structure from local to global scales, including mantle as well as detailed crustal features. For this we develop a multi-scale full waveform inversion technique that assimilates complete teleseismic and regional seismograms in a broad frequency band. Being based on spectral-element modelling and adjoint techniques, our method simultaneously solves multiple regional- and continental-scale inverse problems in order to jointly resolve Earth structure with resolving lengths ranging from around 20 to more than 5000 km. To further increase the exploitable frequency band beyond what can be modelled numerically, we combine full waveform inversion with classical ray tomography that assimilates the arrival times of high-frequency body waves into the tomographic model. This combination results in an improved resolution of Earth structure, especially below 300 km depth.

We apply our method to Europe and Western Asia, where resolution is particularly high beneath the North Atlantic, the Western Mediterranean and Anatolia. Quantitative resolution analysis based on second-order adjoints, as well as comparisons with observed ambient noise correlations, allow us to assess the quality and predictive power of the final model.

1 INTRODUCTION

1.1 Scaling in waveform inversion

During the past decade, full waveform inversion in seismology has developed from a research topic into a mature technique with numerous applications [1, 2, 3, 4]. Factors contributing to this development include the design of misfit functionals that explicitly introduce traveltime information [5, 6, 7], the optimisation of numerical forward modelling tools [8, 9], and advanced data processing and window selection techniques [10, 11].
While growing compute power has contributed as well, the availability of computational resources is still the most significant limitation. Even with the unrealistic assumption of perfect scaling, doubling the maximum frequency in a waveform inversion multiplies the computational requirements by a factor of $2^5 = 32$. A factor $2^3 = 8$ is caused by the necessary refinement of the numerical mesh in three dimensions. An additional factor 2 is imposed by the CFL stability condition that enforces a reduction of the numerical time step. Finally, the volume covered by sensitivity kernels is anti-proportional to frequency, meaning that at least twice as many data - and therefore simulations - are needed to cover the same volume and avoid a loss of resolution.
Current full waveform inversions assimilate seismic waves that have propagated on the order of 100 wavelengths [1, 2, 3, 4]. This is in contrast to the $\mathcal{O}(1000)$ wavelengths that a 1 Hz P wave travels through the Earth. The factor 10 in propagating wavelength translates to a factor of 10^5 by which computational resources would have to increase at least, in order to allow seismologists to assimilate recordings with the complete observable bandwidth into a full waveform inversion.
This simple scaling argument, where storage requirements have not even been considered, illustrates the severity of the problem, and it calls for new methodological developments that allow us to broaden the exploitable bandwidth in tomographic inversions.

1.2 Objectives

The purpose of this contribution is to describe the concept of a new tomographic technique intended to assimilate data in a sufficiently broad frequency range to allow for the resolution of both crustal and mantle structure. The backbone of our method is the coupling of tomographic inversions on different scales and with different forward problem solvers. This strategy includes the combination of full waveform inversion of shorter-period data on regional scales with full waveform inversion of longer-period data on continental scales, but also the coupling with ray tomography that inverts the traveltimes of high-frequency waves that cannot be modelled numerically.

1.3 Outline

This paper is organised as follows: In section 2 we provide a summary of multi-scale full waveform inversion and the coupling with ray tomography. The first application of our approach to European upper-mantle and crustal structure is presented in section 3. Finally, we discuss limitations of our method, as well as future directions in section 4. Since our main goal is to introduce a concept, we will keep the description of mathematical and data processing details at a minimum level, though providing numerous references.

2 THEORY

In order to broaden the exploitable bandwidth of seismic data, we combine tomographic inversions that operate on different scales and are based on different forward problem solvers. Our approach includes (i) multi-scale full waveform inversion through coupled inversions from local to continental scales, and (ii) the coupling of full waveform inversion with classical ray tomography. We describe these components of our method separately in the following paragraphs.

2.1 Multi-scale full waveform inversion

The basic version of our full waveform inversion rests on spectral-element simulations of seismic wave propagation through spherical sections of anisotropic, visco-elastic Earth models [12]. With the help of a semi-automatic window selection algorithm [11], we choose time windows where observed and computed seismograms are sufficiently similar to allow for physically meaningful measurements of time- and frequency-dependent phase differences [7]. From these measurements, we derive adjoint sources used in adjoint simulations to produce Fréchet kernels for anisotropic Earth structure [13, 14, 15]. The Fréchet kernels are then used to iteratively improve the Earth model. To ensure that as many data as possible enter the inversion, the window selection is repeated every few iterations, typically leading to an increase in the number and length of time windows where measurements can be performed. Furthermore, we re-invert for the source location, timing and mechanism of the earthquakes in order to avoid contamination of the Earth model from inaccurate source information.
To jointly assimilate longer-period data on larger scales and shorter-period data on smaller scales, we employ the following inversion scheme [16]: From a multi-scale master model we extract a smaller subvolume that contains both sources and receivers. The limited size of the subvolume allows us to model and invert seismic data at higher frequencies. The updated submodel is then re-introduced into the master model. To compute an update on larger scales, we first employ non-periodic homogenisation in order to construct a smoothed long-wavelength equivalent of the master model [17, 18]. Being smooth, the long-wavelength equivalent can be meshed more coarsely, which reduces the computational requirements to a level where iterative updating with the longer-period data becomes feasible. The long-period update is then interpolated onto the master model, and the procedure is repeated until data are fit to within their errors. Depending on the detail of Earth structure, the homogenisation step may be omitted and replaced by directly meshing with a coarser grid spacing.
The advantage of this approach lies in its inherent scalability. There is no limit on the size and number of the submodels, meaning that high-frequency data for small local domains can be consistently assimilated into the master model. The major limitation is the requirement that sufficiently many sources and receivers must be located within the submodels, though this may be overcome using interferometric techniques [19, 20].

2.2 Ray tomography combined with full waveform inversion

Ray tomography uses traveltimes of distinct seismic phases to infer Earth structure. It relies on the simplifying assumption that seismic waves can be represented by rays. The intensive use of ray theory, which is closely related to geometrical optics, stems from its simplicity, its intuitive interpretation as well as its computational efficiency. Indeed, most seismological inferences concerning the structure of the Earth are based on this assumption.
Within the ray theoretical framework the arrival time of seismic waves solely depends on the

velocity along the geometrical ray path between source and receiver. Instead of simulating the full seismic wavefield, conventional approaches for computing seismic traveltimes try to find the path taken by seismic energy between source and receiver based on Snell's law by shooting (e.g. [21, 22, 23, 24]) or pseudo-/bending methods (e.g. [21, 25, 26]). These schemes may, however, fail to converge to the true two-point path even in mildly heterogeneous media and do not guarantee that the computed ray indeed corresponds to a first arrival. To solve these problems grid based solutions of the infinite frequency approximation of the wave equation, i.e. the eikonal equation, were and are still developed as an alternative approach (e.g. [27, 28, 29]). Most grid-based traveltime solvers can, however, only track first arrivals in continuous media, but it is possible to adapt grid-based schemes to track later arriving reflection and refraction phases in layered media (e.g. [30, 31, 32, 33, 34, 35]). Together with their robustness and advancing efficiency, these schemes are nowadays established as coequal, if not preferable, alternatives to conventional ray tracing methods.

In our application, we use the software package *FMTOMO* [38] for ray tomography. It computes the synthetic traveltimes with a grid based eikonal solver and adjusts the model parameters using a subspace inversion scheme [39]. On continental scales, limitations regarding the maximum amount of grid points for the propagation of information through the model prohibit a detailed representation of the crust and upper mantle. Besides crustal phases we also exclude the highly non-linear transition zone from crustal to upper/lower mantle phases and confine ourselves for now to direct waves for epicentral distances larger than 25°.

Ray tracing as well as grid-based eikonal solvers are only valid in the limit of a hypothetical infinite frequency wave. Its applicability relies on the assumption of weak and relatively large-scale lateral heterogeneities, which is not valid for structures with sizes that are comparable to or less than the dominant wavelength. At finite frequencies seismic waves are sensitive to 3D structure off the ray. Scattering, wave-front healing and other diffraction effects contribute to their traveltimes (e.g. [36]). Neglecting these effects, ray tomography is limited to high frequency information and especially long period waves cannot be inverted for.

Due to computational limitations full waveform inversion is limited to an intermediate period band, typically 10-200 s on regional to continental scales (e.g. [37, 4, 16]). At periods above 200 s, the self-gravitation of the Earth becomes relevant. Since this cannot be modelled with sufficient accuracy by numerical schemes, longer periods are omitted. More severly, the information contained in high frequency P- and S-wave traveltimes is therefore missing. Consequently, full waveform inversion yields promising results within the upper 300 km, where surface wave sensitivity is large. P- and S-velocity heterogeneities at greater depth are, however, less well resolved. Ray tomography explicitly incorporates information from arrivals of high frequency P- and S-waves. By alternating between full waveform inversion and ray tomography in an inversion, we intend to combine their complementary merits and produce 3D Earth models explaining both waveform and traveltime data sets to constrain Earth structure in more detail.

3 APPLICATION

We illustrate our approach with preliminary results from an ongoing tomographic inversion for crustal and upper-mantle structure beneath Europe and western Asia. In order to emphasise the concept and the method, we will mostly focus on the combination of waveform inversion and ray tomography, and on the Western Mediterranean as a smaller-scale subregion. Other subregions such as Anatolia or the North Atlantic will receive less attention.

3.1 Waveform data

The seismic waveform data used in the construction of our model fall into three categories, depending on scale and subregion: (i) On the continental ($10,000$ km) scale we use $14,525$ recordings from 84 earthquakes in the period range from 30 to 200 s, meaning that these data mostly constrain large-scale upper-mantle structure. (ii) Within the Anatolian region, that is on a 10 times smaller scale, we complement the data set with $2,312$ regional recordings from 29 earthquakes in Turkey with periods from 8 - 50 s that provide additional information on crustal heterogeneities [41]. (iii) For the Western Mediterranean region, we added $13,089$ recordings from 52 events in the period range between 12 and 120 s, also in order to constrain the uppermost mantle and the crust. The data coverage for the Western Mediterranean is summarised in figure 1. The waveform data used in the alternating traveltime - full waveform inversion was a sub-sampled version of the continental scale dataset, using 52 events and $13,086$ seismograms, bandpass filtered between 40 and 100 seconds.

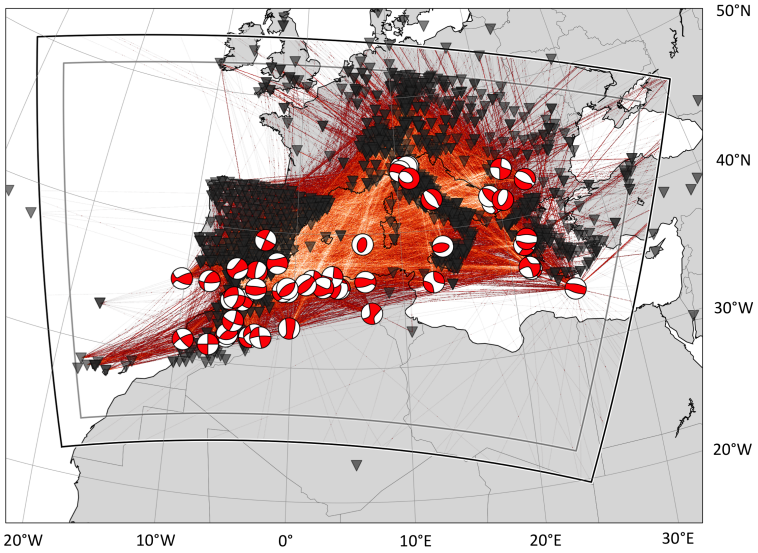


Figure 1: Source-receiver distribution in the Western Mediterranean region. Red-white beachballs indicate the source mechanisms and locations of the 52 earthquakes used in the full waveform inversion for this subregion. The great circles connecting sources and receivers are plotted in lighter colour when coverage is high.

3.2 Traveltime data

The traveltime updates are based on measurements from the International Seismological Center (www.isc.ac.uk). The data set comprises 710 events with a total of $19,010$ S wave traveltimes, measured at a frequency of 1 Hz. Since the measurements are on the transverse component, and are therefore primarily sensitive to SH-velocity, we restrict our velocity updates to the SH velocity component.

3.3 Inversion sequence

We started the inversion sequence with the construction of a long-wavelength model of the European upper mantle using full waveforms with a minimum period of 40 s. Subsequently, smaller-scale refinements within the Anatolian region and the North Atlantic were performed. This was followed by the combined ray and full waveform inversion that primarily updated

structure below 200 km depth. Avoiding difficulties in modeling the complexities in the crust and upper mantle, the traveltime update primarily introduces information in deeper parts of the model. Therefore, the traveltime update is nearly invisible to the waveforms, and the waveform update does not influence the traveltime misfit. Finally, we refined the model in the Western Mediterranean using full waveform inversion.
This sequence is the result of continuing methodological developments rather than a long-term schedule. More systematic updates are planned for the near future, but require further automisation and improved bookkeeping.

3.4 Multi-scale model of the European continent

Figures 2 and 3 summarise the current state of our model. The model is described in terms of the 3D distributions of SH velocity v_{SH}, SV velocity v_{SV}, P velocity v_P, and density ρ. Since most of the data are primarily sensitive to S velocity structure, v_{SH} and v_{SV} are resolved best.
The European model embedded within longer-wavelength global structure [42, 43] is shown in figure 2. Differences between oceans and continents dominate the 25 km slice. At 100 km, the low-velocity imprints of the Iceland-Jan Mayen plume system [4] and the Alpine orogeny [41] are the dominant features. Around 300 km depth, the heterogeneities are weaker and mostly related to the deep structure of the North Atlantic plumes and the deep continental roots of Eurasia.
Close-up views of the regional submodels for Anatolia, the North Atlantic and the Western Mediterranean can be seen in figure 3. The uppermost mantle beneath Anatolia carries the imprint of the North Anatolian Fault Zone and various volcanic fields, all expressed as low-velocity anomalies [41]. The North Atlantic around 250 km depth is marked by the wide-spread plume head of the Iceland-Jan Mayen plume system, also characterised by lower than average seismic velocities [4]. Higher than average velocities associate with the subduction oceanic lithosphere are dominant in a belt stretching from the Strait of Gibraltar though the Western Mediterranean and into Italy.

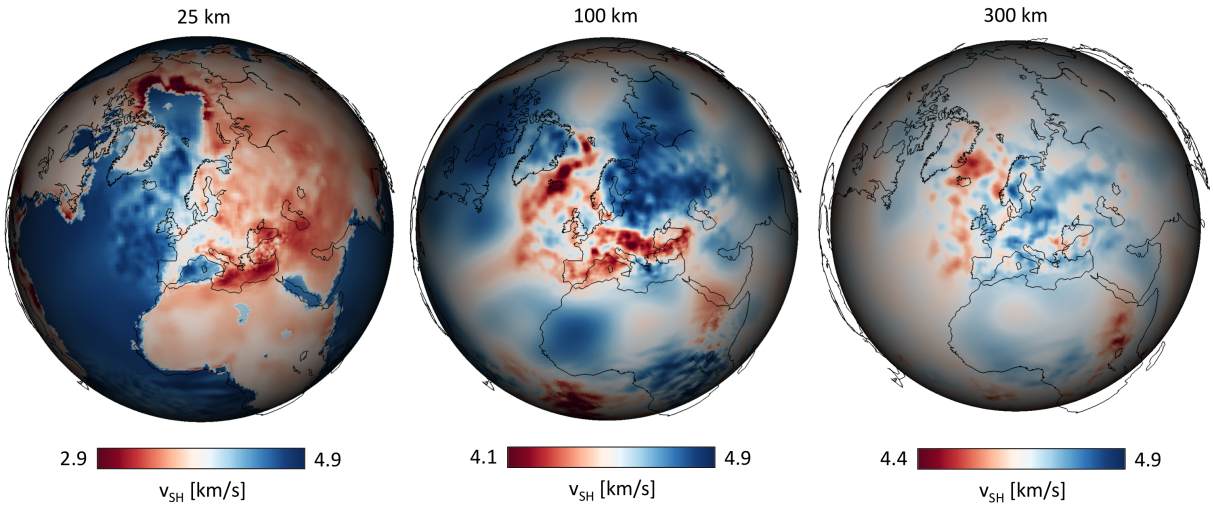


Figure 2: Horizontal slices through the SH velocity structure beneath Europe at depth of 25 km, 100 km and 300 km.

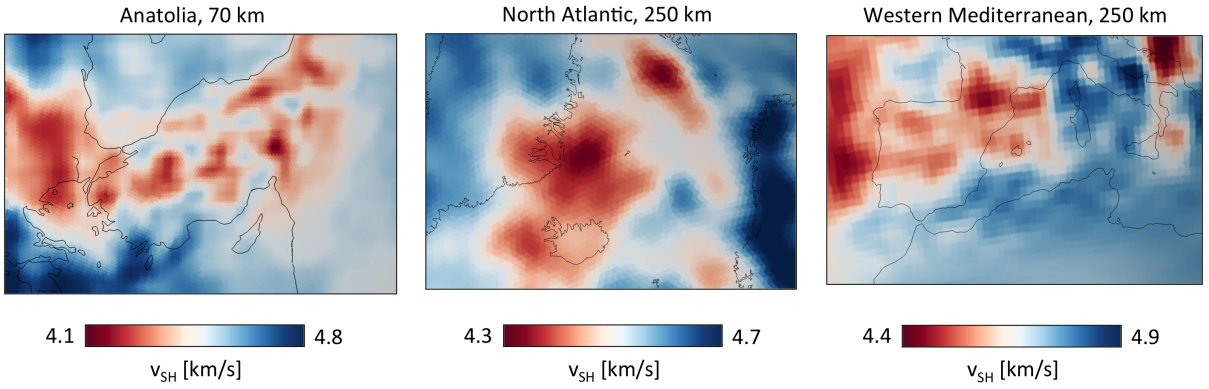


Figure 3: Close-up views of SH velocity structure in the mantle beneath Anatolia, the North Atlantic, and the Western Mediterranean.

3.5 Model validation

The assessment of model quality and uncertainty is among the most challenging aspects of seismic tomography. With the help of second-order adjoints we can compute resolution lengths, that is the width of point-spread functions as a function of position and direction [44]. Maps of resolution length for the Western Mediterranean are shown in figure 4. The maps indicate that resolution is generally better in vertical direction because surface waves dominate the waveform data set. With increasing depth, the resolved volume shrinks, reflecting the decreasing body wave coverage in this regional setting.

In addition to formal resolution analysis, we study the fit to data that have not been used in the inversion. Ambient noise correlations are particularly useful for this purpose as they do not suffer from incorrect earthquake locations and source mechanisms. Furthermore, they probe the model in regions that may be less well covered by earthquake data. To compute noise correlations, we obtained continuous seismic data for the year 2012 from the IRIS DMC (www.iris.edu). The instrument response was removed for the recordings, after which data were cut into overlapping nine-hour-segments, decimated and bandpass-filtered between 4 and 20 s. The normalised cross-correlation was then calculated without further preprocessing. Geometric normalisation of each correlation window ensures the downweighting of high energy signals e.g. from earthquakes.

Figure 5 shows a selection of correlation functions compared to numerical Green functions. Provided that a surface wave clearly emerges from the noise correlation data, it is matched by the Green function to within a few seconds. A remarkable example is shown in the third row of figure 5 where surface waves are not explained but the rare body wave arrivals in the correlation function are explained by the numerical Green function. The above comparison is currently limited to a visual analysis that adds subjective plausibility to the model. A quantitative comparison would require more detailed information on the distribution of noise sources.

4 DISCUSSION AND CONCLUSIONS

In the previous sections we introduced a concept for the construction of multi-scale Earth models based on the solution of tomographic inverse problems on different scales and with forward problem solvers that operate in complementary frequency bands. Specifically, we combined full waveform inversion on regional to continental scales with ray tomography that assimilates high-frequency traveltime data that cannot be modelled numerically due to limited

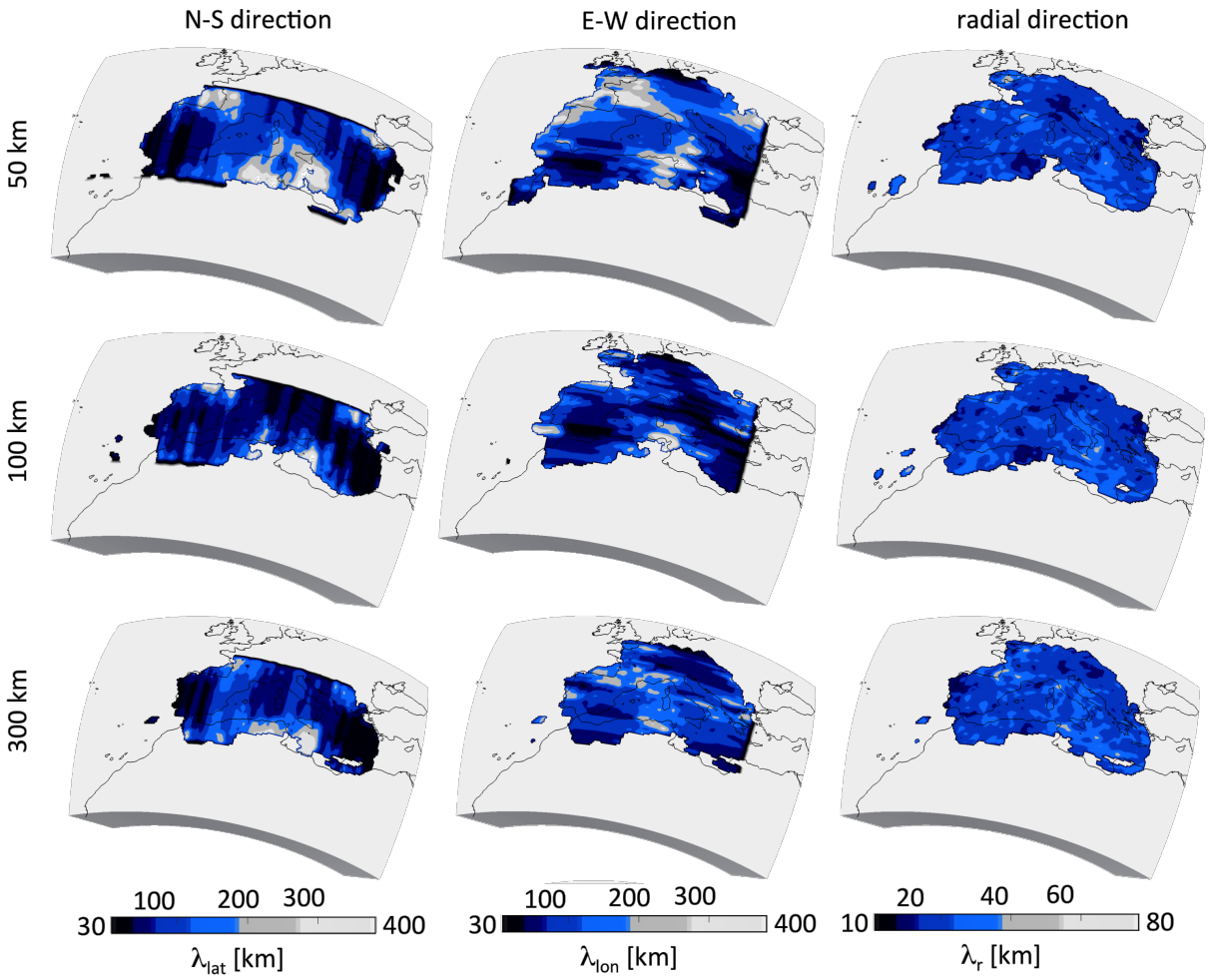


Figure 4: Resolution length as a function of position and direction for the Western Mediterranean.

computational power.

While the focus of this contribution is on the European continent, our developments are ultimately designed to feed into the construction of the Comprehensive Seismic Earth Model (CSEM), a 3D global multi-scale Earth model. As illustrated in Figure 2, the goal of the CSEM is to represent the Earth on all seismically accessible scales, containing high resolution subregions where data and computational limitations allow, and showcasing a smooth 3D Earth in regions where detailed inversions have yet to be performed. By building a high resolution Earth model in this manner, we sidestep the scaling issues outlined in the introduction, which become even more severe when inversions move to the global scale. In addition to the multiscale model of Europe, the CSEM also includes high-resolution images of Japan, Australia, and the South Atlantic, with inversions of Africa and North America currently underway.

With such a variety of models across the scales, analysing the globally-varying resolution becomes a particular challenge. Methods based on second-order adjoints can provide an approximation of resolution in full-waveform inverse problems [40], but the theory extending this method to general multi-scale multi-solver problems remains to be developed.

The incorporation of ambient noise correlations into full waveform inversion consititutes another future challenge. While traveltimes are only weakly affected by heterogeneous and varying noise sources [45], complete waveforms that feed into full waveform inversion are strongly

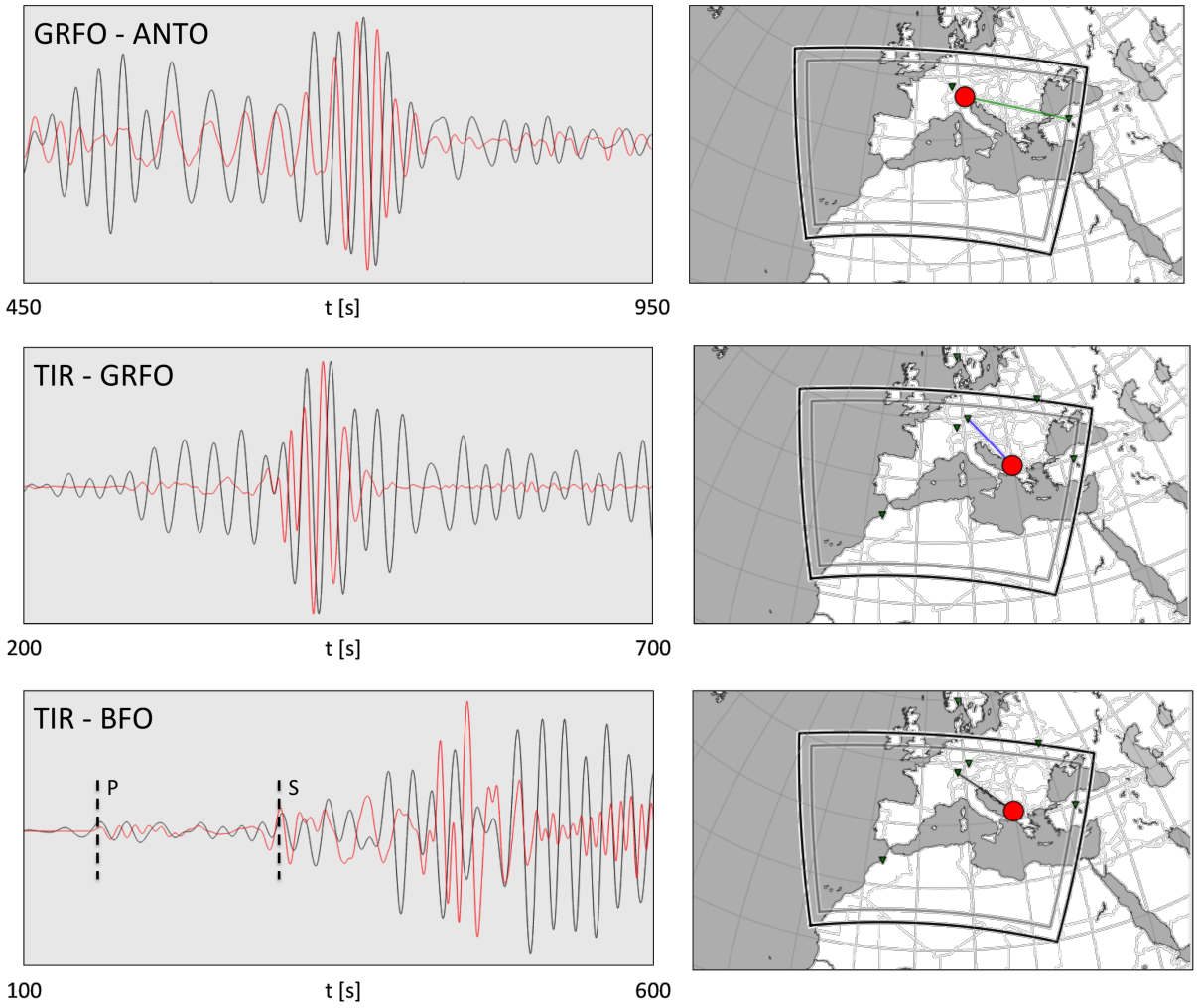


Figure 5: Comparison of ambient noise correlations (black) and numerical Green functions (ref) for three different station pairs. Rarely observed matching P and S wave arrivals for the station pair TIR-BFO are marked by dashed lines.

distorted when the noise source distribution is not isotropic [46, 47]. Properly accounting for the distribution of noise sources is therefore essential before correlations can be used to improve earthquake-based full waveform inversion.

Acknowledgements: This research was supported by the Swiss National Supercomputing Center (CSCS) in the form of the GeoScale and CH1 projects, by the Swiss National Science Foundation (SNF) under grant 200021_149143, and by the Netherlands Organisation for Scientific Research (VIDI grant 864.11.008).

REFERENCES

[1] P. Chen, T. H. Jordan, L. Zhao, Full 3D waveform tomography: a comparison between the scattering-integral and adjoint-wavefield methods, *Geophysical Journal International*, **170**, 175–181, 2007.

[2] A. Fichtner, B. L. N. Kennett, H. Igel, H.-P. Bunge, Full waveform tomography for radially anisotropic structure: New insight into present and past states of the Australasian upper mantle, *Earth and Planetary Science Letters*, **290**, 270–280, 2010.

[3] C. Tape, Q. Liu, A. Maggi, J. Tromp, Seismic tomography of the southern California crust based upon spectral-element and adjoint methods, *Geophysical Journal International*, **180**, 433–462, 2010.

[4] F. Rickers, A. Fichtner, J. Trampert, The Iceland - Jan Mayen plume system and its impact on mantle dynamics in the North Atlantic region: Evidence from full-waveform inversion, *Earth and Planetary Sciences Letters*, **367**, 39–51, 2013.

[5] Y. Luo, G. T. Schuster, Wave-equation traveltime inversion, *Geophysics*, **56**, 645-653, 1991.

[6] L. S. Gee, T. H. Jordan, Generalized seismological data functionals, *Geophysical Journal International*, **111**, 363-390, 1992.

[7] A. Fichtner, B. L. N. Kennett, H. Igel, H.-P. Bunge, Theoretical background for continental- and global-scale full-waveform inversion in the time-frequency domain, *Geophysical Journal International*, **175**, 665–685, 2008.

[8] A. Fichtner, H. Igel, Efficient numerical surface wave propagation through the optimization of discrete crustal models - a technique based on non-linear dispersion curve matching (DCM), *Geophysical Journal International*, **173**, 519–533, 2008.

[9] D. Peter, D. Komatitsch, Y. Luo, R. Martin, N. Le Goff, E. Casarotti, P. Le Loher, F. Magnoni, Q. Liu, C. Blitz, T. Nissen-Meyer, P. Basini, J. Tromp, Forward and adjoint simulations of seismic wave propagation on fully unstructured hexahedral meshes, *Geophysical Journal International*, **186**, 721–739, 2011.

[10] A. Maggi, C. Tape, M. Chen, D. Chao, J. Tromp, An automated time-window selection algorithm for seismic tomography, *Geophysical Journal International*, **178**, 257–281, 2009.

[11] L. Krischer, A. Fichtner, S. Zukauskaite, H. Igel, Large-scale seismic inversion framework, *Seismological Research Letters*, in press, 2015.

[12] A. Fichtner, B. L. N. Kennett, H. Igel, H.-P. Bunge, Spectral-element simulation and inversion of seismic waves in a spherical section of the Earth, *Journal of Numerical Analysis Industrial and Applied Mathematics*, **4**, 11-22, 2009.

[13] A. Tarantola, Theoretical background for the inversion of seismic waveforms, including elasticity and attenuation, *Pure and Applied Geophysics*, **128**, 365-399, 1988.

[14] J. Tromp, C. Tape, Q. Liu, Seismic tomography, adjoint methods, time reversal and banana-doughnut kernels, *Geophysical Journal International*, **160**, 195–216, 2005.

[15] A. Fichtner, H.-P. Bunge, H. Igel, The adjoint method in seismology - I. Theory, *Physics of the Earth and Planetary Interiors*, **157**, 86-104, 2006.

[16] A. Fichtner, J. Trampert, P. Cupillard, E. Saygin, T. Taymaz, Y. Capdeville, A. Villasenor, Multi-scale full waveform inversion, *Geophysical Journal International*, **194**, 534-556, 2013.

[17] Y. Capdeville, J. J. Marigo, Second order homogenization of the elastic wave equation for non-periodic layered media, *Geophysical Journal International*, **170**, 823-838, 2007.

[18] Y. Capdeville, L. Guillot, J. J. Marigo, 2-D nonperiodic homogenization to upscale elastic media for P-SV waves, *Geophysical Journal International*, **182**, 903–922, 2010.

[19] N. M. Shapiro, M. Campillo, L. Stehly, M. Ritzwoller, High resolution surface wave tomography from ambient seismic noise, *Science*, **307**, 1615-1618, 2005.

[20] K. G. Sabra, P. Gerstoft, P. Roux, W. A. Kuperman, Surface wave tomography from microseisms in Southern California, *Geophysical Research Letters*, **32**, doi:10.1029/2005GL023155, 2005.

[21] B.R. Julian, D. Gubbins. Three-dimensional seismic ray tracing. *Journal of Geophysics*, **43**, 95–113, 1977.

[22] M.S. Sambridge. Non-linear arrival time inversion: constraining velocity anomalies by seeking smooth models in 3-D. *Geophysical Journal International*, **102**, 653–677, 1990.

[23] J. Virieux, F. Farra. Ray tracing in 3-D complex isotropic media: an analysis of the problem. *Geophysics*, **56**, 2057–2069, 1991.

[24] N. Rawlinson, G.A. Houseman, C.D.N. Collins. Inversion of seismic refraction and wide-angle reflection traveltimes for three-dimensional layered crustal structure. *Geophysical Journal International*, **145**, 381–400, 2001.

[25] V. Pereyra, W.H.K. Lee, H.B. Keller. Solving two-point seismic-ray tracing problems in a heterogeneous medium. *Bulletin of the Seismological Society of America*, **70**, 79–99, 1980.

[26] J. Um, C. Thurber. A fast algorithm for two-point seismic ray tracing. *Bulletin of the Seismological Society of America*, **77**, 972–986, 1987.

[27] J. Vidale. Finite-difference calculations of traveltimes. *Bulletin of the Seismological Society of America*, **78**, 2062–2076, 1988.

[28] F. Qin, Y. Luo, K.B. Olsen, W. Cai, G.T. Schuster. Finite-difference solution of the eikonal equation along expanding wavefronts. *Geophysics*, **57**, 478–487, 1992.

[29] J. Qian, W.W. Symes. An adaptive finite-difference method for traveltimes and amplitudes. *Geophysics*, **67**, 167–176, 2002.

[30] P. Podvin, I. Lecomte. Finite difference computation of traveltimes in very contrasted velocity models: a massively parallel approach and its associated tools. *Geophysical Journal International*, **105**, 271–284, 1991.

[31] J.A. Hole, B.C. Zelt. 3-D finite-difference reflection traveltimes. *Geophysical Journal International*, **121**, 427–434, 1995.

[32] N. Rawlinson, M. Sambridge. Multiple reflection and transmission phases in complex layered media using a multistage fast marching method. *Geophysics*, **69**, 1338–1350, 2004.

[33] N. Rawlinson, M. Sambridge. Wave front evolution in strongly heterogeneous layered media using the fast marching method. *Geophysical Journal International*, **156**, 631–647, 2004.

[34] N. Rawlinson, M. Sambridge. The fast marching method: an effective tool for tomographic imaging and tracking multiple phases in complex layered media. *Exploration Geophysics*, **36**, 341–350, 2005.

[35] M. de Kool, N. Rawlinson, M. Sambridge. A practical grid-based method for tracking multiple refraction and reflection phases in three-dimensional heterogeneous media. *Geophysical Journal International*, **167**, 253–270, 2006.

[36] Q. Liu, Y.J. Gu. Seismic imaging: From classical to adjoint tomography. *Tectonophysics*, **566–567**, 31–66, 2012.

[37] H. Zhu, E. Bozdağ, D. Peter, J. Tromp. Structure of the European upper mantle revealed by adjoint tomography. *Nature Geoscience*, **5**, 493–498, 2012.

[38] N. Rawlinson, M. Urvoy. Simultaneous inversion of active and passive source datasets for 3-D seismic structure with application to Tasmania. *Geophysical Research Letters*, **33**, L24313, 2006.

[39] B.L.N. Kennett, M.S. Sambridge, P.R. Williamson. Subspace methods for large inverse problems with multiple parameter classes. *Geophysical Journal*, **94**, 237–247, 1988.

[40] A. Fichtner, J. Trampert. Resolution analysis in full waveform inversion. *Geophysical Journal International*, **187**, 1604–1624, 2011.

[41] A. Fichtner, E. Saygin, T. Taymaz, P. Cupillard, Y. Capdeville, J. Trampert, The deep structure of the North Anatolian Fault Zone, *Earth and Planetary Sciences Letters*, **373**, 109–117, 2013.

[42] J. Ritsema, H. vanHeijst, J. H. Woodhouse, Complex shear wave velocity structure imaged beneath Africa and Iceland, *Science*, **286**, 1925-1928, 1999.

[43] U. Meier, A. Curtis, J. Trampert, Fully nonlinear inversion of fundamental mode surface waves for a global crustal model, *Geophysical Research Letters*, **34**, doi:10.1029/2007GL030989, 2007.

[44] A. Fichtner, T. van Leeuwen, Resolution analysis by random probing, *Journal of Geophysical Research*, in review, 2015.

[45] B. Froment, M. Campillo, P. Roux, P. Gouédard, A. Verdel, R. L. Weaver, Estimation of the effect of nonisotropically distributed energy on the apparent arrival time in correlations, *Geophysics*, **75**, SA85-SA93, 2010.

[46] D. Halliday, A. Curtis, Seismic interferometry, surface waves and source distribution, *Geophysical Journal International*, **175**, 1067-1087, 2008.

[47] W. Kimman, J. Trampert, Approximations in seismic interferometry and their effects on surface waves, *Geophysical Journal International*, **182**, 461-476, 2010.

COMPDYN 2015
5th ECCOMAS Thematic Conference on
Computational Methods in Structural Dynamics and Earthquake Engineering
M. Papadrakakis, V. Papadopoulos, V. Plevris (eds.)
Crete Island, Greece, 25–27 May 2015

A FICTITIOUS DOMAIN APPROACH FOR WAVE PROPAGATION PROBLEMS IN UNBOUNDED DOMAINS

S. Falletta[1] and G. Monegato[2]

[1]DISMA - Politecnico di Torino
C.so Duca degli Abruzzi, 24 - 10129 Torino
e-mail: silvia.falletta@polito.it

[2] DISMA - Politecnico di Torino
C.so Duca degli Abruzzi, 24 - 10129 Torino
e-mail: giovanni.monegato@polito.it

Keywords: Time dependent wave equation; fictitious domain; absorbing boundary conditions

Abstract. *We consider the scattering of waves by an obstacle $\mathcal{O} \subset \mathbb{R}^2$ having a sufficiently smooth boundary Γ. By using a fictitious domain approach, we artificially extend the solution inside the obstacle $\mathcal{O}$. Then we solve the original problem in the simpler domain that includes $\mathcal{O}$ and that is artificially bounded by a perfectly transparent boundary $\mathcal{B}$, delimiting the region of interest. We prescribe on $\mathcal{B}$ a Non Reflecting Boundary Condition (NRBC) which is based on a space-time integral equation and that defines a relationship that the solution of the differential problem and its normal derivative must satisfy on $\mathcal{B}$ (see [2]). Further, we enforce the Dirichlet boundary condition on Γ in a weak sense, by means of Lagrange multipliers. The NRBC is discretized on $\mathcal{B}$ by combining a special second order (in time) convolution quadrature and a standard collocation method in space. In the enlarged domain, this discretization is coupled with an unconditionally stable ODE time integrator and a FEM in space. The constraint on Γ is imposed by a matrix B_h that represents a discrete trace operator.*

A particularly useful application of this approach is the scattering of a wave by rotating rigid bodies. In this case the method avoids the complexity of constructing at each time step a new finite element computational mesh and requires only the construction of the discrete trace operator B_h. We present some results we have obtained for rotating (even multiple) scatterers and non trivial data.

1 INTRODUCTION

In recent years, numerical methods for the solution of time dependent problems describing waves scattered by an obstacle have received considerable attention. Boundary Element Methods are particularly useful for treating infinite domain problems and have been successfully used in the solution of linear wave propagation problems in two and three dimensions. In such problems the method offers the great advantage of describing the solution only by its boundary values, thus reducing the problem dimensions by one; hence, only a discretization of the boundary is necessary, which significantly reduces the number of unknowns, if compared to domain-discretization-based methods such as finite element methods. Once the density function is retrieved (by solving the corresponding boundary integral equation), the solution at any point is obtained by computing boundary integrals. This procedure may result costly, especially when the solution is required at many points of the infinite domain.

Alternatively, the use of domain-discretization-based methods requires a finite computational domain with prescribed boundary conditions. A key issue is therefore the choice of a bounded computational domain, where one is interested in studying the behavior of the solution, and the introduction of boundary conditions which guarantee that the solution of the initial boundary value problem inside the finite computational domain coincides with the restriction to the computational domain of the solution of the original problem, which is defined in the infinite region. The method of Artificial (or Absorbing) Boundary Condition (ABC) consists of introducing an artificial boundary $\mathcal{B}$ that truncates the infinite domain and determines two distinct regions: a bounded domain of interest Ω and a residual infinite domain $\mathcal{D}$. By analyzing the problem in $\mathcal{D}$, a Non Reflecting Boundary Condition (NRBC) on $\mathcal{B}$ is derived in order to avoid spurious reflections. Once the NRBC is given, it is used to solve the problem in Ω by using a numerical method such as, for example, finite differences or finite elements.

Many NRBCs have been proposed in the last two-three decades, and most of them are local, both in time and space. For a review, see for example [5], [6], [7]. All these papers, except for [12], Sections 5.5, 5.6, [8], [9], [2], deal with the construction of NRBC with the property of absorbing only outgoing waves, not waves that are either outgoing or incoming. Therefore, known sources must necessarily be included in the computational domain. However, this can be a severe drawback when, for example, sources are far away from the physical domain. Moreover, the NRBC holds only for a single convex artificial boundary having a special shape, like a circle (sphere) or ellipse (ellipsoid). Only in the last years multiple scattering problems have been examined (see [8], [9]). Very recently, in ([2]) we have proposed a (fully) non local NRBC, based on a boundary integral relationship. For its discretization, we have constructed a numerical scheme which is based on a second order Lubich discrete convolution quadrature formula for the discretization of the time integral, coupled with a classical collocation method in space. Among the advantages of this transparent condition we recall the following: it allows the use of (smooth) curve (surfaces) of arbitrary shape; it can be used also in situations of multiple scattering; it allows the treatment of sources and initial data that must not be necessarily included in the finite computational domain; its computational cost is much lower that what it might first appear, due to some special properties of the coefficients of the Lubich convolution quadratures. Indeed, if in the 2D case we choose as $\mathcal{B}$ a circle, the CPU required for the solution of some test problems is similar to that of local NBRCs.

In this paper we aim at using the NRBC proposed in [2] as a transparent condition coupled with a fictitious domain method. In particular, we consider the scattering of a wave by an ob-

stacle $\mathcal{O} \subset \mathbb{R}^2$ having a smooth boundary Γ. By using the fictitious domain approach, we artificially extend the solution inside the obstacle $\mathcal{O}$ and we impose the boundary conditions on Γ in the weak form, by means of Lagrange multipliers. Then, we truncate the infinite external domain by an artificial boundary $\mathcal{B}$ where we impose the transparent boundary conditions proposed in [2]. We solve the original problem in the finite computational domain $\widetilde{\Omega}$ that includes $\mathcal{O}$ and is bounded by the artificial boundary $\mathcal{B}$. To this end, we discretize the space-time integral equation on $\mathcal{B}$ by combining a second order (in time) BDF convolution quadrature and a collocation method in space. Such a discretization is then coupled with an unconditionally stable ODE time integrator and a FEM in space. The main point is that the FEM mesh is defined on the enlarged domain $\widetilde{\Omega}$ and that the constraint on Γ is imposed by a matrix B_h that represents a discrete trace operator.

A significant application of this approach is the scattering of a wave by rotating rigid bodies. In this case the method avoids the complexity of constructing at each time step a new finite element computational mesh and requires only the construction of the discrete trace operator B_h. We will present some new results that we have obtained for rotating (even multiple) scatterers and non trivial data.

2 The model problem

Let $\mathcal{O} \subset \mathbb{R}^2$ be an open bounded domain with a sufficiently smooth boundary Γ; define $\Omega^e = \mathbb{R}^2 \setminus \bar{\mathcal{O}}$. We consider the following wave propagation problem in Ω^e:

$$\begin{cases} u^e_{tt}(\mathbf{x},t) - \Delta u^e(\mathbf{x},t) &= f(\mathbf{x},t) \quad \text{in } \Omega^e \times (0,T) \\ u(\mathbf{x},t) &= 0 \quad \text{in } \Gamma \times (0,T) \\ u^e(\mathbf{x},0) &= u_0(\mathbf{x}) \quad \text{in } \Omega^e \\ u^e_t(\mathbf{x},0) &= v_0(\mathbf{x}) \quad \text{in } \Omega^e. \end{cases} \tag{1}$$

Since in general one has to determine the solution u^e of the above problem in a bounded subregion of Ω^e, surrounding the physical domain $\mathcal{O}$, we truncate the infinite domain Ω^e by introducing an artificial smooth boundary $\mathcal{B}$. This boundary divides Ω^e into two (open) sub-domains: a finite computational domain Ω, which is bounded internally by Γ and externally by $\mathcal{B}$, and an infinite residual domain $\mathcal{D}$. For simplicity, we assume that the initial condition u_0, the initial velocity v_0 and the source term f have a local support which is included in Ω. We impose on $\mathcal{B}$ the exact non reflecting boundary condition

$$\frac{1}{2}u(\mathbf{x},t) = \boldsymbol{\mathcal{V}}\partial_{\mathbf{n}_\mathcal{D}}u(\mathbf{x},t) - \boldsymbol{\mathcal{K}}u(\mathbf{x},t) \quad \mathbf{x} \in \mathcal{B}, \tag{2}$$

where

$$\boldsymbol{\mathcal{V}}\psi(\mathbf{x},t) := \int_0^t \int_\mathcal{B} G(\mathbf{x}-\mathbf{y}, t-\tau)\psi(\mathbf{y},\tau) d\mathcal{B}_\mathbf{y} d\tau,$$

and

$$\boldsymbol{\mathcal{K}}\varphi(\mathbf{x},t) := \int_0^t \int_\mathcal{B} \partial_{\mathbf{n}_\mathcal{D}} G(\mathbf{x}-\mathbf{y}, t-\tau)\varphi(\mathbf{y},\tau) d\mathcal{B}_\mathbf{y} d\tau,$$

are the single and double layer integral operators;

$$G(\mathbf{x},t) = \frac{1}{2\pi}\frac{H(t-\|\mathbf{x}\|)}{\sqrt{t^2-\|\mathbf{x}\|^2}},$$

is the fundamental solution of the wave equation (1) (being $H(\cdot)$ the Heaviside functions); $\partial_{\mathbf{n}_\mathcal{D}} u$ is the outward normal derivative to $\mathcal{B} = \partial\mathcal{D}$. We refer the reader to [2] for details on the derivation of the NRBC and on the regularity of the operators $\boldsymbol{\mathcal{V}}$ and $\boldsymbol{\mathcal{K}}$.

Denoting by $u_\mathcal{B}(\mathbf{x},t) = u(\mathbf{x},t)_{|_\mathcal{B}}$ and $\lambda_\mathcal{B}(\mathbf{x},t) = -\partial_{\mathbf{n}_\mathcal{D}} u(\mathbf{x},t)$, the model problem (defined in the domain of interest Ω) takes the form:

$$\begin{cases} u_{tt}(\mathbf{x},t) - \Delta u(\mathbf{x},t) & = f(\mathbf{x},t) \quad \text{in } \Omega \times (0,T) \\ u(\mathbf{x},t) & = 0 \quad \text{in } \Gamma \times (0,T) \\ \frac{1}{2} u_\mathcal{B}(\mathbf{x},t) + \boldsymbol{\mathcal{V}} \lambda_\mathcal{B}(\mathbf{x},t) + \boldsymbol{\mathcal{K}} u_\mathcal{B}(\mathbf{x},t) & = 0 \quad \text{in } \mathcal{B} \times (0,T) \\ u(\mathbf{x},0) & = u_0(\mathbf{x}) \quad \text{in } \Omega \\ u_t(\mathbf{x},0) & = v_0(\mathbf{x}) \quad \text{in } \Omega, \end{cases}$$

3 The fictitious domain approach

In order to describe the fictitious domain approach, we introduce the extended domain $\widetilde{\Omega} := \Omega \cup \mathcal{O}$ which is bounded by the artificial boundary $\mathcal{B}$ (see Figure 1). The main idea of the fictitious domain method (or domain embedding method) consists in extending artificially the solution of the exterior problem inside the obstacle, and to solve the new problem in the whole extended domain $\widetilde{\Omega}$ (see [4], [11] and their references). The main advantage of this approach is the possibility of solving the problem in a simpler domain by treating the Dirichlet boundary conditions on Γ by Lagrange multipliers, working with a given fixed mesh in the enlarged domain.

Figure 1: Geometry of the problem (left plot) and the fictitious domain approach (right plot)



For a generic function w, we set $w(t)(\mathbf{x}) := w(\mathbf{x},t)$. Following [2] and [4], the problem defined in the domain of interest $\widetilde{\Omega}$ consists in finding the triad of unknown functions $(u(t), \lambda_\Gamma(t), \lambda_\mathcal{B}(t)) \in H^1(\widetilde{\Omega}) \times H^{-1/2}(\Gamma) \times H^{-1/2}(\mathcal{B})$ such that, for all $w \in H^1(\widetilde{\Omega}), \varphi \in H^{-1/2}(\Gamma), \mu \in H^{-1/2}(\mathcal{B})$, the following generalized saddle-point evolution problem

$$\begin{cases} \frac{d^2}{dt^2}(u(t),w)_{\widetilde{\Omega}} + a(u(t),w) - < \lambda_\Gamma(t), w >_\Gamma - < \lambda_\mathcal{B}(t), w >_\mathcal{B} & = (f(t),w) \\ < \varphi, u(t) >_\Gamma & = 0 \\ \frac{1}{2} < \mu, u_\mathcal{B}(t) >_\mathcal{B} + < \mu, \boldsymbol{\mathcal{V}} \lambda_\mathcal{B}(t) >_\mathcal{B} + < \mu, \boldsymbol{\mathcal{K}} u_\mathcal{B}(t) >_\mathcal{B} & = 0 \\ u(0) & = u_0 \\ \frac{du}{dt}(0) & = v_0. \end{cases} , \tag{3}$$

holds in the distributional sense in $(0,T)$, where $a : H^1(\widetilde{\Omega}) \times H^1(\widetilde{\Omega}) \to \mathbb{R}$ is the bilinear form

$$a(v,w) = \int_{\widetilde{\Omega}} \nabla v \cdot \nabla w,$$

and $(v,w)_{\widetilde{\Omega}} = \int_{\widetilde{\Omega}} vw$. The bilinear forms $< \cdot, \cdot >_{\Gamma}$ and $< \cdot, \cdot >_{\mathcal{B}}$ denote the duality pairing between $H^{-1/2}(\Gamma)$ and $H^{1/2}(\Gamma)$, and $H^{-1/2}(\mathcal{B})$ and $H^{1/2}(\mathcal{B})$, respectively.

The weak formulation (3) is the natural setting for the analysis of the method and to deal with convergence issues and error estimates of the associated finite element numerical approximation. However, its numerical solution using methods such as finite and boundary elements, makes it hardly competitive with existing NRBC approaches of local type, in particular when the problem does not have far field sources. From this point of view, replacing the weak formulation of the NRBC with a strong one makes the scheme certainly more appealing, although stronger smoothness conditions on the solution are required. Therefore, in the next section we will consider the coupling of the weak form of the differential equation with the strong form (2) of the NRBC.

At the moment, the theory to justify the validity of the presented approach is still at an early stage. For this reason we have performed an intensive numerical testing to validate the proposed method.

4 Approximation

4.1 Discretization of the NRBC

We start by briefly recalling the main steps of the Lubich-collocation method for the discretization of the NRBC (2) (for more details we refer to [10] and [3]).

The Lubich convolution quadrature formulas have the fundamental property of not using explicitly the expression of the kernel of the integral equation they are applied to, which is instead replaced by that of its Laplace transform. In particular, the discretization in time is based on the splitting of the interval $[0,T]$ into N steps of equal length $\Delta_t = T/N$ and in the collocation of the equation at the discrete time levels $t_n = n\Delta_t$, $n = 0, \dots, N$.

The time integrals appearing in the definition of the single and double layer operators are discretized by means of the convolution quadrature formula associated with the second order Backward Differentiation Method (BDF) for ordinary differential equations (see [3]):

$$\begin{aligned}
(\boldsymbol{\mathcal{V}}\lambda_{\mathcal{B}})(\mathbf{x},t_n) &\approx \sum_{j=0}^{n} \int_{\mathcal{B}} \omega_{n-j}^{\boldsymbol{\mathcal{V}}}(\Delta_t; ||\mathbf{x}-\mathbf{y}||)\lambda_{\mathcal{B}}(\mathbf{y},t_j)\, d\mathcal{B}_{\mathbf{y}}, \quad n = 0,\dots,N \\
(\boldsymbol{\mathcal{K}}u_{\mathcal{B}})(\mathbf{x},t_n) &\approx \sum_{j=0}^{n} \int_{\mathcal{B}} \omega_{n-j}^{\boldsymbol{\mathcal{K}}}(\Delta_t; ||\mathbf{x}-\mathbf{y}||)u_{\mathcal{B}}(\mathbf{y},t_j)\, d\mathcal{B}_{\mathbf{y}}, \quad n = 0,\dots,N
\end{aligned}$$

The coefficients $\omega_n^{\mathcal{J}}$, $\mathcal{J} = \boldsymbol{\mathcal{V}}, \boldsymbol{\mathcal{K}}$, are given by

$$\omega_n^{\mathcal{J}}(\Delta_t; ||\mathbf{x}-\mathbf{y}||) = \frac{1}{2\pi\imath} \int_{|z|=\rho} K^{\mathcal{J}}\left(||\mathbf{x}-\mathbf{y}||, \frac{\gamma(z)}{\Delta_t}\right) z^{-(n+1)}\, dz \tag{4}$$

where in this case $K^{\boldsymbol{\mathcal{V}}} = \widehat{G}$ is the Laplace transform of the kernel G appearing in the definition of the single layer operator $\boldsymbol{\mathcal{V}}$, and $K^{\boldsymbol{\mathcal{K}}} = \widehat{\partial G/\partial \mathbf{n}}$ is the Laplace transform of the kernel $\partial G/\partial \mathbf{n}$ appearing in the definition of the double layer operator $\boldsymbol{\mathcal{K}}$. In particular,

$$K^{\boldsymbol{\mathcal{V}}}(r,s) = \frac{1}{2\pi} K_0(rs), \qquad K^{\boldsymbol{\mathcal{K}}}(r,s) = -\frac{1}{2\pi} sK_1(rs)\frac{\partial r}{\partial \mathbf{n}},$$

where $K_0(z)$ and $K_1(z)$ are the second kind modified Bessel function of order 0 and 1, respectively. The function $\gamma(z) = 3/2 - 2z + 1/2z^2$ is the so called characteristic quotient of the BDF method of order 2. The parameter ρ is such that for $|z| \leq \rho$ the corresponding $\gamma(z)$ lies in the domain of analyticity of $K^{\mathcal{J}}$.

For the space discretization, we introduce a parametrization of the curve $\mathcal{B}$, $\mathbf{x} = \boldsymbol{\psi}(x) = (\psi_1(x), \psi_2(x))$ and $\mathbf{y} = \boldsymbol{\psi}(y) = (\psi_1(y), \psi_2(y))$ with $x, y \in [a, b]$. Then, at every time instant t_j we approximate the unknown function $u_{\mathcal{B}}(\boldsymbol{\psi}(x), t_j)$ and its normal derivative $\lambda_{\mathcal{B}}(\boldsymbol{\psi}(x), t_j)$ by continuous piecewise linear interpolants, associated with a partition $\{x_k\}_{k=1}^{M+1}$ of the parametrization interval $[a, b]$. Denoting by $\{N_i(x)\}$ the classical Lagrangian basis functions of local degree 1 associated with the spatial partition, and collocating the fully discretized equation at the points $\xi_h = x_h$, we obtain (see [2]) the following absorbing condition at time t_n (written in matrix notation):

$$\left(\frac{1}{2}\mathbf{I} + \mathbf{K}_0\right)\mathbf{u}_{\mathcal{B}}^n + \mathbf{V}_0\boldsymbol{\lambda}_{\mathcal{B}}^n = -\sum_{j=0}^{n-1}\mathbf{K}_{n-j}\mathbf{u}_{\mathcal{B}}^j - \sum_{j=0}^{n-1}\mathbf{V}_{n-j}\boldsymbol{\lambda}_{\mathcal{B}}^j, \quad n = 1, \ldots, N. \tag{5}$$

where $\mathbf{I}$ denotes the identity matrix and the matrices $\mathbf{V}$ and $\mathbf{K}$ are given by

$$(\mathbf{V}_{n-j})_{hi} = \int_a^b \omega_{n-j}^{\mathcal{V}}(\Delta_t; \|\boldsymbol{\psi}(x_h) - \boldsymbol{\psi}(y)\|)N_i(y)\|\boldsymbol{\psi}'(y)\|dy,$$

and

$$(\mathbf{K}_{n-j})_{hi} = \int_a^b \omega_{n-j}^{\mathcal{K}}(\Delta_t; \|\boldsymbol{\psi}(x_h) - \boldsymbol{\psi}(y)\|)N_i(y)\|\boldsymbol{\psi}'(y)\|dy.$$

We remark that, since the role of the NRBC is to define on $\mathcal{B}$ a relationship between the wave and its normal derivative, to prevent the raising of spurious waves, the more accurate is the discretized relationship the more transparent this will be. To this end, having chosen a continuous piecewise linear approximant for $u_{\mathcal{B}}$, we use an approximant of the same type also for $\lambda_{\mathcal{B}}$. The integrals appearing in the definition (4) of the coefficients $\omega_n^{\mathcal{J}}$ of the quadrature formula are efficiently computed by using the trapezoidal rule with $L \geq N$ equal steps of length $2\pi/L$. Moreover, they are computed simultaneously by using the FFT algorithm, with $O(N \log N)$ flops.

4.2 Finite element approximation and time discretization of the complete scheme

For the space discretization we consider a regular decomposition of the enlarged domain $\widetilde{\Omega} = \cup_{K \in \mathcal{T}_h} K$ into triangles K of edge length h. We introduce the finite dimensional space

$$X_h = \{w_h \in C^0(\widetilde{\Omega}) : w_{h|_K} \in \mathbb{P}^1(K), K \in \mathcal{T}_h\} \subset H^1(\widetilde{\Omega}),$$

for the finite element approximation of u. We also introduce the space $W_h \in H^{-1/2}(\mathcal{B})$ of piecewise linear (continuous) functions defined on the boundary $\mathcal{B}$ (the traces of the piecewise linear functions defined in X_h) and the space $M_\delta \in H^{-1/2}(\Gamma)$ of piecewise constant functions defined on a partition of Γ into segments of stepsize δ. We remark that the two stepsize parameters h and δ are a priori independent, but their choice is subject to a compatibility relation between the two spaces X_h and M_δ which guarantees the well posedness of the problem (see Lemma 4.1).

We approximate the variational problem (3) by: find $u_h \in X_h$, $\lambda_{\Gamma,\delta} \in M_\delta$, $\lambda_{\mathcal{B},h} \in W_h$ such that

$$\begin{cases} \dfrac{d^2}{dt^2}(u_h, w_h)_{\widetilde{\Omega}} + a(u_h, w_h) - < \lambda_{\Gamma,\delta}, w_h >_\Gamma - < \lambda_{\mathcal{B},h}, w_h >_{\mathcal{B}} & = (f(t), w_h) \quad \forall\, w_h \in X_h, \\ < \varphi_\delta, u_h >_\Gamma & = 0 \qquad\quad \forall \varphi_\delta \in M_\delta \end{cases}$$

For the time discretization we consider the Crank-Nicolson integration method; by introducing the new variable $v := \partial u/\partial t$, with obvious notation, we approximate the variational problem (3) by: find $u_h^{n+1} \in X_h$, $\lambda_{\Gamma,\delta}^{n+1} \in M_\delta$, $\lambda_{\mathcal{B},h}^{n+1} \in W_h$ such that for all $w_h \in X_h$ and for all $\varphi_\delta \in M_\delta$

$$\begin{cases} (u_h^{n+1}, w_h)_{\widetilde{\Omega}} + \frac{\Delta_t^2}{4} a(u_h^{n+1}, w_h) - & \frac{\Delta_t^2}{4} < \lambda_{\Gamma,\delta}^{n+1}, w_h >_\Gamma - \frac{\Delta_t^2}{4} < \lambda_{\mathcal{B},h}^{n+1}, w_h >_{\mathcal{B}} = \\ & (u_h^n, w_h)_{\widetilde{\Omega}} - \frac{\Delta_t^2}{4} a(u_h^n, w_h) + \frac{\Delta_t^2}{4} < \lambda_{\Gamma,\delta}^{n}, w_h >_\Gamma \\ & + \frac{\Delta_t^2}{4} < \lambda_{\mathcal{B},h}^{n}, w_h >_{\mathcal{B}} + \Delta_t (v_h^n, w_h)_{\widetilde{\Omega}} + \frac{\Delta_t^2}{4} (f^{n+1} + f^n, w_h)_{\widetilde{\Omega}} \\ < \varphi_\delta, u_h^{n+1} >_\Gamma = 0 \\ v_h^{n+1} = \frac{2}{\Delta_t}(u_h^{n+1} - u_h^n) - v_h^n \end{cases}$$

which, in matrix form, reads

$$\begin{cases} \left(\mathbf{M_h} + \frac{\Delta_t^2}{4}\mathbf{A_h}\right)\mathbf{u}^{n+1} - \frac{\Delta_t^2}{4}\mathbf{B}_\delta \boldsymbol{\lambda}_\Gamma^{n+1} - \frac{\Delta_t^2}{4}\mathbf{Q_h}\boldsymbol{\lambda}_{\mathcal{B}}^{n+1} & = & \left(\mathbf{M_h} - \frac{\Delta_t^2}{4}\mathbf{A_h}\right)\mathbf{u}^{n} + \frac{\Delta_t^2}{4}\mathbf{B}_\delta \boldsymbol{\lambda}_\Gamma^{n} \\ & & + \frac{\Delta_t^2}{4}\mathbf{Q_h}\boldsymbol{\lambda}_{\mathcal{B}}^{n} + \Delta_t \mathbf{M_h}\mathbf{v}^n \\ & & + \frac{\Delta_t^2}{4}\left(\mathbf{f}^{n+1} + \mathbf{f}^n\right) \\ \mathbf{B}_\delta{}^T \mathbf{u}^{n+1} = 0 \\ \mathbf{v}_k^{n+1} = \frac{2}{\Delta_t}(\mathbf{u}_k^{n+1} - \mathbf{u}_k^n) - \mathbf{v}_k^n \end{cases} \tag{6}$$

where:

- $\mathbf{M_h}$ denotes the mass matrix;
- $\mathbf{A_h}$ denotes the stiffness matrix;
- the rectangular matrix $\mathbf{B}_\delta$ represents a discrete trace operator on Γ;
- the rectangular matrix $\mathbf{Q_h}$ represents a discrete trace operator on $\mathcal{B}$.

Equation (6) is finally coupled with the discretized NRBC equation (5).

We recall that the following result holds (see [4]):

Lemma 4.1. *Suppose that the spaces X_h and M_δ satisfy that the space mesh size used for the discretization of the obstacle Γ is three times larger than the space mesh size used for the discretization of the computational domain $\widetilde{\Omega}$, then there exists a constant $C > 0$ (independent of h and δ) such that the following discrete inf-sup condition holds*

$$\inf_{\lambda_\delta \in M_\delta} \sup_{v_h \in X_h} \frac{< \lambda_\delta, v_h >_\Gamma}{\|\lambda_\delta\|_{-1/2,\Gamma} \|v_h\|_{1,\widetilde{\Omega}}} \geq C \tag{7}$$

Condition (7) guarantees that the rank of the matrix $\mathbf{B}_\delta$ is maximum.

5 Numerical results

In this section, we present some examples of the numerical testing we have performed by using the approach discussed in the previous section. We consider both fix and rotating obstacles. In the first case, to test the accuracy of the approximation obtained by the fictitious domain approach, we construct a reference "exact" solution by applying the Lubich-collocation boundary element method described in [3] with a very fine space and time discretization. Once the density function is retrieved, the solution at any point in the infinite domain is obtained by computing the associated potential (see [3] for details). This solution will be denoted by the acronym BEM.

Example 1 As a first test we consider the scattering of a wave by a fix obstacle, represented by a disk of radius 2. The wave is propagating radially, starting from an initial configuration $u_0(x,y) = e^{-5((x-5)^2+y^2)}$, without the presence of any external source ($f = 0$). Although u_0 does not have a local support (and thus contradicts one of our assumptions), it decays exponentially fast away from its center $x = (5,0)$, in such a way that, from the computational point of view, it can be regarded as compact and supported in a disk with radius smaller than 3 (at distance 2.7 from its center it assumes approximately values of the order $1e-16$). We choose the artificial boundary $\mathcal{B}$ as a circle of radius $R = 10$, so that the support of u_0 is included in $\widetilde{\Omega}$. The disk bounded by Γ represents a soft obstacle that acts as a reflecting body. The enlarged domain $\widetilde{\Omega}$ is the whole disk of radius 10. In Figure 2 we show snapshots of the solution at some time instants. In Figure 3, left plot, we compare the solution obtained by the fictitious approach with the reference one (BEM) at the boundary mesh point $x \approx (10,0)$ and for $t \in [0,20]$. The approximate solution has been obtained by a decomposition of the domain $\widetilde{\Omega}$ into 68724 triangles and by choosing a uniform partition of Γ into 128 segments. With such a choice the spatial step size is $h \approx 7.6e-02$, while $\delta \approx 9.8e-02$. The time interval has been decomposed into $N = 256$ time steps. We note that the solution is zero until the initial data reaches the artificial boundary (around $t = 4$). Approximatively at time $t = 2.5$, the wave reaches the boundary Γ and is perfectly reflected back, so that around $t = 9$ we see another outgoing wave at the artificial boundary $\mathcal{B}$. After that time, the wave is completely out of the annulus, as the reference solution and the approximate solution with the exact NRBC show. In the right plot we show the energy of the system. Since the system is a conservative one, the energy remains constant for the time instants $t \in [0,4]$ after which it starts dissipating because the wave reaches the artificial boundary and leaves the finite computational domain. It is worthwhile noting that the wave bumps the obstacle approximatively at $t = 2.5$ but, since the obstacle is fix, the energy is perfectly preserved up to $t \approx 4$.

In the next two examples we apply the proposed scheme to the diffraction of a wave by rotating bodies. In this case the location of the obstacles depends on t. Boundary element methods seem difficult to apply to such types of problem and standard finite elements would require the reconstruction of the computational mesh at each time step. To avoid such complexity, the fictitious domain approach seems a very attractive solution. In case of rotating rigid obstacles, the modification of the previously described scheme simply consists in replacing the boundary matrix $\mathbf{B_h}$ by a time dependent one.

For the treatment of rotating obstacles, an alternative approach is the one of embedding the rotating body in a domain that rotates together with the scatterer. Such a domain is in turn placed inside a stationary residual domain (see for example [1] where a similar strategy is applied to

Figure 2: Example 1: Snapshots of the solution at different times.

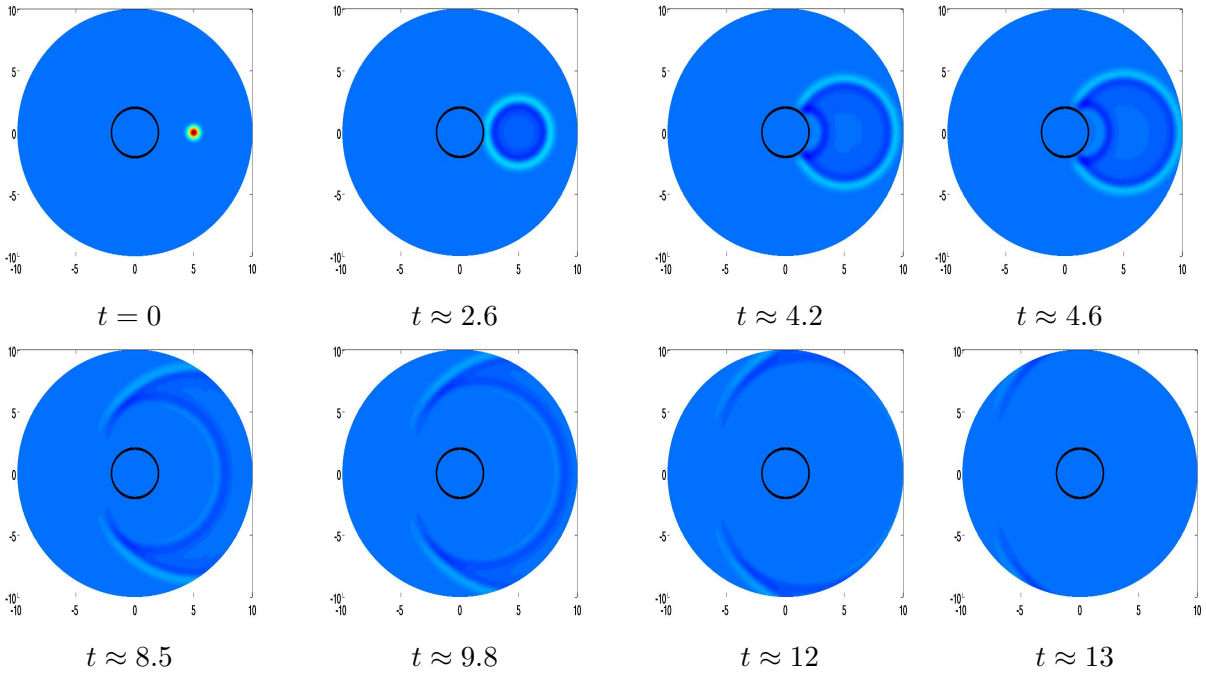
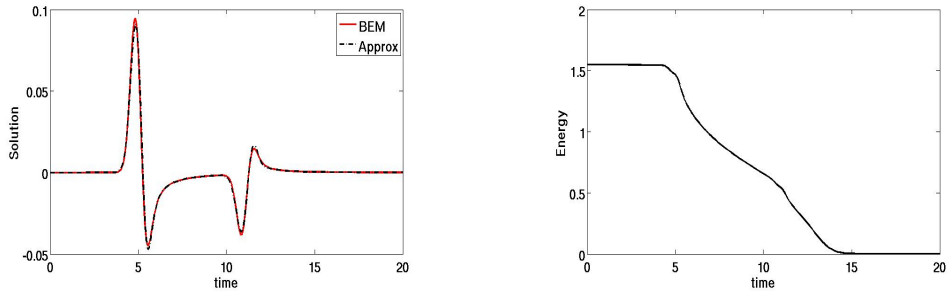


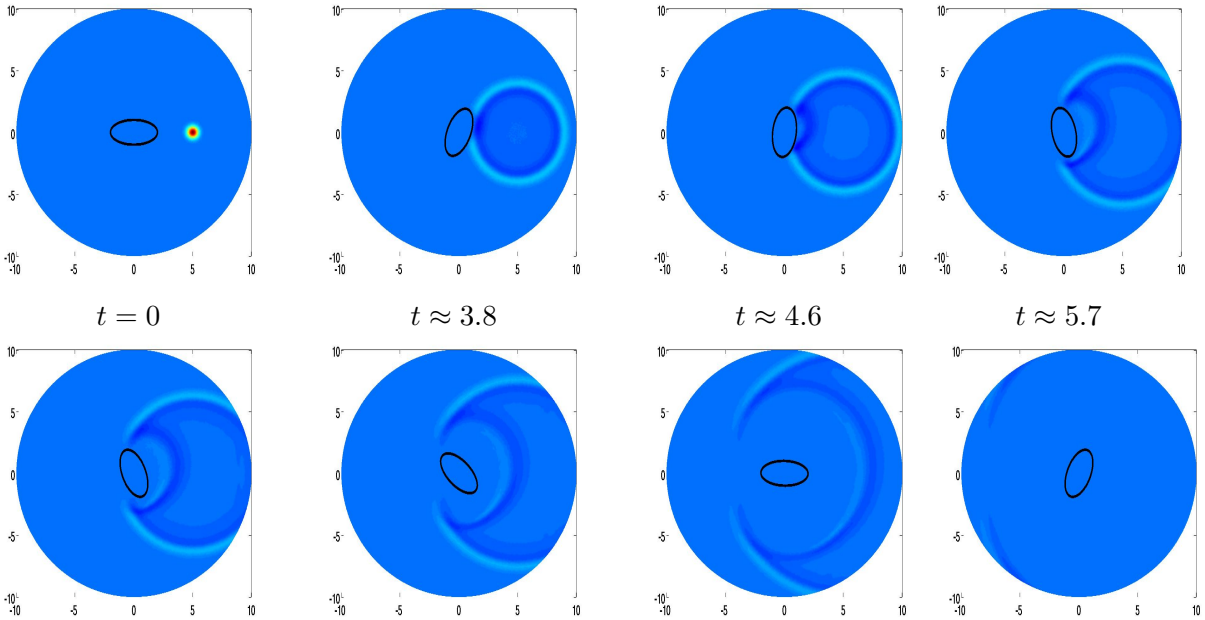
Figure 3: Example 1. Behavior of the solution at $P \approx (10, 0)$ (left plot) and energy dissipation (right plot).



the computation of flows induced by rotating components). By imposing the continuity of the discrete solution weakly on the interface between the rotating and the stationary subdomains, no compatible discretizations are required at the interface. However, in the time marching scheme, an interpolation technique is required to upload the solution at each time step. This increases the computational overhead especially when the discretization of the rotating domain must be chosen sufficiently fine to approximate accurately the boundary of the rotating scatterer.

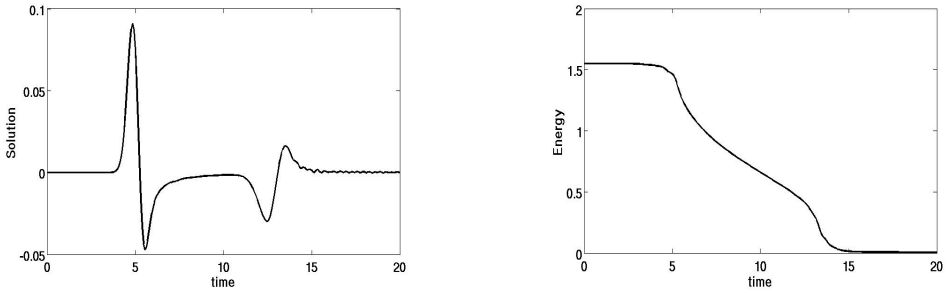
Example 2 We consider a soft ellipsoidal obstacle whose boundary Γ is the ellipse of equation $x^2/a^2 + y^2/b^2 = 1$ with $a = 2$ and $b = 1$. The scatterer rotates around its center with a constant angular velocity equals to $\omega = \pi/128$. We consider a wave with the initial configuration u_0 as in Example 1 and that impinges upon the rotating obstacle. The transparent artificial boundary $\mathcal{B}$ is the circle of radius 10. In Figure 4 we show the snapshots of the solution at different times instants. In Figure 6 we show the behavior of the solution at a point $P \approx (10, 0)$ that belongs to the artificial boundary (left plot) and the energy behavior of the system with respect to time (right plot). The space/time discretization parameters are the same of Example 1. The wave bumps the rotating obstacle around $t = 3.5$, and the energy is preserved up to the time instant $t \approx 5$, when the wave reaches the transparent boundary and leaves the computational domain. We remark that, even if in this case the system is not a conservative one, the velocity of rotation of the obstacle is small if compared to the speed of propagation of the wave, so that the energy remains constant until the wave starts vanishing from the computational domain.

Figure 4: Example 2: Snapshots of the solution at different times.



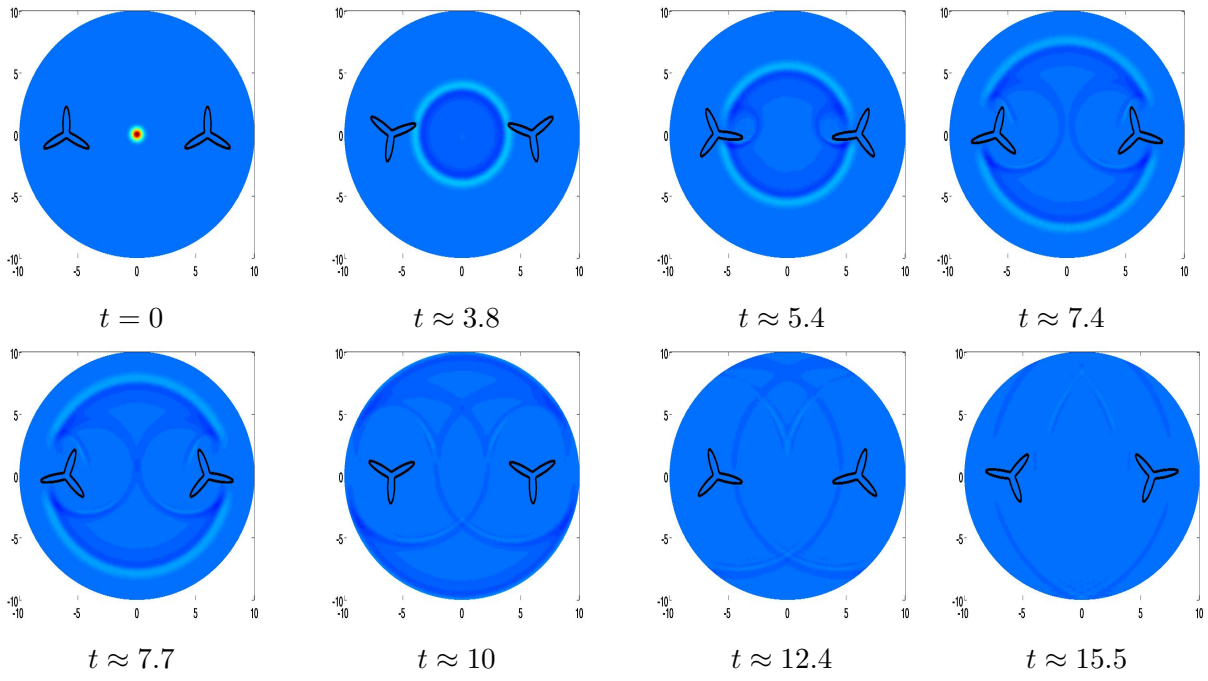
Example 3 In this last example we consider two scatterers, both having helicoidal shape, that rotate around their own center with constant angular velocity $\omega = \pi/128$ and in opposite directions (clockwise direction for the left obstacle and anticlockwise direction for the right one). The two obstacles are surrounded by an artificial circular boundary of radius 10. The initial configuration of the wave is given by the function u_0 of Examples 1 and 2, now centered

Figure 5: Example 2. Behavior of the solution at $P \approx (10, 0)$ (left plot) and energy dissipation (right plot).



at the origin of the axis. In Figure 6 we show the snapshots of the wave propagation at some instants. In Figure 7, left plot, we show the behavior of the solution at a point $P \approx (0, 4)$ for $t \in [0, 20]$ and in the right plot the energy of the system. The solution has been obtained by a decomposition of $\widetilde{\Omega}$ into 69176 triangles, by choosing a uniform partition of the two boundaries of the obstacles into 128 segments and with $N = 256$ time steps. In this case, since the system is not a conservative one, we observe that the energy increases after it bumps the two obstacles (around $t = 4$) and is reflected back.

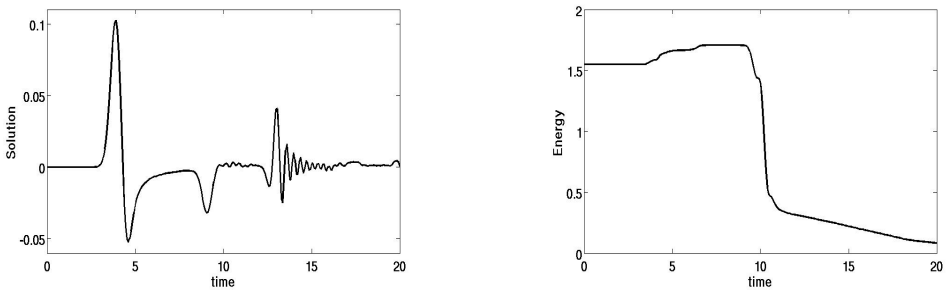
Figure 6: Example 3. Snapshots of the solution at different times.



6 Conclusions

We have considered a fictitious domain method for the solution of wave equation problems in unbounded domains, coupled with a NRBC on a suitably chosen artificial boundary. For its solution, we have used standard finite element methods and an unconditionally stable time marching scheme for the approximation of the domain method, and a convolution quadrature technique in time coupled with a collocation method in space for the approximation of the NRBC. The coupling of the two schemes is a new topic and, although fictitious domain methods

Figure 7: Example 3. Behavior of the solution at $P \approx (0, 4)$ (left plot) and energy dissipation (right plot).



have been successfully applied to time dependent problems with stationary obstacles (see for example [13]), there is still much work to do on numerical methods for the treatment of rotating scatterers. At the moment the theory to justify the validity of the presented approach is still at an early stage, but the first numerical results we have obtained are very promising. Moreover, we emphasize that for the other NRBCs (of local type) that have been proposed in literature, it is not clear whether their application can be extended to the case of rotating obstacles. For these reasons we believe that the proposed method represents a new efficient approach to the diffraction of waves by rotating bodies.

REFERENCES

[1] Y. Bazilevs, T.J.R. Hughes, NURBS-based isogeometric analysis for the computation of flows about rotating components, Comput. Mec. 43 (2008), 143–150.

[2] S. Falletta, G. Monegato, An exact non reflecting boundary condition for 2D time-dependent wave equation problems. Wave Motion 51 (2014), no. 1, 168–192.

[3] S. Falletta, G. Monegato, L. Scuderi, A space-time BIE method for nonhomogeneous exterior wave equation problems. The Dirichlet case. IMA J. Numer. Anal. 32 (2012), no. 1, 202–226.

[4] V. Girault, R. Glowinski, Error analysis of a fictitious domain method applied to a Dirichlet problem. Japan J. Indust. Appl. Math 12 (1995), 487–524.

[5] D. Givoli, Numerical Methods for Problems in Infinite Domains, Elsevier, Amsterdam, 1992.

[6] D. Givoli, Recent advances in the DtN FE method, Archives of Computational Methods in Engineering 6 (1999) 71-116.

[7] D. Givoli, High-order local non-reflecting boundary conditions: A review, Wave Motion 39 (2004) 319-326.

[8] M.J. Grote, Ch. Kirsch, Nonreflecting boundary condition for time-dependent multiple scattering, J. Comput. Phys. 221 (2007) 41-62.

[9] M.J. Grote, I. Sim, Local nonreflecting boundary condition for time-dependent multiple scattering, J. Comput. Phys. 230 (2011) 3135-3154.

[10] Ch. Lubich, Convolution quadrature and discretized operational calculus. I, Num. Math. 52 (1988) 129-145.

[11] P.Joly, Variational methods for time-dependent wave propagation problems. Topics in computational wave propagation, 201264, Lect. Notes Comput. Sci. Eng., 31, Springer, Berlin (2003).

[12] A. Taflove, S.C. Hagness, Computational Electrodynamics. The finite-difference time-domain method, Hartech House, Boston-London, 2005.

[13] Y. Zhang, A fictitious domain method for acoustic wave propagation problems, Mathematical and Computer Modelling 50 (2009) 351–359.

COMPDYN 2015
5th ECCOMAS Thematic Conference on
Computational Methods in Structural Dynamics and Earthquake Engineering
M. Papadrakakis, V. Papadopoulos, V. Plevris (eds.)
Crete Island, Greece, 25–27 May 2015

EFFECTIVENESS OF TUNED MASS DAMPER IN DAMAGE REDUCTION OF BUILDING UNDER FAR-FIELD GROUND MOTIONS

C. Ngamkhanong*, T. Pinkaew

Department of Civil Engineering, Chulalongkorn University
Phayathai Rd., Bangkok 10330, Thailand
chayut.ngam@gmail.com, tospol.p@chula.ac.th

Keywords: Tuned mass damper, Damage reduction, Inelastic structures

Abstract. *Damage reduction of existing tall buildings subjected to earthquake ground motions has been studied in recent decades. Seismic base isolations, strengthening of structural system and installation of damping devices such as viscous dampers, friction damper and buckling restrained brace, have also been introduced to either reduce the seismic demand, improve the strength or dissipation characteristics of the building. However, their applications are very limited since their investment costs seem to be prohibited. A tuned mass damper (TMD) installed at rooftop is proposed as an alternative method to reduce the seismic damage of the existing tall buildings under far-field earthquake excitations. Due to the long duration and narrow band nature of far-field excitation, its application becomes effective. In addition, the cost of the TMD is more attractive comparing to other seismic control systems. However, the performance of TMD might be seriously impaired due to the degradation of structural stiffness caused by severe earthquake. Therefore the real application of the TMD has to be extensively investigated. This paper studies the damage behavior of tall building under various magnitudes of harmonic and recorded ground motions. The dynamic inelastic analysis is employed. The effectiveness of TMD having mass ratio of 5% is evaluated considering the building's damage and performance. The obtained simulation results reveal the effectiveness of the TMD under various intensities of ground motions.*

1 INTRODUCTION

Tuned mass dampers, consist of stiffness, inertia and damping elements, has been used for vibration control of structures under lateral load such as wind [1,2] and earthquake. Tuned mass damper is an inexpensive and effective control device when compare to other applications. Tuned mass damper can greatly reduce the seismic response of the structure within elastic range but when experiences inelastic behavior, the effectiveness of tuned mass damper tend to decreases due to detuning effect under strong ground motion.

Pinkaew et. al. [3] proposed the damage index, based on Park et. al. [4], to describe the effectiveness of TMD instead of displacement reduction of inelastic structure. The efficiency of TMD for control 20 story reinforced concrete building subjected to 1985 SCT is considered. It is found that although TMD cannot reduce the peak displacement after yielding, it can significantly reduce the damages of the building and improve the ability to withstand the severe ground motions. Wong and Johnson [5] studied the seismic energy dissipation of inelastic structure of various placements of multiple TMDs. Their results indicate that placing one TMD at the top floor is the best location to dissipate a large amount of plastic energy. As a result, highest damage reduction in the structure can be expected. Rofooei and Abatahi [6] considered three structural models subjected to seven earthquakes varying the intensity. For the 12 and 15 story buildings, it is found that TMD can greatly reduce the damage of structure, however for the 8 story building, its performance significantly decreases at the same intensity because of the detuning effect. Assuming the building can be modeled by bilinear hysteretic SDOF, Zhang and Balendra [7] proposed a method to obtain the optimal parameters of TMD by minimizing the maximum inelastic response under narrow band excitations of long distance earthquakes. The effectiveness of TMD designed using their proposed method is investigated. It is found that the proposed optimal TMD can provide better damage reduction than traditional design formula.

Nevertheless, the above mentioned researches did not consider the realistic inelastic behavior of the buildings to evaluate the effectiveness of TMD. Therefore, in this study, the nonlinearity characteristics of a three dimensional 20-story reinforced concrete buildings are modeled by the lumped plasticity hinges according to ASCE 41 standard [8]. The Perform 3D program [9] is employed to conduct the inelastic dynamic analysis of the building under harmonic and actual earthquake ground motions with varying peak ground accelerations from zero to collapsed acceleration. The obtained results are used to evaluate the effectiveness of TMD and its control characteristics.

2 AN EXAMPLE REINFORCED CONCRETE BUILDING

In this study, a 20 story reinforced concrete residential building as outlined in Moehle et.al. [10] is considered. The moment resisting frame and shear wall are re-designed to resist the gravity load based on ASCE7-10 and ACI318-08. The plan and elevations are shown in Fig. 1. This building is not designed for earthquake but only gravity loads and uniform wind pressure of 2.0 kN/m^2 are taken into account. Compressive strength of concrete of 30 MPa and yield strength of reinforcement of 400 MPa are used. The thickness of shear wall is 0.15 m with 0.33% and 0.25% of reinforcement in vertical and transverse directions, respectively. The cross-section of columns vary from 0.30 m x 0.30 m to 0.75 m x 0.75 m while the thickness of slabs are 0.2 m in every floors.

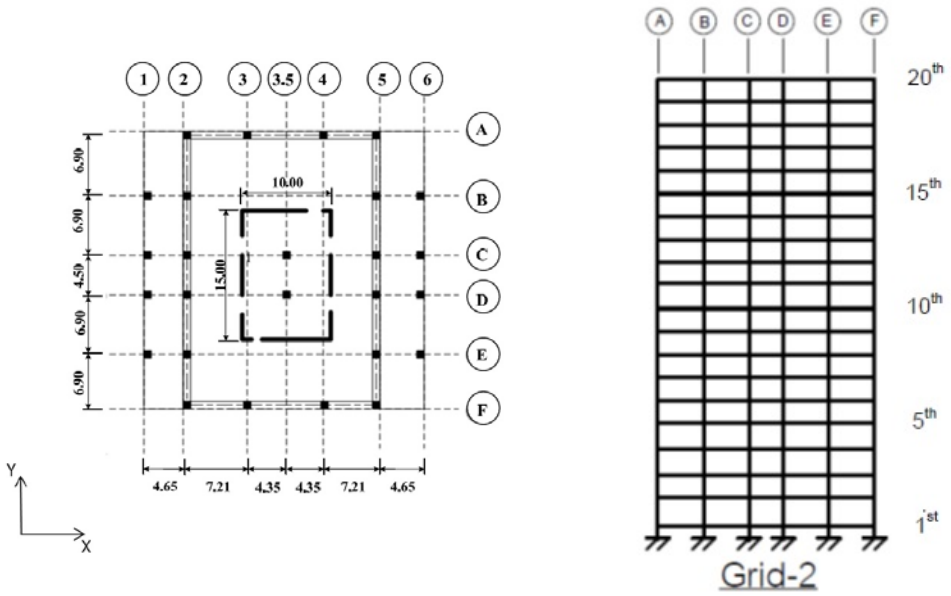


Fig. 1. Plan and elevation

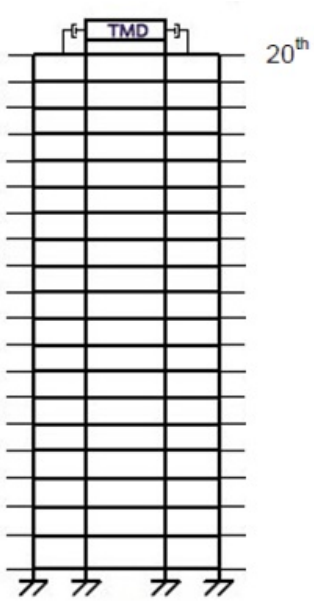


Fig. 2. Example building installed by TMD

3 THE PROPERTIES OF TUNED MASS DAMPER

The example building as previously mentioned is installed by the tuned mass damper (TMD) on the top roof, Fig. 2. To design the optimal parameters of TMD, the equivalent SDOF system of the building is considered based on the fundamental mode of vibration.

In this study, the tuned mass damper with 5% mass ratio is provided to resist both harmonic ground motion and far-field earthquake with varying amplitudes until the collapse of the building. The parameters of TMD are set to the optimal values of the TMD installed on linear structure under harmonic loading given by Den Hartog [11] as shown in Eq.(1)

$$\gamma_{opt} = \frac{1}{1+\mu}$$
$$\zeta_{opt} = \sqrt{\frac{3\mu}{8(1+\mu)}} \quad (1)$$

Where μ, γ and ζ are, respectively, mass ratio, frequency ratio, and damping ratio

Building	Total	Mass = 19,941 tons
	SDOF (Mode 1)	Mass = 5,334 tons, Stiffness = 43,859 kN/m,
		Period = 2.19 s, Damping ratio = 0.015
TMD		Mass = 997 tons, Stiffness = 5,839 kN/m,
		Damping ratio = 0.24

Table 1 : Properties of the equivalent SDOF system and tuned mass damper

4 DAMAGE AND PERFORMANCE OF BUILDING

4.1 Damage Index

4.1.1 Component Damage

To quantify the effectiveness of the tuned mass damper in damage reduction of the building induced by strong ground motion, the modified Park and Ang damage index as proposed by Kunnath et al. [12] is employed. This index consist of term of rotation and dissipated energy as in Eq.(2)

$$DI = \frac{\theta_m - \theta_r}{\theta_u - \theta_r} + \frac{\beta}{M_y \theta_u} E_h \quad (2)$$

Where θ_m, θ_u and θ_r are, respectively, maximum rotation, ultimate rotation, and recoverable rotation (unloading)

M_y is the yielding moment

E_h is the dissipated energy of the element

β is the strength deterioration parameter (assumed to be 0.27 by Ciampoli et. al. [13])

4.1.1 Story Damage

Damage index of story is evaluated by weighted average of dissipated hysteretic energy in the component, Eq.(3) . In this study, the maximum grid damage in each story is represented as a story damage of the building.

$$DI_{story} = DI_{grid}\Big|_{MAX} = \sum_{i=1}^{n} (DI_i)_{component} \left[\frac{E_i}{\sum_{i=1}^{n} E_i} \right]_{component} \quad (3)$$

Where E_i are the total absorbed energy by the component "*i*".

4.1.2 Building Damage

Building damage is assumed to be the maximum story damage of the building.

4.2 Building Performance Levels

Besides the quantitative evaluation of building damage as previously mentioned, this study also calculate the building performance based on the maximum plastic rotation of every structural components according to ASCE41 as following

4.2.1 Operational

Very light damage, no permanent displacement, substantially original strength and stiffness, and backup utility services maintain functions.

4.2.2 Immediate Occupancy (IO)

Very light damage, no permanent displacement and substantially original strength and stiffness, Minor cracking, and The building remains safe to occupy; any repairs are minor.

4.2.3 Life Safty (LS)

Moderate damage, Some permanent displacement, Residual strength and stiffness in all stories. Structure remains stable and has significant reserve capacity; hazardous nonstructural damage is controlled.

4.2.4 Collapse Prevention (CP)

Severe damage, Large permanent displacement, Little residual strength or stiffness, Gravity elements function. Some exits blocked. The building remains standing but near collapse and other damage or loss is acceptable.

5 EFFECTIVENESS OF TMD UNDER ASSUMED HARMONIC GROUND MOTION

The effectiveness of TMD are evaluated under an assumed harmonic ground motion with time-varying amplitudes, as shown in Fig. 3. The amplitude of ground motion is assumed to be linearly increased from t = 0 s to reach its PGA at t = 15 s and is kept constant from t = 15-45 s, then, is assumed to be linearly reduced to zero at t = 60 s. The ground motion frequency is set to the first natural frequency of the building and its PGA is varied from zero until the collapse of the building is obtained.

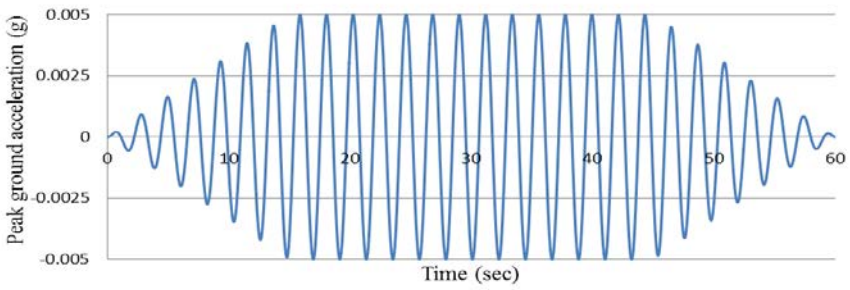


Fig. 3. An assumed harmonic ground motion

Fig. 4. shows the typical roof displacement of the building with and without TMD when PGA of ground motion is 0.02g. Since the excitation frequency is intentionally set to the natural frequency of the building, the resonance vibration of the building is expected. With this magnitude of excitation, it is found that the building without TMD exhibits excessive vibration with building damage = 1.0 and the building performance goes beyond the collapse prevention limit (CP) while that with TMD gets no damage and its performance are well within operational limit. It is noted that about 83% of roof displacement reduction by TMD can be observed.

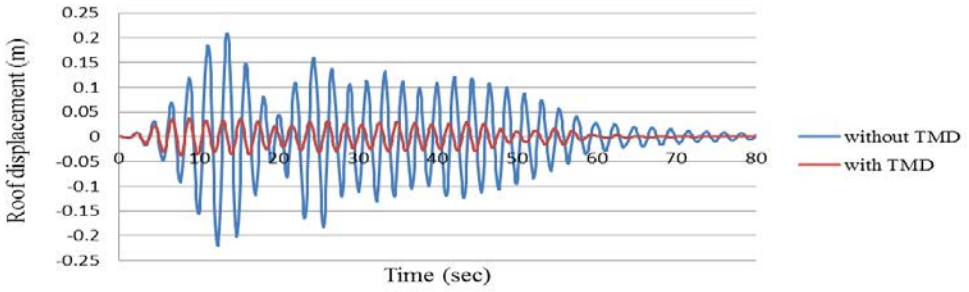


Fig. 4. Roof displacement of the building along X direction with and without TMD under an assumed harmonic ground motion with PGA = 0.02g

Fig. 5 shows the comparison of damage index between building without and with TMD under harmonic ground motion with varying PGA. Damage Index of the building with TMD is equal to 1 when a PGA is 0.115g, while damage index of the building without TMD exceeds the collapse line when PGA is only 0.02g. Fig. 6 show the damage reduction from TMD, for PGA less than 0.002g, there is no damage to both buildings, so the damage reduction is not defined. For PGA between 0.002g and 0.05g, TMD can prevent the building damage. In particular, the building without TMD collapses when PGA reaches 0.02g while that with TMD can resist the ground motion without any damage until PGA = 0.05g. Although, the building with TMD shows some damages when PGA is greater than 0.05g. The building is protected from collapse until PGA reaches 0.115g. In addition, it can be seen that when the structure is vibrated within a range of slight inelasticity, damage reduction slowly decreases. However, due to the de-tuning effect, the damage reduction rapidly decreases when the building is vibrated within a range of significant inelasticity.

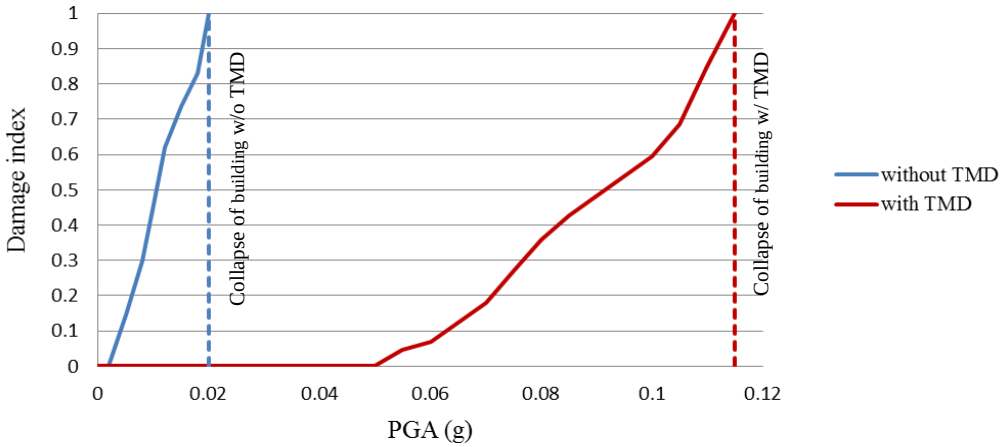


Fig. 5. Damage index of the building against PGA under harmonic ground motion

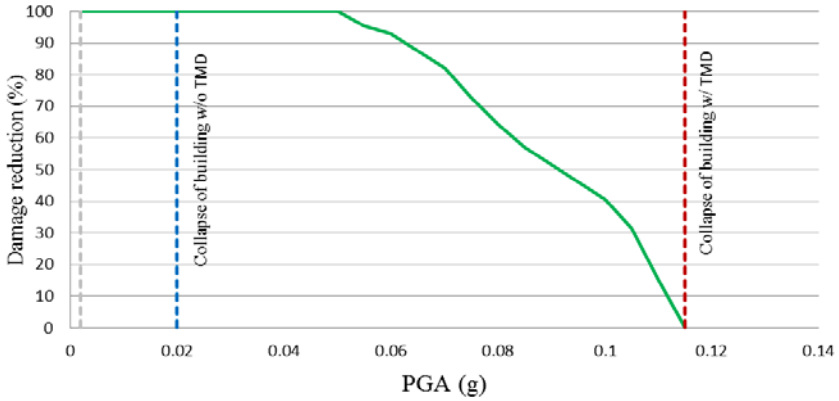


Fig. 6. Damage reduction of the building with TMD under harmonic ground motion

Fig. 7 shows the seismic performances of the critical frames and walls of the building with and without TMD under collapse ground motions. Frames along Grid A and F in the top floor are the most damaged zones of both structures. While the shear wall damages are found only at the ground floor. Fig.7a shows the damage scenario of the building without TMD under PGA = 0.02g, it can be seen that the columns in the upper story get more damage than lower story. In particular, the corner columns in the 18th -19th floor reach CP performance limit, while the performances of internal columns are well within LS limit. The damage in shear walls is found at the ground floor with CP performance limit. Fig. 7b, on another hand, shows the damage scenario of the building with TMD under PGA = 0.115g. It is found that it looks quite similar with that without TMD except the ground motion is about 5.7 times larger.

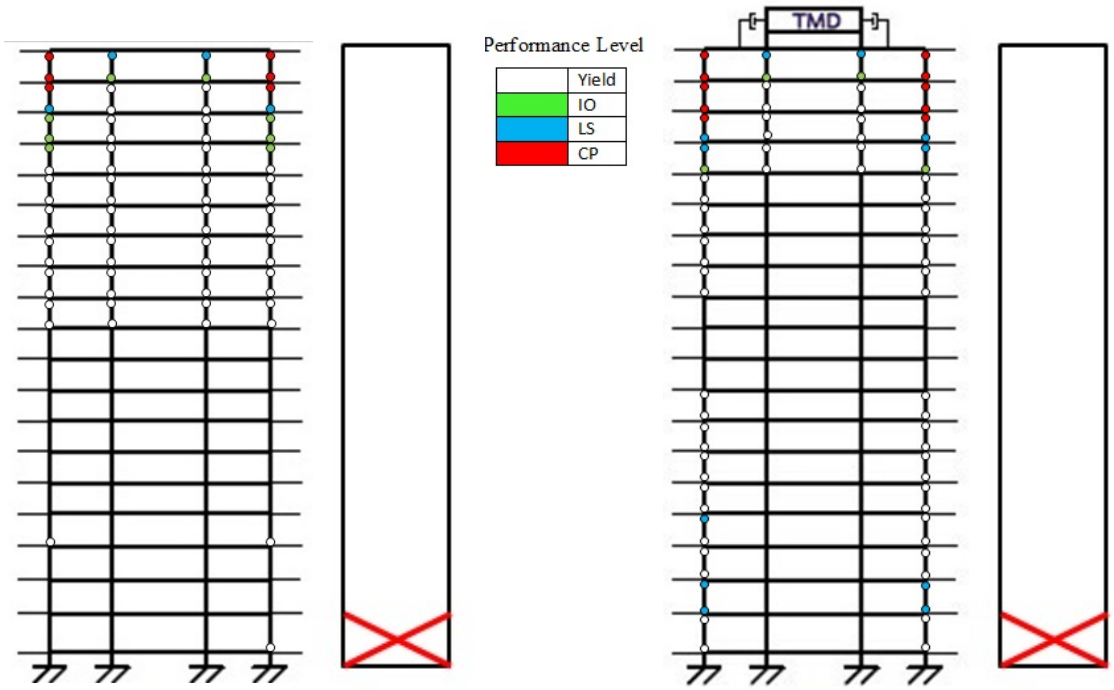


Fig.7. (a) Performance of building without TMD under a harmonic ground motion with PGA = 0.02g
(b) Performance of building with TMD under a harmonic ground motion with PGA = 0.115g

6 EFFECTIVENESS OF TMD UNDER A FAR-FIELD GROUND MOTION

In this study, the Chi-Chi earthquake record (1999) at KAU082 station is adopted as a far-field ground motion as shown in Fig. 8. It is noted that this record has a dominant frequency close to the natural frequency of the building and therefore the resonance vibration of the building can be expected

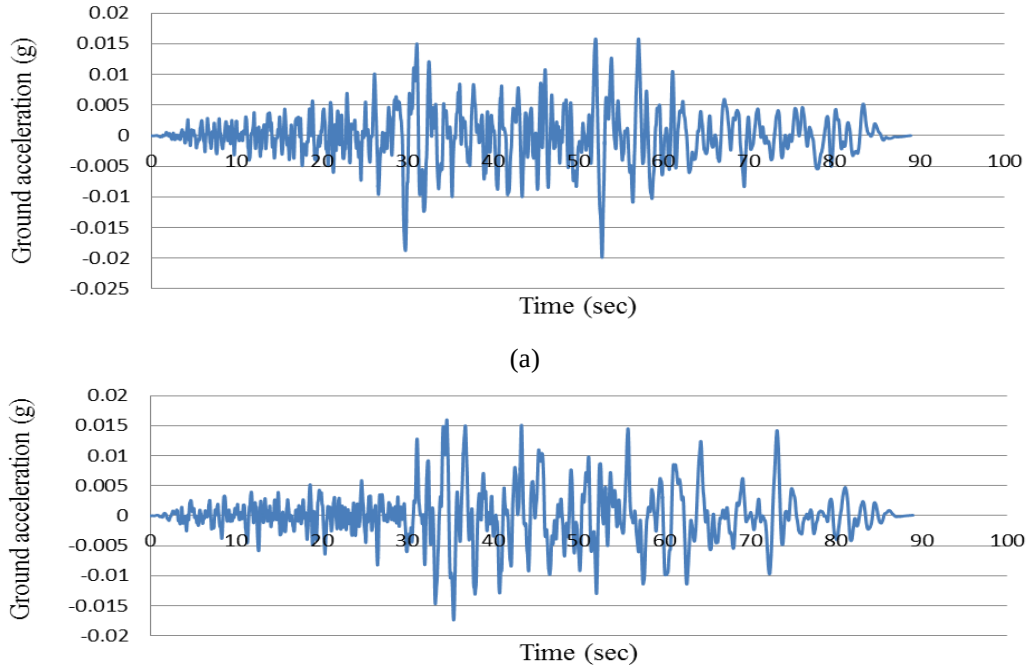


Fig. 8. Chi-Chi (1991) earthquake in, (a) X direction and (b) Y direction

Fig. 9 shows the roof displacement of the building along XX direction with and without TMD under the input ground motion with PGA of 0.0116g. With this magnitude of PGA, both buildings are vibrated within elastic range. It is observed that about 41.7% of displacement reduction can be gained from TMD. Fig. 10 shows the roof displacement of the building with and without TMD when the PGA of the input earthquake is increased to the collapse PGA of the building without TMD at 0.042g. It is clearly seen that TMD is not effective in displacement reduction of the structure. In particular, only 0.04% displacement reduction is obtained. By comparing with elastic range of Building, TMD's effectiveness in roof displacement decreases when PGA increases.

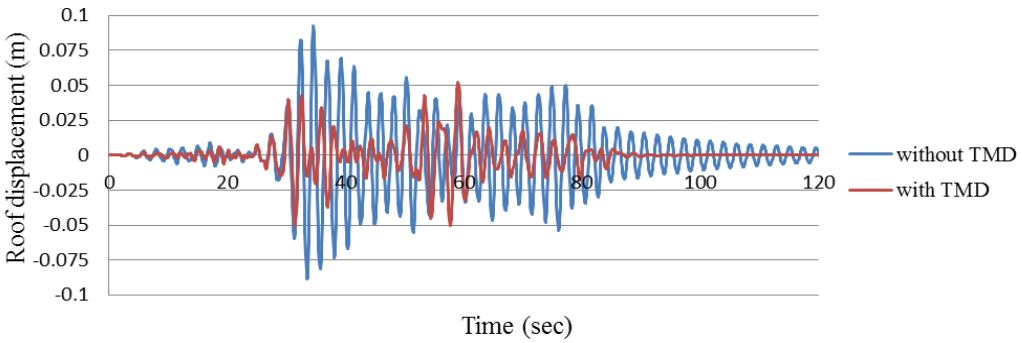


Fig. 9. Roof displacement of the building along X direction with and without TMD under Chi-Chi earthquake with PGA of 0.0116g

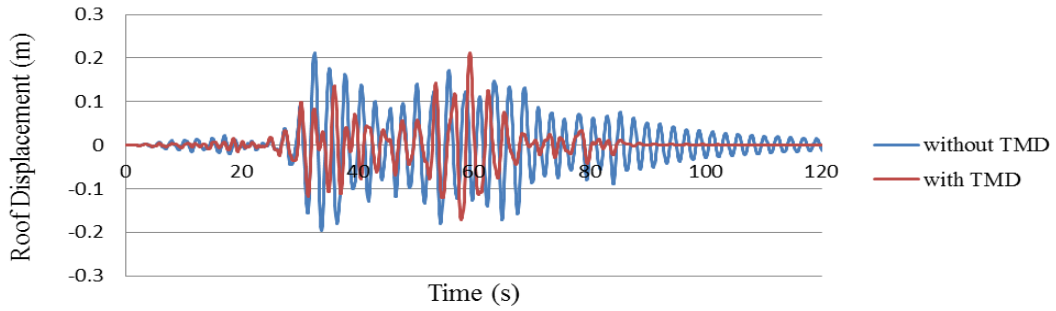


Fig. 10. Roof displacement of the building along X direction with and without TMD under Chi-Chi earthquake with PGA of 0.042g

Fig. 11. shows the comparison of damage index between buildings without and with TMD under input earthquake with varying PGA. It is noticed that the damage index of the building with TMD equals to 1 when PGA is 0.054g, while damage index of the building without TMD equals to 1 when PGA is 0.042g. This indicates about 30% enhancement of collapse prevention by TMD. Fig. 12 shows the damage reduction and roof displacement reduction by TMD. In term of damage reduction, for PGA less than 0.0116g, there is no damage to both building so that the damage reduction is not defined. For PGA between 0.0116g and 0.0193g, although the damages of the building without TMD increase as the PGA increases, there is no damage to the building with TMD in this range of excitation. For PGA between 0.0193g and 0.043g, TMD can reduce the damage of the building, however it effectiveness in damage reduction becomes smaller as the PGA increases. For PGA is greater than 0.054g, the building with TMD also collapses and therefore TMD provides no benefit to the building. In term of roof displacement reduction, TMD can suppress the roof displacement whenever the building vibration is within elastic range or slightly inelastic range.

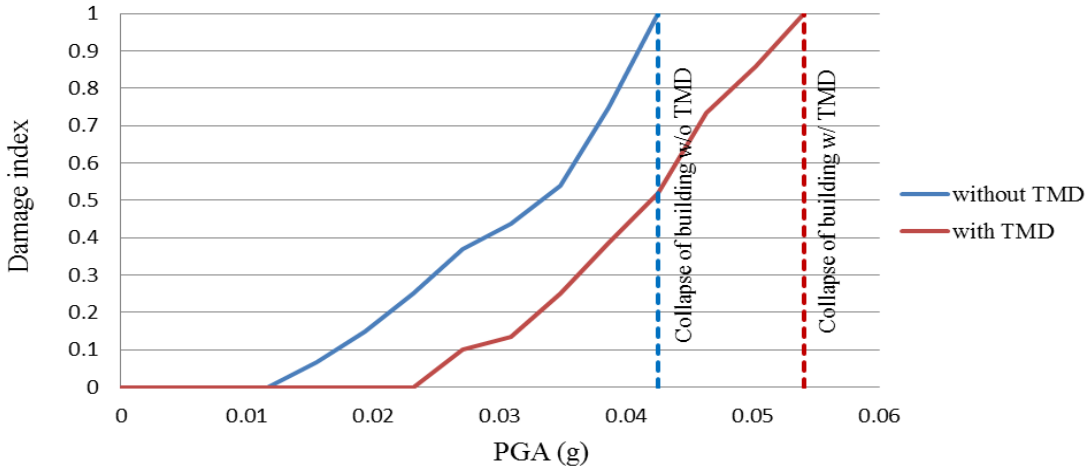


Fig. 11. Damage index of the building against PGA under Chi-Chi earthquake

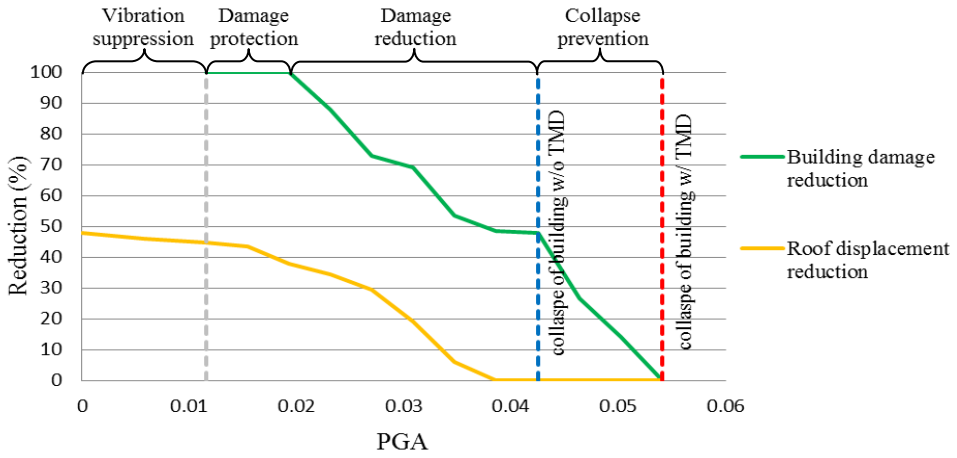


Fig. 12. Vibration and damage reduction of the building with TMD under Chi-Chi earthquake

Fig. 13 shows the seismic performance of critical frames and walls of the building with and without TMD under the input earthquake having PGA = 0.042g. Frames along grid A and F in the top floor are the most damaged zones of both structures. Fig.13a shows the damage scenario of the building without TMD. Similar to the case of harmonic ground motion, it can be seen that the damages occur in only upper story and the most damaged columns in the story are the corner columns. While the shear wall damage occurs only at the first story where the CP performance limit is observed. Fig. 13b shows the damage scenario of the building with TMD under the same magnitude of PGA. Obviously, the damages are not severe comparing with the collapse of the building without TMD. In particular, there is no column and shear wall gets damage of CP performance limit

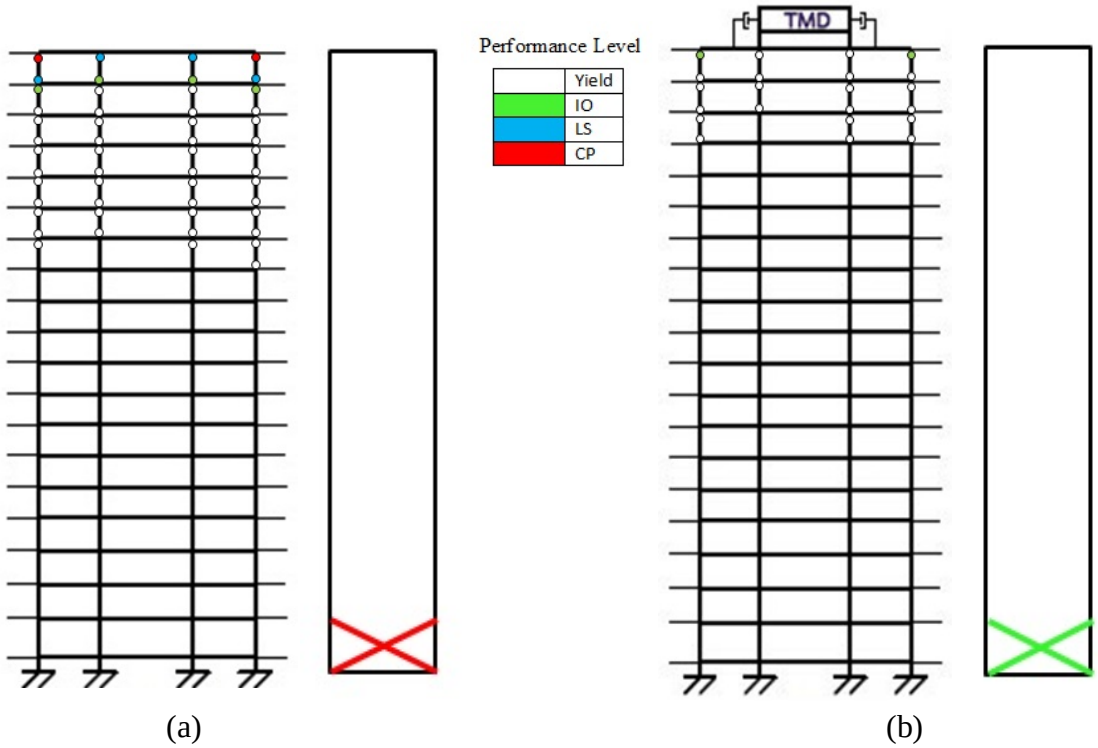


Fig. 13. Comparison of building performance level between (a) buiilding without TMD (b) building with TMD under Chi-Chi earthquake with PGA of 0.042g

7 CONCLUSIONS

In this study, the seismic effectiveness of TMD for a 20 story reinforced concrete building subjected to both harmonic and earthquake record ground motions with varying amplitudes until the building collapse is investigated. The inelastic modeling of the building according to ASCE 41 is employed to realistically represent the building behavior under strong ground motion. The dynamic inelastic analysis of the building with and without TMD is adopted. To evaluate the effectiveness of TMD, the damage index and building performance level are estimated. The obtained results indicate that, for these narrow band ground motions, TMD is effective in displacement reduction whenever the vibration of the building is within elastic or slightly inelastic ranges. When the building gets significant damages, the change in vibration frequency deteriorates its effectiveness due to de-tuning effect. Therefore, TMD cannot provide any significant displacement reduction in this high inelastic range. However, it is clearly found that TMD can protect or reduce the building damages induced by the ground motions. The damage protection and reduction are significant. In addition, it is also observed that TMD can prevent the building from collapse with a significant range of ground motion magnitude. Based on this investigation, the application of TMD to a tall building subjected to far-field ground motions seems to be an attractive alternative to other retrofitting techniques.

8 REFERENCES

[1] K.C.S. Kwok, B. Samali, Performance of tuned mass dampers under wind load. *Engineering Structures*, Vol. 17, No. 9, pp. 655~67, 1995.

[2] C. Meinhardt, Increase of a high rise buildings damping behavior by applying large scale tuned mass dampers. *IABSE Congress Report*, 17th Congress of IABSE, Chicago, pp. 68-69(2), 2008.

[3] T. Pinkaew, P. Lukkunaprasit, P. Chatupote, Seismic effectiveness of tuned mass damper for damage reduction of structure. *Engineering structure 25*, 39-46, 2003.

[4] Y.J. Park et.al., Mechanistic seismic damage model for reinforced concrete. *Journal of Structural Engineering and Structural Engineering*, ASCE,111(4): 722-39, 1985.

[5] K. K.F.Wong, J. Johnson, Seismic energy dissipation of inelastic structures with multiple tuned mass damper. *Journal of Engineering Mechanics*, Vol.135, 2009.

[6] F.R.Rofooei, P. Abtahi, On the performance of passive TMDs in reducing the damage in 2-D concrete structural models. *Procedia Engineering14*, 1665–1671, 2011

[7] Z. Zhang, T. Balendra, Passive control of bilinear hysteretic structures by tuned mass damper for narrow band seismic motions. *Engineering Structures*, 54, 103–111, 2013.

[8] American Society of Civil Engineering, *Seismic evaluation and retrofit of existing buildings*, American Society of Civil Engineering, 2013.

[9] Computer Structures, Inc., *User's Guide: PERFORM 3D version 4.0*, Berkeley, CA., 2008.

[10] J. Moehle et.al., Case studies of the seismic performance of tall buildings designed by alternative means. *Task 12 Report for the Tall Buildings Initiative* , Pacific Earthquake Engineering Research Center, 2011.

[11] J.P. Den Hartog, *Mechanical Vibrations*, 4th Edition, McGraw-Hill, 1956.

[12] S.K. Kunnath et.al., IDARC 2D version 4.0:A Computer Program for the Inelastic Damage Analysis of Buildings. *Report no. NCEER-96-0010*, National Center for Earthquake Engineering and Research, 1996.

[13] M. Ciampoli, R. Giannini, C. Nuti, P.E. Pinto, Seismic reliability of non-linear structures with stochastic parameters by directional simulation. In: *Proceedings of the 5th International Conference on Structural Safety and Reliability*, San Francisco, CA, 1121-28, 1989.

.

COMPDYN 2015
5th ECCOMAS Thematic Conference on
Computational Methods in Structural Dynamics and Earthquake Engineering
M. Papadrakakis, V. Papadopoulos, V. Plevris (eds.)
Crete Island, Greece, 25–27 May 2015

NEURO-FUZZY MODELING OF A SPONGE-TYPE MR DAMPER

Manuel T. Braz-César[1], **Rui C. Barros**[2]

[1] Polytechnic Institute of Bragança
Campus de Santa Aplónia – Apt. 134 – 5301-857 Bragança - Portugal
e-mail: brazcesar@ipb.pt

[2] Faculty of Engineering of the University of Porto
Rua Dr. Roberto Frias, s/n 4200-465 Porto - Portugal
rcb@fe.up.pt

Keywords: MR damper, ANFIS, Fuzzy model.

Abstract. *Numerical modeling of MR dampers based on parametric models constitutes one of the main methodologies to simulate the behavior of this type of devices. However, its highly non-linear nature and also its inherent rheological behavior make this type of numerical modeling harsh and complicated, which hinders the development of simple models capable to cover all aspects associated with the proper numerical simulation of the damper behavior and therefore usually complex parametric models involving several parameters are required to achieve a reliable and accurate representation of its rheological behavior. Hence, non-parametric models represent another feasible approach to simulate the complex non-linear behavior of MR dampers although in this case allowing to obtain a wide-ranging numerical model without the need to define or identify a large number of model parameters. In this context, we attempt to model and predict the response of a sponge-type MR damper using a non-parametric modeling technique based on an Adaptive Neuro-Fuzzy Inference System (ANFIS) model. Initially, the basic structure of this data modeling technique is presented and the main aspects regarding the development of a neuro-fuzzy model for MR dampers are addressed. Then, an ANFIS modeling technique is developed to obtain a non-parametric model for the MR damper. Finally, a comparison between the numerical and experimental results will be presented to validate the selected modeling technique.*

1 INTRODUCTION

Non-parametric models represent an alternative methodology to numerically simulate the complex behaviour of active and semi-active devices. Among these modelling techniques, neuro-fuzzy models incorporate pattern recognition capabilities of neural networks with the non-linear mapping modelling of fuzzy logic systems which make them a particularly suitable non-parametric modelling approach to characterize the highly non-linear behaviour of MR dampers. A generic schematic representation of a neuro-fuzzy model is shown in Figure 1.

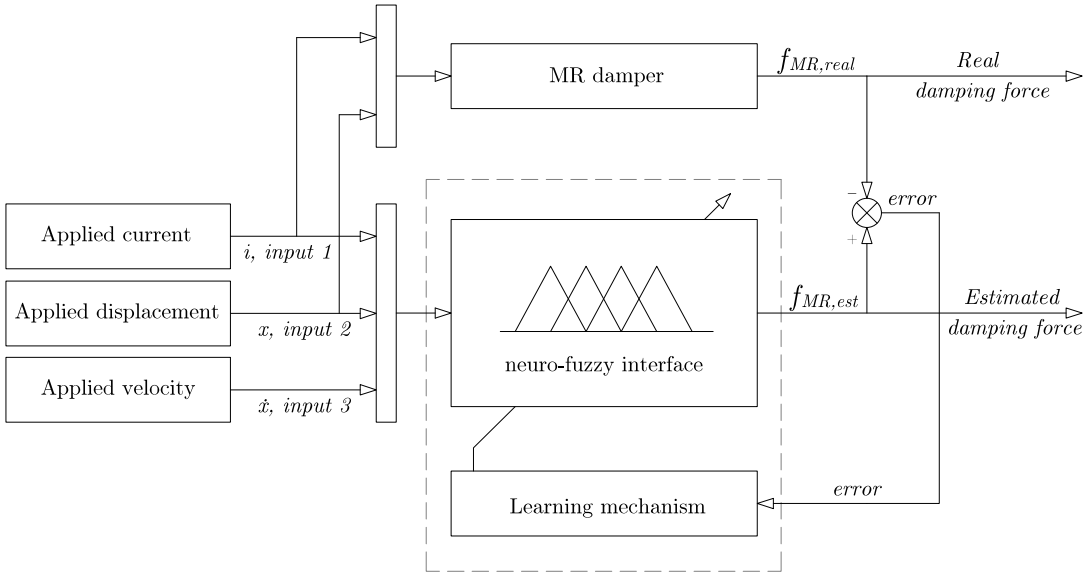


Figure 1: Neuro-fuzzy modeling of a MR damper.

Adaptive Neuro-Fuzzy Inference System (ANFIS) algorithm presents the advantage of providing automatic tuning of a Sugeno-type fuzzy inference system (FIS) to model the relationships of the input variables and their important parameters such as the mechanical excitation and operating current to generate a single output. Moreover, numerical simulation based on fuzzy logic represents a robust and reliable modelling methodology that allows the numerical model to account for some uncertainties associated with the typical hysteretic behaviour of MR devices but, especially due to its ability to represent unpredicted responses that are usually not quantified or considered with more accurate models (e.g., parametric models), since fuzzy logic models use continuous membership functions to relate inputs and outputs. Although FIS models can be considered less accurate than other numerical models, they have been shown to correctly represent the experimental response of MR dampers, presenting a good compromise between computational time and numerical precision [1-6].

Hence, the present paper explores the use of this neuro-fuzzy technique in modelling the response of a sponge-type MR damper. The application of an ANFIS algorithm to emulate the non-linear behaviour of MR dampers device will be investigated to demonstrate the capabilities of this hybrid intelligent system as a feasible modelling approach to map the relationships between inputs and outputs in order to create a fuzzy model for these devices even with uncertain or imprecise knowledge about its behaviour. The proposed modelling approach can be applied to estimate the non-linear hysteretic response of this type of devices between different operating currents and mechanical excitations and is validated over a set of experimental and numerical datasets of the sponge-type MR damper.

2 ADAPTIVE NEURO-FUZZY INFERENCE SYSTEM (ANFIS)

Neuro-adaptive learning techniques represent a simple methodology for the fuzzy modeling procedure to learn information about a dataset in order to compute the membership function parameters that best allow the associated fuzzy inference system to track a given input/output data. ANFIS uses a hybrid learning algorithm that combines the backpropagation gradient descent and least squares methods to create a fuzzy inference system whose membership functions are iteratively adjusted according to a given set of input and output data [3,4]. The reasoning scheme of ANFIS architecture is shown in Figure 2.

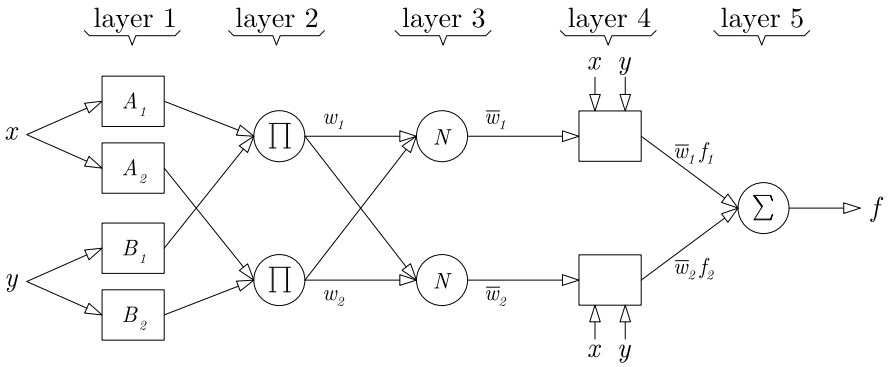


Figure 2: Adaptive Neuro-Fuzzy Inference System or ANFIS.

Soft computing methods represent a relatively recent modeling technique of MR dampers that have been shown to be effective in representing the non-linear response of these devices. The development of a neuro-fuzzy model of a MR damper involve four main steps:

1) Definition of input variables and the corresponding FIS membership functions (the FIS output is the desired damper force);

2) Selection of experimental or artificial data sets to generate training and checking data;

3) Use of ANFIS optimization algorithm for training the FIS membership function parameters to model the set of input/output data by mapping the relationship between inputs and outputs in order to generate a fuzzy model of the MR damper;

4) Validation of the resulting fuzzy model.

ANFIS system training procedure is summarized in the flowchart shown in Figure 3. The process begins by obtaining a training data set and checking data sets. The training data is used to find the premise parameters for the membership functions (MFs are dependent on the system designer). A threshold value for the error between the actual and desired output is determined. The consequent parameters are found using the least-squares method. If this error is larger than the threshold value, then the premise parameters are updated using the gradient decent method. The process end when the error becomes less than the threshold value. Checking data set can then be used to compare the model with the actual system.

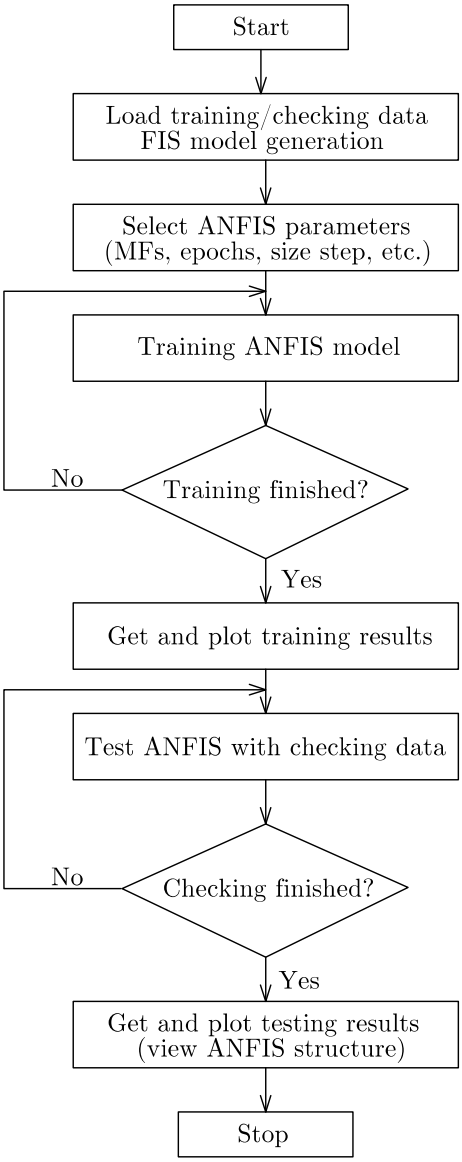


Figure 3: Flowchart of ANFIS training.

After the ANFIS training process is complete, a fuzzy model of the MR damper is obtained based on the training data, training options and type/number of membership functions previously defined by the system designer.

It is important to notice that the fuzzy inference system and the corresponding input (displacement, velocity and operating current) and output (damper force) membership functions produced by the ANFIS training algorithm must be capable to conveniently represent the actual behavior of the device. Although the training data may have significant information about the behavior of the MR damper, the resulting fuzzy model may not accurately represent the damper response (incorrect training data, some wrong or uneven data points, singularities in the device response, etc.). Thus, a final verification is required to ensure realistic results of the fuzzy model, which can be done by performing an assessment of the fuzzy surfaces to confirm realistic input/output magnitudes and geometry.

3 FUZZY MODELING WITH ANFIS

MR dampers are semi-active devices whose damping characteristics can be modified in real time due to the capability to adjust the resistance to flow of a MR fluid within the damper through the application of a magnetic field. The particular properties of the MR fluid allow variations in the damping force that can be controlled by varying an applied current. Thus, the hysteretic behaviour of a MR damper is current dependent but also function of the amplitude of the excitation [9-11].

The present section describes the application of ANFIS to develop a neuro-fuzzy model for a sponge-type MR damper (RD-1097-1 model). It is intended to optimize a fuzzy inference system by training a family of membership functions according to a predetermined input and output data set related with the damper behaviour. Thus, the piston displacement and velocity, and the operating current represent the three fuzzy variables assigned to the input membership functions and the damper force represents the fuzzy output variable. Generalized bell-shaped membership functions are used to represent the input variables. The fuzzy parameters assigned to each fuzzy input variable, i.e., the properties of the selected MFs (number, type and universe of discourse) are summarized in Table 1.

Data	Fuzzy variable	Type	Number of MFs**	Universe of discourse*
Input MFs	- Piston displacement	Generalized bell-shaped	2	$\|-x_{max}, x_{max}\|$ with x_{max}=20 mm
	- Piston velocity	Generalized bell-shaped	3	$\|-\dot{x}_{max}, \dot{x}_{max}\|$ with $\dot{x}_{max}$=14 cm/s
	- Operating current	Generalized bell-shaped	2	$\|0, I_{max}\|$ with I_{max}=0.50 A

Table 1: Fuzzy MFs parameters (RD-1097-1 MR damper).

According with the device specifications the sponge-type MR damper operates with an operating currents up to 1.0 A (intermittent operation). The maximum stroke is around ±25 mm within a damping force range of 9 N (0.0 A) and 100 N (1.0 A). The expected operational ranges for this MR damper are x= ±20 mm, $\dot{x}$= ±14.0 cm/s and I= 0.5 A. Based on the experimental results, the maximum damping force is around 30 N. These values represent the upper and lower boundaries of the proposed neuro-fuzzy model (i.e., f_{min}= 2 N, f_{max}= 30 N, x_{max}= 20 mm, $\dot{x}_{max}$= 14.0 cm/s, I_{min}= 0.0 A and I_{max}= 0.5 A). Hence, the training data should include enough information to cover the entire spectrum of operation of the MR damper within these ranges of values since the precision of the fuzzy model is mainly dependent on the training data used for the FIS optimization with ANFIS.

This type of MR devices are usually commanded through a voltage-to-current controller unit designated as Wonder Box Device Controller and sold as a complementary product for MR devices. The device provides a closed-loop current control to compensate for changing electrical loads up to the limits of the power supply and can be used to investigate the control possibilities of the LORD MR technology since it can be operated as an interface device for PLC or computer control of the MR fluid devices. This controller was connected to a voltage power supply unit in order to feed the MR damper with a constant voltage converted to current supply through the Wonder Box.

In this case, a set of numerical signals based on experimental results was used to develop the neuro-fuzzy model. More specifically, the numerical based fuzzy model was developed from the numerical results of the Bouc-Wen model which in turn was developed from experimental data obtained from several experimental tests. Thus fuzzy model was developed to ensure good performance in solving the fuzzy parameter prediction problem by using artificial data inputs to generate the training data set. The aim is to verify the efficiency of the optimization algorithm to predict the damper response when a smooth, regular and plentiful data set is available for the training procedure. The artificial data set used for training the FIS of the neuro-fuzzy model for the sponge-type MR damper is illustrated in Figure 4.

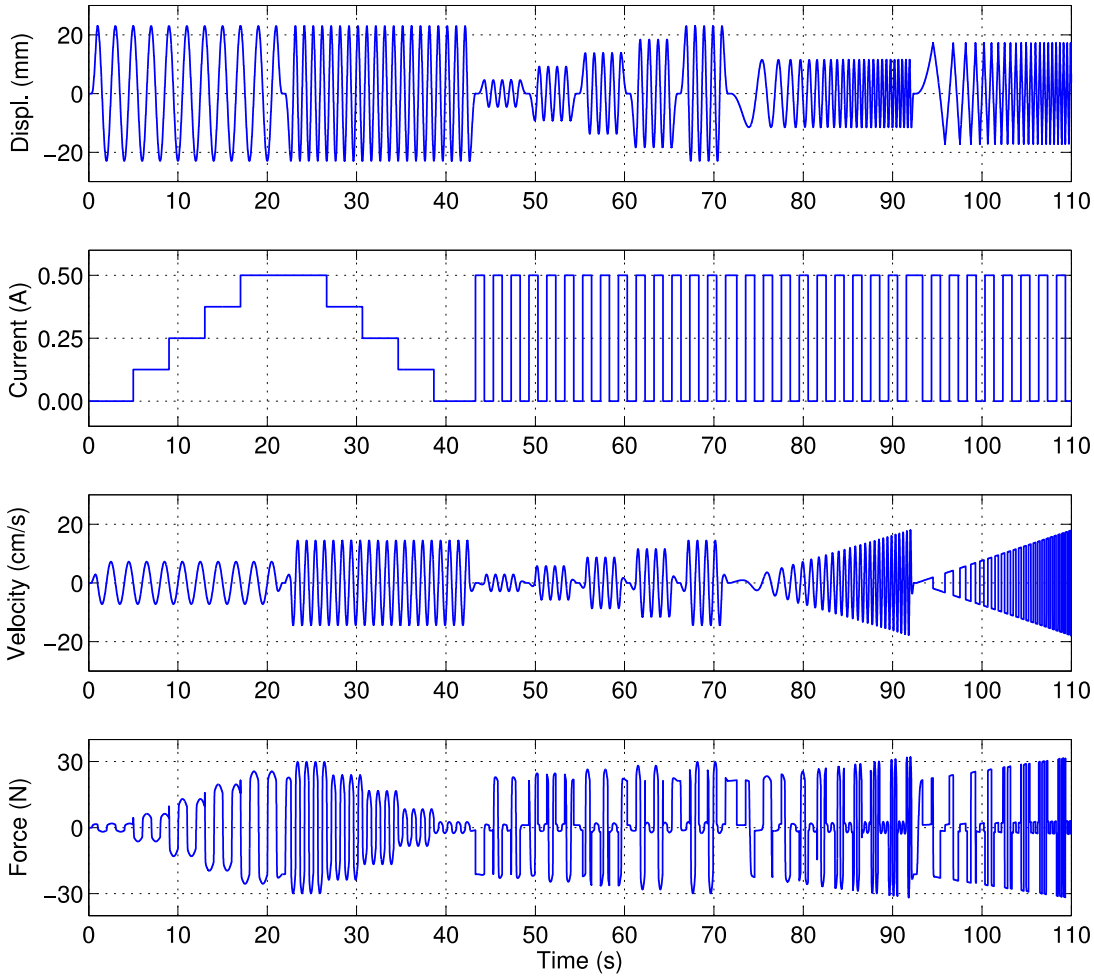


Figure 4: Training data for fuzzy model A (RD-1097-1 MR damper).

Thus, a series of training sequences comprising five types of artificial displacement sequence inputs were used to generate the data set for training the fuzzy inference system of the proposed numerical based fuzzy model. Constant displacement (CD), triangular wave (TW), amplitude-modulated (AM) and frequency-modulated (FM) are the displacement sequences used to represent the MR damper dynamics and the hysteresis behavior under changes in the magnitude and frequency of excitation for stepped increments of the operating current level. To improve ANFIS optimization, displacements outside the expected operating range (i.e., x= ±20 mm) were trimmed. The main characteristics of the five displacement sequences are presented in Table 2.

The signal sequences have 110000 data points. A training data set containing a total of 22000 data points (110 sec.) was generated using a time step of 0.005 sec. In this case, odd numbered values were used for training and even numbered values for checking (50%-50% alternating training-checking partition).

Case	Type of displacement	Amplitude (mm)	Frequency (Hz)	Current (A)
1/2	Constant Displacement (CD)	20*	0.5/1.0	0.0-0.5 (5 steps)
3	Amplitude-Modulated (AM)	4-20* (5 steps)	3.0	0.0-0.5 (5 steps)
4	Frequency-Modulated (FM)	12	0.5-3.0	0.0 and 0.5
5	Triangular Wave (TW)	18	0.5-3.0	0.0 and 0.5

Table 2: Artificial training data (RD-1097-1 MR damper).

The membership function parameter adjustment was performed using the ANFIS training routine included in the MATLAB fuzzy logic toolbox [12]. The input membership functions for command voltage, displacement and velocity before and after training are shown in Figure 5.

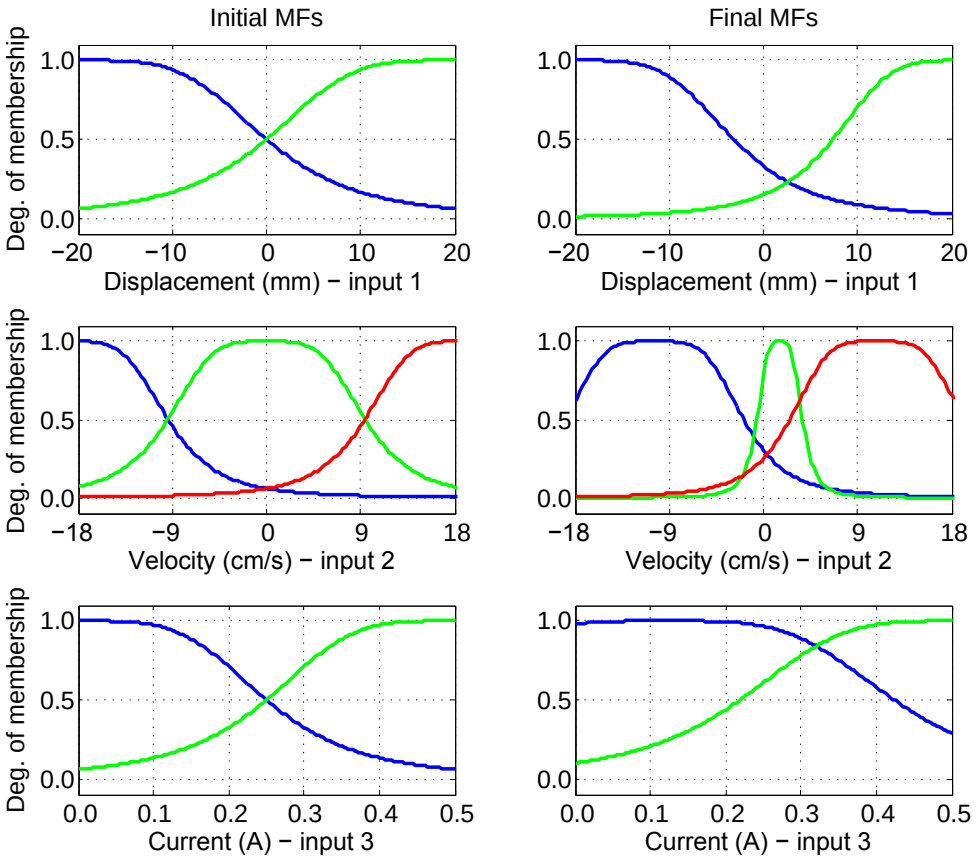


Figure 5: Input membership functions before and after training.

The fuzzy model was obtained after an iterative trial and error process to determine the appropriate number of membership functions and the corresponding training parameters. Several training parameters (number of epochs, initial step size, error tolerance, etc.) must be defined before starting the learning process. The ANFIS training options used in the present study are presented in Table 3.

Number of epochs	Initial step size	Increasing step size	Decreasing step size	Error tolerance
200	0.11/0.15	1.20	0.80	0.1

Table 3: ANFIS training parameters (RD-1097-1 MR damper).

These input MFs were obtained with an initial step size of 0.11, which provided the best ANFIS optimization results in predicting the training data. The units of the fuzzy variables were also scaled to improve the optimization procedure (i.e., [m] to [mm], [m/s] to [cm/s], respectively). In accordance with the estimated MFs, ANFIS generated a FIS structure with a total of 24 if-then rules to map the non-linear response of the MR damper. A plot of the fuzzy surface for the trained FIS model representing the output force as a function of the piston displacement and velocity, $f_{MR}= f(\text{displ}_i,\text{vel}_i)$ is shown in Figure 6.

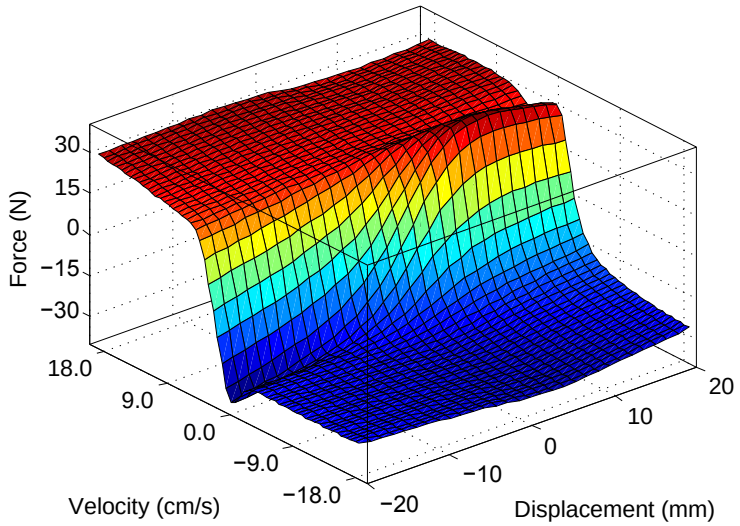


Figure 6: ANFIS estimated fuzzy surface $f_{MR}= f(\text{displ}_i,\text{vel}_i)$.

The fuzzy surface has an appropriate scale with a realistic geometry in accordance with the expected MR damper behavior. Moreover, changing the velocity for small displacements generates a significant change in the damper force while changing one of these input variables when both have the same magnitude has almost no effect in the output force.

Another FIS surface displaying the resultant damping force as a function of the piston displacement and the level of operating current, i.e., $f_{MR}= f(\text{displ}_i,\text{cur}_i)$ is displayed in Figure 7. The behavior depicted in the non-linear mapping of the trained fuzzy model is in line with the expected damper response for different operating current levels.

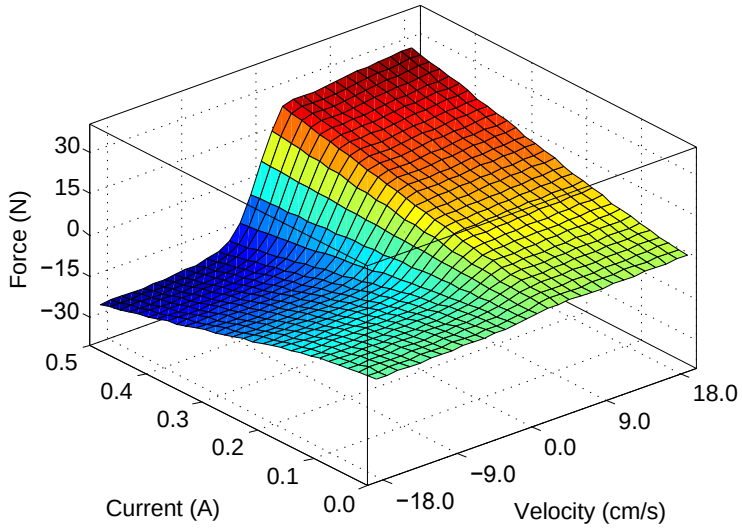


Figure 7: ANFIS estimated fuzzy surface $f_{MR}= f(\text{displ}_i,\text{cur}_i)$.

The non-linear relationship between the damping force and the piston displacement with respect to different levels of operating currents is clearly visible in this fuzzy mapping, i.e., when the operating current is increased for equal values of piston displacement, the resultant damping force is also increased. Additionally, changing the magnitude of the piston displacement for low levels of command current has almost no effect in the damper force producing almost a flat surface while changing the piston displacement for high levels of operating current generates a highly non-linear force-displacement response, especially for a maximum command current where increasing the piston displacement produces a significant increase in the force developed by the MR damper.

A similar fuzzy surface representing the resultant damper force as a function of the piston velocity and the applied operating current, $f_{MR}= f(\text{vel}_i,\text{cur}_i)$ is shown in Figure 8. In this case, this mapping surface emphasizes the highly non-linear relationship between the damping force and the piston velocity.

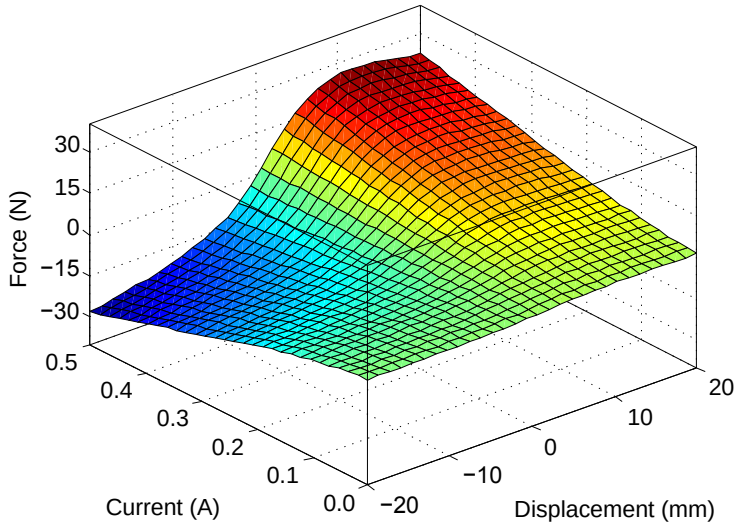


Figure 8: ANFIS estimated fuzzy surface $f_{MR}= f(\text{vel}_i,\text{cur}_i)$.

The level of damping generated by the MR damper is directly related with the damper force and the piston velocity since the gradient of the force-velocity relationship within the fuzzy surface represent the damping level. Due to the typical rheological behavior of this type of controllable devices, the damping level is a function of the current input, i.e., low operating currents generates a low damping state characterized by a flat surface while high command currents produce a high damping state represented by a steep slope in the fuzzy surface. So, increasing the operating current level will increase the resultant damper force and therefore the damping capacity of the MR damper.

The performance of the neuro-fuzzy model can be assessed by examining the convergence trend of the RMS error and step size evolution for the training and checking data over the number of epochs. Figure 9 shows the error plots along with the corresponding step size evolution. As can be seen, there is no model overfitting during the training procedure because the checking data RMSE exhibit nearly the same evolution as the training data error. A steady RMSE is achieved after 60 epochs after which the error curves tend to stabilize without a significant RMSE and step size modification.

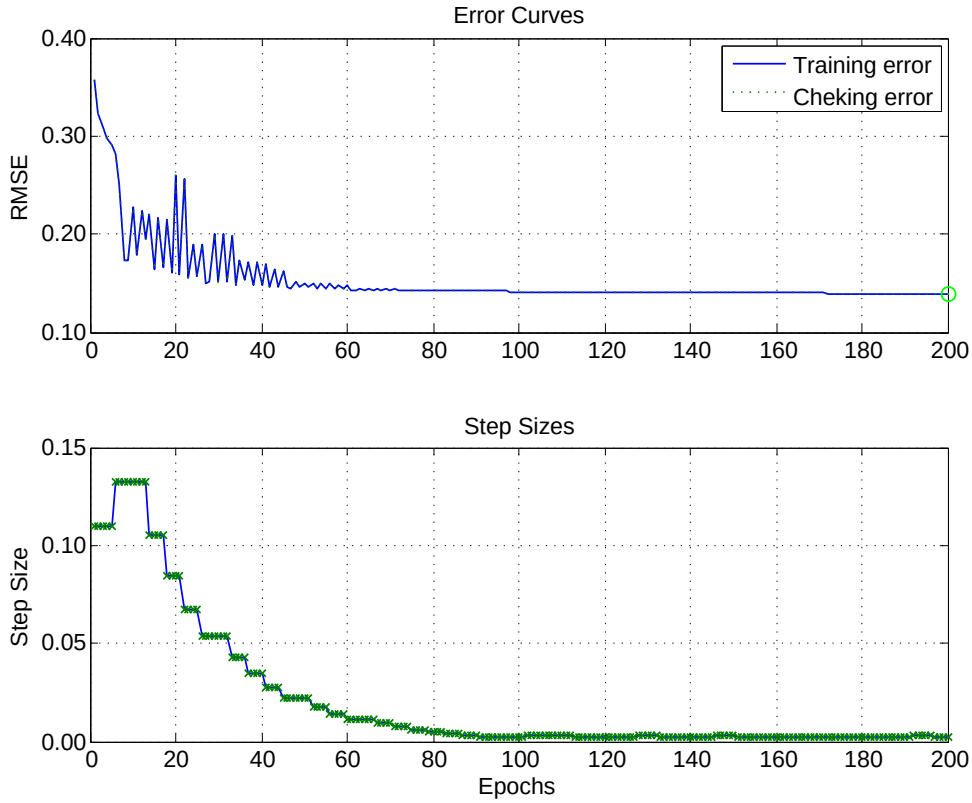


Figure 9: Training and checking errors obtained by ANFIS.

A displacement signal generated by low-pass filtering a white noise signal through a 4th order Butterworth filter with a cutoff frequency of 4.0 Hz was used to generate the testing data set for the fuzzy model (Figure 10). Therefore, a testing data with 20 mm of maximum peak-to-peak displacement amplitude was obtained. The corresponding velocity data set was computed from displacement data using a 4th-order backward difference method. The command current was generated using a PRBS signal to represent a bi-state command signal constrained between 0.0 A to 0.5 A (maximum operating current for intermittent operation of the RD-1097-1 MR damper).

A time step of 0.001 seconds is used to produce a total of 20000 data samples over a 20 seconds numerical simulation. The damper force was also determined from the Bouc-Wen model of MR damper. The testing data and the reference damper force are shown in Figure 10. The results achieved with the fuzzy model were then compared to those found with the reference model for the second validation data set as shown in Figure 11. There is a general good agreement between the damper force estimated with the fuzzy model and the reference data.

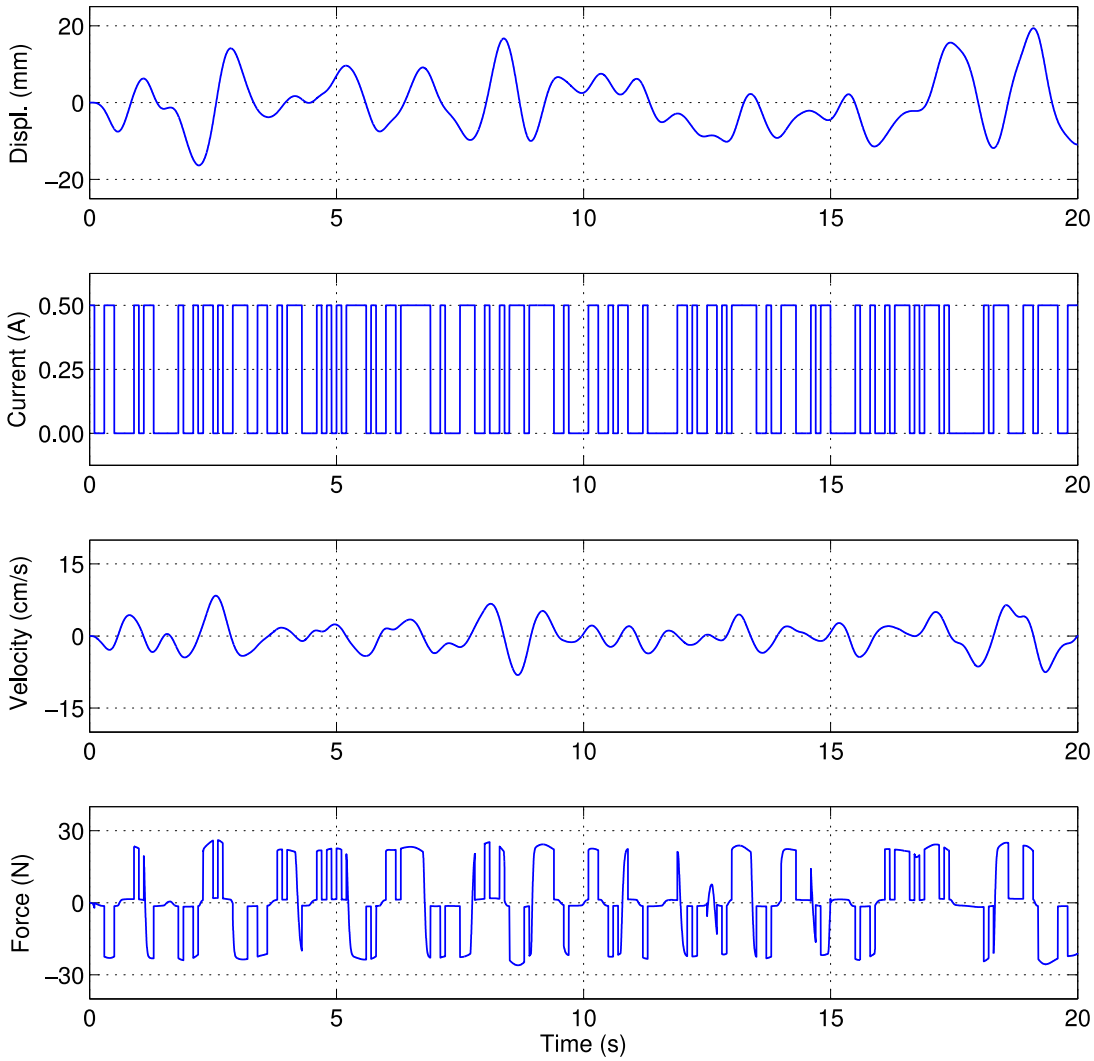


Figure 10: Testing data set for validation of the proposed fuzzy model.

An important aspect in modeling the response of a MR damper is the capability of the numerical model to represent the damper force upon a step change in the load current. It was found that the proposed model is able to represent the transient response during a command current change although the transition from pre-yield to post-yield behavior is not so accurately described. Besides peak damper forces can be slightly under or overestimated although the difference between the reference damping force and the fuzzy output force is small ($|f_{ref} - f_{fuzzy}|_{max}$ = 0.7 N) resulting in a residual error below 3% relatively to the maximum damping force. In conclusion, the results indicate that the proposed neuro-fuzzy model is capable to represent with acceptable accuracy the damper response which in this case was defined using a set of artificial data from a parametric model (i.e., the Bouc-Wen model).

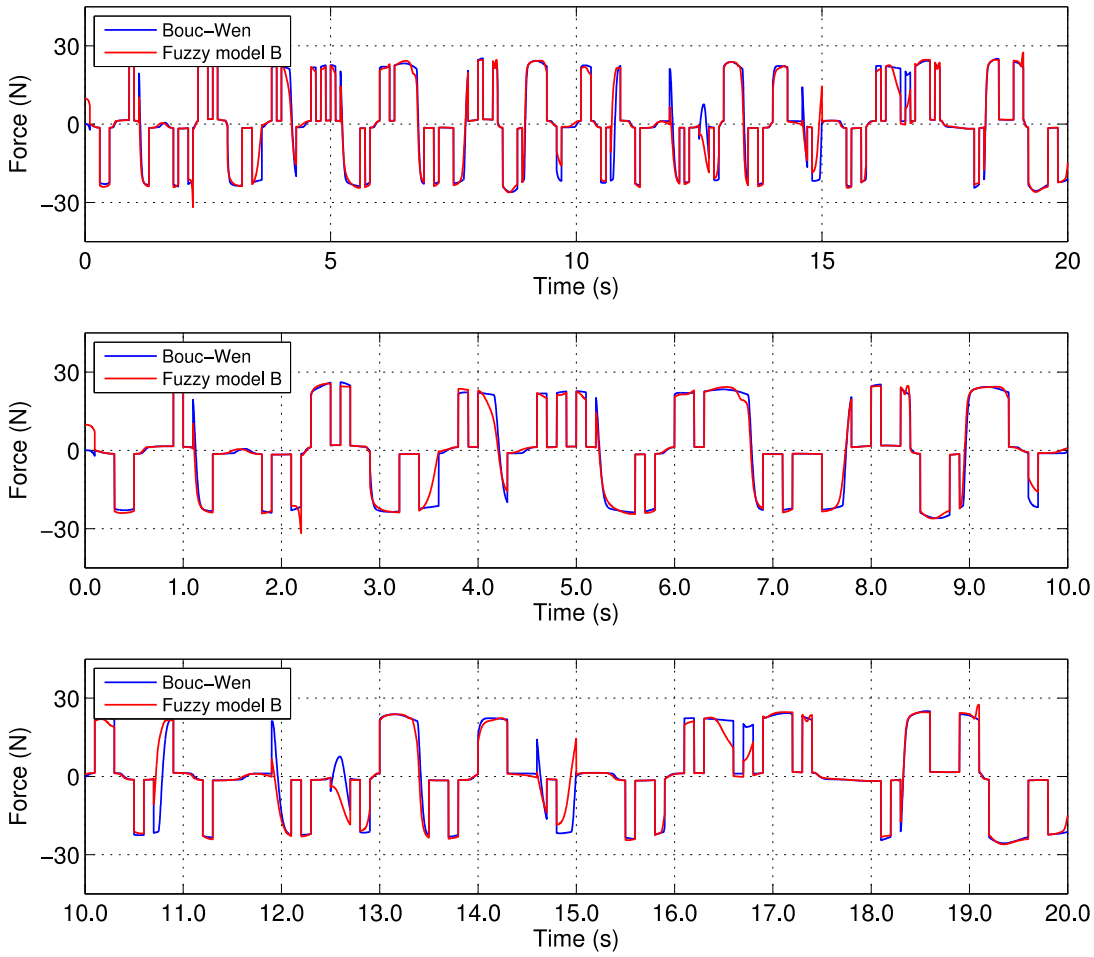


Figure 11: Results obtained with the testing data set.

The last performance assessment will be achieved comparing the experimental results achieved with a sinusoidal excitation and constant current (5 mm amplitude with a frequency of 1.00 Hz and 0.50 A) with the numerical responses obtained with both numerical models, i.e., the estimated fuzzy model and the Bouc-Wen model. The experimental and both numerical responses are displayed in Figure 12. It can be seen that, on the whole, the neuro-fuzzy model estimates the corresponding force-time, force-displacement and force-velocity experimental responses with acceptable reliability and precision being effective in capturing the size and shape of the non-linear hysteresis loop.

The already discussed mismatching between the fuzzy model prediction and the damper response around the yield point region is highlighted in the force-velocity plot (force overshoot). Although this problem affects the accuracy of the model in simulating the damper response, it does not prejudge in a significant way the final outcome by comparison with other numerical models such as the Bouc-Wen model, given that the global behavior of the MR damper can be reliably estimated. Additionally, the results obtained with the fuzzy simulation show a very good agreement with the numerical response obtained with the Bouc-Wen model. Disregarding this slight error around the yield point region, the proposed fuzzy model should be considered adequate to simulate the MR damper behavior since it provides an acceptable prediction of the device response defined by an equivalent Bouc-Wen model or the corresponding experimental data.

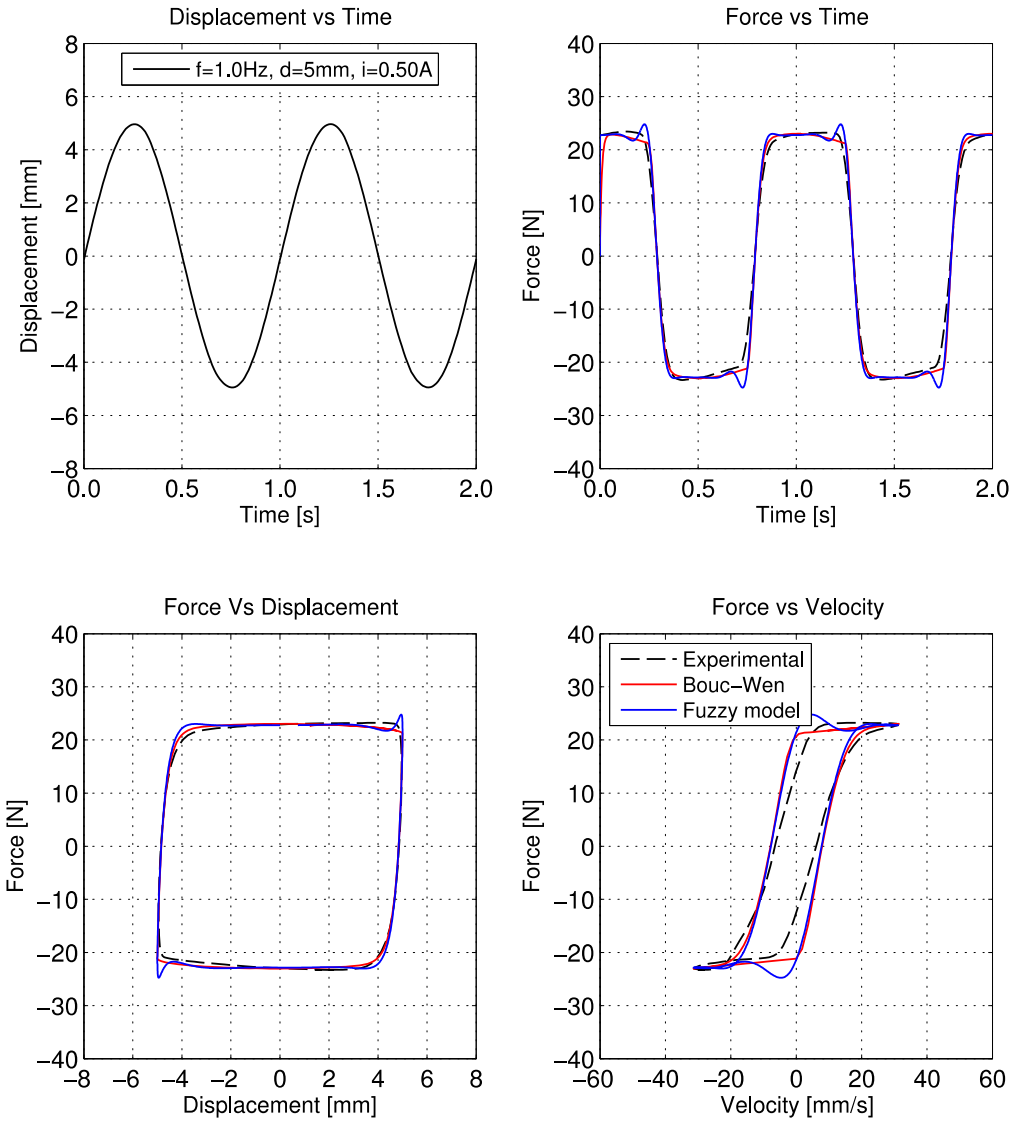


Figure 12: RD-1097-1 MR damper – Fuzzy model vs. Bouc-Wen model response (1.00 Hz, 5 mm amplitude and 0.50 A).

4 CONCLUSIONS

The present paper addressed a non-parametric modeling procedure for MR dampers based on an Adaptive Neuro-Fuzzy Inference System (ANFIS) model. This modeling approach was used to develop a neuro-fuzzy model for a sponge-type MR damper based on artificial training data. It was verified that the fuzzy model presents a similar numerical performance as the equivalent parametric model and therefore the proposed model is considered capable to simulate the hysteretic behavior of the MR damper. Hence, the damper response can be estimated with a relative high level of accuracy by the proposed fuzzy model. The greater the accuracy and usually the complexity of the numerical model, the better the performance in simulating the damper response. The proposed neuro-fuzzy model presents advantages and limitations that should be taken into consideration when planning and implementing a numerical model for a specific engineering application.

REFERENCES

[1] K.C. Schurter, P.N. Roschke, *Neuro-fuzzy control of structures using acceleration feedback*, Smart Materials and Structures, 10, 770-779, 2001.

[2] H.S. Kim, P.N. Roschke, P.Y. Lin, C.H. Loh, *Neuro-fuzzy model of hybrid semi-active base isolation system with FPS bearings and a MR damper*, Engineering Structures, 28(7), 947-958, 2006.

[3] D.A. Shook, *Control of a benchmark structure using GA-optimized fuzzy logic control*, MSc Thesis, 2006.

[4] H. Wang, H. Hu, *The Neuro-Fuzzy Identification of MR Damper*, Sixth International Conference on Fuzzy Systems and Knowledge Discovery, 2009.

[5] H. Wang, *Modeling of Magnetorheological Damper Using Neuro-Fuzzy System*, Fuzzy Information and Engineering Volume 2, Advances in Intelligent and Soft Computing Volume 62, 1157-1164, 2009.

[6] L. Zong, X. Gong, C. Guo, S. Xuan, *Inverse neuro-fuzzy MR damper model and its application in vibration control of vehicle suspension system*, Vehicle System Dynamics: International Journal of Vehicle Mechanics and Mobility, 50:7, 1025-1041, 2011.

[7] J.R. Jang, *ANFIS: Adaptive-network-based fuzzy inference system*, IEEE Transactions on Systems, Man and Cybernetics, 23(3), 665-685, 1993.

[8] A.R. Sadeghian, *Nonlinear Neuro-Fuzzy Prediction: Methodology, Design and Applications Fuzzy Systems*, The 10th IEEE International Conference on Volume 2, 2-5, 1022-1026, Vol 3, 2001.

[9] B.F. Spencer Jr., S.J. Dyke, M.K. Sain, J.D. Carlson, *Phenomenological model of a magnetorheological damper*, Journal of Engineering Mechanics, 123, 230-238, 1997.

[10] D.H. Wang, W.H. Liao, *Magnetorheological fluid dampers: a review of parametric modelling*, Smart Materials and Structures, 20, 023001, 2011.

[11] M. Braz-César, R. Barros, *Properties and Numerical Modeling of MR Dampers*, 15th ICEM - 15th International Conference on Experimental Mechanics, 2012.

[12] The Mathworks, Inc. *Optimization Toolbox User's Guide*, USA, 2012.

COMPDYN 2015
5th ECCOMAS Thematic Conference on
Computational Methods in Structural Dynamics and Earthquake Engineering
M. Papadrakakis, V. Papadopoulos, V. Plevris (eds.)
Crete Island, Greece, 25–27 May 2015

SEISMIC RESPONSE REDUCTION OF BUILDING STRUCTURES USING A SEMI-ACTIVE CONTROL SYSTEM BASED ON A BRAIN EMOTIONAL LEARNING CONTROLLER

Manuel T. Braz-César[1], **Rui C. Barros**[2]

[1] Polytechnic Institute of Bragança
Campus de Santa Aplónia – Apt. 134 – 5301-857 Bragança - Portugal
e-mail: brazcesar@ipb.pt

[2] Faculty of Engineering of the University of Porto
Rua Dr. Roberto Frias, s/n 4200-465 Porto - Portugal
rcb@fe.up.pt

Keywords: BELBIC controller, BEL controller, semi-active control, MR damper.

Abstract. *The present paper investigates the effectiveness of a bio-inspired semi-active controller to reduce seismic-induced vibrations in building structures. The control system is based on the use of a MR damper in combination with the so-called Brain emotional learning based intelligent controller (BELBIC), which is an intelligent controller based on the model of Limbic system of brain. A general case for a three degrees of freedom building structure excited by the El Centro earthquake will be used to demonstrate how a semi-active control system comprising a MR damper in a non-collocated configuration can reduce the structural response under seismic loading. Hence, the key objective of this study will be to evaluate and verify the efficiency of a MR damper in controlling the level of vibrations in a three degrees of freedom building structure by means of a BEL controller. A comparison between uncontrolled and controlled structural responses are used to validate the performance and efficiency of the proposed semi-active controller.*

1 INTRODUCTION

The Brain Emotional Learning (BEL) controller is a novel bio-inpired control model based on the emotional learning mechanism of the brain limbic system, which has been employed to develop feedback controllers for complex control problems [1-5]. Essentially the BEL controller comprises four main components, i.e, the amygdala (Am), the orbitofrontal cortex (OC), the sensory cortex (SC) and the thalamus (Th). The amygdala and the orbitofrontal cortex are used to process the emotional signal (SE) while the sensory cortex and the thalamus receives and processes sensory inputs (SI). Sensory inputs (SI) are processed in the thalamus initiating the process of response to stimuli and passing those signals to the amygdala and the sensory cortex. Then, the sensory cortex operates by distributing the incoming signals properly between the amygdala and the orbitofrontal cortex. In this controller, the learning procedure is mainly processed in the orbitofrontal cortex and is based on the difference between an expected punishment or reward and the received punishment or reward (Rew). The perceived punishment/reward (ES) is processed in the brain using learning mechanisms while the received punishment/reward represents an external input. If these signals are not identical, the orbitofronal cortex inhibits and restrains the emotional response for further learning. Otherwise, the controller generates an output response [1,3].

The BEL controller presents interesting features that can be exploited to design structural control systems for civil engineering applications. Thus, the following semi-active control system was developed based on this bio-inspired controller. The Simulink model of the BEL controller is depicted in Figure 1.

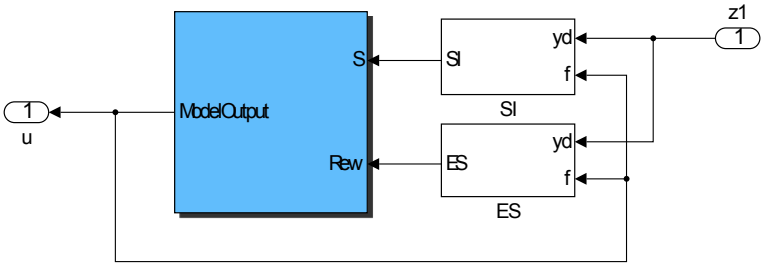


Figure 1: Simulink model of the BEL controller for the three DOFs system.

In this case the sensory input (SI) and the emotional signal (ES) can be related with the system response y_d (interstory drifts in this case) and the BEL model output u, which are determined using the following equations

$$SI = w_1 y_d + w_2 u \tag{1}$$

$$ES = w_3 y_d + w_4 \int u\, dt \tag{2}$$

where w_i are weight factors that define the relative importance given to the drift response ($z_1=y_d$) and the output of the BEL controller ($f=u$). The sensory and emotional outputs are forwarded as the stimuli and the reward/punishment for the BEL controller, respectively. Finally, the BEL control block uses this information to construct a response (model output) that represents the control action.

The BEL algorithm can be also combined with a PID controller to improve the performance of the control system. The PID controller is integrated in the BEL controller as part of the emotional signal, i.e.

$$ES = K_p y_d + K_I \int y_d \, dt + K_D \frac{d}{dt} y_d + w_4 \int u \, dt \tag{3}$$

where K_P, K_I, and K_D are weight factors of the PID controller that must be carefully selected to obtain the desired performance [5]. The learning system of both amygdala (Am) and orbitofrontal cortex (OC) are based on internal weight adjusting rules defined by

$$\frac{dG_{Am,i}}{dt} = \alpha \cdot \mathrm{SI}_i \cdot \max(0, \mathrm{ES} - \sum \mathrm{A}_{m,i}) \tag{4}$$

$$\frac{dG_{OC,i}}{dt} = \beta \cdot \mathrm{SI}_i (\mathrm{MO} - \mathrm{ES}) \tag{5}$$

where α is the learning rate of the amygdala, β is the learning rate of the orbitofrontal cortex, ES and MO are the emotional signal and the model output, respectively. These learning rates represent model parameters that must be adjusted in accordance with the input variables (i.e., structural responses) to achieve the required control action.

The main drawback of the BEL controller is related essentially with the appropriate definition of emotional and sensory signals that are able to represent with sufficient precision the system state and the control objective in order to maximize the performance of the control system. There are numerous optimization methods available for tuning these parameters (e.g. genetic algorithms) although a common approach is to use a trial-and-error procedure.

2 NUMERICAL MODEL

Consider a semi-active controlled system subjected to an earthquake ground motion with a control force applied to the first mass (or the first DOF, x_1) as illustrated in Figure 2. The control force intends to reduce the response of the system and can be achieved placing an actuator between the base and the first mass. The damper force can be changed using a control system comprising a controller that monitors the system response and computes the required damping force that should be applied to the system changes the system response in order to improve its structural performance. An effective semi-active control involves an appropriate control algorithm that can take advantage of the dissipative properties of the control device. There are several approaches available in the literature to control semi-active devices (further information about semi-active control algorithms is provided in [7,8]).

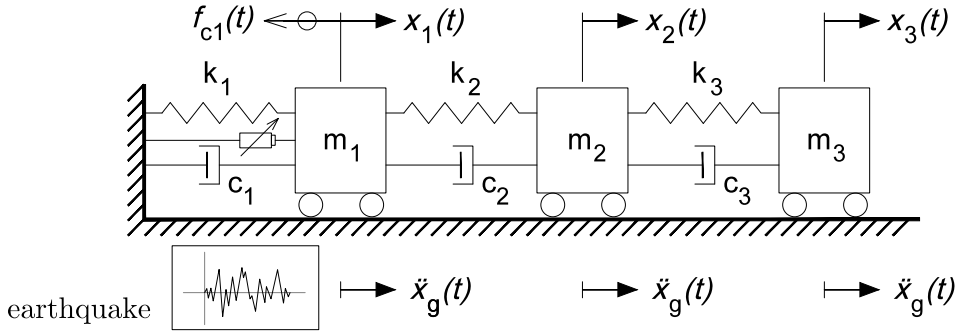


Figure 2: Schematic representation of a 3DOFs system under earthquake excitation - Semi-active control with a MR damper at the first floor.

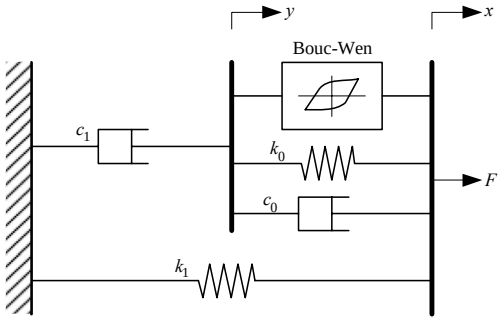
MR dampers are semi-active devices in the sense that they are passive actuators with adjustable properties, i.e., they operate by following the response of the system instead of working against the structure motion like in the case of active devices. Also, they cannot be directly controlled to generate a specific damper force because the damper response is dependent on the local motion of the structure where the device is located. A practical approach to control the MR damper it to adjust the voltage applied to the current driver to change the damper force. In this context, the following rules are used to design the control laws [8]:

i. The control voltage to the device is limited ranging between zero voltage input (passive OFF case) and the maximum value of the operating voltage/current Vmax (passive ON case);

ii. For a fixed set of states, the magnitude of the applied force increases and decreases when the voltage input increases and decreases, respectively.

As already has been stated, the structure is equipped with a passive control system comprising a MR damper (Lord RD-1005-03 model) located between the ground floor and the first floor which can operate in two modes: as a passive energy dissipation device and as a semi-active actuator whose control action is being commanded by a BEL based controller. In this case, the modified Bouc-Wen model was selected to simulate the behaviour of the MR damper. The numerical formulation and the corresponding model parameters are presented in Table 1 [9]. Besides, the first-order time lag involved in the current driver/electromagnet during a step command signal must be included in the numerical model of the device, which in this case is defined by a first order filter (η= 130 sec^{-1}).

Modified Bouc-Wen model



$$F(t) = c_1\dot{y} + k_1(x - x_0)$$

$$\dot{y} = \frac{1}{c_0 + c_1}\left[\alpha z + c_0\dot{x} + k_0(x - y)\right]$$

$$\dot{z}(t) = -\beta\left|\dot{x}(t)\right|z(t)\left|z(t)\right|^{n-1} - \gamma\dot{x}(t)\left|z(t)\right|^{n} + A\,\dot{x}(t)$$

Current **independent** parameters	A [-]	β [mm^{-1}]	γ [mm^{-1}]	k_0 [N/mm]	f_0 [N]	n
	10.013	3.044	0.103	1.121	40	2
Current **dependent** parameters	$\alpha(I) = -826.67I^3 + 905.14I^2 + 412.52I + 38.24$ [N] $c_0(I) = -11.73I^3 + 10.51I^2 + 11.02I + 0.59$ [N.s/mm] $c_1(I) = -54.40I^3 + 57.03I^2 + 64.57I + 4.73$ [N.s/mm]					

Table 1 - Modified Bouc-Wen model - Parameters of the RD-1005-3 MR damper [9].

In what follows, the results of the semi-active control system are compared with the uncontrolled, passive OFF and passive ON responses to evaluate the efficiency of each semi-active control scheme in reducing the structural response. The mass, damping and stiffness matrices of the model structure can be determined as

$$\mathrm{M} = \begin{bmatrix} m_1 & 0 & 0 \\ 0 & m_2 & 0 \\ 0 & 0 & m_3 \end{bmatrix} = \begin{bmatrix} 100 & 0 & 0 \\ 0 & 100 & 0 \\ 0 & 0 & 100 \end{bmatrix} \text{ kg} \tag{6}$$

$$\mathrm{C} = \begin{bmatrix} c_1 + c_2 & -c_2 & 0 \\ -c_2 & c_2 + c_3 & -c_3 \\ 0 & -c_3 & c_3 \end{bmatrix} = \begin{bmatrix} 175 & -50 & 0 \\ -50 & 100 & -50 \\ 0 & -50 & 50 \end{bmatrix} \text{ N} \cdot \text{s/m} \tag{7}$$

$$\mathrm{K} = \begin{bmatrix} k_1 + k_2 & -k_2 & 0 \\ -k_2 & k_2 + k_3 & -k_3 \\ 0 & -k_3 & k_3 \end{bmatrix} = \begin{bmatrix} 12 & -6 & 0 \\ -6 & 12 & -6 \\ 0 & -6 & 6 \end{bmatrix} 10^5 \text{ N/m} \tag{8}$$

In this study, the structure will be subjected to the El-Centro ground motion (1940 N-S component with a peak acceleration of 3.42 m/s^2). Since the mechanical system seeks to represent a small-scale building, the earthquake signal needs to be decreased to represent the magnitude of displacements that would be observed in experiments tests. Thus, the time was scaled to 20% of the full-scale earthquake time history as shown in Figure 3.

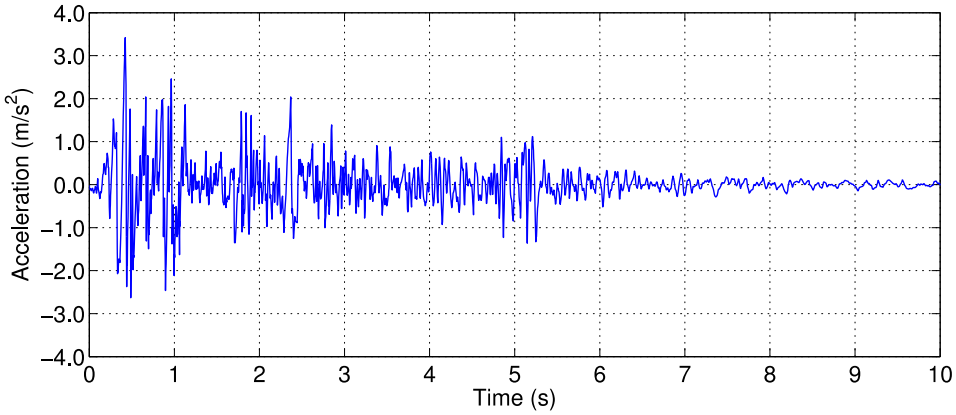


Figure 3: Time-escale El-Centro NS earthquake gound motion (0.2t).

The state space equation of motion is given by

$$\dot{z}(t)_{(6\times1)} = \begin{bmatrix} 0_{(3\times3)} & \mathrm{I}_{(3\times3)} \\ -\mathrm{M}^{-1}\mathrm{K}_{(3\times3)} & -\mathrm{M}^{-1}\mathrm{C}_{(3\times3)} \end{bmatrix} \begin{Bmatrix} \mathrm{X}(t)_{(3\times1)} \\ \dot{\mathrm{X}}(t)_{(3\times1)} \end{Bmatrix} + \begin{Bmatrix} 0_{(3\times1)} \\ -\lambda_{(3\times1)} \end{Bmatrix} \underbrace{\ddot{x}_g(t)}_{\text{El Centro NS}} \tag{9}$$

where the column vector λ represents the location of the earthquake excitation (i.e., the seismic acceleration). Equation 1 can be written in a simplified form as

$$\dot{z}(t)_{(6\times1)} = A_{(6\times6)}\, z(t)_{(6\times1)} + E_{(6\times1)} \ddot{x}_g(t) \tag{10}$$

where matrix A represent the system matrix

$$A_{(6\times6)} = \begin{bmatrix} 0_{(3\times3)} & \mathrm{I}_{(3\times3)} \\ -\mathrm{M}^{-1}\mathrm{K}_{(3\times3)} & -\mathrm{M}^{-1}\mathrm{C}_{(3\times3)} \end{bmatrix} \tag{11}$$

and E is the disturbance locating vector given by

$$E_{(6\times1)} = \{0,\ 0,\ 0,\ -1,\ -1,\ -1\}^T \tag{12}$$

The response of the system can be computed using the state space output vector $y(t)$

$$y(t) = Cz(t) + Du(t) \tag{13}$$

If the system displacements, velocities and accelerations are required, then

$$C_{(9\times6)} = \begin{bmatrix} \mathrm{I}_{(3\times3)} & 0_{(3\times3)} \\ 0_{(3\times3)} & \mathrm{I}_{(3\times3)} \\ -\mathrm{M}^{-1}\mathrm{K}_{(3\times3)} & -\mathrm{M}^{-1}\mathrm{C}_{(3\times3)} \end{bmatrix}, \quad D_{(9\times1)} = \begin{Bmatrix} 0_{(6\times1)} \\ -\lambda_{(3\times1)} \end{Bmatrix} \tag{14}$$

The uncontrolled response is displayed in Figure 4.

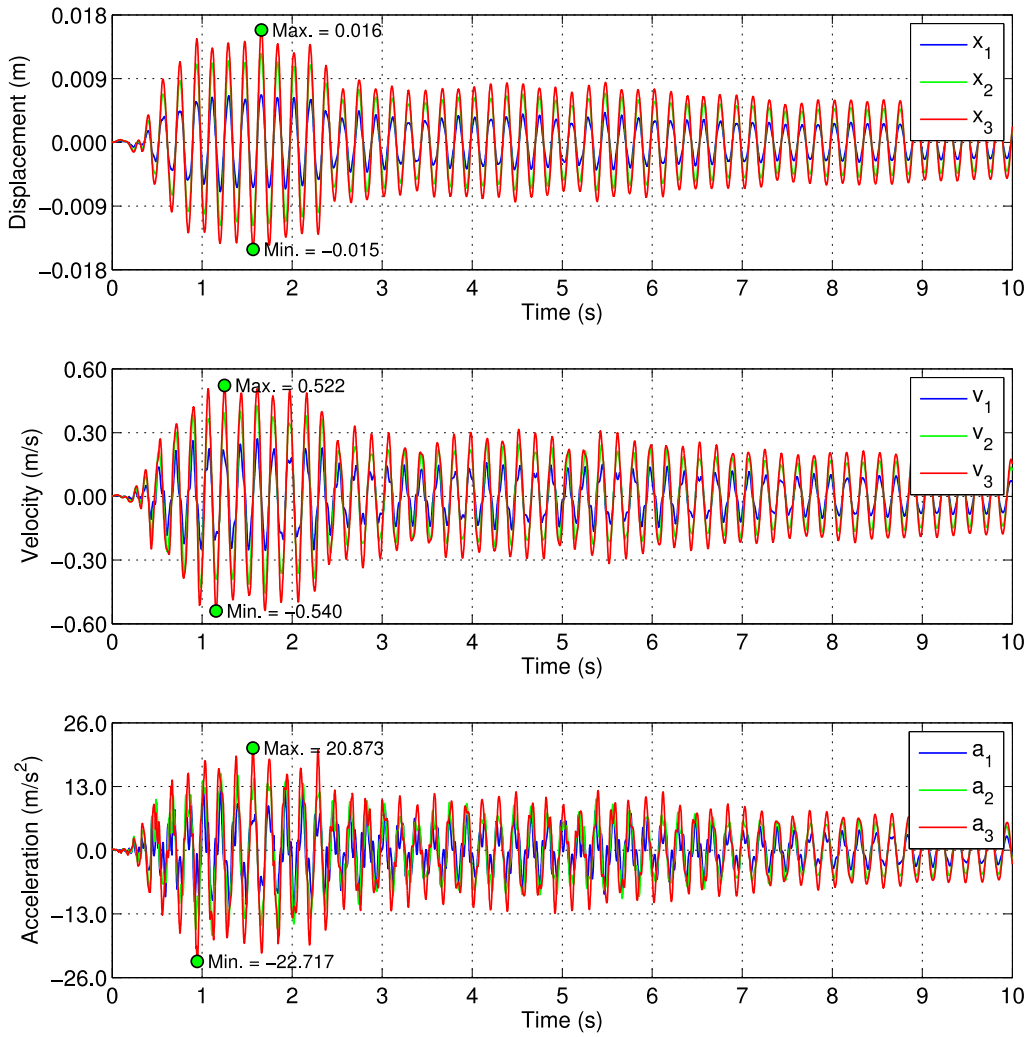


Figure 4: Uncontrolled response of the 3DOFs system.

It should be noted that the response was obtained with a high excitation level of the El Centro earthquake achieved by scaling up the amplitude of the earthquake signal in 150%. This modification in the excitation signal was used only to amplify the magnitude of the displacements making the system response more compatible with the operating range of the MR damper. The equation of motion of the controlled structure can be defined by a state space formulation as

$$\dot{z}(t)_{(6\times1)} = A_{(6\times6)}z(t)_{(6\times1)} + B_{c(6\times1)}f_{c1}(t) + E_{(6\times1)}\underbrace{\ddot{x}_g(t)}_{\text{El Centro NS}} \tag{15}$$

where B_c is an additional matrix accounting for the position of the control forces in the structure and f_c is a column vector with the control forces. The location of the control forces is defined by a location matrix Γ within B_c. In this case there is only one control force applied to the first mass and therefore, it follows that

$$\Gamma_{(3\times1)} = \left\{1,\ 0,\ 0\right\}^T \tag{16}$$

and then

$$B_{c\,(6\times1)} = \left\{0,\ 0,\ 0,\ -\frac{1}{m_1},\ 0,\ 0\right\}^T \tag{17}$$

Equation 15 can be written in a more compact given that

$$B_{(6\times2)} = \left[B_{c(6\times1)} \quad E_{(6\times1)}\right] = \left[\begin{array}{cc} 0 & 0 \\ 0 & 0 \\ 0 & 0 \\ \hdashline -\frac{1}{m_1} & -1 \\ 0 & -1 \\ 0 & -1 \end{array}\right], \quad u(t)_{(2\times1)} = \left\{\begin{array}{c} f_{c1}(t) \\ \ddot{x}_g(t) \end{array}\right\} \tag{18}$$

and finally

$$\dot{z}(t)_{(6\times1)} = A_{(6\times6)}z(t)_{(6\times1)} + B_{(6\times2)} + u(t)_{(2\times1)} \tag{19}$$

The response of the system can be determined using the state space output vector

$$y(t)_{(9\times1)} = C_{(9\times6)}z(t)_{(9\times1)} + D_{c(9\times1)}f_c + F_{(9\times1)}\underbrace{\ddot{x}_g(t)}_{\text{El Centro NS}} \tag{20}$$

where C is the same matrix of Equation 14, D_c comprising the control forces is

$$D_{c(9\times1)} = \left\{0,\ 0,\ 0,\ 0,\ 0,\ 0,\ -\frac{1}{m_1},\ 0,\ 0\right\}^T \tag{21}$$

and the column vector F describing the location of the earthquake signal is given by

$$F_{(9\times1)} = \left\{0,\ 0,\ 0,\ 0,\ 0,\ 0,\ -1,\ -1,\ -1\right\}^T \tag{22}$$

As for the state space equation, $\ddot{x}_g(t)$ represents the seismic excitation loading.

A new numerical simulation was carried out to obtain the response of the three DOF structure to the time-scale earthquake excitation (i.e., El Centro NS). The system response for the passive OFF case along with the maximum and minimum values of each output variable is displayed in Figure 5 and the damper behaviour is characterized in Figure 6.

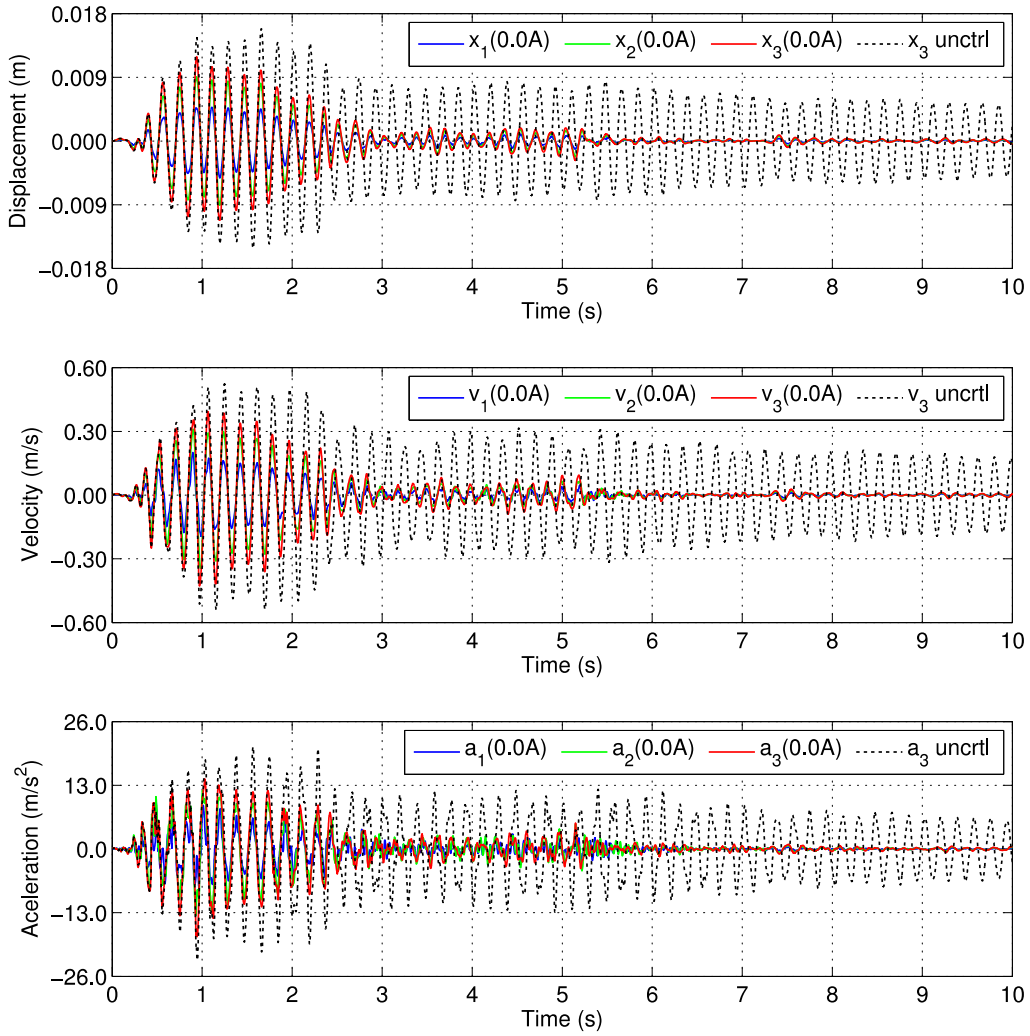


Figure 5: Results with the Modified Bouc-Wen model – Passive OFF case.

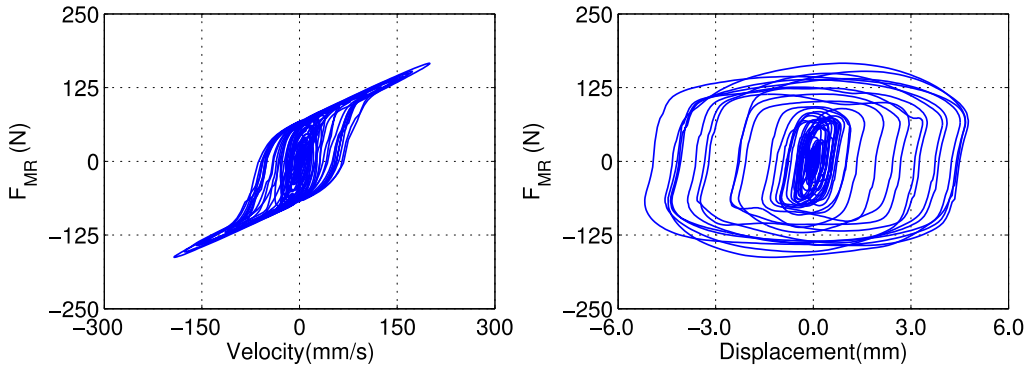


Figure 6: 3DOFs system - RD-1005-03 MR damper control force.
Passive OFF case – Modified Bouc-Wen model

Likewise, a numerical simulation was carried out to obtain the response of the three DOF structure to the time-scale earthquake excitation for the passive ON mode. The corresponding system response along with the maximum and minimum values of each output variable is displayed in Figure 7 and the damper behaviour is characterized in Figure 8.

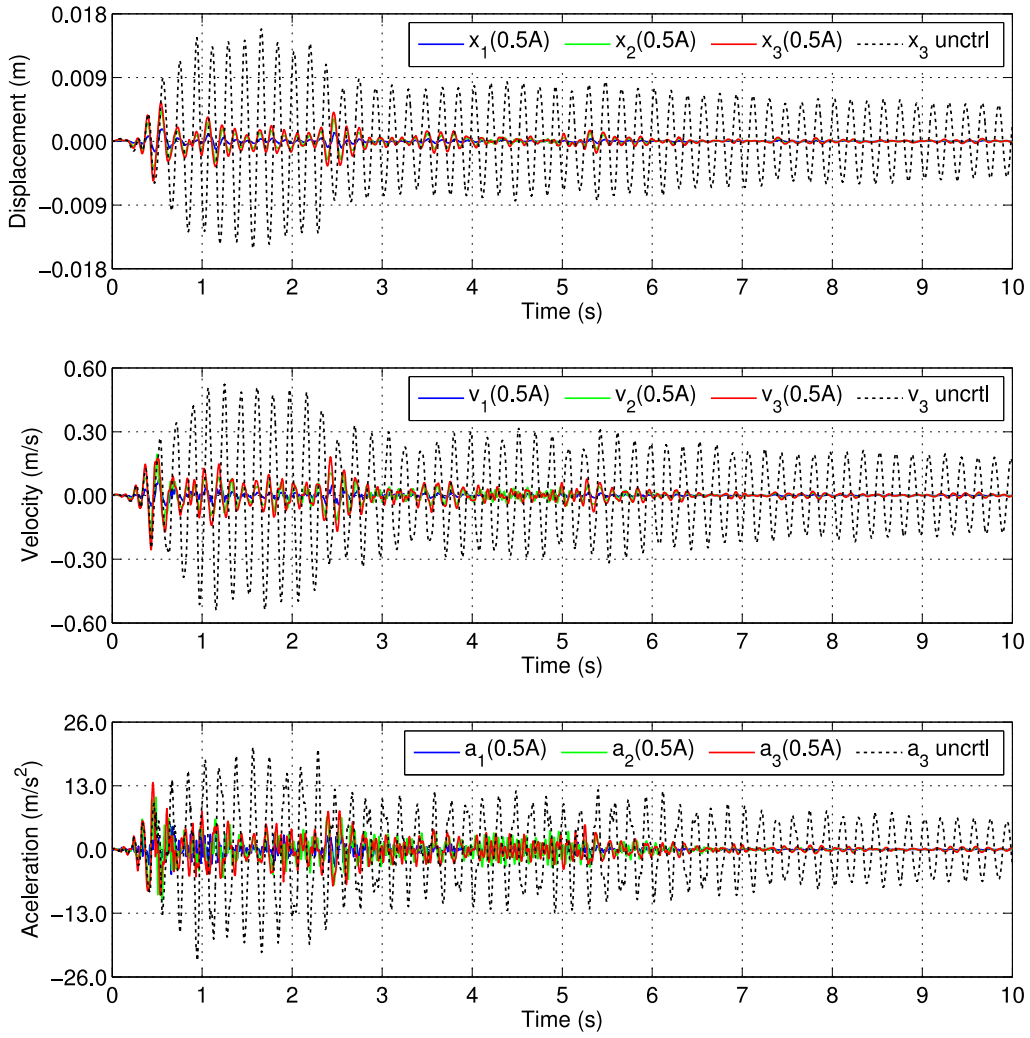


Figure 7: Results with the Modified Bouc-Wen model – Passive ON case.

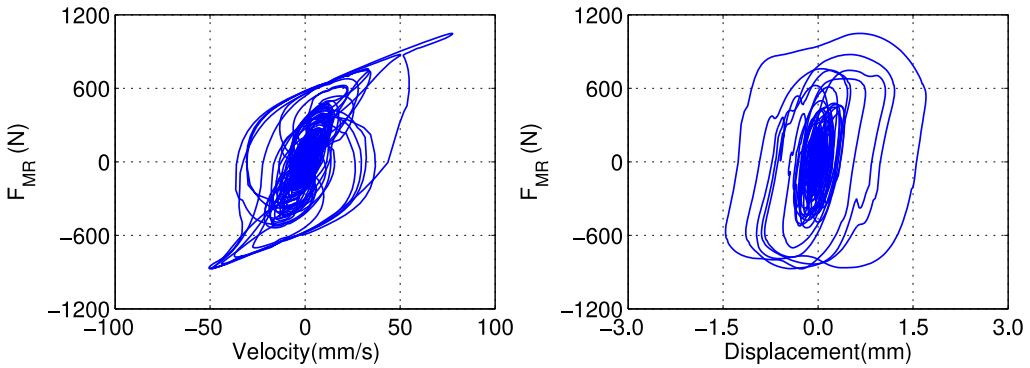


Figure 8: 3DOFs system - RD-1005-03 MR damper control force.
Passive ON case – Modified Bouc-Wen model

The Simulink model of the semi-active control system based on the BEL controller is displayed in Figure 9. As can be observed in this figure, interstory drifs of the building structure constitute the responses of the controlled system used by the BEL controller to determine the desired control force. Subsequently, the required control signal, i.e., the command current is determined from the predicted/desired control force using an inverse Bingham model of the MR damper.

The learning rates for the amygdala and orbitofrontal cortex were defined after a trial-and-error procedure and are computed to be α = 0.8 and β =0.5. Likewise, the sensory and the emotional outputs are determined by applying weight factors w_1 =2, w_2 =0.56, w_3 =2 and w_4 =0.85, which provide the best structural performance.

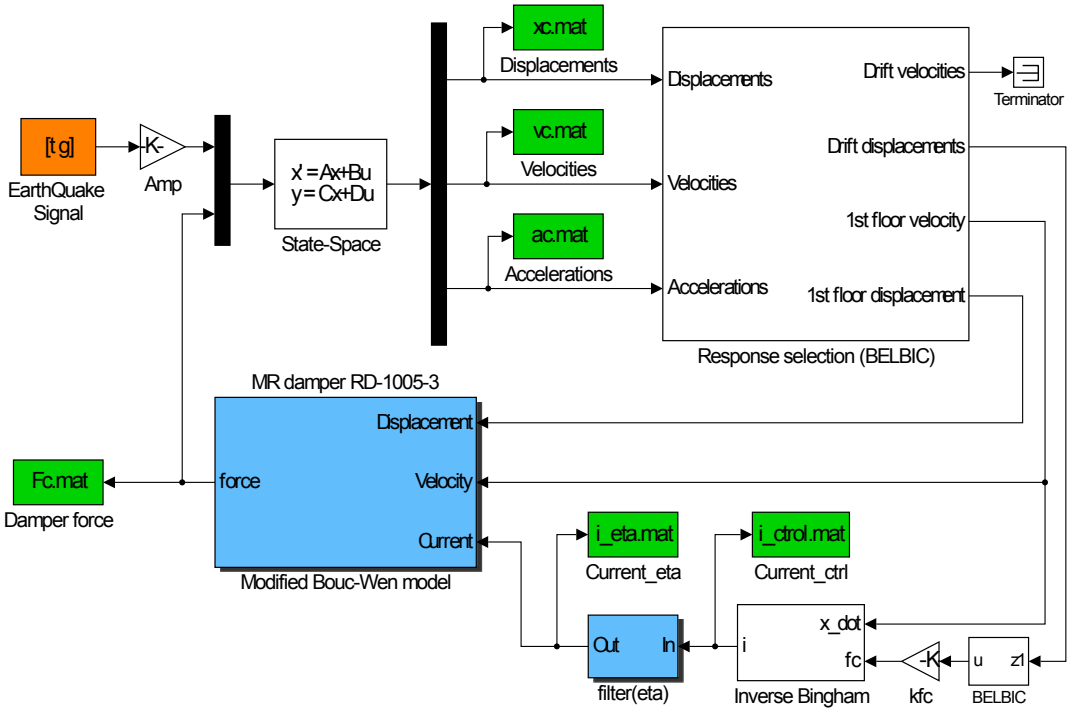


Figure 9: Simulink model of the BEL control system.

The structural responses obtained with the BEL based semi-active control system along with the uncontrolled response of the third floor are displayed in Figure 10. The peak responses of the uncontrolled and controlled systems are listed in Table 2. The results show the effectiveness of the proposed bio-inspired controller in reducing the response of the structure.

As can be seen, the proposed semi-active control system achieves a good performance in reducing the structural responses using only floor displacements as the reference signals to compute the control action. In fact, the main advantage of the BEL based control system is that only interstory drift responses of the structure are required to determine the control action. This means that the damping force generated during the control process does not need to be monitored, as happens in other controllers such as the clipped-optimal algorithm. Obviously, the main drawback regarding the implementation of the BEL based control system is related with the optimization of the controller parameters.

It should be also noted that the combination of a BEL controller with other control techniques (e.g. PID control) is shown to be able to improve the overall performance of the resultant control system [5].

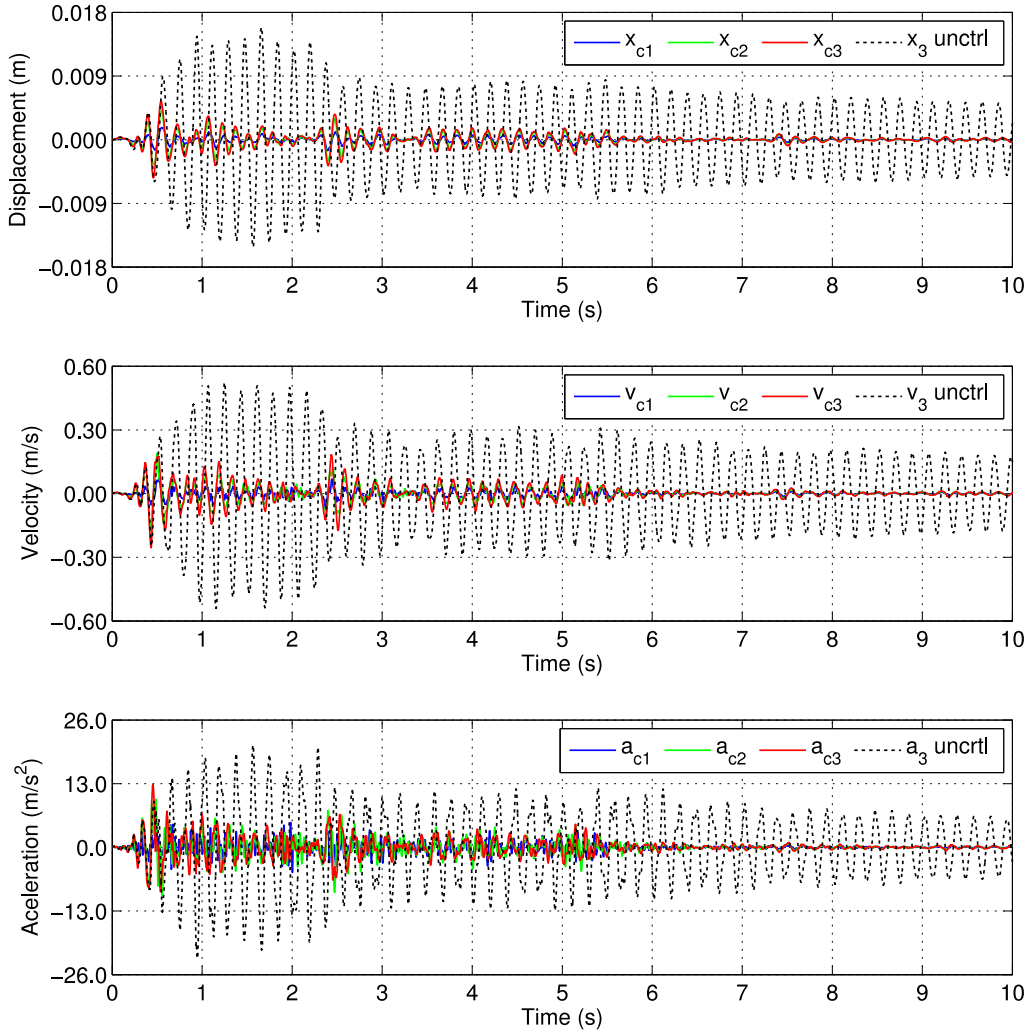


Figure 10: Structural responses obtained with the BEL controller.

Control strategy		$x(\mathrm{cm})$	$\dot{x}(\mathrm{cm/s})$	$\ddot{x}(\mathrm{cm/s^2})$	$f(\mathrm{N})$
Uncontrolled		0.695 1.251 1.587	27.09 45.78 54.02	1305 1736 2272	----
Passive OFF	Modified Bouc-Wen	0.518 0.907 1.191	20.02 34.51 42.79	999 1358 1791	166.4
Passive ON	**Modified Bouc-Wen**	**0.171** **0.423** **0.560**	**7.77** **19.36** **25.58**	**613** **1066** **1366**	**1048.9**
Brain Emotinal Learning		0.164 (-4%) 0.403 (-5%) 0.525 (-6%)	6.80 (-13%) 17.88 (-8%) 24.19 (-5%)	619 (1%) 964 (-10%) 1252 (-8%)	1014.4

Table 2 - Peak responses under the time-scaled El-Centro earthquake.

The damper force and the corresponding control signal are presented in Figure 11. As can be observed, the control system uses a continuous control signal to command the MR damper. The hysteretic behaviour of the MR damper during the numerical simulation is portrayed in the force-displacement and force-velocity plots presented in Figure 12. The proposed control system is capable to explore the dissipative nature of this type of actuators.

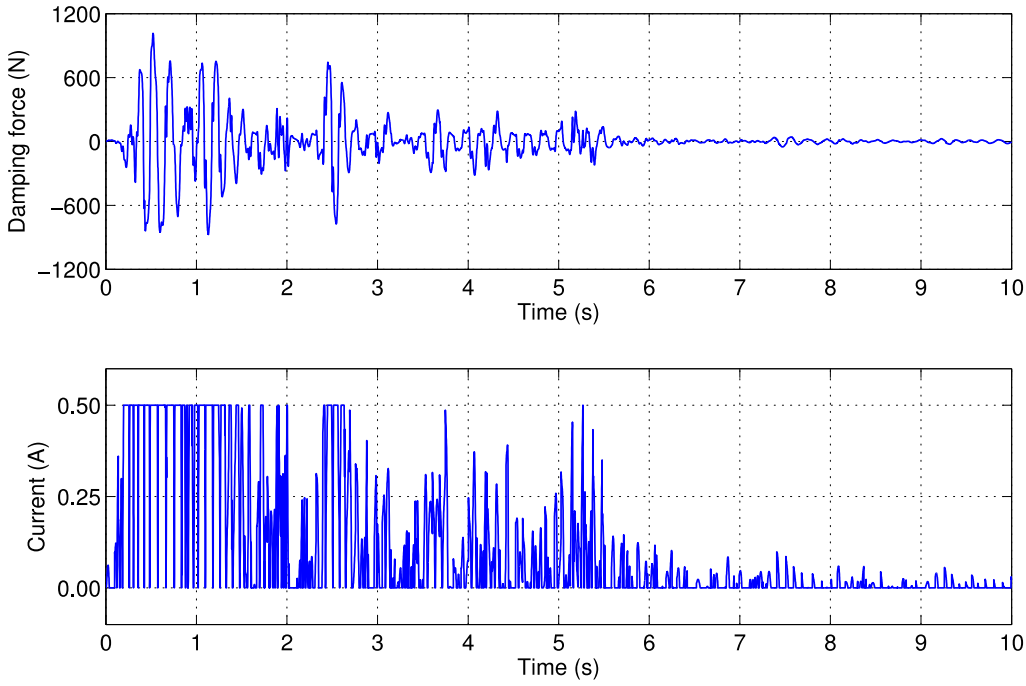


Figure 11: Damper force and corresponding operating current (BEL controller).

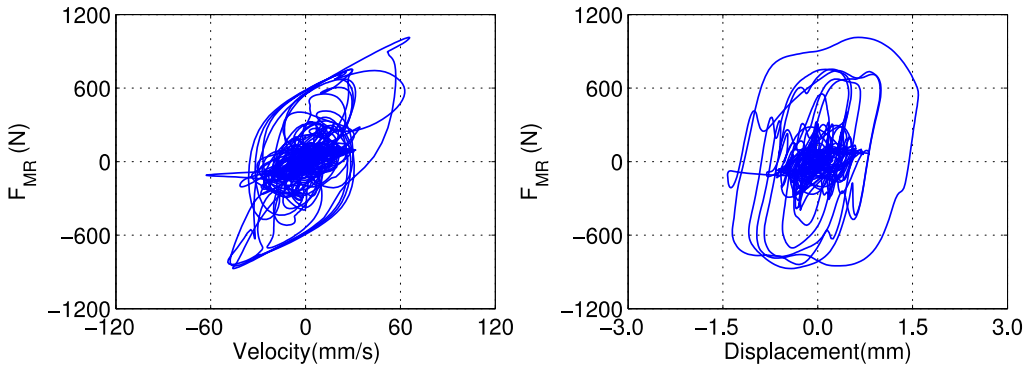


Figure 12: RD-1005-03 MR damper control force (BEL controller).

3 CONCLUSIONS

The present article addressed the non-linear hysteretic properties of MR dampers. An experimental testing procedure was carried out to characterize the response of a commercial MR damper and the experimental data were used to develop a numerical model. Some model parameters that must be initially found to construct a realistic numerical response. Thus, an identification routine was developed and the predicted response was compared with the experimental data. The results showed that the selected numerical model is capable to simulate the hysteretic behavior of the MR damper.

REFERENCES

[1] C. Lucas, D. Shahmirzadi, and N. Sheikholeslami, *Introducing BELBIC: Brain emotional learning based intelligent control*, international journal of Intelligent Automation & Soft Computing, 10 (1): 11–21, 2004.

[2] A. Arami, M. Javan, C. Roshtkhari, C. Lucas, *A Fast Model Free Intelligent Controller Based on Fused Emotions: A Practical Case Implementation*, pp. 596–602, 2008.

[3] M. Javan, A. Arami, C. Lucas, *Emotional Control of Inverted Pendulum System, A soft switching from Imitative to emotional learning*, pp. 651–656, 2009.

[4] M. Javan, A. Arami, C. Lucas, *Imitative Learning Based Emotional Controller for Unknown Systems with Unstable Equilibrium*, International Journal of Intelligent Computing and Cybernetics 2: 334–359, 2010.

[5] Y. Kim, C. Kim and R. Langari, *Novel bio-inspired smart control for hazard mitigation of civil structures*, Smart Materials and Structures, Vol. 19, No. 11, 2010.

[6] B.F. Spencer Jr., S.J. Dyke, M.K. Sain, J.D. Carlson, *Phenomenological model of a magnetorheological damper*, Journal of Engineering Mechanics, 123, 230-238, 1997.

[7] S.J. Dyke, B.F. Spencer, *A comparison of semi-active control strategies for the MR damper*, Proceedings of the IASTED International Conference, Intelligent information Systems, 580-584, 1997.

[8] L.M. Jansen, S.J. Dyke, *Semi-active control strategies for MR dampers: comparative study, Journal of Engineering Mechanics*, Vol. 125, No. 8, 795-803, 2000.

[9] M. Braz-Cesar, R. Barros, *Experimental and numerical analysis of MR dampers*, COMPDYN 2013 – 4th International Conference on Computational Methods in Structural Dynamics & Earthquake Engineering, 2013.

COMPDYN 2015
5th ECCOMAS Thematic Conference on
Computational Methods in Structural Dynamics and Earthquake Engineering
M. Papadrakakis, V. Papadopoulos, V. Plevris (eds.)
Crete Island, Greece, 25–27 May 2015

AN INTEGRATED FRAMEWORK FOR THE ANALYSIS OF MIXED-TYPE REINFORCED CONCRETE STRUCTURES

Vahid Sadeghian[1], Oh-Sung Kwon[1] and Frank Vecchio[1]

[1]University of Toronto Department of Civil Engineering
35 St. George St., M5S 1A4, Toronto, ON, Canada
vahid.sadeghian@utoronto.ca, os.kwon@utoronto.ca, fjv@ecf.utoronto.ca

Keywords: Reinforced concrete, Nonlinear analysis, Integrated simulation, Substructuring technique

Abstract. *The substructuring concept has been used in different forms such as in hybrid simulation and parallel computing methods, all contributing significantly to experimental testing and numerical analysis research programs. In this paper, unlike previous studies, the main goal is to use the substructuring technique to develop a framework which expands the capabilities of current nonlinear programs, enabling detailed analysis of mixed-type reinforced concrete (RC) systems in an integrated fashion, to a degree of accuracy unattained before. To achieve this goal, the primary objective of the proposed framework is to combine different VecTor programs which are among the most advanced nonlinear analysis tools for RC structures, while fully considering the interaction between substructures. This can greatly extend the application of conventional stand-alone nonlinear analysis. For instance, integrating VecTor2 (membrane software) and VecTor5 (frame software) provides a unique and effective solution technique for detailed analysis of disturbed regions in RC frames which is not available in any other stand-alone frame type analysis program. The flexible and object-oriented architecture of the framework facilitates inclusion of new analysis software. The application and effectiveness of the proposed framework are illustrated by modelling and analysis of two experimental case studies.*

1. INTRODUCTION

Nonlinear finite element analysis (NLFEA) of reinforced concrete structures has seen tremendous advancement over the past few decades. There are some situations where using advanced NLFEA tools is essential due to complexity of the analysis or the required level of accuracy. For instance, if the structure is subjected to unintended or extreme loads, if the codes or standards used for its design are deemed to be deficient today, if the structure was incorrectly designed or constructed in the first place, or if the structure is damaged and requires rehabilitation, then a more comprehensive analysis may be warranted. Especially considering the ageing infrastructure, the importance of having an advanced analysis tool is apparent.

Over the past decades, the VecTor programs, a suite of NLFEA software, have been developed on the theoretical basis of the Disturbed Stress Field Model (DSFM) [1]. The computational approach of the programs is based on a secant stiffness formulation using a total-load iterative process. Several experimental programs with a wide range of specimens and loading conditions have been conducted to examine the accuracy of the software [2, 3]. Moreover, analyzing real-world structures including frames, slabs, shear walls, silos, bridges, offshore platforms, and nuclear containment structures have been demonstrated the value of the VecTor programs in evaluating the complex nonlinear behaviour of reinforced concrete structures [4, 5]. Analysis application and element types for each VecTor program are presented in Table 1.

Program	Structure Type	Elements Type	Available DOFs
VecTor2	2D Membrane	Rectangular; Quadrilateral; Triangular; Truss; Link; Contact	Dx and Dy
VecTor3	3D Solid	Hexahedral; Wedge; Truss; Link; Contact	Dx, Dy and Dz
VecTor4	Plates and Shells	Heterosis; Truss	Dx, Dy, Dz, R1 and R2
VecTor5	Plane Frames	Frame	Dx and Dy
VecTor6	Axisymmetric Solids	Rectangular Torus; Triangular Torus; Ring	Dx and Dy

Note: Dx, Dy and Dz are translational DOFs in the X, Y and Z directions, respectively and R1 and R2 are rotational DOFs in the local directions.

Table 1: The analysis application and element types for each VecTor program

In many finite element analysis software, it has become necessary to combine lower-dimensional elements with higher-dimensional elements to provide both global and local assessment of the behaviour of the complex structural systems. In the VecTor analysis programs, each program is specialized for one particular type of problem; for example, VecTor2 can only model 2D planar continuums and VecTor5 can only model 2D plane frames. There are many applications where several types of structural components act together; for example, in a typical building, a moment resisting frame (2D frame) may act compositely with floor slabs (3D plate) and shear walls (2D continuum). Analysis capabilities for such systems or any other mixed-type structures are not available in the VecTor programs. In addition, modelling the entire structural system in detail is not practical due to computational time and memory storage limitations.

The most common approach to analyze integrated structural systems and overcome the above-mentioned limitations is the global-local method. In this approach, the structure is analyzed in two separate steps. In the first step, a global analysis of the entire structure is performed to find the force distribution and reactions. In the second step, using the global analysis results, the critical

components of the structure are analyzed in detail. However, determining the critical regions that needs to be modelled requires expert users with a very good understanding of the force flow in the structure. Also, defining the right boundary conditions for each component is a challenging task. Even if the critical components are chosen and modelled properly, force redistribution due to stiffness changes in the system raises questions about the accuracy of the method.

One effective approach to accurately simulate the response of integrated systems is to develop a multi-scale framework which can combine the best features of different analysis software. UI-SimCor [6] is an example of such framework, which is targeted toward hybrid (experiment-analysis) simulation. In the multi-scale framework approach, each component, based on its mechanical characteristics, can be modelled using the most suitable analysis tool. The components are connected to each other through an integrated framework which coordinates the analysis of the whole system. The coupled nature of the simulation allows one to fully consider the interaction between the substructures, resulting in a more accurate analysis of the system. The framework provides a multi-platform analysis environment which includes a broad range of analysis methods, element types, material models, and load options. Moreover, it enables the use of the parallel processing technique to avoid computational time and memory storage limitations associated with sequential single-platform analyses. Developing such framework for the VecTor programs can greatly extend the application of the software to assess the behaviour of complex integrated reinforced concrete structures to a degree that was difficult or impossible before.

In this paper, the proposed multi-scale simulation framework is presented. The effectiveness of the proposed framework are illustrated with two experimental case studies.

2. PROPOSED INTEGRATED FRAMEWORK

The proposed integrated framework, named as Cyrus, intends to incorporate single-platform NLFEA tools and provide a unique simulation environment which helps to eliminate the limitations associated with analysis of mixed-type reinforced concrete structures. The architecture of the framework is described in detail in subsequent sections.

2.1 Overview of the Framework

Cyrus is written in the C++ programming language using Microsoft Foundation Classes and Open Graphics Library. The architecture of the framework is based on object-oriented methodology, making it suitable to adapt to other analysis tools. Cyrus consists of three main parts: solution algorithms, inter-process communication (IPC) methods, and graphical user interfaces (GUI). Detailed descriptions of each part are provided in the following sections. The framework is linked with advanced C/C++ libraries such as MKL [7] and PARDISO [8] enabling high-performance, memory efficient sparse matrix calculation and fast multi-threaded partial factorization computation which is used in the static condensation phase of the substructuring technique.

By running the simulation, Cyrus connects to all the components. The first stage of the analysis is the initial static equilibrium. In this stage, depending on the solution algorithm, Cyrus collects full or condensed forms of the stiffness and force values of all the substructures, maps them based on an internal numbering format, and solves for the displacements. This satisfies equilibrium for all DOFs of the mixed-type system including the boundaries between the substructures. Then, the framework sends computed displacements to each substructure along with a proceed command to continue their analyses. The boundary displacements between connecting substructures are taken to be identical so that compatibility is satisfied in the system.

For dynamic analysis, after imposing the static loads in the first load stage, Cyrus collects mass and stiffness values of all the components, performs an eigenvalue analysis, and sends the computed Rayleigh damping coefficients to the substructures. In this procedure, the equation of motion is formulated for each substructure separately using numerical integration methods available in the VecTor programs. Based on a total-load secant stiffness formulation of the integration methods developed by Saatci [9], equivalent stiffness matrix and force vector of dynamic effects are calculated in each component and sent to Cyrus. These values will be added to the corresponding static values and will be used to compute displacements.

In each load stage, when a substructure reaches convergence, Cyrus temporarily holds the analysis of that specific substructure and uses its converged stiffness and force values for the analysis of the rest of the system. At the end of the analysis, all the substructures are disconnected from the framework. Figure 1 demonstrates the overall architecture of the proposed framework and its application on a shear wall-frame system. The dotted line steps are only preformed in the dynamic analysis.

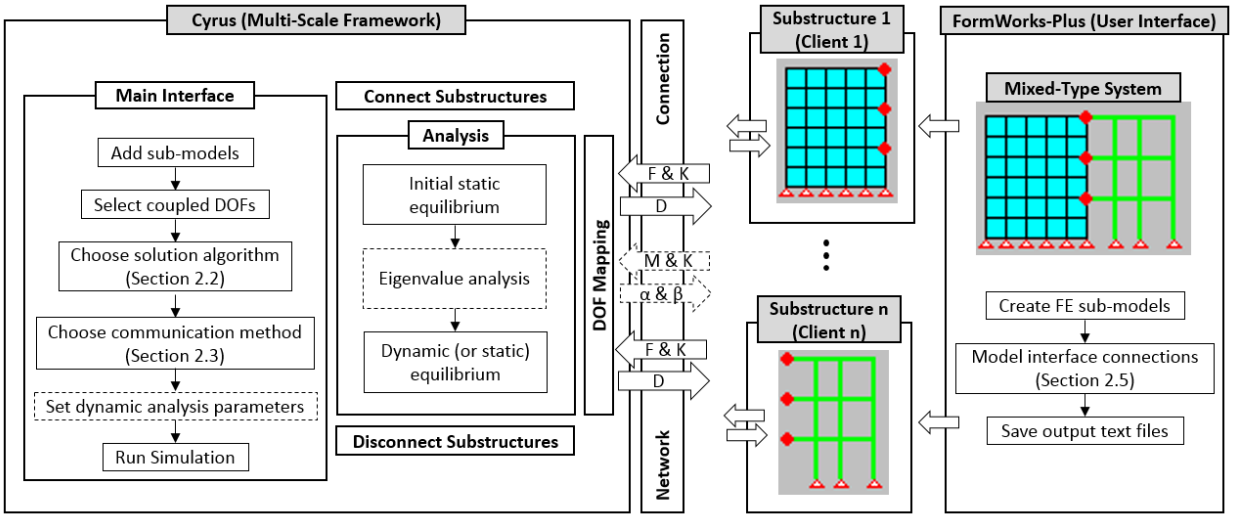


Figure 1. Overall architecture of the proposed multi-scale framework

2.2 Solution Methods

To consider geometry and material nonlinearity of structures, analysis software use different types of iterative solution methods. The majority of these methods can be categorized into two groups: Tangent-Based methods and Secant-Based methods. In the Tangent-Based methods, the displacements are computed from tangent stiffness and unbalanced force values. The unbalanced forces are calculated by subtracting the applied external loads from sectional forces. Since finding the stiffness matrix in each iteration is computationally expensive, some methods use initial stiffness instead of tangent stiffness in their procedure. In the Secant-Based methods, unlike Tangent-Based methods, the force vector is constant and equal to the applied forces through the iterations while the nonlinear behaviour of the structure is taken into account by updating the secant stiffness values. This section intends to demonstrate that, by using reasonably small load steps, the Tangent-Based methods and Secant-Based methods are equivalent; therefore, analysis tools with different solution techniques can be combined.

In the Incremental Tangent method, as shown in Figure 2(a), the next step displacement (u_{n+1}) is estimated from the current displacement (u_n) based on:

$$u_{n+1} = u_n + \frac{F - f_n}{E_{tn}} \tag{1}$$

where F is the external applied force; f_n and E_{tn} are the internal force and tangent stiffness corresponding to the u_n displacement, respectively. In the Incremental Secant method, however, the next step displacement is computed from the intersection of applied force and incremental secant line (E_s) (Figure 2(b)). The equation of the incremental secant line can be described as:

$$E_s(u) = \frac{f_n - f_{n-1}}{u_n - u_{n-1}} u + \frac{u_n f_{n-1} - u_{n-1} f_n}{u_n - u_{n-1}} \tag{2}$$

From $E_s(u_{n+1}) = F$, the next step displacement is computed as:

$$u_{n+1} = \frac{F(u_n - u_{n-1}) + u_{n-1} f_n - u_n f_{n-1}}{f_n - f_{n-1}} \tag{3}$$

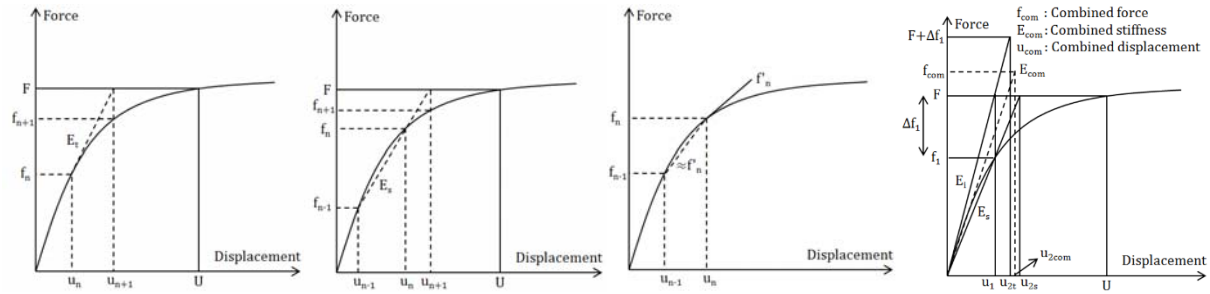


Figure 2. (a) Tangent method; (b) Secant method; (c) Tangent stiffness approximation; (d) Combined method

As illustrated in Figure 2(c), for small load steps one can approximate the tangent stiffness at u_n with $\frac{f_n - f_{n-1}}{u_n - u_{n-1}}$. Substituting this equation into the Tangent method equation gives the following:

$$u_{n+1} \approx \frac{(F - f_n)(u_n - u_{n-1})}{f_n - f_{n-1}} + u_n \tag{4}$$

Expanding this equation results in a similar equation as the one described in the Secant method.

This also can be illustrated graphically. As shown in Figure 2(d), which presents the total form of the Tangent and Secant solutions, combing the two methods results in stiffness values which are not as high as the initial stiffness and not as low as the secant stiffness of the system. Similarly, the combined force values are within the range of the external force and total unbalanced force values. Therefore, the computed displacements from the combined method are always between the values obtained from the Tangent method and Secant method. Assuming small load steps, it can be concluded that the solution of the combined method is equivalent to the solution of Tangent and Secant methods.

All the VecTor programs are formulated based on the Secant solution method except VecTor5 (frame analysis) which uses the Tangent solution method (Newton-Raphson method). The combined solution method analysis results are examined using VecTor2 and VecTor5 programs in the application example section of this paper.

In order to solve the equilibrium equation and find displacements at coupled DOFs, two different solution techniques were implemented in Cyrus: Centralized solution and Distributed solution. While both methods give exact the same results, depending on the number of substructures, amount of communication data, and number of available nodes, their performance can be significantly different.

In the Centralized solution method, substructures compute the stiffness and force values and send them to Cyrus in sparse format (non-zero values). Cyrus generates the global stiffness matrix and force vector and solves for the displacements of all DOFs of the system. This method is used in most previous simulation frameworks. However, for large systems, transferring the stiffness and force values of all the DOFs requires an excessive amount of communication which can significantly affect the analysis time. In addition, storing all the information of the entire system on as single computing node is not memory efficient.

To avoid the aforementioned problems, a new solution technique, Distributed solution method, is implemented in Cyrus, which is not available in any other similar framework. In this method, unlike the Centralized method, only the condensed form of the stiffness matrix and force vector are sent to Cyrus. The simulation framework is responsible for solving equilibrium equations for the coupled DOFs while each substructure solves for the displacements of the internal DOFs. Therefore, the solution step of the analysis is distributed between the framework and components.

2.3 Communication Procedures

To exchange data among substructures, Cyrus is enhanced with several Inter-Process Communication (IPC) methods. These techniques enable transferring data between two or more threads of one or more processors. Processors can be located on multiple computers connected by a network. Figure 3 illustrates the overall architecture of the different communication methods implemented in the simulation framework.

The first communication method available in Cyrus is pipe communication which can be used to redirect input and output of substructures and send them control commands (run and pause). To exchange data in both directions, Cyrus creates two anonymous pipes per substructure. It writes data to one pipe using its write handle, while the substructure reads the data from that pipe using its read handle. Similarly, the substructure writes data to the other pipe and Cyrus reads from it. Pipes have limited size which depends on the system properties. If the size of data is larger than the pipe size, the program transfers data in multiple byte blocks.

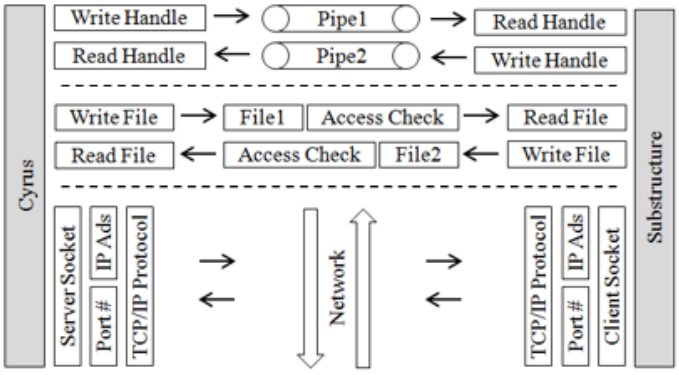


Figure 3. Different communication methods in the multi-scale framework

For large structural systems, using the pipe option to transfer data in multiple byte blocks can be time consuming. To improve the communication performance, binary files are also used in conjunction with pipes. In this configuration, pipes are responsible for sending control commands (run and pause) while binary files are used to send stiffness and force values. Unlike pipes, there is no limited size for files; therefore, all the data can be transferred between server and client in a single file instead of multiple byte blocks.

Both pipes and files are local communication methods and cannot be used over a network. To perform geographically distributed simulation or connect multiple distinct computing nodes to increase the computational performance and storage capacity of the system, a socket communication method is implemented in the framework. The type of socket used is the stream socket, also known as connection-oriented socket, which uses TCP (Transmission Control Protocol) internet protocol for data exchange. In this architecture, Cyrus, the server program, creates sockets on the startup and puts them in the listening state. Then, the sockets wait for initiatives from substructures which are the client programs. Each socket is characterized by a socket address which includes an IP address and a port number.

2.4 Graphical User Interface

Cyrus is compatible with a generalized graphical user interface program, FormWorks-Plus [10], which enables the user to conveniently generate finite element mesh for substructures and model the interface between the components. In addition, Cyrus is enhanced with a graphical user interface which facilitates the process of selecting sub-models, choosing coupled DOFs, and specifying proper analysis options. These developments make the mixed-type modelling process more transparent for engineers, contributing to acceptance and utilization of the simulation framework.

2.5 Interface of Multi-Scale Models

One of the challenges in combining different analysis tools is the modelling of the connecting sections at the interface of sub-models. Each FE program has a different element library and number of DOFs. There are many instances where the rotation at the interface nodes of one program must be transferred to the equivalent displacements for another program which only supports translational DOFs. The connection between the VecTor2 membrane elements and VecTor5 frame elements is an example of this type of mixed-dimensional problem. The common approach to connect the two programs is to use Rigid Constraints at the connecting section. This enables the analysis to transfer rotation from the frame sub-model to equivalent translational displacements in the membrane sub-model based on the plane sections remain plane assumption, while satisfying the compatibility and equilibrium in the multi-scale analysis. However, a set of transverse rigid members at the connection acts as a very strong stirrup which does not allow transverse expansion at the interface and adds additional stiffness to the structure which may affect the response of the system.

To overcome the above-mentioned limitations and model the interface section more accurately, a new interface element, F2M element, is proposed. The F2M element is a two nodded semi-deformable element which can fully transfer translational and rotational displacements at the interface. It does not add any additional stiffness to the system and allows lateral expansion at the connecting section. The stiffness matrix of the proposed element was set up such that it has high stiffness values in the transverse and rotational directions while zero stiffness in the axial direction. Similar to the rigid elements, F2M elements are defined along the membrane elements at the

interface. A master node connects each set of F2M elements to the corresponding frame sub-model. From the shear stress distribution at the master node of the frame sub-model, the equivalent axial forces at the F2M element nodes are computed. To transfer shear between the two sub-models, the computed equivalent forces are applied in the opposite direction on corresponding nodes of connecting membrane elements.

3. APPLICATION EXAMPLES

The application of the newly developed multi-scale framework is demonstrated through modeling and analysis of two different case studies. All the analyses were done according to the default material models and analysis parameters. No "fine tuning" of the analysis was done in an attempt to obtain a better fit to experimental results.

3.1 Beam-Column Joint

Shiohara and Kusuhara [11] conducted an experimental test program to investigate the response of six half-scale reinforced concrete beam-column joints under quasi-statically reversed cyclic load. Specimen A2 was selected for modeling and analysis in this section. The study intended to compare the analysis results against the experimental results and illustrate the improvements in the response of the multi-scale analysis over the stand-alone analysis.

The test setup and experimental crack pattern are illustrated in Figure 4. Also, the cross-sectional dimensions and reinforcement layout are shown in Figure 5. The loading conditions considered in the experimental program were a constant axial force of 216 kN and a horizontal reversed cyclic load in a displacement controlled manner. The loads were applied at the top of the column.

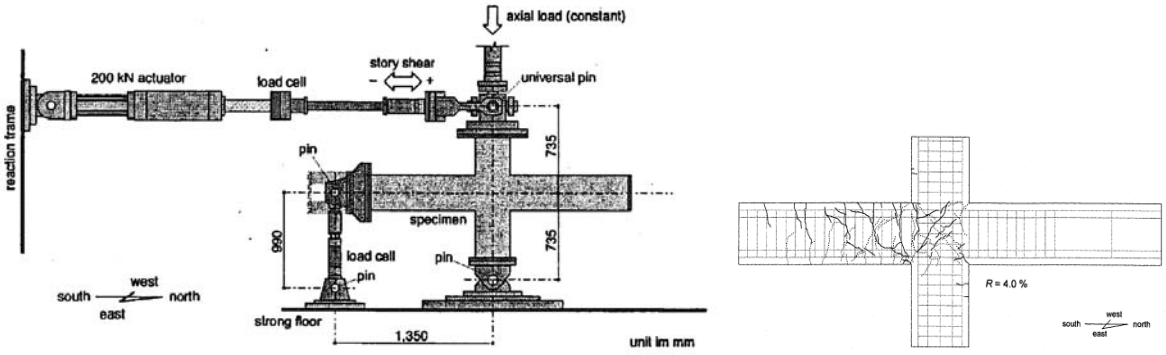


Figure 4. Test setup and experimental crack pattern [11]

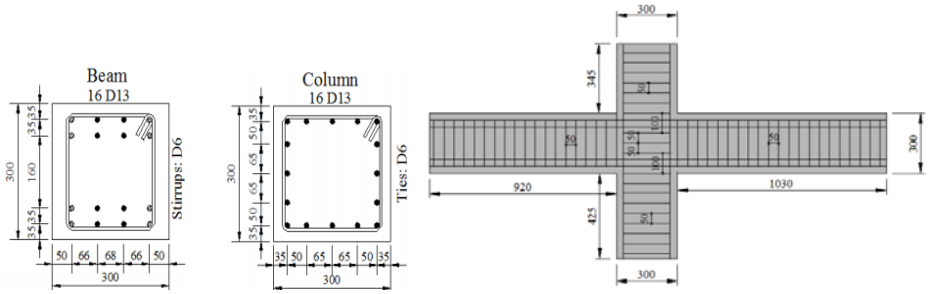


Figure 5. Cross-sectional dimensions and reinforcement layout

A frame model of the entire structure (joint, beams, and columns) was created and analyzed using the frame analysis program, VecTor5 (Figure 6). Based on the analysis results, VecTor5 calculated the overall response of the structure reasonably well. However, the load capacity after the first two cycles was considerably underestimated. Also, the pinching effect in the load-deflection response was not captured accurately and was underestimated. These issues are not exclusively due to the limitations associated with VecTor5 program. Most frame analysis programs, including VecTor5, assume plane section remains plane and perfect bond between reinforcement and concrete in their analysis procedure. However, according to the experimental crack pattern, the test specimen experienced major cracks in the joint panel zone which is considered to be a disturbed region. Also, there were noticeable slips between the reinforcement and concrete at the joint region and extension of the left beam.

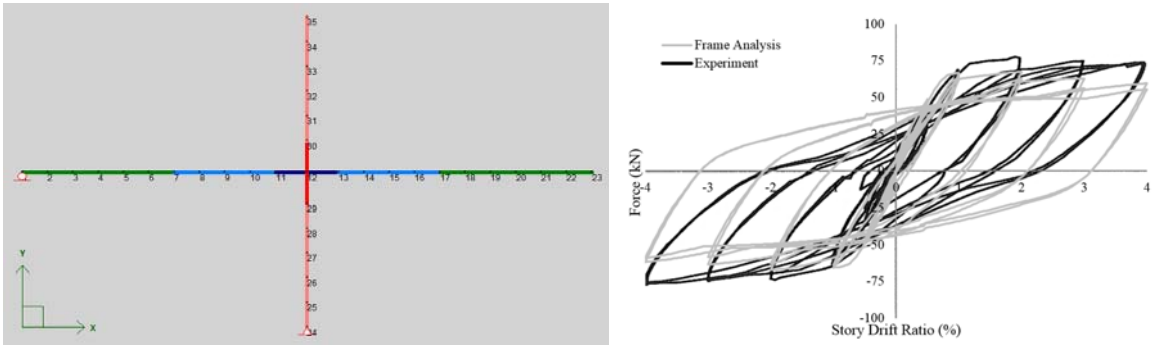


Figure 6. Stand-Alone frame model and load-deflection analysis results

To overcome the limitations associated with VecTor5 program and most frame type analyses, the critical part of the structure can be modelled using VecTor2 which is a more detailed analysis software. The critical zone consists of the joint region and an extension of connecting members in each direction. For the 2D membrane sub-model, rectangular and truss elements were used to model concrete and longitudinal reinforcement, respectively. The transverse reinforcement was modelled as smeared. In addition, link elements were used between rectangular elements and truss elements to capture any possible slip between concrete and longitudinal reinforcing bars. Newly developed F2M elements were used to connect the two finite element sub-models (VecTor2 and VecTor5). Cyrus combined the two sub-models and coordinated the multi-scale simulation.

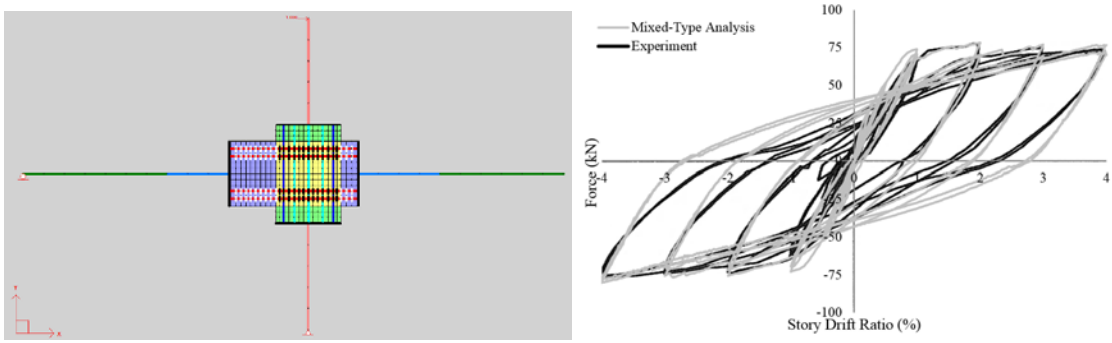


Figure 7. Mixed-Type model and load-deflection analysis results

The experimental and mixed-type analysis load-deflection results are presented in Figure 7. It can be seen that the mixed-type analysis predicted the peak loads and pinching effects with better accuracy than the stand-alone frame analysis. The reason is that unlike frame analysis software, VecTor2 is applicable for the joint panel zone where the strain distribution is significantly nonlinear. In addition, the VecTor2 sub-model was able to compute the slip in the critical part of the structure and consider it in the analysis.

3.2 Three Story Reinforced Concrete Frame

Calvi et al. [12] performed quasi-static cyclic test on a three-story 2/3-scaled reinforced concrete building frame designed only for gravity loads based on typical Italian construction practice common between the 1950s and 1970s (Figure 8). To be consistent with the old design practice, smooth bars were used for the reinforcements and the joint regions were constructed without any transverse reinforcement. Also, instead of bending the longitudinal bars in the exterior joints, they were anchored with end-hooks. The lateral loads were applied in a hybrid force-displacement control manner; the displacement at the top floor was increased in reversed cyclic regime while maintaining a linear force distribution along the height of the structure. In addition, a gravity load of 73 kN was applied on the first and second floors and 54.2 kN on the third floor.

The poor detailing of the reinforcements resulted in a brittle failure mode with most of the damage concentrated in the exterior beam-column joint regions of the first floor (Figure 9). The failure mechanism consisted of the shear cracks in the joint region along with the formation of a wide flexural crack at the interface of the beam due to the slip of smooth bars.

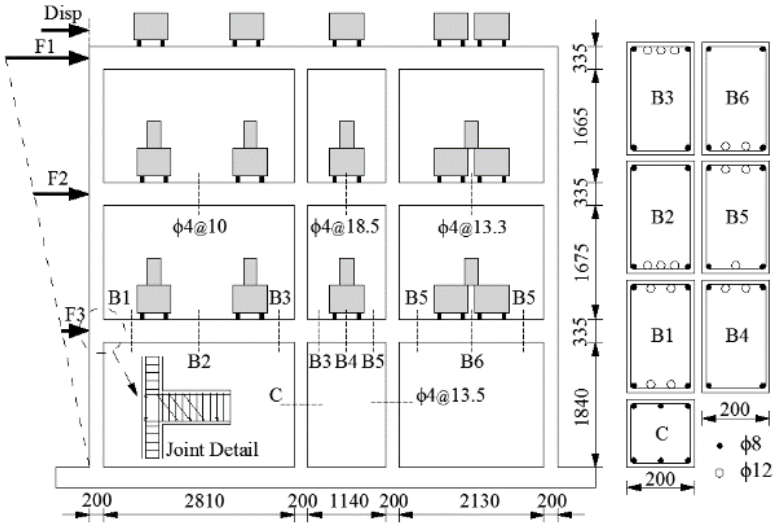


Figure 8. Reinforced concrete frame tested by Calvi et al. [12]

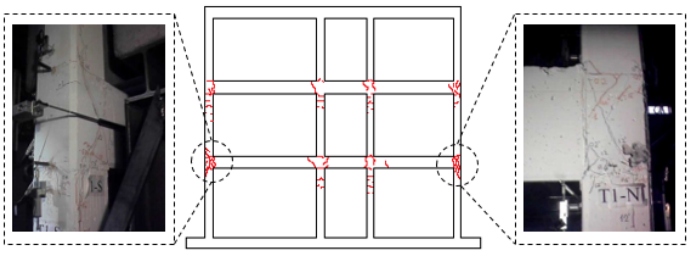


Figure 9. Experimentally observed crack pattern at ultimate load [12]

A frame model of the entire structure was analyzed using VecTor5. Six DOF layered frame elements with member lengths in the range of half of the cross section depth were used. Since like most other sectional analysis procedures, VecTor5 is unable to analyze the disturbed regions, the amount of reinforcement was increased by a factor of two in the beam-column joint regions to avoid artificial damage.

The calculated push-over load-deflection responses are compared to the experimentally observed behaviour in Figure 11. The stand-alone VecTor5 analysis response agreed reasonably well with the experimental results up to the point where joints began to crack. However, beyond this point, the analysis began to overestimate the strength and stiffness, resulting in much higher failure load than the experiment. This is a consequence of the aforementioned limitations associated with most frame analysis software including VecTor5.

The proposed mixed-type analysis procedure can be used to extend frame analysis methods application from a global analysis tool to include local behaviour of critical parts of the structure. Here, based on the stand-alone frame analysis results and experimental crack pattern presented in Figure 9, the external joints in the first floor and an extension of connecting members in each direction (equal to the member height) were selected as critical parts of the structure. These regions were modelled using more detailed analysis software, VecTor2, while the rest of the structure was modelled using frame analysis software VecTor5 (Figure 10). The multi-scale framework, Cyrus, was used to combine the two sub-models and coordinate the mixed-type analysis.

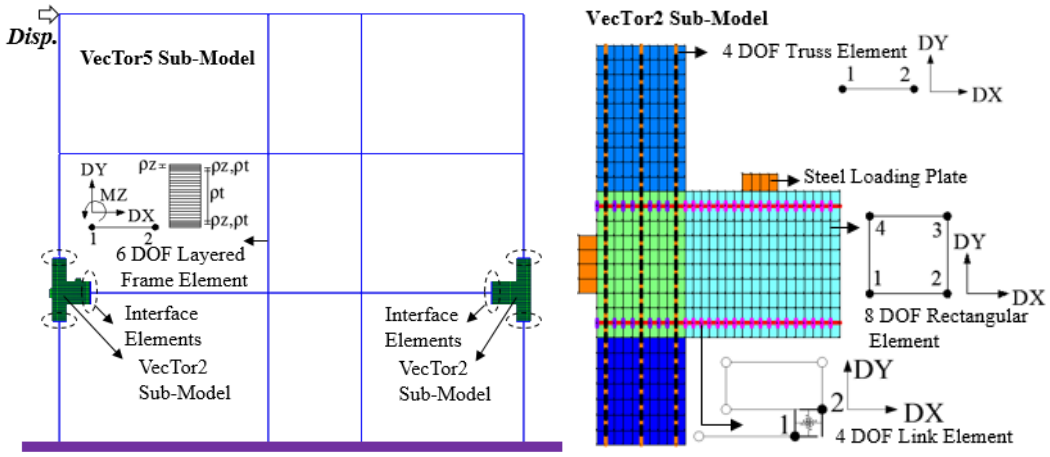


Figure 10. Mixed-type FE model of reinforced concrete frame

Based on the load-deflection results, the mixed-type analysis computed the peak load and stiffness with better accuracy compared to the stand-alone analysis. The mixed-type analysis predicted multiple cracks in the joint panel zone followed by formation of a wide flexural crack at the beam-column interface (Figure 11). Thereafter, a large amount of slip was computed in the longitudinal reinforcement of the beams at the interface section, resulting in significant reduction in the stiffness of the system. The computed crack pattern and bond slip effects agreed well with the experimentally observed behaviour. The analysis also showed the post-peak decay in strength due to the local failure in the joints. It must be noted that none of these mechanisms were captured in the stand-alone frame analysis.

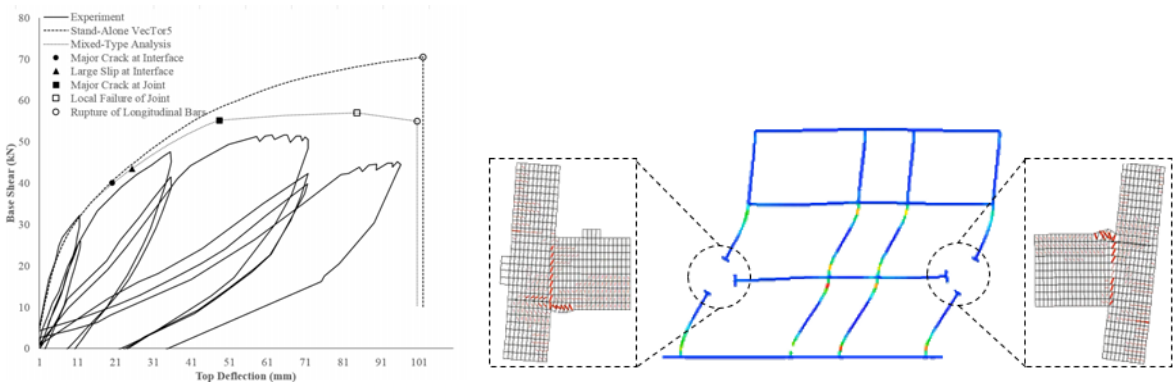


Figure 11. Load-deflection responses and mixed-type analysis crack pattern and deflected shape

4. SUMMARY AND CONCLUSIONS

A multi-scale analysis framework is presented which can integrate different finite element analysis software, enabling accurate simulation of complex mixed-type reinforced concrete systems. The primary goal of the framework is to combine different VecTor analysis programs, while fully considering the coupled nature of the simulation, although other commonly used software (e.g., OpenSees) can also be combined. The proposed framework greatly expands the software application and provides a unique analysis environment where well-recognized behaviour models for reinforced concrete (e.g., DSFM) can be applied to complicated structures. The object-oriented architecture of the framework allows easy inclusion of new analysis tools.

Using substructuring techniques and static condensation procedure, two solution algorithms are developed and implemented into the program to consider the interaction between components. The combined tangent-secant solution method is verified theoretically and numerically, illustrating that analysis tools with different solution algorithms can be integrated. The framework is implemented with a wide range of communication methods including binary file, pipe, and TCP/IP socket. A graphical user interface is implemented into the framework, facilitating the mixed-type structure modelling process. A new interface element is developed to address problems associated with traditional mixed-dimensional coupling approach.

To demonstrate the new capabilities of the framework, two application examples are presented. In these examples, the frame type analysis is enhanced with an effective solution technique for detailed analysis of disturbed regions such as beam-column joints and bond effects between reinforcement and concrete. In both application examples, the mixed-type analysis predicted the behaviour of the structures with a level of accuracy which was impossible or impractical to achieve with most stand-alone analysis tools.

The development of the framework is still in progress. In the near future, the program will have a feature to integrate experimental specimen such that pseudo-dynamic hybrid simulation is possible using the framework. In addition, by using a standardized communication protocol and data exchange format, which is under development at University of Toronto, the framework will be inter-operable with several other analysis tools.

ACKNOWLEDGMENTS

Financial support provided by IC-IMPACTS (the India-Canada Centre for Innovative Multidisciplinary Partnerships to Accelerate Community Transformation and Sustainability) are gratefully acknowledged.

REFERENCES

[1] F.J. Vecchio, Disturbed stress field model for reinforced concrete: Formulation. *J. Struct. Eng.*, 126(9), 1070–1077, 2000.

[2] D. Palermo, F.J. Vecchio, Behaviour of 3-D reinforced concrete shear walls. *ACI Struct. J.*, 99(1), 81-89, 2002.

[3] F.J. Vecchio, W. Shim, Experimental and analytical re-examination of classic concrete beam tests. *J. Struct. Eng.*, 130(3), 460-469, 2004.

[4] M.P. Collins, F.J. Vecchio, R.G. Selby, The failure of an offshore platform. *Can. J. Civil Eng.*, 24(3), 460-470, 1997.

[5] F.J. Vecchio, Contribution of NLFEA to the evaluation of two structural concrete failures. *J. Perform. Constr. Fac.*, 16(3), 110-115, 2002.

[6] O. Kwon, A.S. Elnashai, B.F. Spencer. A framework for distributed analytical and hybrid simulations, *Structural Engineering and Mechanics*, 30(3), 331–350.

[7] E. Indrupska, Intel math kernel library for windows user's guide. 2014.

[8] O. Schenk, K. Gartner, PARDISO user guide version 5.0.0. 2014.

[9] S. Saatci, Behaviour and modelling of reinforced concrete structures subjected to impact loads. Ph.D. thesis, Dept. of Civil Engineering, Univ. of Toronto, 288, 2007.

[10] V. Sadeghian, FormWorks-Plus: improved pre-processor for VecTor analysis software. Master thesis, Dept. of Civil Engineering, Univ. of Toronto, 144, 2012.

[11] H. Shiohara, F. Kusuhara, Benchmark test for validation of mathematical models for non-linear and cyclic behaviour of RC beam-column joints. Report by Dept. of Architecture, School of Engineering, University of Tokyo, 2007.

[12] G.M. Calvi, G. Magenes, S. Pampanin, Experimental test on a three storey RC frame designed for gravity only. Proc., *12th ECEE*, London, Paper n. 727, 2002.

COMPDYN 2015
5th ECCOMAS Thematic Conference on
Computational Methods in Structural Dynamics and Earthquake Engineering
M. Papadrakakis, V. Papadopoulos, V. Plevris (eds.)
Crete Island, Greece, 25–27 May 2015

NUMERICAL SEISMIC ASSESSMENT OF AN EXISTING BRIDGE WITH DIFFERENT SUPPORT CONFIGURATIONS

Ciro Del Vecchio[1], Maria C. Caruso[1], Luigi Di Sarno[2], Oh-Sung Kwon[3] and Andrea Prota[1]

[1]University of Napoli "Federico II", Department of Structures for Engineering and Architecture
via Claudio 21, 80125 Napoli, Italy
ciro.delvecchio@unina.it, mariachiara.caruso@yahoo.it, aprota@unina.it

[2]University of Sannio, Department of Engineering
Piazza Roma, 21, 82100 Benevento, Italy
ldisarno@unisannio.it

[3]University of Toronto, Department of Civil Engineering
35 St. George St., M5S 1A4, Toronto, ON, Canada
os.kwon@utoronto.ca

Keywords: Reinforced concrete, numerical model, shaking table, shear, bridge, isolators.

Abstract. *The assessment of existing infrastructures is a critical issue in the seismic protection of the modern societies. Field surveys in the aftermath of major seismic events have demonstrated the high vulnerability of highway bridges. This led to an increasing interest in the seismic performance assessment of existing bridges. The present paper deals with the seismic assessment of a bridge substructure reproducing typical existing Italian infrastructures. The reference structural system is a reinforced concrete (RC) 1:3 scale single span bridge that will be tested on the shaking table facilities at the University of Naples, Italy. The details of the numerical models adopted in the nonlinear dynamic analysis and the seismic performance prediction required for the test preparation are discussed in details. The record selection, the development of a step-by step validated numerical model are presented for the case study comprising an existing RC bridge designed primarily for gravity loads . The advanced numerical models and the assumptions made to account for the shear behavior of the piers are also illustrated. The preliminary results of the incremental dynamic analysis are presented and analyzed with reference to the effectiveness of the use of base isolation strategy commonly adopted for the seismic retrofit of the bridge deck.*

1 INTRODUCTION

The damage and the collapse experienced by several highway RC bridges worldwide after moderate-to-major earthquakes are caused by the high vulnerability of bridges (e.g. [1]–[5], among many others). A number of existing RC bridges constructed in 1980s or earlier are

designed primarily for gravity loads and require major structural retrofitting. Thus, there is an urgent need to assess the seismic performance of existing bridges, considering also the ageing effects that may detrimentally affect the performance of such structures. The reliable evaluation of the support conditions of highway bridges is essential related to the structural dynamic response. Retrofitting measure may either employ traditional local and/or global interventions or use vibration control techniques, such as base isolation systems and supplemental damping. Adequate structural response parameters, such as pier chord rotations, lateral drift thresholds, shear for circular and hollow sections with smooth bars require experimental and numerical studies.

Towards this aim, a recent comprehensive research program was initiated in the laboratory of structures and materials of University of Naples, Federico II. Such program, funded by the Italian Ministry of Research through the Project PON-FESR 2007-2013 (PON01_02366, STRIT) "Tools and Technologies for the Management of the Transportation Infrastructures" focuses on the assessment of the structural response analysis of as-built and retrofitted RC bridges. This research includes a series of shaking table tests to be carried on substructures reproducing typical existing simply supported highway bridges in Italy, as further discussed in the next paragraphs. A representative bridge system, which is assumed to be located in a region of medium-to-high seismicity in the South of Italy, is first assessed in its as-built configuration with simple supports at both end of the deck and then retrofitted with two types of base isolators that can be installed at the base of the deck. The design of such bridge configuration is based on displacement-based approaches [6].

This paper deals with the numerical seismic assessment procedure carried out in preparation for a set of shaking table tests on 1:3 scale bridge subassemblies. Incremental dynamic analysis are performed in order to characterize the seismic performance of the bridge considering the variability of input motions. A detailed report on the step-by-step validation of the proposed numerical model is presented along with the assumption made to account for the shear behavior. In compliance with the scope of the experimental program, the influence of the pier type (i.e. circular pier with full and hollow cross section) and the support conditions (i.e. with or without isolators) are investigated by means of incremental dynamic analysis.

2 SUBASSEMBLY NUMERICAL MODEL

2.1 Subassembly description

The selected bridge subassembly is a 1:3 scaled specimen representing existing structural systems typical of the Mediterranean area designed with obsolete non-seismic code provisions [7]. The subassembly is a single span bridge with two piers supporting the bridge deck (see Figure 1). Because the objective of the study is to evaluate the response of the bridge piers and supports, the deck was designed to remain in elastic range during the tests. Thus, the deck is used to simulate the inertial force resulting from the structural mass only. Two different RC pier types are investigated; the variable is the member cross-section with its geometry and internal reinforcements. A bridge pier with a circular cross section and a hollow-circular cross sections have been designed according to typical 70-80s Italian practice. The reduced design seismic intensity and the absence of adequate seismic details led to structural systems with insufficient lateral capacity. Such response is caused primarily by insufficient transverse and longitudinal reinforcements. Furthermore, smooth bars have been adopted for internal longitudinal and transverse reinforcements, according to old design practice.

To improve the evaluation of the seismic capacity of the single span bridge, different seismic isolation devices, along with the simply supported configuration, have been properly designed and manufactured for the scaled subassembly. Specific construction details have been in-

stalled in the pier cap to allocate the different supports to be used during the laboratory tests. The specimen geometry and reinforcements details are reported in Figure 1.

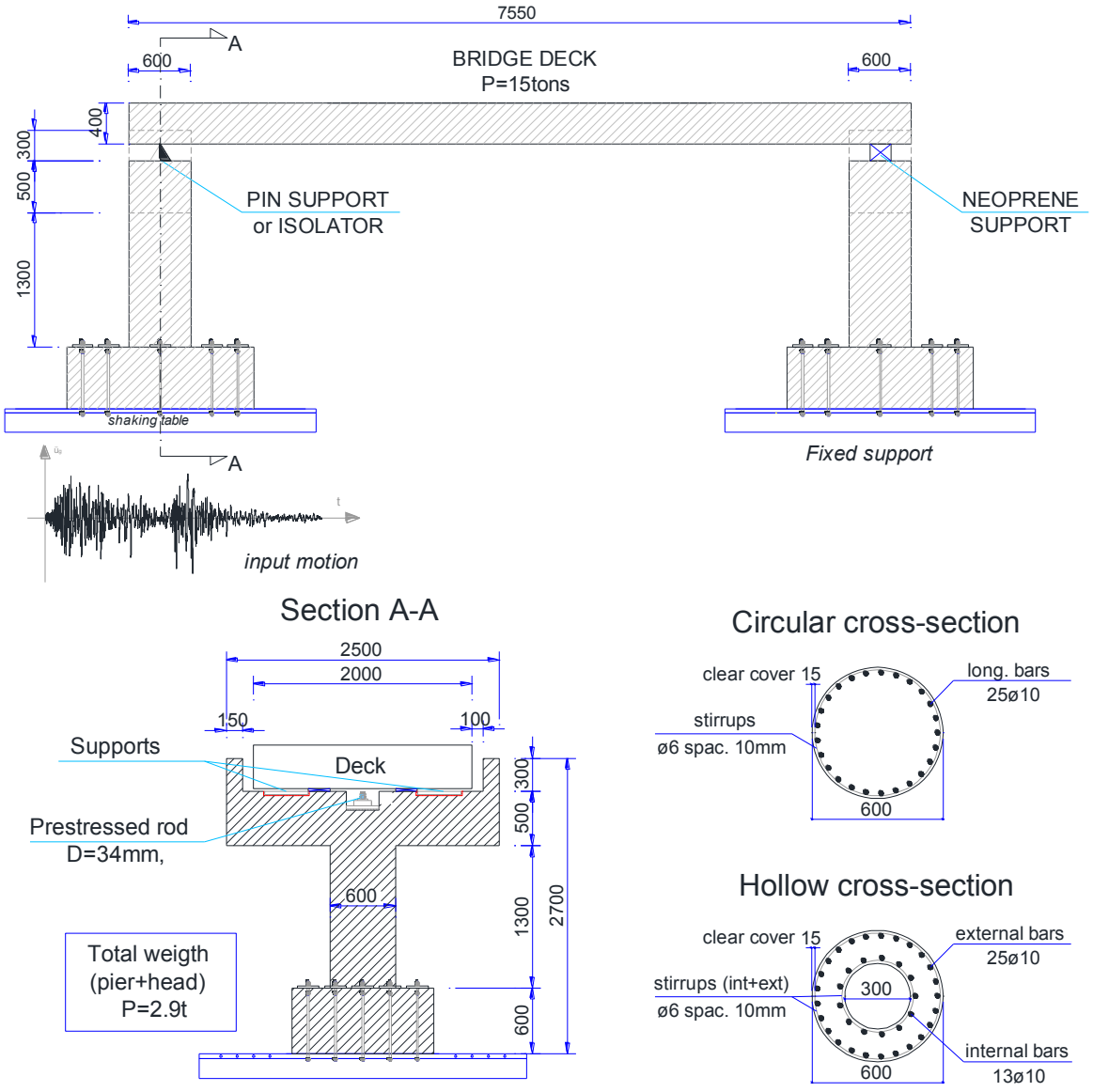


Figure 1: Details of the 1:3 scale bridge subassemblies (dimensions in mm).

The experimental shaking table tests, will be carried out in different configurations, varying the pier and support type and the input motions. However only four configurations, derived from the combinations of two piers and two different support configurations (simply supported or with Friction Pendulum Systems, FPS, isolators) have been analyzed in this study. In compliance with experimental tests, the input motion is applied to the left pier only (see Figure 1). Furthermore, to be representative of the real axial load available on typical bridge piers, further axial force have been introduced in the piers by means of internal prestressed rods. A total axial load about 0.05 (in terms of normalized axial load $\nu=N/(A_c f_c)$) will be adopted for all the tests. The deck supports will be subjected to the deck self-weight.

The specimens have been designed using materials properties commonly adopted in the old construction practice. In particular, a mean concrete compressive strength about 24 MPa

have been adopted in the calculation. The AQ50 steel (f_{ym}=370 MPa) has been adopted for internal reinforcements. Preliminary tests on reference coupons confirmed the assumed mechanical properties.

The adopted friction pendulum (FP) isolators have been experimentally characterized through dynamic tests at different frequencies and displacement amplitudes. Further details on the device specifics are reported in the next paragraphs.

2.2 Numerical models

One of the objectives of present study is to built a reliable and efficient numerical model of the selected bridge subassembly able to represent the real mechanical characteristic of the system until the collapse. Thus, a complete characterization of the specimen behavior with particular care of the seismic relevant response characteristics and failure mode is needed. This aspect has been found to be very sensitive for the seismic assessment of RC structural systems [8], [9]. The low amount of transverse reinforcements strongly reduce the lateral capacity of the piers, resulting in low ductility capacity and potential shear failure. To account for these failure mechanisms, proper numerical models should be adopted for the specimen response prediction. Available literature studies [8]–[10] pointed out that, recently, specific computer programs have been developed to reliably predict the hysteretic behavior of shear critical members. New mechanical models and solution algorithms have been developed and great effort has been made to combine them with the state-of-the-art knowledge in refined tools suitable for the use in the practical applications (e.g., OpenSees [11], VecTor programs [12], among others). The numerical models considered in this study are based on the Modified Compression Field Theory (MCFT) [15] and Disturbed Stress Field Model (DSFM)[13]. Both these theories have been developed at University of Toronto. In this paper, the response of the selected bridge piers will be predicted by mean of two different computer software (Response 2000, R2k [14], and VecTor2, VT2 [18]). The latter software presents an increasing level of difficulty in the modeling and, in turn, higher accuracy in the response prediction.

As described in the previous sections, the two piers of the single span bridge present structural details that could strongly affect the structural response. As well as these details are typical of existing structural viaducts, they can be difficult accounted in the numerical modelling. Furthermore, the dynamic response of the sample columns has been not completely characterized. Thus, due to the peculiarities of these structural members, the simplified numerical models may be approximated and present many sources of uncertainties in the response prediction. To develop a reliable numerical model suitable for shaking table response prediction and parametric studies, a step-by-step validation against experimental tests on specimens with the same structural details is adopted. Once that the proposed VecTor2 numerical model is validated, it is thus adopted to predict the hysteretic response of the two bridge piers. Later, the hysteretic response will be used to calibrate a more efficient OpenSees model of the piers. This model will be included in the dynamic model of the bridge subassembly along with the different support configurations. To move from a static model to a dynamic one a further step of validation against a shaking table test is needed in order to proper understand how to manage the input motion, masses, damping and solution algorithms.

2.3 Step-by-step modelling

Although the shear behavior of RC column subjected to cyclic loads can accurately captured by the MCFT/DSFM [8], [10], difficulties arise in the model definition in the case of circular members, especially if they have an hollow core. In fact, the behavior of a circular

cross section can be accurately reproduced in a 2D model by linearizing the curve shape and preserve the area and the inertia [9], [15], the reduced confinement pressure of the hollow cross section is difficult to be accounted in a 2D model. This phenomena was investigated by Ranzo and Priestley [16] that suggested for practical purpose to reduce the confinement pressure calculated for a circular cross section of the 30% to account of the hollow core. To validate the proposed VecTor2 numerical model for this particular case, the analytical results were compared against experimental evidence for the columns HS2 and HS3 (Ranzo and Priestley, 2000) exhibiting a shear failure. The consolidated modelling procedure [8]–[10] has been adopted to define the member mesh, longitudinal reinforcements, percentage of in-plane and out of-plane transverse reinforcements, applied load and displacement. Also in this case, VecTor2 default material properties and analysis options have been adopted except for the concrete constitutive model by Popovic and Mander [17], [18] is adopted to reproduce concrete compressive behavior.

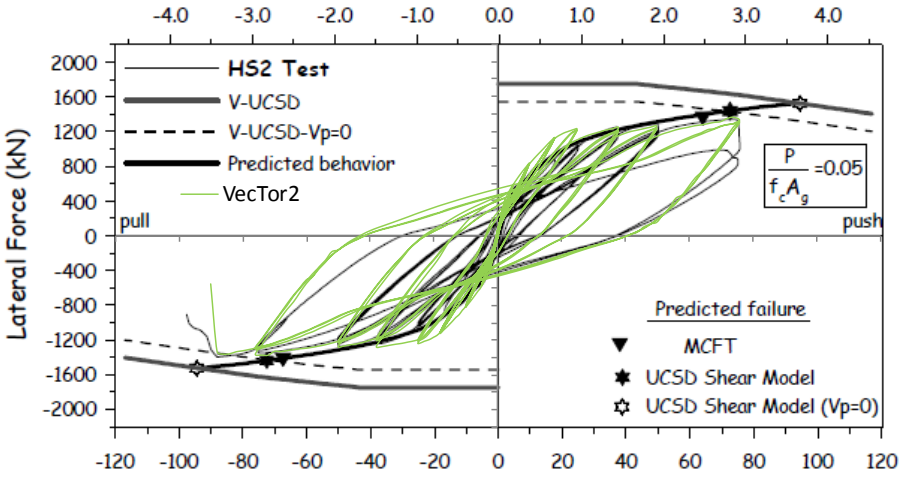


Figure 2: Comparison of experimental and analytical response for HS2 column [16].

The VecTor2 numerical model show a good match with experimental results in terms of strength and deformability subjected to monotonic and cyclic loads. Thus, because no calibrations have been made in order to fit the experimental results, it can be adopted for the prediction of the structural response of hollow circular column that failed in shear. Response 2000 is also adopted to estimate the column shear strength, as a reference value. Although a good match with experimental results has been achieved for the selected hollow circular columns, it is less accurate than VecTor2 in the estimation of the member deformations. This is due to the assumption at the base of the MCFT that assumes no slip on the cracks and could not work properly in the disturbed stress field regions as at the base of the column in which there is a significant flexural-shear interaction.

Another aspect that should be considered in modelling the bridge piers is the presence of smooth longitudinal reinforcements that strongly affects the structural behavior of reinforced concrete columns [19]–[22]. The significant slip at the interface of concrete and reinforcements commonly resulted in a characteristic failure mode, with a large crack at the column base and a significant rocking mechanism. The numerical modelling of the structural members with smooth bars is quite a challenging task. The significant slip between concrete and internal reinforcements fight against the basic assumption of perfect bond of the classic theories of RC. VecTor2 can use a piecewise linear bond slip model in terms of τ-slip to account for the effective slip between concrete and reinforcements at each node of the 2D mesh. The

adopted numerical model was validated against experimental results on a shear critical frame tested by Paolacci and Giannini (2012) (Del Vecchio et al. 2015). However, a more specific validation at the column level is required to evaluate the accuracy of the model predicting the strong nonlinear behavior at high level of ductility characterized by marked rocking mechanism. For this purpose the experimental test on underdesigned RC column tested by Verderame et al. [19], [20] are adopted for the validation. The selected test (M270-A1) allows also to account of the overlap length of the longitudinal reinforcements at the column base. This is a typical construction detail that can be properly accounted only with an accurate modelling of the bond-slip behavior. Furthermore, the base overlapping may strongly affect the structural response due to the stress concentrations at the hooked ends detrimental for other local phenomena such as bar buckling and bond degradation.

The smooth internal reinforcements have been modeled by using link elements in VecTor2. A typical bond-slip behavior in terms of τ-slip directly derived from pull-out tests have been adopted to characterize the link elements along the bar and in correspondence of hooked anchorages [21]. These elements have been inserted in each node of the mesh between the concrete and the truss elements adopted for the longitudinal reinforcements.

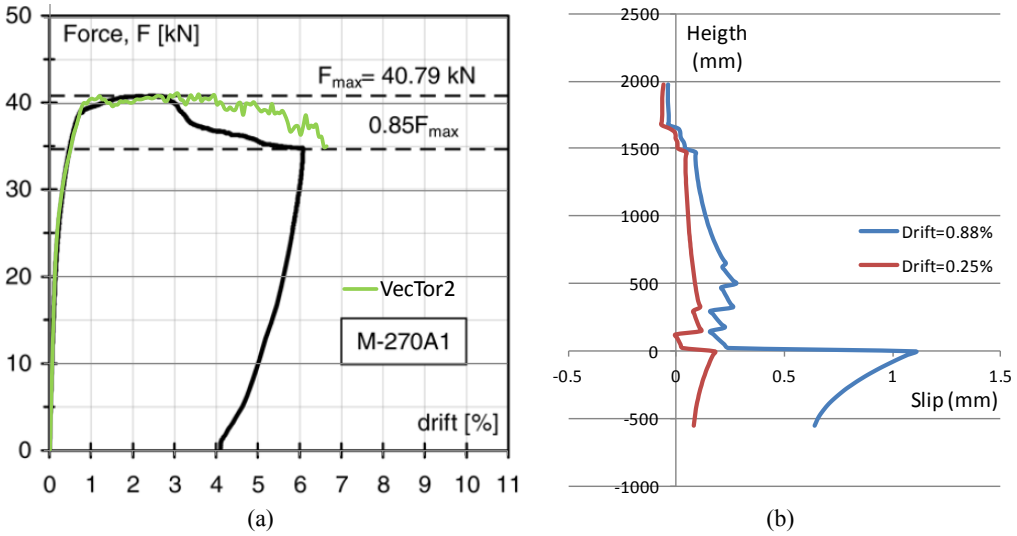


Figure 3: (a) Comparison between experimental results (Verderame et al. 2008) and adopted numerical models (VecTor2); (b) Analytical slip distributions along member height.

The comparison with experimental results in Figure 3a, demonstrated the accuracy of the proposed analytical model reproducing the column monotonic behavior and the failure mode characterized by a significant rocking followed by concrete crushing. The slip distribution in Figure 3b shows that before the first cracking (red line) the slip is uniformly distributed along the specimen height. On the other side, at the yielding of longitudinal reinforcements (blue line) the slip are concentrated at the column base. This allows the use of simplified numerical models (i.e. OpenSees model with strain penetration model at the column base, Bond_SP01 command) to reproduce the nonlinear behavior of columns with smooth internal reinforcements [23]. However, this model can lead to initial stiffness overestimation because of slip concentration at the column base instead of a more realistic uniform distribution along the height in the elastic range. Thus, a proper calibration of the slip at the significant point of the longitudinal reinforcement stress is needed.

2.4 Pier response prediction

A monotonic push-over analysis was carried out with VecTor2 nonlinear FEM model in order to define the nonlinear behavior of the two bridge piers. The member dimensions and the cross section details are those reported in Figure 1. In compliance with the design assumption and preliminary tests, the material properties adopted in the analysis are: concrete compressive strength f_{cm}=24MPa; the steel adopted for the ϕ10 longitudinal reinforcements is characterized by f_{ym}=370MPa and an ultimate stress f_{su}=480MPa. The elastic modulus is about 195000MPa, the strain at the hardening ε_{sh}=0.0032 and ultimate strain ε_{su} = 0.022. The steel adopted for ϕ6 transverse reinforcement is characterized by a f_{ym}=400MPa and an ultimate stress fsu=480MPa. The elastic modulus is about 195000MPa, the strain at the hardening ε_{sh}=0.0035 and ultimate strain ε_{su} = 0.017. The adopted mechanical properties are in compliance with mechanical characterizations of the steel AQ50 reported in available literature studies ([20], [22], [24]).
The column axial load is computed considering a normalized axial ν load equal to 0.05 (where $\nu=N/(A_c f_{cm})$). Because of the differences in the effective column cross section, axial force about 254kN and 340kN loads the hollow and the circular column, respectively.
The Vector2 modelling procedure described in the previous sections (including bar bond-slip, circular-hollow cross section, longitudinal reinforcement overlapping) has been adopted. The pier model includes the foundation block and the pier cap. The imposed external force and displacement have been applied at the pier cap in compliance with test setup for shaking table tests. The response prediction for both the piers is reported in Figure 4.

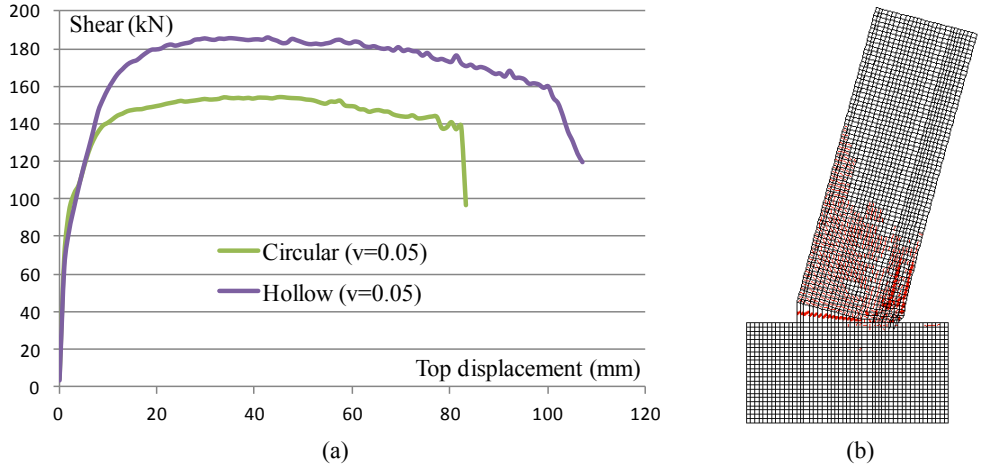


Figure 4: VecTor2 response prediction for both bridge piers: (a) monotonic response; (b) detected failure mode.

The monotonic response of the two piers shows a typical nonlinear behavior of RC column with smooth internal reinforcements. The high initial stiffness depends by the low member aspect ratio (L/h≈2), typical of squat columns. Although a low amount of transverse reinforcement has been adopted, a ductile failure mode occurs. This is related to the significant slip of the longitudinal reinforcements at the column base which allows the concentration of inelastic deformation at the column base. Once that the reinforcement yielding has been achieved, a marked nonlinear behavior without significant hardening phenomena occurs. For large displacement demands, significant rocking phenomena can be detected. The concrete crushing and bar buckling limit the member ductility. The crack pattern analysis at the failure mode, confirmed this trend, also pointed out in other experimental tests [19], [20], [22], [23].

Both sample piers, i.e. the hollow and the circular piers, have a structural behavior characterized by a marked rocking mechanism. Due to the high strength and stiffness degrading phenomena of the pier response, a more accurate characterization can be achieved performing a quasi-static cyclic analysis with increasing top displacement.

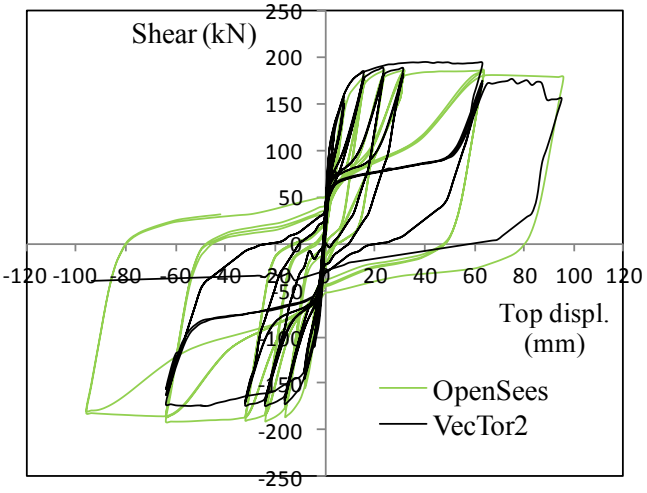


Figure 5: Comparison of the two proposed analytical models for the hollow bridge pier.

The cyclic response is similar to the monotonic response in terms of maximum shear strength both for the circular and hollow piers (see Figure 5). Significant differences can be observed in terms of the ultimate displacement capacity. The cyclic response is characterized by a displacement capacity lower than the monotonic response and this is related to the concrete and bond degradation. The ultimate displacement capacity, conventionally measured in correspondence of a strength reduction of the 20% respect to the peak strength, is about 72 mm (5.3% Drift) for the hollow pier and 58 mm (3.9% Drift) for the circular one. Both the drift and top displacement are measured in correspondence of the pier top end. The cyclic response shows marked pinching effects, typical of rocking mechanism related to significant slips at the column base.

2.5 OpenSees models

With the scope to achieve a wide seismic characterization of the bridge subassemblies by means of nonlinear time-history analysis (NLTH) a more efficient numerical models need to be created. The latter requirement is due to the large computational demand associated with VecTor2 software [8], [9]. In compliance with consolidated modelling procedures for RC columns [8]–[10], an OpenSees non-linear fiber model has been created including the foundation block and the pier cap. In the fiber model, three different materials are used to represent the cyclic behavior of column cross sections: the confined and unconfined concrete is simulated with the nonlinear *Concrete01* material; the longitudinal reinforcement is modelled with the *Reinforcing Steel* uniaxial material with isotropic strain hardening. This command is strongly suggested for dynamic model of RC elements subjected to input motion, in order to accurately reproduce energy dissipation and residual displacements [25]. The confining effects of transverse reinforcement on the mechanical properties of the concrete core are calculated according to Mander et al. [18]. The ultimate compressive strain of confined concrete is calculated according to Fardis [26]. The uniform radial discretization scheme is employed, and each section is divided into 50 fibers in circumferential direction, 8 fibers in the radial direction in the core, and 2 fiber in the radial direction in the cover. The *Bond_SP01* command is used to in-

clude in a *zeroLengthSection* element the effect of bar slip and strain penetration at the column base as suggested by Arani et al. [23] and with opportune calibration of the slip parameters. Five integration points along the finite elements have been adopted, thus allowing the spreading of inelasticity to be accurately described. Applied axial load (P) and cyclic displacement (Δ) are determined in accordance with the VecTor analysis. The P-Δ effects are accounted by means of the geometric transformation tool *PDelta Transformation*. The Newton-Raphson solution algorithm is adopted to solve model nonlinear equations.
The OpenSees model provides a close match to the the VecTor 2 prediction except for the strength loss at the ultimate displacement (see Figure 5). For this reason the ultimate displacements pointed out by the VecTor2 analysis should be adopted to identify the collapse.

In order to validate the OpenSees modelling procedure also for dynamic loads, the proposed analytical model has been adopted to predict the dynamic response of shaking table tests performed by Hachem et al. [27]. The effects of added mass are accounted both in the lateral and rotational displacements. Furthermore additional viscous damping proportional to the current stiffness has been included in the model by means of the *Rayleigh Damping* command with the initial value of 2% as suggested by Petrini et al. [28]. The input motion has been defined by means of the *UniformExcitation* pattern in terms of acceleration history. The analysis has been performed with the *AccelSeries* command with a time step of 0.01s. The results of the comparison is reported in the Figure 6.

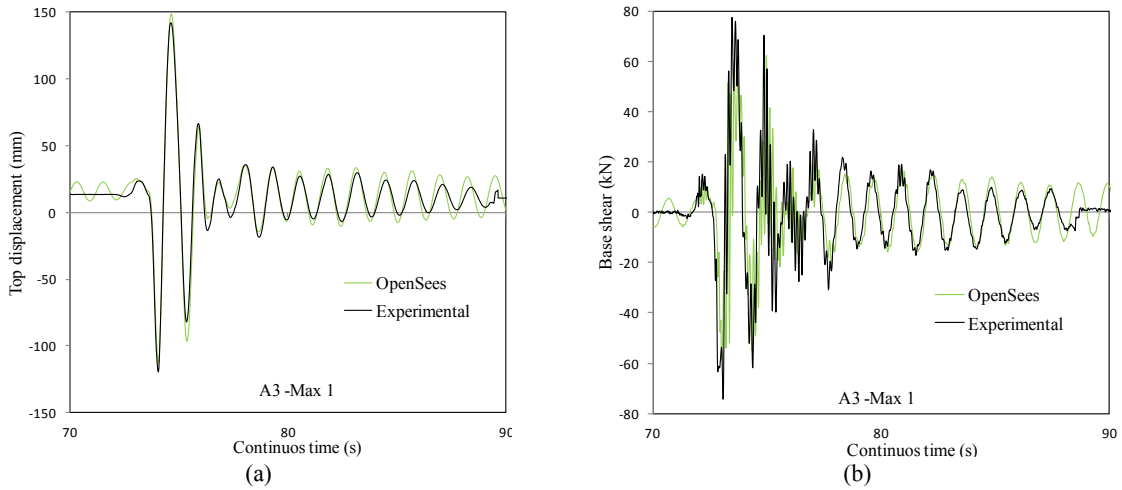


Figure 6: Comparison of experimental test and analytical results in terms of top displacement history; (a) run A3-Max1 (peak displacement); (b) base shear comparison at run A3-Max1.

The results presented in Figure 6 show the accuracy of the numerical modeling in predicting the dynamic behavior of the bridge pier. Comparing the displacements and the base shear history of the A3-Max1 run (Figure 6a and b), a close match with experimental results has been achieved. A low scatter of about 10% has been achieved in the estimation of maximum displacement.

Once that the proposed modelling procedure has been validated for dynamic loads, the numerical model of the entire bridge subassembly has been created. The OpenSees model is composed of two bridge piers modeled in order to reproduce the VecTor2 hysteretic response predictions and including dynamic properties and input motion as proposed for the Hachem et al. [27] pier. In order to include the FP isolator on the top of the left pier, a *zeroLength* element has been introduced between node 7 and 8 not included in the Rayleigh damping calculation. The FP hysteretic behavior has been reproduced by means of the Steel01 uniaxial

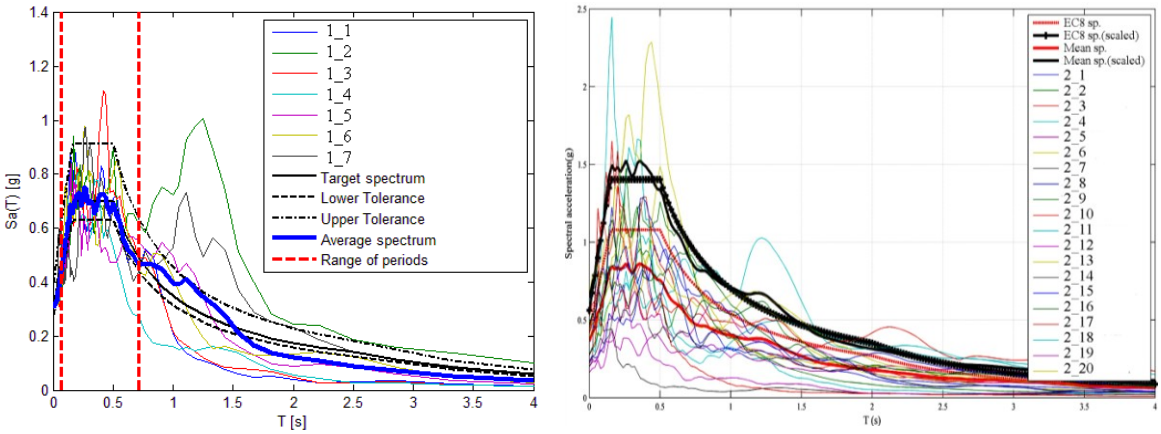
material in the horizontal direction. In order to match the experimental behavior of tested FP and considering that two FP devices support the bridge deck on the left pier, the following parameters have been set: yielding force F_y=5000N, initial elastic modulus E=10000MPa, hardening ratio b=0.0036. The authors want to specify that this model is properly built to have preliminary results to make a subassembly characterization for shaking table tests. Thus, the analyzed support configurations (pin-roll or isolated-roll) may not reflect the real ones.

The eigenvalue analysis and the analysis of the response to a white-noise signal carried out before the record motion analysis showed a fundamental period (T_1) ranging between 0.10 and 0.12s for the simply supported configuration. Using higher amplitude signal the period evolves until 0.4s at the ultimate displacement. A period significant higher has been detected for the isolated bridge. It ranges between 2.2 and 4s.

3 INCREMENTAL DYNAMIC ANALYSIS

3.1 Record selection

Two sets of record motions have been selected for this study. The records have been selected basing on the hazard disaggregation for the site selected for this study. In particular, the sets consists of far-field records with a magnitude in the range 5.2-7.0 and epicentral distance in the range of 10–30 km. The first set of records has been selected respecting the spectrum compatibility with the design response spectrum built in compliance with Italian building code [29] at the life safety limit state for a soil type B by means of the REXEL software [30]. As reported in Figure 7a, the spectrum compatibility is guaranteed in the entire range of variation of the structural period for the as-built configuration. However, it can be observed that by scaling the selected records, the average response spectrum matches the target spectrum also for period larger than 2.0s. Thus, the same set can be used in the seismic assessment of the isolated system. Because few records matching these requirements can be found in the European strong motion database, a new set of records has been selected from the PEER strong motion database of worldwide records. The record selection has been performed with the software ISSARS [31] by matching the EC8-pt2 Bridges spectrum [32]. The target spectrum for a soil type B and reference PGA 0.36 has been adopted to match the average response spectrum. All the records are on a C/D soil type, according to the National Earthquake Hazards Reduction Program (NEHRP) classification. As depicted in Figure 7b, an acceptable spectral matching has been achieved at all the periods and this allow to use the same records both for as-built and isolated configuration. The damage factor (ID) [33] was computed for all records, and only records with a reduced damage were selected. This specific rule was included in the selection of records because it allows the consideration of ground motion properties (e.g., number of plastic cycles and energy content of earthquake) that can strongly affect the dynamic response of SSD systems. More details about the selected records are reported in Table 1and Table 2.



(a) (b)

Figure 7: Spectrum compatibility of the selected records: (a) set 1; (b) set 2.

N°	Event	Location	Station ID	Year	M	EC8 Site Class	Epic. Dist.	PGA	PGV	I_A	I_D
[-]	[-]	[-]	[-]	[-]	[-]	[-]	[km]	[g]	[cm/s]	[cm/s]	[-]
1_1	Patras	Greece	ST178	1993	5.6	B	27	0.05	4.7	2.7	7.3
1_2	Campano-Luc.	Italy	ST276	1980	6.9	B	16	0.16	26.8	104.9	16.0
1_3	Patras	Greece	ST178	1993	5.6	B	27	0.04	2.3	2.1	13.8
1_4	Potenza	Italy	ST103	1990	5.8	B	24	0.04	1.9	1.5	14.4
1_5	Almiros-aftersh.	Greece	ST1300	1980	5.2	B	14	0.07	5.5	4.7	7.6
1_6	aftershock	Montenegro	ST77	1979	6.2	B	20	0.06	4.3	4.1	11.0
1_7	aftershock	Montenegro	ST63	1979	6.9	B	24	0.30	38.5	185.1	10.3

M, earthquake magnitude; EC8, Eurocode 8; Epic. Dist., Epicentral distance; PGA, peak ground acceleration; PGV, peak ground velocity; I_A, Arias intensity; I_D, damage factor.

Table 1: Set 1 of earthquake records selected for the study.

3.2 Scaling procedure

The proposed advanced numerical models have been used to run NLTHs. The intensity measure (IM) is represented by the spectral acceleration for the elastic period $Sa(T_1, 5\%)$, while the pier top displacement, measured in correspondence of the pier top end, is adopted as damage index (ID). The ultimate capacity is fixed at the displacement identifying the collapse of the piers or the FP devices. However, due to the high variability of the nonlinear dynamic response, a proper estimation of the motion intensity at the collapse is not easy. As a result, the nonlinear dynamic analyses have been carried out according to the IDA procedure [17]. The Hunt and Fill optimized scaling procedure has been adopted to scale the record to incremental IMs, optimizing the number of runs to identify the collapse with an accepted level of confidence (i.e. 10%).

A total of 1300 NLTH analyses have been carried out for the four studied structural systems. Twelve runs at different IMs for the two sets of record motions (7 and 20 records, respectively) were required to properly assess the seismic capacity. The results of the analysis in the form of IDA curves are reported in Figure 8. Although the spectral acceleration has been used as IM to scale the selected records, the results are presented in terms of PGA in order to allow the comparison between the as-built and isolated configuration.

N°	Event	Location	Station	Year	M	NEHRP Soil	Epic. Dist.	PGA	PGV	I_A	I_D
[-]	[-]	[-]	[-]	[-]	[-]	[-]	[km]	[g]	[cm/s]	[cm/s]	[-]
2_1	Imp. Vall.-02	California	El Centro Arr #9	1940	7.0	D	13	0.26	29.7	170.4	14.2
2_2	Friuli-01	Italy	Tolmezzo	1976	6.5	C	20	0.35	22.0	78.0	6.5
2_3	Tabas	Iran	Dayhook	1978	7.4	C	21	0.35	20.5	142.3	12.6
2_4	Imp. Vall.-06	California	El Centro Arr #10	1979	6.5	D	26	0.21	47.5	56.8	3.7
2_5	Irpinia-01	Italy	Calitri	1980	6.9	C	15	0.15	16.4	57.8	14.7
2_6	Corinth	Greece	Corinth	1981	6.6	D	20	0.26	23.3	69.3	7.2
2_7	Nahanni	Canada	Site 3	1985	6.8	C	22	0.15	6.1	28.3	19.7
2_8	New Zeal-02	New Zeal.	Matahina Dam	1987	6.6	C	24	0.29	21.7	65.2	6.5
2_9	Super.H.-02	California	Westm. Fire Sta	1987	6.5	D	20	0.21	23.5	80.3	10.4
2_10	Super.H.-02	California	Wildl. Liquef. Arr	1987	6.5	D	29	0.19	29.9	69.4	7.7
2_11	Loma Prieta	California	UCSC Lick Obs.	1989	6.9	C	16	0.46	18.7	266.1	19.9
2_12	Cape Mend.	California	Fortuna-Blvd	1992	7.0	C	30	0.12	29.9	26.1	4.7
2_13	Cape Mend.	California	Rio Dell Over-FF	1992	7.0	D	23	0.42	43.8	152.3	5.2
2_14	Landers	California	Desert Hot Sprin.	1992	7.3	D	27	0.14	20.0	70.7	15.9
2_15	Landers	California	Morongo Valley	1992	7.3	D	21	0.16	16.6	95.8	22.8
2_16	Northrid.-01	California	Arleta-Nord Fire St	1994	6.7	D	11	0.33	40.4	152.3	7.3
2_17	Northrid.-01	California	Glendal -Las Palm.	1994	6.7	C	30	0.26	12.2	117.2	23.8
2_18	Kobe	Japan	Kobe University	1995	6.9	C	25	0.30	54.8	122.3	4.7
2_19	Duzce	Turkey	Lamont 1059	1999	7.1	C	24	0.13	12.0	38.2	15.5
2_20	Hector Mine	California	Hector	1999	7.1	C	27	0.31	28.6	83.0	6.1

M, earthquake magnitude; NEHRP, National Earthquake Hazards Reduction Program; Epic. Dist., Epicentral distance; PGA, peak ground acceleration; PGV, peak ground velocity; I_A, Arias intensity; I_D, damage factor.

Table 2: Set 2 of earthquake records selected for the study.

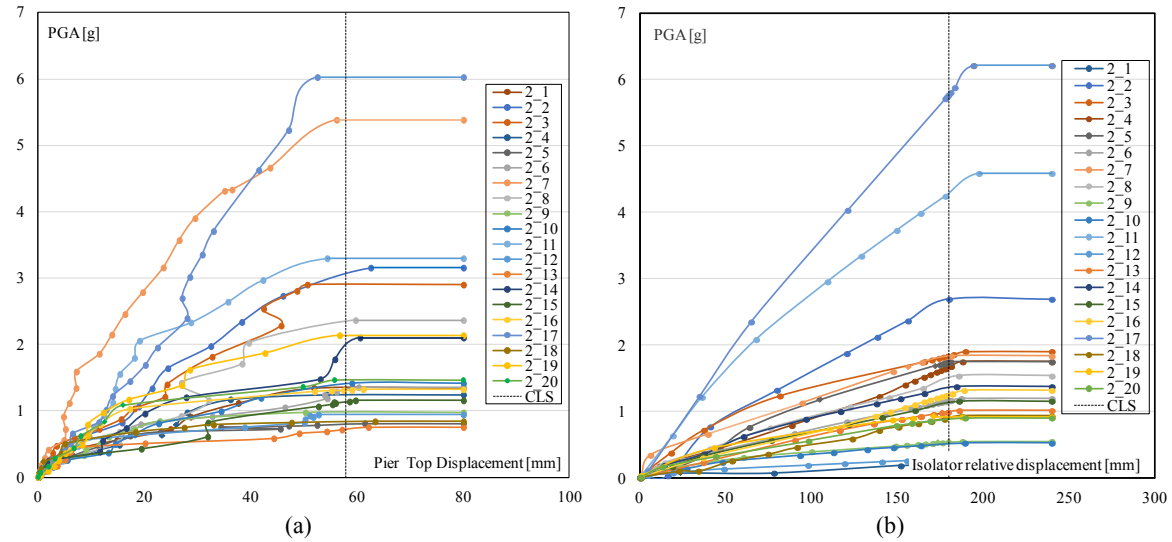


Figure 8: IDA curves for bridge subassembly with circular piers: (a) Set 2 "as-built" configuration; (b) Set 2 isolated.

The results of NLTHs can be useful to make important considerations on the variability of the seismic performances with the input motion, pier type and on the effectiveness of the FP isolators. The median PGA at the collapse limit state are reported in Table 3 for the eight differ-

ent test configurations. The collapse limit state it has been identified with the ultimate placement of column or bearings.

	Median PGA [g] at the collapse			
	as-built		isolated	
Set	Circular (58mm)	Hollow (72mm)	Circular (180mm)	Hollow (180mm)
1 (7 records)	1.253	1.708	3.504	3.304
2 (20 records)	1.403	1.606	1.261	1.103

Table 3: Summary of the Median values in terms of PGA at the collapse of the piers or the FP for the 8 analyzed configurations.

Because the safety check on the seismic demand requirements for the selected bridge is out of the scope of this paper, only some considerations on the effects on the seismic response of pier type, input motion and support configuration are made. The NLTHs confirm the higher seismic capacity of the bridge pier with hollow cross section, due to the displacement capacity higher than the circular pier. The Median PGAs at the collapse of the two piers are almost in the same ratio as for the displacement at the collapse. This because the initial stiffness is very similar and only significant differences in the ultimate displacement and yielding strength can be appreciated (see Figure 5). No significant differences can be observed in the results respect to the input motion variability. The use of FP isolators allow to move the failure from the piers to the devices. In fact, FP devices allow to strongly reduce the acceleration transmitted to the piers, which response becomes essentially elastic not exceeding the flexural cracking. The comparisons in terms of median PGA between the as-built and isolated configuration shows a slight reduction in maximum seismic demand for the isolated systems. This results can be related to the variability of the input, but also to the configuration of the isolators, placed on the left pier only, while they have been designed to be applied on both piers. Further analysis are required to characterize the response of the bridge in the other configurations.

The high variability in the seismic response of the isolated systems respect to the set of input motions can be related to the particular spectral shape in terms of displacements of the records of the set 1. This evidence point out that further analysis, with displacement spectra matching the target displacement spectrum, are needed in order to accurately characterize the seismic response of the isolated systems.

The NLTHs can be used also to select the input motion for shaking table tests. For this purpose, one of the record of the set 2 has been selected. Although, the records of the set 1 are all selected from the European strong motion database, and, thus more representative of the Italian earthquakes, they have a spectral shape in term of displacement irregular with a descending slope for long periods. The selected record should be close, as much as possible, to the median value of the PGA both for the as-built and isolated configuration.

4 CONCLUSIONS

The present paper deals with the numerical seismic assessment of a bridge subassembly which will be tested on shaking tables. A total of 1300 NLTHs have been carried out investigating the variability of pier type (i.e. circular or circular-hollow cross-section), input motion variability and support configuration (with or without FP devices). To be representative of the real behavior of the structural system and provide reliable information to design a shaking table test program, an advanced numerical model has been created. The model was built in the

OpenSees environment, however to reliable predict the pier hysteretic response, preliminary analysis with VecTor2 program have been conducted. In fact, the presence of smooth longitudinal reinforcements and the lack of proper transverse reinforcements may allow the occurrence of premature shear failure or other nonlinear phenomena which is typical of old-type members and difficult to be accounted for in the classical fiber-based program. The model has been validated at different levels against experimental results.

Preliminary results of NLTHs show the influence of pier ductility on the seismic response and the effectiveness of the adopted seismic isolation solution is demonstrated. The use of FP devices as supports for the bridge deck limits the inertial force transmitted to the piers. The piers remained mostly in elastic range. Further considerations can be made on the effectiveness of the proposed record selection for seismic isolated structures. In fact, the spectral matching with the target acceleration spectrum does not allow to control the variability in the response of displacement sensitive systems. High variability in the seismic response is pointed out comparing the response of isolated bridge subjected to the records of set 1 and set 2. This emphasizes that a more appropriate record selection considering the displacement spectra is needed. The final results of this study can be useful to determine the support configurations and the earthquake signal for shaking table tests.

ACKNOWLEDGMENTS

The work carried out was funded by the Seventh Framework Programme of the European Commission under the PIRSES-GA-2009-247567-EXCHANGE-SSI (Experimental & Computational Hybrid Assessment Network for Ground-Motion Excited Soil-Structure Interaction Systems) grant (www.exchange-ssi.net). The experimental test program presented herein is funded by the Ministry of Research through the Project PON-FESR 2007-2013 (PON01_02366, STRIT) “Tools and Technologies for the Management of the Transportation Infrastructures”.

REFERENCES

[1] A. S. Elnashai and L. Di Sarno, *Fundamentals of Earthquake Engineering*. John Wiley & Sons Ltd, 2008, p. 373.

[2] A. Lupoi, P. Franchin, and M. Schotanus, “Seismic risk evaluation of RC bridge structures,” *Earthq. Eng. Struct. Dyn.*, vol. 32, no. 8, pp. 1275–1290, 2003.

[3] E. Choi, R. DesRoches, and B. Nielson, “Seismic fragility of typical bridges in moderate seismic zones,” *Eng. Struct.*, vol. 26, no. 2, pp. 187–199, 2004.

[4] B. Nielson and R. DesRoches, “Analytical seismic fragility curves for typical bridges in the central and southeastern United States,” *Earthq. Spectra*, vol. 23, no. 3, pp. 615–633, 2007.

[5] A. J. Kappos, M. S. Saiidi, M. N. Aydınoğlu, and T. Isaković, *Seismic Design and Assessment of Bridges - Inelastic Methods of Analysis and Case Studies*. Series: Geotechnical, Geological and Earthquake Engineering, Vol. 21 Springer, 2012.

[6] G. Della Corte, R. De Risi, and L. Di Sarno, “Design and analysis of bilinear isolation systems for transverse seismic response of continuous bridges,” *ASCE J. Bridg. Eng.*, vol. 18, no. 11, pp. 1121–1130, 2013.

[7] Regio Decreto Legge (R.D.L.) 2229-1939, “Norme per l’esecuzione delle opere in conglomerate cementizio semplice o armato. [Guidelines for the execution of concrete structures] (in Italian).”

[8] X. Huang and O.-S. Kwon, “Numerical Models of RC Elements and their Impacts on Seismic Performance Assessment,” *Earthq. Eng. Struct. Dyn.*, vol. 44, no. 2, pp. 283–298, 2015.

[9] C. Del Vecchio, O. Kwon, L. Di Sarno, and A. Prota, "Accuracy of nonlinear static procedures for the seismic assessment of shear critical structures," *Earthq. Eng. Struct. Dyn.*, vol. (published, 2015). doi: 10.1002/eqe.2540.

[10] C. Del Vecchio, L. Di Sarno, O. Kwon, and A. Prota, "Validation of Numerical Models for RC Columns Subjected to Cyclic Load," in *COMPDYN 2013, 4th ECCOMAS Thematic Conference on Computational Methods in Structural Dynamics and Earthquake Engineeering*, 2013, no. June, pp. 1958–1974.

[11] The Regents of the University of California, "OpenSees: Open system for earthquake engineering simulation." Pacific Earthquake Engineering Research Center College of Engineering University of California, Berkeley.

[12] P. S. Wong, F. J. Vecchio, and H. Trommels, "VecTor2 & FormWorks User's Manual. Second Edition," Toronto, ON, Canada, 2013.

[13] F. J. Vecchio, "Disturbed Stress Field Model for Reinforced Concrete: Formulation," *ASCE J. Struct. Eng.*, vol. 126, no. 9, pp. 1070–1077, 2000.

[14] F. J. Vecchio, E. C. Bentz, and M. P. Collins, "Tools for forensic analysis of concrete structures," *Comput. Concr.*, vol. 1, no. 1, pp. 1–14, 2004.

[15] M. P. Collins, E. C. Bentz, and J. Kim, "Shear Strength of Circular Reinforced Concrete Columns," *ACI J.*, vol. SP 197–3, pp. 45–85.

[16] G. Ranzo and M. J. N. Priestley, "Seismic performance of large rc circular hollow columns," in *12 WCEE*, 2000, pp. 1–8.

[17] S. Popovic, "A numerical approach to the complete stress-strain curve of concrete," *Cem. Concr. Res.*, vol. 3, no. 5, pp. 583–599, 1973.

[18] J. B. Mander, M. J. N. Priestley, and R. Park, "Theoretical Stress-Strain Model for Confined Concrete," *ASCE J. Struct. Eng.*, vol. 114, no. 8, p. 1804, 1988.

[19] G. Verderame, G. Fabbrocino, and G. Manfredi, "Seismic response of r . c . columns with smooth reinforcement . Part II : Cyclic tests," *Eng. Struct.*, vol. 30, pp. 2289–2300, 2008.

[20] G. Verderame, G. Fabbrocino, and G. Manfredi, "Seismic response of r . c . columns with smooth reinforcement . Part I : Monotonic tests," *Eng. Struct.*, vol. 30, pp. 2277–2288, 2008.

[21] F. Paolacci and R. Giannini, "An experimental and numerical investigation on the cyclic response of a portal frame pier belonging to an old reinforced concrete viaduct," *Earthq. Eng. Struct. Dyn.*, vol. 41, pp. 1109–1127, 2012.

[22] M. Di Ludovico, G. M. Verderame, A. Prota, G. Manfredi, and E. Cosenza, "Cyclic Behavior of Nonconforming Full-Scale RC Columns," *J. Struct. Eng.*, 2014.

[23] K. Arani, M. Di Ludovico, M. S. Marefat, and A. Prota, "Lateral Response Evaluation of Old Type Reinforced Concrete Columns with Smooth Bars," *ACI Struct. J.*, vol. 111, no. 1–6, pp. 1–12, 2014.

[24] G. M. Verderame, P. Ricci, M. Esposito, and F. C. Sansiviero, "Le Caratteristiche Meccaniche degli Acciai Impiegati nelle Strutture in c.a. realizzate dal 1950 al 1980," in *XXVI Convegno Nazionale AICAP*, 2011.

[25] H. I. L. Jeong, J. Sakai, and S. A. Mahin, "PEER report 2008/06: Shaking Table Tests and Numerical Investigation of Self-Centering Reinforced Concrete Bridge Columns," 2008.

[26] M. N. Fardis, *Seismic Design, Assessment and Retrofitting of Concrete Buildings (Based on EN-Eurocode8)*, Series: Ge. Istanbul, Turkey: Springer, 2009.

[27] M. M. Hachem, S. A. Mahin, and J. P. Moehle, "Performance of Circular Reinforced Concrete Bridge Columns under Bidirectional Earthquake Loading," Berkeley, 2003.

[28] L. Petrini, C. Maggi, M. J. N. Priestley, and G. M. Calvi, "Experimental Verification of Viscous Damping Modeling for Inelastic Time History Analyzes," *J. Earthq. Eng.*, vol. 12:S1, no. July 2014, pp. 125–145, 2008.
[29] MI, *D.M. 14 Gennaio 2008 (D.M. 2008). Technical codes for structures (in Italian)*, GU n°29, F. Rome, Italy, 2008.
[30] I. Iervolino, C. Galasso, and E. Cosenza, "REXEL: Computer aided record selection for code-based seismic structural analysis," *Bull. Earthq. Eng.*, vol. 8, pp. 339–362, 2010.
[31] E. I. Katsanos and A. G. Sextos, "ISSARS: An integrated software environment for structure-specific earthquake ground motion selection," *Adv. Eng. Softw.*, vol. 58, pp. 70–85, 2013.
[32] European Commitee for Standardization, *Eurocode 8: Design of structures for earthquake resistance. Part 2: Bridges.*, vol. 3. Brussels, Belgium, 2005, pp. 1–232.
[33] E. Cosenza and G. Manfredi, "Damage indices and damage measures," *Prog. Struct. Eng. Mater.*, vol. 2, no. 1, pp. 50–59, 2000.

COMPDYN 2015
5th ECCOMAS Thematic Conference on
Computational Methods in Structural Dynamics and Earthquake Engineering
M. Papadrakakis, V. Papadopoulos, V. Plevris (eds.)
Crete Island, Greece, 25–27 May 2015

OBJECTIVE EVALUATION OF THE q FACTOR OF IRREGULAR RC BUILDINGS DESIGNED ACCORDING TO EC8 - DESIGN AND ANALYSES PROCEDURES

Vasiliki V. Anagnostopoulou[1], Efstratios K. Volakos[1], and Christos A. Zeris[1]

[1] Laboratory of Reinforced Concrete, School of Civil Engineering
National Technical University of Athens
5, Iroon Polythechniou, Zografou, 15780, Athens, Greece

e-mails: vantua@central.ntua.gr, stratis_v@live.com, zeris@central.ntua.gr

Keywords: Vertical irregularity, Behavior factor, OpenSees, RC buildings, EC8.

Abstract. *The seismic design of reinforced concrete (RC) mass or stiffness irregular buildings, in accordance with the classifications of Eurocode 8, is adjusted through the quantification of irregularity, through the use of irregularity indices and corresponding irregularity criteria. As a consequence, the design behavior factor in this case is no longer constant over a group of structures of similar form and building material, but varies on a case by case basis, since it involves modification of both behavior factors defining the design q, namely q due to structural overstrength (q_Ω) and q due to the local ductility supply of the members (q_μ). The reliability of this design approach is evaluated herein through the investigation of the inelastic performance of a form of irregular building with different degrees of irregularity per EC8. Focusing primarily herein - for the sake of simplicity - on vertical irregularity, an automated and therefore objective design analysis procedure is presented, which has been developed on the Open System of Earthquake Engineering Simulation platform (OpenSees). Following the definition of the basic framing configuration, characteristic loads and material grades, the procedure includes the following automatic steps: i) successive analysis of the frame for all EC8 required combinations, ii) evaluation of the internal design forces and envelopes thereof, iii) evaluation of flexural and shear reinforcement in all member critical regions, iv) evaluation of the local ductility supply of the members, v) formulation of the inelastic three-dimensional model of the structure (base is assumed fixed), using spread damage fiber section finite elements, vi) three dimensional analysis of the model both statically (modal load profiles) and in the time domain (incremental base excitation); and vii) establishment of response details and damage indices, such as seismic shear and deformation profiles, the collapse pattern, local and global ductility and supplied q. Given the module versatility, different levels of vertical and/or torsional irregularities can be established by removing selected structural members in plan, by adjusting selectively the plan or height geometry or by locally increasing the acting vertical loads. The process is applied to a typical tower; the code prescribed design procedure and irregularity indices are imposed and their reliability is established through local damage comparisons with the assumed design values.*

1 INTRODUCTION

Various functional and architectural requirements render important the presence of vertical irregularities in geometry, stiffness or mass between adjacent stories or continuous with height. Such vertical discontinuities increase the sensitivity to damages from earthquake ground motions and there are many examples of building failures in past earthquakes due to vertical irregularities. So, the engineer needs to have a thorough understanding of the seismic response of such irregular structures and reliable guidelines for the establishment of a safe, economic and reliable structural design that accounts for such irregularity, during inelastic response.

Several studies have been carried out in order to evaluate the seismic response of irregular buildings. Concentrating our emphasis on vertically irregular buildings, Aranda [1] and Shahrooz and Moehle [2] compared the ductility demands of regular and setback structures by analyzing such systems. They concluded that setback structures demand higher ductility than regular structures and the effect is more pronounced in the tower portion of the building. Das and Nau [3] observed the same as aforementioned authors. In more detail, they observed that the presence of irregularity alters the inelastic response of the building causing marked increases in the inelastic story drift in the vicinity of the irregularity and results in large increases in curvature ductility demands in plastic regions.

Ruiz and Diederich [4] examined the seismic performance of buildings with a weak first story. They concluded that the behavior of such irregular buildings greatly depends on the ratio of the dominant periods of excitation and response, the resistances of the upper to the first stories and the base shear coefficient used for design. Moreover, Nasaar and Krawinkler [5] evaluated their seismic demand parameters and found that the strength required for a specified target ductility ratio depends on the type of failure mechanisms that developed during severe earthquakes. Finally, they observed that the weak first story led to large variations in ductility and overturning moment demands.

Valmudsson and Nau [6] examined the earthquake response of multi-story framed structures with uniform mass, stiffness and strength distributions. They concluded that the response parameters were not dependent on mass and stiffness requirements, but only on strength. At the same time, Al-Ali and Krawinkler [7] focused on the effects of vertical irregularity by considering height-wise variations of the seismic demand and observed that mass irregularity was the least significant, while strength irregularity was more significant than stiffness irregularity. Moreover, stiffness and strength irregularity, in combination, was shown to be the most unfavorable factor under inelastic response.

Zeris et al. [8] examined the behavior factor q of vertically irregular plane reinforced concrete frames, designed according to Eurocode 8, with different heights in the first story. A computer design-nonlinear analysis algorithm was used in order to estimate q, which adopted collapse criteria of global or interstory drift and local curvature ductility comparisons in all the critical regions. Using the program DRAIN2D for inelastic analysis, the critical base excitation intensity was evaluated for a given earthquake record, at which nominal collapse was obtained due to the exceedance of the above collapse criteria. The procedure was applied in three six story, three bay RC frames with different first story heights; it was concluded that the estimated q were higher than those assumed for design, except from the frame with a relatively taller first story.

Repapis et al. [9] compared the earthquake response of typical regular and irregular in height existing RC buildings, designed with past non-conforming seismic provisions in Greece. The buildings differed in the form of discontinuity of their beams and columns or according to the distribution of masonry infills in height. They concluded that past building

generations with relatively short column spacing behaved relatively better, and that buildings with a taller first story behaved better than buildings with a penthouse recess or with short ground story columns due to the infill. Also, the influence of the distribution in height of the infill walls was significant, causing an increase in inelastic demands.

Chuny et al. [10] observed that irregular buildings in plan and elevation led to severe damage under strong earthquakes. Based on their results they proposed changes in their designs that contributed favorably to the seismic capacity of the irregular structure. Simultaneously, Sarkar et al. [11] investigated the vertical geometric irregularity in stepped building frames. They proposed a measure for vertical irregularity, involving the fundamental period of the stepped building superstructure, as a function of regularity index, which was shown to be more reliable than existing measures.

Contrary to all the above, Athanassiadou [12] examined multistory RC frame buildings, irregular in elevation, which have been designed to the provisions of the EC8 for the High (DCH) and Medium (DCM) ductility classes; the study concluded that the effect of the ductility class on the cost of buildings was negligible, while the seismic performance of all irregular frames appeared to be equally satisfactory, not inferior to (and in some cases superior than) that of their regular counterparts, even for base inputs twice as strong as the design earthquake. Moreover, Elassaly [13] examined the seismic response of irregular in height RC buildings, which had been designed according to the most common type of irregular buildings in Egyptian building environment. This type of buildings was distinguished from other studies in that it exhibited a varying first floor height. The study considered the seismic performance of such vertically irregular RC buildings and concluded that, in some cases, their response was superior to that of regular configuration, in terms of drift ratio and damage index limitations.

The above literature review reveals that the seismic behavior of setback or tower frames is a rather controversial issue, since some works indicate adequate seismic performance, while some others show the opposite for those frames. Therefore, more research work is needed in order to better understand the elastic and inelastic seismic response of such frames.

Several building codes address the seismic design of RC buildings having vertical irregularities. For example, in the recent version of IS 1893 (Part 1) - 2002 (BIS,[14]), an irregular configuration for buildings is being defined explicitly. In fact, five types of vertical irregularity are defined, namely: a) stiffness irregularity, b) mass irregularity, c) setback irregularity (in geometry), d) discontinuity in capacity, e) in-plane discontinuity in lateral-force-resisting elements in the vertical direction. Moreover, in the NEHRP code (BSSC,[15]) vertical irregularities are classified similar to IS 1893 (Part 1) - 2002 (BIS) while a structure is defined as irregular if the ratio of one of the system parameters (such as mass, stiffness or strength) between adjacent stories exceeds a minimum prescribed value. These values have been defined using judgmental criteria. In addition to the issue of irregularity classification, as a common denominator, building codes require the use of dynamic analysis methods for irregular structures to establish the design lateral force distribution, rather than using equivalent lateral force procedures.

In what follows, the irregularity quantification in accordance with the requirements of EC8 [16] are considered in more detail, since this is the design code whose special irregularity provisions are under investigation herein. In order to address more efficiently research with engineering practice, an automated design procedure is developed on the Open System of Earthquake Engineering Simulation (OpenSees) platform [18]. The main features of the procedure are presented in the following sections.

2 CRITERIA FOR REGULARITY OF BUILDINGS WITH SETBACKS IN EC8

In accordance with EC8 [16] building structures are categorized into being regular or non-regular for the purpose of seismic design. Vertical irregularity significantly affects the behavior factor *q*, which should be decreased in the case of the buildings being non-regular in elevation. In particular, for irregular buildings in elevation, the reduced values of the behavior factor are obtained by multiplying the reference values by 0.8. In EC8 [16] the behavior factor *q* is defined as follows (Eqn.1):

$$q=q_o \times k_w \geq 1.5 \tag{1}$$

where

q_o is the basic value of the behavior factor, dependent on the type of the structural system and its regularity in elevation. For buildings that are regular in elevation, in accordance with EC8, the basic values of q_o are given in Table 1, below.

k_w is the factor reflecting the prevailing failure mode in structural systems with walls (see EC8, Section 5.2.2.2, (11)P).

STRUCTURAL TYPE	Ductility Class Medium	Ductility Class High
Frame system, dual system, coupled wall system	3.0 α_u/α_1	4.5 α_u/α_1
Uncoupled wall system	3.0	4.0 α_u/α_1
Torsionally flexible system	2.0	3.0
Inverted pendulum system	1.5	2.0

Table 1: Basic values of the behavior factor q_o for systems which are regular in elevation.

α_u and α_1 as defined in EC8 [16].

For buildings which are regular in plan and for frames or frame - equivalent dual systems the following approximate values of α_u/α_1 may be used:

− One-story buildings: α_u/α_1=1.1.

− Multi-story, one-bay frames: α_u/α_1=1.2.

− Multi-story, multi-bay frames or frame-equivalent dual structures: α_u/α_1=1.3.

Also, for buildings which are not regular in elevation, the value of q_o should be reduced by 20%. A building can be categorized as regular in elevation, if all the following conditions are satisfied:

1) All lateral load resisting systems, for example the structural walls shall extend without interruption from their foundations to the top of the building or to the top of the relevant zone of the building, if setbacks exist at different heights.

2) Both the lateral stiffness and the mass of the individual stories shall remain constant or decrease gradually without abrupt changes, from the base to the top of a particular building.

3) In regard to framed buildings, the ratio of the actual story resistance to the resistance required by the analysis should not vary disproportionally between adjacent stories.

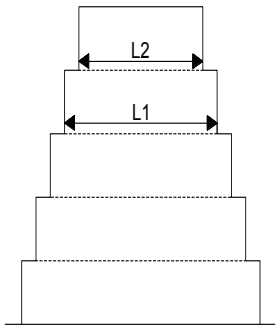
4) In case of existing setbacks, the following additional conditions apply:

a) For gradual setbacks, preserving axial symmetry, the setback at any floor shall be not greater than 20% of the previous plan dimension in the direction of the setback (Fig.1a, b).

b) For a single setback within the lower 15% of the total height of the main structural system, the setback shall be not greater than 50% of the previous plan dimension (Fig.1c). In this case the structure of the base zone within the vertically projected perimeter of the upper stories, should be designed to resist at least 75% of the horizontal shear force that would develop in that zone in a similar building without the base enlargement.

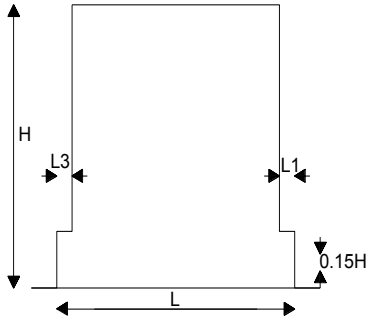
c) In case of setbacks without symmetry, for each face, the sum of the setbacks in all the stories shall be not greater than 30% of the plan dimension at the ground floor above the

foundation or above the top of a rigid basement, and the individual setbacks shall be not greater than 10% of the previous plan dimension (Fig.1d).



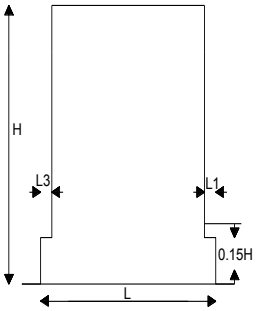
Criterion for (a): $\frac{L1-L2}{L1} \leq 0{,}20$

(a)



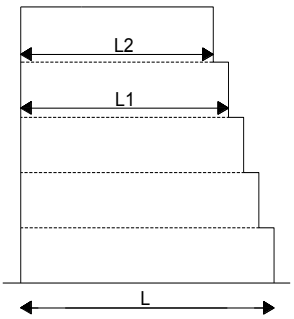
Criterion for (b): $\frac{L3+L1}{L} \leq 0{,}20$

(b) (setback occurs above 0,15H)



Criterion for (c): $\frac{L3+L1}{L} \leq 0{,}50$

(c) (setback occurs below 0,15H)



Criteria for (d): $\frac{L-L2}{L} \leq 0{,}30$

$\frac{L1-L2}{L1} \leq 0{,}10$

(d)

Figure 1: Criteria for regularity of buildings with setbacks following EC8 (2004).

If any one of the above is not satisfied, the building will be assumed as non-regular and the behavior factor *q* shall be decreased. It should be noted, however, that a behavior factor *q* of as low as 1.5 should be used in deriving the seismic actions, regardless of the structural system and the regularity in elevation.

3 DESCRIPTION OF MODELING AND ANALYSIS PROCEDURE

A general frame design and analysis algorithm has been developed for the automated definition of RC frame designs of irregular structures (and their corresponding inelastic analysis models) in an objective manner, in order to evaluate the adequacy of the seismic design provisions of irregular RC buildings according to EC2 [17] and EC8 [16]. The algorithm was developed on the OpenSees platform [18] and is been coded entirely in Tcl, an open source language with which the OpenSees language has also been developed. Due to the versatility of this code and the fact that the entire building definition and simulation is entirely pro-

grammable in the Tcl language syntax and the OpenSees object structure, it is possible to create a fully parametrically automated and therefore objective design procedure for EC8 [16] compliant design generations. This procedure gives the opportunity to the user to define groups of irregular systems compliant to the codes and to perform sensitivity analyses on these, by varying their design parameters. The algorithm includes both static analysis and/or dynamic excitation for the evaluation of the seismic performance of the design. In what follows, the algorithm (outlined in Fig.2 below), is described in some detail.

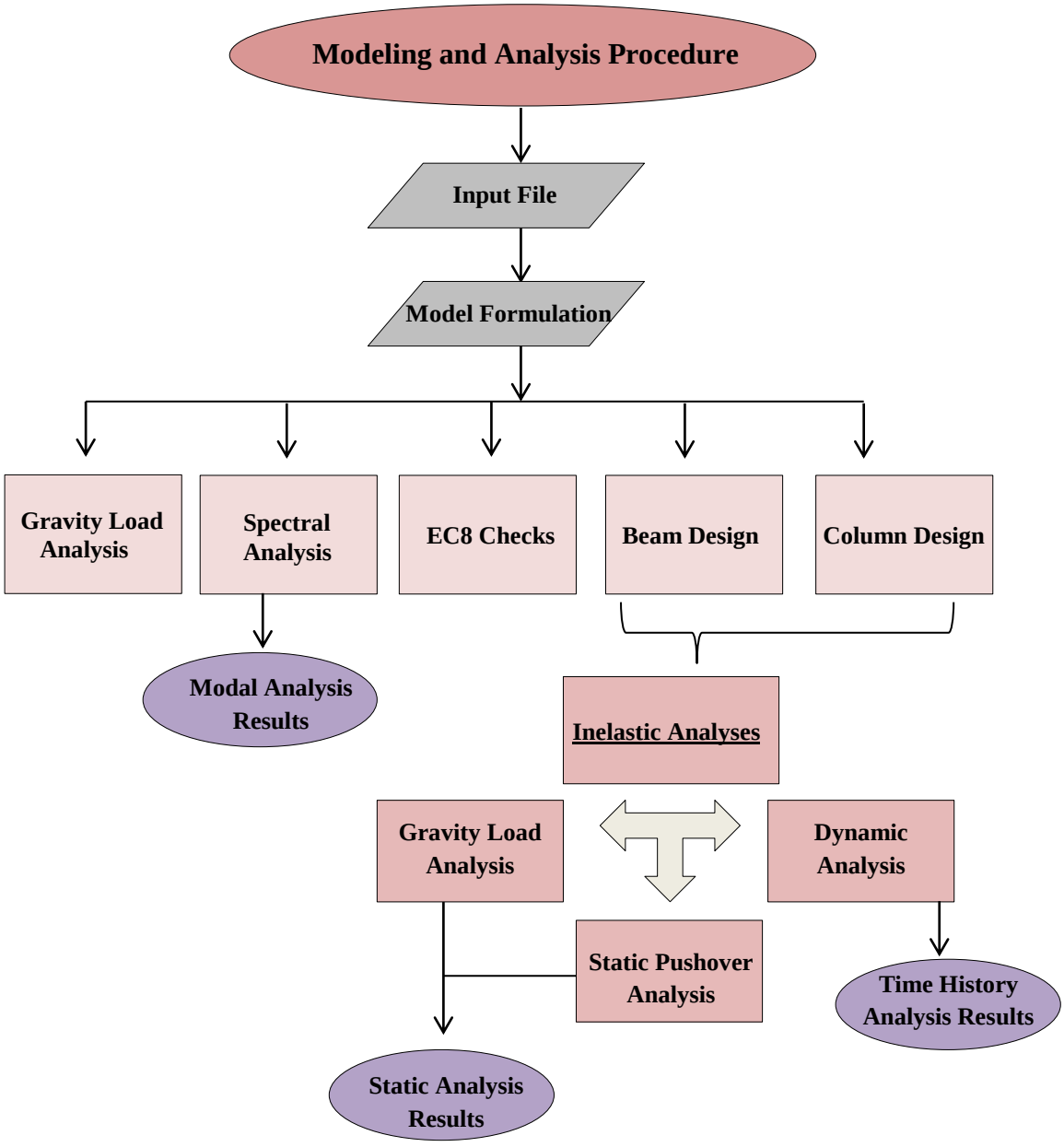


Figure 2: Principal Modules of the EC8 RC frame design and analysis algorithm.

3.1 Input File and Model Formulation

The Input File includes all necessary information for the definition of the geometry of the examined frame and the EC8 design parameters. In more detail, it contains input for: i) the material capacities, ii) the initial design and subsequent analysis properties (partial factors for

load and material strengths, Ductility Class, basic behavior factor q_o, the design spectrum parameters), iii) the proposed cross section dimensions of the elements (namely vertical elements per floor and entire beam lines per floor and per bay), iv) the uniformly imposed area loads in plan (excluding self-weights, which are automatically established) and v) the three-dimensional geometry of the frame. Members with a zero cross section are considered by the algorithm as missing and not contributing to mass and stiffness (e.g. a setback, a "planted" discontinuous column or a discontinuous beam forming an arcade in any location). Moreover, the definition of frame geometry includes the definition of the number of stories, the (variable) heights of these stories and the number of bays in each direction and the length of these bays, respectively. Unequal lengths of entire bays or story heights are possible to define.

In the Model Formulation file then, the three-dimensional frame model is initially defined on a regular orthogonal grid of floor levels along the vertical (y) axis and transversely, along the (x,z) direction of bays, observing the frame geometry and boundary conditions (commands *model*, *node* and *fix*, see [18]). Following this point, the algorithm entirely generates the topological connectivity between elements (slabs and their support boundary conditions each side, beams, columns) and the base constraints. In order to perform the initial elastic analysis model, the connectivity is achieved using "*element elasticBeamColumn*" [18], defining linear finite elements by specifying their Young Modulus, the Shear Modulus, the torsional moment of inertia of cross section and lastly the second moment of area about the local axes, compatible with the input geometry. Eventually, loads are imposed in each element (in slabs, in beams and finally in columns) and the algorithm calculates the nodal coordinates and masses of the frame for all the following analyses (command *mass*, see [18]).

3.2 Gravity Load – Spectral Analyses and EC8 Checks

Linear elastic structural models are successively analyzed and the corresponding design force envelope resultants are obtained for the structural elements for all applicable load cases. These are: i) load combinations of Dead plus Live Loads only, using the proper maximum and minimum partial load factors (favorable and unfavorable) and a checkerboard distribution of Live Loads at each floor; ii) the Dead plus reduced Live (by Ψ_2) plus Seismic Load combinations, using either the equivalent static load distributions or the modal distributions (depending on the system parameters, as per EC8, [18]) and corresponding accidental eccentricities simultaneously applied over the entire height on each side of the floor center of mass. At this stage, serviceability limit state combinations are not considered.

After these analyses, the algorithm evaluates, checks and prints the adequacy of the design according to the restrictions of EC8, including the limit for interstory drift and the limit for second order (P-δ) effects, as well as all relevant irregularity indices and checks. Moreover, this file contains all necessary information about the spectral characteristics of the subject frame, given a first point of view for the frame analysis.

3.3 Member Design

Following the corresponding design force envelope resultants, design procedures are assumed for beams and columns.

Concerning the design of RC beams, the following apply:

Every beam is divided into three sections, namely end *i*, end *j* and midspan section *m* and the beams are designed according to the user defined the Ductility Class per EC8. Consequently, the following are established for every critical section of a beam:

1. Calculation of moments M_{sd} and μ_{sd}.

2. Calculation of A_{s1}, A_{s2} and comparison with maximum and minimum limits from Eurocode 2 and 8 using the reinforcing Tables based on EC2 flexural analysis.
3. Finally, the beam capacity and final steel ratios are evaluated.
4. Inadequate choice of initial dimensions or code requirement violation issue corresponding messages and the procedure stops.

According to the design of RC columns, the following apply:

1. Each column section is checked for maximum permitted normalized compressive load (v_d) under the gravity plus seismic load combinations.
2. The section is designed for uniaxial bending with compressive load for all load combinations. This procedure is repeated four times, once for every axis and critical section of column element (y-axis, z-axis, base section, top section), observing in each case the Code required minima and maxima in each direction (the constructability of the section is also verified, in terms of amount and layout of reinforcement provided).
3. The flexural strength in each direction is defined.
4. The section is verified in biaxial bending. If the maximum steel ratios established are insufficient for the biaxial bending and axial load demands or the layout is improper, a message appears for section inadequacy and the procedure stops. Eventually, the final steel ratios are extracted for all the beams and columns of the frame, satisfying strength and material characteristics limitations.
5. After the design of beams and columns, every beam-column joint is checked, according to EC8 ($\sum M_{\mathrm{Rc}} \geq 1{,}3 \sum M_{\mathrm{Rb}}$, see [18]), so as to take into account the joint overstrength. In case that no restrictions are met, the algorithm corrects the moment of column and redesigns it, ending in final steel ratios.
6. Eventually, columns are checked for confinement in critical and non-critical regions, resulting in the transverse reinforcement (namely $\alpha\omega_d$, see [18]).
7. The column is checked and designed for shear, if confinement steel is insufficient, and new confinement properties ($\alpha\omega_d$) are evaluated.

3.4 Inelastic Analyses

Once the design of the frame is completed, the algorithm creates automatically the entire *RunBuilding.tcl* input file describing the entire inelastic finite element model of the designed structure for inelastic analyses. The file includes all the information for the geometry, the element connectivity, the fiber sections of the members and the corresponding uniaxial materials for concrete and steel, loads and analysis specifications and output information.

As before, for the definition of the design model, the three-dimensional frame geometry and masses with its boundary conditions are defined using commands: *model*, *node*, *fix*, and *mass*, [18]. Section objects are automatically established through the "*Section Fiber*, *patch* and *layer*" (see [18]) commands for all the beams and columns, with each fiber section object being composed of fibers, associated with an assembly of uniaxial materials (commands *uniaxialMaterial Concrete01* and *Steel01* are used, respectively, see [18]), in the corresponding local coordinate system (command *geomTransf*, see [18], also including the rigid offsets of half the contributing member size in each end); all these parameters are established from the design section characteristics (section sizes, material properties and steel reinforcement) previously defined. Figure 3 depicts the using uniaxial materials for concrete and steel and the distributed - plasticity element, from the library of OpenSees [18].

In terms of the finite element model representation per se, beams are created using displacement interpolation spread damage elements (*element dispBeamColumn*, see [18]). All the beams are automatically split into five sub elements per span with three Gauss integration

monitored sections each, in order to handle internal transversely distributed loads in the beam (case Dead plus Ψ_2 Live). Columns, on the other hand, are defined using equilibrium interpolation spread damage elements (*element forceBeamColumn*" (see [18]), with five integration points per column.

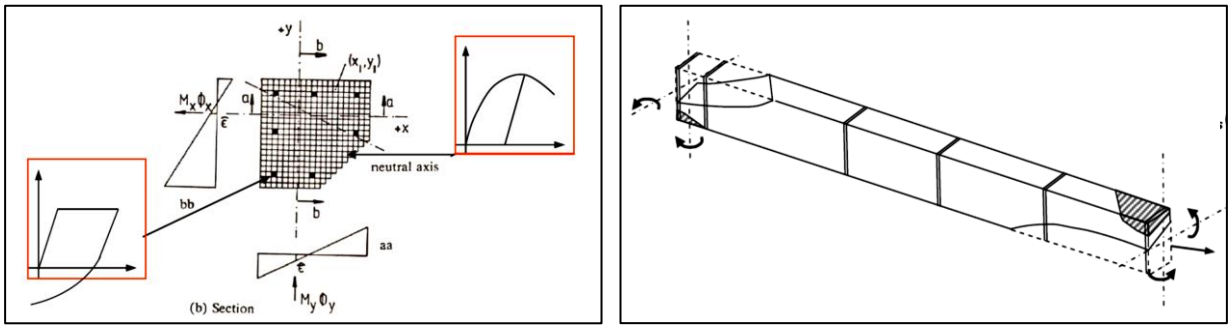


Figure 3: a) Uniaxial Materials and b) Distributed Plasticity Element.

The algorithm proceeds with the analysis of the design, including, in sequence, Gravity Load followed by Static Pushover analyses or/and Dynamic analysis. In the first case, two different Load patterns are defined, one for Gravity Loads and the other for Lateral Loads, (command *pattern Plain*, see [18]). The corresponding Dead plus factored Live Loads are automatically evaluated as vertical loads from the design of beams and columns. The Lateral Loads are applied at the frame nodes, connected to each other using diaphragmatic elastic truss elements (*element truss*, see [18]) of very large stiffness. In case of a time history integration dynamic analysis, the time resets to zero so that the dynamic analysis starts from time zero (command *loadConst* see [18]). In this case, the user defines the acceleration record for examination and applies the ground motion to the structure at the base (command *uniform excitation pattern*, see [18]). Additional user defined information for the dynamic analysis includes the acceleration record time series, the digitization time step of the ground motion and the analysis time step, the scale factor applied to the ground motion and the direction in which the motion is to be applied. In all cases, prior to the analysis, test, convergence, system numbering and the model constraints are also specified by the code.

In the end of the analysis, the response parameters are obtained through a set of output (*recorder*, see [18]) specifications, providing information on nodal displacements, global force components and plastic rotation histories and critical section information of the beams and columns. Nodal profiles, the frame geometry, mode shapes, internal force diagrams and selected time history outputs are subsequently graphically post processed using MATLAB [19].

4 OVERVIEW OF THE CASE STUDY

The algorithmic procedure described above is demonstrated in a six story irregular in elevation RC frame, with four bays along the x-axis and four bays along the z-axis (Fig.4), which has been designed according to the provisions of EC8 for the DCH and DCM ductility classes. The spans are 5m long both in x-axis and z-axis. The irregularity exists from the third floor and above by reducing the bays to two, so as to create a central tower. Live vertical loads for residential construction of 2.0 kN/m^2 and dead loads due to self-weight plus an additional surcharge load, including light partitions, of 2.1 kN/m^2 and a perimeter infill load of 3.6 kN/m^2 of facade area, were assumed. The frame cross section dimensions are shown in Fig.4.

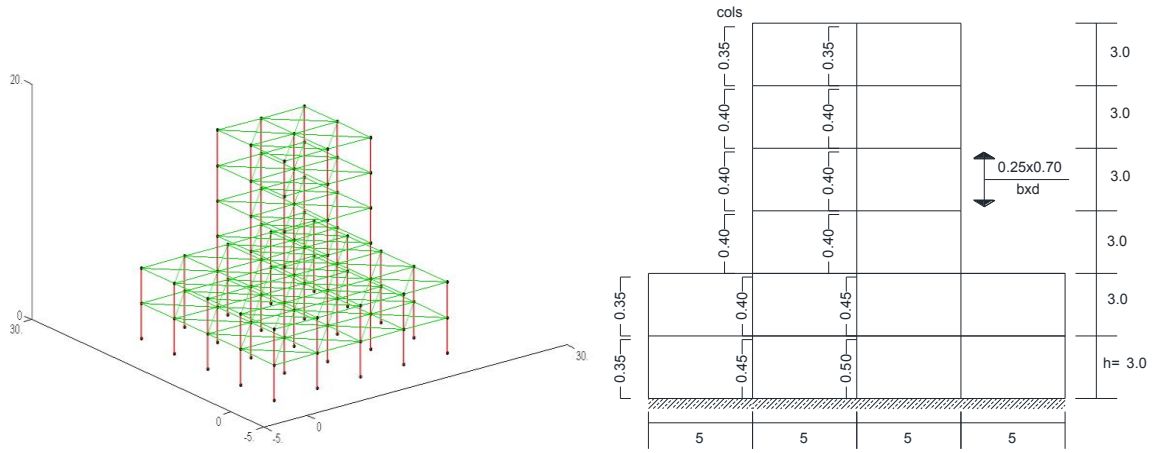


Figure 4: Frame Geometry (dimensions in m).

The structures were designed using a design behavior factor q of 3.12 and 4.68 for DCM and DCH respectively, with the first fundamental mode period of each frame equal to T_1= 0.514sec and T_1=0.535sec and for medium seismicity (design PGA of 0.24g). They were subsequently analyzed under: i) a Static Pushover (SPO) using a monotonically increasing modal load pattern, following the first lateral mode (Fig.5a) and ii) a time history dynamic analysis, using the OTE accelerogram of the 1981 Korinth earthquake (Fig.5b), with a peak ground acceleration (PGA) of 0.28g; in the latter case, two levels of excitation were considered, at 100% of the PGA (denoted PGA1) and at 200% of the PGA (denoted PGA2), respectively.

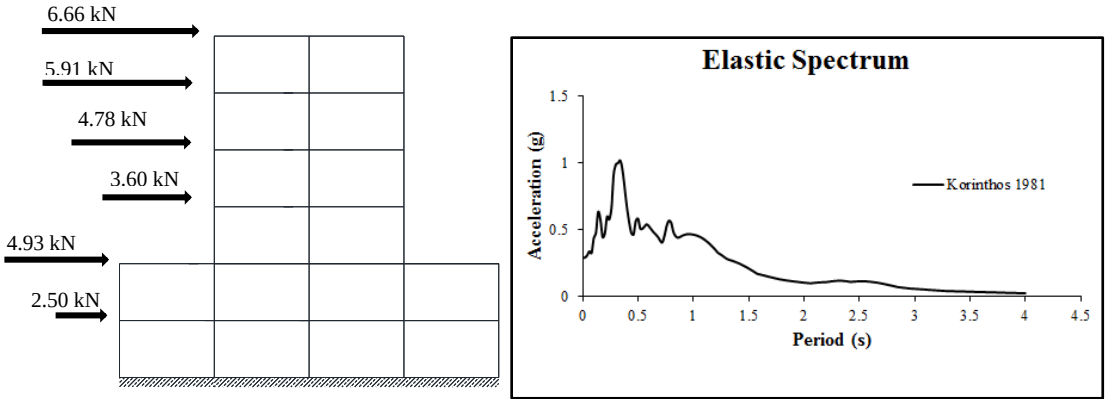


Figure 5: a) Pushover Load Profile and b) Base Input Accelerogram Spectrum.

5 SEISMIC RESPONSE AND ESTIMATION OF THE DESIGN *q*

As mentioned above, the output from the OpenSees model enables the user to obtain information of the model response for nodes and elements, so as to check not only the local damages of elements, but also the global damage of the entire frame. The plastic hinges which are developed in frames during the analyses, are shown in Fig.6 for the External and Internal Frames and they are comparable for both ductility classes. The External Frame developed low demands of plastic hinge rotations ($\theta_{plastic}$ < 0.005 rad), in contrast with Internal Frame, which exhibited large demands of plastic rotations in the bottom and the top of the third floor columns and beams at the recess, at the base of the tower.

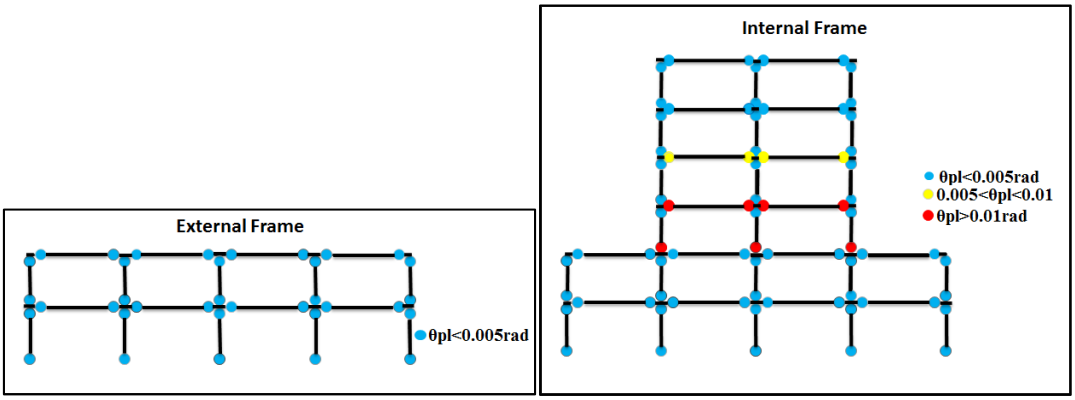


Figure 6: Distribution of Plastic Hinges in External and Internal Frames.

The inelastic demands in terms of plastic rotations for the interior frame column at the third floor are examined further in Fig.7, for SPO and the two dynamic analyses PGA1 and PGA2 and for both ductility classes DCM and DCH; it is seen that the plastic rotation demands of the base (end i, bottom) of the subject column do not exceed the limits of EC8 for the Collapse Prevention Performance level in all load cases, static or dynamic, whereby the maxima refer to the SPO demand at the target point, estimated according to EC8, and to the maximum absolute values, for the time history analyses.

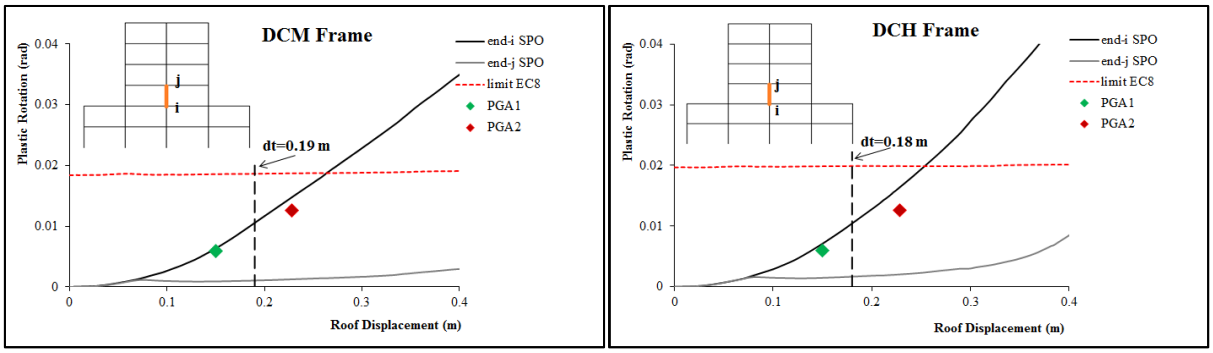


Figure 7: Plastic Rotation – Roof Displacement demands of the third floor column, for DCM and DCH Frames.

The interstory drift profiles of the examined frames for all executed analyses are compared in Fig.8. In all cases, relatively high demands in interstory drift are consistently developed in the third and fourth floor; generally, unlike the DCH frame, for the DCM frame larger interstory drifts are demanded by the SPO analysis, compared to the dynamic analysis under the 100% PGA earthquake.

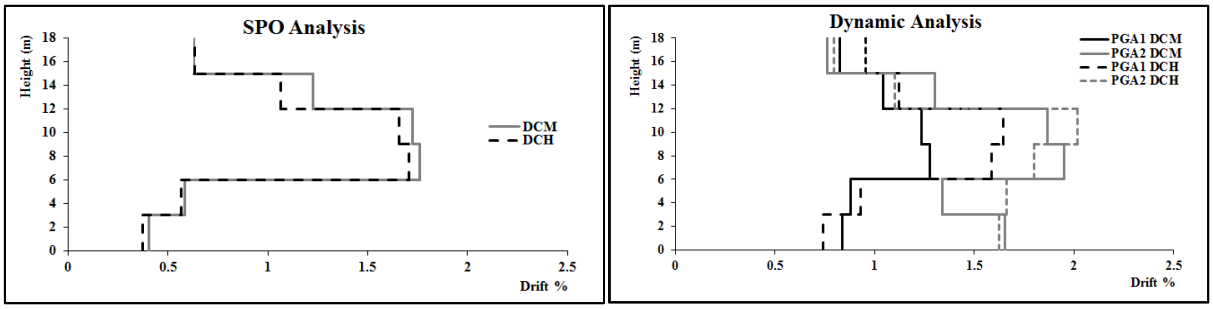


Figure 8: Comparative Profile Drifts DCM – DCH Frames for SPO and Dynamic Analysis.

On the other hand, the response of both frames under dynamic analysis depends strongly on the intensity of imposed excitation, with the interstory drifts reaching values as high as 2% at the tower base and comparable amplitudes at the base of the building, under the extreme event PGA2 (Fig.8).

The corresponding target point demands under SPO analysis are depicted below in Fig.9 for the two frames in normalized base shear - roof displacement characteristics. In both cases the equivalent bilinear base shear - deformation diagrams are also evaluated, following the usual convention of equal areas under the inelastic and bilinear curves and an initial elastic stiffness passing through the point of 60% of the peak base resistance.

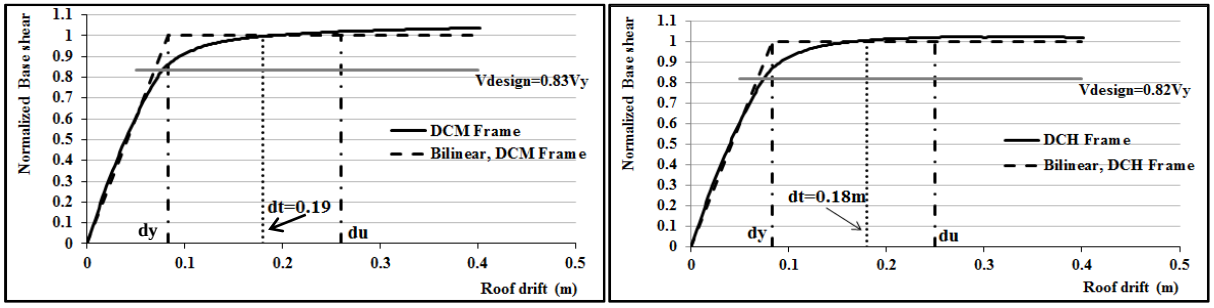


Figure 9: Normalized Base Shear-Roof displacement characteristics of the two frames.

The calculation of the q factor supplied by the structure depends on the type of structural system and on its regularity in elevation, which define both contributing factors, namely the ductility supplied (q_u) as well as the structural overstrength (q_Ω). From the results of the SPO analysis, taking into account the ultimate deformation supply for each frame for the Collapse Prevention Performance level (at column failure), the supplied q_u of the DCM frame is calculated to be 3.0 and of the DCH frame is calculated to be 3.1. Based on the overstrength factors q_Ω from the SPO analysis (Fig.9), it can be concluded that the supplied q exceeds the design value in both frames.

6 CONCLUSIONS

- A computerized procedure is developed on the OpenSees platform, aiming to produce a compliant design and to establish the inelastic seismic performance of a given vertically irregular three-dimensional RC building, according to the limitations of EC2 and EC8.
- The efficacy of the method is demonstrated using two typical RC frames having a central tower configuration (vertical irregularity) at the bottom third of the building, which are designed for Class Medium and High respectively in a zone of medium seismicity.
- For this class of buildings considered, it is shown that in both cases, the base of the tower develops high demands in plastic rotation and drift, concentrating a flexibility in this floor, thereby making it sensitive to the localization of damage.
- Regarding the supplied behavior factor of the structures, q, it is concluded that it is greater than the design q, accounting for irregularity, for both cases considered.
- It is observed that the two frames do not differ in regards to their inelastic response prediction, either using static pushover or dynamic analysis, since they developed similar inelastic characteristics, both in local and global level.

REFERENCES

[1] G.R. Aranda, Ductility Demands for R/C Frames Irregular in Elevation, *Proceedings of the Eighth World Conference on Earthquake Engineering*, San Francisco, U.S.A., Vol. 4: 559-566, 1984.

[2] B.M. Shahrooz, J.P. Moehle, Seismic Response and Design of Setback Buildings, *Journal of Structural Engineering*, ASCE, **116**(5), 1423-1439, 1990.

[3] S. Das, J.M. Nau, Seismic Design Aspects of Vertically Irregular Reinforced Concrete Buildings, *Earthquake Spectra*, **19**(3), pp. 455-477, 2003.

[4] S.E. Ruiz, R. Diederich, The Mexico Earthquake of September 19, 1985 – The Seismic Performance of Buildings with Weak First Storey, *Earthquake Spectra*, **5**(1), pp. 89-102, 1989.

[5] A.A. Nassar, H. Krawinkler, Seismic Demands for SDOF and MDOF Systems, Report No. 95, *The John A. Blume Earthquake Engineering Center*, Department of Civil and Environmental Engineering, Stanford University, Stanford, U.S.A., 1991.

[6] E.V. Valmundsson, J.M. Nau, Seismic Response of Building Frames with Vertical Structural Irregularities, *Journal of Structural Engineering*, ASCE, **123**(1), pp. 30-41, 1997.

[7] A.A.K. Al-Ali, H. Krawinkler, Effects of Vertical Irregularities on Seismic Behavior of Building Structures, Report No. 130, *The John A. Blume Earthquake Engineering Center*, Department of Civil and Environmental Engineering, Stanford University, Stanford, U.S.A.,1998.

[8] C.A. Zeris, T.P. Tassios, Y. Lu, G.F. Zhang, Influence of Irregularity on the q Factor of RC Frames, Proceedings, *Tenth World Conference of Earthquake Engineering*, 1992.

[9] C. Repapis, C. Zeris, E.Vintzileou, Evaluation of the Seismic Performance of Existing RC Buildings II: A Case Study for Regular and Irregular Buildings, *Journal of Earthquake Engineering*, **10**(3), 429-452, 2006.

[10] T. Chunyu, L. Junjin, Z. Hong, C. Jinzhe, Experimental study on seismic behavior of an irregular high-rise building, *15th World Conference on Earthquake Engineering*, Lisbon, Portugal, September 24-28, 2012.

[11] P. Sarkar, A. Meher Prasad, D. Menonb, Vertical geometric irregularity in stepped building frames, *Engineering Structures*, **32**, 2175-2182, 2010.

[12] C.J. Athanassiadou, Seismic performance of R/C plane frames irregular in elevation, *Engineering Structures*, **30**, 1250–1261, 2008.

[13] M.M. Elassaly, Seismic Hazard Evaluation of Regular and Vertical Irregular R.C. Buildings in EGYPT, for Different Ground Motion Characteristics, *15th World Conference on Earthquake Engineering*, Lisbon, Portugal, September 24-28, 2012.

[14] BIS, IS 1893(Part 1) – 2002: *Indian Standard Criteria for Earthquake Resistant Design of Structures. Part 1 – General Provisions and Buildings (Fifth Revision),* Bureau of Indian Standards, New Delhi, 2002.

[15] BSSC, *The 2003 NEHRP Recommended Provisions for New Buildings and Other Structures, Part 2: Commentary (FEMA 450),* Building Seismic Safety Council, National Institute of Building Sciences, Washington, DC, U.S.A., 2003.

[16] EC8, European Committee for Standardization, Eurocode 8: *Design of structures for earthquake resistance - Part 1: General rules, seismic actions and rules for buildings*, 2004.

[17] EC2, European Committee for Standardization, Eurocode 2: *Design of concrete structures - Part 1: General rules and rules for buildings*, 2004.

[18] F. McKenna, G. L. Fenves, B. Jeremic, M. H. Scott, *OpenSees Command Language Manual*, 2007. *http://opensees.berkeley.edu*.

[19] MATLAB Primer, R2015a, the Mathworks Inc, Natick, MA, 2015.

COMPDYN 2015
5th ECCOMAS Thematic Conference on
Computational Methods in Structural Dynamics and Earthquake Engineering
M. Papadrakakis, V. Papadopoulos, V. Plevris (eds.)
Crete Island, Greece, 25–27 May 2015

CRACKING AND FRACTURE OF HSS BRACES UNDER CYCLIC LOADING

M. Haddad[1], R. Tremblay[2], L. Chen[2], and L. Tirca[3]

[1] United Arab Emirates University
madhar@uaeu.ac.ae

[2] Ecole Polytechnique of Montreal
{robert.tremblay,liang.chen}@polymtl.ca

[3] Concordia University
lucea.tirca@concordia.ca

Keywords: Concentrically Braced Frame, Finite Element Analysis, HSS Brace, Fracture.

Abstract. *Concentric-braced steel frames often fracture at the mid-length of the braces during strong ground motions when the members and connections are properly designed and detailed. The paper describes a finite element model incorporating a damage accumulation model that is able to predict fracture of HSS braces under cyclic loading. Crack initiation is predicted through a refined fracture model. It is shown that the fracture life predicted from finite element analysis based on damage model agrees well with the experimental results and the refined fracture model results. Brace fracture performance is examined for an 8-storey inverted-V concentrically braced frame designed in accordance with the Canadian seismic provisions. Time history analysis of four selected ground motions is carried out on the CBF structure using the OpenSees program. Failure of the braces at the 7th storey is investigated with consideration of the deformation history demand.*

1 INTRODUCTION

Concentrically braced frames (CBFs) frequently use hollow structural steel section (HSS) braces to resist lateral loads and seismic excitations. Fracture of HSS braces was reported after the 1994 Northridge and the 1995 Kobe earthquakes [1]-[2]. Failure of HSS braces has also been observed in braced frame test programs [3]-[6] as shown in Fig. 1. When the end connections are properly designed, fracture typically occurs in the plastic hinge forming at the mid-length of the brace upon global buckling, as a result of high strains developing after local buckling. A review of the fracture life prediction criteria's [7]-[25] revealed that a slightly varied form of the Cyclic Void Growth Model (CVGM) model in [23] for ultra-low cycle fatigue is an appropriate candidate to predict fracture life of steel braces under seismic excitations. With respect to the available plastic hardening models proposed in [26]-[34], it is shown in [35] that the kinematic hardening rule in [27] is a sufficient candidate to model the shift in the yield surface in stress space of HSS brace tests by [36].

Two micromechanics models were presented to simulate ultra-low cycle fatigue of moment connections [23]. The first model is the Degraded Significant Plastic Strain model (DSPS) and the second model is the Cyclic Void Growth Model (CVGM). The two models depend on the cumulative plastic strain, the triaxiality ratio and the characteristic length, to predict fracture. The significant cumulative plastic strain concept is introduced to the DSPS and CVGM models. This concept is compatible with the growth and coalescence mechanisms of the ultra-low cycle fatigue problems. The variation of triaxiality ratio with cycles is not considered in the DSPS model. This variation is taken into account in the CVGM model. Triaxiality is the mean stress over the effective or the Von Mises stress. The triaxiality ratio depends on the load history and the geometry of the specimens (thickness for example). The cyclic fracture life predictions of the CVGM are better than the cyclic results of the DSPS model, especially with variable amplitude loadings. The change in triaxiality is considered with cycling in the latter.

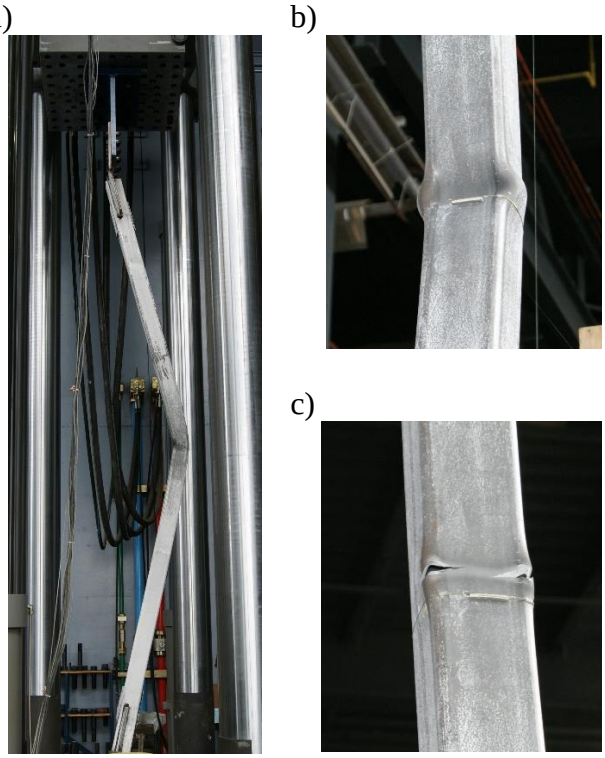


Fig. 1 Quasi-static tests on an HSS127x127x8.0 bracing member [6]: a) Global buckling; b) Local buckling upon brace global buckling; and c) Fracture upon reloading in tension.

Brace fracture prediction represents a critical ingredient for the assessment of the seismic performance of braced steel frames, especially when verifying life safety and collapse prevention limit states. In this paper, a modified finite element model is presented to predict the onset of cracking for HSS specimen 4B of the brace tests in [36]. The significant cumulative plastic strain obtained from the refined CVGM model when cracking first seen is used in a cyclic damage model to predict the fracture life of specimen 4B. The cyclic damage model is needed to simulate the ductile damage initiation when the crack is first seen to failure. The same model is then tested on prediction of the fracture life of a bracing member identical to specimen 4B at the 7th floor level of an 8-storey CBF subjected to seismic ground motion records.

2 FINITE ELEMENT MODEL DESCRIPTION

The combined isotropic kinematic hardening material model was used in the finite element analysis with data type equal to half cycle. This model is capable of simulating the expansion, contraction and the shift of the yield surface in stress space to model the brace behavior under cyclic loading. The shift in the yield surface is a function of the plastic strains and the plastic hardening modulus. The shift (translation) of the yield surface is subtracted from the corresponding stresses according to the kinematic hardening rule in [27], as described in [35]. The engineering stress strain curves obtained from coupon tests on HSS material in [37]-[39] were converted to true stress strain curves that were used here in the finite element model of specimen 4B. The true stress strain curves for walls and corners of specimen 4B in addition to the gusset plates are shown in Fig. 2.

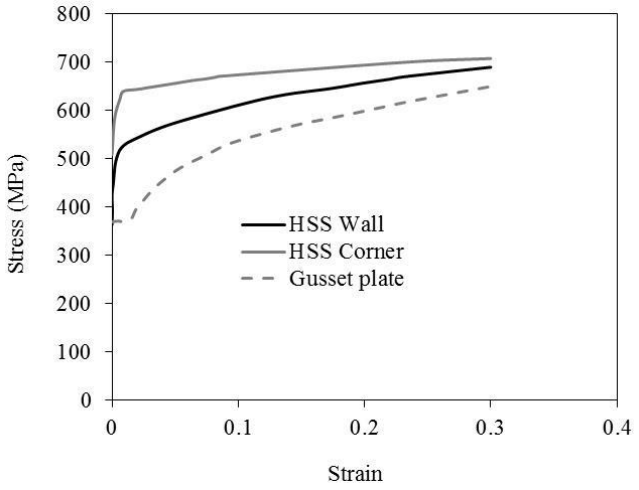


Fig. 2 Stress strain curve

Specimen 4B was designed according to the weak brace strong gusset approach. The tensile capacity of the gusset was greater than the tensile capacity of the brace. Two ways are possible to prevent the net-section fracture. The first way is by using reinforcement plates and the other way is by rounding the fillet weld to close the slot. Both ways are sufficient to prevent net-section fracture. Specimen 4B was tested when rounding the weld even though it is more practical to use reinforcement plates. The detail of the slotted hole at the end of the weld should not affect the brace fracture response since fracture developed at the brace mid-length.

The finite element analysis was performed using the Abaqus code [40]. The use of a four-node quadrilateral shell element (S4R) in modelling steel braces accounts for in-plane and out-of-plane deformations and allows for changes in thickness with deformation. S4R is a re-

duced integration element with three translational and three rotational degrees of freedom per node. Seven integration points were adopted through thickness of the S4R element. A high mesh density was used at the mid-length plastic hinge of the HSS. The element aspect ratio in this region was 1. The gusset plates were connected to the HSS by the nodes on their interfaces. The number of nodes, elements used in modeling specimen 4B, were 16730, 13580, respectively. Fixed brace end conditions were used. It is worth mentioning that using shell elements in modeling braces subjected to cyclic loading is better than using solid elements. The solid elements are not able to simulate the kink at the mid-length of the brace, while this behavior is evident when using shell elements [41]. From experience on modeling concentric braces subjected to cyclic applied displacements, it is more convenient to use multiple integration points through the thickness of one shell element than staking solid elements with one integration point for each solid element. The number of integration points will have an effect on the local behavior and will not have pronounced effect on global behavior. In addition, solid elements are stiffer than shell elements.

The finite element analysis was carried out in two stages. First mode elastic buckling analysis was created in the specimens in the first stage. The initial imperfection to match the measured camber and the cyclic end displacements were then applied in the second stage where nonlinear inelastic analysis was adopted to simulate the hysteresis loops. Large deformations are expected; therefore, the geometric nonlinearity was adopted with the material nonlinearity. The Newton-Raphson method was used to solve the nonlinear equilibrium equations in the stability based approach.

3 VALIDATION OF EXPERIEMNTAL TEST

Specimen 4B, characterized by an HSS 152x152x9.5 mm section with 300x25.4 mm gusset plates at each end of the specimen for end connections, has been selected from the brace tests in [36]. Specimen 4B had the largest cross-section and nearly the longest among the specimens tested. The length of the HSS is 4850 mm. The measured free length of the gusset plates was equal to 32 mm. Thus, the total length of the specimen was equal to 4914 mm. The effective slenderness ratio accounting for end flexural restraint by the gusset plates is 59.7 and the width-to-thickness ratio, $(b\text{-}4t)/t$, is 13.0. The yield strength F_y = 442 MPa and the modulus of elasticity E = 196 GPa of the HSS material were obtained from stub column tests.

The experimental and the finite element's axial hysteresis loops are nearly identical in Fig. 3(a), as well as the lateral hysteresis loops showed in Fig. 3(b). In the experiment and the finite element analysis, the specimen was subjected to four elastic cycles of compression-tension loading. During the compressive side of the fifth cycle, the specimen noticeably buckled into a bow shape. Two plastic hinges formed progressively in the free length of the two gusset plates. The full tension side of the same cycle straightened the specimen. The specimen buckled at lower axial displacements in the sixth compressive cycle than in the fifth. This is mainly attributed to the residual elongation, or camber, and to the plastic hinges which had formed at both ends of the specimens. During the same cycle, the bow shape buckling became larger as shown in Fig. 4(a). The two free length plastic hinges formed completely during the sixth compressive cycle with filet weld cracking noticed in the experiment at both the compression and tension sides of the gusset plate adjacent to free length. The weld was not modeled in the finite element model. The compressive loads showed a marked decrease in capacity in the cycles following the fifth cycle. The tension side of the sixth cycle removed the camber and fully yielded the specimen. Stable plastic behavior of the gusset plates was evident at all times during the test and the finite element model.

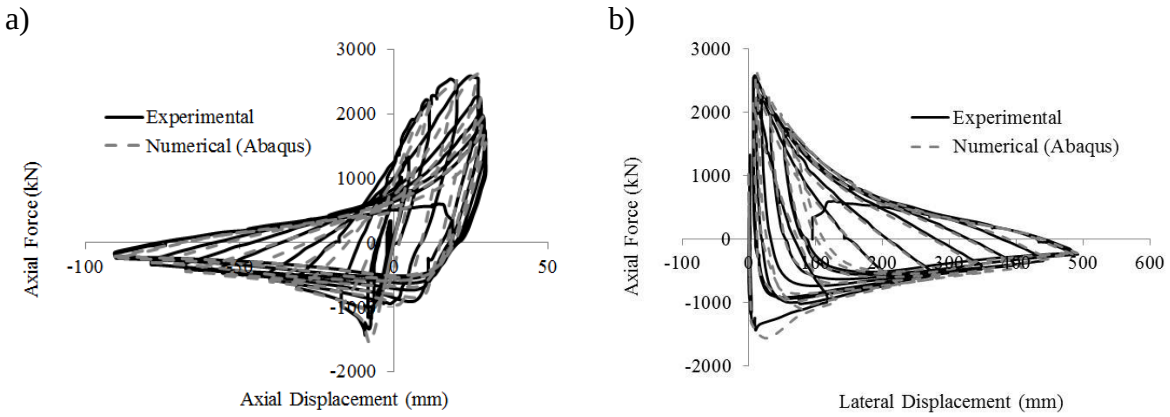


Fig. 3 Hysteresis loops: a) Axial displacement; b) Lateral displacement.

During the compressive side of cycles seven and eight, the specimen shape was changing from a bow shape to a kinked shape, concentrated at the mid-length of the specimen in the experiment and the finite element analysis. This shift in shape indicated the beginning of the development of a plastic hinge at the mid-length of the specimen.

Local buckling at the mid-length plastic hinge began during the compressive side of the ninth cycle, with inward and outward bulging of the specimens' compressive web and flanges, respectively. The outward bulging is closer to the compressive web rather than the tension web. A small inward bow of the tension web was also noticed. The local buckling partially disappeared during the tension side of the same cycle. Local buckling continued to increase in severity during the following cycles. As a result, the buckling shape transformed from a bow shape to a V-shape as shown in Fig. 4(b).

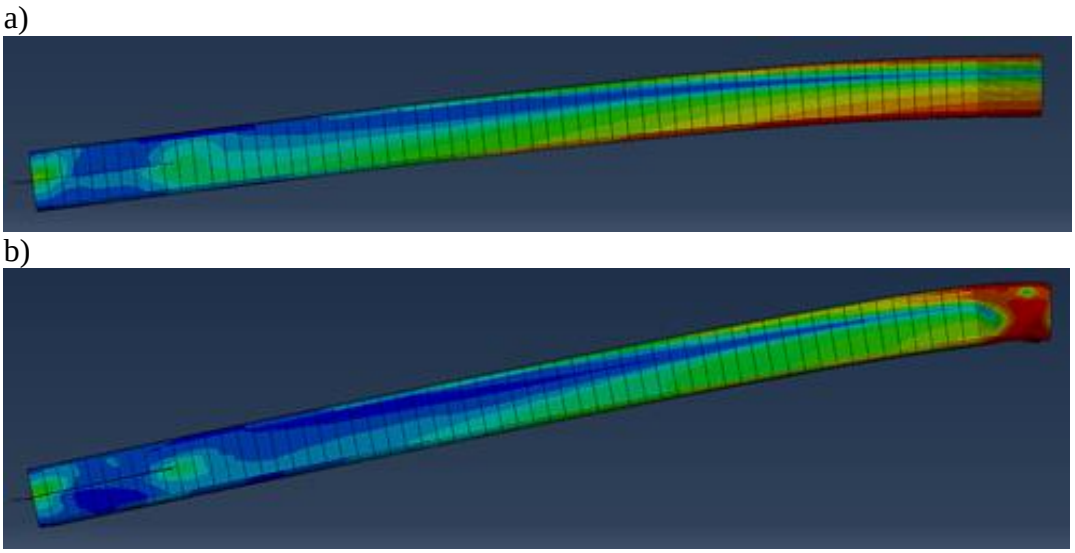


Fig. 4 Lateral buckling: a) Half-bow shape; b) Half-V shape

In the experiment, the continued working of the mid-length region resulted in the tearing of the flanges on the corners at the compressive side of the locally buckled region during the tension excursion of the 11th and final cycle of loading. Small size bent was present at the compressive corners and web at the mid-length plastic hinge upon compressive buckling. This bent is usually severe at the compressive corners (Fig. 5) due to the geometric nature of local buckling and bending. The bent opens during tensile loading and concaves during compres-

sive buckling leading to crack formation due to the cyclic rotational demand and reduction in the cross-sectional area at those locations. Reduction in strain gauge measurements on the compressive side of cycles 11 and 12 is sees in Fig. 6 due to the formation of the small size bent. Tearing and subsequent propagation of the tear resulted in the failure of the specimen upon increasing levels of axial displacement. Failure of the specimen was shifted at a distance of less than the depth of the HSS as shown in Fig. 7.

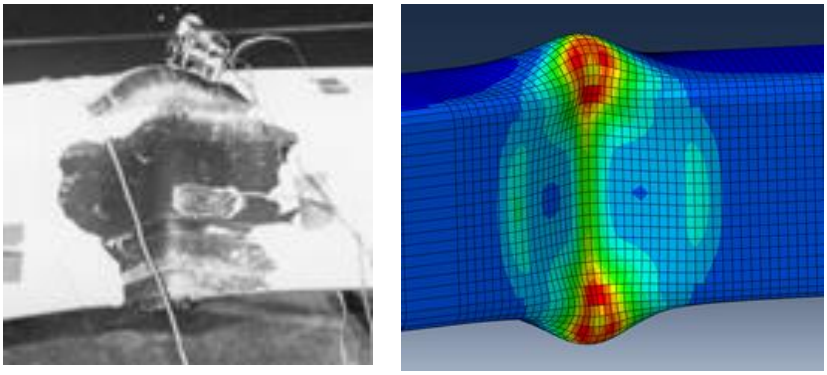


Fig. 5 Small size bent and local buckling

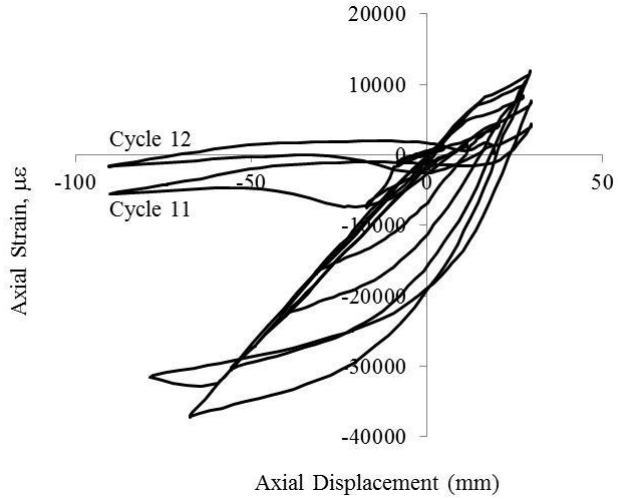


Fig. 6 Axial displacement versus axial strain hysteresis loops

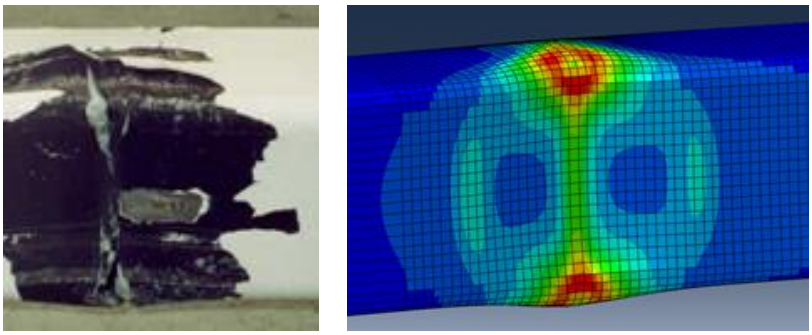


Fig. 7 Fracture of specimen 4B

4 FRACTURE AND DAMAMGE MODELS

During the compressive side of cycles seven and eight, the specimen shape was changing from a bow shape to a kinked shape, concentrated at the mid-length of the specimen in the experiment and the finite element analysis. This shift in shape indicated the beginning of the development of a plastic hinge at the mid-length of the specimen.

An extension to the model proposed in [10] was the CVGM model in [23], which predicts fracture for ultra-low-cycle fatigue (ULCF) braces under cyclic loadings. The CVGM model is based on the following equation (fracture initiates in braces when the degradation in monotonic capacity is less than the cyclic growth in demand):

$$\begin{aligned} &exp(-\lambda_{CVGM}\varepsilon_p)\eta_{monotonic} \leq \\ &\Sigma_{tensile-cycles}\int_{\varepsilon_1}^{\varepsilon_2} exp(|1.5T|)d\varepsilon_t - \\ &\Sigma_{compressive-cycles}\int_{\varepsilon_1}^{\varepsilon_2} exp(|1.5T|)d\varepsilon_c \end{aligned} \tag{1}$$

On the demand side, the equivalent compressive strains are subtracted from the equivalent tensile strains and added incrementally for every cycle of loading taking triaxiality, *T*, into account. Cycles are considered compressive when triaxiality is negative and vice versa.

The capacity side represents the degradation of the monotonic tensile capacity, $\eta_{monotonic}$, due to cyclic loading according to the equation:

$$\eta_{cyclic} = exp(-\lambda_{CVGM}\varepsilon_p)\eta_{monotonic} \tag{2}$$

where:

$$\eta_{monotonic} = \int_0^{\varepsilon_p} exp(1.5T)d\varepsilon_p \tag{3}$$

and ε_p is the cumulative plastic strain.

The monotonic capacity could be obtained from standard coupon or notched bar tests. The monotonic capacity degrades according to the degradation coefficient, λ_{CVGM}. The values of $\eta_{monotonic}$ and λ_{CVGM} were calibrated by conducting notch round bar monotonic and cyclic tests, with two different loading protocols, on seven types of steel made in Japan and the USA [23]. The first loading protocol is to cycle the specimen under constant amplitude high tension and/or low compression cyclic displacements to failure. The second loading protocol is to cycle the specimen under constant predefined low tension and/or compression amplitude displacements, and then to pull the specimen to failure during the last tension cycle. The applied compressive displacements are greater than the applied tensile displacements of specimen 4B (Fig. 3(a)). Strain gauges were deployed at the expected plastic hinge location at the exact mid-length of specimen 4B. The strain gauges were inserted at the neutral axes of the specimen. The strain gauge deployed at the compressive web (Fig. 5) measured the greatest values of strain demand in compression among all strain gauges. Axial strains in compression are greater than axial strains in tension as shown in Fig. 8. Therefore, the significant plastic strains are taken to be compressive minus tensile strains. Plastic strains are accumulated during compressive cycles in the model proposed in [42] where cycles are considered compressive when triaxiality is negative.

For fracture life predictions in the current study, the significant plastic strains are taken to be compressive minus tensile strains on the demand side. Strains are considered compressive when triaxiality is less than -1/3. The -1/3 is a revised simplification for positive maximum principal stress [25]. The maximum principal stress is positive for damage evolution in cyclic loading [18]. For cyclic loading, a slightly modified form of damage evolution by [18] was used in [25]:

$$dD = \begin{cases} (cy)^m d\varepsilon_P & for\, T > -\frac{1}{3}, and \\ 0 & otherwise \end{cases}$$

$$y = \frac{\sigma_{eq}^2}{2E(1-D)^2}\left[\frac{2}{3}(1+\nu)+3(1-2\nu)T^2\right] \tag{4}$$

$$D_c = \int_0^{\varepsilon_P} dD$$

where c and m are material constants, E is the elastic modulus, ν is the Poisson's ratio, σ_{eq} is the effective or the Von Mises stress, dD is damage increment and D_c is the critical damage limit.

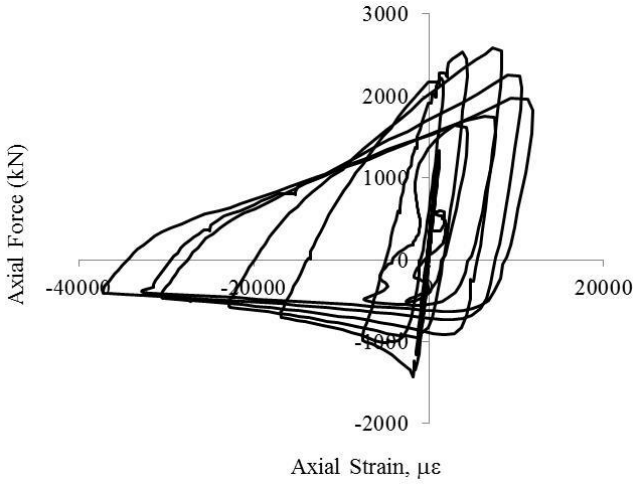


Fig. 8 Axial strain hysteresis loops

For specimen 4B, $\eta_{monotonic}$ is 2.86, which is similar to the value obtained in [23] for AW50 (ASTM A572 Grade 50) steel. In the finite element model, fracture is predicted for specimen 4B during the tensile side of cycle number 12 with λ_{CVGM} equal to 0.11 as shown in Fig. 9. The previous prediction is identical to the fracture of the brace that occurred during the experiment. Using a value of λ_{CVGM} equal to 0.4 or 0.6 for instance results in fracture of the brace during the compressive side of the same cycle (Fig. 9).

The fracture life of specimen 4B is identical to the prediction of the finite element model when considering compressive minus tensile strains. As could be seen from Fig. 9 on the demand side, the critical significant cumulative plastic strain at which tearing or cracking is first seen is 0.67 (tensile side of cycle number 11).

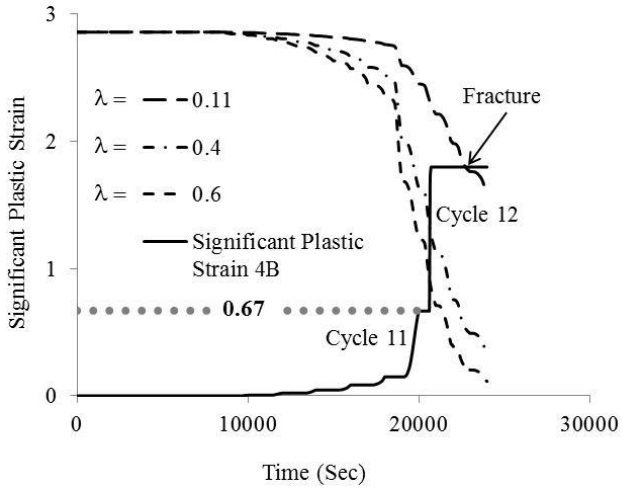


Fig. 9 Fracture life prediction

The cumulative plastic strain is used to specify the location of crack initiation for specimen 4B. The cumulative plastic strain is greater at the external integration point (outer face) than at the internal integration point (inner face) of the element where crack initiates, as shown in Fig. 10. The axial and rotational capacity of the element in consideration is exceeded at the outer faces due to cyclic loading leading to crack initiation at the external face of the element. At these locations, the geometric nature of local buckling leads to early pile up of dislocations that result in formation of slip bands. The continuous cyclic movement along the slip bands or plans leads to the formation of intrusions and extrusions at the outer free surface. At this location, microcracks occur as a result of the formation of slip planes with high shear stress which is often inclined by 45 degrees to the maximum principal stress. Some microcracks join together to form a main crack. When the length of the main crack is sufficient for a stress field to be dominant, the main crack begins to propagate through the brace in the direction normal to the maximum principal stress. The significant plastic strain was equal to 0.67 for the main crack to be dominant for specimen 4B. The main or dominant crack continues to grow until the remaining uncracked cross-section is no longer able to resist the applied load triggering fracture of the brace.

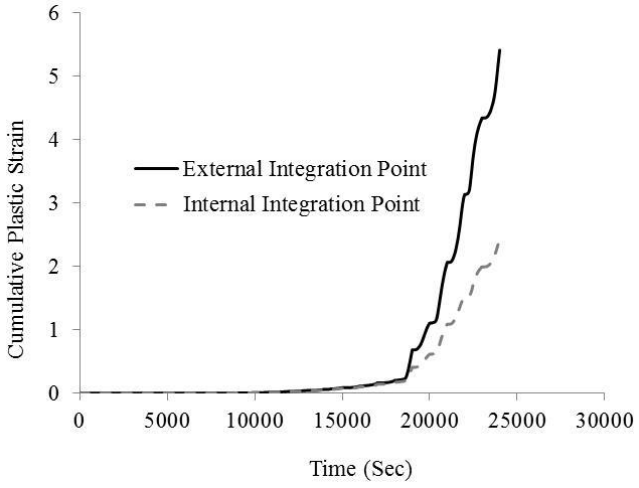


Fig. 10 Cumulative plastic strain at the element where crack initiates

The incremental deformation plasticity theory, based on the significant cumulative plastic strain, was implemented in the damage model to predict the behavior and fracture life of specimen 4B. In the actual test, main crack formed on the compressive side at the mid-length of the specimen where a plastic hinge develops. Hence, the stiffness at this location will gradually decrease causing the specimen to fail. The stiffness in the direction of the maximum principal stress, when the significant cumulative plastic strain reached a value of 0.67, was reduced to zero at the appropriate integration points. The finite element model incorporating the damage model stopped working during the tensile side of the 12th cycle due to numerical error. The axial hysteresis loops of the finite element analysis incorporating the damage model is shown in Fig. 3(a).

5 CASE STUDY

Inverted V-bracing is a popular pattern of brace arrangements for special concentrically braced frames (SCBFs). The brace fracture and fatigue models are used to predict the fracture of braces in a typical 8-storey chevron braced frame located on a site class C in Victoria, British Columbia, subjected to four ground motions. The frame is shown Fig. 11. It is a Type MD (moderately ductile) braced frame designed in accordance with the provisions of NBCC 2010 [43] and CSA S16-09 [44]. The dynamic (response spectrum) analysis method was used to determine seismic design forces in the braces. All braces are square tubing (HSS) conforming to CSA G40.20 with minimum specified F_y = 350 MPa. The braces at the 7th floor level are examined. The size of these braces is HSS 152x152x9.5, which is the same as specimen 4B in [36]. The center line (o/c) length of the brace in the building frame is 5374 mm and the distance between the ductile hinges forming in the gusset plates upon brace buckling is 4836 mm. For specimen 4B, the length between the hinges was 4850 (HSS length) + 32 (two times half the free length) = 4882 mm. The latter is very close to the length of the brace in the prototype building. The same finite element model for specimen 4B is used to examine the fracture life of the brace in the braced frame with a slightly modified version concerning the gusset plate thickness ($t_{Gusset\ plate}$ = 19.1 mm).

Nonlinear seismic response history analyses of the 8-storey structure were carried out using the OpenSees program [45]. The bracing members were modelled using force based nonlinear beam-column elements with fiber discretization of the cross-section [46], [47]. The Giuffré-Menegotto-Pinto (Steel02) material model was selected to account for Bauschinger effect and simulate kinematic-isotropic strain hardening response. The nominal yield strength F_y = 350 MPa was assigned to the steel material. Initial sinusoidal out-of-straightness with maximum amplitude of 1/500 of the unsupported member length was specified for the bracing members. A co-rotational formulation was chosen to consider geometric nonlinearities for the braces. The analyses were performed for four different earthquake records from the PEER ground motion database [48]: Nos. 057, 767, 986, and 1006, as listed in Table I. Hence, a total of eight axial deformation histories were obtained for the two braces, which is of interest because some include several cycles in compression while others have more demand in tension. All records were initially scaled to match the design spectrum.

The time histories axial deformation responses for the two braces (Left and Right) at the 7th floor, as monitored between the two gusset plate plastic hinges in the response history analyses were applied to the finite element model to verify fracture limit states. In the finite element model of the brace, the material properties used for specimen 4B were used after scaling the strength values so that F_y becomes equal to 350 MPa, same as in the response history analyses. The brace axial deformation at yield, δ_y, is 8.3 mm.

In Fig. 12, excellent agreement is found between the brace hysteretic response predicted by the OpenSees and Abaqus models for both braces and all ground motions. In all cases, the braces sustained larger axial deformations in compression as a result of the downward resultant brace load that was imposed at the beam mid-span after buckling of the braces. Yielding in tension only occurred in the Right brace under records Nos. 57, 767, and 1006. Local buckling did not develop in the finite element analysis of the 7th floor braces. These braces did not fracture under the four earthquake records according to the refined fracture and damage models.

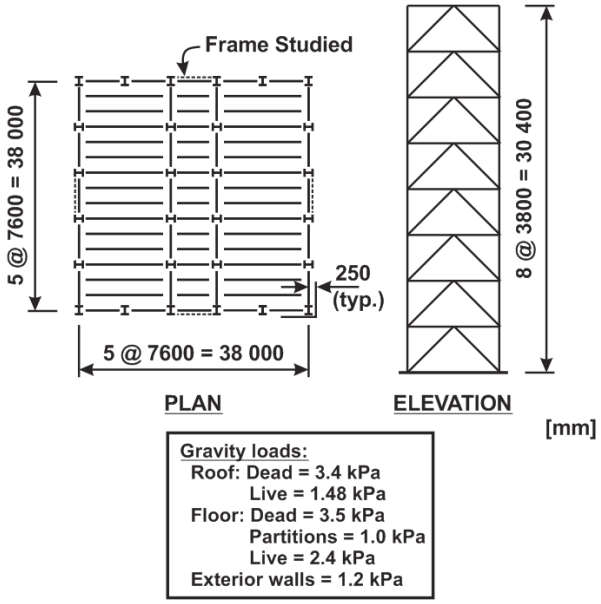


Fig. 11 Prototype building studied

For the ground motion record No. 767, incremental dynamic analysis was carried in OpenSees by applying the following scaling factors, S_F, to the ground motion: 1.5, 2.0 and 2.5. The results for S_F = 1.0, 1.5 and 2.0 are plotted in Fig. 13 for the 4.0-16.0 s time interval. The results are not shown for S_F = 2.5 as inelastic deformations concentrated in braces at another level in the building under that amplified ground motion and the demand on the braces at the 7th floor level reduced. As shown in the figure, the Left brace is subjected to a series of tension excursions before it experiences a series of sequence of significant compression half-cycles. The opposite is observed for the Right brace.

No crack initiation was detected in the Left and Right braces for the previous magnifications of ground motion. For S_F = 2.0, the displacement histories were magnified further by factors of 1.25, 1.5 and 1.75 to detect crack initiation. As could be seen from Fig. 14, crack initiation is detected when magnifying the displacement history by an additional factor between 1.25 and 1.5 for the Left brace while crack initiation is detected when magnifying the displacement history by an additional factor between 1.5 and 1.75 for the Right brace. This particular braced frame therefore possesses significant reserve capacity against fracture of the brace at the 7th floor level. The results also indicate that it is more critical for the brace studied to experience damage when the brace is subjected to a series of tension excursions before compression excursions for the displacement histories used in the case study presented here.

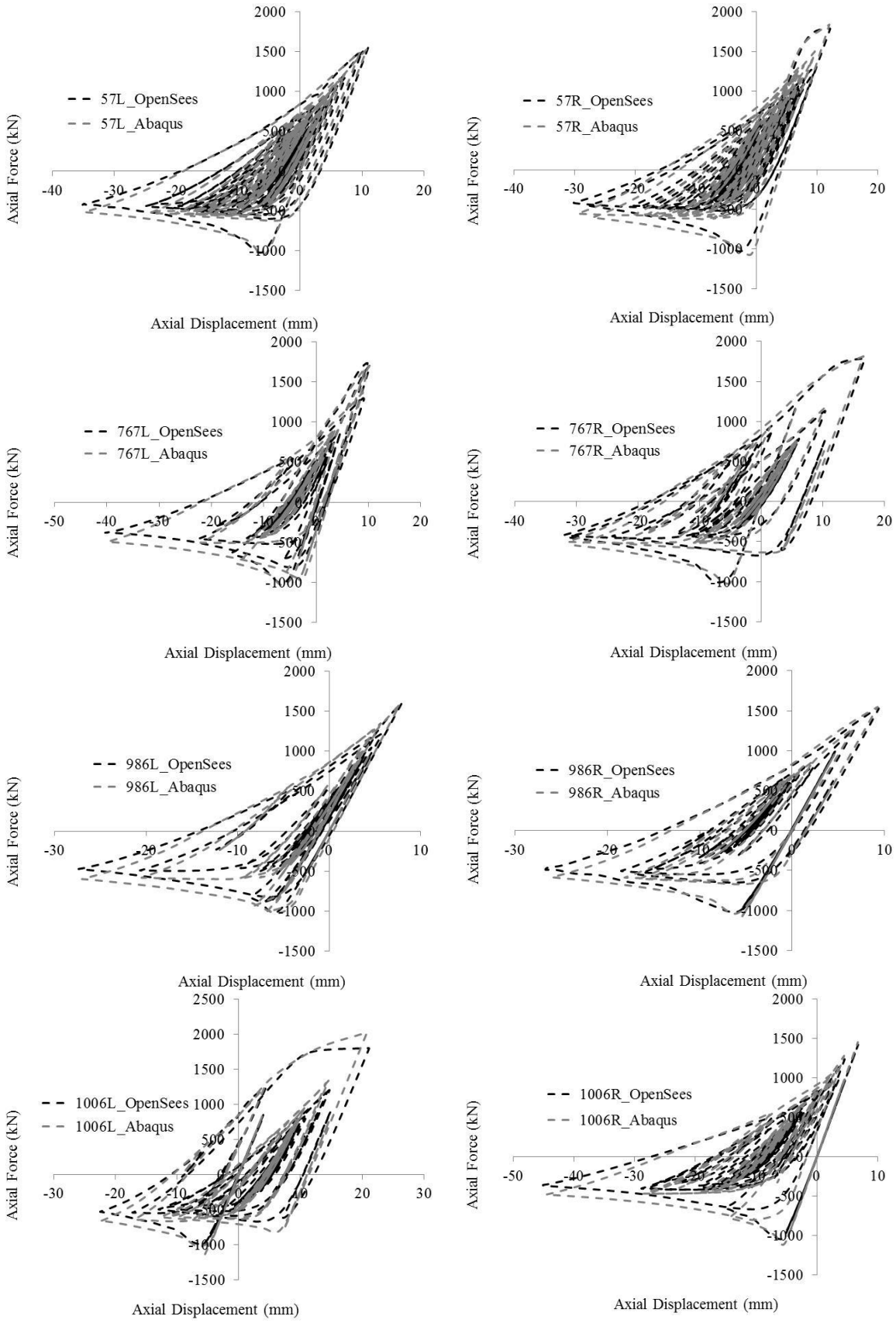


Fig. 12 Axial Hysteresis Loops

No.	Record Sequence Number	Earthquake Name	Station Name	Mag.	Comp.
1	57	1971 San Fernando	Castaic - Old Ridge Route	6.6	291°
2	767	1989 Loma Prieta	Gilroy Array #3	6.9	0°
3	986	1994 Northridge	LA - Brentwood VA Hospital	6.7	195°
4	1006	1994 Northridge	LA - UCLA Grounds	6.7	90°

Table 1: Characteristics of ground motion earthquake records.

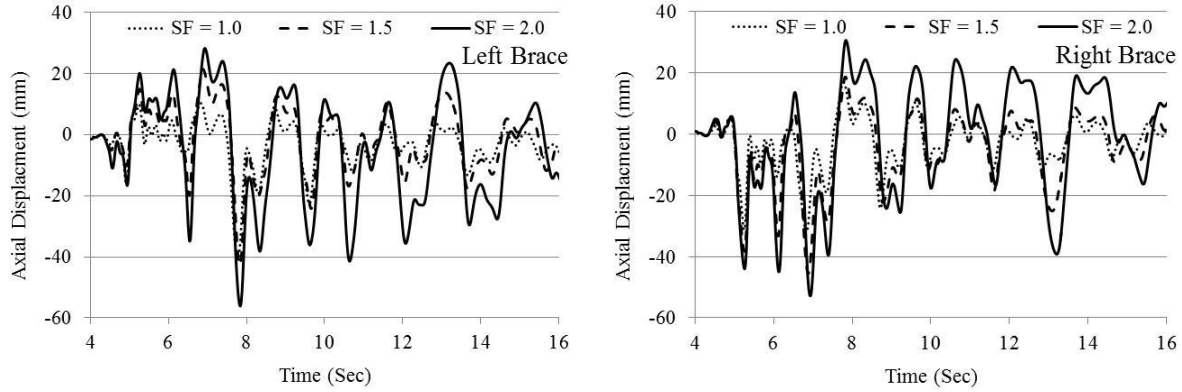


Fig.13 Axial deformation time histories for the Left (L) and Right (R) braces under stepwise incremented ground motion record No. 767.

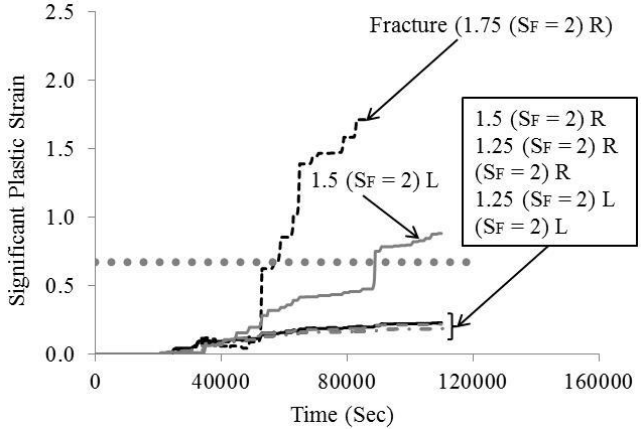


Fig. 14 Significant plastic strain for the Left (L) and Right (R) braces under magnified displacement histories of S_F = 2.0, record No. 767.

6 CONCLUSIONS

Accurate prediction of low-cycle fatigue failure of bracing members is essential for the verification of life safety and collapse prevention limit states when performing seismic assessment of concentrically steel braced frames. A modified finite element model developed in Abaqus was presented to predict the onset of cracking based on the significant cumulative

plastic strain obtained from a refined CVGM model. The model was verified against test data for an HSS specimen. The finite element model could predict the overall cyclic inelastic response of the brace as well as initiation of cracking in the plastic hinge that developed at mid-length of the brace specimen. Nonlinear dynamic analyses were conducted using an OpenSees model in order to obtain time histories of the axial deformation demands imposed to the braces at the 7th floor level of an 8-storey CBF designed in accordance with current Canadian seismic design provisions. The computed time histories of the axial deformation were then applied to the brace finite element model. The analyses showed that fracture of the braces studied would not occur under seismic ground motions corresponding to two times the design earthquake level. Brace fracture was found to be more critical in braces that are subjected to a series of tension excursions before compression excursions are applied.

ACKNOWLEDGMENT

The study was made possible by financial support of the Natural Science and Engineering Council, NSERC Canada and the Individual Research Grant of the UAE University. Many thanks for Brad Shaback, University of Calgary, for providing the experimental data.

APPENDIX

[1] R. Tremblay, M. Bruneau, M. Nakashima, H.G.L. Prion, A. Filiatrault, and R. DeVall, Seismic Design of Steel Buildings: Lessons From the 1995 Hyogoken-Nanbu Earthquake, *Canadian Journal of Civil Engineering*, **23**(3), 727-756, 1996.

[2] R. Tremblay, P. Timler, M. Bruneau, and A. Filiatrault, Performance of Steel Structures During the January 17, 1994 Northridge Earthquake, *Canadian Journal of Civil Engineering*, **22**(2), 138-360, 1995.

[3] X. Tang and S. Goel. Brace Fractures and Analysis of Phase I Structure, *Journal of Structural Engineering*, **115**(8), 1960-1976, 1989.

[4] R. Tremblay, M-H. Archambault, and A. Filiatrault, Seismic Response of Concentrically Braced Steel Frames Made with Rectangular Hollow Bracing Members, *Journal of Structural Engineering*, **129**(12), 1626-1636, 2003.

[5] C.W. Roeder, D.E. Lehman, K. Clark, J. Powell, J.-H. Yoo, K.-C. Tsai, C.-H. Lin, and C.-Y. Wei, Influence of gusset plate connections and braces on the seismic performance of X-braced frames, *Earthquake Engineering and Structural Dynamics*, **40**(XX), 355-374, 2011.

[6] Y. Jiang and R. Tremblay, Influence of PAFs on the inelastic seismic response of steel HSS bracing members, Research Report No. SR14-01, Civil, Geological and Mining Engineering Department, Polytechnique Montreal, Montreal, Canada.

[7] A. M. Freudenthal, The Inelastic Behavior of Engineering Materials and Structures, John Wiley & Sons, New York, 1950.

[8] F. A. McClintock, A. S. Argon, Mechanical Behavior of Materials, Addison-Wesley Publishing Company, 1966.

[9] M. G. Cockcroft, D. J. Latham, Ductility and the Workability of Metals, *Journal of the Institute of Metals*, **96**(2), 33-39, 1968.

[10] J. R. Rice, and D. M. Tracey, On the Ductile Enlargement of Voids in Triaxial Stress Fields, *Journal of the Mechanics and Physics of Solids*, **17**(3), 201-217, 1969.

[11] P. Brozzo, B. Deluka, and R. Rendina, A New Method for the Prediction of Formability in Metal Sheets, *Proceedings of the 7th Biennial Conference on Sheet metal Forming and Formability*, **169**, 41-57, 1972.

[12] L. F. Gillemot, Criterion of Crack Initiation and Spreading, *Engineering Fracture Mechanics*, **8**(1), 239-253, 1976.
[13] D. M. Norris, J. E. Reaugh, B. Moran, and D. F. Quinones, A Plastic-Strain, Mean-Stress Criterion for Ductile Fracture, *Journal of Engineering Materials and Technology*, **100**(3), 279-286, 1978.
[14] M. Oyane, T. K. Sato, Okimoto, and S. Shima, Criteria for Ductile Fracture and Their Applications, *Journal of Mechanical Working Technology*, **4**(l), 65-81, 1980.
[15] A. G. Atkins, Possible Explanation for Unexpected Departures in Hydrostatic Tension-Fracture Strain Relations, *Metal Science*, **15**(2), 81-83, 1981.
[16] V. Tvergaard, Ductile Fracture by Cavity Nucleation between Larger Voids, *Journal of the Mechanics and Physics of Solids*, **30**(4), 265-286, 1982.
[17] V. Tvergaard, and A. Needleman, Analysis of the Cup-Cone Fracture in a Round Tensile Bar, *Acta Metallurgica*, **32**(1), 157-169, 1984.
[18] J. Lemaitre, A course on damage mechanics, Springer-Verlag, 1992.
[19] J. Lemaitre, A continuous damage mechanics model for ductile fracture, *Journal of Engineering Materials and Technology*, **107**(1), 83-89, 1985.
[20] J. Lemaitre, How to use damage mechanics, Nuclear Engineering and Design, **80**(2), 233-245, 1984.
[21] J. Dufailly, and J. Lemaitre, Modeling Very Low Cycle Fatigue, *International Journal of Damage Mechanics*, **4**(2), 153-170, 1995.
[22] P. Matic, G. C. Kirby III, and M. I. Jolles, The Relationship of the Tensile Specimen Size and Geometry Effects to Unique Constitutive Parameters for Ductile Material, NRL Memorandum Report 5936, Mechanics of Materials Branch, Material Science and Technology Division, 1987.
[23] A. M. Kanvinde, and G. G, Deierlein, Micromechanical Simulation of Earthquake-Induced Fracture in Steel Structures, Technical Report 145, John A. Blume Earthquake Engineering Center, Stanford University, California, USA, 2004.
[24] A. M. Kanvinde, and G. G. Deierlein, Cyclic Void Growth Model to Assess Ductile Fracture Initiation in Structural Steels due to Ultra Low Cycle Fatigue, *Journal of Engineering Mechanics*, **133**(6), 701-712, 2007.
[25] Y. L. Huang, and S. A. Mahin, Evaluation of Steel Structure Deterioration with Cyclic Damaged Plasticity, *The 14th World Conference on Earthquake Engineering, Beijing*, China, 2008.
[26] W. Prager, and R. I. Providence, A New Method of Analyzing Stresses and Strains in Work-Hardening Plastic Solids, *ASME Journal of Applied Mechanics*, **23**, 493-496, 1956.
[27] H. Ziegler, A Modification of Prager's Hardening Rule, *Quarterly of Applied Mathematics*, **17**, pp. 55-65, 1959.
[28] Z. Mroz, On the Description of Anisotropic Workhardening, *Journal of the Mechanics and Physics of Solids*, **15**, 163-175, 1967.
[29] Y. F. Dafalias, and E. P. Popov, A Model of Nonlinearly Hardening Materials for Complex Loading, *Acta Mechanica*, **21**, 173-192, 1975.
[30] Y. F. Dafalias, and E. P. Popov, Plastic Internal Variables Formalism of Cyclic Plasticity, *Journal of Applied Mechanics*, **43**, 645-651, 1976.
[31] N. T. Tseng, and G. C. Lee, Simple Plasticity Model of Two-Surface Type, *Journal of Engineering Mechanics*, **109**(3), 795-810, 1983.
[32] P. J. Armstrong, and C. O. Frederick, A Mathematical Representation of the Multiaxial Bauschinger Effect, CEGB Report, RD/B/N/731, Berkeley Nuclear Laboratories, R&D Department, California, USA, 1966.

[33] J. L. Chaboche, Time-Independent Constitutive Theories for Cyclic Plasticity, *International Journal of Plasticity*, **2**(2), 149-188, 1986.
[34] A. F. Bower, Cyclic Hardening Properties of Hard-Drawn Copper and Rail Steel, *Journal of the Mechanics and Physics of Solids*, **37**(4), 455-470, 1989.
[35] M. Haddad, Seismic design of concentrically braced steel frames for earthquakes, PhD Dissertation. Department of Civil Engineering, The University of Calgary, Calgary, A.B., Canada, 2004.
[36] B. Shaback, and T. Brown, Behaviour of square hollow structural steel braces with end connections under reversed cyclic axial loading, *Canadian Journal of Civil Engineering*, **30**(4), 745-753, 2003.
[37] R. K. Bubela, An experimental and analytical study of chevron braced frames with vertical slotted connections, MSc Thesis. Department of Civil Engineering, The University of British Colombia, Vancouver, B.C., Canada, 2003.
[38] J. Aguilera, A. Shaat, and A. Fam, Strengthening T-joints of rectangular hollow steel sections against web buckling under brace axial compression using through-wall bolts, *Thin-Walled Structures*, **56**, 71-78, 2012.
[39] R. Moreau, C. A. Roger, R. Tremblay, and J. A. Packer, Finite element evaluation of the "modified-hidden-gap" HSS slotted tube-to-plate connection, *Connections VII, 7th International Workshop on Connections in Steel Structures*, Timisoara, Romania. 30 May - 2 June, 2012, 10p.
[40] Abaqus, 2011. User's Manual, Version, 11.6, Hibbitt, Karlsson, and Sorensen, Inc., Providence, RI.
[41] S. Santagati, D. Bolognini, and R. Nascimbene, Strain Life Analysis at Low-Cycle Fatigue on Concentrically Braced Steel Structures with RHS Shape Braces, *Journal of Earthquake Engineering*, **16**(S1), 2012, 107-137. doi:10.1080/13632469.2012.675840
[42] A. T. Myers, G. G. Deierlein, and A. M. Kanvinde, Testing and probabilistic simulation of ductile fracture initiation in structural steel components and weldments, Report No. 170. Department of Civil and Environmental Engineering, Stanford University, San Francisco, California, 2009.
[43] NRCC. National Building Code of Canada 2010, 13th ed., National Research Council of Canada, Ottawa, ON, 2010.
[44] CSA. CSA-S16-09, Design of Steel Structures, Canadian Standards Association, Mississauga, ON, 2009
[45] F. McKenna, and G. L. Fenves, Open System for Earthquake Engineering Simulation (OpenSees), Pacific Earthquake Engineering Research Center (PEER), University of California, Berkeley, C.A., 2014. (http://opensees.berkeley.edu/)
[46] A. Aguero, C. Izvernari, and R. Tremblay, Modelling of the Seismic Response of Concentrically Braced Steel Frames using the OpenSees Analysis Environment, *International Journal of Advanced Steel Construction*, **2**(3), 242-274, 2006.
[47] P. Uriz, F. C. Filippou, and S.A. Mahin, Model for Cyclic Inelastic Buckling of Steel Braces, *Journal of Structural Engineering*, **134**(4), 619-628, 2008.
[48] PEER, PEER Strong Ground Motion Database, Pacific Earthquake Engineering Center, 2011. (http://peer.berkeley.edu/nga/)

COMPDYN 2015
5th ECCOMAS Thematic Conference on
Computational Methods in Structural Dynamics and Earthquake Engineering
M. Papadrakakis, V. Papadopoulos, V. Plevris (eds.)
Crete Island, Greece, 25–27 May 2015

CALCULATING THE FREQUENCY OF AN ACTUAL STRUCTURE USING THE RAYLEIGH TECHNIQUE

Alexandre de M. Wahrhaftig[1] and Reyolando M. L. R. F. Brasil[2]

[1] Federal University of Bahia (UFBa)
Polytechnic School, Department of Construction and Structures, Aristides Novís Street, number 02, 5th floor, Federação, Salvador – BA, Brazil, CEP: 40210-910
alixa@ufba.br address

[2] University of São Paulo (USP)
Polytechnic School, Department of Structural and Geotechnical Engineering, Prof. Almeida Prado Av., tv. 2, nbr 83, University Campus, São Paulo – SP, Brazil, CEP: 05508-900
reyolando.brasil@poli.usp.br

Keywords: Actual Structure, Natural Frequency, Rayleigh Technique, Structural Dynamics, Element Finite Method.

Abstract. *Beams and columns constitute a continuous system with infinite degrees of freedom. To study the behavior of these systems the use of discretization techniques is required. However, one can associate them to a system with a single degree of freedom, restricting the form in which the system will deform and write their properties as a function of the generalized coordinate. This technique is the called Rayleigh Method and is a resource largely used to study the vibration of elastic systems. However, actual structures are systems more complex than simple beams and columns, because they have properties varying along its length. In such cases, the use of the Rayleigh Method should be done by parts and its integrals resolved within the limits established for each interval, being the generalized properties calculated for each segment of the structure. The actual structure selected for this study is a metallic high slenderness pole for which the frequency of the first vibration mode was calculated analytically, and as well as by a FEM - Finite Element Method model based computer for comparative purposes, getting a very good result.*

1 INTRODUCTION

The vibration analysis response of framed structures modeled as beams and columns have been studied by many researchers and continue to be treated extensively in the literature. Beams and columns constitute a continuous system with infinite degrees of freedom. To study the behavior of these systems the use of discretization techniques is required, in which the structure is transformed into subsystems defined by points called joints. However, one can associate them to a system with a single degree of freedom, restricting the form in which the system will deform and write their properties as a function of the generalized coordinate. This technique was used by Rayleigh [1] in the study of vibration of elastic systems, being its equations valid in the whole domain of the problem. Leissa [2] claims that the precision obtained through this method depends entirely on the functional form that is used to represent the free vibration mode.

However, actual structures are systems more complex than simple beams and columns, because their properties vary along its length. In such cases, the use of the Rayleigh method should be done by parts and its integrals resolved within the limits established for each interval, being the generalized properties calculated for each segment of the structure, paying special attention to the geometric stiffness because each parcel must take into account the normal force distributed in its range and efforts that operate in the upper segments. The actual structure selected for this study is a metallic high slenderness pole for which the frequency of the first vibration mode was calculated as described above, and a computer model was developed using the Finite Element Method (FEM) for comparative purposes, getting a very good result, hence its importance can be realized independently of sophisticated computational programs.

2 A QUICK OVERVIEW ABOUT THE MATHEMATICS CONSIDERATIONS

The analytical formulation developed in this paper is based on the principle of virtual work combined with a technique similar to that of Rayleigh [1]. Rayleigh assumed that a system containing infinite degrees of freedom can be replaced by a finite SDOF (single degree of freedom) system that approximates their frequency. Applications of the Rayleigh technique to mechanical systems with vibration problems are found in a wide range of scientific studies. It is important to observe that the technique developed by Rayleigh and presented in his first book was only used to calculate the fundamental frequency. Leissa [2] claims that the precision obtained through this method depends entirely on the functional form that is used to represent the free vibration mode. If the exact shape were assumed, the exact corresponding frequency would be generated by this method.

The basic concept behind the Rayleigh method is the principle of conservation of energy in mechanical systems, therefore it is applicable to linear and nonlinear structures, according to Clough [3]. According to Temple [4], the fundamental principles developed by Rayleigh are applied both to systems with finite degrees of freedom and to continuous systems. The purpose is to determine the fundamental period of vibration and to analyze the stability of the elastic systems with the precision required for engineering problems. To do this, the Virtual Works Principles must be described by adequate chosen of generalized coordinates and by a functional form that describes the first mode of vibration. At the end of the calculation, the movement equation is written in terms of the generalized coordinate, from which one can extract the generalized elastic and geometric properties of the system.

Assuming that the well-known trigonometric function

$$\phi(\mathrm{x}) = 1 - \cos\left(\frac{\pi \mathrm{x}}{2\mathrm{L}}\right) \tag{1}$$

one finds the elastic stiffness,

$$K_0 = \int_0^L EI\left(\frac{d^2\phi(x)}{dx^2}\right)^2 dx \tag{2}$$

with *E* being the elasticity modulus and *I* the inertia of the section. The geometrical stiffness is

$$K_g = \int_0^L N(x)\left(\frac{d\phi(x)}{dx}\right)^2 dx \tag{3}$$

where *N(x)* is a function of normal force. The total generalized mass, for their turn is

$$M = m_0 + m \tag{4}$$

where m_0 is the lumped mass at the element joint and

$$m = \int_0^L \bar{m}\left(\phi(x)\right)^2 \tag{5}$$

with $\bar{m}$ the mass per unit length.

Finally, the natural cyclical frequency should be calculated doing

$$\omega = \sqrt{\frac{K}{\Pi}} \tag{6}$$

taking into account that

$$K = K_0 - K_g \tag{7}$$

For a more detailed information about the development this analytical procedure Wahrhaftig *et all* [5] can be consulted.

3 ACTUAL STRUCTURE CHARACTERISTICS

The actual structure selected for this study is a metallic high slenderness pole, showed in Figure 1 and Figure 2. The geometric details also can be seen in Figure 2, where *t* means the thickness of the wall of each segment of the structure.

This is a metal pole for supporting the radiating system of cellular mobile telephone signal. The structure has 48 meters of height and has hollow circular section of external diameter (ϕ_{ext}) and thickness (*t*) variables, having slenderness equal to 310.

Table 1 presents the structure proprieties and model discretization. Table 2 shows the structural parameters and the existent devices on structure.



Figure 1: Actual structure.

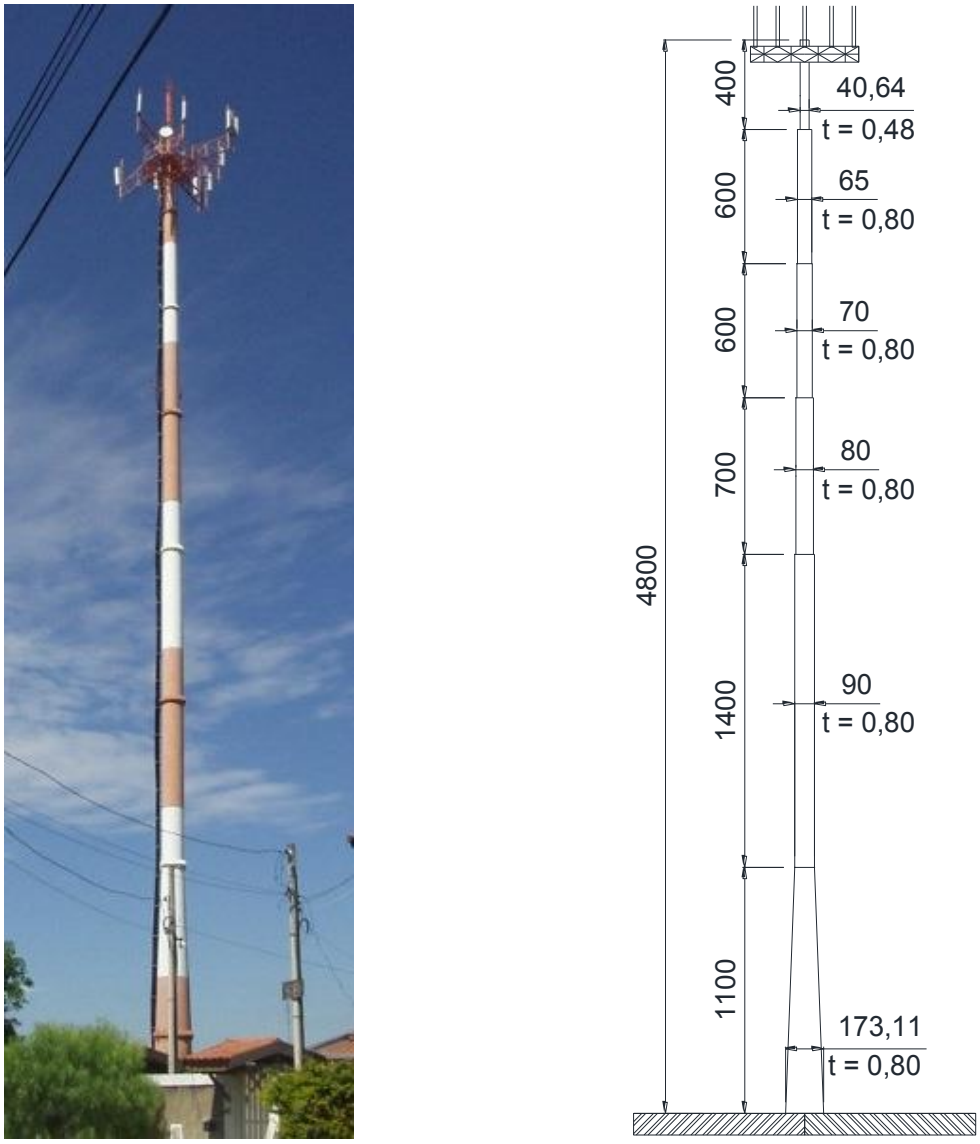


Figure 2: A slender metallic pole – geometric details.

Height (m)	ϕ_{ext} (cm)	t (cm)	Height (m)	ϕ_{ext} (cm)	t (cm)	Height (m)	ϕ_{ext} (cm)	t (cm)	Height (m)	ϕ_{ext} (cm)	t (cm)
48.00	40.64	0.48	30.00	80.00	0,80	20.00	90.00	0.80	10.00	97.56	0.80
46.00	40.64	0.48	29.00	80.00	0,80	19.00	90.00	0.80	9.00	105.11	0.80
44.00	40.64	0.48	28.00	80.00	0,80	18.00	90.00	0.80	8.00	112.67	0.80
42.00	65.00	0.80	27.00	80.00	0,80	17.00	90.00	0.80	7.00	120.22	0.80
40.00	65.00	0.80	26.00	80.00	0,80	16.00	90.00	0.80	6.00	127.78	0.80
38.00	65.00	0.80	25.00	80.00	0,80	15.00	90.00	0.80	5.00	135.33	0.80
36.00	70.00	0.80	24.00	90.00	0,80	14.00	90.00	0.80	4.00	142.89	0.80
34.00	70.00	0.80	23.00	90.00	0,80	13.00	90.00	0.80	3.00	150.44	0.80
32.00	70.00	0.80	22.00	90.00	0,80	12.00	90.00	0.80	2.00	158.00	0.80
31.00	80.00	0.80	21.00	90.00	0,80	11.00	90.00	0.80	1.00	165.56	0.80
									0.00	173.11	0.80

Table 1: Structural geometry and discretization of the FEM model.

Device	Height	Weight and distributed weight
Pole	from 0 to 48 m	7850 kN/m^3
Stair	from 0 to 48 m	0.15 kN/m
Cables	from 0 to 48 m	0.25 kN/m
Antenna and Supports	48 m	3.36 kN

Table 2: Devices and weighs on structure.

4 SIMULATIONS AND RESULTS

4.1 Analytical procedure

4.1.1. Geometric definitions and parameters adopted

The parameters used for application of analytical procedure using the Rayleigh Method are the follows:

- elasticity modulus of steel: E = 205 GPa,
- density of steel: ρ = 7850 kg/m^3,
- lumped mass on the top: m_0 = 342.40 kg,
- distributed mass per unity height: m_e = 40 kg/m,
- acceleration of gravity: g = 9.806650 m/s^2.

The corresponding order the heights in the structure and the geometric properties of the cross sections of the respective segments are given by:

On the base to $x = 0$, one has: $D_1 = 173.11\text{cm}$, $t_1 = 0.80\text{cm}$, $d_1 = D_1 - 2t_1$, $A_1 = \frac{\pi}{4}\left(D_1^2 - d_1^2\right)$, $I_1 = \frac{\pi}{64}\left(D_1^4 - d_1^4\right)$.

To the follow segment, of variable proprieties, one has: $D(x) = \frac{D_2 - D_1}{L_1}x + D_1$, $d(x) = D(x) - 2t_1$, $A(x) = \frac{\pi}{4}\left(D(x)^2 - d_1(x)^2\right)$, $I(x) = \frac{\pi}{64}\left(D(x)^4 - d(x)^4\right)$.

To the ordinate $L_1 = 11\text{m}$, one defines: $D_2 = 90.00\ \text{cm}$, $t_2 = 0.80\text{cm}$, $d_2 = D_2 - 2t_2$, $A_2 = \frac{\pi}{4}\left(D_2^{\,2} - d_2^{\,2}\right)$, $I_2 = \frac{\pi}{64}\left(D_2^{\,4} - d_2^{\,4}\right)$.

To $L_2 = 25.00\text{m}$, one has: $D_3 = 80.00\ \text{cm}$, $t_3 = 0.80\text{cm}$, $d_3 = D_3 - 2t_3$, $A_3 = \frac{\pi}{4}\left(D_3^{\,2} - d_3^{\,2}\right)$, $I_3 = \frac{\pi}{64}\left(D_3^{\,4} - d_3^{\,4}\right)$.

To $L_3 = 32.00\text{m}$, one has: $D_4 = 70.00\ \text{cm}$, $t_4 = 0.80\text{cm}$, $d_4 = D_4 - 2t_4$, $A_4 = \frac{\pi}{4}\left(D_4^{\,2} - d_4^{\,2}\right)$, $I_4 = \frac{\pi}{64}\left(D_4^{\,4} - d_4^{\,4}\right)$.

To $L_4 = 38.00\text{m}$, one has: $D_5 = 65.00\ \text{cm}$, $t_5 = 0.80\text{cm}$, $d_5 = D_5 - 2t_5$, $A_5 = \frac{\pi}{4}\left(D_5^{\,2} - d_5^{\,2}\right)$, $I_5 = \frac{\pi}{64}\left(D_5^{\,4} - d_5^{\,4}\right)$.

To $L_5 = 44.00\text{m}$ and $L_6 = 48.00\text{m}$, one has: $D_6 = 40.64\text{cm}$, $t_6 = 0.48\text{cm}$, $d_6 = D_6 - 2t_6$, $A_6 = \frac{\pi}{4}\left(D_6^{\,2} - d_6^{\,2}\right)$, $I_6 = \frac{\pi}{64}\left(D_5^{\,4} - d_5^{\,4}\right)$.

4.1.2. The calculation of generalized mass

The sub-indices in Roman numerals, introduced from this point on, aim to prevent redundancy of notation in expressions. The generalized mass was measured by the following integral arranged.

To the first segment

$$m_1 = \int_0^{L_1} m_I(x)\phi(x)^2 dx \text{, with } m_I(x) = A(x)\rho + m_e \tag{8}$$

To the second segment

$$m_2 = \int_{L_1}^{L_2} m_{II}\phi(x)^2 dx \text{, with } m_{II} = A_2\rho + m_e \tag{9}$$

Similarly, to the other segments, can be written in the general form

$$m_i = \int_{L_{i-1}}^{L_i} m_i\phi(x)^2 dx \text{, with } m_i = A_i\rho + m_e \tag{10}$$

The generalized distributed mass is obtained by

$$m_R = \sum_{i=1}^{6} m_i \tag{11}$$

and the total generalized mass by:

$$M = m_0 + m_R \tag{12}$$

4.1.3. The calculation of generalized geometric stiffness

To compute the generalized geometric stiffness is necessary to determine the normal efforts for the parts defined in geometry. From top to bottom the structure of the axial forces are

$$F_0 = m_0 g \tag{13}$$

$$F_6 = \int_{L_5}^{L} m_{VI} g dx \tag{14}$$

$$F_5 = \int_{L_4}^{L_5} m_V g dx \tag{15}$$

and so on, or better

$$F_i = \int_{L_{i-1}}^{L_i} m_i g dx \tag{16}$$

The axial force on the first segment, which is linearly variable, was obtained by the following expression

$$F_1 = \int_{0}^{L_1} m_I(x) g dx \tag{17}$$

where *g* is de gravity acceleration. The generalized axial force *F* is so

$$F = \sum_{i=0}^{6} F_i \tag{18}$$

and the geometric stiffness is calculated following the expressions

$$\begin{aligned}
K_{g6} &= \int_{L_5}^{L} \left[F_0 + m_{VI}(L_6 - x) g \left(\frac{d}{dx}\phi(x) \right)^2 \right], \\
K_{g5} &= \int_{L_4}^{L_5} \left[F_0 + F_6 + m_V(L_5 - x) g \left(\frac{d}{dx}\phi(x) \right)^2 \right], \\
K_{g4} &= \int_{L_3}^{L_4} \left[F_0 + F_6 + F_5 + m_{IV}(L_4 - x) g \left(\frac{d}{dx}\phi(x) \right)^2 \right], \\
K_{g3} &= \int_{L_2}^{L_3} \left[F_0 + F_6 + F_5 + F_4 + m_{III}(L_3 - x) g \left(\frac{d}{dx}\phi(x) \right)^2 \right], \\
K_{g2} &= \int_{L_1}^{L_2} \left[F_0 + F_6 + F_5 + F_4 + F_3 + m_{II}(L_2 - x) g \left(\frac{d}{dx}\phi(x) \right)^2 \right], \\
K_{g1} &= \int_{0}^{L_1} \left[F_0 + F_6 + F_5 + F_4 + F_3 + F_2 + m_I(x)(L_1 - x) g \left(\frac{d}{dx}\phi(x) \right)^2 \right].
\end{aligned} \tag{19}$$

So that, the generalized geometric stiffness K_g of structure is obtained by

$$K_g = \sum_{i=1}^{6} K_{gi} \tag{20}$$

4.1.4. The calculation of generalized elastic stiffness

The elastic geometric parcels are

$$K_{01} = \int_0^{L_1} EI(x)\left(\frac{d^2}{dx^2}\phi(x)\right)^2 dx \tag{21}$$

$$K_{02} = \int_{L_1}^{L_2} EI_2\left(\frac{d^2}{dx^2}\phi(x)\right)^2 dx \tag{22}$$

which in the same way, to the others segments, can be written as

$$K_{0i} = \int_{L_{i-1}}^{L_i} EI_i\left(\frac{d^2}{dx^2}\phi(x)\right)^2 dx \tag{23}$$

and the generalized elastic stiffness, is given by the sum of their parcels, so

$$K_0 = \sum_{i=1}^{6} K_{0i} \tag{24}$$

4.1.5. The calculation of frequency

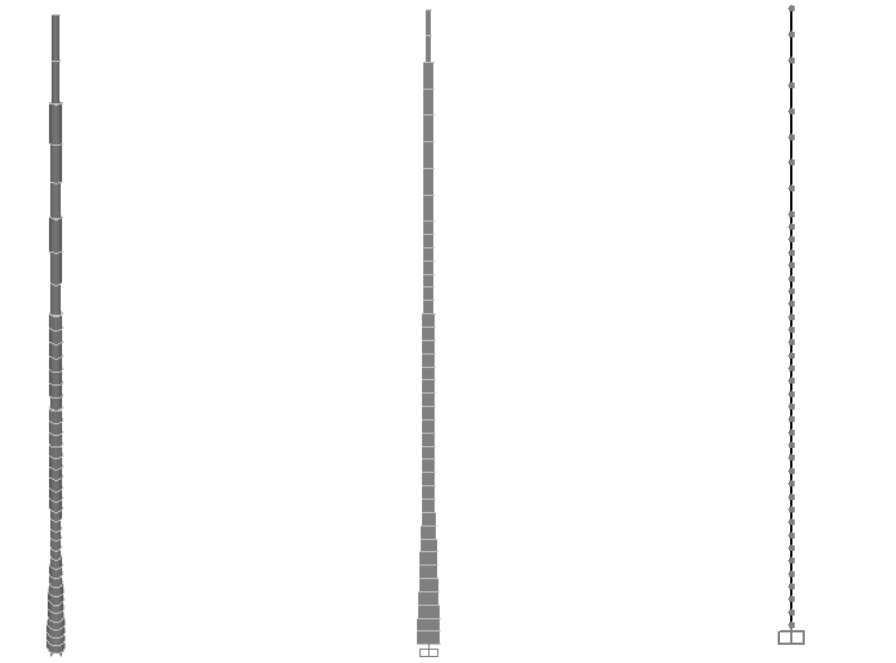
The frequency of the first mode calculated using Eq. (6), transformed to Hertz, is 0.569646 Hz.

4.2 Finite Element Method

To compare the results development above was elaborated a computational modeling by Finite Element Method (FEM). The vibration mode and frequency obtained for that method is listed in Figure 5.

The structure analyzed was modeled using bar elements with constant and variable cross-sections, as appropriate. The model was awarded the forces described in Table 2, with the corresponding masses. Figure 3 shows the three-dimensional model available by the program and the discretization of the built structure with 40 bar elements.

The frequency by FEM was calculated taking into account the effect of normal force, using the correspondent formulation for them, the named geometric nonlinearity (GNL). For more details about the specific formulations in Finite Element Method Clough [3], Cook [6], Bucalem [7] and Zienkiewicz [8] can be consulted.



(a) 3D (b) Lateral view (c) Discretization

Figure 3: Model by Finite Element Method (FEM).

The form and frequency to the first mode vibration by Finite Element Method is presented in Figure 4.

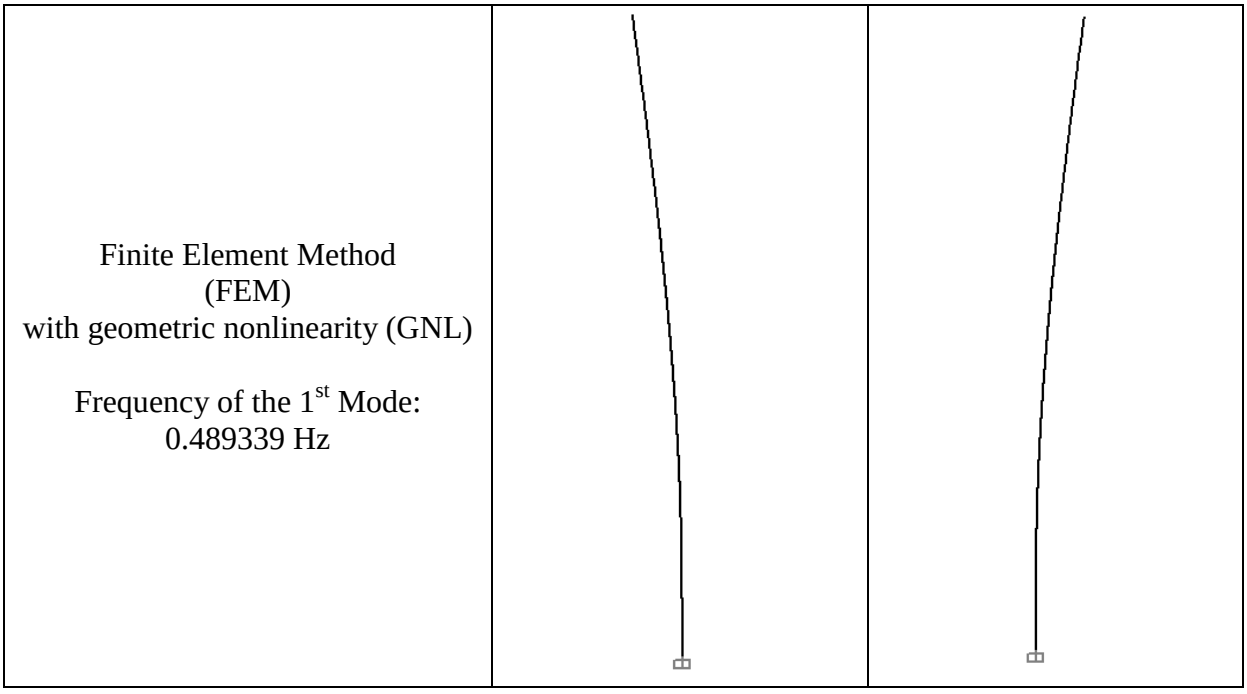


Figure 4: Natural mode and frequencies by Finite Element Method.

A comparison which assesses the quality of analytical results of the development of this work is the appreciation of normal force on each segment of the structure, as shown in Table 3.

L (m)	Analytical procedure (kN)	FEM (kN)	Differences	
			Absolute	(%)
48.00	3.355520	3.355520	0.0000	0.000000
44.00	6.786842	6.786842	0.0000	-0.000001
38.00	16.585633	16.585633	0.0000	-0.000001
32.00	26.964392	26.964392	0.0000	-0.000001
25.00	40.426203	40.426204	0.0000	-0.000002
11.00	70.056344	70.056345	0.0000	-0.000002
0.00	102.174047	102.174049	0.0000	-0.000002

Table 3: Normal effort on structure.

5 CONCLUSIONS

- The formulation for calculating the geometric stiffness of the present study was reviewed by the Finite Element Method (FEM), for comparing the results of axial forces on each segment of the structure (Table 3), without difference between them.
- The difference in relation to the vibration frequency of the fundamental mode, calculated under geometric nonlinearity, proposed for this paper, of 0.569646 Hz and the obtained by the Finite Element Method, of 0.489339 Hz, is different to 16 % upper.
- This paper does not terminate the studies for the application of analytical procedure based in the Rayleigh Method to actual structures. That method can allow the calculation of frequency without the use of sophisticated computer resources, in a correct way and within the limits required by engineering.

REFERENCES

[1] Rayleigh, *Theory of Sound* (two volumes), Dover Publications, New York, re-issued. 1877.

[2] A.W. Leissa, *The historical bases of the Rayleigh and Ritz methods*, Journal of Sound and Vibration, Volume 287, Issues 4-5, 4, pp 961-978, doi:10.1016/j.jsv.2004.12.021, 2004.

[3] R.W. Clough and J. Penzien, *Dynamic of Structures*, McGraw Hill International Editions, Second Edition, Taiwan, 1993.

[4] G. Temple, and W.G. Bickley, *Rayleigh´s Principle and its Applications to Engineering*, Oxford University Press, Humphrey Milford, London, 1933.

[5] A.M. Wahrhaftig, R. M. L. R. F. Brasil, J.M. Balthazar, *The first frequency of cantilevered bars with geometric effect: a mathematical and experimental evaluation*, J Braz. Soc. Mech. Sci. Eng., doi:10.1007/s40430-013-0043-9, 2013.

[6] R.D. Cook, *Concepts and Applications of Finite Element Analysis*. John Wiley and Sons, Inc., NJ, USA, 1974.

[7] Bucalem, M. L., Bathe, K. J.: *The Mechanics of Solids and Structures – Hierarchical Modeling and the Finite Element Solution*, Springer, German, 2011.

[8] O.C. Zienkiewicz, R.C. Taylor, *The finite element method, Vol. I,* 4th Edition. McGraw Hill, 1989.

COMPDYN 2015
5th ECCOMAS Thematic Conference on
Computational Methods in Structural Dynamics and Earthquake Engineering
M. Papadrakakis, V. Papadopoulos, V. Plevris (eds.)
Crete Island, Greece, 25–27 May 2015

EFFICIENT NONLINEAR DYNAMIC ANALYSIS OF FRAME STRUCTURES

Johannes Burtscher

Unit of Applied Mechanics, University of Innsbruck
Technikerstr. 13, 6020 Innsbruck, Austria
e-mail: johannes.burtscher@uibk.ac.at

Keywords: nonlinear dynamic analysis; sparse linear systems; matrix factor modification.

Abstract. *This paper presents the application of multiple-rank modifications to the sparse Cholesky factorization* $\mathbf{LDL}^T$ *for faster nonlinear finite element analysis of moment resisting frames. Such frames resist lateral forces primarily by bending moments at the joints and are often modeled by the concept of concentrated plasticity. That is, the joints are represented by rotational springs with nonlinear material behavior, whereas the beams and columns remain linear elastic. This implies that within a materially-nonlinear-only finite element analysis, large parts of the system matrix remain unchanged. The Cholesky factors, however, are completely recomputed amongst solution steps and no reuse is made of the previous factorization. I address this drawback with a multiple-rank update routine implemented in the publicly available library CHOLMOD. The routine allows an update or downdate of a sparse* $\mathbf{LDL}^T$ *factorization with a runtime proportional to the number of nonzero entries in* $\mathbf{L}$ *and* $\mathbf{D}$ *that change. Exemplary simulations show that the proposed method can be substantially faster if changes to the simulation's system matrix can efficiently be expressed as a multiple-rank update problem. It also becomes apparent that the method is not restricted to frame problems but rather can be applied to any physical phenomenon where nonlinearities are locally bounded.*

1 INTRODUCTION

Realistic analysis of engineering structures often requires nonlinear methods. The occurring nonlinearities stem from various reasons such as inelastic material behavior, large displacements and rotations, or complex boundary conditions. For many practical applications only nonlinear material behavior is of concern. Often, these nonlinearities are further restricted to local domains whereas large parts of the structure remain linear elastic. Standard finite element codes used for structural dynamic analysis do not take advantage of this fact, which leads to simulations that are ultimately slower than necessary.

Finite element methods discretize the governing partial differential equations in space, leading, in case of transient problems, to a set of ordinary differential equations. These can be solved by direct integration, which ultimately means to solve a large sparse linear system in the form of

$$\mathbf{A}\mathbf{x} = \mathbf{b} \tag{1}$$

in each time step. If the underlying physical behavior is nonlinear and an implicit integration scheme is used in combination with a direct solver, the solution of Eq. (1) requires the repeated computation of some decomposition of $\mathbf{A}$. The computation of this factorization is a rather expensive operation and the costs cannot be amortized across time steps. This fact has motivated the search for methods, which allow for modifications of an existing factorization in order to obtain the new factors more efficiently.

In this article I present the application of such an update routine in the context of nonlinear structural dynamic analysis of frame problems. The method is substantially faster than full refactorization and requires only minor extensions to the finite element code.

2 FINITE ELEMENT METHOD

The semi-discrete equations of motion of a structural system read

$$\mathbf{M}\ddot{\mathbf{x}}(t) + \mathbf{C}\dot{\mathbf{x}}(t) + \mathbf{f}_{\text{int}}(\mathbf{x}(t), \boldsymbol{\kappa}) = \mathbf{f}_{\text{ext}}(t) \tag{2}$$

with $\mathbf{M}$ being the mass matrix, $\mathbf{C}$ the damping matrix, $\mathbf{f}_{\text{int}}$ the internal force vector, and $\mathbf{f}_{\text{ext}}$ the external force vector. Both $\mathbf{M}$ and $\mathbf{C}$ are herein assumed to be constant. The global unknowns are contained in the displacement vector $\mathbf{x}$ with $\dot{\mathbf{x}}$ and $\ddot{\mathbf{x}}$ being the first and second derivative with respect to time, that is, velocities and accelerations. $\boldsymbol{\kappa}$ denotes a set of internal variables, needed for the treatment of inelastic, path-dependent materials. The exact derivation of the equilibrium equation is given, together with a thorough introduction to the finite element method, e. g., by Bathe [1].

Eq. (2) is a system of ordinary differential equations of second order and can be solved by direct integration. For this purpose, equilibrium is only satisfied at discrete time intervals Δt apart, and a variation of displacements, velocities, and accelerations is assumed in each interval. Widely used is thereby Newmark's assumption [2] that accelerations vary linearly from time t to time $t + \Delta t$, so that

$$\dot{\mathbf{x}}^{t+\Delta t} = \dot{\mathbf{x}}^{t} + \Delta t \left[(1-\gamma)\ddot{\mathbf{x}}^{t} + \gamma\ddot{\mathbf{x}}^{t+\Delta t}\right] \tag{3}$$

$$\mathbf{x}^{t+\Delta t} = \mathbf{x}^{t} + \Delta t\dot{\mathbf{x}}^{t} + \tfrac{1}{2}\Delta t^2 \left[(1-2\beta)\ddot{\mathbf{x}}^{t} + 2\beta\ddot{\mathbf{x}}^{t+\Delta t}\right] \tag{4}$$

where the parameters β and γ determine integration accuracy and stability. Solving for $\ddot{\mathbf{x}}^{t+\Delta t}$ from Eq. (4) and substituting for $\ddot{\mathbf{x}}^{t+\Delta t}$ into Eq. (3) yields equations for accelerations and velocities

at time $t + \Delta t$ in terms of the unknown displacements $\mathbf{x}^{t+\Delta t}$. Inserting these two equations into Eq. (2) yields now the fully discretized equations of motion as a system of nonlinear algebraic equations

$$\mathbf{M}\left[\tfrac{1}{\beta\Delta t^2}(\mathbf{x}^{t+\Delta t} - \mathbf{x}^t) - \tfrac{1}{\beta\Delta t}\dot{\mathbf{x}}^t - \tfrac{1-2\beta}{2\beta}\ddot{\mathbf{x}}^t\right] + \mathbf{C}\left[\tfrac{\gamma}{\beta\Delta t}(\mathbf{x}^{t+\Delta t} - \mathbf{x}^t) + (1 - \tfrac{\gamma}{\beta})\dot{\mathbf{x}}^t + (1 - \tfrac{\gamma}{2\beta})\Delta t\,\ddot{\mathbf{x}}^t\right] + \mathbf{f}_{\text{int}}(\mathbf{x}^{t+\Delta t}) - \mathbf{f}_{\text{ext}}^{t+\Delta t} = \mathbf{0} \quad (5)$$

The solution for each time step can then be found with iterative procedures.

One commonly applied iterative procedure to solve Eq. (5) is the Newton–Raphson method. It successively finds better approximations to the roots of a vector function $\mathbf{F}(\mathbf{x})$ with its Jacobian $\mathbf{J}_\mathbf{F} = \frac{d\mathbf{F}}{d\mathbf{x}}$ and an already known state $\mathbf{x}_j$, according to

$$\mathbf{J}_\mathbf{F}(\mathbf{x}_j)\,\Delta\mathbf{x}_{j+1} = -\mathbf{F}(\mathbf{x}_j) \quad \text{with} \quad \Delta\mathbf{x}_{j+1} = \mathbf{x}_{j+1} - \mathbf{x}_j \quad (6)$$

The resulting linear system is solved in each iteration j until some error measure lies within a given tolerance. Using Eq. (6) with the discretized equations of motion as $\mathbf{F}(\mathbf{x})$, leads with

$$\left.\frac{\partial\mathbf{f}_{\text{int}}}{\partial\mathbf{x}^{t+\Delta t}}\right|_{\mathbf{x}_j^{t+\Delta t}} = \mathbf{K}(\mathbf{x}_j^{t+\Delta t})$$

finally to a relation in the form of Eq. (1)

$$\left[\tfrac{1}{\beta\Delta t^2}\mathbf{M} + \tfrac{\gamma}{\beta\Delta t}\mathbf{C} + \mathbf{K}(\mathbf{x}_j^{t+\Delta t})\right]\Delta\mathbf{x}_{j+1} = \mathbf{f}_{\text{ext}}^{t+\Delta t} - \mathbf{f}_{\text{int}}(\mathbf{x}_j^{t+\Delta t}) - \mathbf{M}\ddot{\mathbf{x}}_j^{t+\Delta t} - \mathbf{C}\dot{\mathbf{x}}_j^{t+\Delta t} \quad (7)$$

for finding "dynamic equilibrium" within a time step.

3 DIRECT SOLUTION AND UPDATE PROCEDURE

For the solution of Eq. (7) either direct or iterative methods can be used. Direct methods find an exact solution within a predetermined number of operations, whereas iterative methods produce a sequence of approximate solutions that should ultimately converge to the exact one. As long as memory is of no concern, that is, problems with low number of unknowns, direct solvers are preferable because of their accuracy and robustness. I thus use CHOLMOD [3], a sparse direct solver for symmetric, positive-definite matrices authored by Tim Davis.

Direct solution techniques solve a linear system by some decomposition of $\mathbf{A}$, being basically a variation of Gauss elimination [4]. If $\mathbf{A}$ is a real, symmetric matrix, the general form of this decomposition is

$$\mathbf{A} = \mathbf{L}\mathbf{D}\mathbf{L}^{\mathrm{T}}$$

where $\mathbf{L}$ is a unit lower triangular matrix and $\mathbf{D}$ a diagonal matrix. With this factors at hand, a solution for $\mathbf{x}$ can be obtained by forward reduction, diagonal scaling, and backward substitution, which are simple and efficient methods for computing $\mathbf{L}^{-1}\mathbf{b}$, $\mathbf{D}^{-1}(\mathbf{L}^{-1}\mathbf{b})$, and $\mathbf{L}^{-\mathrm{T}}(\mathbf{D}^{-1}\mathbf{L}^{-1}\mathbf{b})$ in succession. The computation of $\mathbf{L}$ and $\mathbf{D}$, however, can be quite time consuming and has obviously to be repeated each time the linearized system's matrix $\mathbf{A}$ changes.

A change to $\mathbf{A}$ can most generally be expressed as $\mathbf{A}_{j+1} = \mathbf{A}_j + \Delta\mathbf{A}_{j+1}$. A special case and one of particular interest is a so-called *rank-one modification*

$$\mathbf{A}_{j+1} = \mathbf{A}_j + \alpha\mathbf{v}\mathbf{v}^{\mathrm{T}}$$

where α is a scalar and $\mathbf{v}$ a vector of appropriate size. Finding the factorization of $\mathbf{A}_{j+1}$ after such a modification is usually described as a problem of *updating* the factors of $\mathbf{A}_j$ and its importance has long been recognized. An overview of several update schemes can be found in the classic paper by Gill et al. [5] published back in 1974. More recently, Davis and Hager [6] took up some ideas given therein and developed an algorithm in regard of modern sparse methods and extended it in further consequence to the multiple rank case [7]. The resulting algorithm is implemented in CHOLMOD as routine `cholmod_updown` and incorporated in the finite element code used for this study.

The update/downdate routine `cholmod_updown` takes an $\mathbf{LDL}^{\mathrm{T}}$ factorization and computes a new factorization according to

$$\overline{\mathbf{LDL}}^{\mathrm{T}} = \mathbf{LDL}^{\mathrm{T}} \pm \mathbf{CC}^{\mathrm{T}}$$

where $\mathbf{A} + \mathbf{CC}^{\mathrm{T}}$ corresponds to an update and, conversely, $\mathbf{A} - \mathbf{CC}^{\mathrm{T}}$ to a downdate. Apparently, it is necessary to express $\Delta\mathbf{A}$ as $\mathbf{CC}^{\mathrm{T}}$ to employ this routine. In so doing, I make use of the idea stated at the beginning that in a materially-nonlinear-only analysis large parts of a structure usually remain linear elastic. This implies that $\Delta\mathbf{A}$ should be extremely sparse and should hold a rank much smaller than the dimension of $\mathbf{A}$. The $n \times n$ matrix $\Delta\mathbf{A}$ can then conveniently be expressed as

$$\Delta\mathbf{A} = \mathbf{PWP}^{\mathrm{T}}$$

where $\mathbf{P}$ is an $n \times m$ sparse incidence matrix consisting solely of zeros and ones, and $\mathbf{W}$ is the the change to the linearized system's matrix in compressed (and dense) form of size $m \times m$ with $m \leq n$. Computing the eigendecomposition

$$\mathbf{W} = \mathbf{Q}\Lambda\mathbf{Q}^{\mathrm{T}}$$

and separating the eigenvalues together with the corresponding eigenvectors in positive and negative ones, yields $\mathbf{C}$ in case of an update as

$$\mathbf{C}^{+} = \mathbf{PQ}^{+}(\Lambda^{+})^{1/2}$$

and in case of a downdate as

$$\mathbf{C}^{-} = \mathbf{PQ}^{-}|\Lambda^{-}|^{1/2}$$

It should be obvious by now that the initial assumption of $\Delta\mathbf{A}$ being extremely sparse is crucial, as the eigendecomposition of the dense matrix $\mathbf{W}$ is an expensive operation where the costs can easily outweigh a refactorization from scratch.

4 EXEMPLARY STRUCTURE AND NUMERICAL RESULTS

I implemented the `cholmod_updown` routine in my finite element code and tested its performance against the standard methods from SuperLU [8] and CHOLMOD. The moment resisting frame depicted in Fig. 1 thereby serves as a benchmark example. Such frames are amongst the most common forms in modern engineering and basically are steel assemblages of beams and columns rigidly connected to each other. They withstand lateral forces primarily by bending and should by design avoid potentially brittle shear failure modes. To achieve a ductile behavior during strong earthquake shaking, the beam ends and column bases are designed to sustain large inelastic rotations and thus provide an energy dissipating mechanism.

For the numerical model, the concept of concentrated plasticity is used. Although these models date back to the 1960s, they are the still amongst the preferred modeling approaches for seismic

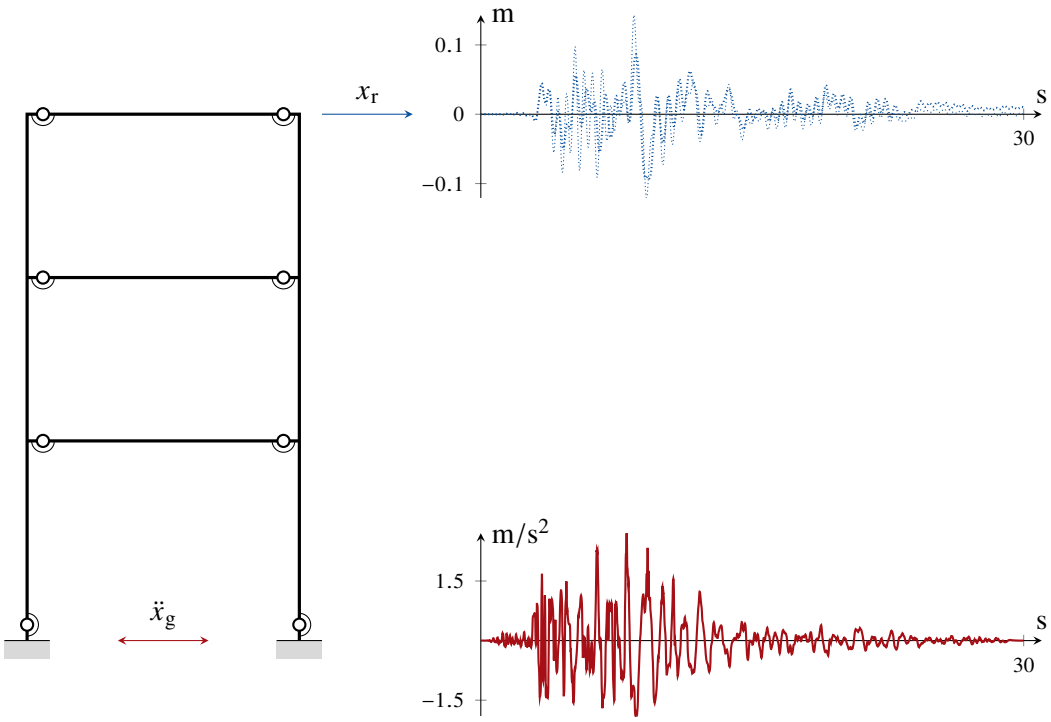


Figure 1: A three story moment resisting frame with nonlinear rotational springs at the beam ends and the column bases, subjected to the ground motion record from the 1994 Northridge earthquake (Beverly Hills, 14145 Mulholland station). The top right time history plot shows the horizontal roof displacement for linear-elastic springs (dotted line) and for perfectly plastic springs (solid line).

performance assessment in earthquake engineering. Within this concept, beams and columns are modeled as two-node linear elastic beam elements, whereas the parts which are designed to experience inelastic deformations, are modeled with rotational springs of zero length. The material behavior of these springs is for the case at hand elastic-perfectly plastic.

The exemplary structure is subjected to ground motions from the 1994 Northridge earthquake (Beverly Hills, 14145 Mulholland station) and the horizontal roof displacement is chosen as engineering demand parameter. The frame is 6 m wide and 11.6 m high, resulting from the first story being 4.4 m and the remaining ones being each 3.6 m high. The flexural rigidity of the beams and columns is assumed to be $1 \cdot 10^6\,\mathrm{kN/m^2}$ and $2 \cdot 10^6\,\mathrm{kN/m^2}$, respectively, and all springs have an elastic stiffness of $210 \cdot 10^6\,\mathrm{kN/m^2}$. The results of a linear elastic simulation is shown in the top right time history plot of Fig. 1 as dotted line. For the nonlinear response, the material behavior of the springs was modified such that they start yielding at a bending moment of 2400 kN m (base), 1300 kN m (first floor), 1000 kN m (second floor), and 800 kN m (roof). The nonlinear results are depicted in the same plot as solid line.

The nonlinear simulation was run three times: with the standard solution procedure, that is, a complete refactorization of $\mathbf{A}$ in each solution step, using first SuperLU and second CHOLMOD. In the third run I used the update routine `cholmod_updown` and applied incremental changes $\Delta\mathbf{A}$ to the system's linearized matrix. The runtime of all three approaches is shown in Fig. 2. The top graph shows the time needed for each individual solve, whereas the bottom graph shows the same data in accumulated form. Of all three solvers, SuperLU is slowest which is apparent as the library is intended to solve non-symmetric linear systems. These timings reflect no weakness of SuperLU, but rather emphasize that only specially tailored routines achieve really high performance. The standard solve from CHOLMOD, designed for symmetric matrices, thus outperforms SuperLU

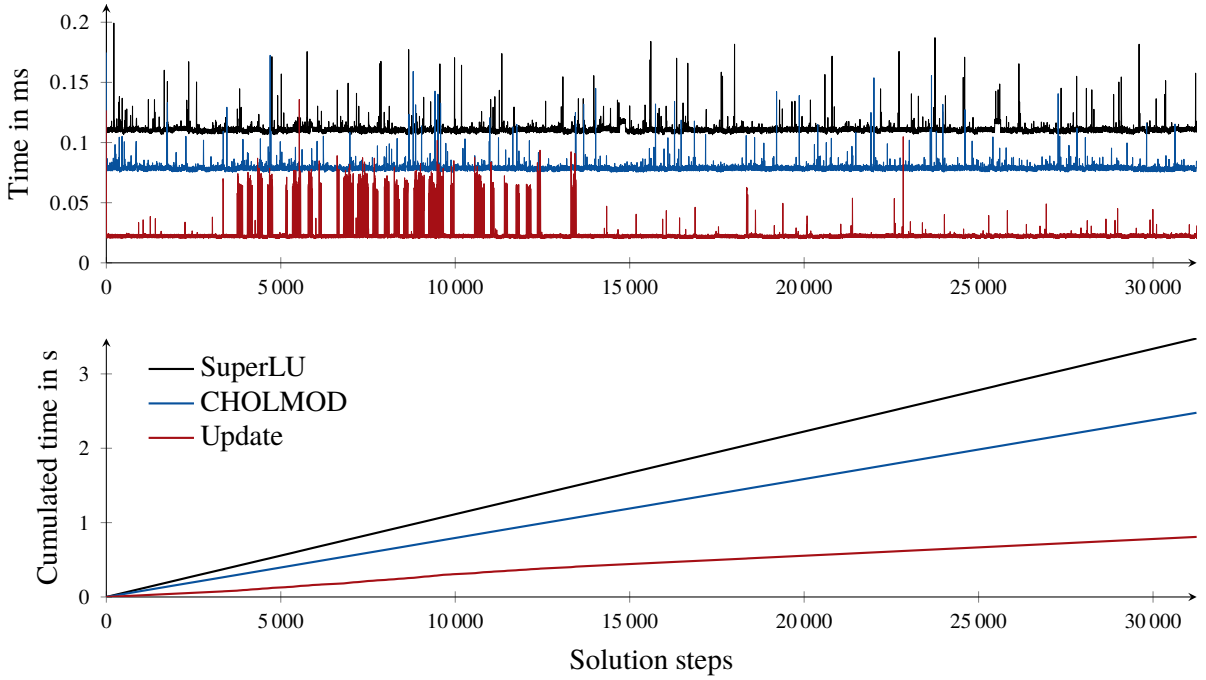


Figure 2: Runtime over solution steps for solving Eq. (7) of the exemplary structure individually (top graph) and in accumulated form (bottom graph) using three different methods. SuperLU is slowest due to its general applicability to non-symmetric linear systems, whereas CHOLMOD exploits this fact and is faster by a factor of 1.4. The update routine logically has erratic performance and is in the best case around 3.8 times faster than CHOLMODs standard solve. If the rank of the update matrix $\Delta\mathbf{A}$ increases, the performance hit is evident.

by a factor of 1.4. The update procedure compares badly with the two previous methods because it obviously has an erratic performance. In the best case where no update is needed, it is 3.8 times faster than the reference solve from CHOLMOD. The time needed therein results only from the solution phase (forward reduction to backward substitution) and eventually poses a lower bound. In the worst-case scenario, the update routine is on par with CHOLMOD.

5 CONCLUSION

The solution of Eq. (7) is one the most time consuming parts in a finite element solution. If a direct solver is used, this can be attributed to the computation of the $\mathbf{LDL}^\mathrm{T}$ factorization. For nonlinear problems, this process has to be repeated in each iteration and can be problematic regarding the overall performance. I address this problem by an update procedure which allows for the modification of an existing factorization.

The runtime of the `cholmod_updown` routine is proportional to the numbers of nonzero entries in $\mathbf{L}$ and $\mathbf{D}$ that change. The problem, however, is the form of the update matrix. The finite element code can easily be modified to return $\Delta\mathbf{A}$, but it can be rather expensive to rewrite it in the form $\mathbf{CC}^\mathrm{T}$. If the compressed update matrix $\mathbf{W}$ is very small, the additional costs are negligible, but with increasing size, they inevitably get higher and will ultimately exceed the costs of a full refactorization. The crucial point is in consequence the central premise of local plastic regions which result in local changes to $\mathbf{A}$. This is, however, only true in the context of materially-nonlinear-only analysis. If geometric nonlinearities have to be considered, the rank of $\Delta\mathbf{A}$ becomes far too big for the update method to still be performant. The exemplary frame structure meets all requirements and thus allows for a considerably faster analysis using the update approach.

In future work, I will address the limiting factor of $\Delta\mathbf{A}$ being of small rank. By implication, the `cholmod_updown` routine has to be ruled out, but I believe that a different updating procedure can be devised which has, in the worst-case scenario, the same runtime as a complete refactorization from scratch.

REFERENCES

[1] K.-J. Bathe. *Finite Element Procedures*. Prentice Hall, 1996.

[2] N. M. Newmark. A Method of Computation for Structural Dynamics. *ASCE Journal of the Engineering Mechanics Division*, **85**, 67–94, 1959.

[3] Y. Chen, T. A. Davis, W. W. Hager, S. Rajamanickam. Algorithm 887: CHOLMOD, Supernodal Sparse Cholesky Factorization and Update/Downdate. *ACM Transactions on Mathematical Software*, **35**, 22:1–22:14, 2008.

[4] G. H. Golub, C. F. Van Loan. *Matrix Computations*, 4th Edition. John Hopkins University Press, 2013.

[5] P. E. Gill, G. H. Golub, W. Murray, M. A. Saunders. Methods for Modifying Matrix Factorizations. *Mathematics of Computation*, **28**, 505–535, 1974.

[6] T. A. Davis, W. W. Hager. Modifying a Sparse Cholesky Factorization. *SIAM Journal on Matrix Analysis and Applications*, **20**, 606–627, 1999.

[7] T. A. Davis, W. W. Hager. Multiple-rank Modifications of a Sparse Cholesky Factorization. *SIAM Journal on Matrix Analysis and Applications*, **22**, 997–1013, 2001.

[8] X. S. Li. An Overview of SuperLU: Algorithms, Implementation and User Interface. *ACM Transactions on Mathematical Software*, **31**, 302–325, 2005.

COMPDYN 2015
5th ECCOMAS Thematic Conference on
Computational Methods in Structural Dynamics and Earthquake Engineering
M. Papadrakakis, V. Papadopoulos, V. Plevris (eds.)
Crete Island, Greece, 25–27 May 2015

A NEW 3D CO-ROTATIONAL BEAM ELEMENT FOR NONLINEAR DYNAMIC ANALYSIS

Thanh-Nam LE[1,2], Jean-Marc BATTINI [2], and Mohammed HJIAJ[1]

[1]Structural Engineering Research Group - INSA de Rennes
20 Avenue des Buttes de Coësmes, 35708, Rennes, France
{Thanh-Nam.LE, Mohammed.Hjiaj}@insa-rennes.fr

[2] Department of Civil and Architectural Engineering
Royal Institute of Technology, SE-10044 Stockholm, Sweden
jean-marc.battini@byv.kth.se

Keywords: Instructions, ECCOMAS Thematic Conference, Structural Dynamics, Earthquake Engineering, Proceedings.

Abstract. *The paper investigates the contribution of the warping deformations and the shear center location on the dynamic response of 3D thin-walled beams obtained with an original consistent co-rotational formulation developed by the authors. Consistency of the formulation is ensured by employing the same kinematic assumptions to derive both the static and dynamic terms. Hence, the element has seven degrees of freedom at each node and cubic shape functions are used to interpolate local transversal displacements and axial rotations. Accounting for warping deformations and the position of the shear center produces additional terms in the expressions of the inertia force vector and the tangent dynamic matrix. The performance of the present formulation is assessed by comparing its predictions against 3D-solid FE solutions.*

1 INTRODUCTION

The purpose of the present paper is to further develop the dynamic formulation proposed in [31] so that beams with arbitrary thin-walled open cross-sections can be studied. For that, two main ideas are used. Firstly, a seventh degree of freedom is added at each node to describe the warping of the cross-section. Consequently, the linear interpolation for the local axial rotation used in [31] is replaced by a cubic interpolation. Secondly, the main difficulty in the nonlinear analysis of beams with arbitrary cross-sections is that, due to the eccentricity of the shear center, the cross-section rotations are usually not defined at the same point. To avoid this difficulty, the kinematic description proposed by Gruttmann et al. [1] is adopted. In this approach, the warping function is modified and all the cross-section rotations are defined at the centroid.

Consequently, the inertia terms are consistent with the static ones developed by Battini and Pacoste in [5] since the same corotational kinematic description is used to derive all the terms. Regarding the dynamic terms, i.e. the inertia force vector and tangent dynamic matrix, the formulation proposed in [31] is extended and several additional terms are introduced. The contribution of these terms in the performance of the formulation is then investigated in the numerical examples. Regarding the static deformational terms, i.e. the internal force vector and tangent stiffness matrix, the corotational beam element developed by Battini and Pacoste [5] is adopted. However, in order to introduce the bending shear deformations, the cubic Hermitian functions are modified as suggested in the Interdependent Interpolation Element (IIE) formulation [39].

2 PARAMETRIZATION OF FINITE ROTATION

In this section, the basic relations concerning the parameterizations of finite rotations are briefly presented. For a more complete description, the reader is referred to textbooks and review papers such as [2, 12, 16, 20, 21, 28].

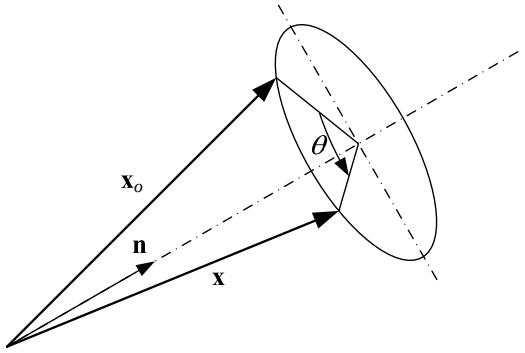


Figure 1: Finite rotation of a vector

The coordinate of a vector $\mathbf{x}_o$ that is rotated into the position $\mathbf{x}$ (see Fig. 1) is given by the relation

$$\mathbf{x} = \mathbf{R}\,\mathbf{x}_o\,. \tag{1}$$

Due to its orthonormality, the rotation matrix $\mathbf{R}$ can be parameterized using only three indepen-

dent parameters. One possibility is to use the rotational vector defined by

$$\boldsymbol{\theta} = \theta\,\mathbf{n}\,, \tag{2}$$

where $\mathbf{n}$ is a unit vector defining the axis of the rotation and $\theta = (\boldsymbol{\theta}^{\mathrm{T}}\boldsymbol{\theta})^{1/2}$ is the angle of the rotation.

The relation between the rotation matrix and the rotational vector is given by the Rodrigues' formula

$$\mathbf{R} = \mathbf{I} + \frac{\sin\theta}{\theta}\widetilde{\boldsymbol{\theta}} + \frac{1-\cos\theta}{\theta^2}\widetilde{\boldsymbol{\theta}}\widetilde{\boldsymbol{\theta}} = \exp(\widetilde{\boldsymbol{\theta}})\,, \tag{3}$$

where $\widetilde{\boldsymbol{\theta}}$ is the skew matrix associated with the vector $\boldsymbol{\theta}$.

The variation of the rotation matrix in spatial and material form is given by

$$\delta\mathbf{R} = \widetilde{\delta\mathbf{w}}\mathbf{R} = \mathbf{R}\widetilde{\delta\boldsymbol{\omega}}\,. \tag{4}$$

Physically, $\widetilde{\delta\mathbf{w}}$ represents infinitesimal spatial rotation superposed onto the rotation $\mathbf{R}$. $\delta\mathbf{w}$, which is also denoted as spatial spin variables, is related to the variation of the rotational vector through

$$\delta\mathbf{w} = \mathbf{T}_s(\boldsymbol{\theta})\,\delta\boldsymbol{\theta}\,, \tag{5}$$

with

$$\mathbf{T}_s(\boldsymbol{\theta}) = \mathbf{I} + \frac{1-\cos\theta}{\theta^2}\widetilde{\boldsymbol{\theta}} + \frac{\theta-\sin\theta}{\theta^3}\widetilde{\boldsymbol{\theta}}\widetilde{\boldsymbol{\theta}}\,. \tag{6}$$

The time derivative of the rotation matrix in spatial and material form is given by

$$\dot{\mathbf{R}} = \widetilde{\dot{\mathbf{w}}}\mathbf{R} = \mathbf{R}\widetilde{\dot{\boldsymbol{\omega}}}\,, \tag{7}$$

where the axis vectors $\dot{\mathbf{w}}$ and $\dot{\boldsymbol{\omega}}$ are spatial and material angular velocities, respectively.

The spatial and material quantities are connected by the relations

$$\delta\mathbf{w} = \mathbf{R}\,\delta\boldsymbol{\omega}\,, \tag{8}$$

$$\dot{\mathbf{w}} = \mathbf{R}\,\dot{\boldsymbol{\omega}}\,, \tag{9}$$

$$\ddot{\mathbf{w}} = \mathbf{R}\,\ddot{\boldsymbol{\omega}}\,. \tag{10}$$

The variation of the material angular velocity is given by (see [8])

$$\delta\dot{\boldsymbol{\omega}} = \dot{\delta\boldsymbol{\omega}} + \widetilde{\dot{\boldsymbol{\omega}}}\,\delta\boldsymbol{\omega}\,, \tag{11}$$

with $\dot{\delta\boldsymbol{\omega}}$ denoting the time derivative of the material spin variables.

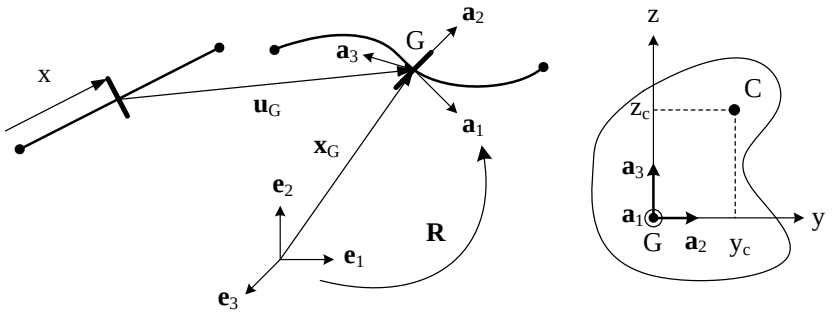


Figure 2: Initial and current configuration of the beam

3 KINETIC ENERGY

In the present paper, the kinematic description proposed by Gruttmann et al. [1] is adopted (see Fig. 2). A beam with an arbitrary cross-section is considered. G and C are the centroid and the shear center of the cross-section. $\mathbf{e}_i$ and $\mathbf{a}_i$ $(i = 1,2,3)$ denote the global and cross-section-attached orthogonal coordinates systems, respectively. The transformation from the global coordinates system to the cross-section-attached one is defined by

$$\mathbf{a}_i = \mathbf{R}\,\mathbf{e}_i\,. \tag{12}$$

Let $\mathbf{x}_{\mathrm{P}}(x,y,z)$ denote the position vector of an arbitrary point P in the current configuration

$$\mathbf{x}_{\mathrm{P}}(x,y,z) = \mathbf{x}_{\mathrm{G}}(x) + y\,\mathbf{a}_2(x) + z\,\mathbf{a}_3(x) + \alpha(x)\,\overline{\omega}(y,z)\,\mathbf{a}_1(x)\,, \tag{13}$$

with $\mathbf{x}_{\mathrm{G}}$ denoting the position vector of G in the current configuration.

The warping function $\overline{\omega}(y,z)$ is defined within the Saint-Venant torsion theory and refers to the centroid G, i.e.

$$\overline{\omega} = \omega - y_c\,z + z_c\,y\,, \tag{14}$$

where ω refers to the shear center C with coordinates $y_c\,, z_c$. Note that in connection with ω, the following normality conditions hold

$$\int_A \omega\,\mathrm{d}A = 0\,, \quad \int_A \omega\,y\,\mathrm{d}A = 0\,, \quad \int_A \omega\,z\,\mathrm{d}A = 0\,. \tag{15}$$

Using Eq. (12), the expression (13) can be put in the form

$$\mathbf{x}_{\mathrm{P}} = \mathbf{x}_{\mathrm{G}} + \mathbf{R}\,(\mathbf{X} + \alpha\,\mathbf{n}_{\overline{\omega}})\,, \tag{16}$$

with $\mathbf{X} = [0\ \ y\ \ z]^{\mathrm{T}}$ and $\mathbf{n}_{\overline{\omega}} = [\overline{\omega}\ \ 0\ \ 0]^{\mathrm{T}}$.

By taking the time derivative of the above expression and using Eq. (7), the velocity is obtained as

$$\begin{aligned}\dot{\mathbf{u}}_{\mathrm{P}} = \dot{\mathbf{x}}_{\mathrm{P}} &= \dot{\mathbf{x}}_{\mathrm{G}} + \mathbf{R}\,\widetilde{\boldsymbol{\omega}}(\mathbf{X} + \alpha\,\mathbf{n}_{\overline{\omega}}) + \mathbf{R}\,\dot{\alpha}\,\mathbf{n}_{\overline{\omega}} \\ &= \dot{\mathbf{u}}_{\mathrm{G}} + \mathbf{R}\,(-\widetilde{\mathbf{X}}\,\dot{\boldsymbol{\omega}} - \alpha\,\widetilde{\mathbf{n}_{\overline{\omega}}}\,\dot{\boldsymbol{\omega}} + \dot{\alpha}\,\mathbf{n}_{\overline{\omega}})\,.\end{aligned} \tag{17}$$

The kinetic energy of the beam is then calculated by

$$K = \frac{1}{2}\int_V \rho\ \dot{\mathbf{u}}_{\mathrm{P}}^{\mathrm{T}}\ \dot{\mathbf{u}}_{\mathrm{P}}\ \mathrm{d}V = \frac{1}{2}\Bigg[\int_{l_o} \dot{\mathbf{u}}_{\mathrm{G}}^{\mathrm{T}}\, A_\rho\ \dot{\mathbf{u}}_{\mathrm{G}}\ \mathrm{d}l + \int_V \rho\ \left(-\widetilde{\mathbf{X}}\,\dot{\boldsymbol{\omega}} - \alpha\,\widetilde{\mathbf{n}_{\overline{\omega}}}\,\dot{\boldsymbol{\omega}} + \dot{\alpha}\,\mathbf{n}_{\overline{\omega}}\right)^{\mathrm{T}}\left(-\widetilde{\mathbf{X}}\,\dot{\boldsymbol{\omega}} - \alpha\,\widetilde{\mathbf{n}_{\overline{\omega}}}\,\dot{\boldsymbol{\omega}} + \dot{\alpha}\,\mathbf{n}_{\overline{\omega}}\right)\ \mathrm{d}V\Bigg]. \tag{18}$$

The following notations are introduced

$$I_{yz} = \int_A y\,z\,\mathrm{d}A\,,\quad I_{yy} = \int_A y^2\,\mathrm{d}A\,,\quad I_{zz} = \int_A z^2\,\mathrm{d}A\,,\quad I_\omega = \int_A \omega^2\,\mathrm{d}A\,, \tag{19}$$

$$I_{\overline{\omega}} = \int_A \overline{\omega}^2\,\mathrm{d}A = I_\omega + z_c^2 I_{yy} + y_c^2 I_{zz} - 2\,y_c\,z_c\,I_{yz}\,, \tag{20}$$

$$I_{yc} = \int_A y\,\overline{\omega}\,\mathrm{d}A = -y_c\,I_{yz} + z_c\,I_{yy}\,, \tag{21}$$

$$I_{zc} = \int_A z\,\overline{\omega}\,\mathrm{d}A = -y_c\,I_{zz} + z_c\,I_{yz}\,, \tag{22}$$

$$\mathbf{J}_\rho = \int_A \rho\ \widetilde{\mathbf{X}}^{\mathrm{T}}\,\widetilde{\mathbf{X}}\ \mathrm{d}A = \rho\begin{bmatrix} I_{yy}+I_{zz} & 0 & 0 \\ 0 & I_{zz} & -I_{yz} \\ 0 & -I_{yz} & I_{yy} \end{bmatrix}, \tag{23}$$

$$\mathbf{J}_{\overline{\omega}} = \int_A \rho\ \widetilde{\mathbf{n}_{\overline{\omega}}}^{\mathrm{T}}\,\widetilde{\mathbf{n}_{\overline{\omega}}}\ \mathrm{d}A = \rho\begin{bmatrix} 0 & 0 & 0 \\ 0 & I_{\overline{\omega}} & 0 \\ 0 & 0 & I_{\overline{\omega}} \end{bmatrix}, \tag{24}$$

$$\mathbf{J}_a = \int_A \rho\ \left(\widetilde{\mathbf{X}}^{\mathrm{T}}\,\widetilde{\mathbf{n}_{\overline{\omega}}} + \widetilde{\mathbf{n}_{\overline{\omega}}}^{\mathrm{T}}\,\widetilde{\mathbf{X}}\right)\ \mathrm{d}A = \rho\begin{bmatrix} 0 & -I_{yc} & -I_{zc} \\ -I_{yc} & 0 & 0 \\ -I_{zc} & 0 & 0 \end{bmatrix}, \tag{25}$$

$$\mathbf{J}_b = \int_A \rho\ \widetilde{\mathbf{X}}^{\mathrm{T}}\,\mathbf{n}_{\overline{\omega}}\ \mathrm{d}A = \rho\begin{bmatrix} 0 \\ -I_{zc} \\ I_{yc} \end{bmatrix}, \tag{26}$$

$$\mathbf{J}_\alpha = \alpha^2\,\mathbf{J}_{\overline{\omega}} + \alpha\,\mathbf{J}_a\,,\quad J_{\overline{\omega}} = \rho\,I_{\overline{\omega}}\,. \tag{27}$$

The expression of the kinetic energy can then be rewritten in the material form as

$$K = \frac{1}{2}\int_{l_o}\left[\dot{\mathbf{u}}_{\mathrm{G}}^{\mathrm{T}}\,A_\rho\ \dot{\mathbf{u}}_{\mathrm{G}} + \dot{\boldsymbol{\omega}}^{\mathrm{T}}\,\mathbf{J}_\rho\ \dot{\boldsymbol{\omega}}\right]\ \mathrm{d}l + \frac{1}{2}\int_{l_o}\left[\dot{\boldsymbol{\omega}}^{\mathrm{T}}\,\mathbf{J}_\alpha\,\dot{\boldsymbol{\omega}} - 2\,\dot{\boldsymbol{\omega}}^{\mathrm{T}}\,\mathbf{J}_b\,\dot{\alpha} + J_{\overline{\omega}}\,\dot{\alpha}^2\right]\ \mathrm{d}l\,, \tag{28}$$

and, using Eq. (9), the spatial form is obtained

$$K = \frac{1}{2}\int_{l_o}\left[\dot{\mathbf{u}}_{\mathrm{G}}^{\mathrm{T}}\,A_\rho\ \dot{\mathbf{u}}_{\mathrm{G}} + \dot{\mathbf{w}}^{\mathrm{T}}\,\mathbf{I}_\rho\ \dot{\mathbf{w}}\right]\ \mathrm{d}l + \frac{1}{2}\int_{l_o}\left[\dot{\mathbf{w}}^{\mathrm{T}}\,\mathbf{I}_\alpha\,\dot{\mathbf{w}} - 2\,\dot{\mathbf{w}}^{\mathrm{T}}\,\mathbf{I}_b\,\dot{\alpha} + J_{\overline{\omega}}\,\dot{\alpha}^2\right]\ \mathrm{d}l\,, \tag{29}$$

with

$$\mathbf{I}_\rho = \mathbf{R}\,\mathbf{J}_\rho\,\mathbf{R}^{\mathrm{T}}\,,\quad \mathbf{I}_{\overline{\omega}} = \mathbf{R}\,\mathbf{J}_{\overline{\omega}}\,\mathbf{R}^{\mathrm{T}}\,,\quad \mathbf{I}_\alpha = \mathbf{R}\,\mathbf{J}_\alpha\,\mathbf{R}^{\mathrm{T}}\,,\quad \mathbf{I}_b = \mathbf{R}\,\mathbf{J}_b\,. \tag{30}$$

The first integrals in Eqs. (28) and (29) are the kinetic energy due to the translation and rotation of the beam cross-section. The variation, in the spatial form, is obtained as

$$\delta K_{Trans+Rot} = -\int_{l_o} \left\{ \delta \mathbf{u}_{\mathrm{G}}{}^{\mathrm{T}} A_\rho \ddot{\mathbf{u}}_{\mathrm{G}} + \delta \mathbf{w}^{\mathrm{T}} \left[\mathbf{I}_\rho \dot{\mathbf{w}} + \widetilde{\dot{\mathbf{w}}} \mathbf{I}_\rho \mathbf{w} \right] \right\} \mathrm{d}l \,. \tag{31}$$

The second integrals in Eqs. (28) and (29), named as $K_{Warping}$, are the additional kinetic energy due to the warping deformations and the eccentricity of shear center with respect to the centroid

$$K_{Warping} = \int_{l_o} k_W \ \mathrm{d}l = \frac{1}{2} \int_{l_o} \left[\dot{\boldsymbol{\omega}}^{\mathrm{T}} \mathbf{J}_\alpha \, \dot{\boldsymbol{\omega}} - 2 \, \dot{\boldsymbol{\omega}}^{\mathrm{T}} \mathbf{J}_b \, \dot{\alpha} + J_{\overline{\omega}} \, \dot{\alpha}^2 \right] \ \mathrm{d}l \,. \tag{32}$$

The variation of k_W is given by

$$\delta k_W = \delta \dot{\boldsymbol{\omega}}^{\mathrm{T}} \ (\mathbf{J}_\alpha \, \dot{\boldsymbol{\omega}} - \mathbf{J}_b \, \dot{\alpha}) + \delta \alpha \, \dot{\boldsymbol{\omega}}^{\mathrm{T}} \mathbf{J}_\alpha{}' \, \dot{\boldsymbol{\omega}} + \delta \dot{\alpha} \ (J_{\overline{\omega}} \, \dot{\alpha} - \dot{\boldsymbol{\omega}}^{\mathrm{T}} \mathbf{J}_b) \,, \tag{33}$$

where

$$\mathbf{J}_\alpha{}' = \frac{1}{2} \frac{\mathrm{d}\mathbf{J}_\alpha}{\mathrm{d}\alpha} = \alpha \, \mathbf{J}_{\overline{\omega}} + \frac{1}{2} \, \mathbf{J}_a \,. \tag{34}$$

In order to derive an expression which only depends on infinitesimal rotations, an integration in time is performed using Eqs. (11) and (33)

$$\begin{aligned} \int_{t_1}^{t_2} \delta k_W \mathrm{d}t = & \int_{t_1}^{t_2} \delta \dot{\boldsymbol{\omega}}^{\mathrm{T}} \ (\mathbf{J}_\alpha \, \dot{\boldsymbol{\omega}} - \mathbf{J}_b \, \dot{\alpha}) \ \mathrm{d}t + \int_{t_1}^{t_2} \delta \boldsymbol{\omega}^{\mathrm{T}} \, \widetilde{\dot{\boldsymbol{\omega}}}^{\mathrm{T}} \ (\mathbf{J}_\alpha \, \dot{\boldsymbol{\omega}} - \mathbf{J}_b \, \dot{\alpha}) \ \mathrm{d}t \\ & + \int_{t_1}^{t_2} \delta \alpha \, \dot{\boldsymbol{\omega}}^{\mathrm{T}} \mathbf{J}_\alpha{}' \, \dot{\boldsymbol{\omega}} \, \mathrm{d}t + \int_{t_1}^{t_2} \delta \dot{\alpha} \ (J_{\overline{\omega}} \, \dot{\alpha} - \dot{\boldsymbol{\omega}}^{\mathrm{T}} \mathbf{J}_b) \, \mathrm{d}t \,. \end{aligned} \tag{35}$$

The first and fourth terms in the above expression are integrated by parts

$$\begin{aligned} \int_{t_1}^{t_2} \delta \dot{\boldsymbol{\omega}}^{\mathrm{T}} \ (\mathbf{J}_\alpha \, \dot{\boldsymbol{\omega}} - \mathbf{J}_b \, \dot{\alpha}) \ \mathrm{d}t = & \ \delta \boldsymbol{\omega}^{\mathrm{T}} \ (\mathbf{J}_\alpha \, \dot{\boldsymbol{\omega}} - \mathbf{J}_b \, \dot{\alpha}) \Big|_{t_1}^{t_2} \\ & - \int_{t_1}^{t_2} \delta \boldsymbol{\omega}^{\mathrm{T}} \ (\mathbf{J}_\alpha \, \ddot{\boldsymbol{\omega}} - \mathbf{J}_b \, \ddot{\alpha}) \ \mathrm{d}t - \int_{t_1}^{t_2} \delta \boldsymbol{\omega}^{\mathrm{T}} \, 2 \, \mathbf{J}_\alpha{}' \, \dot{\alpha} \, \dot{\boldsymbol{\omega}} \, \mathrm{d}t \,, \end{aligned} \tag{36}$$

$$\int_{t_1}^{t_2} \delta \dot{\alpha} \ (J_{\overline{\omega}} \, \dot{\alpha} - \dot{\boldsymbol{\omega}}^{\mathrm{T}} \mathbf{J}_b) \, \mathrm{d}t = \delta \alpha (J_{\overline{\omega}} \, \dot{\alpha} - \dot{\boldsymbol{\omega}}^{\mathrm{T}} \mathbf{J}_b) \Big|_{t_1}^{t_2} - \int_{t_1}^{t_2} \delta \alpha \ (J_{\overline{\omega}} \, \ddot{\alpha} - \ddot{\boldsymbol{\omega}}^{\mathrm{T}} \mathbf{J}_b) \, \mathrm{d}t \,. \tag{37}$$

Due to the arbitrariness of the variations $\delta \boldsymbol{\omega}$ and $\delta \alpha$

$$\delta \boldsymbol{\omega}^{\mathrm{T}} \ (\mathbf{J}_\alpha \, \dot{\boldsymbol{\omega}} - \mathbf{J}_b \, \dot{\alpha}) \Big|_{t_1}^{t_2} = 0 \,, \tag{38}$$

$$\delta \alpha (J_{\overline{\omega}} \, \dot{\alpha} - \dot{\boldsymbol{\omega}}^{\mathrm{T}} \mathbf{J}_b) \Big|_{t_1}^{t_2} = 0 \,, \tag{39}$$

hence, using Eqs. (36) and (37), Eq. (33) can be rewritten as

$$\delta k_W = -\begin{bmatrix} \delta \boldsymbol{\omega} \\ \delta \alpha \end{bmatrix}^{\mathrm{T}} \begin{bmatrix} \mathbf{J}_\alpha & -\mathbf{J}_b \\ -\mathbf{J}_b^{\mathrm{T}} & J_{\overline{\omega}} \end{bmatrix} \begin{bmatrix} \ddot{\boldsymbol{\omega}} \\ \ddot{\alpha} \end{bmatrix} - \begin{bmatrix} \delta \boldsymbol{\omega} \\ \delta \alpha \end{bmatrix}^{\mathrm{T}} \begin{bmatrix} \widetilde{\dot{\boldsymbol{\omega}}} \, \mathbf{J}_\alpha & \mathbf{J}_c \, \dot{\boldsymbol{\omega}} \\ -\dot{\boldsymbol{\omega}}^{\mathrm{T}} \mathbf{J}_\alpha{}' & 0 \end{bmatrix} \begin{bmatrix} \dot{\boldsymbol{\omega}} \\ \dot{\alpha} \end{bmatrix} , \tag{40}$$

where $\mathbf{J}_c = 2\,\mathbf{J}_\alpha^{'} + \widetilde{\mathbf{J}}_b$.

Finally, the variation of the total kinetic energy, in the spatial form, is expressed as

$$\delta K = -\int_{l_o} \left\{ \delta \mathbf{u}_{\mathrm{G}}{}^{\mathrm{T}} A_\rho \ddot{\mathbf{u}}_{\mathrm{G}} + \delta \mathbf{w}^{\mathrm{T}} \left[\mathbf{I}_\rho \dot{\mathbf{w}} + \widetilde{\dot{\mathbf{w}}} \mathbf{I}_\rho \dot{\mathbf{w}} \right] \right\} \mathrm{d}l - \tag{41}$$
$$\int_{l_o} \begin{bmatrix} \delta \mathbf{w} \\ \delta \alpha \end{bmatrix}^{\mathrm{T}} \begin{bmatrix} \mathbf{I}_\alpha & -\mathbf{I}_b \\ -\mathbf{I}_b^{\mathrm{T}} & J_{\overline{\omega}} \end{bmatrix} \begin{bmatrix} \ddot{\mathbf{w}} \\ \ddot{\alpha} \end{bmatrix} \mathrm{d}l - \int_{l_o} \begin{bmatrix} \delta \mathbf{w} \\ \delta \alpha \end{bmatrix}^{\mathrm{T}} \begin{bmatrix} \widetilde{\dot{\mathbf{w}}}\, \mathbf{I}_\alpha & \mathbf{I}_c\, \dot{\mathbf{w}} \\ -\dot{\mathbf{w}}^{\mathrm{T}}\, \mathbf{I}_\alpha^{'} & 0 \end{bmatrix} \begin{bmatrix} \dot{\mathbf{w}} \\ \dot{\alpha} \end{bmatrix} \mathrm{d}l\,,$$

where $\mathbf{I}_\alpha^{'} = \mathbf{R}\,\mathbf{J}_\alpha^{'}\,\mathbf{R}^{\mathrm{T}}$ and $\mathbf{I}_c = \mathbf{R}\,\mathbf{J}_c\,\mathbf{R}^{\mathrm{T}}$.

By introducing the following notations

$$\delta \mathbf{w}^w = \begin{bmatrix} \delta \mathbf{w} \\ \delta \alpha \end{bmatrix}, \quad \dot{\mathbf{w}}^w = \begin{bmatrix} \dot{\mathbf{w}} \\ \dot{\alpha} \end{bmatrix}, \quad \ddot{\mathbf{w}}^w = \begin{bmatrix} \ddot{\mathbf{w}} \\ \ddot{\alpha} \end{bmatrix}, \tag{42}$$

$$\mathbf{I}_\rho^1 = \begin{bmatrix} (\mathbf{I}_\rho + \mathbf{I}_\alpha) & -\mathbf{I}_b \\ -\mathbf{I}_b^{\mathrm{T}} & J_{\overline{\omega}} \end{bmatrix}, \quad \mathbf{I}_\rho^2 = \begin{bmatrix} \widetilde{\dot{\mathbf{w}}}\,(\mathbf{I}_\rho + \mathbf{I}_\alpha) & \mathbf{I}_c\,\dot{\mathbf{w}} \\ -\dot{\mathbf{w}}^{\mathrm{T}}\,\mathbf{I}_\alpha^{'} & 0 \end{bmatrix}, \tag{43}$$

the expression in Eq. (41) can be put in the form

$$\delta K = -\int_{l_o} \left\{ \delta \mathbf{u}_{\mathrm{G}}{}^{\mathrm{T}} A_\rho \ddot{\mathbf{u}}_{\mathrm{G}} + \delta \mathbf{w}^{w\mathrm{T}} \left[\mathbf{I}_\rho^1 \ddot{\mathbf{w}}^w + \mathbf{I}_\rho^2 \dot{\mathbf{w}}^w \right] \right\} \mathrm{d}l\,. \tag{44}$$

4 BEAM KINEMATICS

In this work, the corotational framework introduced by Rankin and Nour-Omid [36,38], and further developed Battini and Pacoste [5] is fully adopted.

The definition of the corotational two noded-beam element, described in this section, involves several coordinate systems, see Fig. 3. First a global reference system is defined by the triad of unit orthogonal vectors $\mathbf{e}_j$ $(j = 1,2,3)$. Next, a local system which continuously rotates and translates with the element is selected. The orthonormal basis vectors of the local system are denoted by $\mathbf{r}_j$ $(j = 1,2,3)$. In the initial (undeformed) configuration, the local system is defined by the orthonormal triad $\mathbf{e}_j^o$. In addition, $\mathbf{t}_j^1$ and $\mathbf{t}_j^2$ $(j = 1,2,3)$, denote two unit triads rigidly attached to nodes 1 and 2. The origin of each unit triad (except the global one $\mathbf{e}_j$) coincides with the centroid of the cross-section.

According to the main idea of the corotational formulation, the motion of the element from the initial to the final deformed configuration is split into a rigid body component and a deformational part. The rigid body motion consists of a rigid translation and rotation of the local element frame. The origin of the local system is taken at node 1 and thus the rigid translation is defined by $\mathbf{u}_1^g$, the translation of the cross-section centroid at node 1. Here and in the sequel, superscript g indicates quantities expressed in the global reference system. The rigid rotation is such that the new orientation of the local reference system is defined by an orthogonal matrix $\mathbf{R}_r$, given by

$$\mathbf{R}_r = [\,\mathbf{r}_1\ \mathbf{r}_2\ \mathbf{r}_3\,]\,. \tag{45}$$

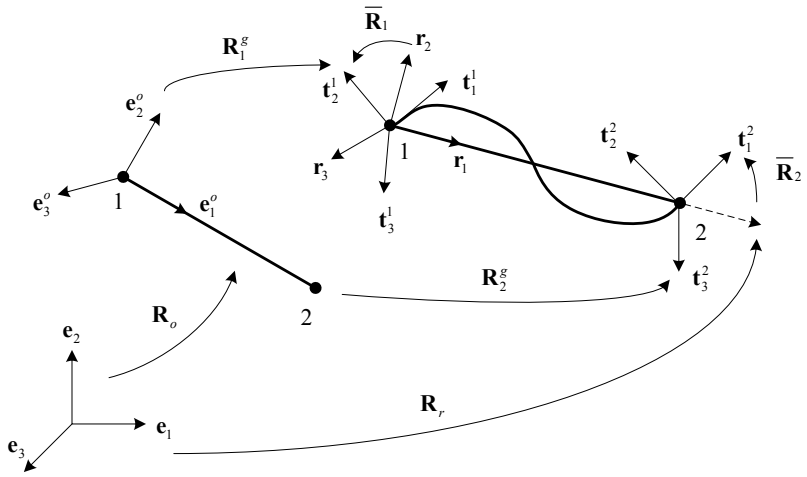


Figure 3: Beam kinematics and the coordinate systems

The first coordinate axis of the local system is defined by the line connecting nodes 1 and 2 of the element. Consequently, $\mathbf{r}_1$ is given by

$$\mathbf{r}_1 = \frac{\mathbf{x}_2^g + \mathbf{u}_2^g - \mathbf{x}_1^g - \mathbf{u}_1^g}{l_n}\,, \tag{46}$$

with $\mathbf{x}_i^g$ $(i = 1,2)$ denoting the nodal coordinates in the initial undeformed configuration and l_n denoting the current length of the beam, i.e.

$$l_n = \|\mathbf{x}_2^g + \mathbf{u}_2^g - \mathbf{x}_1^g - \mathbf{u}_1^g\|\,. \tag{47}$$

The remaining two axes are determined with the help of an auxiliary vector $\mathbf{p}$. In the initial configuration, $\mathbf{p}$ is directed along the local $\mathbf{e}_2^o$ direction, whereas in the deformed configuration its orientation is obtained from

$$\mathbf{p} = \frac{1}{2}(\mathbf{p}_1 + \mathbf{p}_2)\,, \quad \mathbf{p}_i = \mathbf{R}_i^g\,\mathbf{R}_o\,[0\;1\;0]^{\mathrm{T}} \quad (i = 1,2)\,, \tag{48}$$

where $\mathbf{R}_1^g$ and $\mathbf{R}_2^g$ are the orthogonal matrices used to specify the orientation of the nodal triads $\mathbf{t}_j^1$ and $\mathbf{t}_j^2$ respectively, and $\mathbf{R}_o$ specifies the orientation of the local frame in the initial configuration, i.e. $\mathbf{R}_o = [\mathbf{e}_1^o\;\mathbf{e}_2^o\;\mathbf{e}_3^o]$. The unit vectors $\mathbf{r}_2$ and $\mathbf{r}_3$ are then computed by the following vector products

$$\mathbf{r}_3 = \frac{\mathbf{r}_1 \times \mathbf{p}}{\|\mathbf{r}_1 \times \mathbf{p}\|}, \quad \mathbf{r}_2 = \mathbf{r}_3 \times \mathbf{r}_1\,, \tag{49}$$

resulting in the orthogonal matrix $\mathbf{R}_r$ (Eq. (45)) being completely determined.

The rigid motion previously described, is accompanied by local deformational displacements and rotations with respect to the local element axes. In this context, due to the particular choice of the local system, the local translations at node 1 are zero. Moreover, at node 2, the only non zero component is the translation along $\mathbf{r}_1$. This can easily be evaluated according to

$$\overline{u} = l_n - l_o\,, \tag{50}$$

with l_o denoting the length of the beam in the original undeformed configuration. Here and in the sequel, an overbar denotes a deformational kinematic quantity.

The global rotations at node i can be expressed in terms of the rigid rotation of the local axes, defined by $\mathbf{R}_r$, followed by a local rotation relative to these axes. The latter is defined by the orthogonal matrix $\overline{\mathbf{R}}_i$. Consequently, the orientation of the nodal triad $\mathbf{t}_j^i$ can be obtained by means of the product $\mathbf{R}_r\,\overline{\mathbf{R}}_i$. On the other hand, (see Fig. 3) this orientation can also be obtained through the product $\mathbf{R}_i^g\,\mathbf{R}_o$, which gives

$$\overline{\mathbf{R}}_i = \mathbf{R}_r^{\mathrm{T}}\,\mathbf{R}_i^g\,\mathbf{R}_o \quad (i=1,2)\,. \tag{51}$$

The local rotations are then evaluated from

$$\overline{\boldsymbol{\theta}}_i = \log\left(\overline{\mathbf{R}}_i\right) \quad (i=1,2)\,. \tag{52}$$

Due to the choice of the local coordinate system, the local nodal displacement vector $\mathbf{d}_l^w$ has only nine components and is given by

$$\mathbf{d}_l^w = \left[\,\overline{u}\;\;\overline{\boldsymbol{\theta}}_1^{\mathrm{T}}\;\;\overline{\boldsymbol{\theta}}_2^{\mathrm{T}}\;\;\alpha_1\;\;\alpha_2\,\right]^{\mathrm{T}}. \tag{53}$$

with α_i $(i=1,2)$ denoting the additional warping degrees of freedom.

The variation of the local nodal displacement vector is

$$\delta\mathbf{d}_l^w = \left[\,\delta\overline{u}\;\;\delta\overline{\boldsymbol{\theta}}_1^{\mathrm{T}}\;\;\delta\overline{\boldsymbol{\theta}}_2^{\mathrm{T}}\;\;\delta\alpha_1\;\;\delta\alpha_2\,\right]^{\mathrm{T}}, \tag{54}$$

and the global counterpart is given by

$$\delta\mathbf{d}_g^w = \left[\,\delta\mathbf{u}_1^{g\mathrm{T}}\;\;\delta\mathbf{w}_1^{g\mathrm{T}}\;\;\delta\mathbf{u}_2^{g\mathrm{T}}\;\;\delta\mathbf{w}_2^{g\mathrm{T}}\;\;\delta\alpha_1\;\;\delta\alpha_2\,\right]^{\mathrm{T}}, \tag{55}$$

with $\delta\mathbf{w}_i^g$ $(i=1,2)$ denoting spatial spin variables defined by

$$\delta\mathbf{R}_i^g = \widetilde{\delta\mathbf{w}_i^g}\,\mathbf{R}_i^g\,. \tag{56}$$

Since the warping is a deformational quantity, it remains constant during the transformation between the global and local system, see Eqs. (54) and (55).

Further, let $\delta\overline{\mathbf{w}}_i$ and $\delta\mathbf{w}_r^g$ denote the spatial spin variables defined by

$$\delta\overline{\mathbf{R}}_i = \widetilde{\delta\overline{\mathbf{w}}_i}\,\overline{\mathbf{R}}_i, \quad \delta\mathbf{R}_r = \widetilde{\delta\mathbf{w}_r^g}\,\mathbf{R}_r\,. \tag{57}$$

By taking the variation of Eq. (51), one obtains the following relation (see [5])

$$\delta\overline{\mathbf{w}}_i = \delta\mathbf{w}_i^e - \delta\mathbf{w}_r^e \quad (i=1,2)\,, \tag{58}$$

where use of Eq. (51) has been made along the fact that $\mathbf{R}_r$ transforms a vector and a tensor from global to local coordinates according to

$$\mathbf{x}^e = \mathbf{R}_r^{\mathrm{T}}\,\mathbf{x}^g, \quad \widetilde{\mathbf{x}^e} = \mathbf{R}_r^{\mathrm{T}}\,\widetilde{\mathbf{x}^g}\,\mathbf{R}_r\,. \tag{59}$$

Let consider only the global translational and rotational variables

$$\delta \mathbf{d}_g = \left[\delta \mathbf{u}_1^{g\mathrm{T}} \;\; \delta \mathbf{w}_1^{g\mathrm{T}} \;\; \delta \mathbf{u}_2^{g\mathrm{T}} \;\; \delta \mathbf{w}_2^{g\mathrm{T}} \right]^{\mathrm{T}}, \tag{60}$$

and let

$$\delta \mathbf{d}_g^e = \mathbf{E}^{\mathrm{T}} \delta \mathbf{d}_g, \quad \mathbf{E} = \begin{bmatrix} \mathbf{R}_r & \mathbf{0} & \mathbf{0} & \mathbf{0} \\ \mathbf{0} & \mathbf{R}_r & \mathbf{0} & \mathbf{0} \\ \mathbf{0} & \mathbf{0} & \mathbf{R}_r & \mathbf{0} \\ \mathbf{0} & \mathbf{0} & \mathbf{0} & \mathbf{R}_r \end{bmatrix}, \tag{61}$$

with $\mathbf{0}$ denoting the 3×3 zero matrix.

Using the chain rule, $\delta \overline{\mathbf{w}}_i$ is evaluated as

$$\delta \overline{\mathbf{w}}_i = \frac{\partial \overline{\mathbf{w}}_i}{\partial \mathbf{d}_g^e} \frac{\partial \mathbf{d}_g^e}{\partial \mathbf{d}_g} \delta \mathbf{d}_g = \frac{\partial \overline{\mathbf{w}}_i}{\partial \mathbf{d}_g^e} \mathbf{E}^{\mathrm{T}} \delta \mathbf{d}_g \quad (i = 1,2). \tag{62}$$

Then Eq. (58) can be rewritten as

$$\begin{bmatrix} \delta \overline{\mathbf{w}}_1 \\ \delta \overline{\mathbf{w}}_2 \end{bmatrix} = \left(\begin{bmatrix} \mathbf{0} & \mathbf{I} & \mathbf{0} & \mathbf{0} \\ \mathbf{0} & \mathbf{0} & \mathbf{0} & \mathbf{I} \end{bmatrix} - \begin{bmatrix} \mathbf{G}^{\mathrm{T}} \\ \mathbf{G}^{\mathrm{T}} \end{bmatrix} \right) \mathbf{E}^{\mathrm{T}} \delta \mathbf{d}_g = \mathbf{P} \mathbf{E}^{\mathrm{T}} \delta \mathbf{d}_g, \tag{63}$$

where the matrix $\mathbf{G}$ is defined by

$$\mathbf{G}^{\mathrm{T}} = \frac{\partial \mathbf{w}_r^e}{\partial \mathbf{d}_g^e}. \tag{64}$$

For the local coordinate system defined in Eqs. (46) - (49), the above equation yield to

$$\mathbf{G}^{\mathrm{T}} = \begin{bmatrix} 0 & 0 & \frac{\eta}{l_n} & \frac{\eta_{12}}{2} & -\frac{\eta_{11}}{2} & 0 & 0 & 0 & -\frac{\eta}{l_n} & \frac{\eta_{22}}{2} & -\frac{\eta_{21}}{2} & 0 \\ 0 & 0 & \frac{1}{l_n} & 0 & 0 & 0 & 0 & 0 & -\frac{1}{l_n} & 0 & 0 & 0 \\ 0 & -\frac{1}{l_n} & 0 & 0 & 0 & 0 & 0 & \frac{1}{l_n} & 0 & 0 & 0 & 0 \end{bmatrix}, \tag{65}$$

$$\eta = \frac{p_1}{p_2}, \quad \eta_{11} = \frac{p_{11}}{p_2}, \quad \eta_{12} = \frac{p_{12}}{p_2}, \quad \eta_{21} = \frac{p_{21}}{p_2}, \quad \eta_{22} = \frac{p_{22}}{p_2}, \tag{66}$$

where (see Eq. (48)) p_j and p_{ij} are the components of the vectors $\mathbf{R}_r^{\mathrm{T}} \mathbf{p}$ and $\mathbf{R}_r^{\mathrm{T}} \mathbf{p}_i$, respectively.

5 INERTIA FORCE AND TANGENT DYNAMIC MATRIX

5.1 Local beam kinematic description

The local motion of a beam cross-section from the initial (i.e. rotated but still undeformed) configuration to the current configuration is defined by $[\overline{u}_1 \;\; \overline{u}_2 \;\; \overline{u}_3]^{\mathrm{T}}$, the translation of the cross-section centroid G and $\overline{\boldsymbol{\theta}} = [\overline{\theta}_1 \;\; \overline{\theta}_2 \;\; \overline{\theta}_3]^{\mathrm{T}}$, the local rotation of the section (see Figs. 4 and 5) and α, the warping intensity (see Eq. (13)).

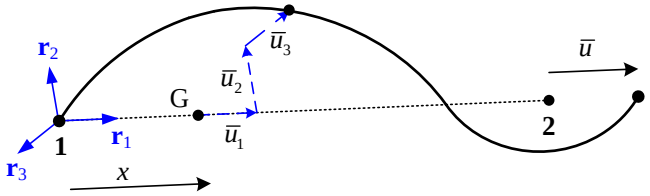


Figure 4: Local beam configuration - Translation.

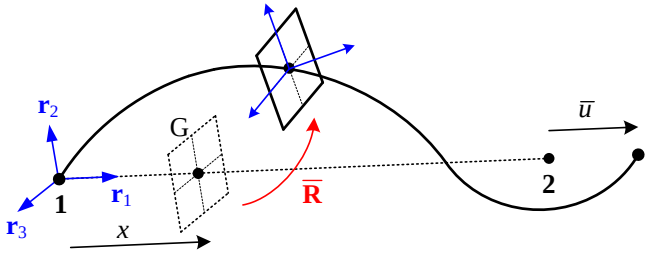


Figure 5: Local beam configuration - Rotation.

The main interest in the separation of the local deformation and the rigid body motion is that different assumptions can be made to represent the local displacements. Hence, linear interpolation is used for the axial displacement whereas cubic interpolations are used for the transverse displacements and for the axial rotation. Then, due to the particular choice of the local degrees of freedom, one has

$$\begin{bmatrix} \overline{u}_1 \\ \overline{u}_2 \\ \overline{u}_3 \\ \overline{\theta}_1 \\ \overline{\theta}_2 \\ \overline{\theta}_3 \\ \alpha \end{bmatrix} = \begin{bmatrix} N_2 & 0 & 0 & 0 & 0 & 0 & 0 & 0 & 0 \\ 0 & 0 & 0 & N_3 & 0 & 0 & N_4 & 0 & 0 \\ 0 & 0 & -N_3 & 0 & 0 & -N_4 & 0 & 0 & 0 \\ 0 & N_7 & 0 & 0 & N_8 & 0 & 0 & N_3 & N_4 \\ 0 & 0 & N_5 & 0 & 0 & N_6 & 0 & 0 & 0 \\ 0 & 0 & 0 & N_5 & 0 & 0 & N_6 & 0 & 0 \\ 0 & N_9 & 0 & 0 & -N_9 & 0 & 0 & N_5 & N_6 \end{bmatrix} \mathbf{d}_l^w , \tag{67}$$

where the local nodal displacement vector $\mathbf{d}_l^w$ is defined by Eq. (53).

The expressions of the interpolation functions are given by

$$N_1 = 1 - \frac{x}{l_o}, \quad N_2 = 1 - N_1, \quad N_3 = x\left(1 - \frac{x}{l_o}\right)^2,$$
$$N_4 = -\left(1 - \frac{x}{l_o}\right)\frac{x^2}{l_o}, \quad N_5 = \left(1 - \frac{3x}{l_o}\right)\left(1 - \frac{x}{l_o}\right), \quad N_6 = \left(\frac{3x}{l_o} - 2\right)\frac{x}{l_o},$$
$$N_7 = 1 - \frac{3x^2}{l_o^2} + \frac{2x^3}{l_o^3}, \quad N_8 = 1 - N_7, \quad N_9 = \frac{6x^2}{l_o^3} - \frac{6x}{l_o^2}.$$

Let $\mathbf{u}_l = [0 \ \overline{u}_2 \ \overline{u}_3]^{\mathrm{T}}$ denotes the local transverse displacement vector. From Eq. (67), this vector

is given by

$$\mathbf{u}_l = \mathbf{P}_1 \begin{bmatrix} \overline{\boldsymbol{\theta}}_1 \\ \overline{\boldsymbol{\theta}}_2 \end{bmatrix}, \tag{68}$$

with

$$\mathbf{P}_1 = \begin{bmatrix} 0 & 0 & 0 & 0 & 0 & 0 \\ 0 & 0 & N_3 & 0 & 0 & N_4 \\ 0 & -N_3 & 0 & 0 & -N_4 & 0 \end{bmatrix}. \tag{69}$$

From Eq. (67), the local rotation and the warping degree of freedom are given by

$$\begin{bmatrix} \overline{\boldsymbol{\theta}} \\ \alpha \end{bmatrix} = \begin{bmatrix} \mathbf{P}_2 & \mathbf{P}_3 \\ \mathbf{P}_4 & \mathbf{P}_5 \end{bmatrix} \begin{bmatrix} \overline{\boldsymbol{\theta}}_1 \\ \overline{\boldsymbol{\theta}}_2 \\ \alpha_1 \\ \alpha_2 \end{bmatrix}, \tag{70}$$

with

$$\mathbf{P}_2 = \begin{bmatrix} N_7 & 0 & 0 & N_8 & 0 & 0 \\ 0 & N_5 & 0 & 0 & N_6 & 0 \\ 0 & 0 & N_5 & 0 & 0 & N_6 \end{bmatrix}, \quad \mathbf{P}_3 = \begin{bmatrix} N_3 & N_4 \\ 0 & 0 \\ 0 & 0 \end{bmatrix}, \tag{71}$$
$$\mathbf{P}_4 = \begin{bmatrix} N_9 & 0 & 0 & -N_9 & 0 & 0 \end{bmatrix}, \quad \mathbf{P}_5 = \begin{bmatrix} N_5 & N_6 \end{bmatrix}.$$

5.2 Translational displacement variables

The position of the cross-section centroid in the global coordinate system is given by (see Fig. 4)

$$\mathrm{OG} = \mathbf{x}_\mathrm{G} = \mathbf{x}_1^g + \mathbf{u}_1^g + (x + \overline{u}_1)\,\mathbf{r}_1 + \overline{u}_2\mathbf{r}_2 + \overline{u}_3\mathbf{r}_3\,. \tag{72}$$

Using Eqs. (46), (50) and (67), the above relation can be put in the following form

$$\mathrm{OG} = N_1\mathbf{x}_1^g + N_2\mathbf{x}_2^g + N_1\mathbf{u}_1^g + N_2\mathbf{u}_2^g + \mathbf{R}_r\mathbf{u}_l\,, \tag{73}$$

with $\mathbf{u}_l$ as defined in Eq. (68).

Then by taking the variation of the above equation, the following expression is obtained

$$\delta\mathrm{OG} = \delta\mathbf{u} = \mathbf{N}\,\delta\mathbf{d}_g + \mathbf{R}_r\delta\mathbf{u}_l + \delta\mathbf{R}_r\mathbf{u}_l\,, \tag{74}$$

with $\mathbf{N} = \begin{bmatrix} N_1\mathbf{I} & \mathbf{0} & N_2\mathbf{I} & \mathbf{0} \end{bmatrix}$.
One interesting property of $\mathbf{N}$ is that

$$\mathbf{N} = \mathbf{R}_r\,\mathbf{N}\,\mathbf{E}^{\mathrm{T}}. \tag{75}$$

The variation $\delta\mathbf{R}_r$ is calculated

$$\delta\mathbf{R}_r = \mathbf{R}_r\,\widetilde{\delta\mathbf{w}_r^e}\,. \tag{76}$$

From Eqs. (61) and (64), $\delta \mathbf{w}_r^e$ is obtained as

$$\delta \mathbf{w}_r^e = \mathbf{G}^{\mathrm{T}} \mathbf{E}^{\mathrm{T}} \delta \mathbf{d}_g \,. \tag{77}$$

By taking the differentiation of Eq. (68), one obtains

$$\delta \mathbf{u}_l = \mathbf{P}_1 \begin{bmatrix} \delta \overline{\boldsymbol{\theta}}_1 \\ \delta \overline{\boldsymbol{\theta}}_2 \end{bmatrix} . \tag{78}$$

In the corotational approach, the local rotations at the nodes $\overline{\boldsymbol{\theta}}_i$ $(i = 1,2)$, defined in Eq. (52), are small and the operator $\mathbf{T}_s(\overline{\boldsymbol{\theta}}_i)$ is close to the identity matrix. Consequently, see Eq. (5), the following approximation is adopted

$$\delta \overline{\mathbf{w}}_i \approx \delta \overline{\boldsymbol{\theta}}_i \,. \tag{79}$$

Then, using Eqs. (63) and (79), the expression in (78) becomes

$$\delta \mathbf{u}_l \approx \mathbf{P}_1 \begin{bmatrix} \delta \overline{\mathbf{w}}_1 \\ \delta \overline{\mathbf{w}}_2 \end{bmatrix} = \mathbf{P}_1 \mathbf{P} \mathbf{E}^{\mathrm{T}} \delta \mathbf{d}_g \,. \tag{80}$$

Inserting Eqs. (75) - (77) and (80) into Eq. (74), one obtains

$$\delta \mathbf{u} = \mathbf{R}_r \mathbf{H}_1 \mathbf{E}^{\mathrm{T}} \delta \mathbf{d}_g \,, \tag{81}$$

where

$$\mathbf{H}_1 = \mathbf{N} + \mathbf{P}_1 \mathbf{P} - \widetilde{\mathbf{u}}_l \mathbf{G}^{\mathrm{T}} \,. \tag{82}$$

Obviously, the translational velocity of the cross-section centroid is given as

$$\dot{\mathbf{u}} = \mathbf{R}_r \mathbf{H}_1 \mathbf{E}^{\mathrm{T}} \dot{\mathbf{d}}_g \,. \tag{83}$$

By taking the time derivative of the above equation, the expression of the translational acceleration reads as follows

$$\ddot{\mathbf{u}} = \mathbf{R}_r \mathbf{H}_1 \mathbf{E}^{\mathrm{T}} \ddot{\mathbf{d}}_g + \left(\dot{\mathbf{R}}_r \mathbf{H}_1 \mathbf{E}^{\mathrm{T}} + \mathbf{R}_r \dot{\mathbf{H}}_1 \mathbf{E}^{\mathrm{T}} + \mathbf{R}_r \mathbf{H}_1 \dot{\mathbf{E}}^{\mathrm{T}} \right) \dot{\mathbf{d}}_g \,, \tag{84}$$

with $\dot{\mathbf{H}}_1$ given in [32].

By noting that $\dot{\mathbf{R}}_r = \mathbf{R}_r \widetilde{\dot{\mathbf{w}}_r^e}$ (see Eq. (76)), one has

$$\dot{\mathbf{E}} = \mathbf{E} \mathbf{E}_t, \quad \mathbf{E}_t = \begin{bmatrix} \widetilde{\dot{\mathbf{w}}_r^e} & \mathbf{0} & \mathbf{0} & \mathbf{0} \\ \mathbf{0} & \widetilde{\dot{\mathbf{w}}_r^e} & \mathbf{0} & \mathbf{0} \\ \mathbf{0} & \mathbf{0} & \widetilde{\dot{\mathbf{w}}_r^e} & \mathbf{0} \\ \mathbf{0} & \mathbf{0} & \mathbf{0} & \widetilde{\dot{\mathbf{w}}_r^e} \end{bmatrix} . \tag{85}$$

$\dot{\mathbf{w}}_r^e$ (see Eq. (77)) is calculated as

$$\dot{\mathbf{w}}_r^e = \mathbf{G}^{\mathrm{T}} \mathbf{E}^{\mathrm{T}} \dot{\mathbf{d}}_g \,. \tag{86}$$

By introducing the notation

$$\mathbf{C}_1 = \widetilde{\dot{\mathbf{w}}_r^e} \mathbf{H}_1 + \dot{\mathbf{H}}_1 - \mathbf{H}_1 \mathbf{E}_t \,, \tag{87}$$

Eq. (84) can be rewritten in a more compact form as

$$\ddot{\mathbf{u}} = \mathbf{R}_r \mathbf{H}_1 \mathbf{E}^{\mathrm{T}} \ddot{\mathbf{d}}_g + \mathbf{R}_r \mathbf{C}_1 \mathbf{E}^{\mathrm{T}} \dot{\mathbf{d}}_g \,. \tag{88}$$

5.3 Finite rotations and warping variables

Combining Eq. (70) with the approximation defined in Eq. (79), the local spatial spin and warping variables are calculated as follows

$$\delta\overline{\mathbf{w}} = \begin{bmatrix}\mathbf{P}_2 & \mathbf{P}_3\end{bmatrix}\begin{bmatrix}\delta\overline{\mathbf{w}}_1\\ \delta\overline{\mathbf{w}}_2\\ \delta\alpha_1\\ \delta\alpha_2\end{bmatrix}, \quad \delta\alpha = \begin{bmatrix}\mathbf{P}_4 & \mathbf{P}_5\end{bmatrix}\begin{bmatrix}\delta\overline{\mathbf{w}}_1\\ \delta\overline{\mathbf{w}}_2\\ \delta\alpha_1\\ \delta\alpha_2\end{bmatrix}. \tag{89}$$

Using Eq. (63), the above equation leads to

$$\delta\overline{\mathbf{w}} = \begin{bmatrix}\mathbf{P}_2 & \mathbf{P}_3\end{bmatrix}\begin{bmatrix}\mathbf{P}\mathbf{E}^{\mathrm{T}} & \mathbf{0}\\ \mathbf{0} & \mathbf{I}_2\end{bmatrix}\delta\mathbf{d}_g^w = \begin{bmatrix}\mathbf{P}_2\mathbf{P} & \mathbf{P}_3\end{bmatrix}\mathbf{E}^{w\mathrm{T}}\delta\mathbf{d}_g^w, \tag{90}$$

$$\delta\alpha = \begin{bmatrix}\mathbf{P}_4 & \mathbf{P}_5\end{bmatrix}\begin{bmatrix}\mathbf{P}\mathbf{E}^{\mathrm{T}} & \mathbf{0}\\ \mathbf{0} & \mathbf{I}_2\end{bmatrix}\delta\mathbf{d}_g^w = \mathbf{H}_3\mathbf{E}^{w\mathrm{T}}\delta\mathbf{d}_g^w, \tag{91}$$

where

$$\mathbf{E}^w = \begin{bmatrix}\mathbf{E} & \mathbf{0}\\ \mathbf{0} & \mathbf{I}_2\end{bmatrix}, \quad \mathbf{I}_2 = \begin{bmatrix}1 & 0\\ 0 & 1\end{bmatrix}, \quad \mathbf{H}_3 = \begin{bmatrix}\mathbf{P}_4\mathbf{P} & \mathbf{P}_5\end{bmatrix}. \tag{92}$$

Using Eqs. (58) and (59), the spatial spin variables, associated to the global rotation of a cross-section, are evaluated using

$$\delta\mathbf{w} = \mathbf{R}_r\delta\mathbf{w}^e = \mathbf{R}_r\left(\delta\mathbf{w}_r^e + \delta\overline{\mathbf{w}}\right). \tag{93}$$

Using Eqs. (77) and (90), the above expression can be rewritten in as

$$\delta\mathbf{w} = \mathbf{R}_r\mathbf{H}_2\mathbf{E}^{w\mathrm{T}}\delta\mathbf{d}_g^w, \tag{94}$$

with

$$\mathbf{H}_2 = \begin{bmatrix}\mathbf{P}_2\mathbf{P} + \mathbf{G}^{\mathrm{T}} & \mathbf{P}_3\end{bmatrix}. \tag{95}$$

$\dot{\mathbf{w}}$ and $\dot{\alpha}$ are calculated with expressions similar to (91) and (94)

$$\dot{\mathbf{w}} = \mathbf{R}_r\mathbf{H}_2\mathbf{E}^{w\mathrm{T}}\dot{\mathbf{d}}_g^w, \quad \dot{\alpha} = \mathbf{H}_3\mathbf{E}^{w\mathrm{T}}\dot{\mathbf{d}}_g^w. \tag{96}$$

$\ddot{\mathbf{w}}$ is obtained by taking the time derivative of $\dot{\mathbf{w}}$

$$\ddot{\mathbf{w}} = \mathbf{R}_r\mathbf{H}_2\mathbf{E}^{w\mathrm{T}}\ddot{\mathbf{d}}_g^w + \mathbf{R}_r\left(\widetilde{\dot{\mathbf{w}}_r^e}\mathbf{H}_2 + \dot{\mathbf{H}}_2 - \mathbf{H}_2\mathbf{E}_t^w\right)\mathbf{E}^{w\mathrm{T}}\dot{\mathbf{d}}_g^w, \tag{97}$$

with $\dot{\mathbf{H}}_2$ given in [32]

$$\mathbf{E}_t^w = \begin{bmatrix}\mathbf{E}_t & \mathbf{0}\\ \mathbf{0} & \mathbf{0}_2\end{bmatrix}. \tag{98}$$

By noting that

$$\mathbf{P}_4\mathbf{P} = \begin{bmatrix} 0 & 0 & 0 & N_9 & 0 & 0 & 0 & 0 & 0 & -N_9 & 0 & 0 \end{bmatrix}, \tag{99}$$

and by taking the time derivative of $\dot{\alpha}$, the expression of $\ddot{\alpha}$ is obtained

$$\ddot{\alpha} = \mathbf{H}_3\,\mathbf{E}^{w\mathrm{T}}\,\ddot{\mathbf{d}}_g^w - \mathbf{H}_3\,\mathbf{E}_t^w\,\mathbf{E}^{w\mathrm{T}}\,\dot{\mathbf{d}}_g^w\,. \tag{100}$$

Introducing Eqs. (91),(94),(96),(97), and (100) into Eq. (42), one obtains

$$\delta\mathbf{w}^w = \begin{bmatrix} \mathbf{R}_r & \mathbf{0} \\ \mathbf{0} & 1 \end{bmatrix} \begin{bmatrix} \mathbf{H}_2 \\ \mathbf{H}_3 \end{bmatrix} \mathbf{E}^{w\mathrm{T}}\,\delta\mathbf{d}_g^w = \mathbf{R}_r^w\,\mathbf{H}_2^w\,\mathbf{E}^{w\mathrm{T}}\,\delta\mathbf{d}_g^w\,, \tag{101}$$

$$\dot{\mathbf{w}}^w = \mathbf{R}_r^w\,\mathbf{H}_2^w\,\mathbf{E}^{w\mathrm{T}}\,\dot{\mathbf{d}}_g^w\,, \tag{102}$$

$$\ddot{\mathbf{w}}^w = \mathbf{R}_r^w\,\mathbf{H}_2^w\,\mathbf{E}^{w\mathrm{T}}\,\ddot{\mathbf{d}}_g^w + \mathbf{R}_r^w\,\mathbf{C}_2\,\mathbf{E}^{w\mathrm{T}}\,\dot{\mathbf{d}}_g^w\,, \tag{103}$$

where

$$\mathbf{C}_2 = \begin{bmatrix} \widetilde{\dot{\mathbf{w}}_r^e}\,\mathbf{H}_2 + \dot{\mathbf{H}}_2 - \mathbf{H}_2\,\mathbf{E}_t^w \\ -\mathbf{H}_3\,\mathbf{E}_t^w \end{bmatrix}. \tag{104}$$

5.4 Inertia force vector and tangent dynamic matrix

By inserting the expressions of $\delta\mathbf{u}$ and $\delta\mathbf{w}^w$ given in Eqs. (81) and (101) into Eq. (44), the inertia force vector is obtained as

$$\mathbf{f}_{\mathrm{k}}^w = \mathbf{E}^w \left\{ \begin{bmatrix} \int_{l_o} \mathbf{H}_1^{\mathrm{T}}\,\mathbf{R}_r^{\mathrm{T}}\,A\rho\,\ddot{\mathbf{u}}\,\mathrm{d}l \\ \mathbf{0} \end{bmatrix} + \int_{l_o} \mathbf{H}_2^{w\mathrm{T}}\,\mathbf{R}_r^{w\mathrm{T}} \left[\mathbf{I}_\rho^1\,\ddot{\mathbf{w}}^w + \mathbf{I}_\rho^2\,\dot{\mathbf{w}}^w \right] \mathrm{d}l \right\}. \tag{105}$$

As shown in the above equation, the inertia force vector depends on $\mathbf{d}_g^w, \dot{\mathbf{d}}_g^w$ and $\ddot{\mathbf{d}}_g^w$. Hence, linearization of this force vector is evaluated as follows

$$\Delta\mathbf{f}_{\mathrm{k}}^w = \mathbf{M}\Delta\ddot{\mathbf{d}}_g^w + \mathbf{C}_{\mathrm{k}}\Delta\dot{\mathbf{d}}_g^w + \mathbf{K}_{\mathrm{k}}\Delta\mathbf{d}_g^w\,. \tag{106}$$

Some authors [8, 18] proposed to keep only the mass matrix $\mathbf{M}$, and to eliminate the gyroscopic $\mathbf{C}_{\mathrm{k}}$ and centrifugal $\mathbf{K}_{\mathrm{k}}$ dynamic matrices. However, in [30], extensive numerical studies have shown that it is advantageous to retain also the gyroscopic matrix as it enhances the computational efficiency. The same approach is used here. The centrifugal matrix, whose derivation is complicated and would give rise to a lengthy mathematical expression, is neglected. Therefore, the iterative scheme of the present formulation is implemented with the following approximative linearization

$$\Delta\mathbf{f}_{\mathrm{k}}^w \approx \mathbf{M}\Delta\ddot{\mathbf{d}}_g^w + \mathbf{C}_{\mathrm{k}}\Delta\dot{\mathbf{d}}_g^w\,. \tag{107}$$

From the expressions (88), (102) and (103), the following linearizations are derived

$$\begin{aligned}\Delta\ddot{\mathbf{u}} &= \mathbf{R}_r\left[\mathbf{H}_1\,\mathbf{E}^{\mathrm{T}}\,\Delta\ddot{\mathbf{d}}_g + \mathbf{C}_1\,\mathbf{E}^{\mathrm{T}}\,\Delta\dot{\mathbf{d}}_g + (\frac{\partial\mathbf{C}_1}{\partial\dot{\mathbf{d}}_g}\Delta\dot{\mathbf{d}}_g)\,\mathbf{E}^{\mathrm{T}}\,\dot{\mathbf{d}}_g\right] + f(\Delta\mathbf{d}_g)\\ &= \mathbf{R}_r\left[\mathbf{H}_1\,\mathbf{E}^{\mathrm{T}}\,\Delta\ddot{\mathbf{d}}_g + (\mathbf{C}_1+\mathbf{C}_3)\,\mathbf{E}^{\mathrm{T}}\,\Delta\dot{\mathbf{d}}_g\right] + f(\Delta\mathbf{d}_g)\,,\end{aligned} \tag{108}$$

$$\Delta\dot{\mathbf{w}}^w = \mathbf{R}_r^w\,\mathbf{H}_2^w\,\mathbf{E}^{w\mathrm{T}}\,\Delta\dot{\mathbf{d}}_g^w + f(\Delta\mathbf{d}_g^w)\,, \tag{109}$$

$$\begin{aligned}\Delta\ddot{\mathbf{w}}^w &= \mathbf{R}_r^w\left[\mathbf{H}_2^w\,\mathbf{E}^{w\mathrm{T}}\,\Delta\ddot{\mathbf{d}}_g^w + \mathbf{C}_2\,\mathbf{E}^{w\mathrm{T}}\,\Delta\dot{\mathbf{d}}_g^w + (\frac{\partial\mathbf{C}_2}{\partial\dot{\mathbf{d}}_g^w}\Delta\dot{\mathbf{d}}_g^w)\,\mathbf{E}^{w\mathrm{T}}\,\dot{\mathbf{d}}_g^w\right] + f(\Delta\mathbf{d}_g^w)\\ &= \mathbf{R}_r^w\left[\mathbf{H}_2^w\,\mathbf{E}^{w\mathrm{T}}\,\Delta\ddot{\mathbf{d}}_g^w + (\mathbf{C}_2+\mathbf{C}_4)\,\mathbf{E}^{w\mathrm{T}}\,\Delta\dot{\mathbf{d}}_g^w\right] + f(\Delta\mathbf{d}_g^w)\,,\end{aligned} \tag{110}$$

with $\mathbf{C}_3$ and $\mathbf{C}_4$ given [32].

Using the above linearizations, the expression of the mass matrix $\mathbf{M}$ is obtained as

$$\begin{aligned}\mathbf{M} &= \mathbf{E}^w\left\{\begin{bmatrix}\int_{l_o}\mathbf{H}_1^{\mathrm{T}}A_\rho\,\mathbf{H}_1\,\mathrm{d}l & \mathbf{0}\\ \mathbf{0} & \mathbf{0}\end{bmatrix} + \int_{l_o}\mathbf{H}_2^{w\mathrm{T}}\,\mathbf{R}_r^{w\mathrm{T}}\,\mathbf{I}_\rho^1\,\mathbf{R}_r^w\,\mathbf{H}_2^w\,\mathrm{d}l\right\}\mathbf{E}^{w\mathrm{T}}\\ &= \mathbf{E}^w\,\mathbf{M}^e\,\mathbf{E}^{w\mathrm{T}}\,.\end{aligned} \tag{111}$$

Regarding the gyroscopic matrix $\mathbf{C}_{\mathrm{k}}$, the following intermediate variation is used

$$\begin{aligned}\frac{\partial\mathbf{I}_\rho^2\dot{\mathbf{w}}^w}{\partial\dot{\mathbf{w}}^w}\Delta\dot{\mathbf{w}}^w &= \begin{bmatrix}\widetilde{\dot{\mathbf{w}}}\,(\mathbf{I}_\rho+\mathbf{I}_\alpha)\Delta\dot{\mathbf{w}} + \widetilde{\Delta\dot{\mathbf{w}}}\,(\mathbf{I}_\rho+\mathbf{I}_\alpha)\dot{\mathbf{w}} + \mathbf{I}_c\,(\Delta\dot{\mathbf{w}}\,\dot{\alpha}+\dot{\mathbf{w}}\Delta\dot{\alpha})\\ -\Delta\dot{\mathbf{w}}^{\mathrm{T}}\,\mathbf{I}_\alpha^{'}\,\dot{\mathbf{w}} - \dot{\mathbf{w}}^{\mathrm{T}}\,\mathbf{I}_\alpha^{'}\,\Delta\dot{\mathbf{w}}\end{bmatrix}\\ &= \begin{bmatrix}\widetilde{\dot{\mathbf{w}}}\,(\mathbf{I}_\rho+\mathbf{I}_\alpha) & \mathbf{I}_c\,\dot{\mathbf{w}}\\ -\dot{\mathbf{w}}^{\mathrm{T}}\,\mathbf{I}_\alpha^{'} & 0\end{bmatrix}\Delta\dot{\mathbf{w}}^w + \begin{bmatrix}\widetilde{(\mathbf{I}_\rho+\mathbf{I}_\alpha)\dot{\mathbf{w}}} + \mathbf{I}_c\,\dot{\alpha} & \mathbf{0}\\ -\dot{\mathbf{w}}^{\mathrm{T}}\,\mathbf{I}_\alpha^{'\mathrm{T}} & 0\end{bmatrix}\Delta\dot{\mathbf{w}}^w\\ &= \left(\mathbf{I}_\rho^2+\mathbf{I}_\rho^3\right)\Delta\dot{\mathbf{w}}^w\,.\end{aligned} \tag{112}$$

Finally, the gyroscopic matrix $\mathbf{C}_{\mathrm{k}}$ is calculated from

$$\begin{aligned}\mathbf{C}_{\mathrm{k}} =&\mathbf{E}^w\left\{\begin{bmatrix}\int_{l_o}\mathbf{H}_1^{\mathrm{T}}A_\rho\,(\mathbf{C}_1+\mathbf{C}_3)\,\mathrm{d}l & \mathbf{0}\\ \mathbf{0} & \mathbf{0}\end{bmatrix} + \int_{l_o}\mathbf{H}_2^{w\mathrm{T}}\,\mathbf{R}_r^{w\mathrm{T}}\,\mathbf{I}_\rho^1\,\mathbf{R}_r^w\,(\mathbf{C}_2+\mathbf{C}_4)\,\mathrm{d}l\right.\\ &\left.+\int_{l_o}\mathbf{H}_2^{w\mathrm{T}}\,\mathbf{R}_r^{w\mathrm{T}}\left(\mathbf{I}_\rho^2+\mathbf{I}_\rho^3\right)\mathbf{R}_r^w\,\mathbf{H}_2^w\,\mathrm{d}l\right\}\mathbf{E}^{w\mathrm{T}} = \mathbf{E}^w\,\mathbf{C}_{\mathrm{k}}^e\,\mathbf{E}^{w\mathrm{T}}\,.\end{aligned} \tag{113}$$

In this work, the warping deformations and the eccentricity of the shear center have been taken into account in deriving the inertial terms, see Eq. (13). Consequently, several additional terms have been introduced in the expressions of the inertia force vector and the tangent (mass and gyroscopic) matrices. The importance of these terms can be discussed. In the five numerical examples presented in Section 7, it has been found, as expected, that the warping deformations

in the dynamic terms have a negligible contribution to the response and can be omitted. This is done by setting $I_\omega = 0$ in Eqs. (19) and (20).

The eccentricity of the shear center with respect to the centroid generates extra dynamic terms whose importance has been investigated. It appears that for slender beams (Examples 7.1), these terms do not affect the results and can be therefore neglected. But as it has bee shown in [32], they may have a significant contribution for short beams.

If $I_\omega = y_c = z_c = 0$ is adopted, then the expression of the inertia force vector in Eq. (105) can be simplified as

$$\mathbf{f}_{\mathrm{k}}^{w} = \mathbf{E}^{w} \left\{ \begin{bmatrix} \int_{l_o} \mathbf{H}_{\mathrm{l}}^{\mathrm{T}} \mathbf{R}_r^{\mathrm{T}} A_\rho \ddot{\mathbf{u}} \mathrm{d}l \\ \mathbf{0} \end{bmatrix} + \int_{l_o} \mathbf{H}_2^{\mathrm{T}} \mathbf{R}_r^{\mathrm{T}} \left[\mathbf{I}_\rho \ddot{\mathbf{w}} + \widetilde{\dot{\mathbf{w}}} \mathbf{I}_\rho \dot{\mathbf{w}} \right] \mathrm{d}l \right\}, \tag{114}$$

and similar simplifications apply also for the expressions of the mass and gyroscopic matrices.

6 Internal force vector and tangent stiffness matrix

The purpose of this section is to present briefly the derivation of the inertial force vector and the tangent stiffness matrix. A complete description can be found in [5].

The local nodal displacements and rotations defined in Eq. (53) are extracted from the global degrees of freedom using Eqs. (50), (51) and (52).

The local internal force vector $\mathbf{f}_{\mathrm{l}}^{w}$ and the local tangent stiffness matrix $\mathbf{K}_{\mathrm{l}}^{w}$ associated with $\delta\mathbf{d}_l^{w}$ (see Eq. (54)) are derived using the same local beam kinematic description as in 5.1. However, to incorporate the bending shear deformations, the Hermitian shape functions for the transverse displacements are slightly modified as suggested in the Interdependent Interpolation Element (IIE) [39]. The Maple codes for $\mathbf{f}_{\mathrm{l}}^{w}$ and $\mathbf{K}_{\mathrm{l}}^{w}$ are given [32]. A low order of geometrical nonlinearity is introduced through a shallow arch strain description and the Wagner term.

The global internal force vector $\mathbf{f}_{\mathrm{g}}^{w}$ and the global tangent stiffness matrix $\mathbf{K}_{\mathrm{g}}^{w}$ associated with $\delta\mathbf{d}_g^{w}$ (see Eq. (55)) are obtained through a change of variables based on the transformation matrix $\mathbf{B}^{w}$ defined by

$$\delta\mathbf{d}_l^{w} = \mathbf{B}^{w}\, \delta\mathbf{d}_g^{w}. \tag{115}$$

By equating the internal virtual work in both the global and local systems, the expression of the global internal force vector $\mathbf{f}_{\mathrm{g}}^{w}$ is obtained as

$$\mathbf{f}_{\mathrm{g}}^{w} = \mathbf{B}^{w\mathrm{T}} \mathbf{f}_{\mathrm{l}}^{w}. \tag{116}$$

By taking the variations of Eq. (116), the expression of the global tangent stiffness matrix $\mathbf{K}_{\mathrm{g}}^{w}$ is obtained

$$\mathbf{K}_{\mathrm{g}}^{w} = \mathbf{B}^{w\mathrm{T}} \mathbf{K}_{\mathrm{l}}^{w} \mathbf{B}^{w} + \left. \frac{\partial (\mathbf{B}^{w\mathrm{T}} \mathbf{f}_{\mathrm{l}}^{w})}{\partial \mathbf{d}_g^{w}} \right|_{\mathbf{f}_{\mathrm{l}}^{w}}. \tag{117}$$

The expressions of $\mathbf{f}_{\mathrm{g}}^{w}$ and $\mathbf{K}_{\mathrm{g}}^{w}$ are given in [5].

7 NUMERICAL EXAMPLE

The purpose of the five numerical examples presented in this section is to assess the accuracy of the proposed corotational dynamic formulation for beam with thin-walled cross-section. For that, additional 3D-solid analyses are performed with the commercial finite element program Abaqus.

Besides, the influence of the warping deformations (I_ω) and the shear center eccentricity (y_c, z_c) in the dynamic terms of the corotational formulation is also studied. In all the examples, and as expected, the same results have been obtained with and without I_ω in the inertia terms. In Example which consists of a slender beams, the same results have been obtained with $y_c = z_c = 0$. However, for the short beam (see [32], different results are obtained with and without account for the eccentricity of the shear center.

Regarding the time integration method, the HHT α method with $\alpha = -0.05$ is used in this work. This energy-dissipative method, which is implemented in several commercial FEM programs (Abaqus, Lusas) and was employed by many authors [8, 11, 27], limits the influence of high frequencies by introducing a numerical damping. However, a numerical damping gives also a dissipation of the total energy, which can affect long time analyses. It can be noted that for beam structures, more robust alternatives to the HHT α method have been proposed in the literature [23].

In the present work, at the beginning of each time step, the predictor proposed by Crisfield [12] for the particular case of linear inertia force vector and further developed for the general case by the authors [30], is adopted. The idea of this predictor is to use the tangent operator at the time instant t_n to predict the values at the time instant t_{n+1}.

Damping is not considered. The following convergence criterion is adopted: the norm of the residual vector must be less than the prescribed tolerance $\varepsilon_f = 10^{-5}$.

The following material properties are used for all the five examples: $E = 210$ GPa, $\nu = 0.33$ and $\rho = 7850$ kg/m^3. All the dimensions in the figures are in meter.

7.1 Example: Cantilever beam with a T cross-section

The nonlinear dynamic behavior of a cantilever beam with a T cross-section, see Fig. 6, is investigated. The eccentricity of the shear center is $y_c = 0.046$ m. At the left end, the beam is clamped and all degrees of freedom, including warping, are set to zero. At the point O of the right end section, two time-varying loads are applied: $F_y^{\mathrm{O}} = -50F$, $F_z^{\mathrm{O}} = 25F$. The time evolution of F is given in Fig. 7.

The cantilever is modeled using 40 corotational beam elements. Besides, the commercial finite element software Abaqus is employed considering both beam and 3D-solid elements.

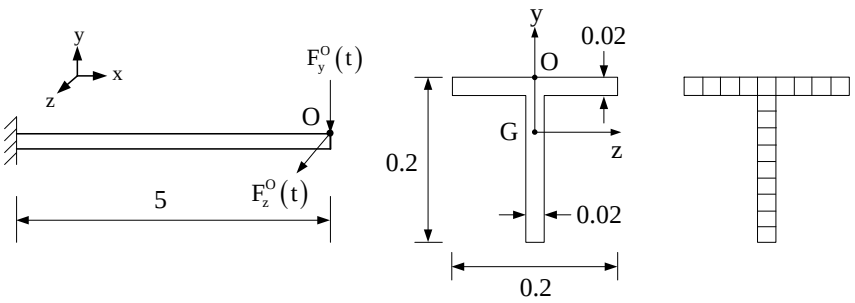


Figure 6: Cantilever beam with T cross-section : geometrical data.

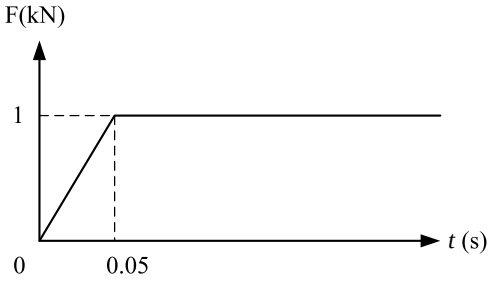


Figure 7: Cantilever beam with T cross-section - Loading history.

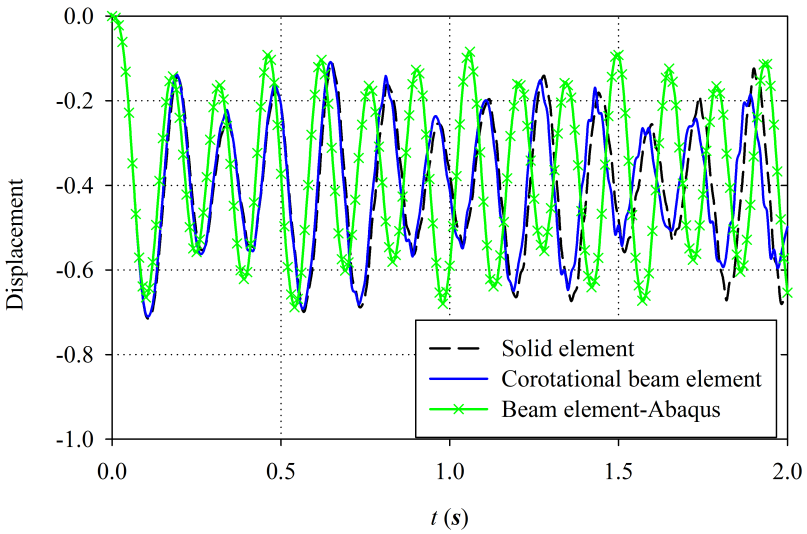


Figure 8: Cantilever beam with T cross-section - Time evolution of the displacement u_y of point G.

For the beam analysis, 80 B31OS elements are used. The beam element B31OS has seven degrees of freedom at each node. The additional degree of freedom represents the warping of the beam cross-section. Linear interpolations are used for all variables. For the 3D-solid analysis, the mesh consists of $18 \cdot 160 = 2880$ isoparametric 20 node elements (see Fig. 6). All analyses are performed with a time step $\Delta t = 10^{-3}$ s.

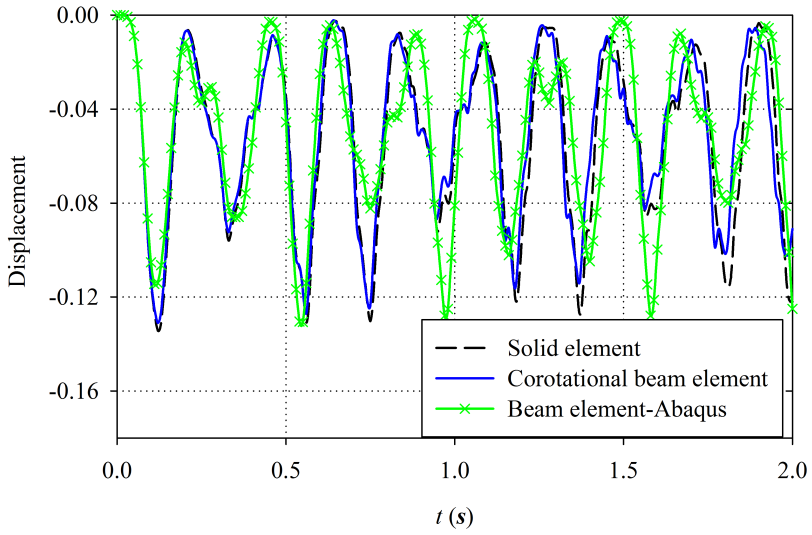


Figure 9: Cantilever beam with T cross-section - Time evolution of the displacement u_x of point G.

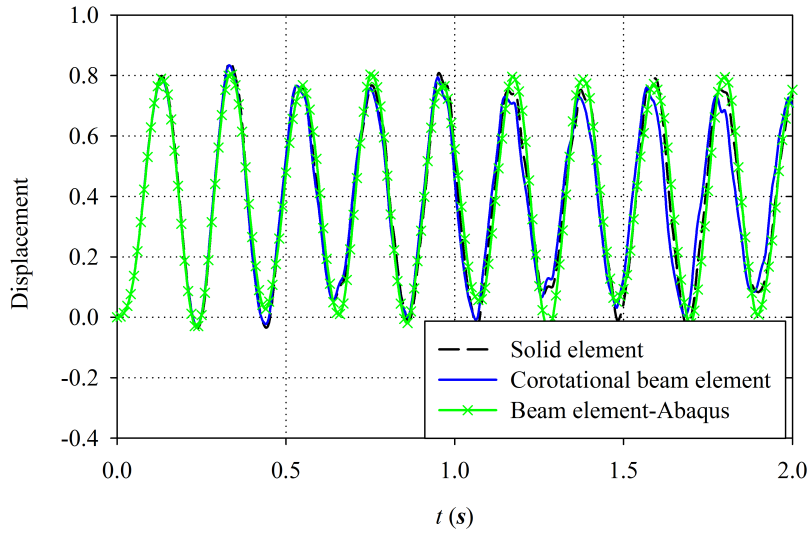


Figure 10: Cantilever beam with T cross-section - Time evolution of the displacement u_z of point G.

The displacements of the right end centroid G are depicted in Figs. 8, 9, and 10. A very good agreement in the predictions of both the corotational beam element and Abaqus 3D-solid analyses is obtained. However, large discrepancies in the predictions of both Abaqus beam and 3D-solid models can be observed, especially in Fig. 8.

A small but increasing phase lead can be observed between the results obtained with the corotational beam element and those obtained with the solid analysis. To investigate this aspect, the problem has been run for a time period of 7 s. The results are shown in Fig. 11. It can be observed that after 7 s the phase lead remains negligible. In fact, this increasing phase lead is due to a small difference in the estimation of natural frequencies between the two models.

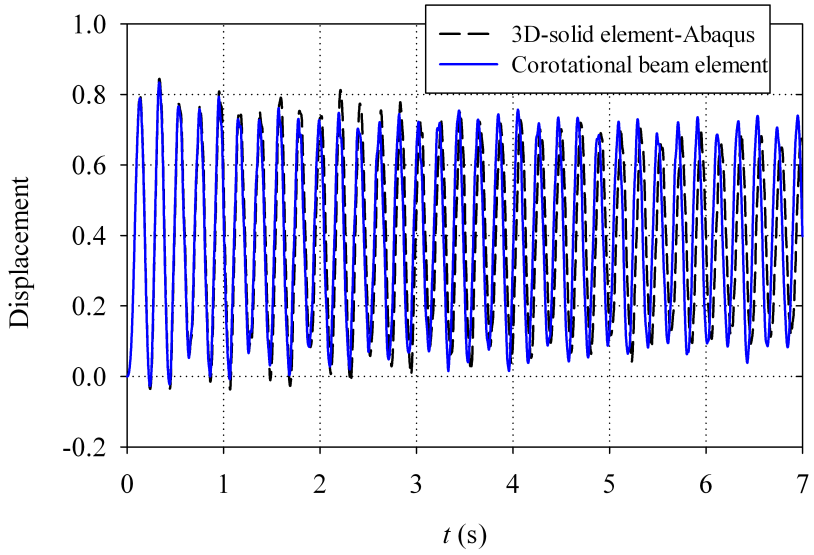


Figure 11: Cantilever beam with T cross-section - Time evolution of the displacement u_z of point G for 7 s.

8 CONCLUSIONS

In this paper, a corotational dynamic formulation for nonlinear analysis of beams with arbitrary thin-walled cross-sections was developed. The formulation is an extension of the one proposed by the authors in [31]. The same kinematic assumptions were used to derive the static and dynamic terms. Hence, the element has seven degrees of freedom at each node and cubic shape functions are used to interpolate local transverse displacements and axial rotations.

The warping deformations and the shear center eccentricity were fully taken into account in the derivation of the dynamic terms. This leads to additional terms in the expressions of the inertia force vector and the tangent (mass and gyroscopic) dynamic matrices.

A very good agreement between the results obtained with the corotational beam element and the 3D-solid element was obtained. Besides, the numerical results also showed that the warping deformations have a negligible influence in the dynamic terms and could be omitted. As shown in [32] However, the additional dynamic terms due to the shear center eccentricity cannot always be neglected.

REFERENCES

[1] R. Grutmann, R. Sauer, W. Wagner, Theory and numerics of three-dimensional beams with elastoplastic behaviour, Int. J. Num. Methods. Engrg., Vol. 48, 1675-1702 (2000).

[2] J. Argyris, An excursion into large rotations, Comput. Methods Appl. Mech. Engrg., Vol. 32, 85-155 (1982).

[3] R. Alsafadie, J.-M. Battini, M. Hjiaj, H. Somja, A comparative study of displacement and mixed-based corotational finite element formulations for elasto-plastic three-dimensional beam analysis, Engerg. Computs., Vol. 28, 7, 939-982 (2011).

[4] K.J. Bathe, E. Ramm, Wilson E.L., Finite element formulations for large deformation dynamic analysis, Int. J. Num. Methods. Engrg., Vol. 9, 353-386 (1975).

[5] J.-M. Battini, C. Pacoste, Co-rotational beam elements with warping effects in instability problems, Comput. Methods Appl. Mech. Engrg., Vol. 191, 1755-1789 (2002).

[6] K. Behdinan, M.C Stylianou, B. Tabarrok, Co-rotational dynamic analysis of flexible beams, Comput. Methods Appl. Mech. Engrg., Vol. 154, 151-161 (1998).

[7] P. Betsch, P. Steinmann, Constrained dynamics of geometrically exact beams, Comput. Mech., Vol. 31, 49-59 (2003).

[8] A. Cardona, M. Geradin, A beam finite element non-linear theory with finite rotations, Int. J. Num. Methods. Engrg., Vol. 26, 2403-2438 (1988).

[9] M.A. Crisfield, J. Shi, An energy conserving co-rotational procedure for non-linear dynamics with finite elements, Nonlinear Dynamics, Vol. 9, 37-52 (1996).

[10] M.A. Crisfield, G.F. Moita, A unified co-rotational framework for solids shells and beams, Int. J. Solids Struct., Vol. 33, 29692992 (1996).

[11] M.A. Crisfield, U. Galvanetto, G. Jelenić, Dynamics of 3-D co-rotational beams, Comput. Mech., Vol. 20, 507-519 (1997).

[12] M.A. Crisfield, Non-Linear Finite Element Analysis of Solids and Structures, Volume 2: Advanced Topics, Wiley, Chischester (1997).

[13] H.A. Elkaranshawy, M.A. Dokainish, Corotational finite element analysis of planar flexible multibody systems, Comput. Struct., Vol. 54, No.5, 881-890 (1995).

[14] U. Galvanetto, M.A. Crisfield, An energy conserving co-rotational procedure for dynamics of planar beam structures, Int. J. Num. Methods. Engrg., Vol. 39, 2265-2282 (1996).

[15] M. Geradin, A. Cardona, Kinematics and dynamics of rigid and flexible mechanisms using finite elements and quaternion algebra, Comput. Mech., Vol. 4, 115-135 (1989).

[16] M. Geradin, A. Cardona, Flexible multibody dynamics : A finite element approach, 120-127. Wiley, Chischester (2001).

[17] K.M. Hsiao, R.T. Yang, A co-rotational formulation for nonlinear dynamic analysis of curved Euler beam, Comput. Struct. , Vol. 54, No.6, 1091-1097 (1995).

[18] K.M. Hsiao, J.Y. Lin, W.Y. Lin, A consistent co-rotational finite element formulation for geometrically nonlinear dynamics analysis of 3-D beams, Comput. Methods Appl. Mech. Engrg., Vol. 169, 1-18 (1999).

[19] K.M. Hsiao, W.Y. Lin, R.H. Chen, Geometrically non-linear dynamic analysis of thin-walled beams, Proc. World Congress Engrg., Vol. II (2009).

[20] A. Ibrahimbegović, F. Frey, I. Kožar, Computational aspects of vector-like parameterization of three-dimensional finite rotations, Int. J. Num. Methods. Engrg., Vol. 38, 3653-3673 (1995).

[21] A. Ibrahimbegović, On the choice of finite rotation parameters, Comput. Methods Appl. Mech. Engrg., Vol. 149, 49-71 (1997).

[22] A. Ibrahimbegović, M.A. Mikdad, Finite rotations in dynamics of beams and implicit time-stepping schemes, Int. J. Num. Methods. Engrg., Vol. 41, 781-814 (1998).

[23] A. Ibrahimbegović, S. Mamouri, Energy conserving/decaying implicit time-stepping scheme for nonlinear dynamics of three-dimensional beams undergoing finite rotations, Comput. Methods Appl. Mech. Engrg., Vol. 191, 4241-4258 (2002).

[24] M. Iura, S.N. Atluri, Dynamic analysis of finitely stretched and rotated three-dimensional space-curved beams, Comput. Struct., Vol. 29, 875-889 (1988).

[25] M. Iura, S.N. Atluri, Dynamic analysis of planar flexible beams with finite rotations by using inertial and rotating frames, Comput. Struct., Vol. 55, No.3, 453-462 (1995).

[26] G. Jelenić, M.A. Crisfield, Interpolation of rotational variables in nonlinear dynamics of 3D beams, Int. J. Num. Methods. Engrg., Vol. 43, 1193-1222 (1998).

[27] G. Jelenić, M.A. Crisfield, Geometrically exact 3D beam theory: implementation of a strain-invariant element for stactics and dynamics, Comput. Methods Appl. Mech. Engrg., Vol. 171, 141-171 (1999).

[28] S. Krenk, Non-Linear Modeling And Analysis Of Solids And Structures, 47-75, Cambridge University Press, New York (2009).

[29] T.-N. Le, J.-M. Battini, M. Hjiaj, Efficient formulation for dynamics of corotational 2D beams, Comput. Mech., Vol. 48, No. 2, 153-161 (2011).

[30] T.-N. Le, J.-M. Battini, M. Hjiaj, Dynamics of 3D beam elements in a corotational context: A comparative study of established and new formulations, Finite Elem. Anal. Des., Vol. 61, 97-111 (2012).

[31] T.-N. Le, J.-M. Battini, M. Hjiaj, A consistent 3D corotational beam element for nonlinear dynamic analysis of flexible structures, Comput. Methods Appl. Mech. Engrg., 2vol. 269: 538-565. (2014).

[32] T.-N. Le, J.-M. Battini, M. Hjiaj, Corotational formulation for nonlinear dynamics of beams with arbitrary thin-walled cross-sections, Computers and Structures, vol.134: 112-127 (2014).

[33] E.V. Lens, A. Cardona, A nonlinear beam element formulation in the framework of an energy preserving time integration scheme for constrained multibody systems dynamics, Comput. Struct. , Vol. 86, 47-63 (2008).

[34] J. Mäkinen, Total Lagrangian Reissner's geometrically exact beam element without singularities, Int. J. Num. Methods. Engrg., Vol. 70, 1009-1048 (2007).

[35] N. Masuda, T. Nishiwaki, M. Minaaawa, Nonlinear dynamic analysis of frame structures, Comput. Struct., Vol. 27, No.1, 103-110 (1987).

[36] B. Nour-Omid, C.C. Rankin, Finite rotation analysis and consistent linearization using projectors, Comput. Methods Appl. Mech. Engrg., Vol. 93, 353-384 1991.

[37] C. Oran, A. Kassimali, Large deformations of framed structures under static and dynamic loads, Comput. Struct., Vol. 6, 539-547 (1976).

[38] C.C. Rankin, B. Nour-Omid, The use of projectors to improve finite element performance, Comput. Struct., Vol. 30, 257-267 (1988).

[39] J.N. Reddy, On locking-free shear deformable beam finite elements, Comput. Methods Appl. Mech. Engrg., Vol. 149, 113-132 (1997).

[40] J.C. Simo, L. Vu-Quoc, On the dynamics in space of rods undergoing large motions - A geometrically exact approach, Comput. Methods Appl. Mech. Engrg., Vol. 66, 125-161 (1988).

[41] Q. Xue, J.L Meek, Dynamic response and instability of frame structures, Comput. Methods Appl. Mech. Engrg., Vol. 190, 5233-5242 (2001).

[42] E. Zupan, M. Saje, D. Zupan, Quaternion-based dynamics of geometrically nonlinear spatial beams using the RungeKutta method, Finite Elem. Anal. Des., Vol. 54, 48-60 (2012).

[43] E. Zupan, M. Saje, D. Zupan, Dynamics of spatial beams in quaternion description based on the Newmark integration scheme, Comput. Mech., Vol. 51, 47-64 (2013).

COMPDYN 2015
5th ECCOMAS Thematic Conference on
Computational Methods in Structural Dynamics and Earthquake Engineering
M. Papadrakakis, V. Papadopoulos, V. Plevris (eds.)
Crete Island, Greece, 25–27 May 2015

ENERGY METHOD FOR COUPLING NEWMARK AND α-SCHEMES TIME INTEGRATORS WITH DIFFERENT TIME STEPS

M. BRUN*, A. GRAVOUIL† AND A. COMBESCURE†

*Université de Lyon, INSA-Lyon, LGCIE, 34 rue des Arts, F-69621 Villeurbanne, France

†Université de Lyon, INSA-Lyon, LaMCoS, CNRS UMR5259, 18-20 rue des sciences, F-69621 Villeurbanne, France.
e-mail: michael.brun@insa-lyon.fr - Web page: ttp://lamcos.insa-lyon.fr/

Keywords: Structural dynamics, Heterogeneous Asynchronous time integrators, Hybrid multi-time methods, Energy conserving methods

Abstract. *The time integration procedure selected in computational structural dynamics must possess at least the stability and accuracy properties required for the convergence to the exact solution. Other desired properties are the unconditional stability for linear dynamics, second-order of accuracy, high frequency dissipation capabilities, self-starting, no overshoot, one step method and no more than one set of implicit equations to be solved for each time step (single-step-single-solve format). In linear dynamics, the stability is classically assessed by a spectral study of the amplification matrix, whereas physical energy bounds are preferred in nonlinear dynamics. Popular a-schemes (HHT-α, WBZ-α, CH-α) are second-order accurate and provides numerical dissipation for spurious high frequencies due to the finite element discretization. To go beyond the standard approach based on the same time integration scheme (homogeneous time integration scheme) and the same time step for all the finite elements of the mesh (synchronous time integration), the purpose of this paper is to describe a general methodology for building Heterogeneous (different time integration schemes such as Newmark or a-schemes) Asynchronous (different time steps) Time Integrators (HATI) for computational dynamics. The proposed HATI methods allow selecting the appropriate time integration scheme with its own time step in each part of the mesh following a dual Schur subdomain decomposition technique by introducing Lagrange multipliers for ensuring the velocity gluing at the subdomain interface. The key point for building the HATI methods is to cancel the interface pseudo-energy as introduced by Hughes in the so-called energy method employed for proving the stability of implicit-explicit algorithms in its pioneer works on heterogeneous time integrators. By canceling the pseudo-energy at the interface between subdomains and assuming a linear time variation of the Lagrange multipliers at the coarse time scale, two HATI methods are derived. The first new method, called BCG-macro method, for which the interface problem involving the Lagrange multipliers is solved at the large time scale, can handle any dissipative a-schemes (HHT-α, WBZ-α, CH-α), while preserving the second-order of accuracy when adopting different time steps. In addition to the energy argument (cancelation of the interface pseudo-energy), the stability and order of accuracy is proved by the spectral study of the amplification matrix. The*

second new method, called BGC-micro, is based on the velocity gluing at the fine time scale and can be viewed as an extension of the method proposed by Gravouil and Combescure (GC method) to the dissipative α-schemes.

1 INTRODUCTION

Partitioning approaches are very appealing with a view of coupling dynamic parts of a complex structure in a hybrid (experimental/numerical) real time testing. These hybrid tests require different explicit or implicit time integration schemes in different subdomains (called substructure in the context of hybrid testing) according to their complexity and characteristics. The purpose of such hybrid experimental/numerical testing such as the continuous pseudo-dynamic testing (PsD) is to test parts of the structure expected to experience some damage while the remainder of the whole structure is dealt numerically. As a consequence, the hybrid numerical-experimental testing techniques need to select high performance coupling methods from the field of computational mechanics in order to be able to make interact physical and numerical parts in real time (*Pinto et al.* [2004], *Brun et al.* [2012]). Typically, a reduced number of degrees of freedom is considered for the tested part but with a large number of small time steps: explicit time schemes are then adopted or other non-iterative time integration schemes (*Combescure and Pegon* [1997], *Bonnet et al.* [2008]).
In the numerical/experimental hybrid context, heterogeneous (different time schemes) asynchronous (different time steps) time integrators (HATI) have been investigated. Gravouil and Combescure proposed an HATI (*Gravouil and Combescure* [2001] and *Combescure and Gravouil* [2002]), called GC method, enabling explicit/implicit multi-time step computations on a partitioned domain: the non overlapping subdomains are coupled following on a dual approach, that is by prescribing the continuity of the velocity at the interface with the help of Lagrange multipliers. The stability of the GC method when considering any Newmark time integration schemes has been proven using the energy method, initially proposed by Hughes for deriving stability conditions for hybrid (implicit/explicit) time integrators. Beyond the widely used Newmark schemes, it is of great interest in structural dynamics to choose more advanced time integration schemes endowed with the following desirable properties: unconditional stability, second-order accuracy, no more than one set of implicit equations involved in the time step, self-starting, and controllable algorithmic dissipation in the higher modes. An excellent state of the art on the generalized single-step-single-solve (GSSSS) framework algorithms that encompasses the class of liner multi-time step methods (LMS) can be found in the works of Tamma and co-authors (*Masuri et al.* [2009c],*Masuri et al.* [2009a],*Masuri et al.* [2009b]).

In the context of the PsD tests, the staggered nature of the GC method (requiring in a first stage the computation of predictors followed by the solving of the interface problem finally completed with the correction of the predictors coming from the interface forces) clearly constitutes a drawback for carrying out experimental and numerical tasks in a concurrent way. Consequently, a new interfield parallel solution method, called the PM method from the authors' name (Pegon and Magonnette), has been described by Bonelli $et\ al.$ (*Bonelli et al.* [2008]) by coupling explicit and implicit time schemes. Recently, further efforts have been done to build coupling method able to handle the Generalized-α schemes proposed by Chung and Hulbert (*Chung and Hulbert* [1993]), well known for being able to control numerical damping and to filter out spurious high-frequency components of the response. The low-frequency are unaffected and the time integration scheme remains second-order accurate. Bursi $et\ al.$ (*Bursi et al.* [2010]) underline that the GC method based on the velocity continuity at the end time of the fine time steps is incompatible with the Generalized-α scheme whose terms involved into the equation of motion are weighted by different parameters. Therefore, in order to adapt the Generalized-α scheme to the end time collocation format of the GC coupling method, a new form of the Generalized-α scheme proposed by Arnold and Bruls (*Arnold and Bruls* [2007]) in

the multibody dynamic context is adopted, enforcing the equilibrium at the end of the time step instead of an averaged form as in the original time integrator. The derived interfield parallel solution method, called the PM-α method, is an extension to the α-schemes of the PM method (*Bursi et al.* [2010]).

Built upon the GC formulation, two other multi-time coupling schemes have been proposed. The first one is the PH method developed by Prakash and Hjelmstad (*Prakash and Hjelmstad* [2004]), assuming a velocity continuity at the macro-time scale (large time step) unlike the GC method based on the micro time scale (fine time step). It enables the dissipative drawback of the GC method to be tackled while optimizing the computation time related to the solving of the interface problem. The authors proved by using the energy-method that the pseudo-energy at the interface remains equal to zero. They concluded that the PH method is energy conserving when coupling non-dissipative Newmark schemes such as the implicit Constant Average Acceleration scheme (CAA) and the explicit Central Difference scheme (CD). Recently, the MGC method based on the macro time scale for the interface problem too, has been built with the focus of canceling the classical measure of the interface energy (*Mahjoubi et al.* [2011]). The derived method turns out to be able to couple Newmark schemes, HHT-α scheme (*Hilber et al.* [1977]), Simo scheme (*Simo and Tarnow* [1992]) and Krenk scheme (Balance Dissipation Scheme, *Krenk* [2008]) in linear dynamics. Nonetheless, the MGC coupling method uses a modified equation of motion for the HHT-α scheme: solving the equation of motion related to a given time step requires quantities one time step before, loosing the single solve single step format of the original HHT-α scheme.

In this paper, a general methodology based on energy considerations is described to obtain asynchronous coupling methods for different time integration schemes (Newmark, HHT-α, WBZ-α and CH-α)(*Brun et al.* [2015],**?**). The gluing of subdomains with their own time integrator and time step is ensured with Lagrange multipliers and velocity continuity. The key point for building stable HATI is to ensure the zero interface pseudo-energy, involved in the energy method for the DAE (Differential Algebraic Equation) stability analysis. On the other hand, the energy method argument is confirmed by carrying out a stability analysis performed from the amplification matrix linking state vectors at the beginning and at the end of the time step. Two new coupling methods, denoted in the following BGC-macro and BGC-micro methods, will be derived. The BGC-macro method is a macro-time-based method, such as the PH and MGC methods. It assumes a linear variation of the Lagrange multipliers over the macro-time step so as to lead to a kinematic condition at the interface, which, used together with the Lagrange multiplier variation assumption, guarantees the zero interface pseudo-energy. The method conserves the second order accuracy as highlighted by the convergence analysis. From the previous kinematic relationship, a second method is derived, called BGC-micro method, which handles the interface problem at the micro-time scale rather than at the macro time scale. Both proposed methods allow coupling α-schemes while conserving their original format, contrary to the MGC algorithm.

2 GENERAL METHODOLOGY FOR COUPLING α schemes

2.1 Unified format for the α-schemes

The time discretization is introduced as the following partition of the time domain: $t_0 < t_1 < \cdots < t_n < t_{n+1} < \cdots < t_f$ and h is the time step size assumed to be constant. Following the concept of weak equilibrium, the discretized equilibrium equation is only ensured at some times inside the time step. For the α-schemes, it corresponds to different weights applied to inertial, stiffness and external terms as given below (viscous terms are omitted in the following for the sake of simplicity):

$$\mathbf{M}\mathbf{a}_{n+\xi_m} + \mathbf{K}\mathbf{u}_{n+\xi_f} = \mathbf{f}_{n+\xi_f} - \mathbf{L}^T\boldsymbol{\lambda}_{n+\xi_f} \tag{1}$$

where $\mathbf{M}$, and $\mathbf{K}$, are the consistent mass matrix and the stiffness matrix. $\mathbf{L}$ is a linear kinematic constraint matrix at the boundary conditions. The discrete displacements, velocities and accelerations are designated by $\mathbf{u}$, $\mathbf{v}$ and $\mathbf{a}$. As external forces, the Lagrange multipliers required by the kinematic constraint is expressed at the time $t_{n+\xi_f}$. Using the two different averaged parameters ξ_m and ξ_f, the averaged displacements, velocities, accelerations and Lagrange multipliers read:

$$\begin{cases} \mathbf{a}_{n+\xi_m} = (1-\xi_m)\mathbf{a}_n + \xi_m\mathbf{a}_{n+1} \\ \mathbf{u}_{n+\xi_f} = (1-\xi_f)\mathbf{u}_n + \xi_f\mathbf{u}_{n+1} \\ \mathbf{f}_{ext,n+\xi_f} = (1-\xi_f)\mathbf{f}_{ext,n} + \xi_f\mathbf{f}_{ext,n+1} \\ \boldsymbol{\lambda}_{n+\xi_f} = (1-\xi_f)\boldsymbol{\lambda}_n + \xi_f\boldsymbol{\lambda}_{n+1} \end{cases} \tag{2}$$

The classical form for the Generalized-α scheme proposed by Chung and Hulbert (*Chung and Hulbert* [1993]) is characterized by two weighting parameters α_m and α_f. It writes:

$$\begin{aligned} (1-\alpha_m)\mathbf{M}\mathbf{a}_{n+1} + \alpha_m\mathbf{M}\mathbf{a}_n + (1-\alpha_f)\mathbf{K}\mathbf{u}_{n+1} + \alpha_f\mathbf{K}\mathbf{u}_{n+1} = \\ (1-\alpha_f)\mathbf{f}_{n+1} + (1-\alpha_f)\mathbf{f}_n - \mathbf{L}^T\boldsymbol{\lambda}_{n+1-\alpha_f} \end{aligned} \tag{3}$$

From the above averaged equilibrium equations in Eq. 1 and in Eq. 3, it can be easily seen that the following relationships between the algorithmic parameters hold: $\xi_m = 1 - \alpha_m$ and $\xi_f = 1 - \alpha_f$.

Optimized algorithmic parameters α_m, α_f, γ and β are given by the authors in order to achieve the unconditional stability, the second-order accuracy as well as the high-frequency dissipation while minimizing low-frequency dissipation. Three α-schemes are investigated : HHT-α (*Hilber et al.* [1977]), WBZ-α (*Wood et al.* [1981]) and CH-α (*Chung and Hulbert* [1993]). For all the three previous α-schemes, it is convenient to define the α_m and α_f parameters as a function of the the spectral radius at the high frequency limit (at infinity), noted as ρ_∞, characterizing the amount of dissipative energy in the high frequency range. The two other algorithmic parameters γ and β are involved in the classical Newmark formulae written below in terms of velocity increments:

$$\begin{cases} \Delta\mathbf{a} = \frac{1}{\gamma h}\Delta\mathbf{v} - \frac{1}{\gamma}\mathbf{a}_n \\ \Delta\mathbf{u} = \frac{\beta h}{\gamma}\Delta\mathbf{v} + h\mathbf{v}_n + \frac{\gamma-2\beta}{2\gamma}h^2\mathbf{a}_n \end{cases} \tag{4}$$

The algorithmic parameters γ and β are expressed in terms of α_m and α_f as it has been resumed in Table 1.

From Eq. 2, the averaged accelerations and displacements can be written as: $\mathbf{a}_{n+\xi_m} = \mathbf{a}_n +$

Scheme	α_m	α_f	γ	β
$HHT-\alpha$	0	$-\alpha_{HHT}=\frac{1-\rho_\infty}{1+\rho_\infty}$	$\frac{1}{2}-\alpha_{HHT}$	$\frac{1}{4}(1-\alpha_{HHT})^2$
$WBZ-\alpha$	$\alpha_{WBZ}=\frac{\rho_\infty-1}{1+\rho_\infty}$	0	$\frac{1}{2}-\alpha_{WBZ}$	$\frac{1}{4}(1-\alpha_{WBZ})^2$
$CH-\alpha$	$\frac{2\rho_\infty-1}{1+\rho_\infty}$	$\frac{\rho_\infty}{1+\rho_\infty}$	$\frac{3}{2}-2\alpha_f$	$(1-\alpha_f)^2$

Table 1: Relations between the spectral radius at infinity and the algorithmic parameters for the α-schemes enabling unconditional stability, second-order accuracy, optimized dissipative features.

$\xi_m\Delta\mathbf{a}$ and $\mathbf{u}_{n+\xi_f}=\mathbf{u}_n+\xi_f\Delta\mathbf{u}$. Incorporating theses expressions and the Newmark formulae in Eq. 4 into the equilibrium equation Eq. 1, we obtain a new format for the Generalized-α schemes as:

$$\mathbf{K}^*\Delta\mathbf{v}_{n+1}=\mathbf{g}_{n+1}-\mathbf{L}^T\boldsymbol{\lambda}_{n+\xi_f} \tag{5}$$

where the dynamic operator matrix is defined by $\mathbf{K}^*=\xi_m\frac{1}{\gamma h}\mathbf{M}+\xi_f\frac{\beta h}{\gamma}\mathbf{K}$. The right hand side vector $\mathbf{g}_{n+1}$ is expressed as:

$$\mathbf{g}_{n+1}=\mathbf{f}_{ext,n+\xi_f}-\mathbf{K}\mathbf{u}_n-\xi_f h\mathbf{K}\mathbf{v}_n+\xi_m\frac{1}{\gamma}M\mathbf{a}_n-M\mathbf{a}_n-\xi_f(\frac{\gamma-2\beta}{2\gamma})h^2\mathbf{K}\mathbf{a}_n \tag{6}$$

With a view to formulating the subdomain coupling algorithm, it is interesting to adopt a compact form for the complete-three stage time-stepping of the α-schemes as:

$$\mathbb{K}^*\Delta\mathbb{U}_{n+1}+\mathbb{L}^T\boldsymbol{\lambda}_{n+\xi_f}=\mathbb{G}_{n+1} \tag{7}$$

The vector $\Delta\mathbb{U}_{n+1}$ gathers the increments of velocities, displacements and accelerations: $\Delta\mathbb{U}_{n+1}^T=\begin{bmatrix}\Delta\mathbf{v} & \Delta\mathbf{u} & \Delta\mathbf{a}\end{bmatrix}$. $\mathbb{L}$ is the constraint matrix: $\mathbb{L}=\begin{bmatrix}\mathbf{L} & \mathbf{0} & \mathbf{0}\end{bmatrix}$. The right hand side vector is given by:

$$\mathbb{G}_{n+1}=\mathbb{F}_{n+\xi_f}-\mathbb{N}\mathbb{U}_n \tag{8}$$

where $\mathbb{F}_{n+\xi_f}^T=\begin{bmatrix}\mathbf{f}_{ext,n+\xi_f} & \mathbf{0} & \mathbf{0}\end{bmatrix}$. The expressions of the matrix $\mathbb{K}^*$ and the matrix $\mathbb{N}$ are:

$$\mathbb{K}^*=\begin{bmatrix}\mathbf{K}^* & \mathbf{0} & \mathbf{0}\\ -\frac{\beta h}{\gamma}\mathbf{I} & \mathbf{I} & \mathbf{0}\\ -\frac{1}{\gamma h}\mathbf{I} & \mathbf{0} & \mathbf{I}\end{bmatrix},\mathbb{N}=\begin{bmatrix}\xi_f h\mathbf{K} & \mathbf{K} & \xi_f\left(\frac{\gamma-2\beta}{2\gamma}\right)h^2\mathbf{K}+\left(1-\xi_m\frac{1}{\gamma}\right)\mathbf{M}\\ h\mathbf{I} & \mathbf{0} & \left(\frac{\gamma-2\beta}{2\gamma}\right)h^2\mathbf{I}\\ \mathbf{0} & \mathbf{0} & -\frac{1}{\gamma}\mathbf{I}\end{bmatrix} \tag{9}$$

2.2 Coupling with heterogeneous time steps

In order to formulate the coupling between two subdomains, we employ the previous unified form of the equilibrium equations at t_{γ_A} for the subdomain Ω_A (macro time scale), and at a series of times $t_{j-1+\gamma_B}$ for the subdomain Ω_B (micro time scale); first, for the macro subdomain Ω_A:

$$\begin{cases}\mathbf{K}_A^*\Delta\mathbf{v}_m^A+\mathbf{L}_A^T\boldsymbol{\lambda}_{\xi_{A,f}}=\mathbf{g}_m^A\\ \Delta\mathbf{u}_m^A=\frac{\beta_A h_A}{\gamma_A}\Delta\mathbf{v}_m^A+h_A\mathbf{v}_0^A+\frac{\gamma_A-2\beta_A}{2\gamma_A}h_A^2\mathbf{a}_0\\ \Delta\mathbf{a}_m^A=\frac{1}{\gamma_A h_A}\Delta\mathbf{v}_m^A-\frac{1}{\gamma_A}\mathbf{a}_0^A\end{cases} \tag{10}$$

Secondly, for the micro subdomain Ω_B:

$$\begin{cases} \mathbf{K}_B^* \Delta \mathbf{v}_j^B + \mathbf{L}_B^T \boldsymbol{\lambda}_{j-1+\xi_{B,f}} = \mathbf{g}_j^B \\ \Delta \mathbf{u}_j^B = \frac{\beta_B h_B}{\gamma_B} \Delta \mathbf{v}_j^B + h_B \mathbf{v}_{j-1}^B + \frac{\gamma_B - 2\beta_B}{2\gamma_B} h_B^2 \mathbf{a}_{j-1} \\ \Delta \mathbf{a}_j^B = \frac{1}{\gamma_B h_B} \Delta \mathbf{v}_j^B - \frac{1}{\gamma_B} \mathbf{a}_{j-1}^B \\ \forall j \in \{1, m\} \end{cases} \tag{11}$$

The above equations can also be given in a compact form as:

$$\mathbb{K}_{\mathbb{A}}^* \Delta \mathbb{U}_m^A + \mathbb{L}_A^T \boldsymbol{\lambda}_{\xi_{A,f}} = \mathbb{F}_{\xi_{A,f}}^A - \mathbb{N}_A \mathbb{U}_0^A \tag{12}$$

and

$$\mathbb{K}_{\mathbb{B}}^* \Delta \mathbb{U}_j^A + \mathbb{L}_B^T \boldsymbol{\lambda}_{j-1+\xi_{B,f}} = \mathbb{F}_{j-1+\xi_{B,f}}^B - \mathbb{N}_B \mathbb{U}_{j-1}^B \; \forall j \in \{1, m\} \tag{13}$$

The kinematic equation at the interface will complete the system of equations for coupling the two subdomains with heterogeneous time steps. It will be shown in the following that ensuring the zero energy at the interface in terms of the pseudo-energy norm as introduced by Hughes in the energy method (*Hughes* [1987]), enables a kinematic condition for velocity increments to be derived.

3 BGC-MACRO METHOD FROM THE ENERGY METHOD

The energy method proposed by Hughes has been widely used for obtaining the stability conditions for coupling schemes, mixing implicit and explicit schemes (*Hughes* [1987]). For example, the stability of the GC method and the PH method has been proven by this way (*Combescure and Gravouil* [2002], *Prakash and Hjelmstad* [2004]). It consists in proving that the interface pseudo-energy is equal or less than zero. Here, the interface pseudo-energy is employed as the starting point of the new coupling methods by ensuring the zero interface pseudo-energy. Thus, the following coupling schemes are built from the discrete balance equation given in the energy method in terms of pseudo-energy. For a given subdomain (by omitting the scripts for belonging subdomains), the pseudo-energy balance equation is given by:

$$\left[\frac{1}{2} \mathbf{a}^T \mathbf{A} \mathbf{a} + \frac{1}{2} \mathbf{v}^T \mathbf{K} \mathbf{v} \right]_n^{n+1} = \frac{1}{h} \Delta \mathbf{v}^T \left\{ (\mathbf{f}_{ext,n+1} - \mathbf{f}_{ext,n}) \right\} - (\gamma - \frac{1}{2}) \left\{ \Delta \mathbf{a}^T \mathbf{A} \Delta \mathbf{a} \right\} \tag{14}$$

in which the matrix $\mathbf{A}$ is defined by $\mathbf{A} = \mathbf{M} + \left(\beta - \frac{1}{2}\gamma\right) h^2 \mathbf{K}$. The previous balance equation can also be noted as:

$$\Delta E_{kin} + \Delta E_{int} = \Delta E_{ext} + \Delta E_{diss} \tag{15}$$

where ΔE_{kin}, ΔE_{int}, ΔE_{ext} and ΔE_{diss} are the increments over the time step of pseudo-energies which can be related to the classical kinetic, internal, external and dissipated energies.

Considering two subdomains Ω_A and Ω_B, the global discrete pseudo-energy balance equation takes into account the above contributions from both subdomains on the macro time step $h_A = [t_0; t_m]$ and on the series of the micro time steps $h_B = [t_{j-1}; t_j]$ for j varying from 1 to m, plus an additional term corresponding to the interface energy. The discrete pseudo-energy balance

equation over the macro time step $h_A = [t_0; t_m]$ for the whole domain is given below:

$$\Delta E^A_{kin,m} + \Delta E^A_{int,m} + \sum_{j=1}^{m} \left\{ \Delta E^B_{kin,j} + \Delta E^B_{int,j} \right\} = \dots$$

$$\Delta E^A_{ext,m} + \sum_{j=1}^{m} \Delta E^B_{ext,j} + \Delta E^A_{diss,m} + \sum_{j=1}^{m} \Delta E^B_{diss,j} + \Delta E_{interface} \tag{16}$$

The interface pseudo-energy (*Prakash and Hjelmstad* [2004]) can be written as:

$$\Delta E_{interface} = -\frac{1}{h_A} \Delta \mathbf{v_m^A}^T \left\{ \mathbf{L}_A^T \left(\boldsymbol{\lambda}_m - \boldsymbol{\lambda}_0 \right) \right\} - \sum_{j=1}^{m} \left\{ \frac{1}{h_B} \Delta \mathbf{v_j^B}^T \left\{ \mathbf{L}_B^T \left(\boldsymbol{\lambda}_j - \boldsymbol{\lambda}_{j-1} \right) \right\} \right\} \tag{17}$$

The pseudo-energy method has to be distinguished from the discretized energy balance equation (*Hughes* [1987] and *Brun et al.* [2014]). The pseudo-energy is dedicated to stability analysis whereas the classical energy balance equation enables to build energy-preserving time integrators. It has to be noted that the above equation can be seen as a generalization of the pseudo-energy method related to the study of ODE (Ordinary Differential Equation) stability to the study of DAE (Differential Algebraic Equation) stability, that is with Lagrange multipliers. This stability method based on the energetic view point will be confirmed in the last section by a classical amplification matrix spectral analysis, with state vectors gathering kinematic quantities and Lagrange multipliers. The coupling method is considered to be stable if the total pseudo-energy variation (kinetic plus internal pseudo-energy variations) over the macro time step under zero external loads is less than or equal to zero. Consequently, it is sufficient to prove that the pseudo-energy at the interface $E_{interface}$ is less than or equal to zero. It has to be reminded that the energy conservative features of the PH method (*Prakash and Hjelmstad* [2004]) has been demonstrated $a\ posteriori$. In contrast to the PH method , the coupling method here enables to satisfy the energy conservative feature $a\ priori$ by ensuring the zero interface pseudo-energy over the macro time step. For this purpose, an assumption related to the time variation of the Lagrange multipliers over the macro time step is required: we assume that the Lagrange multipliers at the micro scale can be linearly interpolated from the Lagrange multipliers given at the beginning and the end of macro time step. So we have:

$$\boldsymbol{\lambda}_j - \boldsymbol{\lambda}_{j-1} = \frac{\boldsymbol{\lambda}_m - \boldsymbol{\lambda}_0}{m} \tag{18}$$

Consequently, the interface pseudo-energy can be simplified as:

$$\Delta E_{interface} = -\left[\frac{1}{h_A} \Delta \mathbf{v}_m^{A\,T} \mathbf{L}_A^T + \sum_{j=1}^{m} \left\{ \frac{1}{m h_B} \Delta \mathbf{v}_j^{B\,T} \mathbf{L}_B^T \right\} \right] \left(\boldsymbol{\lambda}_m - \boldsymbol{\lambda}_0 \right) \tag{19}$$

Finally, the zero interface pseudo-energy requirement leads to the following kinematic equation:

$$\mathbf{L}_A \Delta \mathbf{v}_m^A + \sum_{j=1}^{m} \mathbf{L}_B \Delta \mathbf{v}_j^B = 0 \tag{20}$$

Considering two subdomains Ω_A and Ω_B with different time scales, m being equal to the time step ratio, the interface forces associated with the subdomain Ω_A are computed at the

time $t_{\xi_{A,f}} = \xi_{A,f} t_0 + (1-\xi_{A,f}) t_m$ belonging to the macro-time step $h_A = [t_0; t_m]$, whereas the interface forces associated with the subdomain Ω_B are computed at the time $t_{j-1+\xi_{B,f}} = \xi_{B,f} t_{j-1} + (1-\xi_{B,f}) t_j$ belonging to the micro-time step $h_B = [t_{j-1}; t_j]$ for j varying from 1 to m. By using the linear relationship for Lagrange multipliers, we can write the interface forces for both subdomains as:

$$\left\{ \begin{array}{l} \mathbf{L}_A^T \boldsymbol{\lambda}_{\xi_{A,f}} = \mathbf{E}_{A,m}^T \boldsymbol{\lambda}_0 + \mathbf{C}_{A,m}^T \boldsymbol{\lambda}_m \\ \mathbf{L}_B^T \boldsymbol{\lambda}_{j-1+\xi_{B,f}} = \mathbf{E}_{B,j}^T \boldsymbol{\lambda}_{j-1} + \mathbf{C}_{B,j}^T \boldsymbol{\lambda}_j \end{array} \right. \tag{21}$$

with:

$$\left\{ \begin{array}{l} \mathbf{E}_{A,m}^T = (1-\xi_{A,f}) \mathbf{L}_A^T \\ \mathbf{C}_{A,m}^T = \xi_{A,f} \mathbf{L}_A^T \\ \mathbf{E}_{B,j}^T = \left[(1-\xi_{B,f})(1-\frac{j-1}{m}) + \xi_{B,f}(1-\frac{j}{m}) \right] \mathbf{L}_B^T \\ \mathbf{C}_{B,j}^T = \left[(1-\xi_{B,f})(\frac{j-1}{m}) + \xi_{B,f}(\frac{j}{m}) \right] \mathbf{L}_B^T \quad \forall j \in [1,m] \end{array} \right. \tag{22}$$

Then, the global system of equilibrium equations is obtained by gathering the compact forms of the three-stage time stepping schemes for both subdomains. It writes:

$$\left[\begin{array}{ccccc|c|c} \mathbb{K}_B^* & & & & & & \mathbb{C}_{B,1}^T \\ \mathbb{N}_B & \mathbb{K}_B^* & & & & & \mathbb{C}_{B,2}^T \\ \mathbb{N}_B & \mathbb{N}_B & \mathbb{K}_B^* & & & & \mathbb{C}_{B,3}^T \\ & \ddots & \ddots & \ddots & & & \vdots \\ \mathbb{N}_B & \mathbb{N}_B & \mathbb{N}_B & \mathbb{N}_B & \mathbb{K}_B^* & & \mathbb{C}_{B,m}^T \\ \hline & & & & & \mathbb{K}_A^* & \mathbb{C}_{A,m}^T \\ \hline \mathbb{L}_B & \mathbb{L}_B & \mathbb{L}_B & \cdots & \mathbb{L}_B & \mathbb{L}_A & \mathbf{0} \end{array} \right] \left[\begin{array}{c} \Delta \mathbb{U}_1^B \\ \Delta \mathbb{U}_2^B \\ \Delta \mathbb{U}_3^B \\ \vdots \\ \Delta \mathbb{U}_m^B \\ \hline \Delta \mathbb{U}_m^A \\ \hline \boldsymbol{\lambda}_m \end{array} \right] = \left[\begin{array}{c} \mathbb{F}_{\xi_{B,f}}^B - \mathbb{N}_B \mathbb{U}_0^B - \mathbb{E}_{B,1}^T \boldsymbol{\lambda}_0 \\ \mathbb{F}_{1+\xi_{B,f}}^B - \mathbb{N}_B \mathbb{U}_0^B - \mathbb{E}_{B,2}^T \boldsymbol{\lambda}_0 \\ \mathbb{F}_{2+\xi_{B,f}}^B - \mathbb{N}_B \mathbb{U}_0^B - \mathbb{E}_{B,3}^T \boldsymbol{\lambda}_0 \\ \vdots \\ \mathbb{F}_{m-1+\xi_{B,f}}^B - \mathbb{N}_B \mathbb{U}_0^B - \mathbb{E}_{B,m}^T \boldsymbol{\lambda}_0 \\ \hline \mathbb{F}_{\xi_{A,f}}^A - \mathbb{N}_A \mathbb{U}_0^A - \mathbb{E}_{A,m}^T \boldsymbol{\lambda}_0 \\ \hline \mathbf{0} \end{array} \right] \tag{23}$$

4 BGC-MICRO METHOD FROM THE ENERGY METHOD

From the kinematic relationship at the macro time step in Eq. 20, it is easy to define a similar relationship at the micro time step as:

$$\frac{1}{m} \mathbf{L}_A \Delta \mathbf{v}_m^A + \mathbf{L}_B \Delta \mathbf{v}_j^B = 0 \ \ \forall j \in [1,m] \tag{24}$$

The Lagrange multipliers are computed at the times $t_0 + \xi_{A_f}$ and $t_{j-1} + \xi_{B_f}$ for the subdomains Ω_A and Ω_B as:

$$\left\{ \begin{array}{l} \boldsymbol{\lambda}_{\xi_{A,f}} = \boldsymbol{\lambda}_0 + \xi_{A,f} \sum_{k=1}^m \Delta \boldsymbol{\lambda}_k \\ \boldsymbol{\lambda}_{j-1+\xi_{B,f}} = \boldsymbol{\lambda}_{j-1} + \xi_{B,f} \Delta \boldsymbol{\lambda}_j \end{array} \right. \tag{25}$$

Assuming the increment of the Lagrange multipliers $\Delta \boldsymbol{\lambda}_k$ is constant over the macro time step h_A, the interface equation at the micro time step can be rewritten for the α-schemes as (*Brun et al.* [2015]):

$$\mathbf{H} \Delta \boldsymbol{\lambda}_j = \mathbf{b}_j \tag{26}$$

in which the interface operator at the micro time scale and the right hand side vector are defined by:

$$\begin{cases} \mathbf{H} = \left[\xi_{A,f}\mathbf{L}_A(\mathbf{K}_A^*)^{-1}\mathbf{L}_A^T + \xi_{B,f}\mathbf{L}_B(\mathbf{K}_B^*)^{-1}\mathbf{L}_B^T\right] \\ \mathbf{b}_j = \frac{1}{m}\mathbf{L}_A\Delta\mathbf{v}_{free,m}^A + L_B\Delta\mathbf{v}_{free,j}^B - \frac{1}{m}\mathbf{L}_A(\mathbf{K}_A^*)^{-1}\mathbf{L}_A^T\boldsymbol{\lambda}_0 - \mathbf{L}_B(\mathbf{K}_B^*)^{-1}\mathbf{L}_B^T\boldsymbol{\lambda}_{j-1} \end{cases} \tag{27}$$

5 CONVERGENCE ANALYSIS

The BGC-macro method preserves exactly the pseudo-interface energy, proving the stability of the coupling algorithm. It remains to analyse the accuracy order of the coupling algorithm. Along the lines of *Bonelli et al.* [2008] and *Bursi et al.* [2010], an alternative convergence analysis is investigated by the spectral analysis of the amplification matrix $\mathbf{A}$, linking a state vector at the time $t_n + h_A = t_{n+1}$ to the previous state vector t_n. In addition to the stability, the amplification matrix enables to derive the accuracy order as well as the algorithmic damping ratio and the period elongation error related to the coupling algorithm. The convergence of the BGC-macro method is carried out for a single degree of freedom system, split into two subdomains Ω_A and Ω_B. The BGC-macro method is recast into the following recursive form:

$$\mathbf{X}_{n+1} = \mathbf{A}\mathbf{X}_n + \mathbf{L}_n \tag{28}$$

where $\mathbf{X}$ is an appropriate state vector depending on the formulation of the time integration algorithm, $\mathbf{A}$ is the amplification matrix and $\mathbf{L}$ is the load vector depending on the external forces. The BGC-macro method adopts the following state vector at time t_n:

$$\mathbf{X}_n = \left[\mathbf{X}_n^A \;\; \mathbf{X}_n^B\right]^T \tag{29}$$

where $\mathbf{X}_n^A$, $\mathbf{X}_n^B$ are the state vectors related the subdomains Ω_A and Ω_B, respectively. $\mathbf{X}_n^A$ collects the kinematic quantities of subdomain Ω_A, including the Lagrange multiplier at the macro time scale:

$$\mathbf{X}_n^A = \left[\mathbf{u}_n^A \;\; \mathbf{v}_n^A \;\; \mathbf{a}_n^A \;\; \boldsymbol{\lambda}_n\right]^T \tag{30}$$

It is important to remark that the state vector includes the Lagrange multiplier contrary to the PM method proposed by Bonelli $et\ al$ *Bonelli et al.* [2008] and Bursi $et\ al$ *Bursi et al.* [2010], including instead the free velocity related to the subdomain Ω_A.
$\mathbf{X}_n^B$ collects the kinematic quantities of subdomain Ω_B:

$$\mathbf{X}_n^B = \left[\mathbf{u}_n^B \;\; \mathbf{v}_n^B \;\; \mathbf{a}_n^B\right]^T \tag{31}$$

For the split oscillator, the state vector $\mathbf{X}_n$ gathers 7 components. In the following, we do not consider the load vector $\mathbf{L}_n$ because we assume that the leading error term of its approximation is greater than the order of accuracy of the method. It has been in *Brun et al.* [2014] that Eq. 28 can be developed as:

$$\begin{bmatrix} \mathbf{X}_{n+1}^A \\ \mathbf{X}_{n+1}^B \end{bmatrix} = \begin{bmatrix} \mathbf{A}^{AA} & \mathbf{A}^{AB} \\ \mathbf{A}^{BA} & \mathbf{A}^{BB} \end{bmatrix} \begin{bmatrix} \mathbf{X}_n^A \\ \mathbf{X}_n^B \end{bmatrix} \tag{32}$$

where the matrices $\mathbf{A}^{AA}$, $\mathbf{A}^{AB}$, $\mathbf{A}^{BA}$ and $\mathbf{A}^{BB}$ depend on the time step ratio, noted in the following as ss. The split oscillator is defined by the following mass and stiffness decomposition: $m = m^A + m^B$, $k = k^A + k^B$ with the ratio $b_1 = \frac{m^A}{m^B} = \frac{k^B}{k^A}$. The amplification matrix is

too complex for a closed-form expression as soon as different time steps are used. As a consequence, the amplification matrix is numerically computed for different values of time integrator parameters (ρ_∞ for CH-α schemes), mass and stiffness ratio b_1 and time step ratio ss. To address the accuracy, an alternative form of the amplification matrix is considered (*Bonelli et al.* [2008], *Bursi et al.* [2010]):

$$\bar{\mathbf{A}} = \bar{\mathbf{M}}\mathbf{A}\bar{\mathbf{M}}^{-1} \tag{33}$$

with the state vector modified as:

$$\bar{\mathbf{X}}_n = \left[\mathbf{u}_n^A \;\; \mathbf{v}_n^A \;\; h_A\mathbf{a}_n^A \;\; h_A\boldsymbol{\lambda}_n \;\; \mathbf{u}_n^B \;\; \mathbf{v}_n^B \;\; h_A\mathbf{a}_n^B\right]^T \tag{34}$$

and the matrix $\bar{\mathbf{M}}$ given by:

$$\bar{\mathbf{M}} = block\ diagonal\left[\mathbf{I} \;\; \mathbf{I} \;\; h_A\mathbf{I} \;\; h_A\mathbf{I} \;\; \mathbf{I} \;\; \mathbf{I} \;\; h_A\mathbf{I}\right]^T \tag{35}$$

where $\mathbf{I}$ is the identity matrix (equal to 1 in the case of the split oscillator).

Let us begin with the study of the stability of the BGC-macro method. The absolute stability of the BGC-macro method is investigated by computing the seven eigenvalues of the amplification matrix $\mathbf{A}$ in the case of the split-oscillator. The eigenvectors are linearly independent for each repeated eigenvalues λ_i. Hence, the condition $|\lambda_i| \leq 1$, for $i = 1...7$, is sufficient to demonstrate the A-stability of the method. In Figure 1, the coupling between two CH-α schemes (spectral radii $\rho_\infty = 0.8$ and $\rho_\infty = 0.5$ for the two subdomains at the coarse and fine time scales, respectively) is investigated as a function of the time step ratio ss by plotting the absolute values of the eigenvalues as a function of the reduced angular frequency $\Omega_B = \omega_B h_B$. Among the seven eigenvalues, only one pair is complex conjugate, giving the principal eigenvalues, whereas the five remaining are the spurious ones. In all investigated cases (any ρ_∞ and b_1), the BGC-macro method is found to be unconditionally stable when coupling unconditionally stable time integrators.

The local truncation error $\bar{\tau}_n$ is defined as

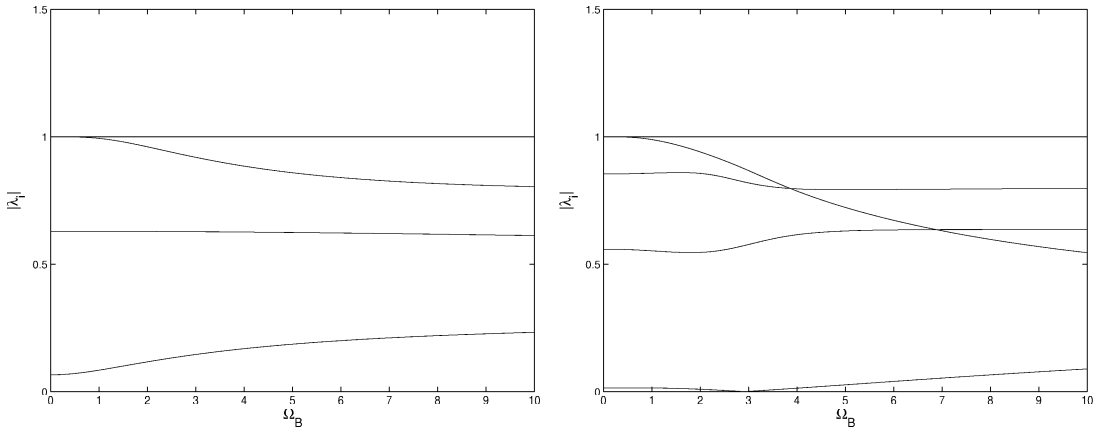
$$\bar{\tau}_n = \bar{\mathbf{A}}\bar{\mathbf{X}}(t_n) - \bar{\mathbf{X}}(t_{n+1}) \tag{36}$$

where $\bar{\mathbf{X}}(t_n)$ and $\bar{\mathbf{X}}(t_{n+1})$ correspond to the exact solutions of the state vector at the time t_n and t_{n+1}. From numerical calculations, the order of the truncation error can be assessed by computing the slope of $\ln(\bar{\tau}_n)$ as a function of the macro time step h_A. Indeed, the power k of the leading term of the local truncation error $\bar{\tau}_n = \alpha h_A^k + O(h_A^{k+1})$ (α being a constant) can be computed as: $k = \frac{\ln(\bar{\tau}_n(h_{2,A})) - \ln(\bar{\tau}_n(h_{1,A}))}{\ln(h_{2,A}) - \ln(h_{1,A})}$, where $\bar{\tau}_n(h_{2,A})$ and $\bar{\tau}_n(h_{1,A})$ are the numerical results of the local truncation error for two different small values of the macro time step h_A, with $h_{1,A} < h_{2,A}$. One obtains

$$\bar{\tau}_n = O(h_A^3) \tag{37}$$

for any values of the time step ratio ss. It is worth noting that the same result has been obtained in *Bonelli et al.* [2008] (Newmark schemes) and *Bursi et al.* [2010] (α-schemes) for the PM method, but only in the case of the same time step in both subdomains. Indeed, as soon as different time steps are adopted, the PM method only exhibits $\bar{\tau}_n = O(h_A^2)$.

For illustration, the local truncation error is plotted in Figure 2 for a time step ratio $ss = 2$. It can be seen that the power k of the leading term of the local truncation error depends on the quantity under consideration (displacement, velocity, acceleration and Lagrange multiplier). In details, we have: $\bar{\tau}_u^A = O(h_A^4)$, $\bar{\tau}_v^A = O(h_A^3)$, $\bar{\tau}_a^A = O(h_A^3)$, $\bar{\tau}_\lambda^A = O(h_A^3)$, $\bar{\tau}_u^B = O(h_A^4)$, $\bar{\tau}_v^B = O(h_A^3)$, $\bar{\tau}_a^B = O(h_A^3)$.



(a) ss=1 (b) ss=2

(c) ss=5 (d) ss=10

Figure 1: $|\lambda_i|$ of the split oscillator ($b_1 = 1$) for the BGC-macro method: CH-α ($\rho_\infty = 0.8$) coupled with CH-α ($\rho_\infty = 0.5$) with different time step ratios ss.

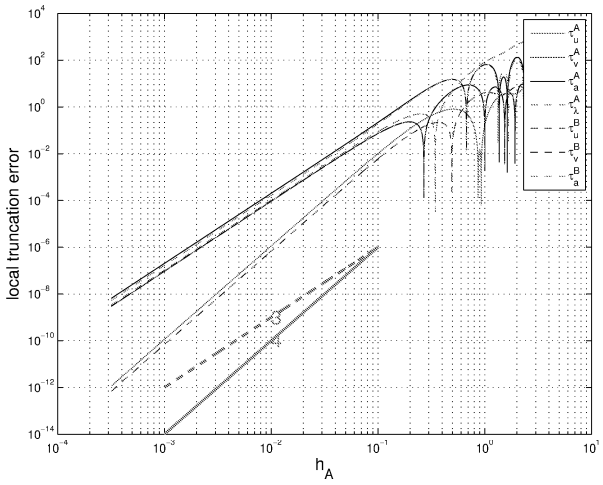


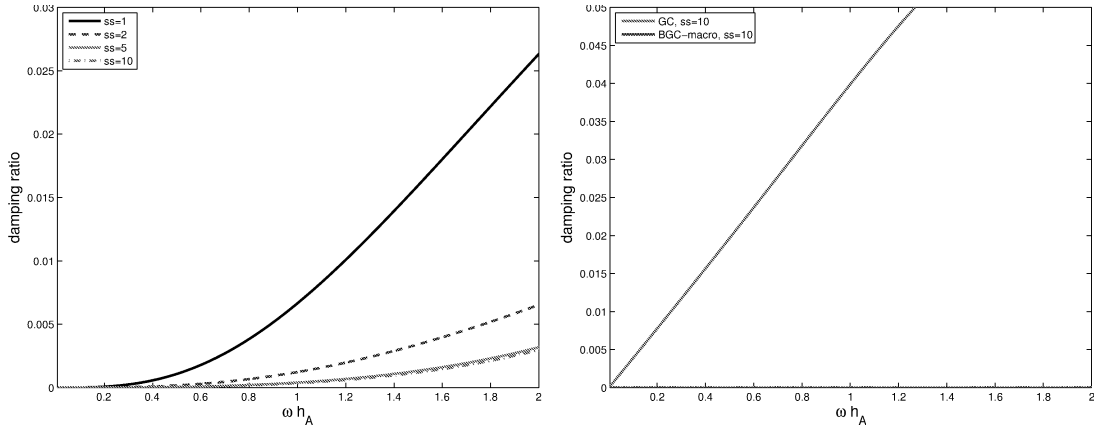
Figure 2: Local truncation error $\bar{\tau}$ of the split oscillator ($b_1 = 1$): CH-α ($\rho_\infty = 0.8$) coupled with CH-α ($\rho_\infty = 0.5$) with time step ratios $ss = 2$.

According to the Lax equivalence theorem (following the arguments of *Bonelli et al.* [2008] and *Bursi et al.* [2010]), a method will be convergent of the order k, if it is stable and consistent of the order k, $i.e.$ $\bar{\tau}_n = O(h_A^{k+1})$. As a result, the BGC-macro method is convergent of the order 2 for any time step ratio.
It is important to underline that the second order accuracy of the α-schemes is preserved through coupling with the BGC-macro method, which is not the case for the algorithms proposed in the literature (*Bursi et al.* [2010]). The last point of this convergence analysis concerns the numerical damping ratio and the relative period error. We define the nondimensional frequency of the whole system as $\Omega = \omega h_A$. The principal complex conjugate eigenvalues of the amplification matrix can be expressed as (*Bonelli et al.* [2008],*Geradin and Rixen* [1993]):

$$\lambda_{1,2} = e^{-\bar{\xi}\bar{\omega}h_A \pm i\bar{\omega}h_A} \tag{38}$$

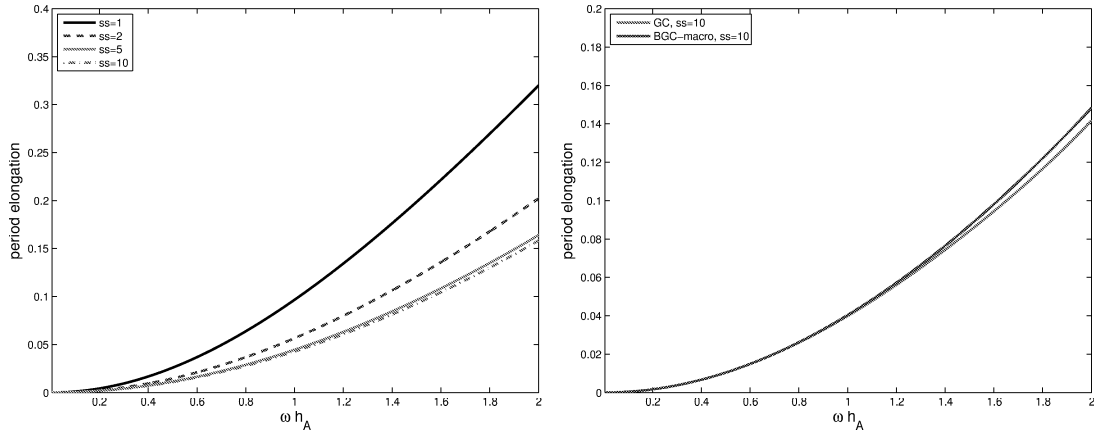
where $\bar{\xi}$ is the numerical damping ratio and $\bar{\omega}$ the numerical angular frequency. In Figure 3, the numerical damping ratio related to BGC-macro method for a time step ratio ss equal to 1 is compared with numerical damping ratio for a time step ratio higher than 1 when coupling CH-α schemes with $\rho_\infty = 0.8$ and $\rho_\infty = 0.5$ for the two subdomains (coarse and fine time scales). It can be checked that the slope at small values of Ω seems not to be altered by the multi-time step algorithm. More precisely, the order of the damping ratio is assessed by computing $\frac{\ln(\bar{\xi}(h_{2,A}))-\ln(\bar{\xi}(h_{1,A}))}{\ln(h_{2,A})-\ln(h_{1,A})}$ where $h_{1,A}$ and $h_{2,A}$ are small values of macro time step. It enables to conclude about the order of the leading low-frequency damping term. One obtains: $\bar{\xi} = O(\Omega^3)$ for any time step ratio ss. It can be verified that this order of accuracy corresponds to the leading low-frequency term of the α-schemes without coupling (*Krenk* [2008], *Krenk and Hogsberg* [2005]). It is also important to highlight that there is a marked difference between classical GC algorithm and the proposed BGC-macro algorithm in the case of Newmark schemes. By carrying out the same analysis for the GC method, along the lines of Bonelli $et\ al$ (*Bonelli et al.* [2008]) conducted for their PM method, the damping ratio obtained for the GC method is compared to the one for the BGC-macro method for two implicit CAA Newmark schemes in Figure 3. It can be seen that the order of the leading term in the damping ratio is equal to 1 for the GC algorithm ($\bar{\xi} = O(\Omega)$) whereas the BGC-macro method maintains the zero damping values of the CAA schemes.

Last, the numerical elongation period is studied. It is defined as $\frac{\bar{T}-T}{T}$, where $\bar{T} = \frac{2\pi}{\bar{\omega}}$. In Figure 4, period elongations for different time step ratios ss are compared when considering CH-α schemes ($\rho_\infty = 0.8$ and $\rho_\infty = 0.5$ for the two subdomains). Again, the leading low-frequency term in the period elongation is assessed and one obtains $\frac{\bar{T}-T}{T} = O(\Omega^2)$, corresponding to the classical result for α-schemes (*Krenk and Hogsberg* [2005], *Geradin and Rixen* [1993]). When coupling CAA schemes, the BGC-macro method generates a very similar period elongation to the one generated by the GC method. The leading low-frequency term is equal to 2, corresponding to the classical result for the Newmark schemes (*Geradin and Rixen* [1993]). Thus, the GC coupling alters the leading low-frequency damping term but not the period elongation one.
To resume, the BGC-macro method provides $\bar{\xi} = O(\Omega^3)$ and $\frac{\bar{T}-T}{T} = O(\Omega^2)$ for the α-schemes and for any time step ratios ss, as offered by the α scheme without coupling, confirming the second order of accuracy. For CAA schemes, the BGC-macro method provides $\bar{\xi} = 0$ and $\frac{\bar{T}-T}{T} = O(\Omega^2)$ for any time step ratios ss, as offered by the CAA scheme without coupling, confirming the second order of accuracy.
In conclusion, the stability, second order accuracy and convergence of the α-schemes are preserved through coupling with the BGC-macro method thanks to its conservation law based on the interface pseudo-energy.



(a) BGC-macro method (α-schemes) (b) BGC-macro and GC methods (CAA schemes)

Figure 3: Numerical damping ratio $\bar{\xi}$ of the split oscillator ($b_1 = 1$): CH-α ($\rho_\infty = 0.8$) coupled with CH-α ($\rho_\infty = 0.5$) with different time step ratios ss. CAA coupled with CAA using BGC-macro and GC methods with $ss = 10$.



(a) BGC-macro method (α-schemes) (b) BGC-macro and GC methods (CAA schemes)

Figure 4: Period elongation $\frac{\bar{T}-T}{T}$ of the split oscillator ($b_1 = 1$): CH-α ($\rho_\infty = 0.8$) coupled with CH-α ($\rho_\infty = 0.5$) with different time step ratios ss. CAA coupled with CAA using BGC-macro and GC methods with $ss = 10$.

6 CONCLUSIONS

The paper presents a general methodology for building Heterogeneous Asynchronous Time Integrators based on energy considerations. It has been sought to cancel the interface pseudo-energy, originally introduced by Hughes in the energy method, for demonstrating the stability of hybrid time integration coupling methods related with homogeneous and heterogeneous time steps. The first method, called BGC-macro method, solves the interface problem, whose Lagrange multipliers at the interface are the unknowns, at the macro time scale by deriving from the zero value of the interface pseudo-energy a kinematic constraint at the interface expressed in terms of velocity increments. A linear assumption on the variation of the Lagrange multipliers over the macro time step is adopted. Then, the kinematic constraint at the macro time scale is modified so as to comply with a micro time scale approach. The second new coupling method, called BGC-micro method, is deduced from the previous macro-time based method, and is also able to couple Newmark and α-schemes.
From energy arguments, both methods are stable. It has been confirmed by the convergence analysis through the spectral analysis of the amplification matrix. In addition to the stability, the BGC-macro method is found to be second-order accurate when dealing with Newmark and α-schemes. The algorithmic damping ratio and the period elongation error are of the same order than the original properties of the α-schemes, despite the addition of Lagrange multipliers (the equations of motion related to the subdomains along with the kinematic constraint constituting a DAE). The BGC-micro method exhibits a first order accuracy when dealing with different time steps but is more versatile for a wide range of engineering dynamics problems, such as non linear dynamics, co-simulations, PsD tests and multiphysics applications (FSI). Developments are in progress to extend the BGC-micro approach at the same level of accuracy than the BGC-macro method.

References

Arnold, M., and O. Bruls, Convergence of the generalized-α scheme for constraint mechanical systems, *Multibody System Dynamics*, *18*, 185–202, 2007.

Bonelli, A., O. Bursi, L. He, G. Magonette, and P. Pegon, Convergence analysis of a parallel interfield method for heterogeneous simulations with dynamic substructuring, *International Journal for Numerical Methods in Engineering*, *75*, 800–825, 2008.

Bonnet, P., M. Williams, and A. Blakeborough, Evaluation of numerical time-integration schemes for real-time hybrid testing, *Earthquake Engineering and Structural Dynamics 2008*, *37*, 1467–1490, 2008.

Brun, M., A. Batti, A. Limam, and A. Combescure, Implicit/explicit multi-time step co-computations for predicting reinforced concrete structure response under earthquake loading, *Soil dynamics and Earthquake Engineering*, *33*, 19–37, 2012.

Brun, M., A. Batti, A. Combescure, and A. Gravouil, External coupling software based on macro- and micro-time scales for explicit/implicit multi-time-step co-computations in structural dynamics, *Finite Elements in Analysis & Design*, *52*, 41–59, 2014.

Brun, M., A. Gravouil, A. Combescure, and A. Limam, Two feti-based heterogeneous time step coupling methods for newmark and alpha-schemes derived from the energy method, *Computer Methods in Applied Mechanics and Engineering*, *283*, 130–176, 2015.

Bursi, O., L. He, A. Bonelli, and P. Pegon, Novel generalized-α methods for interfield parallel integration of heterogeneous structural dynamic systems, *Journal of Computational and Applied Mathematics*, *234*, 2250–2258, 2010.

Chung, J., and G. Hulbert, A time integration algorithm for structural dynamics with improved numerical dissipation: the generalized-α method, *Journal of Applied Mechanics*, *60*, 371–375, 1993.

Combescure, A., and A. Gravouil, A numerical scheme to couple subdomains with different time-steps for predominantly linear transient analysis, *Computer methods in applied mechanics and engineering*, *191*, 1129–1157, 2002.

Combescure, D., and P. Pegon, α-operator splitting time integration technique for pseudodynamic testing - error propagation analysis, *Soil Dynamics and Earthquake Engineering*, *16*, 427–443, 1997.

Geradin, M., and D. Rixen, *Theorie des Vibrations. Application la dynamique des structures.*, Masson, Paris,, 1993.

Gravouil, A., and A. Combescure, A multi-time-step explicit-implicit method for non-linear structural dynamics, *International Journal for Numerical Methods in Engineering*, *50*, 199–225, 2001.

Hilber, H., T. Hughes, and R. Taylor, Improved numerical dissipation for time integration algorithms in structural dynamics, *Earthquake Engineering and Structural Dynamics*, *5*, 283–292, 1977.

Hughes, T., *The Finite Element Method: Linear Static and Dynamic Finite Element Analysis*, Prentice-Hall, Englewood Cliffs, NJ, 1987.

Krenk, S., Extended state-space time intergation with high-frequency energy dissipation, *International Journal for Numerical Methods in Engineering*, *73*, 1767–1787, 2008.

Krenk, S., and J. Hogsberg, Properties of time intergation with first order filter damping, *International Journal for Numerical Methods in Engineering*, *64*, 547–566, 2005.

Mahjoubi, N., A. Gravouil, A. Combescure, and N. Greffet, A monolithic energy conserving method to couple heterogeneous time integrators with incompatible time steps in structural dynamics, *Computer methods in applied mechanics and engineering*, *200*, 1069–1086, 2011.

Masuri, S., A. Hoitink, X. Zhou, and K. Tamma, Algorithms by design: Part ii: A novel normalized time weighted residual methodology and design of a family of symplectic-momentum conserving algorithms for nonlinear structural dynamics, *International Journal for Computational Methods in Engineering Science and Mechanics*, *10*(1), 27–56, 2009a.

Masuri, S., A. Hoitink, X. Zhou, and K. Tamma, Algorithms by design: Part iii: A novel normalized time weighted residual methodology and design of optimal symplectic-momentum based controllable numerical dissipative algorithms for nonlinear structural dynamics, *International Journal for Computational Methods in Engineering Science and Mechanics*, *10*(1), 57–90, 2009b.

Masuri, S., A. Hoitink, X. Zhou, and K. Tamma, Algorithms by design: A new normalized time-weighted residual methodology and design of a family of energy-momentum conversing algorithms for non-linear structural dynamics, *International Journal for Numerical Methods in Engineering*, *79*, 1094–1146, 2009c.

Pinto, A., P. Pegon, G. Magonette, and G. Tsionis, Pseudo-dynamic testing of bridges using non-linear substructuring, *Earthquake Engineering and Structural Dynamics*, *33*, 1125–1146, 2004.

Prakash, A., and K. Hjelmstad, A feti-based multi-time-step coupling method for newmark schemes in structural dynamics, *International Journal for Numerical Methods in Engineering 2004*, *61*, 2183–2204, 2004.

Simo, J., and N. Tarnow, The discrete energy-momentum method: conserving algorithms for nonlinear elastodynamics, *Z. Angew. Math. Phys.*, *43*, 757–792, 1992.

Wood, W., M. Bossak, and O. Zienkiewicz, An alpha modification of newmark's method, *International Journal for Numerical Methods in Engineering*, *15*, 1562–1566, 1981.

COMPDYN 2015
5th ECCOMAS Thematic Conference on
Computational Methods in Structural Dynamics and Earthquake Engineering
M. Papadrakakis, V. Papadopoulos, V. Plevris (eds.)
Crete Island, Greece, 25–27 May 2015

MULTIGRID SOLVER WITH DOMAIN DECOMPOSITION SMOOTHING FOR STEADY-STATE INCOMPRESSIBLE FSI PROBLEMS

Eugenio Aulisa[1], Simone Bnà[2], and Giorgio Bornia[1]

[1]Department of Mathematics and Statistics, Texas Tech University
Lubbock, TX 79409
e-mail: {eugenio.aulisa,giorgio.bornia}@ttu.edu

[2] SCAI-CINECA (Super Computing Applications and Innovation)
Casalecchio di Reno, BO, Italy
e-mail: simone.bna@cineca.it

Keywords: Fluid-Structure Interaction, Finite Element Methods, Multigrid, Domain Decomposition

Abstract. *In this paper we investigate the numerical performance of a monolithic Newton-multigrid solver with domain decomposition smoothers for the solution of a class of stationary incompressible FSI problems. The physics of the problem is described using a monolithic approach, where mass continuity and stress balance are automatically satisfied across the fluid-solid interface. The deformation of the fluid domain is taken into account within the nonlinear Newton iterations according to an Arbitrary Lagrangian Eulerian (ALE) scheme. Due to the complexity and variety of the operators, the implementation of the Jacobian matrix in the nonlinear iterations is not a trivial task. To this purpose, we make use of automatic differentiation tools for an exact computation of the Jacobian matrix. The numerical solution of steady-state problems is particularly challenging, due to the ill-conditioning of the induced stiffness matrix. Moreover, the enforcement of the incompressibility condition calls for the use of incompressible solvers either of mixed or segregated type. At each nonlinear outer iteration the resulting linearized system is solved with a geometric multigrid solver. We consider a GMRES smoother preconditioned by an Additive Schwarz Method (ASM). The domain decomposition of the preconditioner is driven by the natural splitting between fluid and solid domain. The numerical results of some benchmark tests for steady-state cases show agreement with the literature and an increased robustness with our choice of smoothers with respect to standard ones.*

1 INTRODUCTION

Fluid-Structure Interaction problems (FSI) are of great interest because of a large number of applications arising in various fields such as aerodynamics, elasticity, civil engineering, biomechanics and hemodynamics. Examples of interesting problems are the fluttering of wings and bridges, mechanical vibrations or water hammer effects in pipe networks, blood flow in large arteries, parachute modeling and oil flow in porous media.

Nowadays, many challenging questions are still open in the FSI community ranging from mathematical modeling and analysis to numerical discretization and computational issues. The fluid and the structure influence each other in a nonlinear way. Indeed, the structure changes its shape under the action of the fluid force and, conversely, the fluid flow is altered by the structure deformation. The numerical solution of FSI problems is a very challenging task. Several choices are possible for the description of the solid and fluid parts, the determination of the unkwnown variables (velocity, displacement, pressure in fluid and in solid), the treatment of the moving domain (ALE, interface tracking/capturing), the linearization procedure (linearize then discretize or viceversa; fixed point, Newton), the choice of the linear solver.

In this work we intend to address two main difficulties concerning FSI simulations: stationary cases and incompressible materials, both for the fluid and for the solid part. Our intent is to highlight the performance of multigrid methods with domain decomposition smoothers in the case of steady-state saddle-point problems. Pseudo-time stepping schemes, in which a stationary solution is reached as a limit of a time sequence, are typically considered due to a better conditioning of the linear systems to be solved. We do not consider here the use of pseudo-time steppers and we treat the fluid and solid as purely incompressible, without introducing slightly-compressible stabilization terms.

Concerning the coupling between the solid and fluid unknowns, we consider a monolithic approach. Monolithic algorithms solve simultaneously for the fluid and the structure unknowns in a unique solver, so that the solid and fluid regions are treated as a single continuum and the boundary conditions at the interface are automatically satisfied ([9, 12]). Monolithic algorithms are CPU-time expensive. This issue is enhanced in the case of incompressible formulation by the saddle-point character of the system. In this work we consider a monolithic strongly coupled strategy. This approach is the most robust and stable one among the strong coupling approaches, but it requires the development of strategies to reduce the computational time.

We consider the case of large deformations, thus obtaining a nonlinear system of equations for the displacement, velocity and pressure variables. The implementation of the Fréchet derivative of the nonlinear FSI operator needed for building the Jacobian matrix is not a trivial task. We have chosen to compute the exact Jacobian matrix by using Automatic Differentiation (AD) tools provided by the Adept software package [10]. Other variants have been proposed in literature for the linearization. In [11] quasi-Newton outer iterations with line search are performed and the Jacobian matrix is computed by a divided difference approach. A Newton method with the analytical computation of the Jacobian using shape-derivative calculus is considered in [6]. A quasi-Newton method in which the variation of the fluid domain in the fluid equations is neglected is proposed in [5, 4].

Inspired by the Arbitrary Lagrangian Eulerian (ALE) formulation for solving time-dependent PDEs in moving domains, we adopt this approach for the movement of the domain within the nonlinear iterations. An appropriate arbitrary mapping is chosen from the fluid fixed reference configuration to the current domain. The ALE mapping is constructed as a harmonic extension of the trace of the structure displacement on the fluid-solid interface.

The solution of the linear system in each linearization step is the most time-consuming part. Multigrid solvers are taken into account for the solution of large sparse linear systems due to their optimal computational complexity, at least for elliptic problems. In this paper we propose to use a geometric Newton-multigrid solver, in which Newton linearization is performed as an outer iteration and the resulting Jacobian system is solved using a geometric multigrid solver. Multigrid F-cycle schemes are considered with a GMRES smoother preconditioned by an additive Schwarz method (ASM). In this work we observed that the use of domain decomposition methods in the smoothing step guarantees convergence where standard smoothers fail. Another advantage of these methods is to allow for an effective parallel implementation. While the coarse grid solution is obtained by inverting the corresponding matrix with a direct sparse solver, several local subproblems are solved on finer levels over subdomain patches.

Both multigrid and domain decomposition methods draw a lot of attention within the FSI community. In [12] a geometric multigrid solver with a Multilevel Pressure Schur Complement (MPSC) Vanka-like smoother is considered, with applications to nonstationary FSI problems in biomechanics. Applications of this scheme to hemodynamics are also addressed in [22, 14]. Monolithic Newton-Krylov algorithms are studied in [8, 26]. In [8] the inner Krylov iterations are preconditioned with algebraic multigrid methods, while an overlapping additive Schwarz preconditioner is considered in [26] with application to parallel three-dimensional blood flow simulations. A partitioned method in which multigrid is used either within the fluid and solid solves or as an outer iteration is addressed in [16, 18]. Other numerical studies are available in the literature on the use of domain decomposition Vanka-type smoothers for multigrid both in Computational Fluid Dynamics (CFD) and in Computational Solid Mechanics (CSM) [1, 19, 24, 25, 14, 2].

The paper is organized as follows. In Section 2 we present the strong and weak formulations of the stationary incompressible FSI problem under investigation. We describe the linearization procedure by means of automatic differentiation, and we illustrate the features of the multigrid linear solver with domain decomposition smoothing. Numerical results of benchmark problems are presented in Section 3. Finally, we draw our conclusions.

2 FORMULATION OF THE FSI PROBLEM

2.1 Strong formulation

Let $\widehat{\Omega} \subset \mathbb{R}^3$ be a reference undeformed configuration for a given domain. Let $\Omega \subset \mathbb{R}^3$ be the deformed steady-state configuration. Let assume that there is a one-to-one, uniquely invertible, sufficiently smooth mapping $\mathcal{X}$ of the reference configuration $\widehat{\Omega}$ to the deformed configuration

$$\mathcal{X} : \widehat{\Omega} \to \Omega \,.$$

It is clear that the mapping $\mathcal{X}$ depends on the choice of the reference configuration $\widehat{\Omega}$. All the reference configurations are in principle equivalent. For instance, we can set $\widehat{\Omega}$ as the initial (stress-free) configuration. Let us denote an arbitrary material point in the reference configuration $\widehat{\Omega}$ by $\widehat{\mathbf{x}}$. The position of this point in the deformed configuration Ω is given by

$$\mathbf{x} = \mathcal{X}(\widehat{\mathbf{x}}), \quad \text{for all} \quad \widehat{\mathbf{x}} \in \widehat{\Omega} \,.$$

Let Ω^f and Ω^s be the regions occupied by the fluid and the solid at the final deformed configuration, respectively. In the stress-free configuration the fluid and solid region are defined by $\widehat{\Omega}^f$ and $\widehat{\Omega}^s$. Let $\Gamma^i = \Omega^f \cap \Omega^s$ and $\widehat{\Gamma}^i = \widehat{\Omega}^f \cap \widehat{\Omega}^s$ be the interface between solid and fluid in the

final and undeformed configuration, respectively. The deformation of the domain $\Omega = \Omega^f \cup \Omega^s$ can be described by considering the two applications

$$\mathcal{X}^s : \widehat{\Omega}^s \to \mathbb{R}^3\,,$$
$$\mathcal{X}^f : \widehat{\Omega}^f \to \mathbb{R}^3\,,$$

such that $\mathrm{Im}(\mathcal{X}^s(\cdot)) = \Omega^s$, $\mathrm{Im}(\mathcal{X}^f(\cdot)) = \Omega^f$. The application $\mathcal{X}$ maps the position of any material point $\widehat{\mathbf{x}}$ from the given fixed reference configuration $\widehat{\Omega}$ to the deformed configuration Ω. The displacement field $\mathbf{d} : \widehat{\Omega} \to \mathbb{R}^3$ is defined as

$$\mathbf{d}(\widehat{\mathbf{x}}) = \mathcal{X}(\widehat{\mathbf{x}}) - \widehat{\mathbf{x}} = \mathbf{x} - \widehat{\mathbf{x}}\,, \tag{1}$$

$$\mathbf{d} = \begin{cases} \mathbf{d}^s & \text{on} \quad \widehat{\Omega}^s \\ \mathbf{d}^f & \text{on} \quad \widehat{\Omega}^f \end{cases}. \tag{2}$$

In the solid domain $\mathbf{d}^s$ is the actual solid displacement. In the fluid domain $\mathbf{d}^f$ is an artificial displacement with no physical meaning that is used to map the deformation of the fluid domain which occurs because of the deformation of the solid domain. The displacement $\mathbf{d}$ is an unknown of the FSI problem, and its knowledge also defines the unknown steady state configuration $\Omega = \Omega(\mathbf{d})$, where $\mathbf{x} \in \Omega$ is given by

$$\mathbf{x} = \widehat{\mathbf{x}} + \mathbf{d}(\widehat{\mathbf{x}}). \tag{3}$$

The velocity field $u : \widehat{\Omega} \to \mathbb{R}^3$

$$\mathbf{u} = \begin{cases} \mathbf{u}^s & \text{on} \quad \Omega^s \\ \mathbf{u}^f & \text{on} \quad \Omega^f \end{cases} \tag{4}$$

represents the fluid flow velocity $\mathbf{u}^f$ in the fluid domain and the solid velocity $\mathbf{u}^s$ in the solid domain. Since we only consider steady-state solutions we assume $\mathbf{u}^s = \mathbf{0}$ everywhere in the solid domain, including on the solid-fluid interface. Both the displacement $\mathbf{d}$ and the velocity $\mathbf{u}$ are continuous across the interface and are treated as monolithic fields on the whole domain.

In the following we will use the notations $\widehat{\nabla}$ or ∇ to refer to the del operator in the reference or in the deformed configuration, respectively.

The steady state momentum and mass balance equations for the solid and the fluid can be written as

$$\nabla \cdot \boldsymbol{\sigma}^s + \mathbf{f}^s = 0 \qquad \text{in } \Omega^s(\mathbf{d})\,, \tag{5}$$
$$-\rho(\mathbf{u} \cdot \nabla \mathbf{u}) + \nabla \cdot \boldsymbol{\sigma}^f + \mathbf{f}^f = 0 \qquad \text{in } \Omega^f(\mathbf{d})\,, \tag{6}$$
$$J - 1 = 0 \qquad \text{in } \widehat{\Omega}^s\,, \tag{7}$$
$$\nabla \cdot \mathbf{u} = 0 \qquad \text{in } \Omega^f(\mathbf{d})\,. \tag{8}$$

Here, ρ is the fluid density, $\mathbf{f}^s$ and $\mathbf{f}^f$ are the body forces in the solid and fluid domain, respectively. In Eq.(7)

$$J = \det \mathbf{F},$$

where $\mathbf{F}$ is the deformation gradient tensor, $\mathbf{F} = I + \widehat{\nabla}\mathbf{d}$. Notice that the gradient is taken with respect to the reference configuration. The symbol $\boldsymbol{\sigma}$ denotes the stress tensor (or Cauchy stress tensor in the solid). For incompressible fluid flows the stress tensor is given by

$$\boldsymbol{\sigma}^f(\mathbf{u}, p) = -p\boldsymbol{I} + \mu\nabla\mathbf{u} \ \text{ in } \ \Omega^f, \tag{9}$$

where μ is the fluid viscosity. For the solid we consider either the case of an incompressible Neo-Hookean material

$$\boldsymbol{\sigma}^s(\mathbf{d}, p) = -p\mathbf{I} + 2C_1\mathbf{B} \text{ in } \Omega^s\,, \tag{10}$$

or the case of an incompressible Mooney-Rivlin material

$$\boldsymbol{\sigma}^s(\mathbf{d}, p) = -p\mathbf{I} + 2C_1\mathbf{B} - 2C_2\mathbf{B}^{-1} \text{ in } \Omega^s\,, \tag{11}$$

where the constants C_1 and C_2 depend on the mechanical properties of the material and

$$\mathbf{B} = \mathbf{F}\mathbf{F}^T$$

is the left Cauchy-Green deformation tensor. The Neo-Hookean and Mooney-Rivlin hyperelastic models can be used for large strains. In Eqs. (6), (10) and (11) p is the pressure field and has to be computed. In the fluid domain p^f is the actual fluid pressure, while in the solid domain p^s does not have a clear physical meaning and can be regarded mathematically as the Lagrange multiplier associated to the incompressibility constraint (7). Similar mathematical interpretation can also be given to the fluid pressure p^f with respect to the incompressible constraint (8). Although we use a monolithic formulation also for the pressure p, we do not require pressure continuity across the solid-fluid interface.

We remark that the solid and fluid momentum equations are written in the final deformed configuration Ω, as well as the fluid divergence-free condition. The mass conservation for the solid is instead written in the stress-free configuration.

On the solid fluid interface we also enforce the stress continuity condition

$$\boldsymbol{\sigma}^f \cdot \mathbf{n} = \boldsymbol{\sigma}^s \cdot \mathbf{n} \qquad \text{on } \Gamma^i(\mathbf{d}), \tag{12}$$

where $\mathbf{n}$ is the unit normal vector on the deformed interface $\Gamma^i(\mathbf{d})$ whose direction has been fixed either from the fluid to the solid or from the solid to the fluid. No other interface condition is needed for the velocity and the displacement since, as we already pointed out, these are monolithic fields and their continuity is automatically satisfied.

Since these equations are posed on an unknown domain, their linearization will involve a domain update. The kinematic conditions for the movement of the domain are chosen to satisfy

$$\mathbf{0} = \mathbf{u} \qquad \text{in } \widehat{\Omega}^s\,, \tag{13}$$

$$\mathbf{0} = \widehat{\nabla} \cdot (k(\widehat{\mathbf{x}})\widehat{\nabla}\mathbf{d}) \qquad \text{in } \widehat{\Omega}^f\,, \tag{14}$$

where the role of the function $k(\widehat{\mathbf{x}})$ is described below. The mesh deformation is dealt based on the sizes of the elements. Following the work in [15] and [17] we want smaller elements to be stiffer than larger ones. In regions where the mesh would undergo large distortions (e.g. the region near the fluid-solid interface) we refine and build smaller and stiffer elements, in order not to degrade the mesh quality. This is easily achieved setting the function $k(\widehat{\mathbf{x}})$ to be a piecewise-constant function discontinuous across the element boundary and whose value is given by

$$k(\widehat{\mathbf{x}}) = \frac{1}{\mathrm{V}_{el}},$$

where V_{el} is the volume of the mesh element that contains the $\widehat{\mathbf{x}}$ coordinate.

2.2 Weak formulation

In this part of the paper we focus on describing how the weak formulation of the FSI problem is achieved using a monolithic approach. In this section we do not put too much emphasis on the external boundary conditions, rather we assume that they are given, are physically meaningful and compatible with all our assumptions. Different types of boundary conditions require us to modify the Sobolev spaces on which the solution and the shape functions are defined. Later in the numerical example part we will be more specific in choosing and describing the boundary conditions. For the sake of simplicity we assume here physically compatible Dirichlet boundary data everywhere.

Let the domain be divided as $\Omega = \Omega_s \cup \Omega_{sf} \cup \Omega_f$. Here, Ω_s and Ω_f denote the solid and fluid parts respectively, while Ω_{sf} is the union of the supports of the shape functions associated to the interface degrees of freedom. We will also define $\Omega_{sf} = \Omega_{s,i} \cup \Omega_{f,i}$, with $\Omega_{s,i} \cap \Omega_{f,i} = \emptyset$. Namely, we assume the interface Γ^i to be on the boundary of Ω_s and Ω_f and contained inside Ω_{sf}.

Let $\mathbf{d}, \mathbf{u}$ and p denote the displacement, velocity and pressure, respectively. After multiplication by appropriate test functions and integration by parts, the weak problem of the coupled FSI reduces in finding $\mathbf{d}, \mathbf{u}, p$ in $\boldsymbol{H}^1(\Omega) \times \boldsymbol{H}^1(\Omega) \times L^2(\Omega)$ such that

$$\int_{\Omega_s(\mathbf{d})} \sigma(\mathbf{d}, p) : \nabla \boldsymbol{\phi}^{\mathbf{d}} - \mathbf{f}^s \cdot \boldsymbol{\phi}^{\mathbf{d}} = 0, \qquad \forall\, \boldsymbol{\phi}^{\mathbf{d}} \in \boldsymbol{H}^1_0(\Omega_s(\mathbf{d})), \quad (15)$$

$$\int_{\Omega_{s,i}(\mathbf{d})} \sigma(\mathbf{d}, p) : \nabla \boldsymbol{\phi}^{\mathbf{d}} - \mathbf{f}^s \cdot \boldsymbol{\phi}^{\mathbf{d}} + \int_{\Omega_{f,i}(\mathbf{d})} \rho(\mathbf{u} \cdot \nabla \mathbf{u}) \cdot \boldsymbol{\phi}^{\mathbf{d}} + \sigma(\mathbf{u}, p) : \nabla \boldsymbol{\phi}^{\mathbf{d}} - \mathbf{f}^f \cdot \boldsymbol{\phi}^{\mathbf{d}} = 0, \quad \forall\, \boldsymbol{\phi}^{\mathbf{d}} \in \boldsymbol{H}^1_0(\Omega_{sf}(\mathbf{d})), \quad (16)$$

$$\int_{\widehat{\Omega}_f} k(x) \nabla \mathbf{d} \cdot \nabla \boldsymbol{\phi}^{\mathbf{d}} = 0, \qquad \forall\, \boldsymbol{\phi}^{\mathbf{d}} \in \boldsymbol{H}^1_0(\widehat{\Omega}_f), \quad (17)$$

$$\int_{\widehat{\Omega}_s} \mathbf{u} \cdot \boldsymbol{\phi}^{\mathbf{u}} = 0, \qquad \forall\, \boldsymbol{\phi}^{\mathbf{u}} \in \boldsymbol{H}^1(\widehat{\Omega}_s), \quad (18)$$

$$\int_{\Omega_f(\mathbf{d})} \rho(\mathbf{u} \cdot \nabla \mathbf{u}) \cdot \boldsymbol{\phi}^{\mathbf{u}} + \sigma(\mathbf{u}, p) : \nabla \boldsymbol{\phi}^{\mathbf{u}} - \mathbf{f}^f \cdot \boldsymbol{\phi}^{\mathbf{u}} = 0, \qquad \forall\, \boldsymbol{\phi}^{\mathbf{u}} \in \boldsymbol{H}^1_0(\Omega_f(\mathbf{d})), \quad (19)$$

$$\int_{\widehat{\Omega}_s} (J-1)\phi^p = 0, \qquad \forall\, \phi^p \in L^2(\widehat{\Omega}_s), \quad (20)$$

$$\int_{\Omega_f(\mathbf{d})} \phi^p \nabla \cdot \mathbf{u} = 0, \qquad \forall\, \phi^p \in L^2(\Omega_f(\mathbf{d})), \quad (21)$$

with appropriate boundary conditions on Ω. Notice that Eq. (15) represents the momentum balance inside the solid domain, while equation Eq. (19) represents the momentum balance inside the fluid domain. Eq. (16) satisfies the momentum balance on the interface region between the fluid and the solid domain. The test functions in Eq. (15) and Eq. (19) are on $\boldsymbol{H}^1_0(\Omega_s(\mathbf{d}))$ and $\boldsymbol{H}^1_0(\Omega_f(\mathbf{d}))$, respectively, thus the two sets of equations are defined in two disjoint subdomains. The momentum exchange between these regions occurs through Eq. (16) where the test functions are defined on $\boldsymbol{H}^1_0(\Omega_{sf}(\mathbf{d}))$, thus on a domain which overlaps with both the solid and fluid parts. It is worth noting that, by the coupling conditions (12), the two boundary terms that result from integration by parts at the solid-fluid interface Γ^i cancel out. This assures that stresses at the interface are correctly balanced.

Eq. (17) is the auxiliary displacement equation inside the fluid domain. Notice that the test functions are in $\boldsymbol{H}_0^1(\widehat{\Omega}_f)$. In other words the solution of this equation yields a smooth displacement field inside the fluid domain for given values on the boundary of $\widehat{\Omega}_f$. Thus, this equation does not affect directly the value of the displacement on the solid-fluid interface, which is an unknown of the problem that is evaluated by solving the other parts of the system.

Eq. (18) constrains the solid velocity to be equal to zero both inside the solid region and on its boundary, including the solid-fluid interface $\widehat{\Gamma}^i$, since the test functions are taken in $\boldsymbol{H}^1(\widehat{\Omega}_s)$.

Eqs. (20) and (21) represent the mass continuity constraints in the solid and fluid domains, respectively.

An idea of the variable dependence pattern for the equations in the previous system is given in Figure 2.2. Notice that in the figure we shaded in black the variables that appear explicitly in

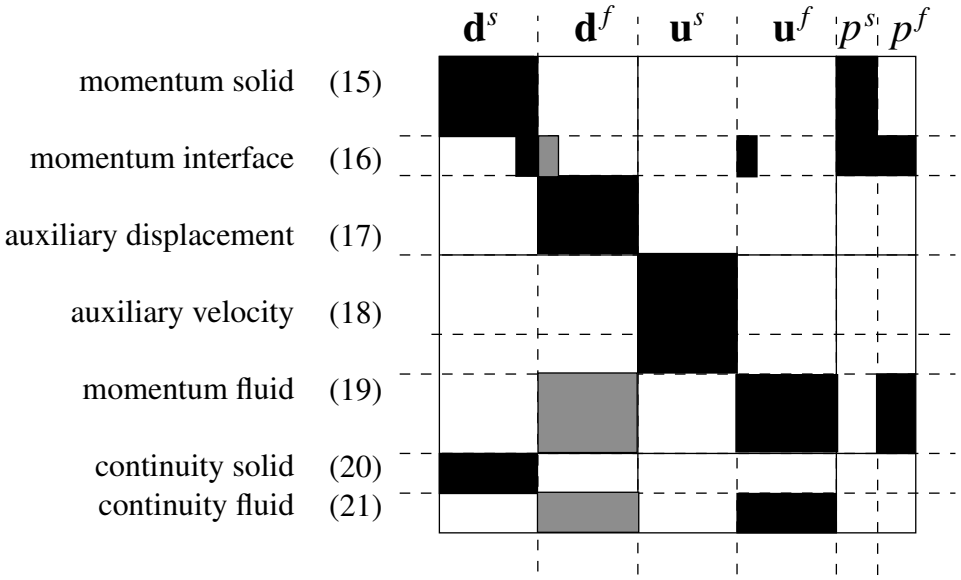


Figure 1: Variable dependence pattern associated to system (15)-(21).

the integrands and in gray the variables that appear indirectly because the integrals are evaluated on the deformed domain $\Omega(\mathbf{d})$. For the sake of clarity we split the solution variables in the solid and fluid parts by adding the corresponding superscripts ^{s} and ^{f}, but we emphasize that the formulation is monolithic and the solution variables are defined on the whole domain Ω.

It is worth nothing that the Jacobian matrix associated to equation system (15)-(21) has exactly the same sparsity pattern as in Figure 2.2. The accurate choice of the equation ordering (and corresponding shape function choice) optimizes the diagonal structure of the Jacobian matrix and is crucial for achieving convergence of the proposed algorithm.

2.3 Automatic differentiation for the evaluation of the tangent operator

The nonlinear system (15)-(21) is solved by using a Newton scheme. Let $\mathbf{v} = (\mathbf{d}, \mathbf{u}, p)$ and rewrite the equation system (15)-(21) in compact notation as

$$\mathcal{F}(\mathbf{v}) = 0. \tag{22}$$

Let $\mathbf{v}^0$ be an initial guess. Then a single Newton iteration is given by

$$\mathbf{v}^i = \mathbf{v}^{i-1} - \mathcal{J}^{-1}(\mathbf{v}^{i-1})\mathcal{F}(\mathbf{v}^{i-1}) \quad \text{for} \quad i \geq 1, \tag{23}$$

and it is repeated till the difference in norm between two successive solutions $\|\mathbf{v}^i - \mathbf{v}^{i-1}\|$ drops below a given tolerance value. Here, $\mathcal{J}(\mathbf{v})$ is the tangent operator (or Jacobian) of $\mathcal{F}$ in $\mathbf{v}$ and it is evaluated as

$$\mathcal{J}(\mathbf{v}^i) = \frac{\partial \mathcal{F}}{\partial \mathbf{v}}(\mathbf{v}^i).$$

This basic iteration exhibits quadratic convergence provided that the initial guess is sufficiently close to the solution. As already pointed out the Jacobian exhibits the same dependence variable pattern as the original system $(15) - (21)$ as described in Figure 2.2.

For the considered problem the symbolic differentiation of $\mathcal{J}$ is cumbersome, due to the presence of the integrals evaluated on the moving domain $\Omega(\mathbf{d})$. An approximate evaluation of $\mathcal{J}$ can be done either by neglecting some of the dependencies or by using approximate differentiation perturbing each component of $\mathbf{v}$ in $\mathcal{F}(\mathbf{v})$. In the current work the authors have instead computed the exact Jacobian using fast reverse automatic differentiation as described in [10]. Automatic differentiation is a set of techniques that numerically evaluate the derivative of a function specified in a computer program. It exploits the fact that every computer program executes a sequence of elementary arithmetic operations (addition, subtraction, multiplication, division, etc.) and elementary functions (exp, log, sin, cos, etc.). By applying the chain rule repeatedly to these operations derivatives of arbitrary order can be evaluated. Among the several libraries available we have chosen Adept, a software library that enables algorithms written in C and C++ to be automatically differentiated using operator overloading strategy.

It is worth noticing that in almost all the other works available in literature the authors prefer to rewrite all the equations in (15)-(21) in the fixed domain $\widehat{\Omega}$ using Kirchhoff-Piola tensor multiplication and Jacobian transformation, in order to avoid differentiation in moving domains. This approach greatly complicates the formulation of the problem, but it is preferred because once the equations are written in the fixed domain then the exact Jacobian $\mathcal{J}$ can be evaluated using symbolic differentiation (however, it still remains a challenging task in both derivation and numerical implementation). In our algorithm such an approach is not needed at all, and we choose to rewrite each equation in the domain configuration that is most convenient and to use automatic differentiation for the evaluation of the Jacobian. This approach results in high clarity for the formulation, as well as exactness and ease of use in the numerical implementation.

2.4 Multigrid discretization and inter-grid operators

We hereby describe the general ideas that lie behind the multigrid algorithm used to discretize and solve the FSI system for the variables $\mathbf{d}$, $\mathbf{u}$, and p. By starting at the coarse level $l = 0$, we discretize the entire domain $\widehat{\Omega}$ into a collection of finite elements, with the constraint that any point on the solid-fluid interface $\widehat{\Gamma}^i$ is located on the boundary between two elements. A geometrically conforming coarse triangulation $\mathcal{T}_h^0$ is then generated not only on the entire domain $\widehat{\Omega}$, but also on the subdomains $\widehat{\Omega}_s$, $\widehat{\Omega}_f$, and $\widehat{\Omega}_{sf}^0$. Recall that we defined $\widehat{\Omega}_{sf}$ to be the union of the supports of all the test functions associated to the interface degrees of freedom. Therefore its extension depends on the triangulation and is given by the collection of all the finite elements adjacent to the interface $\widehat{\Gamma}^i$. For this reason we added the apex notation, $\widehat{\Omega}_{sf}^0$, indicating the level mesh where it is defined.

Based on a simple element midpoint refinement, successive level meshes $\mathcal{T}_h^l$ are built recursively up to the top level $l = n$. Every triangulation $\mathcal{T}_h^l$ is geometrically conforming within all domains $\widehat{\Omega}$, $\widehat{\Omega}_s$, $\widehat{\Omega}_f$ and $\widehat{\Omega}_{sf}^l$. The nodes of the coarser mesh are always included in the nodes of the finer mesh. This is the key point for this kind of discretization and it is always true for different level meshes generated by using midpoint refinement.

Let $\mathbf{V}^l(\widehat{\Omega}) \subset \mathbf{H}^1(\widehat{\Omega})$ be a finite-element space built on the triangulation $\mathcal{T}_h^l$, and let $\mathbf{V}^l(\widehat{\Omega}_s)$, $\mathbf{V}^l(\widehat{\Omega}_f)$, and $\mathbf{V}^l(\widehat{\Omega}_{sf}^l)$ be the corresponding spaces obtained by the restriction of $\mathbf{V}^l(\widehat{\Omega})$ to the subdomains $\widehat{\Omega}_s$, $\widehat{\Omega}_f$, and $\widehat{\Omega}_{sf}^l$, respectively. Then the following nested relations between the spaces hold

$$\mathbf{V}^0(\widehat{\Omega}) \subset \mathbf{V}^1(\widehat{\Omega}) \subset \cdots \subset \mathbf{V}^n(\widehat{\Omega}), \tag{24}$$

$$\mathbf{V}^0(\widehat{\Omega}_s) \subset \mathbf{V}^1(\widehat{\Omega}_s) \subset \cdots \subset \mathbf{V}^n(\widehat{\Omega}_s), \tag{25}$$

$$\mathbf{V}^0(\widehat{\Omega}_f) \subset \mathbf{V}^1(\widehat{\Omega}_f) \subset \cdots \subset \mathbf{V}^n(\widehat{\Omega}_f), \tag{26}$$

but

$$\mathbf{V}^0(\widehat{\Omega}_{sf}^0) \not\subseteq \mathbf{V}^1(\widehat{\Omega}_{sf}^1) \not\subseteq \cdots \not\subseteq \mathbf{V}^n(\widehat{\Omega}_{sf}^n), \tag{27}$$

since the domain Ω_{sf}^l reduces in size as l increases.

Similarly, let $X^l(\widehat{\Omega}) \subset L^2(\widehat{\Omega})$ be a finite-element space built on the triangulation $\mathcal{T}_h^l$, and let $X^l(\widehat{\Omega}_s)$ and $X^l(\widehat{\Omega}_f)$, be the corresponding spaces obtained by restriction of $X^l(\widehat{\Omega})$ to the subdomains $\widehat{\Omega}_s$, and $\widehat{\Omega}_f$, respectively. Then the following nested relations between the spaces hold

$$X^0(\widehat{\Omega}) \subset X^1(\widehat{\Omega}) \subset \cdots \subset X^n(\widehat{\Omega}), \tag{28}$$

$$X^0(\widehat{\Omega}_s) \subset X^1(\widehat{\Omega}_s) \subset \cdots \subset X^n(\widehat{\Omega}_s), \tag{29}$$

$$X^0(\widehat{\Omega}_f) \subset X^1(\widehat{\Omega}_f) \subset \cdots \subset X^n(\widehat{\Omega}_f). \tag{30}$$

We solve for the FSI problem on the finest level spaces $\mathbf{V} = \mathbf{V}^n$ and $X = X^n$. The solution triplet $(\mathbf{d}, \mathbf{u}, p)$ is sought in the finite dimensional space $\mathbf{V} \times \mathbf{V} \times X$. We recall that the pair of spaces $\mathbf{V} \times X$, chosen for coupling either the solution variables $(\mathbf{d}, p)$ or $(\mathbf{u}, p)$ have to be taken appropriately in such a way that the discrete inf-sup condition is satisfied. This guarantees the stability of the approximation for both the incompressible hyperelastic material and the incompressible Navier-Stokes equation. We have chosen for $\mathbf{V}$ the space of biquadratic Lagrangian polynomials and for X the space of linear discontinuous polynomials, where the discontinuity occurs across the element boundaries. This last choice is well suited for the pressure field p since we do not enforce any continuity between the fluid and the solid pressure across the interface.

The coarser spaces are used to define and solve a Full Newton Geometric Multigrid Algorithm scheme, however extra attention should be given to define the inter level transfer operators between levels. The coarse-to-fine (prolongation) operator is classical and is taken to be the natural injection on the whole domain $\widehat{\Omega}$

$$I_{l-1}^l : \mathbf{V}^{l-1} \times \mathbf{V}^{l-1} \times X^{l-1}(\widehat{\Omega}) \longrightarrow \mathbf{V}^l \times \mathbf{V}^l \times X^l(\widehat{\Omega}), \tag{31}$$

given by

$$I_{l-1}^l \mathbf{v} = \mathbf{v}\,, \quad \text{for all} \quad \mathbf{v} \in \mathbf{V}^{l-1} \times \mathbf{V}^{l-1} \times X^{l-1}(\widehat{\Omega}). \tag{32}$$

The fine-to-coarse (restriction) operator is non classical, due both to the choice of the test function support and to the special ordering of the equations in the equation system (15)-(21). Rather than defining it in a formal mathematical setting (that will just over-complicate this discussion) we prefer to emphasize the major differences between a classical restriction operator and the current one.

When the multigrid algorithm is built on nested finite element spaces, the prolongation operator $\mathcal{I}_{l-1}^{l}$ is generally taken to be the natural injection between the two nested level spaces V^{l-1} and V^{l}, with $V^{l-1} \subset V^{l}$, as

$$\mathcal{I}_{l-1}^{l} : V^{l-1} \to V^{l} \ . \tag{33}$$

$$\mathcal{I}_{l-1}^{l} v = v, \quad \text{for all } v \in V^{l-1}. \tag{34}$$

Then, the corresponding restriction operator is defined to be the transpose of $\mathcal{I}_{l-1}^{l}$ with respect to the inner product $(.,.)$. In other words

$$\mathcal{I}_{l}^{l-1} : V^{l} \to V^{l-1} \ , \tag{35}$$

$$(\mathcal{I}_{l}^{l-1} v, w) = (v, \mathcal{I}_{l-1}^{l} w) \quad \text{for all } v \in V^{l} \text{ and } w \in V^{l-1}. \tag{36}$$

This is done under the underlying assumption that the set of partial differential equations associated to a particular test function is defined on the whole domain. In the equation system (15)-(21) this assumption is violated, since the equations have been fragmented, shuffled and defined piecewise on part of the domain. Moreover, in the interface momentum equation 16, the test functions in the target set have support Ω_{sf}^{l-1} larger than the support Ω_{sf}^{l} of the test functions in the original set. Therefore contributions from the other momentum equations are needed. To overcome these obstacles we build the restriction operator for each equation set, with special attention to the momentum interface equations. With reference to Figure 2.4, we have the following:

- the coarse solid momentum equations are obtained by restricting only the fine solid momentum equations;
- the coarse interface momentum equations are obtained by contributions not only from the interface but also from the solid and fluid momentum equations;
- the coarse auxiliary displacement equations are obtained by restricting only the fine auxiliary displacement equations on the fluid domain;
- the coarse auxiliary velocity equations are obtained by restricting the fine auxiliary velocity equations both on the solid domain and on the interface;
- the coarse fluid momentum equations are obtained by restricting only the fine fluid momentum equations;
- mass continuity equations are restricted in a standard way since the test functions associated to them are discontinuous and no interaction occurs between the two subdomains.

2.5 Domain decomposition for the multigrid algorithm

In the Newton-multigrid solver at each level we use a GMRES smoothing algorithm, where the tangent matrix is preconditioned by means of a domain decomposition strategy. In particular, we use an Additive Schwarz Method (ASM) with overlapping subdomains, where first we split the whole domain in the fluid and solid subregions, and then we further divide each subregion into smaller blocks. In each block the equations to be solved are taken following a Vanka-type strategy. The Vanka-type class of smoothers can be seen as a block Gauss-Seidel method (for details see [13, 1, 19, 24]). In each step several small linear systems are solved,

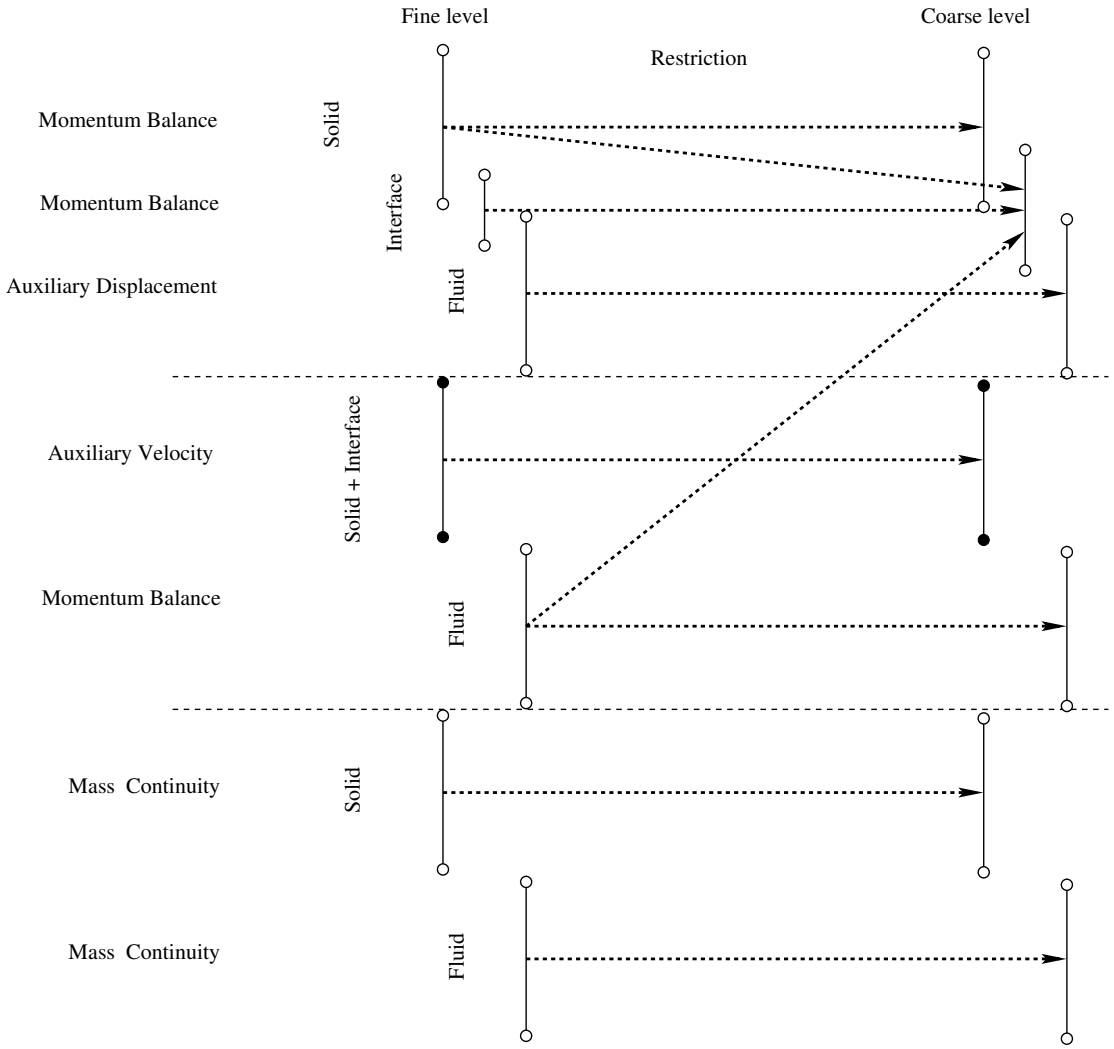


Figure 2: Restriction Scheme

each of which corresponds to all the degrees of freedom (DOFs) associated within the block of elements. Each subsystem is then solved using a direct or iterative solver. Notice that the DOFs associated to an element consists in displacement, velocity and pressure. While the support of the test functions associated to the pressure DOFs is limited to the element itself, the support of the test function associated to the displacement and velocity DOFs extends to the neighboring elements. This extension is responsible for the overlapping and the exchange of information between blocks.

3 NUMERICAL RESULTS

We seek to validate and evaluate the accuracy and performance of the proposed Newton-multigrid solver for a set of FSI benchmark configurations that can be found in the literature (see [3, 7, 23]).

3.1 Steady-state two-dimensional Hron-Turek FSI1 test

In [20] the authors proposed a benchmark for testing and comparing different numerical methods and code implementations for fluid-structure interaction problems. This benchmark is

based on the older successful *flow around cylinder* setting developed in [21] for incompressible laminar flow. The overall setup of this interaction problem consists of an elastic solid object attached to a infinite rigid cylinder in a laminar channel flow. The fluid is supposed to be incompressible and the structure is allowed to be compressible or incompressible. The magnitude of the average inlet velocity is chosen in order to induce a steady flow and stationary deformations.

The computational domain is based on the 2D version of the well-known *flow around cylinder* benchmark and it is shown in Figure 3. The parameters which define the geometry are given as follows:

- the domain dimensions are: length $L = 2.5m$, height $H = 0.41m$;
- the circle center is positioned at $C = (0.2m, 0.2m)$ (measured from the left bottom corner of the channel) and the radius is $r = 0.05m$;
- the elastic structure bar has length $l = 0.35m$ and height $h = 0.02m$; the right bottom corner is positioned at $(0.6m, 0.19m)$, and the left end is fully attached to the fixed and rigid cylinder;
- the control point is A on the tip of the structure, with undeformed coordinates $A_0 = (0.6m, 0.2m)$.

The thickness and the length of the beam are chosen in order to reduce the bending stiffness without introducing additional numerical complications connected with high aspect ratios in the geometry. As reported in [21], the setting is intentionally non-symmetric to prevent the dependence of the onset of any possible oscillation on the precision of the computation.

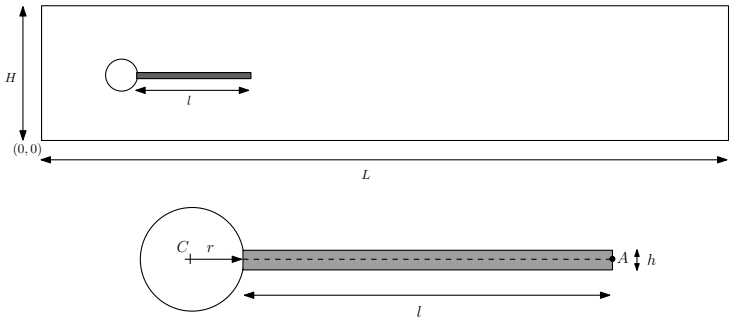


Figure 3: Computational domain and detail of the beam.

The FSI problem at hand needs to prescribe some boundary conditions.

- A parabolic velocity profile is prescribed in the left channel inflow section

$$\mathbf{v}^f(0, y) = 1.5U_m \frac{y(H-y)}{\left(\frac{H}{2}\right)^2} = 1.5U_m \frac{4.0}{0.1681} y(0.41 - y)\,. \tag{37}$$

- As outflow boundary condition the reference pressure at the outflow section is set to have zero mean value. This value has no influence on the solid deformation since fluid and solid are both incompressible. This is not true if the structure is supposed to be compressible.
- The *no-slip* condition is prescribed for the fluid on the other boundary edges. i.e. top and bottom wall, circle and fluid-structure interface.

We point out that the initialization of the nonlinear algorithm is performed by prescribing zero velocity in the fluid and no deformation in the structure.

The results of the benchmark computations are summarized in Table 2: $d_1(A)$ and $d_2(A)$ denote the displacements in $x-$ and $y-$direction of the control point A. The column "ndof" refers to the sum of unknowns for all velocity components, pressure, and displacement components.

Table 1: Parameter settings for the Hron-Turek FSI1 benchmark.

Parameter	symbol	measure unit	FSI1
Fluid density	ρ^f	$[10^3 \frac{Kg}{m^3}]$	1
Fluid viscosity	ν^f	$[10^{-3} \frac{m^2}{s}]$	1
Solid density	ρ^s	$[10^3 \frac{Kg}{m^3}]$	1
Poisson coefficient	ν^s	-	0.4
Shear modulus	μ^s	$[10^6 \frac{Kg}{ms^2}]$	0.5
Density ratio	β	-	1
Dimensionless shear modulus	Ae	-	3.5 $\times 10^4$
Average inlet velocity	U_m	$[\frac{m}{s}]$	0.2
Reynolds number	Re	-	20

All simulations have been performed with a fully implicit monolithic ALE-FEM method with a fully coupled multigrid solver as described in the previous chapter. For the validation of the employed fluid and solid solvers, we performed computations for different levels of spatial discretization (see Table 2).

The FSI test has been performed for an inflow speed resulting in a steady state solution. The parameter values of the test are given in the Table 1. This configuration of the benchmark has been named FSI1 by the authors who proposed it.

Table 2: Results for FSI1.

# of Levels	nel	ndof	$d_1(A)[\times 10^{-3}]$	$d_2(A)[\times 10^{-3}]$	drag	lift
1	792	15,640	0.02277155	0.81681181	14.29122	0.77623
2	3,168	61,376	0.02274210	0.81849791	14.28967	0.77512
3	12,672	243,136	0.02271325	0.81848982	14.28475	0.77456
4	50,688	967,808	0.02269713	0.81855286	14.28432	0.77424
ref.			0.0227	0.818	14.284	0.774

3.2 Steady-state vertical beam test

The second test example is based on a 2D classical benchmark proposed by COMSOL Multiphysics and consists of a narrow vertical structure attached to the bottom wall of a horizontal channel which bends under the force due to viscous drag and fluid pressure. As in the previous benchmark the fluid and solid are both incompressible.

The model geometry consists of a horizontal flow channel in the middle of which an obstacle, a narrow vertical structure, is placed. The fluid flows from left to right, except where the obstacle forces it to flow into a narrow path in the upper part of the channel, and it exerts a force onto the structure wall resulting from the viscous drag and fluid pressure. The deformable structure bends under the applied force thus modifying the path followed by the fluid flow. The parameters which define the geometry are shown in Figure 4:

- the channel dimensions are: length $L = 300\mu m$, height $H = 100\mu m$;
- the elastic vertical structure has length $l = 35\mu m$ and height $h = 5.5\mu m$; the left side is positioned at $d = 100\mu m$ away from the channel's left boundary and the bottom end is fully attached to the bottom wall of the channel; the top end of the beam is semicircular which radius is $r = 5\mu m$;
- the control point is A, attached to the top of the vertical narrow structure, with undeformed coordinates $A_0 = (105\mu m, 55\mu m)$.

As for the previous benchmark, the thickness and the length of the vertical structure are chosen in order to get a significant excursion of the beam without introducing additional numerical complications connected with high aspect ratios in the geometry.

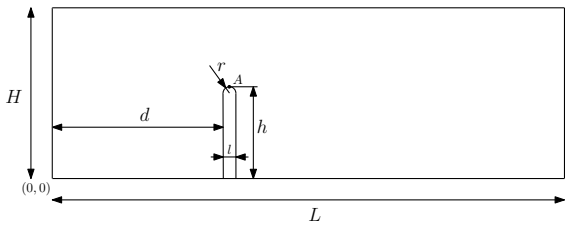


Figure 4: Computational domain.

The fluid flow in the channel is described by the incompressible Navier-Stokes equations for the velocity field $\mathbf{v}$ and the pressure p in the ALE (deformed) moving coordinate system. We assume that no gravitation or other volume forces affect the fluid motion. An incompressible water-like substance with a density $\rho^f = 1000Kg/m^3$ and dynamic viscosity $\mu^f = 0.001Pa \cdot s$ has been used as a fluid.

The structural deformations are solved by using a neo-Hookean hyperelastic material model and a nonlinear geometry formulation to allow large deformations. The structure consists of a narrow vertical flexible material with a density of $\rho^s = 7850Kg/m^3$, Young's modulus $E = 200kPa$ and Poisson coefficient $\nu^s = 0.50$.

At the channel entrance on the left, the flow has fully developed laminar with a parabolic velocity profile. At the outflow (right boundary), a do-nothing boundary condition is prescribed. On the solid (non-deforming) walls, no-slip conditions are imposed, $\mathbf{v} = \mathbf{0}$, while on the deforming interface the continuity of the velocity between fluid and solid is prescribed.

The obstacle is fixed to the bottom of the fluid channel. All other beam boundaries experience a load from the fluid, given by

$$\boldsymbol{\sigma}^s_{|\gamma_i} = (-p^f \mathbf{I} + \mu^f(\nabla \mathbf{v} + (\nabla \mathbf{v})^T)) \cdot \mathbf{n}\,,$$

where $\mathbf{n}$ is the normal vector to the boundary. This load represents the sum of pressure and viscous drag forces.

In this FSI benchmark we are interested in the computation of the displacement of a beam subject to a bending force in order to highlight the potentiality of the multigrid algorithm that has been presented in the previous chapter. The results of the benchmark computations are collected in Table 3. We report the number of refinement, the number of elements, the number of DOFs, the x and y displacements and the drag and lift forces.

The reference values are compared with the results obtained by solving the model using COMSOL Multiphysics.

Table 3: Results for COMSOL benchmark.

# of Levels	nel	ndof	$d_1(\mathbf{A})$	$d_2(\mathbf{A})$	drag	lift
2	1,088	21,188	$1.080789e^{-05}$	$-1.357274e^{-06}$	0.0094275	-0.395467
3	4,352	83,716	$1.081792e^{-05}$	$-1.359843e^{-06}$	0.0083106	-0.384255
4	17,408	332,804	$1.082601e^{-05}$	$-1.361546e^{-06}$	0.0050521	-0.384331
ref.			$1.0826e^{-05}$	$-1.361e^{-06}$	0.005	-0.384

4 CONCLUSIONS

In this work we presented a monolithic Newton-multigrid solver with domain decomposition smoothing for the solution of stationary incompressible FSI problems. This class of problems presents several challenging features due to the nonlinearity of the operators, the ill-conditioning of the matrices for steady-state cases and the enforcement of the incompressibility constraint. The Jacobian matrix in the Newton linearization of the FSI operator has been computed exactly by means of automatic differentiation tools. The numerical results are in agreement with benchmark solutions. Robust computations of FSI steady-state solutions can be performed with the proposed multigrid algorithm. No pseudo-time stepping needs to be introduced, which brings to a drastic reduction in computational time.

REFERENCES

[1] E. Aulisa, S. Manservisi, and P. Seshaiyer. A computational multilevel approach for solving two-dimensional Navier–Stokes equations over non-matching grids. *Computer methods in applied mechanics and engineering*, 195(33):4604–4616, 2006.

[2] E. Aulisa, S. Manservisi, and P. Seshaiyer. A multilevel domain decomposition approach to solving coupled applications in computational fluid dynamics. *Int. J. Numer. Meth. Fluids*, 56(8):1139–1145, 2008.

[3] Klaus-Jürgen Bathe and Gustavo A Ledezma. Benchmark problems for incompressible fluid flows with structural interactions. *Computers & structures*, 85(11):628–644, 2007.

[4] S. Bnà. *Multilevel Domain Decomposition Algorithms for Monolithic Fluid-Structure Interaction Problems with Application to Haemodynamics*. PhD thesis, Alma Mater Studiorum Università di Bologna, 2014.

[5] S. Bnà, E. Aulisa, and S. Manservisi. A Multilevel Domain Decomposition Solver for Monolithic Fluid-Structure Interaction Problems. In *11th International Conference of Numerical Analysis and Applied Mathematics 2013: ICNAAM 2013*, volume 1558, pages 871–874. AIP, 2013.

[6] M.Á. Fernández and M. Moubachir. A Newton method using exact Jacobians for solving fluid-structure coupling. *Computers and Structures*, 83:127–142, 2005.

[7] Miguel Ángel Fernández and Marwan Moubachir. A newton method using exact jacobians for solving fluid–structure coupling. *Computers & Structures*, 83(2):127–142, 2005.

[8] MW Gee, U Küttler, and WA Wall. Truly monolithic algebraic multigrid for fluid–structure interaction. *International Journal for Numerical Methods in Engineering*, 85(8):987–1016, 2011.

[9] M. Heil. An Efficient Solver to the Fully Coupled Solution of Large-Displacement Fluid-Structure Interaction Problems. *Comput. Meth. Appl. Mech. Eng.*, 193:1–23, 2004.

[10] Robin J Hogan. Adept fast automatic differentiation library for c++: User guide.

[11] J. Hron and S. Turek. A monolithic fem/multigrid solver for ale formulation of fluid structure interaction with application in biomechanics. In H.-J. Bungartz and M. Schäfer, editors, *Fluid-Structure Interaction: Modeling, Simulation, Optimization*, volume 53 of *Lecture Notes in Computational Science and Engineering*, pages 146–170. Springer, 2006.

[12] Jaroslav Hron and Stefan Turek. *A monolithic FEM/multigrid solver for an ALE formulation of fluid-structure interaction with applications in biomechanics*. Springer, 2006.

[13] S. Manservisi. Numerical analysis of vanka-type solvers for steady Stokes and Navier–Stokes flows. *SIAM J. Numer. Anal.*, 44(5):2025–2056, September 2006.

[14] M Razzaq, H Damanik, J Hron, A Ouazzi, and S Turek. Fem multigrid techniques for fluid–structure interaction with application to hemodynamics. *Applied Numerical Mathematics*, 62(9):1156–1170, 2012.

[15] PA Sackinger, PR Schunk, and RR Rao. A newton–raphson pseudo-solid domain mapping technique for free and moving boundary problems: a finite element implementation. *Journal of Computational Physics*, 125(1):83–103, 1996.

[16] Michael Schäfer, Marcus Heck, and Saim Yigit. An implicit partitioned method for the numerical simulation of fluid-structure interaction. In *Fluid-structure interaction*, pages 171–194. Springer, 2006.

[17] K Stein, T Tezduyar, and R Benney. Mesh moving techniques for fluid-structure interactions with large displacements. *Journal of Applied Mechanics*, 70(1):58–63, 2003.

[18] DC Sternel, M Schäfer, M Heck, and S Yigit. Efficiency and accuracy of fluid-structure interaction simulations using an implicit partitioned approach. *Computational mechanics*, 43(1):103–113, 2008.

[19] S. Turek. *Efficient solvers for incompressible flow problems: an algorithmic and computational approach*, volume 6. Springer, 1999.

[20] S. Turek and J. Hron. Proposal for numerical benchmarking of fluid-structure interaction between an elastic object and laminar incompressible flow. In H.-J. Bungartz and M. Schäfer, editors, *Fluid-Structure Interaction: Modeling, Simulation, Optimization*, volume 53 of *Lecture Notes in Computational Science and Engineering*, pages 371–385. Springer, 2006.

[21] S. Turek and M. Schäfer. Benchmark computations of laminar flow around a cylinder. In E. H. Hirschel, editor, *Flow Simulation with High-Performance Computers II*, volume 52 of *Notes on Numerical Fluid Mechanics*, pages 547–566. Vieweg, 1996.

[22] Stefan Turek, J Hron, M Madlik, M Razzaq, H Wobker, and JF Acker. *Numerical simulation and benchmarking of a monolithic multigrid solver for fluid-structure interaction problems with application to hemodynamics*. Springer, 2010.

[23] Stefan Turek and Jaroslav Hron. *Proposal for numerical benchmarking of fluid-structure interaction between an elastic object and laminar incompressible flow*. Springer, 2006.

[24] S P Vanka. Block-implicit multigrid calculation of two-dimensional recirculating flows. *Comput. Methods Appl. Mech. Eng.*, 59(1):29–48, November 1986.

[25] Hilmar Wobker and Stefan Turek. Numerical studies of vanka-type smoothers in computational solid mechanics. *Advances in Applied Mathematics and Mechanics*, 1(1):29–55, 2009.

[26] Yuqi Wu and Xiao-Chuan Cai. A parallel monolithic domain decomposition method for blood flow simulations in 3d. In *Domain Decomposition Methods in Science and Engineering XX*, pages 671–678. Springer, 2013.

COMPDYN 2015
5th ECCOMAS Thematic Conference on
Computational Methods in Structural Dynamics and Earthquake Engineering
M. Papadrakakis, V. Papadopoulos, V. Plevris (eds.)
Crete Island, Greece, 25–27 May 2015

OPTIMAL DESIGN FOR HIGH RESISTANT ROCKFALL BARRIERS

J.P. Escallón[1], P. Bartelt[2], and E. Chatzi[2]

[1]WSL Institute for Snow and Avalanche Research SLF and ETH Swiss Federal Institute of Technology Zurich
Flueelastrasse 11 CH-7260 Davos Dorf
e-mail: juan.escallon@slf.ch

[2] WSL Institute for Snow and Avalanche Research SLF and ETH Swiss Federal Institute of Technology Zurich
Flueelastrasse 11 CH-7260 Davos Dorf, Wolfgang-Pauli-Str. 15 CH-8093 Zürich
e-mail: {bartelt@slf.ch, chatzi@ibk.baug.ethz.ch}

Keywords: Rockfall, General Contact, Impact, Contact Interactions, Optimization.

Abstract. *Rockfall barriers are key protection systems in mountainous regions worldwide. They are composed of a netting intercepting structure connected to steel posts by means of wire-rope cables anchored to the ground. Additional energy dissipating devices can be attached to the cables. Rockfall barriers are designed to intercept and capture falling rocks with kinetic energies from 100 to about 10000 kJ. They dissipate rock kinetic impact energies by friction and plasticity. The accurate prediction of the dissipation rate, forces transmitted to the anchors and wire-net deformations depends on the approximation of contact interactions among the different structural components of the system. To treat the complex contact interactions occurring in a rockfall barrier in an efficient and accurate manner a computational scheme relying on a general contact algorithm has been developed in previous work. An issue that arises pertains to the tensile and bending coupling taking place at the connections of the chain-link netting. We considered tensile quasi-static laboratory tests to derive FE models that adequately describe such a behavior. In order to deliver a more resistant connection design, a local enhancement is proposed herein. The modified setup is optimally configured via a numerical optimization procedure and its benefits against the standard design are illustrated by means of numerical simulations. The developed modeling tools prove to comprise a versatile platform for enhancing existing designs of rockfall barriers, thereby extending the efficacy and performance of industrial solutions.*

1 INTRODUCTION

When a block or group of blocks detach from a rock face, they propagate rapidly downslope, endangering settlements and roadways. Rockfall is common problem in mountain regions worldwide, resulting in casualties and damage to infrastructure [1, 2]. Rockfall events are mitigated using either passive or active measures. Concrete shelters, rockfall dams, drapery/netting, and flexible wire-net barriers are common passive protection measures against rockfalls. These systems do not prevent the rockfall phenomenon but attempt to control the outcome. The purpose of passive measures is to dissipate the kinetic energy of rock impact by controlled plasticity and friction.

Today, the use of flexible protection systems is one of the most common rockfall protection measures [3]. These systems deform significantly to dissipate the impact kinetic energy of falling rocks. The forces transmitted to the ground are significantly smaller in comparison to rigid systems such as concrete shelters. Intercepting netting is responsible for slowing down the dissipation process. High-performance wire-netting is therefore engineered to have a non-linear response [4].

Product development in the sector of rockfall flexible systems has been carried out using a classical engineering approach. This approach is based on intuition, experience of the design engineer and extensive number of large scale experiments. As a result, product development in this sector is slow and expensive [4]. The aim of this paper is to show how an accurate FE simulation scheme in conjunction with optimization techniques can be used to develop new designs in a cost-effective manner.

Explicit Finite Element (FE) calculation schemes have been developed to simulate rockfall barriers in multi-purpose commercial codes like LS-DYNA and Abaqus [5, 6, 7, 8, 9, 10]. Initial FE simulations supported in Abaqus/Explicit [11] made use of a Contact Pairs (CP) algorithm [5]. This algorithm was able to only consider the interaction between slave nodes belonging to the wire-net truss elements and the impactor modelled as a rigid body. This approach neglected bending deformations in all structural components. Furthermore, it allowed only small relative motions of the support cables at the connections with the steel posts.

Parametric studies on similar rockfall FE models were carried out to assess several prototype modifications [6, 9]. The computational scheme was therefore developed to obtain results in a short time. This scheme neglects bending deformations and contact interactions between wire-net components. The authors approximated the real ring-net geometry by simpler geometries neglecting contact. Moreover, the sliding of the cables through the posts was roughly approximated by means of special connector elements. With these schemes GC algorithms were used under their capabilities in order to limit the computational effort. The model simplifications cause the barrier model to behave more rigidly in comparison to the real barrier. Therefore, numerically evaluated cable forces were higher and the time to achieve the impactor kinetic energy dissipation was smaller in comparison to experimentally measured values [6, 9]. Furthermore, the use of an "equivalent" numerical panel with different geometry caused the netting deformation pattern to differ from the real net. Recent FE methodologies representing contact in a more accurate manner have been implemented in LS-DYNA to model wire-nets subjected to impact [8] or rockfall barriers [10]. A FE model of a rockfall barrier with wire-rope cables and braces as part of the interception structure was implemented in LS-DYNA [10]. In this approach, a one-side contact algorithm [12] is used to treat the interactions of the impactor with the wire-netting and wire-rope cables. This algorithm only requires the definitions of the slave surface. To enforce contact properly, the slave surface needs to have a relatively fine mesh.

Moreover, the stiffer body needs to play the role of the master. Additionally, a single surface algorithm [12] was used to treat additional interactions in a rockfall barrier. This algorithm considers contact inside a slave surface list. Edge-to-edge and beam contact were considered with this approach. This model takes into account contact between rope elements of the net. The posts and impactor are modelled with solid elements. However, this modelling scheme leaded to significant unresolved penetrations. A detailed FE model of a ring-net attached to support cables that were connected to a rigid frame was accomplished [8]. In this case the impactor was a concrete spherical ball. The simulation results showed a very good match of the deformation pattern and overall stiffness.

Discrete Element (DE) calculation schemes have been developed in special-purpose codes [13, 14, 15, 16]. A pure master-slave contact algorithm was developed to treat contact between ring-net element nodes and the impact block treated as a lumped mass [14]. This algorithm was implemented in the simulation code FARO. In this code, contact is only treated for the block-net pair, which is a severe restriction. A special cable model was developed in FARO to simulate the sliding between cables and posts and wire-net and cables. The netting nodes are part of the cable macro-element. This special element allows these nodes to slide on the cable, thus creating a curtain effect [14]. In this approach, the wire ring-net is modelled as a collection of slave nodes forming a close representation of the real geometry. The nodes are then attached to each other by either purely translational springs [14] or by a combination of rotational and translational springs [13]. Chain-link elements are modelled in FARO as macro-elements in contact at the connection nodes. The tensile forces transmitted from one element to the neighbour at the connections depend on the so-called opening angle [15]. This is an approximate method to consider the influence of the bending deformations of the connections on the tensile response. The shape effects of the impact block are neglected with the contact algorithm of the FARO code. The parameters of the macro-elements and springs are calibrated using quasi-static tensile tests. Only a few parameters are needed for the calibration. However, the calibration process was still time consuming because optimization algorithms were not coupled with the model. Additional DE modelling attempts to determine the mechanical properties of wire-nets modelled with equivalent homogeneous membranes have been performed [16]. DE models have been developed to calculate double-twisted hexagonal wire-nets and to simulate rockfall kinetic energy attenuation with drapery systems. The model considers contact nodes and two types of interactions among them. The model provided good estimates for impact velocity and run-out distance [17].

This paper presents the state-of-art of a novel FE modelling scheme to simulate rockfall barriers which relies on the GC algorithm programmed in the multi-purpose code Abaqus [11]. The GC algorithm in Abaqus is two-sided, and therefore, the user does not need to define pure slave and master bodies for contact interactions, thus facilitating model generation [4]. This GC algorithm uses the penalty constraint method for explicit calculations. This method allows slight penetrations of one surface into another surface. A "spring" stiffness is applied automatically to the surfaces to resist these penetrations [11]. The "spring" stiffness is, in general, determined from stable time increment considerations and masses of the nodes involved in contact [4]. This new computational scheme was developed in order to treat the complex contact interactions occurring in a rockfall barrier in an efficient and accurate manner. The frictional contact behaviour is considered using a Coulomb-type model. The basic idea behind this scheme is to model the contact interactions between structural components as close as possible to those of real systems. Ring-net and loose chain-link rockfall systems have been already modelled with this approach [4, 18, 19, 20, 21].

Another challenge in rockfall barrier numerical modelling is, calibrating the parameters of the wire-net models. An extensive database of quasi-static tests performed on ring and chain-link nets have been collected on the course of several research projects [4, 13, 14, 15, 22]. Therefore, when a numerical model is elaborated, an inverse process needs to be performed to obtain the model parameters. This process have been carried out in the past on the basis of tedious and subjective back-calculations, which are only feasible when few parameters need to be calibrated. However, when the number of parameters constitutes an n-dimensional space as it is the case for the ring and chain-link-net models developed with this novel approach [4], the use of optimization methods becomes necessary. Mastering the use of optimization algorithms is also helpful to optimize new wire-net design as it will be shown in section 3.1.

2 STANDARD CONFIGURATION

This section presents the standard design of a chain-link net with loose connections. Moreover, it presents the standard design of a rockfall barrier where this netting typology is used. These designs have been developed by the technical department of Geobrugg AG. The features of the standard wire-netting design are presented, as well as the configuration of the prototyped rockfall barrier structure. Some aspects of the numerical models are presented. However, more complete details of the state-of-art of the simulation approach that is used are provided in [15, 18, 19, 20, 21]. In particular, a highly detailed explanation of the FE model of the chain-link netting is provided in [21], as well as details on the mode ling of the prototyped rockfall barrier structure.

2.1 Standard Chain-link net

In this particular investigation a chain-link net consisting of a three wire twisted spiral bundle was investigated [21] (Fig. 1). Each wire has a 2 mm radius (r_{wire}). The geometric dimensions of the rhomboidal mesh elements are given in Tab. 1.

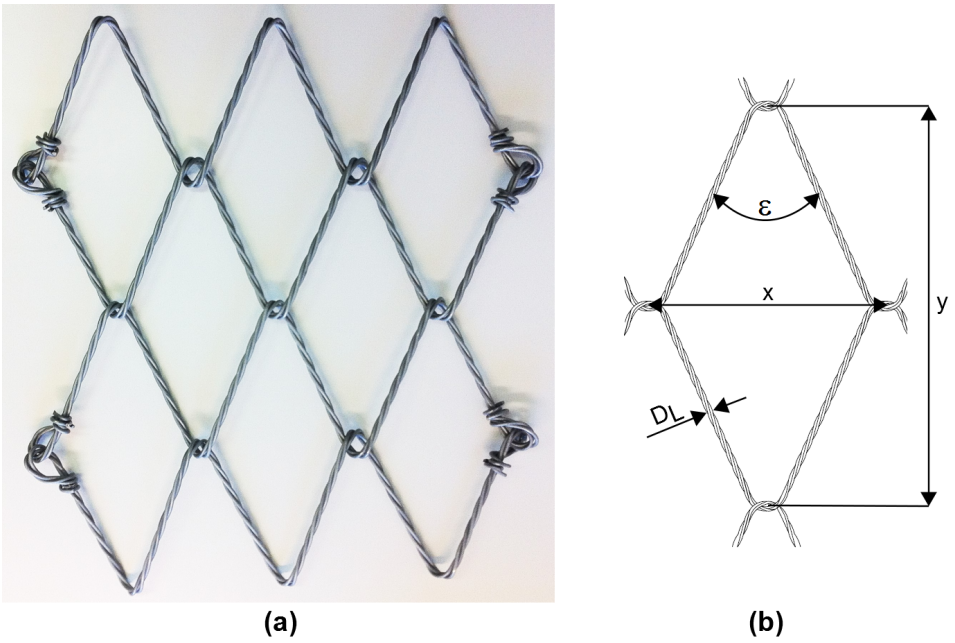


Figure 1: Triple twisted wire chain-link net components and mesh dimensions [21]

wire net producer	Geobrugg
x [mm]	180 (+/-5 %)
y [mm]	300 (+/-5 %)
mesh width D_L [mm]	8.6
mesh angle ε [degrees]	47

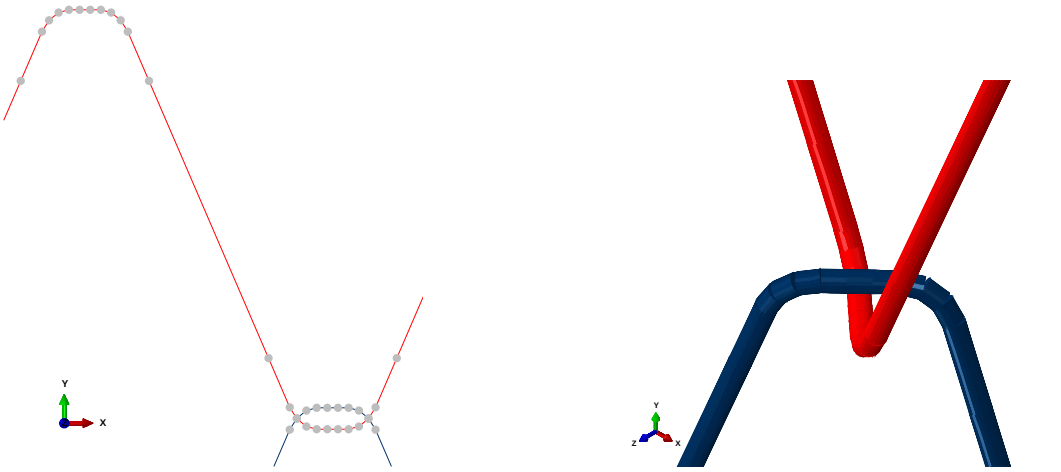
Table 1: Summary of the mesh characteristics and dimensions as indicated in Fig. 1 [21]

A FE model of the triple twisted wire chain-link net with loose connections was developed using the commercially available Finite Element code Abaqus/Explicit 6.14 [21]. An equivalent circular wire cross-section is obtained, which is equal to the sum of the areas of the three wires multiplied by a factor χ. This factor takes into account the fact that the cross-sectional area of the single wires is not perpendicular to the axial load, as it is the case for the simplified area [21]. Furthermore, the bending stiffness is overestimated if the area is not reduced. This approach has been applied and verified for ring net systems [18, 20]. The equivalent wire is modelled with linear elasticity, strain-hardening metal plasticity (Von Mises) and ductile damage. The numerical approach relies on the general contact algorithm of Abaqus/Explicit. The penalty method is used to approximate hard contact. Additionally, Coulomb type sliding friction is included in the contact model.

The input geometry of the chain-link elements and their connectivity is modelled according to the geometrical measurements of the real netting (Figs. 2a-b). A finer mesh is needed in the connections between chain-link elements to reproduce the axial, shear and bending behaviour obtained by the analytical chain-link model discussed in [15, 21]. Three elements in the middle of the connection are required to capture the shear transition while the remaining six elements (three to each side of the centre elements) are needed to capture the bending deformations of the connection, see Fig. 2a. These six elements were also necessary to obtain an accurate pattern of the sliding between chain-link elements. Four elements (two to each side of the centre elements) cannot correctly approximate the curved geometry of the contact zone, causing unrealistic sliding patterns between chain-link elements. Furthermore, a finer mesh having more than 9 elements per connection do not change the results significantly. Therefore, the optimal number of elements converges to 9 per connection.

The knotted connections between the ends of the chain-link elements are simplified. The connections between the border knots of the chain-link net elements are placed at the same coordinate (Fig. 2.1a). Therefore, to avoid initial over-closures [11], contact between chain-link elements is excluded in the region of the knots. Actions are transmitted from one "zig-zag" element to its neighbour at the knots by means of the so-called connector elements available in Abaqus [11]. Cartesian and Revolute connections are used to model the border "zig-zag" chain-link element connections or knots (Fig. 2.1b). The Cartesian component provides a connection between the vertices of adjacent "zig-zag" chain-link elements that allows independent behaviour in three local Cartesian directions that follow the system at the vertex a (Fig. 2.1c). Rigid behaviour is specified in the local 3-direction (z-local), while node b is allowed to change position along 1- and 2-directions (x- and y-local). The relative positions of node b with respect to node a in the local 1- and 2-directions is fixed in a working range by means of the stop option available in Abaqus/Explicit [11]. A close observation of a physical net panel reveals that the available gap for translational movement in the knotted connections is not constant. Such irregularities influence the macroscopic behaviour of the net. It is necessary to take them into account to better reproduce the soft response (stage 1) of the net panel to tensile loading (Fig. 7. In this work, the connector stop in the 1-direction is assumed to be a random number

between 5 mm and 6 mm (with a seed of 0.1 mm). A possible random variation of the gap in the 2-direction has a negligible effect on the net panel response and therefore is assumed to remain constant and equal to 6 mm. The Revolute connection type (Fig. 2.1d) is used to constrain the rotations around the 2- and 3-directions, while the 1-direction rotational component is free.



(a) element nodes

(b) connection three-dimensionality with rendered beam profiles

Figure 2: Modelling of inner connections [21].

To solve the inverse problem of finding the model parameters, a series of quasi-static tensile tests performed in the Geobrugg testing facility in Romanshorn (SG), Switzerland were considered. The tests were used to help quantify (1) the friction between the mesh elements, (2) the onset of material damage [21] and (3) the change in load eccentricity during deformation. For the quasi-static tensile tests, a rectangular net panel of 1100 x 900 mm is connected at three sides via shackles to a fixed frame (in blue Figs. 4). The upper side is connected via shackles to a moving frame (in red Figs. 4). The fixed frame is composed of steel beams which are attached to each other via bolts. The moving frame is composed of two steel plates which are attached by pins and screws. Steel sliding connections are inserted in between the frame beams and pulling machine plates. Two wire-rope cables are attached to the moving frame, which pull at a constant velocity. Prior to the test, the net is slightly pre-tensioned to avoid any possible sag. Fig. 4a shows the initial configuration of the net panel. After applying the pretension, the cables pull the moving frame at a constant velocity of 100 mm/min. The chain-link net strain rate is approximately $0.002/s$, which can be considered as quasi-static. The test machine displacement and force response of the moving frame are automatically recorded. A high-speed camera was placed above the net panel to capture the net deformation in time. Two tests were performed. Both tests lasted approximately 115 s; damage takes place only within the last 0.5 s. The pulling force reaches a peak and then drops as a consequence of damage (Fig. 4b).

To accurately model this test, true contact conditions were considered to ensure that the chain-link parameters were not influenced by significant contact simplifications. Under this approximation, the rigid and moving frames, as well as the sliders were omitted, similar to approach used in the first modelling attempts. However, in the new model, the steel pins connecting the net to the sliders were included as well as the shackles. The presence of the sliders was taken into account by constraining the movement in the z-direction of all the shackles in contact with the sliders. Furthermore, the movement in the z-direction of some beam elements

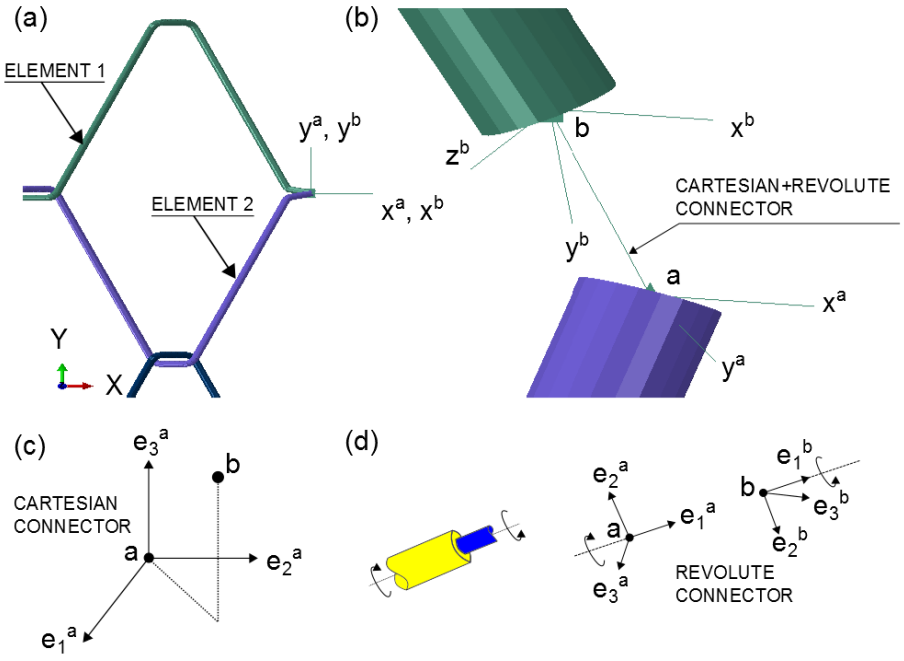


Figure 3: Modelling of the knotted connections: (a) connection type CARTESIAN, (b) connection type REVOLUTE, (c) knotted connection at the initial configuration, and (d) deformed configuration of the knot [21].

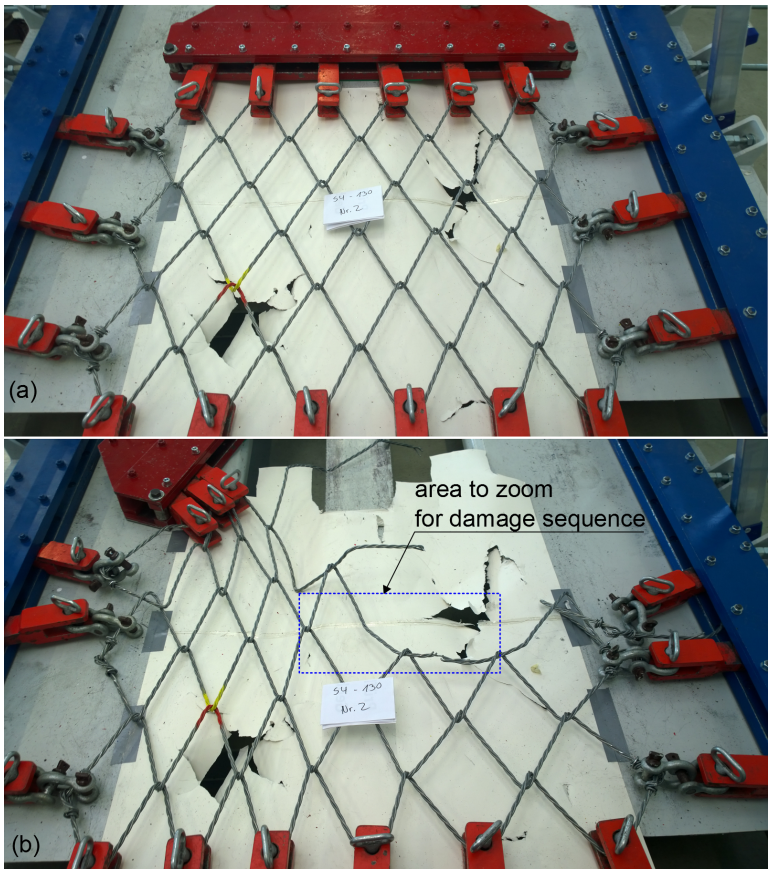
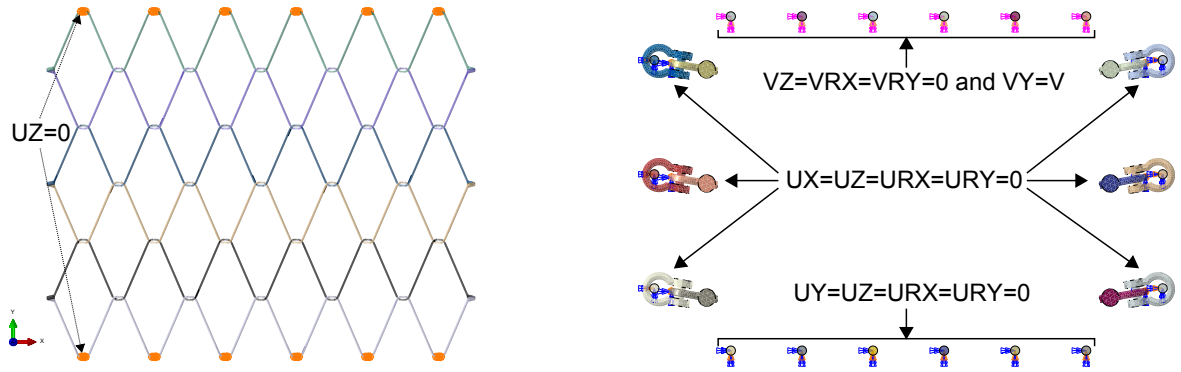


Figure 4: Tensile quasi-static test set-up [21].

was also constrained to simulate the presence of the sliders. The pins attached to the moving frame were pulled quasi-statically. Figs. 5 show the boundary conditions applied in the model. Fig. 5a shows the zones in the chain-link net were the boundary condition $UZ = 0$ was applied to take into account the movement restriction caused by the sliders. Fig. 5b shows the shackles where boundary conditions were applied, and the constrained degrees of freedom in the pins.



(a) applied to the net (b) applied to pins and shackles

Figure 5: Model boundary conditions [21].

The numerical simulation of the tensile test was carried out using an explicit time integration scheme. The calculation time was decreased by artificially increasing the density of the net using the mass-scaling approach [23, 24, 25]. Criteria to verify the quasi-static nature of the simulation was checked [20]. All shackles and pins were modelled as solid three dimensional rigid bodies, because they are one order of magnitude stiffer than the chain-link net. The rigid bodies were still discretized by means of finite elements, in order to have contact facets for the contact calculations.

The measured non-linear force-displacement response curves exhibit a progressive stiffening (Fig. 7) up to 100-120 mm deformation (stage 1) at which point the stiffness is approximately constant until failure (stage 2). The behaviour observed in stage 1 and 2 is a consequence of the different interaction steps between bending and axial behaviour at the connection. The details of this axial-bending interaction are provided in [15, 21]. In [21] it is shown that it is important to consider friction at the contact between chain-link elements.

To determine the best-fit parameters for the chain-link net model, a FEM based optimization scheme was implemented. The software Isight 5.9 [26] is used for this analysis due to its compatibility to the Abaqus software. The parameters to optimize in the bi-dimensional model were set as: (1) the yield curve described by two points (0, σ_y) and (ε_u^p, σ_u), (2) the Young Modulus, (3) the area reduction factor χ, and (4) the damage parameters $\bar{\varepsilon}_0^p$ (plastic strain at the onset of damage), and G_f (fracture energy per unit area). To increase the efficiency of the optimization of the model, a two stage optimization process was performed. In the first stage, damage was excluded, and to enhance the stability of the model, the ultimate plastic strain ε_u^p was assumed to be significantly large (1.5). Damage could be excluded from the first stage of the optimization since it is observed to occur at the last 0.5 sec of the 115 sec long test. The chosen objective function in this case consists in the difference between the numerical and experimental maximum force, which can be expressed as:

$$Objective\ Function = \mid F_{max,exp} - F_{max,mod} \mid \tag{1}$$

where $F_{max,exp}$ is the maximum experimental force, while $F_{max,mod}$ is the maximum force of a model optimization run. The parameters to be optimized are: (1) the equivalent wire cross-section radius $r_{section}$, (2) the elastic modulus E, (3) the yield and ultimate stresses (σ_y, σ_u). The corresponding χ factor of the chain-link net is obtained as:

$$\chi = (r_{section}/r_{wire})^2/3 \tag{2}$$

In this case the optimization surface is a smooth function. The applied scheme allowed us to use a Downhill Simplex Technique (DST), which had a fast convergence to the optimal solution [21]. For more details on the general workings of a DST one can refer to previous work by [27, 28], as well as fundamental literature on this topic [29]. Further details about the parameter optimization process are provided in [21]. Tab. 2 illustrates the optimization parameters for the chain-link net along with their lower and upper search space bounds. These bounds were defined after performing two Design of Experiments (DoEs) using the Latin Hypercube Sampling technique [30]. Finally, the optimization process is formulated as the problem of minimizing the specified objective function. Fig. 6 depicts the radial basis approximation of the objective function vs. the yield stress σ_y and the equivalent wire cross-section radius $r_{section}$. The optimization function surface is smooth and exhibits several local maxima and a region where the global minimum value is found. The simulation results of the model with the best fit parameters, served to select the plastic strain at the onset of damage $\overline{\varepsilon}_0^p$. The value of G_f allowing damage to occur at the end of the experiment was then optimized in the second stage of the optimization cycle [21]. Fig. 7 displays the results from one of the quasi-static tests and of its numerical simulation with the developed finite element model [21].

Parameter	Lower	Upper
σ_y [MPa]	1500	1700
σ_u [MPa]	2800	3000
E [MPa]	100000	110000
$r_{section}$ [mm]	2.4	2.5

Table 2: Chain-link optimization parameters (constitutive)

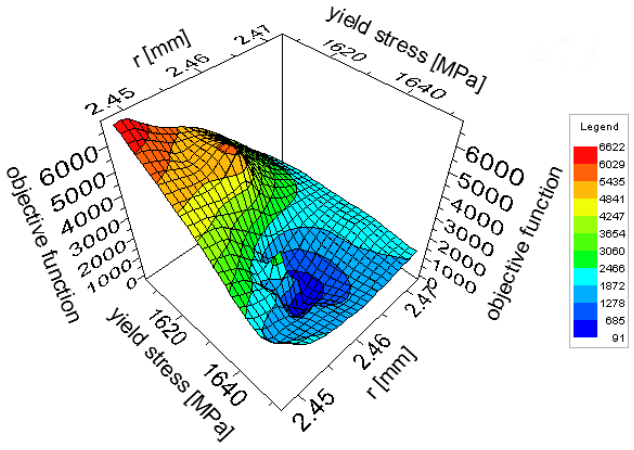


Figure 6: Radial basis function surface approximation of the objective function vs. yield stress and equivalent wire cross-section radius [21].

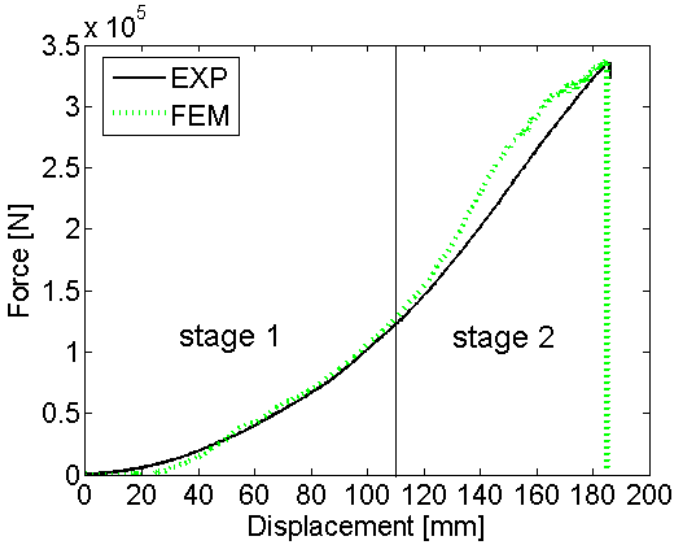


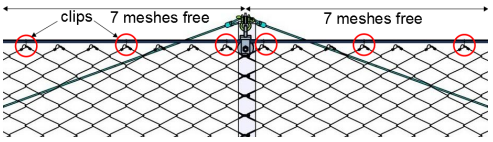
Figure 7: Force vs. displacement curve (experimental and FE simulation with optimal parameters).

2.2 Standard net-to-cables connections

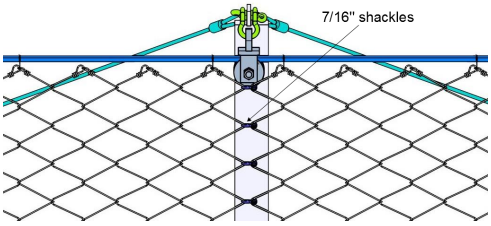
The netting of a rockfall barrier able to dissipate a MEL (Maximum Energy Level) rock impact of 2000 kJ consists of loose chain-links of the typology described in the previous section. This barrier obtained the European Technical Approval according to the ETAG027 [31] guideline in 2010.

Field scale tests were performed to develop the final system. This tests revealed that when all meshes of the netting are in contact with the support cables, local failures in the chain-links take place around the posts. Therefore, through the tests an optimal solution was sought in order to avoid large stress concentrations in the netting. The final solution was to interrupt the contact between the chain-link meshes near the posts and the support cables. This is accomplished by not threading the support cables through seven meshes on each side of the inner posts and on one side of each border post (Fig. 8a). Three of the "free" meshes located on the top and bottom of the net are attached to the support cables by means of round clips (Fig. 8a-c). The round clips are made of galvanized steel wire with a diameter of 3 mm and a tensile strength of $1770 N/mm^2$. Their maximum braking force is 13760 N. The clips have negligible structural importance. All clips will fail in the case of an impact with the SEL (Serviceability Energy Level), which is approximately 700 kJ. Cable-to-net openings are created as these round clips fail progressively. The openings grow until all clips have failed. These gaps alleviate the stresses on the retaining cables and on the chain-link elements in the vicinity of the posts [21].

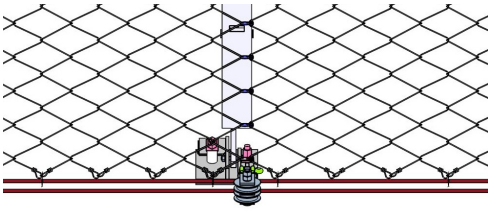
Full scale test data [32] was used to verify the FE model developed to simulate this barrier [21]. This rockfall fence has been modelled by using a novel computational scheme relying on a general contact algorithm [11, 21]. The hard contact behaviour is approximated by using a penalty method to enforce the contact constraint. The frictional behaviour at contact is modelled using a Coulomb-type friction [21]. Further details about the FE model of this rockfall barrier are provided in [21]. Additional features of the numerical modelling approach that has been developed to model rockfall barriers with high accuracy can be seen in [4, 19, 18, 20, 21]. The details pertaining to the test used to verify the FE model of the rockfall barrier are provided in [21]. Fig. 9 depicts the positions of the load cell as well as the anchor and energy dissipating devices in the rockfall barrier. The lateral cables (in yellow) are attached to separate anchors.



(a) free meshes rule



(b) connection between net panel and between net and cables (top) according to the installation kit manual



(c) connection between net panel and between net and cables (bottom) according to the installation kit manual

Figure 8: Connection of chain-link net to cables [21].

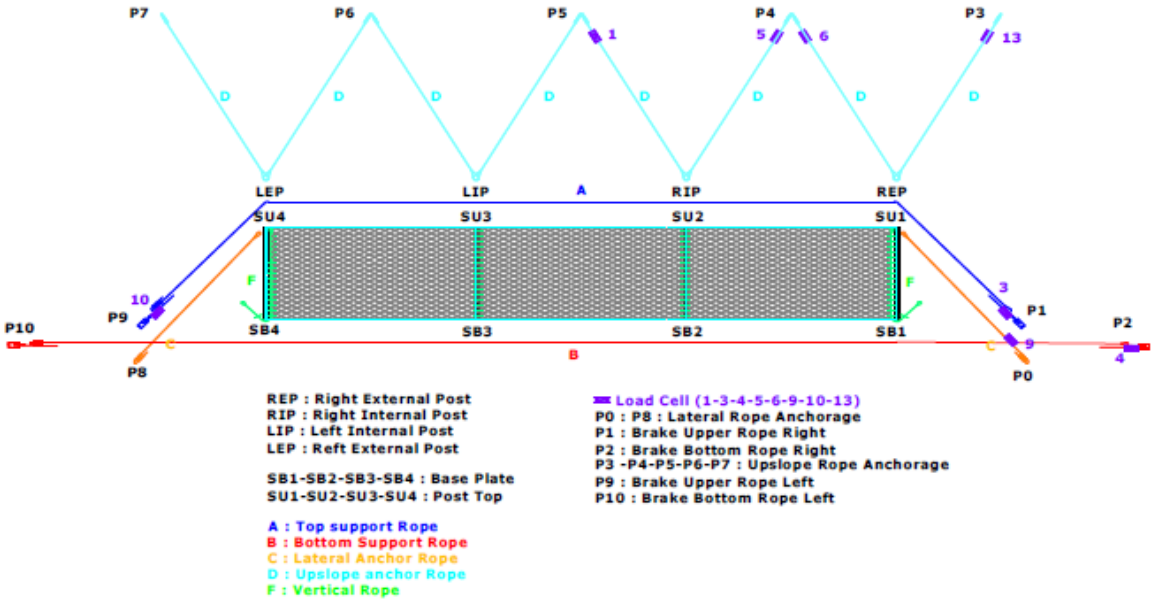


Figure 9: Load cell positions [21, 32].

Fig. 10 compares the experimental measurements (first column) and numerical simulation (second column) of the barrier during the MEL test. The third column depicts the z-location of the concrete block in the simulation. The experimental and numerical results are shown at approximately the same scale. The maximum net elongation during the MEL test (evaluated according to the ETAG No. 027) was 8960 mm, while the calculated deformation is 9013 mm. The sampling frequency of both the experimental and numerical force history data is 1/0.5 ms (2 kHz). The force histories at the load cells (MEL test) are shown in Fig. 11. The experimental force histories (dark) [32] are compared to the FEM force histories (light). Details regarding the simulation steps are provided in [21].

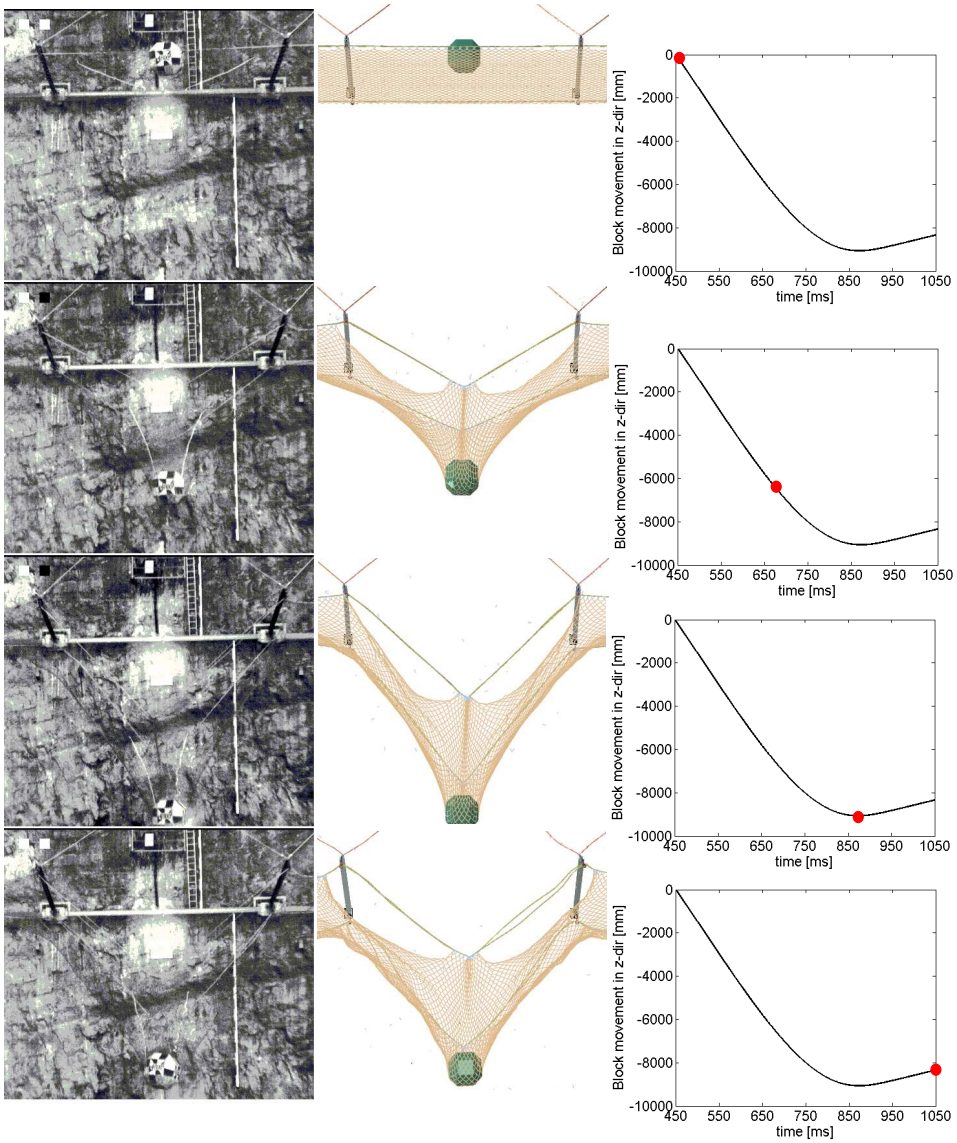


Figure 10: Experimental video frames (first column), simulation video frames (second column), and block movement evolution (third column): (a) t_1 = 0.0 ms (b) t_2 = 220 ms (c) t_3 = 420 ms and (d) t_4 = 600 ms [21].

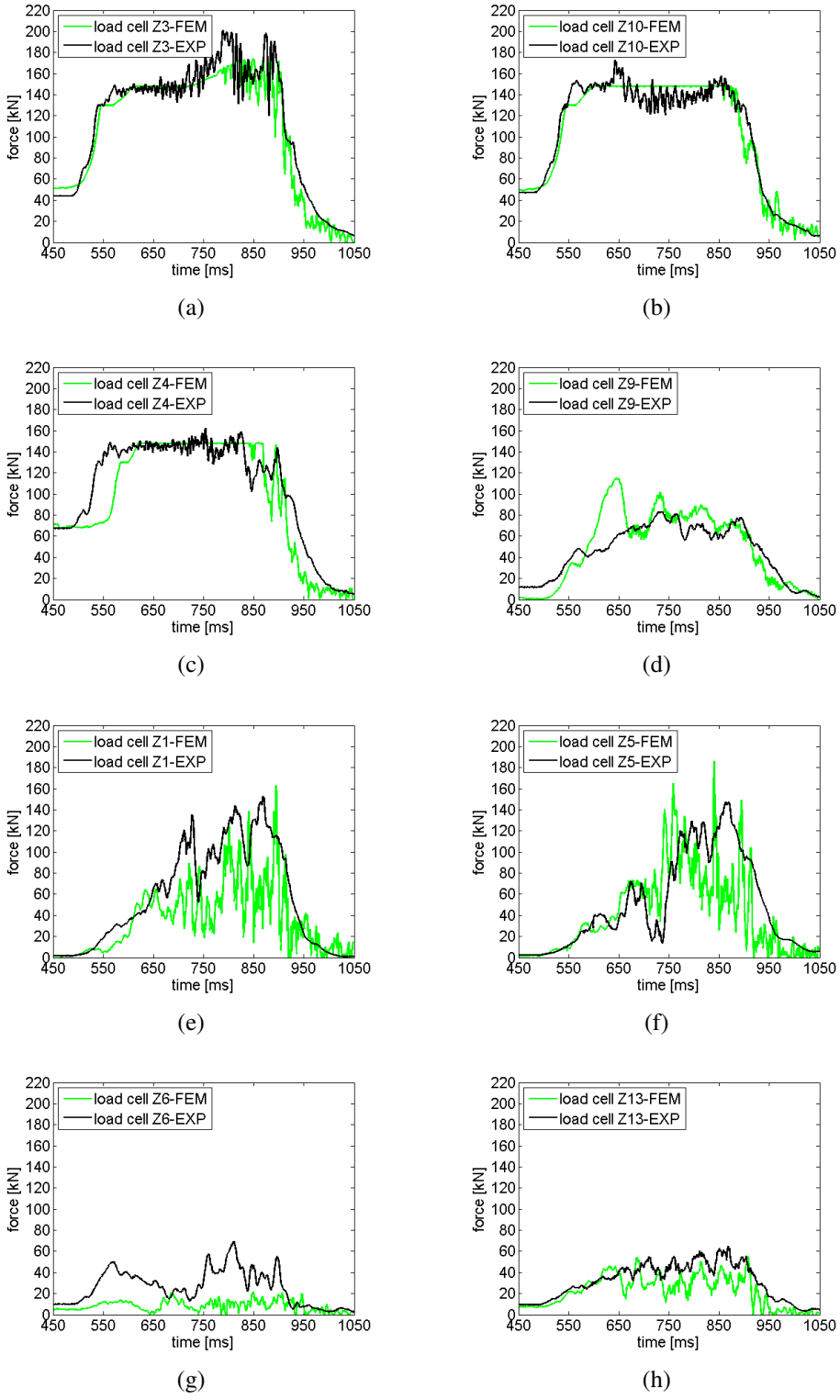


Figure 11: Load cell histories: (a-d) lateral anchors, (e-h) uphill anchors [21].

3 PROPOSED DESIGN

3.1 Optimized Chain-link net

The current chain-link net design exhibits a decrease in axial strength at the contact zones (connections). This is due to the coupling effect between axial and bending behaviour. The maximum value of the bending moment is reached at the connections and as a result the axial capacity is significantly reduced in these zones. In order to increase the axial strength at the connections, a thicker equivalent circular section can be assumed only at the contact points. The larger thickness at the connections can be assumed to be the result of two options: (1) the three wires forming the spiral bundle are thicker at the contact zones, or (2) an additional high-strength wire is winded around the three-wire bundle in a helical manner through the whole length of the connection (Fig. 12). However, in the second case, the friction between chain-links would increase with respect to the standard design. Furthermore, the thickness increase due to the additional wire would need to be determined from laboratory experiments. In this work, we will only present a simple hypothesis.

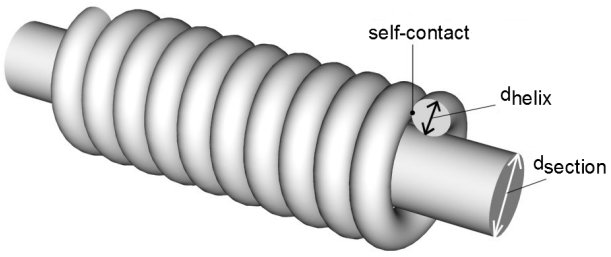


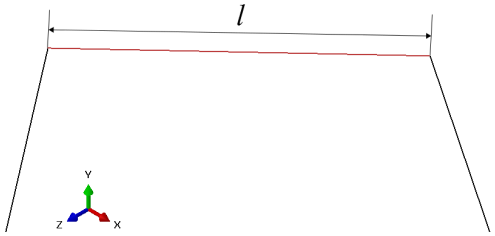
Figure 12: Helical wire wound as tightly as possible on the equivalent chain-link wire (adapted from [33]).

The increase in axial strength due to the larger section area of the equivalent wire will increase the resistance and elongation capacity of the chain-link panel. In this work, an elongation capacity increase of approximately 10% with respect to the tested standard panel is considered. Moreover, it is assumed that the strain energy of the optimized panel is the same to that of the tested panel up to the displacement at which failure occurs in the tested standard panel. The purpose of this assumption is to avoid higher forces to be transmitted to the cables in the rockfall barrier standard design (section 4.2). To fulfil this assumption regarding the strain energy, the dimensions of the three-dimensional chain-link connections need to be optimized (Fig. 13a-c).

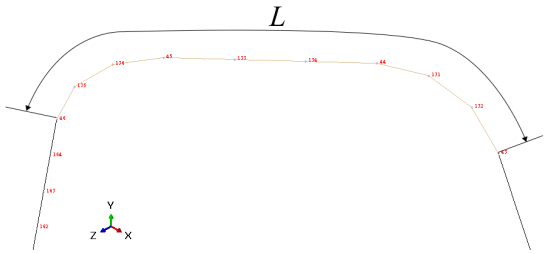
Furthermore, if option two is chosen, the radius of the additional winded helical wire r_{helix} is optimized. In this case, the chain-link is modelled with two circular cross-sections. Namely, a cross-section that takes into account the area increase due to the winded wire along the connections (helix shape), and a cross-section that considers the calibrated area of the equivalent wire in the tested standard panel [21], which is applied to the whole chain-link except for the connections (Fig. 13c). The approximate length of the connection is:

$$L = l + f_r r_{round} \tag{3}$$

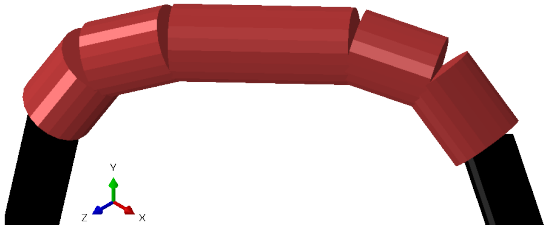
where r_{round} is equal to the radius of the round (Fig. 13b) created between the linear segments shown in Fig. 13a, and f_r is a factor that remains approximately constant for the range of variation considered for r_{round}. The length $l = (L_x^2 + L_z^2)^{0.5}$ is shown in Fig. 13a.



(a) connection before "create round"



(b) finite element discretization at the connection



(c) rendered equivalent wire profiles

Figure 13: Connection dimensions.

The helical wire of radius a and pitch $P = 2\pi b$ is described by the following parametrisation [33]:

$$x(t) = a\cos(t), \tag{4}$$
$$y(t) = a\sin(t), \tag{5}$$
$$z(t) = bt. \tag{6}$$

Where $a = r_{helix} + r_{chain}$, and $t = N_r 2\pi$. Considering a closely packed helix (Fig. 12) [33], the pitch P is equal to $2r_{helix}$. The number of turns N_r of the helix is approximated as:

$$N_r = int(L/P) \tag{7}$$

The volume of the helical wire is equal to:

$$V_{helix} = 2\pi^2 r_{helix}^2 N_r \sqrt{(a^2 + b^2)} \tag{8}$$

The radius of the equivalent wire modelling the connection section is then assumed to be equal to:

$$R_{eq} = (r_{chain}^2 + V_{helix}/(L\pi))^{0.5} \tag{9}$$

The topology variables L_x, L_z, and r_{round} plus r_{helix} are the optimization variables of the problem. A Python script is used to generate the FE model, to calculate it using the Explicit solver and to finally produce a force-displacement curve. The Python script is parametrized, in other words, the definition of the FE model depends on the values of the optimization variables.

The Isight software is used herein to quantify how fit a candidate solution is, i.e., how closely it approximates the sought quantities. The first quantity is a desired force-displacement curve. The optimization function to be minimized is then, the absolute area difference between the sought and simulation curves (Fig. 14). The second quantity is the peak force, which is to be maximized, then constituting a second optimization function. The multi-objective function problem is posed as a single objective by combining both optimization functions into one, where the resulting function is to be minimized:

$$f_{opt} = f_{w1} f_1 - f_{w2} f_2 \tag{10}$$

where f_{w1} and f_{w2} are the weight factors. In this case an equal weight was given to both functions and therefore $f_{w1} = f_{w2} = 1.0$.

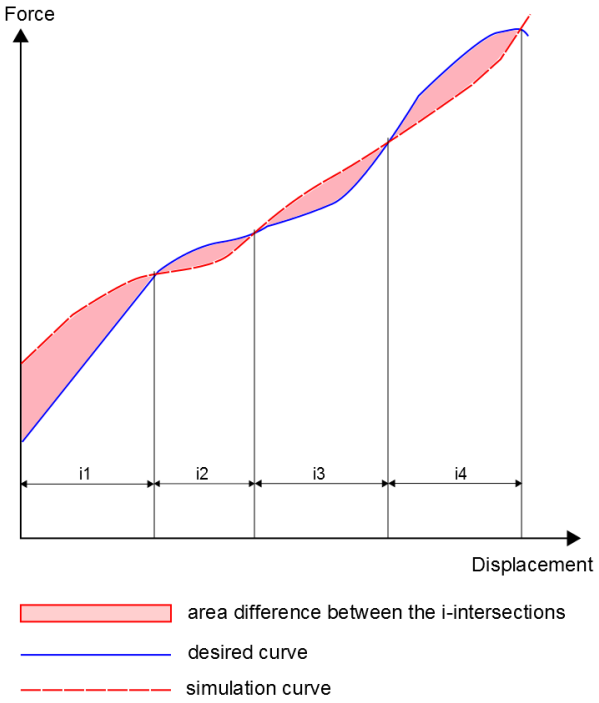


Figure 14: Area difference to be minimized (optimization function 1).

Tab. 3 illustrates the optimization parameters for the chain-link net along with their lower and upper search space bounds. Finally, the optimization process is formulated as the problem of minimizing the specified objective function. The process to obtain the lower and upper bounds of the optimization variables, as long as the details of the solution of a similar optimization problem are provided in [20]. Figure 15 depicts the radial basis approximation of the composed objective function vs. the connection dimensions L_x and L_z. This figure reveals a multi-modal optimization problem. The optimal values of L_x and L_z are approximately 29 mm and 26 mm respectively. These values are larger than those used to model the standard netting design which are: 25 mm and 23 mm respectively. Therefore, in case of using a thicker cross-section (either just at the connection or globally), the optimal solution is to also increase the connection length.

Parameter	Lower	Upper
L_x [mm]	25.0	31.0
L_z [mm]	24.0	28.0
r_{round} [mm]	11.0	13.0
r_{helix} [mm]	1.0	2.0

Table 3: Chain-link optimization parameters (topology and contact equivalent wire section)

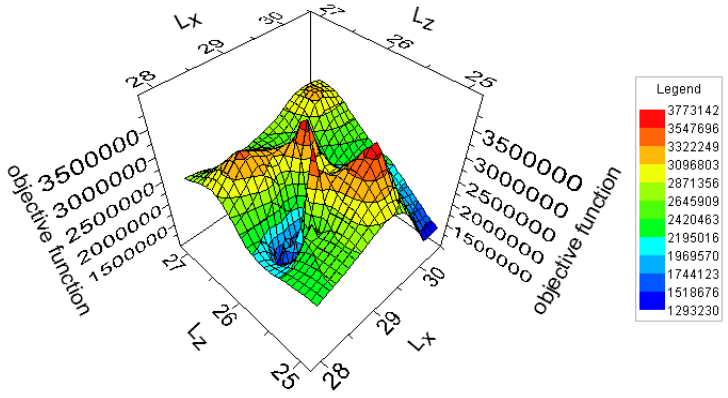


Figure 15: Radial basis function surface approximation of f_{opt} vs. L_x and L_z.

3.2 Net-to-cable connection modifications

The higher resistance achieved by the new chain-link netting design is useful to perform modifications aimed to improve the performance of the rockfall barrier system already discussed. The only modification considered in this work was to reduce the number of "free" meshes from seven to six per post side (Fig. 16). The scheme used to connect the chain-link netting to the support cables is explained in detail in [21]. Basically, there are two types of modelled clips connecting the netting to the support cables: (1) rigid body [11] type clips which by definition cannot fail. They are used in the locations where in the real barrier, the cables are threaded through the netting. Large scale tests have shown that failures do not occur in this type of connection, and therefore assuming rigid body type clips is acceptable [21]; and (2) deformable type clips modelled with metal plasticity and a ductile damage law [21]. These clips represent the realistic clips that connect some of the "free" meshes to the support cables. The clips that fail are highlighted in Fig. 16. The purpose of the implemented modification is to reduce the netting deformation. This is useful in locations where the space allowed for the netting deformation is limited.

Figs. 17a-b shows the deformed state of the modified barrier at two different times (with the same scale), namely: the time where the maximum deformation is achieved (Fig. 17a), and the time where the maximum deformation was achieved in the standard design (Fig. 17b). The maximum deformation of the proposed design with the optimal chain-link netting is 6330 mm, that is 2630 mm. Therefore, the deformation space of the system with the proposed modification is reduced by more than 2 meters. Fig. 17a shows that 3 deformable clips (type 2) did not fail. This fact caused an antisymmetry effect on the model and therefore the impactor takes an inclined direction. Those clips did not fail because the forces transmitted to the support cables are reduced in the modified design. This is because the energy dissipating devices (brakes) connected to the support cables dissipate less energy with the proposed design. The brakes

experience a smaller sliding in comparison to the standard design case. The larger frictional dissipation of the optimal netting compensates the lower energy dissipation of the brakes.

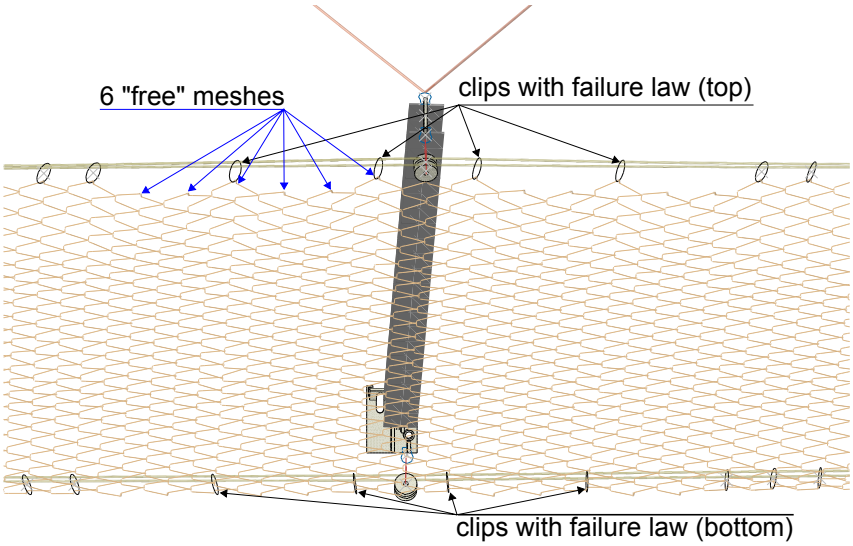


Figure 16: Connection of chain-link net to cables with 6 "free" meshes by post side (bottom and top).

4 COMPARATIVE PERFORMANCE OF PROPOSED VS. STANDARD APPROACH

4.1 Chain-link panel

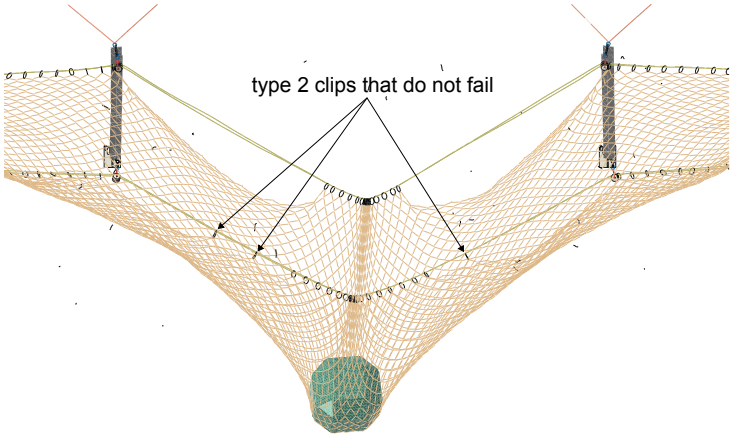
Fig. 18 illustrate the comparison between the simulation results of the standard and optimal chain-link netting design. It can be observed that the modified net has an increase of $\approx 10\%$ in elongation capacity and of $\approx 5\%$ in strength. It is also observed how the strain energy of both curves is similar up to the force-elongation point where failure occurs in the standard design. This in fact is a result of the optimization goal expressed by means of the multi-objective optimization.

4.2 Rockfall barrier

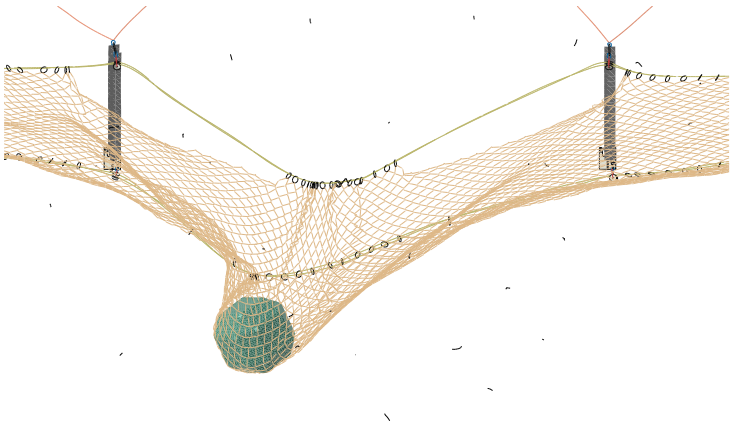
Fig. 19 illustrate the comparison between the simulation results of the standard and modified 2000 kJ rockfall barrier design. It can be observed how the forces decay faster in the modified design because of the smaller brake time. Until the decay time (about 750 ms) the forces in the modified system are slightly larger in comparison to the forces in the standard system. Therefore, it is proved that the optimal netting does not transmit forces that are significantly larger than those transmitted by the standard chain-link netting.

5 DISCUSSION

The solution of a topology optimization problem of a wire-net approximated by an equivalent circular section and discretized by beams elements can be obtained by means of simple algorithms such as the Downhill Simplex (DS) [29]. On the other hand, when the shape of cross-section is not knowing a priori, a three dimensional element discretization of the structural component is needed and the optimal cross-section shape and area is found by means of more complex numerical procedures such as the SIMP (Solid Isotropic Material with Penaliza-



(a) Maximum deformation of the proposed design



(b) Deformation of the barrier at the time where the standard design achieves the maximum deformation

Figure 17: Simulation video frames: (a) t_1 = 260 ms and (b) t_2 = 420 ms.

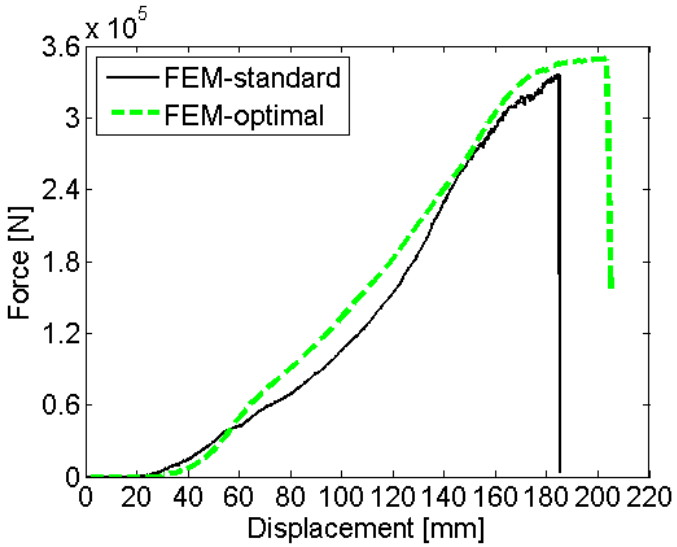


Figure 18: Force vs. displacement curve from FE simulations (standard and optimal designs).

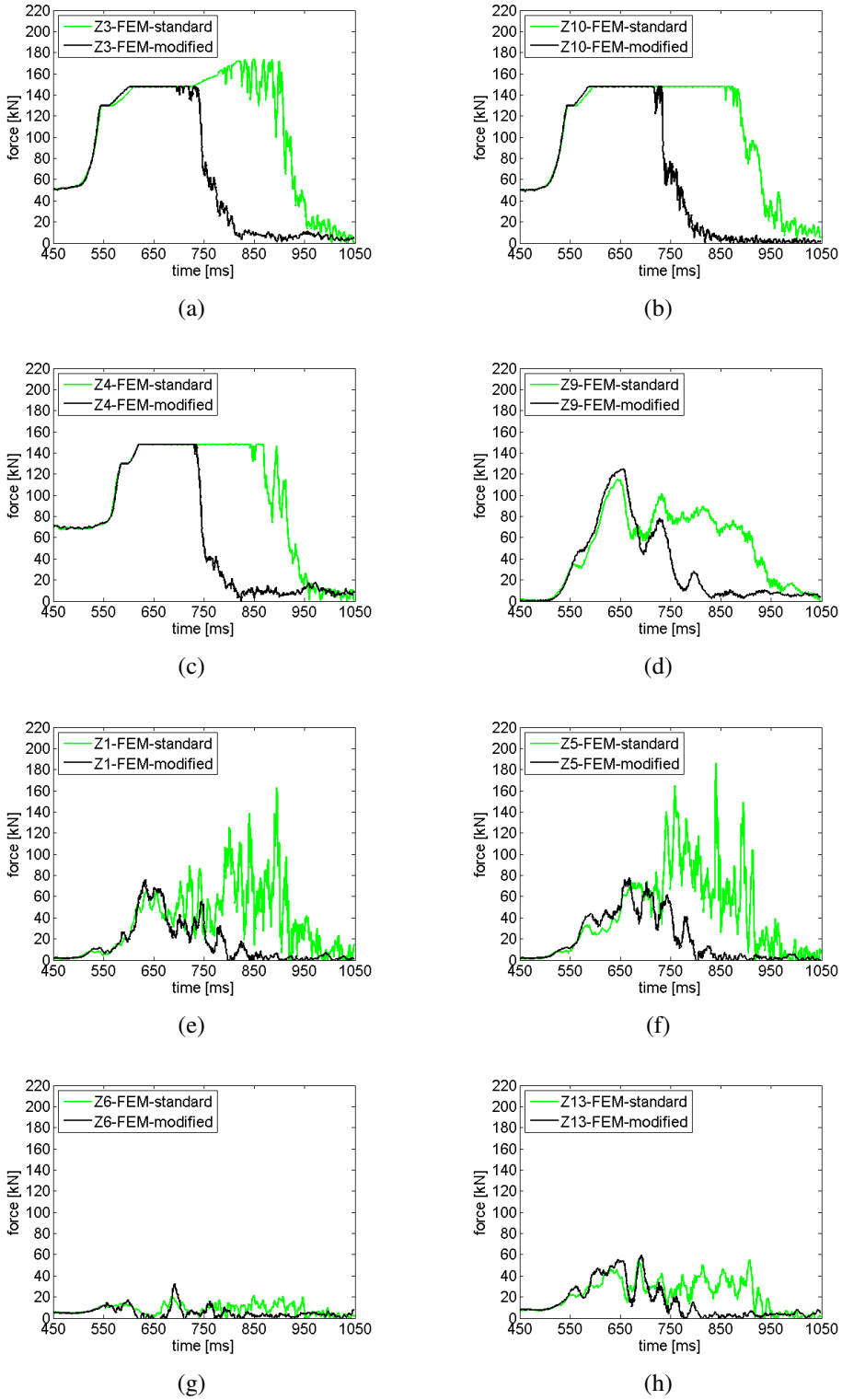


Figure 19: Comparison between the simulation results of the standard and modified 2000 kJ barrier: (a-d) lateral anchors, (e-h) uphill anchors.

tion) approach [34]. For structures subjected to impact, topology optimization problems can be solved with the Hybrid Cellular Automata (HCA) [35] or the Equivalent Static Load (ESL) [36, 37] method. The objective in the impact case is to maximize the internal energy.

Rockfall barrier developers should advance in the design of more efficient energy dissipating devices with larger absorption capacities. In order to optimize new designs, methods such as the HCA and ESL can be used. Software such as Tosca [38] based on standard FE software (Abaqus, ANSYS, MSC Nastran) is used to perform shape and topology optimization of structures under static and dynamic loading. Additionally, LS-TaDSC [39] can be coupled with LS-DYNA to also solve topology optimization problems involving large non-linearities, dynamic loads and contact conditions. Another component where topology optimization would be interesting for cutting costs, is the ground plates. The FE modelling aspects of standard ground plates and their connection with the posts can be seen in [20, 21].

This paper presents an example of how topology optimization can be useful to obtain better performing systems. Rockfall barriers can be therefore optimized using existing methods. In order to speed up product development and to cut costs, the rockfall barrier developers would benefit from an analytical/numerical approach to optimize their designs such as it is already the norm in other industrial sectors [40, 41, 42, 43, 44]. The re-configured design for large scale experiments (after optimization) is already close to optimum [45].

In the structural optimization of the chain-link netting, assumptions regarding the equivalent wire at the connections and the friction coefficient between the modified chain-links were made. In order to validate the results of the simulation, real scale tests need to be performed.

6 CONCLUSIONS

We make the following conclusions:

- Topology optimization of standard netting designs can be carried out using the same techniques already employed to optimize the parameters of the netting FE models.
- Optimized existing wire nets can allow modifications to standard designs aimed to enhance their performance in terms of energy dissipation and barrier elongation.
- Topology optimization of completely new netting designs can also be performed. However, it is first necessary to obtain the equivalent circular cross-section as it has done for ring and chain-link nets [20, 21].
- More advanced methods such as the HCA and ESL are necessary to perform topology optimization of better performing energy dissipating devices. In these cases a 3D model of the brakes and a three-dimensional finite element discretization is necessary.
- New ground plates including dissipation capabilities can also be subjected to topology optimization. Such components will reduce the forces transmitted to the ground, causing the installation costs of the rockfall barriers to be reduced.

REFERENCES

[1] F. Guzzetti, P. Reichenbach, and G. F. Wieczorek. Rockfall hazard and risk assessment in the yosemite valley, california, usa. *Natural Hazards and Earth System Science*, 3(6):491–503, 2003.

[2] F. Agliardi, G. B. Crosta, and P. Frattini. Integrating rockfall risk assessment and countermeasure design by 3d modelling techniques. *Natural Hazards and Earth System Science*, 9(4):1059–1073, 2009.

[3] A. Volkwein, K. Schellenberg, V. Labiouse, F. Agliardi, F. Berger, F. Bourrier, L. K. A. Dorren, W. Gerber, and M. Jaboyedoff. Rockfall characterisation and structural protection - a review. *Natural Hazards and Earth System Science*, 11(9):2617–2651, 2011.

[4] Juan Pablo Escallón Osorio. *Simulation of flexible steel wire-net rock-fall barriers via finite element model updating*. PhD thesis, ETH, 2015.

[5] A. Cazzani, L. Mongiovì, and T. Frenez. Dynamic finite element analysis of interceptive devices for falling rocks. *International Journal of Rock Mechanics and Mining Sciences*, 39(3):303 – 321, 2002.

[6] Cristina Gentilini, Laura Govoni, Stefano de Miranda, Guido Gottardi, and Francesco Ubertini. Three-dimensional numerical modelling of falling rock protection barriers. *Computers and Geotechnics*, 44(0):58 – 72, 2012.

[7] M. Spadari, A. Giacomini, O. Buzzi, and J.P. Hambleton. Prediction of the bullet effect for rockfall barriers: a scaling approach. *Rock Mechanics and Rock Engineering*, 45(2):131–144, 2012.

[8] J. Yiu, Y. Huang, J. Pappin, S.H. Julian, Kwan, and K.S. Ho. Ken. Landslide mobility and flexible barrier numerical modeling using ls-dyna. In *12th International LS-DYNA Users Conference*, 2012.

[9] C. Gentilini, G. Gottardi, L. Govoni, A. Mentani, and F. Ubertini. Design of falling rock protection barriers using numerical models. *Engineering Structures*, 50(0):96 – 106, 2013.

[10] Phuc Van Tran, Koji Maegawa, and Saiji Fukada. Prototype of a wire-rope rockfall protective fence developed with three-dimensional numerical modeling. *Computers and Geotechnics*, 54(0):84 – 93, 2013.

[11] Dassault Systémes Simulia Corp, Providence, RI. *Abaqus Analysis User's Manual, Version 6.14*, 2014.

[12] J.O. Hallquist. *LS-DYNA Keyword User's Manual, LS-DYNA R7.1*. Livermore Software and Technology Corporation, Livermore CA, May 2014.

[13] Hans Gerhard Grassl. *Experimentelle und numerische Modellierung des dynamischen Trag- und Verformungsverhaltens von hochflexibeln Schutzsystemen gegen Steinschlag*. PhD thesis, Swiss Federal Institute of Technology, Zurich, 2002.

[14] Axel Volkwein. *Numerische Simulation von flexiblen Steinschlagschutzsystemen*. PhD thesis, Swiss Federal Institute of Technology, Zurich, 2004.

[15] Albrecht Von Boetticher. *Flexible Hangmurenbarrieren: Eine numerische Modellierung des Tragwerks, der Hangmure und der Fluid-Struktur-Interaktion*. PhD thesis, Technische Universitaet Muenchen, 2012.

[16] Leyla GHOUSSOUB, Cyril Douthe, and Karam Sab. Analysis of the mechanical behaviour of soft rockfall barriers. In *RocExs 2014 - 5th Interdisciplinary Workshop on Rockfall Protection*, page 4 p., Italy, May 2014.

[17] Klaus Thoeni, Anna Giacomini, Cédric Lambert, Scott W. Sloan, and John P. Carter. A 3D discrete element modelling approach for rockfall analysis with drapery systems. *International Journal of Rock Mechanics and Mining Sciences*, 68(0):107 – 119, 2014.

[18] J.P. Escallón and C. Wendeler. Numerical simulations of quasi-static and rockfall impact tests of ultra-high strength steel wire-ring nets using abaqus/explicit. In *2013 SIMULIA Community Conference 1 www.3ds.com/simulia*, 2013.

[19] J.P. Escallón, C. Wendeler, and M. Mrozik. Chapter 64. numerical simulation of rock-fall impact on a flexible barrier using abaqus/explicit 6.12. In *Rock Mechanics for Resources, Energy and Environment, Edited by Marek Kwaśniewski and Dariusz Lydżba, CRC Press 2013, Pages 417-423*, 2013.

[20] J.P. Escallón, C. Wendeler, E. Chatzi, and P. Bartelt. Parameter identification of rockfall protection barrier components through an inverse formulation. *Engineering Structures*, 77(0):1 – 16, 2014.

[21] J.P. Escallón, C. Wendeler, E. Chatzi, and P. Bartelt. Mechanics of chain-link wire nets with loose connections. *Engineering Structures*. under review.

[22] Corinna Simone Isabelle Wendeler. *Murgangrueckhalt in Wildbaechen. Grundlagen zu Planung und Berechnung von flexiblen Barrieren von Corinna Simone Isabelle Wendeler*. PhD thesis, ETH, 2008.

[23] W.J. Chung, J.W. Choand, and T. Belytschko. On the dynamic effects of explicit fem in sheet metal forming analysis. *Engineering Computations*, 15 (6):750–776, 1998.

[24] Haipeng Han, Farid Taheri, and Neil Pegg. Quasi-static and dynamic crushing behaviors of aluminum and steel tubes with a cutout. *Thin-Walled Structures*, 45(3):283 – 300, 2007.

[25] Dassault Systémes Simulia Corp, Providence, RI. *Abaqus Analysis User's Manual, Version 6.13*, 2013.

[26] Dassault Systémes Simulia Corp, Providence, RI. *SIMULIA Isight 5.9. User's Guide.*

[27] J.P. Bardet and M.M. Kapuskar. A simplex analysis of slope stability. *Computers and Geotechnics*, 8(4):329 – 348, 1989.

[28] W. Riedel, K. Fischer, C. Kranzer, J. Erskine, R. Cleave, D. Hadden, and M. Romani. Modeling and validation of a wall-window retrofit system under blast loading. *Engineering Structures*, 37(0):235 – 245, 2012.

[29] J. A. Nelder and R. Mead. A simplex method for function minimization. *The Computer Journal*, 7(4):308–313, 1965.

[30] M. D. McKay, R. J. Beckman, and W. J. Conover. Comparison of three methods for selecting values of input variables in the analysis of output from a computer code. *Technometrics*, 21:239–245, 1979.

[31] EOTA. Etag 027 guideline for european technical approval of falling rock protection kits, 2012.

[32] Z. Sternová. European Technical Approval ETA-09/0369. Technical report, TSUS Building Testing and Research Institute, 2010.

[33] S. Przybył and P. Pierański. Helical close packings of ideal ropes. *The European Physical Journal E*, 4(4):445–449, 2001.

[34] O. Sigmund and J. Petersson. Numerical instabilities in topology optimization: A survey on procedures dealing with checkerboards, mesh-dependencies and local minima. *Structural optimization*, 16(1):68–75, 1998.

[35] Andrés Tovar, Neal M. Patel, Glen L. Niebur, Mihir Sen, and John E. Renaud. Topology optimization using a hybrid cellular automaton method with local control rules. *Journal of Mechanical Design*, 128(6):1205–1216, 01 2006.

[36] Heiner Muellerschoen, Andrea Erhart, Krassen Anakiev, Peter Schumacher, and Heribert Kassegger. Application of the equivalent static load method for impact problems with genesis and ls-dyna. In *World congress on structural and multidisc. Optim*, 2013.

[37] Hyun-Ah Lee and Gyung-Jin Park. Nonlinear dynamic response topology optimization using the equivalent static loads method. *Computer Methods in Applied Mechanics and Engineering*, 283(0):956 – 970, 2015.

[38] FE-Design. *TOSCA User's Manual*. FE-Design GmbH, Karlsruhe, Germany, 2008.

[39] Livermore Software Technology Corporation. *LS-TaSC Manual Topology and Shape Computations for LS-DYNA User's Manual*, version 2.0 edition, 2011.

[40] Marta R. Dias, José M. Guedes, Colleen L. Flanagan, Scott J. Hollister, and Paulo R. Fernandes. Optimization of scaffold design for bone tissue engineering: A computational and experimental study. *Medical Engineering & Physics*, 36(4):448 – 457, 2014.

[41] Maggie Kociecki and Hojjat Adeli. Shape optimization of free-form steel space-frame roof structures with complex geometries using evolutionary computing. *Engineering Applications of Artificial Intelligence*, 38(0):168 – 182, 2015.

[42] Guangyong Sun, Guangyao Li, Shiwei Zhou, Hongzhou Li, Shujuan Hou, and Qing Li. Crashworthiness design of vehicle by using multiobjective robust optimization. *Structural and Multidisciplinary Optimization*, 44(1):99–110, 2011.

[43] Jianguang Fang, Yunkai Gao, Guangyong Sun, Chengmin Xu, and Qing Li. Multiobjective robust design optimization of fatigue life for a truck cab. *Reliability Engineering & System Safety*, 135(0):1 – 8, 2015.

[44] Claudio Comis Da Ronco, Rita Ponza, and Ernesto Benini. Aerodynamic shape optimization of aircraft components using an advanced multi-objective evolutionary approach. *Computer Methods in Applied Mechanics and Engineering*, 285(0):255 – 290, 2015.

[45] P. Eberhard. Optimization of mechanical systems. Institute of Engineering and Computational Mechanics Pfaffenwaldring 9, 4th floor 70563 Stuttgart.

COMPDYN 2015
5th ECCOMAS Thematic Conference on
Computational Methods in Structural Dynamics and Earthquake Engineering
M. Papadrakakis, V. Papadopoulos, V. Plevris (eds.)
Crete Island, Greece, 25–27 May 2015

SMOOTH AND NON-SMOOTH SOLUTIONS FOR GEOMETRICALLY EXACT BEAMS SUBJECTED TO IMPACT

Tien-Long Nguyen[1], Mohammed Hjiaj[1] and Carlo Sansour[2]

[1]Civil Engineering department, Institut National des Sciences Appliques de Rennes
20 Avenue des Buttes de Coesmes, 35708, Rennes, France
{Tien-long.Nguyen, Mohammed.Hjiaj}@insa-rennes.fr

[2] Faculty of engineering, University of Nottingham
NG7, Nottingham, United Kingdom
Carlo.Sansour@nottingham.ac.uk

Keywords: non-linear dynamics, impact, smooth dynamics, non-smooth dynamics, geometrically exact beam theory, finite strain, energy-momentum method.

Abstract. *Shock and Impact problems have been the focus of research for decades in many engineering areas such as structural engineering, automobile industry, aerospace, multibody dynamics. In general, unlike classical dynamics, impact requires specials techniques to correctly model the underlying physics. The solutions for the problems of impact have been developed in different ways by many authors with each of them using different hypothesis. However, formulations of impact of beams have received limited attention. The solution methods for impact can be divided into two main groups: smooth and non-smooth approaches. In this paper we will develop both smooth and nonsmooth formulations for impact between projectiles and beams. The adopted beam kinematics is geometrically exact. In smooth formulations, the velocities and forces are continuous functions. The impact forces is determined by the corresponding deformations of the projectile, the deformation of beam is calculated with the applied impact force. This approach is appropriate when the projectile is deformable and it reflects the reality of many impact scenarios.*
When it comes to impact between rigid projectile and deformable beams, the problem becomes more complex and should be treated using non-smooth formulations where the velocities and the impact forces may have jumps, thus, they are discontinuous. Set-valued force laws are used to account for unilateral conditions on both displacement and velocities. The appropriate framework is differntial measure combined with convex analysis The coefficient of restitution plays also an important role. The integration is also split into smooth and non-smooth part. Though, having stable time integration schemes for geometrically exact beams is not a straightforward task. For both formulations, the use of a newly developed energy-momentum time integration scheme conserve perfectly the total energy and the momentum of the system during and after the impact. A range of numerical applications will be delivered to show excellent performances of the new formulations.

1 Summary of kinematics of beams and strain measure

In this section we briefly introduce the beam's strain measures. We consider a general Cartesian co-ordinate basis $\boldsymbol{e}_i, i = 1, 2, 3$ and a curve $\boldsymbol{X}_0(s)$, with s being the arc-length. We understand $\boldsymbol{X}_0(s)$ as describing the centre line of the rod cross section. However, we restrict the deformations to planar ones in the $\boldsymbol{e}_1 - \boldsymbol{e}_2$ plane and introduce the tangent vector $\boldsymbol{G}_0 = \frac{d\boldsymbol{X}_0(s)}{ds}$. Perpendicular to this vector, we define $\boldsymbol{N}$ to be the normal vector with z as the corresponding coordinate in the direction of $\boldsymbol{N}$.

In addition to the Cartesian system, we define a suitable convected curvilinear coordinate system given by the triple s, z, x_3. We define the vector $\boldsymbol{X}(s, z) = \boldsymbol{X}_0(s) + z\boldsymbol{N}(s)$ as the position vector of points in the direction of $\boldsymbol{N}$ at the reference configuration. In a general cross section the boundary is defined by z being a function of x_3. Note that the third direction is not explicitly included in this equation, though it is implicitly understood that it is in the direction of $\boldsymbol{e}_3$ and that the deformation is independent of that direction. Consequently, a local basis in the reference configuration is defined by the triple $(\boldsymbol{G}, \boldsymbol{N}, \boldsymbol{e}_3)$, with $\boldsymbol{G} = \frac{\partial \boldsymbol{X}}{\partial s}$, $\boldsymbol{N} = \frac{\partial \boldsymbol{X}}{\partial z} = \frac{\partial \boldsymbol{X}}{\partial z}|_{z=0}$ and $\boldsymbol{G}_0 = \boldsymbol{G}\ |_{z=0}$. We have also the following relations $\boldsymbol{G} \cdot \boldsymbol{N} = \boldsymbol{G}_0 \cdot \boldsymbol{N} = 0$, $|\boldsymbol{N}| = 1$, $\boldsymbol{N} = \boldsymbol{e}_3 \times \frac{\boldsymbol{G}}{|\boldsymbol{G}|} = \boldsymbol{e}_3 \times \boldsymbol{G}_0$, where $|\bullet|$ denotes the absolute value of a vector, $\times$ and $(\cdot)$ denotes the cross and scalar product of vectors, respectively. The corresponding contra-variant basis vectors are then given by $(\boldsymbol{G}^*, \boldsymbol{N}, \boldsymbol{e}_3)$, with $\boldsymbol{G}^* = \frac{\boldsymbol{G}}{|\boldsymbol{G}|^2}$.

The deformed configuration is given as $\boldsymbol{x} = \boldsymbol{\varphi}(\boldsymbol{X})$ which defines the actual configuration. For our geometrically exact beam theory we make use of the Bernoulli model where the cross sections are assumed to be rigid and remain perpendicular to the center line. Thus, the corresponding tangent vectors at the deformed configuration are defined as $(\boldsymbol{g}, \boldsymbol{n}, \boldsymbol{e}_3)$ with $\boldsymbol{g}_0 = \boldsymbol{g}|_{z=0}$, and the following relations hold: $\boldsymbol{g} = \frac{\partial \boldsymbol{x}}{\partial s}$, $\boldsymbol{n} = \boldsymbol{e}_3 \times \frac{\boldsymbol{g}}{|\boldsymbol{g}|} = \boldsymbol{e}_3 \times \frac{\boldsymbol{g}_0}{|\boldsymbol{g}_0|}$. The position vector in the direction of $\boldsymbol{n}$ can be characterized by the following relation

$$\boldsymbol{x} = \boldsymbol{X}(s) - z\boldsymbol{N}(s) + \boldsymbol{u}(s) + z\boldsymbol{n}(s) = \boldsymbol{X}_0(s) + \boldsymbol{u}(s) + z\boldsymbol{n}(s), \tag{1}$$

where $\boldsymbol{u}(s)$ is the displacement vector of the centre line. From this we obtain immediately $\boldsymbol{g} = \boldsymbol{X}_{0,s} + \boldsymbol{u}_{,s} + z\boldsymbol{n}_{,s}$. The deformation gradient is written down in the curvilinear basis system as $\boldsymbol{F} = \boldsymbol{g} \otimes \boldsymbol{G}^* + \boldsymbol{n} \otimes \boldsymbol{N} + \boldsymbol{e}_3 \otimes \boldsymbol{e}_3$. The Green strain tensor is defined as $\boldsymbol{E} = \frac{1}{2}(\boldsymbol{C} - \boldsymbol{1})$, where $\boldsymbol{C} = \boldsymbol{F}^T\boldsymbol{F}$. It has only one non-trivial component $E_{11} = \boldsymbol{u}_{,s} \cdot \boldsymbol{X}_{0,s} + \frac{1}{2}\boldsymbol{u}_{,s} \cdot \boldsymbol{u}_{,s} + z\left(\boldsymbol{n}_{,s} \cdot (\boldsymbol{X}_{0,s} + \boldsymbol{u}_{,s}) - \boldsymbol{N}_{,s} \cdot \boldsymbol{X}_{0,s}\right)$, where the term in z^2 has been neglected. E_{11} is split into two components as $E_{11} = \varepsilon_{11} + z\kappa$, the definition of which are given by $\varepsilon_{11} = \boldsymbol{u}_{,s} \cdot \boldsymbol{X}_{0,s} + \frac{1}{2}\boldsymbol{u}_{,s} \cdot \boldsymbol{u}_{,s}$, $\kappa = \boldsymbol{n}_{,s} \cdot (\boldsymbol{X}_{0,s} + \boldsymbol{u}_{,s}) - \boldsymbol{N}_{,s} \cdot \boldsymbol{X}_{0,s}$. The first is the axial strain and the second is the classical change of curvature.

2 Smooth formulation and equations of motion

2.1 Dynamic equations and force integration method

In this section, the projectile is assumed to be elastically deformable and modelled by a spring with a mass, Fig. 1. The mass can only move in the horizontal direction which is parallel to vector $\boldsymbol{e_2}$ with an initial velocity V. Before contact, the projectile moves freely without friction and gravity, therefore the equation of motion of the projectile is:

$$M\ddot{U}_2 = 0, \tag{2}$$

where M is the weight of the projectile, $U_2 = \boldsymbol{U} \cdot \boldsymbol{e}_2$. $\boldsymbol{U}$ denotes the displacement of the mass measured from the moment that the spring hits the beam. Let's call the contact force F, so during contact, the equation of motion of the projectile is written as follows:

$$M\ddot{U}_2 + R_1 (U_2 - u_2) = 0, \quad F = R_1 (U_2 - u_2) . \tag{3}$$

where u_2 is the second component of the displacement vector of the contact point on beam, R_1 is the stiffness coefficient of spring. Starting from Hamilton's principle for our conservative mechanical system, the dynamics equation for our beam is written down as follows

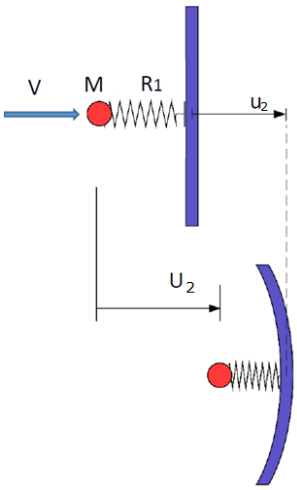


Figure 1: Impact model

$$\int_L \rho A \ddot{\boldsymbol{u}} \cdot \delta \boldsymbol{u} \, ds \, dt + \int_L \rho I \ddot{\boldsymbol{n}} \cdot \delta \boldsymbol{n} \, ds + \int_L \left(EA\varepsilon_{11}\delta\varepsilon_{11} + EI\kappa\delta\kappa \right) ds - F\delta u_2 = 0. \tag{4}$$

where E is Young's Modulus of the material, V is the volume of the system, $\boldsymbol{u}(s)$ is the displacement vector at coordinate s, $F = R_1 (U_2 - u_2) > 0$ during the contact and $F = 0$ otherwise, I is the moment of inertia of the section and L is the length of the beam, ρ is the material density.

2.2 Energy-momentum method and force integration

After the spatial discretisation which is standard as presented in[1], the numerical approach is completed by using a newly developed energy-momentum method for geometrically exact Euler-bernoulli beams which has been proven to have long-term stability and perfect conservation of energy and momentum [1]. The summary of the energy-momentum method is given as follows:

$$\varepsilon_{n+\frac{1}{2}} = \varepsilon_n + \frac{1}{2}\Delta T \dot{\varepsilon}_{n+\frac{1}{2}}, \quad \kappa_{n+\frac{1}{2}} = \kappa_n + \frac{1}{2}\Delta T \dot{\kappa}_{n+\frac{1}{2}}, \quad \dot{\boldsymbol{n}}_{n+\frac{1}{2}} = \dot{\boldsymbol{n}}_n + \frac{1}{2}\Delta T \ddot{\boldsymbol{n}}_{n+\frac{1}{2}}, \tag{5}$$

The mathematical proof of conservations are presented in [1]. The projectile displacement is updated using the classical midpoint rule. The value of force during the contact is integrated flowing $F^{n+\frac{1}{2}} = R1 \left(U_2^{n+\frac{1}{2}} - u_2^{n+\frac{1}{2}} \right)$ with condition $F > 0$ to be verified at each time step, otherwise it's contact free and F is set to be zero.

2.3 Examples

In this example, we study the impact of an elastic projectile with an in-plane Euler-Bernoulli beam Fig. 2. Parameters of the problem are given below:

Projectile's mass: $M = 500\ Kg$
Projectile's initial velocity: $V = 20\ m/s$
Projectile's initial position:
$d = -0.2\ m$ - spring length
Spring stiffness: $R_1 = 7.5E5\ N/m$
Beam length $L = 3\ m$
Cross section area $A = 1E3\ cm^2$
Cross section inertia $I = 8330\ cm^4$
Young's Modulus $E = 0.2E10\ Pa$
Density $\rho = 3000\ Kg/m^3$
Number of elements = 6
Time increment $\Delta T = 1E-4\ s$

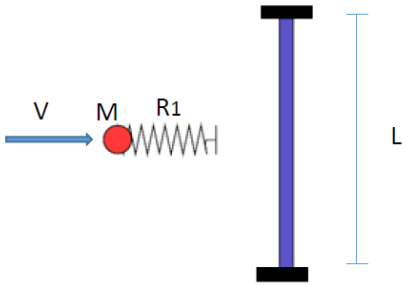


Figure 2: Impact model

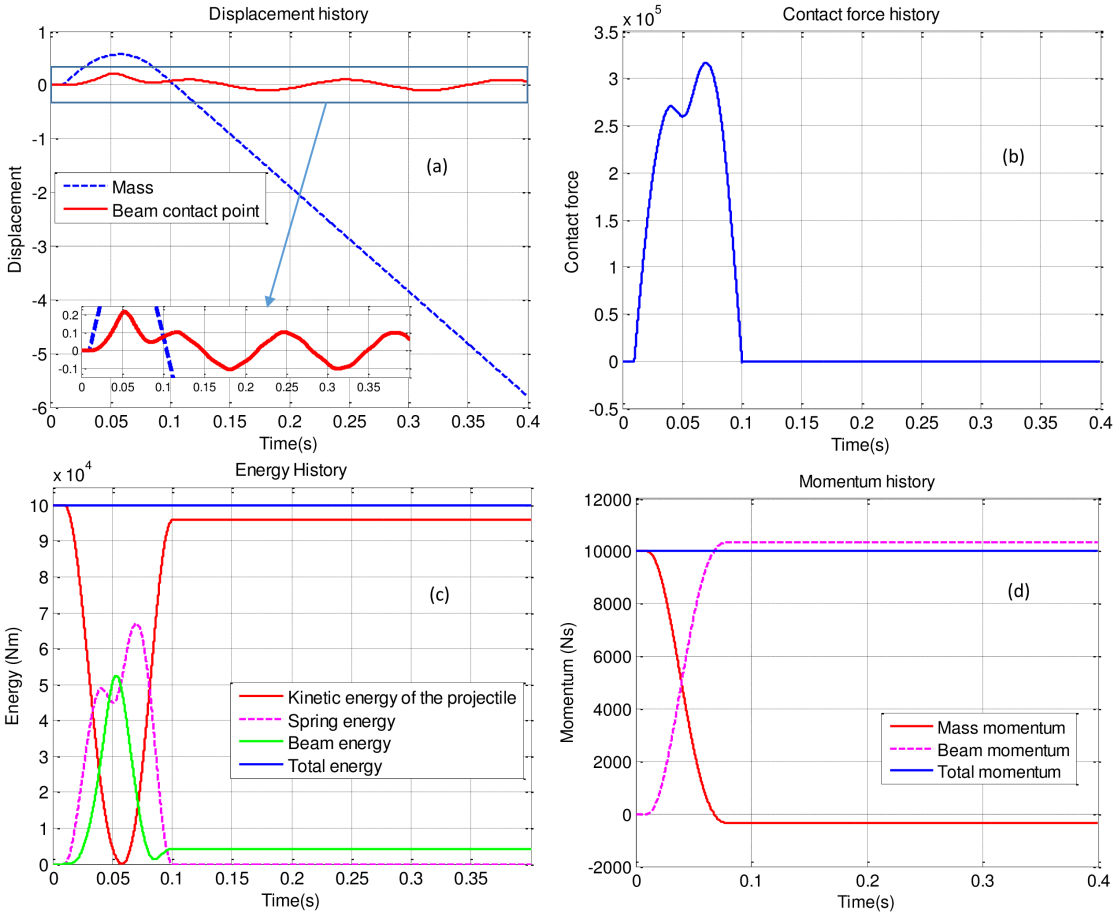


Figure 3: (a)displacement history, (b)contact force, (c)energy history, (d)momentum history

Fig. 3a illustrates the displacement of the mass compared to the displacement of the beam contact point. The segment where the displacement of the mass is larger than the beam corresponds to the contact period which is also represented by a positive contact force period in Fig.3b. Fig.3c shows that the total energy of the system is perfectly conserved. To verify the momentum conservation, the same test has been carried out considering the same beam but without support. The total momentum is also conserved perfectly, Fig. 3d. We note that when increasing the spring stiffness, not only one but several separated contact scenarios can happen.

3 Nonsmooth formulation and impact equations

3.1 Equations of motion

Hamilton's principle in nonsmooth mechanics has been studied by many authors [2, 5]. For our conservative system, the classical form still holds:

$$\delta \int_{t_1}^{t_2} \mathcal{L}\, dt = 0, \tag{6}$$

where t refers to time and t_1 and t_2 are boundaries of the time interval, $\mathcal{L}$ is defined as the Lagrangian given by

$$\mathcal{L} = T - \Psi_{int} - \Psi_{ext}, \tag{7}$$

where T is the kinetic energy of the system and Ψ_{int}, Ψ_{ext} are respectively the internal and the external potential energies. Our body is non-conducting linear elastic solid and thermodynamic effects are not included in the system. The quantities in (7) are defined as

$$\delta T = \int_V \rho \dot{\boldsymbol{x}} \cdot \delta \dot{\boldsymbol{x}}\, dV, \;\; \delta \Psi_{int} = \int_V (E E_{11} \delta E_{11})\, dV, \;\; \delta \Psi_{ext} = \boldsymbol{\lambda}_N \delta \boldsymbol{u}, \tag{8}$$

where E is Young's modulus of the material, V is the volume of the system, L is the length of the beam, $\boldsymbol{\lambda}_N$ is the contact force during the impact time and equal to zero elsewhere. Let t_k be the moment of impact. t_k^- and t_k^+ are the starting and the closing time of the impact event, as a result, $\Delta t = t_k^+ - t_k^- = \frac{1}{n}$, with $n \to +\infty$. The impact event is assumed to happen in an infinitesimal time. The displacement is continuous but the velocity is discontinuous[2, 3, 4, 5], which read $\boldsymbol{x}\left(t_k^-\right) = \boldsymbol{x}\left(t_k^+\right)$, $\dot{\boldsymbol{x}}\left(t_k^-\right) \neq \dot{\boldsymbol{x}}\left(t_k^+\right)$. For $t < t_k^-$ and $t > t_k^+$ the equation of motion has its regular form, from (6), (7), together with an integration over the cross section, and due to the fact that the variations vanish at the boundaries, standard arguments of the calculus of variation deliver

$$\int_L \rho A \ddot{\boldsymbol{u}} \cdot \delta \boldsymbol{u}\, ds + \int_L \rho I \ddot{\boldsymbol{n}} \cdot \delta \boldsymbol{n}\, ds + \int_L \left(E A \varepsilon_{11} \delta \varepsilon_{11} + E I \kappa \delta \kappa\right)\, ds = 0, \tag{9}$$

where A and I is the area and the moment of inertia of the cross section, respectively. The equation of motion for projectile holds

$$M_1 \ddot{\boldsymbol{y}} = 0, \tag{10}$$

where M_1 and $\boldsymbol{y}$ are the mass and the position vector of the projectile, respectively. For $t_k^- < t < t_k^+$, from (6), (7), we have

$$\int_{t_k^-}^{t_k^+} \int_V \dot{\boldsymbol{x}} \delta \dot{\boldsymbol{x}} dV dt - \int_{t_k^-}^{t_k^+} \int_V E E_{11} \delta E_{11} dV dt + \int_{t_k^-}^{t_k^+} \boldsymbol{\lambda}_N \delta \boldsymbol{u} dt = 0. \tag{11}$$

Let's define the acceleration $\{\ddot{\boldsymbol{x}}\}$ as follows $\{\ddot{\boldsymbol{x}}\} \xrightarrow[n \to +\infty]{} \frac{\dot{\boldsymbol{x}}\left(t_k^+\right) - \dot{\boldsymbol{x}}\left(t_k^-\right)}{t_k^+ - t_k^-}$. From (11), the fact that the variations vanish at the boundary and the calculation of the integral over Δt and then the integral over the cross sectio, we obtain

$$\begin{aligned} \int_L A \left(\dot{\boldsymbol{u}}\left(t_k^+\right) - \dot{\boldsymbol{u}}\left(t_k^-\right)\right) \delta \boldsymbol{u} ds + \int_L I \left(\dot{\boldsymbol{n}}\left(t_k^+\right) - \dot{\boldsymbol{n}}\left(t_k^-\right)\right) \delta \boldsymbol{n} ds \\ + \int_L \left(E A \varepsilon_{11} \delta \varepsilon_{11} + E I \kappa \delta \kappa\right) \Delta t\, ds - \boldsymbol{\Lambda}_N \delta \boldsymbol{u} = 0, \end{aligned} \tag{12}$$

where $\boldsymbol{\Lambda}_N = \boldsymbol{\lambda}_N \Delta t$ is the impulsive force during impact. The equation of motion for projectile during impact holds

$$M_1 \left(\dot{\boldsymbol{y}}^+ - \dot{\boldsymbol{y}}^- \right) = -\boldsymbol{\lambda}_N. \tag{13}$$

(9), (10), (12) and (13) are fundamental equations of motion for our system before, after and within the impact event.

3.2 Unilateral constraints

Let's define $\boldsymbol{D}_N$ as the relative displacement between the projectile and the contact point on the beam. On displacement level, we have the following constraint between contact forces and $\boldsymbol{D}_N$ holds $\boldsymbol{D}_N \geq 0$, $\boldsymbol{\lambda}_N \geq 0$ and $\boldsymbol{D}_N \boldsymbol{\lambda}_N = 0$. Due to the equivalence between Signorini's force laws and normal cone inclusion of force laws[2, 3, 4], one can write the previous relations in a very compact form: $\boldsymbol{D}_N \in \mathcal{N}_{\mathcal{B}} \left(-\boldsymbol{\lambda}_N \right)$, where $\mathcal{B}$ is the convex set containing all available values of $-\boldsymbol{\lambda}_N$. Equivalently, at velocity level, the constraint is written as $\boldsymbol{\zeta}_N \in \mathcal{N}_{\mathbb{R}_r^-} \left(-\boldsymbol{\Lambda}_N \right)$, where $\boldsymbol{\zeta}_N$ is the relative velocity between the projectile and the beam contact point. Please refer to [2, 3, 4] for more details on the solution of normal cone inclusion as proximal point.

3.3 Newton's impact laws

Newton's impact laws states: $\boldsymbol{\zeta}_N^+ = -\alpha \boldsymbol{\zeta}_N^-$, where $\boldsymbol{\zeta}_N^-$ and $\boldsymbol{\zeta}_N^+$ are the relative velocities just before and after impact, $\alpha = [0, 1]$ is the coefficient of restitution(CoR). Therefore, the constraint on velocity level can be generalized to have the form:

$$\boldsymbol{\zeta}_N^+ + \alpha \boldsymbol{\zeta}_N^- \in \mathcal{N}_{\mathbb{R}_r^-} \left(-\boldsymbol{\Lambda}_N \right). \tag{14}$$

(14) can be solved using proximal point equation [2, 3, 4] as follows

$$-\boldsymbol{\Lambda}_N = prox_{\mathcal{B}}^{\mathbb{R}_0^-} \left(-\boldsymbol{\Lambda}_N + R^{-1} \left(\boldsymbol{\zeta}_N^+ + \alpha \boldsymbol{\zeta}_N^- \right) \right), \tag{15}$$

where R is a chosen parameter to only speed up the convergence and it doesn't affect the converged numerical results.

3.4 Space and time discretisation and local iteration

Before and after impact ($t < t_k^-,\ t > t_k^+,\ \boldsymbol{D}_N > 0$), the motion of the beam is regular and is described by (9). Thus, the time integration scheme is similar to the smooth case, Cf.5. During impact ($t_k^- < t < t_k^+,\ \boldsymbol{D}_N = 0$), the value of the impulsive force is determined via a internal iteration by solving the proximal point equation [2, 3, 4]:

$$\boldsymbol{\Lambda}_N^{j+1} = max \left(\boldsymbol{\Lambda}_N^j - R^{-1} \left(\boldsymbol{\zeta}_{Nn+1}^+ + \alpha \boldsymbol{\zeta}_{Nn}^- \right) \right),\ \left| \boldsymbol{\Lambda}_N^{j+1} - \boldsymbol{\Lambda}_N^j \right| \leq error. \tag{16}$$

In our case R is chosen to be equal to $\frac{M_1 m}{M_1 + m}$, where m is the weigh of one beam element.

3.5 Examples

To assess the effectiveness of the formulation in dealing with impact problems, we first examine an example of impact between a rigid projectile and a clamped Euler-Bernoulli beam at both ends, Fig 4. The mass; the initial velocity of the projectile and the beam parameters are given below:

Projectile's mass: $M_1 = 100\ Kg$
Projectile's initial velocity: $V_1 = -40\ m/s$
Projectile's initial position: $d = 2\ cm$
Beam length $L = 3\ m$
Cross section area $A = 1E3\ cm^2$
Cross section inertia $I = 8330\ cm^4$
Young's Modulus $E = 0.2E12\ Pa$
Density $\rho = 3000\ Kg/m^3$
Number of elements = 6
Time increment $\Delta T = 1E-5\ s$
Coefficient of restitution = 1

In Fig. 5a, both the motion of the projectile as well as the motion of the contact point on the beam are depicted. Jumps in velocities are illustrated in Fig. 5c. Impulsive force are plotted in Fig. 5b which have value only at the moments of impact. At the same time, Fig. 5d shows clearly the conservation of total energy. To verify the conservation of momentum, the same example has been studied but the beam doesn't have any support. The momentum is perfectly conserved, total momentum is independent of the coefficient of restitution and always equal to the initial momentum of the projectile, Fig. 5e.

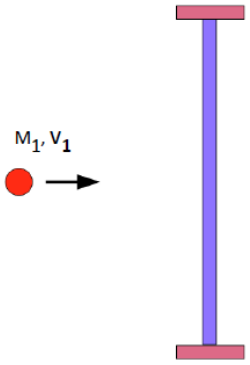


Figure 4: Nonsmooth impact model

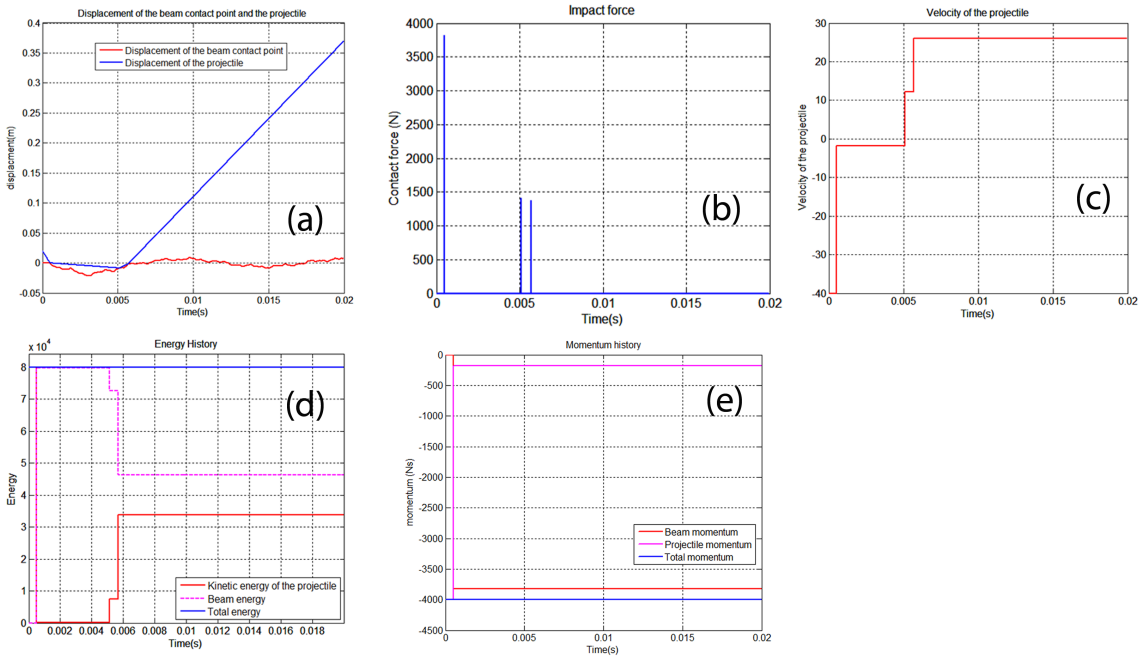


Figure 5: (a)displacement history, (b)contact force, (c)velocity of projectile, (d)energy history, (e)momentum history

The same test has been carried out, but in this case the value of coefficient of restitution is set to be zero. Similar results are obtained Fig.6 but we can see that preserved energy is proportional to the coefficient of restitution (Fig. 6d, 6f, 5d) and total momentum is conserved independently of the coefficient of restitution.

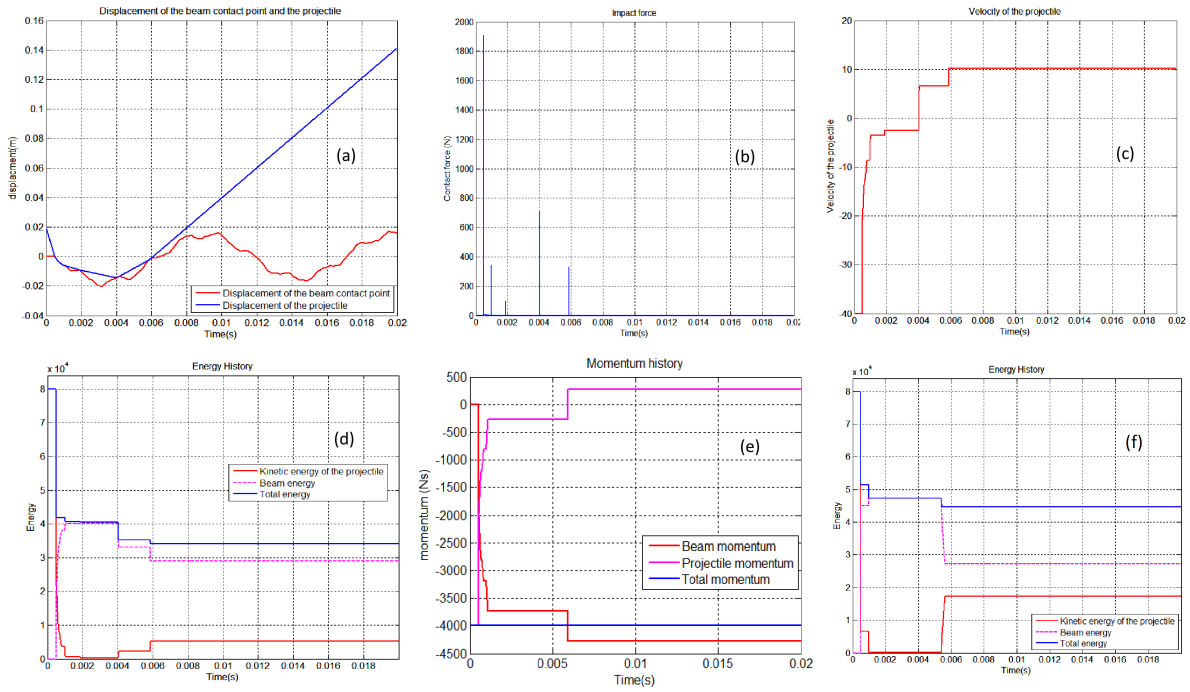


Figure 6: (a)displacement history, (b)contact force, (c)velocity of projectile, (d)energy history, (e)momentum history, (f)energy history (CoR=0.5)

4 Conclusions

In this work, two algorithms for impact on beam have been presented. Both smooth and nonsmooth approaches have shown excellent performances in term of accuracy, stability and conservation properties even for strongly non-linear situations. In the smooth formulation, the impact force is calculated directly from projectile deformations, however the whole together has to respect collision laws, dynamics equations for the beams and the projectile. The nonsmooth ones are specially used when projectiles are rigids. The method is able to tackle perfectly the discontinuities of velocities and impact forces via set-value force laws of normal cone and also Newton's Impact law where coefficient of restitution is incorporated.

REFERENCES

[1] C. Sansour, T.L. Nguyen, M.Hjiaj. An energy-momentum method for in–plane geometrically exact Euler-Bernoulli beam dynamics. *International Journal for Numerical Methods in Engineering*, 2015.

[2] B.Brogliato. *Nonsmooth Mechanics: Models, Dynamics and Control*, 2th. Edition, 1999.

[3] C.Glocker. *Set-Valued Force Laws: Dynamics of Non-Smooth Systems*, Lecture Notes in Applied Mechanics. 2001, Springer.

[4] M.H.Moller. *Consistent Integrators for Non-Smooth Dynamical Systems*, Department of Mechanical and Process Engineering 2011, ETH Zurich.

[5] R. C. Fetecau, J. E. Marsden, M. Ortiz and M. West. *Nonsmooth Lagrangian Mechanics and Variational Collision Integrators*, SIAM J. Appl. Dyn. Syst., Vol. 2, No. 3, 381–416,2003.

[6] C. P. Vyasarayani,Sukhpreet Singh Sandhu and John McPhee. *Nonsmooth Modeling of Vibro-Impacting Euler-Bernoulli Beam*, Advances in Acoustics and vibration, 1, Vol. 2012.

COMPDYN 2015
5th ECCOMAS Thematic Conference on
Computational Methods in Structural Dynamics and Earthquake Engineering
M. Papadrakakis, V. Papadopoulos, V. Plevris (eds.)
Crete Island, Greece, 25–27 May 2015

VARIATIONAL FORMULATION OF DISCONTINUOUS-GALERKIN TIME INTEGRATORS

Pablo Mata A.[1], **Yongxing Shen**[2], **and Vahid Ziaei-Rad**[2]

[1]Centro de Investigación en Ecosistemas de la Patagonia (CIEP), Conicyt Regional/ CIEP R10C1003
Universidad Austral de Chile
c/Bilbao 449, Coyhaique, Chile
e-mail: pmata@ciep.cl

[2]University of Michigan-Shanghai Jiao Tong University Joint Institute, Shanghai Jiao Tong University
200240, Shanghai, China
e-mail: yongxing.shen@sjtu.edu

[3]Laboratori de Càlcul Numèric, Universitat Politècnica de Catalunya (UPC BarcelonaTech)
08034, Barcelona, Spain
vahid.ziaei@upc.edu

Keywords: variational integrators, discontinuous-Galerkin, time integrator.

Abstract. *Variational integrators provide a way to design structure-preserving time integrators for problems presenting a Lagrangian structure. The basic idea consists in obtaining algorithms from a discrete analogue of Hamilton's variational principle. Then, the discrete trajectories are stationary points of a discrete analogue of the action functional. The resulting methods enjoy a number of remarkable properties: i) they exactly conserves the momenta associated to the symmetries of a discrete version of the Lagrangian, ii) they define a discrete symplectic flow on the phase space and iii) they show an error in the total energy that remains bounded for exponentially long periods of time. A particularly interesting family of such methods is given by the so called Galerkin variational integrators. Their construction is based on approximating the trajectory of the system by means of piecewise continuous polynomials and providing suitable quadrature rules to approximate the action functional. Then, increasing the order of the interpolating polynomials and the accuracy of the quadrature rules allow to obtain higher order time integrators. In this work we extend the Galerkin methods to the discontinuous case yielding to a family of discontinuous-Galerkin (dG)-methods. To this end, we resort to using two key ingredients: 1) the trajectory of the system is approximated by means of piecewise polynomials which may presents a finite number of discontinuities across time interval boundaries and 2) we approximate the velocity of the system by means of an appropriate dG-time-derivative of the trajectory following some ideas presented in [1, 2] for static problems in elasticity. The resulting algorithms corresponds to a family of discontinuous-symplectic Runge-Kutta methods.*

1 INTRODUCTION

The construction of integrators for which the trajectories preserve invariants of the original system is the realm of structured or geometric integration, see e.g. [3, 4, 5]. Variational integrators (VI) provide a way to design structure-preserving time integrators for problems whose dynamics is generated by a Hamiltonian. The basic idea behind these methods is to obtain the algorithm from discrete analog to Hamilton's variational principle. In this way, the computed discrete trajectories are stationary points of a discrete action functional, the discrete action sum. As a result, the discrete trajectories approximate the exact trajectories of the system, and nearly exactly preserve the exact energy of the system for long times [4, Ch. 9]. Moreover, if the discrete action sum is designed to respect symmetries of the original action functional, then by virtue of a discrete version of Noether's theorem, the discrete trajectories conserve the momenta conjugate to each one of these symmetries, see e.g. [6]. Finally, the resulting algorithms are symplectic by design. Nowadays it is possible to find a vast literature on VIs. Most of the basic theory and analytical results may be reviewed in [7, 8, 9, 6, 10, 11, 12].

These methods have been successfully applied in numerous fields, such as to the construction of asynchronous integration methods in solid mechanics [6, 10], to problems with constraints [11, 13], to problems with contact [14, 15, 16, 17], with oscillatory solutions [18], to Langevin and stochastic differential equations [19, 20], to problems where the evolution takes place over a nonlinear manifold [21, 22, 23], to thermoelasticity [24, 25, 26] and to incompressible fluids [27], to name some of the most relevant ones.

In this paper, we extend the standard methodology to constructuct (continuous) Galerkin time integrators to the discontinuous case. The basic idea consists in approximating the discrete Lagrangian by means of piecewise discontinuous polynomials. The corresponding discrete approximation to the velocity in the time interval is obtained by means of using the Discontinuous-Galerkin (DG) derivative [1, 2]. The resulting integrators provide a methodology for constructing discontinuous integrators which automatically have a number of properties: (i) they are symplectic, (ii) they exactly preserve the momenta associated to symmetries, (iii) and they have excellent longtime energy behavior (see [6, 10, 12, 28]). The proposed methodology is showcased through some examples.

2 Formulation of variational integrators

We consider a finite-dimensional mechanical system characterized by a Lagrangian function $L(\mathbf{q}, \dot{\mathbf{q}})$ with $\mathbf{q} = (\mathrm{q}^1, ..., \mathrm{q}^n)$ being generalized coordinates defined on a configuration space Q and $\dot{\mathbf{q}}$ the velocities corresponding to time-dependent curves on Q. The action functional over the time interval $[t_a, t_b]$ is formed integrating the Lagrangian function along $\mathbf{q}(t)$ as

$$S[\mathbf{q}(\cdot)] = \int_{t_a}^{t_b} L\left(\mathbf{q}(t), \dot{\mathbf{q}}(t)\right)\ dt. \tag{1}$$

Hamilton's principle states that the system evolves following trajectories that are a stationary point of $S[\mathbf{q}(\cdot)]$ under arbitrary variations in the set of all smooth enough trajectories that leave the end-points fixed. This condition yields the so called *Euler-Lagrange* (E-L) equations, namely

$$\frac{\partial L}{\partial \mathrm{q}^i}(\mathbf{q}(t), \dot{\mathbf{q}}(t)) - \frac{d}{dt}\left(\frac{\partial}{\partial L \dot{\mathrm{q}}^i}(\mathbf{q}(t), \dot{\mathbf{q}}(t))\right) = 0, \qquad i = 1, ..., n. \tag{2}$$

Moreover, Noether's theorem states that there exists a correspondence between the quantities conserved along solution trajectories and the symmetries of the Lagrangian [29].

The Hamiltonian function $\mathsf{H} : \mathsf{T}^*Q \to \mathbb{R}$ is obtained as the *Legendre transformation* of the Lagrangian function in the velocity variables as

$$H(\mathbf{q}, \mathbf{p}) = \mathbf{p} \cdot \dot{\mathbf{q}} - L(\mathbf{q}, \dot{\mathbf{q}}), \tag{3}$$

which considers the change of variables $(\mathbf{q}, \dot{\mathbf{q}}) \to (\mathbf{q}, \mathbf{p})$ after the introduction of the conjugated (mechanical) momenta,

$$\mathbf{p} = \frac{\partial L}{\partial \dot{\mathbf{q}}}(\mathbf{q}, \dot{\mathbf{q}}). \tag{4}$$

Then, taking the time derivative of (3) it is possible to see that the equations of motion (2) may be rephrased in the following completely equivalent (Hamiltonian) form,

$$\dot{\mathbf{z}} = \mathbf{J}\frac{\partial H}{\partial \mathbf{z}}(\mathbf{z}), \qquad \mathbf{z}(t^0) = \mathbf{z}^0, \tag{5}$$

where $\mathbf{z} = (\mathbf{q}, \mathbf{p})$ and

$$\mathbf{J} = \begin{pmatrix} \mathbf{0}_{n\times n} & \mathbf{I}_{n\times n} \\ -\mathbf{I}_{n\times n} & \mathbf{0}_{n\times n} \end{pmatrix}$$

is a cannonical symplectic matrix [29]. Moreover, $\mathbf{0}_{n\times n}$ and $\mathbf{I}_{n\times n}$ are $n-$dimensional zero and identity matrices.

Two significant characteristics of time continuous (autonomous) Hamiltonian systems are:

- The Hamiltonian function H is along solution trajectories of the system (5).
- They define symplectic flows over the phase space (cotangent bundle) T^*Q as explained in [4, Ch. 6] or [30, Ch. 4].

2.1 General discretization procedure

The basic idea behind the formulation of variational integrators consists in a constructing discrete approximations of the action sum instead of developing methods based on the discretization of the Euler-Lagrange equations. A complete review of the methods may be found for example in [31, 6, 10]. Then, we begin by partitioning the time interval of interest into equally spaced intervals of length $h = (t_b - t_a)/N_t$, and set $t^k = t_a + kh$ for $k = 0, \ldots, N_t$. The discrete Lagrangian $L_d : Q \times Q \times \mathbb{R} \to \mathbb{R}$ is constructed to approximate the action integral over a time step $[0, h]$ as

$$L_d(\mathbf{q}^0, \mathbf{q}^1, h) \approx \int_0^h L(\mathbf{q}(t), \dot{\mathbf{q}}(t))\, dt, \tag{6}$$

where $\mathbf{q}(t) : [0, h] \to Q$ is the solution of equations (2) subjected to $\mathbf{q}(0) = \mathbf{q}^0$ and $\mathbf{q}(h) = \mathbf{q}^h$ [11]. Then, the discrete action sum is constructed as

$$S_d(\mathbf{q}^0, ..., \mathbf{q}^{N_t}, h) = \sum_{k=0}^{N_t-1} \mathsf{L}_d(\mathbf{q}^k, \mathbf{q}^{k+1}, h), \tag{7}$$

and a discrete version of Hamilton's principle allows to deduce the discrete Euler-Lagrange equations (DEL) as

$$D_2 L_d(\mathbf{q}^{k-1}, \mathbf{q}^k) + D_1 L_d(\mathbf{q}^k, \mathbf{q}^{k+1}) = 0, \qquad k = 1, ..., N_t - 1, \tag{8}$$

where $D_i L_d$ denotes the partial derivative of L_d with respect the i[th] slot and the time step length h has been omitted in the arguments of L_d to alleviate the notation. The above system of equations defines an update map from $Q \times Q$ to itself known as the *discrete Lagrangian flow map* which takes a point $(\mathbf{q}^{k-1}, \mathbf{q}^k)$ to $(\mathbf{q}^k, \mathbf{q}^{k+1})$. The discrete counterpart of the momenta (4) are defined by means of a discrete Legendre transformation according to

$$\mathbf{\Pi}^k = -D_1 L_d(\mathbf{q}^k, \mathbf{q}^{k+1}), \tag{9a}$$

$$\mathbf{\Pi}^{k+1} = D_2 L_d(\mathbf{q}^k, \mathbf{q}^{k+1}). \tag{9b}$$

The above equations define the *discrete Hamiltonian flow map* wich takes a point $(\mathbf{q}^k, \mathbf{\Pi}^k)$ to $(\mathbf{q}^{k+1}, \mathbf{\Pi}^{k+1})$. This maps defines implicitly a time integrator expressed in the so called *position-momentum* form. The procedure consist in solving (9a) for $\mathbf{q}^{k+1}$ and then replacing it in Eq. (9b) to obtain $\mathbf{\Pi}^{k+1}$.

A convergence result on variational integrators in [11] states that if L_d is an $\mathcal{O}(h^{p+1})$ $(p > 1)$ approximation for the action on a time step and some standard smoothness conditions on L are satisfied, then (i) the discrete Hamiltonian flow maps is an $\mathcal{O}(h^{p+1})$ approximation of the exact flow of the system on T^*Q and (ii) the discrete Legendre transformation of L_d has error that decays at least as h^{p+1}. Therefore, higher-order approximations in (6) result in correspondingly higher-order integrators.

2.2 Continuous Galerkin VI

The basic idea behind the formulation of continuous Galerkin rules consist in extending tow order quadrature rule to higher order. To this end, we consider s control points $\{\mathbf{q}_\nu^0\}_{\nu=0,...,s}$ (with $\mathbf{q}_0^0 = \mathbf{q}^0$ and $\mathbf{q}_s^0 = \mathbf{q}^1$) corresponding to the values of the trajectory at control times $\{d_\nu h\}_{\nu=0,...,s}$ with $0 = d_0 < d_1 < ... < d_s = 1$. Moreover, we assume that the trajectory over $[0, h]$ is approximated by a unique $s-$degree polynomial $\mathbf{q}_p(t; \mathbf{q}_0^0, ..., \mathbf{q}_s^0, h) \in \mathbb{P}^s([0, h])$ such that

$$\mathbf{q}_p(d_\nu h) = \mathbf{q}_\nu^0, \qquad \nu \in \{0, 1, ..., s\}.$$

See Figure 1-a, c. Then, providing an appropriate quadrature rule, the discrete Lagrangian is obtained as

$$L_d(\mathbf{q}^0, \mathbf{q}^1, h) = \inf_{\substack{\mathbf{q}(t)\in\mathbb{P}^s([0,h]) \\ \mathbf{q}(0)=\mathbf{q}^0, \mathbf{q}(h)=\mathbf{q}^1}} \sum_{i=1}^{n_q} w_i L(\mathbf{q}_p(\xi^i), \dot{\mathbf{q}}_p(\xi_i)). \tag{10}$$

Thwn, we obtain that the discrete action sum will be of the form

$$S_d\left(\left\{\mathbf{q}_\nu^0\right\}_{\nu=0,...,s}, ..., \left\{\mathbf{q}_\nu^N\right\}_{\nu=0,...,s}\right), \tag{11}$$

subjected to the continuity constraints

$$\mathbf{q}_s^i = \mathbf{q}_0^{i+1}, \qquad i \in \{1, ..., N-1\}. \tag{12}$$

Enforcing the action sum to be stationary under arbitrary variations $\{\delta\mathbf{q}_\nu^0\}_{\nu=0,...,s}$ that held the endpoints of the trajectory fixed yields to the DEL equations (8) plus the following extra conditions

$$\frac{\partial S_d}{\partial \mathbf{q}_\nu^i}\left(\left\{\mathbf{q}_\nu^0\right\}_{\nu=0,...,s}, ..., \left\{\mathbf{q}_\nu^N\right\}_{\nu=0,...,s}\right) = 0, \qquad \begin{matrix} i = 1, ..., N-1 \\ \nu = 1, ..., s-1 \end{matrix}, \tag{13}$$

which ensures that the values of the trajectory at the control point fulfil the infimum condition (10).

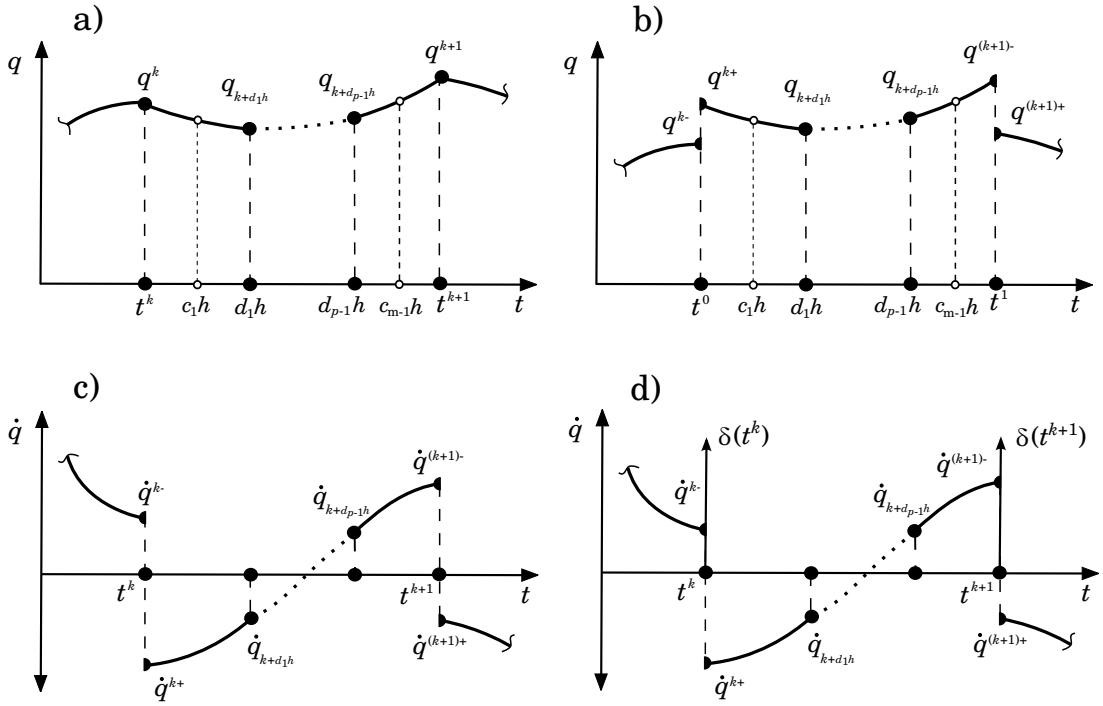


Figure 1: $a)$ Schematic representation of a piecewise-continuous polynonial used to interpolate $\mathbf{q}(t)$ in echa time step. $b)$ Piecewise-discontinuous polynomial. $c)$ Velocity profile obtained for the case $a)$. $d)$ Velocity profile for the case $b)$.

3 Formulation of discontinuous Galerkin VI

In this case we we allow to $\mathbf{q}^p(t; \mathbf{q}_0^0, ..., \mathbf{q}_s^0, h)$ to be discontinuous across time interval boundaries. Thus, relaxing the constraint (12). See figure (1-b). Then, we have that

$$\mathbf{q}^{k+} = \lim_{\epsilon \to 0^+} \mathbf{q}_p(t^k + \epsilon) \neq \lim_{\epsilon \to 0^-} \mathbf{q}_p(t^k + \epsilon) = \mathbf{q}^{k-}. \tag{14}$$

Moreover, we define

$$\begin{aligned} [\![\mathbf{q}]\!]^k &:= \mathbf{q}^{k-} - \mathbf{q}^{k+}, \qquad \text{(jump operator)} \\ \{\mathbf{q}\}^k &:= \frac{1}{2}(\mathbf{q}^{k-} + \mathbf{q}^{k+}), \qquad \text{(average operator)}. \end{aligned}$$

and following [1, 2] we define the Discontinuous-Galerkin approximation to the time derivative (DG-derivative) of $\mathbf{q}_p(t)$ as

$$D_{DG}\mathbf{q}_p := \dot{\mathbf{q}}_p - r([\![\hat{\mathbf{q}} - \mathbf{q}]\!]) - l(\{\hat{\mathbf{q}} - \mathbf{q}\}),$$

where $\dot{\mathbf{q}}_p$ means derivation in each time interval, $\hat{\mathbf{q}}$ is a numerical flux (to be given bellow) and the right and left lifting operators $r(\cdot)$ and $l(\cdot)$ are defined as

$$\begin{aligned} \int_0^T r(\varphi)\tau \, dt &:= -\sum_{k=0}^{N} \varphi^k \{\tau\}^k, \\ \int_0^T l(\varphi)\tau \, dt &:= -\sum_{k=1}^{N-1} \varphi^k [\![\tau]\!]^k, \end{aligned}$$

for all $\tau \in V_h^{n'} := \{v \in L_2(0;T) \ : \ v|_{(t^k,t^{k+1})} \in P^{n'}(t^k;t^{k+1}\}$ with $n' \geq n-1$ and $\mathbf{q}_p \in V_h^n$.

Considering the *Bassi-Rebay* [2] approximation for the flux, $\hat{\mathbf{q}} = \{\mathbf{q}\}$, we obtain that

$$L_d(\mathbf{q}_p, D_{DG}\mathbf{q}_p, h) = \sum_{i=1}^{n_g} w_i L(\mathbf{q}_p(\xi_i), D_{DG}\mathbf{q}_p(\xi_i)) \approx \int_{t^k}^{t^{k+1}} L(\mathbf{q}, \dot{\mathbf{q}})\ dt,$$

where $\{\xi_i, w_i\}_{i=1,\dots,n_g}$ is a set of quadrature points and the corresponding weights used to approximate the action over $[t^k, t^{k+1}]$.

4 Examples

In the following examples we consider separable Lagrangian functions of the form

$$L(\mathbf{q}, \dot{\mathbf{q}}) = \mathbf{M}\dot{\mathbf{q}} \cdot \dot{\mathbf{q}} - V(\mathbf{q}).$$

4.1 Bassi-Rebay

We consider a discontinuous piecewise linear approximation for $\mathbf{q} \in [t^k, t^{k+1}]$. In this case we always have $p^{k-} = p^{(k+1)+}$.

The discrete Lagrangian is

$$\begin{aligned} &L_d\left(q^{k-}, q^{k+}, q^{(k+1)-}, q^{(k+1)+}, \Delta t\right) \\ &= M\frac{\left(-q^{k-} - q^{k+} + q^{(k+1)-} + q^{(k+1)+}\right)^2}{8\Delta t} - \int_{t_k}^{t_{k+1}} V(q)\ dt \end{aligned}$$

The algorithm in position-momentum form thus reads

$$\begin{aligned} p^{k-} &= M\frac{\left(-q^{k-} - q^{k+} + q^{(k+1)-} + q^{(k+1)+}\right)}{4\Delta t}, \\ p^{k+} &= M\frac{\left(-q^{k-} - q^{k+} + q^{(k+1)-} + q^{(k+1)+}\right)}{4\Delta t} + \frac{\partial}{\partial q^{k+}}\int_{t_k}^{t_{k+1}} V(q)\ dt, \\ p^{(k+1)-} &= M\frac{\left(-q^{k-} - q^{k+} + q^{(k+1)-} + q^{(k+1)+}\right)}{4\Delta t} - \frac{\partial}{\partial q^{(k+1)-}}\int_{t_k}^{t_{k+1}} V(q)\ dt, \\ p^{(k+1)+} &= M\frac{\left(-q^{k-} - q^{k+} + q^{(k+1)-} + q^{(k+1)+}\right)}{4\Delta t}. \end{aligned}$$

4.1.1 Piecewise linear $r_k(q)$

In this case, let ψ_k denote the standard $P^1([0,h])$ shape function of node k in time. Then,

$$r_k(1) = \begin{cases} h_{k-1}^{-1}(\psi_{k-1}(t) - 2\psi_k(t)), & t_{k-1} < t < t_k, \\ h_k^{-1}(-2\psi_k(t) + \psi_{k+1}(t)), & t_k < t < t_{k+1}, \\ 0, & \text{otherwise}. \end{cases}$$

As a result, with a constant $h_k = \Delta t$,

$$\begin{aligned} D_{DG}q|_{(t_k,t_{k+1})} &= \frac{q^{(k+1)-} - q^{k+}}{\Delta t} + r_k\left(q^{k-} - q^{k+}\right)(t) + r_{k+1}\left(q^{(k+1)-} - q^{(k+1)+}\right)(t) \\ &= \frac{q^{(k+1)-} - q^{k+}}{\Delta t} + \frac{1}{\Delta t}\left(q^{k-} - q^{k+}\right)(-2\psi_k(t) + \psi_{k+1}(t)) \\ &\quad + \frac{1}{\Delta t}\left(q^{(k+1)-} - q^{(k+1)+}\right)(\psi_k(t) - 2\psi_{k+1}(t)). \end{aligned}$$

We can use Simpson's rule (Lobatto quadrature rule with 3 points) to exactly integrate $M(D_{DG}q)^2$. Doing so yields

$$\begin{aligned}
&\int_{t_k}^{t_{k+1}} M(D_{DG}q)^2\,dt \\
&= \frac{M\Delta t}{6}\left[\frac{q^{(k+1)-}-q^{k+}}{\Delta t}-\frac{2}{\Delta t}\left(q^{k-}-q^{k+}\right)+\frac{1}{\Delta t}\left(q^{(k+1)-}-q^{(k+1)+}\right)\right]^2 \\
&\quad+\frac{2M\Delta t}{3}\left[\frac{q^{(k+1)-}-q^{k+}}{\Delta t}-\frac{1}{2\Delta t}\left(q^{k-}-q^{k+}\right)-\frac{1}{2\Delta t}\left(q^{(k+1)-}-q^{(k+1)+}\right)\right]^2 \\
&\quad+\frac{M\Delta t}{6}\left[\frac{q^{(k+1)-}-q^{k+}}{\Delta t}+\frac{1}{\Delta t}\left(q^{k-}-q^{k+}\right)-\frac{2}{\Delta t}\left(q^{(k+1)-}-q^{(k+1)+}\right)\right]^2 \\
&= \frac{M}{6\Delta t}\Big\{\left[-2q^{k-}+q^{k+}+2q^{(k+1)-}-q^{(k+1)+}\right]^2+\left[-q^{k-}-q^{k+}+q^{(k+1)-}+q^{(k+1)+}\right]^2 \\
&\quad+\left[q^{k-}-2q^{k+}-q^{(k+1)-}+2q^{(k+1)+}\right]^2\Big\}
\end{aligned}$$

Thus

$$\begin{aligned}
&L_d\left(q^{k-},q^{k+},q^{(k+1)-},q^{(k+1)+},\Delta t\right) \\
&= \frac{M}{12\Delta t}\Big\{\left[-2q^{k-}+q^{k+}+2q^{(k+1)-}-q^{(k+1)+}\right]^2+\left[-q^{k-}-q^{k+}+q^{(k+1)-}+q^{(k+1)+}\right]^2 \\
&\quad+\left[q^{k-}-2q^{k+}-q^{(k+1)-}+2q^{(k+1)+}\right]^2\Big\}-\int_{t_k}^{t_{k+1}} V(q)\,dt
\end{aligned}$$

The algorithm reads

$$\begin{aligned}
p^{k-} &= \frac{M}{2\Delta t}\left[-2q^{k-}+q^{k+}+2q^{(k+1)-}-q^{(k+1)+}\right], \\
p^{k+} &= \frac{M}{2\Delta t}\left[q^{k-}-2q^{k+}-q^{(k+1)-}+2q^{(k+1)+}\right]+\frac{\partial}{\partial q^{k+}}\int_{t_k}^{t_{k+1}} V(q)\,dt, \\
p^{(k+1)-} &= \frac{M}{2\Delta t}\left[-2q^{k-}+q^{k+}+2q^{(k+1)-}-q^{(k+1)+}\right]-\frac{\partial}{\partial q^{(k+1)-}}\int_{t_k}^{t_{k+1}} V(q)\,dt, \\
p^{(k+1)+} &= \frac{M}{2\Delta t}\left[q^{k-}-2q^{k+}-q^{(k+1)-}+2q^{(k+1)+}\right].
\end{aligned}$$

It can be checked that when $V\equiv 0$, starting with $q^{0-}=q^{0+}=0$ and $p^{0-}=p^{0+}=M/(2\Delta t)$, we get

$$p^{k-}=p^{k+}=M/(2\Delta t),\quad q^{k-}=q^{k+}=k.$$

4.2 Higher order methods

The lifting operator in terms of Legendre polynomials:

$$r_k(1)=\begin{cases}-(2h_{k-1})^{-1}\sum_{l=0}^{n}(2l+1)P_l(\xi(t)), & t_{k-1}<t<t_k,\\ -(2h_k)^{-1}\sum_{l=0}^{n}(-1)^l(2l+1)P_l(\xi(t)), & t_k<t<t_{k+1},\\ 0, & \text{otherwise.}\end{cases}$$

The first few Legendre polynomials read

$$P_0(\xi) = 1, \quad P_1(\xi) = \xi, \quad P_2(\xi) = \frac{1}{2}\left(3\xi^2 - 1\right).$$

With $n = 0$ and 1 we recover the expressions of $r_k(1)$ above. With $n = 2$,

$$r_k(1) = \begin{cases} -(4h_{k-1})^{-1}\left(1 + 6\xi + 3\xi^2\right), & t_{k-1} < t < t_k, \\ -(4h_k)^{-1}\left(1 - 6\xi + 3\xi^2\right), & t_k < t < t_{k+1}, \\ 0, & \text{otherwise}. \end{cases}$$

The DG derivative with degrees of freedom q^{k+}, $q^{k+1/2}$, and $q^{(k+1)-}$ reads

$$\begin{aligned} & D_{DG}q|_{(t_k,t_{k+1})} \\ &= \frac{1}{\Delta t}\left[(2\xi - 1)\, q^{k+} - 4\xi q^{k+1/2} + (2\xi + 1)\, q^{(k+1)+}\right] \\ &\quad + r_k\left(q^{k-} - q^{k+}\right)(t) + r_{k+1}\left(q^{(k+1)-} - q^{(k+1)+}\right)(t) \\ &= \frac{1}{\Delta t}\left[(2\xi - 1)\, q^{k+} - 4\xi q^{k+1/2} + (2\xi + 1)\, q^{(k+1)+}\right] \\ &\quad - \frac{4}{\Delta t}\left(q^{k-} - q^{k+}\right)\left(1 - 6\xi + 3\xi^2\right) + \frac{4}{\Delta t}\left(q^{(k+1)-} - q^{(k+1)+}\right)\left(1 + 6\xi + 3\xi^2\right) \end{aligned}$$

The discrete Lagrangian reads

$$L_d\left(q^{k-}, q^{k+}, q^{k+1/2}, q^{(k+1)-}, q^{(k+1)+}, \Delta t\right) = \int_{t_k}^{t_{k+1}} \left(\frac{1}{2} M D_{DG} q^2 - V(q)\right) dt$$

The algorithm reads

$$\begin{aligned} p^{k-} &= -D_1 L_d\left(q^{k-}, q^{k+}, q^{k+1/2}, q^{(k+1)-}, q^{(k+1)+}, \Delta t\right), \\ p^{k+} &= -D_2 L_d\left(q^{k-}, q^{k+}, q^{k+1/2}, q^{(k+1)-}, q^{(k+1)+}, \Delta t\right), \\ 0 &= D_3 L_d\left(q^{k-}, q^{k+}, q^{k+1/2}, q^{(k+1)-}, q^{(k+1)+}, \Delta t\right), \\ p^{(k+1)-} &= D_4 L_d\left(q^{k-}, q^{k+}, q^{k+1/2}, q^{(k+1)-}, q^{(k+1)+}, \Delta t\right), \\ p^{(k+1)+} &= D_5 L_d\left(q^{k-}, q^{k+}, q^{k+1/2}, q^{(k+1)-}, q^{(k+1)+}, \Delta t\right). \end{aligned}$$

The Gauss quadrature rule with three points or the Lobatto rule with four points is sufficient to integrate the kinetic energy exactly.

REFERENCES

[1] Y. Shen, A. Lew., A family of discontinuous galerkin mixed methods for nearly and perfectly incompressible elasticity, ESAIM: Mathematical Modelling and Numerical Analysis 46 (5) (2012) 1003–1028.

[2] A. T. Eyck, A. Lew., Discontinuous galerkin methods for non-linear elasticity, International Journal for Numerical Methods in Engineering 67 (9) (2006) 1204–1243.

[3] B. Leimkuhler, S. Reich, Simulating Hamiltonian Dynamics. Cambridge Monographs on Applied and Computational Mathematics, Vol. 14, Cambridge University Press, 2004.

[4] E. Hairer, C. Lubich, G. Wanner, Geometric Numerical Integration. Structure-Preserving Algorithms for Ordinary Differential Equations, Springer-Verlag, 2006.

[5] E. Hairer, C. Lubich, G. Wanner, Geometric numerical integration illustrated by the Störmer-Verlet method, Acta Numerica 12 (2003) 399–450.

[6] A. Lew, J. E. Marsden, M. Ortiz, M. West, Variational time integrators, International Journal for Numerical Methods in Engineering 60 (2004) 153–212.

[7] A. P. Veselov, Integrable discrete-time systems and difference operators, Functional Analysis and Its Applications 22 (2) (1988) 83–93.

[8] J. Moser, A. P. Veselov, Discrete versions of some classical integrable systems and factorization of matrix polynomials, Communications in Mathematical Physics 139 (2) (1991) 217–243.

[9] C. Kane, J. E. Marsden, M. Ortiz, Symplectic-energy-momentum preserving variational integrators, Journal of Mathematical Physics 40 (7) (1999) 3353–3371.

[10] A. Lew, J. E. Marsden, M. Ortiz, M. West, Asynchronous variational integrators, Archive for Rational Mechanics and Analysis 2 (2003) 85–146.

[11] J. E. Marsden, W. West, Discrete mechanics and variational integrators, Acta Numerica 10 (2001) 357–514.

[12] J. E. Marsden, S. Pekarsky, S. Shkoller, M. West, Variational methods, multisymplectic geometry and continuum mechanics, Journal of Geometry and Physics 38 (2001) 253–284.

[13] S. Leyendecker, J. E. Marsden, M. Ortiz, Variational integrators for constrained dynamical systems, ZAMM - Journal of Applied Mathematics and Mechanics / Zeitschrift fr Angewandte Mathematik und Mechanik 88 (9) (2008) 677–708.

[14] R. C. Fetecau, J. E. Marsden, M. Ortiz, M. West, Nonsmooth Lagrangian mechanics and variational collision integrators, SIAM Journal on Applied Dynamical Systems 2 (3) (2003) 381–416.

[15] F. Cirak, M. West, Decomposition contact response (DCR) for explicit finite element dynamics, International Journal for Numerical Methods in Engineering 64 (2005) 1078–1110.

[16] R. Ryckman, A. Lew, An explicit asynchronous contact algorithm for elastic body–rigid wall interaction, International Journal for Numerical Methods in Engineering 89 (7) (2012) 869–896.

[17] D. Harmon, E. Vouga, B. Smith, R. Tamstorf, E. Grinspun, Asynchronous contact mechanics, ACM Transactions on Graphics (TOG) - Proceedings of ACM SIGGRAPH 2009 (Article 87) 28 (3).

[18] A. Stern, E. Grinspun, Implicit-explicit variational integration of highly oscillatory problems, Multiscale Modelling & Simulation 7 (2009) 1779–1794.

[19] N. Bou-Rabee, H. Owhadi, Long-run accuracy of variational integrators in the stochastic context, SIAM Journal on Numerical Analysis 48 (1) (2010) 278–297.

[20] N. Bou-Rabee, H. Owhadi, Stochastic variational integrators, IMA Journal of Numerical Analysis 29 (2) (2009) 421–443.

[21] T. Lee, M. Leok, N. H. McClamroch, Lie group variational integrators for the full body problem, Computer Methods in Applied Mechanics and Engineering 196 (29-30) (2007) 2907–2924.

[22] T. Lee, M. Leok, N. H. McClamroch, Lagrangian mechanics and variational integrators on two-spheres, International Journal for Numerical Methods in Engineering 79 (9) (2009) 1147–1174.

[23] P. Mata, Explicit symplectic momentum-conserving time-stepping scheme for the dynamics of geometrically exact rods, Finite Elements in Analysis and Design 96 (2015) 11–22.

[24] P. Mata, A. Lew, Variational time integrators for finite dimensional thermoelasto dynamics without heat conduction, International Journal for Numerical Methods in Engineering 88 (1) (2011) 1–30.

[25] P. Mata, A. Lew, Variational integrators for the dynamics of thermo-elastic solids with finite speed thermal waves, Journal of Computational Physics 257 (Part B) (2014) 1423–1443.

[26] P. Mata, A. Lew, Structure-preserving time integrators for thermo-elasticity with heat conduction, Abstract in the *European Congress on Computational Methods in Applied Sciences and Engineering* Vienna, Austria, (September, 10-14, 2012).

[27] E. Gawlik, P. Mullen, D. Pavlov, J. Marsden, M. Desbrun, Geometric, variational discretization of continuum theories, Physica D: Nonlinear Phenomena.

[28] C. Kane, J. E. Marsden, M. Ortiz, M. West, Variational integrators and the Newmark algorithm for conservative and dissipative mechanical systems, International Journal for Numerical Methods in Engineering 49 (2000) 1295–1325.

[29] J. E. Marsden, T. S. Ratiu, Introduction to Mechanics and Symmetry, Springer-Verlag, 1999.

[30] K. Feng, M. Qin, Symplectic geometric algorithms for Hamiltonian Systems, Springer and Zhejiang Publishing United Group, 2010.

[31] A. Lew, Variational time integrators in computational solid mechanics, Ph.D. thesis, California Institute of Technology, Pasadena, California, USA (2003).

COMPDYN 2015
5th ECCOMAS Thematic Conference on
Computational Methods in Structural Dynamics and Earthquake Engineering
M. Papadrakakis, V. Papadopoulos, V. Plevris (eds.)
Crete Island, Greece, 25–27 May 2015

SVD FAMILY FOR ANALYSING CAR CRASH BEHAVIOUR

T.T.T. VUONG [1,2], L. JEZEQUEL[1] and Y. TOURBIER[2]

[1]LTDS, Ecole Centrale de Lyon
36 avenue Guy de Collongue, 69134 Ecully Cedex, France
e-mail: louis.jezequel@ec-lyon.fr

[2] Renault S.A.S, 1 avenue du Golf, 78084 Guyancourt cedex, France
e-mail: {thuy-thithanh.vuong,yves.tourbier}@renault.com

Keywords: Reduced Order Model, Optimization, Crash, Singular Value Decomposition, Generalized Singular Value Decomposition, Higher-Order Generalized Singular Value Decomposition, Proper Orthogonal Decomposition, a posteriori, non-intrusive

Abstract. *The car crash simulation describes the deformation of the car structure under high velocity (up to 65 km/h) during a very short simulation time (about 100 ms). The simulation represents many complexities of the finite element method in structural analysis: (i) high number of degrees of freedom (from 5 to 20 M finite elements for a whole vehicle) in order to well take into account of the geometrical and material nonlinearities; (ii) use of direct time-integration, explicit algorithm, which needs very small time step (due to Courant's condition) and consequently long time simulation (till* 24 *hours); (iii) high performance software needed (solver). Furthermore, the crash simulation is transient during all simulation; the contact management is sophisticated and the results are scattered. We are interested in elaborating a reduced crash model in order to cut down the total cost of an optimization study. The method should be a posteriori allowing predicting a new simulation interpolated between existing simulation(s) in a Design Of Experiments (DOE). We choose methods in the Singular Value Decomposition (SVD) family in order to find temporal correlation among crash data in one simulation, spatial and parametric correlation among crash data in several simulations. Two almost industrial use cases (BoxBeam — representing the most important car part for energy absorption and TBeam — representing the engine compartment) are tested with Matlab software.*

1 INTRODUCTION

In the design of a vehicle structure, the crash requirement for the security of occupants must be satisfied before any other requirements such as Durability or Noise Vibration Harshness (NVH). The simple Lumped Mass Spring (LMS) model of which properties are deduced from static crush tests, like Kamal's model [1], was firstly used for a crash simulation. Then, the multibody model MADYMO [2] was developed for both car parts and occupants [3]. Since 20 years, thanks to advances of computer technologies, the nonlinear FE model including geometries and material laws of vehicle parts become more and more popular. It becomes the high-fidelity model because it is believed to be the best approximated model for a car simulation : the physical phenomena are well modeled in particularly at the local level such as plasticity or crack. The crash solver at Renault is Pam-Crash developed by ESI Group. It uses the explicit algorithm which demands very small time steps, about μs (due to the stability condition – Courant's condition) so long time simulation (till 24 hours). As a result, the system is considered in balanced condition for each step. The mass matrix modeled by lumped-mass is already diagonal so there is no need to inverse the mass matrix during in the simulation. That makes the important difference to implicit algorithm.

Renault uses multi-objectives optimization in order to design the vehicle : there are a lot of parameters in a vehicle such as the shapes, the material laws and so on ; engineers must choose the parameters which match the technical specifications (crash, NVH ...) and some objectives such as mass minimization. While searching the best solution for an optimization study with the FE model, it is interesting to increase the number of parameters in order to improve the quality of the optimal solution but it rises dramatically the number of simulations. Nevertheless, it is not possible for the industrial context because of three reasons :

- Firstly, we will not transform our model to a simplified model like LMS or MADYMO because it will loose the "high-fidelity".
- Secondly, methods for parameters reduction are not already available so we can not have fewer parameters than that defined in the car technical specifications. In fact, there are perhaps correlations between parameters which allow us to reduce their number before creating the parametric domain. However, no method is found until now for crash simulation.
- Thirdly, the deadline must be respected : one or two days is needed for an engineer to receive and analyze the results of a simulation ; so there is a limited number of points in the parametric domain which can be explored.

As a result, our objective is to find out a method to reduce the cost of an optimization study, with the same optimal solution if we use the high-fidelity model.

There are many ways to reduce the optimization cost. The first one is to use the meta-model in order to approximate the solution in all parametric domain. However, this method is purely statistical and not really efficient in crash simulation because of the very strong nonlinear characters of car structure. The second one is to reduce the cost of a unique simulation by changing the crash code. As a user of Pam-Crash software, Renault will not tend to reduce a single simulation, which is an intrusive reduction, because it is not belong to Renault skills but the software developers. The last one is the method that we aim for : we are interested in a **non-intrusive** and **a posteriori** method, i.e., no modification of the code is made and some points (crash simulations) are necessarily realized before the reduction, respectively. We will take advantage of the maximum physical outputs of these simulations (displacements, stress, strains, sectional

efforts ... in function of time) in order to interpolate other points in parametric domain and/or to indicate which are next interesting points to simulate. The following reasons help us decide to chose a **non-intrusive** and **a posteriori** method

- The first reason is due to the unpredictable behaviors of crash simulation when we change parameters. It is impossible to calculate the crash results with analytic methods. That's why we should have some simulations done to see at least the crash behaviors of some points in parametric domain .
- The second reason is that we can not modify the crash solver but the number and type of outputs results (we call "**outputs**") are easily controlled so more outputs we get more information we will explore. We hope to find their potential relations that the solver can provide actually .
- The last reason is that the requirement of precision of the reduced model for optimization is not the same as that for a unique simulation. More precisely, we only need to known more exactly where is the optimal solution in the parametric domain without increasing the number of high-fidelity simulations. The precision for each simulation is not really necessary.

Recently, the Model Order Reduction (MOR) methods have been developed in many fields like control systems, dynamical systems, fluid mechanics, heat transfer and structural mechanics. The aim is to reduce the complexity and the time to resolve mathematical systems, usually systems of (partial) differential equations. In industry, a system can have a great number of dimensions or degrees of freedom (about millions) and consequently a big number of equations. In the dynamic context, the resolution is more and more difficult because these degrees of freedom depend on time. The reduction techniques involve the research of subspace that minimize the projection errors of the initial space (space containing the degrees of freedom of the initial problem). The dimension of subspace is much more smaller so the resolution is faster. The subspace is represented by its basis which can approximate the initial space. The non-intrusive and a posteriori reduction techniques are then both physically and mathematically interesting for us because they tend to conserve the physical properties and allow quantifying reduction errors, which are not the same things concerning the simplified models (LMS and MADYMO).

There are a variety of reduction methods of which the major can be found in [17]. Theses methods can be both applied for quasi-static and dynamic analyses, linear and nonlinear cases. We can cite some recent and popular methods such as LArge Time INcrement (LATIN) [4, 5] providing an iterative and non-incremental algorithm to resolve nonlinear problems, Proper Generalized Decomposition (PGD) [6, 7, 8] in which the solution is decomposed in a sum of products of variables (time, space and parameters), Reduced Basis (RB) [9, 10] which find a discretization for parametrized problems , Empirical Interpolation Method (EIM) [12] in which the base is built from points giving the maximum errors of projection, A Priori Hyper-Reduction (APHR)[16] which tends to reduce the number of elements in the high-fidelity model and the POD method [13, 14, 15] that we will detail after. These methods, firstly tested in academic use cases, have been introduced in the industrial contexts. However, the method for car crash simulation has not already been available. Our goal is not to invent another reduction method but try to test and adapt existing ones for our context. The POD method is possibly the best candidate for our **non-intrusive** and **a posteriori** reduction.

The POD method [21] is similar to Karhunen-Loève Decomposition [18, 19] and Principal Component Analysis (PCA) [20] in statistics and Singular Value Decomposition (SVD) [22] in linear algebra. From now on, we call SVD instead of POD because our data for reduction are directly in a matrix form (see section 4).

2 Short review of Singular Value Decomposition family

The SVD allows decomposing one matrix in a product of three ones. The extension to two, there matrices and more than three constitute a family of SVD while staying on the fundamental definition of SVD. In this section, we will review some significant methods. Their application in crash simulation will be detailed in the section 5.

2.1 Singular Value Decomposition

While the eigenvalues and eigenvectors problems deal with square matrix, the SVD try to do the same thing with a rectangle matrix.

Theorem 1. ***The singular value decomposition for real matrices [23, 21].***
If A is a $N_t \times N_x$ real matrix, then there exists real orthogonal matrices U ($N_t \times N_t$) and V ($N_x \times N_x$), i.e. $U.U_t = I_{N_t}$ and $V.V_t = I_{N_x}$

$$U = [u_1 \quad u_2 \dots u_{N_t}]$$

and

$$V = [v_1 \quad v_2 \dots v_{N_x}]$$

such that

$$U^t.A.V = diag(\sigma_1, \sigma_2, \dots, \sigma_p)$$

where

$$p = min(N_t, N_x)$$

$$\sigma_1 \geq \sigma_2 \geq \dots \sigma_r > \sigma_{r+1} = \dots = 0 \qquad rank(A) = r \leq p$$

The σ_i are the singular values of A and the vectors u_i and v_i are respectively the i-th left and i-right singular vector.

Then A can be expressed as :

$$\boxed{A = U.\Sigma.V^t} \tag{1}$$

where

$$\Sigma = diag(\sigma_1, \sigma_2, \dots, \sigma_p)$$

If $r < N_x < N_t$:

$$\begin{aligned} A_{N_t \times N_x} &= U_{N_t \times N_t}.\Sigma_{N_t \times N_x} . V^t_{N_x \times N_x} \\ &= (U_{N_t \times r} \quad U_{N_t \times (N_t - r)}). \begin{pmatrix} \Sigma_{r \times r} & 0 \\ 0 & 0 \end{pmatrix} .(V^t_{N_x \times r} \quad V^t_{N_x \times (N_x - r)}) \\ &= U_{N_t \times r} . \Sigma_{r \times r} . V^t_{Nx \times r} \end{aligned}$$

In all case A can be decomposed by the sum of r matrices of the same dimensions as A :

$$\boxed{A_{N_t \times N_x} = \sum_{i=1}^{r} u_i \, .\sigma_i \, .v_i^t = \sigma_1 \, u_1 \, v_1^t + \sigma_2 \, u_2 \, v_2^t + \dots + \sigma_r \, u_r \, v_r^t} \tag{2}$$

Then

$$\text{Frobenius norm of A :} \qquad \| A \|_F^2 = \sum_{i=1}^{m} \sum_{j=1}^{n} a_{ij}^2 = \sum_{i=1}^{r} u_i \,.\sigma_i \,.v_i^t$$

and

$$\text{2-norm of A :} \qquad \| A \|_2 = max_{\|x\|=1} \| Ax \| = \sigma_1 \qquad \text{where } x \text{ is an real } n \times 1 \text{ vector}$$

We can prove easily that U and V are respectively eigenvectors of hermitian matrices $A.A^t$ and $A^t.A$, respectively. $\sigma_{i,(i=1,\ldots,r)}$ are eigenvalues of both two matrices $A.A^t$ and $A^t.A$ because

$$A.A^t = U \,.\, \Sigma^2 \,.\, U^t$$

$$A^t.A = V \,.\, \Sigma^2 \,.\, V^t$$

2.2 Generalized Singular Value Decomposition

Theorem 2. ***The generalized singular value decomposition for REAL MATRIX pairs***
If A is a $N_t \times N_{x_1}$ matrix with $Nx_1 \geq N_t$ and B is a $N_t \times N_{x_2}$ matrix, then there exists orthogonal matrices $U(N_{x_1} \times N_{x_1})$ and $V(N_{x_2} \times N_{x_2})$ and an invertible $X(N_t \times N_t)$ such that :

$$X \,.\, A \,.\, U = D_A = diag(\alpha_i) \quad \alpha_i \geq 0 \quad i = 1, \ldots, N_t$$

and

$$X \,.\, B \,.\, V = D_B = diag(\beta_i) \quad \beta_i \geq 0 \qquad i = 1, \ldots, q = min(N_t, N_{x_2})$$

where

$$\beta_1 \geq \beta_2 \geq \cdots \geq \beta_r \geq \beta_{r+1} = \cdots = \beta_q = 0 \qquad r = rank(B)$$

The elements of the set $\sigma(A, B)$ are generalized singular values of A and B :

$$\sigma(A, B) = \{\alpha_1/\beta_1, \ldots, \alpha_r/\beta_r\}$$

The generalized singular values corresponding to $\beta_i = 0$ are infinite. While the SVD is to find $\sigma \geq 0$ such as :

$$det(A \,.\, A^t - \sigma I_{N_t}) = 0$$

the GSVD is to find $\sigma(A, B)$ such as :

$$det(A \,.\, A^t - \sigma \,.B \,.\, B^t) = 0$$

Then A and B can be expressed as :

$$\boxed{\begin{array}{ll} A & = X^{-1} \,.\, D_A \,.\, U^t \\ B & = X^{-1} \,.\, D_B \,.\, V^t \end{array}} \tag{3}$$

We remark that the the decomposition above allows A and B, which contain the same number of rows, to have the same left matrix X . If we have 2 matrix A and B having the same number of columns, with $A \in R^{N_{t_1} \times N_x}$, $B \in R^{N_{t_2} \times N_x}$ and $N_{t_1} \geq N_x$, their properties stay the same and their decomposition is call "**BSVD**" by Van Loan[24] :

$$U^t \, A \, X = D_A = diag(\alpha_i)$$

$$V^t\, B\, X = D_B = diag(\beta_i)$$

where $U(N_{t_1} \times N_{t_1})$ and $V(N_{t_2} \times N_{t_2})$ are orthogonal matrices and $X(N_x \times N_x)$ non-singular matrix. $q = min\{N_{t_2}, N_x\}$. Bart de Moor [25, 26] extended to matrices with complex values with Quotient Singular Value Decomposition (**QSVD**) – generalized form of **BSVD** and Product Singular Value Decomposition (**PSVD)** that we will not detail now for the sake of time.

2.3 Higher-Order Generalized Singular Value Decomposition

In many case, we need to work with more than two matrices simultaneously, so the GSVD can not be applied. Van Loan et *al.* [27] developed a new method called "Higher-Order Generalized Singular Value Decomposition" (HO GSVD) which allows the factorization for $N \geq 2$ matrices.

Suppose we have a set of N real matrices $D_i \in R^{m_i \times n}$ and $rank(D_i) = n$, so the HO GSVD of N matrices is :

$$\begin{aligned} D_1 &= U_1 \,.\, \Sigma_1 \,.\, V^t \\ D_2 &= U_2 \,.\, \Sigma_2 \,.\, V^t \\ \vdots &\quad\ \vdots \\ D_N &= U_N \,.\, \Sigma_N \,.\, V^t \end{aligned} \tag{4}$$

where

$$\begin{aligned} &U_i \in R^{m_i \times n} && : \textit{normalized left basis vectors} \\ &\Sigma_i = diag(\sigma_{i,k}) \in R^{n \times n} && : \textit{diagonal with } \sigma_{i,k} > 0 \\ &V \in R^{n \times n} && : \textit{normalized right basis} \end{aligned}$$

We remark that U and V are **not orthogonal**, i.e. $U_i.U_i^t \neq I_{m_i}, i = 1, \ldots, N$ and $V.V^t \neq I_n$ but their columns are still independent and normalized. The interesting point here is that V is the same for all matrices D_i. The following steps show how to calculate U_i, Σ_i and V [27]. We define the S matrix with $S_{ij} = \frac{1}{2}(A_i A_j^{-1} + A_j A_i^{-1})$, $i \neq j$ where $A_i = D_i^t D_i$.

$$S = \frac{1}{N(N-1)} \sum_{i=1}^{N} \sum_{j>i}^{N} (A_i A_j^{-1} + A_i A_j^{-1}) \tag{5}$$

$$S = \frac{2}{N(N-1)} \sum_{i=1}^{N} \sum_{j>i}^{N} S_{ij}$$

S is proven has n independent eigenvectors so it can be decomposed :

$$SV = V\Lambda$$

Where $V = (v_1, \ldots, v_n)$, $\parallel v_k \parallel = 1$ and $\Lambda = diag(\lambda_k), k = 1, \ldots, n, \lambda_k \geq 1$. V and Λ are eigenvectors and eigenvalues respectively. Then we compute matrices B_i by solving N linear

systems :

$$VB^t = D_i^t$$
$$B_i = (b_{i,1}, \ldots, b_{i,n}), \qquad i = 1, \ldots N$$

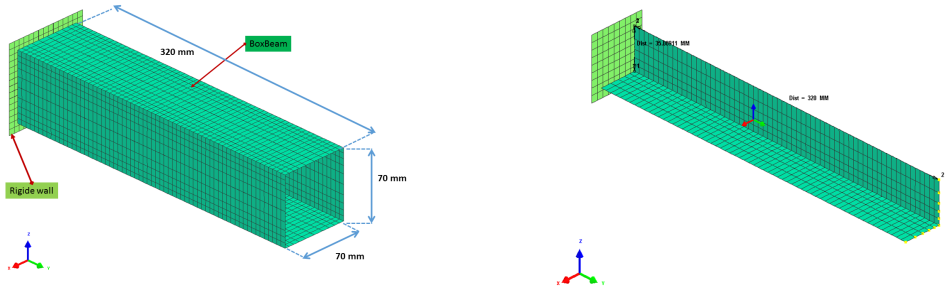
Finally,

$$\begin{array}{rcl} \sigma_{i,k} & = & \parallel b_{i,k} \parallel \\ \Sigma_i & = & diag(\sigma_{i,k}) \\ B_i & = & U_i \Sigma_i \end{array}$$

3 Description of crash use cases

A car is a complex object composing of millions of parts. Before testing a reduction method for a whole car, it is desirable to know how it works for a unit part and then a set of part. As a results, we made two use cases with the increasing complexity – BoxBeam (figure 1 (a)) and TBeam (figure 2).

1. **BoxBeam** : the crushing of a thin-walled beam against a rigid wall at the left section and hit by a rigid body, in the perpendicular direction to the wall, at the right section (the rigid body is not presented in the figure 1). The BoxBeam has square section. Because of the symmetry, we can consider from now on its quarter, see figure 1 (b). This represents the crushing of a side-member during the crash.
2. **TBeam** : This presents some significant parts in the motor compartment. The purple part (a rigid body) hits perpendicularly the dark green part with an initial velocity. In crash, the motor doesn't deform so it is modeled as a rigid body (cylinder int the figure 2).



(a) Complete BoxBeam

(b) A quarter

FIGURE 1: BoxBeam

4 Matrice representation of crash output

After a crash simulation, there are two kinds of outputs : one allows to visualize the temporal evolution of the deformation of the whole structure (like a film of the deformed structure) and other allows to draw plots of interested physical quantities in function of time (ex. displacements of a node, efforts in some sections, ...). We tend to use all available outputs for the reduction.

In order to use the properties of SVD family, we expressed all output in the matrix form. Take a crash simulation, there are 3 kinds of outputs : local, partial and global if we consider a car part.

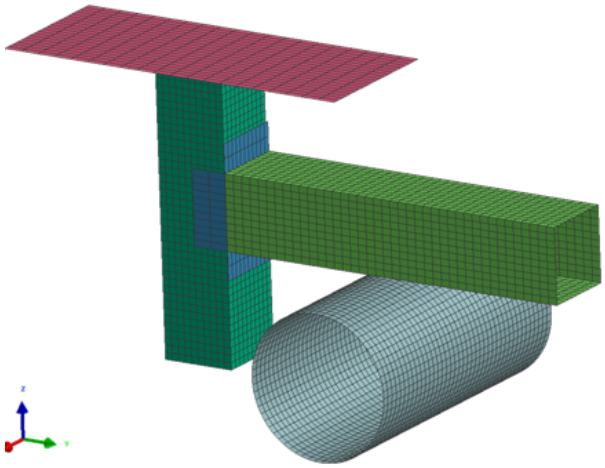


FIGURE 2: TBeam

— **Local** : They are elementary and nodal quantities, such as the displacements of a node or the moment of a element.
— **Parital** : Ex. cross section efforts – the force transmitted from a part to another
— **Global** : Ex. Deformation energy of a part

For each part, we are going to write the output data in a matrix of which each column is the temporal evolution of a physical quantity (local, partial or global) in each direction if this physical quantity is a vector (ex. displacements have 3 components) or tensor (ex. tensor of stress has 6 components). The outputs are taken each 5 time steps (BoxBeam) and 10 time steps (TBeam) of the crash solver Pam-Crash. They are "fine" and "reliable" for the reduction.

The BoxBeam has about $m = 1500$ output time steps and $n = 700$ nodes so the matrix of the X-coordinate of all nodes is A :

$$A = \begin{vmatrix} a_{t_1,N_1} & a_{t_1,N_2} & \dots a_{t_1,N_n} \\ a_{t_2,N_1} & a_{t_2,N_2} & \dots a_{t_1,N_n} \\ \vdots & \vdots & \vdots \\ a_{t_m,N_1} & a_{t_2,N_2} & \dots a_{t_1,N_n} \end{vmatrix}$$

where $t_1, \dots t_m$: increasing time steps and $N_1, \dots, N_n$: identity of nodes from 1 to n. So A_{t_i,N_j} is the X-coordinate at instant t_i of node N_j.

5 SVD family for reduction

In this section, we test the classical SVD to reduce a simulation and then try to interpolate between two simulations when we modify parameters. We would like to rebuild the matrix of all coordinates (concatenation horizontally of X-coordinate, Y-coordinate and Z-coordinate matrices).

5.1 Singular Value Decomposition application

5.1.1 BoxBeam

Reduction of a unit simulation We call the matrix of all coordinates A_{bb}. Its decomposition following the (1) :

$$A_{bb} = U_{bb}.\Sigma_{bb}.V_{bb}^t$$

The number of column of A_{bb} is 3 times the number of nodes, i.e. 2100. So

$$A_{bb} = A_{15000\times2100}$$

The graph 3 shows that the logarithmic values of the first singular values ($\sigma_i, i = 1, \ldots\ldots, 20$) drop rapidly. We don't display others because of their very small values. The graph allows us to expect a possible reduction with crash simulation.

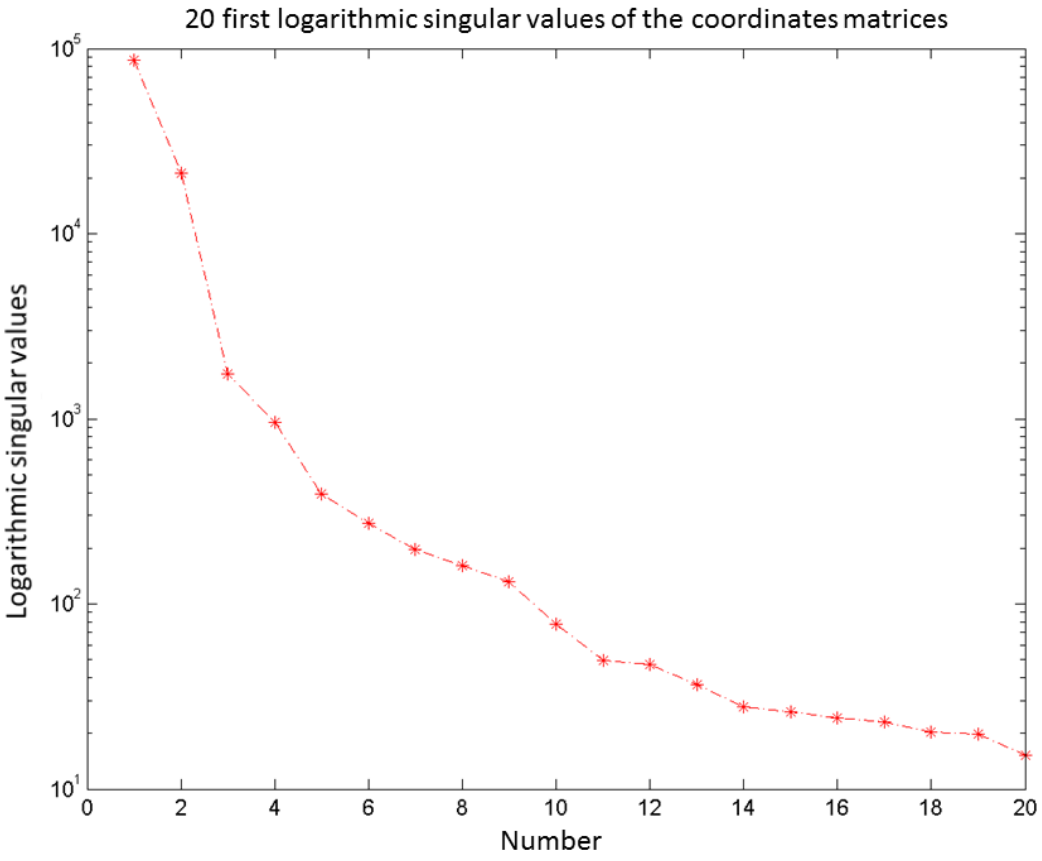


FIGURE 3: Evolution of 20 first logarithmic singular values

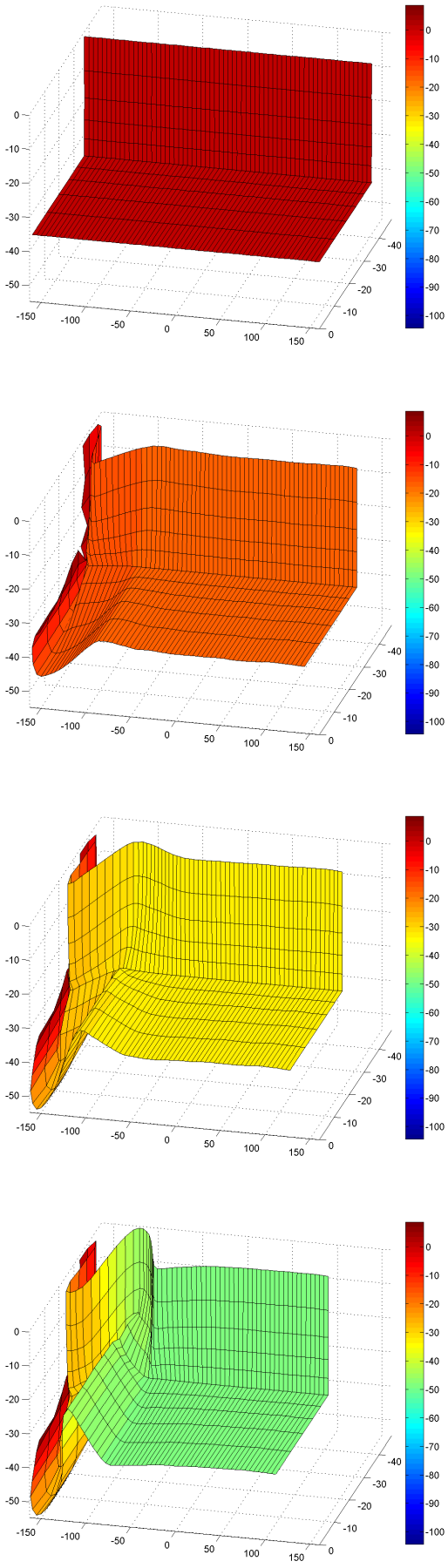
Then we try taking only 3 singular values to approximate A_{bb}, following the formular (2).

$$A_{bb} = \sigma_{(bb),1}\, u_{(bb),1}\, v^t_{(bb),1} + \sigma_{(bb),2}\, u_{(bb),2}\, v^t_{(bb),2} + \sigma_{(bb),3}\, u_{(bb),3}\, v^t_{(bb),3} \tag{6}$$

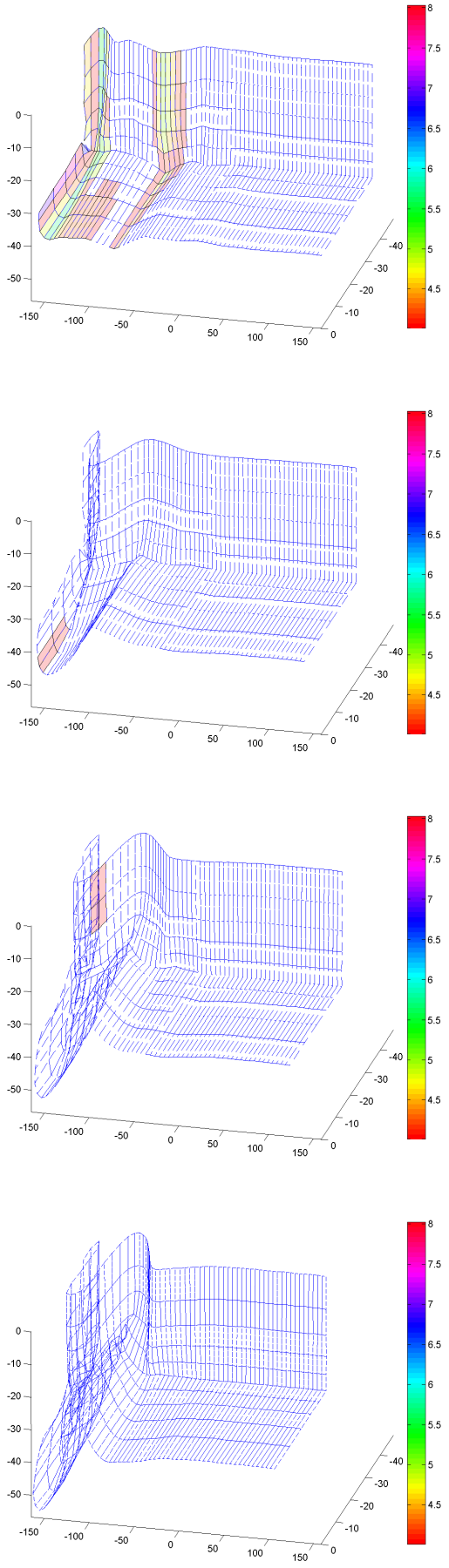
The rebuilt deformation of BoxBeam is showed in the figure 4. The left figures (with colors in the whole surface) are different deformation states (from the beginning to the end of the crash film). The right figures are the same thing but with an approximation of coordinates with the (6) ; the location of a colored element is where euclidean error is greater than 50 % of the maximum euclidean error (50 % quantile) (euclidean error is the distance point by point between approximated mesh and initial mesh). We can conclude :

— Despite strongly nonlinear behaviors of the crash simulation, the SVD can rebuild quite well a crash deformation by only 3 axes.

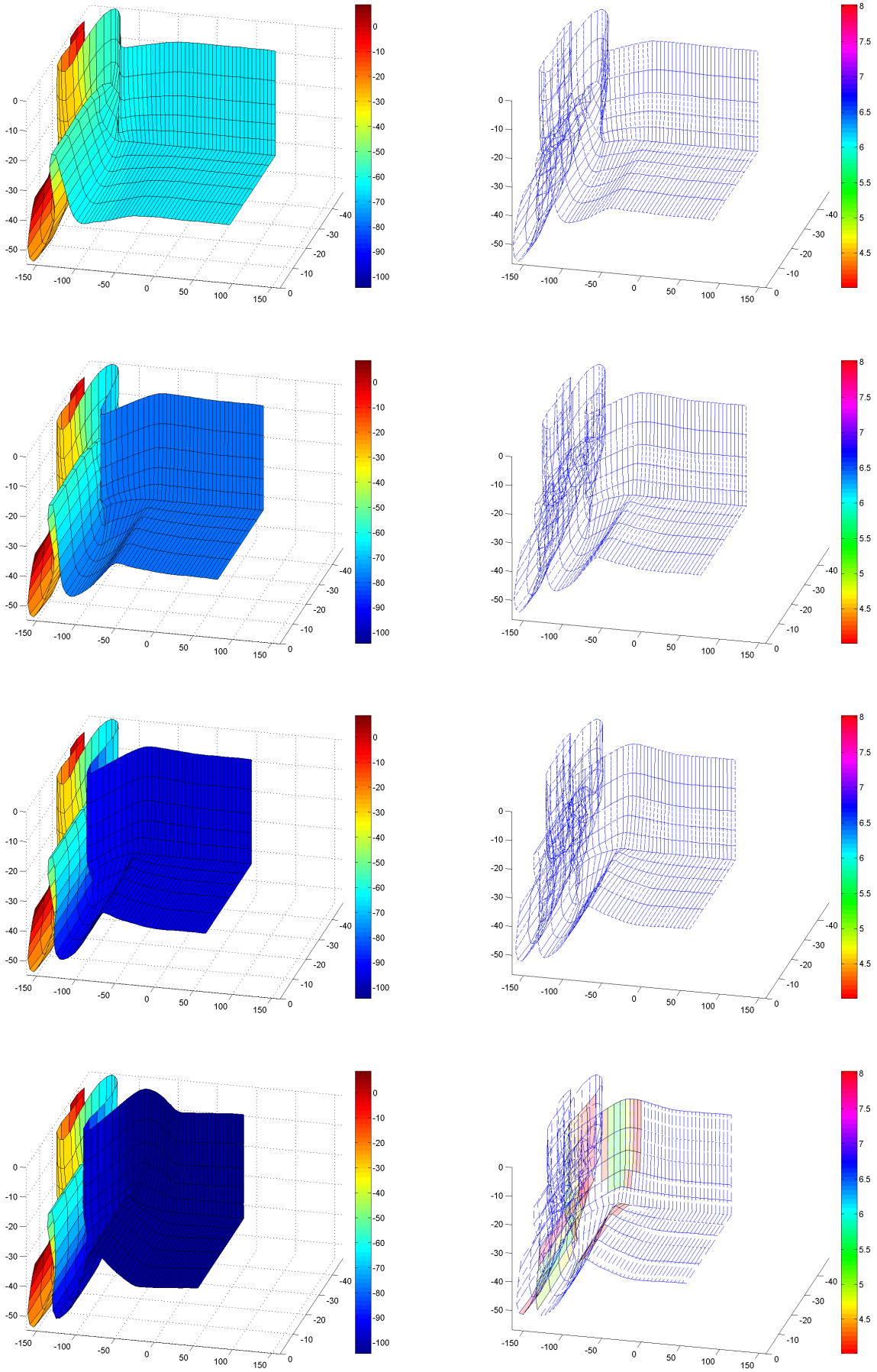
— The errors are located in the folds so they will not spread from a part to another. This is interesting in a system simulation because the total error will not amplify.
— The greatest errors are at the beginning of the simulation which is purely numerical.
— In term of data size, the SVD allows us to keep only 3 columns of U and 3 columns of V so fewer than 300 times the number of columns of the initial matrix A_{bb} (2100).



(a) Without SVD (initial)



(b) With SVD



(a) Without SVD (initial) (b) With SVD

FIGURE 4: Initial deformation v.s. deformation with 3 axes SVD for coordinates

Interpolation We try interpolating the simulation of thickness 1.2 mm between two different thickness 0.8 mm and 1.6 mm, other parameters stay unchanged. These are real part thickness in the car industry. The figure 6 compare the real simulation of 1.2 mm with the linear interpolation of the reduced model by 3 axes SVD of 0.8 mm and 1.6 mm. We remark :

— The interpolation represents quite well the real simulation despite large errors (50 % quantile) in the folds.

— If we increase the number of kept axes SVD, the interpolation errors reduce but stagnate at a certain axis number, see the figure 5.1.1. This means that the linear interpolation is not really good due to the fact than linear interpolation of two SVD is not a SVD. It is desirable to test with other methods.

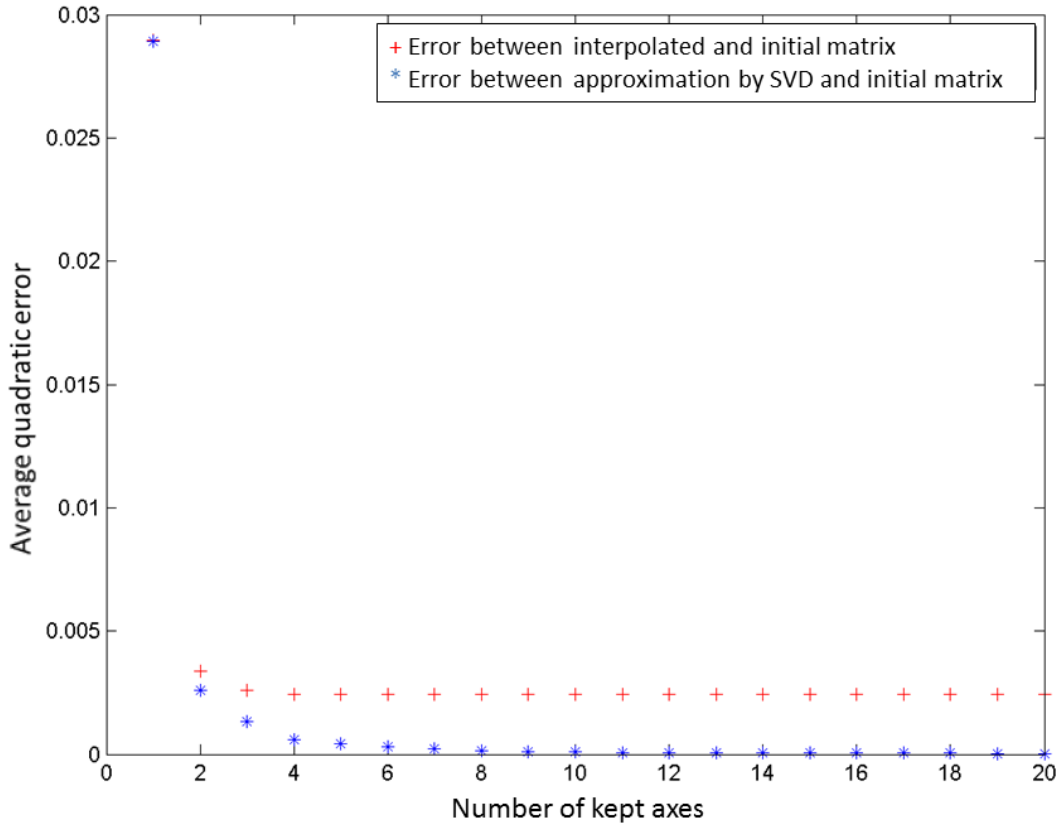
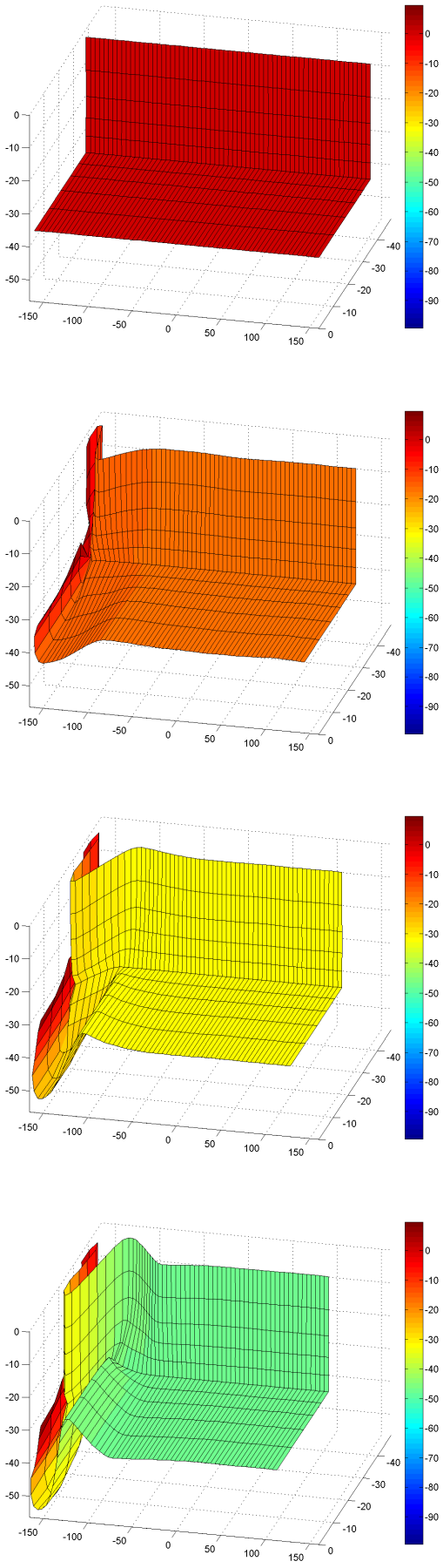
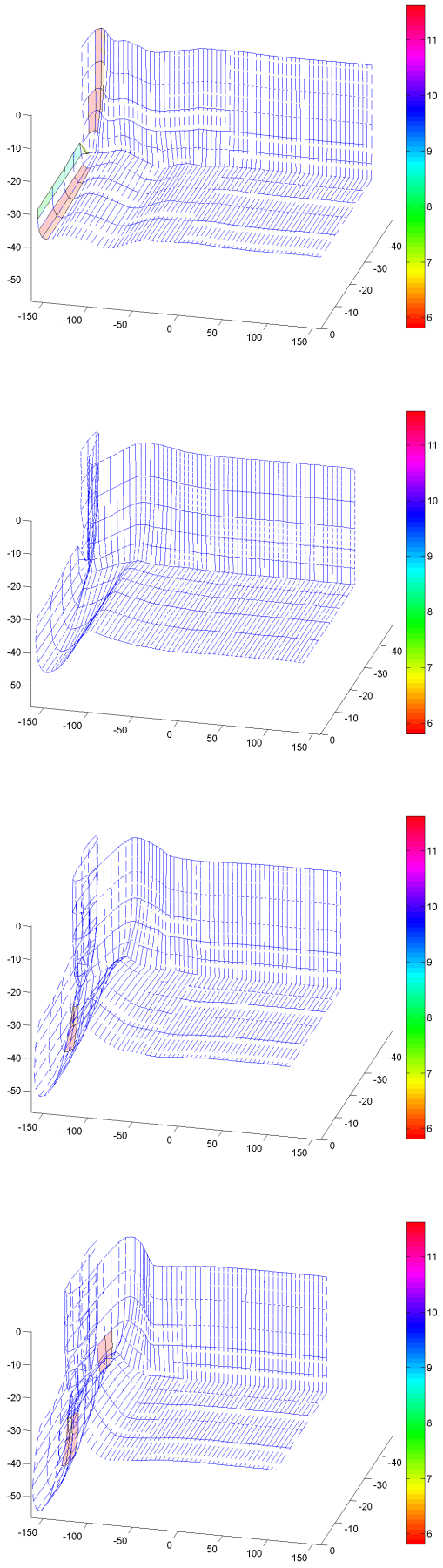


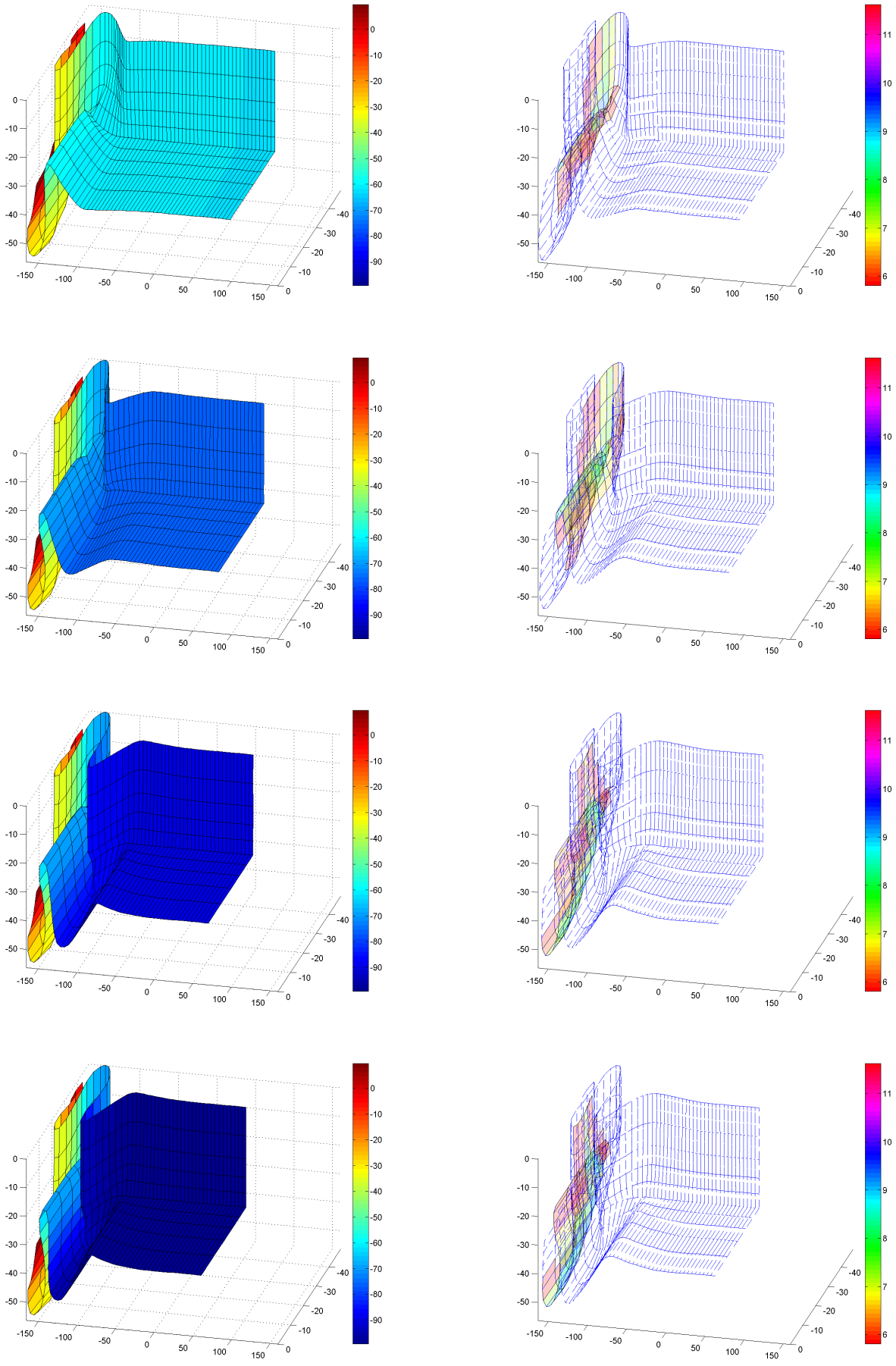
FIGURE 5: Evolution of average quadratic error in function of kept axes



(a) 1.2 mm without SVD (initial)



(b) 1.2 mm with 3 axes SVD then linear interpolation



(a) 1.2 mm without SVD (initial)

(b) 1.2 mm with 3 axes SVD then linear interpolation

FIGURE 6: Initial deformation of 1.2 mm v.s. interpolation of 0.8 mm and 1.6 mm with SVD

5.1.2 TBeam

Reduce a unit simulation We do the same things for the TBeam with the matrix A_{tb}

$$A_{tb} = U_{tb}.\Sigma_{tb}.V_{tb}^t$$

Different deformation states can be seen at the figure 7

The colors of the right figures are the errors between initial TBeam and that rebuilt with 3 axes SVD. The approximation is not really well in light colored area (the right end of the horizontal part) but it can be cut back because these areas have rigid body movements.

For the sake of time, we do not present here the interpolation for TBeam.

5.2 Higher-Order Generalized Singular Value Decomposition application

In the subsection 2.3, the HO GSVD gives the same V, then the same basis for all matrix. If we consider $m_i = N_{t_i}$ – number of time steps of the simulation i and $n = N_x$ – number of nodes of the FE model, we can have the same spacial basis for all simulations. The interpolation is then very easy. That is exactly what we expected in a parametric domain : interpolation all unknown simulations from done simulations.

Unfortunately, there are many restrictions that we can not apply HO GSVD for a coordinate matrix :

— X (Y , Z) - coordinate matrix has not always full columns rank

— The calculation of S is difficult, see (5) because it needs the inversion of matrices.

We conclude that we should not use HO GSVD as a reduction method with local outputs. We expected that may work with partial and global outputs, see definition in 4. In this article,we will present the HO GSVD with a matrix of deformation energies, see 2. We call

— E^1 : Kinetic energy of impactor (purple part)

— E^2 : Deformation energy of dark green part

— E^3 : Deformation energy of green part

— E^4 : Deformation energy of spot-weld

We realized 11 simulation while modifying the velocity of impactor and the thickness of two thin-walled parts. Each matrix D_i can be expressed :

$$D_i = \begin{vmatrix} E^1_{t_1,i} & E^2_{t_1,i} & E^3_{t_1,i} & E^4_{t_1,i} \\ \vdots & \vdots & \vdots & \vdots \\ E^1_{t_m,i} & E^2_{t_m,i} & E^3_{t_m,i} & E^4_{t_m,i} \end{vmatrix}$$

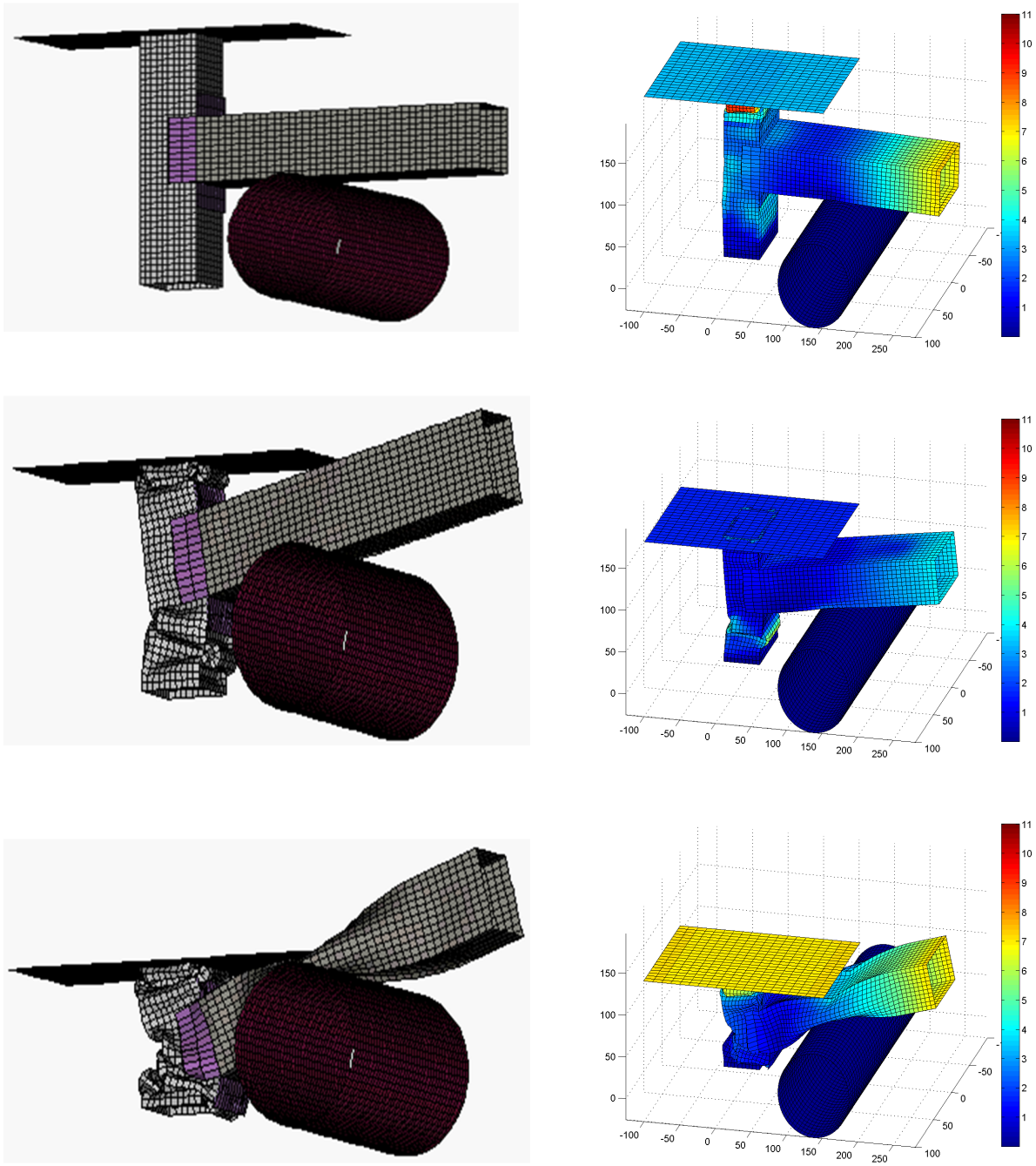
The singular values of 11 matrices are showed in the figure 8.

It is proven in [27] that if a eigenvalue λ_k of S in formula (5) is equal to 1, $\sigma_{i,k} = \sigma_{j,k}$ for all i and j. In analogy with the GSVD, the "common HO GSVD subspace" of the $N > 2$ matrices to be the subspace spanned by the right basis vector v_k corresponding to the eigenvalues of S that satisfy $\lambda_k = 1$. As the result, in the figure 8 the simulation 119 is very "different" from others and the couple (125,126) is quite "similar" which is better for interpolation.

6 CONCLUSIONS

— The classical SVD allows to reduce a unit simulation. To interpolate, we need to find proper methods than linear interpolation.

— With partial and global outputs, the HO GSVD may show the difference and the similarity among simulations. It is very useful before the interpolation.



(a) Without SVD (initial) (b) With SVD

FIGURE 7: Initial deformation v.s. deformation with 3 axes SVD for coordinates

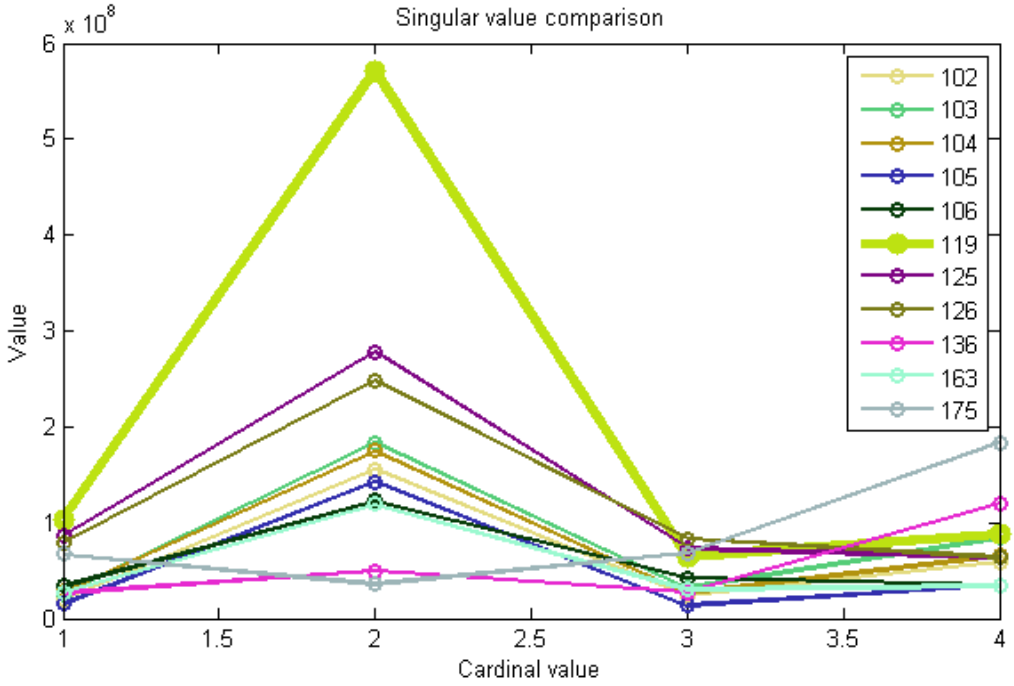


FIGURE 8: Singular values of energy matrices

— Concerning the next work, the PSVD and QSVD may be tested as methods to estimate a physical quantity from another quantity, i.e. if we know how to interpolate the coordinate of an unknown simulation, we can calculate the velocity of this interpolated simulation.

RÉFÉRENCES

[1] Kamal M. M., *Analysis and Simulation of Vehicle to Barrier Impact*. SAE Paper No. 700414, 1970.

[2] Hahm, S-J, Won, Y-H, and Kim, D-S, *Frontal Crash Feasibility Study Using MADYMO 3D frame Model*. SAE International Congress and Exposition, Detroit, Paper No. 1999-01-0072, 1999.

[3] Paul Du Bois, Clifford C. Chou, Bahig B. Fileta, Tawfik B. Khalil, Albert I. King, Hikmat F. Mahmood, Harold J. Mertz, Jac Wismans, *Vehicle crashworthiness and occupant protection*. American Iron and Steel Institute, 2000 Town Center, Southfield, Michigan 48075.

[4] Ladevèze P., *Mécanique non linéaire des structures , nouvelle approche et méthodes de calcul non incrémentales*. HERMES, ouvrage 280 p. 15.5x23.5 cm Broché.

[5] Christophe Heyberger, Pierre-Alain Boucard, David Néron *Multiparametric analysis within the proper generalized decomposition framework*. Comput Mech (2012) 49 :277–289. DOI 10.1007/s00466-011-0646-x.

[6] Amine Ammar, Francisco Chinesta, Elías Cueto and Manuel Doblaré, *Proper generalized decomposition of time-multiscale models*. Int. J. Numer. Meth. Engng 2012 ; 90 :569–596.

[7] Anthony Nouy, *A priori model reduction through Proper Generalized Decomposition for solving time-dependent partial differential equations*. Computer Methods in Applied Mechanics and Engineering (2010), DOI : 10.1016/j.cma.2010.01.009.

[8] Antoine DUMON *Re´duction dimensionnelle de type PGD pour la résolution des écoulements incompressibles*. PhD 2011.

[9] Alfio Quarteroni, Gianluigi Rozza, Andrea Manzoni, *Certified reduced basis approximation for parametrized partial differential equations and applications*. Journal of Mathematics in Industry (2011) 1 :3. DOI 10.1186/2190-5983-1-3.

[10] N.C. Nguyen, G. Rozza, D.B.P. Huynh, and A.T. Patera, *Reduced basis approximation and a posteriori error estimation for parametrized parabolic PDEs ; Application to real-time Bayesian parameter estimation*. Massachusetts Institute of Technology, Department of Mechanical Engineering, Room 3-264, 77 Massachusetts Avenue, Cambridge MA, 02139-4307, USA.

[11] Gianluigi Rozza, *Reduced Basis Approximation and Error Bounds for Potential Flows in Parametrized Geometries*. Commun. Comput. Phys. doi : 10.4208/cicp.100310.260710a

[12] Maxime Barrault, Yvon Maday, Ngoc Cuong Nguyen, Anthony T. Patera, *An "empirical interpolation" method : application to efficient reduced-basis discretization of partial differential equations*. Numerical Analysis, C. R. Acad. Sci. Paris, Ser. I 339 (2004) 667–672.

[13] A. Chatterjee, *An introduction to the proper orthogonal decomposition*, Current Science, vol. 78 (7), pp. 808-817, April 2000.

[14] Seong Woo Hong, *A method to assess dynamic responses in a crash simulation*. A Dissertation submitted to The Faculty of The School of Engineering and Applied Science of The George Washington University in partial satisfaction of the requirements for the degree of Doctor of Philosophy

[15] MURUHAN RATHINAM and LINDA R. PETZOLD. SIAM J. NUMER. ANAL.Vol. 41, No. 5, pp. 1893–1925 *A new look at proper orthogonal decomposition*

[16] D. Ryckelynck, *A priori hypereduction method : an adaptive approach*. Int. J. of Computational Physics, 202 :346–366, 2005.

[17] A.C. Antoulas, *Approximation of Large-Scale Dynamical Systems*. SIAM Book Series : Advances in Design and Control

[18] M. Loève, *Probability Theory*. Van Nostrand, 1955.

[19] K. Karhunen, *Zur spektral theorie stochasticher prozesse*. Ann. Acad. Sci. Fennicae, Ser. A1, 34, 1946.

[20] I.T. Joliffe, *Principal Component Analysis*. Springer-Verlag, 1986.

[21] L. Cordier et M. Bergmann *Réduction de dynamique par Décomposition Orthogonale aux Valeurs Propres*. Ecole de printemps OCET Optimisation et Contrôle des Ecoulements et des Transferts, 12 – 17 Mars 2006, Aussois

[22] G.H. Golub et C.F. Van Loan, *Matrix computations*. The Johns Hopkins University Press, Baltimore, 1990.

[23] Joos Vandewalle and Bart de Moor, *A variety of applications of singular value decomposition in identification of signal processing*. SVD and Signal Processing : Algorithms, Applications and Architectures. E.F.Depretterc, North Holland, Elseviers Science Publishers B.V., 1988, pp. 43-91

[24] Charles F. VAN LOAN, *Generalizing the singular value decomposition*. SIAM J. NUMBER. ANAL., vol. 13 ; No 1.March 1976.

[25] Bart L.R. De Moor, Gene H. Golub, *Generalized Singular Value Decompositions : A Proposal for a Standardized Nomenclature*. Numerical Analysis Project, Computer Science Department, Stanford University Stanford, California 94305.

[26] B. de Moor, *Generalizations of the OSVD Structure, Properties and Applications*. In SVD and Signal Processing, no. 181232, pp. 83-98, 1991.

[27] Sri Priya Ponnapalli, Michael A. Saunders, Charles F. Van Loan, Orly Alter, *A Higher-Order Generalized Singular Value Decomposition for Comparison of Global mRNA Expression from Multiple Organisms*. PLoS ONE, vol. 6, no. 12, December 2011.

COMPDYN 2015
5th ECCOMAS Thematic Conference on
Computational Methods in Structural Dynamics and Earthquake Engineering
M. Papadrakakis, V. Papadopoulos, V. Plevris (eds.)
Crete Island, Greece, 25–27 May 2015

COMPARISON OF INTEGRATION ALGORITHMS FOR REAL-TIME HYBRID SIMULATION USING FREQUENCY DOMAIN-BASED ERROR INDICATORS

Reza Mirza Hessabi[1,*], Ali Ashasi-Sorkhabi[2,*], Yanhui Liu[3,†], and Oya Mercan[4,*]

[*] Department of Civil Engineering, University of Toronto, Toronto, ON, Canada
[1] e-mail: reza.hessabi@mail.utoronto.ca
[2] e-mail: ali.ashasisorkhabi@mail.utoronto.ca
[4] oya.mercan@utoronto.ca

[†]State Key Laboratory for Seismic Reduction/Control & Structural Safety, Guangzhou University, China
[3] e-mail: liuyanhui@gzhu.edu.cn

Keywords: Real-time hybrid simulation, frequency domain-based error indicators, integration algorithms.

Abstract. *Real-time hybrid simulation (RTHS) is a testing method that combines computer simulation (i.e., analytical substructure) with physical testing (i.e., experimental substructure). This enables investigation of dynamic characteristics of load-rate dependent complex structures. To ensure reliable experimental results, even in the presence of sophisticated controllers and compensation methods, it is necessary to evaluate the accuracy of the success of the hydraulic actuators in imposing the command displacements. With recent developments in tracking error monitoring, new indicators have been proposed that are based on frequency domain analysis and can successfully uncouple phase (lag and lead) and amplitude (overshoot and undershoot) errors and quantify them. These new frequency-based error indicators are not structure-specific and can be reliably used to examine the effectiveness of each component of RTHS inner (i.e., servo-control) and outer (i.e., integration algorithm) loops. In this paper, frequency domain-based (FDB) error indicators are employed to evaluate the effectiveness of five commonly-used integration algorithms (i.e. central difference method, explicit Newmark method, discrete state space formulation with a zero-order hold and first-order hold, the state-space formulation by Zhang et al., and the alpha method) in different test scenarios. The applicability of the FDB error indicators to nonlinear systems is first verified through numerical simulations performed on a nonlinear system with predefined parameters. Then these indicators are used to post-process the experimental results obtained from RTHS's with various integration algorithms. The experiments are carried out on a system with a nonlinear analytical substructure and a linear experimental substructure at the University of Toronto. Findings from numerical simulation and experimental results demonstrate that the FDB method is an efficient approach to compare performances of different integration algorithms.*

1 INTRODUCTION

Real-time hybrid simulation (RTHS) is a powerful experimental technique to investigate the dynamic response of complex and rate-dependent structures. In this method, there is an integration algorithm that solves the equation of motion and resulting displacements are imposed on a physical test specimen by using hydraulic actuators. The restoring force and displacement information from the deformed specimen are measured and then used to compute next step command displacements. The block diagram of a typical RTHS is shown in Fig. 1.

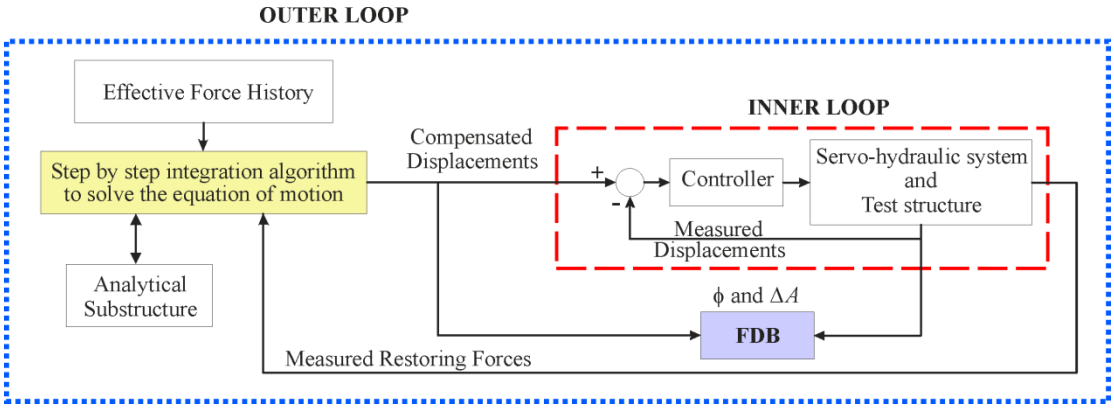


Figure 1: Block diagram of the inner and outer loops of RTHS.

In the process of generating the command displacements, integration algorithms are central and are used to solve the discretized equations of motion of structures. In order for an integration algorithm to be reliable it must be stable and accurate. Several implicit and explicit integration methods such as central difference methods, explicit Newmark method have been used extensively in the past [1, 2] and many other robust integration algorithms have been recently developed for RTHS. The analysis of integration algorithms are typically carried out either in the time domain or frequency domain. List of some of the available criteria for investigating the performance of integration algorithms are listed in [3]. One of the studies on the performance evaluation of integration algorithms was carried out by Mugan in which he found that frequency domain analysis can describe all of the time domain properties of an integration algorithm [4]. A frequency domain analysis will also be used in this paper to evaluate different integration algorithms.

In addition to the accuracy of the integration algorithms, another key factor for obtaining reliable RTHS results is system errors. Errors in a hybrid simulation can be attributed to either the numerical components or the experimental components, and even in the steps required to couple the two together. Due to the vulnerability of RTHS to error propagation, which can affect the accuracy and even the stability of the entire experiment, it is imperative to estimate and monitor the errors. Current available error assessment measures are categorized in [5, 6] and can also be divided into time domain and frequency domain assessment measures. In this paper, the application of one of the most recently developed frequency domain error assessment measures is proposed to evaluate the performance of various integration algorithms.

2 FREQUENCY DOMAIN-BASED ERROR INDICATORS

2.1 Background

Since the introduction of the RTHS, there has been a continuous effort on development and implementation of proper methods to assess the success of the simulation results. Current

methods for estimation of local response error such as the tracking error (i.e., the difference between the command and measured displacements) usually use time domain properties [7], cumulative growth of energy errors [8], synchronization subspace plots [9, 10] or the frequency domain response of the signals [11] to develop error monitors and indicators.

Although the abovementioned indicators are useful in evaluating the quality of the test results and have been successfully used by other researchers, there was a need for a new indicator that was not structure or test specific and was capable of uncoupling the phase and amplitude errors. Mirza Hessabi et al. [12] introduced a new set of error indicators (i.e., Frequency Domain-Based (FDB) error indicators) to solve these problems. Moreover, unlike their predecessors, the implementation of these new indicators is not computationally expensive and therefore they can be executed in realtime and serve as online indicators.

The FDB error indicators are developed using discrete Fourier transform (DFT). These indicators can be employed to find the corresponding values of the amplitude ratio and phase error within each moving time window. As shown in Eq. 1, the amplitude ratio is defined in terms of the ratio of the command over measured displacement amplitudes.

$$\Delta A = A_c / A_m \tag{1}$$

Similarly, a phase error is defined in Eq. 2 based on the discrepancy of the phase shifts between the command and measured signals. Positive and negative phase error values from Eq. 2 show phase lead and lag, respectively. Similarly, a value greater than one obtained from Eq. 1 is an undershoot error and a value less than one represents overshoot.

$$\phi = \phi_c - \phi_m \tag{2}$$

It should be emphasized that the closer ΔA and ϕ values are to 1 and 0, respectively, the more accurate is the actuator control and the more reliable are the RTHS results.

In order to determine the FDB error indicators, first the DFT power spectra of the command and measured signals are computed independently and then, from each power spectrum, the frequency that corresponds to the largest amplitude is located (i.e. $\bar{f}_c$ and $\bar{f}_m$ for command and measured signals, respectively) [12]. As it is shown in Eq. 3, the ratio between the magnitudes of the power spectra at the frequencies of $\bar{f}_c$ and $\bar{f}_m$ can be used to determine the amplitude ratio,

$$\Delta A = \left|U_c(\bar{f}_c)\right| / \left|U_m(\bar{f}_m)\right| \tag{3}$$

Likewise, the phase error defined in Eq. 4 is found as the difference of the DFT phase spectrum values of the two signals at $\bar{f}_c$ and $\bar{f}_m$.

$$\phi = \phi_c^*(\bar{f}_c) - \phi_m^*(\bar{f}_m) \tag{4}$$

2.2 Application of FDB error indicators to nonlinear substructures

Although several numerical simulations were performed in [12] to illustrate the advantages of using the FDB error indicators in comparison to other available error assessment measures, all of the evaluated cases were limited to structural elements with linear behaviour. In order to verify the applicability of the FDB error indicators to nonlinear systems, in this section Simulink is used and numerical simulations are carried out for a test structure that shows a hysteretic behavior as shown in Fig. 2-b. The hysteretic model exhibits elasto-plastic behaviour with strain hardening (the post-yield stiffness is 10% of the initial stiffness). Also, the yield force of the model is 25% of the weight of the analytical structure. The mass and damping ratio of the considered test structure are 1 ton and 5 %, respectively. In addition, a natural period of vibration of 0.7 seconds is assumed for the test structure and the initial stiffness is determined

accordingly. The Simulink models for modeling the servo-hydraulic set-up are the same as [13] and a sinusoidal signal with the amplitude of 0.2 m and frequency of 0.8 Hz is chosen as the input. Finally, the PID controller for the simulation is tuned with the k_p, k_i and k_d coefficients of 25, 1 and 1, respectively. The measured and command displacements for the described system is shown in Fig. 2-a. As it can be seen, the measured displacements have smaller amplitudes (undershoot) and are lagging behind the command signals.

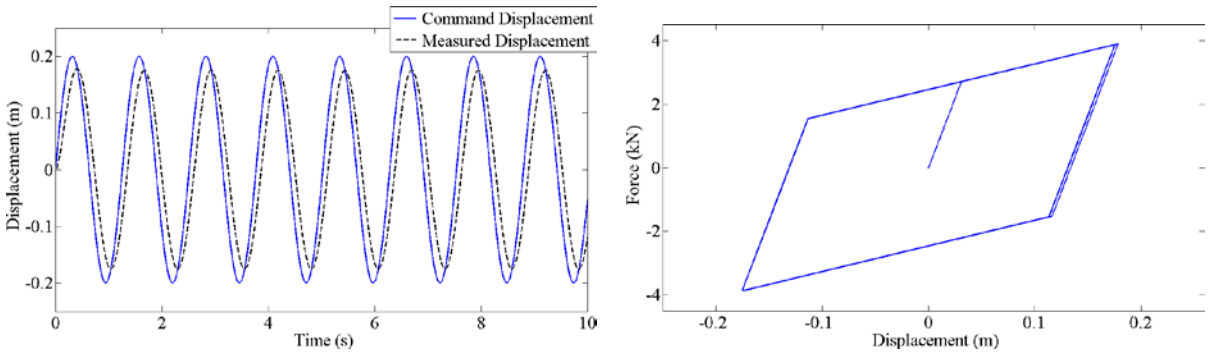


Figure 2: a) Command and measured displacements in time domain, and b) hysteresis loop for the structure with nonlinearity.

In Fig. 3, FDB error indicators are employed to measure the tracking error. The oscillation of the indicators around the mean values is due to the application of moving windows and Fourier transforms in the calculation of these indicators. The average values of FDB amplitude ratio and phase error are 1.160 and -28.189 degrees, respectively.

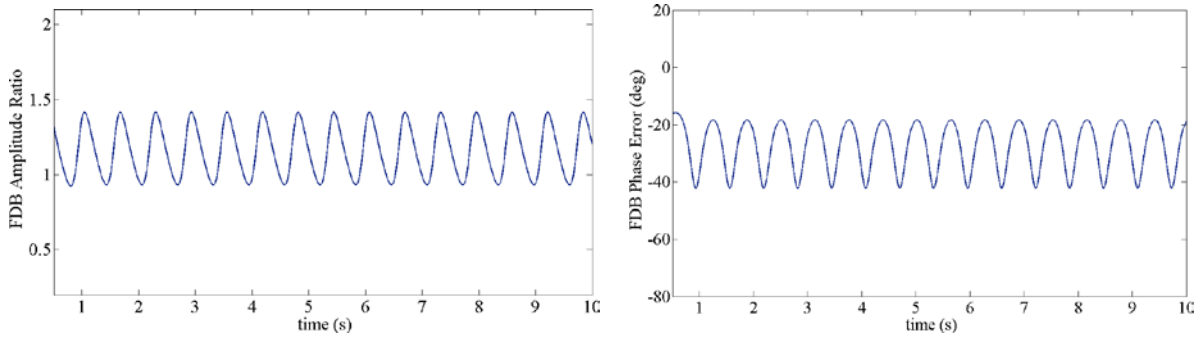


Figure 3: FDB error indicators for the structure with nonlinearity.

In order to verify these values and illustrate the accuracy of the FDB indicators, the time domain plots of command and measured displacements in Fig. 2-a, are enlarged around the 4th and 5th seconds in Fig. 4.

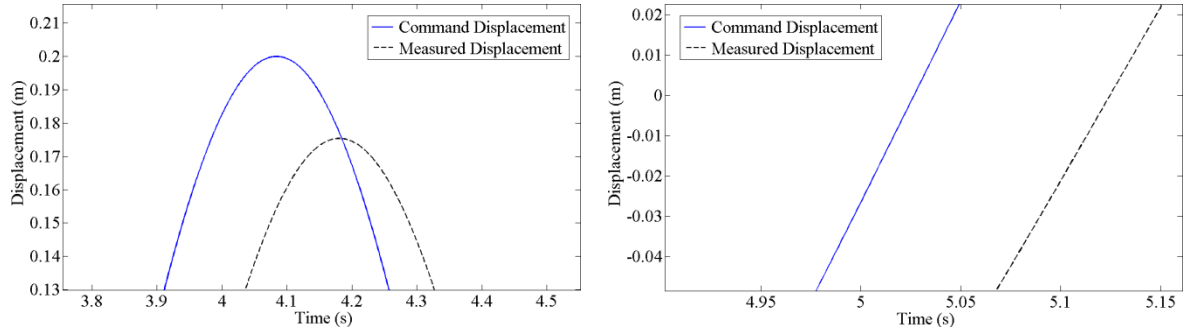


Figure 4: Enlarged time windows around a) 4th and b) 5th seconds to verify FDB error indicator results.

The enlarged view around the 4th second (Fig. 4-a) shows that the peak command displacement maximum (i.e., 0.2 m) is 1.140 times larger than the measured displacement (0.175 m). Also, from a closer look at Fig. 4-b it can be observed that the measured displacement is delayed by 96 time steps. Considering the size of the time steps, (i.e., 1/1024 sec) this translates to a phase lag of 26.857 degrees. These observations are in agreement with the average FDB error indicators from Fig. 3.

3 PERFORMANCE EVALUATION OF THE INTEGRATION ALGORITHMS USING FDB ERROR INDICATORS

In this study, error analysis is not discussed from a mathematical point of view. Rather, FDB error indicators are employed to examine the experimental RTHS results and compare the accuracy of the integration methods with each other. A series of RTHS are carried out for which everything except the integration algorithms is kept identical. This way, the difference in the tracking performance of the simulations can be attributed to the effects of integration algorithms on the accuracy of the simulations. The RTHS were conducted for a system that was comprised of a linear spring with the stiffness of 194 N/mm as the experimental substructure and a nonlinear analytical substructure in which Bouc-Wen model was used to model hysteretic type nonlinearity. The integration methods that are considered in this section were the central difference method [1], explicit Newark method [2], discrete state space formulation with a zero-order hold and first-order hold [14], the state-space formulation by Zhang et al [15] and the Hilber-Hughes-Taylor (HHT) (also called asalpha method) [16]. The system was subjected to the Canoga Park record from the 1994 Northridge earthquake. Fig. 5 shows the measured displacements for one of the RTHS with the central difference integration algorithm.

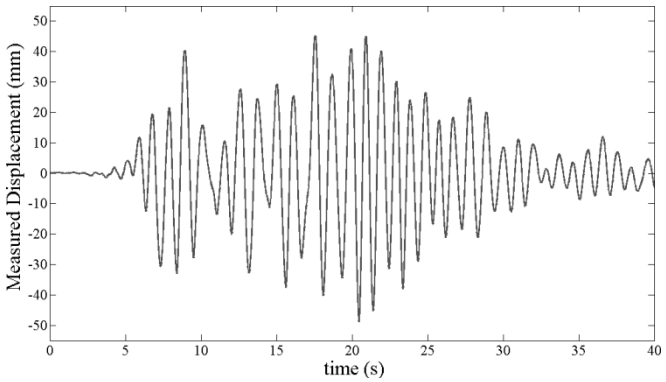


Figure 5: Measured displacement time history for the RTHS with central difference integration algorithm.

Similar to Section 2.2., FDB error indicators are used to measure the errors in each simulation. As a sample, the results for the test with the central difference method are shown below.

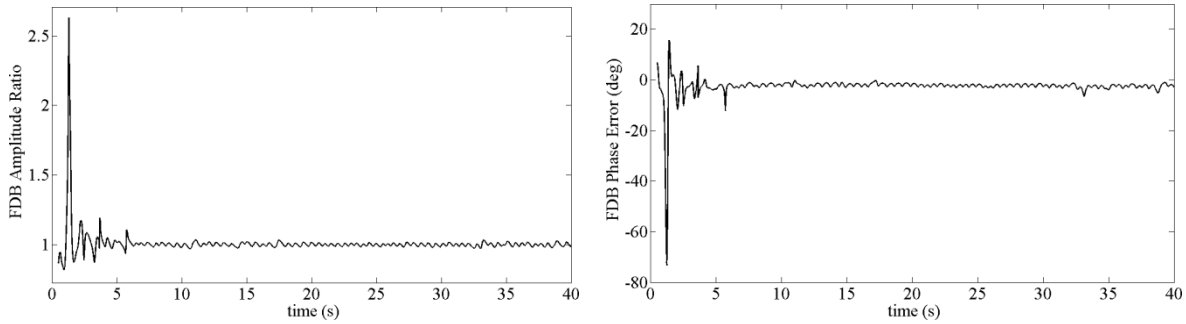


Figure 6: FDB error indicators for the RTHS with central difference integration algorithm.

As it can be seen from Fig. 6 maximum variation in the FDB error indicators occur in the first five seconds of the simulation where the command displacements are small. After the initial five seconds, the amplitude ratio oscillates around one (no amplitude error condition) and the phase error oscillate around -2.5 degrees (phase lag). It should be emphasized again that the closer amplitude ratio and phase error values are to 1 and 0, respectively, the more reliable are the RTHS results. Since the error indicator values for different integration algorithms are relatively close, enlarged views of these indicators are shown in Fig. 7. It can be observed that the application of the central difference method leads to the highest amplitude ratios. The worst results (i.e., the highest phase errors with sudden changes) belong to the simulations with the explicit Newmark and discrete state space formulation with a zero-order hold integration algorithms.

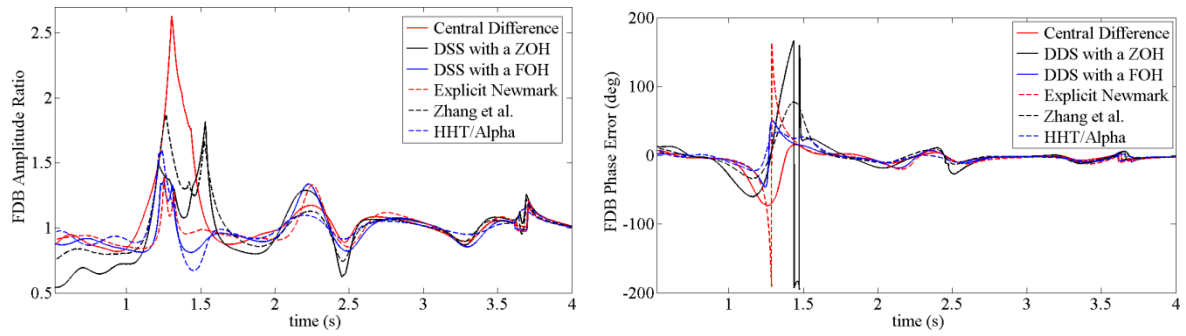


Figure 7: Enlarged views of the FDB error indicators for the RTHS with different integration algorithms.

Finally, in order to compare the abovementioned algorithms numerically, mean values of the FDB error indicators are calculated and reported in Table 1. To have other means to assess the accuracy of the experiment results, the maximum tracking error (MTE) and root mean square (RMS) of the tracking error are also included in Table 1.

Integration Algorithm	MTE	RMS	Amplitude Ratio	Phase Error (deg)
Central Difference Method	2.063	0.590	1.006	-2.679
Explicit Newmark Method	2.093	0.606	0.999	-2.529
DDS with a zero-order hold	2.069	0.600	1.001	-2.534
DDS with a first-order hold	2.116	0.597	0.998	-2.416
Zhang et al. method	2.045	0.583	1.003	-2.157
HHT/Alpha method	2.031	0.620	0.999	-2.230

Table 1: Error assessment measures for RTHS with various integration algorithms.

Table 1 shows that the averaged values fail to fully capture the effects of large local errors. Thus FDB error indicators can be successfully used as an evaluation tool to monitor the performance of RTHS during the entire simulation.

4 CONCLUSIONS

This paper presents a general approach utilizing the FDB error indicators to evaluate the different integration algorithms on the performance of RTHS. The state-of-the-art for error assessment measures is reviewed briefly and the formulation of the FDB error indicators is explained. Then a numerical case study is introduced where a system with a bilinear behaviour is used and the applicability of the FDB error indicators to nonlinear systems is verified. Followed by the numerical simulations, six different integration algorithms are selected to experimentally demonstrate the effectiveness of the FDB error indicators in characterizing the effects of selected integration methods. Based on the assumptions and limitations of this paper, it can be concluded that the effects of an integration algorithms on the performance of the RTHS cannot be judged based on averaged measures. Instead an evaluation tool is needed that can be used to monitor the effects throughout the simulation. FDB error indicators can be successfully used to achieve this goal and can assist in the selection of a suitable integration algorithm.

REFERENCES

[1] A.K. Chopra, *Dynamics of Structures, 4th Edition*. Prentice Hall: Upper Saddle River, New Jersey, 2011.

[2] N.M. Newmark, A method of computation for structural dynamics. *Journal of Engineering Mechanics*, **85**, 67–94, 1959.

[3] C. Chen, J.M. Ricles, Development of direct integration algorithms for structural dynamics using discrete control theory. *Journal of Engineering Mechanics*, **134**, 676-683, 2008.

[4] A. Mugan, Discrete equivalent time integration methods for transient analysis. *International Journal for Numerical Methods in Engineering*, **57**, 2043–2075, 2003.

[5] R. Christenson, S. Dyke, J. Zhang, G. Mosqueda, C. Chen, N. Nakata, P. Laplace, W. Song, Y. Chae, G.A. Marshall, G. Ou, C.A. Riascos Gonzales, C. Song, Hybrid simulation: a discussion of current assessment measures. *https://nees.org/resources/12876*, 2014.

[6] R. Mirza Hessabi, O. Mercan, Assessment measures for hybrid simulation: a discussion of recent developments. *https://nees.org/resources/13483*, 2015.

[7] G. Mosqueda, B. Stojadinovic, S.A. Mahin, Realtime error monitoring for hybrid simulation. Part I: methodology and experimental verification. *Journal of Structural Engineering*, **133**, 1100–1108, 2007.

[8] R. Mirza Hessabi, O. Mercan, A practical approach to the phase and amplitude error estimation of pseudodynamic testing. *Structures Congress, American Society of Civil Engineers (ASCE)*, Pittsburgh, PA, May 2–4, 2013.

[9] O. Mercan, J.M. Ricles, Experimental studies on realtime testing of structures with elastomeric dampers. *Journal of Structural Engineering*, **135**, 1124–1133, 2009.

[10] R. Mirza Hessabi, O. Mercan, Phase and amplitude error indices for error quantification in pseudodynamic testing. *Earthquake Engineering and Structural Dynamics*, **41**, 1347–1364, 2012.

[11] T. Guo, C. Chen, W. Xu, F. Sanchez, A frequency response analysis approach for quantitative assessment of actuator tracking for real-time hybrid simulation. *Smart Materials and Structures*, **23**, 045042, 2014.

[12] R. Mirza Hessabi, A. Ashasi-Sorkhabi, O. Mercan, A new tracking error-based adaptive controller for servo-hydraulic actuator control. *Journal of Vibration and Control*, 1077546314548205, 2014. DOI: 10.1177/1077546314548205.

[13] H. Moosavi, R. Mirza Hessabi, O. Mercan, Numerical simulation and analysis of nonlinear state‐space control design for hydraulic actuator control. *Structural Control and Health Monitoring*, 2015. DOI: 10.1002/stc.1731.

[14] G.F. Franklin, J.D. Powell, M. Workman, *Digital control of dynamic systems, 3rd Edition*. Addison Wesley Longman, Menlo Park, 1997.

[15] Y.F. Zhang, R. Sause, J.M. Ricles, C.J. Naito, Modified predictor-corrector numerical scheme for real-time pseudo dynamic tests using state-space formulation. *Earthquake Engineering and Structural Dynamics*, **34**, 271-288, 2005.

[16] H.M. Hilber, T.J.R. Hughes, R.L. Taylor, Improved numerical dissipation for time integration algorithms in structural dynamics. *Earthquake Engineering and Structural Dynamics*, **5**, 283–292, 1977.

COMPDYN 2015
5th ECCOMAS Thematic Conference on
Computational Methods in Structural Dynamics and Earthquake Engineering
M. Papadrakakis, V. Papadopoulos, V. Plevris (eds.)
Crete Island, Greece, 25–27 May 2015

DE^3: YET ANOTHER HIGH-ORDER INTEGRATION SCHEME FOR LINEAR STRUCTURAL DYNAMICS

Alexandre Depouhon[1,2], Emmanuel Detournay[2], and Vincent Denoël[1]

[1]Structural and Stochastic Dynamics, Université de Liège
1, rue des Chevreuils, 4000 Liège, Belgium
e-mail: v.denoel@ulg.ac.be

[2] Civil, Environmental and Geo- Engineering Department, University of Minnesota
500, Pillsbury Drive S.E., 55455, MN, Minneapolis, USA
e-mail: {depou002, detou001}@umn.edu

Keywords: Structural dynamics, Integration scheme, High-order accuracy, Unconditional stability

Abstract. *In this paper, we present the* DE^3 *integration scheme. This unconditionally stable scheme is dedicated to the numerical integration of linear structural dynamics problems and offers a simple and easy to use high-order alternative to the second-order accurate ones that are usually employed. Its symmetric formulation makes it an interesting candidate to simulate large-scale problems. In addition, the scheme offers the possibility to control the introduced numerical damping via a single algorithmic parameter, which is very convenient for the filtering of the spurious oscillations that can arise from large stiffness contrasts in certain models. The properties of high-order accuracy and numerical damping are illustrated by way of a demonstrative example.*

1 INTRODUCTION

Since Newmark's landmark paper [1], a vast number of integration schemes have been developed to advance in time the canonical equation of motion of linear structural dynamics

$$\mathbf{M}\ddot{\mathbf{u}}(t) + \mathbf{C}\dot{\mathbf{u}}(t) + \mathbf{K}\mathbf{u}(t) = \mathbf{f}(t). \tag{1}$$

These are typically derived from the mathematical treatment of the equation of motion and continuity assumptions of the field to be discretized, *e.g.*, Taylor expansion, finite element approaches based on weak formulations, or finite difference approximations. For linear problems, what matters, though, are the stability and accuracy properties of the derived schemes, their structure-preserving nature (energy conservation for instance), if any, as well as their intrinsic computational cost.

The DE^3 scheme [2] belongs to the class of two-level one-step implicit integration schemes enjoying unconditional stability. It is a reformulation of the scheme proposed by Bottasso and Trainelli [3] by condensation of the original scheme internal variables. As such, it exhibits the same properties. Namely, it preserves the linear momentum of the mechanical system and offers control on the numerical dissipation of mechanical energy, in the high-frequency range, via a single parameter. It is fourth-order accurate when used in its conservative setting; the accuracy drops to third order when numerical damping is present, however. This makes it an ideal candidate for structural dynamics simulations [4] or, even, wave propagation ones in combination with the finite element method [5], as the numerical dissipation enables the control of high-frequency Gibbs oscillations.

The focus of this contribution is set on the derivation of the scheme and the illustration of its superior features by application to an example problem of structural dynamics.

2 THE DE^3 SCHEME

Related to the time discontinuous Galerkin method [6] that is built on the assumption of possible discontinuities of the underlying integrated field, the method proposed by Bottasso and Trainelli [3] is similarly formulated in terms of the left and right limits of the field variables at the time nodes. Assuming equation (1) to hold with constant symmetric stiffness, damping and mass matrices under the typical positiveness assumptions ($\mathbf{K}, \mathbf{C} \geq 0$ and $\mathbf{M} > 0$), the integration scheme they proposed reads

$$\begin{aligned}
&\begin{pmatrix} \frac{1}{2}\mathbf{K} & \frac{1}{h}\mathbf{M} + \frac{1}{2}\mathbf{C} & \frac{1}{2}\mathbf{K} & \frac{1}{2}\mathbf{C} \\ \mathbf{I} & -\frac{h}{2}\mathbf{I} & \mathbf{0} & -\frac{h}{2}\mathbf{I} \\ \mathbf{0} & \frac{h}{6}\mathbf{I} & \mathbf{I} & -\beta\frac{h}{6}\mathbf{I} \\ -\frac{1}{6}\mathbf{K} & -\frac{1}{6}\mathbf{C} & \frac{\beta}{6}\mathbf{K} & \frac{1}{h}\mathbf{M} + \frac{\beta}{6}\mathbf{C} \end{pmatrix} \begin{pmatrix} \mathbf{u}_{n+1} \\ \mathbf{v}_{n+1} \\ \mathbf{u}_{n^+} \\ \mathbf{v}_{n^+} \end{pmatrix} \\
&\qquad = \begin{pmatrix} \mathbf{0} & \frac{1}{h}\mathbf{M} \\ \mathbf{I} & \mathbf{0} \\ \mathbf{I} & (1-\beta)\frac{h}{6}\mathbf{I} \\ \frac{\beta-1}{6}\mathbf{K} & \frac{1}{h}\mathbf{M} + \frac{\beta-1}{6}\mathbf{C} \end{pmatrix} \begin{pmatrix} \mathbf{u}_n \\ \mathbf{v}_n \end{pmatrix} + \begin{pmatrix} \frac{1}{h}\mathbf{I}_1 \\ \mathbf{0} \\ \mathbf{0} \\ \frac{2}{h^2}\left(t_{n+1/2}\mathbf{I}_1 - \mathbf{I}_2\right) \end{pmatrix},
\end{aligned} \tag{2}$$

where

$$\mathbf{I}_1 = \int_{t_n}^{t_{n+1}} \mathbf{f}(t)\,\mathrm{d}t, \qquad \mathbf{I}_2 = \int_{t_n}^{t_{n+1}} t\mathbf{f}(t)\,\mathrm{d}t \tag{3}$$

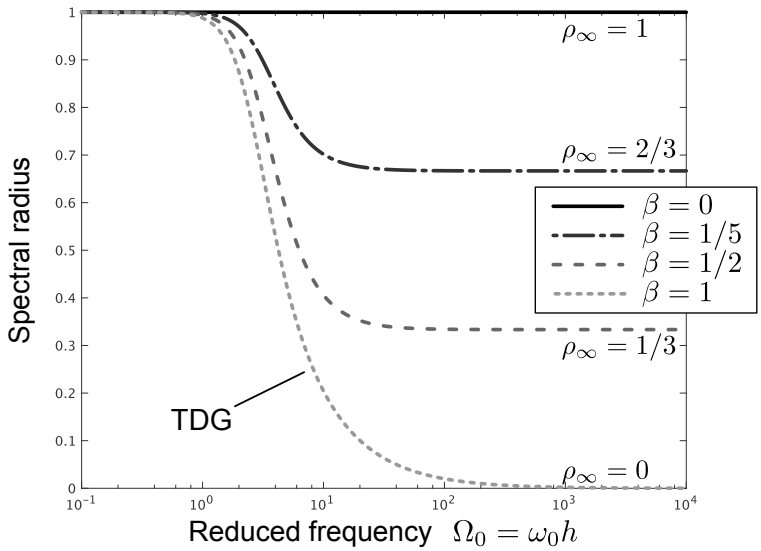


Figure 1: The algorithmic parameter β enables the control of the numerical dissipation introduced by the scheme. For $\beta = 0$, the integration scheme preserves the mechanical energy whereas it numerically dissipates some for $\beta \in (0, 1]$. The time discontinuous Galerkin scheme (TDG) is recovered for $\beta = 1$. After [2].

denote the first- and second-order non-centered time moments of the external forces over the timestep, and $\mathbf{u}, \mathbf{v}$ represent the displacement and velocity fields. The indices refer to the time argument of these fields; the syntax is equivalent to

$$\mathbf{x}_n = \lim_{\epsilon \to 0^-} \mathbf{x}(t_n + \epsilon), \qquad \mathbf{x}_{n^+} = \lim_{\epsilon \to 0^+} \mathbf{x}(t_n + \epsilon). \tag{4}$$

Parameter $\beta \in [0, 1]$ is an algorithmic parameter that controls the numerical dissipation introduced by the scheme. It is related to the spectral radius of the integration scheme amplification matrix at infinite frequency ρ_∞ through the following expression

$$\beta = \frac{1 - \rho_\infty}{1 + \rho_\infty} \quad \leftrightarrow \quad \rho_\infty = \frac{1 - \beta}{1 + \beta}. \tag{5}$$

For $\beta = 0$, the scheme is conservative, in the sense that it preserves the mechanical energy of the system , whereas for $\beta \in (0, 1]$ it is numerically dissipative. In the particular case of $\beta = 1$, the time discontinuous Galerkin method is recovered. This configuration is spectrally annihilating, as can be seen in Figure 1 that shows the evolution of the spectral radius of the scheme in the case of the undamped/unforced single degree of freedom spring/mass oscillator. Furthermore, the study of the balance of mechanical energy over a timestep shows that the scheme is conservative when $\beta = 0$ and dissipative otherwise.

As the right-limit values $\mathbf{u}_{n^+}, \mathbf{v}_{n^+}$ only appear on left-hand side of (1), they can be considered as internal variables to the integration scheme and can be eliminated via static condensation. A double application of the block inversion formula [7] enables the reduction of the four-level formulation (2) to an equivalent two-level formulation based on the displacement and velocity fields only. Completing all the algebra—see [2] for the details—the DE^3 scheme is obtained

$$\mathbf{H}_0 \mathbf{x}_{n+1} = \mathbf{H}_1 \mathbf{x}_n + \boldsymbol{\ell}_n^{n+1}, \tag{6}$$

with

$$
\begin{aligned}
\mathbf{x}_n &= \begin{pmatrix} \mathbf{u}_n \\ \mathbf{v}_n \end{pmatrix}, \\
\mathbf{H}_0 &= \begin{pmatrix} \mathbf{C} + \left(\frac{1}{2} + \frac{\beta}{6}\right) h\mathbf{K} & \mathbf{M} - \left(\frac{1}{12} + \frac{\beta}{12}\right) h^2\mathbf{K} \\ \mathbf{M} - \left(\frac{1}{12} + \frac{\beta}{12}\right) h^2\mathbf{K} & -\left(\frac{1}{2} + \frac{\beta}{6}\right) h\mathbf{M} - \left(\frac{1}{12} + \frac{\beta}{12}\right) h^2\mathbf{C} \end{pmatrix}, \\
\mathbf{H}_1 &= \begin{pmatrix} \mathbf{C} - \left(\frac{1}{2} - \frac{\beta}{6}\right) h\mathbf{K} & \mathbf{M} - \left(\frac{1}{12} - \frac{\beta}{12}\right) h^2\mathbf{K} \\ \mathbf{M} - \left(\frac{1}{12} - \frac{\beta}{12}\right) h^2\mathbf{K} & \left(\frac{1}{2} - \frac{\beta}{6}\right) h\mathbf{M} - \left(\frac{1}{12} - \frac{\beta}{12}\right) h^2\mathbf{C} \end{pmatrix}, \\
\boldsymbol{\ell}_n^{n+1} &= \begin{pmatrix} \mathbf{I}_1 \\ \left(t_{n+1/2} - \frac{\beta}{6}h\right) \mathbf{I}_1 - \mathbf{I}_2 \end{pmatrix}.
\end{aligned}
\tag{7}
$$

As the algebraic manipulations leading to DE^3 scheme do not alter the structure of the scheme (2), it enjoys the same properties. Namely, the algorithmic parameter β controls the spectral radius of the amplification matrix at infinite frequency, in accordance with (5), and therefore the amount of numerical dissipation introduced during integration. It also plays a role on the accuracy of the scheme which can be demonstrated to be fourth-order for $\beta = 0$ (numerically conservative scheme) or third-order for $\beta \in (0, 1]$ (numerically dissipative scheme). Note that high-order accuracy requires that the integrals $\mathbf{I}_1$ and $\mathbf{I}_2$ be computed with at least third degree exactness, as is for instance offered by the Simpson-Cavalieri rule [8]. In such case, after completing the algebra relative to the definition of the error metrics introduced in [2], it can be shown that the local truncation errors for the free and forced responses are asymptotic to

$$L_{\text{free}} \sim \beta\, f_{\text{free}}(\omega_0, \zeta) h^3 + g_{\text{free}}(\omega_0, \zeta, \beta) h^4, \tag{8}$$

$$L_{\text{forced}} \sim \beta\, f_{\text{forced}}(\omega_0, \zeta) h^3 + g_{\text{forced}}(\omega_0, \zeta, \beta) h^4, \tag{9}$$

for $h \ll \omega_0^{-1}$, with functions $g_{\text{free}}(\omega_0, \zeta, \beta)$ and $g_{\text{forced}}(\omega_0, \zeta, \beta)$ not vanishing when $\beta = 0$, and ω_0, ζ denoting the natural frequency and damping coefficient of a single degree of freedom spring/dashpot/mass oscillator periodically excited. Similarly to the original formulation, the two-level one is unconditionally stable.

The two-level formulation of the DE^3 scheme offers a couple of advantages over the original four-level formulation proposed by Bottasso and Trainelli. In particular, it is of lower size, as the update equations no longer involve internal states, and it is symmetric, which is favorable to reducing the storage size of matrices $\mathbf{H}_0, \mathbf{H}_1$ when dealing with large models. Also, in comparison to other integration schemes that can employ multiple algorithmic parameters, the control of numerical dissipation is achieved via a single algorithmic parameter, which makes the integration scheme simple to use.

It is actually found that the DE^3 scheme is very similar to the one proposed by Krenk [9], which was derived from the equation of motion via a weak formulation. A significant difference between the DE^3 scheme and that proposed by Krenk concerns the handling of the contributions of the damping and the external forcing terms, which allow the DE^3 scheme to retain its fourth- (and third-) order accuracy in the conservative (resp. dissipative) setting when integrating forced and/or damped structural models, contrary to Krenk's formulation.

3 DEMONSTRATIVE EXAMPLE

To illustrate the performance of the scheme, we consider the two degree-of-freedom oscillator depicted in Figure 2. This model has a single parameter Ω that is representative of the stiffness contrast that could be encountered in finite element models; in the extreme case $\Omega \gg 1$, the stiff element can be interpreted as a penalty used to enforce a constraint. For this specific

model, the $\Omega \gg 1$ case corresponds to imposing a rigid link between degree-of-freedom 1 and the boundary with imposed displacement.

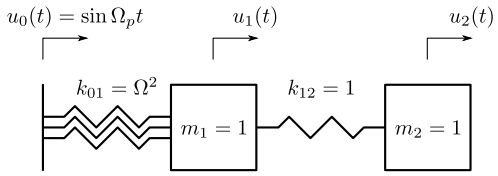


Figure 2: Soft/stiff linear oscillator. External forcing is applied by controlling the displacement $u_0(t)$.

In the first part of this example, we compare the accuracy achieved by the DE^3 scheme to two other well-known integration schemes, namely the ones proposed by Newmark [1] and Bathe [10]. In the second part, we illustrate the utility of numerical damping in structural simulations and, in particular, the property of spectral annihilation that the DE^3 scheme enjoys when used in its most dissipative setting. In both parts, the forcing frequency is set to $\Omega_p = 1.2$.

To quantify the error resulting from the numerical integration of the equations of motion, we use the energy-based metric introduced in [2]

$$\mathcal{E}(t) := \frac{1}{\sqrt{2}} \sqrt{(\mathbf{u}(t) - \underline{\mathbf{u}}\,(t))^T \mathbf{K} (\mathbf{u}(t) - \underline{\mathbf{u}}(t)) + (\mathbf{v}(t) - \underline{\mathbf{v}}(t))^T \mathbf{M} (\mathbf{v}(t) - \underline{\mathbf{v}}(t))}, \qquad (10)$$

where the reference trajectory, denoted by an underlined variable, is calculated using modal superposition [11]. For a proper assessment of the error, the system oscillations must be sufficiently resolved. In other words, the timestep must be small enough to ensure a sufficient number of computed points per period of the highest frequency signals. It is easily shown that this frequency is set by the largest eigenfrequency of the model. For the soft/stiff oscillator, the two eigenfrequencies read

$$\Omega_1 = \frac{\sqrt{4 + 2\Omega^2 - 2\sqrt{4 + \Omega^4}}}{2}, \qquad \Omega_2 = \frac{\sqrt{4 + 2\Omega^2 + 2\sqrt{4 + \Omega^4}}}{2}, \qquad (11)$$

and follow the evolution shown in Figure 3 when parameter Ω is varied. One eigenvalue is always approximately equal to Ω and the other tends to $\sqrt{2}$ or 1 if $\Omega < 1$ or $\Omega > 1$. In the absence of damping, the oscillatory response of the model comprises three frequency component: $\Omega_1, \Omega_2, \Omega_p$. Setting $\Omega = 100$, we have $\Omega_2 > \Omega_p > \Omega_1$ and the resolution constraint is set by $\Omega_2 \simeq 100$. Twelve points per period lead to a timestep requirement of $h \leq 5 \cdot 10^{-3}$.

The evolution of the error $\mathcal{E}(10)$ with the timestep $h \in [5 \cdot 10^{-5}, 5 \cdot 10^{-3}]$ is shown in Figure 4. The high-order nature of the DE^3 scheme is well established over the other considered methods. By order of increasing accuracy, we observe the following ranking: Newmark's scheme ($(\beta, \gamma) = (1/4, 1/2)$) is less accurate than Bathe's method [10]—both are second-order methods—than the DE^3 scheme that is third-order accurate in its dissipative setting ($\rho_\infty = 0.5$) and fourth-order accurate in its conservative setting ($\rho_\infty = 1$). It is observed that the requirement of twelve points per lowest period is not sufficient to ensure proper accuracy with the second-order methods whereas it does for the DE^3 scheme.

Besides offering high-order accuracy integration, the DE^3 scheme can also be tuned to damp Gibbs oscillations that can arise from the finite resolution of the finite elements typically used in structural dynamics. This can be illustrated by setting $\Omega \gg 1$ in the soft/stiff model and

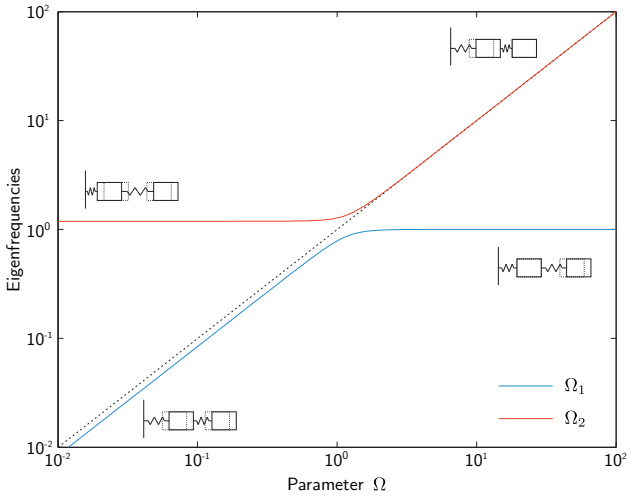


Figure 3: Evolution of the eigenfrequencies with parameter Ω.

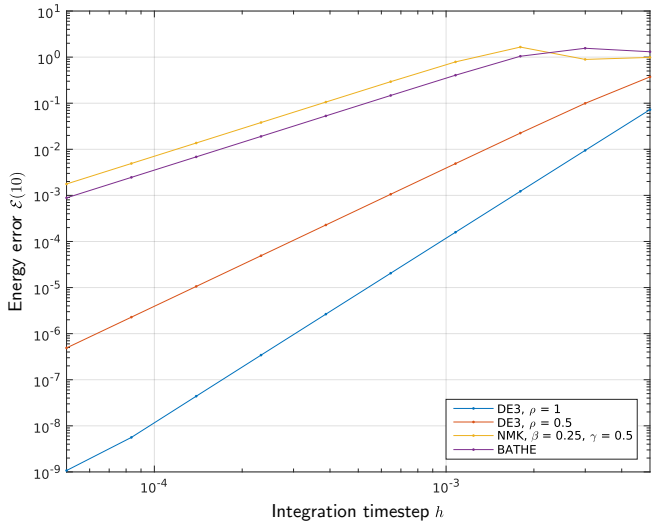


Figure 4: Comparison of the error introduced by the numerical integration procedure for several schemes. The slopes of the lines give the order of accuracy of the schemes.

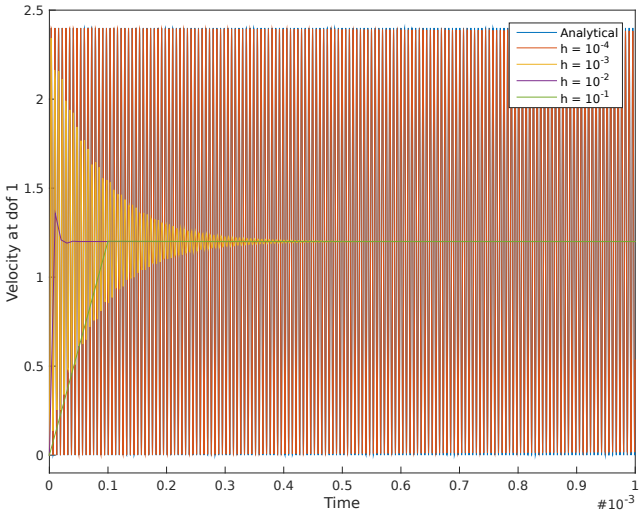


Figure 5: Taming of spurious oscillations via the proper adjustment of the numerical damping introduced by the DE^3 scheme.

by interpreting the high-frequency oscillations at $\Omega_2 \sim \Omega + (2\Omega)^{-1} + O(\Omega^{-3})$ to be spurious ones. Proper filtering should then be achieved to ensure that they do not contaminate the lower frequency components of the model response so that its dynamics is well resolved.

From Figure 1, we see that high-frequency oscillations are very quickly damped by the integration scheme if $\rho_\infty = 0$ (most dissipative configuration) and the frequency-reduced timestep is above 10^2, as the magnitude of the spectral radius of the amplification matrix is indicative of the scaling of the amplitude of harmonic oscillations over a single integration increment. We can thus deduce that spurious oscillations will be fast rejected by the integration scheme provided

$$h > h^* = \frac{10^3}{\Omega_2} \simeq \frac{10^3}{\Omega}. \tag{12}$$

Setting $\Omega = 10^6$ and keeping $\Omega_p = 1.2$, so that there is a timescale separation between the slow dynamics we are interested in and the spurious dynamics, the above criterion reduces to $h > h^* \simeq 10^{-3}$. Figure 5 illustrates the effect of numerical damping on the spurious oscillations, by varying the integration timestep while keeping the numerical setting to $\rho_\infty = 0$. Reducing the timestep is equivalent to moving leftwards along the x-axis of Figure 1 and, thus, the larger the timestep, the more damping is introduced with respect to the frequency set by $\Omega_2 \simeq \Omega$. As expected, the high-frequency oscillations are more quickly damped for large timesteps than for small ones. In fact, they are even annihilated in one increment for $h = 10^{-1}$, whence the name of the spectral annihilation property. The DE^3 scheme thus not only offers high accuracy but also control on the numerical dissipation introduced in the simulations, making it an interesting candidate for structural dynamics computations.

4 CONCLUSION

The DE^3 scheme positions itself as a novel and unconditionally stable high-order alternative to the second-order schemes commonly used in structural dynamics. Its symmetric formulation, combined to the possibility it offers to control numerical damping via a single parameter, make it an ideal algorithmic solution for the simulation of large-scale structural dynamics problems.

Indeed, advantage can be taken from its symmetric nature on the solver side while the controlled numerical damping can be used to tame spurious oscillations that typically arise in problems showing a broad spectrum of eigenfrequencies, with the higher ones being associated with numerical rather than physical eigenmodes.

In this paper, those properties are established and demonstrated by way of an example. In particular, an error analysis shows its superiority on other well-know schemes and the control of numerical damping to remove spurious oscillations is illustrated as well.

REFERENCES

[1] N.M. Newmark. A method of computation for structural dynamics. *Journal of Engineering Mechanics, ASCE*, 85(EM3):67–94, 1959.

[2] A. Depouhon, E. Detournay, and V. Denoël. Accuracy of one-step integration schemes for damped/forced linear structural dynamics. *International Journal for Numerical Methods in Engineering*, 99(5):333–353, August 2014.

[3] C.L. Bottasso and L. Trainelli. An Attempt at the Classification of Energy Decaying Schemes for Structural and Multibody Dynamics. *Multibody System Dynamics*, 12:173–185, 2004.

[4] A. Depouhon, E. Detournay, and V. Denoël. Event-driven integration of linear structural dynamics models under unilateral elastic constraints. *Computer Methods in Applied Mechanics and Engineering*, 276(0):312–340, July 2014.

[5] A. Depouhon, , V. Denoël, and E. Detournay. Numerical simulation of percussive drilling. *International Journal for Numerical and Analytical Methods in Geomechanics*, (Online) 2015.

[6] X.D. Li and N.-E. Wiberg. Structural Dynamic Analysis by a Time-Discontinuous Galerkin Finite Element Method. *International Journal for Numerical Methods in Engineering*, 39(12):2131–2152, 1996.

[7] L. Guttman. Enlargement Methods for Computing the Inverse Matrix. *The Annals of Mathematical Statistics*, 17:336–343, 1946.

[8] A. Quarteroni, R. Sacco, and F. Saleri. *Numerical Mathematics*. Texts in Applied Mathematics. Springer-Verlag New York, Inc., 2010.

[9] S. Krenk. State-space time integration with energy control and fourth-order accuracy for linear dynamic systems. *International Journal for Numerical Methods in Engineering*, 65:595–619, January 2006.

[10] K.-J. Bathe and G. Noh. Insight into an implicit time integration scheme for structural dynamics. *Computers and Structures*, 98–99:1–6, 2012.

[11] M. Géradin and D. Rixen. *Mechanical Vibrations: Theory and Application to Structural Dynamics*. Wiley, 1997.

COMPDYN 2015
5th ECCOMAS Thematic Conference on
Computational Methods in Structural Dynamics and Earthquake Engineering
M. Papadrakakis, V. Papadopoulos, V. Plevris (eds.)
Crete Island, Greece, 25–27 May 2015

A MESHLESS NEURAL NETWORK APPROACH FOR THE DYNAMIC ANALYSIS OF ELASTIC SYSTEMS

Luca Facchini[1] **and Michele Betti**[2]

[1] Department of Civil and Environmental Engineering,
University of Florence
via di S. Marta 3 – I-50139 Florence – Italy
e-mail: luca.facchini@unifi.it

[2] Department of Civil and Environmental Engineering,
University of Florence
via di S. Marta 3 – I-50139 Florence – Italy
e-mail: mbetti@dicea.unifi.it

Keywords: Static and dynamic problem in linear elasticity, Artificial Neural Networks, Meshless methods, Mixed formulation, Hu-Washizu principle, Energy-based training.

Abstract. *A meshless approach is presented for the computation of the approximated solution of static and dynamic problems in linear elasticity in terms of displacement fields. The displacement field is modeled by means of two different kinds of Artificial Neural Networks (ANN). This task is accomplished by means of a meshless approach coupled to a net training based on the weak formulation of the differential problem, related to Hu-Washizu principle. A common benchmark, namely the Timoshenko cantilever beam, is analyzed and discussed in detail; several researches have shown that severe difficulties are encountered with the Galerkin and the collocation approach since the neural networks never satisfy essential boundary conditions (EBC): in the proposed meshless approach, the trial functions can be modified in order to satisfy EBC. A possibility to overcome such difficulty in elasticity is to employ an energy-based training, that is, to employ an approach (such as the Hu-Washizu functional) which can take into account EBC in the error function to be minimized. An example is given in one dimension, analyzing the deflection of a horizontal beam subject to transverse loads. The presented examples clearly show the importance of the optimization of the non-linear pa-rameters of the network, which control the shape and location of the activation functions. It is shown that such parameters can be optimized for a static problem and subsequently employed for a dynamic problem. The paper in fact aims to extend the results investigating the bench-mark problem in the dynamic field.*

1 INTRODUCTION

Meshless approaches which are based on Artificial Neural Networks (ANN) have lately become widely used and investigated by the scientific community to find reliable approximations for the solutions of a great number of problems, described by one or more differential equations. Extensive summaries can be found f.i. in [1] and [2].

In the field of structural mechanics one of the most promising perspectives is the analysis of cracked structures and more generally the behavior of materials which cannot undergo tensile states. One of the most attractive features is that such approaches do not need the definition of a mesh, and many of them need a so-called background mesh of the structure for only numerical integration purposes. This leads, especially in the field of fracture mechanics, to model the cracked materials in a more reliable manner, as the crack pattern computed with a FEM-based algorithm often shows a strong sensitivity in the mesh definition in the surroundings of the crack itself.

Usually, meshless approaches employ a weighted residual method (see f.i. [3] and [4]) to evaluate the solution; the activation functions are defined by means of a set of parameters – called non-linear parameters in the following – which control the shape and location of the support of the functions. The present work emphasizes the importance of the optimization of such parameters, showing that the non-linear parameters can be optimized with respect to a static problem, and subsequently employed to determine the dynamic characteristics of the investigated structure.

2 THEORETICAL REMARKS

A great amount of different kinds of neural networks can be found in specialized literature, but many of them can be represented as a linear combination of nonlinear functions of their arguments in the form

$$\boldsymbol{f}(\boldsymbol{x}) = \sum_{h=1}^{N_\phi} \boldsymbol{w}^{(h)} \phi_h(\boldsymbol{x}) \tag{1}$$

where $\boldsymbol{x} \in \mathbb{R}^n$ is the independent variable and $\boldsymbol{f}: \mathbb{R}^n \to \mathbb{R}^m$ is a vector function. It follows from the definition (1) that $\boldsymbol{w}^{(h)} \in \mathbb{R}^m$ are vectors coefficients and $\phi_h(x)$ are scalar functions of $\boldsymbol{x}$.

Typically, functions $\phi_h(x)$ determine the kind of neural network; in the present work, examples are presented which employ either sigmoid functions (utilized in feed-forward back-propagation – FFBP – networks) or radial basis functions (RBF, giving rise to RBF networks).

2.1 RBF Networks

In the meshless approaches for structural mechanics, RBF are typically employed, such as multi-quadric, Gaussian bells, or compact support functions as the so-called Chebichev's hat or similar functions. RB functions can be expressed by means of the combination of the distance of the generic point $\boldsymbol{x}$ from the so-called center of the associated function, and a real-valued function of a scalar variable which decreases for increasing argument (see f.i. [5], [6] and [7]):

$$\begin{cases} \phi_h(\boldsymbol{x}) = \varphi\left(\| \boldsymbol{x} - \boldsymbol{c}^{(h)} \|\right) \\ \varphi(r) = \exp(-r^2/\sigma^2) \end{cases} \tag{2}$$

In expression (2), $\varphi(r)$ can be seen as an *underlying* function which enables to define the RBFs $\phi_h(\boldsymbol{x})$, and in this case a Gaussian bell is employed (Figure 1); usually, compact support functions are preferred to other kind of functions owing to the difficulty involved in the calculation of integrals, but such difficulty can be overcome by means of proper numerical techniques.

As it is clear from definitions, RB functions depend on a limited number of parameters which control their shape and location. In information theory, trial functions are in fact called activation functions, as they change their value in a limited interval of the real axis: this means that, if the independent variable $\boldsymbol{x}$ falls into a limited region $\Omega_h \in \mathbb{R}^n$, then the activation function attains non-negligible values.

The region Ω_h is typically a hyper-sphere in $\mathbb{R}^n$ in the case of RBFs, so that its characterizing parameters are the coordinates of its center and its radius. Nevertheless, it can also attain different shapes, as its expression is mainly a function of the distance of the generic point $\boldsymbol{x}$ from the so-called center of the associated function as expressed in (2).

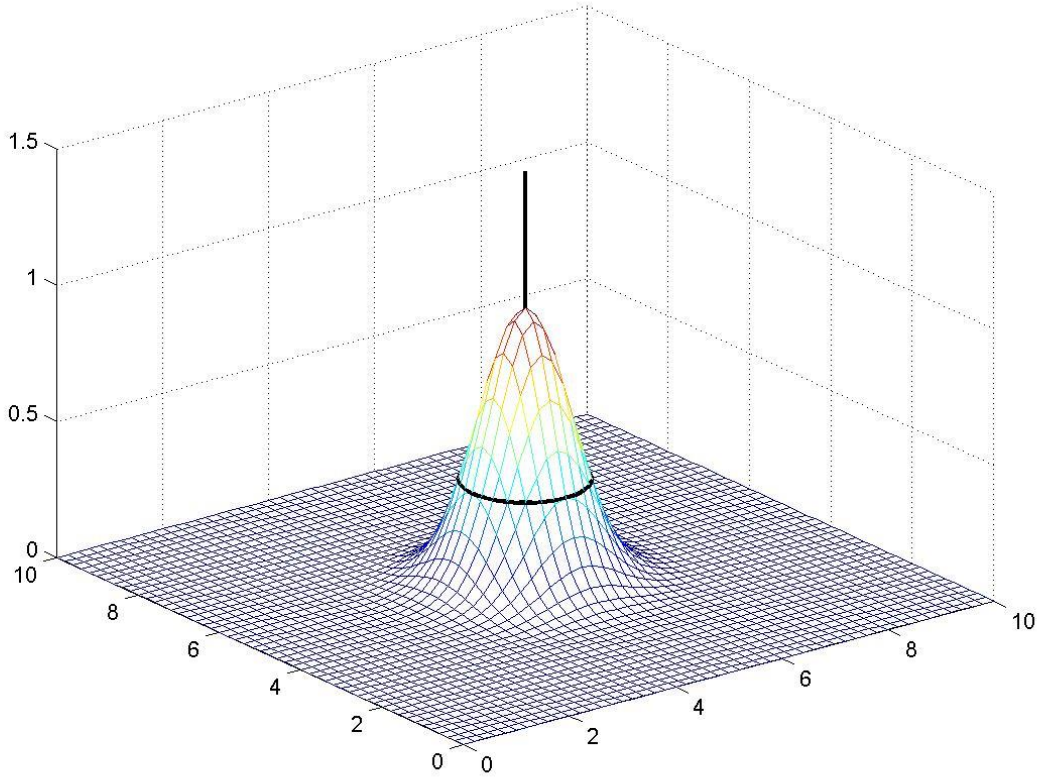


Figure 1: A typical RB function defined by means of a Gaussian bell; the center is located at coordinates (5,5) and is highlighted by the black vertical line, while the parameter σ determines the radius of the black circle.

An interesting example of an RB function is described in [5] and called the *up function*; such function is compactly supported and, if properly scaled and overlapped, possesses the following notable characteristics:

$$\sum_h u_h(x) = 1 \quad ; \quad \sum_h x_h u_h(x) = x \tag{3}$$

2.2 Feed-forward networks

An interesting approach is represented by FFBP networks which make use of sigmoid trial functions: these are monotonically increasing functions of the independent variable, and among the most used are:

$$\text{(sigmoid function)} \begin{cases} \phi_h(\boldsymbol{x}) = \varphi(\sigma_{hk} x_k + b_h) \\ \varphi(r) = \frac{1}{1+\exp(-r)} \end{cases} \tag{4}$$

$$\text{(hyperbolic tangent function)} \begin{cases} \phi_h(\boldsymbol{x}) = \psi(\sigma_{hk} x_k + b_h) \\ \psi(r) = \frac{\exp(r)-\exp(-r)}{\exp(r)+\exp(-r)} \end{cases} \tag{5}$$

The use of functions (4) or (5) as activation functions is equivalent: as a matter of fact, it can be shown that:

$$\psi(r) = \frac{1-\exp(-2r)}{1+\exp(-2r)} = 2\phi(2r) - 1 \tag{6}$$

2.3 Meshless approach for static problem

The described functions are herein utilized to obtain a satisfactory approximation of a linear elastostatic problem, cast in the following terms: given a linearly elastic continuum B subject to body forces $\boldsymbol{b}$ and to surface forces $\hat{\boldsymbol{f}}$ on the boundary ∂B_N (natural boundary conditions, NBC), and to restraints $\hat{\boldsymbol{s}}$ on the boundary ∂B_E, find a displacement field $\boldsymbol{s}(\boldsymbol{x})$ such that:

$$\text{(essential boundary conditions, EBC)} \quad \boldsymbol{s}(\boldsymbol{x}) = \hat{s} \quad \text{on } \partial B_E \tag{7}$$

$$\text{(strain-displacement relation)} \quad \boldsymbol{\epsilon} = Sym(\nabla \boldsymbol{s}) \tag{8}$$

$$\text{(equilibrium equations)} \begin{cases} \text{div}\boldsymbol{\sigma} + \boldsymbol{b} = \boldsymbol{0} & \text{on } B \\ \boldsymbol{\sigma n} = \hat{\boldsymbol{f}} & \text{on } \partial B_N \end{cases} \tag{9}$$

where $\boldsymbol{\sigma} = C[\boldsymbol{\epsilon}]$, C being the elastic tensor. Even though it is simpler than the dynamic case, the solution of the elastostatic problem can nevertheless give some insight on the main issues of the solution procedure: usually, a weighted residual procedure is adopted to determine the unknown parameters $\boldsymbol{w}^{(h)}$ in (1), while the parameters which control the shape and the collocation of the generic function ϕ_h are decided and fixed by the user, and the goodness of the obtained approximation mainly depend on the number N_ϕ of functions chosen.

Some indications can be found in specialized literature on the best possible way to choose the location and shape parameters of the activation functions. As an example, Peng *et al.* [8] observe that a larger support size and higher order of RB functions will yield better convergence results. This fact can be partially explained in the light of the stationarity of the total energy of the continuum, as explained in the following paragraph.

The total energy of the structure, given by the sum of the elastic deformation energy and the potential energy of the applied loads, is defined as follows:

$$E(\boldsymbol{s}) = \frac{1}{2}\int_B \boldsymbol{\sigma} \cdot \boldsymbol{\epsilon}\, dV - \int_B \boldsymbol{b} \cdot \boldsymbol{s}\, dV - \int_{\partial B_N} \hat{f} \cdot \boldsymbol{s}\, dS \tag{10}$$

Finding the vector field which minimizes (10) and satisfies the EBC (7) and the strain-displacement conditions (8) yields the solution of the elastostatic problem.

Functional (10) can usefully be slightly transformed, making use of the symmetries of the elastic tensor and of the deformation and tension components, yielding:

$$E(\boldsymbol{s}) = \frac{1}{2}\int_B \nabla \boldsymbol{s} \cdot C[\nabla \boldsymbol{s}] - \boldsymbol{b} \cdot \boldsymbol{s}\, dV - \int_{\partial B_N} \hat{\boldsymbol{f}} \cdot \boldsymbol{s}\, dS \tag{11}$$

If the displacement is expressed by means of a neural network in the form:

$$\boldsymbol{s}(\boldsymbol{x}) = \sum_{h=1}^{N_\phi} \boldsymbol{w}^{(h)} \phi_h(\boldsymbol{x}) \tag{12}$$

then its gradient is given by the expression:

$$\nabla \boldsymbol{s}(\boldsymbol{x}) = \sum_{h=1}^{N_\phi} \boldsymbol{w}^{(h)} [\nabla \phi_h(\boldsymbol{x})]^t \tag{13}$$

and, by substitution in relation (11), the stiffness matrix $\boldsymbol{K}$ and the load vector $\boldsymbol{q}$ can be computed such that the minimization of the total energy of the system yields:

$$\boldsymbol{K}\boldsymbol{d} = \boldsymbol{q} \tag{14}$$

where $\boldsymbol{d}$ is a vector which groups all the components of the vectors $\boldsymbol{w}^{(h)}$, which are therefore called *linear parameters*. Equation (14) represents the minimization of the structural energy with respect to the linear parameters, but not to the other characterizing parameters of the network, which will be discussed later.

As a matter of fact, the stiffness matrix $\boldsymbol{K}$ and the load vector $\boldsymbol{q}$ are given by the integration, over the continuum body and surface, of the gradient of the displacement field, and therefore depend on the location and shape parameters of the activation functions $\phi_h(\boldsymbol{x})$, which will be grouped in the vector $\boldsymbol{\theta}$ of *non-linear parameters*. In this way, it is possible to write that:

$$\boldsymbol{K} = \boldsymbol{K}(\boldsymbol{\theta}) \quad \boldsymbol{q} = \boldsymbol{q}(\boldsymbol{\theta}) \quad \Rightarrow \quad \boldsymbol{d} = \boldsymbol{K}^{-1}(\boldsymbol{\theta}) q(\boldsymbol{\theta}) = \boldsymbol{d}(\boldsymbol{\theta}) \tag{15}$$

and therefore the total energy of the structure will be approximated by the expression

$$E(\boldsymbol{\theta}) = \frac{1}{2}\boldsymbol{d}^t(\boldsymbol{\theta})\boldsymbol{K}(\boldsymbol{\theta})\boldsymbol{d}(\boldsymbol{\theta}) - \boldsymbol{d}^t(\boldsymbol{\theta})\boldsymbol{q}(\boldsymbol{\theta}) = -\frac{1}{2}\boldsymbol{q}^t(\boldsymbol{\theta})\boldsymbol{K}^{-t}(\boldsymbol{\theta})\boldsymbol{q}(\boldsymbol{\theta}) \tag{16}$$

In other words, the minimum value of the total energy of the structure (with respect to the linear parameters) is a function of the non-linear parameters which define the activation functions, and it is therefore possible to optimize again the energy functional with respect to the non-linear parameters only, as shown in [9].

2.4 Meshless approach for dynamic problem

In the case of an elastodynamic problem, the displacements, deformations, tensions and loads depend, of course, also on time. Following standard approaches for the numerical solution of the dynamical problem, a consistent mass matrix and a damping matrix can be computed such that:

$$\boldsymbol{M}(\boldsymbol{\theta})\ddot{\boldsymbol{d}} + \boldsymbol{C}(\boldsymbol{\theta})\dot{\boldsymbol{d}} + \boldsymbol{K}(\boldsymbol{\theta})\boldsymbol{d} = \boldsymbol{q}(\boldsymbol{\theta}, t) \tag{17}$$

where the dependence of $\boldsymbol{d}$ on time and $\boldsymbol{\theta}$ have been omitted for sake of simplicity. In the following, non-linear parameters will be optimized for the elastostatic problem, and the non-linear parameters determined in this manner will be utilized to compute mass and damping matrices.

3 APPLICATIONS

In order to show the feasibility of the examined approach, two applications will be analyzed and discussed in the following, namely a 1D horizontal beam with a clamped and a hinged end, and a 2D horizontal cantilever, the solution of which can be found f.i. in [10].

3.1 1D application with a clamped-hinged horizontal beam

The considered structure is represented in Figure 2 and is simply a beam with a clamped end on the left and a hinged end on the right.

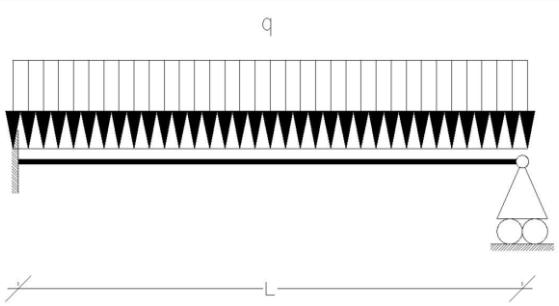


Figure 2: The examined structure.

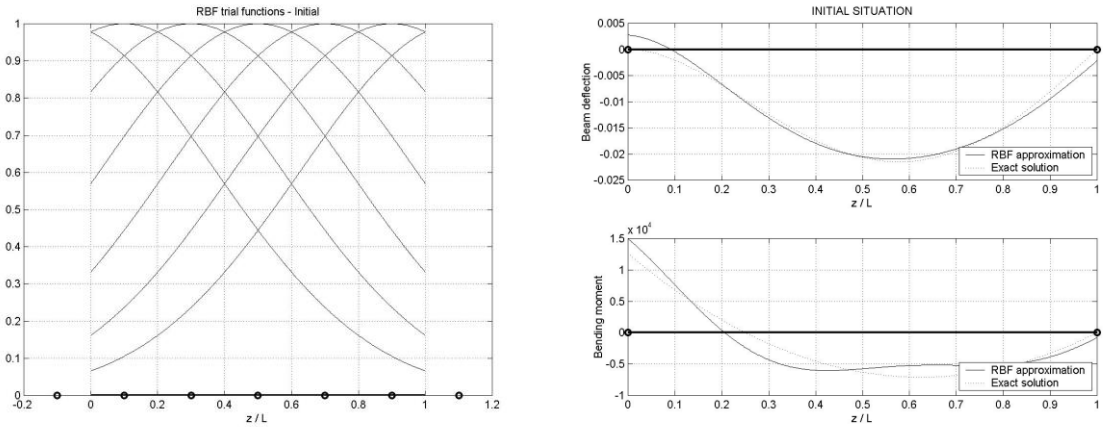


Figure 3: The initial arrangement of the RBFs (left) and the corresponding deflection (top right) and bending moment (bottom right).

At first, a set of 7 RBF were chosen, with centers (shown by the black circles in Figure 3) located at $z_h = [-1.0, 0.10, 0.30, 0.50, 0.70, 0.90, 1.10]L$ where L is the length of the beam.

If the non-linear parameters of the network are left as they are, which means no optimization is carried out on them, but just the linear parameters are evaluated, the obtained

solution is poor from the point of view of both deflections and bending moment, as it is clear from a look at Figure 3 (right).

On the other hand, if the optimization of the non-linear parameters is carried out, the results shown in Figure 4 are obtained, thus demonstrating the importance of the optimization of the non-linear parameters.

As a matter of fact, the optimization of the non-linear parameters is not strictly necessary, but the number of functions N_ϕ employed in equation (12) must be much higher.

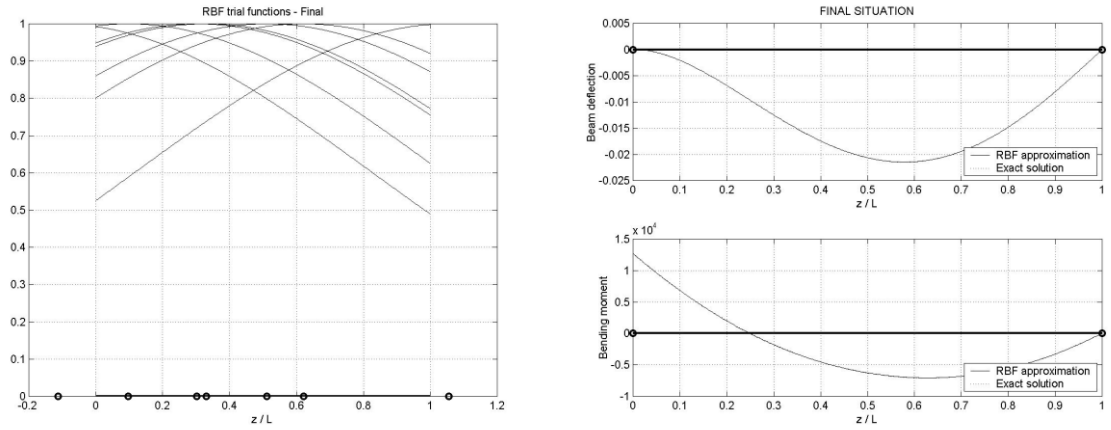


Figure 4: The final arrangement of the RBFs (left) and the obtained solution (top right: deflection, bottom right: bending moment).

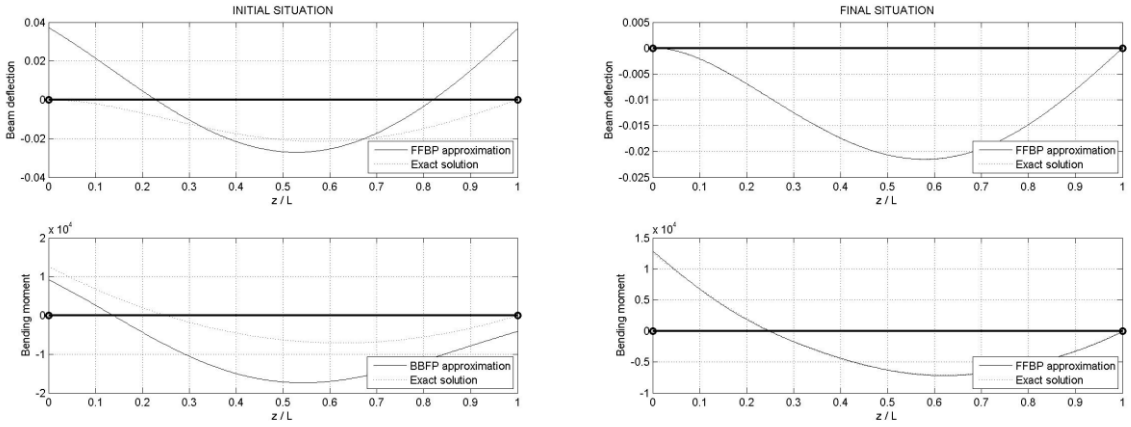


Figure 5: The solution (top: deflection, bottom: bending moment) with hyperbolic tangent activation functions; left: no optimization of non-linear parameters, right: optimized non-linear parameters.

A similar situation is observed with the use of a FFBP network in the form (5) with hyperbolic tangent activation functions, as shown in Figure 5.

3.2 2D application (Timoshenko cantilever)

In this example, a horizontal cantilever is considered, but the displacement is modelled as a bi-dimensional vector field which depends on two independent variables x and y, as shown in Figure 6. The dimensions of the cantilever are 5.00 m (length) by 1.00 m (height).

In the current example, the displacement is modeled by means of equation (12); in order to obtain functions which vanish at $x = 0$, the RBFs were slightly modified, and the following functions were used:

$$\begin{cases} \tilde{\phi}_h(\boldsymbol{p}) = \phi_h(x,y) - \phi_h(0,y) \\ \phi_h(\boldsymbol{p}) = \exp\left(-\| \boldsymbol{p} - \boldsymbol{c}^{(h)} \|^2/\sigma^2\right) \\ \boldsymbol{p} \equiv [x,y]^t \quad ; \quad \boldsymbol{c}^{(h)} \equiv [x_{ch}, y_{ch}]^t \end{cases} \tag{18}$$

Such modification is significant only when the RBF is centered near the clamped end, as is clear from a look at Figure 7.

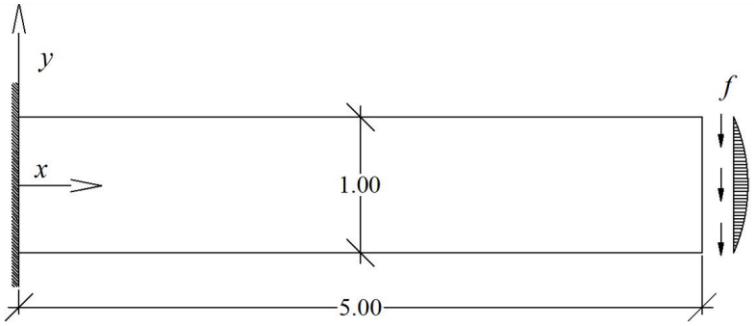


Figure 6: The considered cantilever: the left end is clamped, the right end is free and loaded by a parabolic vertical load *f*(*y*).

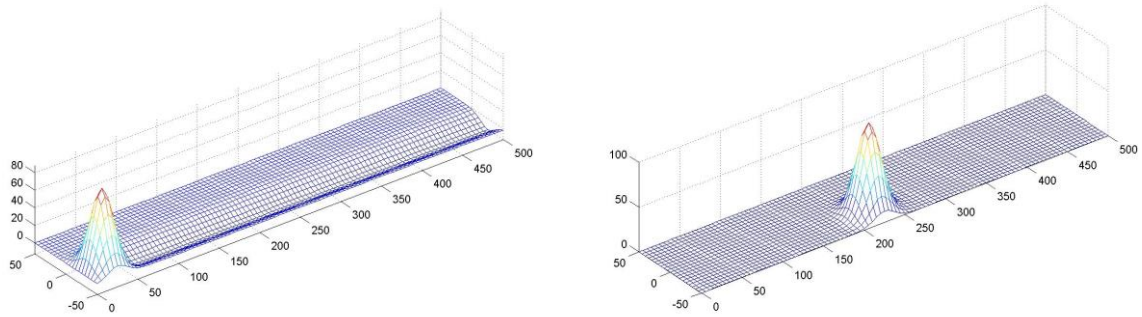


Figure 7: Two examples of the employed RBFs: on the left a function centered near the clamped edge, while on the right a function centered far from the clamped edge.

Element number and type	Degrees of freedom	Tip deflection
20 × CST	40	25,00%
10 × Q4	40	67,00%
10 × LST	48	99,00%
2 × Q8	20	93,00%
2 × Q9	24	95,00%

Table 1: Results reported in [11] for a cantilever beam. The tip deflections are the percentages of the solution obtained for a 1D horizontal slender beam.

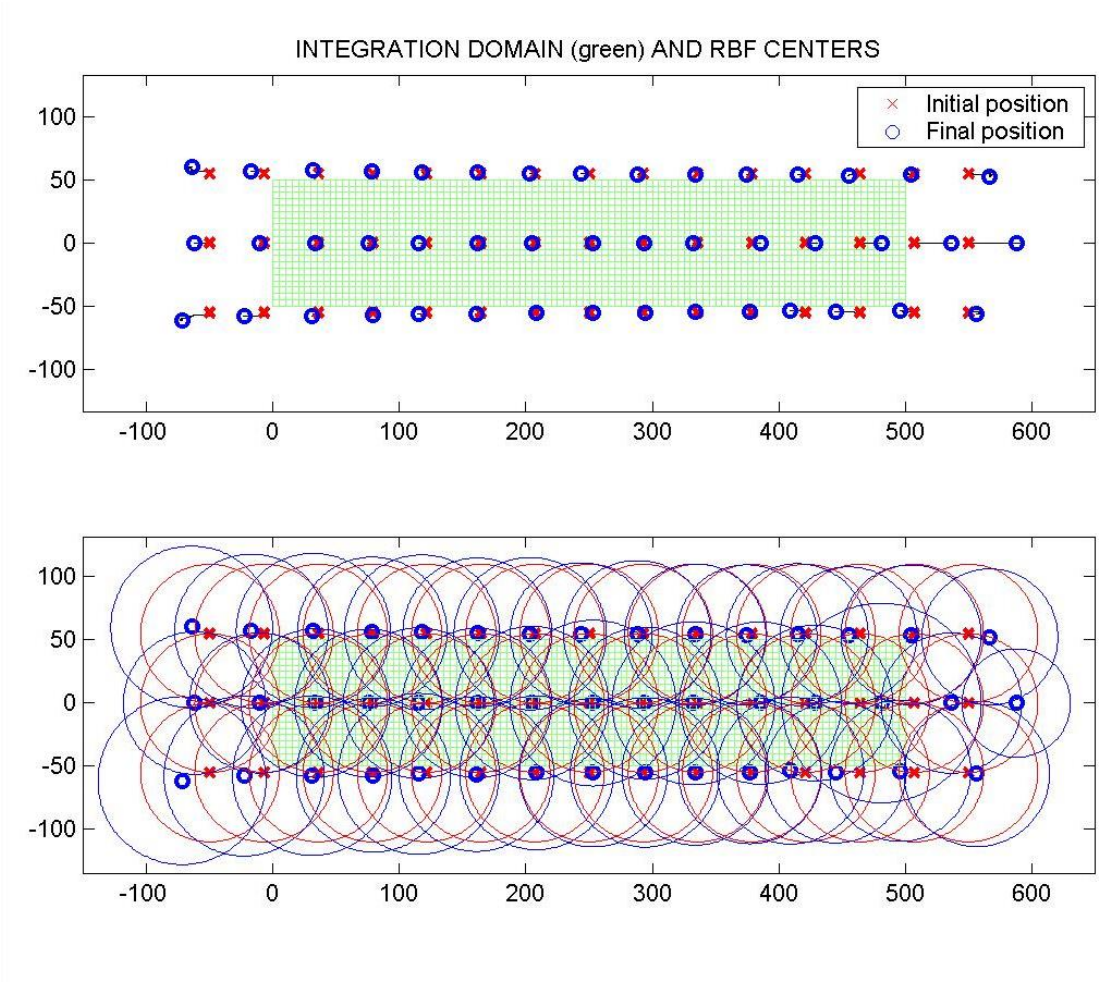


Figure 8: The training of the RBF network in the case of the 2D cantilever: above, the positions of the centers (red crosses denote initial position and blue circles denote final positions), while below the radii of the circles indicate the scaling parameters (red: initial values; blue: final values). The green area indicates the position of the cantilever.

In this case, the optimization of the RBF centers $\boldsymbol{c}^{(h)}$ and scaling parameters σ_h shows that convergence is observed towards a pattern where the centers are placed at more or less equal distances from each other, and the scaling parameters allow a wide overlapping between the functions.

Following such indications, several arrangements of RB functions were tested: a noticeable result is that, after a proper training of the non-linear parameters, a limited number of functions is sufficient to obtain a satisfactory approximation of the solution (see Figure 9 and Figure 10 for details).

For sake of comparison, Table 1 reports results from [11] for a cantilever beam with aspect ratio $L/H = 10$, along with the element types employed in the analysis and the number of degrees of freedom. CST denotes triangular, 3-nodes plane stress elements with linear shape functions. LST denotes triangular, 6-nodes plane stress elements with parabolic shape functions. Q4 denotes quadrilateral, 4-nodes plane stress elements with bi-linear shape functions. Q8 and Q9 denote quadrilateral, 8- and 9-nodes plane stress elements with cubic and quartic shape functions, respectively.

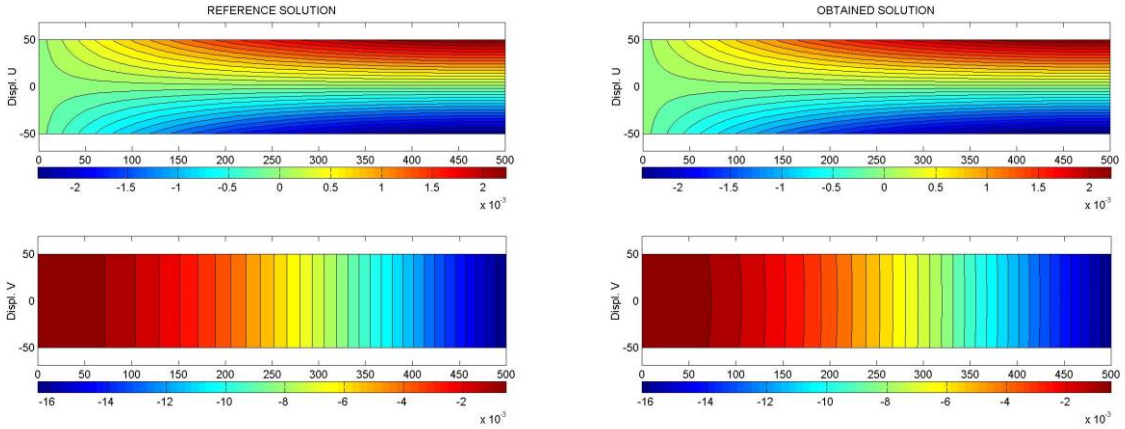


Figure 9: The solution for the horizontal (above) and vertical (below) displacement given in [10] (left) and obtained (right) with a network with only 13 RBFs.

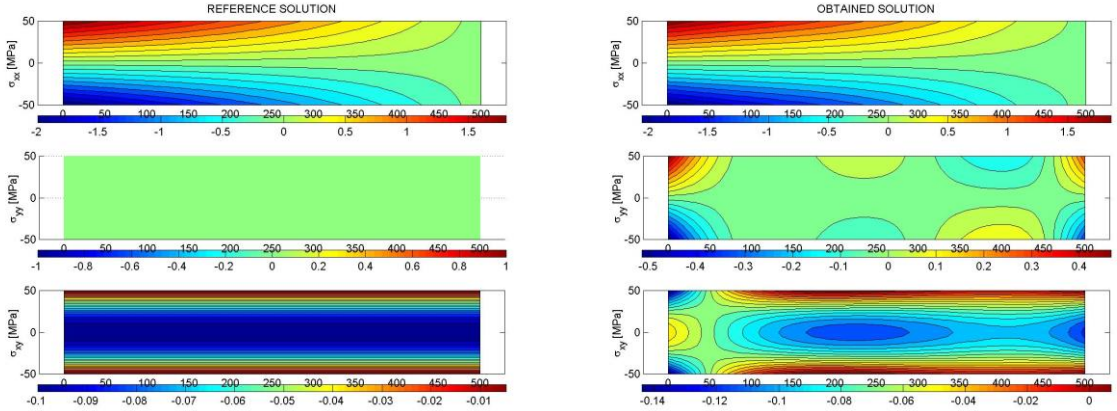


Figure 10: The solution for σ_{xx} (above), σ_{yy} (middle) and τ_{xy} (below) given in [10] (left) and obtained (right) with a network with only 13 RBFs (which corresponds to 26 linear and 39 non-linear parameters).

3.3 2D dynamic application (modal shapes for the 2D cantilever)

The non-linear parameters, optimized for a static load such that of the previous example, can be usefully employed to determine the consistent mass matrix of the structure; in the case of a time-dependent displacement field, equation (12) is changed in

$$\boldsymbol{s}(\boldsymbol{x},t) = \sum_{h=1}^{N_\phi} \boldsymbol{w}^{(h)}(t)\phi_h(\boldsymbol{x}) \tag{19}$$

and, upon differentiation, the velocity field is given by:

$$\boldsymbol{v}(\boldsymbol{x},t) = \dot{\boldsymbol{s}}(\boldsymbol{x},t) = \sum_{h=1}^{N_\phi} \dot{\boldsymbol{w}}^{(h)}(t)\phi_h(\boldsymbol{x}) \tag{20}$$

where the dot indicates differentiation with respect to time.

The kinetic energy of the continuum is therefore given by:

$$E_K(t) = \frac{1}{2}\int_B \boldsymbol{\rho}(\boldsymbol{x}) \parallel \boldsymbol{v}(\boldsymbol{x},t) \parallel^2 dV \tag{21}$$

thus leading to the usual evaluation of the consistent mass matrix $\boldsymbol{M}$; it is to be noted that such matrix can be regarded as a function of the non-linear parameters again: $\boldsymbol{M} = \boldsymbol{M}(\boldsymbol{\theta})$.

It is to be noted that a careful optimization of the non-linear parameters carried out in the case of a static load works well also for the determination of the dynamic characteristics of the structure, as can be seen by Figure 11.

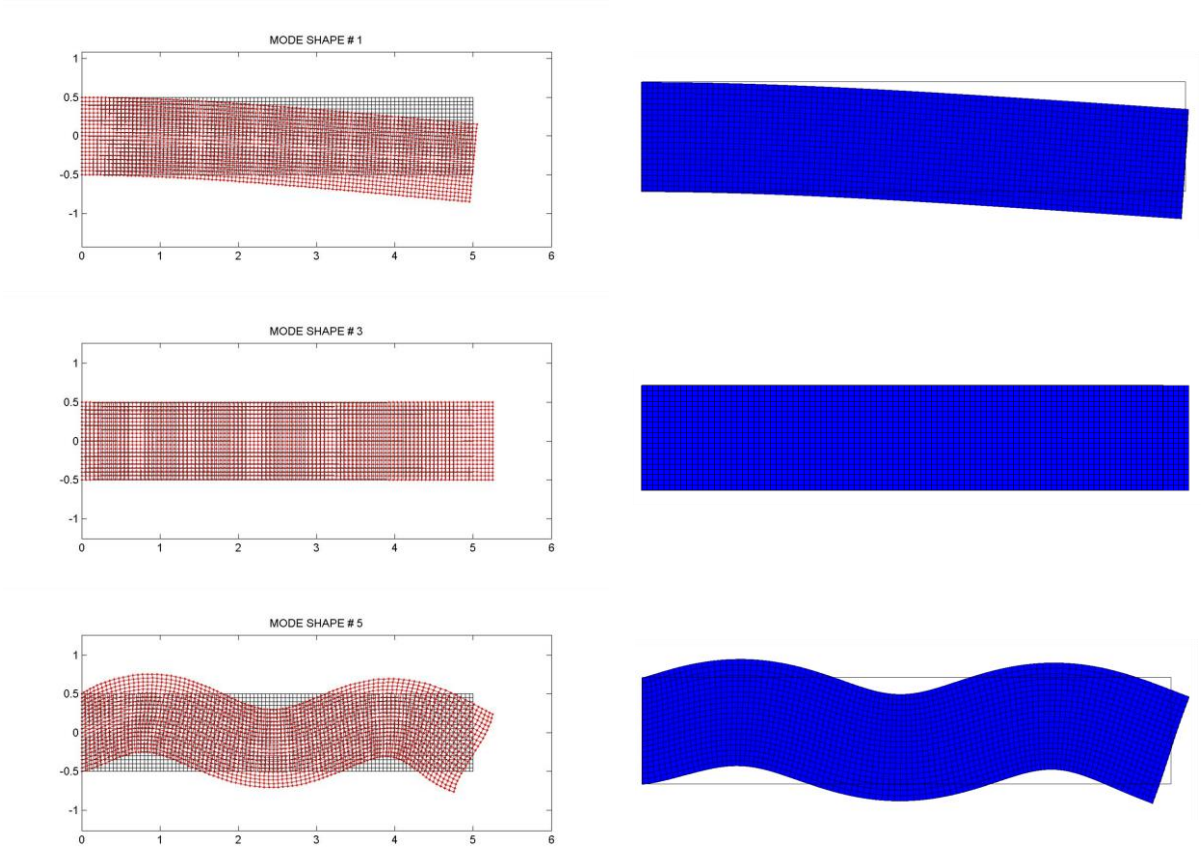


Figure 11: Some examples of the obtained modal shapes of the cantilever: first transverse (top), first axial (middle), fourth transverse (bottom). On the left side the shapes obtained with the meshless approach are shown, while on the right side the results from ANSYS FEM code are shown for comparison.

CONCLUDING REMARKS

The paper presents some results obtained by a RBF meshless approximation of the elastostatic and elastodynamic problems. Following the philosophy of neural networks, a set of non-linear parameters and a set of linear parameters have been defined.

It is clear that the optimization of the non-linear parameters of the network can bring notable benefits on the quality of the obtained approximation, and enable to greatly reduce the numbers of activation functions employed in the network.

The optimization performed for a static load can be extremely effective also in the computation of the dynamic characteristics of the examined structure.

REFERENCES

[1] S.D. Daxini, J.M. Prajapati, A review on recent contribution of meshfree methods to structure and fracture mechanics applications. *The Scientific World Journal*, Article ID 247172, 13 pages, 2014, http://dx.doi.org/10.1155/2014/247172.

[2] T. Belytschko, Y. Krongauz, D. Organ, M. Fleming, P. Krysl, Meshless methods: an overview and recent developments. *Computer Methods in Applied Mechanics and Engineering*, **139**, 3-47, 1996.

[3] G.R. Liu, Y.T. Gu, *An introduction to meshfree methods and their programming*. Springer, Dordrecht 2010.

[4] G. R. Liu, *Meshfree methods: moving beyond the Finite Element Method*. CRC Press, Boca Raton 2010.

[5] B. Gotovac, V. Kozulic, On a selection of basis functions in numerical analyses of engineering problems. *International Journal for Engineering Modelling*, **12(**1-4), 24-41, 1999.

[6] D.S. Broomhead, D. Lowe, Multi-variable functional interpolation and adaptive networks, *Complex Systems*, **2**, 269-303, 1988.

[7] T. Poggio, F. Girosi, Networks for approximation and learning, *Proceedings of the IEEE*, **78**(9), 1481-1497, 1990.

[8] L.X. Peng, S. Kitipornchai, K.M. Liew, Analysis of rectangular stiffened plates under uniform lateral load based on FSDT and element-free Galerkin method, *International Journal of Mechanical Sciences*, **47**(2), 251-276, 2005.

[9] L. Facchini, P. Biagini, Neural networks for meshless and PUFEM approaches, *22nd International Congress of Theoretical and Applied Mechanics (ICTAM 2008)*, Adelaide, Australia, August 24-29, 2008.

[10] S.P. Timoshenko, J.N. Goodier, *Theory of elasticity, 3rd edition*, Mc Graw-Hill International editions, Singapore 1970.

[11] R.D. Cook, D.S. Malkus, M.E. Plesha, R.J. Witt, *Concepts and applications of finite element analysis, 4th edition*, John Wiley and Sons inc., 2002.

COMPDYN 2015
5th ECCOMAS Thematic Conference on
Computational Methods in Structural Dynamics and Earthquake Engineering
M. Papadrakakis, V. Papadopoulos, V. Plevris (eds.)
Crete Island, Greece, 25–27 May 2015

GENETIC OPTIMIZATION OF TOWER VIBRATIONS WITH PENDULUM TMD

Gino B. Colherinhas[1], Maura A. M. Shzu[2], Suzana M. Avila[2], and Marcus V. G. de Morais[1]

[1]Universidade de Brasília - Faculdade de Tecnologia
Departamento de Engenharia Mecânica
Campus Universitário Darcy Ribeiro, Asa Norte - 70.910-900 Brasília, DF, BRAZIL
e-mail: ginobertollucci@hotmail.com; mvmorais@unb.br

[2]Universidade de Brasília - Faculdade UnB-Gama
Campus UnB Gama, Área Especial Indústria e Projeção A - 72.444-240 Gama, DF, BRAZIL
e-mail: {maura,avilas}@unb.br

Keywords: Wind Turbine Tower Vibrations, Tuned Mass Damper, Genetic Optimization, ECCOMAS Thematic Conference, Structural Control, Earthquake Engineering.

Abstract. *The wind turbine is supported by towers, which are slender and flexible due to their geometry and great height. As a consequence, they may experience excessive vibration levels caused by both the operation of the turbine and the wind loads [1]. One solution to this problem is the installation of passive control devices. One common passive device is the Tuned Mass Damper (TMD). Briefly, it is a pendulum-damper which transfers the energy of the vibration from the main structure to itself, working as a passive device. These passive devices need to be finely tuned to work as dampers; otherwise, they could amplify structural vibration levels. In this paper we propose to optimize the vibration performance of a pendulum TMD using Genetic Algorithm (GA). Harmonic analysis is used to describe the tower with pendulum TMD, and restricting the mass and length of the pendulum, we propose two fitness functions for the GA: (a) minimize high peaks of the vibration frequencies; (b) minimize high peaks of the vibration frequencies and maximize the anti-frequency peak (min. max. restriction). We compare the analysis of the GA optimization undertaken by report to Zuluaga [2] gradient approach.*

1 INTRODUCTION

The current energy crises coupled to the depletion of fossil fuel stocks and the need to reduce emissions of carbonic gas, in order to preserve the environment makes wind power generation a viable and attractive mean for producing electricity [1].

The wind turbine is supported by a tower that can experience excessive vibrations caused by both the wind turbine and the wind forces because of its geometry and great height. A detailed analysis of the structural behavior of the tower is of great importance due to its cost, which can represent approximately 20% of the total cost of the system [3].

Given the great progress in analyses and structural dimensioning, with the advances in the material field and construction techniques, higher and slender structures have become more interesting to study. These structures, however, are more vulnerable to excessive vibrations due to dynamic loads such as earthquakes, winds, storms, waves, etc.

An alternative option, widely studied in the last few years, is the structural control. Fundamentally, the structure stiffness and damping properties is changed adding external device or applying external forces. It is classified as passive, active, hybrid, or semi-active control. Several researchers have been studying the use of structural control to help suppress the wind-induced vibrations experienced by wind turbine towers [4].

To minimize these vibrations, we implemented a structural control with a Tuned Mass Damper (TMD) Pendulum type. A TMD is a passive control device composed of a mass-spring-dashpot attached to the structure, aiming to reduce structural vibration response [5], since it exhibits a pendulum absorber geometry. After that, a genetic optimization methodology was loaded with multiple objectives to be compared to an existing mathematical and numerical optimization [2].

In this paper we propose a structural control optimization methodology to assist wind turbine design projects, enabling the selection of a configuration that targets an optimum relation between the min and max frequency peaks (Min.Max optimization). The variable parameters surveyed are: pendulum length and ratio mass between the pendulum and the wind turbine.

Depending on the result obtained for the evaluation of TMD mathematical formulation, fitness is ascribed to each configuration and inputted in a Genetic Algorithm (GA) to optimize the initial values. This optimization method was chosen for its advantages at discontinuous functions with multiple variables and complex formulations.

The following sections describe the modal analysis of a wind turbine tower, the TMD mathematical formulation for the pendulum settings, the optimization method chosen (definitions of the chromosome, fitness function, and convergence criteria), and the results.

2 MODAL ANALYSIS

The goal of the modal analysis is to reduce the complex system of partial differential equation which describes the dynamic behavior of a continuous structure. The motion of a cantilever Bernoulli-Euler beam (Figure 1) is described in Equation 1 using the theoretical treatment of the modal analysis [6].

$$\frac{\partial^2}{\partial z^2}\left(EI\frac{\partial^2 w(z,t)}{\partial z^2}\right)+\rho\frac{\partial^2 w(z,t)}{\partial t^2}=F(z,t) \tag{1}$$

where $w(z,t)$: normal displacement of the beam axis in some directions; z: distance along the beam axis; ρ: mass per unit length of the beam; F: external force per unit length applied normal to the beam axis in the direction of w; E: Young's modulus; I: area inertia moment for bending.

In general, the modulus of the inertia moment and the mass per unit length vary along the span of the beam. However, in this example they may be considered uniform over the span.

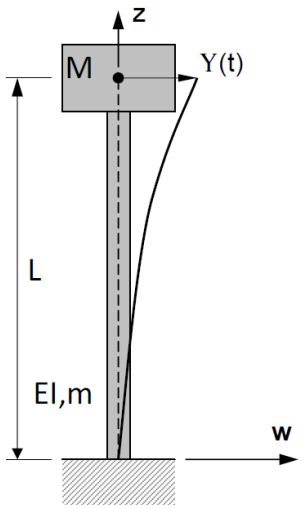


Figure 1: Schematic description of a cantilever beam with a tip mass.

The boundary conditions for a cantilever beam are given by Equation 2.

$$\begin{aligned} w(0,t) &= \partial_z w(0,t) = 0 \\ EI\partial_z^2 w(0,t) &= \omega_n^2 \Phi'(L) J_M \\ EI\partial_z^2 w(L,t) &= \omega_n^2 \Phi(L) M \end{aligned} \tag{2}$$

where M and J_M: mass and corresponding rotatory inertia mass at the free end, respectively.

Separating a space-time function by $w(z,t) = \Phi(z)Y(t)$ and applying the Fourier method into the associated equation for free vibration, we obtain Equation 3.

$$\frac{1}{\Phi}\frac{\partial^4 \Phi}{\partial z^4} = -\frac{m}{EI}\frac{1}{Y}\frac{\partial^2 Y}{\partial t^2} = const. \tag{3}$$

The solution of Equation 3 is given by Equations 4 and 5.

$$\Phi(z) = C_1 \sin \alpha z + C_2 \sin \alpha z + C_3 \sinh \alpha z + C_4 \cosh \alpha z \tag{4}$$

$$Y(t) = A \sin \omega_n t + B \cos \omega_n t, \text{ with } n = 1, 2, 3, \ldots \tag{5}$$

where $\omega_n = (n^2\pi^2/L^2)\sqrt{EI/m}$: natural frequency of vibration; $\alpha_n = \omega_n^2 m/EI$.

Using boundary conditions (Equation 2) and $J_M = 0$ we determined the constants A, B and C_i, $i = 1, 2, 3, \ldots$ Thus the spatial end-conditions of the cantilever beam with tip mass were determined using Equation 6 [7].

$$\frac{\Phi_n(z)}{C_1} = \sin \alpha_n z - \sinh \alpha_n z + \left(\frac{\sin \alpha_n z + \sinh \alpha_n z}{\cos \alpha_n z + \cosh \alpha_n z}\right)\left(\cosh \alpha_n z - \cos \alpha_n z\right) \tag{6}$$

Using the fundamental mode shape $\Phi_1(z)$, as first vector, the Gram-Schmidt orthogonality process is going to be use to orthogonolize the other mode shapes. To determine the equivalent

one-degree-of-freedom (one-DOF) for a dynamic system with distributed mass and stiffness, it can be assumed that the fundamental mode shape is described by Equation 7 [8].

$$w(z,t) = Y(t)\Phi(z) = Y(t)\left[1 - \cos\frac{\pi z}{2L}\right] \tag{7}$$

Substituting Equation 7 into Equation 1, we obtain Equation 8.

$$M_s\ddot{Y} + K_sY = F \tag{8}$$

Then the generalized stiffness and mass of the tower are computed, respectively in Equations 9 and 10.

$$K_s = \int_0^L EI[\Phi''(z)]^2 dz = \int_0^L EI\frac{\pi^4}{16L^4}\cos\frac{\pi z}{2L}dz \Leftrightarrow K^* = \frac{\pi^4}{32L^3}EI \tag{9}$$

$$M_s = M + \int_0^L \left(1 - \cos\frac{\pi z}{2L}\right)^2 dz = M + \frac{mL}{2\pi}(3\pi - 8) \Leftrightarrow M^* = \frac{mL}{2\pi}\left[\pi\left(3 + 2\frac{L_e}{L}\right) - 8\right] \tag{10}$$

where the tip mass $M_s = mL_e$ is defined proportional as an equivalent length L_e.

3 TUNED MASS DAMPER MATHEMATICAL FORMULATION

Figure 2 shows a schematic description of a pendulum TMD attached to a main system composed of a two-DOF. The main system is reduced to a one-DOF model, which corresponds to the mode to be controlled [5]. The motion considering small displacements to the system is given by the matrix of the Equation 11 [2].

$$\begin{bmatrix}(M_s + M_p) & MpL \\ M_pL & M_pL^2\end{bmatrix}\begin{bmatrix}\ddot{y} \\ \ddot{\theta}\end{bmatrix} + \begin{bmatrix}C_s & 0 \\ 0 & C_p\end{bmatrix}\begin{bmatrix}\dot{y} \\ \dot{\theta}\end{bmatrix} + \begin{bmatrix}K_s & 0 \\ 0 & (K_p + M_pgL)\end{bmatrix}\begin{bmatrix}y \\ \theta\end{bmatrix} = \begin{bmatrix}F_s(t) \\ 0\end{bmatrix} \tag{11}$$

where M_s: main system modal mass; C_s: main system modal damping; K_s: main system modal stiffness; M_p: pendulum mass; C_p: pendulum damping; K_p: pendulum stiffness; L: cable length; g: gravity acceleration; $F_s(t) = F_{s0}e^{i\omega t}$: excitation modal force; $y(t)$: main system displacement; $\theta(t)$: pendulum angular displacement.

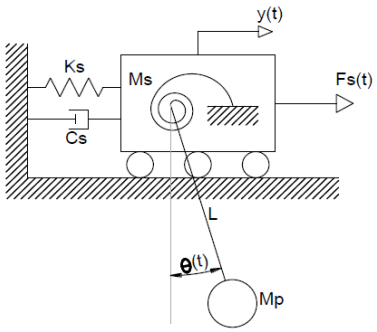


Figure 2: Structure with a linear pendulum attached: excitation due to a force $F_s(t)$.

Considering $F_s(t) = e^{i\omega t}$, then was obtained $y(t) = H_y(\omega)e^{i\omega t}$ $\theta(t) = H_\theta(\omega)e^{i\omega t}$. Substituting in Equation 11, we obtain the linear equation system given by Equation 12.

$$\begin{bmatrix} -(M_s + M_p)\omega^2 + C_s i\omega + K_s & M_p L\omega^2 \\ -M_p L\omega^2 & -M_p L^2\omega^2 + C_p i\omega + (K_p + M_p gL) \end{bmatrix} \begin{bmatrix} H_y(\omega) \\ H_\theta(\omega) \end{bmatrix} = \begin{bmatrix} 1 \\ 0 \end{bmatrix} \quad (12)$$

where $H_y(\omega)$: structure response function in the frequency domain; $H_\theta(\omega)$: pendulum response function in the frequency domain.

Solving this linear equation system (Equation 12), Zuluaga [2] obtained response functions $H_y(\omega)$ and $H_\theta(\omega)$ in the frequency domain. These responses are present in Equations 13 and 14.

$$H_y(\omega) = \frac{-\omega^2 B_2 + i\omega B_1 + B_0}{\omega^4 A_4 - i\omega^3 A_3 - \omega^2 A_2 + i\omega A_1 + A_0} \quad (13)$$

where: $B_0 = K_p + M_p gL$; $B_1 = C_p$; $B_2 = M_p L^2$; $A_0 = M_p K_s gL + K_s K_p$; $A_1 = M_p C_s gL + C_s K_p + C_p K_s$; $A_2 = M_s K_p + M_p K_p + M_s M_p gL + M_p^2 gL + C_s C_p + M_p K_s L^2$; $A_3 = M_s C_p + M_p C_p + M_p C_s L^2$; $A_4 = M_s M_p L^2$.

$$H_\theta(\omega) = \frac{-\omega^2 B_2 + i\omega B_1 + B_0}{\omega^4 A_4 - i\omega^3 A_3 - \omega^2 A_2 + i\omega A_1 + A_0} \quad (14)$$

where: $B_0 = 0$; $B_1 = 0$; $B_2 = M_p L^2$; $A_0 = M_p K_s gL + K_s K_p$; $A_1 = M_p C_s gL + C_s K_p + C_p K_s$; $A_2 = M_s K_p + M_p K_p + M_s M_p gL + M_p^2 gL + C_s C_p + M_p K_s L^2$; $A_3 = M_s C_p + M_p C_p + M_p C_s L^2$; $A_4 = M_s M_p L^2$.

4 OPTIMIZATION

In this section we discuss how to reduce wind turbine vibrations currently, analyzing the analytic formulation and we propose a Genetic Algorithm (GA) optimization to reach this goal, with length pendulum and mass ratio restrictions.

4.1 Current optimization

The structural optimization proposed by Zuluaga [2] considers some criteria such as reducing the mean square displacement, velocity, and acceleration. A mean square value of x is $E[x^2]$, where E is the expected value of a random variable, given by:

$$E[x^2] = \int_{-\infty}^{\infty} x^2 p(x) dx \quad (15)$$

where $p(x)$ is the probability density function of the random variable x.

Some power spectra was used in the optimization. In undamped structures subjected to random excitations with a white-noise spectrum, Zuluaga [2] determined an analytical solution for the TMD optimum parameters, such as: cable length and pendulum damping ratio (Equations 16 and 17, respectively).

$$L_{(optim)} = \frac{\left(2g(\mu+1) + 2\sqrt{(\mu g + g^2) + 2\omega_a \omega_s^2(\mu+2)}\right)(\mu+1)}{2\omega_s^2(\mu+2)} \quad (16)$$

$$\xi_{p(optim)} = \frac{\sqrt{\mu(\mu+2)(3\mu+4)(\mu+1)A}}{2\omega_s^2(\mu+2)^2} \quad (17)$$

where $A = (\mu g+g)^2+\omega_a\omega_s^2(\mu+2)+g(\mu+1)\sqrt{(\mu g+g)^2+2\omega_a\omega_s^2(\mu+2)}$; $\mu = M_p/M_s$: mass ratio; $\omega_s = \sqrt{\frac{K_s}{M_s}}$: structure natural frequency; $\omega_p = \sqrt{\frac{K_p+M_pgL}{M_pL^2}}$: pendulum natural frequency; $\omega_a = K_p/M_p$: ratio between stiffness and pendulum mass.

A white-noise is an idealized spectrum, but it can reach useful approximations of a physically possible excitation. A white-noise has been used by many researchers in the study of random vibrations such as the seism and wind [2, 9, 10].

Taking a damped structure in consideration, it is impossible to ascertain an analytical solution of the best pendulum settings. Therefore it is necessary to perform a numerical search. This procedure consists of a setting search of the minimum value of the mean square response to be controlled (displacement, velocity, and acceleration) of the main system. In this study it was adapted by a Min.Max numerical search, which registers the peak of the frequency response function and the forced frequency ratio corresponding to different setting combinations, searching for minimum peak.

Furthermore, other criteria used by different researchers can be included, such as [5]:

- Maximum dynamic stiffness of the main structure;
- Maximum effective damping of the structure system/TMD;
- A mixed criterion involving tuning frequency using minimum displacement criterion and determining the TMD damping using the criterion of maximum effective damping;
- Minimum force of the main portico structure.

Repeated attempt variations of each parameter were made to reach Zuluaga's goal.

In the study carried out by Zuluaga [2], it was observed that the optimum pendulum length decreases when the mass ratio increases. Therefore the pendulum period also decreases when the mass ratio increases. Also, no significant difference was found between white-noise, Davenport or Kanai-Tajimi spectra. In many cases, the white-noise provides good approximations in random vibrations.

Knowing the hard work in the search of variable combinations (pendulum length and mass ratio between the main system and the pendulum) and the uncertainty to reach analytical solutions, in this paper we propose a best way to optimize the wind turbine vibration, with a pendulum TMD. To reach this goal, a genetic algorithm optimization routine was created using a white-noise spectrum.

4.2 Genetic Algorithm optimization

A Genetic Algorithm (GA) is a stochastic algorithm that mimics natural phenomena as operators, proposed to find the best pendulum setting. GAs are search techniques based on the processes of natural selection for survival through population genetics [11]. For the GAs to start evolving, we can use the steps selection, recombination (crossover), mutation, and replacement, where the survival-of-the-fittest mechanism can be applied to the candidate solutions [12, 13].

In the initialization, the algorithm replies the evolutionary genetics and generates a random population by uniform distribution. The chromosomes represent the elements in evolutionary algorithm space, where their features, called genes (quantified by values called alleles), are the problem inputs to be rated by the fitness function [14].

The selection allocates more copies of those solutions with higher fitness values and the roulette-wheel select is the procedure chosen to accomplish this idea. After that, recombination

combines parts of two parental solutions to create new, possibly better, solutions. The mutation, on the other hand, randomly modifies the solutions' allele. At the end, a percentage of the best elements is simply copied to the next generation using an elitism probability. This is a mechanism to guarantee the best solutions are transmitted to the current generation [12].

The algorithm feeds the system back and evaluates each element from the population. Using the aforementioned evolutionary strategies, the fittest elements will have more probability to pass their features to the next generations.

They are depicted by real base, where each gene matches to the hereditary characteristics to be combined and evaluated. The chromosome is described by the following function:

$$C = [L; \mu] \tag{18}$$

where L: pendulum length; $\mu = M_p/M_s$, where M_p: pendulum mass; M_s: main system mass.

The real base is useful when the parameters to be optimized are continuous variables [15]. Working with any decimal digits of precision the computer uses flow point numbers to represent the chromosome and its size is equal to the vector that represents the problem solution; thereby each gene represents one problem variable [16].

Variable restrictions were inputted to control this optimization faster. The lanes for pendulum length L (m) and mass ratio μ are:

$$0.70 \leq L \leq 2.00 \tag{19}$$

$$0.05 \leq \mu \leq 0.20 \tag{20}$$

The performance of each element of the population is measured by the fitness function. It rates the capability of the element (given a pendulum setting) to minimize high vibration level and minimize high vibration level and the difference of frequency and anti-frequency peaks (Min.Max restriction).

5 RESULTS

Given the presented model (Figure 1), the tower with realistic dimensions was considered for the GA optimization and modeled as a uniform cantilever beam of circular hollow cross-section with a tip mass (nacelle) at its free end. The tower was made of steel with a hub height of $60m$, a width of $3m$, and a shell thickness of $0.015m$, considering elastic modulus and density of the steel with $2.1 \times 10^{11} N/m^2$ and $7850 kg/m^3$, respectively. The tower carries a nacelle and a rotor system mass of $19.876kg$. The pendulum stiffness was calculated as 1% of the system stiffness, $C_s = 0$, and the pendulum damping was fixed in $\xi_p = 0.024$ [3].

Using Equations 9 and 10 and considering wind force as a harmonic excitation, we obtained the following generalized rigidity, mass, and force parameters:

$$M_s\ddot{Y} + K_sY = F_s(t), \text{ where } M_s \cong 34.899kg \text{ and } K_s \cong 46.3671N/m \tag{21}$$

Inputting these values in the algorithm, many tests were made to determine the best probabilities of crossover, mutation, and elitism, as well as the population and generation sizes. The parameters were adjusted with: 7% probability of mutation; 70% crossover; 10% elitism; 150 chromosomes per generation. After 80 generations, the figures were plotted containing the curves of the best general fitness for each generation with their mean values.

Two function fitness were loaded with distinct objectives. First, a simple case aiming to reduce the two high system response peaks. Second, a complex case trying to reduce, simultaneously, the high system response peaks and the difference between the high and low response peaks. These two cases are detailed below.

5.1 Reducing the high peaks

In this first case, the low peak of the response was not considered for the optimization. The best fitness $\times$ generation curve was dramatically converged as shown in Figure 3, maximizing Equation 22.

$$f_{fitness_1} = \frac{1}{\max H_y(\omega)_i}, \text{ where } i = 1, 2, \ldots, N_{ind} \tag{22}$$

where $\max H_y(\omega)_i$: maximum response of each generation; N_{ind}: size of the population.

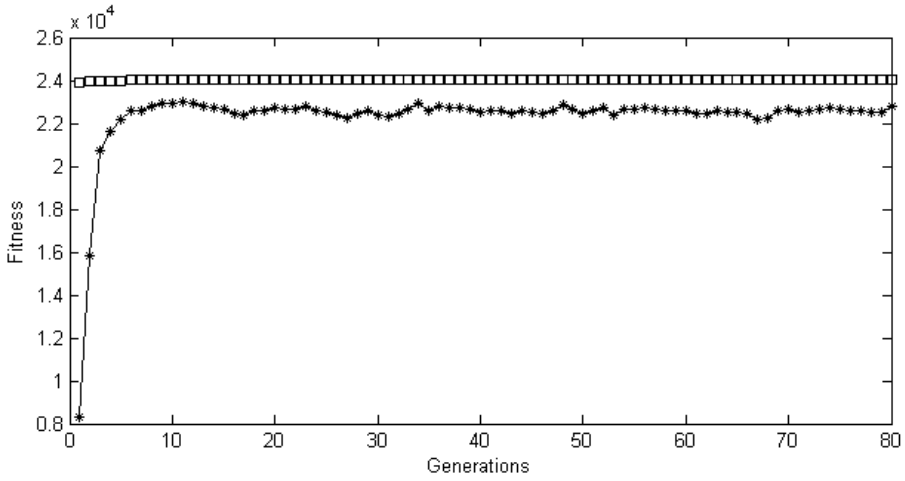


Figure 3: Optimization results by fitness per generation of the best fitness of each generation (squares) and their means (asterisks).

The frequency response of the structure was plotted, as well as the structure without a pendulum TMD (Figure 4).

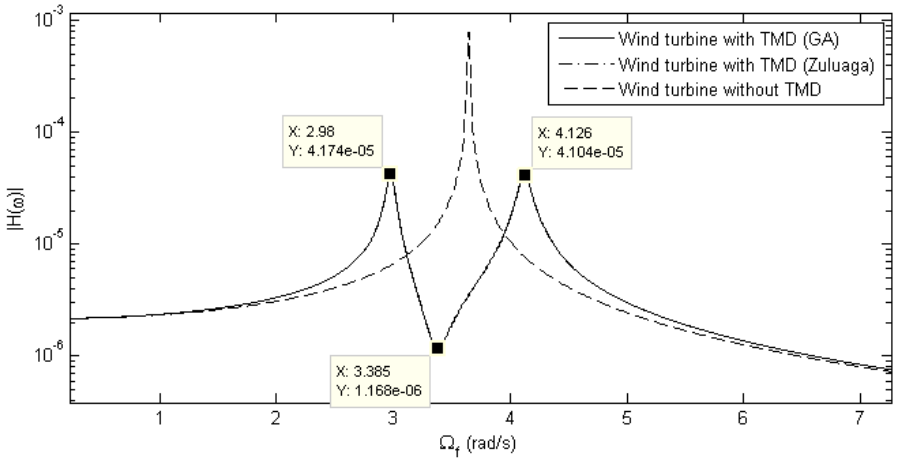


Figure 4: Displacement harmonic response of the wind turbine: with TMD (using GA), with TMD (using Zuluaga optimization), and without TMD.

Although the best fitness values look the same in the Figure 3, the convergence is in the decimal places. The GA gives the best pendulum length and the best mass ratio between the pendulum and the main system, respectively:

$$L = 0.9737m; \mu = 0.1090 \tag{23}$$

Using the mass ratio μ determined by the GA, the optimum pendulum length was calculated using Zuluaga's formulation (Equation 16), which gives:

$$L_{(optim)} = 0.9713m \tag{24}$$

The difference almost cannot be viewed between the best pendulum length given by the GA optimization and Zuluaga optimization $(0,24\%)$. This can validate the GA, because for the same ratio mass μ, we can reach the same goal (L) with distinct ways.

We make a parametric analysis searching the maximum displacement of the transfer function. With the optimum Zuluaga length (Equation 23), we obtained the maximum displacement of harmonic response as function of mass ratio μ (Figure 7). The minimum response found is close to $\mu = 0.1088$.

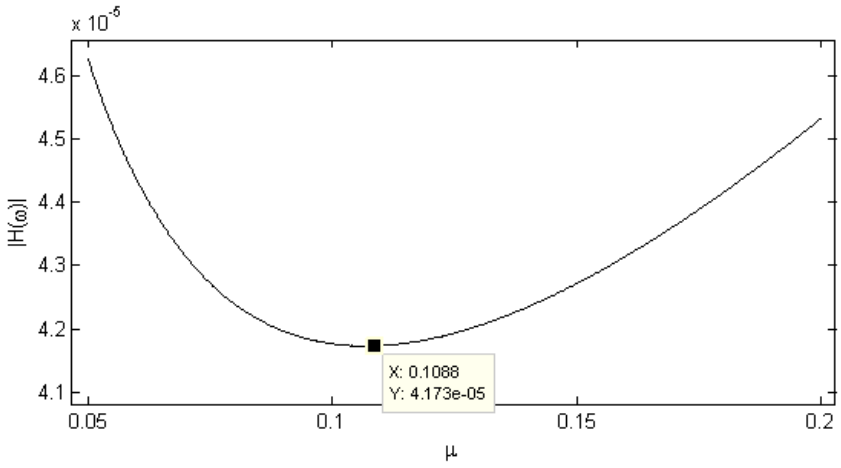


Figure 5: Relation between response function in the frequency domain $H_y(\omega)$ and the mass ratio μ between the pendulum and the main system.

5.2 Reducing the high peaks and increasing the low peak

In this second case, we searched to minimize the main system pole peaks and maximize the zeros peaks. Thus was necessary analyzed more than one situation, because probably existed local maxima. The fitness function it was maximized is given by Equation 25.

$$f_{fitness_2} = \frac{\min H_y^*(\omega)_i}{\max H_y(\omega)_i}, \text{ where } i = 1, 2, \ldots, N_{ind} \tag{25}$$

where $\min H_y^*(\omega)_i$: minimum response of each generation between the natural frequencies $(\lambda_1 \leq \Omega_f \leq \lambda_2)$; N_{ind}: size of the population.

The fitness evolution converges after 10 generations. The optimum combination between the pendulum length L and the mass ratio μ was summarized in Table 1. For the same GA

	$L(m)$	μ	ξ_p
GA	0.76	0.0787	0.024
Zuluaga	0.97	0.0787	0.024

Table 1: Length results obtained by GA and Zuluaga optimization for the same mass ratio μ and pendulum damping ratio ξ_p.

optimum mass ration, we can estimate a pendulum length by Zuluaga (Equation 16). The pendulum damping ratio ξ_p was remain the same of previous case (Subsection 5.1).

Figure 6 compares harmonic responses $H_y(\omega)$ of GA and Zuluaga optimum values. GA results present an harmonic response asymmetric with a pronounced resonant frequency. The pendulum damping ratio ξ_p has a role importance in dynamic response. To obtain better harmonic results, we need set ξ_p as a project variable.

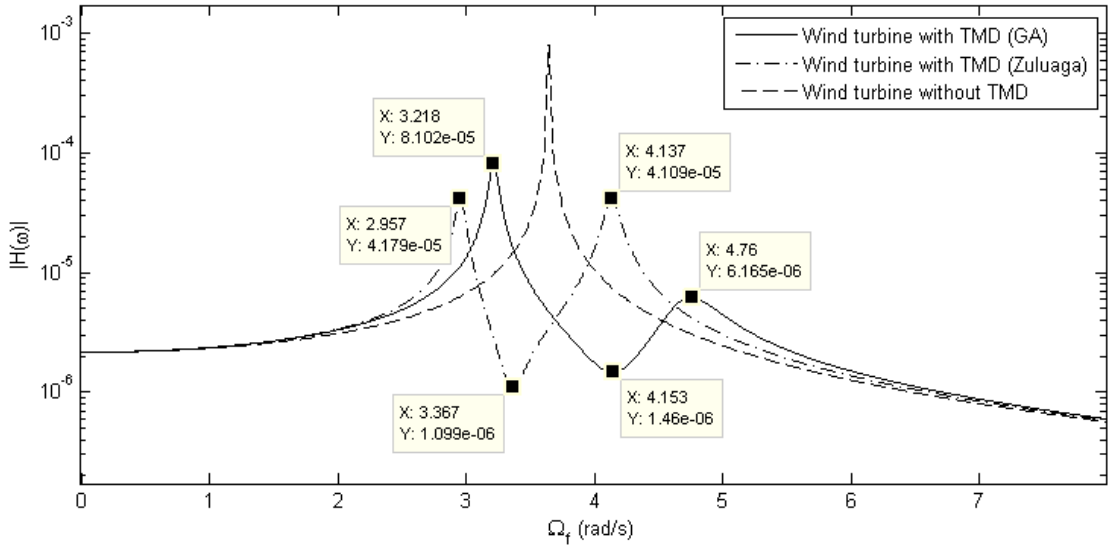


Figure 6: Displacement harmonic response of the wind turbine: with TMD (using GA), with TMD (using Zuluaga optimization), and without TMD.

The pendulum damping ratio has a crucial role to attain a min. max. harmonic response of the structure. We inserted this pendulum damping as a chromosome variable, $C = [L; \mu; \xi_p]$. The interval lane assumed was $0.00 \leq \xi_p \leq 0.20$, limiting the pendulum TMDs to lightly damped oscillator. The assumed range was quite extensive to provide a large amount of possibilities.

Figure 7 compares GA results with Zuluaga approaches. To obtain Zuluaga's length $L_{(optim)}$ and damping ratio $\xi_{(optim)}$ optimum results, we used the mass ratio μ obtained by GA optimization.

The displacement harmonic response of the min.max. optimization shows a flat level similar to reject-band filter. Its harmonic response is worse compared to a Zuluaga optimum values, as expected, due to a pendulum damping ratio increase.

Optimum project variables for GA and Zuluaga approaches was summarized in Table 2. For the same mass ratio μ, the pendulum length was quite similar. Perhaps the min.max. optimization point to underdamped system with highest pendulum mass ratio.

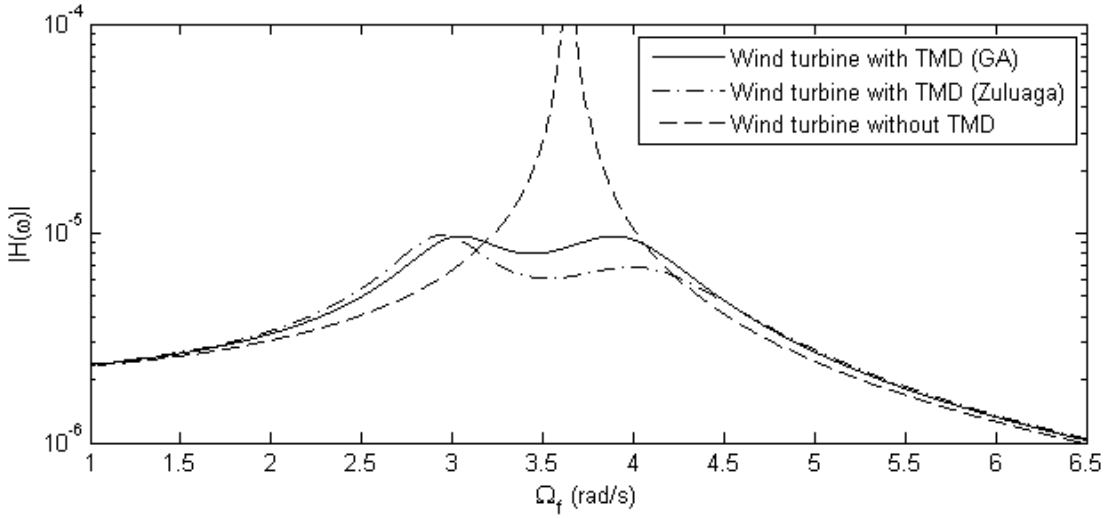


Figure 7: Displacement harmonic response of the wind turbine: with TMD (using GA), with TMD (using Zuluaga optimization), and without TMD.

	$L(m)$	μ	ξ_p
GA	1.01	0.1051	0.18
Zuluaga	0.97	0.1051	0.15

Table 2: Length L and pendulum damping ratio ξ_p results obtained by GA and Zuluaga optimization for the same mass ratio μ.

We undertake a parametric analysis optimizing pendulum length L and damping ratio ξ_p for a fixed mass ratio μ. The mass ratio values was assumed as $\mu \in [0.04; 0.06; 0.08; 0.10; 0.12; 0.14]$. Figure 8 shows a displacement harmonic response for each mass ratio μ.

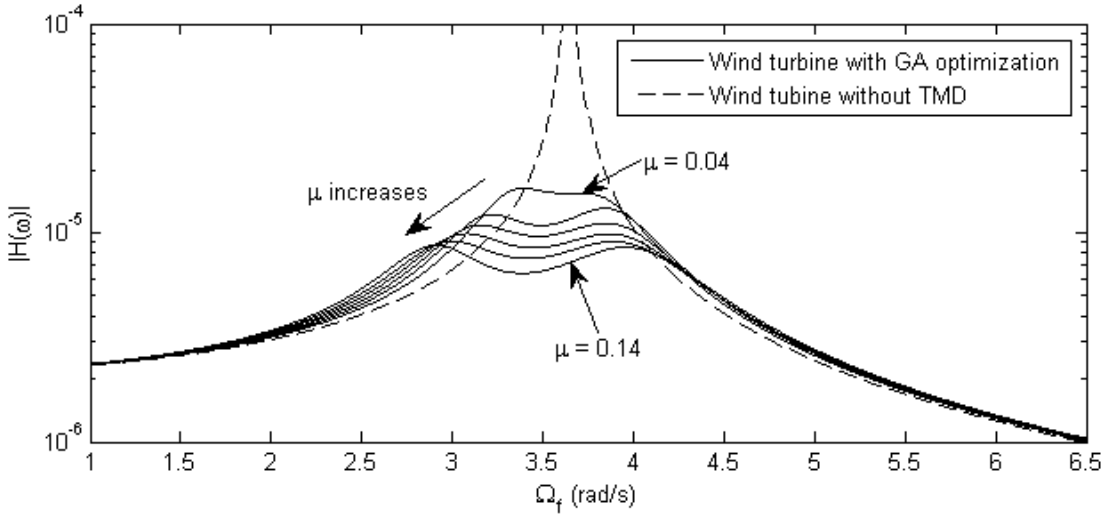


Figure 8: Evolution of displacement harmonic response of the wind turbine: with TMD (using GA) and without TMD.

The increase of mass ratio μ presents an expected reduction of dynamic displacement of the main structure. But reject-band filter shape has a degradation with the μ increase.

6 CONCLUSION

This paper present a GA application to optimize the vibration performance of a pendulum TMD. We use harmonic analysis to obtain the frequency response function of a tower with a pendulum TMD. The continuous system that describe the tower was reduced to the first mode. Then the structure system was described as a 2-DoF dynamic system.

Using a genetic algorithm with floating point chromosome, we propose two restrictions in objective function: (a) minimize high peaks of the vibration frequencies; (b) minimize high peaks of the vibration frequencies and maximize the anti-frequency peak (min. max. restriction).

We compare the analysis of the GA optimization undertaken by report to Zuluaga [2] gradient approach. The first restriction obtain an optimum harmonic response identical to Zuluaga approach, as expected. This result validate present GA implementation. The second restriction provide several results. Pendulum TMD is mainly influenced by mass ratio an damping ratio.

The optimum mass ratio μ to 10% of main structure mass. But the optimum pendulum damping ratio ξ_p has a high value of 18%. More studies must be undertake to analyze damping forces in other mode shapes.

7 ACKNOWLEDGMENTS

The authors greetings CNPq (Brazilian Scientific Conseil) and MCTI (Industrial, Science and Technology Ministry) by financial support (Process 406895/2013-9) referent to scientific project edital MCTI/CNPq 74/2013 ”Capacitação laboratorial e formação de recursos humanos em Energia Eólica (Linha 1)”.

REFERENCES

[1] S.M. Avila, M.A.M. Shzu, W.M. Pereira, L.S. Santos, M.V.G. de Morais, Z.J.G. del Prado, *Numerical Modeling of the Dynamic Behavior of a Wind Turbine Tower*, 11th International Conference on Vibration Problems, Lisbon, Portugal, 2013.

[2] A.L. Zuluaga, *Controle de vibrações em edifícios submetidos á ação de cargas dinâmicas utilizando amortecedor de massa sintonizado na forma de pêndulo*, Master's dissertation in Structures and Civil Construction, Universidade de Brasília, **22-64**, 2007.

[3] M.V.G. de Morais, M. Barcelos, S.M. Avila, M.A.M. Shzu, R.C. Silva, *Dynamic Behavior Analysis of Wind Turbine Towers*, Congreso de Métodos Numéricos en Ingenieria, SEMNI, España, 2009.

[4] G.M. Stewart, M.A. Lackner, *The Impact of Passive Tuned Mass Dampers and Wind-wave Misalignment on Offshore Wind Turbine Loads*, Engineering Structures, Vol 73, **54-61**, 2014.

[5] T.T. Soong, G.F. Dargush, *Passive Energy Dissipation Systems in Structural Engineering*, Wiley and Sons, New York, **368**, 1997.

[6] L. Meirovitch *Analytical methods in vibrations*, MacMillan, 1967.

[7] P.J. Murtagh, B. Basu, B.M. Broderick, *Simple models for natural frequencies and mode shapes of towers supporting utilities*, Computers & Structures, vol. 82, **1745-1750**, 2004.

[8] M. Paz, *Structural Dynamics: Theory and Computation*, Springer, 1997.

[9] G.B. Warburton, E.O. Ayorinde, *Optimum absorber parameters for simple systems*, Earthquake Engineering & Structural Dynamics, Volume 8, 1980.

[10] R.R. Gerges, B.J. Vickery, *Optimum design of pendulum-type tuned mass dampers*, The Structural Design of Tall and Special Buildings, Volume 14, 2005.

[11] J.H. Holland, *Adaptation in Natural and Artificial Systems: An Introductory Analysis with Applications to Biology, Control and Artificial Intelligence*, Cambridge, MA, USA: MIT Press, 1992.

[12] D.E. Goldberg, *Genetic Algorithms in Search, Optimization and Machine Learning*, The University of Alabama: Society of Automotive Engineers, 1989.

[13] R.L. Haupt, S. E. Haupt, *Practical Genetic Algorithm*, John Wiley G. Sons Inc., 1998.

[14] G.B. Colherinhas, P.H.C. Dias, A.C.G.C. Diniz, A.P.S.P. Rodrigues, *Automotive powertrain optimization by genetic algorithm analysing transmission ratios*, EngOpt: 4th International Conference on Engineering Optimization, Lisbon, Portugal, 2014.

[15] Y. Rahmat-Samii, E. Michielssen, *Electromagnetic Optimization by Genetic Algorithms*, John Wiley & Sons, 1999.

[16] A.P.S.P. Rodrigues, *Parametrization and Numerical Simulation of the Hidrokinetic Turbine Optimization Using Genetic Algorithm*, Dissertation in Mechanical Engineering, Universidade de Brasília, UnB, 2007.

COMPDYN 2015
5th ECCOMAS Thematic Conference on
Computational Methods in Structural Dynamics and Earthquake Engineering
M. Papadrakakis, V. Papadopoulos, V. Plevris (eds.)
Crete Island, Greece, 25–27 May 2015

SLENDER LARGE-SCALE PARABOLIC TROUGHS USING SHAPE-OPTIMIZED HOLLOW STRUCTURES MADE OF HIGH-STRENGTH CONCRETE

Christoph Kämper[1], Janna Krummenacker[2], Patrick Forman[1], Peter Mark[1], Jürgen Schnell[2]

[1] Institute of Concrete Structures, Ruhr-University Bochum
Universitätsstrasse 150, 44780 Bochum, Germany
e-mail: christoph.kaemper@ruhr-uni-bochum.de

[2] Institute of Concrete Structures and Structural Engineering, Technical University Kaiserslautern
Paul-Ehrlich-Strasse, 67663 Kaiserslautern, Germany
janna.krummenacker@bauing.uni-kl.de

Keywords: Parabolic trough, high-strength concrete, hollow cross-section, optimization

Abstract. *Parabolic trough collectors focus insolation on receiver tubes to generate electricity in downstream steam cycles. Currently, commercially already established collector modules consist of spatial steel frameworks supporting mirror elements point-wise. The crucial disadvantage hereof is the separation between supporting and reflecting structure. To overcome this drawback, a yet small-scale but continuous concrete shell prototype, that combines both tasks, has been manufactured. It consists of a single thin-walled shell made from high-strength concrete with a thickness of 20 to 30 millimeters only. Tests have proven a considerable optical efficiency of the prototype developed in a cooperation of the universities of Bochum and Kaiserslautern in Germany.*

In line with current trends to reduce costs by economy of scale, an up-scaled structure based on the prototype, but having an aperture of 10 x 30 m and a hollow cross-section, is now aimed for. To account for the specific action effects on such structures, like wind loads and temperature, an initial numerical model has been set up. Employing topology optimization techniques delivers an optimally balanced model candidate with respect to mass and stiffness iteratively. Structural parts that require low densities only are identified and substituted by hollow shapes of simple geometry. That way, the total structure is subdivided into appropriate substructures according to the flux of inner forces along with a significant weight-reduction. Obviously, the emerging partial segments defined by the substructures have to be designed for stability. Accompanying experimental studies of micro-meshed reinforced high-strength concrete elements prove both general feasibility and also manufacturing.

1 INTRODUCTION

State-of-the-art for parabolic troughs is steel frameworks supporting curved mirror elements point-wise like in case of the EuroTrough module with an aperture of 5.77 x 12 m [1]. This kind of collectors has become the most mature technology in concentrating solar light during the last years. Today the worldwide installed power amounts to more than 2 GW. But, a disadvantage of these troughs has been claimed, too. Due to the point-wise supported mirror elements potential energy losses might arise, e.g. from wind-induced, deformation in between the boundary points. Recently, this drawback has been tackled in cooperative investigations of the two universities of Bochum and Kaiserslautern in Germany. A small-scale prototype made from concrete has been developed that merges support and reflection in a shell-like structure. To reflect solar light, a foil is glued plane on the concrete surface. Their small-scale prototype has an aperture of 2.205 x 3.20 m along with a thickness 2-3 cm only. However, it shows the general feasibility of highly accurate concrete collector modules with proven optical performance [2]. Extending these fundamental findings and following current trends to reduce costs by economy of scale, a parabolic trough module of 10 x 30 m is now aimed for. To realize these dimensions with concrete, structural weight must clearly be saved. The massive single-walled concrete shell is dissolved into a hollow structure. Employing topology optimization techniques the cross-section is re-designed claiming volume decrease and stiffness gains simultaneously. In an initial step before, the design space for topology optimization must be restricted with respect to stiffness, low deformation and the concrete's tensile strength pivotal for cracking. First results of this iterative form-finding process are presented in the remainder.

2 CONCEPTUAL DESIGN

Recently published conceptual designs of parabolic trough collector modules consist of thin-walled concrete shells made of high-strength concrete in which reflectors on the inner surface are adapted that do not contribute to structural bearing capacity [3, 4]. They concentrate on the concrete shell and do not comprise detailed analyses of the supports what might be necessary in a holistic optimization. Inspired by the EuroTrough module a small-scale prototype with homogenous cross-section has been manufactured with wall thicknesses of 3 cm at vertex and 2 cm at the free edge [2]. In case of large-scale parabolic troughs similar low wall-thicknesses can be achieved dissolving a homogeneous concrete cross-section into an inhomogeneous hollow one. That way, significant portions of self-weight are saved whereby the adaptive inner lever arm of forces, the distance between compressive and tensile stress resultants in concrete, grants high stiffness. Following the concept of non-cracked concrete, the size of the inner lever arm is restricted by allowable tensile stresses due to concrete's tensile strength with respect to intended wall-thicknesses. Additionally, low deformations must be met to obtain high surface accuracy and total efficiency of the collector. An inhomogeneous cross-section shall be obtained by adjusted hollow shapes describing the inner geometry especially the position of vertical struts. Initial geometry and material properties of an envisaged large-scale trough module are presented in Fig. 1 and Table 1.

Young's modulus	47 593 N/mm²
Bending tensile strength	15.1 N/mm²
Cylindrical compressive strength	109.1 N/mm²
Density of hardened concrete	2524 kg/m³

Table 1: Material properties of hardened Nanodur® concrete (mean values, determined at TU Kaiserslautern).

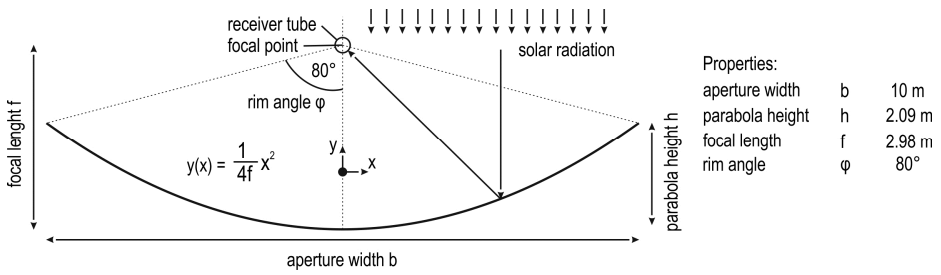


Figure 1: Sketch and dimensions of a large-scale parabolic trough.

While the inner shape of the collector is required to be smooth and can be best described by a general parabolic function, the exterior shape is optional. This gives the opportunity to search for an optimum shape. Eq. 1 relates the focal length f of 2.98 m to a rim angle φ = 80 and an aperture width b = 10 m with respect to a computational module model.

$$y(x)=\frac{1}{4f}x^2 \tag{1}$$

To investigate the exterior contour on bottom side, the cross-section has been modelled as a cantilever beam. Its length is half the aperture width due to symmetry. Further, the so called design space (cf. Fig. 2, top left) is defined by six design variables of local thickness (h1-h6) initially set to 0.35 m. Self-weight and a distributed wind load perpendicular to the inner surface is accounted for. Highly accurate surfaces are achieved penalizing maximum vertical displacements in the analysis.

The numerical model set-up in ANSYS software consists of 8880 quadrilateral plane stress elements (plane 82) with quadratic shape functions in a regular mesh. The elements thickness is constant for all elements (0.20 m) [5]. Consequential, the volume amounts to 0.35 m³. The total strain energy Π follows from Eq. 2 by integration of transposed elemental stresses σ and strains ε over the total volume V and gives 2.23 Nm.

$$\Pi=\frac{1}{2}\int_V \sigma^T \varepsilon \, dV \tag{2}$$

Twice the strain energy is equivalent to structural compliance, the inverted stiffness. Its physical interpretation is hence straightforward. Strain energy is obviously anti-proportional to structural stiffness. If the stiffness decreases, the strain energy rises and vice versa.

3 CROSS SECTIONAL OPTIMIZATION

The optimization process is split into five independent but subsequent steps reducing allowable vertical displacements from initially 9 to 5 mm in the end. In all steps the objective is to maximize the volume reduction by means of minimal local thicknesses (h1-h6). This is mathematically equivalent with finding the minimum structural compliance that grants the pre-scribed displacements. In general two optimization techniques are combined. At first, shape optimization fixes the outer contour of the parabolic trough that serves as the design space in subsequent topology optimization employing artificial material densities. The latter one then identifies domains where material is necessary for stiffness and others where hollow bodies reduce the total weight. Thereby, the output of shape optimization is simultaneously the input of topology optimization. To gain insight in the solution process of shape optimization by ANSYS two consecutive methods, zero-order and first-order-method are combined. They deliver the progress of the objective function and the design variables continuously.

3.1 Outer shape optimization

For the outer shape optimization, three different groups of variables have been defined. First group is the design variables x expressed by six heights (h1-h6) fixing the vertical distances between the radiation surface itself and its exterior end according to Fig. 2. These end points are connected one to another by a cubic spline function. At the very beginning equal heights (h_i=0.35) are stored in an initial vector but changed during iteration. Each iteration starts with the solution of the previous one by means of adapted values of height.
Second group are state variables g(x) used to restrict structural responses. They are formulated with respect to the design variables x and limited by upper (u) and lower (l) bounds (Eq. 3).

$$\begin{aligned} &x = [x_1, x_2, \ldots, x_n] \\ &x_{i,l} \leq x_i \leq x_{i,u} \qquad i = 1,2, \ldots n \\ &g_{j,l} \leq g_j(x_i) \leq g_{j,u} \qquad j = 1,2, \ldots n \end{aligned} \tag{3}$$

Restrictions are made concerning vertical displacements and concrete cracking that happens if stresses top the high-strength concrete's tensile strength. Generally, the higher the structural stiffness is, the lower deflections under constant loads are. Vertical displacements are reduced in five independent steps from initially 9 to finally 5 mm.

The last, third group comprises the objective function to be minimized. Here the volume of the trough subjected to self-weight and wind load shall be reduced to some extent. The wind load pressure according to Beaufort scale 6 is given with q = 0.18 kN/m² assuming an average pressure coefficient c_{pe} = 4 that integrates different load positions due to sun tracking and other but minor effects [2]. Tolerances of the three groups are defined separately. While the objective function's tolerance is set to 0.01 in ANSYS software, the design variables one is two times finer. For state variables a tolerance of 0.0002 is fixed.

Conceptually in this study, a two-step approach for shape optimization of the exterior shell contour is employed. However, the optimum determined this way is intermediate only and serves for subsequent optimization of topology discussed in section 3.2. Here, the focus is on shape optimization.

At first, a so called zero-order-method that relies on the design values, the state variables and the objective function but not on their derivatives is employed. It approximates the objective function by linear or quadratic polynomials according to Eq. 4. The coefficients herein a_0, a_i and b_{ij}, are obtained from regression employing weighted least squares to account for the restrictions set. Acc. to [5] the initially constrained optimization problem is transferred to an explicitly unconstrained one incorporating penalty terms for both, state variables and objective function.

$$f = a_0 + \sum_{i}^{n} a_i x_i \sum_{i}^{n} \sum_{j}^{n} b_{ij} x_i x_j \tag{4}$$

Next is to improve the approximation obtained above by a first-order-method employing derivatives. Here, the derivatives of the objective function are evaluated and stored in a gradient vector. In general, the method is known to be superior to the zero-order-approach since it finds local and global optima more accurate due to steepest descent and conjugate line-search techniques [5, 7]. However, this advantage comes along with a disadvantage. Obeying the total solution process, the method reduces the number of general iterations needed to converge at minimum but also requires a greater number of sub-iterations in intermediate loops. This condenses in higher time-demands for a global iteration but a smaller amount of iterations

compared to the zero-order-method. Additionally, it is possible to use zero-order-solutions obtained before as input for further optimization with the first-order-approach.

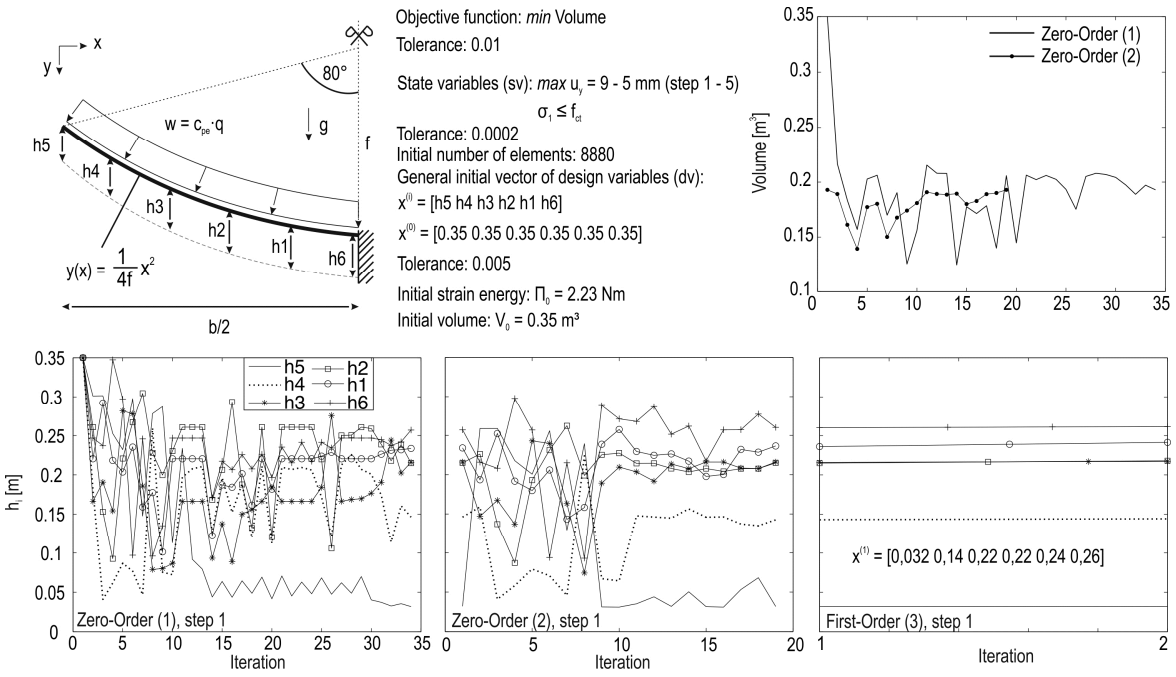


Figure 2: Cantilever beam as reduced cross sectional mechanical model (top left), general variables (top middle), objective function (top right) and design optimization progress for step 1 exemplarily (bottom).

Exemplarily the progress of shape optimization for limited vertical deflections (9 mm, step 1) employing the two consecutive methods discussed above is shown in Figure 2. At bottom three diagrams show the progress of the design variables during optimization. Six curves track the vertical heights (h1-h6) of the trough. While the first two diagrams were obtained from the zero-order-approach using approximation, the last one follows from the enhanced, derivative-based first-order-method. After 34 iterations, contained in the first graph, converging design variables could hardly be identified. Hence, another 17 iterations were performed. Thereafter all design variables have nearly converged. Physical interpretation is as follows: The closer the variable's location to the center, the higher its thickness. The final contour is crescent-shaped as shown in Fig. 4. Two more iterations by the enhanced method leave these results unchanged. However, the convergence rate of the latter shows significantly improved. Additionally, the objective function's progress in course of optimization is tracked in the upper-right graph of Fig. 2.

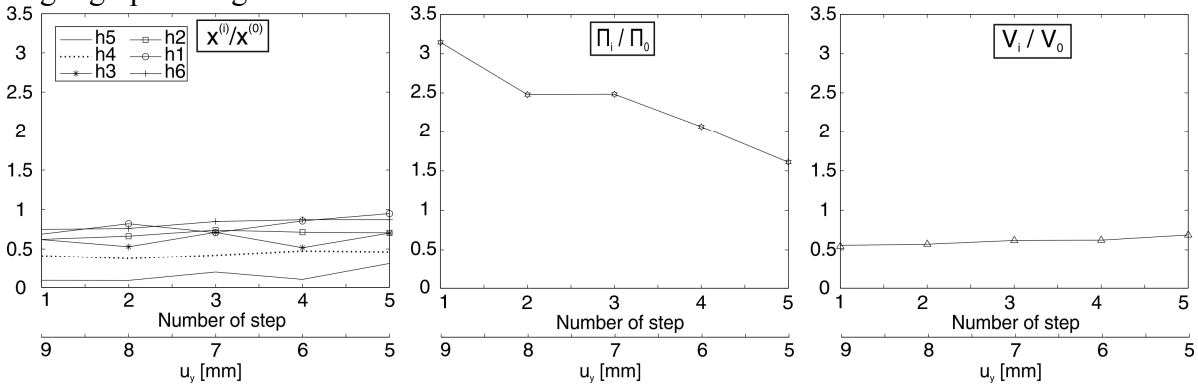


Figure 3: Design variables (h_i), stiffness indicator (strain energy Π_i) and objective function (volume V_i) related to their initial values for step 1-5.

Figure 3 shows the variation of the solution by means of three newly developed dimensionless indicators with step-wise intensified restriction of maximal deflection. On the horizontal axes step number and pre-scribed maximum deflection in mm is plotted, whereas the y-axes show the dimensionless indicators, e.g. design vector x, total strain energy Π and volume V. In general, the indicators relate current to the initial values and reveal global tendencies meanwhile the restriction of deflection is tightened. As expected the volume V as well as the design variables h_i show moderate increases, while the strain energy Π shows a steep descent. This sensitivity qualifies the strain energy as a perfect monitoring variable in structural optimization.

3.2 Topological optimization for identifying hollow shapes

By contrast to shape optimization, the design space in topology optimization is (already) fixed. Here, design variables (η_i) are internal pseudo-densities of finite elements [5, 6]. Thus a finite element mesh, a discretization of the design space, is a prerequisite for this method. Here, the same mesh introduced before has been used. For every element the pseudo-density lies between its limits of zero and one. Intermediate values are theoretically allowed but should be avoided. Physical meaning of a zero density is that belonging elements might be removed in terms of structural stiffness, whereas ones mark the opposite. Of course, the density value depends on boundary conditions and load patterns applied on the mesh but interestingly not on the size of loads. Defining both, loads and boundary conditions, on a mesh leads to a distribution of material according to the inner flux of forces. Besides these two, obviously, the number of elements of the discretization chosen strongly influences the results. Aside the material itself is of minor interest. In practical application it is mostly assumed linear elastic, e.g. defined by Young's modulus and Poisson's ratio. A final driving parameter of the results is the mass reduction factor beta according to Eq. 5.

$$m_{red} = (1-\beta)m_0$$
$$m_0 = \textit{initial mass},\ m_{red} = \textit{reduced mass} \tag{5}$$

It relates initial and final mass, thereby defining the extent of mass reduction allowed for in optimization. A typical strategy for topological optimization is to adapt the optimality-criteria (OC) algorithm. It minimizes the structural compliance, the inverse of structural stiffness, which equals twice the strain energy according to Eq. 2. Thereby, the mass reduction factor beta is fixed as a constraint [5, 6]. Consequently, the convergence of results must be checked to ensure optimality.

For this study, the situation is different. Since the structural stiffness of the concrete trough has already been determined by shape optimization before, the ideal mass reduction factor beta remains to be searched for. Sequential Convex Programming (SCP) is known to be advantageous for this purpose [7, 8, 9]. Figure 4 contains first results of structural optimization. The upper cross-section of the parabolic trough achieves a maximum volume reduction with respect to the here allowed compliance in a range from 7 to 8. Although both parameters - structural compliance and mass reduction factor beta - have converged obviously the material distribution lacks plausibility in parts of the structure. For comparison the compliance for the solid case (about 7.25 Nm) is added to the plot of compliances. It is lower than the one obtained by structural optimization and meets the expectation since the volume has been significantly decreased. Nevertheless, at center, close to the symmetry axis, clear substructures by means of struts and hollow domains, can be identified. Here the wall thickness is low as expected due to the stress limitations set. Aside, at the very end of the structure no material seems to be needed which is unacceptable. A quick workaround excludes these parts from the

optimization not allowing for material reduction at all. The remaining design space is again optimized and results in a more plausible material distribution along the whole structure, which is still subject of current investigations to gain robust hollow structures with maximum material mass reduction factors.

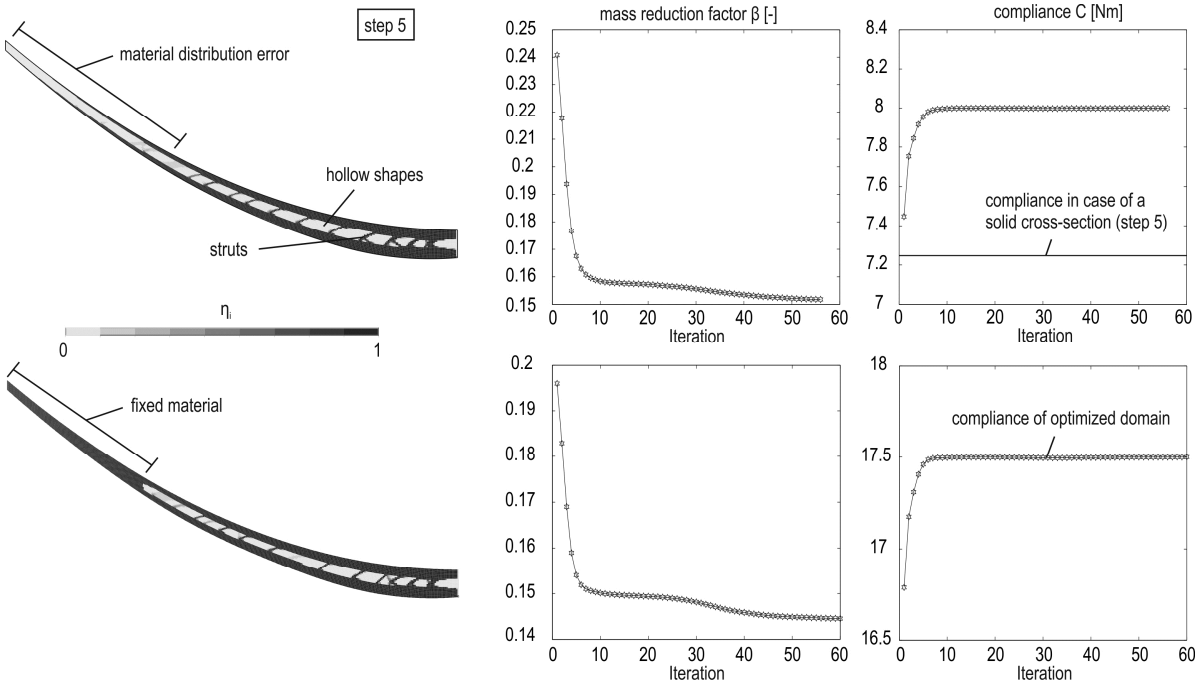


Figure 4: Material distribution (left), reduction factor β (middle) and maximum compliance (right) for initial (top) and reduced design space (bottom) of step 5.

4 CONCLUSIONS AND OUTLOOK

Large-scale parabolic troughs made from high-strength concrete have a high-potential being competitive on market. They can be cost efficient since serial production is a common concrete technology. Therefore, an essential prerequisite is an optimally balanced relation of stiffness and weight, to minimize material costs in construction and maximize bearing capacities subjected to a variety of different load cases expected during operation. In combination of two promising structural optimization methods a true-to scale prototype trough structure is set up and numerically analyzed in detail. Employing shape-optimization techniques in ANSYS software its outer contours are optimized with respect to concrete volume and the flux of inner forces. Meanwhile it also serves as the design space in a subsequent optimization step by means of topology optimization. Here, the solid inner concrete matrix is dissolved in distinct struts and hollow bodies leading to mass reductions about 15 % thereby fulfilling tight deflection limits of few millimeters. All intermediate solution steps and final results allow to be checked for adequacy and plausibility. A newly developed dimensionless progress indicator of the holistic optimization process identifies the total strain energy as the most sensitive parameter which is thus recommended for monitoring.

Remaining tasks for the future are the extrapolation of the hollow cross-section derived from structural optimization in longitudinal direction as well as the experimental verification by means of large-scale trough structures made of high-strength concrete including its smaller sub-structures in view of bearing capacities and structural stability.

5 ACKNOWLEDGEMENT

The authors thank the German Research Foundation (DFG) for the financial support of this project, which is part of the "Concrete Light" DFG priority program SPP 1542.

REFERENCES

[1] P. Forman, S. Müller, M.A. Ahrens, J. Schnell, P. Mark, R. Höffer, K. Hennecke, J. Krüger, Light concrete shells for parabolic trough collectors – conceptual design, prototype and proof of accuracy. *Solar Energy, Volume 111*, p. 364-377, 2015.

[2] S. Müller, P. Forman, J. Schnell, P. Mark, Leichte Schalen aus hochfestem Beton als Parabolrinnen solarthermischer Kraftwerke. *Beton- und Stahlbetonbau*, Ernst & Sohn Verlag, Volume 108, Issue 11, p. 752-762, 2013.

[3] P. Forman, S. Müller, Shape-optimised parabolic trough collectors made of micro reinforced ultra-high performance concrete. *9th fib International PhD Symposium in Civil Engineering,* Karlsruhe Institute of Technology (KIT), 22-25 July, Germany, 2012.

[4] P. Forman, S. Müller, Verformungsoptimierte Parabolrinnenkollektorschalen aus hochfestem Beton. *Tagungsband des 54. Forschungskolloquiums des Deutschen Ausschusses für Stahlbeton (DAfStb)*, Bochum, 2013.

[5] ANSYS® - *Handbook, Theory reference for the mechanical APDL and mechanical applications*. Release 12.1, U.S.A, 2009.

[6] M.P Bendsøe, O. Sigmund, *Topology Optimization – Theory, Methods and Application.* Springer Verlag, Berlin, 2003.

[7] L. Harzheim, *Strukturoptimierung – Grundlagen und Anwendung*. Europa Lehrmittel Verlag, 2. Auflage, Mainz, 2014.

[8] T. Putke, P. Mark, Fachwerkmodellbildung mit topologischen Optimierungsverfahren. *Beton- und Spannbetonbau*, Ernst & Sohn Verlag, Volume 109, Issue 9, p. 618-627 2014.

[9] Q. Ni, Ch. Zillober, K. Schittkowski, Sequential convex programming methods for solving topology optimization problems: implementation and computational results. *Journal of Computational Mathematics*, Volume 23, Issue 5, 2005.

COMPDYN 2015
5th ECCOMAS Thematic Conference on
Computational Methods in Structural Dynamics and Earthquake Engineering
M. Papadrakakis, V. Papadopoulos, V. Plevris (eds.)
Crete Island, Greece, 25–27 May 2015

PROPABILISTIC FATIGUE ANALYSIS OF OFFSHORE WIND TURBINES

Dimitrios V. Bilionis[1], Dimitrios Vamvatsikos[2]

[1] PhD Candidate
Institute of Steel Structures, School of Civil Engineering, National Technical University of Athens
Zografou Campus, Iroon Polytechneiou 9, 15780 Zografou, Athens, Greece
e-mail: dimbilionis@gmail.com

[2]Lecturer
Institute of Steel Structures, School of Civil Engineering, National Technical University of Athens
Zografou Campus, Iroon Polytechneiou 9, 15780 Zografou, Athens, Greece
e-mail: divamva@mail.ntua.gr

Keywords: Offshore Wind Turbine, Monopile Design, Fatigue, Aegean Sea

Abstract. *Wind Turbines constitute a sustainable and effective solution for the production of energy using wind power. Offshore wind turbines especially are becoming of special interest. However, their design poses great challenges, since an offshore structure is subject to combined wind and wave dynamic loading that is characteristic of the site of installation. The purpose of this paper is to provide a case study of fatigue life assessment for the cross-section at mudline (foundation) of a standard offshore wind turbine with a monopile design, under a probabilistic framework and assuming the thickness of the examined cross-section as the design variable. Two potential sites of construction in the Aegean Sea of Greece were examined. A probabilistic approach was employed in order to determine the fatigue life based on anemological data at each of the two sites of interest. At its basis is an extensive Monte Carlo simulation of wind (velocity) and wave (height, period) characteristics. The results show the dependence of fatigue life on the local wind and wave conditions, the cross-section geometry (i.e. the thickness of the foundation's pile) and the welded connection detail. All in all, the more benign conditions in the Aegean allow simpler connection details and smaller thickness of foundation pile's cross-section to still have acceptable performance.*

1 INTRODUCTION

Wind turbines constitute a sustainable and effective solution for the production of energy using wind power. Wind turbines may be constructed either in land areas (onshore) or in sea areas (offshore). Offshore wind turbines are becoming of special interest in recent years. Although an offshore wind turbine usually starts with a higher initial cost, it can outweigh a similar onshore one during its service life in a number of aspects such as: higher productivity due to stronger winds over sea areas, larger available installation areas and lower (or even non-existent) public nuisance. The latter is especially important in countries such as Greece where protracted court battles have hindered most onshore wind farms, inflicting substantial cost and crippling delays.

A wind turbine could be considered as a structure that lies between a civil engineering structure and a machine [1]. In specific, a wind turbine consists of structural elements (tower, substructure etc.) and a number of electrical and machine components with a control system (gear box, drivetrain etc.). Under a civil engineering perspective, the main components of a wind turbine could be considered the tower and the substructure system. The tower is the element on the top of which the mechanical parts of the wind turbine, such as the nacelle and the blades, are installed. The tower is made of steel and has a circular cross-section. It is usually tapered i.e. the cross-section size (e.g. diameter, thickness etc.) decreases with height, typically in a linear fashion. The tower is connected to the substructure, i.e., the part of the wind turbine that is submerged in the water. The substructure may be founded directly in the seabed or based on a floating platform. This type of the substructure's foundation usually distinguishes an offshore wind turbine into two categories, namely fixed and floating. Fixed wind turbines are used especially in sites of low or medium depths, while the construction of a floating wind turbine is cost-effective in the case of deep waters. The most common type of design for fixed wind turbines, which is used for depths up to 30 meters, is the monopile. This is probably the simplest structural concept, where the tower is connected (directly or via a transition piece) to a pile that has been founded at the seabed.

Regardless of the type of an offshore wind turbine, both structure and substructure are subject to dynamic combinations of wind and wave loads with a wide range of frequencies. This fact may raise critical issues during the turbine's service life in terms of fatigue and power efficiency [2]. For this reason, special focus should be devoted on the appropriate analysis and assessment of the dynamic combination of loads during the design phase. Furthermore, since wind turbines are complicated structures including a number of different components, reliability analysis considering consistent reliability levels and taking into account the dynamic nature of loads has received considerable attention by researchers [1, 3]. However, a great challenge in the above analysis is posed by the stochastic nature of the main loading mechanisms, namely wind and wave, as their characteristics tend to vary rapidly. Their stochasticity mainly depends on the climate at the area of construction. Thus, one could say that the design of an offshore wind turbine is a highly site-specific process. For this reason, the use of accurate site anemological and wave data is essential.

As far as the loads are concerned, the aforementioned stochasticity affects their magnitude and also subjects the structure to cyclic stresses making its components vulnerable to fatigue damage. Furthermore, they affect the overall performance and energy output. Research efforts are currently under way to incorporate climate information and relate it directly to the calculation of fatigue damage [4] or the assessment of performance [5]. However the stochastic nature of the wind and waves, as physical phenomena, makes such an analysis very complicated and advanced methods from statistics and probability theory need to be incorporated.

The purpose of this paper is to provide a case study of a probabilistic fatigue life assessment for a standard offshore wind turbine located in the Aegean Sea of Greece. In specific, a fixed offshore wind turbine with a monopile foundation is studied. Two potential sites of construction, one in the north part and another in the south part of Aegean, with different wind and wave characteristics, are considered. For both sites dynamic loading analysis is performed and the corresponding fatigue damage of the pile's cross-section at the mudline of the structure is calculated for different wind-wave states. The estimation of the expected fatigue life is made by incorporating Monte Carlo simulation. Furthermore, the thickness of the cross-section is examined as the design variable. Thus, estimations of the expected fatigue annual damage and corresponding life are made for a range of values of thickness and inferences about the influence of this parameter to fatigue life are made for both sites.

2 THE WIND TURBINE MODEL

The National Renewable Energy Laboratory (NREL) 5MW Baseline Wind Turbine was selected as a standard offshore wind turbine for this study. The rated power is 5 MW. The tower of the turbine is tapered and of steel circular hollow cross-section. The base diameter is 6.00 m and the thickness 27 mm, while the top diameter is 3.87 m with a thickness of 19 mm. The height of the tower at its top point (where the nacelle is based) is at 87.60 m from the Mean Sea Level (MSL). The rotor has three blades. The rotor disk has a diameter of 126.00 m and its center (hub height) is located at 90.00 m from the MSL. The cut-in and cut-out wind speeds are 3 m/s and 25 m/s respectively. For additional details regarding the characteristics of the standard turbine the reader may refer to [6].The tower is connected to a monopile foundation via a transition piece (TP). The monopile is considered to be founded at a depth of 28 m. It has a steel circular hollow cross-section, 6.00 m in diameter. The thickness of the pile's cross-section in the standard model is 60 mm. The connection of the base of the tower to the transition piece is considered to be at 10.00 m of the MSL (Figure 1). Finally, a rigid type of foundation is assumed.

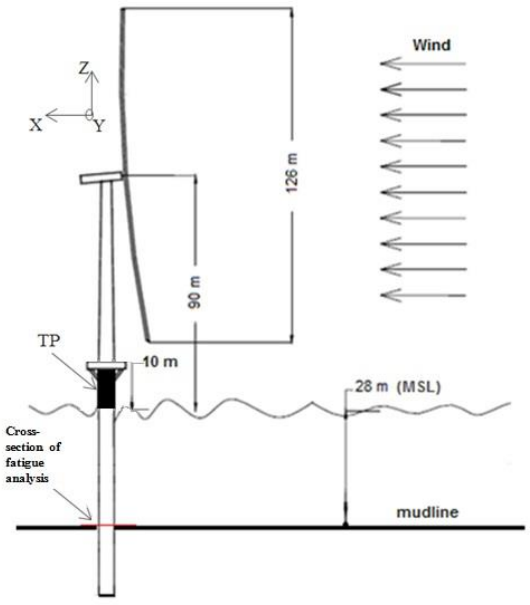


Figure 1: Wind turbine model (adapted from [7]).

3 THEORETICAL BACKGROUND

Design criteria and analysis guidance are provided by published standards. The analysis of offshore wind turbines is mainly based on the IEC 61400-3 standard [8]. It specifies the context for the assessment of external conditions and the design requirements to ensure the engineering integrity of the structure. The IEC standard also provides an appropriate level of protection from all hazards during the planned lifetime of an offshore wind turbine. In addition, the DNV standards [9] can also be used for the assessment of loads on marine structures subjected to wind, wave and current loading.

3.1 Loads

The assessment of wind loads is critical for the analysis of an offshore wind turbine. Although wind is essential for the operation and efficiency of a wind turbine, it is also the environmental factor with the greatest contribution to the loading of the structure. For the assessment of wind loads, time-series of wind speed at the hub height of the wind turbine are used. The time-series may have been developed according to specific spectrums (such as Kaimal or von Karman), based on the characteristic (average) value of a 10-minute wind speed. For this process appropriate software can be used, such as the TurbSim software developed by NREL [10] and adopted in this study. The wind time-series are then used as the input to calculate the values of reactions and deflections at the structure due to the wind. In this study, the authors used the FAST software [11].

Offshore wind turbines are also subject to wave loads which in some cases (e.g. in North Seas) may be very significant. Wave characteristics, such as the significant wave height (H_s) and peak spectral period (T_p), depend on the wind speed and the available sea length, or fetch, over which the wind transfers energy to the sea. Several methodologies and associated wave spectra are available for the calculation of the dynamic wave characteristics. A very widely used spectrum is JONSWAP [8, 9] that will also be our choice. A simplified method to transform wave characteristics into forces on a structure is the Morison equation [12]. This is a semi-empirical method for calculating the acting force on a body (e.g. a pile) that is submerged into moving water. The general form of the equation is as follows:

$$F = C_M \rho A \frac{du}{dt} + C_D \frac{1}{2} \rho D |u| u \tag{1}$$

where: D is the diameter of the member (pile), C_D and C_M are the drag and inertial coefficients respectively, ρ is the water density, A is the cross-sectional area and u is the water velocity relative to the body. The forces and the moments acting on the structure are then calculated by integrating the height-wise contributions of Eq. 1. For more details about the application of the Morison equation, the reader may refer to [9].

3.2 Fatigue

According to Eurocode 3 (EC3) [13], fatigue is considered as the damage in a member of a structure through crack initiation and/or crack propagation due to repeated stress fluctuations. Various standards have been published for the design of steel structures against fatigue. In the Eurocode series, part 1.9 of EC3 [13] provides the analysis context for fatigue design of steel structures. For the estimation of fatigue damage, time-series of stress history associated with the structural member of interest are needed. After those time-series are obtained, the stresses of various magnitudes should be grouped into groups of specific stress magnitude. Then, the

number of cycles (i.e. the frequency) of each group is counted. A very widely used approach for counting the number of cycles is the rainflow counting algorithm [14, 15].

By incorporating rainflow counting, the number of cycles of stress is calculated for each of the different stress amplitudes (or groups). Once the number of cycles for each group is specified, the corresponding fatigue damage can be estimated. In specific, if n_i is the number of cycles observed for stress group i, and N_{fi} is the number of cycles to failure for stress group i, the corresponding damage d_i is:

$$d_i = \frac{n_i}{N_{fi}} \tag{2}$$

The total damage D in a stress history of a specific length is then calculated by the following formula (Palmgren-Miner rule):

$$D = \sum_{i=1}^{k} d_i = \sum_{i=1}^{k} \frac{n_i}{N_{fi}} \tag{3}$$

The fatigue life of a structural member is the time until D reaches the maximum allowable value of 1. Assuming that D has been estimated for a representative enough interval of duration T_D over which its accumulation may be assumed to be stationary, a good estimate (assuming deterministic capacity) of the corresponding fatigue life is equal to T_D/D. For instance, if D is the mean annual fatigue damage of a member, the estimated fatigue life in years is equal to $1/D$ (in this case $T_D=1$).

4 CASE STUDIES FOR GREECE

4.1 Examined Sites

Offshore wind farms have been constructed and are in operation in the northern seas of Europe. On the other hand, none have been installed in the Mediterranean Sea. However, a number of projects are ongoing for examining the potential of design and installation of offshore wind farms by several Mediterranean countries [16]. In this paper, two case studies will be presented for the preliminary assessment of fatigue life for the cross-section at mudline of a standard offshore wind turbine with a monopile foundation for a range of thickness values of the cross-section. In specific, two different sites in the Aegean Sea of Greece were selected, shown in the map of Figure 2.

The first site is located on the North part of the Aegean, while the second site on the South part. Each has its own wind and wave characteristics, in large part due to the difference in the surrounding geography. For the case of the North site, due to the proximity of the mainland, significant difference in fetch (i.e. the uninterrupted length of water over which waves can develop) exists for the various wind directions, with the maximum appearing for a southern wind. In the case of the South site though, no much difference could be assumed between the different directions and a practically uniform fetch could be used for the analysis.

4.2 Analysis Process

For both sites of the study a similar process was followed for the estimation of the fatigue life. First, anemological data was obtained from the National Weather Service of Greece. A statistical analysis for specifying the major trends and the distribution of that data was performed. Given the relatively small fetch distances in the Aegean, the wind speed is reasonably

assumed to fully determine the wave state as well, something that would not be true, for example, in an ocean environment. Thus, the wave characteristics (significant wave height and peak period) were calculated based on the JONSWAP spectrum for each possible value of *local* wind speed. Finally, the joint probability density function (joint PDF) of wind speed *(U)* and significant wave height (H_s) were estimated, a process that will be discussed in more detail in the next section.



Figure 2: Map of Aegean Sea with the examined installation sites.

For the analysis of loads, time-series of wind speed at the hub height were simulated using the TurbSim software. In specific, time-series of 10-minute length, for a number of wind speed values, namely 3 m/s (cut-in), 5 m/s, 10 m/s, 15 m/s, 20 m/s, 25 m/s (cut-out) and 30 m/s (parked turbine) were developed. The aforementioned time-series along with the corresponding wave characteristics constituted the input for the FAST software, where a coupled (i.e. assuming that the wind and waves act simultaneously on the structure) dynamic analysis of wind and wave loadings was performed.

A number of 10 simulations were performed for each mean wind speed. Of course, the above number might be small for some of the more variable wind-wave states, but it was selected as a preliminary value due to the large computational effort that the process requires. At the end of each simulation, 10-minute time-series of reaction forces, moments, deflections and other values on the structure were obtained. Based on those time-series, the 10-minute stress history, by incorporating the reaction forces and moments were calculated for the cross-section of interest. As far as the geometry of the cross-section is concerned, the diameter was kept equal to 6.00 m (as in the standard model) and values from the range between 25 mm to 60 mm (with a step of 5 mm) were examined for the thickness. Rainflow counting and the Palmgren-Miner rule were used for the calculation of the 10-minute fatigue damage. Two different classes of detail, namely 40 MPa and 71 MPa, were assumed for the welded connection and the corresponding S-N curves of EC3 part 1.9 were employed. The Wöhler coefficients (which represent the slope of S-N curve) are equal to m=3 and m=5 as shown in Figure 3. According to EC3, a detail of 40 MPa corresponds to fillet welds, while a detail of 71 MPa corresponds to butt welds for connecting a circular hollow section to a ring-shaped flange plate.

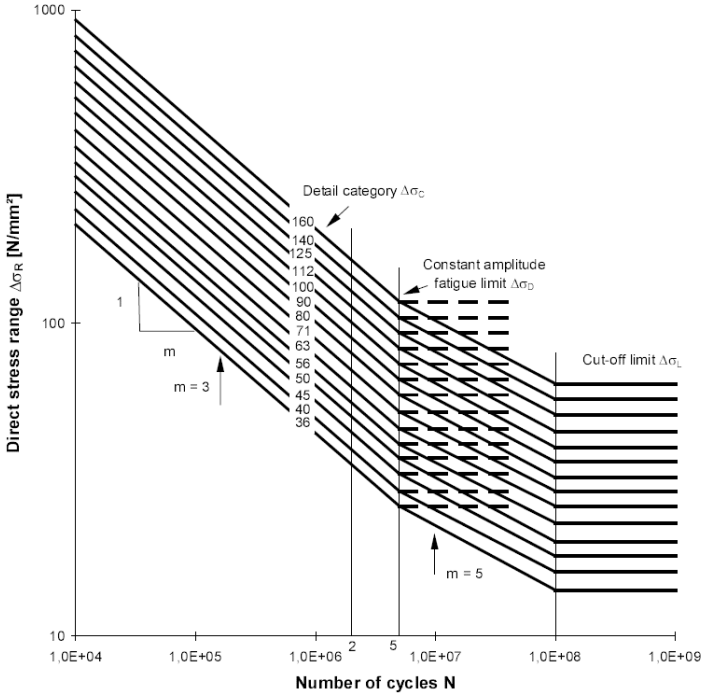


Figure 3: S-N curves for steel from EC3 Part 1.9.

From the above process, 10 potential values of 10-min fatigue damage were estimated for each of the selected wind speeds. Based on those 10 values the empirical cumulative density function of damage for each of the wind speeds was calculated and thus the empirical distribution of the damage was specified. For intermediate values of wind speed linear interpolation was used for determining the corresponding fatigue damage distribution.

The final step was to estimate the annual damage based on the 10-minute damage and the distribution of the annual wind speed data. Once the annual damage is calculated, the estimated fatigue life in years is equal to the reciprocal of that value. The process of calculating the annual damage (and the corresponding fatigue life) can be repeated numerous times since the distributions of the fatigue damage and the anemological data of the site are known. Thus, a Monte Carlo simulation for 100 years was performed in this study, in order to estimate the distribution of the fatigue life in the cross-section of interest. The results of this simulation for both sites and details of connection will be presented in the next section of the paper.

5 ANALYSIS RESULTS

5.1 Case 1: North Aegean Sea

The first site that was examined is in the north part of the Aegean Sea. The distribution of the 10 min mean wind speed at 10 m (U_{10}) of the MSL in a typical year is shown in Figure 4. A statistical analysis also showed that the mean value of wind speed was 5.41 m/s and the standard deviation 2.92 m/s. Furthermore the distribution of the wind speed is best modeled by a lognormal distribution with parameters $\mu = 1.56$ and $\sigma = 0.51$. Regarding the wind direction, North-East (24.6%) and North (12.9%) constitute the preferred directions of winds in a typical year. Finally, as for the surrounding geometry, Table 1 shows the values of fetch for each of the eight main directions considered in this study.

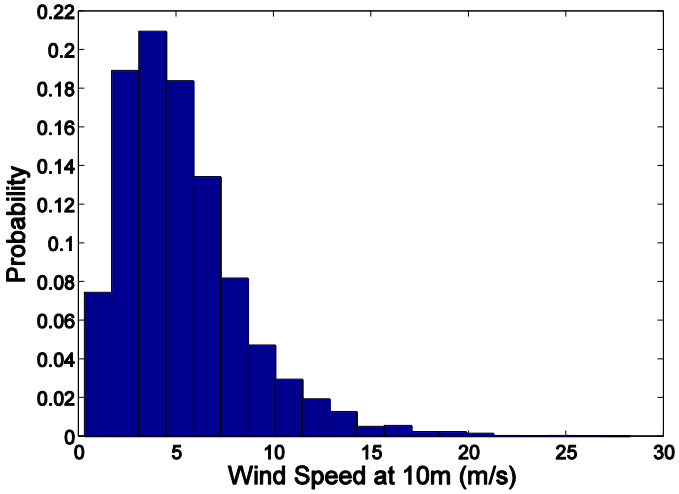


Figure 4: Distribution of non-zero 10 min mean wind speed at 10 m height (North site). There is also a ~30% probability of zero wind occurrence.

Direction	Fetch (Km)
N	5.8
NE	6.0
E	8.8
SE	34.4
S	73.1
SW	113.6
W	86.2
NW	18.9

Table 1: Fetch for each of the directions considered (North site).

The next step in the analysis was to estimate the joint PDF $f(H_s,U_{10})$ of wind speed and significant wave height. The joint PDF is calculated by the following formula:

$$f(H_s, U_{10}) = f_{H_s/U_{10}}(H_s/U_{10}) f_{U_{10}}(U_{10}) \tag{4}$$

where: $f_{U10}(U_{10})$ is the PDF of U_{10}, which is assumed to follow a lognormal distribution, as mentioned above and $f_{Hs/U10}(H_s/U_{10})$ is the conditional PDF of significant wave height H_s given the wind speed U_{10}. The distribution of the conditional PDF during a given storm is assumed to follow a Rayleigh distribution according to IEC 61400-3.

Using Eq. 4, the joint probability between wind speed and significant wave height can be estimated and the associated probability plots can be constructed. Since, the PDF takes into account two variables its plot is depicted as a surface in 3D or in a 2D contour plot. Figure 5 shows a contour plot of the joint PDF for the North site studied. It is noteworthy that in Figure 5, the part of the contours associated with higher H_s corresponds to South directions, where the fetch is higher according to Table 1. This is because according to JONSWAP methodology the higher the fetch the larger is the H_s for a specific U_{10}.

From the specific PDF, one can determine the directions with the higher contribution for different wind speed values. The direction with the highest contribution for wind speed values up to 15 m/s at hub height (U_{90}) was the North-East (NE), and the North (N) direction for

speed values larger than 15 m/s. As shown in Table 1, the aforementioned directions are associated with fetch of 5.9 km and 5.8 km, respectively. Based on these values, the wave characteristics for each speed were calculated, and as expected they are practically negligible. The results are shown in Table 2.

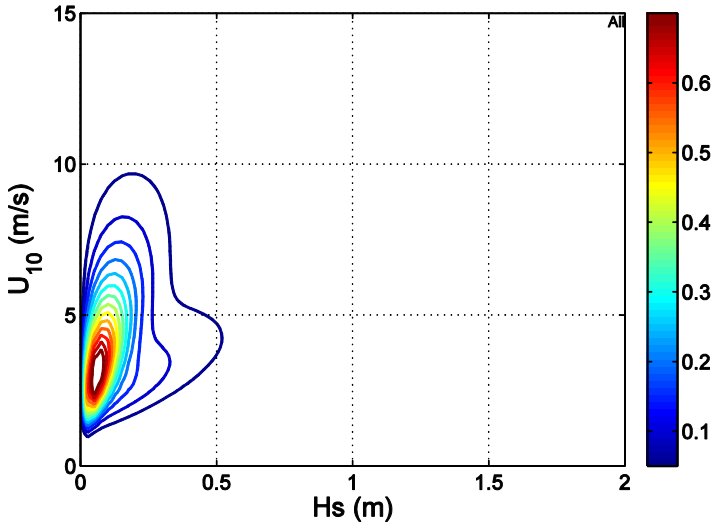


Figure 5: Contour plot of the joint PDF $f(H_s,U_{10})$ (North site).

A power-law wind profile (IEC 61400-3) was assumed for the distribution of the value of wind speed along the height z. According to this, if the wind speed is known at specific height z_0, the wind speed at height z is given by the formula:

$$U(z) = U(z_0)\left(\frac{z}{z_0}\right)^{\alpha} \tag{5}$$

where: α is the power-law exponent, taken to be equal to 0.14, as proposed by IEC 61400-3 for normal wind conditions. For the case at hand, z_0 = 10 m (reference value) and z = 90 m (hub height).

U_{90} (m/s)	U_{10} (m/s)	T_p (s)	H_s (m)	Dominant Direction	Fetch (km)
3	2.21	1.26	0.08	NE	6.0
5	3.68	1.50	0.12	NE	6.0
10	7.35	1.93	0.20	NE	6.0
15	11.03	2.24	0.30	NE	6.0
20	14.70	2.48	0.40	N	5.8
25	18.38	2.70	0.48	N	5.8
30	22.06	2.90	0.52	N	5.8

Table 2: Wind speed and wave characteristics at the North site.

The values of wind speed at hub height and the corresponding wave characteristics constitute the input to FAST, where the coupled dynamic analysis was performed. At the end of each simulation, time-series of stress history were obtained. A typical form of those time-series is shown in Figure 6. The stress time-histories are used in the estimation of fatigue damage and the corresponding fatigue life for the different wind speed values following the methodology of EC3 part 1.9 as mentioned in the theoretical background of this paper. Thus,

the annual fatigue damage and the corresponding fatigue life could be estimated. To this end, a simple Monte Carlo simulation was performed and 100 possible values of annual fatigue damage and corresponding fatigue life were calculated for each of the two details and for the different values of thickness for the cross-section of study.

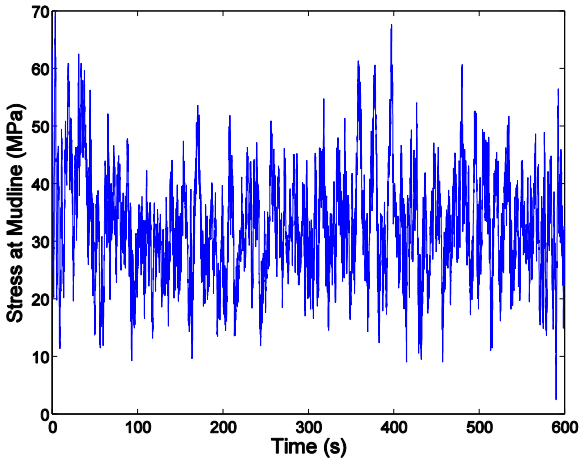


Figure 6: Typical form of stress time-series.

Table 3 shows the results of the analysis for the characteristics of the North Site. In specific, the average values of the annual damage and the corresponding estimated fatigue life for both types of detail, as resulted from the Monte Carlo simulations of 100 years are listed. An interesting finding is that the thickness of the cross-section has a significant effect on the annual damage for both details. In specific, as the thickness increases the annual damage decreases. This trend makes an intuitive sense, since a cross-section with larger thickness is expected to tolerate greater loads and be less vulnerable to fatigue. For instance, for a detail of 40 MPa, the annual damage of a cross-section with 25mm of thickness is around 40 times greater than a cross-section with 60 mm of thickness. The results are also plotted in Figure 7.

Thickness (mm)	DETAIL 40 MPa		DETAIL 71 MPa	
	Annual Damage	Fatigue Life (yrs)	Annual Damage	Fatigue Life (yrs)
25	0.1519	6.58	0.0159	63.06
30	0.0801	12.48	0.0064	156.76
35	0.0449	22.26	0.0026	382.21
40	0.0262	38.16	0.0011	936.09
45	0.0156	64.29	4.043E-04	2473.80
50	0.0094	106.24	1.562E-04	6403.04
55	0.0057	174.55	4.839E-05	20671.37
60	0.0035	285.91	1.337E-05	74830.91

Table 3: Results of Analysis for the North site

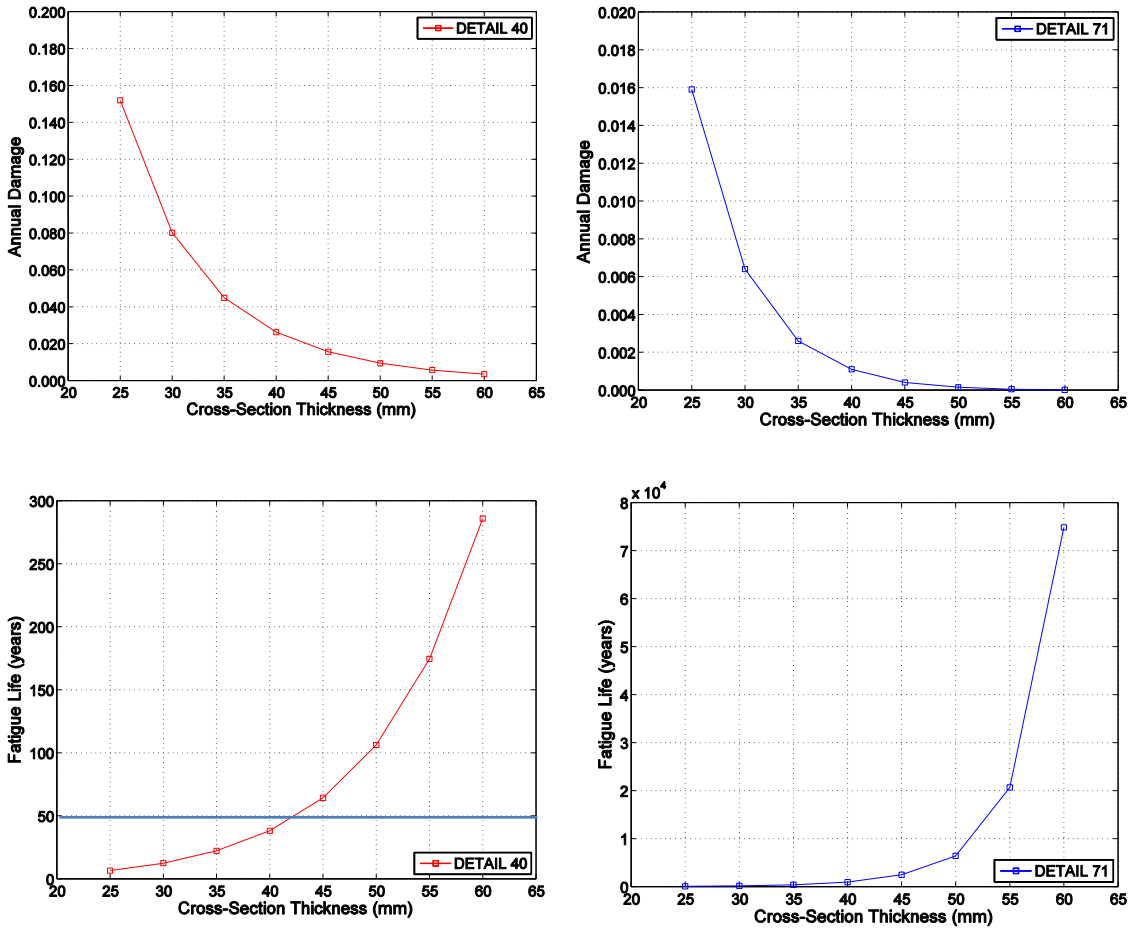


Figure 7: Annual damage and thickness of cross-section (top graphs) and fatigue life and thickness of cross-section (bottom graphs) for North site

The annual damage is directly associated with the fatigue life. As mentioned in a previous subsection, the fatigue life is approximately equal to the reciprocal of the annual damage. From the results listed in Table 3, an inference is that the fatigue life (which is a more tangible magnitude in common sense than damage, since it is measured in years) depends highly on the thickness of the cross-section. In specific, regardless of the detail, as thickness increases the expected fatigue life increases as well. Of course, this finding is intuitively expected, since a long fatigue life is associated with low annual damage.

It is noteworthy that the estimation of the fatigue life may be of special interest during the design phase of an offshore wind turbine. In other words, based on the expected fatigue life the designer is able to select an appropriate thickness for the pile's cross-section. This is because, it could be estimated whether a specific selection of thickness and detail of connection will make the specific cross-section to last during the whole design life of the structure. For example, in the case of an offshore wind turbine the structure's life-time is usually considered to be equal to 50 years. Based on the values of Table 3, one could conclude that if a detail of 40 MPa is selected, the minimum thickness that is expected to last longer than the design life (with respect to fatigue) is 45 mm. If a thickness less than 45 mm is used, then a fatigue failure is expected sooner than the end of the design life, i.e. during the service life of the wind turbine. For this reason a horizontal line is plotted in the bottom left graph of Figure 7 at the level of 50 years. The role of this line is to graphically show the above inference.

On the other hand, if a detail of 71 MPa for the welded connection is used, then no fatigue failure is expected during the life of the wind turbine, even if a thickness of 25 mm is used. This is because a thickness of 25 mm is associated with a fatigue life of around 63 years that is greater than 50 years. It is also noteworthy that if a thickness of more than 40 mm is used, then the fatigue life is estimated to be thousands of years. The latter means that no fatigue failure is expected in those cases. However, the benefit of the absence of fatigue may be associated with a high price such as higher construction costs (larger cross-section, advanced welded connection).

5.2 Case 2: South Aegean Sea

The second site of this study was selected to be in the South Aegean. It was also assumed that this site is far enough from shore in order to use the same fetch (equal to 120 km) regardless of direction. This assumption is of course oversimplified but it has the advantage that it does not require the consideration of wind direction in the analysis. At this point, the authors would like to mention a legal limitation that may arise. As of today, Greece has not declared an Exclusive Economic Zone and its territorial waters are extended up to 6 nautical miles from the shore. Thus, any planned offshore wind farm would have to be placed inside the above 6-mile zone. For this reason, a site with such a large omnidirectional fetch may not yet be available for exploitation in the Aegean Sea. However, the authors performed an analysis in order to evaluate the effect of a duration-limited (rather than fetch-limited) sea state. When the regional politics will allow it, such a case can become more of a practical, rather than a theoretical possibility.

Figure 8 shows the distribution of the wind speed at 10 m at the South site. A statistical analysis showed that the mean value of the wind speed is equal to 7.74 m/s and the standard deviation is equal to 5.10 m/s. Thus, a first inference is that South site is characterized by higher wind speeds than the North site. Finally, it was found that a Weibull (and not a lognormal) distribution with parameters $\lambda = 8.65$ and $k = 1.58$ provides the best fit.

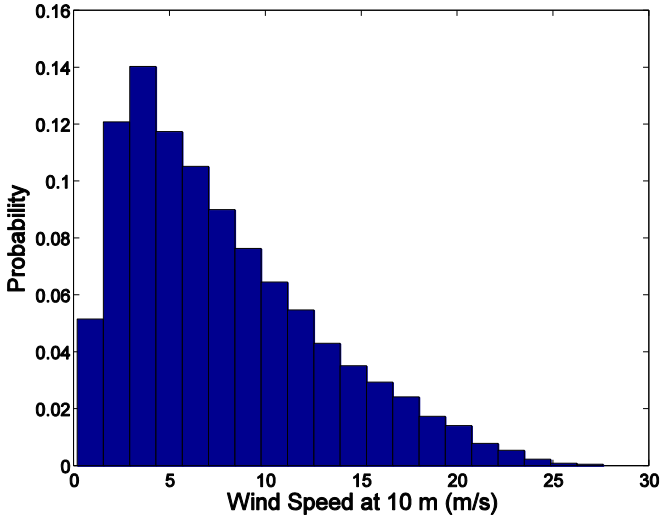


Figure 8: Distribution of Wind Speed at 10 m height (South site).
The zero-wind probability is practically zero.

The same assumptions and analysis process as in the case of the North site were undertaken for the estimation of the fatigue damage. Table 4 shows the wind speed and wave characteristics that were used for the dynamic analysis. From Table 4 it becomes obvious that, as expected, the wave intensity characteristics are quite more significant compared to those of

the North site. Of course this can be attributed to the longer fetch distances that were employed. Figure 9 shows the contour plot of the joint PDF $f(H_s,U_{10})$ for the South site. Now, all contours have an "oval" shape since the same fetch is assumed for all directions. In the North site, only South and South-East winds are practically fetch-unlimited, but generally less frequent, this leading to the lower-right lobe appearing in Figure 5 that is absent from Figure 9.

U_{90} (m/s)	U_{10} (m/s)	T_p (s)	H_s (m)	Fetch (km)
3	2.21	3.42	0.36	120
5	3.68	4.08	0.59	120
10	7.35	5.23	1.24	120
15	11.03	6.08	1.94	120
20	14.70	6.78	2.70	120
25	18.38	7.40	3.50	120
30	22.06	7.96	4.36	120

Table 4: Wind speed and wave characteristics at the South site

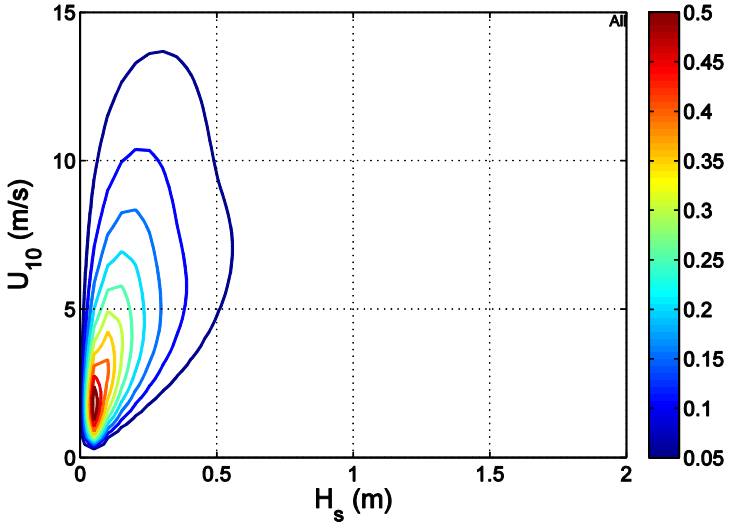


Figure 9: Contour plot of the joint PDF $f(H_s,U_{10})$ at the South site.

The Monte Carlo analysis gave the results shown in Table 5. The results, as expected, follow the same trends as in the case of the North site. However, due to the higher wind and wave conditions of the site, very large values of annual damage and low values of fatigue life were calculated. It is noteworthy that for a detail of 40 MPa, only if a thickness of 60 mm is used, the fatigue life will be slightly greater (only about 6 years) than the design life. For this reason only the combination associated with 60 mm of thickness is above the reference line of 50 years in the bottom left graph of Figure 10. For lower values of thickness a detail of 40 MPa will give fatigue lives lower than 50 years. Moreover, for very low values (lower than 40 mm) the estimated fatigue life is lower than 10 years.

If a detail of 71 MPa is selected, then longer values of fatigue life are expected. However, it should be mentioned that even with the better detail, only if the thickness of the cross-section is larger than 30 mm, the estimated fatigue life is greater than the design life of the wind turbine. Finally, if a value of thickness larger than 50 mm is used then the estimated fatigue is greater than 500 yrs (10 times the design life) and no fatigue failure is expected in practice.

Thickness (mm)	DETAIL 40		DETAIL 71	
	Annual Damage	Fatigue Life (yrs)	Annual Damage	Fatigue Life (yrs)
25	0.5791	1.73	0.0687	14.55
30	0.3130	3.20	0.0304	32.91
35	0.1812	5.52	0.0139	72.02
40	0.1087	9.20	0.0064	157.20
45	0.0676	14.80	0.0031	326.10
50	0.0429	23.29	0.0015	674.38
55	0.0276	36.20	0.0007	1394.30
60	0.0179	55.77	0.0003	3048.30

Table 5: Results of Analysis for the South site.

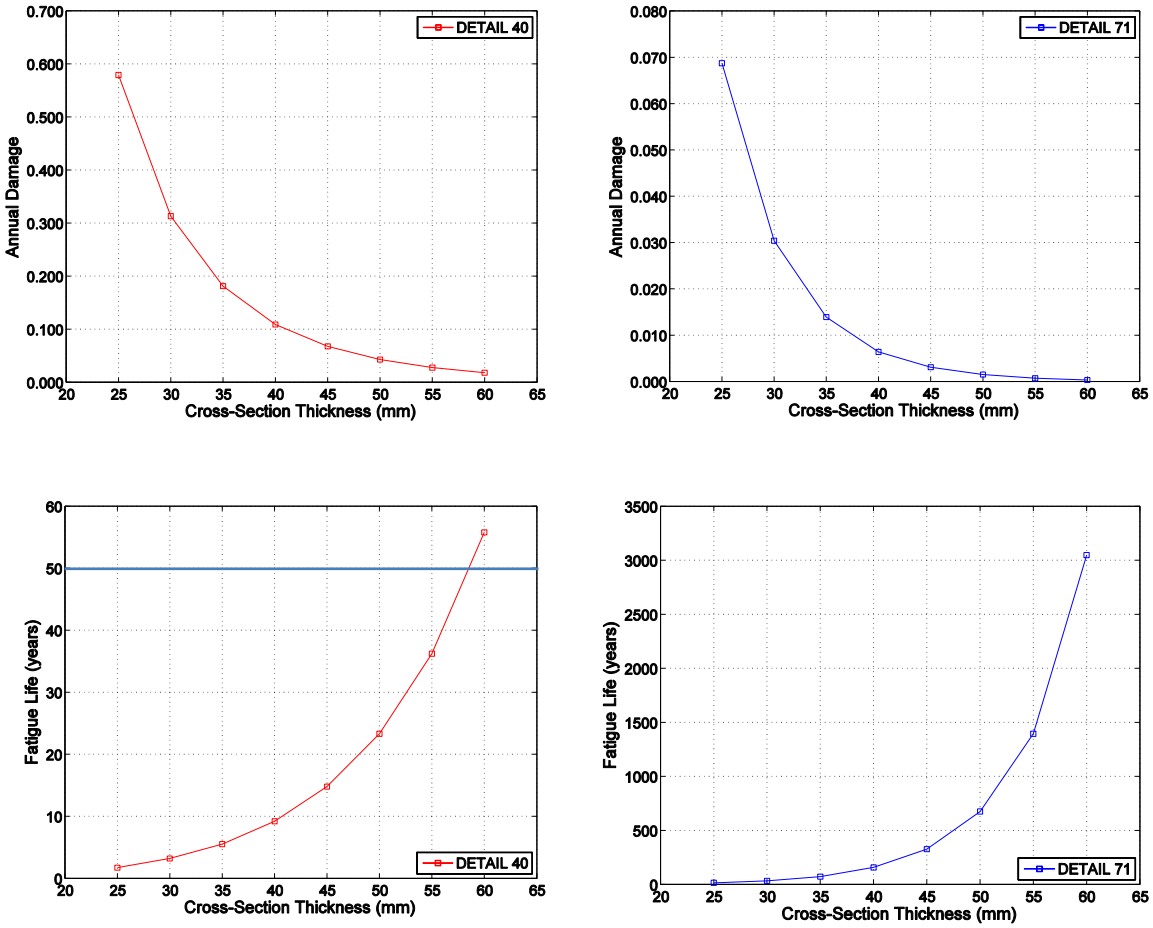


Figure 10: Annual damage and thickness of cross-section (top graphs) and fatigue life and thickness of cross-section (bottom graphs) for South site

5.3 Discussion of findings

Based on the results of both sites, it is inferred that for the site with higher wind and waves (South site) larger fatigue damage is expected for all the values of thickness examined in this study. This finding is associated with shorter fatigue life for the cross-section of interest. This certainly makes sense since larger wind and wave loads are expected to act on the construc-

tion. Finally, as expected, the lower-quality fillet welds (detail 40 MPa) are more vulnerable to fatigue than butt welds. Figure 11 shows that for the case of the South site a fillet weld might not be appropriate since it will result to a fatigue failure before the end of the design life of the wind turbine (with only exception the case of 60 mm thickness). Furthermore, even in the case of North site, where the wind and waves are milder, the use of a fillet weld requires at least 45 mm of thickness in order to last during the whole design life.

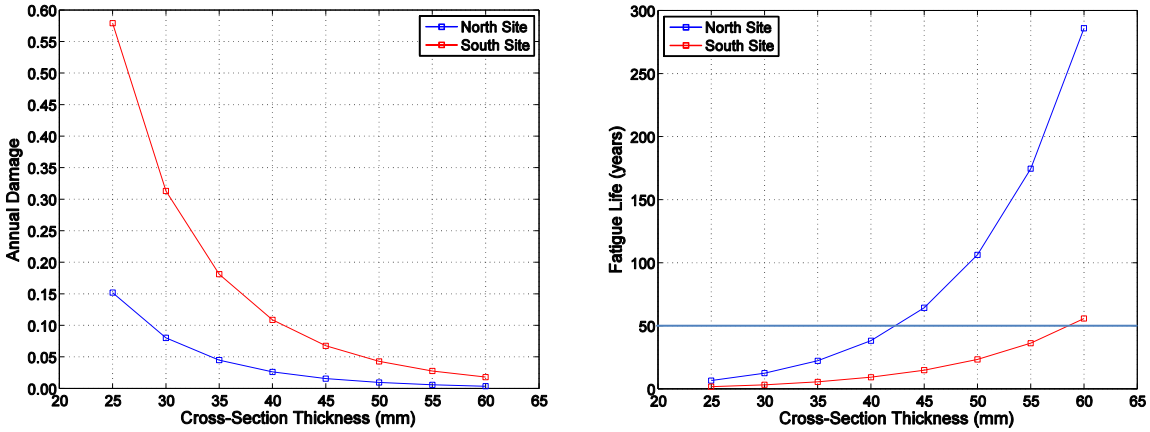


Figure 11: Comparison of annual damage (left graph) and fatigue life versus thickness of cross-section (right graph) for fillet welds (detail 40MPa) for the examined sites

On the other hand, the use of butt welds is found to be a safe (albeit expensive) solution regardless of thickness for the North site, since the expected fatigue life is longer than the design life, even when the smallest thickness is used. For the South site though, the use of butt weld requires a minimum with of 35 mm (see Table 5) in order the fatigue life to be longer than the design life.

The inferences from the above discussion may be useful, especially during the design of the foundation pile. Fillet welds might not be appropriate in a construction site characterized by windy conditions, however they might be a potential cost-reduction technique for sites with less intensive wind loads, since they are much cheaper to execute than butt welds and with an appropriate thickness may last more than the design life.

6 CONCLUSIONS

In this paper, a probabilistic fatigue life assessment for a standard offshore wind turbine with a monopile design was presented. Two potential sites of construction in the Aegean Sea of Greece with different wind and wave characteristics were examined. A fully coupled dynamic analysis for the calculation of loadings due to wind and wave was performed using the freely available FAST software. The assessment of fatigue damage (and corresponding fatigue life) was made considering two different details of welded connections according to EC3 for the cross-section at mudline of the structure.

The results follow the obvious trends: Turbines at windier sites with longer fetch distances are obviously more vulnerable to fatigue. Lower quality fillet welds similarly attract higher fatigue damage compared to more expensive butt welds. The thickness of the cross-section is a crucial parameter for the design, since a small thickness may result in a very quick fatigue failure, especially in the case of fillet welds.

Finally, as an overall conclusion of this work is that the accuracy offered by a detailed probabilistic approach can help in properly quantifying the actual performance of the structur-

al components and thus result to a better compromise between safety and economy. Incorporating further sources of uncertainty and operational states of the wind turbine (e.g., starting and stopping) will only improve the accuracy in such predictions and help offer a cost-effective custom-made solution for a site of interest.

ACKNOWLEDGEMENTS

This research has been co-financed by the European Union (European Social Fund - ESF) and Hellenic national funds through the Operational Program "Competitiveness and Entrepreneurship" of the National Strategic Reference Framework (NSRF 2007-2013) - Research Funding Program: Bilateral R&D Cooperation between Greece and China 2012-2014.

REFERENCES

[1] J.D. Sorensen, Reliability Analysis of Wind Turbines Exposed to Dynamic Loads. A. Cunha, E. Caetano, P. Ribeiro, G. Muller eds. *9th International Conference on Structural Dynamics*, EURODYN 2014, Porto, Portugal, 2014.

[2] J.M. Jonkman, Dynamics of Offshore Floating Wind Turbines-Model Development and Verification. *Wind Energ.* **12**, pp.459-492, 2009.

[3] T. Moan, Stochastic Dynamic Response Analysis of Offshore Wind Turbines in a Reliability Perspective. A. Cunha, E. Caetano, P. Ribeiro, G. Muller eds. *9th International Conference on Structural Dynamics*, EURODYN 2014, Porto, Portugal, 2014.

[4] P. Passon, K. Branner, Condensation of Long-Term wave Climates for the Fatigue Design of Hydrodynamically Sensitive Offshore Wind Turbine Support Structures. *Ships and Offshore Structures*, Taylor & Francis, 1-25, 2014.

[5] S.R. Arwade, M.A. Lackner, M.D. Grigoriu, Probabilistic Models for Wind Turbine and Wind Farm Performance. *ASME Journal of Solar Energy Engineering*, **133**, No. 4: 041006, 2011.

[6] J. Jonkman, S. Butterfiled, W. Musial, G. Scott, Definition of a 5-MW Reference Wind Turbine for Offshore System Development. *Technical Report NREL/TP-500-38060. NREL Technical Report,* National Renewable Energy Laboratory, Golden, Colorado, 2009.

[7] H.J.T. Kooijman, C. Lindenburg, D. Winkelaar, E.L. van der Hooft, DOWEC 6 MW Pre-Design. *Tech Report DOWEC-F1W2-HJK-01-046/9 (Public Version),* Petten, Holland, 2003.

[8] IEC 61400-3, Wind Turbines-Part 3: Design Requirements for Offshore Wind Turbines. *European Committee for Electrotechinal Standardization,* Brussels, Belgium, 2009.

[9] DNV-RP-C205, Environmental Conditions and Environmental Loads. *Det Norske Veritas*, Bærum, Norway, 2010.

[10] B.J. Jonkman, L. Kilcher, TurbSim User's Guide: Version 1.06.00. *Tech Report NREL/EL-xxx-xxx (Draft Version),* National Renewable Energy Laboratory, Golden, Colorado, 2012.

[11] J.D. Jonkman, M.L. Kilcher Jr, FAST User's Guide. *Tech Report NREL/EL-500-38230,* National Renewable Energy Laboratory, Golden, Colorado, 2005.

[12] J. Morison, M.P. O'Brien, J.W. Johnson, S.A. Schaaf, The Force Exerted by Surface Waves on Piles. *Petroleum Transactions,* **189**, 149-154, 1950.

[13] Eurocode 3: Design of Steel Structures, Part 1.9: Fatigue Strength of Steel Structures. *CEN Central Secretariat,* Brussels, Belgium, 2002.

[14] ASTM E1049-85, Standard Practices for Cycle Counting in Fatigue Analysis. *Annual Book of ASTM Standards*, 03.01, 710-718, 1997.

[15] A. Nielsony, Determination of Fragments of Multiaxial Service Loading Strongly Influencing the Fatigue of Machine Components. *Mechanical Systems and Signal Processing*, **23**, 2712-27121, 2009.

[16] MedPAN, Overview of Planned OWF Projects in the Mediterranean. *Network of Marine Protected Area Managers in the Mediterranean*, Marseille, France, 2013.

COMPDYN 2015
5th ECCOMAS Thematic Conference on
Computational Methods in Structural Dynamics and Earthquake Engineering
M. Papadrakakis, V. Papadopoulos, V. Plevris (eds.)
Crete Island, Greece, 25–27 May 2015

ONE YEAR OF CONTINUOUS DYNAMIC MONITORING OF A WIND TURBINE. STRUCTURAL INTEGRITY AND FATIGUE ASSESSMENT

Gustavo Oliveira[1], **Filipe Magalhães**[1], **Álvaro Cunha**[1], **Elsa Caetano**[1]

[1] ViBest, Faculty of Engineering (FEUP), University of Porto
R. Dr. Roberto Frias, s/n, 4200-465 Porto, Portugal
e-mail: gustavo.oliveira@fe.up.pt; acunha@fe.up.pt

Keywords: Wind Turbine, Monitoring, Operational Modal Analysis, Fatigue Assessment.

Abstract. *The paper presents recent results from a research project based on a continuous dynamic monitoring of a wind turbine. The monitoring system was developed with the capacity to detect structural abnormalities based on the continuous tracking of the modal properties of wind turbines (natural frequencies, modal damping ratios and mode shapes). In addition, the system is also capable to estimate the dynamic stress levels of the tower structure, in order to assess the damage condition and evaluate its remaining fatigue life.*
In the first part of the present paper, preliminary results from one year of continuous tracking of the modal properties of the wind turbine vibration modes are introduced. The main characteristics of the tracked modes are shown and the evolution of these modes with rotor rotation speed is characterized.
In a second part, the methodology followed to evaluate the stress condition of the wind turbine tower is introduced. This procedure is illustrated and validated with the help of a numerical analysis of a wind turbine, developed in the HAWC2 aeroelastic code.

1 INTRODUCTION

Wind power exploitation has shown a consistent growth both in onshore [1] and offshore installations [2], with increasingly competitive costs. This growth has been reflected in the installation of wind turbines composed by very flexible support structures and with large rotors. Due to these characteristics, wind turbines became very susceptible to vibration problems and, consequently, to fatigue damage problems.

This paper presents a continuous dynamic monitoring system, under development by the Laboratory of Vibrations and Structural Monitoring (ViBest, www.fe.up.pt/vibest) of FEUP, with the purpose of identifying structural changes (i.e. damage) and estimating the fatigue damage condition of a wind turbine. The system is based on the continuous tracking of modal properties of the structure (frequency values, modal damping ratios and mode shapes), identified during the different operating conditions of a wind turbine. The strategy adopted for the monitoring system has already proved to be suitable to be installed both in onshore and offshore wind turbines [3].

The modal identification of large structures excited by operational conditions, an approach usually named as Operational Modal Analysis (OMA), is a technique widely used in several applications [4]. Some examples of implementation of monitoring systems based on OMA in wind turbines are presented in [5, 6].

The assessment of fatigue condition through acceleration data records was already investigated by some researchers [7, 8]. However, in these works, the authors used the results from modal identification tests to tune a finite element model in order to estimate the stress condition of the structure.

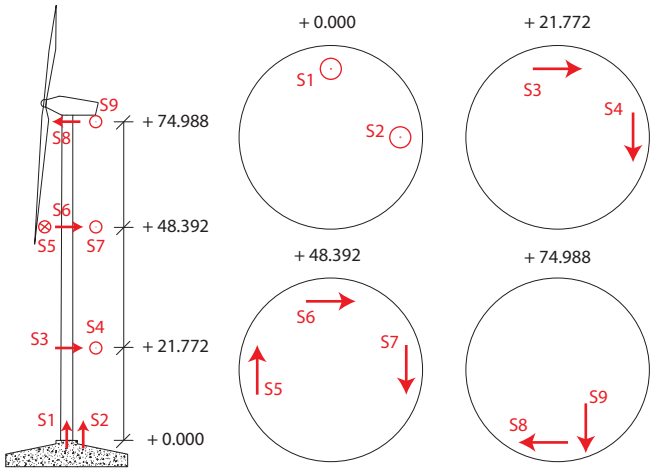
This paper presents some results already achieved with the developed dynamic monitoring. Initially, the results obtained with the continuous tracking of the modal properties of the wind turbine during one year are presented. In the second part, an improved methodology to estimate the stress time history of the tower structure is presented, where only the acceleration data, alongside with a simple stiffness matrix of the tower, is used. This methodology is applied to a numerical example using the HAWC2 aeroelastic code [9].

2 DESCRIPTION OF THE STRUCTURE

The wind turbine under analysis is a 2.0 MW system with a variable-speed generator located at the north of Portugal. It has a hub height of 80 m and an up-wind rotor with a diameter of 80 m. Its support structure is composed by a concrete slab foundation and a steel tower. As usual, the tower is constituted by individual cylindrical segments which are connected to each other by flanged bolted connections.

The implemented dynamic monitoring system is composed by 9 uni-axial force-balanced accelerometers which are linked to a 24-bit digitizer and acquisition system. The sensors are located along the tower height according to Figure 1. Sensors S1 and S2 are not used in the modal identification and fatigue assessment process, since they are only used to evaluate the vibration levels at the foundation.

The monitoring system is configured to record acceleration time series of 10 minutes sampled at a rate of 50 Hz, and then decimated to 25 Hz. Alongside, the systems also uses the data recorded by the SCADA system. This system records the 10 minutes averaged values of several parameters such as rotor speed, yaw angle, wind speed and direction, temperature, among others.



a) b)

Figure 1: Position of the accelerometers at the different levels of the wind turbine: a) front view; b) top view at different sections

3 CONTINUOUS MODAL TRACKING

The results presented in this section are referred to the modal tracking of the wind turbine vibration modes during a period of analysis of one year. During this period, the wind turbine operated under several conditions. In order to cope with this variability of conditions, a strategy to automate the identification process was developed.

3.1 Strategy for automated processing

The strategy implemented for the continuous modal tracking of the turbine modal properties is composed by an initial pre-processing, where the signals are filtered and re-sampled. After this step, the modal properties of the structure are identified through the application of output-only system identification algorithms: SSI-COV [10] and SSI-DATA [11] (both in time domain); and p-LSCF [12] (in frequency domain). Usually, the results obtained with these algorithms are presented in the form of stabilization diagrams. These diagrams show the obtained poles with different model orders at the frequencies of suspected resonance peaks. Thus, if the properties of a pole (modal parameters) are kept constant, it is considered a stable pole and it is very likely to represent a physical pole, in opposition to a spurious one.

Lastly, a methodology for automatic identification of the modal parameters is used. This method is based on a hierarquical clustering algorithm, which tend to cluster poles that are related to the same physical mode [13]. The properties of the cluster are then compared to reference properties of the vibration modes intended to be tracked, in order to classify the cluster as the correct vibration mode.

Due to different operating conditions and, consequently, different structural configurations (e.g. pitch angle variations), 6 operating regimes were considered when defining the reference properties of the vibration modes. These regimes are presented in Table 1.

Operating regime	Wind turbine condition
1	Parked or idling (with high pitch angle)
2	Parked or idling (with lower pitch angle, in conditions to start operating)
3	Transition situation from non-operation to operation (mean value of rotor speed between 0 and the lowest operating rotor speed)
4	Operating situation, defined by the lowest operating rotor speed and the point where the pitch angle starts to increase to avoid excessive rotor torque values
5	Operating situation, between regime 4 and highest operating rotor speed
6	Wind speed higher than cut-out speed

Table 1: Operating regimes considered for reference modal properties of the vibration modes

3.2 Identified vibration modes

The analysis of the collected data clearly evidenced different vibration scenarios of the wind turbine support structure due to the different operating regimes. As an example, Figures 2 and 3 present the results from the modal identification obtained with two different situations. In Figure 2, the stabilization diagram from a non-operating situation, where the wind turbine is idling and the wind speed is low, is shown. In this case, the assumptions for application of OMA are practically fulfilled and the identification of the vibration modes is straightforward. On the other hand, in operating situations, these assumptions are not present [14] and the modal identification is considerably hindered. Figure 3 presents the results from an operating situation (regime 4), where the rotor is rotating at a mean velocity of 14 rpm. As can be seen, there are several resonance peaks that are not present in Figure 2. These peaks, identified as 1, 3, 6, 9 and 12P, are due to the harmonic excitation of the structure from the rotor rotation (where the rotation frequency is denoted as 1P). Although these resonance peaks are indicated as vibration modes from a raw analysis of the results from the modal identification algorithms, they should not be confused as such.

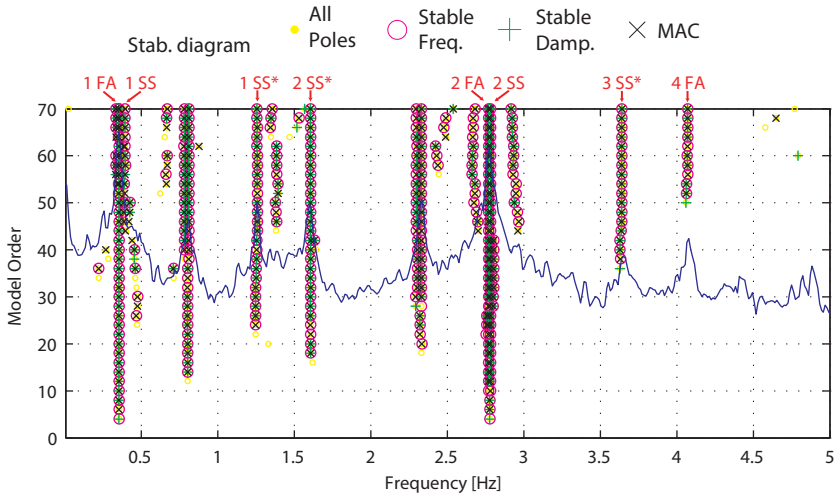


Figure 2: Stabilization diagram from a non-operating situation

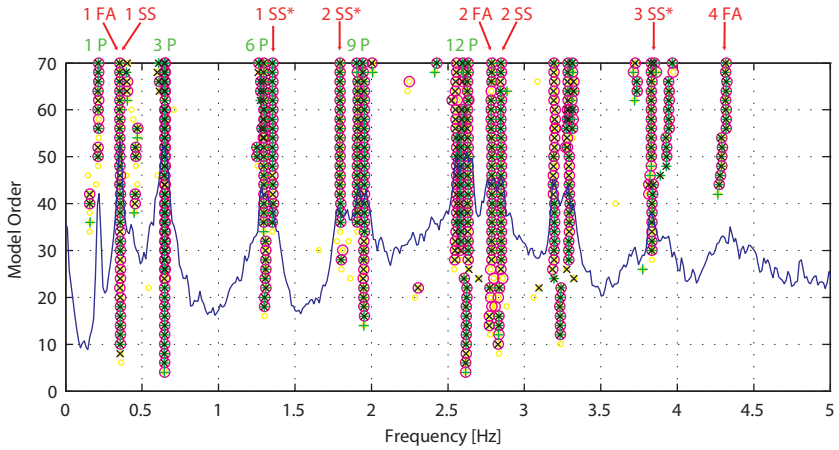


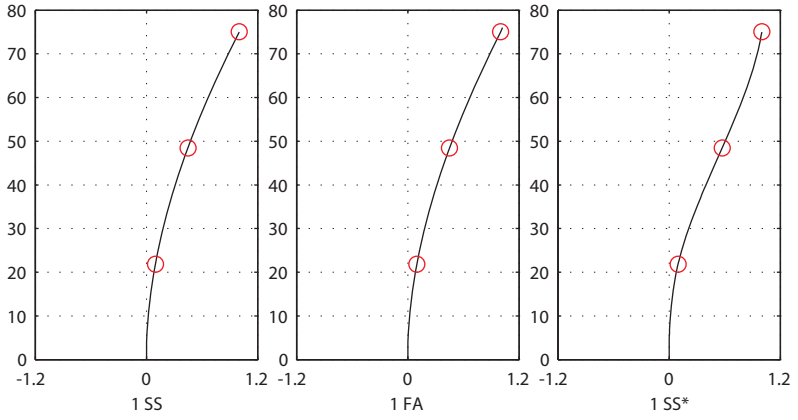
Figure 3: Stabilization diagram from a power production situation

From initial analysis of the data, some vibration modes were selected to be tracked. For this decision, the modes with the higher contribution to the vibration of the structure and with little interference from harmonics excitation were selected. From this analysis, it was decided to track 9 vibration modes within a frequency range of 0 – 4.5 Hz. The mean value of frequency of these modes is presented in Table 2. Although these modes include a support structure component in their mode shape, the modes identified with an asterisk ("*") have a significant rotor motion.

Vibration mode	f [Hz]
1 SS	0.355
1 FA	0.362
1 SS*	1.363
2 SS*	1.796
2 FA	2.801
2 SS	2.843
3 SS	3.700
3 SS*	3.813
4 FA	4.300

Table 2: Mean frequency value of the of the tracked vibration modes

The configurations of the modes are presented in Figure 4.



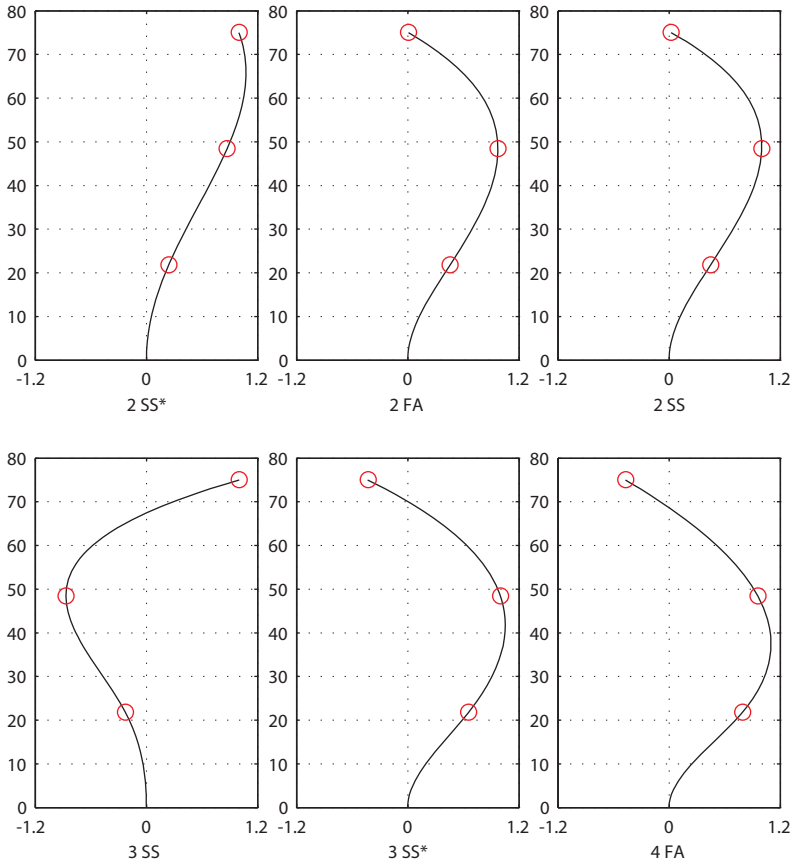


Figure 4: Mode shapes of the selected vibration modes

3.3 First monitoring results

The automated analysis of the data was processed according to the presented strategy. During the period of one year, the 9 selected vibration modes were successfully identified under various operating conditions of the wind turbine.

In order to illustrate the influence of the harmonic excitation in the identification of the vibration modes, Figure 5 shows a Campbell diagram of all identified clusters of stable poles, plotted according to the direction of vibration (FA or SS), where the diagonal dashed lines represents the harmonic frequencies of rotor rotation (multiples of 3P). The vertical dashed lines indicate the non-production situation, a transition state and the operating regimes from the wind turbine. As can be seen, the influence of the harmonics is clearly noticed, particularly from the 3P and 6P, with a large number of clusters around the diagonal dashed lines.

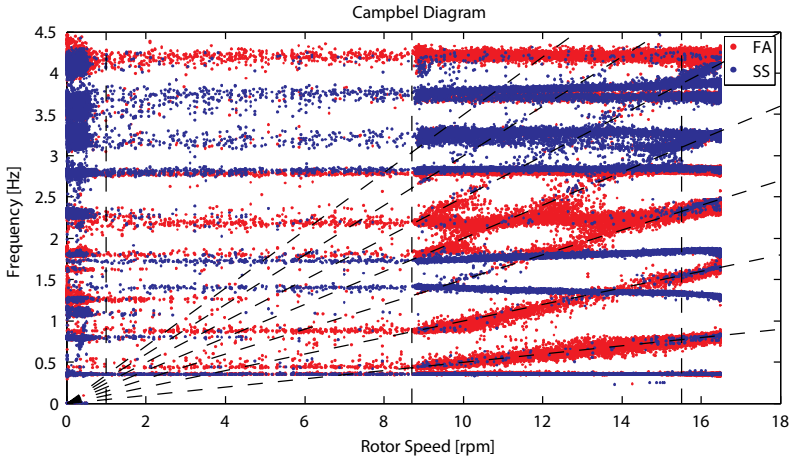


Figure 5: Campbell diagram of identified clusters of stable poles (including vibration modes and external sources of excitation)

Since the aim of the monitoring system is the identification of the modal properties of the wind turbine, an accurate definition of the reference properties from the selected vibration modes was performed. Figure 6 presents the results of the modal identification after comparison of the clusters properties with the reference values of each vibration mode. It is possible to attest the almost inexistence influence of the harmonic excitation.

One interesting phenomenon is observed in Figure 6. It is clearly visible that the frequency value of modes 1 SS*, 2 SS* and 3 SS* presents a clear dependency on the rotor rotation speed. This is a characteristic of rotor vibration modes that, when in operation, develops two whirl modes: one forward and one backward mode. From a non-rotating reference (like the one from the installed sensors on the tower), the frequency values of these modes tend to increase and decrease, respectively for the forward and backward mode, with the increase of the rotor speed.

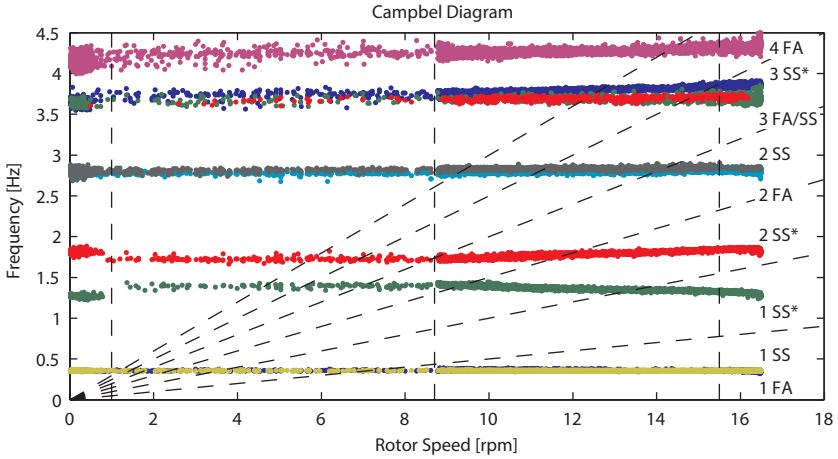


Figure 6: Campbell diagram of the tracked vibration modes

4 FATIGUE ASSESSMENT

The methodology adopted in this paper to assess the fatigue condition of the wind turbine tower is based on the decomposition of the acceleration data records in modal acceleration responses. After this step, the fatigue stress due to each vibration mode or stationary responses to harmonic excitations is computed. Finally, the real dynamic component of stress of the structure is obtained as the sum of every individual contribution.

The presented methodology is illustrated and validated with the help of a numerical example developed with the HAWC2 code.

4.1 Decomposition of the acceleration time series in modal acceleration responses

The decomposition of the acceleration time series into modal responses is based on the approach present in [10]. This starts with the computation of the state-space matrix *A* and the output-matrix *C* from the state-space model of the wind turbine (both obtained from the modal identification algorithms), and with the process and measurement noise covariance matrices *Q*, *R* and *S* (obtained as a post-process of the modal identification algorithms).

After the computation of these matrices, the Lyapunov equation is used to obtain Σ:

$$\Sigma = \mathrm{A}\Sigma\mathrm{A}^{\mathrm{T}} + \mathrm{Q} \tag{1}$$

where ^{T} represents the transpose operation. Then, the correlation and next-state output correlation matrices (R_0 and G) are computed:

$$R_0 = \mathrm{C}\Sigma\mathrm{C}^{T} + \mathrm{R} \tag{2}$$

$$\mathrm{G} = \mathrm{A}\Sigma\mathrm{C}^{\mathrm{T}} + \mathrm{S} \tag{3}$$

in order to solve the Riccati equation for P:

$$P = APA^T + (G - APC)^T(R_0 - CPC^T)^{-1}(G - APC^T)^T \tag{4}$$

Lastly, the Kalman gain (K) is calculated according to:

$$K = (G - APC^T)(R_0 - CPC^T)^{-1} \tag{5}$$

After the Kalman gain is computed, it is possible to define the identified model in a forward innovation model:

$$\begin{aligned} z_{k+1} &= A\, z_k + K\, e_k \\ \ddot{y}_k &= C\, z_k + e_k \end{aligned} \tag{6}$$

where e_k represents the white noise innovation sequence and $\ddot{y}_k$ is the acceleration recorded at k time step. Transforming equations (6) into modal basis equations:

$$\begin{aligned} z_{m,k+1} &= \Lambda_d\, z_{m,k} + K_m\, e_k \\ \ddot{y}_k &= V\, z_{m,k} + e_k \end{aligned} \tag{7}$$

where Ψ and Λ_{d} represents a matrix with the eigenvectors and a diagonal matrix with the eigenvalues of the state-space matrix and:

$$z_{m,k} = \Psi^{-1}\, z_k \tag{8}$$

$$K_m = \Psi^{-1}\, K \tag{9}$$

With the model of the equation (7), an estimation of the acceleration data can be reconstructed with the contribution of n modal responses:

$$\hat{\ddot{y}}_k = \sum_{i=1}^{n} \hat{\ddot{y}}_{k,i} = \sum_{i=1}^{n} \mathrm{V}_i\, z_{m,k,i} \tag{10}$$

Since Λ_{d} is a diagonal matrix, equation (7) allows to decompose the measured acceleration time series into several acceleration time series with the contribution of vibration modes or stationary responses to external harmonic loads.

4.2 Modal fatigue stress

Considering that a reasonable number of accelerometers is available, the resolution of each mode shape (eigenvector) along the tower height can be increased through a cubic spline interpolation. With this step, it is possible to estimate the modal acceleration response at any point of the tower with equation (10).

At this point, it is necessary to integrate the modal acceleration response signal obtained into modal displacements. In this paper, the double integration of the acceleration time series in the frequency domain was performed:

$$\hat{Y}_{k,i} = -\frac{\hat{Y}_{k,i}}{\omega^2} \tag{11}$$

where $\hat{Y}$ represents the estimated displacements of the structure in the frequency domain.

Since the modal displacement field of the wind turbine tower has a sufficient characterization (due to the performed interpolation), equivalent forces imposing the same deformation, for each vibration mode, are calculated according to:

$$F_{k,i}(z) = K\,\hat{y}_{k,i}(z) \tag{12}$$

where z indicates the height of the wind turbine tower and K represents the stiffness matrix of the wind turbine tower. Since the tower structure can be assumed as a simple cantilevered beam, the matrix K can be constructed through simple methods, once the structural characteristics (variation of the bending stiffness along the height) are known.

After obtaining the equivalent forces for each vibration mode, the total dynamic component of the force is obtained as the sum of all modal contributions. The stress at any height of the tower can then be evaluated. Figure 7 illustrates the presented methodology.

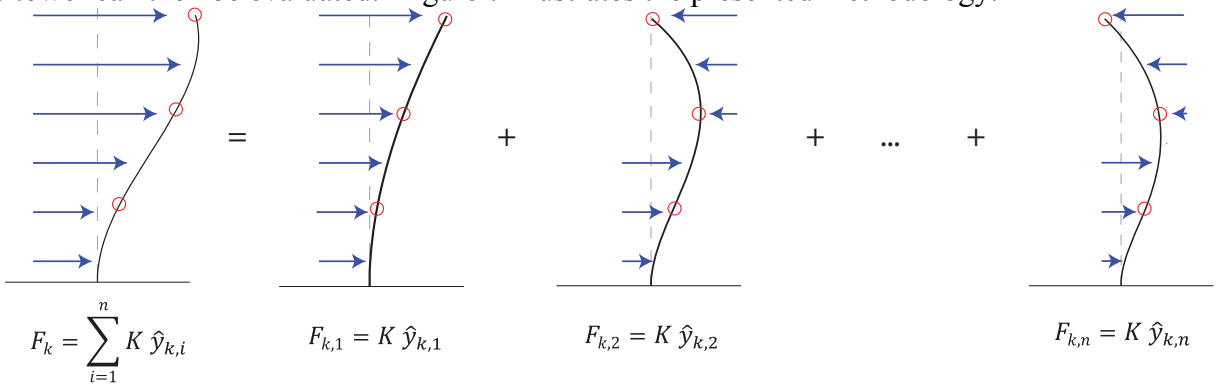


Figure 7: Illustration of the proposed methodology to estimate the dynamic forces along the tower height

4.3 Numerical model of the wind turbine

A numerical model of the studied 2.0 MW wind turbine has been developed using HAWC2 code [9]. HAWC2 is an aeroelastic code developed in Riso DTU, intended for calculating wind turbine response in time domain under aerodynamic loads. It uses the multibody formulation to model the wind turbine structure through beam elements with 6 degrees of freedom.

The aerodynamic model implemented in the HAWC2 code is based on the blade element theory. In the performed analysis, the effect of the tip loss and dynamic stall of the blades were included. Also, the tower shadow effect, due to disturbance of the flow created by the tower, was included.

The wind turbine tower structure was modelled according to the technical drawings made available by the manufacturer. However, since the characteristics of the nacelle and rotor were

not provided, the characteristics from the NREL 5MW [15] reference wind turbine were scaled down to meet the characteristics of the desired wind turbine.

The model was then used to perform a 600 s time-domain analysis with a time resolution of 0.02 s. In the analysis, the wind turbine was subjected to a tridimensional turbulent wind flow field with a mean wind speed of 9 m/s. The time history of the wind speed at hub height is shown in Figure 8. During the analysis, the rotor speed varied between 16.2 and 17.8 rpm (Figure 9).

The same layout of sensors presented in Figure 1 was implemented to record the numerically simulated acceleration time series of the structure (although only the 3 sensors oriented in the FA direction were used in this work).

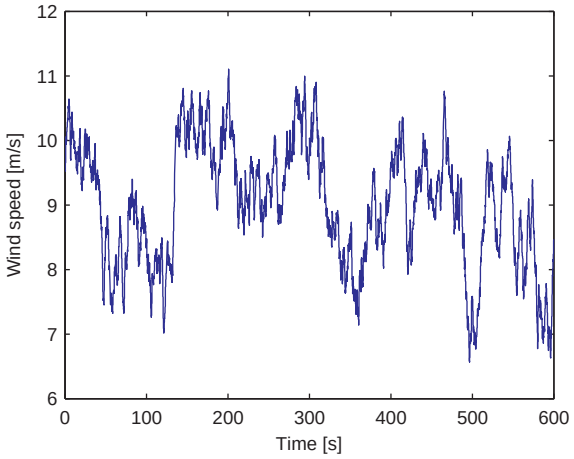


Figure 8: Wind speed at hub height

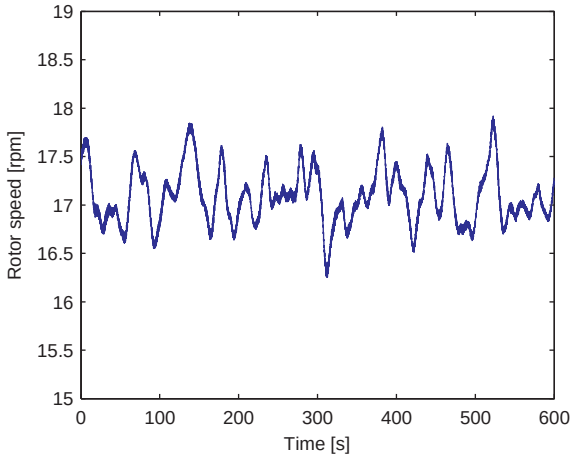
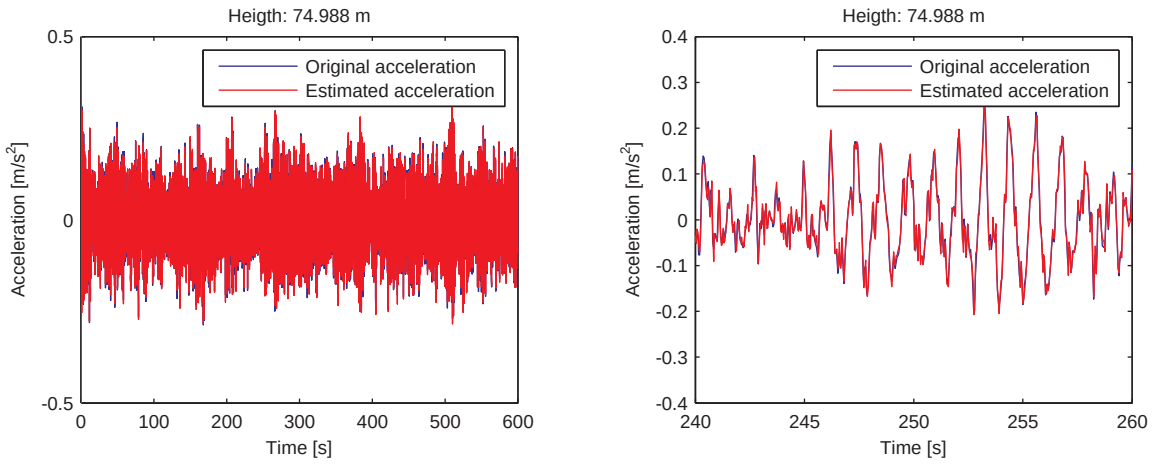


Figure 9: Rotor speed

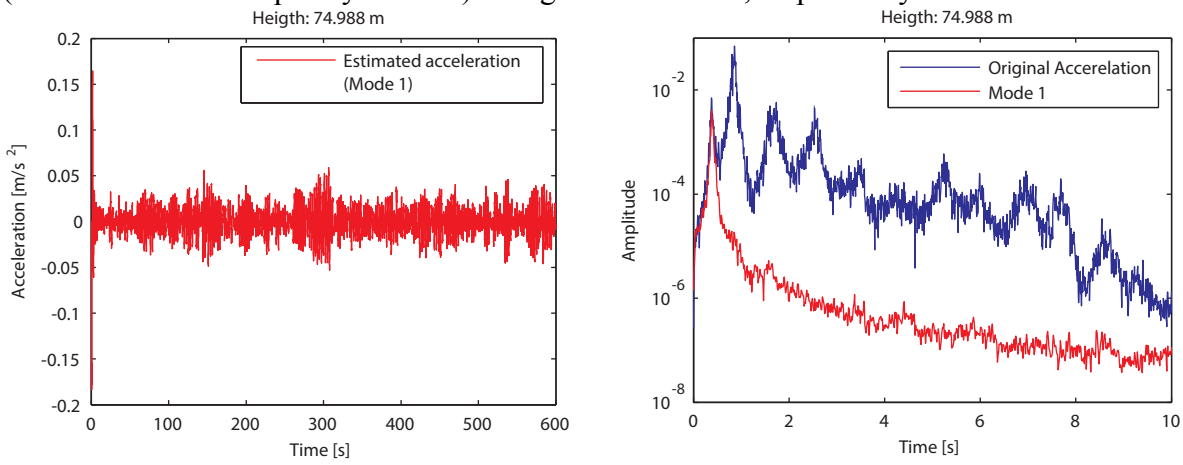
During the analysis, the SSI-DATA modal identification algorithm was used and the results obtained from the analysis were decimated to a sampling frequency of 25 Hz, to be consistent with the settings of the monitoring system. The acceleration time series "recorded" by the top sensor (height of 74.988 m) is presented in Figure 10 a), alongside with the estimated acceleration obtained as the contribution of all identified poles. Figure 11 b) shows a zoom for a period of 20 seconds where it is possible to attest the very good agreement between the two signals.



a) b)

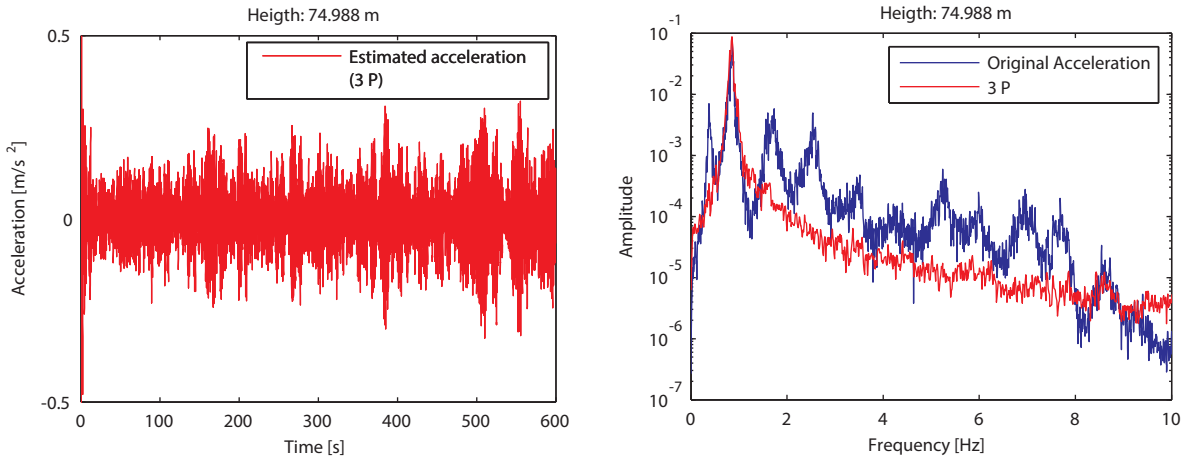
Figure 10: Estimated and recorded acceleration by the sensor: a) complete time series; and b) zoom of a period of 20 seconds

In order to illustrate the procedure presented in 4.1, the acceleration signal obtained for the first vibration mode of the wind turbine and due to the harmonic excitation of 3P is presented (in both time and frequency domain) in Figures 11 and 12, respectively.



a) b)

Figure 11: Estimated acceleration due to the 1st vibration mode in time domain a) and comparison with the recorded acceleration signal in frequency domain b)



a) b)

Figure 12: Estimated acceleration due to the harmonic excitation 3P in time domain a) and comparison with the recorded acceleration signal in frequency domain b)

After the estimation of the acceleration response time series for every vibration mode and harmonic excitation, it is possible to apply the procedure introduced in 4.2. Firstly, the displacement due to each mode and harmonic excitation is estimated. The displacements directly provided by the HAWC2 software (reference displacement) and estimated from simulated acceleration time series (estimated displacement) at the height of 74.988 m are shown in Figure 13. As can be seen, the agreement between the two signals is considerably good for the most important part of the spectrum. It is important to notice that, for very low frequencies (lower than 0.10 Hz), the signal coherence is not so good due to the frequency cut value chosen for the double integration process. However, this fact is not very important when trying to estimate the dynamic component of the displacements. Since standards, such as [16, 17], use an approach based on accumulated damage and S/N curves to estimate the fatigue damage of steel structural components, that does not consider the quasi-static component of the stresses,

this fact has a very low influence in the estimation of the remaining fatigue life of the structure.

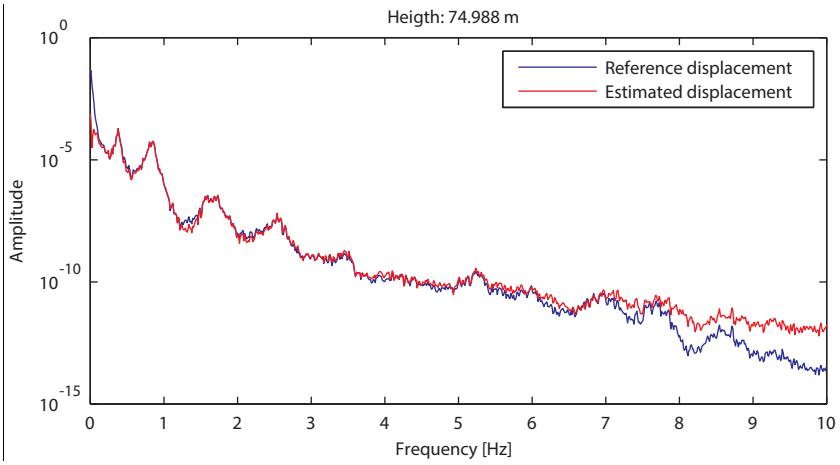


Figure 13: Comparison between reference and estimated displacement at height of 74.988 m

Lastly, after the equivalent forces are computed, it is possible to estimate the bending moment at the foundation level. The estimated bending moment at the foundation level is presented in Figure 14 and compared with the result directly obtained in the numerical analysis.

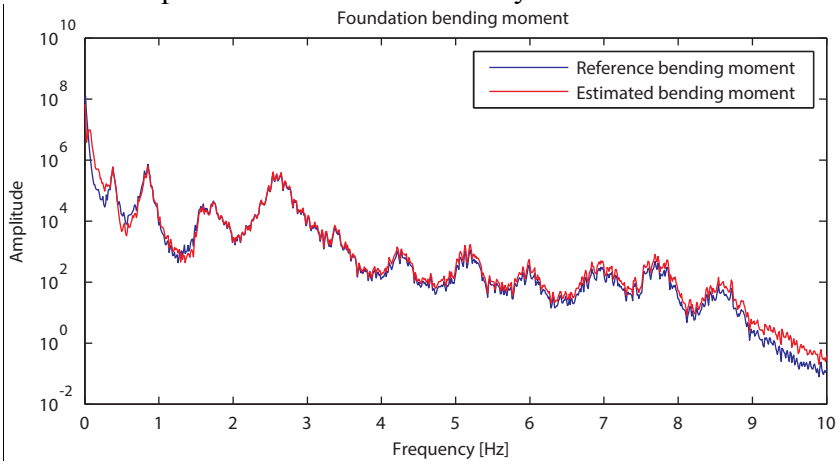


Figure 14: Comparison between the reference and estimated bending moment

In the context of the fatigue analysis, it is usual to use the Rainflow method to count the number of load cycles acting on the structure. This methodology followed in the standards despises the mean value of the stress (or bending moment) cycles for the fatigue analysis of steel towers. The comparison of the load cycles calculated using the bending moments directly obtained from the numerical analysis and the ones estimated from the simulated acceleration time series at the foundation level is presented in the histogram of the Figure 15. Once again, the histogram obtained with both signals is very similar, attesting the low influence of the simplifications adopted in the analysis.

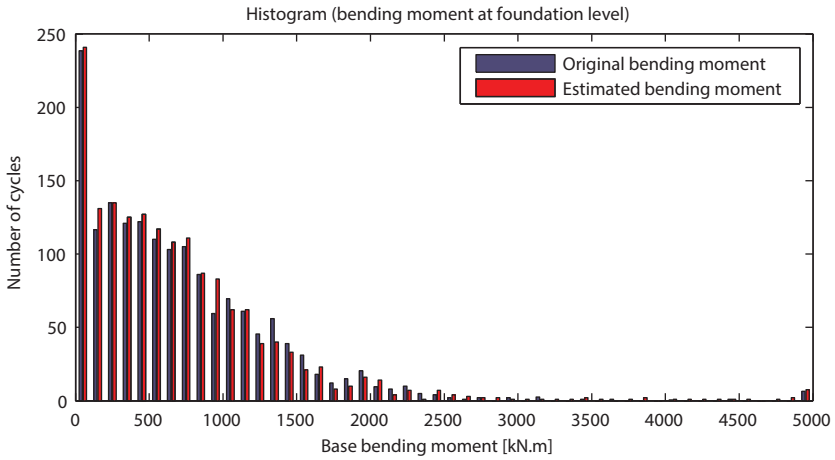


Figure 15: Histogram with the number of cycles from the original and estimated bending moment at the foundation level

5 CONCLUSIONS

The paper presents the work carried out up to the date in the development of a dynamic monitoring system for a 2.0 MW wind turbine system.

In the first part, the strategy for the automated continuous modal identification of the wind turbine is introduced and preliminary results are presented. In addition, the influence of the harmonic excitation in the vibration of the wind turbine is also illustrated.

The second part of the paper introduces a methodology to assess the fatigue stress of the wind turbine tower through the recorded acceleration data. In order to attest the suitability of the approach, a numerical analysis was used to illustrate the method. The good results achieved with the proposed methodology are a good indicator for the application of this approach in continuous processing of real acceleration time series.

REFERENCES

[1] The European Wind Energy Association (EWEA), *Wind in power – 2014 European statistics*, 2015.

[2] The European Wind Energy Association (EWEA), *The European offshore wind industry – key trends and statistics 2014*, 2015.

[3] G. Oliveira, W. Weijtjens, G. D. Sitter, F. Magalhães, Á. Cunha, E. Caetano, C. Devriendt, Dynamic Monitoring of a Wind Turbine: case studies on- and off-shore, *1st International Conference on Renewable Energies Offshore RENEW*, Lisboa, Portugal, 2014.

[4] F. Magalhães, Á. Cunha, Explaining operational modal analysis with data from an arch bridge, *Mechanical Systems and Signal Processing*, **25**, 1431-1450, 2011.

[5] C. Devriendt, F. Magalhães, W. Weijtjens, G D. Sitter, Á. Cunha, P. Guillaume, Structural health monitoring of offshore wind turbines using automated operational modal analysis, *Structural Health Monitoring*, **13(6)**, 644-659, 2014.

[6] W.-H. Hu, S. Thöns, R. G. Rohrmann, S. Said, W. Rücker, Vibration-based structural health monitoring of a wind turbine system. Part I: Ressonance phenomenon, *Engineering Structures*, in press, 2014.

[7] H. Hjelm, R. Brincker, J. Graugaard-Jensen, K. Munch, Determination of stress histories in structures by natural input modal analysis. *XXI International Modal Analysis Conference (IMAC)*, Copenhagen, Denmark, 2005.

[8] P. Fernández, M. L. Aenlle, R. Brincker, A. F. Canteli, Stress Estimation in Structures Using Operational Modal Analysis, *3rd International Modal Analysis Conference (IOMAC)*, Portonovo, Italy, 2009.

[9] T. J. Larsen, A. M. Hansen. How 2 HAWC2, the user's manual. Risø-R-1597(EN), 2007

[10] B. Peeters, G. de Roeck, Reference-based Stochastic Subspace Identification for Output-Only Modal Analysis, *Mechanical Systems and Signal Processing*, **13(6)**, 855-878, 1999.

[11] P. V. Overschee, B. D. Moor, Subspace Identification for Linear Systems. Theory-Implementation-Applications. Kluver Academic Publishers, 1996.

[12] B. Peeters, H. Van der Auweraer, Polymax: a Revolution in Operational Modal Analysis, *1st International Operational Modal Analysis Conference (IOMAC)*, Copenhagen, Denmark, 2005.

[13] F. Magalhães, Á. Cunha, E. Caetano, Online automatic identification of the modal parameters of a long span arch bridge, Mechanical Systems and Signal Processing, 23(2), 316-329, 2009.

[14] D. Tcherniak, S. Chauhan, Applicability Limits of Operational Modal Analysis to Operational Wind Turbines, XXVIII International Modal Analysis Conference (IMAC), Jacksonville, USA, 2010.

[15] J. Jonkman, S. Butterfield, W. Musial, G. Scott, Definition of a 5-MW Reference Wind Turbine for Offshore System Development, NREL/TP-500-38060 National Renewable Energy Laboratory, 2009.

[16] European Committee for Standardization (CEN), EN 1993-1-9: Design of steel structures – Fatigue, Brussels, Belgium, 2005.

[17] Germanischer Lloyd (GL), Guideline for the Certification of Wind Turbines, Hamburg, Germany, 2010.

COMPDYN 2015
5th ECCOMAS Thematic Conference on
Computational Methods in Structural Dynamics and Earthquake Engineering
M. Papadrakakis, V. Papadopoulos, V. Plevris (eds.)
Crete Island, Greece, 25–27 May 2015

A CLOSED-FORM APPROACH TO PREDICT GUST INDUCED FATIGUE DAMAGES

Frank H. Kemper[2]

[1]Institute for Steel Structures
RWTH Aachen University
52070 Aachen
e-mail: frank.kemper@rwth-live.de

Keywords: Structural Dynamics, Wind Engineering, Slender Structures, Stochastic Methods, Fatigue

Abstract. *The investigation of gust induced dynamic responses of structures is still subject of current research in wind engineering. Especially with regard to the fatigue life prognosis, different methods have been discussed in recent years - but all current design codes still have not implemented a general reliable guidance for the determination of stress-range spectra and the application of cumulative damage calculations. The present paper makes use of spectral methods for the determination of responses to stochastic loading and shows, that based on power spectral densities of the structural responses, reliable approximations of the Rainflow stress-range spectra are possible. Consequently, fatigue verifications are possible by means of closed form spectral methods. The reliability has been proven, compared to time-domain solutions. Thereby the bandwidth of the structural response does not affect the prediction quality. Due to the tight manageability of the presented formulas, the application in all cases, where gust excited structural responses may be significant, is advised. The second part of this paper additionally implements an approximative consideration of nonlinear structural behaviour in the closed form solution methodology.*

Convolving with site related wind statistics, realistic predictions of the lifetime related distribution of stress cycles are enabled. Based on the presented methodology, an extensive parameter study has been perfomed in order to discover the dependencies between structural and aerodynamic properties on the resulting stress range distributions. Finally, a simplified approach is presented, which suggests damage equivalence factors, taking into account an individual and realistic shape of the cycle count distribution.

Based on the presented approach, both exact life time predictions and simplified estimations are enabled for wind excited structures. The presented methodoly is demonastrated using the example of a wind turbine tower. For these structures the cyclic loading induced by the wind gust directly into the tower and by the rotor are decisive for the design of the steel structure.

1 Introduction

Wind affected structures generally have to withstand fluctuating load cycles. For an appraisement whether the resulting stress range spectra may lead to structural failures during the designed lifetime, standard methods are still rare because the influencing parameters are manifold. A realistic determination of structural stress range spectra provoked by the natural wind, requires profound knowledge about the statistical properties of the wind flow at the considered site, as well as about the dynamic structural behavior. Eventually, the interpretation of the resulting structural responses in terms of stress amplitudes $\Delta\sigma$ and associated frequencies of occurrence $N(\Delta\sigma)_{Life}$ over the expected lifetime are the main task to allow fatigue verifications.

2 APPROXIMATIVE CLOSED FORM SOLUTIONS

The statistical description of the wind flow succeeds in two time categories, to consider both, the short-termed flow fluctuations which may lead to resonant structural responses and the long-termed fluctuations, which mainly influence the load level at which structural vibrations occur over the expected life-time. Accordingly, the fatigue relevant loading over the lifetime can be expressed as a combination of the short-termed dynamic effects at a mean load level, which is influenced by the long-termed average flow conditions. With respect to possible resonant wind effects under extreme wind conditions, site related power spectral densities (PSD) of the wind velocity are needed.

Already 50 years ago, *Davenport* [2] laid the foundation and introduced the probabilistic theory for a usage in the field of wind engineering. Meanwhile nearly all wind codes in the world adopted procedures which are based on his early work for the rating of extreme (short-termed) gust effects. Concerning the long-termed changes of the wind velocity, the probability density function (PDF), e.g. using the two-parametric Weibull distribution, allows the determination of the wind performance under usual conditions.

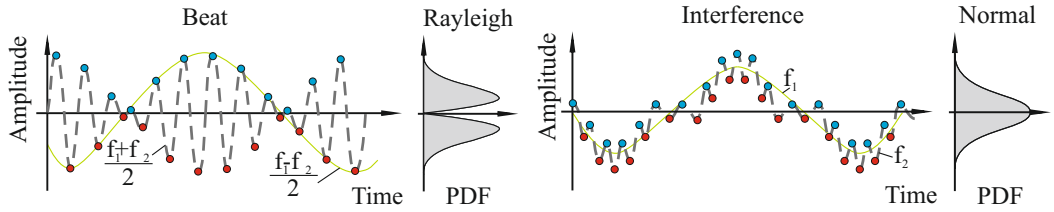
Structural system properties are generally described by the mechanical admittance function $H(i\omega)$, whereat in most cases a simplified consideration of single degree of freedom systems deems to be sufficient. Decisive for the susceptibility to wind induced resonant vibrations and the associated bandwidth of the structural response, are the natural frequency and the damping ratio of the system. Namely, with increasing structural frequency, the excited responses decrease as a consequence of the falling spectral density, furthermore the response becomes wider by reason of the quasi-static range in the structural admittance function up to the natural frequency.

For the interpretation of structural responses with respect to fatigue, the rain-flow counting method is admittedly the best instrument [17]. The procedure has been developed by *Matsuishi* and *Endo* [12] for the application with time histories of stress and can therefore not be used directly in frequency based analyzes. Hence, during the last decades a lot of research effort has been focussed on the finding of approximative solutions.

3 PSD BASED CYCLE COUNTING

Although the numerical rainflow method is an efficient, reliable and widely accepted tool for determining the amplitude distribution of stochastic responses, it requires the existence of plausible stress time series. In case of a non-linear structural behavior a fatigue life prognosis requires a considerable diversity of time series which belong to different wind speeds.

For the above reasons, it is more desirable that the determination of the rainflow classifi-



(a) Narrow-band Signal ($\gamma \approx 1$) (b) Wide-band Signal ($\gamma \approx 0$)

Figure 1: Visualization of Time Series with different Bandwidths and Effect on the Distribution of Extremes

cations of stochastic processes is enabled in the frequency domain. This task has been extensively treated in recent decades by researchers from different disciplines, especially in aviation and space technology. In the following sections different approaches are presented (which are partially described in [6]) and evaluated in the light of the particular problem of gust excited structural responses. All methods have in common that they do not consider an influence of the mean stress amplitude, which is in accordance e.g. with Eurocode 3-1-9 [4].

The initial point of most stochastic fatigue methods represents the level crossing formula from *Rice* according to Eq. (1). It describes the density of the positive crossings of a given amplitude level σ based on the standard deviation σ_σ of the process to:

$$f(\sigma) = \frac{\sigma}{\sigma_\sigma^2} \cdot \exp\left(-\frac{\sigma^2}{2\sigma_\sigma^2}\right) \tag{1}$$

For the determination of stress range collectives, an extension has been proposed by *Bendat*. Using the spectral moments of a response power spectral density $S_{aa}(f)$:

$$m_i = \int_0^\infty f_i \cdot S_{aa}(f)\, df \tag{2}$$

The cycle rate E_P and the rate of the positive level crossings E_0 (as expected value of the frequency ν) is calculated as:

$$E_0 = \nu = \sqrt{\frac{m_2}{m_0}} \qquad\qquad E_P = \sqrt{\frac{m_4}{m_2}} \tag{3}$$

Finally an approach for estimating the probability density of the collective stress can be derived [1]. The *Bendat* solution takes into account the rate of the positive extremes associated with the distribution of these extreme values. It is assumed, that the distribution of the extreme values of a narrowband process can be described by a Rayleigh distribution. Since the number of closed stress cycles are relevant for the fatigue design, the double stress amplitude $\Delta\sigma$ is used for the calculation. Consequently, the estimate of the stress range cycles of a narrow-band process is given by:

$$N(\Delta\sigma) = \nu \cdot T \cdot f_r(\Delta\sigma, \sigma_{\Delta\sigma}) = \nu \cdot T \cdot \frac{\Delta\sigma}{\sigma_{\Delta\sigma}^2} \cdot \exp\left(\frac{-\Delta\sigma^2}{2 \cdot \sigma_{\Delta\sigma}^2}\right) \tag{4}$$

Under gusty wind load narrow-band responses can be expected for low frequent structures and weakly damped systems. A distinction between narrow-band and wide-band signals is shown in Fig. 1(a) and Fig. 1(b). With increasing bandwidth of the signal, the presented methodology fails to calculate appropriate level crossings. With respect to structural responses

of different dynamic systems, alternative methods are needed in order to describe the frequency distribution of the extreme values. The Rice formula overestimates in these cases the actual stress range distributions significantly.

Especially in the field of mechanical engineering an empirical approach for estimating the Rainflow distribution based on the power spectral density is meanwhile well established. *Dirlik* derived this method based on continuous random processes and subsequent numerical Rainflow counting [3]. He discovered an empirical relationship between the frequency range description of the signal and the Rainflow distribution.

His studies were directed to stationary, ergodic random processes with arbitrary bandwidth. Consistently, the *Dirlik* probability density function of peak values of a process with any bandwidth is a weighted sum of a normal distribution and a Rayleigh distribution. In previous studies of *Wirsching* and Shehata [18], a similar approach was chosen, but there an attempt was made to describe the Rainflow distributions by Weibull functions. The simulations of Dirlik, as well as own simulations showed, that the Rainflow distributions of peaks often differs significantly from a Weibull distribution. For this reason, the *Wirsching*-Factor, which has been used for instance from *Holmes* [7], is not realistic in case of higher response bandwidth [9].

With Dirlik's formula, the density of the number of cycle counts N' of a given stress level $\Delta\sigma$ can be computed to:

$$N'(\Delta\sigma) = E_P \cdot T \cdot f_D(\Delta\sigma) \tag{5}$$

$$f_D(\Delta\sigma) = \frac{\frac{D_1}{Q} \cdot e^{\frac{-Z(\Delta\sigma)}{Q}} + \frac{D_2 \cdot Z(\Delta\sigma)}{R^2} \cdot e^{\frac{-Z(\Delta\sigma)^2}{2 \cdot R^2}} + D_3 \cdot Z(\Delta\sigma) \cdot e^{\frac{-Z(\Delta\sigma)^2}{2}}}{2 \cdot \sqrt{m_0}} \tag{6}$$

where:

$$x_m = \frac{m_1}{m_0} \cdot \sqrt{\frac{m_2}{m_4}} \qquad R = \frac{\gamma - x_m - D_1^2}{1 - \gamma - D_1 + D_1^2}$$

$$D_1 = \frac{2 \cdot (x_m - \gamma^2)}{1 + \gamma^2} \qquad D_2 = \frac{1 - \gamma - D_1 + D_1^2}{1 - R}$$

$$D_3 = 1 - D_1 - D_2 \qquad Z(\Delta\sigma) = \frac{\Delta\sigma}{2 \cdot \sqrt{m_0}}$$

$$Q = \frac{1.25 \cdot (\gamma - D_3 - D_2 \cdot R)}{D_1}$$

are auxillary values.

The accuracy of the method has been verified with respect to gust excited structures by comparing the results to corresponding transient simulations. In all cases, the discrepancies between transient Rainflow count and *Dirlik* formula where negligible [10]. Even geometrical nonlinear structures can be analyzed based on the presented spectral approach. The necessary stochastic description of the mechanical system has been presented in [11].

4 FATIGUE BEHAVIOUR AND STRUCTURAL INFLUENCE ON THE LIFETIME

4.1 Assessment of Gust Repsonse with the N_{Life}-Formula

Making use of the presented PSD based cycle count algorithm, the assessment of stress cycles is enabled. But so far, only the impact of a short-termed extreme wind on the stress

range distribution has been considered. For the computation of the expected cycles during the designated life-time with respect to fatigue phenomena, the prevalent wind events during this time period have to be taken into account as well.

Hence, the resulting cycle count spectrum during the foreseen lifetime originates from a convolution of short termed stress range spectra and a long-termed wind statistics. It can be computed by the following expression:

$$N'_{Life}(\Delta\sigma) = \int_0^{\overline{u}} \frac{T_{Life}}{T_{ref}} \cdot f(u) \cdot N'(\Delta\sigma, u) du \tag{7}$$

where: T_{Life} is the designed Lifetime, T_{ref} is the average time of the mean wind speed, $f(u)$ is the probability density function of the wind velocity and $N(\Delta\sigma, u)$ is the stress range spectra for a given mean wind speed within the average time period. The latter expression is computed based on the *Dirlik* formula.

The probability density function for the frequency of occurrence of mean wind speeds can be derived based on the *Weibull*-Distribution:

$$f(\overline{u}) = \frac{k}{A}\left(\frac{\overline{u}}{A}\right)^{k-1} exp\left[-\left(\frac{\overline{u}}{A}\right)^{k}\right] \tag{8}$$

where: A is the scale and k is the form parameter of the distribution. Site dependent values for these parameters can be taken from the European Wind Atlas [16].
Based on appropriate assumptions for the site dependent extreme wind impact and the probability of exceedance of the prevalent wind speeds, a realistic consideration of fatigue impact is possible. Using the direction related Weibull Parameter, even a directional design is possible. Finally, the fatigue verification succeeds based on an appropriate damage accumulation approach in conjunction with a suitable s-N-Curve. For example, using a elementary *Miner*-Rule:

$$D = \int_{\Delta\sigma} \frac{N'_{Life}(\Delta\sigma)}{N_c \cdot \left(\frac{\Delta\sigma_c}{\Delta\sigma}\right)^m} \, d\Delta\sigma \tag{9}$$

It is important to consider, that the cycle count density $N'_{Life}(\Delta\sigma)$ has to be integrated over the range of possible stress amplitudes in order to evaluate the cumulative number of cycles and hence, the total damage.

4.2 Shape of Cycle Count Distribution and influencing Parameters

Due to the analytical formulation of Eq. (7), parametric studies of the relation between structural and aerodynamic characteristics on the resulting cycle count distribution can be studied comparatively easy. The described procedure is significantly faster than time-domain methods, which require wind field generations and transient dynamic analyzes. Nevertheless, in case of linear structural systems, the computation succeeds without limitations.

In order to allow a general usage of the cycle count distribution, a normalization of the curve is necessary. It is postulated, that the maximum stress amplitude $\Delta\sigma_{max}$ occurs exactly once in the designated lifetime. This demand requires the consideration of the cumulative function N_{Life}, as only in this notation a frequency of occurence of $N = 1$ can be found. The cumulative

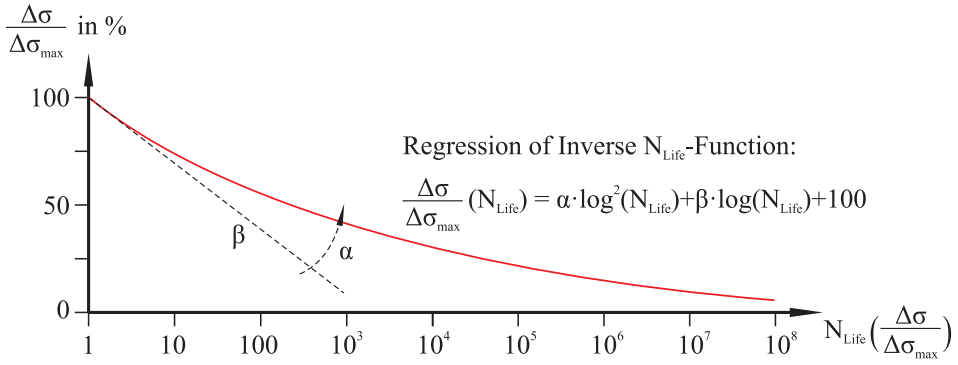


Figure 2: Regression of the Cycle Count Distribution

function is defined as:

$$N_{Life}(s) = \int_0^s N'_{Life}(t)\, dt \tag{10}$$

As a result, the N_{Life}-Function allows a quantifiable description of the influences on the damage life. The individual cumulative stress cycle count distributions can now be normalized by the maximum amplitude $\Delta\sigma_{max}$ at $N = 1$ and finally be fitted by a logarithmic polynomial 2^{nd} order:

$$\frac{\Delta\sigma}{\Delta\sigma_{max}}(N_{Life}) = \alpha \cdot log^2 N_{Life} + \beta \cdot log\ N_{Life} + 100 \tag{11}$$

where the normalized stress $\Delta\sigma/\Delta\sigma_{max}$ is given in percent. A general distinction has to be made concerning parameters, which affect the amplitude (scaling) of the cycle count distribution and those which affect the distribution (shape). Concerning the first, the normalization of stress amplitude to its maximum separates scaling from shape. Concerning the second, the variation in shape is expressed in the polynomial coefficients α and β.

4.2.1 Location

The of the Weibull parameters A and k on the fatigue loading of structures was desribed by *Höffer* and *Görnandt* [15]. Assuming a quasi-static structural behavior, they showed how different Weibull distributions of wind speeds at German sites affect the cumulative number of cycles. They discovered that this influence is significant and a that a simplified, unique assumption for the shape of cumulative cycle counts like in Eurocode 1 is not realistic.

Stochastic calculations have been performed in order to identify the influence of different aerodynamic related parameters on the shape of the cycle count distribution. For these investigations, a designated lifetime of $T_{Life} = 50$ a has been assumed. As structural system a single degree of freedom oscillator with a natural frequency of $f = 1.0$ Hz and a logarithmic damping decrement of $\delta = 0.01$ has been chosen. The cycle count density $N'(\Delta\sigma, u)$ has been determined based on the *Dirlik formula* according to Eq. (6) at a given level of mean wind speed u and for a reference period of $T_{ref} = 3600$ s.

Different aerodynamic values have been modified in order to evaluate the influence on the fatigue life. It has been discovered, that the basic wind speed on site u_b, the turbulence intensity I_u, the integral length scale L_{ux} and the quasi-static force coefficient affect mainly the scaling

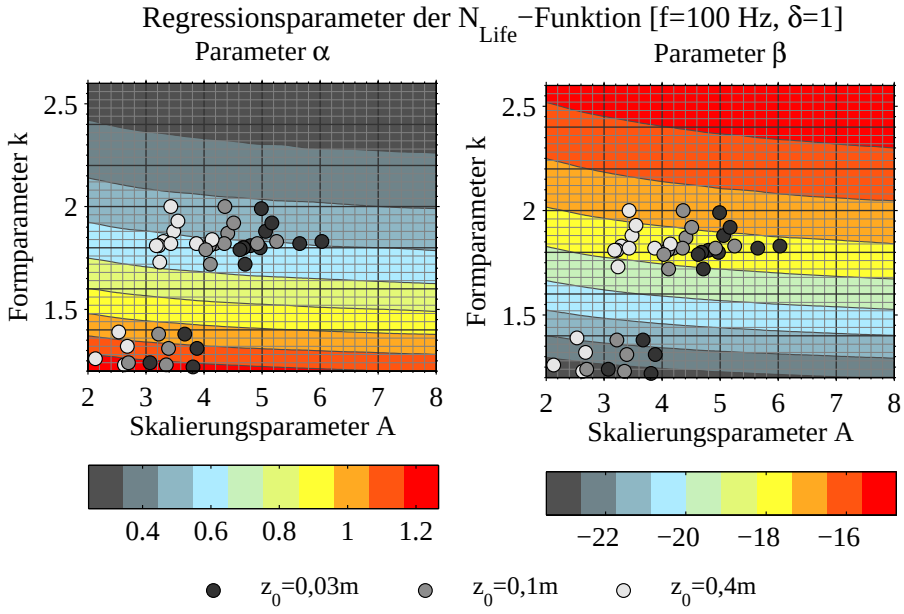


Figure 3: Regression of the N_{Life}-Curve dependent on the Shape and Scaling Parameters of the Weibull Distribution and Visualization of 15 different Locations in Germany with varying Roughness Length z_0

of the cycle count distribution [8]. Hence, all mentioned parameters primarily affect the maximum stress amplitude $\Delta\sigma_{max}$. Therefore, their influence is already covered by a standard gust response factor approach [13], [14].

Nevertheless, also aerodynamic influences on the shape of the cycle count distribution have been observed. Mainly the shape coefficient k of the long-termed wind statistic is to mention in this regard. In the investigations, both parameters of the Weibull modell for the long-termed wind statistic A and k have been modified. In Fig. 3 the regression parameter α and β are plotted for a wide range range of A-k-pairs. Additionally, 18 pairs of Weibull distributions, representing existing German locations and assuming different roughness lengths z_0 have been marked in this plot.

It becomes clear that the parameter of the Weibull distribution have a significant influence on the regression function of the N_{Life} histograms. In order to evaluate the influence on the actual fatigue damage, the obtained cycle count distribution have been used with a linear damage accumulation strategy (modified *Miner* Rule) and based on following assumptions:

- As a quasi-static maximum stress $\Delta\sigma_{max} = 300\ \mathrm{N/mm^2}$ is assumed
- The slopes for the S-N-curve are assumed with $m_1 = 3$ und $m_2 = 5$
- A cut-off level of dynamic stress of $\Delta\sigma_L = 25{,}5\ \mathrm{N/mm^2}$ is considered, below this level no damage growth is considered

In Fig. 4, the effect of different locational wind statistics on the actual fatigue damage is plotted for two different structural notch cases $\Delta\sigma_C$.

4.2.2 Dynamic Properties of the considered Structure

It is well known, that the dynamic structural properties affect the maximum response stress $\Delta\sigma_{max}$ of a structure considering the gust response behavior. Using the presented stochastic approach, it is furthermore of interest, to which extent these properties do effect the shape of the long-termed cycle count distribution as well. For this aim, a parameter study has been

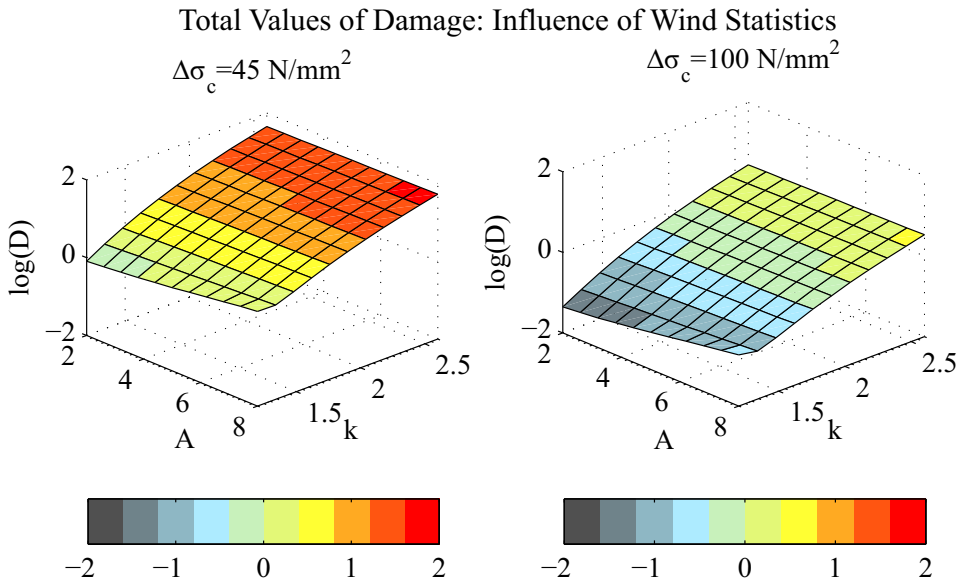


Figure 4: Influence of Long-Term Distribution of Wind Speeds on the Fatigue Damage

performed, in which both parameters eigenfrequency and damping ratio have been changed within structurally relevant limits. The influence on the regression parameter α and β of the N_{Life} function has been plotted in Fig. 5 for a specific pair of Weibull parameters. It becomes apparent that both dynamic properties are of significant importance considering the distribution of cycles.

Again, the influence on the actual fatigue damage has been considered under the same assumptions than in section 4.2.1. In Fig. 6, the associated absolute values of damage are plotted.

4.3 Bilinear Regression of Cycle Count Distributions for various Systems

In the preceding section mainly four parameters have been identified, which affect the shape of the cycle count distribution. These parameters are:

- Eigenfrequency f
- Logarithmic Damping δ
- Scale Parameter A of the Weibull distribution of wind speeds
- Shape Parameter k of the Weibull distribution of wind speeds

In order to enable a combined consideration of all these parameters, besides exemplary calculations (like those presented in Fig. 5), a wide matrix of Weibull pairs A-k has been investigated in order to achieve a broader database concerning the influences on the cycle count distributions. All in all, over 14.000 dynamic calculations have been performed. For a tight provision of these results, in the following a reduction of the 4-dimensional problem is described. The two-dimensional result surfaces for α and β (in the f-δ-plane) of each Weibull-pair can be fitted by an appropriate shape function with a least-squares method (s. Fig. 2). Subsequently, the parameters of the chosen shape function can be plotted dependent on A and k. Hence, the 4-dimensional problem has been broken down into two 2-dimensional problems, which can be easily plotted in surface diagrams.

The mathematical separation of the 4-dimensional result matrices for α and β succeeds with introduction of the auxillary matrices κ and λ and the shape function Ω:

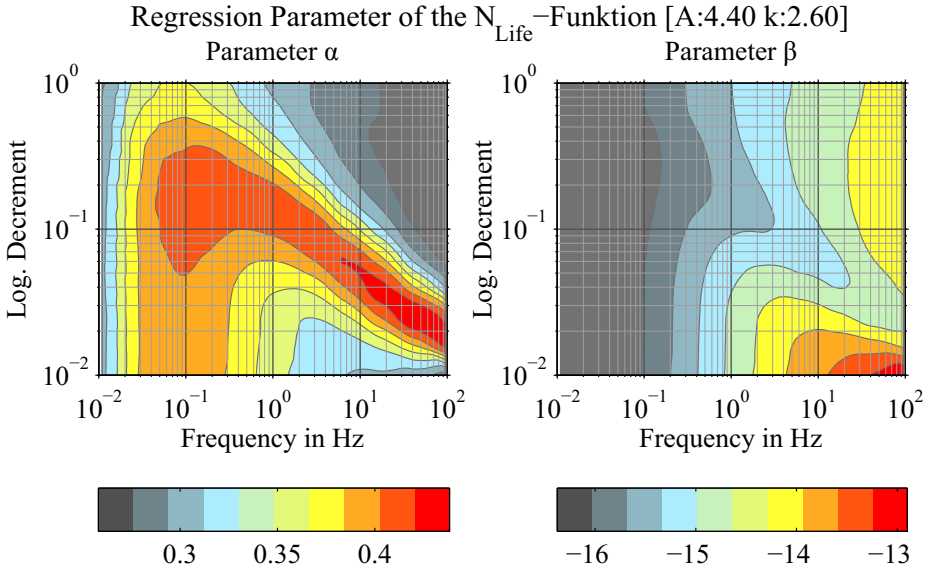


Figure 5: Influence of structural dynamic properties on the cumulative cycle count distribution N_{Life} within 50 years

$$\alpha(f, \delta, A, k) = \kappa(A, k) \cdot \Omega(f, \delta) \tag{12}$$
$$\beta(f, \delta, A, k) = \lambda(A, k) \cdot \Omega(f, \delta) \tag{13}$$

Different shape functions have been investigated. As a most detailed approach, a biquadratic polynominal with 6 parameters has been used. Further simplifications showed, that the number of necessary parameters could be reduced to 3, representing a simplified bilinear approach:

$$\Omega(\delta, f) = c_1 \cdot \log \delta + c_2 \cdot \log f + c_3 \tag{14}$$

Using a two-dimensional optimization according to the least-squares method allowed the description of the surface with the mentioned parameters:

$$\sum_i \sum_j [\Omega(\delta, f) - \Psi(f, \delta, A, k)]^2 \rightarrow \min \tag{15}$$

Where Ψ represents the result matrices for α and β. Accordingly, the conditional equations are given by:

$$\alpha = \kappa_1(A, k) \cdot \log \delta + \kappa_2(A, k) \cdot \log f + \kappa_3(A, k) \tag{16}$$
$$\beta = \lambda_1(A, k) \cdot \log \delta + \lambda_2(A, k) \cdot \log f + \lambda_3(A, k) \tag{17}$$

The planar representation of the regression results of the N_{Life}-distribution showed partially appreciable deviations between the exact calculation and the approximation to the bilinear shape functions, see Fig. **??**. This was mainly caused by the fact that there is a dependency between the variables α and β, so the choice of a slightly larger α-value leads to a slightly smaller β value and vice versa. With regard to the optimization strategy, this means that there may be no clear optima, and the local minimum of Eq. (15) lies in a shallow valley and thus the optimization found is not particularly stable. Therefore, a second constrained optimization step has been

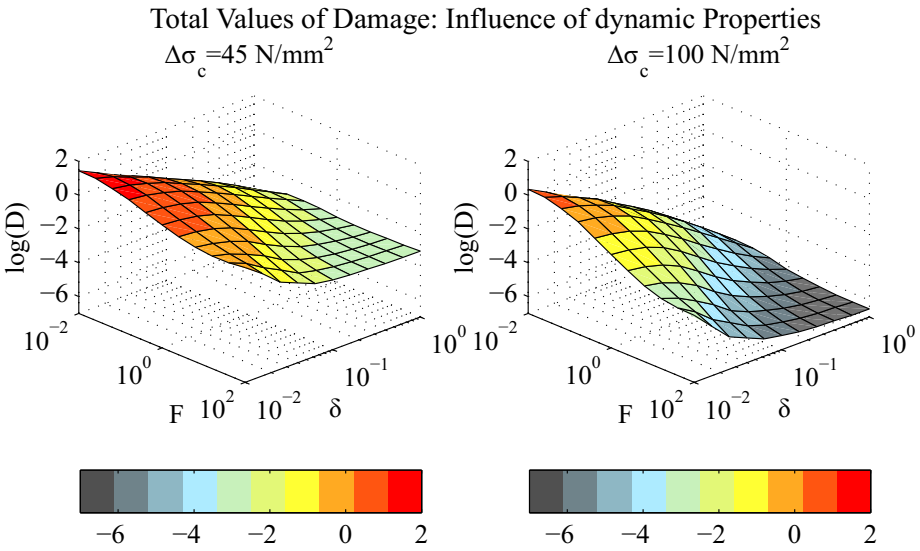


Figure 6: Damage values $log(D)$ for an exemplary structure dependent on dynamic properties and considered notch case $\Delta\sigma_C$

made. In this step, the former linearized results for α have been kept and the corresponding, optimum values for β have been determined.

The final results of the bi-linear optimization of all considered dynamic calculations are plotted in Fig. 8. In combination with Eq. (16) and (17) the values κ_i and λ_i can be used directly to determine a site and structure related cycle count distribution.

5 DAMAGE EQUIVALENCE FACTOR CONCEPT

In the preceding sections the main computation strategy and a simplified possibility for the determination of realistic cycle count distributions is presented. The latter allows a detailed verification of the actual fatigue life considering appropriate S-N curves and damage accumulation strategies. However, at least for a pre-design stage, the damage assessment might be still too extensive, as the damage integral has still to be solved. For this reason some additional considerations have been made, allowing to reduce the fatigue assessment to a really simple check of the fatigue endurance. The following items are addressed in order to allow a further simplification:

- Consideration of a realistic shape of the N_{Life}-curve based on $\alpha(f, \delta, A, k)$ and $\beta(f, \delta, A, k)$
- Assumption of a certain shape of the structural S-N curve (trilinear or single slope)
- Linear damage hypothesis (elementary or modified Miner rule)

Based on these preconditions, an equivalent stress amplitude $\Delta\sigma_E$ at a given number of cycles can be computed which leads to an identical damage than the original collective. The ratio between the maximum stress amplitude $\Delta\sigma_{max}$ and $\Delta\sigma_E$, is therefore denoted as a damage equivalence factor.

In order to calculate the damage due to the N_{Life} cycle count distribution in a general form, the density of cycle numbers $N'_{Life}(s)$ in accordance to Eq. (7) is needed. The deviation of the cumulative cycle count function is given by:

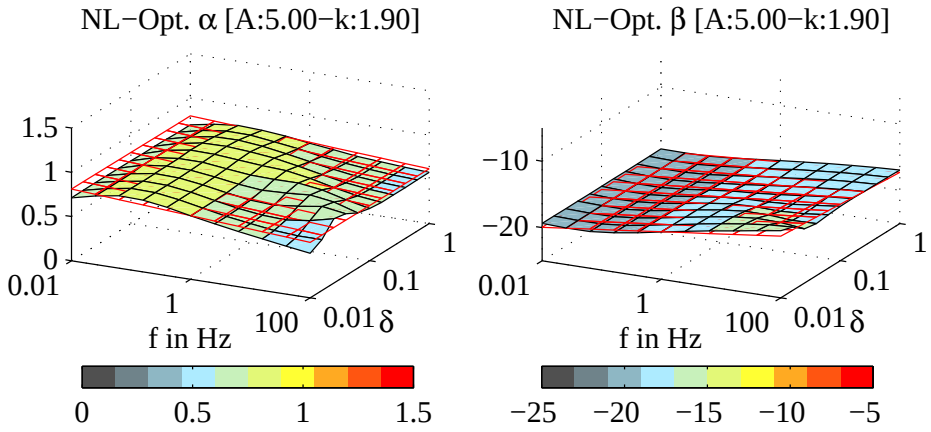


Figure 7: Exemplary fitting of the computation results with a bilinear shape function (Weibull parameter: A=5,0 m/s and k=1,9) after first optimization step

$$N'_{Life}(s) = \frac{dN_{Life}(s)}{ds} = -\frac{\ln(10)}{\gamma(s)} \cdot \exp\left[-\frac{\beta+\gamma(s)}{2\alpha} \cdot \ln(10)\right] \tag{18}$$

where:

$$\gamma(s) = \sqrt{\beta^2 - 400 \cdot \alpha + 4 \cdot s \cdot \alpha}$$
$$s = \Delta\sigma / \Delta\sigma_{max}$$

The general formulation of the structural damage under consideration of the elementary Miner rule leads to:

$$D = \int_{\Delta\sigma} \frac{N'_{Life}(\Delta\sigma)}{N_c \cdot \left(\frac{\Delta\sigma_c}{\Delta\sigma}\right)^m} \, d\Delta\sigma \tag{19}$$

where $\Delta\sigma_c$ is the notch case of the structural detail and m ist the slope of the S-N curve. As the N_{Life} curve represends the cumulative cycle counts within 50 years, Eq. (19) yields to the associated damage within this period.

5.1 Elementary Miner-Rule (acc. to Palmgren)

In this section the steps are described, which allow the development of damage equivalence factors using the elementary Miner rule. The equivalent stress range $\Delta\sigma_E$ can be calculated implicitly by the definition of the number equivalent of cycles $n_E = N_D = 5 \cdot 10^6$ and by the demand of an identity of damages:

$$\frac{n_E}{N_E} = \frac{N_D}{N_E} \stackrel{!}{=} D_{Miner,elementary} \tag{20}$$

The associated stress range amplitude $\Delta\sigma_E$ is defined based on the structural S-N curve:

$$\Delta\sigma_E = \left(\Delta\sigma_D^m \cdot \frac{N_D}{N_E}\right)^{\frac{1}{m}} \tag{21}$$

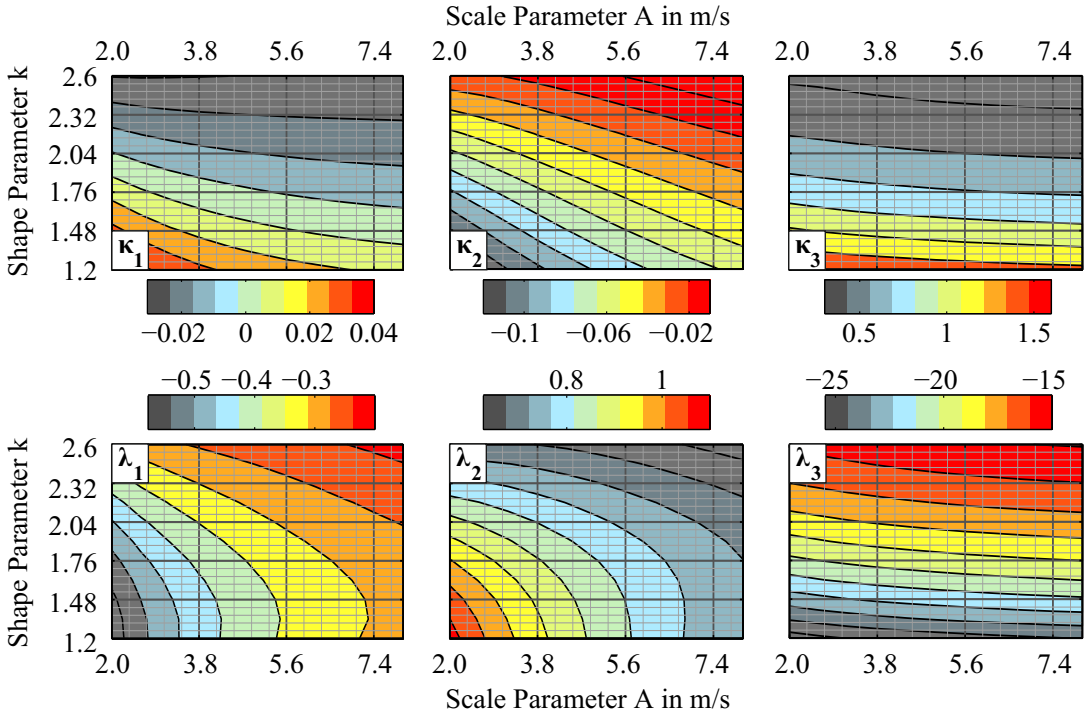


Figure 8: Parameter κ and λ for the simplified determination of realistic cycle count Spectra considering dynamic structural properties and the wind statistic on site

and hence, if the damage D is known:

$$\Delta\sigma_E = (\Delta\sigma_D^m \cdot D)^{\frac{1}{m}} \tag{22}$$

Under consideration of Eq. (19), the equivalent stress amplitude can finally be derived to:

$$\Delta\sigma_E = \left[\frac{1}{N_D} \cdot \int_0^\infty N'_{Life}\left(100 \cdot \frac{s}{\Delta\sigma_{max}}\right) \cdot s^m \, ds\right]^{\frac{1}{m}} \tag{23}$$

The damage equivalence factor K_F for the consideration of the shape of the stress range collective is given by:

$$K_F = \Delta\sigma_{max}/\Delta\sigma_E \tag{24}$$

The fatigue endurance verification can be performed considering characteristic values as follows:

$$\Delta\sigma_{max}/K_F \overset{!}{\leq} \Delta\sigma_D \tag{25}$$

A realistic damage assessment is enabled using the bearable cycle counts N_E, which are associated with the stress amplitude $\Delta\sigma_E$:

$$N_E = \left(\frac{\Delta\sigma_D}{\Delta\sigma_E}\right)^m \cdot N_D \tag{26}$$

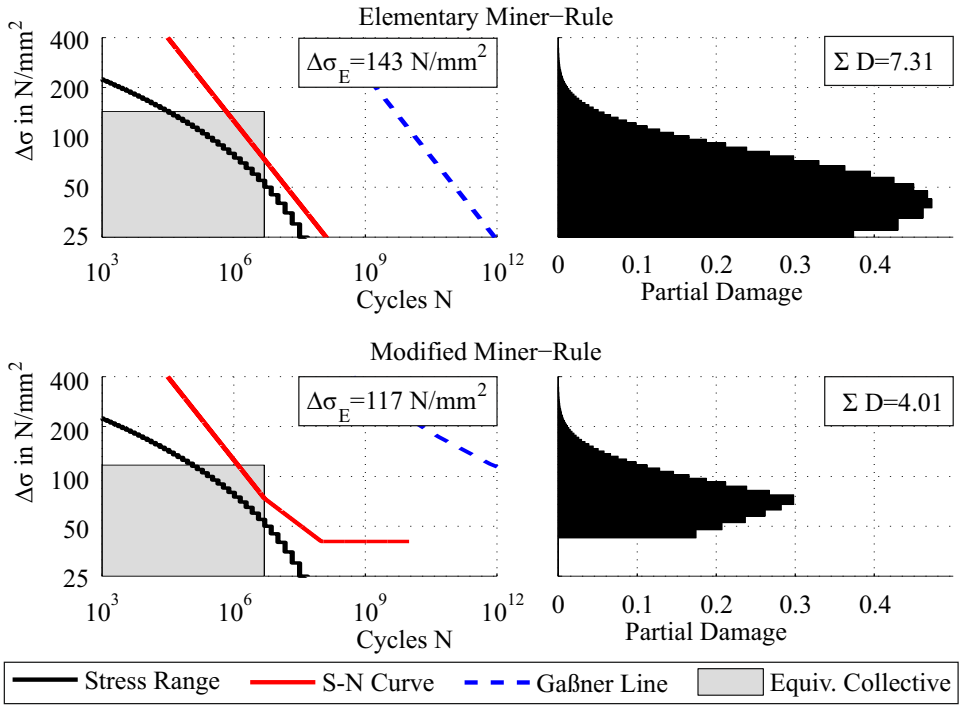


Figure 9: Computation of partial and cumulative Damage for a N_{Life}-function with α=0.7 and β=-17.4 and $\Delta\sigma_{max} = 500\ \mathrm{N/mm^2}$ considering a notch case $\Delta\sigma_C = 100\ \mathrm{N/mm^2}$ according to elementary and modified Miner rule

Finally, the corresponding damage value is defined as:

$$D = \frac{n_E}{N_E} = \frac{N_D}{N_E} \tag{27}$$

The verification now includes implicitly the individual shape of the stress and leads to the same collective damage value as the integral of the actual collective consideration based on Eq. (19).

5.2 Modified Miner-Rule (acc. to Haibach)

The derivation of the damage equivalence factor K_F is slightly more complex, when a S-N curve $\Delta\sigma_W\,(N)$ with different slopes is considered. Depending on the particular slope, the equivalent stress amplitude $\Delta\sigma_E$ can be determined by a distinction of cases to:

$$\Delta\sigma_E = (\Delta\sigma_D^{m_1} \cdot D)^{\frac{1}{m_1}} \qquad \text{for } N_E < N_D \tag{28}$$

$$\Delta\sigma_E = (\Delta\sigma_D^{m_2} \cdot D)^{\frac{1}{m_2}} \qquad \text{for } N_D \leq N_E \tag{29}$$

Using the modified Miner rule in the damage calculation, the value of D is is generally lower, but for most materials more realistic than according to Eq. (27). For the further computation, Eq. (24) till Eq. (27) remain valid.

5.3 Damage Equivalence Factors for Application

For an enabling of a preferably simple and general fatigue assessment concept, it was essential to avoid dependencies of the damage equivalence factor K_F to other parameters than the shape of the cycle count distribution. Especially an influence of the maximum stress amplitude

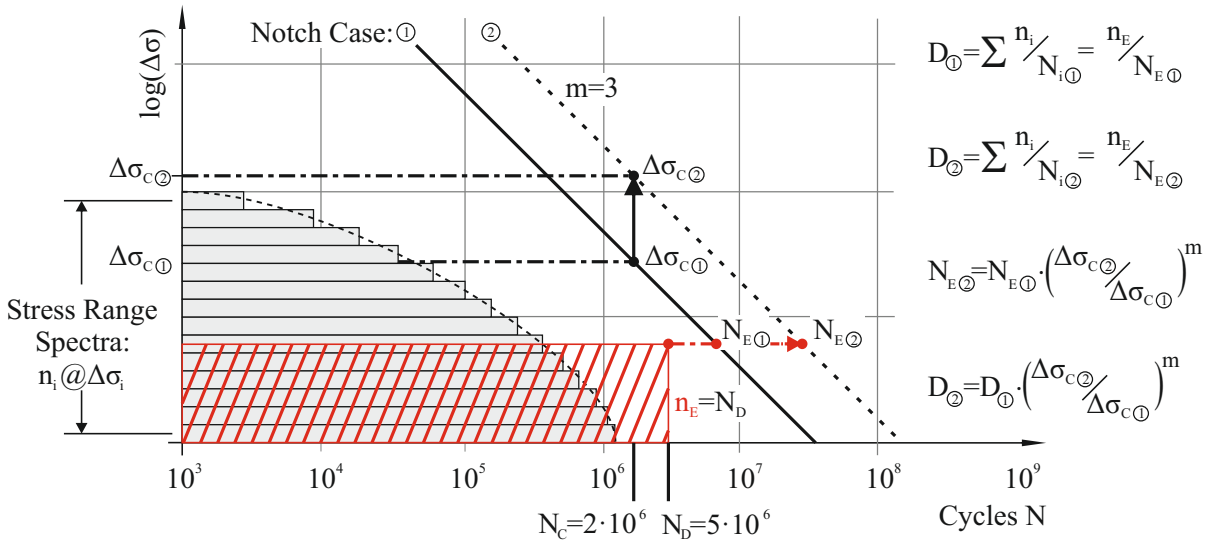


Figure 10: Reduction of a stress range histogram to a damage equivalent block histogram and independence of $\Delta\sigma_E$ on the notch case $\Delta\sigma_C$ under consideration of the elementary Miner rule

$\Delta\sigma_{max}$ and the notch case $\Delta\sigma_C$ would complicate the concept. Considering Eq. (22), it becomes apparent that the equivalent stress range depends on the fatigue endurance limit $\Delta\sigma_D$ in a direct way and indirectly by the damage D. Therefore, the equivalent stress range $\Delta\sigma_E$, and thus the damage equivalence factor K_F, are not dependent on the notch case $\Delta\sigma_C$. However, as soon as a S-N curve with different inclinations is used, this independency is lost, due to the necessary case distinction according to Eq. (28) and (29).

Generally, the maximum value of the stress collective $\Delta\sigma_{max}$ affects the computed structural damage. In case of a simple linear S-N curve (elementary Miner rule) it follows for different collective maximums $\Delta\sigma_{max,1}$ and $\Delta\sigma_{max,2}$:

$$D_2 = D_1 \cdot \left(\frac{\Delta\sigma_{max,2}}{\Delta\sigma_{max,1}} \right)^m \tag{30}$$

Consequently, in conjunction with equation (22) it follows, that the equivalent stress range $\Delta\sigma_E$ acts linear to the maximum stress amplitude $\Delta\sigma_{max}$ of the collective. Thus, the damage equivalence factor K_F is also independent of the collective maximum amplitude $\Delta\sigma_{max}$.

When the modified Miner's rule is used, the damage equivalence factor K_F depends on both the collective maximum and the notch case of the S-N curve. For the establishment of an easy concept it is therefore advantageous to use the conservative elementary Miner rule with a unique slope of $m_1 = 3$.

In Fig. 11, the damage equivalence factors are plotted for arbitrary combinations of the regression parameter α and β of the cycle count distribution N_{Life}. Considering the influence of wind characteristic and structural dynamic properties, the equivalent stress factors can be read directly from the chart. Therefore, the bi-linear regression model from Section 4.3 has been used. As the plot is restricted to three different values for the shape parameter k of the Weibull distribution, the usage is limited to rather approximative calculations, for example as a part of a pre-dimensioning. For the accurate determination of the damage equivalent factors it is recommended to determine the parameter α and β in advance using the equations described in section 4.3.

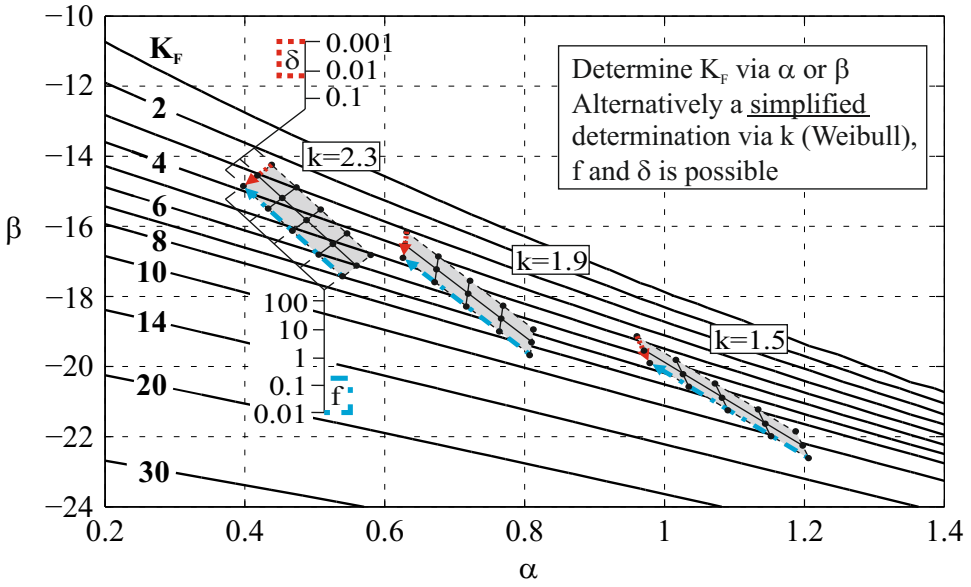


Figure 11: Damage Equivalence Factors K_F dependent on the regression parameter of the N_{Life}-function and assuming the elementary Miner rule

For the fatigue assessment finally Eq. (25) can be simplified to:

$$\gamma_{Ff} \cdot \frac{\Delta\sigma_{max}}{K_F} \overset{!}{\leq} \frac{\Delta\sigma_D}{\gamma_{Mf}} \tag{31}$$

Due to the implicit form of the elementary Miner rule this proof is generally on the safe side. The corresponding damage value can be calculated as follows:

$$D = \left(\frac{\Delta\sigma_D}{\Delta\sigma_{max}} \cdot K_F \right)^{-m} \tag{32}$$

6 EXAMPLE

In this section the presented methods are demonstrated briefly using the example of a steel chimney, which is located at the Institute for Steel Structures, see Fig. 12. Several years ago, *Gahlemann* conducted measurements on-site and he calculated a fatigue Damage, which is associated with measured the gust response behavior of the structure [5]. In his investigations he computed a maximum dynamic stress amplitude of $\Delta\sigma_{max} = 142.9\ \mathrm{N/mm^2}$ and a damage value of $D_{Gust} = 0.21$ within a period of 50 years using the modified Miner rule.

Considering the structural and site dependent aerodynamic parameter, given in Fig. 12, a damage equivalence factor of approximately $K_F = 6$ can be extracted from Fig. 11. For the notch case of $\Delta\sigma_C = 36\ \mathrm{N/mm^2}$, the fatigue endurance limit derives to $\Delta\sigma_D = 26.5\ \mathrm{N/mm^2}$. Based on these values a damage of:

$$D = \left(\frac{26.5}{142.9} \cdot 6.0 \right)^{-3} = 0.72$$

is estimated. Taking into account, that the simplified approach is based on the elementary Miner concept, the correlation of the damage values is quite impressive.

7 CONCLUSIONS

It has been shown, that reliable fatigue verifications based on cumulative damage predictions are possible by means of closed form spectral methods. Due to the tight manageability of the presented formulas, the procedure is advisable for the fatigue verification of arbitrary structures under gusty wind loads.

As main influencing parameters of the stress cycle count distribution, mainly the structural frequency, the damping behavior and the wind statistic on site has been identified. Under consideration of appropriate shape function, the four independent parameters have been brought together in order to enable a simplified, graphical description.

Finally, the damage equivalence factor concepts has been introduced on the base of the regression parameters which describe the actual shape of the cycle count distribution. In combination with the elementary Miner rule it was possible to calculated divisors, which allow a reduction of the maximum stress level in order to consider the distribution of cycle counts. The methodology is very simple in use and it is demonstrated for an exemplary structure.

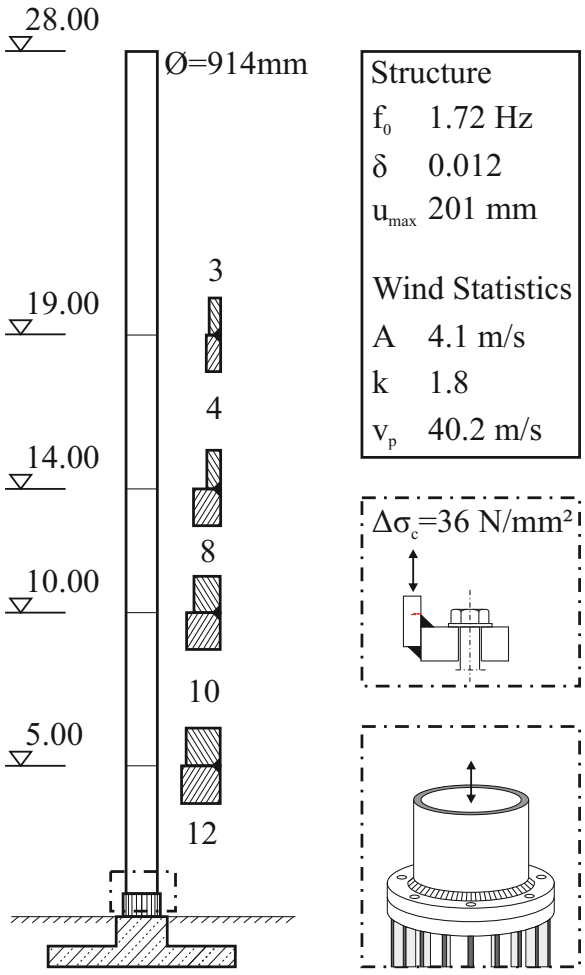


Figure 12: Drawing of the Steel-Chimney and considered Notch case

REFERENCES

[1] J. S. Bendat. Probability functions for random responses: Prediction of peaks, fatigue damage and catastrophic failures. *NASA Technical Report*, (CR-33), 1964.

[2] Alan G. Davenport. The buffeting of structures by gusts. In Teddington Middlesex National Physical Laboratory, editor, *Wind effects on Buildings and Structures*, volume 1, pages 357–391. Her Majesty's stationery office, 1965.

[3] T. Dirlik. *Application of computers to fatigue analysis*. PhD thesis, Warwick University, Warwick, 1985.

[4] Europäisches Komitee für Normung. Eurocode 3: Bemessung und konstruktion von stahlbauten - teil 1-9: Ermüdung, 05.2005.

[5] Thomas Gahlemann. *Messungen der dynamischen Windeinwirkungen auf einen 28m hohen Stahlkamin und Vergleich mit vorliegenden Berechnungsverfahren*. PhD thesis, RWTH Aachen, Aachen, 1994.

[6] Andrew Halfpenny. Rainflow cycle counting and acoustic fatigue analysis techniques for random loading. In *RASD2010*. 2010.

[7] J. D. Holmes. *Wind loading of structures*. Spon Press, London and New York, 2001.

[8] F. H. Kemper. *Böeninduzierte Schwingungsanfälligkeit von durchlässigen Fassadenelementen unter Berücksichtigung nichtlinearer Struktureigenschaften im Grenzzustand der Ermüdung*. PhD thesis, Schriftenreihe des Instituts für Stahlbau, Heft 76, Shaker-Verlag, Aachen, 2013.

[9] F. H. Kemper and M. Feldmann. Appraisement of fatigue phenomena due to gust induced vibrations based on closed-form approaches. In *ICWE 13*. AMSTERDAM, 2011.

[10] F. H. Kemper and M. Feldmann. Fatigue life prognosis for structural elements under stochastic wind loading based on spectral methods: Part 1: Linear structures. In G. de Roeck, editor, *Proceedings of the 8th International Conference on Structural Dynamics, EURODYN 2011*, pages 1629–1635. Leuven, 2011.

[11] F. H. Kemper and M. Feldmann. Fatigue life prognosis for structural elements under stochastic wind loading based on spectral methods: Part 2: Nonlinear structures. In G. de Roeck, editor, *Proceedings of the 8th International Conference on Structural Dynamics, EURODYN 2011*, pages 1636–1643. Leuven, 2011.

[12] M. Matsuishi and T. Endo. Fatigue of metals subjected to varying stress. *Japan Society of Mechanical Engineers*, 1968.

[13] Giovanni Solari. Gust buffeting. i: Peak wind velocity and equivalent pressure. *Journal of Structural Engineering*, 119(2):365, 1993.

[14] Giovanni Solari. Gust buffeting. ii: Dynamic alongwind response. *Journal of Structural Engineering*, 119(2):383, 1993.

[15] Friedhelm Stangenberg, Rolf Breitenbücher, Otto T. Bruhns, Dietrich Hartmann, Rüdiger Höffer, Detlef Kuhl, and Günther Meschke. *Lifetime-Oriented Structural Design Concepts*. Springer-Verlag Berlin Heidelberg, Berlin and Heidelberg, 2009.

[16] I. Troen and E. L. Petersen. *European wind atlas*. Risø National Laboratory, Roskilde, 1989.

[17] P. Watson and B.J Dabell. Cycle counting and fatigue damage. In *Symposium on statistical aspects of fatigue testing*. Warwick University, 1975.

[18] P. H. Wirsching and A. M. Shehata. Fatigue under wide band random stresses using rainflow method. *Journal of Engineering Materials and Technology*, pages 205–211, 1977.

COMPDYN 2015
5th ECCOMAS Thematic Conference on
Computational Methods in Structural Dynamics and Earthquake Engineering
M. Papadrakakis, V. Papadopoulos, V. Plevris (eds.)
Crete Island, Greece, 25–27 May 2015

MULTIVARIATE STOCHASTIC METHODS FOR THE STRUCTURAL DESIGN OF WIND TURBINES

Frank H. Kemper[1] **and Juan Jose Calle Escribano**[1]

[1]Institute for Steel Structures
RWTH Aachen University
52070 Aachen
e-mail: frank.kemper@rwth-live.de

Keywords: Structural Dynamics, Wind Engineering, Wind Turbine, Stochastic Methods, Fatigue

Abstract. *In order to improve the structural design of steel towers for wind turbines, and in order to allow for detailed structural optimizations, a methodology is desirable which allows for quick and reliable considerations of the complex dynamic load situations. Whereat for the design of details for the machinery and the blade optimization time domain methods using multi-body-simulations are well established, their usage is often to extensive due to the needed level of detail to use them for an iterative tower design. Especially with regard to lattice towers, it is therefore desirable to investigate faster stochastic methods which focus on the overall dynamic behavior based on the probability of structural stresses within the tower construction. For this aim, in the present paper a modern stochastic concept is presented and results are compared to NRELS FAST algorithm.*

1 INTRODUCTION

The structural design of blades and the machinery of wind turbines are nowadays based on detailed transient dynamic calculations using multi-body systems (MBS) - which are doubtless indispensable for the construction of the machinery. But with respect to the design of the supporting structure, i.e. the tower and its foundation, the MBS models are unnecessary complex and the obtained results can therefore often only be taken in a simplified manner. With this load input, the design of the structure is carried out afterwards by means of individual calculations. As the dimensioning of the structural components influences the overall dynamic behavior of the wind turbine with respect to the aeroelastic load components and the inherent dynamic amplifications induced by the rotor, the design has to be iterative. With regard to the number of load cases and the time consumption of MBS simulations the structure is often not fully optimized, due to necessary simplifications.

In the field of wind engineering it is common practice to consider the complex stochastic wind load process on flexible structures by means of stochastic methods. An example of this methodology is the gust response factor approach given in Eurocode 1. Besides this simplified approach which is formulated for a single degree of freedom system, it is also possible to consider arbitrary multi-degree of freedom systems as long as the structural dynamic behavior can be treated linear. With application to wind turbines, this approach enables the necessary description of the correlated multivariate wind field and the formulation of the structural dynamic behavior of the response using complex spectral matrices. The main advantage is the algorithm is the allowance for a quick analysis of the load-response chain and to consider the structural interactions between the main components implicitly.

With the presented strategy, a design tool is introduced which especially focusses on the sup-porting structures of wind turbines taking into account the global dynamic behaviour and neglecting machinery details. Due to its faster usability, it might turn out as a useful tool for an optimized design of wind towers and foundations.

2 CONSIDERATION OF RANDOM LOADING

With respect to random loading, the response characteristic of structures is affected by the dynamic properties of a structural system. Dependent on the composition of the natural frequencies, mode shapes and on the damping behavior, the distribution of stress ranges and the maximum amplitudes at the structural details may vary significantly.

Due to the energy composition of the natural wind flow, especially slender structures with low structural frequencies tend to pronounced stress amplification due to this random process. Wind turbines are in particular slender, as their efficiency is highly dependent on hub height and the costs of the tower construction. The latter demands for strong optimization efforts which lowers the stiffness as far as possible. In consequence, wind turbines structures are highly prone to wind excited vibrations which have to be considered in the structural design and optimization process.

Generally there exist two concepts for the computation of structural responses due to random loading. The main difference is the domain in which the random loading is described. Basically, it is advantageous to describe random loads in a stochastic way as this allows for definite description of the turbulence contributions which form the wind speed on a given site. General recommendation for gust spectra are given e.g. in Eurocode 1. With respect to calculation of structural responses it is possible to remain in the stochastic domain or to switch over to the time domain. For the latter it is necessary to generate artificial wind fields. These fields are generally

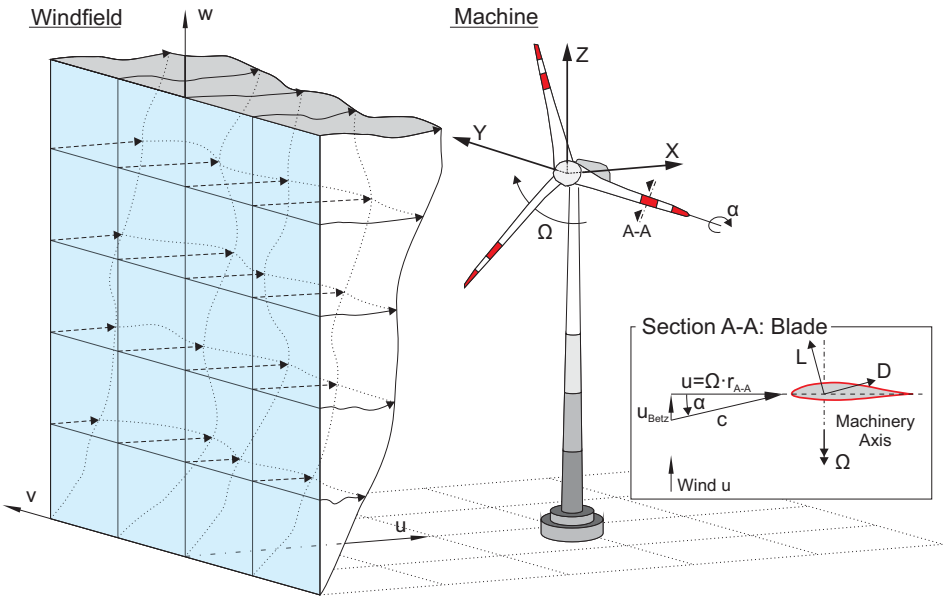


Figure 1: Definition of Axes and Directions of the Wind Turbine

only one representative of the stochastic description, for the needed statistical covering a higher quantity of wind fields has to be considered.

Time-based methods allow for very detailed calculations of the structural dynamic response. Furthermore they are able to consider structural non-linearities and the aeroelastic behavior of structural parts quite easy. With respect to wind turbines time based methods are therefore favored and in most cases performed using multi-body-simulations.

However, remaining in the stochastic domain is possible and it allows the prediction of the stochastic structural responses. Hence, as a result e.g. for the bending moment the spectral density can be obtained which allows the calculation of the statistical moments (e.g. the standard deviation). On a first look, this type of result is less ready to hand than having time series of the bending moment. But in opposite to the time based results, the knowledge of the statistical parameters is definite. Where the transient computations have to be repeated for multiple time-series of loading in order to allow an extreme value prediction, such statistical measures can be achieved directly based on the stochastic structural computation. Furthermore the stochastic method is much quicker, as it is mainly performed by matrix multiplications instead of time step integrations.

With stochastic concepts it is also possible to achieve the expected Rainflow distribution of structural stresses, which is an important measure for the verification of the fatigue stability. And again the method is much quicker the conventional time based procedure.

In the present paper a multivariate stochastic is presented which means that it is applicable for multi-degree of freedom systems. Due the described fast computation algorithm it is expected that the methodology may allow quicker structural optimizations in the future.

3 GENERAL DEFINITIONS

The Hub height of the investigated turbine equals to $H_{Hub} = 90$ m. A rotor diameter of $D_{Rotor} = 125.2$ m has been taken into account. In the study, a conical steel tower with an outer diameter of D_B=6.0m at the bottom and D_T=3.87m at the top respectively. As associated thickness values of T_B=27mm and T_T=19mm have been considered.

4 STOCHASTIC APPROACH FOR STRUCTURAL DESIGN OF WIND TURBINES

4.1 Wind Characteristics

For the description of the natural wind field, the reference values comparable to those of the NREL Study have been taken. The formulation of the resulting wind loading for the spectral method is described in the following subsections.

4.2 Spectral Description of the turbulent Wind Field

Due to the stochastic character of the fluctuating wind field, a general description succeeds with the power spectral density (PSD). In most standards, the *Kaimal* spectrum assuming neutral atmospheric stability has been implemented. For a single point in space with reference height z, the natural turbulence spectrum according to IEC 61400-1 [1] is defined as follows:

$$S_{UU}(f,z) = \frac{4.0 \cdot I_u^2(z) \cdot \overline{u}(z) \cdot L_{ux}(z)}{\left[1 + 6.0 \cdot \frac{f \cdot L_{ux}(z)}{\overline{u}(z)}\right]^{5/3}} \tag{1}$$

where: I_u = turbulence intensity, $\overline{u}$ = mean wind speed and L_{ux} = integral length scale in wind direction at the considered location. In order to take into account the spatial variability of wind speeds, it is common to take into account the coherence function which can be interpreted as the correlation measure of different spectra. According to Davenport [4], the vertical coherence can be expressed as:

$$\gamma_{i,j}(f,\Delta) = \exp\left\{-12.0 \cdot \sqrt{\left(\frac{\Delta \cdot f}{\overline{u}_{Hub}}\right)^2 + \left(0.12 \cdot \frac{\Delta}{L_c}\right)^2}\right\} \tag{2}$$

Where L_c = coherence scale parameter, Δ = spatial distance and $\overline{u}_{Hub}$ = mean wind speed at hub height. Although formula (2) principally only applies to the vertical coherence, it is common to use the formula for the entire spatial coherence, sometimes using adapted decay constants C. To formulate the full coherence relation, the matrix of spatial distances Δ is needed, where each item is defined as follows:

$$\Delta_{i,j} = \sqrt{(x_j - x_i)^2 + (y_j - y_i)^2 + (z_j - z_i)^2} \tag{3}$$

Using Eq. (2) and (3) the nxn coherence matrix $\underline{\gamma}(f)$ for a point vector with n-entries with respect to the flow direction can be assembled.

As the diagonal elements of the distance matrix $\underline{\Delta}$ equal to zero, the diagonal coherence elements are unique. Using the coherence relation, the wind field can be expressed as a nxn-spectral density matrix of wind turbulence as follows:

$$\underline{S}_{UU}(f) = \underline{\gamma}(f) \cdot S_{UU}(f) \tag{4}$$

The formulation of a symmetric gust spectrum neglects phase shifts, which have been reported during on-site measurements. In most cases, this disregardance should be of minor effect on the load formulation. Furthermore, realistic measures for certain locations are not available in the literature.

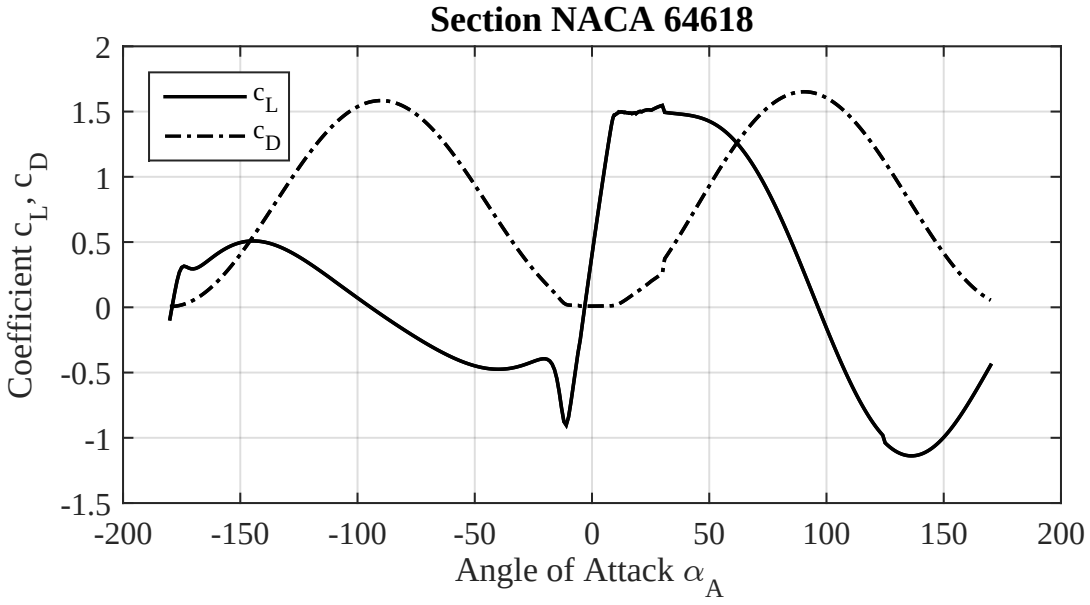


Figure 2: Aerodynamic Coefficients depend on the angle of attack, Exemplary curves of the NACA 64816 profile which is used at the outher third of the blades, here at $Re = 1 \cdot 10^6$

4.3 Aerodynamic Admittance

Wind loads on structures are generated due to a variable pressure fields, distributed over the entire surface. The approaching wind field and rather the individual wind vector at a structural point is responsible for the shape of the resulting pressure distribution at the associated structural section. The integrated pressure distribution leads to the instantaneous wind forces. With respect to line-like structures like the tower sturcture and the blades of wind turbines, it is common to define aerodynamic force coefficients, which can be interpreted as the integral directional wind forces, related to the approaching velocity pressure and normalized to a geometrical measure. The force coefficients are denoted as c_D, c_L and c_M, related to the drag, lift and moment forces and oriented to a wind-fixed coordinate system.

The force coefficients for all blade profiles have been calculated for various Reynolds numbers and angles of attack with the software QBlade [6] using the outer shape polygons. As the force admittance depends on the actual aerodynamic angle of attack α_A and the Reynoldsnumber Re, the values are interpolated appropriately.

For simple cases it is sufficient to formulate a stationary admittance approach, meaning that the time variability does not affect the resulting forces. Actually, with increasing frequency of force attack, the resulting force amplitudes are decreasing, as the spatial extent of the wind gusts are decreasing and consequently the correlation measure decreases as well. This effect is denoted as instationary aerodynamic admittance and considered by the coherence relation according to Eq. (2).

Due to the possible large vibrations, especially of the turbine blades, aeroelastic effects become relevant. In time based calculations it is possible to use the time related relative wind speeds to obtain a realistic aerodynamic damping behavior. Alternatively and suitable for usage with spectral methods, an analytical expression Kuehn [5] can be used:

$$\xi_{Aero} = \frac{3 \cdot \rho_{Air} \cdot \Omega}{8 \cdot \pi \cdot f_0 \cdot M_0} \int_{R_{root}}^{R} \frac{\delta c_l(r)}{\delta \alpha(r)} \cdot c(r) \cdot r \; dr \tag{5}$$

where: Ω = rotational speed of rotor, f_0 first along wind bending mode frequency, M_0 = associated modal mass, $\delta c_l/\delta\alpha$ = slope of lift coefficient with respect to angle of attack and $c(r)$ = chord length at radius r.

Eq. (5) is based on stationary rotor aerodynamics and considers some simplifications concerning the tip speed ratio.

4.4 Blade Aerodynamics

Blades of wind turbines are specially designed with respect to the rotor diameter and the expected wind speed distribution on sited. In this paper the aerodynamic blade properties are taken in dependence on the NREL 5-MW Reference Wind Turbine [2]. The blade sections are defined in table 1.

Table 1: Blade Aerodynamic Characteristics

Blade Section	Start-Pos [m]	End-Pos [m]
DU99W405LM	0	13.07
DU99W350LM	13.07	20.54
DU97W300LM	20.54	24.28
DU91W225LM	24.28	31.75
DU93W210LM	31.75	39.22
NACA 64618	39.22	61.63

For the detailed description of the blade properties reference is made to the NREL report [2]. In the present study, the aerodynamic coefficients for the blade profile sections have been computed with QBlade [6] for various angles of attack α_A and for different Reynolds numbers Re. In Figure 2, some exemplary force coefficients for two blade sections are illustrated.

For the computation, the blades have been discretized in 17 sections, the loads are induced at 16 aerodynamic nodes. For later calculations, the discretization can be simply increased. The aerodynamic properties of turbine blades dependent on the angle of attack and the Reynolds number Re. The presented stochastic computation method has been implemented in Matlab. The code automatically assigns the appropriate aerodynamic coefficients to the aerodynamic blade sections, dependent on the angle of attack and the current Reynolds number, which is computed based on the individual chord lengths and the mean nodal wind velocity.

The power spectral density of the acting wind force is expressed as spectral density matrix $S_{FF}(f)$, where the indiviual items can be obtained as follows:

$$S_{FF,ij}(f) = S_{UU,ij} \cdot \rho_{Air}^2 \cdot \overline{u}_i(z) \cdot c_{f,i}(\alpha_A, \Omega, Re) \cdot A_i \cdot \overline{u}_j(z) \cdot c_{f,j}(\alpha_A, \Omega, Re) \cdot A_j \qquad (6)$$

Based on the spectral density matrix of the wind forces, the instationary wind loading can be described for each DOF of the model. With respect to the necessary consideration of the individual angles of attack, the rotation speed and the Reynolds number, the admittance function has to be updated for each step in rotational discretization.

4.5 Mechanical Properties of the Structural System

Both, blades and tower have been modeled elastically with realistic bending stiffness. However, occurring aeroelastic effects have been neglected in this first setup. The chosen approach

allows for a direct computation of the stationary and instationary rotor loading using the coherence matrix of wind forces at the aerodynamic nodes of the blades. The stiffness matrix K has been set up based on three-dimensional beam elements with the full set of 12 DOF per element. With the prepared algorithm within Matlab, the discretization density of the tower and blade structure can be adjusted individually.

A corresponding mass matrix M has been assembled considering the transversal masses associated with the model nodes. Using a Rayleigh model, a damping Matrix D has been assembled based on a linear combination of mass and stiffness matrix.

$$\underline{D} = \alpha \cdot \underline{M} + \beta \cdot \underline{K} \tag{7}$$

Where the Parameter and are the Rayleigh coefficients, calculated based on two arbitrary frequencies and the desired damping ratio ξ. Due to the resulting frequency dependent characteristic of the obtained damping behavior, it is meaningful to fit the Rayleigh coefficients in order to match the damping ratio at the most relevant Eigenfrequencies. For further explanation reference is made e.g. to [6].

Using all structural matrices, the complex mechanical admittance function can be computed:

$$\underline{H}(f) = \frac{1}{-(2\pi f)^2 \cdot \underline{M} + i\underline{D} + \underline{K}} \tag{8}$$

The complex spectral admittance function of a system includes the complete structural information, including element wise damping and single damping elements (in contrast to the modal analysis concept). In Figure 3, the admittance function is plotted for the computed system.

4.6 Structural Responses of the stopped Machine

Based on the turbulent wind field, the aerodynamic and the mechanical admittance, the stationary and instationary responses of the stopped can be calculated using a multivariate stochastic approach. The spectral density matrix $S_{RR}(f)$ can be computed as follows:

$$\underline{S}_{RR}(f) = \underline{H}(f) \cdot \underline{S}_{FF}(f) \cdot \underline{H}(f)^T \tag{9}$$

The spectral density of the wind loading in this study only comprises the drag load, which is most decisive for the structural design of the supporting tower.

As described in section 2, the usage of a stochastic computation method allows for a full set of all statistically relevant response measures. All results are available within the resulting density matrix of structural deflections $\underline{S}_{RR}(f)$. Based on the mechanical admittance of the structural system, the corresponding frequencies of occurrence of inner forces and stresses can be obtained.

The calculations have been made for $N_f = 500$ frequency steps with a logarithmic spacing between f=0.01 Hz and 10 Hz. The algorithm allows the computation of arbitrary rotor positions Ω and pitch angles Θ.

4.7 Consideration of Operational States

A special challenge is the consideration of the operational states in the stochastic algorithm. The influence of the blade rotation is determined based on calculations for different rotor angles . Dependent on the rotation, the single blade elements are loaded variably due to the changing average wind velocities and turbulence contents with height. In Figure 4, the resulting tip

displacement is plotted over the rotation angle . Due to the consideration of three blades, the relative variability of the out of plane displacement at the top of the tower is much less. However, the periodic load distribution is vulnerable when tower Eigenfrequencies are affected. In Figure 5 the admittance function of a blade tip is plotted over the rotational angle. As the stiffness of the tower support varies dependent on the rotational position, the admittance function is not unique with respect to .

Dependent on the load variability and the angular speed, the periodic load contribution can be calculated. In consequence, a modified stochastic load case is generated which can be superimposed with the load set of a stationary rotor.

5 TIME DOMAIN APPROACH

Time domain calculations have been performed using the FAST program [4]. Wind fields have been computed using TurbSim [3] for different average wind speeds. All settings have been made in accordance the the NREL reference wind turbine [2]. Only the description of the gust spectrum has been formulated divergent (IEC 61400-1 instead of smooth).

The FAST algorithm allows the fully aerodynamic and aeroelastic calculations of a pitch-controlled wind turbine. Various response measures can be chosen for the output files. In this paper the dynamic responses of the tower are mainly focused. In Figure 3, the time related results for the tower deflections are plotted.

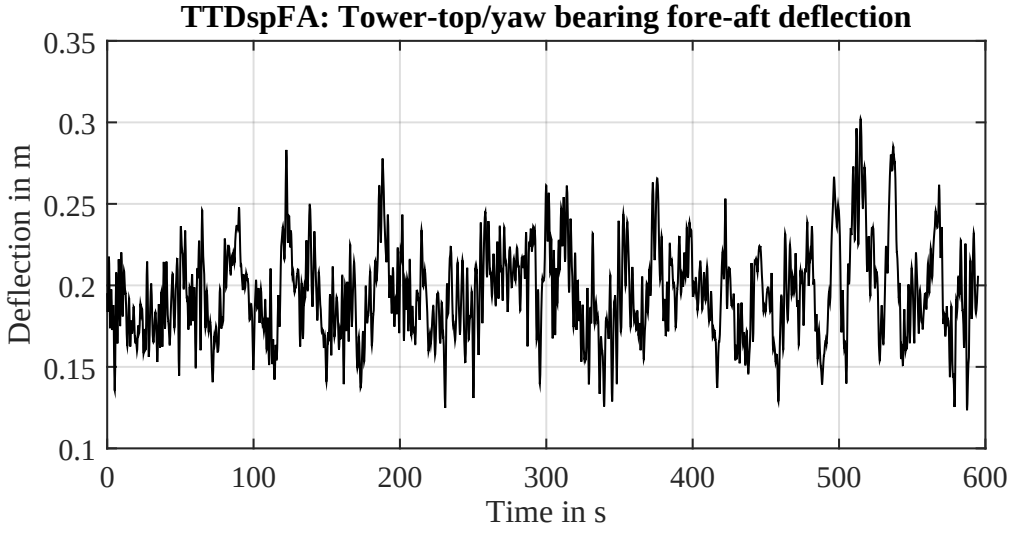


Figure 3: Exemplary Time Series of Tower Deflection, Operation Wind Speed of $v_{Hub} = 18$ m/s

For the design of tower structures the dynamic response at the top of the tower is the most important measure. Therefore, in the following section the corresponding frequency-related results are compared.

6 COMPARISON OF RESULTS

Simulation with FAST have been performed for four different mean wind speed at hub height: $v_{Hub} = 9$ m/s, $v_{Hub} = 14$ m/s, $v_{Hub} = 18$ m/s and $v_{Hub} = 27.5$ m/s. The FAST simulations considered a pitch-control algorithm (conventional variable speed, variable blade-pitch-to-feather configuration). The resulting average rotational speeds have been used for the stochastic computations at the same average wind speeds.

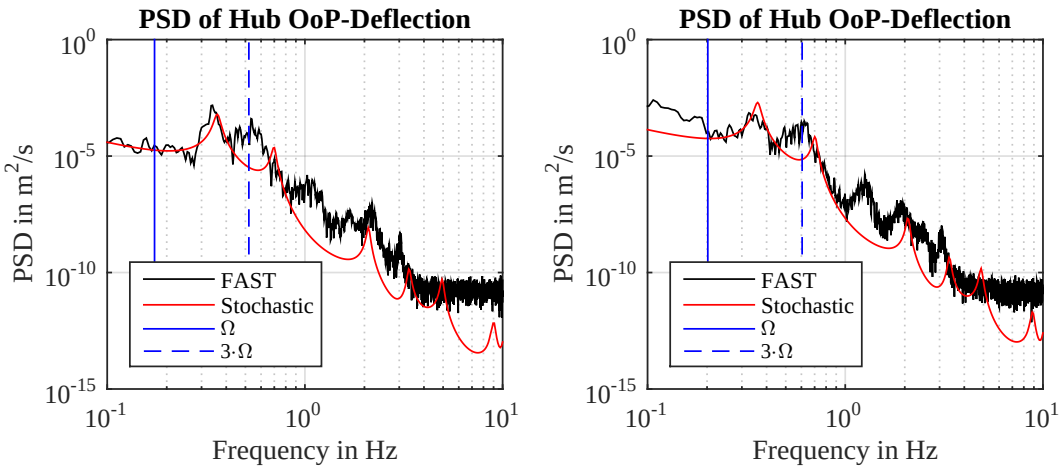


Figure 4: Along-wind Hub Deflection: Operation Wind Speed of $v_{Hub} = 9$ m/s (left) and $v_{Hub} = 14$ m/s (right)

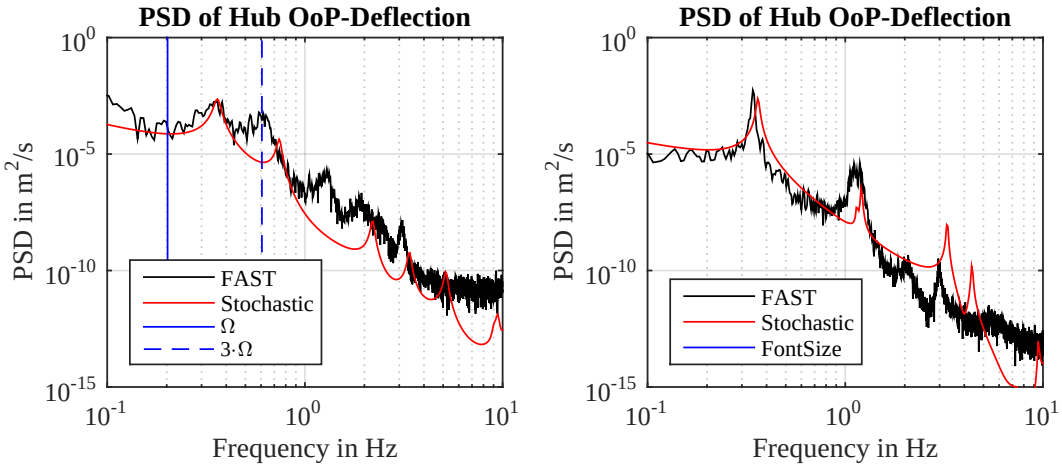


Figure 5: Along-wind Hub Deflection: Operation Wind Speed of $v_{Hub} = 18$ m/s (left) and Cut-Out Wind Speed of $v_{Hub} = 27.5$ m/s (right)

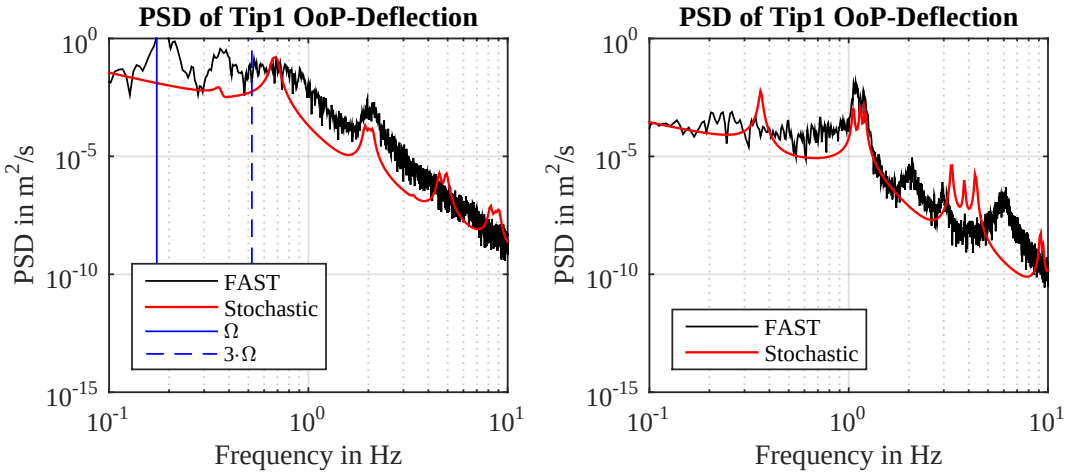


Figure 6: Along-wind Tip Deflection of Blade 1: Operation Wind Speed of $v_{Hub} = 9$ m/s (left) and Cut-Out Wind Speed of $v_{Hub} = 27.5$ m/s (right)

In order to allow a comparison of results, the resulting time series of the FAST algorithm have been analyzed with respect to its frequency domain content. Therefore a windowed spectral analysis has been made using a Hanning-window with a length of one fourth of the total simulation time. Due to the sudden loading at the beginning of the simulation the first 30s of the simulation time has been neglected for all further analyzes (and in the figures as well).

The comparison of the obtained result are presented in Fig. 4 till 6. Aside from the rotational frequency Ω and its multiple (this effect is not implemented yet), the general decay trend and most Eigenfrequencies are represented quite satisfactory using the stochastic method. The spectral sum, which represents the variance of the response process, is comparable.

7 CONCLUSIONS

For a possible future usage of spectral methods for the optimization of tower structures, the computation of structural responses of 3 bladed wind turbine has been performed in the time and the frequency domain. For the former, the well established FAST algorithm has been used. For the latter, a multivariate stochastic approach has been implemented in the programming environment of Matlab. The computation time with FAST averages out at some minutes (which is already extremely fast for a time domain algorithm) whereat the stochastic approach only takes seconds.

The structural and aerodynamic properties have been taken from the 5MW NREL reference wind turbine. Simplified assumptions had to be made for the aeroelastic behavior of the blades in the frequency domain. Furthermore, some inaccuracies remained in the stochastic model with respect to the structural detailing (rotary inertia of hub and nacelle), the eccentricity of the center of masses and the lateral gust components have been made. Additionally, a unique Rayleigh Damping has been assumed. Finally, the stochastic gust model in the present study is just one-dimensional at the moment. Lateral gust components should be included in future work. The mentioned improvements will certainly lead to a further increase of model reliability.

Currently, the stochastic approach considers rotating blade positions but it neglects the periodic loading which is caused by this rotation (Ω and $3 \cdot \Omega$ load contributions). For this aim, an analytical approach will be implemented in further developments.

Results have been obtained in the frequency domain for discrete rotor angle positions Ω. The average power spectral densities of the associated hub displacements have been compared to the results of the operating state based on the FAST calculation.

The obtained structural responses of the tower show wide banded contributions in a range of f =0.3 to 3 Hz. Fundamentally, the multivariate stochastic approach is able to predict the tower responses with respect to the average spectral magnitude and the location of natural frequencies with satisfactory precision. The major aim, a quicker analytical method to estimate dynamic responses for an improved structural optimization, seems reachable. Especially with regard to lattice towers, it seems to be helpful in combination with stochastic optimization algorithms. However, further incorporation of modeling details is necessary.

REFERENCES

[1] IEC 61400-1. Wind turbines - part1: Design requirements, 2005-08.

[2] J. Jonkman, S. Butterfield, W. Musial, and G. Scott. Definition of a 5-mw reference wind turbine for offshore system development, 2009.

[3] B. J. Jonkman and L. Kilcher. *TurbSim User's Guide: DRAFT VERSION: Technical Report NREL/TP-xxx-xxxx*. National Renewable Energy Laboratory, 2012.

[4] Jason M. Jonkman and Marshall L. Buhl Jr. *FAST User's Guide: Technical Report NREL/EL-500-38230*. National Renewable Energy Laboratory, 2005.

[5] Martin Johannes Kühn. *Dynamics and design optimisation of offshore wind energy conversion systems*. DUWIND, Delft University Wind Energy Research Institute, Netherlands, 2001.

[6] D. Marten, Wendler J., G. Pechlivanoglou, and C. N. Nayeri. Qblade: An open source tool for design and simulation of horizontal and vertical axis wind turbines. *International Journal of Emerging Technology and Advanced Engineering*, (3):264–269, 2013.

COMPDYN 2015
5th ECCOMAS Thematic Conference on
Computational Methods in Structural Dynamics and Earthquake Engineering
M. Papadrakakis, V. Papadopoulos, V. Plevris (eds.)
Crete Island, Greece, 25–27 May 2015

SEMI-ACTIVE PENDULUM TO CONTROL OFFSHORE WIND TURBINE VIBRATIONS

Suzana Moreira Avila[1*], **Pedro Varella Barca Guimarães**[1]

[1]University of Brasilia Área Especial de Indústria Projeção A, UNB - DF-480 Gama Leste
Brasília - DF, 72444-240 BRAZIL
avilas@unb.br, pedrobarca@hotmail.com

Keywords: wind turbine, structural control, pendulum, tuned mass damper, semi-active damper, linear optimal control

Abstract. *Wind energy presents itself, nowadays, as one of energy sources in fast development and implementation all over the world. The project, building and maintenance of the so called wind farm still present lots of challenges for engineers and researches. In this context, offshore wind turbine are found: wind turbines installed on ocean next to coast which, between other advantages, gets benefit of more intense and consistent wind with less turbulence in these regions. One of conceptions from this kind of wind turbine is the floating. This kind of structural system can be analyzed like a discrete model of inverted pendulum. This type structure can be vulnerable to excessive vibration caused by wind loads. One of the most used vibration control systems is the Tuned Mass Damper (TMD). It basically consist of a mass-spring-damper system attached to the main structure, the frequency of the damper is tuned to a particular frequency, with the goal of making the TMD vibrate out of phase with the main system, thus transferring the energy system to the damper. However, passive devices only work properly for the design frequency range, and wind forces are random type of excitations. In this sense, a better approach would be design a semi-active device. Semi-active control joins confidence and simplicity typical of passive systems with active control adaptability. It is characterized by not adding mechanical energy due to the structure and to have properties that can change dynamically. These devices can be viewed as controllable passive devices because despite of its changing properties of damping and/or stiffness it action on the structure is passive. This work aims to achieve better results in vibration control of offshore wind turbines proposing a semi-active controller to it, considering an inverted pendulum discrete model.*

1 INTRODUCTION

Wind power is a clear, sustainable source of energy. A great number of wind farms have been installed all over the world in recent years. It appears as an attractive option to reduce carbon dioxide emissions. The wind turbine transforms kinetic energy, generated from wind velocities, in electric power. It is constituted of a supporting structure (tower), a nacelle, a gearbox, a cube, blades and a generator.

Wind farms located at the seaboard, the so called offshore wind turbines, have some advantages compared to the onshore ones: do not have land space limitations; do not have audible or visual impact; at the sea occurs less turbulent winds [1]. Meanwhile, offshore wind turbine stability has to be taken into account, since it has shallower foundations and can even be a floating structure with a mobile base. Floating wind turbines also experience an additional source of dynamical loads: the movement of the sea waves at its base.

Wind turbine towers generally are slender and flexible due to its high altitude and can present excessive vibrations caused by its own operation, as well as, wind action. A detailed analysis of the structural behavior of the tower is of great relevance as it can represent up to 30% of the total system cost [2].

A technology that proposes to reduce excessive vibration of the structures is called structural control. It consists in the addition of external devices such as dampers or application of external forces that change properties of stiffness and/or damping. It can be classified as: passive control, active control, hybrid control and semi-active control. [3]

One widely used device is the tuned mass damper (TMD). It reduces the main structure response amplitudes by transferring energy between the structure and an auxiliary mass. TMD consists of mass-spring-dashpot system that is designed tuning it to a given modal frequency, for high towers, usually the first one [4].

The TMD can also be designed as pendulum system [5], it has the vibration period depending on pendulum length and can only be considered as a linear oscillator when amplitude vibrations are small, and otherwise the system turns to be nonlinear.

However, passive control strategies have disadvantages: they only are efficient within the frequency range for which they were designed. It is a little robust control. In the case of structures subjected to wind loads this fact becomes critical, since this type of loading has a random characteristic.

One alternative to passive control is the so called semi-active control. Semi-active devices do not add energy to the structure and its properties can be varied dynamically [6]. The semi-active systems are more reliable and more robust than active systems. Damping and stiffness properties can be controlled in an active way by a control signal. These are controllable passive devices since they don't apply any additional force to the structure.

Chey et al [7] proposed passive and semi-active tuned mass damper (PTMD and SATMD) building systems to mitigate structural response due to seismic loads.

Zemp et al [8] describes the implementation of a proof-of-concept pendulum tuned inertial mass magnetorheological (TM-MR) damper assembly in a tall building in Santiago, Chile, designed primarily to control building motions, and hence indirectly, interstory deformations.

Rafieipour et al [9] proposed a semi-active TMD with an innovative variable stiffness device called folding variable stiffness springs (FVSS), with the capability to change stiffness between lower and upper bounds through a small change between its supports. It is verified that this damper has an effective performance compared to a passive device.

Despite previous studies and reasonable number of practical applications of structural control in bridges, high towers and buildings, the application of structural control techniques in wind turbines is still a new topic [10-12]. However, despite previous studies, obstacles

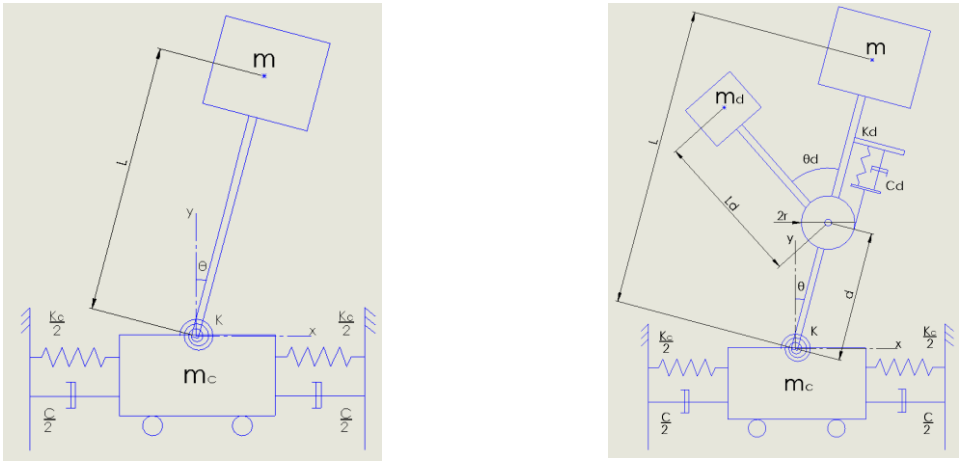
remain to be overcome. These include: reducing cost/maintenance and increase reliability, efficiency and robustness.

On previous studies [13-15] an inverted pendulum model was proposed to study the dynamic behavior and stability of a floating offshore wind turbine. Two passive control systems, a simple pendulum TMD and an inverted pendulum TMD were proposed aiming to reduce the angular amplitude of the main structure. The results obtained showed that inverted pendulum model had a better performance.

In this work a semi-active TMD pendulum is proposed to control excessive vibration of an offshore floating wind turbine. The structure is modeled as an inverted pendulum discrete model. This model is presented as a preliminary model for structural control alternatives studies, the results serve as a basis for real structures design with a more careful modeling. A bang bang control strategy was considered, TMD stiffness and damping values were calculated trough optimal control theory. Satisfactory results were find out compared to those of passive TMD pendulum.

2 FLOATING WIND TURBINE MODEL: INVERTED PENDULUM

For modeling the dynamic behavior of an offshore wind turbine, a discrete model of an inverted pendulum is considered [13] as presented in Fig. 1(a). It is a system with a spring and a damper at the base that simulates fluid resistance of the sea. The excitation of the system is a dynamic force applied to the mass *m*, simulating the wind force on the turbine blades. Figure 1(b) presents the installation of an inverted pendulum TMD to reduce vibration's amplitude of the structure. Some simplifying hypotheses were assumed [14]: (a) angular amplitude is kept within boundaries for a linear behavior; (b) a two dimension vibration system is considered; (c) wave loading is disregarded (d) a top mass represents nacelle+blades [10].



(a) (b)

Figure 1: Model of an inverted pendulum over a mobile base (a) with inverted pendulum TMD installed (b).

Where m is the tip mass at the end of the bar, θ is bar angular amplitude, l is bar's length, K is torsional stiffness, m_c is base's mass, k_c is base's stiffness, c is base's damping coefficient, m_d is TMD pendulum's mass, l_d is TMD pendulum's length, d is the distance from pendulum to bar's base, r is TMD disc's radius, c_d is TMD's damping coefficient, k_d is

TMD's stiffness and θ_d is TMD pendulum's angular amplitude related to the bar. The motion equation of the system with control (Figure 1(b)) is given in matrix form:

$$\begin{bmatrix} M_{1,1} & M_{1,2} & M_{1,3} \\ M_{2,1} & M_{2,2} & M_{2,3} \\ M_{3,1} & M_{3,2} & M_{3,3} \end{bmatrix} \begin{bmatrix} \ddot{\theta} \\ \ddot{\theta}_d \\ \ddot{u} \end{bmatrix} + \begin{bmatrix} 0 & 0 & 0 \\ 0 & c_d.r^2 & 0 \\ 0 & 0 & c \end{bmatrix} \begin{bmatrix} \dot{\theta} \\ \dot{\theta}_d \\ \dot{u} \end{bmatrix} +$$

$$\begin{bmatrix} K - g\left(m.l + \frac{\rho.l^2}{2} + m_d(d + l_d) - \rho_d.l_d\left(d + \frac{l_d}{2}\right)\right) & +m_d.g.l_d + \rho_d.\frac{l_d^2}{2}.g & 0 \\ +m_d.g.l_d + \rho_d.\frac{l_d^2}{2}.g & k_d.r^2 - m_d.g.l_d - \rho_d.\frac{l_d^2}{2}.g & 0 \\ 0 & 0 & k_c \end{bmatrix} \begin{bmatrix} \theta \\ \theta_d \\ u \end{bmatrix} =$$

$$\begin{bmatrix} F(s).l \\ 0 \\ 0 \end{bmatrix} \quad (1)$$

Where:

$$M_{1,1} = \frac{\rho.l^3}{3} + m.l^2 + m_d(d + l_d)^2 + \rho_d.d.l_d(d + l_d) + \rho_d.\frac{l_d^3}{3}$$

$$M_{1,2} = -m_d.d.l_d - m_d.l_d^2 - \rho_d.d.\frac{l_d^2}{2} - \rho_d.\frac{l_d^3}{3}$$

$$M_{1,3} = m.l + \frac{\rho.l^2}{2} + m_d(d + l_d) + \rho_d.d.l_d + \rho_d.\frac{l_d^2}{2}$$

$$M_{2,1} = -m_d.d.l_d - m_d.l_d^2 - \rho_d.d.\frac{l_d^2}{2} - \rho_d.\frac{l_d^3}{3}$$

$$M_{2,2} = m_d.l_d^2 + \rho_d.\frac{l_d^3}{3}$$

$$M_{2,3} = -m_d.l_d - \rho_d.\frac{l_d^2}{2}$$

$$M_{3,1} = m.l + \frac{\rho.l^2}{2} + m_d(d + l_d) + \rho_d.d.l_d + \rho_d.\frac{l_d^2}{2}$$

$$M_{3,2} = -m_d.l_d - \rho_d.\frac{l_d^2}{2}$$

$$M_{3,3} = m_c + m + m_d + \rho.l + \rho_d.l_d$$

Usually, the formulation and solution of control problems present equations of motion Equation (1) as state equations:

$$\dot{\boldsymbol{z}}(t) = \boldsymbol{A}\boldsymbol{z}(t) + \boldsymbol{B}\boldsymbol{u}(t) + \boldsymbol{E}\boldsymbol{f}(t) \quad (2)$$

where ***z(t)*** is the state vector *4n + 2m*; ***A*** corresponds to the matrix system state 4*n + 2m* x 4*n + 2m*; ***B*** and ***E*** are the control and disturbance input matrices; Finally, the vector $\dot{\boldsymbol{z}}(t)$ represents the state of the structural system which contains the relative velocity and responses to acceleration of the structure with respect to the ground. The details of each vector and matrix are listed as follows:

$$\boldsymbol{z}(t) = \begin{bmatrix} \boldsymbol{x}(t) \\ \dot{\boldsymbol{x}}(t) \end{bmatrix}, \quad \boldsymbol{A} = \begin{bmatrix} 0 & I \\ -\boldsymbol{M}^{-1}\boldsymbol{K} & -\boldsymbol{M}^{-1}\boldsymbol{C} \end{bmatrix}, \quad \boldsymbol{B} = \begin{bmatrix} 0 \\ \boldsymbol{M}^{-1}\boldsymbol{D} \end{bmatrix}, \quad \boldsymbol{E} = \begin{bmatrix} 0 \\ \boldsymbol{M}^{-1}\boldsymbol{H} \end{bmatrix} \quad (3)$$

Where $\boldsymbol{x}$(t) and $\dot{\boldsymbol{x}}(t)$ are system displacement and velocities vectors, respectively. Matrices $\boldsymbol{D}$ and $\boldsymbol{H}$ define the location of control forces and of external loading, respectively.

3 SEMI-ACTIVE CONTROL STRATEGY

The Bang Bang control, also called control ON / OFF control, is a feedback controller that suddenly changes between two limit values. This device compares the input with a target value, so that if the output exceeds the input, the actuator is switched off, otherwise, the actuator is now on. Figure (2) shows an example of a bang bang controller block diagram. This is a low cost controller, further its simplicity and convenience.

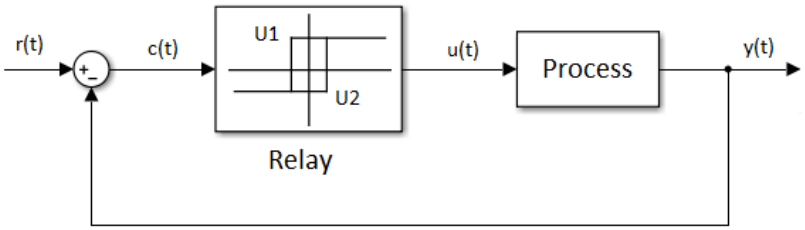


Figure 2: Bang bang control [16].

The control strategy is to control structural response using bang bang control, varying pendulum TMD stiffness k_d and damping c_d, switching from one extreme set of values to the other. The optimal parameter values (k_d and c_d) are obtained based on linear optimal control algorithm (linear quadratic regulator – LQR) [17].

First a LQR controller is designed assuming an active pendulum TMD system and neglecting the actuator dynamics. The optimal actuator force $u(t)$ is defined by the gain matrix $\boldsymbol{G}$. The actuator force is not really applied at the TMD, this force is applied through a semi-active damper.

The linear optimal control problem consist in finding the control vector $\boldsymbol{u}(t)$ that minimizes the performance index J subject to the constraint (3). In structural control, the performance index is usually chosen as a quadratic function in $\boldsymbol{z}(t)$ and $\boldsymbol{u}(t)$, as follows

$$J = \int_{t_0}^{t_f} \left[\mathbf{z}^{\mathrm{T}}(t)\mathbf{Q}\mathbf{z}(t) + \mathbf{u}^{\mathrm{T}}(t)\mathbf{R}\mathbf{u}(t)\right]dt \tag{4}$$

Where $\boldsymbol{Q}$ is a $2n$ x $2n$ positive semi-definite matrix and $\boldsymbol{R}$ is a m x m positive definite matrix. The matrices $\boldsymbol{Q}$ and $\boldsymbol{R}$ are referred to as weighting matrices, whose magnitudes are assigned according to the relative importance attached to the state variables and to the control forces in the minimization procedure. The minimization problem leads to a Riccati differential equation system:

$$\begin{aligned} &\dot{\mathbf{P}}(t) + \mathbf{P}(t)\mathbf{A} - \frac{1}{2}\mathbf{P}(t)\mathbf{B}\mathbf{R}^{-1}\mathbf{B}^{\mathrm{T}}\mathbf{P}(t) + \mathbf{A}^{\mathrm{T}}\mathbf{P}(t) + 2\mathbf{Q} = \mathbf{0}, \\ &\mathbf{P}(t_f) = \mathbf{0} \end{aligned} \tag{5}$$

where $\boldsymbol{P}(t)$ is the Ricatti matrix. The control vector $\boldsymbol{u}(t)$ is linear in $\boldsymbol{z}(t)$. In this case, the linear optimal control law is

$$\mathbf{u}(t) = \mathbf{G}(t)\mathbf{z}(t) = -\frac{1}{2}\mathbf{R}^{-1}\mathbf{B}^{\mathrm{T}}\mathbf{P}(t)\mathbf{z}(t) \tag{6}$$

where $\mathbf{G}(t) = -\frac{1}{2}\mathbf{R}^{-1}\mathbf{B}^{\mathrm{T}}\mathbf{P}(t)$ is the control gain. In most structural applications, numerical analysis show that Riccati matrix $\boldsymbol{P}(t)$ stays constant during the control range, converging fast to zero on the neighborhood of t_f [17]. Thus $\boldsymbol{P}(t)$, in most cases, can be approximated by a constant matrix $\boldsymbol{P}$ and Riccati equation (5) is reduced to

$$\mathbf{PA} - \frac{1}{2}\mathbf{PBR}^{-1}\mathbf{B}^{\mathrm{T}}\mathbf{P} + \mathbf{A}^{\mathrm{T}}\mathbf{P} + 2\mathbf{Q} = \mathbf{0}, \tag{7}$$

and the constant control gain is given by

$$\mathbf{G} = -\frac{1}{2}\mathbf{R}^{-1}\mathbf{B}^{\mathrm{T}}\mathbf{P} \tag{8}$$

As it was stated above the control vector $\boldsymbol{u}(t)$ is proportional to state vector $\boldsymbol{z}(t)$ which contains system displacements and velocities. The elements of control gain matrix $\boldsymbol{G}$ that multiplies θ_d and $\dot{\theta}_d$ are considered to set optimum values for pendulum TMD parameters k_d and c_d.

4 NUMERICAL RESULTS

The present work numerical study considered properties of the turbine NREL 5 MW [18], they are exhibited in Table 1.

Rating	5 MW
Rotor, hub diameter	126.3 m
Hub Height	90 m
Rotor mass	110,000 kg
Tower Mass	347,460 kg

Table 1: Wind turbine's properties [18]

Also the following values were considered for system parameters [14]: l = 90 m, m_c = 240,000 Kg; g = 9.81 m/s^2, K = 8.94 x 10^8 N/rad, m = 110,000 kg, m_d = 49,267 kg, d = 79.6 m. The wind dynamic loading was modeled as an applied load at the inverted pendulum mass. Two loading cases were considered: harmonic force and white noise force. The system without control fundamental frequency is 0,97 rad/s.

In previous studies [15], parameter values for pendulum TMD were found out through a parametric study: kd = 5.9 x 10^6 N/m, cd = 4.4 x 10^5 Ns/m and l_d = 7.4 m. It results on an efficient vibration control of the wind turbine tower when subjected to a harmonic force approximation of wind load and also for a white noise wind load. In order to improve the performance of this structural control device it is proposed in the present work a semi-active pendulum TMD that varies k_d and c_d properties through a bang bang (ON/OFF) control.

Aiming to design an efficient semi-active controller, the values of parameters k_d and c_d were optimized via classical optimal control algorithm (LQR), assuming an active pendulum TMD system. The optimal actuator force $u(t)$ is defined by the gain matrix $\boldsymbol{G}$, obtained through solution of Riccati equation (Equation 7). It is not really applied at the TMD, this force is applied through the semi-active damper.

Optimal control effectiveness is directly related to a proper choice of the weighting matrices $\boldsymbol{Q}$ and $\boldsymbol{R}$. The flexibleness on this matrices choice allows the generation of a family of multiple different controllers; this represents the great advantage, as well as, the great disadvantage of this method. It is extremely important to carry out a detailed parametric study of weighting matrices in order to ensure control robustness [19].

The optimal control algorithm does not lead to a control force truly optimal in certain cases, since the excitation is ignored in obtaining the Riccati matrix [3]. Because of this, in this work two loading cases were considered to obtain the optimum control force $u(t)$: harmonic (HSA) and white noise (WNSA). Parametric studies were performed in both loading cases to set $\boldsymbol{Q}$ and $\boldsymbol{R}$ matrices.

The parametric study for HSA loading case provided the following weighting matrices and the corresponding gain matrix:

$$\boldsymbol{Q} = 5 \times 10^6 \begin{bmatrix} 1 & 0 & 0 & 0 & 0 & 0 \\ 0 & 1 & 0 & 0 & 0 & 0 \\ 0 & 0 & 1 & 0 & 0 & 0 \\ 0 & 0 & 0 & 1 & 0 & 0 \\ 0 & 0 & 0 & 0 & 1 & 0 \\ 0 & 0 & 0 & 0 & 0 & 1 \end{bmatrix} \quad \boldsymbol{R} = 10^{-4}$$

$$\boldsymbol{G} = [2.897 * 10^6 \quad 2.924 * 10^4 \quad 1.677 \quad -1.150 * 10^8 \quad 1.725 * 10^6 \quad -2.633 * 10^6]$$

As for WNSA loading case, the following weighting matrices and the corresponding gain matrix are:

$$\boldsymbol{Q} = 3 \times 10^6 \begin{bmatrix} 1 & 1 & 1 & 1 & 1 & 1 \\ 1 & 1 & 1 & 1 & 1 & 1 \\ 1 & 1 & 1 & 1 & 1 & 1 \\ 1 & 1 & 1 & 1 & 1 & 1 \\ 1 & 1 & 1 & 1 & 1 & 1 \\ 1 & 1 & 1 & 1 & 1 & 1 \end{bmatrix} \quad \boldsymbol{R} = 10^{-4}$$

$$\boldsymbol{G} = [1.444 * 10^6 \quad 1.563 * 10^4 \quad 1.332 * 10^4 \quad -7.220 * 10^7 \quad 1.070 * 10^6 \quad -1.563 * 10^6]$$

Gain Matrix $\boldsymbol{G}$ coefficients are applied to displacements and velocities $\theta, \theta_d, u, \dot{\theta}, \dot{\theta}_d$ and $\dot{u}$, however only the coefficients associated to θ_d and $\dot{\theta}_d$, are considered on the semi-active case. The optimum values of k_d and c_d are obtained adding $\boldsymbol{G}[2,1]$ and $\boldsymbol{G}[5,1]$ to passive k_d and c_d values, respectively, obtaining: k_d = 5.9292 x 10^6 N/m and c_d = 2.1654 x 10^6 Ns/m for HSA case and k_d = 5.9112 x 10^6 N/m and c_d = 1.1886 x 10^6 Ns/m for WNSA case.

Comparing those optimum parameter values to passive parameter values (k_d = 5.9 x 10^6 N/m and c_d = 4.4 x 10^5 Ns/m to the optimum ones it can be observed that a significant increase occurs only for c_d, showing that a semi-active device varying only damping parameters would be satisfactory.

A time domain analysis was performed, four situations were considered for analysis: (1) structure without control, (2) system with passive TMD (sTMD) [14] considered as the semi-

active turned OFF, (3) system with semi-active ON, with optimum parameter for harmonic loading (HSA) and (4) system with semi-active ON, with optimum parameter for white noise loading (WNSA). Time domain simulations for harmonic loading were performed varying forcing frequency in a range from 0 to 2 rad/s.

Figure 3 shows efficiency relation of the semi-active device in ON (HSA) and OFF position (sTMD). This efficiency is measured by *rms* values as follows:

$$EFF = \frac{\theta_{OFF} - \theta_{ON}}{\theta_{OFF}} \text{ x } 100\ \% \tag{9}$$

Figure 3 shows efficiency value as a function of forcing frequency. On the frequency range where efficiency has positive values HSA (ON) is effective and turns to be ineffective for negative values of efficiency.

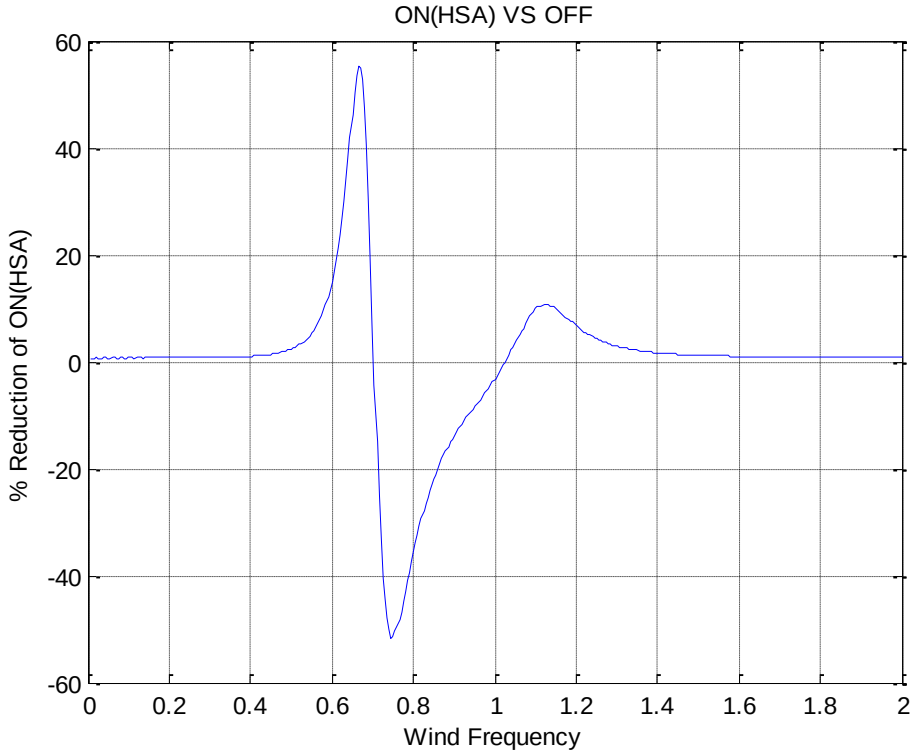
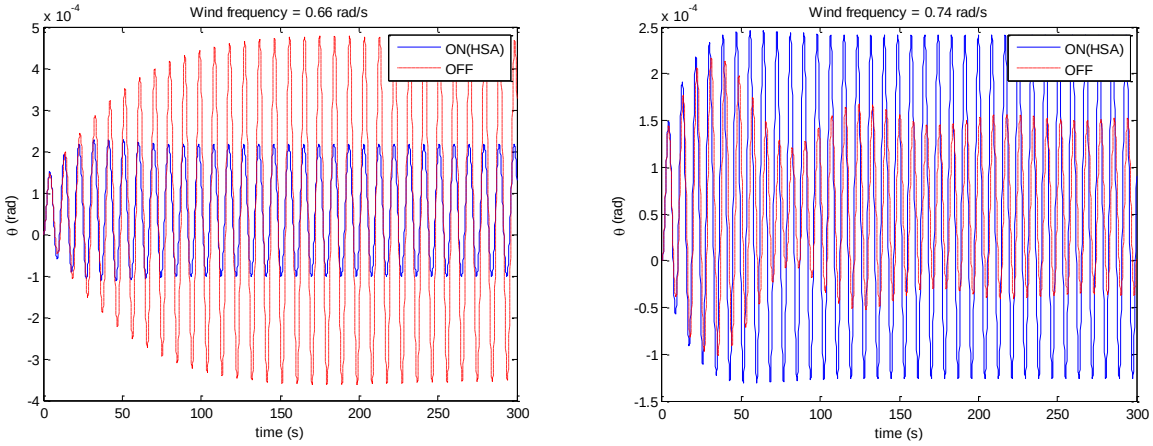


Figure 3: Efficiency of HSA (ON) semi-active control

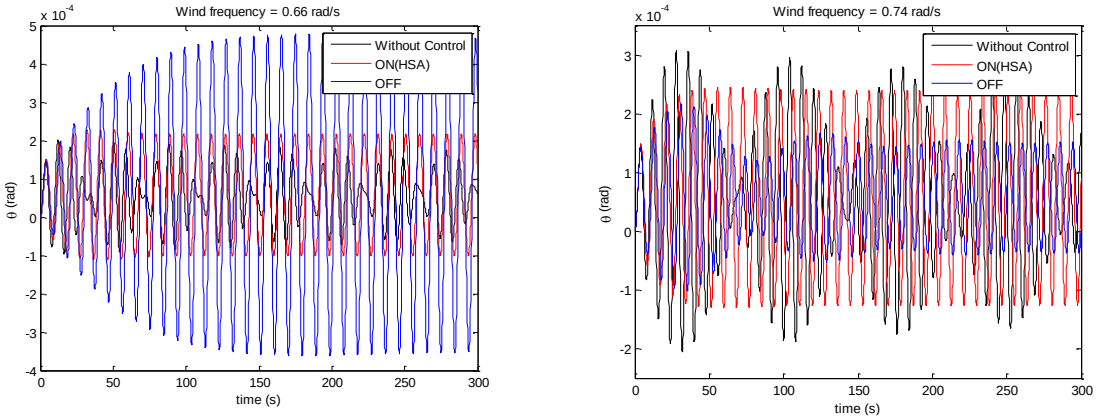
Figures 4(a) and 4(b) shows angular displacement θ time history for OFF and ON(HSA) cases, considering forcing frequencies of 0.66 rad/s and 0.74 rad/s, respectively. These frequencies values match to maximum and minimum efficiency curve peaks of Figure (3).



(a) (b)

Figure 4: Angular displacement time history (a) ω_f=0.66 rad/s; (b) ω_f=0.74 rad/s

It can be noticed, as expected from Figure 3, that for ω_f = 0.74 rad/s HSA(ON) is less effective than OFF position. The same time histories are presented in Figures 5(a) and 5(b) plotting also the system uncontrolled response, in a way to verify semi-active ON/OFF control effectiveness. It can be verified that the semi-active controller presents a good performance on reducing excessive vibration amplitudes.



(a) (b)

Figure 5: Angular displacement time history with and without control

Figure 6 shows angular displacement time history when the structure is subjected to a white noise wind loading. It is verified that HSA(ON) case presents a better efficiency in most of the time response.

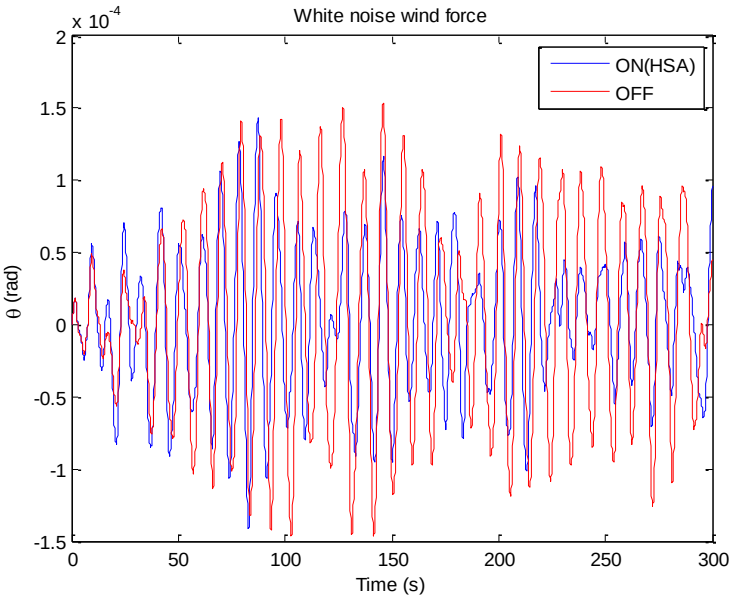


Figure 6: Angular displacement time history: white noise loading.

Similar to Figure 3, Figure 7 shows the efficiency curve for the case ON (WNSA). On the frequency range where efficiency has positive values ON (WNSA) is effective and turns to be ineffective for negative values of efficiency.

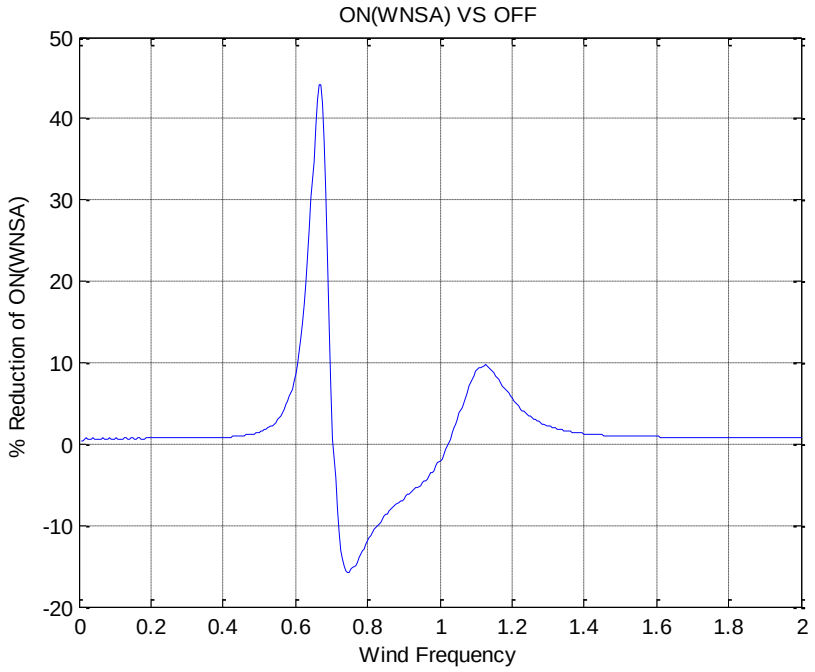
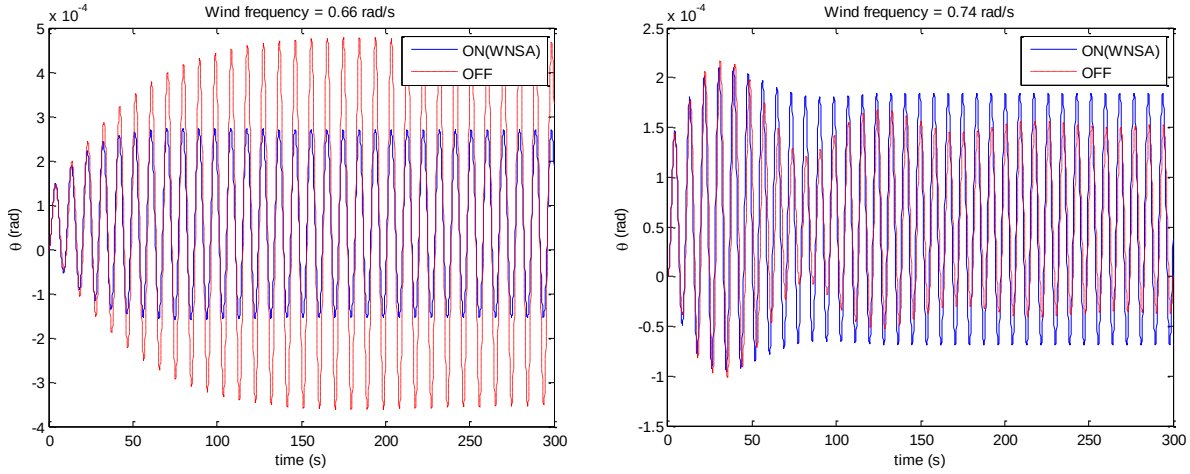


Figure 7: Efficiency of WNSA (ON) semi-active control

Figures 8(a) and 8(b) shows angular displacement θ time history for OFF and ON(WNSA) cases, considering harmonic load with forcing frequencies of 0.66 rad/s and 0.74 rad/s,

respectively. These frequencies values match to maximum and minimum efficiency curve values of Figure 7.



(a) (b)

Figure 8: Angular displacement time history (a) ω_f=0.66 rad/s; (b) ω_f=0.74 rad/s

It can be noticed, as expected from Figure 7, that for ω_f = 0.74 rad/s WNSA(ON) is less effective than OFF position. Figure 9 shows angular displacement time history when the structure is subjected to a white noise wind loading. It is verified that WNSA(ON) case presents a better efficiency in most of the time response.

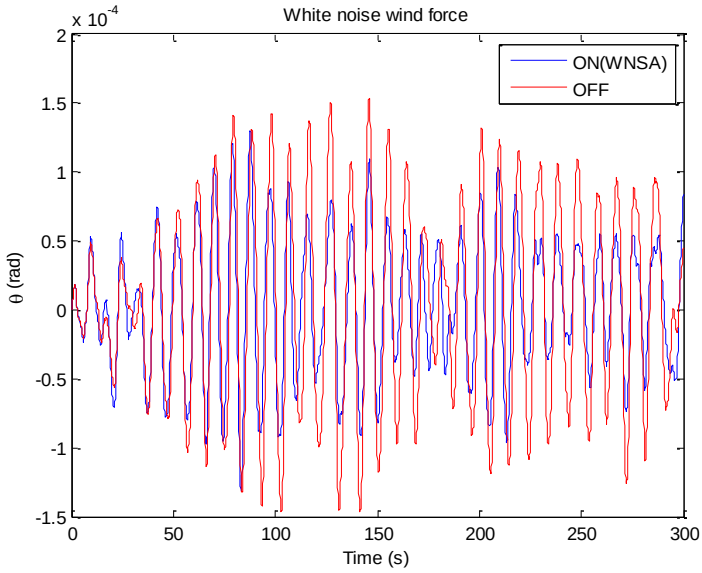


Figure 9: Angular displacement time history: white noise loading.

Comparing efficiency curves on Figures 3 and 7 it can be noticed that HSA present high peak amplitudes than WNSA, this is also visible comparing time histories on Figure 4(a) with Figure 8(a) and Figure 4(b) with Figure 8(b). It can be concluded that HSA(ON) present the

best efficiency and the greater inefficiency compared to WNSA(ON), however semi-active switch ON-OFF supplies this inefficiency.

5 CONCLUSIONS

In this work a semi-active TMD pendulum is proposed to control excessive vibration of an offshore floating wind turbine. The structure is modeled as an inverted pendulum discrete model. This model is presented as a preliminary model for structural control analysis, the results serve as a basis for real structure design with a more careful modeling. A bang bang (ON/OFF) control strategy was considered, semi-active TMD stiffness and damping values were calculated trough optimal control theory. It was held a detailed parametric study of weighting matrices in order to ensure control robustness. Since the excitation is ignored in obtaining the Riccati matrix, two loading cases were considered: harmonic and white noise, leading to a set of two k_d and c_d parameters (HSA and WNSA). It was concluded that HSA parameters are the best choice for setting the semi-active TMD ON position. Satisfactory results were found out compared to those of passive TMD pendulum. Semi-active controller presents a good performance on reducing excessive vibration amplitudes. Further studies would be necessary in order to test other control strategies to semi-active controller design.

6 ACKNOWLEDGEMENTS

The authors gratefully acknowledge the Brazilian agency CNPq (Council of National Scientific and Technological Development) for financial support of this study (MCTI/CNPq Nº 74/2013).

REFERENCES

[1] L.Y. Pao L.Y. and K.E. Johnson, A tutorial on the dynamics and control of wind turbines and wind farms, *Proceedings of the American Control Conference*, St Louis, USA, 2009.

[2] A. Quilligan, A. O´Connor and V. Pakrashi, Fragility Analysis of Steel and Concrete Wind Towers, *Engineering Structures*, **36**, 270-282, 2012.

[3] S.M. Avila, *Controle Híbrido para Atenuação de Vibrações em Edifícios*, PhD Thesis, Pontifícia Universidade Católica do Rio de Janeiro, Rio de Janeiro, 2002. (in portuguese)

[4] T.T. Soong, G.F. Dargush, *Passive energy dissipation systems in structural engineering*, Chichester: John Wiley & Sons, 1997

[5] R. Lourenço, *Design, Construction and Testing of an Adaptive Pendulum Tuned Mass Damper*. Master's Dissertation - Waterloo, Ontario, Canada, 2011.

[6] B.F. Spencer Jr., S.J. Dyke, M.K. Sain and J.D. Carlson, Phenomenological Model of a Magnetorheological Damper, *Journal of engineering mechanics*, **123**, n.3, 230-238, 1997.

[7] Min-Ho Chey, J.G. Chase, J.B. Mander and A.J. Carr1, Semi-active tuned mass damper building systems: Design, *Earthquake Engineering and Structural Dynamics*, **39,**119–139, 2010.

[8] R. Zemp, J.C. de la Llera, and J.L. Almazán, Tall building vibration control using a TM-MR damper assembly, *Earthquake Engineering and Structural Dynamics*, **40**,339–354, 2011.

[9] M. H. Rafieipour, A. K. Ghorbani-Tanha, M. Rahimian, R. Mohammadi-Ghazi, A novel semi-active TMD with folding variable stiffness spring, *Earthquake Engineering and Engineering Vibration*, **13**, n. 3, 509-518, 2014.

[10] P.J. Murtagh, A. Ghosh, B. Basu and B.M. Broderick, Passive control of wind turbine vibrations including blade/tower interaction and rotationally sampled turbulence", *Wind Energy*, v.11, pp.305-317, 2008.

[11] M.A. Lackner. and A.R. Rotea, Passive structural control of offshore wind turbines", *Wind Energy*, v.14, pp.373-388, 2011.

[12] G. Stewart, *Load reduction of floating wind turbines using tuned mass dampers*, Master thesis, University of Massachussets Amherst, 2012.

[13] P.V.B. Guimarães, S.M. Avila, M.A.M. Shzu, Z.J.G. Prado, M.V.G. Morais, Vibration Control of an Offshore Wind Turbine Modeled as an Inverted Pendulum, *Proceedings of International Conference on Vibration Problems, ICOVP*, Lisboa, Portugal, 2013.

[14] P.V.B. Guimarães, M.V.G. Morais and S.M. Avila, Structural Control of Offshore Wind Turbines, *Proceedings of XXXV Iberian Latin American Congress on Computational Methods in Engineering – CILAMCE*, Fortaleza, Brazil, 2014.

[15] P.V.B. Guimarães, M.V.G. Morais and S.M. Avila, Tuned Mass Damper Inverted Pendulum to Reduce Offshore Wind Turbine Vibrations, *Vibration Engineering and Technology of Machinery, Mechanisms and Machine Science* **23**, 379-388 Springer, 2014.

[16] H.F. Moore, *Análise de desempenho de um controlador Bang-Bang em um sistema de freio ABS*, Graduation Project, University of Brasilia, 2014. (in portuguese)

[17] L. Meirovitch, *Dynamics and control of structures*, John Wiley and Sons, 1990.

[18] G.M. Stewart and M.A. Lackner, The Effect of Actuator Dynamics on Active Structural Control of Offshore Wind Turbines, *Engineering Structures*, **33**, 1807-1816, 2011.

[19] S.M. Avila. and P.B. Gonçalves, Procedimento para Determinação das Matrizes de Ponderação do Algoritmo de Controle Ótimo para um Amortecedor de Massa Híbrido (AMH), *Mecânica Computacional* **XXIX**, 1345-1365, 2010. (in Portuguese)

COMPDYN 2015
5th ECCOMAS Thematic Conference on
Computational Methods in Structural Dynamics and Earthquake Engineering
M. Papadrakakis, V. Papadopoulos, V. Plevris (eds.)
Crete Island, Greece, 25–27 May 2015

ANALYSIS OF COUPLED SYSTEMS CONSISTING OF SUPPORT STRUCTURE AND HIGH VOLTAGE SUBSTATION EQUIPMENT WITH VERIFICATION VIA FULL-SCALE SHAKING TABLE TESTS

Shakhzod M. Takhirov[1], Amir S.J. Gilani[2], Frank Blalock[3], and Cary Ahrano[3]

[1] Structures Laboratory, Civil and Environmental Engineering Department, University of California, Berkeley and PEER – UC Berkeley
337 Davis Hall, UC Berkeley, Berkeley, CA 94720-1710, USA
e-mail: takhirov@berkeley.edu

[2] Miyamoto International, Inc.
1450 Halyard Dr, West Sacramento, CA 95691, USA
agilani@miyamotointernational.com

[3] Southern States, LLC.
30 Georgia Avenue, Hampton, GA 30228, USA
f.blalock@SouthernStatesLLC.Com and cahrano@bellsouth.net

Keywords: Seismic qualification, full-scale shaking table testing, sub-structuring, finite element analysis, electrical substation equipment, support structure effect.

Abstract. *According to the current recommended practice for design of substation equipment in seismic regions, high-voltage electrical equipment needs to be tested in a shaking table test. The test is conducted in as-installed configuration that includes a support structure and the electrical equipment mounted on top of the latter. According to the requirement, the equipment has to be re-tested every time a new support structure is introduced. The support structure's design for the same equipment varies from utility to utility and is related to the utility's-specific needs, design practice, and constraints. Therefore, every time a utility company requires a new support structure, a complete assembly of the new support structure and its equipment, needs to be re-tested in a shaking table test which is time consuming and expensive. The main objective of this paper is to study numerically such coupled systems consisting of a support structure and high-voltage substation equipment to provide recommendations on the design of the support structures. Optimization of the support structure design that results in adequate seismic performance of the equipment is studied in this paper. The results of the analysis are verified by full-scale tests of a 500-kV air disconnect switch on the shaking table. The complete assembly of the full-scale switch including the support structure is more than 10 m tall and the equipment is about 5 m tall. The same piece of equipment is seismically tested on different support structures to estimate the effect of the support structure on the overall performance of the coupled system. Moreover, the results of this experimental and analytical research are compared to real-time hybrid simulation results of similar equipment published earlier.*

1 INTRODUCTION

In past and recent earthquakes, high voltage substation components have suffered damage leading to disruption in power distribution [1]. As a result, electric utilities have suffered financial losses and the lag in restoring power delayed the restoration of essential services and post-earthquake recovery. Lengthy power outages may potentially inflict significant economic damage on affected communities or whole regions. The recent earthquakes in New Zealand and Japan serve as representative examples of such failures as well as the challenges of the recovery efforts. The IEEE693 Working Group was formed in part to address the seismic vulnerability of such high voltage equipment and to formulate procedures for seismic qualifications of such equipment in the standard.

The current version of the IEEE standard covering the seismic qualification of substation equipment was published in 2006 [2]. The standard requires that equipment and components of higher voltage classes must be seismically qualified by multi-axial testing on earthquake simulators (shake tables). In general, equipment requiring shake table testing possesses vulnerable characteristics, such as massive tall insulators or other components that have historically performed poorly in earthquakes.

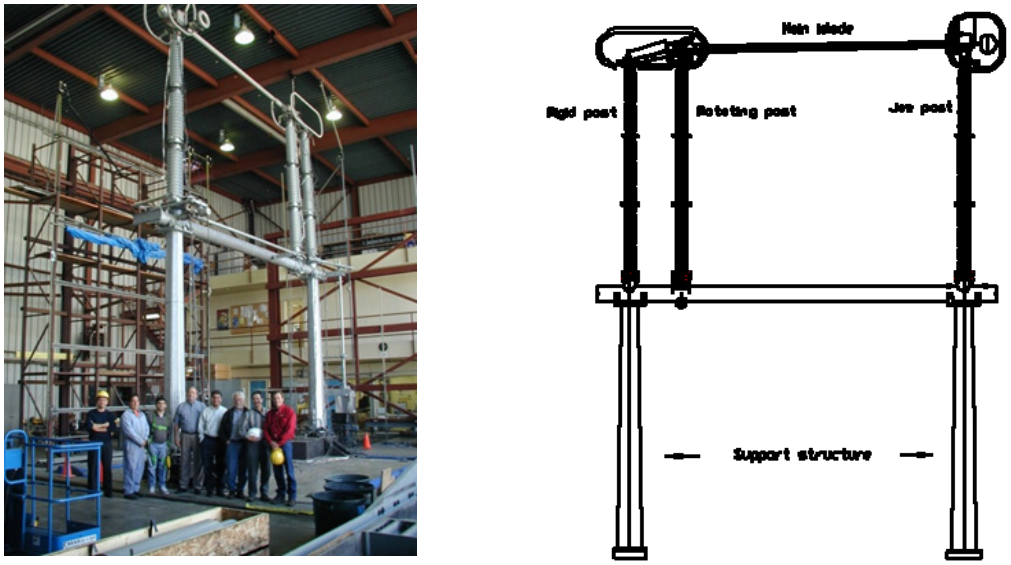
The IEEE693 Working Group is developing the next version of the standard and bases its requirements on the feedback received from open discussions with academia, utility companies, consulting engineers, and equipment manufacturers. The involvement of all interested parties in the development process of the standard has been proven to be very beneficial.

2 EQUIPMENT AND ITS SUPPORT STRUCTURE

Substation components or entire equipment assemblies are often installed on a supporting structure to provide structural integrity as well as achieve electrical clearance from the ground. Examples include: a disconnect switch on a support structure, bushings on top of a transformer, a circuit breaker on a supporting structure and many others. Since all equipment requiring shake table testing must be tested full-scale (preferably in the as-installed configuration), the feasibility of seismic qualification by testing can be limited by the capacity of a test laboratory. These limitations may include the clearance above the shake table, the footprint of the support structure and the equipment itself. The allowed payload of a shake table, displacement and velocity limits are also significant factors to consider. Utilities may often use support structures of their own design, and certain types of equipment may be installed with widely varying support configurations depending on functional needs.

To address these issues, the standard allows the testing of electrical equipment without a support structure under amplified strong motion that accounts for the effects of a support structure. Since no guidance on how that amplification has to be derived, there is some misunderstanding when it comes to testing equipment without a support structure. To some extend this approach is somewhat related to the sub-structuring idea when a system is subdivided into two or many components. These components are interacting with each other ensuring interaction of the components as parts of a coupled system. To achieve this interaction, all six degrees of freedom needed to be imposed at all interfacing nodes between the components. Since the majority of shaking tables can reproduce only three degrees of freedom, this approach is not conservative enough and can miss amplification coming from the remaining degrees of freedom. This shortcoming of this approach is discussed in this paper and is based in part on the extensive research program conducted on the 550-kV vertical break disconnect switch at the University of California, Berkeley as part of the Lifelines Program [3]. The switch was tested using many configurations, including the two major ones: main blade closed and main blade open. The latter configuration was tested with amplified strong motion

obtained from the top of the support structure. The switch in closed configuration is presented in Figure 1. Later on, the same equipment was tested on three different support structures to investigate the effect of support structure with stiffer designs.



a) b)

Figure 1: Photo of 500-kV switch installed on shaking table (left) and its schematic drawing (right).

3 PHYSICAL PROPERTIES OF EQUIPMENT AND SUPPORT STRUCTURES

3.1 Support structure

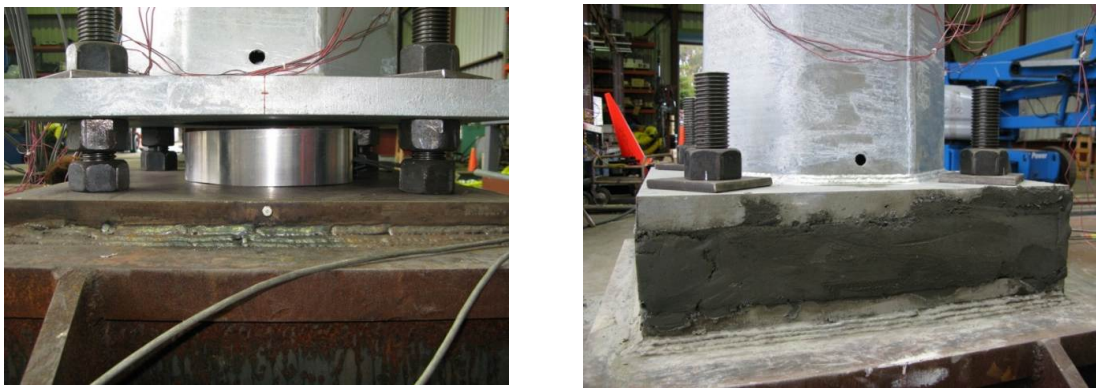
In the recent years following study [3], several support structures were introduced into the investigation and the 500-kV switch was tested on three more support structures. All the support structures had a similar overall design and they consisted of two identical steel columns with octagonal cross sections. The columns were fabricated from 4.76 mm and 7.94 mm thick steel and were tapered as summarized in Table 1. As presented in the table, the distance between opposite flats of column, *D*, measured at its top and bottom, varied from column to column. This distance was incrementally increased to increase the stiffness of the support columns. Here, in *D*, also called AF (Across Flats) distance.

Support	*D* at base, m	*D* at top, m	Wall thickness, mm	Length, m	Reference
SA	0.445	0.305	4.76	4.29	[3]
SB	0.457	0.305	7.94	4.64	[5]
SC	0.508	0.406	7.94	4.64	[6]
SD	0.660	0.406	7.94	4.64	[7]

Table 1: Design details for each support column studied.

As a general practice, a support structure is installed on several anchors embedded into a concrete foundation. An exposed portion of the anchors is long enough to accommodate leveling nuts under the bottom plate of the support column as presented in Figure 2a. In some cases this space is packed with grout or left exposed as presented in Figure 2b. An earlier study [4] showed that the presence of grout under the support structure has a negligible effect on the

stiffness of the support column and its natural frequency. Hence, the effect of grout is neglected in this study.



a) space left between bottom plate and foundation b) the same space packed with a grout

Figure 2: Details of the support structure installation on the anchor rods

The difference between completely rigid installation of the column SA and installation with leveling nuts was also studied earlier [3] and summarized in Table 2. The table also presents a summary of natural frequencies obtained from a numerical analysis of other columns.

Support installation	Cantilever stiffness, kN/m	Frequency, Hz	Damping, %
SA: Rigid	972.0	15.4[1)]	0.5
SA: 8 D44.5 mm rods	796.8	NA	NA
SB	NA	13.6[2)]	NA
SC	NA	14.7[2)]	NA
SD	NA	19.6[2)]	NA

Notes: 1) measured in impact test; 2) estimated from the numerical models of the columns

Table 2: Measured structural response of support column.

3.2 Equipment Components: Insulators

A switch design varies from manufacturer to manufacturer. The switch considered in this study was assembled from several porcelain insulators installed on a tubular base of the switch (please refer to Figure 1b). Two insulators are structurally connected to each other to provide main functionality of the switch – to open and close an electrical connection between terminals of the switch. They're usually called rigid and rotating insulators depending on the function they perform. One terminal of the electrical connection is installed on this group and another terminal is installed on a stand-alone insulator (called jaw insulator). A blade is manufactured from a conductive material (aluminum in this case) and provides a flow of electricity when the switch is in a closed configuration. The structural performance of the switch is controlled by the design details of all its connections and strength capacity of the insulators. Increasing the strength of the insulators usually leads to an increase of the insulators' weight.

Since the switch design is under constant development and enhancement, the switch tested in this study had some variations from specimen to specimen. The enhancements of the switch design are aimed at strengthening the connections while utilizing insulators with greater strength (larger mass).

Structural properties of the insulators used in one of the switch designs tested earlier [3] are summarized in Table 3. The table presents the data obtained for the insulators rigidly fixed to

a strong structural floor, so the frequencies and the stiffnesses represent physical properties of an ideal rigid installation.

Insulator	Cantilever stiffness, kN/m	Frequency, Hz
Rigid and Jaw	164.6	8.3
Rotating	162.9	8.2

Table 3: Measured structural properties of insulators (rigid installation).

3.3 Equipment Assembly

The switch without a support structure was studied in rigid and, so-called, flexible installation. The latter configuration simulated the flexibility of the support's top plate. A summary of this study is presented in Table 4.

Configuration	Direction	Frequency, Hz	Damping, %
Rigid	In-plane	3.9	1.0
	Out-of-plane	3.0	2.0
Flexible (flexibility of sup-port's top plate was simulated)	In-plane	3.4	2.0
	Out-of-plane	2.5	2.0

Table 4: Measured structural response of switch assembly without a support

3.4 Complete Assembly (Support and Switch)

A complete assembly of the switch will combine all the structural properties of each individual component into one interconnected and complex system. Since the attachment details of each component is quite different from an ideal rigid installation, the overall frequency and stiffness of the switch will be much lower than that of its individual components as presented in Table 5.

Direction	Cantilever stiffness, kN/m	Frequency, Hz	Damping, %
In-plane	87.6	1.7	1.0
Out-of-plane	218.9	2.6	1.0

Table 5: Measured structural properties of switch SW1 on Support SA

Other switches were studied in lesser detail and as such, only natural frequencies are summarized in Table 6.

Switch/Support con-figuration	Frequency in-plane, Hz	Frequency in out-of-plane, Hz
SW1 on SA (2003)	2.6	1.7
SW2 on SB (2011)	2.8	2.2
SW3 on SC (2013)	2.9	2.4
SW4 on SD (2014)	3.5	2.8

Table 6: Measured resonant frequencies of all systems

3.5 Complete Assembly Tested on Shaking Table

All the switches presented in Table 6 were tested on a shaking table to evaluate their seismic performance. One of the main performance parameters studied in this paper is a spectral amplification on top of the support structure. In many cases it serves as a good parameter, showing the frequency content of the energy passed to a switch installed on top of a support structure. A typical result is presented in Figure 3 that shows test results for SW2 and SW3 installed on support columns SB and SC, respectively. The spectral amplification peaks at the natural frequencies of the switch: 2.2 Hz for SW2 and 2.4 Hz for SW3. The plot presents results for out-of-plane direction of the switch in a closed configuration which was the most demanding for the switch.

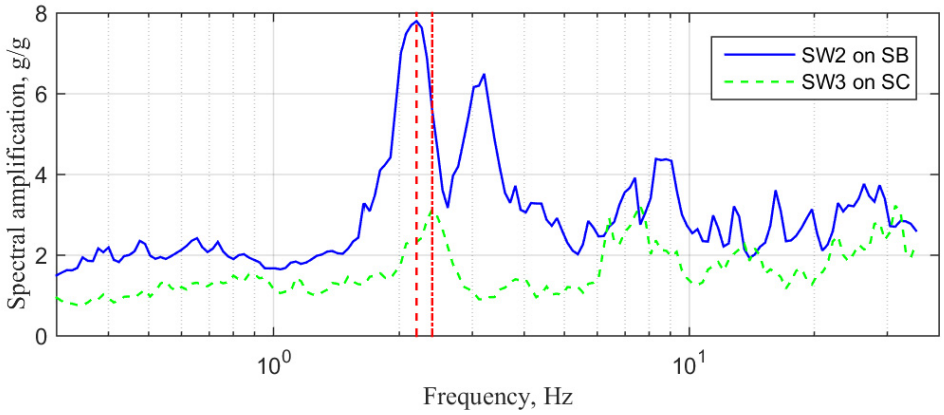


Figure 3: Spectral amplifications estimated from the accelerations recorded during shaking table tests (response on top of support structure versus input at the bottom of the supports)

4 THEORETICAL ESTIMATES AND FINITE ELEMENT ANALYSIS

4.1 Simplified Frequency Estimate for Tubular Columns of Support Structure

As a starting point, it was assumed that the structural performance of the support columns can be closely approximated by thin-walled cylindrical tubes with the same wall thickness as the support columns studied. In this case, the frequency of the column can be estimated from an analytical expression derived from the Euler–Bernoulli beam theory [8]:

$$f_n=(\beta_n)^2 sqrt(EI/\rho A)/(2\pi L^2),$$

where E is the Young modulus of the tube's material, I is the second moment of area of the beam's cross-section, A is the cross-section's area, ρ is the density of the tube's material, (β_n) is the factor obtained from the eigenvalue solution which is equal to 1.875 for the first frequency of a cantilever beam.

If the inner diameter is denoted by R_i and the outer radius of the tube is denoted by R_o, the following expressions can be obtained for I and A:

$$A = \pi(R_o^2 - R_i^2) \text{ and } I = \pi(R_o^4 - R_i^4)/4.$$

The latter equation can be simplified to the following:

$$I = A(R_o^2 + R_i^2)/4.$$

Hence, a change in radius of the tubular support, while keeping its height and wall thickness the same, will result in a new frequency $f_n^{(2)}$ that is related to the original frequency $f_n^{(1)}$ by the following expression:

$$f_n^{(2)}=sqrt((R_o^{(2)2}+ R_i^{(2)2})/(R_o^{(1)2}+ R_i^{(1)2}))\, f_n^{(1)},$$

where it is assumed that the radii of the tube charges from $R_i^{(1)}$ and $R_o^{(1)}$ to $R_i^{(2)}$ and $R_o^{(2)}$. In many practical applications, including the cases considered in the study, the wall thickness is much less than the radius of the tube. Ignoring terms of higher order, the last equation can be simplified to the following:

$$f_n^{(2)}= (R_o^{(2)}/R_o^{(1)})\, f_n^{(1)} \tag{1}$$

Hence, for a thin-walled tubular column the new frequency will be proportional to the ratio of the new radius to that of the original. Therefore, one of the first suggestions in the increasing frequency of the support structure would be the increasing radius of the support column as it was done in the experimental phase of this study. For example, a radius change from 0.222 m to 0.330 m will result in a 49% increase of frequency.

In opposite to that, increasing the height of the support structure leads to drop in the resonant frequency. From the equations provided above, this change will be proportional to the ratio of the heights $L^{(1)}$ *to* $L^{(2)}$ in the second power:

$$f_n^{(2)}= (L^{(1)}/L^{(2)})^2\, f_n^{(1)} \tag{2}$$

For example, a height increase from 4.29 m column to 4.64 m column will result in a 17% percent drop of the resonant frequency.

The combined effect of the height and radius variations on the frequency is presented in Figure 4.

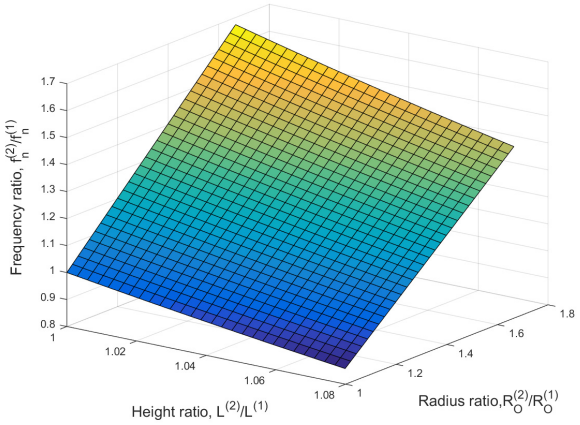
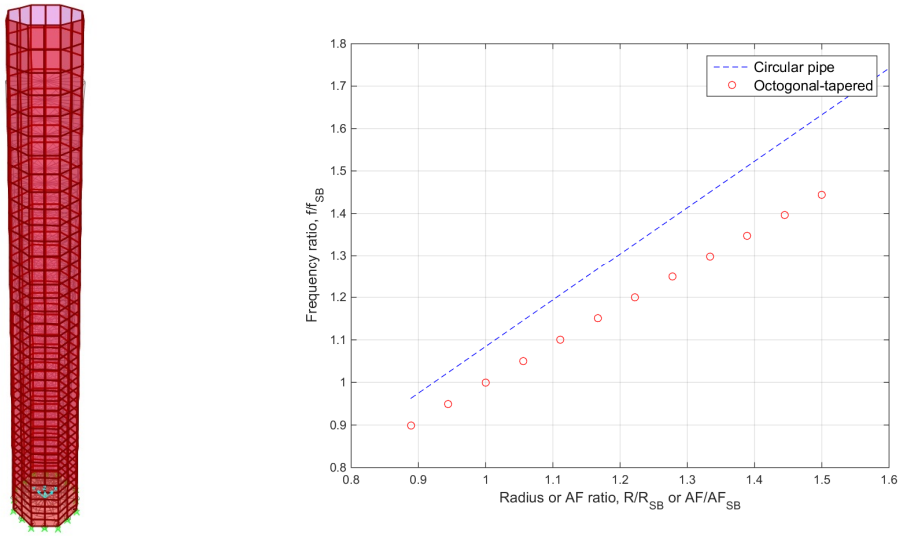


Figure 4: Combined effect of height and radius variation on resonant frequency of thin-walled tubular support column with constant wall thickness.

4.2 Finite Element Analysis of Tapered Columns

A number of finite element models of the tapered columns with octagonal cross sections were created as presented in Figure 5a. The models were generated by generating a mesh in Matlab [9] environment and running analysis in SAP2000 [10]. An extensive parametric study was conducted on a large set of tapered columns, a small subset of which, was represented by the columns used in the testing program. The natural frequencies of the models were compared against that of the straight circular pipe. The taper and the distance across the flats (AF) were varied independently from each other.

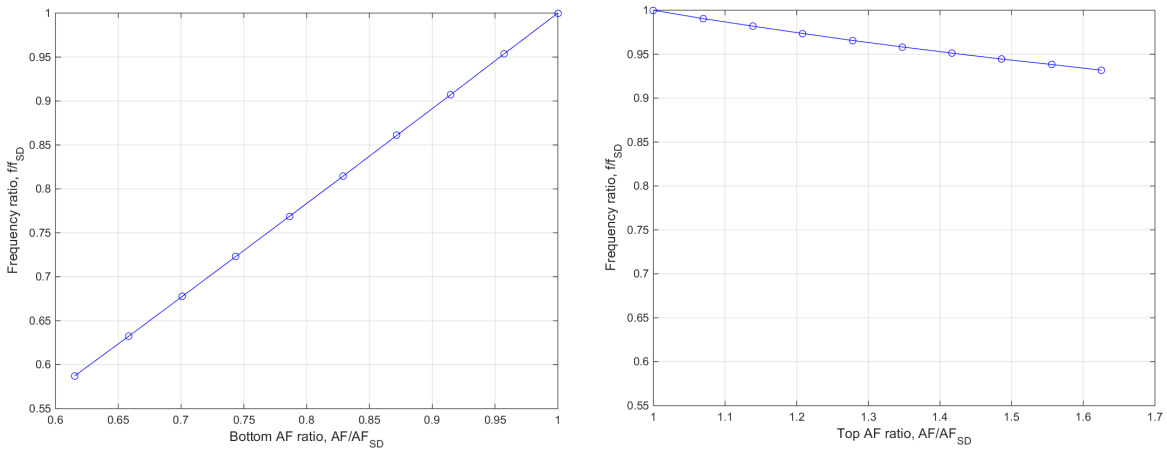
For the parametric study investigating the AF distance effect on the natural frequency, the columns length, its taper, and the wall thickness remained the same from model to model. A taper of column SB was selected as a benchmark. When the taper remains constant, the ratio of frequencies has almost linear relationship with the AF ratio as presented in Figure 5b. This type of a linear correlation between the frequencies and radii of the thin-walled circular columns was discussed earlier and can be closely described by Eq. 1. In the case of the tapered thin-walled columns, the natural frequency of the column is lower than that of the pipe with the same diameter as AF distance and the slope of the frequency change is less than that for the circular column. For example, a 50% increase in AF distance will result in about a 45% increase in the natural frequency (please refer to Figure 5b).



a) Typical FE model b) Relationship between frequency and AF ratio (red)

Figure 5: Comparative analysis for circular versus tapered-octagonal support column (taper is constant).

A taper of the octagonal columns also varied from the largest one studied (support SD) all the way to zero. The latter corresponds to a column with no taper. For this parametric study, the column length, AF distance on top or bottom, and the wall thickness remained the same from model to model. Column SD was selected as a benchmark. Figure 6a shows a significant frequency decrease when the top of AF is fixed and the bottom of AF is reducing. The latter fact is expected, since the second moment of the cross section's area will reduce dramatically at the bottom of the column when the bottom of AF is reducing. This will reduce the column's effective stiffness and natural frequency. It is quite opposite for the case when the cross section at the bottom of the column is fixed and top cross section is changing as presented in Figure 5b (vertical axes in Figure 6a and Figure 6b are in the same scale). These results on Figure 5b are less expected. A significant reduction in the top cross section (to AF is reduced by about 60%) results in only a 6-7% reduction of the natural frequency. This result demonstrates a clear advantage of tapered columns that were utilized in the design of the disconnect switch.



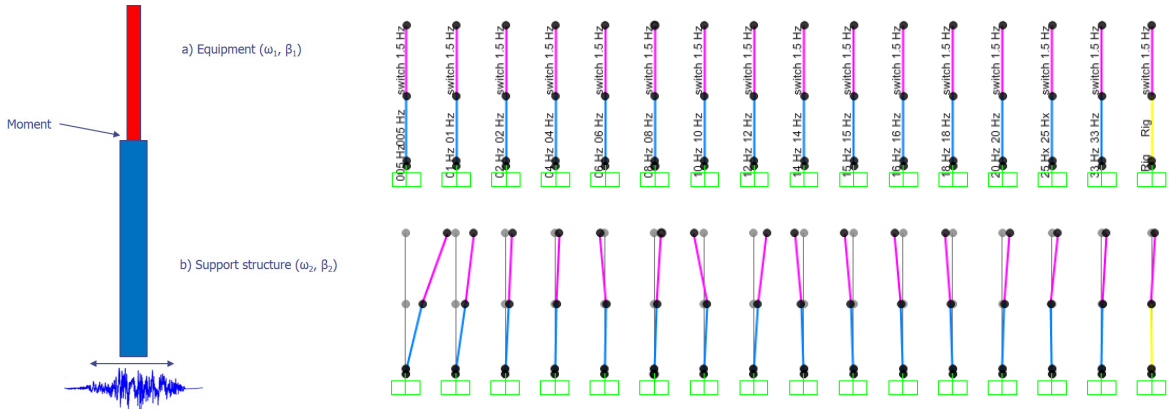
a) Top AF fixed and bottom AF is changing

b) Bottom AF is fixed and top AF is changing

Figure 6: Comparative analysis on variation of column when taper changes from that of column SD to zero (no taper).

4.3 Finite Element Analysis of Complete Switch Assembly

A parametric study on a number of switches installed on different support structures is conducted. The switch's complete assembly is simplified to two Euler–Bernoulli beams installed one on top of another. It is assumed that the switch is the one extensively investigated in [3] with natural frequency of 3 Hz (see Table 4). This beam model of the switch is installed on supports structures with natural frequency varied from 0.5 Hz (very flexible) to 100 Hz (essentially rigid) as presented in Figure 7.



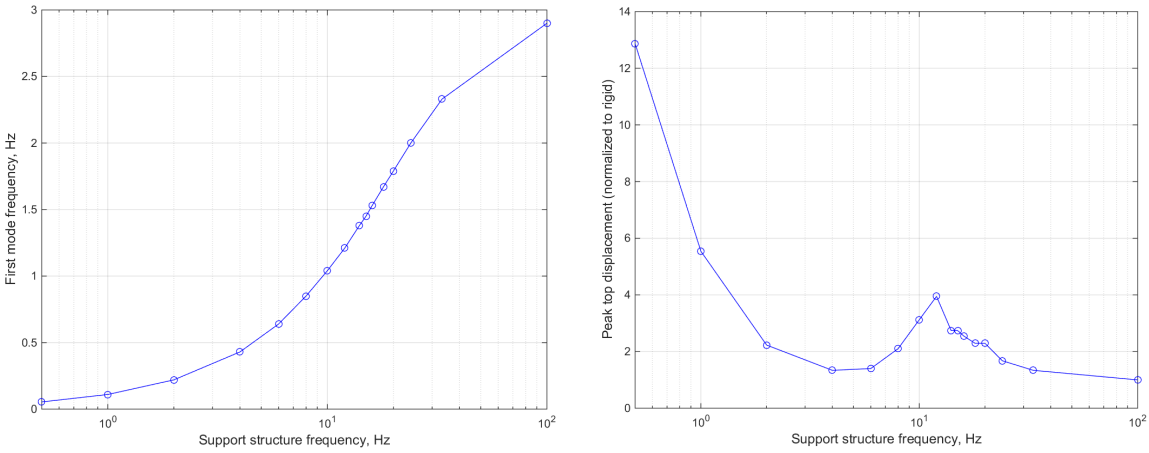
a) FE model of coupled systems

b) Models studied (top) and deformed shapes (bottom

Figure 7: General approach followed for FE model generation of a switch as a coupled system

The overall frequency of the switch as a coupled system will depend on the frequency of the support structure as presented in Figure 8a. A peak displacement on top of the switch has a peak at 12 Hz support structure and drops down after that as presented in Figure 8b. This is consistent with the test results which also showed that the stiffer support structure is more beneficial for reducing spectral accelerations on top of the support structure (please refer to Figure 3) and for reducing peak displacements on top of the switch (as shown in Figure 8b). The variation of the peak moment at the bottom of the equipment from model to model is pre-

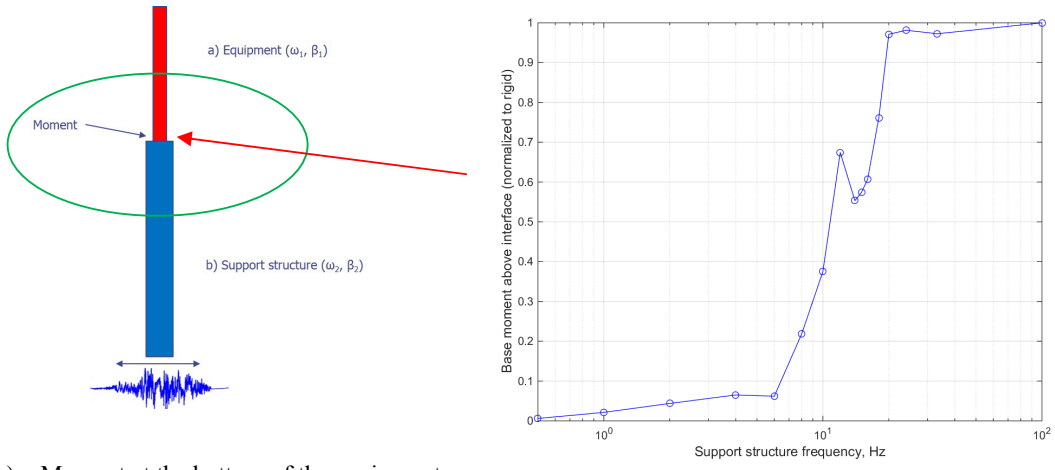
sented in Figure 9. In the case of equipment constructed with porcelain or polymer insulators, strain gages are usually installed at this location to estimate a moment at the bottom of the equipment and correlate it to the insulator's cantilever strength. Clearly, the moment can be minimized by selecting a correct support structure for each equipment and, as such, the seismic performance of the switch can be optimized by means of the proposed finite element analysis.



a) Overall frequency of coupled system

b) Peak displacement versus frequency of support structure

Figure 8: Variation of the system's overall frequency and peak displacement at top of the equipment from model to model



a) Moment at the bottom of the equipment can be correlated to cantilever strength

b) Peak moment at the bottom of the equipment

Figure 9: Variation of peak moment at the equipment's bottom from model to model

Similar conclusions about the feasibility of support structure optimization were made earlier in a hybrid simulation study investigating a coupled system consisting of a FE model of the support structure and a physical object (electrical equipment) [11].

5 CONCLUSIONS

- Similar to a theoretical prediction for a thin-walled cylindrical support column, a frequency of a tapered thin-walled octagonal support column linearly increases when the AF distance increases and it is independent of the wall thickness.
- The increasing taper of the thin-walled octagonal support column results in a relatively small decrease of the natural frequency. Hence, such columns are beneficial for use in support structures.
- Stiffer support structure reduces spectral accelerations on top of the support structure that results in smaller spectral amplifications.
- Stiffer support structures help to minimize peak displacements on top of the switch which is important for interconnected electrical equipment.
- Proper finite element analysis with well-calibrated models can help with optimization of the seismic performance of switches and other electrical equipment installed on support structures.
- The simplified analysis demonstrated the validity of the concept. A numerical analysis of more detailed switch models is required to reconcile test results with the analysis.

6 ACKNOWLEDGEMENTS

Acknowledgements are due to Southern States, LLC for providing access to the test data and sponsoring publication of the test results.

REFERENCES

[1] Eric Fujisaki, Shakhzod Takhirov, Qiang Xie, and Khalid M. Mosalam. *Seismic Vulnerability of Power Supply: Lessons Learned from Recent Earthquakes and Future Horizons of Research.* EURODYN 2014: 9th International Conference on Structural Dynamics, 30 June – 2 July 2014, Porto, Portugal.

[2] *IEEE693: IEEE Recommended Practice for Seismic Design of Substations.* IEEE, 2006.

[3] Takhirov, S., Fenves, G., and Fujisaki, E. (2005). *Seismic Qualification and Fragility Study of Line Break 550-kV Disconnect Switches*. Pacific Earthquake Engineering Research Center, University of California at Berkeley, PEER 2004/08.

[4] K.M. Mosalam, M.A. Moustafa, M.S. Günay, I. Triki and S. Takhirov. *Seismic Performance of Substation Insulator Posts for Vertical-Break Disconnect Switches.* California Energy Commission. Publication number: CEC-500-2012-XXX, March 2012.

[5] Shakhzod M. Takhirov. *Seismic Qualification Study of 550-kV Vertical Break Disconnect Switch, Report No. PEER – STI/2011-02*. Pacific Earthquake Engineering Research Center University of California, Berkeley, September 2011.

[6] Shakhzod M. Takhirov, *2013 Test Program of 500-kV Vertical Disconnect Switch Conducted for Two Different Support Structures. Short Memo/Report 2013/01.* Pacific Earthquake Engineering Research Center, February 2013.

[7] Shakhzod M. Takhirov. *Seismic Qualification Study of 550-kV Vertical Break Disconnect Switch, Report No. PEER – STI/2014-10*. Pacific Earthquake Engineering Research Center University of California, Berkeley, March 2014.

[8] S. Timoshenko, D.H. Young, W. Weaver. *Vibration Problems in Engineering. 4th Edition,* John Wiley & Sons, Inc., 1974.

[9] Matlab R2014b. The MathWorks, Inc., 2014.

[10] SAP2000 Version 16. Computers and Structures, Inc., 2015.

[11] Shakhzod Takhirov, Selim Günay, and Khalid Mosalam. *Real-Time Hybrid Simulation on a Long-Stroke High-Velocity Shaking Table Configuration as a Valuable Tool for IEEE693 Standard Development*, Transactions of SMiRT-22, San Francisco, California, USA - August 18-23, 2013.

COMPDYN 2015
5th ECCOMAS Thematic Conference on
Computational Methods in Structural Dynamics and Earthquake Engineering
M. Papadrakakis, V. Papadopoulos, V. Plevris (eds.)
Crete Island, Greece, 25–27 May 2015

STOCHASTIC REDUCED-ORDER MODELS FOR CALCULATING RESPONSE STATISTICS OF STRUCTURAL SYSTEMS SUBJECTED TO RANDOM INPUT

Alin Radu[1] **and Mircea Grigoriu**[2]

[1]AIR Worldwide
San Francisco, CA 94111
e-mail: aradu@air-worldwide.com

[2] Cornell University
Ithaca, NY 14853
e-mail: mdg12@cornell.edu

Keywords: Stochastic reduced order models, random input, ordinary differential equations, Monte-Carlo simulation, non-linear systems.

Abstract. *Probabilistic characterization of a system's response under random dynamic input is essential for performance-based engineering. Monte Carlo simulation is the only general method available for estimating response statistics. However, the method is computationally expensive for realistic structural systems since it involves repeated deterministic dynamic analyses for a large number of samples of the random input. The framework of random vibration is also inadequate for calculating response statistics for linear systems under non-Gaussian inputs and non-linear systems subjected to both Gaussian and non-Gaussian excitation.*

We propose a novel, highly efficient method for calculating response statistics. The method is based on stochastic reduced-order models (SROM), i.e., stochastic processes that have a finite number of samples selected in an optimal manner from samples of the input process. The SROM-based method can be viewed as a smart Monte-Carlo. Like Monte-Carlo simulation, the method uses random samples of the input to characterize structural response. Unlike Monte Carlo, which uses a large number of samples selected at random, SROM selects just a small number of samples in an optimal way. Numerical examples of the newly proposed method are presented for single-degree-of-freedom linear and non-linear Duffing and Bouc-Wen systems.

1 INTRODUCTION

Calculation of response statistics of structures subjected to seismic loads is an essential part of performance-based seismic design. Monte Carlo is the only general method available for calculating this type of statistics. However, the method is computationally impractical for realistic structural systems since it involves repeated deterministic dynamic analyses for randomly selected samples of seismic load processes. This procedure makes Monte Carlo method computationally expensive.

The framework of linear/non-linear random vibration is also inadequate for calculating response statistics. Classical theory of linear random vibration provides efficient tools for calculating the first two response moments for linear systems. For example, unless the input is Gaussian and the system is linear or the output can be assumed to be Gaussian, the first two moments of the response are insufficient for calculating exceedance probability ([1], Sect. 7.2). This is a significant limitation since structural systems behave non-linearly under strong seismic loads.

The main goal of this paper is to propose two novel, conceptually-simple, accurate, non-intrusive and computationally-efficient methods for calculating response statistics for structures subjected to seismic loads. The methods are based on stochastic reduced order models (SROMs) [2], i.e. stochastic processes that have a finite number of samples selected in an optimal manner from the samples of the target process. Like Monte Carlo simulation, the methods use samples of seismic load processes to characterize structural response and is not intrusive in the sense that their construction uses deterministic solutions. However, the proposed methods use a small number of load samples selected in an optimal manner. In contrast, Monte Carlo simulation uses a large number of samples selected at random.

The first method, referred to as *the first-order SROM*, constructs a SROM using directly the input samples. The second method, referred to as *the second-order SROM*, requires a parametric model, with random parameters, whose samples are evaluated from input samples. A SROM is constructed for the random parameters, which implicitly defines a SROM for the random input.

The use of optimally selected samples allows to reduce the number of simulations required by the Monte Carlo method by one or two orders of magnitude while retaining accuracy. The method has been originally developed for dynamic response [3]. Recently, it has been shown that for static problems the SROM-based method can be improved significantly [4]. Preliminary studies indicate that similar improvements will provide accurate solutions for random vibration problems [5]. Optimization algorithms have been developed for constructing SROMs for random random vectors [2, 6]. Applications of SROM in earthquake engineering, for efficient calculation of fragility surfaces, were already developed in [7].

Response statistics are calculated for linear and non-linear systems subjected to samples of random input through the two new SROM methods and results are compared with the reference Monte-Carlo ones. The SROM match satisfactory the expected results with a fraction of the computational effort.

2 PROBLEM DEFINITION

Simplified models of real systems are often used in structural engineering. Three simple examples of models of single-degree-of-freedom (SDOF) systems are represented by the fol-

lowing three ordinary differential equations:

$$\ddot{Y}(t) + 2\zeta\nu\dot{Y}(t) + \nu^2 Y(t) = X(t) \tag{1}$$

$$\ddot{Y}(t) + 2\zeta\nu\dot{Y}(t) + \nu^2(Y(t) + \rho Y^3(t)) = X(t) \tag{2}$$

$$\ddot{Y}(t) + 2\zeta\nu\dot{Y}(t) + \nu^2(\rho Y(t) + (1-\rho)W(t)) = X(t) \tag{3}$$

$$\dot{W}(t) = -\gamma\dot{Y}(t) + \alpha|W(t)|^{\eta-1}W(t) + \beta\dot{Y}(t)|W(t)|^{\eta}$$

where $X(t)$ is the random input represented by a stochastic process; $Y(t)$, $\dot{Y}(t)$ and $\ddot{Y}(t)$ are the displacement, velocity and acceleration of the SDOF system, respectively; and ν, ζ, α, β, γ, ρ and η are scalars representing system parameters. Equations (1-3) define known systems, i.e. linear, Duffing and Bouc-Wen oscillators, respectively. Parameters ν and ζ in Eq. (1) are also known as the natural frequency and the damping ratio of the linear system.

We want to find statistics of the extrema for the processes $Y(t)$ defined in Eqs. (1-3). For example, we will calculate the probability of exceedance $\mathbb{P}\left(\max_{0\le t\le\tau}|Y(t)| > y_{cr}\right)$, where τ is the duration of the process $X(t)$ and y_{cr} is some critical value of the displacement.

The input process $X(t)$ is a stochastic process and it can represent any type of random loading, such as earthquake or wind. Usually the input process is available in the form of a catalog of recorded events, i.e. samples of $X(t)$. Therefore, for generality we consider that our input is represented by a specified large number n of samples $x(t)$ of $X(t)$.

3 SOLUTION

Two SROM-based methods are used to solve the problem and results are compared with the reference Monte-Carlo results. SROM can be seen as a smart Monte-Carlo method. Like Monte-Carlo, it uses randomly generated samples of the stochastic process $X(t)$. Unlike Monte-Carlo, in which samples are equally likely, in SROM the samples are chosen in an optimal way and are weighed by probabilities.

3.1 Monte-Carlo Solution

The Monte-Carlo method relies on solving the ODEs in Eqs. (1-3) for all available samples $\{x_i(t),\ i = 1, ..., n\}$ of $X(t)$. Then the exceedance probability of interest is calculated as

$$P^{MC}(y_{cr}) = \mathbb{P}\left(\max_{0\le t\le\tau}|Y(t)| > y_{cr}\right) = \frac{1}{n}\sum_{i=1}^{n}\mathbb{1}\left\{\max_{0\le t\le\tau}|y_i(t)| > y_{cr}\right\}. \tag{4}$$

3.2 First-order SROM Solution

The first-order stochastic reduced order model is defined directly for the samples of the input process $X(t)$. Any number m_1 of samples $\{\tilde{x_k}(t),\ k = 1, ..., m_1\}$ of $X(t)$ and probabilities $\{p_k \ge 0,\ k = 1, ..., m_1\}$ such that $\sum_{k=1}^{m_1} p_k = 1$ define a stochastic reduced order model. We denote the SROM as $\tilde{X}(t) = \{(\tilde{x}_k, p_k),\ k = 1, ..., m_1\}$. It is shown [2] that it is possible to find a selection of $\{(\tilde{x_k}(t), p_k),\ k = 1, ..., m_1\}$ such that $X(t)$ and $\tilde{X}(t)$ have similar probability laws for $m_1 << n$.

We are looking for a SROM $\tilde{X}(t)$ with a range $\{\tilde{x_k}(t),\ k = 1, ..., m_1\}$ of a relatively small number m_1 of independent samples of $X(t)$. Our objective is to find an optimal vector $p^{opt} = (p_k^{opt},\ k = 1, ..., m_1)$ that minimizes the discrepancies between the probability laws of $X(t)$ and $\tilde{X}(t)$ [9]. We obtain p^{opt} by solving an optimization problem with an objective function which

measures differences between various statistics of $X(t)$ and $\tilde{X}(t)$. It is suggested in [2] to use an objective function of the form

$$h(p) = \sum_{i=1}^{3} e_i h_i(p), \tag{5}$$

where $h_1(p),\ h_2(p),\ h_3(p)$ measure the differences between the moments, marginal distributions and covariance functions of $X(t)$ and $\tilde{X}(t)$, respectively, where $p = (p_i,\ i = 1, 2, 3)$ and $(e_i \geq 0,\ i = 1, 2, 3)$ are some weights which account for the relative importance of components $h_i(p)$.

Statistics for $X(t)$ can be calculated directly from its probability law if $X(t)$ is well defined. However, in our case, in order to maintain the idea of the input being defined as a catalog of samples, statistics for both $X(t)$ and $\tilde{X}(t)$ are estimated from their samples. Thus, the moments of order q are

$$\mu(t; q) = \mathbb{E}[X^q(t)] = \frac{1}{n} \sum_{i=1}^{n} x_i^q(t), \tag{6}$$

$$\tilde{\mu}(t; q) = \sum_{k=1}^{m_1} p_k \tilde{x}_k^q(t), \tag{7}$$

the marginal distributions are

$$F(\xi_j; t) = \mathbb{P}(X(t) \leq \xi) = \frac{1}{n} \sum_{i=1}^{n} \mathbb{1}\left\{x_i(t) \leq \xi_j\right\}, \tag{8}$$

$$\tilde{F}(\xi_j; t) = \sum_{k=1}^{m_1} p_k \mathbb{1}\left\{\tilde{x}_k(t) \leq \xi_j\right\},\ j = 1, ..., n_F \tag{9}$$

and, finally, the covariance functions can be calculated as

$$\Sigma(t, s) = \mathbb{E}[X(t)X(s)] = \frac{1}{n-1} \sum_{i=1}^{n} x_i(t) x_i(s) \tag{10}$$

$$\tilde{\Sigma}(t, s) = \sum_{k=1}^{m_1} p_k \tilde{x}_k(t) \tilde{x}_k(s). \tag{11}$$

Components of the objective function in Eq.(5) are calculated using the statistics estimated above.

$$h_1(p) = \max_{0 \leq t \leq \tau} \left\{ \sum_{q=1}^{n_q} w_\mu(t, q) \left|\mu(t; q) - \tilde{\mu}(t; q)\right| \right\} \tag{12}$$

$$h_2(p) = \max_{0 \leq t \leq \tau} \left\{ \sum_{j=1}^{n_F} w_F(\xi_j, t) \left| F(\xi_j; t) - \tilde{F}(\xi_j; t) \right| \right\} \tag{13}$$

$$h_3(p) = \max_{0 \leq t, s \leq \tau} \left\{ w_\Sigma(t, s) \left| \Sigma(t, s) - \tilde{\Sigma}(t, s) \right| \right\}, \tag{14}$$

where $w_\mu, w_F, w_\Sigma \geq 0$ are weighing functions. Minimizing the objective function in Eq. (5) results in obtaining the vector p^{opt}. The optimization problem will be repeated for a specified

number of independent sets of m_1 samples of $X(t)$, $\{\tilde{x_k},\ k = 1, ..., m_1\}$. The minimum value of $h(p^{opt})$ indicates a sub-optimal solution p^{opt}.

The selected SROM pairs $\{(\tilde{x_k}(t), p_k^{opt}),\ k = 1, ..., m_1\}$ are used to solve the ordinary differential equations and the target probability is calculated as

$$P_f^{SROM1}(y_{cr}) = \sum_{k=1}^{m_1} p_k^{opt} \mathbb{1}\left\{\max_{0\le t\le\tau} |\tilde{y}_k(t)| > y_{cr}\right\}, \tag{15}$$

where $\tilde{y}_k(t)$ are the solutions of Eqs. (1-3) to $\tilde{x}_k(t),\ k = 1, ..., m_1$.

3.3 Second-order SROM Solution

The second-order SROM method involves using a parametric model for the input process $X(t)$ of the form

$$X(t) = X(t, Z) \approx \sum_{i=1}^{d} Z_i \varphi_i(t), \tag{16}$$

where $Z = (Z_i,\ i = 1, ..., d)$ is a random vector and $\{\varphi_i(t),\ , i = 1, ..., d\}$ are deterministic specified functions of time. Parametric models of this type can be calculated for any stochastic process. We use a truncated Karhunen-Loève model to calculate functions $\{\varphi_i(t),\ i = 1, ..., d\}$ by calibrating it to the first two moments of $X(t)$, that is, the mean and covariance functions [10]. Functions $\varphi_i(t)$ are the eigenvectors of the covariance matrix $\Sigma(t, s)$ defined for $0 \le t, s \le \tau$. Unlike the Karhunen-Loève expansion, for which $X(t) = \lim_{n\to\infty} \sum_{i=1}^{n} \sqrt{\lambda_i} X_i \varphi_i(t),\ t \ge 0$, where λ_i are the eigenvectors and X_i are random variables with zero mean and unit variance, we use the approximation in Eq. (16). The random vector Z_i will be characterized by its samples. Samples $z_{k,i}$ of the random vector Z_i are obtained by minimizing the difference between the actual samples $x_k(t)$ of $X(t)$ and their approximations $\sum_{i=1}^{d} z_{k,i}\varphi_i(t)$, where $z_{k,i}$ denotes the i-th component of sample z_k of Z. In other words, for each sample $x_k(t)$ available we find a sample of $z_k = \{z_{k,i},\ i = 1, ..., d\}$ by minimizing, for example, the mean squared error $\int \left(x_k(t) - \sum_{i=1}^{d} z_{k,i}\varphi_i(t)\right)^2 dt$.

In this second method we construct a SROM $\tilde{Z}$ for Z using the samples of the random vector Z. Let $\tilde{Z}$ be a random vector of the same dimension as Z and samples $\{\tilde{z}_k,\ k = 1, ..., m_2\}$ selected from samples of Z. We associate probabilities $(p_1, ..., p_{m_2})$ for each sample $\tilde{z}_k$ such that $\sum_{k=1}^{m_2} p_k = 1$ and the probability laws of Z and $\tilde{Z}$ are similar, following the same procedure presented in the first-order SROM solution. We call $\tilde{Z}$ a stochastic reduced order model of Z. Moreover, we denote by $\{\Gamma_k,\ k = 1, ..., m_2\}$ the cells of a Voronoi partition of the range of Z, with centers $\{\tilde{z}_k\}$ [4]. A cell Γ_k contains all samples z_i of Z that are closer to $\tilde{z}_k$ than any other $\tilde{z}_l$, i.e. $|z_i - \tilde{z}_k| \le |z_i - \tilde{z}_l|,\ l \ne k$. Note that the probability p_k defines also the probability that Z takes values in cell Γ_k.

The SROM $\tilde{Z}$ of Z also defines a SROM $\tilde{X}(t; Z)$ of $X(t; Z)$ with samples $\{\sum_{i=1}^{d} \tilde{z}_{k,i}\varphi_i(t)\}$ with probabilities $p_k,\ k = 1, ..., m_2$. As in the previous SROM method, $\tilde{X}(t; Z)$ has only m_2 samples $\tilde{x}(t; \tilde{z}_k)$, much smaller than the large number n of available samples of $X(t)$. We denote by $\tilde{y}(t; \tilde{z}_k)$ the solutions of Eqs. (1-3) to $\tilde{x}(t; \tilde{z}_k)$. The response process is approximated by

$$\tilde{Y}(t; Z) = \sum_{k=1}^{m_2} \mathbb{1}\{Z \in \Gamma_k\} \left[\tilde{y}(t; \tilde{z}_k) + \nabla\tilde{y}(t; \tilde{z}_k)(Z - \tilde{z}_k)\right], \tag{17}$$

where $\tilde{y}(t;\tilde{z}_k)$ are the responses as defined previously with their corresponding probabilities p_k and $\nabla\tilde{y}(t;\tilde{z}_k) = \partial Y(t;Z)/\partial Z_i,\ i = 1,...,d$ are called sensitivity factors of the response $Y(t;Z)$ calculated at $Z = \tilde{z}_k$. Function $\mathbb{1}$ denotes the indicator function.

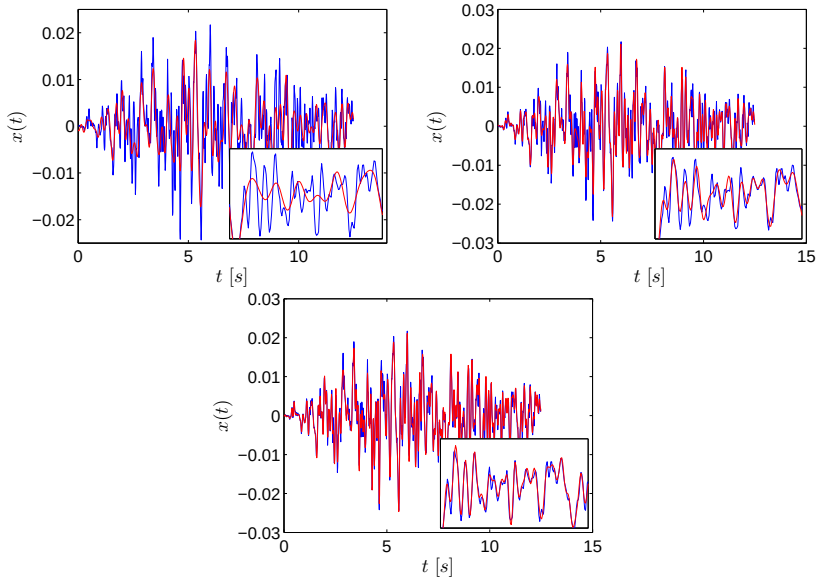


Figure 1: Samples of $X(t)$ and their approximation $\sum_{i=1}^{d} Z_i\varphi_i(t)$ for $d = 100, 200, 300$.

The sensitivity factors can be approximated numerically from the differences between the responses $Y(t;Z)$ calculated at $Z = \tilde{z}_k$ and $Z = \tilde{z}_k + \Delta\tilde{z}_k$, where $\Delta\tilde{z}_k$ denotes a perturbation of $\tilde{z}_k$. They can also be determined by solving deterministic differential equations as illustrated below. The sensitivity factors for the linear system are the solutions of the follwoing ODE with constant coefficients

$$\frac{\partial\ddot{X}(t,Z)}{\partial Z_i} + 2\zeta\nu\frac{\partial\dot{X}(t,Z)}{\partial Z_i} + \nu^2\frac{\partial X(t,Z)}{\partial Z_i} = \varphi_i(t), \tag{18}$$

where $i = 1,...,d$ and they do not depend on the values of $\tilde{z}_k$. The sensitivity factors for the Duffing oscillator in Eq.(2) are the solutions of

$$\frac{\partial\ddot{X}(t,Z)}{\partial Z_i} + 2\zeta\nu\frac{\partial\dot{X}(t,Z)}{\partial Z_i} + \nu^2\frac{\partial X(t,Z)}{\partial Z_i}\left(1 + 3\rho X^2(t;\tilde{z}_k)\right) = \varphi_i(t). \tag{19}$$

Finally, the sensitivity factors $\nabla\tilde{y}(t;\tilde{z}_k)$ for the Bouc-Wen system are the solutions of the following system of deterministic ordinary differential equations

$$\frac{\partial\ddot{X}(t,Z)}{\partial Z_i} + 2\zeta\nu\frac{\partial\dot{X}(t,Z)}{\partial Z_i} + \nu^2\left(\rho\frac{\partial X(t,Z)}{\partial Z_i} + (1-\rho)\frac{\partial W(t,Z)}{\partial Z_i}\right) = \varphi_i(t) \tag{20}$$

$$\frac{\partial W(t,Z)}{\partial Z_i} = -\gamma\frac{\partial\dot{X}(t,Z)}{\partial Z_i} + \alpha\left((n-1)\,\mathrm{sgn}(\tilde{W}_k)|\tilde{W}_k|^{n-2}\tilde{W}_k + |\tilde{W}_k|^{n-1}\right)\frac{\partial W(t,Z)}{\partial Z_i}\bigg|_{Z=\tilde{z}_k}$$
$$+ \beta\left(\frac{\partial\dot{X}(t,Z)}{\partial Z_i}|\tilde{W}_k|^n + n\,\mathrm{sgn}(\tilde{W}_k)\dot{\tilde{X}}_k|\tilde{W}_k|^{n-1}\frac{\partial W(t,Z)}{\partial Z_i}\bigg|_{Z=\tilde{z}_k}\right), \tag{21}$$

where $\tilde{W}_k = (\partial W(t;Z)/\partial Z_i)|Z = \tilde{z}_k$ and $\dot{\tilde{X}}_k = (\partial \dot{X}(t;Z)/\partial Z_i)|Z = \tilde{z}_k$ are deterministic quantities and are calculated from Eq. (3).

Note that the larger the dimension d of vector Z, the better the approximation of $X(t,Z)$ to $X(t)$ is. Figure 1 show one sample of Z using different lengths for the truncation of the KL expansion, i.e. $d = 100$, $d = 200$ and $d = 300$, respectively. Figure 2 shows the mean-squared-error probability density functions between the original samples of $X(t)$ and their approximation by $X(t,Z)$ for various values of d.

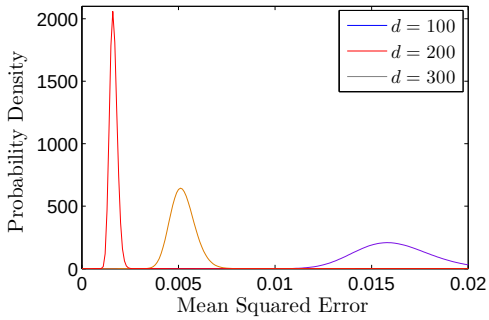


Figure 2: Error densities between samples of $X(t)$ and $\sum_{i=1}^{d} Z_i \varphi_i(t)$ for various d.

The selected SROM pairs $\{(\tilde{z}_k, p_k^{opt}),\ k = 1, ..., m_2\}$ are used to solve the ordinary differential equations and the target probability is calculated as

$$P_f^{SROM2}(y_{cr}) = \sum_{k=1}^{m_2} p_k^{opt} \mathbb{1}\left\{ \max_{0\le t\le \tau} \tilde{y}(t;z_k) > y_{cr} \right\}, \tag{22}$$

where $\tilde{y}(t;z_k)$ are the samples of $\tilde{Y}(t;Z)$ calculated in Eq.(17).

4 Numerical Examples

A numerical example is considered in order to compare the performance of the two SROM-based methods with respect to the reference Monte-Carlo results. We calculate the response statistics for all three systems described above.

For the current example we consider the input process $X(t)$ to be a non-stationary, zero-mean, Gaussian process with known second-order moment properties. We use $n = 10,000$ samples of $X(t)$ in our catalog of input samples. Note that the methodology described in the previous section works also for non-Gaussian processes. The Monte-Carlo statistics are calculated by solving Eqs. (1-3) to all n samples.

First-order SROM The first-order SROM $\tilde{X}(t)$ is calculated using just $m_1 = 20$ samples of $X(t)$. Figure 3 shows the means of processes $X(t)$ and $\tilde{X}(t)$, respectively. Figure 4 and 5 compare marginal distribution and covariance function of $X(t)$ estimated from n samples with the same statistics obtained from the SROM $\tilde{X}(t)$ of $X(t)$.

While the means and the marginal distributions of $X(t)$ and $\tilde{X}(t)$ are reasonably close to each other, it is more difficult to capture the covariance function of $X(t)$ with just the $m_1 = 20$ samples used in the construction of $\tilde{X}(t)$.

Note that the first-order SROM may be improved by either increasing the dimension its dimension m_1 or by improving the selection of the samples in order to minimize the discrepancies between the probability laws of $X(t)$ and $\tilde{X}(t)$.

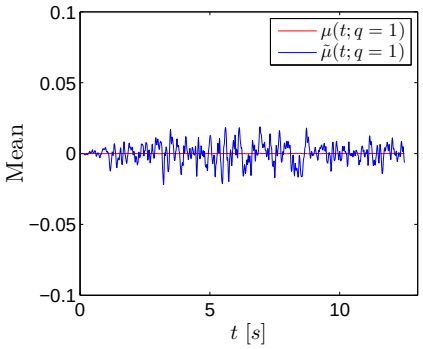


Figure 3: Estimated mean of $X(t)$ and $\tilde{X}(t)$

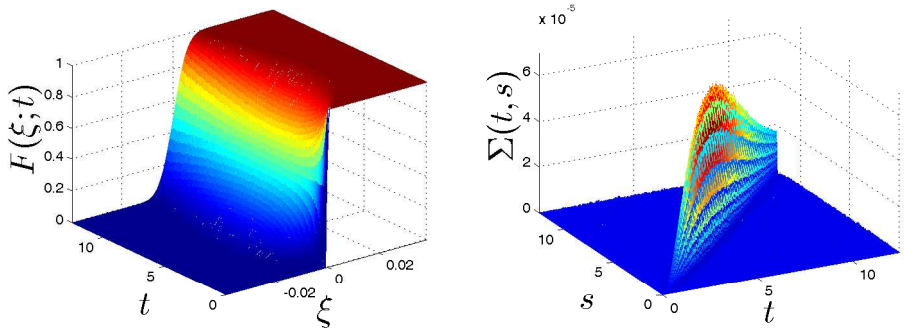


Figure 4: Estimated distribution function and covariance matrix for $X(t)$

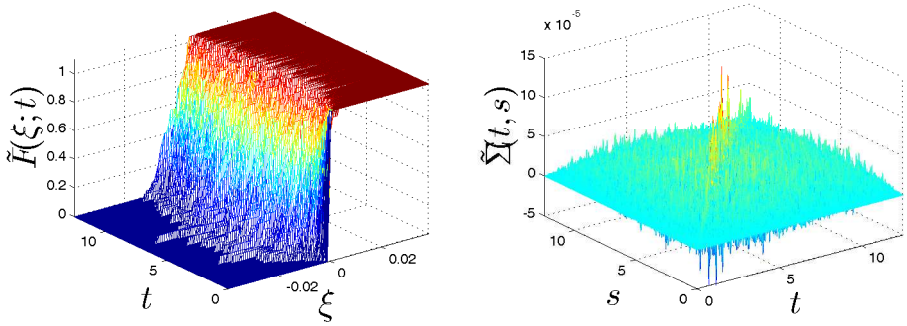


Figure 5: Estimated distribution function and covariance matrix for $\tilde{X}(t)$

Second-order SROM The second-order SROM method involves the construction of a SROM $\tilde{Z}$ for the random-vector parameter Z. We use only $m_2 = 20$ samples of Z. The dimension of Z used is $d = 200$, for which the mean squared error between samples of $X(t)$ and their approximates is around 5×10^{-3} as shown in Figure 2.

Figure 6 shows the means of random-vector parameters Z and $\tilde{Z}$, respectively. Figure 7 and 8 compare the mean, marginal distribution and covariance function of Z and $\tilde{Z}$, respectively. As previously, out of the three statistics, the covariance function is the hardest to match with just $m_2 = 10$ samples of Z.

Note that the second-order SROM built may be improved by either increasing the dimension of the SROM m_2, by increasing the dimension d of the parameter Z, or by using a more efficient methodology of selecting the range of $\tilde{Z}$ in order to optimize the discrepancies between the

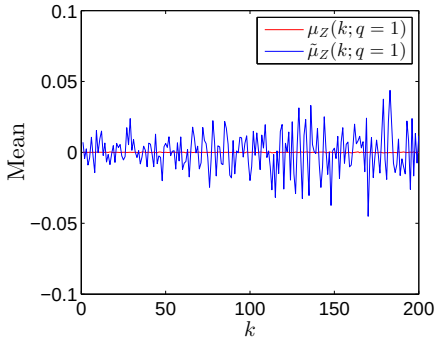


Figure 6: Estimated mean of Z and $\tilde{Z}$

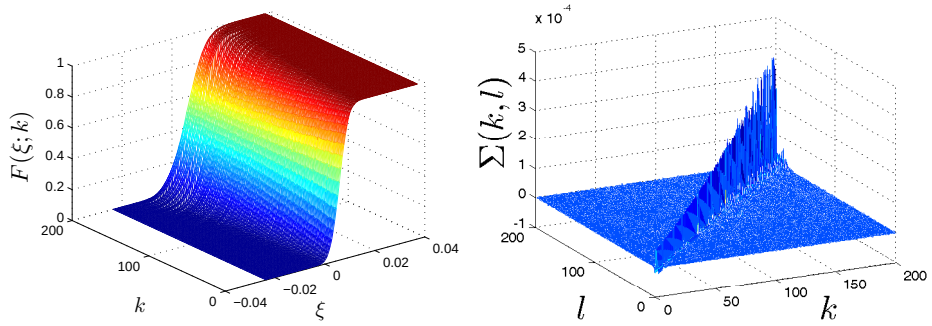


Figure 7: Estimated distribution function and covariance matrix for Z

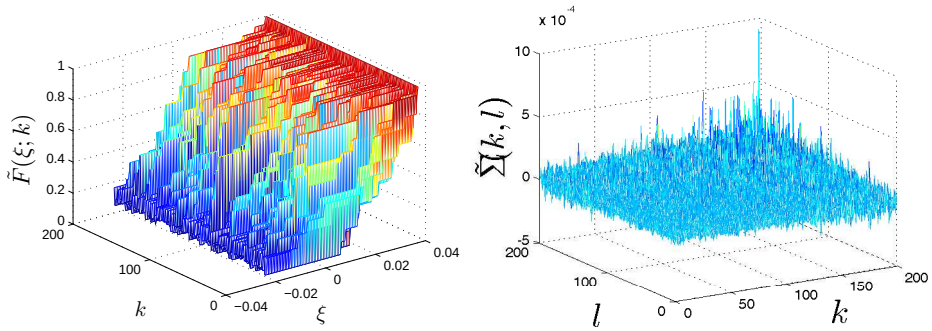


Figure 8: Estimated distribution function and covariance matrix for $\tilde{Z}$

statistics of Z and $\tilde{Z}$.

Once the SROMs are constructed, Eqs. (1-3) may be solved using just the samples selected and exceedance probability curves calculated as shown in Eqs. (15) and (22), respectively. Finally, the probability that the response $Y(t)$ exceeds a critical value y_{cr} is compared in Figure 4 calculated by using each method, i.e. first-order SROM (black dashed line), second-order SROM (red dashed line) and Monte Carlo (solid blue line).

A good approximation within a 5% mean squared error of the Monte-Carlo solution is obtained using the first-order SROM with the least computational effort. The solution obtained by the second-order SROM is almost identical with the Monte-Carlo results. Table 4 summarizes the error and the computational effort in term of the number of dynamic analyses required to calculate the statistics of interest.

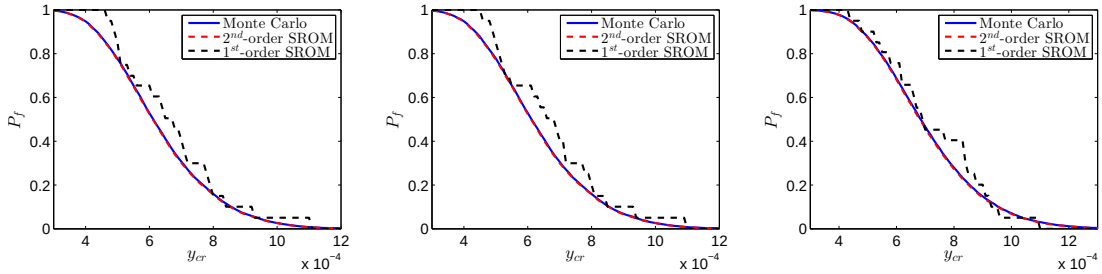


Figure 9: Exceedance probability for Linear, Duffing and Bouc-Wen oscillators

Model	1st order SROM	2nd order SROM	MC
Dynamic Analyses	m_1	$m_2 \times d$	n
Dynamic Analyses (example)	20	$2,000$	$10,000$
Error	$\sim 5\%$	~ 0	0

Table 1: Computational effort vs. relative error by comparing SROM-based methods with Monte Carlo

An important difference between the two SROM-based methods can clearly be noticed in this table. Unlike the first-order SROM, the second-order SROM produces almost zero error with respect to Monte Carlo at the expense of d-times more analayses.

5 CONCLUSIONS

Two novel, highly efficient methods have been proposed to calculate response statistics for structural systems subjected to random input. The methods are based on the stochastic reduced order models that can be viewed as smart Monte Carlo simulations. Unlike the Monte Carlo method which uses a large number of samples selected at random, the new methods use much smaller numbers of samples that are selected in optimal manner. The methods are implemented to calculate exceedance probabilities of linear and non-linear single-degree-of-freedom systems subjected to samples of stochastic processes. The SROM estimates of exceedance probabilities match satisfactorily the Monte-Carlo estimates of these probabilities although they are based on a small number of input samples. Even though both methods produce very good approximations of the reference results, one method produces almost zero error at the expense of more dynamic analyses.

REFERENCES

[1] M. Grigoriu. *Stochastic systems. Uncertainty quantification and propagation.* Springer-Verlag Ltd, London, UK, 2012.

[2] M. Grigoriu. Reduced order models for random functions. application to stochastic problems. *Applied Mathematical Modelling*, 33:161–175, 2009.

[3] M. Grigoriu. Linear random vibration by stochastic reduced order models. *International Journal for Numerical Methods in Engineering*, 82:1537–1559, 2010.

[4] M. Grigoriu. A method for solving stochastic equations by reduced order models and local approximations. *Journal of Computational Physics*, 231(19):64956513, 2012.

[5] M. Grigoriu. A new method for solving random vibration problems. *Proceedings of The Eleventh International Conference on Computational Structural Technology*, 2012.

[6] J. Warner, M. Grigoriu and W. Aquino. Stochastic reduced order models for random vectors. applications to random eigenvalue problems. *Probabilistic Engineering Mechanics*, 31:1–11, 2013.

[7] A. Radu and M. Grigoriu. Structural performance by fragility surfaces for simple systems under non-Gausssian seismic input. *Earthquake Engineering and Structural Dynamics*, (under review), 2015.

[8] A. Radu and M. Grigoriu. An efficient approach on dynamic-response analyses for structural systems. *Proceedings of the 10th National Conference on Earthquake Engineering*, Anchorage, AK, 2014.

[9] A.C. Miller and T.R. Rice. Discrete approximations of probability distributions. *Management Science*, 29(3):352–362, 1983.

[10] M. Grigoriu. Evaluation of Karhunen-Loève, spectral, and sampling representations for stochastic processes *Journal Engineering Mechanics (ASCE)*, 132(2):179–189, 2006.

COMPDYN 2015
5th ECCOMAS Thematic Conference on
Computational Methods in Structural Dynamics and Earthquake Engineering
M. Papadrakakis, V. Papadopoulos, V. Plevris (eds.)
Crete Island, Greece, 25–27 May 2015

SEMI-ANALYTICAL REDUCED-ORDER MODELS FOR THE UNSTEADY AERODYNAMIC LOADS OF SUBSONIC WINGS

Marco Berci

University of Leeds
LS2 9JT, Leeds, UK
M.Berci@leeds.ac.uk

Keywords: Unsteady Loads, Subsonic Aerodynamics, Gust Response, Finite Wings.

Abstract. *Different semi-analytical reduced-order models for calculating the unsteady aerodynamic loads of subsonic slender wings are proposed. The lift-deficiency functions due to a unitary step change in the angle of attack and a unitary sharp-edged vertical gust are first obtained in the (reduced) time domain for both elliptical and rectangular wings of arbitrary aspect ratio, based on previous fundamental works available in the literature. Nonlinear optimisation is then employed to find their best analytical approximation as a series of exponential functions with optimal time constants and amplitudes, as intensively sought for efficient computations of the wing loads as well as aeroelastic stability analyses, especially in the context of aircraft's preliminary multidisciplinary design and optimisation. When the gust penetration effect is also applied, the final curve fitting is performed in the (reduced) frequency domain, where the transfer function between flow perturbation and aerodynamic load is expressed as a series of rational functions with optimal poles and gains; the approximation of the corresponding indicial function is then still obtained as a series of exponential functions with optimal time constants and amplitudes in the (reduced) time domain via Laplace transform. The optimal parameters of the lift-deficiency functions are finally tabulated and analytically expressed as function of the wing's aspect ratio, for each type of wing and flow perturbation. The obtained reduced-order models for unsteady aerodynamic loads are critically discussed and, due to their remarkable computational efficiency and theoretical insights, also suggested for suitable use in the preliminary multidisciplinary design and optimisation of flexible wings in the low-subsonic regime, characterised by attached incompressible flow.*

1 INTRODUCTION

Today's aircraft preliminary design requires a multidisciplinary approach [1] where robust and reliable aeroelastic tools as well as an effective synthesis of the model data are extremely important [2]. Suitable model reduction approaches [3-7] are hence increasingly in demand, among which fast semi-analytical calculations of the aerodynamic loads due to both aircraft motion and wind gusts are still highly desirable [8-10] for efficient aeroelastic stability analysis and structural sizing, especially in the context of wing multidisciplinary design and optimisation (MDO) [11].

For wings undergoing small variations in the effective angle of attack due to either aircraft motion or vertical gust occurrence [12], the circulatory unsteady airload due to each flow perturbation can conveniently be formulated in terms of Duhamel convolution [13] of the latter with the relative lift-deficiency indicial function [14-16]; the contributions of all flow perturbations are then linearly superposed [17-18]. Assuming incompressible potential flow [19], Wagner and Kussner derived the lift-deficiency functions due to a unitary step change in the angle of attack [20] and a unitary sharp-edged vertical gust [21-22] for a thin flat airfoil in the (reduced) time domain, respectively, while Theodorsen [23] and Sears [24-25] solved the same problems in the (reduced) frequency domain. Based on these very fundamental two-dimensional studies [26-28], the lift-deficiency functions due to a unitary step change in the angle of attack and a unitary sharp-edged vertical gust [29] have been investigated for thin flat wings of various shapes [30-38], including elliptical [39-40], rectangular [41] swept trapezoidal [42] and delta wings [43], for which panel-based methods are particularly useful [44-47]. Alternatively, the aerodynamic indicial functions have empirically been obtained by collecting data from dedicated wind tunnel tests [48-53].

More recently, computational fluid dynamics (CFD) [54] has also been employed as the most general high-fidelity aerodynamic tool [55-58], capable of calculating numerically the unsteady load build-up of arbitrary wings in any (practical) flow condition [59-61]. However, CFD simulations are still computationally expensive and rather sensitive to the specific model settings; they often require a significant amount of pre- and post- processing efforts as well as specialist experience to prevent numerical instability and grid singularity [62] (which is a prerequisite for robust and reliable implementations of fully-automatic parametrised MDO routines) and thus grant correct convergence to physically and mathematically sound results, to be confirmed by either rigorous analytical validation or trusted experimental evidence [63]. Indeed, coupling CFD with complex structural solvers [64-65] is still a challenge [66-67].

In order to re-write the aerodynamic load build-up in the state-space form [68-69] suitable for aero-servo-elastic simulations, nonlinear optimisation [70-71] has then been used to obtain the best analytical approximation for the indicial functions as a series of exponential/rational functions with optimal time-constants/poles and amplitudes/gains in the (reduced) time/frequency domain [72-77]; the optimal curve fitting [78] was historically performed in both domains, which are related via Laplace transform [79-80]. Due to fluid dynamics similitude [81], the approximate lift-deficiency functions may finally be parametrised with respect to few fundamental nondimensional numbers, such as Reynolds, Mach and Strouhal numbers of the airflow [82] as well as sweep angle, aspect and thickness ratios of the aircraft wing [42]; correction-based approaches have also been proposed in order to retain the high accuracy of nonlinear CFD at the low computational costs of linear potential-flow aerodynamics [83-86].

In this paper, the lift-deficiency coefficients due to a unitary step change in the angle of attack and a unitary sharp-edged vertical gust are first obtained in the (reduced) time domain for both elliptical and rectangular thin wings of arbitrary aspect ratio, by means of different semi-analytical reduced-order models developed from previous works in the literature [39,42].

Nonlinear optimisation [70] is then employed to find their best approximation as a series of exponential functions with optimal time constants and amplitudes [17,75], where the root mean squared error (RMSE) is set as the objective function to be minimised and the maximum absolute error (MAXE) is monitored [87]. Depending on the availability of the lift-deficiency coefficient, the optimal curve fitting [78] is performed in either the (reduced) time or the (reduced) frequency domain, where the optimal approximation parameters act as the constrained optimisation variables and sequential quadratic programming (SQP) [88-89] is employed as the optimisation algorithm. The optimal coefficients of the approximate lift-deficiency functions are finally tabulated and analytically expressed as function of the wing's aspect ratio, for each type of wing and flow perturbation. The obtained parametric reduced-order models are hence critically discussed and their mathematical features clarified in terms of their main physical assumptions, so to provide with the best theoretical insight.

2 ELLIPTICAL WINGS

Flat elliptical wings (x, y) are geometrically defined as [39]:

$$x = \frac{c_R}{2}\sin\theta\,, \qquad y = \frac{b}{2}\cos\theta\,, \tag{1}$$

where c_R is the root chord, b the span and θ the polar angle; thus, their local chord $c(y)$, surface S and aspect ratio AR are explicitly given by:

$$c = c_R\sqrt{1-\left(\frac{2y}{b}\right)^2}\,, \qquad S = \frac{\pi}{4}bc_R\,, \qquad AR = \frac{4b}{\pi c_R}\,. \tag{2}$$

For such wings, the influence of the tip vortices on the lift distribution along the span may be calculated based on lifting line theory as function of the aspect ratio (which introduces the dependency of the airload on the finite wing span [81,90]) and the unsteady lift of the three-dimensional wing hence obtained from the one of the two-dimensional airfoil [91-92]. In particular, considering a suitable distribution of elementary vortex loops, the lift-deficiency coefficient $C_L^{3D}(t)$ of the wing may be calculated in the (reduced) time domain as [39]:

$$C_L^{3D} = (1-w_{i0})C_L^{2D} - \int_0^\tau \frac{dw_i(\xi)}{d\xi}C_L^{2D}(\tau-\xi)d\xi\,, \qquad \tau = \frac{2V_\infty}{c_R}t\,, \tag{3}$$

where τ and t are the reduced and physical time, respectively, whereas V_∞ is the reference flow speed, $C_L^{2D}(t)$ is the airfoil's lift-deficiency coefficient, $\Gamma_w^{3D}(t)$ the related circulation and $w_i(t)$ the induced wing downwash, which evolve as [39]:

$$\Gamma_w^{3D} = (1-w_{i0})\Gamma_w^{2D} - \int_0^\tau \frac{dw_i(\xi)}{d\xi}\Gamma_w^{2D}(\tau-\xi)d\xi\,, \tag{4}$$

$$w_i = w_\Gamma \Gamma_{w0}^{3D} + \int_0^\tau \frac{d\Gamma_w^{3D}(\xi)}{d\xi} w_\Gamma(\tau - \xi) d\xi \,,$$

with $\Gamma_w^{2D}(t)$ the airfoil circulation induced by a unitary step in the wing downwash and $w_\Gamma(t)$ the wing downwash induced by a unitary step in the wing circulation.

The airfoil's lift coefficient and circulation may be calculated using Peters' inflow theory [91-92] and reciprocity relations [93-95] for thin airfoils and then analytically approximated as a series of n exponential terms as [96]:

$$\begin{aligned} C_L^{2D} &= 2\pi\left(1 - \sum_{j=1}^{n^C} A_j^C e^{-B_j^C \tau}\right), \qquad & \sum_{j=1}^{n^C} A_j^C &= 1 - \frac{C_{L0}^{2D}}{2\pi}, \\ \Gamma_w^{2D} &= 2\pi\left(1 - \sum_{j=1}^{n^\Gamma} A_j^\Gamma e^{-B_j^\Gamma \tau}\right), \qquad & \sum_{j=1}^{n^\Gamma} A_j^\Gamma &= 1, \end{aligned} \tag{5}$$

where all coefficients A_j^C, B_j^C and A_j^Γ, B_j^Γ may be obtained by fitting the exact curves [20-25], as the result of a nonlinear constrained optimisation problem [70] where the approximation error is minimised in a root mean square sense [96] (see Appendix A). Note that the exact asymptotic (steady) conditions $C_{L\infty}^{2D} = 2\pi$ and $\Gamma_{w\infty}^{2D} = 2\pi$ are indeed automatically satisfied and this is also true for the exact initial conditions [91-92], being $C_{L0}^{2D} = \pi$ in the case of Wagner's function for the unsteady lift due to a unitary step change in the angle of attack and $C_{L0}^{2D} = 0$ in the case of Kussner's function for the unsteady lift due to a unitary sharp-edge gust, with $\Gamma_{w0}^{2D} = 0$ in both cases. It is important to stress that Kussner's lift-deficiency function is also the airfoil circulation corresponding to Wagner's lift-deficiency function [93-95].

The wing downwash may be calculated as the vertical velocity induced at the mid-chord by a vortex ring extending along the wake and reads [39]:

$$w_\Gamma = \frac{1}{\pi b}\left\{\frac{2x_w}{b} sK + \frac{b}{2x_w}\left[\left(s - \frac{1}{s}\right)K + \frac{E}{s} - 1\right]\right\}, \qquad s = \left[1 + \left(\frac{2x_w}{b}\right)^2\right]^{-\frac{1}{2}}, \tag{6}$$

where $K(s)$ and $E(s)$ are the elliptic integrals of the first and second kinds [97], respectively, which are functions of the nondimensional spatial variable s, with $x_w = V_\infty t$ the wake length behind the mid-chord; since $s = 1$, $K = \infty$ and $E = 1$ for $t = 0$, the wing downwash is initially $w_{\Gamma 0} = 0$ and then reaches the asymptotic steady condition $w_{\Gamma\infty} = \frac{1}{2b}$, as $s = 0$, $K = \frac{\pi}{2}$ and $E = \frac{\pi}{2}$ for $t = \infty$. In fact, by conveniently fixing $c_R = 2$, with $b = \frac{\pi AR}{2}$ and $x_w = \tau$, the wing downwash can more suitably be rewritten in terms of both wing aspect ratio and reduced time (i.e., the number of travelled semi-chords) as:

$$w_\Gamma = \frac{2}{\pi^2 AR}\left\{\frac{4\tau}{\pi AR}sK + \frac{\pi AR}{4\tau}\left[\left(s-\frac{1}{s}\right)K + \frac{E}{s} - 1\right]\right\}, \qquad s = \left[1+\left(\frac{4\tau}{\pi AR}\right)^2\right]^{-\frac{1}{2}}, \tag{7}$$

and then also analytically approximated as a series of n exponential terms as:

$$w_\Gamma = \frac{1}{\pi AR}\left(1 - \sum_{j=1}^{n^w} A_j^w e^{-B_j^w \frac{\tau}{AR}}\right), \qquad \sum_{j=1}^{n^w} A_j^w = 1, \tag{8}$$

where all coefficients A_j^w and B_j^w may still be obtained by fitting the exact curve and both initial $w_{\Gamma 0} = 0$ and asymptotic $w_{\Gamma\infty} = \frac{1}{\pi AR}$ exact conditions are automatically satisfied. However, as the wing wake actually leaves from the trailing edge, the initial length x_{w0} of the wing wake is set equal to half of the wing's mean geometric chord $\bar{c} = \frac{\pi c_R}{4}$ [39] and the wing downwash may finally be written as:

$$w_\Gamma = \frac{1}{\pi AR}\left(1 - \sum_{j=1}^{n^w} A_j^w e^{-B_j^w \frac{(\tau-\tau_0)}{AR}}\right), \qquad \tau_0 = -\frac{\pi}{4}. \tag{9}$$

Integrating by parts, the three-dimensional lift-deficiency coefficient, related wing circulation and induced wing downwash can conveniently be rewritten as [96]:

$$\begin{aligned} C_L^{3D} &= C_L^{2D} - w_i C_{L0}^{2D} + \int_0^\tau \frac{dC_L^{2D}(\tau-\xi)}{d\xi} w_i(\xi) d\xi, \\ \Gamma_w^{3D} &= \Gamma_w^{2D} - w_i \Gamma_{w0}^{2D} + \int_0^\tau \frac{d\Gamma_w^{2D}(\tau-\xi)}{d\xi} w_i(\xi) d\xi, \\ w_i &= \Gamma_w^{3D} w_{\Gamma 0} - \int_0^\tau \frac{dw_\Gamma(\tau-\xi)}{d\xi} \Gamma_w^{3D}(\xi) d\xi; \end{aligned} \tag{10}$$

due to Laplace transformation [79-80], the integral convolution process in the (reduced) time domain can then be realised by the equivalent differential form:

$$\begin{aligned} C_L^{3D} &= C_L^{2D} - w_i C_{L0}^{2D} - 2\pi \sum_{j=1}^{n^C} A_j^C z_j^C, \\ \Gamma_w^{3D} &= \Gamma_w^{2D} - w_i \Gamma_{w0}^{2D} - 2\pi \sum_{j=1}^{n^\Gamma} A_j^\Gamma z_j^\Gamma, \\ w_i &= \Gamma_w^{3D} w_{\Gamma 0} + \frac{1}{\pi AR} \sum_{j=1}^{n^w} A_j^w e^{-\frac{\pi B_j^w}{4AR}} z_j^w, \end{aligned} \tag{11}$$

where the added aerodynamic states $z(t)$ are defined in the (reduced) Laplace domain p as:

$$z_j^C = \frac{B_j^C w_i}{p + B_j^C}, \qquad z_j^\Gamma = \frac{B_j^\Gamma w_i}{p + B_j^\Gamma}, \qquad z_j^w = \frac{B_j^w \Gamma_w^{3D}}{p + B_j^w}, \tag{12}$$

and evolve in the (reduced) time domain as [96]:

$$\frac{dz_j^C}{d\tau} + B_j^C z_j^C = B_j^C w_i, \qquad \frac{dz_j^\Gamma}{d\tau} + B_j^\Gamma z_j^\Gamma = B_j^\Gamma w_i, \qquad \frac{dz_j^w}{d\tau} + B_j^w z_j^w = B_j^w \Gamma_w^{3D}, \tag{13}$$

with initial conditions $z_j^{C0} = 0$, $z_j^{\Gamma 0} = 0$ and $z_j^{w0} = 0$. The resulting asymptotic conditions are $C_{L\infty}^{3D} = \frac{2\pi AR}{2 + AR}$, $\Gamma_{w\infty}^{3D} = \frac{2\pi AR}{2 + AR}$ and $w_{i\infty} = \frac{2}{2 + AR}$, in perfect agreement with lifting line theory for elliptical wings [90]; therefore, the computed wing's lift-deficiency coefficient may analytically be approximated as a series of n exponential terms as:

$$C_L^{3D} = \frac{2\pi AR}{2 + AR}\left(1 - \sum_{j=1}^{n} A_j e^{-B_j \tau}\right), \qquad \sum_{j=1}^{n} A_j = 1 - \frac{C_{L0}^{3D}}{2\pi}\left(1 + \frac{2}{AR}\right), \tag{14}$$

where all coefficients A_j and B_j are consistently obtained by fitting the numerically integrated curve for each aspect ratio and both asymptotic and initial exact conditions are automatically satisfied, being $C_{L0}^{3D} = \pi$ in the case of a unitary step change in the angle of attack and $C_{L0}^{3D} = 0$ in the case of a unitary sharp-edge gust, with $\Gamma_{w0}^{3D} = 0$ and $w_{i0} = 0$ in both cases. Note that both Wagner's [20] and Kussner's [21-22] functions are correctly obtained in the limit of infinite wing.

In fact, due to the Kutta-Joukowsky condition [98-99], the impulsive start of the wing wake (which initially moves as an extension of the wing) generates some flow inertia which modifies the initial behaviour of the load build-up, especially for a unitary step change in the angle of attack. This further three-dimensional effect may be calculated by considering the two-dimensional distribution of kinetic potential $\Phi(t)$ and pressure difference $\Delta p(t)$ over each wing section in normal motion, namely [39]:

$$\Phi = \frac{w}{E}\sqrt{(1 + x)(1 - x + \tau)}, \qquad \Delta p = -2\rho_\infty V_\infty \left(\frac{\partial \Phi}{\partial \tau} + \frac{\partial \Phi}{\partial x}\right), \tag{15}$$

where ρ_∞ is the reference flow density and the variations in the kinetic potential are due to the apparent variation of the wing shape (although the change in the wing perimeter may be neglected during widening). In particular, with $x = \cos\theta$, right at the wake start it is [39]:

$$\Phi_0 = \frac{w}{E}\sin\theta, \qquad \Delta p_0 = \rho_\infty V_\infty \frac{w(\cos\theta - 1)}{E \sin\theta}, \qquad C_{L0}^{3D} = \int_{-1}^{+1} \frac{\Delta p_0 \, dx}{\rho_\infty V_\infty^2}, \tag{16}$$

where $w = V_\infty$ for a unitary angle of attack; therefore, the approximate initial behavior of the wing's lift-deficiency coefficient may then be estimated by suitably scaling the approximate initial behavior of the airfoil's lift-deficiency coefficient [93] as (see Appendix B):

$$\lim_{\tau\to 0} C_L^{3D} \approx \frac{\pi}{E}\left(1+\frac{\tau}{4}\right), \qquad \lim_{\tau\to 0} C_L^{3D} \approx \frac{2}{E}\sqrt{2\tau}\,, \tag{17}$$

for the case of unitary step change in the angle of attack and unitary sharp-edge gust, respectively. Note that, due to the gust penetration effect, this three-dimensional correction may reasonably be neglected in the latter case [39], since the initial perturbations of both kinetic potential and tip-vortices strength are fairly marginal, the wing's lift-deficiency coefficient starting at zero directly and then increasing very rapidly with an infinite theoretical rate. Thus, by accounting for the flow inertia acting at the impulsive start of the wake, the wing's lift-deficiency coefficient due to a unitary step change in the angle of attack can finally be approximated as:

$$C_L^{3D} = \frac{2\pi AR}{2+AR}\left(1-\sum_{j=1}^{n+1} A_j e^{-B_j\tau}\right), \qquad \sum_{j=1}^{n} A_j = 1-\frac{2+AR}{2AR}, \tag{18}$$

where the two coefficients of the additional exponential term read:

$$A_{n+1} = \frac{2+AR}{2AR}\left(1-\frac{1}{E}\right), \qquad B_{n+1} = \frac{1}{A_{n+1}}\left(\frac{2+AR}{8EAR}-\sum_{j=1}^{n} A_j B_j\right), \tag{19}$$

and Wagner's function [20] is still correctly obtained in the limit of infinite wing.

3 TRAPEZOIDAL WINGS

Flat trapezoidal wings the local chord is explicitly given by [42]:

$$c = c_R\left[1-2(1-\lambda)\frac{y}{b}\right], \qquad \lambda = \frac{c_T}{c_R}\,, \tag{20}$$

where $0 \le \lambda \le 1$ is the taper ratio and c_T the tip chord; surface and aspect ratio then read:

$$S = \left(\frac{1+\lambda}{2}\right) b c_R\,, \qquad AR = \left(\frac{2}{1+\lambda}\right)\frac{b}{c_R}\,, \tag{21}$$

respectively, for any sweep angle Λ. The latter is geometrically defined with respect to the wing's quarter chord line, where the aerodynamic centre of each wing section is assumed in accordance with thin airfoil theory [100]; the downwash control point is then consistently located at the three-quarter chord, where the non-penetration boundary condition for inviscid potential flow is satisfied [47]. In particular, fully symmetrical wings with isosceles trapezoidal planform own $\tan\Lambda = \frac{1}{AR}\left(\frac{1-\lambda}{1+\lambda}\right)$, which gives $\tan\Lambda = \frac{1}{AR}$ for isosceles triangular

wings (with straight symmetry axis); whereas forward and backward swept wings with trapezoidal planform own $\tan\Lambda=\frac{1}{AR}\left(\frac{\lambda-1}{1+\lambda}\right)$ and $\tan\Lambda=\frac{3}{AR}\left(\frac{1-\lambda}{1+\lambda}\right)$, which give $\tan\Lambda=-\frac{1}{AR}$ and $\tan\Lambda=\frac{3}{AR}$ for forward and backward delta wings (with straight leading and trailing edge), respectively; in all cases, a straight wing characterised by two-dimensional flow is correctly obtained in the limit of infinite wing. Rectangular and parallelogram wings have $\lambda=1$, while rhomboidal and delta wings have $\lambda=0$.

Within a simplified yet effective approach [42], a single vortex-ring is considered for modeling the total (lumped) wing circulation and a single control point is then placed at the third quarter of the wing's root chord. Both bound and shed vortex lines are parallel to the wing's quarter chord line, whereas the two wing-tip trailed vortex lines are parallel to the free-stream. All vortices have the same (lumped) intensity and the shed vorticity travels towards infinity with half the reference airflow speed from half the wing's root chord behind the control point, hence stretching the vortex-ring and increasing the wake length; when the wing wake eventually approaches infinity, its influence on the wing flow fades away and the steady condition is asymptotically obtained. The influence of the wing's tip vortices and wake on the (uniform yet time-varying) lift distribution along the span is then calculated with the simplest implementation of the unsteady lifting line theory [47,101-103] and the lift build-up of the three-dimensional wing is hence obtained as function of its aspect ratio, taper ratio and sweep angle. In particular, the lift-deficiency coefficient due to a unitary step change in the angle of attack was calculated in the (reduced) time domain based on Kutta-Joukowsky theorem as [42]:

$$C_L^{3D}=\frac{2\pi AR_e}{b\left(P+Q+R\right)},\qquad AR_e=\left(\frac{1+\lambda}{2}\right)AR, \tag{22}$$

where $P(t)$, $Q(t)$ and $R(t)$ give the vortex-ring contributions due to bound, wing-tip trailed and wake shed vortices, respectively, based on Biot-Savart law [47] and read [42]:

$$\begin{aligned}
bP&=AR_e\left[\frac{AR_e\sec^2\Lambda-\tan\Lambda}{\sqrt{\left(AR_e\sec\Lambda-\sin\Lambda\right)^2+\cos^2\Lambda}}+\tan\Lambda\right],\\
bQ&=\frac{1-AR_e\tan\Lambda}{\sqrt{\left(1-AR_e\tan\Lambda\right)^2+AR_e^2}}+\frac{1+AR_e\tan\Lambda+\frac{\tau}{2}}{\sqrt{\left(1+AR_e\tan\Lambda+\frac{\tau}{2}\right)^2+AR_e^2}},\\
bR&=\frac{AR_e}{1+\frac{\tau}{2}}\left\{\frac{AR_e\sec^2\Lambda+\left(1+\frac{\tau}{2}\right)\tan\Lambda}{\sqrt{\left[AR_e\sec\Lambda+\left(1+\frac{\tau}{2}\right)\sin\Lambda\right]^2+\left[\left(1+\frac{\tau}{2}\right)\cos\Lambda\right]^2}}-\tan\Lambda\right\};
\end{aligned} \tag{23}$$

the wing's lift-deficiency coefficient may finally be approximated as a series of n exponential terms as:

$$C_L^{3D} = C_{L\infty}^{3D}\left(1-\sum_{j=1}^{n} A_j e^{-B_j \tau}\right), \qquad \sum_{j=1}^{n} A_j = 1-\frac{C_{L0}^{3D}}{C_{L\infty}^{3D}}, \tag{24}$$

where all coefficients A_j and B_j are obtained by fitting the exact analytical curve [42] and both asymptotic and initial exact conditions are automatically satisfied.

For the special case of rectangular wing, $\lambda = 1$ and $\Lambda = 0$ and the lift-deficiency coefficient reduces to:

$$C_L^{3D} = \frac{2\pi AR}{\sqrt{1+AR^2}+\dfrac{2}{2+\tau}\sqrt{\left(1+\dfrac{\tau}{2}\right)^2+AR^2}}, \tag{25}$$

with initial behavior and asymptotic (steady) condition given by:

$$\lim_{\tau\to 0} C_L^{3D} \approx \frac{\pi AR}{\sqrt{1+AR^2}}\left[1+\left(\frac{AR^2}{1+AR^2}\right)\frac{\tau}{4}\right], \qquad C_{L\infty}^{3D} = \frac{2\pi AR}{1+\sqrt{1+AR^2}}, \tag{26}$$

respectively, which degenerates into Garrick's approximation [93] of Wagner's function for thin airfoils in the limit of infinite wing. Note that, due to the intrinsic limitations of the simple vortex-system representation employed, it is known that the calculated asymptotic (steady) conditions are not very accurate and should rather be provided by other higher-fidelity sources (e.g., lifting line theory [90] as in Appendix B, vortex or doublet lattice methods [104], computational fluid dynamics [54], wind tunnel tests [51]). In any case, the reported model [42] is better suited for slender thin wings with high aspect and taper ratios as well as small sweep angle, for which the three-dimensional flow and geometry effects are less significant (i.e., the induced downwash speed is smaller and the control points of each wing section are closer to the one at the root section).

Unfortunately, no analytical expression was provided for the lift-deficiency function due to a unitary sharp-edge gust [42]. Nevertheless, this may numerically be obtained in the (reduced) frequency domain by multiplying the Laplace transform of the lift-deficiency function due to a unitary step change in the angle of attack by the transfer function of the gust penetration effect, which is here approximated as the ratio between (modified) Sears' and Theodorsen's functions [23-25] (see Appendix A); the corresponding lift-deficiency function in the (reduced) time domain may then be obtained via inverse Laplace transform [79-80]. Note that this is equivalent to convolving the lift-deficiency function due to a unitary step change in the angle of attack with the delay function given by the inverse Laplace transform of the transfer function of the gust penetration effect [96]. Of course, it is implicitly assumed that all wing sections encounter the wind gust at the same time, even in the case of swept tapered wings [42].

4 NONLINEAR CONSTRAINED OPTIMIZATION FOR BEST APPROXIMATION

The lift-deficiency functions due to a unitary step change in the angle of attack and unitary sharp-edge gust for elliptical wings [39], as well as those due to a unitary step change in the angle of attack for rectangular wings [42], were either numerically obtained or analytically expressed in the (reduced) time domain directly, where their best approximation as a series of

exponential terms with optimal time constants and amplitudes is sought [96]. On the contrary, the lift-deficiency functions due to a unitary sharp-edge wind gust for rectangular wings were numerically obtained in the (reduced) frequency domain, where their best approximation as a series of rational terms with optimal poles and gains is sought [96]; the corresponding best approximation of the lift-deficiency function as a series of exponential functions in the (reduced) time domain is then obtained via inverse Laplace transform [79-80].

Analytical approximation functions with many free coefficients may generally better adapt to the target curve and reproduce its local features but also misbehave between sample points, especially when just few spare are available [78]. An adequate selection of the sample points is hence necessary [105], since their "fixity" drives the "flexibility" of the analytical function, and, in order to avoid focusing on certain regions of the lift-deficiency functions a priori, a uniform distribution of $N=100$ sample points is here first obtained by imposing an equal distance among each couple of consecutive sample points and solving a preliminary nonlinear optimisation problem [96]. Then, with $F(\chi)$ the target curve, the quality of its analytical approximation $\widetilde{F}(\chi)$ is assessed at the sample points χ according to the MAXE and RMSE, namely [87]:

$$\mathrm{MAXE}=\max\left|\widetilde{F}(\chi)-F(\chi)\right|, \qquad \mathrm{RMSE}=\frac{\left\|\widetilde{F}(\chi)-F(\chi)\right\|}{\sqrt{N}}, \tag{27}$$

the latter being set as the objective function to be minimised in the nonlinear optimisation problem, under the constrains given on the approximation function coefficients in order to satisfy the exact limit conditions of the lift-deficiency functions [96]. This choice of the objective function ensures the approximation function being close to the exact curve, as many sample points are indeed readily available in the present case; otherwise, a parametric aggregate objective function where the RMSE of the segments connecting consecutive sample points is also minimised is suggested, which ensures the approximation function being rather smooth without oscillating much around the exact curve [96].

SQP has been employed as gradient-based, iterative optimisation algorithm [88-89], which assumes both the objective function and the constraints are twice continuously differentiable and searches for the point where the gradient of the objective function vanishes within a general Lagrangian formulation, reducing to Newton's method for unconstrained problems [70]. The heuristic gradient-free Nelder-Mead simplex method (NMSM, where the absolute value of the poles was considered for a meaningful unconstrained implementation of the problem) [106] and genetic algorithm (GA, where the initial population was taken as the SQP solution in order to boost convergence) [107] were also employed and the same optimal results eventually obtained, confirming the consistency and robustness of the proposed approach as well as granting confidence the global optimum was actually reached in all cases.

5 LIFT-DEFICIENCY FUNCTIONS AND THEIR OPTIMAL APPROXIMATION

Considering a flat elliptical wing with $AR=3$ and $AR=6$, Jones' preliminary results for the three-dimensional lift-deficiency coefficient due to a unitary step change in the angle of attack [39] are reproduced in Figure 1 (left) for code validation purposes. These results are based on Jones' analytical exponential approximations shown in Figure 1 (right) for the wing downwash build-up as well as Figure 2 for the lift-deficiency coefficient and related circulation due to a unitary step change in the angle of attack of a two-dimensional flat plate. The

proposed analytical approximations (see Appendix A) are also shown in the same figures for direct comparison, along with the exact curves wherever available; the approximations coefficients are summarised in Table 1.

Apart from the initial correction due to the impulsive start of the wing wake [39], Jones's draft results depart from the final ones where his approximations of both wing downwash and especially airfoil circulation depart from the respective exact curves, without approaching the correct asymptotic value and hence artificially increasing the wing's lift coefficient; it is then apparent that accurate analytical approximations are strictly necessary for all flow variables.

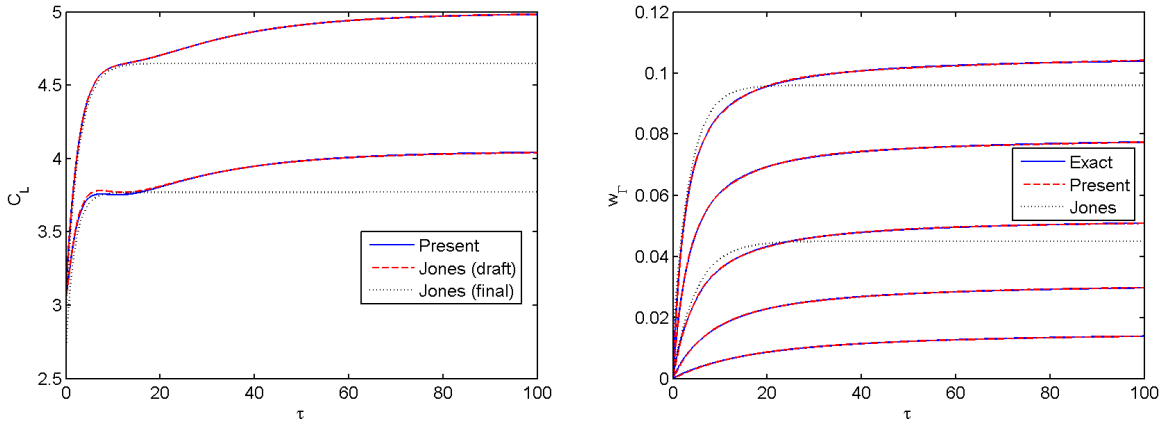


Figure 1. Lift-deficiency coefficient (left) and wing downwash (right) due to a unitary step change in the angle of attack for flat elliptical wing with AR=3,6 (left) and AR=3,4,6,10,20 (right)

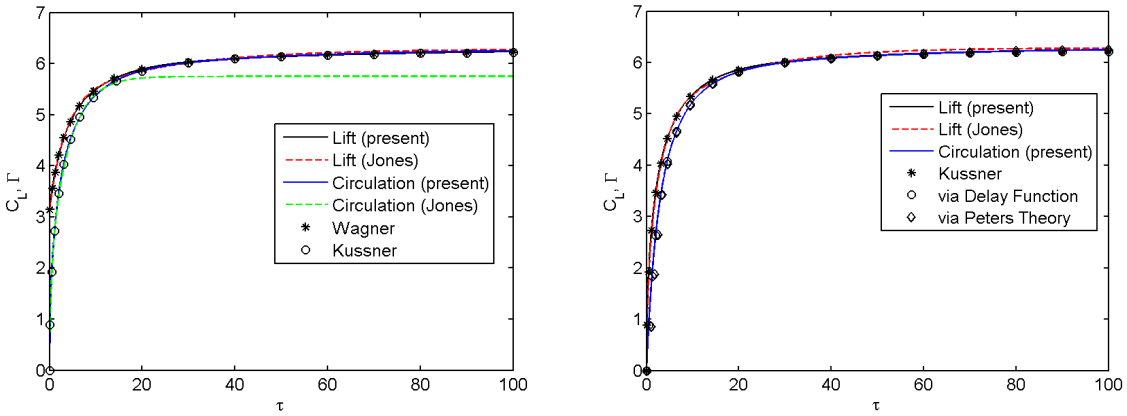


Figure 2. Lift-deficiency function and circulation due to a unitary step change in the angle of attack (left) and unitary sharp-edge gust (right) for flat airfoil

Table 1. Coefficients of the exponential approximation for the fundamental flow variables

	A_1	A_2	A_3	A_4	A_5	B_1	B_2	B_3	B_4	B_5
$C_{L\alpha}^{2D}$	0.0684	0.2657	0.1659	-	-	0.0222	0.1343	0.4915	-	-
C_{Lg}^{2D}	0.0954	0.3836	0.3184	0.1380	0.0646	0.0291	0.1673	0.6602	4.2399	69.585
Γ_{wg}^{2D}	0.0973	0.4522	0.4382	0.0123	-	0.0287	0.1602	0.5011	2.2338	-
w_Γ	0.0924	0.3730	0.5346	-	-	0.0483	0.3788	1.5867	-	-

Figure 3 shows the lift-deficiency coefficient due to a unitary step change in the angle of attack and a unitary sharp-edge gust for elliptical wings with different aspect ratios; the optimal approximation is also shown and the relative coefficients are presented in Table 2, for the case $n = 2$. Indeed, two exponential terms appear sufficient to grant a good approximation; however, an additional one is still needed for reproducing the correct initial behavior of the three-dimensional lift development due to a unitary step change in the angle of attack [39] and would be beneficial to improve the accuracy of the three-dimensional lift development due to a unitary sharp-edge gust [96]. Figures 4 and 5 then show the analytical approximation of these coefficients as function of the inverse of the wing's aspect ratio, as implicitly suggested by the generalised formula for the wing downwash. In particular, a cubic polynomial is generally found sufficient and exhibits a linear behavior for high (inverse) aspect ratios, where all approximation coefficients converge to the ones characterising two-dimensional flow (i.e., the intercepts). Note that Jones' results [39] are rather conservative, as they provide the wing with a faster load build-up and the asymptotic (steady) conditions reached much earlier; this is mainly due to the approximations of both airfoil circulation and wing downwash being conservative in the first place and just a single exponential term being adopted (see Appendix B).

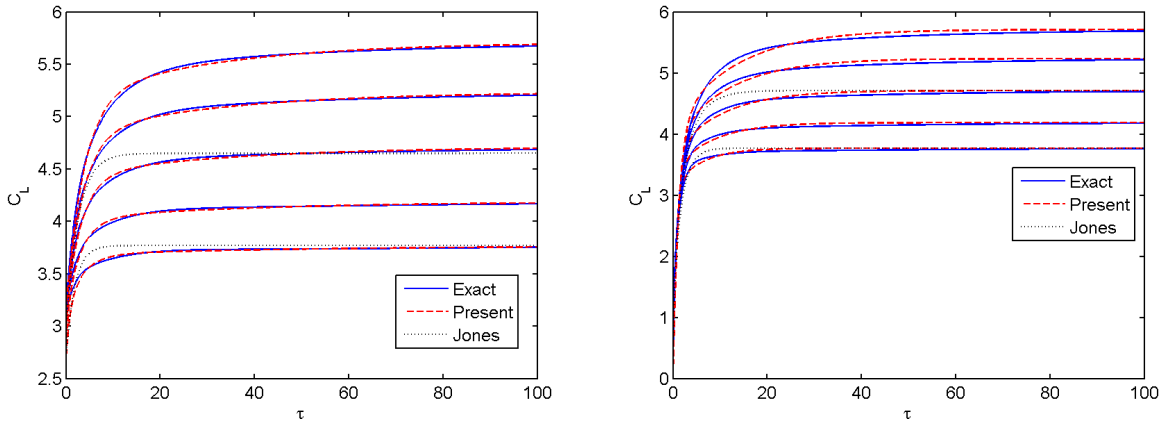


Figure 3. Lift-deficiency coefficient due to a unitary step change in the angle of attack (left) and a unitary sharp-edge gust (right) for flat elliptical wing with AR=3,4,6,10,20

Table 2. Coefficients of the exponential approximation for the lift-deficiency functions of an elliptical wing

	angle of attack				***sharp-edge gust***			
AR	A_1	A_2	B_1	B_2	A_1	A_2	B_1	B_2
3	0.0235	0.1432	0.0190	0.2954	0.1736	0.8264	0.1729	1.5882
4	0.0398	0.2102	0.0257	0.3156	0.1887	0.8113	0.1222	1.3119
6	0.0599	0.2734	0.0297	0.3044	0.2240	0.7760	0.0996	1.1014
10	0.0793	0.3207	0.0315	0.2842	0.2556	0.7444	0.0858	0.9421
20	0.0962	0.3538	0.0320	0.2652	0.2806	0.7194	0.0767	0.8263

Figure 6 shows the lift-deficiency coefficient due to a unitary step change in the angle of attack and a unitary sharp-edge gust for rectangular wings with different aspect ratios; the optimal approximation is also shown and the relative coefficients are presented in Table 3, for the case $n = 2$ which still grants good approximation. Note that the asymptotic (steady) lift-deficiency coefficient for rectangular wing is slightly higher than the corresponding one for elliptical wing since not very accurate [42]; in fact, it should be lower according to lifting line theory [90] (see Appendix B).

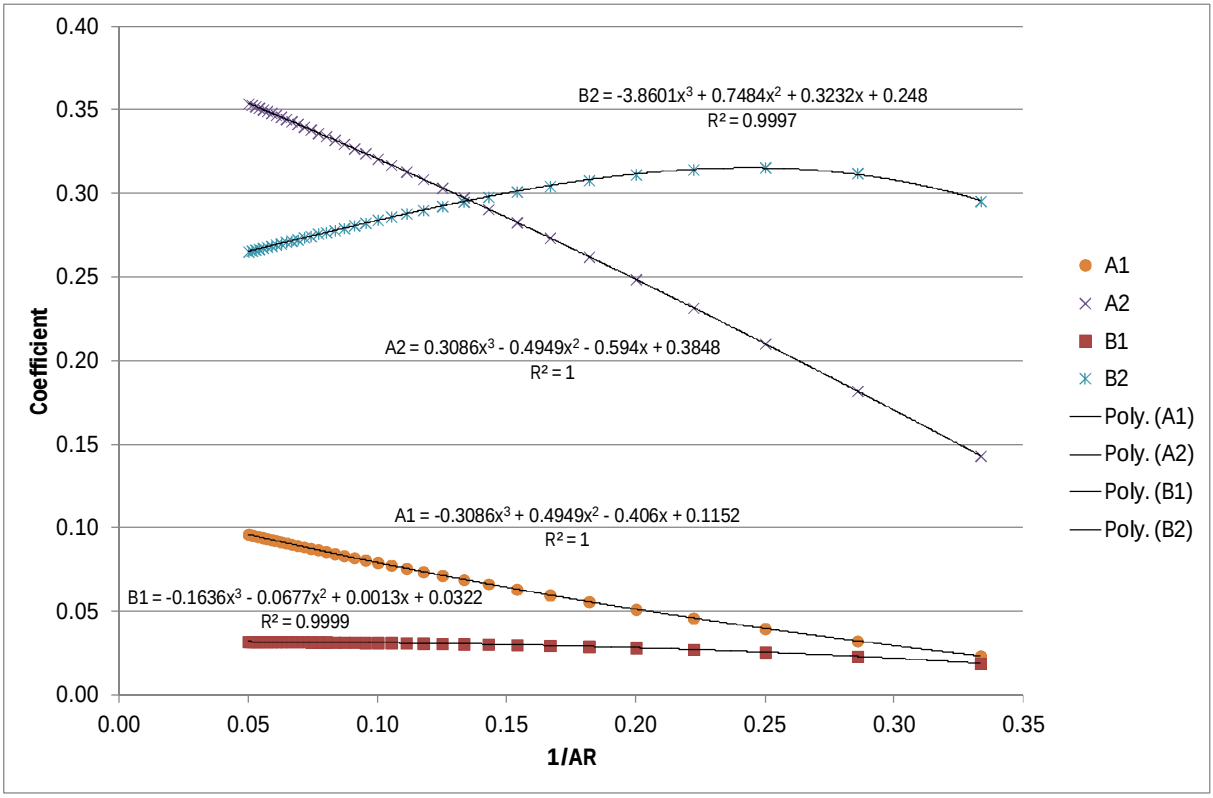


Figure 4. Coefficients of the exponential approximation for the lift-deficiency function due to a unitary step change in the angle of attack for a flat elliptical wing

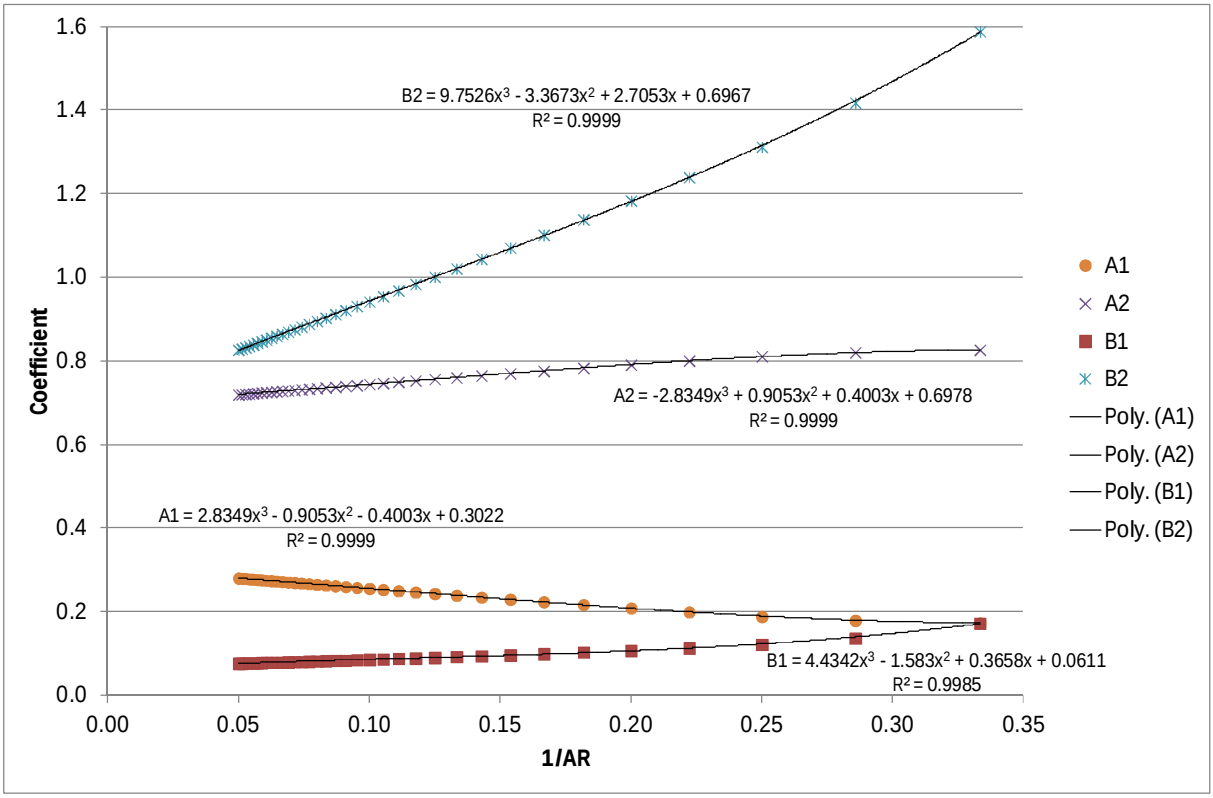


Figure 5. Coefficients of the exponential approximation for the lift-deficiency function due to a unitary sharp-edge gust for a flat elliptical wing

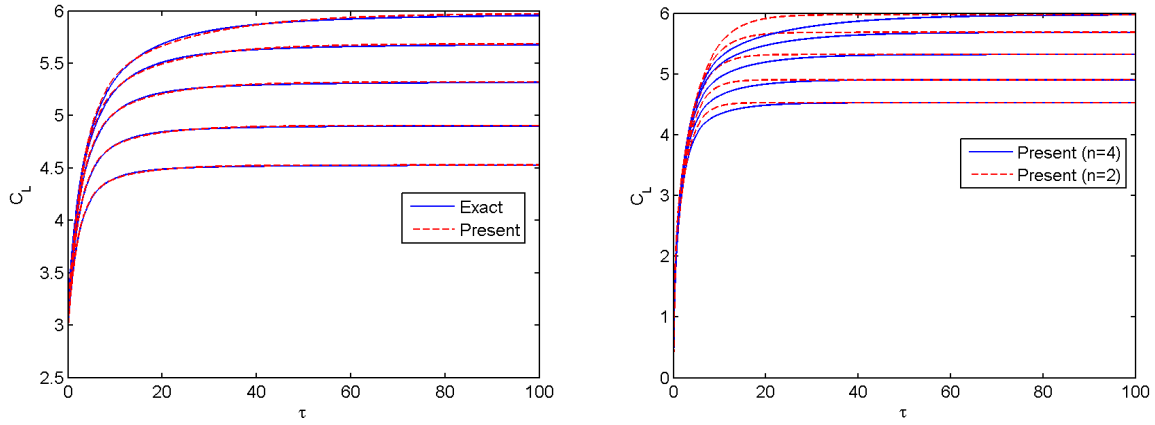


Figure 6. Lift-deficiency coefficient due to a unitary step change in the angle of attack (left) and a unitary sharp-edge gust (right) for flat rectangular wing with AR=3,4,6,10,20

Table 3. Coefficients of the exponential approximation for the lift-deficiency functions of a rectangular wing

	angle of attack				***sharp-edge gust***			
AR	A_1	A_2	B_1	B_2	A_1	A_2	B_1	B_2
3	0.0740	0.2679	0.1038	0.4781	0.6917	0.3083	0.4026	5.7145
4	0.0865	0.2923	0.0930	0.4250	0.6882	0.3118	0.3512	5.0027
6	0.1061	0.3117	0.0808	0.3741	0.6794	0.3206	0.2950	4.1989
10	0.1286	0.3216	0.0676	0.3362	0.6652	0.3348	0.2458	3.4764
20	0.1426	0.3324	0.0514	0.3041	0.6484	0.3516	0.2070	2.9203

Figure 7 shows the complex transfer function of the lift-deficiency coefficient due to a unitary sharp-edge gust for the rectangular wings with $AR = 3$ and $AR = 6$ in the (reduced) frequency domain, as numerically obtained by multiplying the Laplace transform of the lift-deficiency coefficient due to a unitary step change in the angle of attack by the delay function introducing the gust penetration effect (see Appendix A). The corresponding rational function approximations are also shown in the same figure for the cases $n = 2$ and $n = 4$, the former being rather conservative with respect to the latter, which is more accurate and hence generally suggested (note that the curve of the lift-deficiency coefficient due to a unitary sharp-edge gust should approach that of the lift-deficiency coefficient due to a unitary step change in the angle of attack from below, because of the gust penetration effect).

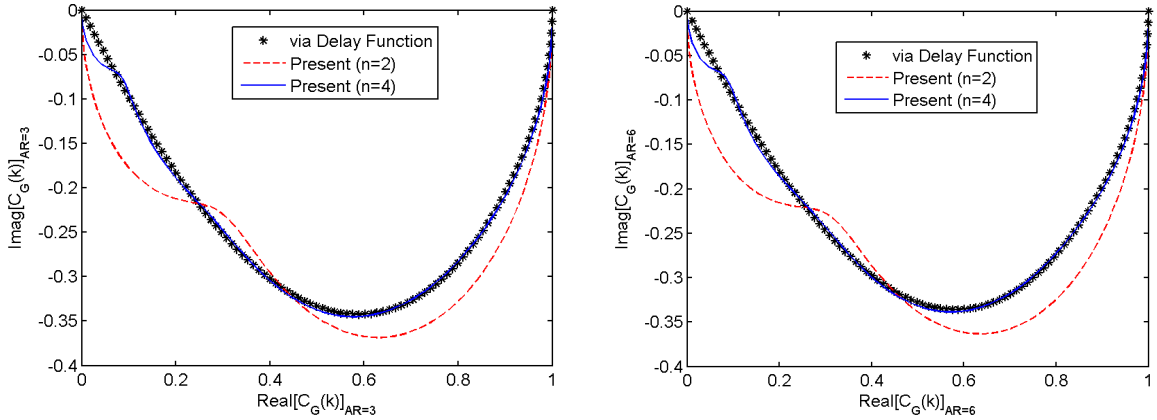


Figure 7. Lift-deficiency coefficient due to a unitary sharp-edge gust for flat rectangular wing with AR=3 (left) and AR=6 (right)

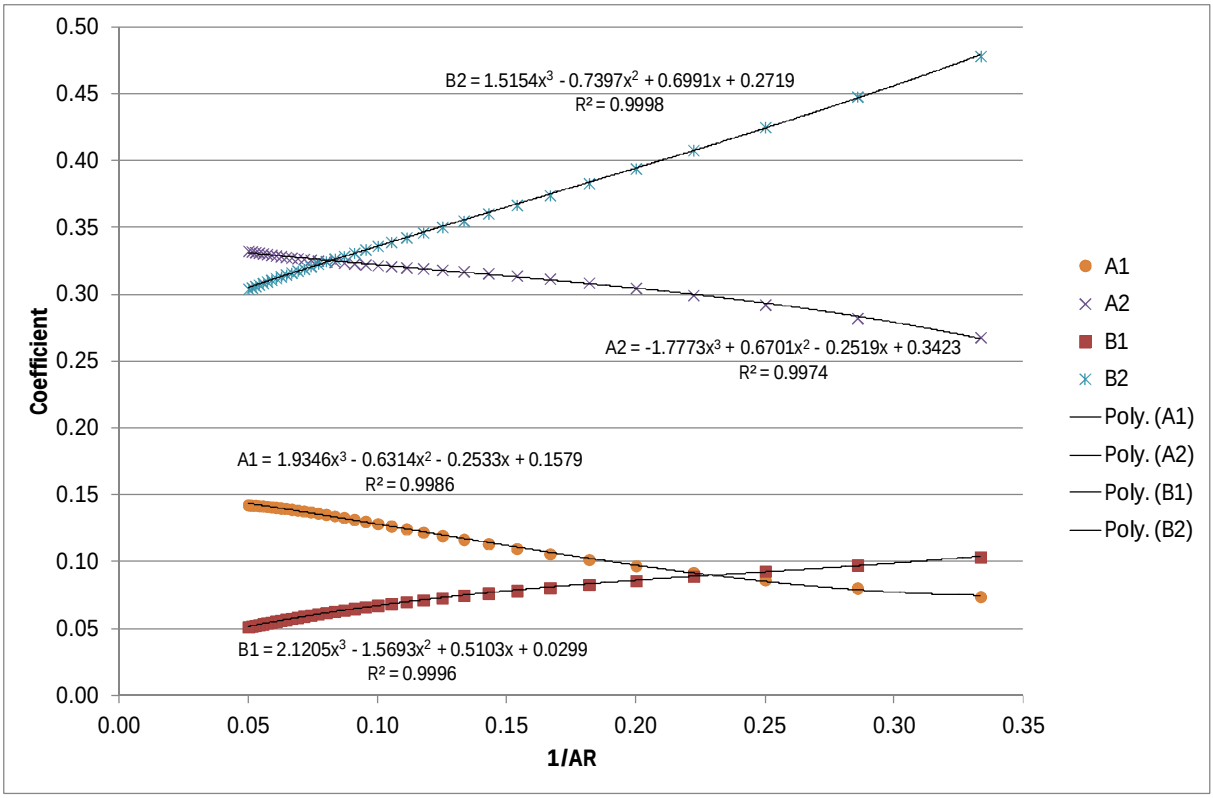


Figure 8. Coefficients of the exponential approximation for the lift-deficiency function due to a unitary step change in the angle of attack for a flat rectangular wing

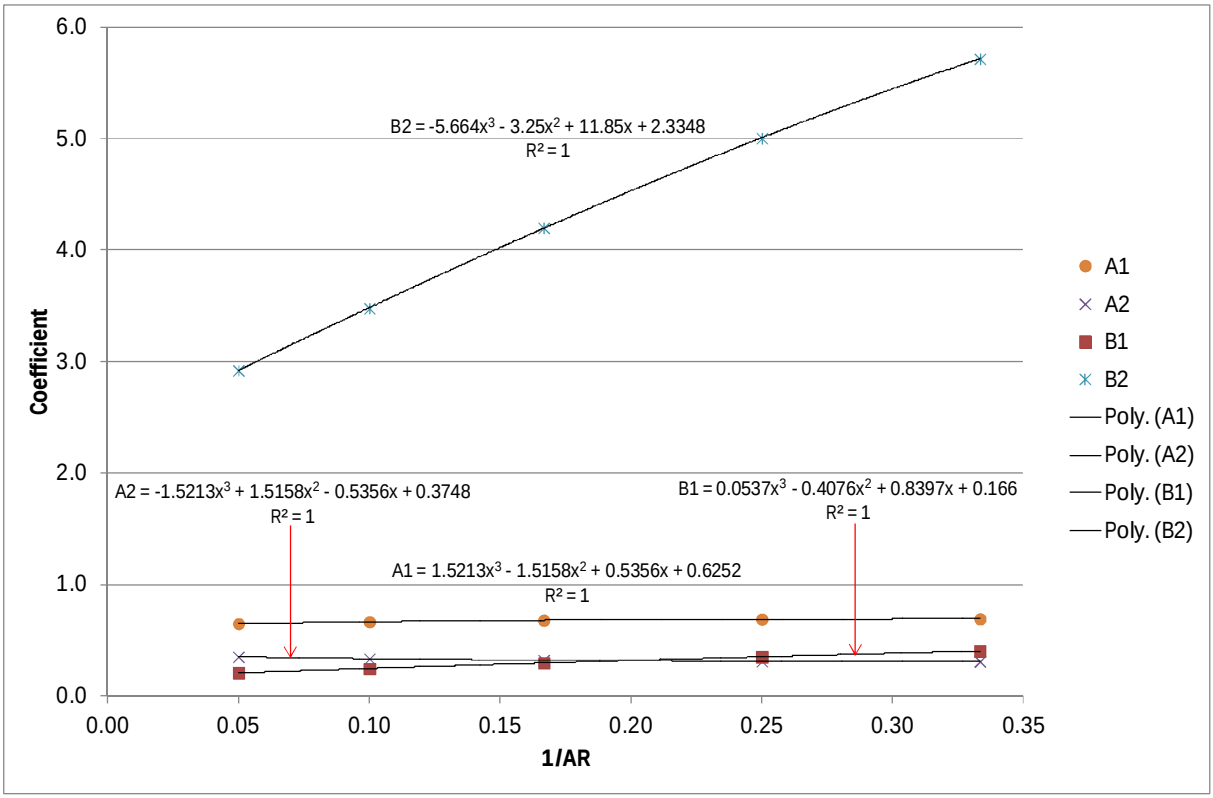


Figure 9. Coefficients of the exponential approximation for the lift-deficiency function due to a unitary sharp-edge gust for a flat rectangular wing

Figures 8 and 9 show the analytical approximation of the optimal parameters for the case $n = 2$, still as function of the inverse of the wing's aspect ratio; a cubic polynomial is again found sufficient and exhibits a linear behavior for high (inverse) aspect ratios, up to the intercept characterising two-dimensional flow. For the lift-deficiency coefficient due to a unitary step change in the angle of attack, both magnitude and trend of the approximation parameters for rectangular wing are rather similar to those for elliptical wing, as the underlying physical principles are substantially the same; for the lift-deficiency coefficient due to a unitary sharp-edge gust, higher discrepancies can be found in the magnitude of the approximation parameters, as different approaches are employed to derive the indicial function.

6 CONCLUSIONS

In this work different semi-analytical reduced-order models for calculating efficiently the unsteady aerodynamic loads of subsonic slender wings have been proposed, as intensively sought in the context of aircraft preliminary MDO. The lift-deficiency functions due to both a unitary step change in the angle of attack and a unitary sharp-edged vertical gust have first been obtained in the (reduced) time domain for both elliptical and rectangular wings of arbitrary aspect ratio, based on previous fundamental works available in the literature. Nonlinear optimisation has then been employed to find their best approximation in terms of a series of exponential functions with optimal time constants and amplitudes, allowing the load build-up to be re-written in the state-space form most suitable for aero-servo-elastic simulations and stability analyses. The approximation error being set as the objective function to be minimised, different optimisation algorithms such as SQP, NMSM and GA have been employed and provided with identical results using the least number of free parameters, thus ensuring the global optimum was reached in all cases under the prescribed constraints. Depending on the availability of the lift-deficiency function, the optimal curve fitting was performed in either the (reduced) time or the (reduced) frequency domain, which are related via Laplace transform; significant improvements were found with respect to previous approximations available in the literature, even without error-weighting. The optimal parameters have then been tabulated and finally expressed as analytical functions of the wing's aspect ratio, for each type of wing and flow perturbation. In order to offer the best theoretical insight, the obtained parametric reduced-order models have critically been assessed with respect to their mathematical features and physical assumptions and useful analogies consistently found in the results for elliptical and rectangular wings, confirming the robustness of the proposed approach. Due to their computational effectiveness, the presented semi-analytical aerodynamic models are suggested for suitable use in the preliminary MDO of flexible wings characterised by attached incompressible flow in the low-subsonic regime and may also be used to assess higher-fidelity aerodynamic tools for unsteady aerodynamics.

APPENDIX A. WAGNER, KUSSNER AND DELAY FUNCTIONS

Assuming small perturbations of incompressible potential flow, analytical solutions have been derived to calculate the unsteady airload around an oscillating flat plate in both the (reduced) time and the (reduced) frequency domains; in particular, Theodorsen [23] and Wagner [20] derived the lift-deficiency function for a unit step-change in the angle of attack, while Sears [24-25] and Kussner [21] derived the lift-deficiency function for a unit step-change in the vertical speed of a "frozen" wind gust. Due to the infinite speed propagating the perturba-

tions, circulatory and noncirculatory load contributions are distinguishable a priori [108]: given a step-change in the boundary conditions, the noncirculatory flow adapts instantaneously and embodies the flow inertia (applied at the airfoil's mid-chord), while the circulatory flow adapts with some delay and embodies the flow circulation (applied at the airfoil's aerodynamic center and control point, located at the first and last quarter-chord, respectively) [28]. Theodorsen $C(k)$ and (modified) Sears $C_G(k)$ functions being defined in the (reduced) frequency domain as [23-25]:

$$C = \frac{H_1^{(2)}}{H_1^{(2)} + \mathrm{j}H_0^{(2)}}, \qquad C_G = \left[C\left(B_0^{(1)} - \mathrm{j}B_1^{(1)}\right) + \mathrm{j}B_1^{(1)}\right]e^{-\mathrm{j}k}, \tag{A1}$$

with $H_n^{(2)}(k) = B_n^{(1)}(k) - \mathrm{j}B_n^{(2)}(k)$ Hankel functions of the second type and n-th order while $B_n^{(1)}(k)$ and $B_n^{(2)}(k)$ Bessel functions of the first and second type and n-th order, Wagner $\phi(\tau)$ and Kussner $\psi(\tau)$ functions are then defined in the (reduced) time domain as [20-21]:

$$\phi = \int_{-\infty}^{\infty} \frac{Ce^{\mathrm{j}k\tau}}{2\pi\mathrm{j}k}dk, \qquad \psi = \int_{-\infty}^{\infty} \frac{C_G e^{\mathrm{j}k\tau}}{2\pi\mathrm{j}k}dk, \tag{A2}$$

and quantify the decaying influence of the wake's inflow speed on the airfoil lift, in terms of semi-chords travelled by the shed vorticity [28].

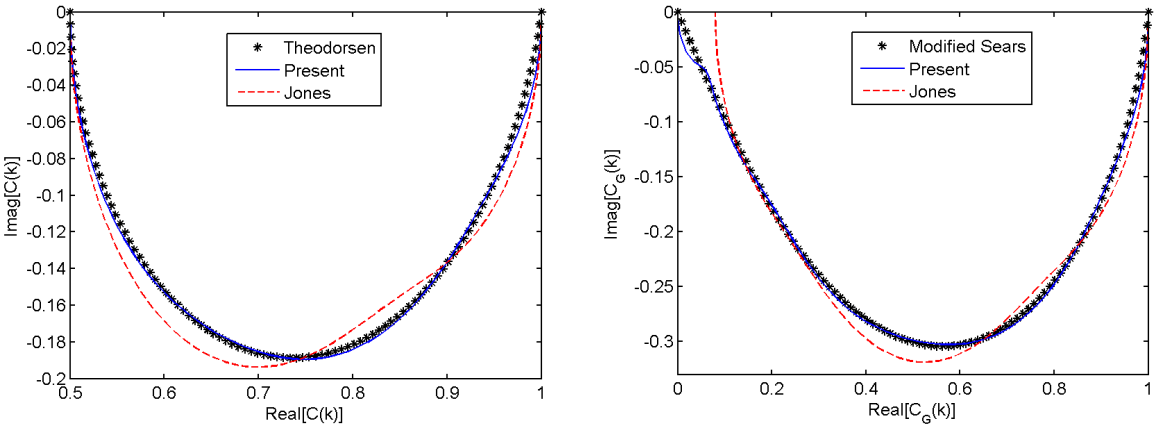


Figure A1. Theodorsen (left) and modified Sears (right) functions and their approximations

Figure A1 shows both Theodorsen and modified Sears functions along with their optimal analytical approximations; the initial guess for the optimal parameters was taken from those found in the literature [39]; deviations have also been investigated but no significant sensitivity found [96]. Note that any error in approximating these functions translates into an error in approximating Wagner and Kussner functions, respectively, and vice-versa; in particular, a good accuracy in approximating the formers at high reduced frequencies (i.e., highly-unsteady flow) translates into a good accuracy in approximating the latter at low reduced time (i.e., transient response), while a good accuracy at low reduced frequencies (i.e., quasi-steady flow) translates into a good accuracy at high reduced time (i.e., asymptotic response). Jones' approximations [39] deviating quite significantly from the exact curves, many other approximations are readily available in the literature [109-116] but the present ones grant the best

agreement along the entire exact curves with the least number of poles [96] (additional poles have been investigated but no significant improvement found) and possess the correct limit values (which is an essential feature for the present applications).

Noting that the gust penetration delays the circulation growth and hence reaching the asymptotic (steady) condition in Kussner's problem [21], the ratio between (modified) Sears and Theodorsen functions [23-25] may be considered as the transfer function of the gust penetration effect in the (reduced) frequency domain; therefore, the delay function $D(k)$ and $\delta(\tau)$ may suitably be defined in the (reduced) frequency and (reduced) time domains as:

$$D = \frac{C_G}{C}, \qquad \delta = \int_{-\infty}^{\infty} \frac{De^{\mathrm{j}k\tau}}{2\pi \mathrm{j}k} dk, \tag{A3}$$

respectively, as shown in Figure A2. Lastly, Figure A3 presents the application of such function to Jones' approximation [39] of the lift-deficiency function due to a unit step-change in the angle of attack and the present curve is in excellent agreement with his approximation [39] of the lift-deficiency function due to a unit step-change in the vertical speed of a "frozen" wind gust.

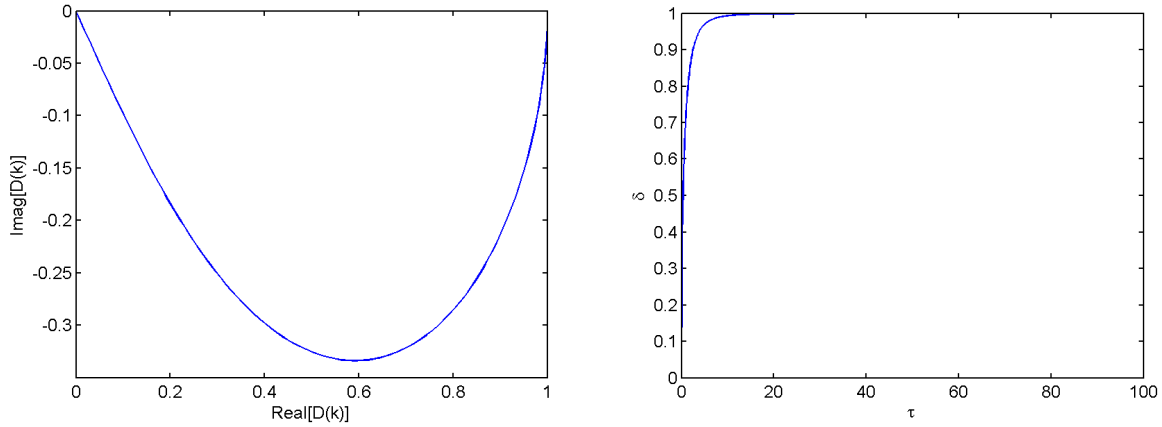


Figure A2. Delay function in the reduced frequency (left) and reduced time (right) domains

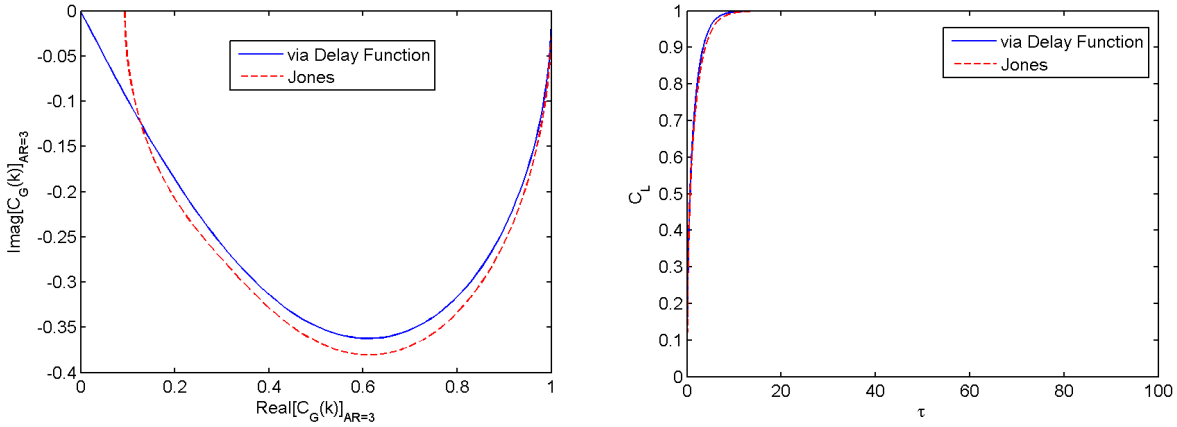


Figure A3. Approximate lift-deficiency coefficient due to a unitary sharp-edge gust for flat elliptical wing with AR=3 in the reduced frequency (left) and reduced time (right) domain

APPENDIX B. SIMPLEST PARAMETRIC APPROXIMATIONS

For thin elliptical wing [39], the simplest approximation of the lift-deficiency coefficient due to a unitary step change in the angle of attack employs a single exponential term connecting initial behaviour and asymptotic (steady) condition directly as:

$$C_L^{3D} = \frac{2\pi AR}{2+AR}\left\{1-\left[\frac{(2E-1)AR-2}{2EAR}\right]e^{-\left[\frac{2+AR}{(2E-1)AR-2}\right]\frac{\tau}{4}}\right\}, \tag{B1}$$

whereas for the case of thin rectangular wing [42] as:

$$C_L^{3D} = \frac{2\pi AR}{1+\sqrt{1+AR^2}}\left[1-\left(\frac{\sqrt{1+AR^2}-1}{2\sqrt{1+AR^2}}\right)e^{-\left(\frac{AR^2}{1+AR^2}\right)\left(\frac{\sqrt{1+AR^2}+1}{\sqrt{1+AR^2}-1}\right)\frac{\tau}{4}}\right]; \tag{B2}$$

selected curves are shown in Figure B1 and compared to those of Jones [39] and Jones [31].

As mentioned, the available steady lift coefficient for thin rectangular wings is not very accurate, due to the intrinsic limitations of the vortex-system representation employed [42]; if calculated according to lifting line theory [81,90], then the simplest approximation of the lift-deficiency coefficient due to a unitary step change in the angle of attack reads:

$$C_L^{3D} = \frac{2\pi}{1+2\pi\kappa}\left[1-\left(\frac{\sqrt{1+AR^2}-1}{2\sqrt{1+AR^2}}\right)e^{-\left(\frac{AR^2}{1+AR^2}\right)\left(\frac{\sqrt{1+AR^2}+1}{\sqrt{1+AR^2}-1}\right)\frac{\tau}{4}}\right], \tag{B3}$$

with κ shown in Figure B2 and initial behavior and asymptotic (steady) condition given by:

$$\lim_{\tau\to 0} C_L^{3D} \approx \frac{\pi\left(\sqrt{1+AR^2}+1\right)}{(1+2\pi\kappa)\sqrt{1+AR^2}}\left[1+\left(\frac{AR^2}{1+AR^2}\right)\frac{\tau}{4}\right], \qquad C_{L\infty}^{3D} = \frac{2\pi}{1+2\pi\kappa}. \tag{B4}$$

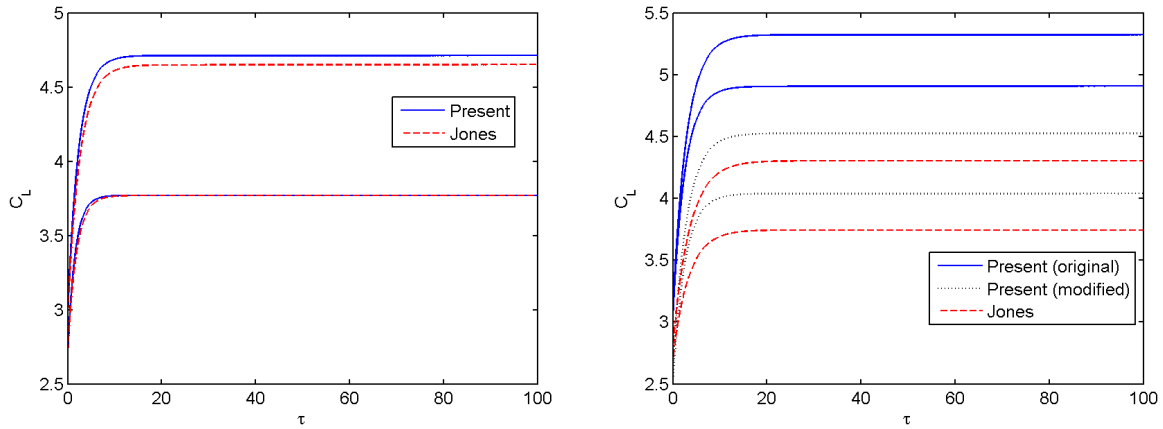


Figure B1. Lift-deficiency coefficient due to a unitary step change in the angle of attack for flat elliptical wing with AR=3,6 (left) and flat rectangular wing with AR=4,6 (right)

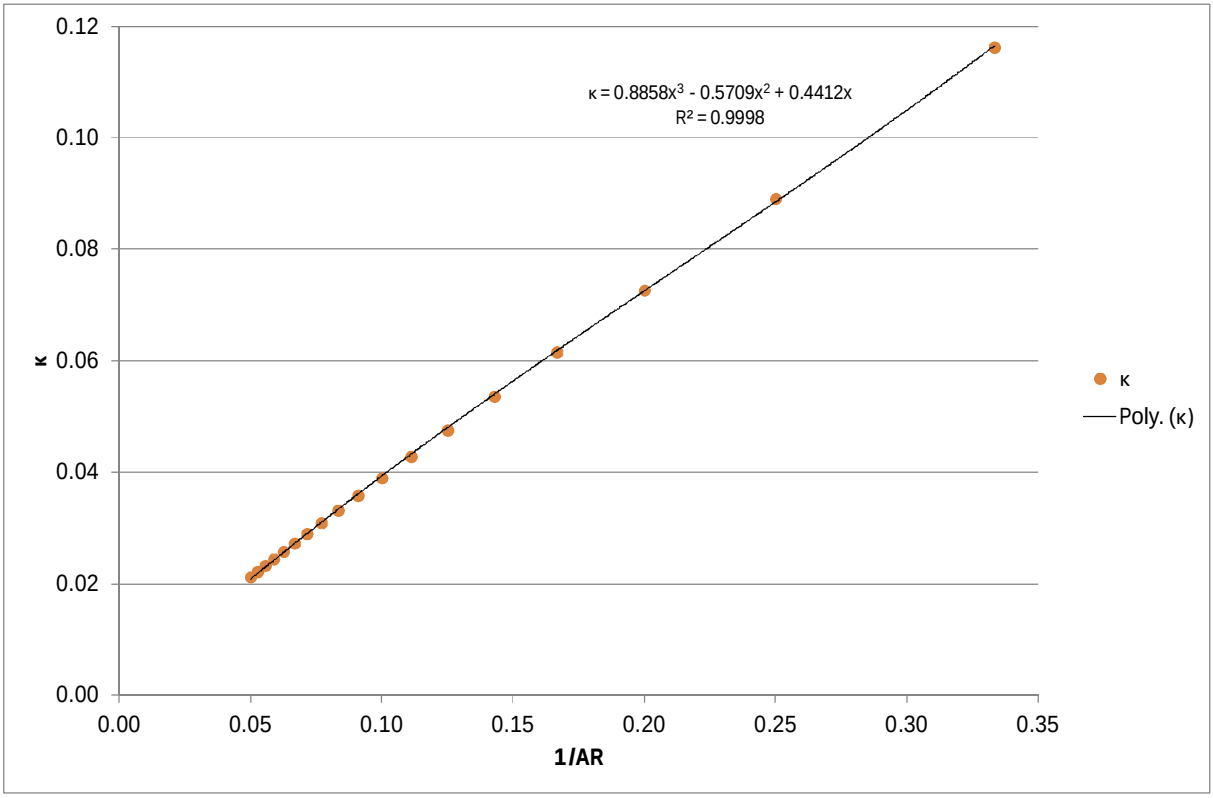


Figure B2. LLT-based coefficient for the asymptotic (steady) lift coefficient for a flat rectangular wing

REFERENCES

[1] N.M. Alexandrov, M.Y. Hussaini, *Multidisciplinary Design Optimization: State of the Art*. Proceedings in Applied Mathematics Series, SIAM, 1997.

[2] E. Kesseler, M. Guenov, *Advances in Collaborative Civil Aeronautical Multidisciplinary Design Optimization*. Progress in Astronautics and Aeronautics Series, AIAA, 2010.

[3] A. Quarteroni, G. Rozza, *Reduced Order Methods for Modeling and Computational Reduction*. Springer International Publishing, 2014.

[4] Z.Q. Qu, *Model Order Reduction Techniques with Applications in Finite Element Analysis*. Springer-Verlag, 2004.

[5] M. Gennaretti, F. Mastroddi, Study of Reduced-Order Models for Gust-Response Analysis of Flexible Fixed Wings. *Journal of Aircraft*, **41** (**2**), 2004.

[6] M. Bianchin, et al., State Space Reduced Order Models for Static Aeroelasticity and Flight Mechanics of Flexible Aircraft. *Proceedings of the 17th AIDAA Conference*, 2003.

[7] D.E. Raveh, Reduced-Order Models for Nonlinear Unsteady Aerodynamics. *AIAA Journal*, **39** (**8**), 2001.

[8] L. Cavagna, et al., Gust Loads Assessment: a Multi-Fidelity Approach. *Proceeding of the 14th IFASD*, 2011.

[9] T.M. Kier, G.H.N. Looye, Unifying Manoeuvre and Gust Loads Analysis Models. *Proceeding of the 13th IFASD*, 2009.

[10] T.M. Kier, Comparison of Unsteady Aerodynamic Modelling Methodologies with respect to Flight Loads Analysis. AIAA-2005-6027, 2005.

[11] E. Livne, The Future of Aircraft Aeroelasticity. *Journal of Aircraft*, **40** (**6**), 2003.

[12] J.R. Wright, J.E. Cooper, *Introduction to Aircraft Aeroelasticity and Loads.* AIAA Education Series, AIAA, 2007.

[13] Y.C. Fung, *An Introduction to the Theory of Aeroelasticity*. Dover, 1993.

[14] P. Marzocca, et al., Development of An Indicial Function Approach for the Two-Dimensional Incompressible/Compressible Aerodynamic Load Modelling. *Proceedings of the Institution of Mechanical Engineers, Part G: Journal of Aerospace Engineering*, **221** (**3**), 2007.

[15] E.C. Pike, Manual on Aeroelasticity. AGARD 578, 1971.

[16] M. Tobak, On the Use of the Indicial-Function Concept in the Analysis of Unsteady Motions of Wings and Wing-Tail Combinations. NACA 1188, 1954.

[17] J.G. Leishman, *Principles of Helicopter Aerodynamics*. Cambridge Aerospace Series, Cambridge University Press, 2006.

[18] R.L. Bisplinghoff, et al., *Aeroelasticity*. Dover, 1996.

[19] E.L. Houghton, et al., *Aerodynamics for Engineering Students*. Elsevier, 2012.

[20] H. Wagner, Uber die Entstenhung des dynamischen Auftriebes von Tragflugeln. *Zeitschrift für Angewandte Mathematik und Mechanik*, **5** (**1**), 1925.

[21] H.G. Kussner, Zusammenfassender Beritch uber den instationaren Auftrieb von Flugeln. *Luftfahrtforsch*, **13** (**12**), 1936.

[22] A. Kayran, Küssner's Function in the Sharp Edged Gust Problem - A Correction. *Journal of Aircraft*, **43** (**5**), 2006.

[23] T. Theodorsen, General Theory of Aerodynamic Instability and the Mechanism of Flutter. NACA 496, 1935.

[24] W.R. Sears, Operational Methods in the Theory of Airfoils in Non-Uniform Motion. *Journal of the Franklin Institute*, **230** (**1**), 1940.

[25] T. Von Karman, W.R. Sears, Airfoil Theory for Non-Uniform Motion, *Journal of the Aeronautical Sciences*, **5** (**10**), 1938.

[26] R.T. Jones, Classical Aerodynamic Theory. NASA RP 1050, 1979.

[27] B.C. Basu, G.J. Hancock, The Unsteady Motion of a Two-Dimensional Aerofoil in Incompressible Inviscid Flow. *Journal of Fluid Mechanics*, **87** (**1**), 1978.

[28] D.A. Peters, Two-Dimensional Incompressible Unsteady Airfoil Theory - An Overview. *Journal of Fluids and Structures*, **24** (**3**), 2008.

[29] F.M. Hoblit, *Gust Loads on Aircraft: Concepts and Applications.* AIAA Education Series, AIAA, 1988.

[30] W.P. Jones, Aerodynamic Forces on Wings in Simple Harmonic Motion. ARC-RM-2026, 1945.

[31] W.P. Jones, Aerodynamic Forces on Wings in Non-Uniform Motion. ARC-RM-2117, 1945.

[32] E. Reissner, Effect of Finite Span on the Airload Distributions for Oscillating Wings – Part I: Aerodynamic Theory of Oscillating Wings of Finite Span. NACA TN-1194, 1947.

[33] E. Reissner, J.E. Stevens, Effect of Finite Span on the Airload Distributions for Oscillating Wings – Part II: Methods of Calculation and Examples of Application. NACA TN-1194, 1947.

[34] H.C. Garner, Multhopp's Subsonic Lifting-Surface Theory of Wings in Slow Pitching Oscillations. ARC-RM-2885, 1956.

[35] D.E. Lehrian, Calculation of Stability Derivatives for Oscillating Wings. ARC-RM-2922, 1956.

[36] D.E. Lehrian, Calculation of Flutter Derivatives for Wings of General Planform. ARC-RM-2961, 1958.

[37] D.E. Lehrian, Initial Lift of Finite Aspect-Ratio Wings due to a Sudden Change of Incidence. ARC-RM-3023, 1957.

[38] B.D. Dore, The Unsteady Forces on Finite Wings in Transient Motion. ARC-RM-3456, 1966.

[39] R.T. Jones, The Unsteady Lift of a Wing of Finite Aspect Ratio. NACA 681, 1940.

[40] A. Hauptman, T. Miloh, Aerodynamic Coefficients of a Thin Elliptic Wing in Unsteady Motion. *AIAA Journal*, **25** (**6**), 1987.

[41] D.E. Lehrian, Vortex-Lattice Treatment of Rectangular Wings with Oscillating Control Surfaces. ARC-RM-3182, 1960.

[42] M.J. Queijo, et al., Approximate Indicial Lift Function for Tapered, Swept Wings in Incompressible Flow. NASA TP-1241, 1978.

[43] D.E. Lehrian, Aerodynamic Coefficients for an Oscillating Delta Wing. ARC-RM-2841, 1957.

[44] E. Albano, W.P. Rodden, A Doublet-Lattice Method for Calculating the Lift Distribution of Oscillating Surfaces in Subsonic Flows. *AIAA Journal*, **7** (**2**), 1969.

[45] F. Woodward, An Improved Method for the Aerodynamic Analysis of Wing-Body-Tail Configurations in Subsonic and Supersonic Flow. NASA CR-2228, 1973.

[46] L. Morino, A General Theory of Unsteady Compressible Potential Aerodynamics. NASA CR-2464, 1974.

[47] J. Katz, A. Plotkin, *Low Speed Aerodynamics*. Cambridge University Press, 2001.

[48] J.A. Drischler, Approximate Indicial Lift Function for Several Wings of Finite Span in Incompressible Flow as obtained from Oscillatory Lift Coefficients. NACA TN-3639, 1956.

[49] C. Scruton, et al., Measurements of the Aerodynamic Derivatives for Swept Wings of Low Aspect Ratio describing Pitching and Plunging Oscillations in Incompressible Flow. ARC-RM-2925, 1957.

[50] G.F. Moss, Low-Speed Wind-Tunnel Measurements of Longitudinal Oscillatory Derivatives on Three Wing Plan-forms. ARC-RM-3009, 1957.

[51] I.H. Abbott, A.E. von Doenhoff, *Theory of Wing Sections: Including a Summary of Airfoil Data*. Dover, 1959.

[52] J.G. Leishman, Indicial Lift Approximations for Two-Dimensional Subsonic Flow as Obtained from Oscillatory Measurements. *Journal of Aircraft*, **30** (**3**), 1993.

[53] M. Gaunaa, et al., Indicial Response Function for Finite-Thickness Airfoils, a Semi-Empirical Approach. AIAA-2011-542, 2011.

[54] T.J. Chung, *Computational Fluid Dynamics*. Cambridge Press, 2002.

[55] L. Cavagna, et al., Efficient Application of CFD Aeroelastic Methods Using Commercial Software. *Proceedings of the 11th IFASD*, 2005.

[56] G. Romanelli, et al., A "Free" Approach to Computational Aeroelasticity. AIAA-2010-176, 2010.

[57] A. Da Ronch, et al., On the Generation of Flight Dynamics Aerodynamic Tables by Computational Fluid Dynamics. *Progress in Aerospace Sciences*, **47**, 2011.

[58] M. Ghoreyshi, et al., Reduced Order Unsteady Aerodynamic Modeling for Stability and Control Analysis Using Computational Fluid Dynamics. *Progress in Aerospace Sciences*, **71**, 2014.

[59] V. Parameswaran, J.D. Baeder, Indicial Aerodynamics in Compressible Flow-Direct Computational Fluid Dynamic Calculations. *Journal of Aircraft*, **34** (**1**), 1997.

[60] W. Silva, Discrete-Time Linear and Nonlinear Aerodynamic Impulse Responses for Efficient Use of CFD Analyses. *PhD Thesis*, College of William & Mary, 1997.

[61] M. Ghoreyshi, et al., Computational Investigation into the Use of Response Functions for Aerodynamic-Load Modeling. *AIAA Journal*, **50** (**6**), 2012.

[62] P.G.A. Cizmas, J.I. Gargoloff, Mesh Generation and Deformation Algorithm for Aeroelasticity Simulations. *Journal of Aircraft*, **45** (**3**), 2008.

[63] C.D. Wieseman, Methodology for Matching Experimental and Computational Aerodynamic Data. NASA TM-100592, 1988.

[64] G. Dhatt, et al., *Finite Element Method*. Wiley, 2013.

[65] K.J. Bathe, *Nonlinear Finite Element Analysis and ADINA*. Pergamon Press, 1977–1999.

[66] C. Farhat, et al., Load and Motion Transfer Algorithms for Fluid/Structure Interaction Problems with Non-Matching Discrete Interfaces: Momentum and Energy Conservation, Optimal Discretization and Application to Aeroelasticity. *Computer Methods in Applied Mechanics and Engineering*, **157** (**1-2**), 1998.

[67] C. Farhat, V. Lakshminarayan, An ALE Formulation of Embedded Boundary Methods for Tracking Boundary Layers in Turbulent Fluid-Structure Interaction Problems. *Journal of Computational Physics*, **263**, 2014.

[68] J.G. Leishman, K.Q. Nguyen, State-Space Representation of Unsteady Airfoil Behavior. *AIAA Journal*, **28** (**5**), 1990.

[69] M. Meyer, H.G. Matthies, State-Space Representation of Instationary Two-Dimensional Airfoil Aerodynamics. *Journal of Wind Engineering and Industrial Aerodynamics*, **92** (**3-4**), 2004.

[70] G.N. Vanderplaats, *Numerical Optimization Techniques for Engineering Design: with Applications*. Series in Mechanical Engineering, McGraw Hill, 1984.

[71] S.H. Tiffany, W.M. Adams, Nonlinear Programming Extensions to Rational Function Approximation Methods for Unsteady Aerodynamic Forces. NASA-TP-2776, 1988.

[72] K.L. Roger, Airplane Math Modeling Methods for Active Control Design, AGARD-CP-228, 1977.

[73] R. Vepa, Finite State Modeling of Aeroelastic System. NASA-CR-2779, 1977.

[74] H. Dunn, An Analytical Technique for Approximating Unsteady Aerodynamics in the Time Domain. NASA-TP-1738, 1980.

[75] T.S. Beddoes, Practical Computation of Unsteady Lift. *Vertica*, **8** (**1**), 1984.

[76] M. Karpel, E. Strul, Minimum-State Unsteady Aerodynamic Approximations with Flexible Constraints, *Journal of Aircraft*, **33** (**6**), 1996.

[77] I. Cotoi, R.M. Botez, Method of Unsteady Aerodynamic Forces Approximation for Aeroservoelastic Interactions. *Journal of Guidance, Control and Dynamics*, **25** (**5**), 2002.

[78] R.B. Holmes, *A Course on Optimization and Best Approximation*. Lecture Notes in Mathematics, Springer, 1972.

[79] D. Poirel, Random Dynamics of a Structurally Nonlinear Airfoil in Turbulent Flow. *PhD Thesis*, McGill University, 2001.

[80] A. Quarteroni, et al., *Numerical Mathematics*. Springer-Verlag, 2000.

[81] J.D. Anderson, *Fundamentals of Aerodynamics*. McGraw-Hill, 2007.

[82] A. Sedaghat, et al., Curve Fitting Approach for Transonic Flutter Prediction. *The Aeronautical Journal*, **107** (**1075**), 2003.

[83] J. Brink-Spalink, J.M. Bruns, Correction of Unsteady Aerodynamic Influence Coefficients Using Experimental or CFD Data. AIAA-2000-1489, 2000.

[84] R. Palacios, et al., Assessment of Strategies for Correcting Linear Unsteady Aerodynamics Using CFD or Test Results. *Proceedings of the 9th IFASD*, 2001.

[85] D. Dimitrov, R. Thormann, DLM-Correction Method for Aerodynamic Gust Response Prediction. *Proceedings of the 15th IFASD*, 2013.

[86] M. Berci, et al., Dynamic Response of Typical Section Using Variable-Fidelity Fluid Dynamics and Gust-Modeling Approaches - With Correction Methods. *Journal of Aerospace Engineering*, **27** (**5**), 2014.

[87] R. Jin, et al., Comparative Studies of Metamodelling Techniques under Multiple Modelling Criteria. *Journal of Structural Optimisation*, **23** (**1**), 2001.

[88] J.B. Hiriart-Urruty, *Optimization: Theory and Algorithms*. Dekker, 1983.

[89] C.T. Leondes, *Optimization Techniques*. Elsevier, 1998.

[90] Prandtl, L., Applications of Modern Hydrodynamics to Aeronautics. NACA TR-116, 1921.

[91] D.A. Peters, et al, Finite State Induced Flow Models – Part I: Two-Dimensional Thin Airfoils. *Journal of Aircraft*, **32** (**2**), 1995.

[92] D.A. Peters, et al, A State-Space Airloads Theory for Flexible Airfoils. *Journal of the American Helicopter Society*, **52** (**4**), 2007.

[93] L.E. Garrick, On some Reciprocal Relations in the Theory of Nonstationary Flows. NACA-629, 1938.

[94] M.A. Heaslet, J.R. Spreiter, Reciprocity Relations in Aerodynamics. NACA-1119, 1953.

[95] G.M. Graham, Aeroelastic Reciprocity: An Indicial Response Formulation. AFOSR-TR-95, 1995.

[96] M. Berci, Optimal Approximations of Indicial Aerodynamics. *Proceedings of the 1st OPTi*, 2014.

[97] B.O. Peirce, *A Short Table of Integrals*. Ginn & Company, 1929.

[98] M.W. Kutta, Auftriebskräfte in Strömenden Flüssigkeiten. *Illustrierte Aeronautische Mitteilungen*, **6** (**133**), 1902.

[99] N.E. Joukowski, Sur les Tourbillons Adjionts. *Traraux de la Section Physique de la Societé Imperiale des Amis des Sciences Naturales*, **13** (**2**), 1906.

[100] H. Glauert, *The Elements of Aerofoil and Airscrew Theory*. Cambridge University Press, 1947.

[101] T. Van Holten, Some Notes on Unsteady Lifting-Line Theory. *Journal of Fluid Mechanics*, **77** (**3**), 1976.

[102] P.D. Sclavounos, An Unsteady Lifting-Line Theory. *Journal of Engineering Mathematics*, **21** (**3**), 1987.

[103] J.L. Guermond, A. Sellier, A Unified Unsteady Lifting-Line Theory. *Journal of Fluid Mechanics*, **229**, 1991.

[104] W.P. Rodden, *Theoretical and Computational Aeroelasticity*. Crest Pub., 2011.

[105] C.F.J. Wu, M. Hamada, *Experiments: Planning, Analysis, and Parameter Design Optimization*. Series in Probability and Statistics, Wiley, 2009.

[106] J.A. Nelder, R. Mead, A Simplex Method for Function Minimization. *Computer Journal*, **7**, 1965.

[107] M. Affenzeller, *Genetic Algorithms and Genetic Programming in Practice: Efficient Algorithm-Design in a Flexible Development Platform*. Chapman & Hall, 2009.

[108] U. Gulcat, *Fundamentals of Modern Unsteady Aerodynamics*. Springer, 2011.

[109] R. Vepa, On the Use of Pade' Approximants to Represent Unsteady Aerodynamic Loads for Arbitrarily Small Motions of Wings. AIAA-76-17, 1976.

[110] R.N. Desmarais, A Continued Fraction Representation for Theodorsen's Circulation Function. NASA-TM-81838, 1980.

[111] E.H. Dowell, A Simple Method for Converting Frequency Domain Aerodynamics to the Time Domain. NASA-TM-81844, 1980.

[112] C. Venkatesan, P. Friedmann, New Approach to Finite-State Modeling of Unsteady Aerodynamics. *AIAA Journal*, **24** (**12**), 1986.

[113] L.D. Peterson, E.F. Crawley, Improved Exponential Time Series Approximations of Unsteady Aerodynamic Operators. *Journal of Aircraft*, **25** (**2**), 1988.

[114] W. Eversman, A. Tewari, Modified Exponential Series Approximation for the Theodorsen Function. *Journal of Aircraft*, **28** (**9**), 1991.

[115] A. Tewari, J. Brink-Spalink, Multiple Pole Rational-Function Approximations for Unsteady Aerodynamics. *Journal of Aircraft*, **30** (**3**), 1993.

[116] S.L. Brunton, C.W. Rowley, Empirical State-Space Representations for Theodorsen's Lift Model. *Journal of Fluids and Structures*, **38** (**1**), 2013.

COMPDYN 2015
5th ECCOMAS Thematic Conference on
Computational Methods in Structural Dynamics and Earthquake Engineering
M. Papadrakakis, V. Papadopoulos, V. Plevris (eds.)
Crete Island, Greece, 25–27 May 2015

VERTICAL ACCELERATION DEMANDS ON NONSTRUCTURAL COMPONENTS IN BUILDINGS

L. Moschen[1], R. A. Medina[2], and C. Adam[1]

[1]Unit of Applied Mechanics, Department of Engineering Science, University of Innsbruck, Austria
Technikerstr. 13, 6020 Innsbruck, Austria
e-mail: {lukas.moschen,christoph.adam}@uibk.ac.at

[2]Department of Civil and Environmental Engineering, University of New Hampshire, U.S.A.
Kingsbury Hall Room W137, 33 Academic Way, 03824 Durham, NH, U.S.A.
e-mail: ricardo.a.medina@unh.edu

Keywords: Design Vertical Acceleration Response Spectrum, Vertical Ground Motion Selection, Perimeter Frames, Peak Vertical Acceleration Demands, Nonstructural Components.

Abstract. *This paper addresses the statistical evaluation of vertical peak floor acceleration (PFA_v) demands on elastic multistory buildings using recorded ground motions. Typical buildings are considered to be relatively flexible in the horizontal (lateral) direction and relatively rigid in the vertical (longitudinal) direction. The vast majority of studies conducted on the quantification of component acceleration demands have considered the flexibility of the nonstructural component (NSC) and its supporting structure primarily in the lateral direction. Studies on the evaluation of vertical component acceleration demands throughout a building are scarce and different opinions exist on the relevance of vertical accelerations in buildings. This paper focuses on the quantification of PFA_v, which implies that NSCs are assumed to be rigid in the vertical direction. Only rigid NSCs located close to columns of moment-resisting frames are considered. Thus, the influence of vertical floor vibrations and their dependence on the properties of the floor system is not addressed. The results demonstrate that the amplification of vertical ground acceleration demands throughout a building depends on the vertical stiffness of the load bearing structure, and hence, the common assumption of rigid-body responses in the vertical direction is highly questionable.*

1 INTRODUCTION

Many studies have been conducted during the last decades to assess seismic acceleration demands on nonstructural components (NSCs, also referred to secondary structures, building contents, mechanical and electrical equipment, architectural components) attached to elastic and inelastic buildings. Most research activities have focused on the horizontal acceleration components of ground motions. As a result, design engineers have relied upon simplified equations provided by building codes [1–3] to estimate the maximum horizontal acceleration demands on NSCs with much less attention been paid to maximum vertical acceleration demands.

Currently, a relatively small number of studies incorporates the effect of the vertical component of ground motions and its corresponding vertical floor motions. Generally, structural systems commonly used in buildings are considered to be relatively flexible in the lateral direction and relatively rigid in the vertical (longitudinal) direction. If columns were axially rigid, negligible amplification of the vertical component of the ground motion would occur for NSCs located at or near columns. On the other hand, for NSCs located at open-bays, i.e., at locations away from columns and relatively close to girders or in the middle of slabs, an amplification of the vertical floor acceleration with respect to ground has the potential to be significant. This is a result of resonance effects due to the out-of-plane flexibility of the girder/slab and the frequency content of the base excitation [4]. Therefore, vertical floor accelerations are highly dependent on the location of the component in a specific floor, the location of the component along the height of the building, and the characteristics and properties of the floor system.

For NSCs of various frequencies, a rigorous and comprehensive evaluation of their response must consider floor response spectra. This is particularly important given the myriad of periods (in this case horizontal vibration periods) associated with secondary structures such as electrical and mechanical equipment. These systems are generally classified as acceleration-sensitive because of their relatively large stiffness. In the United States of America, components are classified as either rigid or flexible based on their horizontal fundamental period, where NSCs with a period $T_s < 0.06\,\mathrm{s}$ are denoted as rigid [5]. Hence, flexible NSCs are susceptible to experiencing significant amplification of acceleration responses with respect to ground. In the specific case of vertical floor motions, and based on the study presented in [4], the flexibility of the girder/slab plays an important role.

Design forces for nonstructural components due to vertical base excitation are proposed in standards of the United States of America [1, 2]. In contrast, the European standard [3] does not provide explicit information on design vertical component accelerations or forces. In the United States of America, the recommended design component forces in the vertical direction $F_{p,v}$ are simply $50\,\%$ of the product of the design horizontal peak ground acceleration PGA_h times the seismic active mass in vertical direction:

$$F_{p,v} = \pm 0.20\, S_{DS} W_p = \pm 0.50\, PGA_h W_p \tag{1}$$

where S_{DS} is the design horizontal spectral acceleration in the short period region, and W_p is the operating mass of the component.

In contrast to the definition in [1], in this study the subscripts v and h are used in order to clearly define the difference between horizontal and vertical direction. However, this simplified estimation is questionable since the proposed equation for vertical component forces is not based on rigorous analyses or reliable experience data. One of the main problems is the lack of recorded vertical responses from buildings due to general unavailability of buildings instrumented with accelerometers able to record vertical motions. Thus, there is the need to quantify peak vertical floor acceleration demands (PFA_v) and their associated vertical floor response spectra.

2 GROUND MOTION RECORD SELECTION

Any ground motion record selection approach based on seismic hazard information necessitates the availability of vertical pseudo-spectral acceleration spectra ($S_{a,v}\left(T,\zeta\right)$). Unfortunately, probabilistic seismic hazard information is only available for the horizontal component of ground motions. Campbell and Bozorgnia [6, 7] developed a procedure to address this challenge without having to conduct a full-blown probabilistic seismic hazard analysis for the vertical component of ground motion. The first step involves converting the $\zeta = 5\,\%$ damped horizontal spectral acceleration at a period of $0.20\,\mathrm{s}$ $S_{a,h}\left(T = 0.20\,\mathrm{s},\zeta\right)$ to vertical spectral accelerations using vertical-to-horizontal (V/H) acceleration ratios for the site class BC boundary [8]. These ratios were estimated based on a study that involves near-source strong ground motions [6]. The second step entails the estimation of vertical spectral ordinates at all periods based on the vertical spectral ordinate at $T = 0.10\,\mathrm{s}$, modified for appropriate site conditions.

As part of the National Earthquake Hazards Reduction Program (NEHRP) in the U.S., a $\zeta = 5\,\%$ damped design vertical acceleration spectrum was proposed in [8]. The design vertical acceleration spectrum is based on modifications made to the procedure proposed by Campbell and Bozorgnia [7]. The primary modification involved estimating design vertical spectral accelerations from horizontal spectral acceleration values, which are available in seismic design maps [9]. These seismic design maps were obtained from hazard analysis using ground motion records that are part of the NGA ground motion database [10], which is the database used in this study to select ground motion records. A modified conversion factor is introduced in [8] to transform design horizontal to design vertical spectral accelerations for all soil conditions. In this process, estimates of design horizontal spectral accelerations are obtained from the $\mathrm{MCE_R}$ (risk-targeted Maximum Considered Earthquake) horizontal spectral acceleration at a period of $T = 0.20\,\mathrm{s}$ (S_S) [1]. These $\mathrm{MCE_R}$ values are provided in seismic design maps. Once this modified conversion is applied, limits are set on the design vertical spectral accelerations, and ordinates at periods other than $0.10\,\mathrm{s}$ are estimated based on relationships that are a function of the period in the vertical direction [8]. This transformation is possible primarily because for most soil conditions, as well as for magnitudes ($M_W > 6.5$) and focal distances ($r_{jb} < 60\,\mathrm{km}$) (Joyner-Boore dinstance) of interest for engineered structures, the (V/H) ratio $S_{a,v}\left(T = 0.10\,\mathrm{s},\zeta\right)/S_{a,h}\left(T = 0.20\,\mathrm{s},\zeta\right)$ is about 0.80 [8].

The approach described above leads to the vertical response spectrum in [8] (from here on referred to in this paper as NEHRP-spectrum). Figure 1 shows the normalized vertical spectral ordinate over the vertical frequency in Hz, $f_v = 1/T_v$. Spectral ordinates are normalized by the acceleration due to gravity g and $C_V S_{DS}$, where C_V can be obtained from Table 1 and S_{DS} is the design horizontal spectral acceleration at short periods according to [1, 8]. The normalized NEHRP-spectrum can be constructed by evaluation of:

$$\frac{S_{a,v}(f_v,\zeta)}{g\,C_V S_{DS}} = \begin{cases} 0.3 & \text{if } f_v \geq 40\,\mathrm{Hz} \\ 2.0\left(1/f_v - 1/40\right) + 0.3 & \text{if } 20\,\mathrm{Hz} \leq f_v \leq 40\,\mathrm{Hz} \\ 0.8 & \text{if } 20/3\,\mathrm{Hz} \leq f_v \leq 20\,\mathrm{Hz} \\ 0.8\left(20/3\,f_v\right)^{3/4} & \text{if } 0\,\mathrm{Hz} \leq f_v \leq 20/3\,\mathrm{Hz} \end{cases} \tag{2}$$

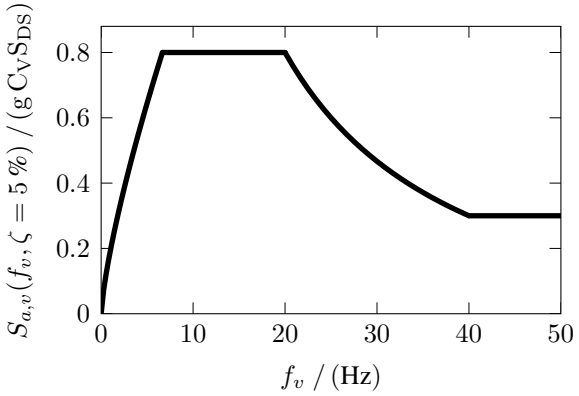


Figure 1: Normalized vertical design response spectrum (NEHRP-spectrum).

S_S	C_V NEHRP Site Class		
	A, B	C	D, E, F
≥ 2.00	0.90	1.30	1.50
1.00	0.90	1.10	1.30
0.60	0.90	1.00	1.10
0.30	0.80	0.80	0.90
≤ 0.20	0.70	0.70	0.70

Table 1: Conversation factor C_V for different site classifications.

2.1 Selection of ground motions for compatibility with the NEHRP-spectrum

Currently, a consensus on how to select ground motions for response history analysis (RHA) is nonexistent. However, an approach that is widely accepted and used in the earthquake engineering community is the use of base accelerations whose spectral ordinates over a desired frequency range are consistent with a target spectrum that is representative of the site. In general, this target spectrum can be obtained from either seismic hazard analysis (e.g., a design response spectrum) or a scenario analysis (e.g., from a ground motion prediction equation, GMPE). A more comprehensive discussion regarding ground motion selection methods as well as their pros and cons can be found in [11].

The ground motion record selection in this paper is based on the NEHRP-spectrum, more specifically, on its spectral shape. Equation (2) shows that the regions of constant acceleration are independent of site conditions. In other words, the corner frequencies are constant (in contrast to those present in NEHRP design horizontal spectra). Therefore, this property of the vertical NEHRP-spectrum facilitates in part the selection of ground motion records from the NGA (PEER) ground motion database [12] based on how consistent the central value and the dispersions of the chosen record set is with the spectral shape of the NEHRP-spectrum. The proposed ground motion record selection method explicitly accounts for the record-to-record variability in the estimation of seismic demands, and hence, provides the means to evaluate seismic demands statistically.

2.2 Spectrum-compatible record sets

In order to evaluate seismic demands statistically, a set of records is required to account for the record-to-record variability. Finding spectrum-compatible ground motion record sets is a computational expensive procedure. Thus, the 3179 earthquake recordings provided by the NGA (PEER) ground motion database were evaluated and a subset of recordings pre-selected based on the following characteristics:

- Moment magnitude: $M_W \geq 5.50$.
- NEHRP Site Classification D (stiff soil, shear wave velocity: $180\,\text{m/s} \leq v_{s30} \leq 360\,\text{m/s}$).
- Fault mechanism (FM): strike-slip (SS), reverse (RV), reverse-oblique (RVO).
- Distance (as defined by Joyner and Boore [13]): $0\,\text{km} \leq r_{jb} \leq 30\,\text{km}$.

A comprehensive overview of the characterization of ground motions (magnitude, fault mechanism, source to site distance, etc.) can be found in [14].

In this paper, the motivation is to find a set of records with the same scale factor α applied to each record according to the following criteria:

- The median spectral acceleration for the set $\widetilde{S}_{a,v}(f_v, \zeta, \alpha)$ should match the normalized NEHRP-spectrum over the frequency range of interest.
- The dispersion, which is measured as the standard deviation of the natural logarithm of the values for a given frequency, $\sigma_{S_{a,v}(f_v,\zeta,\alpha)}$ should be equal to a predefined target dispersion $\sigma_t(f_v) = \sigma_t$.

These two targets constitute two different spectrum-matching requirements. This leads to two coupled objective functions that can be minimized using genetic algorithms implemented in Matlab [15] for multicomponent objective functions:

$$\left.\begin{aligned} F_1(\alpha) &= \left\| S_{a,v}(f_v,\zeta) - \widetilde{S}_{a,v}(f_v,\zeta,\alpha) \right\| \\ F_2(\alpha) &= \left\| \mathrm{e}^{\sigma_t} S_{a,v}(f_v,\zeta) - S_{84,a,v}(f_v,\zeta,\alpha) \right\| \end{aligned}\right\} \longrightarrow \min \tag{3}$$

In order to generate a record set independent of site conditions, the product of the conversion factor and the spectral acceleration at short periods was set to $C_V S_{DS} = 1.00\,\text{g}$ for the optimization procedure. Additionally, spectral accelerations for a given frequency are assumed to be log-normally distributed, which is typical for response quantities in earthquake engineering [16]. Therefore, 84th percentile values $S_{84,a,v}(f_v, \zeta, \alpha)$ can be estimated by the product of the parameter e^{σ_t} and the median spectral acceleration. The implementation of this approach for ground motion selection can be interpreted as semi-probabilistic since the choice of σ_t biases the record selection. However, a variation of the target dispersion of $\sigma_t = 0.4\,\text{g}$, $0.6\,\text{g}$, $0.8\,\text{g}$ and $1.0\,\text{g}$ is used to quantify this influence. This range of values is reasonable and in agreement with the range of dispersions depicted in the spectra of [17].

The solutions of the multi-objective optimization can be graphically interpreted as a Pareto-optimal solution [18], sometimes referred to as Pareto frontier. Possible realizations (i.e., spectrum matching record sets) are shown in Figures 3 to 6. Figures 3a to 6a show the spectra of individual records, their statistical measures, and the NEHRP-spectrum. Figures 3b to 6b show the distribution of the records as a function of magnitude-distance ($M_W - r_{jb}$) coordinates.

No.	recs	σ_t	α
1	55	0.40	1.98
2	62	0.60	1.89
3	91	0.80	2.10
4	82	1.00	2.55

Table 2: Basic characteristics of ground motion record sets compatible with the normalized NEHRP-spectrum.

Table 2 lists the basic properties of each record set; the total number of records in each set is given in the second column.

A qualitative evaluation of the median spectrum of each ground motion set shows that each median spectrum is an adequate approximation of the target spectrum in the region $0\,\text{Hz} \leq f_v \leq {}^{20}/_{3}\,\text{Hz}$ (Figures 3a to 6a). The quality of the approximation in the region around the corner frequency $f_v = 20\,\text{Hz}$ increases with increasing number of records (not with increasing dispersion as discussed later). Furthermore, the median spectrum of each record set fits optimally the NEHRP-spectrum at the frequency of $f_v \approx 27\,\text{Hz}$ and each record set over predicts the target spectrum in the high frequency region.

The distribution of ground motions with respect to magnitude and distance for each record set is shown in Figures 3b to 6b. It is evident that most of the ground motion records belong to earthquakes with moment magnitudes between $6.0 \leq M_W \leq 6.7$, as shown in Table 3.

In order to define an optimal record set out of the four sets presented in Table 2, an understanding of the influence of the number of records and the target dispersion is required. Therefore, the relation between number of records and target dispersion is depicted in Figure 2, where the markers show the data listed in Table 2 and the solid line is a smooth interpolation polynomial.

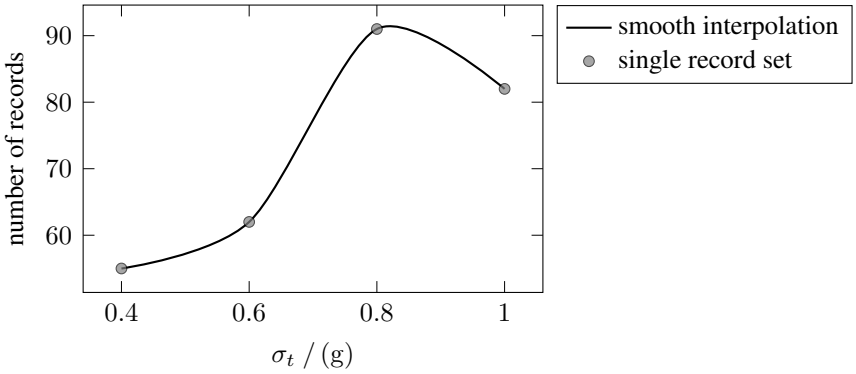


Figure 2: Relation between target dispersion σ_t and number of records (graphical interpretation of Table 2) and its smooth interpolation.

A larger number of records provides a closer and smoother approximation of the median to the NEHRP-spectrum. Moreover, when the target dispersion σ_t approaches zero, the spectrum of each ground motion record should closely match the target spectrum. This condition is only a theoretical consideration since each record has a different spectral shape. The probability density function (PDF) for this theoretical case degenerates from a log-normal distribution to the Dirac delta function. The conclusion is that competing objectives are present and, in general, increasing the number of records is required to obtain larger target dispersion values.

An optimal solution for the proposed record sets used in this paper can be obtained from Table 2 and from the graphical interpretation shown in Figure 2. Record set number three ($\sigma_t = 0.80$ g) consists of the maximum number of records. Comparison of the median spectrum between Figures 5a and 6a as well as a qualitative evaluation of the relative error in Figure 7 leads to a different conclusion than described before - record set number four shows fewer records than set number three but a median spectrum with a better compatibility with the NEHRP-spectrum. It can then be expected that a record set with a target dispersion of $0.80\,\text{g} \leq \sigma_t \leq 1.00\,\text{g}$ should lead to an optimal solution, i.e., a reasonable compromise between number of records, dispersion, and medium spectrum compatibility. Figure 2 shows that, based on the discrete values of dispersion used in this study, the peak value is very close to $\sigma_t = 0.80$ g, thus the median of record set number three is selected as the optimal fit to the NEHRP-spectrum. From here on, in this paper, this record set is referred to as the VGM record set. The basic characteristics of the single ground motion records constituting the VGM record set are listed in Table 3.

A practical tool for selection of spectrum compatible record sets is currently under development of this research group and will be published to the community in the near future.

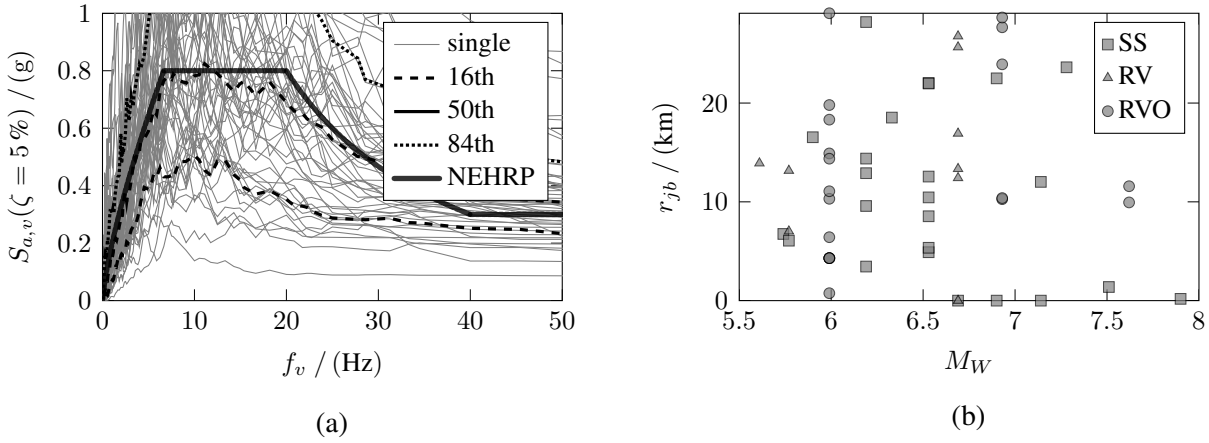


Figure 3: (a) Spectra of ground motion record sets and (b) distribution of records compatible with the normalized NEHRP-spectrum for a given target dispersion $\sigma_t = 0.40$ g.

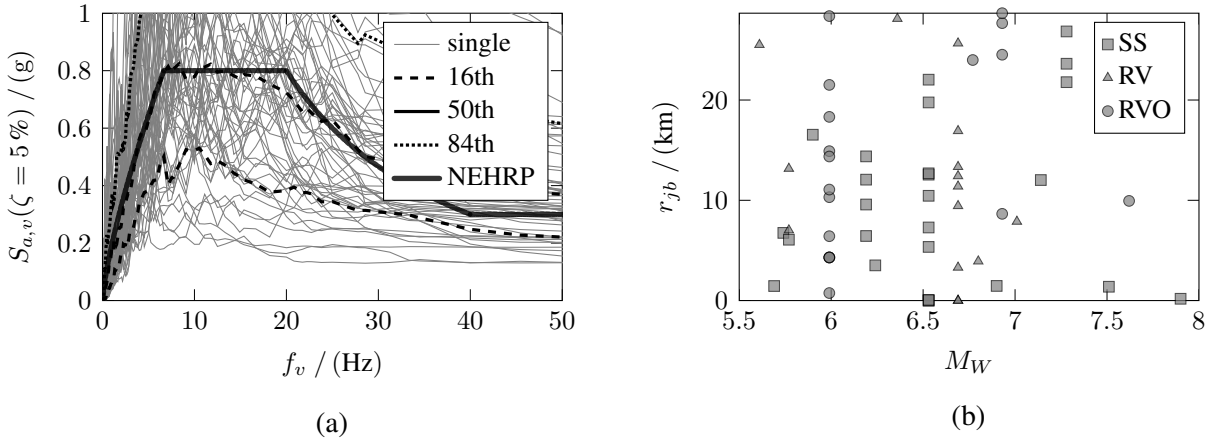
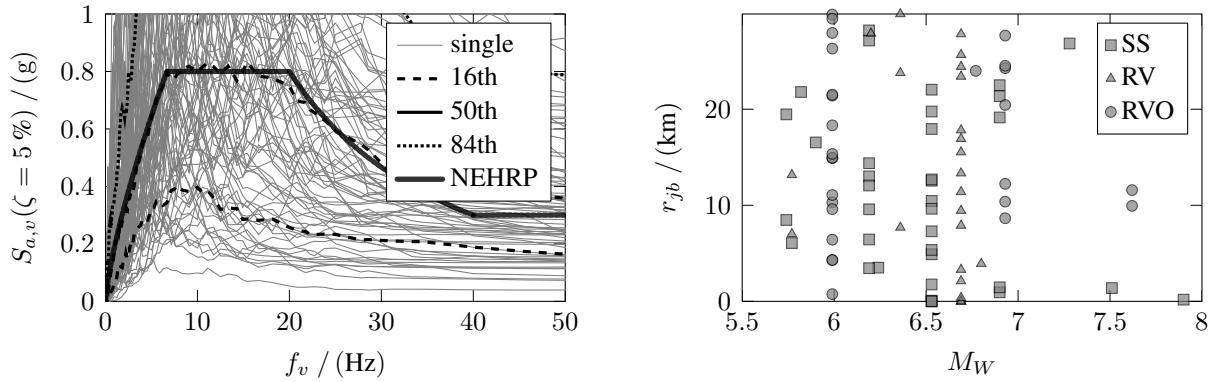
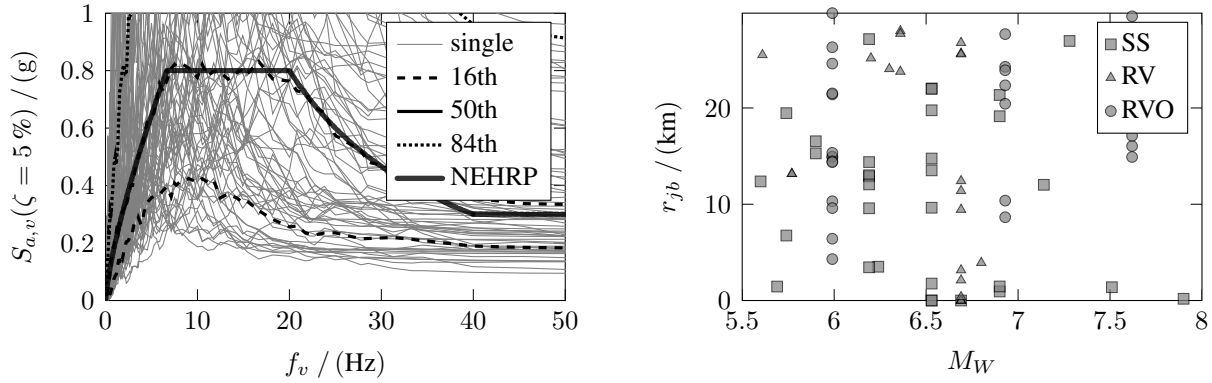


Figure 4: (a) Spectra of ground motion record sets and (b) distribution of records compatible with the normalized NEHRP-spectrum for a given target dispersion $\sigma_t = 0.60$ g.



(a) (b)

Figure 5: (a) Spectra of ground motion record sets and (b) distribution of records compatible with the normalized NEHRP-spectrum for a given target dispersion $\sigma_t = 0.80$ g.



(a) (b)

Figure 6: (a) Spectra of ground motion record sets and (b) distribution of records compatible with the normalized NEHRP-spectrum for a given target dispersion $\sigma_t = 1.00$ g.

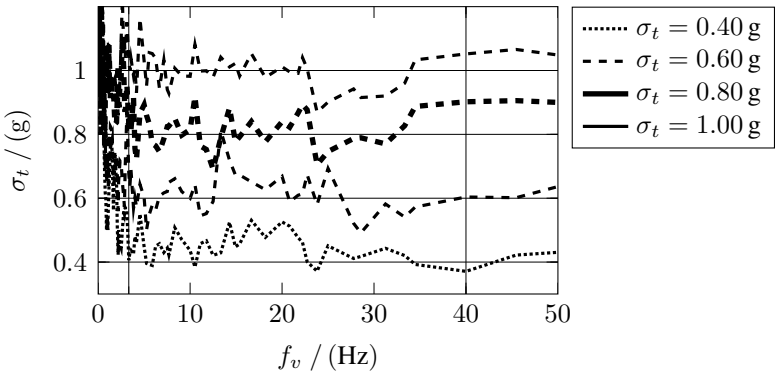


Figure 7: Variation with frequency of the dispersion of ground motion record sets compatible with the normalized NEHRP-spectrum for a given target dispersion.

No.	Earthquake Name	Station Name	Year	M_W	FM	r_{jb}/(km)
1	Parkfield	Cholame - Shandon Array 5	1966	6.19	SS	9.58
2	Managua, Nicaragua-01	Managua, ESSO	1972	6.24	SS	3.51
3	Gazli, USSR	Karakyr	1976	6.80	RV	3.92
4	Coyote Lake	Gilroy Array 2	1979	5.74	SS	8.47
5	Coyote Lake	San Juan Bautista, 24 Polk St	1979	5.74	SS	19.46
6	Imperial Valley-06	Aeropuerto Mexicali	1979	6.53	SS	0.00
7	Imperial Valley-06	Calexico Fire Station	1979	6.53	SS	10.45
8	Imperial Valley-06	Chihuahua	1979	6.53	SS	7.29
9	Imperial Valley-06	Delta	1979	6.53	SS	22.03
10	Imperial Valley-06	El Centro - Meloland Geot. Array	1979	6.53	SS	0.07
11	Imperial Valley-06	El Centro Array 1	1979	6.53	SS	19.76
12	Imperial Valley-06	El Centro Array 11	1979	6.53	SS	12.56
13	Imperial Valley-06	El Centro Array 12	1979	6.53	SS	17.94
14	Imperial Valley-06	El Centro Array 4	1979	6.53	SS	4.90
15	Imperial Valley-06	El Centro Array 5	1979	6.53	SS	1.76
16	Imperial Valley-06	El Centro Array 6	1979	6.53	SS	0.00
17	Imperial Valley-06	Holtville Post Office	1979	6.53	SS	5.35
18	Imperial Valley-06	Parachute Test Site	1979	6.53	SS	12.69
19	Imperial Valley-06	SAHOP Casa Flores	1979	6.53	SS	9.64
20	Westmorland	Parachute Test Site	1981	5.90	SS	16.54
21	Coalinga-01	Cantua Creek School	1983	6.36	RV	23.78
22	Coalinga-01	Parkfield - Fault Zone 7	1983	6.36	RV	29.91
23	Coalinga-01	Pleasant Valley P.P. - yard	1983	6.36	RV	7.69
24	Coalinga-05	Coalinga-14th Elm (Old CHP)	1983	5.77	RV	7.02
25	Coalinga-05	Pleasant Valley P.P. - yard	1983	5.77	RV	13.16
26	Morgan Hill	Gilroy Array 3	1984	6.19	SS	13.01
27	Morgan Hill	Gilroy Array 7	1984	6.19	SS	12.06
28	Morgan Hill	Halls Valley	1984	6.19	SS	3.45
29	Morgan Hill	San Juan Bautista, 24 Polk St	1984	6.19	SS	27.15
30	Bishop (Rnd Val)	McGee Creek - Surface	1984	5.82	SS	21.79
31	Chalfant Valley-01	Zack Brothers Ranch	1986	5.77	SS	6.07
32	Chalfant Valley-02	Bishop - LADWP South St	1986	6.19	SS	14.38
33	Chalfant Valley-02	McGee Creek - Surface	1986	6.19	SS	28.20
34	Chalfant Valley-02	Zack Brothers Ranch	1986	6.19	SS	6.44
35	Whittier Narrows-01	Bell Gardens - Jaboneria	1987	5.99	RVO	10.31
36	Whittier Narrows-01	Carson - Catskill Ave	1987	5.99	RVO	29.85
37	Whittier Narrows-01	Compton - Castlegate St	1987	5.99	RVO	18.32
38	Whittier Narrows-01	Downey - Birchdale	1987	5.99	RVO	14.90
39	Whittier Narrows-01	Downey - Co Maint Bldg	1987	5.99	RVO	14.95
40	Whittier Narrows-01	El Monte - Fairview Av	1987	5.99	RVO	0.75
41	Whittier Narrows-01	Hacienda Heights - Colima	1987	5.99	RVO	9.60
42	Whittier Narrows-01	Inglewood - Union Oil	1987	5.99	RVO	21.41
43	Whittier Narrows-01	LA - Baldwin Hills	1987	5.99	RVO	21.51
44	Whittier Narrows-01	LA - Fletcher Dr	1987	5.99	RVO	11.07
45	Whittier Narrows-01	LA - N Faring Rd	1987	5.99	RVO	27.94
46	Whittier Narrows-01	LA - N Westmoreland	1987	5.99	RVO	15.34
47	Whittier Narrows-01	Lawndale - Osage Ave	1987	5.99	RVO	26.31

Continued on next page

No.	Earthquake Name	Station Name	Year	M_W	FM	r_{jb}/(km)
48	Whittier Narrows-01	Pasadena - Brown Gym	1987	5.99	RVO	4.30
49	Whittier Narrows-01	Pasadena - CIT Calif Blvd	1987	5.99	RVO	4.30
50	Whittier Narrows-01	Playa Del Rey - Saran	1987	5.99	RVO	29.42
51	Whittier Narrows-01	West Covina - S Orange Ave	1987	5.99	RVO	6.42
52	Spitak, Armenia	Gukasian	1988	6.77	RVO	23.99
53	Loma Prieta	Agnews State Hospital	1989	6.93	RVO	24.27
54	Loma Prieta	Capitola	1989	6.93	RVO	8.65
55	Loma Prieta	Coyote Lake Dam (Downst)	1989	6.93	RVO	20.44
56	Loma Prieta	Gilroy Array 2	1989	6.93	RVO	10.38
57	Loma Prieta	Gilroy Array 3	1989	6.93	RVO	12.23
58	Loma Prieta	Hollister - South Pine	1989	6.93	RVO	27.67
59	Loma Prieta	Hollister Differential Array	1989	6.93	RVO	24.52
60	Landers	North Palm Springs	1992	7.28	SS	26.84
61	Northridge-01	Arleta - Nordhoff Fire Sta	1994	6.69	RV	3.30
62	Northridge-01	Beverly Hills - 14145 Mulhol	1994	6.69	RV	9.44
63	Northridge-01	Canoga Park - Topanga Can	1994	6.69	RV	0.00
64	Northridge-01	Canyon Country - W Lost Cany	1994	6.69	RV	11.39
65	Northridge-01	Hollywood - Willoughby Ave	1994	6.69	RV	17.82
66	Northridge-01	LA - Century City CC North	1994	6.69	RV	15.53
67	Northridge-01	LA - Fletcher Dr	1994	6.69	RV	25.66
68	Northridge-01	LA - N Westmoreland	1994	6.69	RV	23.40
69	Northridge-01	LA - Pico Sentous	1994	6.69	RV	27.82
70	Northridge-01	Moorpark - Fire Sta	1994	6.69	RV	16.92
71	Northridge-01	N Hollywood - Coldwater Can	1994	6.69	RV	7.89
72	Northridge-01	Newhall - W Pico Canyon Rd.	1994	6.69	RV	2.11
73	Northridge-01	Pacific Palisades - Sunset	1994	6.69	RV	13.34
74	Northridge-01	Playa Del Rey - Saran	1994	6.69	RV	24.42
75	Northridge-01	Rinaldi Receiving Sta	1994	6.69	RV	0.00
76	Northridge-01	Sylmar - Converter Sta	1994	6.69	RV	0.00
77	Northridge-01	Tarzana - Cedar Hill A	1994	6.69	RV	0.37
78	Kobe, Japan	KJMA	1995	6.90	SS	0.94
79	Kobe, Japan	Kakogawa	1995	6.90	SS	22.50
80	Kobe, Japan	OSAJ	1995	6.90	SS	21.35
81	Kobe, Japan	Shin-Osaka	1995	6.90	SS	19.14
82	Kobe, Japan	Takatori	1995	6.90	SS	1.46
83	Kocaeli, Turkey	Yarimca	1999	7.51	SS	1.38
84	Chi-Chi, Taiwan	CHY025	1999	7.62	RVO	19.07
85	Chi-Chi, Taiwan	CHY101	1999	7.62	RVO	9.94
86	Chi-Chi, Taiwan	CHY104	1999	7.62	RVO	18.02
87	Chi-Chi, Taiwan	TCU038	1999	7.62	RVO	25.42
88	Chi-Chi, Taiwan	TCU110	1999	7.62	RVO	11.58
89	Chi-Chi, Taiwan	TCU112	1999	7.62	RVO	27.48
90	Denali, Alaska	TAPS Pump Station 10	2002	7.90	SS	0.18
91	Chi-Chi, Taiwan-03	CHY025	1999	6.20	RV	27.88

Table 3: Basic characteristics of ground motion records constituting the VGM record set ($\sigma_t = 0.80\,\mathrm{g}$, $\alpha = 2.10$) compatible with the normalized NEHRP-spectrum.

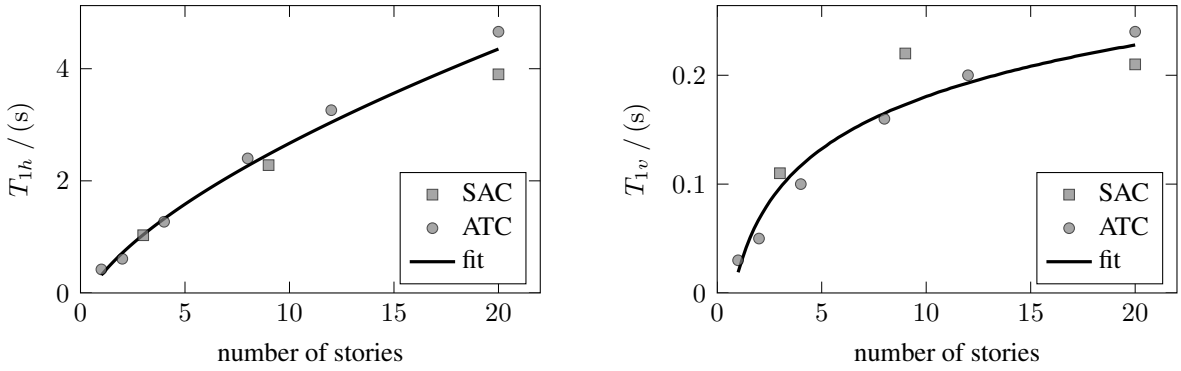
3 GENERIC STICK MODELS

The generic stick models used throughout this paper are developed on the basis of an evaluation of modal properties of the steel frames from the SAC steel project [19] and the ATC-76-1 project [20]. In a pilot study, conducted by this research group [21], the modal properties of the perimeter frames from the aforementioned projects were evaluated. Results demonstrated that linear first-mode shapes are reasonable approximations to the fundamental mode shapes in the lateral and longitudinal direction of these steel frames. Additionally, an analytical expression in terms of a two term power series is used to quantify the relation between the fundamental periods in both lateral, T_{1h}, and longitudinal, T_{1v}, directions, as a function of the total number of stories, N, of the structure:

$$T_{1h} = 0.720N^{0.63} - 0.401 \tag{4}$$

$$T_{1v} = -3.602N^{-0.02} + 3.621 \tag{5}$$

Figure 8 shows a graphical representation of Equations (4) and (5). The squared markers in the scatter highlight the empirical data observed from structural models of the SAC steel project [19], and the circled scatter marks the data from the ATC-76-1 project [20]. Equations (4) and (5) and linear first-mode shapes in the lateral and longitudinal direction are the basis to develop generic stick models as shown below for an interior column of a perimeter frame.



(a) (b)

Figure 8: Relation between (a) the fundamental period T_{1h} respectively (b) the fundamental period T_{1v} and the number of stories for the SAC steel project and the ATC-76-1 project.

Typical perimeter frames consist of two exterior columns and, if required, interior columns to transfer the effects of equivalent lateral forces from the structure to the foundation. Figure 9a shows schematically a six-story, two-bay generic frame. Lumped masses are depicted as gray circles. The degrees of freedom with respect to the ground $(x_g(t), z_g(t))$ are denoted as $x_i(t)$ in the lateral direction and as $z_i(t)$ in the vertical direction, where i is the floor number. In this context, a generic stick model represents an isolated column line of a frame as shown for the 6-story generic frame in Figure 9b for an interior column. In this paper the development of the generic stick model of interior columns is illustrated. The story and the floor numbering as well as the enumeration of the seismic mass are defined in Figure 9b. Figure 9c shows the generic stick model of the interior column consisting of columns, rotational springs $c_{\theta i}$ (representing the flexural stiffness of the frame) and vertical springs c_{ui} (representing the shear stiffness of the girders and the axial stiffness of the exterior columns). An additional rotational spring at the

base $c_{\theta 0}$ is required to make sure that the fundamental mode in the lateral direction is a straight line over the structure's height and to obtain a uniform distribution of the moments of inertia over the height [22].

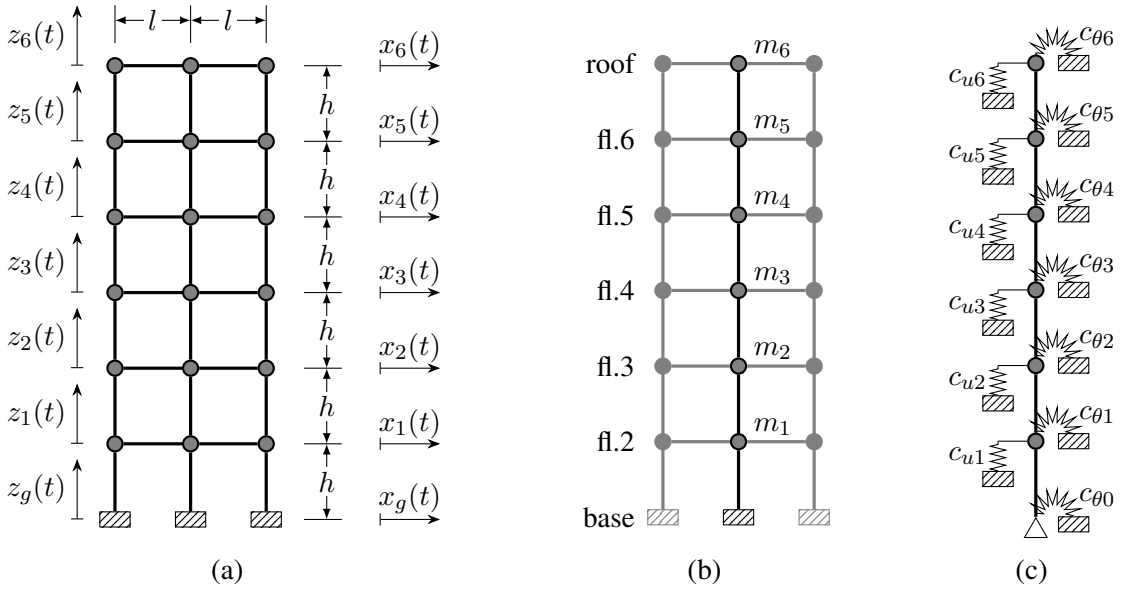


Figure 9: Development of generic stick models for interior columns based on a two-bay generic frame. (a) Complete generic frame, (b) isolated interior column with floor / story / mass numbering and (c) generic stick model including equivalent springs.

Furthermore, the assumptions outlined below are required for the development of models with appropriate flexibility in the vertical and horizontal directions:

- PΔ effects are not included. In other words, modal quantities are based on first-order analyses. Thus, the global stiffness matrix $\mathbf{K}$ does not include the geometric stiffness.
- Lumped masses as shown in Figure 9 are used. When modeling the structure with a generic stick, the mass matrix $\mathbf{M}$ is a diagonal matrix for the lateral as well as the vertical degrees of freedom.
- The story height h is the same for each story and the bay width is l for each one of them (see Figure 9).
- Since SAC and the ATC-76-1 frames are steel frames, Young's modulus of $E = 2 \cdot 10^{11}$ N/m^2 is used.
- Column splices are located at column mid-heights (except the columns of the first story, the splices of those members are located at mid height of the second story). Therefore, column cross sectional properties A_i and I_i between story mid-heights are constant. Furthermore, at each beam-column (BC) connection, column and girder member sizes are assumed to be the same as shown in Figure 10b for the ith floor.

3.1 Structural parameters in the lateral direction

In this study, it is assumed that the first mode dominates the structural response and the fundamental mode shape in the lateral direction is linear over the structure's height. The

deflected shape of the frame under lateral loading assumes points of inflection POIs at column mid-heights and beam mid-spans (Figure 10a). This assumption allows the use of the free-body diagram presented in Figure 10b by constraining the substructure using pinned supports at the POIs.

At each floor level, the same seismic masses $m_{ih}^{(l)}$, $m_{ih}^{(m)}$ and $m_{ih}^{(r)}$ are used at the left, mid, and right of the BC connection as shown in Figure 10b. Thus, the total seismic mass in the horizontal direction acting at each floor level of the perimeter frame equals:

$$m_h^{(story)} = m_{ih}^{(l)} + m_{ih}^{(m)} + m_{ih}^{(r)} \tag{6}$$

For this generic stick model only the mass associated with the interior column is required, therefore, $m_h = m_{ih}^{(m)}$, which implies that floor masses are constant with a value equal to that of the diagonal elements of the mass matrix $\mathbf{M}_h$ (note, the labels of the masses in Figure 9b don't have a subscript h to keep the figure independent from the lateral / vertical direction). The seismic mass can be determined from the dead load of the structure including the weight of cladding.

Equivalent lateral stiffness for the generic stick models can be obtained by imposing the deflected shape shown in Figure 10b to the various substructures along the height of the frame. Both exterior columns are the same. In particular, each BC connection consists of a half column of the lower story, a half column of the upper story, and a half girder. In contrast, the BC connection at the interior column is stiffer since two half girders frame into it.

The stiffness of an isolated BC connection can be expressed in terms of the relative lateral deformation u of the bottom and top column nodes in the free-body diagram of Figure 10b for a unit shear load. Thus, the individual contribution of the half columns below and above the girder to the total horizontal deflection is given by:

$$u^{(col)} = \frac{\left(h/2\right)^3}{3EI_i} \tag{7}$$

The deflection given by Equation (7) is equivalent to the deformation at the tip of a cantilever column of length $h/2$ that frames into a rigid girder when a unit shear load is applied. Now, if the girder is flexible and the column is considered to be rigid in flexure, then, the relative lateral deformation between the bottom and top column nodes in the free-body diagram of Figure 10b for a unit shear load is given by:

$$u^{(gir,int)} = 2\frac{l/2\left(h/2\right)^2}{3EI_i} \tag{8}$$

$$u^{(gir,ext)} = 4\frac{l/2\left(h/2\right)^2}{3EI_i} \tag{9}$$

The total substructure flexibility caused by the flexibility of the columns and the girder(s) is given by:

$$u^{(int)} = 2u^{(col)} + u^{(gir,int)} \tag{10}$$

$$u^{(ext)} = 2u^{(col)} + u^{(gir,ext)} \tag{11}$$

The equivalent lateral stiffness for each column line of the substructure of Figure 10b is then the

inverse of the flexibility given by Equations (10) and (11) and it is equal to:

$$c^{(int)} = \frac{1}{u^{(int)}} \tag{12}$$

$$c^{(ext)} = \frac{1}{u^{(ext)}} \tag{13}$$

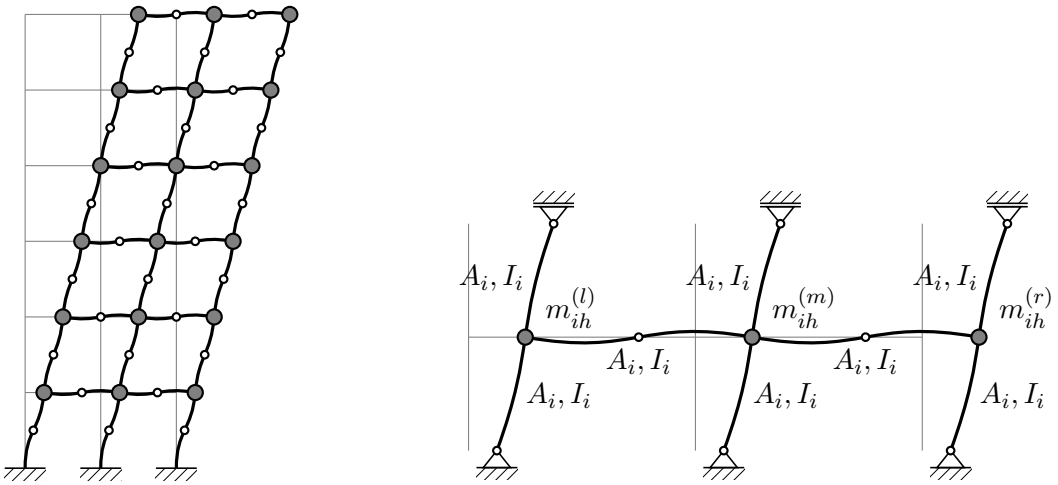
Then, the total lateral story stiffness yields:

$$c^{(story)} = 2c^{(ext)} + c^{(int)} \tag{14}$$

Since the story shear force is directly proportional to the story mass (if damping is neglected), the seismic mass on the exterior columns and the interior column is proportional to the ratio between the individual joint stiffnesses and the total lateral stiffness for the substructure:

$$m_{ih}^{(m)} = \frac{c^{(int)}}{c^{(story)}} m_h^{(story)} = \frac{5}{11} m_h^{(story)} \tag{15}$$

$$m_{ih}^{(l)} = m_{ih}^{(r)} = \frac{c^{(ext)}}{c^{(story)}} m_h^{(story)} = \frac{3}{11} m_h^{(story)} \tag{16}$$



(a) (b)

Figure 10: Generic frame vibrating in its lateral linear fundamental mode. (a) Complete generic frame and (b) isolated substructure.

For vibration in the lateral direction the beam members are assumed to be axially rigid. The equivalent stiffness $c_{\theta i}$ of the rotational spring that represents the girders at the ith floor level (see Figure 10b) can be obtained by evaluation of:

$$c_{\theta i} = 2\frac{3EI_i}{l/2} = \frac{12EI_i}{l} \tag{17}$$

In order to obtain a uniform distribution of the moments of inertia over the structure's height a rotational spring is added at the base, which *simulates* beams framed at the bottom of the first story column:

$$c_{\theta 0} = 2\frac{3EI_1}{l/2} = \frac{12EI_1}{l} \tag{18}$$

Assembling the global mass- and stiffness matrix leads to the eigenvalue problem formulated in terms of the first eigenvalue and the corresponding linear mode shape:

$$(\mathbf{M}_h - \lambda_{1h}\mathbf{K}_h)\,\boldsymbol{\phi}_1 = \mathbf{0} \tag{19}$$

where the first eigenvalue λ_{1h} is the inversion of the square of the fundamental circular frequency ω_{1h}, which can be estimated by using Equation (4):

$$\lambda_{1h} = \frac{1}{\omega_{1h}^2} = \frac{T_{1h}^2}{4\pi^2} \tag{20}$$

Hence, the unknown parameters in the system of nonlinear equations in Equation (20) are the moments of inertia I_i. In other words, there are N unknown moments of inertias if the structure is a N-story frame. Equation (19) can be seen as a simple optimization problem. The roots of the nonlinear system of equations can be found by the function *fsolve*, which is a part of Matlab's *Optimization Toolbox* [15].

3.2 Structural parameters in the vertical direction

For vibration in the vertical direction the seismic mass is simply defined by the associated floor tributary area. From Figure 11b it can be seen that the seismic mass of the exterior column is equal to the half of the mass acting on the interior column:

$$m_{iv}^{(m)} = \frac{1}{2} m_v^{(story)} \tag{21}$$

$$m_{iv}^{(l)} = m_{iv}^{(r)} = \frac{1}{4} m_v^{(story)} \tag{22}$$

When the structure vibrates in its vertical fundamental mode (see Figure 11a) the vertical springs in Figure 9c represent the flexural stiffness of the girders. The POIs are assumed to be located at column mid-heights and beam mid-spans as shown in Figure 11a. The equivalent stiffness of the vertical springs c_{ui} can be obtained from Equation (23), which is analogous to Equation (17):

$$c_{ui} = \frac{3EA_iI_i\,(h + 12l)}{3I_ih^2 + A_ihl^3 + 36I_ihl + 3A_il^4} \tag{23}$$

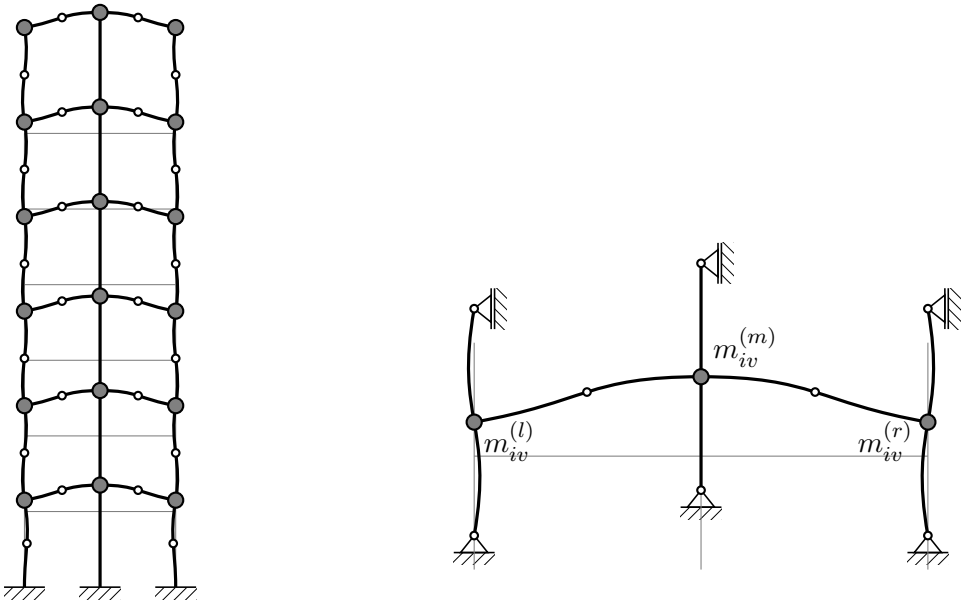
The eigenvalue problem formulated in terms of the linear fundamental mode shape and the corresponding eigenvalue in the vertical direction leads to:

$$(\mathbf{M}_v - \lambda_{1v}\mathbf{K}_v)\,\boldsymbol{\phi}_1 = \mathbf{0} \tag{24}$$

The first eigenvalue in the vertical direction can be estimated by using Equation (5):

$$\lambda_{1v} = \frac{1}{\omega_{1v}^2} = \frac{T_{1v}^2}{4\pi^2} \tag{25}$$

The unknown variables are the cross sectional areas A_i, which can determined using simple optimization techniques.



(a) (b)

Figure 11: Generic frame vibrating in its vertical linear fundamental mode. (a) Complete generic frame and (b) isolated substructure.

3.3 Evaluation of structural parameters

The parameters of the generic stick model are determined based on the mass and geometric characteristics outlined below.

- Seismic active story mass for vibration in the horizontal direction:

$$m_h^{(story)} = 229\,741\,\text{kg} \approx 230\,\text{t} \approx 10\,000\,\text{kip} \tag{26}$$

- Seismic active story mass for vibration in the vertical direction:

$$m_v^{(story)} = 19\,271\,\text{kg} \approx 19\,\text{t} \approx 830\,\text{kip} \tag{27}$$

- Story height, h, and bay width, l:

$$h/l = 1/2, \quad h = 3.96\,\text{m} = 13\,\text{ft} \tag{28}$$

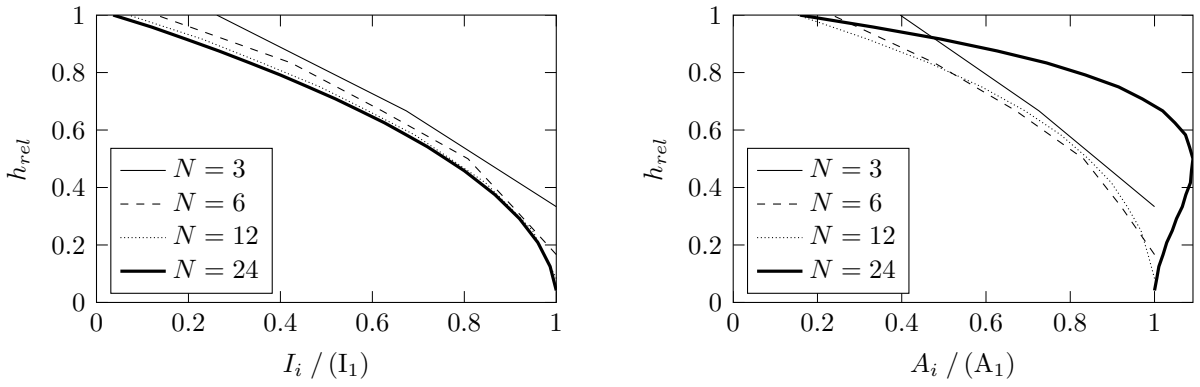
Substituting Equation (28) into Equation (23) leads to a simplified formulation for the stiffness of the equivalent vertical springs:

$$c_{ui} = \frac{1}{\frac{7}{75}\frac{l^3}{EI_i} + \frac{1}{2}\frac{l}{EA_i}} \tag{29}$$

Equations (26) and (27) are substituted into Equations (15) and (21) to define the seismic mass in each story in the vertical and horizontal direction.

Performing the optimization problem defined by the eigenvalue problems in Equations (19) and (24) for generic stick models with $N = 3, 6, 12,$ and 24 stories leads to the moments of inertia I_i and the area A_i of the cross sections of the generic stick.

Figure 12a shows the ratio between the moment of inertia of the cross section in the ith floor I_i and the cross section of the first floor I_1. The same variation of this parameter over the structure's height is applied to all generic stick models with different number of stories. The moment of inertia decreases with an increase in height. This behavior is consistent with the variation of moment of inertia found in real perimeter steel moment-resisting frames [4, 19, 20]. In contrast, the profiles of the normalized area of the cross sectional area A_i/A_1 are shown in Figure 12b. The 3-, 6-, and 12-story structures have distributions of cross sectional area consistent with the corresponding profiles of the moments of inertia. However, for the 24-story generic steel model, the cross sectional area grows with increasing height up to approximately $2/3\, h_{rel}$, which is not consistent with the distribution of cross sectional areas in real perimeter frames. A reasonable explanation is that the generic structure is based on results (fundamental modes and corresponding periods) of real structures. A qualitative evaluation of the difference between the fundamental periods predicted from regression equations and their associated data points, as shown in Figures 8a and 8b, leads to the conclusion that the error is larger for tall structures than for low-rise structures. This is another reason why the profile of the relative cross sectional-areas of the 24-story generic stick model deviates from that of the actual structure.



(a) (b)

Figure 12: Distribution of (a) the moments of inertia I_i and (b) the areas A_i of the cross sections over the relative height for the generic stick models used in this study.

4 RESULTS

4.1 Profiles of the vertical peak floor acceleration demand

Profiles of vertical peak floor acceleration demands PFA_v normalized to the vertical peak ground acceleration PGA_v due to ground motions of the VGM record set are shown in Figure 13. Gray lines show profiles of single records, bold black curves indicate statistical measures.

PFA_v demands increase with the number of stories (or vertical period). The maximum median amplification occurs for all structures at the roof level and it is approximately $4PGA_v$.

The importance of higher modes can be observed by evaluating the behavior of the 6-story frame (Figure 13b). In this case, the structure is tuned to a fundamental period in the vertical direction equal to $T_{1v} = 0.15\,\text{s} = 20/3\,\text{Hz}$. This period lies exactly on the lower corner frequency of the NEHRP-spectrum in Figure 1. Thus, the first few higher modes of the 6-story structure experience relatively high modal spectral acceleration demands, which causes an increase in

accelerations with respect to the 3-story structure. This behavior is also observed for the 12- and 20-story generic stick models.

These results show that, in general, PFA_v demands tend to vary linearly over the structure's height. The taller the structure, the more S-shaped the PFA_v profiles are. This behavior is also reported in a study of R.S. Chaudhuri [23] on the evaluation of PFA_h demands. While regression equations are proposed for the S-shaped PFA_h demand in [23], a very simple linear fitting equation could lead to a useful approximation of the PFA_v demands over the height of the structure.

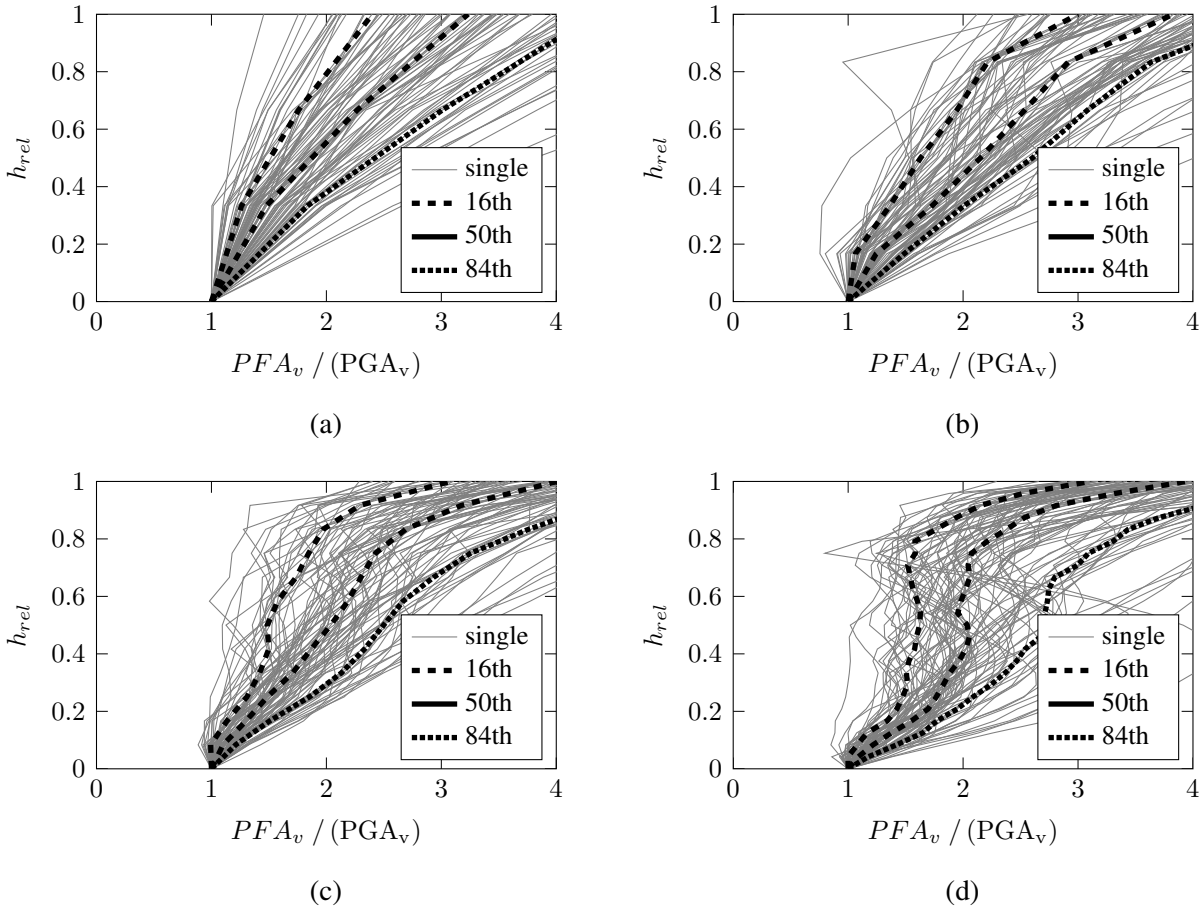


Figure 13: Profiles of the vertical peak floor acceleration demand normalized to the vertical peak ground acceleration for the (a) 3-story, (b) 6-story, (c) 12-story, and (d) 24-story generic stick models exposed to records from the VGM record set.

In order to evaluate the adequacy of Equation (1), which was developed for NSCs [1], Figure 14 shows the ratio of PFA_v to PGA_h. The vertical dash-dotted line at ${}^{PGA_v}/_{PGA_h} = {}^1/_2$ represents Equation (1) in terms of the vertical acceleration demand of a nonstructural component based on seismic design provision in the United States of America. It is evident from Figure 14 that the codified procedure leads to an underestimation of the PFA_v demand in contrast to the median profiles. As already mentioned, a linear variation of PFA_v over the height is a more representative characterization. A reasonable distribution analogous to the PFA_h (i.e. height factor) demand determined from the seismic equivalent lateral forces acting on NSCs defined in [1] would lead to a better approximation based on the results from this study.

At the base of the structures, the resulting PFA_v to PGA_h ratios are consistent with the V/H ratios discussed in the study of Bozorgnia and Campbell [7]. Traditionally, the $^{PGA_v}/_{PGA_h}$ ratio is assumed to be $^2/_3$, which is adequate for a median ratio. However, the 84th percentile value is larger than unity and the peak value is larger than two. Therefore, if the objective is to propose a codified procedure to estimate V/H ratios, a value greater than $^2/_3$ may be warranted.

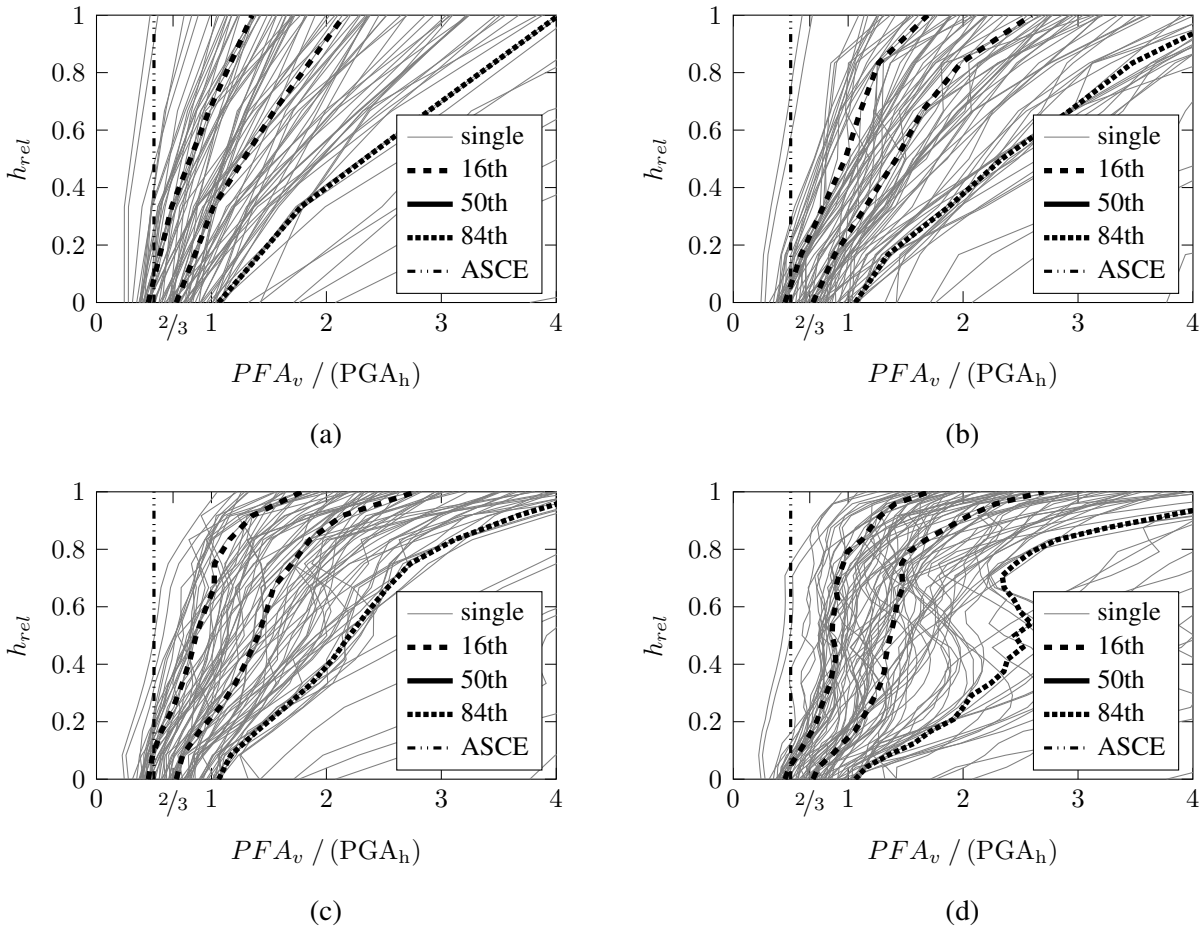


Figure 14: Profiles of the vertical peak floor acceleration demand normalized to the horizontal peak ground acceleration for the (a) 3-story, (b) 6-story, (c) 12-story and (d) 24-story generic stick models exposed to records from the VGM record set.

5 SUMMARY AND CONCLUSION

The focus of this paper is on the evaluation of vertical peak floor acceleration demands in elastic, regular perimeter frames of steel structures designed according to older [24] and more modern generations of U.S. design codes [25]. Rigorous treatment of the vertical peak floor acceleration (PFA_v) demand on NSCs is neglected in building codes since typical civil engineering buildings are assumed to behave rigidly in vertical direction.

This study highlights critical research needs as well as the importance of studying PFA_v demands for NSCs. The most salient observation from the results of this study is that neglecting the vertical component of the base acceleration may lead to a drastic underestimation of the vertical design forces for NSCs. This underestimation may lead to risk of injuries; loss of

functionality; and/or significant repair costs associated with damages to components, their supports, and attachments.

In this paper, a ground motion record set compatible with the recommended vertical design response spectrum in the United States of America [8] (in this report referred as NEHRP-spectrum) is generated and generic stick models of column lines in steel perimeter frames are designed. These generic structures were used to evaluate PFA_v demands close to the locations of columns in the structure.

The results from this study show that the vertical floor acceleration demands are in general much larger (up to a factor of three in the median) than the peak vertical ground acceleration. In addition, peak vertical floor accelerations tend to increase with height. These two observations are not explicitly accounted for in current design provisions in the United States of America, which may lead in many cases to the underestimation of vertical component design forces. However, these conclusions are based on assumptions made on numerical models and ground motion properties consistent with the ones used in this study. In addition, only record-to-record variability was accounted for.

REFERENCES

[1] American Society of Civil Engineers, *ASCE 7-10 - Minimum Design Loads for Buildings and Other Structures*, 2010.

[2] International Code Council, *IBC - International Building Code*, 2012.

[3] European Committee for Standardization, *EN 1998-1 - Design of Structures for Earthquake Resistance - Part 1: General Rules, Seismic Actions and Rules for Buildings*, 2013.

[4] J.D. Wieser, G. Pekcan, A.E. Zaghi, A.M. Itani, E. Maragakis, "Assessment of Floor Accelerations in Yielding Buildings", *MCEER reports*, ed. by University at Buffalo, State University of New York. Vol. 12-0008.

[5] ICC - Evaluation Service Inc., *AC156 - Acceptance Criteria for Seismic Qualification by Shake-Table Testing of Nonstructural Components and Systems*, 2007.

[6] K.W. Campbell, Y. Bozorgnia, Updated Near-Source Ground-Motion (Attenuation) Relations for the Horizontal and Vertical Components of Peak Ground Acceleration and Acceleration Response Spectra. *Bulletin of the Seismological Society of America*, **93**, 314–331, 2003.

[7] Y. Bozorgnia, K.W. Campbell, The Vertical-to-Horizontal Response Spectral Ratio and Tentative Procedures for Developing Simplified V/H and Vertical Design Spectra. *Journal of Earthquake Engineering*, **8**, 175–207, 2004.

[8] Applied Technology Council, *FEMA P-750 - NEHRP Recommended Seismic Provisions for New Buildings and Other Structures*, 2009.

[9] USGS, *Geologic Hazards Science Center - U.S. Seismic Design Maps*, 2010.

[10] K.W. Campbell, Y. Bozorgnia, NGA Ground Motion Model for the Geometric Mean Horizontal Component of PGA, PGV, PGD and 5% Damped Linear Elastic Response Spectra for Periods Ranging from 0.01 to 10 s. *Earthquake Spectra*, **24**, 139–171, 2008.

[11] A.E. Seifried, "Response Spectrum Compatibilization and its Impact on Structural Reponse Assessment", PhD thesis, Stanford CA: Stanford University, 2013.

[12] Pacific Earthquake Engineering Research Center, *PEER - Ground Motion Database*, 2010.

[13] W.B. Joyner, D.M. Boore, Peak Horizontal Acceleration and Velocity from Strong-Motion Records Including Records from the 1979 Imperial Valley, California, Earthquake. *Bulletin of the Seismological Society of America*, **71**, 2011–2038, 1981.

[14] K.W. Campbell, Y. Bozorgnia, "Engineering Characterization of Ground Motion", *Earthquake Engineering*, ed. by Y. Bozorgnia, V.V. Bertero. CRC Press, 2004.
[15] The MathWorks Inc., *MATLAB - Global Optimization Toolbox*, 2013.
[16] N. Shome, "Probabilistic Seismic Demand Analysis of Nonlinear Structures", PhD thesis, Stanford, CA: Stanford University, 1999.
[17] National Institute of Standards and Technology, *NIST GCR 11-917-15 - Selecting and Scaling Earthquake Ground Motions for Performing Response-History Analysis*, 2011.
[18] A. Abraham, L.C. Jain, R. Goldberg. *Evolutionary Multiobjective Optimization: Theoretical Advances and Applications*. Springer, 2005.
[19] A. Gupta, "Seismic Demands for Performance Evaluation of Steel Moment Resisting Frame Structures", PhD thesis, Stanford CA: Stanford University, 1999.
[20] National Institute of Standards and Technology, *NIST GCR 10-917-8 - Evaluation of the FEMA P-695 Methodology for Quantification of Building Seismic Performance Factors*, 2010.
[21] L. Moschen, R.A. Medina, C. Adam, *Final Report for the Marshall Plan Scholarship - Vertical Acceleration Demands on Nonstructural Components in Buildings*, 2014.
[22] R.A. Medina, "Seismic Demands for Nondeteriorating Frame Structures and Their Dependence on Ground Motions", PhD thesis, Stanford CA: Stanford University, 2003.
[23] R.S. Chaudhuri, T.C. Hutchinson. Distribution of Peak Horizontal Floor Acceleration for Estimating Nonstructural Element Vulnerability. *Proceedings of the 13th World Conference on Earthquake Engineering (13WCEE)*, Vancouver, British Columbia, Canada, Paper No. 1721, August 1-6, 2004.
[24] International Conference of Building Officials, *UBC - Uniform Building Code Vol. 2 - Structural Engineering Design Provisions*, 1994.
[25] International Code Council, *IBC - International Building Code*, 2009.

COMPDYN 2015
5th ECCOMAS Thematic Conference on
Computational Methods in Structural Dynamics and Earthquake Engineering
D. Giannopoulos, D. Vamvatsikos
Crete Island, Greece, 25–27 May 2015

INFLUENCE OF ROTATED GROUND MOTION COMPONENTS ON THE RESPONSE DISTRIBUTION OF INELASTIC OSCILLATORS

Dimitrios G. Giannopoulos[1], **and Dimitrios I. Vamvatsikos**[1]

[1] National Technical University of Athens
Iroon Polytechneiou 9, Athens, Greece
e-mail: giandimpapaki@hotmail.com, divamva@mail.ntua.gr

Keywords: Incremental Dynamic Analysis, Angle of Incidence, Probabilistic Risk Assessment, Performance-Based Earthquake Engineering, Nonlinear Dynamic Analysis.

Abstract. *Recent research has shown that structures may experience quite different response when the components of any given ground motion record are rotated in the horizontal plane. On the other hand, significant differences are also associated with using different ground motion records. This paper examines whether it is preferable to use a small set of records, each rotated to multiple incidence angles, or a larger set with fewer (or no) rotations, in the case we wish to perform a fixed number of nonlinear dynamic analyses and we have little site information. To this purpose we collected a relatively large, non-pulsive set of records and applied it to an elastoplastic single-degree-of-freedom (SDOF) system. Finally, bootstrapping was performed to investigate the effect of the number of rotation angles studied versus the number of records on the statistics of response. The results indicate that, in all cases, and especially when a small number of nonlinear analyses is allocated, the effect of record-to-record variability clearly outweighs the incidence angle influence. Using a small set of records can lead to unreliable results by both inaccurate estimation of the central value and severe underestimation of the dispersion.*

1 INTRODUCTION

In the past few years, several researchers have examined the impact of the record orientation on both single-degree-of-freedom (SDOF) and multi-degree-of-freedom (MDOF) systems. As a general conclusion, it can be said that the incidence angle can influence the structural response. On the other hand, various studies have shown that when performing time history analyses, e.g. with Incremental Dynamic Analysis (IDA, Vamvatsikos and Cornell [1]), the use of large sets of records is crucial, for the better probabilistic assessment of the results, due to the substantial record-to-record variability.

Particularly, Rigato and Medina [2] studied the influence of the earthquake direction on seismic demand for both symmetrical and asymmetrical inelastic single-story structures, of various degrees of inelasticity and of a wide range of fundamental periods, and demonstrated that applying bi-directional ground motions only along the principal axes of an inelastic building underestimates the inelastic peak deformation demand when compared to those obtained at other angles of incidence. The same trend, with an increase of up to 37%, for rotated records, in terms of both roof displacements and plastic hinge rotations, was found in the research of Magliulo et al [3], which was based on an L-plan shape multi-story RC building. Kalkan and Kwong [4] examined the merits and demerits of rotating ground motion records to fault-normal (FN) and fault-parallel (FP) for response history analysis in the case of pulsive records, using an instrumented 6-story concrete building. They concluded that though the critical angle varies with the ground motion pair and the response quantity of interest, the use of the larger response among the two values corresponding to the FN and FP directions, compared to no rotation at all, is warranted. Lagaros [5] implemented multicomponent incremental dynamic analysis (MIDA) on both symmetric and non-symmetric, in plan, 3D mid-rise RC buildings, while taking the incidence angle as variable. Based on 15 different records and on Latin Hypercube Sampling (LHS) he came to the conclusion that the use of 30 record-incidence angle pairs is sufficient for probabilistic analysis. The same author [6] researched the impact of the earthquake orientation on the seismic loss estimation in order to perform life cycle cost assessment using MIDA. He concluded that MIDA represents a more suitable way to take into consideration the randomness of both record and incidence angle, while his findings that 5 randomly chosen incident angles are enough for taking the randomness of attack of the earthquake into account, were based on an increasing number of total analyses. In the same study he highlighted that the use of a large number of different records is crucial. Fragiadakis et al [7] pointed up that different ground motion records, stemming from either different seismic events or even different recording stations, will produce different demand that varies considerably. Therefore, in order to get reliable response estimates, an appropriately selected set of several ground motion records is necessary, since a single time history analysis is of limited practical use. The uncertainty in the collapse fragility curve and furthermore in the mean annual frequency of collapse associated with record-to-record variability was examined by Eads et al [8] and it was shown that using a small number of ground motions can lead to unreliable estimates of a structure's collapse risk. Finally, we need to mention that using the seismic codes at their lower limit (of 3 or 7 records), has been the source of criticism for potentially unconservative results by several researchers (e.g. Bradley, [9]).

The objective of this paper is to investigate the effect of the number of both rotations and records on the structural response, based on a statistical approach, and suggest whether it is preferable to use a small set of records, each rotated to various angles, or a larger set of records, without considering more orientations, in the case we can only run a fixed number of analyses and there is little site information that would favor one orientation over another. As a first step we present plots which make clear that both rotations and records can severely influ-

ence the elastic and inelastic response of a SDOF system and then we give the full IDA and statistical analyses for SDOF systems of various periods for the non-pulsive set of records. Based on the aforementioned, it will be shown that the record-to-record variability clearly overshadows the impact of the incidence angle, especially when a small number of non-linear dynamic analyses is conducted.

2 A FIRST APPROACH TO ROTATION-TO-ROTATION AND RECORD-TO-RECORD VARIABILITY

Initially we examine the influence of both rotations and records in the case of an elastic SDOF system that was arbitrarily chosen to have a period of 1 sec. This model is analyzed for 30 different records, each one rotated with a constant step of 1^o in the interval of [0^o, 180^o], and the maximum elastic displacement versus the angle of rotation is shown in Figure 1. From this plot, it is clear that the angle of rotation affects the maximum response of the structure, since every single line, which corresponds to a different record, takes different values while the orientation θ changes. It is also observed that for $\theta = 0^o$, we have a vast range of values for the elastic displacement, which means that different records lead to different responses as well.

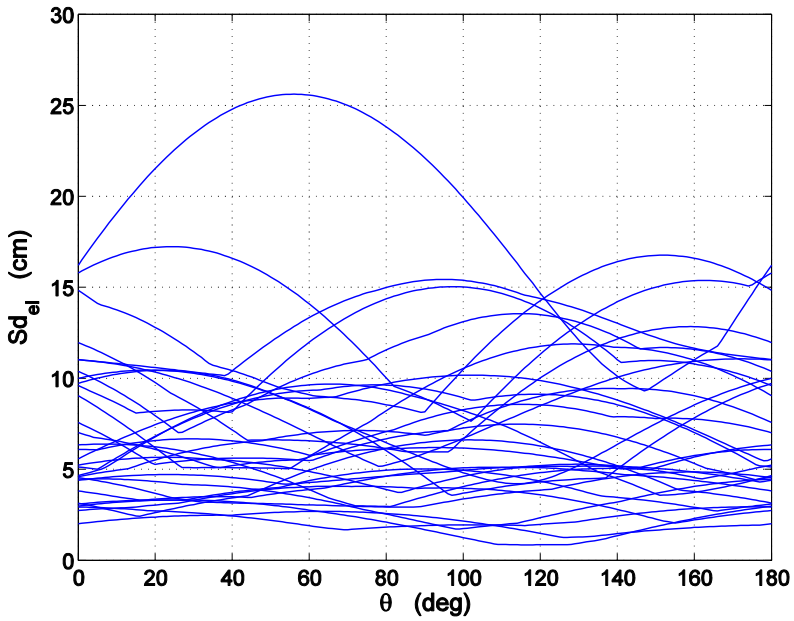
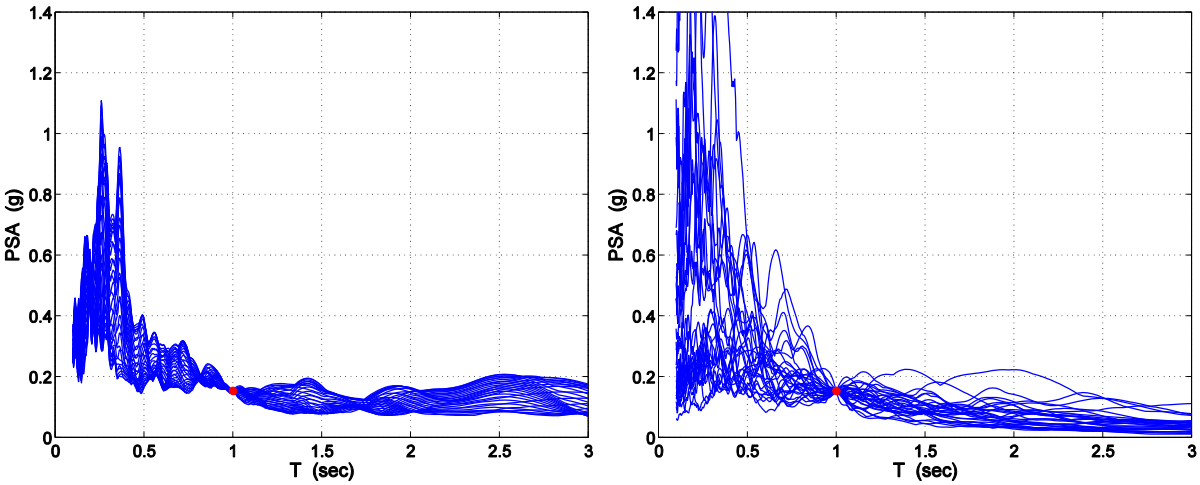


Figure 1: Maximum elastic displacement for 30 records versus angle of rotation. $T = 1$ sec, $\zeta = 5\%$.

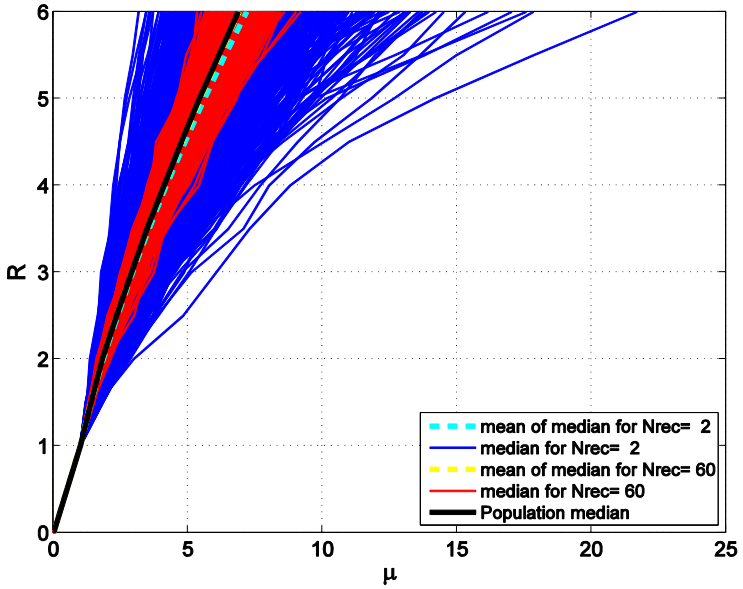
The records used for Figure 1 were of different intensity, as they were applied as originally recorded. On top of that, in real life all structures are designed to yield and reach their plastic region, so the approach based on the response of the elastic SDOF system is insufficient. In order to address this problem, we create the elastic response spectra shown in Figures 2a and 2b, for $\zeta = 5\%$, which are all scaled to the same value of spectral-acceleration for $T = 1$ sec. Particularly, Figure 2a shows 30 spectra of the same record (based on the event of Loma Prieta) rotated with a constant step of 6^o in the interval [0^o, 180^o), while Figure 2b depicts 30 spectra each one from a different recording. In the case of a SDOF system with period $T = 1$ sec, yielding would cause a period larger than 1 sec, clearly leading to uncertainty in terms of structural response as it is evident in both figures for periods greater than 1 sec. Thus, it is obvious that the structural response is a function of both orientation and record, due to the fact that for periods greater than the initial fundamental period, the seismic demand takes values from a wide range.



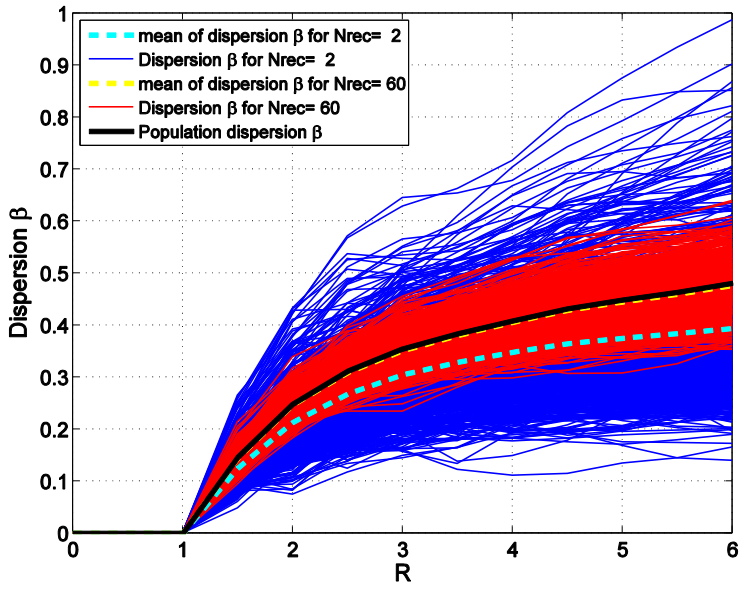
(a) Same record, different orientations. (b) One orientation, different records.

Figure 2: Scaled (T = 1 sec) elastic response spectra for ζ = 5% for (a) various orientations of the same record and (b) various unrotated records. Both figures show 30 spectra.

Thus far, it has been shown that both records and rotations seriously affect the seismic demand. In order to quantify the emerging uncertainty and obtain an idea on which variable is more critical, we implement statistical methods, and particularly bootstrapping [11], on a large number of IDA curves of a SDOF system with T = 1 sec, that originate from 135 records and 60 rotation angles, i.e. 135x60 = 8,100 total analyses. The details regarding these dynamic analyses, the probabilistic assessment methods, the set of records, the SDOF model etc, will be given in the next chapter. We make the assumption that the total number of analyses is constant and equal to 60. That being said, we use two statistical approaches: one with 60 different records for each sample, therefore only 1 angle of rotation, and one with 2 different records for each sample, thus 30 equidistant angles of rotation. From the analyses mentioned before we create Figures 3a and 3b. Figure 3a shows the plasticity μ, defined as the maximum plastic displacement over the yielding displacement, versus the normalized intensity R, defined as the demand acceleration over the yield acceleration. On Figure 3b we plot the dispersion β of each sample, defined as the standard deviation of the logarithm of the data, versus the normalized intensity. From Figure 3a it is apparent that when using a small number of records, the mean of the median value of all samples is close enough to the actual median value that is taken from the whole population. When using only one random sample, which is the case when designing a real structure, the probability of having a large deviation that would lead to unrealistic results, either conservative or unconservative, is much higher than in the case of using a larger number of records. From Figure 3b it is apparent that choosing to use few records rotated in various orientations will lead in both underestimation, in means of central value, of the natural dispersion which is caused by the phenomenon of the earthquake itself, as it is clear by comparing the mean value of all samples with the one of the whole population, and increased estimation error due to the poor sampling. This error is obviously downsized when using a large number of records. From all the previous analyses, it is clear that for this SDOF model the use of a large number of different records will produce much more realistic and reliable results than using a large number of angles of incidence, due to the fact that the record-to-record variability is greater than the rotation-to-rotation one. In the following chapters we investigate whether this trend stands for various values of the period of the SDOF system.



(a) Distribution of the median.



(b) Distribution of the dispersion.

Figure 3: Statistical distribution of a SDOF model with T = 1 sec and ζ = 5%, for (a) Median and (b) dispersion, for a total of 60 analyses.

3 ANALYSIS OF SDOF MODEL WITH NON-PULSIVE SET OF RECORDS

3.1 Assumptions, input data and basic calculations

The SDOF system examined is a relatively simple model. Particularly, we assume that the system is bilinear with elastic-perfectly plastic response, while degradation and hardening have not been taken into account. The damping ratio is 5% and we use a wide range of periods, i.e. 0.2, 0.5, 1.0 and 2.0 sec, so as to investigate both rigid and flexible systems. The yielding displacement is arbitrarily assumed to be d_y = 0.035m.

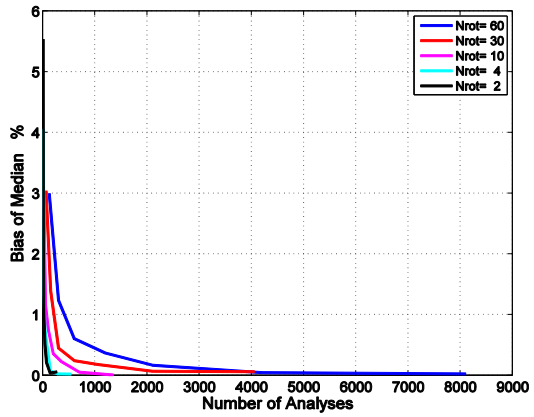
Regarding the earthquake data, we use a set of 135 non-pulsive records from 33 events all around the world from all kinds of faults. The maximum number of records from each earthquake was chosen to be equal to 8 to avoid introducing any bias, caused by over-representing a single event. The moment magnitude ranges from 6.4 to 7.7, while the Joyner-Boore distance ranges from 0 to 30 Km. Despite the small distance, care was exercised to avoid "consensus" pulse-like motions. The site class, according to the NEHRP, is chosen to be C or D, so the soil shear wave velocity takes values from 183 to 762 m/s.

The as-recorded accelerograms are rotated in the horizontal plane using the equations:

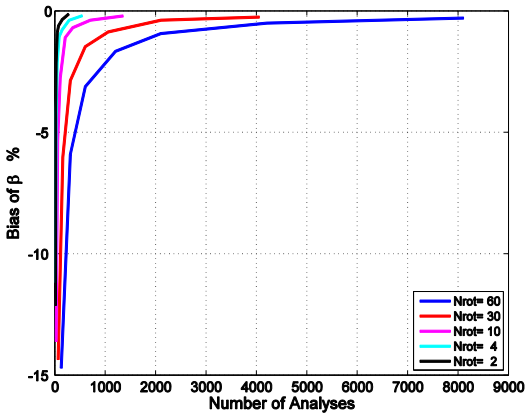
$$x_a = a_x \cos\theta + a_y \sin\theta$$
$$y_a = -a_x \sin\theta + a_y \cos\theta \quad (1)$$

θ being the angle of rotation in the counterclockwise direction, with a constant step of 3° in the [0°,180°) interval, creating 60 different orientations. For the scaling of the accelerograms that is needed to conduct IDA's, we define the normalized intensity R in the interval [1.5, 6] with a constant step of 0.5, thus every IDA has 10 levels of intensity.

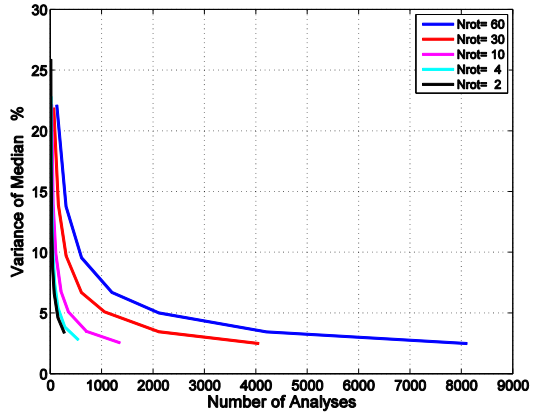
Finally, for the statistical assessment of the results we use bootstrap. Particularly, we create a large number of samples (10,000) for each case and the results produced by this sampling can be assumed to represent the potential variation for the statistical parameters of interest. Based on this methodology, we can easily come to conclusions regarding whether it is better to use more orientations or more records by comparing both central values and dispersions.



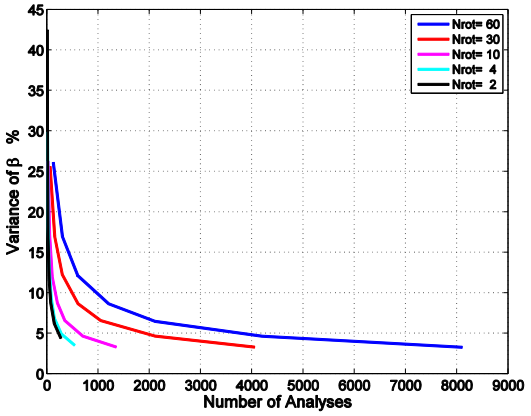
(a) Bias of the median



(b) Bias of the dispersion β



(c) Variance of the median



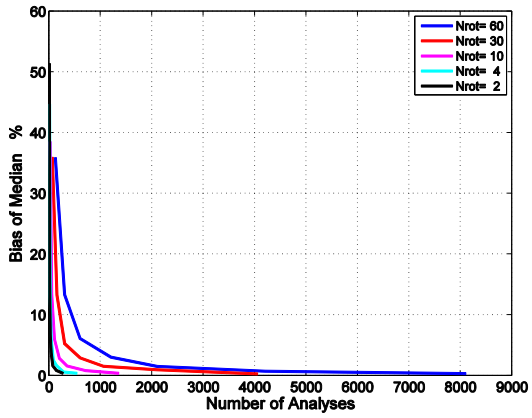
(d) Variance of the dispersion β

Figure 4: Constant number of rotations for T = 1 sec (a) Bias of the median, (b) Bias of the dispersion β, (c) Variance of the median and (d) Variance of the dispersion β.

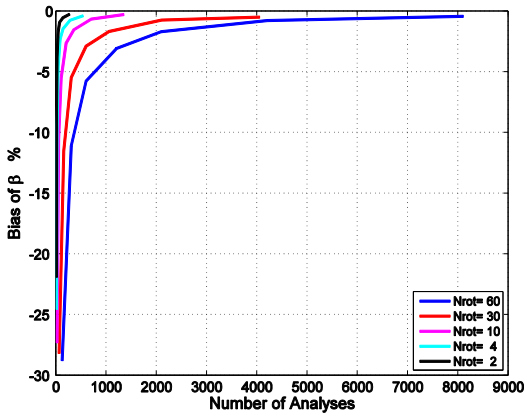
3.2 Results

After running the analyses for the whole set of records, i.e. 135x60 = 8,100 analyses, for each period mentioned before, we choose to use two comparison paradigms: the first one is for constant number of rotations while the number of total analyses, i.e. the number of records, is increasing and the second one is for constant number of total analyses while both numbers of rotations and records are variables. In the next paragraphs we give the results for T = 1 sec and T = 0.2 sec as the results for T = 2 sec and T = 0.5 sec follow the same trends.

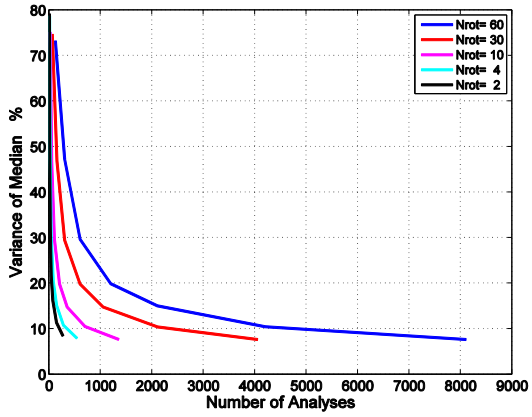
Using the approach of constant number of rotations, we take the graphs shown in Figures 4 and 5. From these figures it is clear that: i) for constant number of total analyses, the more records we use the less error we have in the results, ii) regardless of the number of rotations, the increase in the number of records leads to decreased values of estimation error, iii) the increase in the number of rotations does not decrease the error, iv) by using few records for longer periods, the bias of the median is negligible, while the bias of the dispersion as well as the variance of both the median and the dispersion are not, meaning that by choosing only one single sample for real life applications both the median and the dispersion may include severe errors leading to unreal estimates of the collapse probability and v) by using few records for lower periods, the error in the estimates is much higher and cannot be neglected even for the central value of the median.



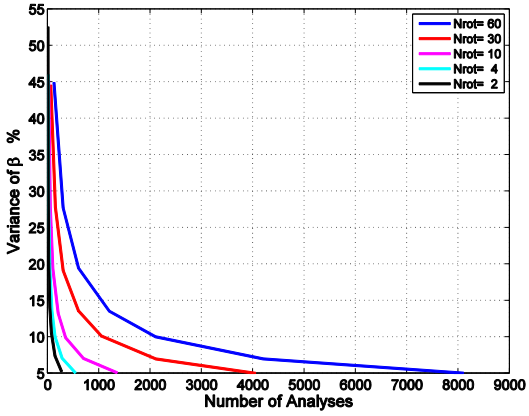
(a) Bias of the median



(b) Bias of the dispersion β

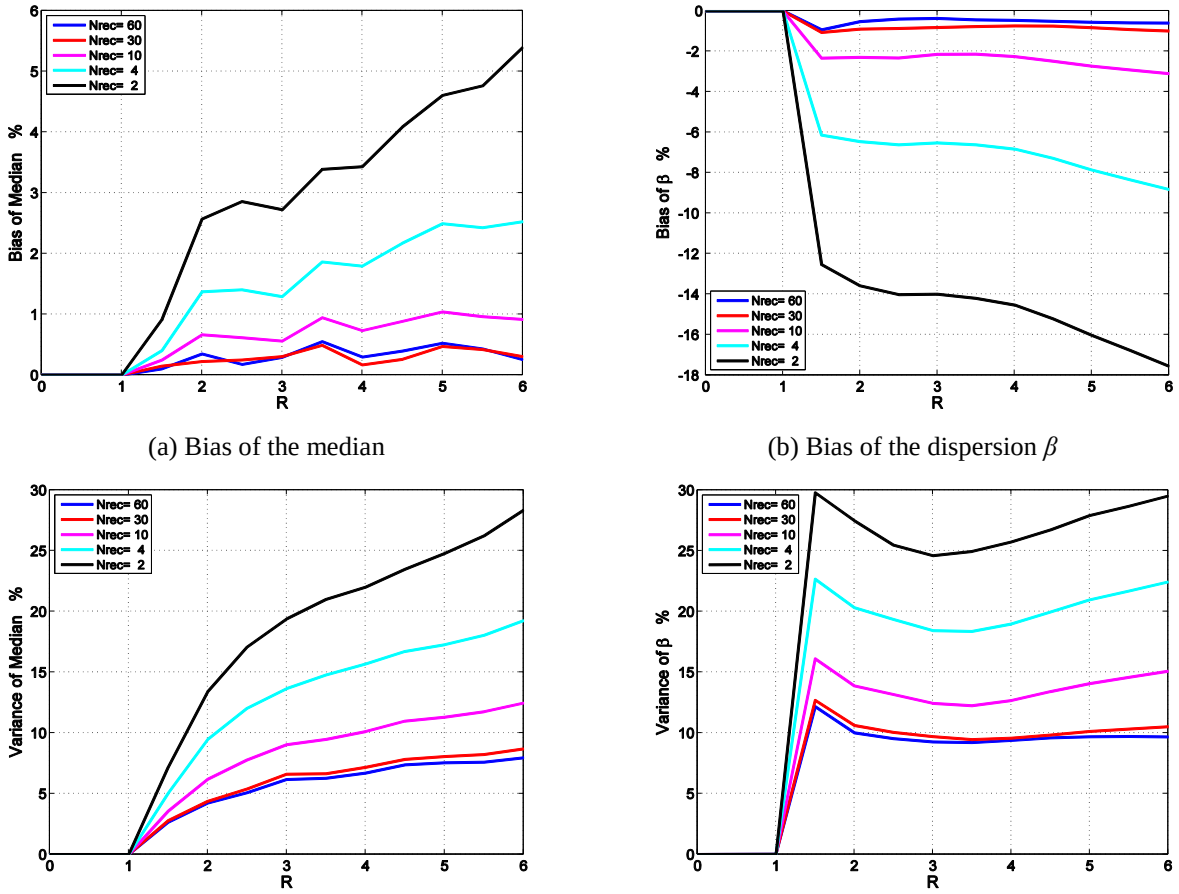


(c) Variance of the median



(d) Variance of the dispersion β

Figure 5: Constant number of rotations for T = 0.2 sec (a) Bias of the median, (b) Bias of the dispersion β, (c) Variance of the median and (d) Variance of the dispersion β.



(a) Bias of the median

(b) Bias of the dispersion β

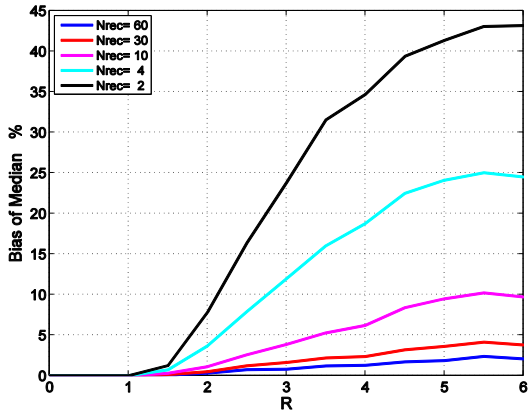
(c) Variance of the median

(d) Variance of the dispersion β

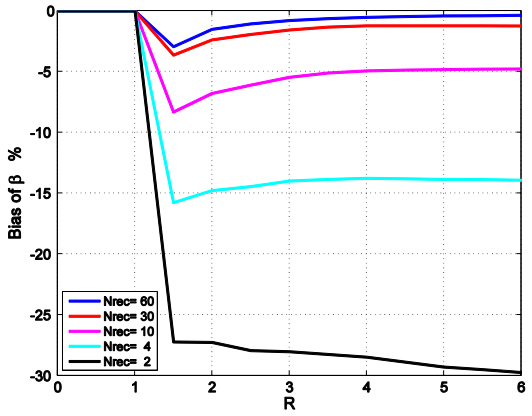
Figure 6: Constant number of analyses *Ntot* = 60 for T = 1 sec (a) Bias of the median, (b) Bias of the dispersion β, (c) Variance of the median and (d) Variance of the dispersion β.

Using the approach of constant number of analyses for *Ntot* = 60 we take the graphs shown in Figures 6 and 7. From these figures we see that: i) the more records used the less error is introduced, ii) for longer periods the bias of the central value tends to be zero regardless of the number of records used, but all the other parameters have severe errors, iii) the error increases for lower periods and iv) the differences between 30 and 60 records are negligible meaning that using 30 records can lead to acceptable results for an elastoplastic SDOF; meanwhile 10 records may lead to wrong estimates so the provisions of the EC8 for using either the maximum response based on 3 records or the mean based on 7 can lead to unconservative calculations.

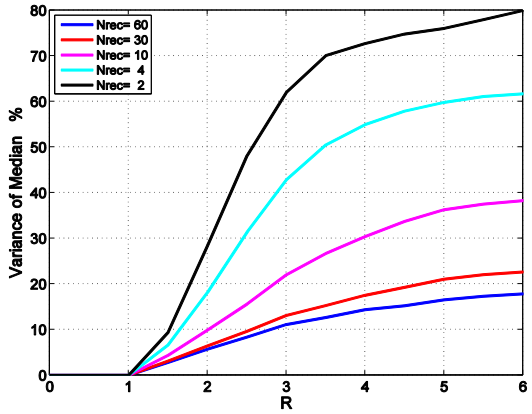
In the aforementioned, when using the term error we mean the bias and the variance of the statistical parameter being examined. Particularly, the bias is defined as the difference between the mean value of the parameter (median or dispersion β) based on all samples and the actual parameter value taken from the whole population over the latter, while the variance is defined as the coefficient of variation, i.e. the standard deviation over the mean of the parameter.



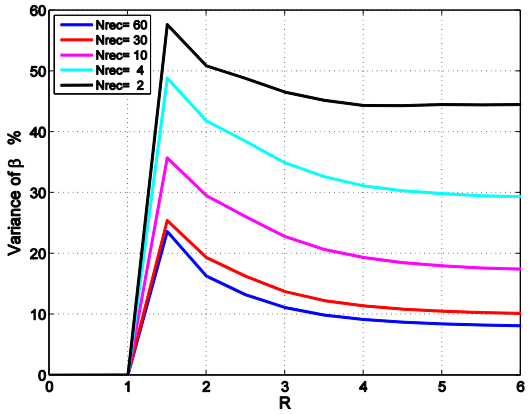
(a) Bias of the median



(b) Bias of the dispersion β



(c) Variance of the median



(d) Variance of the dispersion β

Figure 7: Constant number of analyses N_{tot} = 60 for T = 0.2 sec (a) Bias of the median, (b) Bias of the dispersion β, (c) Variance of the median and (d) Variance of the dispersion β.

4 CONCLUSIONS

The effect of the incidence angle on the structural response has been investigated in probabilistic terms vis-à-vis the number of distinct records used while running time history analyses. The most significant findings of this work can be summarized as follows:

- The record-to-record variability is clearly larger than the one of rotation-to-rotation, so, in the case of having no site information regarding the actual orientation of the fault with respect to the structure, the use of the largest set of records possible is warranted.
- The provisions of EC8 regarding time history analysis that suggest using the maximum response based on 3 records or the mean based on 7 records can lead to unconservative results, especially if one is interested in the dispersion of structural demand. The use of the central value based on 30 records seems to be accurate enough.
- The error induced by poor sampling when using a small number of records is larger for lower periods of the oscillator.

We need to mention that these findings only concern a single-degree of freedom oscillator. Still, we expect that real structures will generally show similar results, unless perhaps there is some directional preference in the structural system. This subject is the current research topic of the authors.

REFERENCES

[1] D. Vamvatsikos, C.A. Cornell, Incremental dynamic analysis. *Earthquake Engineering & Structural Dynamics,* **31**(3), 491–514.

[2] A.B. Rigato, R.A. Medina, Influence of angle of incidence on seismic demands for inelastic single-storey structures subjected to bi-directional ground motions. *Engineering Structures,* **29**, 2593-2601, 2007.

[3] G. Magliulo, G. Maddaloni, C. Petrone, Influence of earthquake direction on the seismic response of irregular plan RC frame buildings. *Earthquake Engineering and Engineering Vibration,* **13**, 243-256, 2014.

[4] E. Kalkan, N.S. Kwong, Pros and cons of rotating ground motion records to fault-normal/parallel directions for response history analysis of buildings. *Journal of Structural Engineering,* **140**, 04013062, 2014.

[5] N.D. Lagaros, Multicomponent incremental dynamic analysis considering variable incident angle. *Structure and Infrastructure Engineering,* **6**, 77-94, 2010.

[6] N.D. Lagaros, The impact of the earthquake incident angle on the seismic loss estimation. *Engineering Structures,* **32**, 1577-1589, 2010.

[7] M. Fragiadakis, D. Vamvatsikos, M. Karlaftis, N.D. Lagaros, M. Papadrakakis, Seismic assessment of structures and lifelines. *Journal of Sound and Vibration,* **334**, 29-56, 2015.

[8] L. Eads, E. Miranda, H. Krawinkler, D.G. Lignos, An efficient method for estimating the collapse risk of structures in seismic regions. *Earthquake Engineering & Structural Dynamics,* **42**, 25-41, 2013.

[9] B.A. Bradley, Design seismic demands from seismic response analyses: A probability-based approach. *Earthquake Spectra,* **27**(1), 213–224, 2011.

[10] A.K. Chopra, *Dynamics of Structures: Theory and Applications to Earthquake Engineering, 4th Edition.* Prentice Hall, 2012.

[11] B. Efron, R. Tibshirani. *An Introduction to the Bootstrap*. Chapman & Hall, 1993.

COMPDYN 2015
5th ECCOMAS Thematic Conference on
Computational Methods in Structural Dynamics and Earthquake Engineering
M. Papadrakakis, V. Papadopoulos, V. Plevris (eds.)
Crete Island, Greece, 25–27 May 2015

A NEXT GENERATION SCALAR INTENSITY MEASURE FOR ANALYTICAL VULNERABILITY STUDIES

Athanasia K. Kazantzi[1] **and Dimitrios Vamvatsikos**[1]

[1] National Technical University of Athens
9 Heroon Polytechneiou, 157 80 Athens,
{kazantzi, divamva}@mail.ntua.gr

Keywords: Intensity Measure, Vulnerability, Significant Duration, Collapse Capacity.

Abstract. *To assess the seismic performance of a structural system within an analytical context, we need, among others, to specify a ground motion Intensity Measure (IM). The wary IM selection is undoubtedly an important step towards the successful implementation of a risk assessment, since insufficient and/or inefficient IMs can induce unwanted bias and variance in the vulnerability estimates. Supplementary issues related to practicality, necessitate the use of IMs for which ground motion prediction relationships exist, such as the elastic response spectral values (i.e. acceleration, velocity and displacement). Several past studies suggested as an improvement the use of IMs defined as the geometric mean of spectral acceleration values computed over a period range. The latter range may span between periods that are below, at or above the fundamental one. Some of these choices were proven to significantly improve both efficiency and sufficiency of the IM compared to more commonly used counterparts.*

This study investigates the efficiency and sufficiency of a newly developed scalar IM that combines the geometric mean IM concept with the significant duration of the ground motions. Improving the geometric mean IMs via including the significant duration of the ground motions, was driven by recent findings suggesting there is a strong tie between the collapse capacity of a structure and the ground motion duration. Hence, the performance of the proposed next generation IM is addressed in detail by means of comparisons and statistical significance tests. The testing is performed at specific levels of local engineering demand parameters that are closely related to losses, using a testbed capacity-designed steel moment-resisting frame. It was demonstrated that ground motion duration is closely related to the collapse capacity whereas its effect at lower demand levels is insignificant. Hence, the proposed IM may be employed to improve the estimates in collapse assessment studies. Nevertheless, at least for steel moment-resisting frame buildings that exhibit moderate cyclic degradation rates and sustain most losses prior to the global collapse state, the significant duration is anticipated to only minimally affect the evaluated vulnerability and consequently may be disregarded.

1 INTRODUCTION

To perform an analytical seismic vulnerability assessment of a structural system, we need, among others, to specify a ground motion Intensity Measure (IM). An IM is actually an interface variable that efficiently separates the seismology and the structural engineering domains. This distinction is manifested in that the seismologists could independently estimate the IM's statistical properties via a probabilistic seismic hazard analysis [1], while the engineers can economize by assessing structural responses, vulnerability and losses conditioned solely on the IM level, rather than on the basis of the several seismological parameters (e.g. magnitude, distance etc). To achieve this desirable decoupling, the IM needs to be (a) practical, (b) efficient and (c) sufficient with respect to the underlying characteristics of the site and source [2].

Practicality necessitates the use of IMs for which Ground Motion Prediction Equations (GMPEs), also known as attenuation relationships, are available. This generally restricts us to the realm of peak ground acceleration/velocity/displacement and pseudo spectral acceleration values. Efficiency means that structural response, measured by appropriate Engineering Demand Parameters (EDPs), at any given level of the IM, should exhibit a low record-to-record variability. This enables the evaluation of the conditional EDP distribution with a small number of time-history analyses without incurring considerable estimate errors. Finally, the sufficiency requirement stipulates that the IM can "cover" the effect of any important seismological parameter, thus removing any bias from considering e.g. ground motions of different magnitudes, distances, fault rupture mechanisms, or epsilons (see [3]).

On account of the above, several past studies suggested as an improvement the use of IMs defined as the geometric mean of spectral acceleration values computed over a period range. For instance, Cordova *et al.* [4] suggested the use of the geometric mean of two S_a components evaluated at two period levels, these being the fundamental period (T_1) and a period that is two times the fundamental one ($2T_1$). The latter period level was introduced at the IM estimation so as to account for the period elongation associated with the structural damage. This choice was proven to significantly improve both the efficiency and the sufficiency of the estimation, compared to $S_a(T)$. It also remains practical, as a GMPE for $S_{agm}(T_i)$ is easily estimated from existing $S_a(T)$ GMPEs, given the correlation of spectral ordinates [4]. In a similar track, Tsantaki & Adam [5] showed that the improvement achieved over the resulted record-to-record variability at collapse, by means of adopting a geometric mean of spectral accelerations, may be further increased by espousing an enhanced period range. For the latter, they proposed a simple analytical expression that links the initial period T_1 to an elongated period and illustrated that the geometric mean of the spectral accelerations evaluated across that period band, leads to a notable reduction in the seismic collapse capacity dispersion. An additional scalar IM based on $S_a(T_1)$ and a parameter N_p that accounts for the spectral shape in a period range, was proposed by Bojorquez & Iervolino [6] and was found to have good efficiency.

Even more recently, Kazantzi & Vamvatsikos ([7], [8]) demonstrated that an efficient and sufficient IM for a class of buildings may be attained by specifying an appropriate period range that includes periods above (to account for the period elongation due to structural damage), at and below (to account for the contribution of higher modes) the class-average first-mode period and using the geometric mean of the spectral accelerations evaluated at these periods. The satisfactory performance of the proposed IM was verified across the entire practical range of peak floor acceleration (PFA) and interstory drift ratio (IDR) values at every floor and story, respectively, for building classes that involved both low and high-rise structures. On that premise, and considering the recent findings suggesting the ground motion duration to affect the collapse capacity of both non ductile and ductile structures [9], we will propose in

this study a new scalar IM that combines the geometric mean IM concept with the significant duration property of the ground motions. The testbed for the present study will be a single contemporary capacity-designed midrise steel moment-resisting frame (MRF) [10]. Nevertheless, it is believed the results being applicable to collapse vulnerability studies that involve either higher numbers of stories or even a class of buildings, but this is up to upcoming ongoing research to prove.

2 SIGNIFICANT DURATION

As discussed in the preceding section, an efficient IM, is one for which the structural response, measured by an appropriate EDP at any given level of intensity, yields a low record-to-record variability. On the other hand, a sufficient IM, renders the structural response at a given level of IM insensitive to seismological parameters, such as the magnitude (M_w) and the source-to-site distance (R). The significant duration of the ground motion is actually a function of the magnitude [11] and hence its effect may be considered masked when using a perfectly sufficient IM. Nevertheless, since the latter could only exist theoretically, the ground motion duration effect on the structural response and/or the collapse risk is likely to be non-negligible. To this end, such field has attracted some research efforts in recent years, which have so far concluded that ground motions with larger durations do not necessarily result in larger peak drift demands [12] but they might trigger a negative correlation with the collapse capacity, more likely due to the higher hysteretic energy demands imposed to the structural system [9].

The term significant or strong motion duration refers, in this study, to the time interval where 5% and 75% of the ground motion Arias Intensity (AI) has been recorded [13]. This time interval is denoted as $T_{5\text{-}75\%}$ (=$T_{75\%}$-$T_{5\%}$) whereas, the AI property may be calculated using the following equation,

$$AI = \frac{\pi}{2g}\int_0^{T_r} a^2(t)\,dt \tag{1}$$

where, $a(t)$ is the acceleration history over time in units of g, T_r is the total recorded time of the accelerogram and g is the acceleration of gravity.

3 DEFINITION OF THE NEW SCALAR IM

In previous studies undertaken by the authors ([7], [8]) it was demonstrated that a geometric mean IM which uses five periods, $S_{agm}(T_i)$, ranging from the second-mode (T_2) to twice the first-mode period ($2{\cdot}T_1$), performs satisfactorily, efficient and sufficient-wise, for both low and high-rise buildings. Despite its apparent advances compared to other commonly used spectral based IMs, this IM still disregards the potential correlation of the collapse risk to the significant ground motion duration, which was recently found to have a non-negligible effect, especially in the case of ductile structures [9]. To deal with this limitation as well as to explore its potential consequences, we introduce a new definition for a scalar IM that combines the $S_{agm}(T_i)$ with the significant duration property, $T_{5\text{-}75\%}$. The newly proposed IM, denoted in this study as $IM(T_{5\text{-}75\%})$ maintains practicality and predictability, since both of its terms are readily available by means of existing GMPEs. Nevertheless, its ability to relate more effectively with the structural response and collapse capacity will be thoroughly investigated by means of a testbed application. The $IM(T_{5\text{-}75\%})$ may be evaluated using the following formula,

$$IM(T_{5-75\%}) = \left(T_{5-75\%}\right)^k \cdot S_{agm}(T_i) \tag{2}$$

where, k is a weight factor that needs to be determined via calibration studies and $S_{agm}(T_i)$ is defined as,

$$S_{agm}(T_i) = \sqrt[5]{S_a(T_2)\cdot S_a(\min[(T_2+T_1)/2, 1.5\cdot T_2])\cdot S_a(T_1)\cdot S_a(1.5\cdot T_1)\cdot S_a(2\cdot T_1)} \quad (3)$$

The effectiveness of the new scalar $IM(T_{5\text{-}75\%})$, will be tested against three IMs, namely $S_a(T_1)$, $S_a(1\text{sec})$ and the $S_{agm}(T_i)$ choice as this is defined in Equation 3.

4 TESTBED APPLICATION

The testbed application of the present study is a capacity-designed steel MRF building. The building consists of four stories, the first being 4.6 m high and the ones above 3.7 m. It was designed as an office building to 2003 IBC and AISC provisions for the Los Angeles area and it has a rectangular floor plan consisting of 3 bays at 9.1 m in the North–South direction and 4 bays at 9.1 m in the East–West direction. Our focus will be the East–West framing, in which only the two middle bays are moment-resisting. The columns of the moment-resisting bays were assumed to be fixed at their bases, whereas they are also spliced at the mid-height of the third story. The beams were designed as reduced sections (RBS) with their 'dogbone' geometries detailed according to FEMA 350 [15]. The building's seismic performance was evaluated using a 2D analytical model with elastic elements in OpenSees [16] were plastic hinge formation (point plasticity) was allowed at column ends as well as at the 'dogbone' location for beams. P–Δ effects were included using a first-order treatment of geometric nonlinearity. In addition, a leaning column was added to account for the destabilizing effect of the gravity frame loads without axially stressing the lateral load resisting columns.

The empirical relationships derived from experimental data and recently proposed by Lignos & Krawinkler [17] are used to model the cyclic behavior of steel components via parameters that determine the pre- and post-capping plastic rotation, the cyclic deterioration in flexural strength and stiffness, the effective yield strength and the post-yield strength ratio of steel components subjected to cyclic loading. The first two vibration periods of the analyzed frame were found to be 1.33 s and 0.40 s, whereas 2% Rayleigh damping was assumed at the first and third-mode of vibration. Figure 1 depicts a 2-D idealization of the East-West MRF along with the beam and column section sizes. A detailed description of the MRF geometry, design and modeling can be found in Lignos *et al.* [18] and Kazantzi *et al.* [10].

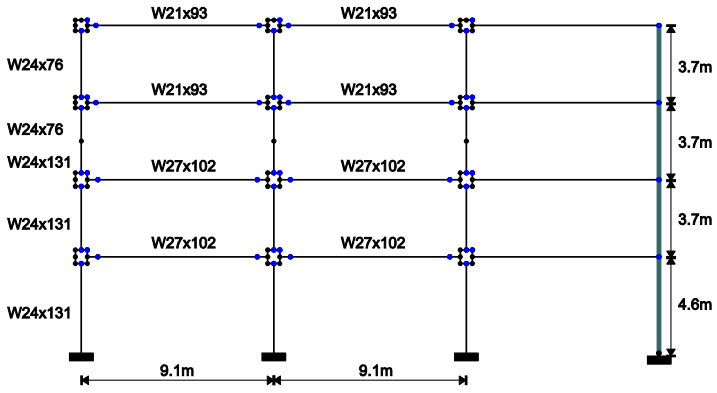


Figure 1: 2D model idealization with leaning column of the analyzed East–West MRF.

5 INCREMENTAL DYNAMIC ANALYSIS AND GROUND MOTIONS

For assessing the seismic performance of the model steel MRF structure, Incremental Dynamic analysis (IDA) was employed [19]. IDA is a powerful tool of structural analysis that involves performing a series of nonlinear time-history analyses for a suite of ground motion records, the latter scaled at increasing intensity levels. To define the IDA curves, two scalars are needed, these being an IM to represent the severity of the seismic input and an EDP to monitor the structural response.

For the needs of this study we have analyzed the testbed MRF under a ground motion set that consists of 76 records. The set contains 68 natural ground motions and 8 simulated ones [21], of which 39 are categorized by Raghunandan & Liel [9] as short duration records, on the basis of having a significant duration $T_{5\text{-}95\%} < 35$ s, whereas the remaining 37 were characterized as long duration records, on the basis of having a significant duration $T_{5\text{-}95\%} > 35$ s. The record set contains ground motions of M_w 4.8 or above, with a maximum of eight records selected from a single earthquake event. The natural records were obtained from the PEER NGA database [20], the COSMOS Virtual Data Center [22] and the USGS National Strong-Motion Project [23] whereas, the simulated ones from the Caltech Virtual Shaker [21]. Table 1 summarizes the main properties of the considered record set. Further details with respect to this set may be found in [9].

6 IM COMPARISON STUDY

The efficiency and sufficiency of the newly defined $IM(T_{5\text{-}75\%})$, which explicitly accounts for the significant duration of the ground motions, was tested against the three IMs defined in Section 3 (i.e. $S_a(T_1)$, S_a(1sec) and $S_{agm}(T_i)$) across the entire structural response range, i.e. from elasticity up to global collapse. The response is monitored by means of two structural response measures, these being the IDR and the PFA. The adopted methodology for undertaking the comparison between the various considered IMs, is novel in that, contrary to past similar studies that exist in the literature (e.g. [3], [24]), (a) it is performed on a IM given EDP (IM|EDP) basis and (b) it employs all IDR and PFA values at each story or floor, respectively, along with the overall maximum drift quantities. The first deviation from the standard practice has the apparent advantage of allowing a detailed point-wise assessment of efficiency and sufficiency that can reach all the way up to global collapse. By contrast, past studies which were performed on an EDP|IM basis were forced to stay away from the collapse state, since in this region EDP becomes either infinite or undefined. The second deviation point yields useful output for selecting an appropriate IM for loss assessment studies, in which case local rather than overall maximum quantities are considered. Hence, in the present study, each IM will be tested for the 4-story MRF against 11 EDPs: One IDR per story (4 total), one PFA per floor (5 total to include the ground level) plus the overall maximum interstory and roof drift. The latter two may not be used *per se* in vulnerability calculations, yet they often appear in fragility estimates used in simpler methodologies and collapse risk assessment studies and, thus should not be discounted.

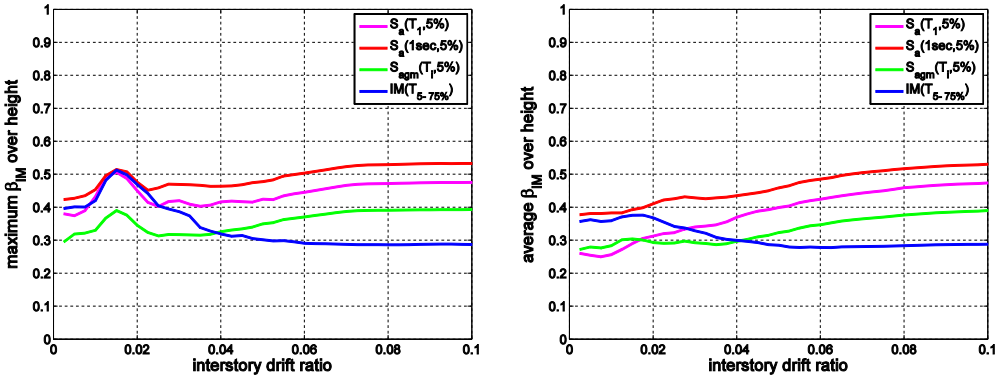
Regarding the weight factor k that appears in the definition of the $IM(T_{5\text{-}75\%})$, calibration studies revealed that a value of 0.2 produces results of satisfactory accuracy. The factor k is likely to be correlated with the cyclic degradation rate of the analyzed MRF but to thoroughly explore that relation is out of the scope of the present study. Nevertheless, in view of this intuition, the presented findings are believed to be valid at least for modern steel MRFs whose structural members experience, in a mean sense, similar cyclic degradation rates.

Year	Earthquake	M_w	Epis. dist. (km)	NEHRP soil type	pga (g)	$T_{5\text{-}95\%}$ (s)	$T_{5\text{-}75\%}$ (s)
1980	Mammoth Lakes	4.8	1.1	D	0.53	1.1	0.3
1935	Helena, Montana	6	6.3	C	0.15	2.2	1.3
1980	Mammoth Lakes	5.7	2.8	D	0.43	3.5	2.4
1976	Friuli, Italy	6.5	20.2	C	0.35	4.2	2.5
1976	Friuli, Italy	6.5	20.2	C	0.30	4.9	2.5
1994	Northridge	6.7	26.5	D	0.48	5.6	2.9
1989	Loma Prieta	6.9	31.4	D	0.54	6.4	1.7
1989	Loma Prieta	6.9	94	D	0.27	7	3.6
1994	Northridge	6.7	16.3	C	0.39	7.6	5.0
1992	Landers	7.3	82.1	D	0.31	8.2	3.8
1999	Duzce, Turkey	7.1	41.3	D	0.73	8.5	2.6
1994	Northridge	6.7	13.4	D	0.42	9.2	6.1
1979	Imperial Valley	6.5	12.4	D	0.29	10	5.7
1999	Kocaeli, Turkey	7.5	98.2	D	0.33	10.6	2.1
1979	Imperial Valley	6.5	17.7	D	0.27	11	5.8
1994	Northridge	6.7	25.5	D	0.47	11.5	5.4
1995	Kobe, Japan	6.9	24.2	D	0.34	12.9	6.5
1987	Superstition Hills	6.5	11.2	D	0.45	13.8	9.8
1979	Imperial Valley	6.5	17.6	D	0.17	14.6	7.2
1992	Cape Mendocino	7	22.6	D	0.24	15.3	4.2
1987	Superstition Hills	6.5	35.8	D	0.36	16	7.0
1989	Loma Prieta	6.9	48.2	C	0.37	16.4	4.6
1989	Loma Prieta	6.9	47.9	D	0.25	17.4	6.4
1992	Landers	7.3	86	D	0.15	18.8	10.9
1987	Superstition Hills	6.5	19.5	D	0.16	19.6	11.8
1986	Taiwan SMART	7.3	77.6	D	0.24	20.3	11.4
1986	Hollister	5.4	14.8	D	0.10	21.2	10.1
1985	Valparaiso	7.8	85.7	A/B	0.53	22.4	12.6
1999	Chi-Chi, Taiwan	7.6	40.5	C	0.30	24.3	5.6
1990	Manjil, Iran	7.4	84	D	0.13	25.7	11.1
1992	Landers	7.3	13.7	C	0.28	26.0	21.7
1992	Landers	7.3	13.7	C	0.27	27.2	20.9
1999	Hector Mine	7.1	48	D	0.18	27.5	12.5
1999	Chi-Chi, Taiwan	7.6	32	D	0.33	28.3	13.3
1990	Manjil, Iran	7.3	40.4	C	0.51	28.9	7.5
1992	Landers	7.3	27.3	D	0.17	31.8	20.9
1992	Landers	7.3	21.3	D	0.13	32.1	22.8
1985	Valparaiso	7.8	115	D/E	0.43	33.7	20.4
1999	Chi-Chi, Taiwan	7.6	28.4	D	0.18	34.6	20.5
1979	St Elias, Alaska	7.5	74.8	D	0.09	35.5	18.2
1992	Landers	7.3	32.3	D	0.11	36.3	23.6
1992	Landers	7.3	32.3	D	0.10	37	25.1
1999	Chi-Chi, Taiwan	7.6	33.8	D	0.12	38.7	28.6
2002	CA/Baja Border	5.3	42.2	D	0.04	39.9	11.6
1985	Valparaiso	7.8	74.3	A/B	0.31	40.4	20.3
1985	Valparaiso	7.8	65	Not available	0.68	42.6	30.4
2002	CA/Baja Border	5.3	42.2	D	0.08	43.5	13.0
1999	Chi-Chi, Taiwan	7.6	41.4	D	0.19	45.9	26.1
1985	Valparaiso	7.8	25.4	Not available	0.30	48.4	31.3
1985	Valparaiso	7.8	25.4	Not available	0.16	49.9	37.1
2007	KM, Indonesia	7.9	164.6	Not available	0.13	50.3	35.5
1979	Imperial Valley	6.5	33.7	D	0.35	50.3	22.4
1979	Imperial Valley	6.5	33.7	D	0.22	51	24.2
2007	KM, Indonesia	7.9	164.6	Not available	0.09	52.9	36.0
1985	Valparaiso	7.9	25.3	Not available	0.20	55.9	28.2
1985	Valparaiso	7.9	25.3	Not available	0.23	56.3	37.0
1995	Kobe, Japan	6.9	47.5	D	0.08	58.3	12.1
1999	Chi-Chi, Taiwan	7.6	69.3	D	0.12	61.4	27.8
1995	Kobe, Japan	6.9	47.5	D	0.06	70.6	21.2
2002	Denali, Alaska	7.9	189.6	C	0.08	73.6	51.5
2002	Denali, Alaska	7.9	189.6	C	0.07	76.6	48.7
1999	Chi-Chi, Taiwan	7.6	71.6	D	0.10	76.9	29.5
1999	Chi-Chi, Taiwan	7.6	71.6	D	0.10	80.1	35.7
2002	Denali, Alaska	7.9	148.1	D	0.04	94.4	25.7
2002	Denali, Alaska	7.9	93.4	C	0.07	97.4	39.3
2002	Denali, Alaska	7.9	93.4	C	0.06	98.7	42.3
2002	Denali, Alaska	7.9	150	C	0.07	104.2	27.8
2002	Denali, Alaska	7.9	296.4	D	0.02	116.1	61.1
n/a	Cascadia	9.2	446.8	B/C	0.16	132.3	59.5
n/a	Cascadia	9.2	446.8	B/C	0.13	137.2	61.8
n/a	Cascadia	9.2	481.3	B/C	0.05	162.2	94.2
n/a	Cascadia	9.2	481.3	D/E	0.13	188	116.4
n/a	Cascadia	9.2	446.8	D/E	0.16	196.7	142.0
n/a	Cascadia	9.2	481.3	D/E	0.14	206	116.3
n/a	Cascadia	9.2	446.8	D/E	0.18	230.1	147.1
n/a	Cascadia	9.2	481.3	B/C	0.04	271.3	116.3

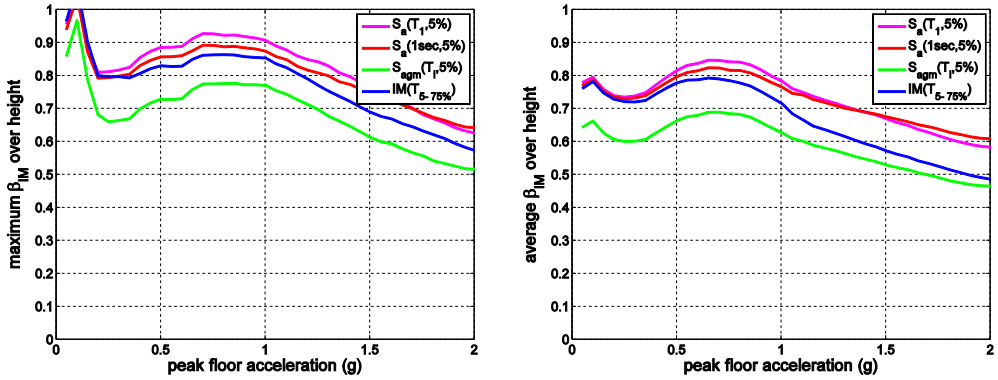
Table 1: Short and long significant duration ground motion dataset.

6.1 IM efficiency testing

Figure 2 illustrates for the testbed application and the four considered IMs, the "maximum over height" dispersions of the IM capacities β_{IM} given IDR or PFA. The range of both EDP types has been selected to span from the elastic up to the inelastic level of structural response. The maximum signifies the worst performance along the height of the building. The "average β_{IM} over height" of the building is also plotted to indicate the average efficiency of each IM at each level of deformation/response.



(a) maximum dispersion of IDR given IM (b) average dispersion of IDR given IM



(c) maximum dispersion of PFA given IM (d) average dispersion of PFA given IM

Figure 2: Maximum and average dispersions of the IM for given values of IDR and PFA response of the steel MRF considering three IMs.

Considering the aforementioned results some characteristic features appear. Quite notably, the IM ranking is not clear across the entire range of IDR values (Figures 2a and 2b). In particular, $S_a(T_1)$ shows the best performance in the early elastic region, $S_{agm}(T_i)$ takes advantage in the post-yield region where the spread of inelasticity results in elongated periods and finally the newly proposed $IM(T_{5\text{-}75\%})$, which combines significant duration with $S_{agm}(T_i)$, performs best in the post-capping range, which at a global level denotes the range from the maximum base shear to collapse. Regarding the IM ranking for the PFAs (Figures 2c and 2d) the dispersions reported for all four IMs are significantly higher than those reported for the IDRs, while the best performing IM is the $S_{agm}(T_i)$. Interestingly though, regardless of the IM, there is significant difficulty in capturing the complex interaction of modes that affects the PFA response and the use of all four IMs was proven to be relatively expensive, i.e. more ground motion records are needed to provide relatively stable PFA dispersion estimates.

Evidently, there does not seem to be a perfect single IM that is optimal for all EDPs and ranges. Hence, when considering both accelerations and drifts in loss assessment studies,

where the majority of the damage occurs prior to the global collapse in modern buildings, then $S_{agm}(T_i)$ seems to be a reasonable choice. By contrast, in the case of collapse vulnerability studies, which are performed on a drift basis considering the responses beyond the capping point, then the significant duration was proven to affect the collapse capacity and hence its inclusion in a scalar IM, such as the $IM(T_{5\text{-}75\%})$, results in an improved efficiency in the region of interest.

6.2 IM sufficiency testing

The sufficiency of the considered IMs is tested against the significant duration $T_{5\text{-}75\%}$. Given that we are only interested in demonstrating the sufficiency of $IM(T_{5\text{-}75\%})$ for use with collapse assessment studies in view of the efficiency findings, the results will be presented only for the testing performed on a drift basis. To accomplish this, a linear regression analysis between ln(IM|EDP), i.e. the logarithm of IM capacity values for a given value of any of the drift related EDPs, and the $T_{5\text{-}75\%}$ value of the record was undertaken as follows,

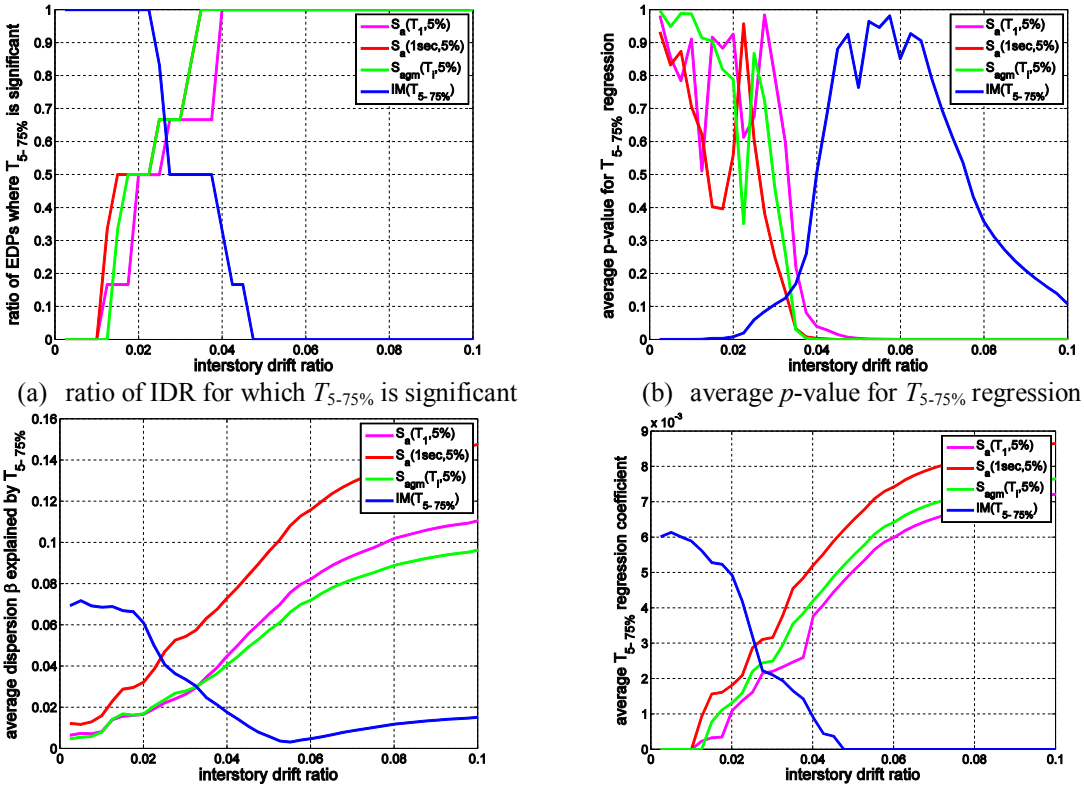
$$\ln(IM \mid EDP) = a + b\,T_{5-75\%} \tag{4}$$

The logarithm of IM|EDP was adopted, since the latter is generally lognormally distributed for the considered range of IMs and EDPs [25]. The proposed methodology for checking sufficiency is advantageous, since it avoids the problems associated with performing the regression analysis over the entire EDP range, an approach that obviously becomes problematic close to collapse (defined here as dynamic instability), but has been found considerable use in previous studies (e.g.[3], [24]). On the other hand, the proposed process reduces the number of data points available for fitting Equation 4 since the fitting process takes place at distinct EDP levels, thus requiring a large number of records for sound interpretation. The results of such tests will be summarized by the following quantities:

(a) The ratio of the number of EDPs for which $T_{5\text{-}75\%}$ is significant over the total number of EDPs considered,
(b) The average *p*-value for significance of the $T_{5\text{-}75\%}$ regression,
(c) The average dispersion β explained by $T_{5\text{-}75\%}$,
(d) The average $T_{5\text{-}75\%}$ regression coefficient.

Figure 3 illustrates the sufficiency testing against $T_{5\text{-}75\%}$. Clearly, across the examined IDR range there is significant scatter. By inspecting Figure 3a we can say that as the structure approaches its collapse state, the sole IM that remains sufficient against $T_{5\text{-}75\%}$ is the one accounting for the significant duration, i.e. the $IM(T_{5\text{-}75\%})$, whereas the remaining three show a significant dependence on $T_{5\text{-}75\%}$ which escalates gradually and becomes absolute for IDR values greater than 4%. The aforementioned finding is further supported by inspecting Figure 3b, where for IDR values beyond 4%, the $S_a(T_1)$, S_a(1sec) and $S_{agm}(T_i)$ exhibit quite a strong dependence on $T_{5\text{-}75\%}$ that is manifested by the small p-values ($p<0.05$) for IDRs>4%. With respect to the dispersion explained by $T_{5\text{-}75\%}$ (see Figure 3c), this was found to be very low for the newly proposed $IM(T_{5\text{-}75\%})$ when the structure is well in the inelastic range, whereas the same quantity for the remaining IMs may reach ~0.1-0.15 close to collapse. This observation demonstrates that adding $T_{5\text{-}75\%}$ in the definition of the IMs can offer a significant reduction in the overall collapse dispersion. Finally, Figure 3d illustrates the average regression coefficient *b*. The maximum reported values for *b* in the close to collapse response range are in the order of $7\text{-}8.5\cdot10^{-3}$. Considering that for the given set of records $T_{5\text{-}75\%}$ ranges from ~0.3-147 s (with a mean of ~27 s) a value of $b=8.5\cdot10^{-3}$ indicates a maximum change due to $T_{5\text{-}75\%}$ for the

worst performing IM by a factor of exp(b·(147-27))=2.8. The magnitude of this factor denotes a significant local bias close to the collapse range.



(a) ratio of IDR for which $T_{5\text{-}75\%}$ is significant

(b) average p-value for $T_{5\text{-}75\%}$ regression

(c) average dispersion β explained by $T_{5\text{-}75\%}$

(d) average $T_{5\text{-}75\%}$ regression coefficient

Figure 3: Variables for testing the sufficiency of the IMs against $T_{5\text{-}75\%}$ across the IDR range.

7 CONCLUSIONS

The efficiency and sufficiency of a scalar IM for use in vulnerability studies that is based on the geometric mean spectral acceleration concept combined with the significant duration was explored in this study. It has been demonstrated that significant duration is closely correlated to the collapse capacity and hence should not be disregarded in collapse vulnerability assessment studies. By contrast, in loss assessment studies of modern structures, where the majority of the losses occur at drift and acceleration levels well before the global instability state, the adoption of a geometric mean of spectral accelerations across the entire range of interest seems to be a reasonable choice while its further refinement with adding the significant duration to the IM definition does not add to the accuracy. The aforementioned findings were obtained on the basis of a capacity-designed steel MRF and hence their projection to other cases should be done with caution.

ACKNOWLEDGEMENT

Financial support was provided by the GEM Foundation through the GEM Vulnerability Consortium, the EU Research Executive Agency via the Marie Curie Continuing Integration Grant No. PCIG09-GA-2011-293855, and Greece and the European Union (European Social Fund) through the Operational Program "Human Resources Development" of the National Strategic Framework (NSRF) 2007-2013. The authors would also like to thank Prof. Abbie B. Liel and Dr. Meera Raghunandan for kindly providing the ground motion record set.

REFERENCES

[1] C.A. Cornell, Engineering seismic risk analysis. *Bulletin of the Seismological Society of America*, **58**(5), 1583-1606, 1968.

[2] N. Luco, C.A. Cornell, Structure-specific scalar intensity measures for near-source and ordinary earthquake ground motions. *Earthquake Spectra*, **23**(2), 357-392, 2007.

[3] J.W. Baker, C.A. Cornell, A vector-valued ground motion intensity measure consisting of spectral acceleration and epsilon. *Earthquake Engineering and Structural Dynamics*, **34**(10), 1193-1217, 2005.

[4] P.P. Cordova, G.G. Deierlein, S.S. Mehanny, C.A. Cornell, Development of a two-parameter seismic intensity measure and probabilistic assessment procedure. *Proceedings of the 2nd US-Japan Workshop on Performance-based Earthquake Engineering Methodology for RC Building Structures*, Sapporo, Hokkaido, 2000.

[5] S. Tsantaki, C. Adam, Collapse capacity spectra based on an improved intensity measure. *Proceedings of the 4th ECCOMAS Thematic Conference on Computational Methods in Structural Dynamics and Earthquake Engineering (COMPDYN 2013)*, Kos, Greece, 2013.

[6] E. Bojorquez, I. Iervolino, Spectral shape proxies and nonlinear structural response. *Soil Dynamics and Earthquake Engineering*, **31**(7), 996–1008, 2011.

[7] A.K. Kazantzi, D. Vamvatsikos, Analytical vulnerability assessment of modern highrise RC moment-resisting frame buildings in the Western USA for the Global Earthquake Model. *Proceedings of the 2nd European Conference on Earthquake Engineering and Seismology*, Istanbul, Turkey, 2014.

[8] A.K. Kazantzi, D. Vamvatsikos, Intensity measure selection for vulnerability studies of building classes. *Earthquake Engineering and Structural Dynamics*, to appear.

[9] M. Raghunandan, A.B. Liel, Effect of ground motion duration on earthquake-induced structural collapse. *Structural Safety*, **41**, 119-133, 2013.

[10] A.K. Kazantzi, D. Vamvatsikos, D.G. Lignos, Seismic performance of a steel moment-resisting frame subject to strength and ductility uncertainty. *Engineering Structures*, **78**, 69-77, 2014.

[11] E.I. Katsanos, A.G. Sextos, G.D. Manolis, Selection of earthquake ground motion records: A state-of-the-art review from a structural engineering perspective. *Soil Dynamics and Earthquake Engineering*, **30**, 157-169, 2010.

[12] J. Hancock, J.J. Bommer, Using spectral matched records to explore the influence of strong-motion duration on inelastic structural response. *Soil Dynamics and Earthquake Engineering*, **27**, 291-299, 2007.

[13] A. Arias, *A measure of earthquake intensity*. Cambridge, MA, 1970.

[14] J.W. Baker, C.A. Cornell, Which spectral acceleration are you using? *Earthquake Spectra*, **22**(2), 293–312, 2006.

[15] FEMA 350, *Recommended seismic design criteria for new steel moment frame buildings*, prepared by Federal Emergency Management Agency, Washington, DC, 2000.

[16] F. McKenna, G. Fenves, B. Jeremic, M. Scott, *Open system for earthquake engineering simulation*, 2000 <http://opensees.berkeley.edu>.

[17] D.G. Lignos, H. Krawinkler, Deterioration modeling of steel components in support of collapse prediction of steel moment frames under earthquake loading. *Journal of Structural Engineering* (ASCE), **137**(11):1291-302, 2011.

[18] D.G. Lignos, H. Krawinkler, A.S. Whittaker, Prediction and validation of sidesway collapse of two scale models of a 4-story steel moment frame. *Earthquake Engineering and Structural Dynamics*, **40**(7), 807-825, 2011.

[19] D. Vamvatsikos, C.A. Cornell, Incremental dynamic analysis. *Earthquake Engineering and Structural Dynamics*, **31**(3), 491-514, 2002.

[20] PEER, *PEER NGA Database*, Pacific Earthquake Engineering Research Center, University of California, Berkeley, California, 2006 <http://peer.berkeley.edu/nga/>.

[21] J. Yang, *Nonlinear responses of high-rise buildings in giant subduction earthquakes*, Ph.D. Thesis, California Institute of Technology, 2009.

[22] COSMOS, *COSMOS Virtual Data Center*, 2011 <http://db.cosmos-eq.org/>.

[23] United States Geological Survey (USGS), *National Strong-Motion Project*, 2012 <http:// nsmp.wr.usgs.gov/>.

[24] P. Tothong, N. Luco, Probabilistic seismic demand analysis using advanced ground motion intensity measures. *Earthquake Engineering and Structural Dynamics*, **36**(13), 1837-1860, 2007.

[25] NIST, *Evaluation of the FEMA P-695 methodology for quantification of building seismic performance factors*, Report No. NIST GCR 10-917-8. Prepared for the US National Institute of Standards and Technology by the NEHRP Consultants Joint Venture, *Gaithersburg*, MD, 2010.

COMPDYN 2015
5th ECCOMAS Thematic Conference on
Computational Methods in Structural Dynamics and Earthquake Engineering
M. Papadrakakis, V. Papadopoulos, V. Plevris (eds.)
Crete Island, Greece, 25–27 May 2015

NEAR -SOURCE PULSE-LIKE SEISMIC DEMAND FOR MULTI-LINEAR BACKBONE OSCILLATORS

Georgios Baltzopoulos[1*], Dimitrios Vamvatsikos[2], Iunio Iervolino[3]

[1,3] Università degli Studi di Napoli Federico II
Via Claudio 21, 80125 Naples, Italy
georgios.baltzopoulos@unina.it , iunio.iervolino@unina.it

[2] National Technical University of Athens
9 Heroon Politechneiou, 157 80 Athens, Greece
divamva@mail.ntua.gr

Keywords: pushover, directivity, incremental dynamic analysis, performance based design.

Abstract. *Nonlinear static procedures, which relate the seismic demand of a structure to that of an equivalent single-degree-of-freedom (SDOF) oscillator, are well-established tools in the performance based earthquake engineering framework and have gradually found their way into modern codes for seismic design and assessment. Initially, such procedures made recourse to inelastic spectra derived for simple elastic-plastic or bilinear oscillators, but the request for demand estimates, which delve deeper into the inelastic range, shifted the trend towards investigating the seismic demand of oscillators with more complex backbone curves.*

Meanwhile, the engineering relevance of near-source (NS) pulse-like ground motions has been receiving increased attention, since it has been recognized that such ground motions can induce a distinctive type of inelastic demand. Pulse-like NS ground motions are usually the result of rupture directivity, where seismic waves generated at different points along the rupture front arrive at a site at the same time, leading to a double-sided velocity pulse, which delivers most of the seismic energy. Recent research has led to a methodology being proposed for incorporating this NS effect in the implementation of nonlinear static procedures.

Both of the aforementioned lines of earthquake engineering research motivate the present study, which investigates the ductility demands imposed by pulse-like NS ground motions on SDOF oscillators who feature pinching hysteretic behavior with trilinear backbone curves. This investigation uses incremental dynamic analysis (IDA) considering a suite of one hundred and thirty pulse-like-identified ground motions. Median, as well as 16% and 84% fractile, IDA curves are calculated, on which an analytical model is fitted. Least-squares estimates are obtained for the model parameters, which importantly include pulse period T_p. The resulting equations effectively constitute an R-μ-T/T_p relation for pulse-like NS motions. A potential application of this result is briefly demonstrated in an illustrative example of NS seismic demand estimation.

1 INTRODUCTION

Estimating the seismic demand for structures expected to respond inelastically to future earthquakes attaining a certain intensity, is one of the key issues in performance based earthquake engineering (PBEE, see for example [1]). What sets near-source (NS) seismic input apart is the fact that NS ground motions often contain significant wave pulses. In fact, the engineering relevance of NS pulse-like ground motions has been receiving increased attention during the past decades, since it has been recognized that such ground motions can be more damaging than ordinary ground motions and can induce a distinctive type of inelastic demand. The primary cause of these impulsive characteristics in NS strong ground motion is rupture *forward directivity* (FD). During fault rupture, shear dislocation may propagate at velocities very near to the shear wave velocity. As a result, there is a *probability* that, at sites aligned along the direction of rupture propagation, shear wave-fronts generated at different points along the fault arrive almost simultaneously, delivering most of the seismic energy in a single double-sided pulse registered early in the velocity recording [2], [3]. See Figure 1 for a schematic representation of this effect and an example of a velocity pulse due to FD.

Procedures relating the structural seismic demand to that of an *equivalent* single-degree-of-freedom oscillator, collectively known as nonlinear static procedures [4], have carved their own niche in the PBEE framework and have gradually found their way into modern codes for seismic design and assessment.

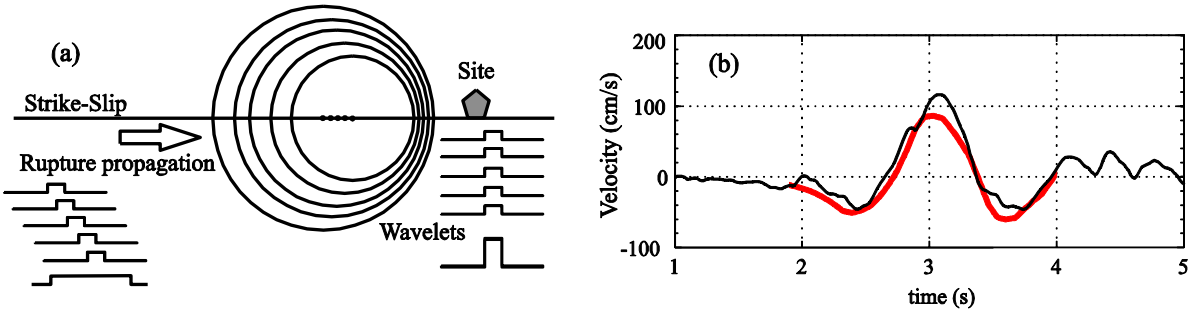


Figure 1: Snapshot of wave fronts; pictorial representation of the directivity of seismic energy adapted from [2] (a) and initial segment of the velocity time history of the fault-normal component of ground motion recorded on the left abutment of the Pacoima Dam, during the 1971 San Fernando (California) earthquake (b).

Initially, these static nonlinear procedures made recourse to inelastic spectra derived for simple elastic-perfectly-plastic or bilinear oscillators. One such procedure applicable in NS conditions has been suggested in [5]. However, the request for demand estimates that delve deeper into the inelastic range and arrive at quantifying *collapse capacity* (definition to follow), led researchers to also investigate the seismic demand of oscillators with more complex backbone curves such as the trilinear backbone depicted in Figure 2.

In order to fully describe this backbone curve mathematically in ductility - reduction factor normalized coordinates, three parameters are required: the slope, α_h, of a plastic or hardening branch that simulates post-yield ductility and the slope, α_c and "capping point" ductility μ_c of a softening branch that is typical of the behavior of most structures, either brittle or ductile, that reach a maximum strength and then exhibit in-cycle degradation that leads them to negative stiffness due to strength loss. The phenomena that actually lead to negative stiffness in a real structure can include P-Δ effects and material strength degradation (often both). Negative stiffness can be encountered on the static pushover curves of many types of structures, such as braced steel frames, moment resisting steel frames, concrete frames or other types of structure that exhibit sensitivity to second order effects.

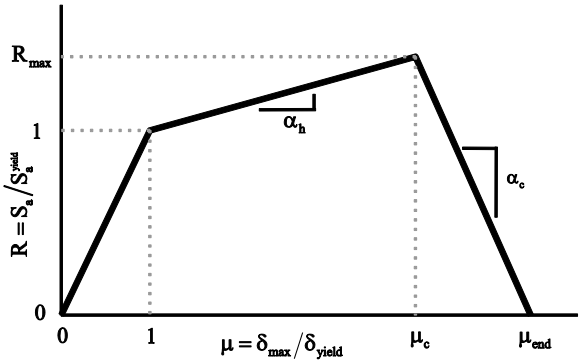


Figure 2: Representation of trilinear backbone curve in normalized coordinates (ductility μ in the abscissa and reduction factor R in the ordinate) and defining parameters: post-yield hardening slope α_h, softening branch negative slope α_c and capping ductility μ_c which separates the hardening and softening branches.

This study employs incremental dynamic analysis (IDA, [6]) in order to investigate the seismic demand of oscillators with tri-linear backbones, when subjected to NS pulse-like ground motions, with the ultimate goal of developing an analytical model. Development of this model closely follows the methodology of Vamvatsikos and Cornell [7] and uses a dataset of one-hundred and thirty pulse-like ground motions exhibiting FD effects [8].

The remainder of this article is structured as follows: after a brief note on the ground motion suite employed, the methodology is laid out in detail followed by a description of the parameter-fitting procedure that leads to the analytical model. Finally, an illustrative example, involving a NS design scenario, is presented to highlight the applicability of the model, followed by a brief discussion on the main conclusions of this study.

2 DATASET OF NS PULSE-LIKE GROUND MOTIONS

The present study employs a dataset of one-hundred and thirty pulse-like NS ground motions, whose impulsive nature is most likely related to rupture directivity. This is motivated by the fact that the stated objective is the characterization of NS structural response in relation to pulse duration T_p. Velocity pulses significantly deviating from the characteristic double-sided, early-arriving waveform associated with directivity, may not exhibit the same type of correlation between inelastic structural response and pulse period.

Having as a starting point the dataset used in [9], the pulse identification approaches suggested in [10] and [11] were used to seek out additional directivity ground motions. This search mainly focused on more recent seismic events which provided a multitude of NS recordings, such as the Parkfield 2004 (California) event, the Darfield 2010 and Christchurch 2011 (New Zealand) events and the South Napa 2014 (California) event. During this search, some effort was made to discern those velocity pulses most likely to have been the result of directivity for eventual inclusion in this investigation. A more detailed account on the methodology employed in order to assemble this dataset, along with a complete list of the ground motion recordings and relevant metadata can be found in [8].

3 MODELLING NEAR-SOURCE PULSE-LIKE SEISMIC DEMAND FOR TRI-LINEAR BACKBONE OSCILLATORS

Incremental dynamic analysis is a procedure to semi-empirically estimate probabilistic seismic structural demand and capacity. This well-established procedure, typically entails a non-linear numerical model of the structure which is subjected to a suite of ground motion records,

all scaled at a common seismic intensity measure (IM) level. This IM level is gradually increased by applying a common scale factor simultaneously to all the records, in order to reveal the entire range of post-yield response of the structure, conditional to several IM values, up to global dynamic instability and consequent collapse.

During IDA, structural response to a single record is usually represented by plotting two scalars against each other: an IM characterizing the various scaled incarnations of the record and an engineering demand parameter (EDP) representing the amplitude of response, to obtain a single record IDA curve. Once a set of IDA curves has been collected, representing the entire suite of ground motions, it is an efficient practice to *summarize* the curves into sample fractile statistics. Typically sample medians, 16% and 84% fractiles are calculated [6].

IDA can be a computationally intensive procedure. This fact motivated Vamvatsikos and Cornell to develop a software tool, which provides a shortcut, at the cost of introducing some approximation in the process [7]. Having observed that summary IDA curves of SDOF systems with multi-linear backbone curves exhibit a consistent behavior in correspondence with each segment of the backbone (elastic, post-yield hardening, post-cap softening and residual strength segments, the first three represented in Figure 1), they used IDA to investigate the response of a large population of oscillators with varying backbone parameters.

Having thus mapped the behavior of many backbone shapes against a suite or ordinary ground motions, not affected by directivity, they proposed a tool, aptly named *SPO2IDA*, capable or reproducing the IDA curves of these SDOF systems without having to run any analysis. Essentially SPO2IDA is nothing less than a complex R-μ-T relation applicable to ordinary ground motions (SPO2IDA tool available online at http://users.ntua.gr/divamva/software/spo2ida-allt.xls , last accessed April 1st, 2015).

The objective of this study is to follow in the footsteps of Vamvatsikos and Cornell [7] and employ IDA on trilinear backbone SDOF systems using a set of pulse-like records, in order to develop the equivalent of an R-μ-T/T_p relation appropriate for NS FD ground motions.

3.1 Predictor variables

A parametric model that predicts the fractile IDA curves of pulse-like FD ground motions (which will occasionally be referred to as *pulse-like IDAs* for brevity in the following) for SDOF oscillators featuring a generic trilinear backbone will necessarily include all the parameters that uniquely define the geometry of the backbone curve. This means α_h, μ_c and α_c (see Figure 1) should all be included as explanatory variables in the model. The effect of varying these parameters on the seismic response to pulse-like ground motions has already been the object of investigation [12]. An additional variable that must be included in the model is pulse period, by virtue of its demonstrable value as a predictor for the inelastic response of this type of ground motion [9], [13]. In this case, pulse period is included as the denominator of the normalized period ratio T/T_p, in a manner analogous to [9]. Consequently, the ground motion IM adopted for the IDAs is strength reduction factor R, defined as per Equation (1). EDP of choice for the SDOF systems is ductility μ defined as the ratio of maximum displacement to displacement at yield – Equation (2).

$$R = \frac{S_a\left(T_i = \kappa \cdot T_{p,i}, \xi = 5\%\right)}{S_a^{yield}\left(T_i, 5\%\right)}, \quad \kappa = \frac{T}{T_p} \in \left[0.10, 2.00\right] \tag{1}$$

$$\mu = \frac{\delta_{max}}{\delta_{yield}} \tag{2}$$

This effectively means that IDA curves computed in this study for given values of the T/T_p ratio, collect the responses of oscillators with different vibration periods (since, in general, every record has a different pulse duration T_p associated with it) and thus only make sense as cross-sectional data when plotted in normalized $\{\mu, R\}$ coordinates. This approach raises the concern that one should avoid mixing the response of very low-period oscillators, which is characterized by high ductility demands even when ordinary records are concerned, with the response of moderate-to-long period oscillators subjected to long duration pulses. To address this concern an additional restriction is imposed, that of only considering response data at each T/T_p cross-section for which $T \geq 0.30s$.

3.2 Hysteretic rule

When oscillators featuring a descending branch are concerned, it was found that a kinematic hardening hysteretic rule is not representative of how actual structures have been observed to behave during experiments [14]. With this information in mind, a peak-oriented, moderately pinching hysteresis rule developed by Ibarra and Krawinkler [15] was adopted for the present study. This hysteretic rule does not include any cyclic strength degradation, but this is considered to be of secondary importance. Strength degradation only tends to supersede the shape of the backbone in importance when severe degradation is encountered in low-period structures. However, given the range of pulse-periods associated with the NS-FD record suite employed in this study [8], the model is more oriented towards moderate to long period structures and cyclic degradation is not included in the hysteretic rule used in the analyses.

3.3 Equivalent ductility concept

A straightforward way of tackling the problem of modelling pulse-like IDAs could be to run a very large number of individual incremental dynamic analyses in an attempt to span the entire parameter space of α_c, α_h, μ_c and T/T_p . However, structural responses exhibit a complicated interdependency with respect to the four parameters (backbone characteristics and normalized period), which cannot be regarded independently one from another; this means that considering all their meaningful combinations leads to a population of SDOF oscillators numbering in the thousands, and an amount of IDAs which can be hard to obtain and manage.

Fortunately, one can take advantage of the experience accumulated in [7] to drastically reduce the amount of necessary analyses. More specifically, it was found that the equivalent ductility μ_{eq} concept (see Figure 3), which was introduced in the analogous study of ordinary ground motion IDAs [7], can also be employed for the case at hand. In that study Vamvatsikos and Cornell found that oscillators with a generic backbone containing both a hardening segment and negative-stiffness softening branches with coincident post-capping slope, such as those shown in Figure 3, have a very similar part of the IDA between capping ductility and the flat-line. The flat-line actually develops at some point slightly prior to reaching zero strength at , which is given by Equation (3).

$$\mu_{end} = \mu_c + \frac{1 + \mu_c \cdot \alpha_h - \alpha_h}{|\alpha_c|} \tag{3}$$

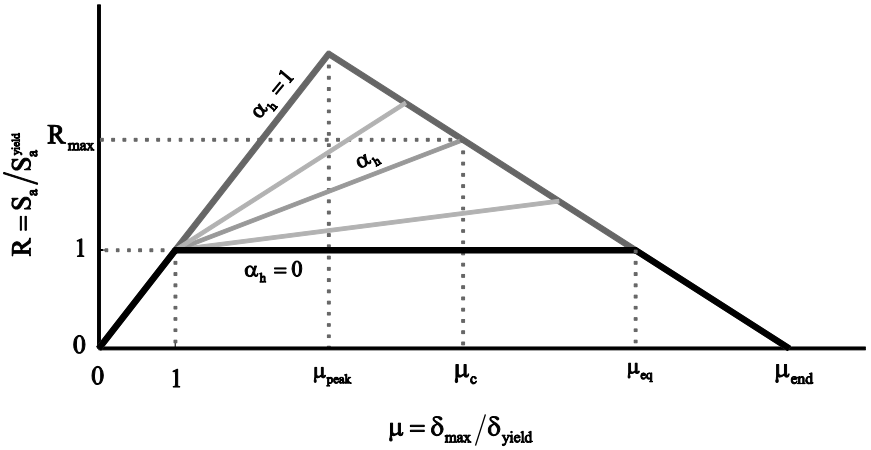


Figure 3: Schematic representation of the "equivalent ductility" μ_{eq} concept.

Furthermore, flat-line height among these oscillators varies in an almost linear fashion between the two extremes marked by $\alpha_h = 0$ and $\alpha_h = 1$ in Figure 3. Therefore, for any tri-linear oscillator with given capping ductility μ_c, one needs only determine ductility at maximum strength reduction factor μ_{peak}, given by Equation (4) and equivalent ductility μ_{eq} where an $\alpha_h = 0$ oscillator meets the common negative branch and is given by Equation (5).

$$\mu_{peak} = \frac{1 + \mu_c \cdot |\alpha_c| + \alpha_h \cdot (\mu_c - 1)}{1 + |\alpha_c|} \tag{4}$$

$$\mu_{eq} = \mu_c + \frac{\alpha_h \cdot (\mu_c - 1)}{|\alpha_c|} \tag{5}$$

As long as a comprehensive model is available for these limit cases, interpolation can be used to provide the IDA curves of the intermediate oscillators, as will be shown in a subsequent example.

4 ANALYTICAL FORM AND FITTING OF THE MODEL

4.1 Bilinear oscillators with hardening post-yield behavior

The analytical functional form selected to model the pulse-like IDA curves for bilinear oscillators with hardening (positive post-yield slope) is given by Equation (6). It is a rational function (in log-space) of ductility given reduction factor fractiles, containing a total of four parameters to be determined by fitting the model to the data.

$$\ln \mu_{x\%} = \frac{a_{x\%} \cdot \ln^2 R + b_{x\%} \cdot \ln R}{c_{x\%} \cdot \ln R + d_{x\%}}, \quad R \in \left(1, R_{(100-x)\%}(\mu_c)\right], \; x = \{16, 50, 84\} \tag{6}$$

The fit follows a *two-stage* procedure: the first stage entails obtaining non-linear least squares estimates of the model parameters $a_{x\%}$, $b_{x\%}$, $c_{x\%}$ and $d_{x\%}$ for each distinct backbone (uniquely characterized by α_h), normalized period T/T_p and x% fractile IDAs, for a total of

nine-hundred instances of parameter estimation. Subsequently, a linear model represented by Equation (7) is fit to each of the parameters, in order to capture their dependence on the remaining variables of the problem, namely α_h and T/T_p. This second stage entails a total of twelve two-dimensional fits, since for each one of the four parameters, three fractile curves must be accommodated.

$$a_{x\%}, b_{x\%}, c_{x\%}, d_{x\%} = \sum_i \theta_{x\%,i} \cdot p_i(\alpha_h) \cdot q_i\left(\frac{T}{T_p}\right),\ \alpha_h \in [0, 0.8),\ T/T_p \in [0.1, 2.0] \quad (7)$$

The terms $p_i(\alpha_h)$ and $q_i\left(\frac{T}{T_p}\right)$ represent simple functions of the variables in parentheses. A sample of the obtained results can be seen in Figure 4, where the fitted curves for all 3 fractile $\mu_{x\%}|R$ IDA curves are plotted against the analysis results for three oscillators with increasing post-yield stiffness and for different T/T_p ratios. Coefficient estimates for Equation (7) can be found in [8].

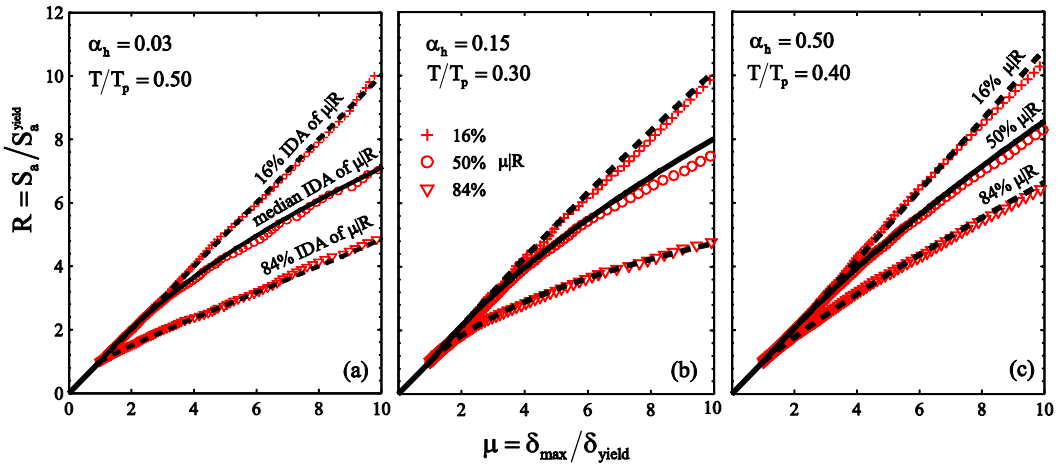


Figure 4: Comparison of the fitted model of Equation (6) with the underlying data for SDOF systems (a) with $\alpha_h = 3\%$ at $T/T_p = 0.50$, (b) $\alpha_h = 15\%$ at $T/T_p = 0.30$ and (c) $\alpha_h = 50\%$ at $T/T_p = 0.40$.

4.2 Bilinear oscillators with softening (negative slope) post-yield behavior

The appearance of a softening on the backbone curve, automatically introduces the question of collapse capacity (i.e. strength reduction factor that causes dynamic instability in the oscillator) into the problem. In the trilinear backbones examined here (where no residual strength part is taken into consideration), the segment with negative post-yield slope will eventually cross the zero capacity axis at μ_{end}; see Equation (4). Dynamic instability, indicated by the typical IDA flat-line will actually occur at a ductility level slightly lower than μ_{end}. The height of the flat-line will be henceforth referred to as collapse capacity R_{cap} while the corresponding ductility will be indicated as μ_{cap} (ductility at capacity, not to be confused with capping ductility μ_c).

In the case of bilinear oscillators, ascending post-yield slopes starting from close to unity and running up to (and including) the horizontal, were examined in the previous section. However, as soon as the slope of the backbone past the yielding point begins to descend, the additional variable of flat-line height R_{cap} must be also accounted for by the model.

Contrary to the hardening case, for which Equation (6) gives fractile μ given R ($\mu_{x\%}|R$) IDAs, for the negative post-yield slope case it was chosen to fit a reduction factor given ductility (fractile $R_{x\%}|\mu$), model, which is given by Equation (8) and supplemented by Equation (9).

$$\ln R_{x\%} = \frac{a_{x\%} \cdot \ln \mu}{\ln \mu + b_{x\%}}, \quad \mu \in \left(1, \mu_{cap(100-x)\%}\right], \quad x=\{16,50,84\} \tag{8}$$

$$a_{x\%}, b_{x\%} = \sum_i \theta_{x\%,i} \cdot p_i\left(|\alpha_c|\right) \cdot q_i\left(\frac{T}{T_p}\right), \ \alpha_c \in [-4.0,-0.05), \ T/T_p \in [0.1,2.0] \tag{9}$$

According to [16], the $\mu_{x\%}|R$ and $R_{(100-x)\%}|\mu$ fractile IDA curves are almost identical, even when the typical IDA properties of continuity and monotonicity are slightly violated. Therefore, collapse capacity $R_{cap,x\%}$ should also appear on the corresponding $\mu_{(100-x)\%}|R$ curve. The motivation behind this modeling choice lies in the prediction of collapse capacity. As can be seen in Figure 5, the tangent slope of each summary IDA curve, progressively decreases as ductility approaches μ_{end}. This means that, as strength reduction factor approaches R_{cap}, small variations in reduction factor correspond to much greater variations in ductility.

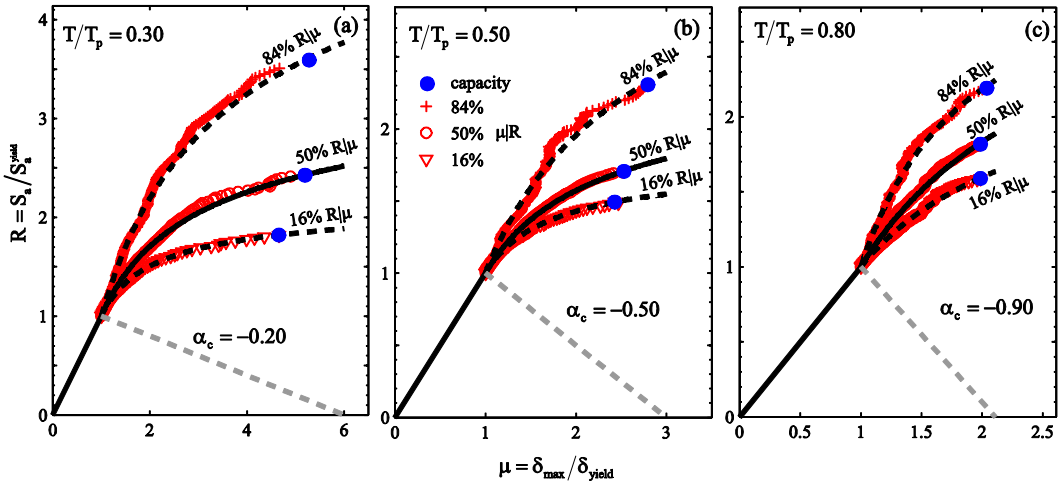


Figure 5: Model fit of Equation (8) plotted over calculated SDOF pulse-like IDAs for oscillators with (a) $\alpha_c = -0.20$ at $T/T_p = 0.30$, (b) $\alpha_c = -0.50$ at $T/T_p = 0.50$ and (c) $\alpha_c = -0.90$ at $T/T_p = 0.80$. Note that the fitted model has been extended past the collapse capacity point only for presentation reasons.

This observation has an important practical implication. Given a *hypothetical* model for $R_{x\%}|\mu$ or $\mu_{(100-x)\%}|R$ fractile IDAs with *misfit* (i.e., a model exactly reproducing the data) and a separate model for R_{cap}, some inevitable misfit in the latter will cause the point of collapse not to fall exactly on the predicted IDA curve. Recalling now the observation about the tangent

slope of the curve, it becomes apparent that a small misfit in predicted flat-line height can cause the flat-line to intersect the IDA "too early" or even unrealistically "late" (beyond μ_{end}).

On the other hand, if one were to adopt a model that predicts ductility at collapse capacity (μ_{cap}), any fitting error would perturb the prediction along the abscissa (assuming μ is plotted on the horizontal axis as in Figure 5) resulting in negligible difference on the corresponding reduction factor. However, modelling μ_{cap} does not automatically resolve the problem; an ordinary least squares fit of Equations (8-9) does not guarantee that the $R_{x\%}|\mu$ curve passes through R_{cap}. For this reason, the finally adopted solution is the combination of a *weighted* least squares fitting scheme for Equation (8) with a model for $\mu_{cap,x\%}$ fractiles given by Equations (10-11).

$$\mu_{cap,x\%} = \mu_c + c_{x\%} \cdot \frac{1+\alpha_h \cdot (\mu_c - 1)}{|\alpha_c|}, \alpha_h \in [0, 0.8),\ \alpha_c \in [-4.0, -0.05),\ x=\{16, 50, 84\} \quad (10)$$

$$c_{x\%} = \beta_{x\%} \cdot \frac{\mu_c - \mu_{peak}}{\mu_{eq} - \mu_{peak}},\ \beta_{x\%} = \{0.85, 1.00, 1.05\} \text{ for } x=\{16, 50, 84\} \quad (11)$$

This concept, employs an adaptive weighting scheme when fitting Equation (8) to the data; the point of collapse capacity is given an increased weight until the fitted curve passes through this point within a prescribed tolerance on the ordinate axis (reduction factor). Essentially, the model is forced to prioritize capturing the point of collapse capacity with increased accuracy. Thus, we may consider that $R_{cap,x\%} \approx R_{x\%}|\mu = \mu_{cap,(100-x)\%}$ as per Equation (8), having ensured that this estimate is less susceptible to fitting error than direct modelling of the flat-line height. Coefficient estimates for Equation (9) can also be found in [8].

5 RESULTS AND DISCUSSION

The analytical models whose development was presented in the preceding paragraphs, can be combined to obtain a prediction for pulse-like IDAs of oscillators in procession of a fully-trilinear backbone curve. The empirical principles underlying this approach have already been either detailed or alluded to in the previous sections. What remains is an illustration of their application. Such an application is shown in Figure 6, for an oscillator characterized by backbone parameters $\alpha_h = 0.20$, $\mu_c = 6$ and $\alpha_c = -0.50$. In order to obtain this composite prediction, Equation (6) is implemented for as long as , with each segment culminating at reduction factor levels indicated as in Figure 6. Subsequently, the negative slope part is modeled, by using Equation (8) for an interval of ductility . This segment is adjusted in height at the intersection with the previous model, so that the points will belong to both segments, in the interest of continuity.

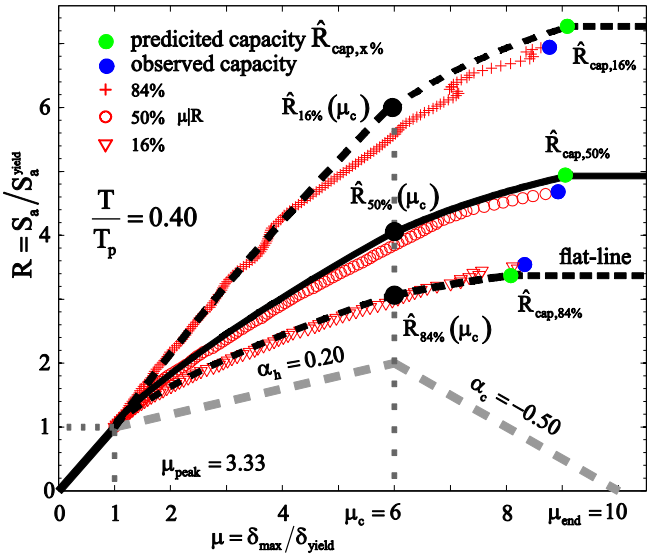


Figure 6: Model prediction of the fractile pulse-like IDAs for a trilinear backbone oscillator ($\alpha_h = 0.20$, $\alpha_c = -0.50$ and $\mu_c = 6$) at $T/T_p = 0.40$.

6 ILLUSTRATIVE APPLICATION

Despite the fact that the model provides output in the form of fractile IDA curves, these should not be employed to directly estimate the probabilistic distribution of EDP given IM. The reason behind this is the fact that the IDA curves refer to a given T/T_p ratio, rather than a specific structure. In fact, the model acts like an R-μ-T/T_p relation, which must be combined with site-specific information on pulse period and likelihood of directivity. As such, it could be employed in a manner analogous to the methodology of [5] in order to render a static non-linear procedure, for example the capacity spectrum method [17], applicable in NS conditions.

An illustrative example of this concept is presented in Figure 7. In the first panel, Figure 7(a), the median SPO2IDA *ordinary* prediction for a bilinear oscillator characterized by a T=1.0s period of natural vibration, post-yield hardening slope $\alpha_h = 0.20$ and spectral acceleration at yield $S_a^{yield} = 0.10\,g$ is compared against various median IDAs which incorporate pulse-like effects in both arbitrary and systematic fashion.

The median IDAs used for the comparison, consist of one curve obtained by running IDA for a set of thirty randomly selected pulse-like ground motions (with an average pulse period $\bar{T}_p = 1.62\,s$), another obtained by means of Equation (6) for $T/T_p = 0.40$ and a third curve obtained by integrating Equation (6) over various potential pulse periods from a site-specific NS design scenario (to follow). A final comparison is made with an IDA curve that accounts for both the ordinary and pulse-like component of seismic demand at the site, each weighted by its respective likelihood.

The NS scenario under consideration refers to a site being affected by a seismic source characterized by a nearly vertical strike-slip mechanism, with seismicity governed by an M7 characteristic earthquake model and maximum rupture area of 1330km^2. The site is 5km distant from the horizontal projection of the assumed fault plane and therefore some directivity effects are to be expected (Figure 8).

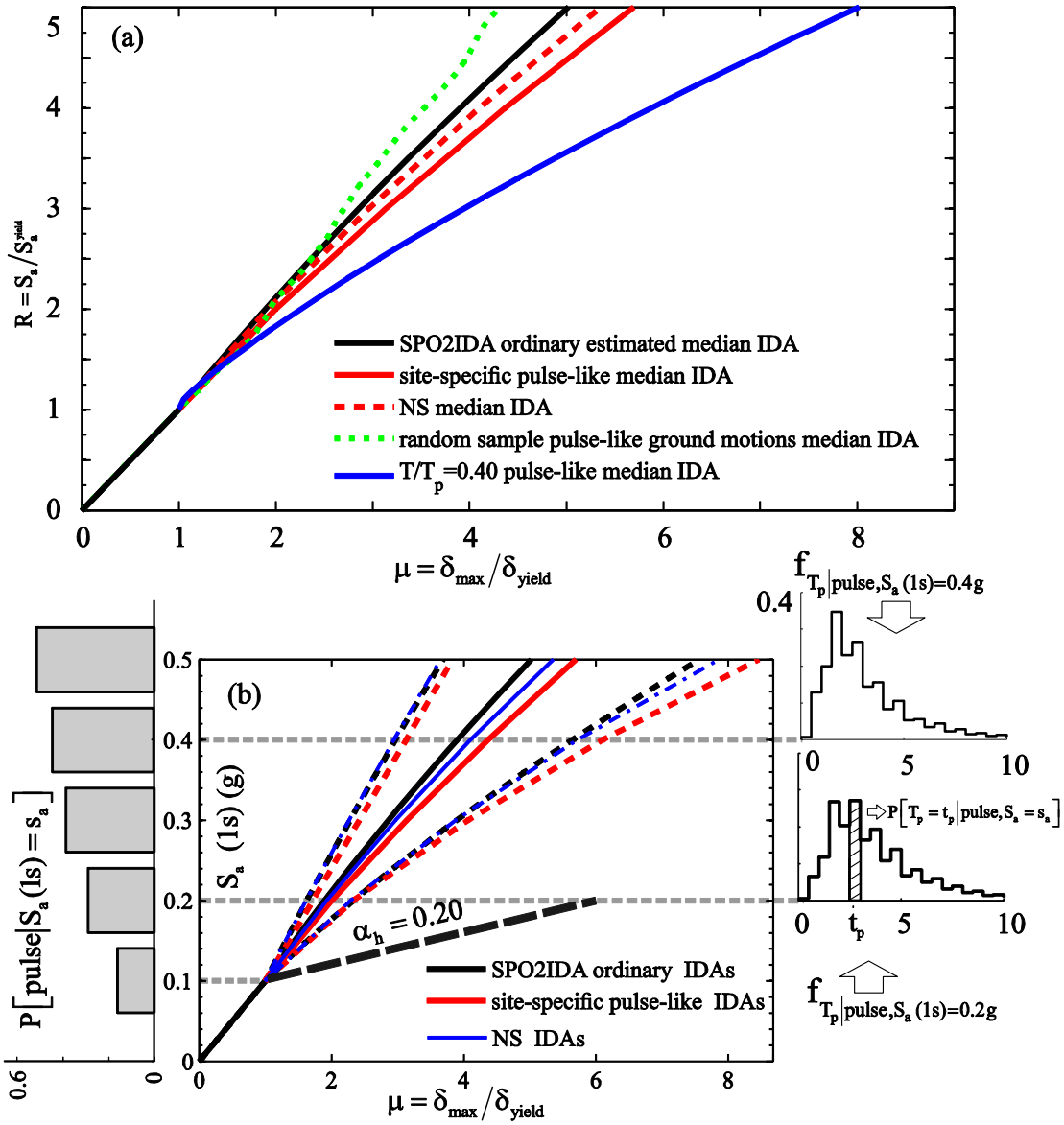


Figure 7: (a) Ordinary SPO2IDA median prediction for a bilinear oscillator with vibration period T=1.0s, post-yield hardening slope $\alpha_h = 0.10$ and spectral acceleration at yield $S_a^{yield} = 0.10\,g$ compared with curves incorporating pulse-like effects in both arbitrary and systematic fashion. (b) Information obtained from site-specific (see Figure 8) NS hazard incorporated into the pulse-like IDA model to obtain site-specific IDA curves.

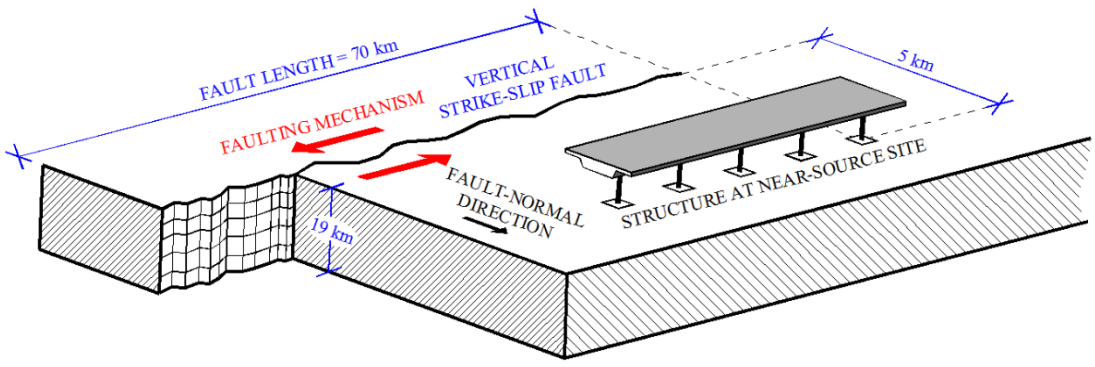


Figure 8: Schematic representation of NS design scenario used in the illustrative example.

NS hazard at the site expressed in terms of spectral acceleration at the oscillator's period was disaggregated for various values of chosen to translate into reduction factors . Thus, the conditional probability density functions of pulse period are obtained at each stripe of reduction factor (the interested reader is referred to [18] and [19] for a detailed treatment of the methodology involved in these NS probabilistic seismic hazard analysis calculations).

This information is incorporated into Equation (6) by assuming that ductility given demand follows a lognormal distribution, leading to Equation (12), where the abbreviated notation is used to indicate the conditional probability mass , resulting from discretizing the random variables involved (see Figure 7b) in order to avoid integral notation when writing the law of conditional expectation.

$$\mathrm{E}\left[\ln\mu\middle|\mathrm{R},\mathrm{pulse}\right]\approx\sum_{\mathrm{i}}\ln\mu_{50\%}\left(\mathrm{R},\mathrm{T}/\mathrm{t}_{\mathrm{p,i}}\right)\cdot\mathrm{P}_{\mathrm{t}_{\mathrm{p,i}}} \tag{12}$$

Under the same assumption of log-normality, the law of conditional variance can be written as in Equation (13), where the notation Var[·] indicates the variance operator. It should be mentioned that in order to maintain a more parsimonious notation, the condition $\mathrm{S_a(T)=s_a}$, which holds for all expected values and variances, is replaced by strength reduction factor R in the following equations (for the specific structure, yield force is known).

$$\begin{aligned}\mathrm{Var}\left[\ln\mu\middle|\mathrm{R},\mathrm{pulse}\right]\approx&\sum_{\mathrm{i}}\mathrm{Var}\left[\ln\mu\middle|\mathrm{R},\mathrm{T}/\mathrm{T_p}\right]\cdot\mathrm{P}_{\mathrm{t}_{\mathrm{p,i}}}+\\&+\sum_{\mathrm{i}}\left[\mathrm{E}\left[\ln\mu\middle|\mathrm{R},\mathrm{pulse}\right]-\ln\mu_{50\%}\left(\mathrm{R},\mathrm{T}/\mathrm{t}_{\mathrm{p,i}}\right)\right]^2\cdot\mathrm{P}_{\mathrm{t}_{\mathrm{p,i}}}\end{aligned} \tag{13}$$

Note that in Equation (13) $\mathrm{Var}\left[\ln\mu\middle|\mathrm{R},\mathrm{T}/\mathrm{T_p}\right]=1/4\cdot\left[\ln\mu_{84\%}\left(\mathrm{R},\mathrm{T}/\mathrm{t}_{\mathrm{p,i}}\right)-\ln\mu_{16\%}\left(\mathrm{R},\mathrm{T}/\mathrm{t}_{\mathrm{p,i}}\right)\right]^2$ due to the log-normality assumption invoked earlier. This procedure and its end result (in terms of both mean and variance), are illustrated in the second panel, Figure 7(b). To the right of the IDA curves plot, the conditional densities of pulse period for two stripes of $\mathrm{S_a}\left(1\mathrm{s}\right)=0.2\mathrm{g}$ and $\mathrm{S_a}\left(1\mathrm{s}\right)=0.4\mathrm{g}$ are shown, while on the left of the vertical axis, the probabilities of pulse occurrence being causal of $\mathrm{S_a}\left(1\mathrm{s}\right)=\mathrm{s_a}$, $\mathrm{P}\left[\mathrm{pulse}\middle|\mathrm{S_a}\left(1\mathrm{s}\right)=\mathrm{s_a}\right]$ are plotted, which are also the result of NS hazard disaggregation.

The final step of the procedure consists of accounting for both cases, i.e. occurrence of directivity pulse and absence thereof, in a single set of IDA curves. As already mentioned, the SPO2IDA prediction serves as an estimate of the ordinary component of seismic demand in this example. Applying the laws of conditional expectation and variance one more time, Equations (14) and (15) are obtained, where $\mathrm{E}\left[\ln\mu\middle|\mathrm{R},\mathrm{nopulse}\right]$ is the logarithm of the median SPO2IDA prediction and the corresponding variance is estimated as $\mathrm{Var}\left[\ln\mu\middle|\mathrm{R},\mathrm{nopulse}\right]=$ $=1/4\cdot\left[\ln\mu_{\mathrm{SPO2IDA},84\%}\left(\mathrm{R}\right)-\ln\mu_{\mathrm{SPO2IDA},16\%}\left(\mathrm{R}\right)\right]^2$. These results lead to the curves labeled "NS IDAs" in Figure 5.7(b).

$$\mathrm{E}\left[\ln\mu\middle|\mathrm{R}\right]=\mathrm{E}\left[\ln\mu\middle|\mathrm{R},\mathrm{pulse}\right]\cdot\mathrm{P}\left[\mathrm{pulse}\middle|\mathrm{R}\right]+\mathrm{E}\left[\ln\mu\middle|\mathrm{R},\mathrm{nopulse}\right]\cdot\left(1-\mathrm{P}\left[\mathrm{pulse}\middle|\mathrm{R}\right]\right) \tag{14}$$

$$\begin{aligned}&\mathrm{Var}\left[\ln\mu\middle|\mathrm{R}\right]=\\&=\mathrm{Var}\left[\ln\mu\middle|\mathrm{R},\mathrm{pulse}\right]\cdot\mathrm{P}\left[\mathrm{pulse}\middle|\mathrm{R}\right]+\mathrm{Var}\left[\ln\mu\middle|\mathrm{R},\mathrm{nopulse}\right]\cdot\left(1-\mathrm{P}\left[\mathrm{pulse}\middle|\mathrm{R}\right]\right)+\\&+\left(\mathrm{E}\left[\ln\mu\middle|\mathrm{R},\mathrm{pulse}\right]-\mathrm{E}\left[\ln\mu\middle|\mathrm{R}\right]\right)^2\cdot\mathrm{P}\left[\mathrm{pulse}\middle|\mathrm{R}\right]+\\&+\left(\mathrm{E}\left[\ln\mu\middle|\mathrm{R},\mathrm{nopulse}\right]-\mathrm{E}\left[\ln\mu\middle|\mathrm{R}\right]\right)^2\cdot\left(1-\mathrm{P}\left[\mathrm{pulse}\middle|\mathrm{R}\right]\right)\end{aligned}\tag{15}$$

7 CONCLUSIONS

The present study saw the use of IDA to investigate the response of oscillators with trilinear backbone curves to NS pulse-like ground motions. To this end, an analytical model was developed for the prediction of pulse-like IDA curves. This model includes the pulse period as a predictor variable and captures central tendency and dispersion of NS pulse-like seismic demand and capacity.

Overall, it can be observed that the assumption of a specific pulse period being considered representative across all scale factors of the IDA can lead to overestimation of NS seismic demand, when said pulse period corresponds to a fraction of structural period associated with aggressive NS FD ground motions. On the other hand, a random sample of pulse-like ground motions, where T_p is not accounted for explicitly, can result in demand which is even less than the ordinary estimate (albeit said ordinary estimate corresponds to an analytical model).

Finally, consideration of T_p in manner consistent with NS hazard, can result in seismic demand which supersedes the ordinary estimate, when site-to-source geometry renders the site prone to FD effects. In the provided example, the NS median seismic demand represented by the corresponding IDA curve shows a trend of increasing detachment from the ordinary curve as S_a levels increase. The example further demonstrates that it is possible to integrate the model into the SPO2IDA tool, in order to extend applicability of the latter into the domain of NS demand. However, such integration will require that the model be extended to also cover a residual strength segment on the backbone curve, as well as lower period ($0.10\mathrm{s} < T < 0.30\mathrm{s}$) oscillators, in order to match the applicability range of the existing SPO2IDA tool.

ACKNOWLEDGEMENTS

The study presented in this paper was developed partially within the activities of *Rete dei Laboratori Universitari di Ingegneria Sismica* (ReLUIS) for the research program funded by the Dipartimento della Protezione Civile (2014–2018) and in part within the AXA-DiSt (*Dipartimento di Strutture per l'Ingegneria e l'Architettura*) 2014-2017 research program, funded by AXA-Matrix Risk Consultants, Milan, Italy.

REFERENCES

[1] H. Krawinkler, E. Miranda, Performance-Based Earthquake Engineering, In: *Earthquake Engineering: From Engineering Seismology to Performance-Based Engineering*, eds. Y. Bozorgina , V.V. Bertero, CRC Press, FL, 2004.

[2] P.J. Singh, Earthquake Ground Motions: Implications for Designing Structures and Reconciling Structural Damage. *Earthquake Spectra*, **1**(2), 239–270, 1985.

[3] P.G. Somerville, N.F. Smith, R.W. Graves, N.A. Abrahamson. Modification of empirical strong ground motion attenuation relations to include the amplitude and duration effects of rupture directivity. *Seismol Res Lett*, **68**, 199-222, 1997.

[4] E. Kalkan, S.K. Kunnath, Assessment of current nonlinear static procedures for seismic evaluation of buildings. *Eng Struct*, **29**, 305-316, 2007.

[5] G. Baltzopoulos, E. Chioccarelli, I.Iervolino, The displacement coefficient method in near-source conditions. *Earthquake Engng Struct. Dyn*, DOI: 10.1002/eqe.2497, 2014.

[6] D. Vamvatsikos, C.A. Cornell, Incremental dynamic analysis. *Earthquake Engng Struct. Dyn*, **31**, 491-514, 2002.

[7] D. Vamvatsikos, C.A. Cornell, Direct estimation of the seismic demand and capacity of oscillators with multi-linear static pushovers through IDA. *Earthquake Engng Struct. Dyn*, **35**, 1097-1117, 2006

[8] G. Baltzopoulos, *Structural performance evaluation in near-source conditions*, PhD Thesis, Doctorate program in Seismic Risk, XXVII cycle, Advisor I. Iervolino, Università degli Studi di Napoli Federico II, Naples, Italy, 2015. http://wpage.unina.it/iuniervo/doc_en/Students.html

[9] I. Iervolino, E. Chioccarelli, G. Baltzopoulos, Inelastic Displacement Ratio of Near-Source Pulse-like Ground Motions. *Earthquake Engng Struct Dyn*, **41**, 2351-2357, 2012.

[10] J.W. Baker, Quantitative Classification of Near-Fault Ground Motions Using Wavelet Analysis. *Bulletin of the Seismological Society of America*, **97**(5), 1486-1501, 2007.

[11] S.K. Shahi, J.W. Baker, An efficient algorithm to identify strong velocity pulses in multi-component ground motions. *Bulletin of the Seismological Society of America*, 104(**5**), 2456–2466, 2014.

[12] V. Dimakopoulou, M. Fragiadaki, C. Spyrakos, Influence of modeling parameters on the response of degrading systems to near-field ground motions. *Eng Struct*, **53**, 10-24, 2013.

[13] S. Akkar, U. Yazgan, P. Gülkan, Deformation limits for simple non-degrading systems subjected to near-fault ground motions. *Proc 13th World Conf Earthq Eng*, Vancouver BC, Canada, Paper no. 2276, 2004.

[14] M. Rahnama, H. Krawinkler, *Effects of soft soils and hysteresis model on seismic demands*. Report No. 108, The John A.Blume Earthquake Engineering Center, Stanford University, Stanford CA, 1993.

[15] L.F. Ibarra, H. Krawikler. *Global Collapse of Frame Structures under Seismic Excitations*. Report No.152, The John A. Blume Earthquake Engineering Center, Dpt. of Civil and Environmental Engineering, Stanford University, Stanford CA, 2005.

[16] D. Vamvatsikos, C.A. Cornell. Applied incremental dynamic analysis. *Earthquake Spectra*, **20**(2), 523–553, 2004.

[17] P. Fajfar, Capacity spectrum method based on inelastic spectra. *Earthquake Engng Struct. Dyn*, **28**, 979-993, 1999.

[18] E. Chioccarelli, I. Iervolino, Near-source seismic hazard and design scenarios. *Earthquake Engng & Struct Dyn*, **42**, 603-622, 2013.

[19] P. Tothong, C.A. Cornell, J.W. Baker. Explicit directivity-pulse inclusion in probabilistic seismic hazard analysis. *Earthq Spectra*, **23**, 867-891, 2007.

COMPDYN 2015
5th ECCOMAS Thematic Conference on
Computational Methods in Structural Dynamics and Earthquake Engineering
M. Papadrakakis, V. Papadopoulos, V. Plevris (eds.)
Crete Island, Greece, 25–27 May 2015

SEISMIC RELIABILITY ASSESSMENT OF ROCKING BEHAVIOUR UNDER NEAR-FAULT EXCITATIONS

Elias G. Dimitrakopoulos[1], **and Themelina S. Paraskeva**[1]

[1] Hong Kong University of Science and Technology
Department of Civil and Environmental Engineering, Kowloon, Clear Water Bay, Hong Kong
e-mail: ilias@ust.hk

Keywords: Rocking, overturning risk, fragility curves, rocking bridges, earthquake engineering.

Abstract. *This paper assesses the seismic reliability of single degree of freedom rocking structures subjected to near-fault excitations within a probabilistic framework. In this context, it proposes a physically consistent and practically useful methodology to scale the rocking behavior for excitations of different intensity and predominant frequency. According to the assumptions of the proposed methodology the definition of both the Engineering Demand Parameter (EDP) and the corresponding limit states is rather straightforward, since when the rocking structure does not overturn it eventually returns to its original configuration without permanent deformation or damage. On the contrary, identifying appropriate intensity measure/s (IM/s) for rocking structures is far from trivial, longstanding challenge. Two groups of dimensionless-orientationless IMs are considered as candidate IMs: one giving the frequency ratio ω_g/p and one equivalent with the dimensionless slenderness $\alpha_g/(g\tan\alpha)$. Using four well-known strong ground motion parameters (the peak ground velocity, the peak ground acceleration, the predominant period of the pulse and the mean period of the CSGM) six different versions of IMs are examined. In addition, this study, introduces a more 'holistic' approach for the description of the rocking fragility using hybrid bivariate IMs. Analytical fragility curves (FCs) for slender, rigid rocking structures are obtained, using either univariate IM/s (conventional FCs) or bivariate IM/s (bivariate FCs). The study shows that while the use of a univariate IM is a simpler approach, it results in increased scatter. On the other hand, the more complex bivariate IM approach utilizes additional information and reduces uncertainty. Further, the study also unveils that when the rocking structure survives the excitation without overturning, the peak response follows a bi-planar distribution. Specifically, it brings forward the existence of critical peak ground motion acceleration, below and above which rocking response scales differently.*

1 INTRODUCTION

The present study focuses on slender rigid structures that exhibit rocking (without sliding) during seismic excitation. This work is part of a broader study [1-3] on the dynamics of rocking structures, which aims to examine the potential merits of rocking behavior as a seismic isolation technique for contemporary structures.

An essential characteristic of rocking dynamics is the negative stiffness that prevents the structure from resonance under constant frequency (e.g., harmonic) excitation [4]. However, the negative stiffness renders also rocking structures inherently unstable, and very sensitive to the characteristics of ground motion. Thus, rocking dynamics remain difficult to predict, especially if one considers the inherent uncertainty related to the specific characteristics of future ground motions. To deal with the non-predictability of rocking response several researchers adopted a probabilistic approach. Housner [5], in his 1963 paper, tackled the problem of rocking behavior also from a stochastic perspective, estimating the probability of overturning via an energy balance equation (see also [6]). Almost two decades later, researchers (e.g., [7]) showed that small changes in size, slenderness, or ground motion could cause drastic differentiation of the rocking response. This prompted the prediction of rocking overturning via probabilistic methods: Spanos and Koh [8] deployed a stochastic linearization technique, Cai et al. [9] assessed the reliability of a rigid block against toppling under nonstationary and nonwhite (random process) base excitations, and Shao and Tung [10] estimated the overturning probability of a rigid body subjected to real earthquake records. Kafle et al. [11] developed overturning fragility curves, for unrestrained blocks, based on physical and numerical experiments, while Roh and Cimellaro [12] and Deng et al. [13] offered fragility curves for frames with rocking columns [14] and bridges with rocking foundations, respectively.

Motivated by the growing interest in rocking, the present study acknowledges the need to tackle the non-predictability of the rocking response probabilistically. Its particular goal is to assess the seismic reliability of (negative stiffness) rocking structures to near-fault excitations. In this context, it integrates two different components: (i) a 'universal' description of rocking response from [2] and (ii) a probabilistic framework, from recent studies of Psycharis et al. [15] and Acikgoz and DeJong [16]. This work brings forward the different sensitivity of rocking response to excitations with low versus high amplitude. In addition it sheds light on the effect of the high-frequency stochastic component of the seismic excitation on rocking behavior and contributes towards improved, specialized intensity measures (*IMs*) for rocking.

2 PROBABILISTIC SEISMIC DEMAND ANALYSIS

2.1 Stochastic model for near-fault ground motions

For the assessment of the seismic reliability of a structure we can use either natural/historic records (e.g., [16]) or synthetic ground motions (e.g., [15]). In the present study, we employ a stochastic synthetic ground motion model [17-19]. First, we model the low-frequency (long period) and high-frequency components of the ground motion, independently (see Figure 1). Then, we superpose the two aforementioned components and generate the combined synthetic ground motions (CSGMs). For economy of space, we keep the presentation of the method (Section 2.1) short, as it is described in detail in [17-19] and references therein.

To model the low-frequency (coherent) pulse of the *CSGM*, we utilize the well-established Mavroeidis and Papageorgiou (M&P) [19] wavelet. Its velocity time-history expression is:

$$\dot{u}_p = \begin{cases} \frac{A}{2}\left[1+\cos\left(\frac{\omega_p}{\gamma_p}(t-t_0)\right)\right]\cos\left(\omega_p\left(t-t_0\right)+\upsilon_p\right), & t \in \left[t_0-\frac{\pi\gamma_p}{\omega_p}\ ,t_0+\frac{\pi\gamma_p}{\omega_p}\right] \\ 0 & otherwise \end{cases} \quad (1)$$

where A, ω_p, υ_p, γ_p and t_0 describe the velocity amplitude of the envelope of the pulse, the angular frequency, the phase angle, the oscillatory character (i.e., number of half cycles), and the time shift to specify the epoch of the envelopes peak, respectively; T_p ($=2\pi/\omega_p$) is the prevailing period of the pulse.

For every earthquake moment magnitude M_w and epicentral distance from the fault R_e, the mean value of the velocity amplitude V_p in centimeters/second and the corresponding mean value of the period T_p in *s* are obtained from [20]:

$$\log(V_p) = -5.17 + 1.98M_w - 0.14M_w^2 - 0.10\log(R_e^2 + 0.562) \quad (2)$$

and

$$\log(T_p) = -2.87 + 0.47M_w \quad (3)$$

where *log* denotes the base *10* logarithm. Equation (2) holds for $M_w \le 7.0$; for higher values ($M_w > 7.0$), M_w is taken as 7.0 [15]. The values of M_w are in the range of 5.5 to 7.5 with a step of 0.5 (i.e., five values); the epicentral distance R_e varies from 5 to 20 km with a step of 2.5 km (i.e., seven values) [15]. For each of the 35 M_w scenarios, we generate 100 samples of the V_p, T_p, υ_p and γ_p with the Latin hypercube sampling procedure [21]. Further, we assume that the logarithms of V_p and T_p follow a normal distribution with standard deviation equal to 0.16 and 0.18, respectively [15], and that γ_p and υ_p follow also a normal distribution with mean values 1.93 and 1.83 and corresponding standard deviations 0.47 and 0.98, accordingly [22]. The distribution of γ_p is left truncated to 1 [15]. Alternatively, the velocity pulse expression of Equation (2) can be utilized with the scaling laws of T_p and V_p proposed by Mavroeidis and Papageorgiou [19] and Halldorsson et al. [22], respectively. Note that the predominant periods estimated by [19] and [20] are not necessarily the same. In addition, the peak ground velocity (PGV) obtained from [20] has not the same value with the V_p estimated by [22].

To model the high-frequency (*>0.1–0.2 Hz*) component (HFC) of the ground motions, we adopt the point source stochastic method of Boore [23]. The method uses a parametric description of the ground motion's radiation spectrum, which is a product of quantities that consider the effect of source, path, site, and instrument (or type) of motion. The duration of the ground motion is incorporated through an envelope function. Both the radiation spectrum and the duration of the ground motion depend on M_w and R_e. The particular parameters used herein are taken from the Atkinson and Silva [24] study.

Finally, the CSGM is obtained by a superposition procedure of the two components (long-period and high frequency), which is described in detail in [17-19]. Overall, the model parameters consist of the seismological parameters M_w and R_e, the additional parameters for the velocity pulse (V_p, T_p, υ_p and γ_p), and the white noise sequence [17, 18]. Figure 1 illustrates the two components, as well as the final (sample) CSGM. All simulations for this section are performed using MATLAB [21].

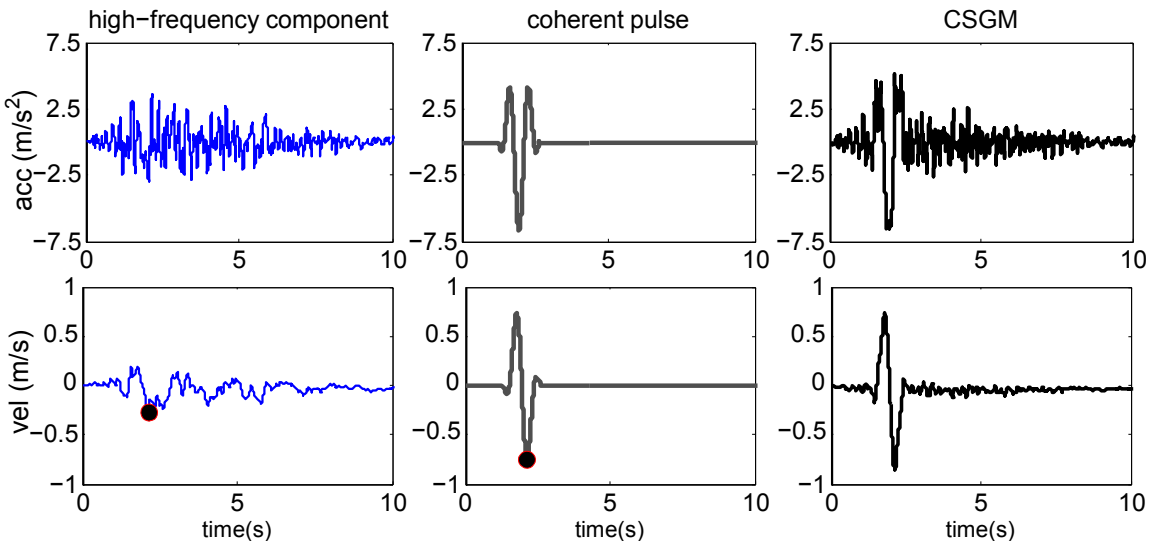


Figure 1: Sample of a CSGM: high frequency component (first column), pure/coherent pulse (second column). Acceleration time history (first row) and velocity time history (second row).

2.2 Structural/Seismic response analysis

The present study examines the seismic response of a rocking frame (see Figure 2). This is a single degree of freedom rocking structure. The equation of motion describing the pure rocking behavior of this structure subjected to a horizontal ground motion with acceleration time history $\ddot{u}_g(t)$ [25] is:

$$\ddot{\theta} = -p^2\left(\sin\left[\alpha\,\mathrm{sgn}(\theta)-\theta\right]+\frac{\ddot{u}_g}{g}\cos\left[\alpha\,\mathrm{sgn}(\theta)-\theta\right]\right) \tag{4}$$

where *sgn()* is the (standard) sign function; α is the slenderness angle; g is the acceleration of gravity; and p ($= p_f$) is the rocking frequency parameter for the rocking frame [25], given as:

$$p_f = \frac{1+2\gamma}{1+3\gamma}\sqrt{\frac{3g}{4R_o}} \tag{5}$$

where, γ is the beam-to-columns mass ratio; and R_o is the semi-diagonal. If sliding is restricted a sufficiently slender frame uplifts and commences rocking once the ground acceleration exceeds a minimum magnitude:

$$\ddot{u}_{g,\min} = \alpha_{g,\min} = g\tan(\alpha) \tag{6}$$

Impact takes place when the structure returns to its initial position (θ=0). Then, the pivot point changes, and the rotation switches sign. To treat impact is with a coefficient of restitution η, which is taken as the ratio of the post-impact ($\dot{\theta}^+$)and pre-impact ($\dot{\theta}^-$) angular velocities. The value of η is material and application dependent (e.g., [1, 2] and references therein) and, therefore, is considered as an additional, independent, governing parameter of the rocking problem. In the present study, we use a coefficient of restitution equal to η=0.92. The rocking response is determined numerically solving the nonlinear equations of motion (4) in MATLAB [21].

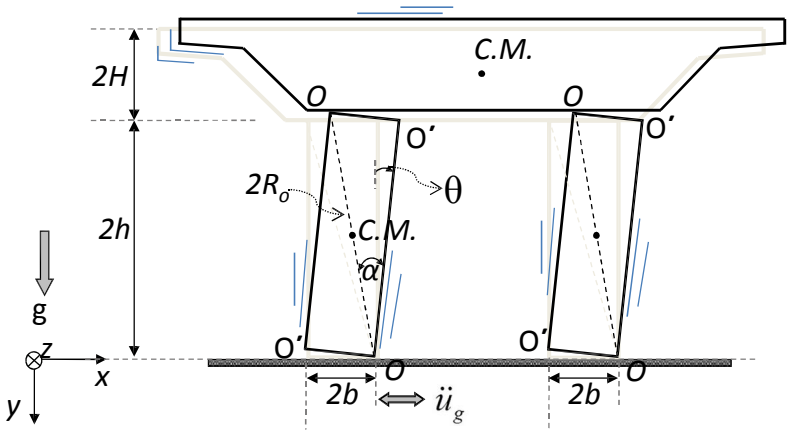


Figure 2: Adopted rocking structure: the single degree of freedom rocking frame.

2.3 Engineering demand parameters and limit states

The definition of appropriate engineering demand parameters (*EDPs*) and limit states (*LS*), for rocking structures, is straightforward, considering the assumptions of the present study. We adopt as *EDP* the absolute peak rocking rotation $|\theta_{max}|$ scaled with respect to the slenderness, a:

$$EDP = \frac{|\theta_{max}|}{\alpha} \tag{7}$$

The dimensionless *EDP* of Equation (7) has a straightforward physical meaning: values larger than zero imply that the structure commences rocking, whereas high values (e.g., $EDP > 1.5$) indicate overturning due to rocking. Accordingly, we define two pertinent performance levels as an upper and a lower limit to assess the response of a rocking structure: the lower limit (LS_l) marks the initiation of rocking and it is equal to zero; the upper limit (LS_{up}) corresponds to overturning due to rocking. Overturning occurs, when the system becomes dynamically unstable, in which case the response tends to numerically infinite values. Thus, the threshold of LS_{up} does not correspond to a particular rotation value (e.g., $EDP = 1.5$), but rather at $EDP \rightarrow \infty$. Intermediate limit states $LS_1, LS_2, ..., LS_n$ can also be defined to indicate observable rocking during seismic response. The values of these limit states are based on engineering judgment to express the level of marginal/limited rocking action that is usually targeted in rocking applications without the substantial danger of overturning. In this context, we define three limit states equal to 0.10, 0.25 and 0.50 to indicate a structure that exhibits rocking without overturning, for different levels of observable damages due to contact (see Figure 10 later on).

Figure 3 plots the *EDP* values of all nonlinear dynamic response analyses (in total 3500) versus the peak ground velocity *PGV* (Figure 3 (b)) (or V_p in the case of pure pulse ground motions, in Figure 3 (a)) and the prevailing period T_p of the pulse. Figure 3 concerns a rocking bridge frame/bent [25] (as shown in Figure 2), with frequency parameter $p = p_f = 1.0$ rad/s and slenderness a=0.149 rad. The structure is subjected to two suites of ground motions: (a) pure M&P pulses (Figure 3(a) top panel), and (b) CSGMs (Figure 3(b) bottom panel). The results are divided in three groups: (i) the 'non-rocking' simulations (crosses), when the peak ground acceleration is less than the minimum acceleration that initiates rocking (Eq.(6)) and hence the structure remains at rest; (ii) the 'safe-rocking' simulations (hollow circles), when the structure commences rocking and does not overturn, and (iii) the 'rocking-overturning'

simulations (solid circles). Recall that a rocking structure becomes statically unstable after $EDP \geqslant 1.0$, because the highly nonlinear nature of rocking dynamics overturning does not necessarily occur when $EDP \geqslant 1.0$. On the contrary, a rocking structure might exhibit significantly higher rotations θ_{max} than α without overturning [3], a behavior counter to the common quasi-static viewpoint of seismic response.

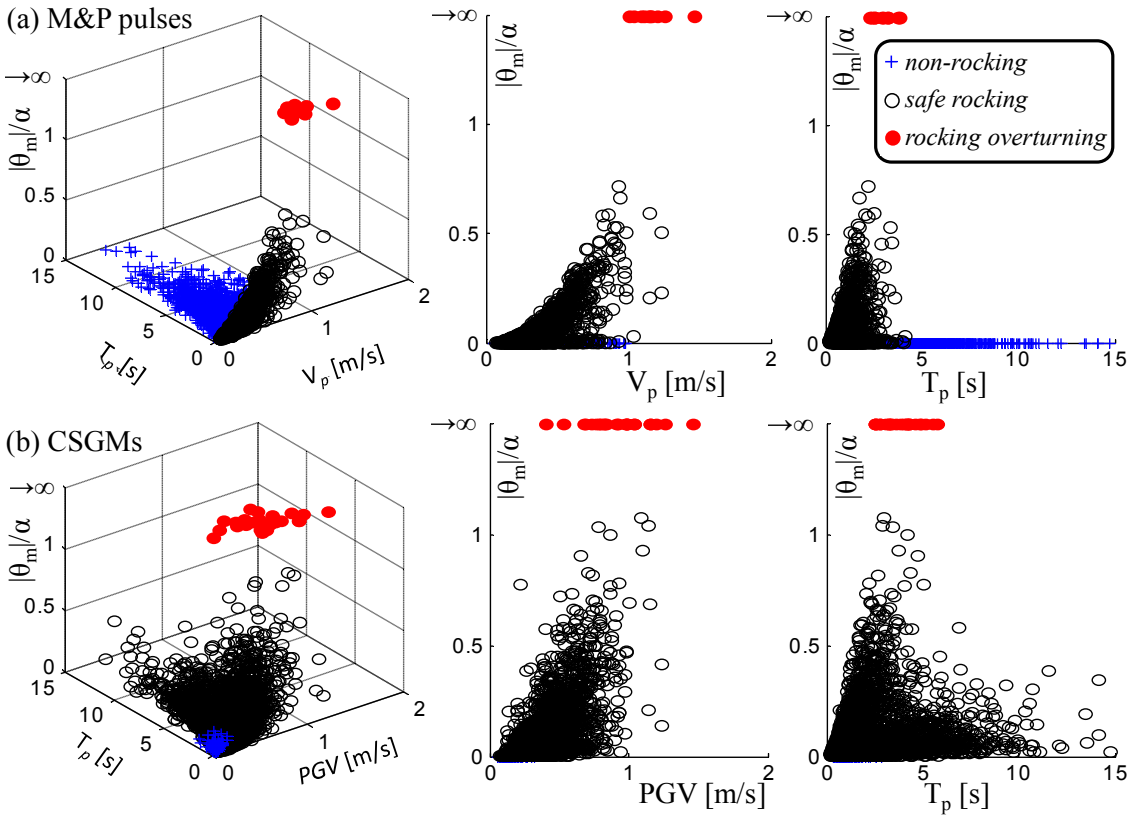


Figure 3: Seismic response analyses of a rocking frame with $p=1.0$ *rad/s* and $\alpha=0.20$ *rad*.

The results of Figure 3 verify the sensitivity of rocking structures to the characteristics of the ground motion and bring forward the influence of the stochastic HFC in the excitation. Note the virtual straight line on the V_p-T_p plane that separates the 'non-rocking' from the rocking simulations in Figure 3 (top left). The slope of this separating limit line on the T_p-V_p plane, corresponds to the minimum ground acceleration (Equation (6)) that triggers (uplifting and) rocking. However, when the stochastic HFC is included in the excitation, this limit line disappears (Figure 3, bottom left), the number of 'non-rocking' simulations is drastically reduced, and rocking response becomes significantly more probable. This is because of the numerous CSGMs for which the presence of the HFC triggers rocking, whereas the (low acceleration M&P) pulse alone would not. Consequently, this introduces observable noise in the results (Figure 3, bottom right), and the response becomes less ordered. Figure 3 verifies also that rocking is sensitive to more than one strong ground motion parameters. Overturning occurs as both PGV and T_p increase, without though a distinguishable pattern.

2.4 Physically similar ('universal') rocking behavior

In this section we propose a physically consistent method to scale the rocking behavior for excitations of different intensities and predominant frequencies. According to this concept, we generate normalized fragility curves, indifferent to the size and the frequency of the rocking structure or the amplitude and the predominant frequency of the near-fault ground motion.

For a given ground motion with a specific waveform (i.e., a specific acceleration time-history shape), for example, the CSGM excitation of Figure 1, the (acceleration) amplitude $\alpha_g = PGA$ and the frequency $\omega_g = 2\pi/T_p$ characterize the length and time scale of the waveform, respectively [26]. Then, the response (e.g., the absolute peak rocking rotation) can be written as a function of the general form:

$$|\theta_{\max}| = f\left(\alpha, p, \omega_g, \frac{\alpha_g}{g}, \eta\right) \tag{8}$$

Equation (8) contains six characteristic variables that involve only one reference dimension, time [T]. The six variables can be grouped into a reduced number of independent dimensionless Π-products according to Buckingham's Π theorem [27], which can be further reduced to a group of dimensionless- orientantionless products, according to the theory of orientational analysis [2, 28] as:

$$\frac{|\theta_{\max}|}{\alpha} = \phi\left(\frac{\omega_g}{p}, \frac{\alpha_g}{g\alpha}, \eta\right) \tag{9}$$

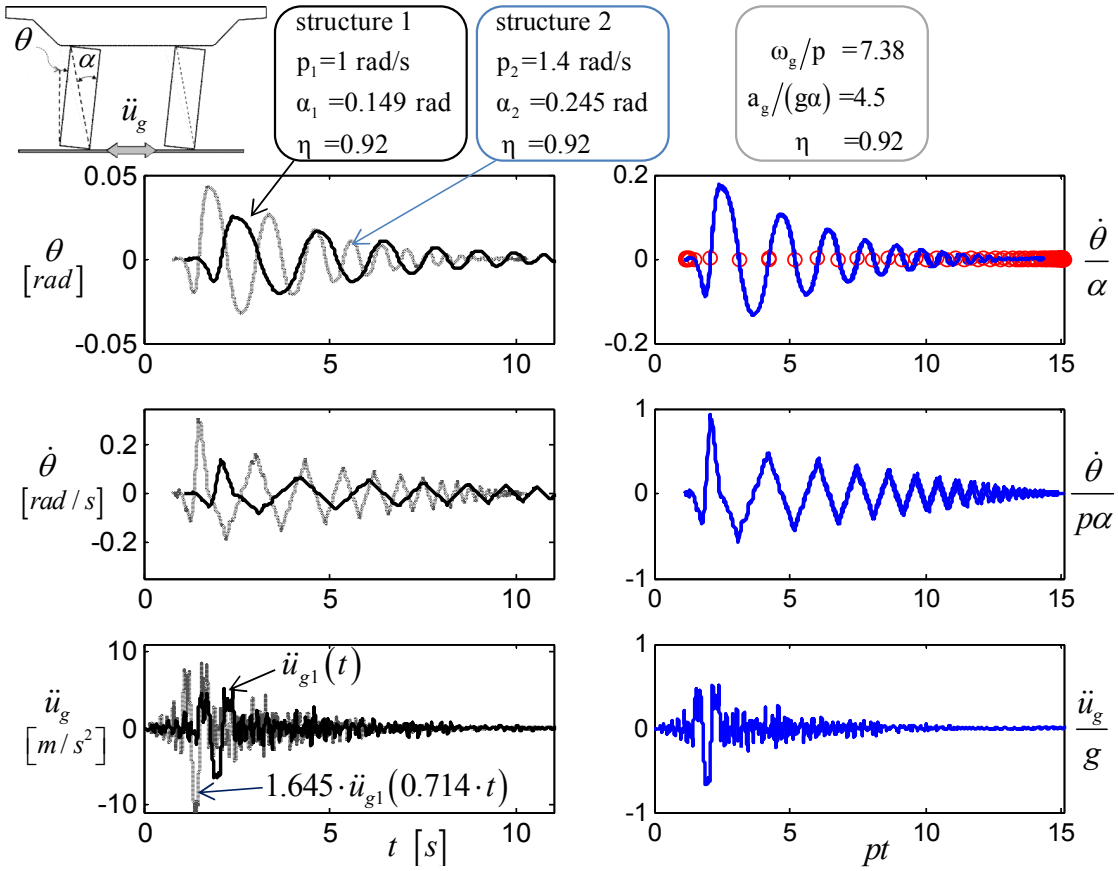


Figure 4: Seismic physically similar rocking response for frame-structures subjected to different CSGMs.

The products of Equation (9) yield an exact representation of the rocking response when the slenderness angle α is small [2]. If α is not small, it should be included explicitly as an additional independent group [2].This study focuses solely on the case of small α (slender rocking structures).

Figure 4 (left) illustrates the time-history response of two different rocking structures, subjected to two CSGM excitations of different amplitude and frequency, but the same waveform (of Figure 1), The two structures differ both in size (p) and in shape (α). However, when the associated dimensionless–orientationless products of Equation (9) take the same values, the response curves of the two different structures are identical (Figure 4 (right)). This *physical similarity* (or self-similarity in [45]) is a special type of symmetry of unique importance for nonlinear phenomena. The dimensionless - orientantionless groups of Equation (9) unveil what matters in rocking response, for example, not the frequency parameter, p or slenderness α but the frequency ratio ω_g/p, or the dimensionless-orientationless slenderness $a_g/(g\alpha)$.

2.5 Intensity measures (*IMs*)

Following the proposed dimensionless–orientationless products of Equation (9), we select *IMs* similar to that in [29] for sliding objects. According to Equation (9), there are two groups that could be considered as candidate *IMs*: the frequency ratio ω_p/p and the dimensionless slenderness $\alpha_g/(g\tan\alpha)$. We examine four common strong ground motion parameters that could be used as α_g or ω_g accordingly: the peak ground velocity *PGV* (= V_p for pulse excitations), the peak ground acceleration PGA, the predominant period T_p of the pulse, and the mean period of the CSGM T_m (see [26] and references therein). Using the four well-known strong ground motion parameters, we construct the following alternative versions of the two groups ω_p/p and $\alpha_g/(g\tan\alpha)$:

$$IM_1 = \frac{\omega_p}{p}, IM_2 = \frac{\omega_m}{p}, IM_3 = \frac{PGA}{pPGV}$$
$$IM_4 = \frac{PGA}{g\tan\alpha}, IM_5 = \frac{pPGV}{g\tan\alpha}, IM_6 = \frac{\omega_m PGV}{g\tan\alpha} \quad (10)$$

where $\omega_p = 2\pi / T_p$ and $\omega_m = 2\pi / T_m$; *IMs* IM_1 to IM_3 reconstruct the frequency ratio (ω_p / p of Equation (9)), whereas IM_4 to IM_6 are alternative dimensionless slenderness ($\alpha_g/(g\tan\alpha)$ of Equation (9)) groups. In the following, we refer to the former as 'frequency ratio' *IMs* and to the latter as 'dimensionless slenderness' *IMs*.

3 FRAGILITY ANALYSIS

In general, fragility (or vulnerability) analysis is the estimation of the conditional probability P_f that an *EDP(=D)*, will exceed a certain capacity limit C(= *c)*, given an *IM* value:

$$P_f = P\left(D > C = c \mid IM\right) \quad (11)$$

Figure 5 illustrates the probability tree diagram that describes the rocking problem and facilitates the calculation of the conditional probability $P_{f|r}$, that the *EDP* of a structure will exceed a certain (capacity) threshold, given an *IM* value and given that the structure is rocking. P_{nr} is the probability that the structure will remain resting on the ground (non-rocking response; Figure 5) during the earthquake excitation; P_{ro} is the probability that the rocking structure overturns. In general, the probability $P_{f|r}$ is derived by the union of two likelihoods (Figure 5): (a) the probability that the structure commences rocking and overturns, and (b) the

rocking structure does not overturn, but during its rocking response, the *EDP* exceeds the capacity limit c. Thus, Equation (11) becomes [15]

$$P_{f|r} = P_{ro} + (1 - P_{ro}) P_{ex}(D > C \mid IM) \tag{12}$$

The overturning probability, P_{ro} (in Figure 5), can be estimated as in [15], from the ratio of the number of simulations (response analyses) that result to rocking overturning to the total number of the simulations. An alternative solution for the estimation of probability P_{ro} is [30], to adopt a maximum likelihood approach (P_{nr}, in Figure 5). The present study, focuses on the calculation of the conditional probability P_{ex} of Equation (12), in which the *EDP* of a rocking structure will exceed a capacity limit, C=c, given an *IM* value without overturning.

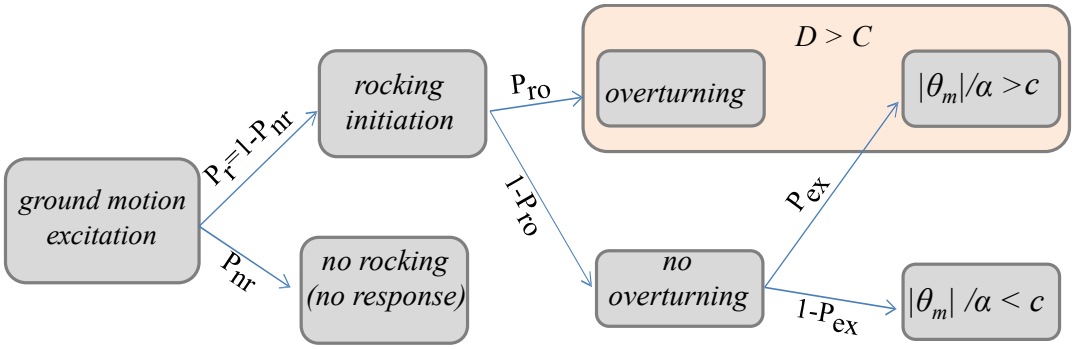


Figure 5: Probability tree diagram for the rocking problem.

3.1 Probability of limit state exceedance during 'safe rocking'.

In this section we present the calculation of the conditional probability P_{ex} (see Figure 5 and Equation (11)) that a rocking structure exceeds a performance/capacity limit C(=c), without the occurrence of overturning ('safe rocking') under a ground motion with $IM = x$. The calculation procedure is based on two typical assumptions.

Firstly, that both the capacity C and the demand D, are random variables following lognormal distributions. Then, P_{ex} is:

$$P_{ex} = P_{ex}(D > C \mid IM = x) = \Phi\left(\frac{\ln x - \mu}{\beta_{D|IM}}\right) \tag{13}$$

where $\Phi(\ )$ is the standard normal cumulative distribution function; μ is the median value of the structural demand as a function of *IM* and $\beta_{D|IM}$ is the dispersion (or logarithmic standard deviation) of the demand conditioned on the *IM* [31].

The second typical assumption ([32]) is that the median demand D_m and the *IM* are related through the function:

$$D_m = \alpha (IM)^b \tag{14}$$

Conveniently, the assumed function (Eq. (14)) becomes a straight line on the lnD_m vs ln*IM* plane:

$$\ln(D_m) = \ln(\alpha) + b \ln(IM) \tag{15}$$

which enables the estimation of parameters α and b by means of linear regression analysis.

Figure 6 presents sample results of the linear regression analyses considering solely rocking without the overturning ('safe rocking' cases of Figure 3). The regression analyses show a significant dispersion in the response for both pure pulse excitations (Figure 6 (a)), as well as, CSGMs (Figure 6 (b)). Regardless which of the *IMs* performs best compared with the others, none of the examined *IMs* shows a strong effect on the response. To some extent, this failure of the well-known strong ground motion parameters (e.g., *PGV, PGA, PGA/PGV*) to predict rocking response should be attributed to the negative stiffness mechanism and further to the lack of resonance of rocking structures under constant frequency ground motions [4].

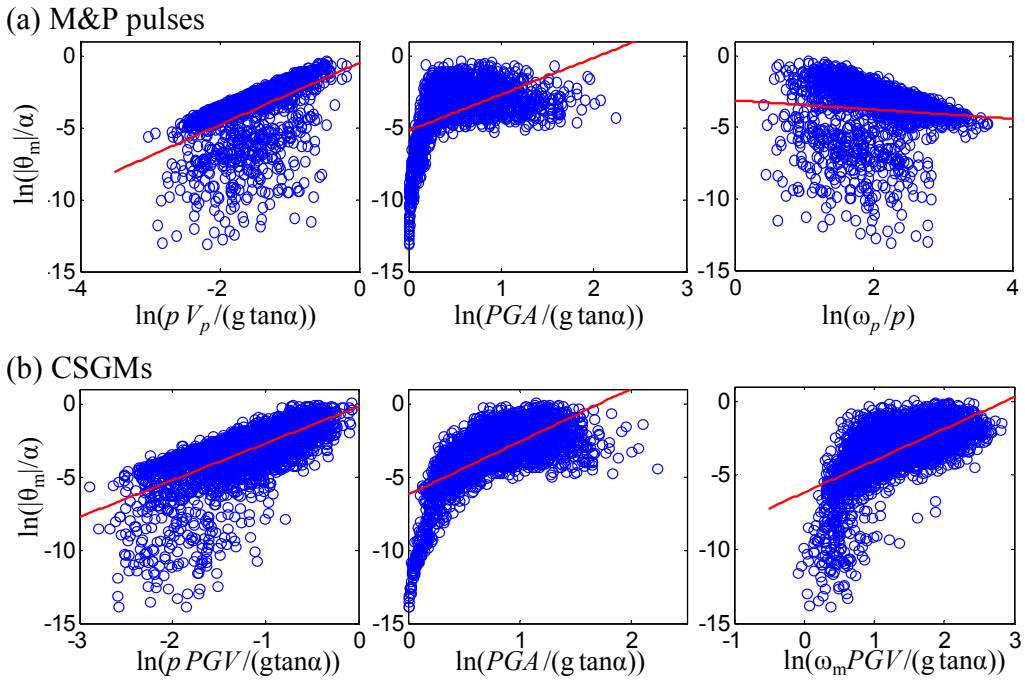


Figure 6: Sample results of the linear-regression analyses for (a) pure M&P pulse excitations and (b) CSGMs.

3.2 Proposed bivariate *IMs*

Alternatively, this section, examines the use of bivariate *IMs*, instead of univariate *IMs*, to capture the rocking response of a structure subjected to seismic (synthetic) excitations [31].

Figures 7 (a) and 8 (a) present a three-dimensional view, $\ln(|\theta_{max}|/\alpha) - \ln V_p - \ln T_p$, of the same 'safe-rocking' simulations (of Figure 3) for pure M&P pulse ground motions and for CSGMs, respectively. In the same Figures, the results are also plotted in the three two-dimensional viewpoints of the 3D plane: (i) a $\ln V_p$-$\ln T_p$ (Figures 7 (b) and 8 (b)), (ii) a $\ln(|\theta_{max}|/\alpha) - \ln V_p$ (Figures 7 (c) and 8 (c)), and (iii) a $\ln(|\theta_{max}|/\alpha) - \ln T_p$ view slice (Figures 7 (d) and 8 (d)). If viewed from the proper viewpoint (compare Figures 7 (a) and 8 (a) with Figures 9(a) and (b), respectively), remarkable order emerges: The response points lie consistently on two distinct planes; a trend hidden in the two-dimensional representations of the same results (e.g., Figure 6). The existence of the two distinct planes unveils that rocking response scales differently for low intensity, versus high intensity, excitations. In particular, rocking is more sensitive to low amplitude excitations, meaning that even slight variations of the excitation characteristics have a strong effect on the peak rocking response. Figure 9 illustrates alternative three-dimensional plots from different viewing angles of the same results of Figures 7 (a) and 8 (a), respectively.

In general, the equation of a plane in a three-dimensional ($\ln(|\theta_{max}|/\alpha)$ – $\ln IM_x$ – $\ln IM_y$) space is given as:

$$\ln(D_m) = b_1 \ln(IM_x) + b_2 \ln(IM_y) + \ln(\alpha) \tag{16}$$

which suggests that the mean demand is given by a bivariate (vector-valued) intensity measure $\hat{IM} = (IM_x, IM_y)$ as

$$D_m = \alpha \left(IM_x^{b_1} IM_y^{b_2} \right) \tag{17}$$

where IM_x and IM_y are two appropriate (scalar) *IMs*, and α, b_1, b_2 are coefficients calculated using multi-linear regression analysis [50]. For IM_x and IM_y, we adopt the dimensionless slenderness IM_4 , and the frequency ratio IM_3 from Eq. (10), respectively, based on [30].

Excitation	1.00<PGA/(g tanα) <1.30				PGA/(g tanα)≥1.30			
	α	b_1	b_2	(R^2)	α	b_1	b_2	(R^2)
M&Ps	0.001	29.40	-1.994	(0.915)	1.490	1.574	-2.004	(0.896)
CSGMs	6.02e-6	28.31	-0.236	(0.737)	0.104	2.640	-1.436	(0.557)

Table 1: The fitted planar distributions for the response analyses of Figure 3.

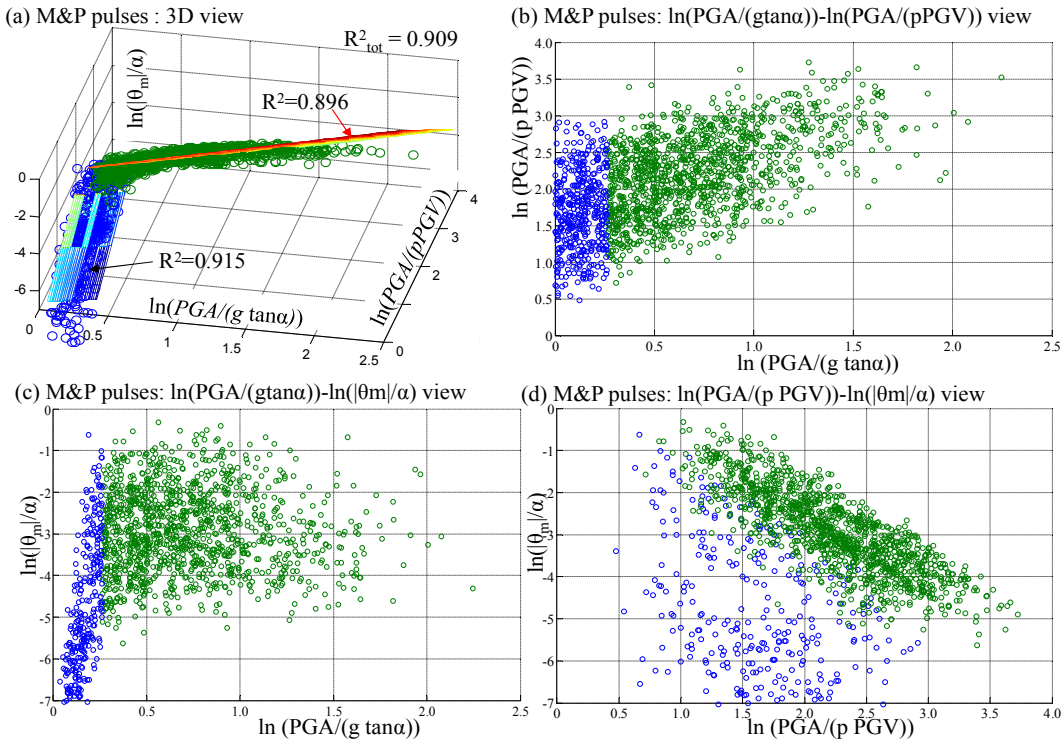


Figure 7: Plots of 'safe-rocking' results (same as Figure 6(a))for M&P pulses excitations in: (a) a 3D plane; (b) a $\ln V_p$-$\ln T_p$, (c) a $\ln(|\theta_{max}|/\alpha)$ – $\ln V_p$, and (d) a $\ln(|\theta_{max}|/\alpha)$ – $\ln T_p$ views.

The transition between the two planes takes place at a constant acceleration boundary (Figures 7 and 8). The estimation of the transition limit can be made with iterative multi-linear regression analyses that minimize the dispersion of both planes of Figures 7 and 8 simultaneously (e.g., through the coefficients of determination R^2). The 'low' (e.g., $PGA < 1.30\ \alpha_{g,min}$)

and the 'high' (e.g., $PGA > 1.30\ \alpha_{g,min}$) amplitudes are then defined according to the minimum rocking acceleration $\alpha_{g,min}=g\tan\alpha$.

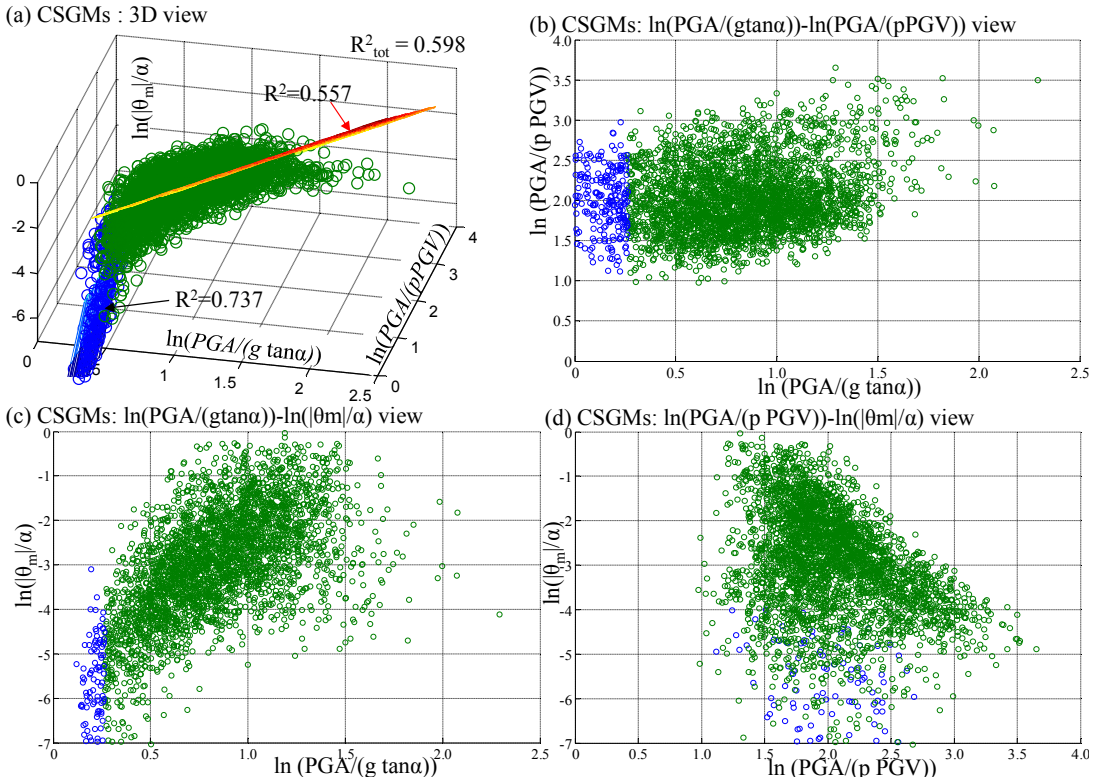


Figure 8: Plots of 'safe-rocking' results (same as Figure 6(b)) for the combined synthetic ground motions for different views: (a) a 3D view; (b) a $\ln V_p$-$\ln T_p$, (c) a $\ln(|\theta_{max}|/\alpha) - \ln V_p$, and (d) a $\ln(|\theta_{max}|/\alpha) - \ln T_p$ views

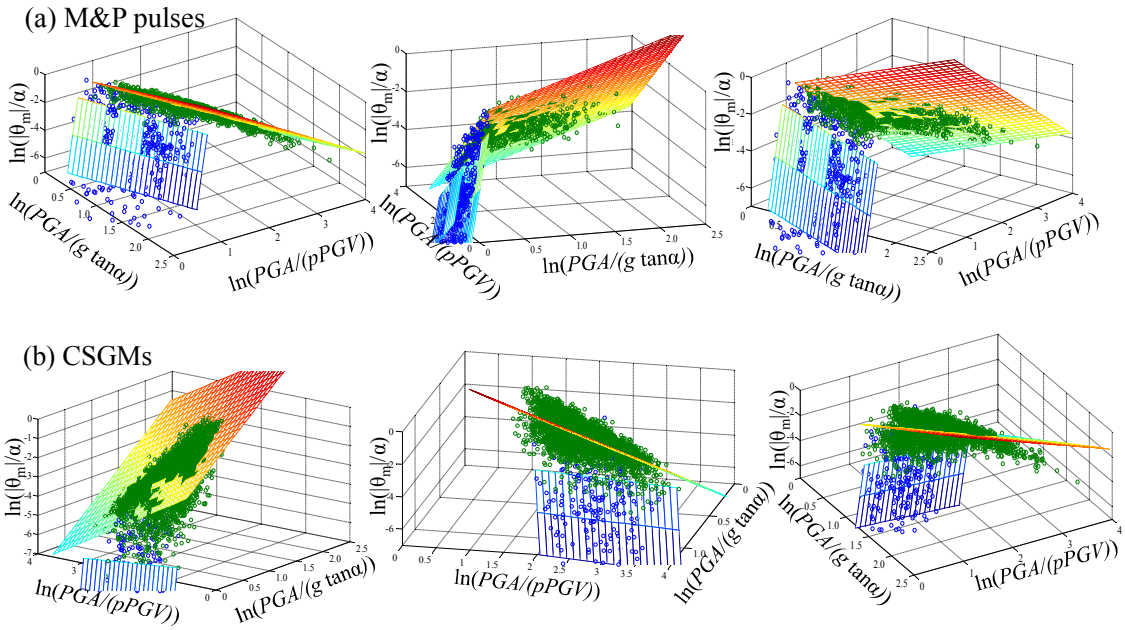


Figure 9: Alternative 3D views from other viewing angles of: (a) Figure 7(a) plot, and (b) Figure 8(a) plot.

In Table 1 are listed all the regression parameters α, b_1, b_2, and the coefficient of correlation R^2 (i.e. the fitted planar distributions) when the structure (e.g., the rocking frame with p= *1.0 rad/s* and α= *0.149 rad*) is subjected either to pure (M&P) pulses or CSGMs.

4 PROPOSED 'UNIVERSAL' FRAGILITY CURVES

In this section, we estimate the probability of a limit state threshold (LS_i) being exceeded during 'safe rocking' P_{ex}. The fragility curves of P_{ex} can be generated using either a univariate or a bivariate *IM*. The use of a univariate *IM* is a simpler approach, but (as shown late in Figure 10) it results in increased scatter. Moreover, the more complex bivariate *IM* approach reduces drastically the uncertainty (Figure 10), but it requires more information about the frequency content of the excitation.

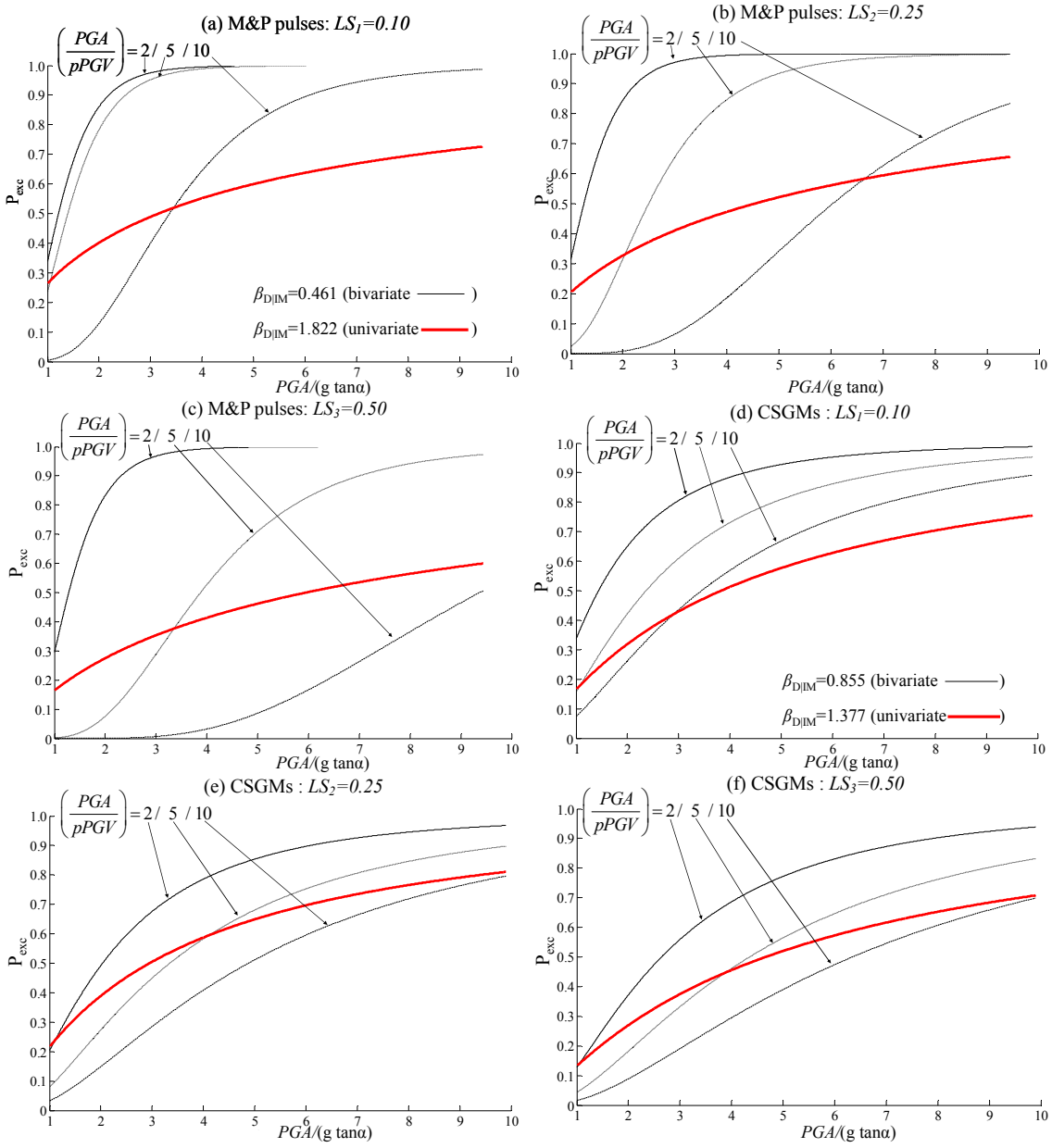


Figure 10: Comparison of bivariate with univariate P_{ex} fragility curves for different *PGA/(pPGV)* values.

Figure 10 plots P_{ex} fragility curves of different limit states using *pPGV/(g tana)* as the univariate *IM* and the pair of *IMs*, (*PGA/(gtana)*, *pPGV/PGA*) as a bivariate *IM*. The fragility curves of Figures 10 (a) to (c) are obtained for M&P pulse excitations (Figure 3(a)), while the fragility curves of Figures 10 (d) to (f) are obtained for CSGMs (Figure 3b). The limit states we adopt herein are: $LS_1=0.10$ (Figures 10 (a) and 10 (d)), $LS_2=0.25$ ((Figures 10 (b) and 10 (e)), and $LS_3=0.50$ ((Figures 10 (c) and 10 (f)). These values are based on engineering judgment, and they express an amplitude of rocking action raging from marginal up to extensive rocking. In particular, LS_1 indicates a rocking structure that may have minor and local damage due to contact. Accordingly, LS_3 corresponds to extensive local damages, while LS_2 demonstrates an intermediate level of observable local damages on the rocking structure. Figure 10, compares the univariate *FC* with bivariate *FCs* for given *PGA/PGV* values. As the *PGA/PGV* ratio increases, the fragility of the rocking structure (Figure 10) decreases a well-known trait of rocking behavior that the univariate *FCs* neglect. In addition, the univariate *FC* is substantially flatter than the bivariate *FCs*, which indicates higher uncertainty.

5 CONCLUSIONS

This paper offers analytical *FCs* for slender, rigid structures rocking under (synthetic) near-fault ground motions. The proposed *FCs* can be generated by either univariate (conventional) *IM* or bivariate *IM/s*. The study shows that the bivariate *FCs* offer a superior estimation of the fragility, compared with the conventional univariate *FCs*. In this context, the study proposes a group of various dimensionless–orientationless *IMs* that offer a normalized (approximately 'universal') description of rocking, indifferent to the characteristics of the structure or to the a_g and ω_g of the (near-fault) ground excitations. Importantly, the paper unveils that rocking response without overturning follows a biplanar distribution with respect to the frequency ratio and the scaled acceleration amplitude of the ground motion. In particular, the paper brings forward the existence of a critical peak ground acceleration, below and above which, rocking response scales differently. This observation is stronger for pure pulse ground motions.

REFERENCES

[1] M.J. DeJong, E.G. Dimitrakopoulos, Dynamically equivalent rocking structures. *Earthquake Engineering & Structural Dynamics,* **43**, 1543-63, 2014.

[2] E.G . Dimitrakopoulos, M.J. DeJong, Revisiting the rocking block: closed-form solutions and similarity laws. *Proceedings of the Royal Society A: Mathematical, Physical and Engineering Science*, **468**, 2294-318, 2014.

[3] E.G. Dimitrakopoulos, A.I. Giouvanidis A.I., Seismic Response Analysis of the Planar Rocking Frame. *Journal of Engineering Mechanics(ASCE)*, accepted for publication, 26/1/2015

[4] M.J. DeJong, Amplification of rocking due to horizontal ground motion. *Earthquake Spectra*, **28**:1405-21, 2012.

[5] G.W. Housner, The behavior of inverted pendulum structures during earthquakes. *Bulletin of the seismological society of America*, **53**, 403-17, 1963.

[6] K. Aydin, C. Tung, Energy balance equation for estimating overturning potential of an unanchored rocking body subjected to earthquake excitation. *Earthquake Spectra*, **17**, 209-20, 2001.

[7] C.S. Yim, A.K. Chopra, J. Penzien, Rocking response of rigid blocks to earthquakes. *Earthquake Engineering & Structural Dynamics*, **8**, 565-87, 1980.

[8] P.D. Spanos, A.S. Koh, Analysis of block random rocking. *Soil Dynamics and Earthquake Engineering*, **5**, 178-83, 1986.

[9] G. Cai, J. Yu, Y. Lin, Toppling of rigid block under evolutionary random base excitations. *Journal of Engineering Mechanics*, **121**, 924-9, 1995.

[10] Y. Shao, C. Tung, Seismic response of unanchored bodies. *Earthquake Spectra*, **15**, 523-36, 1999.

[11] B. Kafle, N.T. Lam, E.F. Gad, J. Wilson, Displacement controlled rocking behaviour of rigid objects. *Earthquake Engineering & Structural Dynamics*, **40**, 1653-69, 2011.

[12] H. Roh, G.P. Cimellaro, Seismic fragility evaluation of RC frame structures retrofitted with controlled concrete rocking column and damping technique. *Journal of Earthquake Engineering*, **15**,1069-82, 2011.

[13] L. Deng, B.L. Kutter, S.K. Kunnath, Probabilistic seismic performance of rocking-foundation and hinging-column bridges. *Earthquake Spectra*, 28:1423-46, 2012.

[14] H. Roh, A.M. Reinhorn, Nonlinear static analysis of structures with rocking columns. *Journal of structural engineering*, **136**, 532-42, 2009.

[15] I.N. Psycharis, M. Fragiadakis, I. Stefanou, Seismic reliability assessment of classical columns subjected to near‐fault ground motions. *Earthquake Engineering & Structural Dynamics*, **42**, 2061-79, 2013.

[16] S. Acikgoz, M.J. DeJong, The rocking response of large flexible structures to earthquakes. *Bulletin of earthquake engineering*, **12,** 875-908, 2014.

[17] A.A. Taflanidis, Optimal probabilistic design of seismic dampers for the protection of isolated bridges against near-fault seismic excitations. *Engineering structures*, **33**, 3496-508, 2011.

[18] A. Lamprou, G. Jia, A.A. Taflanidis, Life-cycle seismic loss estimation and global sensitivity analysis based on stochastic ground motion modeling. *Engineering structures*. **54**, 192-206, 2013.

[19] G.P. Mavroeidis, A.S. Papageorgiou, A mathematical representation of near-fault ground motions. *Bulletin of the seismological society of America*, **93**, 1099-131, 2003.

[20] R. Rupakhety, S. Sigurdsson, A. Papageorgiou, R. Sigbjörnsson, Quantification of ground-motion parameters and response spectra in the near-fault region. *Bulletin of earthquake engineering*, **9**, 893-930, 2011.

[21] The MathWorks Inc., Guide MUs. South Natick MA., 2012.

[22] B. Halldórsson, G.P. Mavroeidis, A.S. Papageorgiou, Near-fault and far-field strong ground-motion simulation for earthquake engineering applications using the specific barrier model. *Journal of structural engineering*, **137**, 433-44, 2010.

[23] D.M. Boore, Simulation of ground motion using the stochastic method. *Pure and applied geophysics*, **160**, 635-76, 2003.

[24] G.M. Atkinson, W. Silva, Stochastic modeling of California ground motions. *Bulletin of the seismological society of America*, **90**, 255-74, 2000.

[25] N. Makris, M.F. Vassiliou, Planar rocking response and stability analysis of an array of free ‐ standing columns capped with a freely supported rigid beam. *Earthquake Engineering & Structural Dynamics*, **42**, 431-49, 2013.

[26] E. Dimitrakopoulos, A.J. Kappos, N. Makris, Dimensional analysis of yielding and pounding structures for records without distinct pulses. *Soil Dynamics and Earthquake Engineering*, **29**, 1170-80, 2009.

[27] E. Buckingham, On physically similar systems; illustrations of the use of dimensional equations. *Physical Review*, **4**, 345-76, 1914.

[28] D.B. Siano DB, Orientational analysis—a supplement to dimensional analysis—I. *Journal of The Franklin Institute*, **320**, 267-83, 1985.

[29] D. Konstantinidis, N. Makris, Experimental and analytical studies on the response of 1/4-scale models of freestanding laboratory equipment subjected to strong earthquake shaking. *Bulletin of earthquake engineering*, **8**, 1457-77, 2010.

[30] E.G. Dimitrakopoulos, T.S. Paraskeva, Dimensionless fragility curves for rocking response to near ‐ fault excitations. *Earthquake Engineering & Structural Dynamics*, DOI:10.1002/eqe.2571, 2015.

[31] J.E. Padgett, B.G. Nielson, R. DesRoches, Selection of optimal intensity measures in probabilistic seismic demand models of highway bridge portfolios. *Earthquake Engineering & Structural Dynamics*, **37**, 711-25, 2008.

[32] C.A. Cornell, F. Jalayer, R.O. Hamburger, D.A. Foutch, Probabilistic basis for 2000 SAC federal emergency management agency steel moment frame guidelines. *Journal of structural engineering*, **128**, 526-33, 2002.

COMPDYN 2015
5th ECCOMAS Thematic Conference on
Computational Methods in Structural Dynamics and Earthquake Engineering
M. Papadrakakis, V. Papadopoulos, V. Plevris (eds.)
Crete Island, Greece, 25–27 May 2015

POST-EARTHQUAKE RECOVERY OF A COMMUNITY AND ITS ELECTRICAL POWER SUPPLY SYSTEM

Max Didier[1], Li Sun[1], Siddhartha Ghosh[2] and Bozidar Stojadinovic[1]

[1] Swiss Federal Institute of Technology (ETH) Zurich
Dept. of Civil, Environmental and Geomatic Engineering, 8093 Zurich, Switzerland
didier@ibk.baug.ethz.ch

[2] Indian Institute of Technology Bombay
Dept. of Civil Engineering, Mumbai 400076, India
sghosh@civil.iitb.ac.in

Keywords: post-earthquake recovery, resilience, infrastructure network, electric power supply system, fragility, sensitivity

Abstract. *Research from the past ten years shows that the seismic fragilities of different infrastructure networks are better understood and estimated than the recovery of a community subjected to these fragilities. Modeling the recovery process for a specific infrastructure system-community-hazard combination is a challenging task due to the lack of data and because the recovery process is subject to a large set of interdependent factors and variables. The primary objective of the present work is to understand how typical modeling assumptions affect the estimated seismic resilience of a community, whose electrical power supply network has been affected by an earthquake. The recovery model relies on component recovery probability functions conditioned on the initial post-disaster damage state of the single components. The loss of resilience (LOR) of a set of systems, composed by an electric power supply system and a community demanding electric power is assessed using a compositional approach to quantify the loss of resilience of the combined system. The modeling assumptions that are considered are: a) the time-varying recovery function, and b) the probabilistic model for recovery. For the recovery function, the adopted probability model of the infrastructure system is found to have a strong influence on the loss of resilience, while it is relatively insensitive to that of the community. LOR is also observed to have a significantly higher sensitivity towards the mean of the used recovery functions than towards their variance.*

1 INTRODUCTION

Seismic resilience assessment of the building stock and of infrastructure systems, like the Electric Power Supply System (EPSS), is essential to estimate the impact of earthquakes to a community and to evaluate pre-disaster mitigation measures or post-disaster emergency plans. The resilience of a system or a community is influenced especially by the robustness of the considered system towards a disastrous event and by its recovery in the aftermath of that event. The fragility of components of the built environment or engineered systems can easily be assessed using, for example, fragility curves, that can be obtained through laboratory tests, finite element analyses of the structure or from diverse databases. However, the computation of recovery is much more challenging. Recovery is a complex, multifaceted and multidimensional process depending on many factors, including especially political decisions and socio-economic considerations which might not be known in advance of the disastrous event and are therefore difficult to model numerically.

The objective of this work is to understand the impact of the modeling assumptions of the component recovery functions to the resilience of a set of systems. The findings should provide guidelines for future modeling of the seismic recovery of infrastructure systems and indicate which parameters need more intricate assessment than others.

2 LITERATURE REVIEW

2.1 Definition of Resilience

The definition of resilience, especially the resilience of a community has been refined during the last decade and the term is often used in different settings (Buffalo). For an engineered infrastructure, the loss of resilience (Figure 1) of a given system can be expressed as the loss of functionality or performance over time [1].

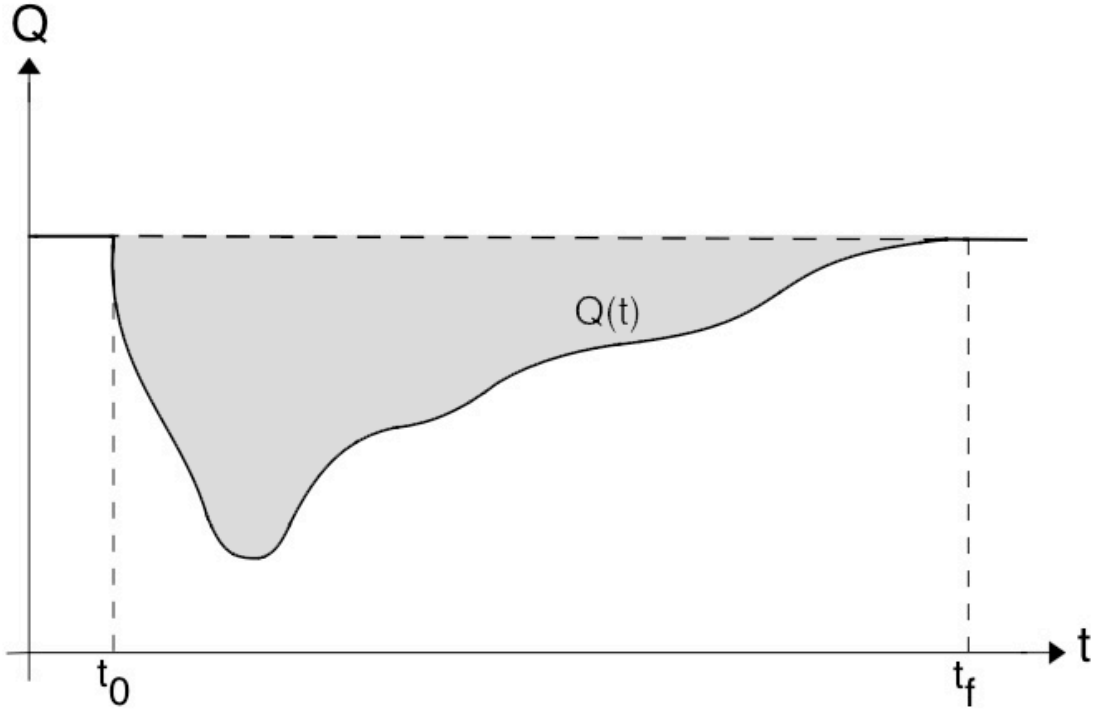


Figure 1: Loss of resilience (shaded area). Adapted from [1]

It can be mathematically defined as

$$R = \int_{t_0}^{t_f} \left[100 - Q(t)\right] dt \tag{1}$$

where, t_0 is the time when the disastrous event (e.g. the earthquake) occurs, t_f the time when the system is fully recovered and Q(t) the performance of the system at a given point in time. The performance function is set at 100% at t_0 [1].

The recovery starts after the absorption phase and ends with the full restoration of the system to its pre-event performance level. Different recovery models have been proposed in the literature. These models can be ordered into five main categories: statistical curve fitting, deterministic resource constraint, Markov processes, network models and discrete event simulations [2].

Statistical curve fitting models usually estimate the parameters of one recovery curve for the whole system using statistical data [3] or a probabilistic parametric approach for a range of parameters [4]. The shape of the system recovery function is predetermined and can take, for example, a trigonometric [4,5], linear or exponential shape [5]. These models do not consider any community or network topology and don't explicitly model the activities that take place during the post-disaster recovery process.

The network approach takes into account the topology of the infrastructure system, which is composed of a number of supply and demand nodes and links between these nodes. It allows the consideration of the temporal and spatial evolution of the systems recovery. This approach has mainly been used in the optimization of the recovery process of the infrastructure system while statistical curve fitting has been used more frequently to model the current recovery process [2].

3 METHODOLOGY

3.1 Estimating the loss of resilience of a set of systems

The definition of the loss of resilience reviewed above only allows to assess the impacts on the performance of a single system - for example, the supply capacity of the electric power supply system over time - and to compare it to its initial performance level. This paper makes use of a compositional approach [6] to calculate the loss of resilience of a set of systems. The compositional approach allows taking into account the changes on the demand side, depending on the performance of a second system, for example a community.

The loss of resilience is therefore the amount of supply that cannot be provided by the damaged supply network in order to cover the demand of a damaged second system or a set of systems (Figure 2). In the example of an EPSS, failure occurs if the post-disaster demand of the community exceeds the available post-disaster power supply capacity of the EPSS. The analytical expression of the loss of resilience (LOR) can be written as

$$LOR = \int_{t_o}^{t_f} \left\langle D(t) - S(t) \right\rangle dt \tag{2}$$

where, D(t) is the demand over time, S(t) is the available supply over time and t_f is the time when both systems have recovered. This quantity is represented by the shaded area in Figure 2.

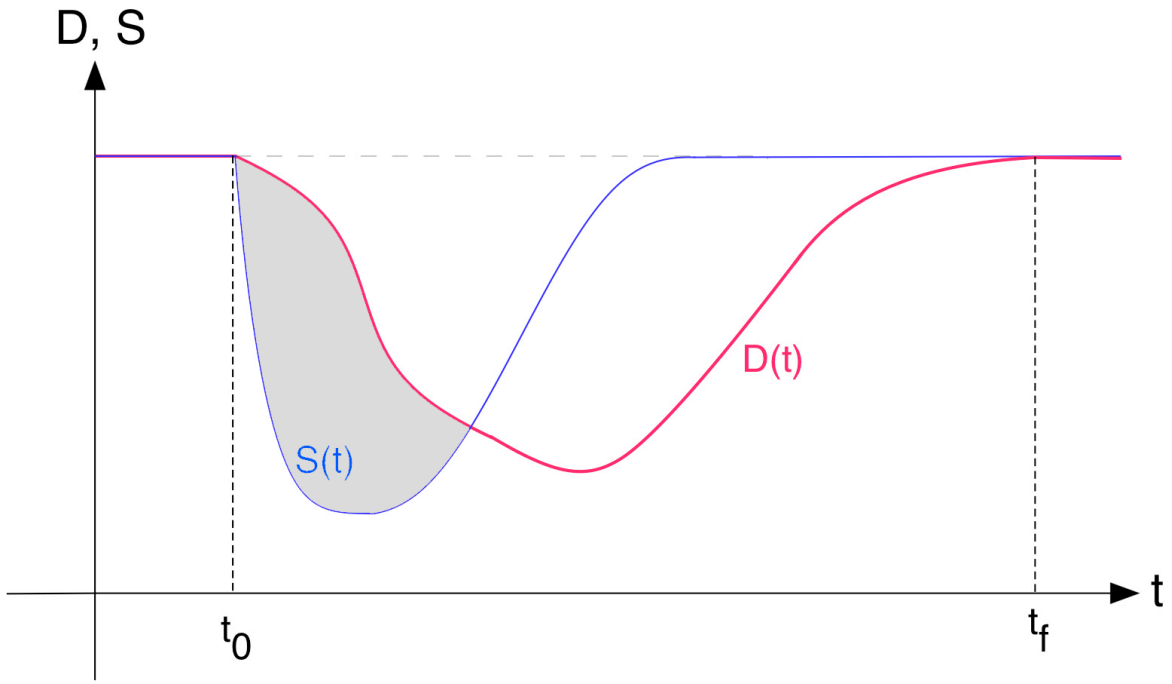


Figure 2: Loss of resilience, compositional approach. Adapted from [6]

3.2 Recovery model

The proposed recovery model combines aspects of the statistical curve fitting and the network approach models. The recovery of every component of the considered systems is expressed by a time-dependent recovery probability distribution conditioned on the damage state of the component. This allows expressing the probability that a certain component of the network has recovered after a certain time after the disastrous event, depending on its initial post-disaster damage state.

It is possible to assign a characteristic recovery distribution to every component in the considered networks and therefore the shape of the system recovery curve is not predetermined. Using the information about the network topology, the available supply and the needed demand at different locations of the considered networks can be calculated and the loss of resilience can be computed using Equation (2).

The advantage of the proposed model is its flexibility and that it only requires few data and no specific knowledge of the detailed recovery process and recovery phases of the considered systems. A specific recovery probability function can be assigned to each component type. The parameters of the used recovery distributions can be estimated using available empirical data, expert opinion or approaches like a discrete event simulation. Different values can be assigned to the parameters depending on the damage state of the components. This allows taking into consideration that heavily damaged components need a longer time to repair than slightly damaged ones [7]. If new information becomes available, all parameters can easily be updated and different recovery speeds can be simulated by simply adapting the parameters of the recovery functions.

4 CASE STUDY

The case study makes use of the introduced concept of loss of resilience (LOR) and the proposed recovery model. In the following, the sensitivity of the LOR of the considered supply-demand system towards the adopted probability distribution type and the probability dis-

tribution parameters is analyzed using an example of an EPSS supplying to a virtual community affected by an earthquake.

4.1 Probability distribution for modeling vulnerability and recovery

To model the probability of recovery of a component at a time t after the disastrous event, two distribution types are compared: the lognormal and the Weibull distributions. The investigated distribution types meet the criterion that the support is defined in $[0,+\infty]$, which is necessary as the probability of recovery is dependent on the time after the disastrous event and can not take place before the event itself.

The lognormal distribution has been chosen for two reasons: the parameters are easy to estimate from available data or expert opinion and most of the fragility curves for structural seismic demand are based on lognormal distributions. The lognormal recovery functions are therefore orthogonal to the vulnerability functions [6]. Its cumulative distribution function reads:

$$F_X(x) = \Phi\left[\frac{\ln x - \mu}{\sigma}\right] \qquad (3)$$

where, Φ is the cumulative distribution function of the standard normal distribution, and μ and σ are the mean and the standard deviation of the associated normal distribution.

The skewness of the lognormal distribution is always positive, which may not reflect the actual recovery process of many systems. The recovery probability might be better represented using a distribution that allows different negative and positive skewness, for example the Weibull distribution. The disadvantage of the Weibull distribution is that the parameters are more difficult to estimate. The cumulative distribution function for a Weibull model reads:

$$F_X(x) = 1 - e^{-(x/\lambda)^k} \qquad (4)$$

where k ($k>0$) is the shape parameter and λ is the scale parameter. The skewness of the Weibull distribution is only dependent on k. For $k=1$ an exponential distribution can be obtained.

4.2 Modeling of the vulnerability of the EPSS and the virtual community

The topology of the EPSS used in the case study corresponds to a part of the IEEE 118 network, which "represents a portion of the American Electric Power System (in the Midwestern US) as of December, 1962" [8]. It is composed of a total of 34 nodes: 15 supply nodes and 19 demand nodes (Figure 3). Two different types of substations are considered in the EPSS, supply substations (220 kV) and distribution substations (35 kV). The substations are modeled using a simplified topology. The supply substation topology includes 3 bus bars (1 reserve) and 7 circuit breakers. Two generators are directly linked to every supply substation [9]. The distribution substations are composed of 3 bus bars (1 reserve), 11 circuit breakers and 3 transformers. Two damage states are considered for bus bars, circuit breakers and transformers: failure and no failure. The corresponding fragility functions are taken from [11]. For generators, three damage states are considered: no damage (DS1), slight / moderate damage (DS2) and extensive damage (DS3), fragility functions are taken from [12].

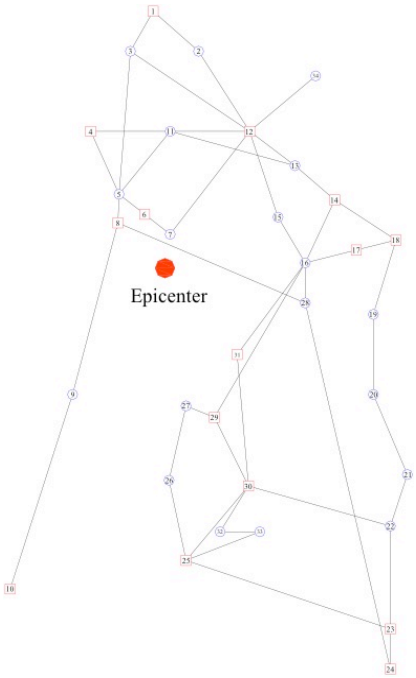


Figure 3: EPSS, virtual community and epicenter. By [6]

The different distribution substations are supplying power to a virtual community, composed of residential buildings, industrial facilities, businesses and critical infrastructure (schools and hospitals), grouped together in several cities, villages and industrial zones situated close to the distribution nodes of the network. 8 different building types are considered and each building type's vulnerability is represented by its own fragility functions [13,14,15,16,17,18]. Three damage states are considered for each building type: no damage (DS1), slight/moderate damage (DS2) and extensive damage/collapse (DS3). The consumption data are obtained from various sources [9]. A power flow balance analysis is run in order to distribute the available supply according to the demand in the network.

The epicenter of the considered seismic event is located close to the geographic center of the considered virtual community environment (Figure 3). The intensity of shaking at the location of each component is measured using peak ground acceleration and peak ground velocity computed using the NGA ground motion model proposed in [19]. The temporal distribution of earthquake recurrence is determined using a Gutenberg-Richter recurrence law, with a=4.4 and b=1 [21].

4.3 Modeling of the recovery

The recovery of the EPSS and the community it supplies to are modeled using different settings (Table 1).

	Setting 1	Setting 2	Setting 3	Setting 4
Components of EPSS	Lognormal	Weibull (k=1)	Weibull (k=1)	Lognormal
Components of community	Lognormal	Lognormal	Weibull (k=5)	Weibull (k=5)

Table 1: Distribution types of the component recovery functions used in the case study.

The mean and standard deviation of the different lognormal component recovery functions of Setting 1 (the 'reference scenario') are estimated for each damage state of each component using existing data for recovery rates from natural hazards [3,7,20]. To account for the longer reconstruction time and uncertainties for severely damaged components, it is assumed that the mean and standard deviation for recovery functions from DS3 back to DS1 are considerably higher as those from DS2 back to DS1 [7].

The shape parameter k of the Weibull recovery functions in Settings 2, 3 and 4 is set according to Table 1. Data from past earthquakes show that considerable effort is put in the fast post-disaster reparation of the EPSS. The recovery of the built environment is much more complex and requires often many preliminary processes (financing, building permit) before the actual reconstruction of repairing can start [20]. For the recovery of the EPSS, k is therefore set to 1 and for the recovery of the built community k is set to 5. The mean of the Weibull component recovery functions is set equal to the corresponding mean of the lognormal component recovery functions used in Setting 1.

The comparison of the LOR for the different settings provides an understanding of the sensitivity of the LOR to the different recovery function types. In order to assess the impact of the mean and standard deviation to the loss of resilience, a sensitivity analysis for these parameters are performed, using Setting 1.

5 RESULTS OF THE CASE STUDY

The described case study is run for 2000 MC simulations for moment magnitudes ranging from 4.5 to 7 with an incremental step of 0.1.

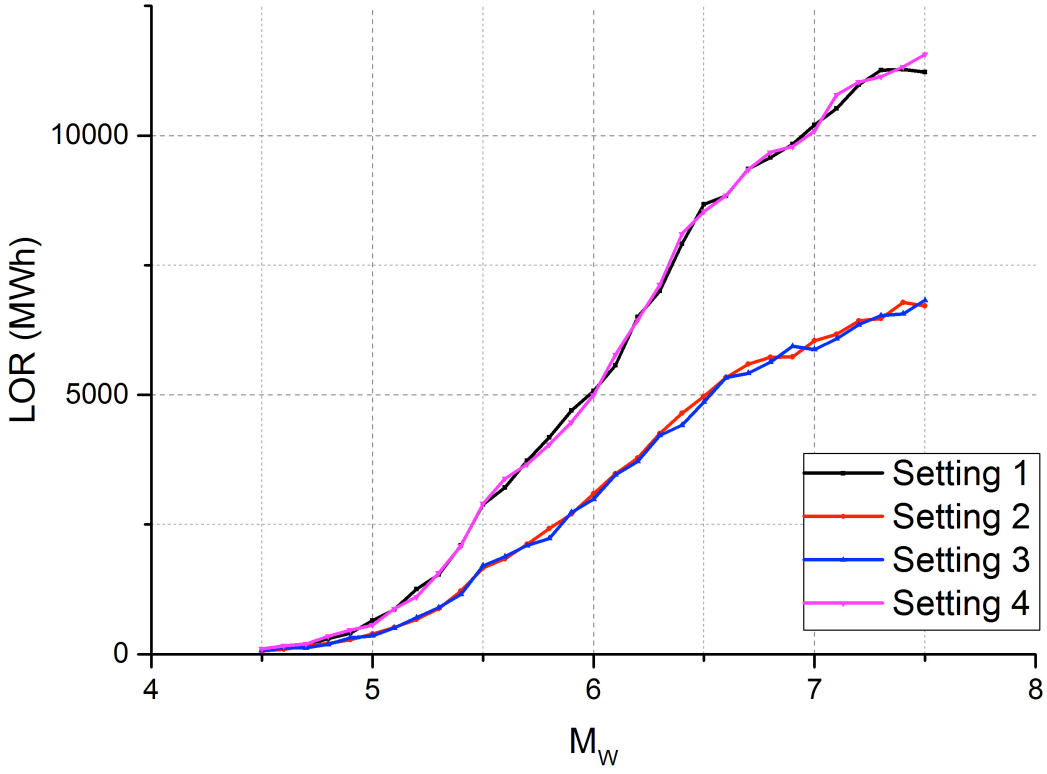


Figure 4: Loss of resilience (LOR) for Settings 1-4 for earthquakes from magnitudes 4.5-7.5.

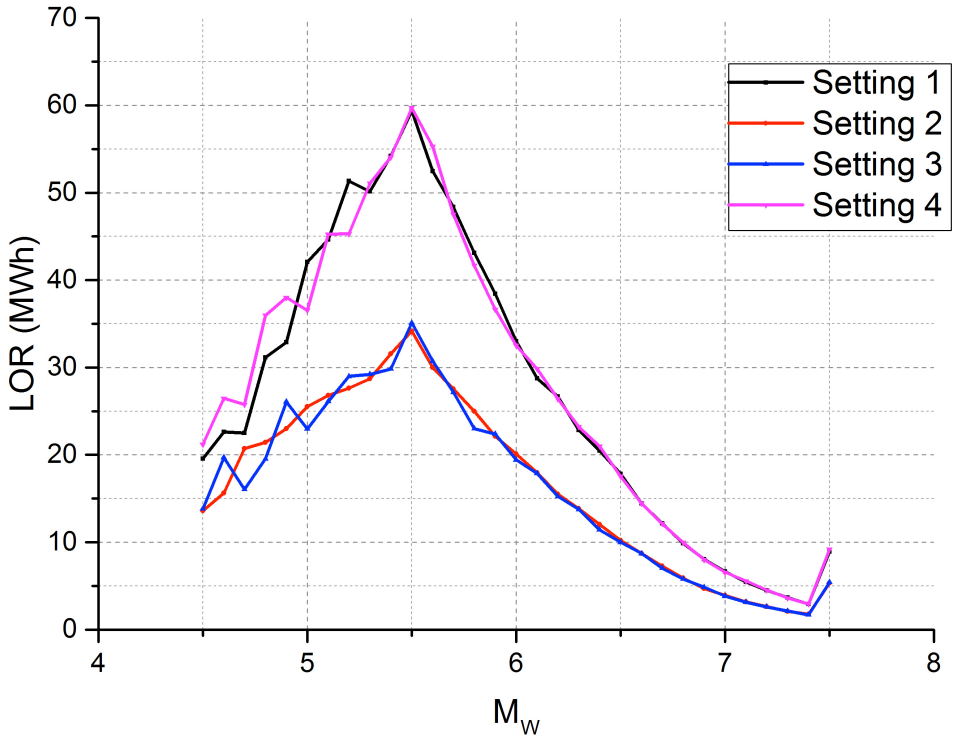


Figure 5: PSHA: Expected loss of resilience (LOR) per year for magnitudes 4.5-7.5.

Figure 4 and Figure 5 illustrate the results for the different recovery settings indicated in Table 1. Figure 4 shows the results of a scenario-based assessment while Figure 5 shows the results of a probabilistic seismic hazard analysis (PSHA). It can be observed that the LOR is higher for the settings, in which the recovery of the EPSS is modeled as lognormal, ie. Setting 1 and Setting 4. This is due to the fact that in Setting 2 and Setting 3, where the recovery of the EPSS is assumed to follow a Weibull distribution, the shape parameter k is set to 1 and the recovery distribution therefore becomes an exponential distribution.

The distribution type of the community recovery function influences the LOR barely. In the modeled set of systems, the recovery of the community is quite slow compared to the one of the EPSS (please note that this may change in other sets of supply-demand systems and the influence of the distribution type of the demand system has to be reassessed for these environments).

Figure 5 indicates that for moment magnitudes ranging from 5 to 6, the difference between Settings 1/4 and Settings 2/3 has the highest impact on the expected LOR per year. If it is assumed that the probability of the recovery of the EPSS following an exponential distribution increases with the preparedness of the community, the elaboration of detailed restoration plans for earthquakes of that range (i.e. M_w 5-6) can considerably reduce the expected LOR.

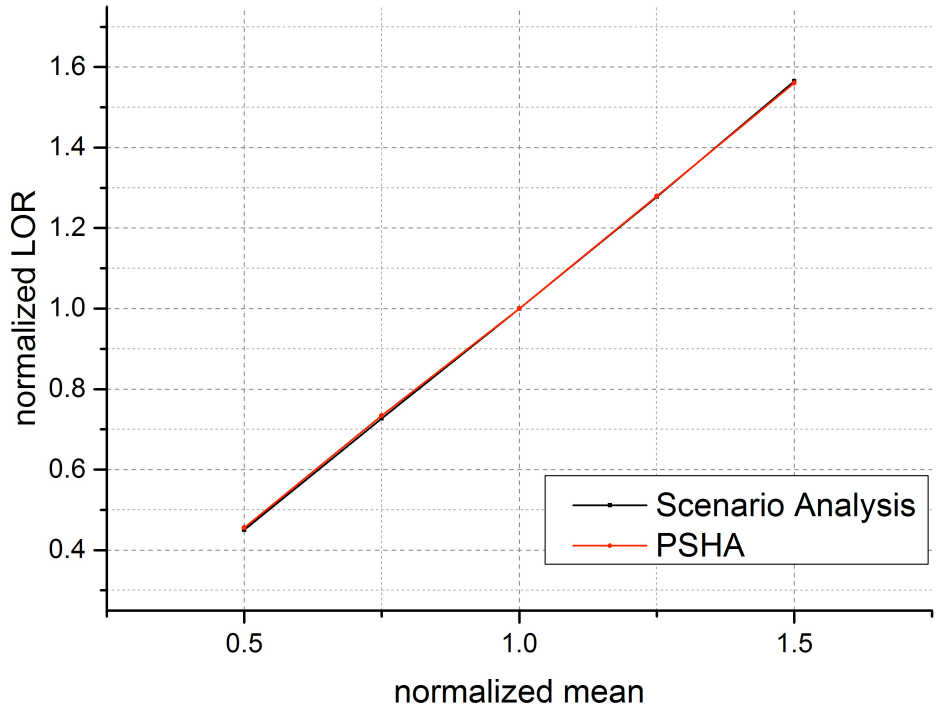


Figure 6: Normalized LOR in function of normalized mean for Scenario Analysis and PSHA.

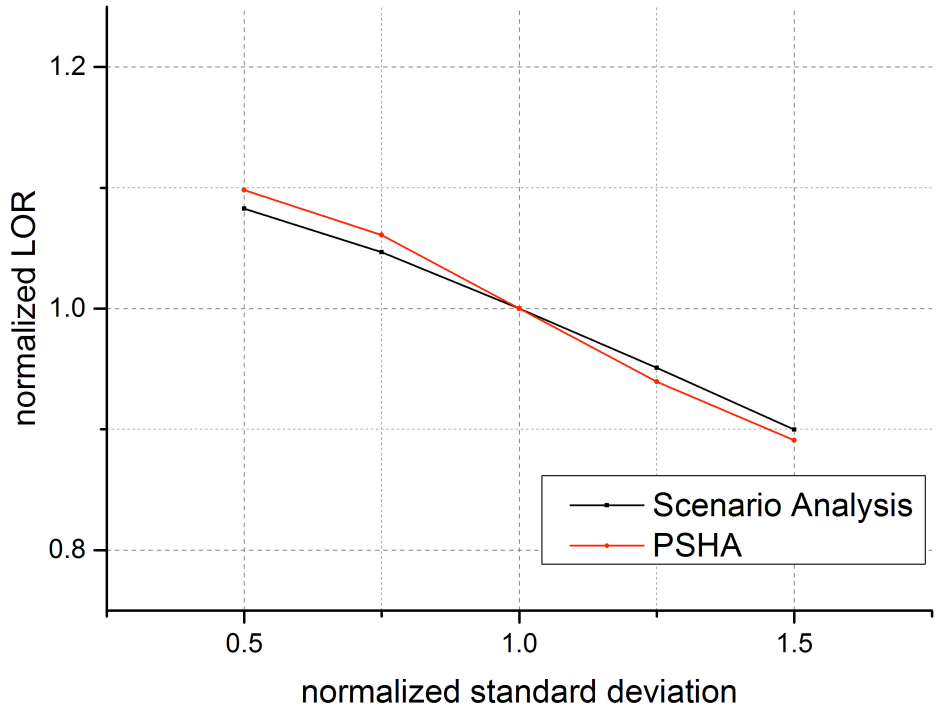


Figure 7: Normalized LOR in function of normalized standard deviation for Scenario Analysis and PSHA.

Figure 6 shows the sensitivity of the LOR towards the variation of the mean of the component recovery functions. It can be seen from the relationship between the normalized LOR and the normalized mean (both normalized to the reference setting) that the LOR is very sensitive to the mean. They change in the same order of magnitude, i.e. a 25% reduction of the mean of the component recovery functions causes a 25% reduction of the LOR of the entire set of systems. The LOR appears to be perfectly correlated to the mean. The sensitivity of the LOR towards the standard deviation of the component recovery functions is relatively smaller (Figure 7). If the standard deviation is reduced for example by 50%, the LOR only changes by 10%. The observations remain the same for the scenario-based simulation and the PSHA.

6 CONCLUSIONS

The loss of resilience of a given set of systems consisting of a supply and a demand system was computed using a compositional approach. It is especially influenced by the recovery of the system. The employed recovery model defines for each component its own time-dependent recovery function conditioned on the component's initial post-disaster damage state. It allows the implementation of the advantages of statistical curve fitting and network approaches. A case study, including a sensitivity analysis, has been carried out in order to determine the influence of the distribution type and the parameters of the recovery functions to the system's total loss of resilience. The distribution type of the recovery of the EPSS has a strong influence on the LOR, while the type of the distribution of the community recovery only causes a slight change in the system's loss of resilience. The results also indicate that the LOR has a higher sensitivity towards the mean of the used recovery functions than towards the standard deviation. These findings should be useful in future modeling of the seismic recovery of infrastructure systems, indicating which parameters need more intricate modeling than others. However, the generality of these outcomes are arguable and should be verified for different network topologies and settings and using different earthquakes sources.

REFERENCES

[1] M. Bruneau, S.E. Chang, R. Eguchi, G. Lee, T. O'Rourke, A. Reinhorn, M. Shinozuka, K. Tierney, E. Wallace, D. von Winterfeldt, A Framework to Quantitatively Assess and Enhance the Seismic Resilience of Communities. *Earthquake Spectra*, **19** (4), 733-752, 2003.

[2] Z. Çağnan, R.A. Davidson, Discrete event simulation of the post-earthquake restoration process for electric power system. *Int. J. Risk Assessment and Management*, **7** (8), 1138-1156, 2007.

[3] D.A. Reed, M.D. Powell, J.M. Westerman, Energy Supply System Performance for Hurricane Katrina. *Journal of Energy Engineering*, **136**, 95-102, 2010.

[4] P. Bocchini, A.Decò, D.M. Frangopol, Probabilistic functionality recovery model for resilience analysis. *Bridge Maintenance, Safety, Management, Resilience and Sustainability – Biondini & Frangopol (Eds)*, 1920-1927, 2012.

[5] G.P. Cimellaro, A.M. Reinhorn, M. Bruneau, Framework for analytical quantification of disaster resilience. *Engineering Structures*, **32**, 3639-3649, 2010.

[6] L.Sun, M. Didier, E. Delé, B. Stojadinovic, Probabilistic Demand and Supply Resilience Model for Electric Power Supply System under Seismic Hazard, *ICASP12*, accepted.

[7] M.C. Comerio, Estimating Downtime in Loss Modeling. *Earthquake Spectra*, **22** (2), 349-365, 2006.
[8] R.D. Christie, Power Systems Test Case Archive. *http://www.ee.washington.edu/research/pstca/pf118/pg_tca118bus.htm* , last access: 21.01.2015.
[9] E. Delé, M. Didier, Time-Varying Seismic Resilience of Electric Supply Systems, Master Thesis, *IBK*, 2014.
[10] M.C. Comerio, Estimating Downtime in Loss Modeling. *Earthquake Spectra*, **22** (2), 349-365, 2006.
[11] M. Shinozuka, X. Dong, T.C. Chen, X.Jin, Seismic performance of electric transmission network under component failures. *Earthquake Engineering and Structural Dynamics*, **36**, 227-244, 2007.
[12] FEMA, *HAZUS MH MR 4 Multi-Hazard Loss Estimation Methodology – Earthquake Model – Technical Manual*, 2003.
[13] T. Rossetto, A.Einashai, Derivation of vulnerability functions for European-type RC structures based on observational data. *Engineering structure*, **25** (10), 1241-1263, 2003.
[14] T. Karantoni, F. Lyrantzaki, G. Tsionis, M.N. Fardis, Analytical Fragility Functions for Masonry Buildings and Building Aggregates – UPAT methodology. *Internal Report, Syner-G Project 2009/2012*, 2011.
[15] S.M. Senel, A.H. Kayhan, Fragility based damage assessment in existing precast industrial buildings: A case study for Turkey. *Structural Engineering and Mechanics*, **34** (1), 39-60, 2009.
[16] S.H.Jeong, A.S. Einashai, Probabilistic fragility analysis parameterized by fundamental response quantities. *Engineered Structures*, **29** (8), 1238-1251, 2007.
[17] SYNER-G, *D3.10 – Fragility functions for elements within healthcare facilities*, 2011.
[18] O.S. Kwon, A.S. Einashai, The effect of material and ground motion uncertainty on the seismic vulnerability curves of RC structures. *Engineered Structures*, **28** (2), 289-303, 2006.
[19] K.W. Campbell, Y. Bozorgnia, NGA Ground Motion Model for the Geometric Mean Horizontal Component of PGA, PGV, PGD and 5% Damped Linear Elastic Response Spectra for Periods Ranging from 0.01 to 10s. *Earthquake Spectra*, **24** (1), 139-171, 2008.
[20] A. Wein, L. Johnson, R. Bernknopf, Recovering from the ShakeOut Earthquake. *Earthquake Spectra*, **27** (2), 521-538, 2011.
[21] S.L. Kramer, *Geotechnical Earthquake Engineering*, 1996.

COMPDYN 2015
5th ECCOMAS Thematic Conference on
Computational Methods in Structural Dynamics and Earthquake Engineering
M. Papadrakakis, V. Papadopoulos, V. Plevris (eds.)
Crete Island, Greece, 25–27 May 2015

ESTIMATION OF CUMULATIVE SEISMIC DAMAGE TO URM BUILDINGS DURING EARTHQUAKE SEQUENCES

Amaryllis Mouyiannou[1], Maria Rota[1] and Andrea Penna[1,2]

[1] European Centre for Training and Research in Earthquake Engineering
Via Ferrata 1, I-27100 Pavia
amaryllis.mouyiannou@eucentre.it, maria.rota@eucentre.it

[2] Department of Civil Engineering and Architecture, University of Pavia
Via Ferrata 3, I-27100 Pavia
andrea.penna@unipv.it

Keywords: earthquake sequence, seismic demand, cumulative damage, unreinforced masonry buildings, SDOF models

Abstract. *During seismic sequences, repeated shocks of varying intensity hit previously damaged and unrepaired building stock. The cumulative damage from repeated shocks affects the building vulnerability to subsequent events. This paper introduces a methodology for estimating the displacement demand, assumed as a damage measure, to existing unreinforced masonry buildings during earthquake sequences in probabilistic terms, only given the intensity levels of each event of the sequence. The damage prediction is based on statistical interpretation of a collection of analytical results derived prior to the occurrence of the seismic sequence. This procedure can be a useful tool when a rapid evaluation of damage is desirable during the earthquake sequence, in order to be incorporated into risk and loss assessment calculations. The analytical results used for damage predictions consist of results of nonlinear dynamic analyses with a large number of unscaled records and a set of SDOF models representing undamaged and damaged URM buildings. In order to investigate the parameters that affect cumulative damage evaluation, application examples are developed by considering records from the Canterbury (New Zealand, 2010-2011) and the Emilia (Italy, 2012) earthquake sequences.*

1 INTRODUCTION

The undesired implications of cumulative damage on the seismic performance of unreinforced masonry buildings (URM) were recently observed during earthquake sequences that occurred in various locations (e.g. the demise of URM buildings after the Canterbury earthquake sequence, New Zealand, 2010-2011 [1][2] and Emilia, Italy, 2012 [3]). The need of developments in the quantification of aftershock risk calculation for pre-damaged buildings became obvious for all buildings, and especially URM buildings, since they constitute a large proportion of the total existing building stock, even in many seismically active countries. This paper proposes a procedure for calculating, in probabilistic terms, the expected seismic demand, by only knowing the intensity level of each earthquake event. This procedure uses the intensity levels of the events that have occurred (during a sequence), for the derivation of a distribution of demand values. Specifically, the procedure takes advantage of the results of state-dependent assessment (results of dynamic analyses performed with pre-damaged models and a large number of unscaled records), to proceed to a quick estimation of seismic demand during an earthquake sequence, without further analysis and by considering only the intensity of the occurring earthquakes and the damage state of the structures due to the preceding earthquake events.

The probabilistic prediction of damage demand for an earthquake sequence can be a useful tool for rapid post-earthquake assessment of a population of buildings, each represented by a model, whose seismic response can be evaluated by means of nonlinear time-history analyses (NLTHA) prior to the occurrence of the sequence. In particular, it can be very useful for emergency assessments, since a quick estimation of damage expectation is possible as soon as the sequence occurs. This could provide, very quickly, a basic idea for the decision-makers regarding the damage distribution among the building population, which was modelled and analyzed with dynamic analyses prior to the occurrence of the earthquake sequence. Moreover, the predictions referring to a single event can be combined with seismic hazard models, in order to derive the seismic risk and loss for expected earthquake events. Alternatively, during the occurrence of seismic sequences, the expected seismic demand can be combined with aftershock seismic hazard and the probability that seismic demand exceeds the limit states of interest can be calculated for given time ranges. Since aftershock hazard is time-dependent [4][5], the calculations can be repeated as the time lapses, by adopting the updated hazard or the updated demand, if more aftershocks are occurring. The outcome of each calculation can be interesting for stakeholders and decision makers for organizing emergency plans.

In the following sections, the methodology for the demand prediction is presented and some necessary considerations for obtaining a reliable prediction are discussed. Then, its applicability is examined through calculations of demand with four real earthquake sequences, for a single case study URM building.

2 OUTLINE OF THE PROPOSED METHODOLOGY

The procedure for deriving a probabilistic estimate of the expected displacement demand (and corresponding damage) for earthquake sequences can be divided in two parts, which will be discussed in the following sub-sections. The first and more time-consuming part should be performed prior to the occurrence of the sequence and includes the modelling and analyses in order to obtain maximum displacement (or other damage index) demand, as a function of the level of pre-existing damage and of the shock intensity, covering an adequate range of intensity measure (IM) values, consistent with the seismic hazard of the area. The second and quicker part (post-earthquake sequence) can be performed either by using the IM values of each event that has occurred during the sequence, in order to assess the accumulated damage,

or by using IM values of hypothetical sequences relevant to the aftershock seismic hazard at the site, in order to assess future demands. The distributions of the expected damage are then calculated for each shock. It should be noted that only the most significant records of the sequence should be used in the calculation. The exclusion of records of intensity below an adequate IM threshold is intended to exclude non-damaging earthquake events in order to speed up the damage prediction. The repetition of events of low intensity could indeed potentially change the expected response, depending on the model and the EDP used.

2.1 Calculation of displacement demand (before earthquake sequence)

The first steps of the procedure are common to those presented in [6], for the derivation of state-dependent fragility curves for URM buildings:

- Step 1: Derivation of appropriate multi-degree-of-freedom (MDOF) models representative of the building typologies of interest and calibration with adequate mechanical properties.
- Step 2 (Optional): Derivation of single-degree-of-freedom (SDOF) models, calibration and verification according to static and dynamic analyses with the MDOF models (if the response can be represented by SDOF models).
- Step 3: Derivation of pre-damaged models, representing the implications of damage experienced due to previous earthquake shocks on the building behavior during subsequent earthquake events, for example with a nonlinear static procedure (cyclic pushover analysis).
- Step 4: Selection of a sufficient number of appropriate records representative of the possible seismic action at the site of interest.
- Step 5: Calculation of seismic demand by means of NLTHA with the selected records and the undamaged and pre-damaged SDOF (or MDOF) models.
- Step 6: Representation of ground motions by appropriate scalar or low-order vector IMs.
- Step 7: Storing of analytical results, in terms of damage (displacement or drift) demands and the corresponding ground motion IM values, for each considered level of pre-existing damage.

2.2 Rapid evaluation of cumulative seismic damage (after earthquake sequence)

The steps to be carried out after the occurrence of a seismic sequence, in order to obtain a rapid evaluation of the cumulative damage consist of:

- Step 1: Representation of the earthquake sequence by a sequence of IM values.
- Step 2: Given the IM value of each earthquake event of the sequence, derivation of maximum displacement demand in probabilistic terms (using the results of the undamaged models for the first earthquake and by combining the results for damaged models for the rest of the events of the sequence). The final prediction regards the maximum damage demand that the building is expected to experience during the whole sequence.

The derivation of the distribution of maximum displacement demand is based on simple probability rules. For the first earthquake of the sequence, given its intensity, the displacement demand distribution (discrete levels) is taken from the previously calculated distributions of displacement from the results of NLTHA with the undamaged model, in a range in the vicinity of the IM value. The latter is based on the assumption that the building under examination is not damaged before the occurrence of the first strong motion of the studied sequence. According to the above, the probability of occurrence of discrete damage levels is

calculated $p(d_{\max,1} = DL_i \mid IM_{EQ1})$, where i corresponds to the damage levels (or bins) that have a non-zero probability of occurrence.

For the next considered earthquake event of the sequence, the probability of occurrence of each discrete damage level is calculated, according to the previously derived damage levels. Particularly, the probability that each damage level DL_j is reached after the second earthquake event is equal to the probability of DL_j, conditional on the pre-existing DL_i:

$$p(d_2 = DL_i \mid EQ_{1,2}) = \sum_{i=1}^{n_{DL}} p(d_{\max,2} = DL_j \mid IM_{EQ2} \mid d_{\max,1} = DL_i \mid IM_{EQ1}) \quad (1)$$

where n_{DL} represents the total number of damage levels (DLs) with non-zero probability of occurrence, during the previous earthquake events. Since the prediction focuses on the maximum experienced damage through the whole sequence, if the probabilistic calculation for the subsequent earthquake event includes damage levels lower than the lowest damage level reached at the preceding event, the probability of these low damage levels is added to the lowest damage level attained from the previous earthquake event.

For the subsequent earthquake of the sequence (3rd event), following the same principles as for calculating the damage demand for the sequence of EQ1 and EQ2, the probability of occurrence of each DL can be calculated according to:

$$p(d_3 = DL_k \mid EQ_{1,2,3}) = \sum_{i=1}^{n_{DL}} p(d_{\max,2} = DL_k \mid IM_{EQ3} \cap d_{\max,2} = DL_j \mid EQ_{1,2}) \quad (2)$$

In the same way, the probabilities of reaching each damage level are calculated for all the earthquakes of the considered sequence. Finally, the probabilistic predictions of damage demand can be compared to the deterministic results of real earthquake sequences derived from NLTHA with the earthquake sequence records.

3 REPRESENTATION OF SEISMIC DEMAND FOR UNDAMAGED AND PRE-DAMAGED MODELS

In this section, application examples of the procedure are presented in order to demonstrate its applicability and indicate the parameters that can affect the reliability of the probabilistic cumulative damage prediction. After a short presentation of the SDOF model used and the results of dynamic analysis (pre-earthquake steps), the probabilistic damage prediction calculations for four real earthquake sequences are presented and the considered parameters are introduced.

3.1 URM building model and considered levels of pre-existing damage

A model of a two-storey typical clay-brick URM building was used for the application examples. The building was assumed to develop a global in-plane failure mechanism, assuming that the out-of-plane failure of the walls is prevented. First, a MDOF model was developed using the software TREMURI [7][8], with mechanical properties adopted from ranges derived from collection and processing of available parameters for clay-brick masonry from experimental studies. Then, in order to reduce the computational burden of the necessary nonlinear dynamic analyses, an equivalent SDOF model was developed, according to the procedure proposed by Graziotti et al. [9], consisting of a static and dynamic calibration. The scheme adopted for the SDOF model is reported in Figure 1. The system is composed of two two-node macro-elements coupled by an axially rigid link, with the scope of allowing an accurate reproduction of the behaviour of the structure, characterised by a combination of flexural (left macro-element) and shear (right macro-element) responses. The degree of freedom corresponds to the horizontal displacement of the mass on top of the system. The

procedure followed for the calibration of the equivalent SDOF system is described in more detail in [6] and [9].

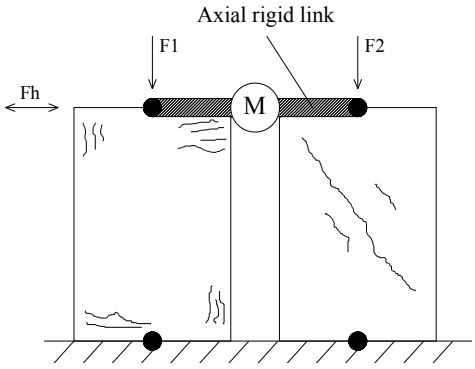


Figure 1: SDOF model of the selected building prototype [9].

This appropriately calibrated SDOF model was then used for the creation of models representing the various levels of pre-damage of the structure. For the applications presented here, the pre-damaged models were derived from the results of nonlinear static analysis, with reference to 15 discrete levels of damage, each represented by a level of top displacement of the MDOF model, starting from 2 mm (damage level 1, DL1) and increasing by 2 mm when moving to the following DL. In order to obtain the damaged model, the undamaged SDOF model was subjected to one loop of a cyclic pushover analysis up to the displacement level characterizing the damage level.

Alternative damage level definitions could obviously be adopted, depending on the application of the damage prediction. For example, the damage levels could correspond to significant damage states (DS), which would allow a direct calculation of loss when the DS are combined with corresponding loss values. Nevertheless, using damage levels independently defined from significant DS is preferred here because it does not require making assumptions on the definition of the limit states, whose uncertainty can have a strong impact on the procedure [10][11]. Lastly, the limit to the number of possible considered damage levels is also set by the need to derive bins with a reasonable number of NLTHA results for the derivation of damage distributions. For the application examples presented in the following, it was assumed that a more detailed discretization of DLs was not likely to be beneficial.

In order to be consistent, the maximum displacement used for deriving the pre-damaged models by cyclic pushover analyses should coincide with the displacement characterizing the *DLi* for the calculations of the post-earthquake assessment. A uniform definition of damage levels allows, during the calculation of seismic demand for sequences, to use results from analyses with pre-damaged model up to the displacement corresponding to *DLi*, if a model has reached *DLi* in a preceding record of the sequence. During all the steps of the procedure, the damage levels can be converted into displacement demand values and vice versa.

Finally, before applying the procedure for predicting the response during earthquake sequences, the maximum considered DL should be decided. Independently from the model used for NLTHA, either MDOF or SDOF, an upper threshold of displacement beyond which the structure is considered collapsed has to be set. For the following applications, a threshold of maximum MDOF displacement equal to 30 mm was selected and the results beyond 30 mm were considered as DL16, which can represent a collapse condition in the assessment scenarios.

3.2 Results of dynamic analyses

The relationships between displacement demand and ground motion intensity were derived from the results of NLTHA with the SDOF model and with the two horizontal components of the 467 real unscaled records of the SIMBAD database [12]. As already mentioned, meaningful intensity measures should be selected to characterise the severity of each accelerogram. For the applications of this paper, two scalar IMs and two two-dimensional vector-based IMs were considered. The aforementioned IMs were derived after a statistical investigation performed on the results of NLTHA, for a significant number of scalar and two-dimensional IMs [13]. In more detail, the selected scalar IMs were the Modified Housner Intensity, *mHI*, and the Average Spectral Acceleration, S_{aavg}, whereas the two vector IMs were composed by one of the aforementioned, as primary component, and the spectral shape factor, N_p [14], as secondary component. Housner Intensity is an energy-based intensity measure, calculated for each earthquake record as the integral of the pseudo-velocity spectrum (5% damping) for periods between 0.1 and 2.5 s [15]. This intensity measure was modified by reducing the period range of integration from 0.1 to 0.5 s (as already done in [9]), to better account for the period range of interest for masonry structures, whose effective fundamental period is rarely beyond 0.5s. Similarly, S_{aavg} was defined as the average of spectral acceleration for periods from 0 to 0.5s. Only combinations of the primary intensity measures with N_p were finally used, since N_p was found to be non-correlated to the primary components, whereas the opposite occurred for other secondary IMs examined (e.g. uniform duration [16] and peak ground acceleration).

Figure 2 shows the maximum displacement demand versus modified Housner Intensity values, obtained from NLTHA of the undamaged SDOF model with unscaled records from the SIMBAD database [12]. Since the number of records is decreasing for increasing intensity levels, the semi-logarithmic scale was used to allow a similar number of records in all the considered bins, in order to avoid giving different weights to the different bins. The green markers in the figure indicate the results considered for the maximum displacement prediction, while the rejected results, shown in red, correspond to values of displacement exceeding the maximum displacement limit (blue horizontal line) and maximum IM value (light blue vertical line). The IM upper limit was set as the level for which almost all the records lead to near collapse conditions (displacements higher than the collapse limit of 32 mm).

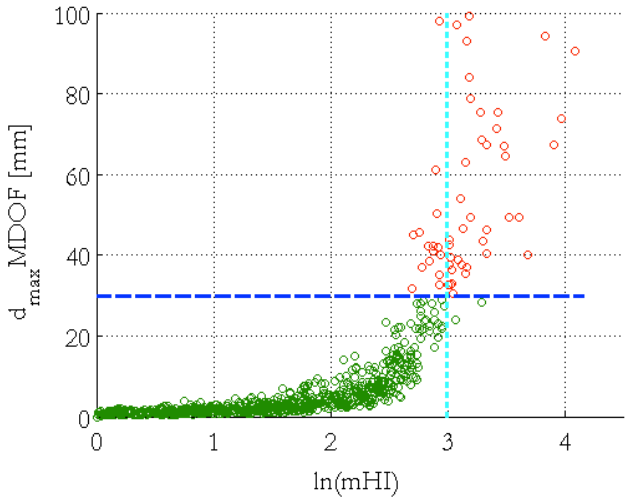


Figure 2 . Maximum displacement demand versus the logarithm of *mHI*

4 EXAMPLE OF QUICK PROBABILISTIC ESTIMATION OF DAMAGE DEMAND DURING A SEISMIC SEQUENCE

4.1 Considered real earthquake sequences

Four real earthquake sequences were considered for this example. The records of the first sequence were obtained from ITACA (Italian Accelerometric Archive, http://itaca.mi.ingv.it/) and were recorded at the Mirandola station (MRN) during the Emilia earthquake sequence in 2012. Additionally, the records of the three Christchurch sequences were obtained from GeoNet, (New Zealand geological database http://geonet.org.nz/) and correspond to the events of the Canterbury earthquake sequence that occurred in 2010-2012. The three considered stations are the Riccarton High School (RHSC), Papanui High School (PPHS) and Christchurch Hospital station (CHHC). A summary of the IM values of the ground motions of the considered sequences is provided in Table 1 and Table 2, for the NS components and EW components of the ground motions, respectively.

Station	Emilia (2012) MRN		Canterbury Earthquake Sequence (2010-2011) RHSC		PPHS		CHHC	
IM	*mHI* (m)	S_{aavg} (ms^{-2})	*mHI* (m)	S_{aavg} (ms^{-2})	*mHI* (m)	S_{aavg} (ms^{-2})	*mHI* (m)	S_{aavg} (ms^{-2})
EQ1	0.117	6.27	0.115	5.91	0.083	4.07	0.090	4.36
EQ2	0.086	4.91	0.145	7.13	0.102	4.89	0.188	8.81
EQ3	0.123	6.62	0.093	4.63	0.070	3.42	0.100	4.55
EQ4	0.056	3.34	0.114	5.87	0.095	4.53	0.090	4.36
EQ5	0.029	1.75	0.050	2.55	0.050	2.48	0.188	8.81
EQ6	-	-	0.094	4.93	0.062	2.90	0.077	4.03
EQ7	-	-	0.100	5.21	0.030	1.52	0.127	5.93
EQ8	-	-	0.090	4.54	0.045	2.25	0.100	4.55
EQ9	-	-	0.070	3.83	0.069	3.34	0.064	3.14
EQ10	-	-	-	-	-	-	0.079	3.86
EQ11	-	-	-	-	-	-	0.074	6.98

Table 1: Intensity measure values of the records of the considered sequences (NS components)

Station	MRN		RHSC		PPHS		CHHC	
IM	*mHI* (m)	S_{aavg} (ms^{-2})	*mHI* (m)	S_{aavg} (ms^{-2})	*mHI* (m)	S_{aavg} (ms^{-2})	*mHI* (m)	S_{aavg} (ms^{-2})
EQ1	0.140	7.11	0.100	5.05	0.088	4.47	0.075	3.56
EQ2	0.059	3.43	0.137	6.79	0.100	4.72	0.170	7.99
EQ3	0.095	5.41	0.152	7.49	0.097	4.59	0.067	3.43
EQ4	0.036	2.35	0.121	6.21	0.102	4.94	0.075	3.56
EQ5	0.043	2.97	0.038	2.08	0.061	2.86	0.170	7.99
EQ6	-	-	0.081	4.34	0.053	2.54	0.049	2.55
EQ7	-	-	0.083	4.41	0.047	2.32	0.065	3.18
EQ8	-	-	0.067	3.52	0.048	2.36	0.067	3.43
EQ9	-	-	0.070	3.75	0.051	2.52	0.055	2.74
EQ10	-	-	-	-	-	-	0.087	4.22
EQ11	-	-	-	-	-	-	0.0903	4.45

Table 2: Intensity measure values of the records of the considered sequences (EW components)

For the application examples presented here, only the events with at least one of the two components with *mHI* equal to or greater than 0.04 m were considered in the prediction calculations. It is worth highlighting (as can be seen from *mHI* values of the records of each sequence) that two moderate intensity sequences of ground motions were considered (recorded at RHSC and MRN), one low intensity sequence (recorded at PPHS) and one high intensity sequence (recorded at CHHC).

The displacement demand of each event and each entire sequence was calculated by NLTHA, in order to provide a measure of comparison to the median prediction of the damage demand, derived from the application of the methodology.

4.2 Evaluation of damage demand with earthquake events represented by scalar IMs

The calculation of cumulative damage demand was carried out for the four considered sequences of records. For each event, only the results from NLTHA with ground motions of IM values close to the IM value of the event were considered for the probabilistic calculation of damage levels. The IM range of interest was centred on the IM value of the considered event, whereas its width was defined taking into account the availability of high intensity ground motions in the adopted accelerometric database. Indeed, even for the highest level of ground motion, the number of records should be sufficient to allow the statistical treatment of the NLTHA results and the derivation of a displacement distribution.

For the presented results, the higher limit of the IM range was set equal to 0.20 m in terms of *mHI* and equal to 10 ms^{-2}, in terms of S_{aavg} and the IM range was divided into 10 bins. The resulting distribution of expected damage levels derived from the results of the undamaged model is shown in Figure 3 (top).

On the other hand, the ranges of the vector-based IMs were defined from adequate ranges of both components of the vectors. Primarily, the range of considered *mHI* or S_{aavg} values was derived and then, from the results contained in the range, only the results with values of N_p around the N_p value of the event were considered for the derivation of the damage distribution. The range of considered spectral shape ratio values was centred on the N_p value of the examined earthquake of the sequence (N_{PE}), plus and minus a fixed deviation of 0.15. It was observed that the deviation was not a governing parameter for the predictions. The limitation was set in order for the range of the second IM to be broad enough to include an adequate number of results for statistical use.

For each subsequent event, values of damage demand were calculated for all the levels of pre-existing damage, as indicated in the two multi-plots of Figure 3, for the two subsequent events of the MRN sequence.

Once the results were sorted in bins of IM and DL, the probabilistic displacement demand after each subsequent event was calculated, as well as the intermediate and final damage demand distributions, as shown in Figure 4 for the sequence recorded at MRN station.

The resulting damage levels for the complete sequences recorded in the four stations under study (components in the two perpendicular directions) are summarized in Figure 5 and Table 3. In Figure 5, each plot contains, for each direction, the median of the predicted damage demand for the sequences, represented either by the scalar *mHI* or S_{aavg}, or by considering them as primary components of vector-based IMs, combined to N_p. The deterministic demand derived from NLTHA with the time histories of the earthquake sequences is also included in the plots.

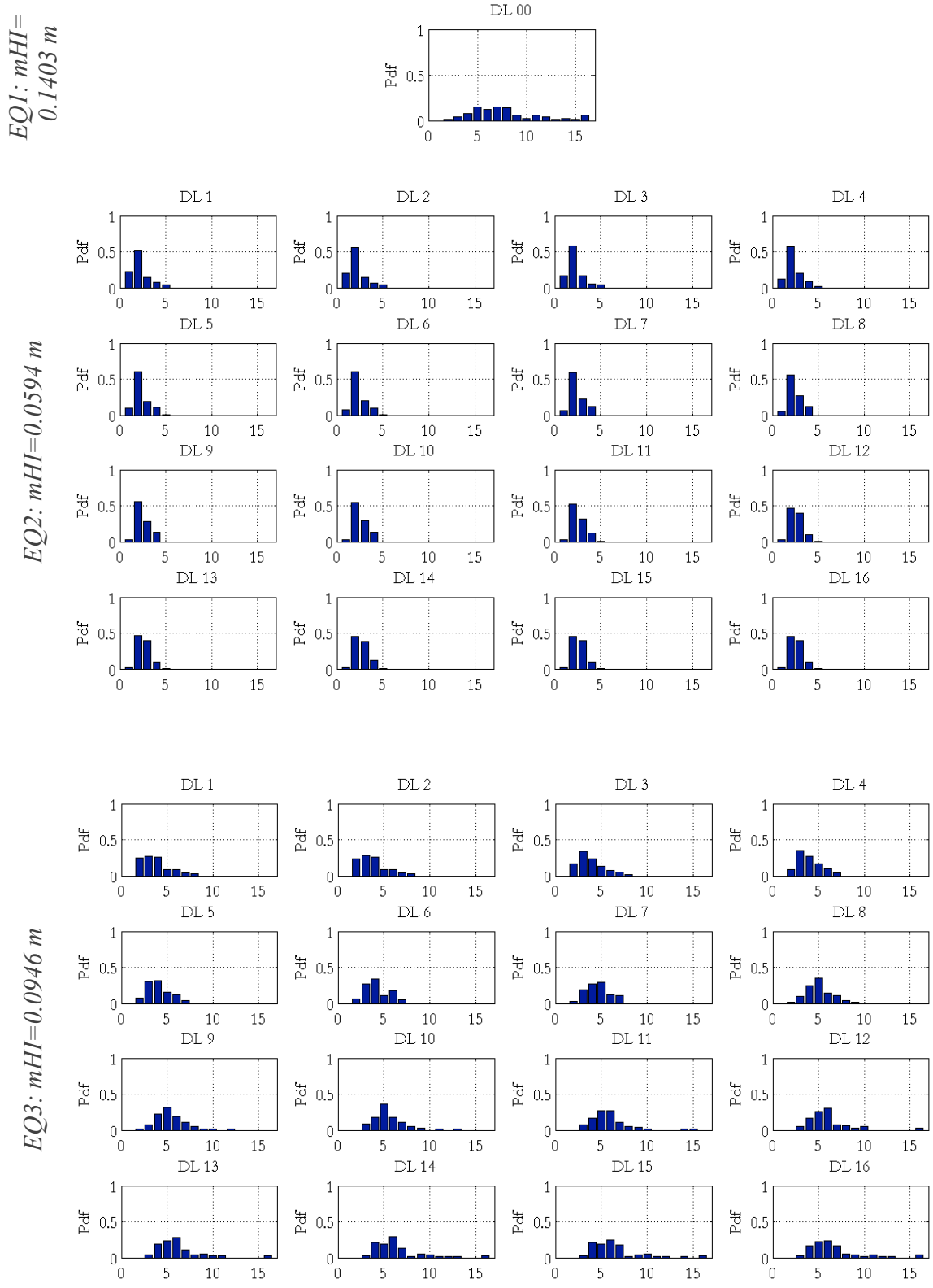


Figure 3: Predicted damage levels, for the undamaged model corresponding to the first earthquake event (top, EQ1) and for increasing levels of pre-existing damage (from DL1, top left, to DL16, bottom right), for the two subsequent events of the MRN sequence (EQ2 and EQ3)

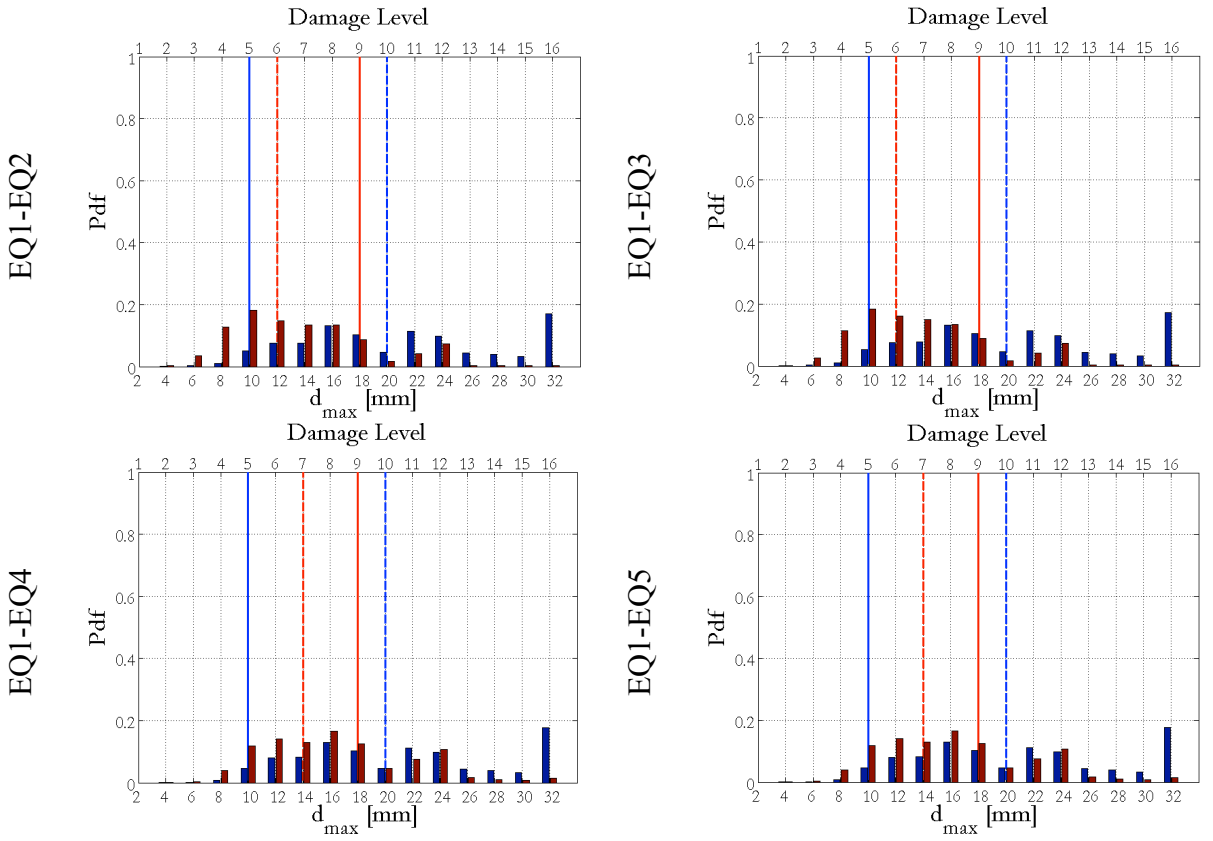


Figure 4: Probabilistic evaluation of seismic damage demand for subsequent events during an earthquake sequence (example of prediction with EW (blue) and NS (red) component of records from MRN station). The median values and the deterministic values for each component are indicated with dashed and continuous vertical lines, respectively, with the corresponding colour.

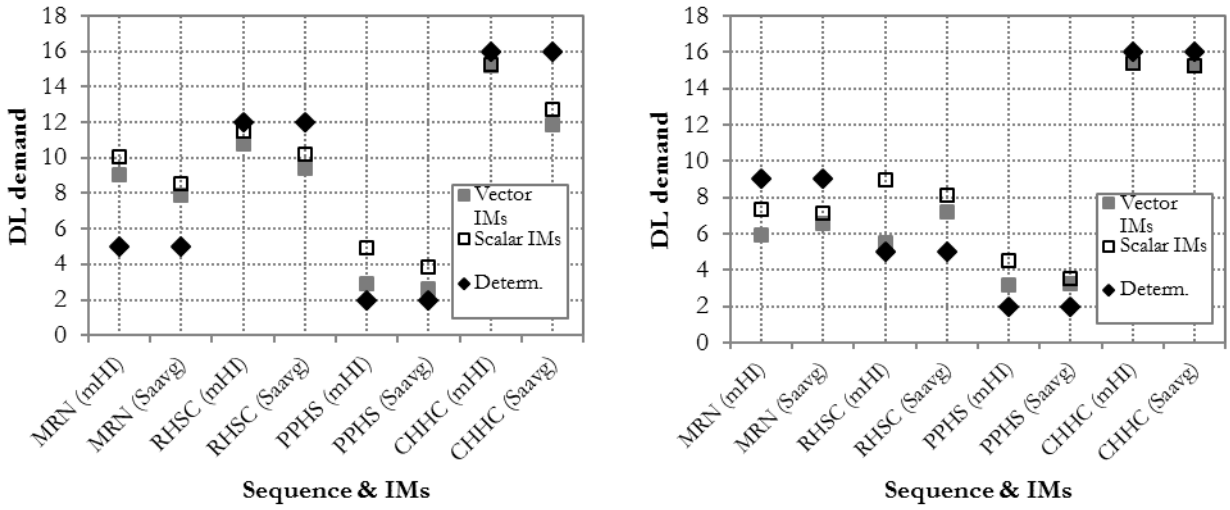


Figure 5: Median predicted damage levels for EW (left) and NS (right) components of the sequences recorded at MRN, RHSC, PPHS and CHHC. The deterministic response is indicated with black points. Each sequence is represented either with scalar IMs (ln(*mHI*) and ln(S_{aavg})) or vector IMs (ln(*mHI*)&Np and ln(S_{aavg})&Np)

The median values of the predicted maximum displacement distributions are found to be slightly lower than the deterministic response for the sequence recorded at the CHHC site (high intensity sequence), while the opposite is observed for the sequence recorded at PPHS (characterized by lower intensities). For the former case, the median of the prediction with *mHI* is closer to the deterministic results than the median of the prediction with S_{aavg} and the use of vector IMs instead of scalar ones does not seem to improve the median prediction. Conversely, for the latter case, prediction with S_{aavg} is closer to deterministic results and the use of vector IMs leads to median predictions closer to the deterministic results than the prediction calculated with scalar IMs. For the remaining sequence examples (recorded at RHSC and MRN), the deterministic response differs significantly between the two components of motion. It can be observed that, for the higher levels of damage, the use of *mHI* in the calculations leads to median values closer to the deterministic result. For the lower levels of damage (DL5), there is an overestimation of damage resulting from both the IMs (NS component of RHSC and EW component of MRN), which is slightly improved by using S_{aavg}. Still, with exception of RHSC (NS component), the use of vector IMs does not significantly affect the median prediction.

The precision of the predicted damage distributions can be evaluated by the scatter of the obtained probability distributions. If the results are assumed to follow a lognormal distribution, this scatter can be defined for example by the standard deviation of the lognormal distribution fitting them. More specifically, lognormal standard deviations can be calculated as one half of the difference of the logarithms of the displacement corresponding to the 84th percentile of the lognormal distribution and the one corresponding to the 16th percentile of the same distribution. The values calculated for all the sequences are shown in Table 3.

In the case of vector IMs, the damage distributions were found to be sensitive to the range of the considered primary IM and to the selected number of bins, especially for the earthquake sequences of moderate intensity (RHSC and MRN). For this reason, Table 3 reports lognormal standard deviation values corresponding to the cases of subdivision of the range of the primary IM both into 10 bins and 6 bins. The shaded cells indicate the lower values for each damage prediction.

	EQ seq.	*Scalar IMs(10bins)*		*Vector IMs(10binsIM1)*		*Vector IMs(6binsIM1)*	
		mHI	S_{aavg}	$mHI\&N_p$	$S_{aavg}\&N_p$	$mHI\&N_p$	$S_{aavg}\&N_p$
NS	*MRN*	0.42	0.44	0.49	0.46	0.52	0.52
	RHSC	0.33	0.40	0.44	0.48	0.55	0.59
	PPHS	0.26	0.22	0.27	0.10	0.35	0.26
	CHHC	0.14	0.32	0.39	0.33	0.19	0.39
EW	*MRN*	0.36	0.39	0.38	0.37	0.48	0.46
	RHSC	0.39	0.39	0.47	0.47	0.47	0.45
	PPHS	0.29	0.28	0.32	0.30	0.34	0.27
	CHHC	0.02	0.14	0.19	0.14	0.03	0.19

Table 3: Lognormal standard deviations of the predicted damage distributions for the four considered earthquake sequences, for the cases of vector and scalar IMs

Table 3 shows that the predictions for moderate intensity sequences leads to large standard deviations for both scalar and vector IMs. By comparing the scatter of the predictions calculated with the two scalar IMs, it seems that the use of *mHI* leads to a slightly lower scatter for the majority of the sequences. For some cases, the scatter calculated with vector IMs was smaller than the scatter resulting from scalar IMs. An example is the case of S_{aavg} and N_p for the low intensity sequence (PPHS).
Nevertheless, given the sensitivity of the scatter to the number of bins used to divide the range of the primary IM, it seems that, for the cases considered in this study, the use of combinations of IMs does not provide a significant improvement over the use of a scalar IM.

4.3 Comparison between main-shock and complete sequence damage demand predictions

In its established form, the calculation of seismic risk is based on the vulnerability of buildings to a single earthquake, i.e. it does not account for the cumulative damage occurring to the buildings for subsequent events. Adversely, as observed during the occurrence of real earthquake sequences, the damage demand due to the main-shock only can be different from the damage demand due to the whole sequence. In this work, the potential differences between the prediction for the main-shocks only and for the entire sequence were investigated.

Figure 6 shows the damage predictions derived for the four investigated sequences, including the results from analyses with both components of earthquake motion, considering S_{aavg} as scalar IM. The damage levels derived from dynamic analyses with the records of the main event and the complete sequence are also reported in the plots, indicated with vertical continuous lines. It is noted that the event with the larger moment magnitude of each sequence was considered as the main-shock, even if the records at the considered stations did not have the largest local intensity value.

With the only exception of the sequence recorded at the PPHS station, considering the complete sequence increases the probability of higher levels of damage with respect to the case of the main-shock only. It is interesting to note that, for the sequence recorded at the MRN station, there is no increase in the damage demand with respect to that obtained from the deterministic values.

This comparison confirms that the use of the median value only of the predicted damage distributions should be avoided, and the scatter in the demand should always be accounted for.

For the majority of the main-shock predictions (with the only exception of the CHHC sequence), the demand distribution obtained for discrete levels of damage could be fitted with a lognormal distribution. This would allow the prediction calculation in a continuous range of damage and the development of a closed-form calculation of the damage demand, when the maximum value of earthquake intensity is known for a main-shock. Nevertheless, from the distributions resulting after damage calculations for complete sequences of events, it seems that the fitting by a mathematical distribution is not a trivial issue.

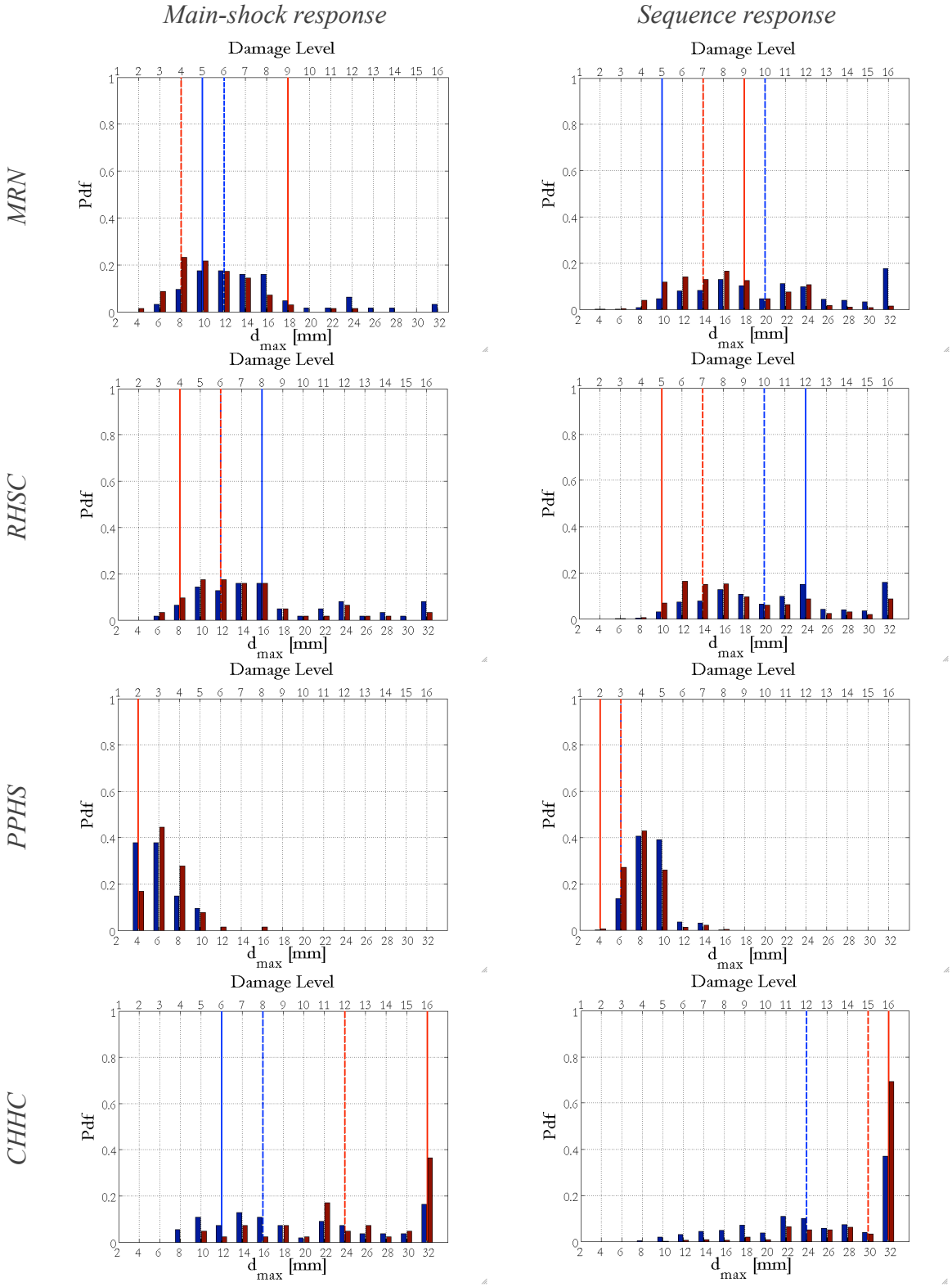


Figure 6: Predicted damage level distributions for main-shock (left) and entire sequence (right) for the four considered earthquake sequences (top to bottom), with EW and NS indicated by blue and red, respectively. The median values and the deterministic values for each component are indicated with dashed and continuous lines, respectively, with the corresponding colour.

4.4 Example of application of the proposed methodology for post-earthquake damage assessment

In several countries worldwide, after the occurrence of an earthquake event, fast-tagging procedures are often applied together with site surveys, where structural engineers are called to quantify the aftershock vulnerability and risk, mainly based on visual inspections, and judge if each building can be reused (green tag), further inspected (yellow) or in danger of collapse (red) in case of aftershocks. The decision is made without any knowledge of the transition probability of the observed damage to collapse. Some guidelines for the quantification of aftershock risk were provided in the past for reinforced concrete buildings [17]. The procedure developed in this work can allow some rapid calculations of damage demand, from the results of previous analytical studies, based on the seismic response of the structures of interest and the intensity of the events of the occurring sequence. This can provide indications for stake-holders and decision makers for organizing fast-assessment plans and prioritizing the operations.

The results of a simple example of this type of fast calculation, based on the results of analyses with pre-damaged SDOF models, are presented in Table 4. The probability distributions were calculated as previously, for the case of only main-shocks and for all events of the considered earthquake sequences. The only additional step required is an adequate definition of the limit state thresholds or, in other words, the translation of DL to significant DS, represented by the tagging colours. For the example presented here, three LS can be considered, consisting of operational limit state (OLS), damage limitation limit state (DLS) and ultimate limit state (ULS). Consequently, four damage states (DS1<OLS, OLS<DS2<DLS, DLS<DS3<ULS, DS4>ULS) are identified. The LS displacement thresholds were defined as the attainment of the first yielding pier for OLS, the attainment of the maximum base shear for DLS and the drop of base shear to 80% of its maximum value for ULS [13].

In this example, the green tag damage state corresponds to damage levels up to OLS, the yellow tag to damage levels between OLS and DLS and the red to damage levels beyond DLS. Making reference to the DLs adopted in this study, DL6 corresponds to the threshold for the attainment of OLS, while DL10 to the attainment of DLS. After DL10 the structure shows a degrading response, with the ULS obtained for DL12. For this example, all damage levels beyond DL10 are considered as red-tagged damage state. Table 4 reports the probabilities of damage occurrence of the three significant damage states, for the four considered sequences, considering either only the main-shock or the entire sequence. It can be observed that the probability of more severe damage is increasing if the entire sequence is considered in the damage prediction calculation.

DL	RHSC		PPHS		CHHC		MRN	
	Main-shock	Sequence	Main.	Seq.	Main.	Seq.	Main.	Seq.
<DL6	0.40	0.05	0.99	0.97	0.16	0.02	0.60	0.24
DL6-DL10	0.50	0.55	0.01	0.03	0.24	0.14	0.32	0.50
>DL10	0.10	0.40	0	0	0.60	0.84	0.08	0.26

Table 4: Example of tagging estimation: probabilistic prediction of damage states for four earthquake sequences (recorded at RHSC, PPHS, CHHC and MRN), considering only main-shocks or entire sequence of events

5 CONCLUDING REMARKS

A methodology for quick estimation of maximum displacement demand during and after earthquake sequences was proposed. The methodology was applied to a single case-study building, with the aim of investigating its applicability and identifying the parameters that can affect the reliability of the damage predictions. In more detail, the ability of the procedure to estimate (in probabilistic terms) the damage demand due to main-shocks and complete sequences was studied by means of four examples with real earthquake sequences and the predictions were compared to the seismic demand calculated with (deterministic) NLTHA with the considered records.

It is recognized that improvements in the procedure can and should be considered. First of all, the proposed procedure currently accounts only for the global response of the buildings, assuming that early local failure modes are prevented. The consideration of local out-of-plane mechanisms should be incorporated as a future development. A further improvement of the methodology could be aiming at deriving predictions of damage demands representative of more general building typologies, represented by similar geometries and varying mechanical properties.

Another possible improvement regards the SDOF model and the representative engineering demand parameter used to recreate the URM seismic response during earthquake sequences. Indeed, an advanced (MDOF) modelling that accounts for out-of-plane failures and allows partial collapses can be significantly more efficient in the prediction of damage. Nevertheless, the downside of the advanced modelling is that the more complex it is, the more case-specific it becomes, and therefore it cannot be adopted in the assessment of a large population of buildings. A compromise between the level of detail in the modelling and its representativeness of a building population should always be considered, taking also into account the inevitable increase of computational time when detailed models are used.

Lastly, former studies (e.g. [18]) showed that, in addition to the ground motion intensities, aftershock ground motion features such as the frequency content and the strong motion duration can affect the post-main-shock response. These aspects should be investigated within the damage prediction procedure and their impact should be studied through applications with more real earthquake examples.

Finally, for the validation of the procedure, empirical data for the observed damage evolution during earthquake sequences should be considered in order to assist the identification of representative thresholds corresponding to significant damage states. The analytical limit state thresholds should be related to more observational damage data, provided that the considered models adequately represent the seismic behaviour of the structures.

REFERENCES

[1] I. Senaldi, G. Magenes, J. Ingham, Damage assessment of unreinforced stone masonry buildings after the 2010-2011 Canterbury earthquakes, *International Journal of Architectural Heritage* [in press], 2015, DOI: 10.1080/15583058.2013.840688.

[2] L. Moon, D. Dizhur, I. Senaldi, H. Derakhshan, M. Griffith, G. Magenes, J. Ingham, The demise of the URM building stock in Christchurch during the 2010/2011 Canterbury earthquake sequence, *Earthquake Spectra*, **30**, 1, 253-276, 2013.

[3] A. Penna, P. Morandi, M. Rota, C.F. Manzini, F. da Porto, G. Magenes, Performance of masonry buildings during the Emilia 2012 earthquake, *Bulletin of Earthquake Engineering*, **12**, 5, 2255–2273, 2015.

[4] B.A. Bradley, R.P. Dhakal, M.Cubrinovski, J.B. Mander, G.A. MacRae, Improved seismic hazard model with application to probabilistic seismic demand analysis, *Earthquake Engineering and Structural Dynamics*, **36**,14, 2211-2225, 2007.

[5] I. Iervolino, M. Giorgio, B. Polidoro, Sequence-based probabilistic seismic hazard analysis, *Bulletin of the Seismological Society of America*, **104**, 2, 1006-1012, 2014.

[6] A. Mouyiannou, A. Penna, M. Rota, F. Graziotti, G. Magenes, Implications of cumulated seismic damage on the seismic performance of unreinforced masonry buildings, *Bulletin of New Zealand society for Earthquake Engineering,* **47**, 2, 157-170, 2014.

[7] A. Penna, S. Lagomarsino, A. Galasco, A nonlinear macro-element model for the seismic analysis of masonry buildings, *Earthquake Engineering and Structural Dynamics*, **43**, 2, 159-179, 2014.

[8] S. Lagomarsino, A. Penna, A. Galasco, S. Cattari, TREMURI program: an equivalent frame model for the nonlinear seismic analysis of masonry buildings, *Engineering Structures*, **56**, 1787-1799, 2013.

[9] F. Graziotti, A. Penna, G. Magenes, Use of equivalent SDOF systems for the evaluation of displacement demand for masonry buildings, *Proceedings of VEESD 2013*, Vienna, Austria, August 28-30, 2013.

[10] A. Mouyiannou, M. Rota, A. Penna, G. Magenes, Identification of suitable limit states from nonlinear dynamic analyses of masonry structures, *Journal of Earthquake Engineering*, **18**, 2, 231 – 263, 2014.

[11] M. Rota, A. Penna, G. Magenes, A methodology for deriving analytical fragility curves for masonry buildings based on stochastic nonlinear analyses, *Engineering Structures*, **32**, 5, 1312-1323, 2010.

[12] C. Smerzini, C. Galasso, I. Iervolino, R. Paolucci, Ground motion record selection based on broadband spectral compatibility, *Earthquake Spectra*, DOI: 10.1193/052312EQS197M, 2015.

[13] A. Mouyiannou, *Implications of cumulative damage on the seismic vulnerability of masonry buildings*, PhD Thesis, IUSS Pavia, 2014.

[14] E. Bojorquez, I. Iervolino, Spectral shape proxies and nonlinear structural response, *Soil Dynamis and Earthquake Engineering,* **31**, 996-1008, 2011.

[15] G.W. Housner, Behavior of structures during earthquakes, *Journal of the Engineering Division*, ASCE, **85**, EM14, 109-129, 1959.

[16] S.K. Sarma, B.J. Casey, Duration of strong motion in earthquakes, *Proceedings of the 9th WCEE*, Tokyo, Japan, 1990.

[17] P. Bazzurro, C.A. Cornell, C. Menun, M. Motahari, Guidelines for seismic assessment of damaged buildings, *Proceedings of 13WCEE*, Vancouver, Canada, 2004.

[18] J. Ruiz-Garcia, Mainshock-aftershock ground motion features and their influence in building's seismic response, *Journal of Earthquake Engineering,* **16**, 5, 719-737, 2012.

COMPDYN 2015
5th ECCOMAS Thematic Conference on
Computational Methods in Structural Dynamics and Earthquake Engineering
M. Papadrakakis, V. Papadopoulos, V. Plevris (eds.)
Crete Island, Greece, 25–27 May 2015

RELATIONSHIP BETWEEN THE VARIATION OF SEISMIC CAPACITY AFTER DAMAGING EARTHQUAKES, COLLAPSE PROBABILITY AND REPAIR COSTS: DETAILED EVALUATION FOR A NON-DUCTILE BUILDING

M. Gaetani d'Aragona[1], **M. Polese**[1] **and A. Prota**[1]

[1] Department of Structures for Engineering and Architecture, University of Naples Federico II
via Claudio 21, 80125 Naples, Italy
{marco.gaetanidaragona, maria.polese, andrea.prota}@unina.it

Keywords: Non-ductile, Residual capacity, Performance loss, Repair costs.

Abstract. *Decisions on reparability for damaged buildings after an earthquake are often controversial, and they should properly take into account the variation of building safety level due to damage and the repair costs. A significant indicator for the appropriate course of action is the so-called Performance Loss (PL), that is a measure of seismic safety decay. PL can be determined as a function of the variation of building seismic capacity from the intact to damaged state. This study investigates, by means of a detailed case study, on the expected PL for increasing seismic demand and its relationship with varied building safety level and repair costs. We simulate the response of an existing non-ductile reinforced concrete building using a finite element model that properly accounts for both flexural, shear and axial failure of members and accounts for joints behavior. Different definitions of building collapse are introduced, and Incremental Dynamic Analyses are performed with a representative set of input ground motions both for the intact and damaged structure. In order to evaluate aftershock fragilities, multiple Mainshock-Aftershock sequences are built through suitable scaling of selected accelerograms. Fragility curves for the intact building and the aftershock fragility curves are used to evaluate PL and the variation of collapse probability for main-shocks of increasing return period T_R. Also, corresponding repair costs are determined. The study shows interesting relations between damage levels and repair costs that may be simulated with detailed analyses and associated PL, representing a first insight in the establishment of relations between PL and repair and/or upgrade decisions.*

1 INTRODUCTION

After a seismic event, a number of possible alternatives for dealing with a building damaged by an earthquake, ranging from the acceptance of the damage up to the building replacement are available. For instance, for buildings complying with modern seismic codes, the upgrading is generally not required, but damage must be repaired to bring the building back to pre-earthquake conditions. On the other hand, existing buildings designed with older seismic codes, or gravity load designed ones, are required to be retrofitted or improved as well as repaired, to make the building more robust in future earthquakes. Indeed, while buildings compliant with modern seismic codes, if damaged, only need to restore pre-earthquake capacity, for older buildings a good strategy is to establish damage "triggers" that require not only repair of damage, but also retrofit to improve seismic performance (e.g. [1]).

The most commonly used damage trigger is a threshold value for the loss of strength in the lateral-force-resisting system above which retrofit is required. The Performance Loss index (*PL*) accounts for the loss in lateral strength due to earthquake.

Acknowledging the need for a standard method for calculating the loss levels triggering repair/upgrade requirements, in ATC52-4 [2] a set of retrofit trigger values for selected building typologies was outlined, and more recently, in [2] further specifications on *PL* thresholds and on their calculation based on FEMA 306 [3] were given. However, the suggested *PL* thresholds are based on previous established values of percent loss triggers (e.g. [4]), without a clear quantitative justification for the proposed values. Therefore, there is a clear need to further investigate on criteria and methods for establishing suitable *PL* thresholds governing damage acceptability.

In Polese et al. [5] tools for simplified assessment of *PL* and related repair costs for existing *RC* building classes were presented; the application of those tools within the performance based policy framework introduced in FEMA 308 [6] allowed to show how it is possible to establish *PL* thresholds that are linked to expected repair costs, therefore supporting informed decisions on reparability [7].

However, although it has been shown that simplified methods for the assessment of the behavior of damaged structures yield comparatively acceptable results with respect to detailed methods, e.g. based on nonlinear time history analyses [8, 9], the quantification of these loss thresholds represent a key issue into a reconstruction policy framework, and requires further investigations through detailed cases.

On the other hand, in addition to detailed evaluation of building safety variation, also suitable assessment of expected repair costs should be pursued. Indeed, along with a clear framework for the assessment of lateral loss strength, the estimate of the costs to repair the building to its original state represents a key aspect for the evaluation of building reparability.

Expected repair costs can be determined based on effective damage amount and distribution on the building structural and non-structural system, allowing for accurate assessment towards reparability decisions. In this sense, the *PEER* approach (e.g., [10]) allows the complete assessment of expected damage and costs within a fully probabilistic framework. Different performance assessment can be carried out using *PEER* framework; a recent introduction is the Time-based assessment [11], that evaluate performance over time, considering all possible earthquakes and their probability of occurrence. This loss assessment can be linked to a Time-based assessment of seismic structural safety in order to obtain a full indication of future building's performances.

This paper presents the results of a detailed case study finalized to the assessment of *PL* and repair costs for an existing building when subjected to earthquakes of increasing intensity. Although other studies addressed *AS* fragility assessment with detailed analyses on representative

buildings (see e.g. [12]), or performed detailed evaluation of expected damage and losses for archetype buildings (see e.g. [13]), the present work performs a time-based assessment of both *AS* fragilities and costs, deriving both with reference to selected T_R. Derivation of results in terms of T_R–dependent indices allows to have an easy term of comparison in case of earthquakes having the same return period in the region, without the need to refer to predefined damage states.

In particular, an existing seven-story non-ductile reinforced concrete (*RC*) structure with moment-resisting frame is considered. The response of the building is simulated with a detailed 2D nonlinear multi-degree-of freedom (*MDOF*) model. The model properly account for cumulative damage due to multiple earthquakes through hysteretic rules, damage progress, as well as both shear and axial failure in structural members. In addition, the definition of collapse modes typical for non-ductile frames are considered.

A clear probabilistic framework is introduced for evaluation of building seismic safety decay after a Mainshock (*MS*) associating it to building *PL* and expected repair costs. Multiple damaging earthquake intensities, representative of specific return periods (T_R) for the studied site are considered. Applying Mainshock – Aftershock (*MS*-*AS*) earthquake sequences, *AS* fragilities are built and used to estimate the variation of collapse probability. Also, the repair costs to ideally restore building's intact capacity were estimated and linked to *PL* for analyzed T_R to obtain a full indication of expected building performance and losses.

After definition of significant performance indices (section 2), section 3 synthetically presents the framework and the formulation to build *AS* collapse fragilities conditioned to multiple T_R. Section 4 describes the case study application introducing two different collapse modes that are typical for older *RC* buildings. The collapse fragilities are derived for both intact and T_R-damaged buildings and first results are shown. Section 5 presents the application of the *PEER* framework for the computation of repair costs for the case study. Finally, section 6 presents first considerations about relationship between *PL* and repair costs.

2 BUILDING PERFORMANCE LOSS

The building capacity after an earthquake may be significantly reduced due to the spread of damage all over the building, while the probability of collapse increases. Seismic behavior of damaged buildings, and their relative seismic safety, may be suitably represented by their seismic capacity modified due to damage, the so-called REsidual Capacity *REC* [14, 15].

REC can be defined as a parameter aimed at representing the building seismic capacity (up to collapse) in terms of a spectral quantity. In particular, *REC* of a building is defined as the smallest ground motion spectral acceleration (at elastic period of the Single Degree Of Freedom *SDOF* system equivalent to the real structure) corresponding to collapse state of the building. The performance index *PL* may be determined based on the value of the residual capacity in the intact and damaged states. In particular, considering the collapse capacity in terms of spectral acceleration of the intact building REC_0 and
the variation of *REC* for a structure that is damaged due to an earthquake with a given return period (T_R), *PL* may be expressed as follows:

$$PL = 1 - \frac{REC_{TR}}{REC_0} \tag{1}$$

with REC_{TR} the residual capacity of the *MS*-damaged structure. As shown in [7] this expression of *PL* is equivalent to the expression introduced in [6], where *PL* is derived as a function of the variation of building displacement capacity.

3 TR-DEPENDENT AFTERSHOCK FRAGILITY FRAMEWORK

REC for building damaged by earthquakes of known intensity can been assessed through a dynamic procedure. Fig. 1 illustrates a schematic view of the framework for the dynamic computation of *REC* of damaged building, and the associated *PL*.

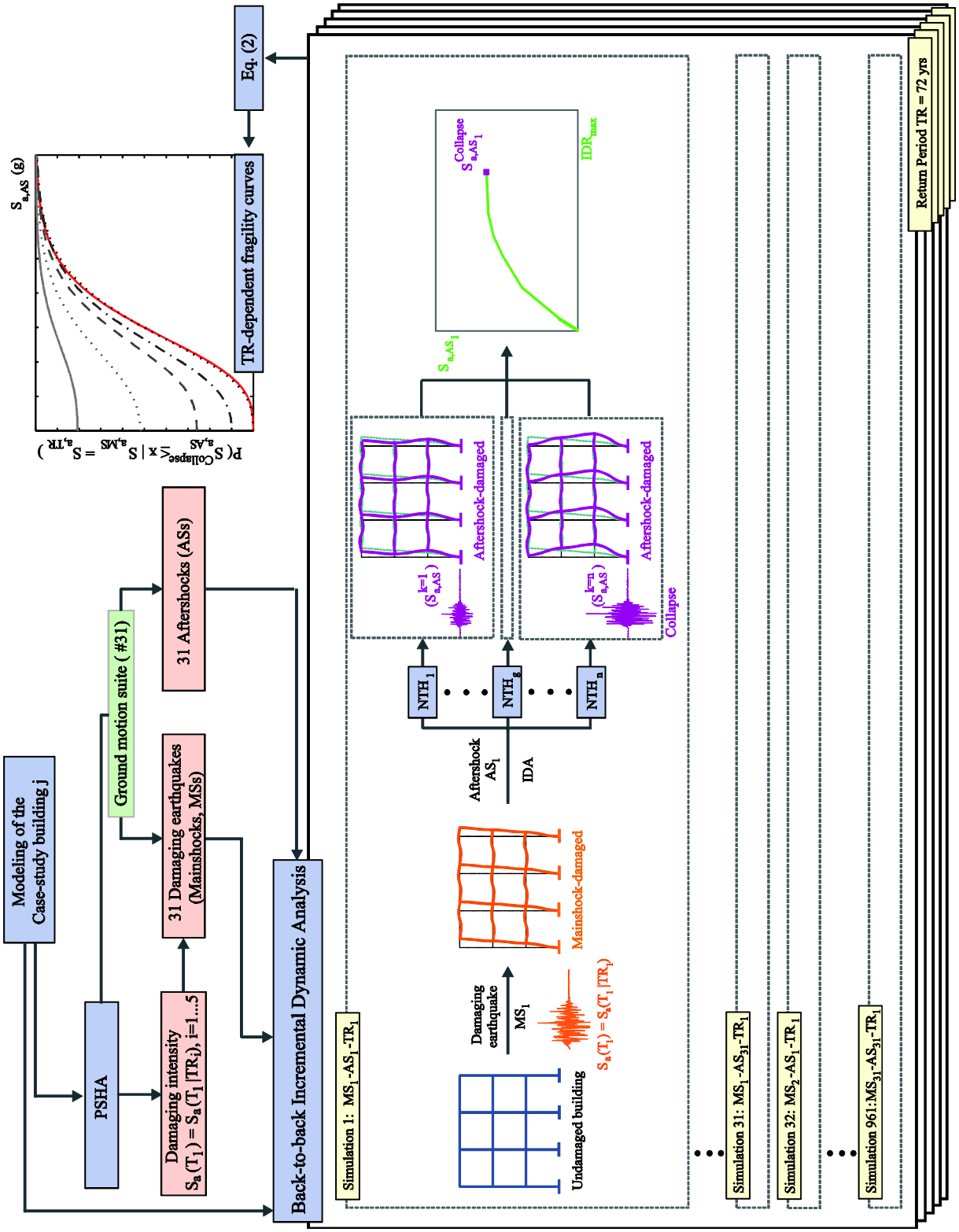


Figure 1: REsidual Capacity assessment framework. Back-to-back *IDA* sequence

The framework is composed of several moduli. After having identified the case-study building, first module entails its elastic and nonlinear structural modeling as well as the assessment of building dynamic properties, such as the fundamental vibration period. This first aspect is addressed for the specific case study in §4.1. Once the properties of the system are calculated, the knowledge of the geographical position of the building and the soil characteristics at the site, allows to perform a Probabilistic Seismic Hazard Analysis (module 2), *PSHA*, the results of which can be used in order to select an appropriate bin of natural ground motions to perform dynamic analyses (§4.2).

Further, *PSHA* allows the computation of earthquake intensities at the site with a given probability of exceedance in a time window (or representative of a given return period T_R). In this study a bin of 31 natural accelerograms was selected to assess the capacity of the intact structure and the REsidual Capacity after damage. With the selected bin of accelerograms, the so called "Back-to-back-*IDA*" (*B2B-IDA*) is used to assess the capacity of building to withstand future earthquakes after damage. Usually, a first earthquake is applied to the undamaged structure in order to reach a specific level of damage; however, in this study the damage level is not known a priori because the sole damaging earthquake intensity is imposed that is representative of a given return period. Once the structure has been damaged, the *IDA* procedure is applied to the damaged structure in order to assess the new capacity of the building. The output of this procedure is an *IDA* curve and an ultimate spectral acceleration capacity of the building for the set Mainshock-Aftershock return period (*MS-AS-*T_R). Note that the accelerograms of the selected bin have been used independently as Mainshock or Aftershock when assessing building's residual capacity.

This simulation must be repeated for each combination *MS-AS* for all considered return periods for a total of 961 simulations for 5 different return periods (4805 simulations) to properly account for record-to-record variability. The result of this framework is a set of fragility curves representing the Residual Capacity of the building conditioned on the return period (i.e., the intensity level of the earthquake conditioned on the site hazard), indicated as "T_R-dependent fragility curves". The simulation of the damaging earthquake and the estimation will be addressed in §4.3, while the mathematical formulation for T_R-dependent fragility curves in §3.1.

In order to evaluate *AS* fragilities, multiple earthquake sequences *MS-AS* are built through suitable scaling of selected accelerograms (see Fig. 2). In particular, the *MS* records are scaled to represent different return periods for the specific area and structure.

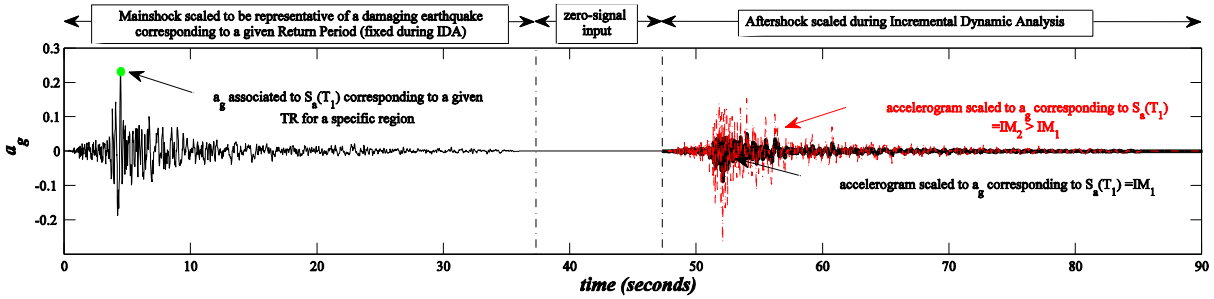


Figure 2: Example of Mainshock-Aftershock sequence.

For the Los Angeles Area and a T_1=1.0 sec, the disaggregation of seismic hazard provides $S_{a,MS}$ values of 0.29, 0.49, 0.65, 0.82 and 1.06g corresponding to the considered T_R = 72, 224, 475, 975, 2475 years respectively (http://geohazards.usgs.gov). For each (scaled) *MS*, nonlinear time history is performed and the response is recorded; then an *AS* record is applied to the *MS*-damaged structure. A time gap of 10 seconds between *MS* and *AS* is considered to allow the

ceasing of vibration produced by the *MS*. Dynamic *AS* analysis is repeated with increasing scale factor applied to the *AS* record, providing *IDA* analysis results for *MS*-damaged structure, until the *MS*-AS sequence causes collapse. To account for the effect of record-to-record variability on structural response *MS*-*AS* sequences are generated using a set of 31 ground motions that are applied as both *MSs* and *ASs*, generating a total of 961 record sequences for each return period.

3.1 Aftershock Fragility Curves Formulation

Starting from the initial damage state produced by a *MS* corresponding to a given T_R, T_R-dependent collapse fragility functions can be built. Because the structure is subject to a series of consecutive events, cumulative damage is accounted for in the estimate of the collapse probability. Considering a seismic sequence consisted of a pair of mainshock *MS* and the consecutive aftershock event *AS*, the aftershock collapse probability conditioned on the *MS* intensity $S_{a,MS}$ can be calculated by considering two mutually exclusive and collectively exhaustive events [16] defined as *C* and *NC*, Eq. (2). *C* accounts for cases where collapse occurs due to the mainshock and *NC* accounts for cases where collapse does not take place due to the mainshock (see [17-19]).

$$\begin{aligned} P(S^C_{a,AS} \le x \,|\, S_{a,MS}) = \\ = P(S^C_{a,AS} \le x \,|\, S_{a,MS}, NC) \cdot P(NC|S_{a,MS}) + P(S^C_{a,AS} \le x \,|\, S_{a,MS}, C) \cdot P(C|S_{a,MS}) \end{aligned} \tag{2}$$

$$\begin{aligned} P(S^C_{a,AS} \le x \,|\, S_{a,MS}, NC) = \int_{\forall \underline{MS}} P(S^C_{a,AS} \le x \,|\, \underline{MS}, S_{a,MS}, NC) \cdot f(\underline{MS}|S_{a,MS}, NC) dMS \approx \\ \approx \frac{1}{N_{NC}} \sum_{i=1}^{N_{NC}} P(S^C_{a,AS} \le x \,|\, \underline{MS_i}, S_{a,MS}, NC) \end{aligned} \tag{3}$$

In Eq. (3) $S_{a,MS}$ is *MS* spectral acceleration corresponding to a specific T_R conditioned on the site hazard, the fundamental vibration period of the intact structure (T_1), and the critical damping ratio assumed; $S_{a,AS}$ is the *AS* spectral intensity at T_1 and $S^C_{a,AS}$ is the *AS* spectral intensity corresponding to collapse. Assuming an equal probability of occurrence for each *MS*, the term $P(NC|S_{a,MS})$ can be estimated as the number of *NC*-cases over the number of *MS* considered (N_{MS}), while $P(C|S_{a,MS})$ can be estimated as the number of *C*-cases over N_{MS} and $P(S^C_{a,AS} \le x|S_{a,MS}, C) = 1$. Hence, the *AS* fragility can be interpreted, for each considered structure and T_R (corresponding to $S_{a,MS}$), as the sum of the mainshock collapse fragility (last term in Eq. (2)), and an inflating term (first term in (3)). $P(S^C_{a,AS} \le x|S_{a,MS}, NC)$ is the collapse probability conditioned on *MS* intensity $S_{a,MS}$ and on *NC* and can be expanded as in Eq. (3). In (4) $\underline{MS}$ stands for the mainshock wave-form vector; $f(\underline{MS}|S_{a,MS}, NC)$ is the joint probability density function for the mainshock wave-form vector given a specific value for $S_{a,AS}$ and given *NC*. The integral in Eq. (3) is an application of the Total Probability Theorem in conditioning on all possible mainshock waveforms conditioned on a given spectral acceleration value. It should be noted that the approximation to the integral in Eq. (3) is based on the assumption that the various mainshock wave-forms have equal probability of occurrence (see [20] for more detail on this kind of approximation).

4 APPLICATION TO A NON-DUCTILE BUILDING

4.1 Description of building's structural model

The building selected for this study is the perimeter moment resisting frame of the Van Nuys Holiday Inn, that is a seven-story eight-bay non-ductile reinforced concrete frame building located in Los Angeles, California, already described in Krawinkler [21].

A two-dimensional finite element *MDOF* model developed using OpenSees [22] is adopted to simulate the seismic response of the building. Beams and columns are modelled using the force-based nonlinear beam–column element [23]. Due to non-ductile details that characterize both of the structures, is expected that the joints may influence the failure mechanism, consequently the joints are modeled using rotational spring elements, the so called "scissor model" by Alath and Kunnath [24], including a pinching hysteric behavior to account for the nonlinear shear deformation of the joint. Similarly, shear and axial failure are expected to occur in non-ductile detailed columns, and consequently shear and axial failure in the columns are modeled using the Limit State material [25]. Bond-slip rotations for beams have been included modifying joint backbone as proposed in [26]. *P-Δ* effects are included. A schematic view of the adopted numerical model is shown in Fig. 3.

The eigenvalue analysis of the intact structure provides a fundamental vibration period of 1.0 sec. A damping of 2% is assigned to the first and third modes using Rayleigh damping. The damping is updated during the first-to-second earthquake analysis at the beginning of each seismic sequence, accounting for the first mode period elongation due to structural damage.

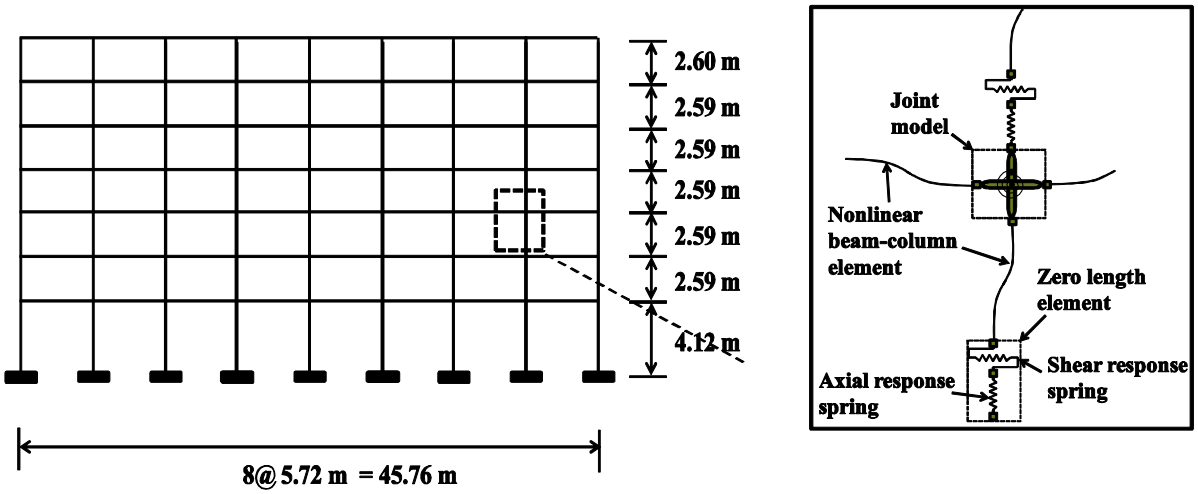


Figure 3: South frame elevation and column, beam and joint models (adapted from Krawinkler, 2005)

4.1.1. Collapse definition

Older RC structures, non-conforming to modern design standards, are likely to experience gravity load collapse prior to side-sway collapse [27]. For this reason, this study considers two possible collapse mechanisms to capture the actual capacity in the model, as firstly proposed in Baradaran Shoraka et al. [28]: Side-sway collapse (*SC*) and Gravity load collapse (*GLC*). The *SC* occurs when a single storey has reached its capacity to withstand lateral loads (i.e., when every column in a given floor has exceeded its residual shear capacity at the same time). *GLC* occurs when vertical load demand exceeds the total vertical load capacity at a given storey. Collapse is detected based on a comparison of storey-level gravity load demands and capacities

(adjusted at each time step to account for member damage and load redistribution). The gravity load demand is considered constant during each analysis.

An internal algorithm monitors the dynamically varying capacity of each element and checks the *GLC* and *SSC* criteria throughout each nonlinear time history analysis to detect the collapse. A bisection algorithm is then implemented to find the collapse capacity with a precision of 0.05g during the *IDA* procedure. The collapse is considered as the first between *GLC* and *SSC*.

4.2 Accelerogram selection

Disaggregation of the seismic hazard for the site is performed based on Bazzurro and Cornell [29]. A shear wave velocity of 218 m/s and a first-mode period of 1 second are assumed. Based on the results of the seismic hazard disaggregation, a set of 31 ground motions is selected from the *PEER* Next Generation Attenuation (NGA) database [30]. To reflect shaking intensity at site, ground motions have been selected using a target $\varepsilon(T_1) = 1.18$ for a reference return period. Ground motions *MS-AS* sequences are generated using this ground motions set where single earthquakes are applied as both *MSs* and *ASs*.

These 31 ground motions have M_w between 6 and 7.6, a closest distance from fault rupture between 7.1 and 48 km and a *PGA* varying between 0.105g and 0.82g. For further information on selection of accelerograms, refer to Baradaran Shoraka et al. [28].

4.3 Fragilities for intact and damaged structure

The fragility computation is based on the use of *IDA* analyses [31], scaled up until collapse is reached; $S_a(T_1)$ is assumed as representative earthquake intensity. To quantify structural response of the intact building, *IDA* is carried out on the nonlinear model of undamaged building using the set of 31 ground motions acting as *MS*. Residual capacity for each *MS* is calculated as the spectral intensity corresponding to the attainment of structural collapse (as defined in previous section); also, median *REC* is determined as the median spectral intensity over all *MSs*, Fig. 4.

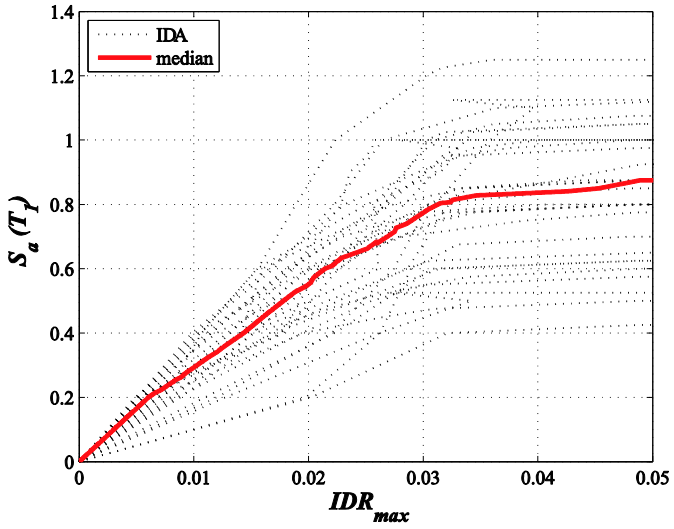


Figure 4: Mainshock incremental dynamic analyses

In order to evaluate *AS* fragilities, multiple earthquake sequences *MS-AS* are built through suitable scaling of selected accelerograms as indicated in §3. In particular, the *MS* record is scaled to represent different return periods for the specific area and structure. The results show

that in the majority of cases a first floor mechanism is activated due to the sole *MS* ground motion; also, usually the Gravity load collapse precede the Sidesway collapse. The type of mechanism usually does not change when considering the *MS-AS* sequence with the same *MS*, this may be attributed to the fact that the damage produced in the building by the *MS*, especially for higher return periods, may significantly affect the future collapse mechanisms that can develop in the building for ASs. *B2B-IDA* is carried out on more than 4800 *MS-AS* sequences (961 *MS-AS* sequence for 5 return periods). The process is computationally intensive, due to the use of a fiber model coupled with the Limit State Material, that allows to account for both shear and axial failure and load redistribution. In order to speed the analyses, OpenSees parallel [22] was used on SCoPE grid at the University of Naples Federico II [32]. Running the analysis on the SCoPE grid in parallel reduces the computation to about 7 days with respect to 240 days required on a desktop computer with 4 processors.

The *REC* of *MS*-damaged building is computed in terms of S_a based on the *IDA* results obtained from *MS-AS* sequences. The results are here represented in terms of fragility curve at collapse. For the undamaged building, the collapse fragility curve is based on the *IDA* results performed on the intact building using the set of 31 ground motions. The collapse fragility curve for damaged building, according to Eq.(2), is calculated based on the *AS* collapse capacities obtained for each of 961 *MS-AS* sequences in which the MS is scaled in order to be representative of the T_R of interest. Fig. 5 illustrates the collapse fragility curves for the intact and damaged building in terms of probability of collapse conditioned on the *MS* for given T_R as a function of *AS* spectral intensity, $S_{a,AS}(T_1)$. The red curve represents the behavior of the intact building.

As the T_R increases, due to the increasing building damage for *MS* application, the collapse fragility curve shift left and up. Because for increasing T_R an increasing number of collapses due to *MS* is detected, the collapse fragility curves for higher T_R have nonzero probability of collapse for $S_{a,AS}$=0.

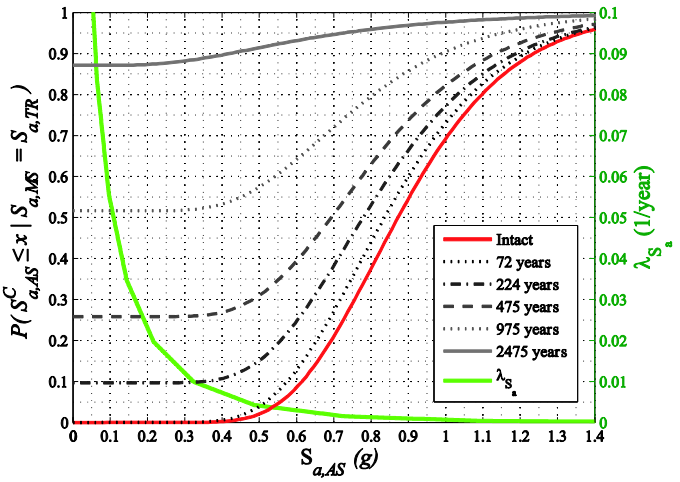


Figure 5: Mainshock TR-dependent aftershock fragility curves and fragility curve for the intact building.

A comprehensive indicator of the structural safety that involves considering both the hazard curve at the site and the collapse fragility curves is the probability of collapse over t years. Under the hypothesis that the occurrence of earthquakes in time follows a Poisson process, the probability of one collapse over t years can be computed as:

$$P_c(\text{in } t \text{ years}) = 1 - \exp(-\lambda_c t) \tag{4}$$

with λ_c the mean annual frequency of collapse. λ_c can be calculated integrating the collapse fragility curve of the structure over the seismic hazard curve (Fig. 5) at the site using the relation $\lambda_c = \int_0^\infty P(C|im)|d\lambda_{IM}(im)|$ [33], where *P(C|im)* is the probability that the structure will collapse when subjected to an earthquake with ground motion intensity level *im*, and λ_{IM} is the mean annual frequency of exceedance of the ground motion intensity *im*. In order to account for the possibility that the *MS* caused collapse, the Eq.(4) can be rewritten using the Total Probability Theorem by separating *C* and *NC* cases for a given T_R.

The "degraded" REC_{TR}, corresponding to each return period, is computed as the median collapse capacity from the Aftershock *IDA* analyses. Then, the corresponding *PL* is calculated with Eq. (1). Fig. 6 shows the relation between *PL*, *REC*, T_R and the probability of collapse in a time window of 50 years. Note that in more than 50% of cases for $T_R \geq 975$ years collapse occurs due to the *MS*, with a median value of *PL* corresponding to 100% (not shown in figure); obviously, in calculating collapse probability the entire fragility is taken into account, resulting in different (increasing) P_C (in 50 years) for T_R 975 (56%) and 2475 (90%). As expected, for increasing T_R the probability of collapse increases. The same trend is observed for *PL*, while the ratio REC_{TR}/REC_0 decreases.

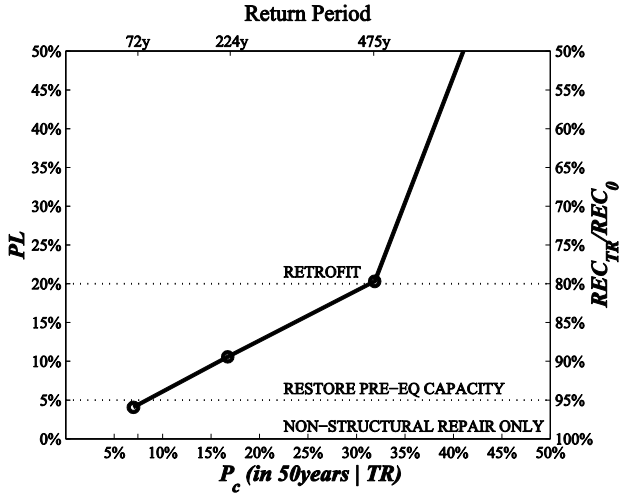


Figure 6: Relations between T_R, P_C in 50 years conditioned to T_R, *PL* and *REC* variation.

The median probability of collapse in 50 years is 6.1% for the intact building while it increases to 7.0% for a 72-years-*MS*-damaged structure and up to a maximum value of 89.6% when considering a return period of 2475 years. In the same figure the restore and retrofit trigger values in terms of *PL*, as suggested in [1] are shown.

Other remarkable observation concern the variation in the fundamental vibration period (T_1), which is strictly related to the global damage [34]. The median variation of the fundamental vibration period with respect to the one for intact building varies with T_R. These values vary in a non-linear way, from a minimum of 0.5% for 72 years return period up to 21% for the 2475 years return period. The same trend is observable for the maximum interstorey drift ratio: the median for T_R=72 years is 0.9% and increases up to 3.7% for T_R=2475 years.

Another interesting parameter is the maximum residual drift, that is often used as limit for technical feasibility of repair intervention and is a directly measurable damage indicator. Its median values vary with T_R from a minimum of 0.02% for T_R=72 years up to 0.46% for T_R=2475 years.

5 ECONOMIC LOSSES

In the previous sections, the collapse performance of a non-ductile *RC* frame was analyzed along with its variation after damaging earthquakes. Here, results are extended to consider economic losses as an additional metric of building seismic performance. In particular, the direct costs associated to repair and/or substitution of the building due to structural and non-structural damage are considered; this metric can support stakeholders' decisions with information, usually in probabilistic terms, about the risk for the building in terms of earthquake economic losses, that is a means of quantifying and communicating risk.

5.1 PEER framework

To evaluate expected economic losses for the studied building, the performance-based framework established by the Pacific Earthquake Engineering Research Center (*PEER*) is adopted [10]. The PEER methodology, briefly summarized in Fig. 7, divides the analysis in 4 subsequent steps, starting from hazard analysis, followed by structural response analysis, evaluation of damage and finally loss analysis; the outcome of each analysis is then integrated using a total probability theorem, allowing to take into account combined numerical integration of all the conditional probabilities and to propagate the uncertainties from one level of analysis to the next, resulting in probabilistic prediction of performance.

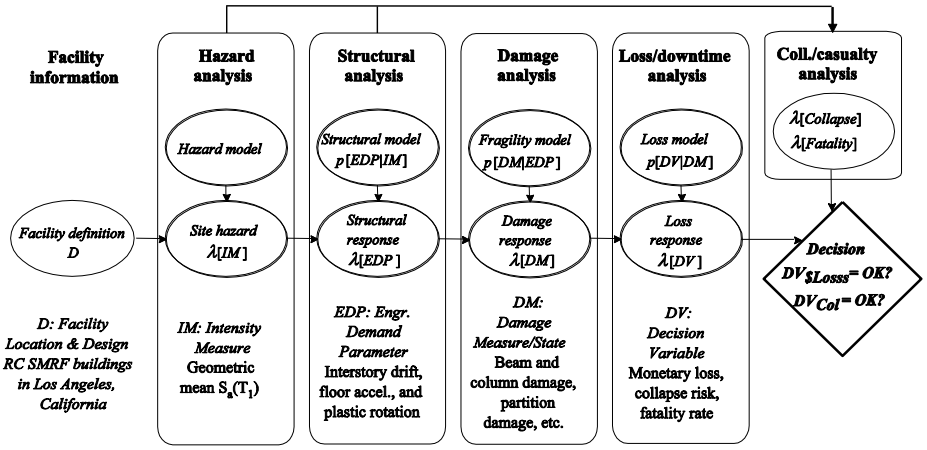


Figure 7: Summary of *PBEE* framework [10]

5.1.1. Hazard Analysis

The first step, the hazard analysis, involves a probabilistic seismic hazard analysis (*PSHA*) [35] to determine the mean annual rate of exceedance of the ground motion of intensity *IM* at the building site. This analysis take into account the earthquake sources, the distance to the fault, local site conditions, etc. The spectral acceleration at the fundamental period is here assumed as *IM*. Using the results of the *PSHA*, a suite of acceleration histories can be selected and scaled to be compatible with the site hazard. This section adopts the same ground motion bin indicated in §4.2.

5.1.2. Response Analysis

The second step involves a suite of nonlinear response history analyses of a structural model of the facility to evaluate its response in terms of engineering demand parameters (*EDPs*), such as peak interstorey drift and peak floor acceleration, conditioned on *IM*. The resulting *EDPs*

will be used as input for the next analysis step to define the damage state reached in each considered component. In this study, the analyses were carried out for the model presented in §4.1, for the five different level of the seismic action corresponding to a 72, 224, 475, 975, 2475 years return period as indicated in §3.1. The response of building is assumed to be the same in two orthogonal directions.

5.1.3. Damage Analysis

The third step, the damage analysis, adopts fragility functions that express the conditional probability that a component (e.g. beam, partition, etc.) reaches or exceeds a particular damage state given the attainment of increasing values of significant *EDPs*. The selected damage states reflect the repair actions needed to restore the component to its undamaged state and corresponding repair costs. Input data for vulnerable components must include information on the types of damage, the structural demands that cause this damage, and the consequences of the damage in terms of repair methods and repairs costs.

Collection of damage fragility functions and unit-repair-cost distribution functions for damageable building components, represent a necessary input to the economic loss analysis. In this study, damage fragilities and repair costs as proposed in [36] were assumed. Ramirez and Miranda [36] provided damage fragility functions for both drift and acceleration-sensitive components, and the expected value of component repair cost expressed as a fraction of component cost as new. It is here noted that lognormal fragility functions are adopted to represent damage distribution, while in this study the uncertainty in repair costs is neglected, adopting expected values as proposed in [36].

Architectural layouts, components and cost of new elements were adopted from Aslani and Miranda [37]; those data are necessary for effective quantification of the amount of damage and costs in the real building. More details can be found in Gaetani d'Aragona [38].

5.1.4. Loss Analysis

The final step of *PBEE* uses the results of previous steps for the computation of the probabilistic losses, which may include repair cost, downtown of activities, and loss of life. In this study, only direct monetary losses (i.e., repair costs) were considered. Further details on the procedure can be found elsewhere (e.g., [11, 39, 40]).

5.2 Evaluation of repair costs

The loss framework outlined in §5.1 was used to carry out the loss simulation for the case-study building. Having simulated the response of the building for different intensities corresponding to return periods ranging from 72 to 2475 years (§3.1), the loss analysis was performed using the fragility data and costs as indicated in §5.1.3. In particular, to solve *PEER* equation integral, a Monte Carlo procedure was adopted. According to Yang et al. [39] and FEMA P-58 [11], the Monte Carlo approach uses inferred statistical distributions of building response obtained from limited suites of analyses to generate additional response parameters (*EDP*) that properly incorporate the effects of modeling uncertainty along with ground motion uncertainty [39]. In this study, 500 realizations were performed for each intensity level. Yang et al. [39] indicated that stable cost estimates can be obtained with as few as 200 realizations. Fragility groups were divided in subsets of group components subjected to the same earthquake demands (i.e., Performance groups, *PG*). For each realization and *PG*, a unique damage state was determined using a uniform random generator over the interval [0,1] considering the probability of the *PG* experiencing each damage state at the *EDP* obtained from structural analysis. Once the damage state for a performance group is identified, the repair action and the associate

repair cost for that performance group is obtained by multiplying cost of new elements by corresponding normalized repair costs by the number of elements in the considered *PG*. If collapse has not occurred, losses are calculated for each realization based on the damage sustained by each component and the consequence functions assigned to each performance group and by summing repair costs of each *PG*. If structural collapse was detected, the total repair cost is calculated using the replacement value of the building plus additional costs related to demolition and debris removal (15% of the replacement value of the building).

Next, direct economic losses are expressed in terms of normalized repair costs (c_r), that are obtained dividing repair costs by the building's replacement value (including expected demolition costs and debris removal as well as cost of new building).

The probability of exceeding a certain level of total normalized repair cost accounting for both the collapse and non-collapse cases can be calculated using the total probability theorem:

$$P(C_r \geq x) = P(C_r \geq x \mid IM, NC)[1 - P(C \mid IM)] + P(C_r \geq x \mid IM, C)P(C \mid IM) \quad (5)$$

where $P(C_r \geq x|IM, NC)$ is the probability conditioned on *IM* when the structure do not collapses that the normalized repair cost exceeds *x*; $P(C_r \geq x|IM, C)$ is the probability of exceeding the normalized repair cost *x* given the collapse, that is actually independent from *IM* and equal to the replacement value of the building; $P(C|IM)$ is the probability of collapse conditioned on *IM*. The complementary cumulative distribution of the total normalized repair costs, is shown in Fig. 8 considering five different hazard levels (i.e. damages due earthquakes characterized by 5 different T_R).

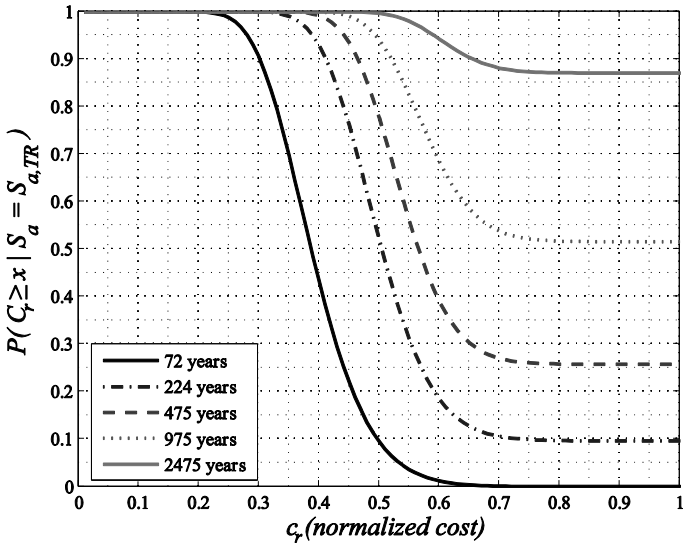


Figure 8: Probability of exceeding normalized cost at five different hazard levels for the American case study.

As it can be seen in Fig. 8, with the increase of the damaging action (i.e., return period) the repair cost inflates making the curve translate rightward. Furthermore, it can be noted that total repair cost of at least 20-25% can be expected even for the lowest considered return period. This high cost is due to the nonstructural components and contents, which significantly contribute to damage and costs even for relatively low levels of seismic action (e.g. for T_R=72 years). It is worth to note that the total normalized repair cost conditioned on the return period of the damaging action at the site is strongly influenced by occurred collapse cases, see second member of the Eq.(5). This effect is particularly evident for higher return periods, for which the curve results translated upward.

6 REPAIR COSTS AND PERFORMANCE LOSS

PL is a measure of variation of building seismic capacity from intact to damaged state and also implicitly account for the seismic safety variation after damage. In addition to performance assessment in terms of safety, repair costs represent a different metric that is normally accounted for in the process of establishing due actions for a damaged building. Hence, it is interesting to observe the relationship between *PL* and repair costs to gather further insights and trend supporting reparability decisions. Fig. 9 shows the median *PL* and the earthquake-induced repair cost c_r determined for the case study building considering increasing return period of the damaging earthquake (the black dots for T_R =72, 224 and 475 years). In order to show the trend for increasing T_R, also dots obtained along the line connecting the *PL*-c_r points of T_R = 475 and T_R = 975 at fixed values of c_r are represented as empty dots.

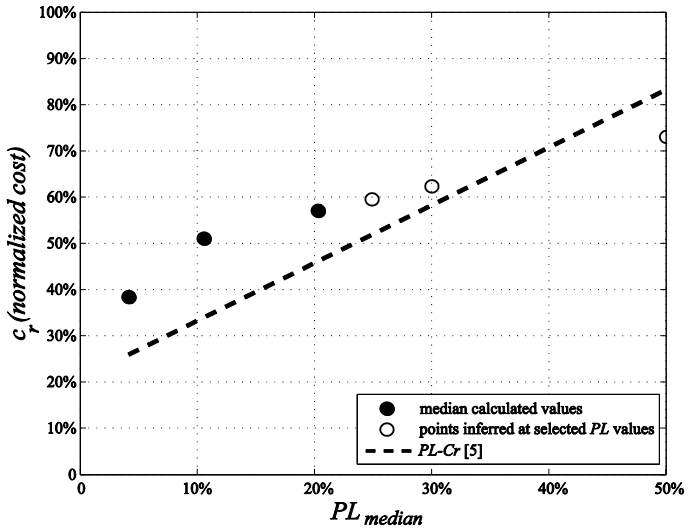


Figure 9: Relation between *PL* and c_r, median values, for the American building and the *PL*-c_r relationship proposed in Polese et al. [5].

In particular, Fig. 9 shows that also for lower *PL* (corresponding to lower return periods) the repair cost is not negligible starting from a median value of about 40%. This effect can be explained considering the source of repair costs, that are structural components, nonstructural components, and building contents. These damageable quantities can be further divided in drift-sensitive and acceleration-sensitive (mainly building contents). The latter quantities result to be severely damaged (contributing to costs) also for lower return periods driving to relatively large repair costs also for a 72 years return period.

The initially increasing trend seems to grow in a less than linear way for higher *PL* (corresponding to higher T_R). This fact suggests some interesting observations. In fact, when the return period increases along with *PL*, then the additional contribution to repair costs is mainly due to drift-sensitive components, whose damage level increases with increasing T_R (and *PL*).

It is interesting to compare *PL*-c_r relationship predicted analytically for this case study, with *PL*-c_r relationship proposed in [5]. This relationship, represented in Fig. 9 with a dotted bold line, was obtained considering a simplified mechanism-based approach that does not account for brittle failures, and observed repair costs after L'Aquila earthquake (2009). In spite of the noticeable simplifications and assumptions for the *PL*-c_r relationship proposed in [5], this first

comparison seems to confirm on the average the proposed trend. Further investigations are required for a better understanding of *PL*-c_r relationship considering different building typologies and hazard level.

7 CONCLUSIONS

The study presented in this paper aims to contribute, with a detailed case study, to the development of tools and applications supporting reparability decisions in a performance based framework. Both the residual capacity variation, that is connected to the variation of safety, and direct economic losses are considered as significant variables for reparability decisions.

In particular, the *PL* index and normalized repair costs were computed with reference to five different return periods, for an existing non-ductile seven-story building in the Los Angeles area.

The response of the building was simulated by means of a detailed 2D nonlinear multi-degree-of freedom (*MDOF*) finite element model. The model properly account for brittle failures and captures typical non-ductile RC frames failure modes.

The analytical model of building was subjected to multiple sequences comprised of two recorded ground motions to simulate the damage produced on the building by main-shocks of a given return period.

The results show that the REsidual Capacity *REC* of a *MS*-damaged building may be significantly smaller (*PL* higher) than the *REC* of an intact building. However, for a *MS* with a T_R=72 years the building capacity is only slightly affected. For increasing T_R, the *PL* increases very fast up to the 100% for *MS* corresponding to T_R= 975 years. For T_R=975 years or larger, the number of collapse cases due to *MS* becomes greater than the non-collapse cases, and the median capacity becomes zero.

Previous studies [12] highlighted that the polarity of the second earthquake may affect the behavior of the building and vary the collapse capacity. However, in this study the effect of polarity on *REC* was neglected and has to be properly taken into account in future works.

Adopting existing component fragilities and repair costs, direct economic losses were computed for the case study building. The results show that repair costs can be significantly high also for low return periods due to the damage of nonstructural components and contents, with a total repair cost of at least 20-25% even for the lowest considered return period. This high cost is due to the nonstructural components and contents, which significantly contribute to damage and costs even for relatively low levels of seismic action.

For increasing T_R the contribution of collapse cases becomes more significant, leading to increasing probability of overcoming the reconstruction costs (c_r=1) already starting from T_R=224 years.

The study performed within this performance-based framework seems to support its applicability for reparability decisions based on quantitative assessment of safety and cost thresholds. Clearly, the level of detail required renders it suitable for specific evaluation of single buildings.

On the other hand, the results can be used to calibrate/verify reparability thresholds to be used in a performance based policy framework of selected building typologies. Indeed, the preliminary comparison with a simplified relationship connecting *PL* and c_r for existing buildings is encouraging towards the possibility to obtain generalized relationships, useful for certain building classes. To this end, further studies are required in order to gather more results on effective thresholds and to assess different factors influencing the trend of variation of repair costs with *PL*, considering different building typologies and hazard levels.

8 ACKNOWLEDGEMENTS

This study was performed in the framework of PE 2014–2016; joint program DPC-Reluis Task 3.3: Reparability limit state and damage cumulated effects and Task 3.5 Methods for the definition of thresholds for seismic retrofit. The S.Co.P.E. computing infrastructure at the University of Naples Federico II was used for parallel computing. The authors would also like to aknowledge Dr. Baradaran Shoraka for sharing OpenSees scripts for the Van Nuys Holiday Inn.

REFERENCES

[1] San Francisco, City of. Post-earthquake repair and Retrofit Requirements, Administrative Bulletins, AB-099, *Department of Building Inspection*, San Francisco, C.A., 2012.

[2] ATC 52–4. Here today—here tomorrow: the road to earthquake resilience in San Francisco, post-earthquake repair and retrofit requirements, applied technology council, prepared for the *Department of Building Inspection (DBI) city and county of San Francisco under the community action plan for seismic safety (CAPSS) project*, 2010.

[3] FEMA 306. Evaluation of Earthquake Damaged Concrete and Masonry Wall Buildings – Basic Procedures Manual. *Federal Emergency Management Agency*, 1998. Washington D.C

[4] CCSF. San Francisco Building Code. *The City and County of San Francisco American Legal Publishing Co.*: Walnut Creek, California, 2010.

[5] Polese M., Di Ludovico M., Marcolini M., Prota A., Manfredi G. Assessing reparability: simple tools for estimation of costs and performance loss of earthquake damaged r.c. buildings, *Earthquake Engineering and Structural Dynamics*, 2014; DOI: 10.1002/eqe.2534.

[6] FEMA 308. Repair of earthquake damaged concrete and masonry wall buildings. *Federal Emergency Management Agency*, Washington D.C., 1998.

[7] Polese M., Marcolini M., Gaetani d'Aragona M., Cosenza E. Reconstruction policies: explicitating the link of decisions thresholds to safety level and costs, *Bull. Earthquake Eng*, submitted, 2015.

[8] Di Ludovico M., Polese M., Gaetani d'Aragona M., Prota A., Manfredi G. A proposal for plastic hinges modification factors for damaged RC columns, *Engineering Structures*, 2013, 51, 99-112, http://dx.doi.org/10.1016/j.engstruct.2013.01.009.

[9] Polese, M., Gaetani d'Aragona, M., Prota, A., Manfredi, G. Seismic behavior of damaged buildings: a comparison of static and dynamic nonlinear approach, paper # 1134, *proceedings of COMPDYN 2013 4th ECCOMAS Thematic Conference on Computational Methods in Structural Dynamics and Earthquake Engineering*, Kos Island, Greece, 12–14 June 2013.

[10] Porter KA. An overview of PEER's performance-based earthquake engineering methodology. *Proceedings of Ninth International Conference on Applications of Statistics and Probability in Civil Engineering*, San Francisco,CA, 2003.

[11] FEMA P-58. Next-generation Seismic Performance Assessment for Buildings, Volume 1 – Methodology, Federal Emergency Management Agency, Washington, D.C., 2012.

[12] Raghunandan, M., Liel, A. B., & Luco, N. Aftershock collapse vulnerability assessment of reinforced concrete frame structures. *Earthquake Engineering & Structural Dynamics*, 2014.

[13] Ramirez, C.M., Liel, A.B., Mitrani-Reiser, J., Haselton, C.B., Spear, A.D., Steiner, J., Deierlein, G.G., Miranda, E. Expected earthquake damage and repair costs in reinforced concrete frame buildings, *Earthquake Engineering Structural Dynamics*; 2012; 41: 1455-1475, DOI: 10.1002/eqe.2216.

[14] Bazzurro, P., Cornell, C. A., Menun, C. A. and Motahari, M. Guidelines for seismic assessment of damaged buildings. *Proceedings of the 13th World Conference on Earthquake Engineering,* 2004. Vancouver B.C., Canada. Paper No. 1708.

[15] Polese, M., Di Ludovico, M., Prota, A., Manfredi, G. Damage-dependent vulnerability curves for existing buildings", *Earthquake Engineering and Structural Dynamics*, 2013; 42 (6), 853-870, DOI: 10.1002/eqe.2249.

[16] Benjamin, J.R. and Cornell, C.A. Probability, statistics and decision for civil engineers, McGraw-Hill, 1970.

[17] Ebrahimian, H., Jalayer, F., Asprone, D., Lombardi, A.M., Marzocchi, W., Prota, A., Manfredi, G. Performance-based Framework for Adaptive Seismic Aftershock Risk Assessment. Earthquake Engineering and Structural Dynamics, Volume 43, Issue 14, pages 2179–2197, November 2014.

[18] Jalayer, F., Asprone, D., Prota, A., Manfredi, G. A decision support system for post-earthquake reliability assessment of structures subjected to after-shocks: an application to L'Aquila earthquake, 2009, *Bull Earthquake Eng*, 2011; 9 (4), pp. 997-1014.

[19] Jalayer F., Asprone D., Prota A., Manfredi G. Multi-Hazard Upgrade Decision-Making for Critical Infrastructure based on Life Cycle Cost Criteria, Earthquake Engng Struct. Dyn, 2011; 40 (10), pp. 1163-1179.

[20] Jalayer, F., Beck, J.L., Zareian, F. Intensity Measures of Ground Shaking Based on Information Theory, *Journal of Engineering Mechanics*, 2012:138 (3), pp. 307-316.

[21] Krawinkler, H. Van Nuys Hotel Building Testbed Report: Exercising Seismic Performance Assessment. P*EER Report 2005/11. College of Engineering*, University of California, Berkeley, 2005.

[22] McKenna, F., Fenves, G. L., Scott, M. H., and Jeremic, B. Open System for Earthquake Engineering Simulation (OpenSees). *Pacific Earthquake Engineering Research Center*, University of California, Berkeley, CA, 2000.

[23] de Souza, R.M. Force-based finite element for large displacement inelastic analysis of frames. *PhD Dissertation*, University of California, Berkeley, USA, California, 2000.

[24] Alath, S., Kunnath, S.K. Modeling inelastic shear deformation in RC beam-column joints. *Engineering Mechanics Proceedings of 10th Conference*, May 21-24, ASCE, Boulder, CO, USA, 1995; 822–825.

[25] Elwood, K. J. Modelling Failures in Existing Reinforced Concrete Columns. *Canadian Journal of Civil Engineering*, 2004: 846-859.

[26] Celik, O.C., and Ellingwood, B.R. Modeling beam-column joints in fragility assessment of gravity load designed reinforced concrete frames. *Journal of Earthquake Engineering*, 2008; *12*(3), 357-381.

[27] Elwood, K.J., Holmes, W.T., Comartin, C.D., Heintz, C., Rojahn, C., Dragovich, J., McCabe, S., Mahoney, M. Collapse Assessment and Mitigation of Nonductile Concrete Buildings: ATC-76-5/ATC-78/ATC-95. *Proceedings of 15th WCEE,* Lisbon, Portugal, 24–28 Sept 2012.

[28] Baradaran Shoraka, M. Collapse assessment of concrete buildings: an application to non-ductile reinforced concrete moment frames. *Ph.D. dissertation*, 2013; Vancouver, BC, Canada.

[29] Bazzurro, P., Cornell, C.A. Disaggregation of seismic hazard. *Bulletin of the Seismological Society of America,* 1999; 89(2): 501–520.

[30] Chiou, B., Darragh, R., Gregor, N., and Silva, W. NGA Project strongmotion database, *Earthquake Spectra*, 2008; Vol. 24, No. 1, pp. 23-44.

[31] Vamvatsikos, D., & Cornell, C. A. Incremental dynamic analysis. *Earthquake Engineering & Structural Dynamics*, 2002; 31(3), 491-514.

[32] Merola L., The S.Co.P.E. Project, *Final workshop of grid projects "PON ricerca 2000-2006, avviso 1575"*, downloadable at http://www.scope.unina.it/datacenter/scopedocs/The_SCoPE_Project.pdf.

[33] Eads, L., Miranda, E., Krawinkler, H., and Lignos, D. G. An efficient method for estimating the collapse risk of structures in seismic regions. *Earthquake Engineering & Structural Dynamics*, 2013; 42(1), 25–41.

[34] Di Pasquale, E., Ju, J. W., Askar, A., & Çakmak, A. S. Relation between global damage indices and local stiffness degradation. *Journal of Structural Engineering*, 1990; 116(5), 1440-1456.

[35] Cornell CA. Engineering seismic risk analysis. Bulletin of the Seismological Society of America 1968; 58(5): 1583.

[36] Ramirez, C.M., & Miranda, E. Building-specific loss estimation methods & tools for simplified performance-based earthquake engineering, *PhD dissertation*, 2009; Stanford University.

[37] Aslani, H., Miranda, E. Probabilistic Earthquake Loss Estimation and Loss Disaggregation in Building. Technical Report No. 157, *John A. Blume Center Earthquake Engineering Center*, Stanford, CA, 2005.

[38] Gaetani d'Aragona, M. Post-Earthquake Assessment of Damaged non-Ductile Buildings: Detailed Evaluation for Rational Reparability Decisions, *Ph.D. Dissertation*, University of Naples Federico II, Italy, 2015.

[39] Yang, T.Y., Moehle, J., Stojadinovic, B., Der Kiureghian, A. Seismic performance evaluation of facilities: Methodology and implementation. *Journal of Structural Engineering,* 2009*;* 135(10): 1146–1154.

[40] Goulet, C.A., Haselton, C.B., Mitrani-Reiser, J., Beck, J.L., Deierlein, G.G., Porter, K.A., Stewart, J.P. Evaluation of the seismic performance of a code-conforming reinforced-concrete frame building - From seismic hazard to collapse safety and economic losses. *Earthquake Engineering and Structural Dynamics,* 2007*;* 36(13): 1973–1997. DOI: 10.1002/eqe.694.

COMPDYN 2015
5th ECCOMAS Thematic Conference on
Computational Methods in Structural Dynamics and Earthquake Engineering
M. Papadrakakis, V. Papadopoulos, V. Plevris (eds.)
Crete Island, Greece, 25–27 May 2015

EARTHQUAKE LOSS ASSESSMENT OF STEEL FRAME BUILDINGS DESIGNED IN HIGHLY SEISMIC REGIONS

Seong-Hoon Hwang[1], Ahmed Elkady[1], Samy Al.Bardaweel[2] and Dimitrios G. Lignos[1]

[1] McGill University
817 Sherbrooke West, Montreal, Quebec, Canada, H3A 2K6
e-mail: seong-hoon.hwang@mail.mcgill.ca, ahmed.elkady@mail.mcgill.ca, dimitrios.lignos@mcgill.ca

[2] The Lane Construction Corporation
Waco, Texas, USA
samy.albardaweel@mail.mcgill.ca

Keywords: Loss Assessment, Steel Special Moment Frames, Special Concentrically Braced Frames, Losses due to Demolition, Collapse.

Abstract. *In recent years, there is an increasing need to quantify earthquake-induced losses throughout the expected life of a building in order to evaluate alternative design options and to minimize repairs in the aftermath of an earthquake. For this reason, the next generation of performance-based earthquake engineering evaluation procedures has formalized procedures that assess several metrics of seismic performance including economic losses. This paper discusses an analytical study that quantifies the expected earthquake-induced losses in typical office steel buildings designed with perimeter special moment frames or perimeter concentrically braced frames at various ground motion intensities. These buildings are designed in urban California in accordance with today's seismic design provisions in North America. The expected economic losses associated with repair are computed based on a refined performance-based earthquake engineering framework developed within the Pacific Earthquake Engineering Research (PEER) center. This framework integrates site-specific seismic hazard, state-of-the-art nonlinear models that incorporate complex deteriorating phenomena of the structural components of a steel frame building, fragility curves of structural and non-structural components that express the probability of being or exceeding a specific damage level, and the resulting repair costs. The effect of residual deformations along the height of steel frame buildings on their earthquake losses is also examined. It is shown that repair costs in the aftermath of earthquakes vary significantly depending on the employed lateral load resisting system, as well as the analytical model representation of the steel frame building itself.*

1 INTRODUCTION

The next generation of performance-based earthquake engineering (PBEE) procedures [1,2] has formalized a framework for assessing the seismic performance of frame buildings through collapse that was established within the Pacific Earthquake Engineering Research Center (PEER) [3]. The same framework can be employed to assess earthquake-induced losses in buildings [4]. This is particularly important for stakeholders and building owners in order to take informed decisions for effective designs that minimize such losses in the aftermath of an earthquake. In building-specific earthquake loss assessment a numerical model representation of the building is typically subjected to a number of ground motions and critical engineering demand parameters (EDPs) associated with structural and non-structural damage are computed. Such EDPs are related with different damage states of each component of the building such that when these components are repaired their undamaged state is restored. Earthquake-induced losses are calculated through component-based fragility functions that express the probability of exceedance of a component being into a damage state given an EDP of interest (e.g., story drift ratio, absolute floor accelerations). A number of researchers introduced the first generation of building-specific loss estimation methodologies [5–7] that was later refined within PEER including a number of studies associated with earthquake-induced losses in reinforced concrete (RC) and wood structures [8, 9]. More recently, Ramirez and Miranda [10] introduced the influence of residual story drift ratios on building-specific earthquake-induced losses. They indicated that losses in RC frame buildings designed according to modern seismic provisions in highly seismic regions in United States are dominated by residual story drift ratios. This could be a fundamental issue in the case of mid- to high-rise steel frame buildings that utilize perimeter steel special moment frames (SMFs) or special concentrically braced frames (SCBFs). Figure 1 shows a 2-story steel building from the 2011 Tohoku earthquake in Japan that although it did not collapse it still had to be demolished due to excessive residual deformations in its second story after the earthquake. Another interesting aspect of the same problem is the effect of the numerical model that is typically employed to conducted the structural analysis and compute the critical EDPs of interest that are employed to compute the expected losses of a building under a seismic event. To the best of our knowledge, both issues have never been addressed in prior studies associated with building-specific economic losses in the aftermath of an earthquake.



Figure 1: Example of a steel building with residual displacements leading to demolition (source from [11]).

This paper employs a building-specific loss estimation methodology that was originally developed by Ramirez and Miranda [10] that explicitly considers the effect of residual defor-

mations along the height of frame buildings on the economic loss estimation after a seismic event. Low- and mid-rise steel frame buildings with perimeter SMFs and SCBFs designed in urban California are utilized to first compute their expected earthquake-induced losses for various seismic intensities from the onset of structural damage through dynamic collapse. The effect of different analytical model representations of the steel frame buildings on their earthquake-induced losses is also assessed. Two loss metrics are employed for this purpose including the expected losses conditioned on the seismic intensity *IM=im* and the expected annual losses (*EAL*) that provide information to compare to annual insurance premiums, assuming no deductible.

2 OVERVIEW OF LOSS ESTIMATION METHODOLOGY

This section presents a summary of the main aspects of the employed loss estimation methodology adopted by Ramirez and Miranda [10] considering the three possible outcomes for a building after an earthquake, namely (a) collapse does not occur and structural and/or non-structural damage in the building is repaired; (b) collapse does not occur, but the building is demolished and rebuilt; (c) collapse occurs and the building is rebuilt. Assuming that these outcomes are mutually exclusive, then the expected value of the loss in the building for a given seismic intensity *IM* can be computed as follows,

$$E\left[L_T\middle|IM\right]=E\left[L_T\middle|NC\cap R,IM\right]P\left(NC\cap R\middle|IM\right)+E\left[L_T\middle|NC\cap D\right]P\left(NC\cap D\middle|IM\right)+E\left[L_T\middle|C\right]P\left(C\middle|IM\right) \quad (1)$$

where, $E[L_T \mid NC\cap R,IM]$ is the expected value of the total loss in the building given that collapse does not occur and the building is repaired given that the seismic intensity was *IM=im*; $E[L_T \mid NC\cap D]$ is the expected loss in the building when there is no collapse but the building is demolished given that the seismic intensity was *IM=im*; and $E[L_T \mid C]$ is the expected loss in the building when collapse occurs given that the seismic intensity was *IM=im* and corresponds to the cost of removing the building from the site plus the replacement cost of the building. Moreover, $P(NC\cap R \mid IM)$, $P(NC\cap D \mid IM)$ and $P(C \mid IM)$ are the probability that the building will not collapse but that it will be repaired, the probability that the building will not collapse but it will be demolished due to large residual deformations and the probability that the building will collapse given that the seismic intensity of the earthquake is *IM=im*. Equation (1) can be rewritten as follows,

$$\begin{aligned}E\left[L_T\middle|IM\right]=&E\left[L_T\middle|NC\cap R,IM\right]P\left(R\middle|NC,IM\right)P\left(NC\middle|IM\right)\\&+E\left[L_T\middle|NC\cap D\right]P\left(D\middle|NC,IM\right)P\left(NC\middle|IM\right)+E\left[L_T\middle|C\right]P\left(C\middle|IM\right)\end{aligned} \quad (2)$$

where, $P(R \mid NC,IM)$, $P(NC \mid IM)$ are the probability that the building will be repaired given that no collapse occurred and the probability that the building did not collapse, respectively, given a seismic intensity *IM=im*; $P(D \mid NC,IM)$ is the probability that the building will be demolished given that it has not collapsed when subjected to an earthquake with seismic intensity *IM=im*. Equation (2) becomes,

$$\begin{aligned}E\left[L_T\middle|IM\right]=&E\left[L_T\middle|NC\cap R,IM\right]\left\{1-P\left(D\middle|NC,IM\right)\right\}\left\{1-P\left(C\middle|IM\right)\right\}\\&+E\left[L_T\middle|NC\cap D\right]P\left(D\middle|NC,IM\right)\left\{1-P\left(C\middle|IM\right)\right\}+E\left[L_T\middle|C\right]P\left(C\middle|IM\right)\end{aligned} \quad (3)$$

In order to estimate the probability that the building will be demolished given that it has not collapsed when subjected to an earthquake with seismic intensity *IM=im* the following relation can be employed,

$$P\left(D\middle|NC,IM\right)=\int_0^\infty P\left(D\middle|RSDR\right)dP\left(RSDR\middle|NC,IM\right) \tag{4}$$

where, $P(D|RSDR)$ is the probability of having to demolish the building conditioned on the maximum residual story drift ratio (*RSDR*) from all stories of the building; $P(RSDR|NC,IM)$ is the probability of experiencing a certain level of *RSDR* in the building given that it has not collapsed and that it has been subjected to an earthquake with seismic intensity $IM=im$. We have assumed that $P(D|RSDR)$ is lognormally distributed with a median of 0.015 and a logarithmic standard deviation of 0.3 as suggested in [10]. This value is purely based on engineering judgment.

3 DESCRIPTION OF CASE-STUDY STEEL FRAME BUILDINGS

In order to quantify the earthquake-induced losses in steel frame buildings with perimeter SMFs and SCBFs, four steel buildings were considered whose seismic response was thoroughly studied through collapse in prior analytical studies [12–15]. In particular, the four steel buildings are as follows: 4- and 12-story steel frame buildings with perimeter SMFs [12–14]; 3- and 12-story steel frame buildings with perimeter SCBFs [15]. All four buildings were assumed to be located in the Bulk Center (34.000°N, 118.150°W) in Los Angeles, which is considered to be a representative location in urban California with high-seismicity [16]. A seismic design category D_{max} and soil class D is considered. The site-specific seismic hazard curves for the four steel buildings considered as part of this paper are shown in log-log scale in Figure 2. All the buildings were designed in accordance with ASCE-7-10 [17], ANSI/AISC 341-10 [18] seismic provisions. A plan view and elevation of a typical 4- and 3-story steel frame building with perimeter SMFs and SCBFs, respectively, are shown in Figure 3. The steel SMFs utilize typical fully restrained beam-to-columns connections with reduced beam sections (RBS) designed according to AISC-358-10 [19]. Details regarding the design of these buildings are summarized in [12–14]. The SCBFs utilize round steel hollow structural sections as braces as discussed in [15]. Their gusset plates have been designed according to a balanced design approach proposed by Lehman et al. [20]. Note that for the 3-story steel frame building with SCBFs only two SCBFs were designed per loading direction (see Figure 3c). The interior gravity framing (i.e., floor system and gravity columns) of the four steel frame buildings was explicitly designed based on ANSI/AISC-360-10 [21]. Note that the orientation of the strong axis of the interior gravity columns is assumed to be perpendicular to the loading direction of interest [i.e., east-west (EW)] as shown in Figures 3a and 3c.

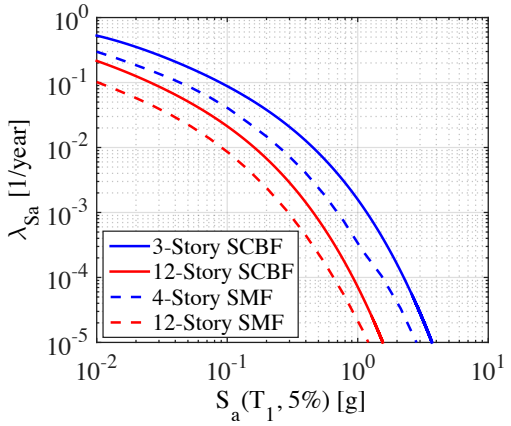


Figure 2: Site-specific hazard curves for the four steel buildings considered.

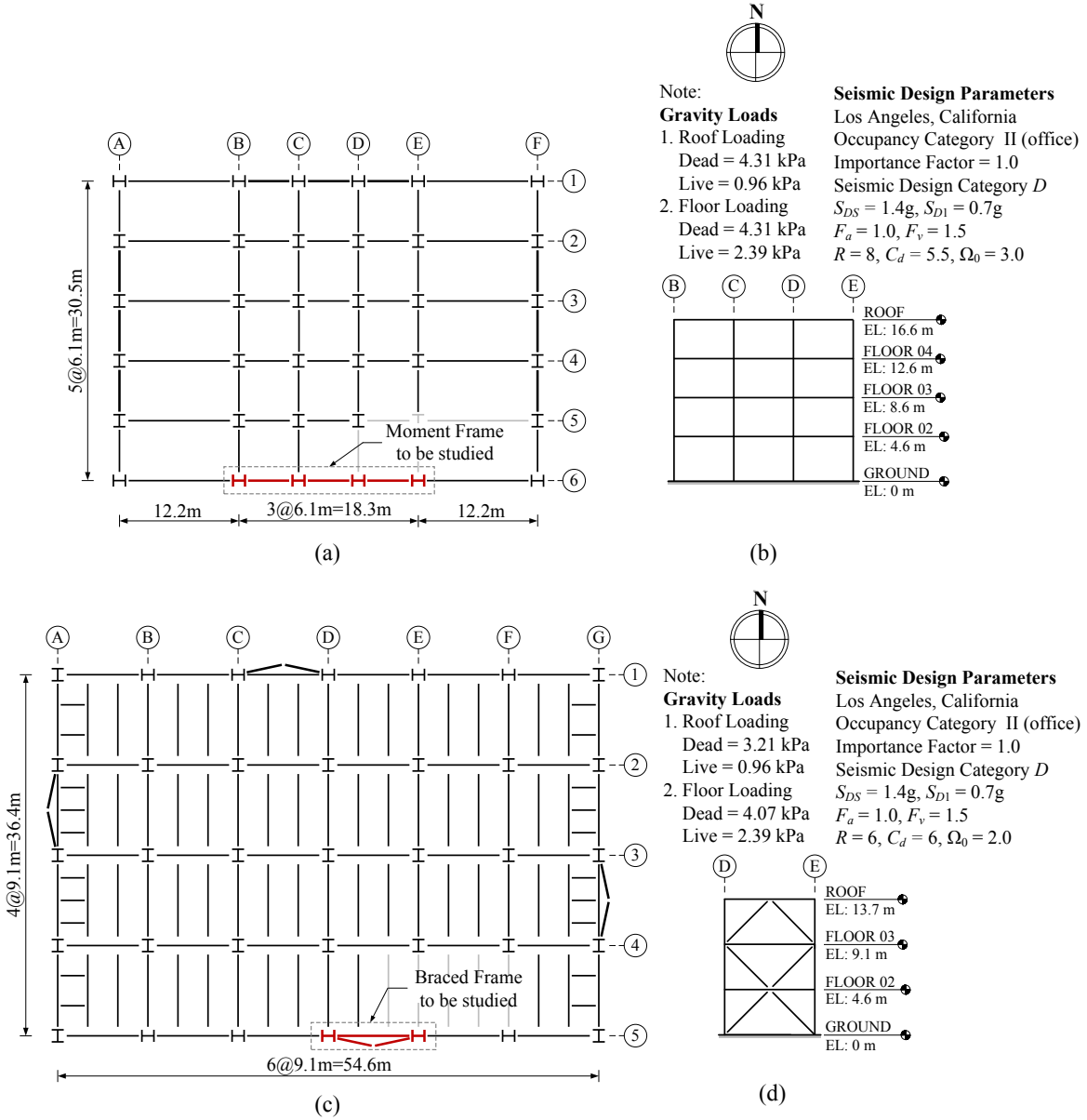


Figure 3: Typical office steel buildings with perimeter steel SMFs and SCBFs.

3.1 Fragility and cost distribution functions

In order to compute realistic loss estimations for the steel frame buildings being considered architectural layouts are developed. A rectangular footprint that is 1,296.25m^2 (14,000 sq.ft) and 1,871.36m^2 (20,144 sq.ft) is developed for the steel frame buildings with perimeter SMFs and SCBFs, respectively (see Figures 3a and c). Prior studies by Aslani and Miranda [22] have demonstrated that a large contributor to earthquake-induced losses in frame buildings is the damage to their nonstructural components even for moderate seismic intensities. The replacement cost estimates for the four buildings that were studied as part of this paper are summarized in Table 1. These replacement cost estimates are employed to normalize the expected losses for the four steel frame buildings at various seismic intensities as discussed later on in Section 5.Cost estimates were developed using the RS Means Cost Estimating Manuals [23] and listed in Table 2 based on the considered damageable components (structural and nonstructural) together with the fragility distribution functions assigned with the repair of the-

se components. Note that the source for each component fragility curve is also noted as part of Table 1.

Building type	Footprint	Area [m^2]	Replacement cost ($)	Cost per m^2 ($)
4-story with perimeter SMFs	42.5m x 30.5m	5,185	7,000,000	1350.1
12-story with perimeter SMFs	42.5m x 30.5m	15,555	21,000,000	1350.1
3-story with perimeter SCBFs	36.4m x 54.4m	5,614	8,100,000	1442.8
12-story with perimeter SCBFs	36.4m x 54.4m	22,456	32,400,000	1442.8

Table 1: Cost estimates for steel frame buildings studied

Assembly description	Damage state	Fragility parameters			Repair cost parameters	
		EDP	x_m	beta	x_m ($)	beta
Columns (base plate) [1,2]	Crack Initiation	SDR (unitless)	0.04	0.40	19224	0.41
	Crack Propagation		0.07	0.40	27263	0.37
	Fracture		0.10	0.40	32424	0.34
Columns (splices) [1,2]	Cracking of the groove welded flange	SDR (unitless)	0.04	0.4	9445	0.32
	Column web failure		0.07	0.4	11246	0.30
	Fracture		0.10	0.4	38473	0.17
Round HSS Braces (Brace weight < 40 plf) [24]	Brace flexural buckling	SDR (unitless)	0.0041	0.51	30897	0.33
	Brace local buckling		0.0096	0.45	39438	0.30
	Brace strength loss		0.0275	0.51	39438	0.30
Round HSS Braces (41 plf < Brace weight < 99 plf) [24]	Brace flexural buckling	SDR (unitless)	0.0041	0.51	30897	0.33
	Brace local buckling		0.0096	0.45	54892	0.28
	Brace strength loss		0.0275	0.51	54892	0.28
Non-RBS beam-column moment connections (beam depth <= W27) [1,2]	Local buckling	SDR (unitless)	0.03	0.30	16033	0.35
	lateral-torsional buckling		0.04	0.30	25933	0.31
	fracture		0.05	0.30	25933	0.31
Non-RBS beam-column moment connections (beam depth >= W30) [1,2]	Local buckling	SDR (unitless)	0.03	0.30	17033	0.33
	lateral-torsional buckling		0.04	0.30	28433	0.28
	fracture		0.05	0.30	28433	0.28

Table 2: fragility and cost distributions.

RBS beam-column moment connections (One side of beam) [25]	Yield Anywhere	SDR (unitless)	0.01	0.17	0	0
	Yielding First in Panel Zone	SDR (unitless)	0.01	0.15	0	0
	Yielding First in Flange	SDR (unitless)	0.0096	0.10	0	0
	Local Buckling	SDR (unitless)	0.0216	0.30	16033	0.352
	Fracture	SDR (unitless)	0.05	0.30	26000	0.305
RBS beam-column moment connections (Both sides of beam) [25]	Yield Anywhere	SDR (unitless)	0.01	0.17	0	0
	Yielding First in Panel Zone	SDR (unitless)	0.01	0.15	0	0
	Yielding First in Flange	SDR (unitless)	0.0096	0.10	0	0
	Local Buckling	SDR (unitless)	0.0216	0.30	24000	0.33
	Fracture	SDR (unitless)	0.05	0.30	41840	0.27
Shear tab connections [1,2]	Yielding of shear tab	SDR (unitless)	0.04	0.40	12107	0.37
	Partial tearing of shear tab		0.08	0.40	12357	0.38
	Complete separation of shear tab		0.11	0.40	12307	0.38
Corrugated Slab (90mm steel; 100mm overlay) [26]	Crack Initiation	SDR (unitless)	0.00375	0.13	18	0.35
	Crushing Near Column		0.01	0.22	33	0.35
	Shear Stud Fracture		0.05	0.35	57	0.35
Drywall partition [1,2]	Visible	SDR (unitless)	0.0039	0.17	90	0.20
	Significant	SDR (unitless)	0.0085	0.23	530	0.20
Drywall finish [1,2]	Visible	SDR (unitless)	0.0039	0.17	90	0.20
	Significant	SDR (unitless)	0.0085	0.23	250	0.20
Acoustic ceiling [1,2]	Collapse	PFA(g)*	92/(l+w)	0.81	2.2×A	0.50
Automatic sprinklers [1,2]	Fracture	PFA(g)*	0.32	1.40	900	0.50
Elevators [1,2]	Failure	PGA(g)+	0.41	0.28	5000	1.00

*PFA: Peak floor absolute acceleration (units of g); + PGA: Peak ground acceleration (units of g)

Table 2 (continued): fragility and cost distributions.

4 NONLINEAR BUILDING MODELS AND COLLAPSE SIMULATIONS

Nonlinear analytical model representations of the steel frame buildings discussed in Section 3 are developed in the OpenSees simulation platform [27]. These models are 2-Dimensional (2-D). In order to assess the effect of the analytical model representation of a steel building on its loss estimation due to earthquake shaking two types of analytical models are developed. The first one is a model that considers the bare steel structural components of the corresponding lateral load resisting system (i.e., bare SMF and bare SCBF: noted as B-model); the second one is a model that considers the effects of the composite slab and the interior gravity framing system on the lateral strength and flexural stiffness of the steel frame building under consideration (noted as CG model).

The SMF steel beams and columns are modeled with concentrated plasticity hinges (i.e., lumped plasticity) employing a phenomenological deterioration model that was developed by Ibarra et al. [28] and was further refined and calibrated by Lignos and Krawinkler [29] with a comprehensive steel beam database [30] (publically available from the following link: http://dimitrios-lignos.research.mcgill.ca/databases/). In order to take into consideration the effect of composite action on the hysteretic response of the beams with RBS modeling recommendations by Elkady and Lignos [13] are employed. Figure 4a shows a comparison of the simulated and measured moment-rotation hysteretic relation of a fully restrained beam-to-column connection with RBS including the composite action. The effect of gravity framing on the overall seismic performance of steel frame buildings is captured as discussed in Elkady and Lignos [14]. This necessitates a realistic representation of typical shear-tab beam-to-column connections that are used for the design of the floor system of a steel frame building. Figure 4b illustrates a comparison of the measured and simulated moment-rotation hysteretic relation of a shear-tab beam-to-column connection including the possibility of beam binding on the column flange as discussed in [14].

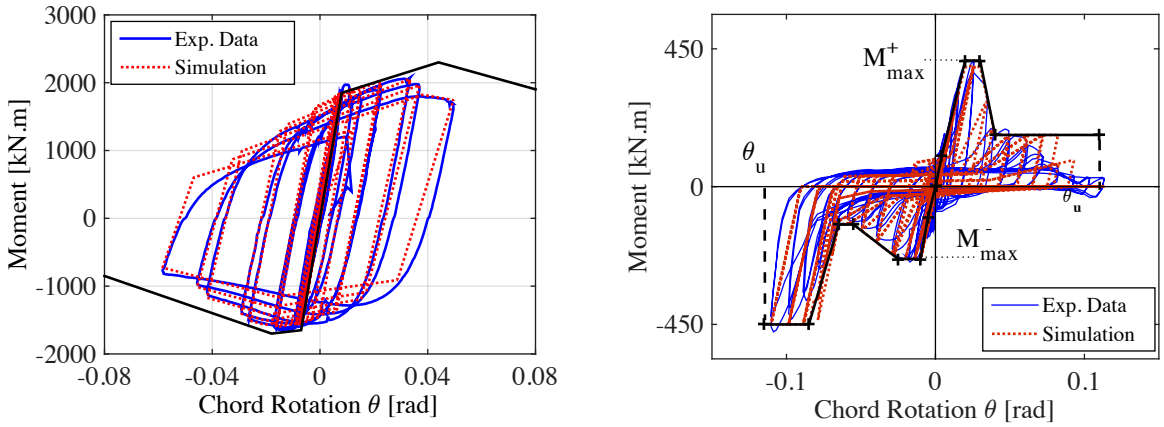
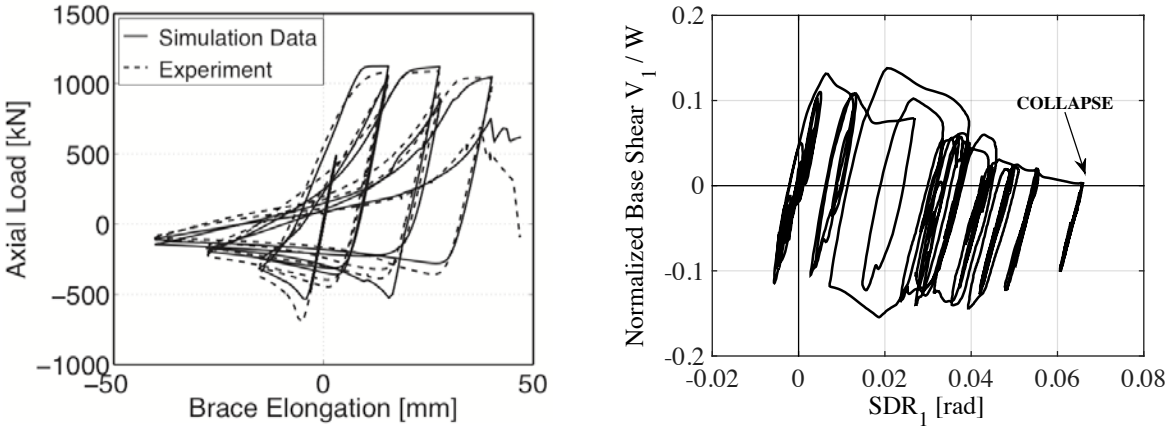


Figure 4: Examples of modeling the moment-rotation hysteretic relation of fully-restrained beam-to-column connections with RBS and typical single-row shear tab beam-to-column connections (data from [30,31])

The SCBFs are modeled based on the computational approach discussed in Karamanci and Lignos [33]. In summary, steel braces are modeled with fiber-based elements that are able to trace flexural buckling as well as fracture initiation due to low-cycle fatigue based on the material model proposed by Uriz et al. [34]. Figure 5a illustrates a comparison of the measured and simulated hysteretic axial force-axial deformation relation of a round HSS steel brace based on the approach discussed in Karamanci and Lignos [33,35]. The flexibility and flexural yielding of the gusset plates at the ends of the steel braces due to out-of-plane brace deformations is explicitly considered based on the model proposed by Hsiao et al. [36]. Cyclic

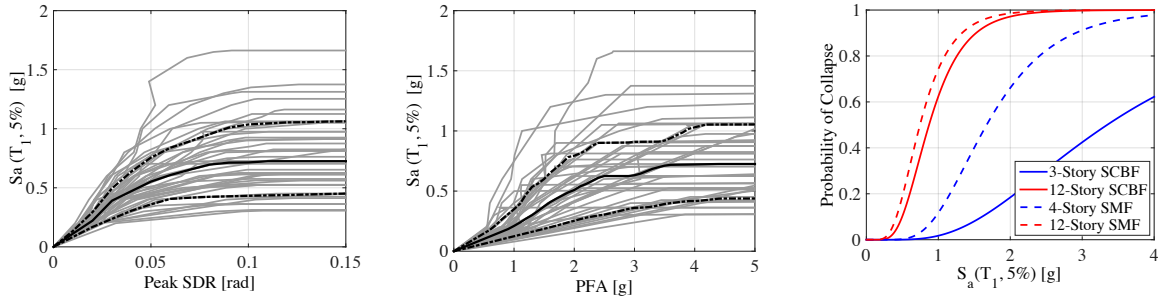
deterioration in flexural strength and stiffness of SCBF beams and columns are simulated based on the approach discussed earlier for SMFs.



(a) modeling inelastic buckling and fracture in steel braces (b) definition of sidesway collapse

Figure 5: Modeling inelastic buckling and fracture in steel braces and definition of sidesway collapse in steel frame buildings (data from [37]).

The analytical model representations of the steel frame buildings discussed earlier are subjected to the Far-Field set of 44 ground motions from FEMA P695 [37]. This set represents large magnitude earthquakes, recorded on rick or stiff soil sites and they represent the seismic hazard of the design location. Incremental dynamic analysis (IDA) is employed as discussed by Vamvatsikos and Cornell [39] in order to trace the dynamic collapse due to sidesway instability for each analytical model. Collapse occurs when a story or a number of stories displaces sufficiently such that P-Delta effects accelerated by component deterioration make the first-order story shear resistance of the respective model equal to zero. Figure 5b illustrates an example of such case for the CG-model of the 12-story steel frame building with SMFs. This definition of collapse is consistent with prior small and full-scale shake table collapse tests of steel frame buildings [39–41]. The *EDPs* of interest [i.e., peak story drift ratios (*SDRs*), peak absolute floor accelerations (*PFAs*), residual story drift ratios (*RSDRs*)] are obtained for each ground motion over the full range or seismic intensities through collapse. Figures 6a and 6b illustrate the peak *SDRs* and *PFAs* versus *IM* [i.e., $S_a(T_1,5\%)$], respectively, for the 12-story steel frame building with perimeter SMFs (CG-model). In the same figures we have superimposed the counted median, 16th and 84th percentiles based on the set of 44 ground motions. Based on the IDA, a collapse fragility curve is computed per analytical model representation that describes the probability of collapse as a function of the first mode spectral acceleration $S_a(T_1,5\%)$. Figure 6c illustrates the collapse fragility curves for the four CG models of the steel frame buildings with perimeter SMFs and SCBFs.



(a) IM versus peak SDRs (b) IM versus PFAs (c) collapse fragility curves

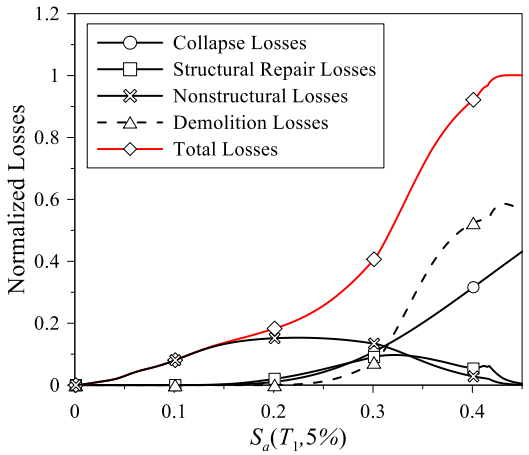
Figure 6: Critical EDPs and collapse fragility curves for steel frame buildings with perimeter SMFs and SCBFs.

5 EXPECTED LOSSES CONDITIONED ON SEISMIC INTENSITY

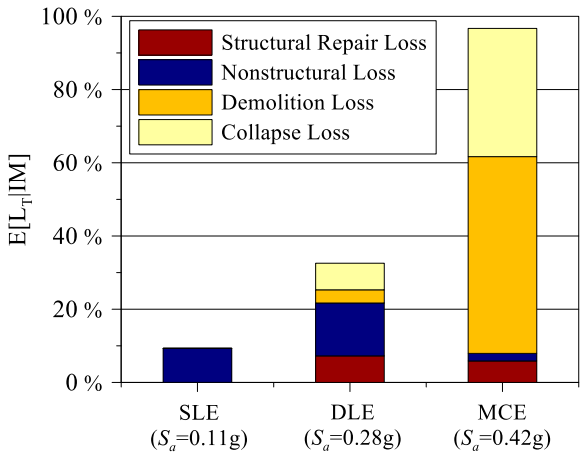
The expected losses are computed for each building conditioned on the seismic intensity, as shown in Figures 7a and c for the 12-story steel frame buildings with perimeter SMFs and SCBFs, respectively, when the bare frame is only considered as part of the analytical model representation of the building under consideration (i.e., B-models). These curves are also known as loss vulnerability curves [10]. The total repair losses conditioned on seismic intensity are further disaggregated into losses due to structural and nonstructural component repair, losses due to demolition given that building collapse has not occurred and losses due to dynamic collapse. In these figures the expected losses for the 12-story steel frame building are normalized with respect to its total replacement cost (see Table 1). For steel frame buildings with perimeter SMFs (see Figure 7a) the total loss vulnerability curves initially increase linearly with respect to the seismic intensity. Note that for the case of the 12-story steel frame building under service level [i.e., SLE: $S_a(T_1,5\%) = 0.11g$] and design level [i.e., DLE: $S_a(T_1,5\%) = 0.32g$] earthquake intensities losses are dominated by damage into nonstructural components (see Figure 7b). This is to be expected based on past reconnaissance reports for steel buildings with moment resisting frames [42,43]. However, from Figure 7c, this is not the case for steel frame buildings with perimeter SCBFs. In particular, under the DLE intensity [i.e., $S_a(T_1,5\%) = 0.40g$] the expected losses equal to the 20% of the replacement cost of the 12-story steel building with SCBFs is attributed to damage due to flexural buckling of its steel round HSS braces (see Figure 7d). This is to be expected due to the fact that steel braces would typically buckle in flexure at about 0.5% story drift ratios as discussed in Lignos and Karamanci [24]. From Figure 7 losses are dominated by the non-collapse losses at lower intensities that have a higher rate of occurrence regardless of the lateral load resisting system. From the same figure, for seismic intensities higher than 0.4g that are associated with maximum considered earthquakes (i.e., MCE: 2% probability of exceedance over 50 years) collapse losses tend to contribute much more to the overall earthquake-induced losses of a steel frame building regardless of its height and its lateral load resisting system. This can be clearly seen in Figures 7b and 7d. From the same figures, another notable observation is that at higher seismic intensities associated with MCE shaking building losses are dominated by demolition given that building collapse has not occurred. This is much more evident for the 12-story steel building with SMFs (see Figure 7b) compared to the 12-story steel building with SCBFs (see Figure 7d). This agrees with earlier findings on code-compliant RC frame buildings [10]. Similar observations hold true for the 4-and 3-story steel frame buildings with perimeter SMFs and SCBFs, respectively.

In order to examine the effect of analytical model representation of a steel frame building on its earthquake loss estimation the same analysis discussed above is repeated for the CG models (see Section 4). Figures 8a and 8c illustrate the loss vulnerability curves for the 12-story steel buildings with perimeter SMFs and SCBFs, respectively, when the gravity framing is considered as part of the analytical model of the respective building. From these figures, the findings associated with (a) the magnitude of earthquake losses and (b) the primary contributors to total losses for low seismic intensities (i.e., SLE, DLE) are practically the same with the ones computed based on the B-models building representations. This can be seen in Figures 8b and 8d for the 12-story steel frame with perimeter SMFs and SCBFs, respectively. It is worth mentioning that for the 12-story building with perimeter SMFs for seismic intensities associated with extreme earthquake events (i.e., MCE intensity) the losses due to demolition become nearly half compared to estimated ones based on the B-model of the same building (see Figure 8b). Losses associated with collapse are also reduced by about 50% as shown in Figure 8b in comparison with Figure 7b (i.e., results are based on the B-model). Similarly, for

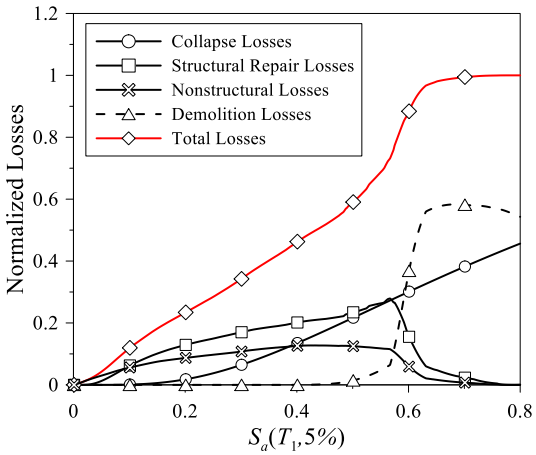
the 12-story steel building with perimeter SCBFs losses due to demolition become very small under a MCE seismic intensity as shown in Figure 8d. This indicates that there is less drift concentration in the bottom stories of steel frame buildings with SCBFs when the interior gravity framing is considered as part of the lateral-force resistance system. This agrees with findings from prior analytical studies on braced frames [45]. Note that for $S_a(T_1,5\%) > 0.7g$ losses due to demolition become fairly large the 12-story steel frame building with perimeter SCBFs. However, losses due to collapse practically are not affected by the analytical model representation of the same building. This is attributed to the fact that in concentrically braced frames it is nearly impossible to achieve a uniform demand-to-capacity ratio along their height and ultimately avoid local story mechanisms that are associated with concentration of plastic deformations that trigger structural collapse [33].



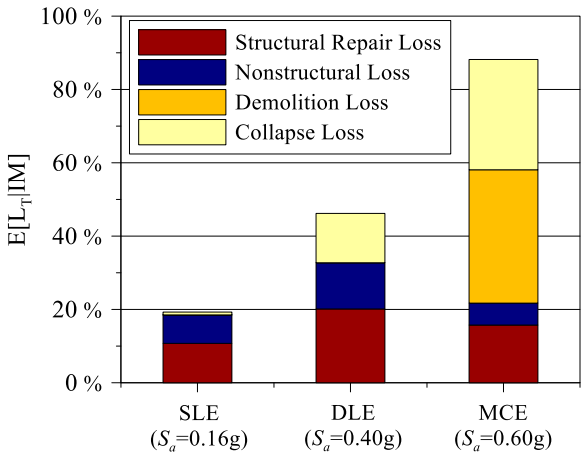
(a) 12-story steel building with SMFs



(b) 12-story steel building with SMFs-three intensities



(c) 12-story steel building with SCBFs



(d) 12-story steel building with SCBFs-three intensities

Figure 7: Normalized loss vulnerability functions for steel frame buildings with perimete SMFs and SCBFs conditioned on seismic intensity without considering the gravity framing system and composite action as part of the analytical model representation (B-models)

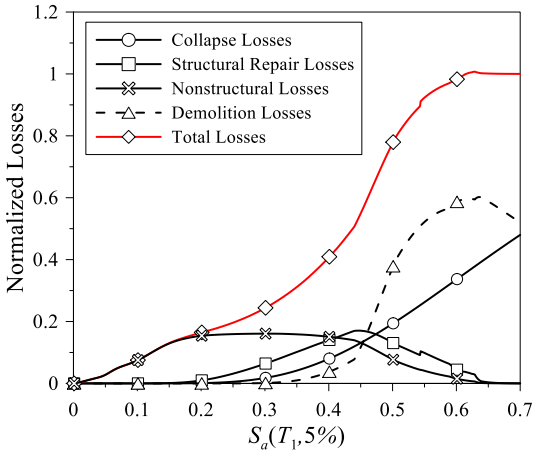
In summary, from a comparison of Figures 7 and 8 it is clear that earthquake induced losses in steel frame buildings may be significantly overestimated under MCE seismic intensities if the contribution of the interior gravity framing and the composite action to lateral strength and stiffness is neglected.

6 EXPECTED ANNUAL LOSSES

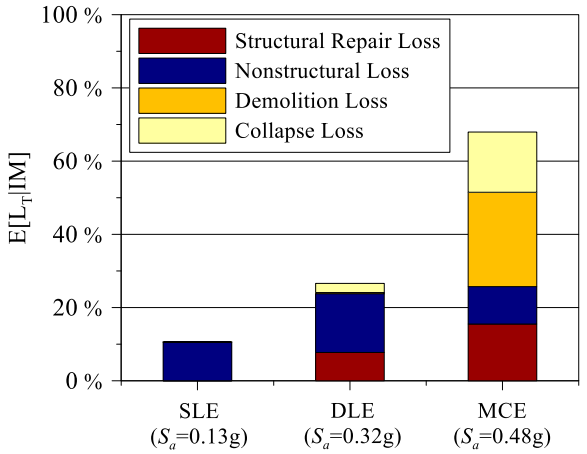
This section summarizes the normalized *EAL* results for the four steel frame buildings that are studied depending on the employed analytical model representation (i.e., B-models versus CG models). The *EAL* is computed as follows,

$$E\left(L_T\right)=\int_0^{\infty}E\left(L_T\middle|IM\right)\mathrm{d}\lambda\left(IM\right)=\int_0^{\infty}E\left(L_T\middle|IM\right)\left|\frac{\mathrm{d}\lambda\left(IM\right)}{\mathrm{d}IM}\right|\mathrm{d}IM \tag{5}$$

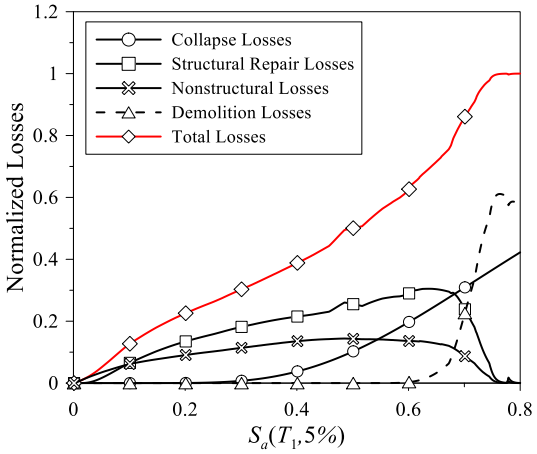
where $\lambda(IM)$ is the mean annual frequency of the ground motion intensity and $|\mathrm{d}\lambda(IM)/\mathrm{d}(IM)|$ is the derivative of the seismic hazard curve (see Figure 2).



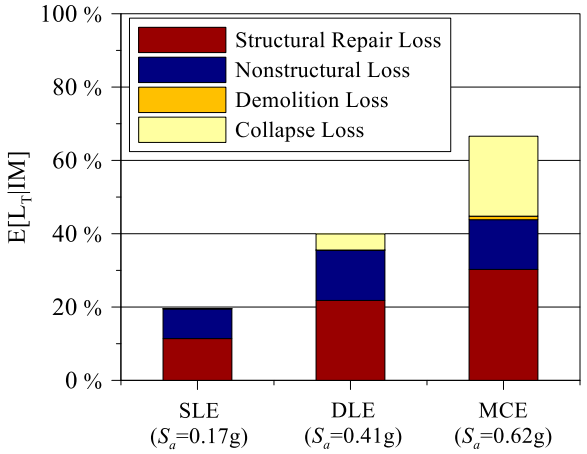
(a) 12-story steel building with SMFs



(b) 12-story steel building with SMFs-three intensities



(c) 12-story steel building with SCBFs



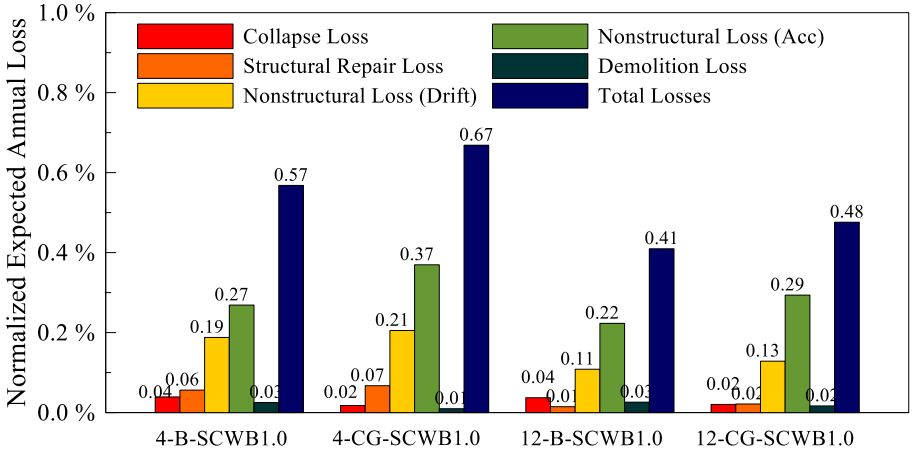
(d) 12-story steel building with SCBFs-three intensities

Figure 8: Normalized loss vulnerability functions for steel frame buildings with perimeter SMFs and SCBFs conditioned on seismic intensity based on analytical mode representations that include the gravity framing system (CG-models).

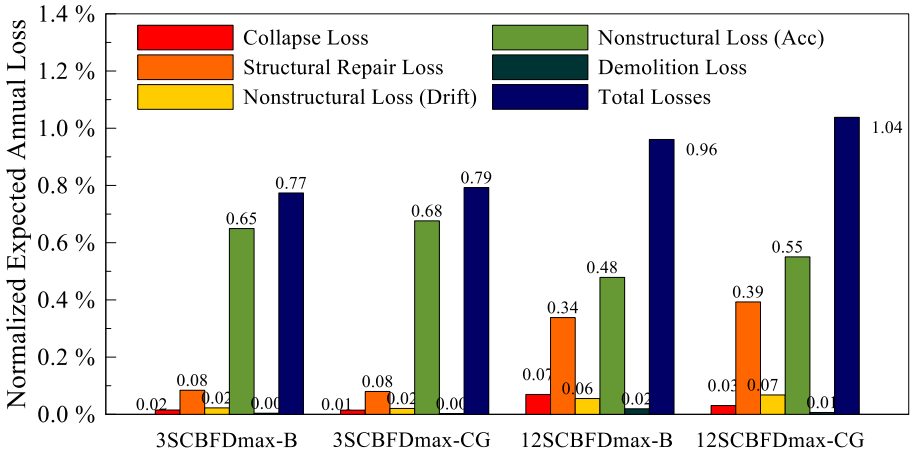
Figure 9a illustrates the normalized *EAL* results for the 4- and 12-story steel frame buildings with perimeter SMFs. Based on this figure the expected annual losses vary between 0.41 to 0.67% of the replacement costs for mid-rise and low-rise steel buildings, respectively. The total normalized annual losses for the 3- and 12-story steel frame buildings with perimeter SCBFs tend to be larger than the equivalent results for steel frame buildings with SMFs as shown in Figure 9b. In order to explain this finding the *EAL* results are further disaggregated into losses due to acceleration- and drift-sensitive nonstructural components, structural repair and demolition losses and collapse losses. For steel frame buildings with perimeter SMFs the

expected annual losses and demolition and collapse expected annual losses. From Figure 9, the drift-sensitive nonstructural components of steel frame buildings with perimeter SMFs contribute more to the total *EAL*s than the equivalent *EAL* results for steel frame buildings with SCBFs. This is to be expected given the flexibility of the former compared to the latter. However, steel frame buildings with perimeter SCBFs tend to have nearly double *EALs* due to acceleration-sensitive nonstructural component repairs compared to steel frame buildings with perimeter SMFs. This is attributed to the fact that SCBFs are typically much stiffer than SMFs with the same height. Another notable observation from Figure 9b is that *EALs* due to structural damage into steel round HSS braces in mid-rise steel buildings with perimeter SCBFs become comparable with *EALs* due to acceleration-sensitive nonstructural component repairs. This is attributed to the relatively small story drift ratios that flexural buckling may occur in steel braces [24]. On the contrary, in steel frame buildings with perimeter SMFs the *EAL* results in terms of repairs of the primary structural components (e.g., beam-to-column connections and/or steel columns) is a negligible fraction of the total *EAL*s. The reason is that such components are typically damaged at story drift ratios larger than 1%.

It is worth mentioning that *EAL* results weight all possible levels of seismic intensity by taking into account their probability of occurrence (see Eq. 5). Therefore, it may be a more comprehensive loss metric than other loss metrics conditioned on a single seismic intensity such as a service, design or maximum considered earthquake in order to evaluate a steel frame building's seismic risk.



(a) Normalized expected annual losses for steel frame buildings with perimeter SMFs



(b) Normalized expected annual losses for steel frame building with perimeter SCBFs

Figure 9: Normalized expected annual losses for steel frame buildings with perimeter SMFs and SCBFs.

7 CONCLUSIONS

This paper evaluated the earthquake-induced losses in four steel frame buildings with perimeter special moment frames (SMFs) and special concentrically braced frames (SCBFs) designed in urban California in accordance with today's regional seismic provisions. Two types of analytical model representations of the steel frame buildings were considered including (a) models that represent the bare structural components of the lateral load resisting system of a building; and (b) models that take into account the composite action and the interior gravity framing of a steel frame building. The earthquake loss assessment was based on two primary loss metrics including (a) the expected losses conditioned on seismic intensity and (b) the expected annual losses. The effect of residual deformations of a building that did not collapse at a given seismic intensity on its earthquake losses was considered based on the approach discussed in [10]. Even though the present assessment is based on four steel frame buildings only, the main findings discussed in this paper are summarized as follows:

- Non-collapse repairs at low seismic intensities associated with service and/or design level earthquakes dominate building earthquake losses. The primary contributor to these losses is damage to the nonstructural content of a building regardless of the selected lateral load resisting system.
- At seismic intensities associated with design level earthquakes, steel buildings that utilize perimeter SCBFs tend to have considerable repairs due to steel brace flexural buckling. This is not the case for steel buildings that utilize perimeter SMFs.
- Demolition and collapse losses tend to dominate building earthquake losses at seismic intensities associated with maximum considered earthquakes. Demolition losses are attributed to large residual deformations that steel frame buildings may experience during a large earthquake.
- Earthquake-induced losses in steel frame buildings may be considerably overestimated when critical engineering demand parameters (EDPs) that control losses are based on analytical models that represent the bare lateral load resisting system only. The consideration of the composite action and the interior gravity framing of a steel frame building in the analytical model representation of a building reduces the earthquake-induced losses due to demolition by more than 50% regardless of the employed lateral load resisting system.
- In steel frame buildings with perimeter SMFs repairs in drift-sensitive nonstructural components followed by acceleration-sensitive nonstructural components primarily dominate the expected annual losses. The expected annual losses in steel frame buildings with perimeter SCBFs are dominated by acceleration-sensitive nonstructural components due to high absolute floor acceleration demands because of the considerable lateral stiffness of a SCBF. An important contributor to the expected annual losses is steel brace repairs due to flexural buckling at fairly small story drift ratios.

REFERENCES

[1] FEMA, "Seismic performance assessment of buildings Volume 1 - Methodology." Federal Emergency Management Agency (FEMA), Washington, DC, 2012.
[2] FEMA, "Seismic performance assessment of buildings, Volume 2 - Implementation Guide." Federal Emergency Management Agency (FEMA), Washington, DC, 2012.

[3] A. Cornell C. and H. Krawinkler, "Progress and challenges in seismic performance assessment.," in *PEER Center News*, Berkeley, California, 2000, vol. 3, pp. 1–4.
[4] H. Krawinkler and E. Miranda, "Performance-based earthquake engineering, Chapter 9," in *Earthquake Engineering: From Engineering Seismology to Performance-Based Engineering*, vol. 1st, 1 vols., Boca Raton, FL: CRC Press, 2004, pp. 9–1 to 9–59.
[5] K. A. Porter, A. S. Kiremidjian, and J. S. LeGrue, "Assembly-based vulnerability of buildings and its use in performance evaluation," *Earthq. Spectra*, vol. 17, no. 2, pp. 291–312, May 2001.
[6] S. Gunturi, "Building-specific earthquake damage estimation," PH.D. Dissertation, John A. Blume Earthquake Engineering Center, Stanford University, Stanford, California, 1993.
[7] A. Singhal and A. Kiremidjian, "A Method for earthquake motion-damage relationships with application to reinforced concrete frames.," John A. Blume Earthquake Engineering Center, Stanford University, Stanford, California, Technical Report 119, 1996.
[8] C. M. Ramirez, A. B. Liel, J. Mitrani-Reiser, C. B. Haselton, A. D. Spear, J. Steiner, G. G. Deierlein, and E. Miranda, "Expected earthquake damage and repair costs in reinforced concrete frame buildings," *Earthq. Eng. Struct. Dyn.*, vol. 41, no. 11, pp. 1455–1475, Sep. 2012.
[9] S. Pei and J. W. van de Lindt, "Methodology for earthquake-induced loss estimation: An application to woodframe buildings," *Struct. Saf.*, vol. 31, no. 1, pp. 31–42, Jan. 2009.
[10] C. M. Ramirez and E. Miranda, "Significance of residual drifts in building earthquake loss estimation," *Earthq. Eng. Struct. Dyn.*, vol. 41, no. 11, pp. 1477–1493, Sep. 2012.
[11] T. Okazaki, D. G. Lignos, M. Midorikawa, J. M. Ricles, and J. Love, "Damage to steel buildings observed after the 2011 Tohoku-Oki earthquake," *Earthq. Spectra*, vol. 29, no. S1, pp. S219–S243, Mar. 2013.
[12] A. Elkady and D. G. Lignos, "Effect of composite action on the dynamic stability of special steel moment resisting frames designed in seismic regions," in *Structures Congress 2013*, pp. 2151–2160.
[13] A. Elkady and D. G. Lignos, "Modeling of the composite action in fully restrained beam-to-column connections: implications in the seismic design and collapse capacity of steel special moment frames," *Earthq. Eng. Struct. Dyn.*, vol. 43, no. 13, pp. 1935–1954, Apr. 2014.
[14] A. Elkady and D. G. Lignos, "Effect of gravity framing on the overstrength and collapse capacity of steel frame buildings with perimeter special moment frames," *Earthq. Eng. Struct. Dyn.*, (available in early view), Nov. 2014.
[15] NIST, "Evaluation of the FEMA P-695 Methodology for Quantification of Building Seismic Performance Factors." National Institute of Standards and Technology (NIST), U.S. Department of Commerce, Gaithersburg, Maryland, 2009.
[16] C. A. Goulet, C. B. Haselton, J. Mitrani-Reiser, J. L. Beck, G. G. Deierlein, K. A. Porter, and J. P. Stewart, "Evaluation of the seismic performance of a code-conforming reinforced-concrete frame building—from seismic hazard to collapse safety and economic losses," *Earthq. Eng. Struct. Dyn.*, vol. 36, no. 13, pp. 1973–1997, Oct. 2007.
[17] ASCE, "Minimum Design Loads for Buildings and Other Structures." American Society of Civil Engineers, Reston, Virginia, 2010.
[18] AISC, "Seismic provisions for structural steel buildings," American Institute for Steel Construction, Chicago, IL, Seismic Provisions ANSI/AISC 341-10, 2010.
[19] AISC, "Prequalified connections for special and intermediate steel moment frames for seismic applications," American Institute for Steel Construction, Chicago, IL, Seismic Provisions ANSI/AISC 358-10, 2010.

[20] D. Lehman, C. Roeder W., D. Herman, S. Johnson, and B. Kotulka, "Improved seismic performance of gusset plate connections," *J. Struct. Eng.*, vol. 134, no. 6, pp. 890–901, 2008.
[21] AISC, "Specification for structural steel buildings," American Institute for Steel Construction, Chicago, IL, Seismic Provisions ANSI/AISC 360-10, 2010.
[22] H. Aslani and E. Miranda, "Probabilistic earthquake loss estimation and loss disaggregation in buildings," John A. Blume Earthquake Engineering Center, Stanford University, Stanford, California, Ph.D. Thesis 157, 2005.
[23] RS Means, *Square foot costs 2015*, 36th ed. Kingston, MA: RS Means Corporation, 2015.
[24] D. G. Lignos and E. Karamanci, "Drift-based and dual-parameter fragility curves for concentrically braced frames in seismic regions," *J. Constr. Steel Res.*, vol. 90, pp. 209–220, Nov. 2013.
[25] D. G. Lignos, D. Kolios, and E. Miranda, "Fragility assessment of reduced beam section moment connections," *J. Struct. Eng.*, vol. 136, no. 9, pp. 1140–1150, 2010.
[26] S. Al Bardaweel and D. G. Lignos, "Indicators for sustainable design of civil engineering systems: Towards earthquake resilient steel frame buildings through loss assessment, Report No. G13-49," Master of Science, McGill University, McGill University, Montreal, Canada, 2013.
[27] F. T. Mckenna, "Object-oriented finite element programming: frameworks for analysis, algorithms and parallel computing," University of California, Berkeley, 1997.
[28] L. F. Ibarra, R. A. Medina, and H. Krawinkler, "Hysteretic models that incorporate strength and stiffness deterioration," *Earthq. Eng. Struct. Dyn.*, vol. 34, no. 12, pp. 1489–1511, Oct. 2005.
[29] D. G. Lignos and H. Krawinkler, "Deterioration Modeling of Steel Components in Support of Collapse Prediction of Steel Moment Frames under Earthquake Loading," *J. Struct. Eng.*, vol. 137, no. 11, pp. 1291–1302, 2011.
[30] D. G. Lignos and H. Krawinkler, "Development and utilization of structural component databases for performance-based earthquake engineering," *J. Struct. Eng.*, vol. 139, no. 8, pp. 1382–1394, 2013.
[31] X. Zhang and J. M. Ricles, "Experimental evaluation of reduced beam section connections to deep columns," *J. Struct. Eng.*, vol. 132, no. 3, pp. 346–357, 2006.
[32] J. Liu and A. Astaneh-Asl, "Cyclic testing of simple connections including effects of slab," *J. Struct. Eng.*, vol. 126, no. 1, pp. 32–39, 2000.
[33] E. Karamanci and D. Lignos G., "Computational approach for collapse assessment of concentrically braced frames in seismic regions," *J. Struct. Eng.*, vol. 15, no. A4014019, pp. 1-15, 2014.
[34] P. Uriz, F. Filippou, and S. Mahin, "Model for cyclic inelastic buckling of steel braces," *J. Struct. Eng.*, vol. 134, no. 4, pp. 619–628, 2008.
[35] D. G. Lignos and E. Karamanci, "Predictive equations for modelling cyclic buckling and fracture of steel braces," in *10CUEE Conference Proceedings*, Tokyo Institute of Technology, Tokyo, Japan, 2013.
[36] P.-C. Hsiao, D. E. Lehman, and C. W. Roeder, "Improved analytical model for special concentrically braced frames," *J. Constr. Steel Res.*, vol. 73, pp. 80–94, Jun. 2012.
[37] B. Fell, A. Kanvinde, G.G. Deierlein, and A. Myers, "Experimental Investigation of Inelastic Cyclic Buckling and Fracture of Steel Braces," *J. Struct. Eng.*, vol. 135, no. 1, pp. 19–32, 2009.
[38] FEMA, "Quantification of Building Seismic Performance Factors." Federal Emergency Management Agency (FEMA), Washington, DC, 2009.

[39] D. Vamvatsikos and C. A. Cornell, "Incremental dynamic analysis," *Earthq. Eng. Struct. Dyn.*, vol. 31, no. 3, pp. 491–514, Mar. 2002.

[40] D. Lignos G., H. Krawinkler, and A. Whittaker S., "Collapse assessment of a 4-story steel moment resisting frame," in *2nd International Conference on Computational Methods in Structural Dynamics & Earthquake Engineering*, Rodos, Greece, 2009.

[41] D. Lignos G., H. Krawinkler, and A. Whittaker S., "Prediction and validation of sidesway collapse of two scale models of a 4-story steel moment frame," *Earthq. Eng. Struct. Dyn.*, vol. 40, no. 7, pp. 807–825, Jun. 2011.

[42] D. G. Lignos, T. Hikino, Y. Matsuoka, and M. Nakashima, "Collapse assessment of steel moment frames based on E-Defense full-scale shake table collapse tests," *J. Struct. Eng.*, vol. 139, no. 1, pp. 120–132, 2013.

[43] S. A. Mahin, "Lessons from damage to steel buildings during the Northridge earthquake," *Eng. Struct.*, vol. 20, no. 4–6, pp. 261–270, Apr. 1998.

[44] M. Nakashima, K. Inoue, and M. Tada, "Classification of damage to steel buildings observed in the 1995 Hyogoken-Nanbu earthquake," *Eng. Struct.*, vol. 20, no. 4–6, pp. 271–281, Apr. 1998.

[45] X. Ji, M. Kato, T. Wang, T. Hitaka, and M. Nakashima, "Effect of gravity columns on mitigation of drift concentration for braced frames," *J. Constr. Steel Res.*, vol. 65, no. 12, pp. 2148–2156, Dec. 2009.

COMPDYN 2015
5th ECCOMAS Thematic Conference on
Computational Methods in Structural Dynamics and Earthquake Engineering
M. Papadrakakis, V. Papadopoulos, V. Plevris (eds.)
Crete Island, Greece, 25–27 May 2015

CATASTROPHE RESILIENCE RELATED TO URBAN NETWORK SHAPE: PRELIMINARY ANALYSIS.

Anna Bozza[1*], Domenico Asprone[1], Alessandro Fiasconaro[2], Vito Latora[2], Gaetano Manfredi[1]

[1]Department of Structures for Engineering and Architecture
University of Naples Federico II
Via Claudio 21, 80125 Naples - ITALY
{anna.bozza, d.asprone, g.manfredi}@unina.it

[2]Department of Applied Mathematics
Queen Mary University of London
Mile end road, London E1 4NS - UK
{a.fiasconaro, v.latora}@qmul.ac.uk

Keywords: complex network, seismic risk, risk management, social resilience, physical resilience, damage assessment.

Abstract. *People living in a city represent the most important agents of the urban system. In fact, people organize bits of the city, while organizing their own lives, hence directly influencing much of the city structure, from both a human point of view and a topological one. Such a self-organizing process reflects on both safety and life quality of citizens and efficiency of city services.*

As a result, in order to better manage a city one should know its inhabitants' behaviour and its topological configuration too. An ambitious goal that can be pursued in the sense of complex networks theory approach, studying the urban centre as a hybrid social-physical network made by both human and physical components (HSPN)[1].

In this study different topological structures and geometric shapes of cities are investigated, focusing on the efficiency of cities themselves, and their resilience. Moreover, due to the current increasing risk of natural and human-induced disaster threatening local communities, urban societies are suffering a gradual reduction of their actual and potential resilience, as their ability to cope and withstand with external events.

To this purpose, seismic events are simulated for each investigated urban geometry, referring to the most common shapes existing worldwide. A novel systemic measure of the expected damage state is here defined, which allows for a vectorial measure of the city efficiency in its entirety. Urban resilience is assessed as an integral measure, before, during and after an extreme event occurs. Thence, a recovery strategy is hypothesized and the efficiency of the HSPN network and the resilience of the city are then evaluated and compared in a time-discrete analysis.

1 INTRODUCTION

Urban environment can be easily studied as a complex system, made by several different components and agents coexisting and mutually interacting. The main constituents of such a structure are the social ones, that are the citizens. They are semi-autonomous agents, which take choices and act following rules, such as laws, codes, guidelines, but also trends and traditions. These are rather like the "DNA" of the city, affecting its shape both from a human point of view and a topological one [2]. In fact, such social dynamic, together with urban planning choices performed by local governments, produces different outcomes, depending on the geographical configuration of the single urban system and on its sociological, cultural and economic background.

Hence, the resulting urban structure shows wide differences from city to city, which can influence the overall behaviour of local centres both in terms of the quality of life and safety of citizens. In order to understand how much and in which way this happens, one need to characterize the topological configuration of the city itself, once the features of both its physical and human components are well known.

To face such an issue, the modeling of the city as a hybrid social-physical network (HSPNs) [1] can be performed. HSPNs' approach is an innovative mean which can lead to the effective enhancement of the city resilience and efficiency, according to a human-centric perspective. Moreover it also allows for the improvement of urban planning instruments and risk management.

HSPNs' modeling allows to focus on connectivity too, in the sense of complex networks theory approach. In fact, it has been studied as a fundamental feature of some human behaviours, depending on "if" and "how" they are linked together to form a city [3].

Several efforts have also been made during last years for enhancing urban planning instruments and control urban evolving dynamics. Actually, one should let a city evolving itself while contextually performing strategic and catalytic interventions, such as in the case of the modern "top-down" approaches, so as to catalyse modern self-organization growth processes around specific areas [4]. The "physiological" behaviour of a city would be thence respected, and actions would be undertaken just acting on the enhancement of the efficiency of city patterns according to citizens' choices and preferences.

The focus of this study is just to investigate different topological structures and geometric shapes of cities, which can already exist and also result from modern urbanization processes. Nowadays modern communities are seriously threaten by global risks, such as climate change, natural catastrophes and human-induced disasters. Moreover they are ever more exposed and vulnerable to such risks, given the high urbanization and the high concentration of economic and strategic activities in urban centres. Modern urban systems are suffering a gradual reduction of their actual and potential resilience, as their capability to face and to bounce back from external events.

A particular focus is done on seismic risk, through the simulation of earthquakes with different values of peak ground acceleration (PGA) for each investigated urban geometry. Thence, a recovery strategy is hypothesized, accounting for cheaper damaged buildings to be repaired and the efficiency of the HSPN network and the resilience of the city are then evaluated in a time-discrete manner.

New paradigms are recognised in the field of damage assessment allowing for a systemic measure of damages to be performed. Efficiency evaluated in the sense of complex networks theory is merged together with engineering damage assessment of buildings and streets, according to the performance based earthquake engineering methodology. As a result an integral measure of the impacts of seismic events on urban centres is assessed.

Urban resilience and city efficiency are evaluated, before, during and after the seismic event occurs according to different typical geometric shapes of the street patterns and building locations. In fact, cities are modeled with different geometric shapes referring to the most common existing worldwide, all having a grid-like layout, which is particular to cities whose shapes are the result of large-scale top-down planning efforts, which represent one of the preferential option for modern urban city planning [7].

The different city shapes which are herein investigated have already been classified within different scientific studies. In particular, circular, rectangular, hexagonal and star shapes are modeled.

Moreover, according to the complex networks approach, it is also accounted for particular aspects concerning the number of nodes (representing citizens, strategic buildings, commercial activities and/or residential buildings), the number of links (streets) and their geographic site. These are variables which deeply influence cities' behaviour, being urban areas modelled as graphs.

Cities' behavior, as they are modelled as graphs, apart from the overall geometry of the network itself, is described by the number of nodes (representing citizens, strategic buildings, commercial activities and/or residential buildings), the number of links (streets) and the geographic site of them. Given that, the research project will be based on three main aspects, accounting for all these variable aspects, within two main subprojects:

1. urban resilience and network efficiency assessment for different urban geometries, having the same number of buildings but different locations together with different number of links, when earthquakes with different magnitude occur;
2. urban resilience and network efficiency assessment for different urban geometries, hence different number of links, being the same for each geometry both the number and location of buildings, when earthquakes with different magnitude occur.

2 CITY MODELING ACCORDING TO THE COMPLEX NETWORKS THEORY

2.1 HSPNs modeling

A system of typical street patterns is constructed for the modeling of each urban geometry, into a GIS environment, which is inspired to the European and US major cities and ancient city centres.

Then the primal graph is constructed whereas a set of nodes represent street junctions and another one represents residential buildings.

In order to model the cities, for each studied configuration some assumptions and hypothesis are made to characterize it. Structural typology is assumed to be frame buildings made of reinforced concrete, with all buildings designed for gravity loads. Referring to the Italian built environment, in fact, and to the building constructing practices in most of the European cities, it is known that reinforced concrete buildings usually exhibits plane parallel frame schemes and regularity both in plane and in height. This is for both, non-seismic designed and seismic designed buildings. Buildings considered for city scenario simulations are assumed to be typical 70s – 80s constructions, with number of storey being comprised between 2 and 5.

Citizens living in each city are accounted depending on the total floor area of each structural typology and assuming about 1 citizen each 30 square meters, as suggested by the database of the Italian Institute of Statistics, ISTAT. 1 dwelling each floor is assumed for 2-storey buildings, hence 100 – 150 sqm of total floor area each storey, 2 dwelling are assumed for 3-storey buildings (180 – 250 sqm), 4 dwelling are assumed for 4-storey buildings (300 – 450 sqm) and 6 dwelling are assumed for 5-storey buildings (500 – 600 sqm).

Moreover, the percentage of buildings with reference to their number of storey is taken fixed, given that the number of inhabitants is calculated depending on the total residential square meters for each simulated urban centre. Residential buildings are modelled for 10% as 2-storey, 40% 3-storey, 30% 4-storey and 20% 5-storey. This allow to compare more accurately and realistically data from scenario simulations, keeping in this way the number of citizens always in the same magnitude.

Also street network configuration is hypothesized assuming denser streets concentrations near the centre, being topologically different for each simulated city, according to its shape.

Different HSPNs are constructed, being divided into two typology, according to the research project:

- for each geometry, being fixed the street patterns and the number of designed buildings, four different configurations of residential HSPNs are designed, where the buildings location is always different (Figure 1 – 4);
- for each geometry, being fixed the number and the location of residential buildings, one different configuration of residential HSPNs is designed (Figure 5a – 5d).

HSPNs are then described by means of a graph with $N = |\mathcal{N}|$ nodes and $K = |\mathcal{U}|$ edges. Being $\mathcal{N} = \{\eta_1, \eta_2, \ldots, \eta_N\}$ and $\mathcal{U} = \{\upsilon_1, \upsilon_2, \ldots, \upsilon_N\}$. Actually the modelled HSPNs consist of two set of nodes and two set of edges, being:

- $\mathcal{N}_i$, the set of node intersections representing crossings in the street network;
- $\mathcal{N}_b$, the set of building nodes;
- $\mathcal{U}_{ss}$, the set of street segments, representing links between couple of node intersections;
- $\mathcal{U}_{sb}$, the set of street segments linking street segments to building nodes.

The city graph can then be defined and is denoted by $G(\mathcal{N}_i \cup \mathcal{N}_b \cup \mathcal{U}_{ss} \cup \mathcal{U}_{sb})$. Different geometries are modelled , being inspired by the major European cities, as shown following:

- Circular (ex. Rome, l'Enfants' plan for Washington DC, Regent's park in London, Karlsruhe)
- Rectangular (ex. Savannah, Regensburg on the southern bank of river Danube, from Roman times [6]), better known as the typical structure of US modern cities, ex. Orlando, New York, Philadelphia, etc., they typically exhibits T-shaped crossing as self-organised urban networks. Also Venice and Cairo shows similar geometric shapes, actually they are not just rectangular but self-organised cities as well;
- Hexagonal/Octagonal (Vitruvius model) [5] [6]
- Star, ideal city model of renaissance, an example is the Italian city of Palma Nuova, outside Venice, originally accredited to the architect Scamozzi.

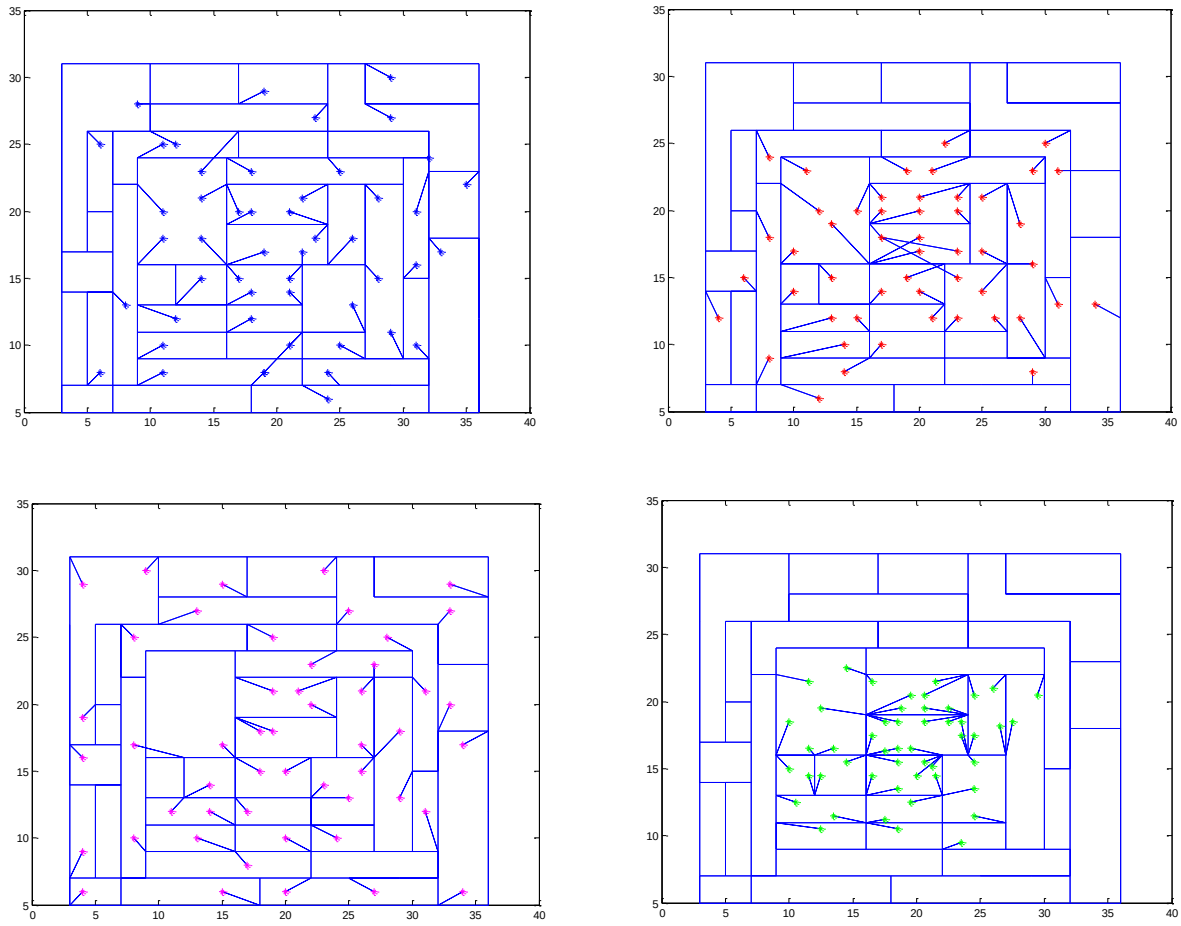


Figure 1 – Four different buildings spatially configuration for rectangular city shape

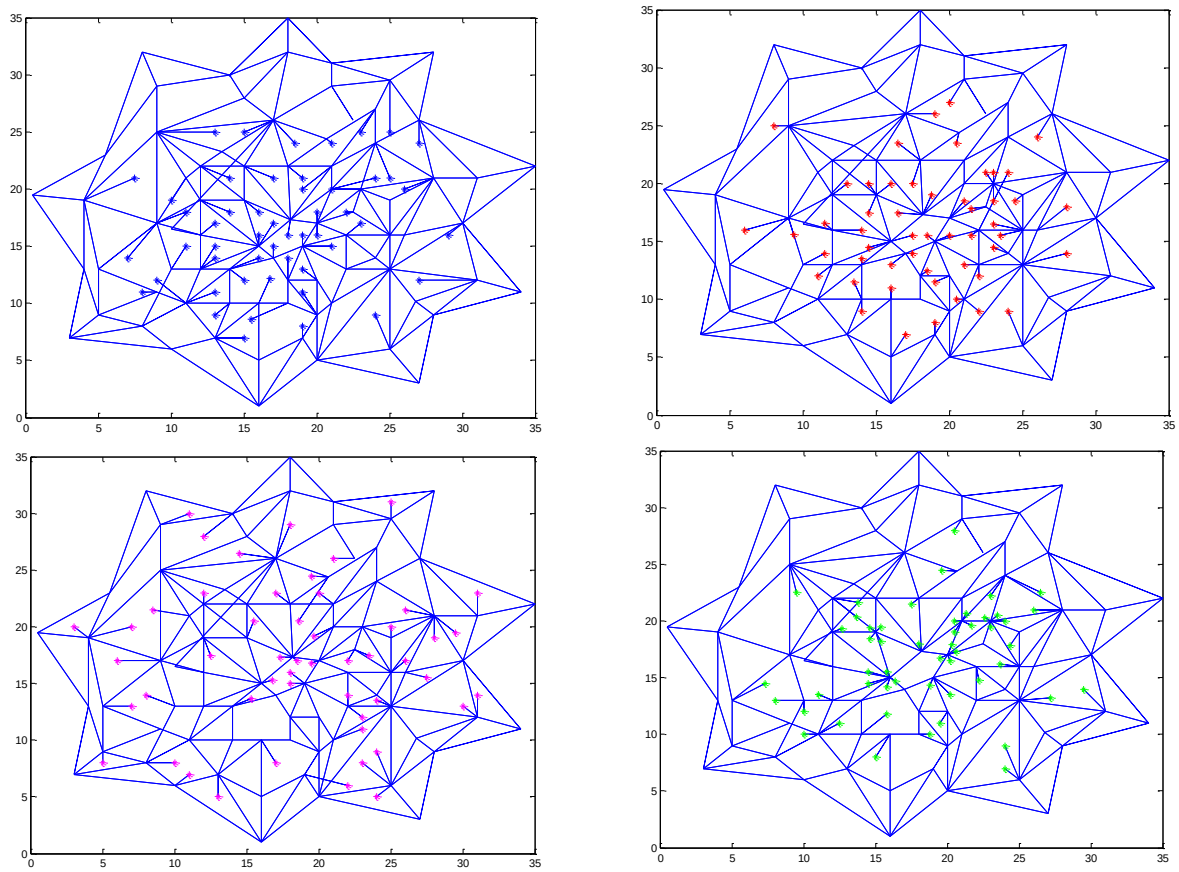
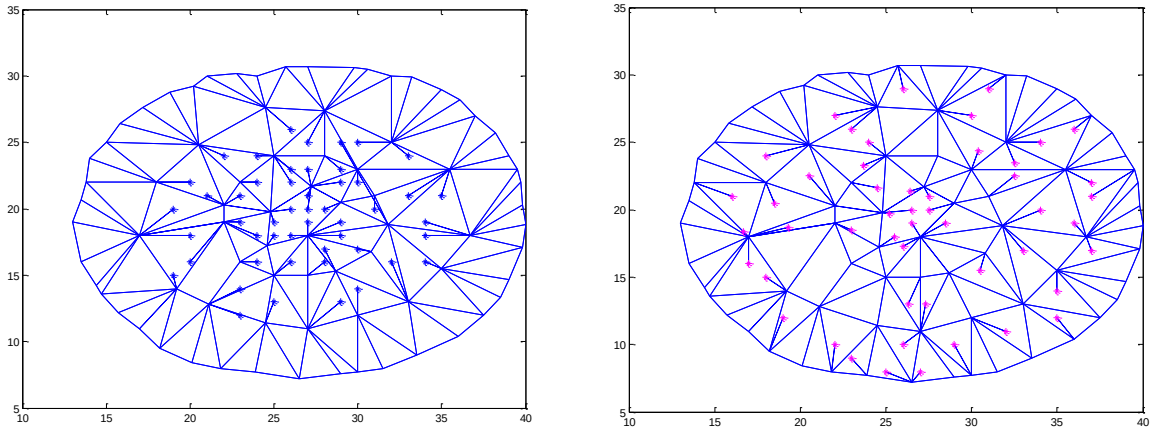


Figure 2 - Four different buildings spatially configuration for star city shape



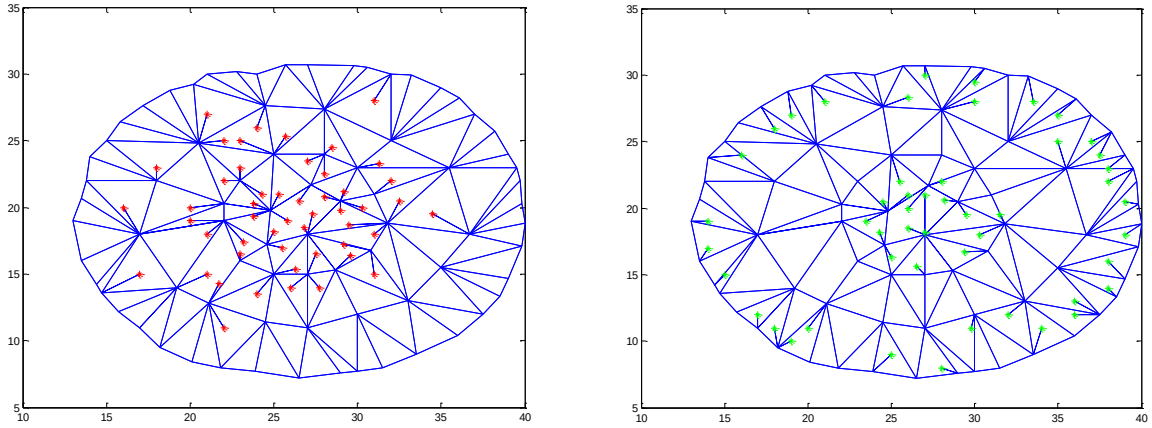


Figure 3 - Four different buildings spatially configuration for circular city shape

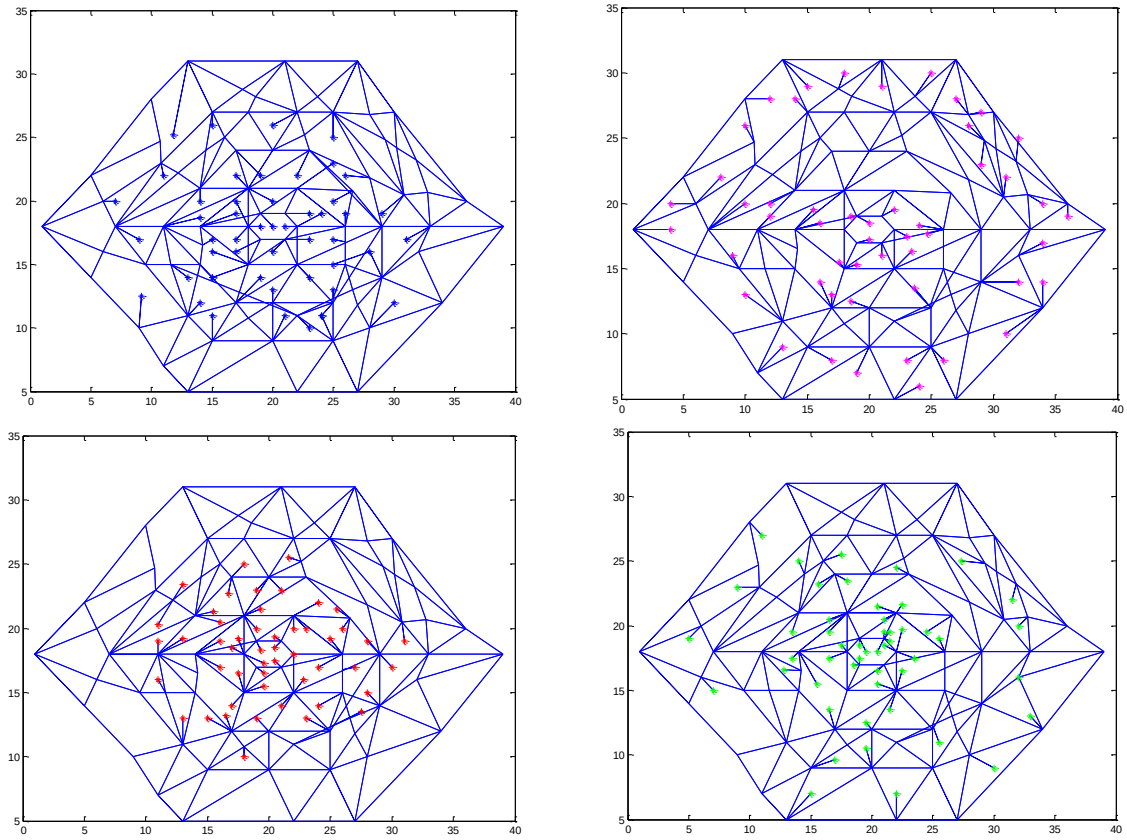


Figure 4 - Four different buildings spatially configuration for hexagonal city shape

Four different urban configurations are modeled according to the case study 1. In Figures a set of discrete links is observed, which represent street patterns. Colored starred nodes represent instead residential building nodes, which are connected to streets by fictitious links. These represent the access point from the main streets to the residential buildings.

The case study 1 considers always the same street patterns, while buildings' location is always different within the four studied topologies. Residential buildings' location is differently modeled for each city, considering for scattered locations, more peripheral locations and more central locations within the urban context.

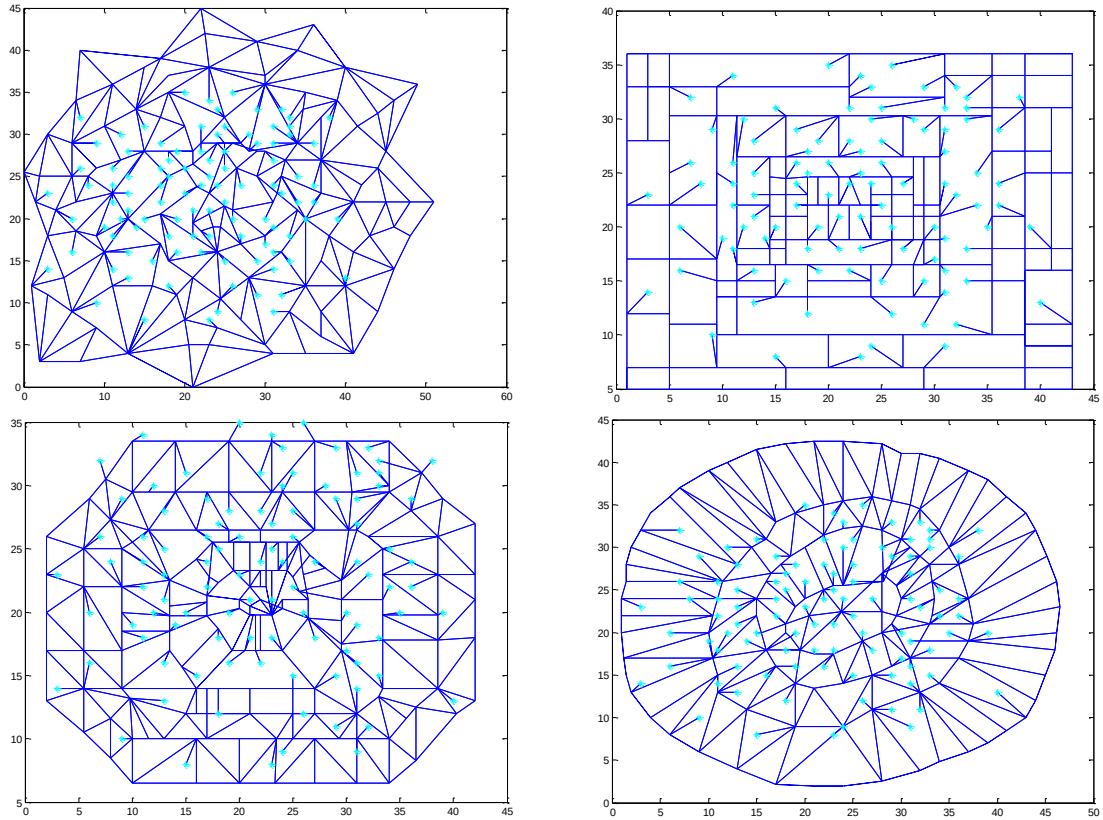


Figure 5 - Four different street patterns configurations with 200 buildings with fixed location

Just four different cities are modeled in the case study 2, one for each urban shape. Here segments shown in Figures, which define the geometric urban shape, represent streets as for the case study 1. Colored starred nodes are the building nodes, whose locations remain always the same for the four shapes, while street patterns change according to the adopted geometry. Links connecting buildings to streets are the same as in case study 1.

2.2 Efficiency assessment

In this study cities are modelled as spatial networks, which are a particular kind of complex networks and they are embedded in a space in turn associated with a metric.

Urban environment is represented through the modeling of a planar graph, usually embedded in a two-dimensional Euclidean space, whose typical metric is the Euclidean distance.

Dealing with spatial networks, it is fundamental to know in which way nodes are connected, to move or send information from a node *i* to a node *j*. A sequence alternating nodes and edges is called a *walk* from *i* to *j*, and whether each node of the walk is traversed only once, it is called a *path*. A cost is then associated to each walk/path, as the sum of all involved edges.

The path from *i* to *j* having the minimal length is called the *shortest path*, having length equal to d_{ij}. One can then gather that the lower is the length of the shortest paths and the better is the communication between any pair of nodes belonging to the network.

The concept of efficiency here is understood as the capability of the urban shape to effectively ensure connection between pair of nodes, even whether a shocking event occurs, like an earthquake.

In order to measure the network efficiency as the average reachability of its nodes, the network efficiency as proposed by Latora and Marchiori (2001) [10] is used. Hence such

reachability can be measured even when the network is not connected, as typically happens in the aftermath of a disaster, when road networks get partially or totally disrupted.

The efficiency between pair of nodes is evaluated as the inverse of the length of the shortest paths connecting them, $e_{ij}=1/d_{ij,}$ and it is minimal when $d_{ij}=\infty$, that is when i and j are disconnected.

Usually the efficiency between two nodes is then normalized as: $e_{ij}= d_{ij}^{\,eucl}/d_{ij}$, where $d_{ij}^{\,eucl}$ is the Euclidean distance. The global efficiency is then assessed as the normalized pairwise efficiency, averaged on all possible pairs of nodes:

$$E = \frac{1}{N(N-1)} \cdot \sum_{\substack{i,j \in N \\ i \neq j}} \frac{d_{ij}^{eucl}}{d_{ij}} \qquad (1)$$

The global efficiency is normalized in [0,1]. This is due to the distance between node i and node j, $d_{ij,}$ being larger than the Euclidean distance between i and j. Such a measurement of the global efficiency allows to consistently compare two distinct graphs, even whether they have a different number of nodes and links.

Actually such an equation does not allow to evaluate efficiency of the residential HSPN, since it does not account for people living in each building. Hence a further equation is defined to calculate the citizen-citizen efficiency, as outlined in Cavallaro et al. (2013) [1], as follows:

$$\begin{aligned} Ecc &= \frac{1}{H_{tot}(H_{tot}-1)} \sum_{i \in N_b} H_i \cdot \left((H_i - 1) + \sum_{j \in N_b, j \neq i} H_j \frac{d_{ij}^{eucl}}{d_{ij}} \right) \\ &= \frac{1}{H_{tot}(H_{tot}-1)} \sum_{i \in N_b} H_i \cdot \left((h_i - 1) + \sum_{j \in (N_b \setminus I)} H_j \frac{d_{ij}^{eucl}}{d_{ij}} \right) \end{aligned} \qquad (2)$$

Where i, j are the indexes of building nodes, H_{tot} is the number of citizens living in the studied city, H_i is the total number of citizens living in building i, N_b is the set of building nodes, d_{ij} is the length of the shortest path connecting node i and node j and h_i is the number of citizens living in buildings, which belong to the set I, of buildings having zero distance from to building i. The result is a measure of connectivity between inhabitants inside buildings, which is obtained by summing over all couples of citizens and imposing $d_{ij}^{\,eucl}/d_{ij} = 1$ for inhabitants living at distance zero. This last is obviously the case in which the efficiency is maximised in communication between couples of citizens.

3 A NOVEL SYSTEMIC DAMAGE ASSESSMENT

3.1 Probability-based earthquake simulation

Earthquake scenarios are simulated for 0.25g and 0.30g PGA, which describes medium intensity seismic phenomena. Resulting building damages are simulated through the implementation of literature fragility curves, as the probability of exceedance of the "onset of damage" of each building belonging to the set of the residential ones. Hence only the exceedance of a very heavy limit state is accounted for, that is buildings are not available for occupation and use any more. Two kind of damages for the urban centre can be considered through the implementation of the vulnerability functions.

First of all, the probability of being damaged or becoming unfit for use when hit by an earthquake of a certain intensity for each building. It is represented by the fragility function, a probability law which is described by a log-normal distribution function, as follows:

$$P_b(PGA;\mu,\sigma) = \Phi\left(-\frac{\ln PGA - \mu}{\sigma}\right) \quad (3)$$

Simulations are performed considering (μ, σ)=(-0.91,0.29) for reinforced concrete buildings fragility curve from Ahmad et al. (2011) [9], which refer to the "moderate" damage state as shown in Table 1.

N° of Limit States	Limit State	Median, μ	Standard Deviation, σ
3	Slight	-1.07	0.22
	Moderate	-0.91	0.29
	Extensive	-0.71	0.27

Table 1: statistics of the fragility curve by Ahmad et al. [9]

Such a choice follows from the need of not being too conservative but also to avoid to overestimate the vulnerability of the built environment, that is clear from fitted curves, shown in Figure 6.

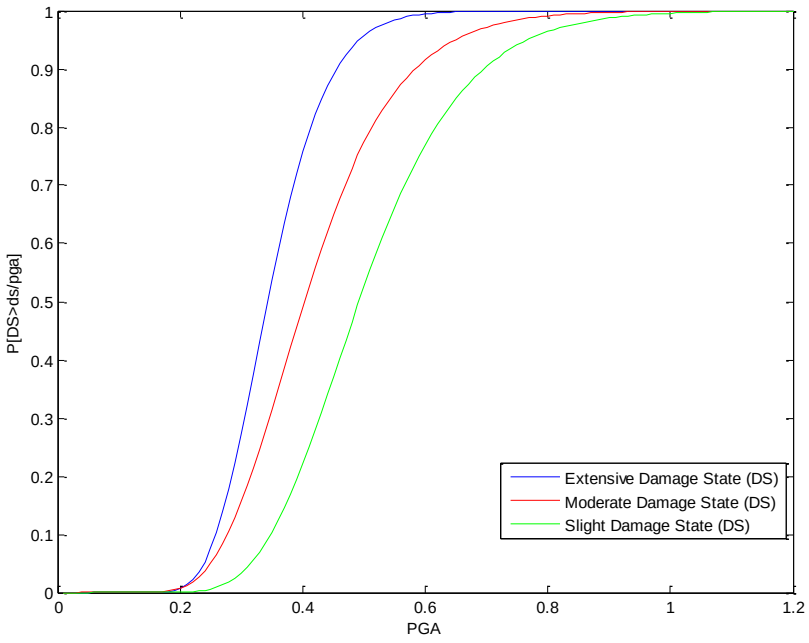


Figure 6 – Fragility curves according to Ahmad et al. for non-ductile reinforced concrete buildings

Then the probability that a damaged building limits or interrupts the transit along a street, that is adjacent to it. In fact, it is well-known that whenever an earthquake occurs, buildings located along a street could suffer damages making it inaccessible, due to the debris fallen. Moreover accessibility to a street, which is adjacent to buildings, could however be limited for safety purposes, from civil protection and other local authorities managing the emergency.

Due to this last dynamics, the street patterns probability of interruption is defined:

$$P_r(h,l) = \begin{cases} 1 & if \quad h \geq l \\ \dfrac{h}{l} & otherwise \end{cases} \qquad (4)$$

Stream of uniform pseudorandom numbers is generated and values from the standard uniform distribution are selected on the open interval (0,1) and compared to the value from the fragility function, related to the PGA value attained by the simulated event. Being such value larger or smaller than those obtained from the stream simulation, decide respectively whether the building will not obstruct the adjacent street or will make it inaccessible.

This has got a further effect on the behaviour of the HSPN itself: due to the street being eventually become inaccessible, the link which represents it, will not be useful for network connectivity purposes. Hence, being the link inactive, it is removed from the network, so as the building which was adjacent to it, and caused the street usage restrictions.

Moreover damages on buildings result, for each simulated earthquake and damaged city configuration, in a certain number of citizens to be reallocated. In fact, as already explained, the number of citizens living in each city is accounted assuming a certain floor area for each storey, depending on the storeys number itself, and assuming an inhabitant each 30 square meters.

Once the city is modelled the methodology allow for the damage assessment right after a seismic event occurred, both in terms of street pattern and damaged buildings which are removed and also in terms of citizens, which remain without their homes and need to be reallocated. Ten scenario analysis are performed for each different urban geometrical configuration, drawing values from the pseudorandom number simulation, which are always different, and giving, as a consequence, different results, as shown in Figure 7 and in Figure 8:

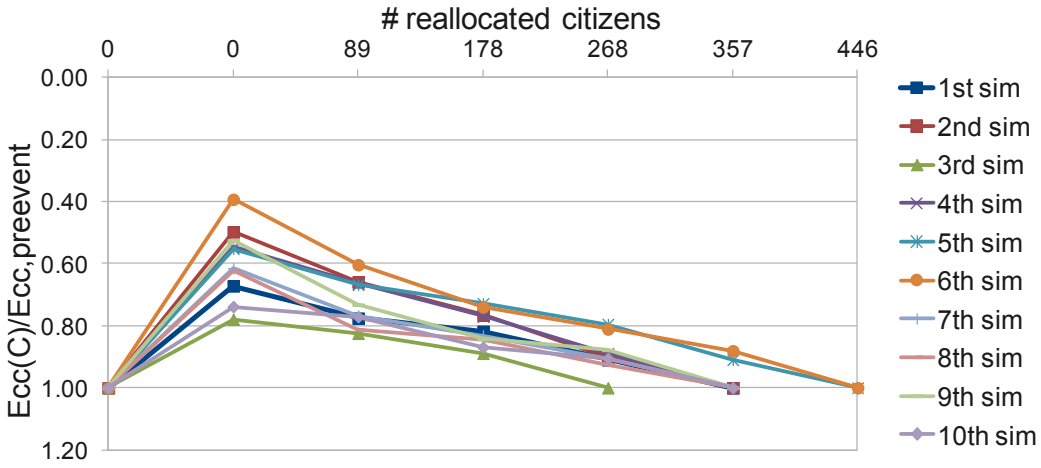


Figure 7 – Normalized efficiency against the number of reallocated citizens for the star shape HSPN, in the case of seismic scenario analysis with PGA=0.30g and 50 residential buildings with different location

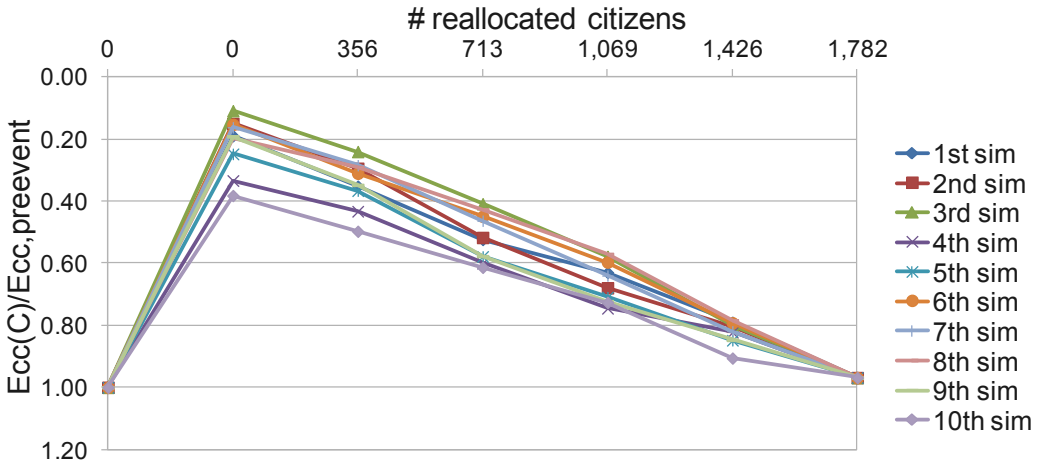


Figure 8 – Normalized efficiency against the number of reallocated citizens for the star shape HSPN, in the case of seismic scenario analysis with PGA=0.30g and 100 residential buildings with fixed location

3.2 Efficiency of damaged urban centres as a measure of the integral urban damage

Since HSPNs are modelled as graphs, the basic principle to measure their overall behaviour in a scientific manner refers to the complex network theory. Damages suffered by a city are measured starting from the single building. This is conceived as a physical structure itself, but also as an "ideal reference point", in which citizens live and from which they are served. Urban services, such as gas and water pipelines and electric grids, and also road infrastructures are linked to such buildings. Hence, once the links between buildings and all urban services are modelled, one can simply assume that when the building goes out-of-service, even all services which are linked to it are useless. Particularly, in this work the link between the couple of nodes representing buildings are modelled based on the street patterns of the studied city. This assumption is easily justified by the fact that in nearly every urban centre urban services infrastructures (pipelines for instance), are located on the streets.

The fragility curve here implemented gives a probability-based measure of the capacity of buildings within an urban centre to withstand a seismic event. Hence, it allows to quantify the vulnerability of the built environment.

Given the assumption made, it also allows to identify which urban areas become useless whenever an earthquake occurs.

Structural measures performed through the fragility function on each single building are then extended to streets and to all urban services which are linked to it. Hence, the engineering assessment is understood as a scattered measure of each urban area usability.

On the other hand, all urban areas are mutually interrelated by further streets and services distribution plants. The evaluation of the quality of such links, the connectivity and the efficiency level leads to the knowledge of the overall behaviour of the investigated urban system. An information which is obtained through the implementation of complex networks measure techniques. Particularly, global efficiency measurement are performed according to Latora and Marchiori (2001) [10].

Finally the novelty in the assessment of the state of service of the urban environment after the occurrence of a catastrophic event is underlined, as the chance to merge civil engineering and complex networks methodologies. Such an approach, allow to perform a measurement of the after-event level of performance of the city which is a systemic and integral one. Further-

more, the performed measures follow the modern multi-scale approach, from the lower to the higher degree of network complexity.

Given the residential HSPN efficiency, as evaluated in Cavallaro et al. (2013), the systemic damage measure can be simply evaluated as:

$$D = E_{cc}^{pre-event} - E_{cc}^{post-event} \quad (5)$$

Whereas the ratio between this two quantities is also defined as the *recovery function*, as well as the normalized efficiency corresponding to the first time step soon after the earthquake has occurred:

$$Y(0) = \frac{E_{cc}^{post-event}}{E_{cc}^{pre-event}} \quad (6)$$

Values for all investigated urban shapes for such a ratio, are shown in Table 2.

City Shape	Mean Pre-event Efficiency [$E_{cc}^{pre\text{-}event}$]	Mean Post-event Efficiency [$E_{cc}^{post\text{-}event}$]	Y(0)	D
Case 1 - Different city shape with different building location				
Hexagonal	3,034	2,512	0,826	0,523
Rectangular	2,643	2,001	0,761	0,642
Star	3,103	2,584	0,833	0,519
Circular	2,977	2,281	0,765	0,696
Case 2 - Different city shape with same building location				
Octagonal	2,603	1,075	0,413	1,529
Rectangular	2,505	1,046	0,417	1,459
Star	2,693	1,077	0,400	1,616
Circular	3,127	1,029	0,329	2,098

Table 2: Pre-event and post-event efficiency values of residential HSPNs according to different modelled geometrical forms, in the case in which building location is modelled as variable and fixed

According to the normalized efficiency values, the star and hexagonal shapes exhibit the best behaviour in case 1, while in case 2 the efficiency for octagonal, rectangular and star show values, which are very similar. From case 1 to case 2 efficiency is almost halved while the number of residential buildings is doubled. This is due to the major effort in case 2 of having efficient links. Obviously a major quantity of buildings is much difficult to get connected. Moreover the lower the distance among people in the urban network, the higher the efficiency of the residential HSPN.

Such a lower efficiency in case 2 has not to be ascribed to the building vulnerability instead, since they are all reinforced concrete buildings, whose percentage in terms of number of storeys is keeping invariant when passing from case 1 to case 2.

4 LINKING URBAN DAMAGE AND RESILIENCE ASSESSMENT

The systemic measure of damages suffered by the urban environment when a seismic event occurs are also understood according to the classical approach to urban resilience.

The recovery function, Y, is the measure of the performance of the system at a certain instant in time, t. Hence, if it is evaluated for each step of the recovery strategy implemented

after the shock, the capability of the city to bounce back to its previous performance level can be assessed as the integral of such quantity in time.

Resilience is, in fact, defined as the area under the recovery curve, divided by the time passed by from the start of the recovery process, t_b, to its completion, t_c, as follows:

$$R = \frac{\int_{tb}^{tc} Y(t)dt}{(t_c - t_b)} \quad (7)$$

According to the implemented HSPN model and to the definition of the recovery function previously given:

$$Y(t) = \frac{E_{cc}(t)}{E_{cc}^{pre-event}} \quad (8)$$

In fact, while Y(0) is the value of the recovery function soon after the occurrence of the earthquake, Y(t) is the same function evaluated for each step of the recovery strategy.

Such formulation requires a good knowledge of the state of service of the city for each step of time, during reconstruction. But it depends on several factors (available monetary budget, promptness of reconstruction, first aid time, etc.) and it is not easy to know in detail, so any dependence on time is removed and the recovery function is calculated depending on the number of reallocated citizens, C, for each step of the recovery strategy:

$$Y(C) = \frac{E_{cc}(C)}{E_{cc}^{pre-event}} \quad (9)$$

Also the dependence on total damage is removed by defining:

$$y(C) = \frac{Y(C) - Y(0)}{1 - Y(0)} \quad (10)$$

Where Y(0) is zero in the aftermath of the seismic event, that is when no citizen has been yet reallocated. And disaster resilience is then calculated through the following:

$$R = \frac{\int_{0}^{C\max} y(C)dC}{C\max} = \frac{\sum_{c=0}^{C\max} y(C)}{C\max} \quad (11)$$

Where Cmax is the total number of citizens to reallocate after the earthquake and the integral is simplified with a summation, being the strategy implemented in a discrete number of steps.

In this study, a recovery strategy is hypothesized according to which first cheaper buildings are restored after the earthquake. Hence, efficiency is evaluated, for each urban shape, for each step of the recovery strategy and then it is integrated by the number of reallocated citizens to compute resilience. Mean values from simulation are fitted against the number of reallocated citizens for each urban geometry in the case of an earthquake of PGA=0.25g and in the case of an earthquake of PGA=0.30g for both the case of study 1 and 2 (Figures 9 – 12).

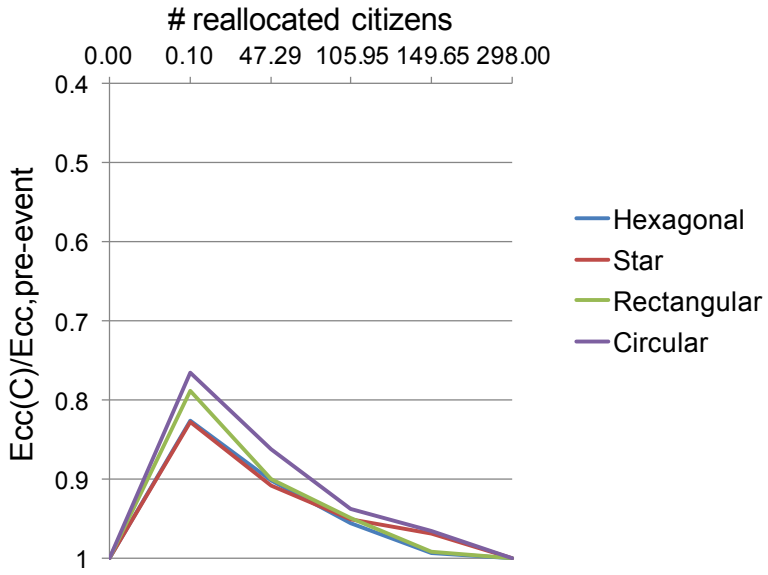


Figure 9 – Normalized efficiency against number of reallocated citizens in the case of different buildings location (Case 1) and PGA=0.25g

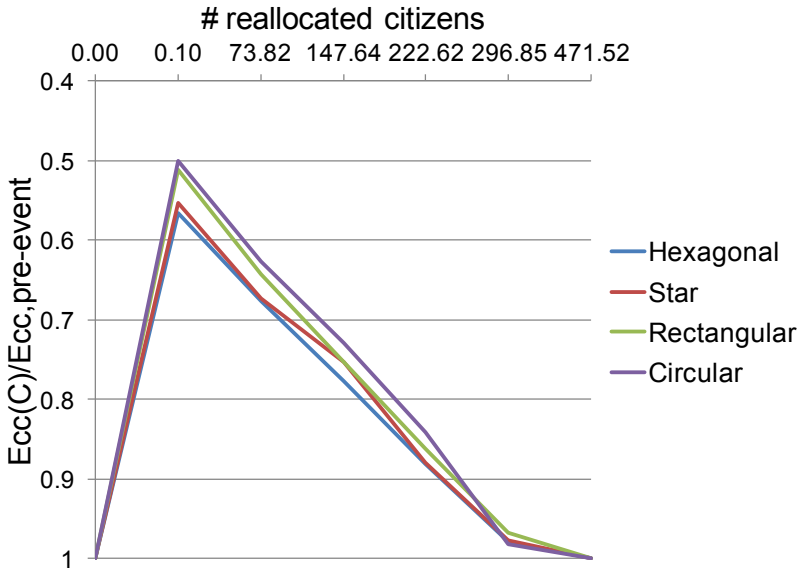


Figure 10 - Normalized efficiency against number of reallocated citizens in the case of different buildings location (Case 1) and PGA=0.30g

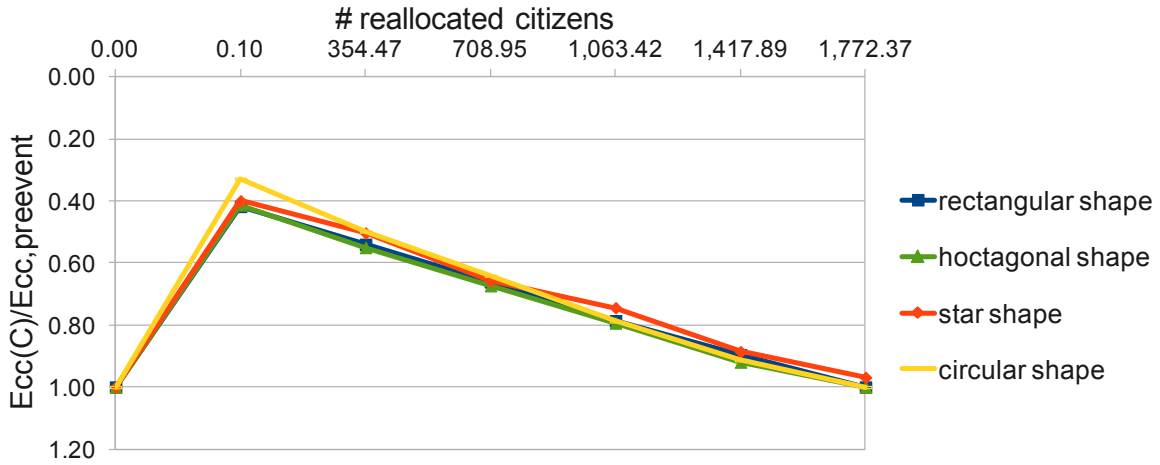


Figure 11 – Normalized efficiency against number of reallocated citizens in the case of fixed buildings locations (Case 2) and PGA=0.25g

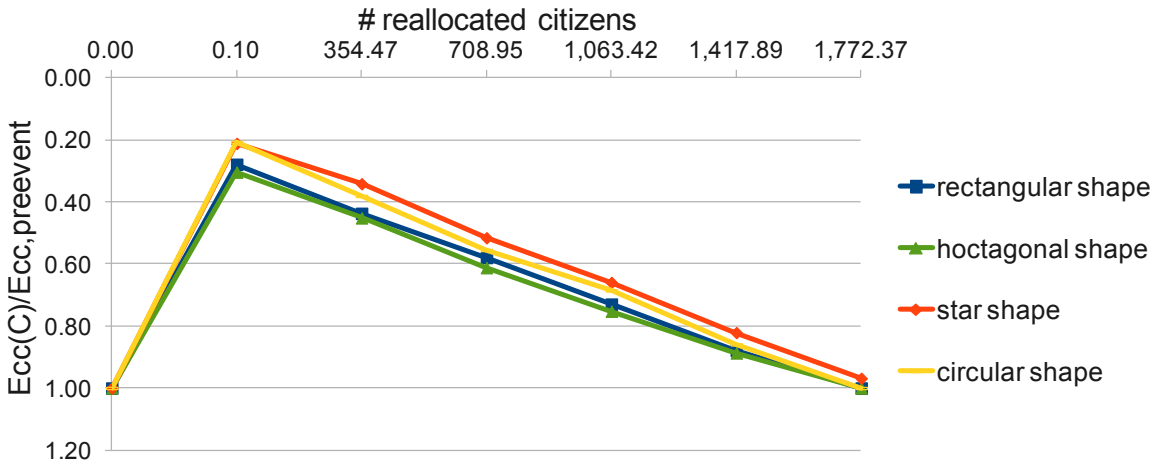


Figure 12 – Normalized efficiency against number of reallocated citizens in the case of fixed buildings locations (Case 2) and PGA=0.30g

Experimental results show a clear major downfall of the efficiency curve in the case of an earthquake occurrence whose PGA is 0.30g. Obviously the more intense is the earthquake the many more buildings are damaged, and many more citizens are deallocated too. A major slope is outlined in case 1 between star and hexagonal shapes, which are clearly more efficient, rectangular and circular shapes. Conversely, in case 2 the behavior seems to be much similar even when geometric shape changes. There are slight differences in the case of an earthquake of PGA=0.25g in which the circular shape reveals to be the less efficient one, and such a behavior is confirmed when PGA=0.30g , together with the star shape.

All things considered no major differences are revealed when comparing results in terms of resilience from case study 1 and case study 2. Hence,

Considerations are validated when performing the resilience assessment for each geometry in the two case studies, which is averaged on the ten scenario simulations performed for each of them, as shown in Table 3.

RESILIENCE		
Case 1 - Different spatial buildings configuration and same links	PGA=0.25	PGA=0.30
RECTANGULAR	0,0168	0,0092
HEXAGONAL	0,0146	0,0086
STAR	0,0200	0,0085
CIRCULAR	0,0142	0,0080
Case 2 - Fixed spatial buildings configuration and different links	PGA=0.25	PGA=0.30
RECTANGULAR	0,0031	0,0024
OCTAGONAL	0,0031	0,0024
STAR	0,0033	0,0021
CIRCULAR	0,0032	0,0022

Table 3 – Mean seismic resilience assessed for each urban geometry in the case of an earthquake with magnitudes, PGA=0.25g and PGA=0.30g

5 CONCLUSIONS

The present study focus on the evaluation of the efficiency of cities when subjected to seismic events according to their topological structure. A methodology merging civil engineering and complex networks metrics is implemented in order to assess the global state of damage and the urban resilience. The equation used for the quantification of resilience allows to appreciate the efficiency in the recovery process of a city after a disaster has occurred. Efficiency is then evaluated closely after the earthquake and has to be compared with as many strategies for reconstruction.

The paper proposes a novel approach which take also into account people living in a city, through the modeling of urban centres as hybrid social-physical networks (HSPNs). Urban street patterns and infrastructures are modelled as undirected graphs, and also citizens are considered as the sensors of urban efficiency and connectivity.

Earthquake scenarios are simulated and a recovery strategy is hypothesized. A probability-based approach is used to evaluate buildings' vulnerability and urban efficiency measure soon after the earthquake occurrence are used as a systemic measure of the overall damage suffered by each investigated urban centre.

Resilience is then evaluated for each urban shape and each earthquake scenario.

Results show some differences in resilience levels, with the star shape in every case the most efficient and the circular one the worst.

Not significant differences have been instead recorded for the different city geometries, while considering the different number of links between fixed building distributions. Even if higher slope in the efficiency level is observed for urban shapes investigated in the case study 2 with respect to those in the case study 1. This can be attributes to the higher number of residential buildings being modelled within the second case study (they are doubled), which makes cities more exposed. Hence, for the same simulated seismic intensity the global response in terms of both efficiency and resilience is quite similar in the two case studies. But if

the urban efficiency is observed within a time-discrete analysis, it is clear that major problems and inconveniences are expected in the case study 2. That is the case in which many more buildings are located within the studied urban area.

Further analysis are needed, with the purpose to model urban networks with many more buildings and real cases to be compared with.

Moreover further developments are needed to compare attained urban resilience when different recovery strategies are implemented.

The proposed methodology can be an effective mean, to used as a support for disaster management. Best practises can be recognised for each investigated topology, by implementing scenario analysis in which different recovery strategies are adopted and by comparing the evaluated resilience and efficiency for each of them.

The proposed methodology has a dual application field, being potentially used as an effective engineering mean to quantify a unique indicator as a vectorial measure of city damages. On the other hand, the quantification of resilience being reiterated for each city, different magnitudes of simulated disaster and different hypothesized recovery strategies, is a very powerful mean to be used as a support for urban planning and disaster management.

REFERENCES

[1] Cavallaro, M., Asprone D., V. Latora, G. Manfredi, V. Nicosia, "Assessment of Urban Ecosystem Resilience through Hybrid Social–Physical Complex Networks", *Computer Aided Civil and Infrastructure Engineering*, 2014.

[2] M. Mehaffy, "Design Technologies for Self-Organizing Cities", *article in Meeting of the minds 2014, http://cityminded.org/design-technologies-for-self-organizing-cities-7100,* 2014.

[3] A. Makse, S. Havlin, H.E. Stanley, "Modeling urban growth patterns", *Nature 377, 608-612,* 1995.

[4] J. Jacobs, "The death and life of great American cities", *Random House LLC,* 1961.

[5] M. Batty, P.A. Longley, "Fractal cities: a geometry of form and function", *Academic Press*, 1994.

[6] A.E.J. Morris, "History of urban from before industrial revolutions", *London: George Godwin,* 1979.

[7] E. Strano, V. Nicosia, V. Latora, V. Porta, M. Barthelèmy, "Elementary processes governing the evolution of road networks", *Scientific reports 2*, 2012.

[8] M. Batty, "The size, scale, and shape of cities", *Science 319, 769-771,* 2008.

[9] Ahmad, N., Crowley, H., Pinho, R., "Analytical Fragility Functions for Reinforced Concrete and Masonry Buildings and Building Aggregates of Euro-Mediterranean Regions", *Department of Structural Mechanics, University of Pavia. WP3-Task* 3, 2011.

[10] Latora V. and Marchiori M., "Efficient behavior of small-world networks." *Physical review letters 87.19 (2001): 198701,* 2001.

COMPDYN 2015
5th ECCOMAS Thematic Conference on
Computational Methods in Structural Dynamics and Earthquake Engineering
M. Papadrakakis, V. Papadopoulos, V. Plevris (eds.)
Crete Island, Greece, 25–27 May 2015

APPLICATION OF A DAMAGE STATE METHOD BASED ON PERIOD ELONGATION FOR TIME VARIANT VULNERABILITY OF DEGRADING REINFORCED CONCRETE BUILDINGS

Konstantinos Trevlopoulos[1], **Philippe Guéguen**[1]

[1] ISTerre : Institut des Sciences de la Terre
BP 53, 38041 Grenoble CEDEX 9, France
konstantinos.trevlopoulos@ujf-grenoble.fr
philippe.gueguen@ujf-grenoble.fr

Keywords: seismic vulnerability, time variation, aftershock sequence, reinforced concrete, structural degradation

Abstract. *We present a method for a probabilistic estimation of the time variation during aftershock sequences of the vulnerability of reinforced concrete structures which deteriorate as they accumulate damage and become more vulnerable. First we describe the steps of the proposed method and then we apply it in the case of two building models and two aftershock sequences. The degradation of the structural elements of the buildings is assumed to be stochastic and computed with time-history analyses using a hysteretic model of bending response. Then the engineering demand parameter of maximum drift is associated with the elongation of the fundamental period of the structure and we define limit damage states using as thresholds values of the period elongation ratio. The numerical models of the buildings that correspond to the defined damage states are defined and analyzed, in order to calculate their fragility curves and the probability of the damaged building models transitioning to higher damage states. The cumulative probability of exceeding a damage state for the selected aftershock sequences is calculated with a Markov chain whose transition matrices are a function of the intensity of the aftershocks. This results to the variation of the probability of exceedance of period elongation thresholds due to damage accumulation as a function of time during the selected aftershock sequences.*

1 INTRODUCTION

Earthquakes is a principal cause of degradation of the properties of structural elements in reinforced concrete buildings. Stiffness degradation is one of the reasons modern seismic codes such as the Eurocode 8 [1] demand the stiffness of structural elements to be taken into account with its effective value, which equals a portion of the stiffness of the geometric section of each member. Apart from stiffness degradation an increase of the damping ratio of the building may accompany seismic damage and affect its vulnerability [2]. Another source of structural degradation is the non-seismic progressive natural deterioration of the structural materials. Pitilakis et al. [3] estimated the detrimental effect of reinforced concrete steel corrosion with time-dependent fragility curves of multistory buildings. Sanchez-Silva et al. [4] proposed a stochastic model that takes into account the effect of gradual non-seismic deterioration of structural materials along with the structural deterioration due to sudden events such as earthquakes and highlighted the importance of both modes of deterioration.

Iervolino et al. [5] focused on earthquake clusters (aftershock sequences) and developed a probabilistic damage accumulation model for elastic-perfectly plastic single-degree-of-freedom (SDOF) structures and estimated the failure probability as an increasing function of time. Repeated earthquakes and the subsequent damage accumulation may lead to an increased inelastic displacement demand of SDOF systems and an increased ratio of the inelastic displacement to the maximum displacement of the elastic system [6]. Apart from displacement demands, strength demands may also be 20 % averagely higher for degrading SDOF structures in comparison to non-degrading structures, if their period is shorter than the predominant period of the excitation [7] and their ductility demand may be higher, if excited with soft soil seismic records.

One way of quantifying the structural degradation of a building is through the elongation of its fundamental period. The degree of cracking in reinforced concrete elements because of static loads as well as the cracking of infill walls during the earthquake are considered to contribute significantly to the elongation of the natural period of buildings [8]. Katsanos et al. [9] estimated the period elongation for the design earthquake and twice the design earthquake at approximately 1.2 and 1.7 on average in the case of moment resisting frames and dual structural system multi-storey buildings designed with Eurocode 8. Only in extreme cases of severely degrading buildings a ratio of 2.0 was estimated. Katsanos and Sextos [10] also proposed an empirical function for period elongation based on the structural period and the force-reduction factor. Moreover, they showed that PGA has a low correlation with the predominant inelastic period in contrast to spectral acceleration. Based on measurements in damaged buildings after the 2011 Lorca earthquake Vidal et al. [11] proposed relationships for the period of the damaged buildings as a function of the number of stories. According to these relationships the period elongation corresponding to EMS-98 [12] damage grade 1, 2 and 3-4 is equal to 20 %, 43 % and 65 % and is independent of the number of storeys. The period elongation ratio has been observed to be in an analogy to the stiffness and the force-reduction factor (ratio of the maximum seismic force to yield force) of SDOF oscillators [10] while the effect of earthquake magnitude, distance and soil conditions has been estimated to be of minor significance.

Given that reinforced concrete buildings may accumulate damage during aftershock sequences and become more vulnerable we deem necessary the development of a model of time-variable vulnerability for the aftershock time-period. This is the aim of this paper and we consider the variation of the vulnerability over these time-periods a significant piece of information for buildings part of critical infrastructures such as the Port of Thessaloniki, whose location we use in one case study. In many cases the structural health of such buildings is monitored with proper instrumentation and since structural degradation can be observed and localized through eigenfrequency variation [13, 14] we are employing limit damage-state thresholds in terms of

the ratio of the periods of the elastic and the degraded building (T_{in}/T_{el}) for developing an operative tool in emergency situation. The properties of the structural elements of the degraded building models are computed based on the stochastic inelastic deformations calculated with finite element time-history analyses of the original building with excitations covering a wide intensity range. Using the derived fragility curves the cumulative probability of exceedance of period elongation thresholds is then calculated for the cases of two real aftershock sequences.

2 SELECTED BUILDING MODELS

For the application of the developed method for time-varying vulnerability two reference mid-rise building models [15] are selected (Figure 1, Table 1). The first is a high-code reinforced concrete moment resisting frame designed with the Greek seismic code of 2001 (EAK 2000) [16] and the second building is a low-code building with a shear wall system, i.e. a structural system with shear walls carrying more than 65 % of the base seismic shear force [17], designed with the first seismic code that came into effect in Greece in 1959. The provisions of the 2001 code bear similarities to EN 1998-1 [17] and demand capacity design with structural member detailing for ductile behavior aiming for energy dissipation in the seismic resisting system and plastic building collapse mechanisms. According to a 2001 survey 32 % of the building stock of Greece predated the 1959 code, 46 % was constructed between 1959 and 1985, when a new seismic code was introduced [18], under which 22 % of the stock was built. Based on more recent data in the city of Grevena in Greece the reinforced concrete buildings built after 1959, 1985 and 2001 consist respectively 49 %, 11 %, and 19 % of the stock [19]. The selected models fall under the C1M and C2M model building types of HAZUS [20] and will be thus referred to for brevity.

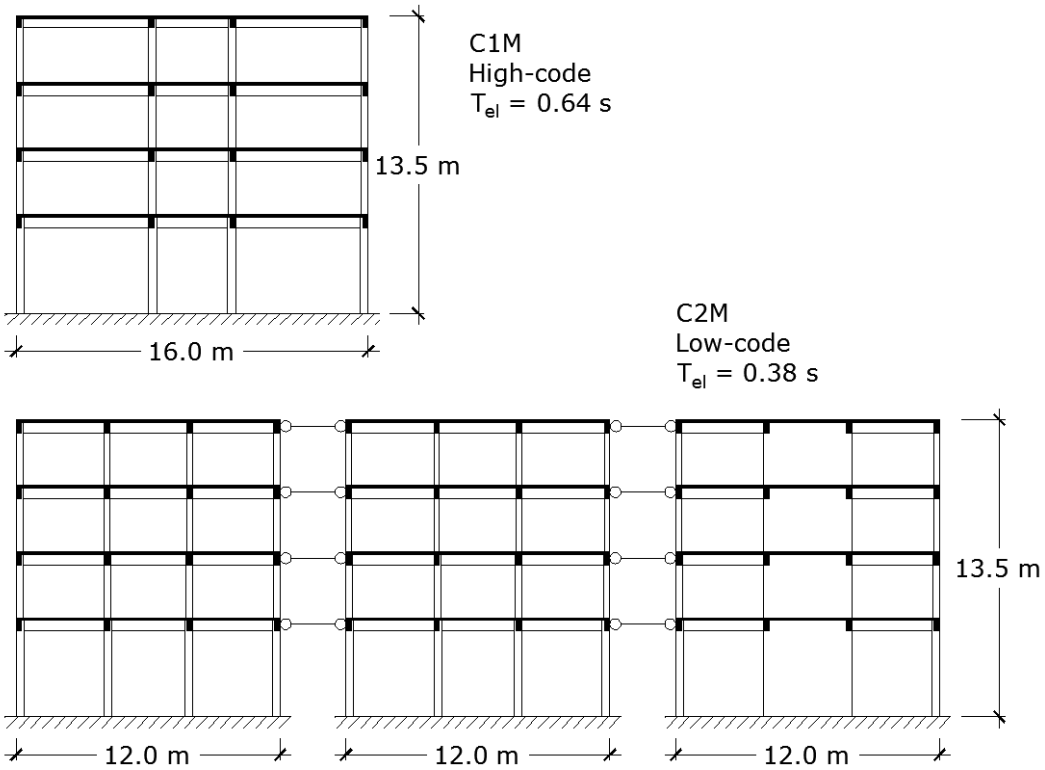


Figure 1: Reference building models: C1M high-code moment resisting frame, C2M low-code coupled shear wall and moment resisting frames.

Type	Structural System	Code	Concrete	Steel	Mass (t)	T_{el} (s)
C1M	Moment resisting frame	High	C20	S400	130.0	0.64
C2M	Shear walls	Low	B225	StI	491.9	0.38

Table 1: Details of the selected building models.

Three types of analyses are performed with OpenSees [21]; fiber, non-linear time-history and modal. The fiber analyses are employed to calculate the yield moment and curvature of each structural element through a bi-linear approximation of the numerical results. This data is then used to model the inelastic response of the elements with a distributed plasticity model of hysteretic response. Pinching in the moment-curvature loops is used only for the structural walls with a factor of 0.3 assuming a strong pinching effect. The modal analyses are used to calculate the fundamental period of the models in their undamaged and structurally degraded states. In the total mass of each model the mass corresponding to structural elements infill walls, live and dead loads of the slab floors are included. According to the code for interventions in existing buildings in Greece [22] the bending stiffness (EI) of structural elements should be reduced to the value of the modulus at yield, which is averagely 25 % or less of the stiffness of the geometric uncracked section (EI_g) [17]. It is assumed that this is intended for pushover analysis with elastic-perfectly plastic springs. Since a hysteretic law is used for bending behavior in the context of dynamic analyses, which models stiffness degradation after yield, the reduced elastic stiffness of the concrete elements is required to account for Stage II cracking. In the C2M model the stiffness is taken equal to 40 %, 60 % and 80 % of the geometric stiffness for beams, perimeter columns and shear walls, and inner columns respectively according to the comments of EAK 2000. This leads to bending stiffness of the elements in agreement with the moment-curvature results from the fiber analyses at the range of small elastic deformations (Figure 2) and to a more effective estimation of the elastic fundamental period of the building (T_{el}).

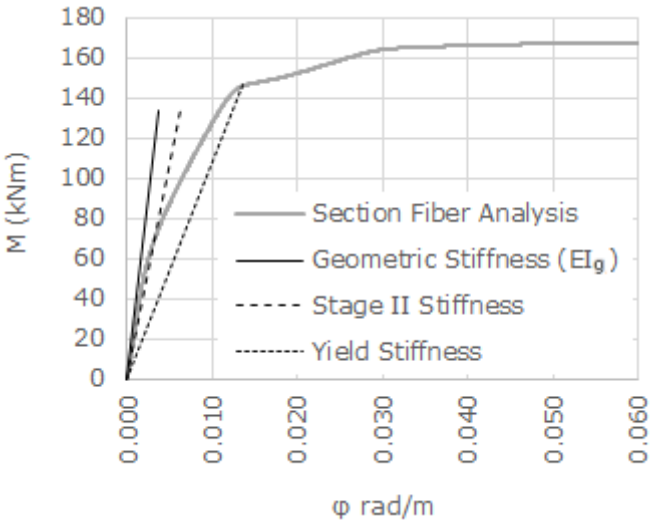


Figure 2: Moment-curvature results at the foot of the perimetric columns of the C1M building compared to the geometric, Stage II and yield stiffness of the section.

3 METHOD DESCRIPTION

The assessment of the variation of the vulnerability of the studied buildings during an after-shock sequence is performed by following steps 1-7:

1. For each seismic event (Magnitude/Distance couple) in the sequence (i = 1-n) compute the corresponding Intensity Measure (a_i), e.g. PGA, with a suitable Ground Motion Prediction Equation either from [23] or [24] for Europe.
2. Calculate the fragility curves of the undamaged building prior to the main shock for each damage state as a function of the selected Intensity Measure(s).
3. Define the damage states of the building in terms of period elongation due to structural degradation (T_{in}/T_{el} or $\Delta T = (T_{in}-T_{el})/ T_{el}$). Calculate the degraded stiffness of the structural elements of the building in each damage state in order to model the building in each state. This step is described analytically in Paragraph 4.
4. For each of the considered damage states (DS_j, j = 1-m) of the building calculate the fragility curves for every higher damage state.
5. Form the vector of the probabilities of exceedance of each damage state (e.g. Table 2 for four DSs) in terms of drift and frequency reduction at the time of the first seismic event (t_1) and its corresponding IM value (a_1) from the computed fragility curves of the undamaged building (Equation 1).

$$P_{(t1),j} = P\left[DS_{(t1)} \geq j \mid IM_{(t1)} = a_1\right],\ j = 1 - m \tag{1}$$

$P_{(t1),01}$	$P_{(t1),02}$	…	$P_{(t1),0m}$

Table 2: Vector of probabilities of exceedance of damage states at the time of the main shock (t_1).

6. Calculate the probability of exceedance of each damage state for the IM values (a_i) that correspond to the events in the catalog (catalog to be defined) from the computed fragility curves (Equation 2) of the building in all considered damaged states (1 - m). These values are then used to form the damage state transition matrices for each seismic event as shown in Table 3.

$$P_{(ti),j} = P\left[DS_{(ti)} \geq j \mid DS_{(ti)} \geq k, IM_{(ti)} = a_i\right],\ k \leq j = 1 - m \tag{2}$$

	$DS_{(ti)} \geq 0$	$DS_{(ti)} \geq 1$	$DS_{(ti)} \geq 2$	…	$DS_{(ti)} \geq m$
$DS_{(ti-1)} = 0$	1.0	$P_{(ti),01}$	$P_{(ti),02}$	…	$P_{(ti),0m}$
$DS_{(ti-1)} = 1$	0.0	1.0	$P_{(ti),12}$	…	$P_{(ti),1m}$
$DS_{(ti-1)} = 2$	0.0	0.0	1.0		$P_{(ti),2m}$
…	…	…		…	…
$DS_{(ti-1)} = m$	0.0	0.0	0.0	…	1.0

Table 3: Transition matrix ($T_{r(ti)}$) consisting of time-variant probabilities of exceedance of a damage at the time of an aftershock (t_i) depending on the damage state of the building prior to the event (t_{i-1}).

7. Calculate the probability of the building exceeding a damage state at the time points of the aftershocks with a discrete-time Markov chain with a discrete time space (Equation 3) using the transition matrices. Markov chains are used to describe systems going through a chain of events or states, in which every following state depends only on the current state. Note that the initial state vector in the right hand side has zero values with the exception of its first element which is equal to 1.0. This way the probability of exceedance of the damage states is computed given that the building is at the beginning of

the calculation in its first state, which here is its original undamaged state. With Equation 3 it is also possible to compute the exceedance probabilities given that the building is in a higher damage state by assigning the 1.0 value to the corresponding element of the vector.

$$[\,P[DS_{tn} \geq 1]\ \ldots\ P[DS_{tn} \geq m]\,] = [1\ 0\ \ldots\ 0] \prod_1^n T_{\mathrm{r}(ti)} \qquad (3)$$

4 PERIOD ELONGATION-BASED DAMAGE STATES

In this paper the damage states that are used are defined using as thresholds values of the elongation of the period of the building (T_{in}/T_{el} or ΔT). Limit damage states are typically defined with thresholds of the maximum interstorey drift (e.g. in HAZUS [20]). The advantage of using such thresholds is that, since the elongation of the first eigenperiod of a building can be measured by means of instrumentation immediately after the mainshocks, the degree of the suffered structural damage can be available remotely and in real time without the need for inspection. These limit damage states are defined using the results of the same set of non-linear analyses used for the calculation of the fragility curves of the building in its original state.

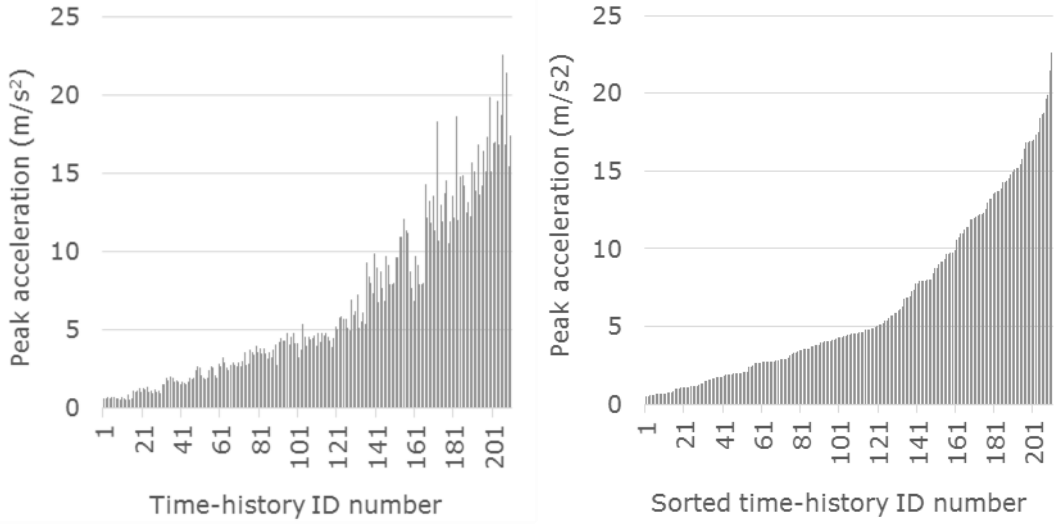


Figure 3: PGAs of the synthetic input motions.

4.1 Seismic input time-histories

The time-history analyses are performed assuming full fixity of the foot all vertical structural elements of the ground floor, where the seismic excitation was applied. Fourteen groups of 15 synthetic acceleration time histories are used as base excitation in the time-history analyses. Each group was generated with Eurocode's Type C spectrum as the average target spectrum. The synthetic time-histories were generated with SeismoArtif [25], which implements a method based on Hallodorson and Papageorgiou [26], for the case of a near field source under an interplate regime, with hypocentral distance of 9 km. The PGA of each of the 14 target spectra ranges from 0.005 m/s^2 to 15.0 m/s^2. However individual time histories have a wider range exceeding 20.0 m/s^2 (Figure 3). By using such a set of synthetic accelerograms with a varying intensity it is assured that the frequency content of each accelerogram corresponds to its intensity. Zacharenaki et al. [27] have shown that the response to time-histories with frequency content resulting from scaling in Incremental Dynamic Analysis [28] may be lower than the response to natural and synthetic records in the case of SDOFs with a period lower than 0.50 s, while being unbiased for SDOFs with period higher than 0.70 s. Although for structures with

multiple degrees of freedom the assessment of this bias may be more complex, we consider the selected time-histories suitable for the C2M building, as its fundamental period is 0.38 s.

4.2 Structural degradation and period elongation

Besides the calculation of the storey drifts for each building from the series of analyses model we calculate the stiffness degradation ratio at selected sections of each structural element (the ratio of the secant modulus (EI_{sec}) of the moment-curvature loops of each section to the elastic (EI_{el}) stiffness of the section) as a function of the first storey drift (Figure 4). HAZUS sets the collapse threshold at a maximum interstorey drift of 0.0333 for C2M buildings, while Kappos [29] at 0.02 for buildings in Greece. Therefore we calculate the degraded stiffness of each structural element with its corresponding power fit function (excluding values equal to 1.0) for a series of first storey drift in the range of $1 \cdot 10^{-4}$ to $4 \cdot 10^{-2}$ and perform modal analyses of the resulting building models. The ratio of the fundamental period of these building models that have undergone inelastic deformations to the period of the elastic building models in its original undamaged state (T_{in}/T_{el}) is shown in Figure 6a. We observe that the period elongation of the C1M building starts at a higher drift compared to the stiffer C2M building and that its period elongation is sharper. The ratio of the total drift to the first storey drift –as expected– is significantly higher for the building with the shear walls in comparison to the moment resisting frame building. Using the computed ratio of total to first storey drift (Figure 5) we then plot the period elongation ratio T_{in}/T_{el} as a function of the total drift (Figure 6b). By defining damage limit state thresholds as period elongation equal to 20 %, 40 % and 60 % we obtain the corresponding drifts (Table 4). We assume that ΔT = 60 % corresponds to a damage state on the verge of collapse based on the observations in Vidal et al. [11]. For these drift values we calculate the stiffness of each element and model the studied buildings in the defined limit damage states.

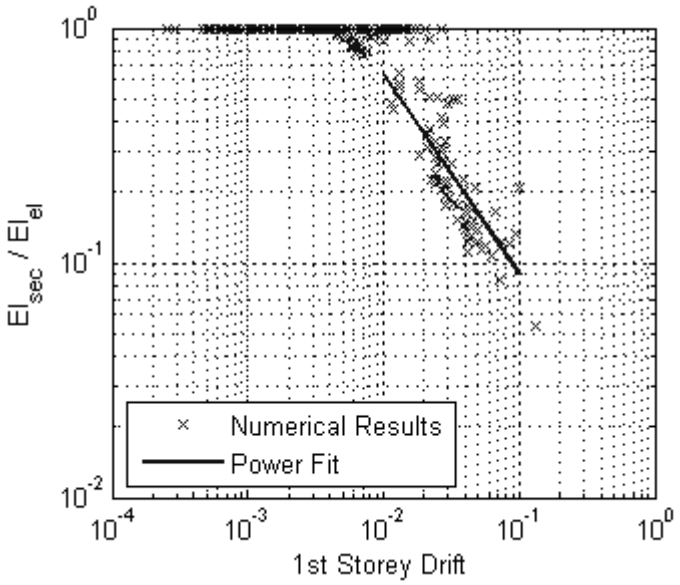


Figure 4: Stiffness degradation ratio at the foot of a corner column; results and power fit.

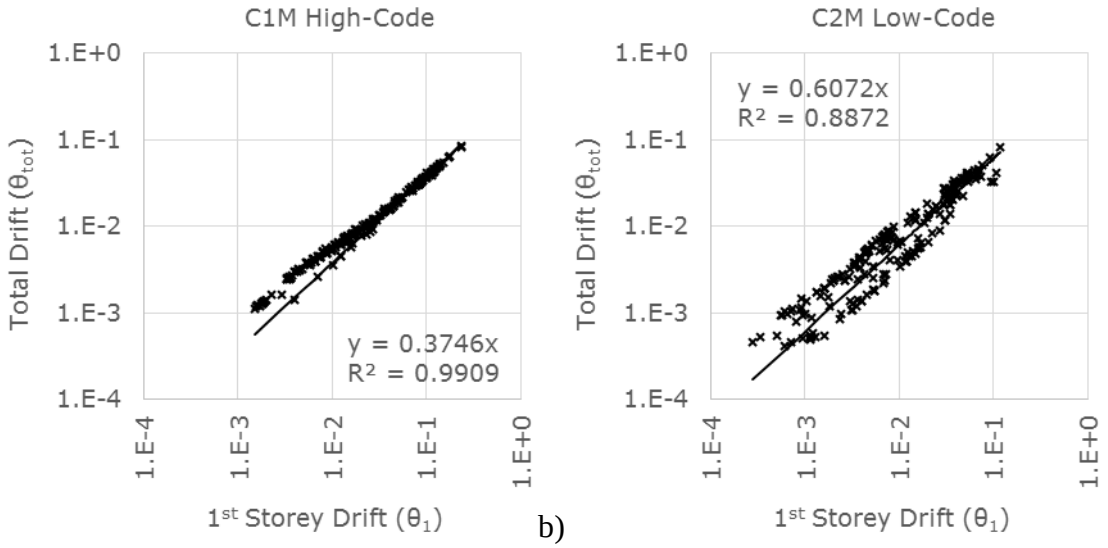


Figure 5: Total versus 1st storey drift in the case of the studied C1M high code (a) and C2M low code building models.

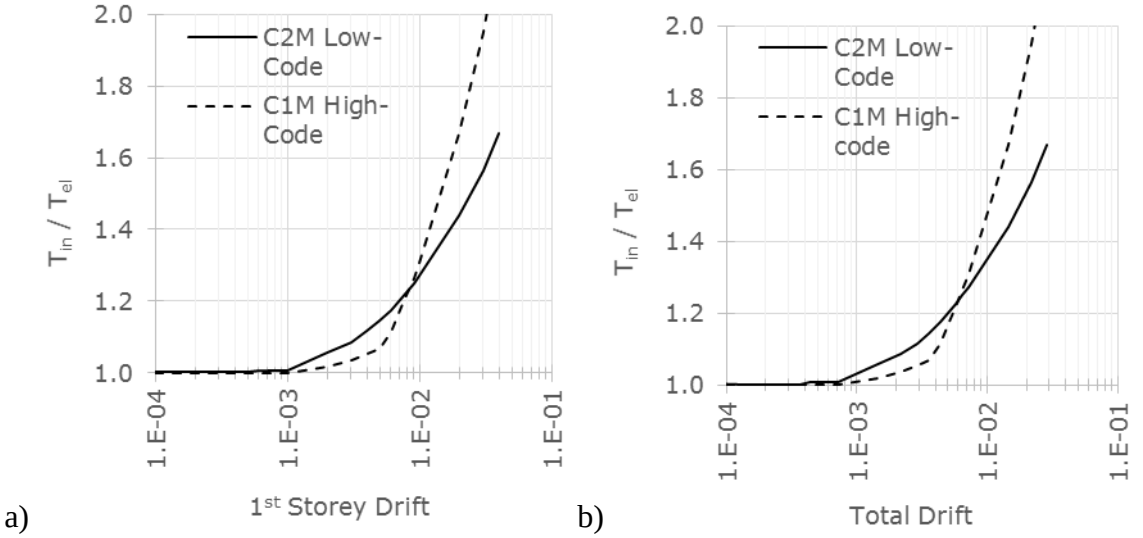


Figure 6: Period elongation ratio (T_{in}/T_{el}) as a function of the first storey drift (a) and total drift (b) of the buildings in this study.

		C2M Low-code			C1M High-code		
ΔT (%)	T_{in}/T_{el}	T_{in}	θ_{max}	θ_{tot}	T_{in}	θ_{max}	θ_{tot}
20	1.2	0.47	0.0070	0.0042	0.769	0.0076	0.0029
40	1.4	0.54	0.0177	0.0107	0.898	0.0125	0.0047
60	1.6	0.62	0.0328	0.0199	1.026	0.0181	0.0068

Table 4: Period elongation thresholds and the corresponding inelastic periods and drifts of the two building models.

5 TIME-VARYING VULNERABILITY

5.1 Structural period elongation-based fragility curves

Having modeled the studied buildings in the defined period-elongation based damage states we perform inelastic time history analyses with the degraded building models with the same set of excitations described in paragraph 4.1 in order to calculate their fragility curves. Typically fragility curves are plotted in groups corresponding to the probability of each limit state being exceeded given that the building is in its original state. These fragility curves for the selected buildings are presented in Figure 8. The fragility curves of the C1M building have higher values than the curves of the C2M building in the considered range of PGAs. Figure 7 shows the numerical results of the first storey drift versus PGA and the corresponding relationships. The scatter of the results is higher in the case of the C2M model, which can be seen both visually and by comparing the values (0.95 versus 0.81) of the coefficient of determination (R^2). A possible explanation for this is the adoption of PGA as an intensity measure [30].

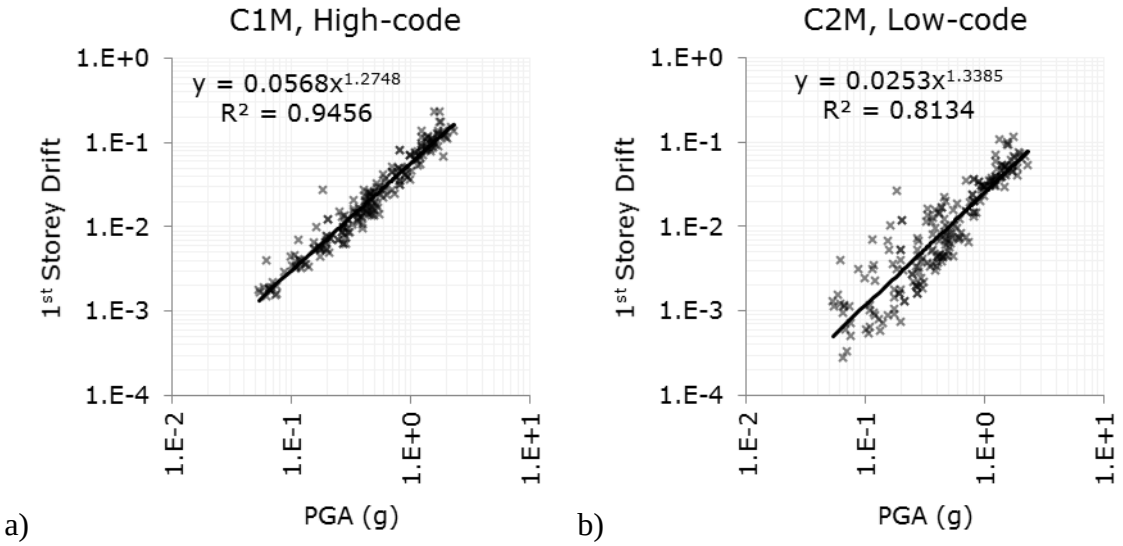


Figure 7: First storey drift versus PGA numerical results for the C1M (a) and C2M (b) buildings.

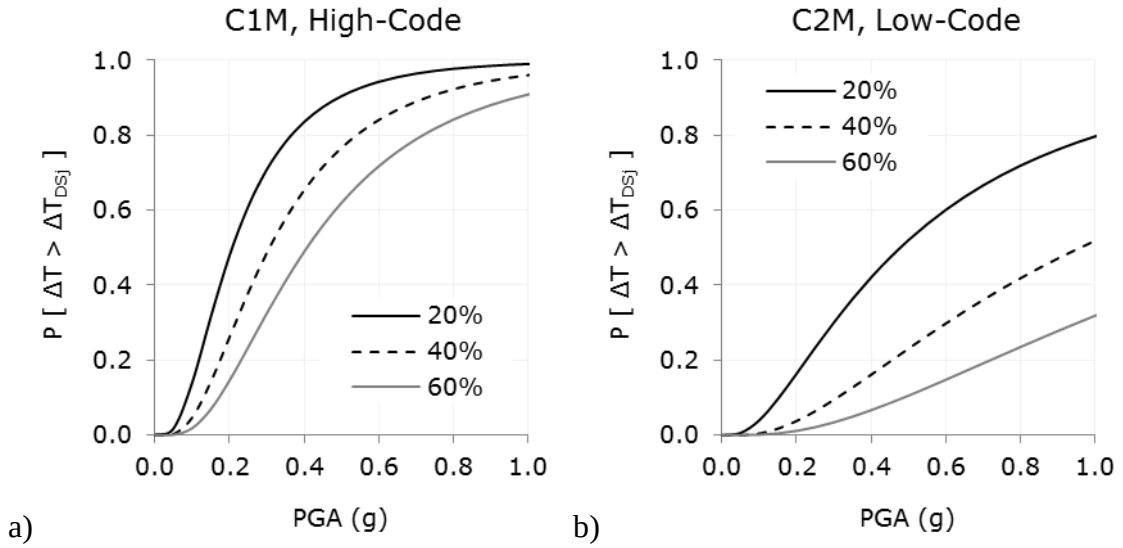


Figure 8: Fragility curves of the C1M (a) and C2M (b) buildings based on period elongation thresholds.

We are proposing an alternative grouping which gives the probability of exceedance of a specific damage state given that the building is in all lower damage states. This way the probability of transition from the current state to a higher damage state is obtained in order to be used in the transition matrices (Paragraph 3). Figure 9 gives the exceedance probabilities of limit damage states with period elongation thresholds of 40 % and 60 % as a function of the PGA given that the building models are in a lower damage state. We observe that the probability of exceedane of $\Delta T = 40$ % is higher for the building models in damage state with $\Delta T = 20$ % than for the building in its original state ($\Delta T = 0$ %) and that the difference is larger in the case of the C2M low-code building.

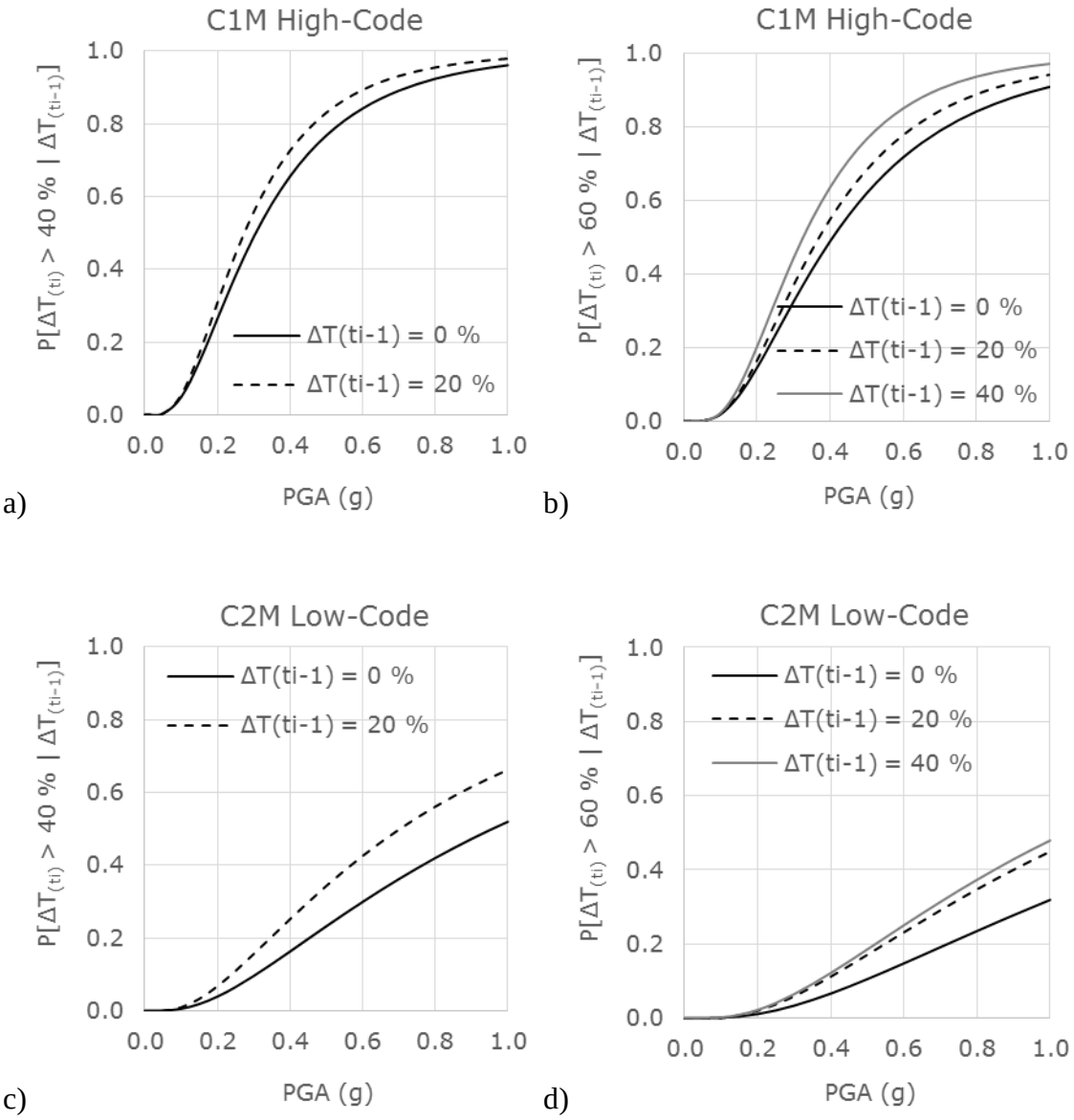


Figure 9: Probability of transition of the studied building models at a time point (t_i) from lower damage states to the damage states defined by the period elongation thresholds of 40 % (a, c) and 60 % (b, d).

5.2 Probability of exceedance of period elongation thresholds over periods of aftershock sequences

The probability of exceedance of the three defined threshold of period elongation are computed for the cases of the aftershock sequences of the 1978 Thessaloniki (events with $M \geq 4.3$ [31]) and 1994 Northridge earthquakes [32, 33] considered as case studies. We assume that the studied buildings have the coordinates listed in Table 5 with a main-shock epicentral distance of 28.2 km and 16.0 km. For the calculations for the 1978 Thessaloniki sequence the building location was selected assuming that the building is part of the critical infrastructure of the port of the city, while for the Northridge case a fictional location is used. In the case of the Thessaloniki sequence the event details from the seismicity catalog [34, 35] were used since the listed magnitudes are practically equal to the moment magnitude [36]. The PGA at the base of the building for each seismic event is estimated with the ground motion prediction equation (GMPE) of Akkar and Bommer [37], as it is considered suitable for the tectonic setting of Thessaloniki [24]. The same equation is also used for the case of the Northridge sequence for demonstration

The prediction of ground motion parameters such as the PGA is characterized by significant uncertainty and an elaborate approach is recommended (e.g. logic tree) including other GMPEs (e.g. [38]) and different types of excitation time series [39] for detailed studies. We limit this study to the computed PGAs by the selected GMPE for simplicity, since our aim is the presentation of the proposed method.

Next we form the transition matrices by computing the values of the fragility curves that correspond to the PGAs of the seismic events in the aftershock sequences. The probability of exceedance of the limit damage state thresholds at the time points of the seismic events is then computed as the product given by Equation 3. Figure 10 shows the results of this calculation for the 1978 Thessaloniki aftershock sequence and Figure 11 for the 1994 Northridge sequence. The largest increase of the exceedance probabilities is observed at the time points of the main shocks. In the Northridge case it takes place at the beginning of the aftershock sequence, while in the case of Thessaloniki on day 43. In both cases the C1M building has a higher probability of sustaining damage in comparison to the C2M building although it's a high-code building and the C2M is low-code.

Case	λ	φ	R (km)
Thessaloniki 1978	40.634 N	22.937 E	28.2
Northridge 1994	34.194 N	-118.376 W	16.0

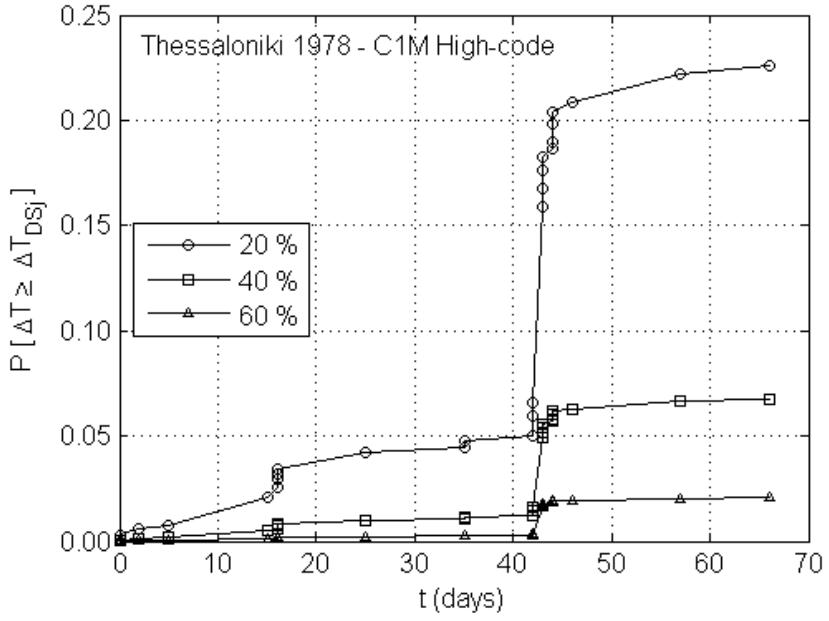
Table 5: Fictional coordinates of the studied buildings for the two case studies and the main shock epicentral distance.

6 CONCLUSIONS

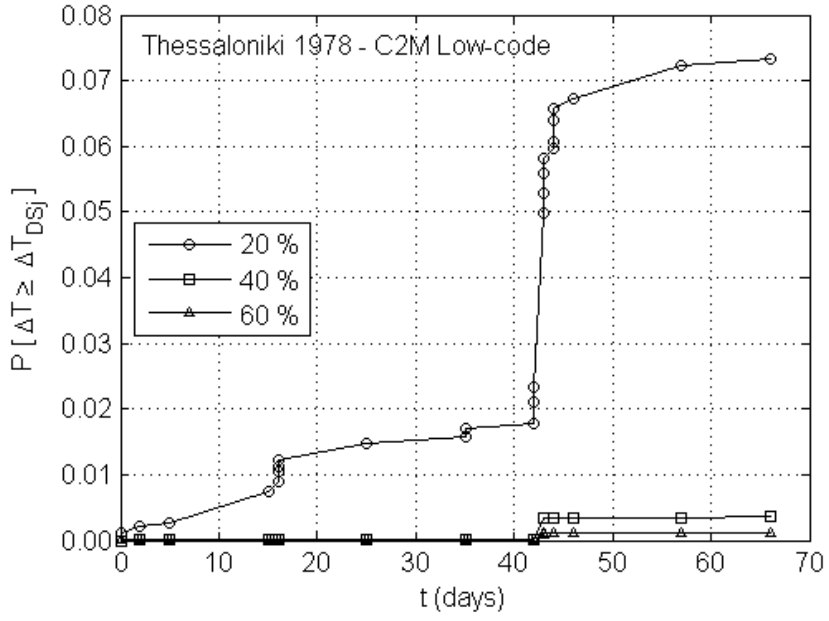
Our main goal was to present a method that calculates the variation of the vulnerability of reinforced concrete structures during aftershock sequences. The proposed method and the numerical results show that reinforced concrete buildings indeed may become more vulnerable due to damage accumulation during aftershock sequences. It is shown that the probability increase due to the main shock is the largest in the presented case studies, but it is only a fraction of the cumulative probability of exceedance of a damage state throughout the aftershock sequences. The probability of damage state exceedance in the numerical results for the case studies of the aftershock sequences of the Thessaloniki (1978) and the Northridge (1994) follows a similar trend to the failure probability during the aftershock sequence period as estimated by Iervolino et al. [5]. Moreover, the assumption that period elongation of $\Delta T = 60$ % corresponds

to a state near collapse is in agreement with the empirical estimations by Katsanos and Sextos [10].

This study makes the hypothesis that the response of plane numerical models is representative of the response of the actual three-dimensional buildings, however this is a common hypothesis in seismic vulnerability studies and it reduces the computational load. We also ignore the variation of the damping of the structure as it accumulates seismic damage and the degradation of strength of the structural elements. Furthermore, the sensitivity of the numerical results on the type of input time-histories is not investigated.

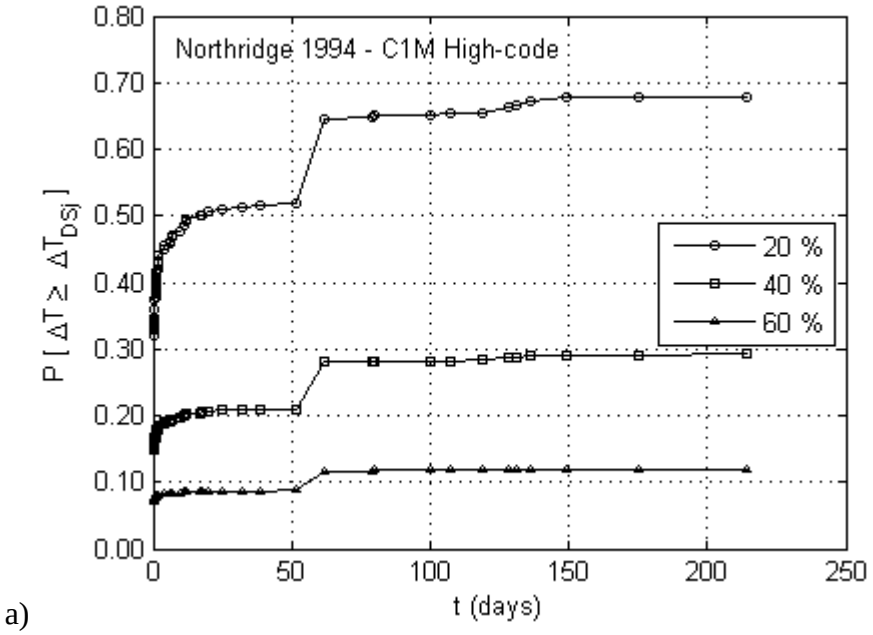


a)

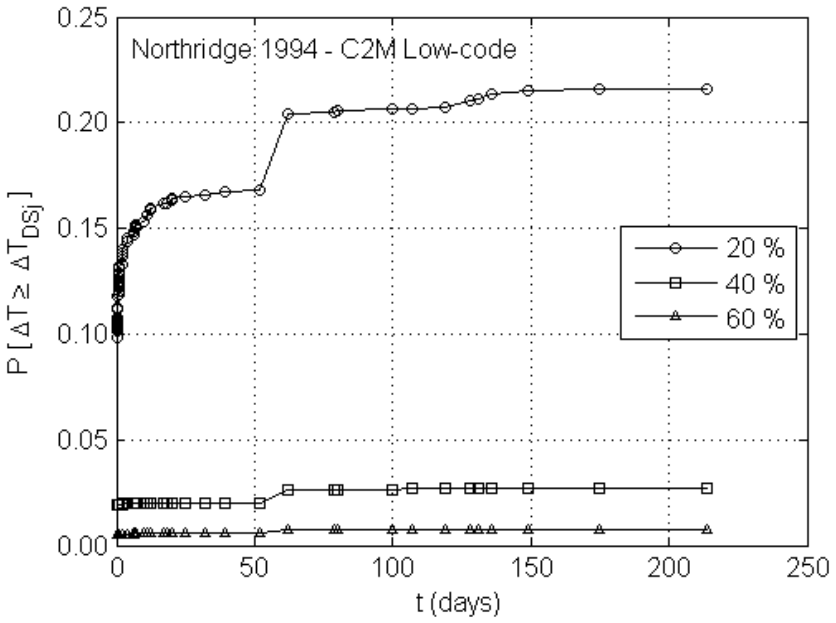


b)

Figure 10: Probability exceedance of limit damage state thresholds in the form of period elongation (ΔT) in the case of the 1978 Thessaloniki aftershock sequence for the C1M high-code (a) and the C2M low-code building (b).



a)



b)

Figure 11: Probability exceedance of limit damage state thresholds in the form of period elongation (ΔT) in the case of the 1994 Northridge aftershock sequence for the C1M high-code (a) and the C2M low-code building (b).

The proposed calculation procedure can be performed for RC buildings with a structural system of moment resisting frames, shear walls, or dual irrelevant of the number of storeys, and for any series of seismic events, e.g. in order to estimate structural deterioration due to small magnitude earthquakes during a time period. Moreover, this method gives the stiffness degradation ratio of the structural elements of a building and therefore the location of seismic damage depending on the frequency content of the excitations and the dynamic characteristics of the building. This is considered an advantage over pushover analyses, during which the locations of the plastic hinges depend significantly on the load pattern.

Improvements upon the presented study may be achieved by accounting for the uncertainties in the prediction of the PGA, and by exploring alternative Intensity Measures and different

types of time-histories as excitation of the numerical models. It is also worth taking into account infill walls and their possible irregularity in height, as well as possible shear and residual deformations of the structural elements.

AKNOWLEDGEMENTS

This study was carried out in the framework of the research programme "STREST" – Harmonized approach to stress tests for critical infrastructures against natural hazards (http://www.strest-eu.org) funded by the European Union's Seventh Framework Programme (FP7/2007-2013, Grant agreement No. 603389).

REFERENCES

[1] Comité Européen de Normalisation, *Eurocode 8: Design of structures for earthquake resistance – Part 1: General rules, seismic actions and rules for buildings*, EN 1998-1:2004:E, 2004.

[2] H. Ziar, *Time variation of fragility curves for seismic vulnerability assessment of reinforced concrete structures*, Research report, Université Joseph Fourier, 2014.

[3] K.D. Pitilakis, S.T. Karapetrou and S.D. Fotopoulou, Consideration of aging and SSI effects on seismic vulnerability assessment of RC buildings, *Bulleting of Earthquake Engineering*, **12**, 1777-1803, 2014.

[4] M. Sanchez-Silva, G.-A. Klutke and D.V. Rosowsky, Life-cycle performance of structures subject to multiple deterioration mechanism, *Structural Safety*, **33**, 206-217, 2011.

[5] I. Iervolino, M. Giorgio and E. Chioccarelli, Closed-form aftershock reliability of damage-cumulating elastic-perfectly-plastic systems, Earthquake Engineering and Structural Dynamics, 43, 613-625, 2014.

[6] G.D. Hatzigeorgiou and D.E. Beskos, Inelastic displacement ratios for SDOF structures subjected to repeated earthquakes, *Engineering Structures*, **31**, 2744-2755, 2009.

[7] E. Miranda and J. Ruiz-Garcia, Influence of stiffness degradation on strength demands of structures built on soft soil sites, *Engineering Structures*, **24**, 1271-1281, 2002.

[8] A. Masi and M. Vona, Experimental and numerical evaluation of the fundamental period of undamaged and damaged RC framed buildings, *Bulletin of Earthquake Engineering*, **8**, 643-656, 2010.

[9] E.I. Katsanos, A.G. Sextos and A.S. Elnashai, Prediction of inelastic response periods of buildings based on intensity measures and analytical model parameters, *Engineering Structures*, **71**, 161-177, 2014.

[10] E.I. Katsanos and A.G. Sextos, Inelastic spectra to predict period elongation of structures under earthquake loading, *Earthquake Engineering and Structural Dynamics*, published online, 2015.

[11] E. Vidal, M. Navarro, C. Aranda and T. Enomoto, Changes in dynamic characteristics of Lorca RC buildings from pre- and post-earthquake ambient vibration data, *Bulletin of Earthquake Engineering*, **12**, 2095-2110, 2014.

[12] Conseil de L'Europe, G. Grünthal (ed), European Macroseismic Scale, *Cahiers du Centre Européen de Géodynamique et de Séismologie*, **15**, 1998.

[13] J. Régnier, C. Michel, E. Bertrand and P. Guéguen, Contribution of ambient vibration recordings (free-field and buildings) for post-seismic analysis : The case of the Mw 7.3 Martinique (French Lesser Antilles) earthquake, November 29, 2007, *Soil Dynamics and Earthquake Engineering,* **50**, 162-167, 2013.

[14] P. Roux, P. Guéguen, L. Baillet and A. Hamze, Structural-change localization and monitoring through a perturbation-based inverse problem, *The Journal of the Acoustical Society of America*, **136**, 2586-2597, 2014.

[15] A.J. Kappos, G. Panagopoulos, C. Panagiotopoulos and G. Penelis, A hybrid method for the vulnerability assessment of R/C and URM buildings, *Bulletin of Earthquake Engineering*, **4**, 391-419, 2006.

[16] Earthquake Planning and Protection. *EAK 2000 - Greek Antiseismic Code 2000*, GG 2184/B/20-12-1999, Hellenic Republic, 2001. (in Greek)

[17] M. Fardis, E. Carvalho, A. Elnashai, E. Faccioli, P. Pinto and A. Plumier, *Designer's guide to EN 1998-1 and EN 1998-5 Eurocode 8: Design of structures for earthquake resistance,* Thomas Telford Publishing ,2005.

[18] G.G. Penelis and G.G. Penelis, *Concrete buildings in seismic regions*, CRC Press, 2014.

[19] A.J. Kappos, G.K. Panagopoulos, A.G. Sextos, V.K. Papanikolaou and K.C. Stylianidis, Development of comprehensive earthquake loss scenarios for a Greek and a Turkish city – structural aspects, *Earthquakes and Structures*, **1**, 197-214, 2010.

[20] Federal Emergency Agency, *HAZUS-MH 2.1 – Technical Manual – Earthquake Model*, Department of Homeland Security, 2012.

[21] S. Mazzoni, F. McKenna, M.H. Scott and G. L. Fenves, *Open System for Earthquake Engineering Simulation - user manual*, Pacific Earthquake Engineering Research Center, University of California, Berkeley, CA, 2009.

[22] Earthquake Planning and Protection, *Code for Interventions*, GG 2187/B/05-09-2013, Hellenic Republic, 2013. (in Greek)

[23] J. Douglas, *Ground-motion prediction equations 1964-2010*, Pacific Earthquake Engineering Research Center - brgm, 2011.

[24] E. Delavaud, F. Cotton, S. Akkar, F. Scherbaum, L. Danciu, C. Beauval, S. Drouet, J. Douglas, R. Basili, M. A. Sandikkaya, M. Segou, E. Faccioli, N. Theodoulidis, Toward a ground-motion logic tree for probabilistic seismic hazard assessment in Europe, *Journal of Seismology*, **16**, 451-473, 2012.

[25] Seismosoft, *SeismoArtif*, Version 2.1, Computer Program, Available at: seismosoft.com, Accessed: 02 February 2015, 2013.

[26] B. Halldorsson and A. S. Papageorgiou, Calibration of the Specific Barrier Model to earthquakes of different tectonic regions, *Bulletin of the Seismological Society of America*, **95**, 1276-1300, 2005.

[27] A. Zacharenaki., M. Fragiadakis, D. Assimaki and M. Papadrakakis, Bias assessment in in Incremental Dynamic Analysis due to record scaling, *Soil Dynamics and Earthquake Engineering,* **67**, 158-168, 2014.

[28] D. Vamvatsikos, C.A. Cornell, Developing efficient scalar and vector intensity measures for IDA capacity estimation by incorporating elastic spectral shape information, *Earthquake Engineering and Structural Dynamics*, **34**, 1573-1600, 2005.

[29] A.J. Kappos, Seismic vulnerability and loss assessment for buildings in Greece, P. Guéguen ed., *Seismic Vulnerability of Structures*, ISTE Ltd and John Wiley & Sons Inc, 2013.

[30] M. Perrault, P. Guéguen, A. Aldea and S. Demetriu, Using experimental data to reduce the single-building sigma of fragility curves: case study of the BRD tower in Bucharest, Romania, *Earthquake Engineering and Engineering Vibration*, **12**, 643-658, 2013.

[31] B.C. Papazachos and P.G. Carydis, The time, magnitude and space distributions of the 1978 Thessaloniki seismic sequence, *The Thessaloniki, Northern Greece, earthquake of June 20 1978, and its seismic sequence*, Technical Chamber of Greece – Section of Central Macedonia, 1983.

[32] E. Hauksson, L.M. Jones and K. Hutton, The 1994 Northridge earthquake sequence in California: seismological and tectonic aspects, *Journal of Geophysical Research*, **100**, 12,335-12,355, 1995.

[33] H.K. Thio and H. Kanamori, Source complexity of the 1994 Northridge earthquake and its relation to aftershock mechanisms, *Bulletin of the Seismological Society of America*, **86**, S84-S92, 1996.

[34] B.C. Papazachos, P.E. Comninakis, G.F. Karakaisis, B.G. Karakostas, Ch.A. Papaioannou, C.B. Papazachos and E.M. Scordilis, A catalogue of earthquakes in Greece and surrounding area for the period 550BC-1999, *Publ. Geophys. Laboratory*, University of Thessaloniki, 2000.

[35] B.C. Papazachos, P.E. Comninakis, E.M. Scordilis, G.F. Karakaisis and C.B. Papazachos, A catalogue of earthquakes in the Mediterranean and surrounding area for the period 1901 - 2010, *Publ. Geophys. Laboratory*, University of Thessaloniki, 2010.

[36] B.C. Papazachos, V.G. Karakostas, A.A. Kiratzi, B.N. Margaris, C.B. Papazachos and E.M. Scordilis, Uncertainties in the estimation of earthquake magnitudes in Greece, *Journal of Seismology*, **6**, 557-570, 2002.

[37] S. Akkar and J.J Bommer, Empirical equations for the prediction of PGA, PGV and spectral accelerations in Europe, the Mediterranean region, and the Middle East, *Seismological Research Letter*, **81**, 195-206. 2010.

[38] A.A. Scarlatoudis, C.B. Papazachos, B.N. Margaris, N. Theodoulidids, C. Papaioannou, I. Kalogeras, E.M. Scordilis and V. Karakostas, Empirical peak ground-motion predictive relations for shallow earthquakes in Greece, *Bulletin of the Seismological Society of America*, **93**, 2591-2603, 2003.

[39] M. Causse, A. Laurendeau, M. Perrault, J. Douglas, L.F. Bonilla and P. Guéguen, Eurocode 8-compatible synthetic time-series as input to dynamic analysis, *Bulletin of Earthquake Engineering*, **12**, 755-768, 2014.

COMPDYN 2015
5th ECCOMAS Thematic Conference on
Computational Methods in Structural Dynamics and Earthquake Engineering
M. Papadrakakis, V. Papadopoulos, V. Plevris (eds.)
Crete Island, Greece, 25–27 May 2015

RECORD-TO-RECORD VARIABILITY IN THE SEISMIC RESPONSE OF RC WALLS BUILDINGS SUBJECTED TO GROUND MOTIONS MATCHED TO THE CONDITIONAL SPECTRUM

Matthew J. Fox[1] **and Timothy J. Sullivan**[2,3]

[1] ROSE Programme, UME School, IUSS Pavia
Via Ferrata 1, Pavia 27100, Italy
e-mail: matthew.fox@umeschool.it

[2] University of Pavia, Department of Civil Engineering and Architecture
Via Ferrata 1, Pavia 27100, Italy
tim.sullivan@unipv.it

[3] EUCENTRE
Via Ferrata 1, Pavia 27100, Italy

Keywords: Performance-based earthquake engineering, simplified seismic assessment, conditional spectrum, record-to-record variability

Abstract. *In Performance-Based Earthquake Engineering, it is often necessary to be able to estimate the response of a structure whilst accounting for various sources of uncertainty. A number of simplified procedures have been proposed whereby record-to-record variability is accounted for using empirical estimates of dispersion. It is shown herein how the calibration of empirical dispersion estimates may prove challenging due to the numerous factors that influence dispersion. An alternative simplified numerical approach is examined, in which record-to-record variability is accounted for through use of the conditional spectrum. This simplified procedure is evaluated through a comparison with results obtained from nonlinear response-history analyses. Both inter-storey drift ratio and base shear are examined, with promising initial results.*

1 INTRODUCTION

Traditionally, in the field of earthquake engineering, the seismic design or assessment of structures has been based around rather prescriptive code provisions. However, over the last couple of decades there has been a realisation that these more simplistic approaches may not be satisfactory and thus there is an ongoing shift towards Performance-Based Earthquake Engineering (PBEE). From the seismic assessment point of view, the core concept of PBEE is that the expected performance of a structure should be able to be expressed to an end user in terms of useful performance metrics. To this extent it is becoming evident that an effective means of expressing performance is to use time-dependent performance metrics such as expected annual economic loss or the annual rate of exceedance of a predefined limit state.

To calculate time-dependent performance metrics, a conditional approach is typically adopted, whereby information on the fragility of the structure is combined with hazard information. For example, the annual rate of exceeding a limit state inter-storey drift ratio, *idr*, can be determined through numerical integration of Equation 1, adapted from [1]:

$$\lambda(IDR > idr) = \int_x P(IDR > idr \mid IM = x) \left| d\lambda(x) \right| \tag{1}$$

where $P(IDR>idr|\text{IM}=x)$ is the probability that IDR exceeds the limit state value (*idr*) conditioned on the occurrence of an event with intensity IM=*x*, in which IM is the specific intensity measure being considered (*e.g.* PGA), and $|d\lambda(\text{x})|$ is the absolute value of the derivate of the hazard curve times *dx*. In simplistic terms $|d\lambda(\text{x})|$ can be considered as the rate of events occurring within an infinitesimal intensity range *dx* about *x*. Alternatively, closed form solutions exist whereby the annual probability of exceeding a given level of demand can be approximated. For example, as shown in Equation 2, again adapted from [1]:

$$P(EDP > edp) = \lambda\left(x^{edp}\right) \exp\left(\frac{1}{2}\frac{k^2}{b^2}\beta^2\right) \tag{2}$$

where $\lambda(x^{edp})$ is the hazard rate corresponding to a median response equal to *edp*, *k* is related to the slope of the hazard curve, *b* is used to described the relationship between intensity and the median conditional response and β is the dispersion in the engineering demand parameter (EDP) being examined.

Regardless of whether the rigorous numerical solution (Equation (1)) or the simplified closed form solution is used, a critical aspect is that for one or more intensity levels the engineer must determine not only the mean (or median) response of the structure but also the dispersion in response. In the case of Equation 1 this uncertainty manifests itself in the $P(IDR>idr|\text{IM}=x)$ term, whereas in Equation 2 the uncertainty is incorporated directly as the term β, which is the standard deviation of the logarithms of the EDP. Note that both epistemic and aleatory uncertainty in demand and capacity should be considered [1]; however, this paper will be limited to consideration of the aleatory component in demand, or record-to-record variability, only.

To obtain the probability distribution of an EDP at a given intensity, it is possible to conduct nonlinear response-history analyses (NLRHAs) using an appropriate set of ground-motions. However, both the numerical modelling and ground-motion selection aspects of this approach may be too demanding in practice. Furthermore, for large structural models the computational time required for the step-by-step integration schemes can be significant. Alternatively, a number of simplified approaches exist in which the median value of an EDP is obtained through simplified analyses, for example using the N2 method [2,3] or Direct Dis-

placement-Based Assessment [4], and then combining the median response with an empirical estimate of dispersion. In most cases a lognormal distribution can be assumed [5]. Some notable examples of the aforementioned simplified approach include FEMA P-58 [5], Fajfar and Dolšek [6], Welch *et al.* [7] and Sullivan *et al*. [8]. The ability to estimate the dispersion, β, is the focus of the remainder of this paper. Section 2 starts by looking at the factors that influence dispersion. Section 3 then discusses a proposed simplified method for determining dispersion numerically, rather than relying on empirical estimates. Section 4 then covers a case study application of this method.

2 FACTORS INFLUENCING DISPERSION

As mentioned in the previous section, a number of proposed simplified procedures rely on empirical estimates of dispersion, such as those provided in FEMA P-58[5]. The values provided in FEMA P-58 [5] are given as a function of the relative intensity and different values are provided depending on the EDP being considered. In addition to the relative intensity and EDP being considered, there are additional factors that will also influence dispersion, in particular, building configuration and local site conditions.

To demonstrate the influence that these factors can have on dispersion, a number of simple numerical analyses are carried out:

- A regular three storey RC wall building, described in [9], is analysed in two configurations, one corresponding to a reduction factor of R=2 and the other corresponding to R=4, to show the influence of relative intensity on dispersion. IDR is investigated as the EDP.
- For the same three storey building with R=4, the dispersion in both IDR and wall curvature, φ_w, are compared to show that dispersion is dependent on which EDP is being considered.
- The same case study building for R=2 is increased in height to six storeys, but with the walls stiffened and strengthened so that the same fundamental mode period and strength reduction factor are retained. The dispersion in IDR is then compared to that for the three storey building to show the influence of structural configuration on dispersion.
- Finally, the three storey building for R=4 is considered at two different sites with different ground types and seismic hazard characteristics.

In all cases the buildings are modelled using Ruaumoko3D [9] and analysed using NLRHA. A set of 40 ground motions (Set 1), selected to match the conditional spectrum [11, 12, 13] is used in the analyses. For the final case, a second set of 40 ground motions (Set 2), selected assuming different site characteristics, is used. The conditional spectra and displacement response spectra of the selected ground motions are shown in Figure 1. The different site characteristics are provided in Table 1. Note that these characteristics have been selected so that the two different conditional spectra differ significantly in their shape, but possess the same value of spectral displacement at the conditioning period, T*, of 1s (equal to the fundamental period of the case study building). The choice to use the conditional spectrum as a target for ground motion selection was made as it is considered a superior alternative to other target spectra, such as the uniform hazard spectrum. In particular, because the conditional spectrum accurately captures the record-to-record uncertainty on a spectrum level (conditioned on $Sd(T^*)$) it is consider as a robust starting point for obtaining estimates of record-to-record variability in structural response. Further discussion relating to the ground–motion sets used in this work and the target conditional spectra is provided in [9].

Set	V_{S30} (m/s)	$\overline{M}$	$\overline{R}$ (km)	ε
1	400	6.0	20	1.45
2	200	7.0	50	0.72

Table 1: Key parameters for conditional spectra and ground-motion selection (from [9]).

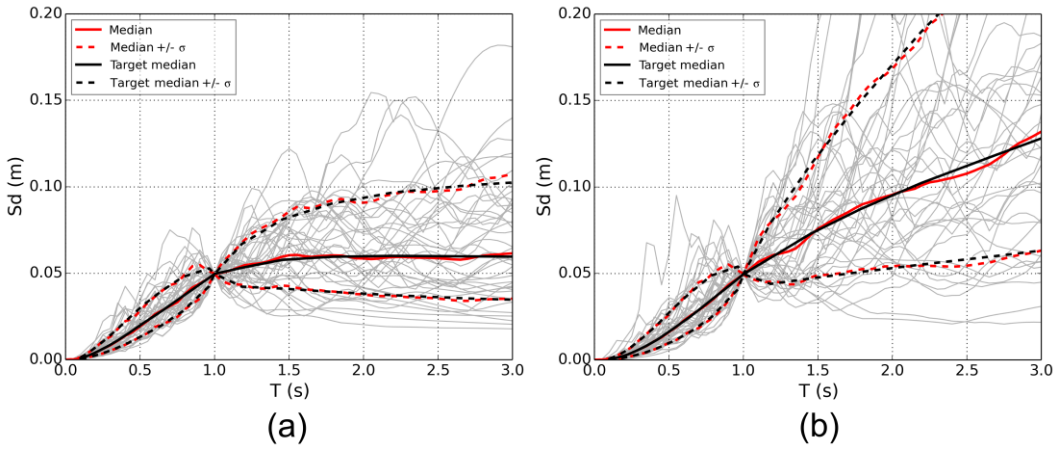


Figure 1. Conditional spectra and displacement response spectra of selected ground motions. (a) Set 1. (b) Set 2 (from [9]).

The results from the four different analyses are presented in Figure 2. In each case the results are plotted as empirical cumulative distribution functions of the EDP being considered. However, in order for the analyses to focus on the differences in dispersion, the results are first normalized by the median value of the EDP being considered. It can be seen that in each case the dispersion of the EDP distributions changes as different factors are varied. In Figure 2a, dispersion increases as *R* increases. This reflects how the empirical dispersion estimates in FEMA P-58 [5] vary with relative intensity. In Figure 2b the dispersion in curvature is observed to be larger than the dispersion in IDR. This is a consequence of curvature starting to increase rapidly once the walls start to yield, whereas the effect of yielding is not as dramatic on drift response. In Figure 2c it is observed that dispersion is larger for the six storey building. This is due to the stronger influence of higher-modes in the taller building, which contribute significantly to the total base shear. Finally, in Figure 2d it is observed that the different sets of ground motions produce very different levels of dispersion in drift response. This is despite the fact that the parameters used to construct the target conditional spectra do not vary too dramatically between the different ground-motion sets.

It is difficult to envisage how all these different factors could be taken into account when compiling empirical distribution data, in particular, the last aspect considering different site characteristics. As such, Fox and Sullivan [9] proposed a simplified numerical assessment procedure capable of estimating, with reasonable accuracy, the dispersion in the structural response of simple RC wall buildings.

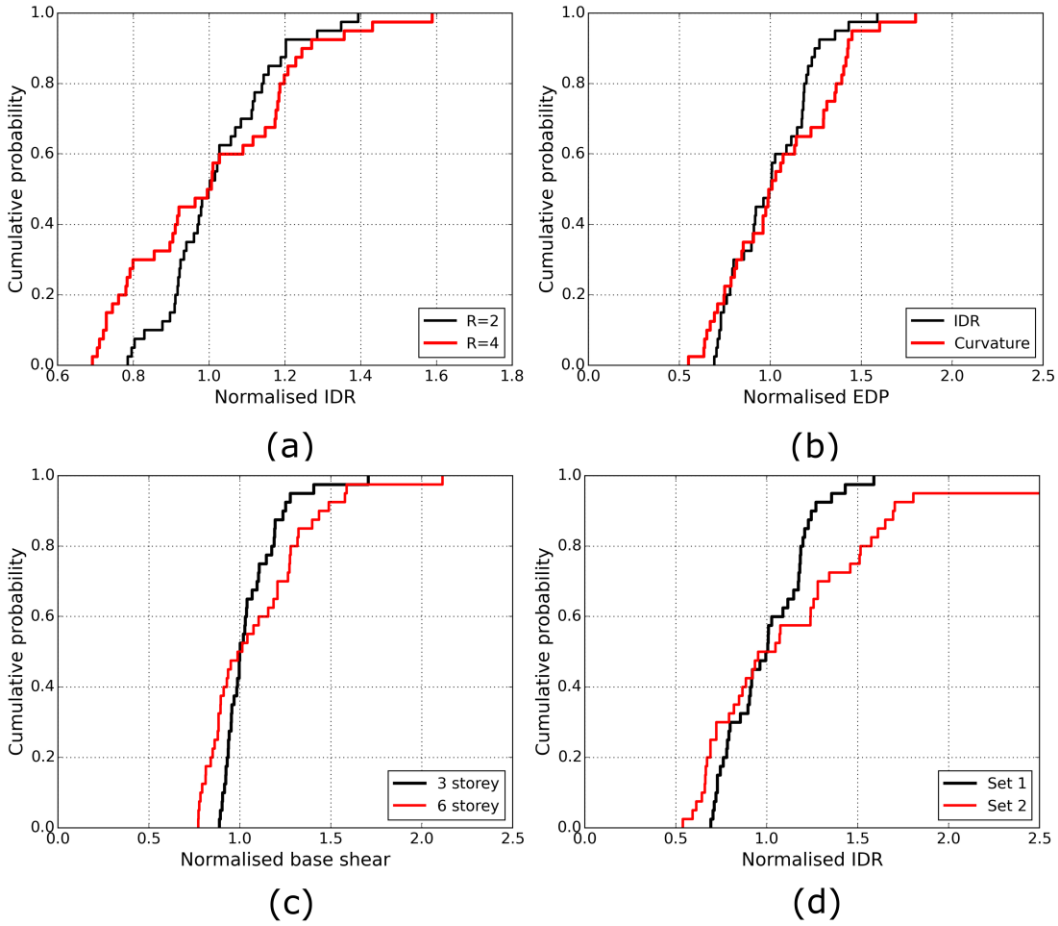


Figure 2. EDP distributions for examining different factors influencing dispersion. (a) Relative intensity, (b) different EDPs, (c) different building configurations, and (d) different site characteristics.

3 SIMPLFIED ASSESSMENT PROCEDURE INCORPORATING RECORD-TO-RECORD VARIABILITY IN STRUCTURAL RESPONSE ESTIMATES

To avoid the need for empirical dispersion estimates, Fox and Sullivan [9] proposed a simplified numerical assessment procedure for estimation of structural response whilst accounting for record-to-record variability. The procedure is considered "simplified" in the sense that ground-motion selection and NLRHA are not required. The key aspect of the procedure is that it relates the displacement response of an equivalent single-degree-of-freedom (SDOF) system to the spectral displacement at the effective period of the structure, $Sd(T_e)$, sampled from the conditional spectrum. The effective period is defined in accordance with [5] as the period of an equivalent linear system with the stiffness equal to the secant stiffness to the maximum displacement of the inelastic system. As this relation between displacement demand and spectral displacement is formed at the effective period, the procedure can capture the influence of the dispersion that is already defined within the conditional spectrum.

To start the procedure it is necessary to convert the multi-degree-of-freedom (MDOF) wall system to an equivalent SDOF system. This can be done using numerous existing approaches, for example, through the equations provided in [14]. Once the equivalent SDOF properties are obtained the following step-by-step procedure is used:

1) Construct the conditional (displacement) spectrum using T_1 as the conditioning period.

2) If $Sd(T_1)$ is greater than the yield displacement, Δ_y, the SDOF system will respond in the inelastic range and so the procedure moves on to step 3. If instead the structure remains in the elastic range then the solution is trivial *i.e.* $\Delta_d = Sd(T_1)$.

3) Make an initial estimate of the displacement demand. A good initial guess is $\Delta_d = Sd(T_1)$ *i.e.* the 'equal displacement rule' [15].

4) Calculate the displacement ductility demand and subsequently the effective period using Equations 3 and 4 respectively.

$$\mu = \frac{\Delta_d}{\Delta_y} \tag{3}$$

$$T_e = \sqrt{\frac{\mu}{(1 - r\mu + r)}} \tag{4}$$

where r is the post-yield hardening ratio.

5) Obtain a randomly sampled value of spectral displacement at the effective period using Equation 5:

$$Sd(T_e) = \exp\left(\overline{\ln Sd}(T_e) + K.\sigma_{\ln Sd(T_e)}\right) \tag{5}$$

where $\overline{\ln Sd}(T_e)$ and $\sigma_{\ln Sd(Te)}$ are the mean and standard deviation of the natural logarithms of spectral displacement obtained from the conditional spectrum at the effective period and K is a randomly sampled value from the standard normal distribution.

6) Calculate a ductility dependent displacement reduction factor (DRF), which is defined as $\eta = \Delta_d / Sd(T_e)$. This can be done in using the concept of equivalent viscous damping as per Priestley *et al.* [4]. Equation 6, which is based on a thin Takeda hysteresis rule and considered appropriate for well detailed RC wall systems, is used to calculate the equivalent viscous damping ratio. Equation 7 is then used to adjust the 5% damped displacement spectrum to that corresponding to the new damping ratio ξ_{eq}.

$$\xi_{eq} = 0.05 + 0.444\sqrt{\frac{\mu - 1}{\mu\pi}} \tag{6}$$

$$\eta = \sqrt{\frac{0.07}{0.02 + \xi_{eq}}} \tag{7}$$

An alternative approach to this step is to use equations that provide DRFs as a function of ductility directly, such as those provided by Pennucci *et al.* [16].

7) Using the DRF found in the previous step, calculate a revised displacement demand from Equation 8. If the difference between the initial estimate of displacement demand (made in step 3) and the revised value is small, say within 2%, then continue to step 7. If not, then start again at step 3 using the revised estimate of displacement demand. Note that within each loop from steps 2 to 6, the same value of K should be used.

$$\Delta_d = \eta.Sd(T_e) \tag{8}$$

8) Record the calculated value of displacement demand and then start again at step 2 with a newly sampled value of K. This process is repeated until the desired number of estimates for displacement demand is obtained. Note that each estimate roughly corresponds to a displacement value calculated using NLRHA for a single ground motion. It is therefore recommended that the number of samples of K be comparable to the number of ground motions one might use in NLRHA.

With the set of displacement estimates, each corresponding to different sampled values of K, the distribution of different EDPs can be obtained. This is achieved by, for each different displacement estimate, converting the SDOF system back to a MDOF system and extracting values of the relevant EDPs. Any desired statistics, such as the median and dispersion, can then be calculated for each EDP. An example of the core part of the procedure is illustrated in Figure 3. In Figure 3a two iterations of steps 2-7 are shown for the case where K=+1.2, which results in a single estimate of displacement response. Figure 3b then shows 10 iterations of steps 2-8, which results in 10 different estimates of displacement demand, each corresponding to a different value of K.

The aforementioned procedure is suitable for obtaining estimates of EDPs that are not strongly influenced by higher-modes of vibration. To account for higher-mode effects Fox and Sullivan [9] proposed an additional procedure based on similar principals; however, it is limited to elastic structures only. To account for higher-mode effects, the contributions from multiple modes of vibration are combined using the square-root-sum-of-the-squares rule. As the conditional spectrum is chosen to be conditioned on $Sd(T_1)$ the first mode (elastic) response is deterministic. On the other hand, for the second mode of vibration there is a known distribution of $Sd(T_2)$ conditioned on the occurrence of $Sd(T_1)$. Therefore, a sampling procedure can again be used to estimate the distribution of different EDPs in the elastic range, considering the distribution of $Sd(T_2)$. It is assumed then that the contribution from the third mode and higher is not significant. Extension of this approach to account for higher-mode effects is a subject of ongoing research; however, for illustrative purposes it be assumed in this work that the SRSS modal combination rule can be extended to inelastic structures. This is approximately equivalent to what is done in Modal Pushover Analysis [17].

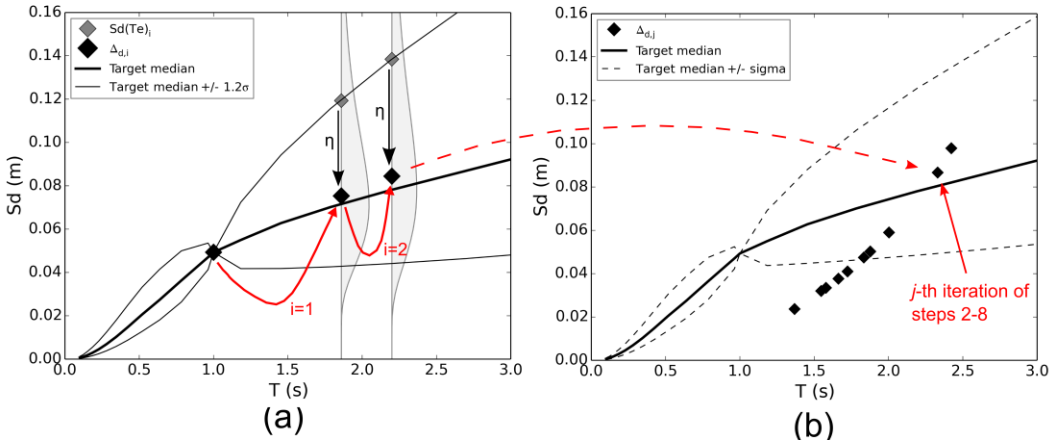


Figure 3. Example of the sampling procedure for an SDOF system. (a) Two iterations of steps 1-7. (b) 10 iterations of steps 1-7 (from [9]).

4 APPLICATION EXAMPLE

To illustrate the performance of the simplified approach of Fox and Sullivan [9], a case study application is examined. The building is the same three storey building used in section three, but with the walls having flexural strength corresponding to a force reduction factor of R=3 for $Sd(T_1)$=0.05m. The site under consideration is in Campobasso, Italy and it is assumed the building is located on Rock/Stiff Soils. The hazard curve for the site is obtained from the Italian National Institute of Geophysics and Volcanology (INGV) website [18] and the corresponding disaggregation data obtained from Barani *et al.* [19].

Conditional spectra are constructed using the same methodology and tools as in Fox and Sullivan [9]. A limitation of this is that the GMPE used for constructing the conditional spectra [20] is inconsistent with those used in the probabilistic seismic hazard analyses (PSHA). Furthermore, hazard is defined in terms of envelope spectral acceleration, whereas it is herein assumed to correspond to a random component of spectral acceleration. Although these limitations mean the resulting conditional spectra are not consistent with the PSHA, they are sufficient for a comparative evaluation of the method of [9].

Nine different levels of hazard are considered, corresponding to those provided by INGV and shown in Figure 4a. The resulting conditional spectra are expressed as conditional mean spectra and dispersion, shown in Figures 4b and 4c respectively. Once the conditional spectra were constructed, ground-motion selection was carried out using the same tools and methodology discussed in [9].

Multiple-stripes analyses were conducted using NLRHA and the simplified [9] approach was used to evaluate the inter-storey drift ratio at roof level and the maximum shear at the base of the wall. The results for the nine intensity levels are shown in Figure 5. It can be observed that the results from the simplified approach match those of the NLRHA rather well.

For drift, the simplified approach tends to give a lower prediction of the median response, but with larger dispersion than the NLRHA results. It is interesting to note that after yield, the inter-storey drift ratio tends to increase less quickly (with increasing demand) than prior to yield. This is a result of post-yield wall deformations being due to essentially rigid body rotation only (refer [21]). Figure 5b shows that after flexural yielding, the shear force at the base of the wall continues to increase, albeit at a slower rate. This is due to the contribution of higher modes, which play a significant role, even though the building is only three storeys. As the first mode contribution to shear cannot increase post-yield, a more appropriate intensity measure for evaluation of shear forces may be $Sd(T_2)$, as discussed in [22].

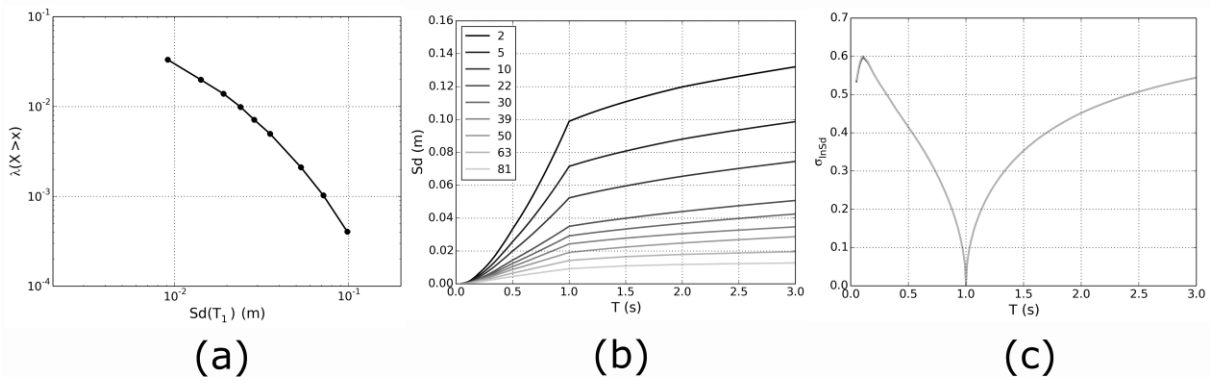


Figure 4. (a) Hazard curve for Campobasso, Italy. (b) Conditional mean spectra. (c) Conditional spectrum dispersion

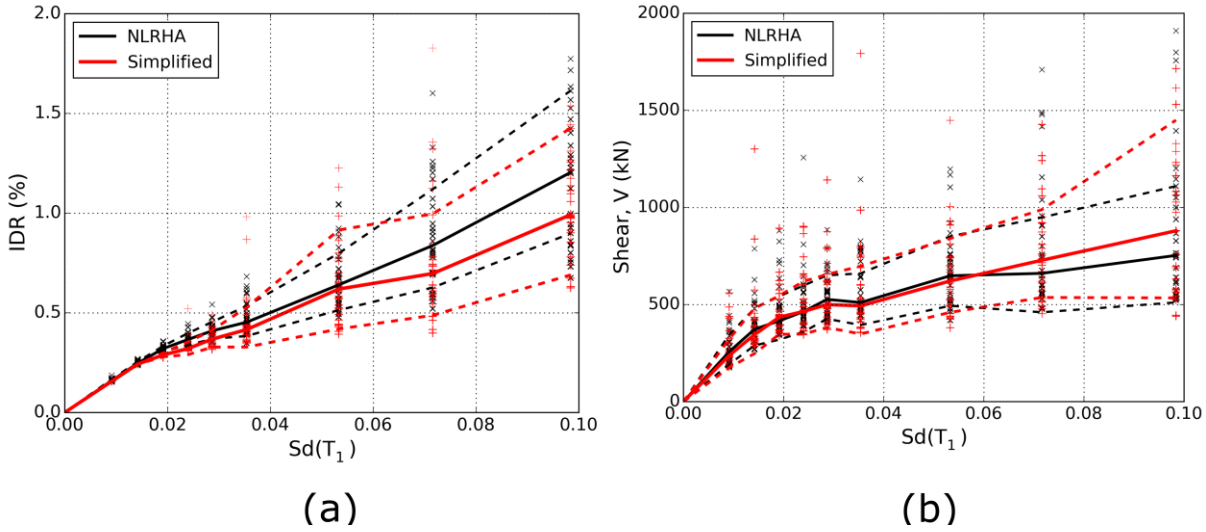


Figure 5. Multiple-stripes analysis curves showing individual data points, median response, and median +/- one standard deviation for (a) inter-storey drift ratio, and (b) base shear.

Using the information obtained from the multiple stripes analyses, fragility curves were constructed for the exceedance of several levels of drift and shear. Specifically, inter-storey drift ratios of 0.4, 0.6, 0.8 and 1.0% are considered and shear forces of 400, 600, 800 and 1000kN. Fragility curves are assumed to be well represented by a lognormal distribution and the data is fitted using maximum likelihood estimation, as discussed in [23]. For drift, the match between the NLRHA results and those obtained using the simplified method is not particularly good, but is still deemed reasonable considering the minimal effort required for the simplified approach. Furthermore, one must keep in mind the inherent uncertainty associated with the use of only 30 ground-motions at each intensity level. For shear, the match between the simplified and NLRHA results is extremely good. One will note, however, the large dispersion for the higher shear limits.

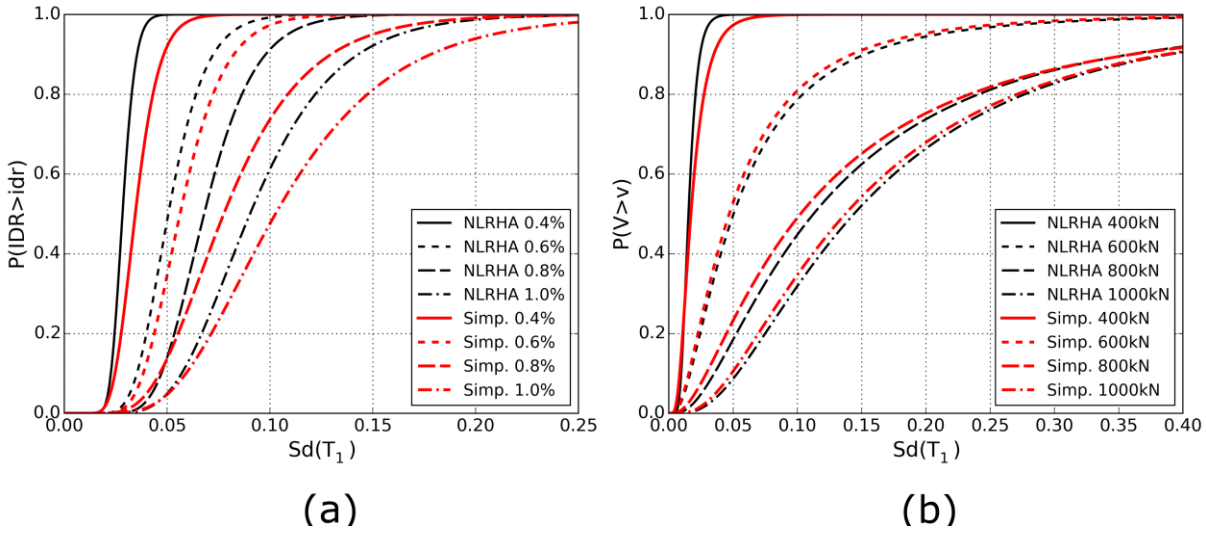


Figure 6. Fragility curves constructed from multiple-stripes analyses. (a) Inter-storey drift ratio. (b) Base shear.

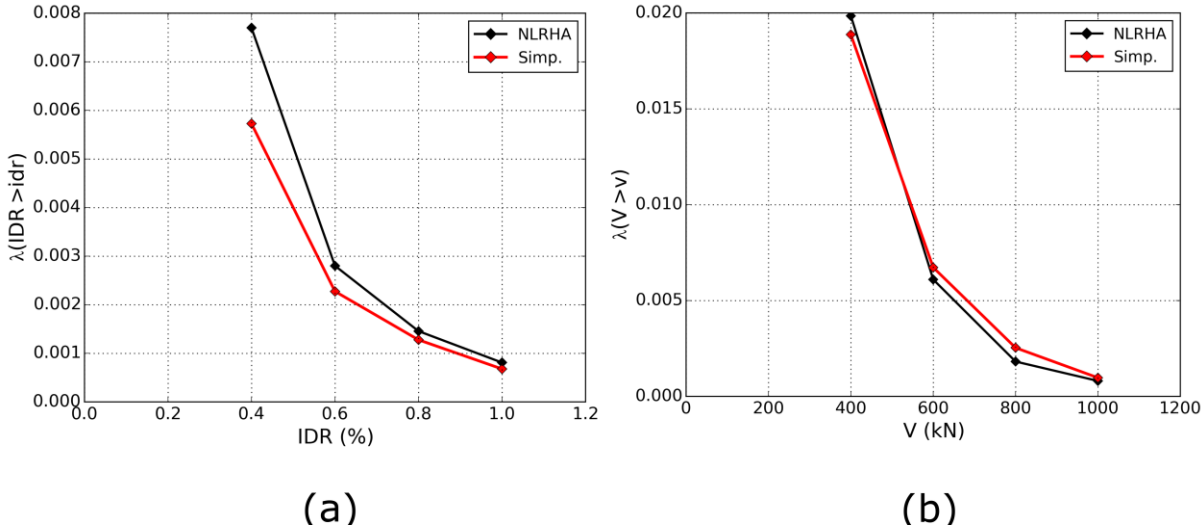


Figure 7. Annual rates of exceedance for various (a) inter-storey drift ratios, and (b) base shear forces.

Using the fragility curves of Figure 6 and the hazard curve from Figure 4a, the annual rate of exceedance is calculated for the different drift and shear limits. This calculation is done numerically using Equation 1. The resulting curves are shown in Figure 7. In general, the curves obtained using the two approaches match rather well. The exception to this is at the low levels of drift (0.4% and 0.6%). This is a result of poor fitting of the fragility curves for large probabilities of exceedance. Because the dispersion for the low drift levels is small, the most significant contribution to the annual rate of exceedance comes from the region above the median intensity *i.e.* the region in which there are large errors.

5 CONCLUSIONS

This paper has examined the record-to-record variability in the response of RC wall buildings subjected to ground motions matched to the conditional spectrum. It was shown through numerical examples that dispersion is a function of relative intensity, the EDP being considered, properties of the structure, and site characteristics. This presents a challenge in the calibration of empirical dispersion estimates for use in simplified probabilistic seismic assessment procedures.

The simplified approach of Fox and Sullivan [9] was investigated as an alternative to overcome this difficulty. For a case study example it was shown to give predictions of response that were comparable to those obtained from NLRHA, in most cases. The results were used to construct fragility curves, which for shear gave an excellent match to those obtained for NLRHA. For drift, the match in fragility curves was not as good. The annual rate of exceedance was calculated for a number of drift and shear limit states. Again in most cases the match between the NLRHA results and those obtained using the simplified method was good, the exception being for low levels of drift.

ACKNOWLEDGEMENTS

Part of the work leading to this paper received funding through the 2015 ReLUIS project, which the authors gratefully acknowledge.

REFERENCES

[1] C.A. Cornell, F. Jalayer, R.O. Hamburger, D.A. Foutch, Probabilistic basis for 2000 SAC Federal Emergency Management Agency Steel Moment Frame Guidelines. *Journal of Structural Engineering*, **128**, 526-533, 2000.

[2] P. Fajfar, Capacity spectrum method based on inelastic demand spectra. *Earthquake Engineering and Structural Dynamics*, **28**, 979-993, 1999.

[3] P. Fajfar, A nonlinear analysis method for performance-based seismic design. *Earthquake Spectra*, **16**, 573-592, 2000.

[4] M.J.N. Priestley, G.M. Calvi, M.J. Kowalsky. *Displacement-Based Seismic Design of Structures*. IUSS Press, Pavia, Italy, 2007.

[5] FEMA P-58. Next-generation methodology for seismic performance assessment of buildings. *Applied Technology Council for the Federal Emergency Management Agency*, Washington DC, 2012.

[6] P. Fajfar, M. Dolšek, A practice-oriented estimation of the failure probability of building structures. *Earthquake Engineering and Structural Dynamics*, **41**, 531-547, 2012.

[7] D.P. Welch, T.J. Sullivan, G.M. Calvi, Development of direct displacement-based procedures for simplified loss assessment in performance-based earthquake engineering. *Journal of Earthquake Engineering*, **18**, 290-322, 2014.

[8] T.J. Sullivan, D.P. Welch, G.M. Calvi, Simplified seismic performance assessment and implications for seismic design. *Earthquake Engineering and Engineering Vibration*, **13**(Supp. 1), 95-122, 2014.

[9] M.J. Fox, T.J. Sullivan, Use of the conditional spectrum to incorporate record-to-record variability in simplified seismic assessment. Submitted to *Earthquake Engineering and Structural Dynamics*, 2015.

[10] A.J. Carr, Ruaumoko Manual – Volume 3: User manual for the 3-dimensional version Ruaumoko3D, Department of Civil Engineering, University of Canterbury, 2012.

[11] J.W. Baker, Conditional mean spectrum: tool for ground motion selection. *Journal of Structural Engineering*, **137**, 322-331, 2011.

[12] N. Jayaram, T. Lin, J.W. Baker, A computationally efficient ground-motion selection algorithm for matching a target response spectrum mean and variance. *Earthquake Spectra*, **27**, 797-815, 2011.

[13] T. Lin, S.C. Harmsen, J.W. Baker, N. Luco, Conditional spectrum computation incorporating multiple causal earthquakes and ground motion prediction models. *Bulletin of the Seismological Society of America*, **103**, 1103-1116,

[14] T.J. Sullivan, G.M. Calvi, M.J.N. Priestley, (eds.). *A Model Code for the Displacement-Based Seismic Design of Structures DBD12*, IUSS Press, Pavia, Italy, 2012.

[15] A.S. Veletsos, N.M. Newmark, Effect of inelastic behaviour on the response of simple systems to earthquake motions. *Proceedings – Second World Conference on Earthquake Engineering*, **2**,895-912, Tokyo, Japan, 1960.

[16] D. Pennucci, T.J. Sullivan, G.M. Calvi, Displacement reduction factors for the design of medium and long period structures. *Journal of Earthquake Engineering*, **15**(S1), 1-29, 2011.

[17] A.K. Chopra, R.K. Goel, A modal pushover analysis procedure for estimating seismic demands for buildings. *Earthquake Engineering and Structural Dynamics*, **31**, 561-582, 2002.

[18] http://esse1-gis.mi.ingv.it/s1_en.php last accessed 1/03/2015.

[19] S. Barani, D. Spallarossa, P. Bazzurro, Disaggregation of probabilistic ground-motion hazard in Italy. *Bulletin of the Seismological Society of America*, **99**, 2638-2661, 2009.

[20] K.W. Campbell, Y. Bozorgni, NGA ground motion model for the geometric mean horizontal component of PGA, PGV, PGD and 5% damped linear elastic response spectra for periods ranging from 0.01 to 10s. *Earthquake Spectra* 2008, **24**, 139-171.

[21] M.J. Fox, T.J. Sullivan, K. Beyer. Evaluation of seismic assessment procedures for determining deformation demands in RC wall buildings. Submitted to *Earthquakes and Structures*, 2015.

[22] B.Ö. Ay, M.J. Fox, T.J. Sullivan, Impact of ground-motion selection criteria on the probabilistic seismic performance assessment of RC wall structures. Submitted to *Journal of Earthquake Engineering*, 2015.

[23] J.W. Baker, Efficient analytical fragility function fitting using dynamic structural analysis. *Earthquake Spectra*, **31**, 579-599, 2015.

COMPDYN 2015
5th ECCOMAS Thematic Conference on
Computational Methods in Structural Dynamics and Earthquake Engineering
M. Papadrakakis, V. Papadopoulos, V. Plevris (eds.)
Crete Island, Greece, 25–27 May 2015

INFLUENCE OF JOINT RESPONSE IN THE ASSESSMENT OF SEISMIC PERFORMANCE OF EXISTING REINFORCED CONCRETE FRAMES

Maria Teresa De Risi[1], Paolo Ricci[1], and Gerardo M. Verderame[1]

[1] University of Naples Federico II – Department of Structures for Engineering and Architecture
via Claudio 21, Naples
e-mail: mariateresa.derisi@unina.it, paolo.ricci@unina.it, verderam@unina.it

Keywords: Earthquake Engineering, Seismic Performance, Reinforced Concrete Frames, Beam-Column Joints.

Abstract. *In the seismic performance assessment of existing Reinforced Concrete buildings, non-ductile failures related to beam-column joint regions can represent a critical issue. Therefore, within the context of Performance-Based Earthquake Engineering, a growing attention should be addressed to the behavior of these non-ductile elements, starting from the classification of their failure typology.*
In particular, in typical existing buildings, seismic performance might be significantly affected by the non-linear behavior of joints which are involved in the failure mechanisms because of poor structural detailing (e.g. lack of an adequate transverse reinforcement in joint panel, deficiencies in the anchorage or absence of any capacity design principle). Nevertheless, conventional modeling approaches consider only beam and column flexibility, although joints can provide a great contribution to the global deformability.
In this study, a numerical investigation on the influence of joint response on the seismic behavior of a case study RC frame – designed for seismic loads according to an obsolete technical code – is performed. A preliminary classification of joint failure typology of the elements within the frames and the definition of the corresponding nonlinear behavior are carried out. Structural models that explicitly include beam-column joints are built. A probabilistic assessment based on nonlinear dynamic simulations of structural behavior is performed to evaluate the seismic response at different performance levels. Uncertainty in seismic ground-motion is accounted for.

1 INTRODUCTION

Assessment of seismic performance of structures requires the development of nonlinear analysis models that can detect all possible local and global collapse modes.

Potential element deterioration and failure modes are a consequence of the design and detailing requirements, materials properties and structural system. Thus, once all failure typologies have been identified for a given structural system, the attention can be focused on a subset of likely collapse mechanisms by means of the analysis of experimental test data, engineering judgment, analytical models, and observations of damage from past earthquakes. The identified collapse modes then serve as the basis for selecting appropriate simulation and damage models that can be used to predict structural seismic performance.

The building code requirements for modern moment-resisting frames are designed to promote ductile and more desirable collapse modes, preventing the formation of the brittle collapse modes ([1]-[3]): the strong column – weak beam requirement promotes flexural hinging in beams before columns; likewise, shear strength capacity design provisions for beams and columns should ensure that shear failure is highly unlikely in beam-column elements. Vice-versa, older RC moment-resisting frames, with minimal detailing requirements used in their design, are vulnerable to a wider range of possible collapse modes ([4]-[7]). These structures have a demonstrated tendency to fail in soft story or column-hinging mechanisms [8], when they are designed for gravity loads only, or to exhibit joint failures [9], also if old seismic codes are adopted for the design [10]. Less stringent detailing requirements may also promote lap-splice failure or pull-out of the bottom beam reinforcing bars anchored into the joint panel. Moreover, column shear failure may occur, depending on the column's design and gravity loading [11].

Therefore, in seismic performance assessment of non-conforming RC buildings, non-ductile failures related to beam-column joint regions and their modeling may represent a critical issue.

In this study, a numerical investigation on the influence of joint failures on the seismic performance at different performance levels of a case study RC frame - designed for seismic loads according to an obsolete technical code - is performed. A preliminary classification of joint failure typology within the frames and the definition of the corresponding nonlinear behavior are carried out. Structural models that explicitly include beam-column joints are built. In particular, the empirical model proposed by the Authors [12] for exterior joints was applied, in conjunction with modeling proposals from literature for interior joints [9] and beam/column behavior [13], as explained in Section 2.

A probabilistic assessment based on nonlinear dynamic simulations of the structural response is performed taking into account record-to-record variability.

2 STRUCTURAL MODELING

Analytical evaluation of seismic performance at different performance levels requires primarily the accurate modeling of nonlinear behavior and deterioration due to seismic loading for each of the constituent element in the structural system, such that all possible local and global collapse modes can be captured. Therefore, to ensure that the model faithfully represents the structure and its possible failure modes, an accurate representation of material properties and deterioration of beam/column elements and joints is needed.

An overview of the frame modeling adopted in this study is shown in Figure 1.

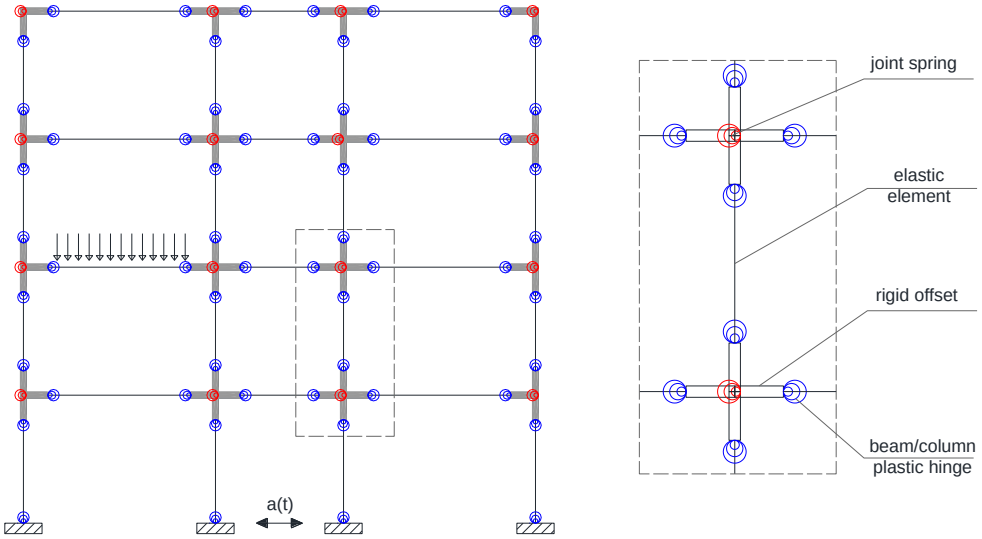


Figure 1: Adopted structural model.

Nonlinear element models for RC beams/columns developed by Ibarra, Medina, and Krawinkler [14] and calibrated by Haselton et al. [13] is adopted in this study to capture the yielding, strain hardening, and spalling and rebar buckling that lead to degradation of strength and stiffness in the structure. The database adopted for the calibration by [13] includes RC columns with both ductile and non-ductile detailing, and varying levels of axial load and geometries. Approximately 35 of the 255 column tests have non-ductile detailing and failed in flexure-shear, as expected for the older RC columns of interest in this study. However, the model cannot capture explicitly the onset of shear failure with the subsequent axial collapse of column, because the column model does not incorporate axial-shear interaction.

Lumped plasticity models also account for bond-slip that occurs in regions of high bond stresses in beam-column joints. Also rebar pull-out and the resulting loss in strength could be accounted for by introducing an additional spring, properly defined as a function of bond stress-slip relationship and anchorage length. However, in the case study analyzed herein, the latter possible failure is excluded, by assuming that a sufficient anchorage length or efficient anchorage devices are guaranteed, as common construction practice provided for, especially for seismic designed structures.

It is worth noting that the simulation model is not able to capture all possible collapse modes, in particular the onset of columns shear failures and the subsequent degrading behavior. To develop flexural behavior, the member shear strength must be larger than the flexural strength, which is the condition typically required in capacity design provisions for seismic design. Where the shear strength is not sufficient to preclude shear failure (such as in most of the existing buildings), shear effects must be considered in the analysis model in addition to flexural and axial load effects. Nevertheless, modeling the cyclic response of a RC element experiencing shear deterioration is complex due to the interactions of shear, moment, and axial forces, as well as the overall brittle nature of this deterioration mode. A review of previous researches on the shear behavior of existing columns [15] have indicated that it is quite difficult that column shear models satisfy all the needed requirements of accuracy, computationally efficiency and compatibility with existing software programs. The problem is still an open and important issue, but, in the present work, shear failures are not accounted for.

Modeling of joint shear behavior in beam-column joints is the focus of Section 2.1.

2.1 Joints modeling

Two main different modes of joint failure can be identified (if no anchorage failure of longitudinal reinforcement anchored into the joint panel occurs, as in the case analyzed in this study): (i) joint shear failure prior to (J-failure) or after than (BJ-failure) yielding of beam longitudinal reinforcement (in hypothesis of strong column-weak beam). In both cases, to capture nonlinear behavior and deterioration associated with degradation of shear strength and stiffness in the beam-column joint regions, the shear panel is modeled with an inelastic rotational spring and rigid offsets spreading into the joint panel, namely by means of the so-called scissors model [16].

In literature there are several models available to reproduce joint shear behavior into numerical analyses of RC frames, basically lumped plasticity approaches, multi-spring macromodels or finite element simulations. It can be pointed out that finite element models are too demanding in terms of computational efforts for a great number of analyses, while models with multiple nodes and multiple springs (e.g. [17]-[19]) require more limited computational efforts allowing to capture realistically the joint panel kinematic behavior and simulate the horizontal translation that can occur between the centerlines of the columns above and below the joint. Vice-versa, the scissors model by Alath and Kunnath [16] does not capture this possible kinematic response, but it is the simplest and computationally less demanding joint model and it seems to be sufficiently accurate in predicting the experimental beam-column joint panel response for simulating the seismic response of non-conforming RC frames for purposes of fragility assessment and performance-based earthquake engineering [9].

Therefore, both for exterior and interior joints, the scissors model has been adopted. No springs at the interface between the joint panel and the adjacent beams/columns representing the bond-slip contribution are introduced in these analyses because the deformability contribution due to bond slip is already accounted for in beam/column rotational springs.

The joint panel model adopted herein is implemented by defining duplicate nodes, node A (master) and node B (slave), with the same coordinates at the center of the joint panel. Node A is connected to the column rigid link and node B is connected to the beam rigid link. A zero length rotational spring connects the two nodes and allows only relative rotation between them through a constitutive model which describes the shear deformation of the joint panel zone, and that is different for exterior and interior joints. In both cases, such a rotational spring is defined as a quadri-linear moment (M_j) – rotation (γ_j) spring characterized by four characteristic points (Figure 2): cracking, pre-peak, peak and residual points.

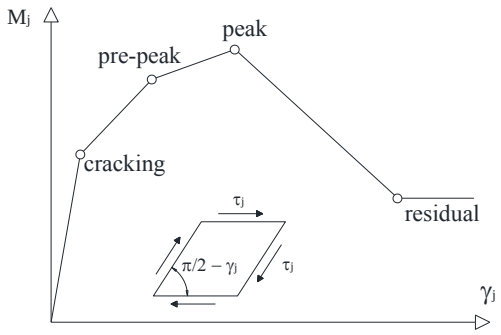


Figure 2: Schematic stress-strain relationship for the rotational spring representing joint panel.

In particular, in this study, the model approach proposed by the Authors [12] is adopted for exterior joints. The proposed model provides only a backbone for the joint moment-rotation

relationship. The calibration of the relative cyclic behavior, that is essential to perform dynamic nonlinear analyses, is carried out herein including cyclic degradation in unloading and reloading stiffness and pinching effects.

Exterior joints

The joint panel zone model for exterior unreinforced joints was calibrated through tests well documented in literature, different for the failure mode they exhibited, namely J-failure (by [20] – here referred to as Pant2, Pant3, Pant5, Pante6) and BJ-failure (by [21] – here referred to as Clyde2, Clyde4, Clyde5, Clyde6), for which experimental shear stress-strain relationships for joint panel were available.

Key parameters defining the quadri-linear backbone of the proposed joint rotational spring for exterior joints are reported in details in [12] and [15] and briefly summarized in Table 1, in terms of shear stress (τ_j) – versus shear strain (γ_j), separately for J- and BJ-mode of failure. From simple equilibrium equation, for each characteristic point of the backbone, the moment transferred through the rotational spring M_j can be obtained as a function of the joint shear stress τ_j.

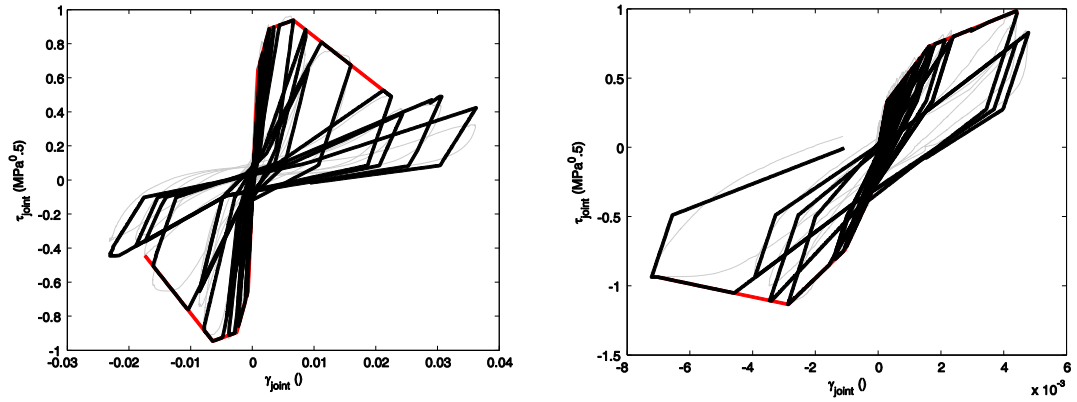
Backbone point	**J-failure**		**BJ-failure**	
	τ_j	γ_j	τ_j	γ_j
cracking	from [22]	0.06%	from [22]	0.06%
pre-peak	0.9 τ_{peak}	0.21%	τ ($M_{yielding,beam}$)	0.26%
peak	from [23]	0.48%	from [23]	0.63%
residual	0.6 τ_{peak}	2.86%	0.7 τ_{peak}	3.03%

Table 1: Summary of the proposed backbone for the joint panel.

The same tests adopted for the calibration of the backbone described above are considered to calibrate the cyclic behavior of the joint shear stress-strain response of this typology of joints. The calibration is performed in OpenSees ([24]) on the basis of the hysteresis rules characterizing the *Pinching4* material, so that the obtained parameters can be practically employed in modeling of RC frames. Pinching4 material is a four-points uniaxial material developed by Lowes et al. ([25]) and belonging to the library of OpenSees, that allows to model the cyclic degradation of unloading and reloading stiffness (through the parameters gk and gD, respectively), degradation in strength (through the parameters gF) and pinching effects (through the parameters rDisp, rForce and uForce). Calibration of these key parameters was performed starting from the experimental shear stress-strain backbones and minimizing the error in terms of energy dissipated between the numerical and the experimental responses. No degradation in strength was introduced since it is already included in the backbone of the joint response obtained from experimental data.

In Figure 3 two examples of the comparison between numerical and experimental cyclic responses are presented: experimental backbone and cyclic response are reported in red and grey, respectively; while numerical cyclic response is reported in black. The graphical numerical versus experimental comparison for each of the eight tests is reported in [15].

Table 2 presents the modeling parameters of the Pinching4 material (in positive "P" and negative "N" loading directions) adopted to obtain a good fit of the experimental response of the analyzed non-ductile exterior beam-column joints. The mean value of these parameters will be utilized in structural analyses for a probabilistic performance assessment.



(a) (b)

Figure 3: Cyclic behavior calibration for tests by Pantelides et al. (2002) [20] – Pantelides6 (a) and Clyde et al. (2000) [21] – Clyde6 (b).

	Pant2	Pant3	Pant6	Pant5	Clyde2	Clyde4	Clyde5	Clyde6	Mean	Adopted
rDisp P	0.2	0.2	0.2	0.2	0.1	0.2	0.2	0.2	0.19	0.16
rDisp N	0.2	0.2	0.2	0.2	-0.1	0.2	-0.1	0.3	0.14	
rForce P	0.2	0.2	0.2	0.2	0.2	0.2	0.2	0.2	0.20	0.23
rForce N	0.2	0.2	0.2	0.2	0.2	0.2	0.4	0.4	0.25	
uForce P	-0.2	-0.2	-0.2	-0.05	-0.05	-0.25	-0.2	-0.5	-0.21	-0.22
uForce N	-0.2	-0.2	-0.2	-0.2	-0.2	-0.2	-0.2	-0.4	-0.23	
gK1	0.9	0.9	0.9	0.8	0.9	0.95	0.95	0.5	0.85	0.85
gK3	0.1	0.1	0.1	0.1	0.1	0.2	0.15	0.1	0.12	0.12
gKlim	0.95	0.95	0.95	0.95	0.95	0.99	0.95	0.95	0.96	0.96
gD1	0.35	0.35	0.35	0.35	0.25	0.35	0.6	0.4	0.38	0.38
gD3	0.15	0.15	0.15	0.15	0.15	0.15	0.9	0.9	0.34	0.34
gDlim	0.95	0.95	0.95	0.95	0.95	0.95	0.99	0.99	0.96	0.96

gF1= gF2= gF3= gF4= gFlim=0; gK2=gK4=0; gD2=gD4=0.

Table 2: Parameters adopted to reproduce the hysteretic behavior of exterior unreinforced joints in Pinching4 material.

Interior joints

The joint moment-rotation constitutive relationship proposed by Celik and Ellingwood [9], within the modeling approach of the scissors model, is adopted in this study for interior joints. This relationship was based on a statistical analysis carried out on the basis of experimental tests.

Celik and Ellingwood also suggested that the shear stress-strain backbone curve for the panel zone in typical non-conforming RC beam-column joints can be defined through four key points, which correspond to joint shear cracking, reinforcement yielding, joint shear strength or contemporary achievement of adjoining beam or column capacity, and residual joint strength, respectively. The ordinates of the backbone points were reduced if the shear failure of the joint occurs before beams or columns reach their capacities. Shear failure of the joint is assumed to depend on the kind of joint (interior/exterior) and the anchorage conditions.

In particular, the abscissas of the four key points $\gamma_{j,cr}$, $\gamma_{j,y}$, $\gamma_{j,max}$, $\gamma_{j,res}$, typicalIy fall within the following ranges: 0.0001-0.0013, 0.002-0.010, 0.01-0.03, and 0.03-0.10 radians, respectively. Joint shear strength $\tau_{j,max}$ is proposed in analogy with ASCE-SEI/41 prescription and it falls within the range 0.75-1.00 $(MPa)^{0.5}$ for interior beam-column joints. Residual strength is

assumed equal to shear stress corresponding to joint cracking (evaluated by means of Uzumeri formulation [22]). Mean values of the proposed ranges are adopted in this study, since modeling uncertainties are not considered in structural analyses herein.

The proposal by Celik and Ellingwood also included joint moment-rotation constitutive relationship for exterior joints. However, from the analysis of the experimental dataset they adopted, it was observed that the proposed joint shear strain values for the four key points are related to interior joints tests only; such values are very high if compared with shear strain values obtained from experimental tests on exterior beam-column joints. Therefore, the proposal by Celik and Ellingwood is adopted for interior joints only.

In the proposal by Celik and Ellingwood [9], anchorage failure was also taken into account through a reduced envelope for the joint shear stress-strain relationship. However, in this study, no reduction of joint shear stress is considered, since the hypothesis that a sufficient anchorage length or efficient anchorage devices are guaranteed, thus excluding this failure mode.

By proposing that joint strength should be assumed as the minimum between empirical shear strength and the maximum joint shear stress related to beam/column flexural capacity, this model is the only one able to reproduce the softening response of the joint panel also when a BJ-failure occurs. This is in accordance with the modeling adopted for exterior joints (since the nature of the strength model by [23] adopted for exterior joints) and with observed experimental results [26], which showed that beam-column intersections always exhibited a degradation response if joint cracking was occurred.

Furthermore, since the proposal by Celik and Ellingwood suggests only pinching parameters to model joints hysteretic response, the parameters calibrated by Jeon et al. [10] for the Pinching4 material in OpenSees for the hysteretic response of interior joints are adopted herein. However, these parameters are modified so that no strength degradation was taken into account (since strength degradation is already included in the backbone of the joint response obtained from experimental data).

It is worth noting that, in order to reproduce the softening response of the joint when a BJ-failure occurs - as observed experimentally (e.g. [26]) – also for interior joints, the adjacent beams have to be modeled with no post-peak strength degradation. In fact, in the case of BJ failure, the peak strength of interior joints is defined as the maximum shear stress corresponding to the contemporary achievement of flexural capacity in both the adjacent beams. If beam response degrades after its peak is reached, it is highly unlikely that this condition can be achieved during the analysis thus leading the interior joint to go through its softening branch. Since the adjacent beams are in series with the joint panel spring, it was necessary to model the response of the beams as perfectly-plastic after the peak strength is reached. In this way, the contemporary achievement of peak strength in the adjacent beams can be obtained and thus the joint can reach its peak strength, then starting to degrade. For the same reasons, no degradation in strength should be modeled in beams.

This simulation model is not able to capture axial failure in beam-column joints. Therefore, both for exterior and interior joints, this non-simulated failure mode is detected in this study by post-processing dynamic analyses results. Such an approach is adopted because of the lack of experimental data and reliable models that allow capturing this failure mode explicitly in numerical modeling. Unfortunately, very few unconfined joint tests are available with confirmed axial failure, since, generally, during laboratory tests, a common practice has been to terminate the test after dropping to 80% of lateral load resistance without testing the axial capacity of the joint.

In this study, the empirical shear-friction capacity model proposed by Hassan and Moehle [27] calibrated on the basis of available experimental data is adopted. The expression of the IDR threshold (IDR_{AxJ}) that identifies the onset of joint axial failure is reported in Eq. (1):

$$IDR_{AxJ} = 0.057 \cdot \left(\frac{P \cdot tg\theta}{A_{sb} \cdot f_{yb}} \right)^{-0.5} \quad (1)$$

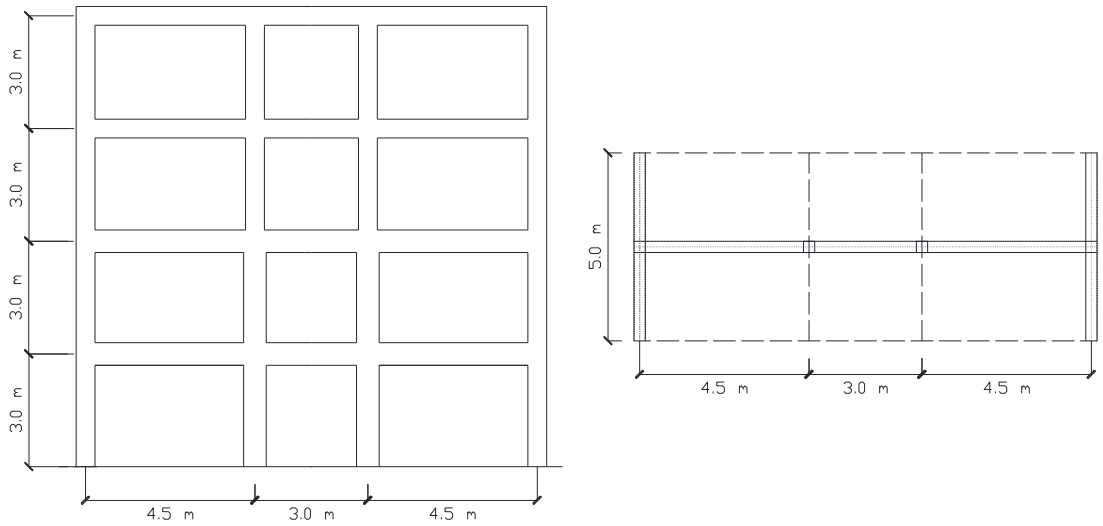
where P is the axial load acting on the joint, A_{sb} and f_{yb} are longitudinal reinforcement area and strength, respectively, of the bottom beam bars, and θ represents the shear critical angle, as reported in [27].

3 CASE STUDY FRAME

A symmetric four-story three-bay frame is designed, modeled as explained in Section 2, and assessed. This case-study frame is the internal frame of a structure with 5 m-transverse bay. Figure 4 represents frontal and in-plane views of the analyzed frame.

Dead load from slab is equal to 5 kN/m^2 for the last story and 7 kN/m^2 for all of the other ones; live load is equal to 1 kN/m^2 for the last story and 2 kN/m^2 for all of the other ones.

The case-study frame (referred to as OLD SLD) is intended to be realized in 1980s and it is designed by means of a simulated procedure according to an obsolete technical code [28] in force in Italy until 1990s, by means of the allowable tensile stress method. The structure is located in a first-category site, corresponding to a design horizontal peak ground acceleration equal to 0.1g. Element dimensions are calculated according to the allowable stresses method; the design value for maximum concrete compressive stress is assumed equal to 6.0 and 8.5 MPa for axial load (σ_c) and axial load combined with bending ($\sigma_{c,f}$), respectively. Reinforcing bars (FeB38K) are deformed and their allowable design stress (σ_s) is assumed equal to 220 MPa.



(a) (b)

Figure 4: Case-study frame: frontal (a) and in plane (b) views.

Section dimensions are (30x50) cm^2 for beams and columns of the third and fourth levels, and (30x60) cm^2 for beams and columns belonging to the first and the second levels.

Longitudinal reinforcement ratio ranges between 2 and 2.5% in columns, whereas longitudinal reinforcement at the end sections of beams varies from 0.75 and 0.9% of the section area

for the top layer, and from 0.34 and 0.4% of the section area for the bottom layer. Stirrups spacing in columns was defined as the minimum amount of transverse reinforcement required by the adopted code, namely ϕ8/240 mm in this case.

Expected values of concrete compressive strength (f_c), and steel yielding strength for longitudinal and transverse reinforcement (f_y) adopted in the assessment phase are 20 MPa and 450 MPa, respectively.

In Table 3, it is shown that column-to-beam flexural capacity (M_c/M_b) is significantly higher than the unity; therefore, strong column-weak beam hierarchy characterizes this frame. By reporting beam flexural capacity to the joint centerline ($M_{j,b}$) and by comparing $M_{j,b}$ and joint moment strength ($M_{j,R}$), it can be observed that prevalently J-failures characterize this frame. $M_{j,R}/M_{j,b}$ is equal to the unity when joint strength is limited to the flexural capacity of the adjacent beams, according to the modeling approach described in Section 2.

story	joint	M_b (kNm)	M_c (kNm)	M_c/M_b ()	$M_{j,R}$ (kNm)	$M_{j,b}$ (kNm)	$M_{j,R}$ / $M_{j,b}$ ()	failure mode
1	ext	376.52	1028.46	2.73	384.12	434.45	0.88	J
	int	582.46	1112.56	1.91	528.27	693.41	0.76	J
2	ext	376.52	896.44	2.38	358.46	434.45	0.83	J
	int	582.46	950.81	1.63	423.42	693.41	0.61	J
3	ext	306.29	767.83	2.51	294.69	344.57	0.86	J
	int	473.82	794.07	1.68	333.49	546.71	0.61	J
4	ext	186.16	375.61	2.02	209.43	209.43	1.00	BJ
	int	281.37	383.27	1.36	324.66	324.66	1.00	BJ

Table 3: Beam/column hierarchy and joints classification.

4 PERFORMANCE LEVELS AND GROUND MOTION RECORDS

In order to perform dynamic analyses, input ground motion records have to be selected and performance levels of interest should be identified.

In this study, natural records representing Italian seismicity are selected and scaled to different levels of seismicity. The records selection has been performed by using REXEL software [29], from ITACA strong-motion database. Earthquakes characterized by a low-medium magnitude levels (between 4.4 and 5.7), with a source-to-site distance ranging between 10 and 40 km, and recorded on soil class B are selected. On the whole 50 ground motion records are selected.

As far as performance levels of interest are concerned, the structural capacities are primarily defined by the maximum interstorey drifts (IDR) that correspond to three widely used performance levels (or limit states) in the earthquake community (e.g. [30]): immediate occupancy (IO), life safety or significant damage (SD), and collapse prevention (CP). Table 4 reports the values of the IDR thresholds (IDR_{LS}) for the selected performance levels, chosen on the basis of previous literature researches ([30], [31]).

	IO LS	SD LS	CP LS
IDR_{LS}	0.2%	2%	5%

Table 4: IDR thresholds for the selected performance levels.

Additional LSs, defined on the basis of the achievement of characteristic points in the nonlinear response of the primary structural elements, are adopted. In particular the first achieve-

ment of a particular condition or a "conventional failure" is detected, in analogy with the approach of typical European code prescriptions (e.g. [2], [3]), as shown in Figure 5.

For columns, green circles represent a pre-yielding condition; yellow, orange and red circles indicate the achievement of yielding, capping and post-peak rotations, respectively.

For beam-column joints, white circle identifies a pre-cracking condition of joint; while green, yellow, orange and red circles represent the achievements of joint cracking, pre-peak point, peak joint strength, and residual strength, respectively. Such a convention will be adopted in Section 5 when damage states in RC elements are presented. The corresponding LSs will be referred to as summarized in Table 5.

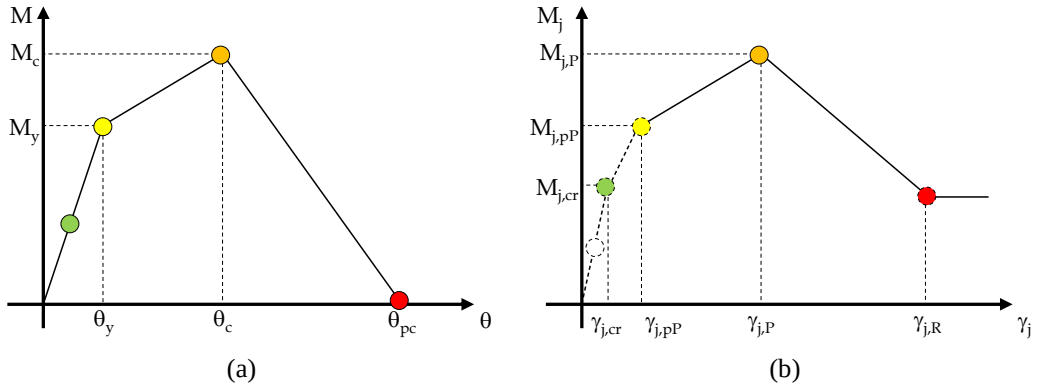


Figure 5: Characteristic points of columns (a) and joints (b) response.

FY	first element at yielding
FC	first element at capping
FPC	first element at post-capping
FcrJ	first joint cracking
FpPJ	first joint at pre-peak point
FPJ	first joint at peak strength
FRJ	first joint at residual strength

Table 5: Additional LSs acronyms.

5 PRELIMINARY NONLINEAR STATIC ANALYSES

Preliminary, nonlinear static analyses with first-mode-shape-proportional lateral load pattern are performed in OpenSees [24] on the structural models (obtained as described in Section 2) in a double condition:

(i) with "rigid joints", assuming a very high stiffness and shear strength for beam-column connections, and

(ii) "with joints", explicitly modeling the nonlinear behavior of joints, as explained in Section 2.1.

Results of this kind of analysis are reported in this Section.

First of all, elastic periods from modal analysis are reported in Table 6 for both conditions ("rigid joints" and "with joints"). An increment of about 8% in elastic period is observed when joint elastic deformability is taken into account.

	Rigid joints	With joints
T_1 (s)	0.694	0.747

Table 6: Elastic periods.

In both cases, for rigid joints condition and when nonlinear response of beam-column joints is modeled, the OLD SLD frame exhibited a global collapse mechanism, as expected due to the strong-column-weak-beam hierarchy observed in Section 3.

Static pushover (SPO) curves and collapse mechanisms and damage levels in each beam/column hinge at the last step are reported in Figure 6 and Figure 7, respectively.

In the case of "rigid joints" no red circle (namely, no beam/column that reach post-peak rotation) is present (see Figure 10a), since SPO was interrupted before the first element reached its post-peak rotation capacity because of a convergence issue. When nonlinear response of beam-column joints is modeled, even if the maximum top displacement at last step is higher with respect to the case of "rigid joints", a lower damage level can be observed in beams (for example at the 2nd and 3rd stories) and a quite distributed damage level in beam-column joints is exhibited, especially from the first to the third story.

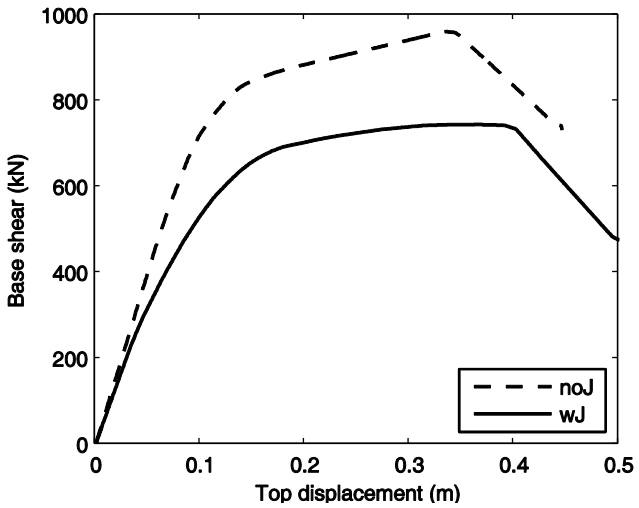
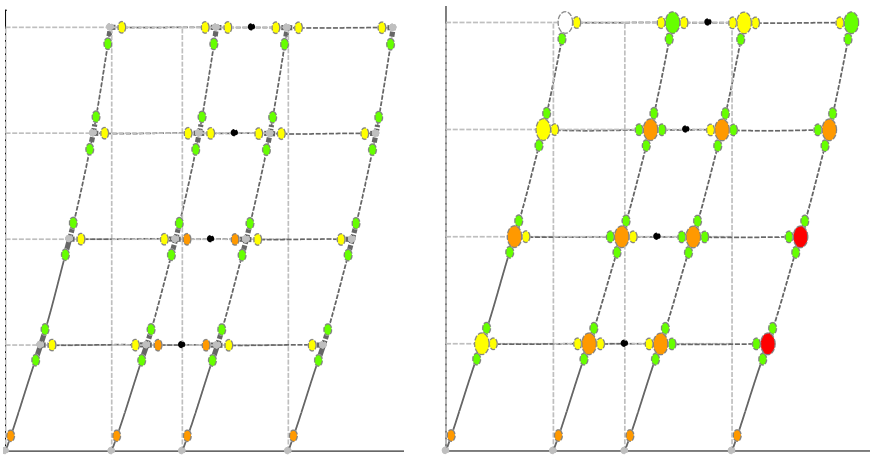


Figure 6: SPO curves: "rigid joints" (noJ) versus "with joints" (wJ).



(a) (b)

Figure 7: Collapse mechanism and damage levels at last step: "rigid joints" (a) versus "with joints" (b).

In Table 7, a comparison in terms of peak base shear ($V_{b.max}$) and the corresponding displacement (D_{max}) in SPO analyses "with joint" (wJ) and with "rigid joints" (noJ) is carried out. It can be observed that the explicit modeling of beam-column joints in the structural analysis

implies a reduction of the maximum base shear (equal to 21%) and a slightly higher peak deformability (that increases of about 6%).

	$V_{b,max}$ (kN)	D_{max} (m)	$V_{b,max\ wJ}$/ $V_{b,max\ noJ}$ (-)	D_{wJ}/D_{noJ} (-)
noJ	959.5	0.343	0.79	1.06
wJ	745.2	0.362		

Table 7: Comparison in terms of peak base shear and peak displacement in SPO – "with joint" (wJ) and "rigid joints" (noJ).

6 INCREMENTAL DYNAMIC ANALYSES

The incremental nonlinear dynamic analyses (IDAs) [32] are conducted in OpenSees [24] with the selected ground motion records with "rigid joints" and "with joints".

Robust convergence algorithms for solving simultaneous equations when strength and stiffness are degrading are implemented.

Five percent mass- and tangent stiffness-proportional Rayleigh damping is applied to the first and third mode of elastic response.

First, IDA curves have been obtained and, then, fragility curves have been calculated, at different LSs taking into account only aleatoric uncertainty, namely record-to-record variability. In this study, the structural demand measure is selected to be the maximum interstory drift in the frame, IDR_{max}, which occurs during its dynamic response to earthquake shaking. At lower levels of excitation, the IDR typically provides insight regarding the potential for damage to non-structural components, while at higher levels it is closely related to structural or local collapse. The adopted seismic intensity measure is the spectral acceleration at the fundamental period of the frame, $Sa(T_1)$, for 5% damping, a measure that is consistent with that used in previous studies and that is generally considered as a more efficient parameter to characterize earthquake intensity than peak ground acceleration [33].

In this Section, IDAs and fragility curves at different LSs for the OLD SLD frame are reported and commented. It is worth noting that IDA curves have been scaled to $Sa(T_1)$, where T_1 is the elastic period of the "with joints" configuration, namely 0.747 s.

6.1 Rigid joints

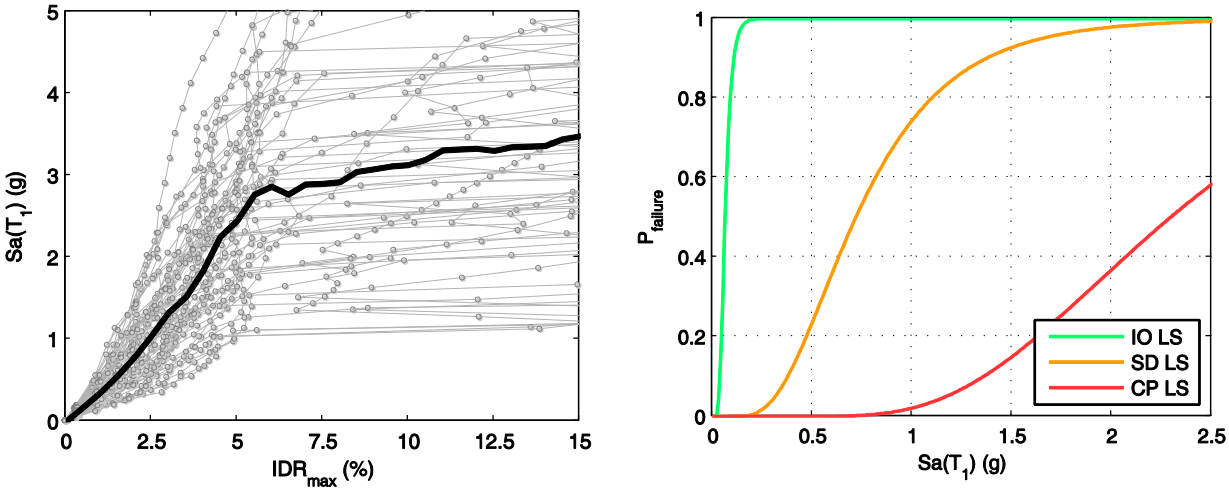
In Figure 8a, IDAs curves related to the "rigid joints" model obtained from all the ground motion records are shown in terms of first-period spectral acceleration $Sa(T_1)$ versus maximum IDR, together with the related median IDA curve.

Starting from such IDAs, fragility curves at LSs defined as the achievement of a given maximum IDR threshold can be easily obtained, by means of a lognormal fit of $Sa(T_1)$ given the value of IDR threshold. In this way, fragility curves shown in Figure 8b have been calculated. Related parameters are reported in Table 8, with μ and β representing the estimated median (expressed in (g)) and logarithmic standard deviation of $Sa(T_1)$ capacity, respectively, at IO, SD, and CP LSs. β-coefficient provides an useful indication about the overall sensitivity of seismic capacity to the variability of the ground motion record, confirming that record-to-record variability is a very important source of uncertainty (β ranges between 41 and 51% for these LSs). Table 8 also reports the maximum IDR threshold (IDR_{max}) corresponding to IO, SD, and CP LSs and the median values ($Sa(T_1)_{median}$) of $Sa(T_1)$, given the maximum IDR.

By means of the same approach based on a lognormal fit of the intensity measure capacities, fragility curves related to the achievement of a certain condition in the elements response for the first time (i.e. in the first element) can be calculated. These fragility curves are report-

ed in Figure 9 and the related parameters in Table 9, where $Sa(T_1)_{median}$ is the median value of $Sa(T_1)$ capacity and IDR_{max} the corresponding median value of maximum IDR.

It can be observed that the yielding condition in the first element (FY LS) occurs for a median value of $Sa(T_1)$ equal to 0.158g, while the achievement of the peak strength for the first time (FC LS) occurs for a quite high value of $Sa(T_1)_{median}$ (1.648g) thanks to the uniform distribution of inelastic demand in the frame. Also in this case, it can be observed that the record-to-record variability provides a logarithmic standard deviation of $Sa(T_1)$ capacity (β) that varies from 42 to 46% for these LSs.



(a) (b)

Figure 8: IDA curves and median IDA (a); fragility curves at IO, SD, and CP LSs (b) – "rigid joints".

LS	$Sa(T_1)_{,median}$ (g)	IDR_{max} (%)	μ (g)	β
IO	0.067	0.20	0.062	0.417
SD	0.783	2.00	0.717	0.506
CP	2.455	5.00	2.293	0.411

Table 8: Fragility parameters at IO, SD, and CP LSs – "rigid joints".

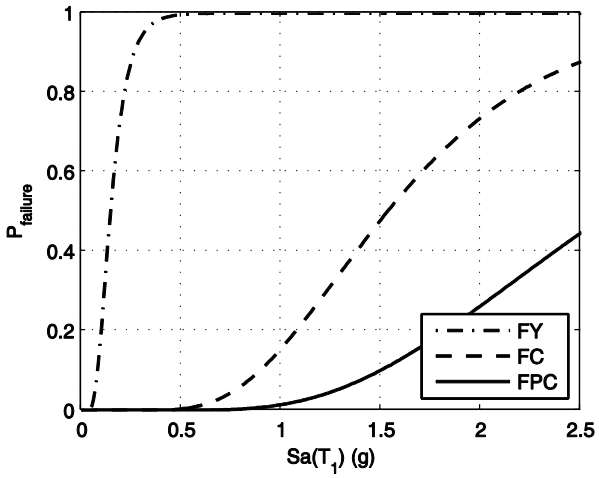


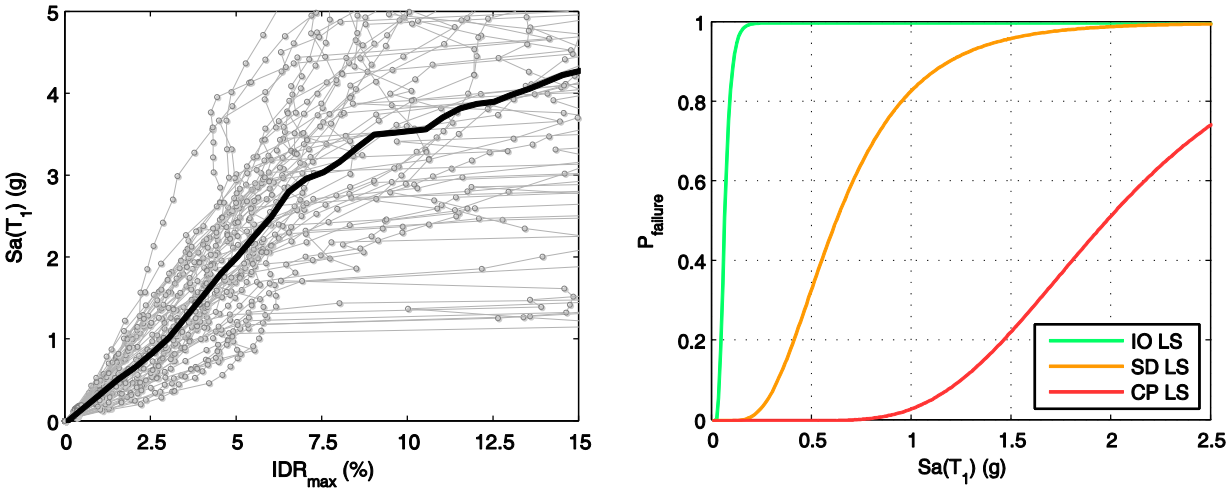
Figure 9: Fragility curves at FY, FC, FPC LSs – "rigid joints".

LS	$Sa(T_1)_{,median}$ (g)	IDR_{max} (%)	μ (g)	β
FY	0.158	0.47	0.145	0.464
FC	1.648	3.71	1.532	0.422
FPC	2.722	5.43	2.656	0.449

Table 9: Fragility parameters at FY, FC, FPC LSs – "rigid joints".

6.2 With joints

The same results are reported also for the structural model that explicitly takes into account joints nonlinear behavior. Figure 10a shows IDAs curves related to the model "with joints" obtained from all the ground motion records, together with the related median IDA curve. Figure 10b reports the fragility curves at IO, SD, and CP LSs, obtained by means of a lognormal fit of $Sa(T_1)$ given the value of IDR threshold for each LS, and Table 10 shows the related parameters.



(a) (b)

Figure 10: IDA curves and median IDA (a); fragility curves at IO, SD, and CP LSs (b) – "with joints".

LS	$Sa(T_1)_{,median}$ (g)	IDR_{max} (%)	μ (g)	β
IO	0.070	0.20	0.059	0.432
SD	0.665	2.00	0.617	0.502
CP	2.034	5.00	1.969	0.362

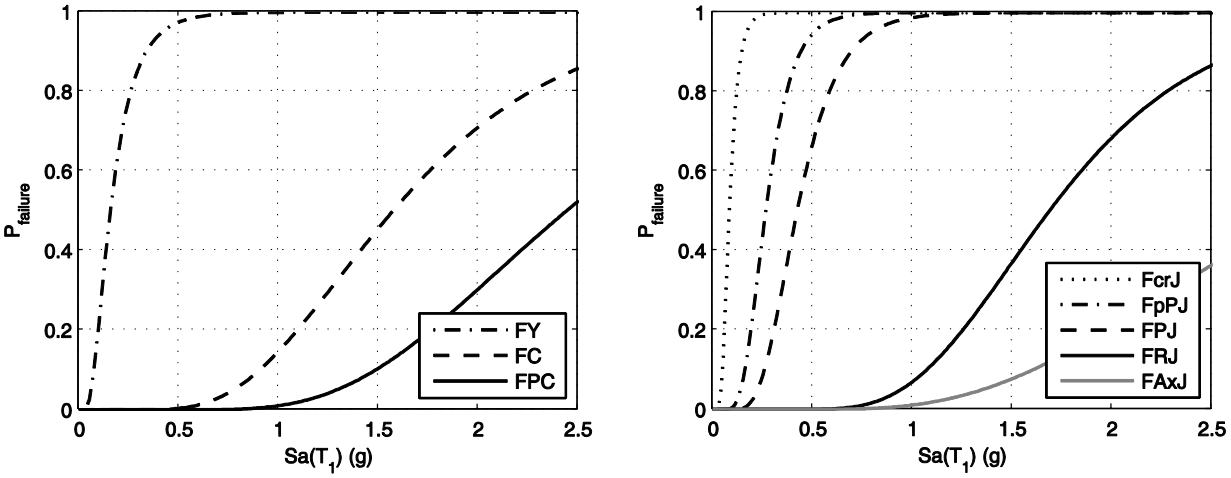
Table 10: Fragility parameters at IO, SD, and CP LSs – "with joints".

Figure 11a and b reports fragility curves obtained in this case at FY, FC, and FPC LSs, but also, at LSs defined as the achievement of particular "limit conditions" in joints response, namely FcrJ, FpPJ, FPJ, and FRJ (defined in Table 5). The related parameters are reported in Table 11, where $Sa(T_1)_{median}$ is the median value of $Sa(T_1)$ capacity and IDR_{max} the corresponding median value of maximum IDR.

It can be observed that the first achievement of peak strength in beam-column joints anticipates the first achievement of capping strength in beams or columns, in terms of $Sa(T_1)_{median}$; the achievement of the peak strength in beams or columns occurs for a value of $Sa(T_1)$ quite

close to that corresponding to the achievement of the first residual strength in joints, thus suggesting that joint damage can be very critical in such a frame, especially for loss estimation.

Moreover, also when joints are explicitly modeled into the numerical model, the possible axial failure of joints cannot be captured directly due to the features of the adopted model. As anticipated in Section 2, a post-processing of the nonlinear analyses can lead to the detection of such kind of failure when the maximum IDR in a story overcomes the minimum IDR capacity (IDR_{AxJ}) among joints at that story. In this way, the achievement of the first axial failure (FAxJ LS) has been detected for each ground motion record and the related fragility parameters has been obtained by means of a lognormal fit (see Table 11 and Figure 11b). A maximum IDR equal to 7.54% leads to the first joint axial failure.



(a) (b)

Figure 11: Fragility curves at FY, FC, FPC LSs (a); Fragility curves at FcrJ, FpPJ, FPJ, FRJ, and FAxJ LSs (b) – "with joints".

DS	$Sa(T_1)_{median}$ (g)	IDR_{max} (%)	μ (g)	β
FY	0.166	0.49	0.157	0.594
FC	1.614	4.14	1.572	0.433
FPC	2.349	5.66	2.441	0.389
FcrJ	0.081	0.24	0.082	0.435
FpPJ	0.296	0.87	0.265	0.394
FPJ	0.470	1.37	0.421	0.385
FRJ	1.706	4.31	1.685	0.354
FAxJ	3.059	7.54	2.947	0.476

Table 11: Fragility parameters at FY, FC, FPC, FcrJ, FpPJ, FPJ, FRJ, and FAxJ LSs – "with joints".

6.3 Comparison

By comparing median IDA curves between the two analyzed frame models ("rigid joints" and "with joints"), as in Figure 12, it can be observed that joint damage leads to lower $Sa(T_1)$ capacity for a given IDR, until about 6% maximum IDR is achieved; successively, when joints involved in the mechanism reach their residual strength - thus starting to go through a constant-strength branch -, IDA curves "with joints" (wJ) keeps increasing, while IDA related to "rigid joints" (noJ) frame goes toward a "flatline".

The difference in $Sa(T_1)$ capacity given IDR that can be observed from the comparison between IDA curves, produces the "distance" between fragility curves that can be observed in Figure 13. The comparison between median $Sa(T_1)$ capacity (from lognormal fitting) with rigid joints (noJ) and with joints (wJ) for the OLD SLD frame is summarized in Table 12 for IO, SD, CP LSs, and also at FY, FC, FPC LSs.

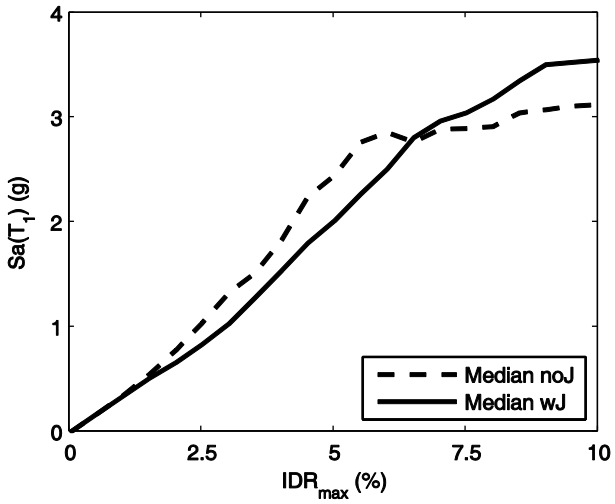


Figure 12: Comparison between median IDA curves.

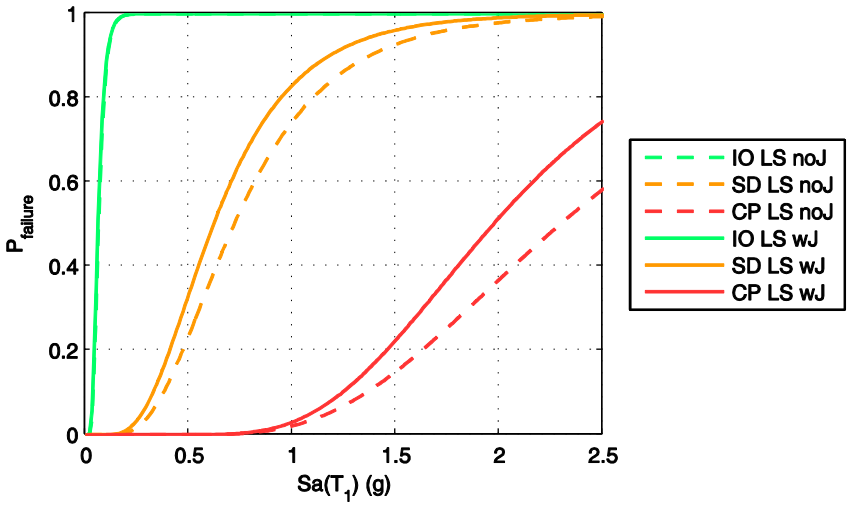


Figure 13: Comparison between fragility curves at IO, SD, and CP LSs.

LS	Sa_{noJ} (g)	Sa_{wJ} (g)	Sa_{wJ}/Sa_{noJ} (-)
IO	0.062	0.059	0.96
SD	0.717	0.617	0.86
CP	2.293	1.969	0.86
FY	0.145	0.157	1.08
FC	1.532	1.572	1.03
FPC	2.656	2.441	0.92

Table 12: Comparison between median $Sa(T_1)$ capacity with rigid joints (noJ) and with joints (wJ).

It can be observed that the minimum ratio between $Sa(T_1)$ capacity with and without nonlinear joint modeling (Sa_{wJ}/Sa_{noJ}) is related to higher seismic intensity, namely at SD, CP and FPC LSs, thus highlighting that the influence of joints in seismic assessment of RC frames becomes more relevant at higher performance levels.

7 CONCLUSIONS

In this paper, a numerical investigation on the influence of joint failures on the seismic performance at different performance levels of a case study RC frame - designed for seismic loads according to an obsolete technical code – has been presented. A preliminary classification of joint failure typology within the frames and the definition of the corresponding nonlinear behavior were carried out. Structural models that explicitly include beam-column joints were built. In particular, the joint model proposed by the Authors has been applied for exterior joints, in conjunction with modeling proposals from literature for interior joints and beam/column behavior. A probabilistic assessment based on nonlinear dynamic simulations of the structural response was performed taking into account record-to-record variability.

The structural capacities were primarily defined by the maximum interstorey drifts (IDR) that correspond to three widely used performance levels in the earthquake community: immediate occupancy, life safety or significant damage, and collapse prevention. Additional LSs, defined on the basis of the achievement of characteristic points in the nonlinear response of the primary structural elements, have been adopted. In particular, the first achievement of a particular condition or a "conventional failure" has been detected, in analogy with the approach of typical European code prescriptions (e.g. Eurocode 8, DM 2008).

Preliminary nonlinear static analyses and incremental nonlinear dynamic analyses under selected ground motion records have been performed in OpenSees in a double condition:

(i) with "rigid joints", assuming a very high stiffness and shear strength for beam-column connections;

(ii) "with joints", explicitly modeling the nonlinear behavior of beam-column intersections.

It was observed that for the analyzed frame (characterized by strong column-weak beam design):

- the minimum ratio between $Sa(T_1)$ capacity with and without nonlinear joint modeling is related to higher seismic intensity levels, thus highlighting that the influence of joints in seismic assessment becomes more relevant at higher performance levels;
- when nonlinear response of beam-column joints is modeled, a lower damage level can be observed in beams/columns and a quite distributed damage level in beam-column joints is exhibited, thus confirming that joint damage can be very critical in such a frame, especially for loss estimation.

Incremental dynamic analysis alone does not account for how well the nonlinear simulation model represents the real frame, since no modeling uncertainties have been considered. These modeling uncertainties are especially important in predicting collapse. Thus, also modeling uncertainties should be accounted for in future works to a more reliable evaluation of seismic performance.

Another important improvement of the study presented herein will be the explicitly modeling of shear failures with degrading behavior after detection and consequent axial failure by means of a reliable, realistic and computational sustainable model.

REFERENCES

[1] ACI. Building Code Requirements for Structural Concrete (ACI 318), 2002.

[2] CEN European standard EN1998-3, Eurocode 8: design provisions for earthquake resistance of structures – Part 3: assessment and retrofitting of buildings. European Committee for Standardisation, Brussels, 2005.

[3] DM 2008, Decreto Ministeriale del 14/1/2008, Approvazione delle nuove norme tecniche per le costruzioni. G.U. n. 29 del 4/2/2008. (in Italian)

[4] L. E. Aycardi, J. Mander and A. Reinhorn, Seismic Resistance of Reinforced Concrete Frame Structures Designed Only for Gravity Loads: Experimental Performance of Subassemblages. *ACI Structural Journal* **91**(5): 552-563, 1994.

[5] S. K.Kunnath, G. Hoffmann A. M. Reinhorn and J. B. Mander, Gravity-Load-Designed Reinforced Concrete Buildings -Part I: Seismic Evaluation of Existing Construction. *ACI Structural Journal* **92**(3): 343-354, 1995.

[6] A.G. El-Attar, R.N. White, P. Gergerly, Behavior of gravity load designed reinforced concrete buildings subjected to earthquakes, *ACI Structural Journal* **94**(2): 133– 145, 1997.

[7] A. Filiatrault, E. Lachapelle and P. La Montagne, Seismic performance of ductile and nominally ductile reinforced concrete moment resisting frames I. Experimental Study. *Canadian Journal of Civil Engineering* **25(**2): 331-341, 1998.

[8] A. B. Liel, Assessing the collapse risk of California's existing reinforced concrete frame structures: Metrics for seismic safety decisions. Diss. Stanford University, 2008.

[9] O.C. Celik and B.R. Ellingwood, Modeling Beam-Column Joints in Fragility Assessment of Gravity Load Designed Reinforced Concrete Frames, *Journal of Earthquake Engineering*. **12**:357-381, 2008.

[10] J. S. Jeon, L. N.Lowes, R. DesRoches, and I. Brilakis, Fragility curves for non-ductile reinforced concrete frames that exhibit different component response mechanisms. *Engineering Structures* **85**: 127-143, 2015.

[11] K. J. Elwood, Modelling failures in existing reinforced concrete columns. *Canadian Journal of Civil Engineering* **31**.5: 846-859, 2004.

[12] M.T. De Risi, P. Ricci, G.M. Verderame, G. Manfredi, A nonlinear macro model of exterior RC joints without transverse reinforcement under seismic load. *Engineering Structures* (submitted), 2015.

[13] C. Haselton, A. Liel, S. L. Taylor and G.G. Deierlein, Beam-Column Element Model Calibrated for Predicting Flexural Response Leading to Global Collapse of RC Frame Buildings, Pacific Earthquake Engineering Research Center 2007/03, University of California at Berkeley, 2007.

[14] L. F. Ibarra, R. A. Medina and H. Krawinkler, Hysteretic Models that Incorporate Strength and Stiffness Deterioration. *Earthquake Engineering and Structural Dynamics* **34**: 1489- 1511, 2005.

[15] M.T. De Risi, Seismic performance assessment of RC buildings accounting for structural and nonstructural elements. Ph.D. Thesis, University of Naples Federico II, Naples, Italy, 2015.

[16] S. Alath, S. K. Kunnath. Modeling inelastic shear deformations in RC beam–column joints. Engineering mechanics proceedings of 10th conference, May 21–24, University of Colorado at Boulder, Boulder, Colorado, vol. 2. New York: ASCE: p. 822–5, 1996.

[17] L.N. Lowes. and A. Altoontash, Modeling Reinforced-Concrete Beam-Column Joints Subjected to Cyclic Loading, *Journal of Structural Engineering*. **129**:1686-1697, 2003.

[18] M. Shin, and J.M. LaFave, Modeling of cyclic joint shear deformation contributions in RC beam-column connections to overall frame behaviour. *Structural Engineering and Mechanics*, **18**(5), 645-669, 2004.

[19] A. Sharma, R. Eligehausen, G. R. Reddy, A new model to simulate joint shear behavior of poorly detailed beam–column connections in RC structures under seismic loads, part I: exterior joints. *Engineering Structures*, **33**(3), 1034-1051, 2011.

[20] C. P. Pantelides, J. Hansen, J. Nadauld, L. D. Reaveley, Assessment of Reinforced Concrete Building Exterior Joints with Substandard Details, PEER Report, No. 2002/18, Pacific Earthquake Engineering Research Center, University of California, Berkeley, USA, 2002.

[21] C. Clyde, C.P. Pantelides, L. D. Reaveley, Performance-Based Evaluation of Exterior Reinforced Concrete Buildings Joints for Seismic Excitation, PEER Report, No. 2000/05, Pacific Earthquake Engineering Research Center, University of California, Berkeley, USA, 2000.

[22] S. M. Uzumeri, Strength and ductility of cast-in-place beam-column joints. *American Concrete Institute Annual Convention, Symposium on Reinforced Concrete Structures in Seismic Zones*, San Francisco, 1974. No. SP-53, 1977.

[23] S. Park and K.M. Mosalam, Analytical model for predicting the shear strength of unreinforced exterior beam-column joints, *ACI Structural Journal* **109**, 149–159, 2012.

[24] F. McKenna, G.L. Fenves, M. H.Scott, OpenSees: Open System for Earthquake Engineering Simulation. Pacific Earthquake Engineering Research Center. University of California, Berkeley, CA, USA. http://opensees.berkeley.edu. Reinforced Concrete Beam-Column Joints, Doctoral Dissertation, Stanford University, 2010.

[25] L. N. Lowes, N. Mitra and A. Altoontash, A Beam-Column Joint Model for Simulating the Earthquake Response of Reinforced Concrete Frames, Pacific Earthquake Engineering Research Center, College of Engineering, University of California, 2004.

[26] S. Park and K. M. Mosalam, Simulation of Reinforced Concrete Frames with

[27] W.M. Hassan and J.Moehle, Quantification of residual axial capacity of beam-column joints in existing concrete buildings under seismic load reversals, *Compdyn 2013* – Kos Island, Greece, 12–14 June, 2013.

[28] Decreto Ministeriale n. 40 del 3/3/1975. Approvazione delle norme tecniche per le costruzioni in zone sismiche. G.U. n. 93 dell'8/4/1975. (in Italian)

[29] I. Iervolino, C. Galasso, E. Cosenza, REXEL: computer aided record selection for code-based seismic structural analysis, *Bulletin of Earthquake Engineering*, **8**(2), 339-362, 2010.

[30] O.C. Celik, and B.R. Ellingwood, Seismic fragilities for non-ductile reinforced concrete frames–Role of aleatoric and epistemic uncertainties, *Structural Safety*, **32**(1): 1-12, 2010.

[31] O.C. Celik. Probabilistic assessment of non-ductile reinforced concrete frames susceptible to Mid-America ground motions. PhD dissertation, School of Civil and Environmental Engineering, Georgia Institute of Technology, Atlanta, GA, 2007.

[32] D.Vamvatsikos, C.A. Cornell, Incremental dynamic analysis. *Earthquake Engineering and Structural Dynamics*, **31**(3), 491-514, 2002.

[33] N. Shome, C. A. Cornel, P. Bazzurro, J. E. Carballo, Earthquakes, records, and nonlinear responses. *Earthquake Spectra* (EERI); **14**(3):469–500, 1998.

COMPDYN 2015
5th ECCOMAS Thematic Conference on
Computational Methods in Structural Dynamics and Earthquake Engineering
M. Papadrakakis, V. Papadopoulos, V. Plevris (eds.)
Crete Island, Greece, 25–27 May 2015

ASSESSMENT OF MULTISTORY RC BUILDINGS SUFFERING INTER-STORY POUNDING

Maria J. Favvata[1], Sofia E. Mochla[1], Maria C. Naoum[1] and Chris G. Karayannis[1]

[1]Democritus University of Thrace, School of Engineering, Department of Civil Engineering
12, V. Sofias street, Xanthi 67100, Greece
{mfavvata, sofimoch, mnaoum, karayan}@civil.duth.gr

Keywords: Seismic Assessment, Inter-story Pounding, Shear Demands, Ductility Requirements, Gap Distance, Non-linear Step by Step Analysis.

Abstract. *The pounding of adjacent RC frames with different heights is studied. The main issue behind this investigation is the influence of the local behaviour of the columns that suffer the hit from the slabs of the adjacent building during the seismic excitation. This column's requirements for ductility and shear capacity have been proven to be the critical parameters for the behaviour and final performance of the whole structure. These parameters can be designed in order the obtained performances to satisfy the seismic demands of the Eurocodes. In this study the critical column's requirements for ductility and shear capacity are evaluated for three seismic demands based on Eurocode 8-part3: (a) demand for Damage Limitation limit state that corresponds to ground motions with return periods of 225 years (b) demand for Significant Damage limit state that corresponds to ground motions with return periods of 475 years and (c) demand for Near Collapse limit state that corresponds to ground motions with return periods of 2475 years. The evaluated requirements are for seven different seismic excitations that have been properly scaled to fit the Eurocode's three seismic demands of low zone of seismic hazard. Afterwards, the minimum required gap distances between the adjacent structures are evaluated taking into account the local capacities of the columns that suffer the inter-story pounding effect. These results are compared with the corresponding limitations for adequate gap distances that are provided by the Eurocode 8. The results show that even in the case of Damage limitation seismic demand special measures have to be taken for the column of the multistory RC frame that suffers the hit. The seismic performance of the columns at a specific limit state of the assessment should be considered for the estimation of an adequate gap distance between the adjacent structures. Thus, the minimum gap distance that is required in order to eliminate the possibility for interaction between adjacent structures depends on the limit state of the assessment. Eurocode's provisions for adequate gap separation do not depend on the seismic demand (limit state) but in any case based on the results of this study these provisions seem to be conservative.*

1 INTRODUCTION

An important issue in the field of the structural engineering is the assessment of the seismic performance of the structures under strong ground motions while the inter-story pounding between adjacent structures has been recognized as the most crucial case of interaction for the integrity of the structural stability. The problem of earthquake induced pounding between adjacent buildings has received substantial attention over the last two to three decades [1–23]. However, most of the studies have been focused on modeling the floor to floor collision. Most of these studies have yielded conclusions not directly applicable for the design or the assessment of multistory buildings potentially under pounding. It has to be stressed (see also Cole *et al* [9]) that the majority of the inter-story (floor to column) pounding research has been undertaken by Karayannis and Favvata [1-6]. In these studies the influence of the structural pounding on the seismic behaviour of adjacent multistory RC structures was investigated taking into account several parameters such as: the height variations between the adjacent structures, the positions of the contact points, the separation gap distances, the beam to column joints damage effect, the infills effect with and without openings, the case of open ground story (pilotis type building) and the seismic excitations. The most important problem in the case of inter-story pounding is the developing critical shear state at the columns that suffer the hit. The local damage of the critical column that suffers the impact as a result of the seismic pounding was investigated for the first time in 2005 by Karayannis & Favvata [1], [2].

2 SCOPE OF THIS STUDY

The main issue behind the inter-story pounding between adjacent structures is the local behaviour of the columns that suffer the hit during the seismic excitation. This column's requirements for ductility and shear capacity have been proven to be the critical parameters for the behaviour and final performance of the whole structure. These parameters can be designed so that performances that could satisfy the seismic demands of the Eurocodes to be obtained. Nevertheless, in the modern seismic design codes there are no provisions to ensure the column that may be suffer the impact effect from critical increase of the flexural and shear capacity requirements.

A key parameter for the elimination of the interaction is the initial gap distance between the adjacent structures. About this issue Eurocode 8 provides gap separation limits between the structures in order to prevent possible pounding problems during strong motion earthquakes. However, none of these limits is directly associated with the seismic demand and the seismic hazard design code approaches for the structures. Furthermore, the new design philosophy of the codes leads to flexible frame structures while the adequate seismic separation that is required by the codes is not always easy to apply.

Based on these thoughts in this study, the minimum required gap distance between the adjacent structures at different seismic demands of the Eurocode 8 is also evaluated taking into account the local capacities of the columns that suffer the inter-story pounding effect. These results are compared with the corresponding limitations that are provided by the Eurocode 8.

3 EXAMINED CASES

The seismic assessment of the 8-storey RC frame structure that suffers the inter-story pounding effect from an adjacent 3-storey structure with unequal interstory heights is investigated. Considering that the level of the seismic hazard for the examined interaction problem is low the seismic performance of the external column that suffers the impact from

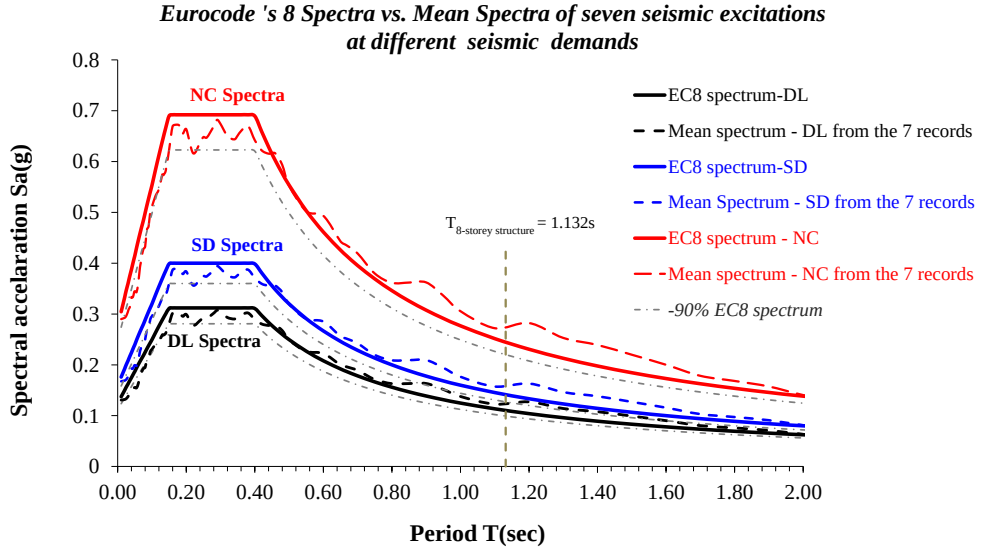
the upper floor slab of the adjacent shorter and stiffer structure is evaluated for three different seismic demands according to the Eurocode 8 - Part3:
(a) seismic demand for Damage Limitation (DL) limit state that corresponds to ground motions with return periods of 225 years and peak ground acceleration 0.13g
(b) seismic demand for Significant Damage (SD) limit state that corresponds to ground motions with return periods of 475 years and peak ground acceleration 0.16g
(c) seismic demand for Near Collapse (NC) limit state that corresponds to ground motions with return periods of 2475 years and peak ground acceleration 0.28g.

For this purpose, both components of seven different seismic excitations extracted from the PEER's database are taken into account. The selected ground motions are scaled to fit Eurocode's 8 elastic spectrum of low zone of seismic hazard at three different seismic demands and ground type A (Fig. 1).

The two adjacent structures are considered to be in contact from the beginning (d_g =0) while the highest contact point of the two structures lies between the levels of the 3rd and the 4th floor of the 8-storey frame at the 1/3 of the height of the column of the 4th floor.

Beams, columns, and walls of the examined structural systems were designed according to Eurocodes 2 and 8, meeting the Ductility Capacity Medium (DCM) criteria of the codes. The structure geometry and reinforcement of the columns of the 8-storey frame are shown in Figure 2. The well known nonlinear dynamic structural analysis program Drain-2dx is used. Non-linear dynamic step-by-step analysis and special purpose elements are employed for the needs of this study. More details about the design of the structures and the structural modelling assumptions can be found in a previous work by Karayannis and Favvata [1].

Results concerning the flexural and the shear demands of the critical external column of the 8-storey frame structure that suffer the impact are presented and compared with the corresponding available capacities at different limit states for low intensity level of seismic hazard. Of course, results in terms of displacements and interstory drift requirements due to pounding effect are presented and compared with the Eurocode's 8 limitations.



Records: *San Fernando, 1971 (EQ59), Italy Auletta, 1980(EQ284), Italy Arienzo, 1980(EQ283), Loma Prieta, 1989 (EQ804), Chi-Chi Taiwan-06, 1999 (EQ3479), Chi-Chi Taiwan-04,1999 (EQ2805), Denali-Alaska, 2002 (EQ2107)*

Figure 1: Eurocode's 8 elastic spectra for three different seismic demands of low seismic hazard in comparison to the corresponding Mean spectra of seven seismic excitations.

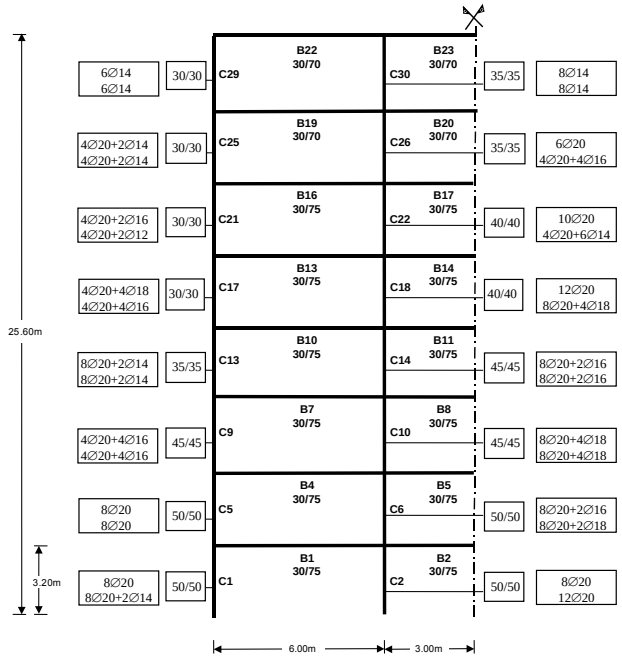


Figure 2: Structural system and column reinforcement of the 8-storey frame structure.

4 RESULTS

The seismic assessment of the 8-storey RC frame structure that suffers the inter-story pounding effect from the adjacent 3-storey structure is investigated. In this study the adjacent structures are considered in contact from the beginning (d_g=0). Based on the provisions of the Eurocode 8, the minimum gap distance that the 8-storey frame structure should have in order to prevent inter-story pounding problems with the adjacent structure is defined and discussed. According to the Eurocode 8 the gap distance between adjacent structures can be considered adequate when it is greater than the maximum plastic design displacement of the structure at the level of pounding. The maximum plastic design displacement ($\delta_{EC8,plastic}$) that can be developed by the structure is the corresponding maximum elastic design displacement ($\delta_{EC8,elastic}$) multiplied by the seismic behavior factor q.

The maximum elastic ($\delta_{EC8,elastic}$) and plastic ($\delta_{EC8,plastic}$) design displacements that can be developed by the 8-storey frame structure at all the story levels are presented in Figure 3a and are compared in the same figure with the maximum displacements (at the pounding side) of the 8-storey frame without and with the inter-story pounding effects at limit states of Damage Limitation (DL) and Near Collapse (NC). It can be observed that in the examined cases the maximum displacements of the 8-storey frame are less than the capacity of the structure for inelastic response. Also, as it was expected the demands for displacement of the structure are depended on the limit state that is used for the evaluation. However, the code's provisions for the minimum gap distance separation do not depend on the limit state. Based on the Eurocode 8 a minimum gap distance of 9.0cm should be adopted in order to prevent the interaction between the 8-storey frame structure and the 3-storey structure at the 4th floor level (Fig. 3a). The maximum displacements of the 8-storey frame at the pounding side are decreased due to the pounding effect.

The maximum interstory drifts at three limit states for low level of seismic hazard due to the interaction of the 8-storey frame with the 3-storey structure are presented in Figures 3b, 3c, 3d and are compared with the ones of the 8-storey frame vibrating without pounding effects. As it was expected the maximum interstory drifts of the 8-storey frame are increased in the

floors above the upper floor level of contact (4th floor level) in comparison with the corresponding ones without pounding effect. It can also be observed that the developing requirements for interstory drift are increased when the limit state for the evaluation of the seismic performance becomes more exigent.

Further, in Figures 3b, 3c and 3d the maximum interstory drifts that can be developed by the 8-storey frame structure without suffering the pounding effect are also presented. These drifts are deduced from the maximum plastic design displacement ($\delta_{EC8,plastic}$) of the frame structure. It can be observed that in the case of evaluating the pounding effect at the Near Collapse limit state the capacity of the structure for interstory drift is exceeded at the last two floor levels (7th and 8th) (Fig. 3d). In Figure 3, each value of drift or displacement requirement is the mean value of fourteen maximum interstory drifts or displacements as resulted from both components of the seven seismic excitations that are used in this study.

Figure 4 presents the maximum curvature ductility requirements that are developed at the critical part of the column of the 4th floor level of the 8-storey frame that suffers the inter-story pounding effect from the slab of the adjacent 3-storey structure. The developed requirements are compared with the corresponding available capacity of the column. Based on these results it can be observed that for the same level of seismic hazard (low) the evaluation of the pounding effect on the column's maximum ductility requirements is influenced by the seismic demand (limit state) under consideration. In fact, the column that suffers the impact appears to be in critical condition due to high ductility demands when the limit state for the assessment is enhanced from Damage Limitation to Significant Damage and to Near Collapse.

The maximum shear requirements of the critical column of the 4th floor level of the 8-storey frame due to the pounding effect at the limit states of Damage Limitation, Significant Damage and Near Collapse are also evaluated for all the seismic excitations. In all the examined cases the requirements for shear exceed the available shear strength of the column, indicating this way that the column that suffers the hit is always in a critical condition due to shear action (Table 1).

Nevertheless, shear failure of the column due to the pounding effect cannot be concluded based only on the number of times that the shear force is exceeding the available strength during the analyses. A parameter that could be used in order to identify possible shear failure is the sequence of the impacts that cause high values for shear strength. In other words, the number of critical demands for shear that are developing at a time or/and at successive times during the seismic analysis at the column that suffers the inter-story pounding problem. Thus, in Figure 5 the time history of the shear requirements that are developing due to the inter-story pounding effect on the critical part of the column of the 4th floor level of the 8-storey frame are presented and compared with the corresponding available shear strength during the analysis. The exact time the demand exceeds the available strength is also depicted in the same figure. Based on these results, it can be observed that different seismic demand (limit state) for the evaluation of the pounding effect on the shear requirements of the column altered the times and the successive times that the column is in critical condition of shear failure. It is noted that the column's behaviour is elastic in flexure and in shear in all the examined cases of this study without the pounding effect.

Also, the adjacent structures suffered the inter-story pounding effect almost from the beginning of both seismic excitations EQ59 and EQ804 and for the three limit states (Fig. 5).

From the beginning of the seismic excitation EQ59 the critical column of the 8-storey frame structure developed high demands for shear that restrict the development of high ductility requirements (see also Fig. 4). However, in the case of the seismic excitation EQ804 that column is in critical condition due to high demands for both shear and flexure strength at all the limit states.

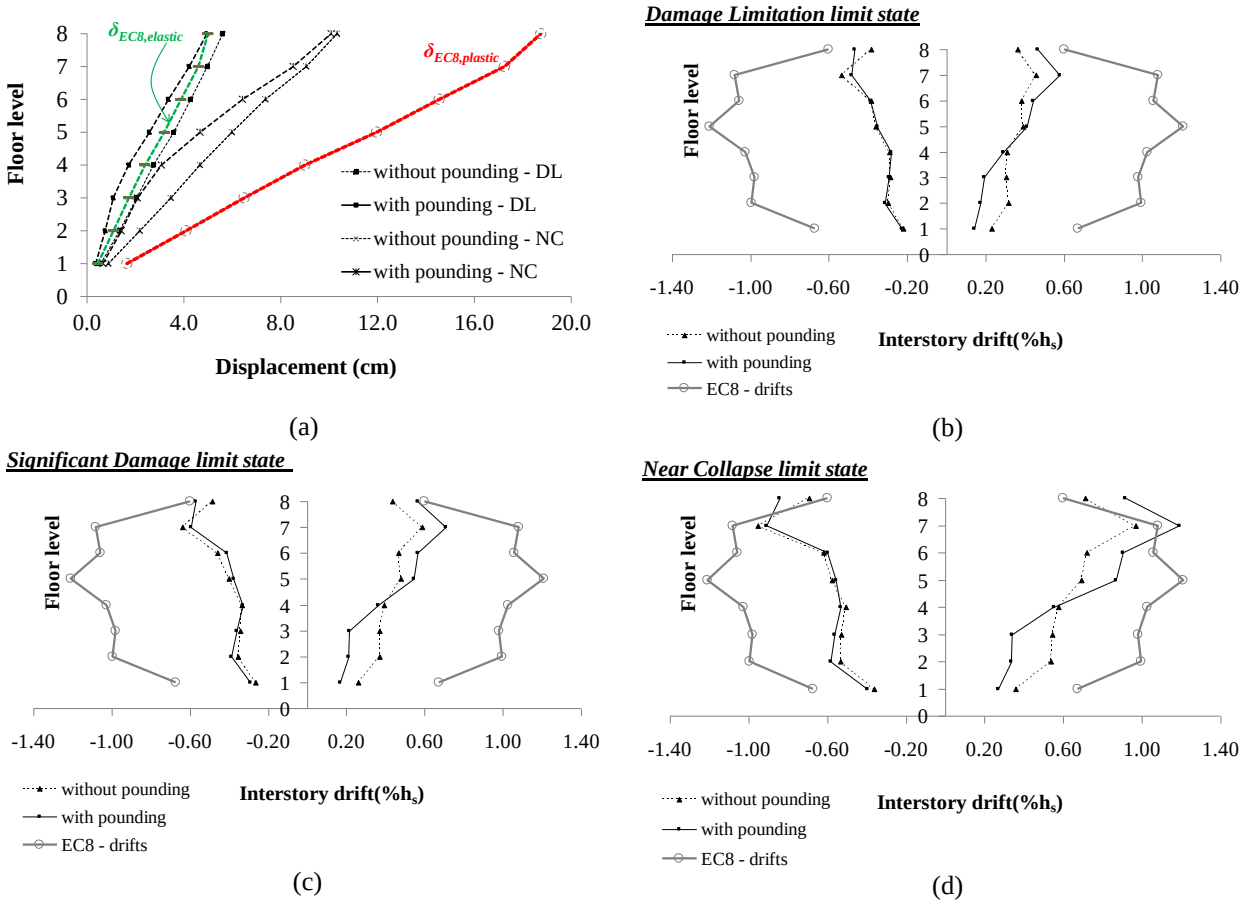


Figure 3: Maximun displacements and interstory drifts requirements of the 8-storey frame structure at three limit states in comparison to the Eurocode's 8 demands for the elimination of the pounding effect between the adjacent structures.

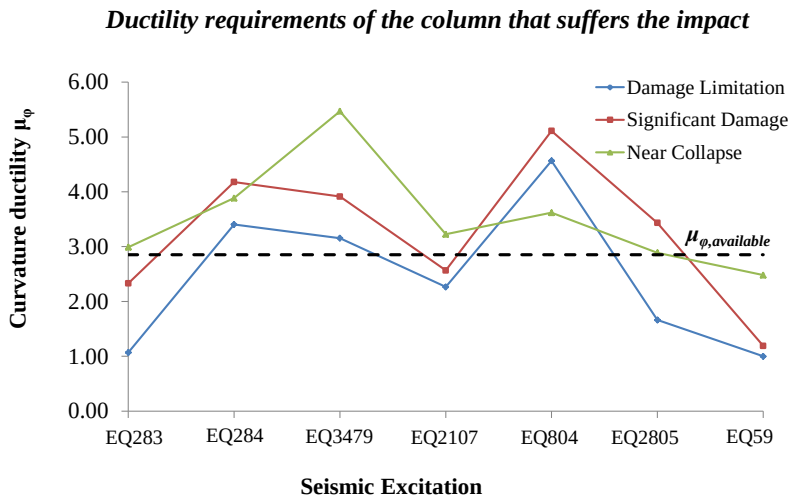


Figure 4: Maximun curvature ductility requirements of the column of the 8-storey frame structure that suffers the hit at three different limit states.

Shear Demands of the critical column of the 4th floor level of the 8-storey frame structure that suffers the inter-story pounding effect at different limit states										
		Damage Limitation			Significant Damage			Near Collapse		
Earthquake		V (kN)		Total times† $V > V_{avail.}$	V (kN)		Total times† $V > V_{avail.}$	V(kN)		Total times† $V > V_{avail.}$
EQ283	FN	582	(1.6)*	56	684	(1.9)*	85	642	(1.7)*	101
	FP	615	(1.6)	94	698	(1.8)	65	791	(2.1)	108
EQ284	FN	705	(1.9)	68	721	(2.0)	76	771	(2.1)	142
	FP	545	(1.5)	75	683	(1.9)	89	769	(2.0)	123
EQ3479	FN	736	(1.9)	90	758	(2.0)	90	771	(2.0)	98
	FP	646	(1.9)	65	681	(1.9)	80	781	(2.1)	116
EQ2107	FN	647	(1.7)	24	777	(2.0)	22	802	(2.0)	38
	FP	675	(1.9)	21	614	(1.7)	31	695	(1.9)	75
EQ804	FN	823	(2.0)	91	829	(2.1)	97	772	(2.0)	98
	FP	677	(1.8)	58	785	(2.0)	56	795	(2.1)	67
EQ2805	FN	630	(1.7)	27	699	(1.8)	42	749	(2.0)	73
	FP	725	(1.9)	38	753	(2.0)	36	761	(2.0)	62
EQ59	FN	551	(1.5)	84	650	(1.7)	92	742	(2.0)	182
	FP	553	(1.4)	79	620	(1.6)	50	688	(1.8)	75
Maximum:		823	(2.0)	94	829	(2.1)	97	802	(2.1)	182
Average:		690	(1.8)	71	741	(1.9)	75	778	(2.0)	113

** Ratio of the maximum shear demand to the available shear strength*

† *Total times steps the shear demand exceeds the available shear strength during the analysis*

Table 1: Shear demands of the multistory RC frame external column that suffers the inter-story pounding at three different limit states for all the examined cases.

Further, as it can be observed in Figure 6a, in the case of the seismic excitation EQ804 at the limit state of Damage Limitation the minimum gap distance (d_g) that is required between the examined adjacent structures in order the critical developing shear forces and ductility demands due to the pounding effect to be minimized is 2cm.

However, for the same gap distance (d_g=2cm) at the limit state of Significant Damage the column is still in critical condition due to shear action (Fig. 6b) while at the limit state of Near Collapse the critical part of the column has increased demands for shear strength and ductility (Fig. 6c). Finally, the local performance of the column can be considered safe due to the inter-story pounding effect at the limit state of Near Collapse when a gap distance (d_g) equal to 4cm is provided (Fig. 6d). Thus, the seismic performance of the column that suffers the impact should also be taken into account for the evaluation of the minimum gap distance between adjacent structures so that the critical shear actions and ductility demands could be eliminated. Similar results also hold for all the examined cases of this study.

It is noted that according to the Eurocode 8 a minimum gap distance of 9cm is required in order to prevent the pounding between the 8-storey frame structure and the 3-storey structure at the 4th floor level (Fig. 3a). This code provision for the gap distance is independent of the seismic demand (limit state) under consideration.

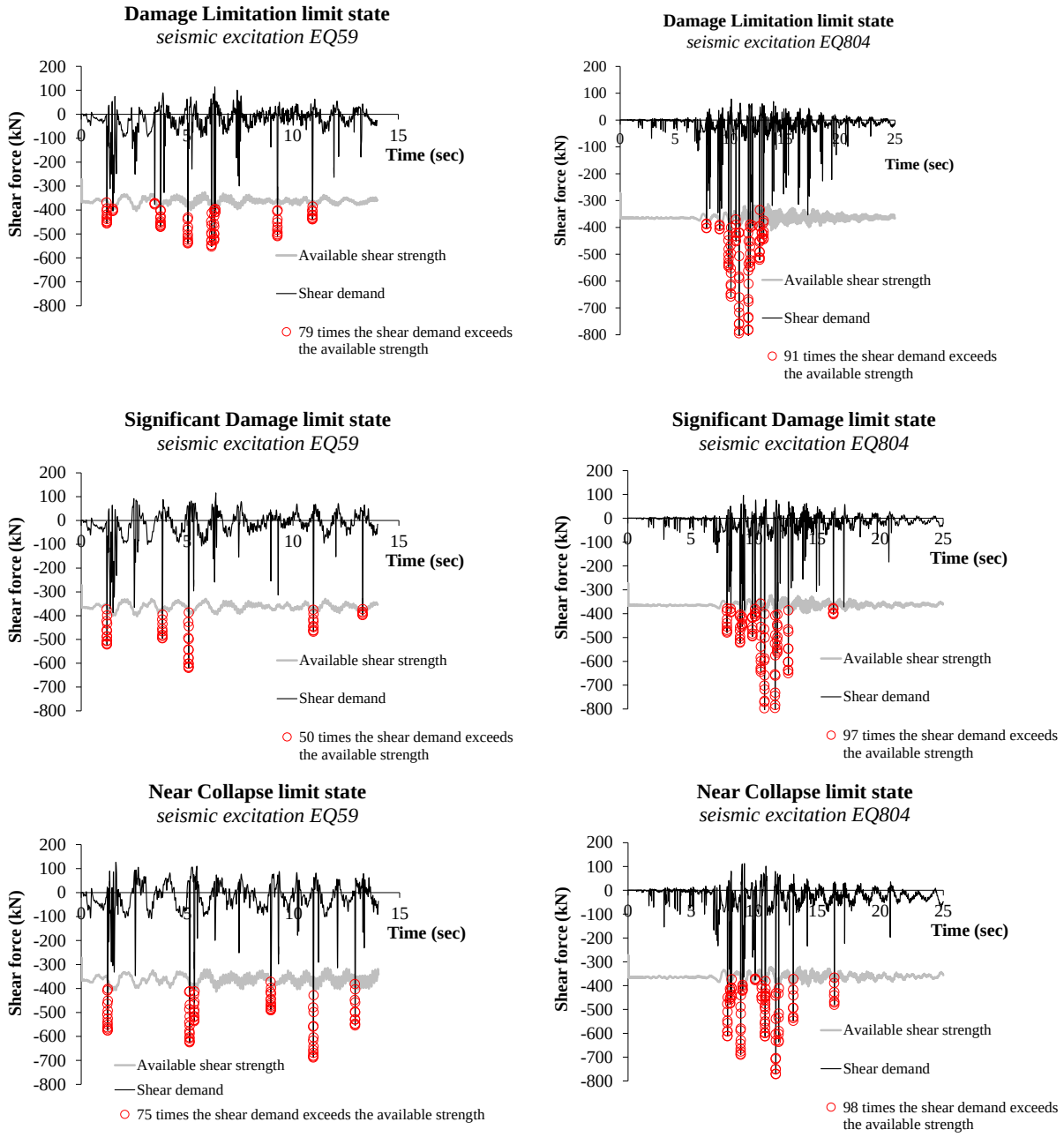


Figure 5: Time history shear requirements of the critical column of the 8-storey frame structure that suffers the hit at three different limit states. Comparison with the available shear strength.

5 CONCLUSIONS

In this study the seismic assessment of the inter-story pounding problem between adjacent structures is evaluated at different limit states for the case of low level of seismic hazard. Dynamic step by step analyses were performed and results in terms of displacement, interstory drifts, ductility requirements and shear requirements were presented. Further, the minimum required gap distance between the adjacent structures at different seismic demands of the Eurocode 8 was evaluated taking into account the local performances of the columns that suffer the inter-story pounding effect. These results are compared with the corresponding limitations that are provided by the Eurocode 8. The main conclusions of this study can be summarized as:

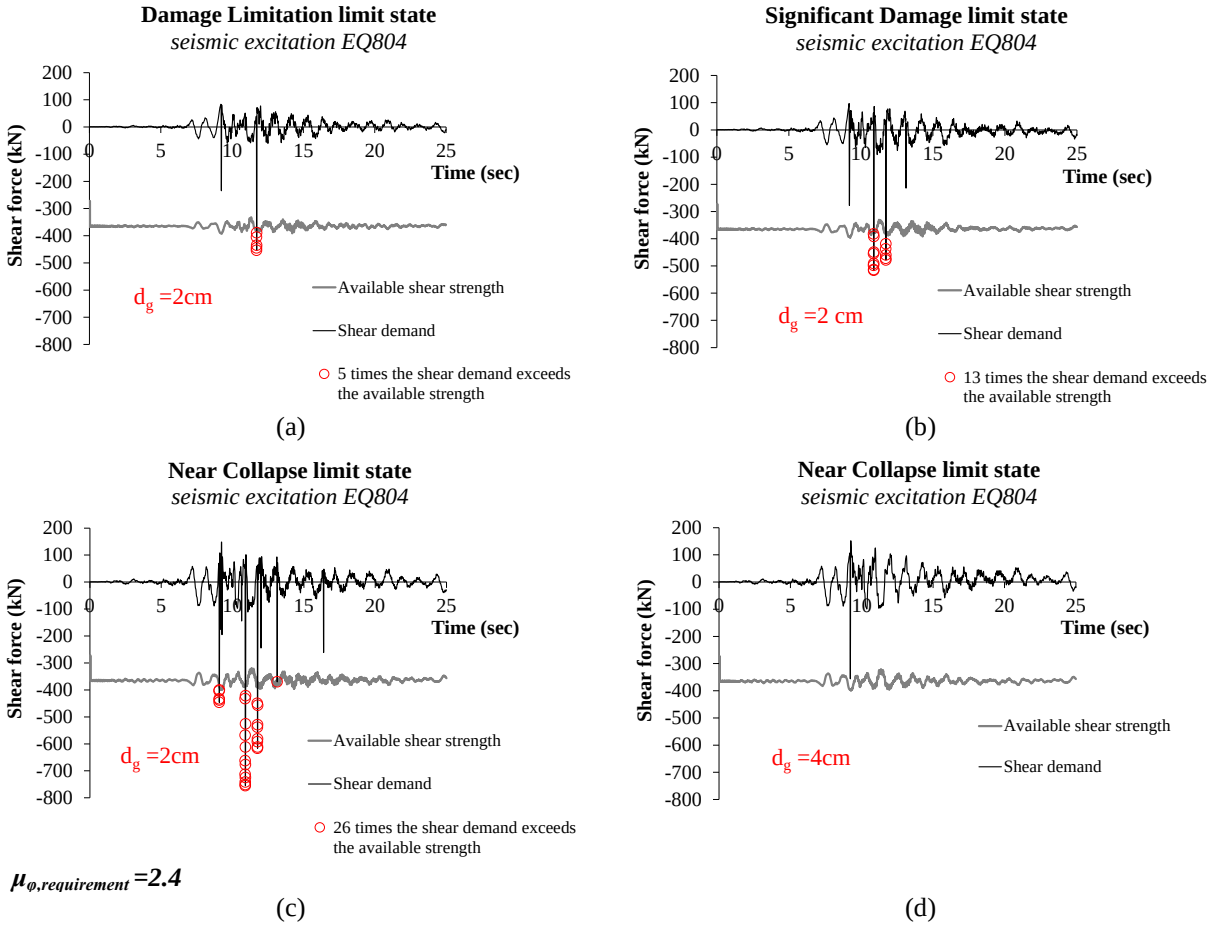


Figure 6: Estimated gap distances between the adjacent structures to prevent the critical shear demands of the critical column of the 8-storey frame structure that suffers the hit at three different limit states.

- The developing requirements for interstory drift are increased when the seismic demand for the assessment becomes more exigent.
- The column that suffers the hit is always in a critical condition due to shear action.
- The column that suffers the impact appears to be in critical condition due to high ductility demands when the limit state for the assessment is altered from Damage limitation to Significant damage and to Near collapse.
- Even in the case of Damage limitation limit state special measures have to be taken for the columns of the multistory RC frame that suffer the hit.
- The seismic performance of the columns that suffer the impact at a specific limit state of the assessment should be considered for the estimation of an adequate gap distance separation between adjacent structures.
- Thus, the minimum gap distance that is required in order to eliminate the possibility for pounding between adjacent structures depends on the limit state of the assessment.
- Eurocode's provisions for adequate gap separation do not depend on the seismic demand (limit state) but in any case based on the results of this study these provisions seem to be conservative.

REFERENCES

[1] C.G. Karayannis, M.J. Favvata, Earthquake-induced interaction between adjacent reinforced concrete structures with non-equal heights. *Earthquake Engineering and Structural Dynamics*, **34(1)**, 1-20, 2005.

[2] C.G. Karayannis, M.J. Favvata, Inter-story pounding between multistory reinforced concrete structures. *Structural Engineering and Mechanics*, **20(5),** 505-526, 2005.

[3] M.J. Favvata, C.G. Karayannis, A.A. Liolios, Influence of exterior joint effect on the inter-story pounding interaction of structures. *Structural Engineering and Mechanics,* **33(2)**, 113-136, 2009.

[4] M.J. Favvata, C.G Karayannis, The inter-story pounding effect on the seismic behavior of infilled and pilotis RC structures. *Geotechnical, Geological and Earthquake Engineering,* **24**, 87-101, 2013.

[5] M.J. Favvata, C.G. Karayannis, V. Anagnostopoulou, Influence of infill panels with and without openings on the pounding effect of RC structures. *15th World on Earthquake Engineering,* Lisbon Portugal, 24-28, 2012.

[6] M.J. Favvata, M.C. Naoum, C.G Karayannis, Earthquake induced Earthquake induced interaction between RC frame and steel frame structures. *WIT Transactions on the Built Environment*, **134**, 839-851, 2013.

[7] S.A. Anagnostopoulos, C.E. Karamaneas, Use of collision shear wall to minimize seismic separation and to protect adjacent buildings from collapse due to earthquake-induced pounding. *Earthquake Engineering and Structural Dynamics,* **37(12)**, 1371-1388, 2008.

[8] S.E. Abdel Raheem, Pounding mitigation and unseating prevention at expansion joints of isolated multi-span bridges. *Engineering Structures*, **31(10)**, 2345-2356, 2009.

[9] G.L. Cole, R.P. Dhakal, A.J. Carr, D.K. Bull, Building Pounding State of the Art: Identifying Structures Vulnerable to Pounding Damage. *New Zealand Society for Earthquake Engineering Annual Conference,* New Zealand, P11, 2010.

[10] R. Jankowski, Non-linear FEM analysis of pounding-involved response of buildings under non-uniform earthquake excitation. *Engineering Structures*, **37**, 99-105, 2012.

[11] E. Tubaldi, M. Barbato, S. Ghazizadeh, A probabilistic performance-based risk assessment approach for seismic pounding with efficient application to linear systems. *Structural Safety*, **36-37**, 14-22, 2012.

[12] G.L. Cole, R.P. Dhakal, F.M. Turner, Building pounding damage observed in the 2011 Christchurch earthquake. *Earthquake Engineering and Structural Dynamics*, **41(5)**, 893-913, 2012.

[13] M. Lu, Q. Yang, N. Yang, Maximum relative displacement of adjacent buildings during ground motions. *Transactions of Tianjin University*, **18(5)**, 366-371, 2012.

[14] D.R. Pant, A.C. Wijeyewickrema, Structural performance of a base-isolated reinforced concrete building subjected to seismic pounding**.** *Earthquake Engineering and Structural Dynamics*, **41(12)**, 1709-1716, 2012.

[15] S. Mahmoud, A. Abd-Elhamed, R. Jankowski, Earthquake-induced pounding between equal height multi-storey buildings considering soil-structure interaction. *Bulletin of Earthquake Engineering*, **11(4)**, 1021-1048, 2013.

[16] S. Efraimiadou, G.D. Hatzigeorgiou, G.D. D.E. Beskos, Structural pounding between adjacent buildings subjected to strong ground motions: Part I: The effect of different structures arrangement. *Earthquake Engineering and Structural Dynamics*, **42(10)**, 1509-1528, 2013.

[17] L. Zou, K. Huang, L. Wang, L. Fang, Pounding of adjacent buildings considering pile-soil-structure interaction. *Journal of Vibroengineering*, **15(2)**, 905-918, 2013.

[18] S. Naserkhaki, M. El-Rich, F.N.A.A. Aziz, H. Pourmohammad, Pounding between adjacent buildings of varying height coupled through soil. *Structural Engineering and Mechanics*, **52 (3)**, 573-593, 2014.

[19] P. Skrekas, A. Sextos, A. Giaralis, Influence of bi-directional seismic pounding on the inelastic demand distribution of three adjacent multi-storey R/C buildings. *Earthquake and Structures*, **6 (1)**, 71-87, 2014.

[20] A. Moustafa, S. Mahmoud, Damage assessment of adjacent buildings under earthquake loads. *Engineering Structures*, **61**, 153-165, 2014.

[21] I. Yüksel, S. Büyükçapar, Structural Performance Degeneration by Inclusion of a Seismic Joint. *Arabian Journal for Science and Engineering*, **39 (8)**, 5991-5999, 2014.

[22] J.G. Chase, F. Boyer, G.W Rodgers, G. Labrosse, G.A. Macrae, Probabilistic risk analysis of structural impact in seismic events for linear and nonlinear systems. *Earthquake Engineering and Structural Dynamics*, **43(10)**, 1565-1580, 2014.

[23] R. Jankowski, A. Seleemah, S. El-Khoriby, H. Elwardany, Experimental study on pounding between structures during damaging earthquakes. *Key Engineering Materials*, **627**, 249-252, 2015.

COMPDYN 2015
5th ECCOMAS Thematic Conference on
Computational Methods in Structural Dynamics and Earthquake Engineering
M. Papadrakakis, V. Papadopoulos, V. Plevris (eds.)
Crete Island, Greece, 25–27 May 2015

SEISMIC RETROFIT DECISION-MAKING OF BRIDGES BASED ON LIFE-CYCLE COST CRITERIA

Hossein Ebrahimian[1], Fatemeh Jalayer[2], and Gaetano Manfredi[3]

[1] Post-doctoral Researcher
Dep. of Structures for Engineering and Architecture, University of Naples Federico II, Naples, Italy
e-mail: ebrahimian.hossein@unina.it

[2] Associate Professor
Dep. of Structures for Engineering and Architecture, University of Naples Federico II, Naples, Italy
fatemeh.jalayer@unina.it

[3] Professor
Dep. of Structures for Engineering and Architecture, University of Naples Federico II, Naples, Italy
gamanfre@unina.it

Keywords: Seismic Retrofit of Bridges, Retrofit Decision-making, Life-Cycle Cost Criteria, Time-dependent Risk, Limit State Probability.

Abstract. *In a decision-making framework within the context of performance-based design, life-cycle cost can be regarded as a suitable benchmark performance variable to quantify and measure performance objectives for a set of (discrete) limit states. Life-cycle cost criteria is identified as an economic term expressed in monetary units; it accounts for the initial construction costs, the repair costs taking into account also the loss of revenue due to down time, and finally the maintenance cost. The expected life-cycle cost is used for retrofit design of an existing reinforced concrete bridge infrastructure that is located in south of Italy. The retrofit design involves decision-making between a set of viable rehabilitation schemes, which mainly isolate the simply-supported bridge deck from the pier cap or force the deck to have a uniform displacement along its longitudinal direction. The proposed methodology for life-cycle cost assessment takes the advantage of a closed- and analytic-form approximation in order to take into account the time-varying profile of the probability of exceeding a set of structural limit states. The presented procedure can be effectively used for screening among alternative proposed upgrading strategies while satisfying prescribed reliability-based criteria. The optimal solution is highlighted based on the minimization of the life-cycle cost.*

1 INTRODUCTION

In the context of performance-based design, several performance objectives (e.g., minimize initial cost of construction, ensure life-safety in case of extreme and rare events) can be considered for a set of discrete limit states. In order to implement the performance objectives in a decision making framework, it is desirable to quantify and measure these objectives in terms of a common benchmark variable. The life-cycle cost has been proposed by many researchers (see e.g. [1-7]) as a suitable benchmark performance variable. Life-cycle cost, which is historically identified as an economic term expressed in monetary units, accounts for initial costs of construction of facility, the regular costs of its maintenance and its functionality over time, loss of revenue in case of damage, re-pair / replacement costs, social losses including eventual loss of life and end-of-life recycling costs. The evaluation of life-cycle cost is subjected to several sources of uncertainty, such as the occurrence and the intensity of future earthquake events, the structural resistance and the service life itself. Life-cycle cost is generally evaluated in terms of its expected value over the life-time of the infrastructure.

The present study aims to apply the life-cycle cost criteria to retrofit design of an existing reinforced concrete (RC) bridge with simply-supported decks built in the 1970s and located in the Campania Region, south Italy. The retrofit design involves decision making between a set of viable options which can be evaluated and compared in terms of their corresponding life-cycle cost and subjected to reliability constraints. In particular, for each upgrade option, the corresponding life-cycle cost is evaluated by calculating in monetary terms, the direct cost of the installation of the upgrade solution, the maintenance cost of the upgraded system, the re-pair/replacement costs in case of damage. After the low-cost option is identified among the set of retrofit schemes, the structural reliability for the corresponding upgraded infrastructure needs to be verified against an acceptable threshold.

The methodology for calculating the life-cycle cost takes into account the time-varying profile of the probability of exceeding a set of structural limit states. Thus, in the first step, a procedure is proposed for calculating the time-dependent probability of exceeding different structural limit states given a sequence of major seismic events. It takes advantage of a recently developed framework by the authors which was proposed for post-mainshock risk assessment [8-10]. Later, a closed- and analytic-form approximation to the time-dependent limit state probability is derived (see also [10]). The calculated time-dependent limit state probabilities based on the closed-form expression are then used in order to estimate the expected life-cycle cost for each retrofit option considered.

For the simplicity of calculations, the three-dimensional (3D) model of the case-study bridge is subjected to ground motions in its longitudinal direction. Five alternative schemes are adopted for rehabilitation of the bridge. They aim mainly at improving the global behavior of bridge deck by using friction pendulum isolators and/or force the deck to have a uniform displacement along its longitudinal direction. The optimal solution is highlighted based on the minimization of the life cycle cost satisfying the acceptable reliability-based criteria.

2 METHODOLOGY

The objective of this methodology is to evaluate the expected life-cycle cost for a bridge that is subjected to seismic actions during its life-time neglecting the effect of aging (given the fact that this methodology is used for optimal decision-making and not for assessment purposes). First, a method is proposed in order to calculate the time-dependent risk in terms of the probabilities corresponding to the exceedance of desired (discrete) limit states during the entire lifetime of the bridge (considering the sequence of seismic events that may take place during the bridge life cycle). It implements the methodology presented primary in [6, 8], and

further developed in [9]. Subsequently, to facilitate the estimation of time-dependent limit state exceedance probability, a simple closed-form and analytical approximation is derived. It employs the standard tools in risk assessment such as the fragility curve for the intact structure and takes into account that the bridge is going to be repaired before the next events takes place. These results are directly used within the calculation of the repair cost.

Accordingly, the expected life-cycle cost is calculated by taking into account the initial construction costs, the repair costs taking into account also the loss of revenue due to down time, and finally the maintenance cost. The calculations involved in this methodology are based on a set of assumption described in the following section. The presented probability-based methodology for evaluation of the expected life-cycle cost herein can be effectively used for screening among various proposed upgrading strategies while satisfying prescribed reliability constraints.

2.1 The Set of Assumptions

The following assumptions are adopted herein:

1. Once a major seismic event (i.e., the one with magnitude greater than a prescribed threshold) hits the bridge, the decision follows the immediate shutdown of the bridge and repairing of the infrastructure.
2. The repair operation is supposed to restore the infrastructure back to its intact initial state.
3. The time of repair, which is also equal to the down-time for the infrastructure, depends only on the state of the damaged bridge. It is likely that major seismic events take place while the bridge is under repair.
4. The bridge is going to be replaced / recycled while the following conditions arise: a) the infrastructure goes beyond the defined ultimate limit states, and b) the cost of repair operations exceeds the replacement costs.
5. The sequence of major seismic events taking place does not include the clustering of seismic events (i.e., aftershocks); previous works by the authors has focused on the clustered events (see [8-10]).
6. The effect of aging is not considered.

2.2 Calculation of Time-dependent Limit State Probability

Assume that $\mathbf{I}_1$ stands for the information as follows: t denotes the life time of the bridge (generally defined in unit of year); N_{ce} represents the maximum number of critical seismic events that can take place during the time interval $[0,t]$ and have magnitude M within the range $M_l \leq M \leq M_u$ (M_l is the lower magnitude and M_u defines the upper-bound magnitude). The probability of first-excursion for the desired limit state LS given $\mathbf{I}_1$, denoted by $P(LS|\mathbf{I}_1)$ can be expanded by using Total probability Theorem [11]:

$$P\left(LS \mid \mathbf{I}_1\right) = \sum_{n=1}^{N_{ce}} P\left(LS \mid n, \mathbf{I}_1\right) P\left(n \mid \mathbf{I}_1\right) \tag{1}$$

where $P(LS|n,\mathbf{I}_1)$ is the probability of exceeding the limit state LS for the first time given that exactly $n=1{:}N_{ce}$ events take place and $\mathbf{I}_1$; $P(n|\mathbf{I}_1)$ is the probability that exactly n events with $M_l \leq M \leq M_u$ take place during t. Assuming that the earthquake occurrence in the life-time of the bridge infrastructure is expressed by a stationary Poisson probability mass function, $P(n|\mathbf{I}_1)$ can be expressed as:

$$P(n \mid \mathbf{I}_1) = \frac{(\nu t)^n e^{-\nu t}}{n!} \tag{2}$$

where ν is the annual rate of seismicity (i.e., annual rate of occurrence of events with $M_l \leq M \leq M_u$). The best-estimate for N_{ce} in Eq. (1) can be adopted herein as the expected value plus two standard deviations ($N_{ce} \approx \nu t + 2[\nu t]^{1/2}$) for the distribution $P(n|\mathbf{I}_1)$ provided by the Poisson model. The term $P(LS|n,\mathbf{I}_1)$ in Eq. (1) can be calculated by taking into account the set of mutually exclusive and collectively exhaustive (MECE) events that the *LS* first-excursion is taken place at one and just one of the previous events (see [6-10]):

$$P\left(LS \mid n, \mathbf{I}_1\right) = P\left(C_1 + \overline{C}_1 C_2 + \overline{C}_1 \overline{C}_2 C_3 + \ldots + \overline{C}_1 \overline{C}_2 \ldots \overline{C}_{n-1} C_n\right) \tag{3}$$

where C_k, k=1:n, is defined by the following statement:

$$\begin{cases} C_k \equiv LS \text{ first-excursion after } k\text{th event} \\ \overline{C}_k \equiv LS \text{ not exceeded after } k\text{th event (read as NOT } C_k) \end{cases} \tag{4}$$

The authors have shown that $P(LS|n,\mathbf{I}_1)$ in Eq. (3) can be written as (see Appendix of [9]):

$$\begin{aligned} P\left(LS \mid n, \mathbf{I}_1\right) &= \sum_{k=1}^{n} \left(P\left(C_k \mid \overline{C}_1 \overline{C}_2 \ldots \overline{C}_{k-1}, \mathbf{I}_1\right) \cdot \prod_{i=1}^{k-1} \left[1 - P\left(C_i \mid \overline{C}_1 \overline{C}_2 \ldots \overline{C}_{i-1}, \mathbf{I}_1\right)\right] \right) \\ &\triangleq \sum_{k=1}^{n} \left(\Pi_k \cdot \prod_{i=1}^{k-1} \left(1 - \Pi_i\right) \right) \end{aligned} \tag{5}$$

where Π_k denotes the probability of *LS* first-excursion due to the occurrence of the kth event given that the limit state has not exceeded in the previous (k-1) events and $\mathbf{I}_1$. For the sake of brevity, the conditioning information that the limit state first-excursion did not take place in the previous events together with $\mathbf{I}_1$ is expressed hereafter as $\mathbf{I}_2$. The probability term Π_k in Eq. (5) can further be expanded with respect to the ground motion intensity measure *IM*, as follows (see also [9]):

$$\Pi_k = \int_{\text{all}\,x} P\left(C_k \mid x, \mathbf{I}_2\right) p\left(x \mid \mathbf{I}_2\right) \mathrm{d}x = \int_{\text{all}\,x} \pi_k\left(x\right) \left[\frac{1}{\nu} \cdot \left| \frac{\mathrm{d}\lambda_{IM}\left(x\right)}{\mathrm{d}x} \right| \right] \mathrm{d}x = \frac{1}{\nu} \int_{\text{all}\,x} \pi_k\left(x\right) \left| \mathrm{d}\lambda_{IM}\left(x\right) \right| \tag{6}$$

where x specifies *IM* associated with the kth event; $\pi_k(x)$ is called *event-dependent* fragility for the kth event given $\mathbf{I}_2$ [9]. The set of event-dependent fragilities $\{\pi_n(x)|n=1{:}N_{ce}\}$ is estimated through a non-linear dynamic analysis procedure named *Sequential Cloud Analysis* which is discussed in Appendix of this paper. The probability $p(x|\mathbf{I}_2)$ is the likelihood of *IM* at x corresponding to the kth event (among the information within $\mathbf{I}_2$, the conditioning that the previous (k-1) events have not led to the exceedance of the limit state *LS* is ignored as it is already seen in calculating π_k); $p(x|\mathbf{I}_2)$ can be derived directly from the site-specific seismic hazard in terms of the mean annual rate of exceeding x, i.e. $\lambda_{IM}(x)$, as shown in Eq. (6) where $\mathrm{d}\lambda_{IM}(x)/\mathrm{d}x$ is the slope of the seismic hazard curve. In general, Π_k is solved using numerical integration by computing the product of the event-dependent fragility and the differential of the seismic hazard curve at discrete values x, adding the results from all x, and then multiplying by $1/\nu$.

Although $P(LS|\mathbf{I}_1)$ is estimated within the time-interval $[0,t]$, the first-excursion probability in the time interval $[0,t+\Delta t]$ denoted as $P(LS|t+\Delta t,\mathbf{I}_1)$ where Δt is a time increment, can be expressed as:

$$P\left(LS \mid t+\Delta t, \mathbf{I}_1\right) = P\left(LS \mid \mathbf{I}_1\right) + P\left(LS \mid [t, t+\Delta t], \mathbf{I}_1\right) \tag{7}$$

where the second term in Eq. (7) denotes the time-dependent limit state first-excursion probability in the time interval $[t, t+\Delta t]$, and equals [8]:

$$P\left(LS \mid [t, t+\Delta t], \mathbf{I}_1\right) = P\left(LS \mid t+\Delta t, \mathbf{I}_1\right) - P\left(LS \mid \mathbf{I}_1\right) \tag{8}$$

Thus, by setting Δt=1 year, the limit state first-excursion probability in one-year time interval $[t, t+1]$ can be attained.

2.3 A Closed-form Approximation to Time-dependent Limit State Probability

The term $P(LS|\mathbf{I}_1)$ in Eq. (1) is approximated with a closed-form analytic expression based on the methodology preliminary proposed in [10]. Assume that the set of probability terms $\{\Pi_k | k=1{:}n\}$ introduced in Eq. (5) is identical and equal to the time- and event-invariant function Π. Thus, $P(LS|n,\mathbf{I}_1)$ in Eq. (5) can be regarded as the sum of a geometric series:

$$P\left(LS \mid n, \mathbf{I}_1\right) = \Pi \cdot \sum_{k=1}^{n} \left(1-\Pi\right)^{k-1} = \Pi \cdot \frac{1-\left(1-\Pi\right)^{n}}{1-\left(1-\Pi\right)} = 1-\left(1-\Pi\right)^{n} \tag{9}$$

Substituting $P(LS|n,\mathbf{I}_1)$ from Eq. (9) and $P(n|\mathbf{I}_1)$ from Eq. (2) into $P(LS|\mathbf{I}_1)$ in Eq. (1), we have:

$$\begin{aligned} P\left(LS \mid \mathbf{I}_1\right) &= \sum_{n=1}^{N_{ce}} \left(1-\left(1-\Pi\right)^{n}\right) \cdot \frac{\left(\nu t\right)^{n} e^{-\nu t}}{n!} \\ &= \sum_{n=1}^{N_{ce}} \frac{\left(\nu t\right)^{n} e^{-\nu t}}{n!} - \sum_{n=1}^{N_{ce}} \left(1-\Pi\right)^{n} \cdot \frac{\left(\nu t\right)^{n} e^{-\nu t}}{n!} \end{aligned} \tag{10}$$

The first term in Eq. (10) equals the sum of the Poisson Probability Mass Function (PMF) terms starting from n=1. Knowing that the sum of the Poisson PMS terms starting from n=0 is equal to unity, the first term in Eq. (10) equals 1-exp(νt). Subsequently, Eq. (10) can be further simplified as follows:

$$\begin{aligned} P\left(LS \mid \mathbf{I}_1\right) &= \left(1-e^{-\nu t}\right) - e^{-\Pi \nu t} \sum_{n=1}^{N_{ce}} \frac{\left(\left(1-\Pi\right) \cdot \nu t\right)^{n} e^{-(1-\Pi)\nu t}}{n!} \\ &= \left(1-e^{-\nu t}\right) - e^{-\Pi \nu t}\left(1-e^{-(1-\Pi)\nu t}\right) \end{aligned} \tag{11}$$

As a result, the closed-form approximation to the time-dependent limit state probability $P(LS|\mathbf{I}_1)$ in Eq. (11) is derived as:

$$P\left(LS \mid \mathbf{I}_1\right) = 1-\exp\left(-\Pi \nu t\right) \tag{12}$$

The closed-form expression in Eq. (12) serves as a simple analytic equation for calculating the time-dependent *LS* first-excursion probability due a sequence of events. There are different proposals that can be drawn for Π, which can be defined based on the alternative decisions for the repair of the bridge system, as will be discussed in the next section.

Nevertheless, it is interesting to note that with reference to Eq. (6), k=1 denotes the occurrence of one event, where π_1 can be interpreted as the structural fragility for the intact bridge, and the limit state exceedance can be described by a homogenous Poisson process with rate λ_{LS}. Thus,

$$\Pi_1 = \frac{1}{\nu} \int_{\text{all}\,x} \pi_1(x) \left| \mathrm{d}\lambda_{IM}(x) \right| = \frac{\lambda_{LS}}{\nu} \tag{13}$$

In case of using $\Pi=\Pi_1$, the exceedance probability in Eq. (12) can be further expressed as:

$$P(LS \mid \mathbf{I}_1) = 1 - \exp(-\lambda_{LS} t) \tag{14}$$

which is respectively the standard and well-known equation of the probability of occurrence of at least one event in a period of time $[0,t]$, considering the fact that the occurrence of events are described by a homogenous Poisson process. In this method, it is assumed that the bridge is going to be repaired immediately after the occurrence of a major seismic event with a repair time, τ, that is assumed to be equal to zero. Thus, the limit state first-excursion becomes a Poisson process. As a convention for the rest of current paper, the calculation of time-dependent limit-state probability by employing Eq. (14) is addressed as "*Standard method*", and is denoted as $P(LS|\tau=0,\mathbf{I}_1)$.

In a research study conducted recently by the authors [10], the closed-form analytical expression was utilized for calculating the post-mainshock limit state probability. It was investigated the even using the fragility of intact structure in Eq. (12) leads to a very good agreement with the computationally extensive and time-consuming exact solution for limit state probability (as described in Section 2.2 by using the sequence of event-dependent fragilities). Therefore, in this study, the fragility of the intact bridge infrastructure, π_1, is used without emphasizing to provide any further comparison with the exact solution introduced in Section 2.2.

2.4 How does the decision for repair affect the probabilistic time-dependent risk formulation?

According to the assumptions previously made in Section 2.1, the objective here is to take into account the repairing decision (addressed in this paper as **R** *decision*) with a predefined repair time $\tau\neq0$. Accordingly, the time-dependent limit state probability by this approach is denoted herein as $P(LS|\tau,\mathbf{I}_1)$. Hence, the limit-state first excursion is not a Poisson process and depends on the history of events taken place. This decision is taken into account while estimating the set of probability terms $\{\Pi_n|n=1{:}N_{ce}\}$. For the Repair (**R**) decision, the set of probability terms $\{\Pi_{n,\mathbf{R}}|n=1{:}N_{ce}\}$ should further break down into the sum of two MECE events considering the fact that event n hits the intact (not damaged) bridge (denoted by D_0) or the damaged bridge (defined by D), as follows:

$$\Pi_{n,\mathbf{R}} = P(C_n, D_0 \mid \mathbf{I}_2) + P(C_n, D \mid \mathbf{I}_2) \tag{15}$$

As noted previously, $\mathbf{I}_2$ comprises the background information $\mathbf{I}_1$ and the information that the previous (n-1) events have not led to the first-excursion of the limit state *LS*. Eq. (15) expands as:

$$\Pi_{n,\mathbf{R}} = P(C_n \mid D_0, \mathbf{I}_2)\, p(D_0 \mid \mathbf{I}_2) + \sum_{j=1}^{n-1} P(C_n \mid D_j, \mathbf{I}_2)\, p(D_j \mid \mathbf{I}_2) \tag{16}$$

where $P(C_n|D_0,\mathbf{I}_2)$ is the conditional probability of *LS* first-excursion due to the occurrence of the nth event given that the bridge is repaired (back to its intact state) right before the last nth event takes place. As a result, this probability term equals Π_1 associated with the intact bridge infrastructure. Accordingly, $p(D_0|\mathbf{I}_2)$ is the probability that the bridge is repaired before occurrence of the nth event, which reveals that the inter-arrival time (IAT) between the last subse-

quent events, i.e. nth and (n-1)th events, is greater than the repair time τ associated with the limit state LS. Thus, $p(D_0|\mathbf{I}_2)$ is the probability that IAT> τ which can be expressed as an Exponential distribution equal to exp(-$\nu\tau$). Consistently, $P(C_n|D_j,\mathbf{I}_2)$ can be interpreted as the LS first-excursion due to the nth event given that the damaged bridge is already subjected to j=1:n-1 seismic events while it have been under repair (the information extracted from $\mathbf{I}_2$ is that the previous j events have not led to the first-excursion of limit state LS). Hence, this probability term is identical to Π_{j+1}. In addition, $p(D_j|\mathbf{I}_2)$ is the probability of experiencing exactly j events (before the last nth event take place) while the bridge is being under repair (i.e., for all of the preceding j events, IAT< τ and the bridge became intact before jth event); hence, there are j independent and exponentially distributed probabilities that the IAT<τ, each can be expressed as 1-exp(-$\nu\tau$) in addition to the probability exp(-$\nu\tau$). As a result, Eq. (16) can be re-written as:

$$\Pi_{n,\mathbf{R}} = \Pi_1 e^{-\nu\tau} + \sum_{j=1}^{n-1} \Pi_{j+1}\, e^{-\nu\tau}\left(1-e^{-\nu\tau}\right)^j \tag{17}$$

With reference to Eq. (17), Π_1 is calculated from Eq. (13), while Π_{j+1} should be estimated from Eq. (6) using the event-dependent fragility π_{j+1}. However, in case of directly using the closed-form expression proposed in Eq. (12) for time-dependent limit state probability, proper assignment should be given to Π. In this case, one can set Π_{j+1}=Π_1, and directly calculate $\Pi_{2,\mathrm{R}}$ to be used as Π. Nevertheless, it would be much more convenient if one uses the so-called damaged bridge (i.e. Π_2) and assign it to all Π_{j+1}, and then set Π=$\Pi_{2,\mathrm{R}}$ in Eq. (12). The time-dependent limit-state probability by considering the repair, **R**, decision is called herein as "**R** *decision*".

2.5 Expected Life-Cycle Cost

The expected life-cycle cost given the information $\mathbf{I}_1$ can be expressed as [1]:

$$\mathbb{E}[C \mid \mathbf{I}_2] = C_0 + C_\mathrm{R} + C_\mathrm{M} \tag{18}$$

where C_0 is the initial construction or upgrade installation cost, C_R is the repair or replacement costs taking into account also the loss of revenue due to downtime, and C_M is the annual maintenance costs. The repair cost C_R can be calculated from the following equation:

$$\begin{aligned} C_\mathrm{R} &= \sum_t \sum_{ls=1}^{N_{LS}} LSC_{ls} \cdot e^{-\lambda_\mathrm{d} t}\left[P\left(LS_{ls} \mid [t,t+1],\mathbf{I}_1\right) - P\left(LS_{ls+1} \mid [t,t+1],\mathbf{I}_1\right)\right] \\ &= \sum_t \sum_{ls=1}^{N_{LS}} LSC_{ls} \cdot e^{-\lambda_\mathrm{d} t} \cdot \Delta P\left(LS_{ls} \mid [t,t+1],\mathbf{I}_1\right) \end{aligned} \tag{19}$$

where N_{LS} is the number of desired limit states ordered from the service up to the collapse, and ls, where ls=1:N_{LS}, accounts for the limit state under consideration; LSC_{ls} is the expected cost of restoring the bridge infrastructure from the lsth limit state LS_{ls} back to its intact state including eventual loss of revenue caused by interruption for repair operations; λ_d is the annual discount rate and exp(-$\lambda_\mathrm{d}t$) denotes the change in the monetary-based evaluations per time; $P(LS_{ls}|[t,t+1],\mathbf{I}_1)$ derived from Eq. (8) is the time-dependent first-excursion probability of limit state LS_{ls} in one-year for the time-interval [t,t+1]. The term $\Delta P(LS_{ls}|[t,t+1],\mathbf{I}_1)$ denotes the annual probability in the time interval [t,t+1] that the infrastructure is between the two subsequent limit states ls and ls+1; needless to say that for the collapse limit state (i.e., the last limit

state $ls=N_{LS}$), this probability differential ΔP becomes $P(LS_{N_{LS}}|[t,t+1],\mathbf{I}_1)$. It is also noteworthy that t starts from one as the relationship in Eq. (8) is meaningful for t_{life} starting from one.

The cost of maintenance C_M can be estimated as:

$$C_M = \int_0^{t_{life}} C_m e^{-\lambda_d t} dt = \frac{C_m}{\lambda_d}[1 - e^{-\lambda_d t_{life}}] \tag{20}$$

where C_m is the (constant) annual maintenance cost.

3 NUMERICAL EXAMPLE

The methodology described in Section 2 is applied to screening of alternative retrofit options associated with an existing bridge infrastructure in order to find the most suitable retrofit solution according to life cycle cost and reliability criteria.

3.1 Bridge Infrastructure Description

The case-study bridge examined in this study is a RC bridge built in the 1970s and located in the Campania Region, south Italy. It consists of six simply supported decks having independent spans of 41.00 meters, as illustrated in Fig. 1. It is worth mentioning that the bridge is representative of the Italian bridge inventory considering the fact that approximately 90% of the Italian highway bridges are represented by multi-span simply supported deck bridges (either with independent spans or with continuous cast in situ top slab above the piers) (see [12,13]).

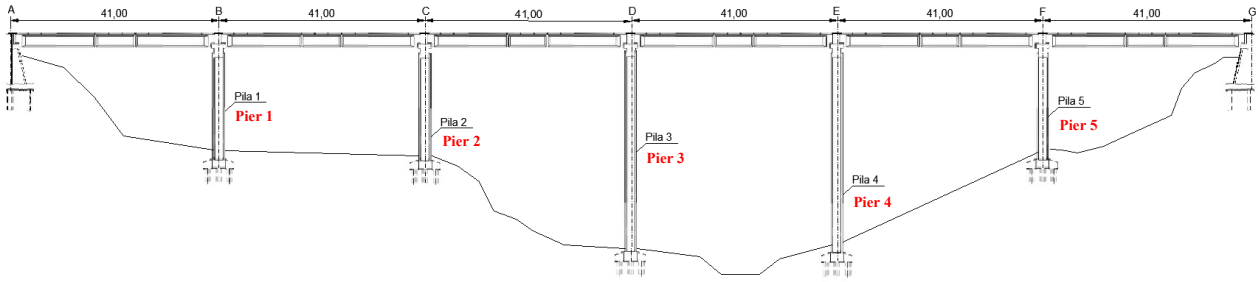


Figure 1: The longitudinal profile of the case-study bridge

The decks are supported by five pairs of box-type piers which are classified into two different types of cross section as shown in Fig. 2: the central piers (numbered as 3 and 4 in Fig. 1) which are approximately 40 m high, and the remaining tree piers defined with numbers 1, 2 and 5 in Fig. 1, with a height of around 20 m.

The simply-supported deck, whose cross section is illustrated in Fig. 3, consists of eight longitudinal beams with an upper cast-in-place slab of thickness 20 cm. The decks are supported on the cap-beams by means of elastomeric (neoprene) bearing supports. The abutments are seat-type, with neoprene bearing pads.

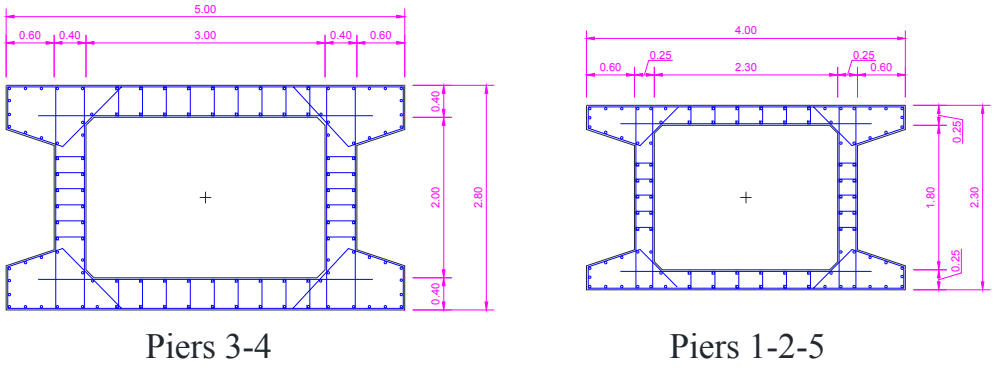


Figure 2: The cross section of piers

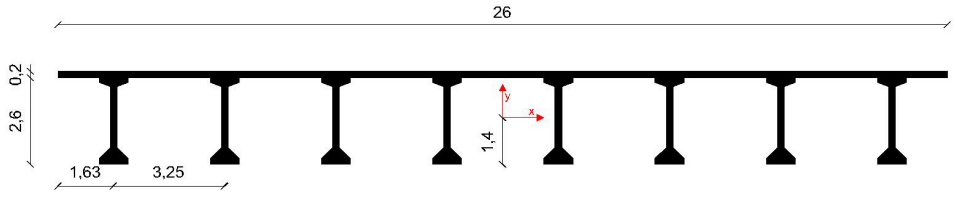


Figure 3: The cross section of simply-supported decks (dimensions are in meters)

3.2 Development of Bridge Model

The three-dimensional (3D) model of the bridge was created in the nonlinear finite element analytical program OpenSees [14], which provides an adequate element and material library for earthquake engineering applications. Illustrative descriptions of the nodal and element designations and boundary conditions corresponding to the spine-line model for the case-study bridge, with line elements located at the centroids of the cross-sections, are shown in Fig. 4. This figure serves as a representative model for a typical double pier and the deck above it as well as the abutment in both longitudinal and transverse directions, which is used as the OpenSees simulation model. The global directions are shown on this figure

In this figure, nodes are shown with hollow black circles. Individual components are included in this figure: (1) pair of piers considered as nonlinear components, (2) deck considered as a linear elastic component, (3) cap-beam shown as rigid element (RE), (4) bearing device defined with zero-length (denoted as *zeroLength*) elements, and (5) the seat-type abutment where the deck beam is seated on the abutment bearing pad defined with *zeroLength* element. It is noteworthy that the connection of the column bent to the pile cap is considered to be rigid for the case-study herein; hence, no pile-soil-structure interaction is taken into account. In addition, many features in the modeling of abutments and its interaction with the soil are neglected herein for simplicity. Important assumptions and main aspects of the modeling process of each individual component are described in the following subsections.

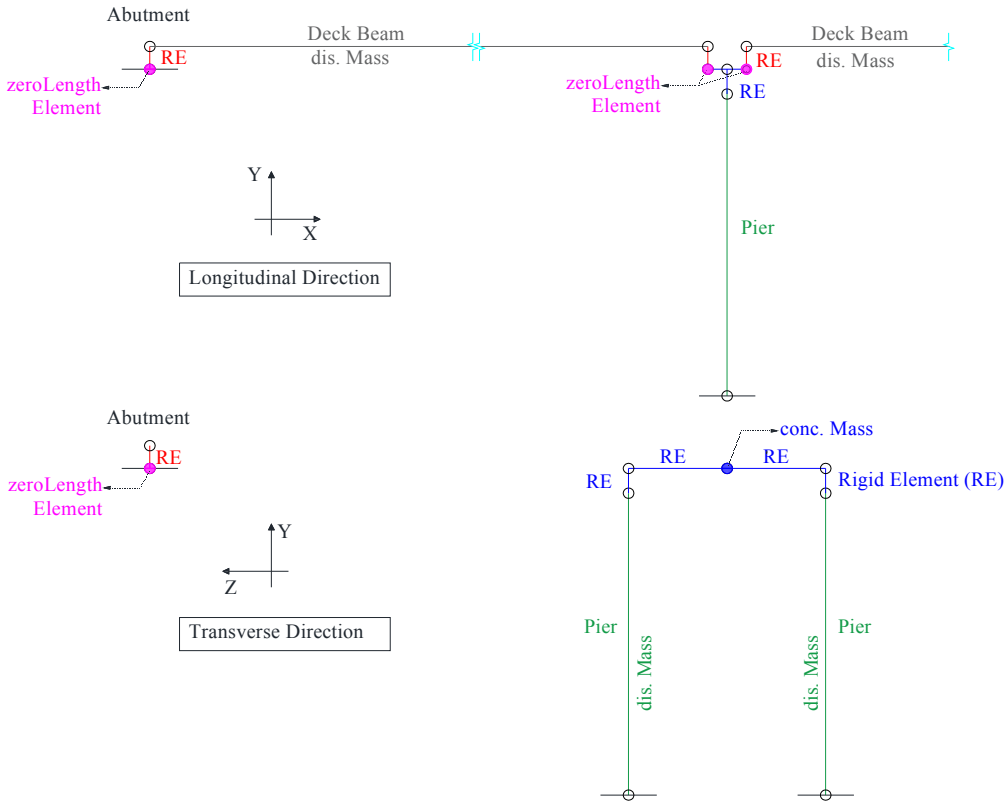


Figure 4: The cross section of simply-supported decks (dimensions are in meters)

3.2.1. Modeling of Deck

Simply-supported Decks are modeled using elastic beam-column elements, since flexural yielding of the deck during seismic response is not expected to take place. Although cracked section properties can obtain realistic values for the infrastructure's period and the seismic demands generated from the analyses, the effective moment of inertia of the deck beams, denoted as I_{eff} is set to that of the gross section (I_g). Needless to say that since all elements are modeled in the centerline of the bridge components (as mentioned earlier), it is required to consider the distance between the centroid of the deck-beam's cross-section (see Fig. 3) and the cap-beam's top. Instead of assigning a rigid joint offset to the deck beams, rigid beam elements (red RE elements in Fig. 4) are modeled which connect the deck beam to the bearing devices on the top of cap-beams. The material properties of deck members are defined subsequently.

3.2.2. Modeling of Cap-beam

A rigid beam element is used to represent the cap-beam, as shown by horizontal blue RE elements in Fig. 4. The cap-beam is connected by the elastomeric bearing supports to the superstructure.

3.2.3. Modeling of Piers

The main source of nonlinearity in this bridge model is reflected in its piers, where the evolution of column yielding and damage are expected under strong ground motions. Hence,

nonlinear force-based beam-column elements are used to represent the nonlinear behavior of piers in Opensees [14]. It is worth mentioning that in the distributed plasticity integration methods for force-based beam-column formulation (e.g. Gauss–Lobatto integration), it is not possible to represent both the spread of plasticity under hardening and member and section response under softening. Therefore, a new plastic hinge integration method based on modified two-point Gauss-Radau quadrature has been implemented which has the capability to overcome the difficulties that arise with Gauss–Lobatto integration for strain-softening behavior in force-based beam-column finite elements (for more details, see [15]).

Accordingly, the nonlinearity is assigned to both end of the piers within the plastic-hinge length and the interior portion of the beam-columns remains elastic. The analytical length of the plastic hinge in the piers is taken herein as the median of the equations suggested in [16], [17], and [18] respectively:

$$L_{\mathrm{p}} = 0.1L_{\mathrm{V}} + 0.17h + 0.24\frac{d_{\mathrm{bL}} f_y(\mathrm{MPa})}{\sqrt{f_c}(\mathrm{MPa})} \tag{21}$$

$$L_{\mathrm{p}} = 0.10L + 0.015 d_{\mathrm{bL}} f_y(\mathrm{MPa}) \cong 0.10L \tag{22}$$

$$L_{\mathrm{p}} = 0.08L + 0.022 d_{\mathrm{bL}} f_y(\mathrm{MPa}) \geq 0.044 d_{\mathrm{bL}} f_y \tag{23}$$

where L_{V} is the shear span (which is equal to the pier height L in longitudinal direction), h is the depth of the cross section, d_{bL} is the diameter of tension reinforcement, f_c is the concrete compressive strength (MPa), and f_y is the estimated mean value of steel yield strength (MPa) (see Section 3.2.5 for the material properties).

Fiber sections are assigned to the two pier sections (see Fig. 2) with two constitutive rules used simultaneously within a cross-section: (1) unconfined concrete, and (2) steel rebar. The concrete and reinforcing steel material properties are defined subsequently. In order to model the portion of the piers that are embedded in the cap-beam, a vertical blue RE elements are defined in the bridge model which connect pier's top to the centroid of the cap-beam (see Fig. 4). It should further be noted that the effect of bar-slip is not considered within the nonlinear modeling of bridge piers in this study. Slip of a pier's reinforcing bars in the base will cause rigid-body rotation of the pier, which cannot be accounted for in a flexural fiber analysis, where the column ends are assumed to be fixed.

3.2.4. Modeling of Abutments

A detailed description of abutment modeling with appropriate references can be found in [19]. In addition to the resistance of distributed bearing pads in both horizontal as well as vertical directions, there are important issues that should be considered in a comprehensive modeling of abutment. In the longitudinal direction of the bridge, the longitudinal stiffness of the zero-length element shown in Fig. 4 should also accounts for the gap between the deck and the abutment backwall as well as the active soil pressure behind the abutment backwall. Similarly, the transverse stiffness of the zero-length element should take into account the shear strength of the backfill soil behind the abutment backwall. In the vertical direction, in addition to the neoprene bearing pad stiffness in vertical direction, the abutment embankment stiffness should also be taken into account. All the assigned nonlinear zero-length elements should work only in compression.

Nevertheless, herein, a very simple abutment modelling is used, where the stiffness assigned to zero-length elements in three directions represents the stiffness of the neoprene bearing pads. The zero-length elements can work in tension and compression simultaneously;

this assumption can introduce a horizontal instability in the model when all the piers' chord rotations go beyond the rotational capacity associated with the maximum strength of piers.

3.2.5. Material Properties

For the reinforced concrete piers, the *Concrete04 UniaxialMaterial* of the OpenSees [14] material library is used in the modeling process which has the capability to consider the concrete model proposed by [20]. The following parameters were employed: unconfined concrete compressive strength f_c=20 MPa, the strain at maximum concrete stress ε_{c0}=0.002, the ultimate unconfined concrete strain ε_{c0}=0.005, and the concrete modulus of elasticity defined as follows:

$$E_C = 0.043 \cdot w^{1.5} \cdot \sqrt{f_c}\,(\text{MPa}) \cong 4700 \cdot \sqrt{f_c} = 21019\,\text{MPa} \tag{24}$$

where w is the unit weight of concrete. It is noteworthy that no tensile strength is considered for the concrete material. In addition, it is also recommended to assign unconfined and confined concrete material to the concrete cover and core of the pier section, respectively; nevertheless, this study assume an unconfined concrete material, as defined previously, for the whole pier section.

For the reinforcing steel material, a uniaxial Giuffre-Menegotto-Pinto steel material object with isotropic strain hardening, called *Steel02*, is used from OpenSees [14] material library. The advantage of this steel material is mainly the smooth translation of backbone curve from elastic range to plastic range, which leads to fewer convergence problems. For this purpose, the steel modulus of elasticity and the mean value of steel yield strength were set as E_s=200000 MPa and f_y=310 MPa, respectively. A strain-hardening ratio (ratio between post-yield tangent and initial elastic tangent) equal to 0.01 is considered.

3.2.6. Assignment of Masses and Damping

In order to achieve an accurate distribution of mass along the length of the bridge deck, a distributed mass is assigned to the elastic beam-column element of the deck beam which has the capability to construct a consistent mass matrix for these elements. In addition, a distributed mass along the height is also considered for the piers (see Fig. 4 for the assigned distributed masses). The mass of the cap-beam (i.e., those portions that are RE in Fig. 4) are concentrated at the mid-node of the cap-beam, as shown in Fig. 4.

Rayleigh damping is employed with a ξ=5% of critical damping coefficient in the first two modes of vibration (see [19, 21]). The classical damping matrix is a linear combination of the mass and stiffness matrices with the coefficients α_M and α_K, respectively [22]:

$$\alpha_M = 2\xi \frac{\omega_1 \cdot \omega_2}{\omega_1 + \omega_2},\ \alpha_K = 2\xi \frac{1}{\omega_1 + \omega_2} \tag{25}$$

where ω_1 and ω_2 are the frequencies associated with the first and second modes, respectively.

3.2.7. Shear Deformation in Pier Sections

In order to account for the shear deformation in piers due to shear force and torsional bending, section aggregator in OpenSees is used. To aggregate the shear deformation in the fiber section analysis of the piers, three elastic uniaxial materials are defined:

1. Two elastic materials with elastic shear stiffness equal to $G_C \times A_{vy}$ and $G_C \times A_{vz}$, which account for the shear deformation in two (local) perpendicular directions of the pier section y and z. G_C is the shear modulus of concrete; A_{vy} and A_{vz} are the effective shear area of the box-type piers which are less that the gross area of the pier, A_g.

2. One elastic material that accounts for the torsional deformation in the fiber section of the pier with the elastic torsional stiffness $0.20 \times G_C \times J_g$ where J_g is the polar moment of inertia of the cross-section of the pier. The reduction factor of 0.20 is used due to cracking of the pier cross-section [21].

It is to note that the shear deformation is calculated by assigning an elastic material. The use of more sophisticated models that account for nonlinear shear deformation is a plan for near future developments.

3.3 Alternative Retrofit Strategies

Five alternative schemes are adopted for rehabilitation of the case-study bridge infrastructure herein. They aim at improving the global behavior of bridge deck by using friction pendulum isolators and/or force the deck to have a uniform displacement along the longitudinal direction (see Table 1). More details about different retrofit options can be found in [23, 24]. The first-mode period, T_1, of the original (as-built) model of the bridge considering also the p-delta effect due to gravity loads is 2.46 sec. The first-more period of alternative retrofit options are outlined in Table 1.

Retrofit option	Description	Implementation in OpenSees (see Fig. 4)
ROD	The simply-supported decks are connected with chains	Impose the same longitudinal displacement to the adjacent nodes of the deck beams in both sides of the pier, T_1 = 1.99 sec
FP-R25	Friction Pendulum isolator with effective radius of concave sliding surface equal to 2.5 m and a Coulomb friction of 2%	Using Single Friction Pendulum Bearing Element together with a Coulomb friction model, T_1 = 3.20 sec
FP-R25-ROD	The combination of ROD and FP-R25	T_1 = 2.84 sec
FP-R31	Friction Pendulum isolator with effective radius of concave sliding surface equal to 3.1 m and a Coulomb friction of 5%	T_1 = 3.47 sec
FP-R31-ROD	The combination of ROD and FP-R31	T_1 = 3.15 sec

Table 1: Alternative retrofit strategies.

3.4 Definition of Limit States

In order to be consistent with recent studies on bridge infrastructures in Italy (see [12, 25]), two limit states (*LS*) or performance levels are considered: *damage* Limit State and *collapse* Limit State. The time-dependent limit state probabilities are evaluated based on both limit states. Each *LS* is associated with states of damage as summarized in Table 2.

According to this Table, *Damage LS* (denoted as DS) defines the condition of having limited structural damages in which it would be prudent to implement structural repairs. This may require traffic interruptions or the installation of temporary bracing systems. For this LS, the only DS that is considered is the pier yielding associated with ductility equal to one. Two important DSs that are not considered in this study are as follows: the bearings' failure when

the displacement exceeds the displacement capacity of the bearing device (it leads to the simple fall of the deck from the bearing seat); attainment of the active resistance of abutments (pulling action).

The *Collapse* LS takes into account the condition in which the extensive damages to bridge retain no margin against collapse. This implies that significant degradation has occurred in the stiffness and strength of the piers, and/or large displacements take place which might cause unseating of the decks. The infrastructure may be technically repairable, but costs could be very high and the closure of the bridge for long time is inevitable. The DSs considered for this limit state are: (1) pier collapse due to the attainment of its ultimate ductility or shear strength, (2) unseating of the deck due to the full loss of support from the cap-beam. It is to note that attainment of the passive resistance of abutments (pushing action) is also an important DS which is not taken into account in current study.

Limit Sate (LS)	State of Damage (SD)	Description
Damage (DS)	Pier flexural yielding	Pier chord rotation exceeds pier chord rotation at yielding, $\theta \geq \theta_y$
Collapse (CS)	Pier flexural capacity	Pier chord rotation exceeds pier chord rotation at collapse, $\theta \geq \theta_u$
	Pier shear capacity	Pier shear force exceeds pier shear resistance, $V \geq V_R(\theta)$
	Unseating of the deck	Deck displacement in the longitudinal direction is greater than the seat length

Table 2: Definition of Limit States.

According to Table 2, the allowable unseating length of the case=study bridge with reference to its original drawings is set to 60 cm. Moreover, Table 2 outlines the two thresholds considered for chord rotation of piers, namely θ_y and θ_u. These values are obtained directly from pushover analysis of single piers (i.e., base shear versus chord rotation) after applying the associated axial force due to gravity loads on each pier. Fig. 5 illustrates the actual pushover curves associated with two types of piers (i.e. piers 1-2-5 and piers 3-4, as shown in Fig. 2) in longitudinal (global X) direction. The onset of damage and collapse limit states are marked on the pushover curves in terms of the chord rotation. It is noteworthy that θ_y is marked by visual inspection on the pushover curve trend, while θ_u threshold is set to 20% drop in ultimate strength of the piers as denoted in [26].

The shear strength, V_R, is calculated by the provisions of [16] (see also [27]), that is commonly suggested for the assessment of existing buildings under cyclic loads. The shear strength is obtained from the following equation:

$$V_R = \frac{1}{\gamma_{\text{el}}}\left(V_N + V_C + V_W\right) \tag{26}$$

where

$$V_N = \frac{h-x}{2L_{\text{V}}} \cdot \min\left(N, 0.55 A_c \frac{f_c}{\gamma_c}\right) \tag{27}$$

$$V_C = \left[1 - 0.05\min\left(5, \mu_\Delta^{\text{pl}}\right)\right] \cdot \left[0.16\max\left(0.5, 100\rho_{\text{tot}}\right) \cdot \left(1 - 0.16\min\left(5, \frac{L_V}{h}\right)\right) \cdot \sqrt{\frac{f_c}{\gamma_c}} A_c\right] \quad (28)$$

$$V_W = \left[1 - 0.05\min\left(5, \mu_\Delta^{\text{pl}}\right)\right] \cdot \rho_w \cdot \frac{f_y}{\gamma_s} \cdot b_w \cdot z \quad (29)$$

where γ_{el}=1.15; x is the depth of the neutral axis at yielding; N is the is axial load; A_c is the area of the section; γ_c=1.50 is the partial safety factor of concrete; μ_Δ^{pl} is the plastic ductility factor which is equal to θ/θ_y-1; ρ_{tot} is the total longitudinal reinforcement ratio; ρ_w is the transverse reinforcement ratio; γ_s=1.15 is the partial safety factor of reinforcing steel; bw is the section width; z is the internal lever arm. In this study, A_c=$b_w \cdot d$ for the box-type section of the piers with the effective thickness b_w equal to two times the web thickness in the direction of loading, and d equal to the effective depth of the section.

The estimated values of the shear strength at the base of the two types of piers as a function of θ are also shown in Fig. 5 for the sake of comparison. It can be depicted that the shear strength is more critical in case of short piers (piers 1-2-5).

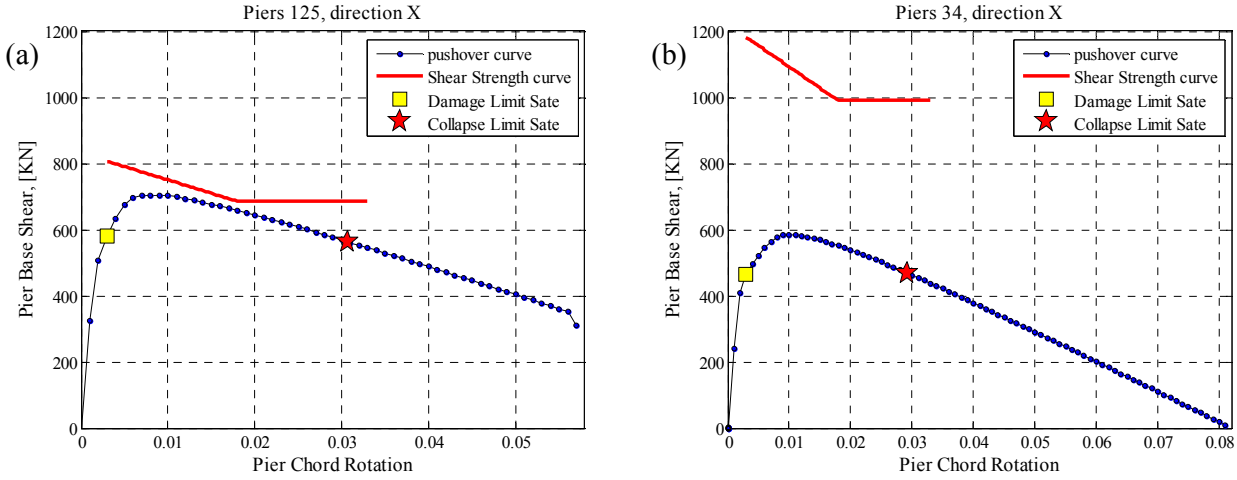


Figure 5: The pushover curve with the onset of both limit states associated with chord rotation marked on it, together with shear strength curve of the bridge piers (a) pier type 1-2-5, (b) pier type 3-4

3.5 Calculation of the structural performance variable Y_{LS}

The structural performance variable Y_{LS}, which is comprehensively defined in the Appendix of this paper as a time and history dependent performance variable, is generally the critical demand to capacity ratio. It is primarily introduced in [28], and further utilized in [9, 29]. It is recently used as a proper decision variable for assessing the existing bridge infrastructures in Italy [25, 30]. Since there are various SD's for a given limit state, Y_{LS} is capable of finding the critical situation while relating the structural behaviour at the component level to its global performance. For the case-study bridge system, a simple scheme of finding the weakest failure mode leads us directly to the global failure. Accordingly, for each limit state LS, Y_{LS} is obtained as:

$$Y_{LS} = \max_i^{N_{\text{SD}}} \max_j^{N_{\text{ele}}} \left(Y_{LS,ji}\right) \quad (30)$$

where N_{SD} is the states of damage for the considered LS, N_{ele} is the number of components taking part in the ith SD, and $Y_{LS,ji}$ is the value of Y_{LS} for the jth component of ith SD. Accordingly, in case of damage limit state, N_{SD}=1 and j=1:6 (as there exists 6 piers). Consequently, for the collapse limit state, N_{SD}=3 (i.e. i=1:3), where i=1:2, j=1:6 correspond to the pier flexural and shear capacities; nevertheless, i=3 denotes the SD corresponding to unseating of the deck with j=1:12 since the displacements at start and end nodes of the 6 simply-supported deck beams should be simultaneously monitored (see Fig. 1).

3.6 Selected Suite of Ground-motion Records

For performing the cloud analysis, a set of 25 European (especially Italian) strong ground motion records are selected from the NGA-West2 database [31], and listed in Table 3. This suite of selected records covers a wide range of magnitudes from 5.50 up to 7.51, and closest distance to ruptured area (R_{RUP}) up to 16 km, as illustrated in Fig. 6(a). This set of ground motions is chosen without emphasizing on detailed record selection which is not a primary focus in this study. The main concern, herein, is to provide a proper cloud response that cover the range of Y_{LS} from lower values to values higher than 1.

The associated spectral shapes are shown in Fig. 6(b). With reference to Table 3, nine records out of 25 are identified as pulse-like based on the algorithm proposed in [32], which can acquire pulses at arbitrary orientations in multi-component ground motions. The outlined pulse periods in Table 3 are obtained from the extracted pulses in the direction of the strongest observed pulse. It is to note that pulses are often found in other orientations due to complex geometry of a real fault; thus, the velocity pulse can be present in orientations other than the computed fault-normal orientation. The spectral accelerations of the nine pulse-like records are shown in Fig. 6(b) with bold lines. In order to draw a point of comparison, the uniform hazard spectra (UHS) for two hazard levels of 10% and 5% exceedance in 50 years are also illustrated on Fig. 6(b). It reveals the appropriateness of the selected set of records which provides a good variability around the UHS (although selecting spectrum compatible records has not been an objective herein).

3.7 Seismicity of the Site

The bridge's site with the coordinate [41.0264N, 14.795E] is located in the Campania region in the boundary of seismic zones 927 and 928, based on the Italian Seismogenic Zonation (ZS9) [33]. Fig. 7(a) shows the seismogenic zonation ZS9 with different zones identified on it; it can be seen that the desired sire is surrounded by the seismic zones 923, 924, 925, 926, 927 and 928, separately indicated in Fig. 7(b). The key seismicity parameters of each zone are outlined in Table 4.

Based on the seismicity data of each zone, a simplified site-specific probabilistic seismic hazard analysis (PSHA) is performed on the bridge site using the MATHAZARD [34]. The Sabetta and Pugliese 1996 attenuation relation [35] is chosen because of its wide use in Italy, and consistency with the INGV hazard maps (Istituto Nazionale di Geofisica e Vulcanologia, Progetto INGV-DPC S1, http://esse1.mi.ingv.it).

NGA Record Number	Earthquake Name	Station Name	Horizontal Component	Magnitude	Closest distance to the ruptured area, R_{RUP} (km)	Fault mecha-nism	NEHRP Site Classification	Lowest Usable Frequency (Hz)	Strongest Pulse Period (sec)
125	Friuli, Italy-01	Tolmezzo	2	6.5	15.82	Reverse	C	0.1625	
126	Gazli, USSR	Karakyr	1	6.8	5.46	Reverse	D	0.1625	
132	Friuli, Italy-02	Forgaria Cornino	2	5.91	14.75	Reverse	C	0.1875	
139	Tabas, Iran	Dayhook	2	7.35	13.94	Reverse	C	0.25	
143	Tabas, Iran	Tabas	2	7.35	2.05	Reverse	B	0.1	6.19
156	Norcia, Italy	Cascia	2	5.9	4.64	Normal	C	0.25	
285	Irpinia, Italy-01	Bagnoli Irpinio	2	6.9	8.18	Normal	C	0.1125	1.71
292	Irpinia, Italy-01	Sturno (STN)	2	6.9	10.84	Normal	C	0.1125	3.27
300	Irpinia, Italy-02	Calitri	2	6.2	8.83	Normal	C	0.1625	
313	Corinth, Greece	Corinth	2	6.6	10.27	Normal-Oblique	C	0.25	
821	Erzican, Turkey	Erzincan	1	6.69	4.38	Strike-Slip	D	0.1125	
1158	Kocaeli, Turkey	Duzce	2	7.51	15.37	Strike-Slip	D	0.1	
1176	Kocaeli, Turkey	Yarimca	1	7.51	4.83	Strike-Slip	D	0.0875	4.95
1602	Duzce, Turkey	Bolu	2	7.14	12.04	Strike-Slip	D	0.0625	0.88
1605	Duzce, Turkey	Duzce	2	7.14	6.58	Strike-Slip	D	0.1	5.94
1633	Manjil, Iran	Abbar	2	7.37	12.55	Strike-Slip	C	0.13	
4040	Bam, Iran	Bam	1	6.6	1.7	Strike-Slip	C	0.0625	2.02
4352	Umbria Marche, Italy	Nocera Umbra	2	6	8.92	Normal	C	0.875	
4367	Umbria Marche (aftershock 1), Italy	Nocera Umbra	2	5.5	9.33	Normal	C	0.75	
4451	Montenegro, Yugo.	Bar-Skupstina Opstine	2	7.1	6.98	Reverse	C	0.1625	1.44
4456	Montenegro, Yugo.	Petrovac - Hotel Olivia	1	7.1	8.01	Reverse	C	0.375	
4480	L'Aquila, Italy	L'Aquila - V. Aterno - Centro Valle	1	6.3	6.27	Normal	C	0.0375	1.07
4481	L'Aquila, Italy	L'Aquila - V. Aterno -Colle Grilli	1	6.3	6.81	Normal	C	0.05	
4509	L'Aquila (aftershock 1), Italy	L'Aquila - V. Aterno -Colle Grilli	1	5.6	14.95	Normal-Oblique	C	0.125	
4510	L'Aquila (aftershock 1), Italy	L'Aquila - V. Aterno - Centro Valle	1	5.6	14.81	Normal-Oblique	C	0.1125	

Table 3: The suite of strong ground-motion records used in this study

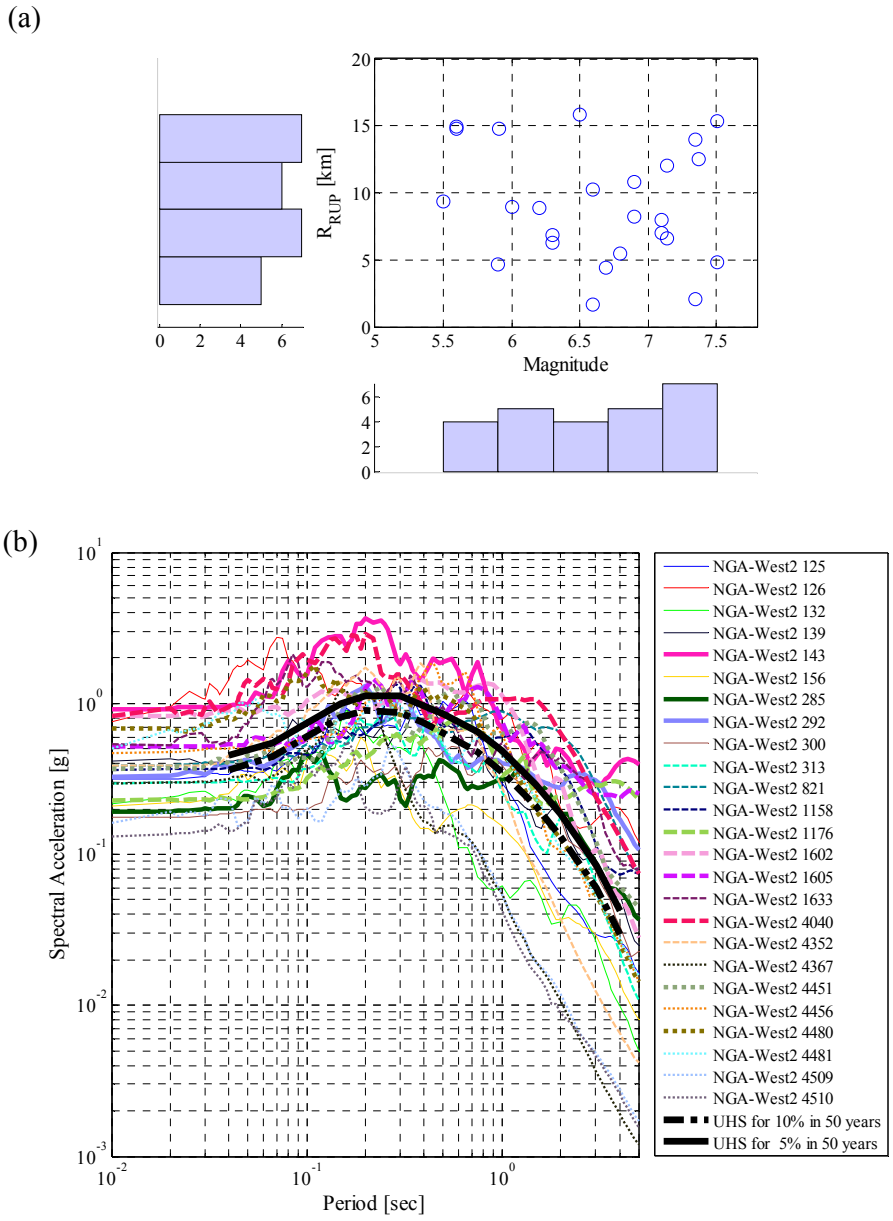


Figure 6: (a) Scatter diagram for the suite of records (Table 3) showing its range of magnitude and closest distance to ruptured area (R_{RUP}), (b) the spectral shape for the suite of records

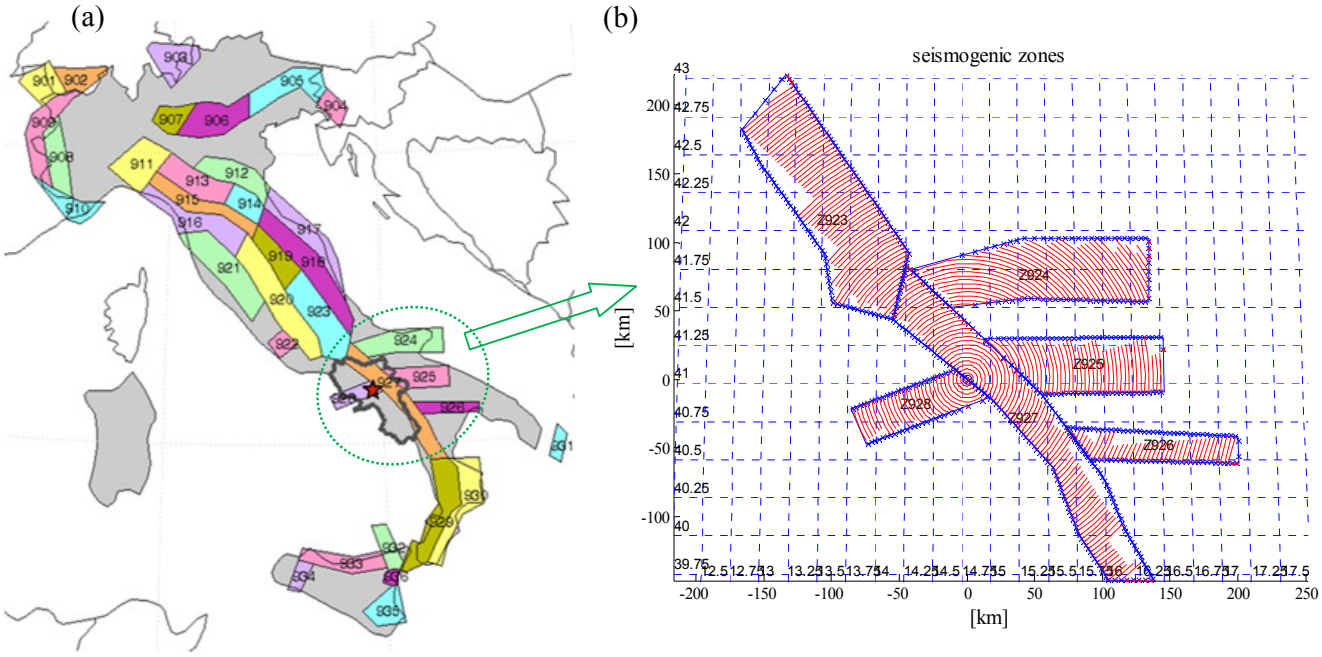


Figure 7: (a) The Italian seismogenic zonation ZS9 with different zones identified, the Campania region highlighted by a gray polyline, and the site of interest is schematically indicated by a pentagram (extracted from [36]), (b) the seismogenic zones surrounding the bridge site

Zone	Seismicity rate ν	Richter b-value	lower magnitude M_l	upper magnitude M_u
923	0.14	1.05	4.76	7.06
924	0.13	1.04	4.76	6.83
925	0.17	0.67	4.76	6.83
926	0.10	1.28	4.76	6.14
927	0.43	0.74	4.76	7.06
928	0.21	1.04	4.76	5.91

Table 4: Parameters of the ZS9 seismic zones surrounding the bridge site.

It is apparent that the selection of a suitable *IM* for representing ground motion uncertainty is a major concern and challenging issue that has to be addressed properly. The stronger is the correlation between the predicted Y_{LS} and the adopted *IM*, the more accurate will be the result of the limit state probabilities. This issue becomes more sensitive in the presence of various retrofit strategies, which are mainly isolation-type rehabilitation schemes. Nevertheless, this is currently not the major concern herein; thus, we opted to use the more simple and well-known *IM*s composed of peak ground acceleration (*PGA*), peak ground velocity (*PGV*), and spectral acceleration at the first-mode period of the bridge, $Sa(T_1)$.

Fig. 8 illustrates the site-specific PSHA in terms of the mean annual rate of exceedance for three aforementioned *IM*s, which was denoted in Section 2 as λ_{IM}. In Fig 8(a, b), the mean rate of exceedance in terms of *PGA* and *PGV* are shown respectively for each of the individu-

al zones as well as for their combination. However, in Fig. 8c, combined PSHA for $Sa(T_1)$ is shown for a range of periods.

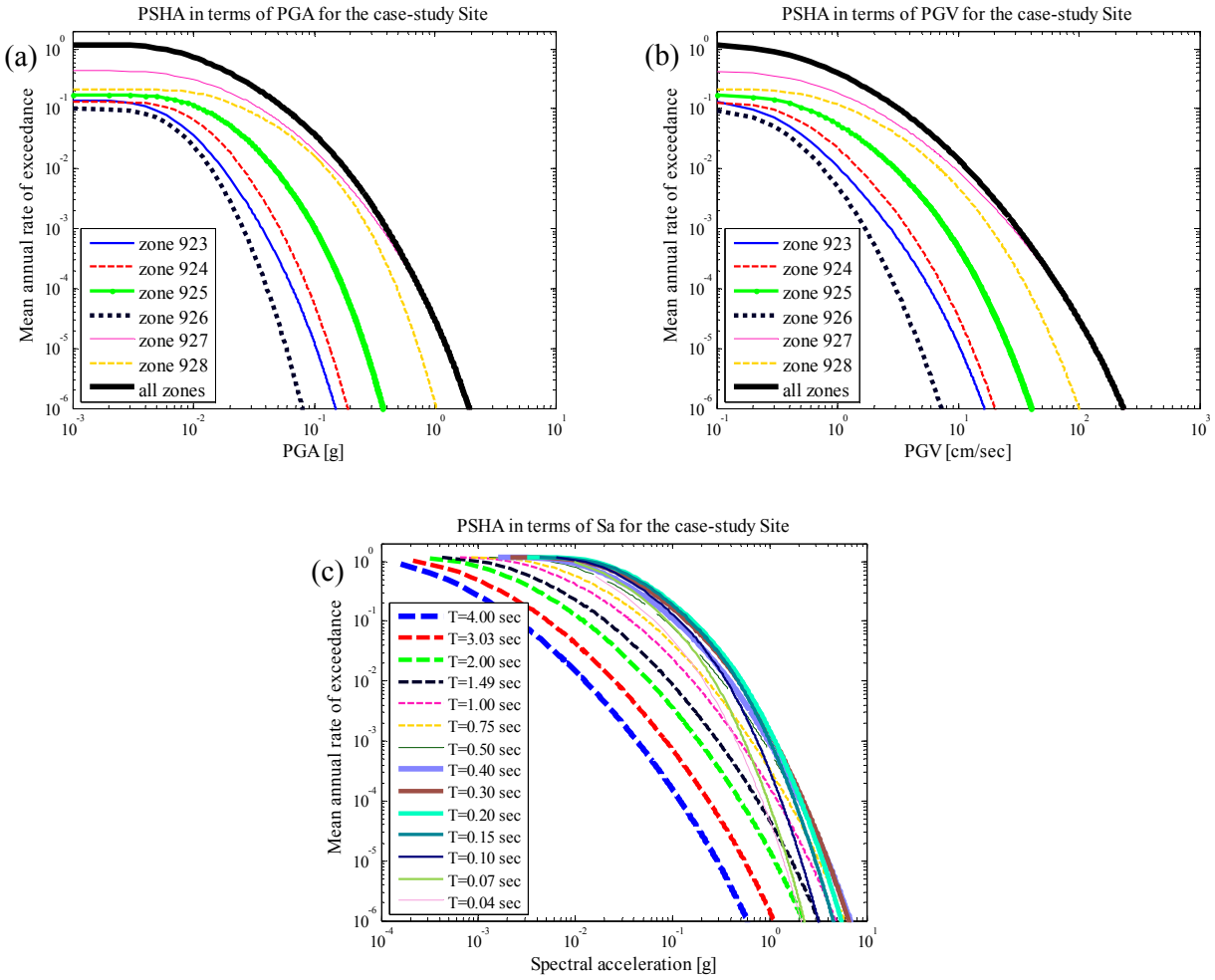


Figure 8: The site-specific seismic hazard results for (a) PGA, (b) PGV, and (c) $Sa(T_1)$

3.8 Estimating the time-dependent limit state probability $P(LS|\mathbf{I}_1)$

This section provides an objective description for calculating the time-dependent limit state probabilities $P(LS|\tau=0,\mathbf{I}_1)$ (denoted in Section 2.3 as *Standard method*) and $P(LS|\tau,\mathbf{I}_1)$ (defined in Section 2.4 as **R** *decision*) for the two desired limit states (see Table 2). The framework described in Section 2 is applied step-by-step to the case-study bridge infrastructure retrofitted with five different schemes outlined in Table 1. Nonetheless, it is worth mentioning that this study aims to use the simple analytic closed-form expression derived in Section 2.3 for estimating the limit state probability $P(LS|\mathbf{I}_1)$. As further explained in Section 2.3, the comparison between the results extracted from the closed-form expression with the exact solution proposed in Section 2.2 in not performed herein.

Step (1): Derive the fragility of the intact infrastructure π_1 based on the Sequential Cloud Analysis methodology described in Appendix. In order to perform this operation, the bridge infrastructure is subjected to the set of ground-motion records outlined in Table 3. In this

study, the records are applied only in the longitudinal direction of the bridge (i.e. bi-directional analysis of the bridge infrastructure is not performed herein). The results of non-linear dynamic analysis in terms of Y_{LS} are calculated based on the methodology described in Section 3.5. The cloud data, which consist of the *IM* of each record and the associated Y_{LS}, are consequently extracted. Fig. 8 illustrates the cloud regressions associated with Y_{CS} vs. *IM* for the Collapse limit state (CS) based on the three different *IM*s considered, respectively. The cloud data corresponding to the original bridge and the five proposed rehabilitation schemes are shown. It can be observed that the cloud data tend to cover the range of Y_{CS} from small values up to $Y_{CS}>1$ (the line corresponds to $Y_{CS}=1$ is marked on each figure). Moreover, the specific SD that has caused Y_{DS} based on Eq. (30) is assigned by a representative color as shown in the title of each regression plot.

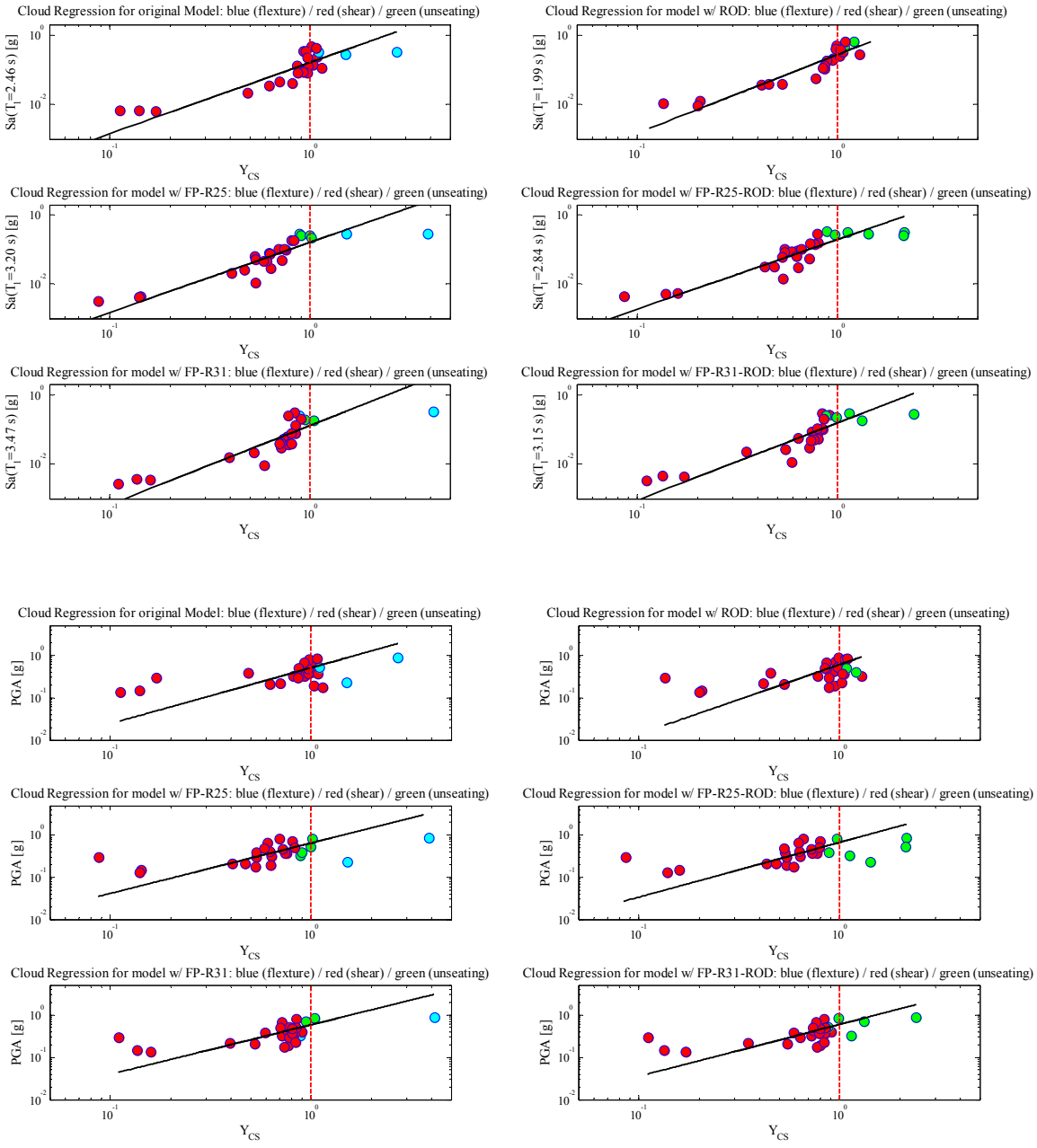
The suitability of one *IM* with respect to another could be evaluated in terms of the average difference in information provided about the predicted Y_{LS}. To accomplish this task, a measure called *Relative Sufficiency Measure* (RSM) proposed in [37] is used herein. The RSM of IM_1 with respect to IM_2, denoted as $I(Y_{LS}|IM_2|IM_1)$, quantifies on average how much more information IM_1 relays to Y_{LS} about the ground motion with respect to IM_2. The RSM herein is calculated in an approximate manner (see [37, 38] and for the corresponding expression). If $I(Y_{LS}|IM_2|IM_1)$, measured in bits of information, is positive, this means that on average IM_2 provides more information about Y_{LS} than IM_1; hence, IM_2 is more sufficient than IM_1. Similarly, if $I(Y_{LS}|IM_2|IM_1)$ is negative, IM_2 is less sufficient than IM_1. The reference intensity (i.e., IM_1) is taken to be $Sa(T_1)$, and the RSM is measured for the other two candidate *IM*s (i.e. *PGA* and *PGV*) relative to $Sa(T_1)$, as summarized in Table 5 for both limit states, DS, and CS, and different bridge models.

Limit state	RSM $IM_1=Sa(T_1)$	Bridge Model					
		original	ROD	FP-R25	FP-R25-ROD	FP-R31	FP-R31-ROD
DS	$IM_2=PGA$	-1.72	-2.09	-1.20	-1.14	-1.30	-1.64
	$IM_2=PGV$	-0.75	-1.15	-0.28	-0.26	-0.38	-0.50
CS	$IM_2=PGA$	-0.81	-1.18	-0.82	-0.92	-0.57	-0.76
	$IM_2=PGV$	-0.24	-0.52	-0.15	-0.20	-0.07	-0.12

Table 5: RSM for *IM*s of *PGA* and *PGV* relative to $Sa(T_1)$ for both limit states DS and CS and different bridge models

With reference to Table 5, it can be concluded that $Sa(T_1)$ is the more efficient compared to *PGA* and *PGV*. Nevertheless, *PGV* is still more informative with respect to *PGA* for various retrofit alternatives of the case-study bridge.

The fragility curves for both limit states and for different bridge models can directly be calculated from the cloud regression data (as explained in the Appendix). Fig. 10 illustrates the fragility curves of various retrofit options based on desired *IM*s and for both limit states.


Cloud Regression for original Model: blue (flexture) / red (shear) / green (unseating)
Sa(T_I=2.46 s) [g]
Cloud Regression for model w/ ROD: blue (flexture) / red (shear) / green (unseating)
Sa(T_I=1.99 s) [g]
Cloud Regression for model w/ FP-R25: blue (flexture) / red (shear) / green (unseating)
Sa(T_I=3.20 s) [g]
Cloud Regression for model w/ FP-R25-ROD: blue (flexture) / red (shear) / green (unseating)
Sa(T_I=2.84 s) [g]
Cloud Regression for model w/ FP-R31: blue (flexture) / red (shear) / green (unseating)
Sa(T_I=3.47 s) [g]
Cloud Regression for model w/ FP-R31-ROD: blue (flexture) / red (shear) / green (unseating)
Sa(T_I=3.15 s) [g]
Y_CS
Cloud Regression for original Model: blue (flexture) / red (shear) / green (unseating)
PGA [g]
Cloud Regression for model w/ ROD: blue (flexture) / red (shear) / green (unseating)
Cloud Regression for model w/ FP-R25: blue (flexture) / red (shear) / green (unseating)
Cloud Regression for model w/ FP-R25-ROD: blue (flexture) / red (shear) / green (unseating)
Cloud Regression for model w/ FP-R31: blue (flexture) / red (shear) / green (unseating)
Cloud Regression for model w/ FP-R31-ROD: blue (flexture) / red (shear) / green (unseating)

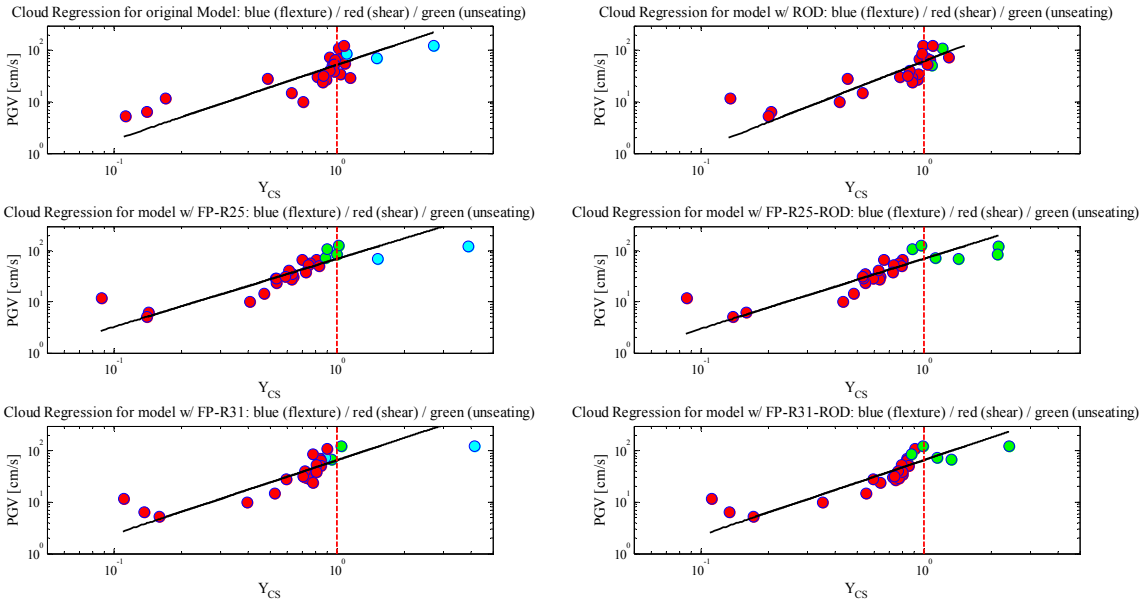


Figure 9: Cloud regression of different bridge models associated with the Collapse limit state (CS) based on the three different *IM*s considered

Step (2): Estimate Π_1 from Eq. (13) by convolving the fragility of the intact structure and the hazard λ_{IM}, for both limit states and different *IM* scenarios. Subsequently, $\{\Pi_{n,\mathbf{R}}|n=1{:}N_{ce}\}$ is evaluated directly from Eq. (17) by substituting $\Pi_{j+1}=\Pi_1$ as defined in Section 2.4. The repair times, denoted as τ, associated with alternative limit states are outlined in Table 6.

Limit state, *LS*	Repair time, τ [year]
Damage	1/2
collapse	1

Table 6: Repair time for alternative limit states

Step (3): Calculate the limit state probability by two different methodology:

(a) Directly substituting the probability Π_1 into Eq. (12) which is addressed as the *Standard method* for calculating the limit state exceedance probability in a given time interval. It is denoted as $P(LS|\tau=0,\mathbf{I}_1)$ and expressed by Eq. (14) (see Section 2.3).

(b) Calculating $\Pi_{2,R}$ from Eq. (17) by substituting $n=2$, and subsequently set $\Pi=\Pi_{2,R}$ in Eq. (12) as noted in Section 2.4. The limit state probability is addressed as **R** *decision* and denoted as $P(LS|\tau,\mathbf{I}_1)$.

Fig. 10 and Fig. 11 reveal the variation in $P(LS|\tau=0,\mathbf{I}_1)$ and $P(LS|\tau,\mathbf{I}_1)$ for both limit states given the desired *IM*s and given the time interval up to 100 years. It can be seen that by consideration of **R** *decision*, the time-dependent limit states will be fairly lower than those estimated by the *Standard method*. Moreover, the ordering of the limit state probabilities given *IM*s $Sa(T_1)$ and *PGV* reveal similar trend among both limit states as well as different limit state probability models. It is concluded that the retrofit strategies FP-R25, and FP-R25-ROD have

the lowest exceedance probabilities. However, this result cannot be clearly reported from those curves that correspond to the intensity *PGA*.

3.9 Calculating the Expected Life-Cycle Cost

The expected cost in the life-time of the bridge infrastructure is calculated for the five retrofit options described in Table 1 using Eq. (18). The initial costs C_0, which are composed of the initial cost of the construction (see [39, 40]) plus the cost of the desired retrofit upgrading [41], are tabulated in Table 7 for various retrofit options. The cost of maintenance C_M is calculated with reference to Eq. (20), where the constant annual maintenance cost C_m is also tabulated in Table 7.

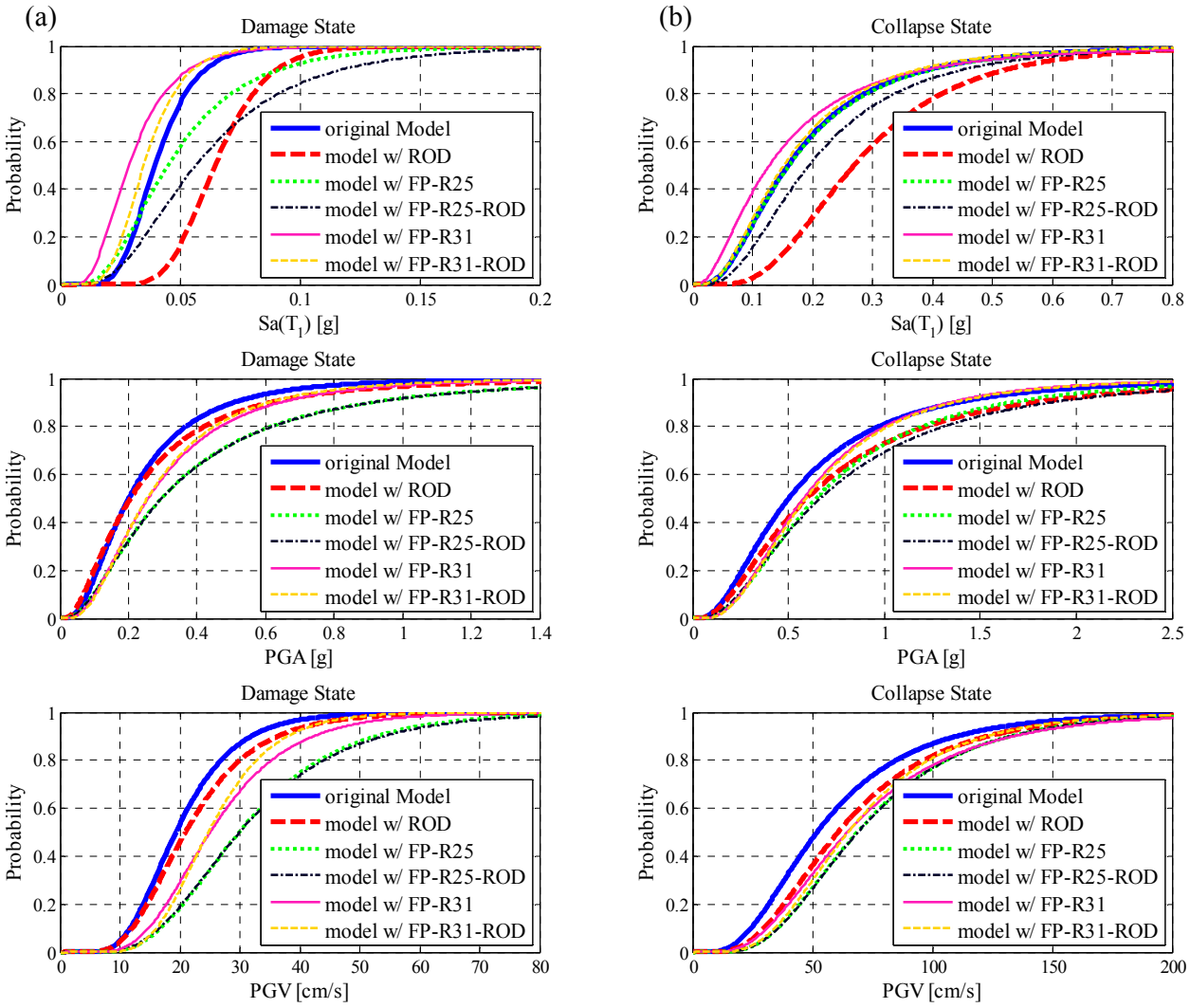


Figure 10: The fragility curves of various retrofit options based on desired *IM*s for (a) Damage and (b) collapse limit states

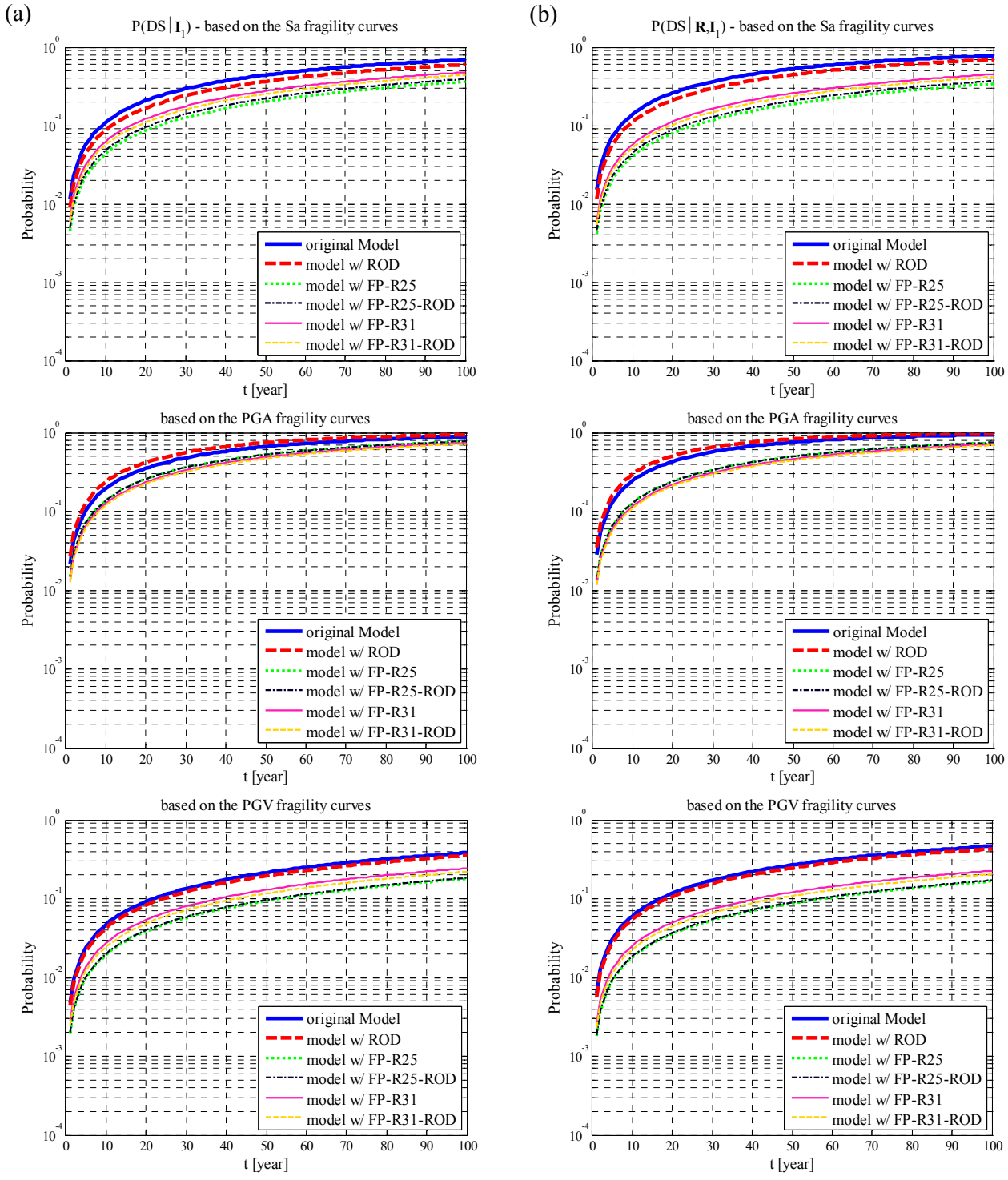


Figure 10: The time-dependent limit state probabilities for *Damage LS* (DS) for the case-study bridge with various retrofit schemes based on (a) *Standard method* - $P(LS|\tau=0,\mathbf{I}_1)$, (b) **R** *decision* - $P(LS|\tau,\mathbf{I}_1)$

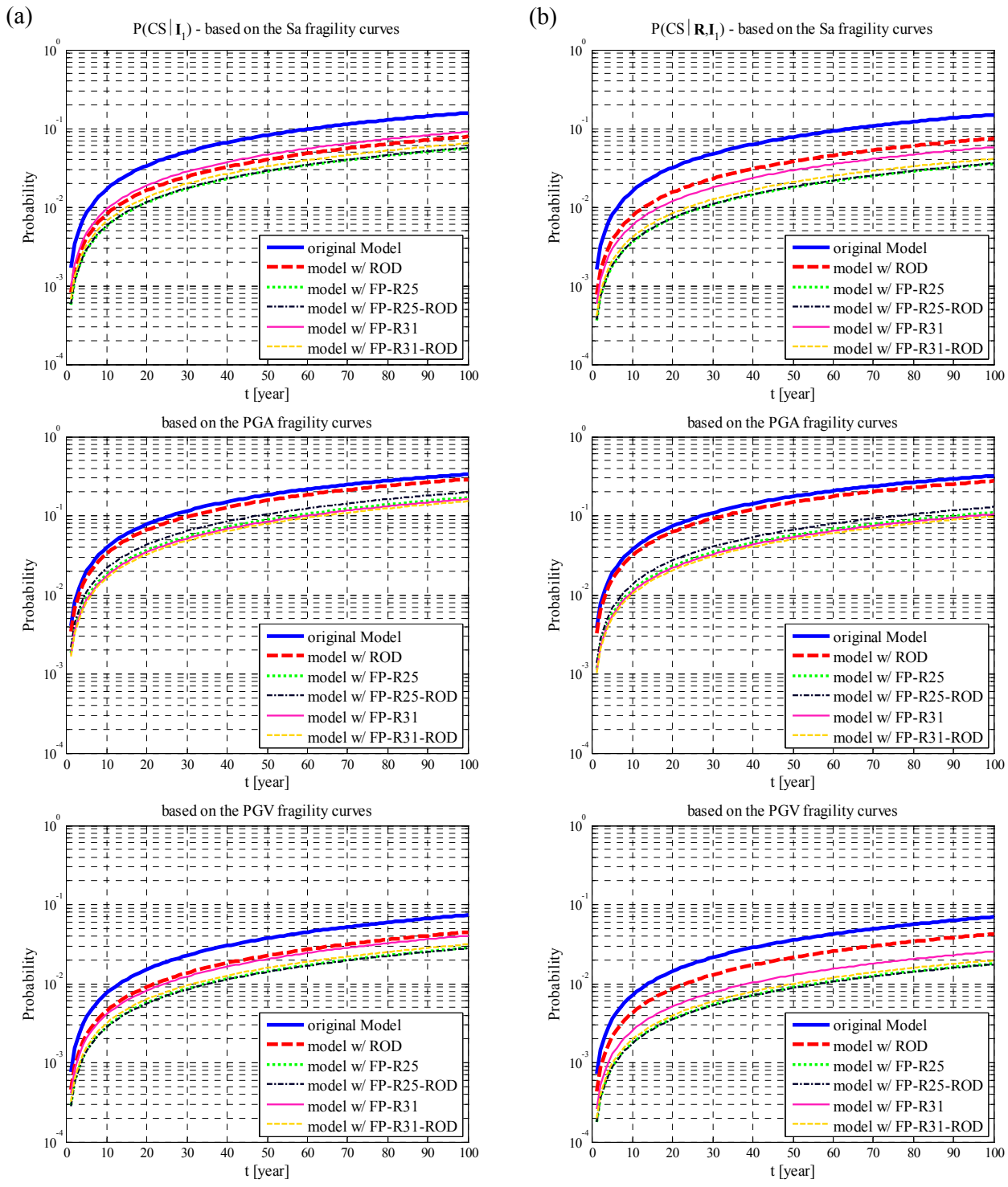


Figure 11: The time-dependent limit state probabilities for *Collapse LS* (CS) for the case-study bridge with various retrofit schemes based on (a) *Standard method* - $P(LS|\tau=0,\mathbf{I}_1)$, (b) **R** *decision* - $P(LS|\tau,\mathbf{I}_1)$

The repair/replacement cost C_R is calculated by using Eq. (19). Accordingly, LSC_{ls} where ls=1:N_{LS}=2, is the annual expected cost of restoring the infrastructure from the lsth limit state LS_{ls} back to its intact state including eventual loss of revenue due to downtime for repair operations. This expression is calculated herein as follows:

$$LSC_{ls} = DTC \cdot e^{-\lambda_d \tau} + RC_{ls} \tag{31}$$

where DTC is the annual cost of downtime outlined in Table 7, $\exp(-\lambda_d \tau)$ denotes the change in the monetary-based evaluations within the repair time where λ_d=0.05; RC_{ls} is the replacement cost associated with desired lsth limit state, ls=1:N_{LS}=2, and tabulated in Table 7; they are extracted from updated data calculated in [39, 40] and considered the same through different retrofit strategies.

Retrofit Option	C_0 ($\times 10^6$, €)	DTC ($\times 10^6$, €/year)	RC_{DS} ($\times 10^6$, €/year)	RC_{CS} ($\times 10^6$, €/year)	C_m ($\times C_0$, €/year)
Original Model	4.906	1	0.44	7.10	0.01
ROD	5.004	1	0.44	7.10	0.01
FP-R25	5.072	1	0.44	7.10	0.01
FP-R25-ROD	5.170	1	0.44	7.10	0.01
FP-R31	5.118	1	0.44	7.10	0.01
FP-R31-ROD	5.216	1	0.44	7.10	0.01

Table 7: Life-cycle cost analysis parameters

With reference to Eq. (19), the probability $P(LS_{ls}|[t,t+1],\mathbf{I}_1)$ is the limit state time-dependent probability in 1-year as a function of time t and for the lsth limit state, LS_{ls}, which is evaluated by using Eq. (8). However, in case of using the closed-from expression in Eq. (12) for time-dependent limit state probability, the following expression can simply be derived:

$$P\left(LS\,|\,[t,t+1],\mathbf{I}_1\right) = \frac{\mathrm{d}}{\mathrm{d}t}\left[1-\exp\left(-\Pi\,\nu t\right)\right]\cdot\left(\Delta t = 1\right) = \Pi\,\nu\exp\left(-\Pi\,\nu t\right) \tag{32}$$

Fig. 12 and Fig. 13 illustrate the resulting annual time-dependent limit state probabilities $P(LS_{ls}|[t,t+1],\mathbf{I}_1)$ for ls=1:2 given the desired *IM*s and given the time interval up to 100 years. Each figure reveals the annual exceedance probabilities in the *Standard method* (i.e. extracting $P(LS_{ls}|[t,t+1],\mathbf{I}_1)$ from $P(LS|\tau=0,\mathbf{I}_1)$ in Eq. 8) as well as considering the **R** *decision* by calculating $P(LS_{ls}|[t,t+1],\mathbf{R},\mathbf{I}_1)$ from $P(LS|\tau,\mathbf{I}_1)$.

In order to have a point of comparison, two threshold levels of 10% and 5% exceedance probability in 50 year are assigned to DS and CS, respectively, as shown by cyan bold line in Fig. 12 and Fig. 13. Thus, the admissible annual exceedance probability P_{adm} will become:

$$P_{adm,DS} = \lambda_{adm,DS}\cdot\exp\left(-\lambda_{adm,DS}\cdot t\right) = \left(2.1\times10^{-3}\right)\cdot\exp\left(-2.1\times10^{-3}\cdot t\right) \tag{33}$$

$$P_{adm,CS} = \lambda_{adm,CS}\cdot\exp\left(-\lambda_{adm,CS}\cdot t\right) = \left(1\times10^{-3}\right)\cdot\exp\left(-1\times10^{-3}\cdot t\right) \tag{34}$$

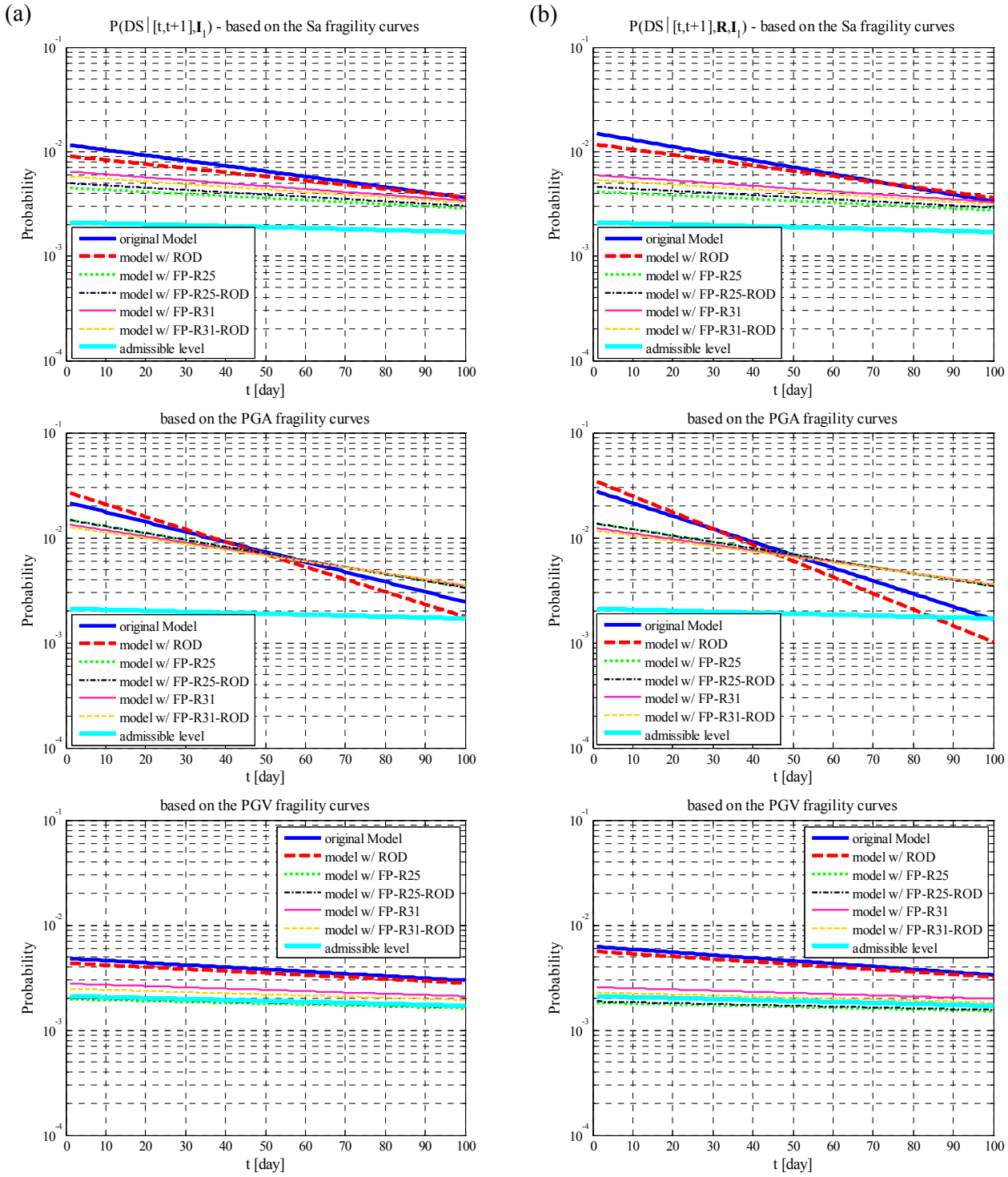


Figure 12: The *Damage LS* exceedance probability in 1-year as a function of time *t* for the case-study bridge with various retrofit schemes based on (a) *Standard method*, (b) **R** *decision*

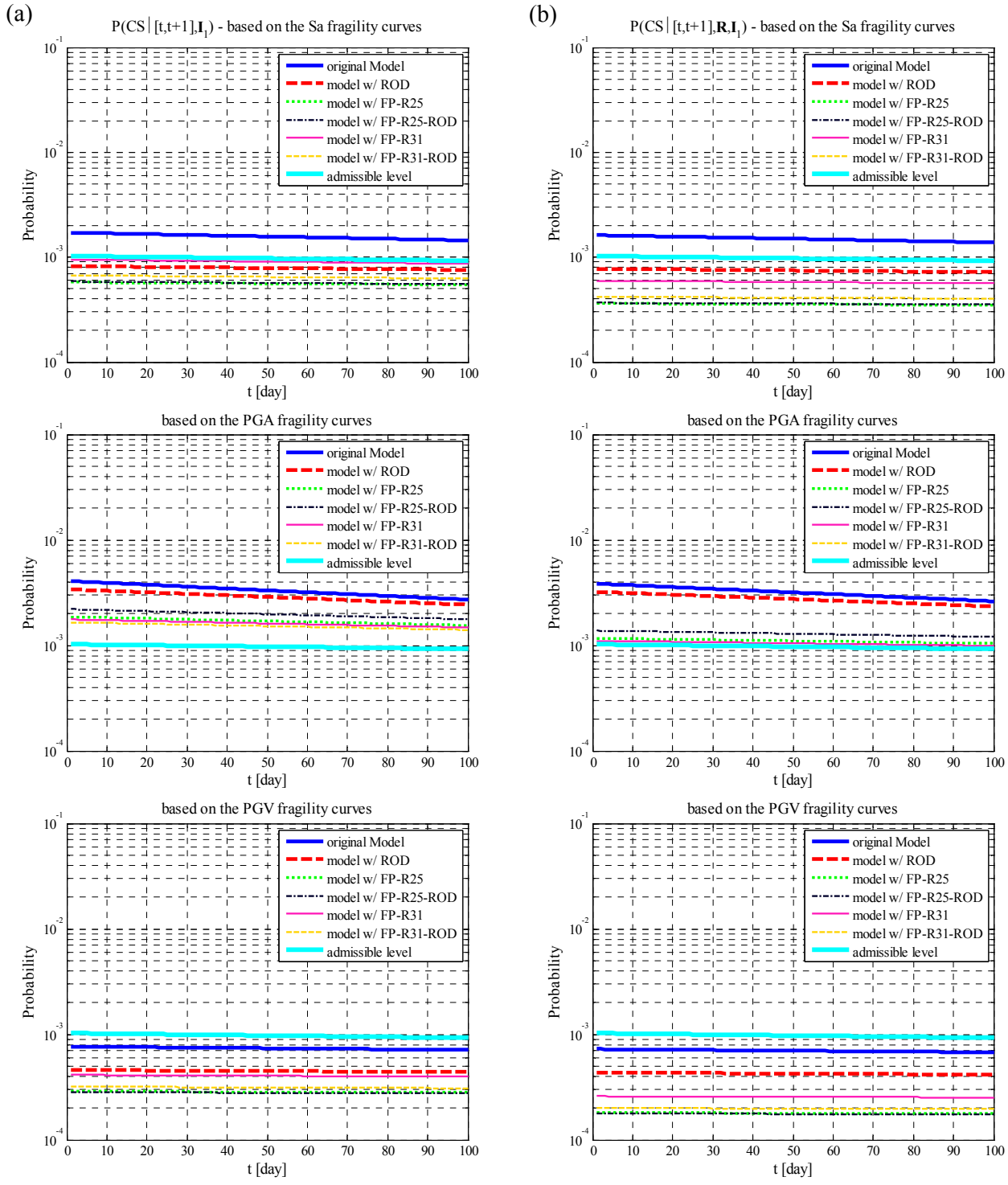


Figure 13: The *Collapse LS* exceedance probability in 1-year as a function of time *t* for the case-study bridge with various retro-fit schemes based on (a) *Standard method*, (b) **R** *decision*

It can be seen the by maintaining the **R** *decision*, the annual limit states probabilities are to some extend different with respect to the *Standard method*; moreover, the differences are more apparent compared to those revealed between $P(LS|\tau=0,\mathbf{I}_1)$ and $P(LS|\tau,\mathbf{I}_1)$ in Fig. 10 and Fig. 11. In addition, the outcomes of annual exceedance probability for CS based on *PGA* as the desired *IM* imply conservative decisions where the probability is higher than the admissible level even for the bridge with different retrofit strategies. The opposite conclusion will be extracted from those based on *PGV* as the desired *IM* where even the original infrastructure lies below the admissible level. However, the annual exccedance probabilities based on $Sa(T_1)$ denote that the original infrastructure is above the admissible level while the alternative retrofit strategies put the infrastructure below the admissible level. Since alternative *IM*s result in different decisions regarding the safety checking which directly affect the life-cycle cost assessment, their selection requires more detailed study.

In terms of life-cycle cost, Fig. 14 demonstrates the resulting expected life-cycle cost for alternative retrofit decisions based on using the *Standard method* or taking the **R** *decision*. It can be observed that:

(a) Based on both methods (i.e. *Standard* and **R** *decision*), the expected life-cycle costs for different retrofit options given the *PGV* as the desired *IM* does not reveal any enhancement in using alternative retrofit options. Hence, in terms of life-cycle cost assessment, the use of this *IM* requires more detailed studies (this conclusion was also drawn in the previous paragraph). However, the expected life-cycle costs given *PGA* or $Sa(T_1)$ reveal that the option FP-R25 (see Table 1) offers the lowest life-cycle cost while renders the bridge infrastructure competitively more reliable for the collapse limit state (see Fig. 13).

(b) Although the FP-R25 options are more expensive in the early stage of life time of the bridge infrastructure, it can be seen that after around 10-20 years (depends on the kind of *IM* for investigation), its corresponding expected cost fall beneath the other retrofit options. On the other hand, the retrofit option FP-R25-ROD has similar costs; however, it will decisively become the more expensive compared to FP-R25 as the time pass.

(c) The distinction between the expected costs of different retrofit options is more apparent while taking into account the repair time τ (i.e. using **R** *decision* with the limit state exceedance probability $P(LS|\tau,\mathbf{I}_1)$) compared to the *Standard method*, which assumes that $\tau=0$. Furthermore, the selection of *IM* affects the decisions regarding the life-cycle cost which requires more detailed studies.

(d) Taking the advantage that the *Standard method* is more convenient in its use, and knowing that it informs the same decision regarding life-cycle costs, it can be used in case of rapid screening among various retrofit options in terms of their life-cycle costs.

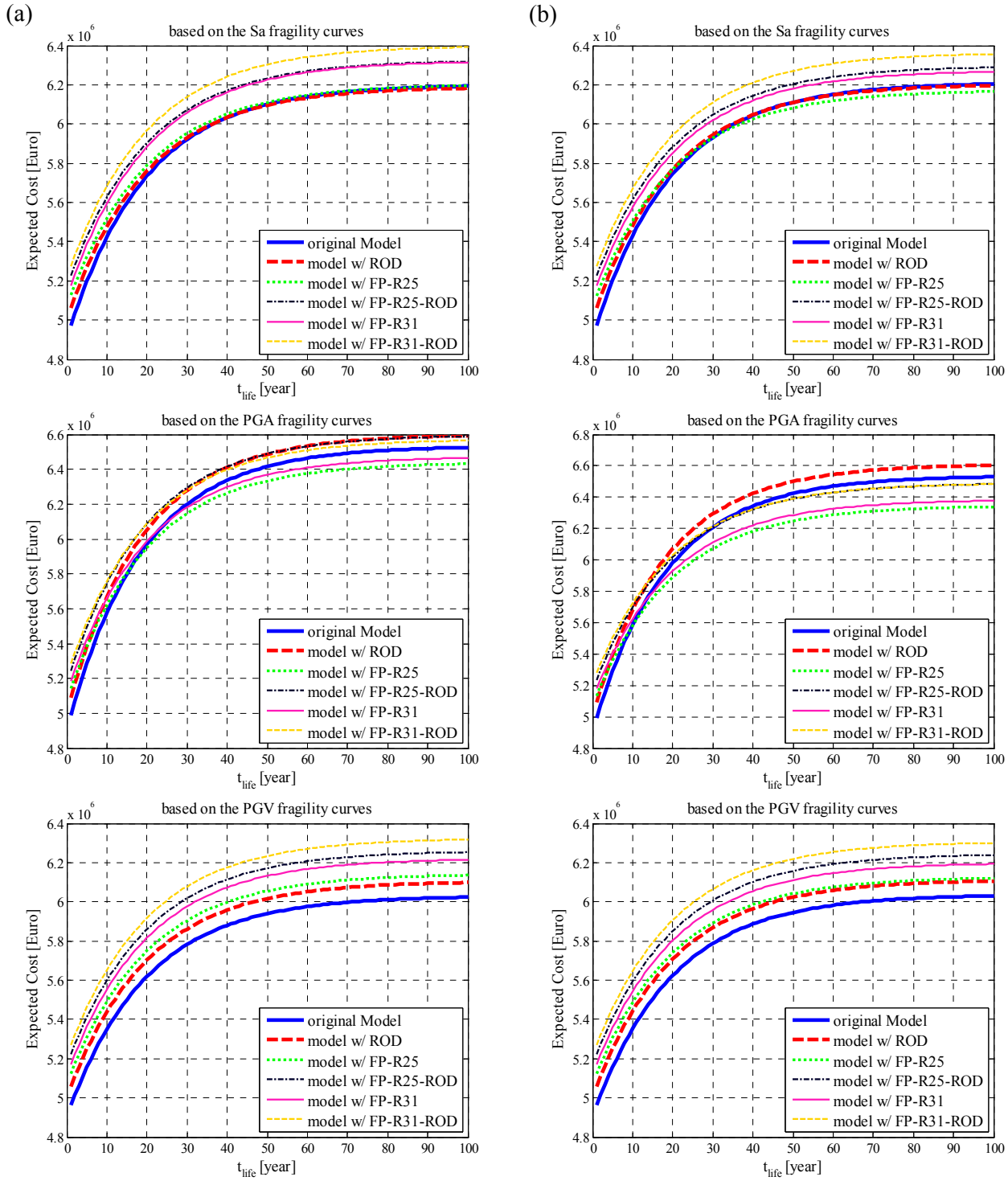


Figure 14: The expected life-cycle cost for alternative retrofit options (a) *Standard method*, (b) **R** *decision*

4 CONCLUSION

- A procedure is presented for retrofit decision-making based on life cycle criteria subjected to safety constraints. It can be effectively used for screening among various proposed retrofit strategies.
- Based on the assumption that a bridge is immediately subjected to repair operations after a major earthquake event, the finite repair time is considered in the life-cycle cost evaluation. This has been done by implementing a procedure developed by the authors for calculating the limit state exceedance probability taking into account the effect of cumulative damage due to a sequence of back-to-back seismic events. In particular, a simplified closed-form analytical expression for the limit state probabilities based on the fragility of intact infrastructure is employed.
- The time-dependent limit state probabilities are then used to calculate the expected life-cycle cost taking into account the total initial construction costs, down time, repair/replacement costs, and regular maintenance costs.
- This methodology is used as a decision-making tool for retrofit design of an existing RC bridge infrastructure in south Italy. The expected life cycle is calculated for the existing bridge (original model), and 5 different retrofit strategies. It is demonstrated that the Friction Pendulum isolator with effective radius of concave sliding surface equal to 2.5 m and a Coulomb friction of 2% (denoted as FP-R25) is the option that leads to the least expected life cycle cost. Although it is among the most expensive options in terms of installation costs, the corresponding expected cost falls beneath the other retrofit options after a certain amount of time.
- Alternative sufficient intensity measures (*IM*s) result in different decisions regarding the safety checking which directly affect the life-cycle cost assessment. Thus, their selection requires more detailed study.

The proposed methodology has its limitations:

- The effect of aging is not considered in the calculation of the limit state probabilities and the expected life cycle costs.
- The effect of cumulative damage is approximated by a simplified closed-form equation and based on the fragility of the intact bridge. That is, no back-to-back analyses are performed.
- The 3D model of the bridge infrastructure is subjected to ground-motion records in its longitudinal direction.
- The spatial variability in ground motion is not considered.
- The soil-structure interaction is not considered.

APPENDIX

The general procedure for calculating the set of event-dependent fragilities $\{\pi_n(x)|n=1{:}N_{ce}\}$ (entered in Eq. 6) in this study is described as follows (see also [6-9]):

1. Construct the nonlinear model of the desired structure.
2. Select a suite of ground motion records.
3. Clone (repeat) each record in the set n times (n=1:N_{ce}) to construct a sequence.
4. Perform a finite element nonlinear dynamic analysis of the representative model of structure by subjecting it to the suite of constructed sequences comprising of the cloned ground motions (previous step). However, exclude those sequences, in which the limit state first-excursion has already taken place in their previous (n-1) events, from the suite of sequences.
5. For each sequence, calculate the time- and history-dependent performance variable $Y_{LS}^{(n)}$ that tends to reflect and to conditionally isolate the effect of the nth event on the desired structure [9]:

$$Y_{LS}^{(n)} = \frac{D_{\max}^{(n)} - D_r^{(n-1)}}{C_{LS} - D_r^{(n-1)}} \tag{A.1}$$

   where $D_{\max}^{(n)}$ is the maximum demand due to the nth event in the sequence; $D_r^{(n\text{-}1)}$ is the residual demand corresponding to the sequence of (n-1) events; C_{LS} is the limit state capacity of the (intact) structure. The term $Y_{LS}^{(n)}$ can be regarded as the ratio of maximum demand increment due to the nth event divided by the reduced capacity right after the sequence of (n-1) events. Needless to say that at the onset of the limit state, $Y_{LS}^{(n)}$=1.
6. For each sequence, register the pair of cloud data [$IM^{(n)}$, $Y_{LS}^{(n)}$] corresponding to nth event.
7. Modify the cloud analysis data at nth step (if required). This issue can be addressed by paying attention to the range of $Y_{LS}^{(n)}$ values, which should manage to especially cover the values greater than or equal to unity (see general notes on cloud analysis while using Y_{LS} in [27]). This modification can be accomplished by deliberately substituting the existing nth cloned record in the sequence with the one that has been excluded (see Step 4) while maintaining $Y_{LS}^{(n)} \geq 1$.
8. Let $N_{gm}(n)$ be the number of ground motions in the suite of records at nth step, carry out a logarithmic linear regression on $N_{gm}(n)$ cloud data by assuming that the conditional distribution of $Y_{LS}^{(n)}$ given a level of $IM^{(n)}$=x is described by a lognormal distribution ([29, 42, 43]); thus, the fragility term $\pi_n(x)$ can be expressed as:

$$\pi_n(x) = P\left(C_n \mid x, \mathbf{I}_2\right) = 1 - \Phi\left(\frac{-\ln \eta_{Y_{LS}|IM}^{(n)}(x)}{\beta_{Y_{LS}|IM}^{(n)}}\right) \tag{A.2}$$

   where Φ is the standardized Gaussian cumulative distribution function (CDF); $\eta_{YLS|IM}^{(n)}$ and $\beta_{YLS|IM}^{(n)}$ are conditional median and standard deviation (dispersion) of the natural logarithm of $Y_{LS}^{(n)}$ given spectral acceleration and given that the structure has already been subjected to n events. The median and dispersion can be calculated as [40]:

$$\ln \eta_{Y_{LS}|IM}^{(n)}(x) = \ln a + b \ln(x), \quad \beta_{Y_{LS}|IM}^{(n)} = \sqrt{\frac{\sum_{i=1}^{N_{gm}(n)} \left[\ln\left(Y_{LS,i}^{(n)} / a \cdot (IM_i^{(n)})^b\right)\right]^2}{N_{gm}(n) - 2}} \tag{A.3}$$

   where ln$a$ and b are the coefficients of the logarithmic linear regression.
9. Repeat steps 3-8 for the same suite of ground motion records until n=N_{ce}.

AKNOWLEDGEMENT

This work was supported in part by project STRIT (Strumenti e Tecnologie per la gestione del Rischio delle Infrastrutture di Trasporto). This support is gratefully acknowledged. Any opinions, findings, and conclusions or recommendations expressed in this material are those of the authors and do not necessarily reflect those of the sponsors. The authors would like to gratefully acknowledge Dr. Luigi Di Sarno and Jonatan Picariello for providing the initial information of the bridge infrastructure and helping in the OpenSees modeling of the bridge. Finally, the authors would like to gratefully acknowledge Dr. Luigi Petti and Alessio Lodato for providing the information for different retrofit options of the bridge.

REFERENCES

[1] Y.K.Wen, Reliability and performance-based design. *Structure Safety*, **23**(4), 407-428, 2001.

[2] M.H. Faber, R. Rackwitz, Sustainable decision making in Civil Engineering. *Structural Engineering International*, **14**(3), 237-242, 2004

[3] K.A. Porter, A.S. Kiremidjian, J.S. LeGrue, Assembly-based vulnerability of buildings and its use in performance evaluation. *Earthquake Spectra*, **17**(2), 291-312, 2001

[4] P. Franchin, P.E. Pinto, M.IJ. Schotanus, Seismic loss estimation by efficient simulation. *Journal of Earthquake Engineering*, **10**(1):31-44, 2006

[5] C.A. Goulet, C.B. Haselton, J. Mitrani-Reiser, J.L. Beck, G.G. DeierLein, K.A. Porter, J.P. Stewart, Evaluation of the seismic performance of a code-conforming reinforced concrete frame building - From seismic hazard to collapse safety and economic losses. *Earthquake Engineering and Structural Dynamics*, **36**(13), 1973-1997, 2007.

[6] F. Jalayer, D. Asprone, A. Prota, G. Manfredi, Multi-hazard upgrade decision making for critical infrastructure based on life-cycle cost criteria. *Earthquake Engineering and Structural Dynamics*, **40**(10), 1163-1179, 2011.

[7] F. Jalayer, D. Asprone, R. Chiodi, A. Prota, G. Manfredi, Seismic Retrofit Decision-Making based on Life Cycle Cost Criteria. *15th Word Conference on Earthquake Engineering (15WCEE)*, Lisbon, Portugal, 2012.

[8] F. Jalayer, D. Asprone, A. Prota, G. Manfredi, A decision support system for post-earthquake reliability assessment of structures subjected to aftershocks: an application to L'Aquila earthquake, 2009. *Bulletin of Earthquake Engineering*, **9**(4), 997-1014, 2011.

[9] H. Ebrahimian, F. Jalayer, D. Asprone, A.M. Lombardi, W. Marzocchi, A. Prota, G. Manfredi, A performance-based framework for adaptive seismic aftershock risk assessment, *Earthquake Engineering and Structural Dynamics*, **43**(14), 2179-2197, 2014.

[10] F. Jalayer, H. Ebrahimian, G. Manfredi, Towards quantifying the effect of aftershocks in seismic risk assessment. *12th International Conference on Applications of Statistics and Probability in Civil Engineering (ICASP12)*, Vancouver, Canada, July 12-15, 2015.

[11] J.R. Benjamin, C.A. Cornell. *Probability, statistics and decision for civil engineers*, McGraw Hill, 684pp, 1970.

[12] D. Cardone, P. Giuseppe, S. Salvatore, A performance-based adaptive methodology for the seismic evaluation of multi-span simply supported deck bridges. *Bulletin of Earthquake Engineering*, **9**(5), 1463-1498, 2011.

[13] ASPI (AutoStrade Per l'Italia S.p.a), *S.A.M.O.A.: Survey, Auscultation and Maintenance of Bridges*, Autostrade per l'Italia S.p.a., Rome, 1992.

[14] OpenSees. *Open system for earthquake engineering simulation*. Pacific Earthquake Engineering Research Center, (PEER), April 2015. (Available from: http://opensees.berkeley.edu).

[15] M.H. Scott, G.L. Fenves, Plastic hinge integration methods for force-based beam–column elements. *Journal of Structural Engineering*, **132**(2), 244-252, 2006.

[16] CEN (Comité Européen de Normalisation), *Eurocode 8: Design of structures for earthquake resistance - Part 3: Assessment and retrofitting of buildings*. EN 1998-3, CEN, Bruxels, 2005.

[17] CEN (Comité Européen de Normalisation), *Eurocode 8: Design of structures for earthquake resistance - Part 2: Bridges*. EN 1998-2, CEN, Bruxels, 2005.

[18] M.J.N. Priestley, F. Seible, G.M. Calvi, *Seismic Design and Retrofit of Bridges*, John Wiley & Sons, Inc., New York, 1996.

[19] P. Kaviani, F. Zareian, E. Taciroglu, *Performance-Based Seismic Assessment of Skewed Bridges*, *Report PEER 2014/01*, Pacific Earthquake Engineering Research Center, University of California, Berkeley, CA, 2014.

[20] J.B. Mander, M.J.N. Priestley, R. Park, Theoretical stress-strain model for confined concrete. *Journal of structural* engineering, **114**(8), 1804-1826, 1988

[21] A. Aviram, K.R. Mackie, B. Stojadinovic, *Guidelines for nonlinear analysis of bridge structures in California*, *Report PEER 2008/3*, Pacific Earthquake Engineering Research Center, University of California, Berkeley, CA, 2008.

[22] R.W. Clough, J. Penzien, *Dynamics of structures*, *2nd Edition*, New York: McGraw-Hill, Inc., 1994.

[23] L. Petti, A. Lodato, A. Mammone, Reliability analysis of seismic isolation in retrofitting of simply supported bridges. *Advances in Civil and Infrastructure Engineering*, Vietri sul Mare, Italy, June 12-13, 2015.

[24] L. Petti, A. Lodato, A. Mammone, Il miglioramento sismico di ponti a travata semplicemente appoggiata mediante isolamento sismico. *XVI Convegno ANIDIS, L'Ingegneria Sismica in Italia*, L'Aquila, Italia, settembre 13-17, 2015 (in Italian).

[25] B. Borzi, P. Ceresa, P. Franchin, F. Noto, G.M. Calvi, P.E. Pinto, Seismic Vulnerability of the Italian Roadway Bridge Stock. *Earthquake Spectra*, In-Press, 2014, DOI 10.1193/070413EQS190M.

[26] CEN (Comité Européen de Normalisation), *Eurocode 8: design of structures for earthquake resistance - Part 1: General rules, seismic actions and rules for buildings*. EN 1998-1 CEN Brussels, 2004.

[27] T. Isaković, L. Bevc, M. Fischinger, Modeling the cyclic flexural and shear response of the RC hollow box columns of an existing viaduct. *Journal of Earthquake Engineering*, **12**(7), 1120-1138, 2008

[28] F. Jalayer, P. Franchin, P.E. Pinto. A scalar damage measure for seismic reliability analysis of RC frames. *Earthquake Engineering and Structural Dynamics*, **36**(13), 2059-2079, 2007

[29] F. Jalayer, R. De Risi, G. Manfredi, Bayesian Cloud Analysis: efficient structural fragility assessment using linear regression. *Bulletin of Earthquake Engineering*, 13, 1183-1203, 2015.

[30] P. Franchin, P.E. Pinto, Allowing traffic over mainshock-damaged bridges. *Journal of Earthquake Engineering*, **13**(5), 585-599, 2009.

[31] T.D. Ancheta, R.B. Darragh, J.P. Stewart, E. Seyhan, W.J. Silva, B.S.-J. Chiou, K.E. Wooddell, R.W. Graves, A.R. Kottke, D.M. Boor, T. Kishida, J.L. Donahue, NGA-West2 Database. *Earthquake Spectra* **30**(3), 989-1005, 2014.

[32] S.K. Shahi, *A probabilistic framework to include the effects of near-fault directivity in seismic hazard assessment*. Dissertation, Stanford University, CA, 2013.

[33] Gruppo di Lavoro, 2004. *Redazione della mappa di pericolosità sismica prevista dall'Ordinanza PCM 3274 del 20 marzo 2003*. Rapporto Conclusivo per il Dipartimento della Protezione Civile, INGV, Milano-Roma, April 2004, 65 pp. + 5 appendixes (in Italian).

[34] MATHAZARD, *A program for seismic hazard analysis*, University of Rome, Italy, December 2000.

[35] F. Sabetta, A. Pugliese, Estimation of response spectra and simulation of nonstationary earthquake ground motions. *Bulletin of the Seismological Society of America*, **86**(2), 337-352, 1996.

[36] L. Elefante, F. Jalayer, I. Iervolino, G. Manfredi, Disaggregation-based response weighting scheme for seismic risk assessment of structures. *Soil Dynamics and Earthquake Engineering*, **30**(2), 1513-1527, 2010.

[37] F. Jalayer, J. Beck, F. Zareian, Analyzing the sufficiency of alternative scalar and vector intensity measures of ground shaking based on information theory. *Journal of Engineering Mechanics*, **138**(3), 307-316, 2011.

[38] H. Ebrahimian, F. Jalayer, A. Lucchini, F. Mollaioli, G. Manfredi, Preliminary ranking of alternative scalar and vector intensity measures of ground shaking. *Bulletin of Earthquake Engineering*, In-Press, 2015, DOI 10.1007/s10518-015-9755-9.

[39] A. Miano, F. Jalayer, R. De Risi, A. Prota, G. Manfredi, A case-study on scenario-based probabilistic seismic loss assessment for a portfolio of bridges. *12th International Conference on Applications of Statistics and Probability in Civil Engineering (ICASP12)*, Vancouver, Canada, July 12-15, 2015.

[40] A. Miano, F. Jalayer, R. De Risi, A. Prota, G. Manfredi, Bridge portfolio seismic loss assessment: simulation of the direct losses due to Irpinia 1980 earthquake, *Bulletin of Earthquake Engineering*, submitted, 2015.

[41] *Prezzi informative opere edili nella regione Abruzzo*, Direzione lavori pubblici ciclo idrico integrato difesa del suolo e della costa protezione civile, servizio tecnico regionale dei ll.pp., 2013 (in Italian).

[42] F. Jalayer, C.A. Cornell, *A Technical Framework for Probability-Based Demand and Capacity Factor Design (DCFD) Seismic Formats*, *Report PEER 2003/08*, , University of California, Berkeley, CA, 2003.

[43] F. Jalayer, C.A. Cornell, Alternative non-linear demand estimation methods for probability-based seismic assessments. *Earthquake Engineering and Structural Dynamics*, **38**(8), 951-972, 2009.

COMPDYN 2015
5th ECCOMAS Thematic Conference on
Computational Methods in Structural Dynamics and Earthquake Engineering
M. Papadrakakis, V. Papadopoulos, V. Plevris (eds.)
Crete Island, Greece, 25–27 May 2015

RISK-BASED DESIGN CHECK FOR COLLAPSE SAFETY USING FEW GROUND MOTIONS

Marko Brozovič[1] and Matjaž Dolšek[2]

[1] University of Ljubljana, Faculty of Civil and Geodetic Engineering
Jamova 2, 1000 Ljubljana, Slovenia
marko.brozovic@fgg.uni-lj.si

[2] University of Ljubljana, Faculty of Civil and Geodetic Engineering
Jamova 2, 1000 Ljubljana, Slovenia
mdolsek@ fgg.uni-lj.si

Keywords: Seismic collapse risk, ground motion selection, characteristic ground motions, nonlinear dynamic analysis, dual structural system, 3R method.

Abstract. *The 3R method (Response analysis, Record selection, Risk-based decision making), which is used to check the adequacy of structural collapse safety by few nonlinear dynamic analyses, is briefly presented. The 3R method uses characteristic ground motions, which are selected by two-step selection procedure. Hazard-consistent set of ground motions is selected in the first step, while in the second step a subset of a few ground motions is obtained on the basis of the seismic response analysis of equivalent single-degree-of-freedom model, which is not computationally demanding. All ground motions are scaled to single intensity level, which corresponds to target collapse risk. The objective of the method is not precise assessment of collapse risk, but decision making whether the collapse risk is lower or greater in comparison to the target collapse risk. For this reason simple decision model may be introduced. If collapse is observed for less than half of characteristic ground motions, it can be decided that the reliability of structure against collapse is appropriate and vice versa. For an example of reinforced concrete dual structural system it is shown that an intensity-based assessment can provide sufficiently accurate risk-based decision making.*

1 INTRODUCTION

Seismic safety of built environment should be guaranteed by an appropriate design of structures for earthquake resistance. Thus it would be appropriate to include an assessment of the seismic risk in design codes. In the simplest case the seismic risk can be communicated in terms of mean annual frequency of exceeding a designated limit state. In this paper collapse safety is taken under consideration, since this is the fundamental performance objective in designing structures for earthquake resistance.

Several procedures for risk-based seismic design of structures were already introduced (e.g. [1, 2, 3]). These procedures are aimed to satisfy the condition that the collapse risk is lower than the target collapse risk, which is assumed acceptable. However, the target collapse risk is to some extent subjective performance measure, which is dependent on potential fatalities, direct and indirect economic losses due to earthquakes in the lifetime of structures.

In general, the calculation of the collapse risk is a complex task, which is performed by integrating the risk equation that combines seismic hazard function with collapse fragility function. For example, definition of collapse fragility function requires large number of computationally demanding dynamic analysis of nonlinear structural model. For practical purposes the estimation of collapse risk was simplified by different procedures. Cornell [4] developed a closed form solution of risk equation, which assumes linear approximation of hazard function in logarithmic space and lognormal distribution of collapse intensities. On this basis Fajfar and Dolšek [5] proposed a practice-oriented estimation of the failure probability of building structures, where the collapse fragility function is determined by assumed standard deviation of collapse intensities and approximate evaluation of median collapse intensity by N2 method [6]. However, different failure modes may strongly impact the seismic behaviour of structures, which can be taken into account by nonlinear dynamic analysis. An important issue of the dynamic analysis is the appropriate selection of ground motions, which should be consistent with seismic hazard at the site and should produce unbiased estimate of seismic demand. Since this is not a trivial task, many ground motion selection procedures were developed (e.g. [7-9]). In addition, different procedures were proposed aiming to reduce the computational time needed to obtain seismic demand by nonlinear dynamic analysis, e.g. [10, 11]. Eads et al. [12] developed a practice-oriented procedure for seismic collapse risk estimation, where lognormally distributed collapse fragility function is determined by nonlinear dynamic analyses at two carefully selected intensities. Such an approach still requires large amount of dynamic analyses due to large sets of ground motions.

Recently, Dolšek and Brozovič [13] proposed the 3R method, which realized a concept of intensity-based assessment for risk-based decision making about adequate seismic collapse safety. Only few dynamic analyses at single intensity are needed to decide whether the seismic collapse risk is adequately low or not. The 3R method uses characteristic ground motions, which are selected by two-step selection procedure. In the first step hazard-consistent set of ground motions is selected, while in the second step a subset of a few ground motions is selected on basis of approximately estimated collapse intensities by using computationally non-demanding seismic response analysis for a proxy of the structural model. All ground motions are scaled to single intensity level, which corresponds to target collapse risk.

In the following the overview of the 3R method is firstly given. Then the application of the 3R method is demonstrated by means of the seismic collapse safety assessment for a dual structural system. At the end evaluation of the accuracy of the 3R method is given.

2 OVERVIEW OF THE 3R METHOD

The building codes, e.g. [14], commonly assume that structures designed according to simple design rules are safe against collapse due to earthquakes. It is clear that such a principal assumption should be checked in the design. To simply check the adequacy of collapse risk the concept of intensity-based assessment for risk-based decision making can be realized by means of the 3R method (Response analysis, Record selection, Risk-based decision making), which was recently proposed [13].

2.1 Decision model

The purpose of the 3R method is not precise assessment of seismic collapse risk, but introduction of the simple decision model to decide whether the collapse risk is lower or greater than then the target collapse risk λ_t,. Such an approach provides slightly less information in comparison to direct estimation of seismic collapse risk λ. However, the adequacy (acceptability) of seismic collapse risk can be estimated and the number of required dynamic analyses of nonlinear structural model is significantly reduced. Assessment of structure is performed only at one intensity, so-called characteristic value of target collapse intensity $S_{a,ct}$, which corresponds to target collapse risk λ_t and seismic hazard at a site. In addition, assessment can be performed only for a few, e.g. seven, hazard consistent ground motions, so-called characteristic ground motions (CGMs), which are scaled to $S_{a,ct}$. Estimation of seismic collapse risk adequacy on basis of results of few dynamic analyses is then straightforward. If less than 50% of CGMs cause the collapse of a structure, it can be concluded that the structure is safe against collapse due to earthquakes. In the opposite case, the performance objective is not met.

2.2 Assumptions

The 3R method uses several assumptions. A type of distribution and standard deviation of collapse intensities have to be assumed in order to definite the characteristic value of target collapse intensity $S_{a,ct}$, at which the seismic assessment is performed. Commonly lognormal distribution of collapse fragility function is used. Lazar and Dolšek [15] showed that standard deviation of natural logarithms of collapse intensities in terms of spectral acceleration at fundamental period in the case of reinforced concrete frames is within the interval from 0.3 to 0.5. To minimize the influence of error in assumed standard deviation of natural logarithms of collapse intensities β_t on the value of $S_{a,ct}$ Dolšek and Brozovič [13] showed that the target collapse intensity should be associated with a low percentile, so-called characteristic percentile, of collapse intensities. Due to simplicity a characteristic percentile was set to 16^{th} percentile. There are several other reasons why the characteristic value of collapse intensity is selected at low percentile of collapse intensities. For example, (i) uncertainties associated with the seismic hazard are controllable at lower intensity levels, (ii) scale factors of ground motions are more likely in the range which still allow unbiased estimates of seismic demand, (iii) the accuracy of simplified methods to provide approximate collapse intensities is greater for those ground motions which cause the collapse of buildings at low intensities [16] and (iv) it is well known that the intensities which have the largest contribution to the collapse risk occur in the lower half of the collapse fragility function, e.g. [12].

In addition, it is assumed that a suitable subset consisting of CGMs can be selected from larger hazard-consistent set using proxy of collapse intensities, which can be obtained by the pushover-based methods. In this paper a number of the CGMs was set equal to seven. In this case the initial set must contain at least 19 ground motions to assure that the median collapse intensity of CGMs is in the vicinity of characteristic value of collapse intensities for the whole hazard-consistent set of ground motions. If there are less than 19 ground motions, the accura-

cy of the method would be reduced. However, the hazard-consistent set can contain a large number of ground motions, since the approximate collapse intensities are obtained by selected simplified method of analysis, which is not computationally demanding.

2.3 Step by step procedure

In the following the algorithm of the 3R method is presented:

1) *Define the target collapse risk* λ_t. The target collapse risk can be defined by code-writing organizations, e.g. [14], or can be adopted on the basis of models of tolerable risk, e.g. [17]. It can also be simply prescribed by the stakeholders due to higher risk aversion.
2) *Obtain detailed information regarding the seismic hazard at the site of interest*. The results of probabilistic seismic hazard analysis are required in order to estimate the characteristic target collapse intensity $S_{a,ct}$ (i.e. the hazard function), and to select a hazard-consistent set of ground motions.
3) *Determine the characteristic value of the target collapse intensity* $S_{a,ct}$. The median value of target collapse intensity $\tilde{S}_{a,t}$ can be determined utilizing risk equation in closed-form or iteratively by numerical integration of the risk equation. In both cases, the standard deviation of collapse intensities in log domain β_t has to be assumed. If the closed-form solution of the risk equation is used, the median value of target collapse intensity $\tilde{S}_{a,t}$ can be determined from the following equation [4]

$$\lambda_t = k_0 \left(\tilde{S}_{a,t} \right)^{-k} \cdot e^{0.5 \cdot k^2 \cdot \beta_t^2} \tag{1}$$

   where k and k_0 represent the slope and intercept of linear approximation to the hazard curve in log domain, respectively. However, the characteristic value of target collapse intensity $S_{a,ct}$ is then estimated at 16^{th} percentile of the target collapse fragility function as follows

$$S_{a,ct} = \tilde{S}_{a,t} \cdot e^{-\beta_t} \tag{2}$$

4) *Select a hazard-consistent set of ground motions.* The results consist of ground motions which are scaled to $S_{a,ct}$. Different procedures can be used to select appropriate ground motions. Disaggregation of the hazard is also required, if, for example, the conditional spectrum approach [8] is used for the selection of the hazard-consistent set of ground motions. Hazard-consistent set of ground motions selected in this step may be large, since the subset of ground motions is selected in the following.
5) *Perform conventional pushover analysis and define a simple model of the structure.* Conventional pushover analysis is performed with invariant distribution of the lateral forces. It is recommended that a load pattern is associated with the most important mode shape. The simple model is represented by an equivalent single-degree-of-freedom model, which can be defined, for example, by analogy to the N2 method [6]. However, the force-displacement relationship of the simple model can be represented by multi-linear idealization of the pushover curve taking into account strength degradation.
6) *Assess approximate collapse intensities.* Dynamic analysis should be performed at the level of the simple model. Each ground motion is scaled until collapse occurs, e.g. by performing incremental dynamic analysis [18].
7) *Determine the characteristic ground motions.* The subset of ground motions from the hazard-consistent set of ground motions (step 4) is obtained gradually, taking into ac-

count approximate collapse intensities from step 6. The selected subset of ground motions corresponds to approximate collapse intensities, which are close to the characteristic value of approximate collapse intensities. It is also required that the median value of approximate collapse intensities corresponding to CGMs closely match with the characteristic value of approximate collapse intensities.

8) *Perform nonlinear response history analysis using a nonlinear model of the entire structure.* The response history analysis is performed for all the CGMs at characteristic value of target collapse intensity $S_{a,ct}$.
9) *Make a risk-based decision.* It can be decided that the collapse risk of the investigated structure is less than the target collapse risk if collapse is observed for less than half of the CGMs. This means that the collapse ratio r_C, which is defined as the number of CGMs causing collapse divided by the total number of all the CGMs is lower than 0.5 (Figure 1). In the opposite case ($r_C > 0.5$), the structure is not safe against collapse due to earthquakes.

More details and description of alternative variants of the 3R method can be found elsewhere [13]. The 3R method requires a lot of steps, which are not computationally demanding, but for practical purposes it would be inconvenient to perform all of these steps manually. For this reason the web application for the selection of CGMs was developed [19], which automatically performs steps 3, 4, 6 and 7 from the above described step-by-step procedure.

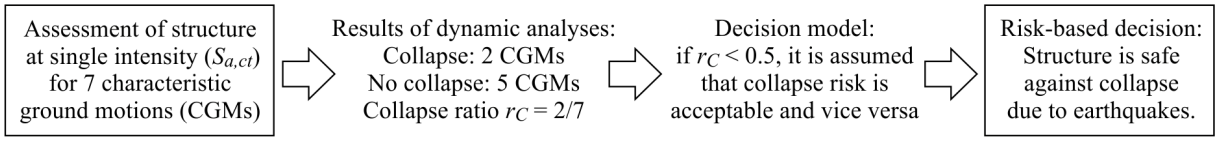


Figure 1: An example of risk-based decision making in the case of the 3R method.

3 CASE STUDY OF SEISMIC COLLAPSE SAFETY ASSESSMENT FOR THE 8-STOREY DUAL STRUCTURAL SYSTEM

3.1 Description of the structure

An 8-storey reinforced concrete dual structural system designed according to Eurocode 8 requirements for medium ductility class was investigated in X direction (Figure 2).

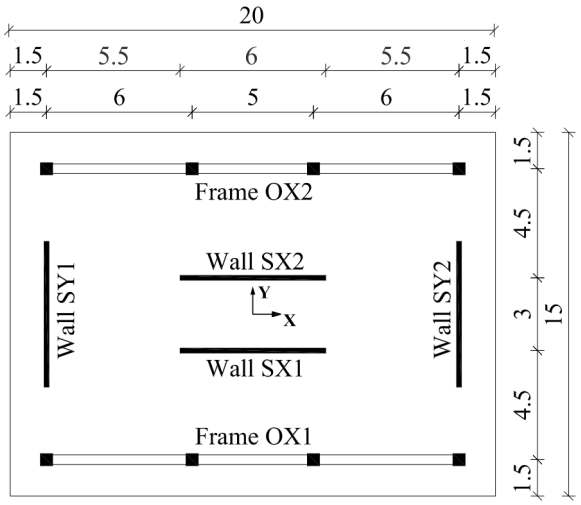


Figure 2: Typical plan view of dual structural system [22].

The height of each storey amounted to 2.8 m. The span of exterior and interior bays amounted to 6 m and 5 m, respectively. Cross sections of all columns and beams were, respectively, 50/50 cm and 40/45 cm. Slabs with 20 cm thickness were considered with beam effective width of 1.6 m. The width and thickness of the wall were 6 m and 20 cm, respectively. Concrete class C30/37 and reinforcement class S500 were prescribed. The structure was modelled with simplified nonlinear model utilizing OpenSees [20] in conjunction with PBEE toolbox [21], which was extended for analysis of dual structures [22]. The fundamental period of the structure was 0.87 s.

3.2 Hazard-consistent ground motion selection

The target collapse risk λ_t was selected to be $5 \cdot 10^{-4}$. The seismic hazard curve and disaggregation was obtained for site in Palo Alto, California from probabilistic seismic hazard analysis computation web tool prepared by United States Geological Survey (https://geohazards.usgs.gov/deaggint/2008/). It should be noted that spectral acceleration at fundamental period of structure $S_a(T_1)$ was used as intensity measure. On this basis the characteristic value of target collapse intensity $S_{a,ct}$ was estimated to 0.96 g by taking into account lognormal fragility function with $\beta_t = 0.4$. The first four steps of proposed 3R method resulted in hazard-consistent set of 40 ground motions, which were selected by matching the conditional spectrum [8] determined for $S_{a,ct}$ (Figure 3a) by using computationally efficient ground motion selection algorithm for matching a target response spectrum mean and variance [23].

3.3 Selection of characteristic ground motions and decision-making

The pushover curve was idealized with a force-displacement relationship (Figure 3b) which was intentionally quite inaccurate at the tail of the pushover curve. This caused an additional bias in the approximate collapse intensities obtained by the SDOF model (Figure 4a). The subset of hazard-consistent ground motions (CGMs) was then selected and the dynamic analysis of the structure was performed taking into account CGMs. Since only two CGMs caused collapse ($r_C = 2/7 = 0.29 < 0.5$), as indicated in Figure 4a, it was decided that structure met the performance objective. Thus it can be concluded that the collapse risk of the investigated dual structure is less than the target collapse risk.

If the analyst would perform dynamic analysis for all ground motions from the hazard consistent set at $S_{a,ct}$, then the decision regarding the adequacy of the structure would be the same. Note that only 3 ground motions caused collapse of the structure (Figure 4a), which means that the $r_C = 3/40 = 0.075$. This is less than threshold value 0.16 associated with the characteristic percentile.

The decision made by 3R method was correct, since the collapse risk of the structure was estimated to $3.5 \cdot 10^{-4}$, which is less than the target (acceptable) collapse risk ($5 \cdot 10^{-4}$). In addition, the risk-based decision making of the 3R method was validated by calculating the collapse ratio r_C for multiple levels of the target collapse risk (Figure 4b). Dynamic analyses have been performed for the CGMs scaled to different intensities $S_{a,ct}$ corresponding to different levels of target collapse risk. On this basis an approximate collapse risk was obtained, which corresponded to the 50% collapse ratio (Figure 4b). Therefore, the decision based on 3R method for this particular example would be incorrect if the target collapse risk would be assumed somewhere in the interval between 'exact' collapse risk ($3.5 \cdot 10^{-4}$) and approximate collapse risk ($4.7 \cdot 10^{-4}$), i.e. the interval of target collapse risk indicated in Figure 4b with grey color. The largest possible error $\varepsilon_{\max}$ in terms of seismic collapse risk would be 32%. The method provide sufficiently accurate decision making in the case of a selected dual structure,

although the intensities causing collapse of SDOF model are significantly different to the corresponding intensities obtained by the entire structural model (Figure 4a).

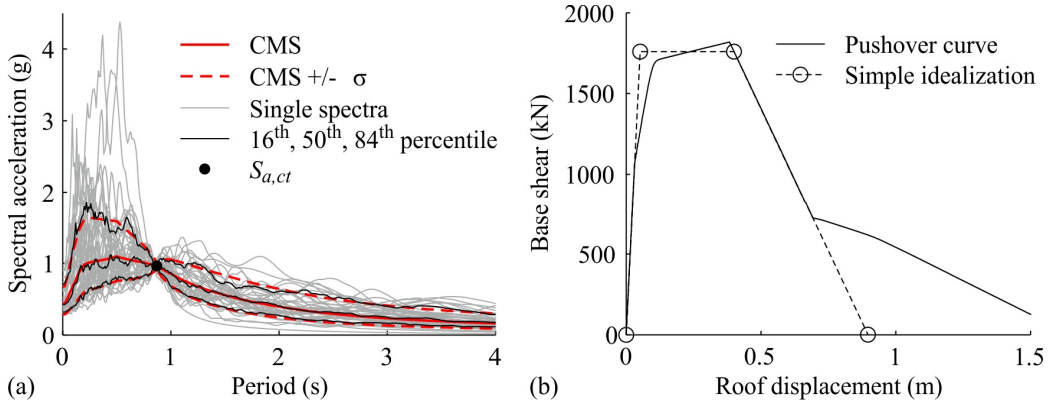


Figure 3: (a) Conditional spectrum consistent with the characteristic value of target collapse intensity $S_{a,ct}$, spectra of selected ground motions and the corresponding 16th, 50th and 84th percentile and (b) the pushover curve with simple idealization of base shear – roof displacement relationship.

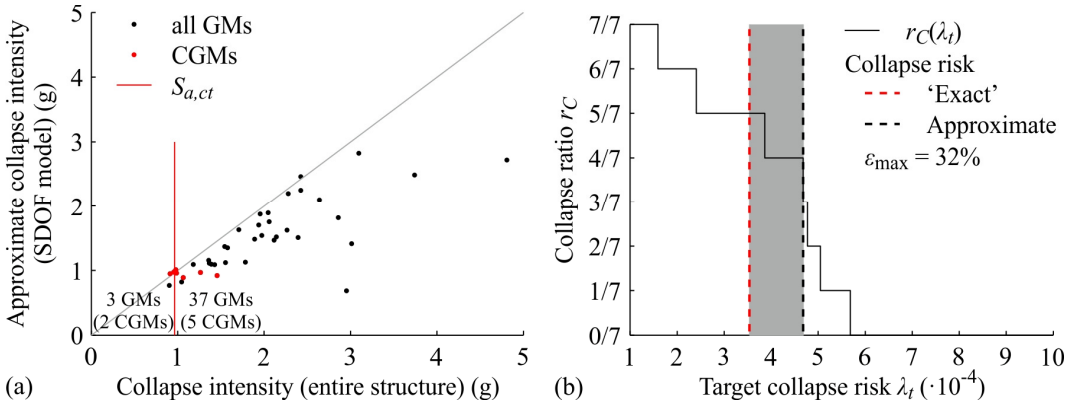


Figure 4: (a) Approximate versus 'exact' collapse intensities for 40 ground motions with indicated CGMs and the characteristic value of target collapse intensity $S_{a,ct}$ and (b) the collapse ratio r_C for multiple levels of the target collapse risk λ_t with the indicated interval of target collapse risk, for which the 3R method would result in an inaccurate risk-based decision making.

4 CONCLUSIONS

The theoretical background and application of the practice-oriented 3R method was briefly presented. The 3R method is intended to be used for checking the adequacy of collapse risk of structures on basis of few nonlinear dynamic analyses. Seismic demand is determined at single intensity, which is associated with target collapse risk, taking into account characteristic ground motions, which are selected by two-step ground motion selection procedure. If collapse is observed for less than half of characteristic ground motions, it can be decided that the design of the structure is appropriate and vice versa. The 3R method is not meant for estimation of precise collapse risk, but to decide whether the collapse risk of investigated structure is larger or lower in comparison to the target collapse risk, which is assumed acceptable.

The method was demonstrated by means of example of checking the seismic collapse safety of the reinforced concrete dual structural system. It was shown that the concept of intensity-based assessment for risk-based decision making can be applied to realistic structures. Decision made by the 3R method was confirmed by direct estimation of collapse risk on the basis of incremental dynamic analysis of the nonlinear structural model.

The proposed seismic analysis method requires only few (e.g. 7) nonlinear dynamic analyses of model of entire structure. This makes it attractive for practical purposes.. Additional work, which should be performed within the 3R method in order to obtain characteristic ground motions and an appropriate characteristic value of target collapse intensity is not computationally demanding and can be automated, which has actually already been realized by means of the web application. An advantage of the proposed method is that scale factors of ground motions are small, which reduces biased estimates of seismic demand.

The 3R method could be used for checking the collapse risk of newly designed and existing structures. Due to computational efficiency it could be also incorporated to iterative risk-based design procedures based on dynamic analysis of nonlinear structural model. However, additional studies are needed in order to assess the applicability of the method for other types of structures and performance objectives.

REFERENCES

[1] M. Dolšek, Concept of risk-based seismic design of buildings using methods of nonlinear analysis. *Proceedings of the 4th International Conference on Computational Methods in Structural Dynamics and Earthquake Engineering (COMPDYN 2013)*, Kos Island, Greece, June 12-14, 2013.

[2] N. Lazar, M. Dolšek, Risk-based seismic design of buildings using an efficient push-over analysis procedure. *Proceedings of the 11th International Conference on Structural Safety & Reliability (ICOSSAR 2013)*, Columbia University, New York, USA, June 16-20, 2013.

[3] N. Lazar Sinković, M. Brozovič, M. Dolšek, Risk-based seismic design for collapse safety. Submitted to *Earthquake Engineering and Structural Dynamics*.

[4] C.A. Cornell, Calculating building seismic performance reliability: a basis for multi-level design norms. *Proceedings of the 11th World Conference on Earthquake Engineering (11WCEE)*, Acapulco, Mexico, June 23-28, 1996.

[5] P. Fajfar, M. Dolšek, A practice-oriented estimation of the failure probability of building structures. *Earthquake Engineering and Structural Dynamics*, **41**, 531-547, 2012.

[6] P. Fajfar, A nonlinear analysis method for performance-based seismic design. *Earthquake Spectra*, **16**, 573-592, 2000.

[7] E.I. Katsanos, A.G. Sextos, G.D. Manolis, Selection of earthquake ground motion records: A state-of-the-art review from a structural engineering perspective. *Soil Dynamics and Earthquake Engineering*, **30**, 157-169, 2010.

[8] J.W. Baker, Conditional mean spectrum: Tool for ground-motion selection. *Journal of Structural Engineering*, **137**, 322-331, 2011.

[9] A.B. Bradley, A generalized conditional intensity measure approach and logistic ground-motion selection. *Earthquake Engineering and Structural Dynamics*, **39**, 1321-1342, 2010.

[10] A. Liel, H. Tuwair, A practical approach for assessing structural resistance to earthquake-induced collapse. *Proceedings of the 19th Analysis and Computation Conference, ASCE Structural Congress*, 2010.

[11] A. Azarbakht, M. Dolšek, Progressive incremental dynamic analysis for first-mode dominated structures. *Journal of Structural Engineering*, **137**, 445-455, 2011.

[12] L. Eads, E. Miranda, H. Krawinkler, D.G. Lignos, An efficient method for estimating the collapse risk of structures in seismic regions. *Earthquake Engineering and Structural Dynamics*, **42**, 25-41, 2013.

[13] M. Dolšek, M. Brozovič, Seismic response analysis using characteristic ground motion records for risk-based decision making. *Earthquake Engineering and Structural Dynamics*, under review.

[14] CEN, *Eurocode 8: design of structures for earthquake resistance - part 1: general rules, seismic actions and rules for buildings, EN 1998-1*. European Committee for Standardisation, 2004.

[15] N. Lazar, M. Dolšek, Incorporating intensity bounds for assessing the seismic safety of structures: Does it matter? *Earthquake Engineering and Structural Dynamics*, **43**, 717-738, 2014.

[16] M. Brozovič, M. Dolšek, Envelope-based pushover analysis procedure for the approximate seismic response analysis of buildings. *Earthquake Engineering and Structural Dynamics*, **43**, 77-96, 2014.

[17] P. Helm, Integrated risk management for natural and technological disasters. *Tephra*, **15**, 5-19, 1996.

[18] D. Vamvatsikos, C.A. Cornell, Incremental dynamic analysis. *Earthquake Engineering and Structural Dynamics*, **31**, 491-514, 2002.

[19] R. Klinc, Ž. Šebenik, M. Dolenc, M. Brozovič, M. Dolšek, Development of web-based system for the selection of characteristic ground motions. Submitted to *Automation in Construction*, 2015.

[20] *Open System for Earthquake Engineering Simulation (OpenSees)*. Pacific Earthquake Engineering Research Center, University of California, Berkeley, CA. http://opensees.berkeley.edu/ [22 Februar 2011].

[21] M. Dolšek, Development of computing environment for the seismic performance assessment of reinforced concrete frames by using simplified nonlinear models. *Bulletin of Earthquake Engineering*, **8**, 1309-1329, 2010.

[22] M. Kosič, *Determination of dispersion measures for seismic response of reinforced concrete buildings*. Doctoral dissertation, University of Ljubljana, Faculty of Civil and Geodetic Engineering, 2014.

[23] N. Jayaram, T. Lin, J.W. Baker, A computationally efficient ground-motion selection algorithm for matching a target response spectrum mean and variance. *Earthquake Spectra*, **27**, 797-815, 2011.

COMPDYN 2015
5th ECCOMAS Thematic Conference on
Computational Methods in Structural Dynamics and Earthquake Engineering
M. Papadrakakis, V. Papadopoulos, V. Plevris (eds.)
Crete Island, Greece, 25–27 May 2015

DYNAMIC ANALYSIS OF TRAIN-BRIDGE SYSTEM SUBJECTED TO EARTHQUAKE ACTION CONSIDERING TOPOGRAPHIC EFFECTS

Hong Qiao[1], He Xia[1], Xianting Du[1] and Yong Nan[1]

[1] School of Civil Engineering, Beijing Jiaotong University
Shangyuancun 3#, Haidian District, Beijing 100044, China
E-mail: CarrieQh@163.com, hxia88@163.com, wadmdxt@163.com, nanyong582613@163.com

Keywords: train-bridge system, dynamic response, earthquake action, topographic effects, viscous- spring artificial boundary.

Abstract. *A method taking into consideration the topographic effects in dynamic analysis of a train-bridge system subjected to earthquake action is presented and the influence of topography on the seismic response of train-bridge system is studied. Based on the theory of viscous-spring artificial boundary, a 3-D finite element model for the site considering topographic effect is established by using the ANSYS. The procedure of wave input is realized by transforming the seismic time history into equivalent loads acting on the artificial boundary, by means of which the seismic time histories at the supports of bridge are obtained. The dynamic model for a train-bridge system subjected to multi-support seismic excitations is established, in which the velocity and displacement time histories of earthquake waves are exerted on the bridge supports. With a train passing through a 480m bridge as a case study, the dynamic response of the train-bridge system under earthquakes considering local topography of the site is analyzed, and compared with those without considering the topographic effect. The results show that when the topographic effect is considered, the dynamic response of the train-bridge system changes on the peak value as well as the time of the peak appearance, showing that it is necessary to consider the topographic effect in dynamic analysis of train-bridge system under earthquakes.*

1 INTRODUCTION

In recent years, the railway transportation has gained rapid development. To ensure the safety and stability of running trains, more and more bridges including viaducts are built, which inevitably increases the possibility of trains on bridges when an earthquake occurs. As a result, the problem of train-bridge interaction during an earthquake has become a research hotspot recently [1-7].

In China, among the extensive railways which have already been built or are under construction, many of them are located in the southwestern regions with mountainous site topographies. On the other hand, these regions are also seismic zones susceptible to earthquakes. The 2008 Wenchuan Earthquake occurring in Sichuan Province is a typical example which caused a wide range of damages on different types of railway bridges [8]. Therefore, it is of significance to study the seismic response of bridges located at these regions. In seismic design, it has been long recognized that the local topography has a significant effect on the amplitude of ground motion during earthquakes. Celebi performed site-response experiments 5 months after the Chile earthquake (Central Chile, M7.8) and found that structures located at ridges suffer more intensive damage than other places [9]. Jibson measured the acceleration peaks across a ridge in Japan and the measurements showed that compared with the base, there was an amplification at the crest varying from 1.8 to 5.5 [10]. In the 2008 Wenchuan Earthquake, the complex topography may be one of the main factors leading to the collapse of the Baihua Bridge as well as the Miaoziping Bridge [11]. Lee et al. [12] investigated the effects of high-resolution surface topography on seismic ground motion and found that the amplification of ground motion mainly occurs at the tops of hills and ridges while the valleys and flat-topped hills experience lower levels of ground shaking. There are also many other papers discussing the topographic effects on the peak of ground motion and on the seismic response of bridges [13-18]. All these publications indicated the necessity of considering the topographic effects in seismic design, but few of them discussed the seismic response of train-bridge coupling system considering this aspect.

In this regard, this paper presents a method for dynamic analysis of train-bridge system subjected to earthquake action considering local topography. In this method, the train-bridge system consists of the bridge subsystem and the train subsystem. The two subsystems are established by mode superposition method and rigid-body dynamics method, respectively and the Newmark-β method is used to solve the dynamic interaction. To take the topographic effects into account, a 3-D analytical model of local site based on the theory of viscous-spring artificial boundary and finite element method is established. The process of wave input is realized by transforming the seismic time history into equivalent loads acting on the artificial boundary, by means of which the seismic time history at each support of bridge can be obtained. Then the dynamic analysis of a train-bridge system subjected to multi-support seismic excitations is carried out, in which the velocity and displacement time histories of seismic excitations obtained by the above method are exerted on the bridge supports. A train passing through a 480m continuous bridge is taken as a case study and the dynamic response of train-bridge system under earthquakes considering local topography are analyzed.

2 SEISMIC EXCITATIONS CONSIDERING LOCAL TOPOGRAPHY

To realize the procedure of earthquake wave propagating in the soil of local site, the finite element method is an efficient way. A key step of this method is to extract a finite domain from the infinite soil medium, which means a verified virtual artificial boundary able to absorb the energy of the scattering waves is necessary. The 3D viscous-spring artificial boundary proposed by Liu [19] not only satisfies the above criterion but also has advantages of high

numerical precision, adequate stability and convenience in application. Therefore, in this analysis, the 3D viscous-spring artificial boundary is used when establishing the model of local site.

2.1 Input method of seismic wave

The problem of how to input the seismic wave can be converted into a wave source problem [20], which means the input motion is converted into equivalent loads acting on the artificial boundary to simulate the procedure of seismic wave input. The equivalent loads F_{BN} and F_{BT}, respectively in the normal and tangential directions, can be expressed as follows.

$$F_{BN} = \sigma_0\left(x_B, y_B, t\right) + C_{BN}\dot{u}_0\left(x_B, y_B, t\right) + K_{BN}u_0\left(x_B, y_B, t\right) \tag{1}$$

$$F_{BT} = \tau_0\left(x_B, y_B, t\right) + C_{BT}\dot{v}_0\left(x_B, y_B, t\right) + K_{BT}v_0\left(x_B, y_B, t\right) \tag{2}$$

where $u_0(x, y, t)$ and $v_0(x, y, t)$ are the normal and tangential displacement of the incident wave, respectively; $\sigma_0(x, y, t)$ and $\tau_0(x, y, t)$ are the normal and tangential stress determined by $u_0(x, y, t)$ and $v_0(x, y, t)$, respectively; x_B and y_B are the node coordinates of the artificial boundary; K_{BN}、K_{BT}、C_{BN}、C_{BT} are the spring coefficients and damping coefficients of the normal and tangential springs respectively, the values of which can be determined according to the following equations [19],

$$\left.\begin{aligned} K_{BN} &= \frac{\alpha_N G}{R} \\ K_{BT} &= \frac{\alpha_T G}{R} \\ C_{BN} &= \rho c_p \\ C_{BT} &= \rho c_s \end{aligned}\right\} \tag{3}$$

where α_N and α_T are the coefficients in the normal and tangential directions respectively, which can be referred to Table 1; G is the shear modulus and ρ is the mass density of the medium, namely the solid of the local site; R is the distance between the load point and the boundary, which can be obtained approximately by simply taking the value of the perpendicular distance from the load point to the boundary.

Parameters	Value range	Recommended value
$\boldsymbol{\alpha_N}$	1.0~2.0	4/3
$\boldsymbol{\alpha_T}$	0.5~1.0	2/3

Table 1: Recommended value of α_N and α_T

2.2 Calculation of equivalent loads

Generally, the focus of an earthquake is deep and there are usually many refractions happening during the propagation process of the seismic wave, which results in the vertical incidence of the earthquake wave when it arrives at the earth surface. Therefore, in this analysis, the seismic wave is assumed to be a plane incident one travelling perpendicularly to the ground surface. The time histories of the incident plane P wave and S wave are $u_P(t)$ and $u_S(t)$ respectively. The *x*-*y* plane of the rectangular coordinate system is parallel to the bottom of the model and the *z*-axis points to the finite domain, as shown in Figure1.

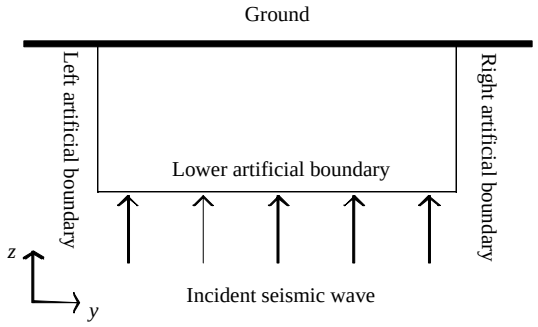


Figure1: Vertical incidence model of seismic wave

Assuming the incident S wave vibrates along the *x*-axis, the equivalent loads acting on each node of the artificial boundary can be obtained based on the wave propagation law and the stress state of the wave field [21], namely,

(1) Under the condition of incident P wave:

$$f_z^{-z}(t) = A\left[K_{\mathrm{BN}}u_{\mathrm{p}}(t) + C_{\mathrm{BN}}\dot{u}_{\mathrm{p}}(t) + \rho c_{\mathrm{p}}\dot{u}_{\mathrm{p}}(t)\right] \tag{4}$$

$$f_x^{-x}(t) = A\lambda\left[\dot{u}_{\mathrm{p}}(t-\Delta t_1) - \dot{u}_{\mathrm{p}}(t-\Delta t_2)\right]/c_{\mathrm{p}} \tag{5}$$

$$f_z^{-x}(t) = A[K_{\mathrm{BT}}u_{\mathrm{p}}(t-\Delta t_1) + C_{\mathrm{BT}}\dot{u}_{\mathrm{p}}(t-\Delta t_1) + K_{\mathrm{BT}}u_{\mathrm{p}}(t-\Delta t_2) + C_{\mathrm{BT}}\dot{u}_{\mathrm{p}}(t-\Delta t_2)] \tag{6}$$

$$f_y^{-y}(t) = -f_x^{+x}(t) = -f_y^{+y}(t) = f_x^{-x}(t) \tag{7}$$

$$f_z^{-y}(t) = f_z^{+x}(t) = f_z^{+y}(t) = f_z^{-x}(t) \tag{8}$$

(2) Under the condition of incident S wave:

$$f_x^{-z}(t) = A\left[K_{\mathrm{BT}}u_{\mathrm{s}}(t) + C_{\mathrm{BT}}\dot{u}_{\mathrm{s}}(t) + \rho c_{\mathrm{s}}\dot{u}_{\mathrm{s}}(t)\right] \tag{9}$$

$$f_x^{-x}(t) = A[K_{\mathrm{BN}}u_{\mathrm{s}}(t-\Delta t_3) + C_{\mathrm{BN}}\dot{u}_{\mathrm{s}}(t-\Delta t_3) + K_{\mathrm{BN}}u_{\mathrm{s}}(t-\Delta t_4) + C_{\mathrm{BN}}\dot{u}_{\mathrm{s}}(t-\Delta t_4)] \tag{10}$$

$$f_z^{-x}(t) = A\rho c_{\mathrm{s}}\left[\dot{u}_{\mathrm{s}}(t-\Delta t_3) - \dot{u}_{\mathrm{s}}(t-\Delta t_4)\right] \tag{11}$$

$$f_x^{+x}(t) = f_x^{-x}(t) \tag{12}$$

$$f_z^{+x}(t) = -f_z^{-x}(t) \tag{13}$$

$$f_x^{-y}(t) = A[K_{\mathrm{BT}}u_{\mathrm{s}}(t-\Delta t_3) + C_{\mathrm{BT}}\dot{u}_{\mathrm{s}}(t-\Delta t_3) + K_{\mathrm{BT}}u_{\mathrm{s}}(t-\Delta t_4) + C_{\mathrm{BT}}\dot{u}_{\mathrm{s}}(t-\Delta t_4)] \tag{14}$$

$$f_x^{+y}(t) = f_x^{-y}(t) \tag{15}$$

$$\left.\begin{aligned} \Delta t_1 &= l/c_{\mathrm{p}} \\ \Delta t_2 &= (2L-l)/c_{\mathrm{p}} \\ \Delta t_3 &= l/c_{\mathrm{s}} \\ \Delta t_4 &= (2L-l)/c_{\mathrm{s}} \end{aligned}\right\} \tag{16}$$

where the subscript of each equivalent load represents the direction of the load, and the superscript represents the outer normal direction of the boundary where the node locates; Δt_1~Δt_4 represent the time delay of the incident P wave, the reflected P wave, the incident S wave and the reflected S wave, respectively; l is the distance between the node and the lower boundary; L is the distance between the lower boundary and the ground surface; A is the representative area of the node on the artificial boundary [19]; λ is the lame constant.

2.3 Realization of the artificial boundary in FE platform

Taking ANSYS as an example, the medium can be modeled with the Solid45 elements, and the springs and dampers in the viscous-spring artificial boundary can be simulated by the Combin14 elements with its one end fixed.

3 DYNAMIC ANALYSIS MODEL OF TRAIN-BRIDGE COUPLING SYSTEM SUBJECTED TO SEISMIC LOAD

The train-bridge system consists of the bridge subsystem and the train subsystem, as shown in Figure 2. A global coordinate system satisfying the right-hand rule is defined for the train-bridge system, in which the *y*-axis is taken as the longitudinal direction of the bridge and the *x*-axis is the lateral direction of the bridge. Before establishing the motion equations of these two subsystems, several assumptions are made,

(1) The train passes through the bridge with a constant speed;

(2) The seismic ground motions at all supports of the bridge are different;

(3) The seismic load only directly acts on the bridge subsystem and the influence on the train subsystem due to earthquake can be realized by the wheel-track interaction relation.

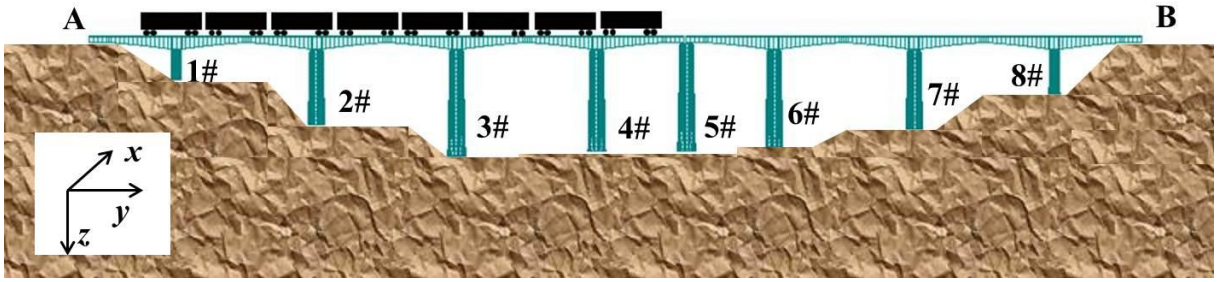


Figure 2: The bridge-train system

The train-bridge dynamic interaction during earthquakes can be described by finite element method and the motion equations of the train subsystem and the bridge subsystem can be expressed as [7]:

$$\boldsymbol{M}_{\mathrm{V}}\ddot{\boldsymbol{u}}_{\mathrm{V}}+\boldsymbol{C}_{\mathrm{V}}\dot{\boldsymbol{u}}_{\mathrm{V}}+\boldsymbol{K}_{\mathrm{V}}\boldsymbol{u}_{\mathrm{V}}=\boldsymbol{F}_{\mathrm{V,B}} \tag{17}$$

$$\begin{bmatrix}\boldsymbol{M}_{\mathrm{ss}} & \boldsymbol{M}_{\mathrm{sb}}\\ \boldsymbol{M}_{\mathrm{bs}} & \boldsymbol{M}_{\mathrm{bb}}\end{bmatrix}\begin{Bmatrix}\ddot{\boldsymbol{u}}_{\mathrm{s}}\\ \ddot{\boldsymbol{u}}_{\mathrm{b}}\end{Bmatrix}+\begin{bmatrix}\boldsymbol{C}_{\mathrm{ss}} & \boldsymbol{C}_{\mathrm{sb}}\\ \boldsymbol{C}_{\mathrm{bs}} & \boldsymbol{C}_{\mathrm{bb}}\end{bmatrix}\begin{Bmatrix}\dot{\boldsymbol{u}}_{\mathrm{s}}\\ \dot{\boldsymbol{u}}_{\mathrm{b}}\end{Bmatrix}+\begin{bmatrix}\boldsymbol{K}_{\mathrm{ss}} & \boldsymbol{K}_{\mathrm{sb}}\\ \boldsymbol{K}_{\mathrm{bs}} & \boldsymbol{K}_{\mathrm{bb}}\end{bmatrix}\begin{Bmatrix}\boldsymbol{u}_{\mathrm{s}}\\ \boldsymbol{u}_{\mathrm{b}}\end{Bmatrix}=\begin{Bmatrix}\boldsymbol{F}_{\mathrm{B,V}}\\ \boldsymbol{0}\end{Bmatrix} \tag{18}$$

where $\boldsymbol{M}$、$\boldsymbol{C}$、$\boldsymbol{K}$ are the mass, damp and stiffness matrices, respectively, $\boldsymbol{u},\dot{\boldsymbol{u}},\ddot{\boldsymbol{u}}$ are the displacement, velocity and acceleration vectors, with the subscript V representing the train subsystem, B the bridge subsystem, s the superstructure and b the base of the bridge, respectively; $\boldsymbol{F}_{\mathrm{B,V}}$ and $\boldsymbol{F}_{\mathrm{V,B}}$ are the interaction forces between the two subsystems which are determined by the wheel-track interaction relation.

From Equation (18), the equilibrium equations of the superstructure with the specified absolute displacement at the bases of the bridge can be written as:

$$\boldsymbol{M}_{\mathrm{ss}}\ddot{\boldsymbol{u}}_{\mathrm{s}}+\boldsymbol{C}_{\mathrm{ss}}\dot{\boldsymbol{u}}_{\mathrm{s}}+\boldsymbol{K}_{\mathrm{ss}}\boldsymbol{u}_{\mathrm{s}}=-\boldsymbol{K}_{\mathrm{sb}}\boldsymbol{u}_{\mathrm{b}}-\boldsymbol{C}_{\mathrm{sb}}\dot{\boldsymbol{u}}_{\mathrm{b}}-\boldsymbol{M}_{\mathrm{sb}}\ddot{\boldsymbol{u}}_{\mathrm{b}}+\boldsymbol{F}_{\mathrm{B,V}} \tag{19}$$

The term $\boldsymbol{M}_{\mathrm{sb}}$ is usually neglected and as a result, Equation (19) can be written as:

$$\boldsymbol{M}_{\mathrm{ss}}\ddot{\boldsymbol{u}}_{\mathrm{s}}+\boldsymbol{C}_{\mathrm{ss}}\dot{\boldsymbol{u}}_{\mathrm{s}}+\boldsymbol{K}_{\mathrm{ss}}\boldsymbol{u}_{\mathrm{s}}=-\boldsymbol{K}_{\mathrm{sb}}\boldsymbol{u}_{\mathrm{b}}-\boldsymbol{C}_{\mathrm{sb}}\dot{\boldsymbol{u}}_{\mathrm{b}}+\boldsymbol{F}_{\mathrm{B,V}} \tag{20}$$

where the first two terms at right side of the equation are the seismic load acting on the bridge.

Applying the mode superposition method to Equation (20), a series of mutually independent modal equations can be obtained, namely:

$$\ddot{q}_i + 2\xi_i\omega_i\dot{q}_i + \omega_i^2 q_i = \boldsymbol{\varphi}_i^T \boldsymbol{M}_{ss}\boldsymbol{R}(2\xi_i\omega_i\dot{\boldsymbol{u}}_b) + \boldsymbol{\varphi}_i^T \boldsymbol{M}_{ss}\boldsymbol{R}(\omega_i^2\boldsymbol{u}_b) + \boldsymbol{\varphi}_i^T \boldsymbol{F}_{B,V} \qquad (i=1,2,\ldots,n) \quad (21)$$

where $\boldsymbol{\varphi}_i$ and q_i are the ith normalized mode shape and generalized coordinate, ω_i and ξ_i are the ith circular frequency and damping ratio, respectively; n is the number of the modes used in the analysis; $\boldsymbol{R}$ is called displacement influence matrix, which can be obtained by the following equation:

$$\boldsymbol{R} = -\boldsymbol{K}_{ss}^{-1}\boldsymbol{K}_{sb} \quad (22)$$

Equation (17) and Equation (21) constitute the basic motion equations of the train-bridge coupling system, and on condition that the wheel-track interaction relation is known, the dynamic response of the train-bridge system can be obtained by solving the above equations by means of numerical step-by-step integration.

4 THE PROCEDURE OF TRAIN-BRIDGE DYNAMIC ANALYSIS DURING EARTHQUAKES CONSIDERING TOPOGRAPHIC EFFECTS

Based on the theory of viscous-spring artificial boundary and the finite element method-based framework for seismic analysis of train-bridge system, the overall procedure of calculating dynamic response of train-bridge system during earthquakes considering local topography can be summarized as follows:

(1) According to the conditions of local topography, establish the 3-D finite element model with viscous-spring artificial boundary;

(2) Calculate the equivalent loads acting on the boundary. If the incident wave is travelling perpendicularly to the ground surface, use Equation (4) ~ (15); if not, there are other equations which are not presented in this paper for the moment;

(3) Apply the loads obtained in step (2) on the nodes at the boundary in the finite element model established in step (1), and then the ground motions considering the local topography at each support can be obtained.

(4) With the ground motions obtained in step (3) taken as seismic excitations, analyze the seismic response of train-bridge coupling system considering topographic effects through the element method-based framework proposed above.

5 CASE STUDY

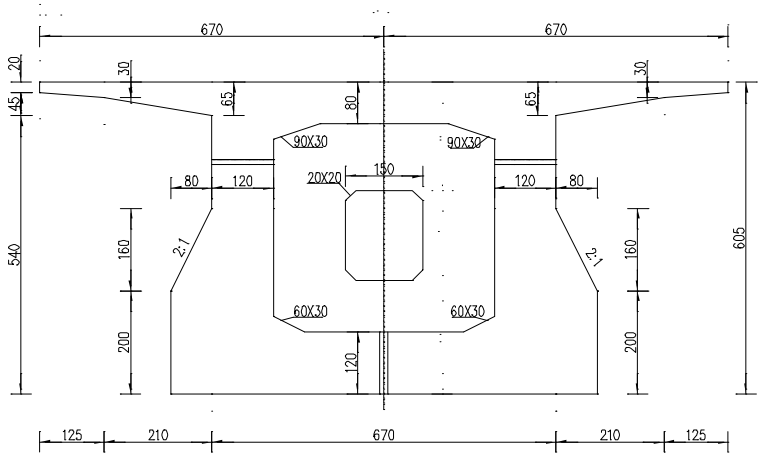
5.1 The bridge model

In order to study the dynamic response of train-bridge system subjected to seismic action considering local topography, a train passing through a 480m bridge is taken as a case study. The local topography at the bridge site can be seen in Figure 2. It is located in a valley, as a result of which the height of the piers are different. The piers are numbered from Pier #1 to Pier #8 and the abutments are expressed as A and B at the ends of the bridge. The highest pier is Pier #5, 49m in height, and the shortest is Pier #1, 13.5m in height.

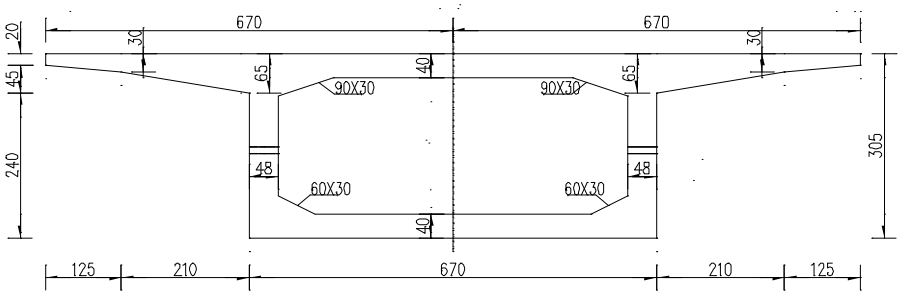
The total length of bridge is 480m composed of two continuous girders and the span layout is (40+64+64+64+40)m+(40+64+64+40)m. The girders have a box section and the configurations of the section can be seen in Figure 3.

A 3-D FE model of the railway bridge is established and the beam elements are used to model the main girder and the piers. The bottoms of Pier #1 to Pier #8 are fixed and the finite

element model is shown in figure 4. The first 100 modes are used for the train-bridge dynamic analysis and the damping ratio is assumed to be 0.05 uniformly.



(a) Section at the top of main piers



(b) Section at the mid-span

Figure 3: The girder section

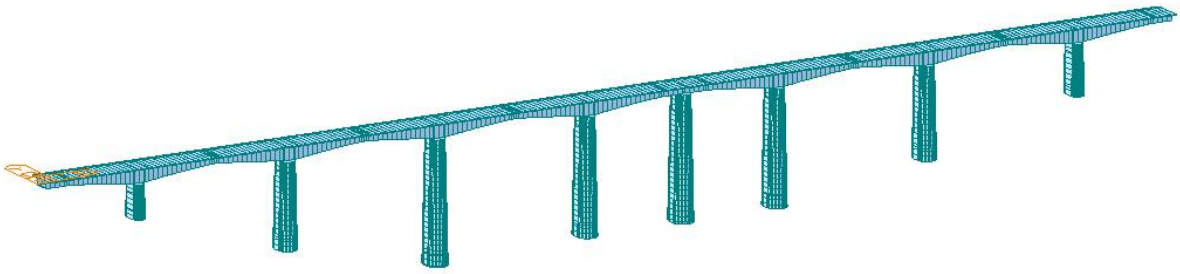


Figure 4: Finite element model of the bridge

5.2 The train model

The train used in this case study is ICE3 high-speed train with 8 vehicles. The fourth and the eighth vehicles are trailer cars and the others are motor cars. Based on the rigid body dynamics method, the model of the train subsystem is established. In this model, each vehicle is a rigid body-spring-damper discrete system and is independent from other vehicles. The mass, damping and stiffness matrices can be obtained based on the D'Alember principle and then the motion equation can be formed [5]. It is assumed that the wheel-track interaction obeys the wheel-track corresponding assumption and the German low disturbance spectra for high-speed railway are used as rail irregularities, whose vertical irregularity curve is shown in Figure 5 for reference.

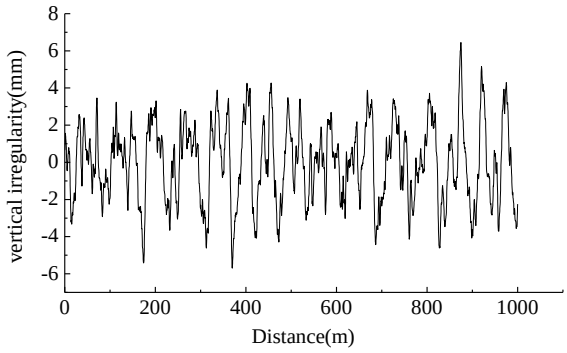


Figure 5: The vertical irregularity curve

5.3 The local topography

According to the actual conditions, the bridge is located in a valley, based on which the FE model of local topography can be established. Then according to the theory of viscous-spring artificial boundary, the equivalent loads acting on the boundary are calculated and finally the ground motions considering the local topography at each support are obtained.

A 3-D FE model of the local topography is built using a general finite element platform ANSYS [22]. The Solid45 elements are used to simulate the soil medium and the Combin14 elements are used to model the viscous-spring artificial boundary. The parameters of the local soil are shown in Table 2. The size of the element is 8m and the overall dimension of the model is 640m ×160m ×160m, which is shown in Figure 6.

Item	Parameter	Item	Parameter
Mass density	2610kg/m^3	Elasticity modulus	5GPa
Poisson's ratio	0.26	Damping ratio	0.05
Velocity of P wave	1530m/s	Velocity of S wave	871m/s

Table 2 The parameters of the soil

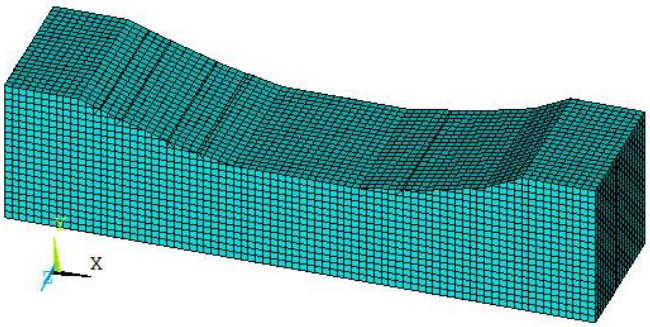
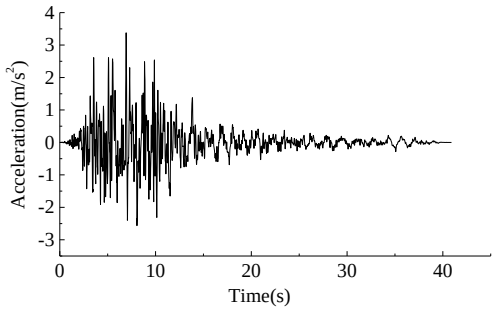


Figure 6: Finite element model of local topography

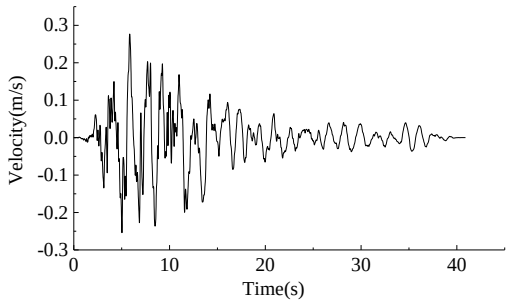
Assuming that the earthquake happens when the train just moves onto the bridge, the computational procedure for the dynamic interaction analysis of the train-bridge system during earthquakes is realized based on the above conditions.

5.4 Ground motions at each support of bridge

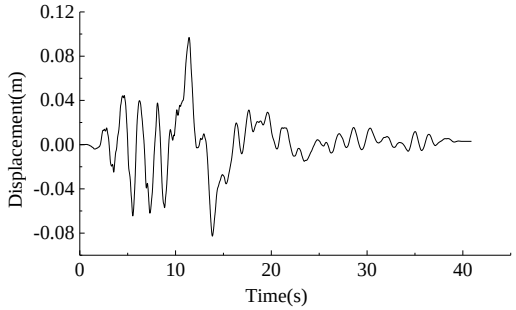
The ground motion time histories of the KOBE earthquake are used in this case study, as shown in Figure 7. It is assumed that the seismic waves are plane P wave and plane S wave, and the corresponding equivalent loads acting on the artificial boundary are obtained by Equations (4)~(8) and Equations (9)~(15), respectively. After the loads applied on the nodes at the boundary in the FE model, the ground motions at all supports of bridge are obtained via time-procedure analysis in ANSYS.



(a) Acceleration time history



(b) Velocity time history



(c) Displacement time history

Figure 7: Seismic time history

The finite element model without considering local topography is also established for comparison, in which the upper surface is taken as free horizontal surface. Through the same procedure, the ground motion time histories without considering topography are obtained.

Listed in Table 3 are the RSDs (Ratios of Seismic Displacement) at different supports, where RSD is defined as the ratio of a seismic displacement maximum with considering the topography to the corresponding one without. It can be seen all the values of RSD are less than 1.0 either in horizontal or in vertical direction, meaning that the displacement maximums

decrease at all the supports after considering the topography, which corresponds to the conclusion in Reference [12].

Direction	A	1#	2#	3#	4#	5#	6#	7#	8#	B
Left(←)	0.9767	0.9540	0.9251	0.9149	0.9177	0.9154	0.9192	0.9194	0.9484	0.9773
Right(→)	0.9763	0.9521	0.9165	0.9025	0.9040	0.9017	0.8984	0.9089	0.9468	0.9766

(a) RSD in horizontal direction

Direction	A	1#	2#	3#	4#	5#	6#	7#	8#	B
Up(↑)	0.9883	0.9736	0.9510	0.9360	0.9334	0.9331	0.9352	0.9474	0.9688	0.9865
Down(↓)	0.9884	0.9711	0.9428	0.9257	0.9237	0.9232	0.9251	0.9387	0.9653	0.9862

(b) RSD in vertical direction

Table 3: RSD at different supports

5.5 Dynamic response of train-bridge system subjected to incident P wave

First, the ratios of displacement response maximums and acceleration response maximums with and without considering the topography are defined as Ratio of Displacement Response (RDR) and Ratio of Acceleration Response (RAR), respectively. Shown in Figures 8 and 9 are, respectively, the vertical acceleration and displacement time histories at mid-span of the first continuous girder at the train speed of 150km/h. It can be seen that the calculated RAR is 1.25 and the RDR is 0.94, namely for this bridge, the vertical acceleration increases while the vertical displacement decreases when the topographic effects are considered.

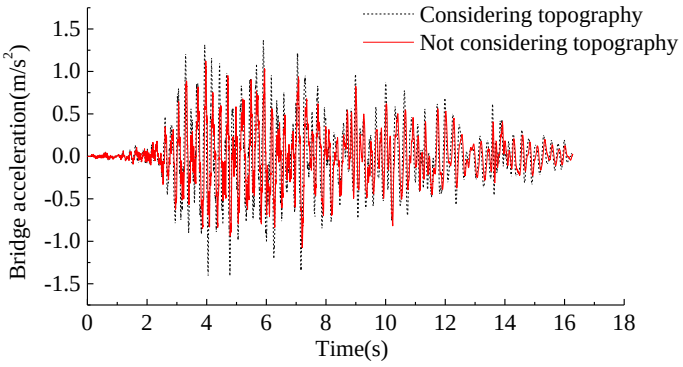


Figure8: Vertical acceleration time history of mid-span subjected to incident P wave

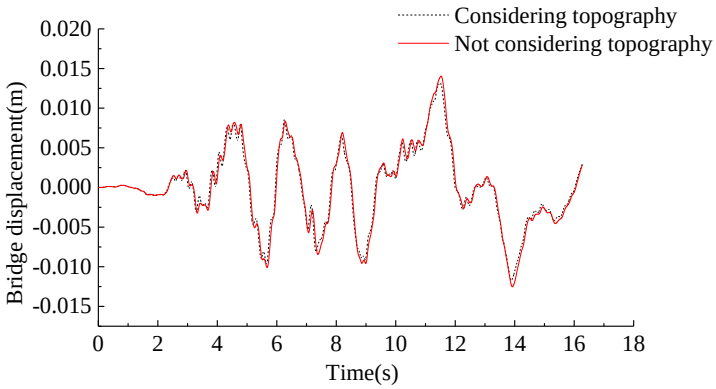


Figure9: Vertical displacement time history of mid-span subjected to incident P wave

Shown in Figures 10 and 11 are, respectively, the vertical acceleration and displacement time histories of the car-body in the first vehicle when the train speed is 150km/h. It can be seen that both the vertical acceleration and displacement of the 1st car-body increase when the topographic effects are considered, and the magnifications are 1.08 and 1.03, respectively, which demonstrates that it is necessary to take topographic effects into consideration when analyzing the dynamic response of train-bridge coupling system and assessing the running safety of trains.

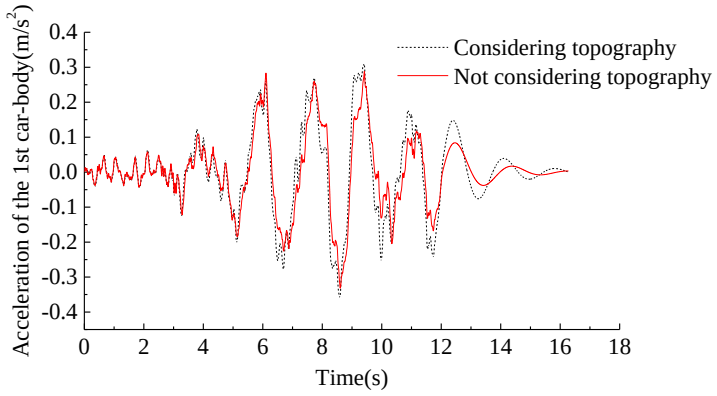


Figure 10: Vertical acceleration time history of 1st car-body subjected to incident P wave

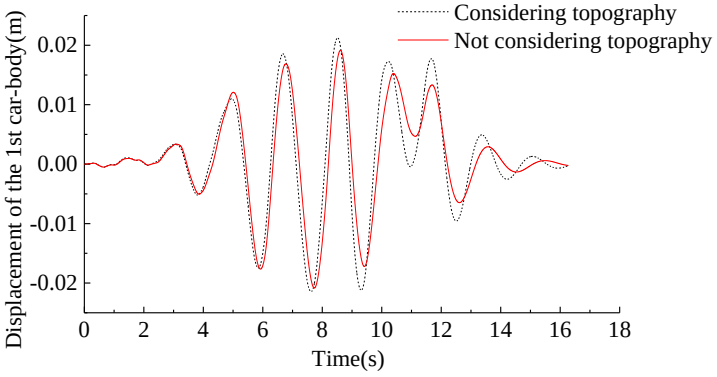


Figure 11: Vertical displacement time history of 1st car-body subjected to incident P wave

5.6 Dynamic response of train-bridge system subjected to incident S wave

Shown in Figures 12 and 13 are, respectively, the horizontal acceleration and displacement time histories at mid-span of the first continuous girder at the train speed of 150km/h. It can be seen that both the horizontal acceleration and displacement of the bridge decrease when the topographic effects are considered and RAR and RDR are about 0.92 and 0.91, respectively.

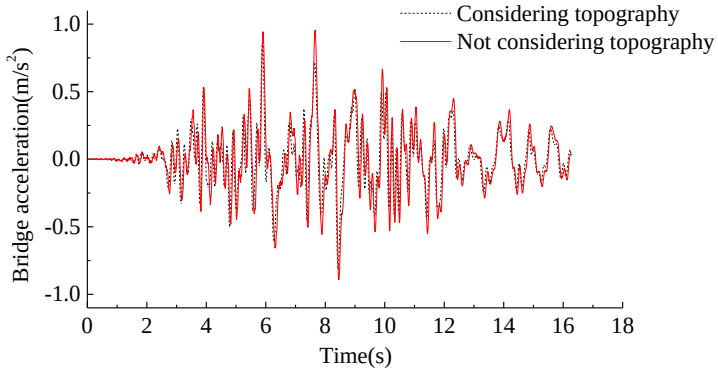


Figure 12: Horizontal acceleration time history of mid-span subjected to incident S wave

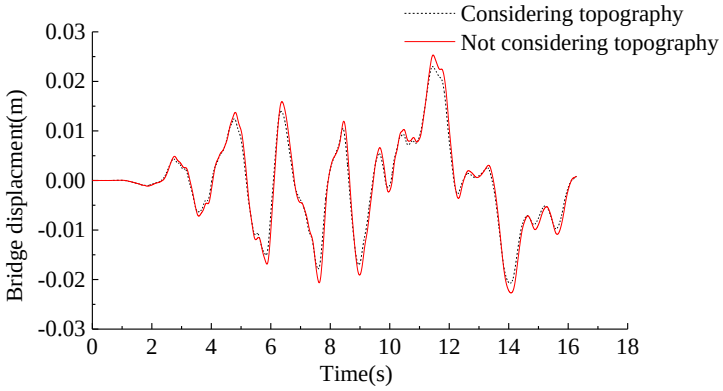


Figure 13: Horizontal displacement time history of mid-span subjected to incident S wave

Shown in Figures 14 and 15 are, respectively, the horizontal acceleration and displacement time histories of the car-body in the first vehicle when the train speed is 150km/h. Similarly, it can be seen that both the acceleration and displacement of the 1st car-body decrease when the topographic effects are considered, and the RAR and RDR of the train subsystem are about 0.80 and 0.97, respectively. The results demonstrate that the local topography of the bridge in this case study is beneficial to the coupling system.

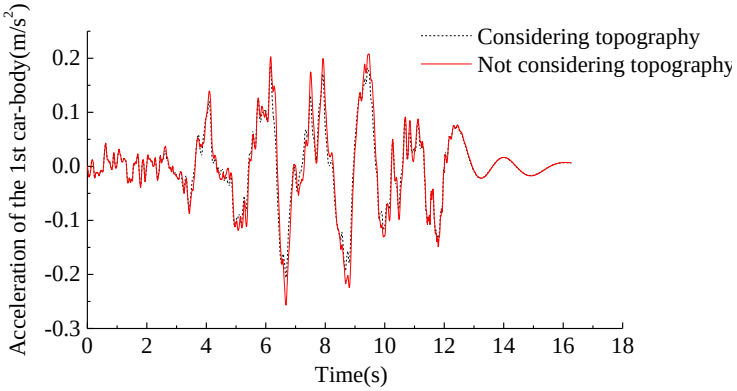


Figure 14: Horizontal acceleration time history of 1st car-body subjected to incident S wave

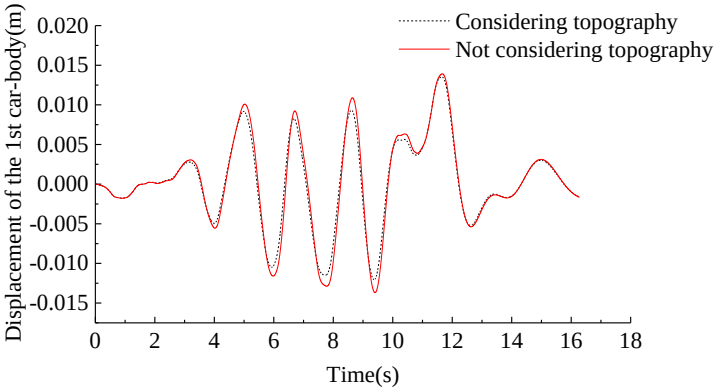


Figure 15: Horizontal displacement time history of 1st car-body subjected to incident S wave

6 CONCLUSIONS

In this paper, a method is presented to take into consideration the topographic effects in dynamic analysis of a train-bridge system subjected to multi-support seismic excitations. The influence of topography on the seismic response of train-bridge system is preliminarily studied by a case study. According to the analysis results, some conclusions can be obtained:

(1) Under the condition of incident P wave, when the topographic effects are considered, the vertical acceleration of the bridge increases while the vertical displacement decreases, and both the vertical acceleration and displacement of train increase, which demonstrate the necessity to consider the effects of local topography in bridge aseismic analysis.

(2) Under the condition of incident S wave, when the topographic effects are considered, the dynamic response of both the train subsystem and the bridge subsystem decrease, which means that in this case study, the valley helps to reduce the seismic response of train-bridge system.

(3) Different bridges may be located in different kinds of sites, as a result of which the influence of the topography on the seismic response of train-bridge coupling system may be different. Besides, there are also many other factors affecting the analysis results. However, the method proposed in this paper has its universal applicability and if necessary, it can be used in other railway bridges for seismic response analysis and running safety assessment.

ACKNOWLEDGEMENTS

This study is financially supported by the National Basic Research Program of China ("973"Project) (Grant No. 2013CB036203), the National Natural Science Foundation of China (Grant No. 51208027) and the Fundamental Research Funds for the Central Universities (Grant No. 2014YJS095)

REFERENCES

[1] T Miyamoto, H Ishida, M Matsuo, Running safety of railway vehicle as earthquake occurs. Japanese National Railway Technical Research Institute Quarterly Reports, **38(3)**, 117-122, 1997.

[2] YB Yang, YS Wu, Dynamic stability of trains moving over bridges shaken by earthquakes. Journal of Sound and Vibration, **258(1)**, 65-94, 2002.

[3] H Xia, Y Han, N Zhang, *et al*., Dynamic analysis of train-bridge system subjected to non-uniform seismic excitations. Earthquake Engineering and Structural Dynamics, **35**, 1563-1579, 2006.

[4] K Nishimura, Y Terumichi, *et al*, Experimental study on the vehicle safety by earthquake track excitation with 1/10 scale vehicle and roller rig. Journal of System Design and Dynamics, **4(1)**, 226-237, 2010.

[5] H Xia, G De Roeck, J M Goicolea, *Bridge Vibration and Controls: New Research*. New York: Nova Science Publishers Inc., 2011.

[6] X He, M Kawatani, T Hayashikawa and T Matsumoto, Numerical analysis on seismic response of Shinkansen bridge-train interaction system under moderate earthquakes. Earthquake Engineering and Engineering Vibration, **10**, 85-97, 2011.

[7] XT Du, YL Xu, H Xia, Dynamic interaction of bridge-train system under non-uniform seismic ground motion. Earthquake Engineering and Structural Dynamics, **41**, 139-157, 2012.

[8] Wang Z, A preliminary report on the great Wenchuan earthquake. Earthquake Engineering and Engineering Vibration, **7(2):** 225-234, 2008.

[9] M Celibi, Topographical and geological amplifications determined from strong-motion and aftershock records of the 3 March 1985 Chile earthquake. Bulletin of the Seismological Society of America, **88(4):** 1147-1167, 1987.

[10] R Jibson, Summary of research on the effects of topographic amplification of earthquake shaking on slope stability. US Geological Survey, Open-file Report 87-268, Menlo Park, California, 1987.

[11] GL Zhou, Canyon topography effects on seismic response of multi-support bridges. Harbin: Institute of Engineering Mechanics, China Earthquake Administration, 2010. (in Chinese)

[12] S J Lee, Y C Chan, D Konatitsch, et al., Effects of realistic surface topography on seismic ground motion in the Yangminshan region of Taiwan based upon the spectral-element method and lidar DTM. Bulletin of the Seismological Society of America, **99(2A)**, 681-693, 2009.

[13] M. J. N. Priestley, F. Seible, G. M. Calvi, *Seismic Design and Retrofit of Bridges*. New York: John Wiley & Sons Inc., 1996.

[14] M Bouchon, Effect of topography on surface motion. Bulletin of the Seismological Society of America, **63**, 615-632, 1973.

[15] D. W. Griffiths , and G. A. Bollinger, The effect of Appalachiam mountain topography on seismic waves. Bulletin of the Seismological Society of America, **69**, 1081-1105, 1979.

[16] D. Assimaki, G. Gazetas, Soil and topographic amplification on canyon banks and the Athens 1999 earthquake. Journal of Earthquake Engineering, 8(1), 1–44, 2004.

[17] GL Zhou, XJ Li, XJ Qi, Seismic response analysis of continuous rigid frame bridge considering canyon topography effects under incident SV waves. Earthquake Science, **23(1):** 53-61, 2010.

[18] HY Jia, DY Zhang, et al., Local site effects on a high-pier railway bridge under tridirectional spatial excitations: nonstationary stochastic analysis. Soil Dynamic and Earthquake Engineering, **52:** 55-69, 2013.

[19] JB Liu, YX Du, XL Du, et al., 3D Viscous-Spring artificial boundary in Time Domain. Earthquake Engineering and Engineering Vibration, **5(1)**: 93-102, 2006.

[20] JB Liu, YD Lu, A direct method for analysis of dynamic soil-structure interaction based on interface idea. CH Zhang and JP Wolf ed. *Dynamic Soil-Structure Interaction*, International Academic Publishers, 258-273, 1997.

[21] XL Du, *Theories and methods of wave motion for engineering*. Beijing: Science Press, 2009. (in Chinese)

[22] P. Kohnke. ANSYS theory reference-release 13.0. ANSYS Inc., 2010.

COMPDYN 2015
5th ECCOMAS Thematic Conference on
Computational Methods in Structural Dynamics and Earthquake Engineering
M. Papadrakakis, V. Papadopoulos, V. Plevris (eds.)
Crete Island, Greece, 25–27 May 2015

DRIVE-BY STRUCTURAL HEALTH MONITORING OF RAILWAY BRIDGES USING TRAIN-MOUNTED ACCELEROMETERS

Cathal Bowe[1], Paraic Quirke[1,2], Daniel Cantero[3], and Eugene J. OBrien[2,3]

[1] Iarnród Éireann - Irish Rail
Technical Department, Engineering & New Works, Inchicore, Dublin 8, Ireland.
e-mail: cathal.bowe@irishrail.ie; paraic.quirke@irishrail.ie

[2] School of Civil, Structural and Environmental Engineering and Earth Institute
University College Dublin, Dublin 4, Ireland.
eugene.obrien@ucd.ie

[3] Roughan O'Donovan Innovative Solutions
Arena House, Arena Road, Sandyford, Dublin 18, Ireland.
daniel.cantero@rod.ie

Keywords: Railway, Bridge, Structural Health Monitoring, Drive-by, Dynamics, Maintenance.

Abstract. *Bridge damage can be detected by observing changes in its spectral properties. In its infancy, bridge health monitoring involved monitoring physical properties via direct instrumentation, i.e. sensors attached to the bridge. In recent years many authors have investigated the ability of indirect methods to assess the structural health of bridges, i.e. the vehicles traversing the bridges are fitted with sensors. This has the potential of reducing monitoring costs as the vehicle may be used to monitor many bridges on the network. Most of the investigation in this relatively new field of study has been on road bridges and road vehicles. A method is proposed in this paper for the detection of the bridge damage through an analysis of vehicle accelerations resulting from the train/track/bridge dynamic interaction. In a train/track/bridge interaction there are additional complications which do not exist on road bridges. The signal generated by the train as it traverses the bridge is normally short in duration. Studies on railway bridges are complicated by the addition of rails, sleepers and sometimes ballast between the tracks and the bridge deck. However, the weight of the train relative to the bridge is considerably larger than previous studies using road vehicles and this will excite the bridge to a higher degree.*

Numerical validation of the drive-by concept is achieved by using a 2-dimensional dynamic vehicle model with 10 degrees of freedom. The finite element interaction model is implemented in MATLAB. The track is modelled as a continuous beam, supported at 0.545m centres on three layers of springs and masses representing sleepers, and ballast lying on a simply supported bridge beam. This paper reports the results of the numerical simulations and the plans that are underway to test the concept in field trials.

1 INTRODUCTION

At present most condition monitoring of bridges on rail networks is carried out by periodic visual inspections and non-destructive testing. This monitoring method is time consuming, prone to human error and as such can be unreliable and inconsistent in its findings. Direct instrumentation of bridges, whereby sensors are attached to the bridge, can be used to detect changes in the spectral properties of the structure and infer damage. This method of structural health monitoring is widely documented in the literature [1]. More recently, indirect methods of assessing the structural health of bridges, whereby the measured response of a vehicle crossing the bridge is analysed to detect damage, have gained increased interest in research projects due to the cost saving potential they offer [2]–[4].

The concept, similar to a track damage detection algorithm presented by Cantero and Basu [5], involves using an instrumented vehicle to regularly record geo-located vehicle acceleration responses, establishing a baseline response to a bridge crossing event. The monitoring method makes comparisons to the baseline to detect large differences which could indicate possible structural damage.

For this study it is proposed to analyse the acceleration response of railway vehicles using a continuous wavelet transform, comparing the response to a baseline, or healthy, analysis in order to detect damage in a bridge. The continuous wavelet transform is a time–frequency analysis that provides more detailed information about non-stationary signals which traditional Fourier analysis miss. It is applied to various fields including civil, mechanical and aerospace engineering, especially for damage detection and structural health monitoring (SHM) [6]. Wavelet analysis has advantages over traditional Fourier transform methods in that frequency information is provided while retaining the corresponding time information. The wavelet transform can analyse smaller portions of larger signals and return the frequency information for that portion. This property of the transform means it has the potential, not only to detect damage, but also to locate it. The wavelet transform was developed by Daubechies [7]. Definitions of the wavelet transform and descriptions of the most common wavelets are published in her work. The wavelets most commonly used in structural health monitoring are investigated by Reda-Taha *et al*, [8] who find that some wavelets perform better in certain situations. A number of authors use the 'Mexican Hat' wavelet in structural health monitoring and bridge damage investigations [9], [10], and is therefore adopted as part of this study.

Zhu and Law [9] use wavelet analysis to detect an irregularity in a beam using its displacement response. Hester *et al.* [10] build on that work by applying the wavelet transform to bridge deck acceleration responses in order to increase the level of accuracy required when assessing vehicle bridge interactions. Hester *et al.* assess the wavelet energy of a signal by squaring the wavelet coefficients over incremental time intervals.

Wimmer *et al.* [11] use experimental data from strain sensors to measure the excitation of a flat steel plate to detect damage in welds along the edge of the plate. This is achieved by comparison of the wavelet transform of the strain data to a baseline state and examining the maximum difference in wavelet transform coefficients.

In this study, the acceleration response of a railway vehicle is generated using a validated finite-element vehicle-bridge interaction model called the Train-Track-Bridge (TTB) model developed by Cantero *et al.* [12]. The model generates acceleration responses at any degree of freedom in the structure or vehicle. Damage is simulated in the bridge structure by reducing the stiffness of affected bridge elements. Acceleration outputs from the TTB model provide the inputs for the wavelet-based damage detection algorithm. Wavelet transforms for vehicle acceleration responses measured for different levels of damage are compared to investigate if damage can be detected and located.

This paper is divided into the following sections. Firstly, the Train-Track-Bridge model used in the investigation is described. This is followed by a brief section describing the wavelet tool and methodology. Results are presented for a range of damage levels, locations and signal noise. Finally, an overview of the results and suggestions for further research are presented.

2 MODEL DESCRIPTION

The Train-Track-Bridge (TTB) model is presented in this section. The vehicle model, track model and bridge model are all described separately before the coupling of the model is briefly described.

2.1 Vehicle Model

The vehicle model used in this study is shown in Figure 1. The vehicle is modelled as a 'half-car' consisting of 10 Degrees Of Freedom (DOF) including 4 wheels (vertical displacements only), 2 bogies (vertical displacement and rotation about the centre of gravity on each bogie) and the main body (vertical displacement and rotation about the centre of gravity of the main body). The wheels are represented as masses (m_{w1}, m_{w2}, m_{w3}, m_{w4}). The bogies are modelled as rigid bars with mass (m_{b1}, m_{b2}) and moment of inertia (I_{b1}, I_{b2}), while the main body of the vehicle is modelled as a rigid bar with mass (m_v) and moment of inertia (I_v). The wheels are connected to the bogies by means of primary suspension systems consisting of springs (k_p) and viscous dampers (c_p) in parallel. Similarly, the bogies are connected to the main body by means of a secondary suspension system consisting of a spring (k_s) and a viscous damper (c_s) in parallel. Assuming small rotations, we can adopt a linearized system of equations of motion. Vehicle properties are gathered from the literature [13] and are listed in Table 1.

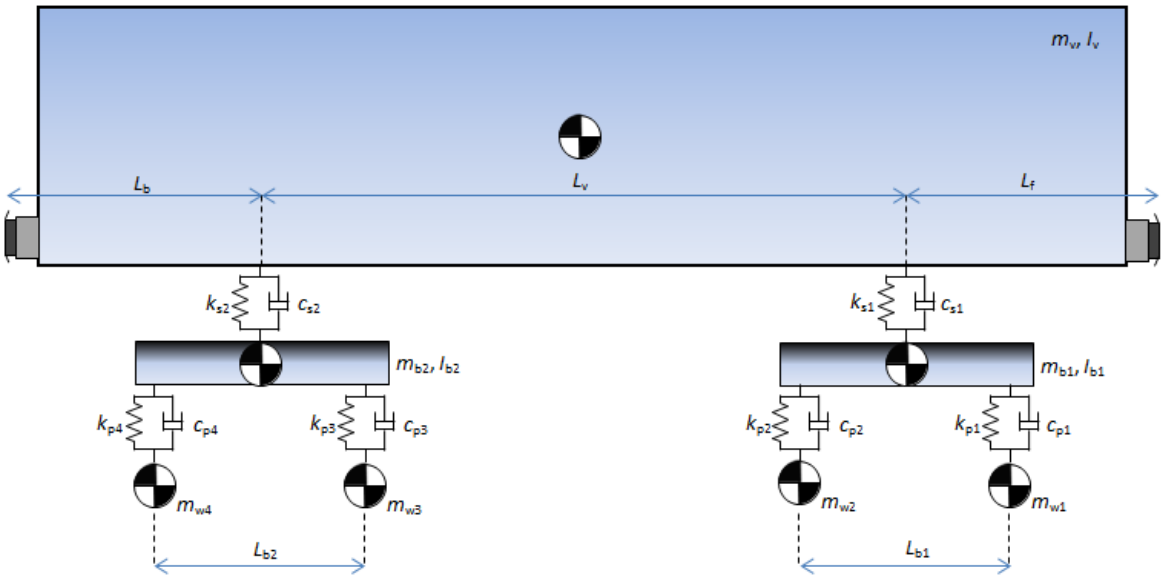


Figure 1: Sketch of vehicle model

Property	Symbol	Value	Unit
Mass of wheel	$m_{w1}, m_{w2}, m_{w3}, m_{w4}$	1843.5	kg
Mass of bogie	m_{b1}, m_{b2}	5630.8	kg
Mass of main body	m_v	59364.2	kg
Moment of Inertia of bogie	I_{b1}, I_{b2}	9487	kg.m^2
Moment of Inertia of main body	I_v	1.723×10^6	kg.m^2
Stiffness of Primary Suspension	$k_{p1}, k_{p2}, k_{p3}, k_{p4}$	4.7992×10^6	N/m
Stiffness of Secondary Suspension	k_{s1}, k_{s2}	1.7716×10^6	N/m
Damping of Primary Suspension	$c_{p1}, c_{p2}, c_{p3}, c_{p4}$	60×10^3	Ns/m
Damping of Secondary Suspension	c_{s1}, c_{s2}	90×10^3	Ns/m
Distance between bogies	L_v	11.46	m
Additional distance (front and back)	L_b, L_f	3	m
Distance between axles	L_{b1}, L_{b2}	3	m

Table 1: Properties of the vehicle – Chinese Star – Power Car.

2.2 Track Model

The track is modelled as a beam supported on a three-layer sprung mass system representing a sleeper, pad and ballast support system as shown in Figure 2. This three-layer system is the structure recommended by the UIC for assessing rail bridges due to dynamic interaction between the train, track and bridge [14]. Track supports are spaced at a regular interval L_s, representing the spacing between the sleepers. The rail is modelled as a finite element Euler-Bernoulli beam with two beam elements per sleeper spacing. Each track element has 2 nodes with 2 DOF at each node. Properties of track structures vary significantly throughout the literature. Values used in this study are taken from Zhai *et al.*[15] and are shown in Table 2. Note that properties marked with an asterisk (*) in the table are for single rail only and are doubled in order to include both rails in the planar TTB model. Ballast is omitted over the bridge where sleepers are fixed directly to the beam. Vibrations are dissipated through sleeper-beam pads, the properties of which are shown in Table 2.

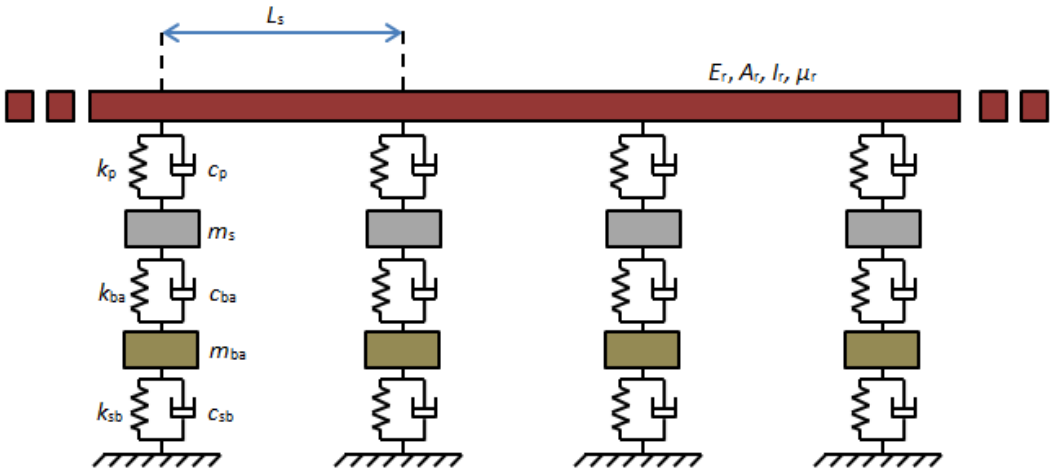


Figure 2: Sketch of track model

Property	Symbol	Value	Unit
Elastic modulus of rail	E_r	2.059×10^{11}	N/m^2
Rail cross-sectional area	A_r	7.69×10^{-3}	m^2
Rail second moment of area	I_r	$*3.217\times10^{-5}$	m^4
Rail mass per unit length	μ_r	*60.64	kg/m
Rail Pad stiffness	k_p	6.5×10^{7}	N/m
Rail Pad damping	c_p	7.5×10^{4}	Ns/m
Sleeper mass (half)	m_s	*125.5	kg
Sleeper spacing	L_s	0.545	m
Ballast stiffness	k_{ba}	137.75×10^{6}	N/m
Ballast damping	c_{ba}	5.88×10^{4}	Ns/m
Ballast mass	m_{ba}	531.4	kg
Sub-ballast stiffness	k_{sb}	77.5×10^{6}	N/m
Sub-ballast damping	c_{sb}	3.115×10^{4}	Ns/m
Beam-sleeper pad stiffness	k_{bs}	77.5×10^{6}	N/m
Beam-sleeper pad damping	c_{bs}	90×10^{3}	Ns/m

Table 2: Properties of the track

2.3 Bridge Model

The bridge used in this study is shown in Figure 3. The bridge is modelled as a simply supported finite element beam with properties listed in Table 3. For the purposes of symmetry the beam element length is equal to the track model element length, i.e. half the sleeper spacing, resulting in a total of 74 elements in the beam. Each beam element has 2 nodes with 2 DOF at each node. Properties of the concrete beam have been taken from the literature [16].

The theory behind global damage detection methods is that damage changes the stiffness, mass or damping properties of a structure, altering its dynamic response. Damage in the beam is modelled simply as a percentage loss of sectional depth in selected elements producing a reduction in the elemental stiffness of the affected elements in the beam.

Rayleigh damping is used in the model to simulate energy dissipation in the beam response.

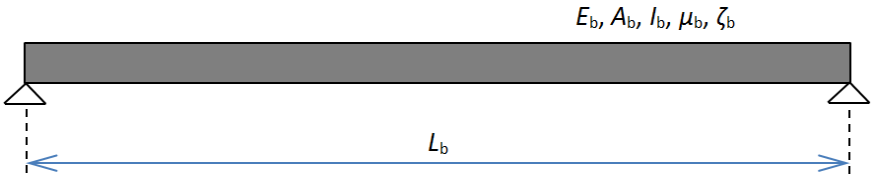


Figure 3: Sketch of beam model

Property	Symbol	Value	Unit
Length	L_b	20	m
Elastic modulus	E_b	25×10^{9}	N/m^2
Second moment of area	I_b	1.46	m^4
Damping ratio	ζ_b	1	%
Cross-sectional area	A_b	1	m^2
Mass per unit length	μ_b	17777	kg/m

Table 3: Properties of the beam

2.4 Coupled Model

The vehicle, track and beam subsystems are combined together to form the TTB model. The model can be visualised in Figure 4. A static analysis is carried out before a dynamic analysis is initiated. Furthermore, a bridge approach distance of 10 m from the leading wheel to the left hand bridge support, is incorporated into the model to allow the vehicle achieve dynamic equilibrium before the first wheel enters the bridge. A section of track is included after the bridge to allow the vehicle to fully exit the bridge and for free vibration of the bridge to take place after the vehicle has passed.

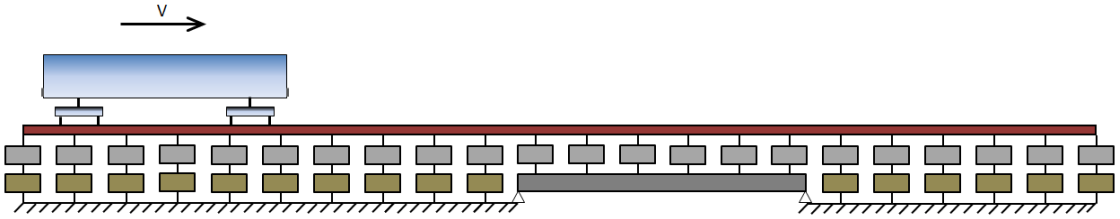


Figure 4: Sketch of TTB model

The vehicle track and beam subsystems can each be defined by a set of second order differential equations that can be represented in matrix format as:

$$M_X \ddot{u}_X + C_X \dot{u}_X + K_X u_X = F_X \tag{1}$$

where M, C and K are the mass, damping and stiffness matrices of the subsystem respectively. The subscript 'x' denotes which subsystem the matrix refers to and may be substituted by V, T, and B to denote the vehicle, track and bridge subsystems respectively. F is the external force vector while $\ddot{u}$, $\dot{u}$ and u are the vectors of accelerations, velocities and displacements respectively. The coupling of the subsystems is expressed mathematically with additional off-diagonal block matrices as shown in Eqn (2).

$$\begin{pmatrix} M_V & 0 & 0 \\ 0 & M_T & 0 \\ 0 & 0 & M_B \end{pmatrix} \begin{Bmatrix} \ddot{u}_V \\ \ddot{u}_T \\ \ddot{u}_B \end{Bmatrix} + \begin{pmatrix} C_V & C_{V,T} & 0 \\ C_{T,V} & C_T & C_{T,B} \\ 0 & C_{B,T} & C_B \end{pmatrix} \begin{Bmatrix} \dot{u}_V \\ \dot{u}_T \\ \dot{u}_B \end{Bmatrix} + \begin{pmatrix} K_V & K_{V,T} & 0 \\ K_{T,V} & K_T & K_{T,B} \\ 0 & K_{B,T} & K_B \end{pmatrix} \begin{Bmatrix} u_V \\ u_T \\ u_B \end{Bmatrix} = \begin{Bmatrix} F_V \\ F_T \\ F_B \end{Bmatrix} \tag{2}$$

The vehicle and track/bridge model are coupled together via the wheel/rail interaction, i.e. the DOF's of the wheels and the DOF's of the rail are combined. The coupling terms in the coupled matrices need to be updated at each time step. The vehicle wheels do not always act at the nodes of the rail and the vehicle's contribution to the coupled terms needs to be distributed to the DOF's of the rail using Hermitian shape functions. This method of distribution is well documented in the literature [17].

The equations of motion are solved using a numerical integration scheme. The Newmark-β method is employed in this study [18]. The TTB model was implemented in Matlab.

3 WAVELET ANALYSIS

A wavelet is a waveform of limited duration with an average value of zero.

$$\int_{-\infty}^{+\infty} \psi(x)dx = 0 \tag{3}$$

where $\psi(x)$ is the base or mother wavelet. The base wavelet can be scaled and translated to create a range of analysing wavelets:

$$\psi(x)_{\bar{x},s} = \frac{1}{\sqrt{s}}\psi\left(\frac{x-\bar{x}}{s}\right) \tag{4}$$

where s is the scaling factor and $\bar{x}$ is the translation parameter. The base wavelet can be a real or complex function; however only real wavelets are used in this study. The continuous wavelet transform of a function, or in this study, a continuous acceleration signal, $y(x)$, is given by the following equation:

$$Y(x,s)_W = \int_{-\infty}^{+\infty} y(x)\frac{1}{\sqrt{s}}\psi\left(\frac{x-\bar{x}}{s}\right)dx \tag{5}$$

where $Y(x,s)_W$ refers to the transformed quantity, or coefficient, of $y(x)$ using the wavelet, $\psi(x)_{\bar{x},s}$.

In a wavelet transform the base wavelet is compared to a portion of the signal being analysed and its coefficient is calculated. The wavelet coefficient is a measure of how closely the base wavelet matches the function in the area of interest. The wavelet is translated along the entire signal resulting in a series of wavelet coefficients in time. The wavelet is then scaled, or stretched, and the process is repeated until the signal has been analysed by all scales in a specified range. The result of the analysis is a 3-dimensional surface or 2-dimensional contour plot in which wavelet coefficients, scales and time can be represented [8].

The scale axis of the plot can be related to a pseudo frequency [10]. A large scaling factor implies a stretched base wavelet that detects low frequency content in the signal. A low scaling factor detects high frequency content in the signal. There exists a relationship between the scale of the base wavelet and a pseudo frequency given by the following equation:

$$F_s = \frac{F_c}{s\Delta} \tag{6}$$

where F_s is the pseudo frequency corresponding to scale, s, in Hz, F_c is the centre frequency of the wavelet in Hz and Δ is the sampling period of the signal being analysed.

In this study the TTB model is used to simulate the passage of a train across a finite element track model featuring a bridge beam as described in Section 2. The acceleration response of the front bogie on the vehicle is chosen as the function analysed in the wavelet transform. Two simulations are carried out to generate a 'healthy' acceleration response, $y_h(x)$ and a 'damaged' response, $y_d(x)$. Wavelet transforms are carried out on both signals independently using the same base wavelet and scale. The difference between the wavelet coefficients for the 'healthy' response and 'damaged' response is given by the equation:

$$Y(x,s)_W = Y_h(x,s)_W - Y_d(x,s)_W \tag{7}$$

where $Y_h(x,s)_W$ represents the wavelet coefficients calculated for the 'healthy' response $y_h(x)$, and $Y_d(x,s)_W$ represents the wavelet coefficients calculated for the 'damaged' response $y_d(x)$. With all other parameters being equal, the difference in the wavelet coefficients will return the magnitude and location of the damage in the beam.

4 RESULTS AND DISCUSSION

In the first simulation, the vehicle is simulated traversing the model with a smooth rail profile and no bridge damage at a constant velocity of 120 km/hr, producing a healthy acceleration response. For the second simulation, damage is introduced into the bridge in elements 22 and 23 (out of a total of 74 elements), and the same vehicle is simulated crossing the model

from the same starting point at the same velocity. A comparison of the wavelet transform produced is shown in Figure 5. It is shown that damage is located where the maximum difference between the healthy and damaged wavelet coefficients occurs.

It is found that scales between 10 and 50 (corresponding to pseudo-frequencies of 20 Hz – 2 Hz) are most successful in finding the damage and damage location using the Mexican hat wavelet for this particular model. The first mode of vibration of the healthy bridge (5.535Hz) is found within the corresponding frequency range. Damage causes a change to the natural frequencies of the bridge which manifests itself in the vehicle response thereby allowing the detection of the damage from the vehicle response.

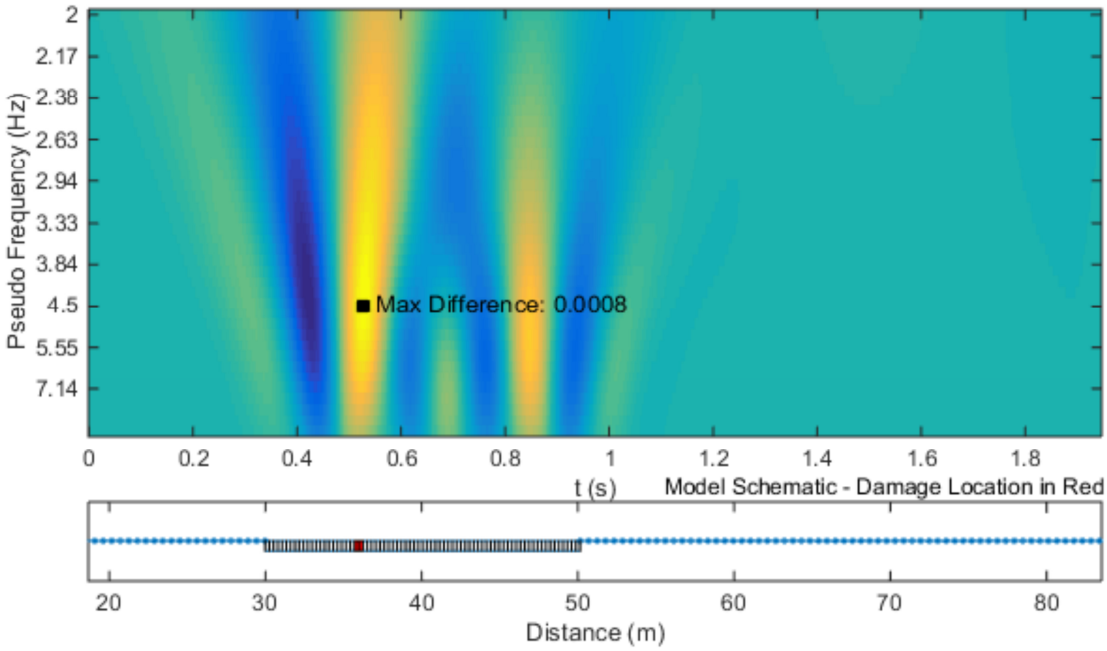


Figure 5: Wavelet contour plot showing difference in Wavelet Coefficients for Bogie1 Accelerations - 0% Noise - 10% Damage

For the next simulation, damage is increased by 10% to 20% in the same beam elements. All other parameters are unchanged. Again, the wavelet transform for the acceleration responses are compared. The differences in the wavelet transform coefficients are shown in Figure 6. As before, the presence of damage, and its location, are determined. By comparison to Figure 5 an estimation of the relative magnitude of the damage can also be made. In Figure 5 the magnitude of the maximum difference was 0.0008 for 10% damage. For 20% damage it is found that the maximum difference is just over twice that (0.0018).

To determine if a relationship exists between the difference in wavelet coefficients and damage level, a number of simulations were carried out and the maximum difference between wavelet functions determined for increasing damage level. Figure 7 shows that the maximum difference between wavelet coefficients increases with damage level suggesting that the level of damage can be estimated using this approach.

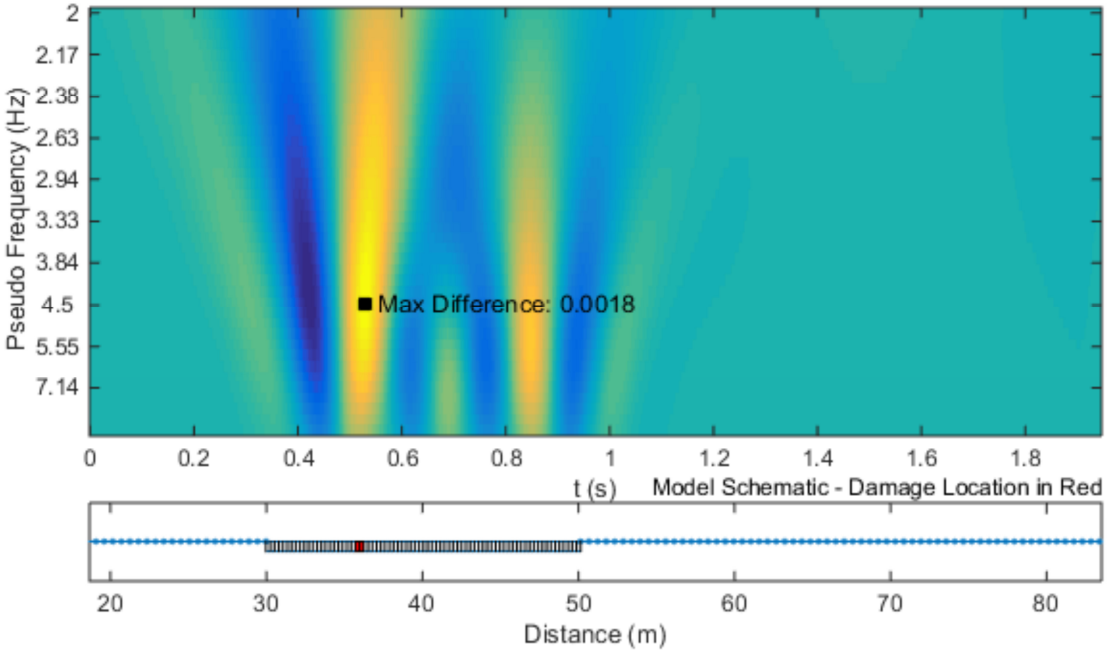


Figure 6: Wavelet Scalogram showing difference in Wavelet Transform Coefficients for Bogie1 Accelerations - 0% Noise - 20% Damage

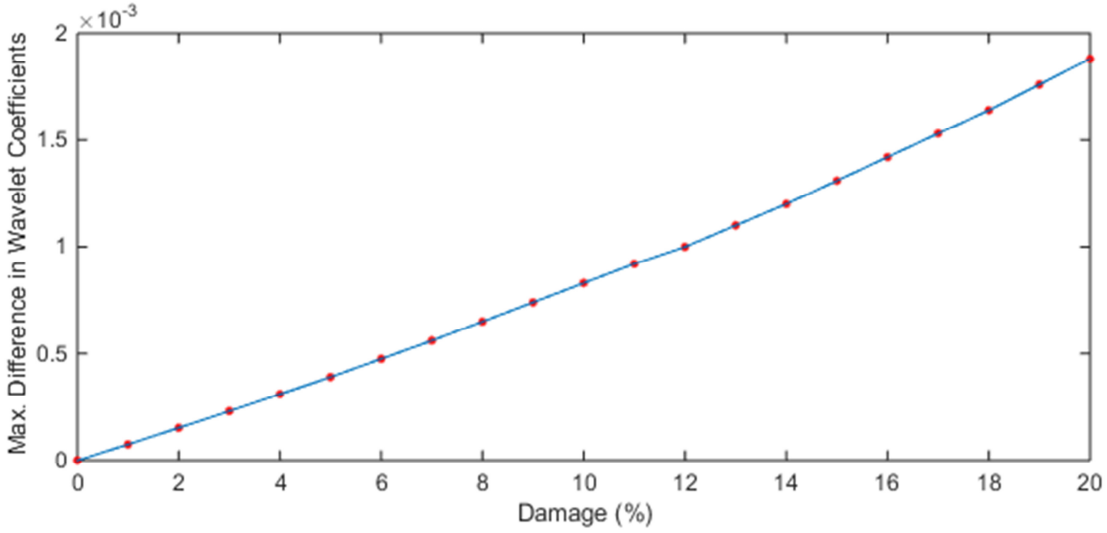


Figure 7: Difference in Wavelet Transform Coefficients vs. Damage

To test the algorithm further, additive white noise related to the signal is introduced to both healthy and damaged signals before wavelet analyses are carried out. Wavelet transforms carried out for both acceleration responses with 1% noise are compared and the differences between the wavelet transform coefficients are shown in Figure 8. As before, the presence of damage, and its location are determined even in the presence of noise. From running multiple simulations for a range of damage levels it is found that damage levels below 5% become generally undetectable in the presence of 1% noise while only damage levels of 8% and above

are detectable when 2% noise is added to the signals. It is found that the addition of noise also reduces the reliability of the damage location capabilities of the algorithm.

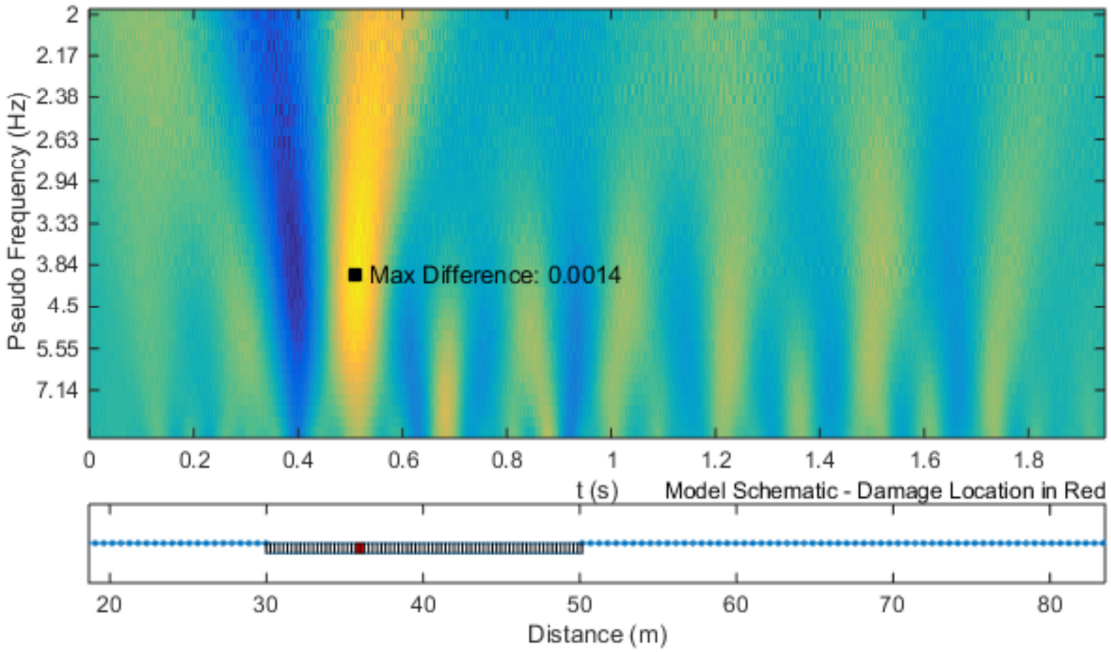


Figure 8: Wavelet contour plot showing difference in Wavelet Transform Coefficients for Bogie1 Accelerations - 1% Noise - 10% Damage

5 CONCLUSIONS

A methodology has been presented whereby damage in a bridge can be detected using instrumentation fitted to a traversing vehicle. A wavelet transform-based damage identification and location technique has been found to be simple, efficient, and independent of damage magnitude and location with an acceptable tolerance to signal noise. The basis of the technique is the comparison of vehicle acceleration response while crossing a damaged bridge to a healthy baseline response. Variations in the acceleration response due to variations in the global properties of the bridge resulting from the bridge damage can be detected as a difference in the resulting wavelet plots.

The authors are in the process of acquiring accelerometers to attach to an Irish Rail train vehicle so that the actual acceleration responses of a vehicle can be obtained while it traverses a section of track featuring a bridge. It is planned to acquire the data at regular time intervals in order to make comparative studies into the structural health of the bridge. A potential challenge with the application of this methodology for structural health monitoring of rail bridges using acquired data is the fact that acceleration responses of vehicles can be influenced by many other factors. Obtaining comparable signals may prove difficult.

6 ACKNOWLEDGEMENTS

The research presented in this paper was carried out as part of the Marie Curie Initial Training Network (ITN) action FP7-PEOPLE-2013-ITN.The project has received funding from the European Union's Seventh Framework Programme for research, technological development and demonstration under grant agreement number 607524 The authors are thankful for the support.

REFERENCES

[1] P. C. Chang, A. Flatau, and S. C. Liu, Review Paper : Health Monitoring of Civil Infrastructure, *Structural Health Monitoring*, vol. 2, no. 3, pp. 257–267, 2003.

[2] P. J. McGetrick, A. González, and E. J. Obrien, Theoretical investigation of the use of a moving vehicle to identify bridge dynamic parameters, *Insight - Non-Destructive Testing and Condition Monitoring*, vol. 51, no. 8, pp. 433–438, Aug. 2009.

[3] J. Keenahan, P. J. McGetrick, A. González, and E. J. Obrien, Using Instrumented Vehicles to detect damage in bridges, in *15th International Conference on Experimental Mechanics, Porto, Portugal, 22-27 July 2012, Paper No. 2934.*, 2012, vol. 1, pp. 07–22.

[4] Y. B. Yang and C. W. Lin, Vehicle–bridge interaction dynamics and potential applications, *Journal of Sound and Vibration*, vol. 284, no. 1–2, pp. 205–226, Jun. 2005.

[5] D. Cantero and B. Basu, Railway infrastructure damage detection using wavelet transformed acceleration reponse of traversing vehicle, *Structural Control and Health Monitoring*, p. a, 2014.

[6] H. Kim and H. Melhem, Damage detection of structures by wavelet analysis, *Engineering Structures*, vol. 26, no. 3, pp. 347–362, Feb. 2004.

[7] I. Daubechies, Ten Lectures on Wavelets, in *CBMS Conference Series 61, SIAM, Philadelphia*, 1992.

[8] M. M. Reda-Taha, A. Noureldin, J. L. Lucero, and T. J. Baca, Wavelet Transform for Structural Health Monitoring : A Compendium of Uses and Features, *Structural Health Monitoring*, vol. 5, no. 3, pp. 267–295, 2006.

[9] X. Q. Zhu and S. S. Law, Wavelet-based crack identification of bridge beam from operational deflection time history, *International Journal of Solids and Structures*, vol. 43, no. 7–8, pp. 2299–2317, Apr. 2006.

[10] D. Hester and A. González, A wavelet-based damage detection algorithm based on bridge acceleration response to a vehicle, *Mechanical Systems and Signal Processing*, vol. 28, pp. 145–166, Apr. 2012.

[11] S. A. Wimmer and V. G. De Giorgi, A wavelet based algorithm for detecting damage, in *Chang, F-K. (ed.), Proceedings of 4th Int. Workshop on Structural Health Monitoring, Stanford, CA, USA.*, 2003, pp. 395–402.

[12] D. Cantero, T. Arvidsson, E. J. Obrien, and R. Karoumi, Train-track-bridge dynamic model, validation and review of parameters., *Submitted for publication*, 2014.

[13] W. Zhai, K. Wang, and C. Cai, Fundamentals of vehicle-track coupled dynamics, *Vehicle System Dynamics: International Journal of Vehicle Mechanics and Mobility*, vol. 47, no. 11, pp. 1349–1376, 2009.

[14] International Union of Railways. Design requirements for rail-bridges based on phenomena between train, track and bridge, UIC 776-2R. 2009.

[15] W. M. Zhai, K. Y. Wang, and J. H. Lin, Modelling and experiment of railway ballast vibrations, *Journal of Sound and Vibration*, vol. 270, no. 4–5, pp. 673–683, Mar. 2004.

[16] S. Rashid, Parametric study of bridge response to high speed trains, 2011.

[17] P. Lou, Finite element analysis for train–track–bridge interaction system, *Archive of Applied Mechanics*, vol. 77, no. 10, pp. 707–728, Mar. 2007.

[18] X. Lei and N.-A. Noda, Analyses of dynamic response of vehicle and track coupling system with random irregularity of track vertical profile, *Journal of Sound and Vibration*, vol. 258, no. 1, pp. 147–165, 2002.

COMPDYN 2015
5th ECCOMAS Thematic Conference on
Computational Methods in Structural Dynamics and Earthquake Engineering
M. Papadrakakis, V. Papadopoulos, V. Plevris (eds.)
Crete Island, Greece, 25–27 May 2015

TEMPERATURE WARPING AND TRAIN-TRACK DYNAMIC ANALYSIS OF CRTS II SLAB BALLASTLESS TRACK

Jingjing Yang[1] **and Nan Zhang**[1]

[1]School of Civil Engineering, Beijing Jiaotong University, Beijing 100044, China
E-mail: 12115292@bjtu.edu.cn, nzhang@ bjtu.edu.cn

Keywords: CRTS II slab ballastless track, track slab, temperature warping, additional rail irregularity, dynamic performance of train-track system.

Abstract. *CRTS II ballastless slab track is widely adopted in high-speed railways in China. The influence of temperature induced deformation of CRTS II slab track on the running safety of high-speed trains is an important issue to be considered. With the temperature field of track slab simulated by applying temperature load on the track slab nodes, the warping of CRTS II track slab under overall temperature change and temperature gradient is analyzed. By applying the vertical rail displacements caused by the slab warping as the additional rail irregularities, the dynamic analysis model for the train-track system is established, to analyze the dynamic performance of the train. With the additional rail irregularities caused by slab warping under the most positive temperature difference as excitations, the dynamic responses of the track and the train vehicles, such as the wheel-rail interaction forces, wheel offload factor, reaction forces of fastener, as well as the accelerations of rail and track slab, are calculated, when the train passes on the track at the speed of 250km/h. The results show that the dynamic responses are larger, especially the accelerations of rail and track slab when considering the additional rail irregularities caused by temperature warping of track slab.*

1 INTRODUCTION

The CRTSII slab ballastless track widely adopted in high-speed railways in China is composed of rail, fasteners, track slab, CA (cement asphalt) mortar layer, concrete supporting layer and anti-frozen layer. A standard track slab is 6.45×2.55×0.2m, as shown in Figure 1. The CA mortar layer is 0.03m thick and 2.55m wide. The concrete supporting layer is 0.3m thick and 2.95m wide.

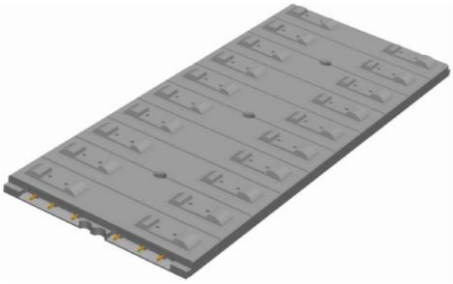


Figure 1: The standard track slab

There are mainly two types of temperature loads to be considered when analyzing the track slab, namely the overall temperature change and the temperature gradient. The temperature gradient of track slab has already been studied thoroughly [1-7], However, the overall temperature change and the temperature gradient happen at the same time, and the concretes at different heights of track slab have different temperature changes to form the temperature gradient in height. The temperature warping of track slab should be caused by the overall temperature change and the temperature gradient.

The warping of track slab under overall temperature change and temperature gradient is analyzed with the temperature field of track slab simulated by applying temperature load on the track slab nodes. By applying the vertical rail displacements caused by the slab warping as the additional rail irregularities, the dynamic analysis model is established, to analyze the dynamic performance of the train-track system.

2 TEMPERATURE WARPING OF CRTS II SLAB BALLASTLESS TRACK

The temperature field of track slab is simulated by applying temperature load on the track slab nodes. The initial temperature is the construction target temperature when track slab has neither temperature difference nor deformation. The final temperature is the measured temperature.

The calculation is simulated with the software Midas. The track slab, the CA mortar and the concrete supporting layer are simulated by solid elements. The track slab and the CA mortar are connected by nonlinear springs which are only compressed. The CA mortar and the concrete supporting layer are concurrent in contact surface. The rail is simulated by beam elements, and the fastener is simulated by the common springs.

The model of a track slab is shown in Figure 2.

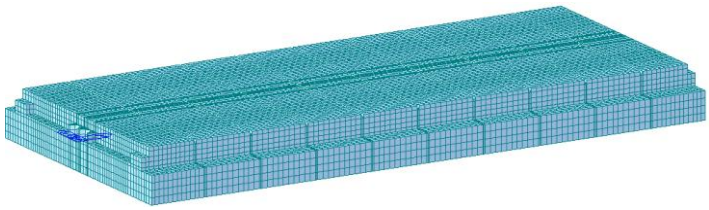


Figure 2: Model of a track slab

The temperature is cited from literature [6] to analyze the warping of track slab during a whole day. The surface temperature, the bottom temperature and the temperature difference of track slab during the whole day are shown in Figure 3. The temperature warping of track slab within 24 hours is shown in Figure 4.

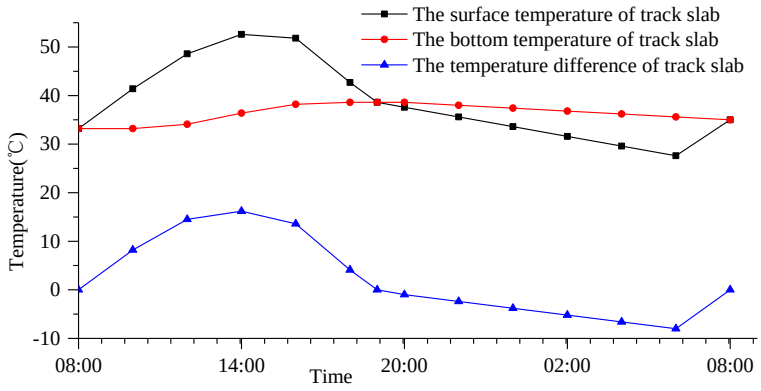


Figure 3: The surface temperature, the bottom temperature and the temperature difference of track slab during the whole day

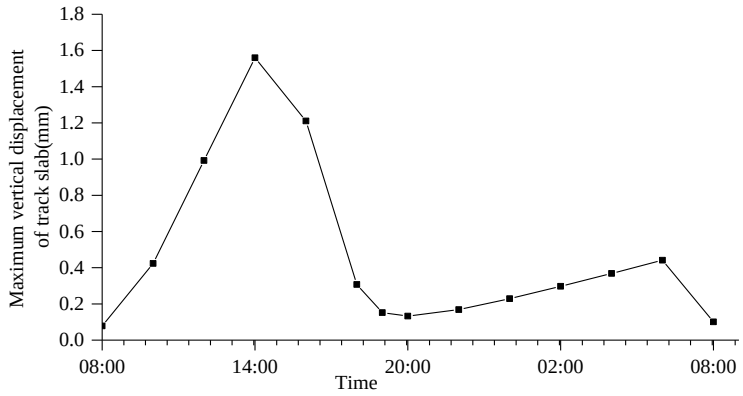


Figure 4: Temperature warping of track slab within 24 hours

The temperature warping of the track slab at the time of the most positive temperature difference and the most negative temperature difference are respectively shown in Figure 5 and Figure 6. The temperature warping is upward in the central area of the track slab at the time of the most positive temperature difference and the temperature warping is upward in the four corners of the track slab at the time of the most negative temperature difference.

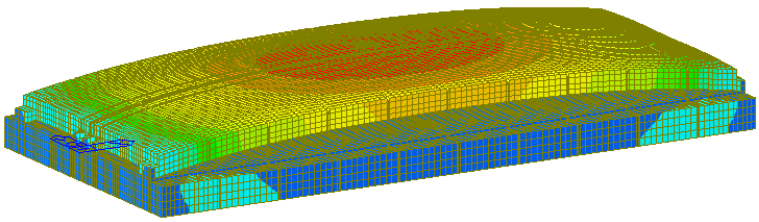


Figure 5: Temperature warping of the track slab at the time of the most positive temperature difference

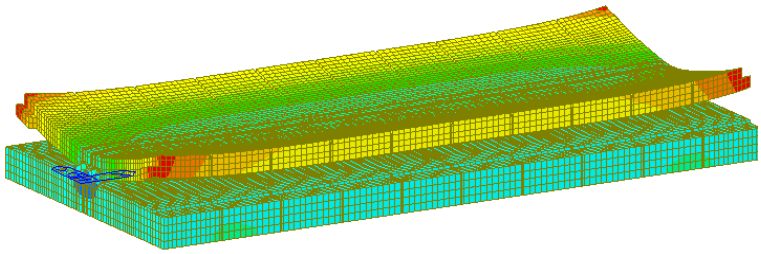


Figure 6: Temperature warping of the track slab at the time of the most negative temperature difference

3 DYNAMIC ANALYSIS OF TRAIN-TRACK SYSTEM UNDER TEMPERATURE LOAD

By applying the vertical rail displacements caused by the slab warping as the additional rail irregularities, the dynamic analysis model for the train-track system is established, to analyze the dynamic performance of the train. With the additional rail irregularities caused by slab warping under the most positive temperature difference as excitations, the dynamic responses of the track and the train vehicles, such as the wheel-rail interaction forces, wheel unloading rates, reaction forces of fastener, as well as the accelerations of rail and track slab, are calculated based on inter-system iteration[8-11], when eight vehicles pass on the track at the speed of 250 km/h.

3.1 The influence of fastener stiffness on the additional rail irregularities

The deformations of the rail and the track slab are calculated under the most positive and negative temperature difference when the stiffness of the fastener is respectively 22.5 kN/m, 60 kN/m and 60000 kN/m. The results are shown in Table 1.

The vertical stiffness of fastener	The maximum vertical displacements of rail		The maximum vertical displacements of track slab	
	The most positive temperature difference	The most negative temperature difference	The most positive temperature difference	The most negative temperature difference
22.5 kN/m	1.34mm	0.09 mm	1.56 mm	0.44 mm
60 kN/m	1.27 mm	0.11 mm	1.50 mm	0.43 mm
60000 kN/m	1.07 mm	0.11 mm	1.32 mm	0.34 mm

Table 1 The maximum vertical displacements of rail and track slab with different fastener stiffness

Table 1 shows that as the vertical stiffness of fastener reduces, the maximum vertical displacements of rail and track slab under the most positive temperature difference decrease. Besides, the maximum vertical displacement of rail under the most negative temperature difference can be ignored compared to the most positive temperature difference. So the additional rail irregularities caused by slab warping under the most positive temperature difference when the stiffness of the fastener is 22.5 kN/m are taken as excitations in this analysis.

3.2 The dynamic index for safety evaluation

The safety indexes of vehicles are composed of the derailment factor, offload factor of the wheel, and the lateral wheel-rail interaction force[12]. However, the lateral wheel-rail interaction force and the derailment factor are zero in this paper, because the lateral rail irregularities

are neglected. So only the wheel offload factor is considered in this paper and it should satisfy: $\Delta P/P \leq 0.6$, according to the <<Code For Design Of High Speed Railway>> in China.

3.3 Dynamic responses under temperature load

With the additional rail irregularities caused by slab warping under the most positive temperature difference when the stiffness of the fastener is 22.5 kN/m as excitations, the dynamic responses of the track and the train vehicles, such as the wheel offload factors, reaction forces of fastener, as well as the accelerations of rail and track slab, are calculated when eight vehicles pass on the track at the speed of 250 km/h. The results are shown in Table 2.

Dynamic indexes	Normal road section	Road section under temperature load	The increase percent
Wheel offload factor	0.300	0.318	6.0%
The maximum vertical reaction force of fastener	24.39/kN	25.25/kN	3.5%
The maximum vertical acceleration of rail	79.49/(m/s^2)	95.93/(m/s^2)	20.7%
The maximum vertical acceleration of track slab	1.72/(m/s^2)	2.08/(m/s^2)	20.7%

Table 2 The dynamic responses under temperature load

Table 2 shows that the dynamic responses are larger when considering the additional rail irregularities caused by temperature warping of track slab. The wheel offload factor increases by 6.0%, the maximum vertical reaction force of fastener increases by 3.5%, and the maximum vertical accelerations of rail and track slab increase obviously by 20.7%.

The wheel offload factor under temperature load is 0.318 and it satisfies: $\Delta P/P \leq 0.6$, so it is safe for the train vehicles.

The vertical wheel-rail interaction forces, the vertical reaction forces of fastener, and the vertical accelerations of rail and track slab are shown respectively in Figures 7 to 10.

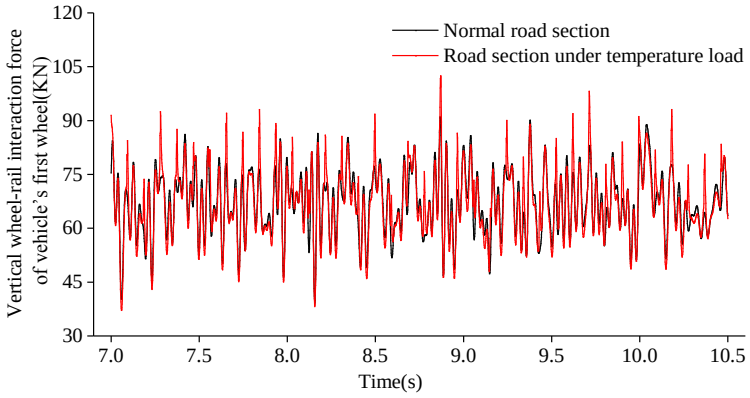


Figure 7: Vertical wheel-rail interaction force histories of vehicle's first wheel

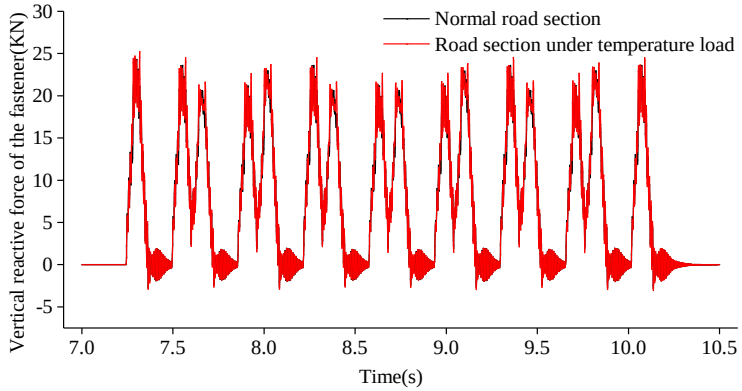


Figure 8: Vertical reaction force histories of fastener

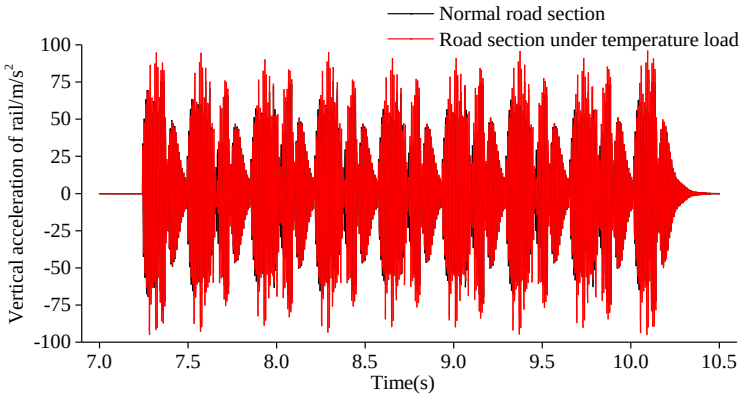


Figure 9: Vertical acceleration histories of rail

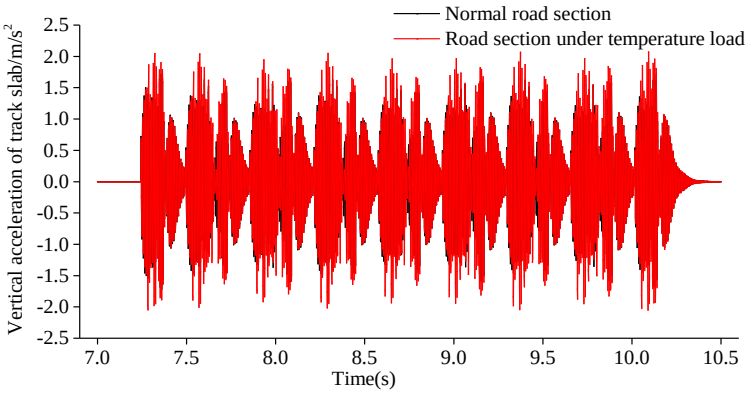


Figure 10: Vertical acceleration histories of track slab

4 COCLUSIONS

In this paper, the warping of track slab under overall temperature change and temperature gradient is analyzed with the temperature field of track slab simulated by applying temperature load on the track slab nodes. By applying the vertical rail displacements caused by the slab warping as the additional rail irregularities, the dynamic analysis model is established, to analyze the dynamic performance of the train-track system. According to the analysis results, some conclusions can be obtained:

(1) The temperature warping is upward in the central area of track slab at the time of the most positive temperature difference and the temperature warping is upward in the four corners of track slab at the time of the most negative temperature difference.
(2) The maximum vertical displacements of rail and track slab under the most positive temperature difference decrease as the vertical stiffness of fastener reduces. Besides, the maximum vertical displacement of rail under the most negative temperature difference can be ignored compared to the most positive temperature difference.
(3) The dynamic responses become larger when considering the additional rail irregularities caused by temperature warping of track slab. The wheel offload factor increases by 6.0%, the maximum vertical reaction force of fastener increases by 3.5% and the maximum vertical accelerations of rail and track slab increase obviously by 20.7%.

ACKNOWLEDGEMENTS

The research is sponsored by the Major State Basic Research Development Program of China (973 Program: 2013CB036203), the 111 Project (Grant No. B13002) and the Doctoral Fund of Ministry of Education of China (Grant No. 20130009110036).

REFERENCES

[1] Ando, K., S. Miura, K. Wataname, Twenty years' experience on slab track. *Proc., Sixth World Conference on Transport Research*, Vol. IV, Lyon, France, July 1992.

[2] Ando, K., S. Mura, J. Okazaki, M. Sunaga, H. Aoki, O. Maruyama, Development and practical use of concrete roadbed for slab track on earthworks. *Proc., Eighth World Conference on Transport Research*, Antwerp, Belgium, July 1998.

[3] Morcher, J, Development of ballastless track in Germany. *Proc., International Conference on Innovations in the Design & Assessment of Railway Track*, Delft University of Technology, Delft, Netherlands, Dec 1999.

[4] Shiraz D. Tayabji, David Bilow, Concrete slab track state of the practice. Transportation Research Record: Journal of the Transportation Research Board, **1742**, 87-96, 2007.

[5] Y Liu, GT Zhao, Analysis of early gap between layers of CRTSII slab ballastless track structure. China Railway Science, **34(4)**, 1-7, 2013. (in Chinese)

[6] Y Liu, P Chen, GT Zhao, Study on the characteristics of early temperature field of CRTSII slab ballastless track structure. China Railway Science, **35(1)**, 1-6, 2014. (in Chinese)

[7] JJ Wang, RL You, M Wang, C Jiang, Research on the slab temperature warping of the unit slab track system. China Railway Science, **31(3)**, 9-14, 2010. (in Chinese)

[8] N Zhang, H Xia, Dynamic analysis of coupled vehicle–bridge system based on inter-system iteration method. Computers and Structures, 114-115, 26-34, 2013.

[9] N Zhang, S Zhou, H Xia, L Su, Evaluation of vehicle-track-bridge interacted system for the continuous CRTS-II non-ballast track slab. Science China, **57(10)**, 1895-1901, 2014.

[10] WM Zhai, H Xia, CB Cai, High-speed train–track–bridge dynamic interactions-Part I: Theoretical model and numerical simulation. International. J Rail Transp, **1**, 3-24, 2013.

[11] WM Zhai, SL Wang, N Zhang, *et al*., High-speed train–track–bridge dynamic interactions-Part II: Experimental validation and engineering application. J Rail Transp, **1**, 25-41, 2013.

[12] H. Xia, G. De Roeck, J. M. Goicolea. *Bridge Vibration and Controls: New Research*, New York: Nova Science Publishers Inc., 2012.

COMPDYN 2015
5th ECCOMAS Thematic Conference on
Computational Methods in Structural Dynamics and Earthquake Engineering
M. Papadrakakis, V. Papadopoulos, V. Plevris (eds.)
Crete Island, Greece, 25–27 May 2015

PARAMETRIC EVALUATION OF VISCOUS DAMPER RETROFIT FOR HIGH-SPEED RAILWAY BRIDGES

Sarah Rådeström[1], Viktor Tell[1,2], Mahir Ülker-Kaustell[1,2] and Raid Karoumi[1]

[1]Division of Structural Engineering and Bridges, KTH Royal Institute of Technology
Brinellvägen 23, 100 44 Stockholm, Sweden
e-mail: sarah.radestrom@byv.kth.se

[2]Department of Bridges, Tyréns AB
Peter Myndes Backe 16, 118 86 Stockholm, Sweden

Keywords: Structural Dynamics, Railway Bridges, High-speed Trains, Passive Damping, Viscous Dampers.

Abstract. *Several of the bridges belonging to the Bothnia Line, located in northern Sweden, do not theoretically fulfil the current design limit for the vertical deck acceleration, when being subjected to high-speed trains. Hence, it is important to find appropriate vibration mitigation strategies that are applicable to railway bridges, in order to reduce the acceleration caused by passing trains. One way of solving this problem is to install external viscous dampers.*

A finite element solution for damper retrofit of high-speed railway bridges is proposed in this paper. The bridge is modelled as a two-dimensional Euler-Bernoulli beam, with inclined dashpots connected between the superstructure and the abutments. Furthermore, this paper highlights the influence of several parameters on the effectiveness of the dampers.

1 INTRODUCTION

The Bothnia Line is a subsection of the Swedish railway system, which stretches along the northern coastline and includes a total of 140 bridges [1]. The tracks and bridges of the line are designed for train speeds of up to 250 km/h. The maximum vertical bridge deck acceleration must not exceed 3.5 m/s^2, for bridges with ballasted tracks, according to the Eurocode [2]. However, theoretical results from previous studies [3] indicate that many of the steel-concrete composite bridges along the Bothnia Line fail to fulfil this requirement.

The demands for analyses of the dynamic behavior of high-speed railway bridges are constantly increasing, due to the combination of higher train speeds and loads together with the decreasing weight of modern railway bridges [4]. One fundamental problem that must be included in the analyses is the risk of resonance in the bridge, caused by train loading. Resonance arises when the forcing frequency from the train coincides with the eigenfrequency of the bridge, which may occur due to the periodic and repetitive action of axle loads.

Consequently, procedures for mitigating the dynamic response of structures have to be employed for both new and existing high-speed railway bridges. An efficient approach is to install control devices, in order to reduce the response of bridges subjected to passing trains [5]. Thus, the structural safety and serviceability of the bridge will be significantly increased.

One example of a damping device, which is a widely accepted application within civil structures, is the tuned mass damper (TMD). The TMD consists of a spring, an added mass and a damper and can relatively easy be attached to structures, in order to efficiently mitigate the vibrations [6]. However, the TMD is tuned to a certain frequency of the structure and will, thus, be inefficient at other ranges of frequencies [7]. Hence, inaccurate estimates of the properties of the bridge can lead to a detuning effect [8]. This results in increased installation and calibration costs, in order to tune the dampers correctly and avoid estimation errors. Furthermore, the TMD may be unsuitable for existing structures, since the structure may not be able to carry the added mass.

The fluid viscous dampers (FVD), on the other hand, provides the robustness necessary for applications in railway bridges. This type of control system covers a wide frequency band, which eliminates the detuning effect. Therefore, the installation and maintenance costs are significantly decreased. Another advantage is that the device does not consist of an added mass and will, thus, not affect the resistance of the bridge to the same extent as a TMD. Figure 1 shows a sketch of a FVD.

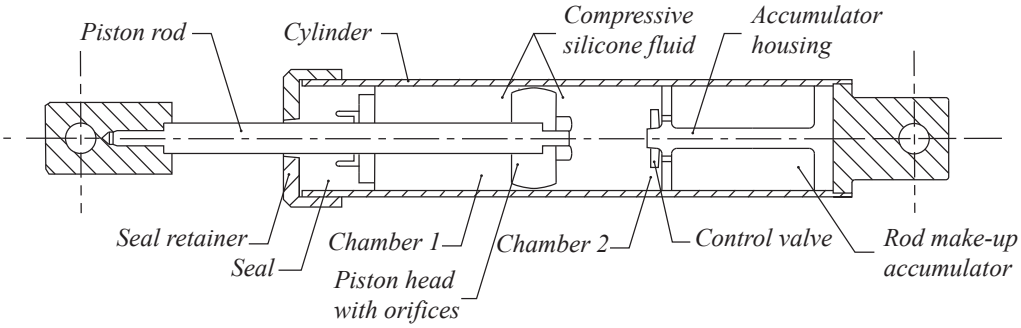


Figure 1: A sketch of a type of FVD, reproduced from [9].

Several studies include investigations of FVDs using auxiliary beams, in order to connect the dampers to the superstructure [7, 10–13]. This retrofit method (as well as installation of TMDs) may, however, be unsuitable for some bridges, where ground conditions or barriers in

the surroundings limit the accessibility for heavy construction machinery. It is expensive to restrict the traffic during the installation of the dampers, wherefore measures that have a small impact on the rail services are desirable.

This study contains a proposal of a retrofit approach, where the FVDs are installed between the superstructure and the abutments. Furthermore, the installation method imposes a distance between the neutral axis of the beam and the connection point of the damper, referred to as eccentricity in the present study. Conclusively, an investigation of some influential parameters on the efficiency of the damping properties is conducted as well.

2 NUMERICAL CALCULATIONS

The bridge is idealized as a two-dimensional Euler-Bernoulli beam, while the FVDs are modeled as dashpots and the eccentricity is obtained through constraint equations. Furthermore, the equation of motion for the system can be described by the viscously damped, linear oscillator

$$M\ddot{u} + C\dot{u} + Ku = F \tag{1}$$

where $\ddot{u}$, $\dot{u}$ and u are the acceleration, velocity and displacement of the structural components. Moreover, M, C and K are the matrices of the mass, damping and stiffness, respectively, and F is the force. The damping consists of the damping contribution from the external dampers C_{d} and the structural damping of the bridge C_{s}. Hence, the governing equation of motion for the bridge-damper system can be expressed as

$$M\ddot{u} + [C_{\mathrm{d}} + C_{\mathrm{s}}]\dot{u} + Ku = F \tag{2}$$

The calculation of the train forces is based on a procedure that is described by Frỳba [14]. The axle distances and loads determine the magnitude and position of the forces at each time instant. These values correspond to the high-speed load model (HSLM) trains that are stated in the Eurocode [2].

The force matrix is assembled by assuming a linear interpolation between the nodes, in order to find the distribution of each concentrated force to the closest vertical degree-of-freedom (DOF) at each time step. The nodal forces at each time instant are shown in Equation (3), where the indices i and $i+1$ correspond to the vertical DOF that the force has already passed and the one it will pass in the immediate future, respectively.

$$F_i(t) = \sum_{n-1}^{N} F_n \epsilon_n(t) \left[\frac{ct - d_n - d_i}{d_{i+1} - d_i} \right] \tag{3a}$$

$$F_{i+1}(t) = \sum_{n-1}^{N} F_n \epsilon_n(t) \left[1 - \frac{ct - d_n - d_i}{d_{i+1} - d_i} \right] \tag{3b}$$

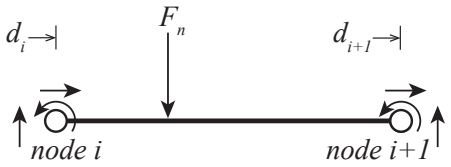


Figure 2: A sketch of the moving concentrated force acting on a beam element.

The quantities in Figure 2 and Equation (3) are the axle force of the nth train axle F_n, the train speed c, the time t and the distance between the first force and the nth force d_n. d_i and d_{i+1} are the positions of the two nodes of the loaded element, whereas $i = 1, 2, 3, ..., N_y - 1$ and N_y is the number of vertical DOFs along the beam. Furthermore, ϵ_n is a function that determines whether or not the force is acting on the beam and is defined as

$$\epsilon_n(t) = H\left[t - t_n\right] - H\left[t - T_n\right] \tag{4}$$

where t_n and T_n are the times when the nth force enters and exits the bridge (with a total bridge length L), respectively

$$\begin{aligned} t_n &= d_n/c \\ T_n &= [L + d_n]/c \end{aligned} \tag{5}$$

and $H(t)$ is Heaviside's function, given by

$$H(t) = \begin{cases} 0 & \text{for } t < 0 \\ 1 & \text{for } t \geq 0 \end{cases}$$

Thereafter, direct time integration using the implicit Newmark's method is conducted, in order to obtain the maximum bridge deck acceleration and velocity at each time instant. The first step is to initialize the values for the force, $F_0 = 0$, and displacement $u_0 = 0$, as well as its derivatives, $\dot{u}_0 = 0$ and $\ddot{u}_0$

$$\ddot{u}_0 = \frac{F_0 - C\dot{u}_0 - Ku_0}{M} \tag{6}$$

The same applies for the Newmark's coefficients, a_1, a_2 and a_3. These depend on the mass and the damping of the system.

$$\begin{aligned} a_1 &= \frac{\beta\Delta t^2}{M} + \frac{\gamma}{\beta\Delta t}C \\ a_2 &= \frac{\beta\Delta t}{M} + \frac{\gamma - \beta}{\beta}C \\ a_3 &= \frac{1 - 2\beta}{2\beta}M + \frac{\gamma - 2\beta}{2\beta}C\Delta t \end{aligned} \tag{7}$$

The constants β and γ in Equation (7) are the Newmark's average acceleration parameters, which are 0.25 and 0.5 respectively. After the initialization, the following procedure is then performed for each time step, Δt.

$$\begin{aligned} \hat{K} &= K + a_1 \\ \hat{F} &= F_{t+1} + a_1 u_t + a_2 \dot{u}_t + a_3 \ddot{u}_t \end{aligned} \tag{8}$$

which gives the displacement, velocity and acceleration at time $t + 1$

$$\begin{aligned} u_{t+1} &= \hat{F}/\hat{K} \\ \dot{u}_{t+1} &= \frac{\gamma}{\beta\Delta t}\Delta u_t + \frac{\beta - \gamma}{\beta}\dot{u}_t + \frac{2\beta - \gamma}{2\beta}\ddot{u}_t\Delta t \\ \ddot{u}_{t+1} &= \frac{1}{\beta\Delta t^2}\Delta u_t - \frac{1}{\beta\Delta t}\dot{u}_t - \frac{1 - 2\beta}{2\beta}\ddot{u}_t \end{aligned} \tag{9}$$

where $\Delta u_t = u_{t+1} - u_t$. Equations (8) and (9) are then repeated for all time steps.

The values for $\dot{u}$ and $\ddot{u}$ in Equation (9) are then used to derive the maximum acceleration and calculate the damper force. The maximum acceleration is found by collecting the maximum value of $\ddot{u}$, at any time instant, for each train speed. Furthermore, the maximum velocity in the dampers must be determined, in order to calculate the required damper force according to Equation (10).

$$f_{\mathrm{d,max}} = c_{\mathrm{d}} |\dot{u}_{\mathrm{max}}| \tag{10}$$

The constant c_{d} in Equation (10) is the damping coefficient for the external damper. The maximum velocity, $\dot{u}_{\mathrm{max}}$, is obtained by extracting the maximum velocity at the damper connections, for all time steps and each train speed.

3 CASE STUDY

A case study of one of the bridges along the Bothnia Line, which theoretically fails to fulfil the Eurocode acceleration requirement, is performed. The investigated bridge (see Figure 3) is called the Banafjäl Bridge. It is a simply supported, single track, steel-concrete composite girder bridge. The relevant bridge properties are shown in Table 1, where the given quantities are: Young's modulus E, the eccentricity e (i.e. the distance between the neutral axis of the bridge and the connection point of the damper, see also Figure 4), the area moment of inertia I, the span length L, the mass of the bridge m and the damping ratio of the constituent materials ξ (chosen according to recommendations in [2]).



Figure 3: The Banafjäl Bridge.

Table 1: Properties of the Banafjäl Bridge.

E	*e*	*I*	*L*	*m*	ξ
[GPa]	[m]	[m^4]	[m]	[kg/m]	[%]
200	2.2	0.61	42	18 400	0.5

Figure 4 shows the proposed retrofit, where c_{d} is the damping coefficient for the external dampers, e is the eccentricity between the bridge deck neutral axis and the connection point of

the dampers (which is assumed to coincide with the vertical coordinate of the support point). Furthermore, α is the inclination of the dampers and x_{d} is the distance between the support and the connection point of the dampers. On this bridge, dampers could be installed using cross beams, attached between the bottom flanges of the main girders.

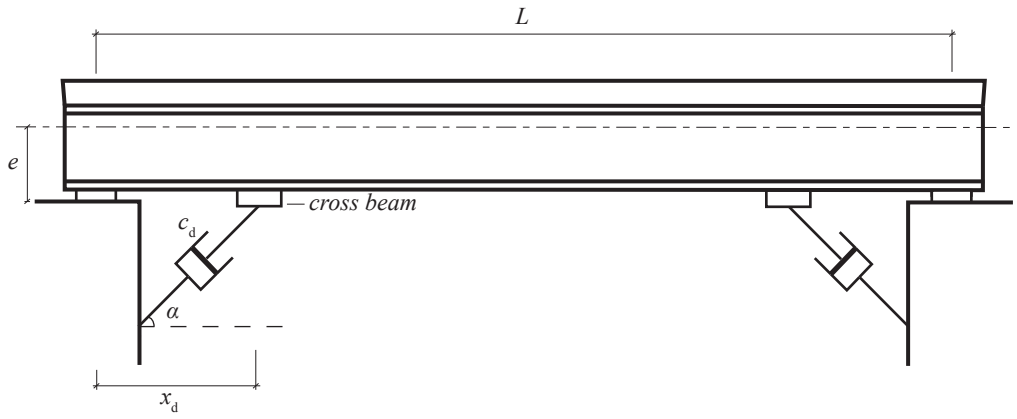


Figure 4: The proposed retrofit method of the dampers.

Previous studies [3] have shown that the critical HSLM-train for this bridge is the HSLM-A4 (see [2]), so the following investigations are limited to this train. The speed of the train, during the passages of the bridge, is varied from 100-300 km/h, with a speed increment of 1 km/h.

4 PARAMETRIC EVALUATION

Four different parameters are varied within the scope of this study, in order to observe the impact on the damping properties, namely;

- the damping coefficient of the dampers
- the eccentricity between the neutral axis of the bridge and the damper connections
- the inclination of the dampers
- the distance from the supports to the connection points of the dampers

Only one of the different parameters are changed within each investigation, while the remaining variables are held constant. The damping coefficient is changed to $c_{\mathrm{d}} = 0, 2, 3, 4.5$ MNs/m. Moreover, the eccentricity is altered between the following values: $e = 0, 2.2, 2.6, 3.0$ m. The first two values, $e = 0$ m and $e = 2.2$ m, correspond to the cases when the dampers are attached directly to the neutral axis of the bridge and to the lower flanges of the girders, respectively. The remaining values are the eccentricity together with two different heights of the additional cross beam (i.e. 0.4 m and 0.8 m). The inclination of the dampers is varied between $\alpha = 30, 45, 60, 75°$ and the distance from the support to the connection point of the dampers is increased within an interval of $x_{\mathrm{d}} = 1, 2, 3, 4$ m. A prerequisite for the evaluations of α and x_{d} is that elongation of the dampers is possible, without introducing any impairments of the stiffness or damping properties. The results in the following sections are presented in the form of maximum acceleration and required damper force as a function of train speed. From Figure 5, it is clear that the bridge has a resonance condition at a speed about 168 km/h.

4.1 The damping coefficient

Figure 5 shows the result of varying the damping coefficient while keeping the eccentricity, inclination and distance from the support constant as $e = 2.2$ m, $\alpha = 45°$ and $x_{\mathrm{d}} = 1$ m, respectively. The top figure shows the acceleration levels for different values of the damping coefficient and train speeds. The bottom figure shows the corresponding damper forces.

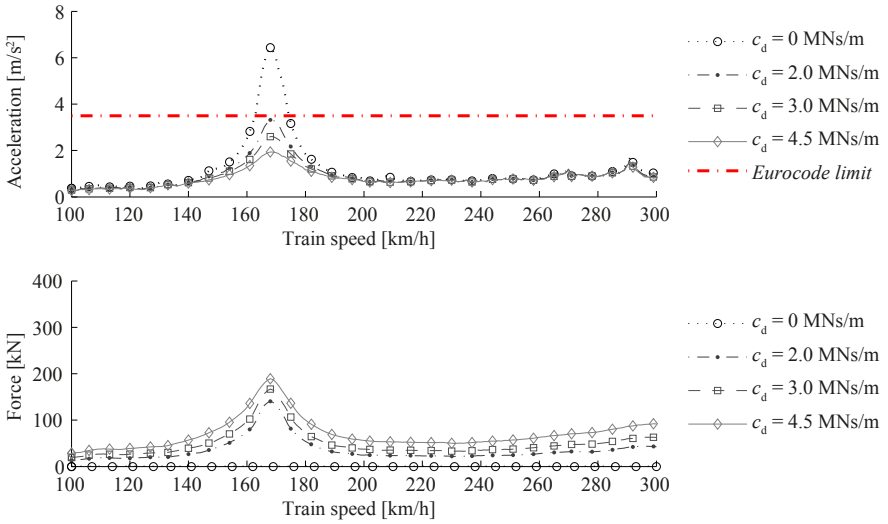


Figure 5: The maximum acceleration and damper force at different train speeds and damping coefficients.

4.2 The eccentricity

Figure 6 includes the results when the height of the cross beam (and, hence, eccentricity) is altered. The upper figure gives the amplitude of the acceleration after the damper retrofit with varying eccentricities and a constant damping coefficient $c_{\mathrm{d}} = 4.5$ MNs/m. Both the damper inclination and the distance from the support is fixed as $\alpha = 45°$ and $x_{\mathrm{d}} = 1$ m, respectively. Moreover, the lower figure shows the required damper force, when altering the same parameter.

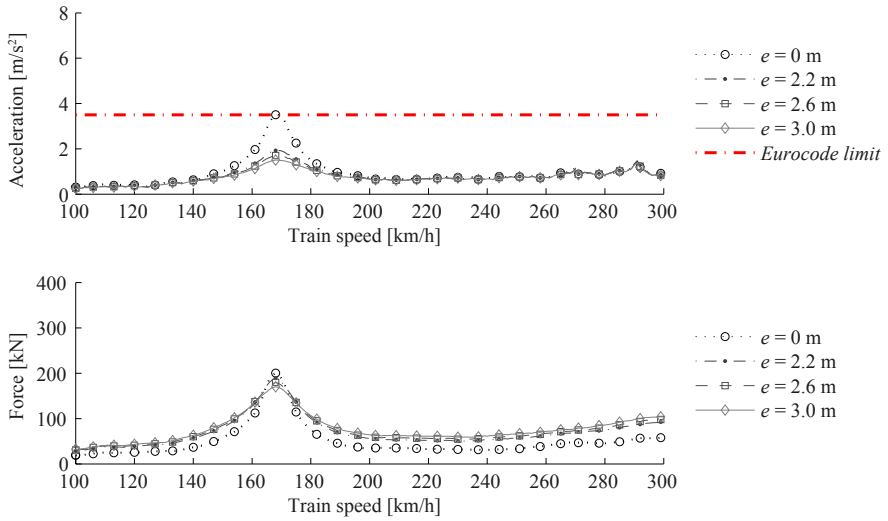


Figure 6: The maximum acceleration and damper force at different train speeds and eccentricities.

4.3 The damper inclination

The results in Figure 7 show the impact on the damping properties when changing the inclination of the damper, with a constant damping coefficient $c_\mathrm{d} = 4.5$ MNs/m, eccentricity $e = 2.2$ m and distance from support $x_\mathrm{d} = 1$ m. The upper and lower figures show the acceleration and force for different inclinations and train speeds, respectively.

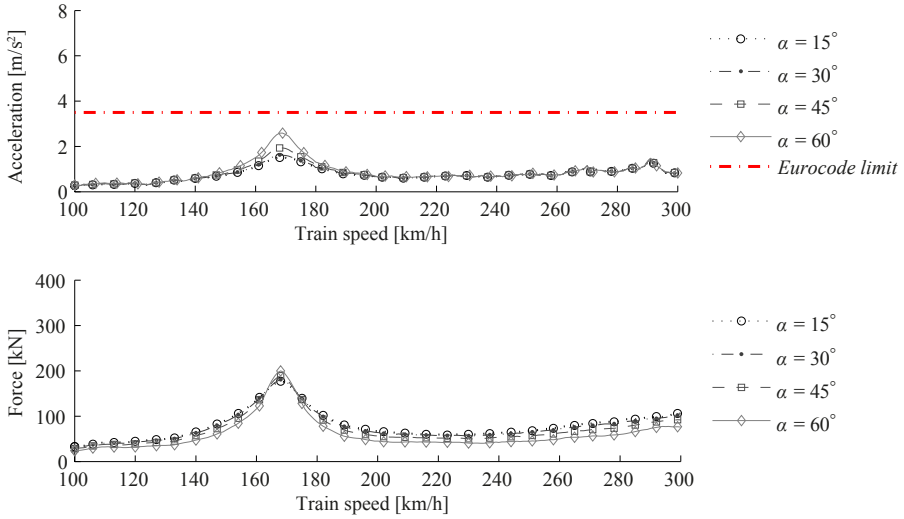


Figure 7: The maximum acceleration and damper force at different train speeds and damper inclinations.

4.4 The distance from the supports

Figure 8 shows the influence of the distance from the supports to the damper connections, while the damping coefficient is $c_\mathrm{d} = 4.5$ MNs/m, the eccentricity is $e = 2.2$ m and the damper inclination is $\alpha = 45°$. The figure shows the impact on the maximum acceleration and the damper force.

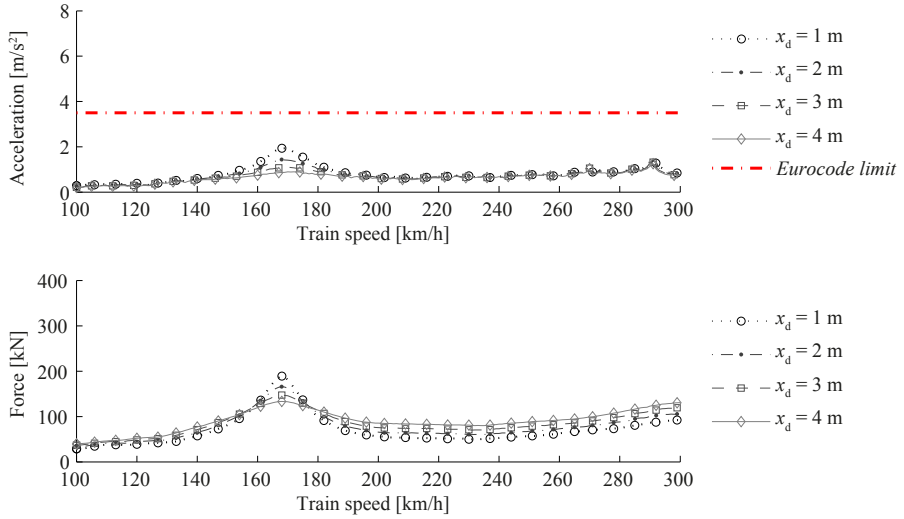


Figure 8: The maximum acceleration and damper force at different train speeds and distances from support.

5 DISCUSSION

The results from Figure 5 to Figure 8 indicate that the bridge deck vertical accelerations can be significantly reduced, when using FVDs according to the proposed attachment method. As expected, the dampers are most efficient for the reduction of the vibrations at resonance, which arises at the critical train speed. The acceleration level only exceeds the design code limit at resonance for this particular bridge, therefore the dampers are efficient for this case.

As shown in Figure 5, the damping coefficient has a major impact on the results. Theoretically, the acceleration can be reduced from 6.4 m/s^2 to 3.3 m/s^2 and 1.9 m/s^2, when using damper coefficients of 2.0 MNs/m and 4.5 MNs/m, respectively. However, the required damper force increases with the damping coefficient. This is important to consider when using FVDs as a retrofit approach for existing bridges.

The height of the cross beam affects the acceleration level, which is shown in Figure 6. Both the acceleration and damper force are lower for a longer distance between the neutral axis and the connection point of the dampers. Thus, an optimal eccentricity exists for each individual bridge, which must be considered in the design of the cross beam.

The dampers are more effective when installed with an angle between 15°-30° to the horizontal plane, than for steeper inclinations (see Figure 7). A reason for this is that the eccentricity of the bridge gives a rotational contribution to the movement of the connection point of the dampers. This results in a more prominent horizontal movement. A less steep angle is, thus, preferred, since the damper device is only able to operate in its axial direction.

From Figure 8, it is clear that the acceleration and the damper force at resonance are further reduced, as the distance to the midpoint of the bridge decreases. Hence, the optimal connection point of the dampers is further out from the support. However, the effect seems to diminish, as the distance between the support and the connection point of the dampers increases. Furthermore, the possible positions of the attachment point are limited, since a connection point further from the support requires a longer damper. This may lead to a lower stiffness of the device and, thereby, a reduced damping capacity.

The proposed solution can be optimized and adapted to many different bridge configurations. However, this retrofit method may lead to problems that have to be investigated and remedied. As seen in the results presented here, the effectiveness of the FVDs is sensitive to changes of certain parameters. Hence, it is important that all uncertainties of the bridge-damper system are accurately and appropriately accounted for in the analysis.

ACKNOWLEDGEMENTS

Deep gratitude is directed to the Department of Bridges at Tyréns AB for helping out in the beginning of the study and, thereby, making this research possible.

REFERENCES

[1] J Wiberg and R Karoumi. *Kontroll av dynamiska effekter av passerande tåg på Botniabanans broar: Sammanfattning*. KTH Department of Structural Engineering and Bridges, 2006. (In Swedish).

[2] European Committee for Standardization (CEN). Eurocode 1: Actions on structures - part 2: Traffic loads on bridges. EN 1991-2, 2003.

[3] C Johansson, A Andersson, C Pacoste, and R Karoumi. *Järnvägsbroar på Botniabanan: Dynamiska kontroller för framtida höghastighetståg – Steg 1*. KTH Department of Structural Engineering and Bridges, 2013. (In Swedish).

[4] JW Kwark, ES Choi, YJ Kim, BS Kim, and SI Kim. Dynamic behavior of two-span continuous concrete bridges under moving high-speed train. *Computers & Structures*, 82(4):463–474, 2004.

[5] HC Kwon, MC Kim, and IW Lee. Vibration control of bridges under moving loads. *Computers & Structures*, 66(4):473–480, 1998.

[6] GL Lin, CC Lin, BC Chen, and TT Soong. Vibration control performance of tuned mass dampers with resettable variable stiffness. *Engineering Structures*, 83:187–197, 2015.

[7] MD Martínez-Rodrigo, J Lavado, and P Museros. Dynamic performance of existing high-speed railway bridges under resonant conditions retrofitted with fluid viscous dampers. *Engineering Structures*, 32(3):808–828, 2010.

[8] JF Wang, CC Lin, and BL Chen. Vibration suppression for high-speed railway bridges using tuned mass dampers. *International Journal of Solids and Structures*, 40(2):465–491, 2003.

[9] DP Taylor and MC Constantinou. *Fluid dampers for applications of seismic energy dissipation and seismic isolation*. Taylor Devices, Incorporated, 1998.

[10] P Museros and MD Martínez-Rodrigo. Vibration control of simply supported beams under moving loads using fluid viscous dampers. *Journal of Sound and Vibration*, 300(1):292–315, 2007.

[11] MD Martínez-Rodrigo and P Museros. Optimal design of passive viscous dampers for controlling the resonant response of orthotropic plates under high-speed moving loads. *Journal of Sound and Vibration*, 330(7):1328–1351, 2011.

[12] J Lavado, A Doménech, and MD Martínez-Rodrigo. Dynamic performance of existing high-speed railway bridges under resonant conditions following a retrofit with fluid viscous dampers supported on clamped auxiliary beams. *Engineering Structures*, 59:355–374, 2014.

[13] M Luu, MD Martínez-Rodrigo, V Zabel, and C Könke. H_∞ optimization of fluid viscous dampers for reducing vibrations of high-speed railway bridges. *Journal of Sound and Vibration*, 333(9):2421–2442, 2014.

[14] L Frỳba. A rough assessment of railway bridges for high speed trains. *Engineering Structures*, 23(5):548–556, 2001.

COMPDYN 2015
5th ECCOMAS Thematic Conference on
Computational Methods in Structural Dynamics and Earthquake Engineering
M. Papadrakakis, V. Papadopoulos, V. Plevris (eds.)
Crete Island, Greece, 25–27 May 2015

TRANSVERSAL VIBRATION CONTROL FOR CATENARY POLES ON A HIGH SPEED RAILWAY BRIDGE

C. Anicotte[1] **and D. Botton**[2]

[1] SNCF Engineering and Projects Direction
6 avenue François Mitterrand 93574 La Plaine Saint Denis, France
e-mail: celine.anicotte@sncf.fr

[2] RFF – Bourgogne Franche-Comté Regional Direction
22 rue de l'Arquebuse - 21078 Dijon cedex France
dominique.botton@rff.fr

Keywords: Catenary supports, resonance, railway bridge dynamics, finite elements modelling, vibration control, tuned-mass dampers

Abstract. *The study presented in this paper deals with the excessive transversal vibrations of the catenary poles located on the Savoureuse viaduct; a railway bridge on high speed line in France. This viaduct across the Savoureuse River opened in 2011 for commercial runs of high speed trains between Dijon and Mulhouse in France. During inspection visits, the maintenance agents on site detected that the catenary poles presented strong transversal vibrations perpendicular to the track axis. RFF and SNCF were then concerned for the integrity of the concrete boxes fastening the catenary poles and the stability of the catenary itself. A full study was carried out by SNCF to explain the phenomenon and to find the best solution to reduce these transversal vibrations.*

1 INTRODUCTION

The viaduct across the Savoureuse River is special bridge with 12 independent spans based on 2 abutments and 11 architecturally designed tetra-pod piers. The bridge deck is composed of two main lateral girders, transversal floorbeams and a filler beam slab resting on the floorbeams. Each span is bearing 2 catenary poles (HEA 240 girders) per track. The poles are located on the filler beam slab at approximately quarter-span on either side.



Figure 1: Aerial photograph of the Savoureuse viaduct

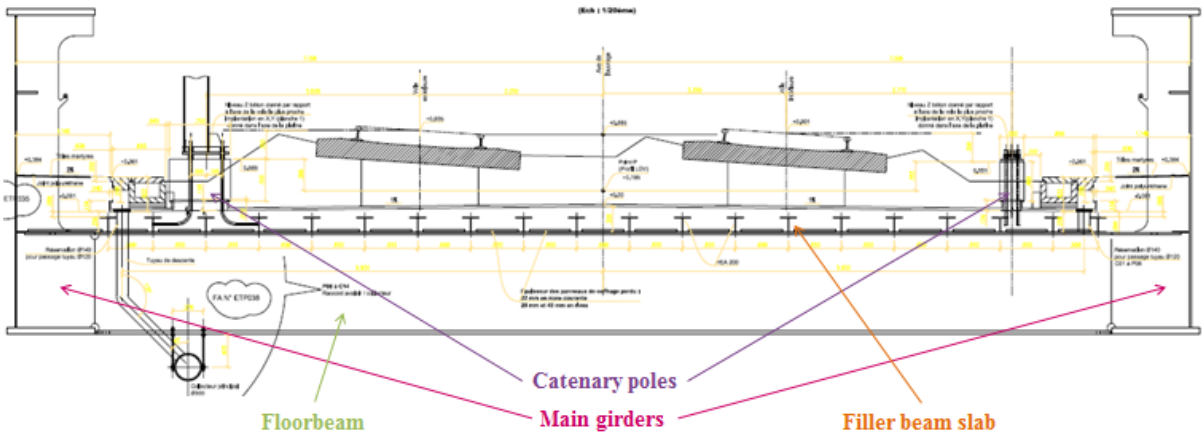


Figure 2: Cross section of the Savoureuse viaduct

During inspection visits, the maintenance agents on site detected that the catenary poles presented strong transversal vibrations perpendicular to the track axis. These vibrations oc-

curred only when TGV trains were passing at 170 km/h to stop at a train station a few kilometres further; TGV trains running at full speed (320 km/h) did not create any important vibrations.

In order to fully explain the phenomenon and to find an adapted solution, it was decided to model the effect of trains passing on the bridge on the dynamic response of the catenary poles. To quantify exactly the transversal vibrations and to validate the model, dynamic measurements were carried out on the bridge and the catenary poles.

2 DYNAMIC MEASUREMENTS ON THE STRUCTURE

The dynamic measures consisted in setting accelerometers and displacement sensors on different points of the structure.

For the bridge, measures were made at the line opening in 2011 with accelerometers and displacement sensors at the middle of spans number 1, 10, 11 and 12. These measures were used to adjust the Finite Elements model of the bridge. The first eigenmode of longitudinal bending was found at 2.23Hz for 66m-long spans (between pier n°2 and pier n°12) and 2.62Hz for 66m-long spans (end spans).

For the catenary poles, transversal accelerometers were placed at the top of 3 poles on the same span of the viaduct. The amplitude of transversal displacement was obtained by integrating twice the acceleration signal.

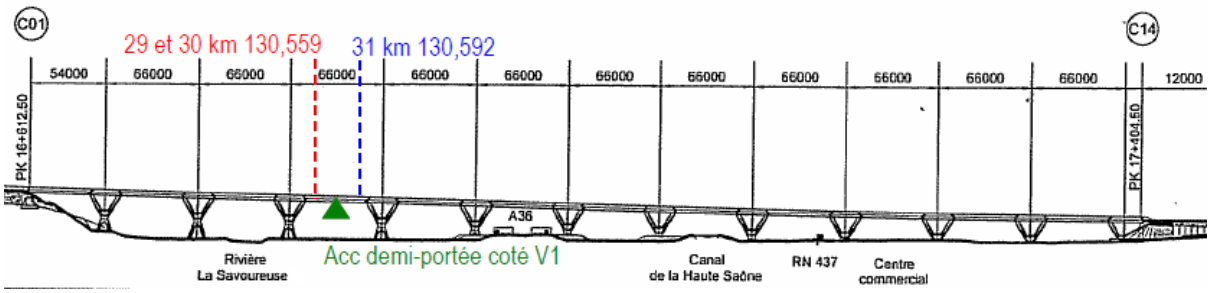


Figure 3: Location on the viaduct of the poles equipped with accelerometers



Figure 4: Fastening of the accelerometer on top of the catenary pole

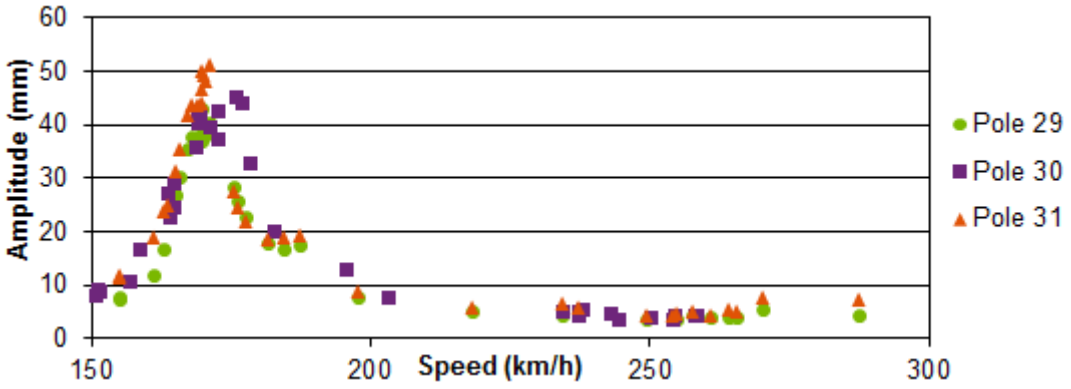


Figure 5: Results of measurement for the 3 equipped poles

These measurements on top of the catenary poles showed that the amplitude of transversal displacements reaches the maximum of 51mm on pole 31 for trains running at 170km/h. This form of curve is characteristic of a resonance phenomenon.

The main frequency measured on all the poles is comprised between 2.5 and 2.6 Hz, which corresponds exactly at the critical speed for TGV of 170 km/h (a bogie passing every 18.7m).

3 MODELLING OF THE STRUCTURE

3.1 Bridge model

To explain perfectly this resonance phenomenon and to find the best solution to reduce the vibration, a Finite Element model of the structure was created.

To reduce the calculation times, only the first three spans of the bridge were modelled and the results were extracted on the central span. The program ANSYS was used to create the model.

All the beams (Main girders, floorbeams, piers, etc.) were represented as BEAM188 elements and the filler beam slab as SHELL181 elements.

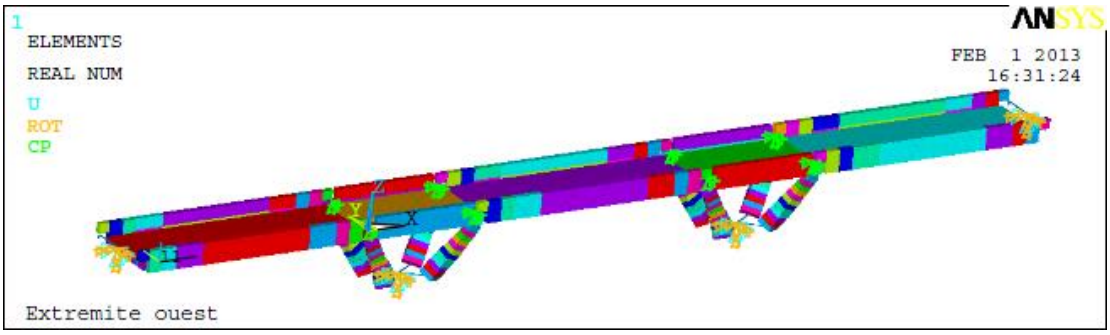


Figure 6: General view of the viaduct Finite Elements model

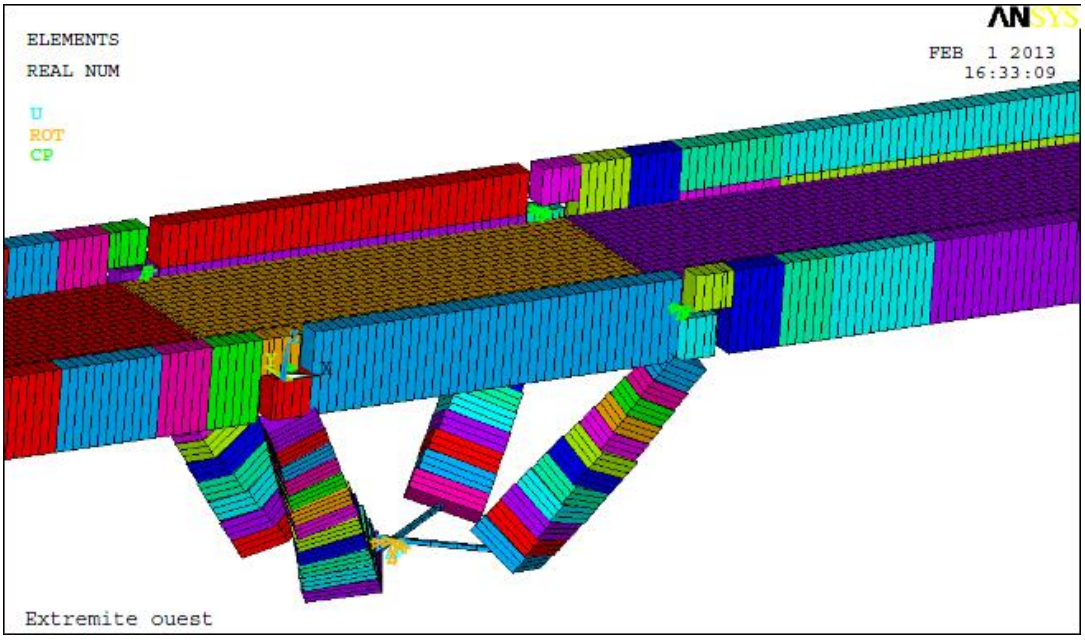


Figure 7: Zoom on the pier of the viaduct Finite Elements model

The young's modulus of the concrete was adjusted to 36GPa to get results as close as possible from the measurements.

The catenary poles were then added as simple beams on the viaduct taking into account the different masses of:

- The HEA 240 girder
- The concrete foundation in which is clamped the girder
- The earth wire
- The cantilever
- The line feeder and its support
- The messenger and contact wires

The transversal offsets of the cantilever, the line feeder and its support and the messenger and contact wires were respected in order to get the exact mass in rotation.

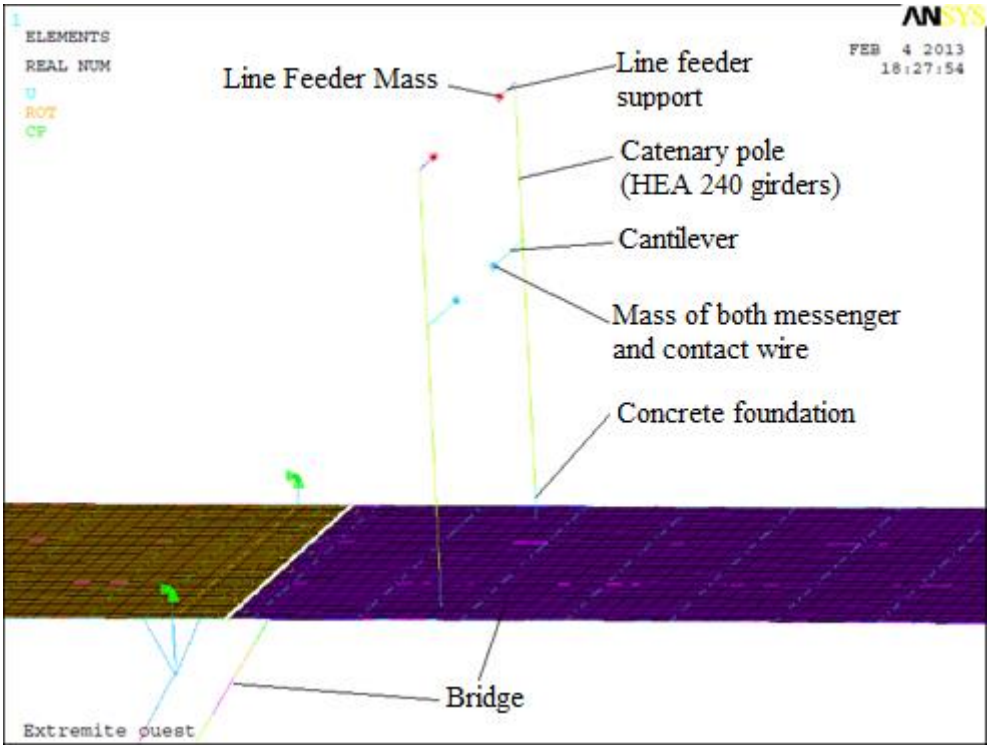


Figure 8: FE Modelling of the catenary poles on the viaduct

The first transversal bending eigenmode for the poles was calculated by Ansys at 2.19Hz (very close to the bridge first bending mode at 2.2Hz). This value is not exactly the value measured on the poles at 2.5Hz. Moreover, the dynamic response of the catenary poles obtained with this model was very far from the measured response. No resonance was highlight with the TGV at a running speed of 170 km/h, nor at 150 km/h (critical speed for TGV with bogies every 18.7m to excite a frequency of 2.2Hz). This model did not seem to represent well what happened really on the viaduct.

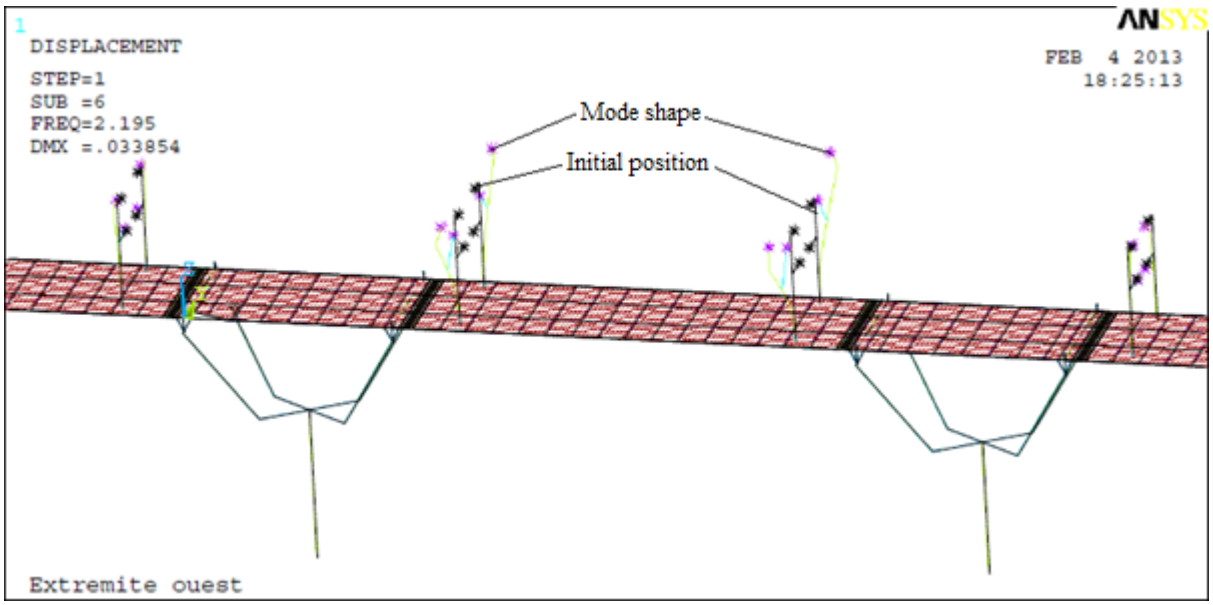


Figure 9: First bending mode of the catenary poles

A more detailed model of the poles seemed then needed to characterize the resonance phenomenon: the interaction between the wire and the poles is probably of great influence. The aspect of all the curves measured on the poles (see Figure 10 for example) validates this hypothesis as a beating phenomenon can be observed: the transversal vibration increases again after the train has left the bridge. These kinds of beats are usually observed in case of coupled systems.

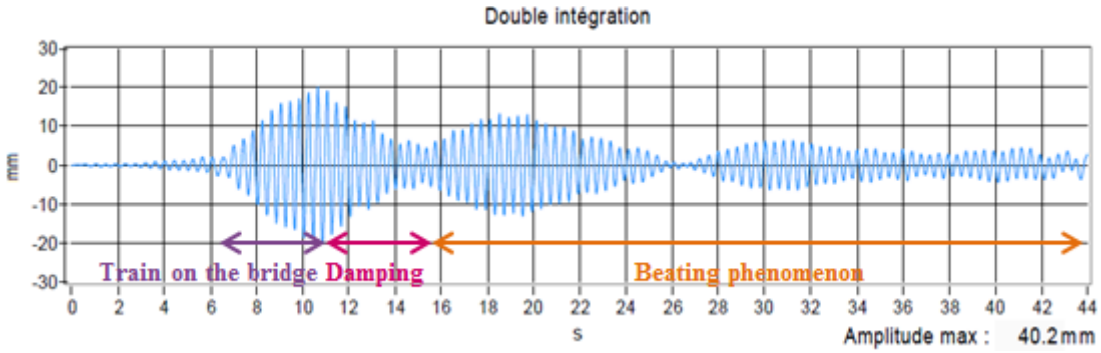


Figure 10: Example of transversal displacement obtained on top of the pole

3.2 Catenary pole model

The different wires (messenger, contact and line feeder) are coupled with the poles and create a coupling between all the poles. This system can be first approximated by a simple system with 2 oscillators as shown in the figure below.

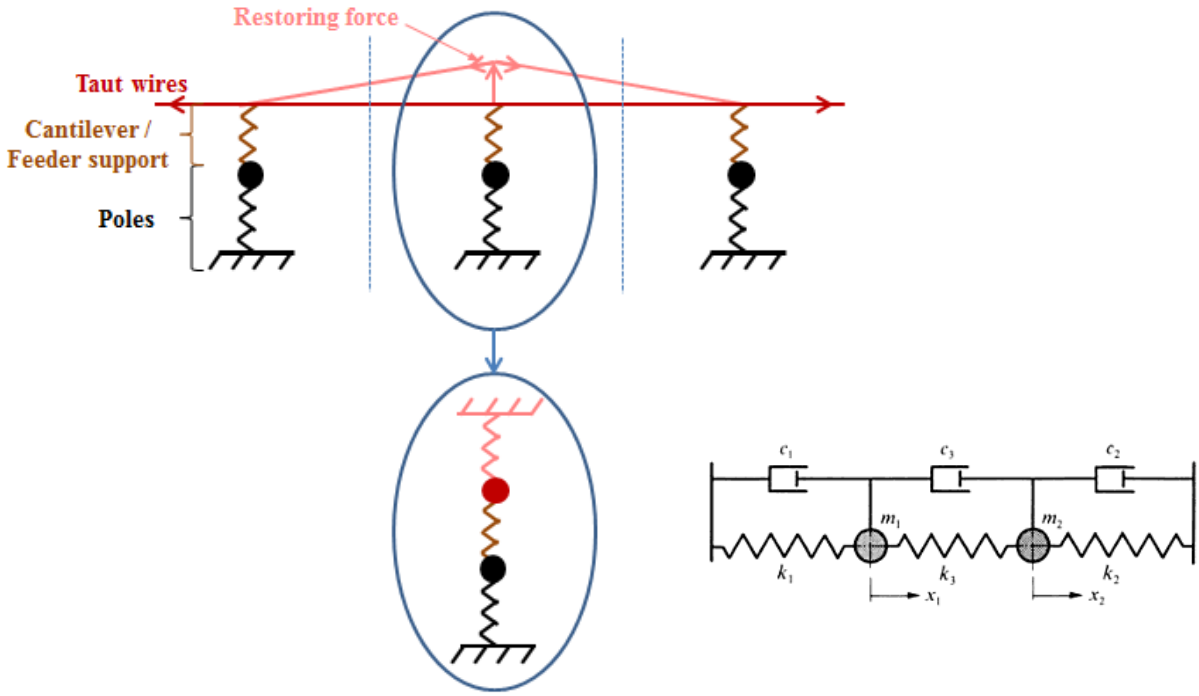


Figure 11: Catenary wires as 2-degrees of freedom oscillating system

Only the effect of the messenger and contact wire is first studied. The effect of the line feeder has then proven to be negligible as the connection to the pole is free to move transversally.

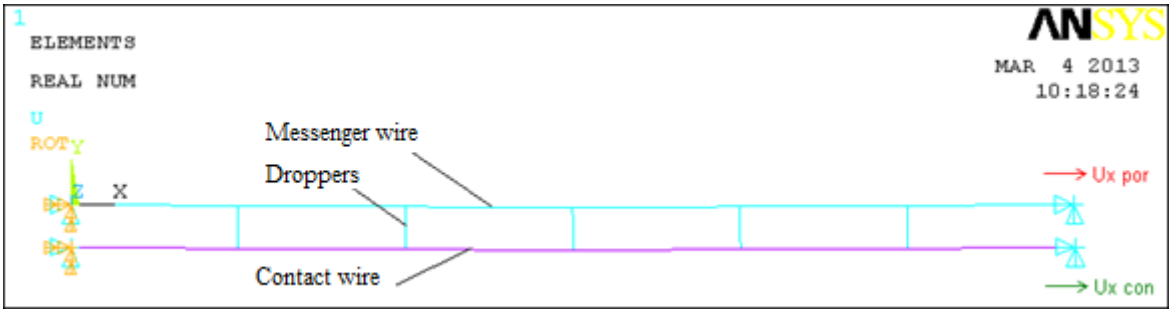


Figure 12: FE modelling of messenger and contact wire

To simplify the calculation with the different wires, it was shown by FE model that the effect of both messenger and contact wires linked by droppers was equivalent to one wire with both masses and initial tensions. By FE model, the first bending frequency was calculated transversally at 2.09Hz and vertically at 2.11Hz.

The frequency calculated analytically by the following equation for a taut wire is equal to 2.08Hz which is sufficiently close to the modelled values.

$$f = \frac{1}{2L}\sqrt{\frac{T}{\mu}} \tag{1}$$

With L: the wire length
μ: the linear mass
T: the wire tension

Taking into account notations of Figure 11, the 2 frequencies of the coupled system are:

$$f_1 = \frac{\sqrt{\left|\frac{-B+\sqrt{B^2-4C}}{2}\right|}}{2\pi}$$
$$f_2 = \frac{\sqrt{\left|\frac{-B-\sqrt{B^2-4C}}{2}\right|}}{2\pi} \tag{2}$$

With

$$B = \frac{k_1+k_3}{m_1} + \frac{k_2+k_3}{m_2}$$
$$C = \frac{k_1k_2 + k_2k_3 + k_1k_3}{m_1 \times m_2} \tag{3}$$

Knowing that the frequency of the pole alone is 2.2Hz and its mass 710 kg, k_1 is calculated as $9.59\text{x}10^4$N/m; and k_2 is calculated equal to $1.11\text{x}10^4$N/m with the frequency of the wires equal to 2.08Hz and its mass to 80kg.

Finally, with the above equations, f_1 is calculated equal to 2.18Hz and f_2 to 2.52Hz with 2.52Hz corresponding to the vibration of the pole. This value is very close to the measured frequency.

The next step in the study was to know which force actually excites the pole to the resonance: vertical displacement or rotation of the bridge deck. A simple model of a pole with the characteristics defined above was made with Ansys (see Figure 13). In this model, the frequencies of 2.18Hz and 2.52Hz were found again. The vertical displacement and rotation of the bridge deck found at the foot of the pole are applied separately at the bottom of the model.

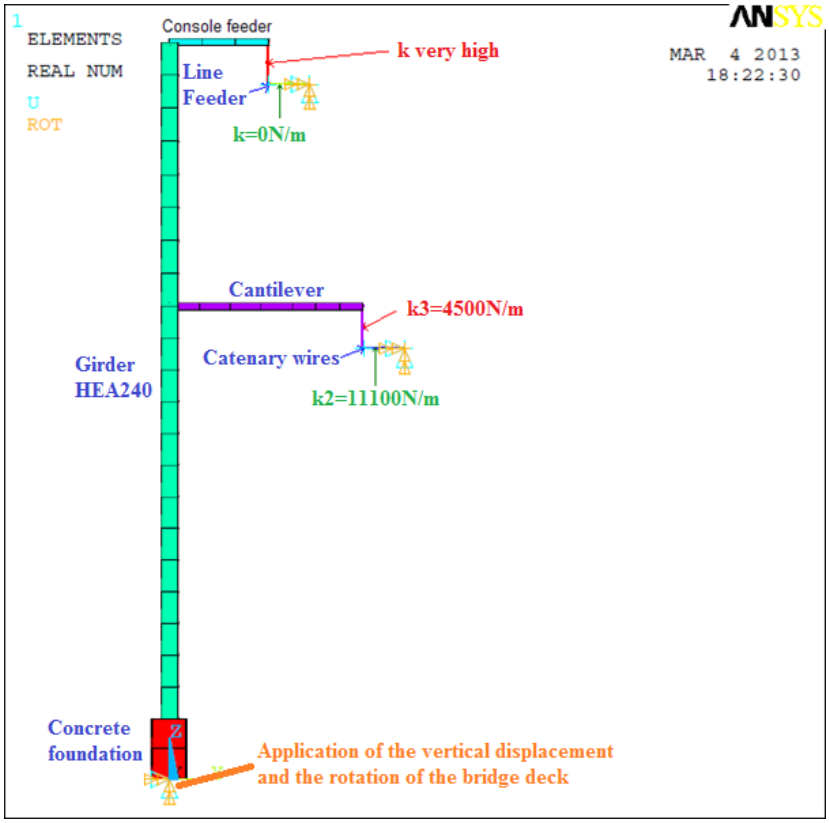


Figure 13: FE modelling of a catenary pole

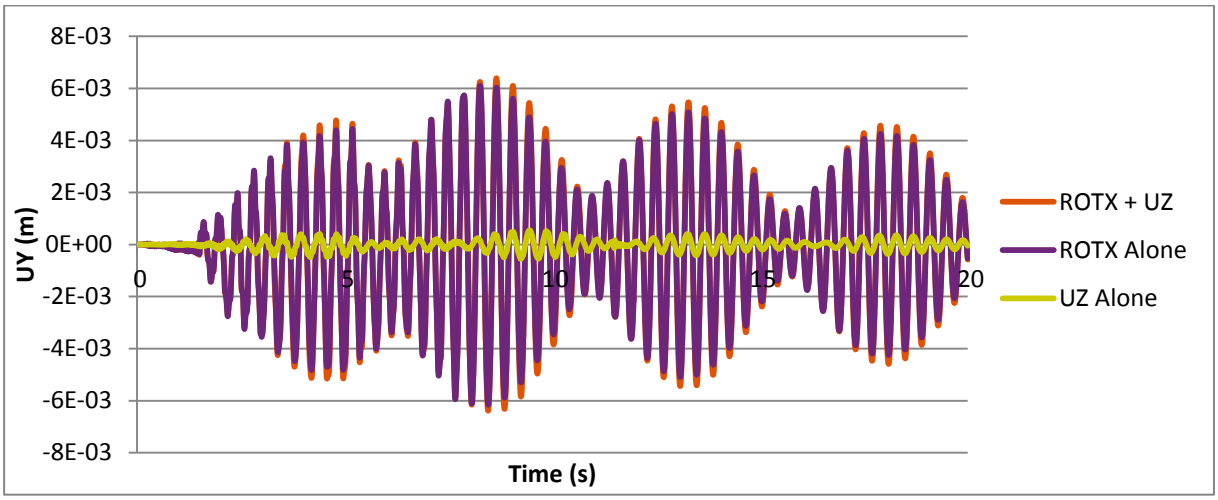


Figure 14: Comparison of transversal displacement on top of the pole under different excitations

With this test, it is clear that most of the resonance comes from the rotation of the bridge slab. This bridge composed of 2 very rigid main girders and a softer slab is more sensible to this type of transversal bending than reinforced concrete slab or bridges with the main girders below the slab.

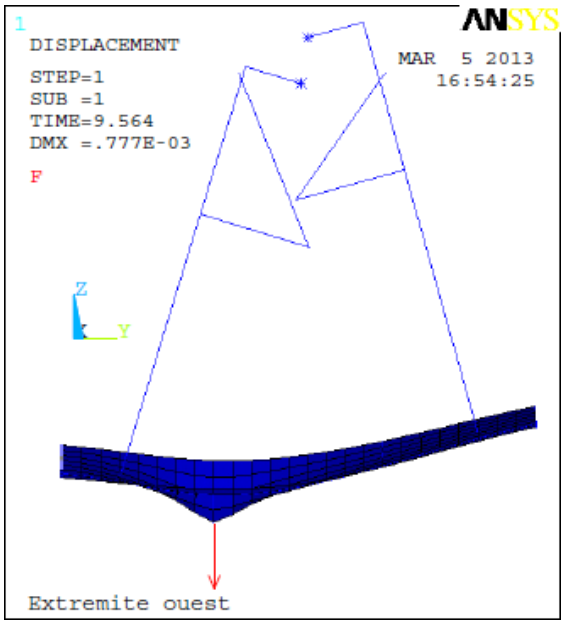


Figure 15: Transversal bending of the deck slab and rotation of the catenary pole when a TGV bogie is passing

Finally, the FE model representing the bridge and the poles was updated to take into account the previous investigations.

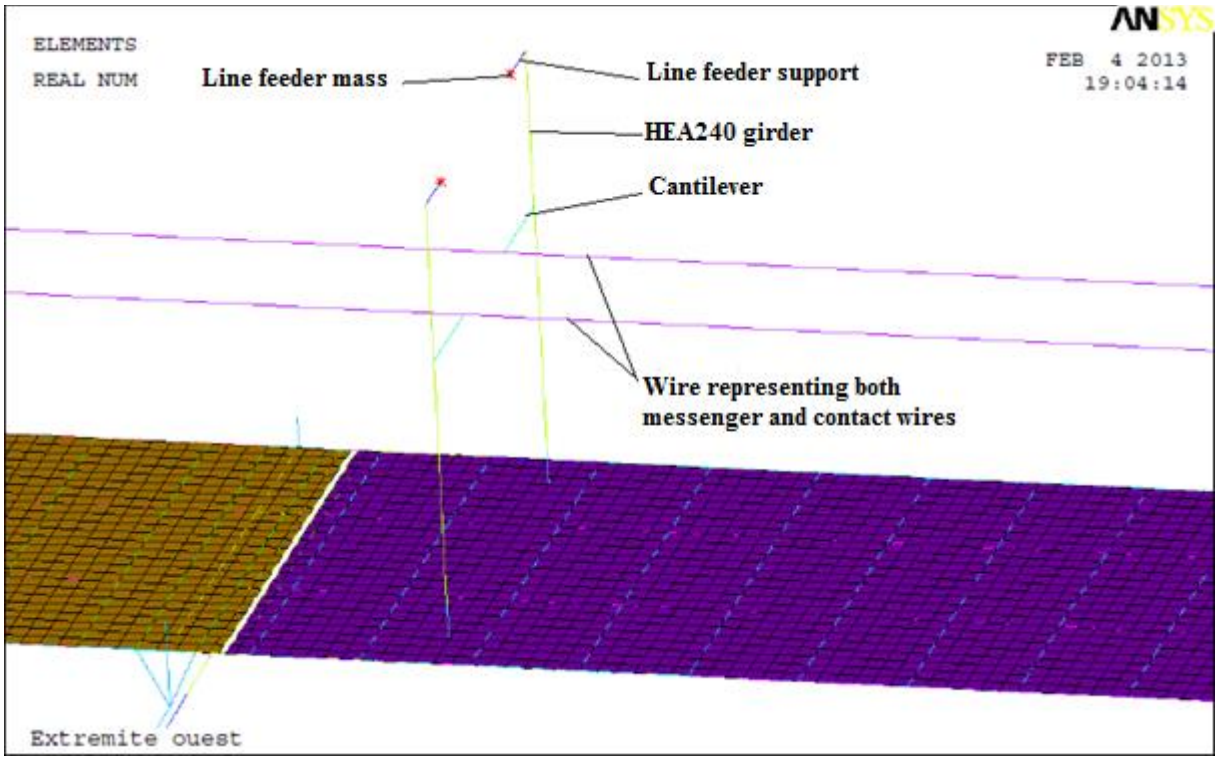


Figure 16: New FE model of the catenary poles on the bridge taking into account the interaction of the wires

The following figure shows that with this FE model, the results of calculations are quite close to the measurements. With this new model, the different solutions could be tested to check their efficiency.

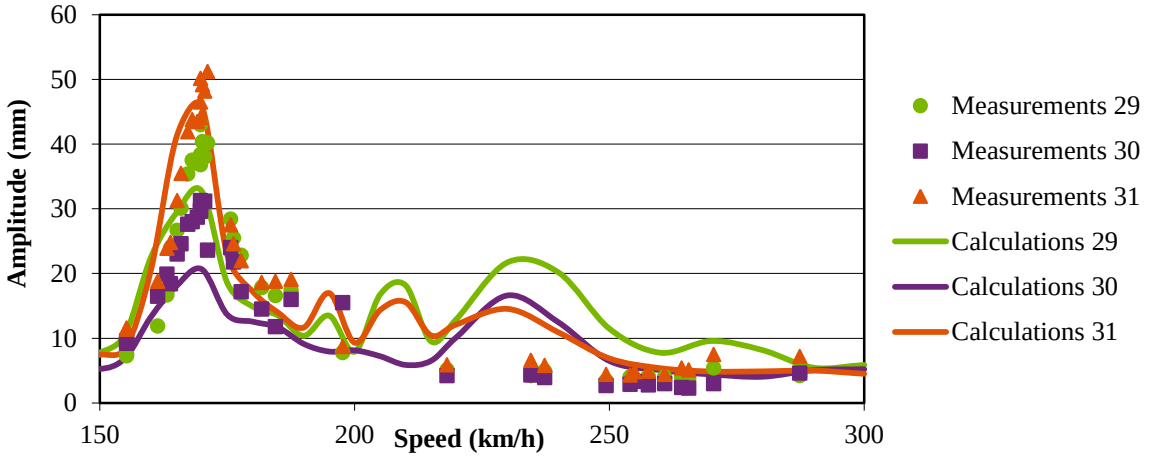


Figure 17: Comparison of the transversal displacement amplitude between calculations and measurements

4 PROPOSAL OF DIFFERENT SOLUTIONS

Different solutions were proposed by SNCF to solve this vibration problem:

- Replacement of the HEA 240 girders by HEA 300
- Setting of an additional crossbar linking the poles on each side of the tracks to create a portal frame effect
- Setting of Tuned Mass Dampers (TMD) on top of the poles

4.1 Replacement of the girders

The first idea submitted to solve this problem was to replace the HEA 240 girders by HEA 300 that are usually recommended by SNCF for high speed lines.

In the model shown in Figure 16, the characteristics of the beam representing the girders are then updated to those of HEA 300. The results of maximum amplitude of transversal displacement regarding the running speed of TGV are given in Figure 18.

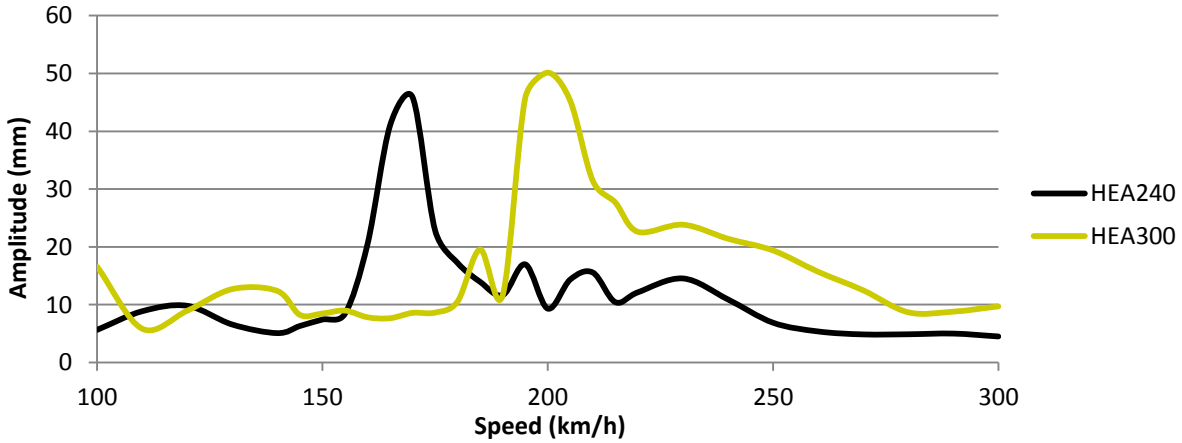


Figure 18: Comparison of the transversal displacement amplitude between HEA 240 and HEA 300

According to the previous figure, it is clear that replacing the girders is not an efficient solution as it offsets the resonance problem to a higher speed. The bending frequency of the catenary pole with a HEA 300 girder is 2.9Hz, corresponding to a critical speed for TGV of 200km/h. The new girder being stiffer, the response at the resonance is expected to be lower. However, the bridge deck rotation increases with the speed. The maximum amplitude obtained at resonance is therefore equal with HEA 300.

4.2 Setting of a crossbar

Another solution proposed by SNCF was to add a crossbar between the poles on each side of the tracks to create a portal frame effect. The position of this crossbar on the poles is very constrained by the isolation offsets to respect regarding the conductors.



Figure 19: Example of crossbar

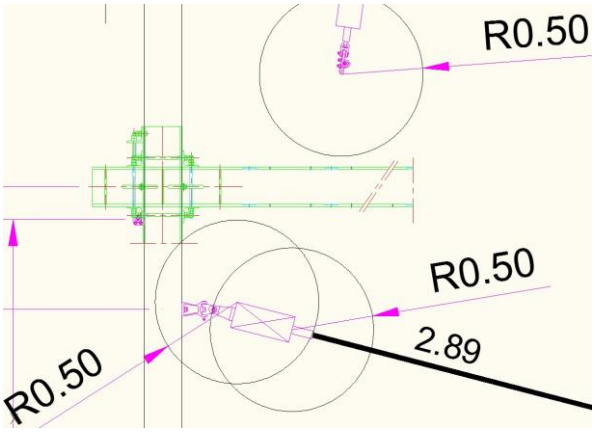


Figure 20: Isolation distances to respect

The crossbar was then modelled in Ansys at its determined position and the transversal response of the catenary poles was calculated with the TGV at different speeds. The first transversal bending frequency of the whole portal was calculated at 1.99Hz.

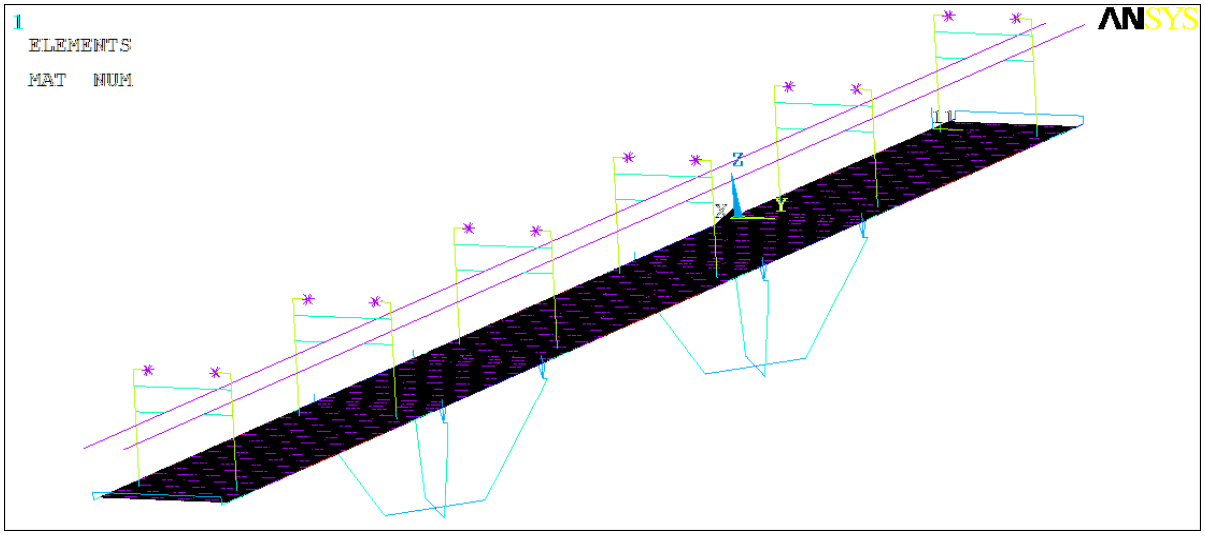


Figure 21: FE model of the Savoureuse bridge with crossbars on the catenary poles

The results for this FE model are given in Figure 22.

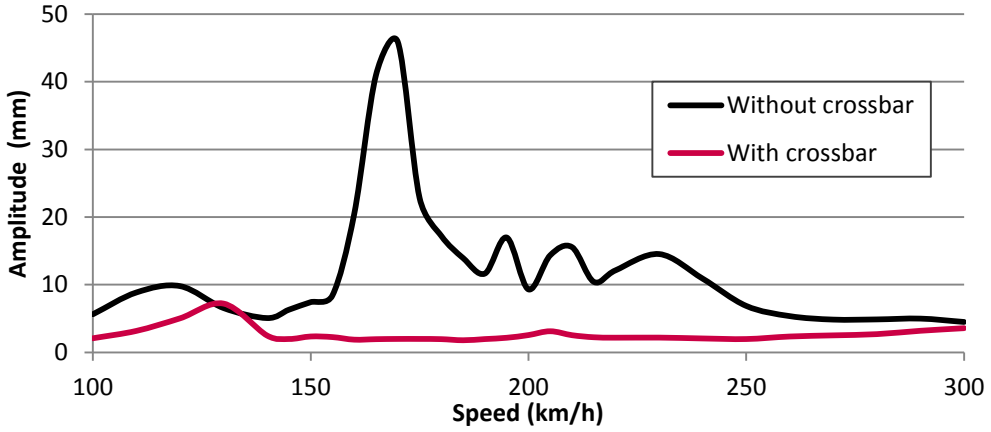


Figure 22: Comparison of the transversal displacement amplitude with and without crossbar

It is clear that the addition of the crossbar is very efficient. However, this solution presents the disadvantages of being:

- Complicated and therefore expensive to implement: the operation would require among others to remove the line feeder and the earth wires.
- Too rigid for maintenance: the position of the crossbar being constrained by the isolation distance it will not be possible to raise the contact wire if needed.
- Quite unsightly on a bridge designed by an architect.

4.3 Setting of Tuned Mass Dampers

Tuned Mass Dampers (TMD) presents interesting characteristics to improve the response of slender structure with low damping ratio (typically the case of catenary poles). They consist in adding a small mass to the structure with a certain stiffness and additional damping. The stiffness of the added system is adjusted to the eigenmode frequency of the main structure, so that the added mass resonates at the same excitation as the main structure. The additional damping dissipates quickly the energy of the resonance.

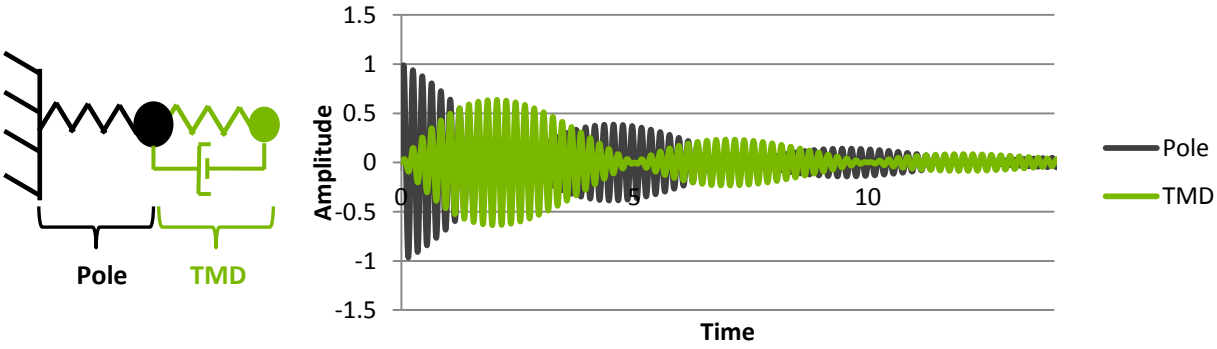


Figure 23: Functioning principle of Tuned Mass Dampers (TMD)

For the catenary poles of the Savoureuse viaduct, the TMD were imagined to fit in a box that could be fixed onto the poles. It was then calculated that the whole system could be located in a 1.2 x 0.18 x 0.18 m box. This box could therefore be fixed inside the flanges of the HEA240 girders for more discretion and aesthetics.

This TMD is composed of a mobile mass fixed on a stainless steel rod turning around a pin at the top of the box. The rod ends at the bottom with a piston able to dissipate the energy in a viscous fluid. The transversal movement of the catenary pole leads the mass to rotate around its axis as a pendulum. The frequency of the mass is adjusted with the height of the mass on the steel rod.

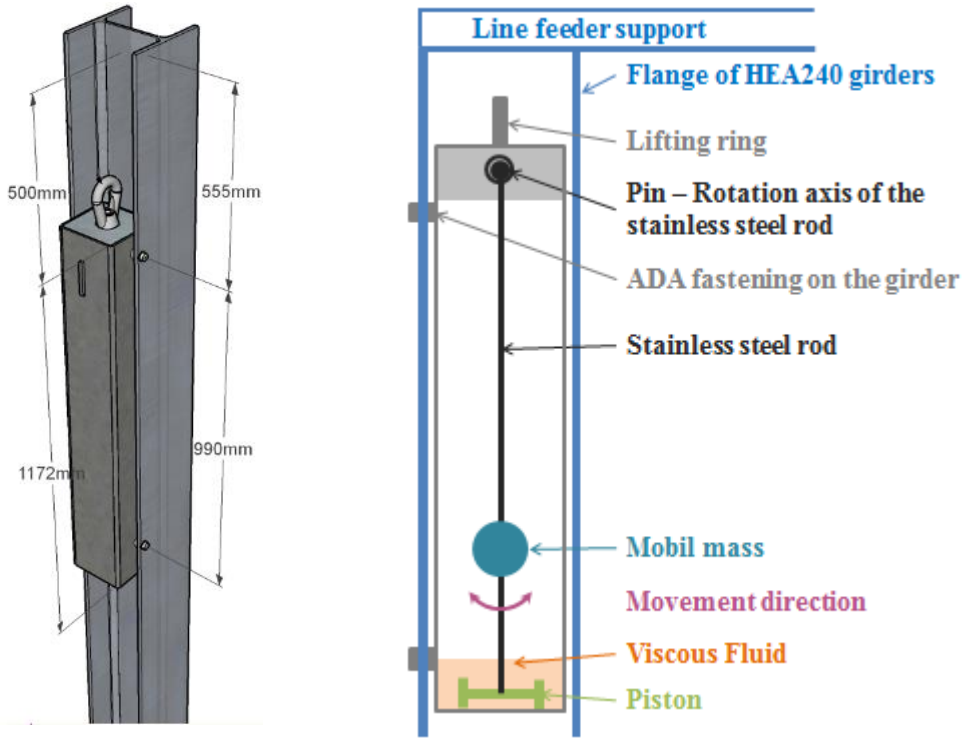


Figure 24: Diagram of TMD for the catenary poles

The effect of these TMD was calculated on the FE model of the bridge.

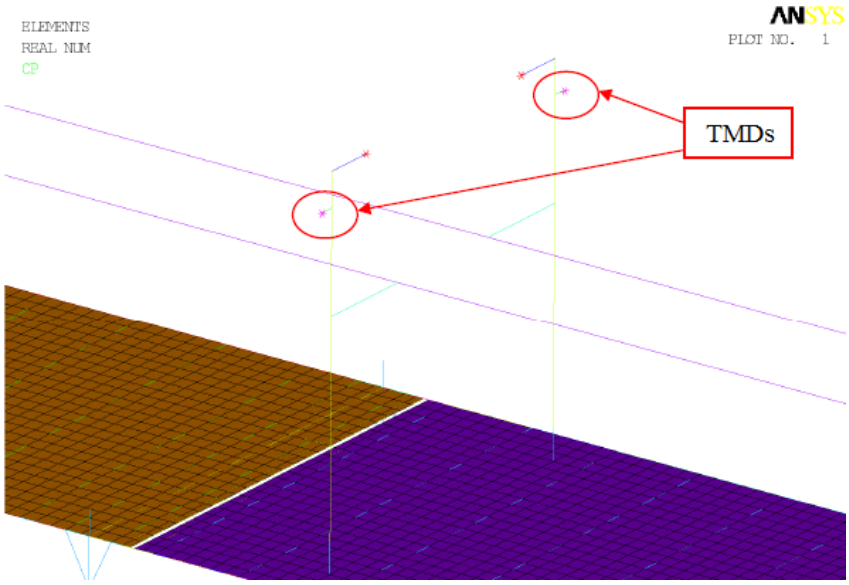


Figure 25: FE model of TMDs on the Savoureuse viaduct

The results of such calculations are shown in Figure 26 regarding the height of the TMD on the girder. It can be seen that when the TMD is placed relatively high on the girder, the system is very effective (displacement reduction around 80%).

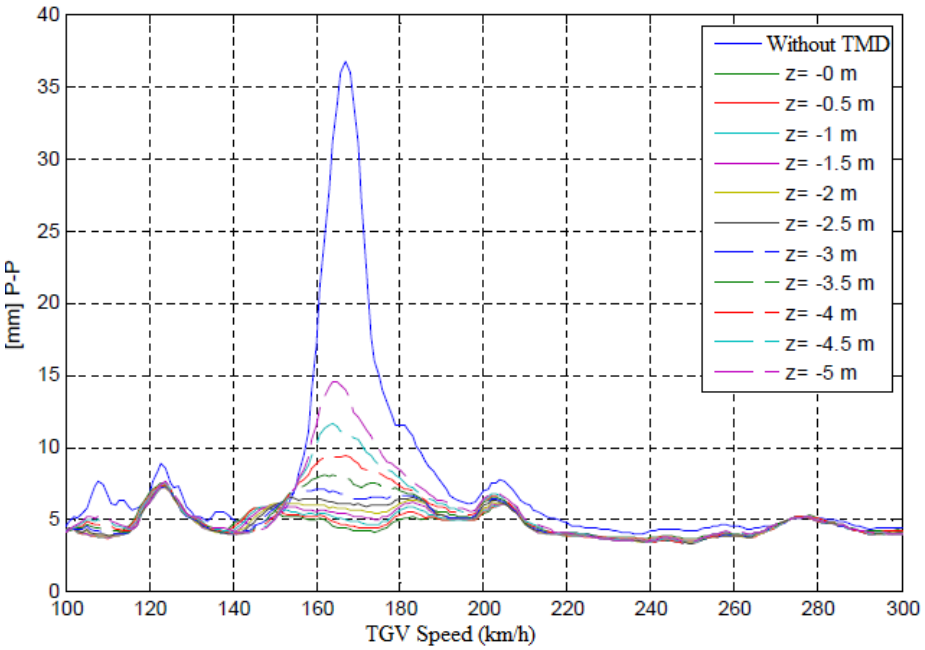


Figure 26: Comparison of the transversal displacement amplitude without and with TMD at different heights

This solution seems to be very efficient and presents different advantages:

- The TMD is easier to set than the crossbar, with a lower calculated implementation cost
- There is less impact on maintenance than the crossbar. The maintenance actions for TMD were identified in a document and adapted to the existing maintenance of the catenary poles.
- The solution is more aesthetic than the crossbar.

In consequence, it is the solution taken on by RFF.

5 IMPLEMENTING TUNED MASS DAMPERS

The TMD were set on the catenary poles of the viaduct and measurements were made before and after their implementation to verify their efficiency.

In a first step, two Φ14mm holes were drilled in the HEA 240 flange. To assure the exact positions of the holes, a drilling template was used.



Figure 27: Drilling in the girder flange

The TMD was then lifting by a crane and fixed with 2 M12 stainless steel bolts. A spacer was placed between the TMD and the girder flange in order to let the air circulating around the TMD.

At the moment of this article writing, only 6 TMD were implemented as a test phase. The equipment of the catenary poles with TMDs has proven to be very easy. The rest of the TMDs will be set in March 2015.



Figure 28: Lifting and fastening of the TMD

The signal measured on top of the pole after the implementation of TMDs was very different than the original signal (See Figure 29). It has to be noted on this figure that the scales of both curves (before and after) are different.

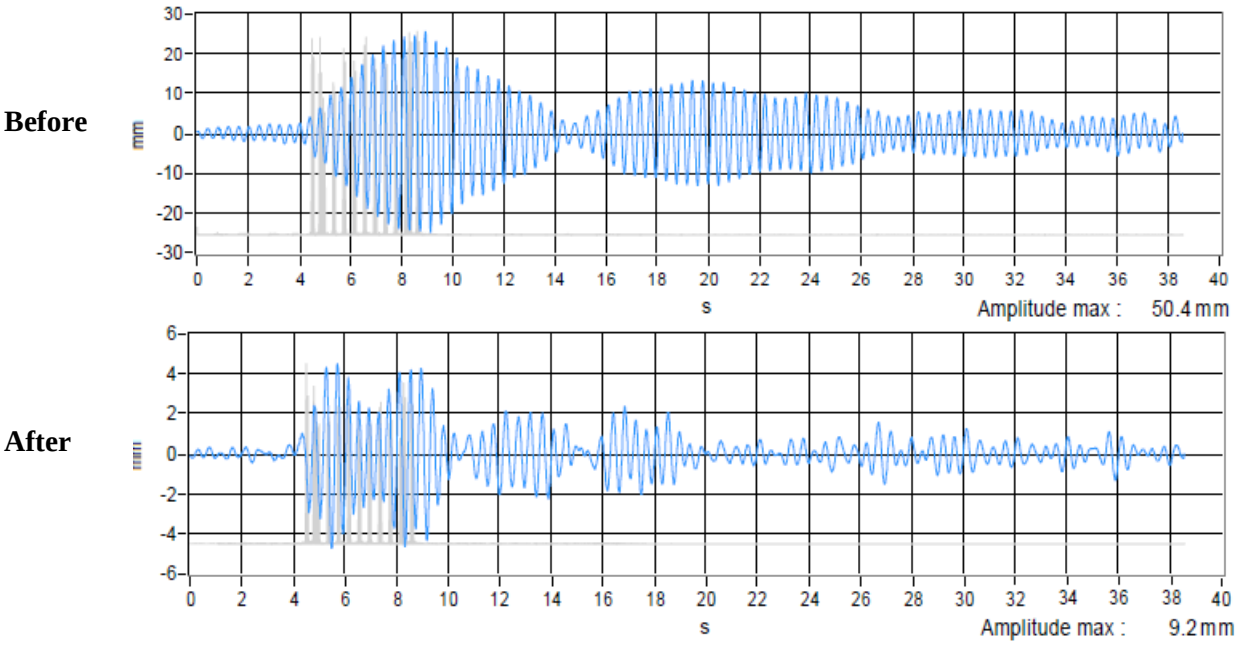


Figure 29: Comparison of the transversal displacement amplitude without and with TMD

It is clear according to this figure that the TMD is very efficient. The following figures show the maximum measured amplitude, the percentage of displacement reduction and the measured damping for the 6 catenary poles equipped with TMD. As it is a system composed of different coupled oscillator, it was not easy to determine the exact damping of the poles. This value was calculated by logarithmic decrement on 1.5 seconds after the train has left the bridge just before the beating phenomenon. This period is relatively short and sometimes the beating phenomenon starts earlier. The values given in Figure 32 should therefore be taken as average values.

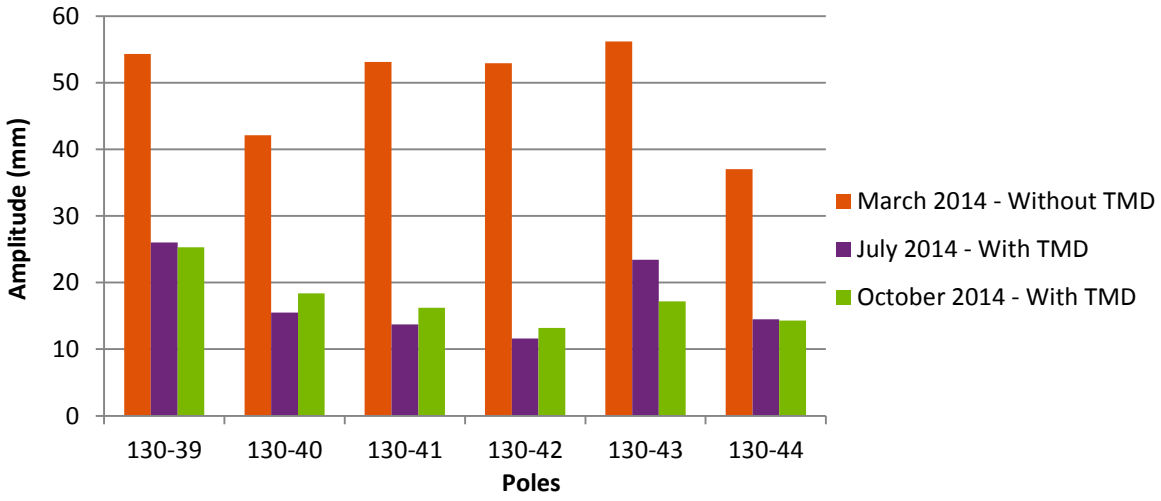


Figure 30: Comparison of the transversal displacement amplitude without and with TMD

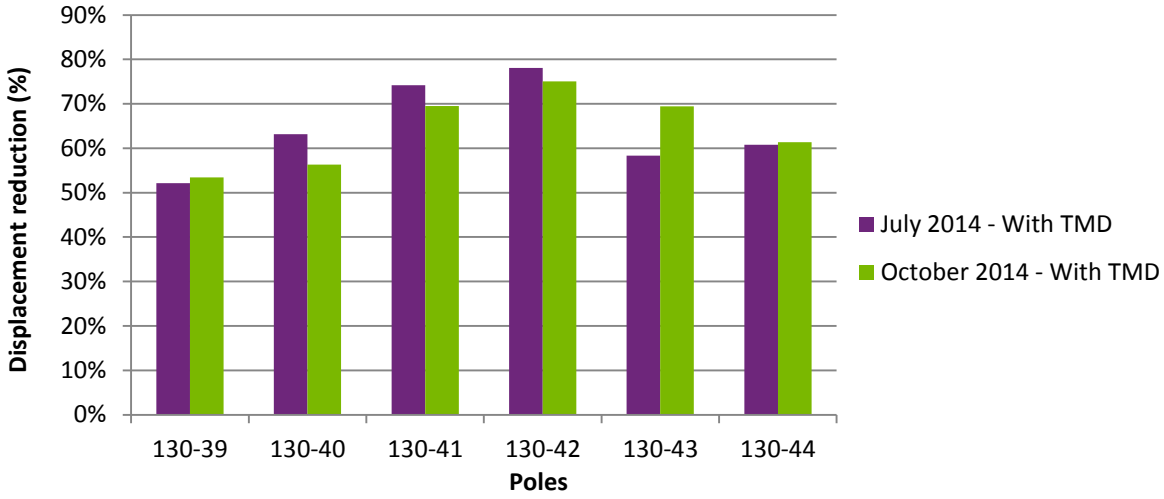


Figure 31: Reduction of the transversal displacements with TMD

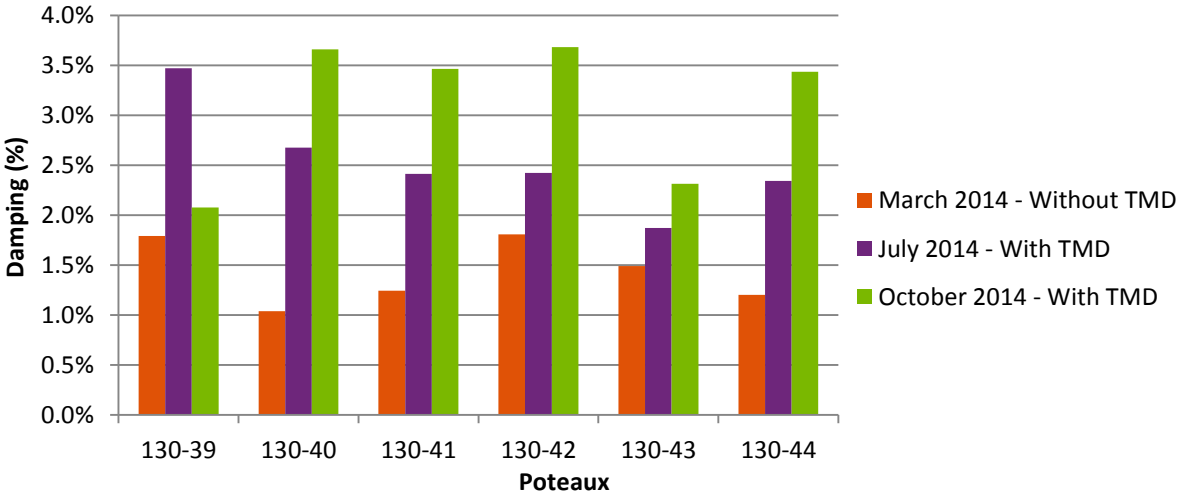


Figure 32: Comparison of the whole system damping without and with TMD

From the above figures, it can been seen that the displacement reduction obtained for catenary poles number 130-41 and 130-42 reaches 75% in average. This value is very close to the 80% obtained by the FE model. These 2 poles are surrounded by poles 130-39, 130-40, 130-43 and 130-44, themselves equipped with TMD. The efficiency of the TMD is then maximal on these 2 poles. For the 4 other poles, the displacement reduction is lower (around 55% in average). This can be explained by the fact that their neighbouring poles have not been equipped yet with TMD. These 4 poles are therefore still sensible to the vibration of these other non-equipped poles. It is expected that when all the poles will be equipped with TMD, the displacement reduction obtain for all the poles will turn around 80%.

For most of the poles, it can be noticed that the damping ratio has notably increased from 1.2% to 3% in average.

6 CONCLUSIONS

- This transversal vibrations phenomenon of catenary poles on a railway bridge was first observed in France in 2011 on the Savoureuse viaduct.
- It was shown in this study that the resonance the poles are subjected to is created by the transversal flexion of the bridge slab on which the poles are fastened.
- FE models and analytic calculations highlighted that the effect of the different wires of the catenary (messenger and contact wires especially) was very important on the global response. Therefore, they had to be taken into account to understand the phenomenon and to design an adapted solution.
- This phenomenon was never observed before because it is linked to a combination of parameters: bridge type (stiff lateral girders with a long transversal slab), train type and speed (TGVs at 170 km/h when stopping at a train station) and position of the poles at quarter span and on the slab close to the track where the rotation is maximal.
- The best solution found to reduce the poles resonance was to set Tuned Mass Dampers on top of the catenary poles.
- SNCF is now thinking about updating some of the rules for the design of catenary poles on railway bridges. Internal reference document will be modified to take this phenomenon into account.

REFERENCES

[1] P. Chapas, Alimentation en énergie des trains – Distribution de l'énergie électrique, Techniques de l'Ingénieur, Ref. 42576210, November 2012

[2] J. Schifter, The Effects of Bending Stiffness on the Dynamics of Catenary Cables, Master thesis, Massachusetts Institute of Technology, August 1996

[3] M. Del Pedro, P. Pahud, Mécanique vibratoire : systèmes discrets linéaires, Presses polytechniques et universitaires romandes, 2003, ISBN 2-88074-243-9

[4] B. Garnier, Isolation antivibratoire et antichoc – Solutions technologiques et industrielles, Techniques de l'Ingénieur, Ref 42424210, May 1994

COMPDYN 2015
5th ECCOMAS Thematic Conference on
Computational Methods in Structural Dynamics and Earthquake Engineering
M. Papadrakakis, V. Papadopoulos, V. Plevris (eds.)
Crete Island, Greece, 25–27 May 2015

SEISMIC RESPONSE OF CABLE-STAYED BRIDGE STEEL TOWER PROVIDED WITH BRACING SYSTEM

Mohamed OMAR
Assistant professor
Civil Engineering Department, Faculty of Engineering, Aswan University, 81542 Aswan, Egypt
moh.omar@aswu.edu.eg, moh_omar77@yahoo.com

Keywords: Nonlinear Analysis, Seismic Response, Steel Tower, Cable-Stayed Bridge, Bracing Systems Instructions.

Abstract. *Cable-Stayed bridges consist of many structural components, which contribute to the overall resistance ability of the system. These structural syntheses give a valuable environment for the nonlinear behavior due to material nonlinearities and geometrical nonlinearities of the relatively large deflection of the structure on the stresses and forces. To improve the bridge seismic performance and to control expected damage, the necessity has arisen to develop more efficient bridge structural systems that can lead to resist the seismic actions. The seismic response of steel structures can be improved by providing bracing elements which can resist the lateral forces affecting the structure. In this paper, the feasibility of providing bracing system as damping elements in cable-stayed bridge steel tower is studied.*

The steel tower of Tappu cable-stayed bridge located in Hokkaido, Japan is considered as model of study. The steel tower is taken out of the bridge and modeled as three-dimensional frame structure. The proposed braced model is to provide the tower by X-bracing elements connecting the upper part of the tower. The study based on comparison of the seismic response of the original un-braced tower and that of proposed braced tower. A nonlinear dynamic analysis program based on total Lagrangian formulation using linearized finite displacement theory and fiber model has been developed to be used in this study. The finite element procedure for the nonlinear time history analysis of the steel tower under seismic loadings is set up. Geometric and material nonlinearities are implemented and bending-axial force interaction is considered. The evaluation of the proposed bracing system response was based on displacements at tower top and vertical forces and moments at supports.

The results of this study show that the seismic response of cable-stayed bridge steel tower can be improved by providing bracing elements which will enhance the seismic ductility of the tower. The proposed bracing system, in this study, can reduce the horizontal displacement of the bridge tower and moment at tower base. In addition, shearing and vertical forces at tower base have slight effect.

1 INTRODUCTION

Thousands of highway bridges throughout the world are located in areas of moderate to high seismicity. The seismic resistance of these bridge structures controls their safety and the functional capability of the associated transportation routes in the aftermath of a major earthquake. Among the various structural forms available for the bridges, cable-stayed and suspension bridges have been researched for several past studies on the seismic response of bridges [1,2]. The damages of highway bridges in the 1989 Loma Prieta, 1994 Northridge and 1995 Hyogoken Nanbu earthquakes together with the research triggered as a consequence of the recent earthquakes have led to significant advance in bridge seismic design and retrofitting [3]. The seismic vulnerability of cable-stayed bridges was made dramatically evident by the failure of many of these structures in recent earthquakes. These earthquakes provided a stimulus to investigate the seismic response of highway bridges and emphasized the need to develop new procedures and specifications to assess existing bridges and to improve the seismic design of new bridges.

The seismic resisting system should provide a reliable and uninterrupted load path for transmitting seismically induced forces into the ground and sufficient means of energy dissipation and/or restraint to reliably control seismically induced displacements. All structural elements of the bridge should be capable of achieving anticipated displacements consistent with the requirements of the chosen mechanism of seismic resistance and other structural requirements. One of the traditional seismic coefficient methods is providing the structures with bracing systems.

Braced system is considered as an effective system in enhancing the stiffness and strength of steel structures where it can exhibit high lateral stiffness [4-12]. The capacity of a steel structure can be greatly strengthen under moderate-to-large magnitude earthquakes by increasing the energy absorption of structures and decreasing the demand imposed by earthquake loads. Though, the connections and foundations which need to be strengthened are affected by using braces.

Due to the high efficiency, braced steel frame systems are widely used. Braced steel frame system is effective if the braces in linear stage. The asymmetrical response is developed when at the nonlinear stage starts whereas the lateral stiffness starts to decrees. To resist seismic loads, braced steel frames have many bracing systems, such as concentric bracing system, eccentric bracing system, knee bracing system and mega bracing system.

Bracing is concentric when the center lines of the bracing members intersect. The concentric bracing used in structures include X, Chevron and Knee bracing. X bracing is the most common type of bracing. The diagonal members of X and Chevron bracing go into tension and compression. Connections for X bracing are located at beam to column joints. The frame lateral stiffness is increased resulting in natural frequency increasing and lateral drift decreasing. A larger inertia force in seismic region is attracted due to stiffness increasing. While the axial compression in the braced connected columns is increased with decreasing the bending moments and shear forces in columns. The beams of frames should be strengthened enough to resist the shear vertical forces developed from the concentric braces.

The present study objective is to investigate the seismic response of steel tower of cable-stayed bridges provided with X-bracing system at tower top in order to enhance the seismic behavior of the tower. A finite element methodology based on theoretical approach and computer simulations for nonlinear dynamic analysis problem is presented. A representative problem of a cable-stayed bridge tower subjected to strong ground motion of Hyogoken-Nanbu earthquake is analyzed. In addition, the maximum displacements at tower top and the vertical forces and moments at tower bases are computed.

2 FINITE ELEMENT OUTLINE

2.1 Finite element model of tower structure

The steel tower of Tappu cable-stayed bridge located in Hokkaido, Japan is considered. Figure 1 shows a general view of the cable-stayed bridge elevation. The steel tower is taken out of the bridge and modeled as three-dimensional frame structure. A fiber flexural element is developed for characterization of the tower structure, in which the element incorporates both geometric and material nonlinearities. The stress-strain relationship of the beam element is modeled as bilinear type with kinematic strain hardening rule. The yield stress and the modulus of elasticity are equal to 355 MPa (SM490Y) and 200GPa, respectively. The plastic region strain hardening is 0.01.

The tower has nine cables in each side; the dead load of the stiffening girder is considered to be equivalent to the vertical component of the pretension force of the cables and acted vertically at the joint of cables. The inertia forces acting on the steel tower from the stiffening girders is neglected. For the numerical analysis, the geometry and the structural properties of the tower is shown in figure 2. The tower has rectangular hollow steel section with internal stiffeners, which has different dimensions along tower height and its horizontal beam; the geometrical properties of the tower are summarized in table 1. A spectral damping scheme of Rayleigh's damping is used to form damping matrix as a linear combination of mass and stiffness matrices, which effectively captures the tower structures damping and is also computationally efficient. The damping ratio corresponding to the frequencies of the fundamental in-plane and out-plane modes of tower free vibration is set to 2%. The natural periods for different modes in three global directions obtained from the linear analysis are shown in table 2.

C. S.	Dim.	Outer dimension				Stiffener dimension			
		A	B	t_1	t_2	A	b	t_{11}	t_{22}
Tower parts	I	240	350	2.2	3.2	25	22	3.6	3.0
	II	240	350	2.2	3.2	22	20	3.2	2.8
	III	240	350	2.2	2.8	20	20	2.8	2.2
	IV	270	350	2.2	2.6	31	22	3.5	2.4

Table 1: Cross section dimensions the tower (cm)

Mode order	Period (sec.)	Mode type
1	2.072	H
2	0.934	L
3	0.773	T
4	0.156	V

Table 2: Principal vibration modes for tower model

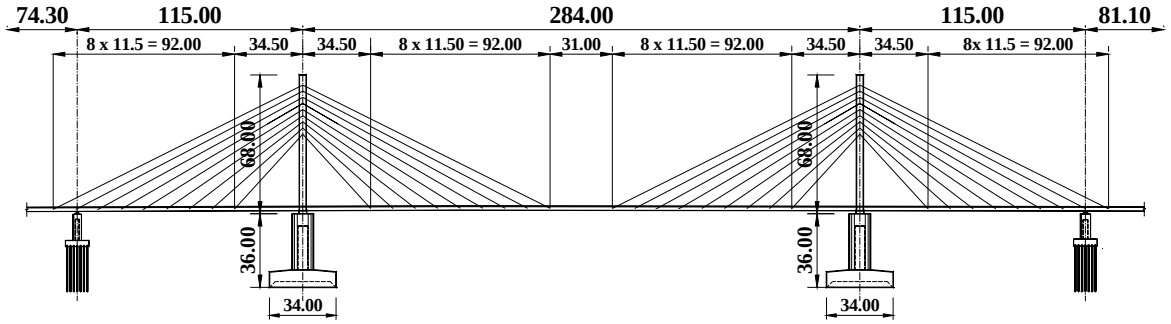
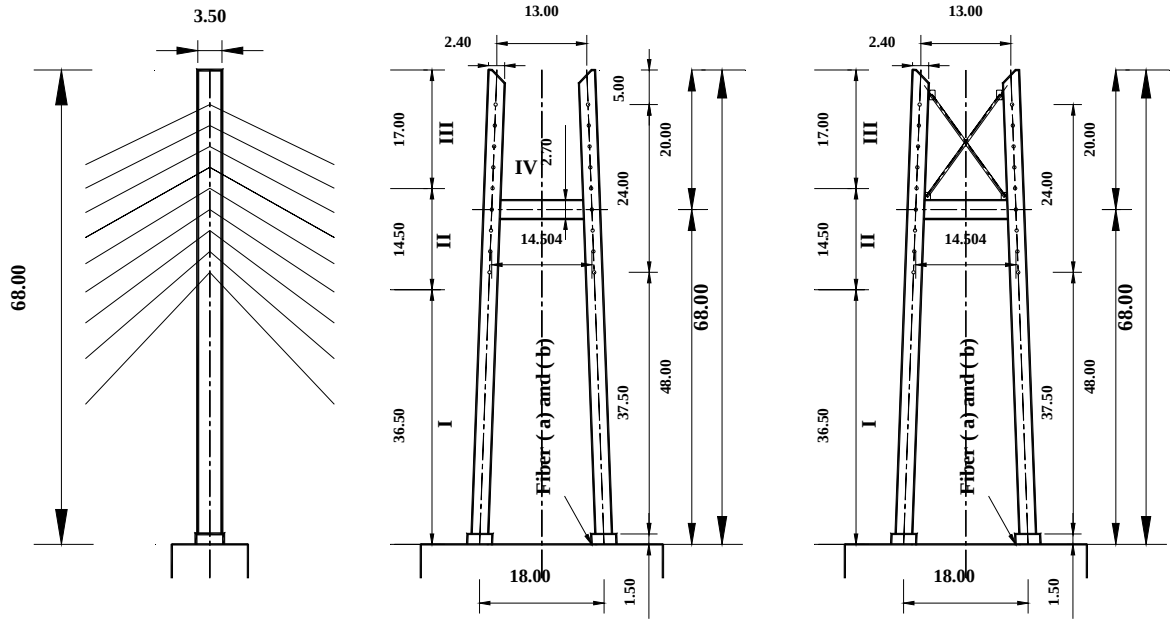
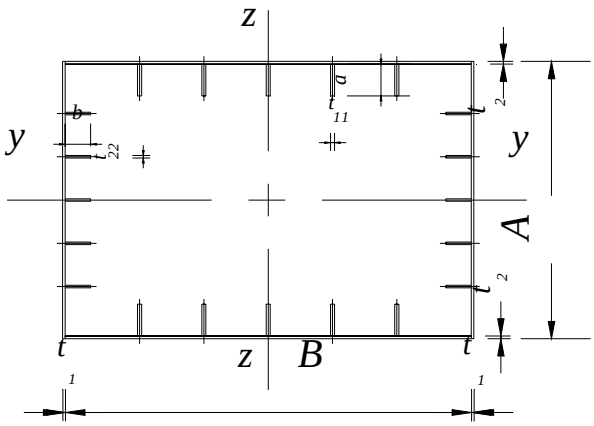


Figure 1: General view of the cable-stayed bridge (m)



(a) Tower geometry (Un-braced and braced tower)



(b) Cross section

Figure 2: Steel tower of cable-stayed bridge

2.2 Nonlinear equilibrium equation solution technique

Based on the total incremental equilibrium equations, finite displacement three-dimensional beam-column element formulation is carried out. The tangent stiffness matrix and nodal point force vectors considering both geometrical and material nonlinearities can be determined by using the fiber model in which the bending-axial force interaction is automatically considered. The initial state of residual stresses effects on both tangent stiffness and force vector is considered. The implicit Newmark step-by-step integration method is used to directly integrate the equation of motion. Since it has been experienced that the Newmark method is the most suitable for nonlinear analysis; it has the lowest period elongation and has no amplitude decay. In addition, the stability concern is not a problem with the variable ratio of time increment to natural period. The equation of motion is solved for the incremental displacement using the Newton Raphson iteration method where the stiffness matrix is updated at each increment to consider the geometrical and material nonlinearities and to speed the convergence rate. As the incremental displacement is determined, the response acceleration and velocity components of the tower can be determined. In addition, attenuation of the steel tower structure is adopted the Rayleigh's viscous damping with damping coefficient equal to 2% to the in-plane and out-plane fundamental natural vibration modes.

Inelasticity of the flexure element is accounted for by the division of the cross section into a number of fiber zones with uniaxial plasticity defining the normal stress-strain relationship for each zone, the element stress resultants are determined by integration of the fiber zone stresses over the cross section of the element. By tracking the center of the yield region, the evolution of the yield surface is monitored, and a stress update algorithm is implemented to allow accurate integration of the stress-strain constitutive law for strain increments, including full load reversals.

To ensure path dependence of the solution, the implementation of the plasticity model for the implicit Newton Raphson equilibrium iterations employs a stress integration whereby the element stresses are updated from the last fully converged equilibrium state. The transformation between element local and global coordinates is accomplished through a vector translation of element forces and displacements based on the direction cosines of the current updated element coordinate system.

3 SELECTED GROUND MOTIONS

In the dynamic response analysis, the ground motion that was recorded during Hyogoken-Nanbu earthquake 1995 with the largest intensity of ground acceleration is used as an input ground motion to assure the seismic safety of bridges. The horizontal and the vertical accelerations recorded at the station of JR Takatori observatory, as presented in figure 3, are suggested for dynamic response analysis of the steel tower of cable-stayed bridge at type II of soil condition, because it is considered to be capable of exciting of this tower well into its nonlinear range. The selected ground motion has maximum acceleration of its components equal to 642 gal (N-S), 666 gal (E-W) and 290 gal (U-D). From Fourier spectrum analysis, the predominant frequencies for N-S and E-W components are 0.83 and 0.81 Hz, respectively, which are relatively low, and that for the U-D component is 7.96Hz, which includes high frequency components and indicates the vertical motion time lag to horizontal motions. The earthquake force of E-W wave is put into the bridge axis direction (out-plane), and N-S wave to the right angle to the bridge axis (in-plane).

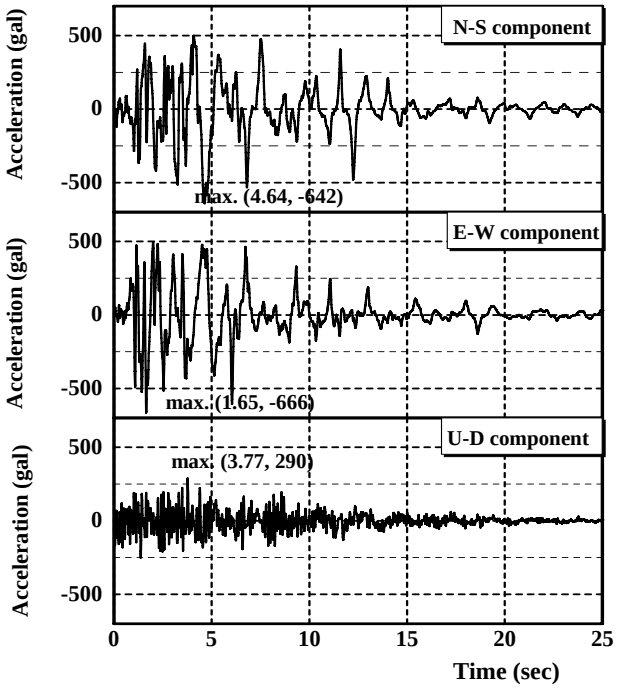


Figure 3: Strong ground motion measured at JR Takatori

4 RESULTS AND DISCUSSION

Seismic response analysis using the time history inputs is required to meet the goals of performance based design. Seismic response behavior of the cable-stayed bridge tower provided with bracing system under a great input ground motion is presented, and compared to the response of un-braced tower.

A finite element analysis of steel tower and provided with suggested bracing system was carried out. A seismic response analysis comparison to un-braced steel tower (original case) is presented. The resulting seismic characteristics of the braced tower model are different from the un-braced tower due to control of the upper part from side sway. The providing tower with bracing system displays more pronounced difference in tower model seismic response as the lateral displacements controlled.

It is noticeable that the results of seismic response vary with different structural system for the same input earthquake motion. The acceleration response for the braced system shows lower acceleration response than the un-braaced system along all the time history. The acceleration response is significantly affected by the tower lateral stiffness. It is interesting to see that the braced and the un-braced systems show similar acceleration responses along the time history with higher amplification of input excitation in the high frequency bridge axis direction as can be illustrated in figure 4.

The displacement response of the tower structure is calculated, the braced system gives much lower displacements in the right angle bridge axis direction, figure 5. This effect is characterized by three cycles of large displacement amplitude related to the large pulse in the input ground motion, decaying rapidly after the peak excursions due to the large plastic deformation caused by the high intensity. Unfavorable residual deformation in the tower structure after earthquake is attained. The bracing system can control the residual deformation. The providing tower with bracing system can affect the tower top displacement global response, where its contribution in the maximum displacement reaches about 30 % of that of the un-braced tower.

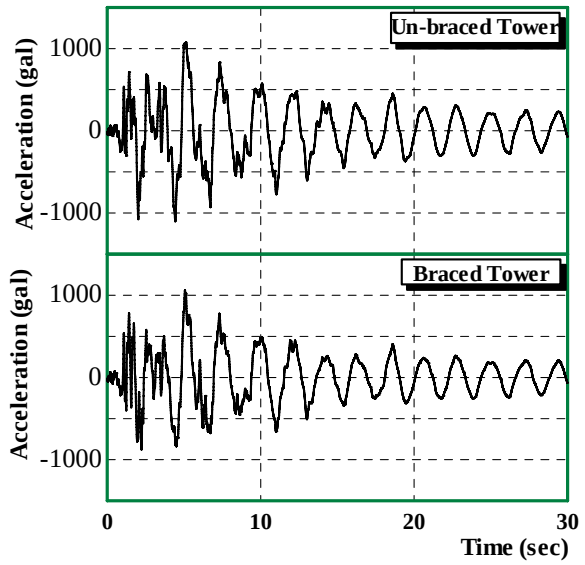


Figure 4: Acceleration time history at tower top

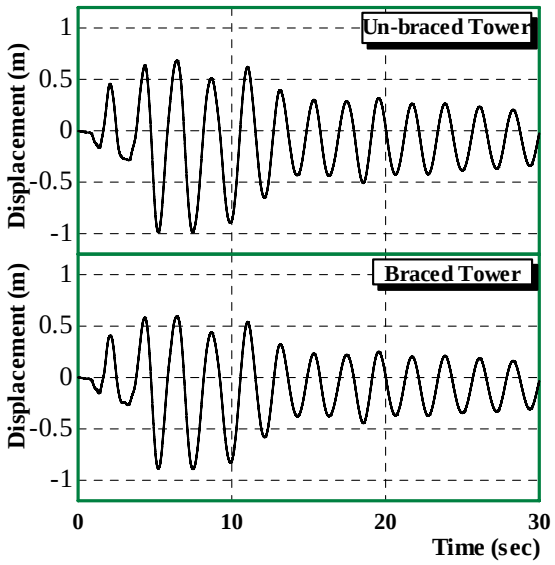


Figure 5: Displacement time history at tower top

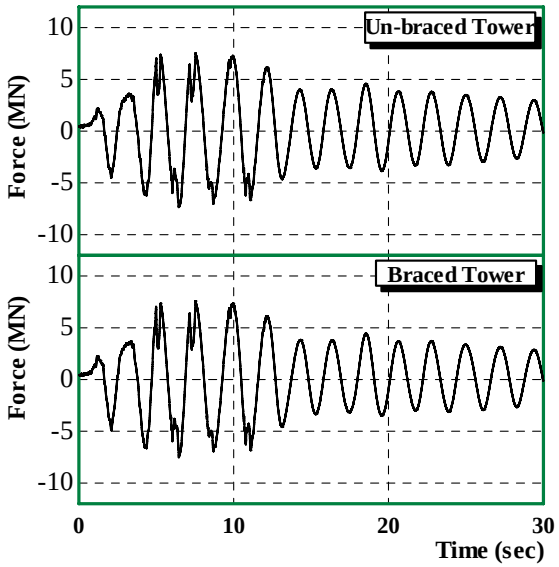


Figure 6: Shear force time history at tower base

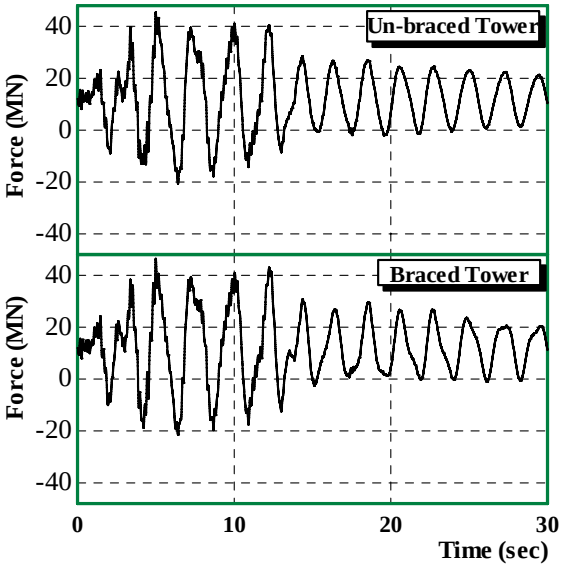


Figure 7: Vertical force time history at tower base

The negative effect of bracing system is increasing the shearing force at supports of structures. Hence, the shearing force is important to be examined at tower base after providing the bracing system. The shear force time history at tower base is shown in figure 6. Providing the tower with bracing system gives negligible increasing in the shearing force magnitude. The increasing of the shearing force can be calculated by 0.5 % only which considered has no obvious effect. By comparing the vertical reaction force time history at the tower base for the two different tower models, it is found that the tower provided with bracing system displays slight increase in the reaction force responses compared to the un-braced tower response (original case), as shown in figure 7. The increase of the vertical reaction force in both negative and positive directions may be reaches around 0.2 % which can be considered has no effect. It can be concluded that the bracing system provided to the tower structure has no effect on the reaction forces at tower base.

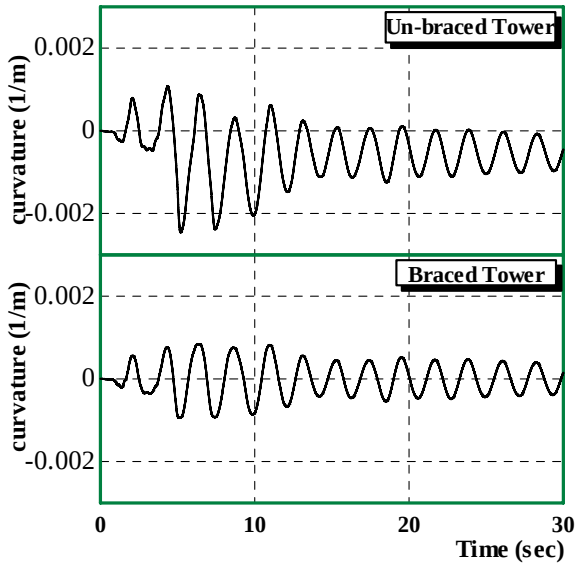


Figure 8: Curvature time history at tower base

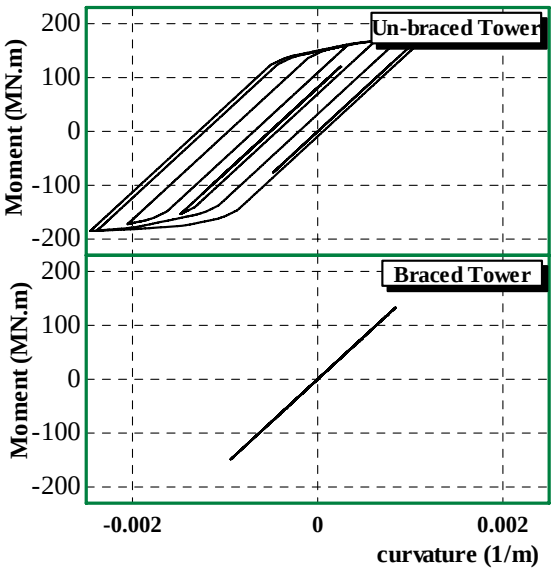


Figure 9: Moment & curvature relationship at tower base

Figure 8 shows the curvature time history which represent the residual curvature at tower base in case of original un-braced tower. It is can be shown the great effect of suggested bracing system which can control this residual curvature after earthquake end. Form the moment curvature relation for the original un-braced tower, figure 9; it can clarify the effect of the near fault acceleration pulse on the tower structural response that tends to be characterized by progressive yielding in one direction starts from tome 5 seconds in the negative direction. The asymmetric accumulation of inelastic deformation in one direction becomes increasingly important as the duration of the ground motion is increased. For the mass proportional damping, it can be observed that the asymmetry strength and moment curvature diagram shift due to fluctuating axial force effect. This asymmetric completely disappears in case of using bracing system. That means using of the bracing system can overcome the effect of near fault acceleration pulse in the input wave and makes equalization of the hysteric response. On the other hand, the axial force-moment interaction which leads to irregular shape due to presence of vertical motion can be balance by the suggested bracing system.

5 CONCLUSIONS

The feasibility of providing bracing system in cable-stayed bridge steel tower is studied. The steel tower of Tappu cable-stayed bridge located in Hokkaido, Japan is considered as model of study. The steel tower is taken out of the bridge and modeled as three-dimensional frame structure. The proposed braced model is to provide the tower by X-bracing elements connecting the upper part of the tower. The study based on comparison of the seismic response of the original un-braced tower and that of proposed braced tower. A nonlinear dynamic analysis program based on total Lagrangian formulation using linearized finite displacement theory and fiber model has been developed to be used in this study. The finite element procedure for the nonlinear time history analysis of the steel tower under seismic loadings is set up. The results of this study show that the seismic response of cable-stayed bridge steel tower can be improved by providing bracing elements which will enhance the seismic ductility of the tower. The proposed bracing system, in this study, can reduce the horizontal displacement of the bridge tower. In addition, the vertical force and bending moments at tower support give more reduced values compared to those of un-braced tower.

From this study, the following conclusions can be drawn as follow:

- Providing the tower with proposed X-bracing system can affect the tower top displacement response, where its contribution in the maximum displacement reaches about 30 % of that of the un-braced tower.
- The proposed X-bracing system provides slight increase in the reaction forces while the moment reduced compared to the un-braced original tower response, moreover the curvature at tower base give symmetrical response.
- The proposed X-bracing system leads to no residual curvature at tower column.

REFERENCES

[1] T. Hayashikawa, and S. E. Abdel Raheem, Nonlinear dynamic behavior of steel tower of cable-stayed bridges with passive energy dissipation system, *Journal of Structural Engineering, JSCE,* Vol. 48A, pp. 863-874, 2002.

[2] M. OMAR, Seismic Performance of Cable-Stayed Bridge Steel Towers, *PhD thesis, Graduate School of Engineering, Hokkaido University*, 2008.

[3] Committee of Earthquake Engineering, The 1995 Hyogoken-Nanbu Earthquake, Investigation into Damage to Civil Engineering Structures, *Japan Society of Civil Engineers*, June, 1996.

[4] M. OMAR: Seismic Response of Braced Steel Frames with Shape Memory Alloy and Mega Bracing Systems, WASET, *International Journal of Civil, Architectural Science and Engineering* Vol:8 No:2, 2014.

[5] M. OMAR and T. HAYASHIKAWA, Improvement of Nonlinear Response of Plan-Irregular Multi-Storey Steel Buildings under Three-Dimensional Earthquake Motion Using Bracing System, *Journal of Steel Construction, JSSC*, Vol.22, 2014.

[6] R. Sabelli, S. Mahin, C. Chang. Seismic demands on steel braced frame buildings with buckling-restrained braces, *Engineering Structures*, 25(5):655-66, 2003.

[7] M. Nakashima, K. Inoue, M. Tada, Classification of damage to steel buildings observed in the 1995 Hyogoken-Nanbu Earthquake, *Engineering Structures*,20(4-6):271-81, 1998.

[8] FEMA. Recommended seismic design provisions for new moment frame buildings, *Federal emergency management agency report* No. 350. 2000.

[9] J. Osteraa, H. Krawinkler, The Mexico earthquake of September 19, 1985 behavior of steel buildings. *Earthquake Spectra*, 5(1):51-88, 1989.

[10] H. Kim, S. Goel, Seismic evaluation and upgrading of braced frame structures for potential local failures, UMCEE 92-24, *Dept. of civil engineering and environmental engineering, Univ. of Michigan, Ann Arbor*,Oct. p. 290, 1992.

[11] R. Tremblay, P. Timler, M. Bruneau, A. Filiatrault, Performance of steel structures during the 1994 Northridge earthquake, *Canadian Journal of Civil Engineering*, 22:338-60, 1995.

[12] R. Trembla, M. Bruneau, M. Nakashima, HGL Prion, A. Filiatrault, R. DeVall, Seismic design of steel buildings: lessons from the 1995 Hyogo-ken Nanbu earthquake, *Canadian Journal of Civil Engineering*, 23: 727-56, 1996.

COMPDYN 2015
5th ECCOMAS Thematic Conference on
Computational Methods in Structural Dynamics and Earthquake Engineering
M. Papadrakakis, V. Papadopoulos, V. Plevris (eds.)
Crete Island, Greece, 25–27 May 2015

MODAL PROPERTIES OF SIMPLY SUPPORTED RAILWAY BRIDGES DUE TO SOIL-STRUCTURE INTERACTION

Christoffer Svedholm[1,2*], Costin Pacoste[1,2] and Raid Karoumi[1]

[1]Division of Structural Engineering and Bridges, KTH Royal Institute of Technology
Brinellvägen 23, 100 44 Stockholm, Sweden

[2] ELU Konsult AB
Valhallavägen 117, 102 51 Stockholm, Sweden
e-mail: christoffer.svedholm@elu.se

Keywords: Bridge, Damping, Soil–structure interaction, Modal properties, Non–proportionally damped

Abstract. *Resonance vibration of railway bridges has become an important design issue during the last decade due to the development of new high-speed lines. At resonance it is well known that the damping of the structure has a great influence on the final response. The current paper presents modal parameters, such as modal damping ratios and natural frequencies, derived based on a simply supported Bernoulli–Euler beam on an elastic half–space.*

In the current chapters of Eurocode dealing with dynamical analysis of railway bridges, the expression for the modal damping ratio is essentially empirical. The novelty of this paper is therefore two-fold: (1) provide modal damping ratios for soil–structure interaction, and (2) show that the damping should not be considered as constant for all modes but it varies depending on the particular mode shape and interaction with the soil.

1 INTRODUCTION

In the field of dynamics, it is well known that damping is of the essence for structures under periodic loading. This would not be a problem in it self but in practice, damping is also the most difficult and complicated problem in vibration. One of the reasons for this seems to be that there exist several mechanisms for energy transfer. Today it is believed that the most important sources of damping for a railway bridge are: (1) bending stresses, (2) friction at supports, (3) wave propagation in soil, and (4) friction in ballast. Given these points, it is not surprising to find that the damping ratios proposed by design handbooks are based on empirical data obtained solely by measuring the free vibration response. The key point is that in this type of measurement the sources of damping are unknown and only the dominant mode is taken into account. For railway bridges, the most well–known and widely used damping ratios (see Fig. 1) are presented in ERRI D-214 [1]. Looking at the figure, it is apparent that there is a pronounced degree of scatter. For example, the ratio of damping for two identical bridges, may vary by a factor 8 [2].

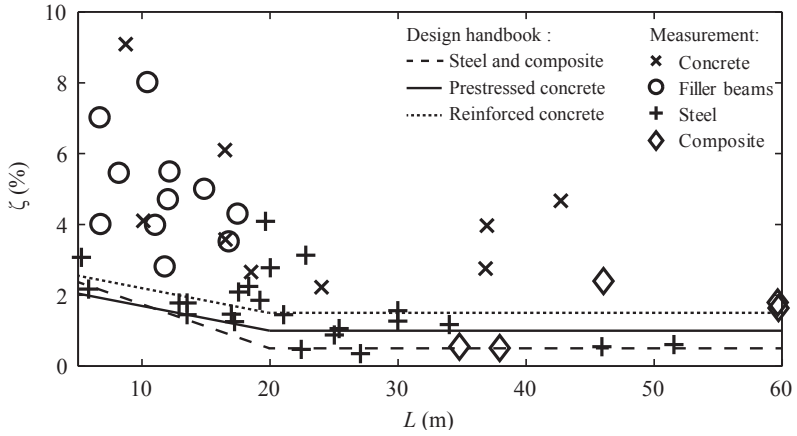


Figure 1: Measured damping values. Reproduced from ERRI D-214 [1]

Therefore, it is the purpose of this paper to provide new insight to this problem. Here, we focus on soil-structure interaction (SSI). Ülker et al. [8] performed the dynamic analysis of a portal frame bridge to study the effect of soil–structure interaction. Through numerical simulation, it was found that the modal damping ratio could vary between 1 and 15%. In another interesting paper, Romero et al. [7] studied soil–structure interaction in resonant railway bridges. It is shown by means of numerical calculations that soft soils have a favourable effect on the response due to geometric damping.

The novelty of this paper is to perform a thorough investigation of modal parameters due to SSI in railway bridges. For this purpose, we begin by deriving an analytical expression for the natural frequencies and modal damping ratios of an elastically–supported beam with two vertical viscous dampers. An approximation of the spring–dashpot parameters can be found from Gazetas model [4]. Based on this model, we are able to address several important questions. In particular, good correspondence is found between theoretical and measured damping values.

2 FORMULATION OF THE PROBLEM

Let us start by considering Fig. 2, a Bernoulli–Euler beam supported by a spring–dashpot system representing the elastic half–space. Then, the equation of motion for free vibration is given by,

$$m\frac{\partial^2 w}{\partial t^2} + EI\frac{\partial^4 w}{\partial x^4} = 0 \tag{1}$$

where the mass per unit length m and bending stiffness EI are assumed constant over the span L.

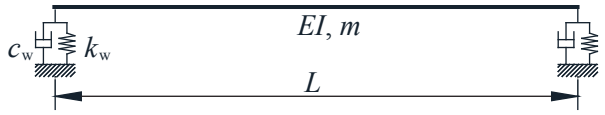


Figure 2: Structural system of an elastically–supported beam with two vertical viscous dampers.

Using the separation–of–variables technique, the transverse displacement $w(x,t)$ can be written as a product of two functions, each depending only on one parameter:

$$w(x,t) = q(t)\phi(x) \tag{2}$$

Here $q(t)$ is the generalized coordinate and $\phi(x)$ is the normal mode. Then, by substituting Eq. 2 into Eq. 1 and grouping all terms involving t and x on the left–hand side and right–hand side, respectively, we obtain Eq. 3.

$$\frac{\ddot{q}(t)}{\frac{EI}{m}q(t)} = -\frac{\phi''''(x)}{\phi(x)} \tag{3}$$

Now Eq. 3 can be reduced to a pair of ordinary differential equations by making each side of the equation equal a constant $-\lambda^4$.

$$\phi''''(x) - \lambda^4\phi(x) = 0 \tag{4a}$$

$$\ddot{q}(t) + \lambda^4\frac{EI}{m}q(t) = 0 \tag{4b}$$

The solution to the above equations are of the form:

$$\phi(x) = A_1e^{\lambda x} + A_2e^{-\lambda x} + A_3e^{i\lambda x} + A_4e^{-i\lambda x} \tag{5a}$$

$$q(t) = Be^{\Lambda t} \tag{5b}$$

A relationship between the separation constant λ and the eigenvalue Λ is obtained by substituting Eq. 5b into Eq. 4b.

$$\lambda^4 = -\frac{m\Lambda^2}{EI} \tag{6}$$

We have now to introduce the boundary conditions to be able to calculate Λ and $A_1 - A_4$. From the free body diagram (Fig. 3) it follows that the sum of forces and moments, at $x = 0$ and

$x = L$, should be zero:

$$EI\phi'''(0) = -Z_w(\Lambda)\phi(0) \tag{7a}$$
$$EI\phi''(0) = 0 \tag{7b}$$
$$EI\phi'''(L) = Z_w(\Lambda)\phi(L) \tag{7c}$$
$$EI\phi''(L) = 0 \tag{7d}$$

where the impedance is evaluated as $Z_w(\Lambda) = c_w\Lambda + k_w$. Now, by substituting Eq. 5a into

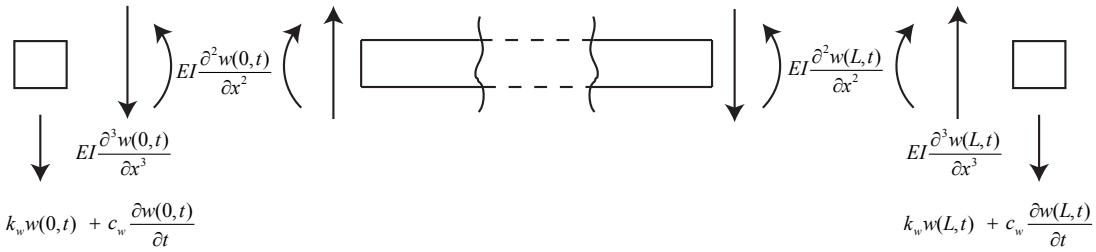


Figure 3: Free body diagram.

Eq. 7 and arranging the four equations into matrix form, i.e. $\Gamma(\Lambda)J = 0$, we obtain:

$$\begin{bmatrix} \eta+1 & \eta-1 & \eta-i & \eta+i \\ -(\eta-1)\,e^{L\lambda} & -(\eta+1)\,e^{-L\lambda} & -(\eta+i)\,e^{L\lambda i} & -(\eta-i)\,e^{-L\lambda i} \\ 1 & 1 & -1 & -1 \\ e^{L\lambda} & e^{-L\lambda} & -e^{L\lambda i} & -e^{-L\lambda i} \end{bmatrix} \begin{bmatrix} A_1 \\ A_2 \\ A_3 \\ A_4 \end{bmatrix} = \begin{bmatrix} 0 \\ 0 \\ 0 \\ 0 \end{bmatrix} \tag{8}$$

where $\eta = Z_w/\lambda^3 EI$. The eigenvalues are calculated by solving $\mathrm{Det}(\Gamma) = 0$. Once the eigenvalues have been estimated, it is possible to calculate the angular natural frequency ω_n and the modal damping ration ζ_n.

$$\omega_n = |\Lambda_n| \tag{9a}$$
$$\zeta_n = \frac{-\Re(\Lambda_n)}{\omega_n} \tag{9b}$$

The angular natural frequency of vibration is given by the familiar equation $\omega_n = 2\pi f_n$, where f_n is the natural frequency of vibration.

3 SOIL–STRUCTURE INTERACTION

Through the years, there have been a number of studies looking at soil–structure interaction (SSI) during dynamic loading. In the authors' opinion, the most comprehensive work in this area is due to Gazetas [4, 3, 5]. The present paper uses Gazetas solution for a rigid slab on an elastic half–space to calculate spring and dashpot coefficients. Hereafter, for the sake of completeness, we provide a brief summary of Gazetas method [4].

First, let us consider a general shape foundation with a soil contact area of A_b and a circumscribed rectangle $2B_1$ by $2B_2$, where $B_1 \geq B_2$. Once the geometry of the slab and the soil properties are known, the dynamic stiffness k_w can be calculated with the following equation:

$$k_w = \frac{2GL}{1-\nu}\left(0.73 + 1.54\chi^{0.75}\right)\tilde{k}_w\left(B_1/B_2, \nu; a_0\right) \tag{10}$$
$$\text{where } \chi = \frac{A_b}{4L^2}$$

Here the dynamic stiffness coefficient $\tilde{k}_w$ (Fig. 4) accounts for the frequency–dependent effects. It is important to note that frequency–dependent parameters only arise if the half space is replaced by a spring-dashpot model. In Fig. 4, the dimensionless circular frequency is defined by $a_0 = \omega B_2/V_\mathrm{s}$, where V_s stands for the shear wave speed. The radiation dashpot, c_w, which accounts for the spreading of elastic waves in the half–space medium, is defined by:

$$c_w = \rho V_\mathrm{La} A_\mathrm{b} \tilde{c}_w\left(B_1/B_2, \nu; a_0\right) \tag{11}$$
$$\text{where } V_\mathrm{La} = \frac{3.4V_\mathrm{s}}{\pi\left(1-\nu\right)}$$

The radiation dashpot coefficient $\tilde{c}_w$ is plotted in Fig. 4. It should also be noted here that $\tilde{c}_w$ varies with frequency. However, from the figure it is evident that frequency dependence is relatively small for $B_1/B_2 < 6$. The variable V_La in Eq. 11 is known as Lysmer's analog wave velocity, which physically represents the velocity of compression waves at the foundation–soil interface.

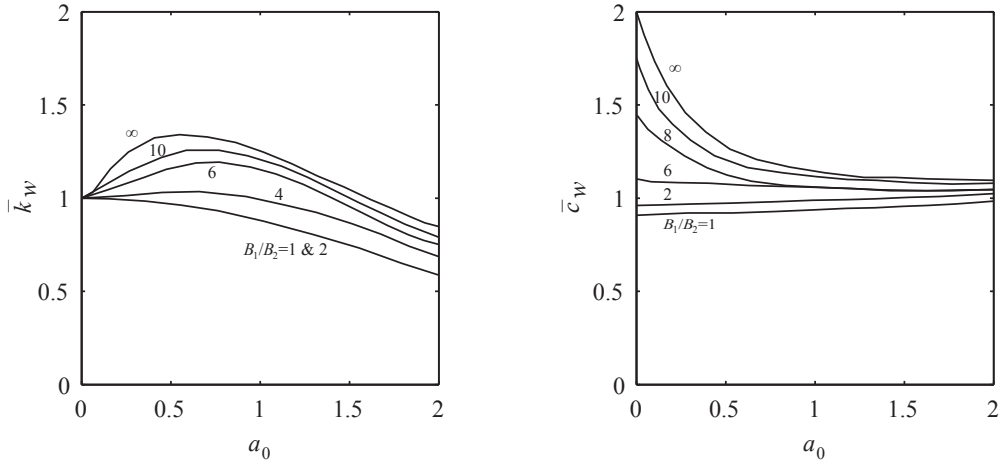


Figure 4: Dynamic stiffness and dashpot coefficient. Reproduction from Gazeta [4]

4 NUMERICAL EXAMPLES

Numerical simulations have been performed on bridges with a span of 5 m (short) to 60 m (long) supported by a granular material with a Young's modulus E_{soil} of 50 MPa (loose) to 800 MPa (dense). The Poisson's ratio and density of the soil was assumed constant $\nu = 0.4$ and $\rho = 1800$ kg/m^3, respectively. Also, the size of the foundation is fixed to a constant value of 8×8 m. Both the mass per unit length m and the bending stiffness EI was assumed to vary with the span L. This relationship was previously derived in Johansson et al. [6], where Eq. 12a and 12b are proposed, for single–track ballasted concrete bridges, by collecting data from "real" bridges.

$$m = 580L + 5350 \text{ [kg/m]} \tag{12a}$$

$$EI = 4(265L^{-1.28})^2 mL^4/\pi^2 \text{ [N/m}^2\text{]} \tag{12b}$$

On the basis of this information, numerical simulation have been carried out in MATLAB R2013a to determine natural frequencies, modal damping ratios and mode shapes.

4.1 Loose granular material

This section presents the results, see Fig. 5 and Table. 2, for a loose soil with an elastic Young's modulus of 50 MPa. Using the parameters presented above, this corresponds to a shear wave speed of $V_s = 99.6$ m/s. By examining the figures, it turns out that the solution consist of a set of underdamped (bending mode 1-6) and overdamped (mode 7-10) modes, hereafter, these modes are referred to as "real" and "imaginary" modes, respectively. If we only consider

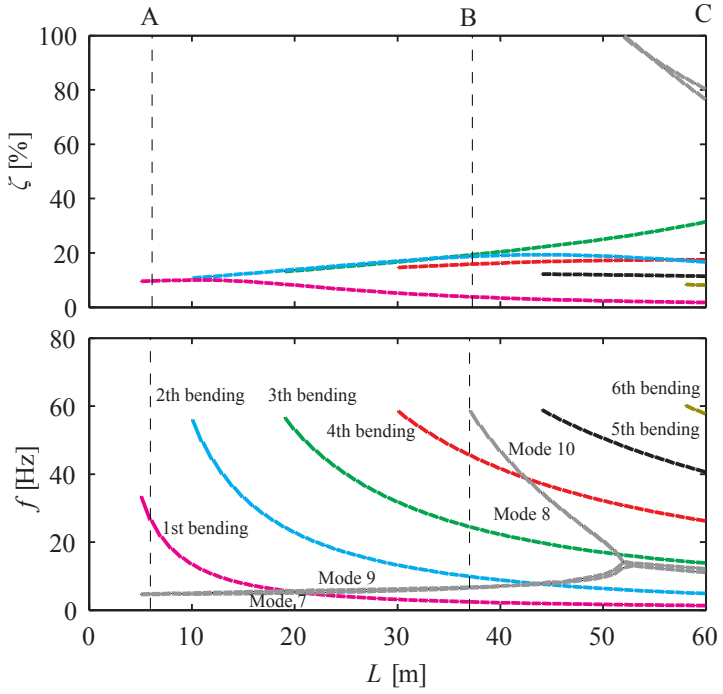


Figure 5: Damping ratios and natural frequencies for $E_{\text{soil}} = 50$ MPa.

the imaginary modes, it seems that something interesting is happening at $L = 52$ m. This is because at $L < 52$ m there exist four imaginary modes with $\zeta > 1$, but at $L > 52$ m these merge into two modes with $\zeta < 1$. The reason for this is not clear, but it could be that the wave

propagation characteristics change. Let us then consider the modal damping ratios of the real modes in Fig. 5. Here the results show that the modal damping ratio varies depending on the particular mode shape and span. The smallest (1.75 %) and largest (31.4 %) damping ratios were, for example, obtained at $L = 60$ m, for the 1st and 3rd bending mode, respectively. This difference is most easily explained by looking at the modal displacement and phase angle of the relevant modes (see Table. 2 Case C). Here it is obvious that the 1st bending mode is dominated by standing wave (all points in–phase or out–of–phase) and the 3th bending mode is vibrating in a combination of traveling and standing wave. Finally, Table. 1 show the maximum damping ratio for the bending modes.

Table 1: Maximum damping ratios for $E_{\text{soil}} = 50$ MPa.

	1st bending	2th bending	3th bending	4th bending	5th bending	6th bending
L [m]	11	42	60	60	44	58
ζ_n [%]	10.0	19.3	31.4	17.5	12.2	8.3

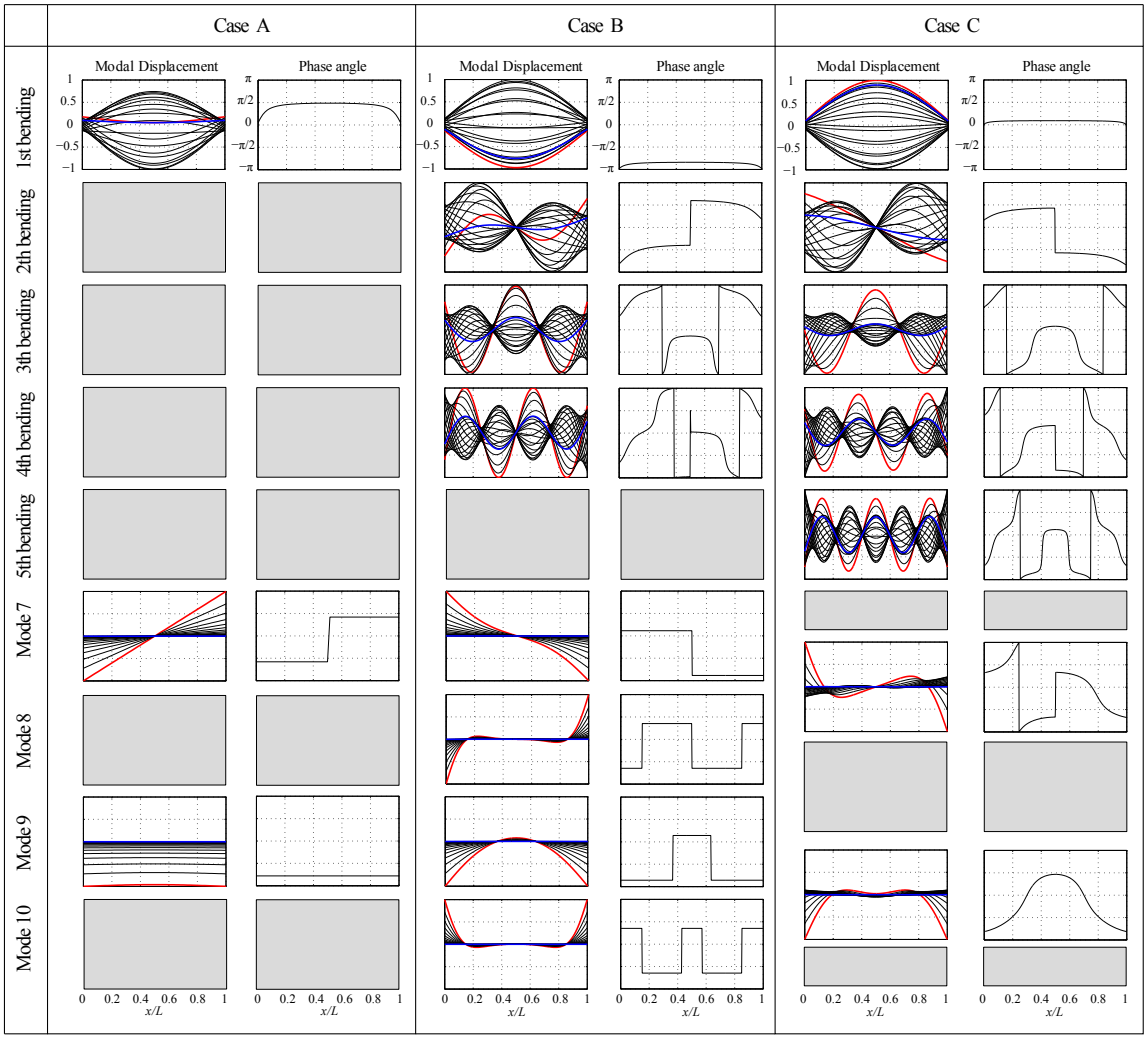


Table 2: Modal displacement and phase angle for $E_{\text{soil}} = 50$ MPa.

4.2 Dense granular material

The results presented in Section 4.1 show that loose soils provide high modal damping values. However, these values are drastically reduced for dense soils. Taking for illustrative purposes $E = 200$ MPa ($V_s = 199.2$ m/s, see Fig. 6 and Table 4), we find that ζ, at $L = 60$ m, varies from 0.3 % (1st bending) to 12.9 % (4th bending). This corresponds to a reduction of the modal damping ratio by 82.9 % and 58.9 %. With this in mind the engineer should, when designing a bridge, use stiff material for the soil in order not to overestimate the damping.

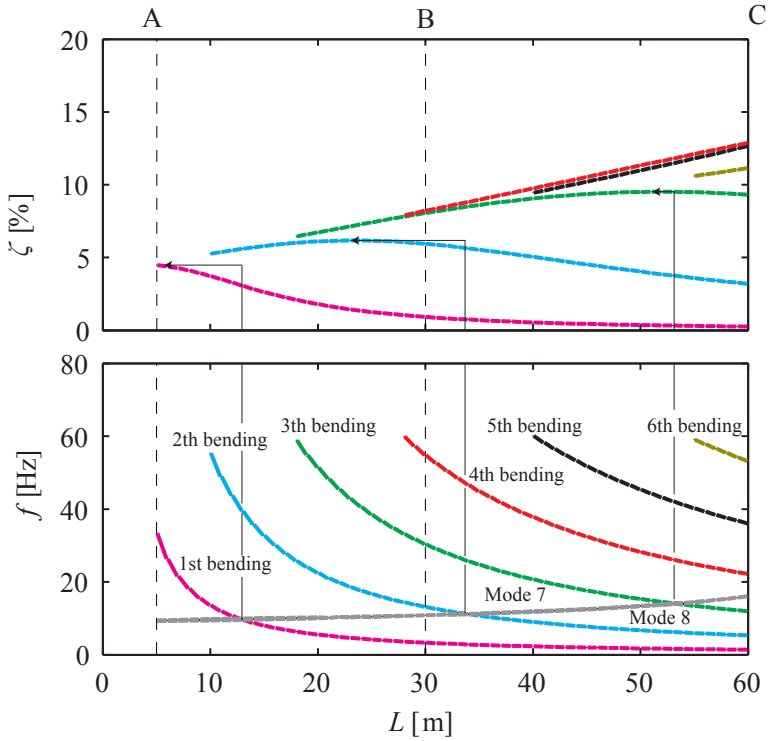


Figure 6: Damping ratios and natural frequencies for $E_{\text{soil}} = 200$ MPa.

For both soil types, it was found that ζ_n tends to $\uparrow$ (increase) with the first few modes, after which ζ_n tends to $\downarrow$ (decreases), see Table. 1 and 3. In fact, if we let $n \to \infty$, then the model shows that $\zeta_n \to 0$. To put the same thing in other words, SSI cannot damp the high frequency oscillation in general. Another aspect that the authors found interesting is that maximum damping seem to occur in the vicinity points where the natural frequencies of real and imaginary modes coincide. This observation, together with previous studies by the authors show that imaginary modes provide damping to real modes if their natural frequencies are closely spaced.

Table 3: Maximum damping ratios for $E_{\text{soil}} = 200$ MPa.

	1st bending	2th bending	3th bending	4th bending	5th bending	6th bending
L [m]	5	23	51	60	60	60
ζ_n [%]	4.5	6.2	9.5	12.9	12.7	11.1

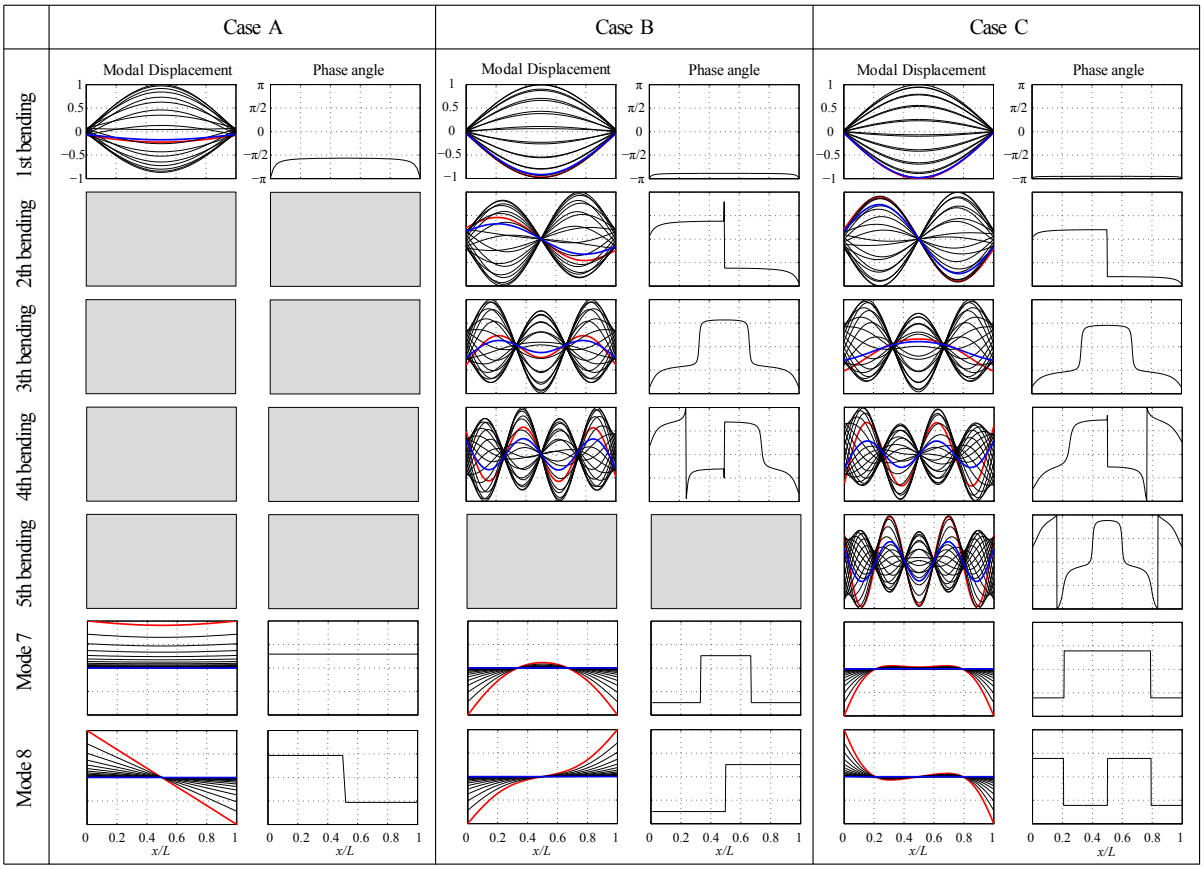


Table 4: Modal displacement and phase angle for $E_{\text{soil}} = 200$ MPa.

4.3 Damping of the fundamental frequency

In this section, we compare measured and calculated modal damping ratios for the 1st bending mode. Higher modes of vibration are not studied due to limited amount of published experimental data. The measured data points, in Fig. 7, are reproduced from a plot in reference [1]. A fairly reasonable interpretation of the scattering in the figure might be that the modal damping ratio cannot be uniquely defined by the span and type of bridge. Here, we propose that the foundation is another important aspect, which needs to be studied in detail to accurately predict the damping of each mode. To exemplify this fact, we also present in Fig. 7 numerically calculated modal damping ratios (solid lines) of the 1st bending mode for soils with $E_{\text{soil}} = 50 - 800$ MPa. Looking at the figure one can see good consistency between experimental and numerical data. Namely, the modal damping ratio is of the right magnitude and tends to decrease with the span. From a practical point of view, a typical soil in Sweden lies between 100 MPa and 400 MPa. Damping ratios for soils outside of this range should therefore be considered as a theoretical exercise. With this in mind, the expected damping ratio from soil alone is between 0.1 % (long span & dense soil) and 6.6 % (short span & loose soil). This findings clearly indicate that geometric damping of soil is one of the main contributor to damping in railway bridges.

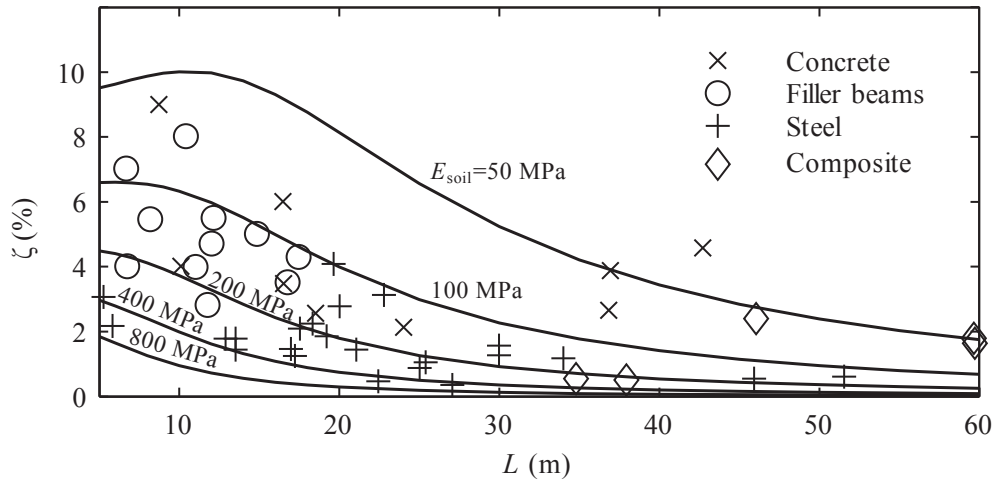


Figure 7: Damping of the 1st bending mode as a function of span. The solid lines are the simulated results.

5 CONCLUSIONS

In this paper, a model for calculating modal properties of a Bernoulli–Euler beam, supported by an elastic half–space, is derived. The model is then used to study the effects of soil–structure interaction (SSI) for ballasted reinforced concrete bridges. From these numerical results, it is possible to draw the following conclusions:

- The expected damping ratio for the 1st bending mode from soil alone is between 0.1 % and 6.6 % for a long span bridge supported by a dense soil and a short span bridge supported by a loose soil, respectively.
- The results of the calculation show that traveling waves provide a damping ratio of 6-12.9 % to the 2-6th bending mode for medium to long span bridges.
- A good correlation is found between theoretical and measured damping values for the 1st bending mode. Higher modes of vibration are not studied due to limited amount of published experimental data.
- SSI will only damp the first few bending modes.
- It is found that imaginary modes provide damping to real modes if their natural frequencies are closely spaced.

REFERENCES

[1] ERRI D-214. Rail bridges for speeds over 200km/h, final report, 1999.

[2] ERRI D-214. Rail bridges for speeds over 200km/h, recommandations for calculating damping in rail bridge decks, 1999.

[3] G Gazetas. Analysis of machine foundation vibrations: state of the art. *International Journal of Soil Dynamics and Earthquake Engineering*, 2(1):2–42, 1983.

[4] G Gazetas. Foundation engineering handbook, chapter 15, 1991.

[5] G Gazetas, K Fan, and A Kaynia. Dynamic response of pile groups with different configurations. *Soil Dynamics and Earthquake Engineering*, 12(4):239–257, 1993.

[6] C. Johansson, A. Andersson, J. Wiberg, M. Ülker-Kaustell, C. Pacoste, and R. Karoumi. Höghastighetsprojekt-bro: Delrapport i: Befintliga krav och erfarenheter samt parameterstudier avseende dimensionering av järnvägsbroar för farter över 200 km/h. 2010.

[7] A. Romero, M. Solís, and P. Galvín. Soil-structure interaction in resonant railway bridges. *Soil Dynamics and Earthquake Engineering*, 2012.

[8] M Ülker-Kaustell, R Karoumi, and C Pacoste. Simplified analysis of the dynamic soil–structure interaction of a portal frame railway bridge. *Engineering structures*, 32(11):3692–3698, 2010.

COMPDYN 2015
5th ECCOMAS Thematic Conference on
Computational Methods in Structural Dynamics and Earthquake Engineering
M. Papadrakakis, V. Papadopoulos, V. Plevris (eds.)
Crete Island, Greece, 25–27 May 2015

SAFETY ASSESSMENT OF A SMALL SPAN HIGH-SPEED RAILWAY BRIDGE USING AN EFFICIENT PROBABILISTIC METHODOLOGY

João M. Rocha[1], António A. Henriques[2], and Rui Calçada[2]

[1] University of Porto - Faculty of Engineering
Rua Dr. Roberto Frias, s/n, 4200-465 Porto, Portugal
e-mail: jmsrocha@fe.up.pt

[2] University of Porto - Faculty of Engineering
Rua Dr. Roberto Frias, s/n, 4200-465 Porto, Portugal
{aarh,ruiabc}@fe.up.pt

Keywords: Efficient probabilistic methodology; Simulation methods; Extreme value theory; Optimized extrapolation; Railway bridges; High-speed traffic.

Abstract. *The behaviour of small span railway bridges is known to be particularly difficult to predict due to the complexity of the coupled train-track-bridge system, as well as for being particularly sensitive to resonant phenomena. The objective of this paper is to present an efficient methodology to evaluate the safety of small span bridges in high-speed railway lines, bearing in mind the real variability of the parameters that influence the dynamic response of the train-track-bridge coupled system. This requires the development of adequate numerical models for the bridge, the track and the train subsystems, as well as the definition of the distributions and variability of all the variables related to the structure, the train, the track and also the wheel-rail contact. Track irregularities are also accounted for in the dynamic analysis. Canelas railway bridge, located in the North of Portugal, was selected as case study. The bridge has six simply supported spans of 12 m each, leading to a total length of 72 m. The deck is a composite structure with two half concrete slab decks with nine embedded rolled steel profiles HEB 500, each supporting one rail track. In order to assess the safety of the bridge two simulation methods were used: the Monte Carlo method and the Latin Hypercube method. Furthermore, both simulation methods are combined with two different approaches to enhance efficiency. One based on the extreme value theory that uses the Generalized Pareto Distribution to model the tail of the distribution. The other uses an approximation procedure based on the evaluation of the failure probabilities at moderate levels to estimate the target probability of failure by extrapolation. The track stability safety due to the deck vibrations level is used as the safety criterion to validate the proposed methodology. The results are extremely promising and indicate the feasibility of this methodology due to the very reasonable computational costs that are required.*

1 INTRODUCTION

Safety has always been one of the main Engineering concerns, particularly for important structures such as bridges. Due to the generalized use of computers and their continuous evolution, the safety assessment techniques have become increasingly sophisticated and complex, allowing more realistic and accurate analysis. In recent years, the use of probabilistic methods to assess the safety of new and existing structures has become more frequent.

Due to the degree of complexity of the safety assessment of railway bridges the use of such methods is not very common. Simulation methods are generally used when probabilistic methodologies are employed to study these problems. The Monte Carlo method [1] is usually selected, but more refined methods like the Latin Hypercube [2] can also be applied. Regardless of the selected method, the objective is always to obtain an accurate assessment using an efficient methodology. The efficiency of a methodology represents its capacity to reduce computational costs without compromising accuracy. Besides accuracy, the quantification of the uncertainties in the predictions is also important.

Despite the potential of the simulation methods, it is observed that for several problems the use of such technique may be computationally prohibitive. For this reason several authors proposed complementary procedures in order to enhance the efficiency of such methods. Naess et al. [3] proposed an approach that estimates the probability of failure by extrapolating the tail probabilities based on the estimates of the failure probabilities at moderate levels. Ramu et al. [4], on the other hand, proposed the estimation of the probability of failure by modelling the tails of the obtained distributions.

In previous research works the safety due to track instability caused by excessive deck vibrations [5] and the running safety of trains [6] on this type of bridges have already been studied using probabilistic approaches. In the present study the safety assessment of a short span composite high-speed railway bridge is performed. The current paper is focused on the analysis of the efficiency of different probabilistic methodologies in the safety assessment of short span railway bridges. Besides the standard Monte Carlo simulation, that has been used in previous works, in this paper a more refined simulation technique, namely the Latin Hypercube sampling method, is also applied. Furthermore, both simulation methods are combined with two different approaches to enhance efficiency. One is based on the extreme value theory and uses the Generalized Pareto Distribution to model the tail of the distribution. The other uses an approximation procedure based on the evaluation of the failure probabilities at moderate levels to estimate the target probability of failure by extrapolation.

The safety of the train-track-bridge system is assessed through the analysis of the track instability due to excessive deck vibrations. The results obtained by different methods are compared in order to identify the most efficient approach.

2 STRUCTURAL RELIABILITY ANALYSIS

The use of analytical techniques for the reliability analysis of complex structural systems, which are often characterized by non-linear limit-state functions, can be extremely difficult. In this section, several alternatives to asses this problem are presented and discussed. The different investigated techniques are used in the safety assessment of a short span high-speed railway bridge presented in Section 3. The obtained results are compared in order to identify the most efficient approach.

2.1 Tail modelling - Generalized Pareto Distribution (GPD)

Since structural reliability problems are determined by the tail of the obtained statistical distributions, the computational cost can be significantly reduced if an extrapolation of the Cumulative Distribution Function (CDF) is made using tail modelling techniques [4]. The classical tail modelling is based on the extreme value theory and consists on approximating the tail portion of the CDF above a certain threshold, *u*, by the Generalized Pareto Distribution [7]. The approximation function, $F_{\xi,\psi}(z)$, can be written as [4]:

$$F_{\xi,\psi}(z) = \begin{cases} 1 - \left(1 + \frac{\xi}{\psi} \cdot z\right)^{-\frac{1}{\xi}} & if\ \xi \neq 0 \\ 1 - \exp\left(-\frac{z}{\xi}\right) & if\ \xi = 0 \end{cases} \quad (1)$$

where z is the exceedance, ξ and ψ are the shape and scale parameters, respectively. This method has been applied in previous research works [5] and proved its efficiency in the analysis of complex multi-modal response problems. However, the tail needs to be modelled accurately, as small variations in the tail of the distribution can result in a variation by an order of magnitude of the safety level. Furthermore, the method relies significantly in the most extreme values, which are the ones that present the largest uncertainty. For this reason the estimated probability of failure may require, in some cases, a larger number of simulations until it stabilizes.

2.2 Enhanced simulation method (ES)

Naess et al. [3] proposed an enhanced simulation method which is able to overcome some limitations of high computational cost due to large samples needed for a robust estimation as in the previously presented method. It exploits the regularity of the tail probabilities to set up an approximation procedure based on the estimates of the failure probabilities at more moderate levels for the prediction of the far tail failure probabilities. The safety margin, *M*, represents the difference between the capacity and the demand to define the probability of failure as $p_f = \text{Prob}(M \leq 0)$ and is extended to a parameterized class of safety margins in the following way:

$$M(\lambda) = M - \mu_M \cdot (1 - \lambda) \quad (2)$$

where μ_M is the mean value of the safety margin *M* and λ is the scaling parameter that assumes values in the interval $0 \leq \lambda \leq 1$, putting the emphasis on the more reliable data points. Thus, the original system is obtained for $\lambda = 1$ while $\lambda = 0$ represents a system highly disposed to failure.

For a sample of size *N* an empirically estimated probability of failure is given by:

$$\hat{p}_f(\lambda) = \frac{N_f(\lambda)}{N} \quad (3)$$

where $N_f(\lambda)$ represents the number of realizations where there was failure for the given λ level. The 95% confidence interval for the value $p_f(\lambda)$ can be reasonably estimated by:

$$C^{\pm}(\lambda) = \hat{p}_f(\lambda) \cdot \left[1 \pm 1.96 \cdot C_v\left(\hat{p}_f(\lambda)\right)\right] \tag{4}$$

Introducing an approximation function fitted to the estimates allows estimating the target probability of failure by extrapolation. As proposed by [3], it is assumed that the probability of failure in the tail is dominated by a function that can be written as a function of λ:

$$p_f(\lambda) \underset{\lambda \to 1}{\approx} q(\lambda) \cdot \exp\left\{-a \cdot (\lambda - b)^c\right\} \tag{5}$$

where $q(\lambda)$ is a function that varies slowly compared with the exponential function $exp\left\{-a(b-\lambda)^c\right\}$. Thus, for practical applications it can be assumed that q(λ) = q and can then be applied in the following form for a suitable value of λ_0 [3]:

$$p_f(\lambda) \approx q \cdot exp\left\{-a \cdot (\lambda - b)^c\right\} \tag{6}$$

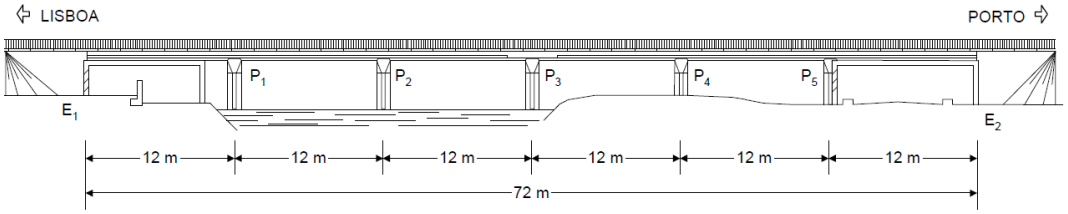
Therefore, an important part of the method is the identification of this suitable λ_0 so that Eq. (5) represents a good approximation of $p_f(\lambda)$ for $\lambda \in [\lambda_0, 1]$, and at least such that $\lambda_0 > b$. The optimum values for the four parameters q, a, b and c can be obtained through a least square optimization method using the Levenberg-Marquardt algorithm to the failure probabilities obtained by the Monte Carlo simulation.

For the estimation of the confidence intervals the empirical confidence band is re-adjusted to the optimal curve through Eq. (4). Then, the optimized confidence intervals are determined using a similar optimization procedure based on the re-adjusted confidence band. The fact that the confidence intervals can also be obtained by extrapolation, reducing significantly the influence of the sample size, is an important feature of this method. This enables it to be used to determine the accuracy of the estimated probability of failure. The fitted curves, extrapolated to the level of interest, will determine an optimized confidence interval of the estimated target failure probability.

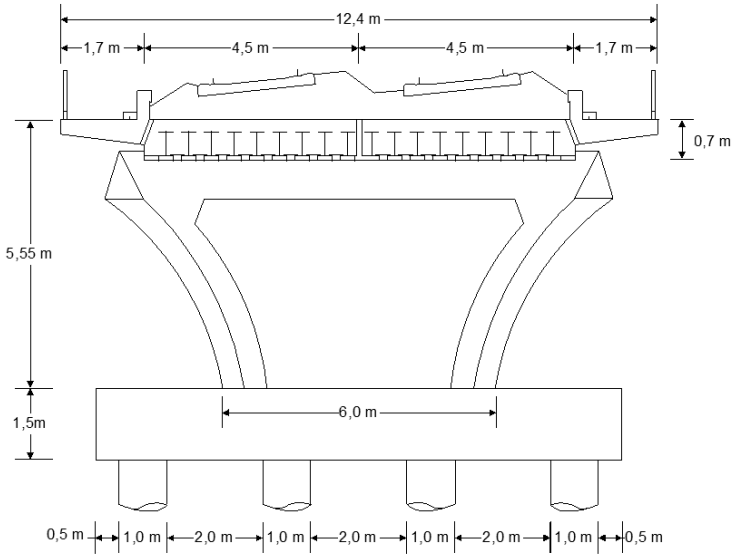
3 CASE STUDY

3.1 Canelas Bridge

Canelas Bridge is selected as case study. It is located in the Northern line of the Portuguese railway and is composed of six simply supported spans of 12 m each, with a total length of 72 m. The bridge deck is a filler beam consisting of two half concrete slab decks, each supporting a single ballasted track, with nine embedded rolled steel profiles HEB 500. Laminated neoprene elastomeric bearings are placed underneath each steel profile, in a total of 9 bearings per half deck. A longitudinal view of the bridge used as case study and the typical deck cross section is shown in Figure 1.



a) Longitudinal view



b) Typical cross section

Figure 1: Canelas railway Bridge.

The main reason for the selection of this bridge is that this is a very common structural system used for the European railway lines. A detailed description of the case study bridge can be found in [8]. The numerical model developed for the bridge is similar to the one used in [5] and is presented in the following section.

3.2 Numerical models

The Finite Element Method is used for the numerical modelling of both the bridge and the train. Regarding the bridge a 2D model is developed and discretized using beam elements. A single span is modelled and only one track is analysed, as the two half slab decks are independent. Furthermore, the model assumes that the bridge is inserted in a straight section of a high-speed railway line.

The deck is modelled as a beam positioned at the corresponding centre of gravity. The bearings are also included in the numerical model as springs positioned at the corresponding centre of rotation. The vertical and horizontal stiffness of the bearings are calculated according to [9]. With respect to the ballasted track, the model includes the rails, modelled as beams, the sleepers which are simulated by lumped masses and also the rail pads and the ballast layer,

modelled as sets of springs and dampers. The shear behaviour of the ballast layer due to composite effects is also accounted for and is computed in accordance with the elastic range of the bi-linear behaviour proposed by [10]. A more detailed description of the numerical model can be consulted in [5]. A schematic representation of the track-bridge numerical model is shown in Figure 2. The zoom in Figure 2 corresponds to the same section that is composed by an overlap of the two represented elements.

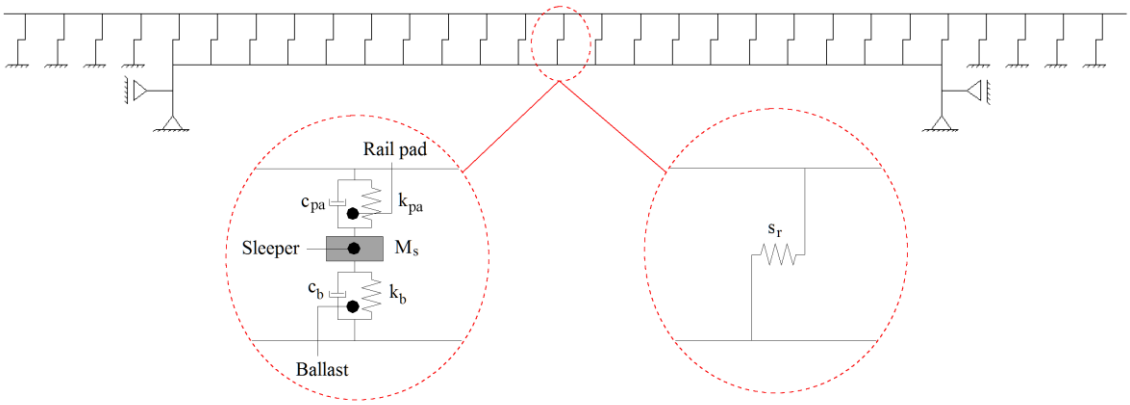


Figure 2: Track-bridge numerical model.

The existence of track irregularities is also taken into account in this paper and they are randomly generated using power spectral density functions according to SNCF proposal, which is limited to wavelengths between 2 m and 40 m [11]. In the current paper the wavelength range D1 defined by [12] is considered, limiting the analysis to wavelengths between 3 m and 25 m. The numerical process used to generate track irregularities can be consulted in [5]. In order to comply with the quality demands of EN13484-5 [12] the maximum standard deviation of the generated track irregularities profiles is limited to 1.5 mm over a track extension of 200 m.

Bearing in mind the bridge case study, variables that might have relevant nondeterministic properties which can lead to a significant change of the dynamic response were identified. This results in the selection of the random variables presented in Table 1. Similarly, the set of selected random variables for the track is specified in Table 2.

Variable	Distribution	Mean (gaussian) or Min. (uniform)	Std. Deviation (gaussian) or Max. (uniform)
Concrete density weight (γ_c)	Gaussian	2.5 t/m^3	0.1 (CV = 4%)
Concrete elasticity modulus (E_c)	Gaussian	36.1 GPa	2.888 (CV = 8%)
Concrete height (h_c)	Gaussian	Nominal value	10 mm
Concrete width (b_c)	Gaussian	Nominal value	5 mm
HEB 500 area (A_s)	Gaussian	Nominal value	0.04 x nominal area
Neoprene shear modulus (G)	Uniform	0.75 MPa	1.2 MPa
Structural damping (ζ)	Gaussian	2 %	0.3 %

Table 1: Bridge random variables.

Variable	Minimum	Maximum
Ballast density weight (γ_b)	1.5 t/m^3	2.1 t/m^3
Ballast elasticity modulus (E_b)	80 MPa	160 MPa
Ballast height (h_b)	0.30 m	0.60 m
Ballast load distribution angle (α)	15 º	35 º
Sleeper weight (M_s)	220 kg	325 kg
Rail pad stiffness (k_p)	100 kN/mm	600 kN/mm
Track shear resistance (R_t)	20 kN/m	60 kN/m
Irregularity amplitude (A)	160	275

Table 2: Track random variables.

Regarding the train, the dynamic behaviour of the bridge is assessed for the crossing of a TGV double high-speed train. This is an articulated train that is composed by a total of 20 coaches: four power cars, four power passenger cars and twelve passenger cars. The train model includes the car bodies, the bogies, the primary and secondary suspensions, the wheel-sets and also the wheel-rail contact stiffness. A schematic representation of the train and the corresponding numerical model is illustrated in Figure 3. A more detailed description of the train numerical model can be consulted in [5].

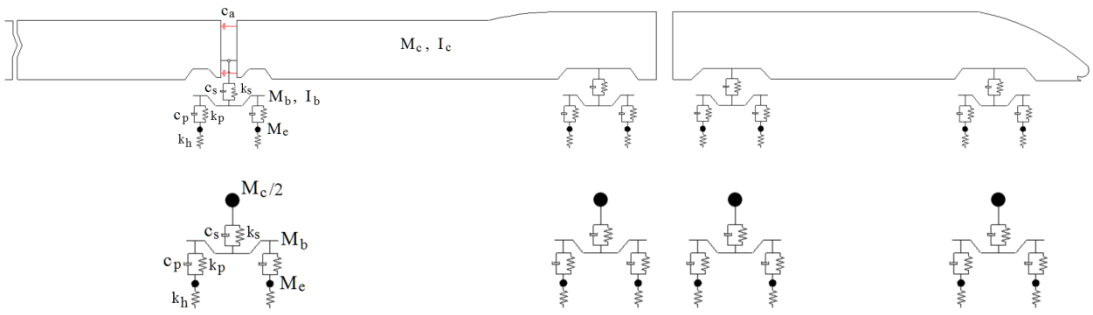


Figure 3: Schematic representation of the TGV double train numerical model.

Adopting the same principle that is considered for the bridge and the track, the random variables selected for the train model are indicated in Table 3. It should be mentioned that the dynamic properties of the train are defined according to the values presented by [10].

Variable	Distribution	Mean (gaussian) or Min. (uniform)	Std. Deviation (gaussian) or Max. (uniform)
Occupancy rate	Uniform	0 %	100 %
Bogie mass	Uniform	2.32 t	3.48 t
Wheel set mass	Uniform	1.6 t	2 t
Primary suspension stiffness	Uniform	1300 kN/m	3900 kN/m
Primary suspension damping	Uniform	6 kN.s/m	18 kN.s/m
Secondary suspension stiffness	Uniform	290 kN/m	870 kN/m
Secondary suspension damping	Uniform	10 kN.s/m	30 kN.s/m
Wheel-rail contact stiffness	Gaussian	1.61x10^6 kN/m	4.1x10^4 kN/m

Table 3: Train random variables.

4 SAFETY ASSESSMENT

In this section the safety assessment of the bridge is discussed. The different methodologies presented in Section 2 are used and the results compared in terms of efficiency. Both Monte Carlo (MC) and Latin Hypercube (LH) simulation are used. Furthermore, each of these simulation methods are combined with the Generalized Pareto Distribution (GPD) fit and also with the Enhanced Simulation method (ES) proposed by [3]. The safety of the train-track-bridge system is assessed through the analysis of the track instability due to excessive deck vibrations. The train-bridge system is considered to be safe if the estimated probability of failure is lower than 10^{-4}, which corresponds to a reference value in the Joint Committee on Structural Safety (JCSS) Probabilistic Model Code [13].

4.1 Track instability

The safety due to track instability is assessed by the bridge deck acceleration. For each simulation the maximum acceleration along the bridge deck is identified and selected as representative to assess the safety. The track instability is characterized by the loss of interlock between ballast grains, leading to the loss of the lateral resistance of the sleepers. Laboratory tests confirmed that the ballast instability only tends to occur for deck accelerations higher than 7 m/s^2 [14]. Below this limit the sleeper hardly moves and no loss of lateral resistance is observed. However, EN1991-2 [15] limits deck acceleration to a maximum of 3.5 m/s^2 for ballasted tracks, which indicates that a safety factor of 2 is applied. Since the safety of the train-bridge system is only at risk when deck accelerations are over 7 m/s^2, the probability of failure of the train-bridge system is established as the probability of the bridge deck reach this acceleration level.

It is observed that the obtained distributions are very similar for both simulation methods, as expected. However, the obtained distribution is not unimodal, due to the existence of two distinct types of response: resonant and non-resonant behaviour. This provides an interesting opportunity to check on how the complexity of the response affects the efficiency of the different methodologies. The estimated probabilities of failure for the different methods are summarized in Table 6, whereas Table 7 shows the required number of simulations to accurately assess the probability of failure due to track instability.

Speed (km/h)	MC	LH	GPD-MC	GPD-LH	ES-MC (C^- ; C^+)	ES-LH (C^- ; C^+)
275	0.20	< 0.1	0.05	0.14	0.08 (0.06 ; 0.31)	0.08 (0.03 ; 0.22)
280	0.40	0.50	0.58	0.70	0.44 (0.26 ; 1.47)	0.48 (0.24 ; 1.24)
285	1.40	1.33	1.32	1.03	1.45 (0.81 ; 3.55)	1.19 (0.82 ; 3.49)
290	5.80	2.67	5.17	4.93	4.40 (2.94 ; 8.17)	3.76 (2.11 ; 8.24)
295	10.30	8.33	13.00	7.81	10.80 (7.45 ; 21.1)	10.30 (8.21 ; 14.4)

Table 6: Estimated probability of failure due to track instability ($\times 10^{-4}$).

Speed (km/h)	GPD-MC	GPD-LH	ES-MC	ES-LH
275	8000	8000	3000	9000
280	14000	7000	3000	4000
285	15000	25000	3000	3000
290	6000	7000	3000	3000
295	5000	5000	2000	9000

Table 7: Number of simulations required to accurately assess the probability of failure due to track instability.

Compared to the GPD approach the ES proves to be more efficient, resulting in reducing the necessary number of simulations to slightly less than 30% (less 34,000 simulations) for the MC simulation and a little over 50% (less 24,000 simulations) for the LH simulation. Regarding the influence of the complexity of the limit state function it became evident that if the response is not monotonic the LH may cause problems thus affecting the efficiency of the ES procedure. Furthermore, it was shown that if the computational costs can be reduced through a refined simulation method then the use of the ES approach will result in even further benefits. Another important feature of the ES procedure that should be pointed out is the fact that it enables quantifying the uncertainties of the estimated probability of failure, thus providing an extra tool to assess the quality of the failure estimation. The GPD approach seems to be much more sensitive to the level of irregularity of the tail of the distribution rather than the complexity of the limit state.

Globally, the safety assessment due to excessive deck acceleration can be accurately analysed with 14,000 simulations by enhanced MC simulation for the critical speed range (275 – 295 km/h). In order to guarantee the track stability the train speed over the bridge should be limited to 280 km/h.

5 CONCLUSIONS

The current work is focused on assessing the efficiency of different probabilistic methodologies for the safety assessment of short span railway bridges. A composite bridge with six simply supported spans of 12 m and ballasted track was selected as case study for the crossing of the TGV-double high-speed train. The variability of parameters related to the bridge, the track and the train were taken into account along with the existence of track irregularities. The selected case study offers the possibility of analysing a failure modes that is characterized by a non-unimodal distribution limit state functions.

Two different simulation techniques (Monte Carlo and Latin Hypercube) are combined with two different procedures: a tail modelling approach based on the extreme value theory that uses the Generalized Pareto Distribution to model the upper tail of the obtained distribution, and an Enhanced Simulation technique which uses an approximation procedure based on the estimates of the failure probabilities at moderate levels for the prediction of the far tail failure probabilities.

The ES approach proves to be more efficient than the GPD, resulting in reducing the necessary number of simulations to slightly less than 30% (less 34,000 simulations) for the MC

simulation and a little over 50% (less 24,000 simulations) for the LH simulation. It also became evident that if the response is not monotonic the LH may cause problems thus affecting the efficiency of the ES procedure. Furthermore, it was shown that if the computational costs can be reduced through a refined simulation method then the use of the ES approach will result in even further benefits. The ES procedure benefits from another important feature which is the fact that it enables quantifying the uncertainties of the estimated probability of failure. This provides an extra tool to assess the quality of the failure estimation. Regarding the GPD approach it seems to be much more sensitive to the level of irregularity of the tail of the distribution rather than the complexity of the limit state.

Globally, the safety assessment due to excessive deck acceleration can be accurately analysed with 14,000 simulations by enhanced MC simulation for the critical speed range (275 – 295 km/h). In order to guarantee the track stability the train speed over the bridge should be limited to 280 km/h.

REFERENCES

[1] Rubinstein, R.Y., *Simulation and the Monte Carlo method*. New York: John Wiley and Sons, 1981.

[2] Mckay M. D., Beckman R. J., Conover W. J., A comparison of three methods for selecting values of input variables in the analysis of output from a computer code. *Technometrics*, **21**, 2: 239–245, 1979.

[3] Naess, A., Leira, B.J., Batsevych, O., System reliability analysis by enhanced Monte Carlo simulation. *Structural Safety*, **31**, 349-355, 2009.

[4] Ramu, P., Kim, N. H., Haftka, R. T., Multiple tail median approach for high reliability estimation. *Structural Safety*, **32**, 124-137, 2010.

[5] Rocha, J. M., Henriques, A. A., Calçada, R., Probabilistic safety assessment of a short span high-speed railway bridge. *Engineering Structures*, **71**, 99-111, 2014.

[6] Rocha, J. M., Henriques, A. A., Calçada, R. Probabilistic assessment of the train running safety on a short span high-speed railway bridge. *Structure and Infrastructure Engineering*, http://dx.doi.org/10.1080/15732479.2014.995106, 2014.

[7] Castillo E., *Extreme value theory in engineering*. San Diego, USA: Academic Press, 1988.

[8] Rocha, J. M., Henriques, A. A., Calçada, R., Safety assessment of a short span railway bridge for high-speed traffic using simulation techniques. *Engineering Structures*, **40**, 141-154, 2012.

[9] Manterola J., *Puentes: apuntes para su diseño, cálculo y construcción*. Servicio de Publicaciones del Colegio de Caminos, Canales y Puertos, 2006 [in Spanish].

[10] ERRI D-214/RP 9. *Rail bridges for speeds > 200 km/h. Final report*. Utrecht: European Rail Research Institute (ERRI), 1999.

[11] Frỳba, L. Dynamics of railway bridges. London: Thomas Telford, 1996.

[12] EN13484-5. *Railway applications - Track - Track geometry quality - Part 5: Geometric quality levels*. European Committee for Standardization (CEN), Brussels, 2008.

[13] Joint Committee on Structural Safety (JCSS). *Probabilistic Model Code – 12th draft*, 2001. (http://www.jcss.ethz.ch/).

[14] Zacher, M., Baeβler, M., Dynamic behaviour of ballast on railway bridges. In: *Proceedings of Dynamics of High-Speed Railway Bridges*. London: Taylor & Francis, 2009.

[15] EN1991-2. *Eurocode 1 - part 2: Actions on structures - traffic load on Bridges*. European Committee for Standardization (CEN), Brussels, 2003.

COMPDYN 2015
5th ECCOMAS Thematic Conference on
Computational Methods in Structural Dynamics and Earthquake Engineering
M. Papadrakakis, V. Papadopoulos, V. Plevris (eds.)
Crete Island, Greece, 25–27 May 2015

OPTIMAL DESIGN AND DYNAMICS OF TRUSS BRIDGES

G. Carpentieri[1], M. Modano[2], F. Fabbrocino[3] and F. Fraternali[1]

[1]Department of Civil Engineering , University of Salerno
Via Giovanni Paolo II, 132, 84084, Fisciano (SA), Italy
e-mail: gcarpentieri@unisa.it (G. Carpentieri), f.fraternali@unisa.it (F. Fraternali)

[2] Department of Structural Engineering, University of Naples
80132, Naples (NA), Italy
e-mail: modano@unina.it (M. Modano)

[3] Department of Engineering, Pegaso Telematic University
80132, Naples (NA), Italy
e-mail: frfabbro@unina.it (F. Fabbrocino)

Keywords: Truss structures, Tensegrity, form-finding, minimum mass, optimal complexity, prestress, vibration modes.

Abstract. *Bridge structures have attracted the interest of Engineers throughout the history because they represent the attempt of men to overcome obstacles. Bridges allow easier connections between two different points and faster displacements of goods and people. The present work makes use of truss structures to search for the most efficient bridges. We first present numerical results for minimal mass truss bridge designs. Our approach creates a network of tensile and compressive members distributed throughout the system at many different scales. We leave the prestress calibration to a second step of our design strategy, to be carried out after the minimal mass topology has been determined, with the aim of optimizing the dynamic performance of the structure. A numerical example shows that the vibration modes of the examined bridge model can be tuned by playing with the prestress of the deck members.*

1 INTRODUCTION

Tensegrity structures are axially loaded prestressable structures. Motivated by nature, where tensegrity concepts appear in every cell, in the molecular structure of the spider fiber, and in the arrangement of bones and tendons for control of locomotion in animals and humans, Engineers have only recently developed efficient analytical methods to exploit tensegrity concepts in engineering design. Previous attempts to judge the suitability of tensegrity for engineering purposes have simply evaluated the tensegrity produced as art-forms, but then judges them according to a different (engineering) criteria. The development of "tensegrity engineering" should allow tensegrity concepts to be optimized for the particular engineering problem at hand, rather than simply evaluating a structure designed only for artistic objectives. The development of such tensegrity engineering methods is the continuing goal of our research.

The tensegrity paradigm used for bridges in this paper allows the marriage of composite structures within the design. Our tensegrity approach creates a network of tension and compressive members distributed throughout the system at many different scales (using tensegrity fractals generates many different scales). Furthermore, these tension and compression members can simultaneously serve multiple functions, as load-carrying members of the structure, and as sensing and actuating functions. Moreover, the choice of materials for each member of the network can form a system with special electrical properties, special acoustic properties, special mechanical properties (stiffness, etc). The mathematical tools of this paper can be used therefore to design metamaterials and structural networks (cf., e.g., [1–9]) with unusual and very special properties not available with normal design methods.

This paper focuses on bridge design for minimal mass. The subject of form-finding of tensegrity structures continues to be an active research area [10–15], due to the special ability of such structures to serve as controllable systems (geometry, size, topology and prestress control), and also because the tensegrity architecture provides minimum mass structures for a variety of loading conditions, [16–19]. Particularly interesting is the use of fractal geometry as a form-finding method for tensegrity structures, which is well described in [16–18, 20]. Such an optimization strategy exploits the use of fractal geometry to design tensegrity structures, through a finite or infinite number of self-similar subdivisions of basic modules. The strategy looks for the optimal number of self-similar iterations to achieve minimal mass or other design criteria. This number is called the optimal *complexity*, since this number fixes the total number of parts in the structure.

The self-similar tensegrity design presented in [16–18] is primarily focused on the generation of *minimum mass* structures, which are of great technical relevance when dealing with tensegrity bridge structures (refer, e.g., to [21]). The 'fractal' approach to tensegrity form-finding paves the way to an effective implementation of the tensegrity paradigm in *parametric architectural design* [11, 12, 22, 23].

Designing tensegrity for engineering objectives has produced minimal mass solutions for five fundamental (but planar) problems in engineering mechanics. Minimal mass for tensile structures, (subject to a stiffness constraint) was motivated by the molecular structure of spider fiber, and may be found in [24]. Minimal mass for compressive loads may be found in [16]. Minimal mass for cantilevered bending loads may be found in [17]. Minimal mass for torsional loads may be found in [18]. Discussions of minimal mass solutions for distributed loads on simply-supported spans, where significant structure is not allowed below the roadway, may be found in [25]. It is also worth noting that tensegrity structures can serve multiple functions. While a cable is a load-carrying member of the structure, it might also serve as a sensor or

actuator to measure or modify tension or length. Other advantages of tensegrity structures are related to the possibility to integrate control functions within the design of the structure. A grand design challenge in tensegrity engineering is to coordinate the structure and control designs to minimize the control energy and produce a structure of minimal mass. This would save resources (energy and mass) in two disciplines, and therefore "integrate" the disciplines [26].

This paper reviews the minimum mass design of tensegrity structures carrying distributed bending loads (Sects. 2, 3), which has been diffusely presented in [25], and investigates on the vibration modes of the examined bridge model by varying the state of prestress applied to the structure (Sect. 4). Prestress design is a typical feature of tensegrity systems. The procedure illustrated in [25] returns the minimal mass structure, for a given loading condition, together with a certain prestress state. By changing such a prestress, while increasing the mass, one can improve the ability of a structure to tolerate larger uncertainties in the external loading, and avoid slackening problems in cables. We leave the prestress calibration to a second step of our design strategy, to be carried out after the minimal mass topology has been determined, with the aim of optimizing the dynamic performance of the structure.

2 TENSEGRITY BRIDGE MODEL

In a famous work dated 1904, A.G.M. Michell examines the problem of finding the minimum volume network of fully stressed truss elements, which transmit a vertical force applied at the middle point C of a given segment AB to two fixed hinge supports applied at A and B [27]. On pages 594-597 of this work, Michell deals with a truss network spanning a 2D continuous domain including the points A, B and C along its boundary (*centrally loaded beam*), and assumes that the material of such a domain is homogenous. Without entering the mathematical aspects of Michell's problem (refer, e.g., to [28]), we notice that the Michell topology under consideration includes a portion DE of a circumference centered in C, the segments DA and EB lying on the tangents in D and F to the arch DE, and all the radii of the circular sector CDE (cf. Fig. 1, where the compressive elements (or *bars*) of the Michell frame are represented through thick black lines, while the tensile elements (or *strings*) are represented through thin red lines). Such a topology can be applied to both the regions placed above and below the applied force F, with the difference that the arch ADEB (hereafter also called Michell arch) works in compression and the radii pointing to C work in tension in the first case (Fig. 1, top), while, on the contrary, the arch ADEB works in tension and the radii pointing to C work in compression in the second case (Fig. 1, bottom). It is worth noting that the central angle of the circular sector CDE gets larger and larger, as the angle α (or β) gets closer and closer to 90 deg (Fig. 1).

We here introduce a parametric model of a tensegrity bridge obtained through n self-similar subdivisions of a basic module. This module is formed by a single Michell arch showing p radii, placed above the deck of the bridge, and two arches, each of them showing $q = p$ radii, placed below the deck. Such a bridge is constrained by a fixed hinge support at one end of the deck, and a rolling hinge support at the other end. We show the basic module corresponding to $n = p = 1$ in Fig. 2, while more complex shapes corresponding to higher values of n and p are shown in Fig. 3 of [25]. Notice how each arch above the deck features p radii, and each arch below the deck features q radii, with $p = q$. The angles α and β can assume arbitrary values, and the horizontal elements at the level of the deck (represented through blue lines in Fig. 2) can work either in tension or in compression (*bidirectional elements*, cf. [19]). Such elements provide the horizontal components of the lateral (supporting) forces of the Michell arch (Fig. 1). The basic module shown in Fig. 2 exhibits a single compressed arch above the deck, two

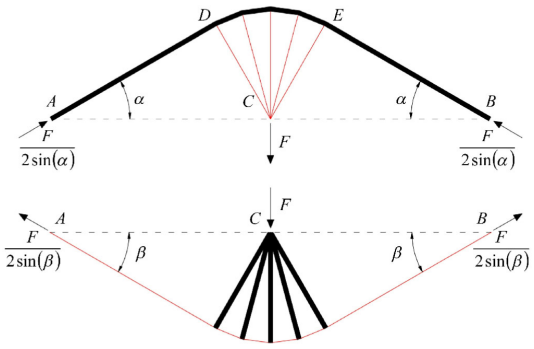


Figure 1: Michell frames for a centrally loaded beam.

tensile chords below the deck and a subdivision of the deck into four elements of equal length. Hereafter, we let f denote the total force transferred from the deck to the bridge structure. For $n > 1$, we assume that the elements of the nested arches placed above the deck can overlap each other. Moreover, to consider a common requirement for bridges over navigable water, we discard the outer arches placed below the deck (indicated by dotted lines in Fig. 3 of [25]), in order to reduce the size of the substructure below the deck, for clearance above the water. In a real bridge structure, the elements placed above the deck would have a 3D geometry that prevents member overlapping. It is worth noting that the geometry corresponding to an arbitrary number n of self-similar subdivisions of the basic module features 2^{n+1} elements at the level of the deck, and show nodal forces equal to $f/(2^{n+1})$ in correspondence with the intermediate nodes placed at the level of the deck. The following variables completely define the geometry of the bridge structure: the total span L, the 'top aspect angle' α, the 'bottom aspect angle' β, and the complexity parameters n, p and q. The total numbers of top arches, n_{ta}, bottom arches, n_{ba}, strings, n_s, bars, n_b, and nodes, n_n, are given by:

$$n_{ta} = 2^n - 1, \quad n_{ba} = 2^n, \tag{1}$$

$$n_s = q n_{ta} + (p+1)\, n_{ba} + 2^{n+1}, \quad n_b = (q+1)\, n_{ta} + p n_{ba} + 2^{n+1}, \tag{2}$$

$$n_n \;=\; q\; n_{ta} + p\; n_{ba} + 2^{n+1} + 1. \tag{3}$$

As to the node coordinates, we observe that the nodes belonging to the 'superstructure' (i.e., the portion of the bridge placed above the deck) lie on n nested circumferences with radii R_{t_i} $(i = 1, ..., n)$, while the nodes of the 'substructure' instead lie on sequential circumferences with radius R_b. Such radii are computed as follows

$$R_{t_i} = \frac{L}{2^i} \sin\alpha, \;\; (i = 1, ..., n); \quad R_b = \frac{L}{2^n} \sin\beta. \tag{4}$$

We look for the optimal values of the complexity parameters n, p and q and the aspect angles α and β, which minimize the mass of the bridge under yielding and buckling constraints. As anticipated, we prescribe $q = p$ and we assume that all bars and strings are made up of the same material, for the sake of simplicity. The removal of such constraints is not a big issue from the theoretical point of view, but might lead to a significant increase in the number of optimization variables.

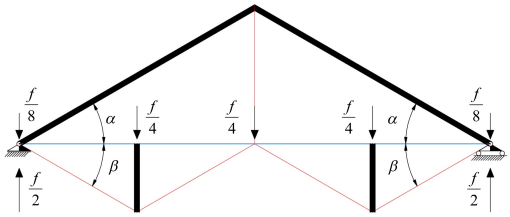


Figure 2: Basic module of the tensegrity bridge ($n = 1$, $p = 1$).

3 MINIMAL MASS DESIGN

In this section we present a collection of numerical results extracted from [25], which aim to illustrate the potential of the minimum mass design under consideration. We use the symbols μ^*, α^* and β^* to denote the minimum mass and the optimal aspect angles of the tensegrity bridge under combined yielding and buckling constraints, respectively, and the symbols μ_Y^*, α_Y^* and β_Y^* to denote the optimal values of the same quantities under simple yielding constraints. In all the examples, we search for a global minimum mass configuration of the bridge, by recursively running the optimization procedure presented in [25], so that the design variables n, p, α and β may range within prescribed search domains. We set the step increments of n and p to 1, the step increments of α and β to 0.01 deg. In addition, we set L, f and ρ to unity, in abstract units, and make use of the following assumptions: $\bar{\sigma}_Y = 6.9 \times 10^8 L^2/f$; $E = 2.1 \times 10^{11} L^2/f$. In order to highlight the relative 'weight' of the elements placed at the level of the deck, we introduce the following ratios,

$$\frac{\mu_{db}^*}{\mu_b^*}, \quad \frac{\mu_{ds}^*}{\mu_s^*}. \tag{5}$$

where μ_{db}^*, μ_{sb}^*, μ_b^*, μ_s^* denote the total mass of the bars placed at the level of the deck, the total mass of the strings placed at the level of the deck, the overall mass of the bars and the overall mass of the strings, respectively, in correspondence with any arbitrary minimum mass configuration under combined yielding and buckling constraints. We remind the reader that the elements placed at the level of the deck are bidirectional, in the sense that they can contemporarily serve as bars or strings [19].

The examined minimum mass design assumes that all the design variables n, p, α, and β may simultaneously vary within the following bounds,

$$n \in [1, 5], \quad p \in [1, 7], \quad \alpha \in (0, 90) \text{ deg}, \quad \beta \in (0, 90) \text{ deg}. \tag{6}$$

The most relevant results corresponding to the present case are illustrated in Tab. 1 and Fig. 3. The results in Tab. 1 highlight that the global minimum mass configuration under combined yielding and buckling constraints is reached for $n = 2$, $p = 7$ ($\mu^* = 333.17$, $\alpha^* = 62.52$ deg, $\beta^* = 17.77$ deg), within the search domain (6). Referring to the case with $n = 2$, in order to detect if the global minimum mass configuration is obtained for finite complexity p or not, we let this parameter grow up to $p = 13$, and determine the corresponding relative minimum mass configurations of the bridge. We find out that the mass of the bridge monotonically decreases when p grows from 1 to 13, and n remains equal to 2. In particular, the relative minimum mass configuration for $n = 2$ and $p = 13$ is the following: $\mu^* = 225.98$, $\alpha^* = 69.45$ deg, $\beta^* = 23.97$ deg. Such results, together with those presented in Tab. 1, indicate that the global minimum mass configuration of the bridge might be achieved either for rather large values of p, or in the limit $p \to \infty$, when $n \geq 2$.

n	p	α_Y^*	β_Y^*	μ_Y^*	α^*	β^*	μ^*
1	1	41.83	24.11	1.1180	26.11	13.77	808.84
1	11	54.44	34.97	0.9867	53.42	33.97	337.69
1	20	54.65	35.18	0.9855	51.98	32.60	352.24
2	1	44.62	9.34	1.5207	26.58	4.77	1086.23
2	3	57.81	14.83	1.3329	45.20	9.53	558.02
2	7	66.42	20.90	1.2534	62.52	17.77	333.17
3	1	44.96	4.08	1.7545	26.58	2.05	1186.33
3	3	59.52	6.92	1.5232	45.31	4.13	607.67
3	7	72.52	12.78	1.4137	63.71	8.23	354.03
4	1	44.96	1.91	1.8761	26.58	1.03	1221.82
4	3	59.73	3.27	1.6256	45.31	1.93	625.75
4	7	75.51	7.35	1.5021	63.82	3.88	363.95
5	1	45.01	0.93	1.9378	26.58	0.75	1234.39
5	3	59.92	1.60	1.6784	45.32	1.44	632.19
5	7	76.80	3.96	1.5489	63.83	1.88	367.65

Table 1: Selected results for the minimal mass design of the examined bridge model.

By adding gravity forces [19], and referring to the case with $n = 2$ and $p = 13$, we obtain $\mu^* = 227.49$, $\alpha^* = 69.48$ deg, and $\beta^* = 23.52$ deg. Such results show that the inclusion of self-weight does not cause a significant change of the minimum mass configuration at hand. As to the elements placed at the level of the deck, we observe the following results: $\mu_{db}^*/\mu_b^* \ll 1$, and $\mu_{ds}^*/\mu_s^* \ll 1$, for $n \leq 3$. The ratio μ_{ds}^*/μ_s^* becomes relevant for $n > 3$, being equal to 0.06 for $n = 4$ and $p = 1$, and 0.3 for $n = 5$ and $p = 1$. Nevertheless, the same ratio decreases with p for fixed n, being equal to $\approx 10^{-4}$ for $n = 4$ and $p = 7$, and $\approx 10^{-5}$ for $n = 5$ and $p = 7$. We can therefore conclude that such elements serve as tensile members (strings) for $n > 1$, and that their structural relevance increases with n and decreases with p. It is also seen from Tab. 1 that, in each of the examined cases, the optimal values of α very slowly increase with n, and rather markedly increase with p. The optimal values of β instead markedly decrease with n, and significantly increase with p. It is worth noting that the two examined design strategies (simple yielding constraints and combined yielding and buckling constraints) lead to rather different aspect ratios of the bridge for $p = 1$, and, on the contrary, to more similar geometries as p gets larger, for any given n (cf. Tab. 1). The results shown in Fig. 3 emphasize that the current minimum mass design of the bridge leads to rather large values of α and considerably small values of β, as the complexity parameters n and p progressively increase. In particular, the bottom height of the bridge dramatical shrinks for $n \geq 3$ (Fig. 3). This is explained by observing that the lower chords of the bridge carry tensile forces $t_{ba} = \frac{f_n}{2Sin(\beta)}$ (cf. Fig. 1), with $f_n = f/(2^{n+1})$. As n goes to infinity and β goes to zero, it can be verified that t_{ba} approaches a finite limit. The solution with $\beta \to 0$ becomes convenient in terms of mass savings as $n \to \infty$, since it reduces the lengths of the tensile chords and compressed rays placed below the deck. We wish to remark, however, that the global minimum mass configuration is achieved for $n = 1$ under simple yielding constraints, and $n = 2$ under combined yielding and buckling constraints.

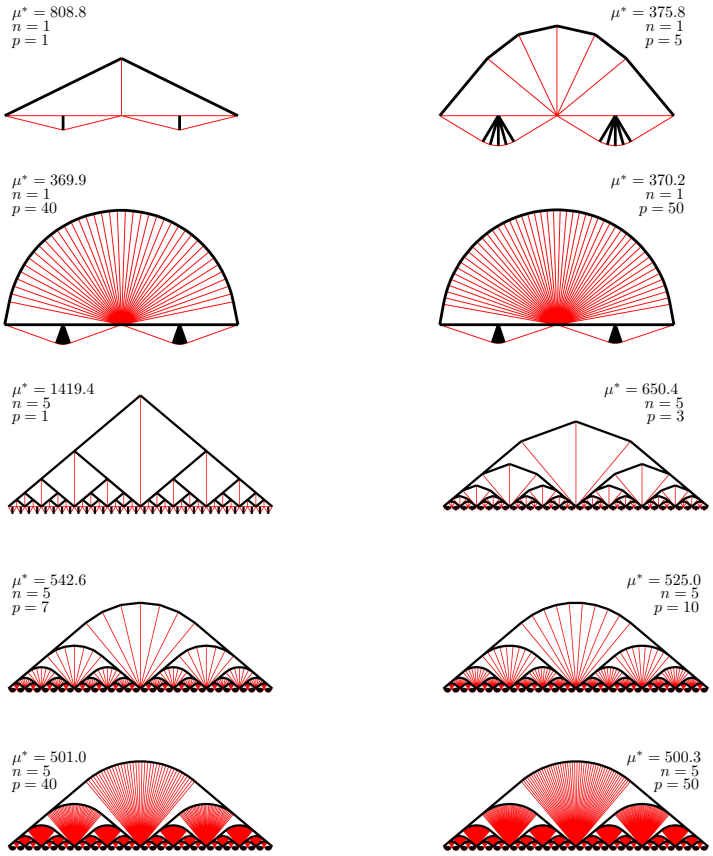


Figure 3: Optimal topologies under combined yielding and buckling constraints for different values of the examined design variables.

4 VIBRATION MODES

It is worth noting that the minimal mass design illustrated in the previous section leads to statically determinate structures with no applied prestress. Nevertheless, the prestress design is of great importance for a number of properties of tensegrity structures, including structural stiffness, stability and dynamics (refer, e.g., to [10–15, 29] and references therein). In particular, an optimal prestress design oriented to control the free vibration modes and frequencies of the structure awaits attention, being at present only partially investigated in the literature [29].

We study the influence of the prestress design on the dynamical response of the present bridge model with reference to the the basic module in Fig. 2, assuming optimal aspect angles ($\alpha = 26.11\ deg$, $\beta = 13.77\ deg$). In order to allow statically indeterminacy, which is necessary to permit the existence of self equilibrated member forces, we replace the roller hinge support of such a structure with a fixed hinge. As a consequence, we allow the string elements placed at the level of the deck to be axially prestrained of an arbitrary quantity p (*deck prestrain*). The assumed material is steel for all members (Young modulus $E = 210\ GPa$, yield strength $\sigma_y = 690\ MPa$); the total span of the bridge is set equal to $30\ m$; and the total bridge weight (including the deck) is set equal to $450\ kN$.

Fig. 4 shows the first vibration modes of the basic module under zero deck prestress ($p = 0$), and deck prestress corresponding to $p = 10^{-3}$. We observe that the vibration mode of the prestressed structure is slightly different from that of the structure under zero prestress. As a matter of fact, the first vibration mode of the structure for $p = 10^{-3}$ features a ratio $\eta = 7.5$ between the vertical displacement at the central node of the deck and the vertical displacements

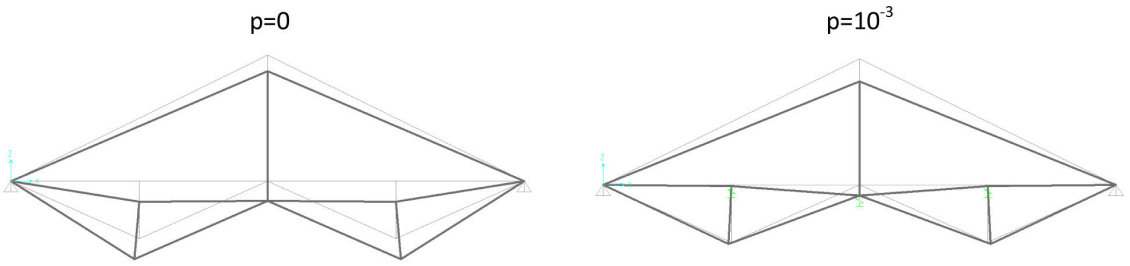


Figure 4: First vibration mode for different prestrains of deck members.

at the nodes of the deck placed at one quarter of the bridge span, i.e. prevalent vertical deflection at the midspan (cf. Fig. 4-right). The vibration mode of the structure under zero prestress instead exhibits $\eta = 0.96$ (cf. Fig. 4-left), i.e. vertical displacements at the lateral nodes of the deck that are comparable to that of the central node. It is also with noting that the structure under $p = 0$ exhibits first natural frequency which is 3.5% lower than the first natural frequency of the structure undergoing $p = 10^{-3}$.

5 CONCLUDING REMARKS

A first goal of the present study has been concerned with the minimal mass design of tensegrity bridge structures. The forces, locations, and number of members of a parametric bridge model in 2D have been optimized to minimize mass subject to both buckling and yielding constraints. We have optimized the complexity of the structure, where structural complexity as the number of members in the design. This can be related to 3 parameters (n, p, q), where 2^n is the number of deck sections along the span; p is the number of compressive members (bars) reaching from the span center to the *substructure*; and q is the number of cables reaching from the span center to the *superstructure*. Hence we refer to (n, p, q) as the three different kinds of *complexities* of the structure. We used a tensegrity structural paradigm which allowed these several kinds of complexities. The complexity n has been determined by a self-similar law to fill the space of the bridge. As the number of self-similar iterations goes to infinity we get a tensegrity fractal topology. The numerical results presented in Sect. 3 have pointed out that the global minimum mass configuration of the examined bridge model shows finite complexity n, and markedly large or infinite complexities $p = q$. We can therefore conclude that such a bridge feature a multiscale, discrete-continuum complexity. Concerning the aspect ratios of the bridge, we have observed that, as the complexity n increases, the height of the portion of the bridge placed above the deck increases, while the height of the structure placed below the deck decreases dramatically.

An illustrative example regarding the first vibration mode of the basic module ($n = p = q = 1$) has demonstrated that the application of a state of prestress to the string elements placed at the deck level may significantly affect the geometry of such a mode and the associated natural frequency. A comprehensive study on the dynamics of tensegrity bridges will follow as future work, to impose suitable design constraints on stiffness issues (vibrational frequencies, mode shapes, displacements for high winds conditions, etc). It is worth noting, however, that the capability all of these choices and adjustments are within the free parameters of the designs in this work. The subsequent dynamics approach will evaluate the value (economics and performance tradeoffs) the use of feedback control for the deployable and service functions, or to adjust the stiffness of the structure (varying the prestress of the cables) to modify stiffness or damping after storm damage.

References

[1] C. Daraio, D. Ngo, V.F. Nesterenko, F. Fraternali, Highly nonlinear pulse splitting and recombination in a two-dimensional granular network. *Physical Review E*, 82:036603, 2010.

[2] D. Ngo, F. Fraternali, C. Daraio, Highly nonlinear solitary wave propagation in Y-shaped granular crystals with variable branch angles. *Physical Review E*, 85:036602, 2012.

[3] F. Fraternali, C.D Lorenz, G. Marcelli, On the estimation of the curvatures and bending rigidity of membrane networks via a local maximum-entropy approach. *Journal of Computational Physics*, **231**, 528-540, 2012.

[4] B. Schmidt, F. Fraternali, Universal formulae for the limiting elastic energy of membrane networks. *Journal of the Mechanics and Physics of Solids*, **60**, 172-180, 2012.

[5] F. Fraternali, L. Senatore, C. Daraio, Solitary waves on tensegrity lattices. *Journal of the Mechanics and Physics of Solids*, **60**, 1137-1144, 2012.

[6] F. Fraternali, I. Farina, G. Carpentieri. A discrete-to-continuum approach to the curvatures of membrane networks and parametric surfaces. *Mechanics Research Communications*, **56**, 18-15, 2014.

[7] A. Amendola, F. Fraternali, G. Carpentieri, M. de Oliveira, R. E. Skelton, Experimental investigation of the softening-hardening response of tensegrity prisms under compressive loading. *Composite Structures*, **117**, 234-243, 2014.

[8] F. Fraternali, G. Carpentieri, A. Amendola, On the mechanical modeling of the extreme softening/hardening response of axially loaded tensegrity prisms. *Journal of the Mechanics and Physics of Solids*,**74**, 136-157, 2015.

[9] F. Fraternali, G. Carpentieri, A. Amendola, R. E. Skelton, V. F. Nesterenko, Multiscale tunability of solitary wave dynamics in tensegrity metamaterials. *Applied Physics Letters*, **105**, 201903, 2014.

[10] K. Koohestani, Form-finding of tensegrity structures via genetic algorithm. *International Journal of Solids and Structures*, 49,739–747, 2012.

[11] L. Rhode-Barbarigos, H. Jain, P. Kripakaran, I.F.C. Smith, Design of tensegrity structures using parametric analysis and stochastic search. *Engineering with Computers*, 26(2),193–203, 2010.

[12] T. Sakamoto , A. Ferrè, M. Kubo, (Eds.), *From Control to Design: Parametric/Algorithmic Architecture*, Actar, 2008.

[13] T. Sokóf, G.I.N. Rozvany, New analytical benchmarks for topology optimization and their implications. Part I: bi-symmetric trusses with two point loads between supports. *Structural and Multidisciplinary Optimization*, 46,477–486, 2012.

[14] A.G. Tilbert, S. Pellegrino, Review of form-finding methods for tensegrity structures. *International Journal of Space Structures*, 18,209–223, 2011.

[15] M. Yamamoto, B.S. Gan, K. Fujita, J. Kurokawa, A genetic algorithm based form-finding for tensegrity structure. *Procedia Engineering*, 14,2949–2956, 2011.

[16] R.E. Skelton, M. de Oliveira, Optimal complexity of deployable compressive structures. *Journal of The Franklin Institute*, 347,228–256, 2010.

[17] R.E. Skelton, M. de Oliveira, Optimal tensegrity structures in bending: the discrete Michell truss. *Journal of The Franklin Institute*, 347,257–283, 2010.

[18] R.E. Skelton, M. de Oliveira, *Tensegrity Systems*. Springer, 2010.

[19] K. Nagase, R.E. Skelton, Minimal mass tensegrity structures. *Journal of the International Association for Shell and Spatial Structures*, 55(1), 37–48, 2014.

[20] F. Fraternali, A. Marino, T. El Sayed, A. Della Cioppa, On the Structural Shape Optimization through Variational Methods and Evolutionary Algorithms. *Mechanics of Advanced Materials and Structures*, 18,224–243, 2011.

[21] N. Bel Hadj Ali, L. Rhode-Barbarigos, A.A. Pascual Albi, I.F.C. Smith, Design optimization and dynamic analysis of a tensegrity-based footbridge. *Engineering Structures*, 32(11),3650–3659, 2010.

[22] M.C. Phocas, O. Kontovourkis, M. Matheou, Kinetic hybrid structure development and simulation. *International Journal of Architectural Computing*, 10(1), 67–86, 2012.

[23] W.F. Baker, L.L. Beghini, A. Mazurek, L. Carrion, A. Beghini, Maxwell's reciprocal diagrams and discrete Michell frames. *Structural and Multidisciplinary Optimization*, Online first, DOI 10.1007/s00158-013-0910-0, 2013.

[24] R.E. Skelton, K. Nagase, Tensile tensegrity structures. *International Journal of Space Structures*, 27,131–137, 2012.

[25] R.E. Skelton, F. Fraternali, G. Carpentieri, A. Micheletti, Minimum mass design of tensegrity bridges with parametric architecture and multiscale complexity. *Mechanics Research Communications*, 58, 124–132, ISSN 0093-6413, doi: 10.1016/j.mechrescom.2013.10.017, 2014.

[26] R.E. Skelton, Structural systems: a marriage of structural engineering and system science. *Journal of Structural Controll*, 9,113–133, 2002.

[27] A.G.M. Michell, The limits of economy of material in frame-structures. *Philosophical Magazine*, 8,589–597, 1904.

[28] G. Bouchittè, W. Gangbo, P. Seppecher, Michell trusses and lines of principal action, *Mathematical Models & Methods In Applied Sciences*, 18,1571–1603, 2008.

[29] S. Dalil Safaei, A. Eriksson, A., G. Tibert, Optimum pre-stress design for frequency requirement of tensegrity structures. *Blucher Mechanical Engineering Proceedings* 1(1), 1258–1270, 2014.

COMPDYN 2015
5th ECCOMAS Thematic Conference on
Computational Methods in Structural Dynamics and Earthquake Engineering
M. Papadrakakis, V. Papadopoulos, V. Plevris (eds.)
Crete Island, Greece, 25–27 May 2015

SEISMIC RESPONSE ANALYSIS OF A COUPLED VEHICLE- BRIDGE SYSTEM

Qing Zeng[1], Elias G. Dimitrakopoulos[1], and Themelina S. Paraskeva [1]

[1] Hong Kong University of Science and Technology
Department of Civil and Environmental Engineering, Kowloon, Clear Water Bay, Hong Kong
ilias@ust.hk

Keywords: Vehicle bridge interaction, truck modelling, earthquake engineering, seismic response, bridges, dynamic analysis.

Abstract. *Traditionally, the traffic and the seismic dynamics have been considered independently when analyzing the seismic response of bridges. Given the ever increasing traffic volume though, vehicles are more likely to encounter an earthquake while crossing a bridge. Hence, there is a growing need to examine the dynamic vehicle-bridge interaction (VBI) under the simultaneous action of seismic ground motions. This study presents an original framework to analyze the seismic response of a coupled vehicle-bridge system during earthquake excitation. The examined dynamical system consists of the vehicle subsystem and the bridge subsystem. The two subsystems are coupled through the contact forces between the vehicle wheels and the bridge. The bridge subsystem is simulated with the finite element method, while the truck vehicles are modelled as rigid body assemblies. The proposed approach relies on the calculation of the coupling contact forces, and results in a system of global equations which provides the response of both the bridge and the vehicle simultaneously. A pilot application of the proposed scheme to a realistic case of (highway) bridge – (truck) vehicles interaction is presented. In this context, the study brings forward new problems encountered when analyzing the seismic response of interacting vehicle-bridge systems. Specifically, the paper underlines the need to consider different positions of the vehicle/s (on the bridge) during earthquake shaking, and highlights the importance of selecting representative parameters for the speed, the number and type of vehicles, which should reflect the site-specific traffic characteristics.*

1 INTRODUCTION

The accumulative experience of past earthquakes (e.g., the 1989 Loma Prieta, the 1994 Northridge and 1995 Kobe earthquakes) unveils the devastating consequences of vehicle accidents due to (any type of) bridge failure [1, 2]. With bridges covering a significant percentage of the existing road network, in many earthquake-prone regions, and with the ever increasing traffic volume, the possibility of vehicles encountering an earthquake while crossing a bridge is also increasing. This observation underlines the growing need to investigate the seismic response of the interacting vehicle- bridge systems instead of focusing solely on the seismic analysis and/or assessment of bridges.

However, the dynamics of traffic and earthquake shaking have been traditionally considered independently when analyzing the response of the bridge. The existing codes and guidelines worldwide [3-5] account for the traffic load solely as an additional live load on the bridge. Research on vehicle - bridge dynamic interaction has shown [6-8] that it is not realistic to treat the vehicle as additional stationary mass; the seismic response of the bridge is reduced when the dynamics of the vehicles are properly simulated and it is amplified when the vehicles are treated as additional vertical masses.

There is a vast body of research on the seismic response of bridges detached from the running vehicles [9, 10], as well as, on the dynamic vehicle bridge interaction (VBI) without considering earthquake shaking (e.g. [11] and references therein). On the other hand, a limited amount of research focuses on the simulation of the effects of earthquakes on the interacting vehicle - bridge system. More specifically, Yang and Wu [12] investigated the stability of train vehicles, stationary or moving, on bridges shaken by earthquakes, and they stressed the importance of the vertical ground motion component on the stability of the vehicle. Tanabe et al. [13-15] studied numerically the behavior of the Shinkansen trains and railway bridges during earthquakes, and verified part of their results experimentally. Matsumoto et al.[16] examined the running safety of railway vehicles on bridges subjected to earthquakes using an in-house computer simulation software. Xia et al.[17] and Du et al. [18] concluded that the vehicle running safety during earthquakes is overestimated when not considering the seismic wave propagation effect.

Another group of studies focuses on the vehicle performance on bridges in windy environments [19-21]. Chen and Cai [22, 23] deployed a framework for the analysis of vehicle accidents on long-span bridges under strong winds. They conducted dynamic interaction analyses of the coupled vehicle-bridge-wind system to predict both the bridge and vehicle response. Zhang and Cai [24], presented an approach for fatigue reliability assessment of existing bridges also considering an interacting vehicle-bridge system. They examined the effects of the road surface condition, vehicle speed and annual traffic increase rate on the fatigue reliability index, using 3D bridge-truck interaction simulations.

The present research is motivated by the need to elucidate the VBI dynamics between vehicles and highway bridges, during seismic excitation. Recently, the authors proposed [11, 25] an analysis approach of the VBI problem for curved (or straight) bridges and different types of vehicles, without considering seismic excitations. Herein the analysis examines a realistic bridge model, and a truck vehicle model under the influence of seismic ground motion excitations. In this context, the study brings forward various new problems which arise when the traffic and seismic loading are accounted for simultaneously.

2 SEISMIC RESPONSE OF THE INTERACTING VEHICLE-BRIDGE SYSTEM: THE PROPOSED METHODOLOGY

The present paper proposes a new approach for the dynamic analysis of the vehicle-bridge interacting (VBI) systems under earthquake ground motions. The examined dynamical system consists of the vehicle subsystem and the bridge subsystem. The two subsystems are coupled through the contact forces between the vehicle wheels and the deck of the bridge. The study simulates the bridge with the finite element method and models the vehicle as a multibody assembly. The proposed approach derives from a previous work of Dimitrakopoulos and Zeng, on vehicle-bridge interaction between trains and straight, or curved in-plan, bridges [11]. The present study adjusts this approach for truck vehicles travelling along the bridge, and adds the simultaneous action of earthquakes.

The VBI problem can be divided into four parts: the simulation of (i) the bridge, (ii) the vehicle model, (iii) the interacting vehicle-bridge system and (iv) the earthquake ground motion shaking. As a first approach, the present study adopts a two-dimensional (2D) vehicle-bridge model. This simplifies the analysis procedure and makes it more economic in terms of computational cost. For brevity we keep the presentation of the VBI analysis short, as it is described in detail in [11, 25].

The finite element model of the bridge is built with the commercial software program, ANSYS [26]. The bridge is modeled with Euler-Bernoulli beam elements [27]. The stiffness matrix $\mathbf{K}^B$, the mass matrix $\mathbf{M}^B$ and the Rayleigh damping matrix $\mathbf{C}^B$ are then exported to an in-house MATLAB[28] algorithm, developed and verified, previously [11]. The equations of motion for the bridge can be written in a general form as:

$$\mathbf{M}^B(t)\ddot{\mathbf{u}}^B+\mathbf{C}^B\dot{\mathbf{u}}^B+\mathbf{K}^B\mathbf{u}^B+\mathbf{W}^B\boldsymbol{\lambda}=\mathbf{F}^B \tag{1}$$

where superscript $(\,)^B$ denotes the bridge subsystem; $\mathbf{u}^B$ is the bridge displacement vector; $\mathbf{F}^B$ is the vector of forces acting on the bridge, in this case the earthquake ground motion; $\mathbf{W}^B$ is the direction matrix of the contact forces for the bridge subsystem and $\boldsymbol{\lambda}$ $\boldsymbol{\lambda}_N$is the vector of the coupling contact forces. Since the analysis herein is 2D, three DOFs are considered per node: two displacements and one rotation with respect to the X-longitudinal and Z-vertical axis, respectively.

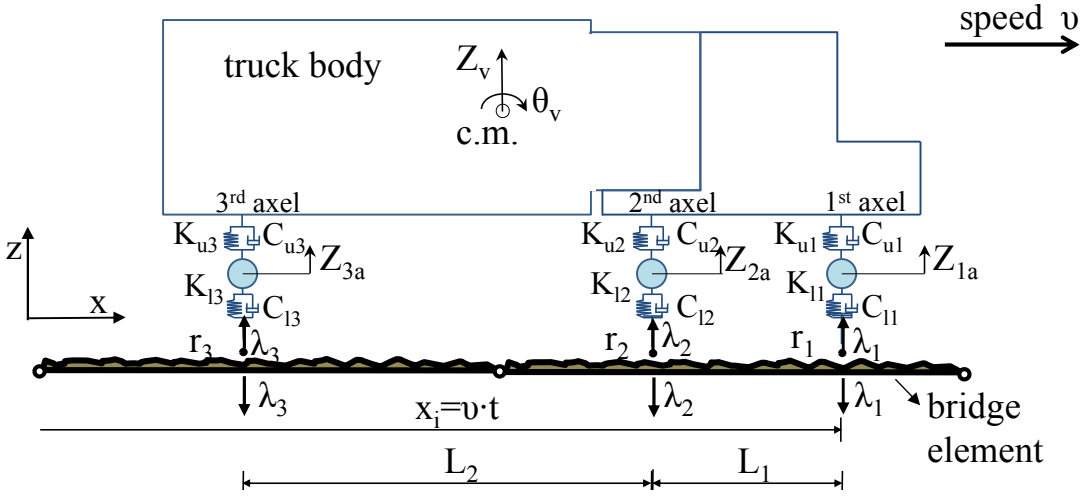


Figure 1: The adopted 3-axle 2D vehicle model.

The truck vehicles are modeled as assemblies of rigid-bodies (representing the car body and the wheel sets) connected with springs and dashpots [11, 23]. Figure 1 presents the *2D* vehicle model utilized in the present study (see for details in Section 3.2). The Newton- Euler equation of motion can describe the motion of the vehicle model in terms of generalized coordinates, as

$$\mathbf{M}^{\mathrm{V}}\ddot{\mathbf{u}}^{\mathrm{V}}+\mathbf{C}^{\mathrm{V}}\dot{\mathbf{u}}^{\mathrm{V}}+\mathbf{K}^{\mathrm{V}}\mathbf{u}^{\mathrm{V}}-\mathbf{W}^{\mathrm{V}}\boldsymbol{\lambda}=\mathbf{F}^{\mathrm{V}} \tag{2}$$

where: superscript $(\ )^{\mathrm{V}}$ denotes the vehicle subsystem; $\ddot{\mathbf{u}}^{\mathrm{V}}$ is the acceleration vector; $\mathbf{M}^{\mathrm{V}}$, $\mathbf{C}^{\mathrm{V}}$ and $\mathbf{K}^{\mathrm{V}}$ are the mass matrix, the damping matrix and the stiffness matrix of the vehicle, respectively; $\mathbf{F}^{\mathrm{V}}$ is the force vector, containing the gravity forces and the earthquake ground motion forces; and $\mathbf{W}^{\mathrm{V}}$ is the direction matrix of the contact forces.

The two sets of equations describing the motion of the bridge (Eq. 1) and the motion of the vehicle (Eq. 2) are coupled by the time-dependent contact forces $\boldsymbol{\lambda}$. Considering one single wheel at contact point j, the coupling contact force can be expressed as:

$$\lambda_{\mathrm{j}}=\mathrm{K}_{\mathrm{lj}}\left((\mathbf{W}^{\mathrm{Bj}})^{\mathrm{T}}\ \mathbf{u}^{\mathrm{B}}-Z_{\mathrm{ja}}+\mathrm{r}_{\mathrm{j}}\right)+\mathrm{C}_{\mathrm{lj}}\left((\mathbf{W}^{\mathrm{Bj}})^{\mathrm{T}}\ \dot{\mathbf{u}}^{\mathrm{B}}-\dot{Z}_{\mathrm{ja}}\right) \tag{3}$$

where: K_{lj} and C_{lj} are the stiffness and damping coefficients of the wheel at contact point j; r_{j} is the road roughness at that point; Z_{ja} and $\dot{Z}_{\mathrm{ja}}$ are the displacement and velocity of the wheel at j, respectively (Figure 1). The superscript $(\ )^{\mathrm{T}}$ denotes the transpose of a matrix.

The final form of the equation of motion of the coupled vehicle-bridge system is:

$$\mathbf{M}\ddot{\mathbf{u}}+\mathbf{C}^{*}\dot{\mathbf{u}}+\mathbf{K}^{*}\mathbf{u}=\mathbf{F}^{*} \tag{4}$$

The global stiffness matrix $\mathbf{K}^{*}$, the global damping matrix $\mathbf{C}^{*}$ and the force vector $\mathbf{F}^{*}$ are defined as:

$$\begin{aligned}\mathbf{K}^{*}&=\mathbf{K}+\mathbf{W}\mathbf{K}_{c}\mathbf{W}^{\mathrm{T}}\\ \mathbf{C}^{*}&=\mathbf{C}+\mathbf{W}\mathbf{C}_{c}\mathbf{W}^{\mathrm{T}}\\ \mathbf{F}^{*}&=\mathbf{F}+\mathbf{W}\mathbf{K}_{c}\mathbf{r}_{c}\end{aligned} \tag{5}$$

where, $\mathbf{r}_{c}$ is the road roughness vector [24] which is given as an expression of irregularities of the road surface [29]; $\mathbf{K}_{c}$ and $\mathbf{C}_{c}$ are the *diagonal* matrices of the stiffness and damping of the wheels (Figure 1), given as:

$$\mathbf{K}_{c}=diag[K_{l1}\quad K_{l2}\quad K_{l3}],\ \mathbf{C}_{c}=diag[C_{l1}\quad C_{l2}\quad C_{l3}] \tag{6}$$

The global mass matrix **M** (of Eq. (4)), the global stiffness matrix **K** and the global damping matrix **C** (of Eq. (5)) are created by gathering the pertinent matrices of the two individual subsystems together as:

$$\mathbf{M}=\begin{bmatrix}\mathbf{M}^{V} & \\ & \mathbf{M}^{B}\end{bmatrix},\quad \mathbf{K}=\begin{bmatrix}\mathbf{K}^{V} & \\ & \mathbf{K}^{B}\end{bmatrix},\quad \mathbf{C}=\begin{bmatrix}\mathbf{C}^{V} & \\ & \mathbf{C}^{B}\end{bmatrix} \tag{7}$$

Accordingly, the displacement vector **u**, the force vector **F** and the direction matrix **W** are:

$$\mathbf{u}=\begin{bmatrix}\mathbf{u}^{\mathrm{V}}\\ \mathbf{u}^{\mathrm{B}}\end{bmatrix},\ \mathbf{F}=\begin{bmatrix}\mathbf{F}^{\mathrm{V}}\\ \mathbf{F}^{\mathrm{B}}\end{bmatrix},\ \mathbf{W}=\begin{bmatrix}\mathbf{W}^{\mathrm{V}}\\ -\mathbf{W}^{\mathrm{B}}\end{bmatrix} \tag{8}$$

Further, this study assumes that the bridge elements and the wheels of the vehicle remain in contact without separation during the analysis.

The equations of motion of the interacting vehicle-bridge system (4) and (5) are numerically solved with MATLAB [28]

3 CASE STUDY: MODELLING, ASSUMPTIONS AND OBTAINED RESULTS

This paper presents a method for estimating the dynamic response of the interacting vehicle-bridge system under seismic excitation. The inelastic response of a bridge under strong ground motions is a topic that has been extensively covered in the literature, but it is not of interest for this study as it corresponds to strong ground motions. On the other hand, the lack of simultaneous consideration of earthquake and traffic loads is the primary motivation for the present analysis. In this study the focus is on R/C bridges that remain elastic during frequently occurring earthquakes.

3.1 Modelling of the adopted bridge

The bridge model adopted herein is based on an actual bridge configuration. The selected R/C highway bridge is a 3-span structure of 246.20m total length (Figure 2), constructed with the cantilever method. The deck consists of a 14.00m wide prestressed concrete box girder section. The spans of the deck have different lengths (63.80m+118.60m+63.80m). The height of the deck varies from 7.00m above the piers up to 3.00m at the midpoint of the middle span and to 2.50m above the abutments. The structure is supported on two single column piers (P1 and P2) of heights 36.00 m and 46.00 m. The deck is monolithically connected to the piers. Piers have a full height hollow rectangular cross section of 3.50m x 7.30m, with 0.74m wall thickness.

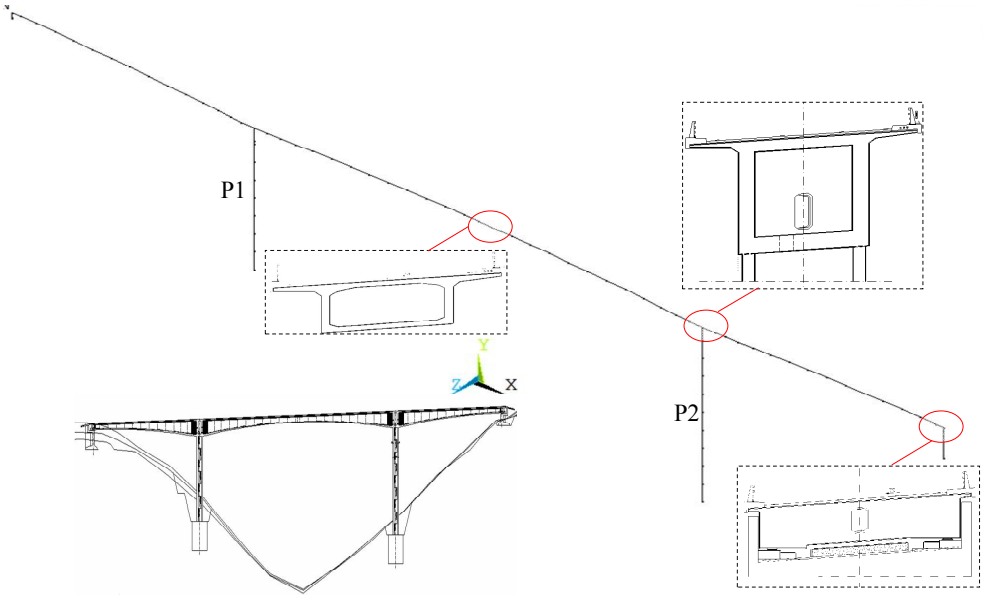


Figure 2: Layout of the bridge configuration and finite element model; inserts in Figure are the deck section (a) in the middle of each span, (b) on top of the piers and (c) on the top of the abutments.

The deck movement at the abutments is free in the longitudinal direction; in the transverse direction, the displacements are restrained by stoppers. The shear keys (Figure 2) at the specific part of the bridge, result in the restraint of the transverse displacements, as well as, the

displacement along and the rotation about the vertical axis. The bridge is assumed to be founded on very stiff soil therefore the boundary condition at the base of the piers is taken as a fully fixed support. Both the deck and the piers are designed to remain into the elastic range during the earthquake excitations.

3.2 Modeling the vehicle

The vehicle model should be representative of the actual traffic load anticipated. In order to define a representative vehicle type and its distribution, the traffic flow information is required. Under real-life conditions, multiple types of vehicles with different distribution patterns may occupy different lanes at the same time randomly. It is still technically difficult to conduct a coupled analysis using all possible vehicles together, based on simulated real traffic flow through current computer techniques. The common practice in analyzing the interaction between vehicles and bridges is to use only one type of vehicle alone or a series of identical vehicles in one line [22, 23, 30]. Therefore, in the present study, it is assumed that vehicles have the same truck geometry, number of axles, axle spacing and gross vehicle weight. The differentiation of the vehicle characteristics and their impacts on the bridge response are not investigated herein. In addition, the traffic loading is based on the assumption that the traffic flow is free-flowing and that traffic is only in a single lane of the bridge.

Parameter	*Description*	Value
Mass	Truck body	30.000 kg
	First axle suspension	490 kg
	Second axle suspension	808 kg
	Third axle suspension	653 kg
Spring stiffness	Upper, 1st axle (K_{u1})	242.604 N/m
	Lower, 1st axle (K_{l1})	875.082 N/m
	Upper, 2nd axle (K_{u2})	1903.172 N/m
	Lower, 2nd axle (K_{l2})	3503.307 N/m
	Upper, 3rd axle (K_{u3})	1969.034 N/m
	Lower, 3rd axle (K_{l3})	3507.429 N/m
Damping coefficient	Upper, 1st axle (C_{u1})	2.190 N.s/m
	Lower, 1st axle (C_{l1})	2.000 N.s/m
	Upper, 2nd axle (C_{u2})	7.882 N.s/m
	Lower, 2nd axle (C_{l2})	2.000 N.s/m
	Upper, 3rd axle (C_{u3})	7.182 N.s/m
	Lower, 3rd axle (C_{l3})	2.000 N.s/m
Length	L_1	2.90 m
	L_2	5.00 m
Total length of the truck	L	13.40 m

Table1: Parameters of the vehicle model (see Figure 1) [24].

The simulated vehicle model used herein is a three-axle truck with gross vehicle weight equal to 30t, which corresponds to a fully loaded truck [31], as shown in Figure 1. The truck body is assigned 2 DOFs: the vertical displacement of the center of mass of the rigid body expressed as Z_v, and the pitching displacement in x-z plane, θ_v. For each wheelset, only 1 DOF is designated: the vertical displacement in the central line of the j axle, Z_{ja}. The displacement vector $\mathbf{u}^V$ for each vehicle is:

$$\mathbf{u}^{V}=\left[Z_{v} \quad \theta_{v} \quad Z_{1a} \quad Z_{2a} \quad Z_{3a}\right]^{T} \tag{9}$$

Table 1 lists the main parameters [24] of the vehicle model used in this study.

Different numbers of vehicles during the earthquake excitation, as well as, different relative distance between them may have important impact on the dynamic response of the bridge. The present study, assumes a series of up to two vehicles moving along the side lane. The typical length of the selected truck is 13.40m. Therefore, a 2m full-stop bumber-to-bumber minimum gap [32] gives 15.40m required length for each truck on the deck. Based on this, we investigate the impact of three different values of relevant distances between the moving vehicles: (i) a distance of 5m, (ii) a distance of 20m and (iii) a distance of 50m, in order to ensure a variety of distances between the moving vehicles. In order to investigate the influence of the speed of the vehicles on the dynamic response of the bridge, we examine three vehicle speeds: (i) 90km/h (25.0 m/s), (ii) 70km/h (19.4 m/s) and (iii) 50km/h (13.8 m/s). In all cases, analyses are conducted with and without considering earthquake excitations.

3.3 Selection of the earthquake records

The aim of the present study is to explore the seismic response of interacting vehicle-bridge systems and not just to assess the seismic response of a bridge. The focus is on frequently occurring earthquake excitations, as they are more likely to happen. Therefore, we adopt a ground motion recorded (CDMG, station 1117) during the historic San Francisco earthquake (22/3/1957) with magnitude 5.28 (PEER) [33]. Specifically, both the east-west (E-W) and the upper-down (U-D) components are considered simultaneously along the longitudinal direction of the bridge, and the vertical axis of the system, respectively. The peak ground accelerations (PGA) are 0.1073g (or 1.053 m/s^2) in the X (longitudinal) direction, and 0.047g (or 0.46 m/s^2) in the Z (vertical) direction.

4 SEISMIC RESPONSE OF THE INTERACTING VEHICLE- BRIDGE SYSTEM

This study examines the following three scenarios: (i) the seismic response of the bridge neglecting the dynamics of the vehicles; (ii) the dynamic interaction between the moving truck vehicles and the bridge, not considering earthquake excitations; and (iii) the seismic response of the interacting vehicle-bridge system. First, a conventional time history response analysis of the bridge model is performed for the earthquake excitation of Section 3.3, without considering the influence of the traffic. Figure 3, illustrates the results in terms of vertical displacements of the midpoint of the bridge versus time. The results of the developed in-house MATLAB algorithm are identical with the pertinent results obtained from ANSYS [11].

Further, the present section examines the response of the interacting vehicle-bridge system considering (and not) the simultaneous action of earthquake ground motions. Interaction starts when the first vehicle enters the bridge and stops when the last vehicle leaves the bridge. Figure 4, illustrates the seismic response of the bridge in terms of vertical displacements of the midpoint of the deck, for three cases: (i) there is no vehicle moving on the bridge (standard approach); (ii) there is only one vehicle moving on the deck, and (iii) there are two vehicles, moving in line, with a relevant distance of 5m between them. For cases (ii) and (iii) it is assumed that vehicles move with a constant speed of 90km/h (or 25m/s). In addition, all the results assuming the earthquake occurs when the first truck enders the bridge. For the first four seconds of the analysis, the response of the midpoint of the bridge is the same for all cases independently of the presence of the moving vehicles. The influence of the trucks on the response of the particular node of the deck can be seen when the first vehicle is at a distance of 23.11m from the observed point. The presence of one vehicle (continuous black line) caus-

es an increase (from 0.2mm to 1.0mm) of the vertical displacements of the observed point, compared to the seismic response without considering the interacting vehicle-bridge system (black dashed line). Higher vertical displacements (up to 1.5mm) can be observed when two vehicles move along the deck (continuous grey line). The influence of the traffic on the response of the bridge stops when the last vehicle leaves the bridge, at 9.85s. As will be seen later, both the vehicle speed and the distance between the moving vehicles have important effect on the response of the bridge.

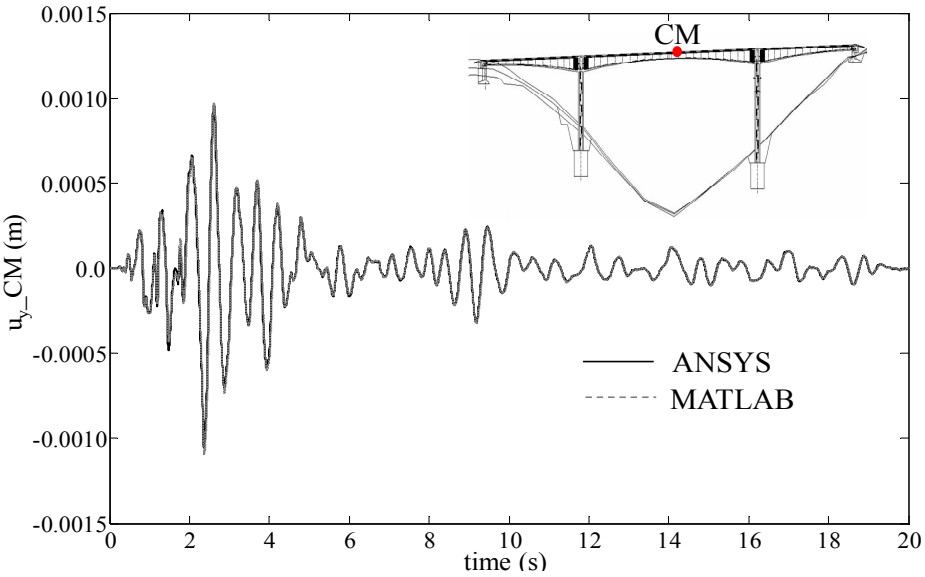


Figure 3: The vertical displacement time history of the midpoint of the bridge.

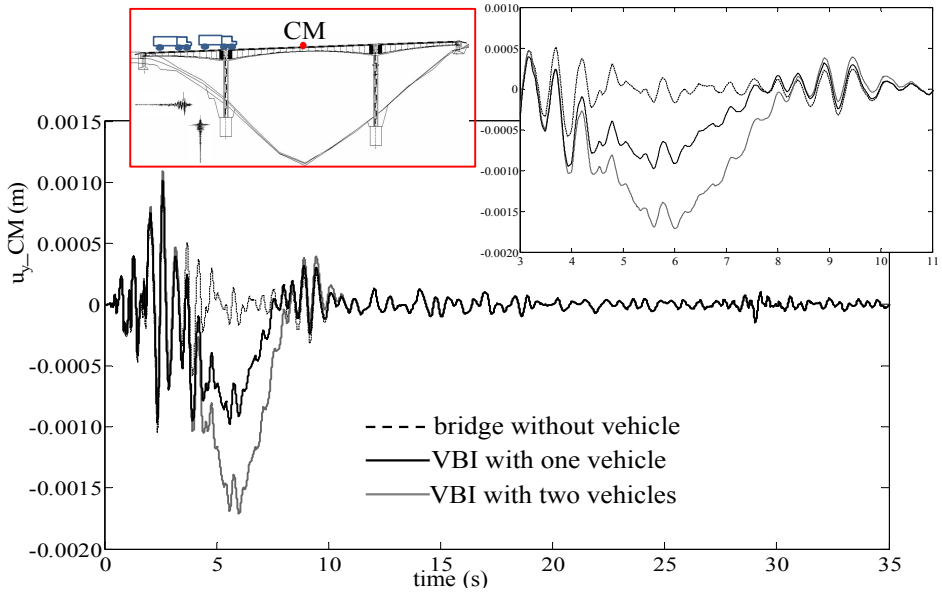


Figure 4: Seismic response of the bridge for the cases: (i) bridge without vehicles; (ii)VBI with one truck, and (iii)VBI with two trucks in line with a relevant distance equal to 5m. The speed of the vehicles 90km/h (25m/s).

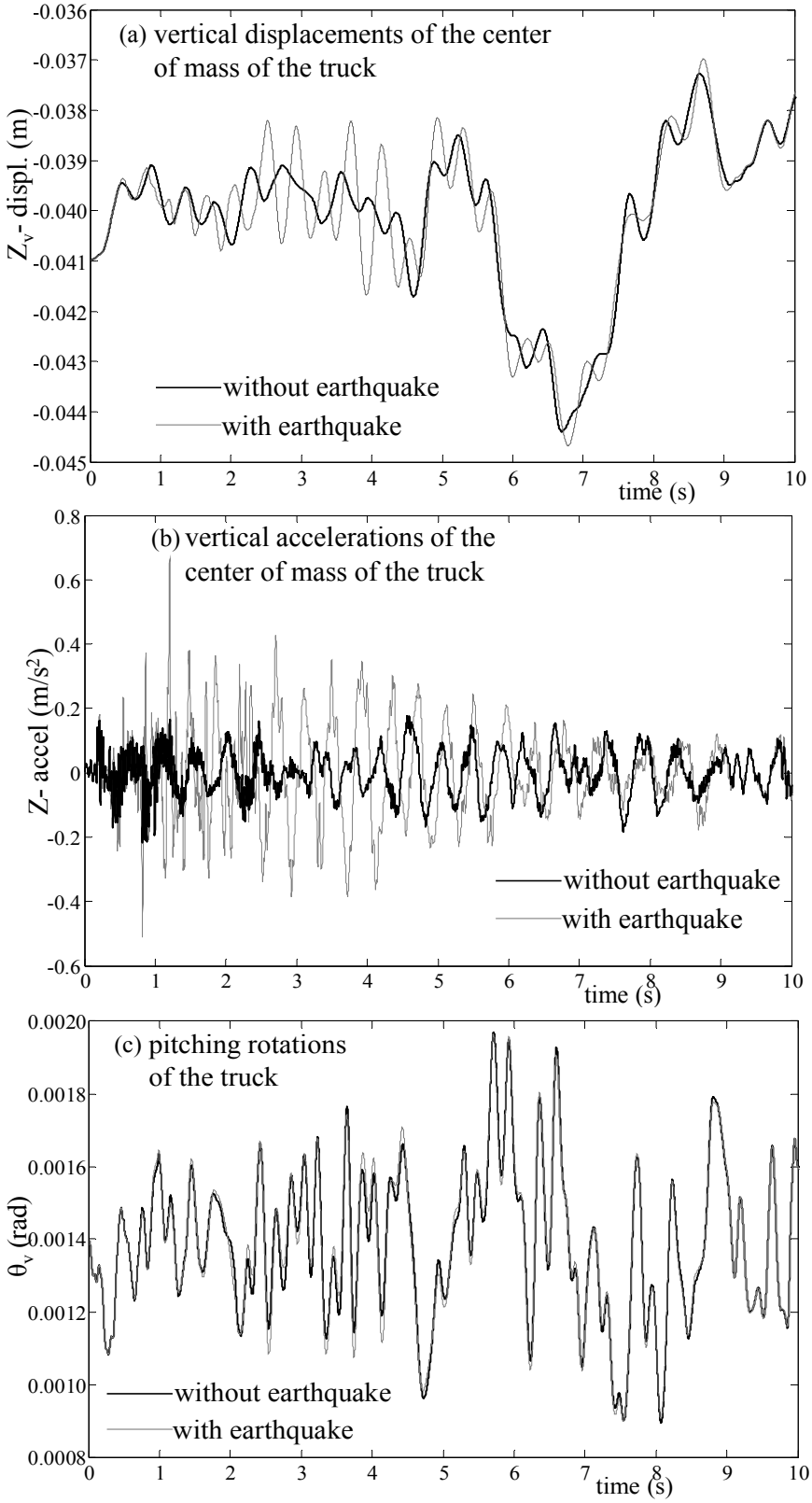


Figure 5: The response of the vehicle in terms of (a) vertical displacements of the rigid body; (b) vertical accelerations and (c) pitching rotations.

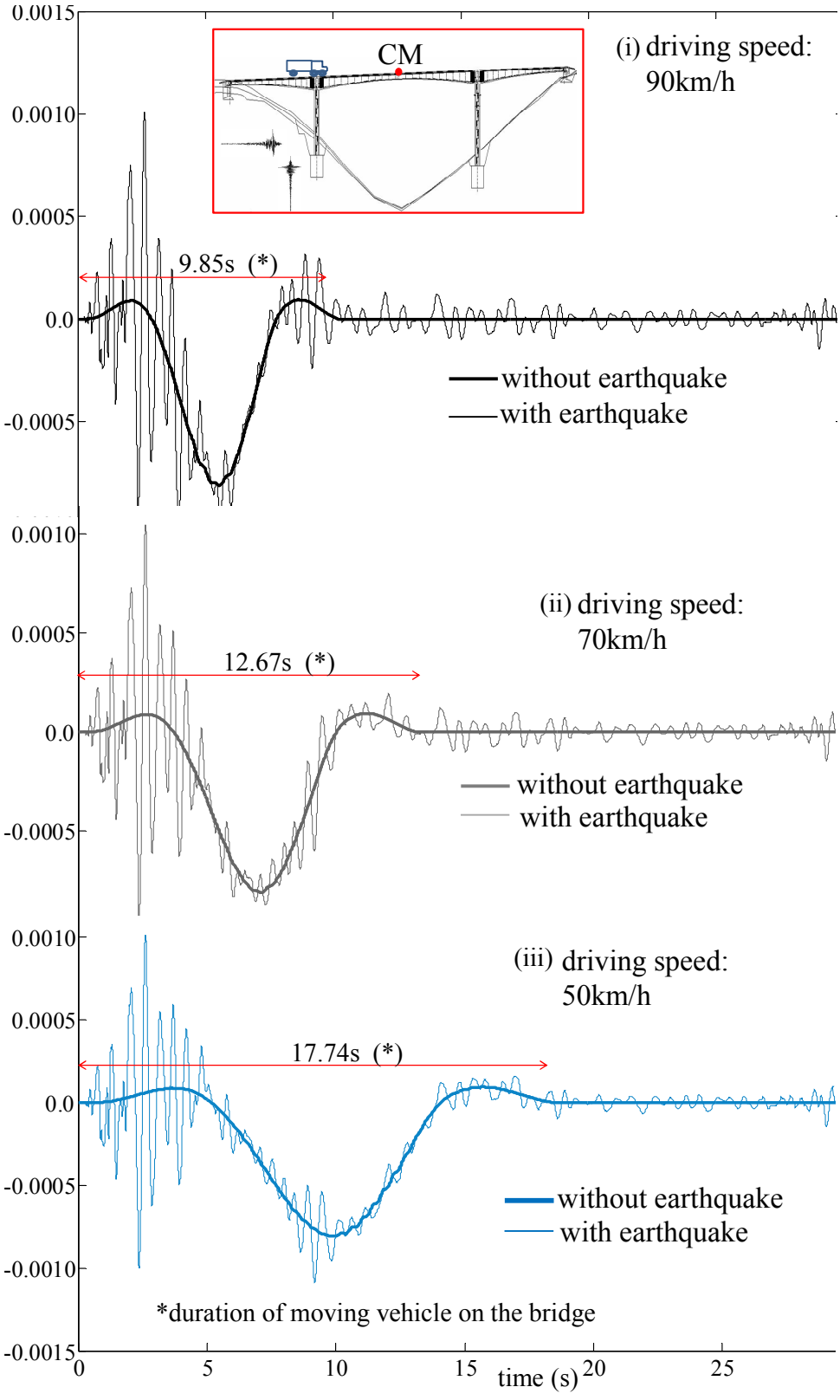


Figure 6: Vertical displacement time histories of the midpoint of the deck considering for vehicle speeds: (i) 90km/h, (ii) 70km/h and (iii) 50km/h.

Figure **5** plots: (a) the vertical displacements Z_v; (b) the vertical accelerations, and (c) the pitching rotations θ_v, versus the time of the center of mass of the truck (see Figure 1), of the first vehicle that moves on the bridge with speed 90km/h. The total duration of the moving vehicle on the bridge is 9.85s. Results are obtained for the interacting vehicle-bridge system with and without the simultaneous action of the earthquake ground motions. When the vehicle enters the bridge (time=0.0s), the study accounts for the non-zero starting values of the vertical displacements and the pitching rotations, due to the steady-state vibration of the moving vehicle. Figure **5**(a) shows significant differences between the vertical displacements of the truck (from the second up to the fifth second of the vehicle response) when the seismic excitation is considered. In Figure **5**(b) the ground motion amplifies the accelerations by a factor of 3. On the contrary, the effect of the earthquake shaking on pitching rotations (Figure **5**(c)) is hardly noticeable.

Figure 6 presents the effect of vehicle speed on the response of the bridge with and without considering the earthquake excitation. In all cases, only one vehicle is accounted for, while all other analysis parameters are as in Figure 5. Different vehicle speeds have significant impact on the peak value of the vertical displacements of the midpoint of the bridge. On the contrary, the VBI last longer, and the amplification of the bridge response increases as the vehicle speed decreases. However, it seems that at a specific time of the response, a higher speed can result in either higher (i.e., at t=5s) or lower (i.e. at t=12s) vertical displacement of the deck. This observation underlines the time-dependency of the problem and the additional complications which emerge from the time superposition of the seismic and the traffic loading.

In order to investigate the influence of the distance between the moving vehicles on the bridge response, the analysis of Figure 6 is repeated for 70km/h considering two moving vehicles with (i) a 5m relative distance between them, (ii) a 20m relative distance and (iii) a 50m relative distance. Figure 7 gives the vertical displacements of the observed point (deck of the midpoint of the deck), during the earthquake excitation, for the aforementioned cases. The maximum response of the bridge appears for the shorter relative distance of the two vehicles. As the distance between the vehicles increases, the influence of the vehicles on the seismic response of the bridge in terms of maximum vertical displacements decreases. This is in agreement with the expected trend based on influence lines.

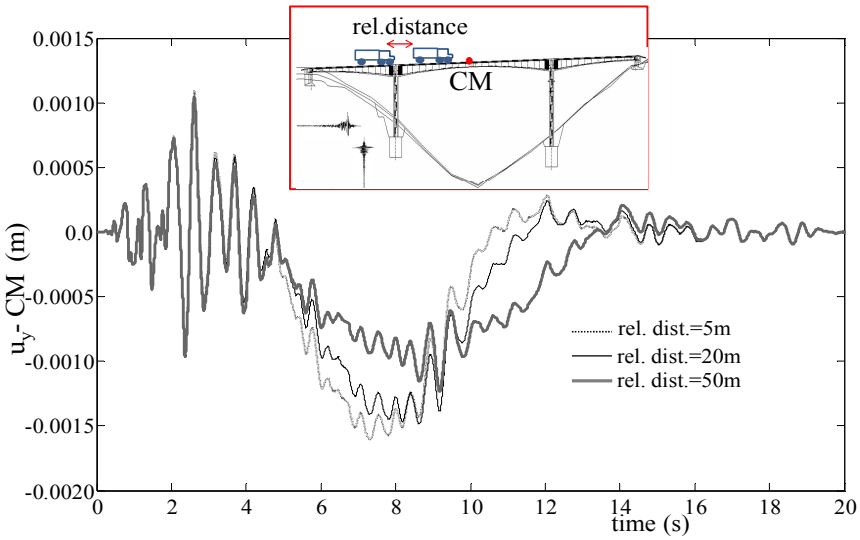


Figure 7: The vertical displacements of the midpoint of the bridge for three different relative distances between the moving vehicles: (i) a 5m relative distance, (ii) a 20m relative distance and (iii) a 50m relative distance.

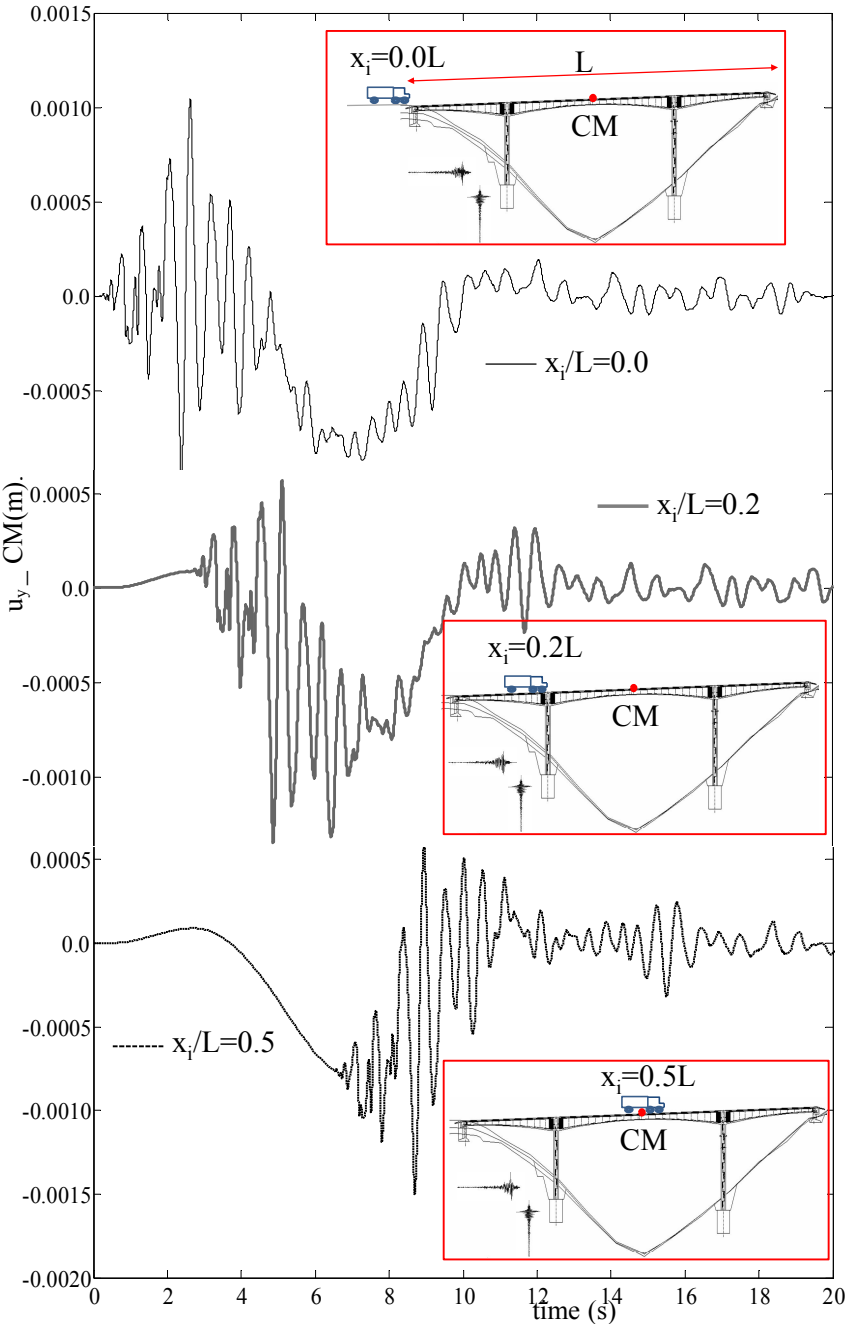


Figure 8: Vertical displacement time histories of the midpoint of the deck for different positions of the vehicle on the deck when the earthquake strikes. The vehicle speed is 70km/h.

Figures 8 and 9 show the seismic response of the bridge for different locations (x_i) of the vehicle, on the deck, when the earthquake excitation occurs. In particular, Figure 8 illustrates the time histories of the vertical displacements of the deck considering three different locations of the truck on the deck: in the first plot, it is assumed that the earthquake occurs when the truck enters the bridge (x_i/L=0.0); in the second plot the vehicle is located at x_i=0.2L(=49m) when the earthquake excitation starts; and in the third plot the earthquake occurs when the vehicle is at the middle of the deck, x_i=0.5L. L is the total length of the bridge. For the adopted earthquake excitation, the seismic response is accentuated the closer to the

midpoint of the deck the vehicle is at the time the earthquake occurs. When the vehicle is passing over the midpoint of the bridge, it maximizes the vertical displacement of the observed point. Therefore, when the earthquake acts at that time, the seismic effects are added on the response of the deck and as a result the deck vertical displacements are maximized.

Figure 9, extends the results of Figure 8 considering ten different positions of the vehicle on the deck when the earthquake excitation occurs. The first set of analyses (the black column in Figure 9) accounts for only one moving vehicle. The second (the grey column in Figure 9) and the third set (the stripes) of analyses assume two moving vehicles with a relative distance between them equal to 5m and 20m, respectively. In all cases, vehicles are crossing the bridge with a constant speed of 70km/h (or 19.4m/s). The stronger influence is observed when the first vehicle is at the middle of the bridge and specifically when it is at position x_i=0.4L (= 98m) at the time the earthquake starts. In most cases, the moving vehicles with a relative distance of 5m, have higher impact on the deck compared to those with a relative distance of 20m. When the first vehicle is at positions x_i equal to 0.7L up to 0.9L, the peak vertical displacements of the midpoint of the bridge are governed by the contribution of the seismic excitation (for the adopted ground motions), and not by the impact of the presence of the vehicles on the bridge. For these cases, the impact of vehicles is not crucial to the peak values of the seismic response of the bridge. In general, and as expected, the presence of two vehicles on the bridge, instead of a single vehicle, induces higher deck vertical displacements.

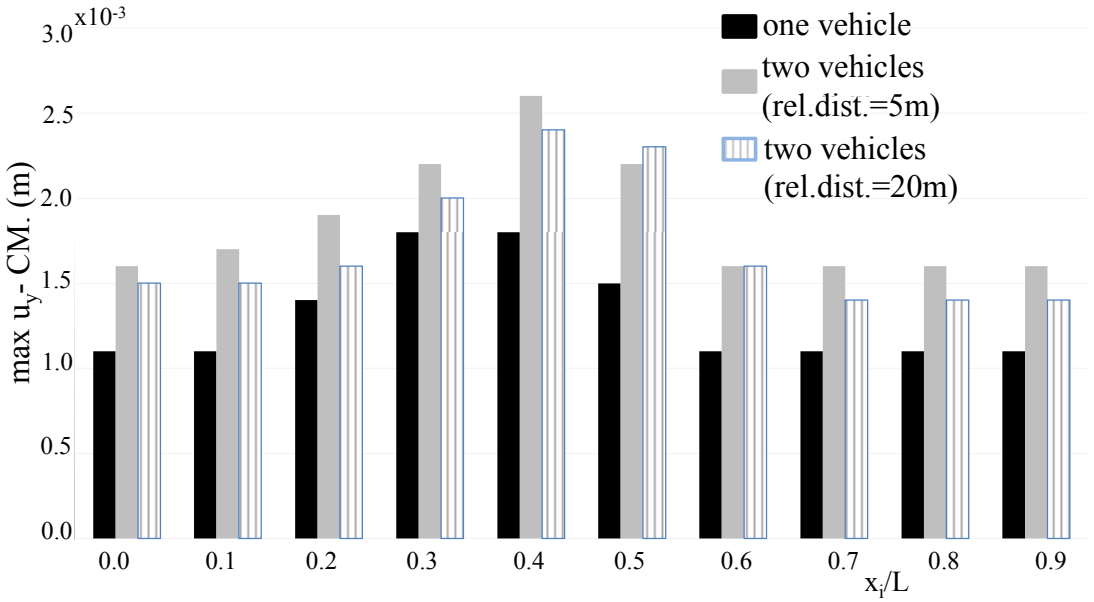


Figure 9: Peak values of the midpoint vertical displacements of the deck for (i) one vehicle; (ii) two vehicles with a 5m relative distance, and (iii) two vehicles with a 20m relative distance. All vehicles have a speed of 70km/h.

5 NEW PROBLEMS ENCOUNTERED DURING THE SEISMIC RESPONSE ANALYSIS OF INTERACTING VEHICLE- BRIDGE SYSTEMS.

In developing the proposed approach of estimating the seismic response of interacting vehicle –bridge systems two new significant problems are encountered. First, given the probabilistic nature of earthquakes, it is practically impossible to predict the position of the moving vehicles on the bridge at the time the earthquake occurs. Each vehicle can be located at any position on the deck when the earthquake strikes. Therefore, different positions of the vehicle

on the deck are equally probable events that should be examined. However, the different positions of the vehicles on the deck may alter substantially the seismic response of the vehicle-bridge system. For instance, when a vehicle enters a bridge ($x_i/L=0.0$) and at the same time an earthquake occurs, the interacting vehicle-bridge system response is different than when the vehicle is in the middle of the deck ($x_i/L=0.5$) at the time the earthquake strikes (Figure 8).

The second very important issue that needs to be addressed, in future studies, is the definition of an accurate interacting traffic vehicle model. The selection of a representative type of vehicle, the number of crossing vehicles, as well as, the distance between them as they move on the deck during the earthquake excitation, are some of the parameters that have to be estimated for an accurate seismic VBI analysis. These parameters are dependent on the site-specific traffic density. The traffic density can be defined as the ratio of the truck flow rate to a constant speed for the traffic stream [31]. Again, when considering the uncertain nature of earthquakes, this problem is far too complicated to be defined deterministically. The study, offers a first insight on the influence of these parameters to the seismic response of the interacting vehicle-bridge system, in order to bring forward these problems.

6 CONCLUSIONS

The present study proposes a framework for the seismic response analysis of interacting vehicle-bridge systems during earthquake excitation. To demonstrate the proposed methodology a numerical example of a realistic case of three–axle trucks on a straight R/C bridge is presented. The particular goal of the work is to unveil new problems encountered when analyzing the seismic response of interacting vehicle-bridge systems.

The study shows that several additional variables may influence the response of the interacting vehicle-bridge system. Thus, for a given ground motion, both the number of moving vehicles and the relative distance between them, influence substantially the seismic response of the vehicle-bridge. As expected, more vehicles induce larger vertical displacements of the deck, whereas different relative distances of the vehicles cause different response of the bridge. The vehicle speed affects significantly the displacement time history of the bridge response. Different vehicle speeds have significant impact on the duration of the VBI, as well as, the amplification of the response of the bridge: it increases as the driving speed decreases. However, for a specific time of the analysis, a higher speed can result in either a larger vertical displacement of the deck or in a lower deck displacement. In the process, the study shows that the position of the moving vehicles on the deck at the time the earthquake occurs, influence significantly the seismic response of the bridge. In this context, the VBI analysis reveals the need for further investigation of all the parameters that influence the seismic response of the interacting vehicle-bridge system under the simultaneous consideration of earthquakes.

REFERENCES

[1] Basoz N, Kiremidjian A., *Evaluation of bridge damage data from the Loma Prieta and Northridge, California earthquakes*. *MCEER Technical Reports*, University at Buffalo, 1998.

[2] SE. Chang, Disasters and transport systems: loss, recovery and competition at the Port of Kobe after the 1995 earthquake. *Journal of transport geography,* **8**, 53-65, 2000.

[3] Japan Road Association, *Design specifications of highway bridges, Part V seismic design*. Maruzen, Tokyo, Japan, 2002.

[4] Eurocode C. E. N., *1: Actions on structures, Part 2: Traffic loads on bridges*. Brussels: European Standard EN 2 (1991), 2003.

[5] American Association of State Highway and Transportation Officials (AASHTO)., *Standard specifications for highway bridges*. Washington, DC, 1996.

[6] CW. Kim, M. Kawatani, S. Konaka, R. Kitaura, Seismic responses of a highway viaduct considering vehicles of design live load as dynamic system during moderate earthquakes. *Structure and Infrastructure Engineering*, 7, 523-34, 2011.

[7] CW. Kim, M. Kawatani, Effect of train dynamics on seismic response of steel monorail bridges under moderate ground motion. *Earthquake Engineering & Structural Dynamics*, **35**, 1225-45, 2006.

[8] X. He, M. Kawatani, T. Hayashikawa, T. Matsumoto, Numerical analysis on seismic response of Shinkansen bridge-train interaction system under moderate earthquakes. *Earthquake Engineering and Engineering Vibration*, **10**, 85-97, 2011.

[9] AJ. Kappos, MS. Saiidi, M.N Aydinoğlu, T. Isaković, *Seismic design and assessment of bridges: inelastic methods of analysis and case studies,* Springer Science & Business Media, 2012.

[10] M.N. Priestley, *Seismic design and retrofit of bridges,* John Wiley & Sons, 1996.

[11] EG. Dimitrakopoulos, Q. Zeng, A three-dimensional dynamic analysis scheme for the interaction between trains and curved railway bridges. *Computers & Structures*, **149**, 43-60, 2015.

[12] YB. Yang, YS Wu, Dynamic stability of trains moving over bridges shaken by earthquakes. *Journal of Sound and Vibration*, **258,** 65-94, 2002.

[13] M. Tanabe, N. Matsumoto, H. Wakui, M. Sogabe, H. Okud, Y. Tanabe, A simple and efficient numerical method for dynamic interaction analysis of a high-speed train and railway structure during an earthquake. *Journal of Computational and Nonlinear Dynamics*, **3**(4), 041002, 2008.

[14] M. Tanabe, N. Matsumoto, H. Wakui, M. Sogabe, Simulation of a Shinkansen train on the railway structure during an earthquake. *Japan journal of industrial and applied mathematics*, **28**:223-36, 2011.

[15] M. Tanabe, H. Wakui, M. Sogabe, N. Matsumoto, Y. Tanabe, An efficient numerical model for dynamic interaction of high speed train and railway structure including post-derailment during an earthquake. *8th International Conference on Structural Dynamics, EURODYN2011*, Leuven, Belgium, 4-6 July, 2011.

[16] N. Matsumoto, M. Sogabe, H. Wakui, M. Tanabe, Running safety analysis of vehicles on structures subjected to earthquake motion. *Quarterly Report of RTRI*, **45**, 116-22, 2004.

[17] H. Xia, Y. Han, N. Zhang, W. Guo, Dynamic analysis of train – bridge system subjected to non - uniform seismic excitations. *Earthquake Engineering & Structural Dynamics*, **35**, 1563-79, 2006.

[18] X. Du, Y. Xu, H. Xia, Dynamic interaction of bridge – train system under non - uniform seismic ground motion. *Earthquake Engineering & Structural Dynamics*, **41**, 139-57, 2012.

[19] W. Guo, Y. Xu, Safety analysis of moving road vehicles on a long bridge under crosswind. *Journal of Engineering Mechanics*, **132,** 438-46, 2006.

[20] S. Chen, J. Wu, Performance enhancement of bridge infrastructure systems: Long-span bridge, moving trucks and wind with tuned mass dampers. *Engineering structures*, **30**, 3316-24, 2008.

[21] W. Guo, *Dynamic analysis of coupled road vehicle and long span cable-stayed bridge systems under cross winds.* PhD thesis, The Hong Kong Polytechnic University, 2003.

[22] S. Chen, C. Cai, Accident assessment of vehicles on long-span bridges in windy environments. *Journal of Wind Engineering and Industrial Aerodynamics*, **92**, 991-1024, 2004.

[23] C. Cai, S. Chen, Framework of vehicle–bridge–wind dynamic analysis. *Journal of Wind Engineering and Industrial Aerodynamics*, **92**, 579-607, 2004.

[24] W. Zhang, C. Cai, Fatigue reliability assessment for existing bridges considering vehicle speed and road surface conditions. *Journal of Bridge Engineering*, **17**, 443-53, 2011.

[25] E.G. Dimitrakopoulos, Q. Zeng, Dynamic interaction between high-speed trains and curved railway bridges. *The 7th International Conference on Bridge Maintenance, Safety and Management*, Shanghai, China, 2014.

[26] ANSYS User's Manual, Version 11.0. Swanson Analysis Systems. Inc., 2007

[27] R.D. Cook, *Concepts and applications of finite element analysis*. John Wiley & Sons, 2007.

[28] The MathWorks Inc., *MATLABUser's Guide*. South Natick, 1994–2012.

[29] L. Deng, C. Cai, Development of dynamic impact factor for performance evaluation of existing multi-girder concrete bridges. *Engineering structures*, **32**, 21-31, 2010.

[30] W. Guo, Y. Xu, Fully computerized approach to study cable-stayed bridge–vehicle interaction. *Journal of Sound and Vibration*, **248**, 745-61, 2001.

[31] J. Ghosh, C.C. Caprani, J.E. Padgett, Influence of Traffic Loading on the Seismic Reliability Assessment of Highway Bridge Structures. *Journal of Bridge Engineering*, **19**(3), 04013009, 2013.

[32] C.C. Caprani, Calibration of a congestion load model for highway bridges using traffic microsimulation. *Structural Engineering International*, **22**, 342-348, 2012.

[33] Pacific Earthquake Engineering Research Center: http://ngawest2.berkeley.edu/

COMPDYN 2015
5th ECCOMAS Thematic Conference on
Computational Methods in Structural Dynamics and Earthquake Engineering
M. Papadrakakis, V. Papadopoulos, V. Plevris (eds.)
Crete Island, Greece, 25–27 May 2015

A STRUCTURAL HEALTH MONITORING DATA MANAGING SCHEME WITH RESILIENCY TO SEISMIC EVENTS: IMPLEMENTATION ON A ROAD NETWORK BRIDGE

George Sergiadis[1], Stelios Hadjidimitriou[1], Vasileios Charisis[1], Panagiotis Panetsos[2], Theodoros Chrysanidis[2]

[1] Department of Electrical & Computer Engineering, Aristotle University of Thessaloniki
University Campus, Building D, GR-54124, Thessaloniki, Greece
stellios22@gmail.com, vcharisis@ee.auth.gr, sergiadi@auth.gr

[2] Egnatia Odos S.A.
Headquarters, 6th km Thessaloniki – Thermi, GR-57001, Thessaloniki, Greece
ppanetsos@egnatia.gr, theodoros_gr@yahoo.com

Keywords: Structural Health Monitoring (SHM), Seismic Event Resiliency, Road Network Bridge, Monitoring Data Management, Energy Supply.

Abstract. *The motivation behind this work is the need for a resilient structural health monitoring (SHM) scheme for road network components that will allow for monitoring continuity and efficient data transfer after major seismic events. We have identified the critical specifications, in terms of resiliency, regarding key components of an SHM system, i.e., data transfer from the structure to the remote end user and energy supply of the SHM components. Based on these specifications, we propose an optimal SHM data managing scheme to be implemented on the already instrumented G9 bridge of the Egnatia motorway, in Western Macedonia, Greece, as a case study. The scheme is based on serial/ optical fiber data transfer from the data loggers to a local communication center, hybrid wired/ cellular/ satellite gateways from the local center to the end user, and uninterruptable power supply unit-based back up energy sources. The collected monitoring data will be made available to the end user/stakeholder - in our case, the RETIS-RISK platform for real-time seismic risk assessment- via web access. The innovative elements of the proposed design are the redundant end user gateways and the use of satellite communication that will provide crucial independence from terrestrial telecommunication networks. The proposed data managing approach meets the identified specifications for resilient SHM and minimizes the possibility of data loss in case of major seismic events.*

1 INTRODUCTION

In the past years, advances in technology have lead to the implementation of highly sophisticated structural health monitoring (SHM) schemes towards a more effective remote monitoring of the integrity of structures. Here, the focus is placed on SHM implementations of large structures such as components of road networks, e.g., bridges, which allow for remote access on monitoring data. Besides the ongoing monitoring of the integrity during the service life of a structure, it is evident that SHM data is of crucial importance during or after individual abnormal events, such as earthquakes, that may cause structural damages [1]. Consequently, SHM implementations must, first and foremost, withstand such events in order to allow for post-event monitoring; in other words, they should be resilient.

Key components of an SHM system are the sensors and their deployment on the structure, the way monitoring data are transferred from the structure to the end user, and the energy efficiency of the SHM system. Common practices concerning sensors deployment can be categorized in two classes, i.e., wired and wireless sensors network (SN) [2]. In the case of the wired SN (for a recent proposed design see [3]), cables are used to provide both power and data connectivity, with initial cost, manipulation, and damage risk of such schemes constituting the main disadvantages. However, they are more reliable and the most cost-effective solution for a long service life. On the other hand, wireless SNs (recent implementation in [4]) rely on over the air data transfer and batteries for energy supply. Such systems may be more cost-effective for short service life and easily manipulated, but, potential problems with over the air propagation and battery life limitations render them more unreliable. Either through wires or wirelessly, monitoring data are usually collected to a nearby data center from where they are further communicated to the remote end user. In most cases, there is a single end user gateway, usually, through a wired internet line or a dedicated wide area network. Certain designs have incorporated wireless end user gateways, such as data transfer over the 2G+ [5] or 3G cellular network [6]. Regarding energy supply, the power grid is the most common source, either directly powering devices, or indirectly, recharging device batteries. During recent years, several technologies [7] have been proposed to replace the power grid as the source of recharging batteries, e.g., photovoltaic panels, but, there is no strong evidence of their reliability and effectiveness. In certain cases, e.g., in [1], [4], battery-based uninterruptible power supply (UPS) units serving as backup power sources of certain components are used, in addition to the power grid. In general, the design of the SHM system depends on several factors, such as the structure itself, especially if it is a large scale one, the surrounding area and weather conditions, as well as the available infrastructure [8].

In this context, the present work addresses, initially, the key specifications, in terms of data transfer and energy efficiency, for an outdoor SHM implementation with resiliency to seismic events, and, secondly and more importantly, it presents such an SHM scheme to be implemented on a already instrumented bridge as a small-scale case study. The design of the proposed scheme focuses on data transfer and energy supply, given the available measuring instruments. The work is part of the RETIS-RISK research project and it aims, eventually, at providing real-time measurement data to the RETIS-RISK platform for real-time seismic risk assessment of urban and interurban road networks in the area of Western Macedonia, Greece.

2 RESILIENT SHM SPECIFICATIONS

The term resilient is used here to describe an outdoor and remote SHM implementation that is designed in such a way as to ensure, to a large extent, that the monitoring continues after natural disasters, such as major seismic events, that may cause damages to the infrastructure. Damages to infrastructure refer to deformation of the structure itself, interruptions of tel-

ecommunication networks or outages of the power grid [9]. Such an SHM implementation should allow for immediate/ continuous assessment of the structural integrity after the event, serving, in this way, as a decision support system. As far as the crucial specifications regarding such a resilient design are concerned, here, we place the focus on data transfer to the end-user and energy supply of the SHM system, highlighted, also, in [1].

Data transfer refers to the whole process of collecting monitoring data from the structure site and making them available to the remote end user/stakeholder. It usually takes place in two stages. The first stage involves the transferring of monitoring data from the structure to a collecting point, i.e., a small room or a building, near the structure, through a dedicated local area network, while the second stage includes the data transferring from the collecting point to the remote end user via a wide area network. Crucial specifications regarding the data transfer process are:

d1) Data transfer from the structure site to the local collection point must be efficient and secured from structural damage. To this end, sensors and networking devices should be protected and of industrial specifications in order to withstand weather conditions and minor structural deformation. In addition, lengthy cables for networking, if any, should be installed in such a way as to avoid damage or cuts.

d2) Data transfer from the collection point towards the end user must be also efficient, in the sense that necessary steps are taken to minimize the possibility of data loss. To this end, availability of redundant end user gateways is considered a good practice. It is of high importance that one of the gateways does not rely on terrestrial telecommunications that suffer from interruptions and congestion in case of emergencies.

In all stages, data transfer speeds, with respect to the monitoring data volume, should suffice for a real-time or on-demand assessment of the structural integrity.

Energy supply refers to the power sources of the individual components that constitute the SHM system. Usually, it takes place through the power grid. However, as local power grid outages are usual in case of seismic events, it is crucial that: e1) every electrical component of the SHM system has a backup power source, and e2) the backup power sources should provide runtimes enough for, at least, an initial assessment of the condition of the structure, immediately after the event.

3 CASE STUDY

Based on the aforementioned specifications, we propose an SHM scheme to be implemented on a part of the road network (Egnatia motorway) that is included in the area of interest, i.e., Western Macedonia, Greece, as a case study. The part of the Egnatia motorway that was selected corresponds to the G9 bridge in the area between Veria city and Kozani city, Greece (Figure 1(a)). The selection was made after the evaluation, in terms of the existing SHM infrastructure, of the road network in collaboration with the motorway administrative body, i.e., Egnatia Odos S.A. (EO S.A.), and it was based on two criteria: 1) it is, currently, the only instrumented part of the road network in the area of interest, and 2) it belongs to second most frequent type of bridges of the Egnatia motorway, built using cantilever construction.

3.1 G9 Bridge Structure and Surrounding Area

The bridge body is T-shaped, consisting of a box-shaped cross-section body with parabolically varying height, which is monolithically connected to the central pier (Figure 1(b)-(c)). The deck has a total length of 173 m. The body is circular in plan view and exhibits a significant slope both along its axis (about 5%) and in the transverse direction due to curvature [5] (Figure 1(d)).



Figure 1: (a) Position of the G9 bridge on the map. (b), (c) Views of the bridge. (d) Overview of the two branches. (e) Abutment of a branch.

On its base, the central pillar is grounded on a compact rectangular box-like foundation socket, and then continues, along its height, as two compact section transverse blades which are monolithically connected to the deck. The connection of the superstructure with the abutments (Figure 1(e)) is made via special type bearings which allow free movement (sliding) along the longitudinal axis of the bridge (for receipt of the temperature expansion and contraction), while functioning as elastomeric in the transverse axis. These bearings operate as elastomeric in the longitudinal axis too, until there is an excess of the static or dynamic (depending on the load) friction between the bridge deck and the Teflon surface of the bearing.

The bridge is situated at an altitude of ~ 600 m (~ 1970 ft) in a rural area. Weather conditions in the area are typical of Northern -Western Greece. Year round, the average lowest temperature is -2 ºC (28 ºF), while the average maximum temperature is 34 ºC (92 ºF). Precipitation ranges from ~60 mm in December (15 rainfall days on average) to ~5 mm in August (five rainfall days on average).

3.2 Current SHM Status and Nearby Infrastructure

The current SHM status of the bridge includes a measuring system that records ambient vibrations on the ground near the bridge. The system consists of triaxial accelerometer that is connected on sight to a GeoSIG GSR-24a data logger (GeoSIG Ltd, Switzerland) with a 24 bit high resolution digitizer [10] (Figure 2(a)). The data logger is also connected to a GPS device and, via a serial RS232 cable, with a Siemens TC35i GSM (Global System for Mobile telecommunications) modem (Siemens A.G., Germany) that is equipped with a SIM card and allows for the remote access to the measurement data over the 2G+ cellular network [11]. Data can also be accessed locally by connecting a laptop via a serial cable to the data logger. The measuring system is powered through the power grid (220 V AC), while, the data logger is also equipped with a battery that offers several hours of system functionality in case of power

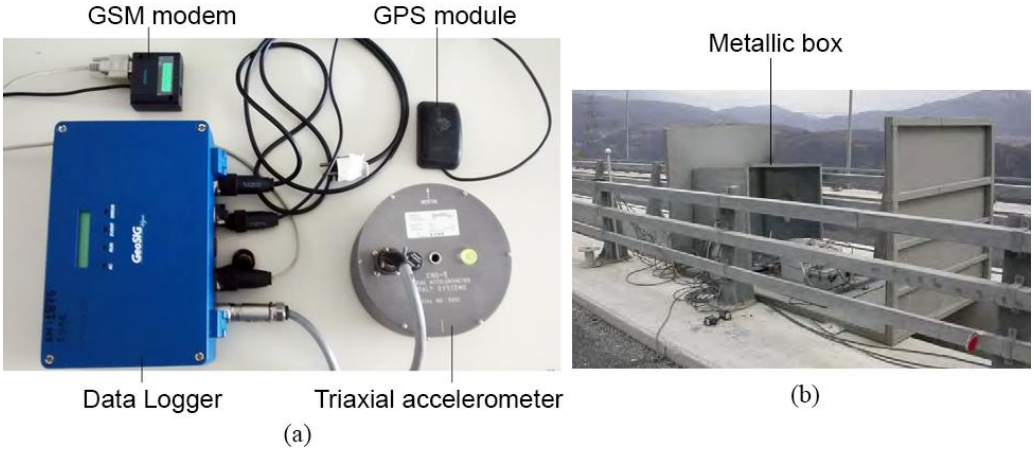


Figure 2: (a) Measuring system of ambient vibrations consisting of a triaxial accelerometer, a data logger, a GPS module, and a GSM modem. (b) Metallic box/ container where the measuring systems are /will be installed.

grid outage. The system is enclosed in a metallic box (Figure 2(b)) that lies on the ground, 62 m away from the bridge entrance lane, with direction from Kozani city to Veria city, Greece, on the right side (Figure 3). According to EO S.A., a second identical measuring system will be installed in a metallic box located midway of the bridge deck, on the right side of the traffic lane with direction from Veria to Kozani, which will record structural vibrations (Figure 3).

In the following, a short presentation of the available infrastructure in the area surrounding the bridge will be given that is not directly related to its current instrumentation, but, it will be taken advantage of during the case study (Figure 3). In particular, on the right side of the exit of the traffic lane with direction from Veria to Kozani, there is a variable-message sign (VMS) on the base of which lies a metallic container where the message routing system is located. The routing system mainly consists of an Ethernet (VMS side) -to-Optical Fiber converter, i.e., a Siemens optical switch module (OSM) (Siemens A.G., Germany) that allows for connection, via an optical fiber, to the nearby traffic control centre (TCC). The TCC building is located on a hill, at a distance of about 1 km from the bridge and within sight of it. There, the optical fiber is converted back to an Ethernet interface that leads to the network switches that constitute the local gateway to the EO S.A. computer network. It must be noted that, from the TCC building, there is visual contact with two nearby villages, the importance of which will be highlighted in a following section. The TCC infrastructure is powered from the grid, while there is also a diesel generator and UPS units that function as backup power sources.

After the evaluation of the current SHM status, the following key conclusions were drawn:

- The measuring instruments that are/ will be installed provide adequate and quality measurements for the assessment of the condition of the bridge. Image monitoring of the bridge would have been useful.
- The way measurement data are accessed remotely, i.e., via the GSM network only, is insufficient and ineffective for two reasons: 1) download speeds of the 2G+ service are low (of the order of 100 Kbit/s, for data the size of several megabytes) [11], and 2) the cellular network suffers from congestion, especially, in cases of emergency, and as a result, it becomes unreliable for data transfer.

3.3 Proposed Data Managing Scheme

Based on the aforementioned conclusions and by taking into consideration the identified specifications, the intervention to the current SHM status of the bridge was designed with the

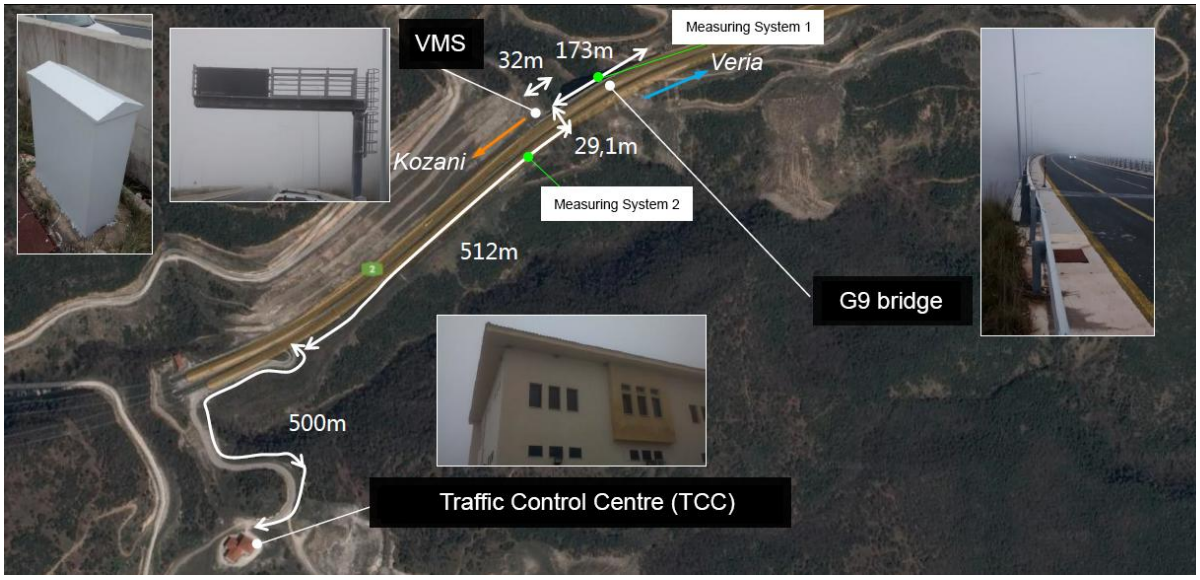


Figure 3: Critical points in the area surrounding the G9 bridge, i.e., the VMS and the metallic container on its base, the TCC, and locations of the two measuring systems.

focus placed on data management that is currently problematic. An overview of the proposed scheme includes the addition of image monitoring, the routing and collection of bridge monitoring data in the TCC (local communication centre), their transfer to the end user through multiple gateways, as well as the efficiency of the whole system in terms of energy supply (Figure 4(a)).

In particular, acceleration data recorded by the two accelerometers will be carried by foil screened twisted pair (FTP) cables, over the RS485 serial protocol, and routed through a local network switch that will be added in the metallic container on the base of the VMS and it will be connected to the OSM. A monitoring camera will be installed on the VMS and connected via Ethernet cable to the network switch. The switch, as well as the OSM system, will be connected to a UPS unit that will be also added to the container and it will serve as a backup power source. The data (accelerations and image) will be carried by the optical fiber to the TCC, where, via optical fiber-to-Ethernet interface conversion, they will be forwarded from the existing EO S.A. network switches to a desktop personal computer (PC) that will be installed and it will serve as a data router to three planned end user gateways: 1) the existing EO S.A. network, 2) an upgraded connection to the 3G cellular network, and 3) a satellite link. Specifically:

1. Data transfer through the EO S.A. network will be realized by routing monitoring data back to the network switches that will then forward them through the EO S.A. computer network to the end user.
2. Connection to the 3G UMTS (Universal Mobile Telecommunications System) cellular network will be realized by forwarding monitoring data to an Ethernet-to-3G converter that will be connected to a UMTS antenna. The latter scheme will allow for significantly higher transfer 3G speeds (of the order of 1 Mbit/s) [11] as compared to the 2G+ service currently used.
3. As far as the satellite link is concerned, data from the PC router will be forwarded to a satellite system that will provide access to fast satellite internet. In this way, monitoring data will be made available through the internet to the end user; there is no need of satellite equipment to be installed to the end user's side.

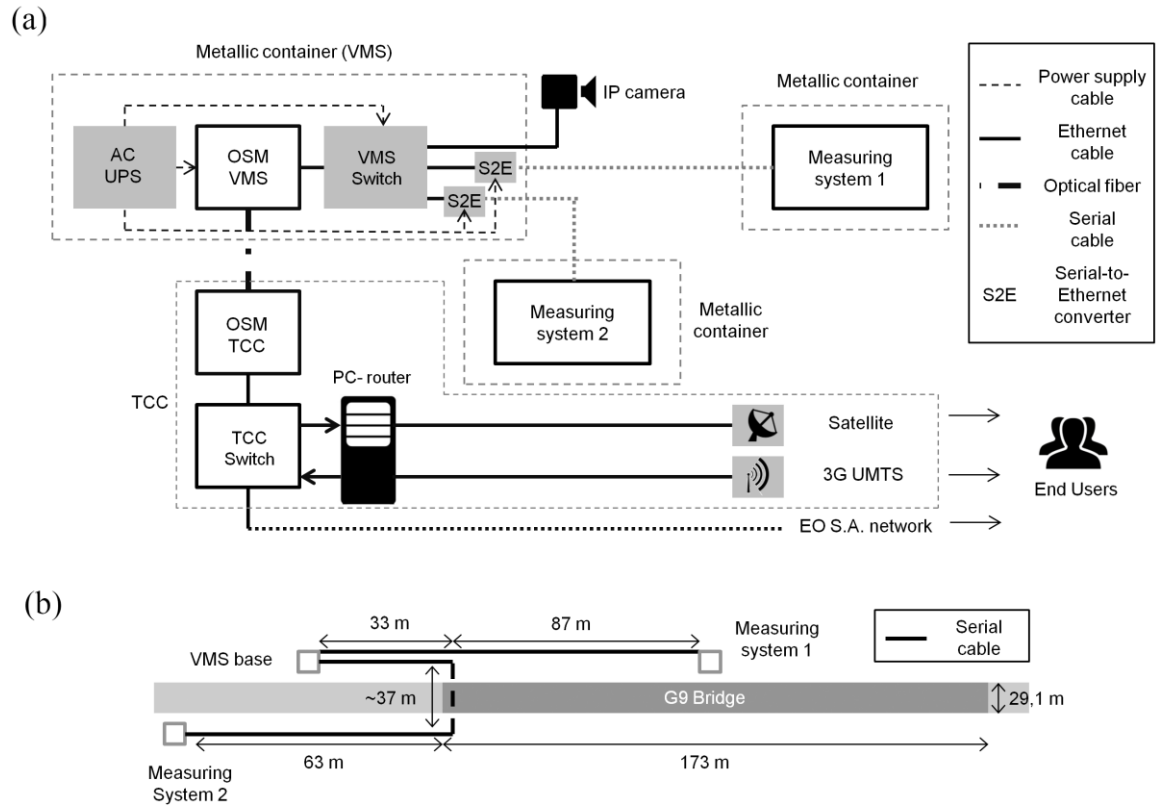


Figure 4: (a) Schematic of the proposed data management scheme. (b) Ethernet cable deployment from the two measuring systems to the metallic container at the VMS base. Dashed line denotes the part of the cabling that will pass under the bridge.

At a given period, monitoring data will be forwarded through one of the aforementioned gateways according to a priority protocol and their availability that will be monitored by the PC-router. Devices that will be added in the TCC will be powered from the grid, and, additionally, they will be connected to the backup power sources that are available, i.e., the diesel generator and the UPS units. Collateral advantages of centralizing the three user gateways in the TCC are the facilitation of network monitoring and the protection of the associated equipment.

3.4 Equipment and Implementation Issues

This section summarizes the required equipment and the implementation issues for the proposed scheme to be realized. On the bridge side, the serial ports on the two data loggers will be connected to RS232-to-RS485 serial protocol converters (Figure 5(a)) in order to allow for long distance transfer [12]. Via FTP cables, data will be transferred to the VMS base, where, via serial-to-Ethernet converters (Figure 5(b)) and Ethernet cables, they will be forwarded to the network switch that will be installed on site. FTP cable deployment is illustrated in Figure 4(b). Since, the distance between both the data loggers and the VMS is long enough, conversion from RS232 to RS485 serial protocol transfer is mandatory in order for satisfactory data transfer rates to be achieved [12]. In particular, a ~120 m-long cable will be used for the data logger that will be installed midway of the bridge, and a ~133 m -long cable will be used for the data logger located on the ground near the bridge. In the case of the latter, part of the cabling will go under the bridge. Rugged foil screened twisted pair (FTP) cables of

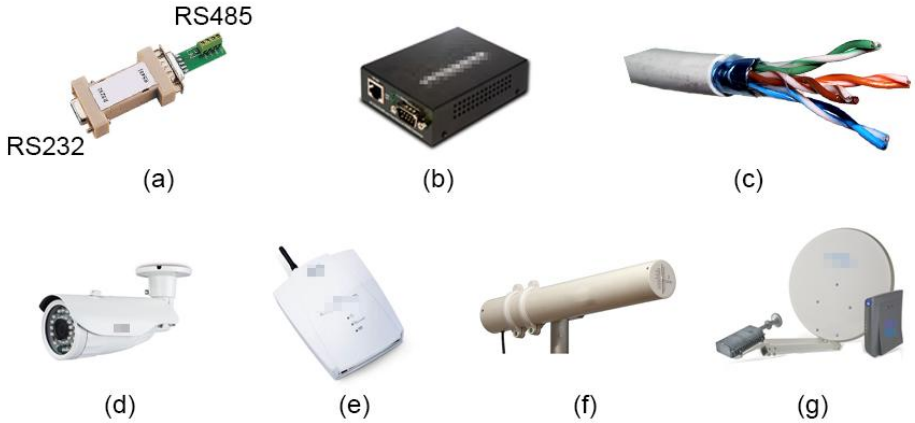


Figure 5: Representative images of parts of the equipment that will be used: (a) RS232-to-RS485 serial protocol converter, (b) Serial-to-Ethernet converter, (c) FTP cable, (d) Day/night IP surveillance camera, (e) Ethernet-to-3G router, (f) directional UMTS antenna, (g) satellite dish.

Category 5e (Figure 5(c)) will be used for both serial and Ethernet-based cabling, which provide insulation from noise interference and allow for outdoor deployment. The day/night monitoring camera will be installed on the top of the VMS scaffolding and it will be IP and PoE-based (Figure 5(d)). It will be connected to the network switch on the base of the VMS via a ~10 m Ethernet cable. The switch will have 5 ports (two ports for the connection with the data loggers, one for the monitoring camera, one for the connection to the OSM and a spare port) and it will be of industrial specifications to withstand weather conditions in the area and with PoE injecting capability to power the IP camera. PoE is a technology, under the IEEE 802.3a(f, t) standards [13], that allows for both data and power to be transferred through an Ethernet cable, and as a result, the main advantage of using PoE-enabled devices is the elimination of additional power sources that would be required to power individual components. A 220V alternating current (AC) UPS unit will be installed that will serve as the back-up power source for the network switch, the OSM, and the serial-to-Ethernet converters with external battery that will provide two hours of runtime.

On the TCC side, the desktop PC serving as a router will be equipped with four Ethernet adapter cards (one for the input data and three for the planned gateways to the end user) and a special version of Linux operating system ('Clear OS', Clear Foundation, New Zealand) that allows for easy configuration of the routing functionality. Regarding the 3G-based end user gateway, an Ethernet-to-3G router (Figure 5(e)) will forward the Ethernet data to a 3G antenna (Figure 5(f)). A directional UMTS antenna with 16 dBi gain, functioning in the 1.9-2.1 GHz range, will be installed on the facade of the TCC building and it will be pointed to one of the nearby villages in order for access to be gained on the 3G enabled-base stations that are located there. The latter configuration is necessary as in the surrounding area of the bridge there is no 3G service (2G+ only). For the satellite-based user gateway, a satellite dish (Figure 5(g)) will be used that will be also installed on the facade of the TCC building in a precisely selected position (elevation and geographical azimuth) in order for a proper pointing and connection with the satellite to be realized. All connections from the PC-router to the three planned end-user gateways will be done via Ethernet cables that will not exceed 30 m in total.

4 MEETING THE SPECIFICATIONS

In the following, the ways that the proposed scheme addresses issues regarding the identified data transfer and energy supply specifications are discussed.

4.1 Data Transfer Efficiency (d1-d2)

On the bridge side, data transfer from the monitoring instruments to the TCC will take place through cabling that is unfolded in such way that the risk of suffering damage due to a seismic event is minimized. In particular, the largest part of outdoor cabling is unfolded on the ground alongside the bridge, rather than on the structure itself, minimizing in this way the possibility of being damaged or cut due to structural deformation. Furthermore, the optical fiber that will carry the data to the TCC is buried deep into the ground and, as a result, it is nearly impossible to suffer catastrophic damage due to a seismic event. It must be also noted that most of the equipment will be installed in metallic boxes that offer protection from extreme weather conditions or/and will be of industrial specifications (e.g., weather proof, wide range of operating temperatures) in order to operate in such conditions.

Regarding the gateways to the end user, the scope of the proposed scheme is to provide redundancy, i.e., multiple ways for the end user to have access to the monitoring data, an issue that is often neglected in SHM designs. In this vein, in case of damage or network congestion, there will be alternative ways to access the monitoring data. Especially in the case of the satellite link, the technology allows for independence from the terrestrial telecommunication networks that can suffer damages from a major seismic event. To the authors' knowledge, this is the first SHM design that incorporates such a number of user gateways and intends to take advantage of satellite communication as one of the means to transfer data to the end user.

4.2 Energy Efficiency (e1-e2)

The proposed design ensures that every component in the network will have backup power sources in order to continue operation in case of power interruption. Specifically, the two measuring instruments have batteries that offer several hours of functionality, while the IP camera is powered over Ethernet. The latter combined with the fact that the serial-to-Ethernet converters and the PoE injecting network switch will be connected to the AC UPS unit ensures that the bridge-side network will continue to function for two hours after a power grid outage. The UPS unit will also serve as a backup power source for the OSM. Finally, on the TCC side, all the devices that will be installed will be connected to the existing backup power sources, i.e., the diesel generator and the UPS units. Consequently, a remote and detailed assessment of the structural integrity of the bridge over a sufficient two hour-interval will be possible, in case of a seismic event that will lead to grid power outage in the area.

5 CONCLUSION

The present work addressed the key specifications regarding an SHM design with resiliency to seismic events and proposed such a scheme to be implemented on a road network bridge as a case study. We consider the proposed data management scheme as an optimal solution for the G9 bridge that not only meets the identified specifications for resilient SHM monitoring, but it also takes advantage of the existing infrastructure in the area, eliminating, in this way, the cost of additional equipment and installation. Apart from the bridge-side data transfer scheme that depends on the structure and the surrounding area, the TCC side data management design, i.e., the three proposed end user gateways, can be applied in most SHM implementations, existing or future, which include a monitoring data collecting point.

Following the implementation of the SHM scheme, acceleration data being acquired from the bridge will be integrated, as additional input, with the novel RETIS-RISK software platform for seismic risk assessment of urban and interurban road networks. Hence, besides statistical data, the platform will be capable of updating models and providing risk assessment feedback for the G9 bridge, based, partially, on valuable real-time measurements.

AKNOWLEDGMENTS

This research has been co-financed by the European Union (European Social Fund – ESF) and Greek national funds through the Operational Program "Education and Lifelong Learning" of the National Strategic Reference Framework (NSRF) – Research Funding Program ARISTEIA II: Reinforcement of the interdisciplinary and/or inter-institutional research and innovation.

REFERENCES

[1] C. Rainieri, G. Fabbrocino, E. Cosenza, Integrated seismic early warning and structural health monitoring of critical civil infrastructures in seismically prone areas. *Struct. Health Monit.*, **10** (3), 291-308, 2010.

[2] G.T. Webb, P.J. Vardanega, C.R. Middleton, Categories of SHM deployments: technologies and capabilities. *J. Bridge Eng.*, 2014, doi: 10.1061/(ASCE)BE.1943-5592.0000735

[3] S. Dinçer, E. Aydin, H. Gencer, A real-time instrumentation approach for structural health monitoring of bridges. *Proceedings of the Istanbul Bridge Conference*, Istanbul, Turkey, August 11-13, 2014.

[4] S. Jang, H. Jo, S. Cho, K. Mechitov, J.A. Rice, S.-H. Sim, H.-J. Jung, C.-B. Yun, B.F. Spencer Jr., G. Agha, Structural health monitoring of cable-stayed bridge using smart sensor technology: deployment and evaluation. *Smart Struct. Sys.*, **6** (5-6), 439-459, 2010.

[5] C. Karakostas, V. Lekidis, K. Papadimitriou, P. Panetsos, E. Ntotsios, T. Salonikios, T. Makarios, I. Nikolaou, I. Sous, Assessment of dynamic characteristics of bridges on Egnatia motorway based on their responses to dynamic excitations. *3rd Panhellenic Conference on Antiseismic Mechanics and Technical Seismology*, Athens, Greece, November 5-7, 2008.

[6] A. Boulis, R. Berriman, S. Attar, Y. Tselishchev, A wireless sensor network test-bed for structural health monitoring of bridges. *36th IEEE International Conference on Local Computer Networks (LCN)*, Bonn, Germany, October 4-7, 2011.

[7] G. Park, T. Rosing, M.D. Todd, C.R. Farrar, W. Hodgkiss, Energy harvesting for structural health monitoring sensor networks. *J. Infrastruct. Syst.*, **14**, 64-79, 2008.

[8] J.M. Ko, Y.Q. Ni, Technology developments in structural health monitoring of large-scale bridges. *Eng. Struct.*, **27**, 1715-1725.

[9] K. Pitilakis, M. Alexoudi, S. Argyroudis, O. Monge, C. Martin, Vulnerability and risk assessment of lifelines. C. Sousa-Oliveira, A. Roca, X. Goula edss. *Assessing and managing earthquake risk*. Springer, 185-211, 2006.

[10] P. Camina, *Geosig GSR-24 / GSD-24 operation manual, 12th edition*. Geosig Ltd., 2009.

[11] F. Adachi, Wireless past and future - evolving mobile communications systems. *IEICE T. Fund. Electr.*, **E84-A** (1), 55-60, 2001.

[12] T. Kugelstadt, *The RS-485 design guide*, Texas Instruments Inc., 2008.

[13] *IEEE Standard for Ethernet*, IEEE Standard 802.3, 2012.

COMPDYN 2015
5th ECCOMAS Thematic Conference on
Computational Methods in Structural Dynamics and Earthquake Engineering
M. Papadrakakis, V. Papadopoulos, V. Plevris (eds.)
Crete Island, Greece, 25–27 May 2015

EVALUATION OF THE STIFFNESS AND DAMPING OF ABUTMENTS TO EXTEND DIRECT DISPLACEMENT-BASED DESIGN TO THE DESIGN OF INTEGRAL BRIDGES

Stergios A Mitoulis[1], Sotiris Argyroudis[2], and Mervyn Kowalsky[3]

[1] Department of Civil and Environmental Engineering
University of Surrey, UK
s.mitoulis@surrey.ac.uk

[2] Department of Civil Engineering
Aristotle University of Thessaloniki, Greece
sarg@civil.auth.gr

[3] Department of Civil, Construction & Environmental Engineering
North Carolina State University, USA
kowalsky@ncsu.edu

Keywords: integral, abutment, bridge, backfill, interaction, damping.

Abstract. *There is an urgent need for maintenance-free transportation infrastructures worldwide. Integral Abutment Bridges (IABs) are robust structures, without bearings or expansion joints that require zero or minimum maintenance. The challenge to the assessment of existing and the application of IABs is the dynamic interaction between the bridge and the backfill soil. In many cases, this interaction is misinterpreted due to the inherent non-linear behavior of the soil during the so-called in-service interaction, which modifies drastically the stresses within the backfill soil under daily displacements of the abutment. A step towards the better understanding of the seismic response of IABs is the evaluation of the resistance of the abutment, which depends upon the geometry of the abutment, the properties of the soil and the successive interactions, i.e. quasi-static, under thermal expansion and contraction of the deck, or dynamic, when the bridge is subjected to seismic excitations and/or breaking loads. Towards this end, this paper attempts to: (a) interpret the condition of the abutment and the backfill soil at the onset of the dynamic excitation based upon the antecedent in-service interaction of the components and (b) to evaluate the stiffness and the damping properties of existing and/or representative integral abutments under dynamic loads to extend the Direct Displacement-Based Design (DDBD) to the design of integral bridges. A typical geometry of the integral abutment and typical backfill soil is investigated based on 2D fully coupled FE simulations adopting a visco-elasto-plastic stress model for the soil (coupled approach) under static and dynamic loads.*

1 INTRODUCTION

Integral Abutment Bridges (IABs) are structures that require minimum or zero maintenance. The barrier for the extended application of IABs is the limited knowledge on the bridge-backfill interaction, namely the in-service displacements of the deck, the consequent movements of the abutment and its non-linear interaction with the backfill soil [1] [2] [3]. On the other hand, there is an acknowledged lack of codes to provide guidance for the design of IABs, as the only standards that support their design are BA 42/96 [4] and BD 37/01 [5], which in principle require that all bridges with a length of less than 60 metres should be integral. More importantly, for earthquake resistant bridges, the use of integral abutments requires the use of a behaviour factor [6] equal to 1 and 1.5 when the bridge is locked in backfills and for abutments rigidly connected to the deck respectively. The aforementioned problems are more challenging in longer bridges, due to the fact that large daily and seasonal movements of the abutment [7] are imposed on the backfill soil. This interaction adversely affects both the long term response of the structure and the condition of the backfill soil, as it imposes settlements and permanent dislocations of the abutment.

It has been recognised that the backfill soil is a source of stiffness [8] [9] [10] and damping due to the highly non-linear response of the soil [11] [12]. This has been addressed by past studies [1] [13] [14] [15] and Caltrans seismic design criteria [8] (section 2.1.5). Despite the large number of numerical and experimental studies on the stiffness of integral abutments there are not many studies available for the estimation of the damping, which influences mainly the displacements of the bridge, but not the overall dynamic response [15]. The design and assessment of integral bridges by the displacement-based design method requires the control of the inelastic lateral displacements. One such method is the Direct Displacement-Based Design (DDBD) approach [14] that utilises the concept of equivalent linearisation to predict the response of inelastic systems with equivalent linear properties of effective stiffness and equivalent viscous damping. Several studies have been conducted to verify the performance of this method for a variety of bridges [16] [17] [18]. However, integral bridges are structures of short fundamental periods, which are expected to remain elastic under the design earthquake, whilst the effective stiffness of the bridge that is strongly dependent on the stiffness of the backfill soil, is required for the equivalent linearisation of the system. Additionally, the yielding of the backfill soil material under the seismic displacements of the deck requires a reliable estimation of the damping ratio to estimate the displacement of the equivalent linear system. Towards this end, bridge systems with fundamental periods ranging from 0.4 to 0.8 sec were analysed. The bridges had a typical integral abutment and backfill soil. Numerical analyses of the coupled abutment-backfill system were performed with the FE code PLAXIS adopting a visco-elasto-plastic stress model for the soil and the equivalent damping ratios were estimated based on the derived force-displacement curves. Subsequently, the concept of equivalent viscous damping that was first proposed by Jacobsen [19] to approximate the steady forced vibration response of linear SDOF damped systems was employed. The results showed that damping is successfully predicted by the proposed method for long-period systems, whilst for short period systems the method seems to underestimate the damping. Also, the method is not able to account for the formation of the voids that are developed between the abutment and the backfill soil, which reduces the stiffness of the system abutment-backfill and hence leads to larger displacements. This effect is described herein as period shift effect.

2 METHODOLOGY FOR DEVELOPMENT OF EQUIVALENT VISCOUS DAMPING MODEL FOR INTEGRAL BRIDGES

The following procedure was applied for the estimation of the equivalent viscous damping model for integral bridges. The successful prediction of the equivalent damping was assessed with three bridge cases having periods ranging from 0.4 to 0.8 sec.

Step 1 Generation of time histories and average compatible design spectrum.

Seven artificial accelerograms compatible to EC8-1 spectrum for soil C and PGA=0.5g were generated with Seismoartif [20] for damping ratios ranging from 5% to 35%. Subsequently, the average displacement response spectra were generated. Figure 1 shows the acceleration response spectra of the artificial accelerograms, the average spectrum of the artificial motions (red line) and the type 1 response spectrum of EC8-1 (blue line) for 5 percent damping.

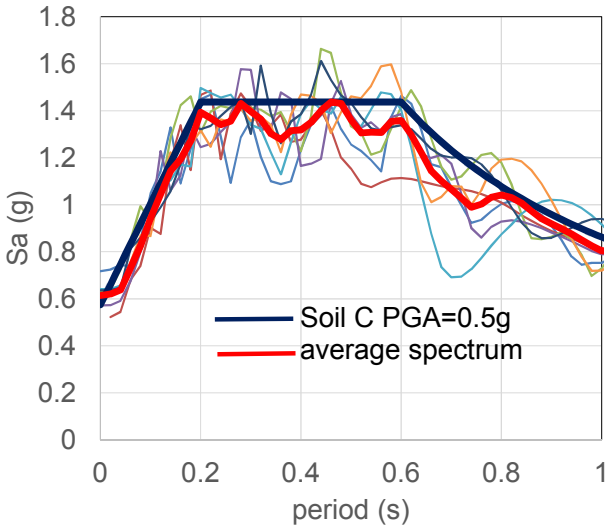


Figure 1: The acceleration response spectra of the artificial accelerograms and the average spectrum (red) and the EC8-1 type 1spectrum for Soil C and PGA=0.5g (blue).

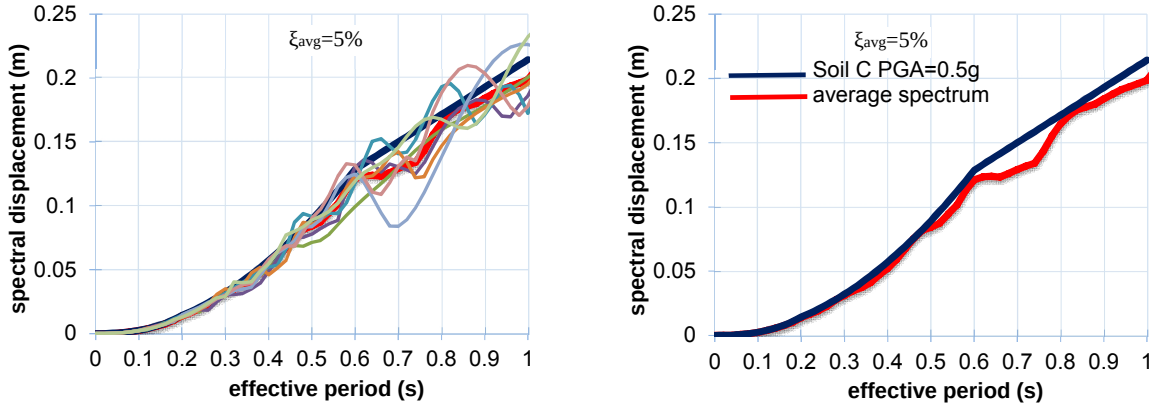
Also, Figures 2a and 2b show the displacement response spectra of the artificial accelerograms, the average spectrum of the artificial motions (red line) and the response spectrum of EC8-1 (blue line) for 5% damping. Small discrepancies are observed in the range of periods between 0.6 and 0.8 sec. The average values of the design spectrum for these seven compatible accelerograms at the corresponding seven values of damping are then obtained, which represent average compatible design spectra for 5% to 35%, Figure 3.

Step 2. **Determination of design displacement demand**

Step 2.1 Hysteretic damping of the abutment-backfill

The effective period is selected and the equivalent viscous damping (ξ_{eq}) is estimated (eq. 1). The simplest approach for estimation of hysteretic damping is proposed by Jacobsen [19], as given by eq. 2, where A_{1oop} is the area of the hysteretic loop and A_{RPP} is the area of the rigid-perfectly plastic rectangle that encloses the loop. Figure 5d shows the graphical representation of the parameters.

$$\xi_{eq}=\xi_{el}+\xi_{hyst} \quad (1)$$



(a) (b)

Figure 2: (a) The displacement response spectra of the artificial accelerograms and the average spectrum (red); (b) comparison of the average response spectrum of the artificial motion (red) with the EC8-1 displacement spectrum (blue) for ζ_{avg}=5%, Soil type C and PGA 0.5g.

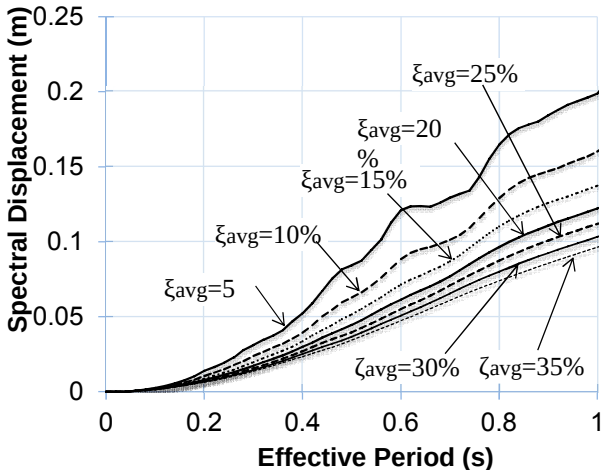


Figure 3: Average displacement response spectra for ξ_{avg} ranging from 5 % to 35 %.

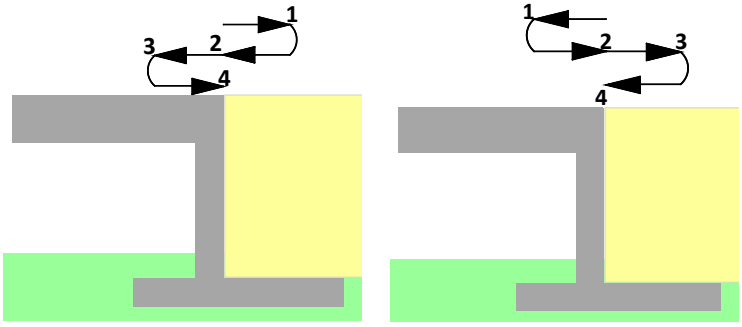
In eq. 1, ξ_{el} corresponds to the damping in the elastic range and ξ_{hyst} corresponds to the damping due to energy dissipation in the abutment-backfill system. Damping in the elastic range is used to represent the damping that is not captured by the hysteretic model adopted for the analysis such as energy dissipation due to nonlinearity in the elastic response. Traditionally, this term is taken as 5 % of critical damping for reinforced concrete structures.

$$\P_{hyst} = \frac{2}{\circledR} \cdot \frac{A_{loop}}{A_{RPP}} \quad (2)$$

For the estimation of the hysteretic damping ratio ξ_{hyst}, two different loading conditions were considered, as shown in Figure 4, for the system abutment-backfill. It was found that the system abutment-backfill has different stiffness and damping when loading 1 or 2 was applied on it. More specifically, it was found that the abutment has greater stiffness and smaller damping when the abutment initially pushes the backfill and subsequently moves away from it (loading 1, shown in Figure 4a). The opposite was found to be valid, i.e. smaller stiffness and higher damping, when the abutment first moves away from the backfill and then pushes the backfill (loading 2), as shown in Figure 4b. This is also given in Table 1.

Subsequently the F-d curves of the bridge-abutment-backfill system were obtained for short period integral bridges. Analysis of bridge-abutment-backfill systems with fundamental periods 0.4 to 0.8 sec was performed. The input motion was a sinusoidal input motion with periods ranging from 0.4 to 0.8 sec. As an example, Figure 6 shows the two loadings that were employed to excite the short period system that had a fundamental period of 0.4 sec. The input motions in Figure 6 are not symmetrical due to the different stiffnesses of the abutment under loading conditions 1 and 2. Target displacements (d_t) in the range of 25mm to 130 mm were obtained for one full cycle of loading.

It is noted that Figure 5 shows the F-d response of the overall bridge system that took into account the equivalent stiffness at maximum displacement of one abutment under loading 1 (K_{ps}), one abutment under loading 2 (K_{pl}) and the stiffness of the bridge (K_b) i.e. the stiffness of the bridge piers. This is further explained in step 2 below and by equation 3. Also, Table 2 summarises the K_{ps} and K_{pl} values for different bridge systems that were analysed. The values of the ξ_{eq} given in Table 1 correspond to the sum of the elastic damping ratio plus the average damping ratio of the two loading conditions (cond. 1 and 2), because when one abutment is pushing the backfill soil, the other one is moving away from the relevant backfill soil.



(a) push-pull (b) pull-push

Figure 4. (a) loading 1: the abutment first pushes (ps) the backfill soil and (b) loading 2, the abutment first pulls (pl) the backfill soil.

bridge period (sec) **target displ. d_t (mm)**	**ξ_{el} (%)**	**$\xi_{hyst,1}$ (%)** loading 1: push	**$\xi_{hyst,2}$ (%)** loading 2: pull	**ξ_{eq} (%)** ξ_{el}+aver($\xi_{hyst,1}$+$\xi_{hyst,2}$)
0.4 sec 25 mm	5%	11.3%	14.8%	18%
0.62 sec 60 mm	5%	12%	15%	18.5%
0.8 sec 130 mm	5%	8.0%	9.8%	13.9%

Table 1: Calculation of ξ_{eq} for short period integral bridges.

bridge period (sec)/(d_t)	**K_{ps}** (kN/m)	**K_{pl}** (kN/m)
0.4 sec / (25mm)	75829.8	30716.5
0.62 sec / (60mm)	56587.4	21193.3
0.8 sec / (130mm)	32224.5	10901.3

Table 2: The stiffness of the abutment-backfill for different effective periods and target displacements ranging from 25 to 130 mm.

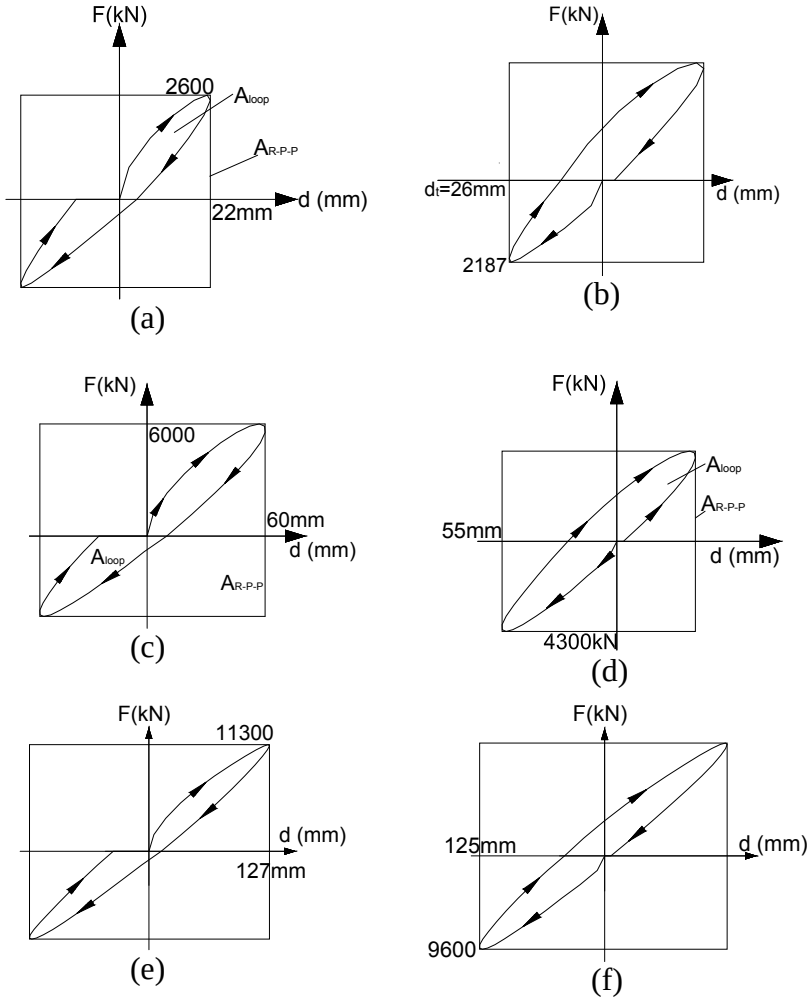


Figure 5: The F-d curves for loading condition 1: (a), (c), (e) and for loading condition 2: (b), (d), (f). Figures (a) and (b) are for T_{eff}=0.4sec and d_t=25mm, figures (c) and (d) are for T_{eff}=0.62sec and d_t=60mm and figures (e) and (f) are for T_{eff}=0.8sec and d_t=130mm (see Table 1).

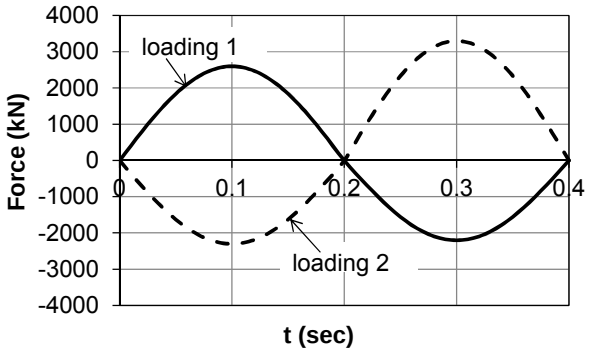


Figure 6: The input motion at the abutment for the systems with effective period 0.4 sec.

For the first iteration the equivalent viscous damping is estimated using the damping Eq. (2) for ξ_{hyst}=10%. The design displacement demand (d_t) is obtained by entering the average design spectra with the effective period (T_{eff}) to the point of the estimated equivalent viscous damping value as shown in Figure 3. Linear interpolation is used to find the damping value if it lies between two damping values of the average design spectra.

Step 3: Determination of SDOF system properties

For the analysis of the SDOF there are three components that define the stiffness, (see eq. 3), and the damping of the system, namely: (a) the bridge, which was considered to respond in an elastic manner with stiffness K_b and mass m_b, (b) the abutment that pushes the backfill soil and has an effective stiffness K_{ps} that corresponds to the target displacement d_t and (c) the other abutment that moves away from the backfill soil that has a smaller effective stiffness of K_{pl}, due to the fact that the backfill soil resists to the movement of the abutment mainly due to its self-weight that sits on the surface foundation of the abutment. Hence, the effective stiffness of the bridge-abutment-backfill system is:

$$K_{eff}=K_b+K_{ps}+K_{pl} \tag{3}$$

whilst eq. 4 relates the effective stiffness of the bridge, the mass of the bridge and the effective period of the equivalent SDOF system:

$$K_{eff}=\left(\frac{2®}{T_{eff}}\right)^2 m_b \tag{4}$$

Step 4 Characterisation of SDOF systems for nonlinear time history analysis (NLTH) of the SDOF-Determination of the Δ_{NL}.

NLTH analysis is performed to a SDOF that has ξ_{el}=5%, stiffness K_b and mass m_b, which correspond to the stiffness and mass of an integral bridge. No yielding of the structural components of the bridge was taken into account, i.e. the bridge remains elastic. The only non-linearity that was taken into account here was due to the elasto-plastic behaviour of the backfill soil. The mass of the backfill soil was not considered in m_b. The equivalent linear SDOF is given in Figure 7a. The SDOF that accounted for the non-linearities of the soil is given in Figure 7b. The SDOF is in series connected to four non-linear links that represent the non-linear response of the abutments as shown in Figure 7b. Two links that receive only compression and represent the cases where the abutment is pushing the backfill soil and two links that receive only tension and correspond to the case that the abutment is moving away from the backfill soil. The F_{ps}-d and F_{pl}-d curves were obtained by PLAXIS under two different conditions that were either push (ps) or pull (pl) of the backfill soil. For the modal analysis half of the K_{ps}^{eff} and K_{pl}^{eff} values were used as these springs in fact receive only compression or tension. The stiffnesses K_{ps}^{eff} and K_{pl}^{eff} were estimated at the target displacement that is given in Table 1, for periods of the systems ranging from 0.4 to 0.8 sec. The resulting displacements of the NLTH were averaged and the displacement Δ_{NL} was compared to the Δ_{el} (i.e. the one we obtain from Figure 3).

The F_{ps}-d F_{pl}-d curves were produced based on the bi-linearisation shown in Figure 8a. The dashed line shows the response of the system abutment-backfill soil for the push and pull conditions as calculated with the FEA in PLAXIS that is described below. The solid lines show the bi-linear curve that was used to model the non-linear response of the backfill soil. Figure 8a also shows the secant stiffness of the system abutment-backfill under loading condition 1. Figure 8b shows the response of the equivalent SDOF system of Figure 7b when the response of abutment-backfill was idealised as per Figure 8a. Figure 8b corresponds to a target displacement d_t=60mm. Similar bilinear models were used for the smaller 25 mm and larger 130mm target displacements. The figure shows that there is a reasonable agreement

between the predicted and the actual response of the system abutment-backfill for both loading conditions, i.e. push and pull. Also, Figures 8a and 8b show that indeed the system abutment has different stiffness and prospected damping for the two different loading conditions.

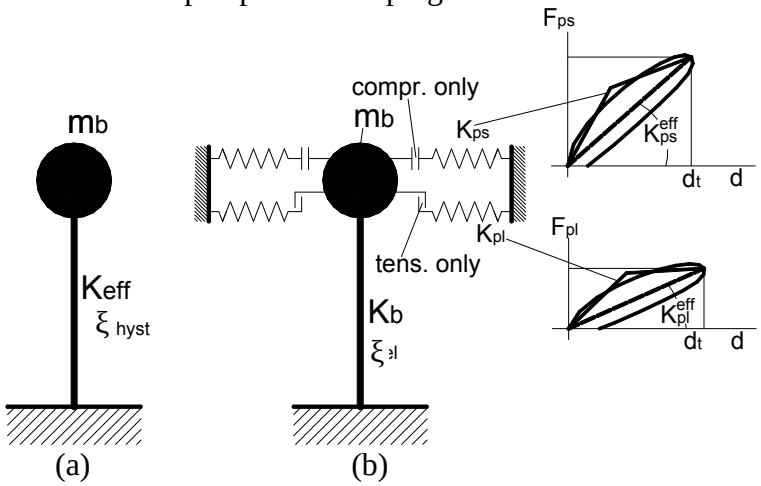


Figure 7: (a) The equivalent linear SDOF and (b) SDOF bridge model employed for the non-linear analysis.

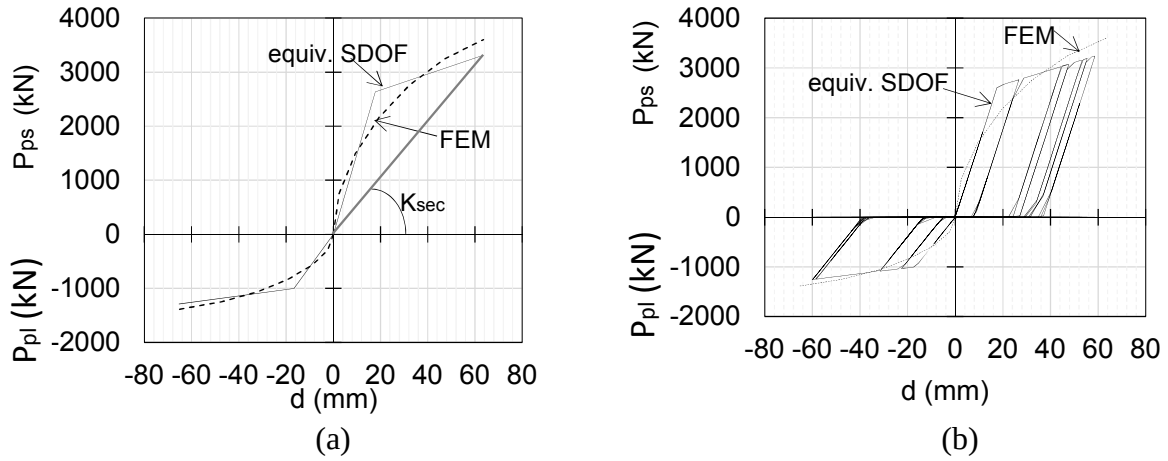


Figure 8: (a) Bi-linearisation of the F-d at target displacement (for d_t=60mm) for push (ps) and pull (pl) loading conditions 1 and 2 and (b) comparison of the F-d response bilinear curve to the response of the non-linear SDOF system.

3 MODELLING OF ABUTMENT-BACKFILL SYSTEM IN PLAXIS

The coupled integral abutment-backfill interaction analyses were performed with the 2D (plane strain) finite element code PLAXIS v8.2 [21] as shown in Figure 7 The basis was assumed to be rigid and the lateral sides were characterized by standard earthquake boundaries. The total width of the model is 250m, which is sufficient to avoid boundary effects. The domain was discretised in a total of 2682 15-node plain strain triangular elements. In the area around the abutment the mesh was refined (Figure 9). The foundation soil domain was modeled with 10 horizontal layers to account for the variable stiffness with depth. In particular, a clay material is used with shear wave velocity (V_s) that varies from 180 m/s at the surface to 310 m/s at the bottom layer, corresponding to soil type C according to the Eurocode 8. The backfill was modeled in 17 horizontal layers. A sandy material with an average V_s equal to 270m/s was selected for the backfill. The values of other soil properties were consistently selected. The integral connection of the abutment to the bridge deck is modeled through a rotation fixity and a fixed-end anchor at the top of the abutment. The axial stiffness of the anchor

has been estimated equal to E·A/L where E·A=2.637·10^7 kN/m for 1.0m of the abutment width and L is 240.0m the length of the bridge.

Initial stage analysis was performed to simulate the initial geostatic stresses. Then the dynamic analyses followed where the sinusoidal force with specific fundamental periods as described in Step 2.2 is applied at the top of the abutment. The analyses were characterised by the assumption of elasto-plastic behavior (i.e. Mohr-Coulomb criterion) for the soil and elastic behavior for the concrete elements. Proper interface elements with a friction coefficient of R_{inter}=0.70 were used to model the interface between the backfill and foundation soil with the abutment [11].

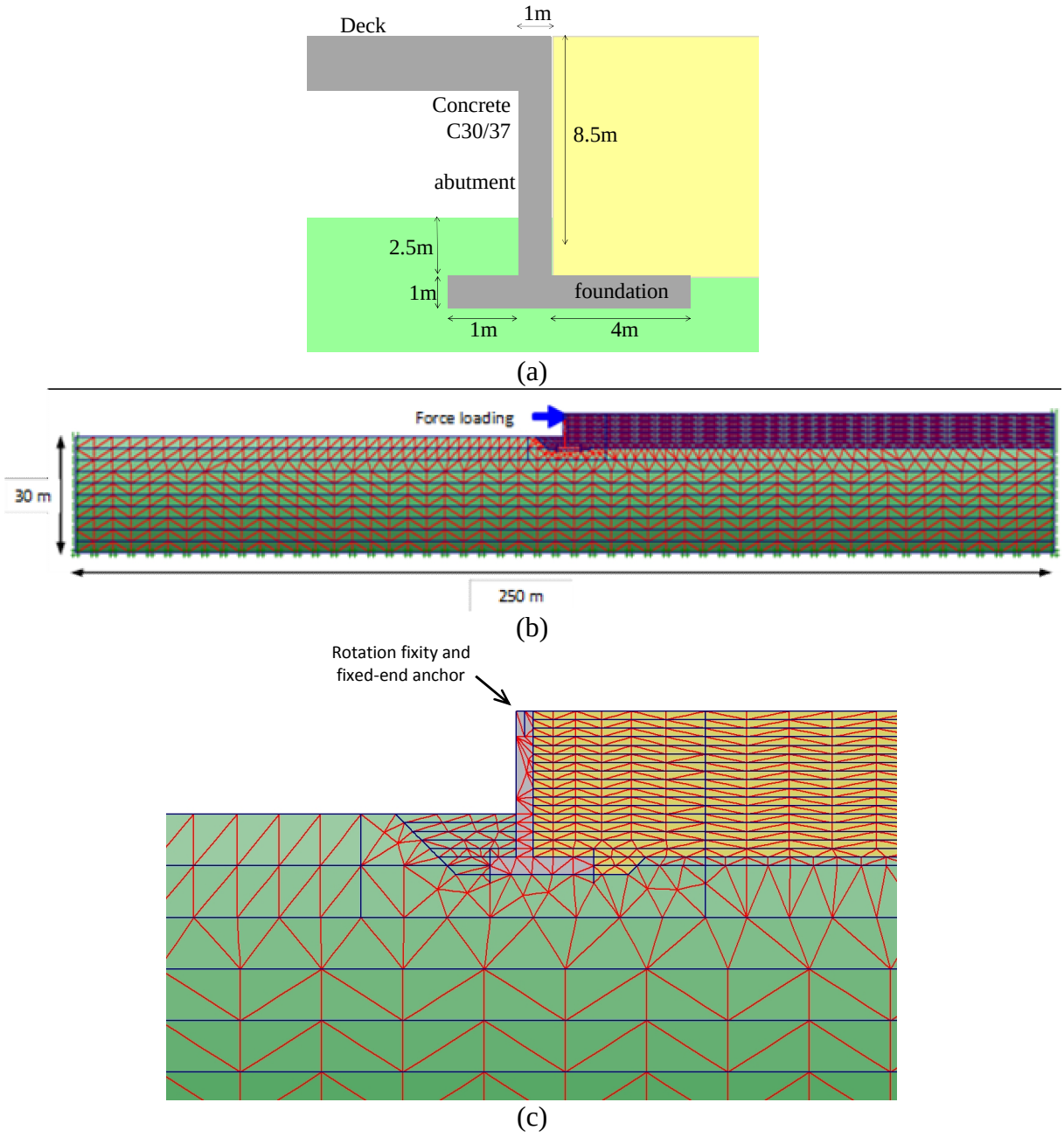


Figure 9: (a) The geometry of the typical abutment, (b) the model of the integral abutment with the backfill soil, (c) detail of the modelling in the vicinity of the integral abutment.

4 RESULTS

The results obtained and the discrepancies of Δ_{el} and Δ_{NL} are given in Table 3.

bridge period (sec)/(d_t)	**Δ_{el}** (mm)	**Δ_{NL}** (mm)	**Δ_{el}/Δ_{NL}**
0.4 sec / (25mm)	31.4	24.5	1.28
0.62 sec / (60mm)	71.6	80.9	0.89
0.8 sec / (130mm)	114.0	115.0	0.99

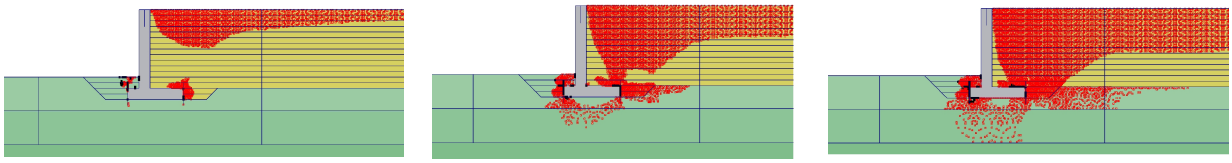
Table 3: Comparison of Δ_{el} and Δ_{NL}.

For the short period bridge system that has a period of 0.4 sec it seems that the proposed procedure underestimates the hysteretic damping, which was found to be equal to 13%, according to the hysteretic damping that is proposed by Jacobsen. If Δ_{NL} is considered to be the accurate displacement of 24.6mm, this displacement corresponds to an equivalent damping ratio of approximately ξ_{eq}=30%, based on the response of the equivalent linear SDOF system, given in Figure 3. It was also found that the permanent displacement of the abutment, for a target displacement of 25 mm, was of the order of 1 mm (i.e. 4% of the d_t) for loading condition 1 and 0.8 mm for loading 2. Therefore, no considerable permanent deformation of the backfill soil is expected and hence the change in the stiffness of the system during the seismic motion due to the creation of voids between the abutment and the backfill soil is negligible.

For bridge systems with a period of 0.6 sec and a target displacement of 60mm the NLTH showed that the displacement was underestimated by the equivalent linear SDOF and hence the hysteretic damping ratio, which was found to be 12-15%, was overestimated. However, the non-linear response of the backfill soil results in the formation of clearances behind the abutment, i.e. gap are formed between the abutment and the backfill soil during the dynamic response of the system. The magnitude of this gap increases during the seismic displacements of the abutment, as it is becoming larger gradually when the abutment pushes the backfill soil and the latter yields, and also when the abutment moves away from the backfill soil. Hence, the stiffness of the system abutment-backfill soil decreases along the earthquake motion and this is described here as period shift effect. This effect is important as the increase in the period was found to be of the order of 18% for the bridge that has an effective period of 0.6 sec. The permanent displacement of the abutment top, for a target displacement of 60 mm, was 14 mm (i.e. 25% of the d_t) for loading 1 and 10 mm for loading 2. This has also been described by Dwairi [16] as softening effect. One way to account for this effect is to use the secant stiffness at maximum deformation, which will account for the formation of the gaps as per Kowalsky et al. [22]. Hence, it is believed that the non-linear displacements Δ_{NL} are larger than the elastic ones Δ_{el} due to the fact that gaps are being formed behind the abutment.

For the bridge system with a period of 0.8 sec, it seems that equivalent damping ratio is predicted successfully as the equivalent elastic system and the non-linear analysis of the SDOF yielded approximately the same displacements. In this case, the absolute permanent displacement of the abutment top for the target displacement of 130mm, was 57 mm for loading 1 and 61 mm for loading 2.

Also, Figure 10 shows the areas of the backfill soil that exhibited plastic deformations when the abutment displacement was 20, 60 and 80 mm. The Figure suggests that the permanent dislocations (displacement and rotation) of the abutment is very small when the displacements are 20mm and hence no significant permanent displacement of the abutment is observed. On the contrary, when the displacement of the abutment is 60 or 80mm both the foundation of the abutment and the backfill soil yields and as a result the abutment exhibits significant permanent, dislocations which is in line with the above findings.



(a) (b) (c)

Figure 10: Points in the backfill soil where plastic deformation of the soil material is developed for 20, 60 and 80 mm.

5 CONCLUSIONS

The response of short period systems was studied for integral abutment bridges. The aim of the research was to define the stiffness and the equivalent damping ratio of the system bridge-abutment-backfill to extend the use of DDBD method to existing and new IABs. FEM software PLAXIS was used to obtain the force-displacement curves of the system abutment-backfill under dynamic loads having fundamental periods ranging from 0.4 sec to 0.8 sec. Non-linear response of the system was considered due to both the material non-linearities (soil) and due to the development of voids between the abutment and the backfill soil. The equivalent damping ratio of the integral bridge system (bridge-abutment-backfills) accounted for the elastic damping (ξ_{el} =5%) and the hysteretic damping (ξ_{hyst}) due to the inelastic behaviour of the backfill soil. The damping model did not take into account the mass of the backfill soil or other types of damping. The results showed that for the bridge systems with periods in the range of 0.6 to 0.8 sec the equivalent damping ratio can be predicted with adequate accuracy by the proposed methodology. For the short period systems the methodology was found to underestimate the damping ratio and hence overestimate the displacement by 28%.

It was evident throughout the analyses of different bridge systems that the hysteretic damping of the system abutment-backfill was not strongly dependent on the magnitude of the target displacement, as for greater target displacements the damping ratio, was not increased significantly. On the contrary, greater frequencies of the input motion lead to larger damping ratios. The equivalent damping ratios for bridge systems having periods in the range of 0.4 – 0.8 sec was found to be in the range of 14-18.5%.

The softening of the system due to the yielding of the backfill soil, the gaps that are formed between the abutment and the backfill soil during an earthquake and the significantly different response of the abutment when it pushes the backfill soil and when it moves away from it, complicate the interaction problem. The above, along with the geometry of the abutment, the foundation soil and the properties of the backfill soil will be the object of further investigation.

REFERENCES

[1] J. Lu, A. Elgamal, K. Mackie, A. Shamsabadi, A framework for performance-based earthquake engineering of bridge-abutment systems. RD. Hyrciw, A. Athanasopoulos-Zekkos, N. Yesiller eds *Geo-Congress 2012: State of the Art and Practice in Geotechnical Engineering*, Geotechnical Special Publication No.225, ASCE Geo-Institute, March 25-29, 2012.

[2] S. Mitoulis, Seismic design of bridges with the participation of seat-type abutments, *Engineering Structures*, **44**, 222-233, 2012.

[3] S. Mitoulis, S. Argyroudis, K. Pitilakis, Green rubberised compressible inclusions to enhance the longevity of integral abutment bridges. *2nd European Conference on Earthquake Engineering and Seismology*, Istanbul, Turkey, 25-29 August, 2014.

[4] BA 42/96, The design of integral bridges, *Highways Agency*, UK, 2003.

[5] BD 37/01, Design manual for roads and bridge, *Highways Agency*, UK, 2001.

[6] EN 1998-2, Eurocode 8: Design of structures for earthquake resistance, Part 2: Bridges, 2005.

[7] A. Lemnitzer, E. Ahlberg, R. Nigbor, A. Shamsabadi, J. Wallace, J. Stewart, Lateral perfor-mance of full-scale bridge abutment wall with granular backfill, *Journal of Geotechnical and Geoenvironmental Engineering*, **135**, 506-514, 2009.

[8] California Department of Transportation (CalTrans), Seismic design criteria, Version 1.7, April, 2013.

[9] O. Taskari, A. Sextos, Probabilistic assessment of abutment-embankment stiffness and implications in the predicted performance of short bridges, *Journal of Earthquake Engineering*, doi:10.1080/13632469.2015.1009586, 2015.

[10] P. Wilson, A. Elgamal, Large-scale passive earth pressure load-displacement tests and numerical simulation, *Journal of Geotechnical and Geoenvironmental Engineering*, **136,** 1634-1643, 2010.

[11] S. Argyroudis, AM. Kaynia, K. Pitilakis, Development of fragility functions for geotechnical constructions: Application to cantilever retaining walls, *Soil Dynamics and Earthquake Engineering*, **50**, 106-116, 2013.

[12] A. Shamsabadi, P. Khalili-Tehrani, J. Stewart, E. Taciroglu, Validated simulation models for lateral response of bridge abutments with typical backfills, *Journal of Bridge Engineering*, **15,** 302-311, 2010.

[13] A. Shamsabadi, S-Y. Xu, E. Taciroglu, A generalized log-spiral-Rankine limit equilibrium model for seismic earth pressure analysis, *Soil Dynamics and Earthquake Engineering*, **49**, 197-209, 2013.

[14] MJN. Priestley, GM. Calvi, MJ. Kowalsky, *Direct displacement-based design of structures*. IUSS Press, Pavia, Italy, 2007.

[15] J. Wilson, B. Tan, Bridge abutments: assessing their influence on earthquake response of Meloland road overpass, *Journal of Engineering Mechanics*, **116**, 1838-1856, 1990.

[16] H. Dwairi, M. Kowalsky, J. Nau, Equivalent damping in support of direct displacement-based design, *Journal of Earthquake Engineering*, **11**, 512-530, 2007.

[17] E. Khan, TJ. Sullivan, MJ. Kowalsky, Direct displacement–based seismic design of reinforced concrete arch bridges, *Journal of Bridge Engineering*, **19**, 44-58, 2014.

[18] W. Kwan, S. Billington, Influence of hysteretic behavior on equivalent period and damping of structural systems, *Journal of Structural Engineering*, **129**, 576-585, 2003.

[19] LS. Jacobsen, Steady forced vibrations as influenced by damping. *Transactions of the American Society of Mechanical Engineers*, **52**, 169-181, 1930.

[20] SeismoSoft. Earthquake Engineering Software Solutions. Seismoartif, ver. 2.1.0, 2015.

[21] Plaxis 2D, *Reference Manual*, Version 8, 2008.

[22] MJ. Kowalsky, MJN. Priestley, GA. MacRae, Displacement-based design of RC bridge columns in seismic regions, *Earthquake Engineering and Structural Dynamics*, **24,** 1623-1643, 1995.

COMPDYN 2015
5th ECCOMAS Thematic Conference on
Computational Methods in Structural Dynamics and Earthquake Engineering
M. Papadrakakis, V. Papadopoulos, V. Plevris (eds.)
Crete Island, Greece, 25–27 May 2015

METHODOLOGY FOR THE DEVELOPMENT OF STRUCTURE-SPECIFIC FRAGILITY CURVES FOR BRIDGES IN A ROADWAY NETWORK

Sotiria P. Stefanidou[1], **Andreas J. Kappos**[2]

[1] Department of Civil Engineering, Aristotle University of Thessaloniki
University Campus, Thessaloniki, 54124, Greece
e-mail: ssotiria@civil.auth.gr

[2] Department of Civil Engineering, City University London
Northampton Sq., London EC1V 0HB, UK
Andreas.Kappos.1@city.ac.uk

Keywords: Bridges; roadway networks; fragility curves; seismic capacity; uncertainty estimation; nonlinear analysis.

Abstract. *Recognising the key role of bridges within a roadway network and the substantial direct and indirect losses related to bridge damage, a new methodology for the development of bridge-specific fragility curves is proposed, intended for application to the bridges forming part of a roadway network. with a view to estimating seismic losses in the network. The key features of the proposed methodology are the explicit definition of critical limit states (damage thresholds) for bridge components, considering the effects of geometry, material strength, reinforcement, and loading properties on the component capacity; the methodology also includes the correlation of local to global damage and the estimation of uncertainty in both capacity and demand. Advanced analysis methods and tools (nonlinear static and response history analysis, IDA) are used for bridge component capacity and demand estimation, whereas Latin Hypercube Sampling is used for uncertainty treatment. Based on processing of a large volume of results from analyses of full bridges, a simplified methodology is developed for seismic demand assessment, involving the use of an elastic (generic) bridge model and response spectrum analysis; demand is then related to component capacity and bridge-specific fragility curves are readily derived. The methodology can be applied, using an ad-hoc developed software, to a large number of bridges(having different geometries and properties) within a network, and direct and indirect losses can then be assessed.*

1 INTRODUCTION

Damage due to recent earthquakes worldwide highlights the role of bridges as the most vulnerable component of a roadway system. In view of this, during the last two decades, several methodologies have been developed for the assessment of bridge vulnerability, mainly in the context of developing fragility curves.

Since fragility is the probability that bridge damage exceeds a specific threshold limit state value for a given level of earthquake intensity, the key issue in the methodologies proposed in the literature is the estimation of capacity and demand at the system [1] or component level [2]. Threshold limit state values for critical components are quantified in terms of local (curvature, rotation) [3], [4] or global parameters [5] based on experimental data [6]. The capacity spectrum (or capacity and demand spectra) method and nonlinear response history analysis are commonly proposed for the demand calculation, while in most cases analytical fragility functions are derived using the Probabilistic Seismic Demand Model (PSDA or IDA) [7], or response surface metamodels [8]. Finally, it should be noted that in most cases uncertainties in demand and capacity are considered in a 'lumped' way.

The main drawback of the existing methodologies is that they are either based on advanced analysis tools, increasing dramatically the computational cost when applied to a large bridge inventory, or on approximate methods that do not account for the seismic performance of all critical structural components, hence risking to miss potential failure modes in some cases.

In view of the above, the key objective of this paper is to put forward a new methodology for the derivation of bridge-specific fragility curves, feasible for application to a bridge inventory with a view to estimating seismic losses in the bridges, as well as in the roadway network [9]. In general, bridges in a roadway network have different geometries, structural systems and component properties, due to differences in the topography and the construction method selected (figure 1). Therefore, the proposed methodology aims to reconciliate two conflicting requirements, namely the need for a detailed and reliable estimation of bridge capacity and demand, and the broad and efficient applicability. To this purpose, the end product of the methodology involves an elastic (generic) 3d bridge model and elastic response spectrum analysis results for the derivation of fragility curves. However, different component (i.e. pier) types have been previously analysed in order to correlate local to global damage, assess the effect of different geometry, material, reinforcement and loading properties on component capacity, and finally derive empirical relationships for component threshold limit state values. Moreover, the seismic performance of bridges with different structural systems is investigated using advanced analysis methods (nonlinear response history analysis, IDA) and the results are incorporated in the simplified methodology proposed.



Figure 1: Different bridge types within a roadway network

2 BRIDGE CLASSIFICATION SCHEME

In the frame of a network loss assessment, the vulnerability of bridges having different geometries, structural systems and properties should be estimated. The most important step prior to fragility analysis is the definition of a classification scheme for the bridges in the network, based on the parameters deemed as the most significant with respect to the seismic response. Therefore, a slightly enhanced version of the classification system developed in the framework of the research programme ASProGE [1], was adopted for the bridges of the roadway network of Greece. A three-digit code is used for each bridge type; the first digit denotes the pier type, the second the deck type, and the third the type of pier-to-deck connection (Table 1).

Code X1 *Pier Description*	**Code X2** *Deck Description*	**Code X3** *Pier-Deck Connection*
1 : Single Column (Solid)	1 : Slab (Solid or with voids)	1 : Monolithic
2 : Single Column (Hollow)	2 : Box girder	2 : Bearings
3 : Multi-column	3 : Simply supported pre-cast- prestressed beams	3 : Combination of monolithic & bearing
4 : Wall-type		
5 : V-shaped		

Table 1: Classification scheme proposed for Greek bridges.

3 DESCRIPTION OF THE METHODOLOGY FOR THE DERIVATION OF BRIDGE SPECIFIC FRAGILITY CURVES

Seismic performance of bridges is highly dependent on the structural system and properties of different components, namely piers, abutments, and bearings. Therefore, the first stage of the proposed methodology is to define the capacity of components, based on the results of inelastic analysis, considering different failure modes. Component limit states (minor, moderate, major and collapse), are qualitatively described based on experimentally observed damage sequence and performance and quantified defining threshold limit state values in terms of global engineering demand parameter (displacement), dependent on component geometry, reinforcement, material and loading properties. Uncertainty in capacity, namely in the damage threshold definition, is estimated using reduced Monte Carlo (Latin Hypercube Sampling) simulation for each component. The second stage is the development of a simplified 3d model

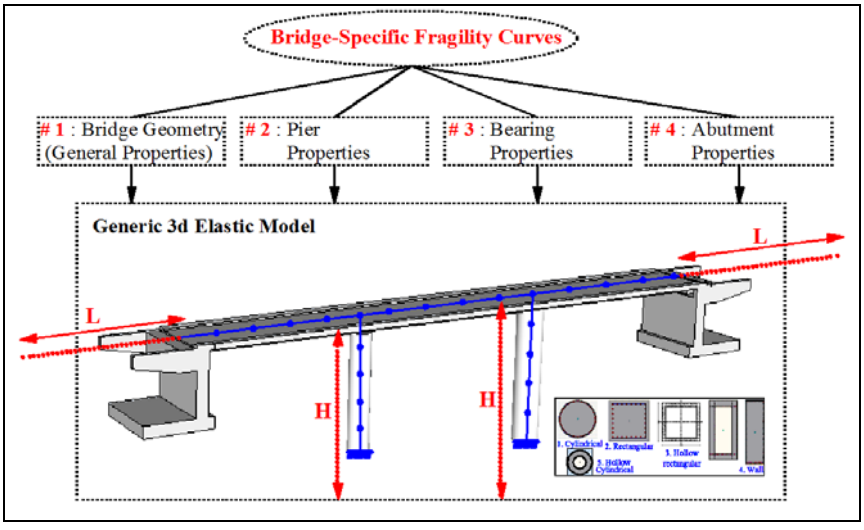


Figure 2: Input data for the derivation of bridge-specific fragility curves

(linear springs for bearings and abutments) in order to estimate seismic demand on each component. Seismic analysis is performed at bridge level, in order to consider the correlation of different components during the evaluation of bridge seismic performance for different levels of earthquake intensity. However, since the main target of the methodology is the feasibility to apply to a large bridge inventory, elastic response spectrum analysis is used for the demand calculation. To account for inelastic performance of the bridge system under seismic actions, the uncertainty in demand is calculated using nonlinear response history analysis for selected accelerograms and various intensity levels (Incremental Dynamic Analysis). Representative bridges of each category (according to the classification scheme described in §2) are selected and Monte Carlo simulation with Latin Hypercube sampling is performed in order to quantify the uncertainty in seismic demand; in a practical context, uncertainty in demand is assumed to be the same for bridges classified in the same category. Having defined capacity and demand at a component level, bridge fragility is calculated assuming (conservatively) series connection between components (except for limit state 4, see §4). Since the demand calculation is based on the results for an elastic model (linear springs), the effect of gap closure should be accounted for, considering two models (open and closed gap), retaining the results of the first model until gap closure. The methodology outlined above, is described in detail in the following paragraphs.

3.1 Step 1 : Component Threshold Limit State values (Capacity) and correlated uncertainty

During the first step, threshold limit state (capacity) values are defined in terms of global engineering demand parameters. Displacement of the component control point is used, since it can be easily recorded during analysis and is a representative measure of the system's seismic performance (damage); therefore it should be correlated to local (component) damage. As far as bridge piers are concerned, the main objective is to develop a database including all different pier types shown in Table 1. Damage is initially quantified at section level (figure 3), using local engineering demand parameters (curvature) corresponding to material strain limits and developed crack widths. Moment - curvature analyses for varying geometric, material,

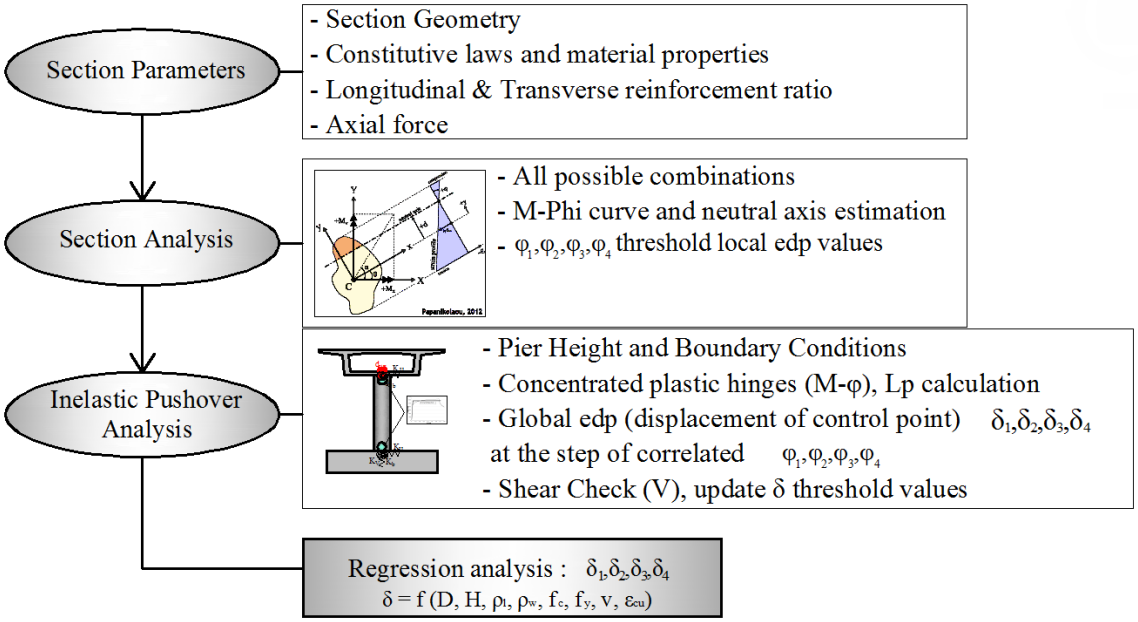


Figure 3: Component (piers) threshold limit state values in displacement terms

reinforcement and loading properties are performed, defining threshold limit state values in curvature terms and the secant stiffness of the fully cracked section at yield ($EI_{eff}=M_y/\varphi_y$), to be used as input in component analysis. Varying pier heights are considered for each different pier type and inelastic pushover analyses of piers are performed. Displacement values at pier top (component control point) for the time step that section curvature exceeds the threshold limit state value are recorded in order to define threshold limit state values in displacement terms. Shear failure modes are also considered, therefore shear checks of the pier model are performed, comparing the shear force to shear capacity ($V_u = V_c(\mu_\varphi)+V_w+V_p$). Displacement value at the time step that the developed shear force exceeds the relevant capacity is recorded and the relevant threshold displacement value is corrected, i.e. the minimum of the top displacements corresponding to flexural and shear failure modes is considered. Regression analysis for every different pier type is performed and empirical closed-form relationships are proposed for each case (pier type). The proposed empirical relationships can be used when the relevant properties are known, however it should be noted at this point that threshold values in displacement terms (capacity) are strongly dependent on the boundary conditions, namely the pier to deck connection and the foundation support. Since, as depicted in figure 3, the control point displacement (cantilever top) can be correlated to the top/bottom moment ratio (point of contraflexure), modal analysis for the first translational mode of the 3d generic beam model of the bridge studied should be initially performed to define the height x_o of the contraflexure point and subsequently calculate threshold limit state values using the proposed closed-form relationships and considering the effect of the component boundary conditions.

Uncertainty in the threshold limit state value definition in displacement terms (d_1,d_2,d_3,d_4) is calculated for each pier type separetely. Uncertainty in material properties, namely the concrete compressive strength (f_c) and steel yield strength (f_y), the ultimate concrete stain (e_{cu}) and the plastic hinge length (L_{pl}) is considered and Monte Carlo simulation with Latin Hypercube sampling is carried out for N=100 statistically different, yet nominally identical, realizations. Analyses results are processed and logarithmic standard deviations β_c are derived for every different pier type. Finally, uncertainty in the limit state definition (β_{LS}) is calculated based on statistical analysis of data (threshold values) available in the literature.

Threshold limit state values are defined in displacement terms for bridge bearings and abutments, based on the literature [10], [11], considering different failure modes, namely yielding of steel shims, lift-off, rotation and unseating for elastomeric bearings, and backwall damage, as well as abutment soil yielding and deformation for seat-type abutments. Damage states for pot bearings are additionally defined based on experimental data [12]. Uncertainty in limit state definition is calculated for abutments and bearings as well (β_{LS}).

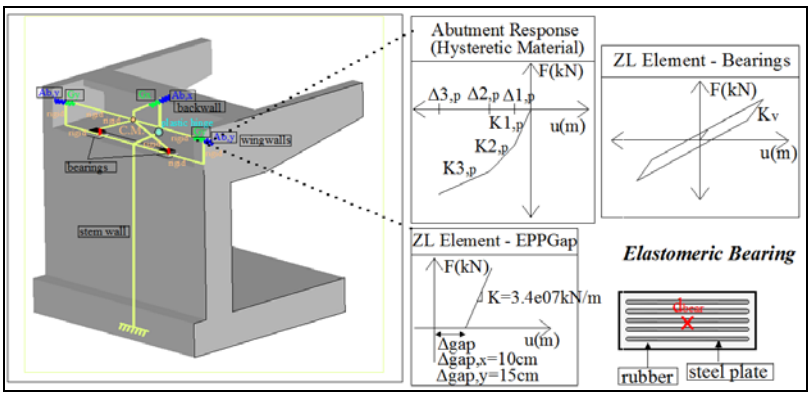


Figure 4: Component (abutments &piers) threshold limit state values in displacement terms

3.2 Step 2 : Component Demand and Bridge System Fragility

So long as threshold limit state values (capacity) and the associated uncertainty are defined, the demand at the control point of every component should be estimated in order to derive fragility curves for each limit state. The proposed methodology is based on elastic response spectrum analysis, and the equal displacement approximation ($d_{elastic}=d_{inelastic}$) for the seismic demand estimation, a reasonable assumption for T>0.5~0.6sec, which is the case for most bridges. A simplified elastic model, as depicted in figure 2 (linear springs for bearings and abutments) has to be set up, to which member properties are fed. The pier cracked stiffness ($EI_{eff}=M_y/\varphi_y$) is calculated for all piers based on empirical relationships proposed for yield moment and curvature (e.g. $\varphi_y=f\,[(f_c/f_y,v,\rho_l,\rho_w)/D]$ for cylindrical sections/bilinear M-φ section diagram). It should be noted that in the longitudinal direction of the bridge, analysis of a single-degree-of-freedom system is generally sufficient; however this is not the case for the transverse direction, since the displacement profile is strongly dependent on the deck geometry and the boundary conditions at the abutments.

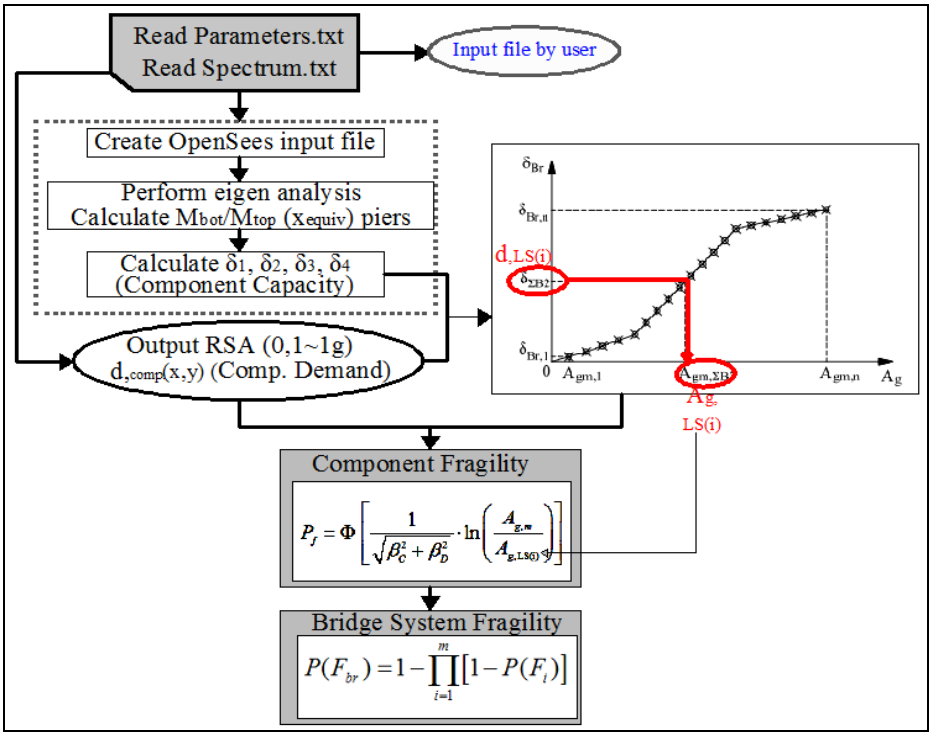


Figure 5: Outline of the proposed methodology for the derivation of bridge-specific fragility curves

Response spectrum analysis (for a site-specific spectrum or mean spectrum of selected accelerograms scaled from 0.1g to 1.0g) is performed and the displacement demand at the component control point versus earthquake parameter is plotted, representing the evolution of damage parameter (displacement) with increasing earthquake intensity (PGA=0.1g~1.0g in this case). From this diagram, median threshold values of the earthquake intensity parameter can be obtained for every damage state (figure 5). Apart from mean values, the standard deviation corresponding to the total demand and capacity uncertainty value, under the assumption of statistical independence, should be defined. Since uncertainty in capacity is calculated in step 1, uncertainty in demand is defined at this step, based on the results of detailed structural models and nonlinear analysis of representative bridge types (according to the classification scheme described above). Uncertainty in material properties, gap size, bearing stiffness and soil properties are considered during analysis of representative bridges; as noted previously,

reduced Monte Carlo simulation for N=100 samples is used and Incremental Dynamic Analysis for selected accelerograms scaled to different levels of earthquake intensity is performed in order to calculate β_d for the relevant bridge class.

Bridge-specific fragility curves are calculated on the basis of the above (mean and standard deviation values), assuming series connection between components, except for LS4 corresponding to bridge collapse and related to collapse of bridge piers only. As already outlined, fragility analysis is based on the response spectrum results of two simplified models (open and closed gap), retaining results of the first model until gap closure.

Application of the methodology presented herein is presented in the following paragraphs, providing the empirical closed-form relationships for the quantitative definition of threshold limit state values (capacity) of all different bridge pier types, the relevant β_c and β_{LS} values, as well as the β_d values for 3 different bridge classes (#221, #232, #221).

4 BRIDGE COMPONENT CAPACITY AND ASSOCIATED UNCERTAINTIES

Different geometric, reinforcement, material and loading parameters affect the available strength and ductility, and eventually the seismic performance of piers. The fact that a cylindrical pier designed according to the provisions of EC2 and EC8 will eventually have a different threshold limit state value (considered limit states are 1 to 4, see Table 2) compared to a similar pier not being designed according to code provisions (reinforcement ratio, confinement) or a pier with different axial load and even more, compared to a hollow rectangular or a wall pier, is recognised. The effect of different pier types, dimensions, material properties and constitutive laws, longitudinal and transverse reinforcement ratio and finally axial load on the threshold limit state values was evaluated and closed form relationships are proposed here for different pier types.

Limit State (LS)	Threshold values of curvature (φ)	Quantitative Performance Description
LS 1 – Minor/Slight damage	$\boldsymbol{\varphi_1}$:φ_y	Quasi-elastic behaviour – Cracks barely visible.
LS 2 – Moderate damage	$\boldsymbol{\varphi_2}$: min (φ: $\varepsilon_c > 0.004$, φ: $\varepsilon_s \geq 0.015$)	Spalling of the cover concrete, strength may continue to increase – Crack width 1-2mm.
LS 3 – Major/Extensive damage	$\boldsymbol{\varphi_3}$: min (φ: $\varepsilon_c \leq 0.004 + 1.4 \cdot \rho_w \cdot \frac{f_{yw}}{f_{cc}}$, φ: $\varepsilon_s \geq 0.06$)	First hoop fracture, buckling of longitudinal reinforcement, initiation of crushing of concrete core – Crack width>2mm.
LS 4 – Failure/Collapse	$\boldsymbol{\varphi_4}$: min (φ: $M < 0.85 \cdot M_{max}$, φ: $\varepsilon_s \geq 0.075$)	Loss of load-carrying capacity - Collapse

Table 2: Component Piers: Threshold limit state values (local edp)

In line with the above, different properties for all the aforementioned parameters are selected and moment-curvature analysis of all possible combinations is performed as described in figure 6. It should be noted that the parameters considered fall, in most cases, within the prescribed code requirements, however lower strength classes for concrete and steel are additionally considered, in order to include cases of older bridge piers. In-house developed software [13] that incorporates stress-strain models for confined, unconfined concrete [14], [15] and steel is used for moment-curvature analysis. Threshold values for the different limit states are initially defined in curvature terms (local engineering demand parameter) as depicted in

table 2. Empirical relationships for the estimation of secant stiffness of the fully cracked section at yield ($EI_{eff}=M_y/\varphi_y$) are proposed for every different pier type (equation 1, figure 7 – cylindrical piers).

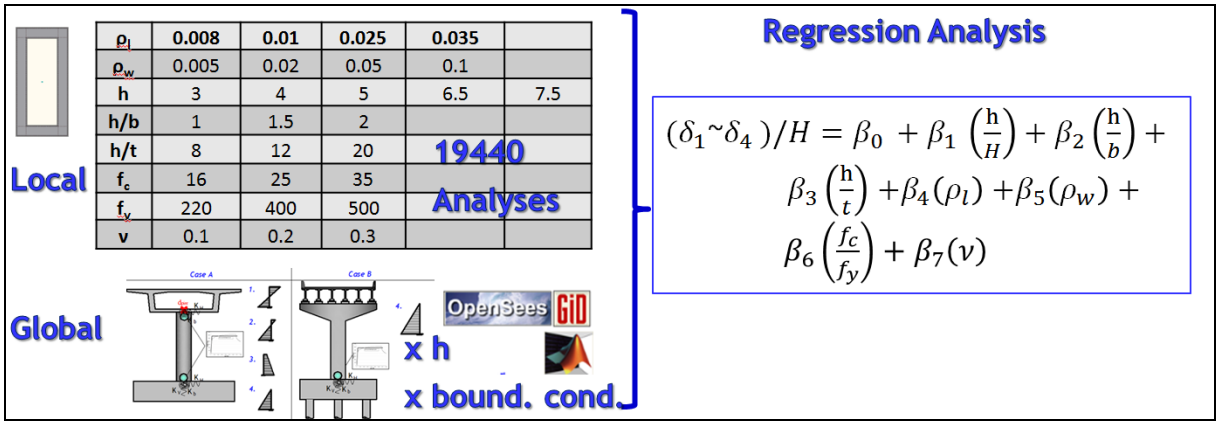


Figure 6: Bridge piers: Local to global engineering demand parameter mapping

$$\varphi_y = \exp[-5.76 - 0.736 \cdot \ln(f_c / f_y) - 0.01 \cdot \ln(v) + 0.295 \cdot \ln \rho_l + 0.091 \cdot \ln \rho_w] \cdot D$$
$$M_y = \exp[-0.339 - 0.638 \cdot \ln(f_c / f_y) + 0.224 \cdot \ln(v) + 0.5578 \cdot \ln \rho_l + 0.0557 \cdot \ln \rho_w] \cdot (2 \cdot \pi \cdot R^3 \cdot f_{cd}) \quad (1)$$

Since the main goal is to define bridge capacity and threshold limit state values in displacement terms, an inelastic generalised single-degree of freedom model is set up. All different bridge pier section types are analysed, namely cylindrical, hollow cylindrical, rectangular, hollow rectangular and wall type, while different pier height range is considered according to the pier type (i.e. 5~20m for cylindrical pier type and 20~50m for hollow rectangular). It should be noted that both weak and strong axis orientation were examined for rectangular shaped piers. Lumped plasticity model is used (bilinear moment-curvature curve), while the plastic hinge length is taken equal to $L_{pl}=0.09L_s+0.2h$ for rectangular, hollow rectangular and wall type piers and $L_{pl}=0.09L_s+2D/3$ for circular and hollow circular according to [16] .

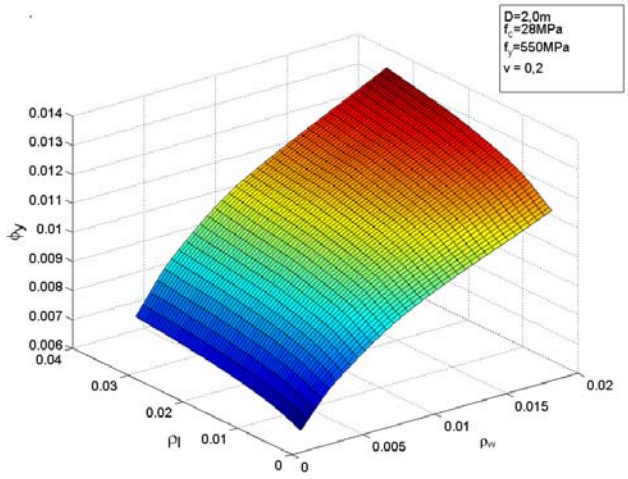


Figure 7: φ_y-ρ_l-ρ_w diagram for cylindrical piers

Nonlinear static (pushover) analyses of the single-degree of freedom models are performed individually for each pier type case (and both strong and weak axis orientation) and the displacement of cantilever top (component control point) at the time step that the deformation of

the plastic hinge exceeds threshold limit state values (φ_1,φ_2,φ_3,φ_4 in table 2) is recorded. Shear failure mode is considered, since the shear demand at each step is compared with the ultimate shear capacity and the displacement value associated with LS4 is recorded and compared with the one derived considering flexural failure. It should be recalled at this point that the reduction in the V_c contribution with increasing curvature ductility is considered.

Practically all possible combinations of properties and pier heights are considered (e.g. ~51800 analyses for the case of hollow rectangular piers) and threshold limit state values in displacement terms (δ_1,δ_2,δ_3,δ_4) are obtained. Analysis results are processed using the advanced least squares method (robust fit) and empirical relationships for threshold δ_i values are provided for every different pier type (equations 2 for the case of cylindrical piers).

Depending on the boundary conditions, i.e. the type of pier to deck connection and the type of foundation, the moment pier diagram may vary, as shown in figure 8. Therefore the equivalent cantilever height x_o, corresponding to the height of the contraflexure point should be estimated in order to use the proposed empirical relationships, derived from cantilever analysis.

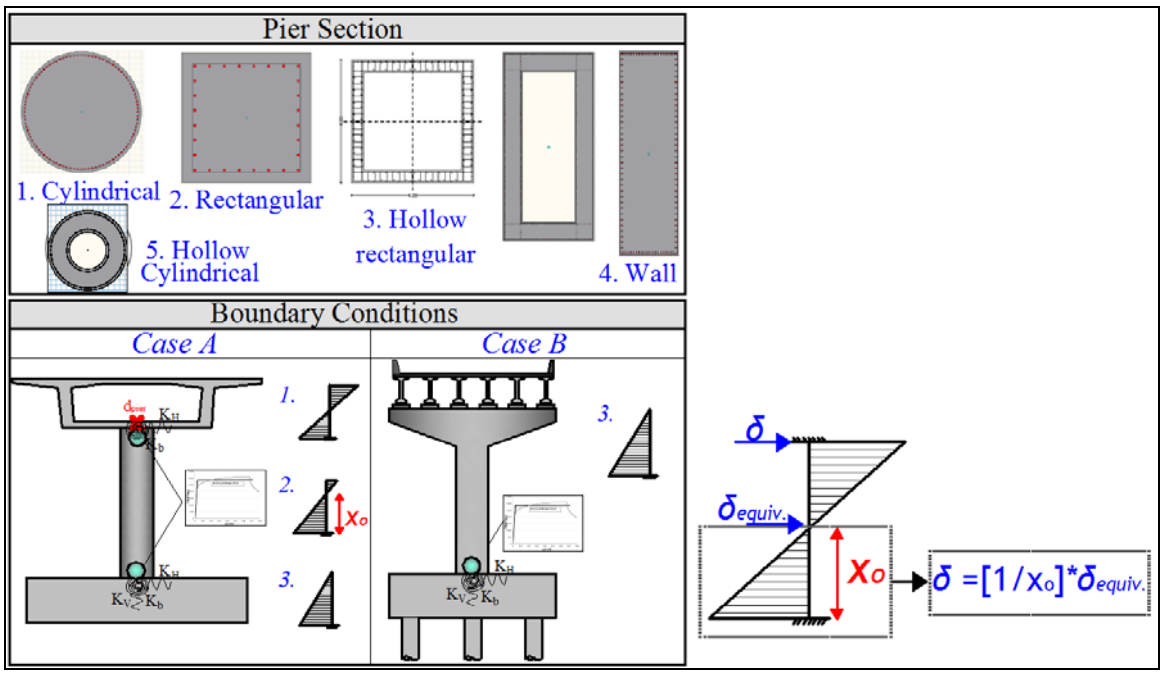


Figure 8: Pier types and boundary conditions

$$\begin{aligned}
\delta_1 &= \exp[-6.600 - 0.892\cdot\ln(D/H) - 0.003\cdot\ln(\mathrm{v}) - 0.700\cdot\ln(f_c/f_y) + 0.089\cdot\ln(\rho_w) + 0.275\cdot\ln(\rho_l)]\cdot H \\
\delta_2 &= \exp[-5.594 - 0.553\cdot\ln(D/H) - 0.288\cdot\ln(\mathrm{v}) + 0.027\cdot\ln(f_c/f_y) + 0.026\cdot\ln(\rho_w) - 0.110\cdot\ln(\rho_l)]\cdot H \\
\delta_3 &= \exp[-2.909 - 0.415\cdot\ln(D/H) - 0.243\cdot\ln(\mathrm{v}) - 0.403\cdot\ln(f_c/f_y) + 0.505\cdot\ln(\rho_w) - 0.122\cdot\ln(\rho_l)]\cdot H \\
\delta_4 &= \exp[-2.560 - 0.369\cdot\ln(D/H) - 0.339\cdot\ln(\mathrm{v}) - 0.398\cdot\ln(f_c/f_y) + 0.384\cdot\ln(\rho_w) + 0.019\cdot\ln(\rho_l)]\cdot H
\end{aligned} \quad (2)$$

The empirical relationships proposed are applied and results regarding all different pier types examined are presented in figures 9 and 10 in terms of dimensionless parameters (displacement ductility and drift) for them to be comparable. Curvature at yield and available curvature ductility (related to displacement ductility via the plastic hinge length) of hollow rectangular and wall pier type sections is less compared to circular, hollow circular and rectangular section. However, the fact that different constitutive models for confined concrete are used for the case of circular [14] and rectangular sections [15] should be highlighted, since the results are dependent on the ultimate strain value ε_{cu}.

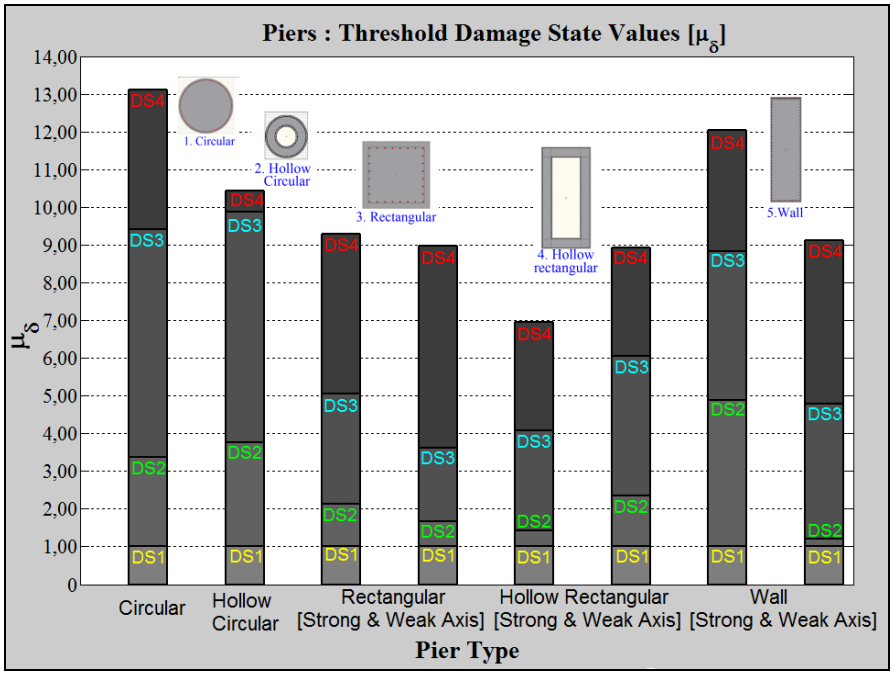


Figure 9: Displacement ductility for all limit states and pier types

As depicted, the threshold capacity values for the four limit states considered (minor, major, extensive and collapse), vary depending on the pier type, therefore a uniform value may either overestimate or underestimate the component's capacity. Detailed results regarding pier component capacity can be found in the technical report of RETIS-Risk (Aristeia II) research programme (expected to be available in July 2015).

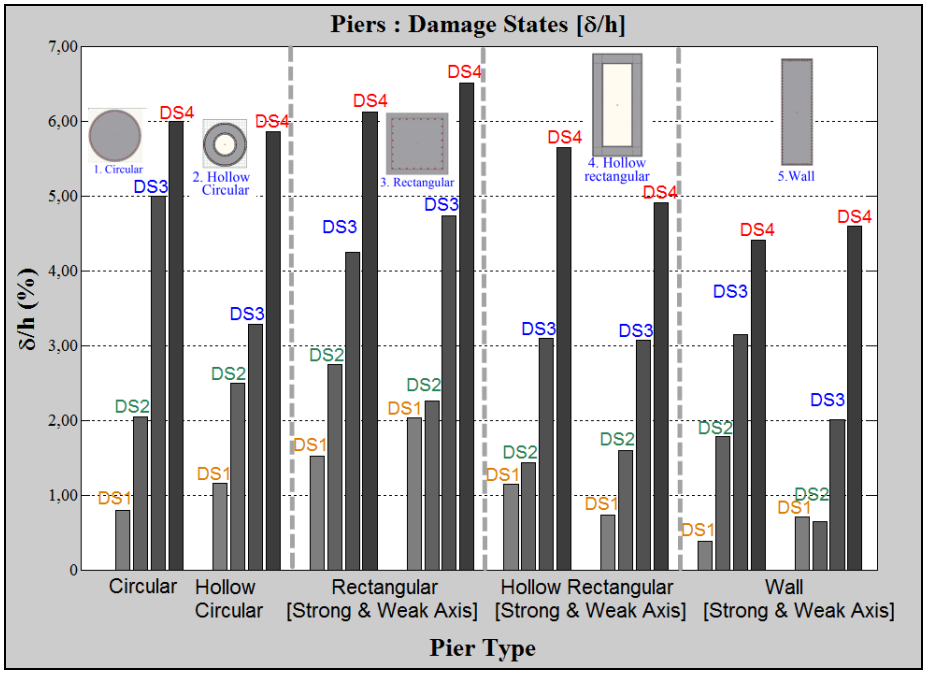


Figure 10: Drift for all limit states and pier types

Uncertainty in capacity is considered, assuming the distribution of random variables with mean and standard deviation values as shown in Table 3, according to [11], [17]. Again, Latin Hypercube sampling is used for 100 realizations of each different pier type. Analysis results

are processed and β_c values are proposed for every different pier type and limit state. For example, analysis of the sample size of cylindrical bridge piers resulted in different β_c values for every limit state, in particular β_{c1}=0.22, β_{c2}=0.35, β_{c3}=0.44, β_{c4}=0.53.

Random Variable	Distribution	Mean	COV
f_c (MPa)	normal	34.5	18%
f_y (MPa)	normal	463	8%
$\varepsilon_{cu}/\varepsilon_{cu,conf.\ model}$ (%)	normal	0.99	35.8%
L_{pl} / $L_{pl(Biskinis)}$	uniform	0.96	47.4%

Table 3: Assumed distributions for random variables related to pier capacity)

Limit state definitions for the abutments are given in Table 4 [11]. Inelastic static (pushover) analysis is performed for the abutment subsystem in order to define the threshold value in terms of displacement of the control point for the first limit state (the other three states are directly expressed in terms of fractions of the backwall height).

Limit State	Threshold values	Quantitative Performance Description
LS 1 – Minor/Slight damage	$\mu_{\varphi,backwall}$=1.5	Cracking and significant damage to the backwall
LS 2 – Moderate damage	$d = 0.01 \cdot h_{backwall}$	First yield of the abutment soil
LS 3 – Major/Extensive damage	$d = 0.035 \cdot h_{backwall}$	Excessive deformation of abutment soil
LS 4 – Failure/Collapse	$d = 0.1 \cdot h_{backwall}$	Ultimate deformation of abutment soil (cohessionless soil)

Table 4: Component Abutments: Threshold limit state values (global edp)

Limit State	Threshold values of shear strain (γ)	Quantitative Performance Description
LS 1 – Minor/Slight damage	100%	Initiation of nonlinear behaviour, potential yielding of anchor bolts and cracking of pedestals.
LS 2 – Moderate damage	150%	Visible damage to the bearing. Yield of steel shims.
LS 3 – Major/Extensive damage	200%	Lift off at the edge of the bearing, uplift and rocking. May cause delamination, bonding failure between rubber layers and steel shim plates.
LS 4 – Failure/Collapse	250%	Lift-off, rotation. Unseating, failure of bearings.

Table 5: Component Bearings: Threshold limit state values (global edp)

The engineering demand parameter used to define threshold limit state values for elastomeric bearings is the shear strain (γ=d/$t_{,rubber}$); threshold values based on information from the literature are given in Table 3. Pot bearings, frequently used in modern motorway bridges, have different failure modes and therefore threshold limit state values. Minor damage is related to the displacement that the lateral load exceeds 10% of the vertical load [12], while moderate, major and collapse limit states are defined according to [12].

5 BRIDGE COMPONENT SEISMIC DEMAND AND ASSOCIATED UNCERTAINTIES

As already mentioned, the median threshold value of the earthquake parameter (PGA,S_a,S_d) for every damage state is calculated using response spectrum analysis results for scaled accelerograms, based on the equal displacement approximation ($d_{elastic}$=$d_{inelastic}$). The main objective of the proposed methodology is the derivation of fragility curves for the longitudinal and transverse direction of the bridge, representing the conditional probability of reaching or exceeding a limit state as a function of the selected ground motion intensity parameter. Fitting of fragility analysis results to a lognormal distribution to express results in a probabilistic manner, requires the mean and standard deviation value for each component.

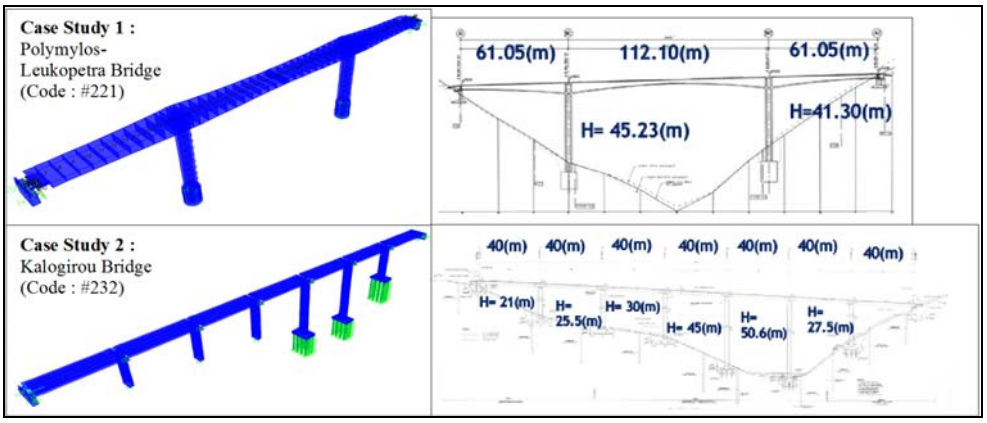


Figure 11: Case Study Bridges

Random Variable	Distribution	Mean	COV
f_c	normal	34.5 MPa	18%
f_y	normal	506 MPa	8%
gap size	normal	24.5 cm	20%
bearings	uniform	G=0.9 MPa	22%
soil properties	uniform	G=663 MPa	20%

Table 6: Assumed distributions for random variables (uncertainty in demand)

A Probabilistic Seismic Demand Model (PSDM) is used to estimate the dispersion value, representing the uncertainty in demand. It is recalled that there are two approaches regarding the implementation of the PSDM, namely the "cloud" (Probabilistic Seismic Demand Analysis) and the "scaling" (Incremental Dynamic Analysis) approach, with the latter having the advantage of not requiring an a priori assumption for the probabilistic distribution of seismic demands for fitting fragility curves [7]. The approach implemented herein is IDA for different levels of seismic action ranging from 0.1~1g. The limit state probability of exceedance at a specific IM level equals the occurrence ratio of the specific limit state, defined as the ratio of the number of damage cases n_i, for the damage state i over the number of simulations N, i.e.

$$P[(\mathrm{D} \geq \mathrm{DS}_i \,|\, I_M) = \frac{n_i}{N} \quad (\mathrm{i} = 1 to\, 4) \tag{3}$$

$$P[(\mathrm{D} \geq \mathrm{LS} | I_M) = \int_{-\infty}^{I_M} \frac{1}{I_M \cdot \sqrt{2\pi \cdot \hat{\beta}}} \cdot e^{\left\{ -\frac{[\ln(I_M) - \hat{\mu}]}{2 \cdot \hat{\beta}^2} \right\}} d(\mathrm{I}_M) \quad (4)$$

Standard deviation, is calculated for every bridge component (piers, bearings, abutments) based on the results of nonlinear response-history analysis of all the realizations considered and different levels of A_g. Their values are obtained from equation 5, where *M* is the number of realizations and a_i is associated with the onset of collapse for the i^{th} realization [18].

$$\hat{\beta} = \sqrt{\frac{1}{(\mathrm{M}-1)} \cdot \sum_{i=1}^{\mathrm{M}} (\ln(\mathrm{a}_i) - \hat{\mu})^2} \quad (5)$$

Two representative bridges of the most common categories in Greek motorways (#221-Polymylos-Leukopetra bridge and #232-Kalogirou bridge according to the classification scheme presented in §2) are studied. Another common category (overpass #121) has been studied and results can be found elsewhere [19], however they are briefly presented herein as well. Both case study bridges are part of the Egnatia Motorway. The structures are modelled and analysed using the OpenSees platform. For the formulation of the 3d model, elastic beam-column elements are used for the deck and beam-column with hinges (lumped plasticity) elements for the piers, as depicted in figures 12 and 13. Cross section analysis was performed for the piers to obtain moment-curvature diagrams for the potential plastic hinges (pier top and bottom for the case of monolithic pier-to-deck connection and pier bottom only for the case of connection through bearings), while the plastic hinge length L_p was calculated according to [16]. The abutment-backfill interaction (passive earth pressures) after gap closure was considered according to [11] .

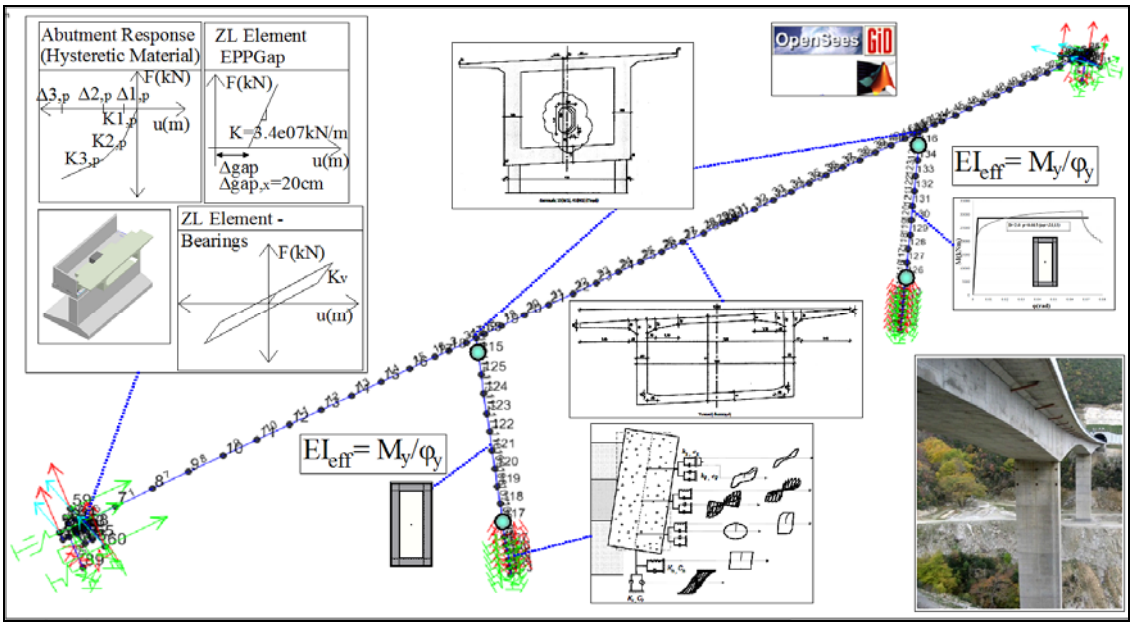


Figure 12: Polymylos-Lefkopetra Bridge (#221)

Uncertainty in demand is considered, assuming the distribution of random variables with mean and standard deviation values as shown in Table 6 [17], [20], [21]. Again Latin Hypercube sampling is used for 100 realizations of each different bridge. Accelerograms (7) for re-

sponse history analysis were selected using ISSARS (M=6.6~6.8 and R=20~40) and scaled according to EC8-Part 2 provisions [22]. A Matlab-code was generated in order to perform analysis for all realizations and various levels of earthquake intensity (i.e. 0.1~1g) resulting in a total of 7×10×100=7000 analyses for every bridge and every direction, and standard deviation value was calculated for all components considered.

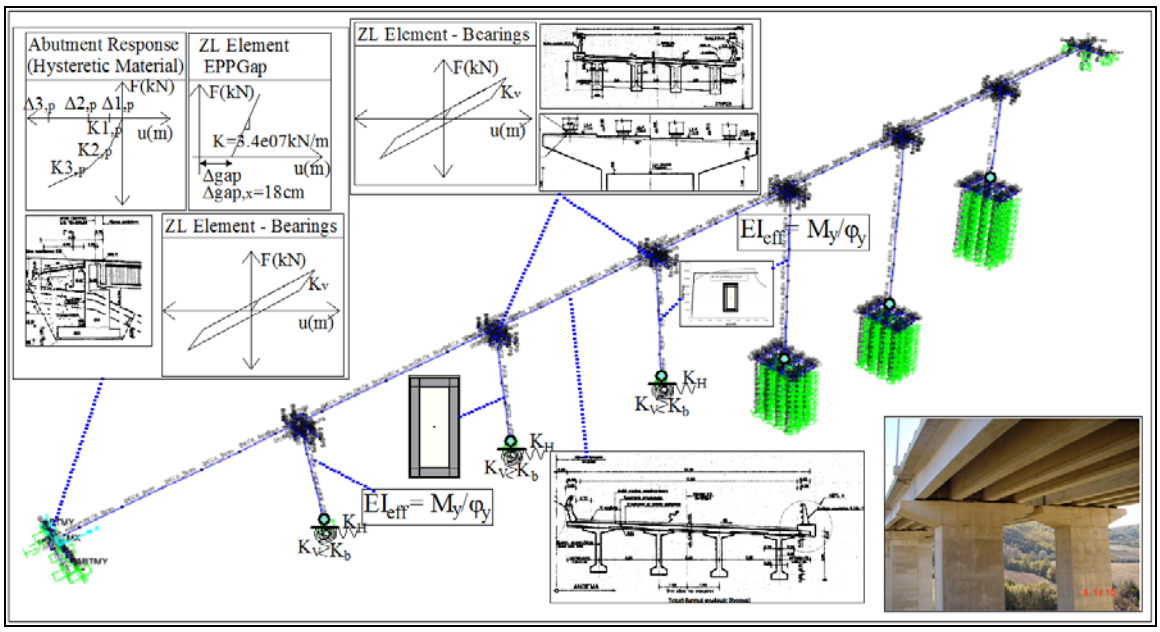


Figure 13: Kalogirou Bridge (#232)

Both cases studies involve long bridges, constructed in the early 2000s, having tall hollow rectangular piers monolithically connected to the deck in the case of Polymylos-Leukopetra bridge and connected through bearings in the case of Kalogirou bridge. Bridge piers are designed according to current provisions. Dispersion values for piers and bearings of the bridges studied are presented in tables 7 and 8. Uncertainties regarding the abutment response have not been taken into account at this stage of development (only uncertainty in gap size is included); therefore the relevant dispersion value is not presented herein.

	Polymylos_X (#221)				Kalogirou_X (#232)			
Component	$\beta_{d,LS1}$	$\beta_{d,LS2}$	$\beta_{d,LS3}$	$\beta_{d,LS4}$	$\beta_{d,LS1}$	$\beta_{d,LS2}$	$\beta_{d,LS3}$	$\beta_{d,LS4}$
Piers	26%	24%	13%	8%	30%	21%	15%	10%
Bearings	20%	18%	12%	10%	26%	19%	15%	11%

Table 7: Uncertainty in demand - β_d values for Polymylos and Kalogirou Bridge (X direction)

	T7_X OverPass (#121)			
Component	$\beta_{d,LS1}$	$\beta_{d,LS2}$	$\beta_{d,LS3}$	$\beta_{d,LS4}$
Piers	36%	30%	18%	12%
Bearings	29%	28%	22%	20%

Table 8: Uncertainty in demand - β_d values for T7 Overpass (X direction)

6 BRIDGE SYSTEM FRAGILITY

Bridge component capacity and demand as well as related uncertainties are calculated utilising the proposed methodology. The total uncertainty value is calculated for every component according to equation 6, under the assumption of statistical independence.

$$\beta_{tot} = \sqrt{\beta_C^2 + \beta_D^2 + \beta_{LS}^2} \tag{6}$$

Series connection between components is assumed for the calculation of bridge fragility, according to equation 7 (i: bridge components considered; namely bridge piers, bearings, abutments).

$$P(F_{br}) = 1 - \prod_{i=1}^{m} [1 - P(F_i)] \tag{7}$$

Since collapse of the bridge system is not expected to occur if bearings or abutments reach LS4 as described previously at a component level, limit state 4 at bridge (as a system) level is related to pier collapse only. Therefore series connection assumption is not invoked for the estimation of system fragility for the collapse limit state.

Fragility analysis is based on the results of response spectrum analysis of the simplified 3d bridge model described above. Two alternative connections of bearing and abutment linear springs depicted in figure 14 are considered for seat type abutments for the case of open and closed gap, respectively. Bridge-specific fragility curves are derived using the first model analysis results up to gap closure.

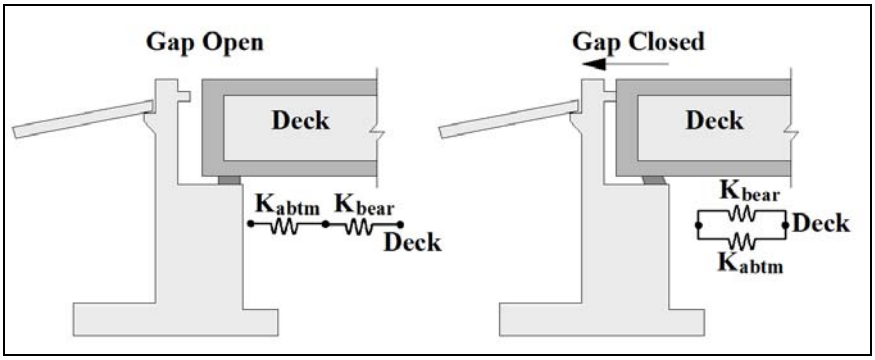


Figure 14: Pier types and boundary conditions

7 SOFTWARE DEVELOPMENT

A Matlab-based software was developed for the implementation of the previously described methodology and the derivation of bridge-specific fragility curves, briefly described in figure 15. The software is based on a generic simplified 3d bridge model created using the OpenSees platform [23]. Input data provided by the user are depicted in figure 15 and concern general bridge geometry and loading properties, component (pier, bearing, abutment) properties, and the (site-specific) response spectrum. Threshold limit state values for piers are automatically calculated according to the geometric, material, reinforcement, loading properties and boundary conditions of each case, while dispersion values, calculated in line with the previously described procedure, are included. Different boundary conditions at abutments are considered for the case of open and closed gap, and fragility curves are automatically calculated for longitudinal and transverse directions separately. The software developed is applied to 76 bridges of a Egnatia Motorway (Western Macedonia section), for the seismic assessment of the road network in the frame of RETIS-Risk (Aristeia II) research programme and

will be included in a GIS-based freeware for the management of seismic risk of roadway networks.

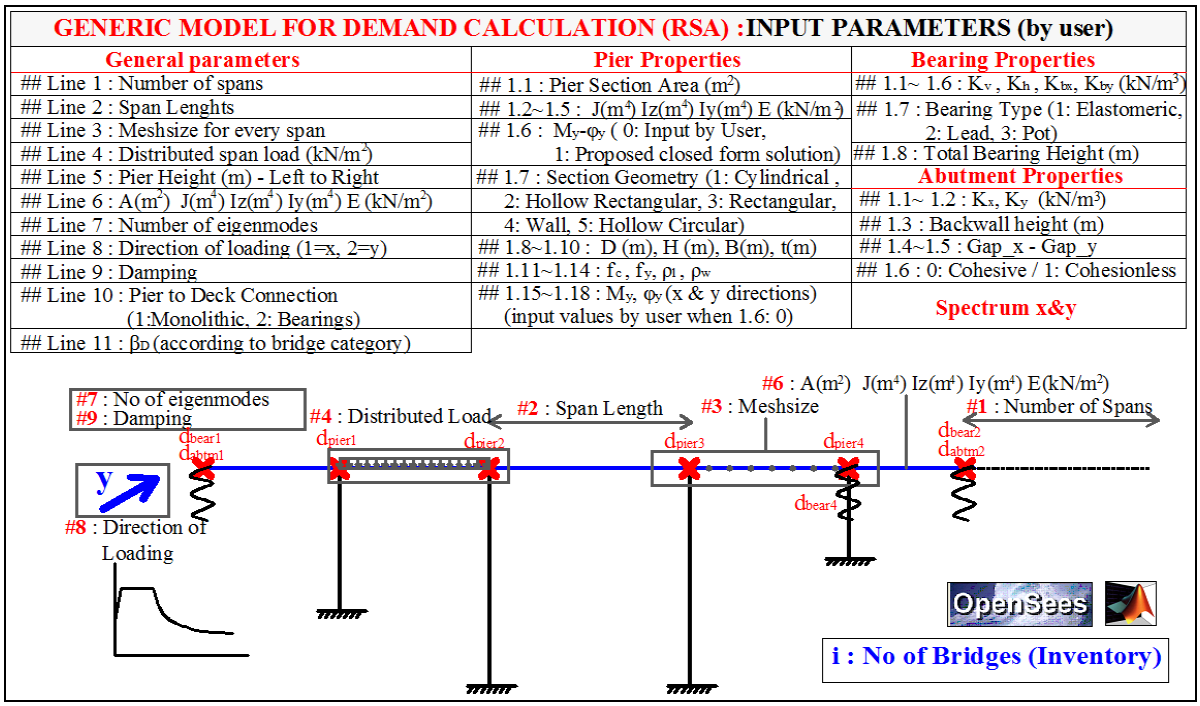


Figure 15: Input data 3d generic beam model

8 EXAMPLES OF BRIDGE-SPECIFIC FRAGILITY CURVES

Fragility curves of the two case study bridges described above are presented in Figures 16 and 17. Since bridges are designed according to code provisions, the probability that demand exceeds bridge capacity is low even for higher levels of earthquake intensity. For both bridges, the lower limit states are controlled by bearing damage, since the yielding of piers occurs for higher levels of earthquake intensity. Regarding the collapse limit state for the system, it is controlled by pier collapse limit state only, as discussed in section 6.

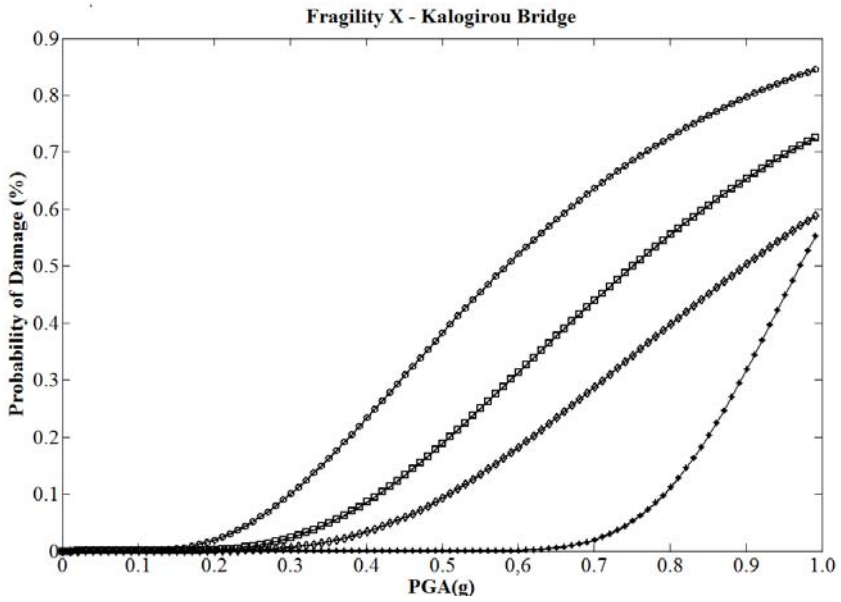


Figure 16: Fragility longitudinal direction (Kalogirou bridge)

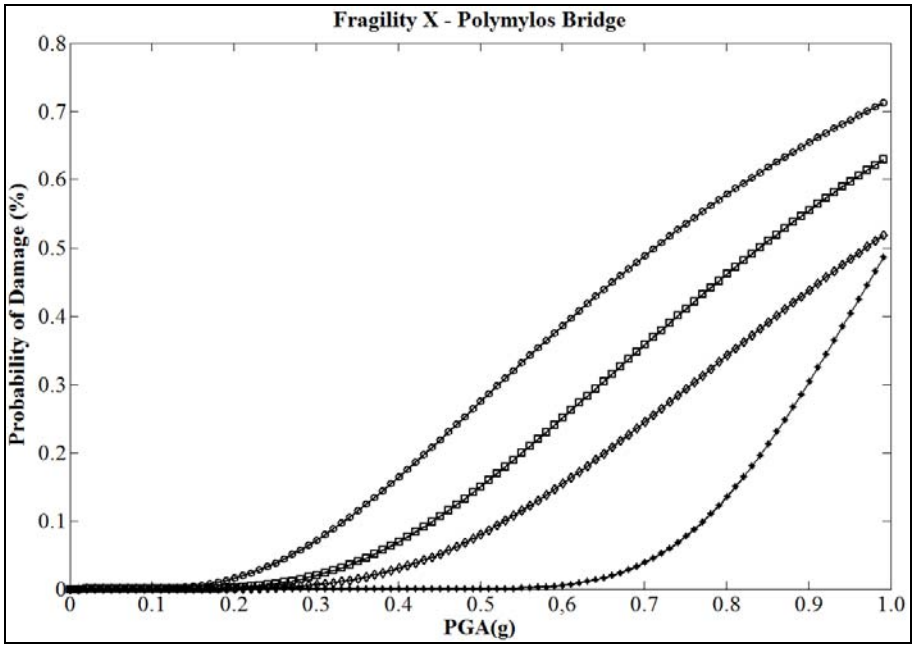


Figure 17: Fragility longitudinal direction (Polymylos Bridge)

It has to be noted that, as evident from Figures 16 and 17, the uncertainty (β_{tot}) associated with each individual fragility curve is generally different (see also Tables 7, 8), hence the different shape of the curves and the possibility of intersecting curves (e.g. for Polymylos Bridge when PGA exceeds about 1.0g). This is still a controversial issue worldwide, since while it is widely recognised that the uncertainty is different for each type, intersection of fragility curves is conceptually incorrect.

9 CONCLUSIONS

The conclusions reached at this stage of this ongoing study can be summarised as follows:

- All critical components should be considered for the derivation of bridge fragility curves. In addition to those addressed herein (piers, abutments, bearings), one could also consider foundation elements that might be critical in some bridge types.
- Threshold limit state values of components should be expressed in global terms (typically displacements) and correlated to relative local damage.
- Different geometry, material, reinforcement, loading properties as well as boundary conditions, affect component capacity and threshold limit state values and should be taken under consideration during fragility analysis.
- Uncertainty in capacity, demand, and limit state definition should be estimated for every component and limit state separately.
- Bridge-specific fragility curves should be based on the results of a simplified 3d model in order to account for the correlation between different components and the dependence of the displacement profile on deck geometric properties and boundary conditions.
- Feasible methodologies for the derivation of bridge-specific fragility curves are those that can be readily applied to a bridge inventory with a view to estimating earthquake losses of a roadway network.

Acknowledgement

This research has been co-financed by the European Union (European Social Fund – ESF) and Greek national funds through the Operational Program "Education and Lifelong Learning" of the National Strategic Reference Framework (NSRF) – Research Funding Program: *ARISTEIA II: Reinforcement of the interdisciplinary and/or interinstitutional research and innovation*



The authors would like to acknowledge the fruitful discussions and the coooperation of other members of the research team of the above programme, in particualrly those working on Work Packages 2 and 8.

REFERENCES

[1] I.F. Moschonas, A.J. Kappos, P. Panetsos, V. Papadopoulos, T. Makarios, P. Thanopoulos, Seismic fragility curves for greek bridges: methodology and case studies. *Bulletin of Earthquake Engineering*, 7(2), 439-468, 2008.

[2] R. DesRoches, B. Nielson, J. Pagett, Fragility Curves for Mid-America Bridges. *8th U.S. National Conference on Earthquake Engineering*. San Fransisco, California, 2006.

[3] E. Choi, R. DesRoches, B. Nielson, Seismic fragility of typical bridges in moderate seismic zones. *Engineering Structures*, 26(2), 187-199, 2004.

[4] S. Banerjee, M. Shinozuka, Nonlinear Static Procedure for Seismic Vulnerability Assessment of Bridges. *Computer-Aided Civil and Infrastructure Engineering*, *22*(4), 293–305, 2007.

[5] D. Cardone, G. Perrone, M. Dolce, Seismic risk assessment of highway bridges. *1st US-Italy Seismic Bridge Workshop*. Pavia, Italy,2007.

[6] M. Berry, M. Eberhard, *Performance Models for Flexural Damage in Reinforced Concrete Columns*. PEER Report 2003/18, University of Washington.

[7] J. Zhang, Y. Huo, Evaluating effectiveness and optimum design of isolation devices for highway bridges using the fragility function method. *Engineering Structures,* 31, 1648-1660, 2009.

[8] P. Towashiraporn, Building Seismic Fragilities using Response Surface Metamodels. *Ph.D. Thesis,* Georgia Institute of Technology, 2004.

[9] Kappos, A., Sextos, A., Stefanidou, S., Mylonakis, G., Pitsiava, M., Sergiadis, G., "Seismic Risk of Inter-Urban Transportation Networks", Procedia-Economics & Finance vol. 18, 2014, 263 – 270.

[10] A. Mori, P.J. Moss, N. Cooke, A.J. Carr, The Behavior of Bearings Used for Seismic Isolation under Shear and Axial Load. *Earthquake Spectra,* 15(2), 199-224, 1999.

[11] B.G. Nielson, Analytical Fragility Curves for Highway Bridges in Moderate Seismic Zones. *Ph.D. Thesis,* Georgia Institute of Technology, 2005.

[12] J.F. Stanton, C.W. Roeder, T.I. Campbell, *High-Load Multi-Rotational Bridge Bearings.* NCHRP Report 432, National Academy Press, Washington, 1999.

[13] V.K. Papanikolaou, Analysis of arbitrary composite sections in biaxial bending and axial load. *Computers and Structures*, 98-99, 33-54, 2012.

[14] J.B. Mander, M.J.N. Priestley, R. Park, Theoretical Stress-Strain Model for Confined Concrete. *Journal of Structural Engineering*, 114(8), 1804-1826,1988.

[15] A.J. Kappos, Analytical Prediction of the Collapse Earthquake for R/C Buildings: Suggested Methodology. *Earthquake Engineering and Structural Dynamics*, 20, 167-176, 1991.

[16] D. Biskinis, Strength and deformation capacity of as-built and retrofitted R/C members. *Ph.D. Thesis,* University of Patras, 2007. (in greek)

[17] C. Dymiotis, A.J. Kappos, M.K. Chryssanthopoulos, Seismic Reliability of R/C Frames with Uncertain Drift and Member Capacity. *Journal of Structural Engineering*, 125(9), 1038-1047 ,1999.

[18] K. Porter, R. Kennedy, R. Bachman, Creating Fragility Functions for Performance-Based Earthquake Engineering. *Earthquake Spectra*, 23(2), 471-489, 2007.

[19] S.P. Stefanidou, A.J. Kappos, Optimum Selection Of Retrofit Measures For R/C Bridges Using Fragility Curves. *4th ECCOMMAS Thematic Conference on Computational Methods in Structural Dynamics and Earthquake Engineering*. Kos Island, Greece, 12-14 June 2013.

[20] D. Tavares, J.Padgett, P. Paultre, Fragility curves of typical as-built highway bridges in eastern Canada. *Engineering Structures*, 40, 107-118, 2012.

[21] M. Fardis, V. Kolias, T. Panagiotakos, C. Katsaras, T. Psychogios, *Guide for Bridge Design with emphasis on Seismic Aspects.* Report No. SEE 2012-01, University of Patras.

[22] E.I. Katsanos, A.G. Sextos, ISSARS: An intergrated software environment for structure-specific earthquake ground motion selection. *Advances in Engineering Software*, 58, 70-85, 2013.

[23] F. McKeena, G.L. Fenves, *Open System for Earthquake Engineering Simlation*. Pacific Earthquale Engineering Research Center, Version 2.4.5, 2015.

COMPDYN 2015
5th ECCOMAS Thematic Conference on
Computational Methods in Structural Dynamics and Earthquake Engineering
M. Papadrakakis, V. Papadopoulos, V. Plevris (eds.)
Crete Island, Greece, 25–27 May 2015

SEISMIC RETROFITTING OF R/C BRIDGES WITH THE USE OF UNBONDED TENDONS

Olga G. Markogiannaki[1], **Ioannis S. Tegos**[2]

[1] Aristotle University of Thessaloniki
54124, Thessaloniki
e-mail: markogiannaki.olga@gmail.com

[2] Professor, Aristotle University of Thessaloniki
54124, Thessaloniki
itegos@civil.auth.gr

Keywords: Seismic Retrofit, Unbonded Tendons, Bridge, Restrainer.

Abstract. *It is widely known that retrofit processes are based on two different retrofit approaches that depend on the treatment of the general safety inequality which requires the capacity to always exceed the demand. The first retrofit approach, direct, includes strengthening of specific bridge members which refers to an increase in capacity that shows focus on the first term of the safety inequality. The second retrofit approach, indirect, includes force limitation or response modification that lowers the demand (second term of the safety inequality) to the level of the existing member's capacity. Characteristic examples of indirect retrofit approaches are seismic isolation and, in general, methods that include the addition of new structural members in the bridge system and/or the activation of non-seismic members. It can be claimed that the advantage of indirect retrofit approaches when compared to direct ones is that they do not depend on the existing member's capacity, while they transfer the seismic forces to new structural members that are highly reliable. In view of the above, the key objective of this paper is to present an alternative retrofit system that follows the indirect retrofit approach that involves the use of unbonded tendons. In this study the tendons are used innovatively for restraining the longitudinal seismic direction. The proposed system is based on previous studies on the use of common steel rebars, which are placed in the bridge superstructure and activated as struts - ties under longitudinal earthquake. Regarding the proposed system, the tendons are placed in the bridge sidewalks at the outer spans through the abutments and the struts - ties response is achieved with appropriate prestressing. The research work performed focuses on evaluating the effectiveness of the application of the proposed retrofit system on R/C multi-span bridges while dealing with in-service issues, as well. The retrofitted bridges were properly modeled with nonlinear elements. The demand of the structural systems was computed using time-history analysis. The time history analyses were performed using a suite of representative ground motions and multiple parameters regarding bridge and the proposed system characteristics were studied. The results of the analyses are presented and show the significant restraining response of the proposed system.*

1 INTRODUCTION

In the last decades, there have been several research efforts for developing effective seismic retrofit methods [1]. Generally, retrofit solutions aim on complying with the safety inequality [2], Eq.(1), which requires the structural capacity of bridge members to exceed seismic demand at all times.

$$Capacity \geq Demand \quad (1)$$

According to Rustum (2012), [3], the various retrofit methods can be summarized in two retrofit philosophies depending on the focus of each procedure on the first or second term of Eq.(1). The first retrofit philosophy which is the direct approach involves methods that are applied on the as-built bridge components with the goal to increase their capacity against seismic loads. For instance, these methods include pier retrofit with steel or concrete jackets or FRP materials,[4]. It shall be noted that the structural capacity of the existing bridge members can be determined with a series of tests, but since the capacity estimation depends on sample measurements it is not considered equally reliable to the estimation of the new structural member's capacity and it may result in misidentifying hidden deficiencies that are not apparent and have severe consequences on the effectiveness of a direct approach retrofit method or in overdesigning the retrofit solution. The second retrofit philosophy, indirect approach, involves the addition of new members in the bridge structural system. The new bridge components are intended to reduce the seismic demand on the as-built bridge members at the level of their structural capacity and they are properly designed for contributing to the seismic resistance by receiving the seismic forces. Such common indirect approach retrofit methods include the use of bearings or energy dissipating devices, i.e. dampers[5], or restrainer cables[6]–[8]. It can be claimed that the advantage of indirect retrofit approaches when compared to direct ones is that they do not depend on the existing member's capacity, while they transfer the seismic forces to new structural members that are highly reliable. A key point in the effectiveness of such methods is the timely activation of the mechanism installed on the bridge; otherwise it is possible that the capacity of the existing components will be exceeded before the activation of the seismic contribution of the retrofit system. In the case of continuous monolithic concrete bridges appropriate indirect retrofit methods are devices like dampers, whilst bearings and restrainer cables are more often used for simply supported bridges, [9],[10].

The key objective of the present study is to study an alternative indirect retrofit approach method which aims on upgrading bridge seismic response by restraining the longitudinal seismic movements. The proposed method involves unbonded tendons and is based on other restraining systems that have been proposed by the authors for limiting longitudinal bridge movements that use steel rebars ,[11], [12] and FRP strips [13] that are applied longitudinally in the bridge superstructure receiving tension and compression loading. The mechanism involving the unbonded tendons has already been proposed by the authors for the design of new bridges[14]. The system can be applied in common monolithic bridges, mainly, and the expected tendons response that reduces their longitudinal movements can be characterized similar to that of seismic links,[15], and dampers which dissipate seismic energy in seismically isolated bridges,[16].

Prestressing in bridges is mostly used for providing necessary resistance to the superstructure's vertical loading and to ensure that concrete stays within its tensile and compressive capacity under the range of the loads applied, [17]. It can be applied with tendons (wires, strands, bars) that are of high strength steel. They can be either internal or external,[18], to the concrete member and can be bonded or unbonded to the structure's concrete. External prestressing can be a rational strategy for strengthening existing bridge superstructures against

increased traffic loading demands, as well,[19].Some research efforts have been conducted for utilizing prestressing for upgrading bridge's seismic response, as well. These methods belong to the direct retrofit approach, focus on increasing the pier's capacity against seismic demand and take several forms, such as enhancing pier's flexural resistance with prestressed tendons and rebars [20],[21], introducing prestressed confinement systems for piers, i.e. prestressed FRP strips [22] or prestressing pile and pier caps [1]. Some researchers have investigated the use of unbonded prestressing tendons for limiting the horizontal displacements but their applications are limited to beams in building frame and wall systems [23],[24].

In view of the above, the proposed method can be an alternative approach of the use of unbonded tendons in seismic retrofitting.

2 UNBONDED TENDONS PROPOSED MECHANISM

The restraining system can be described as a mechanism that reduces bridge seismic movements through the activation of its components for both earthquake signs in the longitudinal direction. The restraining system involves the installation of four symmetric groups of unbonded tendons in the sidewalks of the deck of the bridge. The tendons are of high strength steel (i.e. S1570). They are installed along the longitudinal direction of the bridge and each two groups are placed in the outer spans of the bridge extending beyond the abutments' wing walls. The unbonded tendons avoid bonding with the concrete of the bridge. At the positions where the unbonded tendons are installed the sidewalks are replaced with new ones of high strength concrete and the new sidewalks are connected with the deck with dowels. The tendons are anchored at a new pile-diaphragm structure behind the wingwalls, where the seismic forces can be transferred safely without increasing seismic demand on the abutments. The pile diaphragm consists of concrete members which have equal width to that of the wingwalls.

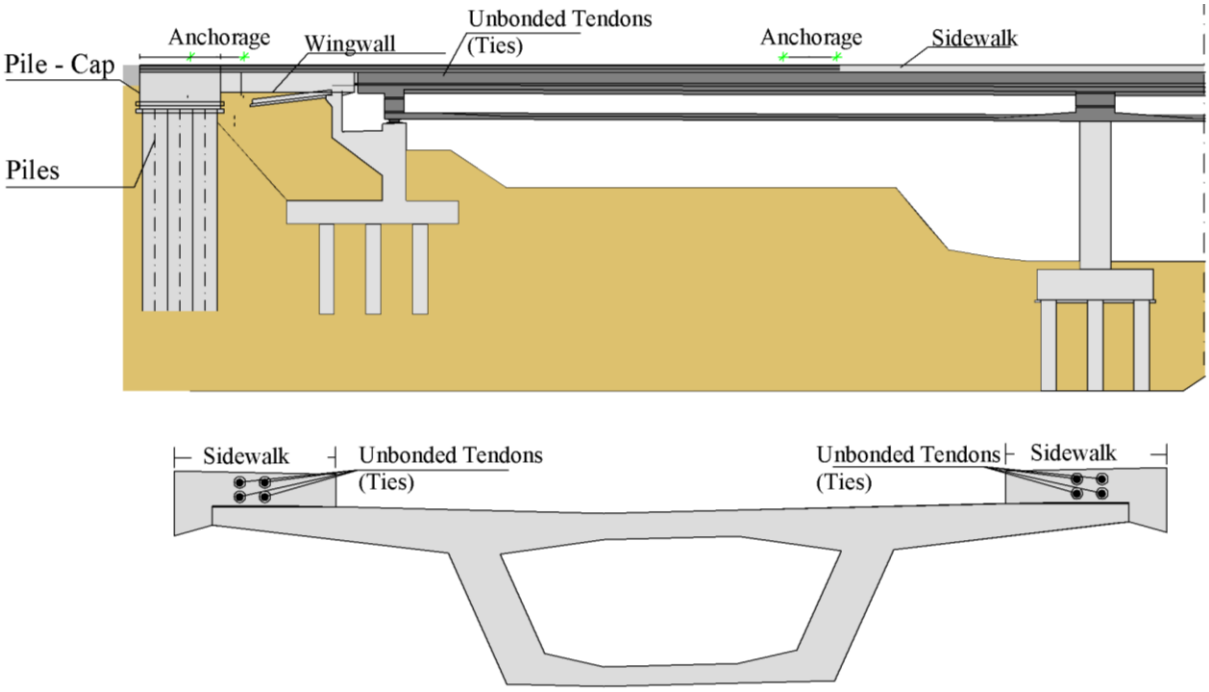


Figure 1: Restraining System. a. Longitudinal view of the bridge, b. Detail 1: cross section of the deck of the bridge

The unbonded tendons receive seismic forces under seismic excitation and limit the longitudinal seismic displacements. The proposed restraining system is an evolution of the struts-ties system that has been proposed by the authors, which uses common steel rebars placed in the superstructure instead of tendons. Although the steel rebars are a reliable solution, as well, they require special care for buckling protection at the positions of the outer expansion joints in order to respond as a struts-ties system. Prestress allows the tendons to receive "compression" loading in terms of lower tensile stresses. Therefore, the prestressed tendons are considered as an efficient alternative system that can develop a "strut" behavior by decreasing their initial prestress (tensile stress). Since the tendons cannot receive compression stresses, the design of the system shall ensure that the seismic demand in the "compression direction will not exceed the tension region. Figure 2 shows the tendon's response

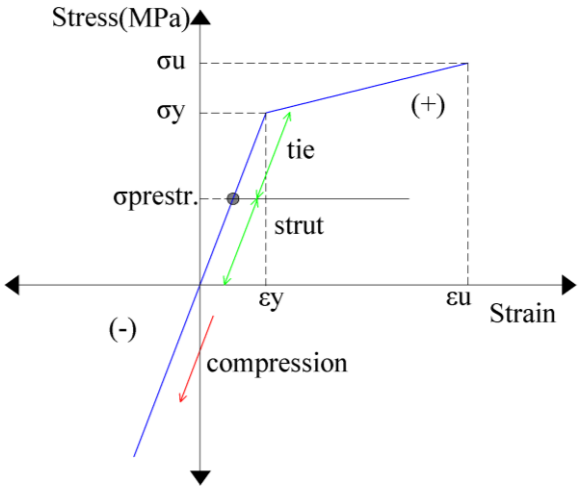


Figure 2: Unbonded tendon response

Furthermore, the proposed mechanism is activated by in service loading, as well. The tendons are in tension during deck contraction and are "compressed" during deck expansion. It is ensured that with in-service loading the proposed mechanism does not arise any issues related to the response of the deck (early cracking) due to the imposed eccentric moments by the mechanism. Analytical investigation shows that an exaggerate size of the mechanism would be required in order to increase the in-service demand on the deck.

In view of the above the determination of the initial prestress shall take into account both seismic and service loads. The initial prestress shall be equal to half of the yielding stress plus a stress caused by in service loads, which is decreased by a factor of 0.5 according to Eurocode 8 provision that service loads are accounted with low values during earthquake events, as shown in Equation 2. In Equation 2 σ_{yd} is yielding stress, E_s is the modulus of elasticity, ΔT is uniform load temperature which corresponds to the critical in service load, L_{tot} is the length of the bridge, l_{eff} is the length of the tendons inside the bridge, l is the total tendon length.

$$\sigma_{prestr.} = \frac{\sigma_{\max}}{2} = \frac{1}{2}\sigma_{yd} + \sigma_{\Delta T_{AV}} = \frac{1}{2}\sigma_{yd} + (E_s * \frac{0.5 * \alpha * \Delta T * (\frac{L_{tot}}{2} - leff + l)}{l}) \quad (2)$$

Regarding the design of the system the elastic response of the tendons under in-service loading is considered as a prerequisite. More specifically, the maximum allowable strain(or stress) for service loading is determined equal to 70% of the yielding strain(or stress). The

minimum tendon length can be determined by equations 3 and 4, based on similar equations for the previous systems ([11], [12]), where $\Delta T_{,con}$ is the contraction temperature which corresponds to the critical in service load and ε_{smax} is the yielding stress.

$$\Delta l = a * \Delta T_{N,con} * \left[\frac{L_{tot}}{2} - l_{eff} \right] + a * \Delta T_{N,con} * \left(l - 2l_b \right) \tag{3}$$

$$\frac{\Delta l + \Delta l_{prestr}}{l - 2l_b} = 0.7 * \varepsilon_{s\max} \tag{4}$$

Regarding the seismic design of mechanism, the size of the tendons is determined according to the seismic demand in order to avoid excess seismic loads beyond the capacity of the prestressed tendons.

3 DESCRIPTION OF REFERENCE BRIDGE

The Reference Bridge that was used foe the analytical study is a monolithic three span prestressed R/C bridge. The end spans are 45.10m, the middle is 45.60m and the total length is 135.80m. The deck is a concrete box section, connected to the piers monolithically, and is supported on the abutments by low friction sliding bearings. The piers are circular and are founded on 3x3 pile groups. The bridge's abutments are seat-type and have transverse seismic links-stoppers. The bridge is founded on ground type B and the area is in seismic zone I, [25]. A 3-D finite element bridge model, Fig. 3, was generated in the analysis software OpenSees, [26], accounting for abutment-embankment interaction.

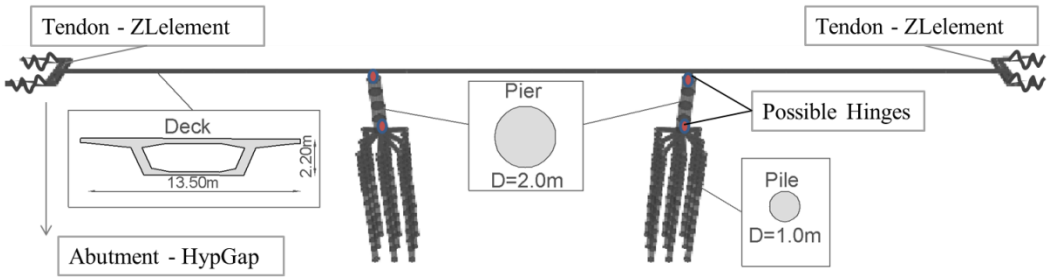
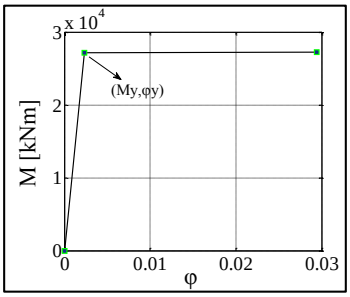


Figure 3 : 3-D Reference Model

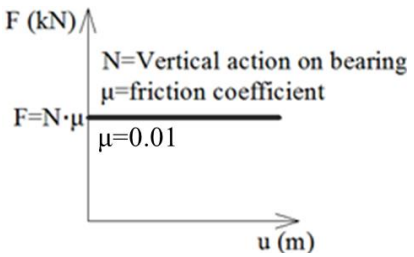


(a)

$$F_{(X)} = \frac{x}{\frac{1}{K_{max}} + R_f \frac{x}{F_{ult}}}$$

Kmax [Kn/m]	81000
Rf	0.7
Fult [kN]	-2739
Gap [m]	-0.07

(b)



(c)

Figure 4 : a)M-φ curve, b) Abutment P-Y curve, c) Sliding Bearing

Bridge members are modeled with frame elements with material nonlinearities. The section analysis, Fig 4(a), for the assignment of concentrated plasticity (hinges) at the top and bottom of piers was performed with AnySection v4.0.6,[26,27]. The foundation springs were provided by the geotechnical report. The passive resistance of the abutments due to embankment

mobilization was simulated according to Shamsabadi guidelines [12],[13] and the HyperbolicGap compression material was used in OpenSees, Fig 4(b). The sliding Bearings were modeled as shown in Fig 4(c).

The proposed mechanism is modeled as nonlinear springs as shown in Fig. 5, where K s the initial stiffness of the group of tendons equal to EA/L, (E is the modulus of Elasticity, A cross section of tendons, L length of tendons

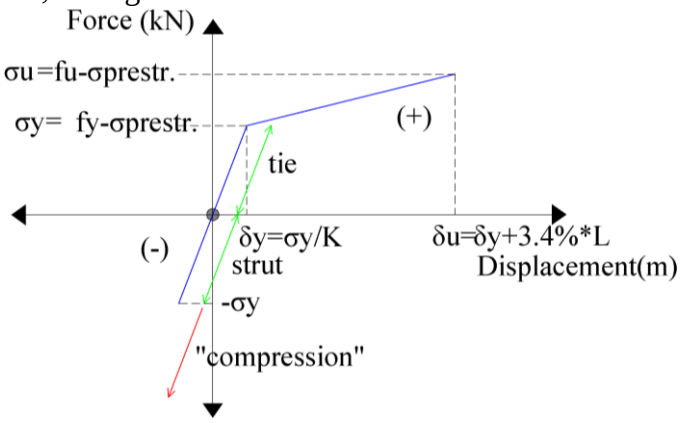


Figure 5 : Tendon nonlinear model

4 ANALYTICAL STUDY

4.1 Parameters

A number of parameters are utilized to screen the effects of the application of the proposed mechanism on the seismic response of continuous concrete box girder bridges. The parameters considered involve the mechanism characteristics and the earthquake intensity.

The first set of parameters consists of the mechanism characteristics. In particular, the effect of the cross-section and the number of tendons each bundle that are installed in the outer spans of the bridge is screened. The variable characteristics correspond to various effective stiffness values of the mechanism that influence the seismic response and the distribution of forces on the bridge. Regarding seismicity, all parameters are screened for the three seismic design intensity levels (I, II and III) according to Eurocode 8, [1]. Seismic zone I is the design intensity level, while the other two levels are used for upgrading the bridge with the same pier dimensions to higher seismic levels by installing in the bridge system the proposed mechanism. For each seismic design level, five artificial accelerograms were used that were compatible to the respective spectrum of Eurocode 8. The parameter values used in the study are presented in Table 1. In Table 2 the specific tendon characteristics are shown. The minimum length of the longitudinal tendons is determined based on equations (3) and (4).

PARAMETERS	VALUES
Diameter of Tendons (mm)	7T15 15T15
No. of Tendons/Bundle	1 2 3 4
Seismicity	0.16g 0.24g 0.36g

Table 1: Parameter Values

5.2 Results Discussion

Table 3 includes the analysis results for the Reference Bridge for the three intensity levels and maximum longitudinal movements, moments and shear forces on piers.

E=190 GPa Fy=1570 MPa										
Tendons	L [m]	A [cm2]	K [kN/M]	σprestr[Mpa]	σy [Mpa]	σu [Mpa]	Fy [kN]	δy [m]	Fu [kN]	δu [m]
1*7T15	41.00	12.37	5732.45	701.56	663.44	776.70	820.68	0.14	960.78	1.54
2*7T15	41.00	24.74	11464.90	701.56	663.44	776.70	1641.36	0.14	1921.57	1.54
3*7T15	41.00	37.11	17197.35	701.56	663.44	776.70	2462.04	0.14	2882.35	1.54
4*7T15	41.00	49.48	22929.80	701.56	663.44	776.70	3282.72	0.14	3843.13	1.54
1*15T15	41.00	26.51	12283.82	701.56	663.44	776.70	1758.60	0.14	2058.82	1.54
2*15T15	41.00	53.01	24567.64	701.56	663.44	776.70	3517.20	0.14	4117.64	1.54
3*15T15	41.00	79.52	36851.46	701.56	663.44	776.70	5275.80	0.14	6176.46	1.54
4*15T15	41.00	106.03	49135.28	701.56	663.44	776.70	7034.39	0.14	8235.28	1.54

Table 2 : Tendon Properties

0.16g	max U1 [m]	max V2 [KN]	max M3[KNm]
	0.08	4826	18968
0.24g	max U1 [m]	max V2 [KN]	max M3[KNm]
	0.12	6143	27193
0.36g	max U1 [m]	max V2 [KN]	max M3[KNm]
	0.14		$>M_u$(27268)

Table 3 : Reference Bridge Analysis Results

Figure 6 demonstrates the effect of the tendon mechanism on the seismic response of the three span concrete bridge for seismic level I. The significant reductions close to 30% on the longitudinal seismic movements the pier moment and shear forces are the first indicators of the effectiveness of the proposed mechanism. The amount forces that are developed on the tendons under seismic level I earthquake, show that a pile diaphragm of 3x0.3x0.7m dimensions has the capability to receive them safely and the stress and strain plots demonstrate the elastic response of the tendons for both earthquake signs, a behavior which is expected for the proposed system.

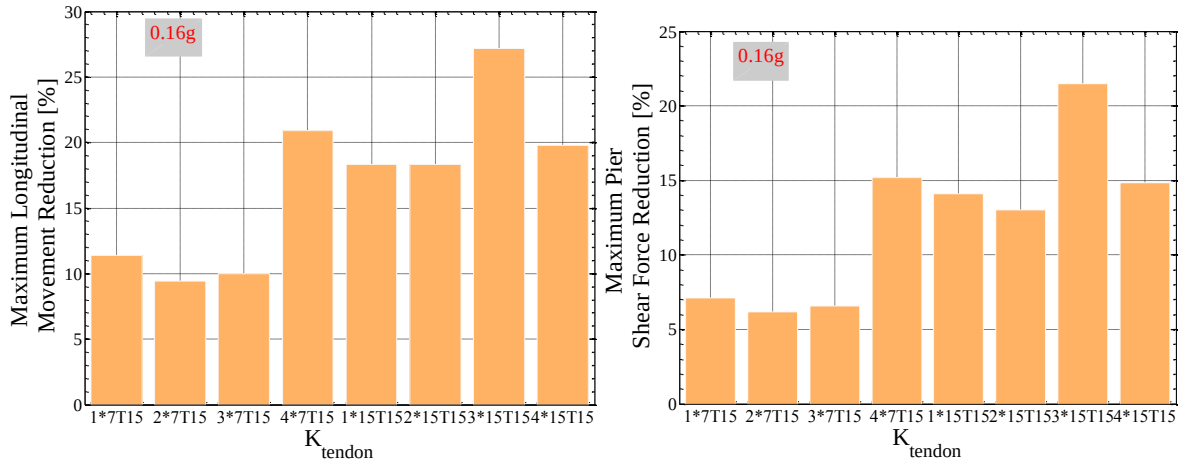


Figure 6: Analysis Results, 0.16g

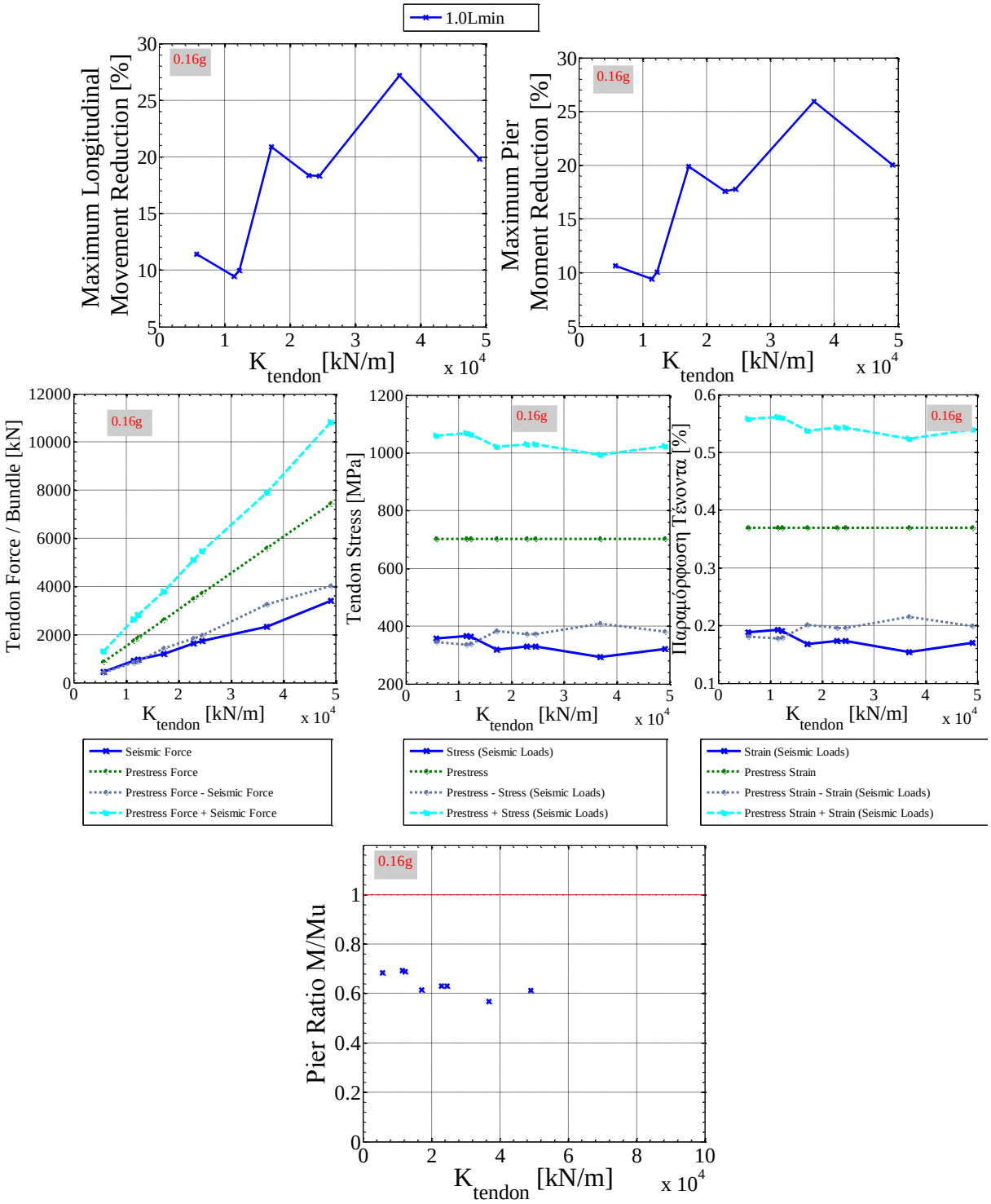


Figure 6 (continued) : Analysis Results, 0.16g

Regarding the capacity of the piers it is observed that since the bridge is designed for this seismic level the initial moment is lower than the Mu. However, the ratio of M/Mu for the bridge systems with the mechanism can be an indicator of the effectiveness of the restraining system on reducing seismic actions, as well. In the results of the two next seismic intensity levels the upgrade of the bridge can be even more obvious.

In Figure 7 the displacement reduction results for seismic levels I and II are shown, while in Figure 8 the ratios or pier moments M/Mu, respectively for the two levels. From the displacement reduction plots, it can be derived that the efficiency of the proposed mechanism is decreased as the earthquake intensity increases, especially for 0.36g when the tendons of small cross section have even negative effect on the seismic movements. However, it can be claimed that the proposed mechanism can upgrade the seismic resistance of the bridge to the higher than the design level seismic intensities. The pier moment ratios in Figure 8 show that, firstly, regarding 0.24g the maximum pier moments are reduced below the yield moment(ratios<0.9) and, secondly, regarding 0.36g the maximum pier moments are reduced below the ultimate moment(ratios<1), which demonstrates the capability of the piers to receive the increased seismic forces in comparison the piers in the Reference Bridge that fail for this specific seismic level.

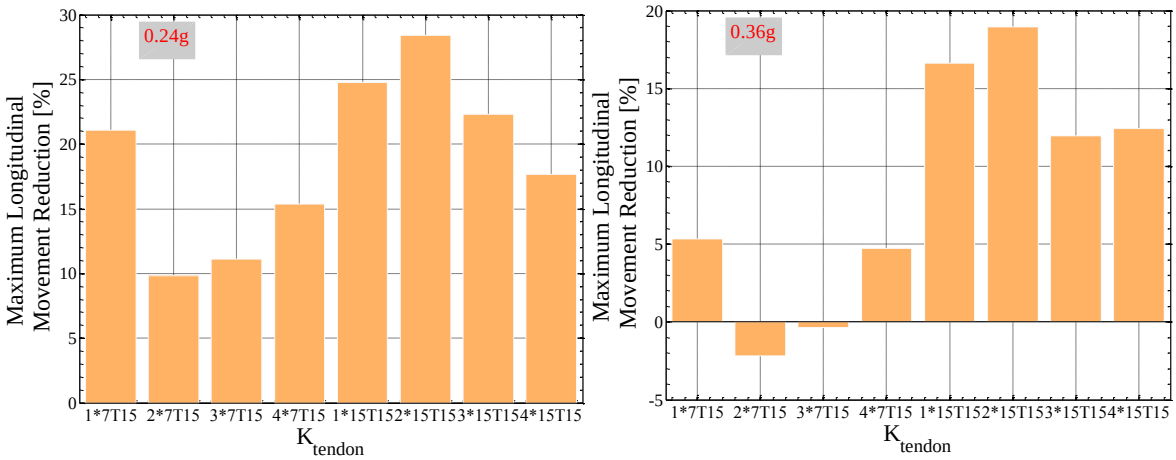


Figure 7 : Long. Movement Reduction, 0.24g and 0.36g

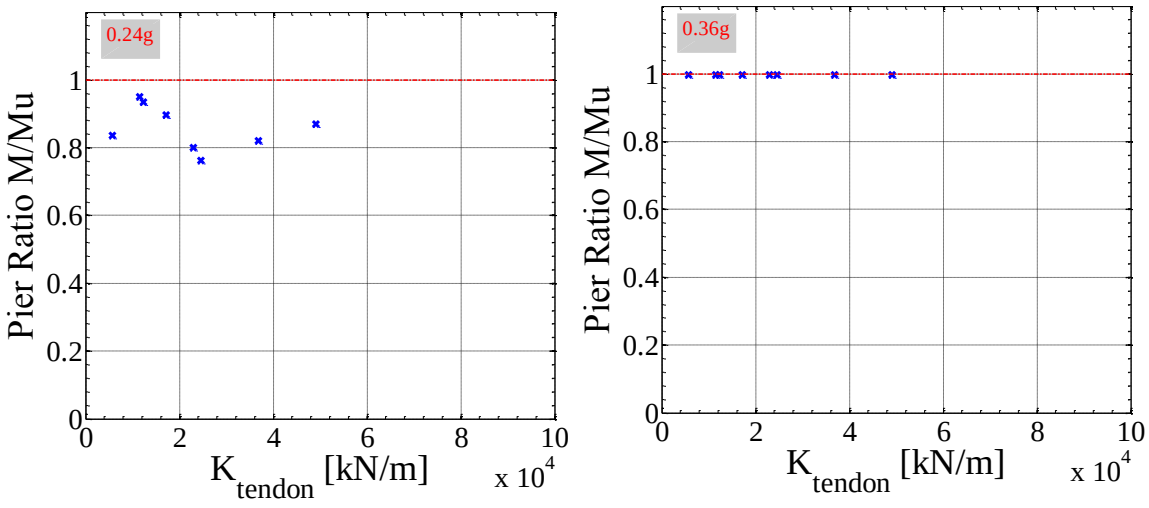


Figure 8 : Pier M/Mu, 0.24g and 0.36g

For selecting an optimum tendon size for the two retrofit cases of 0.24g and 0.36g the level of forces developed at the mechanism is taken into account, as well. Figure 9 presents the response of the tendons for both seismic intensities, where it is apparent that the response of the proposed mechanism is elastic for both earthquake signs. The combination of low seismic

forces and significant reduction results in movements and pier moments is required for selecting the appropriate size of the tendons. From the observation of the Figures 7-9 it can be concluded that the cross section of 1*7T15 is sufficient for the seismic retrofit-upgrade of the reference bridge to seismic level II, while a larger cross section with increased stiffness equal to 2*15T15 is required for the seismic retrofit-upgrade of the reference bridge to seismic level III. The maximum forces developed at the selected tendon sizes are included in Table 4 which indicates that they can be transferred to the pile diaphragm without raising any capacity issues.

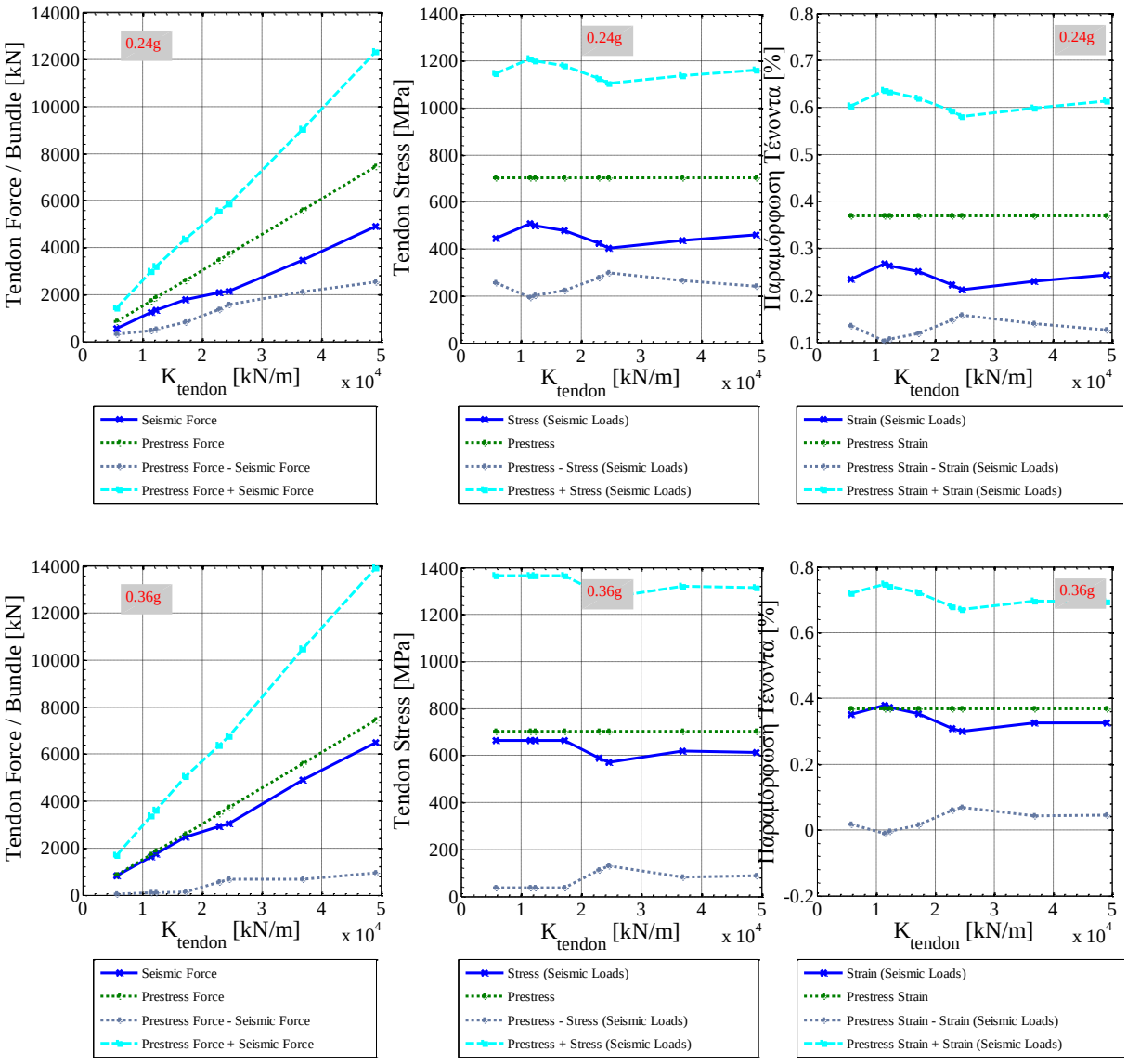


Figure 9 : Tendon Response, 0.24g and 0.36g

Tendons	Forces	
	0.24g	0.36g
1*7T15	1750kN	1900kN
2*15T15	5900 kN	6100 kN

Table 4 : Tendon forces, 0.24g and 0.36g

5 CONCLUSIONS

The key objective of the present study was to investigate the efficiency of a system consisting of prestressed unbonded tendons that is proposed for seismic retrofit of bridges by limiting longitudinal seismic movements. The investigated system belongs to indirect approach retrofit methods due to the addition of new members to the bridge system. The main conclusions derived are the following:

- The indirect accommodation of the increased seismic demand is, in general, the safest way to perform retrofit solutions. Therefore, regarding the longitudinal requirements, the surplus of the seismic actions was driven through the use of the proposed restraining system of tendons to new structures behind the abutments. More specifically, the high seismic demand in combination with the low available additional bearing capacity of the abutments was accommodated with the introduction of tendons in the bridge structural system.
- The proposed system presented high efficiency in limiting longitudinal bridge movements and pier seismic actions for all seismic intensity levels up to 30%. Since the bridge was designed for seismic level I it was taken into account as an indicator of the efficiency of the system. The possible upgrade of the Reference Bridge was more evident for the next two seismic levels. Especially for seismic level III, the seismic demand at the reference bridge exceeded pier capacity, while the installation of the mechanism lowered the seismic demand on the piers to the level of their capacity.
- The tendons are advantageous regarding their response, since they can develop a “strut-tie” behavior with the use of prestress without developing any compression stresses. Analyses for all seismic levels have shown that the proposed system can remain in the elastic region.
- The efficiency in reducing longitudinal movements and in seismic retrofit, the long lifetime of the tendons and the simplicity of the application contribute to the high reliability of the proposed system, as an alternative indirect retrofit method.

ACKNOWLEDGMENTS

The authors would like to acknowledge the assistance of METESYSM Company and EGNATIA ODOS A.E, since they provided all the necessary data and drawings for the investigated reference bridge.

REFERENCES

[1] I. Buckle, I. Friedland, J. Mander, M. Geoffrey, R. Nutt, and M. Power, Seismic Retrofitting Manual for Highway Structures : Part 1 – Bridges, 2006.

[2] CEN[Comité Européen de Normalisation], Eurocode 2 : Design of concrete structures - Part2: Concrete Bridges, 2001.

[3] A. Rustum, Evaluating the Retrofit of Highway Bridges Using Fluid Viscous Dampers, 2012.

[4] J. E. Padgett, Seismic Vulnerability Assessment of Retrofitted Bridges Using Probabilistic Methods, 2007.

[5] K. Kawashima, Seismic Isolation of Highway Bridges, *J. JAEE*, vol. 4, no. 3, pp. 283–297, 2004.

[6] E. Choi, J. Park, S.-J. Yoon, D.-H. Choi, and C. Park, Comparison of seismic performance of three restrainers for multiple-span bridges using fragility analysis, *Nonlinear Dyn.*, vol. 61, no. 1–2, pp. 83–99, Dec. 2009.

[7] B. Andrawes and R. DesRoches, Unseating prevention for multiple frame bridges using superelastic devices, *Smart Mater. Struct.*, vol. 14, no. 3, pp. S60–S67, Jun. 2005.

[8] R. Desroches and G. L. Fenves, Design of Seismic Cable Hinge Restrainers for Bridges, *J. Struct. Eng.*, no. April, pp. 500–509, 2000.

[9] J.-M. Kim, M. Q. Feng, and M. Shinozuka, Energy Dissipating Restrainers for Highway Bridges, *Soil Dyn. Earthq. Eng.*, vol. 19, no. 1, pp. 65–69, Jan. 2000.

[10] R. Desroches, T. Pfeifer, R. T. Leon, and T. Lam, Full-Scale Tests of Seismic Cable Restrainer Retrofits for Simply Supported Bridges, *J. Bridg. Eng.*, vol. July, pp. 191–198, 2003.

[11] O. Markogiannaki and I. Tegos, Seismic reliability of a reinforced concrete retrofitted bridge, in *Safety, Reliability, Risk and Life-Cycle Performance of Structures and Infrastructures*, G. Deodatis, B. R. . Ellingwood, and D. M. . Frangopol, Eds. CRC Press, 2014, pp. 4229–4236.

[12] O. Markogiannaki and I. Tegos, A smart and costless solution for upgrading the seismic resistance of bridges Description of the proposed struts-ties system, in *IABSE Conference*, 2012.

[13] I. A. Tegos and O. G. Markogiannaki, Analytical Investigation on the Use of FRP Materials as Seismic Restrainers in Concrete Bridges, in *Istanbul Bridge Conference*, 2014.

[14] O. Markogiannaki, I. Tegos, and S. Vasileiou, The Use of Unbonded Tendons on Bridges in Seismic Regions, in *IBSBI*, 2014.

[15] CEN [Comité Européen de Normalisation], *Eurocode 8 — Design of Structures for Earthquake Resistance — Part 2: Bridges*, vol. 3. 2005.

[16] A. Rustum, Evaluating the Retrofit of Highway Bridges Using Fluid Viscous Dampers, University of Waterloo, Ontario, Canada, 2012.

[17] N. Hewson, *Prestressed Concrete Bridges*. Thomas Telford Publishing, London, UK, 2003.

[18] O. Burdet and M. Badoux, Comparison of Internal and External Prestressing for Typical Highway Bridges Highway bridge models, in *16th Congress of IABSE*, 2000.

[19] Y. H. Park, C. Park, and Y. G. Park, The Behavior of an In-Service Plate Girder Bridge Strengthened with External Prestressing Tendons, *Eng. Struct.*, vol. 27, no. 3, pp. 379–386, Feb. 2005.

[20] P. M. Davis, T. M. Janes, M. O. Eberhard, and J. F. Stanton, Unbonded Pre-Tensioned Columns for Bridges in Seismic Regions, 2012.

[21] H. M. Dawood and M. ElGawady, Performance-based seismic design of unbonded precast post-tensioned concrete filled GFRP tube piers, *Compos. Part B Eng.*, vol. 44, no. 1, pp. 357–367, Jan. 2013.

[22] C. Zhou, X. Lu, H. Li, and T. Tian, Experimental Study on Seismic Behavior of Circular RC Columns Strengthened with Pre-stressed FRP Strips, *Earthq. Eng. Eng. Vib.*, vol. 12, no. 4, pp. 625–642, Dec. 2013.

[23] K. Q. Walsh and Y. C. Kurama, Behavior and Design of Unbonded Post-Tensioning Strand / Anchorage Systems for Seismic Applications, 2009.

[24] B. D. Weldon, Behavior, Design, and Analysis of Unbonded Post-Tensioned Precast Concrete Coupling Beams, University of Notre Dame, Indiana, USA, 2010.

[25] CEN[Comité Européen de Normalisation], Eurocode 8 : Design of structures for earthquake resistance — Part 1: General rules, seismic actions and rules for buildings, 2003.

[26] M. C. Constantinou, T. T. Soong, and G. F. Dargush, Passive Energy Dissipation Systems For Structural Design and Retrofit, 1998.

[27] V. K. Papanikolaou, Analysis of arbitrary composite sections in biaxial bending and axial load, *Comput. Struct.*, vol. 98–99, pp. 33–54, May 2012.

[28] V. K. Papanikolaou, AnySection : Software for the analysis of arbitrary composite sections in biaxial bending and axial load. Aristotle University of Thessaloniki, Greece, 2015.

[29] A. Shamsabadi, K. M. Rollins, and M. Kapuskar, Nonlinear Soil – Abutment – Bridge Structure Interaction for Seismic Performance-Based Design, *J. Geotech. Geoenvironmental Eng.*, no. June, pp. 707–720, 2007.

[30] J. P. Stewart, E. Taciroglu, J. W. Wallace, A. Lemnitzer, C. Hilson, A. Nojoumi, S. Keowan, R. Nigbor, and A. Salamanca, Nonlinear Load-Deflection Behavior of Abutment Backwalls with Varying Height and Soil Density, 2011.

COMPDYN 2015
5th ECCOMAS Thematic Conference on
Computational Methods in Structural Dynamics and Earthquake Engineering
M. Papadrakakis, V. Papadopoulos, V. Plevris (eds.)
Crete Island, Greece, 25–27 May 2015

EXPERIMENTAL AND NUMERICAL ANALYSIS ON THE CYCLIC BEHAVIOR OF BRIDGE PIERS WITH AND WITHOUT CFRP RETROFIT

Pedro Delgado[1], Frutuoso Sousa[1], Patrício Rocha[1], António Arêde[2], Nelson Vila Pouca[2], Aníbal Costa[3], and Raimundo Delgado[2]

[1] Instituto Politécnico de Viana do Castelo
Apartado 574, 4901-908 Viana do Castelo, Portugal
pdelgado@estg.ipvc.pt, frutuososousa@ipvc.pt, procha@estg.ipvc.pt

[2] Universidade do Porto - Faculdade de Engenharia
R. Dr. Roberto Frias, s/n 4200-465 Porto, Portugal
aarede@fe.up.pt, nelsonvp@fe.up.pt, rdelgado@fe.up.pt

[3] Universidade de Aveiro
Campus Universitário de Santiago, 3810-193 Aveiro, Portugal
acosta@civil.ua.pt

Keywords: RC hollow piers, numerical analysis, experimental tests, retrofit strategies

Abstract. *The main objective of this paper is to evaluate the cyclic behavior of RC hollow piers, with and without with CFRP retrofit, by comparison of experimental tests results with structural numerical modeling. The retrofit techniques aim to increase the shear strength and the ductility capacity through the establishment of principles and strategies applied in an experimental cyclic campaign of RC hollow piers, carried out in the Laboratory for Earthquake and Structural Engineering (LESE) of the Faculty of Engineering of University of Porto (FEUP). The evaluation and calibration of the efficiency of several retrofit solutions is also performed. The numerical simulations are carried out using two different methodologies: (i) fiber model and (ii) damage model. The fiber models based in a finite element discretiztion with non-linear behavior distributed along the elements length and cross-sectional area, while the damage model is supported on refined finite element (FE) meshes, with high complexity and detail levels in the constitutive laws defined for both concrete and steel. The concrete is simulated with a continuum damage model where several applications for bridges with hollow section piers can be found at Faria et al. [1]. Results of the experimental campaign allow to discuss and conclude about the efficiency of each numerical method, namely regarding the shear strength and the ductility capacity assessment.*

1 INTRODUCTION

Hollow piers have large section dimensions, with reinforcement bars spread along both wall faces, and unlike common solid section columns, quite often the shear effect has great importance on the pier behavior. Thus, special attention should be given to this issue when the numerical assessment and retrofit of such type of section piers is envisaged. In line with this concern, an experimental campaign has been carried out at LESE – FEUP (Laboratory of Earthquake and Structural Engineering of the Faculty of Engineering of University of Porto), on a set of RC piers. The test setup characteristics and more detailed results are available in previous reports [2-5]. This set of specimens was based on square piers tested at the Laboratory of Pavia University, Italy [6, 7], consisting on hollow section RC piers with 450mm x 450mm exterior dimensions and 75mm thick walls, and is being tested in order to understand the influence of the cross section geometry of rectangular hollow piers on the cyclic behavior, bearing in mind the purpose of assessing retrofitting solutions.

2 PROTOTYPES

Ten prototypes with square and rectangular hollow section (see Table 1 and Figure 1) were tested with different transverse reinforcement details, namely: piers N2, N3 and N4 - simple stirrups with 2 legs (representative of the old bridge construction); piers N5 - more detailed transverse reinforcement with 2 legs, with EC8 type, and piers N6 - also detailed stirrups (like piers N5), but with 4 legs (twice cross section area of transverse reinforcement).

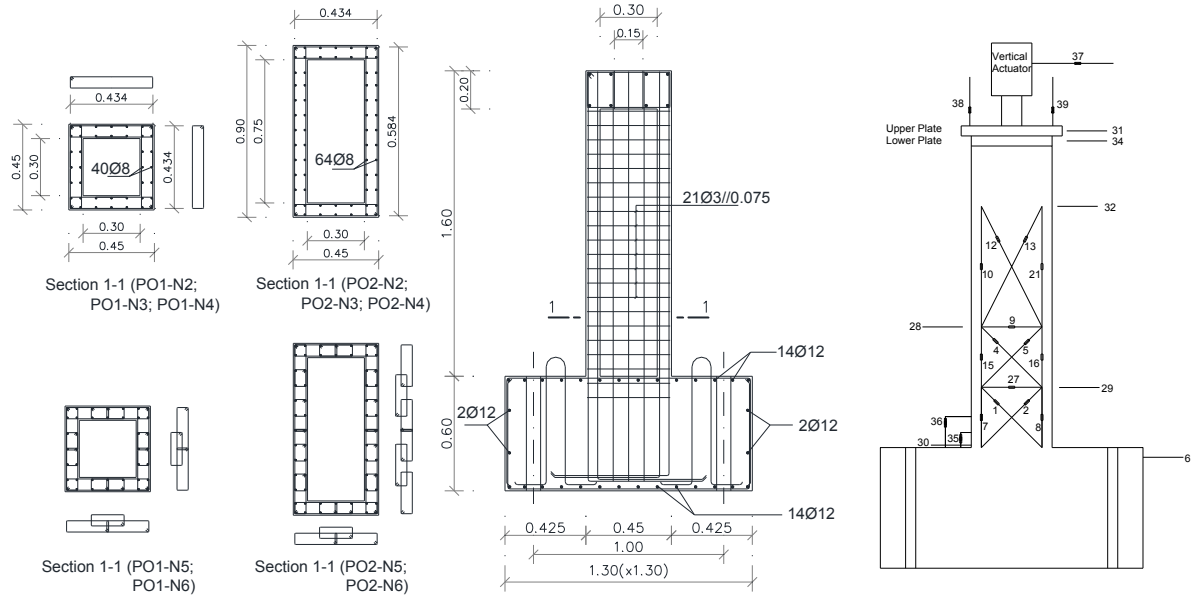
Piers	Square Section	Rectangular Section
2ª Construction series	PO1-N2	PO2-N2
	PO1-N3	PO2-N3
3ª Construction series	PO1-N4	PO2-N4
	PO1-N5	PO2-N5
	PO1-N6	PO2-N6

Table 1: Construction series.

The unconfined concrete compressive strength (f_c) is 28 MPa and the longitudinal and transversal reinforcement yielding strengths (f_{sy} and f_{swy}) are represented in Table 2. The model schemes shown in Figure 1a correspond to ¼ scale representations of bridge piers with square and rectangular hollow section, herein referred to as PO1 and PO2, respectively. Instrumentation to measure curvature and shear deformations was included along the pier height, because important shear deformations were expected in these tests. The LVDT configuration used in both specimens is shown in Figure 1b.

Designation	Geometry	Concrete	Long. Reinf.		Transv. Reinf.		
		f_c (MPa)	area	f_{sy} (MPa)	ϕ (mm)	f_{swy} (MPa)	type
PO1-N2	Square	28	40ϕ8	435	2.6	440	2 legs
PO1-N3	Square	28	40ϕ8	435	2.6	440	2 legs
PO1-N4	Square	28	40ϕ8	560	2.6	440	2 legs
PO1-N5	Square	28	40ϕ8	560	2.6	440	2 legs (EC8)
PO1-N6	Square	28	40ϕ8	560	2.6	440	4 legs (EC8)
PO2-N2	Rectangular	28	64ϕ8	435	2.6	440	2 legs
PO2-N3	Rectangular	28	64ϕ8	435	2.6	440	2 legs
PO2-N4	Rectangular	28	64ϕ8	560	2.6	440	2 legs
PO2-N5	Rectangular	28	64ϕ8	560	2.6	440	2 legs (EC8)
PO2-N6	Rectangular	28	64ϕ8	560	2.6	440	4 legs (EC8)

Table 2: Hollow piers characteristics.



a) b)

Figure 1: Hollow RC piers: a) geometry of specimen and b) lateral LVDT layout.

To define the values of Table 3, simple calculation were carried out for the cross section to compute the flexural capacity, while to evaluate the shear capacity the methodology suggested by Priestley [8] was adopted, usually referred in the bibliography as original UCSD shear model [9], being the shear strength (V_d) obtain for these piers through equation 1:

$$V_d = V_c + V_s + V_p \quad (1)$$

where V_c, V_s and V_p are the shear force components accounting, respectively, for the nominal strength of concrete (which depends on the pier displacement ductility), the transverse reinforcement shear resisting mechanism and the axial compression force. These values were obtained for an axial load of 250 kN (except pier PO2-N3 with 440kN) that corresponds to a normalized axial force of 0.08 and 0.05, respectively for the square and rectangular pier cross sections [2].

Designation	Geometry	Flexural Capacity (kN)		Shear Capacity (kN)	
		yielding	ultimate	ductility of 2	ductility of 8
PO1-N2	Square	155	180	170	105
PO1-N3	Square	155	180	170	105
PO1-N4	Square	185	215	170	105
PO1-N5	Square	185	215	170	105
PO1-N6	Square	185	215	220	160
PO2-N2	Rectangular	230	265	170	105
PO2-N3	Rectangular	255	290	200	135
PO2-N4	Rectangular	280	320	170	105
PO2-N5	Rectangular	280	320	170	105
PO2-N6	Rectangular	280	320	220	160

Table 3: Flexural and shear capacities.

To define the cyclic behavior of piers for experimental tests, was followed a displacement history with three cycles repeated for each range, represented in Table 4.

Displacement. (mm)	***Drift* (%)**
1	0,07
3	0,21
5	0,35
10	0,70
4	0,28
14	1,00
17	1,20
7	0,50
25	1,80
30	2,10
33	2,40
40	2,90
45	3,20

Table 4: Displacement history of experimental tests.

3 RESULTS OF ORIGINAL PIERS

The damage of flange walls (face north and south, which are the perpendicular to the applied force) exhibited mainly horizontal cracking along the pier height. On the other hand it becomes clear that the pier webs (lateral faces east and west) were the most damaged zones of all specimens, exhibiting inclined cracking and concrete spalling on extensive zones, Figure 2. Generally, these damage patterns are associated with shear mechanisms, reveling insufficient shear capacity provide by transverse reinforcement. However, some square piers have shear capacity slightly above the flexural capacity (see Table 5), which have resulted on a mixed collapse mechanism, bending/shear.



(a) square – flange (b) square – web (c) rectangular – flange (d) rectangular – web

Figure 2: Typical final damage on the webs and flange for square and rectangular cross sections piers.

In the Table 5 is presented a summary of shear and flexural capacities, the values of experimental results, as well as the collapse mechanism. The definition of collapse displacement corresponds to the value when the horizontal force applied to the pier reached 80% of the maximum force. For almost all the piers the shear capacity is clearly below the flexural capacity, being the maximum experimental force closer to the numerical estimation of shear strength, although in some cases the experimental response has reached a peak force slightly above the expected values.

Piers	Numerical Flexural Cap. (kN)	Numerical Shear Cap. (kN)	Experimental Max. Force (kN)	Experimental Collapse Displ. (mm)	Collapse mechanism
PO1-N2	155 / 180	170 / 105	130	33	Flexural / Shear
PO1-N3	155 / 180	170 / 105	130	33	Flexural / Shear
PO1-N4	185 / 215	170 / 105	170	25	Shear
PO1-N5	185 / 215	170 / 105	170	25	Shear
PO1-N6	185 / 215	220 / 160	210	30	Shear
PO2-N2	230 / 265	170 / 105	190	25	Shear
PO2-N3	255 / 290	200 / 135	220	25	Shear
PO2-N4	280 / 320	170 / 105	190	30	Shear
PO2-N5	280 / 320	170 / 105	200	30	Shear
PO2-N6	280 / 320	220 / 160	250	40	Shear

Table 5: Resume of forces and collapse mechanism for square and rectangular cross section piers.

For illustration purpose the cyclic response of two piers (PO2-N5 and PO2-N6) are shown in Figure 3, where it is also included the shear capacity lines for both piers (equation 1). In comparison with PO2-N5, a significant improvement was observed in the cyclic response of pier PO2-N6, due to the effect of doubling the transverse reinforcement. This pier has reached the expected level force determined numerically, but, not enough to achieve the strength level needed to yielding of the longitudinal reinforcement. However, the residual strength level obtained at the end of this experimental test is only slightly lower than the maximum peak value of the experimental test PO2-N5, those values occurring for a displacement, relative to PO2-N5, almost double, as demonstrated in Figure 3. Since both piers have the same maximum flexural force of about 300kN, associated with the yielding of the longitudinal reinforcement, premature shear failure was found for both piers, PO2-N5 and PO2-N6.

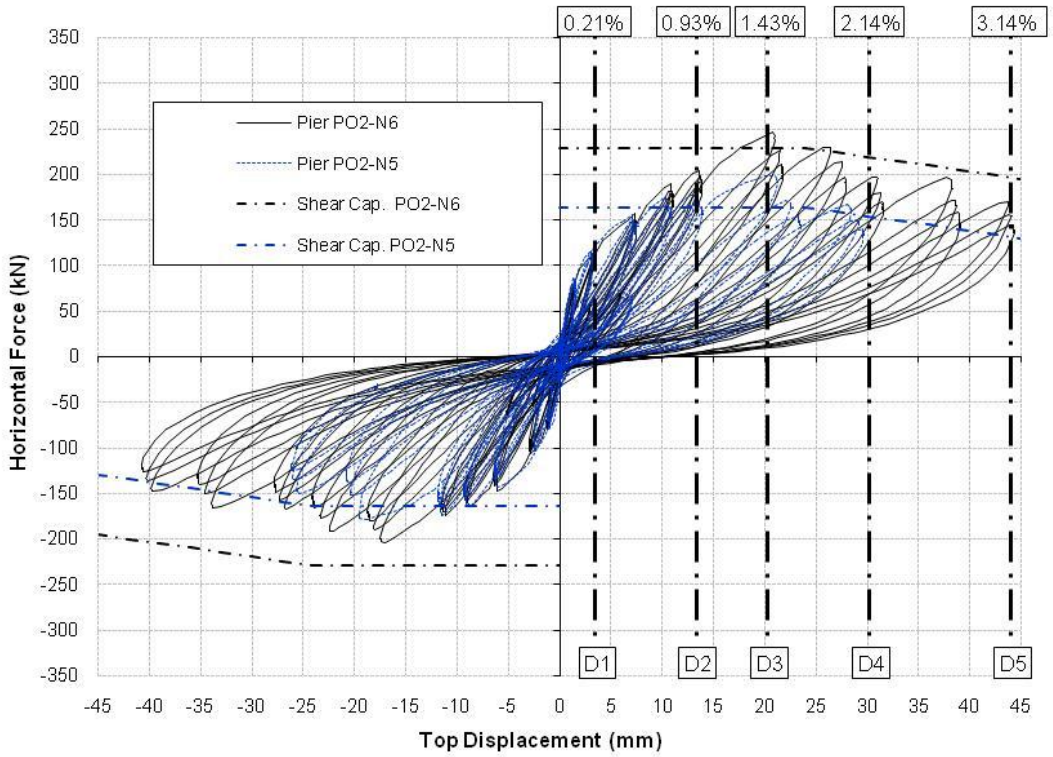


Figure 3: Experimental results comparison - PO2-N5 vs PO2-N6

4 RESULTS OF RETROFIT SOLUTIONS

The main objective of reinforcement techniques are improve the strength and ductility of structural elements. Therefore, the specimens used in previous experimental tests will be subject to a retrofit process in order to evaluate the increase of shear strength and ductility capacities of the retrofit solutions.

4.1 Retrofit process

After the original specimen cyclic tests, piers were repaired and retrofitted by an external contractor (S.T.A.P.) according to the following steps: 1) delimitation of the repair area; 2) removal and cleaning of the damaged concrete; 3) inside retrofit with transversal steel bars; 4) alignment or replacement of the longitudinal rebars; 5) application of formwork and new concrete (Microbeton, a pre-mixed micro concrete, modified with special additives to reduce shrinkage in the plastic and hydraulic phase); 6) outside retrofit with the CFRP sheets. In order to provide a general idea of the pier damage and of the retrofit process, the following pictures show the piers during repair and after retrofit with CFRP sheet jacketing (Figure 4). The inside retrofit with transversal steel bars (only for pier PO2-N3) was designed taking in account the feasibility for future real retrofits; such bars were concentrated at the bottom, in correspondence with the outer CFRP jackets, for improving the plastic hinge confinement.

In order to design the outside shear retrofit with CFRP jackets, the methodology suggested by Priestley [8, 9] was adopted to evaluate the thickness of the rectangular hollow pier jacket for increasing the shear strength above the maximum flexural force while keeping the initial

section conditions. According to this methodology the shear strength can be conveyed by equation 2:

$$V_d = V_c + V_s + V_p + V_{sj} \quad (2)$$

where V_c, V_s and V_p are the shear force components accounting, respectively, for the nominal strength of concrete, the transverse reinforcement shear resisting mechanism and the axial compression force; the term V_{sj} corresponds to the possible retrofit contribution with CFRP or metal jackets and can be estimated according to equation 3:

$$V_{sj} = \frac{A_j}{s} f_j \cdot h \cdot \cot\theta \quad (3)$$

where h is the overall pier section dimension parallel to the applied shear force, f_j is the adopted design jacket stress, A_j is the transverse section area of the jacket sheets spaced at distance s and inclined of the angle θ relative to the member axis.

4.2 Experimental results of PO2-N5-R1 and PO2-N5-R2

For PO2-N5-R1 pier, one strip layer of CFRP sheet with 0,177 mm thick and 100 mm wide was applied. The spacing was 100 mm along the pier height in order to increase the shear capacity, but it was decided to leave a 100 mm distance at the base in order to analyze the available ductility of the pier if shear collapse mechanism was avoided [2].

When it reached 2.5% drift, occurred a premature rupture of CFRP sheet in west side, as can be seen from in Figure 4. As the purpose of this experimental test was the evaluation the flexural behavior of pier, the test was interrupted and the pier was conveniently retrofitted in all its height to avoid any weakness to the shear effect.



a) east side b) south side c) north side d) west side

Figure 4: Final damage of pier PO2-N5-R1, for 2,5% drift.

After this second retrofit with the objective to prevent collapse mechanism by shear, the pier was renamed to PO2-N5-R2. However, when it reached 2.9% drift, the four strips of CFRP closest to the bottom of the pier suffered a sudden rupture in west side, causing a collapse mechanism of pier by shear effect. In Figure 5, it can be observed the fiber and concrete damage, as well as the cracks that appear during the test.

By analyzing the results depicted in Figure 6, it can be concluded that the retrofit executed showed an unsatisfactory behavior, particularly in terms of maximum displacement achieved. However, this retrofit presented a higher strength capacity in compared to the original pier. But, indeed, this retrofit failed to prevent the shear collapse mechanism [2].



a) east side b) south side c) north side d) west side

Figure 5: Final damage of pier PO2-N5-R2, for 2,9% drift.

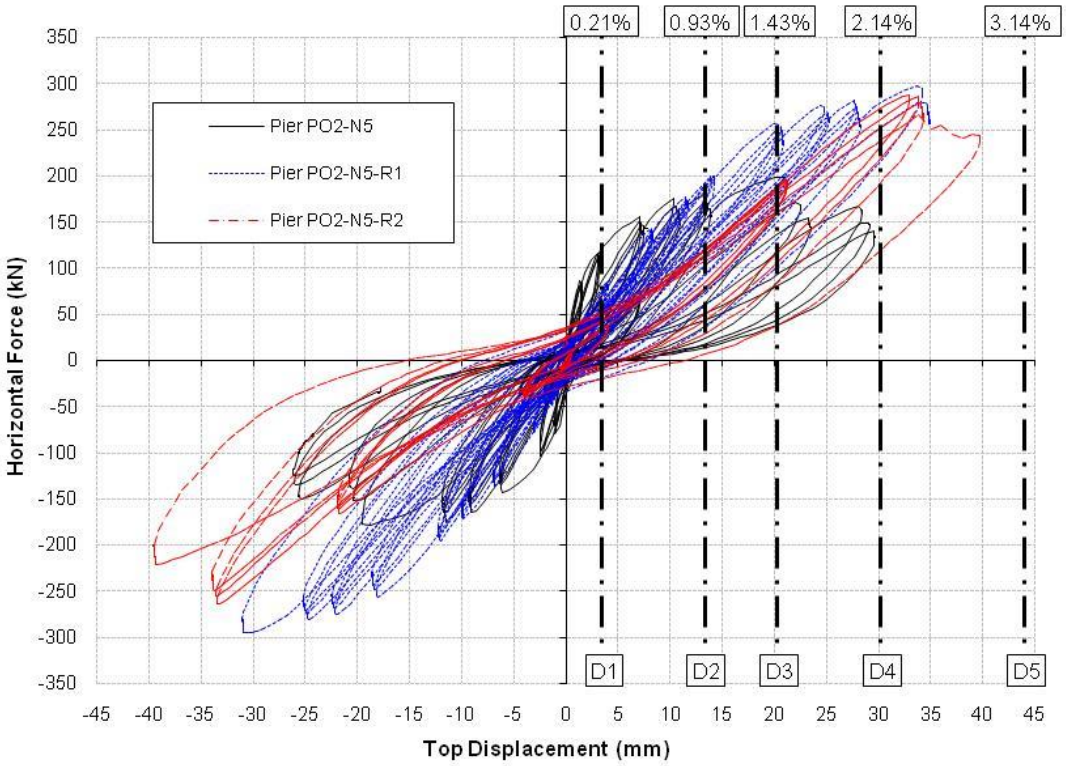


Figure 6: Experimental results comparison - PO2-N5 vs PO2-N5-R1 vs PO2-N5-R2.

4.3 Experimental results of PO2-N6-R1

For this specimen, one strip layer of CFRP sheet was used, which was 0.177 thick, 100 mm wide and spaced at 100 mm along the pier height in order to increase the shear capacity. As considered in pier PO2-N5-R1, it was decided to leave a 100 mm distance at the base in order to analyze the available ductility of the pier if shear collapse mechanism was avoided.

When 3.0% drift was achieved, corresponding to 45 mm of top pier displacement, the second strip of CFRP (counting for the bottom) broke up in the northeast corner. In the subsequent cycles, broke up the 3º, 4º, 5º and 6º fiber strips, in ascending order, in the same

corner as the second strip, Figure 7. After the abrupt rupture of the fibers, the pier lose the concrete confinement, causing the desegregation of the material on the east side wall pier, as can be seen in Figure 7. Finally, after the experimental test has been stopped, high deterioration of the concrete and some buckling phenomena of longitudinal rebars were observed [10].



a) east side b) south side c) north side d) west side

Figure 7: Final damage of pier PO2-N6-R1, for 3.0% drift.

Although the failure mechanism of the pier PO2-N6-R1 was achieved by shear mechanism, it can be observed from Figure 8 that the maximum strength increased about 50% in comparison with the original pier (PO2-N6).

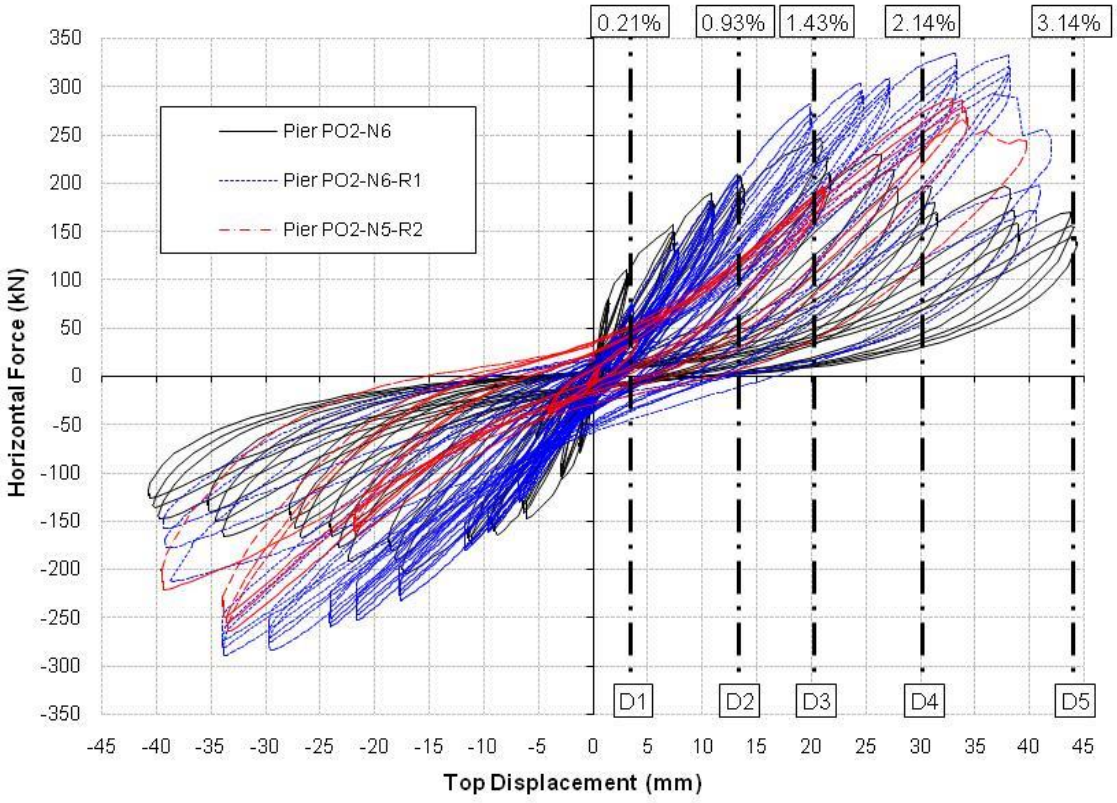


Figure 8: Experimental results comparison - PO2-N6 vs PO2-N6-R1 vs PO2-N5-R2.

Therefore, a higher bending contribution was obtained in the pier behavior (in comparison with the original pier), despite the shear deformation effects that occurred during the test. But in terms of displacement, this pier retrofit just have reached the ductility between 3 and 4, due to CFRP strips failed to accommodate the pier web deformation and broken.

Also in Figure 8, it can be observed an increase of the maximum force achieved for the same displacement level exceeding 50 kN in relation to PO2-N5-R1. These differences may be due to the difference in amount of transverse reinforcement, because the retrofit of both piers was exactly the same. In fact, as already mentioned, N6 piers have the double area of transverse reinforcement in relation to N5.

5 NUMERICAL ANALYSIS

After the interpretation of the results obtained by experimental tests, will be carried a numerical analysis of pier PO2-N6 to explain all phenomena involved, namely the failure mechanisms by shear and bending. The first numerical tool used to perform these analyzes was the fiber method, the freeware Seismostruct [11]. The numerical analyzes were performed with the displacement history used in the experimental tests (Table 4) and with the characteristics and properties of piers shown in Table 2.

In Figure 9 are shown the results of experimental tests and numerical PO2-N6, with and without retrofit in a diagram force - displacement.

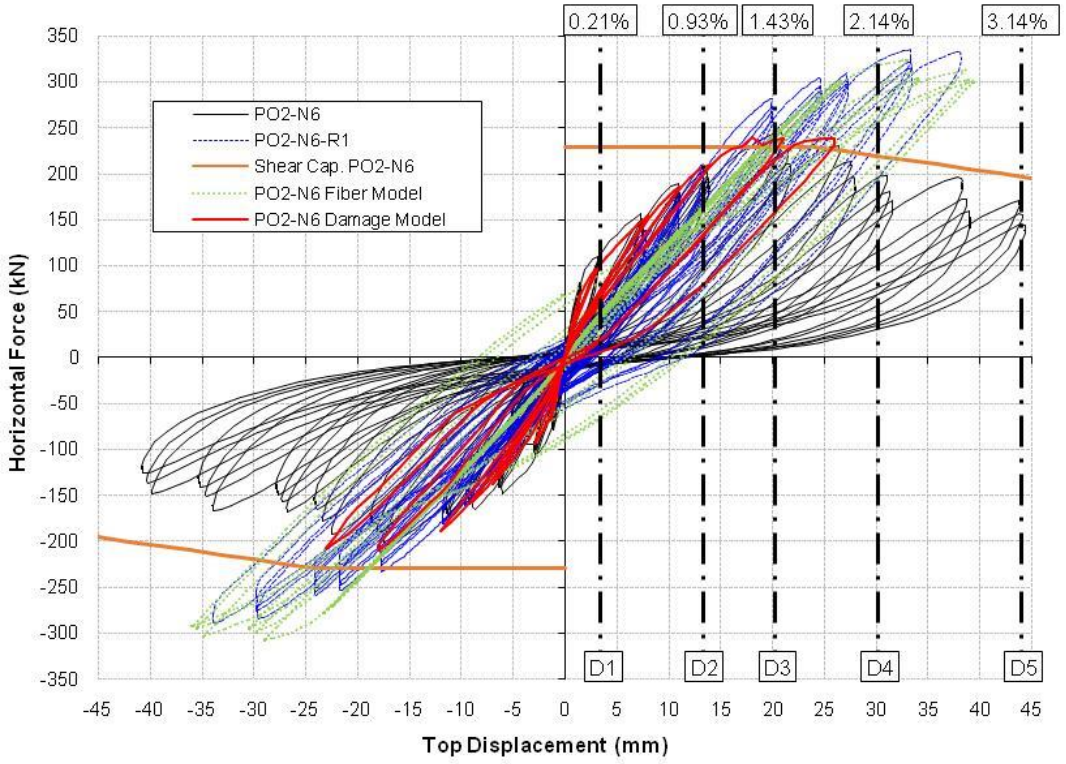


Figure 9: Experimental results vs Numerical results

The difference between the results of the fiber model and the experimental test of pier PO2-N6 is due to a limitation of this numerical model to simulate the shear effects. Namely, the fiber model of Seismostruct [11] assumes that the pier is governed by bending behavior, which leads to a maximum forces achieved similar to those obtained in the experimental test

of the retrofit pier (PO2-N6-R1), once it is capable to explore a higher bending component due to the CFRP strips retrofit. This numerical model does not consider the deformation and stiffness degradation from shear effects, which is quite relevant for the piers behavior when inclined cracks occurs in its webs. This inability to consider the shear effect leads to maximum forces of fiber model (in Figure 9) similar to those shown in Table 5 for flexural capacity (about 320 kN) [10].

The deformation and strength mechanisms associated to shear are related to the concrete tensile behavior [5]. The damage model [1] makes use of "effective stress tensors" decomposed in compression and tensile stresses that lets you explore the deformation and stiffness degradation by shear. As can be seen in figure 9, the damage model results show a good approximation to the experimental test of pier PO2-N6, with a quite accurate simulation of the shear effects.

6 CONCLUSIONS

The comparison of the experimental tests of original piers, PO2-N5 with PO2-N6, allowed to confirm the importance of transverse reinforcement to control the shear deformation. Despite rupture of both piers has been obtained by a shear mechanism, the solution with the twice transverse reinforcement achieved a significant increase in the maximum strength and maximum displacement, exploring a higher bending component.

The comparison of original and retrofit piers, allow concluding that this retrofit technique increases the achieved maximum strength, with similar values of those determined by simple expressions of the bending capacity.

After the tests of retrofitted piers was observed that was difficult to achieve high levels of ductility, due to the difficulty of the CFRP sheets to follow the piers web deformation. This resulted in the collapse of the CFRP sheets to ductility levels below 4.

The numerical analysis were quite useful for helping to understand some phenomena observed in the experimental tests, as for example the formation of failure modes. Through the damage model was possible to observe the influence of the concrete tensile behavior in the results, due to the significant shear component that occurred during the tests. Therefore, it is quite important the accurate simulation of the tensile behavior of reinforced concrete, to account for deformations due to shear effect. The numerical analysis through the fibers method allowed capturing the behavior of retrofit pier, PO2-N6-R1, once the model considers the behavior dominated by bending. The fiber model, which usually only take in account the bending failure mechanism, does not consider the piers web cracking due to shear and, therefore, cannot account for the stiffness degradation due to this piers cracking.

ACKNOWLEDGEMENT

The authors wish to acknowledge the “Irmãos Maia, Lda” company, for the construction of the tested piers and S.T.A.P.- Reparação, Consolidação e Modificação de Estruturas, S. A. company for the repair and retrofit works. Final acknowledgements to the laboratory staff, mainly Mr. Valdemar Luís, for all the care on the test preparation. This experimental tests were performed with the financial support of the “FCT- Fundação para a Ciência e Tecnologia" through the Project PTDC/ECM/72596/2006, ”Seismic Safety Assessment and Retrofitting of Bridges”.

REFERENCES

[1] R. Faria, J. Oliver, M. Cervera, A strain-based plastic viscous-damage model for massive concrete structures. *International Journal of Solids and Structures*, **35**(14), 1533-1558, 1998.

[2] P. Delgado, Avaliação da Segurança Sísmica de Pontes, FEUP: Porto, 2009. (in Portuguese) (http://ncrep.fe.up.pt/web/artigos/PDelgado_PhD_Thesis.pdf)

[3] R. Delgado, P. Delgado, N. Vila Pouca, A. Arêde, P. Rocha, A. Costa, Shear effects on hollow section piers under seismic actions: experimental and numerical analysis, *Bulletin of Earthquake Engineering*, **7**, 377-389, 2009 (DOI: 10.1007/s10518-008-9098-x).

[4] P. Delgado, A. Arêde, N. Vila Pouca, P. Rocha, A. Costa, R. Delgado, Retrofit of RC Hollow Piers with CFRP Sheets, *Composite Structures*, **94**, 1280–1287, doi:10.1016/j.compstruct.2011.11.032, 2012.

[5] P. Delgado, A. Monteiro, A. Arêde, N. Vila Pouca, R. Delgado, A. Costa, Numerical simulations of RC hollow piers under horizontal cyclic loading, *Journal of Earthquake Engineering*, **15**(6), 833-849, 2011.

[6] G.M. Calvi, A. Pavese, A. Rasulo, D. Bolognini, Experimental and Numerical Studies on the Seismic Response of R.C. Hollow Bridge Piers, *Bulletin of Earthquake Engineering*, **3:3**, 267-297, 2005.

[7] A. Pavese, D. Bolognini, S. Peloso, FRP seismic retrofit of RC square hollow section bridge piers, *Journal of Earthquake Engineering*, **1 SPEC. ISS**, 225-250, 2004.

[8] M.J.N. Priestley, F. Seible, G.M. Calvi, *Seismic design and retrofit of bridges*, New York: John Wiley & Sons, 1996.

[9] M.J. Kowalsky, Priestley, Improved Analytical Model for Shear Strength of Circular Reinforced Concrete Columns in Seismic Regions, *ACI Structural Journal*, **97:3**, 388-396, 2000.

[10] F. Sousa, Metodos de análise e avaliação de segurança sísmica de pontes em betão armado, MSc thesis, IPVC: Viana do Castelo, 2015. (in Portuguese) (waiting for publication).

[11] Seismosoft, SeismoStruct. computer program for static and dynamic nonlinear analysis of framed structures, 2006. Available online at: http://www.seismosoft.com.

COMPDYN 2015
5th ECCOMAS Thematic Conference on
Computational Methods in Structural Dynamics and Earthquake Engineering
M. Papadrakakis, V. Papadopoulos, V. Plevris (eds.)
Crete Island, Greece, 25–27 May 2015

META-MODELING FOR CONSISTENT SEISMIC RESPONSE ANALYSIS

Muneo Hori[1,2], Seizo Tanaka[1], Tsuyoshi Ichimura[1], W.L.L. Wijerathne[1] and J.A.S.C. Jayasinghe[1]

[1]Earthquake Research Institute, The University of Tokyo, 1-1-1 Yayoi, Bunkyo, Tokyo 113-0032
e-mail: {hori,stanaka,ichimura,lalith,spoon}@eri.u-tokyo.ac.jp

[2]Advanced Institute for Computational Science, RIKEN, 7-1-26 Minatoshima Minamimachi, Chuo, Kobe, Hyogo 650-0047
e-mail: muneo.hori@riken.jp

Keywords: Continuum Mechanics, Structure Mechanics, Consistent Modeling, Lagrangian.

Abstract. *Depending on the numerical accuracy required, we can choose a simple mass spring system or a solid element model in carrying out structural seismic response analysis. The important issue is the consistency of the models, and meta-modeling proposed by the authors gives a solution to this issue. Presuming that continuum mechanics is the foundation of structural seismic response, for which a suitable Lagrangian is formulated, a model is constructed by making suitable mathematical approximations, and hence the model is consistent in the sense that it is used to solve the identical physical problem of estimating structural seismic responses. In this paper, we explain the basic concepts of meta-modeling and present numerical experiments of constructing consistent models for actual structures such as a large scale tunnel and a freeway bridge.*

1 INTRODUCTION

In earthquake engineering, the use of a structure element, such as truss, beam, plate, or shell is a usual practice; see, for instance, [8, 9]. It is rare that solid element analysis is made for a structure of complicated configuration, even though solid element analysis becomes much easier and less expensive due to the progress of computer hardware and software. While there are several reasons for rare use of solid element analysis, a major reason is that it is believed that the structure element analysis is able to make more accurate estimation, compared with the solid element analysis.

The authors are proposing a *meta-modeling* theory [1]. The essence of this theory is that there are structure mechanics modelings that are *consistent* with continuum mechanics modeling. Hence, the structure element analysis that stems from consistent structure mechanics modeling is mathematical approximation of the solid element analysis that corresponds to continuum mechanics modeling. That is, structure mechanics modeling solves the physical problem of continuum mechanics modeling by applying suitable approximation.

There is a trade-off relation between computational cost and numerical accuracy; see Table 1. According to meta-modeling, solid element analysis that uses a model of high fidelity is an extreme case of high accuracy and high cost. Structure element analysis ends up much less computational cost, with some loss of the numerical accuracy. A key issue here is that the same physical problem is solved; due to difference in mathematical approximation, the physical problem is converted to different mathematical problems. The meta-model theory clarifies this point, and it is the choice of a user whether he employs solid or structure element analysis considering the trade-off relation between the computational cost and the numerical accuracy of solving the same physical problem.

The content of this paper is as follows. First, the meta-modeling theory is briefly summarized in Section 2. As illustrative examples, we study lumped mass modeling and beam theory and present beam theory that is consistent with continuum modeling in Section 3. Numerical examples of applying meta-modeling to tunnel and highway networks are presented in Section 4. Concluding remarks are made at the end.

2 SUMMARY OF META-MODELING

We start from a Lagrangian of an elasticity body, V. For simplicity, we assume that the body is homogeneous and has isotropic elasticity tensor and density, denoted by $\mathbf{c}$ and ρ, respectively. Denoting velocity and strain by $\mathbf{v}$ and $\boldsymbol{\epsilon}$, respectively, we write the Lagrangian as

$$\mathcal{L}[\mathbf{v}, \boldsymbol{\epsilon}] = \int_V \frac{1}{2}\,\rho\mathbf{v}\cdot\mathbf{v} - \frac{1}{2}\boldsymbol{\epsilon} : \mathbf{c} : \boldsymbol{\epsilon}\,\mathrm{d}v, \tag{1}$$

where $\cdot$ and $:$ are the inner product and the second-order contraction. For displacement $\mathbf{u}$ which satisfies suitably prescribed boundary and initial conditions, we compute $\mathbf{v} = \dot{\mathbf{u}}$ and

Table 1: Trade-off relation between computational cost and numerical accuracy.

	soil-structure interaction	computation cost	data	distribution of accuracy
solid element	interface condition	large	material	uniform
structure element	special arraignment	small	structure component	high at measured point

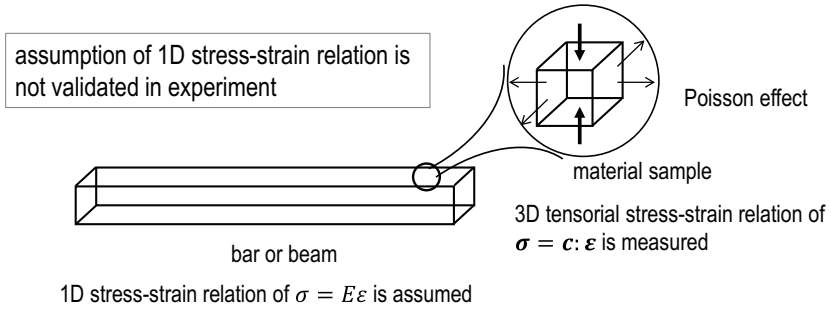


Figure 1: Assumption of one-dimensional stress-strain relation.

$\boldsymbol{\epsilon} = \mathrm{sym}\boldsymbol{\nabla}\mathbf{u}$ with $\dot{(.)}$ and $\boldsymbol{\nabla}(.)$ being temporal and gradient of $(.)$ and sym standing for the symmetric part of a second-order tensor.

Structure mechanics does not use the fourth-order tensor $\mathbf{c}$ as material property of V. It uses Young's modulus, E, instead. More specifically, structure mechanics employs a one-dimensional stress-strain relation expressed in terms of E. For instance, in the Cartesian coordinate of $\{x_1, x_2, x_3\}$, the normal stress and strain components in the x_1-direction are related as

$$\sigma_{11} = E\,\epsilon_{11},$$

rather than $\boldsymbol{\sigma} = \mathbf{c} : \boldsymbol{\epsilon}$ or

$$\sigma_{11} = c_{1111}\epsilon_{11} + \cdots = \frac{(1-\nu)E}{(1+\nu)(1-2\nu)}\epsilon_{11} + \cdots .,$$

where $\boldsymbol{\sigma}$ is stress tensor. While it is usually used, it is not understood that the assumption of the one-dimensional stress-strain relation is not validated in experiments, which assure the tensorial relation of $\boldsymbol{\epsilon}$ and $\boldsymbol{\sigma}$ via the fourth-order tensor $\mathbf{c}$; see Fig. 1.

Meta-modeling does not employ the one-dimensional stress-strain relation [1]. Instead, it modifies the Lagrangian as

$$\mathcal{L}^*[\mathbf{v}, \boldsymbol{\epsilon}, \boldsymbol{\sigma}] = \int_V \frac{1}{2}\rho\,\mathbf{v}\cdot\mathbf{v} - (\boldsymbol{\sigma} : \boldsymbol{\epsilon} - \frac{1}{2}\boldsymbol{\sigma} : \mathbf{c}^{-1} : \boldsymbol{\sigma})\,\mathrm{d}v. \tag{2}$$

where $\mathbf{c}^{-1}$ is the inverse fourth-order tensor of $\mathbf{c}$. It is readily shown that, if non-zero components of $\boldsymbol{\epsilon}$ and $\boldsymbol{\sigma}$ are ϵ_{11} and σ_{11} only, the second term in the integrand becomes $\sigma_{11}\epsilon_{11} - \frac{1}{2}\sigma_{11}^2/E$, and the variation with respect to σ_{11} is

$$\delta\left(\sigma_{11}\epsilon_{11} - \frac{1}{2}\frac{\sigma_{11}^2}{E}\right) = \frac{\delta\sigma_{11}}{E}(E\epsilon_{11} - \sigma_{11}).$$

As is seen, the one-dimensional stress strain relation is derived from the mathematical operation of taking variation. It is readily shown that $\mathcal{L}^*$ of Eq. (2) is equivalent with $\mathcal{L}$ of Eq. (1) in the sense that $\mathbf{u}$ that stationarizes $\mathcal{L}^*$ coincides with $\mathbf{u}$ for $\mathcal{L}$.

Meta-modeling leads to consistent modeling which solves the variational problem of $\mathcal{L}^*$. If no approximation is made for $\mathbf{u}$ (that produces $\mathbf{v}$ and $\boldsymbol{\epsilon}$) and $\boldsymbol{\sigma}$, it results in continuum mechanics modeling, and the governing equation for $\mathbf{u}$ is the wave equation, i.e.,

$$\rho\,\ddot{\mathbf{u}}(\mathbf{x}, t) - \boldsymbol{\nabla}\cdot(\mathbf{c} : \boldsymbol{\nabla}\mathbf{u}(\mathbf{x}, t)) = \mathbf{0}; \tag{3}$$

see, for instance, [4]. If certain approximations are made for $\mathbf{u}$ and $\mathbf{v}$, it results in a consistent modeling that solves the same variational problem of the Lagrangian using different partial differential equations.

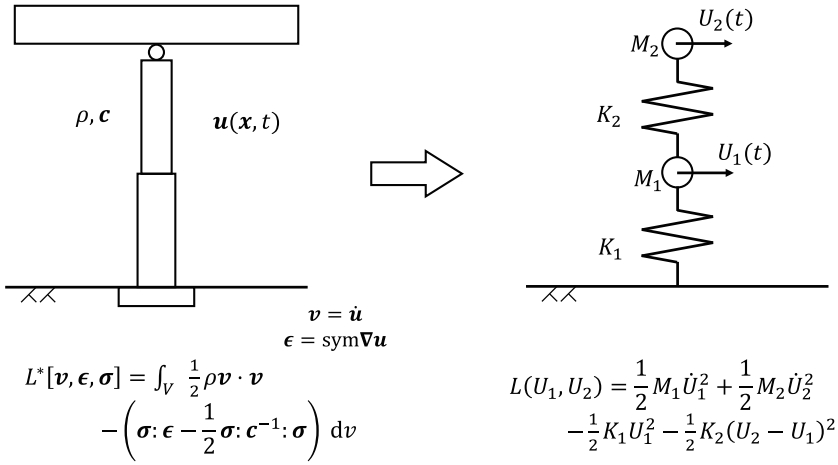


Figure 2: Schematic view of mass spring system consisting of two mass points.

3 EXAMPLES OF META-MODELING

In this section, we present two examples of applying the meta-modeling theory to make consistent modeling. They are modeling for mass spring system and modeling for beam theory.

3.1 Mass spring system

As the simplest case, we consider a mass spring system which consists of two mass points, as shown in Fig. 2. According to the meta-modeling theory, we consider an approximate displacement function of the following form:

$$\mathbf{u}(\mathbf{x},t) = \sum_{\alpha=1}^{2} U^{\alpha}(t)\boldsymbol{\phi}^{\alpha}(\mathbf{x}), \tag{4}$$

where U^{α} is a certain direction component of the α-th mass point and $\boldsymbol{\phi}^{\alpha}$ is displacement mode; by definition, a component of $\boldsymbol{\phi}^{\alpha}(\mathbf{x}^{\alpha})$ which corresponds to U^{α} takes on a value of 1, with $\mathbf{x}^{\alpha}$ being the location of the α-th mass point, and $\boldsymbol{\phi}^{\alpha}(\mathbf{x}^{\beta}) = \mathbf{0}$ for $\alpha \neq \beta$.

For simplicity, we substitute $\mathbf{u}$ of Eq. (4) into $\mathcal{L}$ of Eq. (1) rather than $\mathcal{L}^*$ of Eq. (2) which requires setting of $\boldsymbol{\sigma}$. We obtain

$$\mathcal{L} = \sum_{\alpha,\beta} \frac{1}{2} m^{\alpha\beta}\dot{U}^{\alpha}\dot{U}^{\beta} - \frac{1}{2}k^{\alpha\beta}U^{\alpha}U^{\beta}$$

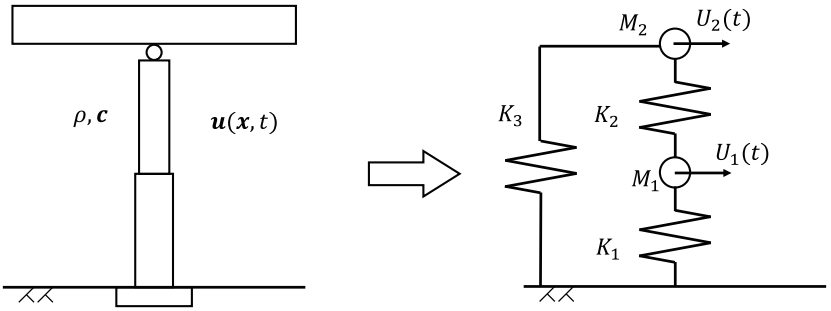
where

$$m^{\alpha\beta} = \int_V \rho\,\boldsymbol{\phi}^{\alpha}\boldsymbol{\phi}^{\beta}\,\mathrm{d}v, \quad k^{\alpha\beta} = \int_V \boldsymbol{\nabla}\boldsymbol{\phi}^{\alpha} : \mathbf{c} : \boldsymbol{\nabla}\boldsymbol{\phi}^{\beta}\,\mathrm{d}v. \tag{5}$$

We choose $\{\mathbf{u}^{\alpha}\}$ so that some elements of $\{m^{\alpha\beta}\}$ and $\{k^{\alpha\beta}\}$ vanish and the above $\mathcal{L}$ becomes

$$\mathcal{L} = \frac{1}{2}M^1(\dot{U}^1)^2 + \frac{1}{2}M^2(\dot{U}^2)^2 - \frac{1}{2}K^1(U^1)^2 - \frac{1}{2}K^2(U^2 - U^1)^2. \tag{6}$$

As is seen, this $\mathcal{L}$ corresponds to a Lagrangian of the mass spring system shown in Fig. 2; M^1 and M^2 are the bottom and top masses, and K^1 and K^2 are the spring connecting the bottom mass to the ground and the top mass to the bottom mass, respectively.



$$L^*[\boldsymbol{v},\boldsymbol{\epsilon},\boldsymbol{\sigma}] = \int_V \frac{1}{2}\rho\boldsymbol{v}\cdot\boldsymbol{v} - \left(\boldsymbol{\sigma}:\boldsymbol{\epsilon} - \frac{1}{2}\boldsymbol{\sigma}:\boldsymbol{c}^{-1}:\boldsymbol{\sigma}\right) \mathrm{d}v \qquad L(U_1,U_2) = \frac{1}{2}M_1\dot{U}_1^2 + \frac{1}{2}M_2\dot{U}_2^2 - \frac{1}{2}K_1U_1^2 - \frac{1}{2}K_2(U_2-U_1)^2 - \frac{1}{2}K_3U_2^2$$

Figure 3: Schematic view of consistent mass spring system consisting of two mass points.

It is easily seen that in order to derive $\mathcal{L}$ of Eq. (6), $\{\boldsymbol{\phi}^\alpha\}$ must satisfy

$$\int \rho\,\boldsymbol{\phi}^1\cdot\boldsymbol{\phi}^2\,\mathrm{d}v = 0, \quad \int (\boldsymbol{\nabla}\boldsymbol{\phi}^1 + \boldsymbol{\nabla}\boldsymbol{\phi}^2) : \mathbf{c} : \boldsymbol{\nabla}\boldsymbol{\phi}^2, \mathrm{d}v = 0.$$

Choosing $\{\boldsymbol{\phi}^\alpha\}$ that satisfy the first condition is relatively easy, compared with choosing $\{\boldsymbol{\phi}^\alpha\}$ that satisfy the second condition.

It is of interest to use the first two dynamic modes of V, denoted by $\{\boldsymbol{\psi}^\alpha\}$ with natural frequency $\{\omega^\alpha\}$ ($\alpha = 1$, 2). By definition, $\boldsymbol{\psi}^\alpha$ and ω^α satisfy

$$\rho\,(\omega^\alpha)^2\boldsymbol{\psi}^\alpha + \boldsymbol{\nabla}\cdot(\mathbf{c}:\boldsymbol{\nabla}\boldsymbol{\psi}^\alpha) = \mathbf{0},$$

and $\int \rho\boldsymbol{\psi}^\alpha\cdot\boldsymbol{\psi}^\beta\,\mathrm{d}v = 0$ and $\int \boldsymbol{\nabla}\boldsymbol{\psi}^\alpha : \mathbf{c} : \boldsymbol{\nabla}\boldsymbol{\psi}^\beta\,\mathrm{d}v = 0$ for $\omega^\alpha \neq \omega^\beta$. As is seen, $\{\boldsymbol{\psi}^\alpha\}$ decouple the kinematic energy but do not decouple the strain energy. That is, if $\{\boldsymbol{\psi}^\alpha\}$ are used for $\{\boldsymbol{\phi}^\alpha\}$ of Eq. (4), the Lagrangian becomes

$$\mathcal{L} = \frac{1}{2}M^1(\dot{U}^1)^2 + \frac{1}{2}M^2(\dot{U}^2)^2 - \frac{1}{2}K^1(U^1)^2 - \frac{1}{2}K^2(U^2-U^1)^2 - \frac{1}{2}K^3(U^2)^2. \tag{7}$$

Figure 3 shows a spring system which correspond to the above Lagrangian. This system has a third spring, denoted by K^3, that connects the top mass (M^2) to the ground. This spring is essential to make the system consistent so that the natural frequency coincides with that of the continuum. It should be noted that $\{\boldsymbol{\phi}^\alpha\}$ are set to satisfy the condition that a component of $\boldsymbol{\phi}^\alpha(\mathbf{x}^\alpha)$ which correspond to U^α is 1, but that they do not have to satisfy $\boldsymbol{\phi}^\alpha(\mathbf{x}^\beta) = \mathbf{0}$ for $\alpha \neq \beta$.

3.2 Beam theory

According to the meta-modeling theory, a governing equation of beam theory is derived from $\mathcal{L}^*$ of Eq. (2), by using $\{\mathbf{u}, \boldsymbol{\sigma}\}$ of the following non-zero components:

$$u_1 = -z\,w'(x,t), \quad u_3 = w(x,t), \quad \sigma_{11} = z\,s(x,t). \tag{8}$$

Here, the x_1- and x_3-axes are the longitudinal and (bending) transverse directions, and x and z are used instead of x_1 and x_3.

Since $\mathcal{L}^*$ becomes a functional of w and s, the variation of $\mathcal{L}^*$ with respect to these functions is

$$\delta\mathcal{L} = \int \delta w\left(\rho(\ddot{w}^2 - z^2\ddot{w}'' + z^2s''\right)\delta s z^2(\frac{s}{E} + w'')\,\mathrm{d}x\mathrm{d}y\mathrm{d}z. \tag{9}$$

Recall that $\mathbf{c}$ is assumed to be homogeneous and isotropic; Young's modulus and Poisson's ratio are E and ν. It thus yields $s = -E\,w''$ and

$$\rho\,A\,\ddot{w}^2 - \rho\,I\,\ddot{w}'' - (E\,I\,w'')'' = 0, \tag{10}$$

where $A = \int \mathrm{d}z\,\mathrm{d}y$ and $I = \int z^2\,\mathrm{d}z\,\mathrm{d}y$. As is seen, this equation for w coincides with the governing equation of Rayleigh beam theory; at quasi-static state, Eq. (10) yields the governing equation of Bernoui Euler beam theory, too.

A beam element solution is now regarded as an approximate numerical solution of solving the variational problem of $\mathcal{L}^*$. A beam element solution which is *closest* to a solid element solution is determined by minimizing a suitable distance in the function space of $\{\mathbf{u}, \boldsymbol{\sigma}\}$. For instance, when a solid element solution $\{\overline{\mathbf{u}}, \overline{\boldsymbol{\sigma}}\}$ is given, we measure the distance of a beam element solution given by w as follows:

$$N(w) = \frac{1}{|\overline{\mathbf{u}}|^2}\int (w - \overline{u}_1)^2 + (-zw' - \overline{u}_3)^2\,\mathrm{d}v + \frac{1}{|\overline{\boldsymbol{\sigma}}|^2}\int (\overline{\sigma}_{11} - zEw'')^2\mathrm{d}v, \tag{11}$$

where $||^2$ is the L2 norm of $\overline{\mathbf{u}}$ and $\overline{\boldsymbol{\sigma}}$; $\frac{1}{|\overline{\mathbf{u}}|^2}$ and $\frac{1}{|\overline{\boldsymbol{\sigma}}|^2}$ are necessary so that N does not have physical dimension of length nor stress.

It is a usual practice of the beam element analysis that a rotation function, θ, is introduced besides for deflection, w. This θ provides $u_1 = -z\theta$ and $\sigma_{11} = -Ez\theta'$, since it is defined as $\theta = -w'$. In numerical computation, θ is discretized separately from w in order to obtain a more accurate solution. Hence, w' is replaced by θ in N of Eq. (11) when θ is used in the beam element analysis.

The conversion from the solid element solution to a beam element solution is readily made by minimizing N. In discretized index form, $\overline{\mathbf{u}}$ and $\overline{\boldsymbol{\sigma}}$ are expressed as

$$\overline{\mathbf{u}} = \sum_\alpha \overline{\mathbf{u}}^\alpha \phi^\alpha(\mathbf{x}), \quad \overline{\boldsymbol{\sigma}} = \sum_\alpha \mathbf{c} : (\overline{\mathbf{u}}^\alpha \otimes \boldsymbol{\nabla}\phi^\alpha(\mathbf{x})), \tag{12}$$

where $\mathbf{u}^\alpha$ and ϕ^α are the α-th nodal displacement and shape function, respectively. Similarly, w and θ are expressed as

$$w = \sum_\beta w^\beta \psi^\beta(x), \quad \theta = \sum_\beta \theta^\beta \psi^\beta(x), \tag{13}$$

where w^β, θ^β and ψ^β are the β-th nodal displacement, rotation and shape function, respectively. In order to minimize N, $\{w^\beta\}$ and $\{\theta^\beta\}$ satisfy

$$\sum_\beta A^{\gamma\beta} w^\beta + \sum_\alpha B^{\gamma\alpha}\overline{u}_3^\alpha = 0, \quad \sum_\beta C^{\gamma\beta}\theta^\beta - \sum_\alpha D^{\gamma\alpha}\overline{u}_i^\alpha = 0, \tag{14}$$

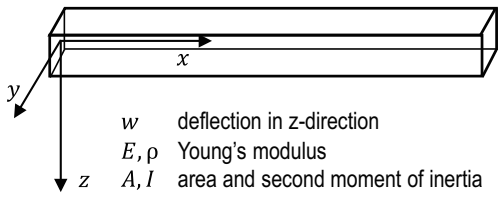


Figure 4: Schematic view of beam and coordinate system.

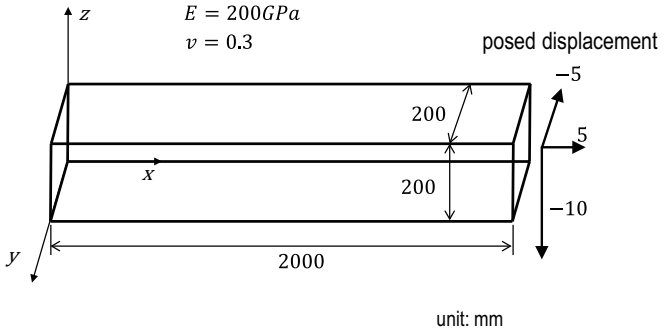


Figure 5: Schematic view of cantilever beam.

for $\gamma = 1, 2, \cdots$, where

$$A^{\gamma\beta} = (\psi^\gamma \psi^\alpha), \quad B^{\gamma\alpha} = (\psi^\gamma \phi^\alpha), \quad C^{\gamma\beta} = (z^2 \psi^\gamma \psi^\beta) + \frac{(\overline{\mathbf{u}} : \overline{\mathbf{u}})}{(\overline{\boldsymbol{\sigma}} : \overline{\boldsymbol{\sigma}})} E^2((\psi^{\gamma\prime}(\psi^{\beta\prime}),$$
$$D_i^{\gamma\alpha} = \delta_{3i}(z\psi^\gamma \phi^\alpha) + \frac{(\overline{\mathbf{u}} : \overline{\mathbf{u}})}{(\overline{\boldsymbol{\sigma}} : \overline{\boldsymbol{\sigma}})}(E\psi^\gamma c_{33ij} \frac{\partial \phi^\alpha}{\partial x_j}). \tag{15}$$

Here, for simplicity, $()$ is used to denote the volume integration taken over V, and summation convention is employed (repeated indices are summed).

4 NUMERICAL EXPERIMENTS FOR CONSISTENT MODELS

4.1 Cantilever beam

Biaxial bending in beam or column is encountered in structural analysis [5]FF. Prediction of bidirectional bending made by ordinary methods is not a simple task due to coupling of biaxial bending with axial force; the ordinary methods employs interpolation and curve fitting of element stress (or nodal stress that is computed from element stress) in order to compute biaxial bending moment. The meta-modeling theory is readily able to decouple biaxial bending moment without introducing any assumption, since it uses genuinely mathematical approximation of functions. In this subsection, we examine the capability of the meta-modeling theory of handling the de-coupling of biaxial bending moment.

A cantilever with uniform square (200 $\times$ 200 mm) cross section is used in the present numerical experiment; see Fig. 5 for the problem setting of the cantilever. Three boundary conditions of displacement are posed at one end, while the other end is clamped. Sufficiently fine mesh is used for both the solid and beam element models. This is essential for the numerical model that is used in the meta-modeling, in order to remove (or minimize) numerical errors caused by coarse meshing.

A solid element solution is converted to a beam element solution, according to the procedures present in the preceding section. The cross-section forces which are computed by the converted beam element solution are shown in Fig. 6. For comparison, the cross sectional force which are computed by the conventional method that uses interpolation and curve fitting of element stress are shown in the figure, too. As is seen, there are some differences in the converted forces and the estimated ones. However, the difference is not significant, suggesting that the cross sectional force computed by the converted beam element solution is sufficiently accurate.

It should be emphasized that de-coupling of the biaxial bending moment is successfully made in the proposed conversion method that is based on the meta-modeling theory. The converted

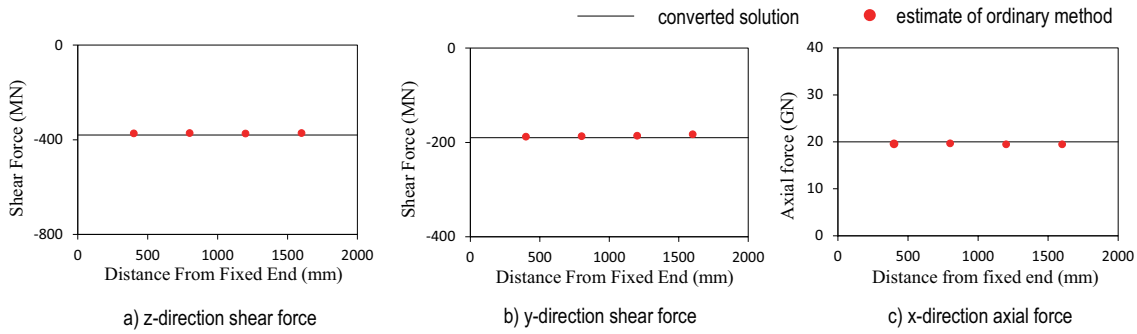


Figure 6: Distribution of cross-sectional force of cantilever computed by converted beam element solution.

beam element solution has a set of displacement and cross-sectional force. The conventional method which calculates cross-sectional force from element stress does not produce such a set. Moreover, interpolation and curve fitting of element stress is laborious when cross sectional force and moment are computed at every cross section. The proposed conversion method is much simpler, since it casts a solid element solution to a beam element solution just by solving Eq. (14) so that the closest beam element solution is found.

4.2 Tunnel structure

A tunnel needs a ramp tunnel which connects the main tunnel to the ground level. By this nature, the ramp tunnel has a complicated configuration and the resulting seismic response ought to be complicated; it often passes through several soil layers of different wave velocities. Therefore, two-dimensional analysis of cross-section has limited accuracy in estimating such complicated responses. Three-dimensional solid element analysis is needed if the seismic response has to be evaluated at highest accuracy [2, 3]. For the purpose of design, cross sectional forces and moment are of primary importance, and hence the results of the three-dimensional solid element analysis must be converted to cross sectional force and moment, in the same manner as shown in the preceding subsection.

A solid element model of a main tunnel connected by a ramp tunnel is used in the present numerical experiment; see Fig. 7 for a schematic view of the tunnel. It should be mentioned that this model is a part of a solid element model that is used for large-scale numerical computation of the main tunnel, the length of which is longer than 2,000 m. A targeting frequency range of the present model is 0 to 6 Hz, and suitably fine meshing is made for the model. Longitudinal ground motion is input to the tunnel; see Fig. 8 for the wave form of the input ground motion.

For simplicity, we convert a solid element solution at an instant at when displacement takes on a maximum value. It is indeed laborious to convert a time series of the solid element solution to that of the beam element solution. However, this conversion is much easier than computing cross sectional force and moment by the conventional method that uses interpolation and curve fitting of element stress. Spatial distribution of three cross sectional forces which are computed from the converted beam element solution are presented in Figs. 9 and 10; the latter shows rapid change in the cross sectional forces along the longitudinal direction of the tunnel. At three cross sections, the forces that are computed by the converted beam element solution are compared with those computed by the ordinary method; see Table 2 for the values of the cross sectional forces.

As is seen in Fig. 10, the main part of the tunnel behaves like rod rather than beam, since the axial force is dominant in the cross sectional forces and the shear force and bending moment

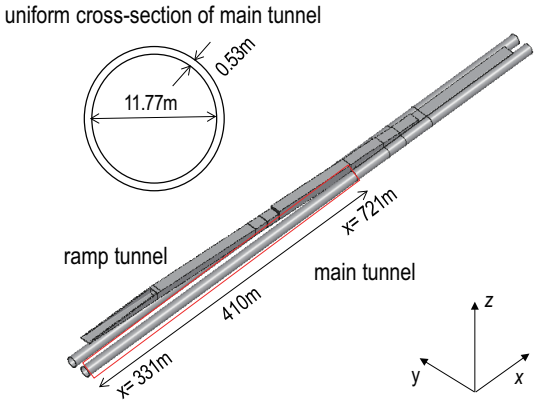


Figure 7: Schematic view of large scale tunnel with ramp tunnel.

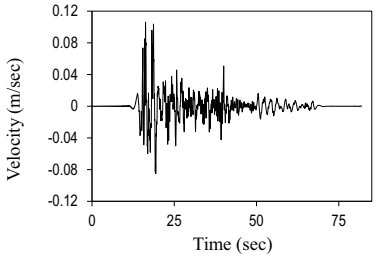


Figure 8: Input ground motion of tunnel.

Table 2: Comparison of cross sectional force of tunnel computed by converted beam element solution.

a) z-direction shear force

location	proposed	ordinary
400	-109.21	-105.22
500	-23.15	-30.22
600	-36.88	-32.24

b) y-direction shear force

location	proposed	ordinary
400	59.66	65.25
500	1.27	3.21
600	1.45	3.25

is small. It is also easily seen that the distribution of the cross sectional forces is not uniform; concentration is observed between 400 m and 500 m along the tunnel longitudinal direction. Choosing a part of the tunnel in which the cross sectional forces are concentrated is easily found. The location of such concentration of the cross sectional force could be different from that of stress. For the purpose of design, it is surely better to use the cross sectional forces if they are easily computed.

Difference in computing the cross sectional force between the present conversion method and the ordinary method is not negligible. Larger relative difference is found for the shear force compared with the axial force. But this is probably because the shear force is smaller than the axial force. These results suggest that the numerical accuracy of computing the cross sectional force from the converted beam element solution is sufficiently high, just like the cantilever of the preceding subsection. We can see a potential usefulness of the conversion method that is based on the meta-modeling theory, since it accurately estimates cross sectional forces that are associated with the converted displacement of the beam theory.

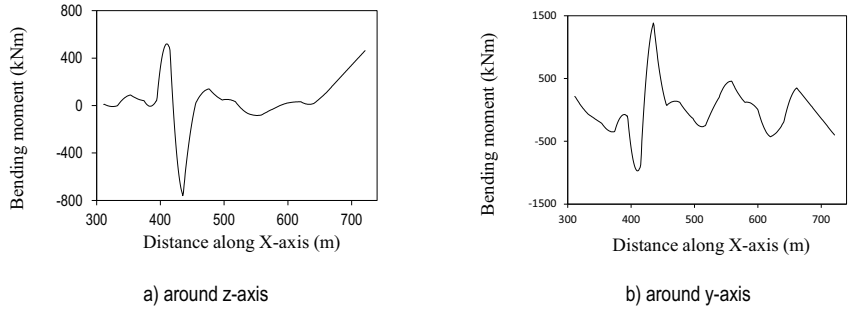


Figure 9: Distribution of cross-sectional force of tunnel computed by converted beam element solution.

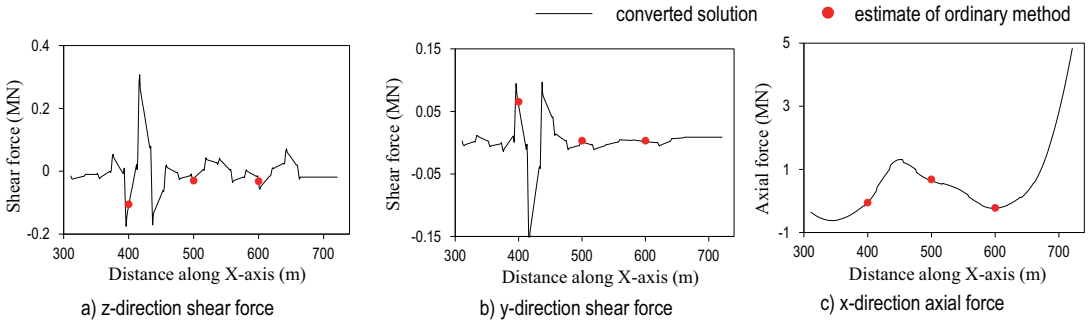


Figure 10: Detailed distribution of cross-sectional force of tunnel computed by converted beam element solution.

4.3 Freeway bridge structure

A freeway bridge which consists of a few pier and a deck is large in scale and complicated in configuration, and it is another target of seismic response analysis that uses the three-dimensional solid element analysis. Modeling connection between the pier and the deck is not straightforward since shoes and bearings that have distinct friction characteristic are used there. Indeed, there are cases when analysis models have natural frequencies different from the observation. The meta-modeling theory could help us to construct a solid element model of high fidelity by gradually increasing the complexity of consistent models.

As an example, we consider a freeway bridge as shown in Fig. 11; it has a curved deck supported by fourteen piers. The material properties are summarized in Table 3. Beside for the deck being curved, the height of the piers is not uniform and each pier has its own configuration. For simplicity, however, we assume that all the piers share the identical cross section, as shown in Fig. 12, while the height of the piers is different.

According to the meta-modeling theory, we construct a mass spring system for each pier; the system consists of one mass and one spring. The mass and stiffness of each pier are presented in Fig. 13. And the natural frequency of the mass spring system of each pier is summarized in

Table 3: Material properties of freeway bridge.

density of pier (concrete)	$2400kg/m^3$
density of deck (steel)	$7800kg/m^3$
Young's modulus (concrete)	$25GPa$
Young's modulus (steel)	$200GPa$
damping ratio (concrete)	5%

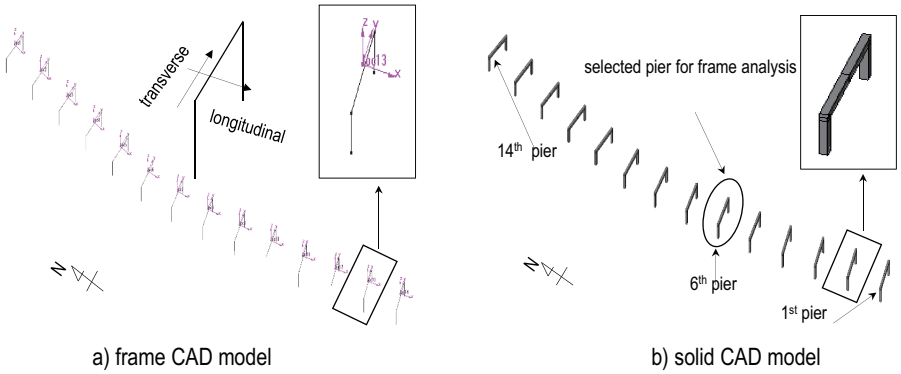


Figure 11: Schematic view of freeway bridge.

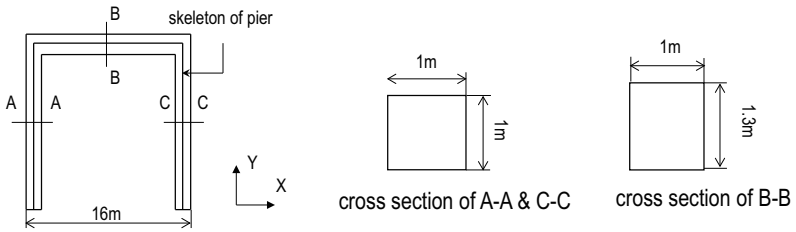


Figure 12: Cross section of freeway bridge.

Table 4: Comparison of natural frequency of freeway bridge computed by converted beam element solution.

	transverse (Hz)	longitudinal (Hz)
lumped mass	3.426	3.426
frame	3.420	3.421

Table. 4.

For some piers, the maximum displacement of the mass spring system is compared with that of the frame model; see, for intance, [6, 9, 11, 12] for the comparison of the seismic response of bridge piers. The frame model is made by manual work, while the mass spring system is automatically constructed according to a given data of the freeway bridge; the mass spring system is much simpler than the frame model and hence we can make such automated model construction. While there are some differences in the natural frequency, they are not significant; see Table 4. This suggests that, for the natural frequency of the first mode, the mass spring system that is constructed by the meta-modeling theory is sufficiently accurate.

We compute seismic response of the piers of the free bridge using the mass spring system. Input ground motion is shown in Fig. 15. For comparison, we carry out the seismic response analysis using the frame model. The difference in the displacement response of the two models is presented in Fig. 16.

As is seen in Fig. 16, there are some difference in the response. This difference is inevitable since even the natural frequency of the mass spring system is different from that of the frame model; see Table 4. However, this difference is not significant since the peak displacement reaches a few ten centimeter. Again, this suggests high accuracy of the consistent mass spring system in computing the seismic response analysis.

Small difference in the seismic response is partial due to the nature of input ground motion which does not have large contribution of the higher modes of the bridge piers. It is inevitable

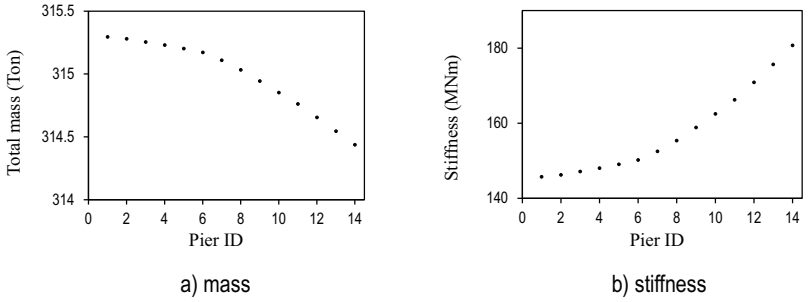


Figure 13: Mass and stiffness of mass spring system for bridge piers.

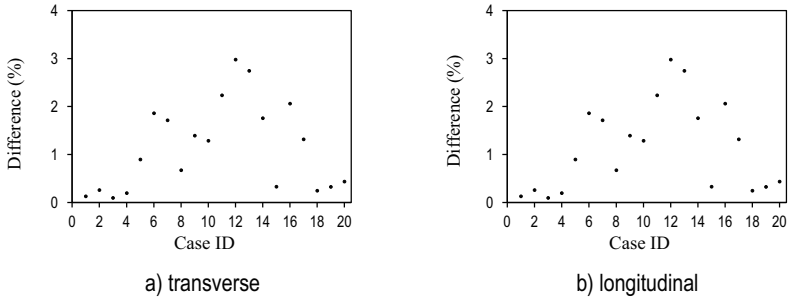


Figure 14: Maximum displacement of freeway bridge computed by converted beam element solution.

for a simple mass spring system to fail computing higher modes accurately. A simple solution to overcome this shortcoming of the mass spring system is to use a more complicated mass spring system which consists of a few masses and springs. Consistency is surely required for such a mass spring system which may need additional springs; compare Fig.3 with Fig. 2.

5 CONCLUDING REMARKS

This paper presents the meta-modeling theory and its application, in order to construct a set of consistent models for structure seismic response analysis. The consistency of modeling is that it solves the same variational problem of continuum mechanics by using different mathematical approximation. Consistent mass spring system and beam theory are explained. Numerical experiments demonstrate that for actual structures, this theory is applicable to construct a set of consistent models.

The present numerical experiments use linear analysis only. It is surely necessary to study the material and kinematic non-linearity, in applying the meta-modeling theory to construct consistent non-linear models. The key issue of this study is to find a Lagrangian for the non-linear case.

REFERENCES

[1] M. Hori, W.L.L. Wijerathne, T. Ichimura, S. Tanaka, Meta-modeling for constructing model consistent with continuum mechanics, *Journal of Stuctural Mechanics and Earthquake Engineering*, Vol. 9, No. 4, 2014.

[2] H. Dobashi, T. Hatsuku, T. Ichimura, M. Hori, T. Yamada, N. Ohbo, M. Moriguchi, H. Itami, Full 3d seismic response analysis of underground ramp tunnel structure using large-

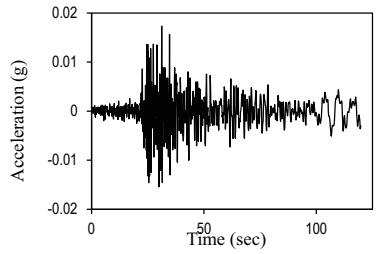


Figure 15: Input ground motion of freeway bridge.

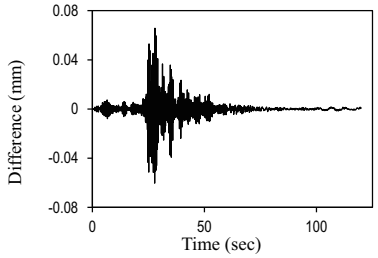


Figure 16: Difference in displacement response of freeway bridge computed by converted beam element solution.

scale numerical computation, *The 14th World Conference on Earthquake Engineering october*, Beijing, China, August, 2008.

[3] H. Dobashi, Y. Terashima, M. Hori, T. Ichimura, N. Ohbo, T. Yamada, T. Obara, Seismic performance analysis of underground ramp tunnel structure using 3-D massive numerical computation, *III ECCOMAS Thematic Conference on Computational Methods in Structural Dynamics and Earthquake Engineering*, Corfu, Greece, May, 2011.

[4] J. F. Doyle, *Wave Propagation in Structures*, Mechanical engineering series, 2nd edition, pp. 43–73, 1997.

[5] G. Li, J. Li, A tapered Timoshenko-Euler beam element for analysis of steel portal frames, *Journal of construc-tional steel research*, Vol. 58, No. 12, pp. 1531–1544, 2002.

[6] C. K. Wang, Stability of rigid frames with nonuniform members, *Journal of Structural Division*, Vol. 93, No. 1, pp. 275–294, 1967.

[7] H. V. S. G. Rao, Closed form series solutions of boundary value problems with variable properties, *Computers & Structures*, Vol. 23, No. 2, pp. 2110–215, 1986.

[8] A. K. Chopra, *Dynamics of Structures*, Prentice Hall Inter-national, 2nd edition, pp. 305–343, 2000.

[9] R. W. Clough, J. Penzien, *Dynamics of Structures*, McGraw-Hill International, 2nd edition, pp. 133–160, 2000.

[10] B. Jang, R. T. Chin, Analysis of Thinning Algorithms Using Mathematical Morphology, *Transactions on Pattern Analysis and Machine Intelligence*, Vol. 12, No. 6, 1990.

[11] M. J. Kowalsky, Deformation limit states for circular reinforced concrete bridge columns, *Journal of Structural Engineering*, Vol. 126, No. 8, 2000.

[12] M. J. Kowalsky, M. J. N. Priestley, G. A. Macrae, Displacement-based design of RC bridge columns in seismic regions, *Earthquake Engineering And Structural Dynamics*, Vol. 24, pp. 1623–1643, 1995.

COMPDYN 2015
5th ECCOMAS Thematic Conference on
Computational Methods in Structural Dynamics and Earthquake Engineering
M. Papadrakakis, V. Papadopoulos, V. Plevris (eds.)
Crete Island, Greece, 25–27 May 2015

PARAMETRIC NUMERICAL STUDY OF THE SEISMIC RESPONSE OF CLASSICAL COLUMNS

Ioannis E. Kavvadias[1] **and Lazaros K. Vasiliadis**[1]

[1] Democritus University of Thrace, Dept. of Civil Engineering,
Institute of Structural Mechanics and Earthquake Engineering
Vas. Sofias 12, 67100 Xanthi, Greece
{ikavvadi, lvasilia}@civil.duth.gr

Keywords: Classical columns, Seismic response, Heritage structures.

Abstract. *This paper presents a numerical investigation of the seismic response of monolithic and multidrum columns. The effect of the column size and the effect of the input motion characteristics on the dynamic response of free standing columns are studied. Single columns and two columns coupled with an architrave subjected to a set of 20 ground motions are examined. The selection of the seismic excitations was made in order to provide a wide spectrum of structural damage due to statistical reasons. Further various prototype geometry sections are considered in order to include as key parameter the column size effect on the seismic behavior of these structural systems. Correlation study is performed to estimate the interrelationship between the most substantial ground motion parameters and the damage indices. Moreover the effect of the column geometry on the seismic response of classical column structural systems is studied based on the results of the linear regression analysis. Finally the relation between the maximum developed rotations and the residual displacements is examined. For the purposes of this study finite element models for the in space simulation of the members are adopted and results in term of relative rotations and relative residual displacements between the drums are presented.*

1 INTRODUCTION

The investigation of the seismic response of ancient structural systems such as ancient columns and colonnades has received increasing attention during the last decades. Different types of columns with numerous variations in their geometrical characteristics can be found in the Eastern Mediterranean region. Usually these are constructed of limestone or marble blocks (drums), which are placed on top of each other, without connecting mortar between them. These rigid-body assemblies display a very different dynamic response compared to modern structures, as their response is composed primarily of the rocking and the sliding among the individual drums of the structure. This behavior can be characterized as highly nonlinear due to the continuously changing of the geometry and boundary conditions of the structural system during a strong earthquake.

Early studies on the rocking response of a rigid block undergoing horizontal motion were presented by Housner [1]. Extensive investigation specifically on the response of single multidrum columns or of columns connected with each other at the top level by architraves has been presented by several researchers [2-7]. A numerical study of the seismic response of ancient columns conducted in two dimensions based on the distinct element method has been presented by Psycharis et al[2] while, Papantonopoulos et al [3] used a three dimension modeling in order to predict the experimental results of a scale multidrum column model[4]. Furthermore, Konstantinidis and Makris [6] examined the effect of wooden poles installed in ancient times, in the dynamic response of multidrum columns. Additionally Papaloizos and Komodromos [7] investigated the seismic response of ancient columns and colonnades with epistyles using a custom-made software based on the Discrete Element Method (DEM).

It is concluded that the dynamic behavior of free standing columns is very sensitive even to trivial changes in the ground motion characteristics or of the geometry of the model. Classical columns are, in general, earthquake resistant, as proven from the fact that many classical monuments have survived many strong earthquakes over the centuries. The predominant period of the excitation significantly affects the response, with low frequency pulses being much more dangerous while, the size of the column is another important parameter, with bigger structures being much more stable than smaller ones with the same slenderness.

In this paper, we present a numerical investigation of the seismic response of classical columns. The parameters we examined refer to the column geometry and the excitation characteristics. Regarding the numerical model, four prototype geometry sections are considered in order to examine the column size effect on the seismic behavior of these structural systems. Both monolithic and multidrum columns are simulated so as to provoke the beneficial drum dislocation. In addition two columns coupled with a varying geometry architrave is considered as to arise its influence on the dynamic response of colonnades. Regarding the excitations a set of 20 ground motions is used.

Correlation coefficients are evaluated to express the grade of interdependency between seismic parameters and the structural damage. Correlation between seismic parameters and structural damage has been studied mainly for RC buildings [8]. The ground motion parameters considered are the peak parameters (PGA, PGV and PGD) and the spectra parameters provided by the Fourier spectrum. Due to the fact that such structures do not possess natural modes in the classical sense and the periods of free vibrations are amplitude dependent the Fourier spectrum is used to find out the period and the amplitude of the main pulse of each ground motion record. The structural damages are represented in terms of relative rotation and relative residual displacements between the drums.

Moreover, linear regression analyses have been performed between the seismic parameter which has the strongest correlation with the overall structure damage, so as to compare the

seismic response between the various models. Especially is examined the size and the slenderness influence, the construction technic (monolithic against multidrum) and the colonnade with epistyle against the single column response. Finally, is presented the interrelationship between the two damage indices which are the maximum developed relative rotation and the relative residual dislocation, in order to arise the dominant response responsible for the collapse of classical columns.

2 NUMERICAL MODEL

For the purpose of this study finite element models are adopted for the in space simulation of the members, in which the blocks are simulated as deformable elements and the ground as a rigid surface. Specifically Young's modulus (E=84.5 GPa), the poison ratio (ν=0.23) and the density of the marble (d=2750 kg/m3) are defined.

Of particular significance of the simulation are the appropriate modeling of the contact between the drums. A Mohr-Coulomb model is adopted to describe the mechanical behavior of the joints. For both normal and tangential direction of the contact element the stiffness is assumed as infinite. In the normal direction no tensile strength is considered while the shear strength is governed by the Coulomb friction coefficient. Typical values of the friction coefficients for marble blocks are μ=0.7.

Prototype geometry columns with two different heights and two different ratios of the heights over the columns diameter are studied. Table 1 presents the dimensions of the examined models. The selection of the dimension was made to be in accordance with the size and the slenderness of recorded ancient columns. Regarding the multidrum columns, a drum of 1m height is considered for every model. Concerning the effect of the architrave existence, two varying geometry architraves are examined. The values of the architrave height defined as a ratio over the columns diameter taking values h/2B =0.5, 1. The axial distance between the columns is L=3m and is spanned with a single block architrave. Figure 1 shows the dimensions specified in the models.

Model	2H (m)	H/B	Number of Drums
I	5	6	5
II	5	7	
III	8	6	8
IV	8	7	

Table 1: Examined models geometry

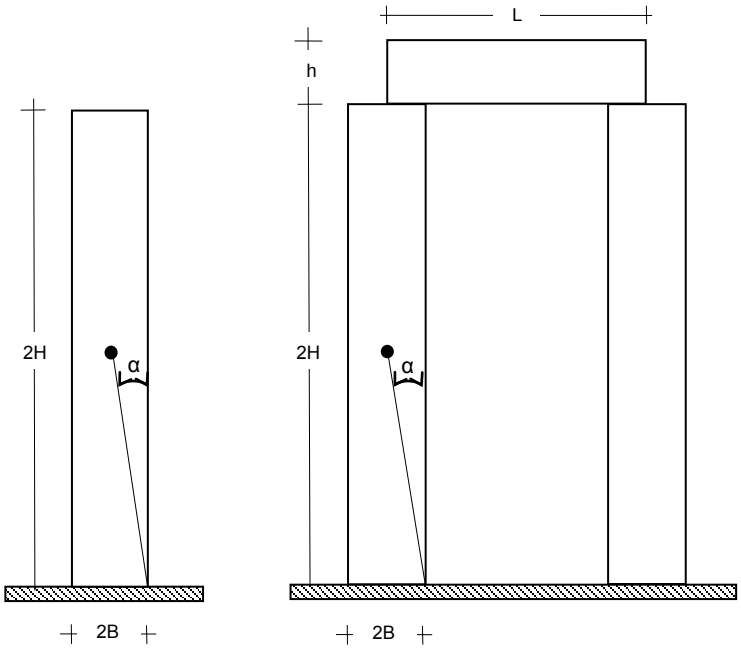


Figure 1: Columns and colonnades with epistyle geometry.

3 SELECTION OF GROUND MOTIONS

Our analyses used a set of 20 ground motions (Table 2) with different characteristics in order to investigate how the response of the columns is influenced by the characteristics of the seismic excitations. The events have been chosen from worldwide well-known sites with strong seismic activity. A further aspect which has been taken into consideration is the expected damage potential of the seismic excitation on the structure to be analyzed. Seismic excitations which provide a wide spectrum of structural damage, from negligible to severe, are taken into account due to statistical reasons. The selected ground motion are in the range of Mw=6.2-7.62. As the predominant period of the ground motion seems to be the main parameter which affects the stability of the column, the ground motion acceleration signal must be converted from a time domain to a frequency domain.

Due to the fact that the free standing columns do not possess natural modes in the classical sense, we do not use the response spectrum parameters. On the contrary, the period of the maximum Fourier amplitude spectrum is not dependent on the structural response and therefore is a more accurate method to find out the period of the main pulse which affects the seismic response of these structures. The term $\alpha_p \bullet T_p = v_p$ seems to be representative as it combines the amplitude with the period of the main pulse. Also the product $\alpha_p \bullet T_p^2 = L_p$ is examined which is a characteristic length scale of the main pulse [9, 10]. Several peaks are shown in the Fourier spectrum. The combination α_p - T_p selected is the one that maximizes the products $\alpha_p \bullet T_p$ and $a_p \bullet T_p^2$ which do not necessarily correspond to the maximum acceleration amplitude spot.

Earthquake	Record	M_w	PGA (g)	PGV (cm/s)	PGD (cm)	T_p (s)	α_p (g)	v_p (m/s)	L_p (m)
Bucharest 04/03/1977	Bucharest	7.50	0.20	73	126	1.71	0.31	5.31	9.06
Chi-Chi 20/09/1999	TCU52	7.62	0.34	159	184	2.28	0.48	10.64	24.2
Chi-Chi 20/09/1999	TCU88	7.62	0.52	35	29	0.10	0.24	0.23	0.02
Chuetsu 16/06/2007	Kariwa	6.80	0.36	103	54	2.34	1.03	23.7	55.6
Corinth 24/02/1981	Corinth	6.60	0.30	25	7	0.85	0.14	1.20	1.02
Duzce 12/11/1999	Lamont 531	7.14	0.16	13	8	0.39	0.15	0.59	0.22
Erzincan 19/03/1992	Erzincan	6.69	0.52	84	28	2.28	0.30	6.64	15.1
Friuli 06/05/1976	Tolmezo	6.50	0.31	31	5	0.67	0.23	1.50	1.01
Gazli 17/05/1976	Karakyr	6.80	0.72	71.6	23.7	0.52	0.32	1.65	0.87
Imperial Valley 19/05/1940	El Centro Array #9	6.95	0.31	30	13	0.85	0.26	2.16	1.84
Imperial Valley 15/02/1979	El Centro Array #7	6.53	0.33	48	25	1.20	0.17	1.98	2.39
Kalamata 13/09/1986	Kalamata	6.20	0.25	29	9	1.22	0.10	1.13	1.39
Kobe 16/01/1995	Nishi - Akashi	6.90	0.51	37	10	0.47	0.40	1.88	0.90
Landers 28/06/1992	Joshua Tree	7.28	0.28	43	14	1.51	0.31	4.62	7.02
Loma Prietta 18/10/1989	UCSG 16 LGPC	6.93	0.97	109	66	2.93	0.40	11.54	33.7
Northridge 17/01/1994	Jensen Filter Plant	6.69	1	68	25	2.05	0.27	5.38	11.0
Parkfield 28/06/1966	Cholame #2	6.20	0.48	75	22	1.37	0.19	2.61	3.56
San Fernando 09/02/1970	Paicoma Dam	6.61	0.32	16	2	0.34	0.15	0.52	0.18
Superstition Hill 24/11/1987	Mtn Camera	6.54	0.68	33	5	0.66	0.27	1.72	1.14
Tabas 16/09/1978	Dayhook	7.35	0.33	20	11	0.64	0.14	0.87	0.56

Table 2: Ground motion used in the analyses

4 RESULTS

Numerical analyses are performed in order to examine the correlation between the parameters of the earthquake excitations and the seismic response of the examined columns. Subsequently the effect of the structural system geometry is performed comparing the lines exported by the linear regression analyses. The overall structure damage index is presented in terms of maximum rotation and residual relative displacement. Both indices are introduced as a ratio over the critical overturning rotation and the critical relative displacement respectively. The critical overturning rotation (θcr) is equal to the slenderness (α) and take the value

$$\theta_{cr} = \alpha = \arctan(B / H) \tag{1}$$

Finally for the multidrum columns, the two indices are plotted in order to display the interrelationship of both and as a result to highlight the most crucial phenomenon between the rocking and the sliding response.

4.1 Correlation analysis

To estimate the degree of the correlation between the ground motion parameters and the damage indices, the linear rank correlation coefficients after Spearman is calculated. Table 3 presents the correlation coefficients regarding all the models (monolithic, multidrum, colonnade connected with architrave) of the 8m height column with dimensional ratio H/B=6 and h/H=1.

Excitation Parameters	Monolithic	Multidrum	Colonnade
PGA	0.353	0.396	0.515
PGV	0.852	0.903	0.929
PGD	0.768	0.746	0.792
T_p	0.845	0.843	0.775
α_p	0.752	0.748	0.847
v_p	0.930	0.912	0.917
L_p	0.876	0.860	0.821

Table 3: Correlation coefficients

Examining Spearman's rank correlation coefficient in Table 3, easily reconcilable is the maximum correlation of the maximum developed rotation with PGV and v_p. Significant values of correlation coefficient also have with T_p and L_p. The lower correlation occurred with PGA, PGD and α_p. It is obvious that the seismic parameters associated with the predominant period of the ground motion exhibit better correlation. It is known that the period of the excitation affects the response of the classical columns, with long period pulses being more dangerous. As expected the columns overturn when they are subjected to excitations with predominant period longer than $T_p > 2$s. Concerning the correlation coefficients from all 24 modes, v_p is the highest correlated seismic parameter whose coefficient ranges from 0.713 to 0.93.

4.2 Linear regression analysis

Linear regression analyses have been performed considering all of the results for each particular model, to notice the relations of maximum developed rotation to v_p, which is the highest correlated seismic parameter with that damage index. Furthermore by comparing the linear regression results between the models are extracted considerable results as regards the effects of the geometry alteretions. Comparative presentation of the performed linear regression analyses results are shown in Figures 2-7.

The response of the 8m height monolithic columns exhibit important stability when excited by ground motion with v_p < 4m/s. Comparing the two columns with same height but with different slenderness ratio H/B (Figure 2) is apparent that both columns overturn when exited by long period ground motions. Only for the Erzincan earthquake the bulkier column developed rotation 72% of columns slenderness without overturns in contrast with the less slender column. Comparing the maximum rotations, the main difference occurred for ground motion with low values of v_p where an increased value of rotation developed to the thinner column.

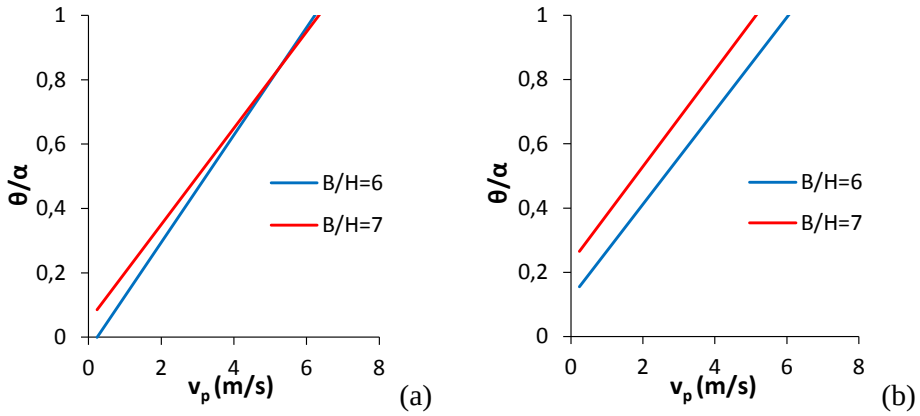


Figure 2: Maximum rotations (a) of the 8m height column, (b) of the 5m height column.

The 5m height columns seismic response demonstrates a significant rocking instability. As it can be observed in Figure the column with slenderness ratio H/B=7 is vulnerable when it is subjected to ground motions with low values of v_p. Overturn of the column occur even when excited by El Centro Array #7 which takes value v_p=1.98m/s. The bulkier column show smaller rotations in relation with the thinner one. Moreover, comparing the columns with the same slenderness ratio but with different actual size (Figure 3) the taller columns displays increased stability

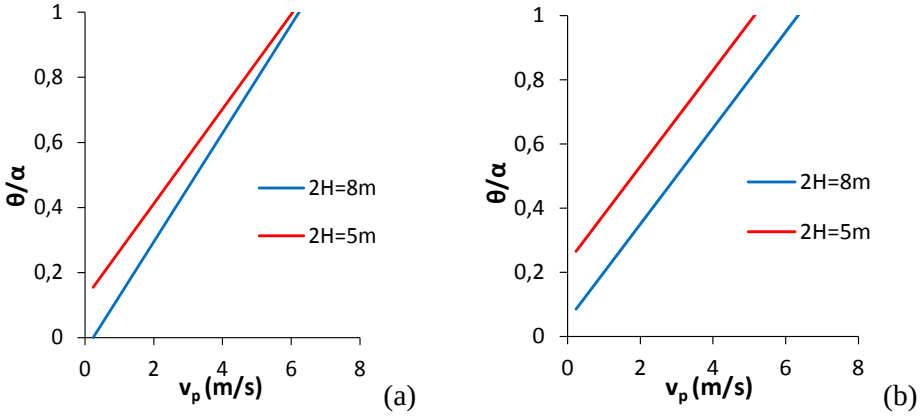


Figure 3: Maximum rotations of columns with slenderness ratio (a) B/H=6, (b) B/H=7.

The seismic response of a structural system composed of two columns linked with an architrave is also examined. Comparative presentations of the maximum developed rotations of the examined columns with and without architrave are shown in Figure 4. It can be observed that the 8m height colonnade request lower values of rotation in contrast with the single column. The epistyle geometry do not significantly affects the response of the structural system. Nevertheless, regarding the 5m height colonnade the geometry of the architrave seems to be of crucial importance.

The seismic response of the colonnade with an architrave with dimensional ratio h/2B=0.5 displays important similarities with the single column models. The maximum developed rotation is almost the same while overturn of the structural system occurs for the same excitations as to the single column. In the examine case when the architraves dimensional ratio is h/2B=0.5 the colonnade system exhibit reduction of the developed rotations. Moreover in contrast with the single columns response the colonnade systems do not overturn excited by the Gazli ground motion.

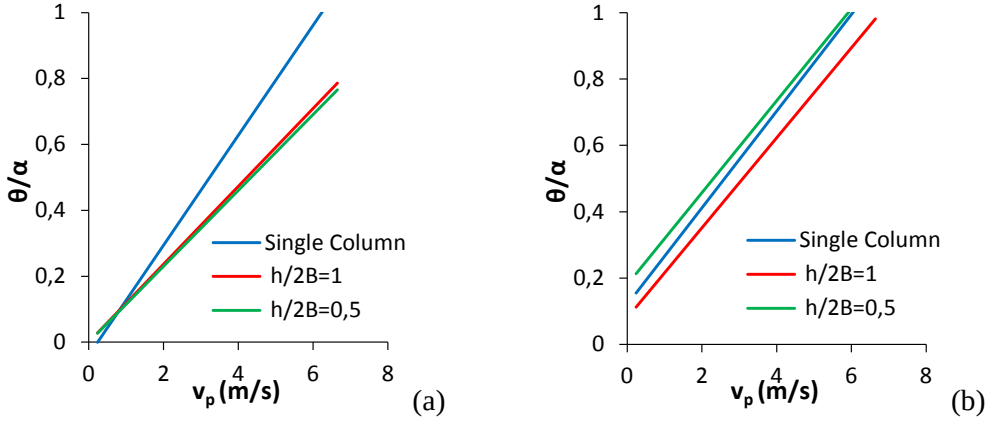


Figure 4: Developed rotations of colonnade systems with (a) 8m height column, (b) 5m height column.

Multidrum columns exhibit very complicated, highly nonlinear seismic response that depends on numerous parameters. Their response are very complex containing both sliding and rocking when they are subjected to low predominant period pulses. On the other hand rocking is the prevailing phenomena when they are subjected to high period pulses. Subjected to ground motion such as Erzincan (v_p=6.67m/s), Chi-Chi TCU52 (v_p=10.60m/s) or to the rest of the earthquakes with greater value of v_p, the columns overturn regardless of whether is monolithic or multidrum column. Comparing the monolithic with the multidrum columns the developed rotation on average does not present large alterations.

Figure 5 demonstrates the comparison of the developed rotations between the monolithic and multidrum 8m height columns. The requested rotations is slight reduced to the multidrum column with slenderness H/B=6. When excited by ground motion which overturn the monolithic column, the drums tend to rotate in a single group with similar to the monolithic column response. Regarding the more slender column did not overturn when it is subjected to long predominant period excitation such as Erzincan's and Northridge's. Nevertheless, it overturns partially when subjected to Gazli and Superstition Hills excitations.

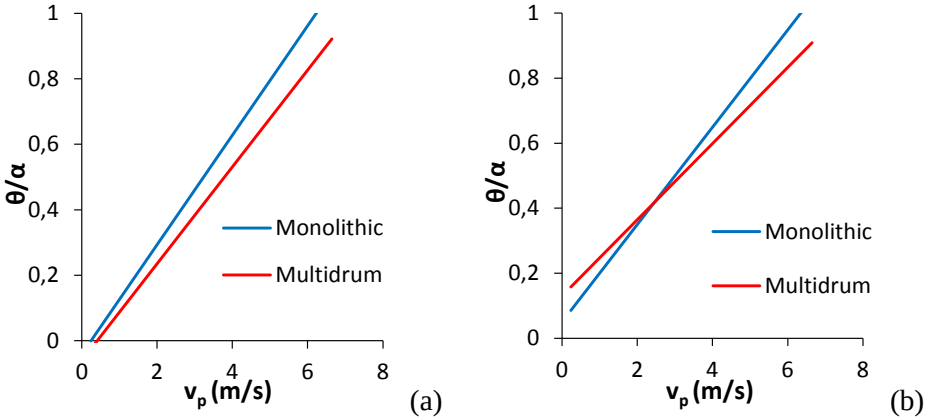


Figure 5: 8m height multidrum column developed rotations (a) for slenderness B/H=6, (b) for slenderness B/H=7.

It is apparent from the Figure 6 that regarding the 5m height column the developed rotations are smaller in the case of the multidrum columns when subjected to excitations with small values of v_p. This remark is common for both considered slenderness's. Subjected to ground motions which have higher values of v_p the demanded rotations of the multidrum models are bigger than those of the monolithic columns especially for the bulkier one. Particularly, subjected to the Landers excitation the monolithic column developed 78% of it slenderness in comparison with the multidrum column which overturn. Similar response occur also to the less slender column.

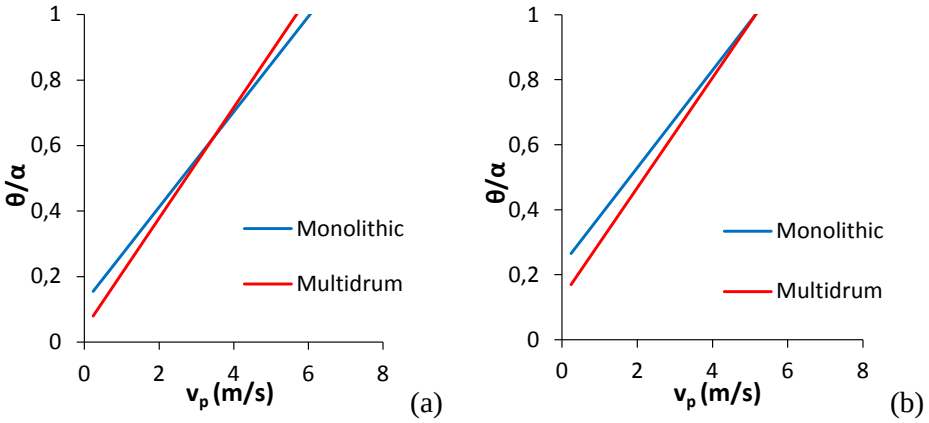


Figure 6: 5m height multidrum column developed rotations (a) for slenderness B/H=6, (b) for slenderness B/H=7.

The seismic response of two columns connected with architrave is studied also for multidrum columns. It is clear that the effect of the architrave to the dynamic response of the structural system is similar among the monolithic and the multidrum column. Regarding the 8m height column the colonnade exhibit significant stability when is excited to ground motion wictht demand large values of rotation. On the other hand the 5m height column models exhibits grate instability and therefore the effect of the architrave on the seismic response of the structural system minor.

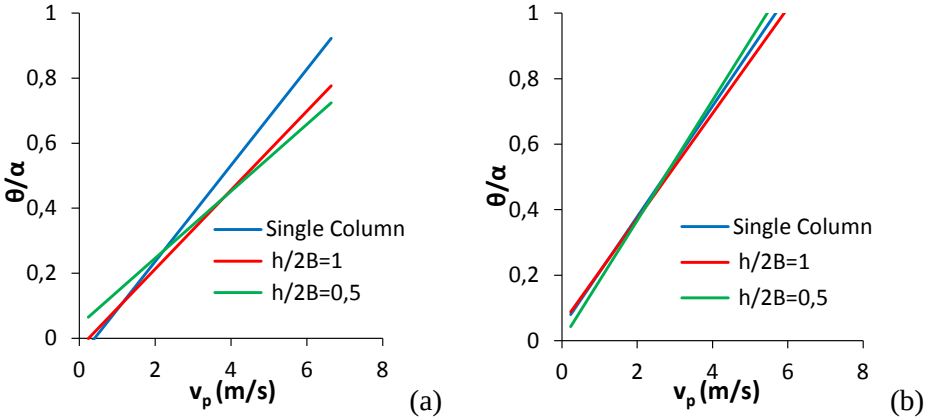


Figure 7: Colonnades developed rotation (a) for the 8m height column, (b) for the 5m height column.

4.3 Relationship between the residual displacement and the maximum rotation

Noticed from the correlation analysis regarding the multidrum column models, results in term of residual displacements did not interrelated with none of the examined seismic parameters. In addition even results in terms of maximum developed rotation did not correlate with the residual dislocation of the drums. The maximum relative dislocation is demonstrated between the drums in which is presented the maximum rotation and specifically they are induced during impacts when the rocking drums alternates pivot points.

Figure 8 displays the maximum relative rotation versus the relative residual displacement. It can be easily observed that rocking is the dominant response of multidrum columns excited by earthquake excitations and the prevailing phenomenon that occur ancient columns collapse. Even for rotation which reached the 65% of the columns slenderness the relative dislocation is restricted to 15%. This Figure data correspond to the 8m height with slenderness H/B=6 column and is representative of all the analyzed multidrum models

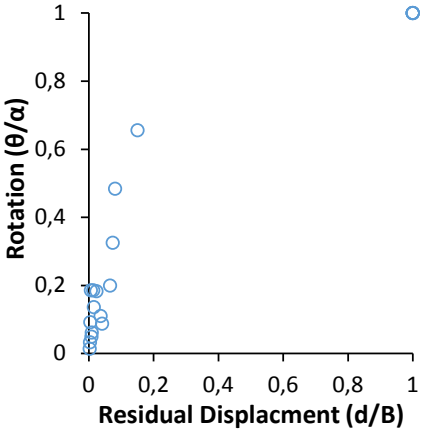


Figure 8: Relation between the developed maximum rotations and the residual relative displacements.

5 CONCLUSIONS

This paper presents an extensive numerical investigation on the seismic response of classical columns. Standalone monolithic and multidrum columns, as well as colonnades with epistyles subjected to a set of 20 excitations are analyzed. The effect of the ground motion characteristics and the effect of the structural system geometry on the dynamic response of these structures are studied.

The effect of the ground motion characteristics was examined through a correlation study between the main seismic excitation parameters and the damage occurred to the structure in terms of maximum rotations. The estimation of the interrelationship has been expressed by the linear Spearman rank correlation coefficient. The results have shown that the developed rotation exhibit strong interrelation with the product $\alpha_p \bullet T_p = v_p$, the values of α_p and T_p are extracted from the Fourier spectra. This product combines the amplitude with the period of the main pulse which is significantly affects the rocking response of these structures.

The effect of the geometry on the seismic response of these structural systems is based on the results of the linear regression analysis in terms of maximum developed rotations. The 5m height columns displays significant vulnerability even when they are subjected to excitations with limited values of v_p. In general the bulkier columns demonstrated increasing stability as they are requested smaller values of rotation. The 8m height colonnade regardless of the architrave geometry present restricted values of developed rotation in contrast to the single column model. However, regarding the 5m height colonnade the dynamic response do not appear great difference in comparison with the single column model.

Multidrum columns presented very complicated dynamic response and sensitive even to minor changes of the excitation characteristics. Subjected to ground motions with long predominant period their response are similar with the corresponding monolithic columns as the drums tend to rotate in a single group while when they are excited by short predominant period ground motions the relative developed rotations are restricted. The colonnade structural systems with multidrum columns present similar response with the multidrum columns.

Furthermore, comparing the maximum developed rotations with the residual relative displacements between the drums is obvious that rocking is the dominant response that occur ancient column collapse as the drum dislocations are minor even when notable rotations are developed.

REFERENCES

[1] G.W. Housner, The behavior of inverted pendulum structures during earthquakes. *Bulletin of the Seismological Society of America*, **53**, 403-417, 1963.

[2] I.N. Psycharis, D.Y. Papastamatiou, A.P. Alexandris, Parametric investigation of the stability of classical columns under harmonic and earthquake excitations. *Earthquake Engineering and Structural Dynamics*, **29**, 1093–1109, 2000.

[3] C. Papantonopoulos, I.N. Psycharis, D.Y. Papastamatiou, J.V. Lemos, and H. Mouzakis Numerical prediction of the earthquake response of classical columns using the Distinct Element Method. *Earthquake Engineering and Structural Dynamics*, **31**, 1699–1717, 2005.

[4] H.P. Mouzakis, I.N. Psycharis, D.Y. Papastamatiou, P.G. Carydis, C. Papantonopoulos, C. Zambas, Experimental investigation of the earthquake response of a model of a marble classical column. *Earthquake Engineering and Structural Dynamics*, **31**, 1681–1698, 2002.

[5] I.N. Psycharis, J.V. Lemos, D.Y. Papastamatiou, C. Zambas, Numerical study of the seismic behaviour or a part of the Parthenon Pronaos. *Earthquake Engineering and Structural Dynamics*, **32**, 2063 –2084, 2003.

[6] D. Konstantinidis and N. Makris, Seismic response analysis of multidrum classical columns. *Earthquake Engineering and Structural Dynamic*s, **34**, 1243–1270, 2005.

[7] L. Papaloizou and P. Komodromos, Planar investigation of the seismic response of ancient columns and colonnades with epistyles using a custom-made software. *Soil Dynamics and Earthquake Engineering*, **29**, 1437–1454, 2009.

[8] A. Elenas, Correlation between seismic acceleration parameters and overall structural damage indices of buildings. *Soil Dynamics and Earthquake Engineering*, **20**,93-100, 2000.

[9] N. Makris, C.J. Black, Dimensional analysis of rigid-plastic and elastoplastic structures under pulse-type excitations. *J. Eng. Mech. (ASCE)*, **130**, 1006–1018, 2004.

[10] N. Makris, C.J. Black, Dimensional analysis of bilinear oscillators under pulse-type excitations. *J. Eng. Mech. (ASCE)*, **130**, 1019–1031, 2004.

COMPDYN 2015
5th ECCOMAS Thematic Conference on
Computational Methods in Structural Dynamics and Earthquake Engineering
M. Papadrakakis, V. Papadopoulos, V. Plevris (eds.)
Crete Island, Greece, 25–27 May 2015

ASSESSMENT OF SEISMIC VULNERABILITY OF HISTORICAL DEFENSIVE WALLS

Graziano Leoni[1], **Alessandro Zona**[1], **Quintilio Piattoni**[1], **Alessandra Meschini**[1], **Enrica Petrucci**[1], **Andrea Dall'Asta**[1], **Luigino Dezi**[2]

[1] School of Architecture and Design, University of Camerino
Viale della Rimembranza, 63100, Ascoli Piceno, Italy
{graziano.leoni, alessandro.zona, quintilio.piattoni, alessandra.meschini,
enrica.petrucci, andrea.dallasta}@unicam.it

[2] Department of Construction, Civil Engineering and Architecture, Marche Polytechnic University
Via Brecce Bianche, 60131, Ancona, Italy
l.dezi@univpm.it

Keywords: Cultural heritage, Defensive walls, Historical structures, Masonry, Seismic vulnerability.

Abstract. *This paper presents a study on the behaviour of the walls of the Rocca Roveresca of Senigallia in Italy built in the XIV century on the ruins of a former Roman defensive structure. This is a peculiar example of a small fortress that had undergone in the XV century important modifications of the plant in order to enhance its defensive performances. A linear finite element model is first developed in order to understand the dynamic behaviour of a generic portion of the wall and to detect the probable incipient failure mechanisms. A subsequent static nonlinear analysis is carried out, with the same finite element model, to investigate the formation of the cracking layout and to detect the position of plastic hinges. The last analysis level is carried out with a tailored macro-element constituted by three bodies, namely the two external curtains and the inner fill for which a degradation of the behaviour is considered. The results obtained demonstrates the efficiency of the wall against earthquakes characterized by return times typical for ultimate limit states. Same issues that deserve further investigation are highlighted.*

1 INTRODUCTION

Historical defensive systems, including fortresses, castles, defensive walls, and towers, are often characterized by very specific construction technologies and seismic vulnerability problems. In general, the core of the construction is always very ancient because located in strategic places, e.g. a mountain pass, a junction of rivers or roads, and such core experienced a lot of restorations, upgrades, and changes. The history of the defensive systems follows the history of offensive weapons and the upgrades and modifications usually consist of adding new elements to the previous construction. For example, with the advent of cannons in the XV century, obsolete defensive walls were strengthened by constructing a second line of walls and by filling with incoherent or slightly coherent material (stones or other materials) the space in between so that the derived systems were such to absorb the energy of fire weapon shots. The juxtaposed strata are characterized by different behaviours and by well definite discontinuity surfaces [1][2].

Under the point of view of the seismic risk, this type of construction are characterized by a vulnerability associated to hidden discontinuity surfaces and cavities that can be potentially very hazardous during a seismic event, as demonstrated by a number of damages in the past: Krak des Chevaliers, Syria, 1170, 1202; Poenari Castle, Romania, 1913, 1940, 1976; San Pedro de la Roca, Cuba, 1675-1679, 1757-1766, Arc-e-Bam citadel, Iran, 2003, St George Castle, Kefalonis, 1953; Santo Stefano di Sessanio Tower, Italy, 2009; Emilia fortresses, Italy, 2012. All of these examples involved monuments that constitute cultural heritage, and the most part considered as UNESCO World Heritage Sites. So, the global seismic risk is enhanced by the unlucky combination of seismic hazard of their location, vulnerability of the construction, and tangible and intangible value of the object.

The assessment of the seismic vulnerability usually cannot be developed by standard methods essentially because this type of construction are not organized by vertical panels and horizontal floors. The failure mechanisms that can be activated by the horizontal forces due to the earthquake are mainly controlled by the internal hidden structure and this requires different approaches for structural analysis, survey techniques, and diagnostic test planning. Only some recent studies focused on the seismic response of defensive systems, e.g. [3][4][5][6].

This paper traces a methodology for the seismic vulnerability assessment by starting from a very specific case study involving the most diffused problems: massive walls, internal discontinuity surfaces, cavities and internal passages organized in a complex three-dimensional geometry. Given that the resisting mechanisms involved in buildings organized as a combinations of walls and floors do not apply to the considered case, and given that survey and diagnostic are more complex, the knowledge of the historical evolution is indispensable as a guide to achieve the required information for seismic vulnerability assessment. The considered case study presents the analysis of the behaviour of the walls of the Rocca Roveresca of Senigallia in Italy built in the XIV century on the ruins of a former Roman defensive structure. This is a peculiar example of a small fortress that had undergone in the XV century important modifications of the plant in order to enhance its defensive performances. A linear finite element model is first developed in order to understand the dynamic behaviour of a generic portion of the wall and to detect the probable incipient failure mechanisms. A static nonlinear analysis is then carried out, with the same finite element model, to investigate the formation of the cracking layout and to detect the position of plastic hinges. The last analysis level is carried out by supposing the wall to behave as a set of rigid blocks constituting a kinematic chain subjected to a finite displacement field typical for the collapse situation by introducing the degradation of the behaviour of the inner (the less consistent) stratum. The results obtained demonstrates

the efficiency of the wall against earthquakes characterized by return times typical for ultimate limit states.

2 CASE STUDY

2.1 General characteristics and historical evolution

The fortress Rocca Roveresca of Senigallia, Italy, presented here as a case study, is characterized by construction stratifications starting from the second half of the XIV century over a pre-existing Roman structure. The historical investigation permitted to identify in details the main evolution phases of the building depicted in Figure 1, each phase associated to parts that are generally homogeneous in terms of constructive methodologies and adopted materials. Such construction sequences have determined a structural system with important discontinuities, e.g. those at the interface between the various layers that constitute the walls.

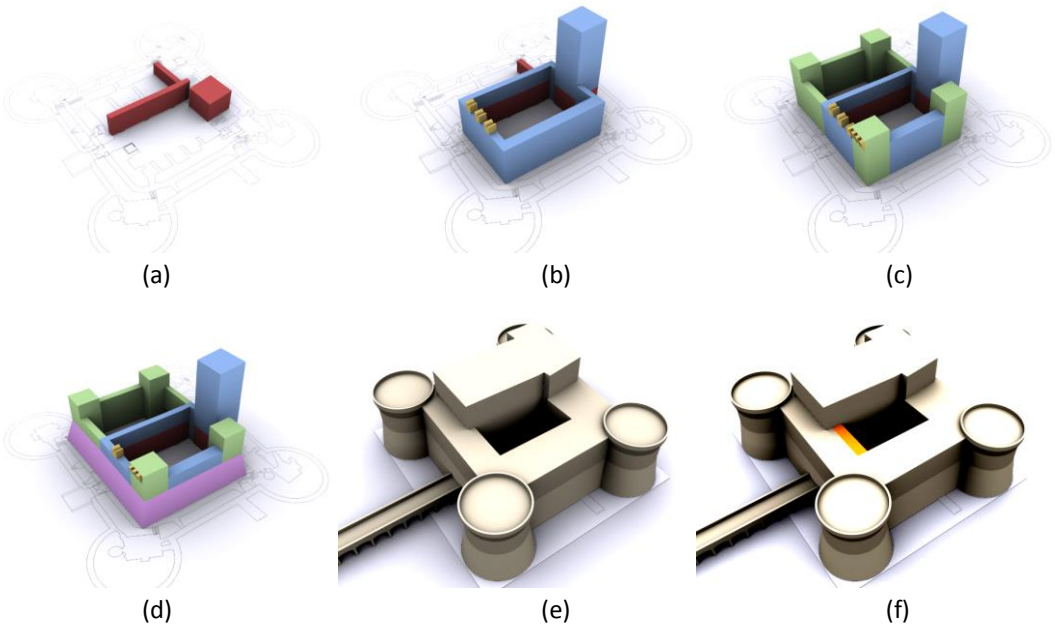


Figure 1: Rocca Roveresca construction phases: (a) Roman ruins; (b) Late Medieval Period fortress; (c) Malatesta family fortress expansion and (d) wall strengthening; (e) building of the Rocca under the Della Rovere family over the Malatesta fortress; (f) internal enlargement at the main entrance.

Since 1965 restoration and strengthening works were undertaken by the regional authority for cultural heritage (*Soprintendenza per i Beni Architettonici e Paesaggistici delle Marche*) in order to eliminate local seismic vulnerabilities, e.g. possible overturning of parapets facilitated by the deteriorated stone elements, cracking in the circular walls of the corner bastions due to the induced horizontal tractions. The works involved the substitution of the damaged stone elements, the realization of reinforced concrete curbs and slabs, and the use of steel tendons.

2.2 Survey and in situ experimental investigations

The technical drawings and documentations of the Rocca Roveresca available from the national (*Ministero per i Beni e le Attività Culturali*) and regional authorities, were verified through systematic floor by floor inspections that allowed to identify some missing infor-

mation, mostly concerning the position of the vertical openings, the typology and thickness of the walls, the nature and dimension of the flooring systems. Afterwards, a large scale survey of external and internal spaces was made based on laser scanning technology. This allowed the definition of a three-dimensional model of the Rocca Roveresca that was the starting point for the development of the structural models later described. The inspections confirmed that the construction has an overall good grade of conservation as no significant active damage mechanisms or damages due to past events are evident. Only some cracking in the spiral staircase at the second level, some sporadic material degradations, some cracking in the circular towers due to their geometry and to the poorer quality of the adopted materials are present. The absence of diffused cracking patterns, vertical misalignments, and other geometric abnormalities are a proof of the soundness of the foundation system. Thus, investigations on the foundation geometry as well as on the soil bearing capacity were not made during the survey. The only studies that involved the soil regarded the characterization of the seismic input, as described in a dedicated paragraph.

Given the need to verify the hypotheses regarding the construction phases, in situ experimental testing was undertaken to identify the various construction layers with their materials and constructive techniques. The evaluation of the homogeneity of the internal parts of the walls that are part of the same stratification is also an important information for the sake of the vulnerability assessment of the single walls. Such information is also fundamental in order to identify the geometry of the analysis model (global model and macro-elements) and the mass distribution required to determinate the entity of the seismic actions. To this end, endoscopic tests in the sub-horizontal and vertical directions were made from the internal and external of the North tower as well as sub-horizontal endoscopic tests were made from the walking path internal to the South-West defensive wall. Such tests confirmed the hypotheses made on the wall stratification with sufficient confidence. In addition, inspections were made to evaluate the conservation of the strengthening works made in the recent past (from 1975 to 1983) through non-destructive tests on the reinforced concrete curbs and on the steel tendons.

2.3 Mechanical characteristics of the materials and confidence factor

The masonry typologies in the Rocca Roveresca can be divided in three subsets according to their expected mechanical behaviour: 1) masonry made by squared stone blocks, used in the lower and older parts of the structure as well as in some of the subsequent construction layers, e.g. internal elements in the towers; 2) masonry made by clay bricks and thin layers of mortar, mostly dated XV Century, with homogenous properties except for some minor reconstructions and good conditions for both the bricks and the mortar; 3) rubble masonry, constituting the massive elements, characterized by a compact arrangement with very few voids and uniform characteristics along the thickness, as evidenced in the endoscopic tests and well in the observations made possible in some openings. An estimation of the mechanical parameters was made based on the prescripts of the current Italian structural code [7][8], based on the masonry typology and conditions as well as on the conducted investigations. The obtained results are reported in Table 1.

Masonry typology	f_m N/cm^2	τ_0 N/cm^2	E N/mm^2	G N/mm^2	w kN/m^3
1 Squared stone blocks	720	9,9	2880	936	22
2 Bricks and mortar	360	7.5	1800	600	18
3 Rubble masonry	150	3.0	1035	345	19

Table 1: Estimated mechanical parameters of the identified masonry typologies.

Given the amount of information obtained from the documentations in the archives of the regional authority for cultural heritage providing details on the restoration and static refurbishment works conducted in the past, considering that most of the wall layout and stratifications are visible, it was deemed possible to achieve the structural knowledge of the Rocca Roveresca through historical studies as well as geometric survey, with reduced use of experimental testing, mostly used to confirm the made hypotheses. Hence, the determination of the confidence factor (F_C), defined according to the indications of the Italian recommendations on seismic risk of cultural heritage [9]:

$$F_C = 1 + \sum_{k=1}^{4} F_{Ck} \tag{1}$$

was defined from the following values deduced from Table 4.1 of the recommendations. The geometric survey was conducted with an high level of completeness, including the cracking patterns and the deformation fields, hence $F_{C1} = 0$. The investigation of the materials was made in a detailed way thanks to the fact that masonry typologies can be easily inspected, hence $F_{C2} = 0$. The material parameters were deduced from available sources based on the undertaken field inspections, hence $F_{C3} = 0.12$. Regarding the foundations and the underneath soil, the available data are considered to provide a good confidence level, hence $F_{C4} = 0.03$. As a result, the obtained confidence factor is $F_C = 1.15$. Such value works as a strength reduction coefficient in strength-based structural verifications and as an acceleration capacity reduction factor in kinematic chain models where materials are assumed without strength limit.

2.4 Local seismic hazard and design seismic input

The evaluation of the local seismic hazard was conducted by the Italian National Research Council (CNR) that produced seven accelerograms at the foundation of the Rocca Roveresca, used to generate the information needed for the structural analyses of the presented case study.

The nonlinear static analyses as well as the kinematic analyses requires the acceleration and displacement response spectra averaged over the assigned seven accelerograms. Figure 2 and Figure 3 depict the averaged spectra (solid red curves), the code spectra [7] for rock (dashed blue curves) and for ground type C (solid blue curves), as well as the spectra from each of the seven accelerograms, for the two return periods (T_R = 201 years and T_R = 712 years) that are considered for the Damage Limitation State and Ultimate Limit State assessments.

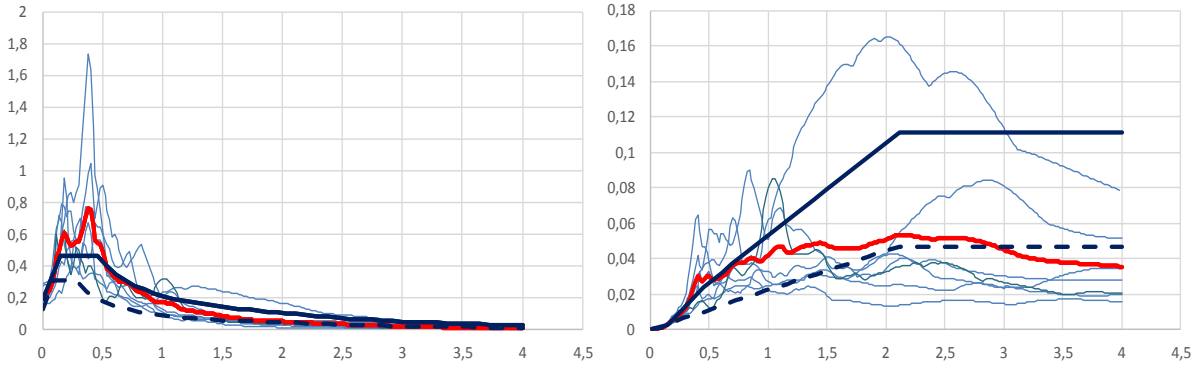


Figure 2: Acceleration (left) and displacement (right) response spectra for returning period 201 years.

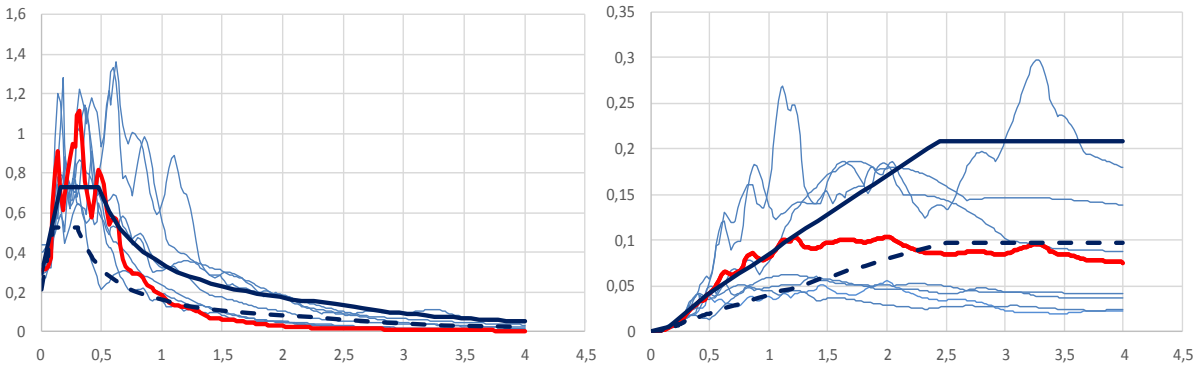


Figure 3: Acceleration (left) and displacement (right) response spectra for returning period 712 years.

3 PRELIMINARY ANALYSIS OF THE DEFENSIVE WALLS

The structural analysis was carried out using representative models comprising the stratified walls and the rubble stone infill thorough the definition of a tailored macro element (Figure 4).

The seismic response of the defensive walls was investigated in their transverse direction in order to assess the influence of the discontinuity surfaces on the failure mechanisms. Specifically, the following analyses were carried out: (1) modal analysis in order to obtain preliminary results on the structural behaviour under seismic loadings; (2) static nonlinear analysis in order to define the incipient failure mechanisms and to highlight the probable cracked layout and the position of the plastic hinges; (3) nonlinear kinematic analysis of a structural model, i.e. kinematic chain made of rigid blocks, defined starting from the results of the previous analyses.

A finite element model of a section of the defensive wall was developed in the structural software Straus7 by using triangular elements with plane strain state. The mesh is generated taking into account the different strata of the masonries with their specific material properties. The discontinuity surfaces were modelled by reduced mechanical properties to allow slip and simulate their failure mechanisms.

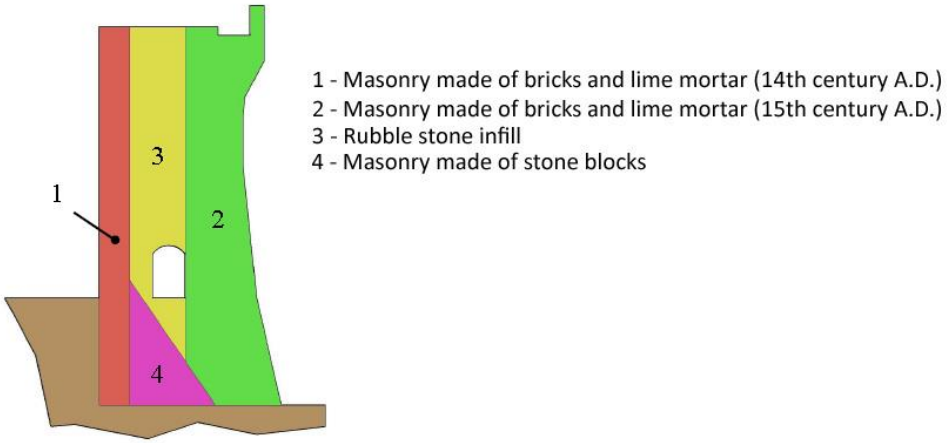


Figure 4: Model for the defensive walls.

3.1 Modal analysis

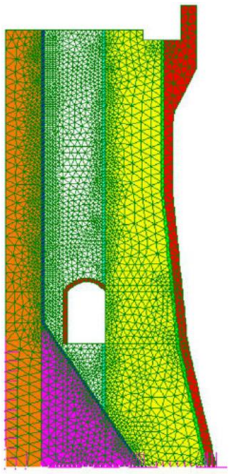
The results of the modal analyses highlight the relevant stiffness of the investigated structural model. The percentage of participant mass relative to the first mode of vibration is equal to 57%. Thus, the first mode of vibration is representative of the dynamical behaviour of the considered masonries. The values of the stress (Figure 5) relative to the first mode of vibration highlight a possible failure mechanism characterised by a hypothetic hinge at the lower part of the first layer of the considered model. The position of this hinge is determined by the sloping surface of the stone block masonries at the base of the defensive wall as well as by the ground level of the inner ward at and higher level than that of the external zone. The inner rubble stone infill influences the modes of vibration of the defensive walls. The peak values of the stress highlighted near the inner tunnel than suggest a failure mechanism of the masonry vaults due to the global behaviour of the model. The external strata of the defensive walls is interested by stress values lower than those of the other strata of the model. The other vibration modes are characterized by low period of vibration and their behaviour is influenced by the discontinuity surfaces between the masonry blocks.



Figure 5: Considered modes of vibration.

3.2 Nonlinear static analysis

The elastic-plastic behaviour of the materials was defined according to the Mohr-Coulomb criteria. The values of the material parameters were obtained from the mechanical properties assessed as previously described (Figure 6). The nonlinear analysis was carried out by force control in two steps: (i) only the gravitational loads are applied to the model; (ii) horizontal static forces proportional to the mass are added. The loading increases are equal to 0.01 g in order to assess the maximum value of the multiplier of the horizontal forces. The last loading step relative to the numerical convergence of the used parameters resulted equal to 0.51 g (horizontal loadings) for the horizontal loading direction towards the inside and equal to 0.40 g for the horizontal loading direction towards the outside (Figure 7).



	E [N/mm^2]	ν	ρ [kg/m^3]	ϕ [°]	c [N/mm2]
Bricks and lime mortar	1.80E+03	3.00E-01	1.80E+03	7.00E+01	3.20E-01
Bricks and lime mortar	1.80E+03	3.00E-01	1.80E+03	7.00E+01	3.20E-01
Bricks and lime mortar	1.80E+03	3.00E-01	1.80E+03	7.00E+01	3.20E-01
Bricks and lime mortar	1.80E+03	3.00E-01	1.80E+03	7.00E+01	3.20E-01
Rubber stone infill	1.80E+01	3.00E-01	1.90E+03	2.00E+01	1.30E-01
Stone blocks and mortar	2.88E+03	3.00E-01	2.20E+03	7.40E+01	5.20E-01
Rubber stone infill	1.04E+03	3.00E-01	1.90E+03	7.00E+01	1.30E-01
Rubber stone infill	1.80E+01	3.00E-01	1.90E+03	2.00E+01	1.30E-01

Figure 6: Material properties for nonlinear analysis.

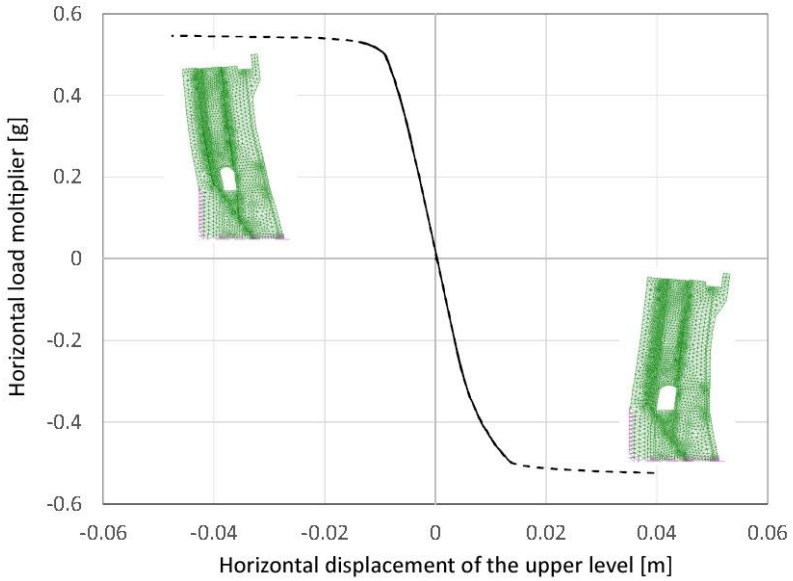


Figure 7: Nonlinear static analysis global response curves.

Low values of the normal and tangential stresses (Figure 8), less than 0.20 MPa, are observed under gravitational loads with peak values at the base of the external part of the defensive walls. These stress concentrations are caused by the sloping discontinuity surface of the stone block masonry at the base of the walls. Another stress concentration is highlighted at the base of the inner block due to both the rotation of the external wall and the presence of the sloping surface of the stone block masonry. The last stress concentration could be uncertain due to the constraints applied to the considered model.

The normal and tangential stress values under gravitational loads plus horizontal loads (0.40 g) toward the inside or the outside of the fortress are reported in Figure 9 and Figure 10, respectively. The performed analyses are representative of the seismic behaviour of the defensive walls under earthquakes characterised by significant intensity. These analyses allow to investigate the considered failure mechanism deriving from the results of the modal analyses. The masonry cracks occur in the white areas while the compressive stress concentrations are highlighted in red, where plastic hinges can be located.

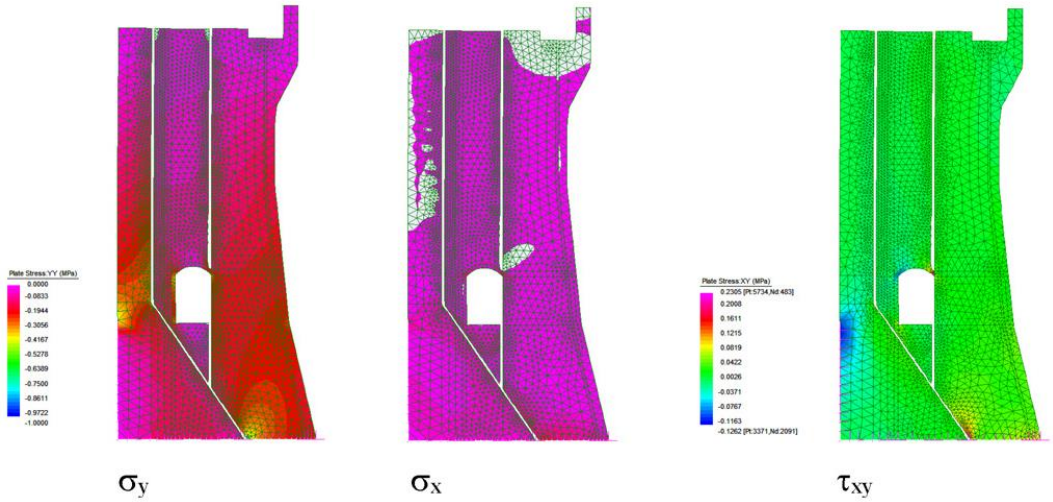


Figure 8: Stress state under gravitational loads.

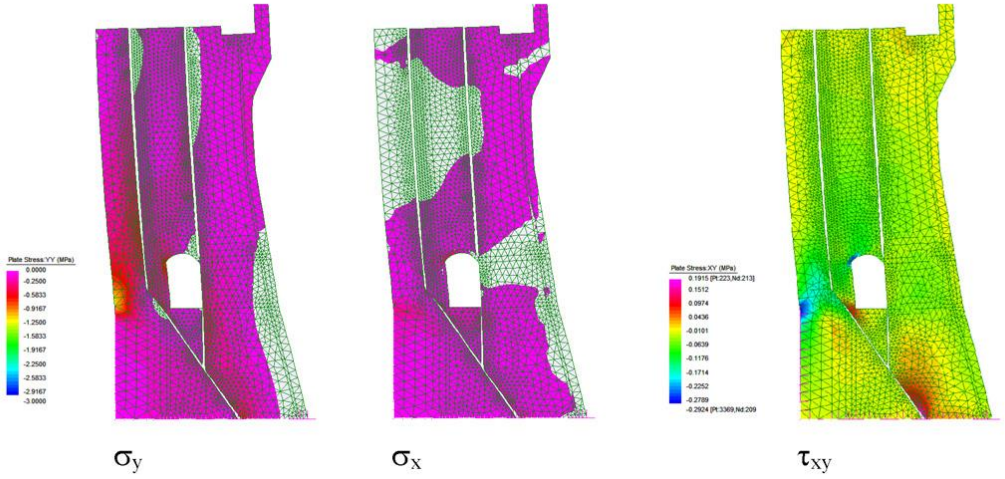


Figure 9: Stress states under gravitational loads and horizontal loads applied toward the inside.

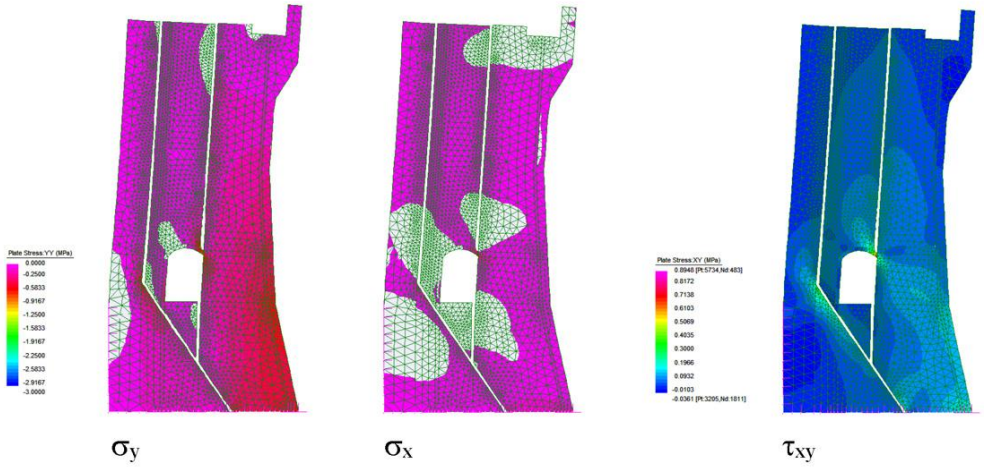


Figure 10: Stress states under gravitational loads and horizontal loads applied toward the outside.

4 KINEMATIC ANALYSIS

The kinematic analysis was carried out by considering a new tailored macro-element constituted by three bodies, namely the external curtains and an intermediate infill. In the case under examination, the first body is that built in the Malatesta family period (internal layer of the defensive wall), it is constituted by brick and lime mortar masonry. The second body (external layer of the wall), built under Della Rovere family, is also constituted by brick and lime mortar masonry. The third body is constituted by the cemented inner rubble stone infill (Fig. 4). The inner batter, made of stone block masonry juxtaposed to the first body, constitutes a sharp sloping surface. Stratifications due to the construction phases, geometry of the layers and the partial buried wall produce a non-symmetric behaviour of the system, as already demonstrated by the nonlinear static analyses. For this purpose, two different overturning mechanisms, one towards the inside of the fortress and the other towards the outside, were considered.

In both the cases, the bodies were assumed to interact each other depending on the magnitude of the displacements imposed to the system. For the incipient mechanism, when the material has not yet cracked and when interlayer slips have not yet occurred, interlock actions and tensile reactions were considered at the discontinuity surfaces of the bodies. Tensile strength and interlock strength were assumed to be equal to τ_0 values reported in Table 1, for the incipient mechanism, and were suitably reduced to account for the degradation occurring in the collapse mechanism. The effects of the limited compression strength was accounted for by placing the hinges according to the stress state detected in the static nonlinear analyses.

4.1 Wall overturning towards the inner ward

Incipient mechanism (linear analysis)

Overturning incipient mechanism is characterized by the undeformed configuration of the system. In this phase, it is assumed that masonry is still undamaged and that the rubble stone infill, characterized by a slight cohesion, is still capable to behave as a rigid body. The mechanism is thus characterized by the rotation of the three bodies that also slip with respect to one another. The three base hinges are placed according to the results of the nonlinear static analysis (Fig. 9): for the internal curtain (body 1), hinge C_1 is assumed at the ground level; hinge C_2 of the external curtain (body 2) is assumed taking place over the discontinuity of inner batter at a lower level with respect to C_1 and, hinge C_3 takes place at the base of the fill (body 3) at the internal discontinuity. It is also assumed that the three bodies undergo rotations keeping in touch each other; this mechanism is constrained by considering that points C_{13} e C_{23} at the top of the curtains undergo the same horizontal displacements while vertical displacements remain unconstrained. The incipient mechanism is depicted in Fig. 11a. Weights of the three bodies, applied in the relevant centroids, tensile forces applied orthogonally to crack surfaces, friction forces applied to the interface surfaces between the various bodies and horizontal forces proportional to masses are considered. The limit equilibrium condition of the system permits to calculate the horizontal acceleration that triggers the overturning mechanism.

Collapse mechanism (nonlinear analysis)

The collapse mechanism is characterized by the finite displacements of the system. In this phase, only bodies 1 and 2 are supposed to be still whole whereas the weakly cemented rubble stone fill is assumed to be in a disgregation phase. The mechanism is thus characterized by rotations of bodies 1 and 2 whereas body 3 becomes and interposed deformable stratum (Fig. 11b). In particular, bodies 1 and 2 are restrained at the base by hinges C_1 e C_2, placed at the same positions of the incipient mechanism, and are constrained to undergo the same finite

rotations. The fill undergoes a shear deformation that produces interaction with the external brick curtains.

The level of the resisted horizontal forces is derived from the equilibrium conditions of the system written with respect to the deformed configuration. The equilibrium conditions involve weights of bodies 1 and 2, applied at the relevant centroids, and the horizontal forces due to inertia of the three strata. Interlock forces and friction forces, suitably penalized to account for degradation under increasing displacements, are applied at the interface surfaces.

In order to assess the seismic vulnerability of the wall, results of the kinematic analysis have to be post-processed to define an equivalent nonlinear 1dof system [8]. For this purpose, the acceleration of the equivalent 1dof is given by

$$a = \frac{1}{F_C}\frac{\alpha}{e^*}g \tag{2}$$

where α is the multiplier of the horizontal loads calculated from the equilibrium conditions, F_C is the previously defined confidence factor, introduced here to account for uncertainties, and e^* is the participating mass (derived considering the virtual displacements of the incipient mechanism as a vibration mode) calculated with the formula

$$e^* = \frac{\left[\sum_{k=1}^{N}\left(P_k\delta_{Px,k} + Q_k\delta_{Qx,k}\right)\right]^2}{\left[\sum_{k=1}^{N}\left(P_k + Q_k\right)\right]\left[\sum_{k=1}^{N}\left(P_k\delta_{Px,k}^2 + Q_k\delta_{Qx,k}^2\right)\right]} \tag{3}$$

where P_k is the weight of the k-th body and Q_k are weights not applied to the k-th body whose masses produce horizontal forces in the k-th body. Finally, the displacement of the equivalent 1dof system can be calculated as

$$d = d_C\frac{\sum_{k=1}^{N}\left(P_k\delta_{Px,k}^2 + Q_k\delta_{Qx,k}^2\right)}{\delta_{Cx}\sum_{k=1}^{N}\left(P_k\delta_{Px,k} + Q_k\delta_{Qx,k}\right)} \tag{4}$$

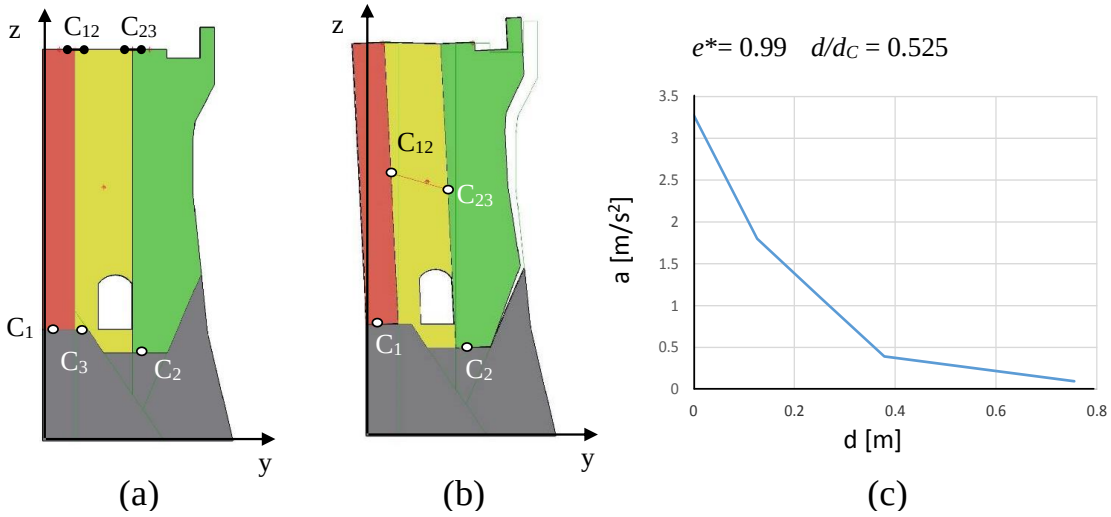


Figure 11: Overturning toward the inner ward: (a) incipient mechanism; (b) collapse mechanism; (c) capacity curve of the equivalent 1dof system

where d_C is the displacement of the control point of the mechanism and δ_{Cx} is the relevant virtual displacement. The curve of capacity of the equivalent 1dof system obtained for the defensive wall is plotted in Fig. 11c.

4.2 Wall overturning towards the outside

Incipient mechanism (linear analysis)

As in the previous case, in this phase the masonry curtains are considered to be undamaged and the rubble stone infill, characterized by a slight cohesion, is capable to behave as a rigid body. Position of hinges at the bases of bodies are derived from the static nonlinear analysis (Fig. 10). Hinge C_1 of the internal curtain (body 1) is supposed to take place at the ground level of the inner ward. Hinge C_2 of the external curtain (body 2) is placed at the foundation level. Internal hinges C_{13} e C_{23} are placed at the interface surfaces between curtains and fill so that the formation of a strut within the fill is reproduced as highlighted by the static nonlinear analysis. Fig. 12a depicts the assumed incipient mechanism.

Collapse mechanism (nonlinear analysis)

In this phase only bodies 1 and 2 are supposed to be undamaged whereas the rubble stone fill is assumed to be in a disgregation phase. The mechanism is thus characterized by rotations of bodies 1 and 2 (Fig. 12b) and by the interaction of the fill that undergoes a mechanical degradation under the increasing displacements.

Hinges C_1 e C_2 take place at the same position of the incipient mechanism whereas the internal hinges are placed so that the two masonry curtains are subjected to the same rotations; it is worth noting that position of internal hinges varies with the increasing displacements. The fill undergoes a shear deformation that produces interaction with the external brick curtains. As in the opposite mechanism previously analysed, interlock forces and friction forces applied at the interface surfaces are suitably penalized to account for the mechanical degradations. Fig. 12c reports the curve of capacity of the system reduced to an equivalent 1dof system.

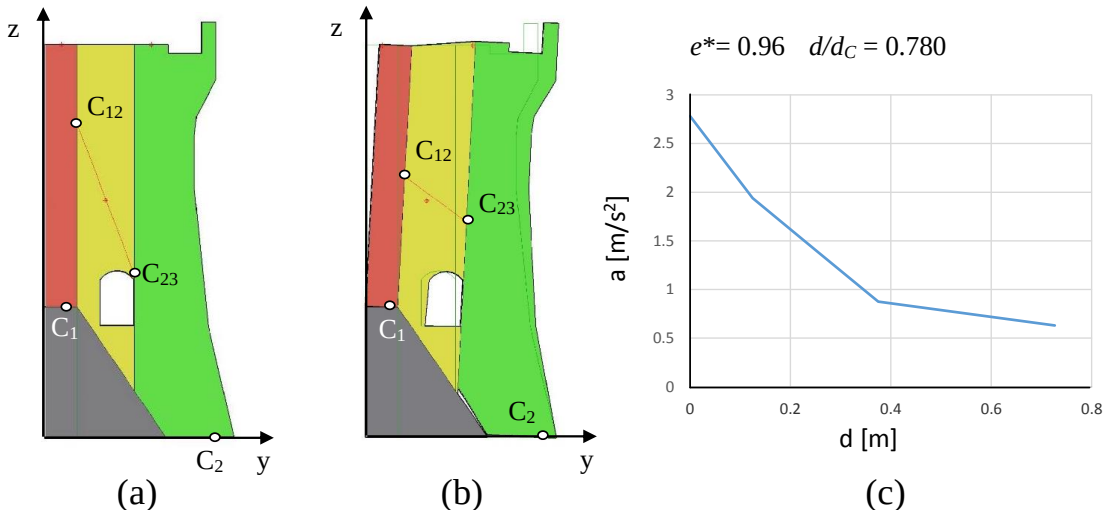


Figure 12: Overturning toward the inner ward: (a) incipient mechanism; (b) collapse mechanism; (c) capacity curve of the equivalent 1dof system

4.3 Remarks on the results

Results obtained from the nonlinear kinematic analysis highlight some peculiarities of the system.

The asymmetric geometry leads to different levels of triggering for the two incipient mechanisms: overturning towards the outside is more probable even if a minor softening behaviour is evident due to the geometry of the external curtain that is characterised by an important batter.

Influence of the weakly cemented rubble stone fill on the overall behaviour of the defensive walls is positive but uncertainties about its real cohesion may change the results of the assessment and also may modify the collapse mechanism.

Results obtained with the kinematic analysis seems to be more conservative with respect to the nonlinear static analysis for what concern the resistance of the wall (maximum base shear); this is due to the mechanical characteristics of the material that were not penalised with the confidence factor in the static non linear analysis.

The displacements obtained with the kinematic analysis are very high due to the aspect ratio of the external layers of the defensive wall (brick curtains). This issue is critical as disgregation of the masonry, not considered in the kinematic analysis, may occur in the early overturning phases of the wall depending on the quality of the masonry.

4.4 Vulnerability assessment

Seismic vulnerability is assessed by comparing the results obtained from the nonlinear kinematic analysis and the seismic demand for fixed return periods. According to the Italian standards the Damage Limitation State is satisfied if the spectral acceleration that triggers the mechanism is greater than the expected PGA. For the case under examination, a return period T_r = 201 years was considered. The expected PGA obtained from the local site analysis is 2.16 m/s^2 that is lower than the minor trigger accelerations of 2.78 m/s^2 obtained for the incipient mechanism of overturning towards the outside.

For what concern the Ultimate Limit State, the verification consists in the comparison of the seismic capacity in terms of displacements with the relevant demand defined conventionally as the spectral displacement corresponding to the secant period T_s at the 40% of the ultimate displacement of the system. The verification is satisfied if

$$d_u \geq S_{De}(T_s) = S_e(T_s)\frac{T_s^2}{4\pi^2} \tag{5}$$

d_u m	0.4 d_u m	T_s s	S_{De} m
0.100	0.040	0.751	0.067
0.200	0.080	1.159	0.100
0.300	0.120	1.600	0.100
0.400	0.160	1.987	0.103
0.500	0.200	2.375	0.087
0.600	0.240	2.870	0.086
0.700	0.280	3.505	0.084
0.755	0.302	3.641	0.080

(a)

d_u m	0.4 d_u m	T_s s	S_{De} m
0.100	0.040	0.795	0.078
0.200	0.080	1.184	0.100
0.300	0.120	1.559	0.098
0.400	0.160	1.883	0.100
0.500	0.200	2.221	0.090
0.600	0.240	2.556	0.084
0.700	0.280	2.938	0.084
0.726	0.291	3.042	0.087

(b)

Table 2: Verification at ULS: (a) overturning towards the inside; (b) overturning toward the outside

As previously discussed, the displacements obtained from the kinematic analysis are quite high and disgregation of the masonry may likely occur. For this reason, the verification is carried out by assuming as ultimate displacements a set of values within the maximum displacement obtained in the analysis. For what concerns the displacement demand, reference is made to the mean spectrum obtained from the site amplification analysis with return time T_r = 712 years. Table 2 reports the results for the two opposite mechanisms; the verifications are satisfied for all the selected ultimate displacements but it is worth to notice that verifications for the lower ultimate displacements are satisfied with a minor margin. This is due to the spectral values obtained from the site response analysis that for the highest periods are quite low (Fig. 3). This point is crucial and rises doubts about the earthquake selected in the definition of the seismic actions even if the fortress has overcome important earthquakes without undergo important damages.

5 CONCLUSIONS

A study on the seismic vulnerability of particular historical defensive walls was presented with reference to the case study of the Rocca Roveresca of Senigallia that underwent in the XV century important modifications of the plant in order to enhance its defensive performances.

A generic portion of the stratified walls was considered. A linear finite element model was first developed in order to understand the dynamic behaviour of the wall and to detect the probable incipient failure mechanisms. A static nonlinear analysis was then carried out to investigate the formation of the cracking layout and to detect the position of plastic hinges. The last analysis consisted in a nonlinear kinematic analysis. A new tailored macro-element constituted by three bodies, namely the two external curtains and the inner infill, is presented. Interaction forces between the bodies are introduced by considering empirical degradations under the increasing displacements. Special emphasis is placed on the behaviour of the weakly cohesive rubber stone fill. The results obtained demonstrated the efficiency of the wall against earthquakes characterized by return times typical for Damage Limitation State and Ultimate Limit State. At the same time, some issues that deserve further investigation were highlighted:

1. influence of weakly cemented rubble stone fills on the behaviour of stratified defensive walls is positive but uncertainties about the real cohesion of the material are crucial as this can affect the collapse mechanism;
2. the displacements obtained with the kinematic analysis carried out by considering the proposed macro-element are very high due to the aspect ratio of the external layers of defensive walls; this issue is critical as disgregation of the masonry may occur in the early overturning phases of the wall depending on the quality of the masonry.

REFERENCES

[1] S. Toy. *A History of Fortification from 3000 BC to AD 1700*. Pen & Swords Ltd, Barnley, England, 2006.

[2] J.E. Kaufmann, H.W. Kaufmann. *The Medieval Fortress: Castles, Forts, and Walled Cities Of The Middle Ages*, Da Capo Press, 2004.

[3] V. Bosiljkov, M. Uranjek, R. Zarni, V. Bokan-Bosiljkov. An integrated diagnostic approach for the assessment of historic masonry structures. *Journal of Cultural Heritage*, Vol.11, 239–249, 2010.

[4] V. Greif, J. Vlcko. Key block theory application for rock slope stability analysis in the foundations of medieval castles in Slovakia, *Journal of Cultural Heritage*, Vol. 14, 359–364, 2013.

[5] A. Baratta, I. Corbi, S. Coppari. A Method for the Evaluation of the Seismic Vulnerability of Fortified Structures. COST ACTION C26: *Urban Habitat Constructions under Catastrophic Events*, Taylor & Francis Group, ISBN:978041560685, 2010.

[6] L. Binda, C. Modena, F. Casarin, F. Lorenzoni, L. Cantini, S. Munda, Emergency actions and investigations on cultural heritage after the L'Aquila earthquake: the case of the Spanish Fortress, *Bulletin of Earthquake Engineering*, Vol. 9(1), 105-138, 2011.

[7] Repubblica Italiana, Ministero delle Infrastrutture e dei Trasporti, *Nuove norme tecniche per le costruzioni*, D.M. 14 gennaio 2008. Gazzetta Ufficiale n. 29 del 4 febbraio 2008 - supplemento ordinario n. 30.

[8] Repubblica Italiana, Ministero delle Infrastrutture e dei Trasporti e Consiglio Superiore dei Lavori Pubblici, *Istruzioni per l'applicazione delle Nuove norme tecniche per le costruzioni di cui al decreto ministeriale 14 gennaio 2008*. Circolare 2 febbraio 2009, n. 617. Gazzetta Ufficiale n. 47 del 26 febbraio 2009 - supplemento ordinario n. 27

[9] Repubblica Italiana, Ministero per i Beni e le Attività Culturali, *Linee guida per la valutazione e la riduzione del rischio sismico del patrimonio culturale con riferimento alle Norme tecniche per le costruzioni di cui al decreto del Ministero delle Infrastrutture e dei trasporti del 14 gennaio 2008*. Gazzetta Ufficiale n.47 del 26 febbraio 2011 - Supplemento ordinario n. 54.

COMPDYN 2015
5th ECCOMAS Thematic Conference on
Computational Methods in Structural Dynamics and Earthquake Engineering
M. Papadrakakis, V. Papadopoulos, V. Plevris (eds.)
Crete Island, Greece, 25–27 May 2015

VULNERABILITY OF TORSIONALLY SENSITIVE HISTORICAL BUILDINGS UNDER SEISMIC LOADS

Stylianos I. Pardalopoulos[1] and Stavroula J. Pantazopoulou[2]

[1] University of Cyprus
Dept. of Civil & Environmental Engineering, Nicosia, Cyprus
sjpard@gmail.com

[2] University of Cyprus
Dept. of Civil & Environmental Engineering, Nicosia, Cyprus
pantaz@ucy.ac.cy

Keywords: Historical buildings, Torsion, Seismic Assessment, Monuments, Masonry.

Abstract. *The paper explores the effects of asymmetry in plan owing to the occurrence of slender wings in massive monumental and historical URM buildings that belong to the post-renaissance neoclassical school of architecture. Although it is common in buildings with flexible diaphragms to disregard the implications of torsion, in this particular case these effects are significant causing important differential displacements and therefore a high risk of damage in the wings. To study the problem, three-dimensional finite element models of a neoclassical building with asymmetric plan shape located in Thessaloniki, Greece, are analyzed to a strong ground motion that has been recorded in the region and their maximum seismic response is explored. This response is then compared with results obtained from application of the rapid seismic assessment procedure of unreinforced masonry buildings, which has been recently introduced by the authors and conclusions on the procedure's accuracy are derived. Emphasis is placed on the sensitivity of the torsional aspects of the response to the stiffness of horizontal diaphragms that is provided by the architectural forms of the era under investigation. Application of this rapid methodology enables easy inspection over the building's geometry to identify those characteristics that may predispose the tendency for a strong torsional component of response, but it may also help identify the efficacy of retrofitting through the addition of diaphragms as a strengthening approach that may mitigate the occurrence of damage.*

1 INTRODUCTION

Monumental unreinforced masonry (URM) buildings built during and after the Renaissance were constructed to house government or state activities (palaces, universities, hospitals, etc) in many European cities, symbolizing at the same time the economical, political or cultural maturity of the society to which they belonged. Having a lifetime ranging from one to more than five centuries, today this category of buildings are a living part of the European history, serving as a reminder of the era in which they have been constructed.



Figure 1: Examples of massive monumental structures across Europe [1]: (a) the palace of Versailles (1770), (b) the Schoenbrunn palace (1750), (c) the Hellenic parliament (1847).

During their long period of existence, buildings of this class of massive load-bearing masonry have suffered significant damages in their structural system, especially in countries of the eastern Mediterranean basin that have high seismicity. Due to those buildings' historical importance, preservation and restoration of their unique architectural and structural characteristics is among the main priorities of the states that own them, often regulated by international treaties for noninvasiveness and reversibility of the intervention (Charters adopted by the general assembly of ICOMOS, [2]). Assessment of the residual strength of those buildings is therefore a necessary task in order to identify those cases that are most vulnerable and have a

disposition for torsional response components owing to their plan morphology. Although in most of these cases retrofitting solutions for strengthening are restricted due to international treaties, an assessment methodology can shed light to the most pertinent strategies that might mitigate a possible accidental loss of part of this heritage in the future.

Assessing the residual strength of monumental URM buildings is a much more demanding task as compared to assessment of residential buildings of the same era, not only because of their massive volume but mostly because this type o buildings possesses special dynamic characteristics due to their Architectural design that may cause significant damages during an earthquake. In order to achieve the desired harmony, which was inspired from highly regarded classical forms of Hellenic antiquity, monumental multi-unit buildings have a system-plan organized along a main axis of symmetry, whereas in many cases a transversal axis of symmetry in plan also exists. To achieve the desired symmetry in plan, Architects of that era organized the building volumes in the form of an ***H***, an ***L,*** a ***Π*** or a ***T***, with courts located in the recesses of these shapes so that the overall plan could be thought to form a concave prism, whereas at each building volume long corridors are usually spanning from one end of the building volume to the other (Fig. 2). The long and slender wings are always susceptible to out of plane action; but in many cases of uniaxial symmetry the plan arrangement of monumental buildings is responsible for the development of in-plan torsional phenomena during a seismic excitation in direction orthogonal to the axis of symmetry, and this can cause significant damages at locations of the building that are remote relative to the center of twist of the complex building plan. This is why systematic development of structural damages mainly at the locations where separate building volumes are joined, as well as at the walls of corridors with significant length between successive transverse walls, due to dynamic displacements in the out-of-plane direction is frequently reported in post earthquake reconnaissance reports of monumental URM buildings (Fig. 2).

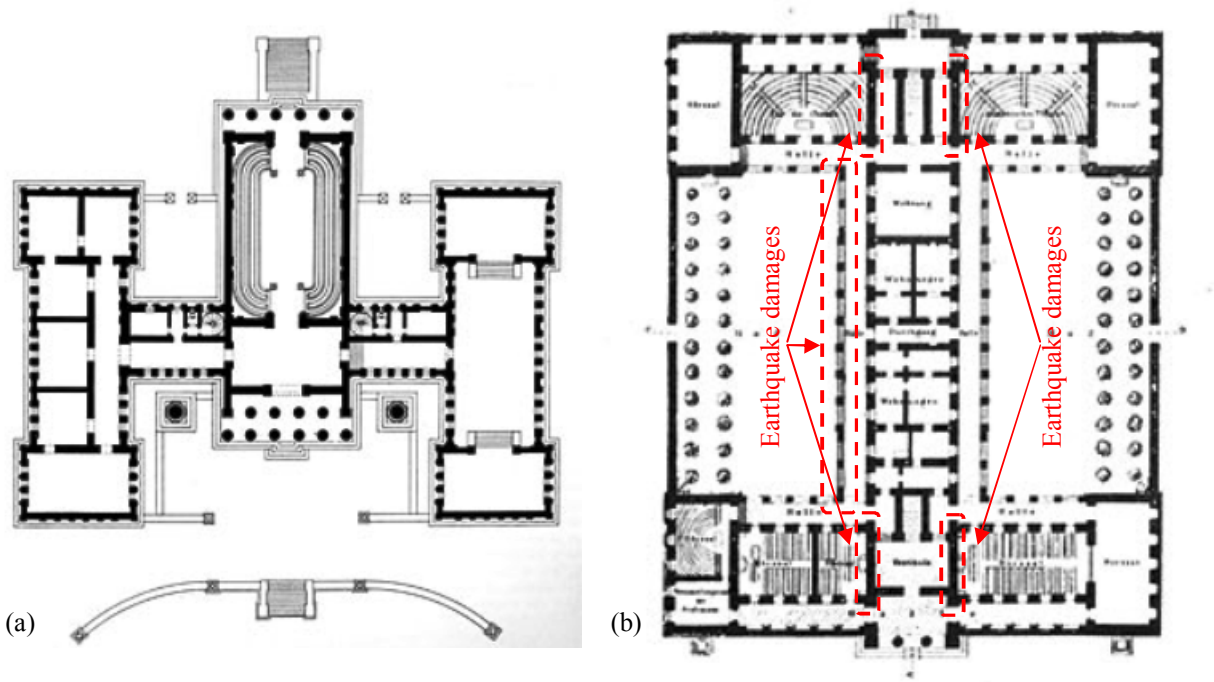


Figure 2: Plans of neoclassical monumental buildings (Athens [3]) and notation of locations of developed damages during the 1999 Athens earthquake: (a) the Academy of Athens (1887), (b) the University of Athens Central Building (1864).

In the present study the torsional response excited by the plan shape morphology of monumental and historical URM buildings is investigated. This is achieved via time-history dynamic analyses of three-dimensional finite element models of a neoclassical building with asymmetric plan shape located in Thessaloniki, Greece. Emphasis is given into investigating the effect of horizontal diaphragm stiffness provided by the architectural forms of that era to the overall torsional response of this class of buildings. This building is then assessed utilizing the latest version of the rapid seismic assessment procedure for URM building, which was recently introduced by the authors [4 - 6] enabling the evaluation of the accuracy of the rapid procedures when torsional behavior is prevalent.

2 RAPID SEISMIC ASSESSMENT PROCEDURE OF URM BUILDINGS

To facilitate seismic assessment of historical and heritage URM buildings a rapid procedure has been recently introduced by the authors [4 - 6], which produces results of equivalent accuracy to detailed time-history dynamic analysis based assessment procedures while requiring significantly less effort and shorter computational time. This procedure consists of the following two steps:

Step 1: Determination of envelope of the developed deformations along the examined building The first step of the introduced rapid assessment procedure is the determination of the envelope of the developed horizontal deformations along the structural system of the examined building during its seismic excitation. To do so, a three-dimensional finite element model of the examined building is subjected to a notional gravitational field that acts horizontally in each of the two principal plan directions of the building and then is analyzed statically. Taking into consideration the brittle response of URM, which cannot secure a positive definite stiffness of pier members after cracking, the examined building can be simulated as a linear finite element model with localized points of non-linear response at contact points. To capture both in-plane and out-of-plane actions, basic element unit in the discretization of the piers and spandrels is a typical thick shell with elastic properties. Each static analysis provides a deflected shape of the examined building analogous to the one corresponding at the instant of the building's maximum seismic response when subjected to a seismic excitation capable of mobilizing the biggest possible fraction of the building's total mass in the corresponding plan direction; note that the percentage of the total mass of a vibrating structure that can be activated during a seismic excitation depends of the correlation between the structure's dynamic characteristics and the earthquake's frequency content and height-wise mass distribution - in the case of URM historic buildings it ranges up to 50% [4]. The envelope of developed deformations along the structural system of the examined building corresponding to the spectral demand imposed at the building's site by the associated seismic code is then calculated by amplifying the deflected shape obtained from the static analysis in the i-th plan direction (i = X or Y) with the amplification factor f_i:

$$f_i = S_{Dd,i}(T_1) / U_{roof,i} \tag{1}$$

where, $S_{Dd}(T_1)$ is the spectral relative displacement demand corresponding to the building's fundamental period of vibration, T_1, and $U_{roof,i}$ is the average horizontal translation at the roof level of the building in the corresponding plan direction i, as calculated from static analysis. The same scaling (through f_i) maybe applied in the estimated member forces from the static analyses in order to obtain a rough estimate of peak member stresses/forces during the ground excitation. $S_{Dd}(T_1)$ can be evaluated according to EC8-1 [7], as per:

$$S_{Dd}(T_1) = S_d(T_1) \cdot \left[\frac{T_1}{2 \cdot \pi}\right]^2 \quad ; \quad S_d(T_1) = \gamma_I \cdot a_{gR} \cdot S \cdot 2.5 \tag{2}$$

where, γ_I is the importance factor of the building, a_{gR} is the reference peak ground acceleration on type A ground and S is the soil factor; $S_d(T_1)$ in Eq. 2 is the total spectral acceleration for a SDOF system with a period of T_1. The building's fundamental period of vibration, T_1, is approximated as (EC8-1 [7]):

$$T_1 = 0.050 \cdot H^{3/4} \tag{3}$$

where, H is the total building height, in m, measured from the level of foundation or the level of rigid basement.

Step 2: Determination of local seismic demand and application of acceptance critiria Bearing capacity in URM historical structures can be best identified by the amount of deformation occurring in the various components of the structure. Using deformation demand for the purpose of seismic assessment is more meaningful than force demand estimation as, based on equal displacement rule, elastic displacement demands are close to the inelastic ones, whereas analogous similarities do not exist between the forces calculated from inelastic and elastic analyses. In the framework of the introduced rapid seismic assessment procedure, local seismic demand is specified in terms of relative drift ratios referring to the in-plane relative deviation of the piers' and walls' ends from vertical, θ_{in}, and to URM facades deviating from the horizontal initial orientation out-of-plane, θ_{out}. The relative drift ratio in plane, θ_{in}, is defined as the horizontal relative displacement (i.e. the difference) that occurs between two points along the building height, (i.e. ends of a pier or a wall), divided by their distance. θ_{out} is defined as the outwards relative deflection between successive points in the building plan. Meaningful indices include the relative displacement between the midspan and corners of walls oriented normal to the direction of seismic action, depicting the out-of-plane action; also the relative displacement at the end points of wings relative to the main structure, indicating the tendency for torsional response, θ_{tor}. This may be examined at the floor levels and at the crest of the building. Definitions of θ_{in}, θ_{out} and θ_{tor} are presented in Figure 3. Thus, the fraction of the θ_{in} value which is owing to the torsional response is equal to $\theta_{tor} \cdot L/H$, where L is the length of wing from the point of support and H the height of the structure at the point considered.

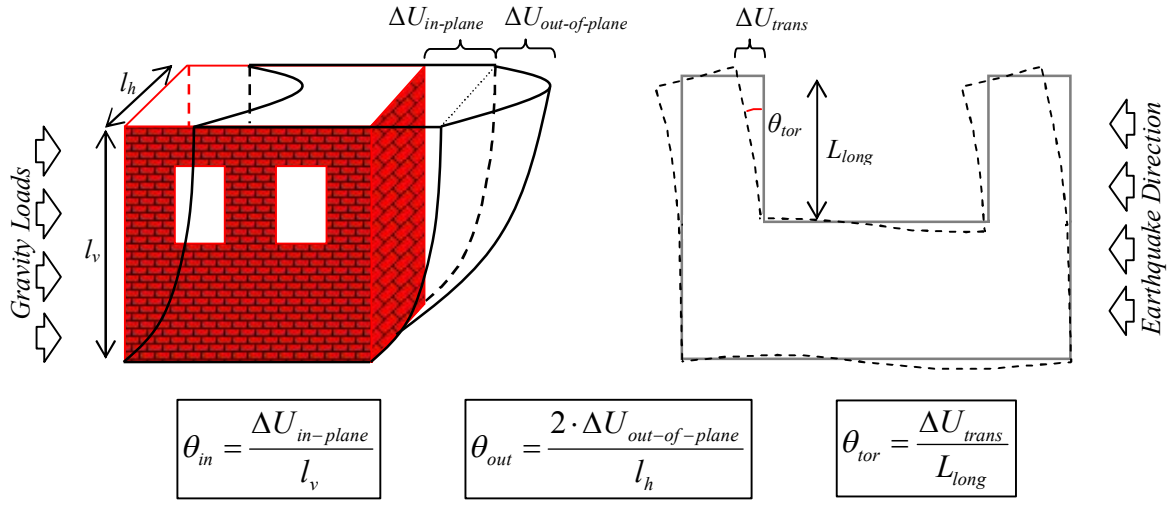


Figure 3: Definitions of θ_{in}, θ_{out} and θ_{tor} relative drift ratios.

The values of θ_{in}, θ_{out} and θ_{tor} calculated above are then compared to the corresponding performance levels imposed by the seismic code applicable at the site. Cracking rotations (drift ratios) in masonry elements, θ_y, are in the order of 0.15% for in-plane and 0.20% for out-of-plane wall deformation (corresponding to the *Operational/Immediate Occupancy* limit state). The Hellenic code for assessment and structural interventions in masonry buildings (KADET 2014, [8]) classifies as *Significant but Repairable Damage* performance level values of relative drift ratios that vary between θ_y and $3/4 \cdot \theta_u$ (i.e. ductilities $\mu < 2.5$), whereas for higher values of θ_{in} and θ_{out} ranging up to the limit of $4/3 \cdot \theta_u$ damages occurring to the structural elements are classified as having attained the *Life-Safe/No collapse* performance level. The value of ultimate drift ratio, θ_u, according to the same code depends on the kind of deformation imposed on the examined wall. For in-plane deformations, θ_u equals:

$$\theta_u = 0.008 / L \tag{4}$$

whereas, for out-of-plane deformations:

$$\theta_u = \min \{\theta_{u,1}, \theta_{u,2}\} \;\; ; \;\; \theta_{u,1} = 0.003 \cdot H_o / t \;, \;\; \theta_{u,2} = \theta_{R,u} \cdot (1 - M_y / M_{Rd}) \tag{5}$$

In Equations 4 and 5, L is the length of the wall (measured in the horizontal direction), t is its width, $\theta_{R,u} = t/H_o$, $M_y = f_{wt} \cdot \left(B \cdot t^2\right)/6$, f_{wt} is the tensile strength of the wall, B is the dimension of the wall pier or spandrel that defines the width of the section that is bending, H_o is the distance from the point about which rotation of the wall occurs, $M_{Rd} = F_{Rd} \cdot H_o / 2$, $F_{Rd} = S_d(T_1) \cdot t \cdot \gamma \cdot A_{L,w}$ and $A_{L,w} = L \cdot H_w$, and H_w is the total wall height.

3 DEMONSTRATION OF THE SEISMIC RESPONSE OF MONUMENTAL URM BUILDINGS

To investigate the seismic response of torsionally sensitive monumental and historical buildings a series of time-history dynamic analyses have been performed to different types of finite element models of a monumental building located in Thessaloniki, Greece. The building, known as "Papafeion", was constructed in 1902 according to the designs of the architect Xenofon Paionidis and the sponsorship of Ioannis Papafis in order to function as an orphanage for the children of the Hellenic community of Thessaloniki, which at the time was under Ottoman rule. Since 1903 the building is being continuously in operation, functioning mainly as an orphanage or a hospital, with the most recent function to be a boarding school for orphan boys under the management of the Orthodox Church.

3.1 Description of the examined building

The Papafeio building is a three storey neoclassical building, consisting of three building wings which in plan forms the shape of the capital letter ***E*** (Fig. 4), codifying the initial letter of the words *Ελλάς*, *Ελευθερία* and *Ειρήνη*, the Greek words for *Greece*, *Freedom* and *Peace* which at the time were the object of national struggle. The entire building complex is enclosed within a rectangle of external dimensions of 81.50 by 55.44 m, whereas the building height measured from the floor of the first storey to the top of the third storey (the height of the timber roof is omitted) is 16.23 m (foundation height: 1.20 m, 1st storey: 3.60 m, 2nd storey: 5.65 m, 3rd storey 5.78 m) except of the central part of the central wing, where the corresponding height is 19.03 m due to an elevation of the roof of the building's ceremonial hall (Fig. 4(e)). The walls of the first storey are made of stone, having a thickness equal to 0.80 m at the perimeter of the building and 0.70 m at the inner plan. Walls of the second storey were built of solid bricks, whereas third storey walls are made of voided bricks. Perimeter walls are

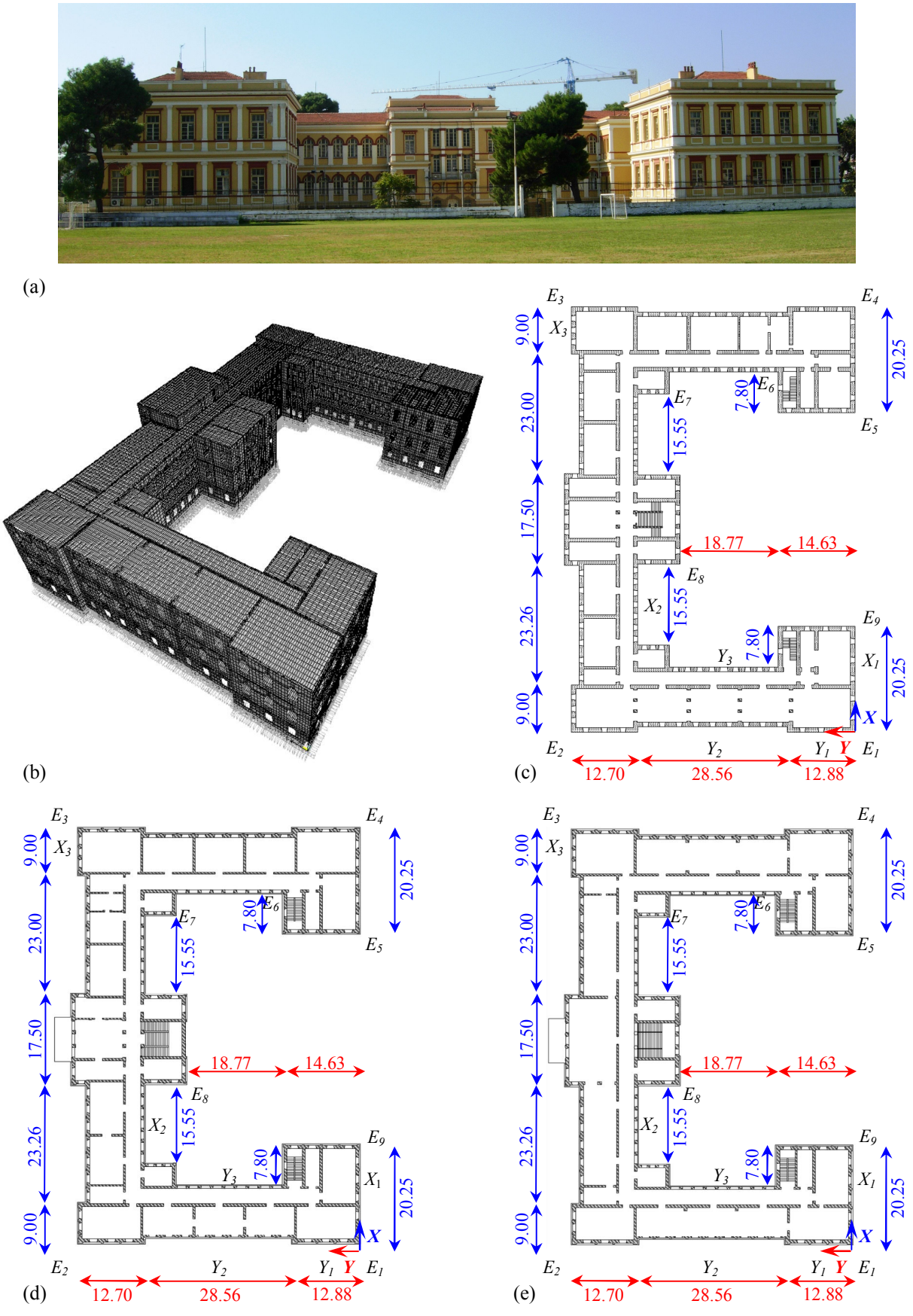


Figure 4: The Papafeio building: (a) North view, (b) 3D finite element model, (c - e) plan views of the 1st, the 2nd and the 3rd storey.

0.55 m in width, whereas internal walls are 0.40 m thick at both storeys. Floors of the first and the second storey are made of double T iron beams having a 100 x 180 mm and a 80 x 180 mm cross section at each storey, respectively, spacing along the small sides of the rooms and the corridors at 0.65 m at the first and 0.67 m at the second storey. The roof of the third storey is also made of double T iron beams, oriented similarly to the iron beams of the 1st and the 2nd storey floors, having a cross section of 80 x 200 mm and spacing at 0.85 m. At all floors and the roof brick–arches spanning in the transverse direction between successive iron beams are encased between the upper and lower flanges of the double T beams. The total thickness of the building's horizontal structural elements (including the finishing) at the location of the iron beams is 0.34 and 0.30 m at first and second storey floor and 0.20 m at third storey roof, whereas the thickness at highest point of the arches is about 0.10 m smaller. The last storey is covered by a roof made of timber, trusses spanning along the longitudinal dimensions of the building's wings, yet this roof is not part of the structural system of the building.

3.2 Modeling and analysis of the examined building

Investigation of the seismic response of the Papafeio building was achieved via simulation of the building as a three-dimensional finite model (Fig. 4(b)) by subjecting the model to time-history dynamic analyses [9]. In the building model walls were idealized using four-node shell elements, capable of supporting in plane and out of plane forces and moments (6 d.o.f. per node), whereas floors were simulated using linear elements for the iron beams and shell elements to represent the brick arches spanning between steel beams. A total number of more than 91000 area and 16000 frame elements were utilized, resulting in the formation of a finite element model of an input size of 180 MB. Response of the shell and the linear elements was considered elastic. The modulus of elasticity of stone and bricks was considered 1000 times the value of the corresponding compressive strength, f_k; this variable was taken equal to: (a) for stone f_k = 5.5 MPa, (b) for solid bricks f_k = 4.0 MPa and (c) for voided bricks f_k = 1.5 MPa. In the case of frame elements (iron beams), the modulus of elasticity was taken equal to 150 GPa. In all cases self weight of the building was calculated according to the material density; for stone 25 kN/m^3, for solid bricks 18 kN/m^3 and for voided bricks 14 kN/m^3. A roof weight equal to 1.5 kN/m^2 was assumed, uniformly distributed along the area elements of the third storey roof. Service loads were considered equal to 2.50 kN/m^2 for the roof and 3.50 kN/m^2 for the floors of the building. Masses considered in the dynamic analyses were automatically calculated by the program, by multiplying each element (shell or linear) volume by their respective density.

In order to investigate the influence of floor and roof stiffness within their plane to the overall seismic response of torsionally vulnerable URM buildings, two different versions of the produced building model were considered in the dynamic analyses. Note that according to the construction practices used from Renaissance until the 20th Century all over Europe, different types of floors and roofs were used in this category of buildings, providing different types of stiffness within their plane. In the first version of the considered building, the stiffness of the horizontal structural elements (floors and roof) was omitted, accounting for a building response which is controlled only by the response of the building's walls. The second version of the examined building model had full diaphragm action established at its floors and roof levels, accounting for the theoretical case where the horizontal structural elements of the same level at height in all building wings respond in plan as if they belong in the same undeformed horizontal plane. The actual seismic response of the building lies somewhere within the response of the two examined versions of the building model, which form the envelope of seismic response that can be developed from it.

Each of the two versions of the building model were subjected to time-history dynamic analyses for the case of the 1978 Thessaloniki earthquake record, selected from the ITSAK earthquake database [10]. From among the three components recorded for the specific earthquake case (two horizontal and one vertical) the record used in dynamic analyses corresponds to the horizontal component with the maximum recorded absolute peak ground acceleration (*PGA*). This component was applied separately in each of the two principal directions in plan of the examined building in each case of dynamic analysis. The absolute acceleration and relative displacement response spectra of the acceleration record used in the dynamic analyses, S_a and S_d respectively, as those were calculated considering a viscous damping equal to ξ = 5%, are presented in Figure 5 in comparison to the corresponding spectra imposed by EC8-1 for seismic assessment of URM historical buildings at the building's site (γ_I = 1.3, S = 1.20).

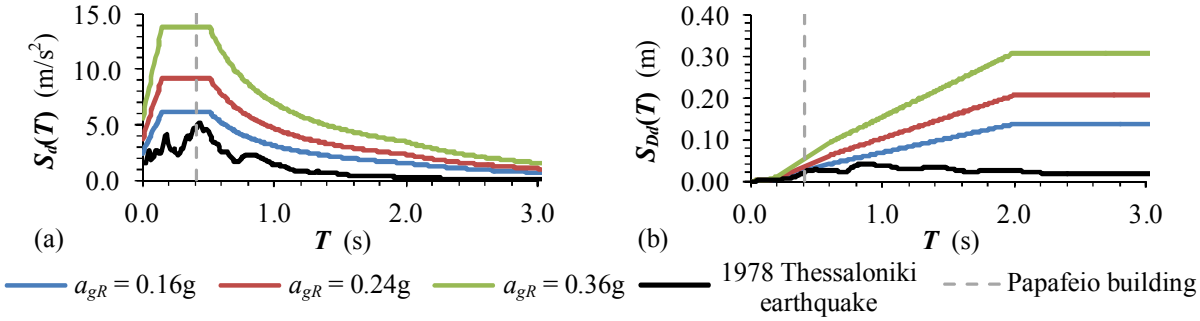


Figure 5: Response spectra of the earthquake record used in the analyses (calculated for 5% damping) and imposed by EC8-1 for assessment: (a) absolute acceleration spectra, (b) relative displacement spectra.

3.3 Examination of the results of time-history analyses

To understand the seismic response of torsionally sensitive, monumental, URM buildings, first the time-history of the horizontal displacements at the roof of the third storey of the Papafeio building is investigated. Figures 6 and 8 depict the time-history of the horizontal displacements parallel to both the X and Y plan directions, U_X and U_Y, at selected locations of the building's plan (for the location of each control point see Fig. 4(e)). U_i ($i = X$ or Y) at those two figures derived from the dynamic analyses of the building model with no floor and roof stiffness, subjected to seismic excitation parallel to X and Y directions, respectively. Each plot depicts a time interval of 1.5s before and after the instant of maximization of the horizontal displacement of the control point in the same direction with the earthquake excitation. Note that time-histories of U_i are presented as a ratio of the maximum value of the time-history of the maximum horizontal displacement developed at the examined locations, estimated from, $U_{max} = \sqrt{(U_X^2 + U_Y^2)}$, so as to investigate the degree of influence of torsional phenomena owing to the building's plan shape. Similar graphs corresponding to the dynamic analyses of the building model with established diaphragm action at floors and roof levels are presented in Figures 7 and 9.

As depicted in Figs. 6 - 9, the degree of provided stiffness within the horizontal structural elements at this category of buildings plays a crucial role at the building's overall seismic response. In the case where floor stiffness is omitted (Figs. 6 and 8), each of the control points of the building displaces not only parallel to the earthquake excitation but also in the orthogonal direction by a significant amount, which may exceed up to 50% of the magnitude of its principal displacement. This applies at the edges of the building and at walls whose plane is parallel to the direction of the earthquake excitation, whereas walls oriented orthogonal to the ground excitation displace mainly in their out-of-plane direction (Figure 6, Facade Y_3). On the contrary, when full diaphragm action is achieved within building's floors and roof, all control

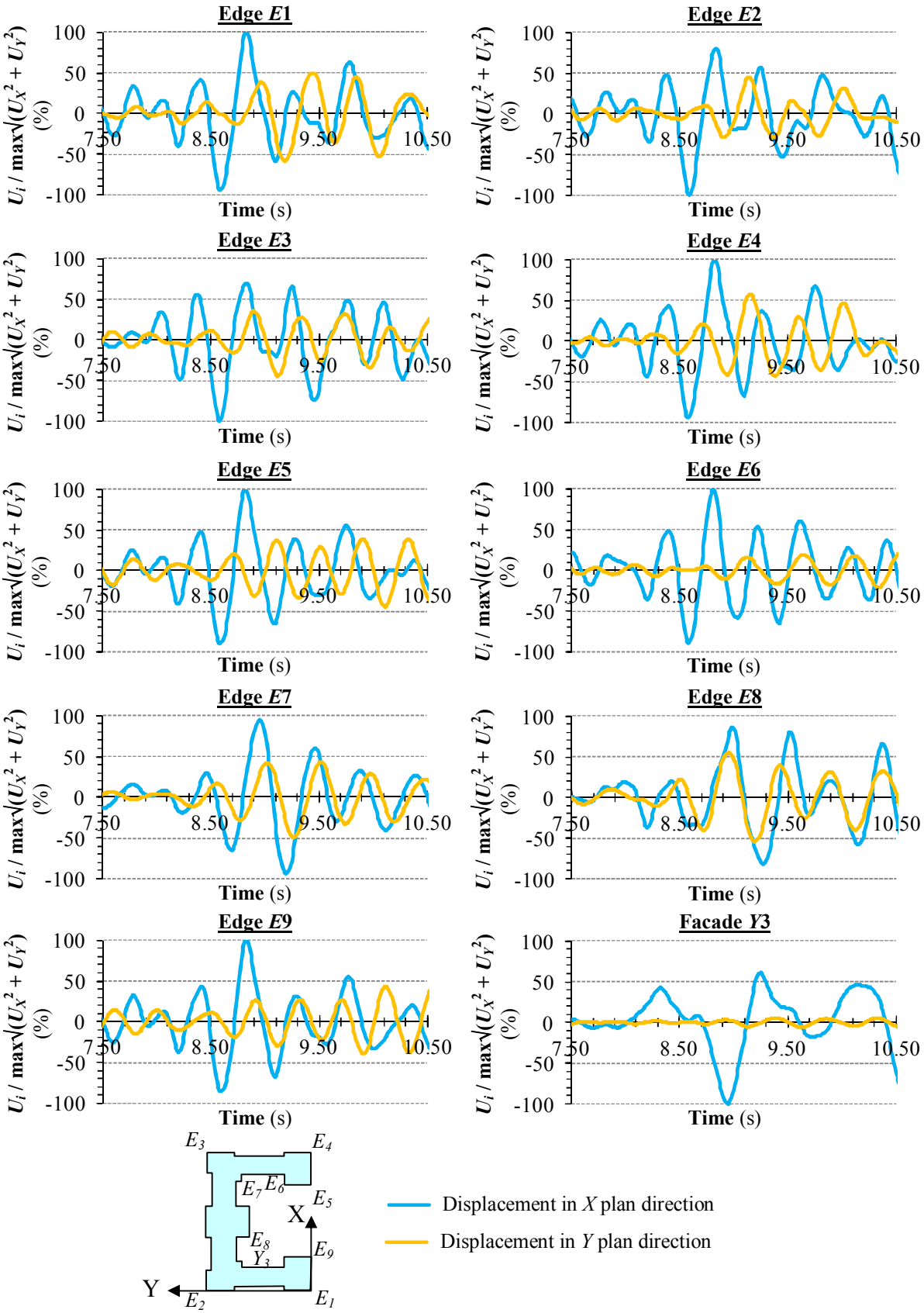


Figure 6: Time-histories of the developed horizontal displacements at roof level of the Papafeio building when zero stiffness is considered within its floors and roof levels - Earthquake action parallel to *X* plan direction.

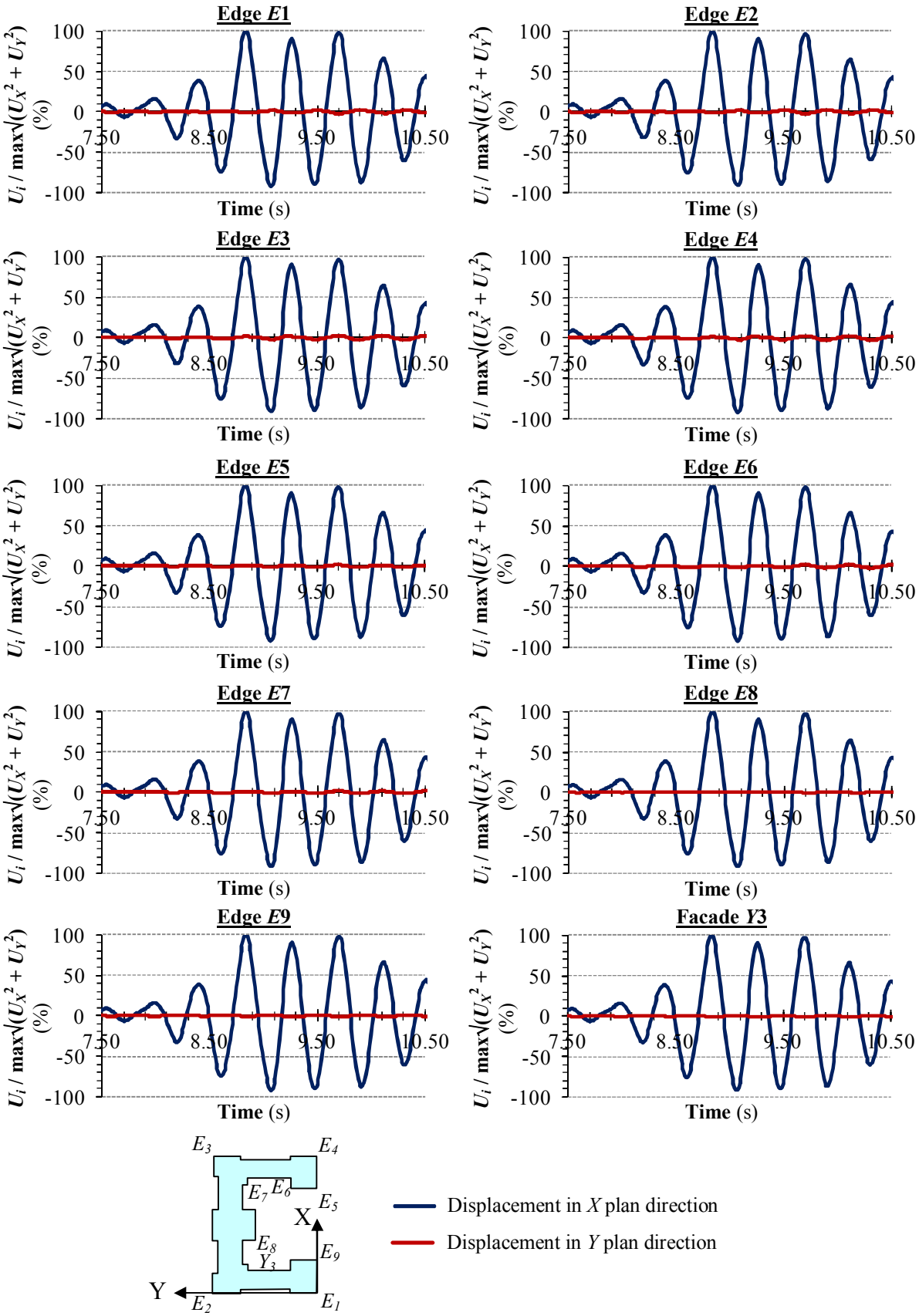


Figure 7: Time-histories of the developed horizontal displacements at roof level of the Papafeio building when full diaphragm action is considered within its floors and roof levels - Earthquake action in *X* plan direction.

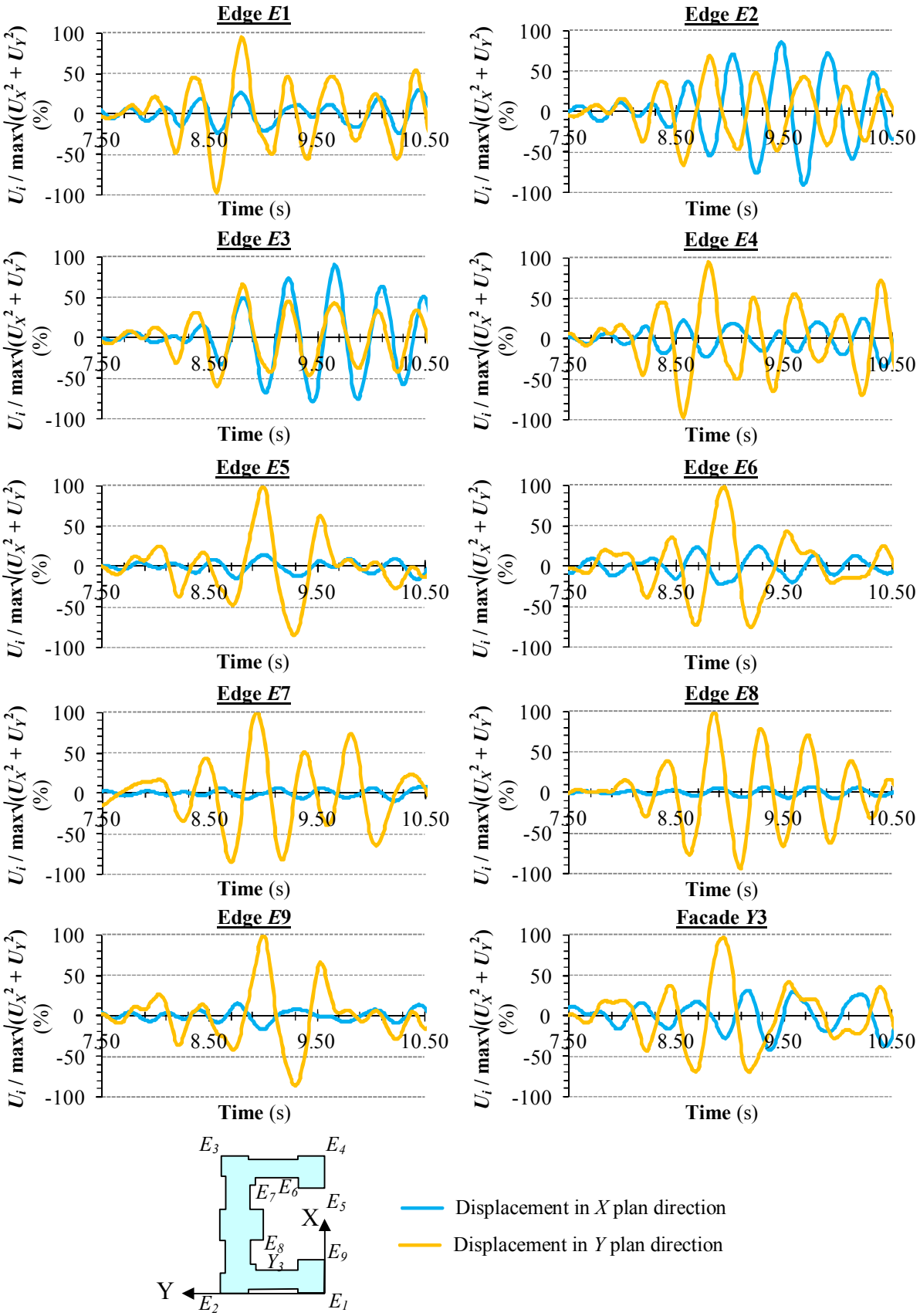


Figure 8: Time-histories of the developed horizontal displacements at roof level of the Papafeio building when diaphragm action is neglected in its floors and roof levels - Earthquake action parallel to *Y* plan direction.

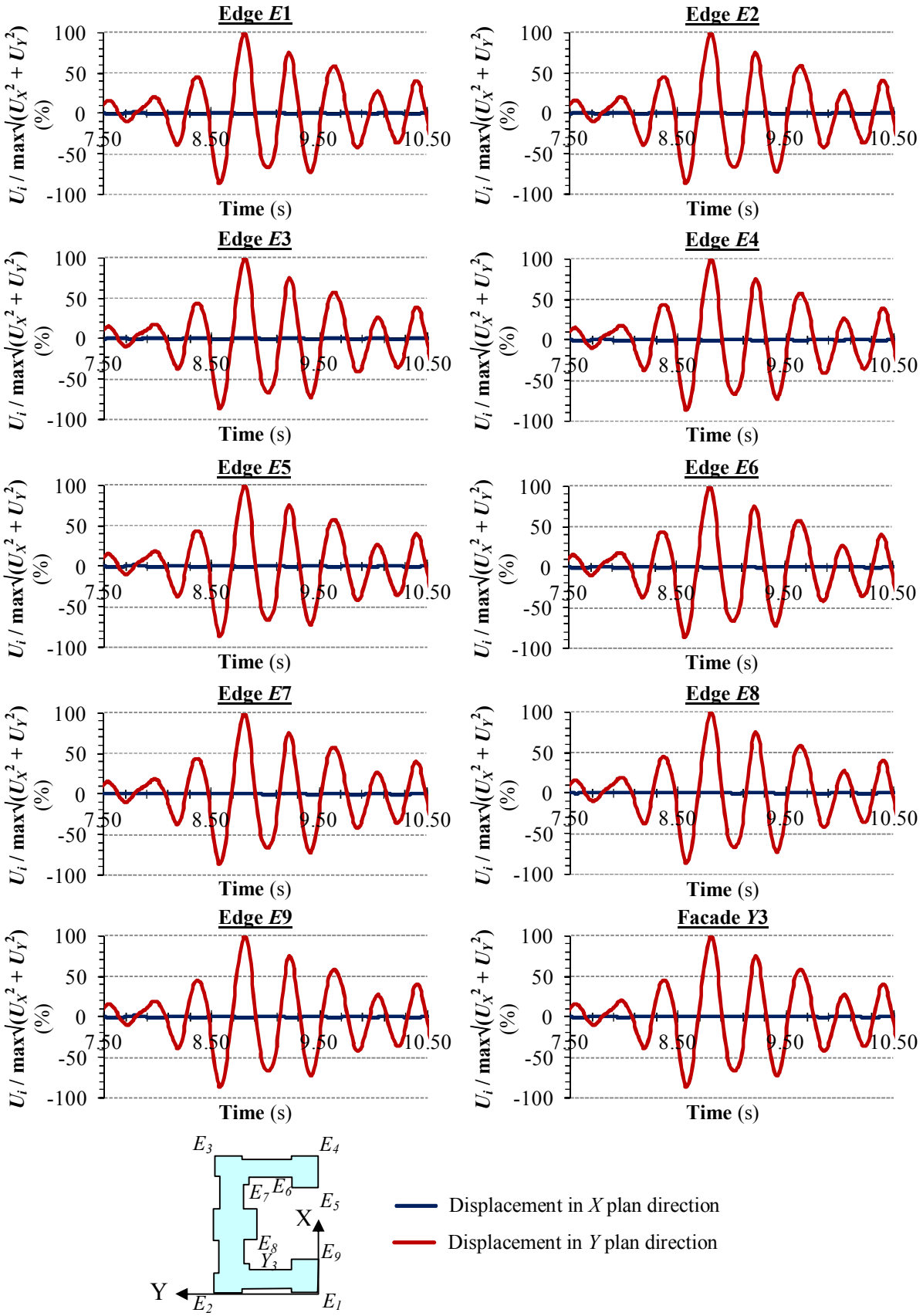


Figure 9: Time-histories of the developed horizontal displacements at roof level of the Papafeio building when full diaphragm action is considered within its floors and roof levels - Earthquake action in *Y* plan direction.

points displace mainly parallel to the direction of the earthquake action, regardless of orientation of the walls to whom they belong with respect to the earthquake's direction (Figs. 7 and 9). Also note that in the case of zero stiffness within the plane of the floors and roof the waveform of developed displacements varies among the different control points of the building, indicating a differential movement within locations of the same horizontal level of the building.

To further understand the influence of torsional effects developing at monumental URM buildings in association to the degree of achievable diaphragm action at their floors and roof to the structures' overall seismic response, Figures 10 and 11 depict the lateral displacements occurring height-wise at control locations at the instant of maximization of the horizontal roof displacement. The two figures present the deflected shapes of the same ten control locations examined at Figs. 6 - 9 at X and Y plan directions respectively, when the earthquake acts in the corresponding direction. Lines in light blue and orange in Fig. 10 and 11 respectively refer to the responses obtained from the building model with no-diaphragm action within its floors and roof, whereas lines in dark blue and red in the same figures correspond to the seismic response of the building model with full diaphragm action. Continuous lines plot the deformed shape of the control locations at the instant of their maximum roof displacement. Also plotted with dashed lines are the corresponding deformed shapes obtained after performing the proposed static analysis procedure for rapid determination of the building's maximum seismic response. These shapes have been amplified by the f_i factors (Eq. 1) so as the maximum horizontal displacement of the respective control location obtained from time-history dynamic analysis be equal with the horizontal displacement occurring from the proposed static analysis procedure at the same building height (this location in height corresponds to the roof level at all control locations except of the case of facade Y_3 when full diaphragm action is considered, which is at 91% of the total building height).

As illustrated in both figures, the horizontal deformations occurring at the building's control locations when the earthquake excitation acts in the same plan direction and full diaphragm action at the floors and roof level is considered are greater as compared to the corresponding displacements obtained in the absence of a diaphragm action. This difference is greater when the earthquake acts in X plan direction (perpendicular to the building's axis of symmetry) ranging up to the value of 3. Also depicted at Figs. 10 and 11 is the very good correlation between the deformed shapes of the control locations obtained by the two analysis procedures, whereas even when there is some discrepancy in the results, the interstorey drift calculated from the static analysis procedure results is greater than the corresponding one derived from the results of time-history dynamic analysis.

Therefore, in terms of determination of the lateral displacement profiles, application of the rapid analysis procedure yields results of the same accuracy as a time–history dynamic analysis. Yet, application of the introduced rapid analysis procedure requires significantly smaller computational time and means. Among the examined analyses cases, the volume of produced output files in the case of time–history dynamic analyses is in the range of 57 GB, requiring an execution time of about 18 h, whereas execution of the rapid analysis procedure in the same 3-D finite element models required less than two minutes for each plan direction of the examined building models and the volume of the produced output files were is the range of 1 GB (note that the input file of the Papafeio building alone has a volume of 0.18 GB). Thus, the proposed static analysis procedure is much simpler to process and handle than the time-history dynamic analysis procedure, especially in cases of massive structures, such as the monumental URM buildings; this renders the rapid approach a useful tool in the hands of practitioners in the field of seismic assessment.

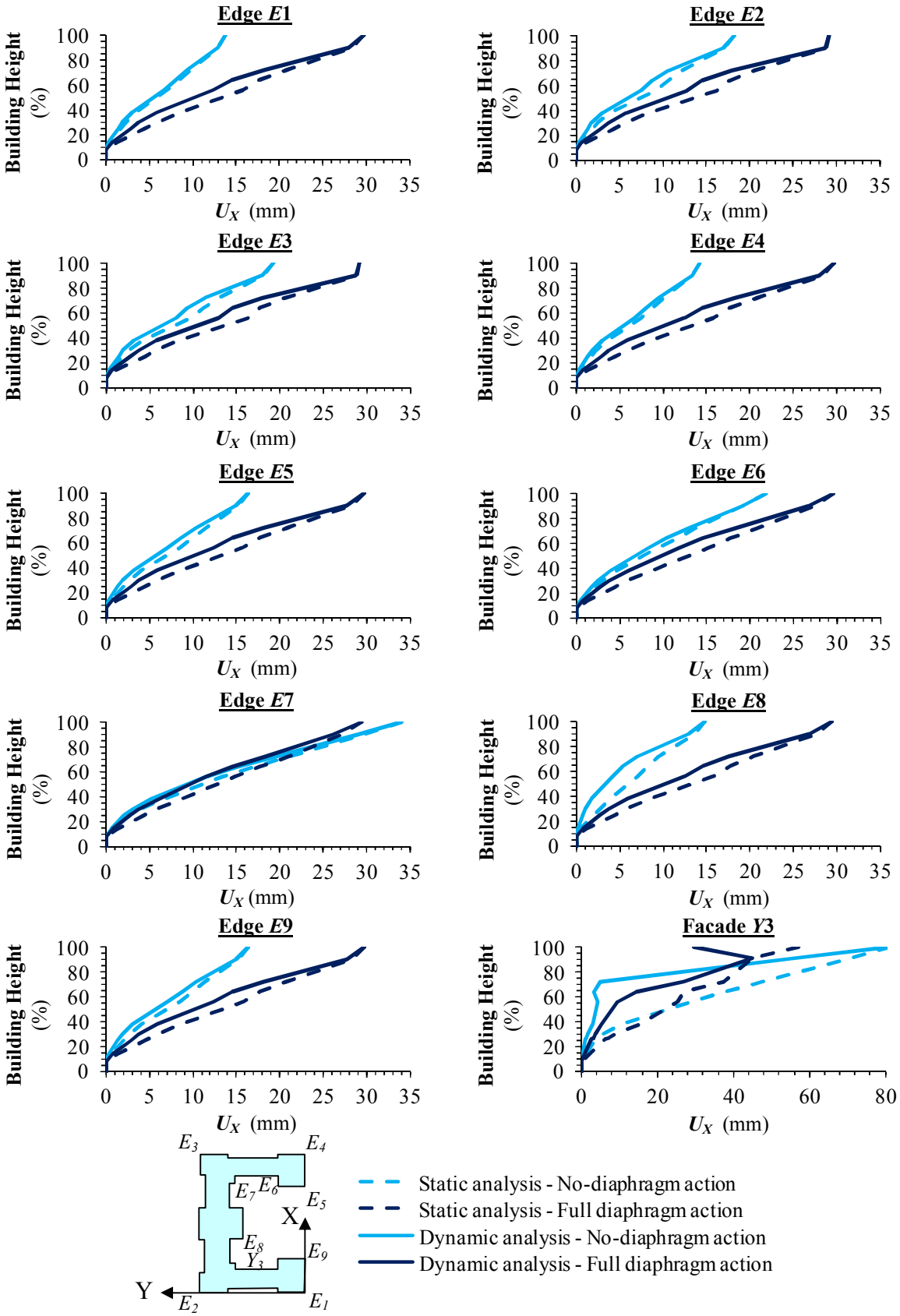


Figure 10: Lateral displacements at control locations of the Papafeio building (for identification of location see Fig. 4) in the *X* plan direction at the instant of the maximum roof displacement, when the building is subjected to earthquake excitation in the same direction.

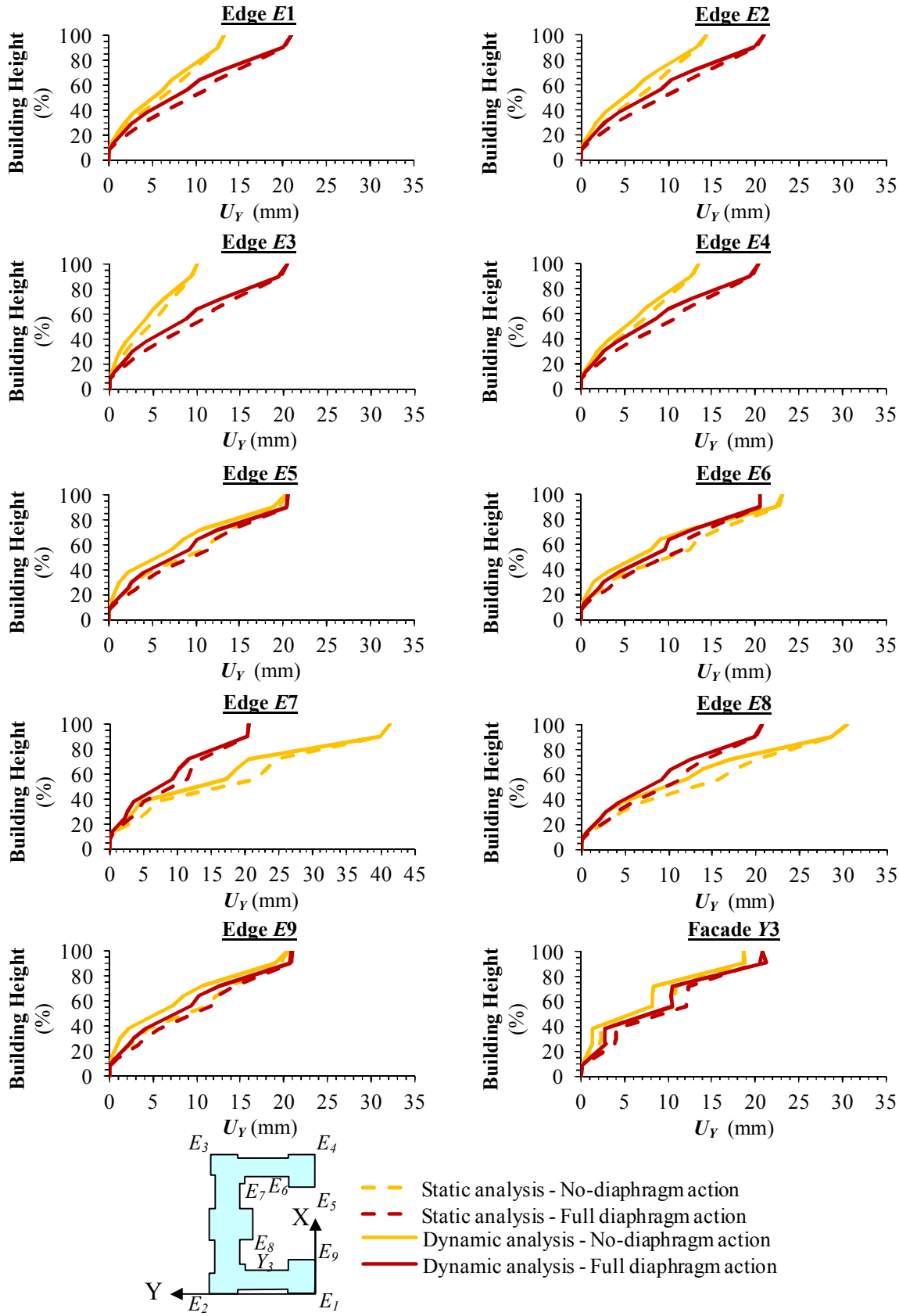


Figure 11: Lateral displacements at control locations of the Papafeio building (for identification of location see Fig. 4) in the *Y* plan direction at the instant of the maximum roof displacement, when the building is subjected to earthquake excitation in the same direction.

4 SEISMIC ASSESSMENT OF THE PAPAFEIO BUILDING

As demonstrated from the seismic response of the two versions of the Papafeio building model, the different degree of diaphragm action provided at floor levels of historic URM buildings due to the vast variety of construction practices used at horizontal structural elements in association with the influence of torsion due to the shape in plan of many of this type of buildings can lead to very different responses of their structural system. Therefore, seismic assessment of monumental and historical URM building is essential, especially in countries that suffer from high seismicity, so as to identify potential locations of damage at the case of the earthquake scenario applied in the greater region and to select the appropriate retrofit strategy that will secure the integrity of the structure as well as the preservation of its unique historic and architectural characteristics. In this framework, the rapid seismic assessment procedure introduced by the authors provides accurate results in a relatively straightforward manner. In this section an example application of the proposed procedure to the two versions of the Papafeio building model is presented for the case of the EC8-1 earthquake scenario applied at the building's site (a_{gR} = 0.16 g, Fig. 5) and the results are compared to the building's actual seismic response during the 1978 Thessaloniki earthquake (Fig. 5).

Application of the rapid seismic assessment procedure first requires the determination of the envelope of the structure's horizontal displacements caused by the earthquake scenario imposed at the building's site. Considering the height of the Papafeio building, measured from its foundations to the roof of the third storey as H = 16.23 m the building's fundamental period of vibration in both of its principal plan directions can be estimated according to Eq. 3 as T_1 = 0.40 s. According to EC8-1 (Eq. 2) the value of spectral absolute acceleration used for the building's seismic assessment is $S_d(T_1) = 1.3 \cdot 1.57 \cdot 1.20 \cdot 2.50 = 6.121$ m/s^2 (intersection of blue and gray lines, Fig. 5(a)), whereas the target roof displacement valid for both the building's principal plan directions is $S_{Dd}(T_1) = 6.121 \cdot (0.40 /(2 \cdot \pi))^2 = 24.81$ mm (Fig. 5(b)). The average horizontal displacement of the third storey roof in the X plan direction, as this was derived from the proposed static analysis procedure, is 21.88 and 19.92 mm when diaphragms were neglected and when full diaphragm action at floor levers was considered, respectively (i.e., practically the same). The corresponding values in the Y plan directions are 5.80 and 4.79 mm. Therefore, calculation of the developed displacements or stresses for conducting seismic assessment can be obtained by multiplying the corresponding parameter from the static analysis with the amplification factors (Eq. 1) f_x = 24.81 / 21.88 = 1.13 and f_y = 24.81 / 19.92 = 1.25 when floor stiffness is neglected and with f_x = 24.81 / 5.80 = 4.28 and f_y = 24.81 / 4.79 = 5.18 in the case of full diaphragm action at the building's floors. Consider for example the building's external wall Y_1 (Fig. 4(c-e)), whose length is L = 12.88 m. In the case of the building model with zero diaphragm action at floors and roof levels the horizontal displacements U_X at midspan (out-of-plane wall response) resulting from the proposed static analysis procedure in the X plan direction at roof levels of the 3rd, the 2nd and the 1st storey are 38.418, 22.876 and 4.626 mm, whereas the corresponding displacements at the northern end of the wall (Y = 0 m) are 6.245, 3.814 and 1.036 mm and at the wall's southern end (Y = 12.88 m) are 9.830, 6.031 and 2.955 mm. Therefore, the out-of-plane deflection of the Y_1 wall at the instant its maximum seismic response, θ_{out}, calculated according to Fig. 3 and the amplification factor f_x = 1.13, will be 0.58%, 0.34% and 0.05% at roof levels of the 3rd, the 2nd and the 1st storey, respectively. Note that when full diaphragm action is considered at floors and roof levels θ_{out} = 0, as all points of the same level move as if they belong in a perfectly undeformed plane. In the case of in-plane wall seismic response, the U_Y horizontal displacements at the roofs of the 3rd, the 2nd and the 1st storey and the floor of the 1st storey of wall Y_1 resulting from the proposed static analysis procedure in the Y plan direction are [4.172, 2.521, 0.708,

0.095] mm when no-diaphragm action is considered and [4.818, 2.838, 0.924, 0.116] mm in the case of full diaphragm action at floors and roof. With the corresponding values of f_y and the storey heights (see §3.1) the maximum value of in-plane relative drift ratios, θ_{in}, of the 3rd, the 2nd and the 1st storey of the wall Y_1 at the instant of their maximum seismic response will be [0.04, 0.04, 0.02] % and [0.18, 0.18, 0.12] % in the case of negligible and full diaphragm action, respectively.

The rapid seismic assessment procedure leads to the evaluation of performance of the Papafeio building for the EC8-1 earthquake scenario from the local seismic deformation capacities, as calculated from Eqs. 4 and 5. Table 1 presents the results of the seismic assessment procedure in terms of θ_{in} and θ_{out} at selected locations of the external walls denoted at Fig. 4(c-e) of the two versions of the building model (note that in the case of the building model with complete diaphragm action at its floors and roof $\theta_{out} = 0$). The relative drift ratios along the height of the building edges that belong to the walls presented at Table 1 are equal to the corresponding values of θ_{in} (for example, the relative drift ratios along the height of the edge E_1 in the X plan direction equal to θ_{in} of the wall X_1, whereas those in the Y plan direction equal to θ_{in} of the wall Y_1). Furthermore, Table 2 presents the values of θ_{tor} which are expected at selected locations of the exterior of the building when the earthquake acts perpendicular to the examined locations, as the result of the torsional phenomena developing at the floors and the roof of the building due to its plan shape. Note that in the case of complete diaphragm action at floors and roof of the building the values of θ_{tor} are systematically lower than the corresponding ones when no diaphragm action is considered, by as much as 200 times. Exception to this rule is the response of the southern façade of the Papafeio building (the $E_2 - E_3$ façade) where in the case of complete diaphragm action the values of θ_{tor} at the floors and roof levels are greater by 8 to 73 times as compared to the corresponding values when no diaphragm action is considered.

		No Diaphragm Action		Complete Diaphragm Action	
Location	Storey	θ_{in} (%)	θ_{out} (%)	θ_{in} (%)	θ_{out} (%)
X_1	3rd	0.05	0.52	0.21	0
	2nd	0.05	0.32	0.21	0
	1st	0.03	0.06	0.15	0
X_2	3rd	0.08	1.10	0.21	0
	2nd	0.09	0.48	0.22	0
	1st	0.04	0.08	0.15	0
X_3	3rd	0.08	0.26	0.21	0
	2nd	0.08	0.16	0.22	0
	1st	0.04	0.03	0.15	0
Y_1	3rd	0.04	0.58	0.18	0
	2nd	0.04	0.34	0.18	0
	1st	0.02	0.05	0.12	0
Y_2	3rd	0.04	0.30	0.16	0
	2nd	0.04	0.25	0.18	0
	1st	0.02	0.01	0.09	0
Y_3	3rd	0.08	1.75	0.33	0
	2nd	0.09	0.81	0.37	0
	1st	0.03	0.11	0.14	0

Table 1: Values of θ_{in} and θ_{out} at selected locations of the external walls of the Papafeio building. Values in red correspond to development of moderate damages.

In the case of in-plane response of the building's walls, the value of θ_u derived from Eq. 4 according to the walls' geometric characteristics equals to 0.80%. Therefore, the onset for the *Repairable Damage* and *No-Collapse* performance levels equal to 0.60% and 1.07%, respectively. When out-of-plane response is considered, given the geometric characteristics of the walls at the selected locations, the onset for the *Repairable Damage* performance level ranges between 1.16% and 3.44%, whereas the corresponding value range for the *Life-Safe/No-Collapse* performance level is between 2.05% and 6.12%. Considering the values of θ_{in} and θ_{out} presented at Table 1, moderate damages are expected to occur at the external walls of the Papafeio building in the form of flexural cracking of the walls due to out of plane action. The results of the rapid seismic assessment are confirmed by the actual response of the building during the 1978 Thessaloniki earthquake, whose response spectra approximate those of EC8-1, calculated for a_{gR} = 0.16 g (Fig. 5).

Location	Storey	No Diaphragm Action θ_{tor} (%)	Complete Diaphragm Action θ_{tor} (%)
$E_1 - E_2 = E_3 - E_4$	3rd	0.006164	0.000169
	2nd	0.003268	0.000265
	1st	0.000460	0.000193
$E_2 - E_3$	3rd	0.000048	0.000411
	2nd	0.000042	0.000321
	1st	0.000003	0.000225
$E_6 - E_7$	3rd	0.035967	0.000178
	2nd	0.016499	0.000257
	1st	0.002991	0.000198
$E_1 - E_9 = E_4 - E_5$	3rd	0.030183	0.000427
	2nd	0.017470	0.000321
	1st	0.003281	0.000214

Table 2: Values of θ_{tor} at selected locations of the Papafeio building.

5 CONCLUSIONS

This paper investigates the seismic response of monumental buildings built during the post-renaissance era in many European cities. Buildings of this category often have a unidirectional plan symmetry, whereas in the other principal plan axis asymmetry occasionally triggers torsional phenomena during a seismic excitation, which can lead to important differential displacements along their structural system and therefore a high risk of damage localization in the remotest edges of the structure. Given the historical value of those buildings, which in many cases are inseparably connected with political, economical or cultural national milestones, seismic assessment of them is an essential step towards identifying potential locations of damage and towards selecting the appropriate retrofit strategy that will secure the integrity of those structures as well as the preservation of their unique historic and architectural characteristics.

In this framework, the rapid seismic procedure for unreinforced masonry buildings, which has recently been developed by the authors, has been applied to a monumental neoclassical building of Thessaloniki, Greece and results have been evaluated to assess the extent of anticipated damage. It was shown that the assessment procedure yielded results of equivalent accuracy to detailed time-history dynamic analysis based assessment procedures, as well as to the actual seismic response of the examined building. Yet, the introduced procedure required significantly shorter computational time and effort, and produced significantly smaller volume of

output files, which makes it ideal for use in the case of massive structures such as the monumental buildings, where, even when powerful computational means are utilized seismic assessment can be an especially demanding task.

Acknowledgments This paper was funded by the Greek State Scholarships Foundation in the framework of the Short Terms scholarship program, under the 2013-ΠΕ2-SHORT TERMS-18496 contract.

REFERENCES

[1] Google search engine. http://www.google.com

[2] Charters and other doctrinal texts. *ICOMOS – International Council On Monuments and Sites*, Charenton-le-Pont, France, http://www.icomos.org/en/charters-and-texts.

[3] Archaeology of the City of Athens. *National Foundation of Research*, Athens, Greece, http://www.eie.gr/archaeologia/En/Index.aspx

[4] S.I. Pardalopoulos, S.J Pantazopoulou, M.Th. Kontari, Rapid seismic assessment procedure of masonry buildings with historic value. *Seismic Assessment, Behavior and Retrofit of Heritage Buildings and Monuments*, Computational Methods in Applied Sciences 37, Springer, Chapter 5, 2015.

[5] S. Pardalopoulos, M.Th. Kontari, S.J Pantazopoulou, Analytical procedure for seismic assessment of masonry buildings with historical value. *COMPDYN 2013 - 4th ECCOMAS Thematic Conference on Computational Methods in Structural Dynamics and Earthquake Engineering*, Kos Island, Greece, June 12-14, 2013.

[6] S. Pardalopoulos, S. J. Pantazopoulou, Seismic assessment of 19th century heritage building through simulation. *COMPDYN 2011 – 3rd ECCOMAS Thematic Conference on Computational Methods in Structural Dynamics and Earthquake Engineering*, Corfu, Greece, May 26-28, 2011.

[7] EN 1998-1 Eurocode 8: Design of Structures for Earthquake Resistance – Part 1: General Rules, Seismic Actions and Rules for Buildings. *European Committee for Standardization (CEN)*, Brussels, 2004.

[8] Hellenic code for assessment and structural interventions in masonry buildings - KADET 2014. *OASP - Organization for Seismic Design and Earthquake Protection*, Athens, Greece, 2014.

[9] SAP2000. *Computers and Structures, Inc.*, University Avenue, Berkeley, California 94704, USA.

[10] ITSAK, *Institute of Technical Seismology and Earthquake Resistant Structures*, Thessaloniki, Greece, www.itsak.gr.

COMPDYN 2015
5th ECCOMAS Thematic Conference on
Computational Methods in Structural Dynamics and Earthquake Engineering
M. Papadrakakis, V. Papadopoulos, V. Plevris (eds.)
Crete Island, Greece, 25–27 May 2015

ASSESSMENT OF STONE MASONRY WALLS WITH DETERIORATION AT THEIR BASE USING NON-LINEAR FINITE ELEMENT ANALYSES

Georgios Papadopoulos, Dimos C. Charmpis and Rogiros Illampas

Department of Civil and Environmental Engineering, University of Cyprus,
75 Kallipoleos Str., P.O. Box 20537, 1678 Nicosia, Cyprus,
E-mails: giwrgospapadopoulos35@gmail.com, charmpis@ucy.ac.cy, rilamp01@ucy.ac.cy

Keywords: Structural safety, local failure, damage tolerance, damage scenario, non-linear finite element analysis, notional material removal, progressive collapse.

Abstract. *Masonry walls are exposed to various potentially damaging factors, which arise due to common environmental effects or accidental actions. Local damage on a masonry wall operating as a primary load carrying component may trigger partial or full collapse of the wall and of the structural system it is supporting. Therefore, reliably assessing (potentially) damaged masonry walls is a crucial aspect in maintaining the desired safety level and decide the appropriate retrofit measures possibly required.*
In the present work, the influence of deterioration at the base of stone masonry walls on their structural response is investigated. For this purpose, plane stress non-linear Finite Element (FE) analyses are performed for various wall configurations and base deterioration scenarios. Hence, the in-plane lateral strength is computed for walls, which are artificially damaged by notionally removing masonry material from the walls' base. By comparing the remaining carrying capacity of a 'damaged' wall with the carrying capacity of the corresponding intact wall, the structural damage tolerance of the deteriorated wall can be quantitatively assessed. The results obtained demonstrate the effects of base deterioration on the lateral resistance of stone masonry walls and facilitate the decision making process for a possible small- or large-scale intervention.

1 INTRODUCTION

Stone masonry walls operating as primary load carrying components are encountered in several historic/traditional as well as contemporary structures. As any structural component, such walls are exposed to various potentially damaging factors, which arise due to common everyday or frequent environmental effects, as well as infrequent severe/accidental actions [1-5]. Local damage may trigger partial or full collapse of a masonry wall and of the structural system it is supporting. Therefore, the understanding of the structural behaviour and the estimation of the remaining carrying capacity of a damaged masonry wall are crucial aspects in its assessment with respect to the safety level provided and the retrofit measures possibly required.

Typically, the part most prone to deterioration is the base of the masonry wall. Hence, the present work is concerned with the influence of deterioration at the base of stone masonry walls on their structural response. Base deterioration develops primarily due to rising damp, which penetrates into the wall and then evaporates causing disintegration of the wall constituents (stone/mortar). This deterioration process starts from the foundation level, at the external wall surface, and proceeds upwards and inwards, undercutting this way the wall structure. Depending on the extent of deterioration, possible interventions may aim at eliminating or at least diminishing the impacts of the deterioration factor (e.g. reduce damp by installing more effective drainage system) and/or at repairing/strengthening the damaged wall (e.g. through stone/mortar replacement or injection grouting).

In this work, plane stress non-linear Finite Element (FE) analyses are performed to examine the in-plane lateral resistance of stone masonry walls under various base deterioration scenarios. The length of the masonry walls considered is 6m, the height is 3m and the thickness is 50cm, while various configurations of door/window openings are assumed. For each case investigated, the intact (non-deteriorated) wall is first analysed. Then, several base deterioration scenarios are defined through the notional thickness reduction of certain elements of the wall FE mesh. The results obtained for the FE models with notionally removed masonry material allow the estimation of the structural damage tolerance of the deteriorated wall. Such results can greatly assist in establishing rational damage control and retrofit strategies for masonry walls with deterioration at their base.

The remainder of this paper is organized as follows. Section 2 provides the geometrical characteristics of the masonry walls analysed in the present work. Section 3 describes the base deterioration scenarios assumed for the analysed masonry walls. Section 4 presents the way the walls are simulated using non-linear FE analysis. FE simulation results are reported in section 5. Finally, the conclusions of the paper are given in section 6.

2 GEOMETRICAL CHARACTERISTICS OF ANALYSED MASONRY WALLS

Four different stone masonry wall configurations are examined in this work (Fig. 1). In all 4 configurations, the same basic geometrical wall characteristics are assumed: 6m×3m×50cm (length×height×thickness of the wall). The difference in these configurations is made by the presence of window/door openings. Hence, the 4 configurations correspond to: (a) a wall without openings, (b) a wall with a central window opening, (c) a wall with a central door opening and (d) a wall with a door and a window opening. Window openings have dimensions 1m×1m, while door openings have dimensions 1m×2m (width×height). Timber lintels are assumed to be installed above all openings. The detailed geometrical characteristics for the 4 wall configurations are given in Fig. 1.

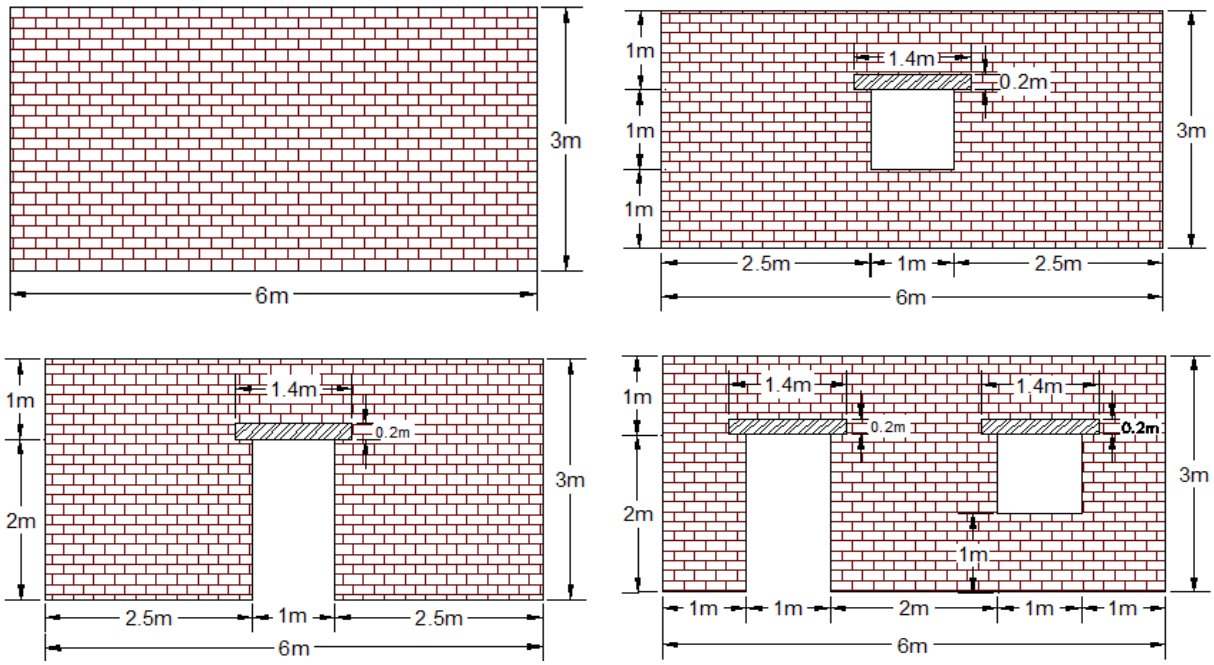


Figure 1: Geometrical characteristics of analysed masonry walls.

3 ARTIFICIAL DETERIORATION THROUGH NOTIONAL MATERIAL REMOVAL

In the present work, deterioration is simulated by the notional material removal from the base of a wall. It is assumed that deterioration develops uniformly over the wall's length. Hence, 3 longitudinal deterioration zones are defined, as shown in Fig. 2; the height of zone 1 is 10cm, while the height of each of zones 2 and 3 is 20cm. Masonry material is notionally removed from the 'deteriorated' wall region (i.e. from the 3 deterioration zones) in 15 phases, as described in Table 1. In each phase, the masonry material removed from a zone has a constant thickness 0-25cm within this zone, i.e. the deterioration thickness is constant over the length and height of a zone. At any phase, each zone may have a different deterioration thickness, however the deterioration thickness in a lower zone is always larger or equal to the one of a higher zone. The maximum height of the 'deteriorated' wall region is 50cm, which is encountered when all 3 zones have non-zero deterioration thicknesses. Characteristic deterioration phases are illustrated in Fig. 3.

Each of the 15 material removal phases defined corresponds to a deterioration scenario of the masonry wall. A FE analysis is conducted to determine the load carrying capacity of the wall for each deterioration scenario. Through the 'gradual' material removal in phases and the FE analysis in each phase, we can monitor the wall's structural behaviour for deterioration effects of increasing severity.

In order to facilitate the reference to deterioration phases, a deterioration index I_{det} is defined, which quantitatively describes the extent of artificial deterioration assumed. Referring to the rectangular cross-section 50cm×300cm (thickness×height) of the masonry wall, we concentrate on its lowest square of 50cm×50cm, which includes the 3 deterioration zones mentioned earlier; this base part of the wall has a cross-sectional area A_b=2500cm^2. Hence, the deterioration index is expressed as:

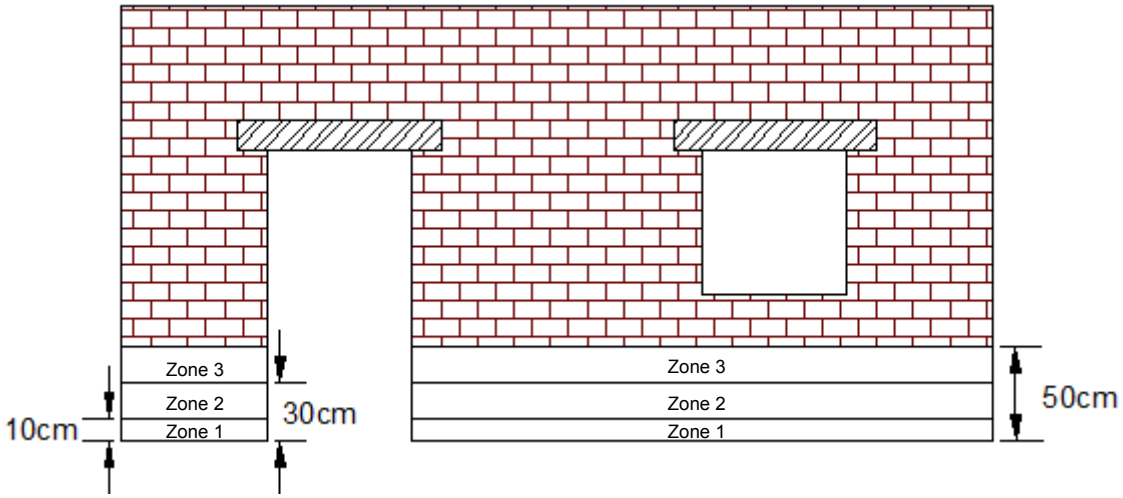


Figure 2: Side view of typical masonry wall showing the 3 longitudinal deterioration zones at the base.

Deterioration phase	I_{det}	Deterioration thickness [cm]		
		Zone 1	Zone 2	Zone 3
0	0.00	0	0	0
1	0.02	5	0	0
2	0.04	10	0	0
3	0.08	10	5	0
4	0.12	10	10	0
5	0.14	15	10	0
6	0.18	15	15	0
7	0.22	15	15	5
8	0.26	15	15	10
9	0.30	15	15	15
10	0.32	20	15	15
11	0.36	20	20	15
12	0.40	20	20	20
13	0.42	25	20	20
14	0.46	25	25	20
15	0.50	25	25	25

Table 1: Definition of deterioration phases.

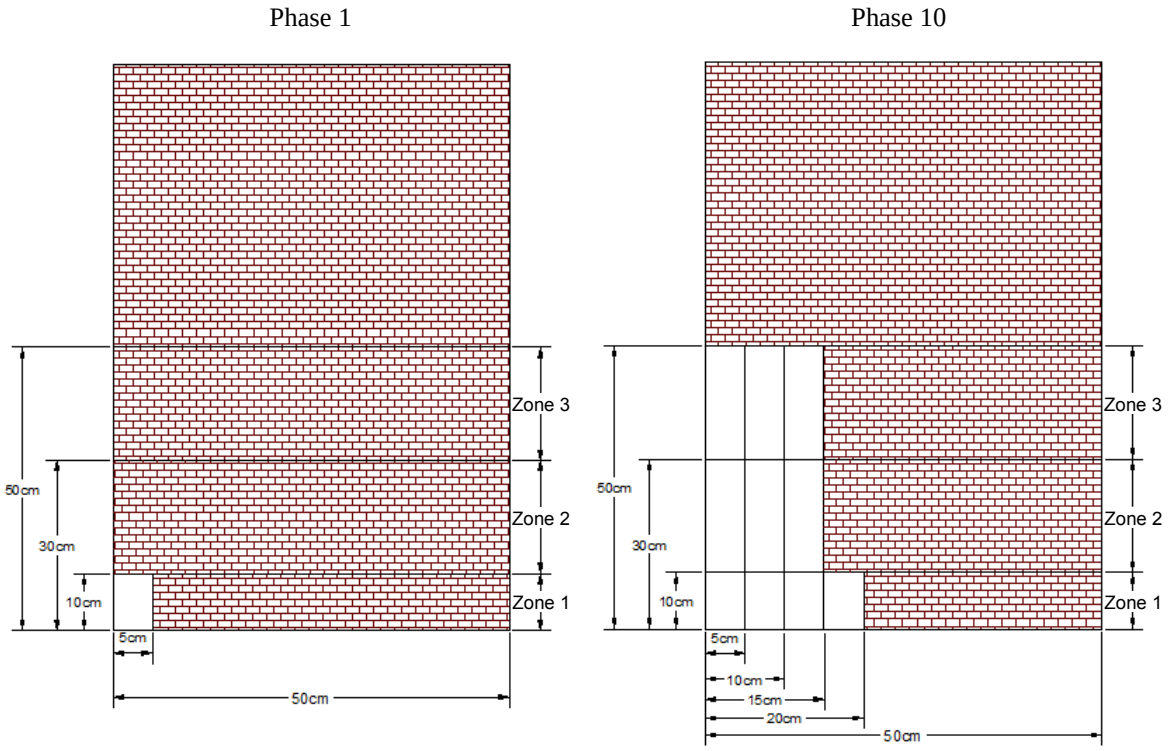


Figure 3: Cross-sectional view at the base of a masonry wall – illustration of characteristic deterioration phases.

$$I_{det} = \frac{A_{b,det}}{A_b}, \tag{1}$$

where $A_{b,det}$ is the cross-sectional area of the wall, which is notionally removed to simulate the masonry material lost due to base deterioration. For example, in deterioration phase 10 (Fig. 3), the removed wall material has a cross-sectional area $A_{b,det}$=20cm×10cm+15cm×40cm=800cm^2, which yields a deterioration index I_{det}=800/2500=0.32. Thus, I_{det} expresses the reduction of the effective load-bearing section at the base of the wall and takes values between 0 (no deterioration – phase 0) and 0.5 (maximum deterioration – phase 15). Table 1 gives the indexes I_{det} for all deterioration phases considered.

4 FINITE ELEMENT MODELLING AND ANALYSIS OF MASONRY WALLS

Various analysis and assessment approaches for masonry structures can be found in the literature (e.g. [6]). In the present work, computational analysis of the in-plane response of masonry wall configurations is conducted with Abaqus/CAE [7] using plane stress FE continuum models (Fig. 4). In the numerical models examined, both the masonry walls and the openings' timber lintels, which are commonly incorporated in traditional constructions, are represented. All bodies are discretized into structured meshes composed of 4-noded 2D bilinear plane stress quadrilateral elements with reduced integration and hourglass control (CPS4R). The plane stress thickness of the undamaged masonry elements and of the lintels is defined as 50cm. Depending on the damage pattern examined, different plane stress thicknesses are assigned to areas of the masonry subjected to deterioration.

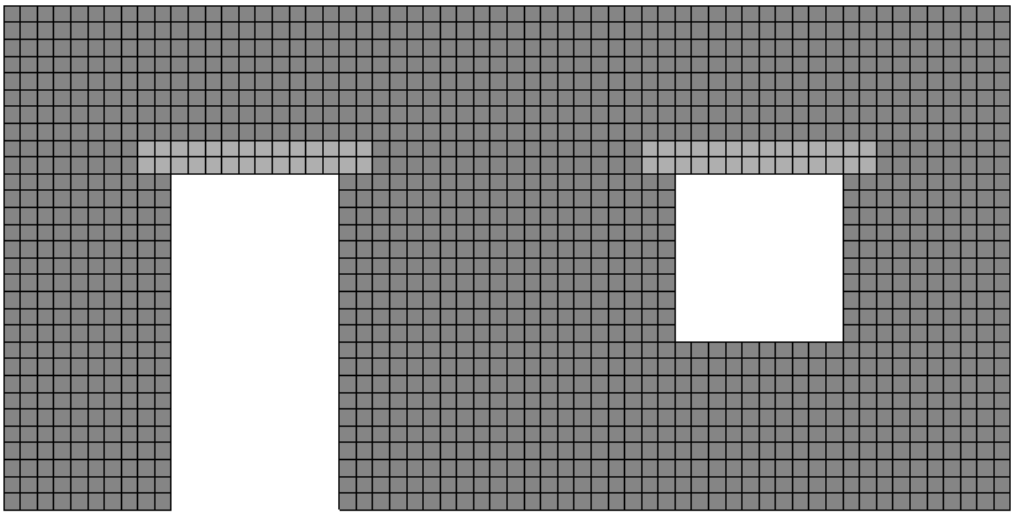


Figure 4. Side view of typical masonry wall and its FE mesh.

Masonry is numerically handled in the context of a macro-modelling strategy. The masonry constituents (i.e. the units, mortar and the unit-mortar interfaces) are hence smeared out into a fictitious homogeneous continuum represented by a FE mesh. The behaviour of the homogenized masonry medium is simulated using the damaged plasticity constitutive model [8], which has been successfully used in FE analyses of masonry structures [9,10]. The adopted model uses brittle fracture concepts in combination with scalar (isotropic) damage plasticity to represent the inelastic response of a material. Two principal damage mechanisms are assumed: tensile cracking and compressive crushing.

The modelling parameters used for the formulation of the constitutive law are based on relevant experimental data reported in the literature. Density is specified as ρ=2500kg/m^3 according to the properties assessed in [11] and the parameters used in [12] for the simulation of stone masonry structures. The elastic modulus and Poisson's ratio are defined as E=3000MPa and ν=0.15, respectively, in line with the information given in [13] and [14] for single-leaf calcarenite stone masonry walls and the range of experimental results summarized in [15].

Under uniaxial compression, initial yielding is assumed to be followed by hardening behaviour up to the maximum allowable stress. After the ultimate strength is attained, stress softening is assumed to develop. Compressive response is specified by expressing compressive stresses as a function of plastic (crushing) strains (Fig. 5(a)). For this purpose, the polynomial stress-strain relation developed in [16] for tuff masonry is adopted:

$$\bar{\sigma}_c = \begin{cases} -0.7144\bar{\varepsilon}_c^3 + 0.4549\bar{\varepsilon}_c^2 + 1.2595\bar{\varepsilon}_c & \text{for } 0 \le \bar{\varepsilon}_c \le 1.12 \\ -0.0107\bar{\varepsilon}_c^3 + 0.1388\bar{\varepsilon}_c^2 - 0.6487\bar{\varepsilon}_c + 1.545 & \text{for } 1.12 \le \bar{\varepsilon}_c \le 4 \end{cases} \quad (2)$$

In the above equation, $\bar{\sigma}_c$ and $\bar{\varepsilon}_c$ are normalized values obtained by dividing the stress with the compressive strength ($\bar{\sigma}_c = \sigma / f_c$) and the axial deformation with the strain at peak stress ($\bar{\varepsilon}_c = \varepsilon / \varepsilon_c$). A stress-strain expression analogous to (2) has been derived in [17] for adobe masonry. Material non-linearity in compression is considered to initiate at stresses exceeding 30% of the bearing capacity. Compressive strength is set as f_c=2MPa based on the data quoted in [16], while strain at peak compressive strength is computed as ε_c=0.00094mm/mm after solving Eq. (2).

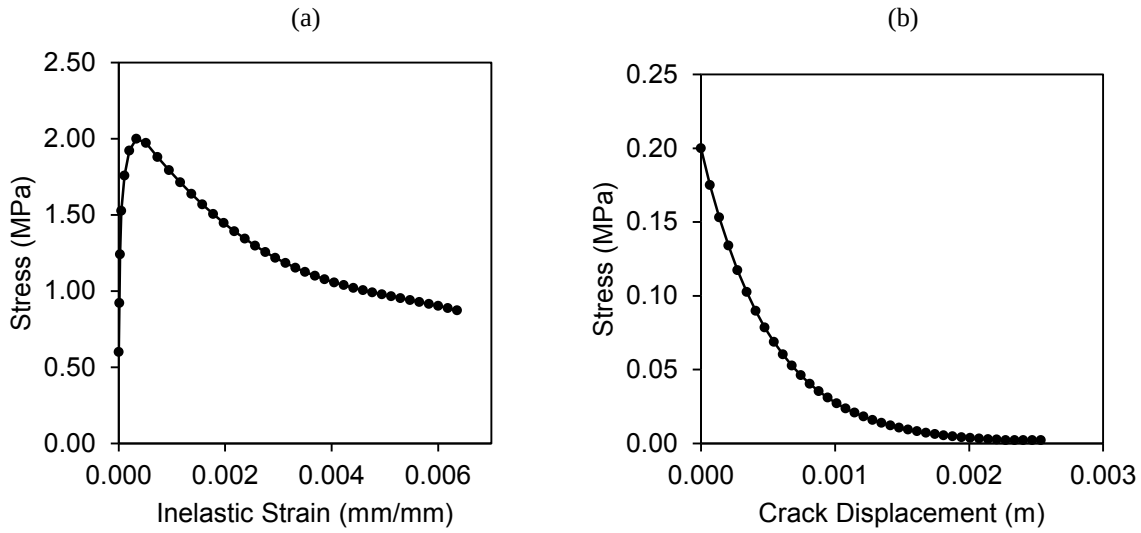


Figure 5: Compressive stress-plastic strain and tensile stress-crack displacement input data specified for the homogenized stone masonry medium in compression (a) and tension (b), respectively.

Under uniaxial tension, masonry's behavior is presumed to be linearly elastic up to the point where the failure stress is reached. Beyond the failure stress, softening stress-strain response is specified using the exponential model proposed in [18]:

$$\sigma_t = f_t \exp\left(-\frac{h f_t}{G_f}\varepsilon_t^{ck}\right). \tag{3}$$

In equation (3), f_t is the tensile strength of the masonry, assumed equal to 10% of the compressive strength, G_f is the tensile fracture energy, selected as G_f=100N/m [19], ε_t^{ck} is the tensile cracking strain and h is the characteristic crack length that is estimated from the elements' average dimensions (h_x, h_y) as $h = \sqrt{2h_x h_y}$ [20]. The global size of the masonry elements' sides is set as h_x=h_y=10±1cm, in order to satisfy the energy criterion associated with the tension softening model used:

$$h \le \frac{G_f E}{f_t^2}. \tag{4}$$

Softening behaviour is assigned by converting tensile plastic strains to equivalent cracking displacements using the elements' characteristic crack length and by specifying stress-cracking displacement tabular data (Fig. 5(b)).

The complete description of the yield surface, in addition to the above, requires the definition of four plasticity parameters. Default values suggested in [7] for concrete and cement-based materials are hereby adopted. The rate at which the hyperbolic flow potential approaches its asymptote is set as e=0.1. The ratio between the initial equibiaxial and the initial uniaxial compressive yield stresses is defined as σ_{b0}/σ_{c0}=1.16. Parameter K_c that affects the shape of the yield surface in the deviatoric plane is set equal to 0.67. Based on [21], a value of ψ=12º is specified for the dilation angle controlling the plastic volumetric strain developed upon plastic shearing.

The timber lintels of the masonry structures examined are modelled to exhibit linearly elastic and isotropic behaviour. The material parameters used are also drawn from the literature [22,23] and are as follows: density ρ=670kg/m^3; Young's modulus E=7000MPa; Poisson's ratio v=0.3.

Perfect bonding is assumed to exist between the timber members and the walls. Therefore, common nodes are assigned at the areas where the lintels are in contact with the masonry. The walls' base is considered to be pinned and hence translational degrees of freedom in the x- and y-directions are constrained.

As regards gravitational loads, the self-weight of each wall analysed is taken into account, as well as a dead load corresponding to a 20cm thick concrete slab supported by the wall; moreover, a live load of 2kN/m^2 is applied. The wall is also subjected to a horizontal seismic load, which is simulated as a lateral displacement enforced at the top of the wall. Specifically, a lateral displacement of up to 5mm is incrementally imposed at each top node of the wall.

Each FE analysis is conducted in two phases: first, the gravitational (dead and live) loads are applied in up to 100 increments; then, the lateral displacements are imposed in up to 1000 increments at the wall's top nodes. Both phases are performed using a general non-linear static procedure with automatic stabilization employing the full Newton solution scheme. The effects of geometric non-linearities are taken into account in both analysis phases.

5 FINITE ELEMENT SIMULATION RESULTS

The main structural response quantity monitored during a masonry wall's FE simulation is the base shear developed due to the lateral top displacement imposed. The base shear is calculated by summing the lateral reactions developed at all base nodes of the wall, which are pinned. Thus, force-displacement curves are constructed, which describe the relation between the incrementally enforced lateral displacement and the corresponding base shear developed. The maximum base shear observed at any instance of the FE analysis represents the lateral in-plane strength (carrying capacity) of the masonry wall analysed.

Figure 6 presents the force-displacement curves derived by the FE analyses performed for the 4 masonry wall configurations without removed material to simulate base deterioration. The 4 curves have similar highly non-linear shapes, which are typical in masonry structural analysis: a non-linear ascending branch is followed by a post-peak softening branch. In all 4 intact walls, the maximum base shear is attained for a lateral top displacement of 1.0-1.5mm, while a significant residual carrying capacity is observed at the end of the FE analysis (at lateral top displacement of 5mm). It is noted that, in all other FE analyses conducted with assumed base deterioration, force-displacement curves have shapes that are similar to the ones depicted in Fig. 6.

The effect of openings on the intact wall's lateral strength is evident in Fig. 6. The maximum base shear for the wall without openings is 473kN; for the walls with openings, it reduces to 370kN (window opening), 326kN (door opening) and 311kN (door and window openings). The 4 configurations exhibit differences also in terms of the crack pattern sustained by the structure at the end of the FE analysis (Fig. 7). The tensor diagrams with the maximum tensile plastic strains computed at the elements' integration points, which are presented in Fig. 7, actually illustrate crack patterns, because the direction of the vector normal to a crack plane is assumed to be parallel to the direction of the maximum principal plastic strain [7]. Thus, due to the different configurations of openings, the 4 walls have significantly different lateral strengths, but also quite different failure modes.

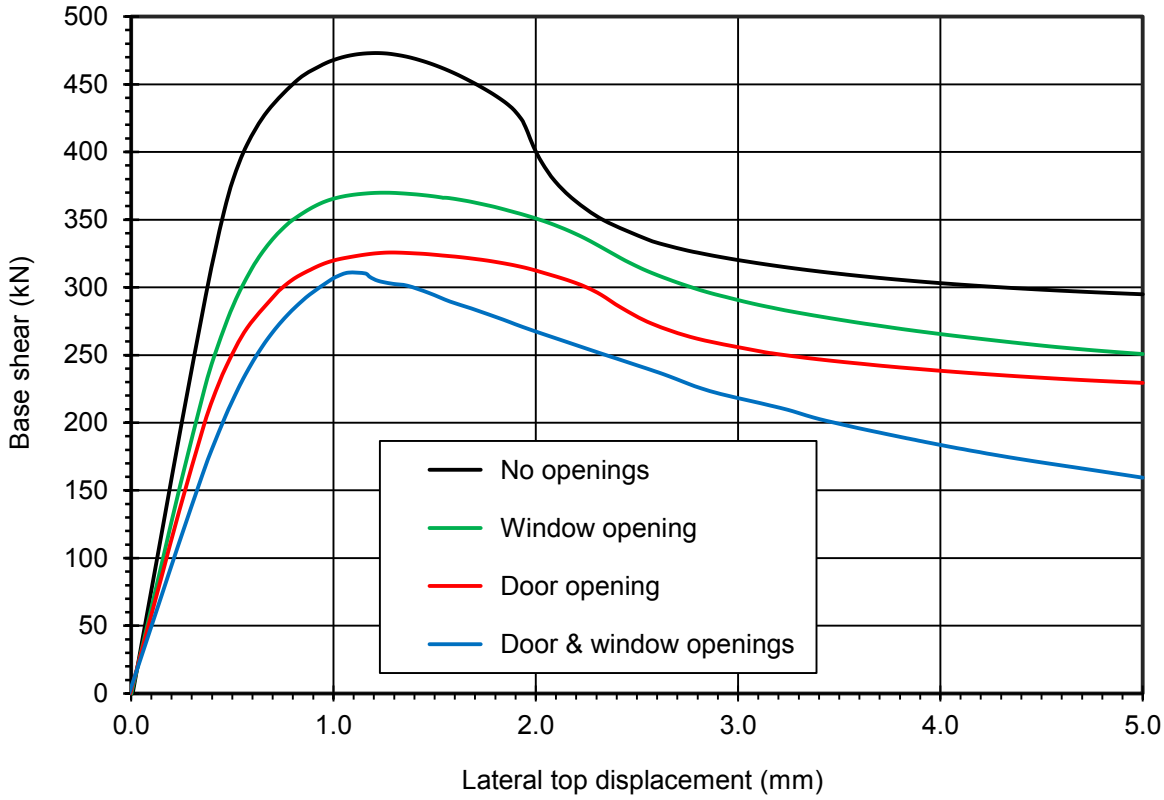


Figure 6: Force-displacement curves obtained for the 4 masonry wall configurations in their intact state (without induced base deterioration, I_{det}=0).

For the deterioration phases of Table 1, the variation of the wall's lateral strength is depicted in Fig. 8. Increasing the extent of deterioration generally leads to lower lateral strength for all 4 masonry wall configurations. However, the most significant effect is observed for the wall without openings. More specifically, compared to the intact state (I_{det}=0), the maximum deterioration phase (I_{det}=0.50) results in about 27% reduction of the maximum base shear for the wall without openings; for the walls with openings, the corresponding reductions are about 19% (window opening), 20% (door opening) and 11% (door and window openings). It is also interesting to notice that the wall with the door opening, in its intact state, is stronger that the wall with door and window openings. But, when base deterioration is induced, the wall with the two openings is stronger.

As regards the developed failure modes when base deterioration is induced, the wall without openings and the wall with the door opening actually exhibit the crack patterns of Figs 7(a) and 7(c), respectively, regardless of the adopted I_{det}-value. In the other two wall configurations, however, base deterioration changes the developed crack pattern after a certain I_{det}-value. Hence, Fig. 9 illustrates the crack pattern of the wall with window opening for I_{det}=0.50, which presents some differences compared to the crack pattern of Fig. 7(b). Moreover, Fig. 10 shows two crack patterns of the wall with door and window openings that are completely different compared to the crack pattern of Fig. 7(d). Thus, the presence of base deterioration may significantly affect not only the strength of a masonry wall, but also the cracking initiation and propagation mechanism and the ultimate failure mode.

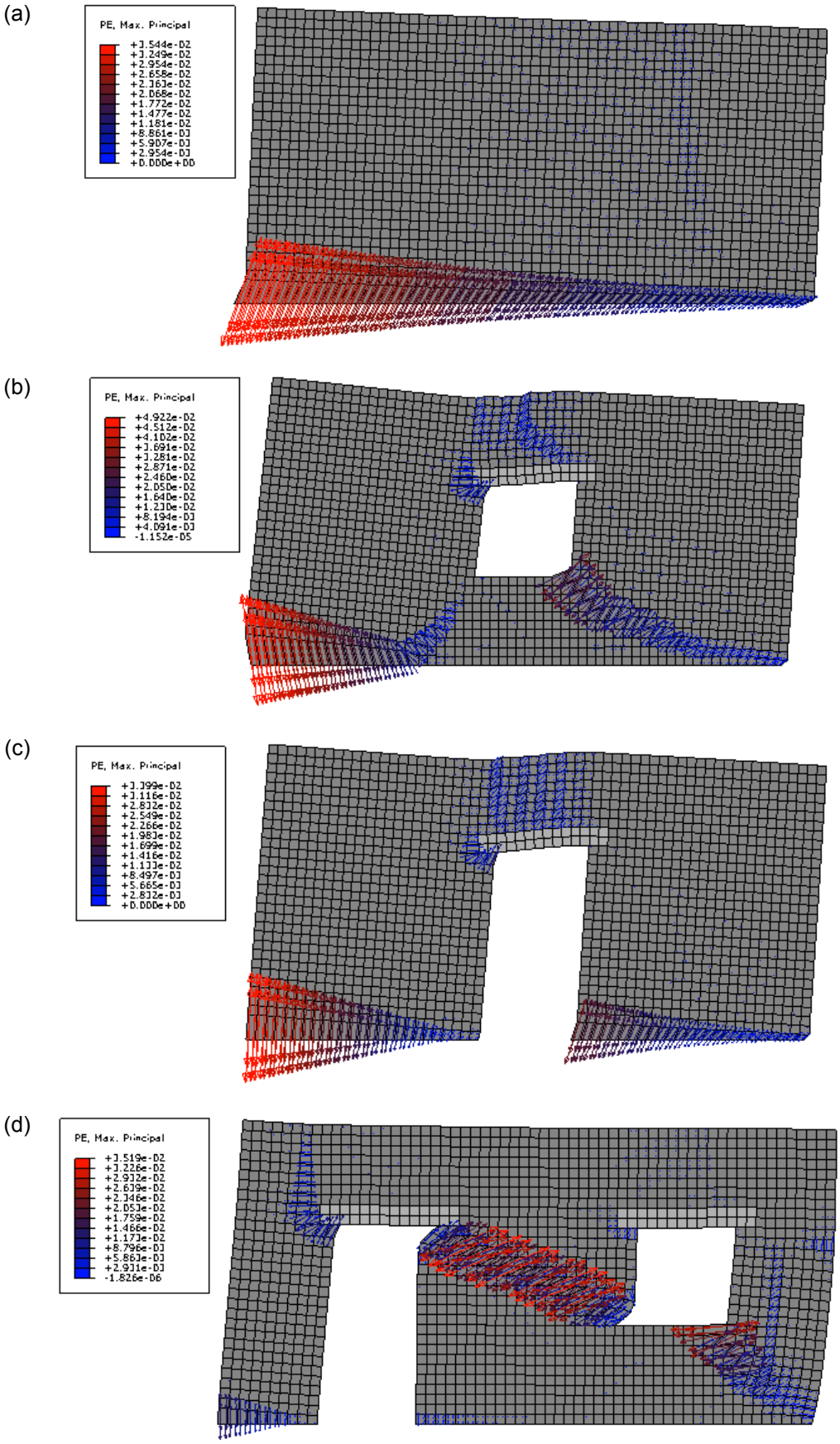


Figure 7: Deformed meshes at the final FE analysis step with tensor diagrams showing the maximum tensile plastic strains computed at the element integration points for the 4 intact masonry wall configurations (I_{det}=0).

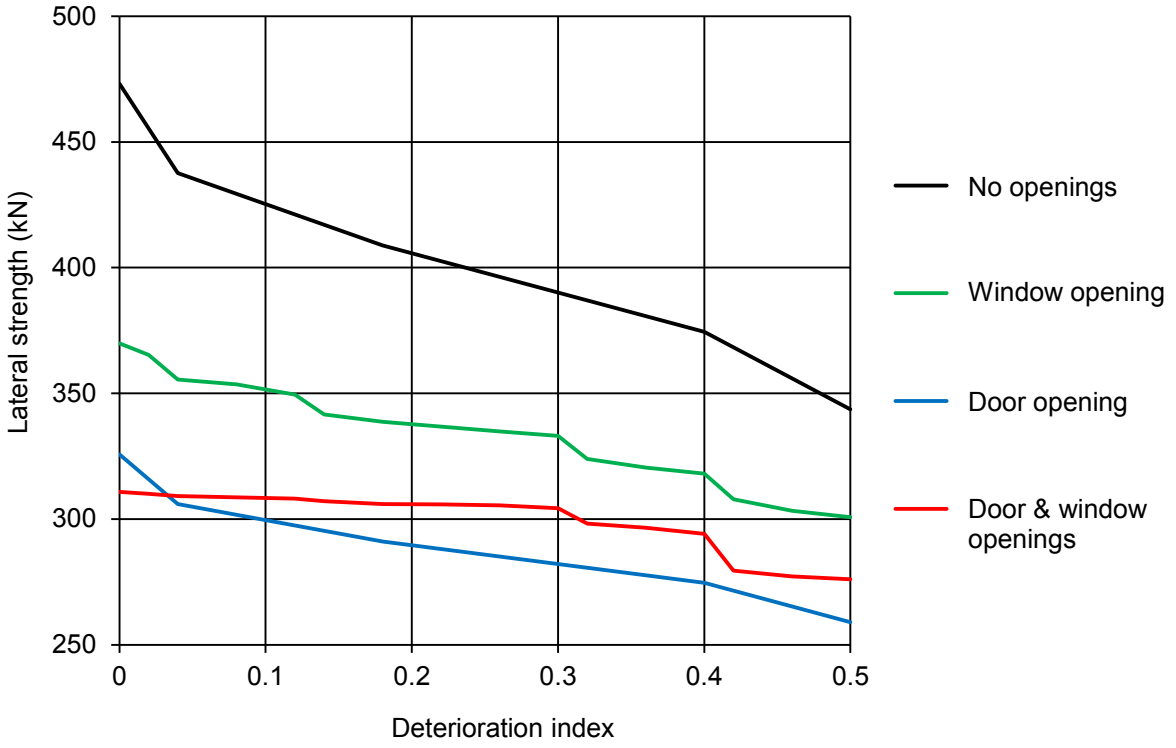


Figure 8: Lateral resistance versus deterioration index (I_{det}) relation obtained for the 4 masonry wall configurations.

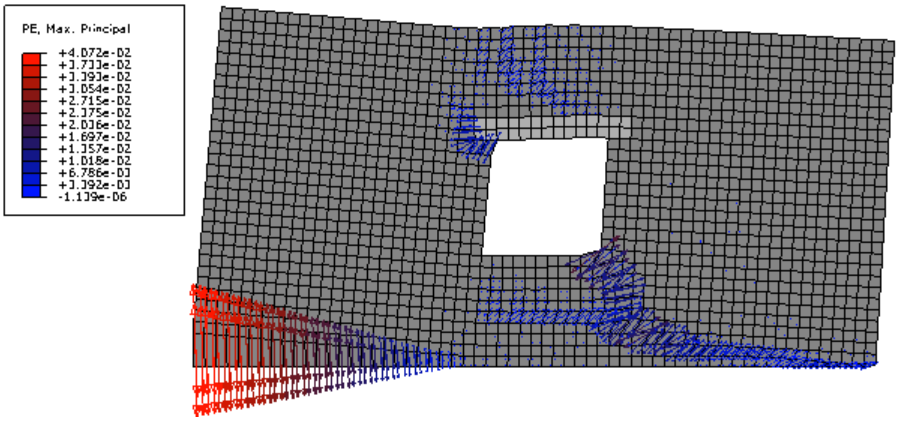


Figure 9: Deformed mesh at the final FE analysis step with tensor diagram showing the maximum tensile plastic strains computed at the element integration points for the deteriorated masonry wall with window opening (I_{det}=0.50).

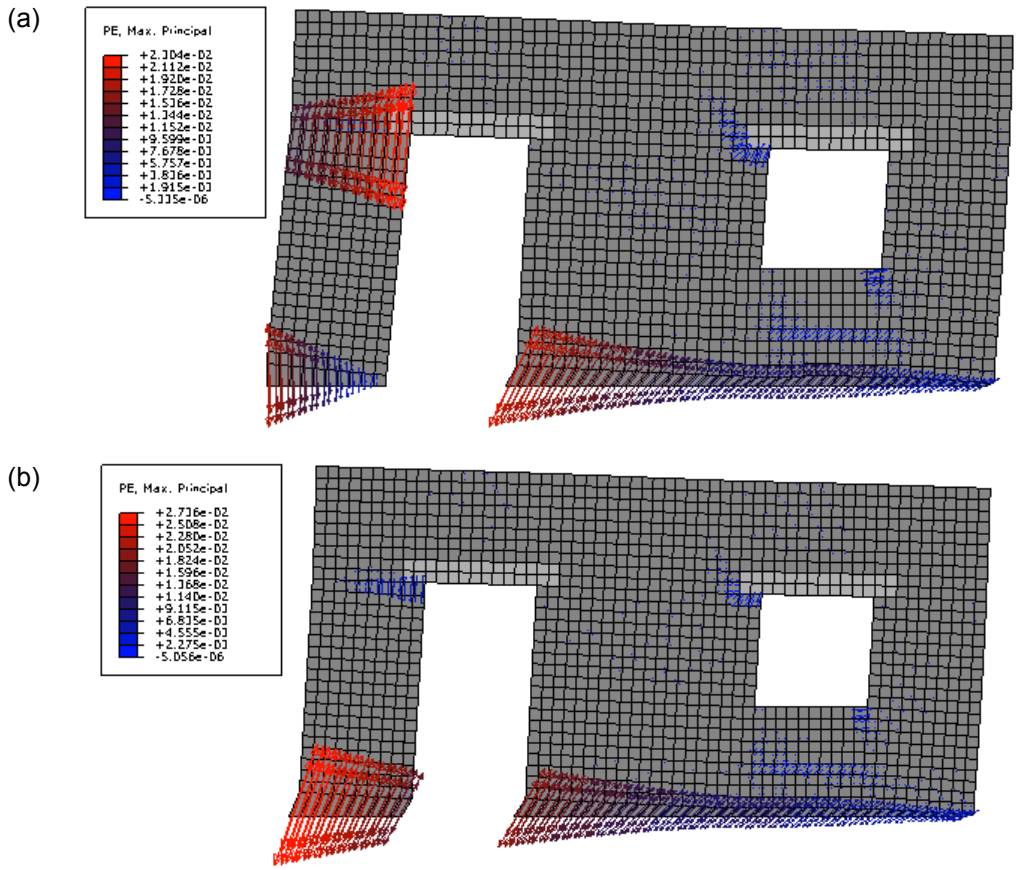


Figure 10: Deformed meshes at the final FE analysis step with tensor diagrams showing the maximum tensile plastic strains computed at the element integration points for the deteriorated masonry wall with door and window openings; (a) I_{det}=0.32, (b) I_{det}=0.50.

6 CONCLUSIONS

In this work, the aim was to numerically investigate the capability of masonry walls to sustain local damage without allowing extensive or global failure, i.e. to estimate their structural damage tolerance. More specifically, plane stress non-linear FE analyses were performed to examine the lateral in-plane strength of masonry walls under various deterioration scenarios, which were realized by notionally removing material from the base of the walls. Four wall configurations without or with window/door openings were assessed with respect to the deterioration scenarios specified. According to the obtained FE analysis results, the presence of openings and/or base deterioration in a wall result in significantly reduced lateral strength compared to an intact wall without openings. The presence of openings and/or base deterioration can also have an effect on the crack pattern developed in the wall and its eventual failure mode.

More work along the research path followed in this paper is certainly needed. It is planned to examine also masonry walls with other geometrical characteristics. In addition, the influence of the boundary conditions assumed at the foundation level could be assessed. Last but not least, future work will investigate the effect of base deterioration on the out-of-plane structural response of masonry walls damaged by base deterioration.

REFERENCES

[1] L. Binda, A. Anzani, Structural behavior and durability of stone masonry. In: *Saving our Architectural Heritage*, Chichester, Wiley, 1997.

[2] E. Doehne, C.A. Price, *Stone conservation: An overview of current research*. Getty Conservation Institute, Los Angeles, 2010.

[3] M. Steiger, A.E. Charola, K. Sterflinger, Weathering and deterioration. In: *Stone in Architecture: Properties, Durability*, Berlin, Springer, 2011.

[4] F.G. Dimes, J. Ashurst, *Conservation of building and decorative stone*. Routledge, New York, 2011.

[5] R. Illampas, I. Ioannou, D.C. Charmpis, Overview of the pathology, repair and strengthening of adobe structures. *International Journal of Architectural Heritage*, **7**, 165-188, 2013.

[6] S.J. Pantazopoulou, *State of the art report for the analysis methods for unreinforced masonry heritage structures and monuments*. OASP, Athens, 2013.

[7] Simulia Corp., *Abaqus 6.10 theory manual*. Dassault Systèmes, Rising Sun Mills, 2009.

[8] J. Lubliner, J. Oliver, S. Oller, E. Oñate, E. A plastic-damage model for concrete, *International Journal of Solids and Structures*, **25**, 299-326, 1989

[9] P. Agnihotri, V. Singhal, D.C. Rai, Effect of in-plane damage on out-of-plane strength of unreinforced masonry walls. *Engineering Structures*, **57**, 1-11, 2013.

[10] R. Illampas, D.C. Charmpis, I. Ioannou, Laboratory testing and finite element simulation of the structural response of an adobe masonry building under horizontal loading. *Engineering Structures*, **80**, 362-376, 2014.

[11] N. Mazzon, *Influence of grout injection on the dynamic behaviour of stone masonry buildings*. PhD Thesis, University of Padova, Italy, 2010.

[12] B. Silva, A. Pappas, M.R. Valluzzi, F. da Porto, C. Modena, Calibration of a material behavior model for the simulation of multi-leaf stone masonry structures: Experimental case study application. In: *Proceedings of 15th World Conference on Earthquake Engineering*, Lisbon, Portugal, 2012.

[13] S. Ganduscio, L. La Mendola, G. Zingone, Comportamento ciclico di sezioni presso inflesse in muratura. *Atti del Convegno Nazionale 'La Meccanica delle murature tra teoria e progetto'*, Messina, Italy, 1996.

[14] M. Stella, Murature in tufo calcareo: Aspetti sperimentali sulle resistenze meccaniche. *Atti del Convegno Internazionale su 'Le pietre da Costruzione in Puglia'*, Quaderno IRIS-CNR n.16, Unione Tipografica Ed., Bari, Italy, 1993.

[15] G. Marcari, G. Fabbrocino, P.B. Lourenco, Mechanical properties of tuff and calcarenite stone masonry panels under compression. In: *Proceedings of 8th International Masonry Conference*, Dresden, Germany, 2010.

[16] N. Augenti, F. Parisi, Constitutive models for tuff masonry under uniaxial compression. *Journal of Materials in Civil Engineering*, **22**, 1102-1111, 2010.

[17] R. Illampas, I. Ioannou, D.C. Charmpis, Adobe bricks under compression: experimental investigation and derivation of stress-strain equation. *Construction and Building Materials*, **53**, 83-90, 2014.

[18] P.B. Lourenço, Anisotropic softening model for masonry plates and shells. *ASCE Journal of Structural Engineering*, **126**, 1008-1016, 2000.

[19] N. Mendes, P.B. Lourenço, Comparison of different seismic non-linear analyses of an ancient masonry building. In: *Proceedings of 11th Canadian Masonry Symposium*, Toronto, Ontario, 2009.

[20] M. Dhanasekar, Review of modelling of masonry shear. *International Journal of Advances in Engineering Sciences and Applied Mathematics*, **2**, 106-118, 2010.

[21] P.B. Lourenco, *Computational strategies for masonry structures*. PhD Thesis, Faculty of Civil Engineering, Delft University of Technology, 1996.

[22] E.S. Katsaragakis, *Timber construction*. NTUA Academic Publications, Athens, 2000.

[23] D.W. Green, J.E. Winandy, D.E. Kretschman, Mechanical properties of wood. In: *Wood handbook: Wood as an engineering material*, General Technical Report FPL-GTR-113, U.S. Department of Agriculture, Forest Service, Forest Products Laboratory, Madison WI, 1999.

COMPDYN 2015
5th ECCOMAS Thematic Conference on
Computational Methods in Structural Dynamics and Earthquake Engineering
M. Papadrakakis, V. Papadopoulos, V. Plevris (eds.)
Crete Island, Greece, 25–27 May 2015

FROM THE NOTIONS OF NONLINEARITY TOLERANCES TOWARDS A DEFICIENCY IN COMMERCIAL TRANSIENT ANALYSIS SOFTWARES AND ITS SOLUTION

A. Soroushian[1], P. Wriggers[2], and J. Farjoodi[3]

[1] Structural Engineering Research Center, International Institute of Earthquake Engineering and Seismology (IIEES)
S.Lavasani (Farmaniyeh), North Dibaji, West Arghavn, No. 21, Tehran 19537, Iran
a.soroushian@iiees.ac.ir

[2] Institute of Continuum Mechanics, University of Hannover
Applestrasse 11, Hannover 30167, Germany
wriggers@ikm.uni-hannoer.de

[3] School of Civil Engineering, University College of Engineering, University of Tehran
Enghelab Avenue, Tehran 11365
jfarjood@ut.ac.ir

Keywords: Nonlinear Analysis, Static, Dynamic, Tolerance, Halt of Analysis, Accuracy.

Abstract. *The notions of nonlinearity tolerances in static and dynamic analyses are reviewed. A deficiency in conventional nonlinear dynamic analysis, also existing in the transient analysis commercial soft wares, is recognized. A simple approach to practically eliminate the deficiency is proposed, and its adequacy is demonstrated numerically.*

1 INTRODUCTION

The true behavior of structural systems is nonlinear and dynamic. For nonlinear dynamic analysis of structural systems, the broadly accepted approach is to define the structural and mathematical models, discretize the mathematical models in space, and solve the resulting ordinary initial value problems in time. In view of the typical initial value problem defining the structural motion, stated below [1-3]:

$$\begin{aligned} &\mathbf{M}\ddot{\mathbf{u}}(t)+\mathbf{f}_{\text{int}}(t)=\mathbf{f}(t) \qquad 0\le t<t_{end}\\ &\mathbf{u}(t=0)=\mathbf{u}_0\\ &\dot{\mathbf{u}}(t=0)=\dot{\mathbf{u}}_0\\ &\mathbf{f}_{\text{int}}(t=0)=\mathbf{f}_{\text{int}_0}\\ &\mathbf{Q}\le 0 \end{aligned} \tag{1}$$

(t and t_{end} imply the time and the duration of the dynamic behavior; $\mathbf{M}$ is the mass matrix; $\mathbf{f}_{\text{int}}$ and $\mathbf{f}(t)$ stand for the vectors of internal force and excitation; $\mathbf{u}(t)$, $\dot{\mathbf{u}}(t)$, and $\ddot{\mathbf{u}}(t)$ denote the vectors of displacement, velocity, and acceleration; $\mathbf{u}_0$, $\dot{\mathbf{u}}_0$, and $\mathbf{f}_{\text{int}_0}$ define the initial status of the model (regarding the essentiality of considering $\mathbf{f}_{\text{int}_0}$ in Eqs. (1), also see [4]); and finally, $\mathbf{Q}$ represents some restricting conditions, in problems involved in nonlinearity; see [5, 6]), the most versatile analysis method is time integration [7, 8]. The process of time integration is schematically displayed in Figure 1, and in addition, for nonlinear analyses, at time stations, where nonlinearities are detected, some iterative computation, for localizing the nonlinearities, is strongly recommended [3, 9-12]. Before each nonlinearity iteration, conditions not to implement the iteration are being checked, and lead to either stop of the iteration and continuation of the analysis, repeat of the iterative computation, or stop of the iteration and halt of the analysis, i.e. (a) stop of the iteration after k iterations and continuation of the analysis, expressed as:

$$\begin{aligned} i=1,2,3\ldots k-1 \;:\quad & \left\| {}^{i}\delta \right\| > \bar{\delta}\\ i=k<K \;:\quad & \left\| {}^{i}\delta \right\| \le \bar{\delta} \end{aligned} \tag{2}$$

(b) Another iteration, formulated as

$$\begin{aligned} & i=1,2,3\ldots k \;:\quad \left\| {}^{i}\delta \right\| > \bar{\delta}\\ & k<K \end{aligned} \tag{3}$$

and (c) Stop of the iteration and halt of the analysis, stated as

$$\begin{aligned} & i=1,2,3\ldots k \;:\quad \left\| {}^{i}\delta \right\| > \bar{\delta}\\ & k=K \end{aligned} \tag{4}$$

In Eqs. (2)-(4), i is an indicator for the nonlinearity iteration, k stands for the number of iterations carried out, equivalently introducing the last or current iteration, ${}^{i}\delta$ implies the residual of a balance equation in terms of force, displacement, energy, momentum, etc. at the i^{th} iteration, $\bar{\delta}$ is the tolerance introducing the maximum residual acceptable, and finally, K denotes the maximum number of iterations acceptable, at each detection of nonlinearity, essential to prevent useless unending iterations in presence of dominating round off errors.

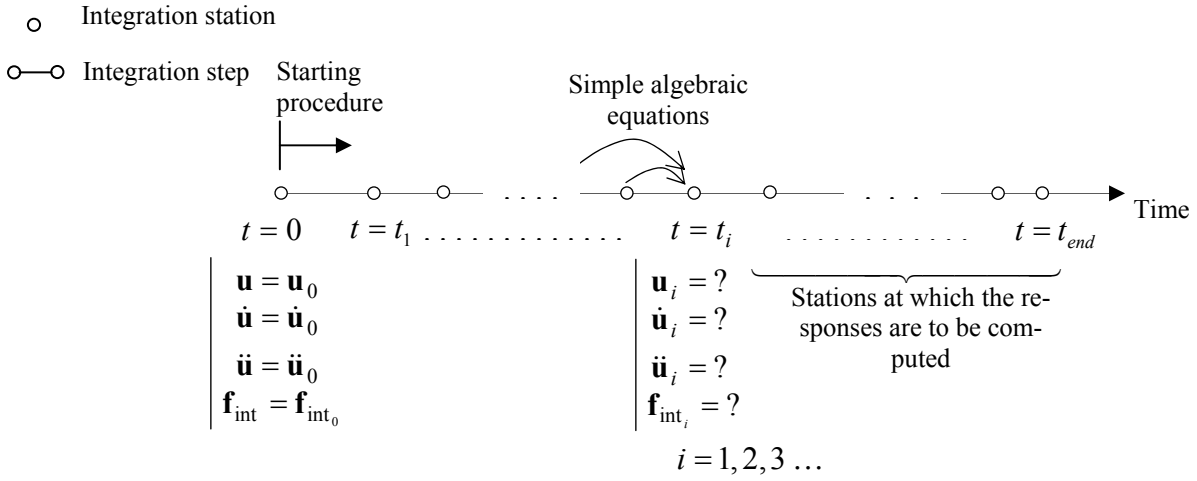


Figure 1: A schematic illustration of the time integration process.

In static nonlinear analyses, Eq. (1) is replaced with

$$\begin{aligned} &\mathbf{f}_{\text{int}} = \mathbf{f} \\ &\mathbf{Q} \le 0 \end{aligned} \tag{5}$$

and the step-by-step consideration of the $\mathbf{f}$ at sequential time instant throughout the time interval $[0 \quad t_{end}]$ is being replaced with incremental implementation of $\mathbf{f}$, i.e.

$$\begin{aligned} &{}_0\mathbf{f} = \overline{\mathbf{O}} \\ &{}_j\mathbf{f} = {}_{j-1}\mathbf{f} + \Delta\mathbf{f} \quad , \quad j = 1, 2, \ldots n \\ &\Delta\mathbf{f} = \frac{\mathbf{f}}{n} \end{aligned} \tag{6}$$

where, n denotes the total number of the increments and a left subscript implies the amount and value of the argument. Nevertheless, Eqs. (2)-(6) remain unchanged and valid in both static and dynamic analyses (see [9-11, 13]). Therefore, it is reasonable to expect differences between the notions of the parameters in Eqs. (2)-(4), in static and dynamic analyses. This paper is dedicated to this purpose, based on which, a deficiency in the current analysis soft wares is also introduced and suggestions for overcoming the deficiency are stated.

2 NOTIONS OF THE TOLERANCES IN STATIC AND DYNAMIC ANALYSES

In a static analysis, the analysis in each increment is exact, unless some nonlinearity is detected. To say better, at the j^{th} increment,

$$\begin{aligned} &\mathbf{K}\ {}_j\Delta\mathbf{u} = {}_j\Delta\mathbf{f} \\ &{}_j\mathbf{u} = {}_{j-1}\mathbf{u} + {}_j\Delta\mathbf{u} \\ &\qquad\qquad j = 1, 2, 3, \ldots \end{aligned} \tag{7}$$

where, ${}_j\mathbf{K}$ is a constant matrix representing the stiffness, at the application of the j^{th} increment of loading

$${}_j\Delta\mathbf{f} = \Delta\mathbf{f} \tag{8}$$

Accordingly, ${}_j\Delta\mathbf{u}$ is available exactly, and hence, when detecting nonlinearities, the residuals are representations of deviations from the exact solutions. Therefore, the tolerances stand for the maximum acceptable inaccuracy, at the detections of nonlinearities.

In the dynamic case, Eq. (7) is replaced with

$$\begin{aligned} {}_j\mathbf{M}\ddot{\mathbf{u}}+{}_j\mathbf{C}\dot{\mathbf{u}}+{}_j\mathbf{K}\mathbf{u}={}_j\mathbf{f} \quad &, \quad t_{j-1}\le t<t_j \\ \mathbf{u}\left(t=t_{j-1}\right)&=\mathbf{u}_{j-1} \\ \dot{\mathbf{u}}\left(t=t_{j-1}\right)&=\dot{\mathbf{u}}_{j-1} \end{aligned} \tag{9}$$

to be generally and conventionally solved for $\mathbf{u}_j$ and $\dot{\mathbf{u}}_j$, by a time integration scheme. Time integration methods generally result in approximate responses [4, 14, 15]. Consequently, different from static analyses, where, ${}_j\mathbf{u}$ can be computed exactly, in dynamic analyses, $\mathbf{u}_j$ and $\dot{\mathbf{u}}_j$ are available approximately (even in totally linear analyses). Therefore, the residuals can not represent deviations from exact solutions, but only, stand for the differences between the carried out analyses and the ideal analyses, for which, throughout the analyses,

$$\delta = 0 \tag{10}$$

Accordingly, in dynamic analyses, tolerances are merely upper bound controls for the above mentioned differences, and do not necessarily control the inaccuracy of the computations at the detected nonlinearities. In other words, different from the tolerances in static analyses, the tolerances in dynamic analyses do not represent upper limits for the computational errors, and hence, disregarding them would not necessarily deteriorate the accuracy. This is specifically true, when the contribution of the errors because of the approximate formulation of time integration is considerable compared to the errors originated in nonlinearity.

3 A DEFIECIENCY IN TRANSIENT ANALYSIS COMMERCIAL SOFTWARES AND A SIMPLE SOLUTION FOR IT

As implied in the last lines of Section 2, in nonlinear dynamic analyses, no accuracy can be guaranteed, by nonlinearity iterations and considering specific tolerances. Consequently, Eq. (4), and the halt of the analyses, via Eq. (4), loses its essentiality.

Currently, the commercial soft wares, dedicated to structural dynamic analysis, consider Eq. (4) and stop the analysis when incapable of arriving at residuals not larger than the tolerances, in a maximum number of iterations (K in Eq. (4)). This halt of analyses is in fact a deficiency causing the analyzer/operator to repeat the analyses with different values of the parameters, e.g. integration step size, nonlinearity tolerance, K, nonlinearity iterative method, etc. entailing additional computational cost.

Since, with attention to the explanation in Section 2, the source of the above mentioned halt is independent of the analysis accuracy, as a solution to the deficiency above, even when the residuals are not small enough after K iterations, the analyses can be continued. In simpler words, in nonlinear dynamic analyses, we can replace Eqs. (2)-(4) and: (a) stop the iterations and continue the analysis, when

$$i=1,2,3\ldots k-1: \quad \left\|{}^i\delta\right\| > \bar{\delta} \quad \text{and} \quad \left(\left\|{}^k\delta\right\| \le \bar{\delta} \quad \text{or} \quad k=K\right) \tag{11}$$

and (b) implement another repetition when

$$i=1,2,3\ldots k: \quad \left\|{}^i\delta\right\| > \bar{\delta} \quad \text{and} \quad k<K \tag{12}$$

In other words, we claim that replacing Eqs. (2)-(4) with Eqs. (11) and (12), leads to non-stop analysis of nonlinear structural dynamic problems (even when the residuals are not necessarily smaller than or equal to the tolerances), with no significant effects or at least practically acceptable effects on the accuracy of the analyses. The implementation of this idea is simple and merely needs disregarding the control of residuals, when $k = K$; see [4, 16]. In view of the conventional approach, i.e. Eqs. (2)-(4), the approach proposed above can be also considered as temporarily changing the tolerance to infinity, in order to prevent the halt of the analysis; see [17].

4 NUMERICAL STUDY

Consider the two shear buildings in Figure 2(a), with the structural members introduced in Table 1, subjected to the ground acceleration displayed in Figure 2(b). Obviously, the behavior is potentially nonlinear, because of the linear-elastic/perfectly-plastic characteristics, and meanwhile the possibility of poundings. The behavior is actually nonlinear in view of the responses depicted in Figure 3, where, the superposition principle [18] is violated. Implementing the average acceleration time integration [19], integration step sizes equal to the steps of the ground motion's record, the fractional time stepping nonlinearity solution method [20-22], and nonlinearity iterations over displacements, considering $K = 5$, and $\bar{\delta} = 10^{-6}$, lead to the

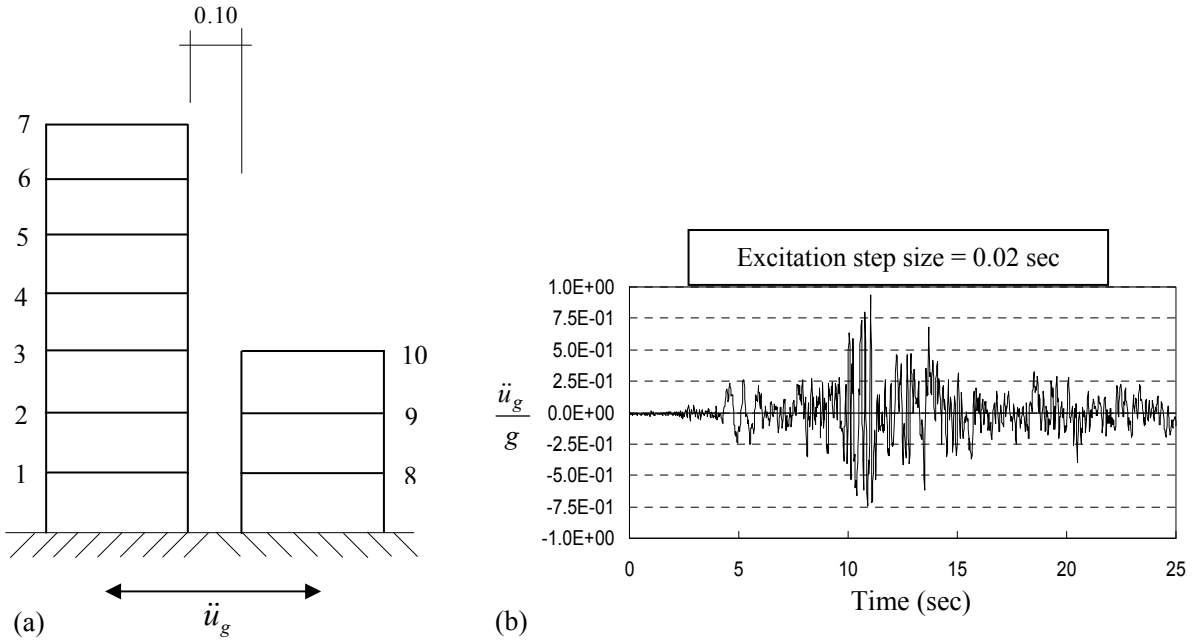


Figure 2: The structural system in the second example: (a) configuration; (b) excitation.

Floor	1	2	3	4	5	6	7	8	9	10
Mass $\times 10^{-3}$	2068	2064	2060	2056	2052	2048	2044	2052	2048	2044
Stiffness$\times 10^{-6}$	840	820	700	680	660	640	620	660	640	620
Yielding displacement $\times 10^{3}$	18.5	19	20	20.5	21	21.5	22	21	21.5	22
Damping	Negligible (considered zero)									
Restitution factor	1.0									

Table 1: The characteristics of the system introduced in Figure 2.

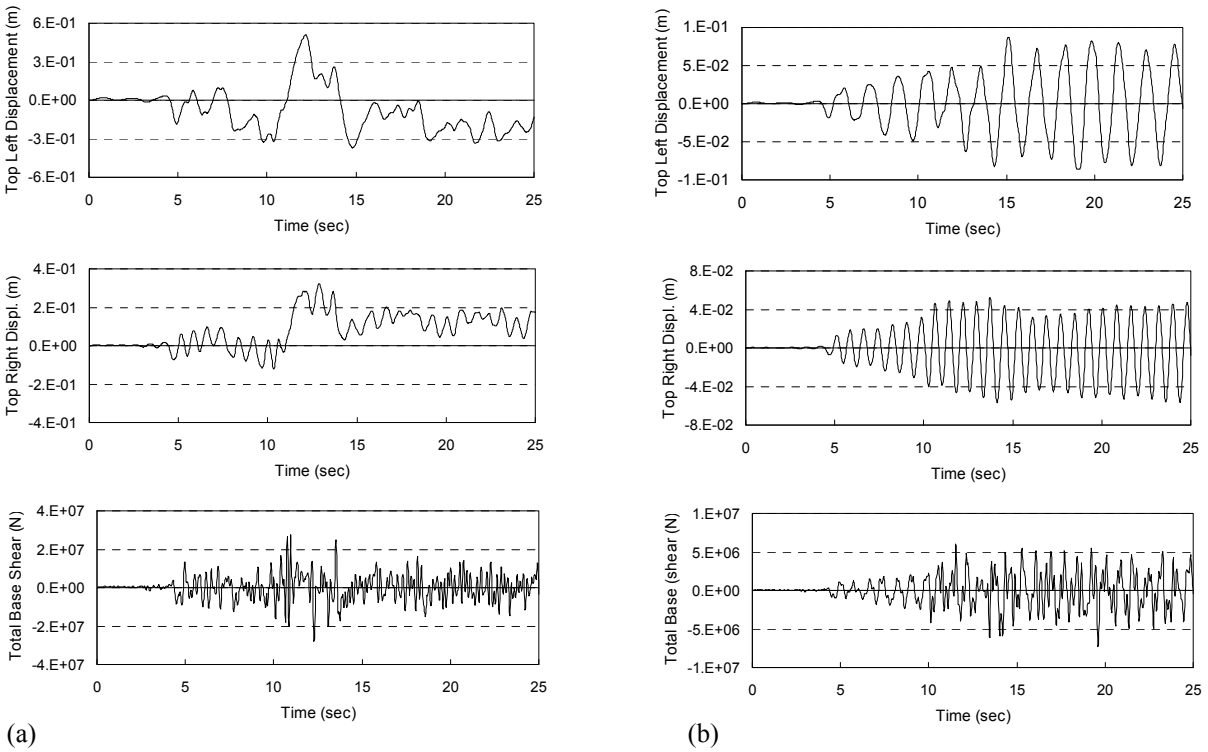


Figure 3: Highly precise responses histories for: (a) the system introduced in Figure 2 and Table 1, (b) the system introduced in Figure 2 and Table 1 after dividing the excitation to ten.

responses displayed in Figure 4. Apparently, by using Eqs. (11) and (12), we have arrived at responses histories throughout the total integration interval (different from the conventional analyses, where the analysis is stopped at $t = 4.58$ sec). Comparing these responses (reported in Figure 4(b)), with the highly precise responses in Figures 3(a), reveals the acceptable accuracy provided by the proposed approach, specifically, in practical areas like earthquake engineering. The study is repeated, as below:

(a) After changing the nonlinearity tolerance twice to 10^{-8} and 10^{-4}.
(b) After omitting one of the two sources of nonlinearity, and once considering only the piece-wise linear/perfectly plastic behavior and once considering only the pounding.
(c) after changing the time integration method, once to the Wilson-θ ($\theta = 1.42$) method [23-25], and once to the Generalized-α ($\rho = 0.8$) method [26].
(d) After changing the nonlinearity solution method.
(e) After adding nonzero classical damping equal to two and five percent.
(f) After scaling the excitation and causing nonlinear behaviors with different severities.
(g) After changing the excitation to excitation different in peak acceleration and frequency content.
(h) After changing the structural system to systems with different complexities.

The results were conceptually similar, revealing the validity of the claims in Section 2, not reported here for the sake of brevity.

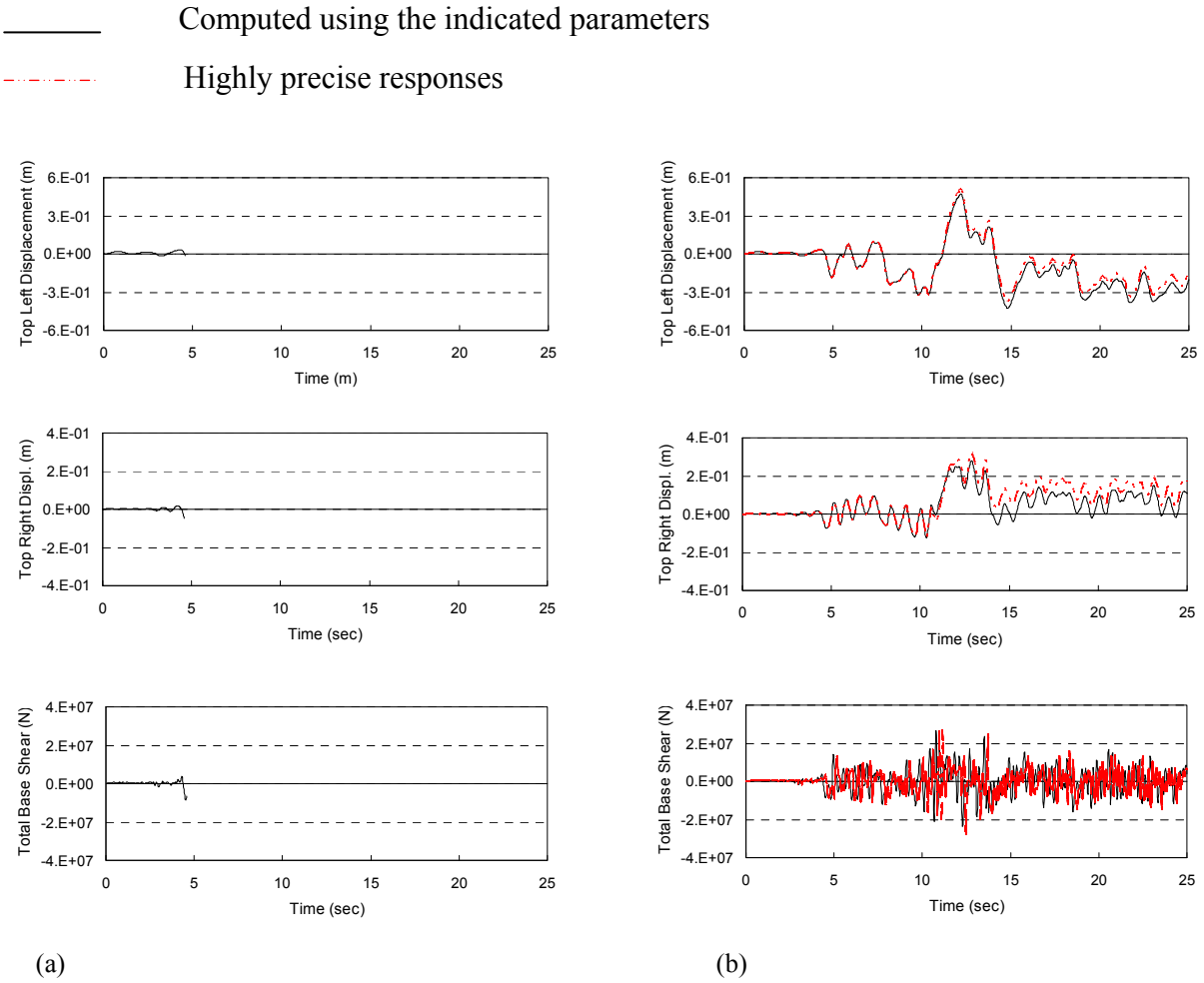


Figure 4: Responses histories computed by average acceleration for the system in Figure 2 and Table 1: (a) conventional, i.e. using Eqs. (2)-(4), (b) when implementing Eqs. (11) and (12) instead of Eqs. (2)-(4).

5 CONCLUSION

Concentrating on the notions of nonlinearity residuals and tolerances in static and dynamic analyses, we in this paper demonstrated that, different from static analyses, in dynamic analyses, nonlinearity tolerances do not necessarily imply upper bounds on the computational errors at nonlinearity detections/localizations. Accordingly, no analysis needs to be stopped when the nonlinearity residuals are not small enough after the maximum acceptable number of nonlinearity iterations. This is both computationally possible, and also leads to accuracies practically acceptable. The claims are discussed theoretically and demonstrated numerically.

REFERENCES

[1] J. Henrych, *Finite models and methods of dynamics in structures*. Elsevier, 1990.

[2] J. Argyris, J.P. Mlejnek, *Dynamics of structures*. Elsevier, 1991.

[3] T. Belytschko, W.K. Liu, B. Moran, *Non-linear finite elements for continua and structures*, John Wiley & Sons, 2000.

[4] A. Soroushian, *New methods to maintain responses' convergence and control responses' errors in the analysis of nonlinear dynamic models of structural systems*, *PhD Thesis*. University of Tehran, 2003. (in Persian)

[5] P. Wriggers, *Computational contact mechanics*, John Wiley & Sons, 2002.

[6] T.J.R. Hughes, K.S. Pister, R.L. Taylor, Implicit-explicit finite elements in nonlinear transient analysis. *Computer Methods in Applied Mechanics and Engineering*, **17/18**, 159-182, 1979.

[7] A.K. Chopra, *Dynamics of structures: theory and application to earthquake engineering*. Prentice-Hall, 1995.

[8] J. Chung, G.M. Hulbert, A family of single-step Houbolt time integration algorithms for structural dynamics. *Computer Methods in Applied Mechanics and Engineering*, **118**, 1-11, 1994.

[9] O.C. Zienkiewicz, R.C. Taylor, *The finite element method, Vol. I, 4th Edition*. McGraw Hill, 1989.

[10] K.J. Bathe, *Finite element procedures*. Prentice-Hall, 1996.

[11] E.L. Allgower, K. Georg, *Numerical continuation methods, an introduction*. Springer, 1980.

[12] A. Soroushian, With nonlinearity iterations towards better control of accuracy in explicit time integration analysis. P.M. Pimenta. *10th World Congress on Computational Mechanics (WCCM2012)*, Sao Paulo, Brazil, July 8-13, 2012.

[13] R.D. Cook, D.S. Malkus, M.E. Plesha, R.J. Witt, *Concepts and applications of finite element analysis*. John Wiley & Sons, 2002.

[14] T. Belytschko, T.J.R. Hughes, *Computational methods for transient analysis*. Elsevier, 1983.

[15] W.L. Wood, *Practical time stepping schemes*. Oxford, 1990.

[16] A. Soroushian, P. Wriggers, J. Farjoodi, Practical integration of semidiscretized nonlinear equations of motion: proper convergence for systems with piecewise linear behaviour. *Journal of Engineering Mechanics (ASCE),* **139**, 114-145, 2013.

[17] Personal Communication with Dr. A.M. Kermani, 2013.

[18] L. Meirowitch, *Fundamentals of vibration.* McGraw Hill, 2001.

[19] M.N. Newmark, A method of computation for structural dynamics. *Journal of Engineering Mechanics (ASCE)*, 85, 67-94.

[20] S.A. Mahin, J. Lin, *Construction of Inelastic Response Spectra for Single Degree-of-freedom Systems*, *Report No. UCB/EERC-83/17, Earthquake Engineering Research Center.* University of California, Berkeley, 1983.

[21] J. Nau, W.J. Hall, Scaling methods for earthquake response spectra. *Journal of Structural Engineering (ASCE)*, **110**, 1533-1548, 1984.

[22] A. Soroushian, An enhanced fractional-time-stepping method for structural dynamics. M.J. Crocker. *17th International Congress on Sound and Vibration (ICSV 17)*, Cairo, Eygypt, July 18-22, 2010.

[23] E.L. Wilson, *A computer program for the dynamic stress analysis of underground structures, Report No. 68-1*. University of California, Berkeley, 1968.

[24] K.J. Bathe, E.L. Wilson, Stability and accuracy analysis of direct integration methods. *Earthquake Engineering and Structural Dynamics*, **1**, 283-291, 1973.

[25] E.L. Wilson, I. Farhoomand, K.J. Bathe, Non-linear dynamic analysis of complex structures. *Earthquake Engineering and Structural Dynamics*, **1**, 241-252, 1973.

[26] J. Chung, G.M. Hulbert, A time integration algorithm for structural dynamics with improved numerical dissipation: the generalized-α method. *Journal of Applied Mechanics (ASME)*, **60**, 371-375, 1993.

COMPDYN 2015
5th ECCOMAS Thematic Conference on
Computational Methods in Structural Dynamics and Earthquake Engineering
M. Papadrakakis, V. Papadopoulos, V. Plevris (eds.)
Crete Island, Greece, 25–27 May 2015

ON THE CONVENTIONAL FINITE ELEMENT SIZES IN PSEUDO-STATIC SEISMIC ANALYSES OF 2D FRAMES

Amir Hossein Pariz[1], Bahram Kordbagh[2], Kiyanoush Ghazvini[3], Seyed Mohsen Borghei Razavi[4], Abbas Ali Jalalabadi[5]

[1] Structural Engineering Research Center
International Institute of Earthquake Engineering and Seismology (IIEES)
S. Lavasani (Farmaniyeh), North Dibaji, West Arghavan, No.21, Tehran, 19537, Iran
a.pariz@iiees.ac.ir

[2] Structural Engineering Research Center
International Institute of Earthquake Engineering and Seismology (IIEES)
S. Lavasani (Farmaniyeh), North Dibaji, West Arghavan, No.21, Tehran, 19537, Iran
b.kordbagh@iiees.ac.ir

[3] Structural Engineering Research Center
International Institute of Earthquake Engineering and Seismology (IIEES)
S. Lavasani (Farmaniyeh), North Dibaji, West Arghavan, No.21, Tehran, 19537, Iran
k.ghazvini@iiees.ac.ir

[4] Structural Engineering Research Center
International Institute of Earthquake Engineering and Seismology (IIEES)
S. Lavasani (Farmaniyeh), North Dibaji, West Arghavan, No.21, Tehran, 19537, Iran
m.razavi@iiees.ac.ir

[5] Structural Engineering Research Center
International Institute of Earthquake Engineering and Seismology (IIEES)
S. Lavasani (Farmaniyeh), North Dibaji, West Arghavan, No.21, Tehran, 19537, Iran
a.jalalabadi@iiees.ac.ir

Keywords: Seismic Analysis, Finite Elements, 2D Frame, Element Sizes, Accuracy.

Abstract. *Pseudo-static analysis is an analysis approach in many seismic codes. With attention to the dependence of the results to the finite elements sizes, this paper examines the sufficiency of the finite elements as large as the structural element, for 2D frames' pseudo-static analyses, using Euler-Bernoulli theory. As the consequence, structural elements' sizes are adequate to be considered for finite elements sizes. Further study is however recommended.*

1 INTRODUCTION

Earthquakes are of major disasters, and the infrastructures, and in general buildings, should be designed such that to stand or damaged slightly against earthquakes. Many national codes are prepared, presenting comments for better seismic designs, e.g. see [1-4]. Nevertheless, the designs are all based on seismic analyses, which can be divided in the two categories of static and dynamic analyses, both including sub-categories. Pseudo-static is a linear static analysis approach belonging to the first category. Regardless of the analysis approach, conventionally the first step of seismic structural analysis is discretization of the models in space and arriving at MDOF (Multi-Degree-Of-Freedom) structural properties at the degrees of freedom. Finite Element Method (FEM) is broadly accepted for discretization in space, conventional in practical seismic analyses. Specially, because of the approximation in the shape functions, discretization by finite elements is involved in errors and inexactness, inversely depending on the number of the degrees of freedom, or to say better, directly on the elements sizes. Being concentrated on seismic analysis of frame structures, traditionally we consider each beam or column as one finite element, e.g. see Figure 1.

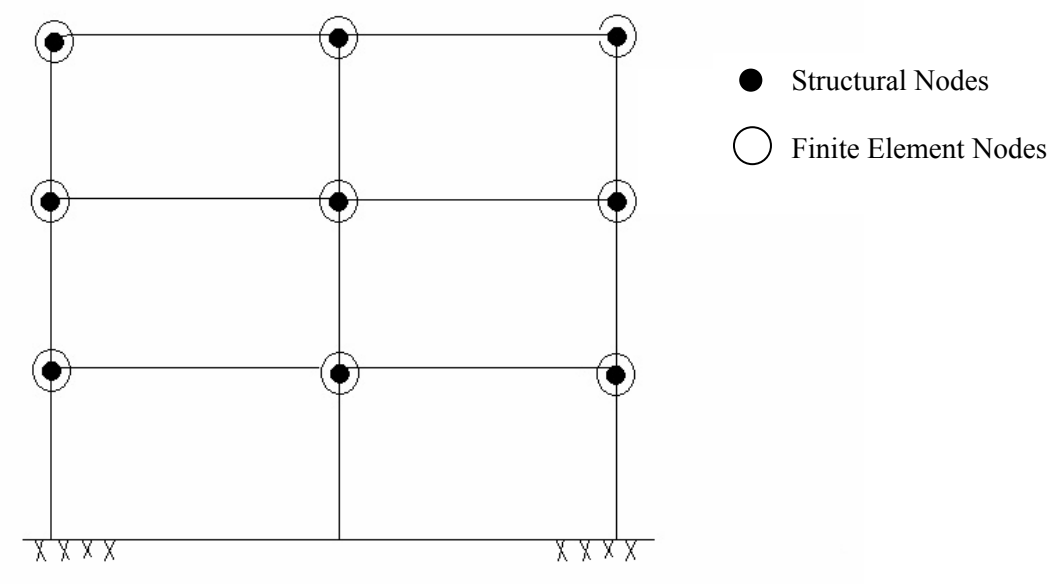


Figure 1: Typical placement of finite elements' nodes and elements in seismic analyses.

The objective in this paper is to briefly study the amount of inaccuracy caused by this convention in linear static analysis of frames against earthquakes, i.e. pseudo-static analyses. For the numerical study the designs are considered in accordance with the seismic standards of Iran [4-6]. In Section 2, a brief theoretical study on the inaccuracy caused by finite elements sized as large as the structural elements is presented. Numerical study of the claims, in Section 2, is presented, in Section 3; and finally, with a brief review on the achievements, the paper is closed in Section 4.

2 THEORITICAL STUDY

In pseudo-static analysis of structures against earthquakes, a total design lateral load, i.e. base shear force, is being determined, taking into account the structural system, it's importance, and the soil type and seismicity of the region; then, the lateral load is being distributed

between the frames potentially resisting against this load according to the stiffness of the frames; later, the lateral load for each frame is being distributed between the floors levels, with special attention to the top floor, leading to the typical case displayed in Figure 2, for each 2D frame [1-4]. The resulting distribution of forces and displacements in the 2D frame

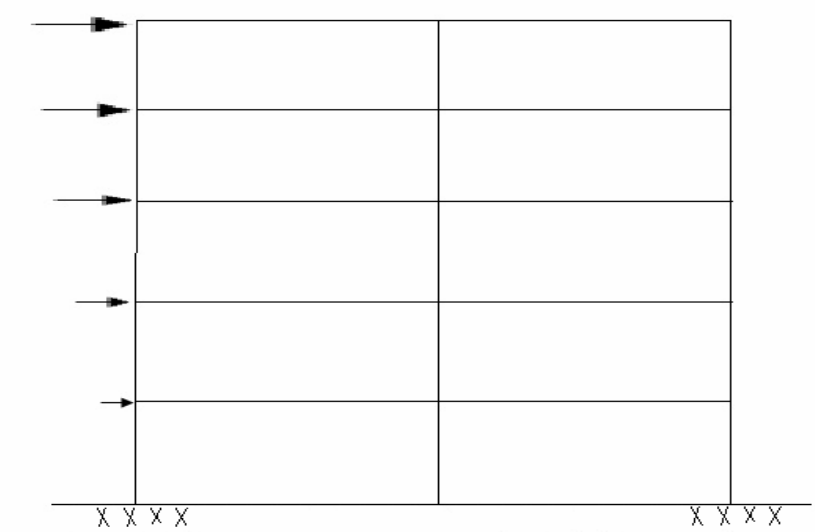


Figure 2: Typical distribution of the lateral load of earthquake in pseudo-static analyses.

need to be added to the distribution of forces and displacements caused by the dead and live loads, according to the seismic code, e.g.

$$\begin{matrix} D+L \\ 0.75[D+L\pm(E \text{ or } W)] \\ 0.75[D\pm(E \text{ or } W)] \end{matrix} \quad (1)$$

(D stands for the dead load; L implies the live load, E denotes the load of earthquake, and W represents the wind load), according to the Iranian codes [4,6].by considering the typical distributions of live and dead loads as displayed in Figure 3, and putting it besides the distribution in Figure 2 and also Eq. (1), and not forgetting the superposition principle in linear analyses [7], it would be apparent that pseudo-static analysis is a static analysis against loads that do not change, unless at structural nodes (see Figure 1). Consequently, in view of the considerations in the simplest column-beam theory [8] and strength of materials [9], it is reasonable to except sufficient accuracies, when locating the finite elements nodes on the structural nodes. This is studied numerically in Section 3.

3 NUMERICAL STUDY

The 2D frame in Figure 4 with structural members introduced in Table 1, located on a type II soil [4], and designed according to Iranian codes (see [4-7, 10-12]) is undergone pseudo-static seismic analysis, considering the beam column members using Euler-Bernoulli beam theory, and elements sized according to Figure 1. Separately, the much more accurate results are obtained using about twenty times smaller elements. Accordingly, the errors of top and mid-floor displacements in the direction of the earthquake load are reported in Table 2. The structural system is changed to a special moment resisting frame (see also Table 3) and the study is repeated, resulting in Table 4, similar to Table 2, displaying the sufficiency of the provided accuracy.

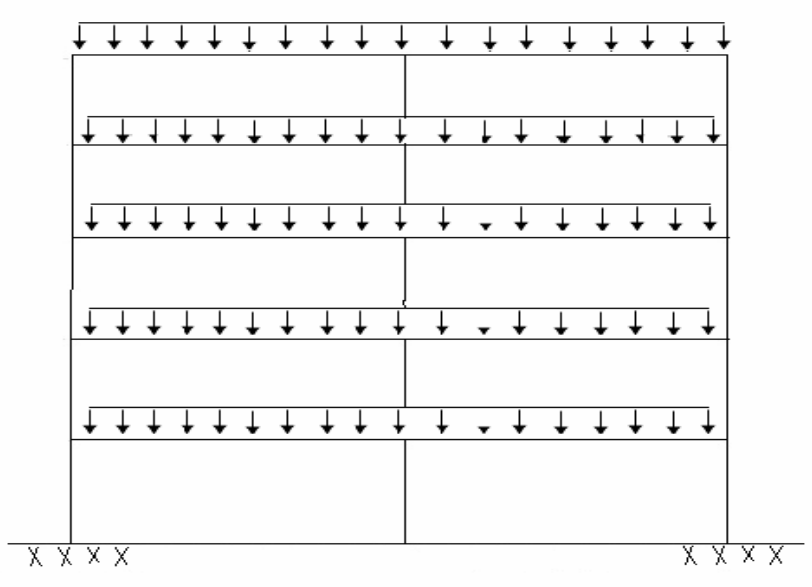


Figure 3: Typical distribution of live and dead loads in pseudo-static analyses against earthquake.

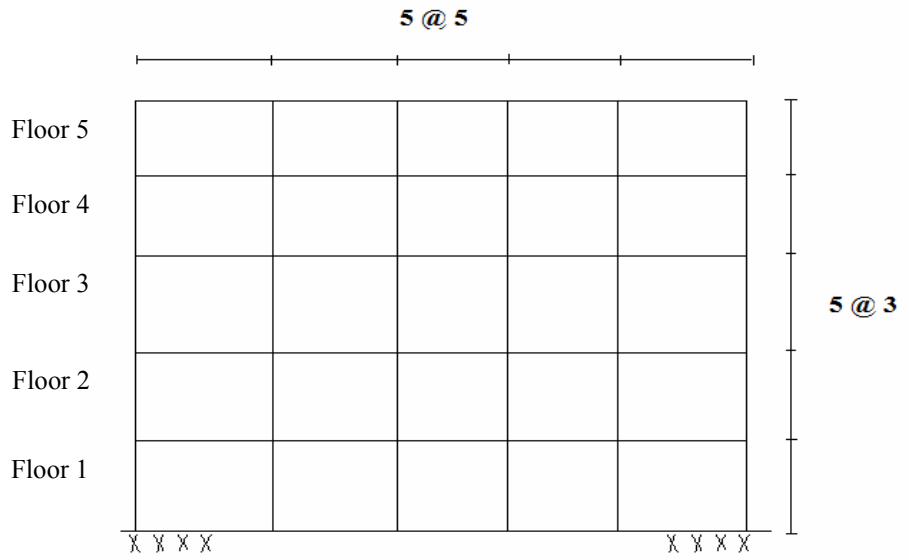


Figure 4: Some main features of the frame under study.

Floor	Side column	Middle column	Beam
1	TUBO 250*250*15	TUBO 260*260*20	IPE 360
2	TUBO 220*220*15	TUBO 240*240*15	IPE 330
3	TUBO 220*220*15	TUBO 240*240*15	IPE 330
4	TUBO 200*200*15	TUBO 200*200*15	IPE 270
5	TUBO 200*200*15	TUBO 200*200*15	IPE 270

Table 1: Structural members of the frame in Figure 4 considering ordinary moment resisting structural system for the frame.

Loading	Top Floor Displacement in the Direction of Earthquake	Mid-height Floor Displacement in the Direction of Earthquake
Earthquake Load	0.062	0.067
Combined Dead Live and Earthquake	0.083	0.030

Table 2: Errors of the analysis of the frame introduced in Figure 2 and Table 1 (%).

Floor	Side column	Middle column	Beam
1	TUBO 220*220*15	TUBO 240*240*15	IPE 330
2	TUBO 200*200*15	TUBO 220*220*15	IPE 330
3	TUBO 200*200*15	TUBO 220*220*15	IPE 330
4	TUBO 160*160*12	TUBO 180*180*12	IPE 300
5	TUBO 160*160*12	TUBO 180*180*12	IPE 300

Table 3: Structural members of the frame in Figure 4 while change the system to special moment resisting frame.

Loading	Top Floor Displacement in the Direction of Earthquake	Mid-height Floor Displacement in the Direction of Earthquake
Earthquake Load	0.049	0.076
Combined Dead Live and Earthquake	0.065	0.101

Table 4: Errors of the analysis of the frame introduced in Figure 2 and Table 3 (%).

4 CONCLUSION

After brief theoretical and numerical study on the analyses of two dimensional frames designed against earthquakes, we can claim about the adequacy of the finite elements' sizes equal to the structural elements sizes. Further study, specifically for cases with complicated geometries and loadings' discontinuities along structural members, or analyses involved in nonlinearities are recommended.

REFERENCES

[1] F. Naeim, S. Zhongzhi, *The seismic design handbook*, Kluwer, 2001.

[2] ICC (International Code Council), *IBC - International building code*, 2003.

[3] NZS (New Zealand Standards), *NZS 1170.5: 2004 Structural design actions, Part 5: Earthquake actions*, 2004.

[4] BHRC (Building and Housing Research Centre), *Standard no.2800, 3rd Edition. Iranian code of practice for seismic resistant design,* 2007. (in Persian)

[5] INBR (Iranian National Building Regulations), *Iranian national building code, Part 6-Loading*, 1993. (in Persian)

[6] INBR (Iranian National Building Regulations), *Iranian national building code, Part 10-Steel Structures*, 1993. (in Persian)

[7] L. Meirovitch, *Fundamentals of vibrations*, McGraw Hill, 2001.

[8] K.J. Bathe, *Finite element procedures*, Prentice Hall, 1996.

[9] S. Timoshenko, *Strength of materials, Part II, 3rd Edition*, Van Nostrand Reinhold, 1956.

[10] A. Soroushian, *Optimization of geometry and structural system of residential complexes*, M.Sc. thesis, Shiraz University, 1995. (in Persian)

[11] A. Sabzei, *On the performance of a recent technique for seismic analyses computational cost reduction when applied to buildings structural systems*, M.Sc. thesis, International Institute of Earthquake Engineering and Seismology (IIEES), 2013. (in Persian)

[12] S. Amiri, *On the adequacy of integration step sizes recommended for nonlinear time integration analyses*, M.Sc. thesis, International Institute of Earthquake Engineering and Seismology (IIEES), 2015. (in Persian)

COMPDYN 2015
5th ECCOMAS Thematic Conference on
Computational Methods in Structural Dynamics and Earthquake Engineering
M. Papadrakakis, V. Papadopoulos, V. Plevris (eds.)
Crete Island, Greece, 25–27 May 2015

ON THE PERFORMANCE OF A TECHNIQUE TO ACCELERATE TIME INTEGRATION WHEN APPLIED TO SPACE STRUCTURES ANALYSES

Alireza Garakaninezhad [1,2], **Reza Kamyab Moghadas**[2]

[1] Structural Engineering Research Centre
International Institute of Earthquake Engineering and Seismology (IIEES), Farmaniyeh (S.Lavasani),
North Dibajee, West Arghvan, No. 21, Tehran 19395, Iran
a.garakani@iiees.ac.ir

[2] Iranian Academic Center for Education, Culture and Research
Kerman 7616914111, Iran
r_kamyab_m@yahoo.com

Keywords: Time integration, Space Structures, computational Cost, Accuracy.

Abstract. *The true behaviors of structures, specifically when subjected to earthquakes, are dynamic. Time integration is a versatile tool in analysis of the semi-discretized equations of motion. Although the implementation of time integration is simple, the computational costs are considerable and the responses are inexact. The integration step size is the main parameter affecting the accuracies and computational costs. When the excitations are available as digitized records, conventionally, the integration step sizes are to be set not larger than the excitation steps. In 2008, a technique is proposed, providing the capability to analyze with steps larger than the excitation steps, leading to considerable less computational cost. This technique is implemented in analyses of different structural systems, including bridges, tall buildings, residential buildings, etc., and the observed losses of accuracies were negligible. In this paper, after brief theoretical discussions, the technique is applied to the analysis of the three space structures, where the structural members are sized, with attention to the existing national codes. The average acceleration method of Newmark is considered as the integration method; an El Centro as well as a Loma Prieta strong ground motion record are considered as the excitations applied in the vertical direction, and the analyses are carried out considering the linear behaviors. To address the main consequence, though the smallest oscillatory periods with considerable contribution in the response were estimated approximately, the losses of accuracy in cases with the applicability of the technique were small, still depending on the structural system and excitation.*

1 INTRODUCTION

In many cases, the true performance of structural systems is dynamic that, cannot be simplified to static. In order to study dynamic behaviors of structures, the widely accepted approach is to define the structural models, set the mathematical models, and, discretizing them in space then semi-discritized model is as follows:

$$\mathbf{M}\ddot{\mathbf{u}}(t)+\mathbf{f}_{\text{int}}=\mathbf{f}(t), \qquad 0\le t\le t_{end}$$

$$\text{initial conditions}: \begin{vmatrix} \mathbf{u}(t=t_0)=\mathbf{u}_0 \\ \dot{\mathbf{u}}(t=t_0)=\dot{\mathbf{u}}_0 \\ \mathbf{f}_{\text{int}}(t=t_0)=\mathbf{f}_{\text{int}_0} \end{vmatrix}, \qquad \text{additional constraints}: \mathbf{Q} \tag{1}$$

Where, t and t_{end} imply the time and the duration of the dynamic behavior; **M** is the mass matrix; f_{int} and **f**(t) stand for the vectors of internal force and excitation; **u**(t), $\dot{\mathbf{u}}$(t), and $\ddot{\mathbf{u}}$(t) denote the vectors of displacement, velocity, and acceleration; u_0, $\dot{\mathbf{u}}_0$, and $\mathbf{f}_{int0}$ define the initial status of the model (regarding the essentiality of considering $\mathbf{f}_{int0}$ in Equations (1), also see [1]); and finally, **Q** represents some restricting conditions, e.g. additional constraints in problems involved in impact or elastic–plastic behavior [2, 3], all in view of the degrees of freedom set for the model.

Equation (1) can be analyzed with an appropriate method [4-6]. The most versatile method to analyze equation (1) is direct time integration [7]. However, the time integration methods are accompanied by some errors and are inexact. The integration step size is the main parameter affecting the accuracies and computational costs. In general, the accuracies of obtained results depended on the integration step size and the shorter one, the more accuracy can be obtained. However, time integration analysis using so small time step significantly increases computational costs. One of the broadly accepted comments is as follows:

$$\Delta t = \text{Min}(h_s, \frac{T}{10}, {}_f\Delta t) \tag{2}$$

Where, T is the smallest dominant period in the response, in general, approximated with the smallest natural period of the system at $t = 0$, likely effectual in the response, h_s is the largest value of the integration step, providing numerically stable responses ($h_s = \infty$ for unconditionally stable methods), and ${}_f\Delta t$ is the digitization step size for excitations available as digitized records. Considering equation (2), if ${}_f\Delta t$ is much smaller than $\text{Min}(h_s, \frac{T}{10})$, the time integration step size must be smaller than be required for convergence or accuracy. Hence, computational cost should be expensive. In 2008, a technique is proposed, providing the capability to analyze with steps larger than the excitation steps, leading to considerable reduction of computational cost. The technique changes time step ${}_f\Delta t$ to the longer one ${}_f\Delta t'$. In fact, the technique replaces the excitation with a new one which is digitized at time steps equal to ${}_f\Delta t'$ responses convergence and the rate of convergence are preserved after the replacement of excitation. This technique implemented in analyzing for some different structural systems,. i.e. a tall building [8], a fuel storage tank [9], and a silo [10], and also subjected to further theoretical investigation [11].

In this paper, we aim to evaluate this method for some specific kinds of space structures. A brief review of the technique is presented in the following section.

2 THE BRIEF REVIEW OF THE TECHNIQUE

The main idea backing this technique is to replace the digitized records of seismic excitations, with records, digitized, at larger steps, such that the loss of integration accuracy resulting from considering the new excitation (instead of the original excitation) is tolerable.in brief, provided the assumptions bellows:

1. The excitation steps, ${}_f\Delta t_i$ i =1,2,… , are equally sized,

$$\forall i,j \quad {}_f\Delta t_i = {}_f\Delta t_j = \Delta t = {}_f\Delta t > 0 \tag{3}$$

2. The integration steps, Δt_i $i = 1,2,\ldots,$, are equally sized,

$$\forall i,j \quad \Delta t_i = \Delta t_j = \Delta t > 0 \tag{4}$$

3. The excitation steps are embedded by the integration steps (the first time station, i.e. t_0 , is a station for both excitation and integration),

$$\exists\ n\epsilon\ Z^+ \quad \frac{\Delta t}{{}_f\Delta t} = n < \infty \tag{5}$$

4. The **f**(t) in equations (1) is a digitized representation of an actual excitation, **g**(t), smooth [12] with respect to time, i.e.,

$$\mathbf{f}(t) = \mathbf{g}(t)\delta(t-\alpha_i)$$
$$\mathbf{g}(t)\text{: smooth with respect to time}$$
$$\alpha_i = i\ {}_f\Delta t\,, \quad i = 1,2,\ldots \tag{6}$$
$$\delta(t-\alpha_i) = \begin{cases} 1 & t = \alpha_i \\ 0 & t \neq \alpha_i \end{cases}$$

We can replace the excitation in equations (1), **f**, with the new excitation, $\hat{\mathbf{f}}$, digitized at steps equal to $n\ {}_f\Delta t$, according to:

$$t_i\text{:}\quad \tilde{\mathbf{f}}_i = \mathbf{f}(t_i)$$
$$0 < t_i < t_{end}\text{:}\quad \mathbf{f}_i = \frac{1}{2}\mathbf{f}(t_i) + \frac{1}{4\acute{n}} \tag{7}$$
$$t_i = t_{end}\ \tilde{\mathbf{f}}_i = \mathbf{f}(t_i)$$

where,

$$t = \Delta t\text{:}\quad \acute{n} = n-1$$
$$\Delta t < t < t_{end} - \Delta t\text{:}\quad \acute{n} = \begin{Bmatrix} \frac{n}{2} \\ \frac{n-1}{2} \end{Bmatrix} \tag{8}$$
$$t = \Delta t\text{:}\quad \acute{n} = n-1$$

and Δt, n ($n\epsilon\ Z^+$) are the largest values satisfying

$$\Delta t = n\ {}_f\Delta t \leq \text{Min}\left(h_s, \frac{T}{10}\right) < t_{end} \tag{9}$$

with generally small loss of accuracy in time integration. Since, the new excitation, $\hat{\mathbf{f}}$, is digitized at steps equal to $n\ {}_f\Delta t$,when considered instead of the original excitation, can lead to a reduction in computational cost.

3 NUMERICAL STUDY

In this paper, three different space structures, a barrel vault, a diamatic dome, and a double layer grid, as shown in figure (1), are considered. The span of the diamatic dome and barrel vault is 46.3 and 30 meters, respectively and the height of them is 36 and 18 meters respec-

tively. For double layer grid the span is 10 meters and the layer thickness is 1.5 meters. Young's modules, mass density, and yield stress are 2.1×10^{10} kg/m^2, 7850 kg/m^3, and 2.4×10^6 kg/m^2, respectively. These structures are designed considering national code [13].

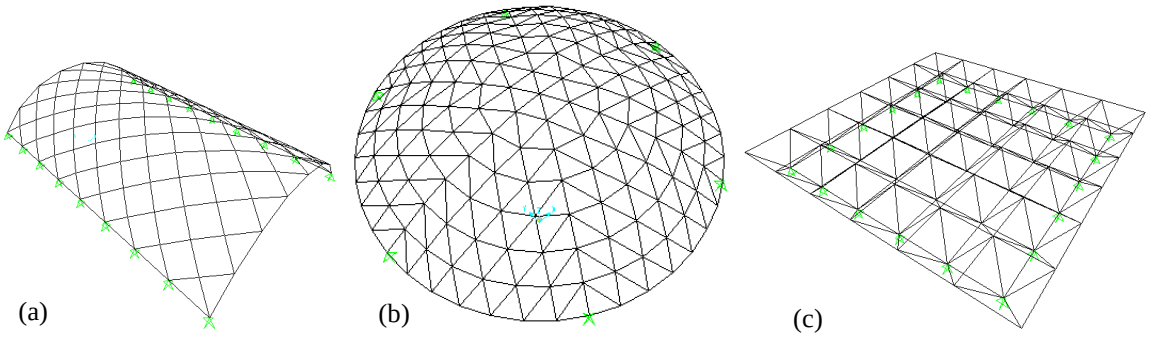
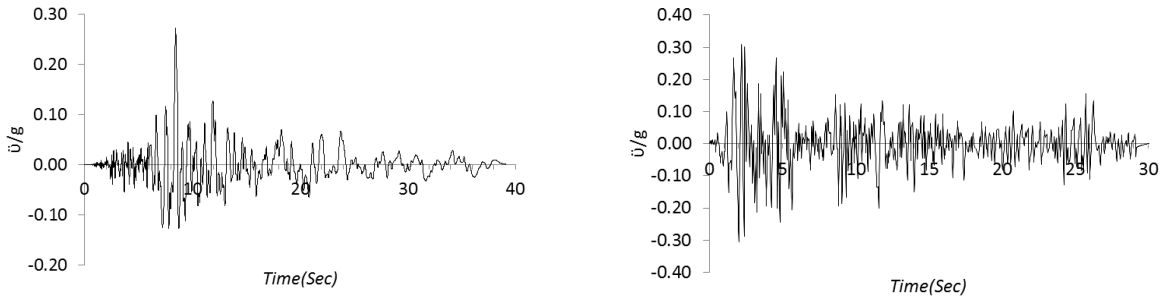


Figure 1: The three space structures under consideration: (a) barrel vault, (b) diamatic dome,(c) double layer grid.

The average acceleration method of Newmark is considered as the integration method, an El Centro and a Loma Prieta strong ground motion record are considered and their time step sizes are 0.02 and 0.005 Sec, respectively, shown in figure 2. Considered to study the performance of the technique.



(a) (b)

Figure 2: The ground motion applied to the structural model, (a) the Loma Prieta and (b) El Centro strong ground motion record

These models are subjected to the considered excitations applied in vertical direction. In view of the approximate response partially reported in Figure 3, studying the response shows the technique is applicable for the barrel vault for both considered excitation and double layer grid only for the Loma Perieta ground motion record. In other hand, dominate period of structures considered is small and the technique application is limited, hence, the time history analysis implement only for n=2. A point displacement is shown in figure (4). The results show the application of this technique can reduce computational costs without considerably compromising the accuracy of responses. Although the technique considering Loma Perieta strong ground motion record is not applicable, comparison the displacement results after implementing the technique are shown in figure (4c).

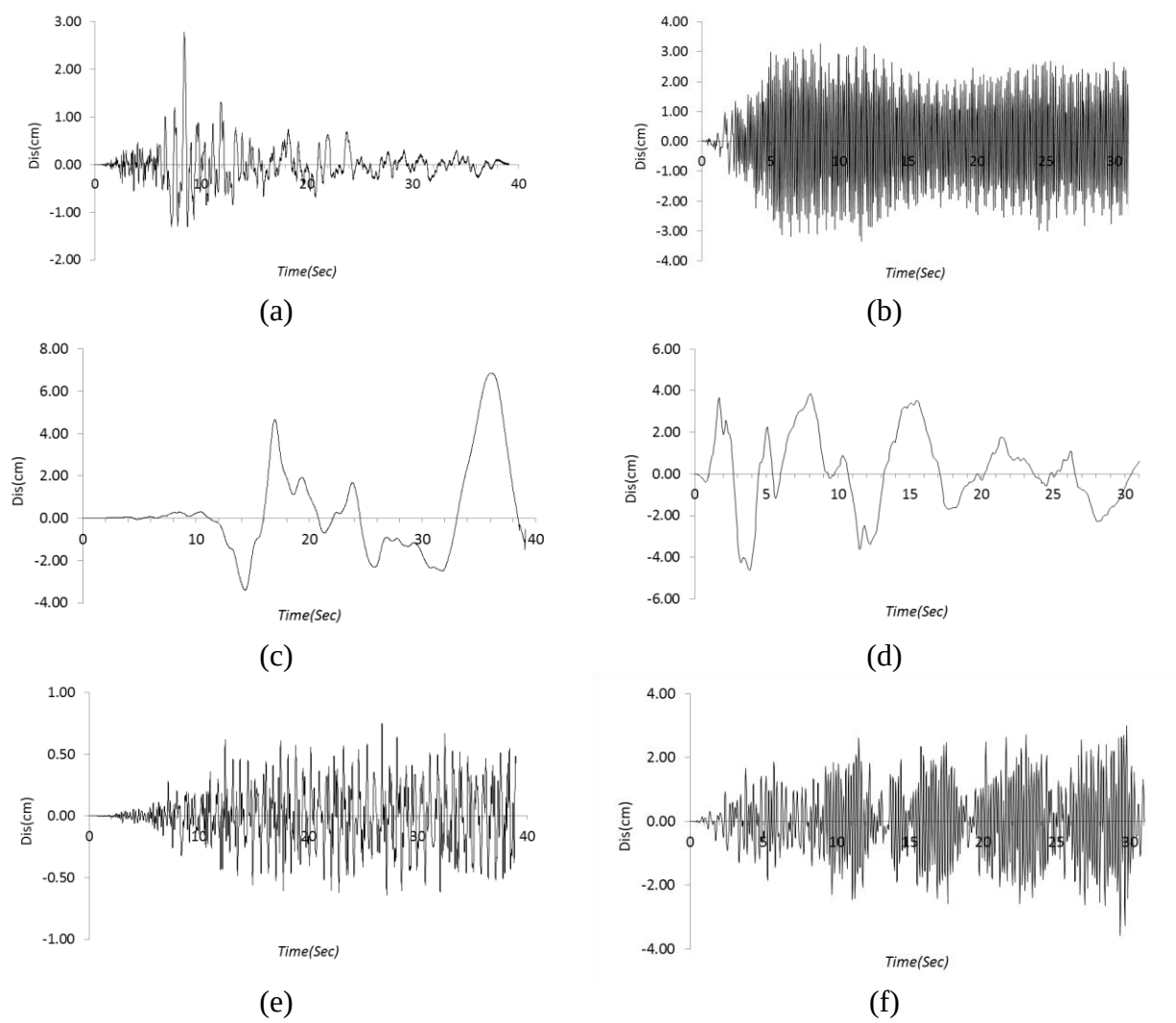


Figure 3: approximate point displacement, (a) and (b) the double layer grid, (c) and (d) the barrel vault, and (e) and (f) the diamatic dome when applying the Loma Preita and El Centro ground motion record respectively.

4 CONCLUSION

The performance of the technique proposed for accelerating of seismic analysis by time integration is examined considering space structures analysis. The results show, though the smallest oscillatory periods with considerable contribution in the response were estimated approximately, the losses of accuracy in cases with the applicability of the technique were small, still depending on the structural system and excitation. The results show, in some cases, the performance of the technique depends on the excitation that needs further study to investigate this effect. Further study in this regard, considering different ground strong motions, and nonlinear time history analysis is suggested.

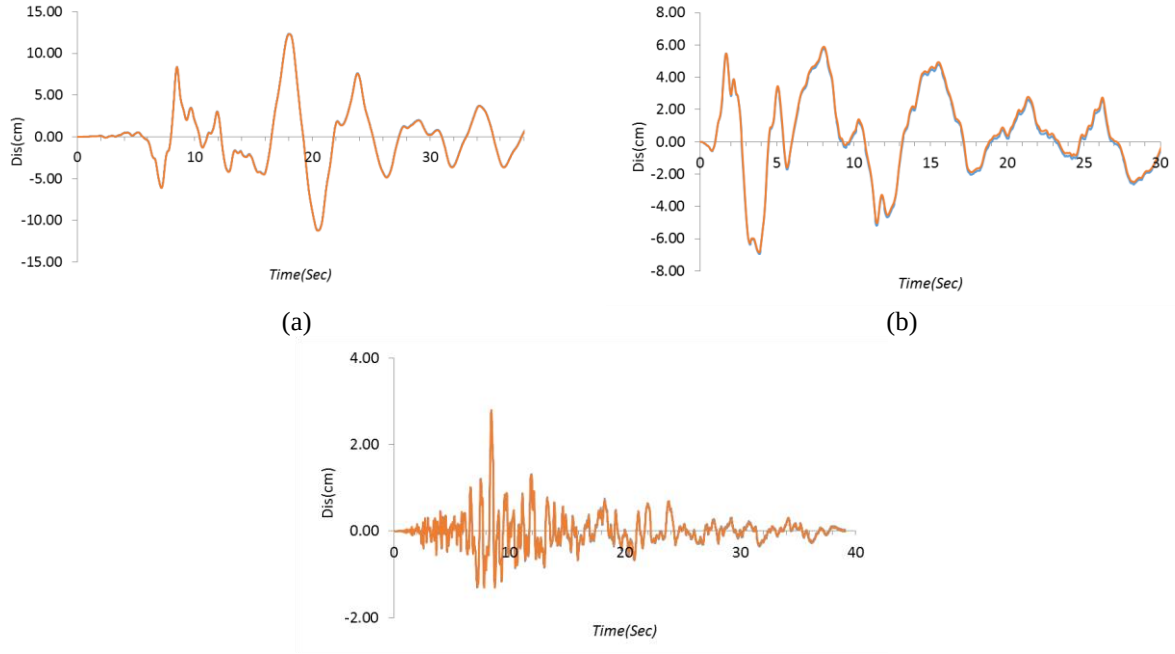


Figure 4: The performance of the technique when applied to, (a) and (b), the barrel vault subjected to the El Centro and Loma Prieta strong ground motion record respectively, and (c) double layer grid subjected to Loma Prieta strong ground motion record.

REFERENCES

[1] A. Soroushian, *New methods to maintain responses' convergence and control responses' errors in the analysis of nonlinear dynamic models of structural systems, Ph.D. Thesis*. University of Tehran, 2003 (in Persian).

[2] P. Wriggers, *Computational contact mechanics*. John Wiley & Sons, 2002.

[3] J T.J.R. Hughes, K.S. Pister, R.L. Taylor, Explicit–explicit finite elements in nonlinear transient analysis. *Computer Methods in Applied Mechanics and Engineering*, **17/18**:159–182, 1979.

[4] J. Henrych, *Finite Models and Methods of Dynamics in Structures*. Elsevier, 1990.

[5] J. Argyris, J.P. Mlejnek, *Dynamics of structures*. Elsevier, 1991.

[6] T. Belytschko, W.K. Liu, B. Moran, *Non-linear Finite Elements for Continua and Structures*. John Wiley & Sons, 2000.

[7] A.K. Chopra, *Dynamics of Structures: Theory and Application to Earthquake Engineering, 1st Edition*. Prentice-Hall, 1995.

[8] A. Soroushian, A. Aziminejad, More efficient seismic analysis of tall buildings by implementing a recently proposed technique. A. Tasnimi ed., *6th International Conference on Seismology and Earthquake Engineering (SEE6)*, Tehran, Iran, May 16-18, 2011.

[9] A. Soroushian, A. Saaed, M. Arghavani, M.Rajabi, M.M. Sharifpour, Less computational costs in the analysis of reservoirs seismic behaviors by time integration. B. Marvalova ed., *10th Biennial International Conference on Vibration Problems*, Technical University of Liberec, Prague, Czech Republic, September 5-8, 2011.

[10] F. Nateghi, M. Yakhchalian, On less computational costs for the analysis of silos seismic behaviors by time integration. M. Papadrakakis, M. Fragiadakis, V. Plevris eds. *3rd ECCOMAS Thematic Conference on Computational Methods in Structural Dynamics and Earthquake Engineering*, Corfu, Greece, May 25-28, 2011.

[11] A. Soroushian, A comparison between two methods for disregarding excitation steps in seismic analyses. A. Tasnimi ed., *6th International Conference on Seismology and Earthquake Engineering (SEE6)*, Tehran, Iran, May 16-18, 2011.

[12] J.W. Brown, R. Churchill, *Fourier series and boundary value problems*. McGraw-Hill, 1993.

[13] *Code of Practice for Skeletal Steel Space Structures*. No.400, vice presidency for Strategic Planning and Supervision, IRAN, 2010.

Using energy -based pushover methods in Seismic Evaluation of Steel Bracing Structures

Kaveh Nezamisavojbolaghi
[1]Department of Civil Engineering, College of Structure Engineering, Mahabad Branch, Islamic Azad University
Mahabad, Iran
nazmbonye@gmail.com

Abstract:

Nonlinear static analysis is a simple and practical method to evaluate seismic demands in structures that has been considered in most of seismic instructions in recent years. Since the concept of energy is more theoretic than other similar methods, the present article evaluated the models of lateral loads discussed in the concept of energy. This approach can be updated in the steps of nonlinear static analysis or remains constant in all steps of the analysis. One of updated pushover models called “story shear-based pushover" has used the concept of energy to estimate the target displacement; so that instead of control point displacement, all stories displacement has been used. Multiple mode load model (MPA) has used energy method to adjust single freedom degree curve and eliminate the problems of rood point displacement reverse in loading models. In the present research, different bracing structures have been subject to lateral loading to evaluate energy-based methods, and the results were compared and assessed by dynamic analytical results. The results of Steel Bracing structural analysis show that energy-based methods have been successful to estimate the storey shear values as the most important parameter in the design of structures.

Keywords: Lateral load pattern, energy, non-linear analysis time history; pushover

۱- Introduction

It seems that nonlinear static analysis methods are one of the most popular analysis methods due to the ease of use, and also present an effective graphical display of general response of structure directly to the pushover curve. This curve is directly related to the system capacity, usually defined by base shear with an important structural node (controller node) response. This kind of overall response allows a direct idealization of structure as a single degree of freedom (SDOF) system that simplifies design or evaluation. Essential steps to perform a nonlinear static analysis method would be as follows:

Conducting a static pushover analysis.

Defining an equivalent SDOFS, based on pushover curve, obtained from a static pushover analysis.

Estimating maximum total displacement demand, based on a selected design response spectrum.

Equivalent and Actual SDOFS response of structure are related by a shape factor, usually determined in the first mode participation factor.

Finally, the response parameters, in-floor drift and forces on each structural member can be evaluated through pushover curve (or capacity curve) by knowing the overall demand of the system. All non-linear static methods have been proposed are different, especially in defining the overall displacement demand (step ۳) and they can vary in two main groups: equivalent linearization and coefficient classification methods. Among the equivalent linearization methods, Rosenblueth and Herrera,

Gülkan and Sozen, Iwan, Priestley and Kowalsky, Freeman CSM, and adjusted CSM (Chopra and Goel) can be pointed out. Methods of Newmark and Hall, Miranda, Federal Emergency Management Agency (FEMA) ٣٥٦, and N٢ method of Fajfar can be implied for coefficient methods. Some researchers such as Hernàndez-Montes and Shakeri have used the energy concept to define structural capacity curve with single degree of freedom for equivalent linearization and obtained better results with stronger theories. In this research, these methods have been evaluated.

٢- Literature Review

As it was described by Kunnath, the term "pushover analysis" makes a new change in classic collapse analysis, thereby a repetitive-incremental solution of static equilibrium equations will be done to obtain the response of a structure under bilateral incremental lateral load pattern. The structural strength is evaluated and stiffness matrix is updated at each step of the loading function. The solution will continue until (1) a predetermined level of performance is reached, (2) collapse of structure is formed or (3) the program fails to converge. In this manner, each point of the basic shear capacity curve shows a state of effective and equivalent stress against displacement, in other words, indicates a state of the deforming directly corresponded to the vector of applied external load.

Even by the simplified analytical tool against nonlinear dynamic analyses, important information for structural response, such as the followings may be provided:

Recognizing the progress of overall capacity curve of the structure.

Recognizing the critical areas, where large inelastic deformations may occur.

Recognizing resistance irregularities in plan and height which could cause significant changes in the inelastic dynamic response characteristics (for example, Krawinkler and Seneviratna, 1998).

Energy demand estimation in the potential fragile elements.

Predicting sequence submission or failure in structural members.

Modal pushover analysis (MPA) has been proposed by Chopra and Goel. In this method, Pushover analyses in each mode have been performed independently, using lateral load profiles showing the expected response in any of the modes. Pushover curve related to each modal pushover analysis is idealized as a bilinear SDOF system. And the responses were combined with each other using SRSS or CQC to define overall answer of the system.

One of the main deficiencies of MPA, as shown in Figure 1, is reversible capacity curve for the higher modes. Since the roof displacement changes in higher modes is not appropriate with the changes of other modes, the roof displacement in the higher modes of some structures are reduced by the increase of base shear after the establishment of structure and formation of plastic hinges, then the pushover curve is moved reversibly that make it difficult to use this method and its application in engineering offices as an alternative approach to the regulations methods.

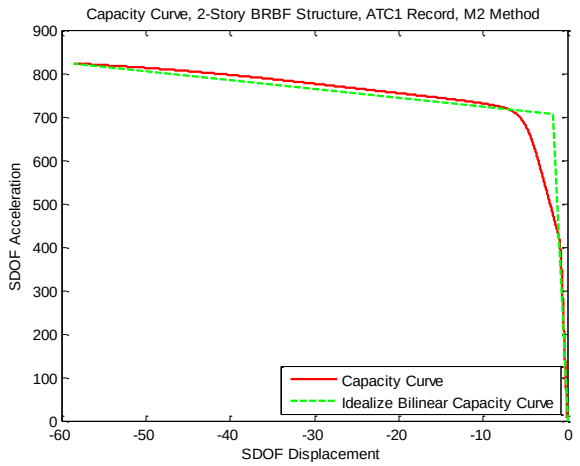


Figure 1: The pushover curve of a two story building, buckling bracing for the second mode

Hernàndez-Montes in 2004 solve this problem focusing on the concept of energy. So in order to determine displacement characteristic in the capacity spectrum of single degree of freedom system, the displacement of all stories is used. The increase of displacement characteristic in capacity spectrum curve in each stage is obtained by dividing the work done in all stories due to the increased load on the base shear at the same story.

In recent years, FIMA 440 (ATC, 2005) has compared this approach with another pushover model. The results show that, although this method has been advanced to the most of simple load mode vectors, the estimations of in-story drift on the total height of structure might be unreliable. It seems that the main limitations of MPA is in connection with the precision of engineering parameters such as forces and rotation of plastic hinges, structural characteristics, and specific details of the method.

A new pushover method called SSAP has been proposed by Shakeri and Shayanfar, in which the energy concept is used to obtain the target displacement of the structure. Such new pushover procedures have the following features:

- Are based on the energy method and solve the problems associated with displacement of roof control.
- Calculate the effects of higher modes by combining multiple response modes.
- Have very simple concepts that applicable in seismic codes and simple programming.
- Apply progressive degeneration and loss of stiffness and strength directly to the load pattern.

۳- complete description of the research methodology

The accuracy of SSAP, FAP, DAP, ELF, EMPA, the distribution of the first mode, the inverted triangular distribution, regulative distribution, and uniform distribution based on mass by using dynamic time history as the most accurate method were compared and evaluated in this research. Except traditional pushover methods, first three modes have been used for the rest of nonlinear static methods to include the effects of higher modes. The target displacement is obtained by maximum inelastic deformation resulted from nonlinear dynamic analysis of a single degree of freedom system.

A nonlinear dynamic analysis has been used to analyze this system, and then the submission and failure of the member is considered. Thus, system capacity is not based on initial submission or even the failure of single member, and it is defined

when the rate of lateral displacement increase of the system is exceeded. Therefore the predicted seismic capacity of this method is different for each earthquake.

The parameters selected for assessing the accuracy of different methods include drift ratios of the stories, the displacement of stories and storey shear. The drift ratios within the storey indicate the maximum values of in-storey drift between two adjacent balances, which are calculated for each storey over time and are normalized to the height of associated storey. The results of the mean and standard deviation are shown based on the maximum values obtained in the building height for each earthquake record. To estimate the maximum peak of in-storey drifts created in each of these structures for the earthquake records, nonlinear dynamic analyses have been used. In this study, the normal in-storey drift (normalized to the height of each floor) is used as a parameter to describe the damage to the overall structure. It is expected that, in-storey drift is related to the maximum plastic deformations in the structural elements, the degree of damage to sensitive- to-displacement non-structural elements, and inclination of the structure to create general instability due to P-Δ effects. In this study, in order to detect damage imposed to the building in a certain earthquake, the maximum in-storey drift of each floor is used. Considering a set of earthquakes and assuming a normal probability distribution, the mean and standard deviation for the maximum in-storey drift were calculated and also were used as an index to express the dispersion of answers.

Also storey shears were compared as one of the most important engineering parameters.

The error criterion used to evaluate the accuracy of estimation obtained by different pushover methods is the index proposed by Lopez and Mengivar that is presented as formula (1). It should be noted that this criterion is applicable only to describe the difference between methods and do not represent the absolute error.

$$\text{Error}_{\Delta}\ (\%) = 100 \times \frac{1}{n}\sqrt{\sum_{i=1}^{n}\left(\frac{\Delta_{i-NSP} - \Delta_{i-NTHA}}{\Delta_{i-NTHA}}\right)^2} \quad (1)$$

In this equation, n represents the number of floors, Δ_{i-NTHA} the mean of maximum response obtained by dynamic time history analysis, and Δ_{i-NSP} the mean of response obtained from nonlinear static analysis.

٤- structural models

Index model for BRBF system has been designed in accordance with the requirements of AISC 341-05 design, Seismic Provisions for Structural Steel Buildings, ASCE / SEI 7-05 regulations, Minimum Design Loads for Buildings and other structures. The beams, columns, and bracing components are designed such that excessive strength doesn't create in the structure. These samples have adapted from the reference [21] and have been analyzed and evaluated in the software OpenSEES.

In this research, two 6-storey and 12-storey braced samples were used as the representatives of average and high structures; the gap between columns is 30 feet as type and the height is 15 feet. Buckling braces are arranged as two story- X. Additional information on these models are available in [21].

Ground motions used to evaluate the performance of different pushover methods in converging braced steel frames in this study have been prepared by FEMA P-695 which are the representative of far-fault ground motions scaled for soil type SD and risks corresponding to a probability of 10% at 50 years in downtown Los Angeles. These earthquakes include 7 ground's motions, these movements are scaled such that their average response spectrum is consistent with the spectrum of ASCE / SEI

7-05 [20] of the same risk level and soil. The technical specifications of these records are presented in Table 1.

Table (1):

EQ label	PEER-NGA Rec. Num.	Description	Earthquake Magnitude	Campbell Distance (km)	Joyner-Boore Distance (km)	Number of Points	Time Step (sec)	PGA (g)
GM۱	۹۵۳	۱۹۹۴, Northridge, Beverly Hills - Mulhol	۶,۷	۱۷,۲	۹,۴	۲۹۹۸	۰,۰۱	۰,۵۲
GM۲	۹۶۰	۱۹۹۴, Northridge, Canyon Country-WLC	۶,۷	۱۲,۴	۱۱,۴	۱۹۹۸	۰,۰۱	۰,۴۸
GM۳	۱۷۸۷	۱۹۹۹, Hector Mine, Hector	۷,۱	۱۲	۱۰,۴	۴۵۲۹	۰,۰۱	۰,۳۴
GM۴	۱۶۹	۱۹۷۹, Imperial Valley, Delta	۶,۵	۲۲,۵	۲۲	۹۹۹۰	۰,۰۱	۰,۳۵
GM۵	۱۱۱۱	۱۹۹۵, Kobe, Japan, Nishi-Akashi	۶,۹	۲۵,۲	۷,۱	۴۰۹۵	۰,۰۱	۰,۵۱
GM۶	۱۱۵۸	۱۹۹۹, Kocaeli, Turkey, Duzce	۷,۵	۱۵,۴	۱۳,۶	۵۴۳۶	۰,۰۰۵	۰,۳۶
GM۷	۱۱۴۸	۱۹۹۹, Kocaeli, Turkey, Arcelik	۷,۵	۱۳,۵	۱۰,۶	۵۹۹۹	۰,۰۰۵	۰,۲۲

۵- Results and interpretation

Following figures show the results of the seismic response of structures under dynamic time history analysis and different nonlinear static analyses.

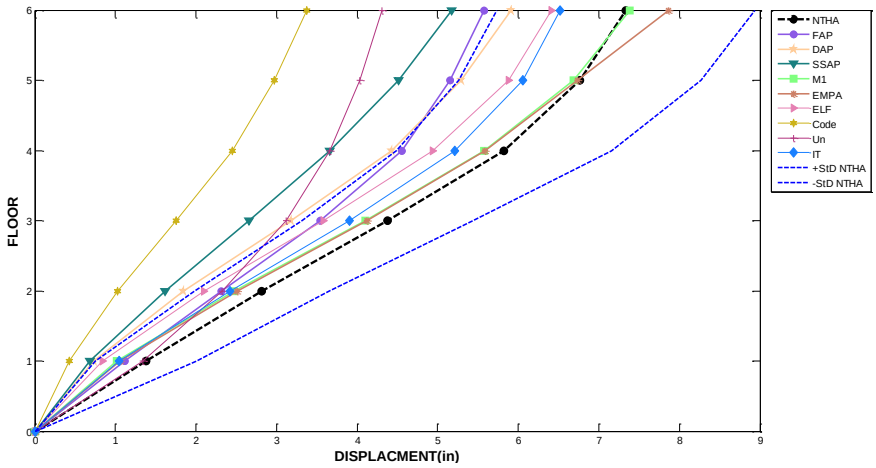


Figure 2: Mean of maximum displacement obtained from all selected records in the height

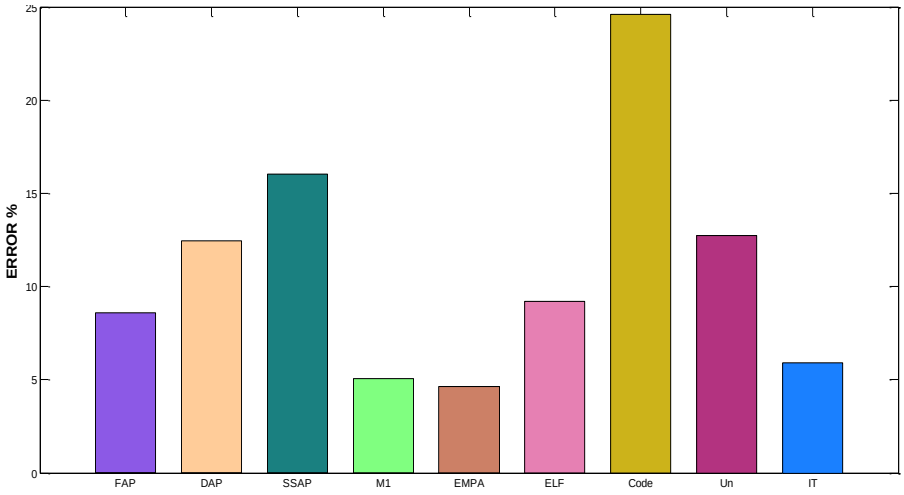


Figure 3: The displacement error obtained by different methods towards time history analysis for all selected records

Figure 2 shows the mean of maximum displacement of the 6-storey building in the height for the average of all selected records with the standard deviation values. Figure 3 shows the error rates of different methods toward non-linear time history analysis.

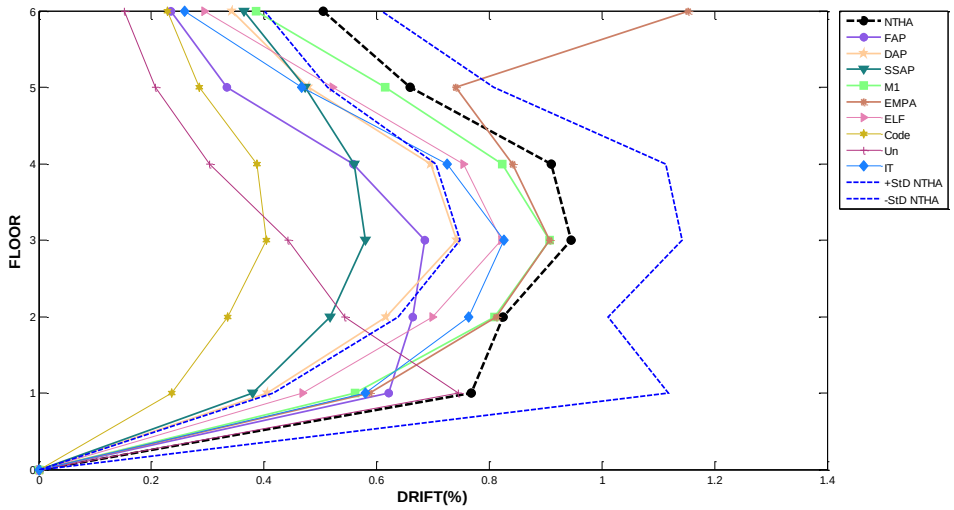


Figure 4: Mean of maximum in-story drift obtained from all selected records, in the height

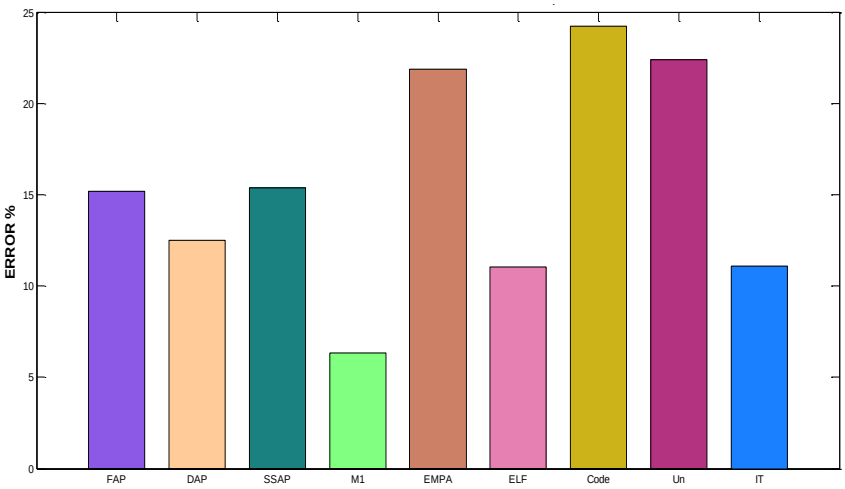


Figure 5: Error of in-story drift obtained from different methods toward time history analysis for all selected records

Figure 4 shows the mean of maximum in-story drift of ٦-storey structure for all selected records with the standard deviation values. Figure ٥ shows the error rates of different methods toward non-linear time history analysis.

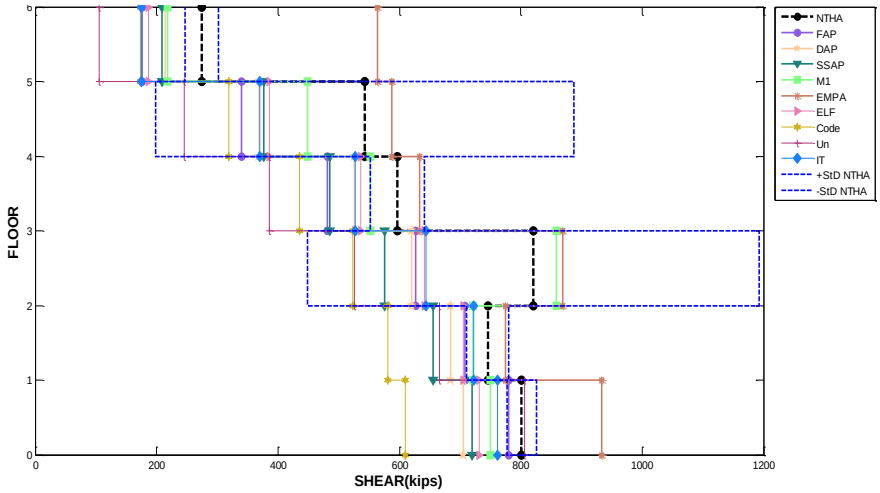


Figure 6: Mean of maximum story shear obtained from all selected records, in the height

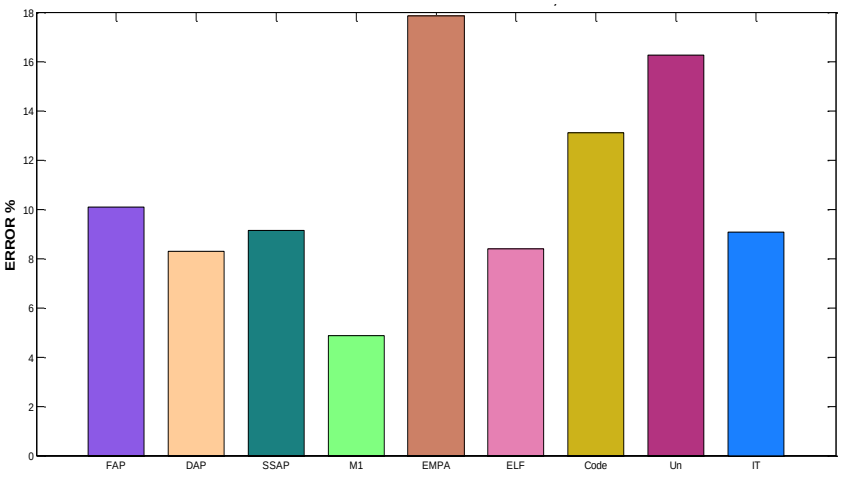


Figure 7: Error of in-story shear obtained from different methods toward time history analysis for all selected records

Figure 6 shows the mean of maximum in-story shear of 6-storey structure for all selected records with the standard deviation values. Figure 7 shows the error rates of different methods toward non-linear time history analysis.

As it can be seen in above figures, SSAP method still presents reliable estimations of maximum structural response. Another point can be observed in these figures is

that, unlike most of engineers who estimate stroey shear forces by the distribution recommended in regulations, it seems that inverted triangular simple method is considerably better than the state where whip force is applied in roof balance. It should be noted that the results are calculated for converging braced structures with buckling bracings and necessitate the evaluation of other structures to present definite results.

As it is evident in above figures, M١ method in shorter structures presents better performance of displacement and drift, as one of the most important parameters of damage control. Regulative methods as well as other advanced updated methods did not achieve such accuracy. It can be due to the lateral behavior of bending bracing structures and overall deformation of the structure appropriate for the first mode of vibration. It can be also observed that EMPA method has a weak performance to estimate the storey shear that can be due to the selected combination law and requires further expertise revisions.

Although regulative methods couldn't cover the results of time history analysis with acceptable accuracy, the results show that conservative estimations are presented which can reduce the concerns about sufficient strengths.

As it can be inferred from above figures, SSAP method among updated methods showed a good estimation of displacement and drift and also had the least standard deviation. It also provide better performance in storey shear estimation by increasing the height.

As above, Figures ٨, ١٠, ١٢ show the mean of maximum displacement, in-storey drift and shear of a ١٢-storey structure for all selected records with the standard deviation values. Figures ٩, ١١, ١٣ show the error rates of different methods toward non-linear time history analysis.

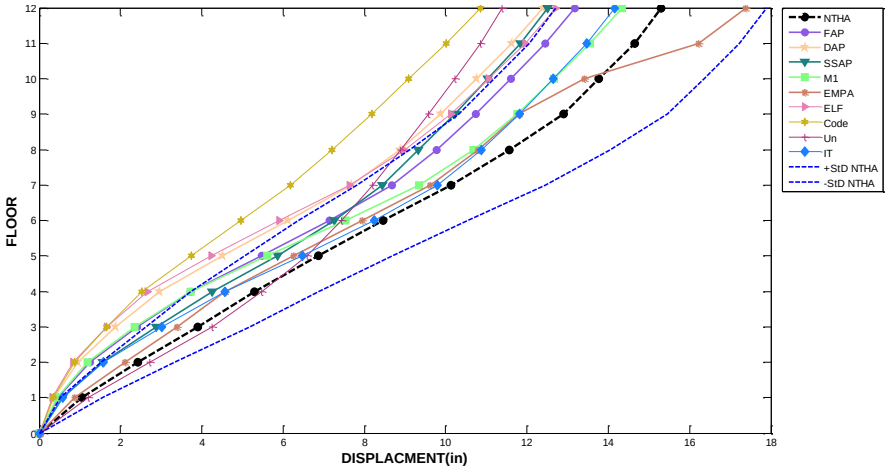


Figure ۸: Mean of maximum displacement obtained from all selected records, in the height

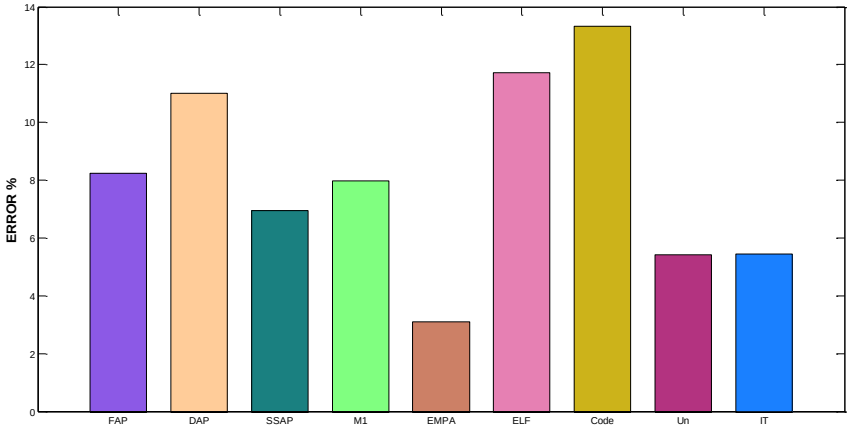


Figure ۹: The displacement error obtained from different methods toward time history analysis for all selected records

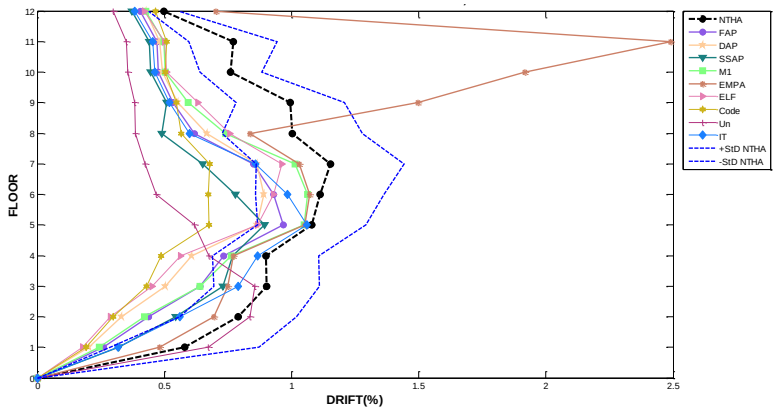


Figure ١٠: Mean of maximum in-storey drift obtained from all selected records, in the height

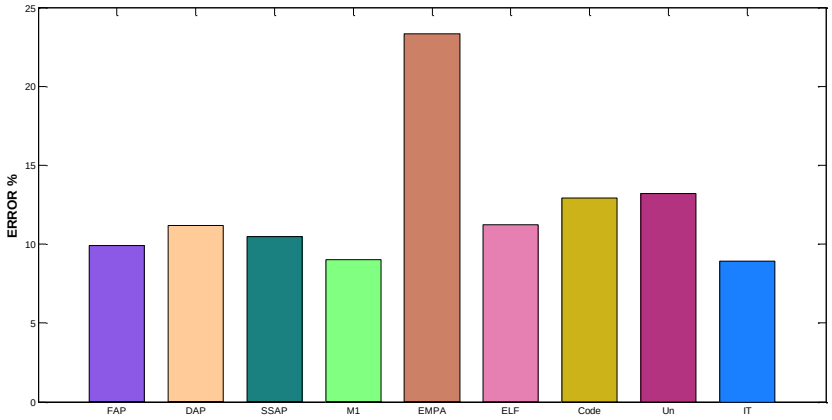


Figure ١١: Error of in-storey drift obtained from different methods toward time history analysis for all selected records

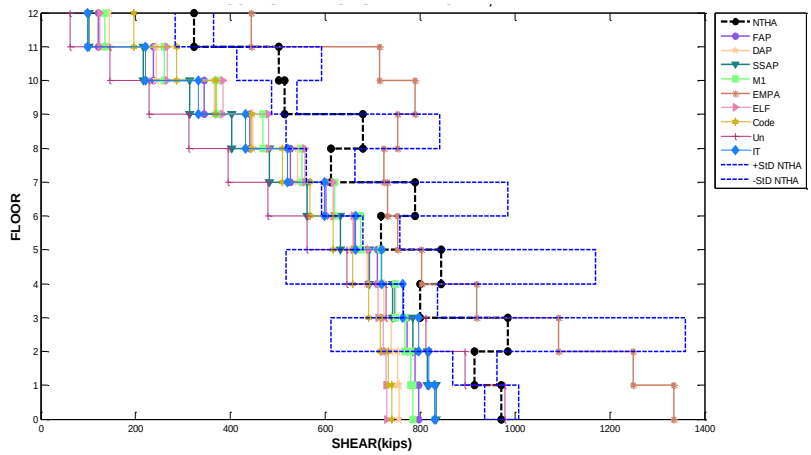


Figure ١٢: Mean of maximum in-storey shear obtained from all selected records, in the height

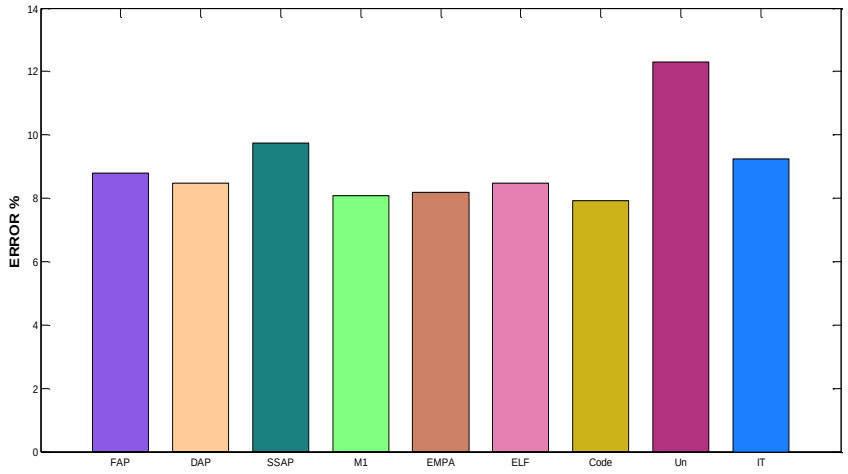


Figure ١٣: Error of in-storey shear obtained from different methods toward time history analysis for all selected records

The above figures show that the performance of storey shear-based methods such as SSAP is increased by increasing the height and inclination to shear behaviors; and the performance of methods such as DAP will be decreased.

The above figures for ١٢-storey model show that EMPA, unlike the poor performance in short structures, has shown better results in the high structures. It shows that SRSS combination principle has greater error within elastic responses rather than resilient responses. However, achieving better results in storey shear requires further researches that seems to be related to the higher modes' response (as three modes used in this study).

٦- Conclusion

As evident, SSAP method has the lowest standard deviation among the existing methods and thus increase the reliability of the results. By increasing the height, the precision of SSAP method for the estimation of response is increased and present better results of response values, especially for storey shear. Another point is that,

the difference between seismic provisions for load distribution estimations toward time history method requires a revision in these methods.

Although regulative methods couldn't cover the results of time history analysis with acceptable accuracy, the results show that conservative estimations are presented which can reduce the concerns about sufficient strengths. It is interesting that inverted triangular simple method is considerably better than the state where whip force is applied in roof balance.

Despite the poor performance of EMPA method in short structures, has shown better results in the high structures. It shows that SRSS combination principle has greater error within elastic responses rather than resilient responses.

The results show that in low to average structures, M١ method gives better and acceptable results, and it is better to use updated methods for higher structures. SSAP method gives good results in the high structures. Among non-updated methods, M١ in the short and medium height structures and EMPA method for high structures are recommended.

References:

١. Rosenblueth E. and Herrera I., ١٩٦٤, On a kind of hysteretic damping, Journal of Engineering Mechanics Division, ASCE, Vol. ٩٠, pp. ٣٧-٤٨.

٢. Gulkan P. and Sozen M.A., ١٩٧٤, Inelastic response of reinforced concrete structures to earthquake motions, ACI Journal, Vol. ٧١, pp. ٦٠٤-٦١٠.

٣. Iwan W.D., ١٩٨٠, Estimating inelastic response spectra from elastic response spectra, Earthquake Engineering and Structural Dynamics, No. ٨, pp. ٣٧٥-٣٨٨.

٤. Priestley M.J.N. and Kowalsky M.J., ٢٠٠٠, Direct displacement-based design of concrete buildings, Bulletin of Earthquake Engineering, Vol. ٣٣, No. ٤.

٥. Freeman S.A., ١٩٩٤, The capacity spectrum method for determining the demand displacement, ACI Spring Convention.

٦. Chopra A.K. and Goel R.K., ١٩٩٩, Capacity-demand-diagram methods based on inelastic design spectrum, Earthquake Spectra, Vol. ١٥, No. ٤, pp. ٦٣٧-٦٥٦.

٧. Newmark N.M. and Hall W.J., ١٩٨٢, Earthquake spectra and design, Earthquake Engineering Research Institute, Berkeley, CA.

٨. Miranda E., ٢٠٠٠, Inelastic displacement ratios for structures on firm sites, Journal of tructural Engineering, No. ١٢٦, pp. ١١٥٠-١١٥٩.

٩. ASCE, ٢٠٠٠, Prestandard and commentary for the seismic rehabilitation of buildings, FEMA ٣٥٦ Report, prepared by the American Society of Civil Engineers for the Federal Emergency Management Agency, Washington, D.C.

١٠. Fajfar P., ١٩٩٩, Capacity spectrum method based on inelastic demand spectra, Earthquake Engineering and Structural Dynamics, No. ٢٨, pp. ٩٧٩-٩٩٣.

١١. Hernàndez-Montes E., Kwon O-S and Ascheim M., ٢٠٠٤, An energy-based formulation for first- and multiplemode nonlinear static (pushover) analyses, Journal of Earthquake Engineering, Vol. ٨, No. ١, pp. ٦٩-٨٨.

١٢. Shakeri K, Shayanfar MA, Kabeyasawa T. A story shear-based adaptive pushover for estimating seismic demands of buildings. Eng Struct ٢٠١٠; ٣٢:١٧٤–٨٣

١٣. Kunnath S.K., ٢٠٠٤, Identification of modal combination for nonlinear static analysis of building structures, Computer-Aided Civil and Infrastructure Engineering, Vol. ١٩, pp ٢٤٦-٢٥٩.

١٤. Krawinkler H. and Seneviratna G.D.P.K., ١٩٩٨, Pros and cons of a pushover analysis of seismic performance evaluation, Engineering Structures, Vol. ٢٠, No. (٤- ٦), pp. ٤٥٢-٤٦٤.

١٥. Chopra A.K. and Goel R.K., ٢٠٠٢, A modal pushover analysis procedure for estimating seismic demands for buildings, Earthquake Engineering and Structural Dynamics, Vol. ٣١, pp. ٥٦١-٥٨٢.

١٦. ATC, ٢٠٠٥, Improvement of nonlinear static seismic analysis procedures, FEMA ٤٤٠ Report, Applied Technology Council, Redwood City, California.

١٧. Hamburger, R. O. (٢٠٠٣). "A Vision for the ATC-٥٨ Project: Development of Performance-Based Seismic Design Guidelines." Applied Technology Council, Sacramento, California.

١٨. López-Menjivar M.A., ٢٠٠٤, Adaptive pushover of ٢-D reinforced concrete buildings, Ph.D. Thesis, European School for Advanced Studies in Reduction of Seismic Risk (ROSE School), University of Pavia, Italy.

١٩. AISC (٢٠٠٥). "Seismic Provisions for Structural Steel Buildings." American Institute of Steel Construction {AISC}, Chicago, Illinois ٦٠٦٠١.

٢٠. ASCE, ٢٠٠٦, Minimum Design Loads for Buildings and Other Structures, ASCE/SEI ٧-٠٥, American Society of Civil Engineers, Reston, Virginia.

٢١. NIST, "Applicability of Nonlinear Multiple-Degree-of-Freedom Modeling for Design," prepared by the NEHRP Consultants Joint Venture for the National Institute of Standards and Technology GCR ١٠-٩١٧-٩, ٢٠١٠.

٢٢. Mazzoni, S., et al. (٢٠٠٦). "OpenSees command language manual." Pacific Earthquake Engineering Research (PEER) Center.

٢٣. ATC-٦٣ (٢٠٠٩). Quantification of Building System Performance and Response Parameters,FEMA P٦٩٥ Report, Applied Technology Council, Redwood City, California.

COMPDYN 2015
5th ECCOMAS Thematic Conference on
Computational Methods in Structural Dynamics and Earthquake Engineering
M. Papadrakakis, V. Papadopoulos, V. Plevris (eds.)
Crete Island, Greece, 25–27 May 2015

ANALYSIS OF INFLUENCE OF SHORT MAGNETORHEOLOGICAL DAMPING ELEMENTS ON VIBRATIONS ATTENUATION OF RIGID ROTORS

Jaroslav Zapomel[1,2], **Petr Ferfecki**[3]

[1] Institute of Thermomechanics
Dolejskova 5, 180 00 Prague, Czech Republic
e-mail: jaroslav.zapomel@vsb.cz

[2] VSB - Technical University of Ostrava
17. listopadu 15, Ostrava - Poruba, 708 33, Czech Republic
e-mail: jaroslav.zapomel@vsb.cz

[3] VSB - Technical University of Ostrava
17. listopadu 15, Ostrava - Poruba, 708 33, Czech Republic
e-mail: petr.ferfecki@vsb.cz

Keywords: Rigid Rotors, Controllable Squeeze Film Dampers, Magnetorheological Oils, Delayed Yielding, Vibrations Damping, Computing Method.

Abstract. *A frequently used technological solution for reducing lateral vibrations of rotating machines as a result of their unbalance consists in adding damping devices to the rotor supports. To achieve their optimum performance their damping effect must be adaptable to the current operating conditions. This is offered by magnetorheological squeeze film dampers. Magnetorheological oils belong to the class of liquids with a yielding shear stress. In the developed mathematical model of a short magnetorheological squeeze film damper the lubricant is represented by Bingham material. Then the pressure distribution in the lubricating layer is governed by the Reynolds equation adapted for Bingham fluid. The yielding shear stress depends on magnetic induction. Its stationary value can be approximated by a power function and its dependence on its time history in the past (characterized by a time constant) by a convolution integral that is consequently transformed to a linear differential equation of the first order. Efficiency of the studied magnetorheological damper was investigated by means of computational simulations. The obtained results show that the rising magnetic flux passing through the layer of the magnetorheological oil arrives at increasing attenuation of the rotor vibrations. On the other hand the damping effect is going down with increasing magnitude of the delayed yielding time constant.*

1 INTRODUCTION

A technological solution frequently used to reduce lateral vibrations of rotors induced by their unbalance consists in adding damping devices to the rotor supports. To achieve their optimum performance their damping effect must be adaptable to the current operating conditions. There are several possibilities based on different physical phenomena how to control the damping force. Some mechanical and hydraulic approaches are discussed in [1-2]. A new concept is represented by application of squeeze film dampers lubricated by magnetorheological oils. The derivation of the relations governing the pressure distribution in the lubricating layer can be found in [3-4]. Some results of the experimental research of the vibration attenuation of a small test rotor damped by magnetorheological dampers are reported in [5].

Magnitude of the damping forces developed by magnetorheological damping devices depends on formation of a chain structure of ferromagnetic particles dispersed in carrying oil by acting of a magnetic field. This paper deals with the study of effect of the time history of magnetic induction on the formation process and thus on efficiency of attenuation of the rotor lateral vibrations.

2 DETERMINATION OF THE DAMPING FORCES

The main parts of magnetorheological squeeze film dampers (Fig. 1) are two concentric rings. The inner one is firmly fixed to the damper housing while the outer one is coupled with the rotor journal by a rolling element bearing and with the damper body by a squirrel spring. The gap between the rings is filled with magnetorheological oil. The rotor journal lateral vibration arrives at squeezing the lubricating layer which produces the damping effect. An important part of the damper is an electric coil generating magnetic flux passing through the lubricating layer. As resistance against the flow of magnetorheological fluids depends on magnetic induction, the damping effect can be controlled by the change of electric current feeding the coil.

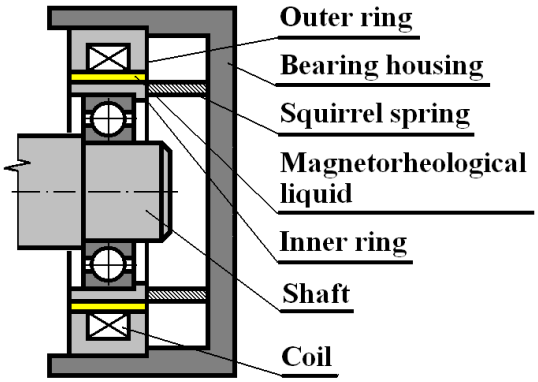


Figure 1: The arrangement of a magnetorheological squeeze film damper.

The developed mathematical model of a magnetorheological squeeze film damper is based on assumptions of the classical theory of lubrication [6-7] except those for the lubricant. As the magnetorheological oil behaves as liquid with a yielding shear stress, it is modelled by Bingham material. In addition, it is assumed that the damper is symmetric relative to its middle plane perpendicular to the journal axis and that its design and geometry make it possible to consider it as short [6-7].

Then the pressure distribution in the thin film of the lubricating oil is described by the Reynolds equation modified for Bingham material [3]

$$h^3 p'^3 + 3\left(h^2 \tau_y - 4\eta_B \dot{h} Z\right) p'^2 - 4\tau_y^3 = 0 \text{ for } Z > 0 \tag{1}$$

where

$$p' = \frac{\partial p}{\partial Z} \tag{2}$$

p denotes the pressure, p' is the pressure gradient in the axial direction, h is the thickness of the oil film, τ_y, η_B are the yielding shear stress and the Bingham viscosity, Z is the axial coordinate referred to the frame of reference describing positions in the oil film (Fig. 2) and $(\dot{})$ denotes the first derivative with respect to time. The details on calculation of the film thickness h can be found in [6-7].

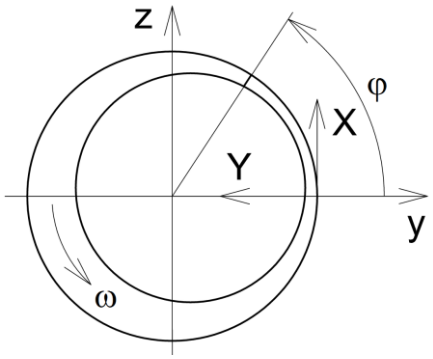


Figure 2: The damper coordinate system.

The Reynolds equation (1) holds only at locations where the beeing squeezed lubricant flows in the direction outside from the damper gap (where the pressure gradient is negative). In areas where the clearance between the inner and outer rings rises with time the lubricant is sucked into the gap from the ambient space and therefore, occurrence of a cavitation is assumed there. In cavitated regions a constant pressure equal to the pressure in the outer space is supposed.

With regard to the assumed damper symmetry, the damping force components are calculated by integration of the pressure distribution p_d in the oil film taking into account a different pressure determination in non cavitated and cavitated regions

$$F_{dy} = -2R \int_0^{2\pi} \int_0^{\frac{L}{2}} p_d \cos\varphi \, \mathrm{d}Z \, \mathrm{d}\varphi \,, \tag{3}$$

$$F_{dz} = -2R \int_0^{2\pi} \int_0^{\frac{L}{2}} p_d \sin\varphi \, \mathrm{d}Z \, \mathrm{d}\varphi \,. \tag{4}$$

F_{dy}, F_{dz} are the y and z components of the damping force, R is the middle radius of the damper gap, L denotes the length of the damping device and φ is the circumferential coordinate.

3 DETERMINATION OF THE YIELDIG SHEAR STRESS

Magnetorheological fluids are formed by carrying liquid in which tiny ferromagnetic particles of micrometre size are randomly dispersed. After application of a magnetic field they

start to form a chain structure which causes that the liquid starts to flow only after the shear stress between two adjacent layers exceeds a limit magnitude (the yielding shear stress).

The steady state value of the yielding shear stress τ_{ys} can be expressed by a power function of magnetic induction B

$$\tau_{ys} = k_y B^{n_y} . \tag{5}$$

k_y, n_y are the proportional and exponential material constants of the magnetorheological oil.

The formation of the chain structure of ferromagnetic particles is a process that is rapid but not instantneous. This implies the yielding shear stress depends on the whole time history of magnetic induction in the past which can be suitably described by a convolution integral

$$\tau_y = k_y \int_0^t \frac{1}{T_y} e^{-\frac{1}{T_y}(t-\vartheta)} B^{n_y} \mathrm{d}\vartheta . \tag{6}$$

Relation (6) is consequently transformed to the differential form

$$T_y \dot{\tau}_y + \tau_y = \tau_{ys} . \tag{7}$$

ϑ denotes the time in the past history before the moment of time t and T_y is the time constant of the delayed yielding process whose value is usually of order of units of miliseconds.

The design arrangement of the damper makes it possible to consider the inner and outer rings as a divided core of an electromagnet with the gap filled with magnetorheological oil. Then the magnetic induction in the lubricating layer can be expressed

$$B = k_B \mu_0 \mu_r \frac{I}{h} . \tag{8}$$

μ_0 is the vacuum permeability, μ_r is the magnetorheological fluid relative permeability, I is the applied current and k_B is the design parametre whose value depends on the number of the coil turns and on the design arrangement of the damping device. After inserting (8) into (5) and introducing the damper design parametre k_{DP}

$$k_{DP} = k_y \left(k_B \mu_0 \mu_r\right)^{n_y} \tag{9}$$

the steady state value of the yielding shear stress reads

$$\tau_{ys} = k_{DP} \left(\frac{I}{h}\right)^{n_y} . \tag{10}$$

4 THE INVESTIGATED ROTOR SYSTEM

The analyzed rotor is rigid. It consists of a shaft and of one disc (Fig. 3). At both its ends it is supported by rolling element bearings and squeeze film magnetorheological dampers. The rotor turns at constant angular speed and is loaded by its weight and unbalance. The squirrel springs of the damping elements are prestressed to be eliminated their deflection resulting from the rotor dead loading.

The task was to investigate the rotor lateral vibrations after the current feeding the magnetorheological dampers is switched on and to analyze influence of the delayed yielding process on amplitude of the resulting transient and steady state oscillations.

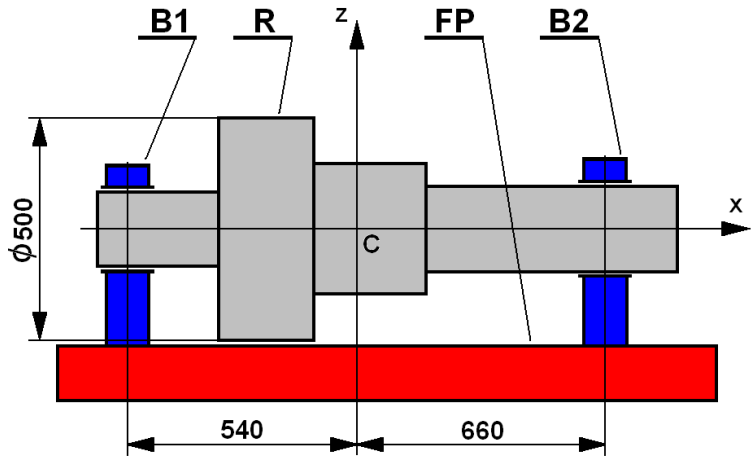


Figure 3: Scheme of the investigated rotor.

In the computational model the rotor is represented by an absolutely rigid body and the dampers by spring elements and nonlinear force couplings. Axis x of the introduced coordinate system is identical with the shaft centre line in the rotor undeformed position and its origin is placed in its intersection with the plane perpendicular to the shaft axis going through the rotor centre of gravity. The rotor can perform four independent motions, displacements in two mutually perpendicular directions (in the directions of axes y and z) and two rotations about y and z axes. Therefore, its oscillations are governed by a set of four equations of motion

$$m\ddot{y} = -b_{TP}\dot{y} + F_{S1y} + F_{S2y} + me_T\omega^2\cos(\omega t + \psi_T)\,, \tag{15}$$

$$m\ddot{z} = -b_{TP}\dot{z} + F_{S1z} + F_{S2z} + F_{PS1} + F_{PS2} - mg + me_T\omega^2\sin(\omega t + \psi_T)\,, \tag{16}$$

$$J_D\ddot{\varphi}_y + \omega J_A\dot{\varphi}_z = -b_{RP}\dot{\varphi}_y + F_{S1y}x_{TS1} - F_{S2y}x_{TS2}\,, \tag{17}$$

$$J_D\ddot{\varphi}_z - \omega J_A\dot{\varphi}_y = -b_{RP}\dot{\varphi}_z - (F_{S1z} + F_{PS1})x_{TS1} + (F_{S2z} + F_{PS2})x_{TS2}\,. \tag{18}$$

m is the rotor mass, J_D and J_A are the diametre and axial moments of inertia the rotor, b_{TP} , b_{RP} are the external damping coefficients referred to the rotor translational and rotational motions, x_{TS1}, x_{TS2} are the distances between the rotor supports and the rotor centre (intersection of the shaft centreline and the perpendicular plane going through the rotor centre of gravity), ω is angular speed of the rotor rotation, e_T is eccentricity of the rotor unbalance, g is the gravity acceleration, F_{S1y} is F_{S1z} are the y and z components of the support force (hydraulic and elastic) acting on the shaft at location of support B1, F_{S2y} is F_{S2z} are the y and z components of the support force (hydraulic and elastic) acting on the shaft at location of support B2, F_{PS1}, F_{PS2} are the prestress forces at supports B1, B2, ψ_T is the phase shift of the unbalance force, y, z are the y and z displacements of the rotor centre, φ_y, φ_z are the rotor rotations about axes y and z and ($\ddot{}$) denotes the second derivative with respect to time.

To solve the motion equations the Adams-Moulton direct integration method was applied.

5 THE SIMULATIONS RESULTS

The technological and geometric parameters of the studied rotor are: the rotor mass 425.9 kg, the rotor diametre and axial moments of inertia 18.9 kgm^2, 9.9 kgm^2 respectively, the external damping coefficients referred to the rotor translational and rotational motions 10 Ns/m, 10 Nms/rad respectively, the squirrel spring stiffness 30 MN/m, the damper diame-

tre/length 150/60 mm, the damper clearance 1 mm, the oil dynamical viscosity (no influence of a magnetic field) 0.3 Pas, the exponential coefficient of the yielding shear stress in its dependence on magnetic induction 2, the damper design parameter 0.001 N/A^2 and the rated speed of the rotor rotation 400 rad/s. At the moment of time of 0.1 s the electric current feeding the coils of both magnetorheological dampers is switched on and reaches its final value of 2.5 A during the time period of 10 ms.

Fig. 4 shows the steady state orbits of the rotor centre (R) and of the journal centres in supports B1 and B2 before switching the current on. The orbits are concentric as the squirrel springs of both dampers are prestressed to be eliminated their deflection caused by the rotor weight.

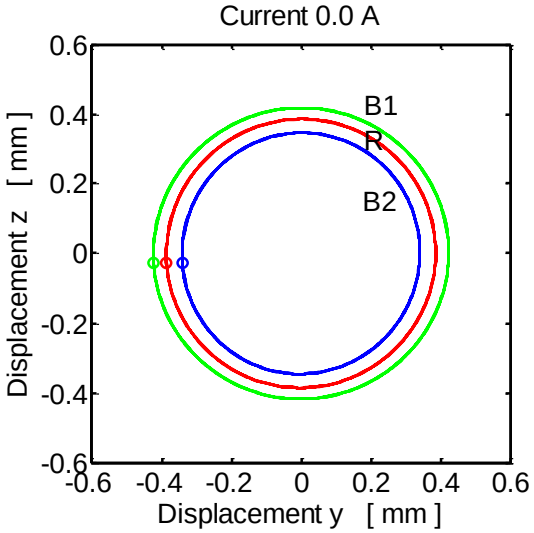


Figure 4: Orbits of the rotor (R) and journal centres (B1, B2) before switching on the current.

Time histories of the horizontal displacement of the rotor centre for three values of the delayed yielding time constant (1 ms, 5 ms, 9 ms) are drawn in Fig. 5-7. It is evident that application of the current increases the damping effect which leads to reducing amplitude of the vibrations. The results also show that the oscillations amplitude after switching the current on strongly depends on the delayed yielding phenomenon. The rising time constant considerably decreases the damping effect which leads to lower suppresion of the rotor oscillations.

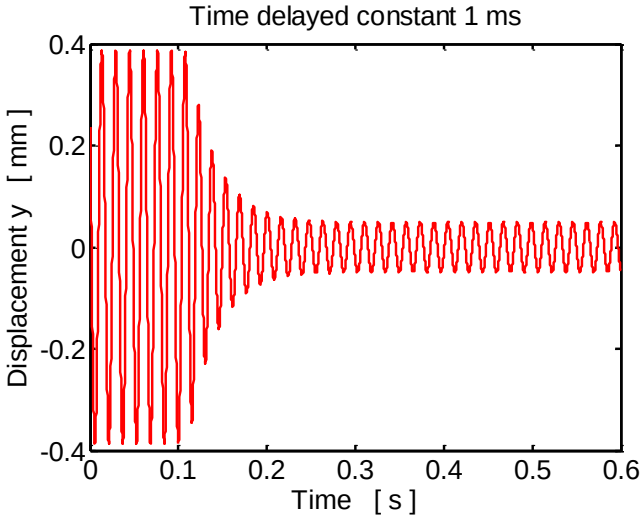


Figure 5: The horizontal displacement of the rotor centre of gravity - 1 ms delayed yielding time constant.

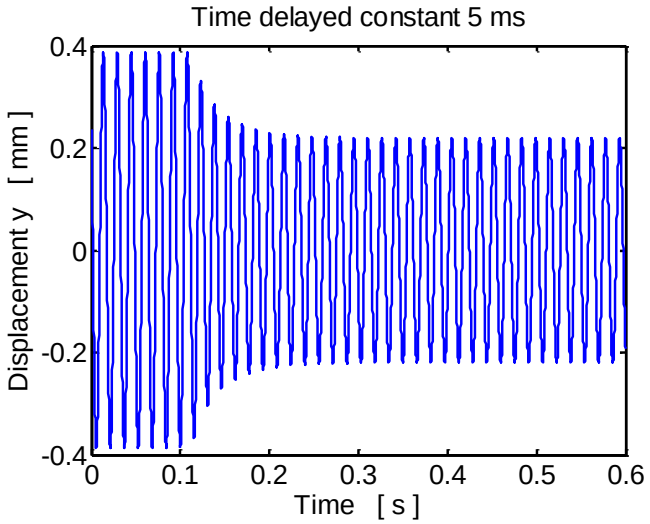


Figure 6: The horizontal displacement of the rotor centre of gravity - 5 ms delayed yielding time constant.

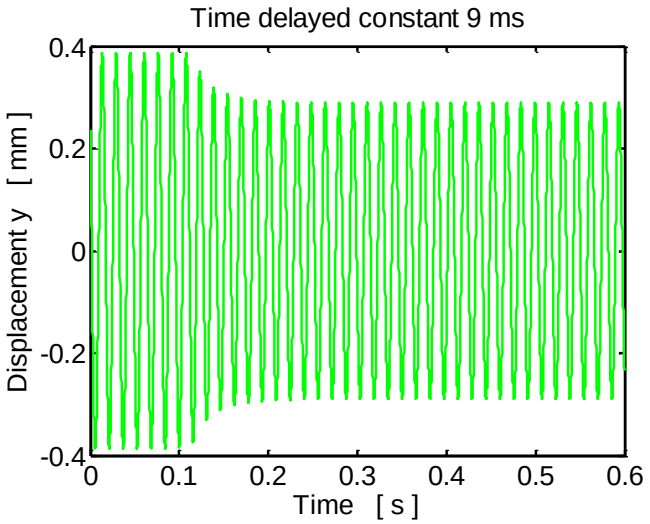


Figure 7: The horizontal displacement of the rotor centre of gravity - 9 ms delayed yielding time constant.

6 CONCLUSIONS

The principal aim of the carried out study was to investigate influence of the delayed yielding process occuring in thin lubricating films of magnetorheological squeeze film dampers on the vibration attenuation of asymmetric rigid rotors performing a complicated spatial motion. The magnetorheological oil was modelled by Bingham material and influence of the time history of magnetic induction on the yielding shear stress was described by a convolution integral. The carried out computational simulations proved that the rising applied current reduces amplitude of the rotor vibrations. On the contrary, the delayed yielding decreases the damping force and the decrease rises with increasing value of the delayed yielding time constant. Such behaviour can reduce efficiency of magnetorheological squeeze film damping devices during the working regimes when fast responses on varying operation conditions or control manipulations are needed.

Acknowledgement: This work has been supported by the grant project of the Czech Science Foundation no. 15-06621S and the European Regional Development Fund in the IT4Innovations Centre of Excellence (CZ.1.05/1.1.00/02.0070).

REFERENCES

[1] C. Mu, J. Darling, C.R. Burrows, An appraisal of a proposed active squeeze film damper, *ASME Journal of Tribology*, **113**(4), 750-754, 1991

[2] A. El-Shafei, M. El-Hakim, Experimental investigation of adaptive control applied to HSFD supported rotors, *ASME Journal of Engineering for Gas Turbines and Power*, **122**, no. October 2000, 685-692, 2000

[3] J. Zapoměl, P. Ferfecki, P. Forte, A computational investigation of the transient response of an unbalanced rigid rotor flexibly supported and damped by short magnetorheological squeeze film dampers, *Smart Materials and Structures* **21**(10), 105011, 2012

[4] J. Zapoměl, P. Ferfecki, Mathematical modelling of a long squeeze film magnetorheological damper for rotor systems, *Modelling and Optimization of Physical Systems*, 97-102, 2010

[5] C. Carmignani, P. Forte, E. Rustighi, Design of a novel magneto-rheological squeeze-film damper, *Smart Materials and Structures*, **15** (1), 164-170, 2006

[6] J. Zapoměl, *Computer modelling of lateral vibration of rotors supported by hydrodynamical bearings and squeeze film dampers*. VSB-Technical University of Ostrava, Ostrava, 2007 (in Czech)

[7] A.Z. Szeri, *Tribology: Friction, Lubrication, and Wear*. Hemisphere Publishing Corporation, Washington, New York, London, 1980

COMPDYN 2015
5th ECCOMAS Thematic Conference on
Computational Methods in Structural Dynamics and Earthquake Engineering
M. Papadrakakis, V. Papadopoulos, V. Plevris (eds.)
Crete Island, Greece, 25–27 May 2015

DESTRUCTION OF THIN FILMS WITH A DAMAGED SUBSTRATE AS A RESULT OF WAVES LOCALIZATION CAUSED BY PERIODIC IMPACT

Andrei K. Abramian[1], **Sergey A. Vakulenko**[2]

[1]Institute of Problems in Mechanical Engineering
St. Petersburg, Russia
e-mail: andabr55@gmail.com

[2] Institute of Problems in Mechanical Engineering
St. Petersburg, Russia
e-mail: vakulenfr@mail.ru

Keywords: thin film,damage substrate,wave localization,string

Abstract. *The present paper is devoted to an issue of possible localization of waves propagating within a structure that consists of a film connected to a backing material through a substrate. The substrate is initially damaged.In the first approximation the film model in the present paper is assumed to be a string on an elastic foundation with a coefficient depending on the substrate damage degree. The elastic foundation imitates the substrate and backing material effects on the film.Initiation of a string delamination resulted from the structure damaged at localized oscillations caused by a periodic impact load has been considered.At loading the initial damage of the substrate is changing in time and space according to the proposed law of the damage growth.It has been shown that at impact the cause of the string substrate material damage increase can be localized oscillation modes. The localized mode existence depends on relation between the initial substrate rigidity and the main material rigidity.There is also possible a passage through a sequence of resonances under the action of a periodic impact force.*

1 INTRODUCTION

Multilayered structures coated with thin films are widely used in various fields of engineering. An illustrative example is auto windshields that either are coated with special films or are laminated structures consisting of thin films bound together by some other material [1]. Shock resistance capability of such multilayered structures depends on a backing material strength and parameters of the film itself. Thin films coating a backing material are employed in microelectronics of flexible screens that can be rolled up, electronic skin production and flexible solar batteries convenient for transportation and application. One of the main problem of developing and application of the aforementioned multilayered structures is their shock resistance capability. An important aspect of the problem is wave processes in the multilayers structures initiated by an impact action. Issues of the multilayered structure shock resistance, in particular the composite material structure, have been investigated during the last 50 years and are still of great interest. The in-depth review of the problem can be found in [2, 3]. The present paper is devoted to an issue of possible localization of waves propagating within a structure that consists of a film connected to a backing material through a substrate. The substrate is initially damaged. Modeling and analysis of waves propagation in elastic solids undergoing damage and growth process were reported in [4]. It was found that a certain low-frequency band exists where the group velocity is antiparallel to the phase advancement,thus indicating an acoustic metamaterial phenomenon. In the first approximation the film model in the presenting paper is assumed to be a string on an elastic foundation with a coefficient depending on the substrate damage degree. The elastic foundation imitates the substrate and backing material effects on the film.A similar spring model has been used by the authors of [5, 6] for comparing the calculated results with the obtained experimental data on ultrasonic investigation of defects in multilayered structures. Papers [7, 8, 9] have revealed that in structures with delamination zones the oscillations localization is possible in those zones. It is explained by the fact that rigidity and density parameters of the delamination zones differ from those in other parts of the structure. The present paper studies initiation of a string delamination resulted from the structure damaged at localized oscillations caused by impact loads. The thin film is simulated as a string in the present paper, and, therefore the substrate and backing material reactions to outside impact effects are taken into account only as the Winkler foundation. The elastic string foundation coefficient is equal to the total rigidity of substrate strings linked together in series plus the rigidity of the backing materials. At loading the initial damage of the substrate is changing in time and space according to the proposed law of the damage growth. The spring model, as the name implies, substitutes the problem of a wave propagation in a medium with the analog problem of exciting an equivalent set of springs. The method is stable and convergent as long as the equivalence between the two problems is justified.The 1-D case is, of course, very elementary. Nevertheless, it is discussed because it allows us to define in a very natural way the ingredients - internal springs,and condition of a string defoliation, which can later be extended to 2D.

2 STATEMENT OF PROBLEM

The main equation of the string dynamics has the form:

$$\gamma u_{xx} - K(n)u - \rho_0 u_{tt} = Q(t,x), \quad x \in (-\infty, +\infty), \quad t \geq 0 \tag{1}$$

Where $K(n)$ is the reduced coefficient of the elastic foundation, n is the damage function (see for the classical definition of n [10]), u is the vertical displacement of the string, ρ_0 is the string material density, $Q(x,t)$ is the external force. In order to underline the purposes of our approach

let us introduce the following definitions.The total volume of a substrate V of M particles is divided into equal cells $w = V/M$,every cell being either filled by "damaged" particles (N is the number of "damaged" particles per cell) or occupied by an undamaged particle(N_0 is number of undamaged particles per cell). The nature of these cells can,in principle,be choose arbitrarily;in practice,it would probably be most satisfactory to chose cells sufficiently small so that the probability of two particles occupying a single cell is negligible.Thus, we can introduce the damaged function n as follows: $n = 1 - \frac{N_0}{N+N_0}$. There is the following expression for the damage function n (see [11]): $\frac{\partial n}{\partial t} + n\nabla V_* = J$, where V_* is the velocity of the particles of the substrate, J is the damage growth source.The term $n\nabla V_*$ in that equation is neglected in the first approximation , i. e. the particle diffusion of the damaged material is not taken into consideration. Assume, that $G = G_0(1-n)$ is the tension/compression rigidity of the substrates, where G_0 is the rigidity of the interstitial layer of the acoustic medium (substrate) with compression modulus $G = \rho_1 c^2$. Here c is a wave speed in the material of substrate, and ρ_1 is the density of the substrate material.Then, a pressure value in the substrate layer in quasi-static approximation is $p_* = \frac{\rho_1 c^2 (u-v)}{h}$, where v is the vertical displacement of the foundation,h is the substrate layer thickness, and $\frac{u-v}{h}$ defines the relative deformation . Assume , that $J = \beta H(p_* - p_{cr})$. Here H is the Heaviside function. Thus, we assume that the damage growth source starts increasing the damage when the pressure in the layer reaches its critical value $p_{cr} = G_0\Delta$. Note, that $\frac{\Delta}{h}$ is the maximum value of the interstitial layer relative deformation. Finally, as a result we have :$J = \beta H[(u-v) - \Delta]$. Since the substrate rigidities and the rigidity of the main material of the structure (designated as k_0) are joint in series, one has : $v = \frac{Gu}{k_0+G}$ and $u - v = \frac{k_0 u}{k_0+G}$. Thus, finally the following system of equations describing dynamics of a film connected to an elastic foundation and containing damaged material has been obtained:

$$\begin{gathered}\gamma u_{xx} - K(n)u - \rho_0 u_{tt} = Q(x,t), \quad x \in (-\infty, +\infty), \quad t \geq 0, \\ K(n) = \mu(n)G(n), \\ \mu(n) = \frac{k_0}{k_0+G(n)}; \\ \frac{\partial n}{\partial t} = \beta H(u\frac{k_0}{k_0+G(n)} - \Delta)(1-n),\end{gathered} \tag{2}$$

where $n = n(x,t), n_0 = n(x,0)$; $k_0 > 0$ is a constant,

$$G(n) = G_0(1-n), \quad 0 \leq n \leq 1,$$

$$G(n) = 0, \quad n > 1,$$

In the case when $n = 1$ the film comes off the substrate. It may be assumed that the film separation starts at some critical value of the damage coefficient $n = n_*$. Thus, the present paper investigates the process of the damage growth leading to the initial film detachment. Let us consider the system of Eqs.(2) describing the elastic system model with the damaged substrate. Here $K(n)$ is the complicated functional of u that includes a damage function n.

The time evolution of the damage function $n(x,t)$ is defined by the following differential equation

$$\frac{\partial n}{\partial t} = \beta H(\mu(n)u - \Delta)(1-n), \tag{3}$$

where $\beta, \Delta > 0$ are positive constants, and H is the Heaviside step function. It is assumed that Q is a smooth function fast decreasing in $|x|$, and the boundary and initial conditions are as

follows:

$$u(x,t) \to 0 \quad (|x| \to \infty) \tag{4}$$

$$u(x,0) = 0, \quad u_t(x,0) = 0, \quad x \in (-\infty, +\infty) \tag{5}$$

$$n(x,0) = n_0(x), \quad x \in (-\infty, +\infty) \tag{6}$$

where n_0 also is a smooth function fast decreasing in $|x|$.

For bounded domains, if $x \in [-h, h]$, we set the Dirichlet boundary condition

$$u(h,t) = u(-h,t) = 0. \tag{7}$$

Below we will show that weak solutions for the case $x \in (-\infty, +\infty)$ can be obtained as a limit of solutions satisfying (7) as $h \to +\infty$.

Note that Eq. (3) implies $0 \le n(x,t) \le 1$ for all n if $0 \le n(x,0) \le 1$. This can be shown by the maximum principle. In fact, if $n > 1$ at some $x_0, t_0 > 0$, then there is a point (x_*, t_*) where $n_t > 0$ and $n = 1$, but this is in contradiction with Eq.(3). Therefore, Eq. (3) correctly defines the damage function. There are possible alternative versions of Eq.(3) for the damage function but they are not considered in the paper. Eq. (3) means that the destruction (the damage growth) starts when the displacement reaches the particular threshold.

To describe the time of the elastic system destruction the criterion of critical damage level is used.

Criterion of critical damage level

Assume that the elastic material is destroyed at point x and at the moment t when the damage function $n(x,t)$ reaches some critical level n_* at that moment:

$$n(x,t) = n_* \tag{8}$$

The minimal time T_F such that Eq.(8) holds for some x, is called the full destruction time.

The front of full destruction $L_F(t)$ is defined by the following relation

$$n_* = n(L_F(t), t), \tag{9}$$

where n_* is a critical damage level. In the general case when $u(x,0) \neq 0$ the function $L_F(t)$ is increases in time.

3 ASYMPTOTIC FOR SMALL β

If β is small, then $dn/dt = O(\beta) << 1$ and the coefficient $K(n)$ is a function of the slow time $\tau = \beta t$. Therefore, we can use a quasi-stationary approximation by the two time scales perturbation method. Let us use the ansatz

$$u = U_0(x,t,\tau) + \beta U_1(x,t,\tau) + ...$$

Then, by substituting this series into Eq.(2) one obtains for terms of the order $O(1)$ the following equation

$$\gamma U_{0xx} - K(n)U_0 - \rho_0 U_{0tt} = Q(t,x), \quad x \in (-\infty, +\infty), \quad t > 0 \tag{10}$$

In this equation $n = n(x,\tau)$ can be considered as a slow parameter. Different asymptotic of U_0 will be found in coming sections. The parameter n is defined, in the first approximation, as follows:

$$\frac{\partial n}{\partial \tau} = H(\frac{k_0 U_0(x,t,\tau)}{k_0 + G(n)} - \Delta), \quad \tau = \beta t. \tag{11}$$

The destruction process starts in points where the following conditions hold:

$$\frac{k_0 U_0(x,t,\tau)}{k_0 + G_0(1-n(x,\tau))} = \Delta. \tag{12}$$

The roots $T_{beg}(x,\tau)$ of eq. (12), can be named the *time when the destruction process start*. The correction U_1 can be found from the following equation :

$$\gamma U_{1xx} - K(n)U_1 - \rho_0 U_{1tt} = Q_1(t,x,U_0), \quad x \in (-\infty,+\infty), \quad t > 0$$

where $Q_1 = 2\rho_0 U_{0t\tau}$. In general, it is not easy to find explicit relations for U_0 and U_1, and because of that, different cases where asymptotic can be obtained in the coming sections are considered.

4 PERIODIC FORCES AND RESONANCE EFFECT

4.1 Resonance condition

In some experiments one studies external loads consisting of some periodical strikes. This can be described by equation (1), where

$$Q(x,t,\epsilon) = \delta_\epsilon(x-x_0)\sum_{j=0}^{M}\delta(t-j\Delta t), \quad x \in (-\infty,+\infty), \quad t > 0. \tag{13}$$

where Δt is a time step for the strikes. The solution depends on the localization parameter ϵ and M. Let us assume that the initial data are as follows:

$$u(x,0,\epsilon) = \phi_0(x), \quad u_t(x,t,\epsilon)|_{t=0} = \phi_1(x).$$

Let us construct some particular solutions of (1) describing resonances between the time periodic external load and localized modes. We consider the limit $\epsilon \to 0$ and suppose that $M >> 1$. To investigate this initial value problem, we can use the Fourier transformation :

$$u(x,t,\epsilon) = 2\pi^{-1/2}\int_{-\infty}^{\infty}\exp(i\omega t)\hat{u}(x,\omega,\epsilon)d\omega,$$

$$Q(x,t) = 2\pi^{-1/2}\int_{-\infty}^{\infty}\exp(i\omega t)\hat{Q}(x,\omega)d\omega, \quad i = \sqrt{-1}$$

The Fourier coefficients $\hat{Q}(x,\omega)$ can be computed and have the form:

$$\hat{Q}(x,\omega) = \delta_\epsilon(x-x_0)2\pi^{-1/2}\hat{S}(\omega), \quad \hat{S}(\omega) = 2\pi^{-1/2}\sum_{j=0}^{M}\exp(-ij\omega\Delta t).$$

Let us make a remark. For large M the quantity $\hat{Q}(x,\omega)$ has the order M only if $\Delta t\omega \approx 2m_0\pi$, where m_0 is a positive integer. Indeed, if $|\Delta t\omega - 2m_0\pi| >> M^{-1}$, then $\hat{S}(\omega)$ is bounded for large M

$$\sum_{j=0}^{M}\exp(-ij\Delta t\omega) = \frac{1-\exp(-(M+1)i\omega\Delta t)}{1-\exp(i\omega\Delta t} = O(1),$$

and it is large if $|\omega\Delta t - 2m_0\pi| = 0$ for some integer m_0. Then

$$\sum_{j=0}^{M}\exp(-ji\omega\Delta t) = M$$

Therefore, we observe a resonance for ω close to $\omega(m_0) = 2m_0\pi(\Delta t)^{-1}$.

For $\hat{u}(x, \omega, \epsilon)$ one finds the following equation

$$\gamma\hat{u}(x,\omega,\epsilon)_{xx} - K(n)\hat{u}(x,\omega,\epsilon) + \rho_0\omega^2\hat{u}(x,\omega,\epsilon) = \delta_\epsilon(x - x_0)\sqrt{2\pi}^{-1/2}\hat{S}(\omega). \tag{14}$$

The left hand side of (14) is the Schrödinger operator, which has the localized eigenfunctions $\Psi_j(x)$ with eigenvalues E_j, and non-localized eigenfunctions $\Psi(x, k)$ with eigenvalues $E(k)$, where k is a wave number. Note that E_j is a complicated functional of $n(x, \tau)$, and these quantities depend on slow time τ as a parameter.

4.2 Asymptotics describing resonance effect

There is also possible a passage through a sequence of resonances. We consider the following cases: (**a**) initial stage of destruction when n is small, (**b**) final stage where $n \approx 1$.

Remind some facts about the Schrödinger operator with shallow potentials wells. Consider the operator

$$H\Psi = (-\Delta + \rho\Phi(x))\Psi$$

in $\mathbf{R}^1$, where $\Phi(x)$ is a smooth function fast decreasing as $|x| \to \infty$. Then, under condition

$$I_\Phi = \int_{-\infty}^{+\infty} \Phi(x)dx < 0 \tag{15}$$

for sufficiently small $\rho > 0$ we have a single eigenfunction $\Psi_1(x)$ with the eigenvalue $E_1(\rho)$ defined by

$$E_1 = -\eta^2, \quad \eta = \frac{\rho I_\Phi}{2}. \tag{16}$$

If $I_\Phi > 0$, we have no eigenfunctions. For Ψ_1 we have asymptotics

$$\Psi_1 = \eta^{3/2}\int_{-\infty}^{+\infty} \exp(ipx)a(p)(p^2 + \eta^2)dp, \quad a(p) = \frac{\tilde{\Phi}(p)}{\tilde{\Phi}(0)}, \tag{17}$$

where

$$\tilde{\Phi}(p) = (2\pi)^{-1/2}\int_{-\infty}^{+\infty} \Phi(x)\exp(-ipx)dx$$

is the Fourier image of the potential Φ.

Let us apply these results to the cases (**a**) and (**b**).

In the first case (**a**) the expression $K(n)$ has the form $a_0^2 - b_0 n + O(n^2)$, where $a_0^2 = k_0G_0/(k_0 + G_0)$ and $b_0 = k_0/(k_0 + G_0) > 0$. Then we obtain a Schrödinger operator with a small potential well. The condition (15) holds. Thus we have a single localized mode and the corresponding energy E_1 admits the estimate $E_1 = -a_0^2 + O(n)$. For $n << 1$ The resonance condition takes the form

$$k_0G_0/(k_0 + G_0) + O(||n||) = \rho\omega(m_0)^2 \tag{18}$$

for some integer m_0. To obtain this condition in a more precise and general form, below we consider a particular case when Φ is a rectangle potential, where resonance condition can be derived by a straight forward way, and after we derive this condition in general form.

Let us introduce the detuning parameter κ by

$$\kappa^2 = \gamma^{-1}(a^2 - \rho\omega(m_0)^2), \quad a^2 = k_0G_0/(k_0 + G_0). \tag{19}$$

Let us investigate the resonance effect in more detail. Suppose $n << 1$, then we can use asymptotics

$$K(n) = a^2 - \frac{k_0 G_0}{(k_0 + G_0)^2} n(x) + O(n^2) = a^2 + \gamma W(x)$$

for the case when $\Phi(x)$ is a rectangle potential

$$\Phi(x) = -h, \quad |x| < l, \quad \Phi = 0, \quad |x| > l. \tag{20}$$

Equation (14) takes the form

$$\hat{u}(x,\omega)_{xx} - \bar{k}_0 \hat{u}(x,\omega) - \Phi(x)\hat{u}(x,\omega) = \gamma^{-1}\delta_\epsilon(x - x_0)\sqrt{2\pi}^{-1/2}\hat{S}(\omega). \tag{21}$$

Due to the basic properties of the Schrödinger equation mentioned above the localized eigenfunction exists if

$$h - \kappa^2 = \beta^2 > 0, \quad \kappa > 0.$$

We assume that these conditions hold. In the case (20) and $\epsilon \to 0$ the solution of eq. (21) can be found. The solution $U = \lim_{\epsilon \to 0} \hat{u}(x,\omega,\epsilon)$ has the form (we assume that $|x_0| < l$, i.e., the external force is localized within the destruction zone). For $x < x_0$ we have

$$U = C_-(\frac{\kappa}{\beta}\sin(\beta(x+l)) + \kappa\cos(\beta(x+l)), \quad x \in (-l, x_0), \tag{22}$$

$$U = C_- \exp(\kappa(x+l)), \quad x < -l \tag{23}$$

and for $x < x_0$ we obtain

$$U = C_+(-\frac{\kappa}{\beta}\sin(\beta(x-l)) + \cos(\beta(x-l)), \quad x \in (x_0, l), \tag{24}$$

$$U = C_+ \exp(-\kappa(x-l)), \quad x > l. \tag{25}$$

Let $x_0 = 0$. Then the constants $C_\pm$ are defined by

$$C_+ = C_{--} = \frac{1}{2(\kappa\sin(\beta l) - \beta\cos(\beta l))}. \tag{26}$$

Finally, the resonance condition has the form

$$\kappa\sin(\beta l) - \beta\cos(\beta l) = 0. \tag{27}$$

The left hand side of this equation is the eigenvalue E_1 of the corresponding Schrödinger operator. This condition does not depend on x_0 however the solution U depends on x_0.

It is clear that the general form of the resonance condition is

$$k_0 G_0/(k_0 + G_0) + E_j = \rho\omega(m_0)^2, \quad j = 1, ... \tag{28}$$

where E_j are eigenfunctions of the corresponding Schrödinger operator. An explicit expression for E_j can be obtained only in some cases. For small damage densities $n_0(x)$ we obtain, by asysmptotics (16)

$$E_1 = \frac{k_0 G_0}{(k_0 + G_0)^2}\int n_0(x)dx. \tag{29}$$

4.3 Wave regime

Consider the case when the external load is defined by (13) and $n \approx 1$. In the case (**b**) the expression $K(n)$ has the form $G_0(1-n) + ((1-n)^2)$. Then again we obtain a Schrödinger operator with a small potential well. However, now condition (15) does not hold. We have no single localized modes and no resonances. Therefore, we conclude that close to a final destruction stage, localized mode and resonances vanish. In this case we observe purely wave regime. Namely, taking into account that $K(n) \approx 0$, we note that eq. (1) takes the form

$$\gamma u_{xx} - \rho_0 u_{tt} = Q(x,t,\epsilon), \quad x \in (-\infty, +\infty), \quad t > 0. \tag{30}$$

Using (13) in limit $\epsilon \to 0$ we can find the following solution of this equation. One has $u(x,t,\epsilon) \to u(x,t)$ as $\epsilon \to 0$ and

$$u = (2c)^{-1} \sum_{j=1}^{M} (H(x - c(t - j\Delta) - (H(x - c(t + j\Delta))H(t - j\Delta t), \quad t > 0. \tag{31}$$

where H is the Heaviside step function. This solution describes M propagating waves.

5 DESTRUCTION FRONT DYNAMICS.

The formal solution of Eq.(3) can be written down as follows:

$$n(x,t) = 1 + (n_0(x) - 1)\exp(-\beta S(x,t)), \quad S = \int_0^t H(\mu u - \Delta) ds. \tag{32}$$

The equation for L_F is as follows

$$n_* = 1 + (n_0(L_F) - 1)\exp(-\beta S(L_F, t)). \tag{33}$$

It is natural to assume that the critical parameter $n*$ is close enough to 1. The integral S can be computed using expression for u. This gives the following asymptotic for large t:

$$S = C_1 t, \quad |x - x_0|/c < t,$$

$$S = 0, \quad |x - x_0|/c > t,$$

where C_1 is a constant depending on the system parameter in a complicated way. Therefore, if $|x - x_0| > ct$, i.e., the wave does attain x within time t, Eq.(33) has no solutions for $n* \approx 1$ since $n_* > \max n_0(x)$. If the right hand side of Eq.(33) is smaller than n_*, then there are no solutions for all x and the destruction process does not start. If the right hand side of Eq.(33) is bigger than n_* then the solution L_F of (33) exists. So, finally, the following result is obtained: for large t we have two destruction fronts such that

$$L_F(t) \approx \pm c\, t + O(1). \tag{34}$$

Consider an influence of the wave contribution W and the localized mode contribution V to a destruction process. It is seen that this effect depends on x and t. For some x the localized mode contribution reinforces the destruction process, while for others that contribution diminishes it. So,we have two qualitatively different dynamics of a destruction front. If the localized mode amplitude is smaller than the amplitude of the wave term, then the dynamics of the front is linear. If the localized mode amplitude has the same order as the wave term amplitude, we have

alternation of time intervals,where L_F increases, and time intervals where $L_F(t)$ is a constant. The transition from oscillating dynamics to wave dynamics with a linear growth, when the front leaves the zone where the localized mode is not small, can be observed. Finally, for large times the front moves in a linear manner, and for very large times the front stops since the amplitude of the wave contribution slowly decreases as $t^{-1/2}$. The time when the front stops can be estimated roughly with the help of the asymptotic for the wave contribution, which finally gives the following expression:

$$T_{stop} \approx A\epsilon^2 \bar{k}_0 \gamma^{-1} \sqrt{\rho_0}.$$

Moreover, there is a possibility for a transition region in which oscillating front dynamics with stop intervals change to the monotone linear dynamics if the zones of the impact force application, and the localized mode concentration, are different.

6 PASSAGE OF FAST LOCALIZED IMPULSE THROUGH DESTRUCTION ZONE

An inhomogeneous distribution of the damage parameter influences the localized solution propagation. The goal of this section is to estimate the impulse amplitude. Experimental data show that the impulse amplitude decreases during this propagation process. In this section, we will find asymptotic solutions, which are valid for any $\beta > 0$ and also for not small inhomogeneities. We can describe a localized solution by the asymptotic solution in the form:

$$u(x,t,\epsilon) = a(x,t)\exp(-\epsilon^{-1}S(x,t)), \tag{35}$$

where $S(x,t) \geq 0$ is a smooth function such that $S(x,t) = 0$ at a point $x = X(t)$, $\epsilon > 0$ is a small parameter. Then this solution describes a displacement impulse localized at $x(t)$. One can get the following equation

$$\epsilon^{-2}a(\gamma S_x^2 - \rho_0 S_t^2) + \epsilon^{-1}(\gamma(-2a_x S_x - aS_{xx}) + \rho_0(2a_t S_t + aS_{tt}) + K(n)a) + \gamma a_{xx} - \rho_0 a_{tt} = 0. \tag{36}$$

We consider first terms of the orders ϵ^{-2}. Then one has the eikonal equation in the form:

$$\gamma S_x^2 - \rho_0 S_t^2 = 0. \tag{37}$$

For $a(x,t)$ one has

$$\gamma(-2a_x S_x - aS_{xx}) + \rho_0(2a_t S_t + aS_{tt}) + \epsilon(K(n)a + \gamma a_{xx} - \rho_0 a_{tt}) = 0. \tag{38}$$

One of simple solutions of equation (37) is $S = \frac{(x-ct)^2}{2}$. Then $X(t) = ct$. The form of solution for $a(x,t)$ (which is not so simple, in general) can be simplified. In fact, in this case we can set $a(x,t) \approx a(ct,t) = A(t) + O(\epsilon)$ and $n(x,t) \approx n(ct,t) + O(\epsilon) = \bar{n}(t) + O(\epsilon)$ with accuracy ϵ, since for $|x - ct| >> \epsilon$ the solution u is exponentially small. It is difficult, however, to use (38) in order to find $a(t)$. We apply the energy balance equation. Let us compute the main asymptotic contribution of the localized solution into the energy, up to small corrections. This gives

$$E[u, u_t] = \frac{1}{2}\int_{-h}^{h}(\gamma u_x^2 + \rho_0 u_t^2 + K(n)u^2)dx \approx R(\epsilon,t)\frac{\bar{a}^2(t)}{2}, \tag{39}$$

where

$$R(\epsilon,t) \approx \int_{-\infty}^{\infty}\exp(-2S/\epsilon)(\epsilon^{-2}(\gamma S_x^2 + \rho_0 S_t^2) + K(\bar{n}(t)))dx. \tag{40}$$

Let us denote

$$M_0(\epsilon) = \int_{-\infty}^{\infty}\exp(-2S/\epsilon)dx.$$

For $S = (x-ct)^2/2$ the third term $K(\bar{n}(t)$ in the right hand side of the equation can be removed, since the contributions of the first and second ones have the order $O(\epsilon^{-1}M_0)$, where the third term give $O(M_0)$. Then $R(\epsilon, t) = R_0(\epsilon)$ is independent on t, and up to small corrections vanish as $\epsilon \to 0$. For the dissipative functional D one has:

$$D(\epsilon, a) \approx \frac{1}{2}\bar{n}_t\bar{a}^2(t)\frac{dK}{dn}(\bar{n}(t))H, \quad M_0 = \int_{-\infty}^{\infty} \exp(-2S/\epsilon)dx. \tag{41}$$

If we suppose that the impulse is powerful enough to start the destruction process at $x = ct$,then:

$$\frac{da}{dt} = M_0R_0^{-1}(\epsilon)\beta K_n(\bar{n}(t))a. \tag{42}$$

So, the impulse amplitude decrease according to the following expression:

$$a(t) = \Theta(t)a(0), \quad \Theta(t) = \exp(M_0R_0^{-1}(\epsilon)\int_0^t \frac{K(\bar{n}(s)}{d\bar{n}}ds). \tag{43}$$

For a small β we can replace $\bar{n}$ in this formula to $\bar{n}_0(t) = n_0(ct)$, where n_0 is initial damage distribution. Finally,we obtain for Gaussian impulses with $S = (x - ct)^2/2$ that

$$\Theta(t) = \exp(-const\epsilon\gamma^{-1}\beta k_0^2G_0\int_0^t (k_0 + G_0(1 - n_0(cs)))^{-2}ds, \tag{44}$$

and for small G_0 or $n_0 \approx 1$ one has:

$$\Theta(t) = \exp(-const\epsilon\gamma^{-1}\beta k_0G_0t). \tag{45}$$

7 CONCLUSIONS

In the paper an influence of the wave contribution and the localized mode contribution to a destruction process has been considered. This effect depends on x and t. For some x the localized mode contribution reinforces the destruction process, while for others that contribution diminishes it. So,we have two qualitatively different dynamics of a destruction front. If the localized mode amplitude is smaller than the amplitude of the wave term, then the dynamics of the front is linear. If the localized mode amplitude has the same order as the wave term amplitude, we have alternation of time intervals,where L_F increases, and time intervals where $L_F(t)$ is a constant. The transition from oscillating dynamics to wave dynamics with a linear growth, when the front leaves the zone where the localized mode is not small, can be observed. Finally, for large times the front moves in a linear manner, and for very large times the front stops since the amplitude of the wave contribution slowly decreases as $t^{-1/2}$. Some particular solutions describing resonances between the time periodic external load and localized modes has been obtained. Also possible passage through a sequence of resonances has been observed. The conclusion that close to a final destruction stage, localized mode and resonances vanish can be made. In this case one can observe purely wave regime. An inhomogeneous distribution of the damage parameter influences the localized solution propagation. It has been shown that at impact the cause of the string substrate material damage increase can be localized oscillation modes. The localized mode existence depends on a relation between the initial substrate rigidity and the main material rigidity. The impact energy is redistributed between propagating waves and localized waves in such a way that the latter may make the main contribution to the growth of the material damage.

8 ACKNOWLEDGEMENTS

This work is supported by a RFBR grant 13-1-00814.

REFERENCES

[1] Nanshu Lu et al.,Failure by simultaneous grain growth,strain localization, and interface de-bonding in metal films on polymer substrates,*J.Mater.Res.*, **24** ,375-385,(2009).

[2] Phaong Tran et al.,Dynamic delamination of patterned thin films: a numerical study, *Int.J.Fract.*, **162**,77-90,(2010).

[3] E.Maeva at al.,Acoustical methods for the investigation of adhesively bonded structures:A review,*Can.J.Phys.*, **82**,981-1025,(2004).

[4] D.Roy Mahapatra, Wave propagation in elastic solids undergoing damage and growth process *Acta Mech*,**203**,163-181,(2009).

[5] Shihong Huo and Henrique Reis, Estimation of adhesive bond strength in laminated safety glass using guided mechanical waves;Part 1.An energy velocity approach,*Insight*, **50**,3,146-152,(2008).

[6] P.P.Delsanto and M.Scalerndi,A spring model for the simulation of the propagation of ultrasonic pulses through imperfect contacy interfaces,*J.Acoust Soc.Am.*, **104**,2584-2591,(November 1998).

[7] Abramyan A.K. et al.,Influence of dynamic processes in a film on damage development in an adhesive base, *Mechanics of Solid*,**47**,5,pp.498-504,(2012).

[8] Indeitsev D.A.,A.K.Abramyan,Bessonov N.M., Motion of the exfoliation boundary during localization of wave processes,*Doklady Physics*,**57**,4,pp.179-182,(2012).

[9] Abramyan et al.,Influence of oscillation localization on film detachment from a substrate,*Vestnik St.Petersburg University:Mathematics*,**44**,1,pp.5-12,(2011).

[10] L.M.Kachanov, *Introduction to continuum damage mechanics*, Martinus Nijhoff Publishers ,Dordrecht Boston Lancaster(1986).

[11] A.V.Kashtanov at al.,Dynamic fracture as a process of nonlinear damage wave propagation,*Int.J.Fract.*, **150**,150,227-240,(2008).

COMPDYN 2015
5th ECCOMAS Thematic Conference on
Computational Methods in Structural Dynamics and Earthquake Engineering
M. Papadrakakis, V. Papadopoulos, V. Plevris (eds.)
Crete Island, Greece, 25–27 May 2015

PRESTRESS TUNING OF THE NONLINEAR DYNAMICS OF TENSEGRITY METAMATERIALS

F. Fraternali[1], A. Amendola[1], E. Hernández-Nava[2], R. Goodall[2], R.E. Skelton[3] and V.F. Nesterenko[3]

[1]Department of Civil Engineering, University of Salerno, 84084, Fisciano (SA), Italy
e-mail: {f.fraternali, adaamendola1}@unisa.it
(A. Amendola, F. Fraternali)
[2] Department of Materials Science and Engineering, University of Sheffield, Mappin Street, Sheffield, S1 3JD, UK
e-mail: {mtq10eh, r.goodall}@sheffield.ac.uk
(E. Hernández-Nava, R. Goodall)
[3]University of California San Diego, MAE/Aero, 9500 Gilman Dr., La Jolla, CA 92093, USA
e-mail: {bobskelton, vnesterenko}@ucsd.edu
(R.E. Skelton, V.F. Nesterenko)

Keywords: Tensegrity Prisms, Additive Manufacturing, Electron Beam Melting, Nonlinear Response, Mechanical metamaterials.

Abstract. *We investigate the experimental response of additively manufactured tensegrity prisms under compression loading and different states of internal prestress. Physical models of tensegrity prisms are additively manufactured through an electron beam melting facility. Spectra strings are applied to the 3D printed models through a post-tensioning approach, which endows the structure with the desired prestress. Experimental tests highlight that the examined structures exhibit strongly nonlinear mechanical response under compression, which appears to be useful for the construction of a new class of nonlinear mechanical metamaterials featuring solitary wave dynamics to be controlled by internal and external prestress.*

1 INTRODUCTION

One of the most common techniques nowadays employed for the fabrication and the rapid prototyping of innovative periodic structures and lattice materials is additive manufacturing (AM). Several fabrication methods have been proposed in this field, with resolution ranging from the centimetre- to the nanometre-scale. It is worth mentioning polyjet 3d printing technologies; Electron Beam Melting (EBM); x-ray lithography; deep UltraViolet lithography; soft lithography; two-photon polymerization; atomic layer deposition; and projection micro-stereolitography, among other available methods (refer to [1]-[5], and references therein). The processing of detailed components through the consecutive addition of small quantities of material, usually in thinner layer than 100 μm, makes AM capable of producing highly complex structures at different scales. EBM is a popular AM technique used to fabricate metallic structures. Its name is down to the technique's deposition, in which, it makes use of a beam of electrons to fully melt powder particles of a conductive material. This melting operation is performed in a selective way to produce a structure corresponding to a surface file, commonly STL. The use of EBM has been successfully demonstrated in several studies of structured materials including; lattices with graded porosity [4], metallic foams [6], optimized topologies [7] and structures with negative Poisson's ratio [8] to name a few.

Tensegrity structures are axially loaded prestressable structures. Motivated by nature, where tensegrity concepts recurrently appear [9], engineers have only recently developed efficient analytical methods to exploit tensegrity concepts in engineering design. Traditional construction of tensegrity structures through manually assembling of different components can represent a challenging task. Potentially resulting in a series of mitigated results because of structural and connecting issues; eccentricities at the joints, unwanted movements and friction (refer, e.g., to [10] and references therein). Hence in order to systematically study complex tensegrity systems, the development of fabrication techniques based on AM would be of great help. The paper begins by describing the Computer Aided Design (CAD) of the tensegrity prisms to be manufactured, which consist of three titanium alloy (Ti6Al4V) bars; two Ti6Al4V plates (bases), and three Spectra fibers connecting the base plates (Sect. 2). Sect. 3 describes the EBM process used for the AM manufacturing of temporary models without the Spectra fibers, while Sect. 4 illustrates the placement and the post-tensioning of such elements within the final models. The experimental part of the study presents quasi-static compression tests that investigate on the response of the examined structures under compressive axial loading. The given results validate the theoretical predictions presented in [10, 11], highlighting the geometrically non-linear nature of the axial force vs. axial displacement response of such structures (Sect. 5). Sect. 6 illustrates the wave dynamics of chains of tensegrity prisms featuring either hardening-type or softening-type nonlinear response, highlighting that hardening-type chains support compression solitary waves, while softening-type chains support rarefaction solitary waves. We end in Sect. 7, by drawing the main conclusions of the present study and future research lines.

2 GEOMETRIC MODELS OF TENSEGRITY PRISMS

We focus in the present Section on the computer aided design of provisional models of structures showing tensegrity prisms endowed with rigid bases as building blocks [10]. Each prism is composed of three struts, two rigid bases (a top-base, and a bottom-base), and three cross-cables. Fig. 1 shows a computer model of metallic structures formed by the struts and the terminal bases of the building blocks, plus some sacrificial supports connecting the bases of the building blocks (vertical elements in Figs. 1). The connections between the bars and the

bases are realized through hemispherical joints (cf. Fig. 1). Such provisional structures will be additively manufactured in a titanium alloy (Ti6Al4V) through the EBM facility Arcam S12 (cf. Sect. 3). Next, the 3D printed structures will be finished with the addition of tensioned Spectra strings connecting the struts and the terminal bases of the building blocks. Once the insertion of the Spectra strings is completed, and a suitable prestress is applied to the structure, the sacrificial supports will be removed (*post-tensioning approach*, cf. Sect.4). We will now show in detail how we design the building blocks of the structures under investigation. To ensure zero bending moments, the extremities of the bars composing such units should have almost zero diameter at the nodes. Unfortunately, it is impossible to additively manufacture elements with nearly zero diameter, due to the limited precision tolerance of the available printing equipment. In the present case the ARCAM S12 EBM facility allows to smoothly manufacture features with size down to 0.5 mm [6]. Such a limitation also affects the manufacturing of the tensile elements (cables or strings) of the building blocks, due to the small diameter that is needed for such elements. As already explained, our fabrication strategy makes use of 3D printed partially complete models in which the strings are replaced by sacrificial supports with diameter $d^* = 0.5$ mm. The latter are removed in a second phase, when Spectra strings are manually inserted into the building blocks, with the aim of 'sewing' the 3D printed models (Sect.4). To this end, the models to be 3D printed show holes passing through the joints, which will host the Spectra strings in the post-tensioning phase. We design the compressive elements (bars or struts) of the temporary models with a bi-conic shape obtained by joining two truncated cones. The latter feature decreasing radii towards the extremities (Fig. 1), so as to minimize the bending rigidity of the nodes. Let d denote the minimum diameter of the struts (at the extremities), and let D denote the maximum diameter of such elements (at the mid-span). Following [12] we make use of the following tapering ratio: $\beta = D/d = 6$. Overall, each building block to be 3D printed is composed of three truncated bi-cones (bars), three sacrificial supports, two triangular plates of thickness t (bases), and six hemispherical joints with radius r (Fig. 1). Table 1 shows the geometric properties of such elements, making use of the symbols s_N, b_N and h_N to respectively denote the length of the edges of the base plates; the length of the struts; and the height of the prism (measured from the centre to centre of the bases), in correspondence with the unstressed (or natural) configuration of the structure.



Figure 1: Graphical model of a building block composed of three sacrificial supports (yellow), six hemispherical joints (orange), three struts (blue) and two terminal plates (gray).

t (mm)	r (mm)	s_N (mm)	b_N (mm)	D(mm)	d (mm)	d^* (mm)	h_N (mm)
1.0	1.5	34.0	44.1	3.0	0.5	0.5	22.3

Table 1: Geometrical properties of the building blocks of the examined models.

3 ADDITIVE MANIFACTURING OF PHYSICAL MODELS

The present section focuses on the EBM technique employed to process the CAD model illustrated in the previous section. We begin by describing the geometrical and chemical characteristics of the employed Ti6Al4V alloy. Next, we briefly describe the employed manufacturing process. We end by presenting an experimental study on the influence of the direction in which the part is built (i.e. how the layers are built up) on the mechanical properties of the melted Ti-6Al-4V alloy.

3.1 Raw materials

The manufacturing process examined in the present work starts with the spreading out of a layer of Ti4Al6V prealloyed powder into the build platform of the printing machine (Arcam EBM S12). Such a powder is provided by the manufacturer and is made of spherical particles with $45 - 100$ μ m diameter. The raw material is grade 5 under the standards of the American Society of Testing and Materials (ASTM Grade 5, 6Al-4V). It must be considered, however, that the continuous material reuse, which is a common practice in the EBM manufacturing, might slightly change the chemical composition of the Ti6Al4V powder (for example by gradual pick up of oxygen). Tab. 2 provides the chemical composition experimentally determined for the powder employed in the previous study.

Ti	Al	V	Fe	C	N	O
88.28	6.88	4.27	0.18	0.007	0.026	0.33

Table 2: Chemical composition of the Ti-6Al-4V prealloyed powder in wt%.

3.2 Manifacturing process

EBM works in vacuum conditions at 1.9×10^{-3} mbar, and heats the base of the build area up to the temperature of $720°$C. Layers of Ti-6Al-4V powder are progressively deposited, heated and melted, according to a sliced version of the CAD model to be manufactured, which is prepared by an internal preprocessor of the Arcam EBM S12. Layer heating (using a defocused beam) is employed to reduce the energy needed for the melting phase. The EBM working parameters are varied for the bars, joints and plates, with the aim of ensuring uniform material density throughout the model, as much as possible (cf. Tab, 3). The voltage is kept constant at 60kV. Once manufactured, all remnants of unmelted powder are removed using compressed air.

3.3 Parent material properties

We printed twelve tensegrity prisms with two different building orientations for material characterization purposes. The main goal of such a study was to detect the influence of the EBM build direction on the mechanical properties of the melted Ti-6Al-4V alloy. We built six samples along the vertical direction (V specimens: prism bases parallel to the building plate), and six other samples along the horizontal direction (H specimens: prism bases perpendicular to the building plate). Parts of such specimens, manually cut using shears, were subject to tensile

	Beam current (mA)	Beam speed (mm/s)	Focus Offset
Preheat	30	14600	50
Plates	17	500	19
Spheres	1.7	200	0
Bars	1.7	200	0

Table 3: Beam parameters employed for the manufacturing of the model parts.

tests according to the ASTM standard E8-13a [13]. The data obtained from tensile tests include the 0.2 % Yield strength (YS), ultimate tensile strength (UTS), and Young's modulus (YM), see Table 3.3. The yield strength of V- and H-specimens was found to be slightly different (V-specimens more resistant than H-specimens, cf. Table 3.3), hought to be due to changes in material porosity with the deposition angle [14]. It is worth mentioning that the reproducibility of material properties in the AM of lattice materials in general is subject of debate. This is as the fraction of defects, such as internal porosity and surface roughness, dramatically affect the material strength, especially in the case of small features, such as, e.g., the nodal junctions [6]. The results presented in Table 3.3 led us to prefer the vertical deposition technique for the manufacturing of the final specimens (Fig. 2).

Build orientation	0.2 % Y.S.	UTS	Young's modulus
	(MPa)	(MPa)	(GPa)
Horizontal	881± 8.4	1040±6.7	110±2.1
Vertical	923±10.7	1042±9.2	116±2.8

Table 4: Bulk material properties based on tensile tests for two build orientations.



Figure 2: EBM-printed left-handed (left) and right-handed (right) tensegrity prisms.

4 POST-TENSIONING OF 3D-PRINTED SPECIMENS

As anticipated, we 'sewed' the 3D printed structures by slipping Spectra® fibers with 0.1 mm diameter through the holes crossing the joints. We used Spectra fibers supplied by Shimano American Corporation (Irvine, CA, USA), with declared maximum load bearing capacity of 5 kg. Hereafter, we assume that such string elements have Young modulus E_s=$5.48GPa$, based on the results of the experimental study presented in [10]. Since the cross-section area of the strings is $A_s = \pi\, 0.1^2/4 = 0.0078$ mm^2, their axial stiffness is computed as: $E_s A_s = 0.043$ kN.

After slipping the Spectra strings through the holes crossing the joints, we fixed them in correspondence with the top-base of the structure through slipknots (Fig. 3). Next, we removed the sacrificial supports of the 3D printed structure (cf. Figs. 2,), and we tensioned the strings by fixing them to the bottom-base. A level was placed on the top-base of the structure during the post-tensioning phase, in order to ensure that such a base was horizontal, and the strings approximatively carried equal tensile forces. We applied the post-tension approach to manufacture single prisms, either left-handed (L-prisms, Fig. 3-left) or right-handed (R-prisms, Fig. 3-right).

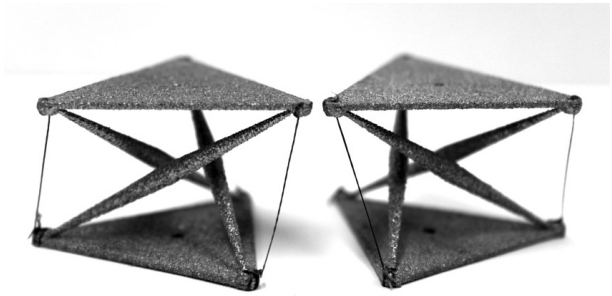


Figure 3: L-prims (left) and R-prism (right) prisms obtained by 'sewing' the EBM-printed models with Spectra strings.

5 QUASI-STATIC COMPRESSION TESTS

We investigated on the experimental response of the tensegrity prisms illustrated in the previous section under quasi-static compression loading, on employing a strain rate of $1 \cdot 10^3\ s^1$. The testing apparatus consisted of a Zwick/Roell Z050 testing machine equipped with 20 kN load cell (Fig.4). To minimize the frictional effects between the terminal bases of the prisms and the testing machine plates, we carefully lubricated all such surfaces, before initiating the compression tests. We lubricated the joints of the tested structures as well, in order to reduce the friction between the strings and the rough internal surface of the joints.

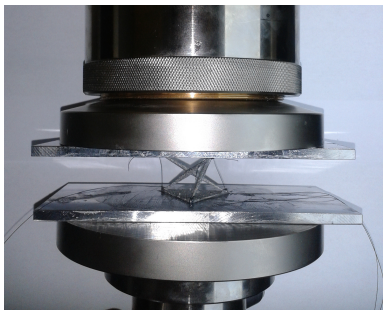


Figure 4: Experimental set-up for the compression testing of post-tensioned structures.

Fig. 5 shows the results of compression tests on different L-prisms and R-prisms, which differ from each other for the value of the applied prestress. The cross-string prestrain p [11] was estimated by comparing the lengths of the cross-strings in the unstressed and prestressed configurations (cf. Fig. 5). The axial force F vs. axial-displacement δ plots in Fig. 5 highlight

a marked hardening behavior of the L- and R-prisms (tangent stiffness increasing with δ), up to the specimen failure. Such an elastic hardening (or hardening) effect is magnified by increasing the internal prestress (cf. Fig. 5), in agreement with the theoretical results presented in [11] for tensegrity prisms endowed with rigid bases. The specimen collapse was due to the detachment of one or more bars from the joints. It is worth mentioning that we did not observe plastic yielding of the strings or buckling of the bars up to the specimen failure.

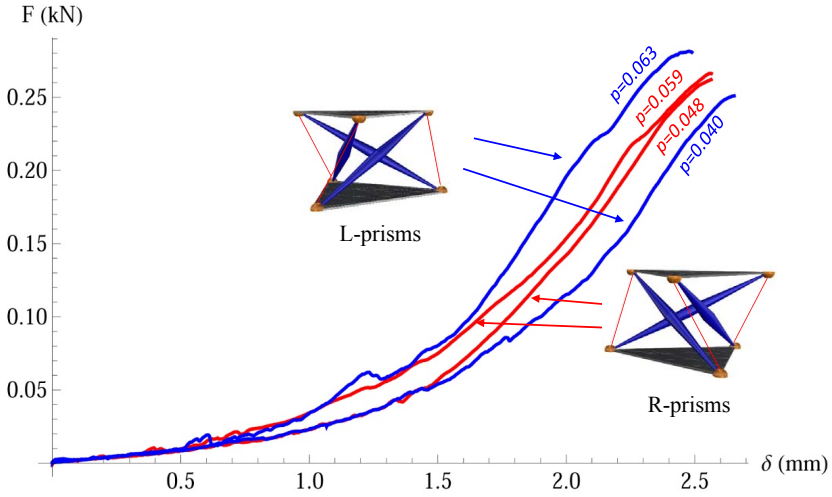


Figure 5: Axial force F vs. axial-displacement δ curves of single-prism structures under axial compression loads.

6 NONLINEAR DYNAMICS OF TENSEGRITY METAMATERIALS

Ordinary engineering materials typically exhibit either elastic hardening (e.g., crystalline solids), or elastic softening (e.g., foams). More puzzling is the geometrically nonlinear response of structural lattices based on tensegrity prisms, which may gradually change their elastic response from hardening to softening through the modification of mechanical, geometrical, and prestress variables. Recent studies have indeed shown that the elastically hardening regime observed in the tensegrity prisms analyzed in Fig. 5 can switch to an elastically softening regime when the rigid bases are replaced with deformable string networks, and the prism features suitable aspect ratios between the height and the radius of the circumference circumscribed to the base triangles [10, 11, 19]. In particular, it has been shown that a low acoustic impedance chain of prisms with with elastic hardening response (LIEH chain) supports compression solitary waves, while a high acoustic impedance chain of prisms with elastic softening response (HIES chain) supports compression solitary waves [19].

Fig. 6-top illustrates the behavior of a compression solitary pulse approaching the interface between two chains in tensionless contact with each other: a LIEH branch with 700 masses and a HIES branch with 2200 masses (refer to [19] for numerical data). The two branches are subjected to different *global prestrains* ε_{s_0} (initial axial strains of the prisms composing the branches) and *local prestrains* $p_0 \equiv p$ (cross-string prestrains). Fig. 6-top shows the evolution of strain pulses in the examined system under the impact velocity $v_0 = 5.0$ m/s. We observe that initial solitary compression wave travels along the LIEH branch. The interaction of such waves

with the LIEH-HIES interface generates a gap between the branches and unexpected transmitted solitary rarefaction waves with oscillatory tail in the HIES branch. A train of reflected solitary compression waves is observed in the LIEH branch [19]. The results in Fig. 6-bottom instead deal with the interaction of a rarefaction solitary wave with an interface between a HIES lattice of 5000 masses and LIEH lattice of 1000 masses under the the impact velocity $v_0 = 5.0$ m/s (refer to [19] for numerical data). It is seen that HIES system supports an incident solitary rarefaction pulse with oscillatory tail. Its interaction with the given interface results in a train of transmitted solitary compression waves in LIEH system. A reflected solitary rarefaction wave followed by oscillatory tail propagates back into the HIES branch. The results in Fig. 6-bottom suggest that the oscillatory tail of the incident rarefaction pulse degenerates into an infinitely small amplitude trail.

7 CONCLUSIONS

We have investigated on the fabrication of physical models of tensegrity prisms, by combining the additive manufacturing of metallic models, via EBM, with the manual insertion of tensioned Spectra strings in 3D printed structures. Compression tests have been performed with the aim of characterizing the nature of the mechanical response of such structures under large or moderately large axial displacements. We have observed a markedly nonlinear response of the examined structures, and elastic hardening effects under large axial displacements. Such results confirm the outcomes of previous theoretical and experimental studies available in the literature on the mechanical response of tensegrity prisms endowed with rigid bases [15, 10, 11].

Elastically hardening mechanical metamaterials support compressive solitary waves and the unusual reflection of waves on material interfaces [16]-[19] (cf. Fig. 6). Solitary wave dynamics has been proven to be useful for the construction of a variety of novel acoustic devices. These include: acoustic band gap materials; shock protector devices; acoustic lenses; and energy trapping containers, to name some examples (refer, e.g., to [20] and references therein). The present study represents a first step towards the additive manufacturing and testing of nonlinear tensegrity metatamerials to be employed for real-life engineering devices. We address the formulation and implementation of innovative, multimaterial deposition techniques that are able to apply internal prestress in AM-fabricated tensegrity structures to future work. We plan to fabricate macro- and small-scale models of such structures using materials with different coefficients of thermal expansion for struts and cables. In addition, we plan to manufacture micro-scale tensegrity models through projection micro-stereolitography [5], employing swelling materials for the tensile members [21], and accounting for material fracture [22]. Once dried, the tensile members will contract, creating internal prestress. Engineering applications of the such metamaterials will deal with novel, tunable focus acoustic lenses, impact mitigation devices, bio-inspired membranes and innovative tools for monitoring structural health and damage detection in materials and structures [18],[23]-[30].

Acknowledgements

Support for this work was received from the Italian Ministry of Foreign Affairs, Grant No. 00173/2014, Italy–USA Scientific and Technological Cooperation 2014–2015 (‘*Lavoro realizzato con il contributo del Ministero degli Affari Esteri, Direzione Generale per la Promozione del Sistema Paese*’).

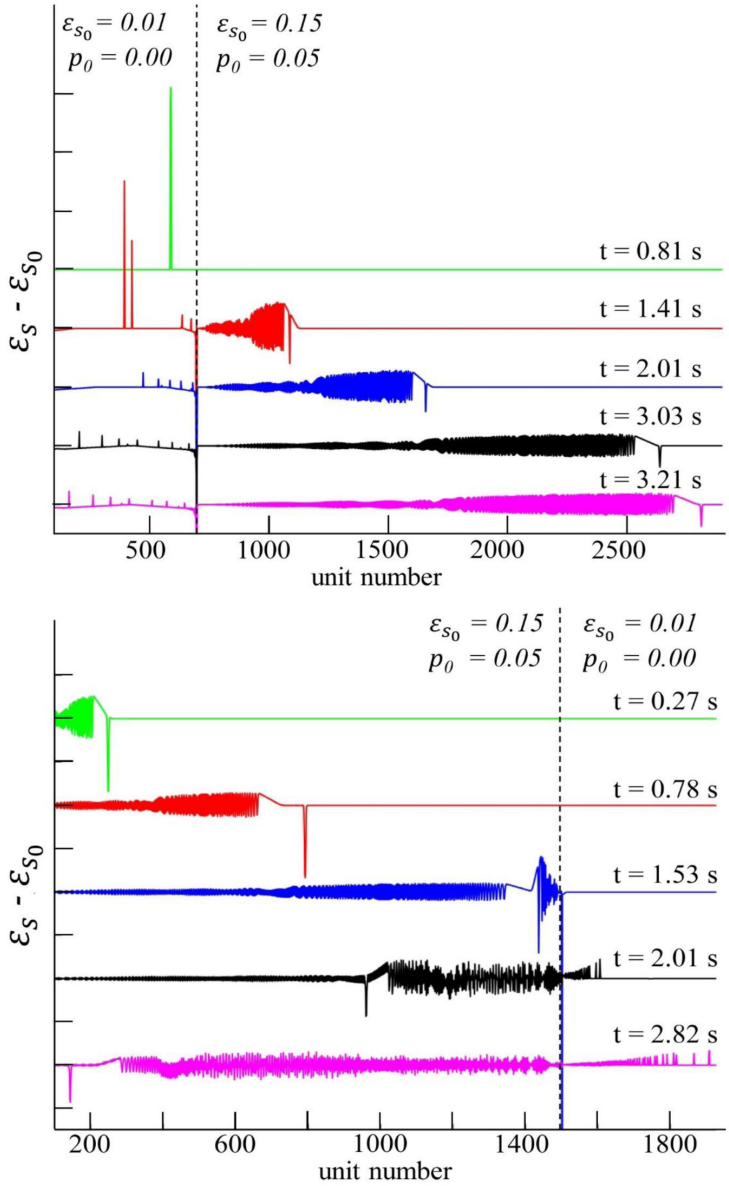


Figure 6: Top: Interaction of a rarefaction solitary wave with the interface between LIEH (left) and HIES (right) chains of tensegrity prisms. Bottom: Interaction of a rarefaction solitary wave with the interface between HIES (left) and LIEH (right) chains of tensegrity prisms.

REFERENCES

[1] T. Bückmann, M. Thiel, M. Kadic, R. Schittny, M. Wegener, An elastomechanical unfeelability cloak made of pentamode metamaterials. *Nature Communications*, **5**, 4130, 2014.

[2] M. Maldovan, Sound and heat revolution in phononics. *Nature*, **503**, 209-217, 2013.

[3] L. R. Meza, S. Das, J. R. Greer, Strong, lightweight, and recoverable three-dimensional ceramic nanolattices. *Science*, **345**, 1322-1326, 2014.

[4] W. van Grunsven, E. Hernandez-Nava, G.C. Reilly, R. Goodall, Fabrication and mechanical characterisation of titanium lattices with graded porosity. *Metals*, **4**(3), 401–409, 2014.

[5] X. Zheng, J. DeOtte, M. P. Alonso, G. R. Farquar, T. H. Weisgraber, S. Gemberling, H. Lee, N. Fang, C. M. Spadaccini, Design and optimization of a light-emitting diode projection micro-stereolithography three-dimensional manufacturing system. *Review of Scientific Instruments*, **83**, 125001, 2012.

[6] E. Hernández-Nava, C. J. Smith, F. Derguti, S. Tammas-Williams, F. Léonar, P. J. Withers, I. Todd, R. Goodall, The effect of density and feature size on mechanical properties of isostructural metallic foams produced by additive manufacturing. *Acta Materialia*, **85**, 387-395, 2015.

[7] C. J. Smith, F. Derguti, E. Hernandez-Nava, S. Tammas-Williams, S. Gulizia, D. Fraser, I. Todd, Dimensional accuracy of Electron Beam Melting (EBM) Additive Manufacture with regard to weight optimized truss structures. Journal of Materials Processing Technology (in press).

[8] L. Yang, O. Harrysson, H. West, D. Cormier, Compressive properties of Ti6Al4V auxetic mesh structures made by electron beam melting. *Acta Materialia*, **60**, 3370-3379,2012.

[9] R. E. Skelton, M. C. de Oliveira, *Tensegrity Systems*. Springer, 2010c.

[10] A. Amendola, F. Fraternali, G. Carpentieri, M. de Oliveira, R. E. Skelton, Experimental investigation of the softening-hardening response of tensegrity prisms under compressive loading. *Composite Structures*, **117**, 234-243, 2014.

[11] F. Fraternali, G. Carpentieri, A. Amendola, On the mechanical modeling of the extreme softening/hardening response of axially loaded tensegrity prisms. *Journal of the Mechanics and Physics of Solids*,**74**, 136-157, 2015.

[12] M. Kadic, D. Bückmann, N. Stenger, M. Thiel, M. Wegner, On the practicability of pentamode mechanical metamaterials. *Applied Physics Letters*,**100**, 191901, 2012.

[13] ASTM E8 - 13a. Standard Test Methods for Tension Testing of Metallic Materials, DOI 10.1520/E0008 E0008M.

[14] L.E. Murr, S.M. Gaytan, F. Medina, E. Martinez, J.L. Martinez, D.H. Hernandez, B.I. Machado, D.A. Ramirez, R.B. Wicker, Characterization of Ti6Al4V open cellular foams fabricated by additive manufacturing using electron beam melting. *Materials Science and Engineering A*, **527**, 1861-1868, 2010.

[15] I. Oppenheim, W. Williams, Geometric effects in an elastic tensegrity structure. *Journal of Elasticity*, **59**, 51–65, 2000.

[16] V. F. Nesterenko, *Dynamics of Heterogeneous Materials*. Springer-Verlag, New York, 2001.

[17] C. Daraio, D. Ngo, V.F. Nesterenko, F. Fraternali, Highly nonlinear pulse splitting and recombination in a two-dimensional granular network. *Physical Review E*, **82**, 036603, 2010.

[18] F. Fraternali, L. Senatore, C. Daraio, Solitary waves on tensegrity lattices. *Journal of the Mechanics and Physics of Solids*, **60**, 1137-1144, 2012.

[19] F. Fraternali, G. Carpentieri, A. Amendola, R. E. Skelton, V. F. Nesterenko, Multiscale tunability of solitary wave dynamics in tensegrity metamaterials. *Applied Physics Letters*, **105**, 201903, 2014b.

[20] G. Theocharis, N. Boechler, C. Daraio, Nonlinear phononic structures and metamaterials. *P.A. Deymier (ed.) Acoustic Matematerials and Phononic Crystals, Springer Series in Solid State Sciences*, **173**, 217-251, 2013.

[21] H. Lee, J. Zhang, H. Jiang, N. X. Fang, Prescribed pattern transformation in swelling gel tubes by elastic instability. *Phys. Rev. Lett.*, **108**, 214304, 2012.

[22] F. Fraternali, Free Discontinuity Finite Element Models in Two-Dimensions for In-Plane Crack Problems. *Theoretical and Applied Fracture Mechanics*, **47**, 274–282, 2007.

[23] J. R. Raney, F. Fraternali, A. Amendola, C. Daraio, Modeling and in situ identification of material parameters for layered structures based on carbon nanotube arrays. *Composite Structures*, **93**, (11):3013–3018, 2011.

[24] M. Modano, F. Fabbrocino, A. Gesualdo, G. Matrone, I. Farina, F. Fraternali, On the forced vibration test by vibrodyne. *CompDyn 2015*, 25-27 May 2015.

[25] T. El Sayed, W. Mock, A. Mota, F. Fraternali, M. Ortiz, Computational assessment of ballistic impact on a high strength structural steel/polyurea composite plate. *Computational Mechanics*, **43**(4), 525-534, 2009.

[26] C. Donahue, P. Anzel, L. Bonanomi, T. Keller, C. Daraio, Experimental realization of a nonlinear acoustic lens with a tunable focus. *Applied Physics Letters*, **104**, 014103, 2014.

[27] F. Fraternali, C.D Lorenz, G. Marcelli, On the estimation of the curvatures and bending rigidity of membrane networks via a local maximum-entropy approach. *Journal of Computational Physics*, **231**, 528-540, 2012.

[28] B. Schmidt, F. Fraternali, Universal formulae for the limiting elastic energy of membrane networks. *Journal of the Mechanics and Physics of Solids*, **60**, 172-180, 2012.

[29] F. Fraternali, I. Farina, G. Carpentieri. A discrete-to-continuum approach to the curvatures of membrane networks and parametric surfaces. *Mechanics Research Communications*, **56**, 18-15, 2014.

[30] X. Ni, *Nondestructive Evaluation And Structural Health Monitoring Based On Highly Nonlinear Solitary Waves*. Phd Dissertation, University of Pittsburgh, USA, 2012.

COMPDYN 2015
5th ECCOMAS Thematic Conference on
Computational Methods in Structural Dynamics and Earthquake Engineering
M. Papadrakakis, V. Papadopoulos, V. Plevris (eds.)
Crete Island, Greece, 25–27 May 2015

COMPARISON OF NUMERICAL AND SEMI-ANALYTICAL SOLUTION OF A SIMPLE NON-LINEAR SYSTEM IN STATE OF THE STOCHASTIC RESONANCE

Jiří Náprstek[1], Cyril Fischer[1], Radomil Král[1] and Stanislav Pospíšil[1]

[1]Institute of Theoretical and Applied Mechanics, v.v.i.
Prosecká 76, CZ-190 00 Prague 9, Czech Republic
e-mail: {naprstek,fischerc,kral,pospisil}@itam.cas.cz

Keywords: Stochastic resonance, interwell hopping, non-linear vibration, aeroelastic divergence, Fokker-Planck equation.

Abstract. *Stochastic resonance (SR) is a phenomenon which can be observed at some non-linear dynamic systems under combined excitation including deterministic harmonic force and random noise. The Duffing single degree of freedom oscillator is treated and the Gaussian white noise as the random excitation component is considered. Mathematical basis of this phenomenon follows from properties of the Duffing system with negative linear part of the stiffness. Under certain combinations of the system and excitation parameters the SR can emerge. It manifests by stable periodic hopping between two nearly constant limits perturbed by random noises. SR is observed and practically used in a number of disciplines in physics, biophysics, chemistry, etc. However it seems to be promising as a theoretical model of several aeroelastic post-critical effects arising at a prismatic beam in a cross flow.*

Three independent theoretical solution methods have been addressed and tested in order to compare results of the system response. The first kind is semi-analytic dealing with the relevant Fokker-Planck Equation (FP). It is solved by means of the stochastic moment procedure. The multiharmonic non-stationary solution of the Probability Density Function (PDF) is expected. The Galerkin approach is adopted. The second way is based on the FEM solution of the FP equation. It is analyzed in an original evolutionary form which enables an analysis of transition effects starting the Dirac type initial conditions. The last procedure represents simulation regarding the original Duffing or relevant Ito stochastic system. Comparison of results provided by the above three methods has revealed appropriate domains of their application to particular problems regarding a preliminary analysis or careful detailed inspection in specific small domains in final stage of an engineering system design.

1 INTRODUCTION

Stochastic resonance (SR) is a phenomenon which can be observed at some non-linear dynamic systems under combined excitation including deterministic harmonic force and random noise, see for instance papers [1], [2], monograph [3] and many other resources. This phenomenon manifests by stable periodic hopping between two nearly constant limits perturbed by random noises. SR is observed in a number of disciplines in physics, life sciences and industry (optics, plasma physics, chemistry, biophysics, etc.). The occurrence of this phenomenon depends on certain combinations of input parameters, which can be determined theoretically and verified experimentally. The long-term experience shows that SR can be assumed either as a dangerous effect of a post-critical system response which should be avoided (plasma physics, aeroelasticity, etc.) or oppositely as a requested process representing functionality of the system itself (optics, special excitation devices, etc.).

With reference to wind channel observations in a wind channel, it seems that SR is promising as a theoretical model inherent for several aeroelastic post-critical effects arising at a prismatic beam in a cross flow. In particular the divergence or buffeting of a bridge deck can be modeled as a post-critical process of the SR type at an SDOF or TDOF system. Dealing with a particular project these post-critical effects should carefully investigated in order to eliminate any danger of the bridge deck collapse due to aeroelastic effects.

The mathematical basis of SR follows in the most simple case from properties of the Duffing equation with negative linear part of the stiffness. Therefore in this study the Duffing SDOF oscillator is treated under excitation by a Gaussian white noise together with a deterministic harmonic force with a fixed frequency. It should be noticed that also other types of nonlinearity can produce a significant periodic part of the response when excited by additive random noise. See for instance [4], where influence of bistable nonlinear damping is discussed.

Let us assume the nonlinear mass-unity oscillator with one degree of freedom:

$$\begin{aligned} \dot{u} &= v; \\ \dot{v} &= -2\omega_b \cdot v - V'(u) + P(t) + \xi(t). \end{aligned} \tag{1}$$

$V(u)$ - potential energy being introduced in a form corresponding with the Duffing equation:

$$V(u) = -\frac{\omega_0^2}{2}u^2 + \frac{\gamma^4}{4}u^4 \qquad \Rightarrow \qquad V'(u) = dV(u)/du = -\omega_0^2 \cdot u + \gamma^4 \cdot u^3 \tag{2}$$

$\xi(t)$ - Gaussian white noise of intensity $2\sigma^2$ respecting conditions:

$$\mathbf{E}\{\xi(t)\} = 0\,; \qquad \mathbf{E}\{\xi(t)\xi(t')\} = 2\sigma^2 \cdot \delta(t-t') \tag{3}$$

$P(t) = P_o \exp(\mathrm{i}\Omega t)$ - external harmonic force with frequency Ω. Amplitude P_o should be understood per unit mass.

Symbols ω_0 and ω_b have a usual meaning of the circular eigen-frequency and circular damping frequency of the associated linear system. The linear part of the $V'(u)$ is negative making the system metastable in the origin, while the cubic part acts as stabilizing factor beyond a certain interval of displacement u. The system is drafted in the Fig. 1 in two versions: (a) system with symmetric potential typical by an equivalent energy needed for hopping from the left into the right potential well and in opposite direction (b) system with asymmetric potential due to the supplementary linear string which could be able (when rising its stiffness) to bring the oscillator to monostable type.

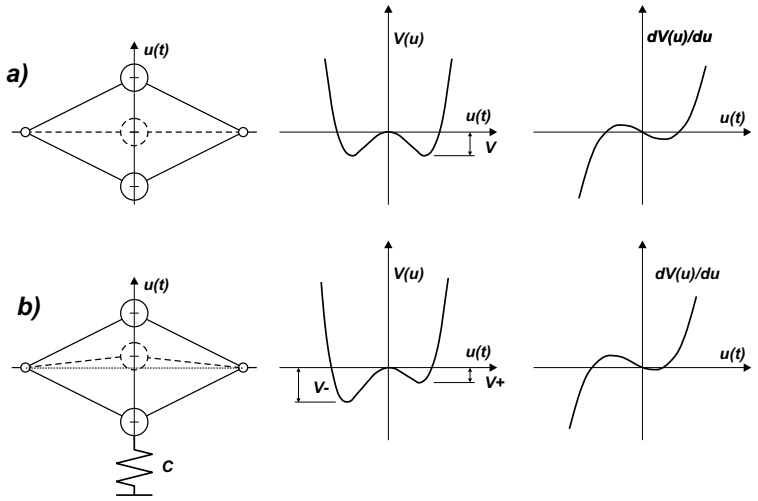


Figure 1: Bistable nonlinear system: a) Symmetric potential; b) Non-symmetric potential.

Response of the system defined by Eq. (1) can be significantly enhanced introducing an optimal amount of additive random noise, which results in the phenomenon called stochastic resonance. The traditional interpretation of stochastic resonance involves the concept of photon inter-well hopping in nonlinear optics, see e.g. [1]. For the symmetric potential ($\Delta V- = \Delta V+$) and in the absence of periodic forcing the approximate frequency of escape from one well into the second (bistable system of type (2)) is given by the following estimate published in the comprehensive study [5]:

$$\omega_e = \sqrt{2} \cdot \exp(-\Delta V/T) \tag{4}$$

where ΔV is height of the barrier separating potential minima and T absolute temperature. It is obvious that T is proportional to σ^2 introduced in Eq. (3). The formula (4) is a result of theoretical and empirical investigation motivated by problems of nonlinear optics. However, it is widely used and works very well. During the last decade a number of areas of optics, quantum mechanics, chemistry, neurophysiology, etc. investigated this formula attempting to use the phenomenon of stochastic resonance for description of various effects arising in their branches using both experimental and theoretical ways of investigation, see e.g. [2, 6].

The Duffing equation under above excitation is treated addressing three independent theoretical solution methods in order to compare results of the system response in general and mainly looking for system and excitation parameters leading to the SR phenomenon.

2 FOKKER-PLANCK EQUATION – SEMI-ANALYTIC SOLUTION

The first procedure considered is based on a manipulation with the response probability density function of the system (1). It is commonly supposed that input and output can be regarded as Markov type processes. In such a case the most effective analytic tool of investigation offers the Fokker-Planck Equation. We try to formulate a semi-analytic solution using the stochastic moment procedure with non-Gaussian closure. The multiharmonic solution is suggested and therefore the solution in a periodic form is fixed. The transition effects due to initial conditions are omitted and only quasi-stationary part is investigated.

Taking into account that random noise in Eq. (1) has an additive character, no Wong-Zakai correction terms emerge, see e.g. [7, 8, 9]. Then the relevant FP equation, e.g. [10] can be

easily written out:

$$\kappa_u = v \; ; \quad \kappa_v = -2\omega_b \cdot v - V'(u) + P(t) \; ; \quad \kappa_{vv} = 2\sigma^2 \tag{5}$$

$$\frac{\partial p(u,v,t)}{\partial t} \; = \; -v\frac{\partial p(u,v,t)}{\partial u} + \frac{\partial}{\partial v}[2\omega_b \cdot v + V'(u) - P(t)]p(u,v,t) + \sigma^2 \frac{\partial^2 p(u,v,t)}{\partial v^2} \tag{6}$$

together with boundary and initial conditions:

$$\lim_{u,v\to\pm\infty} p(u,v,t) = 0 \;\; \text{(a)} \qquad p(u,v,0) = \delta(u,v) \;\; \text{(b)} \tag{7}$$

Provided $P_0 = 0$ and the external excitation is limited to random component only, the right side of Eq. (6) becomes time independent and it is meaningful to investigate the FP equation with canceled left side. In such a case it admits the closed form time independent solution of the Boltzmann type. For details, see e.g. [11, 12, 13], and other papers and monographs. The appropriate solution has the form:

$$p_o(u,v) = D \cdot \exp\left(-\frac{2\omega_b}{\sigma^2} H(u,v)\right) \tag{8}$$

where D is the normalizing constant and $H(u,v)$ represents the Hamiltonian function of the basic system. In particular:

$$H(u,v) = \frac{1}{2}v^2 + V(u) = \frac{1}{2}v^2 - \frac{1}{2}\omega_o^2 u^2 + \frac{1}{4}\gamma^4 u^4 \tag{9}$$

which implicates:

$$\begin{gathered} p_o(u,v) = p_u(u) \cdot p_v(v), \\ p_u(u) = D_u \cdot \exp(-\frac{2\omega_b}{\sigma^2}(\frac{1}{2}\omega_o^2 u^2 + \frac{1}{4}\gamma^4 u^4)), \quad p_v(v) = D_v \cdot \exp(-\frac{2\omega_b}{\sigma^2}\frac{1}{2}v^2) \end{gathered} \tag{10}$$

indicating that u, v are stochastically independent processes.

It is obvious that solution of type Eq. (8) or (10) type can be provided for any arbitrary symmetric/non-symmetric potential including cases leading the system into monostable type. PDF of the response has significantly non-Gaussian form in displacement u (see Fig. 2) and Gaussian form in velocity v. The final shape is influenced by quotient $2\omega_b/\sigma^2$, i.e. approaching zero as quickly as the damping ω_b rises and white noise intensity σ^2 decreases.

When excitation force consists of both component ($P_0 > 0$), time independent solution of Eq. (6) no more exists. In order to approximate its solution, the formula (8) can be used as a basic part which should be multiplied by a space and time dependent series. The PDF can be expected periodic or cyclic-stationary in a certain meaning of the term in time coordinate for $t \to \infty$ and the Floquet theorem or the maximum entropy principle, e.g. [11] could also be alternatively used as a basic tool for the solution.

With respect to the linearity of the FP equation the periodicity of the PDF should be relevant to the frequency of the deterministic excitation component Ω and its integer powers. Therefore the series can be written in the following form:

$$p(u,v,t) = p_o(u,v) \sum_{j=0}^{J} q_j(u,v) \cdot \exp(\mathrm{i}j\Omega t) \tag{11}$$

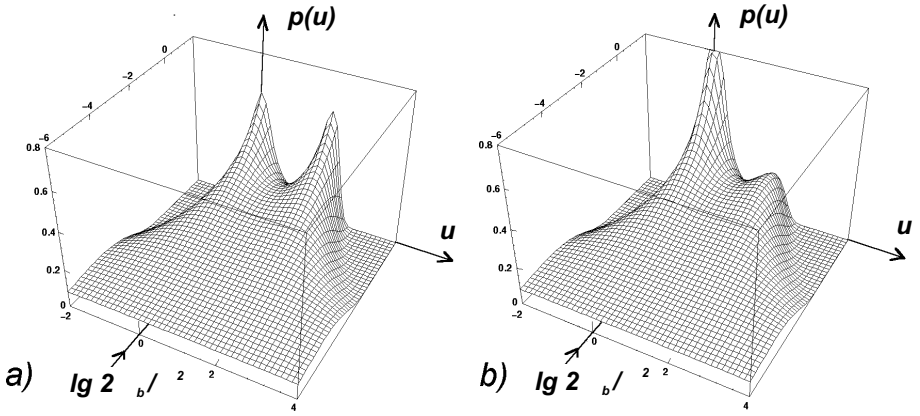


Figure 2: Response PDF of the system excited by white noise only: (a) Symmetric potential; (b) Non-symmetric potential.

where Ω is the harmonic component excitation frequency. The series Eq. (11) represents an approach of a weak solution of FP equation, which repeats in the period $T = 2\pi/\Omega$. It gives a true picture of solution within one period, but cannot express any influence of initial conditions.

The unknown functions $q_j(u, v)$ in Eq. (11) can be searched for using the generalized method of stochastic moments as it can be found e.g. in [10]. Using the Galerkin method approach, the expression (11) should be substituted into Eq. (6) and the whole equation should be multiplied by the testing functions $\alpha(u, v)$.

The testing functions $\alpha(u, v)$ and unknown function $q_j(u, v)$ are assumed to have a following advantageous form:

$$\alpha(u,v) = \alpha_{r,s}(u,v) = u^r \cdot H_s(\beta v)\ ; \quad r = 0, ..., R\ ;\ s = 0, ..., S \tag{12}$$

$$q_j(u,v) = \sum_{k,l=0}^{R,S} q_{j,kl} u^k \cdot H_l(\beta v) \tag{13}$$

where $H_s(\beta v)$ are l'Hermite polynomials and $\beta = \sqrt{\omega_b/\sigma^2}$. After applying the mathematical mean operator with respect to probability density function $p_o(u, v)$, see (8), and employing orthogonality of l'Hermite polynomials a linear algebraic system for unknown coefficients $q_{j;k,l}$ arises ($q_o(u, v) = 1,\ q_{-1}(u, v) \equiv 0$):

$$2\beta(\mathrm{i}j\Omega + 2\omega_b s)\mathbf{A}\mathbf{q}_{j,s} - 2(s+1)\mathbf{C}\mathbf{q}_{j,s+1} + \mathbf{B}\mathbf{q}_{j,s-1} = 2\beta^2 P_o \mathbf{A}\mathbf{q}_{j-1,s-1} \tag{14}$$

$\mathbf{q}_{j,s} = [q_{j,0s}, q_{j,1s}, ..., q_{j,Rs}]^T$ - column vector ($R + 1$ components) and $\mathbf{A}, \mathbf{B}, \mathbf{C} \in \mathbb{R}^{(R+1)\times(R+1)}$ - square arrays containing moments:

$$A_{r,k} = \int_{-\infty}^{\infty} u^{r+k}\Phi(u)du\ ; \quad B_{r,k} = \int_{-\infty}^{\infty} k u^{r+k-1}\Phi(u)du\ ; \quad C_{r,k} = \int_{-\infty}^{\infty} r u^{r+k-1}\Phi(u)du \tag{15}$$
$$\Phi(u) = \exp(\beta\omega_o^2 u^2 - \tfrac{1}{2}\gamma^4 u^4)$$

Function $\Phi(u)$ is symmetric with respect to zero and therefore $A_{r,k} = 0$ for odd $r + k$, while $B_{r,k}, C_{r,k}$ vanish for even $r + k$.

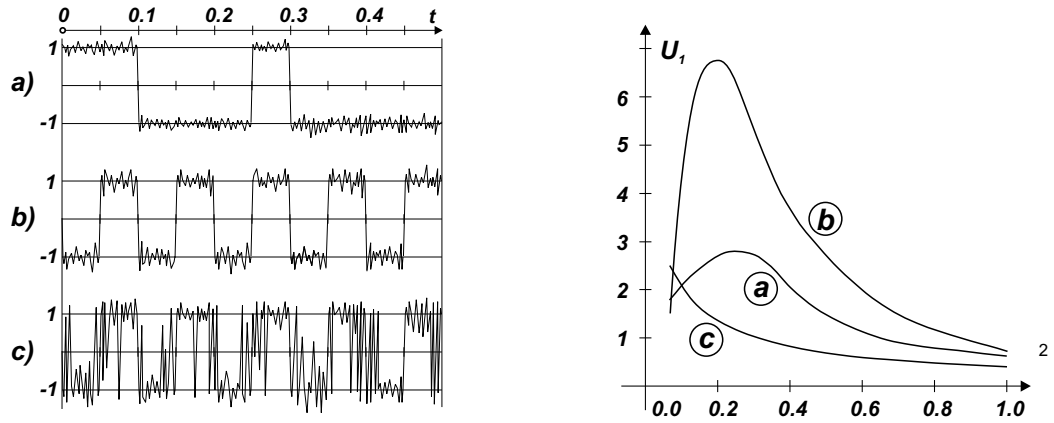


Figure 3: Typical response of a system with combined excitation - white noise and harmonic (left). The spectral amplification of the system response due to stochastic resonance effect (right). Three levels of noise are assumed: a) low noise, b) optimal noise – stochastic resonance occurs, c) high noise .

For each j the three-term recurrence formula (14) forms an algebraic system of size $(S+1)(R+1)\times(S+1)(R+1)$ for all unknown coefficients $q_{j,rs}$. The block diagonal of the system matrix consists from scaled regular matrices $\mathbf{A}$, see (15), and thus it is invertible.

Let us deal with the main idea of the solution method from other point of view. The Eq. (6) represents a linear partial differential equation of the second order with non-symmetric operator defined on an infinite domain, with homogeneous boundary conditions and parametric "excitation". It can be shown, that the weak solution exists and can be found using variational methods. Nevertheless some properties of the operator (non-symmetry, etc.) are limiting in a choice of methods. For instance Ritz method cannot be used due to operator non-symmetry. The modified Galerkin method seems to be acceptable. The presented solution process corresponds in principle to this method. The basic series employed is given by the formula (11) together with Eq. (13). Because $q_j(u,v)$ are polynomials and $p_o(u,v)$ can be interpreted as a weight function, every term of the series (11) separately fulfills the boundary conditions requested for the unknown $p(u,v,t)$ and its derivatives in u, v. The series (11) with respect to Eqs (8,9) is then substituted in fact into the Eq. (6) and then the orthogonality to the function $\alpha(u,v)$ for any arbitrary r,s is requested. The proces of orthogonalization corresponds to the application of mathematical mean value operator with respect to the PDF defined by Eq. (8). Equivalence appeared ascertains the convergence of the approximate formula (13), see e.g. [14]. Therefore the PDF can be reached with any prescribed accuracy. Due to structure of Eq. (11) the same holds also for stochastic moments which are to be used studying various physical effects related with PDF.

In order to validate the approaches presented in the this paper, the differential system (1) will be examined using several numerical methods. The following values of the individual parameters are adopted: $\omega_b = 0.5\,\mathrm{rad.\,s^{-1}}, \omega_0^2 = 1\,\mathrm{rad.\,s^{-2}}, \gamma^4 = 1\,\mathrm{rad.\,m^{-2}\,s^{-2}}, P_o = 0.4\,\mathrm{m.s^{-2}}, \Omega = 0.0942\,\mathrm{rad.s^{-1}}$. The stochastic resonance occurs for noise level $\kappa_{vv} = 2\sigma^2 = 0.25$, where the signal-to-noise ratio curve reaches its maxima, cf. the case b) in Fig. 3.

To approximate the time dependent probability density function according to relation (11) the coefficient matrices $\mathbf{A},\mathbf{B},\mathbf{C}$ has been computed according to relation (15) and the block tridiagonal matrix was set up following the three-term recurrence formula (14). The values of R,S has been selected to $R=S=8$ because for higher polynomial degrees the system matrix became badly conditioned and serious numerical errors were introduced in the solution.

The resulting probability density function varies in time with periodicity, which correspond

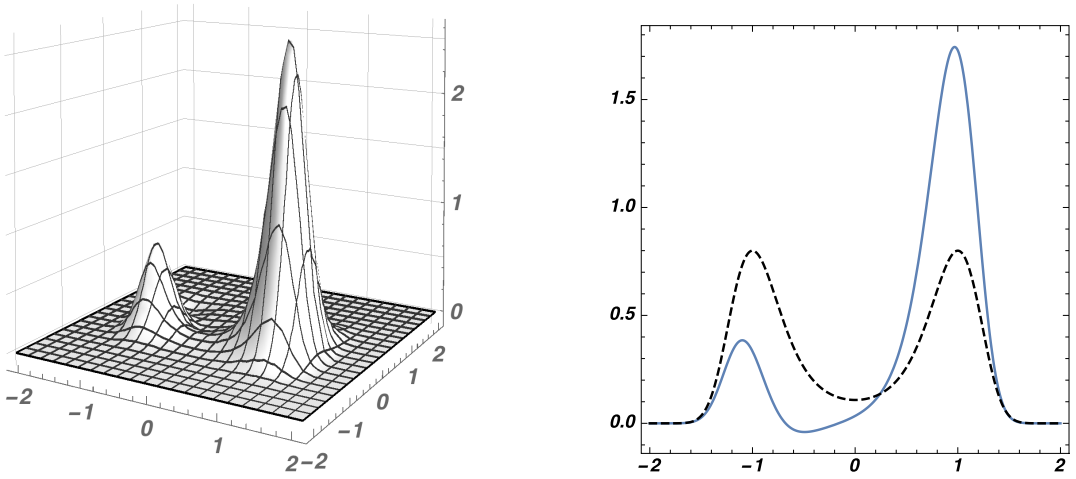


Figure 4: Left: the probability density function according to approximate relation (11) for $t = 30$. Right: the corresponding planar section for $v = 0$ (solid line) and stationary solution of the Boltzmann type (dashed).

to the frequency of external loading Ω. The individual peaks alternate but the lower peak never vanishes completely, see Fig. 4. The computed joint probability density is shown in the left figure, the corresponding curve for the displacement variable u (section for $v = 0$) is in the right graph. The solid line shows the computed time-dependent probability density for $t = 30$, the dashed line corresponds to the stationary solution of the Boltzmann type $p_o(u, v)$, see Eq. (8). Only $J = 5$ terms of expansion Eq. (11) was used in this case, the shape of the curves was not influenced by higher terms of Fourier expansion.

Despite of good theoretical properties of the polynomial ansatz Eqs (12-13) the current model does not fit well the expected flat (low probability) areas. Moreover, there is no theoretical reason preventing subtle overshoots into the negative values. Occurrence of these overshoots is understandable from numerical point of view, however, it can cause problems in subsequent analysis of the approximate probability density function. On the other hand, the presented approach brings results which can provide insight into the problem and mediate a good qualitative analysis of the stochastic resonance effect.

3 FOKKER-PLANCK EQUATION – FEM NUMERICAL SOLUTION

The second solution procedure is based on the FEM solution of the FP. The FP is analyzed in an original evolutionary form which enables an analysis of transition effects starting the (nearly) Dirac type initial conditions. The FEM efficiency when solving FP which follows from the Duffing stochastic differential equation without external harmonic forces was already studied by the authors in [15]. With the periodic force taken into account, certain difficulties arise due to the time inhomogeneity of the corresponding stochastic process.

The method is based on the approximaltion solution of Eq. (6) in the Galerin-Petrov meaning on the piecewise smoothly bounded domain $\Psi \in u \times v$, in $\mathbb{R}^d, d = 2$. The initial conditions at $t = 0$ s for PDF are considered in a form of the Gauss distribution function with an initial system position at the point $u_0 = 0, v_0 = 0$. For a small values of standard deviation it approaches to the Dirac function as it is primarily requested.

After a spatial discretizating of Ψ onto the rectangular finite elements using the bilinear approximation functions and implying boundary condition $p(\partial\Psi, t) = 0$, the system of ordinary differential equations emerge with global matrices $\mathbf{M}$, $\mathbf{K}(t)$ and vector of PD values $\mathbf{p}(t)$ in

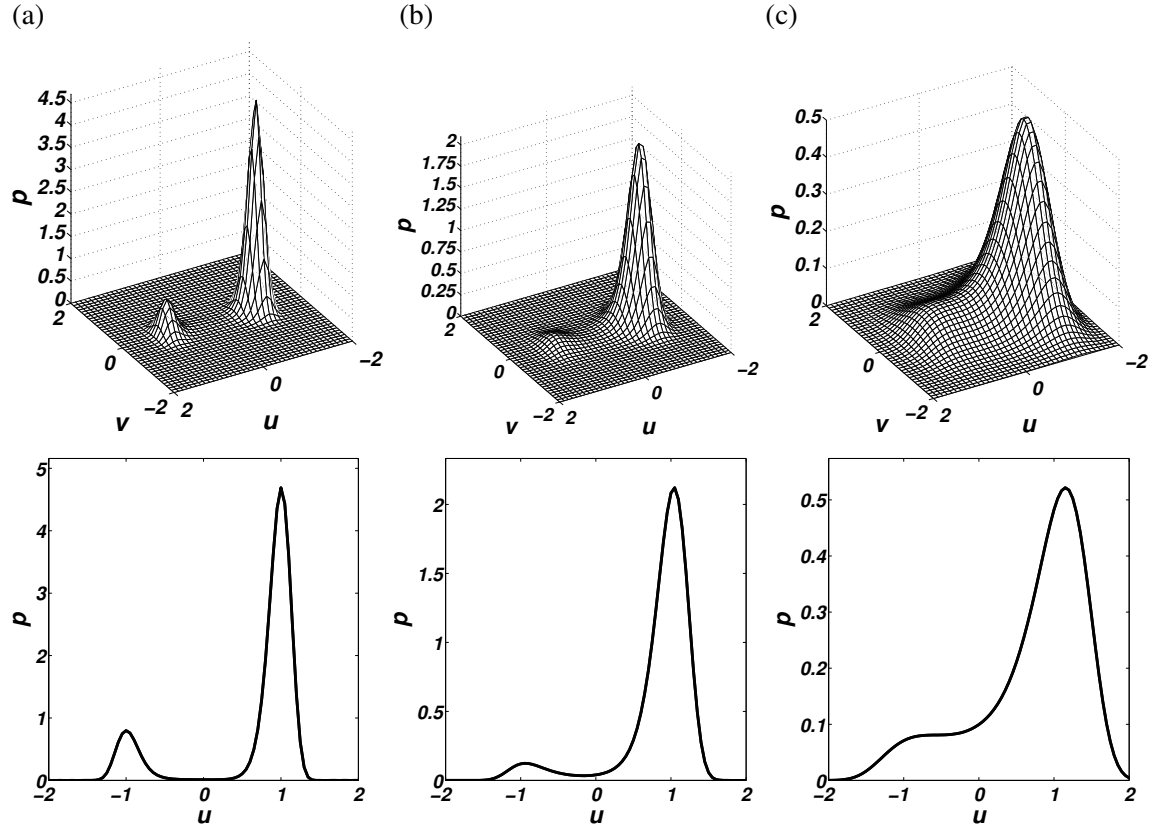


Figure 5: Axonometric and sectional display of the PDF at the highest value of probability of residing in selected potential well: a) $\kappa_{vv} = 0.10$; b) $\kappa_{vv} = 0.25$ - Stochastic resonance c) $\kappa_{vv} = 1.0$.

nodes of the mesh:

$$\mathbf{M}\dot{\mathbf{p}}(t) = \mathbf{K}(t)\mathbf{p}(t). \tag{16}$$

The matrix $\mathbf{K}(t)$ is time-dependent due to the periodic perturbation entering the drift term of FP and, in the result, the solution oscillates periodically between the potential wells. In the regime of SR, the switchings are in phase with the external periodic signal $P(t)$ and the mean residence time is most close to half the signal period $2\pi/\Omega$.

Since convection indicators of SR such as Spectral Power Amplification (SPA), the Signal-to-Noise Ratio (SNR) or the residence-time distribution density are not applicable in the present approach, other way of treating the stochastic response in SR regime is adopted. As a specific measure of optimally selected noise intensity, the integral value of PD distribution over one potential well, $u \in (0, \infty)$, for various κ_{vv} is introduced as:

$$P_N(t; \kappa_{vv}) = \int_{-\infty}^{\infty} \left(\int_0^{\infty} p(u, v, t; \kappa_{vv}) \mathrm{d}u \right) \mathrm{d}v \tag{17}$$

that is periodic in time with the amplitude $A_p(\kappa_{vv})$. The stochastic resonance occurs for such κ_{vv} for which the amplitude $A_p(\kappa_{vv})$ assumes its maximum.

Let us solve Eq. (6) with the identical parameters as introduced in the previous section. The computational domain in size of $u, v \in \langle -10, 10 \rangle$ is adopted and split onto the structured mesh grid with an element edge size of 0.1 m. Selected results of the FEM solution are depicted in Fig. 5. It contains a response PDF in the axonometric view and vertical section under various noise intensities. The figures represent the solution taken in the time instant corresponding

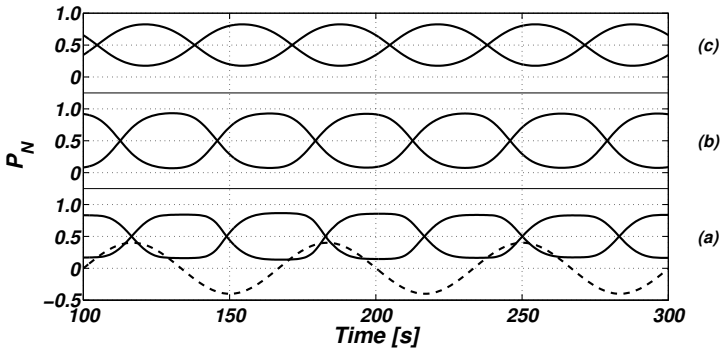


Figure 6: Time history of integral value of PDF over positive and negative domains $P_{N,\langle -10,0\rangle}$ and $P_{N,\langle 0,10\rangle}$ for a) $\kappa_{vv} = 0.10$; b) $\kappa_{vv} = 0.25$ - Stochastic resonance c) $\kappa_{vv} = 1.0$.

to the highest value of probability of residing in one selected potential well. In the temporal evolution case, the peaks periodically oscillate between the relevant potentials with a period close to the excitation frequency. Note that the role of transient effect following from the initial condition has subsided.

Fig. 5(a) shows the approximation PDF at a low noise intensity $\kappa_{vv} = 0.10$ with regards to the stochastic resonance. The solution forms a bimodal shape with two strong peaks around the stable points at $(u, v) = (\pm 1, 0)$ separated by a deep saddle point at $(u, v) = 0$. As the noise intensity increases to the optimal value for the stochastic resonance $\kappa_{vv} = 0.25$, the PDF becomes wider over Ψ and consequently, its peak values drop while still maintaining the evident bistable character, see Fig. 5(b). For higher excitation densities the bistable shape together with the saddle point disappear as pointed out for $\kappa_{vv} = 1.0$ in Fig. 5(c).

The results given by Eq. (17) are illustrated in Fig. 6 that depicts the time history of integral value $P_N(t; \kappa_{vv})$ for three sets of noise intensities. Each set consists of one couple of the integral value determined for both the positive and negative integral domain $u \in (\langle -10, 0\rangle, \langle 0, 10\rangle)$. Starting at low density of noise with $\kappa_{vv} = 0.1$, plot (a), the flattened sine-like functions emerge with the amplitude of $A_p(0.1) = 0.864$. As the intensity grows, the curves change the shape towards a typical sine form and the phase shift between the external excitation and integral value function decreases. At optimal dose of noise in sense of stochastic resonance, the system reaches maximum amplitude $A_p(0.25) = 0.927$, plot (b). Beyond this point the amplitude decreases again, as presented in plot (c) for which yields $A_p(1.0) = 0.825$.

4 STOCHASTIC SIMULATION

The last procedure represents simulation regarding the original Duffing or relevant Ito stochastic system. This way is used, among other things because it allows an effective procedure of searching domains of adequate parameters leading to SR phenomenon.

Introducing the potential energy $V(u)$ Eq. (2) into the general oscillator equation (1), the detailed Duffing system reads:

$$\begin{aligned} \dot{u} &= v; \\ \dot{v} &= -2\omega_b \cdot v + \omega_0^2 u - \gamma^4 u^3 + P_o \exp(\mathrm{i}\Omega t) + \xi(t). \end{aligned} \tag{18}$$

The equation Eq. (18) is solved numerically with the same parameters as used before. The time period taken into account was $T = 1000\,\mathrm{s}$ with the time step $\delta_t = 0.05\,\mathrm{s}$. The white noise was simulated as a finite sum of harmonic functions with uniformly distributed random frequencies $\omega_i \in (0, \omega_{max}\rangle$ and phases $\varphi_i \in (0, 2\pi\rangle$, cf. Eq. (19). The parameter ω_{max} represents the noise

cut-off frequency, value $\omega_{max} = 10\,\mathrm{rad.s}^{-1}$ was used in the simulation.

$$\xi(t) = \sqrt{2}\sigma \sum_{i=1}^{N} cos(\omega_i t + \varphi_i) \tag{19}$$

The results of the stochastic resonance analysis are illustrated starting by Fig. 7 which presents the signal-to-noise ratio as the function of the noise intensity expressed by $2\sigma^2 = \kappa_{vv}$ and the results (Fourier spectra) of the numerical simulations using the basic system Eqs (18). In the individual spectral lines it can be seen the influence of rising white noise intensity, which acts together with a harmonic force onto the system. For very low level of the noise the harmonic component is hardly able to overcome the inter-well barrier and therefore only seldom irregular jumps between stable points occur.

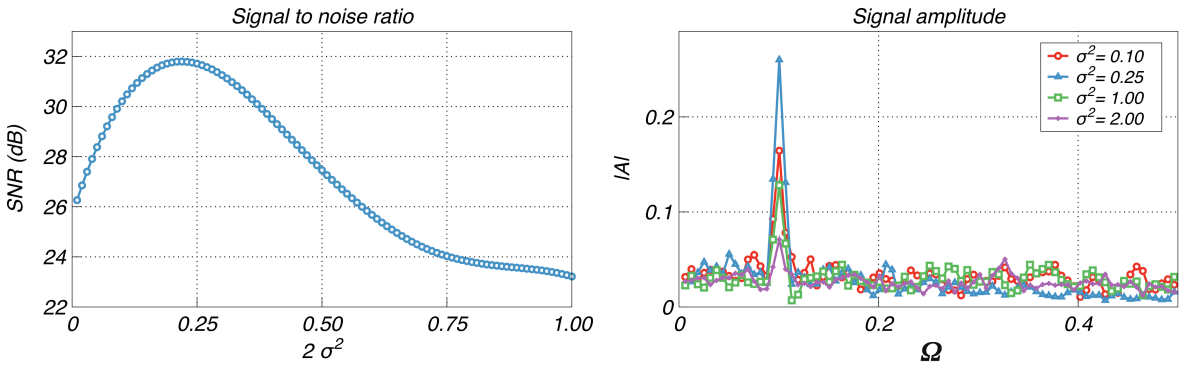


Figure 7: The spectral amplification of the system response due to stochastic resonance effect. The signal-to-noise ratio (SNR) as the function of various noise strengths (σ^2) due to stochastic resonance. Right - Fourier spectra of the response obtained by numerical solution of Eqs (18).

In local regimes the system response is relatively small and nearly linear. Optimal ratio of the noise intensity and the amplitude of the harmonic force results for its certain frequency in the system response containing a visible spectral peaks (amplification) corresponding with the frequency of the external harmonic modulation. The single peak (in the case of coloured noise more peaks may appear) and thus the ”optimal” noise strength can be identified.

5 CONCLUSIONS

The response of a dynamic non-linear single degree of freedom system with cubic characteristic to a combination of additive random noise and external deterministic periodic force were studied. Three different approaches have been addressed in order to compare results obtained using various definitions of the problem.

The effect of stochastic resonance has been described firstly theoretically using the FP equation and method of generalized stochastic moments for its approximate solution. The convergence of this method is expected with respect to theoretical properties of the solution process being similar to Galerkin method applied to the equations with non-symmetric operator. The convergence has also been observed when numerical evaluation of formula and algorithms obtained has been done. The non-stationary character of the response PDF with the basic and the higher harmonics has been verified and used for periodic component detection in the input signal containing both random and deterministic parts. Therefore adding noise to a system can improve its ability of information transfer.

The FEM solution of the FP equation exhibits with a high accuracy the effect of stochastic resonance. Concurrently acting additive deterministic input and random excitation lead to the periodically driven differential system with the time-dependent stiffness matrix. In order to identify the effect of stochastic resonance, the transition response of such a noise-controlled stochastic system was examined using integral formula applied over one potential well. This treatment fully detected the optimal dose of noise for the stochastic resonance regime.

The paper describes also the numerical simulation of the Duffing system. It shows, that under certain "optimal" value of the parameters, the signal-to-noise ratio of the response increases and the resonant-like peak occurs in the amplitude spectra. This makes an optimistic perspective for the experimental analysis, which together with the analytical and numerical ones should continue to obtain better insight into the general tendencies when individual parameters of the system and the input signal are changed.

Possibilities of other analytical solution procedures should be also investigated (Floquet theorem, maximum entropy principle, etc.). Also other types of non-linearities in the system stiffness (especially non-symmetric) should be carefully studied. Other application areas like post-critical processes in aero-elasticity or vehicle dynamics should be thoroughly examined from the point of view of the adverse effects of the response amplification due to stochastic resonance effects.

ACKNOWLEDGEMENT

The kind support of the Czech Science Foundation project No. 15-01035S and of the RVO 68378297 institutional support are gratefully acknowledged. The research related to the third section was carried out with the support of the Czech Science Foundation project No. GP14-34467P.

REFERENCES

[1] Gammaitoni, L., Hänggi, P., Jung, P., Marchesoni, F.: Stochastic resonance. *Reviews of Modern Physics*, 70, 1, 1998, pp. 223-287.

[2] Inchiosa, M.E., Bulsara, A.R.: Signal detection statistics of stochastic resonators. *Physical Review E*, 53, 3, 1996, pp. 2021-2024.

[3] McDonnell M.D., Stock N.G., Pearce C.E.M. & Abbott D. (2008). *Stochastic Resonance*, Cambridge University Press, Cambridge, New York.

[4] Náprstek, J.: Non-linear self-excited random vibrations and stability of an SDOF system with parametric noises. *MECCANICA*, 33, 1998, pp. 267-277.

[5] Kramers, H.A.: Brownian motion in a field of force and the diffusion model of chemical reactions. *Physica*, VII, 4, 1940, pp. 284-304.

[6] Dykman, M.I. et al.: Resonant subharmonic absorption and second-harmonic generation by a fluctuating nonlinear oscillator. *Physical Review E*, 54, 3, 1996, pp. 2366-2377.

[7] Wong, E., Zakai, M.: On the relation between ordinary and stochastic equations. *International Journal of Engineering Sciences*, vol.3, 2, 1965, 213-229.

[8] Lin, Y.K., Cai G.Q.: *Probabilistic Structural Dynamics – Advanced Theory and Applications*. McGraw-Hill, NewYork,1995.

[9] Náprstek, J.: Real and Markov processes in stochastic systems. In: *Proc. Dynamics of Machines 2003* (I. Dobiáš edt.). IT ACSR, Prague, 2003, pp.127-134.

[10] Pugachev V.S., Sinitsyn I.N.: *Stochastic Differential Systems - Analysis and Filtering*. J. Willey, Chichester, 1987.

[11] Náprstek J.: Application of the maximum entropy principle to the analysis of non-stationary response of SDOF/MDOF systems. In: *Proc. 2nd European Nonlinear Oscillations Conference - EUROMECH* (L. Púst and F. Peterka eds.), IT ASCR, Prague, 1996, pp.305-308.

[12] Cai, G.Q., Lin, Y.K.: On exact stationary solutions of equivalent non-linear stochastic systems. *International Journal of Non-Linear Mechanics*, vol.23, 4, 1988, pp. 315-325.

[13] Zhu, W.Q., Cai, G.Q., Lin, Y.K.: On exact stationary solutions of stochastically perturbed Hamiltonian systems. *Probabilistic Engineering Mechanics*, vol.5, 2, 1990, pp.84-87.

[14] Mikhlin, S.G.: *Variational Methods in Mathematical Physics* (in Russian). Nauka, Moscow, 1970.

[15] Náprstek, J., Král, R.: Finite element method analysis of Fokker-Planck equation in stationary and evolutionary versions. *J. Advances in Engineering Software* 72, pp. 28-38, 2014.

COMPDYN 2015
5th ECCOMAS Thematic Conference on
Computational Methods in Structural Dynamics and Earthquake Engineering
M. Papadrakakis, V. Papadopoulos, V. Plevris (eds.)
Crete Island, Greece, 25–27 May 2015

TIME DOMAIN SIMULATION OF VORTEX-INDUCED VIBRATION OF A CURVED BEAM USING A WAKE OSCILLATOR MODEL

Y. Qu[1], **A.V. Metrikine**[1]

[1] Delft University of Technology
Faculty of Civil Engineering & Geosciences
Stevinweg 1, 2628CM Delft, the Netherlands
e-mail: Y. Qu@tudelft.nl，A.Metrikine@tudelft.nl

Keywords: Time Domain, Vortex-induced Vibration, Wake Oscillator, Flexible Cylinder, Curved Beam.

Abstract. *A general model capable of simulating the vortex-induced vibration of a flexible curved cylinder is presented. The 3-D motion of the cylinder is modeled using a curved Euler-Bernoulli beam, which accounts for bending, extensibility and geometrical nonlinearity. The finite element method is used to solve the beam equation. The hydrodynamic forces are modelled with the help of the van der Pol wake oscillators attached to the nodes of the FE model of the beam. Such phenomenological oscillators are conventionally used for the prediction of vortex-induced vibration of rigid cylinders subjected to cross flow perpendicular to their axis. In order to cope with the curvature of the beam, a local reference frame is introduced and the tangential component of the flow velocity is neglected. Comparison is performed of the predictions of the proposed model with experimental observations of the vortex-induced vibration of a curved cable available in the literature. The comparison showed that the proposed model can reproduce some features observed in the experiment, such as the location of power-in region and the travelling wave.*

1 INTRODUCTION

In offshore engineering applications, slender structures such as risers, cables and pipelines are widely used. These types of structures usually have very large aspect ratio (L/D) and have to be considered as flexible. When exposed to marine currents, these slender structures undergo vortex-induced vibrations (VIV) due to the space-time varying hydrodynamics associated with vortex shedding. The prediction of VIV is one of the key issues in the analysis and design of offshore slender structures because these vibrations result in significant fatigue damage.

Although VIV of a short rigid cylinder has been well documented in many reviews [1, 2, 3], the features of VIV of long slender structures have not been fully understood. A review of the recent studies on the VIV of long slender cylinders can be found in [4].

In the prediction of VIV of a short rigid cylinder, nonlinear wake oscillator models have been widely used in recent years and gained popularity due to the low computational effort and acceptable accuracy. In [5], a classical van der Pol oscillator is used to model the near wake dynamics and the effects of several types of linear coupling terms (displacement, velocity and acceleration) modelling the fluid-structure interaction are investigated. It was found in [5] that the acceleration coupling is most appropriate for the modelling of most of the features of VIV. This van der Pol oscillator model was further improved by properly including the effect of stall term dropping the assumption of a small angle of attack [6].

Several papers can be found in the literature, which employ the wake oscillator models for the prediction of VIV of straight flexible cylinders exposed to a normal cross flow. In contrast, the VIV of curved cylinders has not been widely addressed. In all known to the authors works on this matter, strong simplifications have been made regarding either the flow direction [7, 8] or the motion of the cylinder [9].

The main novelty of this paper lies in the improved model of the cylinder-wake interaction, which includes the geometric nonlinearity of the structure and a projection of the initially inclined to the cylinder axis flow direction.

2 MODEL DISCRIPTION

2.1 Nonlinear structural model

In theoretical studies of VIV of slender cylinders, the latter are usually modelled by straight tensioned beams or cables whose equations of motion (excluding the hydrodynamic forces) are assumed to be linear. However, in practical applications many slender structures, such as catenary risers, pipelines during the laying process and mooring cables have a curved shape. So a general Euler-Bernoulli beam model valid for both curved and straight cylindrical structures is used here. It accounts for bending, extensibility and geometrical nonlinearity. The description of the beam position is based on the differential geometry of 3D curves [10] where the arbitrary point on the beam axis can be described by a position vector $\mathbf{r}$:

$$\mathbf{r}(s,t)=\begin{bmatrix} x(s,t) \\ y(s,t) \\ z(s,t) \end{bmatrix}, \tag{1}$$

where s is the Eulerian coordinate measured along the stretched beam and t is the time. Let us introduce the tangential unit vector $\mathbf{t}=\partial\mathbf{r}/\partial s$, the principle normal unit vector $\mathbf{n}$ and the binormal unit vector $\mathbf{b}$, such that $\mathbf{b}=\mathbf{t}\times\mathbf{n}$, $\mathbf{n}=\mathbf{b}\times\mathbf{t}$ and $\mathbf{t}=\mathbf{n}\times\mathbf{b}$. The curvature vector of the beam is $\mathbf{k}=\partial\mathbf{t}/\partial s=\partial^2\mathbf{r}/\partial s^2$, and the axial strain of the beam is $\varepsilon=|\partial\mathbf{r}/\partial p|-1$, where p is the Lagrangian co-

ordinate measured along the unstretched beam. It should be noted that the torsion of the beam is ignored here. For the convenience of writing, the following notation will be used to represent the partial derivative with respect to s: $\mathbf{r}_{,s}=\partial\mathbf{r}/\partial s$.

The weak form of the equations of motion of the beam is derived from the Lagrange-D'Alembert equation:

$$\delta W_E - \delta W_S = \delta W_I, \tag{2}$$

where δW_E denotes the virtual work of the external forces, δW_S is the virtual work done by the internal forces and δW_I is the virtual work of the inertial forces. The elastic internal forces are split into two parts, namely a part due to bending based on the curvature of the deformed beam, and a part due to axial strain. The virtual work done by the axial force is given as

$$\delta W_A = \int_0^l EA\varepsilon\mathbf{r}_{,s}\bullet\delta\mathbf{r}_{,s}ds, \tag{3}$$

while the virtual work due to bending reads

$$\delta W_B = \int_0^l \left(EI\mathbf{r}_{,ss}\bullet\delta\mathbf{r}_{,ss} - EI\kappa^2\mathbf{r}_{,s}\bullet\delta\mathbf{r}_{,s} \right)ds, \tag{4}$$

where EI is the bending stiffness, EA is the axial stiffness and l is the length of the beam in deformed configuration. Then the total virtual work of internal forces can be written as

$$\delta W_S = \int_0^l \left(EI\mathbf{r}_{,ss}\bullet\delta\mathbf{r}_{,ss} - EI\kappa^2\mathbf{r}_{,s}\bullet\delta\mathbf{r}_{,s} + EA\varepsilon\mathbf{r}_{,s}\bullet\delta\mathbf{r}_{,s} \right)ds. \tag{5}$$

For the virtual work of the inertial forces, the rotational inertia is ignored and only the inertia due to the linear acceleration is considered. Thus

$$\delta W_I = \int_0^l m\ddot{\mathbf{r}}\delta\mathbf{r}ds \tag{6}$$

where m is the mass of the beam per unit length in the deformed configuration. When this model is applied in the simulation of the VIV, m includes the ideal added mass $m_a=1/4\,\pi C_a\rho D^2$, in which ρ denotes the density of the fluid, D is the outer diameter of the cylinder and C_a is the added mass coefficient which is assumed to be equal to one in this paper.

As the formulas presented above are derived in the frame of the Eulerian description, they need to be transformed to the Lagrangian description where the original length of the beam L is already known. The relations used for the transformation are

$$\mathbf{r}_{,s} = \frac{1}{\left|\mathbf{r}_{,p}\right|}\mathbf{r}_{,p},\ \mathbf{r}_{,ss} = \frac{1}{\left|\mathbf{r}_{,p}\right|^3}\left(\left|\mathbf{r}_{,p}\right|\mathbf{r}_{,pp} - \frac{\mathbf{r}_{,p}\bullet\mathbf{r}_{,pp}}{\left|\mathbf{r}_{,p}\right|}\mathbf{r}_{,p} \right) \text{ and } ds = \left|\mathbf{r}_{,p}\right|dp. \tag{7}$$

Applying these relations to Eq. (4) and (5), we obtain

$$\delta W_A = \int_0^L EA\frac{\left(\left|\mathbf{r}_{,p}\right|-1\right)}{\left|\mathbf{r}_{,p}\right|}\mathbf{r}_{,p}\bullet\delta\mathbf{r}_{,p}dp \tag{8}$$

and

$$\delta W_B = \int_0^L EI \frac{1}{\left|\mathbf{r}_{,p}\right|^5}\left(\left(\left|\mathbf{r}_{,p}\right|^2 \mathbf{r}_{,pp} - \left(\mathbf{r}_{,p}\bullet\mathbf{r}_{,pp}\right)\mathbf{r}_{,p}\right)\bullet\delta\mathbf{r}_{,pp} + \left(\left(\frac{\mathbf{r}_{,p}\bullet\mathbf{r}_{,pp}}{\left|\mathbf{r}_{,p}\right|}\right)^2 \mathbf{r}_{,p} - \left(\mathbf{r}_{,p}\bullet\mathbf{r}_{,pp}\right)\mathbf{r}_{,pp} + \kappa^2\left|\mathbf{r}_{,p}\right|^4\mathbf{r}_{,p}\right)\bullet\delta\mathbf{r}_{,p}\right)dp, \tag{9}$$

where

$$\kappa = \left|\mathbf{r}_{,ss}\right| == \frac{1}{\left|\mathbf{r}_{,p}\right|^3}\left|\mathbf{r}_{,pp}\times\mathbf{r}_{,p}\right|. \tag{10}$$

A two nodes beam element, the same as the one described in [11], is used in this paper. The vector of nodal coordinates of the element consists of 12 degrees of freedom

$$\begin{aligned}\mathbf{e}^T = \big[&x(0) \quad y(0) \quad z(0) \quad x_{,p}(0) \quad y_{,p}(0) \quad z_{,p}(0)\\ &x(L_0) \quad y(L_0) \quad z(L_0) \quad x_{,p}(L_0) \quad y_{,p}(L_0) \quad z_{,p}(L_0)\big],\end{aligned} \tag{11}$$

where L_0 is the length of the beam element. Based on that, the global position vector of an arbitrary point, originally placed at p of the undeformed beam axis, in the deformed configuration can be interpolated in terms of the nodal coordinates and the element shape function as

$$\mathbf{r} = \begin{bmatrix} x \\ y \\ z \end{bmatrix} = S\mathbf{e}. \tag{12}$$

A cubic polynomial shape function is employed to describe each components of the position vector. Thus, the global shape function S can be written as

$$S = [S_1\mathbf{I} \quad S_2\mathbf{I} \quad S_3\mathbf{I} \quad S_4\mathbf{I}], \tag{13}$$

where $\mathbf{I}$ is the 3×3 unit matrix and the function $S_i = S_i(p)$ are given by

$$\begin{aligned} &S_1 = 2\left(\frac{p}{L}\right)^3 - 3\left(\frac{p}{L}\right)^2 + 1, S_2 = L\left(\frac{p}{L}\right)^3 - 2L\left(\frac{p}{L}\right)^2 + p,\\ &S_3 = 3\left(\frac{p}{L}\right)^2 - 2\left(\frac{p}{L}\right)^3, S_4 = L\left(\left(\frac{p}{L}\right)^3 - \left(\frac{p}{L}\right)^2\right).\end{aligned} \tag{14}$$

2.2 Wake oscillator model

In this study, a van der Pol wake oscillator model proposed in [6] is used to compute the hydrodynamic forces due to vortex shedding. In order to introduce the model, let us consider a case where cylinder is rigid and flow is perpendicular to its axis. By assuming that the flow around the cylinder is two-dimensional (uniform along the cylinder axis), the interaction between the cylinder and the flow can be simplified as shown in Fig. 1. The total vortex force acting on per unit length of the cylinder is decomposed into a drag part F_{VD} and a lift part F_{VL}, where the drag and the lift are defined as, respectively, being in-line with and perpendicular to

U, the latter being the total flow velocity relative to the moving cylinder. The lift force $F_{VL}(s,t)$ is expressed through the wake variable $q(s,t)$ as

$$F_{VL} = \frac{1}{2}\rho D U^2 C_{VL}, \qquad C_{VL} = \frac{C_L}{2} q, \tag{15}$$

where C_L is the lift coefficient measured for a stationary cylinder. Furthermore, the inertial coupling is assumed between the wake oscillator and the structure:

$$\frac{d^2 q}{dt^2} + \varepsilon \omega_s \left(q^2 - 1\right)\frac{dq}{dt} + \omega_s^2 q = \frac{A}{D}\frac{d^2 Y}{dt^2} \tag{16}$$

where ω_s is the Strouhal frequency, whereas A and ε are tuning parameters.

The drag force $F_{VD}(s,t)$ is defined as

$$F_{VD} = \frac{1}{2}\rho D U^2 C_{VD}, \qquad C_{VD} = C_D, \tag{17}$$

where C_D is the drag coefficient measured for a stationary cylinder.

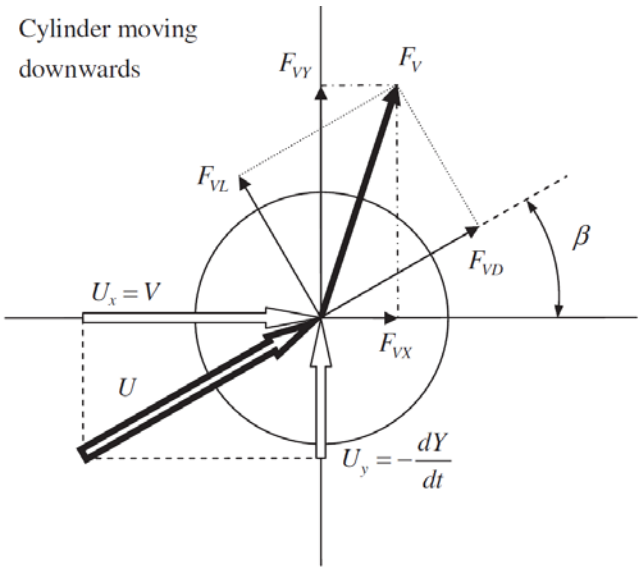


Figure 1: Decomposition of the vortex fluid force in drag, lift, X and Y direction [6].

The force acting on the cylinder in the Y (vertical) direction due to the vortex shedding is given as

$$F_{VY} = \frac{1}{2}\rho D V^2 C_{VY} = \frac{1}{2}\rho D \sqrt{V^2 + \left(\frac{dY}{dt}\right)^2}\left(C_{VL} - C_{VD}\left(\frac{dY}{dt}\right)\right). \tag{18}$$

In order to gain insight into the conditions under which the VIV may occur, let us assume that the cylinder is forced to vibrate in the cross-flow direction harmonically with an amplitude y and a frequency ω_c:

$$Y(t) = y \sin(\omega_c t). \tag{19}$$

Substituting Eq.(19) into Eq. (15) and then using the following dimensionless parameters

$$\tau = \omega_s t,\ \Omega_c = \omega_c / \omega_s,\ \hat{y} = y/D, \tag{20}$$

we obtain

$$\frac{d^2 q}{d\tau^2} + \varepsilon\left(q^2 - 1\right)\frac{dq}{d\tau} + q = -A\Omega_c \hat{y}\sin\left(\Omega_c \tau\right). \tag{21}$$

Applying the same procedure to Eq. (18), the following expression can be obtained for C_{VY}:

$$C_{VY} = \left(-2\pi \mathrm{St}\hat{y}\Omega_c \cos\left(\Omega_c \tau\right) C_{VD} + C_{VL}\right)\sqrt{1 + 4\pi^2 \mathrm{St}^2 \Omega_c^2 \cos^2\left(\Omega_c \tau\right)} \tag{22}$$

According to the harmonic balance method and accounting for the contribution of the fundamental frequency only, the solution to Eq. (21) is sought for in the form $q = q_0 \sin\left(\Omega_c t + \varphi\right)$. Substituting the latter expression in Eq. (22) and considering only the main harmonic contribution of the nonlinearities, collection of multipliers of $\sin\left(\Omega_c t\right)$ and $\cos\left(\Omega_c t\right)$ yields two algebraic equations with two unknowns q_0 and φ. Then the component of C_{VY} that in phase with the velocity of the cylinder can be approximated as

$$C_{yv} \approx \left(-2\pi \mathrm{St}\hat{y}\Omega_c C_{VD} + \frac{1}{2} C_L q_0 \sin\left(\varphi\right)\right)\sqrt{1 + 4\pi^2 \mathrm{St}^2 \Omega_c^2} \tag{23}$$

It is the sign of C_{yv} in Eq. (23) that implies whether the flow provides the cylinder with the energy or extracts it from the moving cylinder. If C_{yv} is positive, the flow increases the energy of the cylinder while otherwise the energy of the vibration of the cylinder will be reduced due to interaction with the flow. As can be seen from Eqs. (21) and (23), if tuning parameters A and ε are fixed, the sign of C_{vy} depends on the dimensionless amplitude $\hat{y}$ and dimensionless frequency Ω_c. In Fig 2 the density plots of C_{vy} are shown in the plane of the reduced velocity $V_c = 1/\mathrm{St}/\Omega_c$ and the normalized amplitude $\hat{y} = y/D$ for two sets of the tuning parameters. For both cases, the following figures for the other parameters are used: St=0.17, C_{VD}=1.2, and C_L=0.3842.

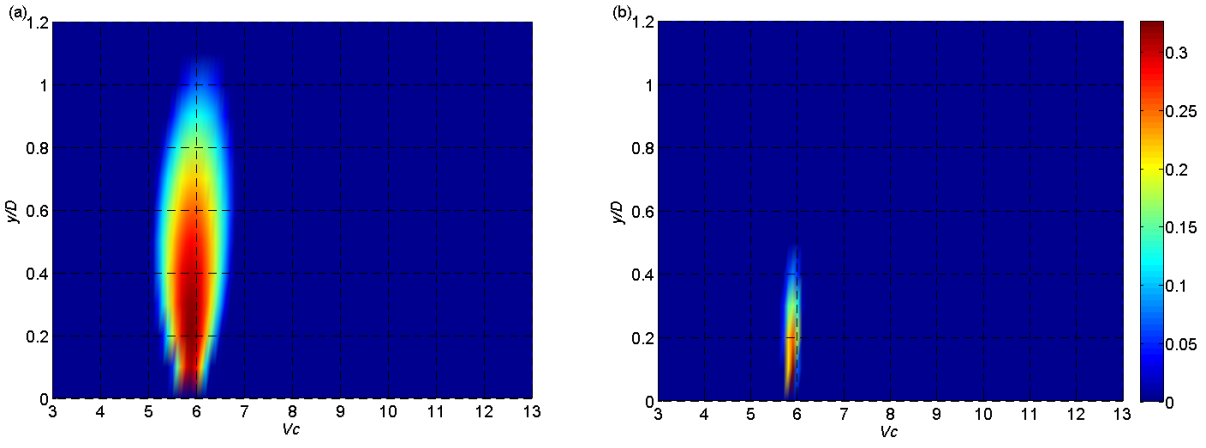


Figure 2: Force coefficient C_{yv} in phase with the velocity of the cylinder: (a) A=4, ε=0.05, (b) A=1, ε=0.1.

As can be seen from Fig 2, the power-in range can depends significantly on the tuning parameters. In Fig 2a, the power-in region is located approximately between reduced velocity 5 and 7, and the maximum amplitude in this range is about 1D. In Fig 2b, due to the small pa-

rameter A, the power-in range is extremely narrow and is localized around the reduced velocity of 6. The maximum amplitude in the power-in range in the latter case is less than 0.5D.

2.3 Coupled system

As mentioned before the wake oscillator model described above has been developed for rigid cylinders subject to the normal cross flow. However, for the VIV of long flexible cylinder, the attack angle and relative to the flow velocity of the cylinder depend on the position along the cylinder. In this paper, by assuming that the Independence Principle is valid and the vortex shedding is correlated within certain length of the cylinder, the wake oscillators are attached to the nodes of beam elements where local frames are used so the wake oscillator described before is applicable.

Using the local frame described by the tangent, principal normal and binormal unit vectors, the 2-D vortex shedding process is assumed to happen in the plane (i.e., **b**-**n** plane) that is perpendicular to the orientation of the beam, see Fig 3.

The absolute normal flow velocity and the relative normal flow velocity are given by

$$\begin{aligned} \mathbf{V}_N &= \mathbf{V} - \left(\mathbf{V}\bullet\mathbf{t}_s\right)\mathbf{t}_s, \\ \mathbf{U}_N &= \mathbf{U} - \left(\mathbf{U}\bullet\mathbf{t}\right)\mathbf{t}, \end{aligned} \tag{24}$$

where $\mathbf{V}$ is the flow velocity in the earth-bound reference frame, $\mathbf{U}$ is the relative flow velocity and $\mathbf{t}_s$ is the unit tangent vector measured under the initial static configuration due to the mean in-line forces.

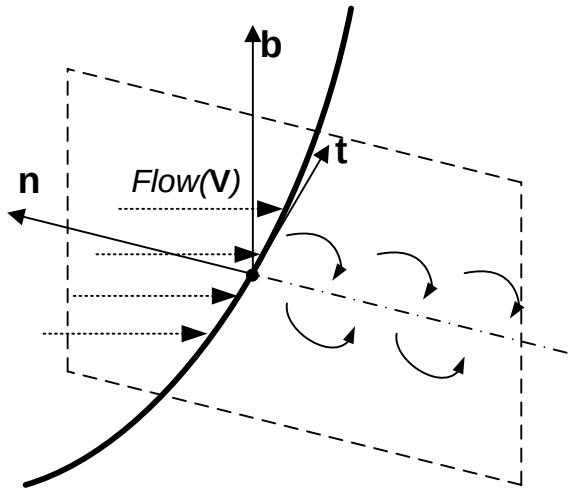


Figure 3: Local vortex shedding for a spatial curved cylinder.

The lift and drag forces are defined as

$$\mathbf{F_L} = \frac{1}{2}\rho DL\frac{C_L}{2}q\left|\mathbf{U_N}\right|^2\mathbf{D_L}, \tag{25}$$

$$\mathbf{F_D} = \frac{1}{2}\rho DLC_D\left|\mathbf{U_N}\right|\mathbf{U_N}, \tag{26}$$

where $\mathbf{D_L}$ is the direction of the lift force:

$$\mathbf{D}_{\mathrm{L}} = \frac{\mathbf{U}_{\mathrm{N}} \times \mathbf{t}}{\left|\mathbf{U}_{\mathrm{N}} \times \mathbf{t}\right|}. \tag{27}$$

The coupling term in the wake oscillator equation is also changed accordingly:

$$\ddot{q} + \varepsilon\omega_s \left(q^2 - 1\right)\dot{q} + \omega_s^2 q = \frac{A}{D}\ddot{\mathbf{r}} \bullet \mathbf{D}_{\mathbf{a}}, \tag{28}$$

where

$$\mathbf{D}_{\mathbf{a}} = \frac{\mathbf{V}_{\mathrm{N}} \times \mathbf{t}_s}{\left|\mathbf{V}_{\mathrm{N}} \times \mathbf{t}_s\right|}. \tag{29}$$

One of the major drawbacks of the approach adopted in this paper is that the Independence Principle is not applicable for large angles between the flow and the cylinder axis. Experiments showed that there is a critical angle above which the relatively wide plateau of the large amplitude oscillations observed in the case of small attack angles disappears and, instead, large-amplitude oscillations occur in a very narrow range of normalized reduced velocities [12]. This means that the parameters of the wake oscillator model should be dependent on the local inclination of the cylinder. For convenience, in this paper only two sets of tuning parameters are used. One set corresponds to the inclination smaller than the critical angle, and the other one is used when inclination is bigger than the critical angle.

3 COMPARISON WITH EXPERIMENTAL RESULTS

In this section, results of a case study are presented and compared with those of a large-scale field test. The objective is to check if experimentally observed results can be reproduced by the model introduced in the previous sections.

A series of field tests were conducted by MIT and the Deepstar Consortium in and near the Gulf Stream in 2004 and 2006. The specific test selected for comparison in this paper is described in [13]. In the tests, a fiber glass composite pipe of 152.4 meters long and 3.63 cm in outer diameter was towed in Gulf Stream with a railroad wheel attached to the tip of the pipe to provide tension. A diagram of the test configuration is shown in Fig. 4. The properties of the pipe are summarized in Table 1.

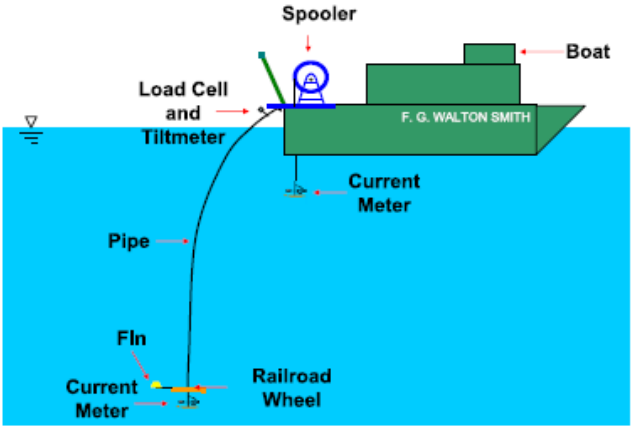


Figure 4: Set-up of the Gulf Steam experiments 2006 [14].

When towed in water, due to the tension applied at the tip and the drag forces acting on the pipe, it will assume a curved shape. This shape defines the angle of attack at various positions

along the pipe. In [13], no information about the pipe shape is given. Only the distribution of the normal velocity of the current relative to the deformed shape is given. In order to get the shape of the pipe, static analysis of the pipe under uniform current is carried out. The drag coefficients were iterated until the calculated and the given in [13] normal current profiles matched each other. Since the wake oscillator model underestimates the amplification of drag forces due to VIV, extra in-line forces were applied during dynamic analysis to maintain the shape.

Parameters	Value
Inner Diameter	0.0249 m
Outer Diameter	0.0363 m
EI	613 Nm^2
EA	3.322e6 N
Weight in sea water	0.1972 kg/m
Weight in air	1.2682 kg/m
Effective Tension	3225 N
Length	152.4 m

Table 1: Gulf Stream 2006 pipe properties.

In view of many uncertainties involved in the experiment, the focus of this paper is placed on the qualitative reproduction of the test results. According to [14, 15], the power-in region is set to belong in the reduced velocity interval from 5 to 7, and the critical angle of inclination is set to 45 degrees. The adopted parameters of the wake oscillator model are given in Table 2.

Parameters	Value
St	0.17
A	4 ($\theta < 45$) 1 ($\theta > 45$)
epsilon	0.05 ($\theta < 45$) 0.1 ($\theta > 45$)

Table 2: Parameters of wake oscillator.

Fig 5 shows the time evolution of the cable response as resulted from both the test and the simulation. The time period from 20 to 30 seconds of the simulation is chosen. Similar to the test, a strong presence of traveling waves along the cable is observed. The dominant waves are generated from the power-in region at the bottom of the cable and then propagate upwards. There are also differences between the simulation results and test data. The most obvious one is that the simulation also predicts waves with lower frequency generated at the top of the cable which then propagate downwards. Intermittent standing waves are observed in the region where the waves travelling upwards and downwards interact. Another difference is that in experiments standing waves are observed at the bottom of the cable due to the reflective boundary condition at the tip. The simulations do not show such a phenomenon. The first difference may be attributed to additional factors that could influence the test results. For example, the VIV generated at the top of the cable might be significantly suppressed by the waves or the motions of the boat.

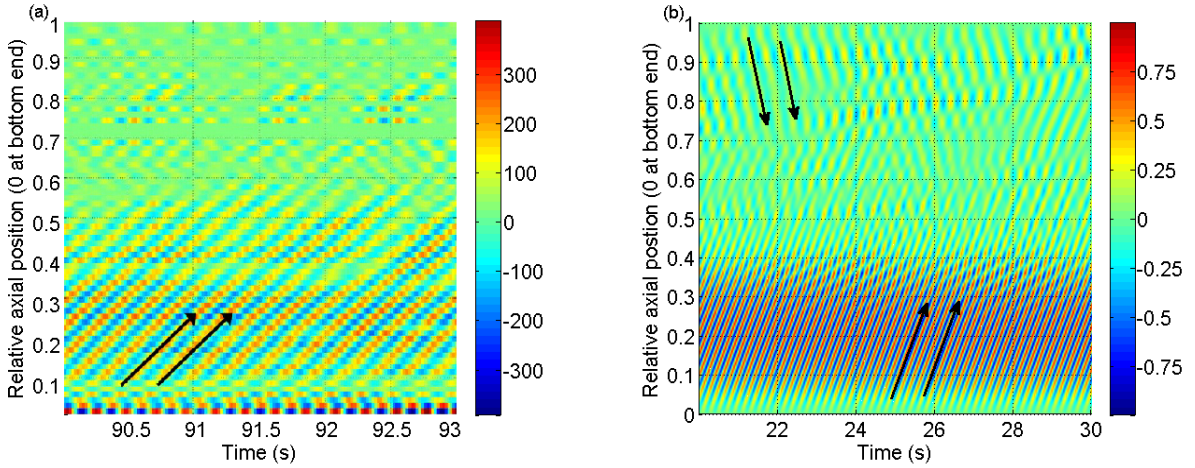


Figure 5: Evolution of the cable response in time and space: (a) fundamental harmonic strain observed in the test; (b) dimensionless cross-flow displacement obtained in simulations.

In order to find a reason for the absence of the standing waves near the tip in the simulations and to understand whether the response of the cable is dependent on the initial conditions, several simulations are conducted with varying initial conditions.

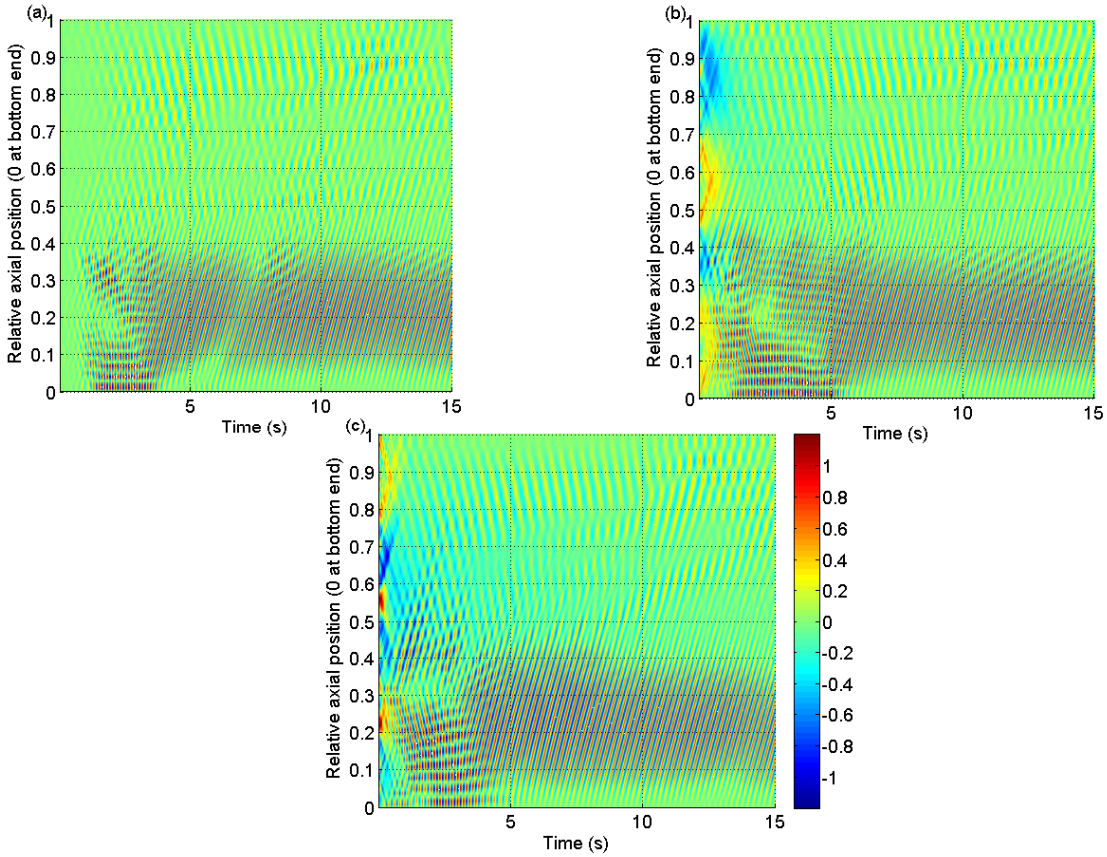


Figure 6: Time evolution of the cross-flow dimensionless displacement in three simulations with different initial conditions.

Fig. 6 shows results of three simulations with different initial conditions. It can be seen that initial conditions do not have apparent influence on pattern of the cross-flow response. For all three cases, the dominant waves are generated at the tip of the pipe and propagate upwards. It

is also noticeable that, in the beginnings of all three simulations, standing waves occur near the tip. However, these standing waves seem to be unstable and are replaced by travelling waves within a few seconds.

Fig. 7 gives a zoom in on the time evolution of the fluctuating lift force (in terms of the wake variable q) acting on lower half of the cable. Results of the same simulation are presented as used for plotting Fig. 6b. Fig. 7 shows that the excitation force is also in the form of a travelling wave which is expectable. However, the evolution of the pattern of the lift force in time is quite interesting. First, a standing wave seems to be present, which is later transferred into a travelling wave. An additional investigation is needed in order to conclude whether such an evolution is generic or it occurs only for specific combinations of the system parameters.

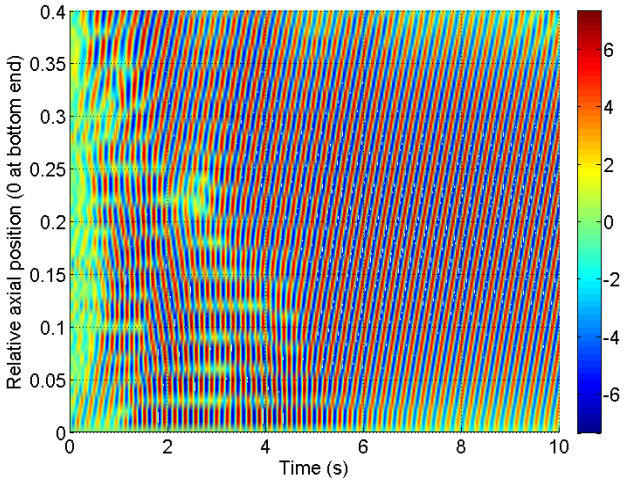


Figure 7: Time evolution of wake variable q .

4 CONCLUSIONS

A model capable of simulating the vortex-induced vibrations of a curved flexible cylinder has been developed. The cylinder model is based on the Euler-Bernoulli beam theory and accounts for bending, extensibility and geometrical nonlinearity. The spatial configuration of the cylinder is described by a position vector, and the 3D motion of the cylinder is solved for using the finite element method. Wake oscillators are attached to the nodes of the structural model to mimic the fluctuating lift and drag forces due to the hydrodynamic interaction of the cylinder with the flow.

A comparison with results of a large-scale test has shown that the developed model can predict main features of the VIV of a long curved cable. The presence of travelling wave that has been observed in the test has been successfully reproduced and the power-in region has been located correctly. However, the model failed to capture the standing waves observed near the tip of the cable in the test. The standing waves generated near the tip at the beginning of simulations seem to be unstable and are gradually replaced by travelling waves within a few seconds. Simulations have also shown that the initial conditions do not have perceptible influence on the steady-state response of the cable.

REFERENCES

[1] T. Sarpkaya, A critical review of the intrinsic nature of vortex-induced vibrations. *Journal of Fluids and Structures*, 19, 389-447, 2004.

[2] R.D. Gabbai, H. Benaroya, An overview of modelling and experiments of vortex-induced vibration of circular cylinder. *Journal of Sound and Vibration*, 282, 575-616, 2005.

[3] P.W. Bearman, Circular cylinder wakes and vortex-induced vibrations. *Journal of Fluid Mechanics*, 27, 648-658, 2011.

[4] X. Wu, F. Ge, Y. Hong, A review of recent studies on vortex-induced vibrations of long slender cylinders. *Journal of Fluids and Structures*, 28, 292-308, 2012.

[5] M.L Facchinetti, E. de Langre, F. Biolley, Coupling of structure and wake oscillators in vortex-induced vibrations. *Journal of Fluids and Structures*, 19 (2), 123-140, 2004.

[6] R.H.M. Ogink, A.V. Metrikine, A wake Osicllator with Frequency Dependent Coupling for the Modelling of Vortex-Induced Vibration. *Journal of Sound and Vibration*, 329, 5452-5473, 2010.

[7] N. Srinil, M. Wiercigroch, P. O'Brien, Reduced-order modelling of vortex-induced vibration of catenary riser. *Ocean Engineering*, 36, 1404-1414, 2009.

[8] N. Srinil, Multi-mode interactions in vortex-induced vibrations of flexible curved/straight structures with geometric nonlinearities. *Journal of Fluids and Structures*, 26, 1098-1122, 2010.

[9] W. Qin, Z. Kang, R. Song, L. Sun, Y. Wu, A New Wake Oscillator Modeling of Vortex-Induced Vibration of SCR in Two Degrees of Freedom. *23rd International Offshore and Polar Engineering (ISOPE 2013),* Anchorage, Alaska, USA, June 30-July 5, 2013.

[10] B. O'Neil, Elementary Differential Geometry, 2nd Edition, San Diego, 2006.

[11] J. Gerstmary, A.A. Shabana, Analysis of Thin Beams and Cables Using the Absolute Nodal Co-ordinate Formulation. *Nonlinear Dynmaics*, 45, 109-130, 2006.

[12] A. Jain, Y. Modarres-Sadeghi, Vortex-induced vibration of a flexibly-mounted inclined cylinder. *Journal of Fluids and Structures*, 43, 28-40, 2013.

[13] J. Kim Vandiver, V. Jaiswal, V. Jhingran, Insights on vortex-induced, traveling waves on long risers. *Journal of Fluids and Structures*, 25, 641-653, 2009.

[14] S.B. Swithenbank, J. Kim Vandiver, Identifying the power-in region for vortex-induced vibrations of long flexible cylinders. *26th International conference on Offshore Mechanics and Arctic Engineering (OMAE 2007),* San Diego, California, USA, June 10-15, 2007.

[15] V. Jaiswal, A. Sheshadri, J. Kim Vandiver, Modelling Traveling Waves using Mode Superposition. *29th International conference on Ocean, Offshore and Arctic Engineering (OMAE 2010),* Shanghai, China, June 6-11, 2010.

COMPDYN 2015
5th ECCOMAS Thematic Conference on
Computational Methods in Structural Dynamics and Earthquake Engineering
M. Papadrakakis, V. Papadopoulos, V. Plevris (eds.)
Crete Island, Greece, 25–27 May 2015

PROBLEM OF NON-STATIONARY WAVES IN VISCOELASTIC ORTHOTROPIC STRIP SOLVED USING ANALYTICAL METHOD

Vítězslav Adámek[1], **František Valeš**[2], **and Jan Červ**[3]

[1] NTIS - New Technologies for Information Society, University of West Bohemia,
Univerzitní 8, 306 14 Pilsen, Czech Republic
e-mail: vadamek@kme.zcu.cz

[2] Institute of Thermomechanics AS CR, v.v.i.,
Veleslavínova 11, 301 14 Pilsen, Czech Republic
e-mail: vales@it.cas.cz

[3] Institute of Thermomechanics AS CR, v.v.i.,
Dolejškova 1402/5, 182 00 Prague 8, Czech Republic
e-mail: cerv@it.cas.cz

Keywords: Infinite Strip, Orthotropic Strip, Viscoelastic Material, Transient Wave Phenomena, Analytical Solution.

Abstract. *The transient response of an infinite orthotropic strip subjected to a transverse load is investigated using an analytical method in this work. The material properties of the strip are described by the discrete model of standard linear viscoelastic solid. In this study, the case of special orthotropy is assumed, i.e., the principal material and geometric axes of the strip are coincident. Once the final system of equations describing the plane-stress problem solved is derived, the integral transform method is used to obtain the Laplace transforms of displacement and velocity components. The inversion of the resulted formulae back to time domain is carried out by the help of numerical inverse Laplace transform. In particular, an algorithm based on the FFT and Wynn's epsilon accelerator was used for this purpose. In the last part of this work, the analytical results obtained for selected orthotropic material are compared to those resulted from numerical simulation performed in the finite element code MSC.Marc. The comparison made showed good agreement between analytical and numerical results and proved their correctness. Finally, the efficiency of both approaches is discussed.*

1 INTRODUCTION

In-plane loaded thin orthotropic and general anisotropic structures are of intensive research interest for many years. This interest is related to the use of thin ribs and panels in many industrial applications, e.g. fuselages and wings of aircrafts, stiffeners in car bodies etc. With respect to high demands on the weight reduction, such structural elements are more often made from composite materials. Due to the fact that these components are mostly subjected to dynamic loading (stationary or transient), it is necessary to be able to describe and analyse their behaviour under such operating conditions.

Since the composite materials have low resistance to crack propagation, most of existing works dealing with the elastodynamics of strip-like solids focus on the stationary problems of fracture mechanics. The number of works dealing with the transient response of orthotropic strips of elastic or viscoelastic properties is very small, especially those which present analytical or semi-analytical approaches.

In this work, the transient response of an infinite viscoelastic orthotropic strip subjected to transverse load is investigated. The integral transform method and numerical inverse Laplace transform are used for solving this plane-stress problem. This study follows [1, 2] in which similar isotropic problems of elastic and viscoelastic strips are solved using analytical methods.

2 PROBLEM FORMULATION

Let us assume an infinite thin orthotropic strip of total height $2d$. The lower boundary of the strip will be free of traction and the upper one will be loaded by a pressure which will be non-zero only for $x_1 \in \langle -h, h \rangle$, see Fig. 1. The amplitude of the pressure will be constant through the strip thickness and its dependence on x_1 will be the same as in [2]. This means that the boundary conditions of this problem can be written as:

$$\sigma_{22}(x_1, d, t) = \begin{cases} -\sigma_a \cos\left(\frac{\pi}{2}\frac{x_1}{h}\right) H(t) & \text{for } x_1 \in \langle -h, h \rangle, \\ 0 & \text{otherwise}, \end{cases} \tag{1}$$

$$\sigma_{22}(x_1, -d, t) = 0\,, \quad \sigma_{12}(x_1, d, t) = 0\,, \quad \sigma_{12}(x_1, -d, t) = 0\,,$$

where σ_{ij} $(i, j = 1, 2)$ denotes normal $(i = j)$ and shear $(i \neq j)$ stress components. From the above mentioned, it is clear that the plane-stress problem in $x_1 - x_2$ plane will be solved and that σ_{11}, σ_{22} and σ_{12} are the only non-zero stress components. Further, zero initial conditions will be considered for simplicity, i.e., the strip is free of load and in a rest at $t = 0$.

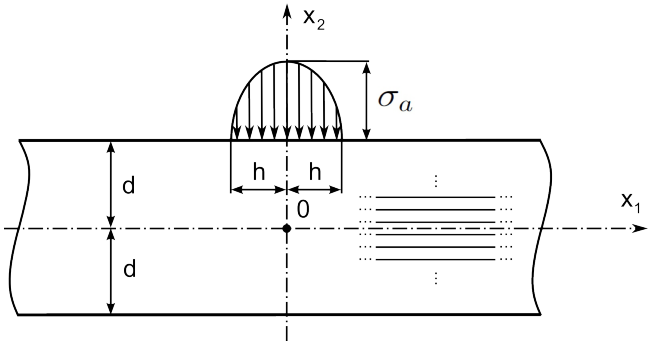


Figure 1: The scheme of the problem.

The orthotropic properties of the strip will be such that the principal geometric and material axes x_1 and x_2 are coincident. Moreover, the memory effect of the material will be taken into account. This will be modelled by using the discrete model of standard linear viscoelastic solid in the Zener configuration [3] in both directions x_1 and x_2. It means that the viscoelastic model consists of a spring and the Maxwell element in parallel, while the Maxwell element contains a spring and a dashpot in series. It is well known that the behaviour of an orthotropic elastic material under the state of plane-stress is described by four independent parameters [4]. They can be denoted by $E_{0,1}$, $E_{0,2}$, $G_{0,12}$ and $\nu_{0,12}$ for the alone-standing spring of the model and they represent two Young's moduli in the direction of principal axes, shear modulus and Poisson's ratio in sequence. Analogously, the parameters of the spring present in the Maxwell element will be introduced in the same way omitting the subscript 0, i.e., E_1, E_2, G_{12} and ν_{12}. Finally, the viscous properties of the dashpot will be characterised by two coefficients of normal viscosity λ_1, λ_2, by the coefficient of shear viscosity η_{12} and by the viscous Poisson's ratio μ_{12}. It is known, see [3, 4], that there hold

$$\frac{\nu_{12}}{E_1} = \frac{\nu_{21}}{E_2} \quad \text{and} \quad \frac{\mu_{12}}{\lambda_1} = \frac{\mu_{21}}{\lambda_2}\,. \tag{2}$$

Additionally, hereinafter we will consider that $\mu_{12} = \nu_{12}$ and $\mu_{21} = \nu_{21}$, i.e., the corresponding viscous and elastic Poisson's ratios are equal for simplicity.

Based on the assumptions made, it is clear that the actual state at an arbitrary point of the strip is described by two independent functions $u_1(x_1, x_2, t)$ and $u_2(x_1, x_2, t)$ which are the displacement components in x_1 and x_2 directions, respectively, and which will represent the solution of the problem solved.

3 ANALYTICAL SOLUTION

3.1 Governing equations

The equations of motion describing the general plane-stress problem of elastodynamics have the form [5]

$$\rho\,\frac{\partial^2 u_1}{\partial t^2} = \frac{\partial \sigma_{11}}{\partial x_1} + \frac{\partial \sigma_{12}}{\partial x_2}\,, \quad \rho\,\frac{\partial^2 u_2}{\partial t^2} = \frac{\partial \sigma_{22}}{\partial x_2} + \frac{\partial \sigma_{12}}{\partial x_1}\,, \tag{3}$$

where ρ denotes the density of the strip material. In the following, constitutive and kinematic equations will be introduced into (3).

The kinematic equations giving the relationship between the displacement and strain components can be expressed as [2]

$$\varepsilon_{11} = \frac{\partial u_1}{\partial x_1}\,, \quad \varepsilon_{22} = \frac{\partial u_2}{\partial x_2}\,, \quad \gamma_{12} = \frac{\partial u_1}{\partial x_2} + \frac{\partial u_2}{\partial x_1}\,. \tag{4}$$

The functions $\varepsilon_{11}(x_1, x_2, t)$, $\varepsilon_{22}(x_1, x_2, t)$ and $\gamma_{12}(x_1, x_2, t)$ represent two normal and one shear strain components in sequence.

The constitutive relations valid for an orthotropic Zener model can be simply derived based on the superposition principle of stresses and strain rates applied to the appropriate parts of the Zener model [3]. Doing so and taking into account the zero initial conditions, the resulting constitutive equations have the form

$$\sigma_{11} = b_{0,11}\left(\varepsilon_{11} + \nu_{0,21}\varepsilon_{22}\right) + b_{11}\left(\varepsilon_{11} + \nu_{21}\varepsilon_{22}\right) - \alpha_1 b_{11}\int_0^t \left(\varepsilon_{11} + \nu_{21}\varepsilon_{22}\right) e^{-\alpha_1(t-\tau)}\,d\tau\,, \tag{5}$$

$$\sigma_{22} = b_{0,22}\left(\varepsilon_{22} + \nu_{0,12}\varepsilon_{11}\right) + b_{22}\left(\varepsilon_{22} + \nu_{12}\varepsilon_{11}\right) - \alpha_2 b_{22}\int_0^t \left(\varepsilon_{22} + \nu_{12}\varepsilon_{11}\right) e^{-\alpha_2(t-\tau)} d\tau\,,$$

$$\sigma_{12} = \left(b_{0,66} + b_{66}\right)\gamma_{12} - \beta b_{66}\int_0^t \gamma_{12}\, e^{-\beta(t-\tau)} d\tau\,,$$

where b_{ij} are the so-called reduced stiffnesses for a plane-stress state in the plane $x_1 - x_2$ and there hold [4]

$$b_{11} = \frac{E_1}{1-\nu_{12}\nu_{21}}\,, \quad b_{22} = \frac{E_2}{1-\nu_{12}\nu_{21}} \quad \text{and} \quad b_{66} = G_{12}\,. \tag{6}$$

The parameters $b_{0,ij}$ in (5) corresponding to the alone-standing spring in the Zener model are defined analogously. The coefficients α_i were introduced as $\alpha_i = E_i/\lambda_i$ and they represent the reciprocal values of relaxation times. The constant β is defined in similar way as $\beta = G_{12}/\eta_{12}$. Using the relations (2) and the assumption $\mu_{ij} = \nu_{ij}$ made in the section 2, it is clear that it holds $\alpha_1 = \alpha_2 = \alpha$.

Based on these assumptions and substituting (5) and (4) into (3), the equations of motion take the form

$$\begin{aligned}\frac{\partial^2 u_1}{\partial t^2} &= c_{0,11}^2\left(\frac{\partial^2 u_1}{\partial x_1^2} + \nu_{0,21}\frac{\partial^2 u_2}{\partial x_1 \partial x_2}\right) + c_{11}^2\left(\frac{\partial^2 u_1}{\partial x_1^2} + \nu_{21}\frac{\partial^2 u_2}{\partial x_1 \partial x_2}\right) \\ &+ c_{0,12}^2\left(\frac{\partial^2 u_1}{\partial x_2^2} + \frac{\partial^2 u_2}{\partial x_1 \partial x_2}\right) + c_{12}^2\left(\frac{\partial^2 u_1}{\partial x_2^2} + \frac{\partial^2 u_2}{\partial x_1 \partial x_2}\right) \\ &- \int_0^t \left[\alpha c_{11}^2\left(\frac{\partial^2 u_1}{\partial x_1^2} + \nu_{21}\frac{\partial^2 u_2}{\partial x_1 \partial x_2}\right) e^{-\alpha(t-\tau)} + \beta c_{12}^2\left(\frac{\partial^2 u_1}{\partial x_2^2} + \frac{\partial^2 u_2}{\partial x_1 \partial x_2}\right) e^{-\beta(t-\tau)}\right] d\tau\,,\end{aligned} \tag{7}$$

$$\begin{aligned}\frac{\partial^2 u_2}{\partial t^2} &= c_{0,22}^2\left(\frac{\partial^2 u_2}{\partial x_2^2} + \nu_{0,12}\frac{\partial^2 u_1}{\partial x_1 \partial x_2}\right) + c_{22}^2\left(\frac{\partial^2 u_2}{\partial x_2^2} + \nu_{12}\frac{\partial^2 u_1}{\partial x_1 \partial x_2}\right) \\ &+ c_{0,12}^2\left(\frac{\partial^2 u_2}{\partial x_1^2} + \frac{\partial^2 u_1}{\partial x_1 \partial x_2}\right) + c_{12}^2\left(\frac{\partial^2 u_2}{\partial x_1^2} + \frac{\partial^2 u_1}{\partial x_1 \partial x_2}\right) \\ &- \int_0^t \left[\alpha c_{22}^2\left(\frac{\partial^2 u_2}{\partial x_2^2} + \nu_{12}\frac{\partial^2 u_1}{\partial x_1 \partial x_2}\right) e^{-\alpha(t-\tau)} + \beta c_{12}^2\left(\frac{\partial^2 u_2}{\partial x_1^2} + \frac{\partial^2 u_1}{\partial x_1 \partial x_2}\right) e^{-\beta(t-\tau)}\right] d\tau\,,\end{aligned} \tag{8}$$

where the quantities c_{11}, c_{22} and c_{12} are defined as

$$c_{11}^2 = \frac{b_{11}}{\rho}\,, \quad c_{22}^2 = \frac{b_{22}}{\rho} \quad \text{and} \quad c_{12}^2 = \frac{b_{66}}{\rho}\,. \tag{9}$$

Analogous relations hold also for $c_{0,11}$, $c_{0,22}$ and $c_{0,12}$.

Hereinafter we will further assume that $\beta = \alpha$ and that the Poisson's ratios of both springs in the Zener model are the same, i.e., $\nu_{0,ij} = \nu_{ij}$. These assumptions will lead to the simplification of the system (7) - (8).

3.2 Application of Laplace and Fourier transforms

In this subsection, the Laplace transform will be applied to the simplified system (7) - (8). Introducing a new complex variable p and taking into account the zero initial conditions specified in the section 2, the transform of the system (7) - (8) takes the form

$$p^2 U_1 = C_{11}^2 \left(\frac{\partial^2 U_1}{\partial x_1^2} + \nu_{21} \frac{\partial^2 U_2}{\partial x_1 \partial x_2} \right) + C_{12}^2 \left(\frac{\partial^2 U_1}{\partial x_2^2} + \frac{\partial^2 U_2}{\partial x_1 \partial x_2} \right), \tag{10}$$
$$p^2 U_2 = C_{22}^2 \left(\frac{\partial^2 U_2}{\partial x_2^2} + \nu_{12} \frac{\partial^2 U_1}{\partial x_1 \partial x_2} \right) + C_{12}^2 \left(\frac{\partial^2 U_2}{\partial x_1^2} + \frac{\partial^2 U_1}{\partial x_1 \partial x_2} \right),$$

where the functions $U_1(x_1, x_2, p)$ and $U_2(x_1, x_2, p)$ denote the Laplace transforms of the unknown displacement components $u_1(x_1, x_2, t)$ and $u_2(x_1, x_2, t)$, respectively, and the complex functions $C_{11}(p)$, $C_{22}(p)$ and $C_{12}(p)$ are defined as follows:

$$C_{11}(p) = \sqrt{c_{0,11}^2 + \left(1 - \frac{\alpha}{p+\alpha}\right) c_{11}^2}\,, \quad C_{22}(p) = \sqrt{c_{0,22}^2 + \left(1 - \frac{\alpha}{p+\alpha}\right) c_{22}^2}\,, \tag{11}$$
$$C_{12}(p) = \sqrt{c_{0,12}^2 + \left(1 - \frac{\alpha}{p+\alpha}\right) c_{12}^2}\,.$$

In contrast to the problem of isotropic viscoelastic strip solved in [2], the system (10) cannot be rewritten to an uncoupled system of PDEs.

Now we will suppose that the solutions U_1 and U_2 of (10) can be written in the form of Fourier integrals. With respect to the fact that the applied load (1) is an even function of x_1, the functions of displacement components u_1 and u_2, as well as their Laplace transforms, will be odd and even functions of this variable, respectively. Therefore one can write

$$U_1(x_1, x_2, p) = \frac{1}{\pi} \int_0^\infty A(\omega, x_2, p) \sin(\omega x_1)\, d\omega\,, \tag{12}$$
$$U_2(x_1, x_2, p) = \frac{1}{\pi} \int_0^\infty B(\omega, x_2, p) \cos(\omega x_1)\, d\omega\,.$$

Substituting the relations (12) into (10), taking the assumption that all necessary functions are integrable and after rearrangement of terms, the equations (10) give the coupled system

$$\frac{\partial^2 A}{\partial x_2^2} - a_1 A - a_2 \frac{\partial B}{\partial x_2} = 0\,, \quad \frac{\partial^2 B}{\partial x_2^2} - b_1 B + b_2 \frac{\partial A}{\partial x_2} = 0 \tag{13}$$

for the unknown Fourier spectra $A(\omega, x_2, p)$ and $B(\omega, x_2, p)$. The function $a_i(\omega, p)$ and $b_i(\omega, p)$ present in (13) are given by

$$a_1(\omega, p) = \left[\left(\frac{C_{11}}{C_{12}} \right)^2 + \left(\frac{p}{\omega C_{12}} \right)^2 \right] \omega^2\,, \quad a_2(\omega, p) = \left[1 + \nu_{21} \left(\frac{C_{11}}{C_{12}} \right)^2 \right] \omega\,, \tag{14}$$
$$b_1(\omega, p) = \left[\left(\frac{C_{12}}{C_{22}} \right)^2 + \left(\frac{p}{\omega C_{22}} \right)^2 \right] \omega^2\,, \quad b_2(\omega, p) = \left[\nu_{12} + \left(\frac{C_{12}}{C_{22}} \right)^2 \right] \omega\,.$$

After some calculus, it is possible to show that the solution of (13) can be expressed as

$$A(\omega, x_2, p) = P \sinh(\Lambda_1 x_2) + Q \cosh(\Lambda_1 x_2) + R \sinh(\Lambda_2 x_2) + S \cosh(\Lambda_2 x_2)\,, \tag{15}$$

$$B(\omega, x_2, p) = L_1 \left(P \cosh\left(\Lambda_1 x_2\right) + Q \sinh\left(\Lambda_1 x_2\right)\right) + L_2 \left(R \cosh\left(\Lambda_2 x_2\right) + S \sinh\left(\Lambda_2 x_2\right)\right),$$

where

$$L_1(\omega, p) = \frac{\Lambda_1^2 - a_1}{\Lambda_1 a_2}, \quad L_2(\omega, p) = \frac{\Lambda_2^2 - a_1}{\Lambda_2 a_2}, \tag{16}$$

$$\Lambda_1(\omega, p) = \sqrt{\frac{1}{2}\left(k + \sqrt{s}\right)}, \quad \Lambda_2(\omega, p) = \sqrt{\frac{1}{2}\left(k - \sqrt{s}\right)},$$

$$k(\omega, p) = a_1 + b_1 - a_2 b_2, \quad s(\omega, p) = a_2^2 b_2^2 - 2a_2 b_2 \left(a_1 + b_1\right) + \left(a_1 - b_1\right)^2.$$

The complex functions $P(\omega, p)$, $Q(\omega, p)$, $R(\omega, p)$ and $S(\omega, p)$ present in (15) are unknown at this moment and they will be determined by using the boundary conditions (1).

3.3 Final formulae for displacement and velocity components in Laplace domain

In this subsection we will focus on finding the functions P, Q, R and S and then on the derivation of final formulae for displacement and velocity components in Laplace domain.

First, the Laplace transform needs to be applied to the boundary conditions (1) and the Laplace transforms of stress components σ_{22} and σ_{12} have to be determined in terms of U_1 and U_2. Let us denote $\Sigma_{22}(x_1, x_2, p)$ and $\Sigma_{12}(x_1, x_2, p)$ the transforms of stresses. Then using the constitutive equations (5) and the zero initial conditions, one can write

$$\Sigma_{22} = h_{22}\left(\frac{\partial U_2}{\partial x_2} + \nu_{12}\frac{\partial U_1}{\partial x_1}\right), \quad \Sigma_{12} = h_{12}\left(\frac{\partial U_1}{\partial x_2} + \frac{\partial U_2}{\partial x_1}\right), \tag{17}$$

where the functions $h_{11}(p)$ and $h_{12}(p)$ were introduced by the following relations:

$$h_{22}(p) = b_{0,22} + \frac{p}{p+\alpha} b_{22}, \quad h_{12}(p) = b_{0,66} + \frac{p}{p+\alpha} b_{66}. \tag{18}$$

When we introduce (17) into the left hand sides of transformed conditions (1) and substituting (12) and (15), a non-homogeneous system of four equations for the unknown functions $P(\omega, p)$, $Q(\omega, p)$, $R(\omega, p)$ and $S(\omega, p)$ is obtained. If we define the functions

$$k_1(\omega, p) = h_{22}\left(\nu_{12}\omega + L_1\Lambda_1\right), \quad k_2(\omega, p) = h_{22}\left(\nu_{12}\omega + L_2\Lambda_2\right), \tag{19}$$

$$k_3(\omega, p) = h_{12}\left(\Lambda_1 - \omega L_1\right), \quad k_4(\omega, p) = h_{12}\left(\Lambda_2 - \omega L_2\right),$$

$$k_5(\omega, p) = k_2 k_3 \cosh\left(d\Lambda_1\right)\sinh\left(d\Lambda_2\right) - k_1 k_4 \cosh\left(d\Lambda_2\right)\sinh\left(d\Lambda_1\right),$$

$$k_6(\omega, p) = k_2 k_3 \cosh\left(d\Lambda_2\right)\sinh\left(d\Lambda_1\right) - k_1 k_4 \cosh\left(d\Lambda_1\right)\sinh\left(d\Lambda_2\right),$$

the solution of the mentioned system can be written in the following compact form:

$$P(\omega, p) = -\frac{1}{2}\frac{a(\omega) k_4 \cosh\left(d\Lambda_2\right)}{p k_5}, \quad Q(\omega, p) = -\frac{1}{2}\frac{a(\omega) k_4 \sinh\left(d\Lambda_2\right)}{p k_6}, \tag{20}$$

$$R(\omega, p) = \frac{1}{2}\frac{a(\omega) k_3 \cosh\left(d\Lambda_1\right)}{p k_5}, \quad S(\omega, p) = \frac{1}{2}\frac{a(\omega) k_3 \sinh\left(d\Lambda_1\right)}{p k_6},$$

where

$$a(\omega) = \frac{4\pi\sigma_a h \cos(\omega h)}{\pi^2 - 4\omega^2 h^2}. \tag{21}$$

The final formulae for the Laplace transforms of displacement components $u_1(x_1, x_2, t)$ and $u_2(x_1, x_2, t)$ can be now simply obtained by the substitution of (20) and (15) into the relations (12). The Laplace transforms $V_1(x_1, x_2, p)$ and $V_2(x_1, x_2, p)$ of the velocity components $v_1(x_1, x_2, t)$ and $v_2(x_1, x_2, t)$ then can be derived analogously because it holds

$$V_1(x_1, x_2, p) = p\, U_1(x_1, x_2, p) \quad \text{and} \quad V_2(x_1, x_2, p) = p\, U_2(x_1, x_2, p). \tag{22}$$

4 ANALYTICAL AND NUMERICAL RESULTS

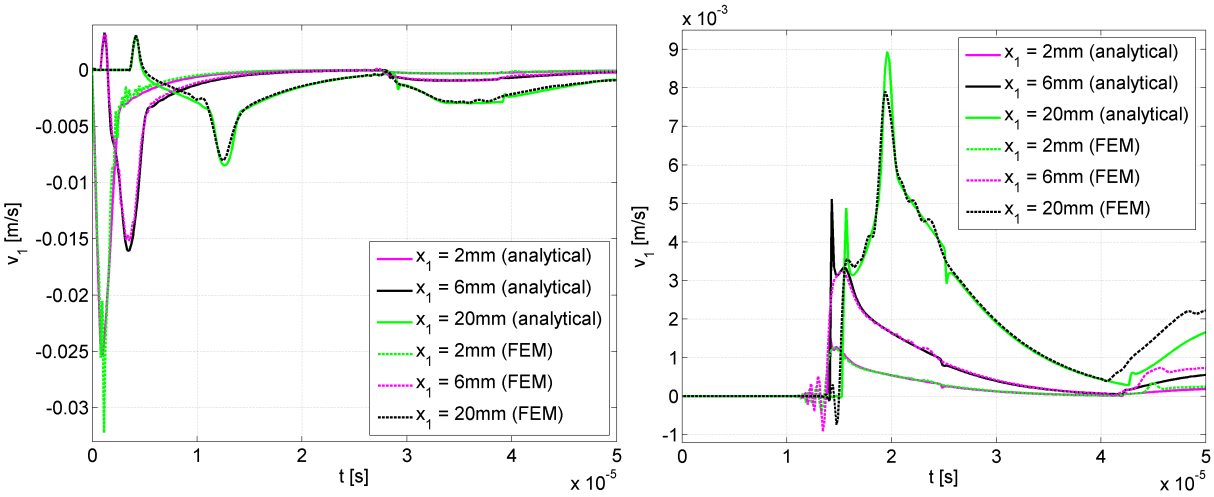
To obtain analytical results in time domain, the inverse Laplace transform (ILT) of U_1 and U_2 (or V_1 and V_2) has to be performed. Basically, there exist two possible approaches. The analytical one is based on the evaluation of the Bromwich integral defining the ILT by using the theorem of residue [6]. This approach is feasible in this case but it involves the process of finding the solution of dispersion equation, i.e., the dispersion curves need to be investigated, which is very computer time consuming process. The application of a suitable and sufficiently precise numerical algorithm to ILT is the next possibility. With respect to the complexity of the formulae derived and to authors' previous good experiences with this procedure, the numerical code based on FFT and Wynn's epsilon accelerator was used for ILT of required functions. This code has been previously tested and verified by authors on different transient wave problems (e.g. radial impact on a thin isotropic viscoelastic disc [7], transverse impact on an isotropic viscoelastic strip [2], impact on functionally graded beams [8] etc.) such that it can be said that its use does not mean the loss of analytical results accuracy.

The results obtained by this procedure were then compared to those of numerical simulation performed in the commercial FE code MSC.Marc. This comparison served both for the verification of the derivation process of the final formulae in the Laplace domain and for finding the limits of the FE model used.

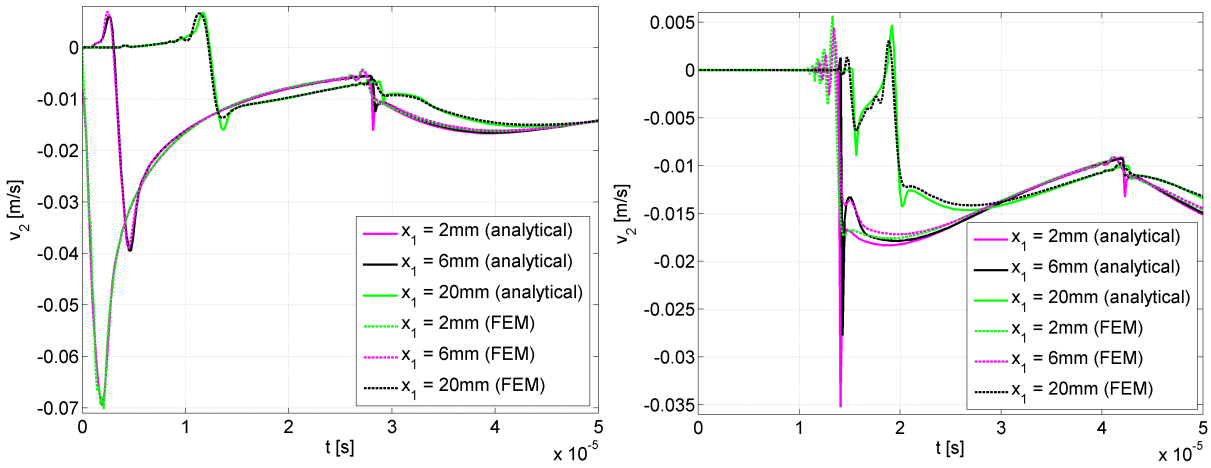
Considering the symmetry of the problem, see Fig. 1, the geometry of the finite element model consisted only of one-half of the strip of total length $200\,\mathrm{mm}$. The spatial discretisation was done by regular bilinear isoparametric elements for 2D plane-stress problem. The basic size of elements was $0.4 \times 0.4\,\mathrm{mm}$ and the mesh was once refined in the area close to the applied load such that the total number of elements was about 25000. Using the procedure described in [9], the frequency limit of the model can be estimated as $0.9\,\mathrm{MHz}$. The implicit Newmark algorithm with constant step $4 \times 10^{-8}\,\mathrm{s}$ was used for the integration in time domain.

The evaluation of analytical solution and the numerical simulation were performed for the following parameters: $d = 20\,\mathrm{mm}$, $\sigma_a = 1\,\mathrm{MPa}$, $h = 2\,\mathrm{mm}$. The material properties of the strip were assumed to be the same as in [10], i.e., $\rho = 2250\,\mathrm{kg\,m^{-3}}$, $E_{0,1} = 35 \times 10^9\,\mathrm{Pa}$, $E_{0,2} = 11.584 \times 10^9\,\mathrm{Pa}$, $G_{0,12} = 4 \times 10^9\,\mathrm{Pa}$, $\nu_{0,12} = 0.278$, $E_1 = 18.48 \times 10^9\,\mathrm{Pa}$, $G_{12} = 1.83 \times 10^9\,\mathrm{Pa}$ and $\lambda_1 = 5 \times 10^4\,\mathrm{Pa\,s^{-1}}$. The other parameters were then determined by using the assumptions mentioned in the previous sections. All the constants have been chosen in such a way to roughly correspond to the parameters of orthotropic material Gevetex (E-Glass 21xK43) which can be found in [11].

The comparison of analytical and numerical results was made at several points lying on the upper ($x_2 = 20\,\mathrm{mm}$) and bottom ($x_2 = -20\,\mathrm{mm}$) edge of the strip. Figs. 2(a) - 2(d) show this comparison for horizontal v_1 and vertical v_2 velocity component for $x_1 = \{2, 6, 20\}\,\mathrm{mm}$. It is clear from these figures that the analytical (*solid lines*) and the numerical (*dotted lines*) solutions are in a very good agreement. Additionally, it is clear that this agreement is better for $x_2 = 20\,\mathrm{mm}$ than in the case of $x_2 = -20\,\mathrm{mm}$. This is mainly caused by too large finite elements which cannot suppress the dispersion due to spatial discretisation when the waves are



(a) Upper strip edge ($x_2 = 20\,\mathrm{mm}$) (b) Bottom strip edge ($x_2 = -20\,\mathrm{mm}$)



(c) Upper strip edge ($x_2 = 20\,\mathrm{mm}$) (d) Bottom strip edge ($x_2 = -20\,\mathrm{mm}$)

Figure 2: Comparison of horizontal v_1 and vertical v_2 velocities determined by analytical and FEM approaches for $x = \{2, 6, 20\}\,\mathrm{mm}$ at the upper and the bottom edge of the strip.

propagated through the whole strip height. The numerical results could be further improved, especially in the vicinity of the steep wave fronts (see Figs. 2(b) and 2(d)), when the element size is reduced. Naturally, this improvement of numerical model will leads to significant increase of computational time. For comparison, the numerical simulation for $t \in \langle 0, 50\rangle\ \mu\mathrm{s}$ takes about $48\,\mathrm{mins}$ whereas the evaluation of analytical solution for the same spatial grid only about $7\,\mathrm{mins}$.

5 CONCLUSIONS

Non-stationary wave problem of an infinite viscoelastic strip of special orthotropic properties was solved for a specific type of external load. The method used was based on the combination of the classical method of integral transforms and the numerical inverse Laplace transform. The analytical results were compared to the numerical ones obtained by using an existing FE code. The agreement of both types of results proved the correctness of the derivation process and showed the limits of the FE model used. Due to the efficiency and accuracy of the algorithm used for the evaluation of analytical solution, the presented solution can be used e.g. for solving

the problems of material parameters identification. For instance, the evaluation of the time history of velocity at one particular point composed of 256 time steps takes less than $13\,\mathrm{s}$ using one core of $2.4\,\mathrm{MHz}$ CPU. Moreover, this solution will be used for solving the problem of general orthotropic viscoelastic strip in future, which will find even more practical applications.

Acknowledgement: This work was supported by the project GA CR P101/12/2315 with the institutional support RVO: 61388998.

REFERENCES

[1] F. Valeš, H. Šebková, The state of stress in non-stationary loaded thin belt. *Acta Technica*, **4**, 439–458, 1976.

[2] V. Adámek, F. Valeš, Analytical solution for wave propagation in a viscoelastic wall strip under transverse impact loading. Z. Dimitrovová, J.R. de Almeida, R. Gonalves eds. *11th International Conference on Vibration Problems (ICOVP-2013)*, Lisbon, Portugal, September 9-12, 2013.

[3] Z. Sobotka, *Rheology of materials and engineering structures*. Elsevier, 1984.

[4] R.M. Jones, *Mechanics of composite materials, 2nd Edition*. Taylor & Francis, 1999.

[5] K.F. Graff, *Wave Motion in Elastic Solids, Reprint*. Dover Publications, Inc, 1991.

[6] D.G. Duffy, *Transform methods for solving partial differential equations, 2nd Edition*. Chapman & Hall/CRC, 2004.

[7] V. Adámek, F. Valeš, Analytical solution of transient in-plane vibration of a thin viscoelastic disc and its multi-precision evaluation. *Mathematics and Computers in Simulation*, **85**, 34–44, 2012.

[8] V. Adámek, F. Valeš, Analytical solution for a heterogeneous Timoshenko beam subjected to an arbitrary dynamic transverse load. *European Journal of Mechanics A/Solids*, **49**, 373–381, 2015.

[9] R. Brepta, F. Valeš, J. Červ, B. Tikal, Rayleigh wave dispersion due to spatial (FEM) discretisation of a thin elastic solid having non-curved boundary. *Computers & Structures*, **58**, 1233–1244, 1996.

[10] V. Adámek, F. Valeš, A viscoelastic orthotropic Timoshenko beam subjected to a general transverse loading. *Applied and Computational Mechanics*, **2**, 215–226, 2008.

[11] P.D. Soden, M.J. Hintonb, A.S. Kaddoura, Lamina properties, lay-up configurations and loading conditions for a range of fibre-reinforced composite laminates. *Composites Science and Technology*, **58**, 1011–1022, 1998.

COMPDYN 2015
5th ECCOMAS Thematic Conference on
Computational Methods in Structural Dynamics and Earthquake Engineering
M. Papadrakakis, V. Papadopoulos, V. Plevris (eds.)
Crete Island, Greece, 25–27 May 2015

PROBABILISTIC ASSESSMENT OF PIPELINE – FAULT CROSSING

Vasileios E. Melissianos[1], Dimitrios Vamvatsikos[2], and Charis J. Gantes[3]

[1] JB ATE
30, Itanou Str., GR-71307 Herakleion, Crete
e-mail: melissianosv@gmail.com

[2] National Technical University of Athens
9, Iroon Polytechneiou Str., GR-15780 Zografou Campus, Athens
divamva@central.ntua.gr

[3] National Technical University of Athens
9, Iroon Polytechneiou Str., GR-15780 Zografou Campus, Athens
chgantes@central.ntua.gr

Keywords: buried steel pipeline, fault crossing, fault displacement, seismic risk assessment, probabilistic approach.

Abstract. *Buried steel pipelines transporting oil and oil products play a vital role in the energy supply chain. Pipelines extend to long distances and thus intercepting tectonic faults, when a seismic area is crossed, is often inevitable and may heavily threat the pipeline integrity. Earthquakes and the associated fault displacements are naturally random events and therefore the imposed large ground displacements on the pipeline have to be considered through a probabilistic perspective. In the present study, a comprehensive seismic risk analysis of buried pipeline – fault crossing is presented, consisting of two steps. The first step is the probabilistic assessment of the fault displacement accounting also for the pertinent uncertainties. The second step is the pipeline structural analysis. The transition from the seismological data to the structural analysis is realized through the fault displacement components as the selected vector intensity measure. The outcome of the proposed methodology is the strain hazard curves for both tensile and compressive longitudinal strains. The resulting strain capacities are compared to strain demands from structural codes in order to assess the potential of pipeline failure due to local buckling or tensile fracture. Furthermore, uncertainty and disaggregation results from the fault displacement hazard analysis are presented for the selection of the appropriate deterministic design scenario and the evaluation of the fault displacement hazard parameters. Lastly, the proposed process is a reliable estimation tool for seismic risk assessment of pipeline – fault crossing and a decision making tool for route selection and application of preventive measures against the consequences of faulting on pipelines.*

1 INTRODUCTION

Industrial experience has demonstrated over the years that the most efficient way for transporting hydrocarbonates over long distances is buried steel pipelines with continuous welded joints. Pipelines are structures of high importance acknowledging that any potential failure may have devastating consequences on the environment, nearby residential areas, as well as economic losses. Thus, pipelines are designed and constructed within a stringent framework of standards and regulations as societies are highly concerned about such projects. So, the combination of the route selection restrictions and pipelines' extended length between oil producers and oil consumers leads several times to the transverse of seismic areas that usually incorporate areas prone to large ground displacements, such as tectonic faults. Fault activation due to earth plate movement imposes large ground displacements that the pipeline has to accommodate safely. Investigation of previous earthquake events has demonstrated that the premier cause of pipeline failure is the imposed large differential ground displacement due to fault offset, compared to other seismic induced actions, such as seismic wave propagation, liquefaction induced lateral spread or landslide [1]. Possible failure modes in such situations are wall local buckling/wrinkling due to compressive strains, tensile fracture of girth welds due to tensile strains and in case of reverse fault type, upheaval buckling due to compressive forces.

Hydrocarbonate pipelines are classified as hazardous structures given the consequences of a potential failure. Thus, it is deemed appropriate to perform a comprehensive risk analysis of pipeline – fault crossing hazard by incorporating the uncertainty of the loading, i.e. fault offset, and the response of the pipeline – soil interaction system. Even though fault rupture is a rare event, most pipeline operators are willing to accept the damage related to fault activation, as long as the pipeline's integrity is maintained, i.e. no leak or rupture. However, earthquakes and the associated fault displacements are naturally random events and thus the dominant question during the design pertains to the appropriate magnitude of fault offset that has to be taken into account. Additionally, the seismic risk analysis is useful in order to design or evaluate financial (insurance) or physical mitigating measures (retrofitting or upgrading) against the fallouts of fault offset. Regarding the construction of a new pipeline project, hazard estimation is necessary so that the appropriate measures are taken to control the subsequent levels of risk through redirecting the design procedure. With reference to the financial loss estimation for insurance purposes, the quantification of failure hazard is the vital information required to fix premiums [2].

The proposed procedure for seismic risk analysis of buried pipeline – fault crossing consists of two parts: (i) conduct the probabilistic analysis of fault displacement hazard, (ii) perform pipeline structural analysis and then merge the results to conduct the seismic risk analysis. The basic aspects of the theoretical background of the proposed procedure for pipeline – fault crossing have been presented in previous work of the authors [3]. The appropriate tool for the probabilistic analysis of the fault displacement hazard is the Probabilistic Fault Displacement Hazard Analysis (PFDHA) introduced by Youngs et al. [4], which aims at quantifying the mean annual rate of exceeding various fault displacement levels at the site of pipeline – fault crossing. PFDHA integrates available geological and seismological data including, for example, the probability of fault activation, rupture location, fault slip rate, distribution of earthquake magnitudes and their associated uncertainties. Then, the seismic risk analysis is the combination of the results for developing the hazard curves for the selected intensity measure and the quantification of the potential of pipeline failure.

2 SEISMIC HAZARD ASSESSMENT

2.1 Probabilistic vs. determinist approach

In seismic engineering there are two approaches for seismic risk assessment: the first one is the deterministic that is implemented through the Deterministic Seismic Hazard Analysis (DSHA) and the second is the probabilistic one applied trough the Probabilistic Seismic Hazard Analysis (PSHA).

The aim of DSHA is the development of earthquake scenarios that consist of a postulated occurrence of an earthquake of a specified magnitude, namely the characteristic or critical earthquake at a specific location, which could affect the structure under consideration. The DSHA implementation does not provide any information regarding the expected level of shaking or fault displacement during the structure's life time; it does not account for the earthquake occurrence probability or the effect of uncertainties throughout the various methodology steps. In proportion to DSHA that deals with ground shaking (e.g. PGA estimation), the Deterministic Fault Displacement Hazard Analysis (DFDHA) has been developed to deal with fault offset hazard.

PSHA, then, aims at quantifying the probabilistic nature of earthquake effects. The hazard derived from different seismic sources is considered separately and the influence of every source on the final outcome is transparent [2]. On the other hand, the contribution of all sources under consideration is combined through PSHA into a single exceedance rate for the specified ground-motion parameter (e.g. PGA). This leads to the estimation of a range of parameters, such as the spectral ordinates at several periods; thus the results may not be compatible with any physically feasible earthquake scenario. The pipeline – fault crossing derives special attention both during the design and the life-cycle of a pipeline project, as the consequences of a potential pipeline failure are usually grave. Thus, the probabilistic approach is selected for the seismic risk assessment of pipeline – fault crossing assisted by our generally incomplete knowledge about the variable nature of earthquake loading and the complex properties of the coupled pipeline – soil system. Within the probabilistic framework the most suitable tool for seismic risk assessment of buried pipeline – fault crossing is the Probabilistic Fault Displacement Hazard Analysis (PFDHA) that quantifies the probabilistic nature of the loading. The basis of PFDHA was presented in [5] where the required data for assessing the probability of rupture for a given fault and its effect on a site under investigation were presented. Then, Youngs et al. [4] presented the framework of PFDHA in order to quantify the mean annual rate of exceeding various fault displacement levels at a site by considering the fault location, the fault slip rate, the strongest expected earthquake, as well as their epistemic uncertainties.

2.2 Pipeline – fault crossing geometry

A straight pipeline segment without any bends is considered that intercepts a single fault at a specific location and thus the crossing site is represented by a single point. The fault is assumed to be planar appearing on the ground surface as a straight line and the fault thickness is approximated to zero. The pipeline – fault crossing is schematically illustrated in Figure 1, therein β is the pipeline – fault crossing angle, LF the fault length, L_p the crossing site from the fault closest edge and ψ the fault dip angle. The fault displacement is defined by D and is related to the spatial components $[\Delta_1,\Delta_2,\Delta_3]$, where Δ_1 and Δ_2 are the fault parallel and fault perpendicular horizontal components, while Δ_3 represents the vertical component:

$$D = \sqrt{\Delta_1^2 + \Delta_2^2 + \Delta_3^2} \tag{1}$$

$$\Delta_3 = \Delta_2 \tan\psi \tag{2}$$

When rotating the fault coordinate system (1,2,3) horizontally by the angle β, then Δ_1 and Δ_2 are transformed to Δ_x and Δ_y, i.e. the longitudinal and the transverse displacements with respect to the pipeline axis, while the vertical displacements Δ_3 and Δ_z coincide:

$$\begin{aligned} \Delta_x &= \Delta_1 \cos\beta + \frac{\Delta_3}{\tan\psi}\sin\beta \\ \Delta_y &= -\Delta_1 \sin\beta + \frac{\Delta_3}{\tan\psi}\cos\beta \end{aligned} \tag{3}$$

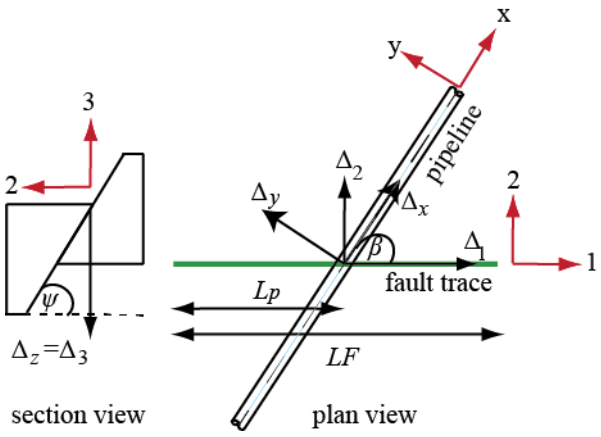


Figure 1: Pipeline fault crossing plan and section view.

2.3 Probabilistic fault displacement hazard analysis

The PFDHA methodology includes two discrete approaches within it: the "earthquake approach" and the "displacement approach". The "earthquake approach" is directly derived from the PSHA, as developed by Cornell [6], and explicitly relates the occurrence of fault displacement on a fault at a site near or at the ground surface to the occurrences of earthquakes in the site region. On the other, the "displacement approach" needs extensive recorded or paleoseismic data. However, these data are not always available and thus within the proposed methodology, the "earthquake approach" is adopted. Furthermore, in the "earthquake approach" of PFDHA the distinction among two types of faulting is introduced, namely the "principal faulting" and the "distributed faulting". The former type is adopted hereinafter, assuming that pipeline crosses a single and sufficiently recorded fault that its displacement may be represented along a single narrow trace or over a zone that be may a few meters wide.

The required information to assess any potential consequences of faulting on pipeline integrity is provided by PFDHA. This information assists engineers on risk-informed decisions regarding site suitability when geological investigations are inconclusive. The outcome, then, of PFDHA is the fault displacement hazard curve on pipeline crossing site, where the fault displacement is presented versus the mean annual rate of exceeding every fault displacement values:

$$v_k(d) = \sum_n \alpha_n(m^0) \times \int_{m^0}^{m_n^u} f_n(m) \times \left[\int_0^{\infty} f_{kn}(r \mid m) \times P_{kn}^*(D > d \mid m, r)\, dr \right] dm \tag{4}$$

where $\alpha_n(m^0)$ is the rate of all earthquakes on source n above a minimum magnitude of engineering significance m^0, $f_n(m)$ is the probability density of earthquake size that seismic source

n can produce between values m^0 and m_n^u estimated using the Gutenberg – Richter Bounded Recurrence Law [7], $f_{kn}(r|m)$ is the conditional probability density function for distance from site k to an earthquake of magnitude m occurring at source n. Finally, $P^*(D>d|m,r)$ is the conditional probability that, given an earthquake of magnitude m at distance r from crossing site, the fault displacement will exceed displacement d. In practice it relates the occurrence of fault displacement at the crossing site to the occurrence of an earthquake through an attenuation model and thus is referred as the Displacement Attenuation (or prediction) Function, which differs from the usual ground motion prediction. Moreover, this term is the product of the conditional probability of slip and the conditional probability of exceedance.

3 PROPOSED METHODOLOGY

3.1 Conceptual algorithm

The estimation of fault displacement hazard in terms of practical applications depends on three factors: (i) the earthquake magnitude as the key factor for describing a seismic source, which ranges from a minimum value M_{min} to a maximum value M_{max} and is discretized into a numbers of bin to account for all possible values, (ii) the surface rupture length (SRL) along the fault trace, acknowledging that different earthquakes may rupture lengths of different size and (iii) the SRL position on the fault trace, as the location of a given earthquake may not encounter the pipeline – fault crossing.

The uncertainty of fault rupture intercepting the pipeline crossing site is handled by considering a variety of potential SRLs, each at a different location. Without more detailed data being available, SRLs of the same size are considered to be equiprobable. Additionally, for simplicity of bookkeeping, a minimum SRL size is determined as for example corresponding to the minimum magnitude of interest via empirical Equations and all subsequent larger sizes are simply integer multiples. So, every SRL size is accounted for at all possible positions, keeping track of those where the rupture crosses the pipeline and thus contributing to the pipeline displacement hazard.

The PFDHA, as presented in section 2.3, is employed as an application of the total probability theorem trough a conceptual algorithm that deals with only one seismic source, i.e. n=1. The mean annual rate of exceeding a defined fault displacement value $\lambda_D(d)$ at the pipeline crossing site is estimated as:

$$\lambda_D(d) = \nu_o \times \sum_i P(D > d \mid m_i) \times f_M(m_i) \tag{5}$$

where ν_o stands for the rate of all earthquakes above a minimum magnitude of engineering significance and is calculated based either on the Equation describing the seismicity of the investigated seismic source zone or provided by the engineer as an input parameter and $f_M(m_i)$ is the earthquake probability calculated according to Gutenberg-Richter Bounded Recurrence Law [7]. Probability function $P(D>d|m_i)$ estimates the probability that fault displacement exceeds a defined value d given earthquake magnitude m_i and is summed over all magnitude values as centers of bins. Further breakdown of Equation (5) yields to:

$$P(D > d \mid m_i) = \sum_i \sum_j \sum_k P(D > d \mid m_i, SRL_j, FD_k, Pos_l) \times P(SRL_j, FD_k, Pos_l \mid m_i) \tag{6}$$

In order to calculate the probability function $P(D>d|m_i)$ of Equation (5), apart from earthquake magnitude range discretization in i bins and rupture length discretization in j bins, a third discretization for the fault displacement option (FD) of PFDHA is necessary. It is pointed out that the proposed conceptual algorithm applies equally for the maximum fault dis-

placement (MD) and the average fault displacement (AD) option of PFDHA. Then, Equation (6) has two constituent elements, the first term is the conditional probability of exceedance and the second term is the conditional probability of SRL, rupture position along the fault trace and the FD approach of PFDHA given an earthquake magnitude.

The conditional probability of exceedance (6) is the term $P(D>d|m_i,SRL_j,FD_k,Pos_l)$ that stands as the core of the PFDHA and necessitates detailed calculations that are carried out over each combination of bins of earthquake magnitude, rupture length, fault displacement and all possible positions of SRL_j along the fault trace. The second element of Equation (6) is the conditional probability of SRL, rupture position along the fault trace and the *FD* approach of PFDHA given an earthquake magnitude m_i, which is decomposed in:

$$P\left(SRL_j, FD_k, Pos_l \mid m_i\right) = P\left(SRL_j, FD_k \mid m_i\right) \times P\left(Pos_l \mid m_i\right) = P\left(SRL_j, FD_k \mid m_i\right) \times \frac{1}{N_l} \quad (7)$$

where the first term is the probability of a given range of fault displacement and size of SRL to occur given an earthquake magnitude. However, SRL_j and FD_k are well correlated given the earthquake magnitude. Therefore, for each combination (i,j,k) the value of $P(SRL_j,FD_k|m_i)$ needs to be estimated with the appropriate joint distribution $f(SRL_j,FD_k|m_i)$. The best known such distribution comes from Wells and Coppersmith [8] and allows the definition of $f(SRL_j,FD_k|m_i)$ as a joint lognormal with positive correlation. Assuming that the discretization is sufficiently fine, the probability of *SRL* and *FD* falling in a bin given the magnitude can be approximated via a single PDF value at its center:

$$\begin{aligned} P\left(SRL_j, FD_k \mid m_i\right) = P_{i,j,k} &= \int_{FD_k-\frac{FD_{step}}{2}}^{FD_k+\frac{FD_{step}}{2}} \int_{SRL_j-\frac{SRL_{step}}{2}}^{SRL_j+\frac{SRL_{step}}{2}} f\left(SRL_j, FD_k \mid m_i\right) dFD\, dSRL \\ &\cong f\left(SRL_j, FD_k \mid m_i\right) \times \Delta FD \times \Delta SRL \end{aligned} \quad (8)$$

Still, the sum of $P_{i,j,k}$ over j and k for all SRL_j and FD_k should equal one. Thus, the required probability function is renormalized as:

$$P\left(SRL_j, FD_k \mid m_i\right) = \frac{P_{i,j,k}}{\sum_j \sum_k P_{i,j,k}} \quad (9)$$

3.2 Interface variable

In seismic risk analysis the roles of the seismologist and the structural engineer are linked by the use of an interface variable, known as the intensity measure (IM). In pipeline – fault crossing seismic risk analysis the structural engineer needs to estimate the mechanical behavior of the pipeline to given IM values. The proper such values are the fault displacement spatial components Δ_1, Δ_2 and Δ_3, as defined in section 2.2. The spatial distribution of fault components is not only necessary for the fault characterization as normal, strike-slip or reverse, but also dominates the pipeline's response. The latter is of great importance as normal faulting leads to pipeline bending and tension, strike-slip faulting leads to pipeline bending and tension or compression, while reverse fault leads to pipeline bending and compression. Thus, it is deemed necessary to define a vector intensity measure [9]. The appropriate such vector IM consists of two components, namely $[\Delta_1,\Delta_3]$, which are structure independent and can fully describe the loading of the structural model, given that Δ_2 component is functionally

dependent to them. Moreover, the selected IM covers the design goal of assessing the structural behavior of the pipeline due to faulting. However, if the proposed methodology needs to be extended to encompass frequency related events, such as low-cycle fatigue, then the adopted IM might be insufficient.

3.3 Fault displacement components

The outlined PFDHA methodology deals with the magnitude of fault displacement norm, neglects its spatial orientation and passes up the fact that fault displacement in nature is usually three-dimensional. Thus, the necessity arises to introduce a calculation procedure of components' magnitude with reference to fault type. So, fault types are divided into two categories, namely strike-slip type where offset is dominated by Δ_1 component and normal or reverse type where the Δ_3 component is dominant. However, there are not sufficient published data regarding the spatial distribution of the components. Hence, within the scope of the proposed methodology, the dominant component is calculated assuming it is normally or uniformly distributed. Due to the lack of adequate data, the distributions adopted are reasonable assumptions and shall be adjusted or replaced if reliable data are available in the future.

In case the dominant fault component is assumed to be uniformly distributed, it is estimated as:

$$\Delta_1 \text{ or } \Delta_3 = \left(0.70D \div 0.90D\right) \tag{10}$$

where the discretization, the lower and the upper bound are input engineering parameters. The proposed lower and upper bounds stand for a reasonable estimation to indicate the dominance of the component that characterizes the fault type and at the same time to assure that fault offset remains three-dimensional.

In case the dominant fault component is assumed to be normally distributed, it is estimated using the parameters listed in Table 1.

Parameter	Value
μ	$0.80D$
σ	$0.20\times\mu$
Upper bound	$0.90D$
Lower bound	$0.70D$

Table 1: Normal distribution parameters for dominant fault component calculation.

The component's mean annual rate of density, whether Δ_1 is the dominant component for strike-slip fault, or Δ_3 for normal/reverse fault, respectively, is estimated as:

$$\lambda'\left(\Delta_1,\Delta_3\right) = f\left(\Delta_1 \mid D\right)\times\frac{d\lambda_D}{dD}\times\frac{\partial\Delta_3}{\partial D} \tag{11}$$

$$\lambda'\left(\Delta_3,\Delta_1\right) = f\left(\Delta_3 \mid D\right)\times\frac{d\lambda_D}{dD}\times\frac{\partial\Delta_1}{\partial D} \tag{12}$$

where $f(\Delta_1|D)$ is the distribution probability density function (either normal or uniform) of the dominant component (either Δ_1 or Δ_3), $d\lambda_D/dD$ is the rate density for given D, while $\partial\Delta_1/\partial D$ or $\partial\Delta_3/\partial D$ is the derivative of the dominant fault component over D that is necessary in order to change the variable [10]. It should be noted that $\lambda'(\Delta_1,\Delta_3)$ is not rate, but rate density and thus

an integration of $\lambda'(\Delta_1,\Delta_3)$ over a two-dimensional interval of Δ_1 and Δ_3 yields the mean annual rate of events occurring in this interval.

3.4 Pipeline strain hazard curves

Fault offset is the primary cause of pipeline failure due to earthquake events, as the differential ground movement imposes large permanent ground displacements on the buried pipeline that the pipeline has to accommodate. Thus, high levels of tensile and compressive strains are developed and endanger the pipeline's integrity. Compressive strains may lead to local buckling of the wall, while tensile strains may lead to fracture of the girth welds between adjacent steel parts. So, the primary consideration for pipeline earthquake resistant design is the determination of strain capacity and for this reason, strain hazard curves are the most suitable tool to perform a probabilistic estimation of any potential pipeline failure throughout the pipeline life-time. However, whilst structural analyses provide strain demands, strain capacity terms are adopted by code recommendations. ALA [11] provisions suggest for the longitudinal strains resulting from ground movement due to fault offset the tensile strain limit $\varepsilon_{t,c}$=2% and the compressive limit $\varepsilon_{c,c}$ of:

$$\varepsilon_{c,c} = 0.5\left(\frac{t}{D'}\right) - 0.0025 + 3000\left(\frac{pD_e}{2Et}\right)^2 \quad \text{where } D' = D_e / \left[1 - 3\left(D_e - D_{\min}\right)/D_e\right] \tag{13}$$

where t is the pipeline wall thickness, D_e is the pipeline external diameter, D_{min} is the internal diameter, p is the internal pressure and E the pipeline steel modulus of elasticity. Equation (13) includes a term for internal pressure, which acts as a relief against the external earth pressure. In the present study the internal pressure is assumed to be equal to zero, as a less favorable situation, thus the pertinent term is neglected.

Strain hazard curves present the mean annual rate of exceeding a defined strain value $\lambda_E(\varepsilon)$ and are evaluated as:

$$\lambda_E(\varepsilon) = \sum_{\varepsilon(\delta_{1i},\delta_{3j})\geq\varepsilon}\sum \Delta\lambda\left(\delta_{1i},\delta_{3j}\right) \tag{14}$$

where $\Delta\lambda(\delta_{1i},\delta_{3j})$ is the mean annual rate of equaling or reaching a given range of fault displacement with components δ_{1i} and δ_{3j}. It is estimated by integrating the mean annual rate of density $\lambda'(\Delta_1,\Delta_3)$ in the appropriate range of components displacement δ_{1i} and δ_{3j}. Finally, this result is in turn summed over all i and j values of Δ_1 and Δ_3 respectively that are found in the structural analysis to correspond to strain values larger than ε.

3.5 Uncertainty

PFDHA, from its origins, can incorporate any quantifiable uncertainty, as identification and quantification of uncertainties is integral to the seismic hazard analysis. Uncertainties are usually divided into two main categories, namely aleatory and epistemic. The division of uncertainties demands a distinct treatment and it is good practice to treat them separately, in order to identify the key uncertainties, although this is not always an easy task. The aleatory uncertainties refer to the inherent variability of the nature over time, while epistemic uncertainties are related to the inadequate understanding of the nature and can be in time reduced with better observations. In the present study, epistemic uncertainties are handled though a logic tree, as the latter is considered to be the state-of-the art tool to quantify and incorporate epistemic uncertainties [12]. The set-up of a logic tree includes the production of alternative

models for various input variables and then the assignment of weight factors to tree branches. These factors represent the engineer's degree of belief in the alternative models or in other words they represent the degree of belief in one model with respect to another. Epistemic uncertainties are considered in the present study through the logic tree that is presented in Figure 2 and includes three parameters.

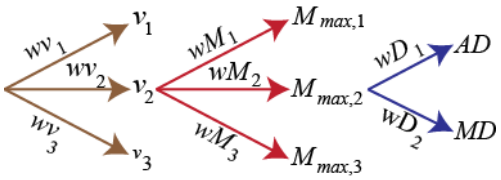


Figure 2: Uncertainty analysis logic tree.

The first parameter is the seismic rate v as the main characteristic of the seismic source that is under question, given that seismologists usually provide the mean value. The second is the maximum expected earthquake magnitude M_{max}. While the minimum earthquake magnitude is selected based on the assumption that lower magnitudes do not contribute to seismic hazards of engineering significance, the maximum earthquake magnitude is uncertain. The third uncertainty parameter is the choice of the average fault displacement (AD) or the maximum earthquake displacement (MD) approach of PFDHA, as presented in section 3.1.

4 ILLUSTRATIVE EXAMPLE

The proposed methodology for seismic risk assessment of buried pipeline – fault crossings consists of two interrelated steps: (i) the seismological part, where the probabilistic fault displacement hazard analysis is conducted to extract the mean annual rate of exceeding fault displacement and the intensity measure on crossing site and (ii) the structural part, where the structural analysis of the buried pipeline is performed to extract the strain demands. Then, the results of both steps are combined, yielding the pipeline strain hazard curves. To demonstrate the proposed methodology a numerical example and its associated results are hereinafter presented.

4.1 Example of fault displacement hazard analysis

A normal fault is considered with length equal to LF=100km, fault dip angle ψ=70^o and average seismic rate v=1.2. Pipeline crossing is located L_p=40km from the fault closest edge, while pipeline – fault crossing angle equals β=80^o, with reference to Figure 1. The minimum earthquake magnitude under consideration is selected as M_{min}=4.5 and the average maximum earthquake magnitude is M_{max}=7.3. Analysis is carried out for fault displacement values ranging from 0.01m to 3m. Uncertainty parameters considered in the analysis are listed in Table 2 with respect to Figure 2. Regarding the AD or MD approach of PFDHA, they are both assigned a weight factor of 0.50, given that there is not sufficient data to favor one approach compared to the other. For the same reasoning, both the normal and the uniform distribution approach for estimating the dominant fault component are assigned a weight factor of 0.50. In addition, the component calculation procedure is an approximation and thus one cannot favor the uniform distribution against the normal distribution.

Parameter value	Weight factor
v_1=1.1	v_1=0.30
v_2=1.2	v_1=0.40
v_3=1.3	v_1=0.30
$M_{max,1}$=7.2	vM_1=0.20
$M_{max,2}$=7.3	vM_2=0.60
$M_{max,3}$=7.4	vM_3=0.20
AD approach	vA_1=0.50
MD approach	vA_2=0.50
Normal distribution	vF_1=0.50
Uniform distribution	vF_2=0.50

Table 2: Uncertainty parameters considered in the illustrative example.

The output of PFDHA is the weighted average fault displacement hazard curve that is illustrated in Figure 3, where in logarithmic scale the mean annual rate or exceedance $\lambda_D(d)$ is presented on the horizontal axis, while the fault displacement on crossing site d is presented on the vertical axis. The descending curve shape is predictable as the larger the fault displacement is, the lower the mean annual rate of exceedance is. The fault displacement components hazard surfaces are estimated according to section 3.3 and depicted in Figure 4, where on the vertical axis the mean annual rate of density is presented, while on the horizontal axes the two structural independent fault displacement components Δ_1 and Δ_3 are presented.

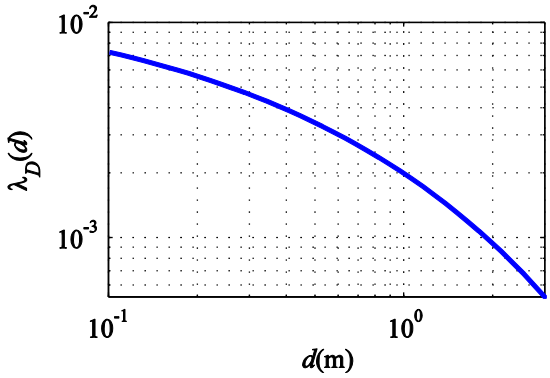


Figure 3: Weighted average fault displacement hazard curve on pipeline crossing site.

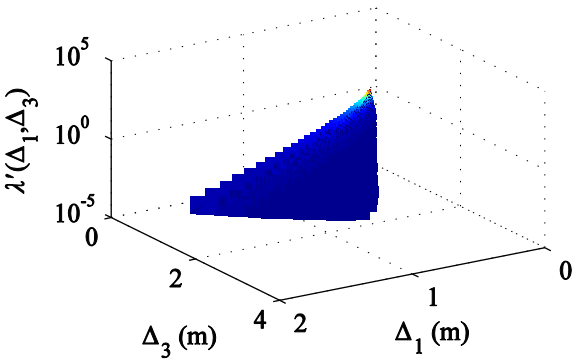


Figure 4: Weighted average fault components hazard surface on pipeline crossing site.

4.2 Disaggregation and uncertainty

Uncertainties are an integral part of seismic risk assessment and are incorporated in the proposed methodology through the logic tree of Figure 2, where weight factors are assigned to tree branches. So, there are in total 18 "triplets" of (wv_i,wM_j,wA_k) weight factors and in practice each branch corresponds to a single factor being the product of partial factors:

$$w_{i,j,k} = wv_i \times wM_j \times wA_k \tag{15}$$

Therefore, the weighted average hazard curve is produced as:

$$\overline{\lambda}_D = \sum_{i,j,k} w_{i,j,k} \times \lambda_D^{i,j,k}(d) \tag{16}$$

For the sake of simplicity, a Monte Carlo simulation approach can be adopted, assuming that the mean value μ and standard deviation σ for a sample size of N are evaluated as follows:

$$\mathrm{E}[\lambda_D] = \frac{\sum_{i=1}^{N} \lambda_D^i}{\mathrm{N}} = \frac{w_1 \times \lambda_D^1 + w_2 \times \lambda_D^2 + \ldots + w_{18} \times \lambda_D^{18}}{\mathrm{N}} \tag{17}$$

$$\sigma = \sqrt{\frac{1}{N} \times \sum_{i=1}^{N} \left(\overline{\lambda}_D - \lambda_D^i\right)^2} \tag{18}$$

Then, the weighted average fault displacement hazard curve is illustrated in Figure 5 along with its dispersion, together with the mean minus one standard deviation.

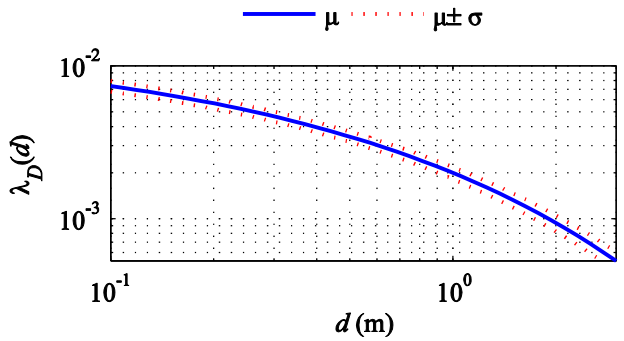


Figure 5: Weighted average fault displacement hazard curve with dispersion.

The conditional probability of exceedance that is incorporated in the fault displacement hazard calculation offers two approaches regarding the normalization of the displacement along the length of the rupture, i.e. the average fault displacement and the maximum fault displacement. As indicated previously, there are not adequate data to favor one approach against the other. Thus, disaggregation results are presented in order to evaluate the selection impact among the two approaches on the fault hazard curve. So, Figure 6 presents the weighted average fault displacement hazard curve adopting the AD or the MD approach of PFDHA, which indicates that for small displacement values the AD approach leads to higher values of mean annual rate of exceedance and vice versa for the MD approach.

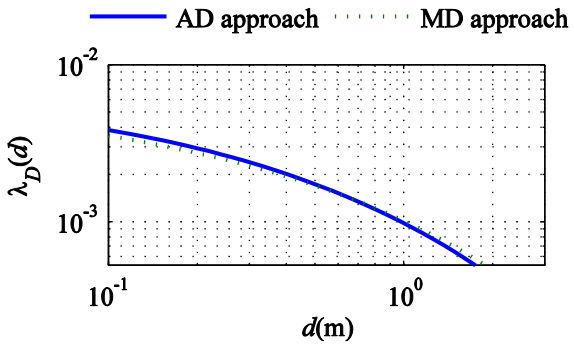


Figure 6: Weighted average fault displacement hazard curve adopting AD or MD approach of PFDHA.

In Eurocode 8 – Part 4 [13] two limit states are introduced for buried pipelines, namely the Ultimate Limit State (DLS) related to a return period of T_{NCR}=475years or 10% probability of exceedance in 50 years and the Damage Limit State (DLS) related to a return period of T_{DLR}=95years or 10% probability of exceedance in 10 years. The probability of exceedance is related with the mean annual rate of exceedance through the Equation (19).

$$P = 1 - \exp\left(1 - t / T_{return}\right) \Rightarrow P = 1 - \exp\left(-\lambda \times t\right) \Rightarrow \lambda = \frac{-\ln\left(1-P\right)}{t} \tag{19}$$

Thus, the mean annual rate of exceeding the ULS is λ_{ULS}=0.0021 and the DLS is λ_{DLS}=0.0105. It is also useful to associate the limit states with earthquake magnitude in order to highlight the contribution of earthquake magnitude values, ranging from M_{min}=4.5 to $M_{\max}$=7.3, to the limit states. Then, using the weighted average fault displacement hazard curve, by neglecting the uncertainty of the M_{max}, it can be found through linear interpolation that the fault displacement corresponding to the ULS is D_{ULS}=0.86m. For the DLS, there is no practically permanent fault offset for the fault under consideration for such low intensity and frequent earthquakes. The disaggregation on earthquake magnitude regarding the ULS is evaluated though:

$$P_{m_i} = \frac{\lambda_D(D \mid m_i)}{\lambda_D(D)} \tag{20}$$

The implementation of Equation (20) leads to Figure 7, where on the horizontal axis the earthquake magnitude values are plotted in bins and on the vertical axis their contribution to the limit states. Disaggregation results indicate that magnitude m=7 contributes most to the ULS. Larger magnitudes may cause larger displacements yet they are apparently too rare for this fault to figure more prominently for ULS.

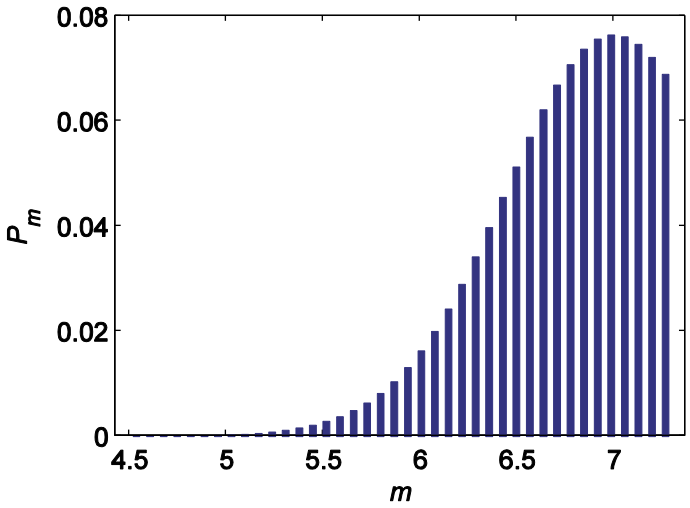


Figure 7: Disaggregation on earthquake magnitude with reference to Eurocode 8 pipeline ultimate limit state.

The spatial distribution of fault components is assessed in the present study through an approximate procedure. Due to the lack of sufficient data, the dominant component is calculated by adopting a uniform or a normal distribution. However, it is essential to demonstrate the differences among the two assumptions in terms of fault components hazard surfaces. Thereby, the independent Δ_1 and Δ_3 components are presented on the horizontal axes, while on the vertical axis their mean annual rate of density $\lambda'(\Delta_1,\Delta_3)$ is presented. The hazard surface using the normal distribution is lower than the corresponding using the uniform distribution. It is also essential to recall that the mean annual rate of density is not a rate but a rate density and thus if an integration is carried out over a two-dimensional interval of Δ_1 and Δ_3 one can estimate the mean annual rate of occurrence in that interval.

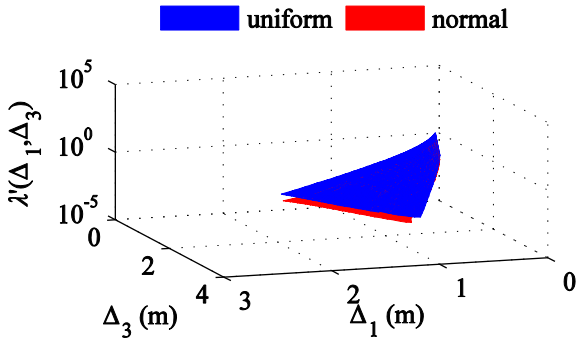


Figure 8: Fault displacement hazard surfaces adopting a uniform or a normal distribution.

4.3 Pipeline structural analysis

Pipeline structural analysis can be carried out either numerically or analytically in order to assess the pipe response due to faulting. The usual design process includes the use of analytical approaches in the preliminary design stage and then numerical simulations in the final stage. For the purposes of the illustrative example, the pipeline structural analysis is performed using the analytical procedure presented by Karamitros et al. in [14],[15] as a reliable approach to estimate the maximum and the minimum developing strain on the pipeline.

A typical high-pressure natural gas API5L-X65 pipeline is considered, featuring an external diameter of D_e=0.914m (36in) and a wall thickness of t=0.0127m. The pipeline steel is considered to be elastic with isotropic hardening, while its properties are listed in Table 3.

Parameter	Value
Yield stress	448.50MPa
Ultimate stress	531.00MPa
Ultimate strain	4.00%
Young's modulus	210GPa
Yield strain	0.233%
Hardening modulus	1.088GPa

Table 3: API-5L X65 steel properties considered in the structural analyses.

The pipeline is assumed to be buried under 1.30m of medium-density sand and coated with coal-tar. Backfill sand's friction angle is φ=36^o and unit weight is equal to γ=18kN/m^2. The surrounding soil is modeled as a series of mutually independent elastoplastic springs according to Winkler soil model, while their properties are estimated according to ALA [11] provisions and listed in Table 4.

Spring type	Force (kN/m)	Displacement (m)
Axial (frictional) springs	22.7	3.0
Transverse horizontal springs	134.4	35.7
Vertical upward springs	41.2	2.6
Vertical downward springs	1021.8	95.3

Table 4: Soil spring properties considered in the structural analyses.

4.4 Pipeline strain hazard curves

Within the scope of the present illustrative example, strain hazard curves are derived by combining structural analysis results and a basic determinist approach, where fault displacement hazard is represented by its weighted average (Figure 3), considering epistemic uncertainties. Also, strain capacities are considered to be deterministic, rather than uncertain, i.e. uncertainty regarding the pipeline steel properties and the soil properties and hence the pipeline mechanical behavior is neglected. The mean annual rate of exceeding a defined strain value is estimated via Equation (14). For the pipeline under investigation, the tensile strain limit equals 2%, while the compressive strain limit yields 0.35%. Then, the combination of analytical results with PFDHA results leads to the estimation of the pipeline strain hazard curves that are illustrated in Figure 9 and Figure 10 for the tensile and the compressive strains respectively. Strain hazard curves indicate that there is no risk of pipeline failure either due to tensile failure of girth welds, or due to local buckling.

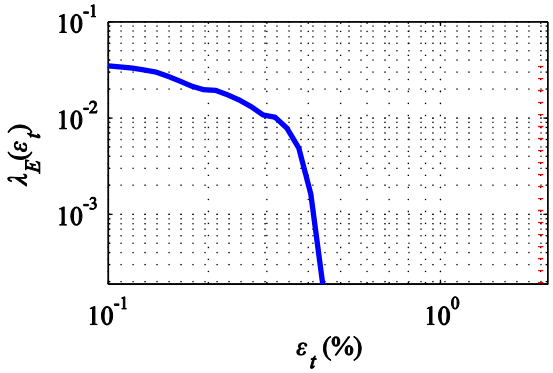


Figure 9: Tensile strain hazard curve.

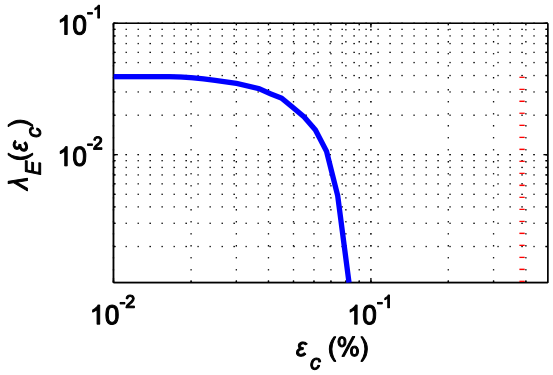


Figure 10: Compressive strain hazard curve.

5 CONCLUSIONS AND REMARKS

A two-step methodology for seismic risk assessment of buried steel pipelines crossing active faults is presented. The first step includes the Probabilistic Fault Displacement Hazard Analysis methodology as adjusted for pipeline fault crossing. The conceptual algorithm of the proposed methodology is also presented, by taking into account epistemic uncertainties. The second step is the "transition" from seismological data to structural analysis through the vector intensity measure of fault displacement components. Strain hazard curves are derived by associating results from pipeline mechanical behavior to hazard analysis in order to compute the mean annual rate of exceedance of longitudinal strains, which are compared to code-based strain failure criteria. Moreover, an illustrative example is presented to demonstrate the proposed methodology. Results regarding the uncertainty of adopting the average fault or the maximum fault displacement are presented to identify its impact on the mean annual rate of exceeding fault displacement on pipeline crossing site. Additionally, the fault components are estimated through an approximate calculation procedure and thus the differences between assuming a uniform or a normal distribution to estimate the dominant component are presented. Disaggregation results on earthquake magnitude with reference to Eurocode 8 limit states are displayed to evaluate the contribution of earthquake magnitude to the limit states.

The proposed approach offers a path for comprehensive performance-based assessment of buried pipelines crossing active faults. Using an adjusted PFDHA implementation for pipeline – fault crossing together with the pipeline response pipeline due to faulting using a reliable analytical approach, the hazard of pipeline crossing in terms of strains can be estimated. The proposed methodology provides engineers with a reliable estimation tool, admittedly requiring programing of the conceptual algorithm, but offering both seismic risk and pipeline structural analyses at low computational effort.

ACKNOWLEDGMENTS

Financial support was provided by the European Research Executive Agency via Marie Curie grant PCIG09-GA-2011-293855 and by Greece and the European Social Funds through the Operational Program "Human Resources Development" of the National Strategic Framework (NSRF) 2007-2013.

REFERENCES

[1] M.J. O' Rourke, X. Liu, *Response of buried pipelines subject to earthquake effects, Multidisciplinary Center for Earthquake Engineering Research*. Buffalo, New York, 1999.

[2] J.J. Bommer, Deterministic vs. probabilistic seismic hazard assessment: an exaggerated and obstructive dichotomy. *Journal of Earthquake Engineering*, **6**, Special Issue I, 43-73, 2002.

[3] V.E. Melissianos, D. Vamvatsikos, C.J. Gantes, Seismic risk assessment of buried pipelines at active fault crossings. *Second European Conference on Earthquake Engineering and Seismology*, Istanbul, Turkey, August 25-19, 2014.

[4] R.R. Youngs, W.J. Arabasz, R.E. Anderson, A.R. Ramelli, J.P. Ake, D.B. Slemmons, J.P. McCalpin, D.I. Doser, D.J. Fridrich, F.H. Swan III, A.M. Rogers, J.C. Yount, L.W. Anderson, K.D. Smith, R.LS. Bruhn, P.L.K. Knuepfer, R.B. Smith, C.M. dePolo, D.W. O'Leary, K.J. Coppersmith, S.K. Pezzopane, D.P. Schwartz, J.W. Whitney, S.S. Olig, G.R. Toro, A methodology for probabilistic fault displacements hazard analysis (PFDHA). *Earthquake Spectra*, **19**(1), 191-219, 2003.

[5] K.L. Coppersmith, R.R. Youngs, Data needs for probabilistic fault displacement hazard analysis. *Journal of Geodynamics*, **29**, 329-343, 2000.

[6] C.A. Cornell, Engineering seismic risk analysis. *Bulletin of the Seismological Society of America*. **58**, 1583-1606, 1968.

[7] R. Gutenberg, C.F. Richter, Frequency of earthquakes in California. *Bulletin of the Seismological Society of America*, **34**, 185-188, 1944.

[8] D.L. Wells, K.J. Coppersmith, New empirical relationships among magnitude, rupture length, rupture width, rupture area and surface displacement, *Bulletin of Seismological Society of America*, **84**, 974-1002, 1994.

[9] P. Bazzuro, C.A. Cornell, Vector-valued probabilistic seismic hazard analysis (VPSHA). *7th U.S. National Conference on Earthquake Engineering*, Boston, M.A., 2002.

[10] J.R. Benjamin, C.A. Cornell, *Probability, Statistics and Decision for Civil Engineers*. McGraw-Hill, New York, 1970.

[11] ALA American Lifelines Alliance, *Guidelines for the Design of Buried Steel Pipe-July 2001 (with addenda through February 2005)*, 2001.

[12] J.J. Bommer, F. Scherbaum, The use and misuse of logic trees in probabilistic seismic hazard analysis. *Earthquake Spectra*, **24**(4), 997-1009, 2008.

[13] European Committee for Standardization, *Eurocode 8: Design of Structures for Earthquake Resistance, Part 4: Silos, Tanks and Pipelines.* Brussels, 2004.

[14] D.K. Karamitros, G.D. Bouckovalas, G.D. Kouretzis, Stress analysis of buried steel pipelines at strike-slip fault crossings. *Soil Dynamics and Earthquake Engineering*, **27**, 200-211, 2007.

[15] D.K. Karamitros, G.D. Bouckovalas, G.D., Kouretzis, V. Gkesouli, An analytical method for strength verification of buried steel pipelines at normal fault crossings. *Soil Dynamics and Earthquake Engineering*, **31**, 1452-1464, 2011.

COMPDYN 2015
5th ECCOMAS Thematic Conference on
Computational Methods in Structural Dynamics and Earthquake Engineering
M. Papadrakakis, V. Papadopoulos, V. Plevris (eds.)
Crete Island, Greece, 25–27 May 2015

SEISMIC PERFORMANCE OF INDUSTRIAL PRESSURE VESSELS: PARAMETRIC INVESTIGATIONS OF SIMPLIFIED MODELING APPROACHES FOR VULNERABILITY ASSESSMENT

Christos Z. Karakostas[1], Ioannis F. Moschonas[2], Vassilios A. Lekidis[1], and Savvas P. Papadopoulos[4]

[1] Research Director, EPPO-ITSAK
address
christos@itsak.gr, lekidis@itsak.gr

[2] Consulting Engineer
16 Agias Lauras str., Katerini, Greece
imosxonas@teemail.gr

[3] Civil Engineer, MSc, PhD Candidate, Aristotle University of Thessaloniki
Thessaloniki, Greece
savvaspp@civil.auth.gr

Keywords: Pressure vessels, pushover analysis, vulnerability and fragility assessment, surrogate models.

Abstract. *The present paper presents the up-to-date results of an on-going research effort aiming to develop novel, efficient and reliable computational (analytical) methods for assessing the vulnerability of pressure vessel structures as well as at advancing their performance-based seismic design framework. More specifically, various potential simplifications of a refined model of a pressure vessel in order to develop a surrogate one are investigated in detail and the derived results and conclusions lead to the proposal of guidelines for the development of surrogate, cost-effective yet reliable, models for pressure vessels.*

1 INTRODUCTION

Until now the various procedures in the literature used to assess the vulnerability of pressure vessels are focused to a specific structural type and as a result refined (detailed) finite element models were used [1]. In a previous research effort by the authors [2], a methodology was proposed for the derivation of fragility curves for various types of industrial pressure vessels. In order for this methodology to be applicable to a large number of pressure vessels the computational effort for analyses has to be minimized; for this reason, the proposed methodology was based on static nonlinear analysis and four damage states were defined directly on the derived pushover curves. A further significant reduction of the time for analyses can be achieved by using surrogate models instead of refined ones, the development of which is the subject of the present paper. Such models were also used in other studies [3, 4] to assess the seismic performance of pressure vessels, but without any investigation of the effect of their inherent simplification assumptions on their accuracy in describing the seismic response of pressure vessels. For this reason, in the present work several simplification approaches that can be applied to a refined model so as to produce a surrogate one are extensively studied and the derived conclusions are then used to form specific guidelines for the development of surrogate models for pressure vessels that can be reliably used in assessment procedures.

2 INVESTIGATION OF SIMPLIFICATION APPROACHES FOR THE DEVELOPMENT OF SURROGATE MODELS

The structural system of a pressure vessel consists of the the spherical shell, the supporting columns and, in some cases the column-bracing trusses. In a refined model the first two parts are modeled with shell elements; the latter one is modeled either with frame elements or, in case wherein braces cannot resist compression forces due to their negligible buckling strength, with hook elements placed at the end of each brace which are activated only in tension.

The development of a surrogate model is usually based on the following modeling approaches:

- Simplified modeling of braces,
- Simplified modeling of the spherical shell,
- Simplified modeling of columns

In the following, these modeling simplifications are parametrically investigated in order to determine the range and limits of their applicability and their effect on the accuracy of the derived surrogate models.

In a previous paper by the authors [2] two actual pressure vessels were used for investigation purposes, one without braces (PV1) and one with braces (PV2). For these two vessels two refined finite element models were developed in ABAQUS (AB1 and AB2, respectively) using the S4R and S3R shell elements for the discretization of the spherical shell and columns and the T3D2 truss element for braces. Based on these two models, 12 additional finite element models (Fig. 1) were derived for parametric investigations, through addition or removal of braces and through differentiation of the column thicknesses so as to correspond to EC3 classification thresholds for section classes 1, 2 and 3. The same models and terminology are used in the present research effort. The interested reader can refer to [2] for further details.

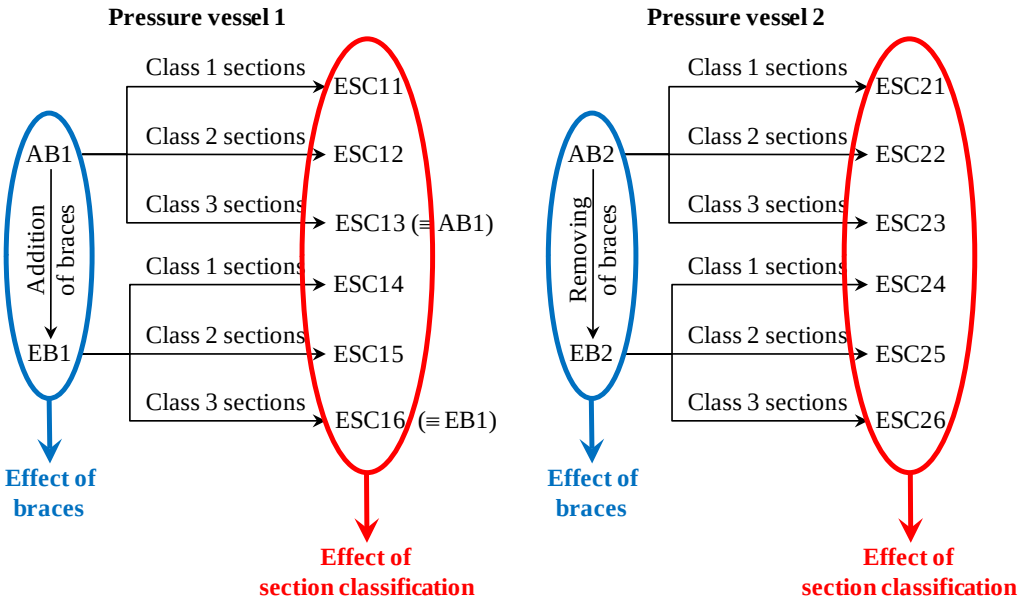
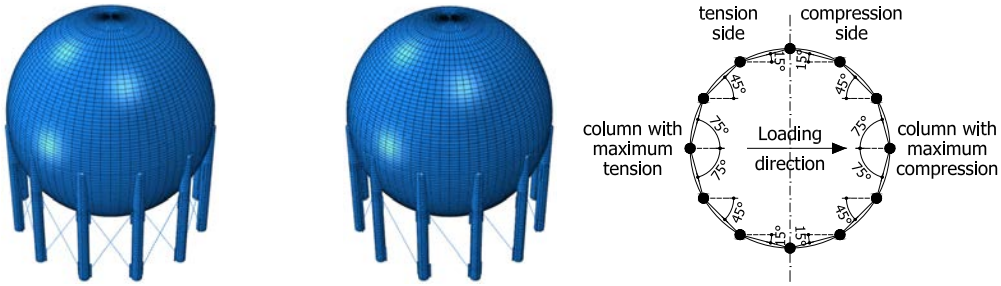


Figure 1: Pressure vessel models used for parametric investigations.

2.1 Simplified modeling of braces

According to the refined method for modeling braces (Fig. 2a), i.e. placing of hook (i.e. tension-only activated) elements at one of their ends, the horizontal elastic stiffness of the vessel is successively increased, due to the successive activation of braces in tension, resulting in a corresponding decrease to the eigenperiod of the translational mode. For this reason, it is very difficult to use this method in response spectrum analysis and also, in performance-based design, to define an appropriate inelastic equivalent single degree of freedom (ESDOF) system to estimate the target displacement on the basis of pushover analysis procedures.

A simplified approach to tackle these problems is to remove any hook elements, keeping only braces in tension in the model (Fig. 2b). In this way, the horizontal elastic stiffness of the vessel, and consequently the period of its translational mode, are constant making this method more appropriate to use in response spectrum analysis and in the definition of the inelastic ESDOF system. However, modeling only the tension braces results in an antisymmetric structural system, which, for the symmetric operating loads, i.e. the internal pressure and the self weight, leads to a small horizontal displacement that actually does not exist.



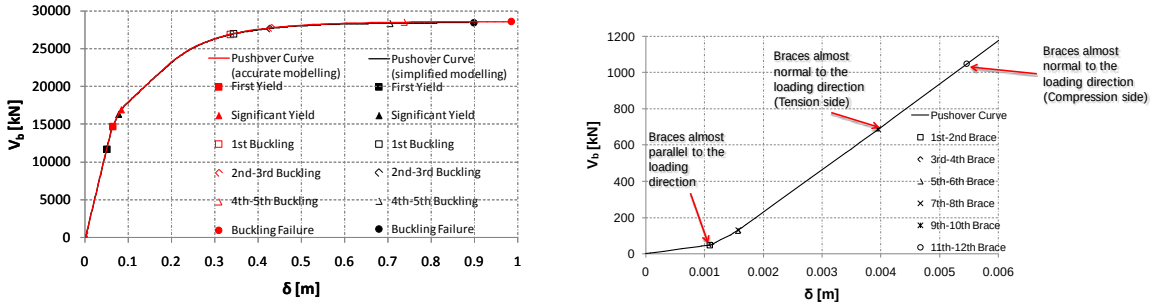
a. Refined modelling (all braces and hook elements at one of their ends)

b. Simplified modelling (only braces in tension)

c. Modelling details (pushover)

Figure 2: Modeling of braces.

Both aforementioned modeling methods are applied to the pressure vessel AB2 and the derived pushover curves are shown in Fig. 3, while the results at their characteristic points are given in Table 1. When all braces are modeled, the derived pushover curve (Fig. 3a – red line) has an increasing slope at its initial stage (Fig. 3b) due to the successive activation of braces in tension. At first, due to the self weight and the internal pressure all braces are inactive, since they cannot carry the resulting compression force. Then, when the horizontal force is applied the stiffness of the vessel has its minimum value, corresponding to an unbraced vessel, until a displacement of 0.011m wherein the first two braces (the nearest parallel ones to the loading direction on the tension side of the vessel – see Fig. 2c) are activated.. The other two braces at the compression side of the vessel are activated at the next step. Then, the slope remains constant until the activation of the next four braces at two successive steps for a horizontal displacement of 0.016m, firstly the two at the tension side and then the two at the compression side. These braces are the ones with an angle of 45° with respect to the loading direction. The last four braces that are activated are the almost normal ones to the loading direction. Again, the two braces at the tension side of the vessel are activated first and next the two at the compression side for displacements 0.040m and 0.055m, respectively. After all tension braces are activated the horizontal stiffness of the vessel remains constant, reaching its maximum value until the first yield.



a. Pushover curves

b. Successive activation of braces at the beginning of the pushover curve

Figure 3: Simplified modeling of braces – Pushover curves.

Quantity	Refined modeling	Simplified modeling	Difference [%]
Yield displacement [m] (Yield of braces)	0.064	0.050	-28.0
Ultimate displacement [m]	0.985	0.898	-14.8
Yield force [kN] (Yield of braces)	14703	11693	-25.7
Ultimate force [kN]	28595	28454	-0.5

Table 1: Simplified modeling of braces – Values at characteristic points of pushover curves.

Tension braces with smaller angle to the loading direction (almost parallel) are activated first and the ones with larger angle (almost normal) are activated last. In other words, the activation sequence is proportional to the contribution of tension braces to the horizontal stiffness of the structure. It should be noted that all tension braces are activated for a horizontal displacement of 0.055m which is very small compared to the ultimate displacement

of 0.985m. For this reason, the derived pushover curve (Fig. 3a – red line) can be practically considered as linear in the elastic range with a slope that corresponds to the stiffness of the vessel with all tension braces activated.

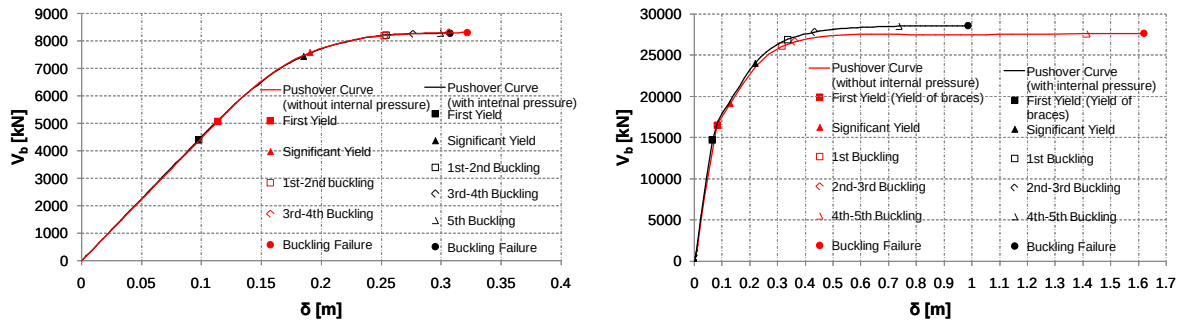
From the comparison between the refined and the simplified modeling methods (Fig. 3a and Table 1) it observed that in the simplified model (i.e. when only tension braces are taken into account) the first yield takes place earlier at an average percentage of 28%, while the ultimate displacement at a smaller and acceptable percentage of 14.8%. The significant yield, i.e. the point that corresponds to 10% reduction of the secant stiffness, and all column buckling (with a small exception at the first column buckling), also take place slightly (i.e. 3% to 5%) earlier. The horizontal displacement for the symmetric operating loads due to the antisymmetry of the structural system of the simplified model is only 0.0011m, i.e. very small compared to the yield displacement of 0.050m and of course the ultimate displacement of 0.898m. Hence, it is concluded that in pushover investigations, modeling only the braces in tension is an acceptable simplification.

2.2 Simplified modeling of the spherical shell

A next step and probably the most critical issue in the development of a surrogate model is the modeling of the spherical shell in a simplified manner. An approach that is commonly used [3, 4] is the substitution of the spherical shell with a rigid body connection of the column heads. In the following, the applicability range of this simplification is investigated.

2.2.1 Effect of internal pressure

Due to the in plane rigidity of the assumed rigid body connection, moments and shear forces at columns mainly due to the internal pressure and secondary due to the self weight are not taken into account. In order to investigate the effect of the internal pressure, models AB1 and AB2 are analyzed with and without the corresponding internal pressure. The derived pushover curves are shown in Fig. 4. It is observed that in model AB1 the overall shape of the two pushover curves is the same and only specific characteristic points differ at percentages varying from 17.5% for the first yield to 4.3% for the ultimate displacement. In model AB2 the ultimate displacement is significantly larger (64.3%) when the internal pressure is ignored, while the difference for the ultimate force (strength) is only 3.3%.



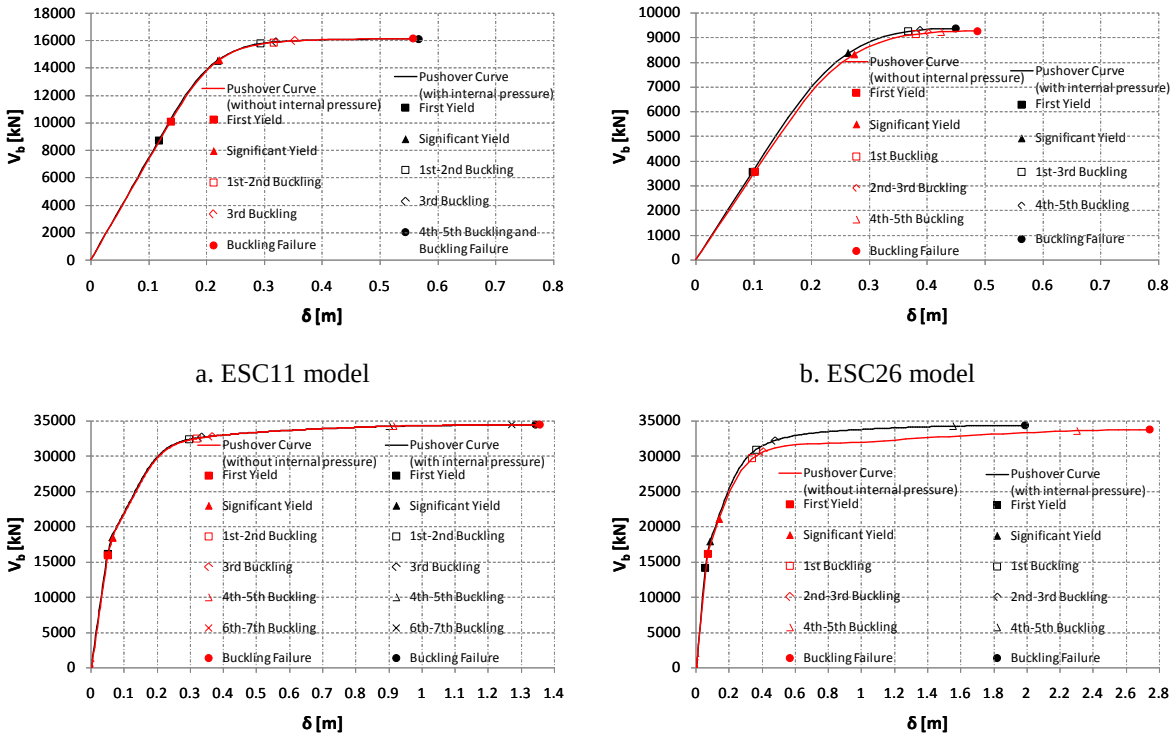
a. AB1 model

b. AB2 model

Figure 4: Effect of internal pressure – Pushover curves of AB1 and AB2 models.

The next step is to investigate whether the presence of braces and/or the class the column sections cause the observed overestimation of the ultimate displacement in model AB2. For this reason all models used for parametric analyses in [2] are analyzed for both cases, i.e. with

and without internal pressure. Some of the derived pushover curves are shown in Fig. 5 and the comparison of the corresponding ultimate displacements is given in Table 2.



a. ESC11 model

b. ESC26 model

c. ESC14 model

d. ESC21 model

Figure 5: Effect of internal pressure – Pushover curves of models in [2].

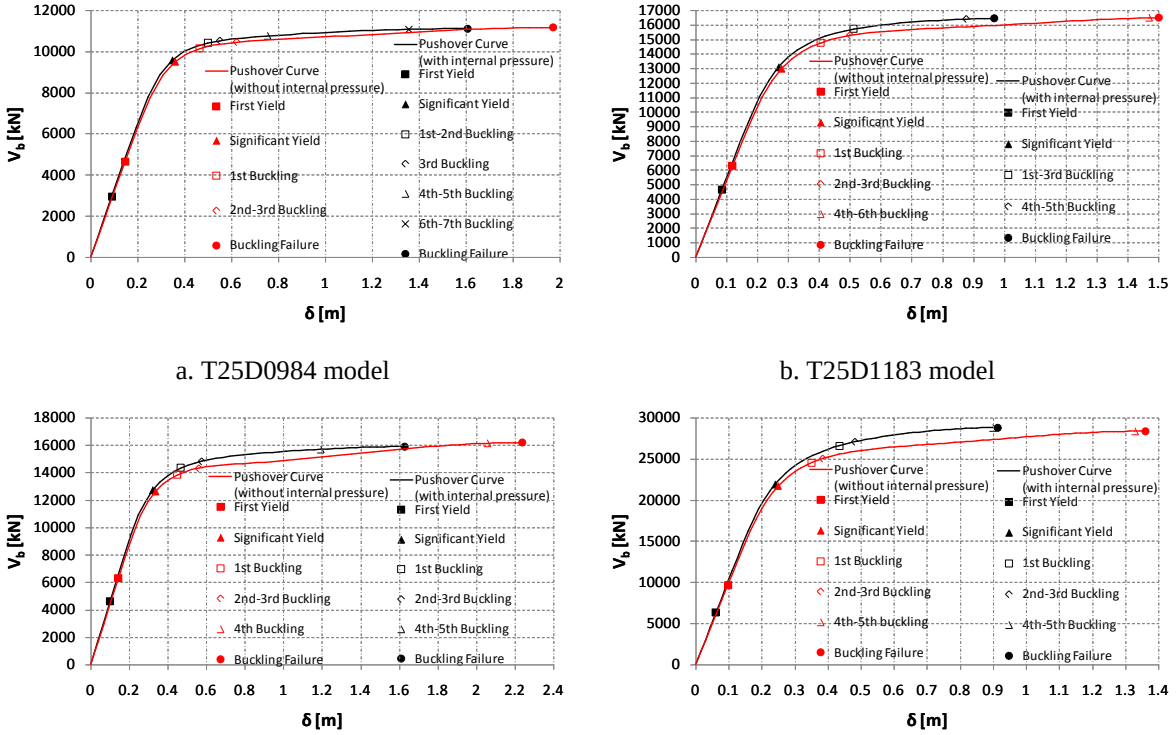
MODEL	t [mm]	D [mm]	BRACES	$d_{ultimate}$ [m] With internal pressure	$d_{ultimate}$ [m] Without internal pressure	Difference [%]
ESC11	33	1016	NO	0.566	0.556	-1.8
ESC12	23	1016	NO	0.378	0.370	-2.1
ESC13≡AB1	18	1016	NO	0.315	0.318	0.9
ESC14	33	1016	YES	1.344	1.356	0.9
ESC15	23	1016	YES	0.747	0.740	-0.9
ESC16≡EB1	18	1016	YES	0.522	0.532	1.8
AB2	25-30	1100	YES	0.985	1.618	64.2
ESC21	40	1100	YES	1.989	2.743	37.9
ESC22	28	1100	YES	0.990	0.660	-33.3
ESC23	22	1100	YES	0.794	0.599	-24.6
EB2	25-30	1100	NO	0.534	0.549	2.8
ESC24	40	1100	NO	0.765	0.628	-18.0
ESC25	28	1100	NO	0.536	0.558	4.1
ESC26	22	1100	NO	0.449	0.487	8.6

Table 2: Effect of internal pressure –Comparison of ultimate displacements of models in [2].

From Fig. 5 and Table 2 it is observed that in all models derived from the original pressure vessel PV1, the pushover curves for the two cases, i.e. with and without internal pressure, practically coincide and the corresponding ultimate displacements differ only at negligible percentages varying from 0.9% to 2.1%. Only specific characteristic points are significantly different, e.g. the first yield in model ESC11. On the contrary, in all models derived from the original pressure vessel PV2 the derived pushover curves differ in both strength (with small variations up to 4%) and ultimate displacement (with significant variations ranging from a 33.3% underestimation up to a 64.2% overestimation). Consequently, the similarities in all models of PV1 and the differences in all models of PV2 are not due to the presence of braces or the column section class.

The other major difference between the two pressure vessels is the thickness of the spherical shell, which in PV1 is 74.5mm and in PV2 is 42mm, i.e. significantly smaller. Hence, in order to investigate whether the reduced shell thickness is responsible for the observed differences in PV2 models, a set on 14 new models without braces are created on the basis of EB2 model. More specifically, in all new models the shell thickness is 42mm and the internal pressure 1120 kN/m^2 (i.e. same as those of vessel PV2). In seven models the thickness of column sections is 25mm and in the other 7 is 30mm. At three of the seven models the diameter of columns corresponds to the limit of each of three section classes (Class 1, 2 and 3), while in the remaining four models columns' diameter corresponds to 1/3 and 2/3 of the difference in diameter between two subsequent classes. The derived pushover curves of some models are shown in Fig. 6 and the comparison of the corresponding ultimate displacements are given in Table 3.

.



a. T25D0984 model

b. T25D1183 model

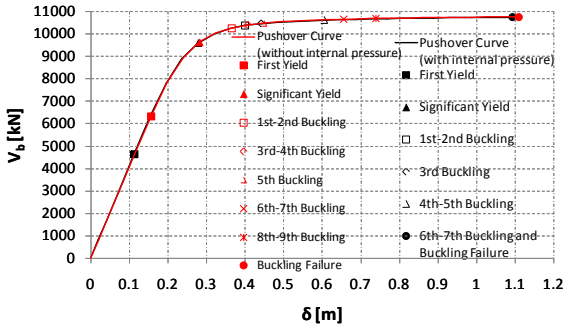
c. T30D1057 model

d. T30D1433 model

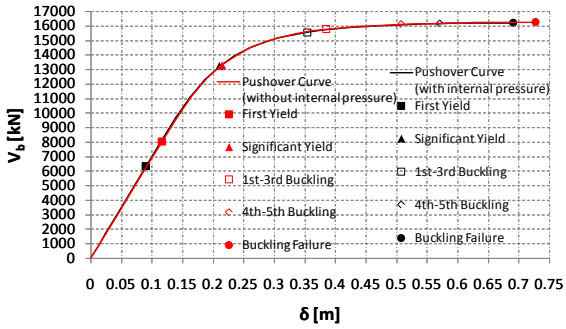
Figure 6: Effect of internal pressure – Pushover curves of new models based on EB2 – Shell thickness 42 mm.

MODEL	t_{shell} [mm]	t_{column} [mm]	D [mm]	Section Class	$d_{ultimate}$ [m] With internal pressure	$d_{ultimate}$ [m] Without internal pressure	Difference [%]
T25D0750	42	25	750	1	1.072	1.405	31.1
T25D0867	42	25	867		1.562	1.834	17.4
T25D0984	42	25	984		1.606	1.971	22.7
T25D1100	42	25	1100	2	0.536	0.558	4.1
T25D1183	42	25	1183		0.966	1.499	55.2
T25D1267	42	25	1267		0.898	1.289	43.6
T25D1350	42	25	1350	3	0.711	0.972	36.7
T30D0930	42	30	930	1	2.158	2.493	15.5
T30D1057	42	30	1057		1.627	2.235	37.4
T30D1184	42	30	1184		1.335	1.930	44.6
T30D1310	42	30	1310	2	1.179	1.679	42.4
T30D1433	42	30	1433		0.913	1.360	48.9
T30D1557	42	30	1557		0.889	1.378	55.1
T30D1680	42	30	1680	3	0.716	1.037	44.9

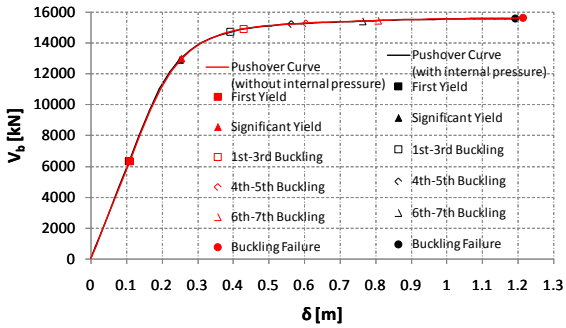
Table 3: Effect of internal pressure – Comparison of ultimate displacements of new models based on EB2 – Shell thickness 42mm.



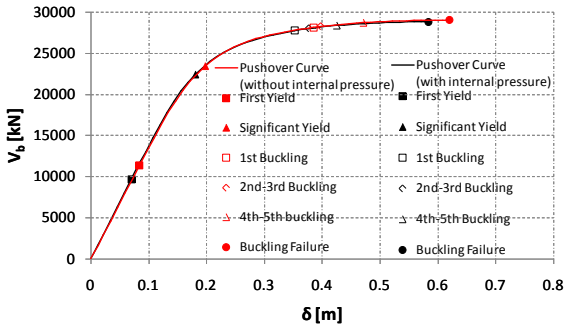
a. T25D0984 model



b. T25D1183 model



c. T30D1057 model



d. T30D1433 model

Figure 7: Effect of internal pressure – Pushover curves of new models based on EB2 – Shell thickness 74.5 mm.

MODEL	t_{shell} [mm]	t_{column} [mm]	D [mm]	Section Class	$d_{ultimate}$ [m] With internal pressure	$d_{ultimate}$ [m] Without internal pressure	Difference [%]
T25D0750	74.5	25	750	1	0.670	0.678	1.3
T25D0867	74.5	25	867		0.812	0.823	1.4
T25D0984	74.5	25	984		1.093	1.110	1.6
T25D1100	74.5	25	1100	2	0.431	0.439	1.7
T25D1183	74.5	25	1183		0.691	0.727	5.3
T25D1267	74.5	25	1267		0.624	0.635	1.8
T25D1350	74.5	25	1350	3	0.555	0.565	1.7
T30D0930	74.5	30	930	1	1.232	1.252	1.6
T30D1057	74.5	30	1057		1.191	1.213	1.8
T30D1184	74.5	30	1184		0.912	0.950	4.2
T30D1310	74.5	30	1310	2	0.748	0.779	4.1
T30D1433	74.5	30	1433		0.583	0.620	6.3
T30D1557	74.5	30	1557		0.624	0.623	-0.3
T30D1680	74.5	30	1680	3	0.581	0.593	2.2

Table 4: Effect of internal pressure – Comparison of ultimate displacements of new models based on EB2 – Shell thickness 74.5 mm.

It is observed that in all models the derived pushover curves for the two cases (with and without internal pressure) show small differences (up to 5%) in strength, and significant differences (up to 55.2%) in the ultimate displacement. Furthermore, in all cases the ultimate displacement is constantly overestimated when the internal pressure is not taken into account.

Then, the thickness of the spherical shell is increased to 74.5 mm and the internal pressure to 2400 kN/m^2, i.e. same as those of vessel PV1, and the 14 models are analyzed again. Some of the derived pushover curves are shown in Fig. 7 and the comparison of the corresponding ultimate displacements are given in Table 4. In this case, in all models the derived pushover curves practically coincide and the ultimate displacements differ only at an acceptable maximum percentage of 6.3% (similar to the case of all models derived from PV1)

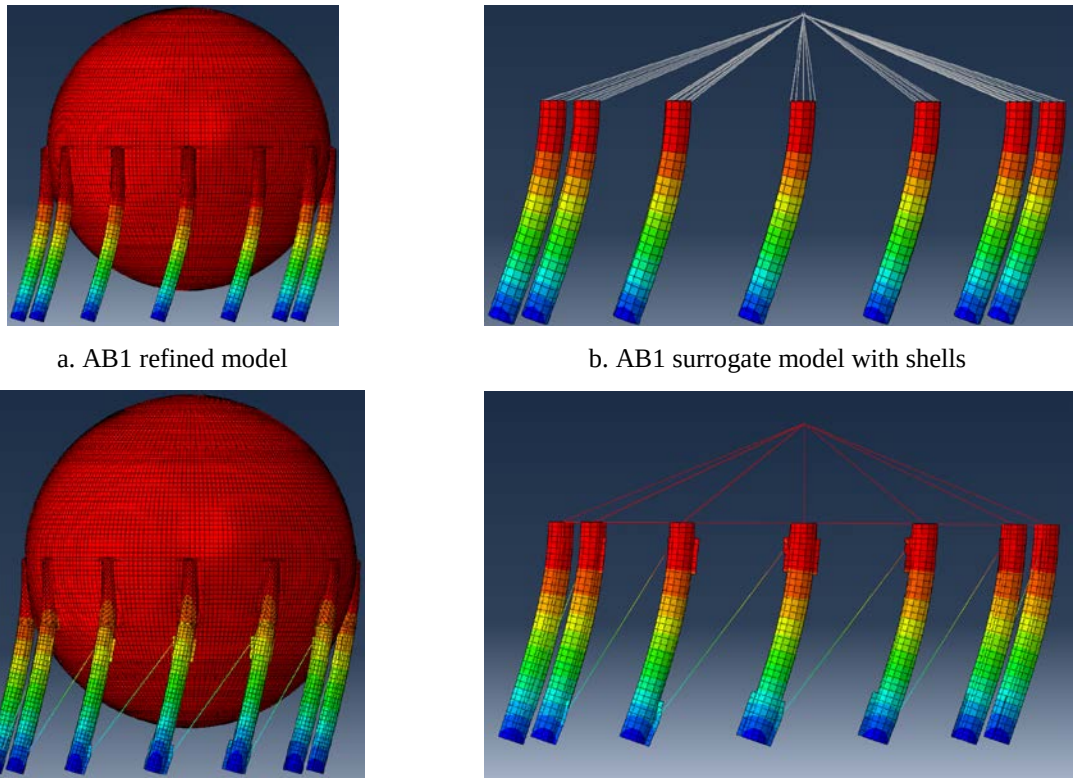
The above analysis shows that when the shell thickness is relatively small, the ultimate displacement is mainly overestimated when the internal pressure is not considered. Of course, this is not on the safety side, since the vessel seems to have significantly larger ductility than it really has. When the thickness of the spherical shell is increased, the overestimation in the ultimate displacement, and consequently in the ultimate ductility, decreases. Hence, the substitution of the spherical shell with a rigid body connection between the heads of columns that does not take into account the stresses from internal pressure is a valid simplification only when the shell thickness is sufficiently large so as to be practically undeformable.

2.2.2 Effect of the consideration of column heads as rotationally fixed

In a refined model columns allow for a small rotation at their heads, which cannot be modeled during the substitution of the shell with a rigid body connection (due to its out of plane rigidity) and, as a result, column heads are considered as rotationally fixed.

In order to investigate the effect of this simplification a surrogate model is created with the shell substituted by a rigid body connection and the columns modeled with shell elements and having their real height, i.e. from their base up to the beginning of their connection to the shell.

Then, modal and pushover analysis are performed; the derived mode shapes for the translational mode are shown in Fig. 8 and the corresponding periods are given in Table 5, while the pushover curves are shown in Fig. 9 (a and c) and the corresponding differences at characteristic points are given in Table 6.



a. AB1 refined model

b. AB1 surrogate model with shells

c. AB2 refined model

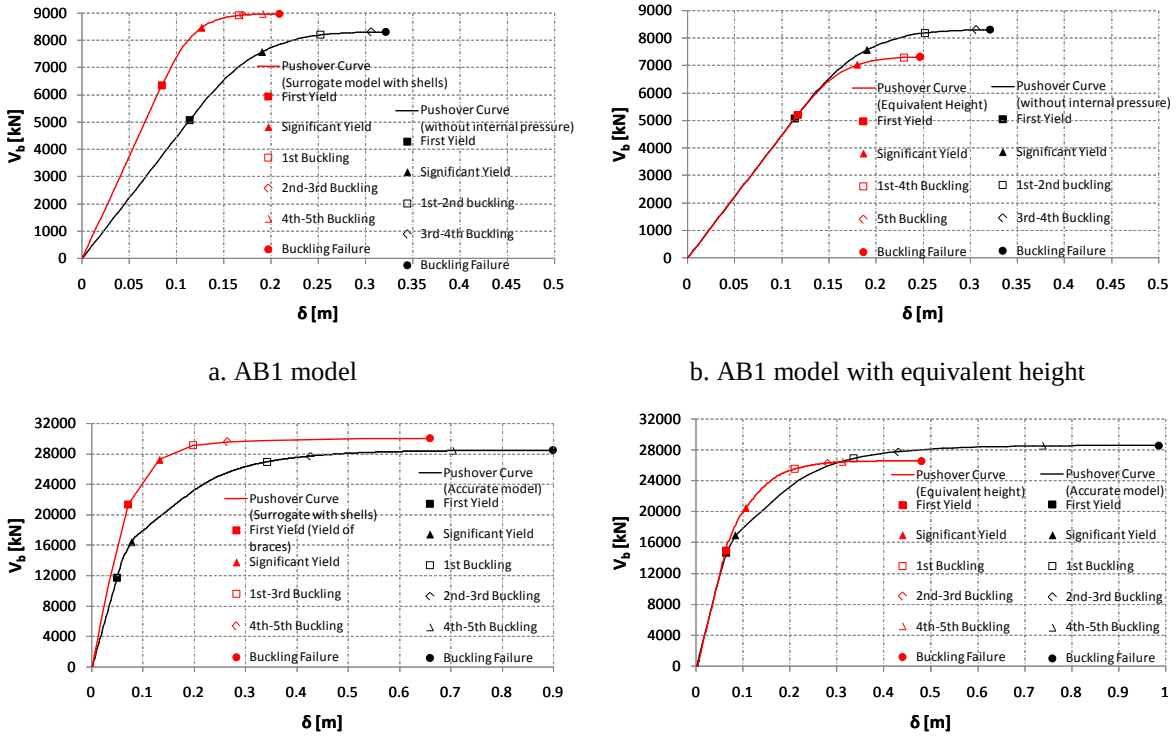
d. AB2 surrogate model with shells

Figure 8: Effect of the consideration of column heads as rotationally fixed – Translational mode shapes of : (a) AB1 and (c) AB2 refined models and (b,d) surrogates with shell-modeled columns.

MODEL	Period [sec] Refined model	Surrogate model with shells	Difference [%]
AB1	1.53	1.22	20.3
AB2	0.72	0.61	15.3

Table 5: Effect of the consideration of column heads as rotationally fixed – Translational modal periods of AB1 and AB2 refined and surrogate with shells models.

From Table 5 it is observed that the eigenperiod of the translational mode in PV1 is significantly increased by 20.3% when the column heads are considered as rotationally fixed, since columns in the surrogate model are stiffer than those in the refined one, resulting to a 68.6% increase of the horizontal elastic stiffness (see Table 6). In case of PV2, the contribution of columns in the horizontal stiffness of the pressure vessel is smaller, due to the presence of braces, and the corresponding increases are somewhat smaller (15.3% for the eigenperiod and 43.8% for the horizontal elastic stiffness - see Table 7).



a. AB1 model

b. AB1 model with equivalent height

c. AB2 model

d. AB2 model with equivalent height

Figure 9: Effect of the consideration of column heads as rotationally fixed – Pushover curves of AB1 and AB2 refined and surrogate with shells models.

From Fig. 9 (a and c) and Table 6 it is firstly observed that in both cases surrogate models are stiffer than the refined ones when column heads are considered as rotationally fixed, not only in the elastic range, as previously mentioned, but in the whole range of the response. More specifically, the ultimate displacements are smaller by 34.9% for AB1 and 33.0% for AB2, while the strength is larger, varying from a 25.0% increase at the yield point to 8.0% at the ultimate point for AB1 and from a 45.3% increase at the yield point to 5.0% at the ultimate point for AB2.

Height of columns	Quantity	Refined model	Surrogate model with shells	Difference [%]
Real	Yield displacement [m]	0.114	0.084	-26.3
	Ultimate displacement [m]	0.321	0.209	-34.9
	Yield force [kN]	5079	6348	25.0
	Ultimate force [kN]	8310	8971	8.0
	Elastic stiffness [kN/m]	44660	75300	68.6
Equivalent	Yield displacement [m]	0.114	0.117	2.6
	Ultimate displacement [m]	0.321	0.247	-23.1
	Yield force [kN]	5079	5213	2.6
	Ultimate force [kN]	8310	7321	-11.9
	Elastic stiffness [kN/m]	44660	44660	0.0

Table 6: Effect of the consideration of column heads as rotationally fixed – Values at characteristic points of pushover curves for models of AB1.

Height of columns	Quantity	Refined model	Surrogate model with shells	Difference [%]
Real	Yield displacement [m]	0.064	0.072	12.5
	Ultimate displacement [m]	0.985	0.660	-33.0
	Yield force [kN]	14703	21367	45.3
	Ultimate force [kN]	28595	30036	5.0
	Elastic stiffness [kN/m]	240000	345000	43.8
Equivalent	Yield displacement [m]	0.064	0.063	-1.6
	Ultimate displacement [m]	0.985	0.480	-51.3
	Yield force [kN]	14703	15016	2.1
	Ultimate force [kN]	28595	26603	-6.7
	Elastic stiffness [kN/m]	240000	240000	0.0

Table 7: Effect of the consideration of column heads as rotationally fixed – Values at characteristic points of pushover curves for models of AB2.

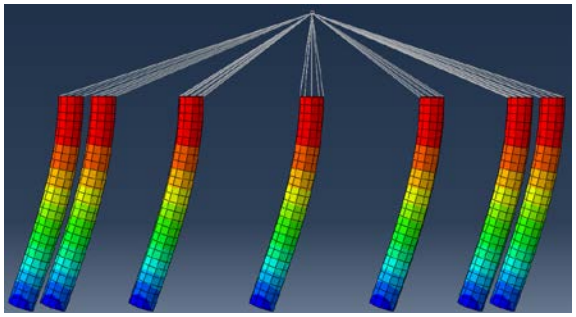
In order to make the surrogate models less stiff in order to comply with the refined ones, a common practice is to increase the height of the columns [3, 4] keeping their heads rotationally fixed. In the present study the column height is increased until the elastic stiffness of the surrogate model becomes equal to the elastic stiffness of the refined one. Following an iterative procedure it was found that for AB1 the column height has to be increased by 50% of the height of the shell-to-column connection, while in AB2 by 33% of the same height. In the two new surrogate models pushover analyses were performed and the derived pushover curves are shown in Fig. 9 (b and d), while the differences at characteristic points are given in Tables 6 and 7. It is observed that for both models the response in the elastic range is almost similar, as expected, and the differences at the yield point are negligible (about 2%). Going to the inelastic branch of the response curve it is observed that now both strength and ultimate displacements are smaller in the surrogate models the former at a acceptable percentage (11.9% for AB1 and 6.7% for AB2) and the latter with a significantly larger percentage (23.1% for AB1 and 51.3% for AB2). In addition, in the surrogate model of AB2 the stiffness after the yielding of braces is not reduced as sharply as in the corresponding refined model (after the significant yield, Figs. 9c and 8d), because the increase of the column height results to larger length of braces, thus smaller stiffness, and to larger angle with respect to the horizontal direction, hence a smaller contribution to the horizontal stiffness of the pressure vessel. In conclusion, since the use of an equivalent column height describes the elastic response sufficiently and the inelastic response on the safety side (regarding the vulnerability of the pressure vessel), it is a acceptable method to implement in order to counteract the increase in stiffness caused by the consideration of column heads as rotationally fixed.

2.3 Simplified modeling of columns

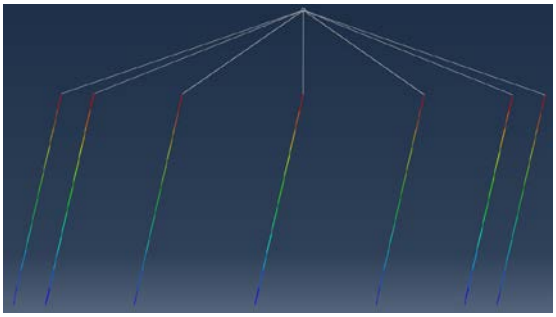
Having substituted the spherical shell with a rigid body connection between column heads, the next step is to model the columns in a simpler manner with frame elements. The major aspect that has to be dealt with is the proper modeling of the inelastic behavior. More specifically, in the refined model a distributed plasticity model is used, wherein each shell element is provided with the inelastic stress-strain relationship of steel. In case of the surrogate model the use of frame elements implies the use of a lumped plasticity model, wherein point hinges are placed at the ends of frame elements.

In each point hinge the inelastic behavior is implemented through use of a specific moment-chord rotation (M-θ) diagram. In general, such a diagram can be adopted by various

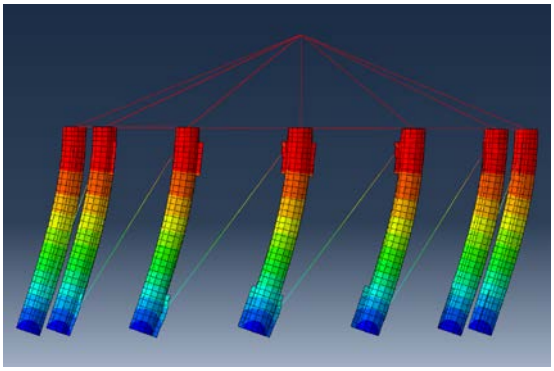
proposals found in the literature [4] but it is not ensured that it will (and most probably will not) match the inelastic behavior of the distributed plasticity model of the refined model (or the surrogate model with shell-modeled columns). Hence, in order to eliminate the differences between the two plasticity models, and consequently modeling of columns with shell and frame elements to become directly comparable, pushover analysis of each shell-modeled column with its corresponding axial force was performed and the derived pushover curve was converted to a M-θ diagram which was then used for the plastic hinge at the end of columns. In our study, since the columns of the vessels under investigation are pinned at their bases, a plastic hinge was introduced only at the top of each column. In the new surrogate model with frame elements, modal and pushover analyses were performed; the derived mode shapes are shown in Fig. 10 and the modal periods are given in Table 8. The derived pushover curves are shown in Fig. 11 and the comparison of strength and displacements at characteristic points are given in Table 9.



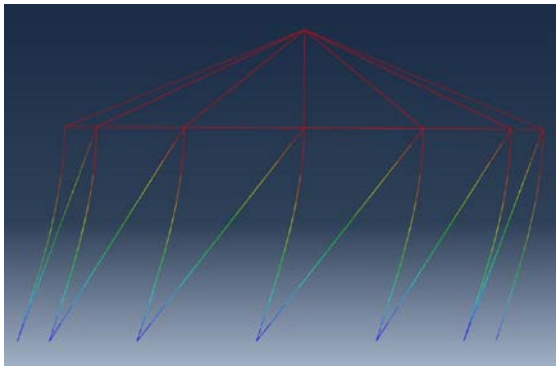
a. AB1 surrogate model with shells



b. AB1 surrogate model with frames



c. AB2 surrogate model with shells



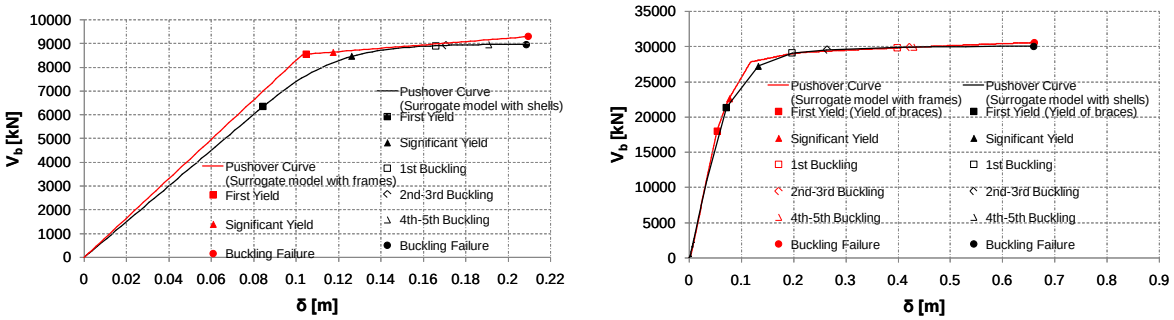
d. AB2 surrogate model with frames

Figure 10: Simplified modeling of columns – Translational mode shapes of AB1 and AB2 surrogate models with shells and frames.

MODEL	Period [sec] Surrogate model with shells	Surrogate model with frames	Difference [%]
AB1	1.220	1.250	2.5
AB2	0.606	0.614	1.3

Table 8: Simplified modeling of columns – Modal periods of AB1 and AB2 surrogate models with shells and frames.

In regard to the modal analysis results it is observed that in both AB1 and AB2 models the difference in modal periods is negligible (2.5% and 1.3%, respectively). In regard to the pushover analysis results it is observed that for model AB1 there is an acceptable difference of 10.2% in the elastic stiffness, which in case of AB2 model becomes negligible (only 1.2%) due to the presence of braces. Also negligible are the differences in the ultimate strength with (3.6% and 1.8% for each model), while there is no difference for ultimate displacements in either model. Conversely, the observed difference at the yield point is significant (varying from 15.7% to 34.9%), since the interaction between moment and axial force (M-N interaction) is not taken into account at the lumped plasticity model. However, overall the observed differences are acceptable, and it can be concluded that modeling of columns with frame elements produces similar results with shell modeling provided that appropriate measures are taken so that the corresponding distributed and lumped plasticity models are compatible.



a. AB1 model

b. AB2 model

Figure 11: Simplified modeling of columns – Pushover curves of AB1 and AB2 surrogate models with shells and frames.

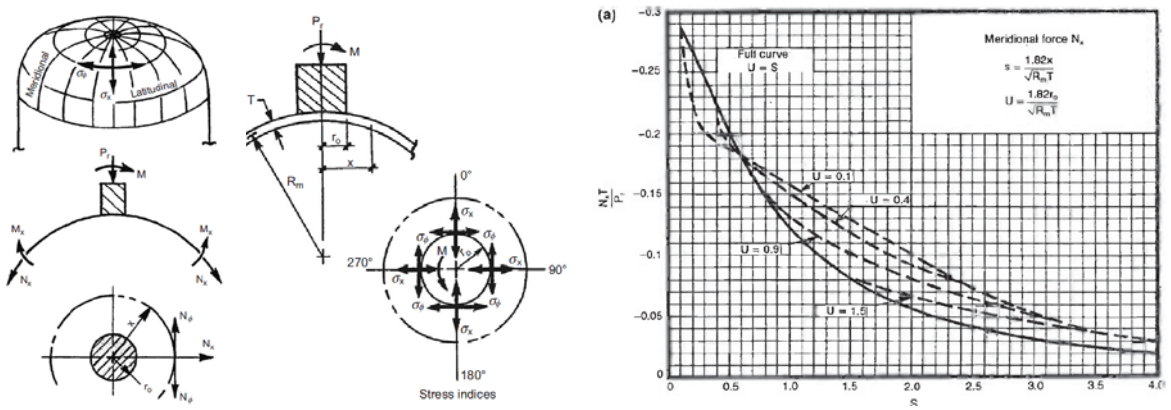
Pressure vessel	Quantity	Surrogate model with shells	Surrogate model with frames	Difference [%]
	Yield displacement [m]	0.084	0.105	25.0
	Ultimate displacement [m]	0.209	0.209	0.0
PV1	Yield force [kN]	6348	8562	34.9
	Ultimate force [kN]	8971	9298	3.6
	Elastic stiffness [kN/m]	75300	83000	10.2
	Yield displacement [m]	0.072	0.054	-25.0
	Ultimate displacement [m]	0.660	0.660	0.0
PV2	Yield force [kN]	21367	18017	15.7
	Ultimate force [kN]	30036	30575	1.8
	Elastic stiffness [kN/m]	344100	348300	1.2

Table 9: Simplified modeling of columns – Values at characteristic points of pushover curves for AB1 and AB2 surrogate models with shells and frames.

2.4 Analytical calculation of stresses at shell-to-columns connections

When a surrogate model with shell or frame-modeled columns is used, the connection between the pressure vessel and the columns is not modeled as in the case of a refined model. However, the developing stresses at the interconnection points in general have to be calculated, so as to check whether the material has reached its yield or in the worst case, its failure point.

For this reason a theoretical procedure proposed in [6] was used in order to estimate the elastic stresses developed at the shell-to-column connection (Fig. 12). It is noted that to the authors' knowledge, no analytical procedure is proposed in the literature for the calculation of stresses developed in the inelastic range of the response. According to this procedure (named as *Procedure 7-5* in [6], pp. 465-472), the elastic stresses in a spherical shell due to external loads (moment M and radial force P_r) imposed by a circular attachment with radius r_0 at a distance $x \geq r_0$ (Fig. 12a) are calculated using nomograms (Fig. 12b) derived from [7] and [8].



a. Stress and sign conventions b. Nomograms

Figure 12: Calculation of elastic stresses at the shell-to-column connection (from D.R. Moss, M. Basic, *Pressure vessel design manual, 4th Edition*).

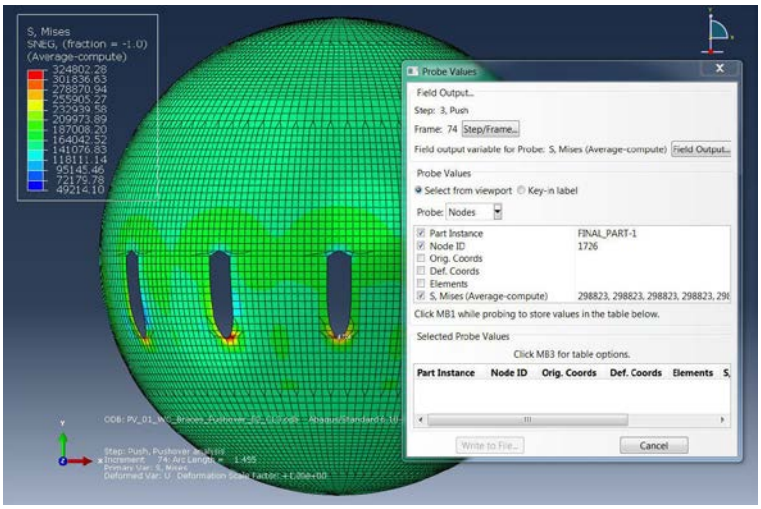


Figure 13: Von Mises stress at the shell-to-column connection of the column with the maximum compression – AB1 model.

The aforementioned procedure is applied to pressure vessel PV1 and specifically to the column with the maximum compression, since it is the critical one regarding the stresses at the shell-to-column connection at the ultimate point of the pushover curve. The derived results are then compared with those from the corresponding numerical model AB1 in Table 10, while in Fig. 13 the derived Von Mises stress at the shell at the bottom of its connection to the column with maximum compression is shown. The observed results between the theoretical procedure and those of the numerical model are negligible (0.25%), thus confirming the validity of the FE model, at least within the elastic behavior range.

Stress	Numerical Model	Theoretical	Difference [%]
Latitudinal [kPa] (Circumferential)	279267	278581	-0.25%
Meridional [kPa]	315139	315684	0.17%
Von Mises [kPa]	298823	298865	0.01%

Table 10: Analytical calculation of stresses in shell-to-column connections – Comparison of results between refined model and analytical procedure.

Given the absence of a theoretical procedure, the FE models were used to numerically predict the inelastic stresses at shell-to-column connections. More specifically, for all cases the developed stresses were checked and it was found that at the ultimate displacement point the stresses at all shell-to-column connections were below the failure point of steel. This means that in general a properly designed pressure vessel will not fail due to stress failure of the spherical shell, since the failure due to buckling of columns typically precedes it.

3 CONCLUSIONS

In the present study various approaches for the development of surrogate models for pressure vessels in order to be used in assessment procedures, such as vulnerability (fragility) assessment methodologies, were extensively investigated resulting to the following conclusions and guidelines :

- For pushover analysis purposes, modeling of braces in tension only by common frame elements is an acceptable simplification over the refined modeling, wherein all braces are taken into account, together with hook (tension-only activated) elements at one of their ends.
- The spherical shell can be substituted by a rigid body connection with the column heads in cases where its thickness is large enough for the shell to be practically undeformable.
- The height of columns should be increased in order to alleviate the increase in their stiffness due to the restriction of the rotation at their top imposed by the substitution of the spherical shell with the rigid body connection. In case of pressure vessels without braces this increase is around 50% of the height of the shell-to-column connection, while in case of pressure vessels with braces this increase is around 33% of the interconnection height.
- Modeling of columns with frame elements will produce similar results as with their modeling with shell elements only in case where the lumped plasticity model used in frames is derived using the results from a pushover analysis of the column modeled with shells.
- In properly designed vessels, the stresses developed at the shell-to-column connections are in general not expected to be the critical failure factor, since the failure due to buckling of columns typically precedes it. However, if the need arises a theoretical procedure described in [6] can be applied with an acceptable accuracy at the results, but only in the elastic range of the response. Regarding inelastic stresses there is not any procedure in the literature for their analytical calculation and resort to numerical analysis using refined FE models is necessary.

4 ACKNOWLEDGEMENTS

The present research effort (research program *"Vulnerability and Risk Assessment for the seismic protection of industrial facilities-RASOR"* 2012-2015) has been co-financed by the European Union (European Social Fund – ESF) and Greek national funds through the Operational Program "Education and Lifelong Learning" of the National Strategic Reference Framework (NSRF) - Research Funding Program: THALES. Investing in knowledge society through the European Social Fund.

REFERENCES

[1] O. Curadelli, Seismic reliability of spherical containers retrofitted by means of energy dissipation devices. *Engineering Structures*, **33**, 2662-2667, 2011.

[2] I. Moschonas, C. Karakostas, V. Lekidis, S. Papadopoulos, Investigation of seismic vulnerability of industrial pressure vessels. *2nd European Conference on Earthquake Engineering and Seismology (2nd ECEES),* Istanbul, Turkey, August 25-29, 2014.

[3] M. Wieschollek, M. Kopp, B. Hoffmeister, M. Feldmann, Seismic design of spherical liquid storage tanks. *3rd ECCOMAS Thematic Conference on Computational Methods in Structural Dynamics and Earthquake Engineering (COMPDYN 20111),* Corfu, Greece, May 26-28, 2011.

[4] M. Wieschollek, K. Diamanti, M. Pinkawa, B. Hoffmeister, M. Feldmann, Guidelines for seismic design and analysis of pressure vessels. *ASME 2013 Pressure Vessels & Piping Division Conference (PVP 2013),* Paris, France, July 14-18, 2013.

[5] F.E.M.A.-A.S.C.E., *FEMA 356 – Prestandard and commentary for the seismic rehabilitation of buildings*. Federal Emergency Management Agency, 2000.

[6] D.R. Moss, M. Basic, *Pressure vessel design manual, 4th Edition*. Elsevier, 2013.

[7] Wichman KR, Hopper AG, Mershon JL. Local Stresses in Spherical and Cylindrical Shells Due to External Loadings. *Welding Research Council Bulletin* No. 107; April 1972.

[8] BS 5500: *Specification for Unfired Fusion Welded Pressure Vessels*. British Standard Institute, 1985.

COMPDYN 2015
5th ECCOMAS Thematic Conference on
Computational Methods in Structural Dynamics and Earthquake Engineering
M. Papadrakakis, V. Papadopoulos, V. Plevris (eds.)
Crete Island, Greece, 25–27 May 2015

SEISMIC PERFORMANCE ASSESSMENT OF OIL & GAS PIPING SYSTEMS THROUGH NONLINEAR ANALYSIS

Oreste S. Bursi[1] , **Fabrizio Paolacci**[2], **Md Shahin Reza**[1]

[1]University of Trento
Department of Civil, Environmental and Mechanical Engineering
Via Mesiano 77, 38123, Trento, Italy
oreste.bursi@unitn.it, md.shahin.reza@unitn.it

[2]Roma Tre University, Department of Engineering
Via Vito Volterra 62, Rome, Italy
fabrizio.paolacci@uniroma3.it

Keywords: Piping Systems, Oil & Gas Piping, Seismic Analysis, Non-linear Analysis

Abstract. *Piping systems, a vital part of energy industries, e.g. petrochemical, oil & gas and chemical plants, have been found particularly vulnerable under earthquake loading, as reported in recent publications. During past earthquakes, piping systems and their components suffered significant damages causing severe consequences. Thus, seismic assessment/evaluation of these structures has become an imperative for their proper design to safeguard them against seismic events. Nevertheless, there exists an inadequacy of proper seismic analysis and design rules for petrochemical piping systems, and designers have to follow seismic standards conceived for other structures such as buildings and nuclear plants. Moreover, the modern performance-based design approach is still not widely adopted for piping systems, where the allowable design method is the customary practice. Along these lines, this paper presents a performance-based seismic analysis of petrochemical plants through two case studies. Initially, main issues on seismic analysis and design of industrial piping systems and components are addressed followed by a discussion on the selection of proper seismic inputs. The current allowable stress and strain based seismic verification methods are presented afterward. Then, nonlinear finite element analyses of two typical petrochemical piping systems under modern design earthquake levels are presented. Finally, performance of these piping systems is commented by comparing the maximum stress and strain levels -found from the analyses- with the allowable design values that exhibited a favourable behaviour of the analysed systems under earthquake limit state levels.*

1. INTRODUCTION

Piping systems play a critical role in meeting the increasing global energy demand. Currently, there exists about 3.5 million kilometers of transmission pipelines, while about 231900 km of oil and gas pipelines are under construction or planned (www.dnv.com); a great portion of which is located in high seismic-prone areas. A piping system consists several components and support structures, e.g. flange joints, tee joints, elbows, valves, pressure vessels and storage tanks, where failures in a single component may hinder the whole transmission process and cause catastrophic consequences. Hence, such systems deserve particular attention to safeguard them against any accidental event such as earthquakes. Nevertheless, piping systems and their components have been found particularly vulnerable under seismic events and suffered severe damages during past earthquakes causing serious accidents both to human lives and to the environment [1, 2, 3, 4].

Current seismic design approach to petrochemical piping systems are mainly based on the allowable design method; the most modern Performance-Based design approach is not strongly implemented yet. One of the main reasons of this is the scarcity of information about the definitions of limit states for pipes and the structural modelling, which have not yet been treated in a satisfactorily manner. Moreover, most seismic codes and standards don't contain enough rules and details for the proper design of industrial piping systems in seismic-prone areas. For example, [5], the Structural Eurocodes that introduce novel seismic design concepts for industrial structures, lacks adequacy for seismic design of pipelines [6]. Also, seismic problem is only partially treated in EN 13480-3 (2002) [7], the main European contribution for piping system design. EN 13480-3, like American codes ASME B31.1 (2001) [8] and ASME B31.3 (2006) [9], prescribes an allowable stress verification method under a design/operating basis (OBE) and a safe shutdown (SSE) earthquake, the latter being addressed only in EN 13480-3. However, no indications on the selection of earthquakes and analysis methods are provided in these standards, instead they refer to general seismic standards conceived for buildings, e.g. [10, 11], or for nuclear plants, e.g. [12]. Some standards have recently been developed in the US that specifically addresses natural gas plants, e.g. [13]; but, in general, there exists a clear scarcity of adequate seismic design rules for petrochemical/Oil & Gas piping systems.

To this end, this paper presents a performance-based seismic analysis of petrochemical piping systems through two realistic case studies. In a greater detail, several aspects of seismic analysis and design of piping systems, such as proper modelling of support structures, straight pipes, elbows etc., dynamic interaction analysis, selection of seismic inputs and analysis methods, have been discussed. Current allowable stress and strain based verification methods for piping systems are presented, which are followed by non-linear analyses of two case studies that investigate two realistic petrochemical piping systems under several limit states. Finally, performance of the piping systems is commented by comparing stress and strain values found from these analyses with allowable stress and strain limits suggested by relevant codes and standards.

2. SEISMIC DESIGN ISSUES OF PIPING SYSTEMS

The seismic design of a piping system entails a number of issues. They are essentially related to overall structure modelling, to a correct definition of the seismic action, to a proper analysis method to be applied, and finally, to an appropriate design method to be used. In the following, relevant aspects are analysed under the light of the current standards recalled above and, in particular, of the European (EN13480-3) and the American (ASME 31.3) standards.

2.1 Definition of numerical models of piping systems

A synthetic scheme of what European and American Standards prescribe for a correct numerical modelling of a piping system and the definition of the seismic conditions is reported in [6]. In that occasion it was clearly shown that the suggested numerical model to use in seismic analysis is always elastic both for EN13480 and ASME B31.3. This choice comes certainly from the old way to evaluate the safety level of a structure: the allowable stress method still diffused in designing of piping systems. Usually, only the piping system is modelled, using the supporting structure only to evaluate the seismic action at pipes level (e.g., in-structure spectra). The supporting structure (e.g. pipe-tack) is treated as elastic too. The assumption of elastic behaviour would not be a strong limitation if a correct value of the behaviour factor were adopted.

A key point in modelling a piping system is the possibility to neglect the interaction (static and dynamic) between the pipes and the supporting structure. EN13480 does not provide any indication about it, whereas ASME B31.3, by means of ASCE-07, prescribes a crude rule based on the ratio, W, between the weights of pipes and supporting structure. In particular, if W< 25% the interaction can be excluded and the piping system can be considered as a non-building structure, loaded by a seismic action coming from the supporting structure at pipes level.

This rule has been recently analysed by several authors. For example, in [14] the rule has been analysed using time-history analysis. From the results and discussion, the author concluded that in some cases this decoupling rule could produce gross errors in the evaluation of the dynamic behaviour of piping systems. In particular, it seems that in dynamic assessment of such systems, in addition to the primary-secondary system weight ratio criteria, attention should be paid to other aspects as “end conditions of pipes”, “relative stiffness of supporting structure to piping system” and “relative stiffness of pipes to pipe-supports”, even though only partial conclusions where reached by the authors, that suggested more investigations on this matter.

Another relevant aspect about modelling of piping systems is the adoption of a proper model for pipes and fittings (elbows, tee-joints, nozzles, etc.). At this regards, usually beam elements with hollow section are used for straight pipes. The fittings are also modelled using beam elements, but modifying the stiffness for the effect of geometry. For this purpose, both European and American Codes define a flexibility factor (k >1) using which the moment of inertia of the pipe is reduced. In addition, to take into account the stress concentration effect, the Stress Intensification Factor (SIF) is used to increase the stress calculated using the beam theory. The values of k and SIF calculated according to EN13480 and ASME B31.3 are very similar. Alternatively, it is possible to use shell elements to model fittings [15]. This approach is appropriate to account for ovalization of the section and stiffening pressure effect also in non-linear field [16]. For these reasons, this model has been used for the Case Study and a comparison with beam model has been carried out. We can anticipate that the numerical simulations have shown a similar behaviour of both the models and the reliability of modified beam element, at least for standard fittings, like pipe elbows.

A last but not less important aspect regards the boundary conditions of the pipes. In fact, because a piping system is realized by hundreds of miles of pipes, the analysis involves necessarily a limited part of the structure. Consequently, proper boundary conditions have to be accurately adopted to simulate the remaining part of the structure. Also, for this delicate aspect no indications are provided by European and American Standards. As already shown in literature, uncertain boundary conditions may significantly influence the dynamics of the piping system; however, their proper modelling vary from case to case [14, 17].

2.2 Seismic actions and analysis methods

Both European and American Standards assume the following two types of analysis for pipes:

- Movements due to inertia effects.
- Differential movements of the supports (within the supporting structure or between adjacent pipe-racks).

The first type of analysis is essentially related to the effects of the absolute acceleration on the pipe mass. The second one is due to the relative movements between two supports, within the supporting structure or belonging to adjacent structures. Often the relevant effects are due to the displacement effect rather than acceleration effects.

Concerning the inertia effects the seismic action for pipe-racks is usually represented by design response spectra or accelerograms (natural records or synthetic accelerograms). For the analysis of pipes only, "In-structure" spectra or "filtered response spectra" are instead used. The design spectra are the main representation of a seismic action and usually are defined by the seismic codes in terms of hazard conditions of the site, the level of dissipation capability of the supporting structure and pipes (response or behaviour factor), the right level of damping to be employed, and the level of structure reliability to impose, identified by the importance factor. For the support structure, hazard conditions apart, the damping usually adopted is equal to 5%, as suggested by Eurocode 8 and 3 for steel structures, whereas the behaviour factor, q, depends on the type of structure used for the pipe-rack. While for building-type structure this aspect has been well identified and quantified, for structures like pipe racks that may often be considered as non-building structures [10], the problem may be quite different.

The current American and European seismic codes provide a q factor for steel racks equal to 3 ½ and 4 respectively. This choice probably derives from the hypothesis of no-coupling between the rack (primary system) and the pipes (secondary system). In fact, usually the level of dynamic coupling between pipes and rack can be neglected. But in other some cases its influence cannot be excluded a priori [14]. The spectral responses of the modal oscillators are then combined to obtain the resultant response of the system. Moreover, the resultant forces and displacements from bi-directional analysis are typically obtained by the square root sum of square of the response in each direction, or by applying the well-known 100-30 rule.

The in-structure spectra allow a seismic action to be defined for single pipes at several floors of the pipe-rack, in which the pipe is placed. Both European and American Codes provide their explicit expressions. They are defined as the spectrum acceleration multiplied by an amplification factor AF defined by codes. The behavior factor provided by the Codes, especially by the American one, seems to be overestimated. For example, ASCE-07 prescribes the use of a behavior factor 6 or 12 according to the deformability of the material used. In some cases this hypothesis may not be totally true [18].

A time history seismic input is rarely used for the design or retrofit of piping systems. Often it is used to generate facility specific response spectra analyses, or as a research tool, to study in detail the full non-linear behavior of a component or system as a function of time. Nowadays, the scientific community has widely accepted the use of natural records to reproduce a real input, for several reasons. For many engineering applications, the purpose of selection and scaling of real earthquake is to fit the Code design spectrum considering the seismological and geological parameters of the specific site. To help engineers in selecting a proper set of records, some tools have already been proposed in the literature.

Seismic anchor motion (or "SAM") is the differential motion between pipe support attachment points (for example, supports attached to an upper floor would sway with the build-

ing, with a larger amplitude than supports attached at a lower elevation), or the differential motion between equipment nozzles and pipe supports. Seismic anchor movements are input as displacements (translations and rotations) at the support attachments or at equipment nozzles. The resulting stresses and loads in the piping system can be properly combined to obtain stress and loads in the pipes.

No specific indications are provided by EN13480:3, whereas, ASCE-07 provides a simplified criterion based on the elastic analysis of the pipe-rack. Here, it is suggested to evaluate first the relative displacements between two connection points within the structure and at the same level for each vibration modes and then to combine them using a proper combination rule as the SRSS rule.

2.3 Verıfıcatıon methods

One of the fundamental steps for the qualification of a pipe system is the fulfillment of some limits of the pipe stress or strain, for a given working condition. For a seismic action, usually two working conditions, namely an Operating Basis Earthquake (OBE) and a Safe Shutdown Earthquake (SSE) as will be discussed later, are used.

Both European and American standards, e.g., EN 13480-3, ASME B31.1, ASME B31.3, provide guidelines for allowable stress based verifications of pipes subject to earthquakes. For instance, ASME B31.1 and EN 13480-3 provide a similar formula expressed as,

$$\sigma = p_c\, d_o / (4e_n) + 0.75i\, M_A/Z + 0.75i\, M_B/Z \leq kf_h \tag{1}$$

where 0.75i is the stress intensity factor whose value is 1 for straight pipes; M_A is the moment from sustained mechanical loads; M_B defines the moment from occasional loads; Z is the modulus of inertia; p_c defines the internal pressure; d_o represents the pipe outer diameter; e_n is equal to the pipe wall thickness and f_h represents the allowable stress as defined in these Codes. For an Operating Basis Earthquake ground motion (OBE), the value of k is given as 1.2 and 1.33 in EN 13480-3 and ASME 31.3, respectively; conversely, the Safe Shutdown Earthquake ground motion (SSE) entails values of k equal to 1.8 for EN 13480-3; no value is foreseen for ASME 31.3. Corresponding moments are indicated as $M_{a,OBE}$ and $M_{a,SSE}$, respectively.

A strain based verification method is also provided in the newly developed strain-based design equation [19] that entails an ultimate design load for a pipe based on the maximum strain, i.e.,

$$\varepsilon_c^{crit} = 0.5t/D - 0.0025 + 3000\,((P_i - P_e)D / (2tE_s))^2 \tag{2}$$

where ε_c^{crit} defines the ultimate compressive strain capacity of a pipe wall; P_i is equal to the internal pressure; P_e defines the external pressure; t is equals to the pipe wall thickness; D is the pipe outer diameter; E_s is the modulus of elasticity of pipe material.

Moreover, several standards provide tensile strain limits in pipes [20] as reported in Table 1.

Table 1. Tensile strain limits in pipelines

Code	Tensile strain limit
CSA-Z662 (2007)	2.5%
DNV-OS-F101 (2000) [31]	2.0%
ASCE (2005) [32]	2.0%

3. APPLICATIONS RELEVANT TO TYPICAL PETROCHEMICAL PIPING SYSTEMS

3.1 Selection of seismic loading

The definition of the levels of earthquake motions to be considered for analysis requires extra attention and assumptions. In fact, several standards dealing with seismic analysis of onshore petrochemical and process plants, e.g., EN 13480-3, ASME B31.1, ASME B31.3 and NFPA 59A, among others, in view of enhanced performance and damage limitation, use the same seismic hazard definitions adopted by nuclear standards [12]. Nonetheless, intended safety objectives are different: in fact, (i) conventional facilities are designed for human lives protection and damage limitation, see for instance Eurocode 8, Part 1 [11], and therefore, crossing to elastoplastic domain is allowed; conversely, (ii) nuclear seismic rules enforce integrity and functionality of structures systems and components important to safety; as a result, incursions in the elastic plastic domain is not allowed. Thus in moderate seismicity regions, one can establish a correspondence between the 10% probability of exceedance in 50 years, i.e. 475 years return period used in Eurocode 8 Part 1 and the OBE ground motion defined in nuclear standards. For clarity, the OBE can be defined as the ground motion for which those features of the –nuclear power- plant necessary for continued operation without undue risk to the health and safety of the public will remain fully functional. Increased return periods can be achieved through additional peak ground acceleration (pga) multipliers; for instance, the importance factor γ_I can reach a value of 1.4 for power plants of vital importance [11].

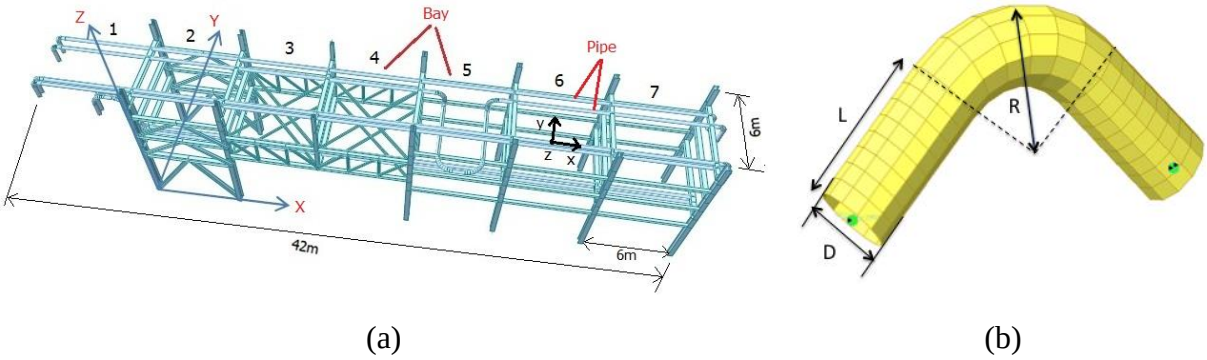
The link of the return periods corresponding to the SSE (pga) is more involved; in fact in NFPA 59A (2013) the SSE pga at the site can be defined as the "risk-adjusted maximum considered earthquake (MCER) ground motion" per the definition in [10]. For most locations except near active faults, ASCE 7 adjustment establishes a uniform probability of failure criteria for a 1% probability of exceedance within a 50 year period corresponding to 4975 year return period. However, ASCE 7 requires the base design level earthquake to be 2/3 of MCER; thus, setting γ_I = 1.5 for structures containing extra hazardous materials results in a design level equal to MCER. Also in France the return period for new "special risk" plants corresponds to 5000 years [21]; whilst the corresponding value defined in nuclear seismic standards is based on 0.5% to 0.05% probability of exceedance in 50 years, e.g. 10000 to 100000 years return period. We recall that the SSE is the ground motion in which certain structures, systems and components important for - nuclear- safety must be designed to remain operational.

For each of the two case studies presented and analysed in the following, the seismic input is represented by the elastic spectrum provided by the current seismic European and Italian codes, based on which a set of natural records have been selected and used to perform linear non-linear analysis.

3.2 Case Study #1

The first Case Study (CS) is relevant to a typical petrochemical piping system as illustrated in Fig. 1(a); details of the CS can be found in [6]. The support steel structure was composed of seven transverse moment resisting frames placed every 6 m, made of commercial steel profiles. The piping system presented a typical layout with pipes having different diameters. In order to simplify the analysis, only the structural contribution of 8" pipes was considered; the remaining pipes acted only as weight. Several flanged elbows were present within the pipe-rack and at both ends of the piping system. Columns and beams of the support structure were modelled by using inelastic fibre-discretized beam elements, whereas straight truss elements

were used both for vertical and horizontal bracings. The straight braches of pipes were modelled by linear beam elements whilst shell elements were used to better capture the behaviour of elbows as depicted in Fig. 1(b). In order to better simulate the boundary conditions/flexibility of elbows, that is the connection between the straight portions of pipe and elbows, a portion of the connected straight pipes of length (L) was modelled using shell elements as well. In this specific case, we assumed L=1100 mm, R=8'' and R/D=1.5.



(a) (b)

Figure 1. (a) The piping system considered in the Case Study; (b) shell element assemblage used for each pipe elbow.

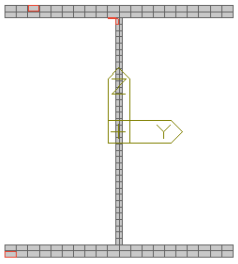


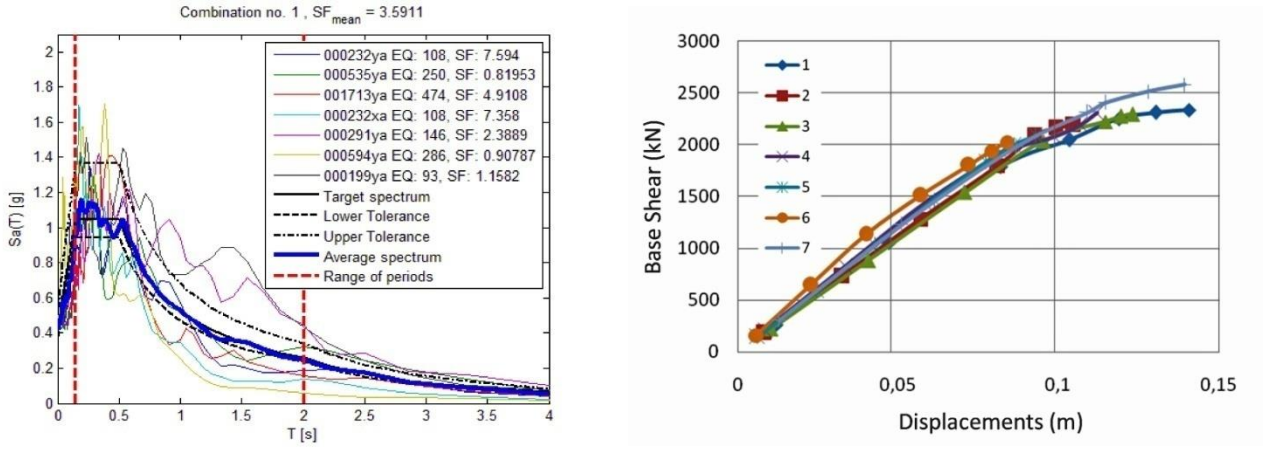
Figure 2. Fiber discretization of an element section of the support frame

Given the fact that this Case Study (CS) is not part of a hazardous facility and is located in a site characterized by a PGA=0.24g, the OBE ground motion was firstly considered, associated with a 5% damped response spectrum foreseen in EN 1998-1, with 475 years return period. The far field spectrum associated with Soil B for the CS is illustrated in Fig. 2(a). Because of unintended consequences of the plant associated with possible failure, a value of γ_I=1.2 foreseen for the plant was assumed [11]. The elastic spectrum was employed to select a set of compatible accelerograms; in greater detail, they have been extracted from the European strong motion database (ESD, http://www.isesd.hi.is/ESD_Local/frameset.htm) according to a Magnitude range 6-7, a distance from the epicentre less than 30 km, and a pga in the range 0.25-0.35 g. The natural accelerograms selected using the REXEL software [22] were characterized by the mean spectrum -bold blue line- shown in Fig. 2(a). The accelerograms were scaled to ensure full compatibility with the target elastic spectrum of Eurocode 8 Part 1, being endowed with a mean spectrum within the lower (-10%) and upper bound (+30%) spectra (line-dot graphs) with respect to the target spectrum.

The selected accelerograms have been used to perform a series of non-linear analyses on the CS evaluating the response both at pipes and support structure. The dynamic characterization of the system provided vibration periods of the support structure equal to T_x=0.35 sec and

T_y=0.46 sec in longitudinal and transversal directions, respectively, which correspond to an excited mass of 53% and 68%. The period of the first modes with and without pipes was similar, whereas the excited mass was higher in the second case, showing some coupling effect of the transverse frames along the Y-axis owing to pipes.

The obtained level of non-linear behaviour of the analysed system was limited and mainly concentrated in the support structure. This is clearly shown in Fig. 2(b) where the results of an incremental dynamic analysis [23] applied to the piping system are shown in terms of dynamic pushover curves, plotted for each accelerogram. Each dot corresponds to the maximum base-shear calculated for a given value of pga and the corresponding displacement measured at the pipe level. The limited plastic deformations level exhibited by the steel structure suggest an actual value of behaviour factor q – equivalent to the response modification factor R_p of ASCE 7- of about 1.8.



(a) (b)

Figure 2. (a) Elastic spectra of the set of seven chosen accelerograms; (b) Dynamic pushover curve of the piping system.

This value underlines that the use of q factors for support structures from [11] must be done with care. In fact, the value of q=4 suggested in that Standard is unsafe for this particular CS, because the layer of present pipes cannot ensure a rigid floor behaviour in the Y direction, see Fig. 1(a), typical of buildings. On the other hand also [13] allows a maximum R_p value of 6 for Seismic Categories II and III. Only for Seismic Category I, the use of R_p is not allowed.

Results of the analysis in terms of moments along local axes y, M_y and z, M_z (see Fig. 1(a)) of the pipe are reported in Table 2. The resultant moments M_R of the single moments M_y and M_z calculated according to the [7] are reported too. ASME B31.3 does not provide a definition of M_R whereas the definition contained in the ASME B31.1, the standard for power piping, is the same. For this reason the same definition has been adopted for the American standard for process piping. The maximum moment was found near the left edge of the rack (bay 2); similar values were also obtained within bay 6 and 7. The average values of the maximum moment was found to be 16.79 kNm; the maximum axial force corresponding to the maximum tensile stress, i.e., 86.41 MPa, was about 180.50 kN.

Table 2. Maximum bending moment and tensile stress in the pipes of the Case Study (OBE)

Moment	Bay						
	1	2	3	4	5	6	7
M_y (kNm)	1.56	6.91	5.98	4.94	5.04	3.47	2.50
M_z(kNm)	13.72	15.30	14.15	7.01	8.75	15.84	15.84
M_R (kNm)	13.81	**16.79**	15.36	8.58	10.10	16.22	16.04
Tensile stress (MPa)	76.71	**86.41**	81.76	59.67	64.62	84.54	83.96

These values were far from the leakage and yield loads of pipe itself and bolted flange joints typically used in piping systems, as already evidenced in [24, 25]. It is, therefore, evident that piping systems like the analysed one possess a good capacity to operate safely under a typical OBE ground motion. The level of stress is well under the elastic limit of the material, i.e. 241 MPa, and allowable stresses at OBE, i.e. 165.60 MPa and 183.50 MPa according to EN13480-3 and ASME B31.3, respectively (see [6]). Moreover, the maximum strain, i.e. about 0.04%, in the pipes was much lower than the allowable limits suggested by standards; see Table 1 in this respect.

In order to evaluate the seismic behaviour of the structure also in beyond-design conditions the response at SSE level has been evaluated. As stated before, SSE can be identified with the Near Collapse condition that corresponds to a return period T_L=2475 years [11] and thus to a importance factor γ_L=2.2 that is a peak ground acceleration a_g= 0.55g. All records of Fig.2 have been scaled accordingly, and used for another set of non-linear analyses. The average values of bending moment and stress in the pipes at several bays are reported in Table 3.

Table 3. Maximum bending moment and tensile stress in the pipes of the Case Study (SSE)

Moment	Bay						
	1	2	3	4	5	6	7
M_y (kNm)	1,78	5,28	6,94	5,67	5,62	3,36	2,39
M_z(kNm)	23,09	26,11	22,18	10,07	10,01	16,94	16,9
M_R (kNm)	23,16	**26,64**	23,24	11,56	11,48	17,27	17,07
Tensile stress (MPa)	132,44	**147,57**	132,80	82,00	81,66	106,84	105,96

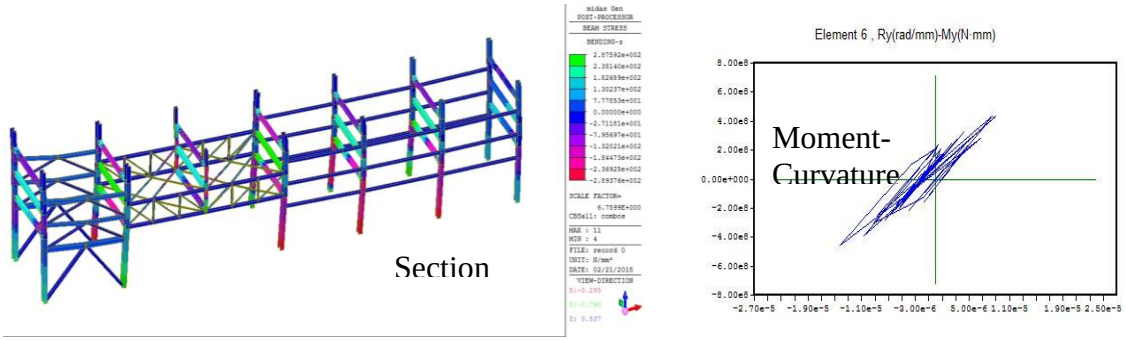


Figure 3. SSE: (a) Stress in the support structure, b) Moment-Curvature - Section A (Acc. 1)

The maximum moment was found to be 26.64 kNm that correspond to a maximum stress equal to 147.57 MPa. The maximum stress in the support structure is located in the col-

umns, whose value is about 280 MPa, slightly greater than the yielding strength, symptom of a slight plasticity in the elements (Fig. 3).

In conclusion, even in presence of a stronger seismic action, the stress level in the pipe at SSE is still confined in the elastic range, as already shown applying the pushover analysis (Fig. 2b). This demonstrates once again the strong conservatisms generally adopted in designing this kind of structures and fully justify the typical usage of linear models for their seismic analysis.

3.3 Case Study #2

The piping system considered within Case Study #2 is a typical petrochemical piping system placed on a steel support structure as illustrated in Fig. 3(a) and 3(c). General dimensions and other geometrical properties of the piping system –presented in Fig. 3(b)- were taken from [15]. The piping system contained 8" and 6" scheduled 40 straight pipes, several elbows, a Tee joint and an EN 1092-1 Standard PN 40 weld-neck bolted flange joint. The pipes were made of API 5L Gr. X52 steel (nominal yield and ultimate strengths: 418 MPa and 554 MPa, respectively) and were filled with water at an internal pressure of 3.2 MPa, corresponding to 80% of the maximum allowable pressure of the piping network.

The support structure was a steel frame structure, 12m high, mainly composed by steel HE and IPE profiles and some vertical and horizontal cross or K-steel bracings. Only a single pipeline ran on the frame supported by sub-frames placed at 3rd floor of the main frame. Two edges of the frame were connected to cylindrical storage tanks whereas the third one was connected to the frame by an anchor. Some design parameters considered for the structure are presented in Table 3.

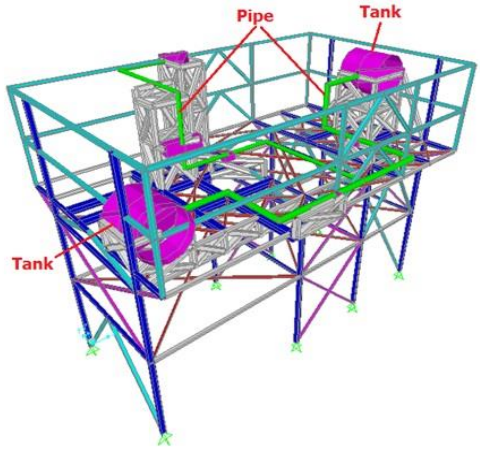


Figure 3(a). A 3D FE model of the support structure of the piping system.

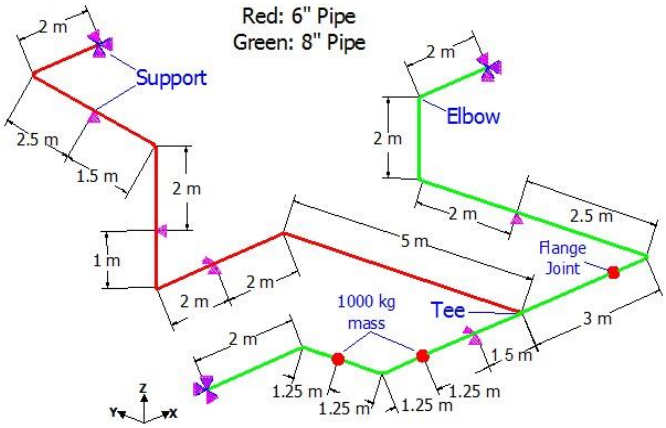


Figure 3(b). Specifications and dimensions of the piping system.

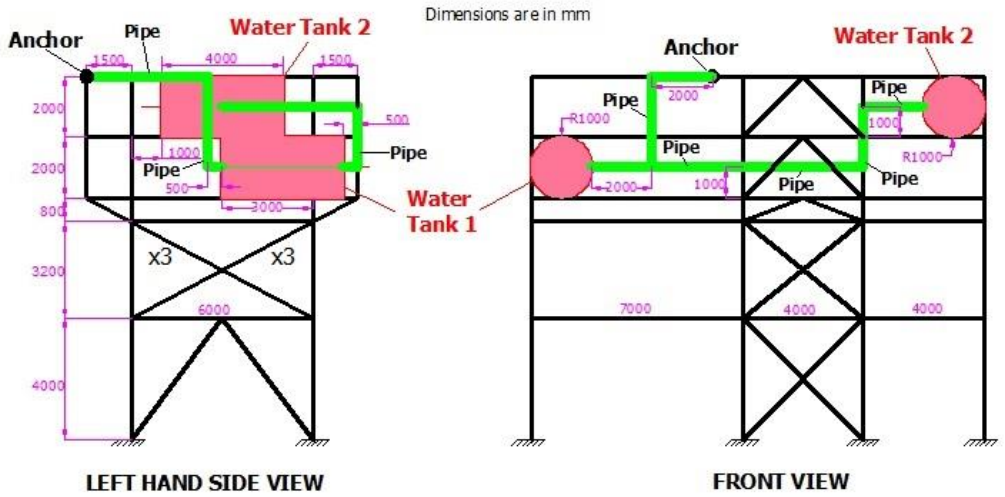


Figure 3(c). Dimensions and lateral views of the support structure.

In order to perform non-linear seismic analysis, a 3D Finite Element (FE) model of the piping system was developed in [26] software. The pipes including elbows were modelled using straight elements with pipe sections. Mass of the water present inside pipes was considered by increasing the mass density of the pipe material. Although elbows were modelled using straight elements in the FE model, flexibilities (see [7]) of these elements were adjusted based on an ABAQUS-based [27] FE analysis. Each elbow had a radius equal to 1.5 times the outer diameter of the connecting pipe; moreover, we considered that the effect of flexibility of an elbow spreads across a distance, L equal to two times the mean diameter of the pipe as illustrated in Fig. 4. The adjusted geometry and properties of elbow elements including the dimensionless flexibility factor, k_B, considered in the piping system model are reported in Table 4.

Table 3. Some design parameters of the support structure.

Location	High Seismic-prone region
pga	0.33g
q factor	3.2
Ground type	C
Return Period	712 years
Importance Class	III*

*Industries with dangerous activities; Reference life, Vr = 75 years

As discussed before, these types of structures with piping systems are normally modelled elastically. However, in order to exploit ductility of the support structure, some nonlinearity was introduced in the model, but only in some brace members. In a greater detail, plastification was allowed only in the some vertical cross and k-bracings of the structure by introducing nonlinearities to those members based on the US standard [28]; see Fig. 5 in this respect which shows the nonlinear model adopted for the vertical cross bracing x3 as shown in Fig. 3(c).

Table 4. Elbow properties considered in the piping system model

Property	8" Elbow		6" Elbow	
	Original	Modified	Original	Modified
Thickness, e_n (mm)	8.18	6.61	7.11	4.35
Flexibility factor, k_B	6.84	1.35	5.97	2.46
Moment of inertia, J^* (mm^4)	3.02 x 10^7	2.49 x 10^7	1.17 x 10^7	7.53 x 10^6

The support structure was placed in Sicily, a high seismic region in the south of Italy. As can be noted from Table 3, soil type C and an important class III was considered for the support structure. Thus, the support structure was designed for an earthquake with a return period T_R equal to 712 years corresponding to the Safe Life Limit State (SLLS) suggested in the Italian standard [29] which, differently from EN 1998-1, prescribes four limit states, as listed in Table 5, in the spirit of performance-based earthquake engineering. Corresponding pga values are also reported in Table 5.

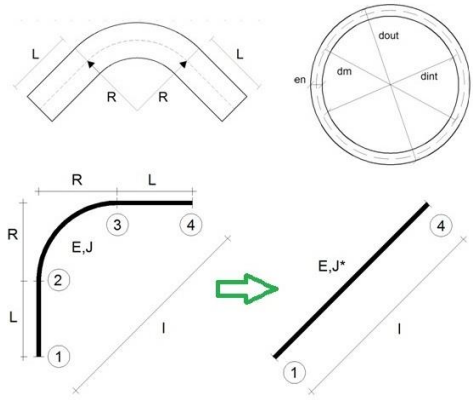


Figure 4. Elbow geometry and equivalent straight elbow element

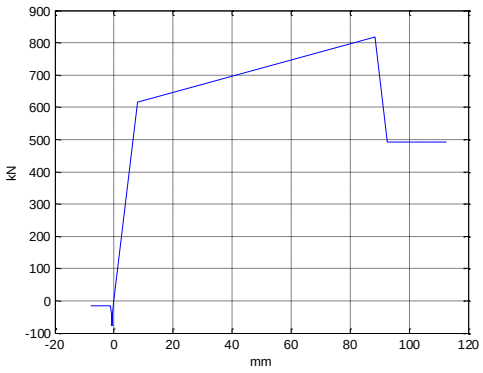


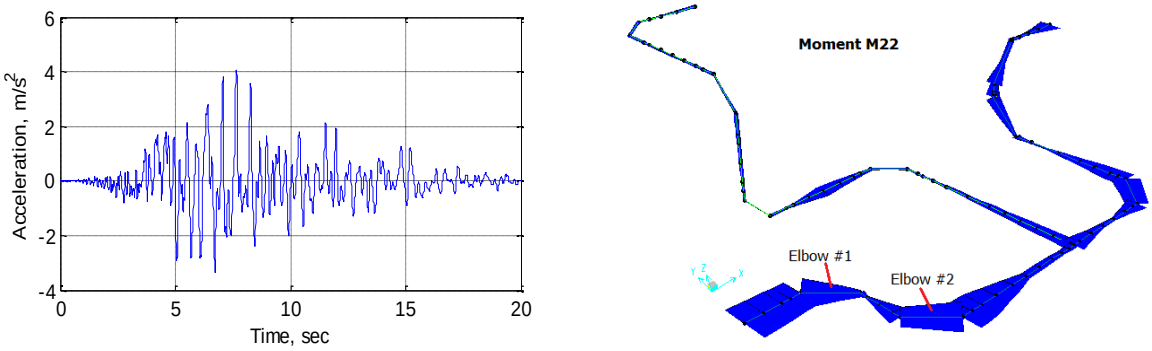
Figure 5. Nonlinear model for cross bracing x3.

Since the piping system considered herein represents a moderately hazardous facility, the SLLS was considered equivalent to the OBE earthquake. However, as discussed above the SSE ground motion would be too severe. Nonetheless and in order to consider a ground motion beyond the OBE, the one associated with the CLS earthquake reported in Table 5 - corresponding to a T_R equal to 1462 years- was considered. Along this line, the input earthquake for the analysis was generated using the Italian spectrum specific of the place where the structure was placed; see in this respect Fig. 6(a) that shows the input accelerogram corresponding to the CLS.

Table 5. pga values corresponding to different limit states

Limit States			pga (g)
Serviceability limit state	Operational limit state	OLS	0.05
	Damage limit state	DLS	0.08
Ultimate limit state	Safe life limit state	SLLS	0.29
	Collapse limit state	CLS	0.41

The piping system was analysed with the four levels of earthquakes listed in Table 5. Seismic loadings were applied in the horizontal x direction (see Fig. 3(b)) adopting a Rayleigh damping considering a 4% damping for the structure suggested in [30]. The maximum stresses and strains in pipes at SLLS and CLS were then compared to the $M_{a,OBE}$ and $M_{a,SSE}$, respectively. Analysis were also carried out at OLS and DLS level earthquakes to check the performance of piping systems at those levels.



(a) (b)

Figure 6. (a) Input earthquake accelerogram and (b) Moment about z axis in the piping system at CLS.

Moments about z axis, M_z in the piping system at CLS is presented in Fig. 6(b); the maximum moment was observed in Elbow #1. Stresses and strains were then compared with corresponding allowable values (see Table 8) calculated according to Eq. (1) and (2) listed in Table 6 and 7. One can see from Table 8 that both the maximum stress and strain at SLLS were below the allowable stress at OBE, $\sigma_{a,OBE}$, while these values at CLS were below the allowable stress at SSE, $\sigma_{a,SSE}$. One may note that while the maximum stress levels are below the allowable limits by a lower margin, maximum strains were found to be far below the allowable limits suggested by standards. In fact, a higher level of plastification is allowed by the strain based design methods. Nevertheless, the above analysis indicates that the piping system remains below its nominal yield strength, i.e. 418 MPa, under an OBE or SSE level earthquake.

Table 6. Allowable stress at OBE, $\sigma_{a,OBE}$ and at SSE, $\sigma_{a,SSE}$

	Stress limit	
Code	$\sigma_{a,OBE}$ (MPa)	$\sigma_{a,SSE}$ (MPa)
EN 13480-3	195.99	293.99
ASME B31.1 & B31.3	217.23	-

Table 7. Allowable strain in pipes

	Strain limit	
Code	Tension limit	Compression limit
CSA-Z662 (2007)	2.5%	1.6%
DNV-OS-F101 (2000)	2.0%	-
ASCE (2005)	2.0%	-

Table 8. Maximum stresses and strains in the piping system at SLLS and CLS

Limit States	Elbow	Stress (MPa)	Strain
SLLS	Elbow #1	186.46	0.093%
	Elbow #2	184.02	0.092%
CLS	Elbow #1	251.53	0.126%
	Elbow #2	248.11	0.124%

4. CONCLUSIONS

Due to the scarcity of adequate and uniform seismic design guidelines for petrochemical, oil & gas piping systems, designers are compelled to follow standards conceived for other struc-

tures, such as buildings and nuclear plants. In this paper, a performance-based seismic analysis of petrochemical piping systems through two realistic case studies was presented. Several issues related to the seismic design and analysis of piping systems were addressed, and relevant design/analysis rules suggested by international codes and standards were discussed. Current allowable stress- and strain-based verification methods were commented. In this respect, a discussion on the selection of proper seismic inputs was offered showing the limits of current guidelines. Two realistic piping systems were analysed in the nonlinear regime for limit states suggested by modern performance-based earthquake standards; and a comparison between computed stresses and strains and allowable code-based design values were made. A favourable performance of both the piping systems under chosen limit states was found. It was found maximum stress and strain values in both the piping systems remained below their yield strengths and allowable limit values even at the collapse limit state.

ACKNOWLEDGEMENTS

The work presented herein was carried out with a financial grant from the Research Fund for Coal and Steel of the European Commission, within the research projects INDUSE (Grant No. RFSR-CT-2009-00022) and INDUSE-2-SAFETY (Grant No. RFS-PR-13056).

REFERENCES

[1] 1 Sezen H, Whittaker AS (2006). “Seismic Performance of Industrial Facilities Affected by the 1999 Turkey Earthquake”, Journal of Performance of Constructed Facilities, Vol. 20, No. 1.

[2] Krausmann E, Cruz AM, Affeltranger B (2010). “The impact of the 12 May 2008 Wenchuan earthquake on industrial facilities”, Journal of Loss Prevention in the Process Industries, 23, 2, 242-248.

[3] Zare MR, Wilkson S (2010). “Resilience of wastewater pipelines in earthquakes”, Proceedings of the 9th U.S. National and 10th Canadian Conference, Toronto, O

[4] Paolacci F, Giannini R, Angelis MD (2013). “Seismic response mitigation of chemical plant components by passive control systems”, Journal of Loss Prevention in the Process Industries, 26 (5), 924-935.

[5] EN 1998-4 (2006). “Eurocode 8 - Design of structures for earthquake resistance – Part 4: Silos, tanks and pipelines”.

[6] Paolacci F, Reza MS, Bursi OS (2011). “Seismic design criteria of refinery piping systems”, COMPDYN 2011-III ECCOMAS Thematic Conference on Computational Methods in Structural Dynamics and Earthquake Engineering, Corfu, Greece, 2628.

[7] EN 13480-3 (2002). “Metallic industrial piping – Part 3: Design and calculation”.

[8] ASME B31.1 (2001). “Power Piping, ASME Code for Pressure Piping, B31”, American Society of Mechanical Engineers.

[9] ASME B31.3 (2006). “Process Piping, ASME Code for Pressure Piping, B31”, American Society of Mechanical Engineers.

[10] ASCE/SEI 7-05 (2005). “Minimum Design Loads for Buildings and Other Structures”, American Society of Civil Engineers.

[11] EN 1998-1 (2005). “Eurocode 8: Design of structures for earthquake resistance – Part 1: General rules, seismic actions and rules for buildings”.

[12] NEA/CSNI/R (2007)17 (2008). “Differences in approach between nuclear and conventional seismic standards with regard to hazard definition”, CSNI Integrity and Ageing Working Group, Nuclear Energy Agency Committee on the Safety of Nuclear Installations.

[13] NFPA 59A (2009). “Standards for the production, storage and handling of liquefied natural gas (LNG)”, Quincy, MA, National Fire Protection Association.

[14] Azizpour O, Hosseisni, M (2009). “A verification of ASCE Recommended Guidelines for seismic evaluation and design of combination structures in petrochemical facilities,” J. of Applied Sciences.

[15] DeGrassi G, Nie J, Hofmayer C (2008). “Seismic Analysis of Large-Scale Piping Systems for the JNES-NUPEC Ultimate Strength Piping Test Program”, U.S. NRC NUREG/CR-6983, BNL-NUREG-81548-2008.

[16] Karamanos SA, Tsouvalas D, Gresnigt AM (2006). "Ultimate Bending Capacity and Buckling of Pressurized 90 deg Steel Elbows," Journal of Pressure VesselTechnology, ASME, Vol. 128, No. 3, pp. 348-356, August 2006.

[17] Bursi OS, Abbiati G, Caracoglia L, Reza MS (2014). “Effects of Uncertainties in Boundary Conditions on Dynamic Characteristics of Industrial Plant Components”, Proceedings of the ASME 2014 Pressure Vessels & Piping Division Conference, PVP 2014, July 20-24, 2014, Anaheim, California, USA.

[18] Okeil A, Tung C (1996). “Effects of ductility on seismic response of piping systems and their implication on design and qualification,” Nuclear Engineering and Design, 166: 69-83

[19] CSA-Z662 (2007). “Canadian standards association. Oil and gas pipeline systems”, Exdale, Ontario, Canada.

[20] Liu B, Liu XJ, Zhang H (2009) “Strain-based design criteria of pipelines”, Journal of Loss Prevention in the Process Industries, 22 (2009) 884-888.

[21] Arrête du 24 janvier 2011 fixant les regles parasismiques applicables a certaines installations classes, DEVP1102251A, Ministère de l’écologie du développement durable des transports et du logement, Journal Official de la République Française. Texte 14 sur 239.

[22] Iervolino I, Galasso C, Cosenza E (2009). “REXEL:computer aided record selection for code-based seismicstructural analysis,” Bulletin of Earthquake Engineering, 8:339-362. DOI 10.1007/s10518-009-9146-1.

[23] Vamvatsikos D and Cornell CA (2002). “Incremental dynamic analysis”, Earthquake Engineering and Structural Dynamics, 31, 491–514.

[24] Bursi OS, Reza MS, Paolacci F, Kumar A (2012). “Seismic Performance of Bolted flange Joints in Piping Systems for Oil and Gas Industries," 15th World Conference on Earthquake Engineering, Lisbon, Portugal, 24-28 September 2012.

[25] Reza MS, Bursi OS, Paolacci F, Kumar A (2014). “Enhanced Seismic Performance of Non-Standard Bolted Flange Joints for Petrochemical Piping Systems,” Journal of Loss Prevention in the Process Industries. Vol. 30, pp 124-136.

[26] SAP2000 (2004). "Linear and Nonlinear Static and Dynamic Analysis and Design of Three-Dimensional Structures. v9", Computers and Structures, Inc., Berkeley, California, USA.

[27] Hibbit HD, Karlsson BI, Sorensen (2003). "Theory Manual, ABAQUS version 6.3", Providence, RI. USA.

[28] FEMA-273 (1997). "NEHRP Guidelines for Seismic Rehabilitation of Buildings. Building Seismic Safety Council, FEMA, Washington, D.C".

[29] Norme Techniche (2008). "Norme Techniche per le costruzioni", DM Infrastrutture, 14 gennaio 2008 (in Italian).

[30] ASME Boiler and Pressure Vessel Code, Code Case N-411-1 (1986). "Alternative Damping Values for Response Spectra Analysis of Class 1, 2 and 3 Piping. Section III, Division 1", American Society of Mechanical Engineers, New York, February 20, 1986.

[31] DNV-OS-F101 (2000). "Submarine Pipeline Systems[S]", HØvik Norway.

[32] ASCE (2005). "Guidelines for the design of buried steel pipe (with addenda through February 2005)", USA.

COMPDYN 2015
5th ECCOMAS Thematic Conference on
Computational Methods in Structural Dynamics and Earthquake Engineering
M. Papadrakakis, V. Papadopoulos, V. Plevris (eds.)
Crete Island, Greece, 25–27 May 2015

SEISMIC FRAGILITY ANALYSIS OF STEEL STORAGE TANKS

Fabrizio Paolacci[1], Hoang N. Phan[1], Daniele Corritore[1], Silvia Alessandri[1], Oreste S. Bursi[2], M. Shahin Reza[2]

[1] Roma Tre University, Department of Engineering
Via Vito Volterra 62, Rome, Italy
fabrizio.paolacci@uniroma3.it, hoangnam.phan@uniroma3.it, daniele.corritore@uniroma3.it, silvia.alessandri@uniroma3.it

[2] University of Trento, Department of Civil, Environmental and Mech. Engineering
Via Mesiano 77, Trento, Italy
oreste.bursi@unitn.it, rezam@ing.unitn.it

Keywords: Elevated Tanks, Simplified Model, Fragility Curve, Probabilistic Analysis, Seismic Response.

Abstract. *Earthquakes can cause significant damages to industrial liquid storage tanks resulting in losses of functionality, fires or environmental contamination due to the leakage of hazardous chemicals. Typical damages of ground supported tanks during past earthquakes were in the form of cracking at the corner of the bottom plate and compression buckling of tank wall due to uplift, sliding of the base, anchorage failure, sloshing damage around the roof, failure of piping systems and plastic deformation of base plate. Liquid tanks can be also located at some elevated positions due to operational purposes. This makes them susceptible to collapse due to increased base shears and overturning moments. The seismic response of elevated tanks has been widely investigated in the past considering different materials and configurations of support structures. This paper addresses the problem of elevated tanks with particular attention focused on the steel storage tanks resting on short RC columns. The vulnerability of a real example of elevated tanks is assessed though the probabilistic analysis performed using non-linear lumped mass models. Consequently different fragility curves are built for identifying the most important damage states and calculating the corresponding probability of occurrence. The results show how the support structure, especially when composed by RC columns, is the most influencing one, whereas the remaining damage states have a limited influence.*

1 INTRODUCTION

Earthquakes can cause severe damages to the tank structures and other facilities in industrial sites resulting in losses of functionality, fires or environmental contamination due to the leakage of hazardous chemicals [1], [2], [3], [4], [5], [6], [7], [8], [9]. Above ground liquid storage tanks have suffered serious damages during past earthquakes. These typical damages were in the form of cracking at the corner of the bottom plate and compression buckling of tank wall (elephant's foot buckling) due to uplift, sliding of the base, anchorage failure, sloshing damage around the roof, failure of piping systems and plastic deformation of base plate.

Liquid tanks can also be elevated due to operational purposes. Steel storage tanks upon reinforced concrete columns represent a typical structural configuration. Moreover, in case of reinforced concrete supports, the high lateral stiffness may induce premature failure in the columns, as shown in recent seismic events. For example, during Izmit earthquake (1999) in Turkey, a group of elevated tanks for the storage of liquefied oxygen were seriously damaged or collapsed [10], [11], [12], [13].

On the basis of the above-depicted framework, this paper addresses the problem of the vulnerability assessment of elevated tanks with particular attention focused on the steel storage tanks resting on short RC columns. The seismic response of one of the liquefied oxygen storage steel tanks collapsed during the 1999 Izmit earthquake due to premature failure of columns has been analyzed under seismic excitation using a 3D model implemented in OpenSEES [14].

Consequently, after a brief review of existing methods for the evaluation of fragility curves and the definition of damage limit states for steel storage tanks, the vulnerability analysis of the selected case study has been assessed using two different methods, namely Cloud method and Increment Dynamic Analysis highlighting the most frequent damage conditions for the tank under seismic action [15].

2 DAMAGE STATES OF STORAGE TANKS

The seismic vulnerability of a structure is generally expressed as probability of exceeding one of more structural limit states. Existing data concerning post earthquake damage observations for steel storage tanks have been collected in order to propose the limit state classifications of equipment response. In fact, according to HAZUS damage state list [16], the effects of seismic actions have been related to structural damage and its reparability. Possible damage limits for steel storage tanks are reassumed in Table 1.

#	Failure mode
1	Overturning
2	Elastic buckling
3	Sliding
4	Elasto-plastic buckling
5	Tank roof damage
6	Uplift

Table 1: Possible failure modes for tanks

These failure modes are usually collected in a limited number of damage states, as reported in Table 2 [16].

In this work, the attention is paid on elevated tanks, whose typical configuration does not include any floating roof. In order to estimate the seismic vulnerability and to derive fragility

curves, extensive (buckling) and complete damage states (complete collapse due to the failure of the support system) have been here considered.

#	Damage state	Description
1	No damage	---
2	Slight damage	Roof and pipes damages, sliding without leakage
3	Moderate damage	Elastic buckling, yielding of tank wall and uplift without leakage
4	Extensive damage	Elastic buckling, uplift, pipes detachment with leakage
5	Complete damage	Complete damage (boilover, injections, complete LOC, total collapse)

Table 2: Damage states for tanks

The damage state associated to instability phenomena in the tank wall can be quantified with the level of stress that activates buckling. Three distinct buckling phenomena have been observed during past seismic events: Diamond Shape Buckling (DSB), Elephant's Foot Buckling (EFB) and Secondary Buckling (SB) [17]. An example of both the buckling phenomena is illustrated in Figure 1.



Figure 1: EFB and DSB observed after the 2012 Emilia Earthquake in Italy [8]

DSB is due to excessive meridional stresses so that to induce lateral instability of the wall in the elastic field. This form of buckling has been observed in those parts of the shell where the thickness is reduced with respect to the thickness of the base and/or the internal pressure (which has a stabilizing effect) is also reduced with respect to the maximum value attained at the base. EFB normally occurs close to the base of the tank, due to a combination of vertical compressive stresses and tensile hoop stresses inducing an inelastic biaxial state of stress.

These two buckling types are explicitly mentioned in current codes as Eurocode 8 [18] and New Zealand guidelines [19] and implicitly accounted for in the API formulation [20]. For example, Eurocode 8 and New Zealand guidelines suggest the Rotter [21] formula to compute the buckling capacity with respect to elastic–plastic buckling:

$$f_{pb} = \sigma_{c1}\left[1-\left(\frac{pR}{t_w f_y}\right)^2\right]\left(1-\frac{1}{1.12+\mathrm{r}^{1.5}}\right)\left(\frac{r+f_y/250}{r+1}\right) \quad (1)$$

where $\sigma_{cl} = 0.605E_w t_w R$ is the Euler's critical axial compressive stress, R is the tank radius, p is the total internal pressure, E_w and t_w are the elastic modulus and the thickness of the tank walls, f_y is the steel yielding stress, and r is a coefficient defined as $r = R/(400t_w)$.

In addition to the well-known elephant's foot and diamond shape buckling modes, a third kind of buckling, due to external pressure and cavitation, is mentioned by Rammerstofer et al. [22] and confirmed also by observations on real tanks after earthquakes. However, this buckling mode is not covered by current codes, and until now, no empirical formula associated to it exists in literature.

Failure conditions in the support structure can be usually treated using common approaches adopted for civil structures. For example, it is frequent to find RC columns as support structure. In this case, the ultimate capacity can be calculated in accordance to the current codes for the assessment of existing RC structures, both for ductile and fragile mechanisms [23].

3 FRAGILITY ASSESSMENT METHODS

In this paper, a fragility function, $P[D_{EDP}>LS|IM]$ is developed for the liquid storage tanks to investigate the damage likely to occur during a seismic event. This function represents the probability of the response, D_{EDP}, of the selected engineering demand parameter, EDP, exceeding a selected structural limit state, LS, for a specific intensity measure, IM, of seismic excitation.

Different methods to build fragility curves have been already proposed in literature, considering or not the randomness of the structure characteristics [15]. The most common used is the Cloud method. This method implements non-linear dynamic analyses through (linear) regression-based probabilistic model [24]. When the seismic demand and the structural limit states are assumed to follow a lognormal distribution, the probability of exceeding a specific damage state can be estimated with the lognormal cumulative distribution function, given as:

$$P\left[D_{EDP} > LS \mid IM\right] = 1 - \Phi\left(\frac{\ln\left(LS_m\right) - \ln\left(D_m\right)}{\sqrt{\beta_{d|IM}^2 + \beta_{LS}^2}}\right) \tag{2}$$

where $\Phi(\cdot)$ is the standard normal cumulative distribution function, LS_m is the median estimate of the structural limit state, D_m is the median estimate of the demand, $\beta_{d|IM}$ is the dispersion of the demand conditioned on the IM, and β_{LS} is the dispersion of the structural limit state.

The estimate of the median demand can be predicted by a power function:

$$D_m = a\left(IM\right)^b \tag{3}$$

where a and b are regression coefficients based on the collection of d_i and IM_i from the time-history seismic analyses of the analyzed tank and from the selected a suite of n ground motions. The dispersion of the demand conditioned on the IM can also be estimated from the regression analysis of the seismic demands:

$$\beta_{d|IM} = \sqrt{\frac{\sum_{i=1}^{n}\left[\ln\left(d_i\right) - \ln\left(aIM_i^b\right)\right]^2}{n-2}} \tag{4}$$

The Cloud method is very attractive because it allows deriving closed-form solutions of the fragility curves. However, the power-law form of the demand is, at best, only a good estimate of the behavior of a structure under earthquake excitation in the interval of values where

the locally linear fit is made. In addition, the dispersion is considered as constant, when in reality there is a clear dependency of the level of *IM* analyzed.

In order to correctly incorporate the above-mentioned variability of mean and dispersion with *IM*, many alternative methods have been proposed. One of them is the Incremental Dynamic Analysis (IDA) method that was initially derived only for collapse condition [25] but can be adopted for different damage levels. This method produces a set of *IM* values associated with the onset of collapse for each ground motion. Fragility function parameters can be estimated by taking logarithms of each ground motion's intensity measure value associated with onset of collapse or damage, and computing their mean and standard deviation:

$$\ln \hat{\mu} = \frac{1}{n}\sum_{i=1}^{n} \ln IM_i \tag{5}$$

$$\hat{\beta} = \sqrt{\frac{1}{n-1}\sum_{i=1}^{n}\left(\ln\left(IM_i / \mu\right)\right)^2} \tag{6}$$

where n is the number of ground motions considered, IM_i is the *IM* value associated with onset of collapse or damage for the i_{th} ground motion.

Consequently, given the limit state, the *IM* is now a random variable, whose probability of being lower than given *IM* is the following that also represents the analytical expression of the fragility curve:

$$P[D_{EDP} > LS \mid IM] = \Phi\left(\frac{\ln\left(IM / \hat{\mu}\right)}{\hat{\beta}}\right) \tag{7}$$

Other possible methods can be derived from the reliability theory, as for example the Effective Fragility Analysis, already proposed for the vulnerability assessment civil and industrial structures [26], [27], [28]. This method makes use of the Response Surface technique.

In this work, Cloud method and IDA will be used to derive fragility curves of the elevated tank described in section 4.

4 PROBABILISTIC SEISMIC RESPONSE ANALYSIS

4.1 Numerical model of elevated tanks

In this paper, the probabilistic seismic analysis of elevated liquefied gas storage tanks at the Habas facility in Izmit, Turkey is presented [10], [12]. The two tanks containing 80% full liquid oxygen were collapsed during the Kocaeli Earthquake in 1999 while the tank and supporting structure containing 25% full liquid nitrogen was undamaged except for some hairline cracks in the columns, as shown in Figure 2.

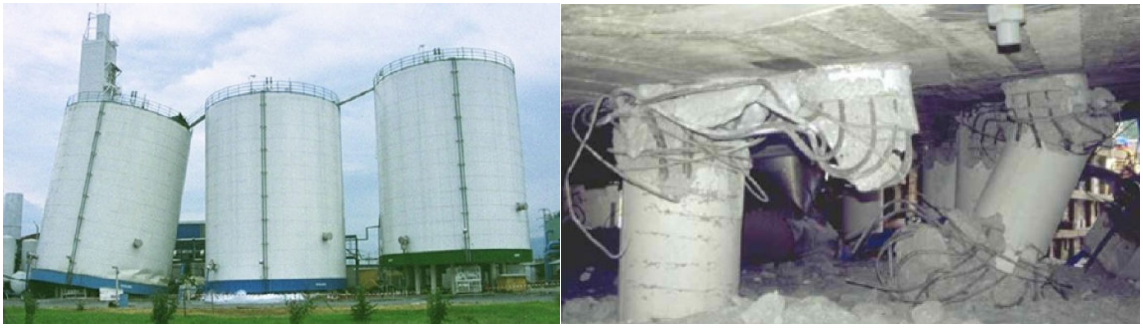


Figure 2: Storage tanks of Liquid Oxygen at Habas plant after the strong event of Izmit (1999)

These tanks were built in 1995 and each tank consisted of two concentric stainless steel shells, one with an outside diameter of 14.6 m and the other with an outside diameter of 12.8 m. The gap between the shells is filled with insulation. Both shells were supported on a 14.6 m-diameter and 1.07 m-thick reinforced concrete slab that was in turn supported by sixteen 500 mm-diameter reinforced concrete columns. Each column was 2.5 m in height and reinforced with sixteen 16 mm-diameter longitudinal bars and 8 mm-diameter ties at 100 mm on the center. According to [10], the concrete used for the columns and the bottom slab was of class C30/37, whereas the steel bars had a yielding strength of 430 MPa. The density of the oxygen was 11.50 kN/m^3.

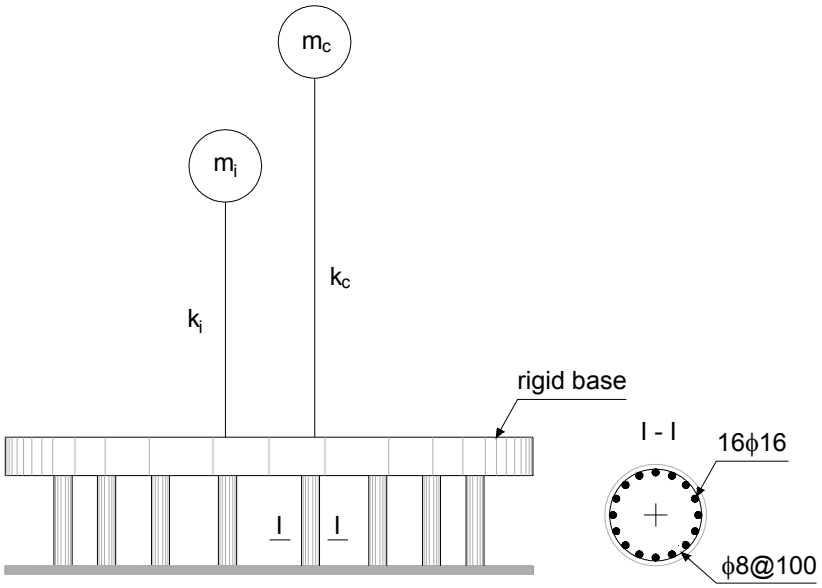


Figure 3: Numerical model of 3D elevated tanks

Based on the typical details taken from the examined elevated tank, 3D numerical model is generated using the finite element platform OpenSEES [14]. The hydrodynamic pressure acting on the tank wall during earthquake loading can be easily performed using the simplified model shown in Figure 3, in which the liquid mass is lumped and subdivided in two components: impulsive and convective masses named m_i and m_c, respectively [29], [30], [31]. The impulsive and convective masses are connected to the tank wall by springs of stiffness k_i and k_c. The RC base is assumed to be rigid and the RC supporting columns are modeled using 3D nonlinear beam–column elements with fiber-defined cross-sections. Concrete is modeled according to Kent-Park model, which include the confinement effect of stirrups whereas the steel bars are modeled using the Menegotto-Pinto model.

The seismic response of the elevated tank is evaluated by using a set of time-history analyses using the nonlinear 3D model of Figure 3. In this respect, the system is subjected to 30 natural records selected from PEER Strong Ground Motion Database. They have been identified according to the following hazard criteria:

- Magnitude: $5 < M < 7$
- Distance from the fault: $0 < d < 20$ km
- S-waves velocity between 360 m/s and 760 m/s

The response spectra of all un-scaled records are shown in Figure 4 together with the elastic spectrum imposed by the EN1998:1 [32]. The design ground acceleration of 0.4g is selected for a soil condition A.

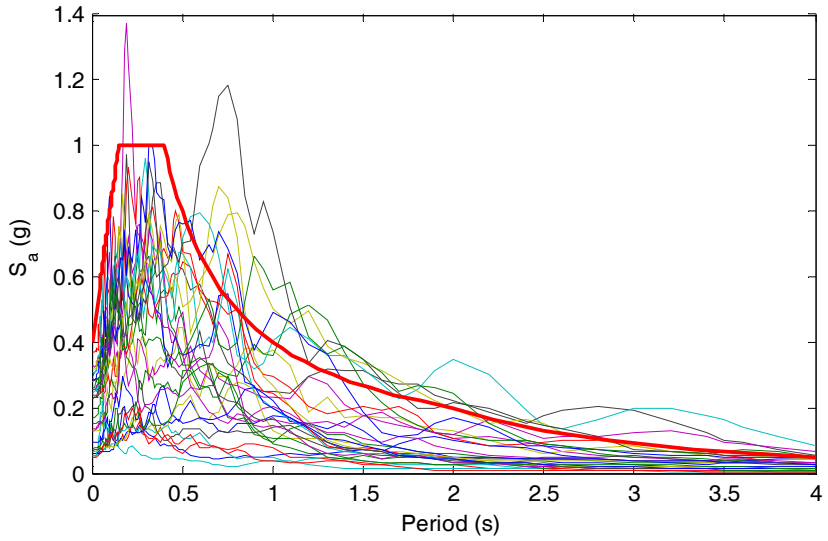


Figure 4: Response spectra of the 30 un-scaled accelerograms

4.2 Probabilistic seismic response analysis of the case study

Concerning the Cloud method, for each ground motion a series of non-linear time-history analyses are performed, where the peak value of seismic response for each accelerogram is recorded. For example, Figure 5 shows the maximum lateral displacement, δ, of the tank base for each of the 30 accelerograms. In this work, the selected demand parameters (EDPs) include the drift ratio of supporting columns, δ/H, and the meridional stress in the tank wall, σ_z.

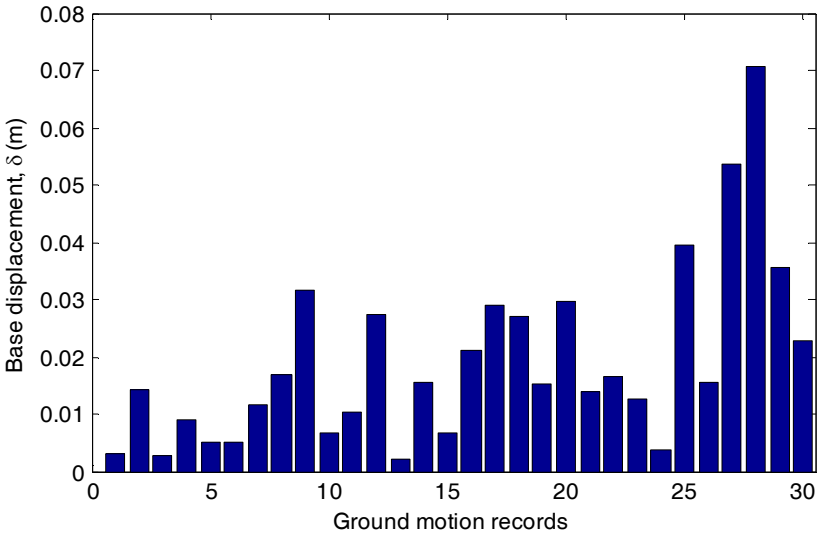


Figure 5: Peak displacement response of tank base for each selected ground motion

Given the high axial stiffness of columns, the drift well approximates the chord rotation that is $\theta \approx \delta/H$. This latter is usually adopted as a parameter for the seismic assessment of ductile mechanism of columns [23]. The meridional stress has been calculated according to the approximated formula provided by the standard API 650 [20].

A linear regression analysis has been performed to determine the regression coefficients of the probabilistic seismic demand model. The coefficient *a* and *b* have been identified using a log-log representation of the EDP-PGA relationship (Figure 6). The fragility curves can be developed using Eq. (2).

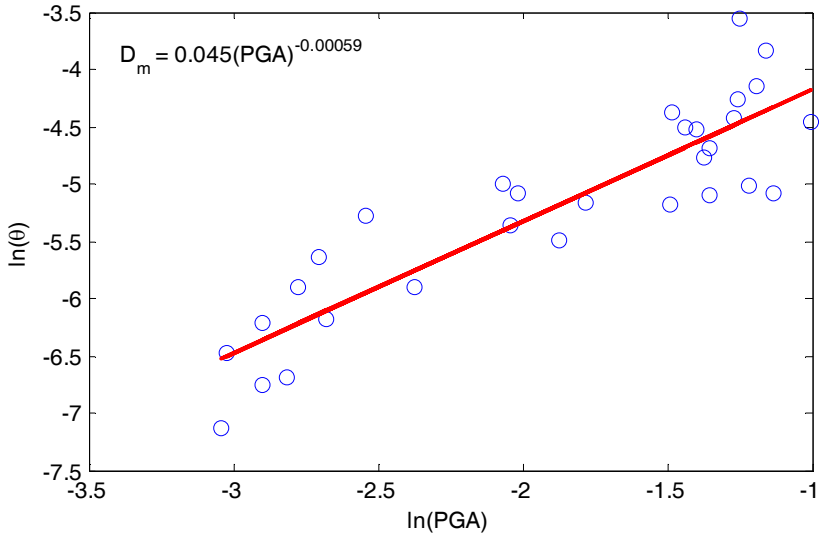


Figure 6: Linear regression analysis for peak drift ratio of supporting columns

With IDA, the ground motions are scaled to a given *LS*. This process produces a set of PGA values associated with the onset of the *LS*. Fragility function parameters for each EDP are then estimated from these values by using Eq. (5-6). Figure 7 shows the IDA results for supporting columns in terms of maximum column drift ratio.

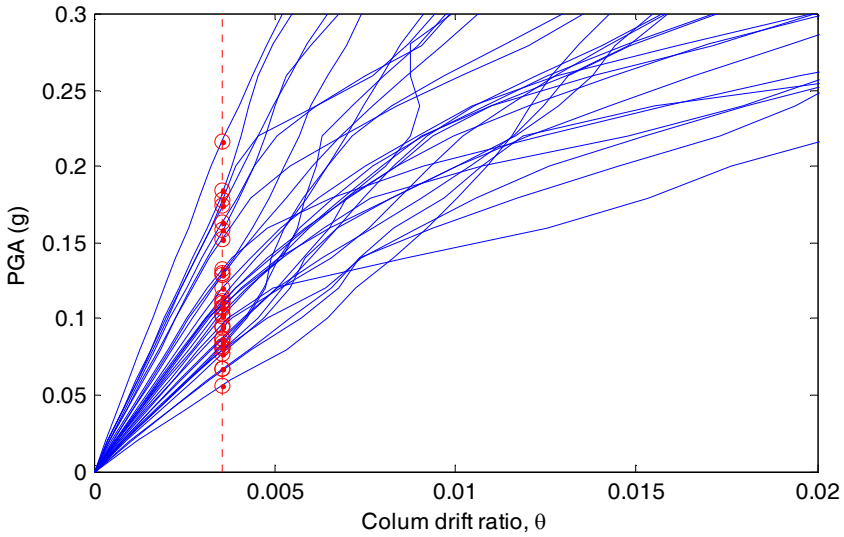


Figure 7: IDA results for peak drift ratio of supporting columns

4.3 Fragility curves estimation

According to the methods presented in section 3, fragility curves of the tank as shown in Figure 8 have been constructed for the several above-described damage states. However, given that the prevalent damage condition is represented by the damage in the RC columns for excessive lateral displacement of the tank base, the fragilities have been calculated under the hypothesis that the other failure modes due to the buckling phenomenon would be excluded. This has also been demonstrated in the reality where the collapse was uniquely caused by the failure of the columns. In this respect, the ultimate capacity of the columns is evaluated in terms of chord rotation θ_u under the hypothesis of ductile mechanism. The ultimate chord rotation can be evaluated according to EN1998:3 [23] as follows:

$$\theta_u = \frac{1}{\gamma_{el}}\left(\theta_y + \left(\phi_u - \phi_y\right)L_{pl}\left(1 - \frac{0.5L_{pl}}{L_V}\right)\right) \tag{8}$$

where γ_{el} = 1.5 is the safety coefficient, $\theta_y = \phi_y L_v/3$ is the chord rotation at yielding, ϕ_u and ϕ_y are the ultimate and yielding section curvatures, L_{pl} is the plastic hinge height and L_v is the distance between the zero moment point and one of the two edges.

Given that the model of Figure 3 includes the overturning effect of the tank, and thus the variation of axial force in the columns during the earthquake, θ_u = 0.0036 has been calculated as the minimum value obtained during the time-history analyses.

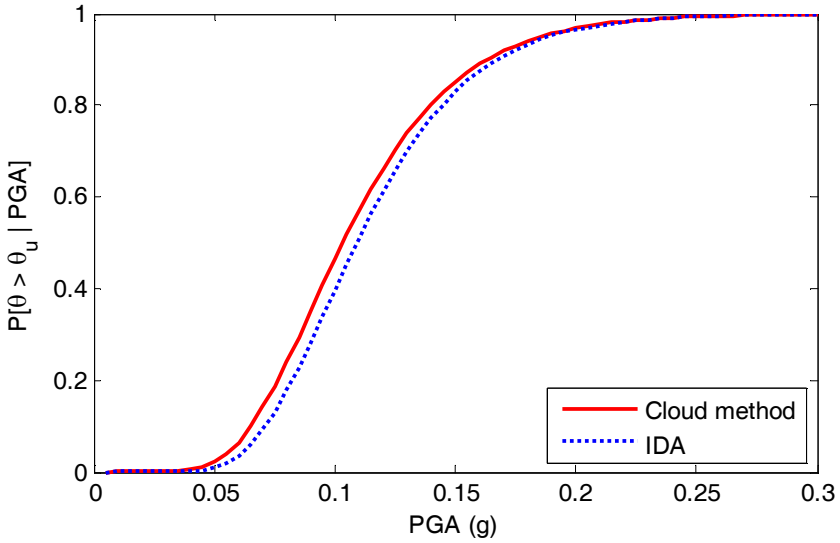


Figure 8: Fragility functions obtained by Cloud method and IDA for ductility of columns

The fragility curves obtained based on the Cloud and the IDA methods are presented in Figure 8. For a given PGA, the probability of exceedance of the ductile mechanism in the support columns is similarly predicted by the two methods. However, IDA method appears to be slightly more conservative. It can be noticed that for a PGA = 0.2g, the probability of failure is approximately equal to 95%. This is a clear demonstration of the high seismic vulnerability of the tank, as dramatically demonstrated during the 1999 Izmit earthquake [10].

For completeness, the fragility curve relative to the failure mode of the tank due to elephant's foot buckling has been calculated. As previously mentioned, because an eventual collapse due to the failure of the columns avoids any buckling phenomena in the tank wall, the

fragility curve has been built assuming for the columns a linear elastic behavior whose stiffness has been calculated according to the secant modulus of the concrete. The curve is illustrated in Figure 9 compared with the fragility curve for columns collapse condition.

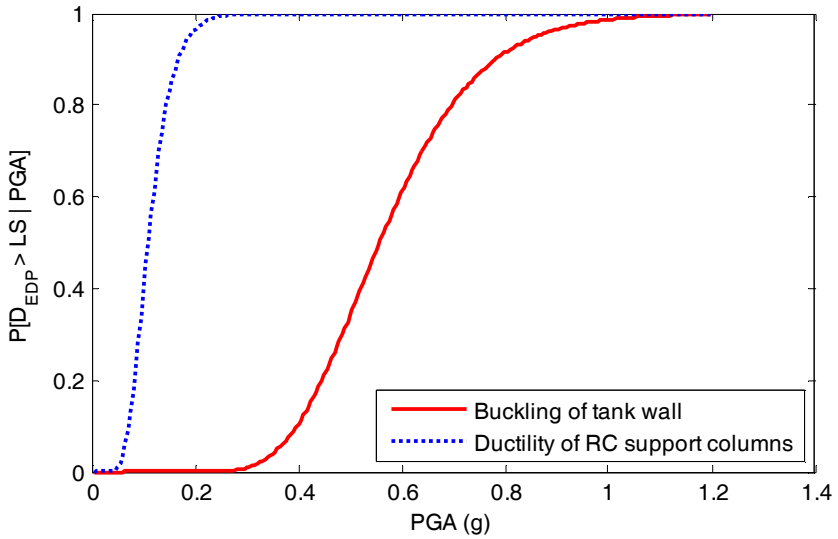


Figure 9: Fragility functions obtained by IDA for ductility of columns and buckling of tank wall

5 CONCLUSIONS

Typical damages of above-ground and elevated tanks during past earthquakes were in the form of cracking at the corner of the bottom plate and compression buckling of tank wall due to uplift, sliding of the base, anchorage failure, sloshing damage around the roof, failure of piping systems and plastic deformation of base plate. The high vulnerability of this typical industrial component is thus evident. A typical tool for a quantitative evaluation of the vulnerability of a structure is the fragility analysis, whose outcome is represented by evaluation of the probability of exceeding a certain damage state for a given intensity measure (e.g. the PGA).

In this respect, the present paper addressed the problem of steel storage tanks. The seismic vulnerability has been assessed though the probabilistic response analysis (Cloud method and IDA) performed using non-linear lumped mass models. As case study, an emblematic example of elevated tank collapsed during the Kocaeli Earthquake in 1999 at Habas pharmaceutics plant in Turkey was considered. Different fragility curves were built identifying the most important damage states and calculating the corresponding probability of occurrence. The results have shown that the use of different methods provides similar results. In particular, it was evidenced that failure in support structure columns is the most influencing one. This is fully in accordance with the real collapse mode.

ACKNOWLEDGEMENTS

The work presented herein was carried out with a financial grant from the Research Fund for Coal and Steel of the European Commission, within the research project INDUSE-2-SAFETY (Grant No. RFS-PR-13056).

REFERENCES

[1] Campedel, M., Analysis of major industrial accidents triggered by natural events reported in the principal available chemical accident databases. *JRC Scientific and Technical Reports*, EUR 23391 EN, 2008.

[2] Hatayama, K., Lessons from the 2003 Tokachi-oki, Japan, earthquake for prediction of long-period strong ground motions and sloshing damage to oil storage tanks. *Journal of Seismology*, 12, 255-263, 2008.

[3] Krausmann, E., Cruz, A., Affeltranger, B., The impact of the 12 May 2008 Wenchuan earthquake on industrial facilities. *Journal of Loss Prevention in the Process Industries*, 23, 242-248, 2010.

[4] Moat, A. M., Morrison, A. J. T., Wong, S., Performance of industrial facilities during 1999 earthquakes: implications for risk managers. *In EuroConference on Global Change and Catastrophe Risk Management: Earthquake Risk in Europe*, Laxenburg, Austria, 2000.

[5] Nishi, H., Damage on hazardous materials facilities. *In International Symposium on Engineering Lessons learned from the 2011 Great East Japan Earthquake*, Tokyo, Japan, 2012.

[6] Sezen, H., Whittaker, A. S., Seismic performance of industrial facilities affected by the 1999 Turkey earthquake. *Journal of Performance of Constructed Facilities*, 20(1), 2006.

[7] Suzuki, K., Earthquake damage to industrial facilities and development of seismic and vibration control technology - based on experience from the 1995 Kobe (Hanshin-Awaji) earthquake. *Journal of System Design and Dynamics*, 1-11, 2008.

[8] Brunesi, E., Nascimbene, R., Pagani, M., Beilic, D., Seismic performance of storage steel tanks during the May 2012 Emilia, Italy, Earthquakes. *J. Peform. Constr. Fac.*, 2014.

[9] Paolacci, F., Giannini, R., De Angelis, M., Seismic response mitigation of chemical plant components by passive control systems. *Journal of Loss Prevention in Process Industries*, 26(5), 879-948, 2013.

[10] Sezen, H., Lıvaoğlu, R., Doğangün, A., Dynamic analysis and seismic performance evaluation of above-ground liquid-containing tanks. *Engineering Structures*, 30, 794-803, 2008.

[11] Korkmaz, K. A., Sari, A., Carhoglu, A. I., Seismic risk assessment of storage tanks in Turkish industrial facilities. *Journal of Loss Prevention in the Process Industries*, 24, 314-320, 2011.

[12] Paolacci, F., On the effectiveness of two isolation systems for the seismic protection of elevated tanks. *Proceedings of the ASME 2014 Pressure Vessels & Piping Conference PVP2014*, Anaheim, California, USA, 2014.

[13] Paolacci, F., On the effectiveness of two isolation systems for the seismic protection of elevated tanks. *Journal of Pressure Vessels and Technology*, 137(3), 2015.

[14] McKenna, F., Fenves, G. L., Scott, M. H., OpenSEES: open system for earthquake engineering simulation. *PEER*, University of California: Berkeley, 2007.

[15] Jalayer, F., Cornell, C. A., A technical framework for probability-based demand and capacity factor design (DCFD) seismic formats. *Pacific Earthquake Engineering Research Center Report*, 08, 2003.

[16] HAZUS, Earthquake Loss Estimation Methodology. *National Institute of Building Science, Risk Managment Solution*, Menlo Park, CA, USA, 2001

[17] Buratti, N., Tavano, M., Dynamic buckling and seismic fragility of anchored steel tanks by the added mass method. *Earthquake Engng. & Structural Dyn.*, 43, 1-21, 2014.

[18] CEN (2006) Comité Européen de Normalisation, Eurocode 8: Design of Structures for Earthquake Resistance—Part 4: Silos, Tanks and Pipeline, EN 1998-4, Brussels, Belgium.

[19] NZS 3106 (1998), Code of practice for concrete structures for the storage of liquids. *New Zealand: Standard Association*.

[20] API (2008), Welded Tanks for Oil Storage.

[21] Rotter, J. M., Teng, J. G., Elastic stability of cylindrical shells with weld depressions. *Journal of Structural Engineering*, 115(12), 44-63, 1989.

[22] Rammerstorfer, F. G., Scharf, K., Fisher, F. D., Storage Tanks Under Earthquake Loading. *Applied Mechanics Reviews*, 43(11), 261-282, 1990.

[23] CEN (2006) Comité Européen de Normalisation, Eurocode 8: Design of structures for earthquake resistance—Part 3: Assessment and retrofitting of buildings, Bruxell.

[24] Benjamin, J. R., Cornell, C. A., Probability, statistics and decision for civil engineers. *McGraw-Hill*, New York, 1975.

[25] Vamvatsikos, D., Cornell C. A., Applied incremental dynamic analysis. *Earthquake Spectra*, 20 (2), 523-553, 2004.

[26] Paolacci, F., Giannini, R., Seismic reliability assessment of a disconnect switch using an effective fragility analysis. *Journal of Earthquake Engineering*, 13, 217-235, 2009.

[27] Paolacci, F., Giannini, R., Alessandri, S., De Felice, G., Seismic vulnerability assessment of a high voltage disconnect switch. *Soil Dyn. and Earthquake Enggn.*, 67, 198-207, 2014.

[28] De Felice, G., Giannini, R., An efficient approach for seismic fragility assessment with application to old reinforced concrete bridges. *Journal of Earthquake Engineering*, 14(2), 2010.

[29] De Angelis, M., Giannini, R., Paolacci, F., Experimental investigation on the seismic response of a steel liquid storage tank equipped with floating roof by shaking table tests. *Earthquake Engng. & Structural Dyn.*, 39, 377–396, 2010.

[30] Abali, E., Uckan, E., Parametric analysis of liquid storage tanks base isolated by curved surface sliding bearings. *Soil Dyn. and Earthquake Engng.*, 30(1-2), 21-31, 2010.

[31] Shrimali, M. K., Seismic response of elevated liquid storage steel tanks under bi-direction excitation. *Steel Structures*, 7, 239-251, 2007.

[32] CEN (2004) Comité Européen de Normalisation, Eurocode 8: Design of structures for earthquake resistance—Part 1: General rules, seismic actions and rules for buildings. EN 1:2004.

COMPDYN 2015
5th ECCOMAS Thematic Conference on
Computational Methods in Structural Dynamics and Earthquake Engineering
M. Papadrakakis, V. Papadopoulos, V. Plevris (eds.)
Crete Island, Greece, 25–27 May 2015

SURROGATE MODELLING OF LIQUID STORAGE TANKS FOR SEISMIC PERFORMANCE DESIGN AND ASSESSMENT

Konstantinos Bakalis[1], Michalis Fragiadakis[2], and Dimitrios Vamvatsikos[3]

[1] National Technical University of Athens
Institute of Steel Structures
Zografou Campus, 9 Iroon Polytechneiou str, 15780 Zografou, Athens, Greece
e-mail: kbakalis@mail.ntua.gr

[2] National Technical University of Athens
Laboratory for Earthquake Engineering
Zografou Campus, 9 Iroon Polytechneiou str, 15780 Zografou, Athens, Greece
e-mail: mfrag@mail.ntua.gr

[3] National Technical University of Athens
Institute of Steel Structures
Zografou Campus, 9 Iroon Polytechneiou str, 15780 Zografou, Athens, Greece
e-mail: divamva@mail.ntua.gr

Keywords: Instructions, ECCOMAS Thematic Conference, Structural Dynamics, Earthquake Engineering, Proceedings.

Abstract. *The finite element method (FEM) is often employed to create detailed models for the seismic assessment and design of liquid storage tanks. This comprehensive approach offers accuracy, which is counter-balanced however by its computational inefficiency, especially for the case of large-scale engineering problems. Regardless of the continuous evolution of computer technology, surrogate models are necessary when such problems of engineering practice are encountered. This study, attempts to develop an appropriate surrogate modelling approach, tailored for the design and seismic risk assessment of liquid storage tanks. A formulation that disregards fluid-structure-interaction is employed in view of providing a reasonable compromise between modelling complexity and error. At the same time, a simplified methodology based on nonlinear static procedures is proposed for the assessment of atmospheric tanks. The comparison with Incremental Dynamic Analysis reveals a reasonable, yet conservative in some cases, match for the damage states considered, thus offering an alternative methodology that may easily be incorporated within code-based provisions.*

1 INTRODUCTION

Large-capacity cylindrical tanks are widely used to store a variety of liquids, such as petroleum and liquefied natural gas. The seismic risk of such industrial facilities is considerably higher compared to ordinary structures, since the damage induced by a strong ground motion may trigger uncontrollable consequences, not only on the actual facility but also on the environment. Recent earthquakes, e.g., Kocaeli (1999) and Tohoku (2011), have shown that heavy damage on tanks may lead to temporary loss of essential facilities, usually followed by leakage and/or fire. In order to meet a desired level of safety, Performance-Based-Earthquake-Engineering (PBEE) concepts can be employed to account for any potential sources of uncertainty. However, recent codes of practice have not fully adopted the PBEE concept, and its application to industrial facilities is limited to simple code provisions.

2 PROBLEM DEFINITION

Recent earthquakes have highlighted the need for innovative engineering concepts in order to mitigate the devastating consequences following a strong ground motion. Although extensive research takes place to date, earthquakes remain a major threat to the community both from a social and a financial point of view. The PBEE concept forms the state-of-the-art approach for evaluating the seismic risk, and should also be extended to critical infrastructure, such as the liquid storage tanks found in industrial complexes. Various approaches serve under this framework, ranging from simplified deterministic to comprehensive probabilistic. In the latter case, the structural model adopted constitutes a key parameter for the successful performance evaluation, due to the computational time required during the analysis. This remark is highlighted for the case of atmospheric liquid storage tanks, where the simulation of the fluid-structure-interaction may result in complex finite element models (FEM) that require a considerable amount of time even for a single dynamic analysis [1]. Similar studies have developed numerical approximations for the contained liquid [2,3], in an attempt to minimise the estimated computational time. Although the aforementioned FEM-based procedures may be able to capture complex modes of failure (e.g. local buckling), their suitability within a probabilistic framework may become computationally prohibitive. Still, at least two studies have attempted to develop simplified simulation techniques that blend efficiency and accuracy. Malhotra and Veletsos [4–6] presented a simplified model for the two-dimensional (2D) analysis of liquid storage tanks, while Cortes et al. [7] developed a model based on rigid beams and equivalent springs that can be used for rapid dynamic analysis. Still, neither of the two models can be easily applied out-of-the-box with commercial software: The first approach is based on custom-made analysis software, while the second needs to be calibrated with a detailed finite element model (originally taken from the NZEE standards [8] by the authors).

3 MODELLING OF LIQUID STORAGE TANKS

The response of liquid storage tanks can be idealised using a two-degree-of-freedom (2DOF) system, where the two masses (impulsive and convective) are considered decoupled [9–11]. The geometric and modal characteristics of the hydrodynamic problem are determined using equivalent parameters for the impulsive and convective masses. For the purpose of this study, the recommendations of Eurocode 8 [12] are adopted featuring Part 4 [13], where the design of tanks is discussed in detail. Under the assumption that the impulsive pressure is acting on the tank walls only, estimates for parameters such as the natural period coefficients (C_i and C_c), the masses (m_i and m_c) and the effective height components (h_i and h_c) are obtained. Subscripts "i" and "c" are used to denote "impulsive" and "convective" respectively. Previous studies have shown that the contribution of the convective mass to the overall response of the structure can

be ignored, as the impulsive mass is held responsible for the majority of the damage that tanks suffer during a strong ground motion event [2,14].

A simplified modelling methodology for liquid storage tanks was recently proposed by Bakalis et al. [15]. The surrogate modelling approach offers a compromise between computational efficiency and accuracy for the nonlinear static or dynamic analysis. It is based on the work of Malhotra and Veletsos [6] for liquid storage systems, where the uplifting mechanism of unanchored tanks is modelled analytically. According to the modelling procedure adopted the base plate is divided into an even number of strips and one of them is subjected to an incremental uplifting static load (V) in order to determine the associated resistance (Figure 1). The strip model consists of force-based fibre beam column elements with element length equal to approximately 15 times the base plate thickness, t_b. A uniaxial elastoplastic material is assigned to the fibres in order to capture the inelastic behaviour of the base plate during uplift. Geometric nonlinearities are taken into account through the co-rotational formulation. The foundation of the tank is modelled using Winkler springs to account for the soil (or concrete slab) stiffness beneath the plate. The Winkler springs are also assigned an elastic-no-tension material which is suitable for the simulation of the base plate uplift. The base plate itself is modelled using rigid beams that are supported on elastic multilinear springs. The latter simulate the nonlinear uplifting resistance for each of the '*N'* beam-spokes, representing equal-area sectors of the circular base plate. One may notice that the convective component of the fluid is not considered in the model. This decision is twofold. Obviously, the contribution of the long-period convective component to the rigid-impulsive response of a broad tank may be deemed negligible [2]. That essentially provides a single rather than a double degree-of-freedom (DOF) system, the efficiency of which can only be appreciated within a probabilistic framework. As a result, the impulsive mass (m_i) of the system is connected to the base using the elastic element shown in Figure 2(a). The deflected shape shown in Figure 2(b) presents the uplifting mechanism of the tank, where the base shear (V_b) induces a certain amount of uplift (w) on the beam-spokes of the model. This mechanism offers the ability to estimate all major modes of failure, when they are expressed as a function of uplift. Sloshing response on the other hand is only affected by parameters such as the convective mass of the fluid and the available freeboard, and may be calculated though a simple response spectrum analysis for the convective component, following the Eurocode 8 [13] provisions.

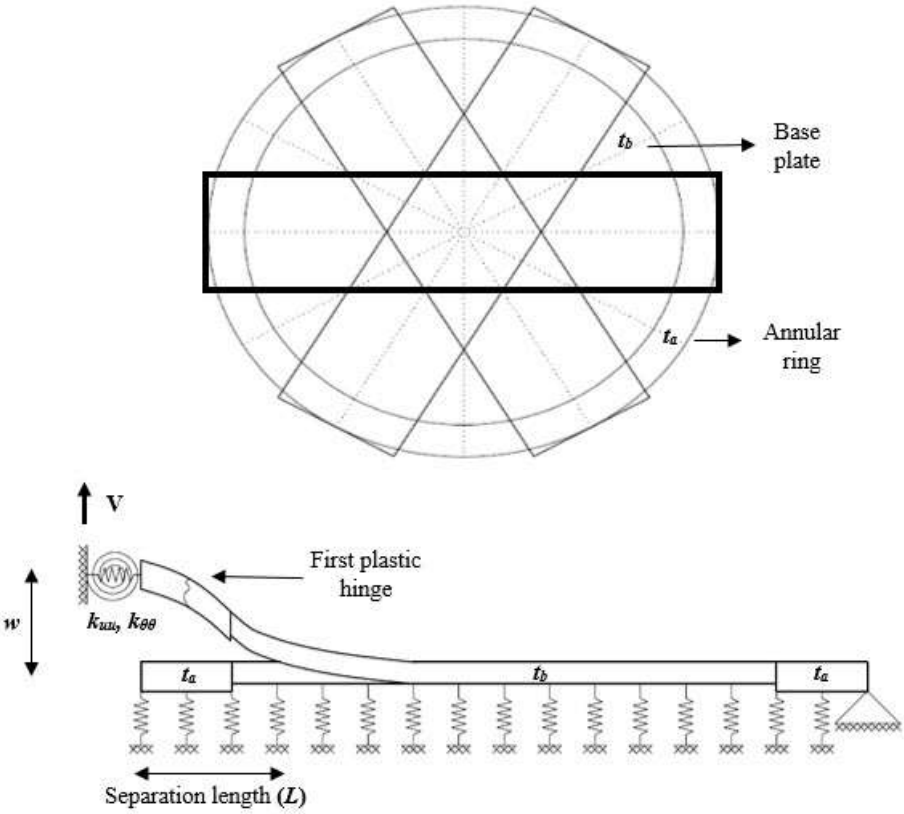


Figure 1: Strip model explained.

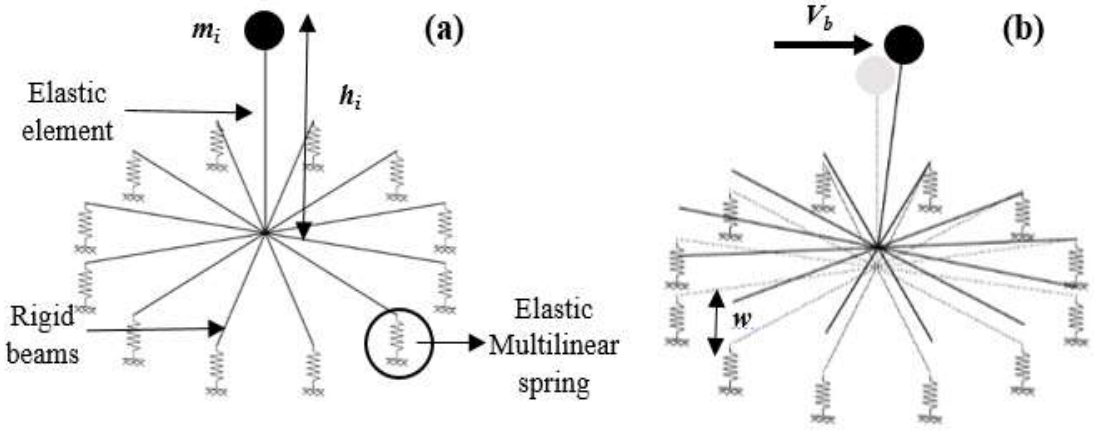


Figure 2: (a) Tank model and (b) its deflected shape.

3.1 Case Study

As a case study the liquid storage tank with the following geometric characteristics is adopted. The tank considered has a radius (R) equal to 13.9m and a total height (h_t) of 16.5m. The bottom course wall (t_w) is 17.7mm thick, while the corresponding base plate (t_b) and annular ring (t_a) thickness are 6.4mm and 8.0mm, respectively. The fluid stored in the tank is assumed to reach the maximum allowable fluid height of h_f=14m, resulting to a 'fluid height over radius' ratio (h_f/R) equal to 1.01. The properties of the liquid storage system adopted are summarised on Table 1.

Table 1. Properties of the tank examined.

	Variable description	Notation (units)	Numerical values
Tank properties	Radius	R_t (m)	13.9
	Height	h_t (m)	16.5
	Wall thickness per course	t_w (mm)	17.7/15.7/13.7/11.7/9.7/7.8/6.4/6.4/6.4
	Base plate thickness	t_b (mm)	6.4
	Annular ring thickness	t_a (mm)	8.0
	Roof mass	m_r (ton)	35
	Yield strength	f_y (MPa)	235
	Steel Young's Modulus	E_s (GPa)	210
Fluid properties	Height	h_f (m)	14.0
	Density	p_f (kg/m^3)	1000

3.2 Validation

Figure 3 presents a comparison of the overturning moment obtained with our model and with the detailed finite element model of Vathi et al. [2]. Good agreement between the two curves is observed, despite the discrepancies found in the post yield zone. The modelling procedure developed herein presents a practically perfect match close to the yield point, although it seems to underestimate the response of the unanchored tank for larger deformations. In all, the modelling procedure adopted provides a good match to the FEM solution, as the differences found do not exceed 15%.

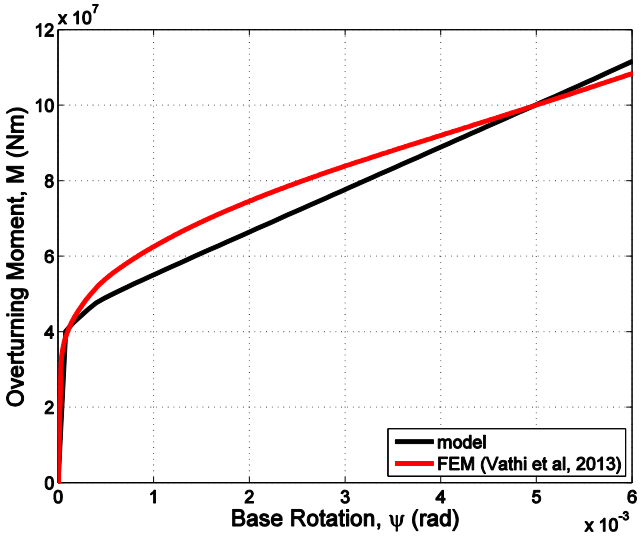


Figure 3. Base plate rotational resistance.

4 PERFORMANCE OBJECTIVES

Field investigations after major earthquakes have revealed a variety of failure modes on atmospheric tanks. They may be summarised to shell buckling, base sliding and sloshing damage to the upper tank shell and roof. EC8-part 4 [13] provides special provisions for these modes of failure, as shown by Vathi et al. [2]. For instance, when partial uplift is allowed, either for design purposes or due to poor detailing of the anchors, the rotation of the plastic hinge developed on the base plate of the tank should not exceed a certain rotational capacity. Moreover, the excitation of the long period convective mass may cause sloshing of the contained liquid,

which can in turn damage the upper parts of the tank (roof, upper wall course). During strong ground motion events, hydrostatic and hydrodynamic effects may lead to high internal pressure on the tank walls. Overturning for those thin shell structures is resisted by compressive meridional stresses on the wall. Although high pressure may increase the capacity against buckling by introducing high hoop stress, local yielding may trigger an elastic-plastic buckling failure around the lower course of the tank's perimeter, known as the "Elephant's Foot Buckling".

The most damaging failure modes are mainly associated with plate/shell rupture, as they may result in loss of the contained liquid. Rupturing either the bottom layers of the tank wall or the base plate is expected to trigger uncontrolled loss of the stored material, with all the associated consequences considered. Recently, Bakalis et al. [16] developed a performance-based assessment methodology for atmospheric steel liquid storage tanks. The PBEE framework considers three damage states of increasing severity, namely minor (DS1), severe without leakage (DS2) and loss of containment (DS3). Although this classification may seem reasonable for roughly understanding the extent of damage, the accurate assessment of loss may become tricky as, for example, the different mechanisms involved in a single damage state may be associated with varying degrees of component damage. For instance, the sloshing height response represents relatively easy-to-repair damage at the top of the tank, compared to an exceedance of a plastic rotation limit at the base. Thus, it becomes more informative to also classify damage based on the actual component that has failed. Figure 4 presents the associated failure modes on the median Incremental Dynamic Analysis (IDA) curve [17] for the unanchored liquid storage tank considered. The FEMA P695 [18] far field ground motion set is used for the nonlinear dynamic analysis. The base uplift is adopted as one of the Engineering Demand Parameters (EDP) and the impulsive period spectral acceleration $S_a(T_{imp})$ or the peak ground acceleration PGA (similar due to low T_{imp}) are employed as suitable Intensity Measures (IM) that adequately capture the response of a liquid storage system. It is evident that a component-based classification of damage is quite informative, where the upper course of the tank (SL=sloshing), its lower course (EFB), the base plate (θ_{pl}=plastic rotation), and the anchors (AN=yielding/fracture of anchors) are individually examined. Failure modes such as buckling and plastic rotation are revealed during the nonlinear time-history analysis. Sloshing damage at the top of the tank wall is also considered. Still, as shown in Figure 4, this may only appear at excessive spectral acceleration values for large tanks due to the ultra-long convective period (T_{con}).

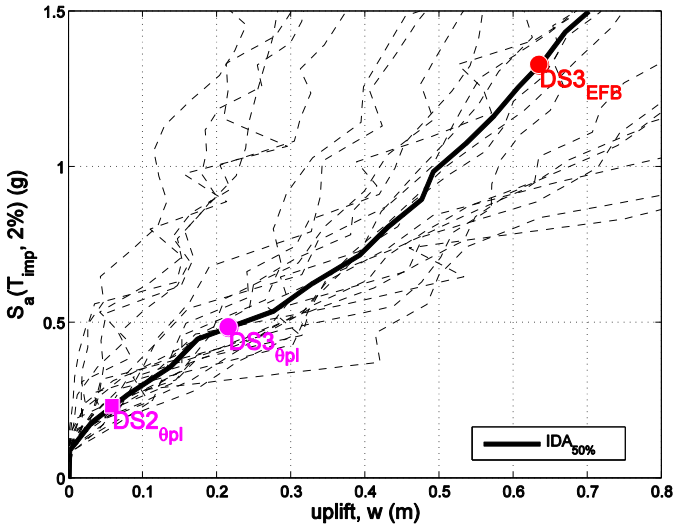


Figure 4: Single record and median IDA curves for the unanchored tank examined. Sloshing damage appears well beyond the limits of the graph.

The local performance objectives summarised in Table 2 may indeed offer a comprehensive procedure for understanding the extent of damage on a liquid storage unit, even offering the potential for assigning detailed repair cost estimates. However, it may often be the case that a global classification is required, suitable for characterising one or more tanks without specific reference to the component that has been damaged. In that sense, DS1 represents minor damage induced by a sloshing wave height of the contained liquid equal to the freeboard. DS2 refers to severe damage at any component of the tank without leakage, where the exceedance of either a sloshing wave height equal to 1.4 times the available freeboard or a plastic rotation of 0.2 rad at the base plate triggers the damage state violation. DS3, finally, provides information on the loss of containment through the exceedance of either the axial EFB capacity (N_{EFB}) or the base plate plastic rotation of 0.4 rad. As far as anchored systems are concerned, the yielding of the anchors is considered for DS1, while the fracture of the connection for DS2. Global performance objectives are presented on Table 3.

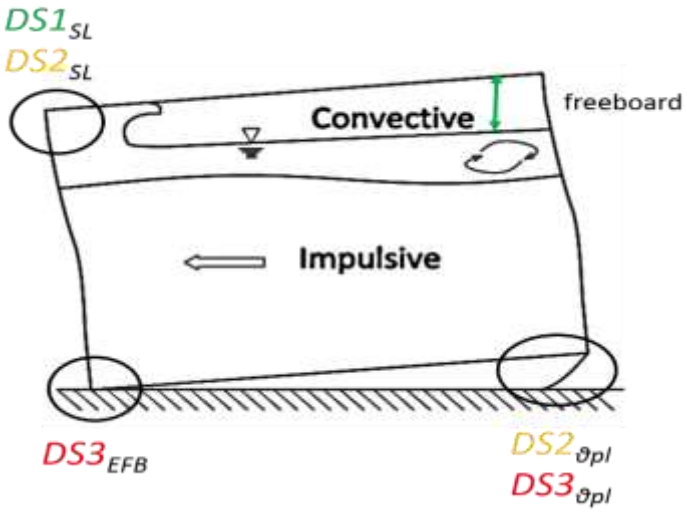


Figure 5: Global versus Local performance objectives for unanchored tanks.

Table 2: Local performance objectives.

Local DSi	DS Capacities
$DS1_{SL}$	freeboard
$DS1_{AN}$	Anchorage yielding
$DS2_{SL}$	1.4* freeboard
$DS2_{AN}$	Anchorage fracture
$DS2_{\theta pl}$	0.2rad
$DS3_{\theta pl}$	0.4rad
$DS3_{EFB}$	EFB strength

Table 3: Global performance objectives

Tank Description	Global (DSi)	DS Capacities
Unanchored	DS1	$DS1_{SL}$
	DS2	$DS2_{SL}$ or $DS2_{\theta pl}$
	DS3	$DS3_{\theta pl}$ or $DS3_{EFB}$
Anchored	DS1	$DS1_{SL}$ or $DS1_{AN}$
	DS2	$DS2_{SL}$ or $DS2_{AN}$ or $DS2_{\theta pl}$
	DS3	$DS3_{\theta pl}$ or $DS3_{EFB}$

5 SIMPLIFIED INELASTIC RESPONSE FOR LIQUID STORAGE TANKS

Performance objectives may be well defined, however, their application within a code-based methodology is still out of the box without the enforcement of nonlinear dynamic analysis. From the early days of earthquake engineering [19] till the development of more sophisticated methods [20–22], several research efforts exist for the prediction of inelastic response of structures. In spite of the miscellaneous approaches developed to date, there is common ground related to the translation of complex engineering concepts to simpler solutions that are more appropriate for practicing engineers. In that sense, the Static Pushover analysis (SPO) plays an important role in the assessment as well as the design of structures, where the well-known reduction factor (R)–ductility (μ)–period (T) relationship is required to determine the nonlinear response of the equivalent SDOF oscillator. Such relationships are available for a variety of structural systems (see Ruiz-Garcia and Miranda [21] for elastoplastic systems, Vamvatsikos and Cornell [20] for oscillators with complex quadrilinear backbones). Malhotra and Veletsos [6] have already shown that liquid storage tanks develop a nonlinear-elastic response with post-yield hardening behaviour. Unfortunately, to the authors' knowledge, such R-μ-T relationships are not available in the existing literature, while Malhotra and Veletsos chose to use instead an equivalent linearization technique that was also calibrated for elastoplastic systems. Left alone with an 'accuracy versus rapidness' dilemma, the generation of new relationships that correspond to the system examined is preferred over an obscure approximation that is based on existing R-μ-T relationships.

5.1 Fitting the hardening branch

A SDOF model with a bilinear backbone and a hardening ratio a_h=1% is used to simulate the response for a wide range of periods (0.1-1sec). A series of Incremental Dynamic Analyses is performed for the given periods in order to form a set of data that will allow the fitting of the hardening branch response. A pattern in log-space is adopted for the regression of the μ|R set of data, as shown in Eq. (1). A pattern in the form of Eq. (2) is adopted for the regression of the Eq. (1) coefficients ($\beta i_{x\%}$) versus the system period. The entire fitting procedure is presented below, where Figure 6 depicts the IDA curves and Figure 7 the Eq. (1) coefficient fits. Table 4 summarises the results of the fitting procedure.

$$\ln \mu_{x\%} = \beta_{0,x\%} + \beta_{1,x\%} \ln R + \beta_{2,x\%} (\ln R)^{1.5} \quad (1)$$

$$\beta_{i,x\%} = b_{1,x\%} + b_{2,x\%} T + b_{3,x\%} (1/T) \quad (2)$$

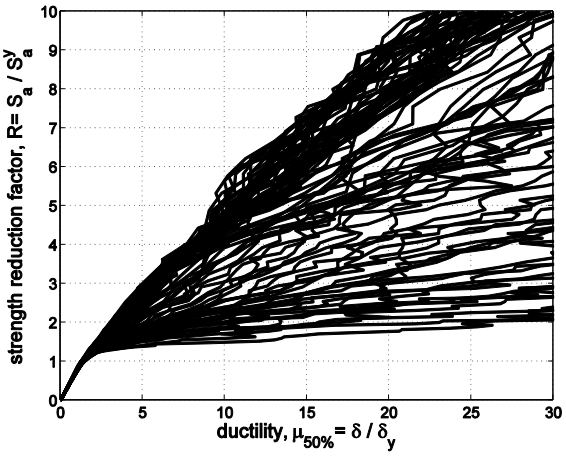


Figure 6. Strength reduction factor versus median ductility for T=0.1–1.

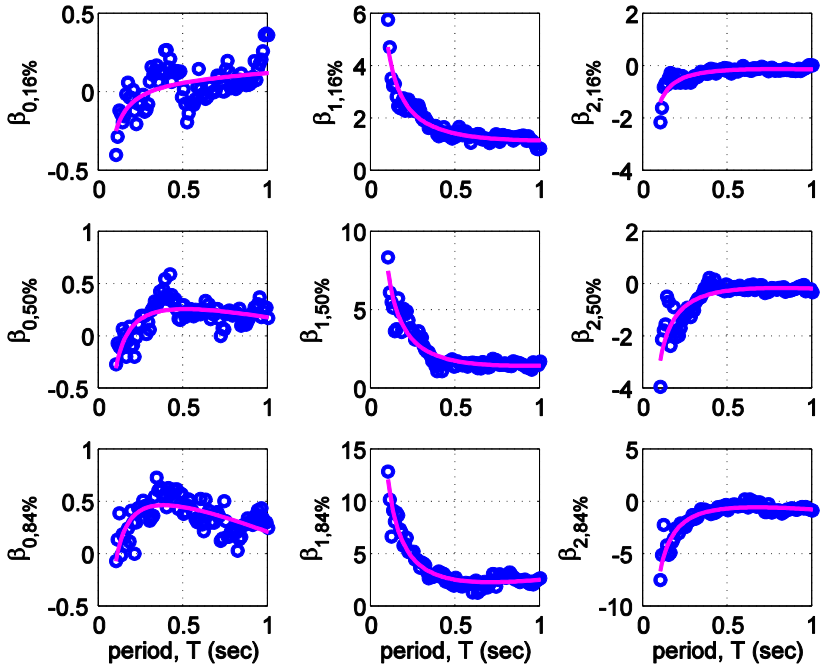


Figure 7: Regression on the Eq. (1) coefficients.

Table 4: Coefficients and functions for the IDA hardening branch fit.

	$bi_{x\%}$ for $\beta_{0,x\%}$			$bi_{x\%}$ for $\beta_{1,x\%}$			$bi_{x\%}$ for $\beta_{2,x\%}$		
hardening	16%	50%	84%	16%	50%	84%	16%	50%	84%
1	0.1056	0.6032	0.9851	0.4134	-0.2010	-1.4072	0.3221	0.7521	2.0113
T	0.0551	-0.3320	-0.6725	0.3290	0.9319	2.6714	-0.26667	-0.5504	-1.8568
$1/T$	-0.0354	-0.0868	-0.0979	0.4275	0.7613	1.3283	-0.1659	-0.3598	-0.8404

6 FRAGILITY CURVES BASED ON STATIC PUSHOVER ANALYSIS

Several methodologies for estimating fragility curves have been proposed based on nonlinear static procedures. The Static Pushover analysis is often employed to evaluate the system performance in view of the simplicity offered to practicing engineers. Despite the approximating nature of the method, there is a major drawback related to record-to-record variability which

is in turn propagated to the seismic fragility estimation. Thus, an inherently probabilistic problem is treated in a deterministic way, simply due to pushover analysis. Using the aforementioned expressions, record-to-record variability can be incorporated explicitly, while limit-state capacity uncertainties can also be included for a structural system that can adequately be approximated by a SDOF oscillator. The aforementioned procedure finds application for the case of liquid storage tanks when a model similar to the one developed by Bakalis et al. [15,16] is used. Following a Static Pushover analysis performed on the full tank model, a bilinear idealisation of the system's performance is necessary to obtain the yield point (δ_y, V_{by}). Figure 8 presents the impulsive mass displacement (here noted as δ_{roof} for compatibility reasons with the pushover terminology) versus the horizontal force (i.e. base shear) V_b.

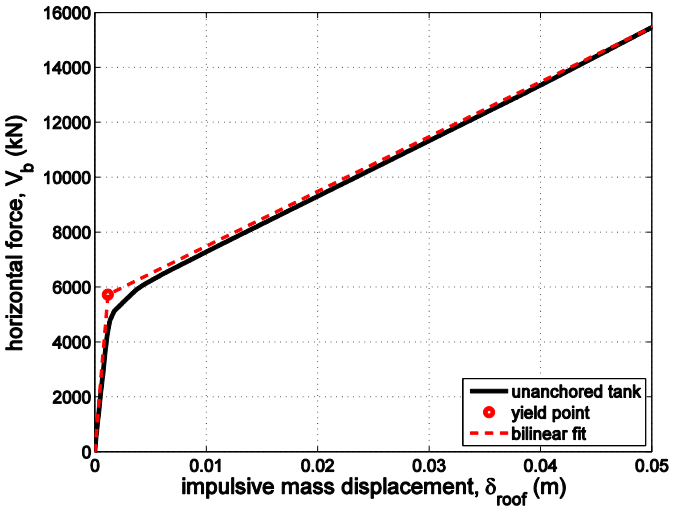


Figure 8: Pushover curve and bilinear fit for the unanchored tank examined.

Converting the damage state capacities outlined above to δ_{roof} terms constitutes a very simple task due to the direct mapping offered through the pushover analysis. For the case of plastic rotation, the estimation is fairly obvious due to the underlying correlation with uplift. On the contrary, EFB capacity is slightly trickier to estimate, as according to Eurocode 8 [13], the buckling stress σ_m is not only a function of the tank wall thickness but also of the internal pressure (p) acting on the walls in the seismic design situation (see Eq. (3)-(5)). The internal pressure is nothing more but the direct sum of the hydrostatic and hydrodynamic (i.e. impulsive) components. The latter involves the impulsive mass acceleration response (A) as shown in Eq. (6), which implies that the inelastic fundamental spectral acceleration should be used instead of the corresponding elastic one.

$$\sigma_m = \sigma_{c1}\left[1-\left(\frac{pR}{t_w f_y}\right)^2\right]\left(1-\frac{1}{1.12+r^{1.15}}\right)\left[\frac{r+f_y/250}{r+1}\right] \tag{3}$$

$$\sigma_{c1} = 0.6E\frac{t_w}{R} \tag{4}$$

$$r = \frac{R/t_w}{400} \tag{5}$$

$$p_i(\xi,\zeta,\theta,t) = C_i(\xi,\zeta)\rho H\cos\theta A(t) \tag{6}$$

The bilinear approximation adopted allows decoupling of the elastic and inelastic regions, when the corresponding stiffness (k_{el}, k_h) is considered. Simply put, at the time of maximum deformation, the inertia force equals the maximum spring restoring force. If we let S_a^{el} *and* S_a^{inel} denote the absolute spectral accelerations in elasticity and inelasticity, respectively, and S_d^{el}, S_d^{inel} stand for the corresponding spectral displacements, then, equilibrium for an elastic system would be expressed as:

$$k_{el} S_d^{el} = m S_a^{el} \tag{7}$$

leading to the well-known expression $S_a^{el} = \omega^2 \cdot S_d^{el}$. Instead, the equilibrium of an inelastic system would appear as

$$\begin{aligned} m S_a^{inel} &= k_{el}\delta_y + k_h\left(S_d^{inel} - \delta_y\right) \Leftrightarrow \cdots \Leftrightarrow \\ S_a^{inel} &= \omega^2\left[\delta_y\left(1-a_h\right) + a_h S_d^{inel}\right] \end{aligned} \tag{8}$$

that allows us to conveniently use the impulsive mass displacement (available from a pushover analysis) to estimate the corresponding inelastic spectral acceleration that influences EFB failure. As far as sloshing damage is concerned, one may rush into the conclusion that an accurate seismic fragility estimation is not possible using pushover analysis, due to the inherent decoupling between the impulsive and convective response. From a first point of view, this is a valid comment as the pushover analysis fundamentally refers to the first-mode loading pattern only. However, in view of providing an approximate solution for the derivation of fragility curves, the median convective spectral acceleration $S_a(T_{con}, 0.5\%)$ may be converted to $S_a(T_{imp}, 2\%)$ terms in order to allow for the corresponding limiting δ_{roof} displacement estimation. In our case, the FEMA P695 far-field ground motion set [18] was used to derive the relationship between the central (i.e. median) value of the impulsive and convective spectral accelerations. Although one may follow the scaling procedure for a given set of records shown in Figure 9, in practice the design spectrum could also be employed with the aid of a damping adjustment factor. Care should be exercised though for long convective periods (i.e. T_{con}>4 sec), as the spectral acceleration shape is not adequately captured through the corresponding design (uniform hazard) spectrum, something that can also be said for accelerograms that have been excessively high-pass filtered.

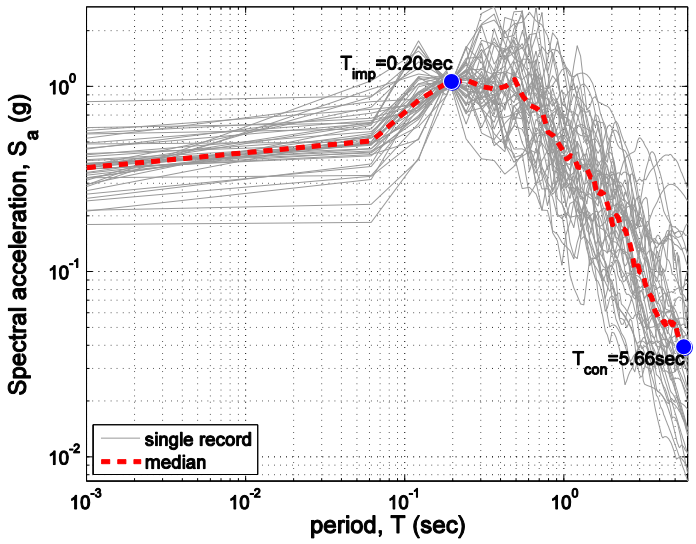


Figure 9: Single record and median spectra featuring the impulsive versus the convective component.

With the limiting capacities defined, the associated impulsive spectral accelerations may be estimated by inverting the well-known control node displacement response equation found in FEMA 440 [23] (see Eq. (10)). The inelastic displacement ratio C_R (also noted as C_1 in FEMA 440) can be estimated though Eq. (9), where the limiting reduction factor is known from the linear regression equation, for a given ductility. Unlike the majority of static pushover applications, the fundamental-mode participation factor (C_0) is set equal to one, as the capacity curve shown in Figure 8 is a product of a simple SDOF model. Similarly, the stiffness degradation modifier (C_2) is also equal to one due to the nonlinear elastic response of the liquid storage system.

$$C_R^{\lim} = \frac{\mu_{\lim}}{R_{\lim}} \tag{9}$$

$$S_a^{\lim} = \delta_{roof}^{\lim} \left(\frac{2\pi}{\mathrm{T}} \right)^2 \frac{1}{C_R^{\lim}} \frac{1}{C_0} \frac{1}{C_2} \tag{10}$$

The seismic fragility estimation forms a very simple procedure within a probabilistic framework, where the capacities are considered lognormally distributed around the corresponding limiting median estimates. The probability that demand exceeds the median limit state capacity, for a given earthquake intensity, may be calculated through the standard normal cumulative distribution function Φ shown in Eq. (11). Following a power law approximation for the median demand (valid for performance levels away from the global instability region) [24], the latter can also be given in the form of Eq. (12), where $\beta^2_{\delta_{roof}^{\lim}}$ and β^2_{μ} are the median capacity and demand dispersions, and b the slope corresponding to the power law equation (see Eq. (13)). The FEMA P-58 [25] guidelines are recommended for the median capacity dispersion estimation. The proposed strength (EFB), ductility (plastic rotation) and displacement-based (sloshing) procedures are employed for the damage state dispersion estimation. Obviously, for the case that relevant data is available, the corresponding dispersion should be used in view of providing a rather smaller margin of error in the final fragility estimation. Demand dispersion on the other hand should be calculated through the 16% and 84% R-μ fractiles, as shown in Eq. (14).

$$P\left(C < D \mid S_a\right) = \Phi\left(\frac{\ln \hat{\delta}_{roof}\left(S_a\right) - \ln \hat{\delta}_{roof}^{\lim}}{\sqrt{\beta^2_{\delta_{roof}^{\lim}} + \beta^2_{\mu}}} \right) \tag{11}$$

$$P\left(C < D \mid S_a\right) = \Phi\left(\frac{\ln \hat{S}_a - \ln \hat{S}_a^{\lim}}{\frac{1}{b}\sqrt{\beta^2_{\delta_{roof}^{\lim}} + \beta^2_{\mu}}} \right) \tag{12}$$

$$b = \frac{\ln \mu_{\lim}}{\ln R_{\lim}} \tag{13}$$

$$\beta_{\mu} = \frac{\ln \mu_{84}\left(R_{\lim}\right) - \ln \mu_{16}\left(R_{\lim}\right)}{2} \tag{14}$$

In order to accurately assess the seismic risk involved in liquid storage tanks, an intensity measure that characterises the structural system's response in an optimal manner must be identified. There could be a lot of discussion regarding which intensity measure better represents the structural response during the seismic risk assessment procedure. Unfortunately, such a discussion is not valid when the pushover analysis is used, as the fundamental-mode load-pattern adopted mandates the use of the corresponding spectral acceleration. For the case of liquid storage tanks that would be the impulsive mass spectral acceleration $S_a(T_{imp})$.

Figure 10 presents the seismic fragility evaluation based on the simplified procedure outlined above. Fragility curves are provided for all local damage states given in Table 2, and a comparison with the IDA-based assessment procedure discussed by Bakalis et al. [16] is performed in view of evaluating the proposed SPO-based methodology. It appears that fragility curves are in good agreement for the sloshing and plastic rotation damage states, although minor discrepancies exist throughout the intensity considered, that can be attributed to the fitting procedure of the cumulative distribution function. The Elephant's Foot Buckling failure mode also presents a good match for low to moderate seismic intensities. Discrepancies are noticed though as the impulsive spectral acceleration is increased, where the response seems to be significantly overestimated when the pushover analysis is employed. Although further research is necessary to verify the results of Figure 10, the complexity of the EFB mode of failure as well as the associated uncertainties is of an extent that cannot probably be captured through a SDOF model pushover analysis. Still the seismic fragility product presents a rather conservative illustration of the system's performance, and hence its application within a code-based methodology could be considered.

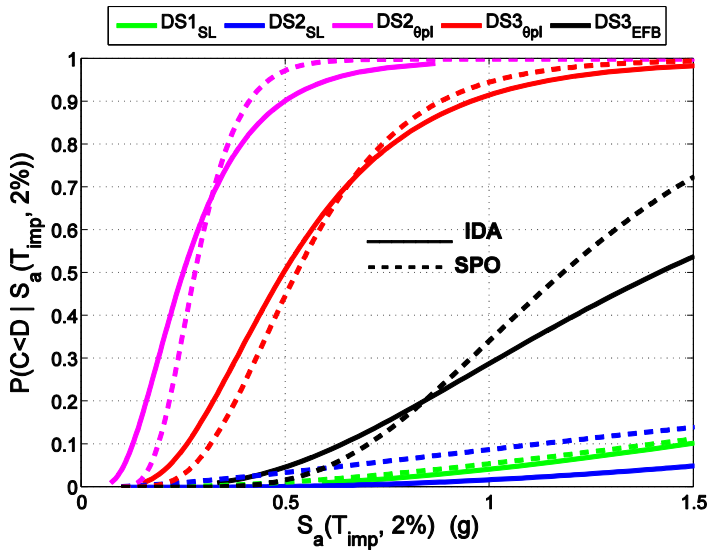


Figure 10: A comparison between IDA and SPO-based fragility curves for the local DS classification.

7 CONCLUSIONS

A surrogate, yet robust, beam element model has been presented for the analysis of liquid storage tanks. Its accuracy in comparison with computationally expensive finite element models make it appealing for design applications. Since the computational effort for a single nonlinear response history analysis does not exceed a few seconds, one may realise that the applicability of the SDOF model can be extended to a seismic risk assessment framework. Incremental Dynamic Analysis is employed for the identification of the most damaging failure modes. Local as well as global damage states are defined, favouring the seismic risk assessment of either a

single liquid storage system or an entire group of tanks, respectively. Following the damage state definition, a simplified assessment methodology is presented based on static pushover analysis, where the estimation of the corresponding limiting capacities is discussed in detail. The evaluation of the pushover-based seismic risk assessment methodology is performed through the extraction of fragility curves that correspond to all local damage states. The comparison with an IDA-based methodology shows the pushover to offer a conservative estimate for the Elephant's Foot Buckling damage state, but a reasonable agreement for the remaining failure modes. The proposed assessment methodology is not intended to substitute well-tested procedures based on nonlinear dynamic analysis. Instead, it attempts to form a simplified technique that may serve under a code-based framework the majority of practicing engineers.

REFERENCES

[1] Kilic S and Ozdemir Z. "Simulation of Sloshing Effects in Cylindrical Containers under Seismic Loading." *Proceedings of the 6 LS-DYNA Anwenderforum, Frankenthal*, 2007.

[2] Vathi M, Pappa P and Karamanos SA. "Seismic Response of Unanchored Liquid Storage Tanks." *Proceedings of the ASME 2013 Pressure Vessels & Piping Division Conference, Paris, France*, 2013.

[3] Talaslidis DG, Manolis GD, Paraskevopoulos E, Panagiotopoulos C, Pelekasis N and Tsamopoulos J. "Risk analysis of industrial structures under extreme transient loads." *Soil Dynamics and Earthquake Engineering*, Vol. 24, No.6, 2004, pp. 435–48.

[4] Malhotra PK and Veletsos AS. "Beam Model for Base- Uplifting Analysis of Cylindrical Tanks." *Journal of Structural Engineering*, Vol. 120, No.12, 1994, pp. 3471–88.

[5] Malhotra PK and Veletsos AS. "Uplifting Analysis of Base Plates in Cylindrical Tanks." *Journal of Structural Engineering*, Vol. 120, No.12, 1994, pp. 3489–505.

[6] Malhotra PK and Veletsos AS. "Uplifting Response of Unanchored Liquid- Storage Tanks." *Journal of Structural Engineering*, Vol. 120, No.12, 1994, pp. 3525–47.

[7] Cortes G, Prinz GS, Nussbaumer A and Koller MG. "Cyclic Demand at the Shell-Bottom Connection of Unanchored Steel Tanks." *15th World Conference on Earthquake Engineering, Lisboa, Portugal*, 2012.

[8] NZEE. "Seismic Design of Storage Tanks." *New Zealand National Society for Earthquake Engineering Wellington, New Zealand*, 2009.

[9] Malhotra PK, Wenk T and Wieland M. "Simple Procedure for Seismic Analysis of Liquid-Storage Tanks." *Structural Engineering International*, Vol. 10, No.3, 2000, pp. 197–201.

[10] Priestley MJN, Wood JH and Davidson BJ. "Seismic Design of Storage Tanks." *Bulletin of the New Zealand Society for Earthquake Engineering*, Vol. 19, No.4, 1986, pp. 272–84.

[11] Calvi GM and Nascimbene R. "Progettazione sismica dei serbatoi." *Progettare i gusci, IUSS Press*, 2011. p. 537–672.

[12] CEN. "Eurocode 8: Design Provisions Of Structures For Earthquake Resistance - Part 1: General rules, seismic actions and rules for buildings, CEN, Brussels." *CEN [Comité Européen de Normalisation]*, 2004.

[13] CEN. "Eurocode 8: Design of structures for earthquake resistance–Part 4: Silos, tanks and pipelines." European Committee for Standard. *Brussels*, 2006.

[14] Malhotra PK. "Seismic Response of Soil-Supported Unanchored Liquid-Storage Tanks." *Journal of Structural Engineering*, Vol. 123, No.4, 1997, pp. 440–50.

[15] Bakalis K, Vamvatsikos D and Fragiadakis M. “Surrogate Modelling and Sensitivity Analysis of Steel Liquid Storage Tanks.” *8th Hellenic National Conference of Steel Structures, Tripoli, Greece, 2-4 October 2014*, 2014.

[16] Bakalis K, Vamvatsikos D and Fragiadakis M. “Seismic Reliability Assessment of Liquid Storage Tanks.” *2nd European Conference on Earthquake Engineering and Seismology, Istanbul, Turkey, 24-29 August 2014*, 2014.

[17] Vamvatsikos D and Cornell CA. “Incremental dynamic analysis.” *Earthquake Engineering & Structural Dynamics*, Vol. 31, No.3, 2002, pp. 491–514.

[18] FEMA. “Quantification of Building Seismic Performance Factors.” *FEMA P-695, prepared by Applied Technology Council for Federal Emergency Management Agency, Washington, D.C.*, 2009.

[19] Veletsos A and Newmark NM. “Effect of inelastic behavior on the response of simple systems to earthquake motions.” *Proceedings of the 2nd World Conference on Earthquake Engineering*, 1960. p. 895–912.

[20] Vamvatsikos D and Cornell CA. “Direct estimation of the seismic demand and capacity of oscillators with multi-linear static pushovers through IDA.” *Earthquake Engineering and Structural Dynamics*, Vol. 35, No.April 2004, 2006, pp. 1097–117.

[21] Ruiz-García J and Miranda E. “Probabilistic estimation of maximum inelastic displacement demands for performance-based design.” *Earthquake Engineering and Structural Dynamics*, Vol. 36, No.March, 2007, pp. 1235–54.

[22] Kreslin M and Fajfar P. “The extended N2 method taking into account higher mode effects in elevation.” *Earthquake Engineering and Structural Dynamics*, Vol. 40, 2011, pp. 1571–89.

[23] FEMA. “Improvement of Nonlinear Static Seismic Analysis Procedures.” *FEMA 440, prepared by the Applied Technology Council for the Federal Emergency Management Agency, Washington D.C*, 2005.

[24] Cornell CA, Jalayer F, Hamburger RO and Foutch D a. “Probabilistic Basis for 2000 SAC Federal Emergency Management Agency Steel Moment Frame Guidelines.” Journal of Structural Engineering. 2002. p. 526–33.

[25] FEMA. “Seismic Performance Assessment of Buildings.” *FEMA P-58, prepared by the Applied Technology Council for the Federal Emergency Management Agency, Washington D.C*, 2012.

COMPDYN 2015
5th ECCOMAS Thematic Conference on
Computational Methods in Structural Dynamics and Earthquake Engineering
M. Papadrakakis, V. Papadopoulos, V. Plevris (eds.)
Crete Island, Greece, 25–27 May 2015

BURIED PIPELINES SUBJECTED TO GROUND DEFORMATION CAUSED BY LANDSLIDE TRIGGERING

Angelos Tsatsis[1], **Rallis Kourkoulis**[1] **and George Gazetas**[1]

[1] National Technical University of Athens
Heroon Polytexneiou 9, Athens, Greece
ag_tsa@yahoo.gr, rallisko@sgm-engineering.com, gazetas@ath.forthnet.gr

Keywords: Pipelines, Landslide, Permanent Ground Deformation, Soil-Structure Interaction, Geotechnical Earthquake Engineering.

Abstract. *Permanent ground deformation is one of the most damaging hazards for buried lifelines such as gas and oil pipelines. The most frequent cause of permanent ground deformation is a landslide. Landslides can be triggered by a variety of causes, yet the factors responsible for the most damaging landslides are water and especially earthquake. The scope of this study is to investigate the response of a continuous buried pipeline subjected to ground deformation caused by landslide triggering, considering two characteristic cases: (a) the pipeline running perpendicularly to the soil movement vector and (b) the pipeline is parallel to the soil movement vector. An idealized landslide of 3D geometry is considered. Due to the inconsistency between the colossal dimensions of the landslide and the much smaller pipe geometry (a combination that would call for a numerical model of several millions elements), the problem is decoupled. In the first step, a "global" free-field model is employed to simulate the landslide evolution, ignoring the presence of the pipeline. The free field analysis provides the input for the second step, in which a "local" detailed model of the pipeline, along with the surrounding soil, is used to simulate its distress. This allows the use of adequately large elements for the global model, and reasonably small elements for the local one, circumventing the aforementioned scale-related problem.*

1 INTRODUCTION

Oil and gas pipelines typically run for very long distances (of the order of hundreds or even thousand kilometers) crossing various topographic anomalies such as slopes. Many of these slopes can be prone to failure during an earthquake or heavy precipitation incident and therefore potentially hazardous for landsliding occurrence. Past experience has proved that pipelines are quite vulnerable to permanent ground deformation (such as landslide) compared to other geohazards such wave propagation [1] [2]. Therefore, it is of paramount importance to be able to realistically simulate the response of pipelines subjected to ground deformation caused by landslide triggering. To this end, this study presents an integrated numerical methodology for the simulation of both the landslide triggering and evolution as well as the response of the pipeline that crosses the critical area.

2 ANALYSIS METHODOLOGY

The 3D nature of the problem is accounted for and the simulation is conducted in 3D. Since the simultaneous simulation of the pipe and the landslide is practically impossible the problem is decoupled. This happens because in order to simulate pipe instability issues, such as local buckling, a very fine mesh is needed for the pipe and the soil at its vicinity. On the other hand, this demand cannot be combined with the large dimensions of the landslide. According to the decoupled methodology, the landslide evolution is first analyzed ignoring the presence of the pipe assuming that the presence of the pipe does not affect the landslide at a global level. The free field analysis provides the input for the second step, in which a "local" detailed model of the pipeline, along with the surrounding soil, is used to simulate its distress. This allows using adequately large elements for the global model, and reasonably small elements for the local one, circumventing the aforementioned scale-related problem.

3 NUMERICAL SIMULATION OF THE LANDSLIDE

Landslides can be of various types. The most widely used classification system was devised by Varnes [3]. Varnes identified five principal categories: falls, topples, slides, spreads, and flows. With respect to the distress of the pipeline, falls and topples may cause damage to above-ground pipelines by direct impact of falling rocks. These types of landslide have little effect on buried pipelines though given that the embedment depth is adequate. In cases of spreads and flows the transported material behaves as a viscous fluid, for which the properties must be defined with caution. On the other hand, in an earth slide, the soil moves more or less as a block, with the materials retaining approximately the same properties with their initial state. For the purposes of this study, an idealized rotational slide is considered. The geometry of the slope and the properties of the soil remain constant. A distinct zone of weakness is predefined, representing the interface between the stable "healthy" soil and the unstable part of the slope, consisting of a loose material (a hypothesis of deposits from a previously triggered landslide is made).

A section of the analyzed slope is presented in Figure 1a (i.e., the two dimensional geometry of the landslide). The elevation difference between the foot and the crest of the slope is 20 m, while the length of the slope is 70 m, yielding a slope angle of 16º. Regarding the sliding surface geometry, a circular failure surface is assumed, described by the intersection of the slope with a circle of radius R = 100 m, with its center 95 m higher and 15 m to the left of the toe of the slope foot. In order to obtain the 3D geometry of the landslide, it is tactically assumed that the 2D section of Figure 1 corresponds to the middle cross section of the landslide, where the largest volume of material is mobilized, while the sliding surface is getting shallower as it moves away from the middle cross section. The 3D geometry of the sliding soil

mass is introduced through the intersection of the 3D slope with the cutting shape that is presented in Figure 1b. This cutting shape comprises a circular middle section in the z–x plane, identical to that presented above. However, in both x–y and y–z plane the adopted shape comprises elliptical sections in order to simulate a smooth sliding mass shape fade out.

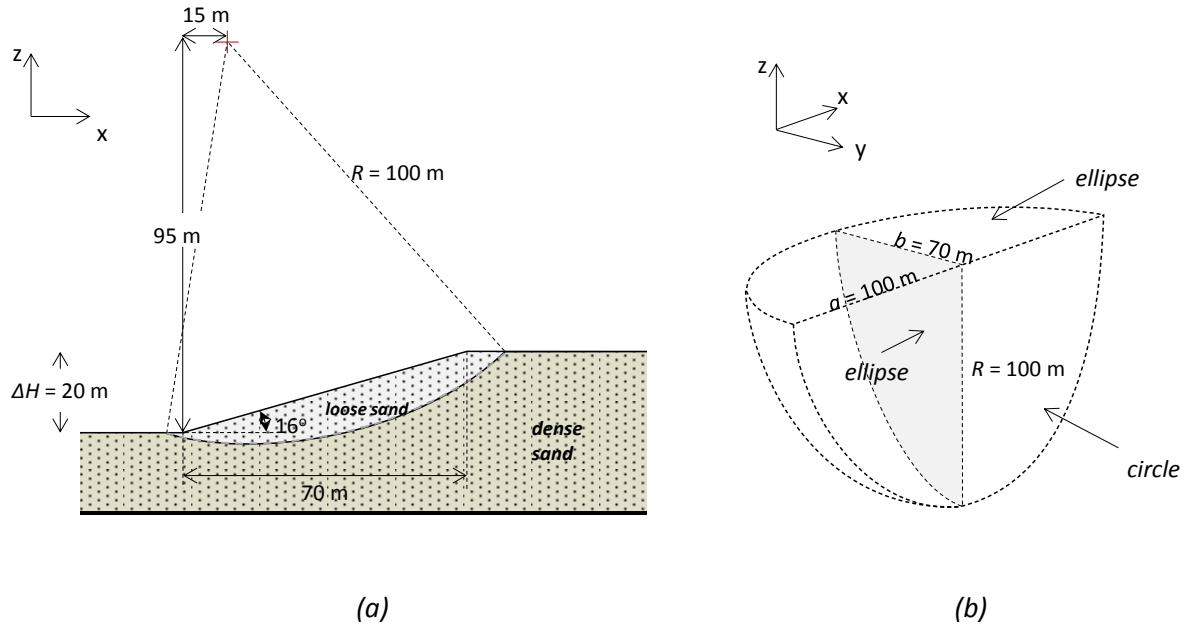


Figure 1: (a) The 2D geometry of the slope and the selected circular cutting plane and (b) the cutting shape used to derive the 3D geometry.

In Figure 2 the finite element model used is briefly presented. Taking advantage of the symmetry of the problem geometry, half of the slope is examined. The middle section, where the largest volume of material is mobilized, is the surface of symmetry. The sliding mass is assumed to consist of a loose material and therefore simulated with a loose sand of Young's modulus E = 10 MPa and friction angle $\varphi = 32^o$. The stable soil surrounding the sliding mass comprises dense sand of E = 25 MPa and $\varphi = 45^o$. The soil is modeled with 8-noded brick type elements, while its strength and nonlinear response is described with a Mohr-Coulomb constitutive model. The sliding plane is simulated with a row of elements of reduced stiffness and strength (E = 8 MPa and $\varphi = 30^o$) between the sliding mass and the stable soil. The landslide is triggered by progressively reducing the strength of these elements with time from $\varphi = 30^o$ to $\varphi_{res} = 5^o$.

Figure 3 presents snapshots of the triggering and evolution of the landslide. As expected, due to the 3D depiction of the geometry of the slide, the soil does not dislocate in a uniform manner throughout the sliding mass; both displacement magnitude as well as the vector of the displacement vary along the sliding mass. It is worth noting that for this slope, the landslide triggering takes place near the crest of the slope, since the inclination of the failure surface is larger in this area. As observed from the displacement contours, during the initial stages of the phenomenon, the soil near the crest of the slope displaces significantly more than the soil near the toe of the slope (top right snapshot). Subsequently, there comes a point where the landslide fully mobilizes and the displacement of the sliding mass becomes more uniform (bottom left snapshot for maximum displacement U = 1 m). In the ensuing the displacement of the point lying on the crest line and on the plane of symmetry (called hereon reference point) is used as an index to describe the evolution of the landslide.

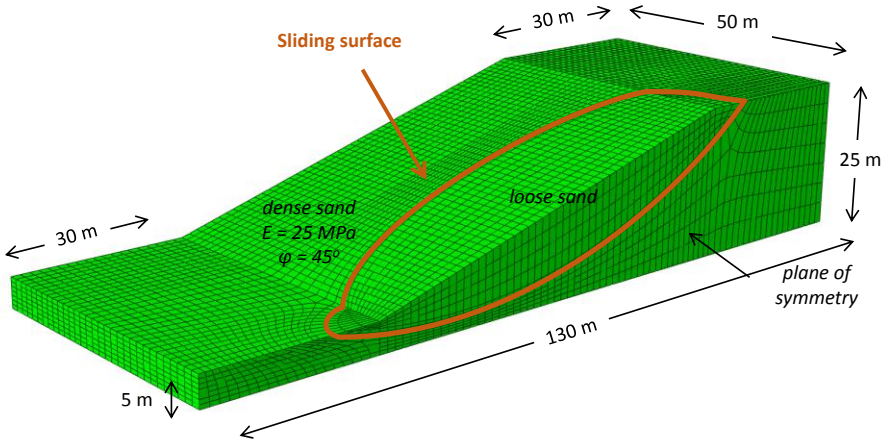


Figure 2: The finite element model of the landslide.

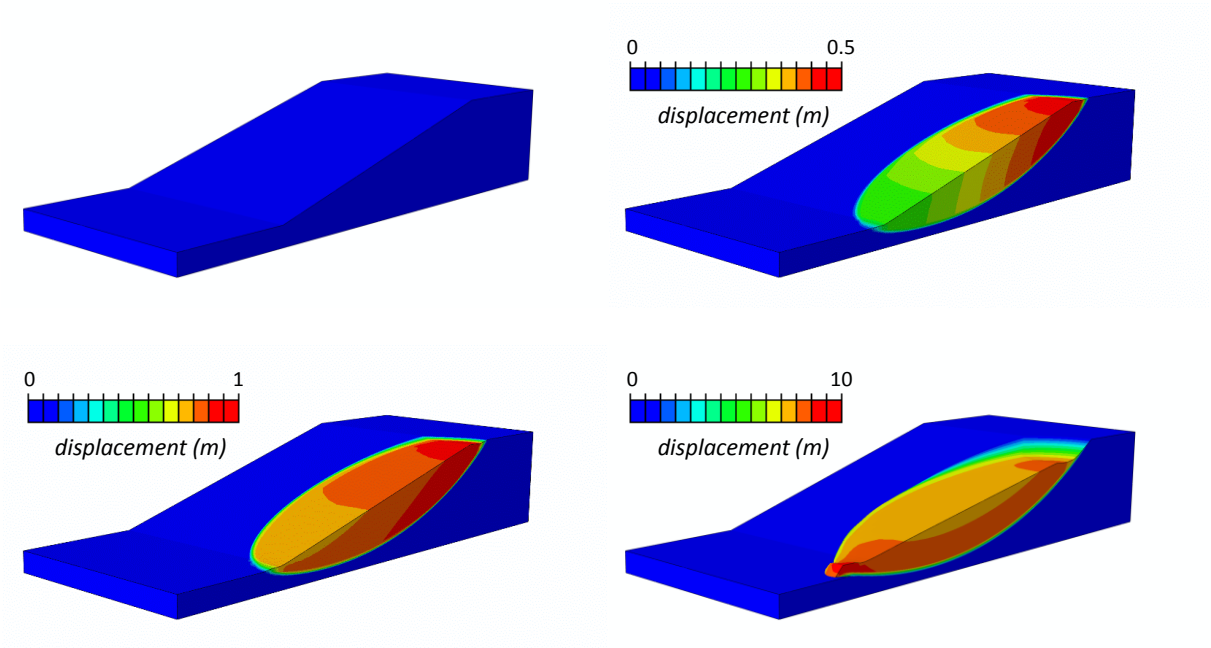


Figure 3: Representative snapshots of the landslide evolution.

4 PIPELINE – LANDSLIDE INTERACTION

A continuous steel pipeline is considered that crosses the aforementioned slope. Two extreme cases are investigated: (a) the pipeline crosses perpendicularly the slope and the potential soil movement direction is parallel to its axis and (b) the pipeline runs in parallel with the slope contour lines and the soil movement direction is perpendicular to its axis. The pipe is made of X65 steel with yield stress σ_y = 450 MPa and maximum stress σ_{max} = 545 MPa at strain ε_{max} = 0.2. The pipe is of diameter D = 36'' and it is designed for a maximum internal pressure of p_{max} = 9 MPa. Its thickness is calculated at t = 12.7 mm as dictated by the expression:

$$p_{max} = 0.72 * \left(\frac{2\sigma_y t}{D}\right) \quad (1)$$

To make the results more realistic the pipeline is considered to be functional under operating pressure p_{oper} = 6 MPa. The pipe is assumed to be embedded in depth 1.5 m from the surface to the crown pipe.

4.1 Pipeline axis parallel to the soil movement

To begin with, the case where the pipe axis is normal to the contour lines of the slope is considered. The centerline of the pipe is at 2 m away from the plane of symmetry of the slope. In order to accommodate the change in the axis inclination two bends are used, one at the toe and one at the crown of the slope. Those bends have a radius of curvature 40 times the pipe diameter (representative of cold bends).

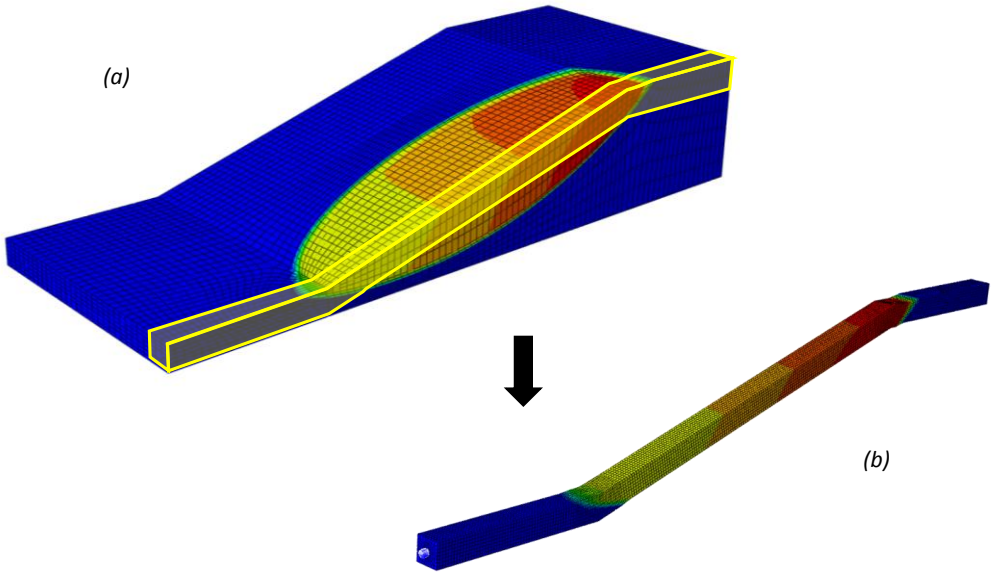


Figure 4: The displacement time histories are extracted from the "global" free field model and imposed as input at the boundaries of the "local" pipeline - soil interaction model.

After the installation of the pipe the aforementioned landslide occurs. As already stated, the analysis is decoupled (Figure 4). Figure 5 presents the local finite element model, used to model soil–pipeline interaction and its various components. Only a soil prism around the pipe is modeled. The pipeline is modeled with 4-noded reduced integration shell elements. 48 elements along the pipe circumference are used of length d_{FE} = 2.5 cm, aiming to realistically capture local instability phenomena.

For the correct simulation of the pipe response, the behavior of the pipe beyond the boundaries of the 3D model has to be accounted for. The soil displacement is expected to cause (among others) axial stressing to the pipe. Axial distress may affect large length of the pipe (of the order of several hundred meters or even kilometers), rather than the limited segment that is simulated in this analysis. In order to account for the axial response of the pipe along its theoretically infinite length the following procedure is followed. First, the soil reaction to axial pulling of the pipe is calculated. For this, a full 3D finite element model of a pipe segment within the soil is employed. The model accounts for the inelastic behavior of the soil and the contact between the pipe and the soil considering interface friction (in this case friction coefficient between the pipe and the surrounding soil is μ = 0.5). The pipe is considered rigid. Knowing the soil reaction per meter to a potential axial movement of the pipe, a simpli-

fied model is used to calculate the force – displacement response of the soil pipe system to an imposed axial displacement. This simplified model is lengthy enough to be considered infinite (the stresses developed on the pipe dissipate within the length simulated). The soil reaction is simulated with distributed springs along the pipe length that are calibrated against the force-displacement behavior of the soil derived from the first step. The pipe is simulated with beam elements accounting for the steel material nonlinearity. An axial displacement is applied at the end of the pipe and the reaction of the pipe–soil system is measured. This reaction (in terms of force – displacement) is attributed to a nonlinear spring at the ends of the pipe at the boundaries of the 3D pipe – landslide interaction model.

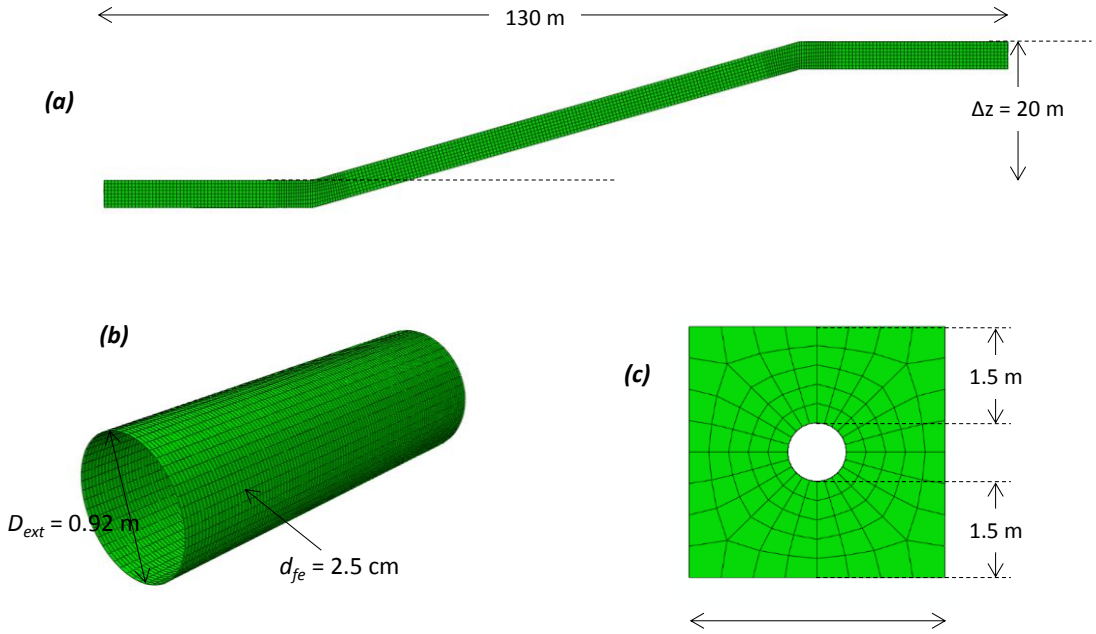


Figure 5: The finite element model that focuses on the soil–pipeline interaction for the case of pipeline positioned parallel to the soil movement: (a) longitudinal view of the model, (b) a detailed view of the pipeline mesh, (c) Cross section showing the meshing of the soil and the dimensions of the soil prism.

Figure 6 presents the deformed mesh of the pipe–landslide interaction model corresponding to displacement magnitude of the reference point U_{ref} = 0.75 m. Figure 6a presents the deformed mesh of the soil prism with superimposed displacement contours, while Figure 6b presents the deformed mesh of the pipe with superimposed stress contours. It is proven that the two bends are the most stressed components by the downslope movement of the soil. Figure 6c concentrates on the top bend (i.e. the one at the crown of the slope). The stressing mechanism can be seen as mechanically analogous to a normal fault. The failure surface where the sliding of the soil mass occurs can be seen as the rupture. Therefore, a part of the bend is fixed within the stable soil while the rest is dragged downwards and outwards by the moving soil. The fixed part bends as cantilever developing tension at the top side and compression at the bottom side, while the dislocating part develops compression at the top side and tension at the bottom side. The bottom bend exhibits similar response, only this time the response mechanism is analogous to a reverse fault. Due to the geometry of the sliding surface, at the intersection with the pipe at the vicinity of the slope toe the soil goes upwards with the simultaneous compression component. The part of the pipe that follows the sliding mass is stressed by the underlying soil (bending) resulting in compression at the bottom side and tension at the top side of the pipe. The part of the pipe that lies within the stable soil bends due to reactions from the overlying soil with the top side under compression and the bottom side un-

der tension. Yet, the downward movement of the soil prevails with the pipe ultimately failing due to local buckling at the part of the bend that is within the stable soil.

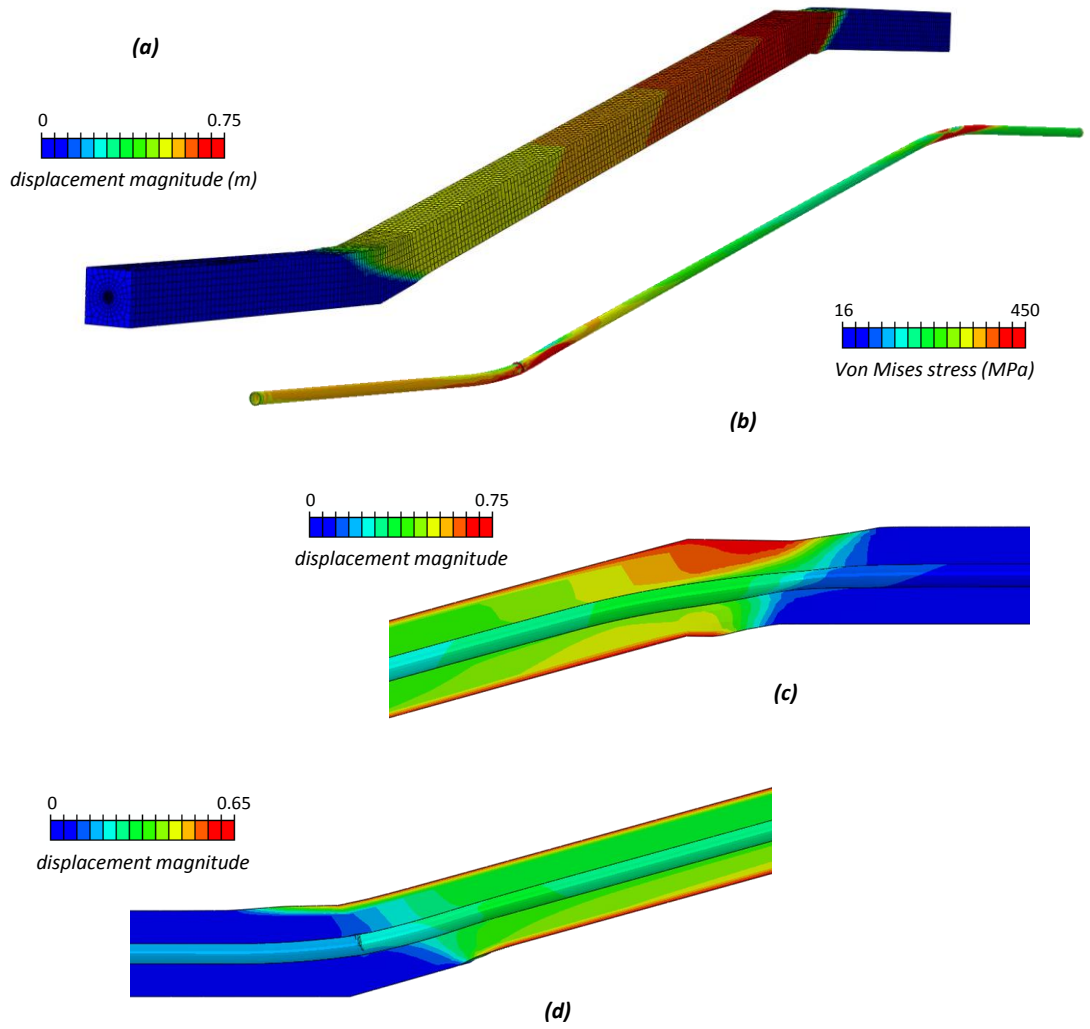


Figure 6: Deformed mesh of the pipeline – landslide interaction problem for displacement magnitude of the reference point U_{ref} = 0.75 m. (a) Deformed mesh of the soil prism. (b) Deformed mesh of the pipe. (c) Cross section of the deformed model concentrating on the top bend. (d) Cross section of the deformed model concentrating on the bottom bend.

Figure 7 and Figure 8 present a closer look at the response of the two bends. Figure 7a presents the deformed mesh of the top bend with superimposed axial strain contours depicting the response mechanism described above. Figure 7b presents the axial strain distribution along the tensile side of the critical area. Considering a tensile failure criterion of ε_{max} = 3% [3], the pipe ultimately fails for U_{ref} = 0.46 m of displacement of the reference point. Figure 8a presents the deformed mesh of the bottom bend with superimposed axial strain contours, while in Figure 8b the axial strain distribution along the compressive side of the critical area of the bottom bend is presented. As evidenced by the shape of the distribution, wrinkling occurs for displacement of the reference point (at the slope crest) U_{ref} = 51 cm. Practically, the two bends fail at the same time, with a minor difference in the critical displacement of the reference point (51 cm for the bottom bend compared to 46 cm for the top bend). However, we

have to remind that this displacement is not uniform throughout the sliding mass; when the reference point at the crest line of the slope has been displaced by 51 cm the respective point at the toe line has displaced 28 cm.

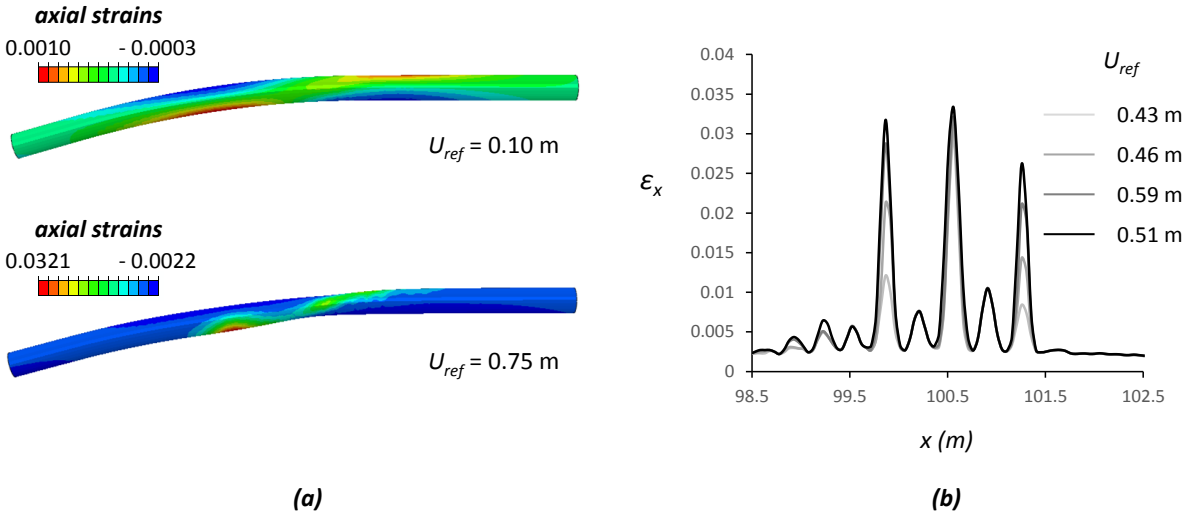


Figure 7: The finite element model that focuses on the soil–pipeline interaction for the case of pipeline positioned parallel to the soil movement: (a) longitudinal view of the model, (b) a detailed view of the pipeline mesh, (c) Cross section showing the meshing of the soil and the dimensions of the soil prism.

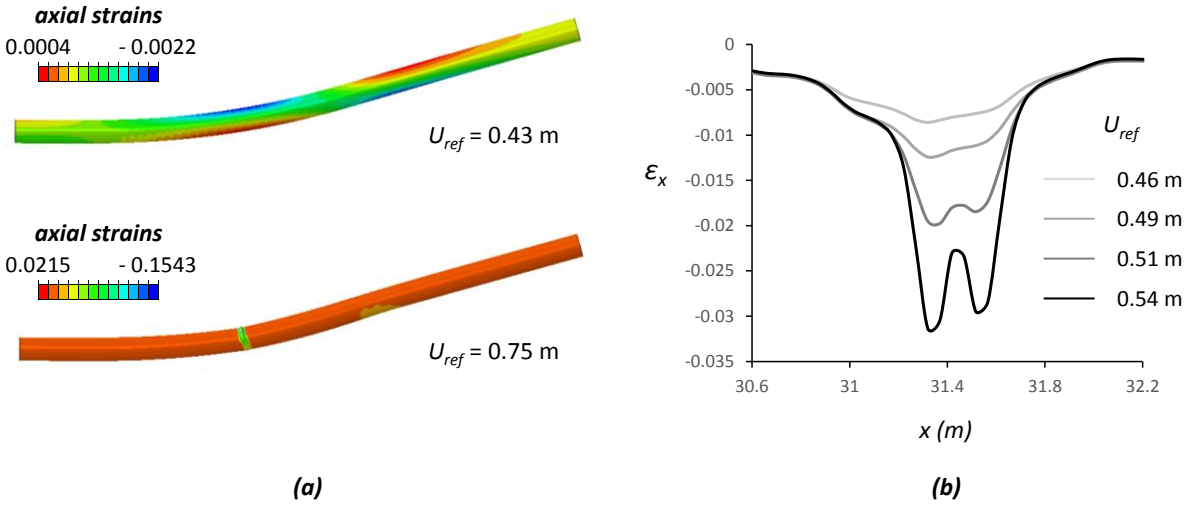


Figure 8: The finite element model that focuses on the soil–pipeline interaction for the case of pipeline positioned parallel to the soil movement: (a) longitudinal view of the model, (b) a detailed view of the pipeline mesh, (c) Cross section showing the meshing of the soil and the dimensions of the soil prism.

4.2 Pipeline axis perpendicular to the soil movement

In this section, the other extreme case is considered where the pipe runs in parallel with the contour lines of the slope intersecting at 90^o with the potentially unstable soil deposit. As an illustrative example of such case, the pipe axis is assumed to be located at the middle of the slope between the toe and the crest of the slope. As explained before, in order to analyze the response of the pipeline subjected to the landslide actions the problem is decoupled. The free

field analysis provides the input for the second step, in which a "local" detailed model of the pipeline, along with the surrounding soil, is used to simulate its distress as shown in Figure 9.

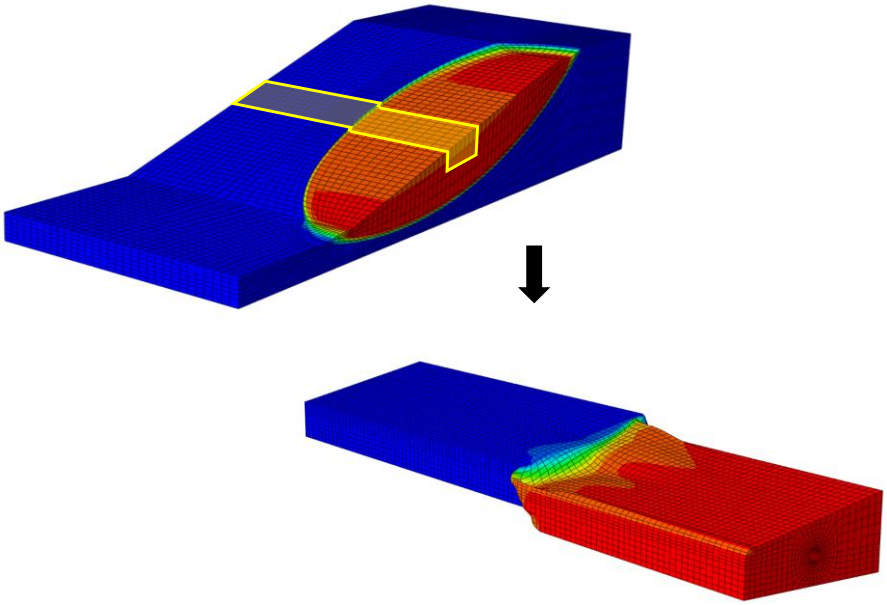


Figure 9: The finite element model that focuses on the soil–pipeline interaction for the case of pipeline positioned parallel to the soil movement: (a) longitudinal view of the model, (b) a detailed view of the pipeline mesh, (c) Cross section showing the meshing of the soil and the dimensions of the soil prism.

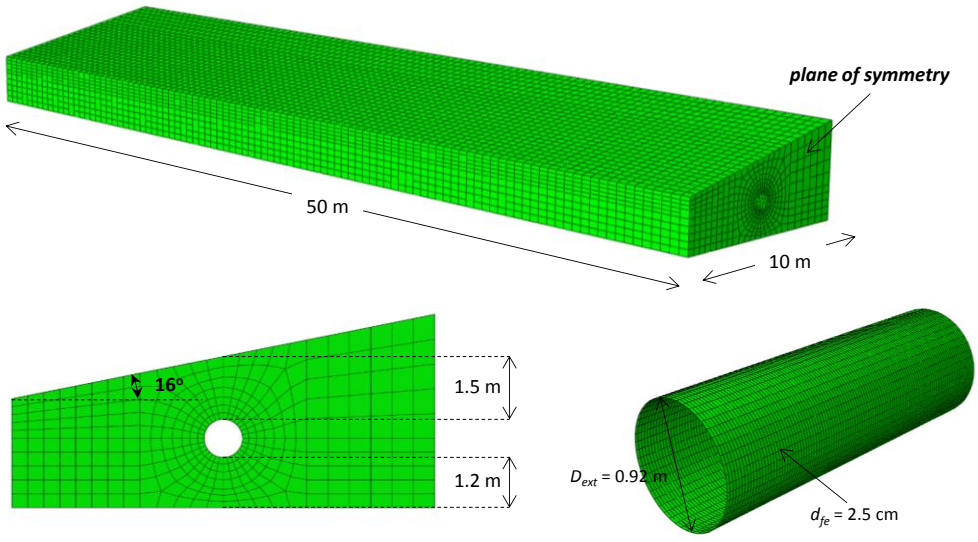


Figure 10: The finite element model that focuses on the soil–pipeline interaction for the case of pipeline positioned perpendicular to the soil movement: the dimensions of the soil prism, a cross section of the prism and a detail of the pipeline mesh.

The finite element model that focuses on the pipeline – landslide interaction is presented in Figure 10. As with the free field model, taking advantage of the symmetry of the problem only half of the pipeline is modeled. In the plane of symmetry all the appropriate degrees of

freedom are constrained. On the other end of the 3D model the pipeline – soil behavior is taken into account using nonlinear springs. The displacements calculated from the free field analysis are imposed at the bottom of the model and at the two sides parallel with pipe axis. Therefore, the distance of these two sides from the pipe axis is equal to 5 diameters to minimize any boundary effects, and to allow any interaction phenomena between the pipe and the surrounding soil to take place.

Figure 11 presents the deformed mesh of the pipe – landslide interaction model for displacement magnitude of the reference point U_{ref} = 1.07 m. It should be noted that at this specific moment, the soil that lies on the plane of symmetry at the immediate vicinity of the pipe (and therefore the pipe end at the plane of symmetry) has been displaced U = 0.95 m. The pipe deforms due to the landslide induced actions and axial strains are developed as shown in for the same Figure 11b displacement. Two maximum curvature points are observed, where the concentration of the axial strains is substantial. The pipe ultimately fails due to excessive tensile strains at the tensile side of the maximum curvature point within the stable soil (Figure 11c). This is expected since the stable soil is of greater strength than the sliding soil, resulting in increased actions on the pipe. Finally, Figure 11d presents the evolution of the axial strain distribution along the most stressed generator at the critical area. Considering a failure criterion of maximum tensile axial strain ε_{max} = 3 % the pipe fails for displacement magnitude of the reference point U_{ref} = 1.0 m (which translated to 0.89 m of displacement of the pipe end lying on the plane of symmetry).

5 CONCLUSIONS

In this study, a two-step analysis methodology has been developed, allowing realistic simulation of pipeline distress due to landslide displacement. Landslides have a 3D geometry, which depends on a variety of factors, which are quite unique for each case. In terms of an illustrative example, an idealized landslide was selected and analyzed. To overcome numerical difficulties, arising from the scale differences between the landslide and the pipeline, the problem is decoupled and the analysis is conducted in two steps. In the first step, a global free-field model is used to simulate the evolution of the landslide, ignoring the presence of the pipeline. In the second step, a more detailed local model is developed, comprising the pipeline and the surrounding soil. The computed displacement time histories from the first step (global model) are imposed as boundary conditions to the local model. The methodology was employed for an illustrative example. A 36'' pipeline of thickness t = 12.7 mm and internal pressure of 6 MPa crosses an idealized rotational landslide considering two characteristic cases: one where the pipeline axis is parallel to the soil movement and one where it is perpendicular to the soil movement. In the first case the bends prove to be most vulnerable components and the pipeline fails for U_{ref} = 0.46 m of displacement of the reference point. In the second case the pipe fails for U_{ref} = 1 m of displacement of the reference point.

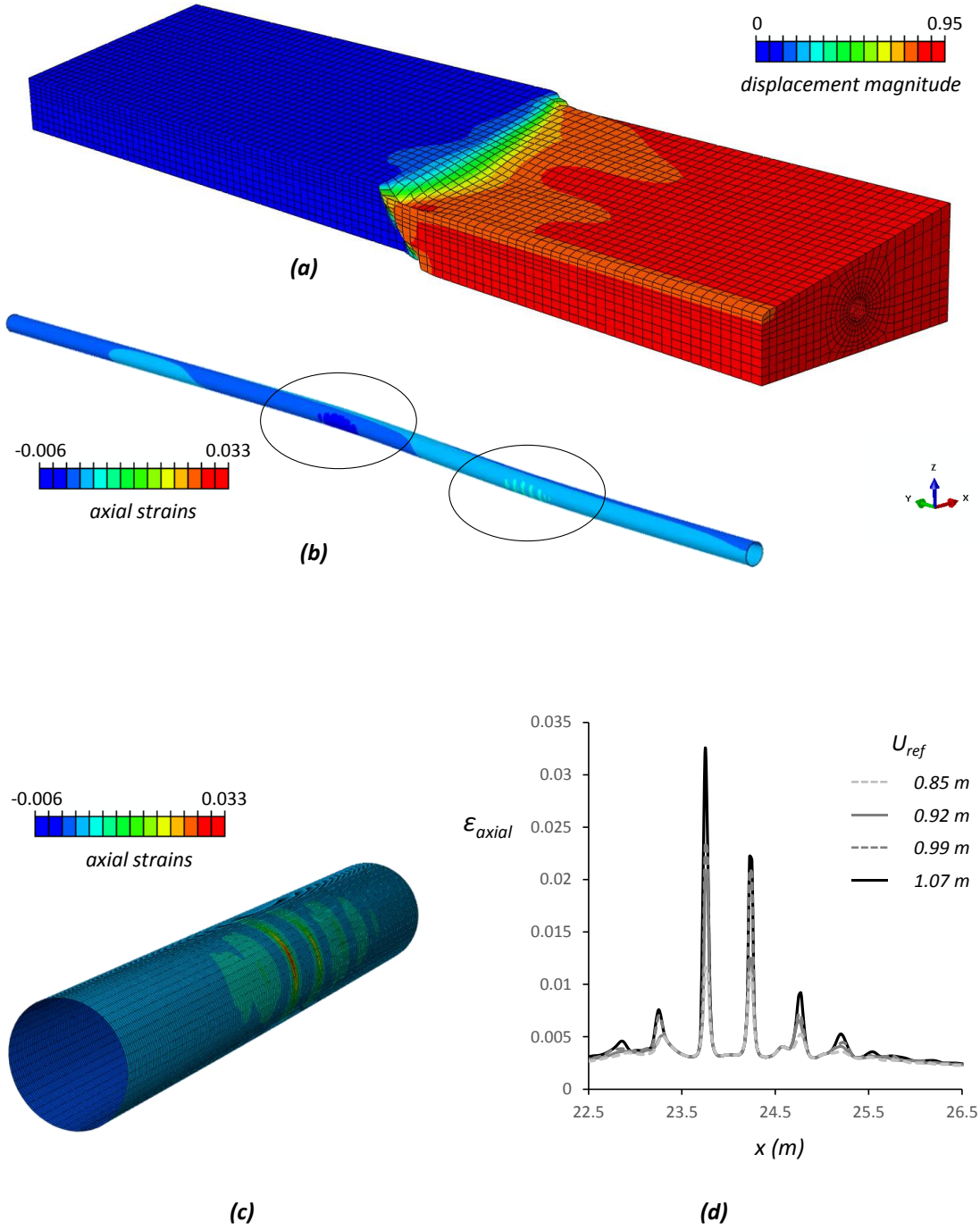


Figure 11: (a) The deformed mesh of the pipeline – landslide interaction model with superimposed displacement contours for displacement of reference point U_{ref} = 1.07 m. (b) Deformed pipe with superimposed axial strain contours for the same displacement. (c) Detail of the pipe mesh at the area of the maximum curvature point within the stable soil (critical area). (d) Evolution of the axial strains at the most stressed generator of the critical area of the pipe with the increase of the pipe displacement.

ACKNOWLEDGEMENT

This research has been co-financed by the European Union (European Social Fund – ESF) and Greek national funds through the Operational Program "Education and Lifelong Learning" of the National Strategic Reference Framework (NSRF) – Research Funding Program: Thales. Investing in knowledge society through the European Social Fund, Project ID "UPGRADE".

REFERENCES

[1] Ariman T, Muleski GE. A review of the response of buried pipelines under seismic excitations. *Earthquake Engineering and Structural Dynamics* 1981;9:133-51

[2] Liang J, Sun S. Site effects on seismic behaviour of pipelines: a review. ASME Journal of Pressure Vessel Technology 2000;122(4):469-75.

[3] EN 1998-4 (1993). "Eurocode 8: Design of structures for earthquake resistance. Part 4: Silos, Tanks and Pipelines", CEN, Brussels.

COMPDYN 2015
5th ECCOMAS Thematic Conference on
Computational Methods in Structural Dynamics and Earthquake Engineering
M. Papadrakakis, V. Papadopoulos, V. Plevris (eds.)
Crete Island, Greece, 25–27 May 2015

PERFORMANCE EVALUATION OF BURIED STEEL PIPES SUBJECT TO STRIKE SLIP FAULT OFFSETS

E. Uckan[1], B. Akbas[2], F. Cakir[3], J. Shen[4], M. O'Rourke[5], M. Caglar[1], F. Paolacci[6]

[1] Bogazici University
Kandilli Observatory and Earthquake Research Institute, Istanbul, Turkey
eren.uckan@boun.edu.tr, nmervec@gmail.com

[2] Gebze Technical University
Deparment of Earthquake and Structural Engineering, Kocaeli, Turkey
akbasb@gtu.edu.tr

[3] Amasya University
Dept. of Architecture, Amasya, Turkey
ferit.ckr@gmail.com

[4] Iowa State University
Dept. of Civil, Construction and Environmental Engineering, Ames, IA, US
jshen@iastate.edu

[5] Rensselaer Polytechnic Institute
Dept. of Civil and Environmental Engineering, Troy, NY, US
orourm@rpi.edu[3]

[6] University of Roma Tre
Deparment of Engineering, Roma, Italy
fabrizio.paolacci@unirome3.it

Keywords: Buried Steel Pipes, Continous Pipelines, Fault Crossings, Perforrmance-Based Design..

Abstract. *Buried steel pipes are commonly used in oil and gas industry for transmitting hydrocarbon products. Fault crossing is considered as one of the most important extreme events. Buried steel pipes are more vulnerable to compressive strains as compared to tensile strains. In this study, a numerical study is carried out on a simplified numerical model to determine the seismic demand on steel pipes at fault crossings. The proposed model permits plastic hinge formation in the pipe due to incrementally applied fault movements, allow determining the critical length of the pipeline and measure strains developed on the tension and compression sides in the pipe. Based on the analyses carried out on the simple model and previous studies, two performance levels are defined for pipelines; namely, fully functional and partially functional.*

1 INTRODUCTION

Buried steel pipes are commonly used in oil and gas industry for transmitting hydrocarbon products from sources to end points. Critical hazard locations for such pipes are in spatially varying permanent ground deformation (PGD) zones (liquefaction and landslide) and fault-crossing locations. Among these, the fault crossing is considered as one of the most important extreme events since the axial strains in the pipe can reach to very high values due to combined effects of bending and axial deformations.

Past earthquakes (1999 Kocaeli earthquake, Turkey; 1999 Chi-Chi earthquake, Taiwan) revealed the fact that the strain demand on pipes crossing active faults may be quite extreme due to relative movement of the fault with respect to the pipe axis [1]. When a continuous pipe is subjected to permanent ground deformation due to fault rupture, the damage pattern depends on the type of the fault, material and geometric properties of the pipe. Pipes with high D/t ratios are usually more vulnerable than the pipes with low D/t ratios, where D and t are the diameter and thickness of the pipe, respectively [2, 3]. In Turkey, most of the pipe damage data is available for segmented pipes in PGD zones [4]. O'Rourke et al. [5] calculated the data points to develop the fragility curves for segmented pipes in Turkey using damage data from 1999 Kocaeli earthquake. Possibly, one of the best documented case study of buried continuous pipe response to fault offsets is the Thames Water Pipeline during the 1999 Izmit (Turkey) event [6, 7]. A welded steel, D= 2.2m water transmission pipe with (D/t = 122) crossing the Sapanca Segment of the North Anatolian Fault at an angle $\beta = 125$ degrees in Kullar, southeastern Izmit, Kocaeli, Turkey (Figure 1) was subject to right lateral fault ruptured with an offset of 2.45 m in Kullar, Izmit. The fault offset caused two major wrinklings and one minor buckling at three different locations on the pipe.

The limit states for buried steel pipes are: a) the maximum tensile strain, b) local buckling due to axial compressive strain (critical buckling strain), c) distortion of pipeline cross section, and d) tearing of the pipe wall [2]. The amount of the strain depends on the type and orientation of the fault with respect to the pipe axis, geometric and material properties of the pipe (steel grade, pipe diameter and thickness), burial depth (deep or shallow), and the properties of the surrounding soil [2, 8].



Figure 1. A close-up view to the wrinkled pipe in Kullar, Izmit during the 1999 Kocaeli Earthquake

In this study, a numerical study is carried out on a simplified numerical model which takes into account the plastic hinge formations and nonlineat soil springs is constructed. The response of the nonlinear pipe-soil interaction system to incrementally applied fault displacements (perpendicular to the pipe axis) is calculated. Critical length of the pipeline, L_{cr} (the distance between the first plastic hinges at both sides of the fault line), and strain demand on compression and tension sides of the pipes are selected as the major response parameters. Large displacement analyses are first verified on a benchmark problem and then applied to the model. The proposed model permits plastic hinge formation in the pipe due to incrementally applied fault movements, allow determining the critical length of the pipeline and measure strains developed on the tension and compression sides in the pipe. The model also considers the effect of bending minimum performance criteria for pipelines are proposed. Based on the analyses carried out on the simple model and previous studies, minimum performance criteria for pipelines are proposed. Two performance levels are defined for pipelines; namely, fully functional and partially functional.

2 STEEL PIPELINES AT FAULT CROSSINGS

Design of steel pipelines crossing a major fault line is based on the determination of axial strain. In general, two types of axial strains are involved in the pipe [3]:

a. Axial bending strains due to the transverse component of fault offset,
b. Net axial deformations of the pipe due to the axial (longitudinal) component of the fault offset.

The magnitude of the pipe strain, in general, depends on the orientation of the pipeline with respect to the pipe axis as well as the slip direction. A strike slip fault movement will induce an axial as well as transverse movement on steel pipes. Axial component will cause uniform axial strain in the forms of tension or compression. In the fault normal direction (90^0 to the pipeline axis), axial strain will be equal to zero, whereas axial strain (tension/compression) will gradually increase with increasing fault movement. As the fault movement increases, the tensile strains will develop due to stretching of the pipe in reversed direction. This will cause reduction in the compressive strains after the peak compressive strain has been reached [3]. The most significant deformation will happen in an effective length, L, of the S shaped segment of the pipeline (Figure 2). L is determined analytically and is based on the elastic behavior of the pipe. In this study, L is calculated numerically as the length of the pipe segment, L_{cr}, which is defined as the distance between the points where first significant yielding occurs in the pipe on both sides of the fault (Figure 2). Seismic design and analyses of steel pipes crossing fault lines are provided by ALA [9], Eurocode 8 [10] and ASCE [11] in detail. Seismic evaluation of these pipes should be based on performance-based design principles as proposed in this paper.

3 NUMERICAL ANALYSES

As a case study, seismic response of a steel pipe is investigated. The pipe is assumed to be perpendicular to the strike slip fault line in the horizontal plane. A structural model consisting of two segments (1^{st} block and 2^{nd} block) is constructed with a total length of 100.0 m; width of 10.0 m, and depth of 5.0 m (Figure 2). Incremental fault displacement is applied gradually to the 2^{nd} block up to the total fault displacement of 3.0 m, while keeping the 1^{st} block fixed.

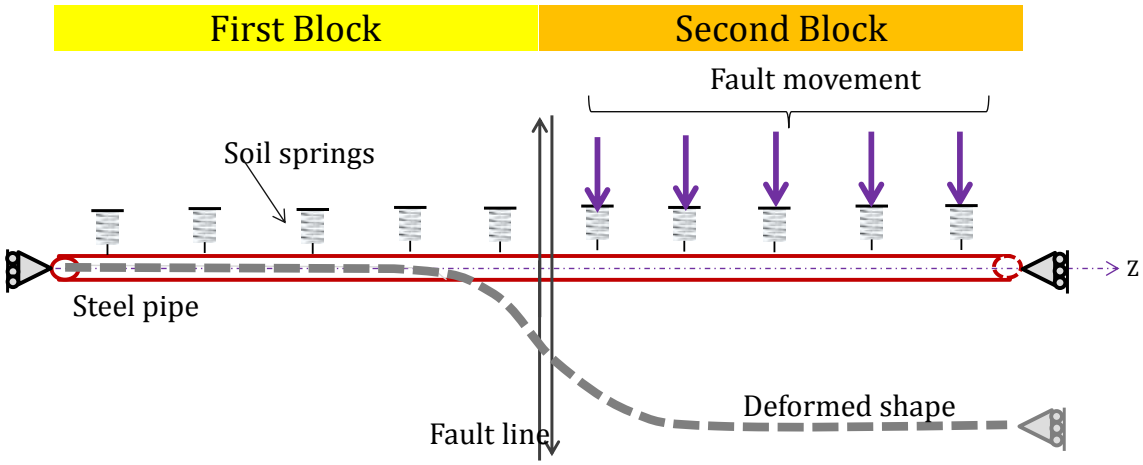


Figure 2. A plan view of the simple model representing pipe behavior under prescribed fault movement perpendicular to the pipe axis (Z axis)

A simplified model consisting of a nonlinear beam element to represent the pipe and linear/nonlinear soil springs attached to the pipe at discrete points is proposed to determine the seismic response of the pipe (Figure 2). Detailed information about the model can be found in [12]. The prescribed displacements are applied to the support nodes of the 2nd block (moving block) only. Nonlinear static analysis is performed to compute the deformations and strains in the pipe of the soil-pipe interaction system (Figure 2). SAP2000 V15 software [13] is used for the analyses. SAP2000 V15 [13] allows to consider large displacement and strain in the analyses. This is verified in a simple arc structure.

The steel pipe used in the study has a diameter (D) of 914.4 mm and thickness (t) of 12.7 mm (Figure 3). Steel grade is assumed as A992Grade50. To determine the plastic hinge formation, axial force (P)-moment (M) hinges are assigned along the pipe at 2.5 m intervals (Figure 4). Soil cohesion for soft clay is assumed to be 10 kPa at a depth of 3.0 m. The beam elements used in the analysis provide stresses and bending moments at nodal points. For further verification of the simplified model, a detailed 3-D finite element (FE) model of a similar pipeline with material and geometric nonlinearities has been constructed as well (Figure 5). Critical pipe length, L_{cr}, axial force and bending moments in the pipe, and strain demand in the pipe on the tension and compression sides are selected as response parameters.

The response of a buried pipeline due to fault offset consists of three phases. In Phase I (small offsets), both axial and bending strains are important, and both increase with fault offsets. Bending strains are large enough such that there is a non-zero net compressive strain. In Phase II (intermediate offsets), the axial strain is beyond yield, and bending stiffness (and hence bending strain) are decreasing and the net compressive strains approach zero. In Phase III (large offsets), the bending strain remains constant while axial strain increases with increasing fault offsets [6] .

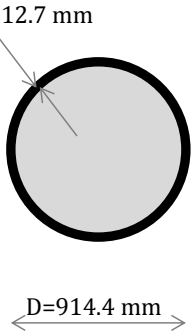


Figure 3. Steel pipe cross-section (A_g=36,000 mm^2)

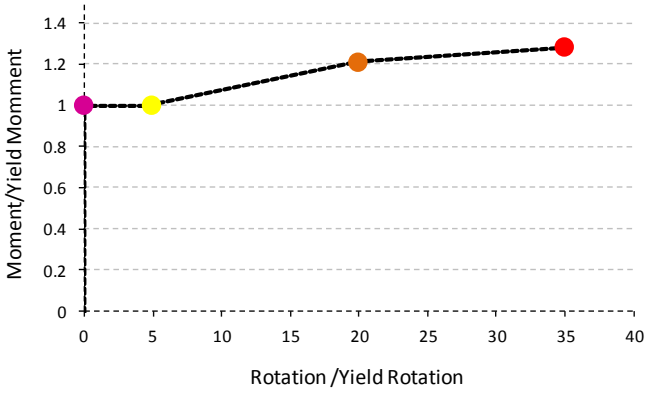


Figure 4. Moment hinge properties for the steel pipe

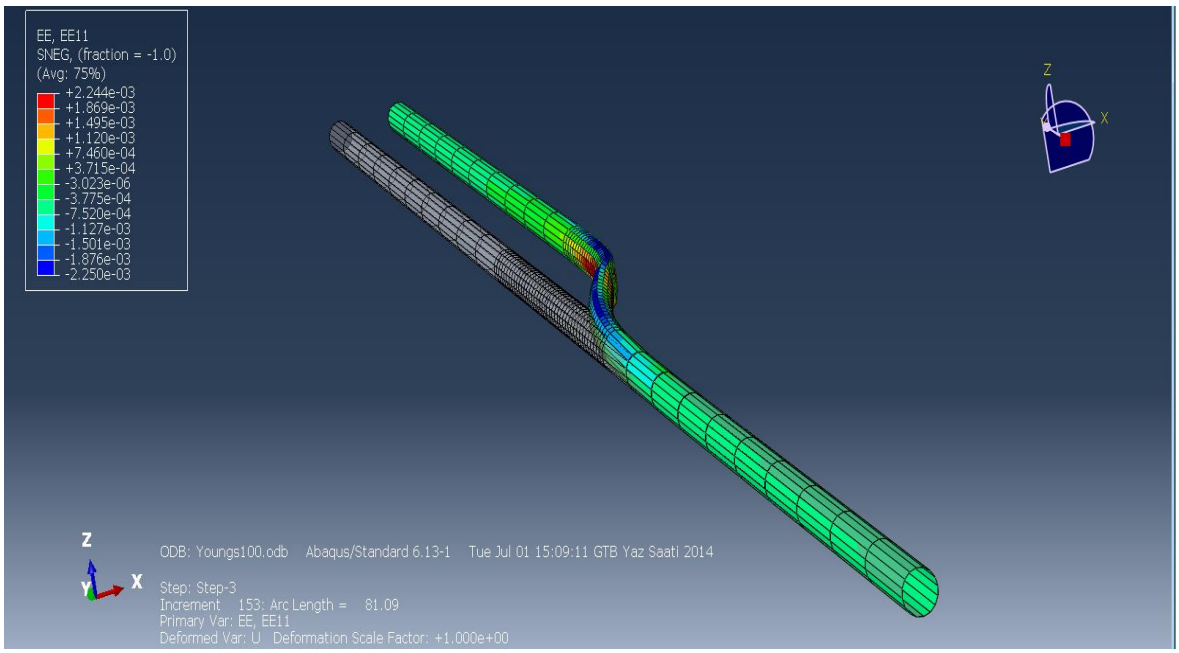


Figure 5. Stress analyses on 3-D FE model of a pipe [14]

4 DISCUSSION OF ANALYSES RESULTS

As a result of nonlinear static analyses, plastic hinge formation indicates L_{cr} of 12.5 m for the pipe. L_{cr} according to Vazouras et al. [3] is found to be 15.5 m for the pipe. Vazouras et al.' [3] expression is based on *D/t* ratio and soft clay as well as steel grade of X65, fault clearance of 33 cm and no internal pressure. Results can be considered as in reasonable agreement.

Fault movement is applied at small increments, *d*=0.2 m, 0.4 m, 0.6 m, 1.0 m, 1.50 m , 2.0 m, 2.5 m, and 3.0 m. The variation in the axial forces developed in the pipe is shown in Figure 6. The axial force is uniformly distributed throughout the pipeline and reaches to 10,900 kN for the pipe at *d*=3.0 m. The critical fault displacement (d_{cr}) corresponding to the first plastic hinge formation with low *D/t* ratio is found to be 1.28 m (Figure 7). As the fault movement increases, the plastic hinge formation spreads to the vicinities of the first plastic hinge formations at both sides of the pipe segment, L_{cr}. The variation of bending moment diagram for the pipe is plotted in Figure 8.

The pattern of the bending moment diagram remains the same along the pipe axis and is symmetrical with respect to the inflection point which is nearly in the middle of the L_{cr}. The peak bending moment is about 2,700 kNm at *d*=3.0 m at which the axial load is the maximum. It is about 4,750 kNm at d_{cr}=1.44 m which corresponds to the fault movement where the first plastic hinge is observed, at which the axial load is only 2,900 kN. Strains along L_{cr} on the tension and compression sides of the pipe are also plotted in Figure 9. The maximum tensile strains are about 0.04 and 0.05 at d_{cr}=1.28 m and *d*=3.0 m, respectively. On the other hand, the maximum compressive strain is about 0.03 at d_{cr}=1.28 m and occurs at a distance for about 7.5 from the fault line. It tends to decrease as the fault moves further from d_{cr}.

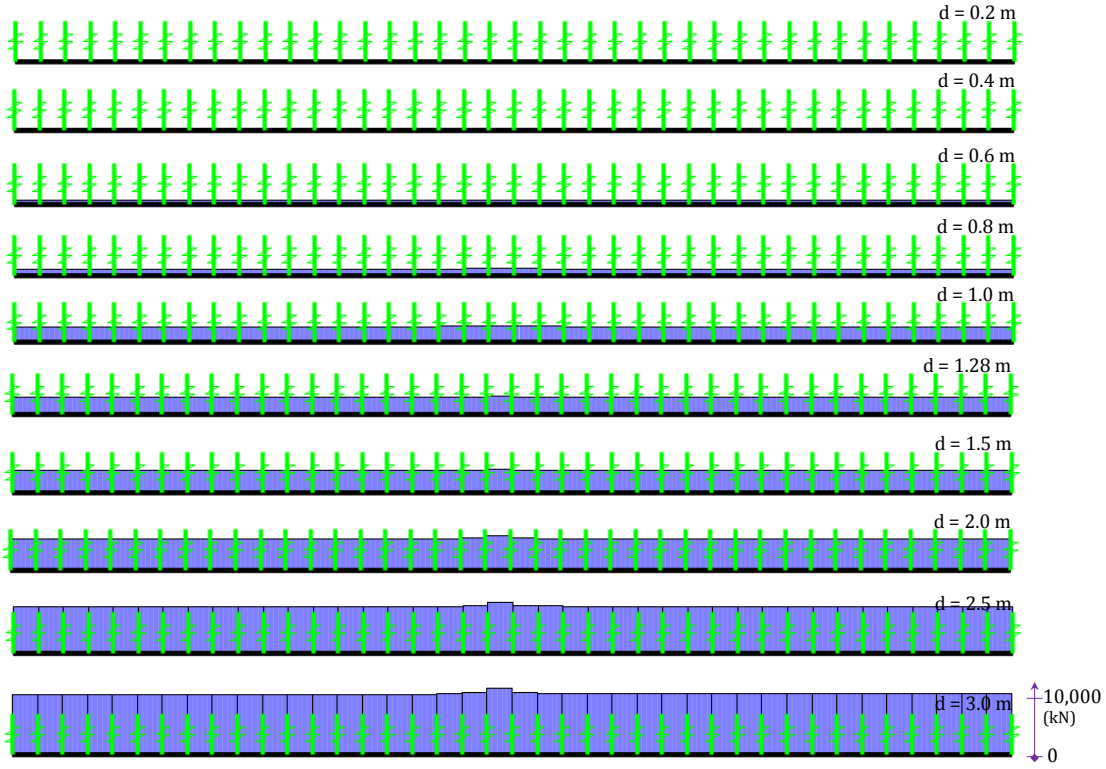


Figure 6. Axial forces developed in the pipe due to stretching at different fault movements

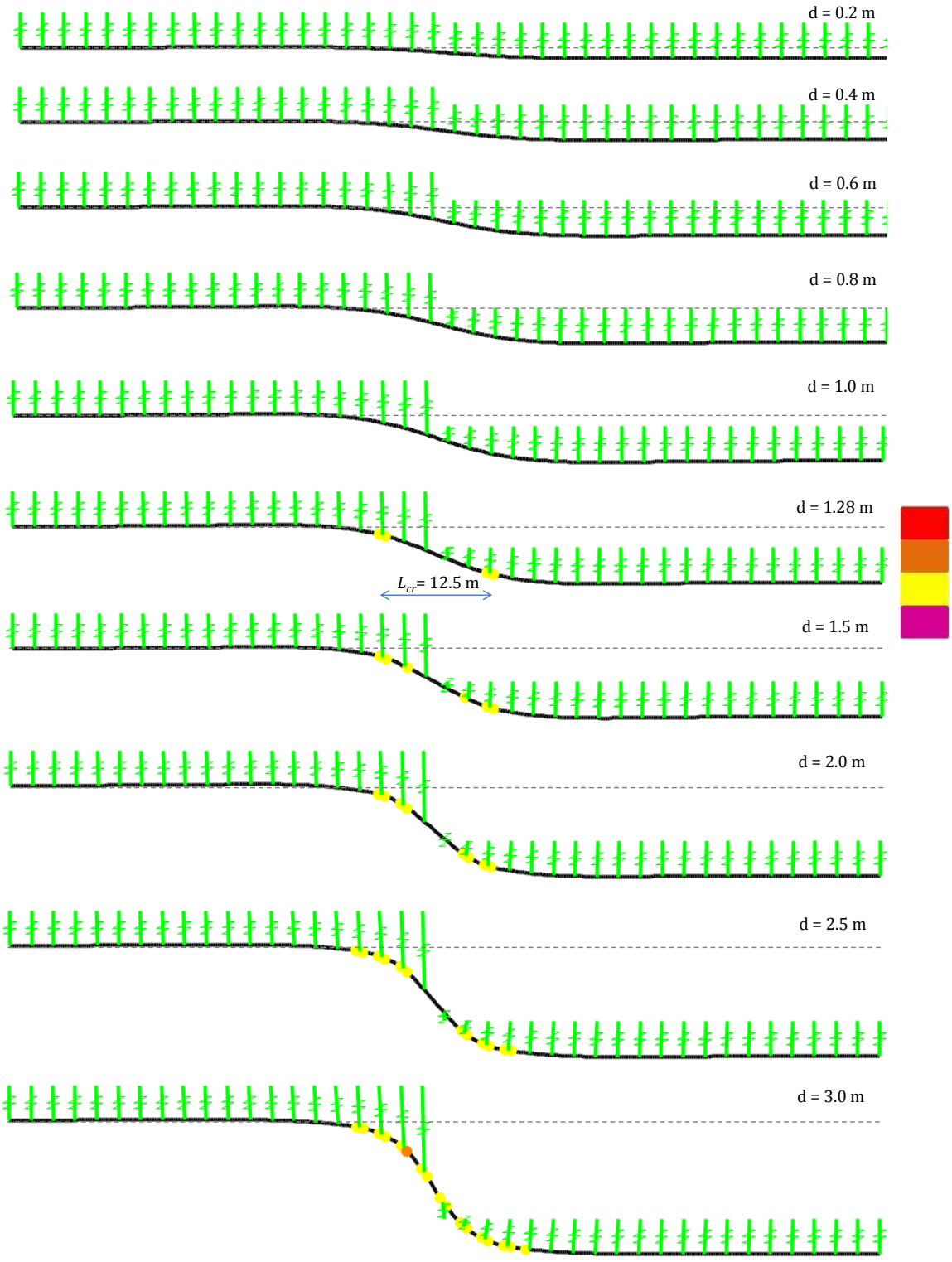


Figure 7. Deformed shape of the pipe at different fault movements (scale factor=5)

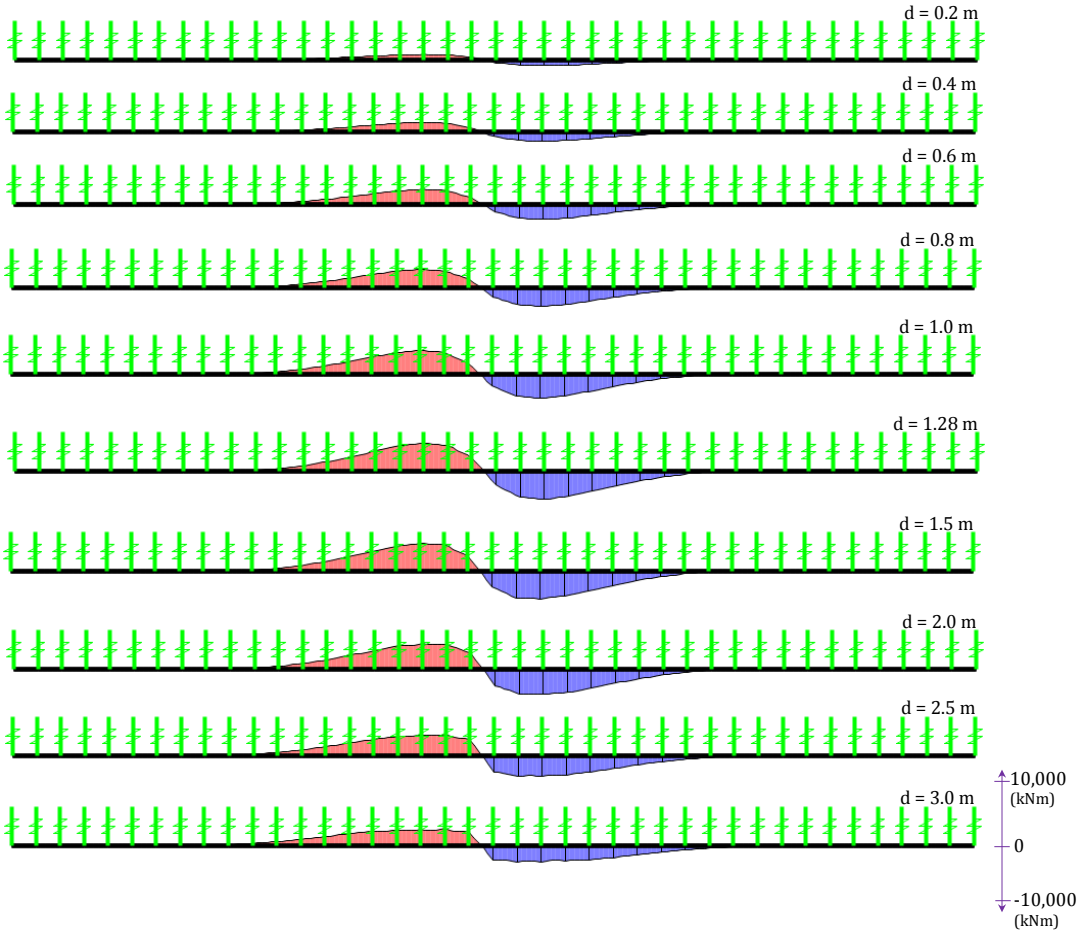


Figure 8. Bending moment diagram of the pipe at different fault movements

5 PERFORMANCE CRITERIA FOR PIPES

Depending on the ductility of the pipe, the pipeline can still be operational after the formations of plastic hinges. However, some micro-cracks or stress concentrations might have been occurred in the pipe during this stage [2]. Therefore, in the post earthquake phase, pressure fluctuations due to service loads may cause initiation of fatigue related fractures. Pipe rupture-/tearing of the pipe wall and loss of the pressure boundary, on the other hand, clearly constitute failure. Thus, performance criteria of the pipe in response to fault movement should be defined considering the critical length, the extent of the plastic hinge zone, geometric and material properties of the pipe and surrounding soil.

Two performance levels are defined for the pipelines; namely, fully functional (no permanent deformation such as wrinkling of the pipe wall) and partially functional (permanent deformation but no tearing/rupture of the pipe wall) (Table 1). Both limit states envision pressure integrity of the pipeline as a whole. Fully functional performance level is defined as the one where no significant damage occurs to the pipeline and the pipeline is fully operational after the earthquake. Partial functional performance level corresponds to the deformed shape of the pipeline where plastic deformations occur within the critical length and approximately 60% of the rupture capacity of the pipe has been reached. Suggested acceptability criteria corresponding to these two performance levels; fully functional and partially functional are 0.01% and 0.04% strain levels, respectively (Figure 10).

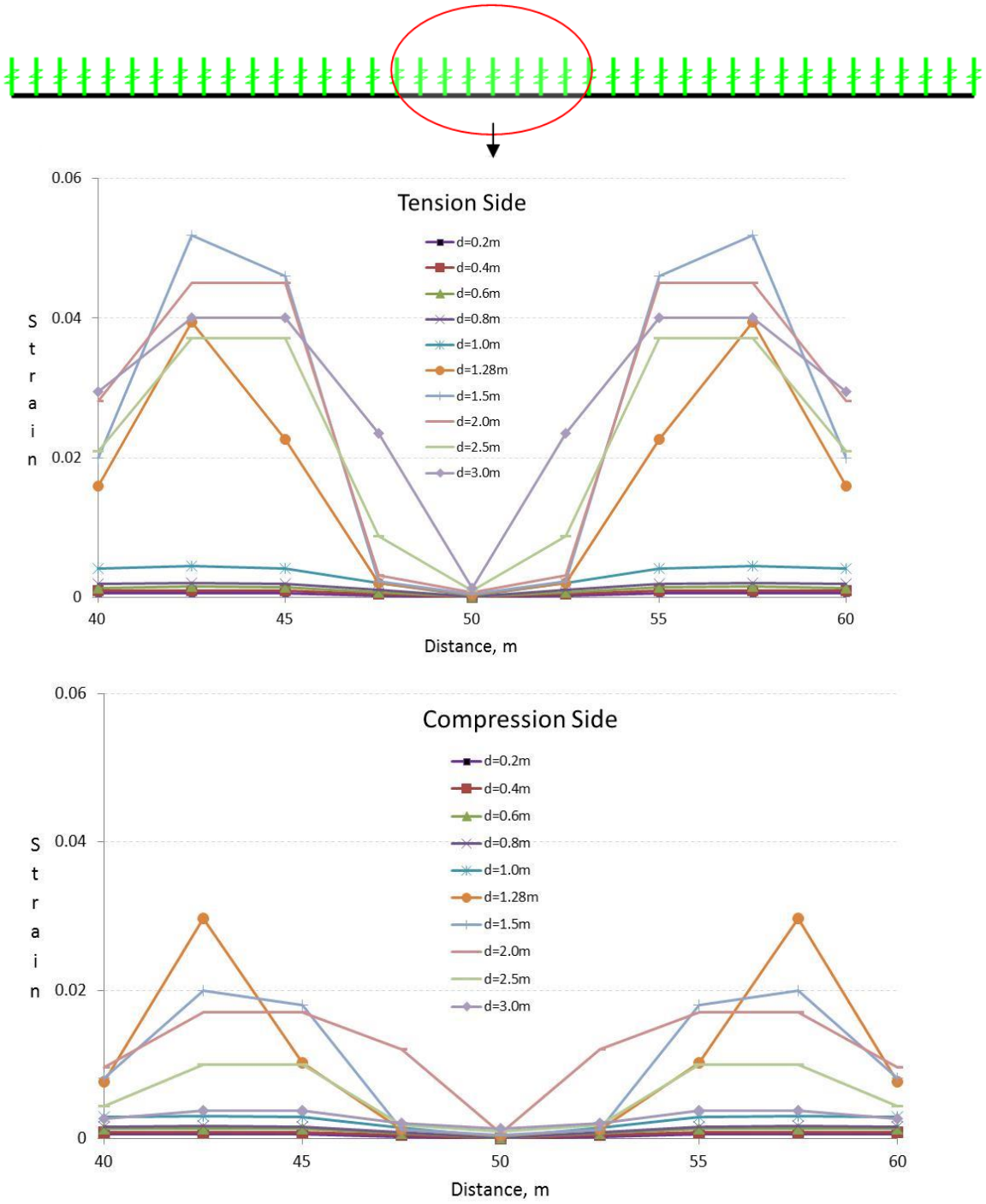


Figure 9. Strains along critical length of the pipe: a) on tension side; b) on compression side

Table 1. Minimum performance criteria for pipelines

	Earthquake Performance Level		
Earthquake Design Level	Probability of exceedance in 50 years	Fully functional (operational)*	Partially functional (operational)**
	Occasional (50%)		
	Rare (10%)		
	Very rare (2%)		

Note: yellow zones indicate minimum acceptance criteria, whereas red zones are not allowed.
*Fully functional: no significant damage has occurred to the pipeline system and the pipeline is fully operational after the earthquake.
**Partially functional and operational: Plastic deformations occurred within the critical length. 60% of the rupture capacity of the pipeline has been reached.

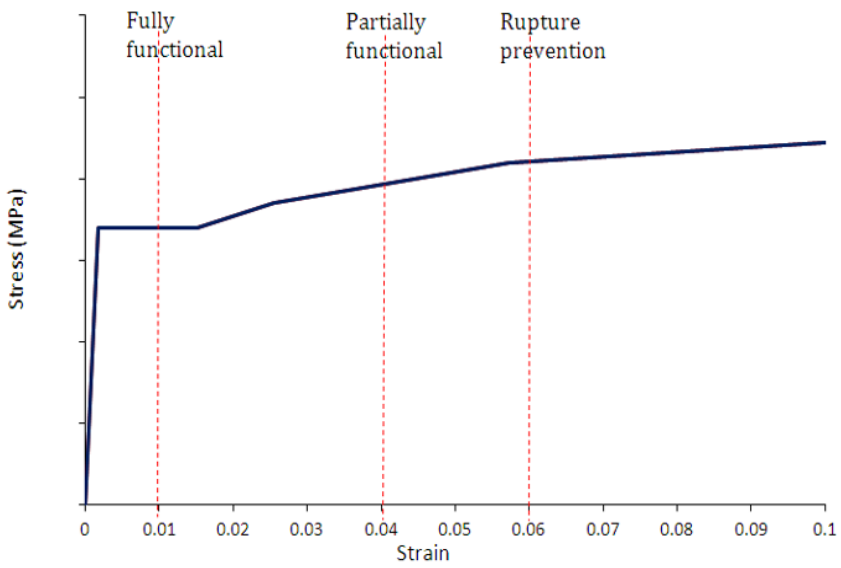


Figure 10. Suggested acceptibility criteria for buried pipelines corresponding to different performance levels

6 CONCLUSIONS

The present paper investigates the seismic response of buried steel pipes crossing strike-slip faults in the horizontal plane causing stress and deformation in the pipeline and proposes performance based design criteria for the pipes. A practical analysis model is presented for determining the critical design and response parameters. The proposed model is intended to be adopted for use in design and engineering practice. The buckling of the steel pipe is not considered in the proposed model. Large displacement and strain are included in the model to estimate the pipe response to PGD due to fault rupture. The distortion of the pipe cross section is ignored. The main outcomes of this study can be summarized as follows:

a. *D/t* ratio and steel grade affect the behavior of the pipe.

b. Axial load level in the pipe during the fault movement due to stretching is independent of the *D/t* ratio and increases almost linearly with respect to fault displacement.
c. The peak axial strain in the compression side of the pipe occurs nearly at a fault movement of twice the diameter of the pipe. This is consistent with the previous published research papers based on analytical formulations [2].

The results of this study are expected to enhance the available performance-based design methodologies for buried steel pipelines in engineering offices. Recommendations for further studies are given as follows:

a. Fragility expressions for buried pipelines at fault crossings should be developed by simplified methods.
b. The effects of stiffness of the steel pipes and the surrounding soil on the seismic response should be studied through a parametric study.

REFERENCES

[1] S. Takada, N. Hassani, K. Fukuda, A new proposal for simplified design of buried steel pipes crossing active faults. *Earthquake Engineering and Structural Dynamics*, **30**, 1243-1257, 2001.

[2] P. Vazouras, S.A. Karamanos, P.D. Dakoulas, Finite element analysis of buried steel pipelines under strike-slip fault displacements. *Soil Dynamics and Earthquake Engineering*, **30**, 1361-1376, 2010.

[3] P. Vazouras, S.A. Karamanos, P.D. Dakoulas, Mechanical behavior of buried steel pipes crossing strike-slip faults. *Soil Dynamics and Earthquake Engineering*, **41**, 164-18, 2012.

[4] Uckan, E., Lifeline Damage Caused In the 23 October (Mw=7.2) 2011 and 9 November (M=5.6) 2011, Van Earthquakes in Eastern Turkey. *International efforts in Lifeline earthquake Engineering, Technical Council on Lifeline Earthquake Engineering, Monograph No: 38,* ASCE Edited by: Davis C, Miyajima M., Yan L. 2013,

[5] M. O'Rourke, E. Filipov, E. Uckan, Towards robust fragility relations for buried segmented pipe in ground strain areas. *Earthquake Spectra* (in press) (2014).

[6] M. O'Rourke and X. Liu, Seismic Design of Buried and Offshore Pipelines. *MCEER-12-MN04*, 2011.

[7] J.M. Edinger, M. O'Rourke, J. Bachhuber, Performance of a pipeline at a fault crossing. *Proc 7th U.S. Nat. Conf. on Earthquake Engineering*, Oakland, California, 2002.

[8] D.K. Karamitros, G.D. Bouckovalas, G.P. Kouretzis, V. Gkesouli, An analytical method for strength verification of buried steel pipelines at normal fault crossings. *Soil Dynamics and Earthquake Engineering*, **31**, 1452-1464, 2011.

[9] ALA, *American Lifelines Alliance Guidelines for the design of buried steel pipes*, 2005.

[10] Eurocode 8 : *EN 1998-4, Design of structures for earthquake resistance – Part 4: Silos, tanks and pipelines*, 2006.

[11] ASCE, *Guidelines for the seismic design of oil and gas pipeline systems*. Committee on Gas and Liquid Fuel Life- lines, Technical Council on Lifeline Earthquake Engineering, American Society of Civil Engineers ASCE, New York, 1984.

[12] E. Uckan, B. Akbas, J. Shen, R. Wen, F. Paolacci, M. O'Rourke, A Simplified Analysis Model for Determining the Seismic Response of Buried Steel Pipes at Strike-Slip Fault Crossings. *Soil Dynamics and Earthquake Engineering* (under review), 2015.

[13] SAP2000 V15, *Structural Analyses Software*, CSI, 2013.

[14] E. Uckan, B. Akbas, J. Shen, R. Wen, O. Seker, F. Paolacci, E.S. Kaya, Soil Effect on Response of Buried Steel Pipes at Strike-Slip Fault Crossings. *Second European Conference on Earthquake Engineering and Seismology*, Special Session: Seismic Assessment of Lifelines, Istanbul, August 25-29, 2014.

COMPDYN 2015
5th ECCOMAS Thematic Conference on
Computational Methods in Structural Dynamics and Earthquake Engineering
M. Papadrakakis, V. Papadopoulos, V. Plevris (eds.)
Crete Island, Greece, 25–27 May 2015

SHEAR STRENGHT AND DEFORMATION MECHANISMS OF COMBINED AND CONFINED MASONRY WALLS SUBJECTED TO CYCLIC LOADING

Arturo Tena-Colunga[1], Artemio Juárez-Ángeles[2], and Víctor Hugo Salinas-Vallejo[3]
[1] Universidad Autónoma Metropolitana
Departamento de Materiales
Av. San Pablo 180, 02200 México, DF, MEXICO
e-mail: atc@correo.azc.uam.mx

[2] ICA Ingeniería
México, DF, MEXICO
e-mail: arjuan_uam@hotmail.com

[3] EuroEstudios
México, DF, México
e-mail: vicusalva@hotmail.com

Keywords: Confined Masonry, Combined Masonry, Shear Strength, Deformation Capacity, Cyclic Testing.

Abstract. *The experimental masonry research in Mexico has concentrated in confined masonry walls, primarily those made with brick, However, a modality named as "combined and confined masonry", where courses of lightweight concrete blocks (cheap in Mexico), are alternated with courses of bricks (more expensive) is being widely used in seismic zones of Mexico. Since there were no tests available for the described combined and confined masonry walls, Mexicans have no information about the performance of such walls under alternated earthquake loading. Therefore, an experimental program was needed in order to evaluate the strength and deformation mechanisms of such walls subjected to cyclic loading. The results of the first cycling testing conducted for combined and confined masonry walls are reported in this paper. The cyclic testing followed the protocol established by Mexican guidelines, which is similar to that used worldwide for the cyclic testing of wall structures. The research not only evaluates resisting mechanisms and deformation characteristics of such walls, but also defines values of useful parameters for analysis and design.*

1 INTRODUCTION

The great demand of housing in Mexico for low income people living in small cities, towns and suburbs, has forced these people to look for alternative constructive systems that would allow them to build their homes with a reduced budget, using then some of the cheapest materials available. One of the new systems used for this purpose is what we call here "combined and confined masonry", where courses of lightweight concrete blocks (cheap in Mexico), are alternated with courses of bricks (more expensive), as depicted in Figure 1. This type of masonry construction allows important saving in costs and execution time, besides having an aesthetic appearance.



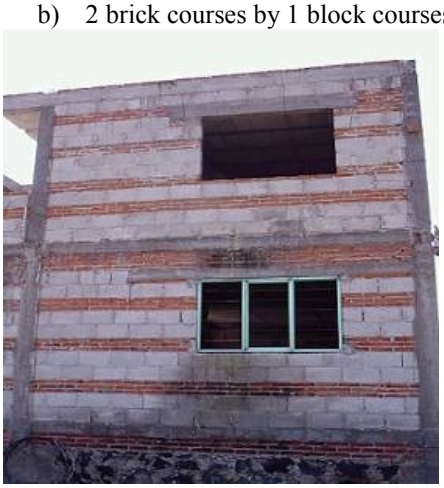
a) 3 bricks courses by 1 block course



b) 2 brick courses by 1 block courses



c) 3 brick courses by 3 block courses



d) 3 brick courses by 2 block courses

Figure 1. Combined and confined masonry construction

This modality of construction has historical background in old construction in Europe in places like Istanbul, Turkey or Athens, Greece (Figure 2) and in few buildings of the XVII or XVIII century in Mexico (Figure 3), where natural stones were alternated with fired bricks. However, this newer version became popular in recent times by the initiative of the inhabitants of the Mexican states of Puebla, Tlaxcala and Oaxaca. They tried to solve with this modality the cracking problem observed in walls made with concrete blocks due to differential settlements. As a matter of fact, their idea of alternating courses of bricks with concrete blocks was successful to solve that problem.



a) Acropolis Archeological site area b) Acropolis Museum area

Figure 2. Existing old combined masonry buildings in Athens, Greece



a) Downtown Mexico City b) Downtown Mérida

Figure 3. Existing old combined masonry buildings in México

This modern version of combined and confined masonry has been being used since early 1990s. Different arrangements to combine and alternate brick courses with block courses have been used [1-4, Figure 1], but the one that it is more commonly used is the one depicted in Figure 1a, where three courses of clay bricks alternate with a course of concrete blocks.

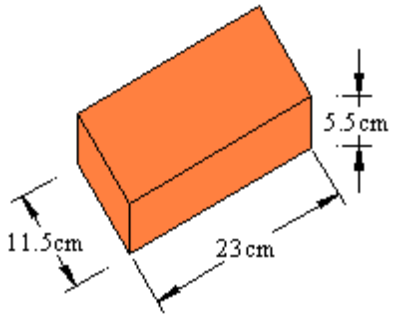
Previous experimental masonry research in Mexico that started in the late 1960s has concentrated in confined masonry walls, primarily those made with brick [for example, 5-10], although there are also some testing with confined walls made with concrete blocks [for example, 11]. Since there were no tests available for the described combined and confined masonry walls, Mexicans have no information about the performance of such walls under alternated earthquake loading, other than the satisfactory performances observed for one and two stories houses at small towns in Puebla and Tlaxcala states during the moderate June 15, 1999 Tehuacán earthquake (M=6.5). The described system is being used in seismic regions of Mexico where the earthquake hazard is high, and the number of applications is growing very fast. In fact, this system is starting to be used in Mexico City as well. Therefore, an experimental program was needed in order to evaluate the strength and deformation mechanisms of such walls when subjected to strong lateral cyclic loading.

The results of the first cycling testing conducted for combined and confined masonry walls are reported in this paper. The cyclic testing followed the protocol established by Mexican guidelines, which is similar to that used worldwide for the cyclic testing of wall structures.

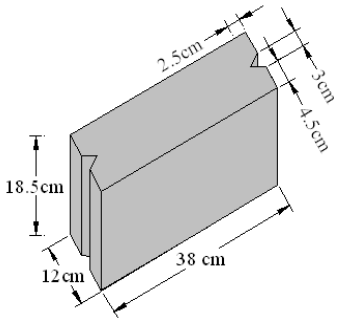
The research not only evaluates resisting mechanisms and deformation characteristics of such walls, but also defines values of useful parameters for analysis and design.

2 MATERIAL PROPERTIES

The combined and confined masonry construction currently used in Mexico for non-engineered construction is composed of non-industrial fired clay bricks and lightweight concrete blocks with no quality control, which dimensions are depicted in Figure 4.



a) Typical clay brick used



b) Typical concrete block used

Figure 4. Pieces commonly used in recent combined and confined masonry construction

The mortar bed joint ranges from 1 cm (3/8") to 1.5 cm (5/8") in thickness. Head joints are filled with mortar and they are usually 1 cm (3/8") thick. The mortar mix used by the people has the following volumetric proportions:1:2:6 (cement: lime: sand). It is worth noting that the proportion used for non-engineered construction in Mexico does not satisfy the minimum volumetric requirements proposed by NTCM-2004 [12], but it is used as it is an inexpensive mortar and workability is good. However, it is also worth noting that this mortar mix has better volumetric proportioning than mortar type O (1:2:9) allowed by masonry codes of the United States like ACI 530-14 [13] for non-seismic regions.

The best mortar mix proportion (a volumetric mortar mix 1:¼:3½) recommended by NTCM-2004 [12] for structural application, known as "Mortar Type I" was also used. The purpose of using this mix is that most lateral loading cyclic tests conducted in Mexico for confined masonry walls have used this mortar type [5-11], and cross comparisons with the dominant masonry construction in Mexico is also desirable.

Therefore, it was also necessary to assess physical and mechanical properties of the materials and the masonry used in this type of construction, as well as determine these properties if a code-based mortar mix is used. These testing are documented in detail elsewhere [1-3], and is summarized in Tables 1 to 6.

Property	Bricks	Blocks
Number of Tested Units	19	18
Volumetric Weight γ (Ton/M^3)	1.57	1.08
Absorption	18.3%	26.5%
Initial Rate of Absorption (Gr/Min)	59.4	32.7
Saturation Coefficient	0.94	0.94
Modulus of Rupture, F_r (MPa)	0.86	0.96
Compressive Strength		
Mean: $\overline{f}_p$ (MPa)	10.1	4.2
Design: f^*_p (MPa)	5.4	2.4

Table 1. Index properties for bricks and blocks

Property	Type I	Non-Engineered
Number of Cubes	30	35
Volumetric Weight γ (Ton/M^3)	1.57	1.51
Compressive Strength		
Mean: $\overline{f}_j$ (MPa)	24.1	7.8
Design: f_j^* (MPa)	13.4	4.3

Table 2. Index properties for mortar

Mexican standards are similar to ASTM guidelines, particularly in testing procedures; however, they differ in the sampling and statistical criterion, particularly to define mechanical design properties denoted with and asterisk (*).

For example, the design compressive strength of a masonry unit f_p^* according to NTCM-2004 [12] should be computed as:

$$f_p^* = \frac{\overline{f}_p}{1 + 2.5c_p} \tag{1}$$

where $\overline{f}_p$ is the mean value from test results and c_p is the coefficient of variation of the test results that shall not be taken less than recommended minimum values established by NTCM-2004. As the c_p value obtained during test results [1, 2] was smaller than the minimum values allowed by NTCM-2004, then minimum values established by NTCM-2004 [12] were used for the reported values in Table 1, that is, $c_p = 0.3$ was used for concrete blocks (mechanized production with no quality control) and $c_p = 0.35$ for the fired clay bricks (non-industrial production).

2.1 Axial compression prism tests

Given the particularity of the combined masonry, where brick layers alternate with block layers, and that bricks and blocks have very different properties (Table 1), two different arrangements were constructed for each mortar type used (Figure 5). It is worth noting that guidelines worldwide for masonry prism tests assume that the same material (brick or block) is used to build the prisms, so combined masonry is not really fully addressed at this time.

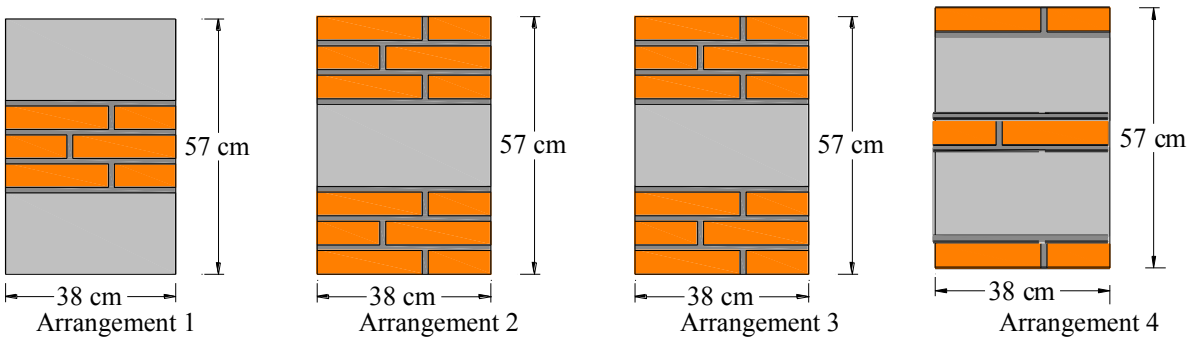


Figure 5. Prisms arrangements for the walls under study

Nine prisms were tested for each arrangement, according to the minimum required by NTCM-2004. The slenderness ratio for the prisms was 4.78, within the range $2 \le h/t \le 5$ established by NTCM-2004.

Test results for prisms with mortar type I are summarized in Table 3, where it can be observed that although higher values for the mechanical properties are obtained under arrangement 1, differences are no significant: around 20% for compressive strength and 5% for the modulus of elasticity. Therefore, for practical purposes it would be convenient to take the weighted properties obtained from the data of both arrangements, that is, f^*_m=19.7 kg/cm^2 (1.9 MPa) and E_m=12,245 kg/cm^2=1,201 MPa (E_m=621.6f^*_m).

Arrangement	$\overline{f}_m$	c_m	f^*_m	E_m
	MPa		MPa	MPa
1	3.1	0.15	2.2	1,233
2	2.6	0.17	1.8	1,171
1 and 2	2.8	0.18	1.9	1,201

Table 3. Index properties from prism tests using mortar type I

Test results for prisms with non-engineered mortar are summarized in Table 4, where it can be observed that there are no differences between arrangements 3 and 4 for practical purposes. Therefore, the weighted properties obtained from the data of both arrangements are f^*_m=15.7 kg/cm^2 (1.5 MPa) and E_m=15,572 kg/cm^2 =1,527 MPa (E_m=991.8f^*_m).

Arrangement	$\overline{f}_m$	c_m	f^*_m	E_m
	MPa		MPa	MPa
3	2.3	0.20	1.5	1,604
4	2.3	0.20	1.5	1,458
3 and 4	2.3	0.19	1.5	1,527

Table 4. Index properties from prism tests using non-engineered mortar

It is worth noting that there are no significant differences between the design compressive strength f^*_m for the prisms built with mortar type I and non-engineered mortar, as it is around 25.5%, perhaps good enough for design under gravitational loading.

2.2 Diagonal compression wallet tests

According to NTCM-2004 [12], small square masonry subassemblies (wallets) as depicted in Figure 6 can be tested under axial compression (commonly using an universal press machine) in order to define an indirect shear (diagonal tension) strength v^*_m for design and the shear modulus G_m.

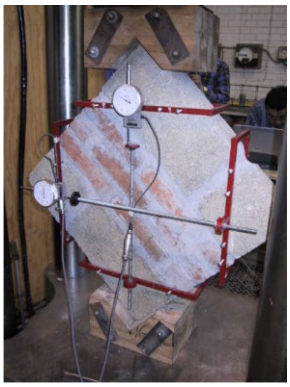


Figure 6. Axial compression test of NTCM-2004 to determine v^*_m and G_m.

Given the particularity of the combined masonry and the reasons stated in the previous section, two different arrangements of wallets were also constructed for the diagonal compression tests for each mortar type used (Figure 7).

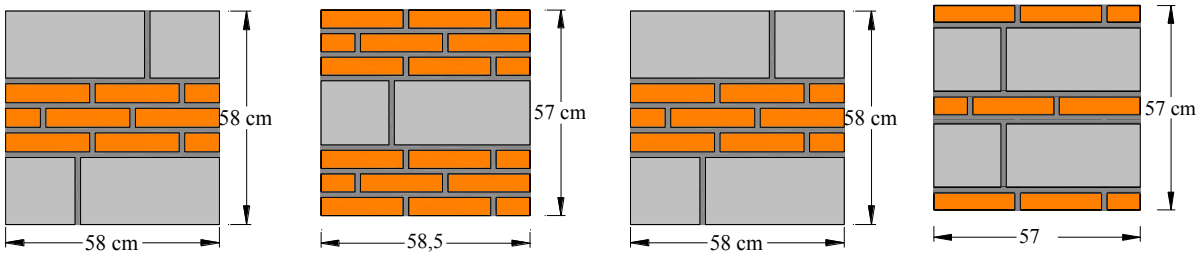


Figure 7. Small wallet arrangements built for axial compression tests

The arrangements were selected based upon the combined masonry walls that were finally tested (Figures 8a and 8b). Nine specimens were tested under diagonal compression for each arrangement, according to the minimum required by NTCM-2004. The aspect ratio for the specimens was almost square, as recommended by NTCM-2004.

Test results for specimens jointed with mortar type I are summarized in Table 5, where it can be observed that, in contrast to what was observed from prism tests, important differences are obtained for shear strength indices values v^*_m between the small wallet arrangements 1 and 2. The most notorious scatter of the data and the smallest values were obtained for arrangement 1. These can be explained by the different predominant modes of failure observed in the tested specimens. For arrangement 1, the predominant mode of failure was sliding along bed joints, whereas for arrangement 2 the predominant mode of failure was diagonal tension. In contrast, no important differences were observed between arrangements 1 and 2 to obtain the average shear modulus G_m (Table 5).

Arrangement	$\bar{v}_m$ **MPa**	c_v	v^*_m **MPa**	G_m **MPa**
1	0.28	0.51	0.13	420
2	0.38	0.18	0.25	393
1 and 2	0.33	0.37	0.17	415

Table 5. Index properties from diagonal compression tests using mortar type I

Test results for specimens jointed with non-engineered mortar are summarized in Table 6, where it can be observed that differences are also obtained for shear strength indices values between the small wallet arrangements 3 and 4. The most notorious scatter of the data and the smallest values were obtained for arrangement 4. However, in contrast to what was observed for mortar type I, a predominant mode of failure was not observed in the tested specimens, as failures in diagonal tension and sliding along bed joints were observed for both arrangements 3 and 4. A 35% difference is observed between the average shear modulus G_m obtained for arrangements 3 and 4 (Table 6), in contrast to what was observed for mortar type I.

Test results lead one to conclude that there is a reasonable doubt on how representative is the axial compression test to define shear strength indices for combined masonry, which can only be answered by relating these index values to estimate the lateral shear strength of wall specimens subjected to lateral loading, as shown in following sections.

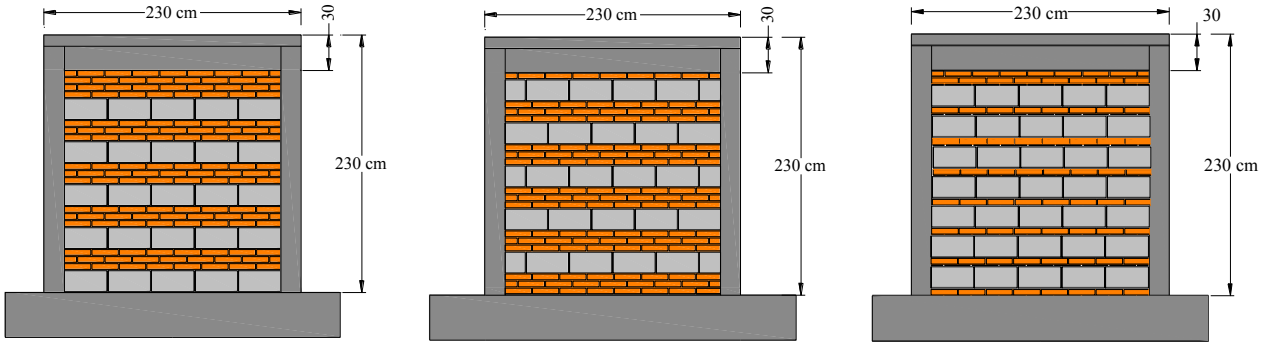
Arrangement	$\bar{v}_m$ MPa	c_v	v^*_m MPa	G_m MPa
3	0.27	0.29	0.16	417
4	0.25	0.44	0.12	310
3 and 4	0.26	0.35	0.14	367

Table 6. Index properties from diagonal compression tests using non-engineered mortar

3 TEST SPECIMENS

Four walls were constructed and tested under cyclic lateral loading. The cryptogram for identification of each wall is MCC-*i* , where *i* is an index to identify the number of wall sequentially tested. The first two walls (MCC-1 and MCC-2) were jointed with mortar type I and the last two walls (MCC-3 and MCC-4) with non-engineered mortar.

The geometry of the walls is schematically depicted in Figure 8. The general dimensions of walls and their confinement elements were selected to make these walls as close as possible to the dimensions of a confined brick masonry wall previously tested [7] at Cenapred (wall M-0-E6), to do some cross comparisons.



a) Walls MCC-1 and MCC-3 b) Wall MCC-2 c) Wall MCC-4

Figure 8. General geometry of tested walls

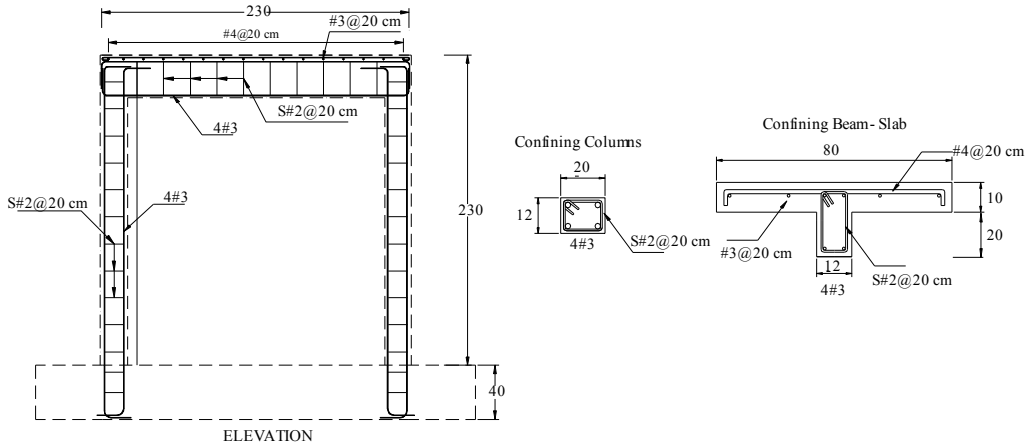


Figure 9. Reinforcement of confining elements

In fact, the confining RC tie-columns, bond-beam and beam on grade have the same dimensions, reinforcement and concrete strength with respect to those of the wall of reference [7], as depicted in Figure 9 and specified in Table 7. Confining tie-column elements are 12x20 cm. The confining rectangular bond-beam is 12x20 cm. A slab 10x80 cm was cast at the top of the confining beam. The compressive strength of the concrete used for the confining tie-

columns and bond-beams was specified as f'_c=150 kg/cm^2 (14.7 MPa) and for the slab was f'_c=250 kg/cm^2 (24.5 MPa). Results of controlled cylinder tests are reported elsewhere [1, 2].

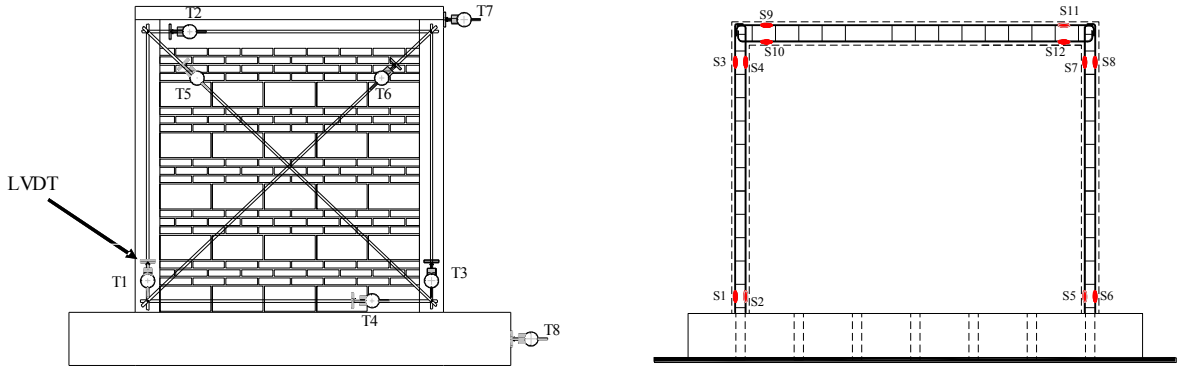
Columns		Beam		Slab	
Longitudinal	Transverse	Longitudinal	Transverse	Longitudinal	Transverse
4#3	S#2@ 20 cm	4#3	S#2 @ 20 cm	#3 @ 20 cm	#4 @ 20 cm

Notes: #3 bars = bars 3/8" in diameter, f_y = 412 MPa
#2 bars= bars 2/8" in diameter, f_y = 216 MPa

Table 7. Reinforcement of the confining RC elements of walls

The external instrumentation for the walls was composed of 8 LVDT (Figure 10a) and a load cell (Figure 11). The internal instrumentation consisted of 12 strain gages placed on the longitudinal reinforcement of the confining elements, as depicted in Figure 10b.

The testing of the walls was done with the help of the reaction braced frame and strong floor schematically depicted in Figure 11. A special C steel beam was designed to apply a uniformly distributed vertical loading of 1 Ton/m (9.81 kN/m) and to help applying with a hydraulic jack the cyclic lateral loading.



a) External wall instrumentation b) Internal wall instrumentation

Figure 10. Instrumentation for the walls

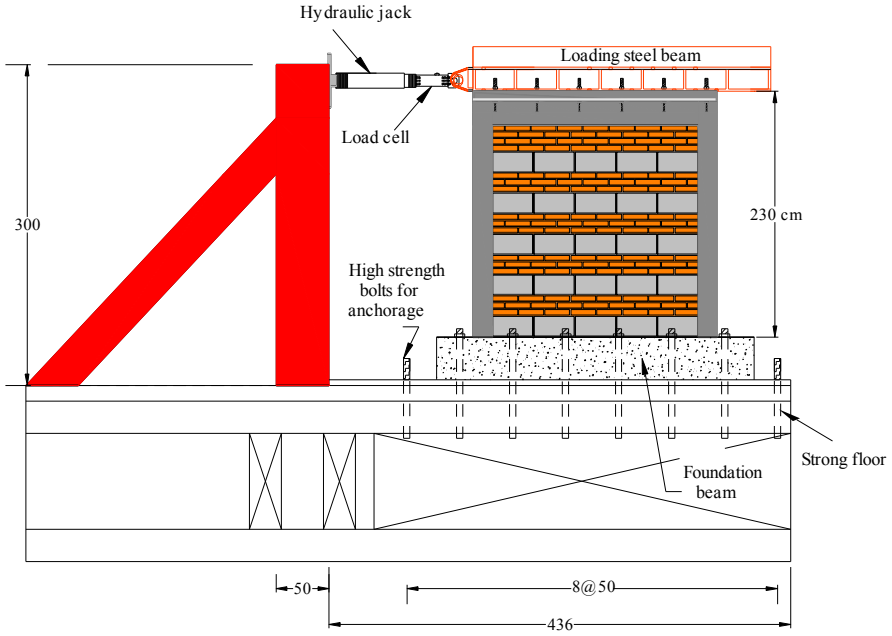


Figure 11. Testing setup

The cycling testing of the walls was done following the general guidelines of Appendix A of NTCM-2004 [12] required for earthquake-resistant masonry wall systems. According to the testing protocol of reference, masonry walls have to be subjected to repeated cycles of at least 25%, 50% and 100% the estimated cracking load for the walls (load control, Figure 12) and, after the first cracking, walls have to be subjected to repeated cycles of increasing drift ratios of at least 0.2% (displacement control, Figure 12). In this research, both the load and the displacement control were done using additional steps, as schematically illustrated in Figure 12.

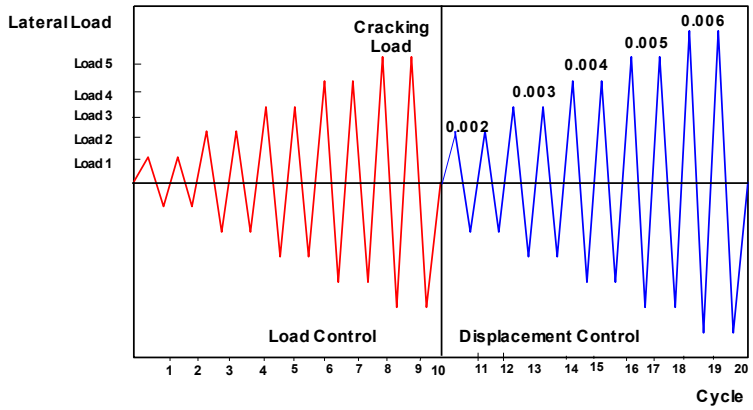


Figure 12. Cyclic testing protocol used

4 EXPERIMENTAL RESULTS

4.1 Hysteretic behavior

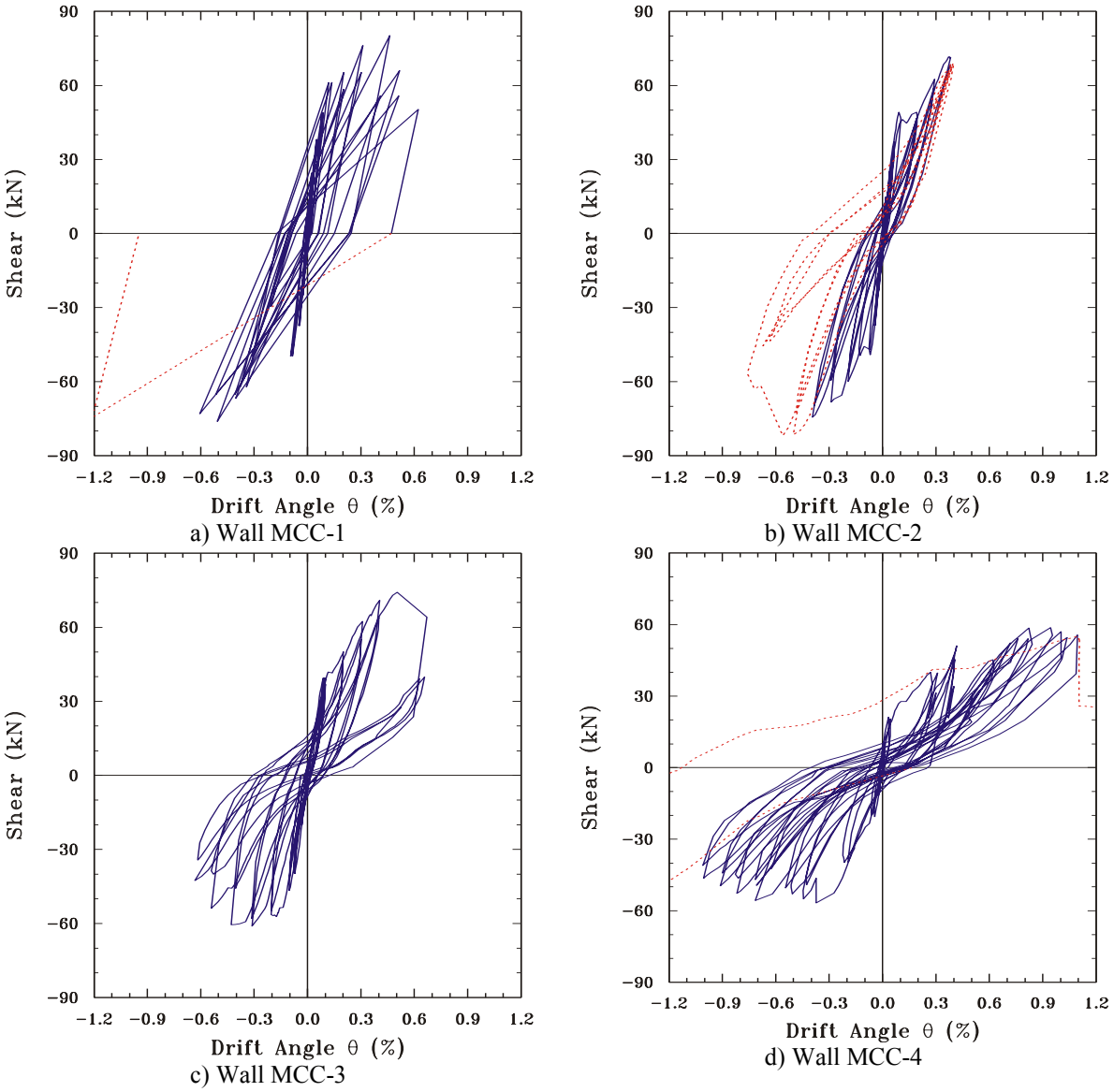
The hysteretic loops obtained for each wall from the cyclic testing protocol described before are depicted in Figure 13. Given the limitations of lab equipment at the time of each testing, it is worth noting the following observations regarding the testing of each wall. During the testing of wall MCC-1 a load cell was not available, so applied lateral forces were obtained indirectly from a previously calibrated manometer, that is why the curves in Figure 13a look rough. During the testing of wall MCC-2 the hydraulic jack "stock" for positive cycles (pulling) after a lateral drift angle of 0.4%, so that is the reason of the asymmetric loops, which are marked with a red-broken line. Fortunately, there were no further technical problems during the testing of walls MCC-3 and MCC-4.

From all the hysteretic loops it is observed a reasonably symmetric and stable response for positive and negative cycles up to a drift angle of 0.6%, except for wall MCC-2 for the reason stated above (loops were rather symmetric up to a drift angle of 0.4%, where the jack problem aroused).

Instability in the wall response triggered for a drift angle of 0.6% for wall MCC-1 after a major shear crack penetrated the confining column (Figure 14); this last half cycle is marked with a broken red line in Figure 13a.

The instability of wall MCC-2 also started because of a shear crack penetration in the confining column at a drift ratio around 0.6%, where an important strength and stiffness degradation was observed (Figure 13b).

For wall MCC-3 an important pinching behavior triggered after a lateral drift of 0.4% (Figure 13c) and the important shear crack penetration of the confining column started at a drift of 0.5%, the testing was stopped at a drift of 0.6% as extensive damage with crack penetration of top and bottom of the confining column was evident.



a) Wall MCC-1 b) Wall MCC-2

c) Wall MCC-3 d) Wall MCC-4

Figure 13. Hysteretic loops for the tested walls



a) Top right corner b) Bottom left corner

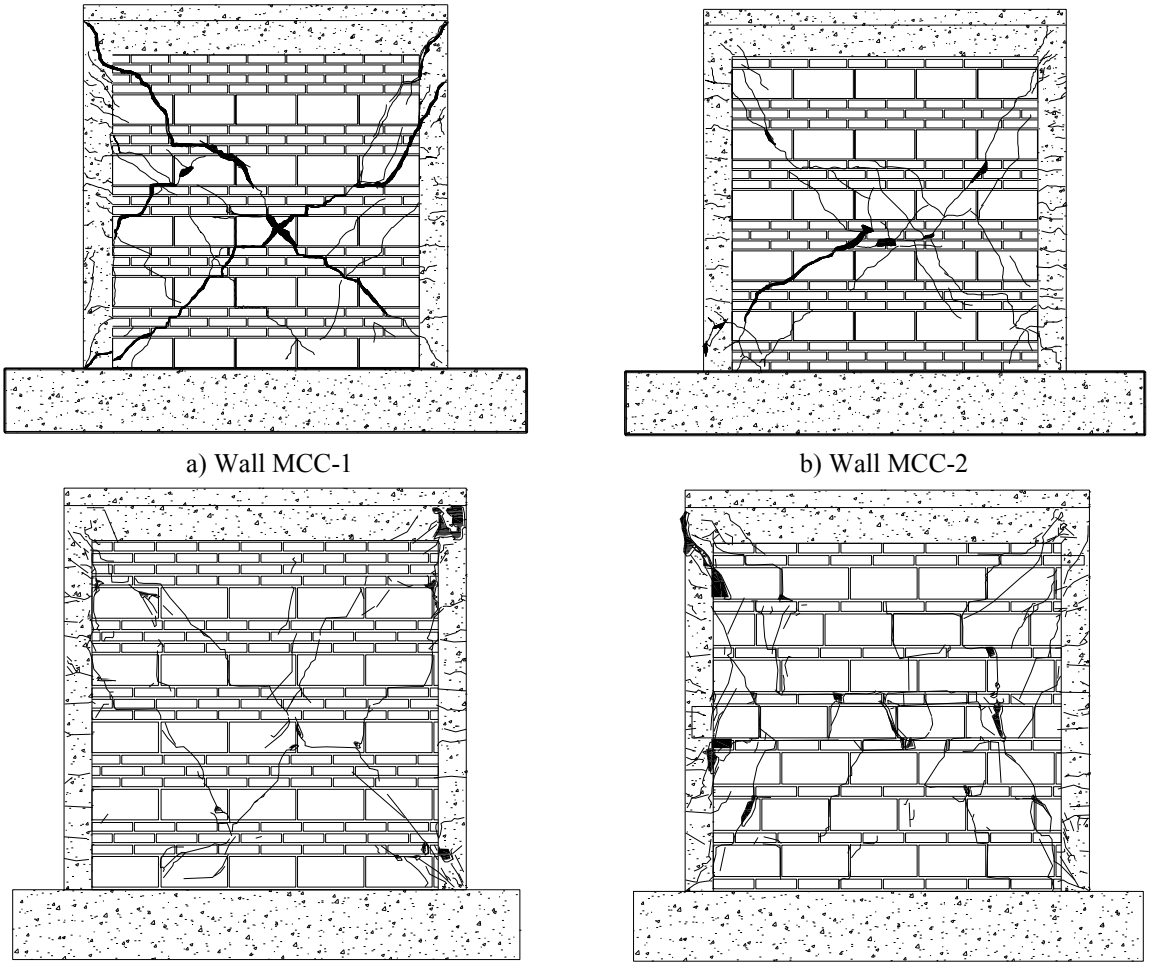
Figure 14. Shear crack penetration of confining RC columns of wall MCC-1 that lead to failure

For wall MCC-4, an important pinching behavior was developed after a drift angle of 0.4% (Figure 13d), basically a frictionless sliding mechanism along bed and head joints during load reversals of a stair-like shear cracking pattern (significant gaps were observed during testing,

particularly at the head joints). Although the important shear crack penetration at the confining column happened at a lateral drift of around 0.6%, this wall presented a very important frictionless sliding mechanism along the bed and head joints that allowed it to sustain stability up to a drift angle of 1%, after that the wall failed because of the shear crack penetration of the confining RC column (dotted red lines, Figure 13b).

4.2 Cracking patterns

The final cracking patterns for all tested walls are depicted in Figure 15, where it can be observed that they are typical diagonal tension shear patterns. It is also worth noting that the shear crack that penetrated the confining column elements started to appear in all walls at a drift angle as low as 0.3%.



a) Wall MCC-1 b) Wall MCC-2

c) Wall MCC-3 d) Wall MCC-4

Figure 15. Final cracking patterns of tested walls

From a gross assessment viewpoint, from the crack patterns, the obtained hysteretic loops and the response envelopes (not shown), it can be observed that the main difference in the cyclic behavior of the walls jointed with mortar type I of NTCM-2004 (walls MCC-1 and MCC-2) and the walls jointed with non-engineered mortar is due to the diagonal crack pattern exhibited for the walls. A well-defined main diagonal crack that crosses and breaks bricks and block layers are developed for the walls jointed with the stronger engineered mortar (walls MCC-1 and MCC-2, Figures 15a and 15b). In contrast, a stair-like, frictionless sliding joint

cracking patterns are developed for the walls jointed with the weaker non-engineered mortar (walls MCC-3 and MCC-4, Figures 15c and 15d), particularly for wall MCC-4 (Figure 15d). This frictionless sliding joint mechanism during load reversals was favored because of the relatively low applied normal stress. That is the reason why more pinching is observed in the hysteretic loops of the walls joined with non-engineered mortar (Figure 13).

4.3 Characteristic parameters from response envelopes

Walls MCC-1 and MCC-2 first cracked at a higher drift angle and shear force than walls MCC-3 and MCC-4 (Table 8). In fact, walls MCC-1 and MCC-2 also developed slightly higher shear forces than walls MCC-3 and MCC-4 (Table 8). However, the difference between the shear force resisted by walls MCC-1 and MCC-3, that have the same configuration, is only 8%.

Wall	First Cracking		Peak Shear Force			
	V_{cr} (KN)	θ_{cr}	$V^{+}_{\max}$ (KN)	θ^{+}	$V^{-}_{\max}$ (KN)	θ^{-}
Mcc-1	49.0	0.0009	80.4	0.0046	76.5	0.0054
Mcc-2	49.0	0.0009	71.6*	0.0038*	82.4	0.0056
Mcc-3	39.2	0.0006	74.5	0.0050	60.8	0.0031
Mcc-4	21.6	0.0006	58.8	0.0090	57.9	0.0070
* Previous reported problem with the hydraulic jack during testing						

Table 8. Characteristic parameters obtained from peak response envelopes

The major difference regarding peak shear forces is observed between walls MCC-3 and MCC-4, which were both jointed with non-engineered mortar, where the difference is 26% (Table 8). This higher difference seems directly related to the fact that a different masonry combination exist where more blocks (weakest material) are used in wall MCC-4 with respect to wall MCC-3.

4.4 Cyclic stiffness degradation

An important parameter for the design and evaluation of structures, masonry included, is to assess their stiffness degradation with respect to increasing drift angle. This parameter is useful to help define drift angle limits for design purposes (i.e., serviceability, collapse prevention, etc). Therefore, from the hysteretic curves depicted in Figure 13, peak-to-peak secant stiffnesses were defined for each cycle at the same drift angle, and then normalized with respect to the computed initial (elastic) stiffness for each walls. The computed curves for all walls are depicted in Figure 26, where first and second cycles at the same drift angle are plotted in separate curves.

It can be observed from Figure 16 that there are no significant differences between the curves of the first and second cycles for all walls except wall MCC-4. The lateral stiffness of all walls degrades very fast, being 0.4 or less of its initial uncracked stiffness K_e for a drift angle as low as 0.2%. For the drift angle where the shear crack starts to penetrate the confining column elements (θ=0.3%), the K/K_e ratio is lower than 0.3 for the walls joined with engineered mortar (walls MCC-1 and MCC-2, Figures 16a and 16b), whereas the walls joined with non-engineered mortar developed a K/K_e ratio higher than 0.3 (walls MCC-3 and MCC-4, Figures 16c and 16d). Spalling of masonry started close to a drift angle of 0.4% or less, where all walls have $K/K_e < 0.25$.

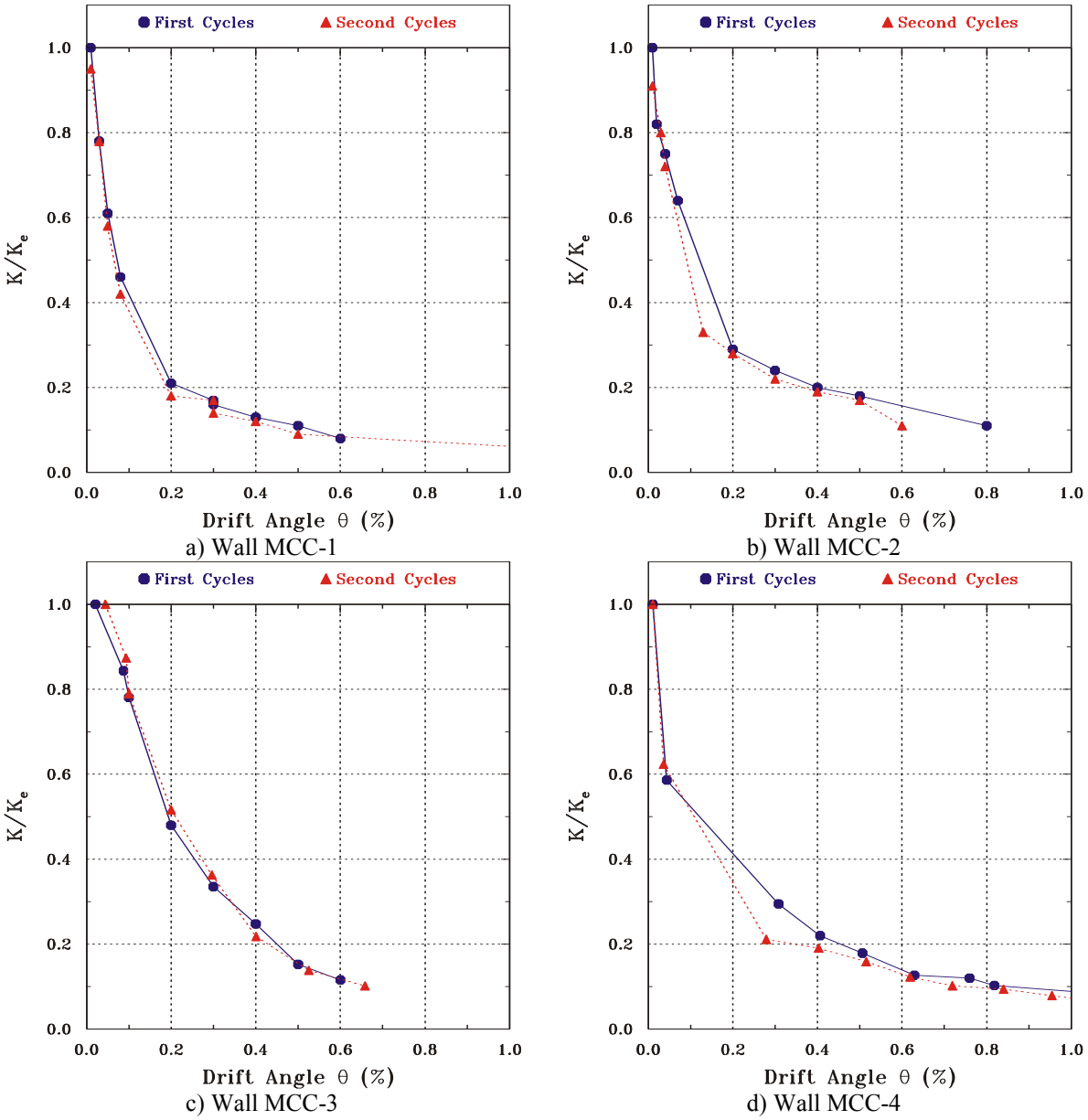


Figure 16. Normalized peak-to-peak secant stiffness vs. drift angle for tested walls

5 DAMAGE INDEX

Structural engineers need simple quantitative evaluation methods to assess the safety of existing structures under an expected level of seismic demand, particularly to take decisions regarding rehabilitation and/or demolition. Damage indices are suitable tools for such purposes.

Therefore, the damage index originally proposed by Kwok and Ang [14] for unreinforced brick masonry walls based on a reliable database of experiments conducted in China in the late 1970s was calibrated with the experimental data obtained in this research study for confined and combined masonry walls.

The Kwok-Ang damage index is defined with the following general expressions:

$$D = D_u + D_e \tag{2}$$

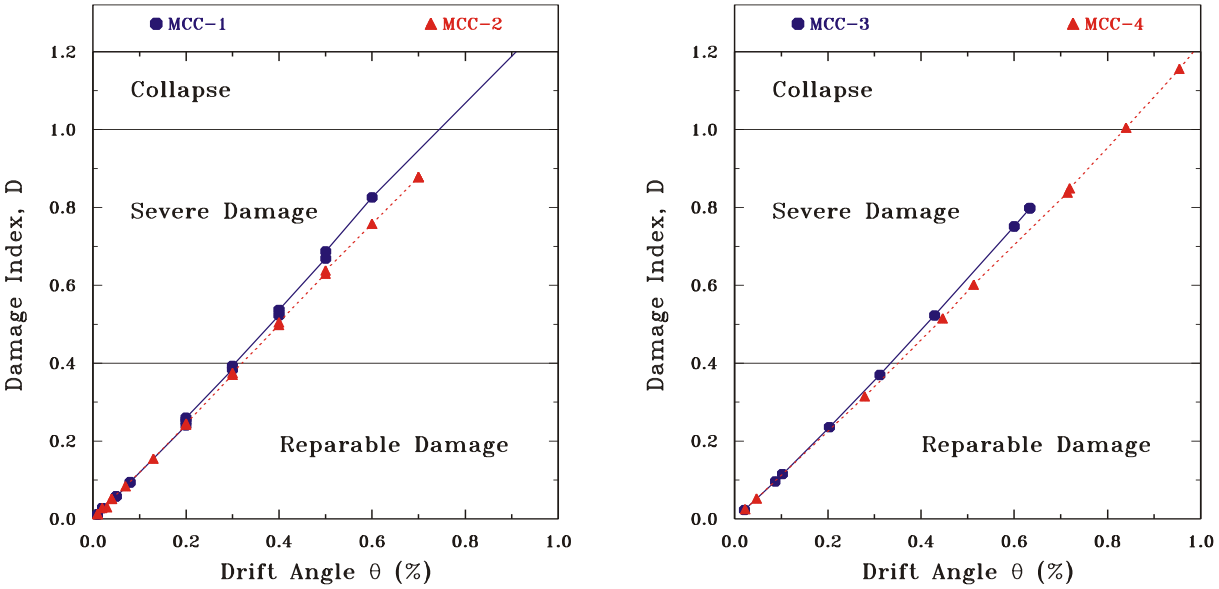
$$D_u = \frac{u_m}{u_f} \tag{3}$$

$$D_e = \varepsilon \frac{\int dE}{q_u u_f} \tag{4}$$

where u_m is the displacement at maximum load, u_f is the displacement at failure, $\int dE$ is the total (cumulative) dissipated energy, q_u is the ultimate shear strength and ε is a constant obtained from regression analysis of experimental data.

Kwok and Ang [14] obtained from the regression analysis of their extensive database that ε=0.075 for unreinforced masonry walls. In addition, they proposed the following damage scale for their index: a) No damage: $D = 0$, b) Reparable damage: $0 < D \leq 0.25$, c) Severe damage: $0.25 < D < 1.0$, d) Collapse: $D \geq 1$.

It is clear that there are some differences in the cyclic behavior under lateral loading of plain unreinforced masonry and the combined and confined masonry described in this study, so some adjustments to the damage index originally proposed by Kwok and Ang were needed for combined and confined masonry walls. For example, the value of constant ε should be assessed from experimental data. Also, the limiting boundary value between reparable and severe damage should be also redefined with the observed experimental behavior to take into account the beneficial presence of confining elements that provide further stability in these walls under lateral loading.



a) Walls with engineered mortar b) Walls with non-engineered mortar

Figure 17.Modified Kwok-Ang damage index vs drift angle for combined and confined masonry walls.

Therefore, from the reduced database of the experiments described here, a preliminary value of ε =0.046 was obtained for combined and confined masonry walls, as reported elsewhere [1-2]. Also, from the analysis of experimental data that allowed defining the limiting lateral drift ratio $\theta = 0.003$ for earthquake-resistant design purposes [1-3], it was clear that the limiting boundary value between reparable and severe damage should be $D = 0.4$ for combined and confined masonry. Therefore, the proposed damage index scale for combined and confined masonry is: a) No damage: $D = 0$, b) Reparable damage: $0 < D \leq 0.4$, c) Severe damage: $0.4 < D < 1.0$, d) Collapse: $D \geq 1$. The obtained damage index vs. drift ratio curves for the tested combined and confined masonry walls are depicted in Figure 17, where it can be

observed the proposed adjustments for the Kwok-Ang damage index seem reasonable for both the walls jointed with engineered (Figure 17a) and non-engineered (Figure 17b) mortar.

6 CONCLUDING REMARKS

From the experimental program summarized in this paper, the following observations can be made:

1. The major difference in the cyclic behavior of the combined and confined masonry walls jointed with engineered and non-engineered mortar is related to the resisting shear mechanism that leads to failure. In the walls jointed with engineered mortar, the failure mechanism is characterized by diagonal tension cracks that favor primarily spalling and crushing of the masonry in the central zone of the main diagonal crack with reasonable energy dissipation characteristics. In contrast, in the walls jointed with non-engineered mortar, the initial diagonal tension cracks that broke the masonry units lessened after a drift ratio θ=0.003, when a stair-like shear mechanisms with friction-less sliding along the bed and head joints triggered, leading to an important pinching of the hysteretic loops and therefore, a reduced energy dissipation characteristics due to the low normal compression stress applied to the walls.
2. From the different wall combinations tested for combined and confined masonry walls jointed with non-engineered mortar (walls MCC-3 and MCC-4), it was observed that wall MCC-3, that has more brick layers, resisted a peak shear force 26% higher than wall MCC-4, that has more concrete blocks. Therefore, this difference seems to be directly related to the fact that a different masonry combination exists where more blocks (weakest material) are used in wall MCC-4 with respect to wall MCC-3.
3. Given that the mechanical properties of the concrete blocks currently used in combined and confined masonry walls are very weak, it will be worth testing in the future combined and confined masonry walls where higher quality concrete blocks are used, to discern if this practice would lead to improved performances under lateral cyclic loading.
4. It was shown that the Kwok-Ang damage index for unreinforced brick masonry walls can be adjusted in a simple manner, as proposed in this paper, to be helpful for the seismic evaluation of combined and confined masonry walls also.

Extensive additional experimental research is needed to discern the impact of many variables, but this research study lead one to believe that the following variables are important to assess in future experimental works: (a) the impact of other wall combinations, (b) the impact of the applied axial load, (c) the impact of other mortar mixes allowed by seismic codes and, (d) the impact of using concrete blocks of better quality, with similar mechanical properties to the ones of clay bricks. Reference confined masonry walls made of: (a) bricks only and, (b) concrete blocks only should be included in the future testing protocols.

7 ACKNOWLEDGEMENTS

This experimental study was possible because of the enthusiastic collaboration of several students and technicians at Universidad Autónoma Metropolitana. Technicians Leopoldo Quiroz (RIP), Rubén Barreda and José Luis Caballero assisted us in all the prototype and material testing. Prof. Hans Archundia-Aranda assisted us in the planning and in data acquisition of the cyclic tests. The construction of test specimens was possible because of the enthusiastic collaboration of several students: César Carpio, José Manuel Alonso, Misael Bahena, Daniel Miranda, Sergio López, Eder Gudiño, Rosaura Ramírez, Efraín Joaquín Diego, Marco Antonio Rico, René Espinoza, Richard Véliz, Roberto Moreno, Elías Josué Moral and Gerardo Ibarra.

REFERENCES

[1] A. Juárez-Ángeles, Mecanismos de resistencia y de deformación de muros de mampostería combinada y confinada, *MSc. Thesis*, División de Ciencias Básicas e Ingeniería, Universidad Autónoma Metropolitana Azcapotzalco, 2009. (in Spanish)

[2] V. H. Salinas-Vallejo, Comportamiento ante cargas laterales de muros de mampostería combinada unidos con morteros de autoconstrucción, *MSc. Thesis*, División de Ciencias Básicas e Ingeniería, Universidad Autónoma Metropolitana Azcapotzalco, 2009. (in Spanish)

[3] A. Tena-Colunga, A. Juárez-Ángeles, V. H. Salinas-Vallejo, Cyclic behavior of combined and confined masonry walls, *Engineering Structures*, **31** (1), 240-259, doi:10.1016/j.engstruct.2008.08.015, 2009.

[4] A. Tena-Colunga, A. Juárez-Ángeles, V. H. Salinas-Vallejo, Housing Report: Combined and confined masonry structures, *World Housing Encyclopedia, an Encyclopedia of Housing Construction in Seismically Active Areas of the World*, Earthquake Engineering Research Institute (EERI) and International Association for Earthquake Engineering (IAEE), Report No. 160, 1-15, 2010.

[5] S. M. Alcocer, R. Meli, Test program on the seismic behavior of confined masonry structures, *The Masonry Society Journal*, **13** (2), 68-76, 1995.

[6] S. M.. Alcocer, Implications derived from recent research in Mexico on confined masonry structures, *Proceedings, CCMS Symposium*, American Society of Civil Engineers, Chicago, 82-92, 1996.

[7] G. Aguilar, R. Meli, R. Diaz, R. S. Vazquez-del-Mercado, Influence of the horizontal reinforcement on the behavior of confined masonry walls, *Proceedings, 11th World Conference on Earthquake Engineering*, Acapulco, Mexico, Paper No. 1380, CDROM, 1996.

[8] L. E. Flores, S. M. Alcocer, Calculated response of confined masonry structures, *Proceedings, 11th World Conference on Earthquake Engineering*, Acapulco, Mexico, Paper No. 1830, CDROM, 1996.

[9] S. M. Alcocer, J. A. Zepeda, Behavior of multi-perforated clay brick walls under earthquake-type loading, *Proceedings, Eighth North American Masonry Conference*, Austin, Texas, EUA, CDROM, 1999.

[10] S. M. Alcocer, J. G. Arias, A. Vazquez, Response assessment of Mexican confined masonry structures through shaking table tests, *Proceedings, 13th World Conference on Earthquake Engineering*, Vancouver, Canada, Paper No. 2130, CDROM, 2004.

[11] E. L. Treviño, S. M. Alcocer, R. Larrúa, L. E. Flores, Estudio experimental de muros de mampostería confinada de bloques de concreto. Primera parte: comportamiento general de los especímenes, *Ingeniería Civil*, Centro de Estudios y Experimentación de Obras Públicas CEDEX, Ministerio de Fomento, Madrid, España, No. 150, ISSN 0213-8468, 2008. (in Spanish)

[12] NTCM-2004, Normas Técnicas Complementarias para Diseño y Construcción de Estructuras de Mampostería*, Gaceta Oficial del Distrito Federal*, October, 2004. (in Spanish)

[13] ACI 530-14, Building Code Requirements for Masonry Structures (ACI 530-14/ASCE 5-14/TMS 402-14), *American Concrete Institute*, 2014.

[14] Y.-H.- Kwok, A. H.-S. Ang, Seismic damage analysis and design of unreinforced masonry buildings, *Structural Research Series No. 536*, University of Illinois at Urbana-Champaign, June, 1987.

COMPDYN 2015
5th ECCOMAS Thematic Conference on
Computational Methods in Structural Dynamics and Earthquake Engineering
M. Papadrakakis, V. Papadopoulos, V. Plevris (eds.)
Crete Island, Greece, 25–27 May 2015

ASSESSMENT OF THE LATERAL STIFFNESS OF WALLS WITH OPENINGS

Arturo Tena-Colunga[1] **and Germán Rivera-Hernández**[2]
[1] Universidad Autónoma Metropolitana
Departamento de Materiales
Av. San Pablo 180, 02200 México, DF, MEXICO
e-mail: atc@correo.azc.uam.mx

[2] Procuraduría General de la República
México, DF, MEXICO
e-mail: germanriverahdez@gmail.com

Keywords: Walls with Openings, Asymmetric Distribution of Openings along the Height, Elastic Lateral Stiffness, Lateral Displacements.

Abstract. *Approximations obtained with different simplified methods to assess the elastic lateral stiffness of walls with openings are compared to results obtained with the finite element method using reasonably fine meshes. Multistory walls were studied, considering symmetric and asymmetric distribution of openings with respect to a vertical axis. From the obtained results it can be* observed *that for a single strip of asymmetric perforated walls, the best approximations are obtained using the equivalent frame method more commonly used in Mexico, the method proposed by Coull and Choudhury, as well as the method baptized as the equivalent no prismatic wide column analogy, particularly as the number of stories of the wall increases.*

1 INTRODUCTION

In displacement-based design is very important to estimate accurately the lateral displacements of a given structural system. Buildings with structural walls are very commonly used in seismic regions, mostly for reinforced concrete and masonry structures. Often, these structural walls have openings, particularly at the facades. Although regular opening patterns are often used, sometimes for architectural requirements (illumination, ventilation, aesthetics), complex opening patterns are not uncommon in seismic regions.

The impact of openings in the lateral stiffness of shear walls captured the attention of researchers and designers in the 1960s. In fact, many expressions, approximations and simplified analysis methods date back to those dates, because during that decade several midrise buildings with shear walls were built, which fostered practical research studies. Among other methods proposed at the times, one can highlight for their simplicity the methods proposed by Coull and Choudhury [1, 2] and the Equivalent Frame Method (EFM) proposed by Schwaighofer and Microys [3]. The approximations obtained with these methods were calibrated then with the results of few low rise walls with symmetrical openings patterns with respect to a vertical axis.

The practical modeling of walls with openings is a complex task that has not yet been fully addressed. In this case the use of the finite element method is essential if the aim is to obtain reliable results, both to estimate deformations, stiffnesses and stresses. In the absence of simple analytical methods that could estimate easy and reasonably the lateral stiffness matrix of walls with complex opening patterns (including asymmetries), Tena-Colunga [4-6] proposed the equivalent condensed beam method, a mixed method where the lateral stiffness matrix is obtained from equivalent condensed beams using the flexibility method and the finite element method. Although the method is accurate for practical purposes because, in essence, is a static condensation done numerically, it has the disadvantage that finite element meshes are required to define the equivalent condensed beams.

The development or improvement of simple models to analyze walls with openings has received relatively little attention in recent years, perhaps because the capabilities of personal computers since 1997 have facilitated the use of commercial finite element programs to model them reasonably. However, even today is still impractical modeling with the required rigor, complete medium to high rise buildings with several walls with openings using refined finite element meshes, especially if the distribution of the openings is irregular or complex in elevation. In many instances, practicing engineers do not have the time and experience needed to develop rigorous and detailed three-dimensional finite elements models that would allow them to analyze and design this type of structures, although they currently have access to the computer software (e.g. SAP 2000 or similar) and hardware to do it. Although the finite element method allow one to model such complex geometries, this method is not always practical for the analysis and design of complex and large buildings having walls with openings.

Therefore, approximate methods are still needed and used by structural engineers worldwide to estimate their lateral displacements using a reasonable number of degrees of freedom. Such methods would allow obtaining reasonable estimates of their corresponding dynamic characteristics (periods and mode shapes), lateral displacements, story drifts, etc. Once lateral deformations are reasonably assessed, relative distributions of forces and stresses can be obtained using also simple methods that would allow realizing suitable structural designs without the imperative need to perform more complex analyses with finite elements.

In this paper, the approximations obtained with different simplified methods to assess the lateral stiffness of walls with openings are compared to results obtained with the finite ele-

ment method using reasonably fine meshes. Multistory walls were studied, considering symmetric and asymmetric distribution of openings with respect to a vertical axis.

2 SIMPLIFIED METHODS UNDER STUDY

2.1 Equivalent frame method

The equivalent frame method, which was originally proposed by Schwaighofer and Microys [3], consider a wall system with central openings (Figure 1), so it can be understood as an equivalent frame with two lines of walls or "wide-columns" connected by wide central beams. The general modeling assumptions were:

1. Centroidal axes for the cross sections of walls and connecting beams form an equivalent frame.
2. Cross section properties for all columns in the equivalent frame are identical to the corresponding sections for the walls.
3. Full cross section properties for the central beams are considered.
4. Rigid end zones in flexure are considered for the extreme sections of beams.

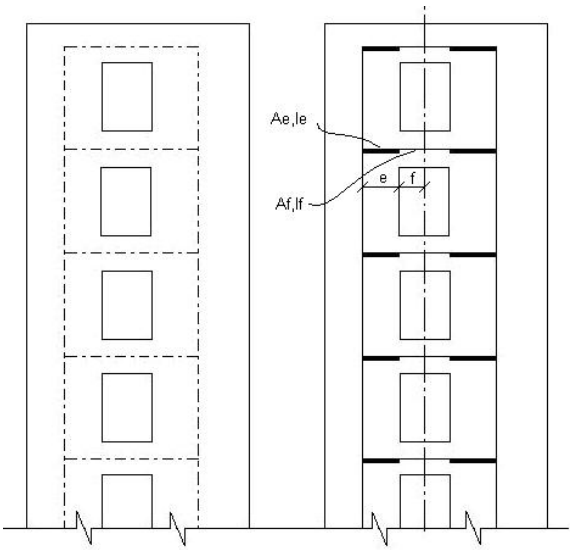


Figure 1. Equivalent frame proposed by Schwaighofer and Microys

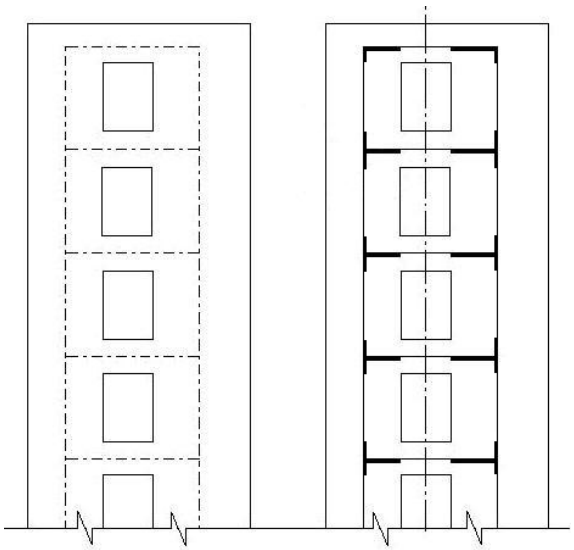


Figure 2. Equivalent frame under SM3 modeling

Schwaighofer and Microys [3] proposed equivalent areas (A_e) and moments of inertia (I_e) for the rigid-end zones, as function of the opening parameters e and f (Figure 1), where e is defined as the distance between the centroidal wall axis and the edge of wall/opening and f is the distance between the centroid of the opening and the edge of the wall/opening. These equivalent properties are computed as:

$$A_e = K_1 A_f \tag{1}$$

$$I_e = K_2 I_f \tag{2}$$

where the proposed values for constants K_1 and K_2 are identified in Table 1.

e/f	K_1	K_1
0.5	50	238
1.0	100	700
2.0	200	2600
3.0	300	6300
5.0	500	21500

Table 1. Constants proposed by Schwaighofer and Microys

From the data provided in Table 1, the following equivalent equations were obtained:

$$K_1 = 100\left(\frac{e}{f}\right) \tag{3}$$

$$K_2 = 0.0593\left(\frac{e}{f}\right)^4 + 99.348\left(\frac{e}{f}\right)^3 + 302.43\left(\frac{e}{f}\right)^2 + 296\left(\frac{e}{f}\right) + 1.7778 \tag{4}$$

Although the equivalent frame method is widely used for the modeling of walls with openings, it is uncommon that engineers would compute constants K_1 and K_2 as proposed by Schwaighofer and Microys. For example, in Mexico beam end zones are considered as infinitely rigid ends zones in flexure, and modeled as rigid links according to what it is described in the literature [4, 7]. Some other people consider that infinitely rigid end zones should be considered also for the equivalent wide columns that represent the walls (Figure 2). Therefore, three different modelings were evaluated for the equivalent frame method:

a) Model SM1. The equivalent frame method as originally proposed by Schwaighofer and Microys (computing A_e and I_e, Figure 1).
b) Model SM2. The equivalent frame method assuming perfectly rigid end zones at beam ends ($A_e \rightarrow \infty$ and $I_e \rightarrow \infty$, Figure 1).
c) Model SM3. The equivalent frame method assuming perfectly rigid end zones at beam and wall ends (Figure 2).

2.2 Method proposed by Coull and Choudhury

Coull and Choudhury [1, 2] proposed a simple method to estimate the peak lateral displacement of walls coupled by slabs or beams (Figure 3), where the lateral loads are resisted entirely by the walls. They proposed a simplified model where the coupling slabs or beams are replaced by an equivalent continuum shear media; that is, the coupling beams with individual stiffnesses EI_p are replaced by an equivalent continuum which stiffness per unit height (h) is EI_p/h. Therefore, they proposed to idealize the system as having two flexural members (walls) connected to a continuum shear media (Figure 3). Coull and Choudhury formulated the second order differential equation for such system and they were able to arrive to a close form solution.

The size of central openings has an important impact in the behavior of coupled shear walls. In the model proposed by Coull and Choudhury, openings are located in a regular, well defined vertical strip, as depicted in Figure 3. Coull and Choudhury proposed the parameter αH (where H is the total height of the structure) to evaluate the overall behavior of the coupled wall system, where:

$$\alpha = \sqrt{\beta\mu l} \tag{5}$$

$$\beta = \frac{12 I_p l}{h b^3 (I_1 + I_2)} \tag{6}$$

$$\mu = 1 + \frac{(A_1 + A_2)(I_1 + I_2)}{A_1 A_2 l^2} \tag{7}$$

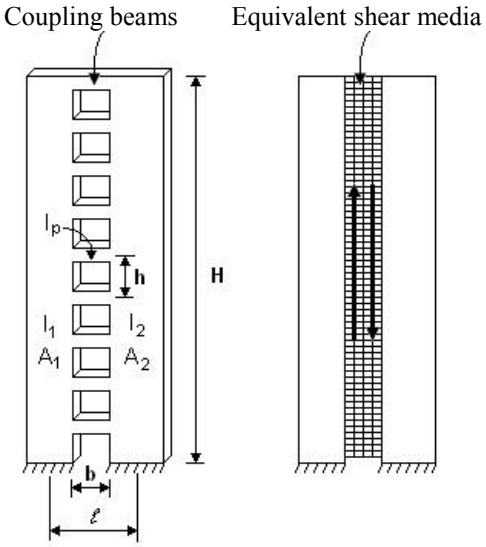


Figure 3. Model proposed by Coull and Choudhury

When αH>8, the coupling wall system tends to behave as a single cantilever wall, whereas when αH<4, the behavior is closer to an equivalent frame. Therefore, for a single vertical strip of openings, the impact of the openings in the lateral stiffness of the coupled wall system can be assessed by using the following stiffness parameters:

$$K_w = \frac{3EI_w}{H^3} \tag{8}$$

$$K_{wo} = \frac{3E(I_1 + I_2)}{H^3 K_4} \tag{9}$$

where K_w and K_{wo} are the lateral stiffnesses of the wall without or with openings respectively, E is Young´s modulus for the walls, I_w is the moment of inertia of the wall considering that there are no openings and:

$$K_4 = 1 - \frac{3}{\mu}\left(\frac{1}{3} + \frac{sinh(\alpha H)}{(\alpha H)^3 \cosh(\alpha H)} - \frac{1}{(\alpha H)^2}\right) \tag{10}$$

The peak top lateral displacement (Δ) for a given lateral load (F) is computed as:

$$\Delta = \frac{F H^3 K_4}{3E(I_1 + I_2)} \tag{11}$$

Coull and Choudhury only proposed how to assess the peak lateral displacement at the top of the building. Therefore, in order to estimate how displacements vary along the height for a

given coordinate x along the height ($0 \leq x \leq H$), three simple functions were evaluated, as described lines below.

Model CC1:

$$\Delta(x) = \frac{Fx^3 K_4}{3E(I_1 + I_2)}; \quad 0 \leq x \leq H \tag{12}$$

Model CC2:

$$\Delta(x) = \frac{FH^{3/4} x^{7/4} K_4}{3E(I_1 + I_2)}; \quad 0 \leq x \leq H \tag{13}$$

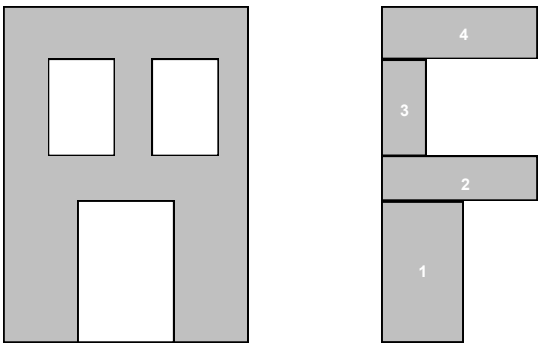
Model CC3:

$$\Delta(x) = \frac{FH^{3/4} x^{7/4} K_4}{3E(I_1 + I_2)}(1 - e^2); \quad 0 \leq x \leq H \tag{14}$$

where e is the opening eccentricity parameter described in section 3.2.

2.3 Equivalent non-prismatic wide column analogy

Another simple method that could be used to estimate lateral displacements of wall systems with openings is to represent such system along the height as a series of equivalent solid segments, ending with an equivalent non-prismatic wide column (Figure 4). With such discretization it is considered that the impact of openings is to diminish the effective cross section properties (area and inertia) of the wall in the segment that the opening is located. For example, the wall system depicted in Figure 4a can be substituted by the equivalent non-prismatic column with four segments depicted in Figure 4b. Therefore, once the effective cross section properties are defined for each segment, the lateral stiffness for the element can be assessed using methods for nonprismatic elements available in the literature [6, 8]. Alternatively, as equivalent prismatic cross sections are defined for the opening segments, available structural analysis software can be used to conduct the required analyses.



a) Wall with openings b) Tapered column

Figure 4. Discretization of a wall with openings as an equivalent nonprismatic wide column

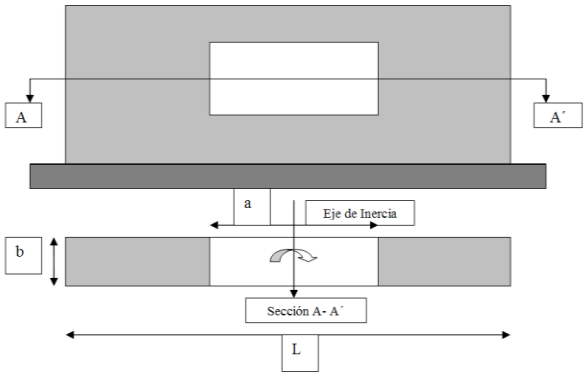


Figure 5. Cross section of the wall in the opening area

The key assumption for this simple method is how to assess the equivalent cross section properties (effective areas A_{eq} and effective moment of inertia I_{eq}) for the segments with openings. Three different assumptions were evaluated.

In Model CE1, it is assumed that in the opening area, the effective section is stiff enough to sustain its theoretical moment of inertia along the opening height. Therefore, taking as reference the section and dimensions depicted in Figure 5, the equivalent cross section properties under this assumption are:

$$I_{eq} = \frac{b}{12}\left(L^3 - a^3\right) \tag{15}$$

$$A_{eq} = b\left(L - a\right) \tag{16}$$

$$A_{ceq} = \frac{A_{eq}}{1.2} \tag{17}$$

In Model CE2, it is assumed that in the opening area, the effective section is basically a solid section which length is the sum of the two solid wall sections (in this case, from Figure 5 the total length would be: $L_{eq} = L_1 + L_2 = L\text{-}a$). Therefore, taking as reference the section and dimensions depicted in Figure 5, the effective areas are those identified in Eqs. 15 and 16 and the equivalent moment of inertia would be assessed as:

$$I_{eq} = \frac{b}{12}\left(L - a\right)^3 \tag{18}$$

In Model CE3, it is assumed that the flexibility in opening area is very important, so each wall section responds separately, so the effective cross section properties at that section are the sum of the properties of the individual solid segments. Under this assumption, and taking as a reference the wall segment depicted in Figure 5, assuming that the wall is completely symmetric, the effective areas are also those identified in Eqs. 15 and 16, but the equivalent moment of inertia would be computed as:

$$I_{eq} = 2\left[\frac{b}{12}\left(\frac{L-a}{2}\right)^3\right] \tag{19}$$

3 GEOMETRIC PARAMETERS FOR OPENINGS

3.1 Opening size parameter λ

The opening size parameter λ is defined, for a given story, as the ratio (in percentage) between the area (in elevation) of the opening and the gross area (in elevation) for the wall segment. Taking as reference the wall segment elevation depicted in Figure 6, this parameter is assessed as:

$$\lambda = 100\left(\frac{l_0 h_0}{Lh}\right) \tag{20}$$

3.2 Opening eccentricity parameter *e*

The opening eccentricity parameter *e* is defined, for a given story, as the normalized distance (in percentage) *d* between the centroidal axis of the opening and the centroidal axis of the wall with the available distance to the edge of the wall, as depicted in Figure 7. If the total length of the wall in Figure 7 is also *L* and the length of the opening is l_0 (Figure 6), then the opening eccentricity parameter is computed as:

$$e = 100\left(\frac{2d}{L - l_0}\right) \tag{21}$$

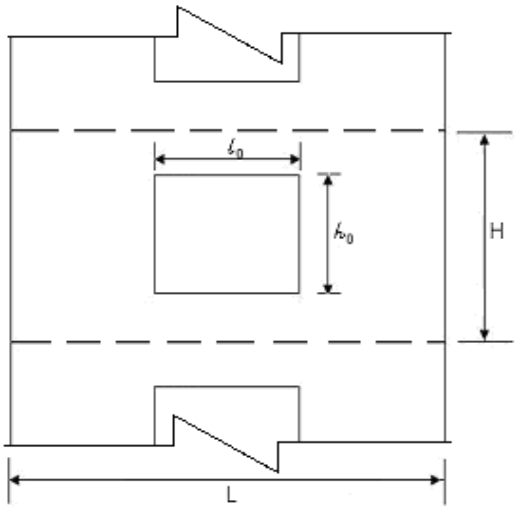


Figure 6. Definition of the opening size parameter λ

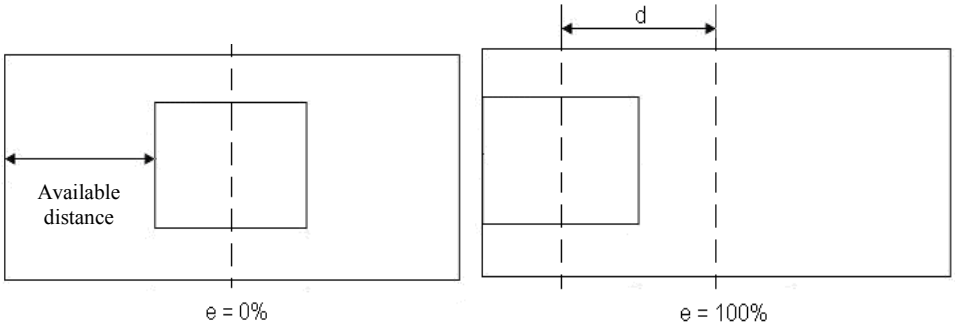


Figure 7. Definition of the opening eccentricity parameter *e*

4 EQUIVALENT OPENING FOR MULTIPERFORATED WALLS

For simplicity, most of the available simplified methods already proposed to assess the lateral stiffness of multi-story walls with openings have considered a well-defined central strip of openings (Figures 1 to 3). However, it is common to have perforated walls with various openings. In many instances, they are not regular (Figure 8). To try to extend such simple methods to more complicated opening geometries, Rivera [9] proposed a simple method to define an equivalent opening (Figure 8).

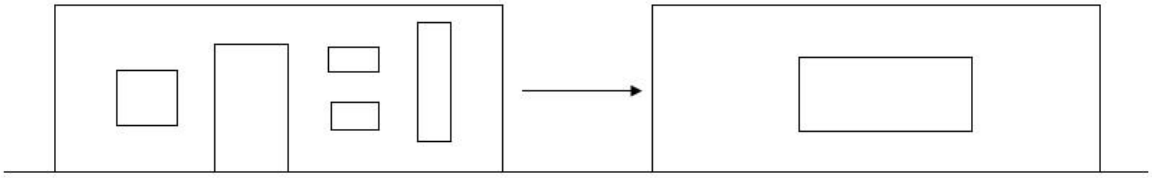


Figure 8. Simplification of multi-perforated walls into a wall with an equivalent single opening

The proposed procedure can be summarized as follows:

1. First, all openings are grouped together around the largest opening, to define a large rectangle with some rectangular appendices around (Figure 9).

2. The area for the equivalent rectangle, A_e, is simply the sum of all individual opening areas A_i.
3. The height to length proportion ratio for the equivalent opening is computed as a weighted average of the individual openings:

$$\frac{H_e'}{L_e'} = \frac{\sum_{i=1}^{n} H_i A_i}{\sum_{i=1}^{n} L_i A_i} \tag{22}$$

4. The dimensions of the equivalent opening are then computed as:

$$L_e = \sqrt{A_e \left(\frac{L_e'}{H_e'} \right)} \tag{23}$$

$$H_e = \sqrt{A_e \left(\frac{H_e'}{L_e'} \right)} \tag{24}$$

5. The centroidal axis for the equivalent opening is located in the centroidal axis of the original openings.

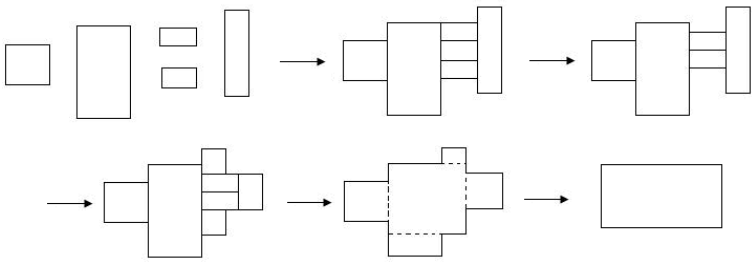
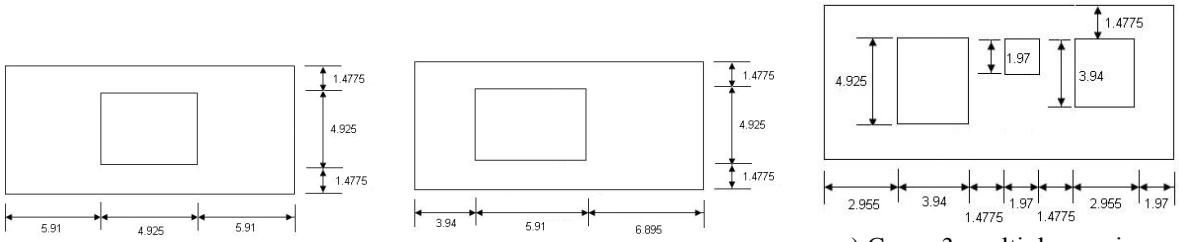


Figure 9. Example of the assessment of an equivalent opening

5 APPROXIMATIONS FOR MULTI-STORY PERFORATED WALLS

In order to assess the degree of approximation of the simple methods under evaluation, a series of multi-story walls with different opening layouts at each story were considered, as depicted in Figure 10. Walls with a single symmetric opening with an opening size parameter λ=18.4% were considered (Group 1, Figure 10a), as well a walls with a single asymmetric opening with λ=18.4% (Group 2, Figure 10b) and walls with multiple asymmetric openings with λ=26.5% (Group 3, Figure 10c). For the walls of Group 3, an equivalent opening as described in section 4 was defined for all the approximate methods under study.



a) Group 1, symmetric b) Group 2, asymmetric c) Group 3, multiple openings

Figure 10. Typical perforated wall configurations (at each story) under study (dimensions in ft)

For each group type, four different elevations were considered: 3, 6, 12 and 18 stories, as schematically depicted in Figure 11, where the walls for Group 1 are identified as A, B, C and D for the 3, 6, 12 and 18 stories respectively, E, F, G and H for Group 2 and I, J, K and L for Group 3. All stories have a story height h=7.88 ft and a length L=16.745 ft (Figure 10). Therefore, the global slenderness ratios for the studied walls vary from H/L=1.41 for the three-story models to H/L=8.47 for the eighteen-story models.

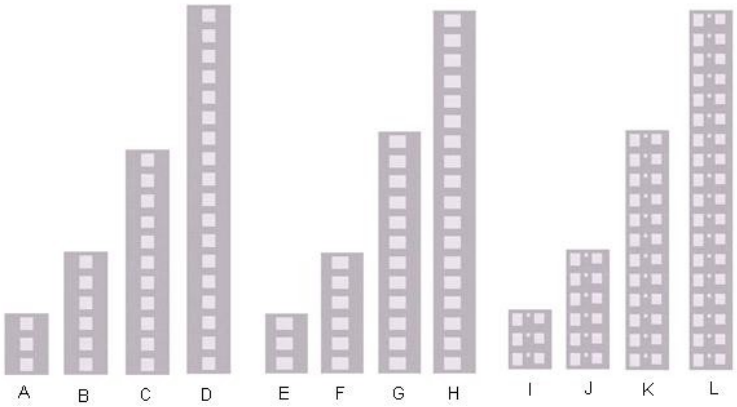


Figure 11. Elevations for the perforated wall models under study

All the described walls (Figures 10 and 11) were rigorously modeled in SAP-2000 using refined meshes with thick shell elements. The assumed elastic properties were E=1.728x10^8 lb/ft^2, v=0.15 and a thickness t=0.7083 ft were considered for all walls. A total lateral load F=350,000 lb was uniformly distributed at the top of each walls. The average lateral displacements at the top of the walls computed from the results of SAP-2000 are reported and identified as "FEM" in Table 2. From the results reported in Table 2, it is observed that average lateral displacements are amplified in walls with asymmetric openings (Group 2) with respect to symmetric openings (Group 1), granted they have the same dimensions and the same opening areas.

Wall	FEM	CC	SM1	SM2	SM3	CE1	CE2	CE3
A (1)	1.115	0.577	1.106	0.968	0.841	0.556	0.629	0.973
B (2)	4.710	3.560	4.842	4.458	4.062	3.431	3.715	5.046
C (3)	28.477	26.170	28.969	28.084	26.376	25.408	26.524	31.760
D (4)	90.175	86.826	91.142	89.754	84.886	84.471	86.966	98.682
E (5)	1.314	0.703	1.254	1.142	0.974	0.567	0.674	1.012
F (6)	5.347	4.0188	5.384	5.066	4.558	3.456	3.868	5.177
G (7)	31.178	28.573	31.584	30.842	28.805	25.464	27.088	32.232
H (8)	97.684	94.0938	98.749	98.585	92.494	84.563	88.196	99.706
I (9)	1.299	0.870	1.532	1.446	1.1796	0.565	0.742	1.351
J (10)	5.916	4.519	5.966	5.730	5.0544	3.454	4.153	6.547
K (11)	38.262	30.848	33.134	32.624	30.562	25.474	28.247	37.741
L (12)	123.451	100.670	102.124	101.332	96.601	84.601	90.821	112.121

Table 2. Average lateral displacements (in) at the top of the walls with openings under study

Also, the results obtained with SAP-2000 are compared with the estimates obtained with the simplified methods under study: Coull and Choudhury (CC), the three described variations for the equivalent frame method (SM1, SM2 and SM3) and for the equivalent non-prismatic wide column analogy (CE1, CE2 and CE3). These approximations are also compared graphically in Figures 12 to 14, where numbers are used to identify the letters, equivalence that is identified in parenthesis in the column named "wall" in Table 2. In Figures 12 to 14, displacements are

normalized with respect to the solution obtained with SAP-2000, which for practical purposes can be considered as "exact"; therefore 100% percent should be interpreted as the exact result.

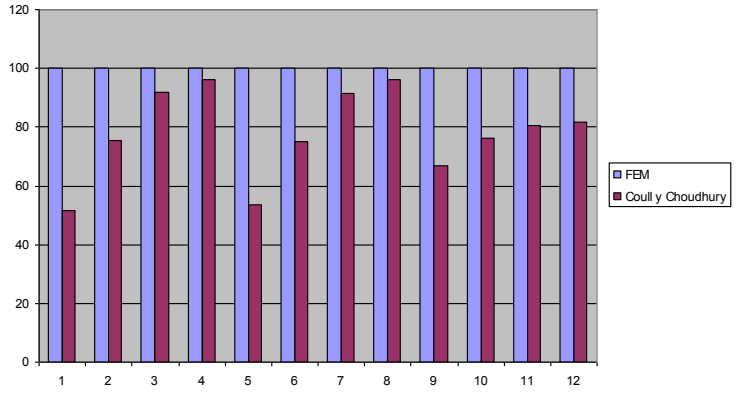


Figure 12. Approximations of the top lateral displacement between SAP-2000 (FEM) and the method of Coull and Choudhury. Displacements are normalized with respect to the FEM solution (100=exact)

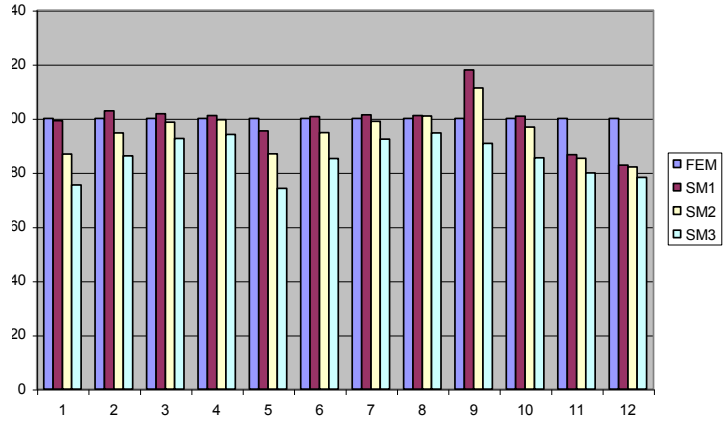


Figure 13. Approximations of the top lateral displacement between SAP-2000 (FEM) and variations of the equivalent frame method (SM1, SM2 and SM3). Displacements are normalized with respect to the FEM solution (100=exact)

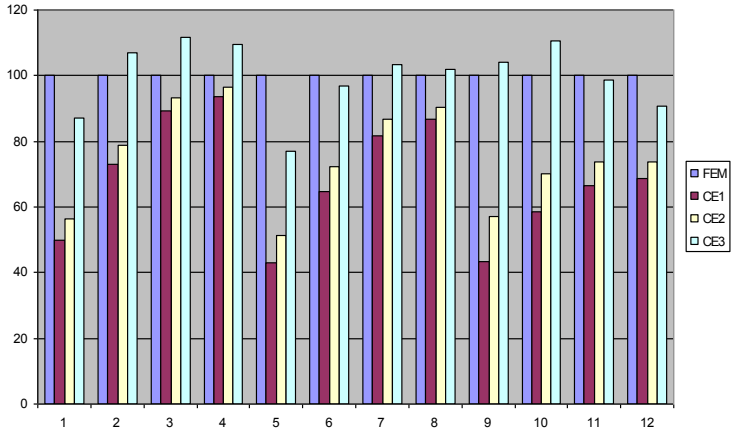


Figure 14. Approximations of the top lateral displacement between SAP-2000 (FEM) and variations of the equivalent non-prismatic wide column analogy (CE1, CE2 and CE3). Displacements are normalized with respect to the FEM solution (100=exact)

It is observed from Figures 12 to 14 that for all simplified methods, the degree of approximation increases as the number of stories increases, that is, as the global slenderness ratio H/L increases. Approximation are reasonable (higher than 70%) from the six story models, that is, when $H/L \geq 2.82$.

It can be observed from Figure 12 that, for the method proposed by Coull and Choudhury, the degree of approximation for a well-defined single opening layout is very similar independently if these openings are symmetric (Group 1, walls 1 to 4) or asymmetric (Group 2, walls 5 to 8). For multi-perforated walls (Group 3, walls 9 to 12), the approximation does not improve as much as the number of stories increases, but it is reasonable, taking into account the inherent simplicity in the definition of an equivalent opening.

It can be observed from Figure 13 that, for the equivalent frame method, the approximation is "exact" for practical purposes for multi-story walls with a single opening layout if the original proposal of Schwaighofer and Microys (SM1) is used, independently if the openings are symmetric (Group 1, walls 1 to 4) or asymmetric (Group 2, walls 5 to 8). However, for walls with multiple openings (Group 3, walls 9 to 12), the method losses accuracy as a consequence of using an equivalent opening. The degree of approximation is reduced when infinitely rigid end zones are considered for the beams (SM2). The worst approximations for this method are obtained when infinitely rigid en zones are also considered for the wall section (SM3).

Finally, it can be observed from Figure 14 that under the equivalent non-prismatic wide column analogy, best approximations are obtained when it is assumed that, in the opening region, each wall section responds separately (CE3); however, under such modeling average displacements can be overestimated with respect to finite element solutions. Under this modeling, the worst approximation was obtained when it is assumed that, in the opening area, the effective section is stiff enough to sustain its theoretical moment of inertia along the opening height (CE1), and as expected, much stiffer results were obtained.

5.1 Assessment of the impact of the opening eccentricity parameter *e*

From the results shown in the previous section it was observed that, for a single strip of openings along the height, average lateral displacements are affected by the asymmetry of the wall opening. Therefore, a parametric study was designed to assess the impact of the eccentricity of the wall opening in terms of the opening eccentricity parameter e described in section 3.2. For this purpose, perforated walls with typical length L=16.745 ft and story height h=7.88 ft with an opening size parameter λ=25% were considered. The considered values for e were e = 0% (symmetric), 20%, 40%, 60% and 80%. Perforated walls of 3, 6, 9, 12, 15 and 18 stories were considered, so their corresponding global slenderness ratio were H/L=1.41, 2.82, 4.24, 5.65, 7.06 and 8.74. In this study, average lateral displacements were computed for each story, so displacement profiles were obtained.

The described walls were rigorously modeled in SAP-2000 using refined meshes with thick shell elements (40 x 40 elements per story). The assumed elastic properties were E=1.728x10^8 lb/ft^2, ν=0.15 and a thickness t=0.7083 ft were considered for all walls. A total lateral load F=1x10^6 lb was uniformly distributed at the top of each walls. The average lateral displacement profiles are depicted in Figure 15, where it can be clearly observed that average lateral displacements increases as the opening eccentricity parameter increases, particularly when e>40%.

The average lateral displacements profiles obtained with the FEM and depicted in Figure 15 are compared with those obtained with the different approximate methods under study in Figures 16 to 21. In order to ease the comparison, for each model under study (number of stories and eccentricity parameter under consideration), average lateral displacements were normalized with respect to the average lateral displacement obtained at the top of each wall model under the finite element method (Δ_{FEM}). In fact, in each subplot the normalized average

lateral displacement profile under the finite element modeling is presented as FEM (red continuous line with open square symbols).

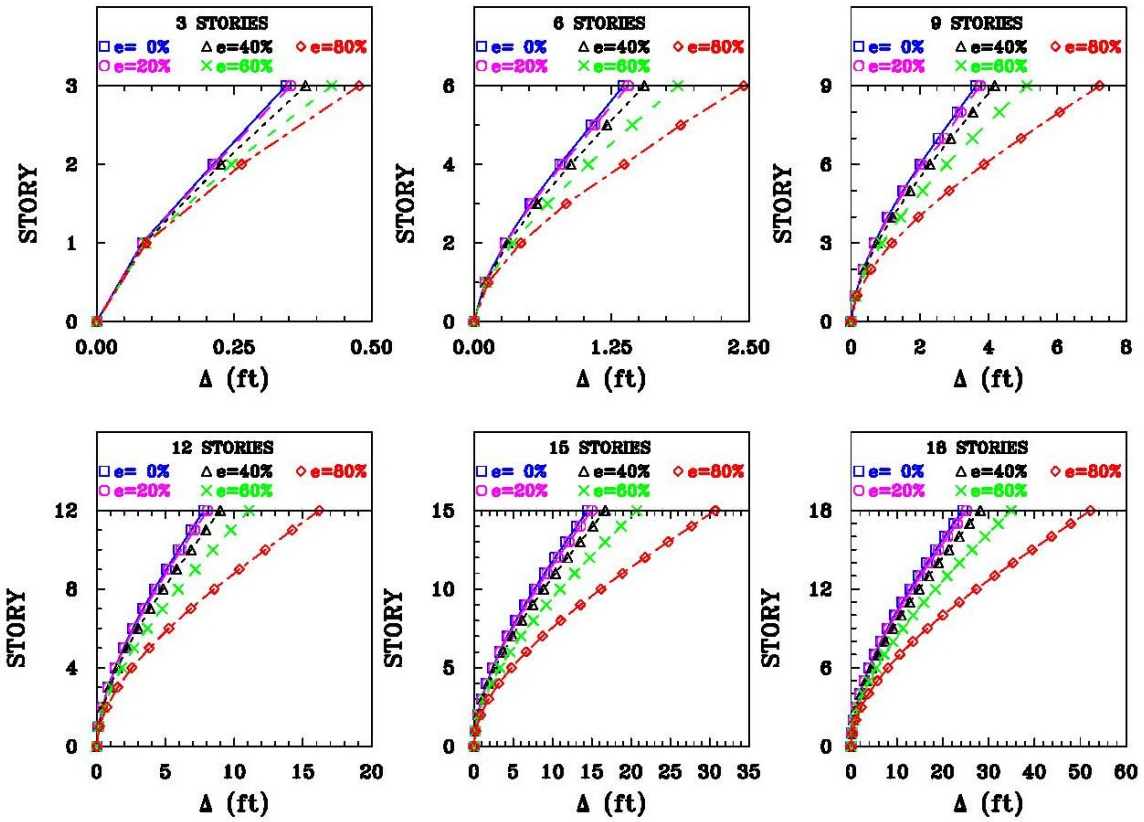


Figure 15. Average lateral displacement profiles for the walls with assymetric openings under study obtained from FEM analyses

It is observed from Figures 16 to 21 that approximations under the Coull and Choudhury method (CC1, CC2 and CC3) depend on the wall height or the global wall slenderness ratio. For example, it is observed from Figure 16 that approximations for the three-story walls (H/L=1.41) are poor (about 50% the average lateral displacement obtained with FEM models), even for walls with symmetric openings (e=0%). However, approximations improve as the number of stories increases, being greater than: a) 70% for the 6-story walls (H/L=2.82, Figure 17), b) 80% for the 9-story walls (H/L=4.24, Figure 18), c) 90% for the 12-story walls (H/L=5.65, Figure 19) and, d) 95% for the 15-story walls (H/L=7.06, Figure 20) and 18-story walls (H/L=8.74, Figure 21). It is worth noting that it was not observed an important reduction on the degree of approximation of this method when the opening eccentricity parameter e increases, that is, approximation obtained for e=20%, 40%, 60% and 80% were similar to those obtained for e=0% for each elevation under consideration (Figures 16 to 21). Regarding the proposed variation of displacement profiles along the height, it is observed from Figures 16 to 21, but particularly from Figures 19 to 21, that the assumption behind model CC2 (Eq. 13) is reasonable. In fact, there is not a significant difference with the assumption behind model CC3, where a correction to account for the eccentricity is proposed (Eq. 15). Therefore, in sake of keeping approximate methods as simple as possible, it is recommended to use the Coull and Choudhury method under the CC2 proposal for walls with global wall aspect ratios (total height H over base dimension L) $H/L \geq 4$, for any given opening eccentricity parameter (e), for walls with a single opening region well defined along the height of the wall, as approximations near or greater than 80% the average lateral displacements are obtained.

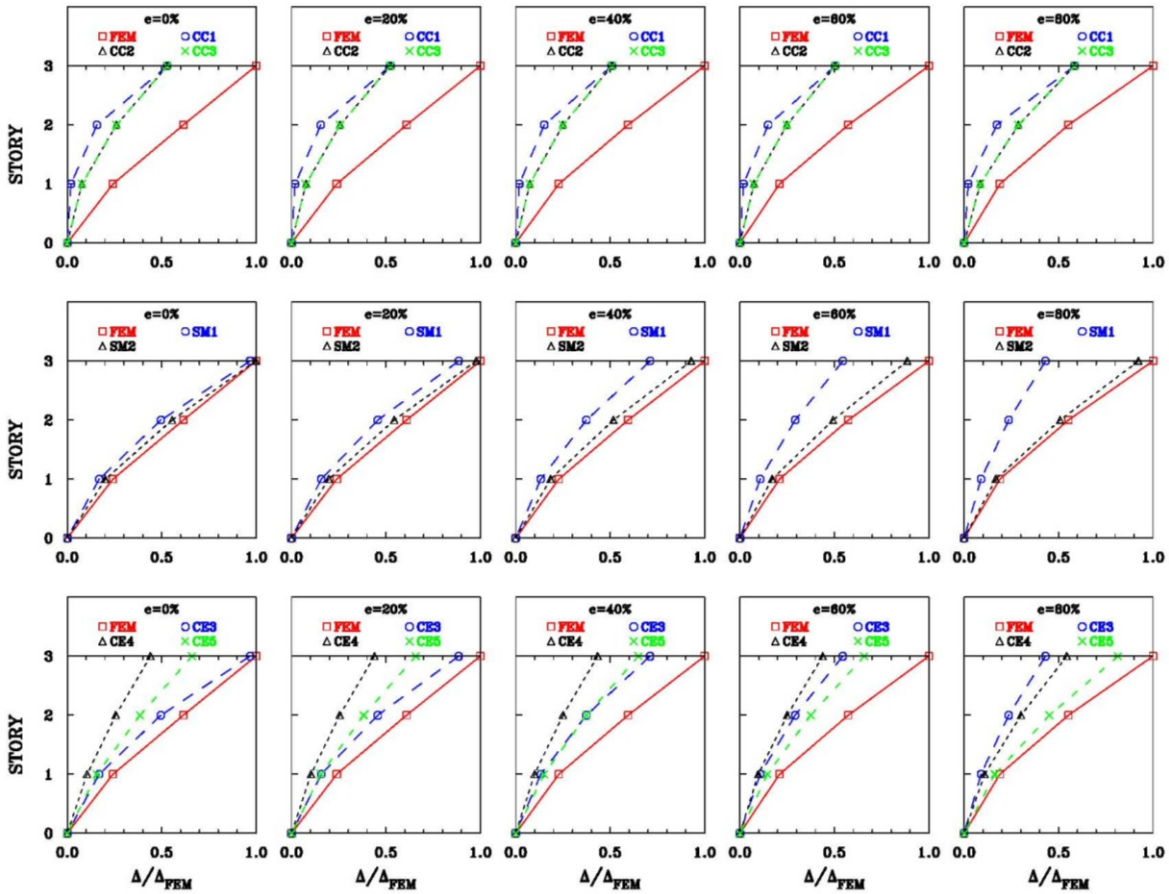


Figure 16. Comparison of normalized average lateral displacement profiles (approximate methods vs FEM) for the 3-story walls with assymetric openings under study

It is observed from Figures 16 to 21 that the original proposal of Schwaighofer and Microys for the equivalent frame method (SM1) is excellent for walls with a single symmetric opening along the height (e=0%), as average lateral displacements are just slightly underestimated or overestimated. It is observed from Figure 16 that for the 3-story models, average lateral displacements are underestimated less than 5% for model SM1 when e=0%; whereas from Figures 17 to 21, an overestimation around 10% is observed for model SM1 for walls from 6 to 18 stories when e=0%. In fact, approximations are still good enough for e=20% and perhaps for e=40%. However, it is also observed from Figures 16 to 21 that approximations under SM1 modeling are notably reduced as the opening eccentricity parameter e increases. This occurs because as the opening eccentricity parameter e increases, the e/f relationship proposed by Schwaighofer and Microys (Figure 1) also increases. Therefore, the proposed constants K_1 and particularly K_2 also increases (Table 1, Eqs.3 and 4) and, as consequence, the equivalent moment of inertia considerably augments (Eq. 2) and the resulting system is much more stiffer. From the observation of Table 1 and equations 1 to 4, it is clear that an increment in the e/f ratio increases more rapidly the bending stiffness (Eqs. 2 and 4) than the shear stiffness (Eqs. 1 and 3).

It is worth noting from Figures 16 to 21 that the equivalent frame method version which it is employed in Mexican design practice (SM2) has a good approximation for all the wall heights and opening eccentricity parameters under study. Nevertheless, it is also observed that the degree of approximation diminishes as the opening eccentricity parameter e increases. Nevertheless, it is also worth noting that in this research we considered only walls with a geometrically well-defined, single opening line along the height of wall, which is the key as-

sumption for the method (Figure 2). It was shown before that such degree of approximation cannot be obtained for more complex opening geometries, even defining an equivalent regular opening.

Based upon the reported results, it can be concluded that the equivalent frame method version which is widely used in Mexican design practice (SM2) lead to better approximation than the original version proposed by Schwaighofer and Microys (SM1) for walls with a geometrical well-defined single line of openings along the height, particularly when the opening eccentricity parameter is 40% or greater ($e \geq 40\%$). For $e \leq 20\%$, both options (SM1 and SM2) lead to reasonable approximations.

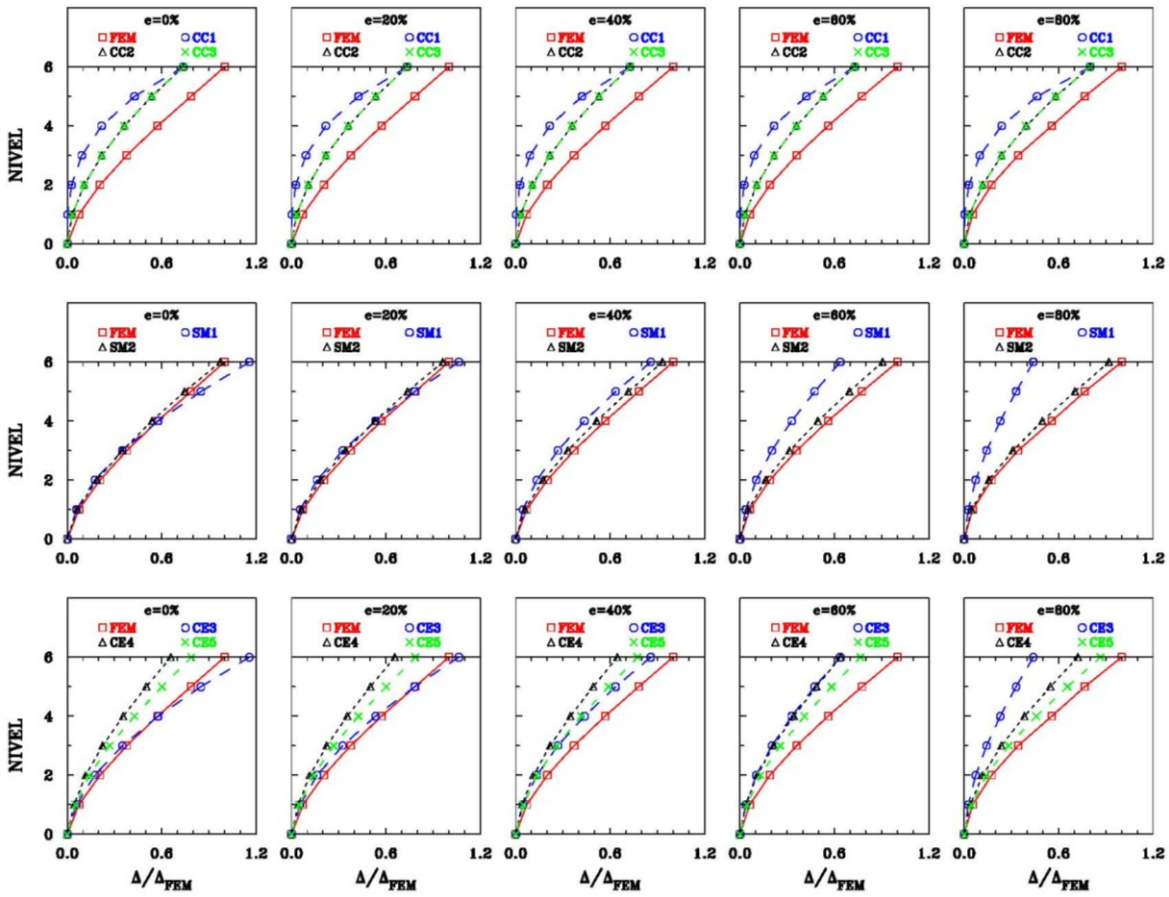


Figure 17. Comparison of normalized average lateral displacement profiles (approximate methods vs FEM) for the 6-story walls with assymetric openings under study

With respect to the equivalent non-prismatic wide column analogy, it is observed from Figures 16 to 21 that the proposed CE3 modeling lead to similar profiles to the equivalent frame method version originally proposed by Schwaighofer and Microys (SM1). Therefore, good approximations are obtained when openings are symmetric (e=0%) or the asymmetry is not very large (e=20%), whereas average lateral displacements are considerably underestimated as the opening eccentricity parameter e increases, as the equivalent moment of inertia increases cubically.

In order to try to improve the approximations for the proposed equivalent non-prismatic wide column analogy, other two options were evaluated. It was observed that although the CE1 model might be the easiest to apply, approximations were not good enough as it leads to very stiff approximations (Figure 14). Then, a simple improvement for the CE1 model was evaluated to take into account the opening eccentricity parameter e, so basically the equiva-

lent moment of inertia (Eq. 15) is multiplied by (1 - e^2) and this is identified as model CE4 in Figures 16 to 21. Finally, another simple expression was evaluated to correct the underestimation of displacements, particularly for low-rise walls, by multiplying CE4 models by 1/(1-1/N), where N is the number of stories. These models are identified as CE5 models in Figures 16 to 21.

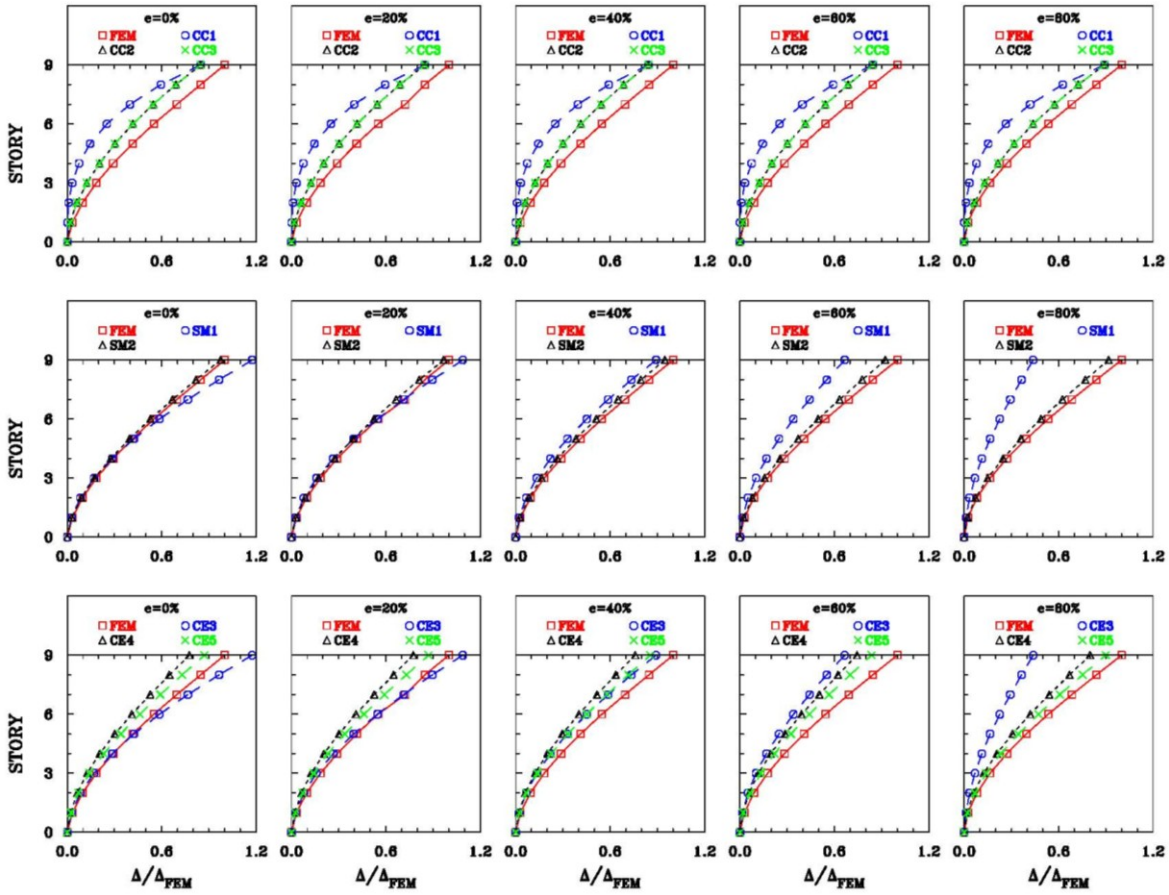


Figure 18. Comparison of normalized average lateral displacement profiles (approximate methods vs FEM) for the 9-story walls with assymetric openings under study

It is observed from Figures 16 to 19 that the proposed correction for eccentricity (models CE4) does not have an important impact on improving the obtained approximations for the simplified methods, independently of the number of stories and the opening eccentricity parameter e, that is, no improvement was observed in the approximations obtained when e=0% with respect to e=80%, except for 3-story models (Figure 16). However, when the opening eccentricity parameter and the proposed flexibility correction in terms of the number of stories are simultaneously accounted for (models CE5), the obtained approximations substantially improved. As expected, improvements were much more notorious for lowrise walls (Figures 16 to 17), where imprecisions were higher when only the correction for the opening eccentricity was accounted for (models CE4).

Based upon the described results, it is concluded that under the equivalent non-prismatic wide column analogy, still the most promising method is the CE3 modeling. However, as under such modeling, the lateral stiffness is considerably overestimated for lowrise walls (H/L<2), therefore, it seems reasonable to amplify the obtained results in terms of the number of stories and/or, more correctly, in terms of the global slenderness ratio for the wall. There-

fore, for future studies, it is proposed to correct the approximations obtained with CE3 modeling using the following global slenderness correction factor F_{sld}:

$$F_{sld} = \frac{1}{1-\frac{1}{N}} = \frac{1}{1-\frac{0.47}{\frac{H}{L}}} \quad if \quad N>1 \quad or \quad \frac{H}{L}>0.47 \tag{25}$$

Also, a correction for the opening eccentricity parameter e is also important to consider, so the following opening eccentricity correction factor F_{ecc} should be used:

$$F_{ecc} = 1-e^2 \tag{26}$$

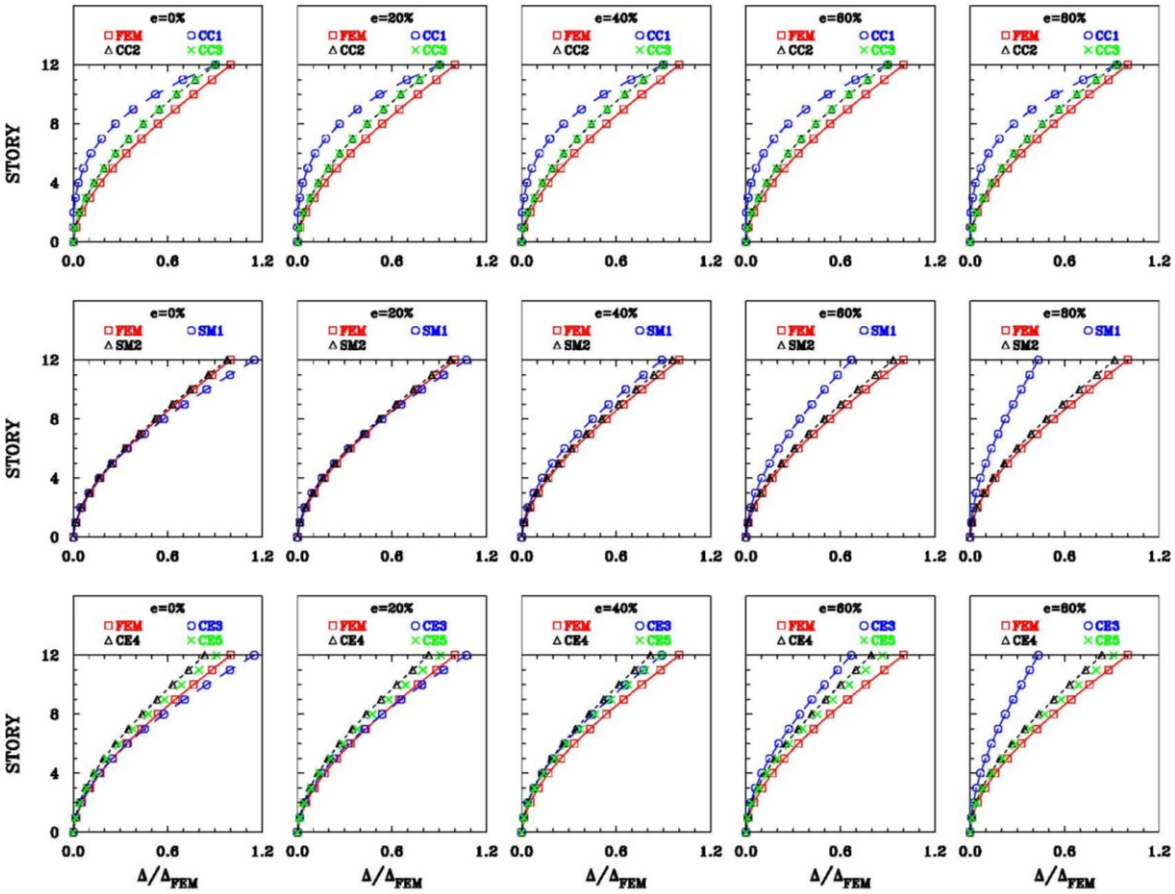


Figure 19. Comparison of normalized average lateral displacement profiles (approximate methods vs FEM) for the 12-story walls with assymetric openings under study

6 CONCLUDING REMARKS

The approximations obtained with different simplified methods to assess the lateral stiffness of walls with openings were compared to results obtained with the finite element method using reasonably fine meshes. Multistory walls were studied, considering symmetric and asymmetric distribution of openings with respect to a vertical axis.

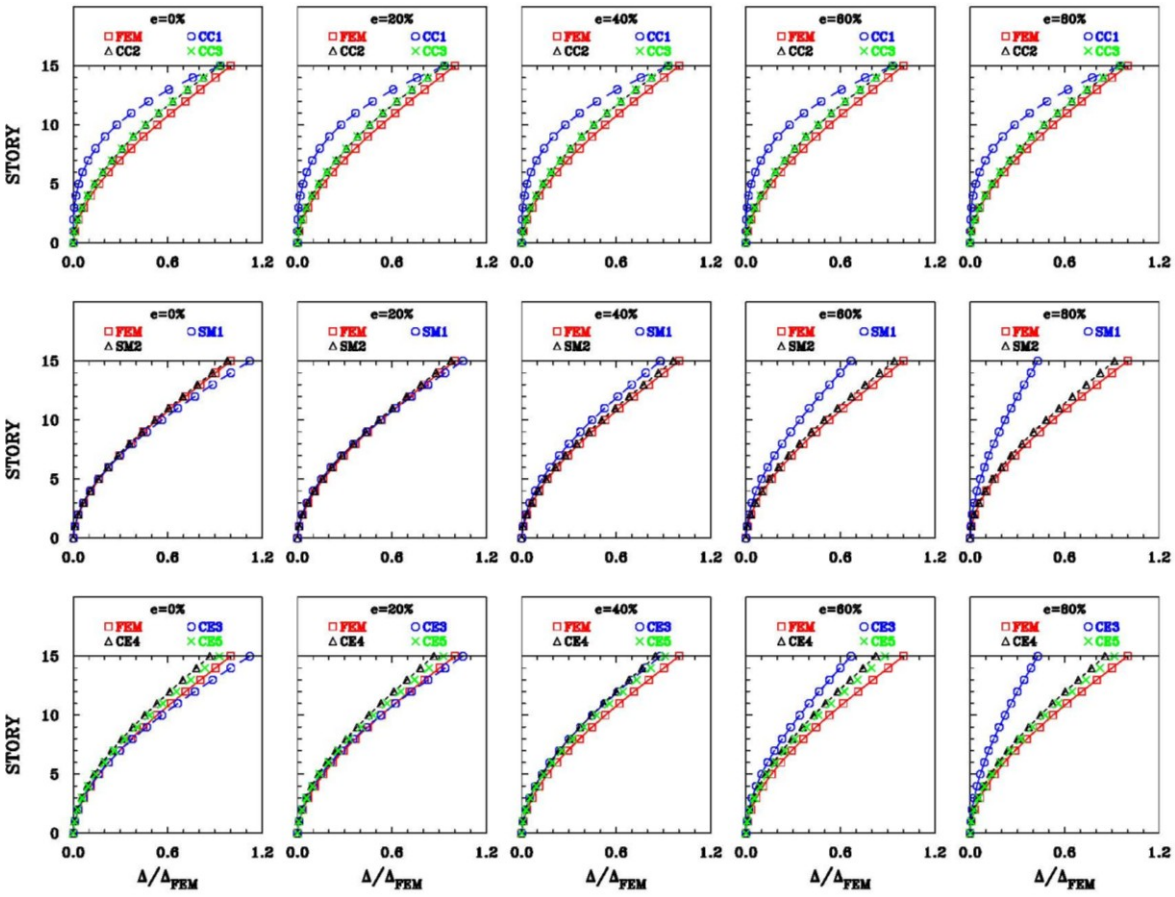


Figure 20. Comparison of normalized average lateral displacement profiles (approximate methods vs FEM) for the 3-story walls with assymetric openings under study

From the obtained results, the following observations can be done:

1. Approximations obtained with the method proposed by Coull and Choudhury depend on the global wall slenderness ratio H/B (wall total height divided by its width). Approximations are poor (around 50%) for relatively stocky walls ($H/L<2$) when compared to finite element results, even for walls with symmetric openings (e=0%). However, the accuracy improves as H/L increases, being higher than 80% for slender walls ($H/L<4$).
2. It was not observed an important reduction on the degree of approximation obtained with the method proposed by Coull and Choudhury when the opening eccentricity parameter e increases, that is, approximation obtained for e=20%, 40%, 60% and 80% were similar to those obtained for e=0%, for each elevation under consideration.
3. As expected, approximations obtained with the method proposed by Coull and Choudhury for multi-story, multi-perforated walls was much smaller when compared to those obtained for walls with a well-defined single opening distribution along the height, given both the original hypothesis for the method and the simple hypothesis explored to define an equivalent single opening.
4. The method proposed by Coull and Choudhury could be improved using the proposed expression (Eq. 13) to estimate how displacements vary along the height (CC2 modeling).
5. It can be recommended to use the method proposed by Coull and Choudhury when $H/L\geq4$ and for any value of the opening eccentricity parameter e, for walls with a well-

defined single layout of openings in elevation, as estimations of average lateral displacements are near or greater 80% when compared to FEM solutions.

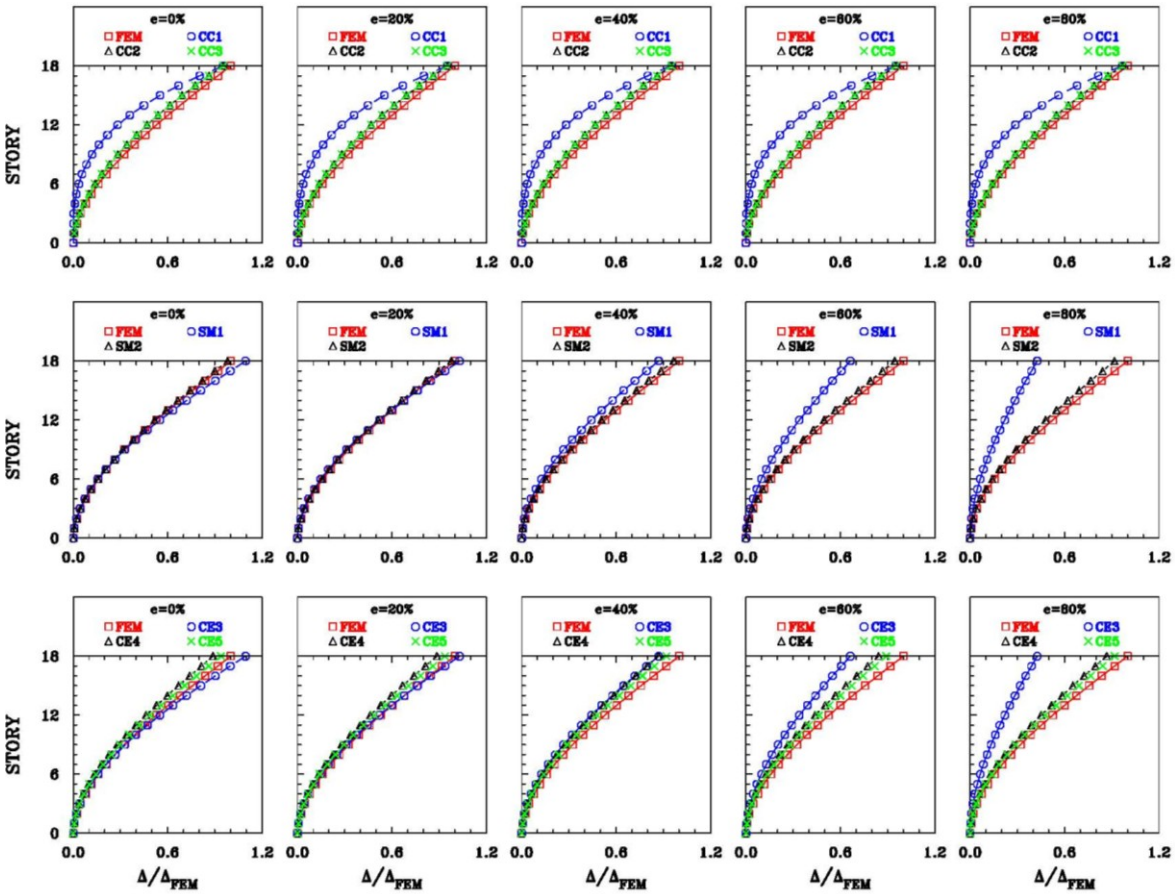


Figure 21. Comparison of normalized average lateral displacement profiles (approximate methods vs FEM) for the 3-story walls with assymetric openings under study

6. For walls with a well-defined single layout of openings in elevation, approximations obtained with the equivalent frame method as originally proposed by Schwaighofer and Microys (models SM1) can be considered exact for practical purposes. The accuracy increases as H/L increases when the opening is completely symmetric (e=0%), or the opening eccentricity parameter is not very large (e≤20%). However, the method notably looses accuracy when the opening eccentricity parameter is large (e>40%) or for complex multi-story, multi-perforated walls.
7. For walls with a well-defined single layout of openings in elevation, approximations obtained with the equivalent frame method most widely used in Mexican design practice (models SM2) can be considered exact for practical purposes, for all the wall heights and opening eccentricity parameters under study. The accuracy increases as H/L increases, but the degree of approximation diminishes as the opening eccentricity e parameter increases. As expected, the method notably looses accuracy for complex multi-story, multi-perforated walls, because key assumptions for the method do not consider such geometries.
8. From the results obtained in this study, it can be recommended to use the equivalent frame method most widely used in Mexican design practice (SM2) when H/L≥1.4 and for any value of the opening eccentricity parameter e, for walls with a well-defined single layout of openings in elevation. The original proposal of Schwaighofer and

Microys can also be used with confidence when $H/L \geq 1.4$ and $e \leq 20\%$, but its reliability diminished when $e > 40\%$.

9. The proposed equivalent non-prismatic wide column analogy lead to reasonable approximations when it is assumed that the flexibility in the opening area is very important, so each wall section responds separately and the effective cross section properties at that section are the sum of the properties of the individual solid segments (model CE3). Similarly to what it was observed in the equivalent frame method as originally proposed by Schwaighofer and Microys (models SM1), for walls with a well-defined single layout of openings in elevation, approximations under CE3 modeling increases as H/L increases, when openings are completely symmetric (e=0%) or the opening eccentricity parameter is not very large ($e \leq 20\%$). However, the method notably looses accuracy when the opening eccentricity parameter is large ($e > 40\%$).

It can be concluded that all the evaluated approximate methods (Coull and Choudhury, equivalent frame method and the equivalent non-prismatic wide column analogy) lead to reasonable approximations for walls with a well-defined single layout of openings in elevation when the perforated walls: a) are slender ($H/L \geq 4$), b) have symmetric openings or the opening eccentricity parameter is not large ($e \leq 20\%$) and, c) openings are reasonably large (opening size parameter $\lambda > 18\%$). With the exception of the version of the equivalent frame method most widely used in Mexican design practice (SM2), the accuracy of these methods is reduced as the opening eccentricity parameter (e) increases, particularly for relatively stocky walls ($H/L < 2$) when $e \geq 40\%$.

All evaluated approximate methods looses accuracy for multi-story, multi-perforated walls, particularly if opening patterns are complex along and across the wall, even with the definition of a single equivalent opening. Therefore, in order to try to expand the applicability of these simple methods, it seems important to keep exploring simple expressions to account for the following parameters: a) the impact of the opening eccentricity parameter e in the amplification of average lateral displacements, b) explore other simple forms to obtain an equivalent opening for multi-perforated walls that may improve approximations and, c) the impact of the stiffness of different floors systems on the lateral displacement profiles of walls with openings. Such parameters should be considered in future research studies, where multi-perforated wall opening patterns commonly used in urban buildings may also be evaluated.

REFERENCES

[1] A. Coull and J. R. Choudhury, Stresses and deflections in coupled shear walls, *ACI Journal*, Title No. 64-6, 1967.

[2] A. Coull and J. R. Choudhury, Analysis of coupled shear walls, *ACI Journal*, Title No. 64-51, pp. 587-593, 1967.

[3] J. Schwaighofer and H. F. Microys, Analysis of shear walls using standard computer programs, **ACI Journal**, Title No 66-89, 1005-1007, 1969.

[4] A. Tena-Colunga, Response of an unreinforced masonry building during the Loma Prieta Earthquake, *Ph.D. Thesis*, Department of Civil Engineering, University of Illinois at Urbana-Champaign, May, 1992.

[5] A. Tena-Colunga, Seismic evaluation of unreinforced masonry structures with flexible diaphragms, *Earthquake Spectra*, **8** (2), 305-318, May, 1992.

[6] A. Tena Colunga, *Análisis de estructuras con métodos matriciales*, first edition, Limusa, ISBN-13: 978-968-18-6980-9, 2007. (in Spanish).

[7] W. McGuire, R. H. Gallagher and R. D. Ziemian, *Matrix structural analysis*, second edition, John Wiley & Sons, 2000.

[8] A. Tena-Colunga, Stiffness formulation for nonprismatic beam elements, *ASCE Journal of Structural Engineering*, **122** (12), 1484-1489, 1996.

[9] G. Rivera, Determinación de la rigidez lateral en muros con aberturas, *Proyecto Terminal I*, Departamento de Materiales, Universidad Autónoma Metropolitana, 2006. (in Spanish).

COMPDYN 2015
5th ECCOMAS Thematic Conference on
Computational Methods in Structural Dynamics and Earthquake Engineering
M. Papadrakakis, V. Papadopoulos, V. Plevris (eds.)
Crete Island, Greece, 25–27 May 2015

DEM & FEM/DEM MODELS FOR LATERALLY LOADED MASONRY WALLS

Daniele Baraldi[1], **Emanuele Reccia**[2], **and Antonella Cecchi**[3]

Department of Architecture Construction Conservation (DACC)
University IUAV of Venezia
Dorsoduro 2206, 30123 Venezia, Italy

[1] e-mail: danielebaraldi@iuav.it

[2] e-mail: emreccia@iuav.it

[3] e-mail: cecchi@iuav.it

Keywords: Masonry Structures, Discrete Models, Discrete/Finite Element Models, Nonlinear Analysis, Mohr-Coulomb Yield Function.

Abstract. *The wide amount of historic masonry constructions in Italy and other European countries makes of paramount importance the development of reliable tools for the evaluation of their structural safety. Masonry is a heterogeneous structural material obtained by composition of blocks connected by dry or mortar joints. The use of refined models for investigating the in-plane nonlinear behavior of periodic brickwork is an active field of research. The mechanical properties of joints are usually considerably lower than those of blocks, therefore it can be assumed that damages occur more frequently along joints. Thus, a key aspect is represented by the evaluation of the effective behavior of joints and its reliable description into numerical models. With this purpose, in this contribution, different models are defined to simulate, with an appropriate accuracy, the behavior of masonry: Discrete Element Model (DEM) and a combined Finite Element and Discrete Element Model (FEM/DEM). Models are based on rigid block hypothesis and joints modeled as Mohr-Coulomb interfaces. These assumptions may be suitable for historical masonry, in which block stiffness is larger than joint stiffness, allowing to assume blocks as rigid bodies, moreover joint thickness is negligible if compared with block size. Analysis is performed in the nonlinear field to investigate the behavior of masonry walls subject to lateral loads, in order to simulate their seismic response, with particular attention to the determination of limit load multipliers.*

1 INTRODUCTION

Masonry is an heterogeneous structural material obtained by the juxtaposition of natural or artificial bricks joined by mortar layers. In the last years several models have been developed based on the micromechanical analysis of the masonry. In the literature [1] different constitutive masonry models have been proposed according to some assumptions: arrangement of the masonry; model of the bricks; models of the mortar; macroscopic model obtained by homogenization or other identification procedures. In this contribution, masonry panels subject to in plane actions are analyzed by means of both FEM/DEM and DEM models, taking into account their nonlinear behavior.

The FEM/DEM i.e. the combination of discrete elements with finite elements allows studying both linear and non-linear masonry behavior. The model is here based on the assumption of both rigid and elastic block and mortar joints modeled as zero thickness linear elastic and Mohr-Coulomb interfaces. Blocks are modeled by means of finite elements while interfaces are modeled as discrete elements. The FEM/DEM analysis is carried out by using an open source code, Y2D, developed by prof. A. Munjiza [2] and implemented by Toronto Group [3,4], who is one of the pioneers of this coupling technique.

Instead in the DEM, a discrete model is considered: the model is based on the assumption of rigid block and mortar joints modeled as zero thickness elastic-plastic interfaces, adopting a Mohr-Coulomb yield criterion. Hence masonry is seen as a "skeleton" [5] in which the interactions between the rigid blocks are represented by forces and moments depending on their relative displacements and rotations and that are limited by the yield criterion chosen. The analysis is performed in this case by extending to more general interfaces an ad-hoc code originally developed by the authors [6,7].

Both models considered fall in the field of discrete or distinct element methods, introduced by the research group of Lemos [8,9] and frequently adopted in the field of rock mechanics.

Recently, a comparison between FEM/DEM and DEM has been carried out for studying masonry linear behavior [10]; in this contribution, such comparison is extended to the nonlinear field. Masonry panels having different height-to-width ratios, subject to self-weight and lateral forces, are considered and incremental analyses are performed for determining the limit load multiplier of lateral forces with respect to self-weight and the corresponding collapse mechanism.

2 GEOMETRIC MODEL

The blocks which form the masonry wall are modeled as rigid bodies connected by interfaces (mortar or dry thin joints). A standard running bond periodic masonry is considered, with block dimensions *a* (height), *b* (width) and *t* (thickness); hence each block has six neighboring blocks (Figure 1).

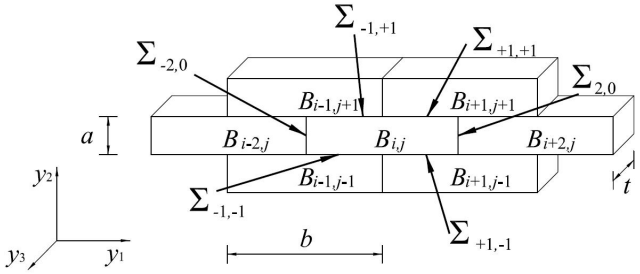


Figure 1: Geometric model adopted.

Let $\mathbf{y}^{i,j}$ denote the position of the center of the generic $B_{i,j}$ block (see Fig. 1), in the Euclidean space; it should be noticed that j can actually take arbitrary values while i is such that $i+j$ is always an even number. Each block exhibits a rigid body motion given by:

$$\mathbf{u}^{i,j}(\mathbf{y}) = \mathbf{u}^{i,j} + \mathbf{\Omega}^{i,j}(\mathbf{y} - \mathbf{y}^{i,j}) \tag{1}$$

where $\mathbf{u}^{i,j}$ is the translation vector of the block characterized by two components and $\mathbf{\Omega}^{i,j}$ is its rotation skew tensor, characterized by one component $\omega_3^{i,j}$, representing block rotation with respect to its center. Due to the regularity of the structure, each block is surrounded by six blocks by means of six interfaces or joints Σ_{k_1,k_2}, with k_1, $k_2 = \pm 1$ for horizontal interfaces and $k_1 = \pm 2$, $k_2 = 0$, for vertical interfaces. For example, the interfaces of the $B_{0,0}$ block are:

$$\begin{aligned}
&\Sigma_{-1,-1}, \Sigma_{-1,+1} = \{-b/2 \le y_1 \le 0,\ y_2 = \pm a/2, -s/2 \le y_3 \le s/2\},\\
&\Sigma_{+1,+1}, \Sigma_{+1,-1} = \{0 \le y_1 \le b/2,\ y_2 = \pm a/2, -s/2 \le y_3 \le s/2\},\\
&\Sigma_{2,0}, \Sigma_{-2,0} = \{y_1 = \pm b/2, -a/2 \le y_2 \le a/2, -s/2 \le y_3 \le s/2\}.
\end{aligned} \tag{2}$$

3 INTERFACE CONSTITUTIVE MODEL

Interfaces between blocks are modeled following an elastoplastic costitutive law, based on a Mohr-Coulomb yield criterion.

3.1 Elastic interface and isotropic joint

If the mortar joint is modeled as an elastic interface [11] the deformation between two blocks may be written as a function of the displacement jump across the interface [[**u**]]. The constitutive prescription for the contact is a linear relation between the tractions on the block surfaces and the jump of the displacement field: $\boldsymbol{\sigma}\mathbf{n} = \mathbf{K}[[\mathbf{u}]]$ on Σ_{k_1,k_2}, where $\boldsymbol{\sigma}$ is the stress tensor, $\mathbf{n}$ is the unit normal to the interface and the stiffness matrix of the interface, $\mathbf{K}$, is given by:

$$\mathbf{K} = \frac{1}{e}\left[\frac{E^M}{2(1+\nu^M)}\left(\mathbf{I} + \frac{1}{(1-2\nu^M)}(\mathbf{n}\otimes\mathbf{n})\right)\right] \tag{3}$$

where E^M and ν^M are the Young's modulus and the Poisson's ratio of mortar, and $\mathbf{I}$ is the identity tensor. Note that tensor $\mathbf{K}$ has, in this case, a diagonal form.

3.2 Interface with Mohr-Coulomb response

If the mortar joint is modeled as a Mohr-Coulomb interface, the yield criterion depends on cohesion $c \ge 0$ and friction angle $0 < \phi < \pi/2$. Adopting a statically admissible approach, the interfacial failure condition can be expressed as

$$f(\sigma_n, \sigma_t) = |\sigma_t| + \sigma_n \tan\phi - c \le 0, \tag{4}$$

where σ_n and σ_t denote the normal and shear component of the stress vector acting on the interface Σ. Adopting a kinematically admissible approach, for any point along the interface, the Mohr-Coulomb yield criterion is expressed by

$$\pi(\mathbf{n}, [[\dot{\mathbf{u}}]]) = \begin{cases} c \cdot \mathrm{ctg}\phi\, [[\dot{\mathbf{u}}]]\cdot\mathbf{n} & \text{if } [[\dot{\mathbf{u}}]]\cdot\mathbf{n} \ge |\mathbf{[[\dot{u}]]}| \sin\phi \\ +\infty & \text{otherwise} \end{cases} \tag{5}$$

where [[**u̇**]] denotes the velocity jump across the interface Σ when following the normal **n** to the Σ interface. The first case may be also expressed as $u^{\perp} \geq u^{\parallel} \cdot \tan\phi$.

4 DISCRETE MODEL

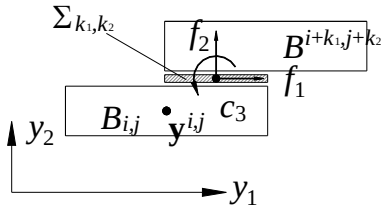


Figure 2: Interface between adjacent blocks and interfacial actions.

The discrete model presented here is based on the implementation of a numerical method already formulated in the case of regular periodic masonry [6]. The interactions between the blocks $B_{i,j}$ and $B_{i+k_1,j+k_2}$ through the interface are represented by unknown distribution of actions $\mathbf{f} = \{ f_1^{k_1,k_2} \quad f_2^{k_1,k_2} \quad c_3^{k_1,k_2} \}^T$ (Fig. 2), that are related to the relative displacements and rotations between adjacent blocks by means of the constitutive relation is **f** = **K**[[**u**]], where $[[\mathbf{u}]] = \{ d_1^{k_1,k_2} \quad d_2^{k_1,k_2} \quad d_3^{k_1,k_2} \}^T$ collects the relative displacements or displacement jumps. The degrees of freedom of block $B_{i,j}$ are globally denoted by $\mathbf{q}^{i,j} = \{ u_1^{i,j}, u_2^{i,j}, \omega_3^{i,j} \}^T$ and **q** collects the degrees of freedom of the entire masonry panel.

The equation of motion of the discrete system is:

$$\mathbf{M}(\partial^2 \mathbf{q} / \partial t^2) + \mathbf{F}_{int} = \mathbf{F}_{ext} . \tag{6}$$

Where $\mathbf{F}_{ext}$ is the vector of the applied in plane actions, **M** is the (diagonal) mass matrix of the panel collecting block mass and polar inertia and $\mathbf{F}_{int}$ is the vector of internal forces. Such vector is equal to $\mathbf{K}_{panel}(\mathbf{q} + \mu \partial \mathbf{q} / dt)$ if the masonry assemblage lies in the elastic field, where $\mathbf{K}_{panel}$ is the in plane stiffness matrix and μ is the damping coefficient (neglected for simplicity). The equilibrium equation above may be solved adopting a molecular dynamics solution method [14,15]. Starting from an external load $\mathbf{F}_{ext}$ characterized by forces and/or couples applied to block centers, the equation of motion may be solved adopting a the predictor-corrector algorithm GEAR of order 2 [6] without determining explicitly panel matrices. At time *t*, for a given increment $\{\delta d_n \quad \delta d_t \quad \delta d_3\}^T$ in the time increment δt, with $n = 1$, $t = 2$ for a vertical interface or $n = 2$, $t = 1$ for a horizontal one, the new interfacial actions are computed by evaluating for first the elastic contribution:

$$\begin{aligned} f_n^{el} &= f_n(t) + K_n \delta d_n, \\ f_t^{el} &= f_t(t) + K_t \delta d_t, \ . \\ c_3^{el} &= c_3(t) + K_m \delta d_3. \end{aligned} \tag{7}$$

Where $\{K_n \quad K_t \quad K_m\}$ are normal, tangential and rotational stiffness of the interface. The elastic guess is correct and $\{ f_n(t+\delta t) \quad f_t(t+\delta t) \quad c_3(t+\delta t) \}^T = \{ f_n^{el} \quad f_t^{el} \quad c_3^{el} \}^T$ if interfa-

cial forces $\{f_n^{el} \quad f_t^{el} \quad c_3^{el}\}^T$ satisfy the following Mohr-Coulomb conditions, that represent, respectively, the detachment, sliding and rotational failure modes:

$$\begin{aligned} f_n &= \mathbf{f} \cdot \mathbf{e}_\perp \le f_c, \\ |f_t| &= |\mathbf{f} \cdot \mathbf{e}_\square| \le (f_t - f_n)\tan\phi, \\ |c_3| &\le (f_c - f_n) l_c. \end{aligned} \tag{8}$$

where $f_c = c\,S/\tan\phi$ is the tensile strength of the interface, with $S = S_v = at$ or $S_h = bt/2$ and l_c is the characteristic length of the interface, represented by the distance of the interfacial normal force with respect to block center.

If $f_n^{el} > f_c$, then $\{f_n(t+\delta t) \quad f_t(t+\delta t) \quad c_3(t+\delta t)\}^T = \{f_c \quad 0 \quad 0\}^T$, otherwise the normal projection according to the tangential force criterion is done:

$$\begin{aligned} f_n' &= f_n^{el} - \lambda_t K_n \tan\varphi\, d_n, \\ f_t(t+\delta t) &= f_t^{el} - [sign(f_t^{el})]\lambda_t K_t d_t, \\ \lambda_t &= [|f_t^{el}| + (f_n^{el} - f_c)\tan\phi] / [K_t + K_n \tan^2\phi] \end{aligned} \tag{9}$$

Then $\{f_n' \quad f_t(t+\delta t) \quad m^{el}\}^T$ is projected according to the moment criterion obtaining:

$$\begin{aligned} f_n(t+\delta t) &= f_n' - \lambda_m K_n l_c, \\ c_3(t+\delta t) &= c_3^{el} - [sign(c_3^{el})]\lambda_m K_m, \\ \lambda_m &= [|c_3^{el}| + (f_n' - f_c) l_c] / [K_m + K_n l_c^2]. \end{aligned} \tag{10}$$

Eq. 6 may be also solved by determining explicitly the stiffness matrix of the entire panel and solving as usual the system of equations: $\mathbf{q} = (\mathbf{K}_{panel})^{-1}\mathbf{F}_{ext}$, moreover panel stiffness matrix may be updated taking into account Mohr-Coulomb yield criterion. Panel stiffness matrix was determined in [16] for performing modal analysis of masonry structures and further details may be found in [17].

5 FEM/DEM MODEL

In the early 1990s FEM and DEM have been combined and the resulting method was termed the combined FEM/DEM [2]. It is in essence a discrete element method with individual elements meshed into finite elements. Finite elements allow to model elastic deformation (if any), while discrete element algorithms allow to model interaction, fracture and fragmentation processes. The FEM/DEM method provides a consistent procedure to study masonry structures [10,18] thanks to the possibility of creating models made of separated blocks. In particular, these models can properly represent the behavior of historical masonry constructions, which could be considered as made of dry stone blocks exhibiting a periodic pattern. The combination of DEM and FEM provided by the open source code Y2D, developed by prof. A. Munjiza [2] and implemented by Geo Group of Toronto University [3,4] allows to further extend the study to both linear and nonlinear masonry behavior. In particular blocks can be assumed to behave (differently from DEM described above) as elastic bodies while mortar joints might be idealized as elastic or elastic-plastic zero-thickness Mohr-Coulomb interfaces. In the present case blocks have been modeled by means of finite elements while interfaces are modeled as discrete elements.

6 FEM/DEM AND DEM MODEL PROCEDURES

DEM and FEM/DEM models are different for several aspects.

The structural model of DEM consists of rigid blocks, with loads and restraints applied at block centers and joint between blocks are modeled as interfaces having translational and rotational stiffness. The parameters involved in the DEM are block geometry, joint stiffness (translational and rotational) values, that depend on mortar elastic modulus E^M, Poisson ratio and joint dimensions (thickness, area and inertia). As described in the 4th paragraph, joints are modelled as Mohr-Coulomb cohesive interfaces. If dry joints are considered, fictitious mortar stiffness values may be adopted with very low value of cohesion. DEM is characterized by a small number of degrees of freedom involved in numerical analysis, hence it requires a relatively small computational effort with respect to models based on finite elements.

The structural model of the FEM/DEM consists of a mesh of Finite Elements, made with triangular elements, hence loads and restraints are applied at nodes. The height of each element is $h = a/2$, thus each block has been meshed with 16 elements. In FEM/DEM, the interfaces are made by specific "crack elements", dedicated four nodes cohesive elements which are embedded between the hedges of all adjacent triangular elements pairs since the beginning of simulation [19]. The potential crack path can open everywhere in the mesh, here in order to simulate the behavior of historic masonry panels, in which cracks usually occur mainly in the mortar joints [20,21], two different joints have been used: one inside the blocks and the other between adjacent blocks. The former has a very high cohesion value in order to avoid the breaking of blocks, while the latter has a very low cohesion value, in order to model dry joints. The parameters involved in the FEM/DEM are block mechanical properties and joint properties: cohesion, tensile strength, friction ratio and fracture energy. In order to emulate the behavior of rigid blocks, the adopted Young modulus is $E^B = 1000\ E^M$, while the Poisson ratio has been set $\nu^B = 0$.

In order to calibrate the two models, cohesion and friction adopted for joints are the same, whereas the fracture energy in FEM/DEM [19] joints has been evaluated on the base of mortar elastic modulus adopted in DEM. As previously stated, in the DEM, due to rigid block hypothesis, forces are applied at block centers, whereas in the FEM/DEM, forces are lumped at the inner nodes of each block subdivision (Fig. 3).

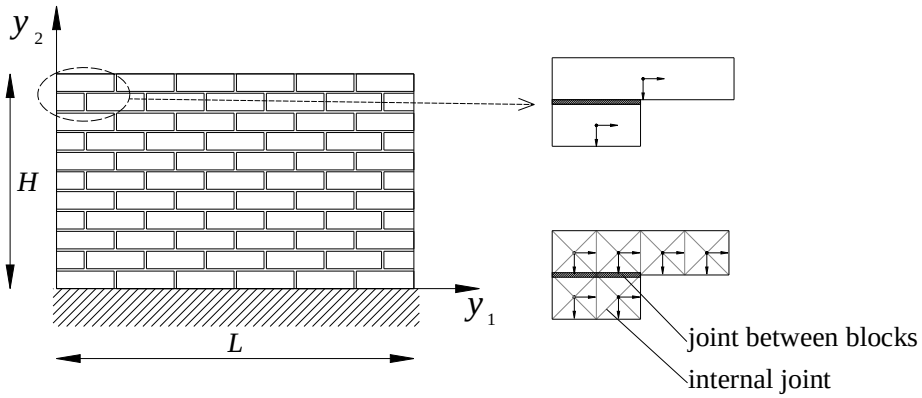


Figure 3: Generic masonry panel modelled with DEM and FEM/DEM.

7 STRUCTURAL ANALYSIS

The stability problem of a masonry panel subject to its own weight and horizontal body forces may be solved analytically by adopting a homogenization procedure based on the definition of a homogeneous material, equivalent to the heterogeneous one in its geometry and in the properties of its constituent materials [22]. The representative elementary volume (REV) adopted for the homogenization is one half of the assemblage in Fig. 1.

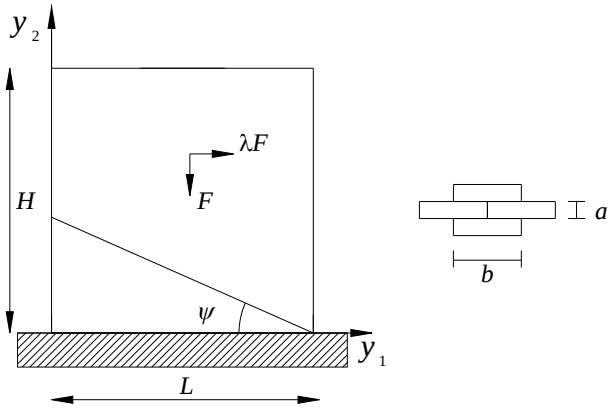


Figure 4: Homogenized masonry panel with rigid block failure and detail of the REV considered.

Considering the hypotheses of rigid blocks and Mohr-Coulomb interfaces, following De Buhan and De Felice [12], the support function $\pi(\varepsilon)$ and the yield criterion $G(\mathbf{y})$ on the REV are defined as:

$$\pi(\varepsilon) = sup\{\boldsymbol{\sigma} \cdot \dot{\boldsymbol{\varepsilon}},\ \boldsymbol{\sigma} \in G(\mathbf{y})\} \quad \Leftrightarrow \quad G(\mathbf{y}) = \{\boldsymbol{\sigma} \mid \boldsymbol{\sigma} \cdot \dot{\boldsymbol{\varepsilon}} \le \pi(\varepsilon), \forall\ \varepsilon\}\,. \tag{11}$$

Where ε denotes a second-order strain rate tensor. The Mohr-Coulomb failure condition at the interfaces provides:

$$< \pi(\mathrm{grad}^s(\dot{\mathbf{u}}) >= \begin{cases} \dfrac{1}{ab}\displaystyle\int_\Sigma \left(\frac{c}{tan\phi}\right)[[\dot{\mathbf{u}}]]\cdot\mathbf{n} & \text{if } [[\dot{\mathbf{u}}]]\cdot\mathbf{n} \ge |\mathbf{[[\dot{u}]]}|\sin\phi \\ +\infty & \text{otherwise} \end{cases}. \tag{12}$$

Details of the macroscopic yield criterion may be found in the works of De Buhan and De Felice, Cecchi and Vanin [12,13].

Then, a homogeneous rectangular panel width L, height H and thickness t is considered (Fig. 4). Vertical forces depend on the specific weight of the panel and horizontal forces are denoted by the multiplier λ that is gradually increased. An upper-bound estimate of the ultimate value of λ, corresponding to the collapse of the panel, is obtained by applying a yield design kinematic approach to the homogenized structure [12]. Following the procedure adopted by Cecchi and Vanin [13], at the collapse, when joints exhibit only frictional strength properties, the free mechanism condition is estimated through the collapse multiplier λ, that is a function of $m = 2a/b$, ϕ and $r = H/b$. In case of shear failure the collapse multiplier is:

$$\lambda = \tan\phi \tag{13}$$

In the case of flexural failure, a rigid block mechanism is considered in which the part of the panel above the line having inclination ψ is given a virtual rigid body motion. Then, a relation between the rotation angle ψ in the homogenized panel, representing the highest slope

of the fracture line, and ϕ in the elementary cell is established by equating the power spent in the macroscopic homogenized panel and in microscopic structure:

$$\tan\psi \le \left(\frac{m}{\tan\phi}\right)^{-1/2} \tag{14}$$

Therefore the flexural failure depends both on the mechanical properties and the geometry of the micro-structure and on the geometry of panel and collapse multiplier is given by:

$$\lambda = \begin{cases} \dfrac{1}{2}\left(\dfrac{m}{\tan\phi}\right)^{-1/2} & \text{if } r = \dfrac{H}{L} \le \left(\dfrac{m}{\tan\phi}\right)^{1/2} \\ \dfrac{3r - 2\left(\dfrac{m}{\tan\phi}\right)^{-1/2}}{3r^2 - \left(\dfrac{m}{\tan\phi}\right)} & \text{otherwise} \end{cases} \tag{15}$$

In particular the first expression of Eq. 15 represents the load multiplier for a local crisis characterized by a flexural failure depending only on m and ϕ parameters, while the second expression of Eq. 15 represents the load multiplier for a global crisis of the panel (flexural failure depends not only on the m and ϕ parameters, but also on the $r = H/b$ ratio).

The values of λ provided by the equations 13 and 15 are adopted as reference solutions for the analyses performed with DEM and FEM/DEM.

8 NUMERICAL TESTS

A set of base supported panels having height H, base L and thickness t is considered. Block dimensions are: b = 240 *mm*, a = 60 *mm*, t = 120 *mm*, 6 blocks along panel width are considered and three different panel height-to-width ratios are taken into account (H/L equal to 0.5, 1.0 and 2.0, Fig. 5). As stated in the 6th paragraph, negligible cohesion c is considered, whereas a friction ratio $\tan\phi$ = 0.6 is assumed, corresponding to a friction angle of about 30°.

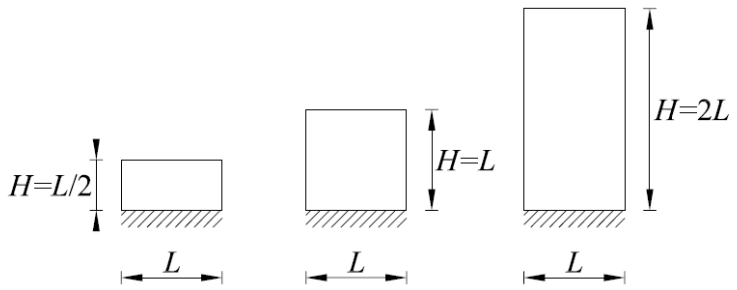


Figure 5: Case studies considered.

Each panel is subject to a uniform vertical load representing its self-weight and to a horizontal increasing force representing a lateral acceleration statically applied. For representing this loading condition in the DEM, due to rigid block hypothesis, each block is subject to a vertical force $F_{2,i}$ and a horizontal one $F_{1,i} = \lambda F_{2,i}$, whereas in the FEM/DEM, horizontal and vertical forces are lumped at the inner nodes of each block subdivision (Fig. 6).

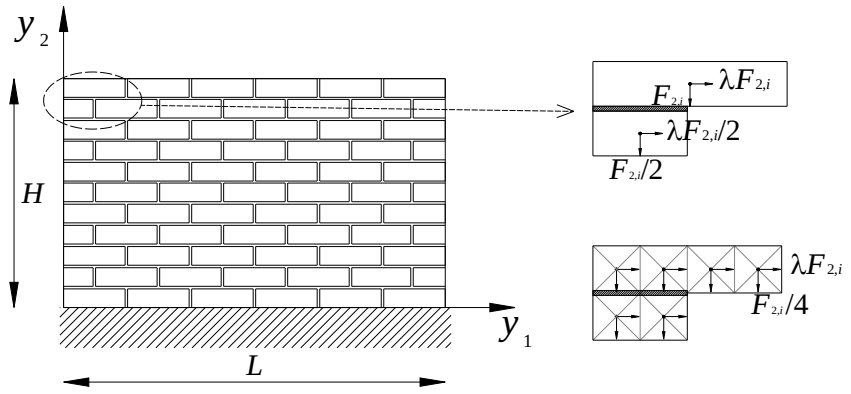


Figure 6: Generic masonry panel subject to self-weight and proportional lateral loads modelled with DEM and FEM/DEM.

Nonlinear incremental analyses of the panels considered are performed in order to determine their ultimate load multiplier (λ_{DEM} and $\lambda_{FEM/DEM}$) and the corresponding collapse mechanisms. Dry joints are taken into account, hence analytic solutions determined in the 7th paragraph are taken as reference (λ_{REF}) and evaluated for increasing H/L ratio and constant $2a/b$ ratio based on block dimensions (Fig. 7).

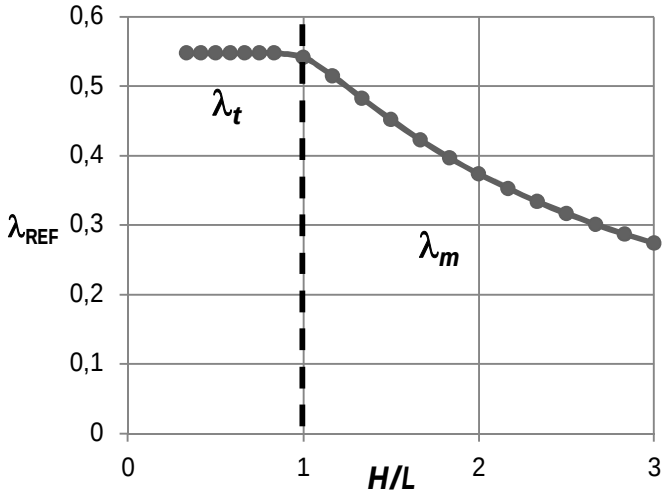


Figure 7: Ultimate load multipliers for masonry panels and increasing H/L ratio.

Fig. 8 shows load multiplier values versus displacement values for the three panels considered and obtained with DEM and FEM/DEM, together with the ultimate load multiplier obtained analytically. Displacements are evaluated at the upper-right corner of the panel. Moreover, limit load multipliers are collected in Tab. 1.

Results are in good agreement between the reference values of multipliers obtained analytically and the ones obtained by DEM and FEM/DEM. Instead some differences may be found in the values of displacements obtained by the two models, due to the different aspects of the two methods previously highlighted in the 6th paragraph. In particular, displacements in DEM are influenced by the Young modulus of joints E^M which is not taken into account in FEM/DEM. The two models have been calibrated calculating the fracture energy adopted in joints in FEM/DEM on the base of mechanical parameters adopted in DEM: Young modulus and cohesion. But, being the joints assumed as dry, so without cohesion, the behavior of joints

is mainly related to friction ratio $\tan\phi$, thus the differences in the displacements obtained by the two models are sensible. In the next step of this research it will be taken into account cohesion and the differences in the displacements should decrease.

Fig. 9 shows collapse mechanisms for the three panels considered obtained with DEM and FEM/DEM.

Results show that both models are suitable to describe the global behavior of masonry walls, and in particular they are able catch the non-linear behavior of masonry panels subjected to lateral loads. Panels with a ratio $H/L<1$ collapse with a sliding mechanism, while panels with a ratio $H/L>1$ collapse with a overturning mechanism, as shown by the mechanisms obtained by the two models, which are in a good agreement. Small differences may be found in panels with a ratio $H/L=1$, for which the mechanism can be either sliding that overturning. Crack patterns obtained by the two models are very close, but DEM provides a mechanism in which the upper part of the panel exhibits a small rotation, while the mechanism obtained by FEM/DEM shows sliding in the upper part of the panel.

H/L	$\lambda_{FEM/DEM}$	λ_{DEM}	λ_{REF}
0.5	0.550	0.550	0.548
1.0	0.450	0.510	0.542
2.0	0.350	0.360	0.374

Table 1: Comparison between ultimate load multipliers.

9 CONCLUSIONS

- The DEM and FEM/DEM models represent a simple and effective tool for the study of non-linear behavior of masonry structures, in particular with reference to masonry panels subjected to lateral loads.
- The DEM and FEM/DEM models are able to take into account the real texture of masonry walls, thus they are able to describe with accuracy the real cracks pattern that may develop in masonry walls and to catch the potential mechanisms of collapse.
- The next step of the research will involve the adoption of real mechanical parameters of mortar joints, in particular with reference to cohesion, and will consider different texture and geometry of panels.
- The behavior of masonry panels will be compared with experimental results, with the purpose of the evaluation of in-plane and out-of-plane behavior of masonry walls.

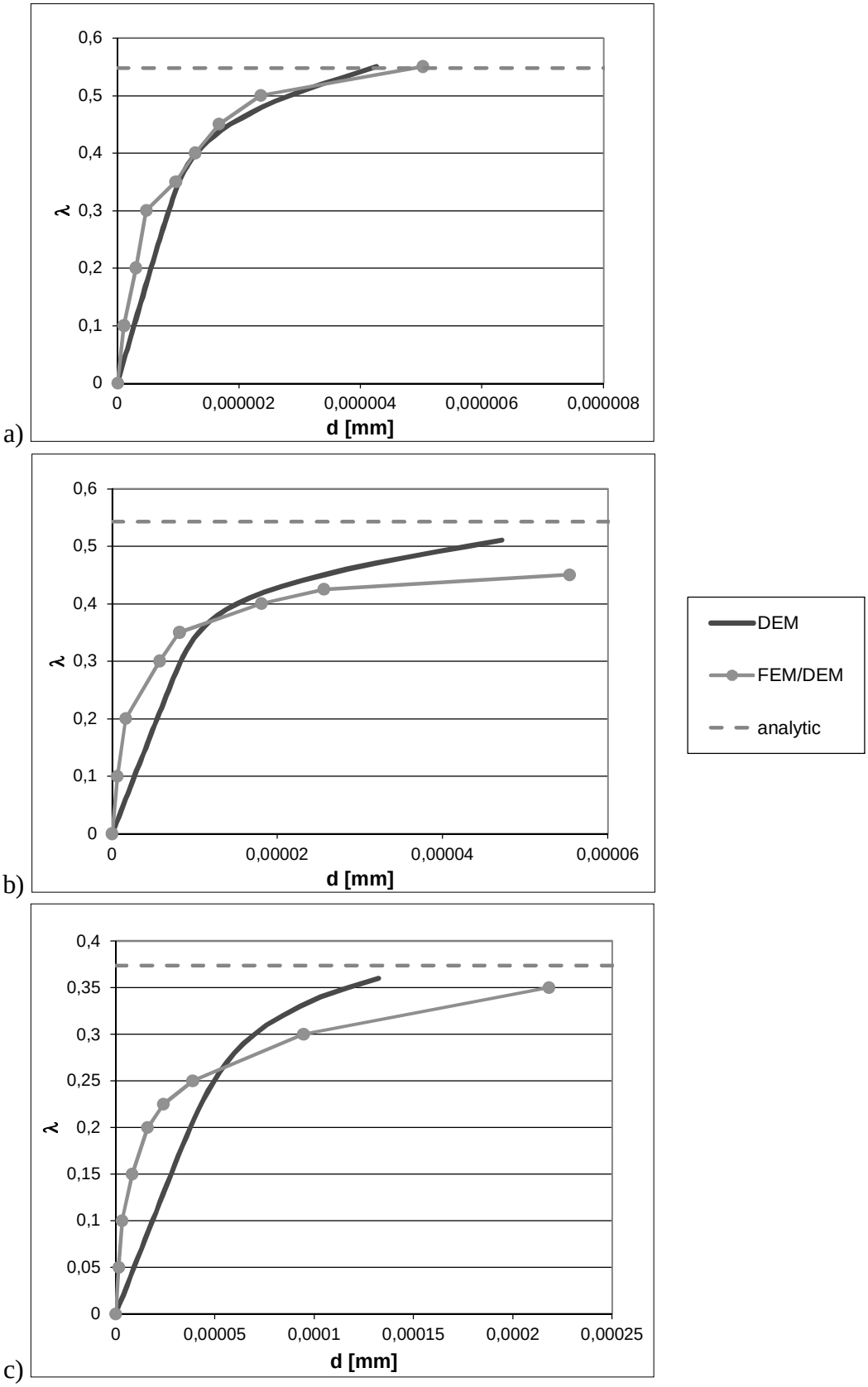


Figure 8: Incremental analyses, load multiplier vs. displacement at the upper-right corner of the panel. (a) H/L = 0.5, (b) H/L = 1, (c) H/L = 2.

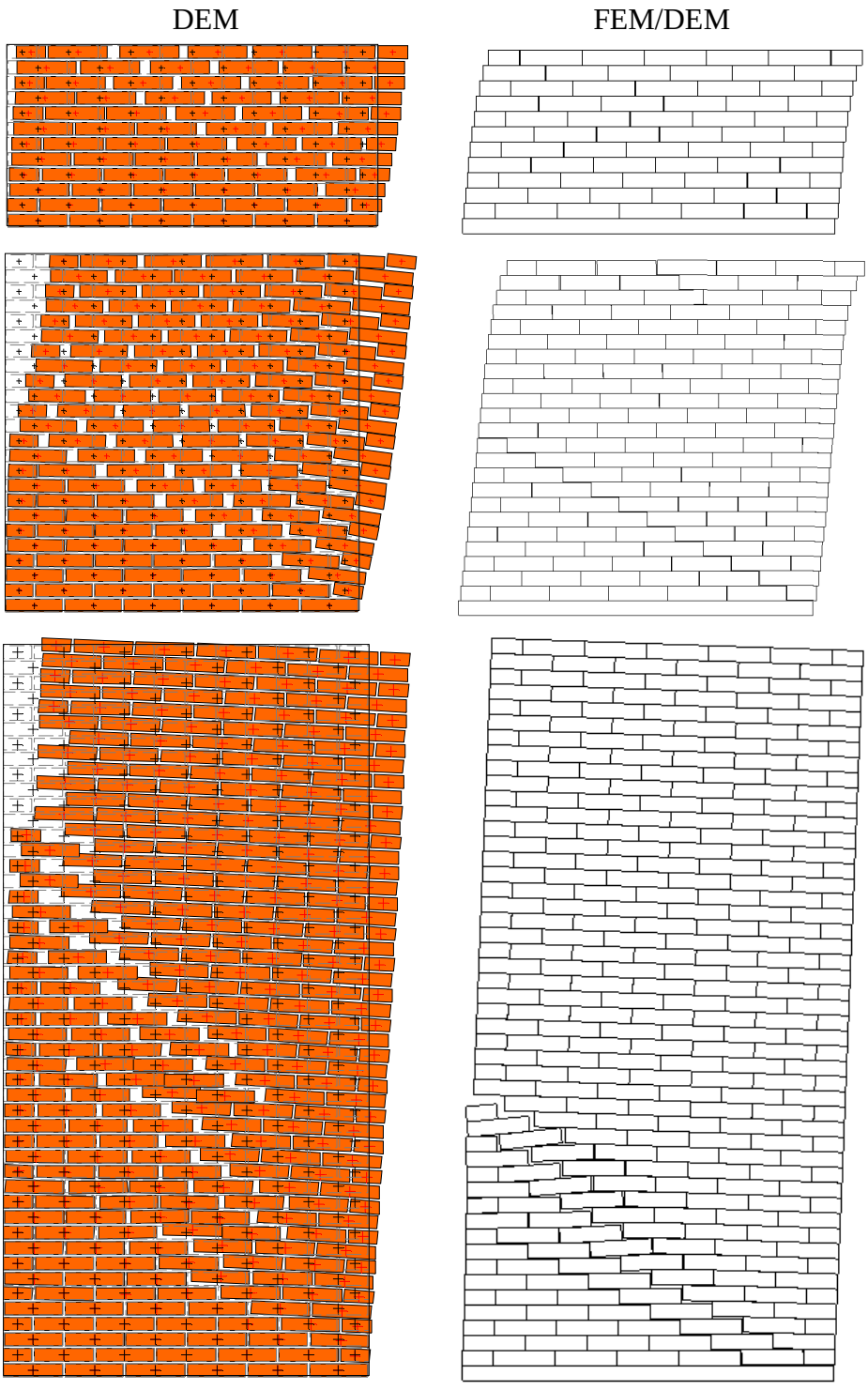


Figure 9: Collapse mechanisms of masonry panels.

REFERENCES

[1] Addessi D. and Sacco E., A multi-scale enriched model for the analysis of masonry panels, *International Journal of Solids and Structures*, **49**, 865–880, 2012.

[2] Munjiza A., *The finite/discrete element method*, John Wiley and Sons, Chicester 2004.

[3] Mahabadi O.K., Grasselli G. and Munjiza, A., Y-GUI: A graphical user interface and preprocessor for the combined finite-discrete element code, Y2D, incorporating material inhomogeneity, *Computer and Geosciences*, **36**, 241–252, 2010.

[4] Mahabadi O.K., Lisjak A., Munjiza A. and Grasselli G., Y-Geo: a new combined finite-discrete element numerical code for geomechanical applications, *Geomechanics*, **12**, 676–688, 2012.

[5] Markov K.Z., Elementary micromechanics of heterogeneous solids. In: Markov K.Z., Preziosi L. Eds., *Heterogeneous MediaMicromechanics ModelingMethods and Simulations*, Birkhauser, Boston, 1999.

[6] Cecchi, A. and Sab, K., A comparison between a 3D discrete model and two homogenized plate models for periodic elastic brickwork, *International Journal of Solids and Structures*, **41**, 2259–2276, 2004.

[7] Baraldi, D., Cecchi, A., Discrete Element Model for in plane loaded viscoelastic masonry, *International Journal for Multiscale Computational Engineering*, **12**, 155-175, 2014.

[8] Lemos, J.V., Discrete Element Modeling of Masonry Structures, *International Journal of Architectural Heritage*, **1**, 190-213, 2007.

[9] Itasca, UDEC (Universal Distinct Element Code) Version ICG1.5 User's Manual, 1989.

[10] Baraldi, D., Reccia, E., Cazzani, A., Cecchi, A., Comparative analysis of numerical discrete and finite element models: the case of in-plane loaded periodic brickwork, *Composites: Mechanics, Computations, Applications, an International Journal*, 4, 319-344, 2013.

[11] Klarbring A., Derivation of model of adhesively bounded joints by the asymptotic expansion method. *International Journal of Engineering Sciences*, **29**, 493–512, 1991.

[12] De Buhan, P., De Felice, G., A homogenization approach to the ultimate strength of brick masonry, *Journal of the Mechanics and Physics of Solids*, **45**(7), 1085-1104, 1997.

[13] Cecchi, A., Vanin, A., From micro to macro models for in plane loaded masonry walls: proposition of a multiscale approach, *Composites: Mechanics, Computations, Applications, an International Journal*, **11**(2), 139-159, 2013.

[14] Allen, M.P., Tildesley, D.J., *Computer simulations of liquids*, Oxford Science Publications, 1994.

[15] Owen, D.R.J., Hinton, E., *Finite elements in plasticity: theory and practice*, Pineridge Press Limited, Swansea U.K., 1980.

[16] Baraldi, D., Cecchi, A., Discrete and continuous models for the in plane Modal analysis of masonry structures. *5th European Conference on Computational Mechanics (ECCM V)*, Barcelona, Spain, 2014.

[17] Baraldi, D., Bullo, S., Cecchi, A., Multi-model approach for periodic masonry: continuous and discrete strategies for modal analysis. Submitted to *European Journal of Mechanics A/Solids*.

[18] Reccia, E., Cazzani, A., Cecchi, A., FEM-DEM Modeling for Out-of-plane Loaded Masonry Panels: A Limit Analysis Approach, *Open Civil Engineering Journal*, **6**(SPEC.ISS.1), 231-238, 2012.

[19] Lisjak, A., Liu, Q., Zhao, Q., Mahabadi, O.K., Grasselli, G., Numerical simulation of acoustic emission in brittle rocks by two-dimensional finite-discrete element analysis, *Geophysical Journal International*, **195**(1), 423-443, 2013.

[20] Luciano, R., Sacco, E., Homogenization technique and damage model for old masonry material, *International Journal of Solids and Structures*, **34**(24), 3191-3208, 1997.

[21] Lourenço, P.B., Rots, J.G., Multisurface interface model for analysis of masonry structures, *Journal of Engineering Mechanics*, **123**(7), 660-668, 1997.

[22] Anthoine, A., Derivation of the in-plane elastic characteristics of masonry through homogenization theory, *International Journal of Solids and Structures*, **32**(2), 137-163, 1995.

COMPDYN 2015
5th ECCOMAS Thematic Conference on
Computational Methods in Structural Dynamics and Earthquake Engineering
M. Papadrakakis, V. Papadopoulos, V. Plevris (eds.)
Crete Island, Greece, 25–27 May 2015

3D FE PUSHOVER AND NON-LINEAR DYNAMIC ANALYSES OF A MASONRY CHIMNEY BEFORE AND AFTER SHORTENING

E. Bertolesi[1], A. del Grosso[2], G. Milani[1], F. Minghini[2]and A. Tralli[2]

[1] Technical University of Milan
Piazza Leonardo da Vinci 32,20133 Milan (IT)
e-mail: elisa.bertolesi@polimi.it, gabriele.milani@polimi.it

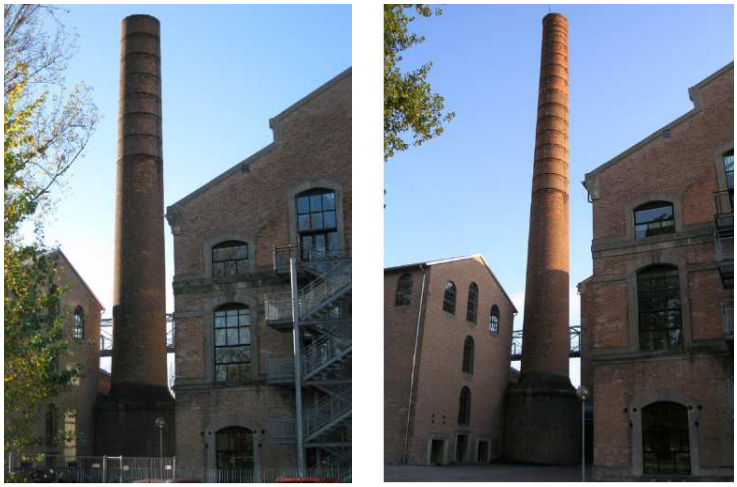
[2] University of Ferrara
Via Saragat 1, 44100 Ferrara (IT)
e-mail: antonio.delgrosso@student.unife.it, fabio.minghini@unife.it, atralli@ing.unife.it

Keywords: masonry chimney; seismic-risk assessment; pushover; nonlinear analysis; vibration mode.

Abstract. *A masonry chimney 50 meters high, severely damaged by the May 2012 Emilia-Romagna (Italy) seismic sequence is numerically analyzed by means of non linear static and dynamic FE techniques. The state of damage on the upper part of the structure led to take the decision to shorten the chimney for security reasons, with a reduction of the height up to 37 meters. A modal pushover analysis (MPA) where force distributions based on the principal vibration modes is used to analyze the structure, finding for the 50 meters case crack patterns consistent with the observed ones. In addition, it is shown how, before and after shortening, the behavior factor to be used in modal response spectrum analyses, estimated directly from the MPA results, is slightly higher than unity, indicating a very low dissipative capacity. To validate static approach results, non-linear dynamic analyses are carried out using natural accelerograms and for the masonry material a damage-plasticity model. The residual deformations obtained and the crack patterns found exhibit convincing similarities with the real behaviour and address how the shortening may be beneficial to improve stability.*

1 INTRODUCTION

In recent years, mainly with the aim of improving the dynamic behavior of the heritage buildings, the seismic analyses of masonry structures have become an important issue in civil engineering. Among the others, slender structures such as chimneys or towers require particular attention in the evaluation of the seismic behavior. Nowadays, the difficulties concerning such structures are mainly related to the complexity, from a computational point of view, in reproducing the nonlinear masonry response in the dynamic field. The strong influence of the higher modes of vibration often increases the problem. One of the first studies on the possible failure mechanisms of masonry chimneys under earthquake excitation is reported in [1], whereas in [2] Riva and co-workers used a simplified model composed by elastic beam elements connected through nonlinear joints, to study the seismic vulnerability of a 97.2 m high masonry tower in the historical centre of Bologna, Italy. More recently, the increased computing power allowed for more advanced analyses using two- or three-dimensional finite elements, some studies dealing with this topic are [3]-[4]. An interesting state-of-the-art review of seismic assessment and strengthening techniques of masonry chimneys is reported in [5].
The present paper deals with the seismic damage assessment of an unreinforced masonry chimney built at the beginning of the 20th century in the service of a sugar factory in Ferrara, Italy. A survey campaign performed after the 2012 earthquake sequence in Northern Italy (Emilia earthquake), evidenced diagonal cracks in the outer surface of the stack at an altitude of approximately 45 m. The damages mainly were composed of large open cracks, grossly inclined at 45°, but also a deterioration of the mortar along the cross section circumference or even partially missing was detected. Due to the position of the masonry chimney, close to the university buildings, the structure has required a subsequent shortening of the upper part. In the current form the chimney is 37.6 m high. The structures after and pre shortening are depicted in Figure 1. In order to explain the causes of the widespread damages and to analyze the different seismic behaviors pre and after the shortening activities, a series of numerical analyses of the chimney previous and in the current form are presented in the paper. In particular, both Modal Pushover Analyses (MPA) and nonlinear Response History Analyses (RHA) using three-dimensional nonlinear finite elements are utilized.



a b

Figure 1. The chimney (a) after and (b) before shortening.

2 NUMERICAL MODELS

The FE analyses presented in the paper are performed using a tridimensional model composed by 8-node solid (brick) elements. The mesh was generated assuming 75 subdivisions along vertical axis while 16 subdivisions were adopted in in the planes of the cross sections. The resultant model is composed by 1200 finite elements and 2432 nodes.
The original 50m-high chimney was discretized using 100 and 16 equal subdivisions along the vertical axis and in the planes of the cross sections, respectively, resulting in 1600 solid elements and 3232 nodes (for a detailed description the reader is referred to [6]-[7]). All the simulations previously presented are performed by means of two different software packages. In particular, pushover analyses are developed using DIANA [9][8], while response history analyses are performed with ABAQUS [10]. The nonlinear behavior of masonry is involved into both simulations. Concerning the DIANA software, the material nonlinearities are reproduced by means of a traditional total strain crack model, belonging to the family of the smeared crack constitutive laws. In particular, the effects due to cracking are taken into account by using a linear softening for the stress-strain relationship in tension and a shear retention factor $\beta = 0.05$. The model parameters are summarized in Table 1.

Young's modulus	Poisson's ratio	Strengths Compressive	Tensile	Ultimate tensile strain	Shear retention factor
E	ν	f_c	f_t	ε_t	β
MPa		MPa	MPa	‰	
1500	0.15	3.5	0.1	0.5	0.05

Table 1. Material properties used in the pushover analyses.

The material properties, such as the compressive strength, are estimated from laboratory test results [6]-[7], whereas, in the absence of a specific experimental characterization, the value of Young's modulus was chosen in agreement with the indications reported by the Italian Building Code [8], for existing masonry structures. The constitutive model used for the numerical simulations in ABAQUS, the so called Concrete Damage Plasticity (CDP) model, is based on the assumption of a scalar isotropic damage with distinct damage parameters in tension and compression and is particularly suitable for applications in which the material is subjected to loading-unloading conditions such as dynamic analyses. Masonry is assumed to obey a Drucker-Prager strength criterion with non-associated flow rule. A value equal to 10° is adopted for the dilatation angle. Software ABAQUS allows for smoothing the strength domain by means of an eccentricity parameter, which in the *q*-*p* plane represents the distance between the points of intersection with the *p*-axis of the cone and the hyperbola. A value of 0.1 is adopted in the simulations.

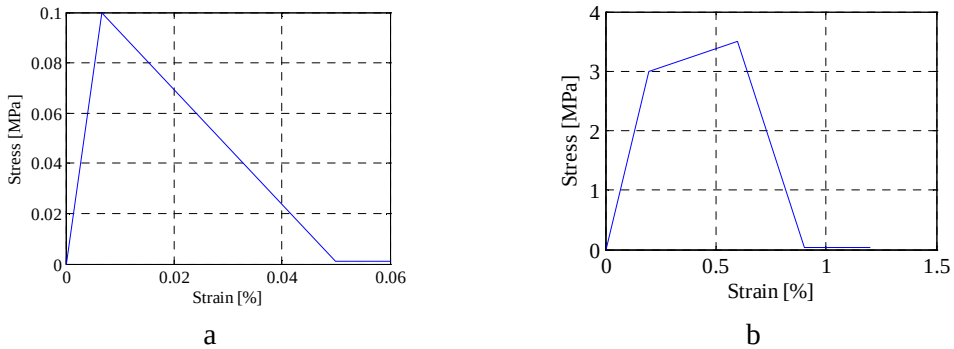


Figure 2. Representation of the masonry constitutive behavior in (a) tension and (b) compression.

During the analyses performed the ratio between the ultimate compressive strength in a biaxial stress state and that in uniaxial conditions must be also considered. Such ratio is reasonably set equal to 1.16. The final stress-strain relationships in tension and in compression adopted for the dynamic analyses are depicted in Figure 2. The damage variables in tension (index "t") and compression (index "c") are defined by means of the following standard relations:

$$f_t = E_0(1 - d_t)(\varepsilon_t - \varepsilon_t^{pl}) \quad (1)$$

$$f_c = E_0(1 - d_c)(\varepsilon_c - \varepsilon_c^{pl}) \quad (2)$$

where f_t, f_c = uniaxial stresses; E_0 = initial elastic modulus; ε_t, ε_c = uniaxial total strains; ε_t^{pl}, ε_c^{pl} = equivalent plastic strains; and, finally, d_t, d_c = damage parameters. Geometric nonlinearities is accounted for in all analyses. The masonry mass density assumed in the simulations is w = 1800 kg/m^3 ([6]-[7]).

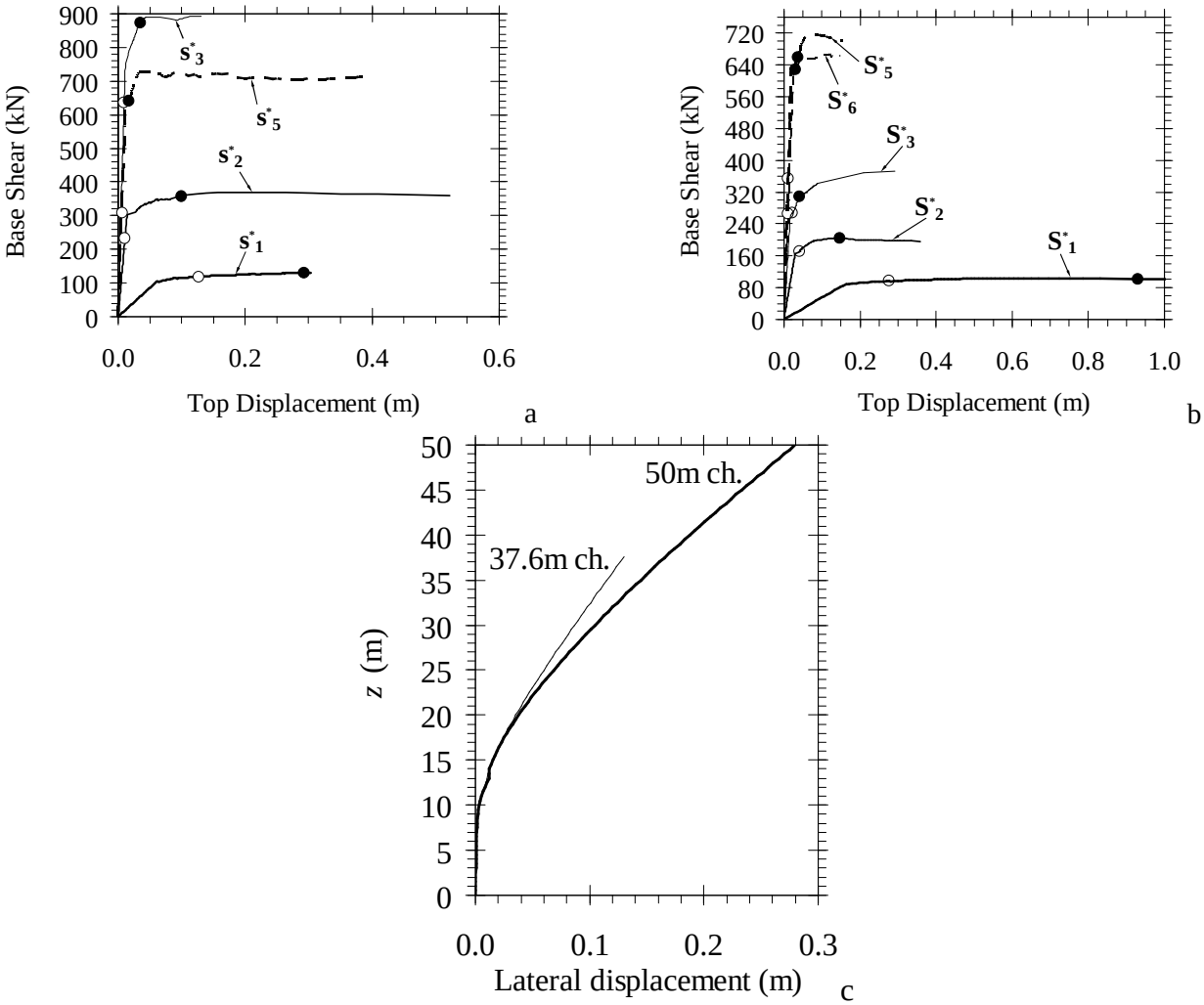


Figure 3. Pushover curves for (a) the shortened, and (b) the original chimney and (c) final profiles of the lateral displacement obtained from the analyses. Open and solid circle data points in Figure 3a,b locate the target displacements obtained assuming a ground motion multiplier equal to 1 and 3, respectively.

3 MODAL PUSHOVER ANALYSIS (MPA)

The Modal Pushover Analysis (MPA) was introduced in [11] for multi-storey framed structures to improve the pushover methods based on force distributions proportional to one single mode of vibration. The basic idea of MPA is to combine the results of N pushover analyses, the n-th of which is based on the invariant force distribution proportional to $\mathbf{s}^*_n = \mathbf{M}\boldsymbol{\phi}_n$, with $\mathbf{M}$ and $\boldsymbol{\phi}_n$ being the global mass matrix and n-th elastic mode shape, respectively.
In this section a series of analyses using the MPA procedure are discussed. All modes with effective mass larger than 5.5% of the total mass are used for the MPA of the shortened chimney. The amount of activated mass for the modes considered is approximately 71%. The lateral loads are reproduced by body forces applied to the FE mesh. The corresponding plots of the total base shear versus the horizontal displacement of one of the nodes located at z = 37.6m are reported in Figure 3a.
In order to estimate the possible damage evolution of the chimney undergoing seismic excitations of increasing intensity, two different ground motion multipliers (GM_{ER}) were used in evaluating the inelastic response spectrum, i.e., $GM_{ER} = 1$ (open circle data points of Figure 3), and $GM_{ER} = 3$ (solid circle data points). It can be noted by inspection that, for $GM_{ER} = 1$, only the target point for mode m1 turns out to be located on the "plastic" branch of the corresponding pushover curve, whereas no damage is to be expected for the other modes. In the present paper also the results obtained by the original 50m high chimney ([6]-[7]) are reported in order to compare its seismic response to that of the shortened chimney. For these simulations, all modes with effective mass larger than 4.5% of the total mass were used for the MPA. In analogy to the case of the shortened chimney, the amount of activated mass for the selected modes is approximately 71%. The corresponding pushover curves referred to the horizontal displacement of one of the nodes located at z = 50m are reported in Figure 3b. The target points for modes M1, M2 and M3 and ground motion multiplier $GM_{ER} = 1$ are located beyond the elastic branch of the corresponding pushover curves, indicating that these modes may contribute to the damage pattern of the chimney. The lateral displacement profiles obtained for the chimneys, 37.6 m and 50 m tall structures, from the MPA for $GM_{ER} = 1$ are reported in Figure 3c. These displacements were computed by combining the four target displacements using the Square-Root-of-Sum-of-Squares (SRSS) rule. The maximum lateral displacement attained at the top resulted to be approximately 0.13m for the shortened structure, while for the 50 m tall chimney was reached the value of 0.28 m. It can be remarked that, for the 50 m tall chimney, the total base shear obtained from the combination of the five modal contributions is 554 kN, approximately corresponding to 9.5% of the self weight, while for the shortened structure the total base shear estimated (combining the four modal contributions with the SRSS rule) is 754 kN, approximately corresponding to 14% of the self weight. The damage patterns corresponding to $GM_{ER} = 1$ are reported in Figure 4a and Figure 4b for the shortened and the original chimney, respectively. Because of the high masonry thickness, the base of the chimneys turns out to be never affected by damages. In the shortened chimney the cracks are triggered only by the fundamental mode (m1) at elevations lying in the range 8–21 m. Conversely, the higher-mode effects play a crucial role for the original chimney. This feature reflects on the final damage map obtained from the combination of the "modal" maps (comb. in Figure 4b). The combination of the modal damage maps for $GM_{ER} = 3$ are reported in Figure 4c and Figure 4d for the shortened and the original chimney, respectively. In this case, with the exception of the top 5 meters, the stack of the 37.6m-high chimney turns out to be damaged, because of the contributions of modes m2, m3 and m5. More and more evident are the higher-mode effects for the original chimney, where cracks form up to z = 46 m.

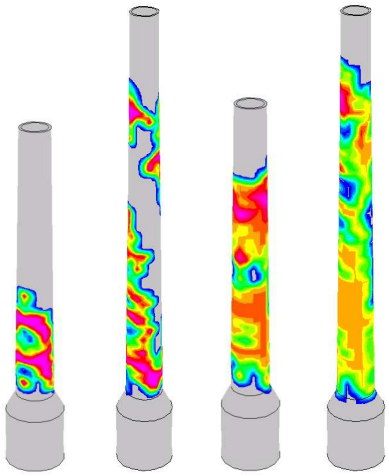


Figure 4. MPA damage patterns for the shortened chimney, with target displacements corresponding to ER ground motion multiplier equal to (a-b) 1, and (c-d) 3.

4 NONLINEAR RESPONSE HISTORY ANALYSIS (RHA)

In this section, a series of nonlinear dynamic analyses (RHA) are compared in order to have an insight into the behavior of the structures under different input accelerograms. To perform the numerical analyses, real registrations available in internet databases, are used. Four ground motions are considered, namely Christchurch (CH), Irpinia (IR), Niigata (NI), and Emilia Romagna (ER). It is worth mentioning that ER is the accelerogram registered in Mirandola –i.e. very near the epicenter- during the first shock (20th May 2012). Both horizontal and vertical components of acceleration are considered in the simulations, after proper scaling, to obtain compatibility with horizontal and vertical elastic response spectra. The horizontal component of the ground motion used during the analyses is the east-west one. The horizontal displacements obtained by the dynamic analyses of one node located at the top of the chimney are depicted in Figure 5, both for the 37.6 m and 50 m tall chimney.
As expected, the residual displacement found for the 50 m tall chimney is generally higher. To evaluate the diffusion of damages over the chimney and to compare the seismic behavior of the structures in the previous and in the current form, a series of damage patches depicted at different time steps are shown in Figure 6 for the 50 m (NI ground motion) and in Figure 7 for the 37.6 m tall structure (ER ground motion), respectively.
The damage patches at the end of simulations confirm that damages over the 50 m tall structure is much more concentrated on the upper part, where diagonal cracks were in-situ observed.

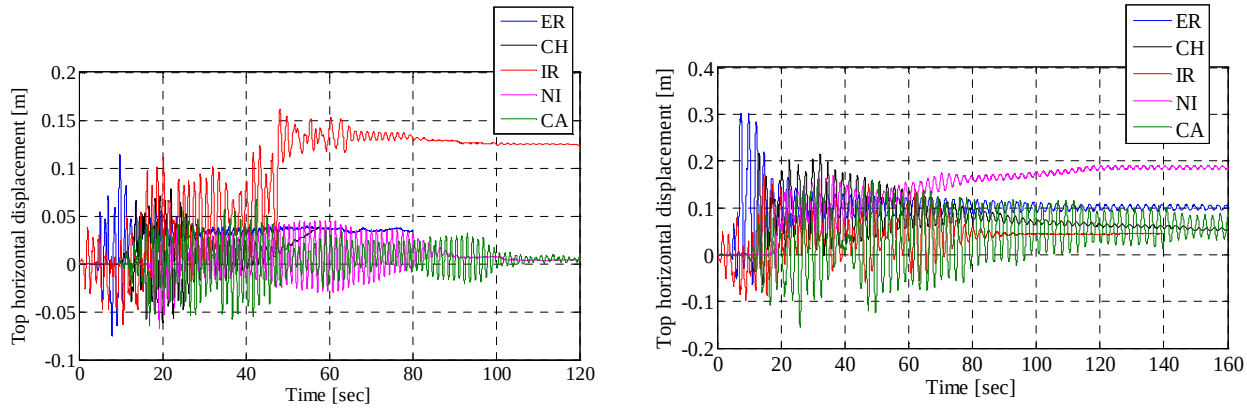


Figure 5. Top displacement time histories for (a) the shortened and (b) the original chimney (CA indicates a further accelerogram registered during the 2012 seismic sequence in Casaglia, a town not far from the cimney).

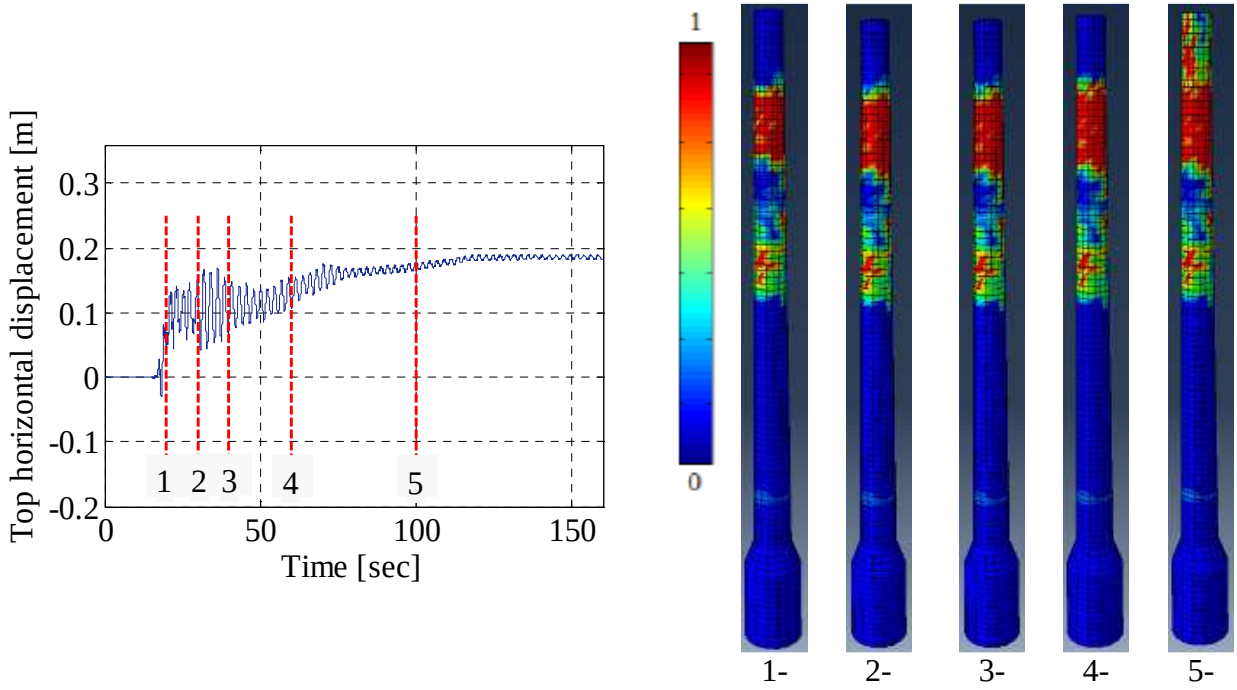


Figure 6.Damage map in tension at different time steps - NI ground motion.

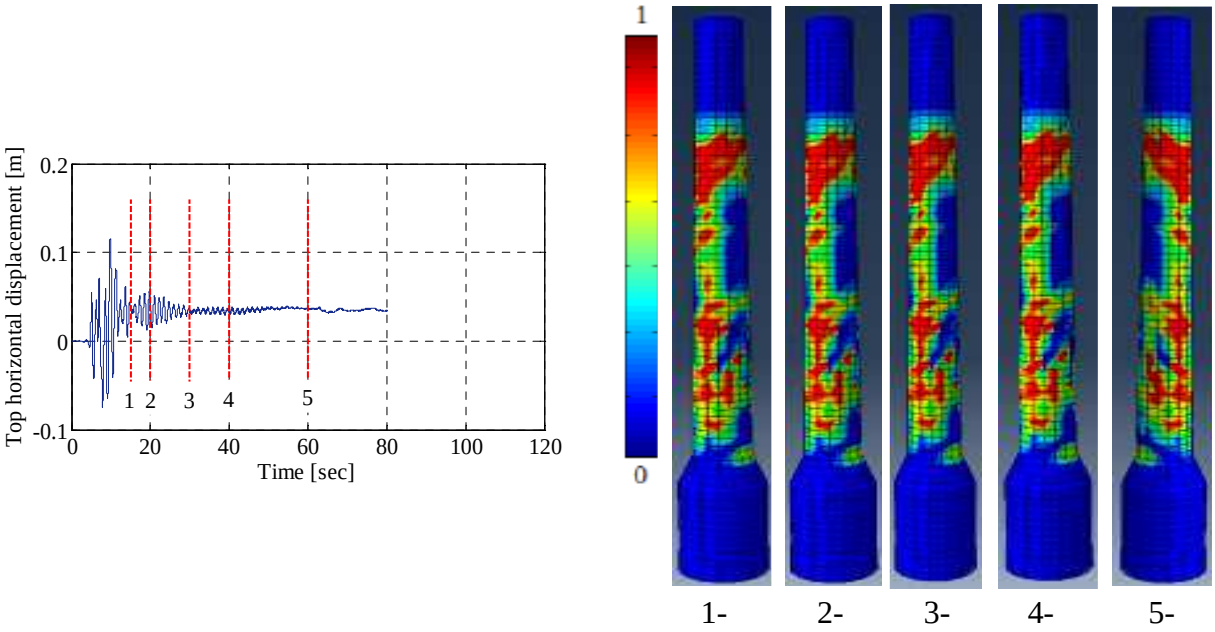


Figure 7.Damage map in tension at different time steps - ER ground motion.

In all the other simulations, depending on the type of accelerogram used, the damage tends to widespread along the entire height of the structure, but mostly affecting the last 10 meters. In the case of the 37.6 m tall chimney, the results seem to suggest again that the more susceptible part to seismic damage coincides with the medium/upper zone of the structure, but a clear trend is visible, with damage in tension spreading over a larger zone from the top to the bottom. The comparison between the horizontal top displacement of the original and of the shortened chimney, confirmed also by the two series of damage patches, suggested that the general seismic behavior of the chimney seems to slightly improve after shortening, even if the conclusion on this issue is contrasted.

5 CONCLUSIONS

In the present paper, the results obtained by a series of nonlinear analyses on a masonry chimney before and after shortening are discussed. The masonry chimney, object of the present study, evidenced severe damages after the Emilia's earthquake occurred on May 29, 2012. At the end of the survey campaign, conducted with the aim of detecting possible damages occurred after the main shock such as cracks or mortar deterioration, it was decided to shorten the structure at the height of 37.6 m, to permit a rapid re-opening of the area. The simulations performed concerned two geometric models, the original 50 m tall chimney and the 37.6 m one. Modal Pushover Analyses (MPA) and Response History Analyses (RHA) were performed using the same tridimensional finite element model, involving both the geometries. The results obtained by the 50 m tall structure shown that the chimney was particularly prone to higher mode effects, as expected by authors and confirmed by the damage maps obtained with the MPA and RHA analyses. In general a good agreement was found between MPA and RHA results. Comparing the results obtained by the MPA and RHA analyses, it was found that the new shortened structure, whose seismic behavior is the objective of the analyses presented, exhibits a slightly different seismic behavior. In general, it can be underlined that the shortening of the original structure produces a global small improvement of the seismic behavior of the chimney. This is proved by the results obtained with the MPA analyses, which

showed a lateral displacement equal to 0.13 m, instead of 0.28 m reached with the previous geometry. Damage maps obtained by means of the RHA analyses indicate that also the upper part of structure suffered of severe damages while MPA results suggested that damages mostly affect the lower part of the stack. The differences detected in the two type of simulations performed are probably connected to the vertical component of the ground motion that was not possible to consider into the MPA analyses.

REFERENCES

[1] Ghobarah A, Baumer T. Seismic response and retrofit of industrial brick masonry chimneys. *Canadian Journal of Civil Engineering* 1992; **19**(1): 117−128. DOI: 10.1139/l92-012.

[2] Riva P, Perotti F, Guidoboni E, Boschi E. Seismic analysis of the Asinelli Tower and earthquakes in Bologna. *Soil Dynamics and Earthquake Engineering* 1998; **17**(7−8): 525−550. DOI: http://dx.doi.org/10.1016/S0267-7261(98)00009-8.

[3] Pallarés FJ, Aguero A, Martin M. Seismic behaviour of industrial masonry chimneys. *International Journal of Solids and Structures* 2006; **43**(7-8): 2076−2090. DOI: 10.1016/j.ijsolstr.2005.06.014.

[4] Pallarés FJ, Aguero A, Ivorra S. A comparison of different failure criteria in a numerical seismic assessment of an industrial brickwork chimney. *Materials and Structures* 2009; **42**(2): 213−226. DOI: 10.1617/s11527-008-9379-5.

[5] Pallarés FJ, Ivorra S, Pallarés L, Adam JM. State of the art of industrial masonry chimneys: A review from construction to strengthening. *Construction and Building Materials* 2011; **25**(12): 4351−4361. DOI: doi:10.1016/j.conbuildmat.2011.02.004.

[6] Minghini F, Milani G, Tralli A. Seismic risk assessment of a 50 m high masonry chimney using advanced analysis techniques. *Engineering Structures* 2014; **69**: 255−270. DOI: 10.1016/j.engstruct.2014.03.028.

[7] Minghini F, Bertolesi E, Del Grosso A, Milani G, Tralli A. Modal pushover and response history analyses of a masonry chimney before and after shortening. *Engineering Structures* (Under review).

[8] Italian Ministry of Infrastructure and Transport. *Italian Building Code-D.M. 14/01/2008*. Rome, Italy, 2008 (in Italian).

[9] DIANA Finite Element Analysis, Release 9.3. *User's Manual*. TNO DIANA BV: Delft, 2009.

[10] ABAQUS Finite Element Analysis, Release 6.6. *Theory Manual*. SIMULIA, Inc.: Maastricht, 2006.

[11] Chopra AK, Goel RK. A modal pushover analysis procedure for estimating seismic demands for buildings. *Earthquake Engineering and Structural Dynamics* 2002; **31**(3): 561−582. DOI: 10.1002/eqe.144.

COMPDYN 2015
5th ECCOMAS Thematic Conference on
Computational Methods in Structural Dynamics and Earthquake Engineering
M. Papadrakakis, V. Papadopoulos, V. Plevris (eds.)
Crete Island, Greece, 25–27 May 2015

SEISMIC PERFORMANCE OF HOLLOW BRICK INTERNAL PARTITIONS

Crescenzo Petrone[1], Gennaro Magliulo[1], Marco Russo[1], and Gaetano Manfredi[1]

[1] University of Naples Federico II, Department of Structures for Engineering and Architecture
via Claudio 21, 80125 Naples, Italy
{crescenzo.petrone,gmagliul,gamanfre}@unina.it, marcorusso1986.mr@gmail.com

Keywords: Nonstructural components, Hollow brick, Seismic performance, Shake table, Natural frequency, Damping.

Abstract. *Bidirectional shaking table tests are performed on standard hollow brick partitions, subjecting the partitions simultaneously to interstory relative displacements in their own plane and accelerations in the out of plane direction. Five couples of accelerograms are selected matching the target response spectrum provided by the U.S. code for nonstructural components, i.e. AC156, in order to investigate a wide range of seismic demand. Three damage states are considered and correlated to an engineering demand parameter, i.e. the interstory drift ratio. The tested specimen exhibits significant damage for 0.3% interstory drift and extensive damage for displacement close to 1.0%. The tested partition exhibits a very large frequency, i.e. about 30 Hz, which is larger than the fundamental frequencies of typical structures. A 1.93% damping ratio is assessed for the tested brick partition. It is also concluded that very simple models can adequately approximate the dynamic behavior of the tested nonstructural components.*

1 INTRODUCTION

Nonstructural components (NSCs) are those systems and components attached to the floors, roof and walls of a building or industrial facility that are not part of the main load-bearing structural system, but may also be subjected to large seismic actions. Taghavi and Miranda [1] pointed out that NSCs give represent a large portion of the total cost of a building; for this reason the NSCs contribution should not be neglected in the evaluation of the economic loss due to an earthquake. Their economic impact is much more severe if losses of inventory and downtime cost are considered: the cost related to nonstructural components failure may exceed the replacement cost of the building [2].

Very limited studies were conducted in the past on the seismic behavior of hollow brick internal partitions, even though they are very common in the European area. Furthermore, recent earthquakes, such as L'Aquila earthquake in 2009, evidenced that brick partitions usually exhibit extensive damage jeopardizing the practicability of the whole building, in which they are installed.

Full-scale experimental tests on standard hollow brick partitions are described in the paper. In particular, bidirectional shaking table tests are performed in order to investigate the seismic performance of hollow brick partitions, subjecting the partition simultaneously to interstorey relative displacements in their own plane and accelerations in the out-of-plane direction. A steel test frame is properly defined in order to simulate the seismic effects at a generic building storey. A set of five couples of accelerograms are selected matching the target response spectrum provided by the U.S. code for nonstructural components, i.e. AC156, in order to investigate a wide range of seismic input. Three damage states are considered in this study and correlated to an engineering demand parameter, i.e. the interstorey drift ratio, through the use of a damage scheme.

The nonstructural components, as well as the structural elements, should be subjected to a careful and rational seismic design, in order to reduce the economic loss and to avoid threats to the life safety. They are subjected to severe seismic actions due to the dynamic interaction with the primary system. The design of acceleration-sensitive nonstructural components is based on the evaluation of the maximum inertia force, which is related to the floor spectral accelerations. The floor spectral accelerations are, in turn, influenced by the dynamic properties, i.e. the natural frequency and the damping ratio, of the nonstructural components. At this purpose, low-intensity random excitations are selected as input motions for the bare and infilled test frame in order to evaluate the influence of the internal partitions on the natural frequency of the undamaged test setup in both the horizontal directions. Moreover, the natural frequency of the component in the out-of-plane direction is evaluated.

2 EXPERIMENTAL TESTS

The shake table tests are performed in the laboratory of the Department of Structures for Engineering and Architecture of the University of Naples Federico II, Italy. As shown in Figure 1, the test setup consists of: (a) a shake table simulator; (b) an existing 3D steel test frame, used in a test campaign on plasterboard partitions [3], able to transfer the seismic input to the partitions; (c) the specimen, i.e. hollow brick partitions.

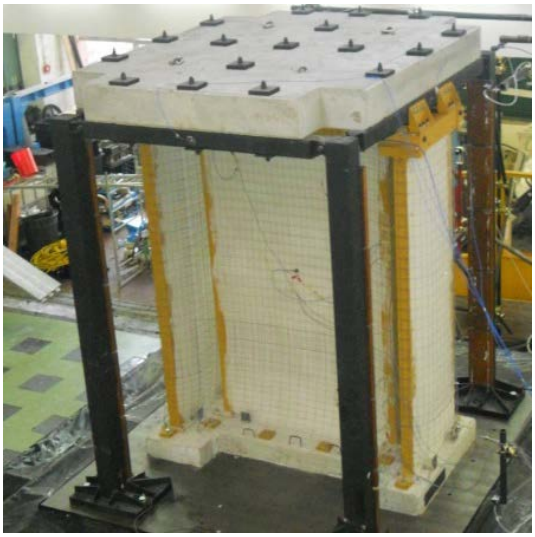


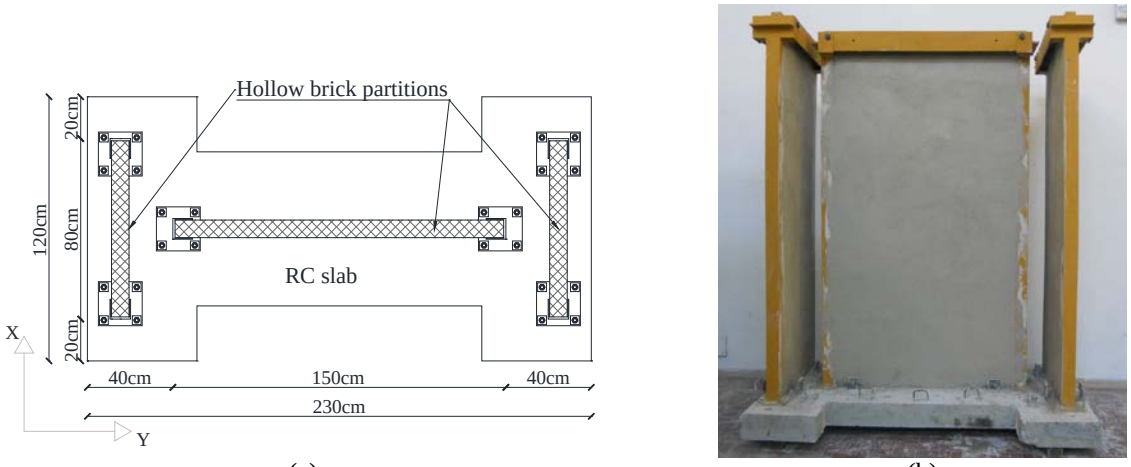
Figure 1: Global view of the test setup.

The function of the existing test frame is to dynamically excite the specimen, subjecting the partitions to a wide range of interstory drifts and accelerations. Indeed, internal partitions are architectural nonstructural components that are displacement-sensitive in their own plane and acceleration-sensitive in their out of plane direction. A steel test frame is therefore designed in order to simulate the seismic behavior of a generic story of a structure located in a high seismicity area [3]. In particular, it is characterized by: (a) a realistic value of mass, i.e. specific mass ratio equal to 1.0 t/m^2; (b) a realistic stiffness: the interstory displacement d_r is assumed to be equal to 0.005 times the interstory height, for a "frequent" (i.e. 50 years return period) earthquake typical of high seismicity areas.

The columns of the test frame are 150x150x15 mm box sections; each column is 2.9 m high. Steel horizontal beams, consisting of 120x120x15 mm cross section profiles, are connected to the columns through pin connections. At the top of the structure a reinforced concrete slab is placed; its plan dimensions are 2,15 m x 2,65 m and its thickness is equal to 250 mm. The total mass of the test frame is 5.215 t.

The specimen consists of three partitions and steel frames surrounding them placed on an "I" shape RC slab (Figure 2): the steel frames and the slab connect the specimen with the existing test frame and the shake table. The partitions are constituted by hollow bricks jointed and plastered with mortar; the vertical joints among the bricks are staggered. The design and the geometry of the setup are defined to simulate the realistic conditions to which a standard hollow brick partition is typically subjected. The specimen is doubly symmetric and presents a 150 cm wide partition and two smaller 80 cm wide partitions in the orthogonal direction.

A steel frame is defined around the partition (Figure 2b) in order to connect the specimen to the existing test frame and to reproduce the partition typical conditions, in which it is disposed between two restraining orthogonal panels. The total mass of the specimen, i.e. RC slab, partitions and surrounding steel frame, is 2.24 t. The plan layout of the panels ensures the global system to have a comparable stiffness in both orthogonal directions; indeed, two 80 cm wide walls are arranged orthogonally with respect to the larger, 150 cm wide, partition (Figure 2a).



(a) (b)

Figure 2: Specimen: (a) plan view; (b) general view.

The width of the larger partition is determined by making a compromise between two different requirements. In particular, the width should be:

- sufficiently large, i.e. a width larger than 1.00 m, in order to test a realistic partition;
- sufficiently narrow to allow the investigation of the whole damage states range of the nonstructural component up to the failure of the component.

The partition width should be less than one meter according to the typical amount of partitions contained in the floor area of the test setup. However, a 1.50m wide partition is chosen in order to test a more realistic specimen.

Preliminary analyses are conducted to evaluate the capacity of the chosen partition, in order to define the partition as large as possible and, simultaneously, bring the partition to collapse at least at the highest intensity level. Preliminary nonlinear dynamic analyses (omitted for the sake of brevity) show the collapse of the partition in Y-direction at the test no. 5.

Accelerometers, strain gauges and displacement laser sensors are used to monitor the response of both the test frame and the specimen. One accelerometer, placed inside the shake table, measures the input accelerations in both the directions. Seven accelerometers are also arranged in order to monitor different points of the setup. Six laser-optical sensors are used to monitor the displacements in specific points of the test setup. Three lasers are placed at steel base plate mid-height (base plate that connects column to shaking table); the other three ones are placed halfway on the concrete slab.

The input to the table is obtained from time histories representative of a target ground motion and acting simultaneously along the two horizontal directions; the time histories are artificially defined to match the required response spectrum (RRS) provided by the AC156 code "Acceptance criteria for seismic qualification testing of non-structural components" [4]. According to AC156, the RRS is obtained as a function of the spectral acceleration at short periods, i.e. SDS. Two artificial acceleration time histories are defined so as their response spectra, i.e. test response spectra, envelope the target spectrum over the frequency range from 1.3 to 33.3 Hz. Further details are given in [5].

The input levels for the test campaign range from SDS equal to 0.30 g to SDS equal to 1.50 g [6], in order to generalize the execution of the test and to make it representative of a large range of real earthquakes. Five bidirectional tests with increasing intensity values, i.e. a 0.30g SDS increase is considered, are defined.

3 RESULTS AND DISCUSSION

The top acceleration, representative of the total inertia force, is plotted versus the relative displacement for different intensity levels (Figure 3) in order to analyze the partition behavior and its contribution to the global behavior of the test setup. A dotted line denotes the behavior of the bare test frame based on its natural frequency and assuming to be in absence of damping.

From the analysis of the so-obtained hysteretic curves it can be noted that:

- a significant interaction between the partitions and the hosting structure is exhibited during the first tests; during the fifth test, the hysteretic behavior is very close to the bare frame response;
- the secant stiffness, evaluated at the maximum displacement of each test, decreases as the relative displacement increases;
- the negligible influence of the partitions during the fifth test denotes the collapse of the specimen.

In this study three damage states are considered for the seismic response definition of the partitions, i.e. minor damage state (DS1), moderate damage state (DS2) and major damage state (DS3).

DS1 achievement implies the need of repairing the specimen, in order to restore its original condition, e.g. plaster replacing. DS2 achievement, instead, implies that the nonstructural component is damaged so that it must be partially removed and replaced. DS3 implies that the damage level is such that the partition needs to be totally replaced or the life safety is not ensured. The damage state definitions and their correlation to the visual damage are indicated in Petrone et al. [6].

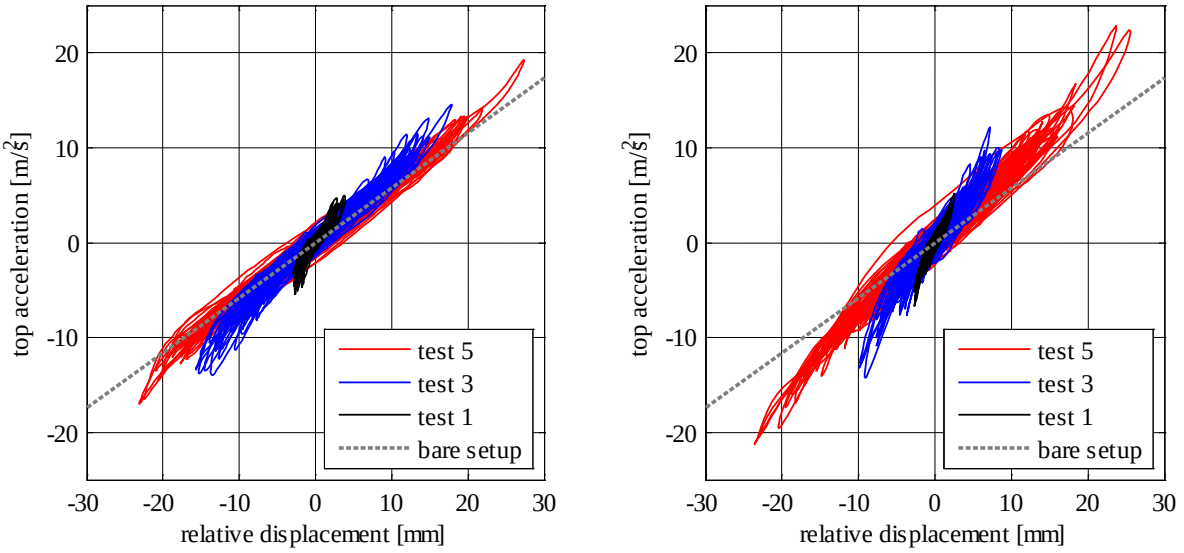


Figure 3: Top acceleration vs relative displacement plot for different seismic tests in (a) X direction and (b) Y direction.

Bidirectional tests show a slight damage already up to 0.35% drift in X direction and 0.20% in Y direction. The damage level increases according to the shaking test intensity and the following damages are noticed:

- cracks along the perimeter of the specimen due to the partitions slip from the surrounding frame in test no. 2;

- fall of plaster and pieces of brick from the top of the specimen from test no. 3 with increasing intensity as the demand increases;
- horizontal cracks, wider than 0.3 mm, in the lower part of the walls in test no. 3 (Figure 4a);
- wide sliding cracks in the mortar, crushing of the mortar at the corner of the specimen and collapse of a brick in the top of the partition in test no. 4 (Figure 4b and Figure 4c);
- deep extended horizontal cracks in the mortar in the lower part of the walls, that let the part above the crack moves as a rigid block with a rocking behavior with respect to the surrounding frame in test no. 5 (Figure 4d). At this damage level, the specimen does not offer any resistance against lateral displacements since it rigidly moves and rotates within the surrounding frame that restraints it in the out of plane direction.

It should be noted that during the tests the specimen is wrapped with a metallic grid without any connection, only for safety purposes. The grid does not give any contribution to the specimen in absorbing the horizontal load.

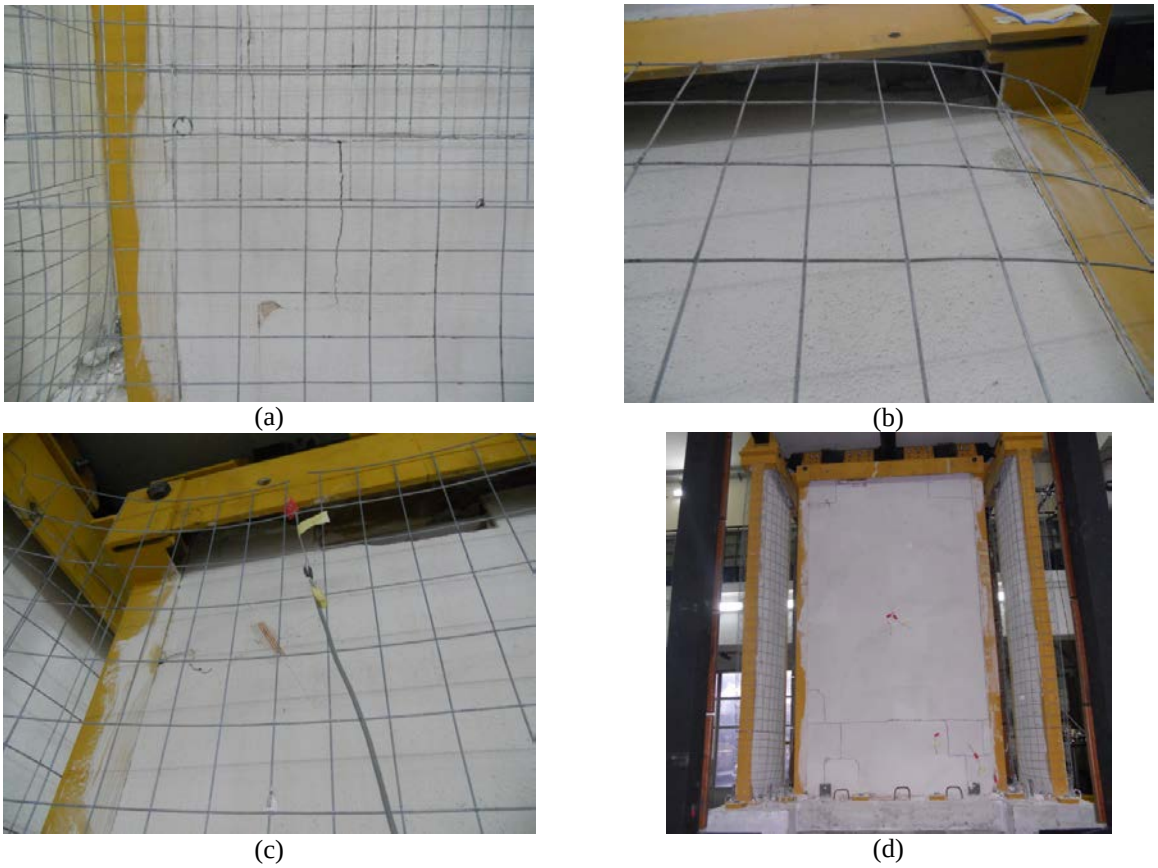


Figure 4: Recorded damage after different shaking tests: (a) wide sliding cracks in mortar in the joints between the bricks; (b) crushing of mortar at the corner; (c) collapse of a brick in the top of the partition; (d) deep extended horizontal cracks in mortar in the lower part of the wall.

A correlation between EDP (Engineering Demand Parameter), i.e. interstory drift, and the DS (Damage State) is also established (Table 1). DS1 is attained in test 2 due to the need of restoring the cracked plaster along the perimeter of the wall; DS2 is attained in test 3, due to the formation of cracks wider than 0.3 mm and the need of partially replacing the partition; finally DS3 is attained for an interstory drift close to 1% in the three specimens, due to the

significant damage and the consequent need of replacing the whole partition. The correlation between the damage states and the engineering demand parameters is based upon the assumption that the damage occurs at the maximum engineering demand parameter that the specimen experiences during a single test.

test no.	Direction	1	2	3	4	5
drift [%]	X	0.13	0.36	0.67	0.99	1.01
Damage State		DS0	DS1	DS2	DS3	DS3
drift [%]	Y	0.12	0.21	0.34	0.66	0.97
Damage State		DS0	DS1	DS2	DS2	DS3

Table 1: Interstory drifts and damage states in X and Y directions for the different tests.

In order to evaluate the natural frequency in the out-of-plane direction of the tested brick partition, the transfer curve method is applied considering the base acceleration and the partition out-of-plane acceleration recorded by an accelerogram at the centroid of the tested component. The method is applied to a random vibration test in which the partition is subjected to acceleration in the out-of-plane direction. The shaking is performed on an undamaged specimen. The random vibration is characterized by a root mean square amplitude equal to 0.90 m/s^2.

The transfer function in Figure 5 yields two peaks: one with lower frequency, denoting the natural frequency of the test frame, while the latter peak is associated to the natural frequency of the brick partition in the out-of-plane direction. The frequency of the undamaged component is slightly larger than 30 Hz, i.e. 31.25 Hz.

The results confirm that the frequency of the tested brick partition is well above the typical structural fundamental frequencies. Hence, the ratio between the period of the nonstructural component (T_a) and the period of the building (T_1), considered in Eurocode 8 [7] for the evaluation of the seismic demand on the component, could be assumed equal to zero.

The damping ratio, estimated according to the half power bandwidth, is equal to 1.93%. This value is smaller than the typical damping ratio assumed for the estimation of the floor response spectrum.

The need to estimate the natural frequency of the component during the design phase is related to the definition of the acceleration seismic demand on the component. Question arises as to whether simple models are able to estimate the fundamental frequency of the components. At this aim, an attempt to estimate the natural frequency through simple model is included in this paragraph.

The tested partition is modelled as a simply supported beam with distributed mass and stiffness. The natural frequency of a simply supported beam [8] with a uniform mass and stiffness distribution is equal to:

$$f_n = \frac{\pi}{2} \cdot \sqrt{\frac{E \cdot I}{\mu \cdot L^4}} \tag{1}$$

where E is the Young's modulus, I is the moment of inertia, μ is the mass per unit length of the beam, and L is the length of the beam.

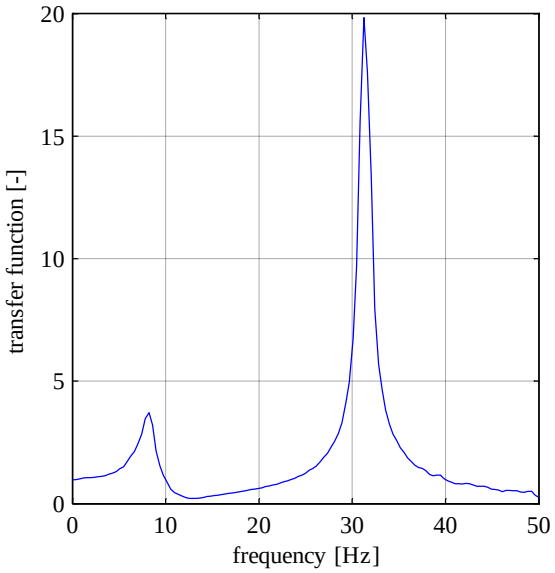


Figure 5: Transfer function from the base to the partition center in the out-of-plane direction for random vibration tests.

In particular, a horizontal 1 m wide strip is considered, since the tested brick partition is characterized by a 1.50 m width and 2.60 m height (Figure 6). The 2-D panel is therefore modelled with a simply supported horizontal beam, which neglects any contribution in the vertical direction, for the sake of simplicity. As above mentioned, the brick partition panel is made with hollows bricks 250x250x80 mm connected together and plastered with mortar. The weight per unit area of the panel is 75 N/m^2. The modulus of elasticity is assumed to be equal to 3500 N/mm^2, according to typical literature values [9].

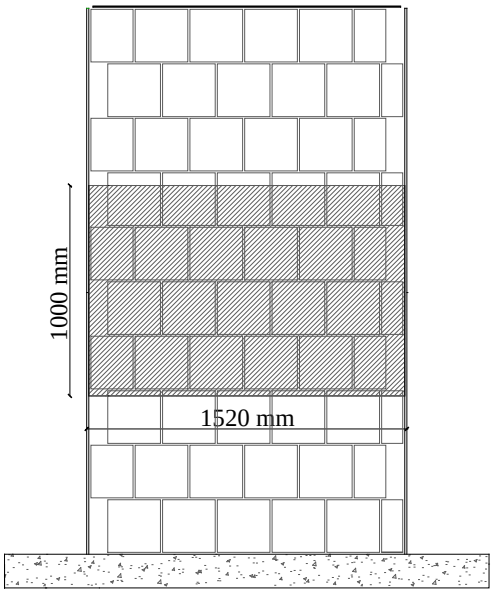


Figure 6: Horizontal strip of the brick partition considered in the analysis.

The flexural stiffness EI of the considered cross-section is equal to 149333 Nm^2 whereas the mass per unit length is equal to 75 kg/m and the total length of the horizontal strip is equal to 1.52 m. The resulting natural frequency, equal to 30.32 Hz, gives a good approximation of the experimental natural frequency.

Finally, it can be concluded that very simple models can adequately approximate the elastic dynamic behavior of the tested nonstructural components.

4 CONCLUSIONS

Shaking table tests are carried out by the earthquake simulator facility available at the Department of Structures for Engineering and Architecture at the University of Naples Federico II in order to investigate the seismic behavior of hollow brick internal partitions. The tested nonstructural component is widespread in the European area.

A steel test frame is adopted in order to simulate the seismic action acting at a generic building story and the specimen boundary conditions. The tests are performed shaking the table simultaneously in both horizontal directions in order to subject the partition simultaneously to interstory relative displacements in its own plane and accelerations in the out of plane direction. A set of five couples of accelerograms are selected matching the target response spectrum provided by the U.S. code for nonstructural components to investigate a wide range of interstory drift demand and damage. Three damage states are considered in this study in order to characterize the seismic behavior of the specimen. The dimensions of the specimen are adequately chosen in order to (a) test a realistic partition and (b) allow the investigation of the whole damage states range.

The hollow brick partition is subjected to interstory drift up to 1.0%. It exhibits minor damage for 0.2% interstory drift, moderate damage for 0.34% interstory drift and major damage for 0.97% interstory drift.

The transfer curve method is applied for the evaluation of the natural frequency of the tested component, i.e. a brick partition, in the out-of-plane direction. The results highlight that the frequencies of the tested partitions in the out-of-plane direction are larger than the typical structural fundamental frequencies. The damping ratio of the tested component in the out-of-plane direction is also estimated, since the damping ratio of the nonstructural component strictly influences the maximum acceleration acting on the component. A 1.93% damping ratio is assessed for the tested brick partition.

An attempt to estimate the natural frequency through a simple model is also performed. In particular both the partition is schematized with a simply supported beam with uniform mass and stiffness. The resulting natural frequencies give a good estimation of the experimental natural frequencies, considering the very simple models adopted for this assessment. It is concluded that very simple models can adequately approximate the elastic dynamic behavior of the tested nonstructural components.

ACKNOWLEDGEMENTS

This research study has been funded by Italian Department of Civil Protection through the national project DPC - ReLUIS 2014, task RS8.

REFERENCES

[1] S. Taghavi, E. Miranda, Response assessment of nonstructural building elements, PEER report 2003/05. College of Engineering, University of California Berkeley, USA, 2003.

[2] Earthquake Engineering Research Institute (EERI), Nonstructural Issues of Seismic Design and Construction, Publication 84-04. Berkeley, CA, USA, 1984.

[3] G. Magliulo, C. Petrone, V. Capozzi, G. Maddaloni, P. Lopez, G. Manfredi, Seismic performance evaluation of plasterboard partitions via shake table tests. *Bulletin of Earthquake Engineering*, **12**, 1657-1677, 2014.

[4] International Conference of Building Officials (ICBO), AC 156 Acceptance Criteria for the Seismic Qualification of Nonstructural Components. ICBO Evaluation Service, Inc., Whittier, California, USA, 2000.

[5] G. Magliulo, V. Pentangelo, G. Maddaloni, V. Capozzi, C. Petrone, P. Lopez, R. Talamonti, G. Manfredi, Shake table tests for seismic assessment of suspended continuous ceilings. *Bulletin of Earthquake Engineering*, **10**, 1819-1832, 2012.

[6] C. Petrone, G. Magliulo, G. Manfredi, Shake table tests for the seismic assessment of hollow brick internal partitions. *Engineering Structures*, **72**, 203-214, 2014.

[7] CEN, Eurocode 8: design of structures for earthquake resistance - Part 1: general rules, seismic actions and rules for buildings. EN 1998-1. Brussels, Belgium., 2004.

[8] A.K. Chopra, *Dynamics of structures: Theory and Applications to Earthquake Engineering*, Englewood Cliffs, New Jersey, USA, Prentice Hall, 1995.

[9] Consiglio Superiore dei Lavori Pubblici, Circolare 2 febbraio 2009, n. 617, Istruzioni per l'applicazione delle «Nuove norme tecniche per le costruzioni». G.U. n. 27 del 26-2-2009 (in Italian), 2009.

COMPDYN 2015
5th ECCOMAS Thematic Conference on
Computational Methods in Structural Dynamics and Earthquake Engineering
M. Papadrakakis, V. Papadopoulos, V. Plevris (eds.)
Crete Island, Greece, 25–27 May 2015

DEFINITION OF MECHANICAL PROPERTIES OF EXISTING MASONRY ACCOUNTING FOR EXPERIMENTAL KNOWLEDGE BY BAYESIAN UPDATING

Stefano Bracchi[1], Maria Rota[2], Andrea Penna[2,3] and Guido Magenes[2,3]

[1] ROSE Programme, UME School, Institute for Advanced Studies
via Ferrata, 1 I-27100 Pavia, Italy
stefano.bracchi@umeschool.it

[2] European Centre for Training and Research in Earthquake Engineering
via Ferrata, 1 I-27100 Pavia, Italy
maria.rota@eucentre.it

[3] University of Pavia, Department of Civil Engineering and Architecture
via Ferrata, 3 I-27100 Pavia, Italy
{andrea.penna, guido.magenes}@unipv.it

Keywords: Bayesian updating, masonry buildings, seismic assessment, uncertainty on material properties, pushover analysis.

Abstract. *The current approach of the Italian and European building codes to account for knowledge-based uncertainties in the seismic assessment of masonry buildings consists in selecting a knowledge level and reducing material strengths by means of the associated value of confidence factor. Previous works showed that, in the case of masonry structures, the codified approach leads in many cases to inconsistent and unrealistic results and does not properly consider the experimental tests performed. This paper proposes a methodology for taking into account the knowledge on material properties acquired by experimental tests, using Bayesian updating techniques. The use of the Bayesian approach allows to update the values of the material properties assumed a priori as knowledge on the building increases, by taking into account all the information (experimental or judgement-based) gained during the assessment process. The material parameters resulting from this method could be used as input in numerical models, with the aim of calibrating confidence factors on material properties. Finally, analytical expressions are provided, which approximate the results obtained by Bayesian updating, allowing the analyst to obtain the values of material properties to be used in the analysis, as a function of the experimental information gained, without the need of performing a case-by-case Bayesian updating.*

1 INTRODUCTION

The approach currently proposed by the European [1] and Italian [2][3] codes for the seismic assessment of an existing building consists in the definition of three discrete knowledge levels (KLs) and the association to each of them of a value of the so-called confidence factor (CF). The latter has to be applied to material strengths and it is supposed to account for all sources of uncertainty involved in the assessment. This approach was proven to provide in many cases inconsistent and unexpected results, at least for the case of nonlinear static analysis, for both reinforced concrete and stone masonry buildings [4][5].

Some attempts have been proposed in the literature to overcome the main limitations of the current code approach. For example, [6] proposed a probabilistic approach to the seismic assessment of masonry buildings considering all the uncertainties involved, whereas Cattari et al. [7] developed a procedure based on systematic use of a simplified sensitivity analysis, leading to the definition of confidence factors to be applied to the parameters most influencing the response. Neither of these approaches, however, specify how the available experimental results should be used to improve the definition of the material parameters to be adopted in the numerical analyses.

With respect to the aforementioned works, which do not account for the experimental information eventually gained, the Commentary to the Italian code [3] includes, at least for KL3, a rough procedure for updating the initial information on mechanical properties (based on the masonry typology selected at KL1 and KL2), as a function of the experimental value of strength measured at KL3. For example, in case one or two experimental values of strength are available, the Commentary suggests to use the maximum/mean value of the codified interval for the selected typology or the mean of the experimental results, depending on the location of the mean of the experimental results with respect to the proposed interval. However, this seems to represent only a first attempt of updating the available knowledge, since it is not applied to the case of KL2 and it only regards the material property that is directly measured (i.e. the shear strength at KL3).

Starting from these considerations, Rota et al. [8] proposed a probabilistic framework for the seismic assessment of existing masonry buildings, in which the effects of the different sources of uncertainty are explicitly taken into account by means of variability factors and of the confidence factor accounting for uncertainty in material properties. Calibration of the variability factors accounting for modelling uncertainties and for the uncertainty in the definition of limit state thresholds is presented in previous works [8][9]. The confidence factors accounting for uncertainty on material properties, CF_{mat}, take into account the imperfect knowledge on material parameters and, hence, they should explicitly consider any additional information, acquired for example by means of experimental tests. However, appropriate values of these CF_{mat} were not yet calibrated, nor a methodology allowing to take advantage of the experimental information was proposed. This work moves therefore from the need to develop a rigorous and efficient procedure for taking into consideration the additional information obtained from experimental tests at the higher levels of knowledge (KL2 and KL3). This methodology, based on Bayesian updating, allows integrating the additional information on material properties with the prior information. The adoption of the mechanical parameters deriving from Bayesian updating into appropriately defined numerical models will allow to calibrate the confidence factors on material properties and hence to complete the methodology proposed in [8].

Bayesian updating techniques have been recently applied to the problem of the assessment of existing buildings (e.g. [10], [11]), with the aim of updating the distributions of material parameters and the corresponding evaluation of structural reliability, as a function of the experimental tests and inspections performed. In some cases (e.g. [11], [12]), these techniques were

applied to calibrate new values of confidence factors. However, the largest part of previous literature work was concerned with reinforced concrete buildings, whereas, to the author's knowledge, the only attempt to apply Bayesian updating with reference to a masonry structure was performed in [13], but with reference to a church. Furthermore, in previous works, a direct experimental information is always required to update the value of any mechanical property. Although this could be the case in reinforced concrete structures, where an experimental information is usually available for the mechanical parameters of interest (i.e. the strengths of both concrete and steel), this is rarely the case for masonry structures, for which very often only a single mechanical property is measured during the assessment process. This work is hence intended to propose a methodology based on Bayesian inference to update the knowledge on material properties taking advantage of the available experimental results. Based on the results obtained, analytical expressions will be calibrated, which provide the values of the material properties representing the input for the numerical model of the assessed building, as a function of the additional information gained through experimental tests. These equations would allow to take advantage of the results of a rigorous Bayesian updating approach, without the need to perform it on a case by case basis, with a view on the possible consideration of this approach in a future revision of the code.

2 PROPOSED PROCEDURE TO ACCOUNT FOR UNCERTAINTY IN MATERIAL PROPERTIES BY BAYESIAN UPDATING

As already mentioned, the aim of this work was to take into account the additional information obtained by in-situ tests for the definition of the material properties to be used in the seismic assessment at the higher levels of knowledge (KL2 and KL3). To this aim, a Bayesian updating framework was developed, allowing to modify the a-priori knowledge of the different mechanical parameters (represented by the so-called prior distributions), taking into account any additional information acquired either experimentally or by exploiting empirical correlations of material parameters with other parameters that have been directly measured. The result of the updating are the so-called posterior distributions.

The proposed procedure is discussed in the following, for the three knowledge levels considered in the Italian code [2][3]. It results in values of the different mechanical parameters, to be used as input in the numerical models of the buildings to be assessed.

2.1 KL1

At knowledge level 1, the knowledge of the structure is only based on a visual survey of the building, since no experimental test is required. The first step of the assessment consists in choosing a masonry typology among those proposed by [3]. In this work, only stone masonry typologies were considered. The possibility of selecting a typology that does not correspond to the actual typology of the building (as highlighted in [14]) was taken into account by defining, for each actual typology, a list of typologies that could be erroneously selected, with the corresponding probability of selection (Table 1).

At KL1, the values of the mechanical parameters to be used as input for numerical models can be taken as the central values of the intervals suggested by [3] for the selected masonry typology. It is recalled that [3] indicates to use the minimum value of the interval for the shear strength τ_0 and the masonry compressive strength f_m, but we would suggest to use the central value, for consistency with the other mechanical parameters and knowledge levels. Finally, for the unit weight of masonry, the single value given for the chosen typology could be used.

Actual typology	Description	Selected typology	Probability
1	Rubble stone masonry (pebbles, fieldstones, irregular stones)	1	90%
		2	10%
2	Undressed stone masonry with facing walls of limited thickness and infill core (sacco)	1	10%
		2	60%
		3	20%
		4	10%
3	Partially dressed stone masonry with good bonding (usually double-leaf)	2	20%
		3	60%
		4	20%
4	Soft stone masonry (tuff, limestone, etc.)	2	10%
		3	20%
		4	60%
		5	10%
5	Dressed rectangular stone masonry	4	10%
		5	90%

Table 1: Typologies that can be selected and probability of selection for the five stone masonry typologies of [3].

2.2 KL2

At knowledge level 2, in addition to the visual survey of the building, [3] recommends to perform at least one double flat-jack test, obtaining a direct experimental measure of the elastic modulus *E*. The experimental test was simulated by randomly selecting a structural member of one of the perfectly known structures[1] on which the test is performed (taking into account the different probability of choosing an internal vs. external wall, as well as a wall at a different storey) and extracting the experimental result from a uniform distribution defined on the interval identified by the exact value plus or minus the error intrinsic in this type of test, which was estimated as being plus or minus 15% of the actual result (based on experimental results, e.g. [15]). For further details about this simulation approach, the reader is referred to [5], in which a similar procedure was followed.

Four random variables were considered, consisting of elastic modulus *E*, compressive strength f_m, shear modulus *G* and shear strength τ_0 (shear strength associated with diagonal cracking to be used within the Turnsek-Sheppard strength criterion [16]). The four parameters considered in the application of the Bayesian approach consist of the mean of the distributions of these four random variables, i.e. μ_E, μ_{fm}, μ_G and $\mu_{\tau 0}$.

At KL2, it is assumed that a single observation of the random variable *E* is available, consisting of the experimental measure obtained by a single double flat-jack test (in case of multiple observations the procedure would not change significantly). This experimental observation will be simply indicated as *E*, whereas the parameters μ_{fm}, μ_G and $\mu_{\tau 0}$ will be indicated for simplicity as f_m, *G* and τ_0, respectively. Since observations of the other mechanical properties are not available, empirical correlations between the different parameters were exploited to derive the posterior distributions of the four parameters, starting from prior distributions and the single observation of *E*. The empirical correlation between f_m and μ_E was expressed by the variable α,

[1] The perfectly known structures represent the real building to be assessed and are defined with material properties varying within different sub-intervals of the intervals defined in [3] for the masonry typology of interest, taking into account element-to-element variability.

assumed to vary in the interval between 500 and 1000 and defined as the ratio between μ_E and f_m.

Since, for stone masonry, significant statistical analyses are not available in the literature, the interval of variation of α was assumed to be consistent with available data and dispersion for other masonry typologies (e.g. [17], [18]).

Similarly, the empirical correlation between the parameters G and μ_E was represented through the variable β, defined as the ratio between G and μ_E and assumed to vary between 0.15 and 0.40. The upper limit of the interval of β (0.4) corresponds to a Poisson's ratio equal to 0.25, a value commonly accepted for this type of material [19]. The lower limit (0.15) corresponds instead to a ratio E/G equal to 6, which is a value historically used and codified for masonry buildings [20]. It should also be noticed that the ratios implicit in the values reported in [3] are around 0.33 and thus they are included in the defined range.

Since a reliable empirical correlation between the shear strength τ_0 and one of the other parameters involved in this problem is not available in the literature, a linear correlation between τ_0 and μ_E was assumed, based on the intervals of variation reported in [3], under the assumption that, for the same masonry typology, if a material has for example a value of E higher than the central value of the interval, it is likely to have as well a value of τ_0 higher than the central value. For simplicity, this correlation can be represented by the variable η, defined as the ratio between μ_E and τ_0.

Four prior distributions were defined for μ_E, μ_α, μ_β and μ_η, which will be indicated as $\pi(\mu_E)$, $\pi(\alpha)$, $\pi(\beta)$, $\pi(\eta)$. Notice that μ_α, μ_β and μ_η were replaced by α, β and η and this notation will be used in the following for simplicity. The prior distribution of μ_E was defined as a normal distribution, with mean μ' equal to the central value of the interval given by [3] for the typology selected at KL1 and standard deviation σ' equal to the 25% of the width of the same interval. This value of standard deviation corresponds, for a normal distribution, to the assumption that about 95% of the values fall inside the considered interval of variation. As regards the random variable E, Bayesian inference was applied only to μ_E, assuming the standard deviation of E, σ, to be equal to 7.5% of the experimental observation of E obtained from the test, i.e. equal to one fourth of the width of the interval of variation of the error of the experimental test.

The prior distributions of α and β were assumed to be normal distributions, with mean equal to the central value of the interval of variation of each parameter and standard deviation equal to 1/8 of the width of this range of variation. The low value of standard deviation is necessary to limit the number of values falling outside the defined interval of variation during Monte Carlo sampling and to avoid the presence of values too far from the defined range. The prior distribution of η was calculated numerically, with values of μ_E extracted from its prior distribution and values of τ_0 extracted from a normal distribution with mean equal to the central value of the interval indicated by [3] and standard deviation equal to 1/4 of the width of the same interval.

The posterior distributions of the four parameters can be calculated numerically, starting from the joint posterior distribution conditioned to the experimental observation E of the random variable E, $\pi(f_m, G, \tau_0, \mu_E | E)$, given by:

$$\pi\left(f_m, G.\tau_0, \mu_E \mid E\right) = \frac{f\left(E \mid \mu_E\right) \cdot \pi\left(\mu_E, f_m, G, \tau_0\right)}{\int_{-\infty}^{\infty}\int_{-\infty}^{\infty}\int_{-\infty}^{\infty}\int_{-\infty}^{\infty} f\left(E \mid \mu_E\right) \cdot \pi\left(\mu_E, f_m, G, \tau_0\right) d\mu_E dG df_m d\tau_0} \tag{1}$$

In the following it is assumed that the parameters μ_E and α (and similarly μ_E and β and μ_E and η) are independent and consequently uncorrelated, whereas the four mechanical parameters

are dependent and the correlation among them was taken into account by means of the empirical correlations previously discussed.

The posterior distribution of μ_E can be easily calculated from the prior distribution of μ_E, the observation E and the standard deviation σ. In particular, in case n observations are available, the posterior distribution is a normal distribution with mean and variance given as in Eq. (2):

$$\mu_E \mid E = N\left(\frac{(\sigma')^2}{\sigma^2/n + (\sigma')^2} \overline{E} + \frac{\sigma^2/n}{\sigma^2/n + (\sigma')^2} \mu', \frac{\sigma^2/n}{\sigma^2/n + (\sigma')^2} (\sigma')^2 \right) \tag{2}$$

where μ' and σ' are the mean and standard deviation of the prior distribution, $\overline{E}$ is the mean value of elastic modulus measured from the tests (equal to the measured E in case of a single test), σ is the standard deviation of the random variable E and n is the number of observations (in this case $n = 1$).

The posterior distributions of the other three parameters can be calculated numerically by extracting, at each step of a Monte Carlo procedure (with Latin hypercube sampling) a value of μ_E from its posterior distribution (Eq. (2)) and a value of α, β and η from their prior distributions. The corresponding values of f_m, G and τ_0 are hence obtained using the empirical correlations previously defined. The posterior distributions of the four considered parameters obtained at KL2 are reported in Figure 1.

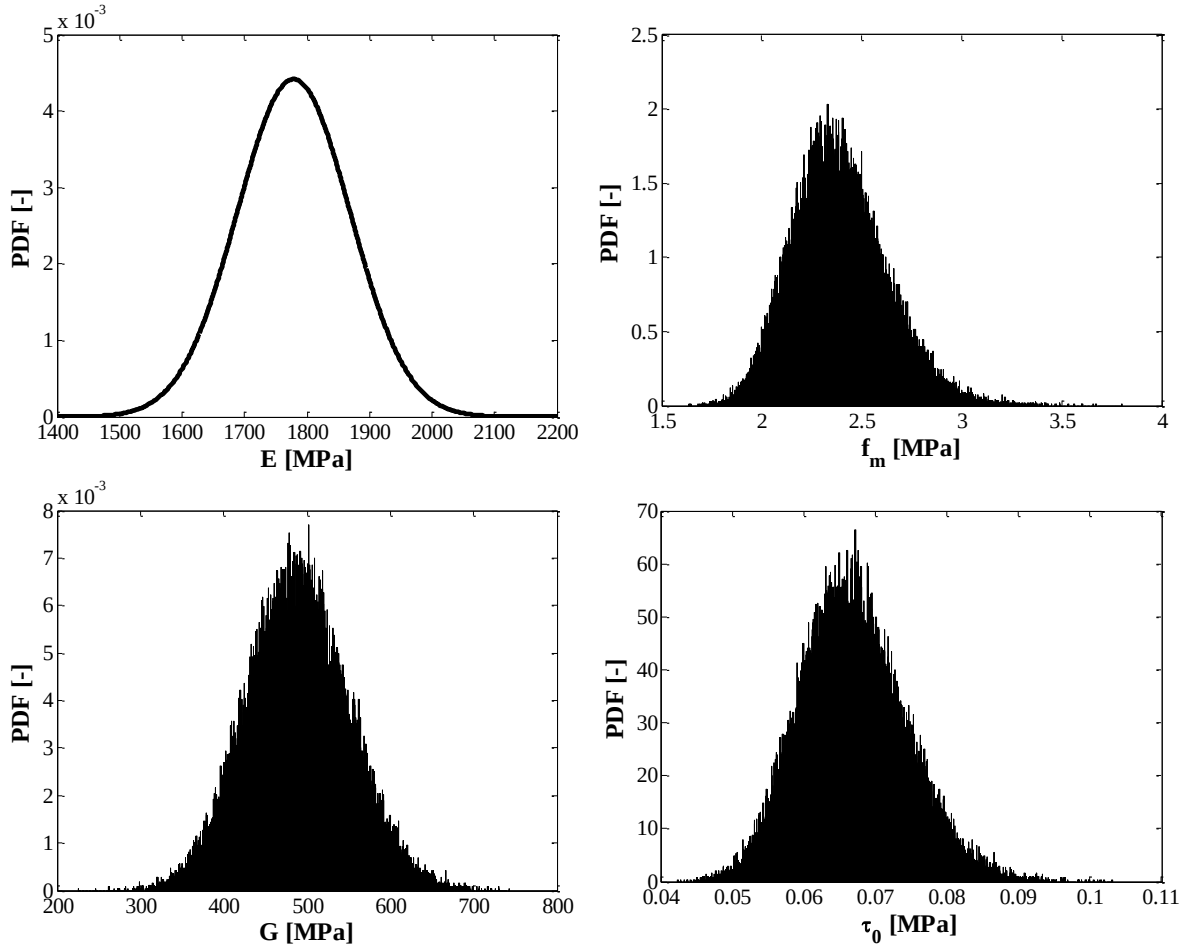


Figure 1: Posterior distributions of the four considered parameters at KL2, constructed either analytically (E, top left) or numerically (f_m top right, G bottom left and τ_0 bottom right).

2.3 KL3

At knowledge level 3, in addition to the visual survey and the test already performed at KL2, [3] requires the performance of additional experimental tests, such as diagonal compression tests. It was assumed that either one, two or three tests, with different probabilities, could be performed, providing a direct measure of the shear strength τ_0. Similarly to KL2, each experimental test was simulated by randomly selecting a structural member of one of the reference structures assumed to be perfectly known on which the test is performed (taking into account the different probability of choosing an internal vs. external wall, as well as a wall at a different storey) and considering an intrinsic error of plus or minus 20% of the actual result (based on [15]). The diagonal compression test theoretically allows to measure also the shear modulus G, but it is not easy to obtain a reliable measure of G and thus it is not very common to measure it.

At KL3, Bayesian updating was used to find the posterior distributions of the four mechanical properties, starting from the prior knowledge (represented by the posterior knowledge obtained at KL2) and from the available observations of τ_0. Similarly to KL2, prior distributions were introduced for the mean value of τ_0 and for the three parameters defining the empirical correlations between the different properties, i.e. α, β and η, defined as for KL2. The prior distribution of $\mu_{\tau 0}$ was modelled as a normal distribution, with mean equal to the mean of the numerically built posterior distribution of τ_0 at KL2 and standard deviation equal to the standard deviation of the same distribution divided by the square root of the ratio k between the number of double flat-jack tests and diagonal compression tests performed. This ratio, proposed in [12], allows to take into account the different reliability of the two types of test performed.

As regards the random variable τ_0, Bayesian inference was applied only to $\mu_{\tau 0}$, assuming the standard deviation of τ_0 equal to

$$\sigma = \frac{1}{n}\sqrt{\sum_{i=1}^{n}\sigma_i^2} \tag{3}$$

where n is the number of diagonal compression tests performed and σ_i is the standard deviation (defined based on the error intrinsic in this type of test) associated with the results of each test, which are assumed to be a random variable. The prior distributions of α and β were assumed equal to the ones used at KL2, whereas the prior distribution of η was defined as done at KL2, with the only difference that the values of E and τ_0 were extracted from the posterior distributions obtained at KL2.

As for KL2, the parameters $\mu_{\tau 0}$ and α (and similarly β and η) were assumed to be independent and consequently uncorrelated, whereas the correlation between the four mechanical parameters was taken into account. The joint posterior distribution of the four parameters $\mu_{\tau 0}$, f_m, G and E, conditioned to the experimental observations of τ_0 was hence derived. Using the formulas of the Bayesian inference already employed at KL2 (Eq. (2)), with the prior distribution of $\mu_{\tau 0}$ previously defined, the posterior distribution of $\mu_{\tau 0}$ turned out to be a normal distribution with mean equal to

$$\mu'' = \frac{\tau_0 \cdot \zeta + k \cdot \mu'}{\zeta + k} \tag{4}$$

where

$$\zeta = \left(\frac{\sigma'}{\sigma}\right)^2 \tag{5}$$

In the previous equations μ' and σ' indicate the mean and standard deviation of the prior distribution, before dividing the standard deviation by the square root of k, τ_0 is the mean of the observations and σ is the standard deviation of τ_0. This formula corresponds to the one used in [12] for combining data from different types of tests. The standard deviation of the posterior distribution was instead given by:

$$\sigma'' = \sqrt{\frac{\sigma^2}{k\sigma^2 + (\sigma')^2}(\sigma')^2} \tag{6}$$

Similarly to KL2, the posterior distributions of the other three parameters could be calculated numerically by extracting a value of $\mu_{\tau 0}$ from its posterior distribution (Eq. (4) and (6)) and a value of α, β and η from their prior distributions. The corresponding values of f_m, G and E were hence obtained using the empirical correlations previously defined for KL2. For both KL2 and KL3, the values of mechanical properties to be used as input for the numerical model of the building to be assessed should be taken as the expected (mean) values of the different posterior distributions obtained after Bayesian updating. It should be remarked that [3] also provides (single) values of the weight of the masonry, for each masonry typology. This parameter was not considered in the Bayesian updating, mainly because it is not common to measure it experimentally and it is impossible to define a correlation between the weight and any other mechanical property.

2.4 Considerations on the dispersion of the mechanical parameters

As already discussed, some of the posterior distributions were calculated numerically using a Monte Carlo approach. The number of Monte Carlo simulations was selected as to guarantee stability of the mean of the four mechanical properties of interest. Furthermore, if the obtained parameters were to be used in numerical analyses of a building, the proposed Bayesian approach would need to be applied a number of times sufficient to reach stability of the mean and standard deviation of the parameter representing the result of the assessment procedure (e.g. the acceleration leading the building to a limit state of interest).

The effectiveness of the proposed Bayesian approach was evaluated by looking at the distribution of values of the four mechanical properties representing the input for the numerical model. As an example, Figure 2 shows the distributions of E and τ_0 obtained for one of the considered case study buildings, for KL2 and KL3. The grey bars in the figure represent the values obtained by applying the proposed procedure, the shaded areas indicate the range of variation of the mechanical properties of the perfectly known structure and the continuous black lines denote the mean values obtained for the considered property. The continuous grey lines and the dashed grey lines represent the mean plus or minus one and two standard deviations of the obtained results, respectively. It is recalled that the perfectly known structure represents the real structure to be assessed, in which element-to-element variability of the mechanical properties within some specified ranges is taken into account. Figure 2 shows that, moving from KL2 to KL3, the dispersion of E and τ_0 decreases, the distribution and its mean value shift towards the range of values of the reference structure and a larger fraction of the values tends to be included in the range of the reference structure. Therefore, the applied Bayesian updating framework appears to be effective.

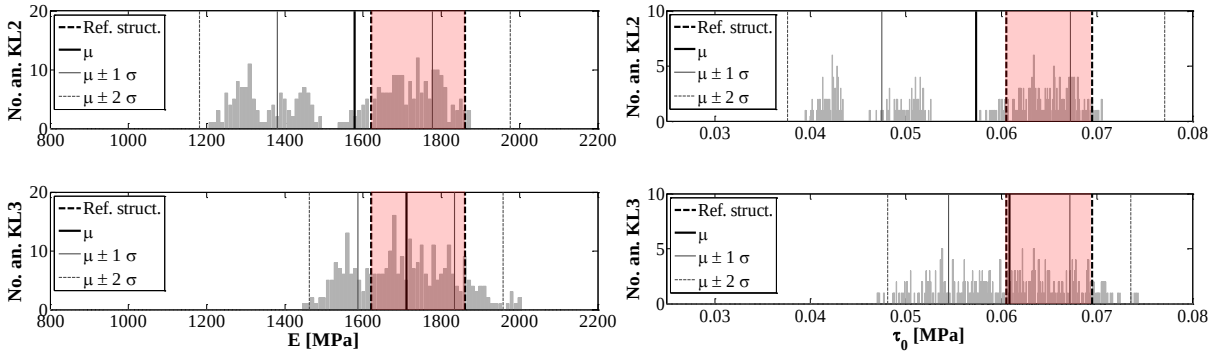


Figure 2: Distribution of E (left) and τ_0 (right) obtained for one of the case study buildings, at KL2 (top) and KL3 (bottom). The shaded areas indicate the range of variation of the mechanical properties of the perfectly known structure, continuous black lines indicate the mean values, whereas continuous and dashed grey lines indicate mean plus or minus one and two standard deviations, respectively.

3 ANALYTICAL EXPRESSIONS PROVIDING VALUES OF THE MATERIAL PROPERTIES AS A FUNCTION OF EXPERIMENTAL RESULTS

For each of the five stone masonry typologies considered in [3], the results of the proposed Bayesian approach were used to calibrate equations providing the values of mechanical properties representing the input for structural analyses, as a function of the experimental information gained at KL2 and KL3.

At KL2, for each typology, an interval of variation of the experimental value of E (E_{exp}) was defined as to cover all the intervals of variation of E corresponding to the typologies which can be confused with the considered typology, accounting also for the intrinsic error of the experimental test. This interval was then discretized into sufficiently small sub-intervals and the central value of each sub-interval was considered as a possible result of the double flat-jack test carried out at this knowledge level. Bayesian approach was then applied, using the prior distributions previously defined and the central value of each sub-interval as experimental observation of E. For each value of E_{exp}, Bayesian updating provided four values of the mechanical parameters representing the input for the analyses, as shown in Figure 3 (referring to typology 2 of Table 1, selected as an example). The shaded areas in the figure indicate the intervals used for the definition of the prior distribution of μ_E. As expected, when the experimental value of E is lower than the mean of the prior distribution of μ_E , the input value of E is larger than E_{exp}, whereas when E_{exp} is larger than the mean of the prior, the input value of E is lower than E_{exp} .

At KL3, for each typology, the experimental value of E was defined with the same sub-intervals used at KL2. The interval of variation of the experimental value of τ_0 ($\tau_{0,exp}$) was discretized into sub-intervals and it was defined as to cover all the intervals of variation of τ_0 corresponding to the typologies which can be confused with the considered typology. Similarly to KL2, the central value of each sub-interval was considered as a possible result of the experimental test. The Bayesian approach was then applied for each couple of experimental values of E and τ_0, using a prior distribution of τ_0 equal to the posterior distribution obtained at KL2. Figure 4 shows the input values of the mechanical properties, as a function of the experimental values of both E and τ_0.

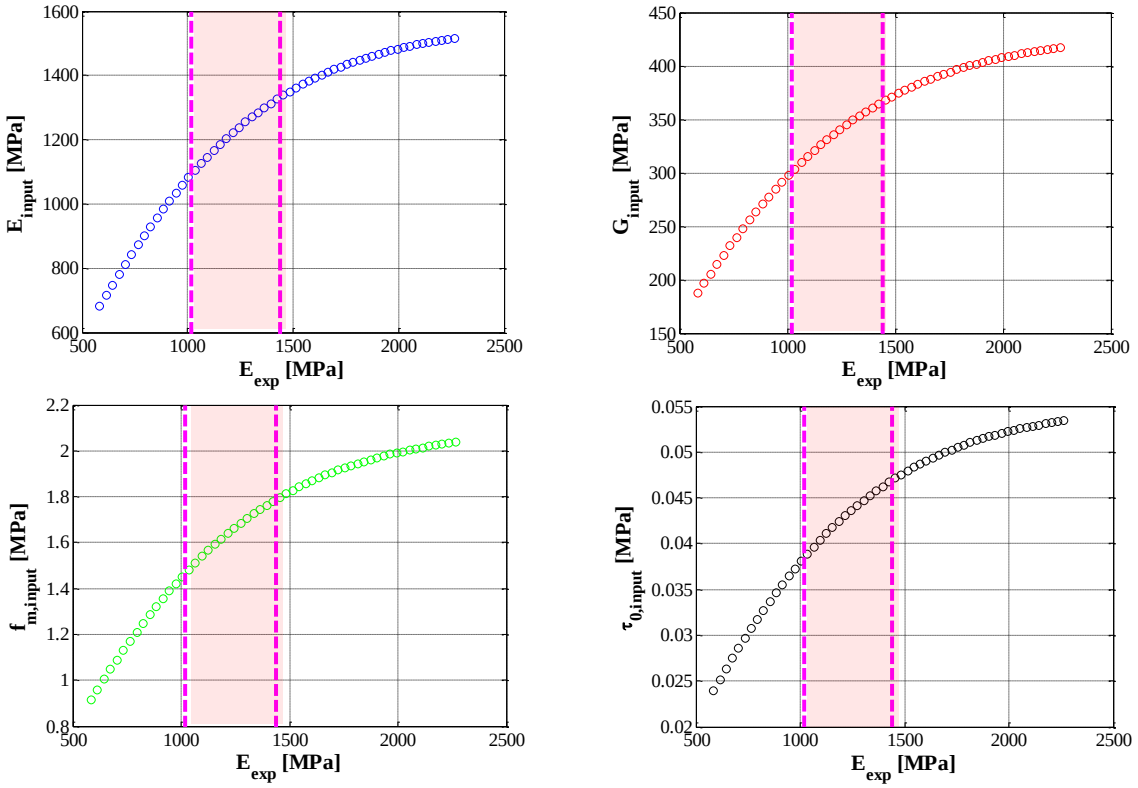


Figure 3: Input values of the four mechanical properties obtained from Bayesian updating at KL2 for typology 2.

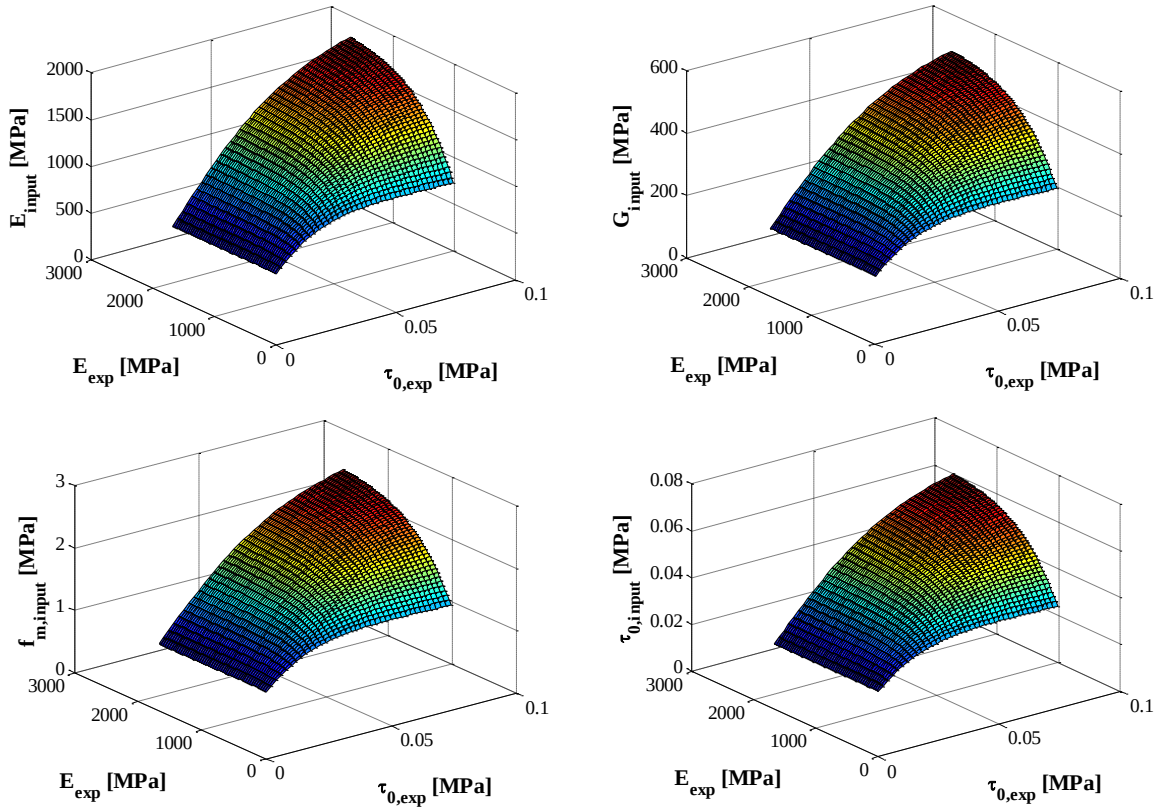


Figure 4: Input values of the four mechanical properties obtained from Bayesian updating at KL3 for typology 2.

The curves and the surfaces obtained from Bayesian updating at KL2 and KL3 were then fitted using a simple mathematical model, in order to find analytical equations providing the values of the mechanical properties representing the input for the structural model, as a function of the obtained experimental values of E and τ_0.

As regards KL2, a 2nd order polynomial provides a good fitting for all the typologies. It should be remarked that, although the use of a polynomial of a higher degree always provides a better fitting of the available data, a compromise has to be found between the goodness-of-fit and the number of coefficients defining the polynomial equation. In this work, it was decided to use a polynomial of low degree in order to limit the number of coefficients. The model adopted for the fitting is thus represented by the following equation:

$$y = p_1 \cdot x^2 + p_2 \cdot x + p_3, \tag{7}$$

where y is the a posteriori value, x is the value of the observation and p_1, p_2 and p_3 are the polynomial coefficients specific for the considered typology.

The parameters calibrated for typology 2, selected as an example, are reported in Table 2, together with the coefficient of determination R^2, which represents a classically adopted measure of the goodness of the fitting (a value closer to 1 indicates a better fitting).

Mechanical property	p_1	p_2	p_3	R^2
E	-3.24E-04	1.39E+00	-4.02E+00	0.998
G	-8.90E-05	3.83E-01	-1.10E+00	0.998
f_m	-4.35E-07	1.87E-03	-5.41E-03	0.998
τ_0	-1.14E-08	4.91E-05	-1.44E-04	0.998

Table 2: Parameters of the models fitting the data and values of R^2 at KL2 for typology 2.

As regards KL3, a 2nd order polynomial surface was selected for all the typologies, in order to limit the number of coefficients, as explained for KL2. The adopted model is now represented by the following equation:

$$y = p_{00} + p_{10} \cdot x_1 + p_{01} \cdot x_2 + p_{20} \cdot x_1^2 + p_{11} \cdot x_1 \cdot x_2 + p_{02} \cdot x_2^2, \tag{8}$$

where x_1 and x_2 are the values of the observations at KL2 and KL3, respectively.

The polynomial coefficients p_{00}, p_{10}, p_{01}, p_{20}, p_{11}, and p_{02} calibrated for typology 2 are reported in Table 3, together with the corresponding values of the coefficient of determination R^2.

Mech. property	p_{00}	p_{10}	p_{01}	p_{20}	p_{11}	p_{02}	R^2
E	-2.77E+02	2.67E+04	5.94E-01	-2.24E+05	8.57E+00	-2.68E-04	0.990
G	-7.61E+01	7.34E+03	1.63E-01	-6.17E+04	2.36E+00	-7.36E-05	0.990
f_m	-3.72E-01	3.59E+01	7.98E-04	-3.01E+02	1.15E-02	-3.59E-07	0.990
τ_0	-9.57E-03	9.21E-01	2.05E-05	-7.74E+00	2.96E-04	-9.25E-09	0.990

Table 3: Parameters of the models fitting the data and values of R^2 at KL3 for typology 2.

In order to check the efficiency of the fitting, the percentage differences between the values of the mechanical properties obtained from Bayesian updating and the ones obtained from the calibrated equations were calculated. For the considered typology, the mean values of these percentage differences are approximately equal to 0.7%, with a maximum of about 3%, for KL2 and 3%, with a maximum of 29%, for KL3. Although the maximum value is significantly larger at KL3, the fitting is still acceptable, since this maximum difference is concentrated only at the corners of the surfaces, as confirmed by the low mean values.

The calibrated equations could be useful to provide the input values of the mechanical properties, updated as a function of the experimental information, without requiring the analyst to perform the Bayesian updating previously described.

4 CONCLUSIONS

This paper proposed a procedure for updating the initial knowledge of mechanical parameters, taking into account additional experimental information by means of a Bayesian approach. In particular, the procedure moves from the selection, performed at KL1, of one of the five stone masonry typologies proposed by [3] and the definition of the prior information based on the intervals provided for each typology. At the higher knowledge levels, this prior information is updated based on the results of the performed experimental tests. The mean values of the obtained posterior distributions could be used as input for the numerical model of the building to be assessed.

For each masonry typology and for each KL, the developed methodology was then used to calibrate analytical expressions providing the input parameters for the numerical model, as a function of the results of the experimental tests. These relationships could be used by the engineer during the assessment of an existing building in order to obtain the material properties to be used in the analysis of the building, taking into proper consideration the results of the Bayesian updating approach, without the need of applying it on a case-by-case basis.

ACKNOWLEDGEMENTS

This work was carried out within the framework of different EUCENTRE Executive Projects in the years 2009-2014, funded by the Italian Department of Civil Protection. The valuable help of prof. Federico Bassetti of the University of Pavia for the mathematical derivation of the methodology is gratefully acknowledged.

REFERENCES

[1] EN 1998-3. Eurocode 8: Design of structures for earthquake resistance - Part 3: Assessment and retrofitting of buildings. CEN, Bruxelles, 2005.

[2] NTC08 Decreto Ministeriale 14 Gennaio 2008: "Norme tecniche per le costruzioni," Ministero delle Infrastrutture. S.O. n.30 alla G.U. del 4.2.2008, No. 29, 2008.

[3] MIT Ministry of Infrastructures and Transportation Circ. C.S.Ll.Pp. No. 617 of 2/2/2009 "Istruzioni per l'applicazione delle nuove norme tecniche per le costruzioni di cui al Decreto Ministeriale 14 Gennaio 2008", Consiglio superiore dei lavori pubblici. S.O. n.27 alla G.U. del 26.02.2009, No. 47, 2009.

[4] P. Franchin, P.E. Pinto, P. Rajeev, Confidence factor? *Journal of Earthquake Engineering*, **14**(7), 989-1007, 2010.

[5] M. Tondelli, M. Rota, A. Penna, G. Magenes, Evaluation of uncertainties in the seismic assessment of existing masonry buildings. *Journal of Earthquake Engineering*, **16**(S1), 36-64, 2012.

[6] CNR Consiglio Nazionale delle Ricerche. Istruzioni per la valutazione affidabilistica della sicurezza sismica di edifici esistenti. CNR-DT 212/2013, 2014 – in Italian.

[7] S. Cattari, S. Lagomarsino, V. Bosiljkov, D. D'Ayala, Sensitivity analysis for setting up the investigation protocol and defining proper confidence factors for masonry buildings. *Bulletin of Earthquake Engineering*, DOI: 10.1007/s10518-014-9648-3, 2014.

[8] M. Rota, A. Penna, G. Magenes, A framework for the seismic assessment of masonry buildings taking into account different sources of uncertainty. *Earthquake Engineering & Structural Dynamics*, **43**(7), 1045–1066, 2014.

[9] S. Bracchi, M. Rota, A. Penna, G. Magenes, Consideration of modelling uncertainties in the seismic assessment of masonry buildings by equivalent-frame approach. *Bulletin of Earthquake Engineering* (accepted).

[10] F. Jalayer, I. Iervolino, G. Manfredi, Structural modeling uncertainties and their influence on seismic assessment of existing RC structures. *Structural Safety*, **32**(3), 220-228, 2010.

[11] G. Monti, S. Alessandri, Application of Bayesian techniques to material strength evaluation and calibration of confidence factors. *Proceedings of the Reluis Research Project Final Workshop*, Naples, Italy, 2009.

[12] X. Romao, R. Gonçalves, A. Costa, R. Delgado, Evaluation of the EC8-3 confidence factors for the characterization of concrete strength in existing structures. *Materials and Structures*, **45**(11), 1737-1758, 2012.

[13] L.F. Ramos, T. Miranda, M. Mishra, F.M. Fernandes, E. Manning, A Bayesian approach for NDT data fusion: The Saint Torcato church case study. *Engineering Structures*, **84**, 120-129, 2015.

[14] A. Penna, Seismic assessment of existing and strengthened stone-masonry buildings: critical issues and possible strategies. *Bulletin of Earthquake Engineering*, DOI: 10.1007/s10518-014-9659-0, 2014

[15] G. Magenes, A. Penna, A. Galasco, M. Rota, Experimental characterization of stone masonry mechanical properties. *Proceedings of 8th International Masonry Conference*, Dresden, Germany, 2010.

[16] V. Turnšek, P. Sheppard, The shear and flexural resistance of masonry walls, *Proceedings of the International Research Conference on Earthquake Engineering*, Skopje, 1980.

[17] R.G. Drysdale, A.A. Hamid, L.R. Baker, *Masonry Structures. Behavior and design*. The Masonry Society, 1999.

[18] S. Sahlin, *Structural masonry*. Prentice-Hall, 1971.

[19] V. Bosiljkov, Y. Totoev, J. Nichols, Shear modulus and stiffness of brickwork masonry: an experimental perspective, *Structural engineering and mechanics*, **20**(1), 21-43, 2005.

[20] MPW Ministry for Public Works Circ. No. 21745 of 30/7/1981 "Istruzioni relative alla normativa tecnica per la riparazione ed il rafforzamento degli edifici in muratura danneggiati dal sisma", Legge 14 Maggio 1981, n. 219, Art. 10.

[21] S. Lagomarsino, A. Penna, A. Galasco, S. Cattari, TREMURI program: an equivalent frame model for the nonlinear seismic analysis of masonry buildings, *Engineering Structures*, DOI: 10.1016/j.engstruct.2013.08.002, 2013.

[22] A. Penna, S. Lagomarsino, A. Galasco, A nonlinear macro-element model for the seismic analysis of masonry buildings, *Earthquake Engineering and Structural Dynamics*, **43**(2), 159-179, 2013.

[23] A. Galasco, S. Lagomarsino, A. Penna, On the use of pushover analysis for existing masonry buildings, *First European Conference on Earthquake Engineering and Seismology*, Geneva, Switzerland, ISBN-10:2-8399-0190-0, 2006.

[24] EN 1998-1 Eurocode 8: Design of structures for earthquake resistance - Part 1: General rules, seismic actions and rules for buildings. CEN, Bruxelles, 2004.

[25] P. Fajfar, A nonlinear analysis method for performance-based seismic design. *Earthquake Spectra*, **16**(3), 573–592, 2000.

COMPDYN 2015
5th ECCOMAS Thematic Conference on
Computational Methods in Structural Dynamics and Earthquake Engineering
M. Papadrakakis, V. Papadopoulos, V. Plevris (eds.)
Crete Island, Greece, 25–27 May 2015

EVALUATION OF SEISMIC VULNERABILITY ASSESSMENT PARAMETERS FOR PORTUGUESE VERNACULAR CONSTRUCTIONS WITH NONLINEAR NUMERICAL ANALYSIS

Javier Ortega[1], Graça Vasconcelos[1], Mariana Correia[2], Hugo Rodrigues[3], Paulo B. Lourenço[1], and Humberto Varum[4]

[1] ISISE, Department of Civil Engineering, University of Minho
Campus de Azurém, 4800-058, Guimarães, Portugal
{javier.ortega,graca,pbl}@civil.uminho.pt

[2] CI-ESG Research Centre, Escola Superior Gallaecia, Portugal
marianacorreia@esg.pt

[3] School of Technology and Management, Polytechnic Institute of Leiria, Portugal
hugo.f.rodrigues@ipleiria.pt

[4] Civil Engineering Department, Faculty of Engineering, University of Porto, Portugal
hvarum@fe.up.pt

Keywords: Vernacular architecture, rammed earth, seismic vulnerability, parametric analysis, numerical analysis, Finite Element Method.

Abstract. *Considering that vernacular architecture may bear important lessons on hazard mitigation and that well-constructed examples showing traditional seismic resistant features can present far less vulnerability than expected, this study aims at understanding the resisting mechanisms and seismic behavior of vernacular buildings through detailed finite element modeling and nonlinear static (pushover) analysis.*

This paper focuses specifically on a type of vernacular rammed earth constructions found in the Portuguese region of Alentejo. Several rammed earth constructions found in the region were selected and studied in terms of dimensions, architectural layout, structural solutions, construction materials and detailing and, as a result, a reference model was built, which intends to be a simplified representative example of these constructions, gathering the most common characteristics.

Different parameters that may affect the seismic response of this type of vernacular constructions have been identified and a numerical parametric study was defined aiming at evaluating and quantifying their influence in the seismic behavior of this type of vernacular buildings. This paper is part of an ongoing research which includes the development of a simplified methodology for assessing the seismic vulnerability of vernacular buildings, based on vulnerability index evaluation methods.

1 INTRODUCTION

This paper addresses a critical gap in knowledge regarding vernacular architecture earthquake preparedness. It has been developed under the framework of the FCT funded research project 'SEISMIC-V: Vernacular Seismic Culture in Portugal', which focuses on the study of Local Seismic Cultures in Portugal and on the identification of adequate retrofitting techniques for vernacular buildings, empirically developed by local populations to prevent or repair earthquake damage [1]. The existence of Local Seismic Cultures was identified in the nineties by Ferrigni [2] and consists of the systematic efforts taken by local communities for protecting their built-up environment from earthquakes by the comprehensive ensemble of architectural elements with technical knowledge to efficiently reduce their impact. The study of Local Seismic Cultures is relevant because the continuity of traditional building systems and techniques is fundamental for the vernacular expression, and essential for its preservation.

Following this research line and results obtained from a preliminary report on the topic [3], Portuguese vernacular architecture is the case study also selected for this study (Figure 1). Portugal has a moderate seismicity but several devastating earthquakes have struck the country, as in 1755, 1909 and 1969 [4], and more are likely to occur in the future. Earthquakes come unexpectedly, endangering in-use vernacular architecture and the population who inhabits it. Most studies regarding seismic resistant Portuguese traditional architecture focus on '*pombalino*' buildings [5], while research in vernacular architecture has been mostly focused on building typologies and spatial organization [6]. In the last years, there has been a growing interest on the experimental characterization of the seismic behavior of representative vernacular constructive systems [7-10]. Still, very little research has been made in terms of proposing strengthening solutions, particularly those emerging from the vernacular architectural heritage [11].



Figure 1: Examples of Portuguese vernacular architecture and traditional materials commonly applied: (from left to right) stone [6], earth [9] and timber

The valorization and preservation of the vernacular heritage is crucial, not only as a record of the past but also as a privileged factor of local development, boosting local economies [12]. The revival of small industries of traditional local materials, developed to be adapted to a specific territory and climate can also reduce waste and energy consumptions in production and transportation. In addition, and opposite to this current world's homogenizing tendency, vernacular architecture is extremely heterogeneous and constitutes and invaluable heritage throughout the world worthy of preservation and a key element of cultural identity. Nonetheless, due to this great variety of building types, work on the built vernacular heritage requires a deep knowledge and investigation of the place, the traditional techniques and materials, and should be cautiously approached in order to undertake a successful intervention. Moreover, the vernacular heritage has a dynamic nature and thus, it should not only be recorded and preserved but its constant evolution should be ensured.

There is another undesirable effect resulting from this current global urbanization tendency, which is the replacement of traditional building materials and the adoption of new modern alien techniques and technologies which enable structures to be erected quickly and cheaply, but not necessarily safely [13]. This tends to increase the vulnerability of the communities because they do not have any more their own tools to prevent earthquake damage and become extremely dependent on external agents, circumstance which ends up diluting Local Seismic Cultures. Indigenous construction practices acquired from ancestors and experience are thus being gradually abandoned and replaced because local communities rely less on them [14]. An increase in knowledge in Local Seismic Cultures and in the seismic behavior of vernacular architecture is therefore justified because it can also prevent further changes in the existing buildings that contribute to the increase of seismic vulnerability by avoiding the usage of inadequate construction practices that can result from an inappropriate juxtaposition of old and new technologies.

This paper consists of an extensive numerical contribution for the better insight of the structural behavior of specific Portuguese vernacular architecture typology under seismic loading, and is part of an ongoing wider research aiming at contributing for the awareness and protection of the Portuguese vernacular heritage by reducing its seismic vulnerability with traditional strengthening solutions. For that purpose, one of the fundamental objectives embraced by the ongoing research was the development of a simplified methodology for the seismic vulnerability assessment of vernacular architecture.

This envisaged vulnerability assessment methodology aims at the identification of building fragilities, thus addressing an essential aspect in which the engineering research can intervene [15], since the evaluation of the seismic vulnerability of existing constructions can be used to evaluate the need of retrofitting solutions and to assess their efficiency in reducing the seismic vulnerability. In conclusion, this proposed methodology is planned to lead to the definition and optimization of building retrofitting strategies based on those traditional practices emerging from vernacular architecture, resulting from a Local Seismic Culture.

The seismic vulnerability of a structure can be defined as its intrinsic proneness to suffer damage as a result of a seismic event of a given intensity. Therefore, the main objective of vulnerability assessments is to measure the probability of reaching a given level of damage [16]. Given the big variety of methodologies proposed by different authors, choosing a certain seismic vulnerability assessment methodology will depend on the goal, scale and nature of the study and, additionally, it should always be adapted to the local techniques, materials and constructive solutions to account for the particularities of the regional construction.

The methodology proposed for this research is based on the vulnerability index methods, initially proposed by Benedetti and Petrini [17], which are based on a vast set of post-seismic damage survey data and on the identification of those constructive aspects that influence the most in the control of the seismic structural damage, i.e. plan and elevation configuration, quality of materials or state of conservation. This type of methodology has been already extensively used for masonry residential buildings in Italy [18] and in several Portuguese historical city centers [10,15,19], obtaining useful and reliable results as a first level approach. Its main advantage is that they allow assessing the different constructions individually, based on their vulnerability characteristics, rather than evaluate the buildings solely as part of a building typology. However, the main disadvantage is that these potential seismic deficiencies are qualified and weighted according to their relative importance mainly through expert judgment and thus has a degree of uncertainty, which is not normally taken into account [16].

The determination of the seismic vulnerability index thus requires the identification and characterization of those parameters affecting the seismic response of the building and their qualification by points. Qualitative and quantitative parameters are defined and the

vulnerability index is calculated as the weighted sum of these parameters, classifying the buildings according to their vulnerability. This index can be used to estimate structural damage after correlation to a specified seismic intensity, supported by post-earthquake recordings and statistical studies.

This paper presents a series of numerical nonlinear parametric analyses that were defined in order to assess and try to quantify the influence of the parameters initially selected for a representative Portuguese vernacular rammed earth construction typology chosen as a case study. This numerical simulation intends to understand in a more detailed way the resisting mechanisms of the different structural elements of this typology under seismic loading, based on these nonlinear static (pushover) analyses. Besides, finite element modeling based on nonlinear numerical analysis of rammed earth vernacular buildings represents a step forward in technical and scientific knowledge, as few results are available in literature.

2 RAMMED EARTH CONSTRUCTIONS IN ALENTEJO

2.1 Selection of a case study

A first vernacular typology was selected as a first case study, consisting of a type of vernacular rammed earth construction commonly found in the south Portuguese region of Alentejo. The choice of these vernacular constructions is twofold: (i) they can be encountered in regions that were previously identified as prone to have developed a Local Seismic Culture, such as Setúbal, Beja or Évora, where the seismicity is characterized by frequent earthquakes of low intensity; and (ii) traditional seismic strengthening solutions were already identified, such as buttresses, ties and timber reinforcements inserted within the rammed earth wall as a reinforcement (Figure 2).

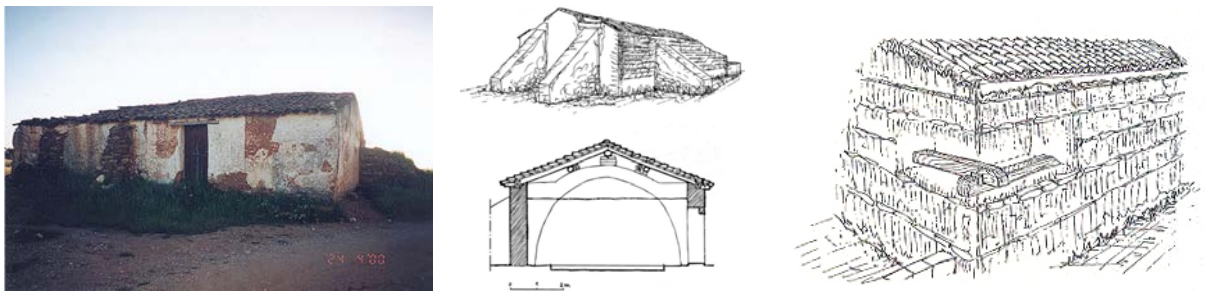


Figure 2: Traditional seismic strengthening solutions identified in characteristic rammed earth constructions of Alentejo [20]

Rammed earth construction, known as *taipa* in Portugal, consists of compacting the earth using a timber formwork for the construction of free standing walls. This has traditionally been the most widespread technique in these regions and, even though its use decreased significantly in the last forty years, is still in use in some places. These buildings have generally small dimensions, simple rectangular shape and only one floor, having predominant horizontal dimensions. They present massive shapes with few or no openings, other than a single door, and are isolated from other buildings. Other materials are also used, such as stone or brick masonry for reinforcing the corners and in order to build a base course or *soco*, which aims at protecting the rammed earth from the humidity and rain penetration by preventing the action of rising damp. The roofs are commonly mono-pitched roofs or gable roofs, usually presenting a low slope, and made with a simple framework of timber beams. The studied buildings can be found in '*Taipa no Alentejo*' [20], which includes an extensive study of their geometry, structural solutions, construction materials and detailing.

2.2 Proposed parameters for the seismic vulnerability assessment methodology

Developing specific and relevant seismic vulnerability assessment tools for this vernacular building typology is difficult due to its great heterogeneity, resulting from the uncertainty of many construction aspects, such as the constituent materials or different geometry configurations, often modified by previous structural or architectural interventions, among others. A methodology based on vulnerability index methods is proposed for obtaining an indicative measure of the seismic vulnerability, assuming that it can overcome this intrinsic heterogeneity by selecting qualitative and quantitative parameters that most influence their seismic response taking into account the particularities of this regional constructional typology so it will be particularly adjusted to this building typology.

The construction characteristics highly influence the seismic behavior of structures and the parameters were selected according to them. The selection was made mainly based on other parameters chosen in similar vulnerability assessments and on literature review of post-earthquake damage observation [21-23], which is a decisive tool for the understanding of the structural behavior of vernacular constructions, since earthquakes are tests that prove the adequacy or inadequacy of construction practices and prove that the vulnerability does not rely solely on the age of a structure or the construction quality, but on many parameters. Table 1 shows the final parameters selected for this specific typology.

Proposed parameters for the seismic vulnerability assessment methodology
1. Location and position within urban fabric
P1: Location and soil condition
2. Geometry: plan and elevation configuration
P2: Plan configuration
3. Construction solutions and materials: vertical resisting elements (rammed earth walls)
P3: Distribution of resisting elements
P4: Wall slenderness
P5: Maximum distance between walls
P6: Rammed earth quality
P7: Connection between perpendicular walls
4. Construction solutions and materials: horizontal elements (roofs)
P8: Type of roofing system
5. Opening characteristics
P9: Number and area of wall openings
P10: Position and misalignment of wall openings
6. Maintenance, previous damage, alterations and traditional strengthening solutions
P11: Structural history of the building
P12: Non-structural elements
P13: Conservation state and previous damage
P14: Traditional strengthening solutions

Table 1: Vulnerability assessment parameters selected for rammed earth vernacular buildings in Alentejo

Most of the parameters selected are common to other vulnerability assessment methodologies, as they represent building features common to most of the typologies. For example, P1 (location and soil conditions) concerns characteristics such as the type of soil, foundations land slope, presence or absence of foundations and seismic micro-zonation of the building. P2 (plan configuration) accounts for the possible in-plan irregularities, which can enhance the torsional effects of the earthquakes and can be due to an excessive in-plan

slenderness or an irregular shape configurations that leads to an eccentricity of the mass center with respect to the stiffness center. P3 (distribution of resisting elements) takes into account the conventional shear resistance of the walls, specifically addressing their distribution, since vernacular buildings usually present an irregular distribution and an unbalanced area of resisting walls in the two orthogonal directions, which may jeopardize the seismic resistance of the building. P4 (wall slenderness) measures the ratio between the effective height of the wall and its thickness, since the most slender elements are the most vulnerable to the seismic action. P5 (maximum distance between walls) measures the span to thickness ratio, since the longest elements without intermediate support are also more vulnerable to out-of-plane collapse. P7 (connection between perpendicular elements) takes into account the organization of the vertical structure system and the level of connection between perpendicular walls, which have a decisive role in the seismic behavior of the building, particularly at the corners. P9 and P10 concern the opening characteristics in terms of number and position, since the presence of many openings always indicates a potential vulnerability of the building, particularly if they are too close to each other or to the edges of the walls. P13 takes into account the degree of deterioration presented by the building, which is strictly correlated with an increase in the vulnerability of the building.

Nevertheless, some of these parameters are, as previously stated, specific of this typology. For instance, P6 takes into account the morphology of the vertical resisting elements, which in this case are rammed earth walls. An essential aspect of this parameter concerns the material mechanical properties, which are always difficult to measure and very variable in vernacular buildings, but have a decisive role in the seismic performance of the structure. A sensitivity analysis is foreseen in order to overcome the uncertainty resulting from the big variability of these properties that was observed in the literature. Not only the rammed earth properties but also the stone masonry properties need to be assessed because the buildings always present a stone masonry base course (Figure 3), whose influence should also be evaluated. Other constructive details that could be taken into account when assessing the influence of the morphology of the rammed earth walls in the seismic behavior are the horizontal brick courses that can be often found between the layers of rammed earth (Figure 3).

The type of roofing system (P8) should be assessed, firstly, in terms of the efficiency of wall-to-roof connections, which are commonly very poor in this typology and, secondly, in terms of the type of roof. Different type of roofs can be commonly observed applied in these buildings, which may have an influence on the seismic behavior of the building. Particular attention should be paid to the thrust exerted by some of these types.

The structural history of the building (P11) is also important in this typology because these buildings traditionally expands. These new parts are usually built in different materials and are poorly connected to the original building, which may increase the vulnerability of the building. Chimneys are the only relevant protruding non-structural element (P12) that can be systematically found in this type of buildings (Figure 3). The vulnerability of the building may increase according to the height of this element.



Figure 3: (left) Stone base course [20]; (middle) brick masonry horizontal course within rammed earth walls [20]; chimney [20]

Finally, P14 accounts for those traditional strengthening solutions that have a direct influence on the seismic behavior of the building, such as buttresses, which is a common element usually observed attached to this type of buildings. This parameter only takes into consideration those techniques that do not have a direct influence over specific parameters, since some of these traditional techniques, i.e. ties, have a direct influence on other parameters selected, like the connection between perpendicular elements.

3 REFERENCE NUMERICAL MODEL

3.1 Reference building geometry

Resulting from the analysis of the buildings from the database found in the literature [20], a reference model was built, which intends to be a simplified representative example of these constructions, gathering common characteristics in terms of dimensions and architectural layout that are able to typify more precisely the rest of the buildings present in the database. The dimensioned plan and elevations of the reference building used are shown in Figure 4.

The plan has a simple rectangular shape, symmetrical in both orthogonal directions, regarding also the distribution of the interior load bearing walls. The height of this type of buildings rarely surpasses 3 meters at the front and back walls. The gable walls are not very high either, keeping the roof slope low, between 15-20 degrees. The height of the stone masonry base course is very variable but was established as 0.4 meters. Regarding the openings, the position of the two doors and two windows has also a symmetrical configuration. Timber lintels were considered over the openings, as this is also the common practice observed in almost every building of the database. Chimneys or other non-structural elements were not added to the reference building at this initial step.

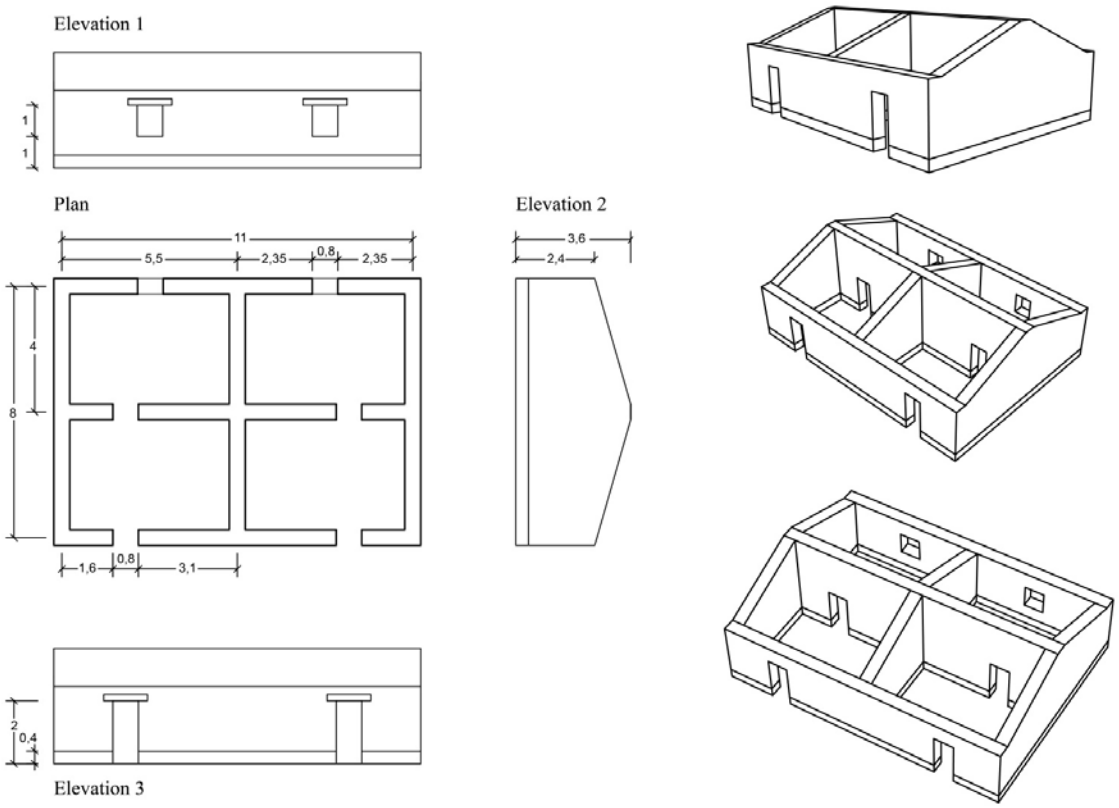


Figure 4: Plan and elevations of the reference building adopted for the construction of the reference model

3.2 Finite element model

The numerical model was constructed taking into consideration the geometry of the reference building previously defined. With regard to the material properties and data, few studies have focused on the finite element modeling of rammed earth buildings [24-30], and most of them have adopted simple models, assuming simple constitutive laws, mainly linear elastic isotropic. However, in order to understand and simulate accurately the seismic behavior of rammed earth constructions, it is important to describe accurately the nonlinear behavior through more complex constitutive models, since relevant deformation of the structural elements is expected. Nevertheless, this requires detailed information of the mechanical properties of the material, which is not always possible. In this case, the material properties were obtained from data collected from different authors. A big variability was noticed, which brings up more uncertainties.

The material model finally adopted to represent the nonlinear behavior of the rammed earth in the analyses is a standard isotropic Total Strain Rotating Crack Model (TSRCM), which describes the tensile and compressive behavior of the material with one stress-strain relationship and assumes that the crack direction rotates with the principal strain axes. It was implemented in DIANA software [31]. An isotropic model was chosen because despite its layered structure, experimental tests found in the literature have shown that the mechanical properties of rammed earth do not behave in an anisotropic way and only has an influence on crack mechanisms [30]. This model is very well suited for analyses which are predominantly governed by cracking or crushing of the material. The tension softening function selected is exponential and the compressive function selected to model the crushing behavior is parabolic.

The model is built with solid 3D elements: (i) twenty-node isoparametric solid brick elements (CHX60) with three-by-three Gauss integration in the volume; and (ii) fifteen-node isoparametric solid wedge elements (CTP45) with a four-point integration scheme in the triangular domain and a three-point scheme in the orthogonal direction, used to adjust the mesh to the geometry resulting from the triangular gable walls.

Three different materials are considered. Stone masonry is used for the base course, which is usually built with an irregular schist or granite masonry and thus, poor material properties are assumed. It is noted that the same isotropic material model (TSRCM) is also used for the stone masonry. Rammed earth is used for the structural walls, both interior and exterior. Timber is used for the lintels over all the openings. The final reference model has two elements in the thickness direction of the wall and therefore, the resulting generated mesh has 31,264 nodes and 7,993 elements, see Figure 5. The roof is only considered as a distributed load on the top of the walls and the displacements of the elements at the base are fully restrained. The total mass of the model is 150 tons.

The rammed earth and the stone masonry are considered to present nonlinear behavior, while for the timber only the elastic properties are considered, as the structural nonlinearities are not expected to concentrate there. For the timber lintels, an elasticity modulus of 10 GPa and a Poisson's ratio of 0.2 were used [27]. Regarding the stone masonry elastic properties, a modulus of elasticity of 1500 MPa and a Poisson's ratio of 0.2 were adopted. Its compressive strength and specific weight were obtained from reference values given by the Italian code [32], assuming the lowest quality masonry class, an irregular rubble stone masonry composed of rubble and irregular stone units of different sizes and shapes. The remaining nonlinear properties of the masonry were computed directly from the compressive strength, based on recommendations given by Lourenço [33]. The compressive fracture energy was obtained using a ductility factor of 1.6 mm, which is the ratio between the fracture energy and the

ultimate compressive strength. The tensile strength was estimated at 1/10 of the compressive strength. Finally, an average value of 0.012 N/mm is adopted for the mode I fracture energy.

Concerning the rammed earth material elastic properties, an elasticity modulus of 300 MPa and a Poisson's ratio of 0.3 were used. A compressive strength of 1 MPa was adopted, which seem to be in agreement with the scattered values observed in the literature, but acknowledging the relevance of a sensitivity analysis. The remaining nonlinear properties were again calculated directly from the compressive strength following the same recommendations [33]. The only difference with respect to the stone masonry lies in the value used for the mode I fracture energy. According to [30], the fracture energy of rammed earth should be increased in about ten times because rammed earth behaves more as a monolithic and less as a brittle material in comparison with stone masonry due to its broad particle size distribution, which includes large particles that may have a significant contribution for the interlocking at the crack surface, by promoting its roughness. A value of 0.1 N/mm was adopted for this reason. Table 2 presents the material properties finally used for the analyses.

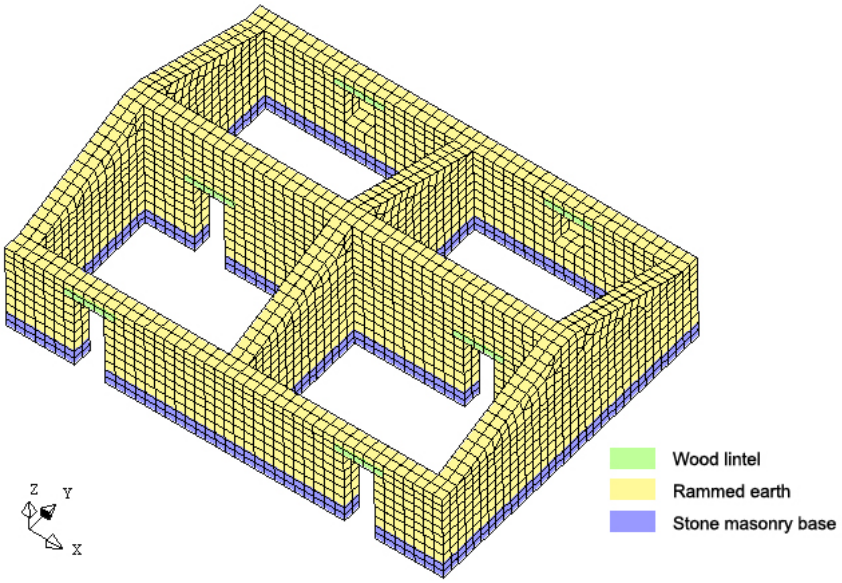


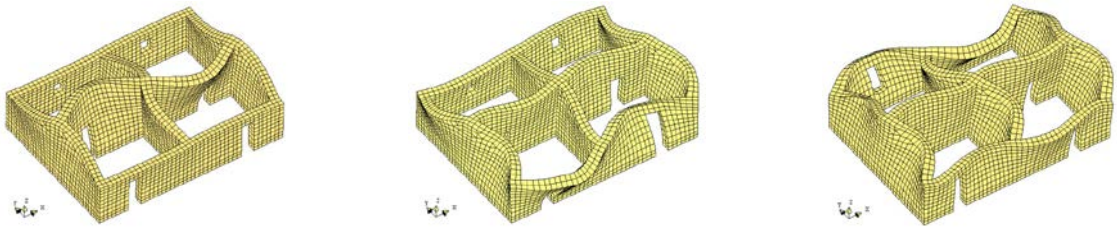
Figure 5: Numerical model: mesh categorized by materials

Material	E (MPa)	ν	f_c (MPa)	G_{fc} (N/mm)	f_t (MPa)	G_{fI} (N/mm)	β	W (kN/m^3)
Stone masonry	1500	0.2	1.5	2.4	0.15	0.012	0.05	20
Rammed earth	300	0.3	1	1.6	0.1	0.1	0.05	20
Timber	10000	0.2	-	-	-	-	-	6

Table 2: Mechanical properties adopted for the three materials used in the reference model

3.3 Seismic performance of the reference model

Before carrying out the numerical parametric study, the main dynamic characteristics of the reference model were obtained, showing that most of the modes are associated with local deformations, involving only specific structural elements at a time and that there is no global modes affecting the whole structure. This effect is enhanced by the fact that the roof is not modeled and the walls get to vibrate independently. The first modes are associated with local out-of-plane deformations of the walls in the Y direction, particularly the taller inner walls, less resistant to local deformations, see Figure 6.



Mode 1:
T = 0.150 s
f = 6.66 Hz

Mode 3:
T = 0.099 s
f = 10.13 H

Mode 6:
T = 0.094 s
f = 10.68 H

Figure 6: Shape of the first, sixth and sixth mode of the reference building

A nonlinear static (pushover) analysis was performed on the reference building, which is a common procedure used for the seismic assessment of buildings. First, only the dead weight and the distributed load on top of the walls, simulating the roof, are considered. After that, an incremental monotonic loading proportional to the mass is applied on the structure in the main horizontal directions (X and Y), as recommended by [34] for masonry structures. Only the positive directions are considered, since the behavior of the building is practically symmetric.

Figure 7 shows the capacity curve for the reference building in both horizontal directions. The analysis shows that the structure capacity is higher than could have been expected for this kind of buildings, obtaining maximum load coefficients of around 0.8g in +Y direction and over 1.1g in +X direction. This might be due mainly because the structural elements of the buildings are considered to be perfectly connected between them, avoiding their premature local out-of-plane collapse. Nevertheless, results were deemed satisfactory for the purpose of the study, which is a comparative analysis between different geometric and structural characteristics.

Figure 7 also shows the evolution of the maximum principal strains in the building in both +X and +Y direction, which can be used as a cracking measure. As could be expected, the parts of the building presenting more damage are the middle walls because they are higher than the rest and show flexural vertical cracks in the mid-span. However, the main damage is located at the connections between perpendicular walls. Horizontal cracking at the stone base is also substantial, as well as in the connection between both materials. In the case of the pushover analysis in +X direction, the middle interior walls present a clear in-plane failure.

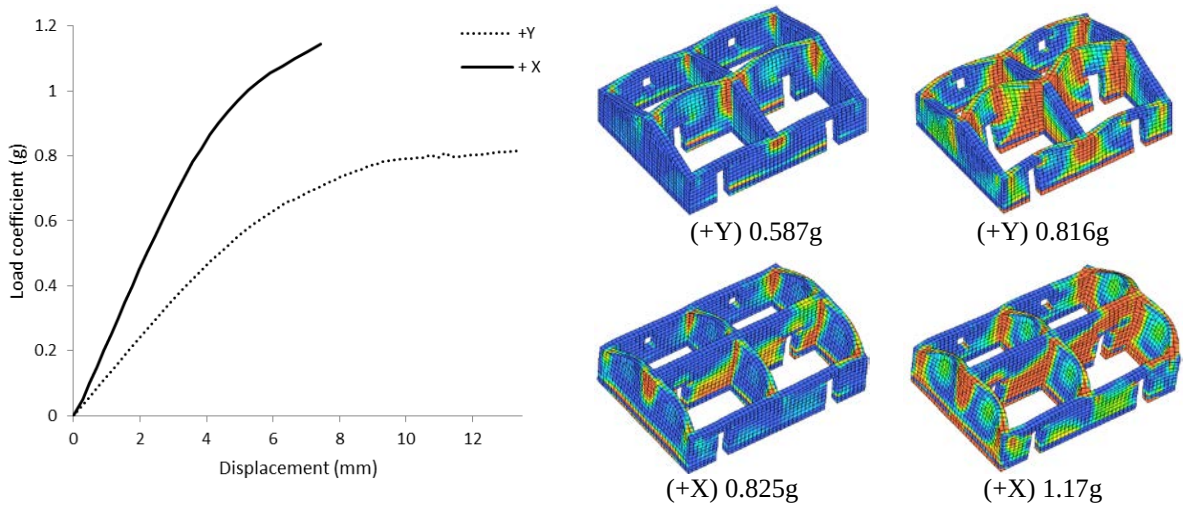


Figure 7: Capacity curve of the pushover analyses on the reference building and evolution of maximum principal strains along the building depicted on deformed mesh for the analysis in booth +X and +Y direction

4 NUMERICAL PARAMETRIC ANALYSIS

Numerical nonlinear parametric analyses were defined in order to assess the influence of the different parameters selected and in order to understand in a more detailed way the seismic behavior of this typology. Therefore, the initial configuration of the reference model was changed in terms of geometry and construction characteristics and new models were built according to the parameters. The comparison between the new models and the reference one is made in terms of capacity curves. This approach intends to identify the most relevant parameters before addressing their calibration, required for the development of a seismic vulnerability assessment methodology. Table 3 shows the comparison, in terms of capacity curves, of the parameters that seem to have more influence in the building seismic response.

For example, the analysis assessing the influence of the plan configuration, particularly the influence of an irregular shape configuration, is shown. Particularly, it can be observed that when those parts of the building projecting have a significant dimension, such as in the case of building P2b_1, the capacity of the building decrease, probably due to the fact that these independent cells are freer to deform and allow some torsion effects to occur.

Parameters P4 and P5, which take into account the wall slenderness and the maximum span between walls shows an important difference in terms of peak loads. With respect to P4, when the height of the walls increases (P4_1 and P4_2), the flexural damage and the damage at the connections between perpendicular walls also increase, both in the interior and the exterior walls. Another two models were built modifying the thickness of the inner walls, which are usually thinner than the exterior ones (P4_3 and P4_4). Expectedly, reducing this thickness decreases the seismic capacity of the building. With respect to P5, when the span covered by the walls is very large, the elements get to behave practically as free standing walls, reducing much more their horizontal resisting capacity.

The influence of the stone masonry base course in the seismic behavior of the building was also evaluated by constructing two more models. First, the stone base was completely removed and the walls were considered to be built only with rammed earth. A second model was built with the stone base reaching a height of 1.0 m. The main difference in the results consists on the variation in the stiffness of the model, mainly resulting from the difference in stiffness between both materials, confirming its influence.

The type of roof has a decisive influence since the type of roof used has a direct influence on the geometry of the building. For instance, if a truss roof is considered, the height of the middle wall is significantly reduced, down to the same height as the exterior walls and, therefore, the capacity of the building may increase. On the other hand, these changes can lead to the formation of new vulnerable elements, such as the gable wall. The lack of a middle wall bracing the gable end wall increases the vulnerability of this element, which becomes highly susceptible to collapse. Therefore, the influence of this parameter, which affects mainly the geometry, should be carefully assessed, particularly when evaluating those roof configurations that exert a thrust on the walls (P8a_2).

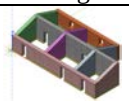
Another type of situation was considered regarding the wall-to-roof connections and another model was built simulating proper coupling between the parallel walls (P8b_1). A notable improvement in the seismic performance can be observed, particularly in the global stiffness of the model, since the resisting walls now respond to the horizontal action simultaneously.

The influence of the relative position of the openings with respect to the wall edges and other openings was also confirmed. A reduction in the size of the resisting piers (model P10_2), because of openings too close to the edges of the wall especially affects the in-plane resistance of the walls and leads to a considerable decrease of the capacity in +X direction.

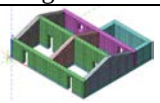
P2. Plan configuration: irregular shape configuration



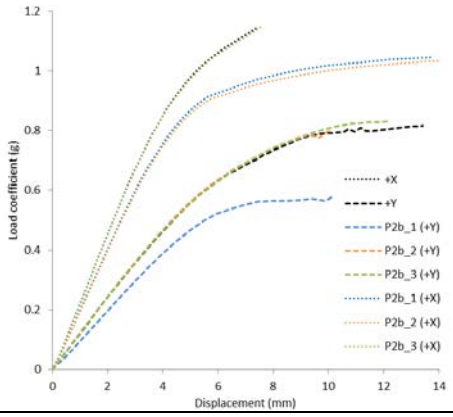
P2b_1



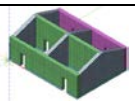
P2b_2



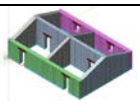
P2b_3



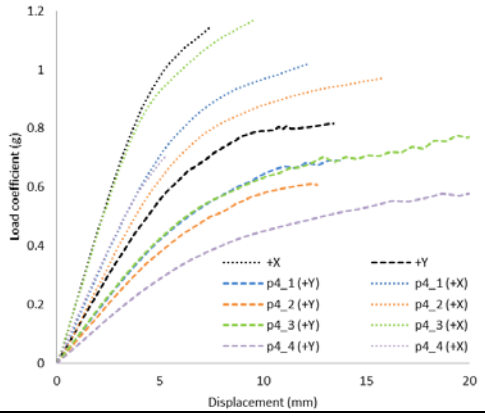
P4. Wall slenderness



P4_1 / P4_2



P4_3 / P4_4



P5. Maximum distance between walls



P5_1



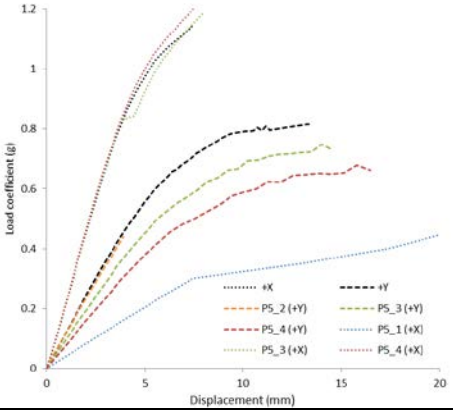
P5_2



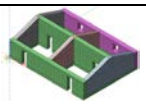
P5_3



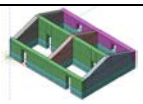
P5_4



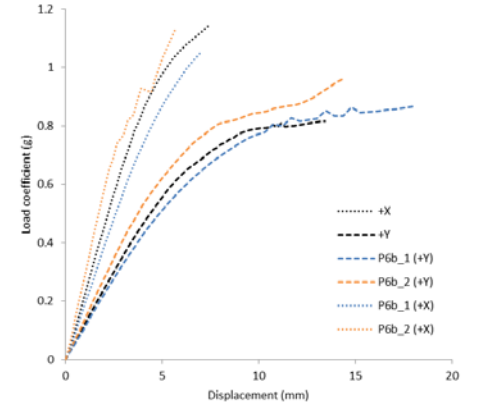
P6. Rammed earth quality: Stone base course



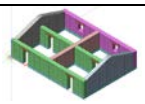
P6b_1



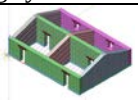
P6b_2



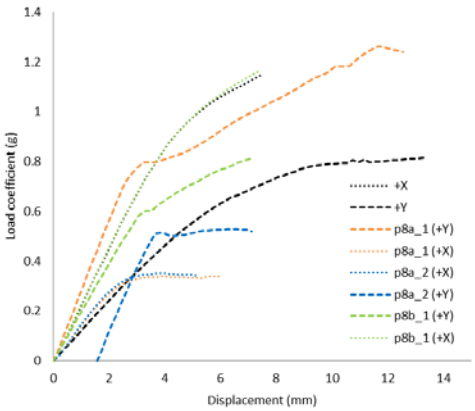
P8. Type of roofing system



P8a_1 / P8a_2



P8b_1



P10. Position and misalignment of walls openings



P10_1



P10_2

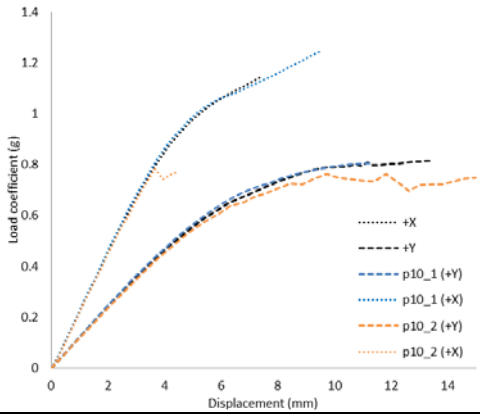


Table 3: Numerical parametric analyses carried out according to the parameters selected and comparisons in terms of capacity curves

5 CONCLUSIONS

As part of an ongoing research that aims at the development of a seismic vulnerability assessment methodology of vernacular architecture, a numerical parametric study was carried out using pushover analysis proportional to the mass. The objective was to evaluate the variation of the seismic response adopting changes in the geometrical and construction characteristics of a Portuguese vernacular typology, consisting of rammed earth buildings.

Different parameters that were assumed to have a relevant influence in the seismic behavior were selected adjusted for the specific building typology studied. Construction aspects such as the plan configuration, the wall slenderness, the distance between walls and the relative position of the openings were among those considered. A reference model was first built, trying to effectively represent this vernacular typology, gathering common architectural characteristics. The model was constructed with DIANA software and the material properties used were obtained from the literature. Different models were then built adopting changes in the dimensions and construction characteristics according to those parameters selected.

Nonlinear static (pushover) parametric analyses were carried out and a comparison between the seismic performance of the reference model and the rest of the models was made, in terms of capacity curves. The results obtained confirm that the parameters selected have a relevant influence in the seismic behavior of the building. The results of the analysis of the reference building show that the building is more sensitive to out-of-plane failure, which can be expected due to the height to thickness ratio of the rammed earth walls assumed. The interior walls present more vulnerability as well because of their bigger height. The points of connection between orthogonal walls are also very vulnerable, showing big concentration of stress. This is particularly important given the fact that a perfect connection between the walls was assumed in this first set of analyses. This is not usually true for this type of buildings, which are many times characterized by poor wall-to-wall connections. The parameter addressing this characteristic assumes a greater importance for later analyses.

Following these analysis aimed at understanding the seismic behavior of this construction typology and the influence of certain specific construction characteristics, the calibration of the weights of the parameters need to be carried out at a further step, in order to develop the seismic vulnerability assessment methodology. Finally, another important future step will be the modeling of the distinct retrofitting solutions identified that are commonly applied in these buildings, such as buttresses. This will lead to a comparative analysis on the efficiency of the different strengthening techniques in improving the seismic global behavior of these vernacular buildings and will result in the calibration of one of the parameters proposed that is expected to be one of the main contributions of this research: the influence of traditional strengthening solutions in the reduction of the seismic vulnerability of vernacular architecture.

ACKNOWLEDGEMENT

The authors wishes to express their gratitude to the Portuguese Science and Technology Foundation (FCT) for the scholarship granted in the scope of the research project ‘SEISMIC-V – Vernacular Seismic Culture in Portugal’ (PTDC/ATP-AQI/ 3934/2012).

REFERENCES

[1] M. Correia, G. Carlos, S. Rocha, P.B. Lourenço, G. Vasconcelos, H. Varum, SEISMIC-V: Vernacular seismic culture in Portugal. M. Correia, G. Carlos, S. Rocha eds. *Vernacular Heritage and Earthen Architecture: Contributions for Sustainable Development*. Taylor & Francis Group, London, U.K., 663-668, 2014.

[2] F. Ferrigni, *S. Lorenzello, à la recherché des anomalies qui protégent*. Conseil de l'Europe et Centre Universitaire Européen pour les Biens Culturels, Ravello, Italy, 1990.

[3] M. Correia, J. Merten, *Preliminary Report of the Local Seismic Culture in Portugal*. Taversism Project – Atlas of Local Seismic Cultures, EUCCH, Ravello Italy, 2001.

[4] V.J. Moreira. Sismicidade Histórica de Portugal Continental. *Revista do Instituto Nacional de Meteorologia e Geofísica*, Março, 1984.

[5] J.M.D. Mascarenhas, Baixa Pombalina, Algumas Inovações Técnicas. *2º Encontro Sobre Conservação e Reabilitação de Edifícios*, LNEC, Lisboa, Portugal, 1994.

[6] A.A.P., *Arquitectura Popular em Portugal, 3ª Edição*. Associação dos Arquitectos Portugueses, Lisboa, Portugal, 1988.

[7] G. Vasconcelos, P.B. Lourenço. Experimental characterization of stone masonry in shear and compression. *Construction and Building Materials*, **23**(11), 3337-3345, 2009.

[8] G. Vasconcelos, P.B. Lourenço. In-Plane Experimental Behavior of Stone Masonry Walls. *Journal of Structural Engineering (ASCE)*, **135**(10), 1269-1278, 2009.

[9] H. Varum, A. Figueiredo, D. Silveira, T. Martins, A. Costa. Outputs from the research developed at the University of Aveiro regarding the mechanical characterization of existing adobe constructions in Portugal. *Revista Informes de la Construcción*, **63**(523), 127-142, 2011.

[10] F. Neves, A. Costa, R. Vicente, C.S. Oliveira, H. Varum. Seismic vulnerability assessment and characterisation of the buildings on Faial Island, Azores. *Bull. Earthquake Eng.*, **10**(1), 27-44, 2012.

[11] M. Correia, Metodología Desarrollada para la Identificación en Portugal de Arquitectura Local Sismo Resistente. *SismoAdobe2005, Seminario Internacional de Arquitectura, Construcción y Conservación de Edificaciones de Tierra en Áreas Sísmicas*, Lima, Perú, 2005.

[12] J. Fernandes, R. Mateus, Energy efficiency principles in Portuguese vernacular architecture. *International conference BSA 2012*, Porto, Portugal, 2012.

[13] M.R. Degg, J. Homan. Earthquake vulnerability in the Middle East. *Geography*, **90**(1), 54-66, 2005.

[14] S.J. Halvorson, J.P. Hamilton. Vulnerability and the Erosion of Seismic Culture in Mountainous Central Asia. *Mountain Research and Development*, **27**(4), 322-330, 2007.

[15] R. Vicente, S. Parodi, S. Lagomarsino, H. Varum, J.R.M. Silva. Seismic vulnerability and risk assessment: case study of the historic city centre of Coimbra, Portugal. *Bulletin of Earthquake Engineering*, **9**(4), 1067-1096, 2011.

[16] G.M. Calvi, R. Pinho, G. Magenes, J.J. Bommer, L.F. Restrepo-Vélez, H. Crowley. Development of Seismic Vulnerability Assessment Methodologies Over the Past 30 Years. *ISET Journal of Earthquake Technology*, **43**(472), 75-104, 2006.

[17] D. Benedetti, V. Petrini. Sulla vulnerabilità di edifici in muratura: proposta di un método di valutazione. *L'industria delle Costruzioni*, **149**(1), 66-74, 1984.

[18] GNDT, *Scheda di esposizione e vulnerabilità e di rilevamento danni di primo livello e secondo livello (muratura e cemento armato)*. Gruppo Nazionale per la Difesa dai Terremoti (GNDT), Roma, Italia, 1994.

[19] T.M. Ferreira, R. Vicente, J.R.M. Silva, H. Varum, A. Costa. Seismic vulnerability assessment of historical urban centres: case study of the old city centre in Seixal, Portugal. *Bulletin of Earthquake Engineering*, **11**(5), 1753-1773, 2013.

[20] M. Correia, *Taipa no Alentejo*. Argumentum, Lisboa, Portugal, 2007.

[21] G. Minke, *Manual de construcción para viviendas antisísmicas, 2ª Edición*. Universidad de Kassel, Alemania, 2001.

[22] M. Blondet, M.G. Villa García, S. Brzev, A. Rubiños, *Earthquake-Resistant Construction of Adobe Buildings: A Tutorial*. Earthquake Engineering Research Institute (EERI), 2011.

[23] J. Bothara, S. Brzev, *A Tutorial: Improving the Seismic Performance of Stone Masonry Buildings*. Earthquake Engineering Research Institute (EERI), 2012.

[24] Q.-B. Bui, J.-C. Morel, S. Hans, N. Meunier. Compression behavior of non-industrial materials in civil engineering by three scale experiments: the case of rammed earth. *Materials and Structures*, **42**(8), 1101-1116, 2008.

[25] P.A. Jaquin, *Analysis of Historic Rammed Earth Construction*. Ph.D. Thesis, Durham University, U.K., 2008.

[26] A.M. Braga, J.M.C. Estêvão, Os sismos e a construção em taipa no Algarve. *Sísmica 2010 - 8º Congresso de Sismologia e Engenharia Sísmica*, Aveiro, Portugal, 2010.

[27] M.I. Gomes, M. Lopes, J. de Brito. Seismic resistance of earth construction in Portugal. *Engineering Structures*, **33**(3), 932-941, 2011.

[28] Q. Angulo-Ibáñez, Á. Mas-Tomas, V. Galvañ-Llopis, J.L. Montesinos. Traditional braces of earth constructions. *Construction and Building Materials*, **30**, 389-399, 2012.

[29] R. Gallego, I. Arto, Evaluation of Seismic Behavior of Rammed Earth Structures. Mileto, Vegas, García-Soriano, Cristini eds. *Versus2014, International Conference on Vernacular Heritage, Sustainability and Earthen Architecture*. Taylor & Francis Group, London, U.K., 2014.

[30] L. Miccoli, D.V. Oliveira, R. Silva, U. Müller, L. Schueremans. Static behaviour of rammed earth: experimental testing and finite element modelling. *Materials and Structures*, 2014.

[31] TNO, *DIsplacement method ANAlyser (DIANA)*. User's manual, Release 9.4., Netherlands, 2009.

[32] NTC08, *Circolare del Ministero delle Infrastrutture e dei Transporti 2 Febbraio 2009, n. 617. Istruzioni per l'applicazione delle nuove norme tecniche per le costruzioni di cui al Decreto Ministeriale 14 gennaio 2008*. Suppl. Ordinario n. 27 alla G.U. n. 47 del 26-02-2009, 2009.

[33] P.B. Lourenço, Recent advances in masonry structures: micromodelling and homogeneization. U. Galvanetto, M.H. Ferri Aliabadi eds. *Multiscale modeling in solid mechanics: computational approaches*. Imperial College Press, London, U.K., 251-294, 2009.

[34] P.B. Lourenço, N. Mendes, L.F. Ramos, D.V. Oliveira. On the analysis of masonry structures without box behavior. *International Journal of Architectural Heritage: Conservation, Analysis, and Restoration*, **5**(4), 369-382, 2011.

COMPDYN 2015
5th ECCOMAS Thematic Conference on
Computational Methods in Structural Dynamics and Earthquake Engineering
M. Papadrakakis, V. Papadopoulos, V. Plevris (eds.)
Crete Island, Greece, 25–27 May 2015

MODELLING OF DIAGONAL COMPRESSION MASONRY WALLETS BY FINITE ELEMENTS WITH EMBEDDED DISCONTINUITIES

Gelacio Juárez-Luna[1] and Arturo Tena-Colunga[2]

[1,2] Departamento de Materiales, Universidad Autónoma Metropolitana
San Pablo 180, Azcapotzalco, México D.F. 02200, Mexico
e-mail: [1]gjl@azc.uam.mx, [2]atc@azc.uam.mx

Keywords: Wallets, Combined Masonry, Embedded Discontinuities, Cracking, Damage.

Abstract. *This paper investigates the behaviour of small square masonry subassembly, wallets, subject to axial compression, involving their crack pattern and the shear stress-shear strain curves. Masonry and mortar were discretized with quadrilateral finite elements with embedded discontinuities, which have three degrees of freedom per node. The constitutive behaviours of blocks, bricks and mortar consider the softening deformation after reaching a failure surface. The numerical modelling of experimental tests for combined masonry wallets were performed in the Finite Element Analysis Program (FEAP). The computed shear stress-shear strain curves with finite elements with embedded discontinuities showed a fairly good agreement in terms of the initial stiffness, strength, ultimate load and dissipative behaviour; also, the computed cracking patter is congruent with the experimental one.*

1 INTRODUCTION

The modelling of masonry structures is a demanding task in structural engineering. This laborious work is attributed to the geometry and to the constitutive behaviour of bricks and mortar materials, which include anisotropy and nonlinearity. The different numerical procedures could be summarized in three levels of refinement [2][3]: 1) macro-modelling, bricks, mortar and the brick–mortar interface are smeared out in a homogeneous continuum; 2) simplified micro-modelling, bricks are represented as fictitious expanded bricks by continuum elements with the same size as the original bricks dimensions plus the real joint thickness. The mortar joint is also discretized with interfaces of zero thickness; and 3) detailed micro-modelling, units and mortar in the joints are discretized by continuum elements whereas the brick–mortar interface is represented by discontinuous elements.

This papers uses a kind of the detailed micro-modelling, where perfect bond in the brick-mortar interface was assumed. Small square masonry wallets, subject to axial compression, were modelled. Bricks, block and mortar were discretized with hexahedral finite elements with embedded discontinuities (FEED). The constitutive behaviour of blocks, bricks and mortar considers the softening deformation after reaching a discrete failure surface. The computed shear stress-shear strain curves with FEED are stiffer than the experimental curves, a fact attributed that the sliding in the brick-mortar interface was neglected.

2 EMBEDDED DISCONTINUITY MODEL

2.1 Variational formulation

The FEED are formulated from an energy functional which has the displacement, **u**, and the displacement jump [|**u**|] as independent variable ([1], [5], [6], [12]). This functional is given by:

$$\Pi\left(\mathbf{u},\left[\left|\mathbf{u}\right|\right]\right)=\int_{\Omega\setminus S}\left[\Psi(\bar{\boldsymbol{\varepsilon}}^{u})-\mathbf{b}\cdot\mathbf{u}\right]d\Omega-\int_{\Gamma_{\sigma}}\mathbf{t}^{*}\cdot\mathbf{u}\,d\Gamma+\int_{\Gamma_{S}}\phi_{S}(\left[\left|\mathbf{u}\right|\right])d\Gamma \tag{1}$$

where the free energy density, $\Psi(\bar{\boldsymbol{\varepsilon}}^{u})$, depends on the continuous strain field $\bar{\boldsymbol{\varepsilon}}^{u}$, and the free discrete energy density, $\Psi_{S}(\left[\left|\mathbf{u}\right|\right])$, depends on the jump. These energy densities are respectively given by:

$$\Psi(\bar{\boldsymbol{\varepsilon}}^{u})=\int_{0}^{\bar{\boldsymbol{\varepsilon}}}\boldsymbol{\sigma}(\bar{\boldsymbol{\varepsilon}})\,d\bar{\boldsymbol{\varepsilon}} \tag{2}$$

$$\phi_{S}(\left[\left|\mathbf{u}\right|\right])=\int_{0}^{\left[\left|\mathbf{u}\right|\right]}\mathbf{T}_{S}(\left[\left|\mathbf{u}\right|\right]_{n,s})\,d\left[\left|\mathbf{u}\right|\right] \tag{3}$$

where the elastic stresses, $\boldsymbol{\sigma}$, are defined by:

$$\boldsymbol{\sigma}=\mathbf{C}\;:\;\bar{\boldsymbol{\varepsilon}} \tag{4}$$

and $\mathbf{T}_S$ is the traction vector at the discontinuity.

2.2 Approximation of the displacement and strain fields

The regular displacement field is approximated by:

$$\hat{\mathbf{u}} = \mathbf{Nd} \tag{5}$$

where **N** is the standard vector of shape functions of the element

$$\mathbf{N} = \sum_{i=1}^{i=n} N_i^{(e)} \tag{6}$$

and, **d**, is the nodal displacement vector. The function, $M_S(\mathbf{x})$, is defined in the finite element approximation as:

$$M_S^e(\mathbf{x}) = H_S^e\left(\mathbf{x}\right) - \phi^e \tag{7}$$

where ϕ^e is constructed by:

$$\phi^e = \sum_{i^+=1}^{n_e^+} N_{i^+} \tag{8}$$

where N_{i^+} are the shape functions corresponding to the nodes placed on Ω^+ of the finite element which contains the discontinuity. The displacement is given by

$$\mathbf{u} = \mathbf{Nd} + \underbrace{M_S^e}_{\mathbf{N}_c}\left[\left|\mathbf{u}\right|\right]_{x,y} \tag{9}$$

The continuous strain field is approximated as:

$$\overline{\boldsymbol{\varepsilon}} = \mathbf{B}\cdot\mathbf{d} - \underbrace{\nabla\phi^e}_{\mathbf{B}_c}\cdot\left[\left|\mathbf{u}\right|\right]_{x,y} \quad \forall\mathbf{x}\in\Omega\ /\ S \tag{10}$$

Where **B**, is the standard strain interpolation matrix, containing the derivatives of the standard shape functions ∂(**Nd**)=**Bd**.

The equilibrium equations corresponding to this formulation are obtained by substituting Eqs. (9) and (10) into the energy functional of Eq. (1), and setting the derivatives with respect to the independent variables (**d** and [|**u**|]) to zero,

$$\frac{\partial\Pi}{\partial\mathbf{d}} = 0 = \int_{\Omega\setminus S}\mathbf{B}^T\boldsymbol{\sigma}\left(\overline{\boldsymbol{\varepsilon}}\right)d\Omega - \int_{\Omega}\mathbf{N}^T\cdot\mathbf{b}\,d\Omega - \int_{\Gamma_\sigma}\mathbf{N}^T\cdot\mathbf{t}^*d\Gamma \tag{11}$$

$$\frac{\partial\Pi}{\partial\left[\left|\mathbf{u}\right|\right]} = 0 = -\int_{\Omega\setminus S}\mathbf{B}_c^T\boldsymbol{\sigma}\left(\overline{\boldsymbol{\varepsilon}}\right)d\Omega + \int_{\Gamma_S}\mathbf{T}_{x,y}d\Gamma \tag{12}$$

In Eqs. (11) and (12), $\boldsymbol{\sigma}\left(\overline{\boldsymbol{\varepsilon}}\right)$ and $\mathbf{T}_{x,y,z}$ are nonlinear, their respective linearizations with Taylor series give [5]:

$$\begin{bmatrix} \int_{\Omega\setminus S}\mathbf{B}^{\mathbf{T}}\cdot\mathbf{C}\cdot\mathbf{B}\,d\Omega & -\int_{\Omega\setminus S}\mathbf{B}^{\mathbf{T}}\cdot\mathbf{C}\cdot\mathbf{B}_c\,d\Omega \\ -\int_{\Omega\setminus S}\mathbf{B}_c^{\mathbf{T}}\cdot\mathbf{C}\cdot\mathbf{B}\,d\Omega & -\int_{\Omega\setminus S}\mathbf{B}_c^{\mathbf{T}}\cdot\mathbf{C}\cdot\mathbf{B}_c\,d\Omega + \int_{\Gamma_S}\mathbf{R}^T\cdot\mathbf{T}\cdot\mathbf{R}\,d\Gamma \end{bmatrix}^{(n,0)} \begin{Bmatrix} \Delta d \\ \Delta\left[\left|\mathbf{u}\right|\right]_{x,y} \end{Bmatrix}^{(n,1)} = \begin{Bmatrix} R_1 \\ R_2 \end{Bmatrix}^{(n,0)} \tag{13}$$

where **R** has the direction cosines, R_1 and R_2 are defined as:

$$R_1 = F_{ext}^{(n)} - \int_{\Omega\setminus S}\mathbf{B}^T\boldsymbol{\sigma}\left(\overline{\boldsymbol{\varepsilon}}\right)d\Omega^{(n,0)} \tag{14}$$

$$R_2 = \int_{\Omega\setminus S}\mathbf{B}_c^T\boldsymbol{\sigma}\left(\overline{\boldsymbol{\varepsilon}}\right)d\Omega^{(n,0)} - \int_{\Gamma_S}\mathbf{T}_{x,y}d\Gamma^{(n,0)} \tag{15}$$

To reduce the size of the system given in Eq. (13), the additional degrees of freedom, Δ[|**u**|], may be condensed. In Eq. (14), R_1 means the equilibrium between the external and the internal forces in the domain $\Omega\setminus S$, whereas R_2, in Eq. (15), the equilibrium between the forces in the domain $\Omega\setminus S$ and forces in the discontinuity Γ_S.

Tractions at the discontinuity are:

$$\mathbf{T}_{x,y,z} = \frac{1}{A_d}\int_{\Omega\setminus S}\mathbf{B}_c^T\boldsymbol{\sigma}\,d\Omega \tag{16}$$

which expressed in the local system becomes

$$\mathbf{T}_{n,s,t} = \frac{1}{A_d}\mathbf{R}\int_{\Omega\setminus S}\mathbf{B}_c^T\boldsymbol{\sigma}d\Omega \tag{17}$$

The definitions of the traction vector in Eqs. (16) and (17) are dependent on the discontinuity area, A_d, and the direction cosines to the normal vector **n**, as shown in Figure 1.

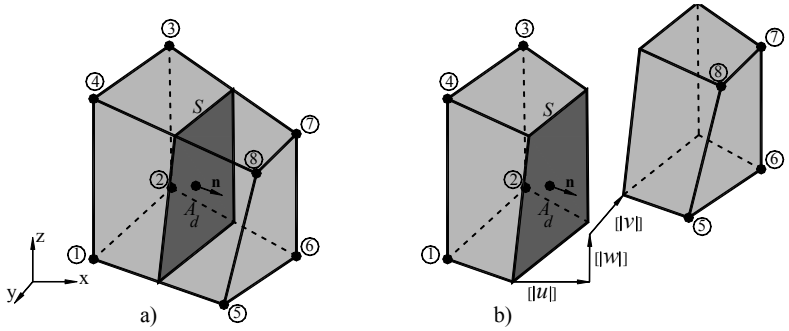


Figure 1: Finite element: a) discontinuity area and b) displacement jumps.

The FEED, given in Eq. (13), were implemented in the finite element analysis program (FEAP), developed by [10]. These FEED capture a discontinuity surface at their geometric centre, which is placed perpendicular to the major principal stress direction. The discontinuity surfaces of the surrounding elements are not aligned and the displacement jump is constant into these FEED. It is important to say that these elements do not have problems of spurious shear deformations and they satisfied the following requirements: (1) equilibrium, traction continuity across the discontinuity interface and (2) kinematics, free relative rigid body motions of the two portions of an element split up by a discontinuity [5].

3 CONSTITUTIVE MODELS

3.1 Concrete

The concrete and mortar behaviour were modelled with a discrete damage model, which has different threshold values under tension and compression, as shown in Figure 2a. This model is equipped with softening after reaching the ultimate tensile strength, T_{ut}, or the ultimate compressive strength, T_{uc}, shown in Figure 2b. This model is defined by the following equations:

$$
\begin{array}{ll}
\text{Discrete free energy density} & \phi\left(\left[\left|\mathbf{u}\right|\right],\bar{\alpha}\right)=\left(1-\omega\right)\phi_0\left(\bar{\alpha}\right),\begin{cases}\phi_0\left(\left[\left|\mathbf{u}\right|\right]\right)=\frac{1}{2}\left[\left|\mathbf{u}\right|\right]\cdot\mathbf{Q^e}\cdot\left[\left|\mathbf{u}\right|\right]\\ \mathbf{Q^e}=\mathbf{n}\cdot\mathbf{C}\cdot\mathbf{n}\end{cases}\\
\text{Constitutive equation} & \mathbf{T}=\frac{\partial\phi\left(\left[\left|\mathbf{u}\right|\right],\bar{\alpha}\right)}{\partial\left[\left|\mathbf{u}\right|\right]}=(1-\omega)\mathbf{Q^e}\cdot\left[\left|\mathbf{u}\right|\right]\\
\text{Damage variable} & \omega=1-\frac{\bar{q}\left(\bar{\alpha}\right)}{\bar{\alpha}};\ \ \omega\in\left[-\infty,1\right]\\
\text{Evolution law} & \dot{\bar{\alpha}}=\dot{\bar{\lambda}}=\frac{\partial}{\partial t}\left(\bar{\alpha}\right),\ \ \bar{\alpha}\in\left[0,\infty\right]\\
\text{Damage criterion} & f(\mathbf{T},\bar{q})=\tau_{\mathbf{T}}-\bar{q};\ \ \tau_{\mathbf{T}}=\left\|\mathbf{T}\right\|_{\mathbf{Q^{e-1}}}=\sqrt{\mathbf{T}\cdot\mathbf{Q^{e^{-1}}}\cdot\mathbf{T}}\\
\text{Hardening rule} & \dot{\bar{q}}\left(\bar{\alpha}\right)=\bar{H}\dot{\bar{\alpha}};\quad \bar{H}=\bar{q}'\left(\bar{\alpha}\right)\le 0\\
\text{Loading-unloading conditions} & f\le 0;\quad \bar{\lambda}\ge 0;\quad \bar{\lambda}f=0;\quad \bar{\lambda}\dot{f}=0\ \text{(consistency)}
\end{array}
\tag{18}
$$

where ϕ is the discrete free energy density, $\mathbf{T}$ is the traction vector. The damage variable ω is defined in terms of the hardening/softening variable $\dot{\bar{q}}$, which is dependent on the hardening/softening parameter. The damage multiplier $\bar{\lambda}$ determines the loading-unloading conditions, the function $f(\mathbf{T},\bar{q})$, bounds the elastic domain defining the damage surface in the tractions space. The tangent constitutive equation, in terms of rates from the model in Eq. (18), is:

$$\dot{\mathbf{T}}=\mathbf{C}_d^T\cdot\left[\left|\dot{\mathbf{u}}\right|\right] \tag{19}$$

where $\mathbf{C}_d^T$ is the tangent constitutive operator, relating the traction and the displacement jump of the nonlinear loading interval, which is defined by

$$\mathbf{C}_d^T=\left(1-\omega\right)\mathbf{Q^e}-\frac{\bar{q}-\bar{H}\bar{\alpha}}{\bar{\alpha}^3}\left(\mathbf{Q^e}\cdot\left[\left|\mathbf{u}\right|\right]\otimes\left[\left|\mathbf{u}\right|\right]\cdot\mathbf{Q^e}\right) \tag{20}$$

and for the elastic loading and unloading interval ($\dot{d}=0$ and $\dot{\omega}=0$):

$$\mathbf{C}_d^T=\left(1-\omega\right)\mathbf{Q^e} \tag{21}$$

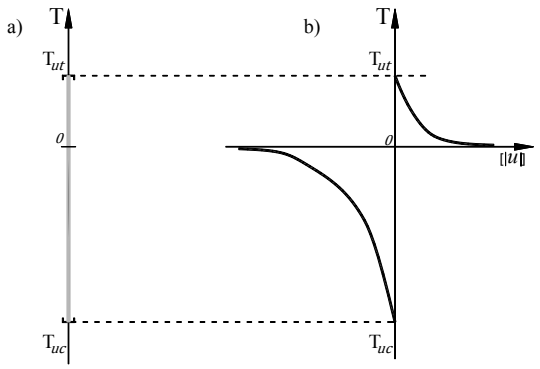


Figure 2: 1D discrete damage model with softening: a) elastic space and b) traction-displacement jump curve.

4 NUMERICAL MODELS

4.1 Description of the wallets

To define an indirect shear strength v_m^* for design and the shear modulus G_m^* under diagonal tension, small square masonry subassemblies, called wallets, can be tested under axial compression according to NTCM-2004 [7], as shown in Figure 3. This test is commonly performed using an universal press machine [11].

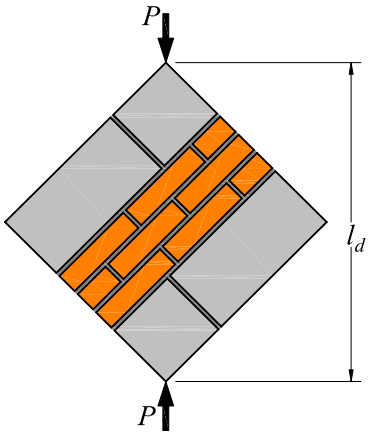


Figure 3: Axial compression test of NTCM-2004.

The shear stress τ was computed by the following relationship:

$$\tau = \frac{P}{l_d t} \tag{22}$$

where P is the vertical load, l_d is the diagonal length, measured from the bottom to the top of the wallet and t is the thickness of the wallet, as shown in Figure 3.

The shear strain γ was computed as follows:

$$\gamma = |\varepsilon_c| + |\varepsilon_t| \tag{23}$$

$$\varepsilon_c = \frac{\delta_c}{lo_c}; \quad \varepsilon_c = \frac{\delta_c}{lo_t} \tag{24}$$

where ε_c is the average of the compression diagonal strain, ε_t is the average of the tension diagonal strain, δ_c is the shortening which is measured along the length of the calibrated compression diagonal, δ_t is the shortening which is measured along the length of the calibrated tension diagonal, lo_c is the calibrated length between transducers of the compression diagonal and lo_t is the calibrated length between transducers of the tension diagonal. Both lengths, lo_c and lo_t, were measured before the test as shown in Figure 4.

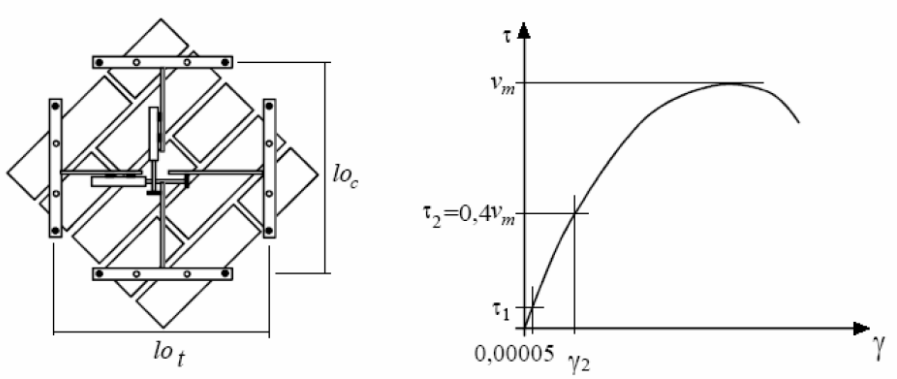


Figure 4: Computation of the shear stress (adapted from [9]).

In this paper, only two arrangements shown in Figure 5 were modelled, with mortar type I, although others two arrangement with mortar type II were also tested by [11]. The mechanical properties of the blocks are: Young´s modulus E=1.1 GPa, Poisson ratio υ=0.2, ultimate tensile strength σ_{tu}=0.84 MPa, ultimate compressive strength σ_{uc}=4.26 MPa and fracture energy density G_f=15.2 N/m. The mechanical properties of the fired clay bricks are: Young´s modulus E=2.0 GPa, Poisson ratio υ=0.1, ultimate tensile strength σ_{tu}=2.02 MPa, ultimate compressive strength σ_{uc}=10.1 MPa and fracture energy density G_f=13.6 N/m. The mechanical properties of the mortar are: Young´s modulus E=2.0 GPa, Poisson ratio υ=0.2, ultimate tensile strength σ_{tu}=4.82 MPa, ultimate compressive strength σ_{uc}=24.1 MPa and fracture energy density G_f=7.5 N/m. The fracture energy density and Young´s modulus were computed by [8].

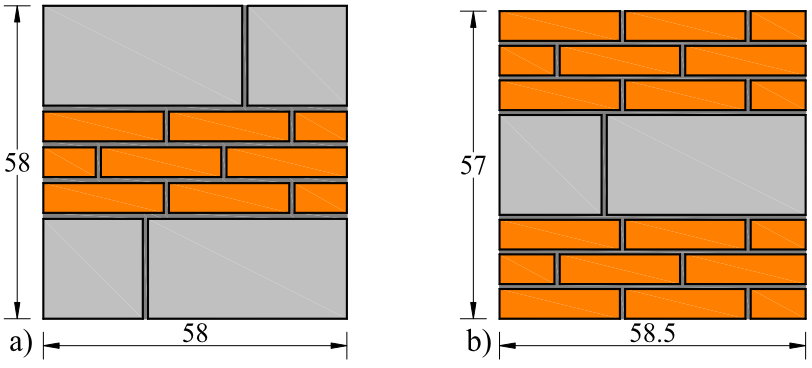
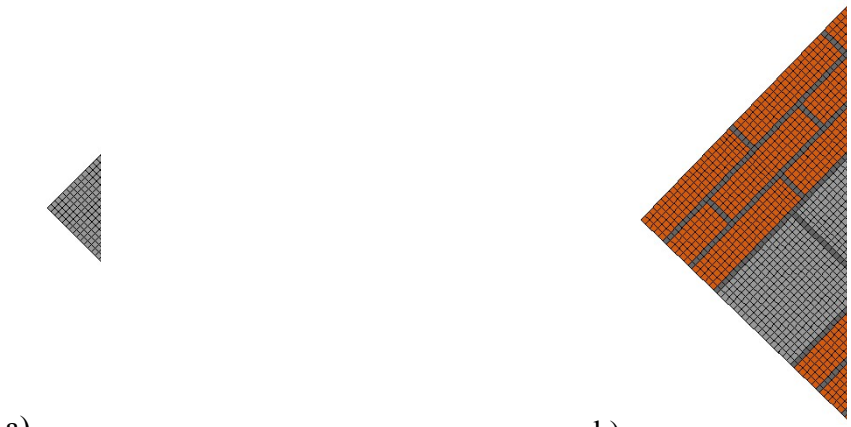


Figure 5: Small wallet arrangements: a) 1 and b) 2 (adapted from [11]).

4.2 Numerical test

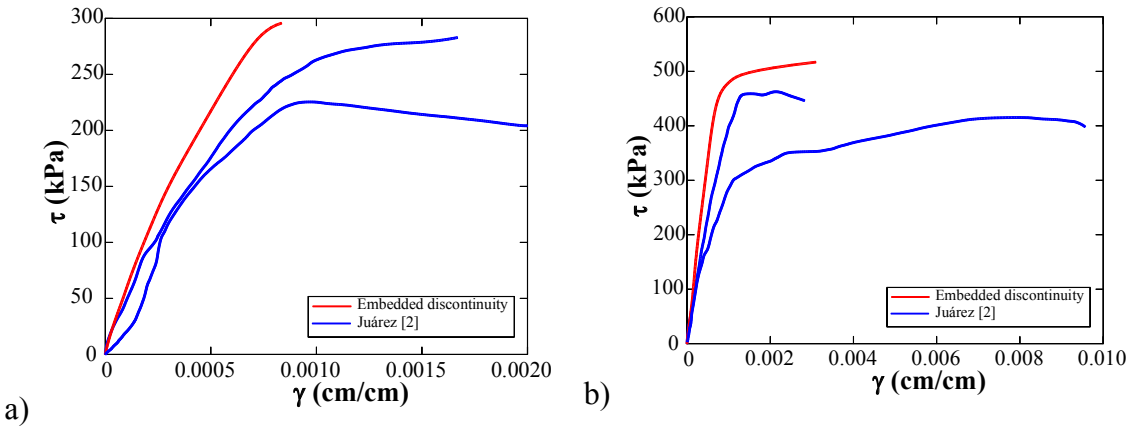
The wallet of the arrangement 1 was discretized with quadrilateral elements, 2052 elements for blocks, 840 elements for bricks and 298 for joints as shown in Figure 6a; whereas the wallet of the arrangement 2 was discretized with 1008 elements for blocks, 1650 elements for bricks and 298 for joints as shown in Figure 6b. Homogenization techniques were not use, so the mechanical properties of the blocks, bricks and joints were assigned to the corresponding discretized elements.



a) b)

Figure 6: Discretization of the wallets, arrangement: a) 1 and b) 2.

The average shear stress *vs* shear strain curves are shown in Figure 7. The computed curve with FEED shows numerical results, which are congruent at the ascending branch with the experimental curve reported by [4]. It is observed that both curves are similar at the beginning; however, the curves computed with FEED are stiffer that the experimental curves. This difference may be attributed to the fact that the sliding between mortar and blocks or bricks were not considered.



a) b)

Figure 7: Shear stress *vs* shear strain for arrangement a) 1 and b) 2

In both arrangements, cracking initiated at both corners, on the top and on the bottom, growing to the centre. Discontinuities along bed joints occurred in arrangement 1 as shown in Figure 8a, whereas discontinuities along the diagonal occurred in the arrangement 2 as shown in Figure 8. These crack patterns at both arrangements were congruent with the experimental results reported by [4] and [11].

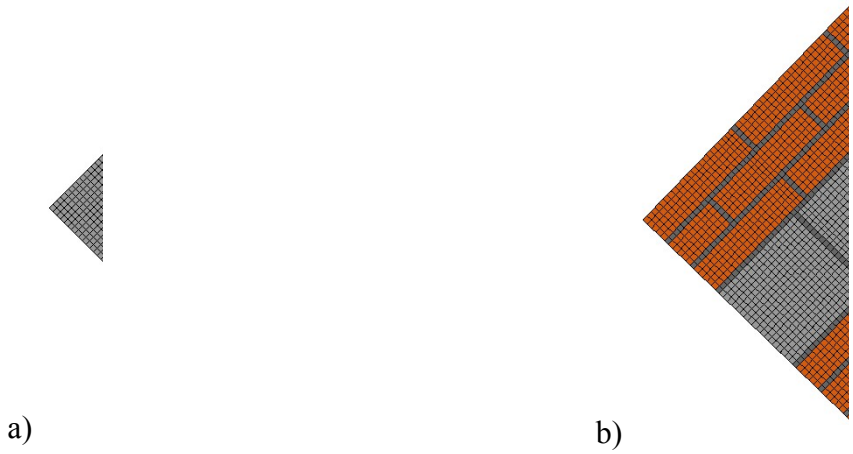


Figure 8: Cracking patterns for arrangement: a) 1 and b) 2

5 CONCLUSIONS

- The FEED with a discrete damage model were used for modelling wallets under compression load, involving their crack pattern and the shear stress-shear strain capacity curve. The discrete damage model considers a constitutive behaviour equipped with softening for the blocks, bricks and joints elements limited for a damage surface.
- The coupling of bricks or block with the mortar yield a shear stress- shear strain curve stiffer than the experimental curves, because sliding is neglected.
- In the wallet 1, discontinuities occurs along bed joints, whereas in the wallet 2, discontinuities occur along the diagonal, which are congruent with the experimental results.
- The ultimate shear stresses computed with FEED were greater than experimental values. These effect is attributed to absence of the sliding in the brick–mortar interface. Forcoming work will include the sliding of brick–mortar interfaces.

Acknowledgements

The first author acknowledges the financial support given by CONACYT under the agreement number I010/176/2012, in the context of the research project: "Analysis and design of concrete slabs". Both authors acknowledge the sponsorship by the project 269222 entitled Analysis and Design of Earthquake Resistant Structures (ADERS) and the support given by the Universidad Autónoma Metropolitana.

REFERENCES

[1] J. Alfaiate, A. Simone, L.J. Sluys, Non-homogeneous displacement jumps in strong embedded discontinuities. *International Journal of Solids and Structures*, **40(21)**, 5799-5817, 2003.

[2] P.G. Asteris, D.M. Cotsovos, C.Z. Chrysostomou, A. Mohebkhah, G.K. Al-Chaar, Mathematical micromodeling of infilled frames: state-of-the-art. *Engineering Structures*, 56, 1905-1921, 2013.

[3] P.G. Asteris, M.P. Chronopoulos, C.Z. Chrysostomou, H. Varum, V. Plevris, N. Kyriakides, V. Silva, Seismic vulnerability assessment of historical masonry structural systems. *Engineering Structures*, **62-63**,118-134, 2014

[4] A. Juárez, *Mecanismos de resistencia y de deformación de muros de mampostería combinada y confinada*. M. Sc. Thesis. División de Ciencias Básicas e Ingeniería, Universidad Autónoma Metropolitana Azcapotzalco, 2008. (In Spanish).

[5] G. Juárez-Luna, G.A. Ayala, Improvement of some features of finite elements with embedded discontinuities. *Engineering Fracture Mechanics*, **118**, 31-48, 2014.

[6] H.R. Lotfi, P. Shing, Embedded representation of fracture in concrete with mixed finite elements. *International Journal for Numerical Methods in Engineering*, **38(8)**, 1307-1325, 1995.

[7] NTCM-2004, Normas Técnicas Complementarias para Diseño y Construcción de Estructuras de Mampostería. *Gaceta Oficial del Distrito Federal*, October, 2004. (in Spanish)

[8] R. Illampas, Personal communication, 2015.

[9] V. Salinas, *Comportamiento ante cargas laterales de muros de mampostería combinada unidos con morteros de autoconstrucción*. M. Sc. Thesis. División de Ciencias Básicas e Ingeniería. Universidad Autónoma Metropolitana Azcapotzalco, 2008. (In Spanish).

[10] L.R. Taylor, A finite element analysis program (FEAP) v8.2. Department of Civil and Environmental Engineering, University of California at Berkeley, Berkeley, CA 2008.

[11] A. Tena-Colunga, A. Juárez-Ángeles, V.M. Salinas-Vallejo, Cyclic behaviour of combined and confined masonry walls. *Engineering Structures*, **31(1)**, 240-259, 2009.

[12] G.N. Wells, L.J.Sluys, A new method for modelling cohesive cracks using finite elements. *International Journal for Numerical Methods in Engineering*, **50(12)**, 2667-2682, 2001.

COMPDYN 2015
5th ECCOMAS Thematic Conference on
Computational Methods in Structural Dynamics and Earthquake Engineering
M. Papadrakakis, V. Papadopoulos, V. Plevris (eds.)
Crete Island, Greece, 25–27 May 2015

ON THE SEISMIC RISK OF MEDIEVAL ITALIAN MASONRY TOWERS

Gianni Bartoli[1], Michele Betti[2], and Silvia Monchetti[3]

[1] Department of Civil and Environmental Engineering,
University of Florence
via di S. Marta 3 – I-50139 Florence – Italy
e-mail: gbartoli@dicea.unifi.it

[2] Department of Civil and Environmental Engineering,
University of Florence
via di S. Marta 3 – I-50139 Florence – Italy
e-mail: mbetti@dicea.unifi.it

[3] Department of Civil and Environmental Engineering,
University of Florence
via di S. Marta 3 – I-50139 Florence – Italy
e-mail: silvia.monchetti@dicea.unifi.it

Keywords: Historic masonry tower, Italian guidelines, Seismic assessment, Finite element modelling, Nonlinear static analysis, Linear time-history analysis.

Abstract. *The paper, after a brief discussion of the methodologies of the research project RiSEM (Seismic Risk of Monumental Buildings), a research project started in 2011 and concluded at the end of 2013, discusses on the seismic assessment of historic masonry towers according to the Italian "Guidelines for the assessment and mitigation of the seismic risk of the cultural heritage". The RiSEM project aimed at developing and testing innovative and expeditious methodologies (i.e. without direct contact with the masonry building) to evaluate all the main structural features of the monumental buildings that are required for the assessment of their seismic safety. As a relevant case study the historic towers of the city of San Gimignano (Italy) in the UNESCO list of the World Cultural Heritage was selected, and the paper summarizes the analyses and the results obtained on three of the analysed towers. The Italian Guidelines identify a methodology of analysis based on three different levels of evaluation, according to an increasing path of knowledge (or requirement) of the structure, namely: LV1 (analysis at territorial level), LV2 (local analysis) and LV3 (global analysis). The paper, summarizing the results obtained for two of the above three levels, highlights a few issue concerning the seismic risk of historic masonry tower.*

1 INTRODUCTION

The quality of the life of a community is strongly affected by the safety and the functionality of the buildings and the infrastructures that constitute the urban environment [1] [2]. In case of Italy (and Tuscany in particular), where the territory is characterized by a massive presence of historical and monumental buildings, life quality is strongly connected with the presence and the functionality of these historical structures. These buildings, as recently demonstrated by the earthquakes of L'Aquila (April 2009) [3] [4] and Reggio Emilia (May 2012) [5], are extremely vulnerable to seismic loads. In addition, although the earthquake which affected L'Aquila was a seismic event of exceptional power (the main shock had a moment magnitude equal to 6.3 MW, with PGA equal to 0.68g) not infrequently damage, and in some cases collapse, of monumental buildings or parts of them were also recorded as a result of not extremely violent earthquakes (e.g. the damage to the Basilica of San Francesco d'Assisi after the seismic shock in November, 2007). It is then clear the need of developing and test methods of investigation and analysis that may allow to carry out a fairly expeditious seismic risk quantification, developing at the same time technologies that can be used with a certain repetitiveness and on a territorial scale, to provide general guidelines to establish priority of intervention to protect historical monuments.

Among the different typologies of historic monumental buildings, the masonry towers represent a hallmark of many Italian and European town centres. Their construction, in the most ancient cases, dates back to the late-medieval age, and today there are many historic towns that owe their notoriety, and even their economic welfare, to their towers. This is the case of the town of San Gimignano, a small medieval village between Florence and Siena in Tuscany included in the UNESCO World Cultural Heritage list since 1990. In its period of maximum splendour San Gimignano had over seventy towers-houses (some as high as 50 m). Today only 13 of these towers have survived.

The seismic risk of the historic towers of San Gimignano was recently analysed, as an illustrative case study, within the 2-year research project RiSEM "Seismic Risk of Monumental Buildings". The project aimed at developing and testing expeditious and innovative methodologies (i.e. without direct contact with the masonry construction) to assess the structural data needed for the subsequent evaluation of the seismic risk. The whole project, funded by the Tuscany Region, was developed by a consortium which included two Italian Universities (Florence and Siena) through four University Departments from different scientific areas. The methodology adopted in the research was based on the following elements: a) assessment of seismic hazard and soil-structure interactions; b) acquisition of the geometric characteristics and reconstruction of the historical evolution of masonry buildings; c) evaluation of the static and dynamic behaviour of towers (structural identification) through non-conventional and innovative investigation techniques; d) evaluation of seismic vulnerability (through the definition of proper limit states aimed at identifying the safety levels for cultural heritage, considering both the problem of preservation and safety); and finally e) evaluation of the seismic risk. The final goal of the project was therefore to develop guidance for the assessment of the seismic vulnerability of historic masonry towers, according to the Italian Recommendations (NTC2008 [6]).

The town of San Gimignano was identified as an exemplary case study due to the typological structural homogeneity of its historic tall masonry towers (in fact the presence of several buildings with a similar dynamic behaviour makes the case study particularly significant for "testing" new techniques of investigation and analysis).

The seismic assessment of the towers, was developed according the provisions of the Italian Guidelines for the assessment and mitigation of the seismic risk of the Cultural

Heritage (DPCM2011 [7]). The Guidelines propose a methodology of analysis based on three different levels of evaluation, according to an increasing knowledge of the structure. The first level of analysis (LV1, analysis at territorial scale) allows to evaluate the collapse acceleration of the structure by means of simplified models based on a limited number of geometrical and mechanical parameters (and qualitative tools such as visual inspections). The second level (LV2, local analysis) is based on a kinematic approach performed to analyse the local collapse mechanisms that can develop on several macro-elements. The identification of proper macro-elements is based on the knowledge of structural details of the building (cracking pattern, construction technique, connections between the architectonic elements, etc). The last level of evaluation (LV3, global analysis) requires a global analysis of the whole building under seismic loading by suitable numerical models. Compared to the previous two levels, the LV3 should be the most accurate but it requires a large amount of input data and, depending on the employed numerical approach, great computational effort.

The paper, as a first step toward the synthesis of the results obtained within the project, summarizes the analysis executed and the results obtained for three of the analysed towers: the Becci tower, the Coppi-Campatelli tower and the Chigi tower (Figure 1). After a short description of the towers, the methodology employed to cover the unknowns deriving from the knowledge process and the performed parametric analyses are critically discussed.

2 THE HISTORIC TOWERS OF SAN GIMIGNANO

The historic towers of San Gimignano date back to XII-XIII century. The sustaining walls of the towers are multi-leaf stone masonry walls with the internal and external face usually made with the same typology of material (and also, presumably, the same thickness); the internal, and thick, core is composed of heterogeneous stone blocks tied by a good mortar.

A section of the three analysed towers, together with the base cross-section, is reported in Figure 1. Slenderness of the towers ranges between 3.4 (Coppi-Campatelli tower) and 5.9 (Becci tower) and the thickness of the walls is almost uniform for all the three towers. At the lower level the towers are largely incorporated into the neighbouring buildings and hence the lower sections present several openings (in most cases subsequent to the tower construction) to allow communication with the confining buildings.

The internal and external faces of the towers are made by a local cavernous limestone except the upper part of the Chigi tower that was built with masonry bricks (Table 1). Due to the lack of information (tests, core drilling, mineralogical surveys etc.), apart from the visual inspection, the mechanical properties of the walls were characterized by taking into account the provisions of the Circular 2009 [8]. In particular several typologies of masonry walls were considered (Table 1). The first is the scheme of uncut stone masonry with facing walls of limited thickness and infill core (USM). The second is the scheme of soft stone masonry (tuff, limestone, etc.) (SSM). The third is the scheme of dressed rectangular stone masonry (DRS). The fourth, characterizing only the upper part of the Chigi tower, is the scheme of full brick masonry with lime mortar (FBM). The reference intervals for the value of the mechanical properties reported in the table C8A.1 of the Circular 2009 were selected according to the mechanical characteristics of the masonry typologies existing in the Italian territory. These values refer to masonry with mortar of poor mechanical characteristics. Furthermore, the values proposed by the Circular 2009 assume, in case of multi-leaf stone masonry, disconnected facing walls and/or lack of systematic transverse connecting elements (or interlocking between the masonry facing walls). To account for good quality mortar, for the presence of a thick inner core and for the presence of thin joints the correction factors proposed by the Circular 2009 (table C8A.2.) were employed.

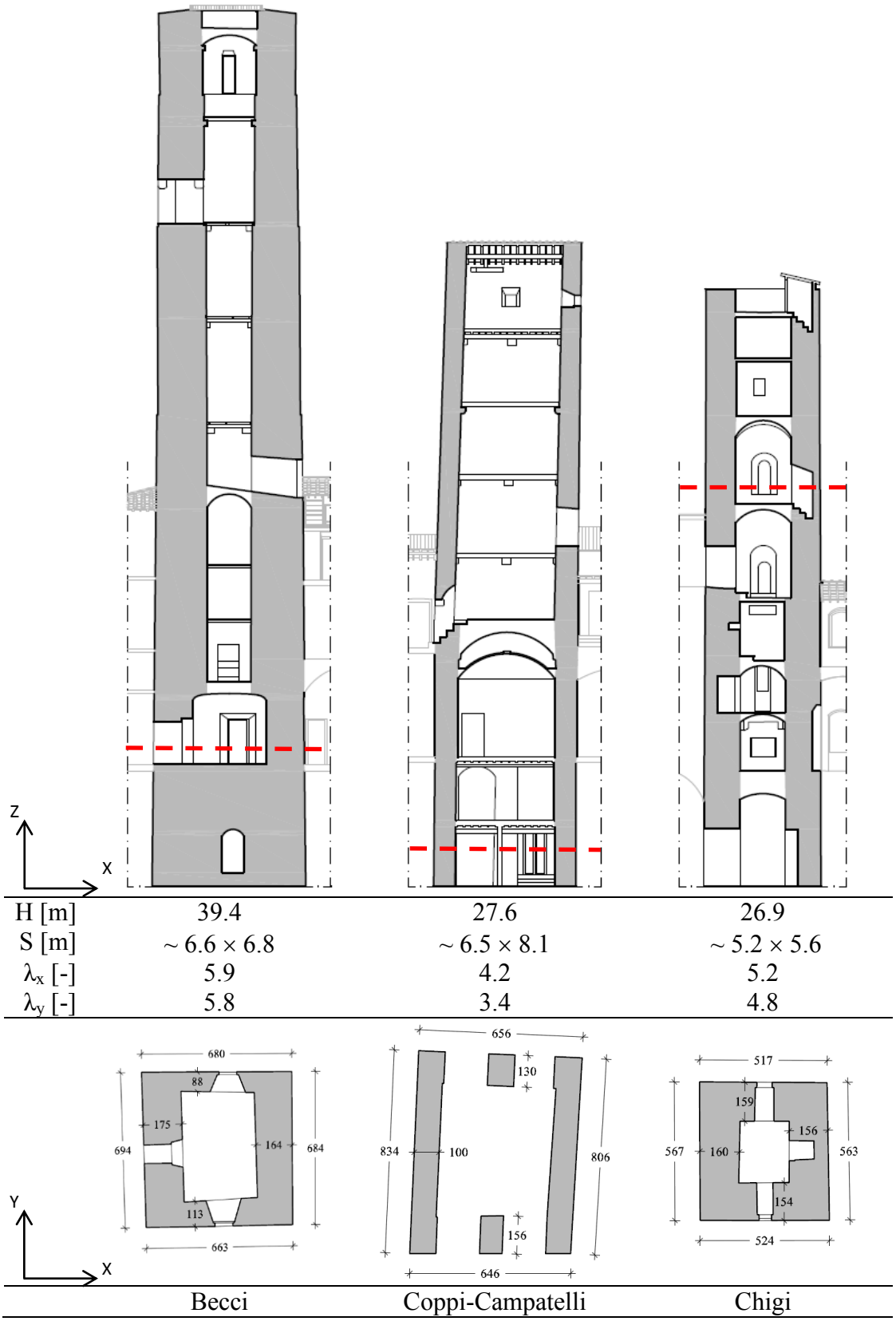


Figure 1: Towers sections and cross sections (H – height, S – base section dimension, $\lambda_{x,y}$ – slenderness).

Tower	Masonry typology	Tower walls	View
Becci	**D**: Soft stone masonry (SSM).	internal and external faces similar / thick inner core / good quality mortar.	
Coppi-Campatelli	**B:** Uncut stone masonry with facing walls of limited thickness and infill core (USM). **E**: Dressed rectangular stone masonry (DRS).	internal and external faces similar / thick inner core / good quality mortar.	
Chigi (lower part) Chigi (upper part)	**D**: Soft stone masonry (SSM). **F**: Full brick masonry with lime mortar (FBM).	internal and external faces similar / thick inner core / good quality mortar. internal and external faces similar / thick inner core / good quality mortar.	

Table 1: Visual characterization of the masonry typologies.

Type of masonry	Mechanical characteristics			Correction factors		
	f_m [N/cm^2]	τ_0 [N/cm^2]	E [N/mm^2]	thick or poor internal core	good quality of the mortar	thin joints
B	200 300	3.5 5.1	1020 1440	0.8	1.4	1.2
D	140 240	2.8 4.2	900 1260	0.9	1.5	1.5
E	600 800	9.0 12.0	2400 3200	0.7	1.2	1.2
F	240 400	6.0 9.2	1200 1800	0.7	1.5	1.5

Table 2: Mechanical properties evaluated according to [8]
(f_m – compressive strength, τ_0 – shear strength, E - modulus of elasticity).

Specifically, considering that a limited level of knowledge (KL1 according to the Code [6], corresponding to a confidence factor of 1.35) was reached, the standard prescribes to employ as resistance parameters (f_m and τ_0) the minimum values of the ranges given in table C8A.2.1 of the Circular 2009, while for the elastic moduli (E and G) the mean values were assumed. According to what the standards suggest, and in the absence of more accurate investigations, the correction factors (table C8A.2. Circular 2009) reported in Table 2 were applied to the mechanical parameters.

The performed estimation of the masonry mechanical parameters through literature results was in accordance with the project's goals, aiming the research to test expeditious techniques to assess the seismic risk of monumental buildings without direct contact with the masonry construction. In this respect the selected types of masonry (Table 1), similar for morphology to those visually detected in situ, were assumed as lower and upper bound for the actual masonry parameters to be employed in the subsequent analysis models.

3 RISK ASSESSMENT

The evaluation of the seismic risk of the tower was performed according to the three levels of evaluation introduced by the Italian DPCM2011 ("Guidelines for the assessment and mitigation of the seismic risk of the cultural heritage" [7]). The Guidelines, that represent an innovative tool in the European context, propose an assessment methodology organised on three levels:

- Level 1 (LV1) is a territorial risk model, in which the input is represented by the macroseismic intensity parameters and the vulnerability is evaluated according to a qualitative knowledge of the relevant structural parameters. The safety indexes are based on typological studies, related to the kind of the building (palace, church, tower), at a territorial scale;
- Level 2 (LV2) is a local mechanical risk model, in which the spectral coordinates of the earthquake represent the input and the vulnerability is evaluated analysing the activation of partial collapse mechanisms in a single part of the structure (macroelement). The evaluation of the safety indexes still requires a few geometrical and mechanical parameters;
- Level 3 (LV3) is a global mechanical risk model, in which the spectral coordinates of the earthquake represent the input and the vulnerability is evaluated performing nonlinear analyses (through a capacity curve if a pushover approach is employed). The model asks for a detailed analysis of the single building, considered as a whole (or as an assembly of macroelements).

Among the three level of analysis the paper reports, for three of the thirteen analysed towers of San Gimignano, the results obtained with the models LV1 and LV3. The two level are compared through the examination of two safety indexes, evaluated with reference to the limit states of Life Safety (SLV).

The first index is the seismic safety index ($I_{S,SLV}$), the ratio between the return period of the seismic action which brings the tower to the Life Safety limit state (T_{SLV}) and the expected return time of the earthquake of the site, corresponding to the Life Safety limit state ($T_{R,SLV}$ = 475), defined as follows:

$$I_{S,SLV} = \frac{T_{SLV}}{T_{R,SLV}} \quad (1)$$

A seismic safety index greater than one corresponds to a safe state for the tower (with respect to the assumed reference period V_R and for its coefficient of use c_u). A safety index lower than one highlights possible critical issues that require in-depth investigations.

The second examined index is the acceleration factor ($f_{a,SLV}$), the ratio between the acceleration which brings the tower to the Life Safety limit state (a_{SLV}) and the reference acceleration for the Life Safety limit state ($a_{g,SLV}$), both referred to a rigid ground (ground type A):

$$f_{a,SLV} = \frac{a_{SLV}}{a_{g,SLV}} \tag{2}$$

The acceleration factor, while considering only one of the parameters that define the seismic action spectrum, has the advantage of providing a quantitative indication of any deficiency in terms of mechanical strength of the structural system. The acceleration factor $f_{a,SLV}$ is a purely mechanical parameter, which may be useful for an evaluation of the weakness of the structure in terms of strength. The seismic safety index $I_{S,SLV}$, being based on the return periods of the seismic demand and the capacity of the structure, provides a direct evaluation of the eventually present vulnerability of the tower over time.

The indexes were evaluated according to the two principal directions of each section of the towers, in both directions, being not (usually) possible to identify in advance the most critical section. In addition the nominal life V_N (which is obtained from the value of the return period of the seismic demand that brings to the achievement of the SLV) and the corresponding return time were also calculated.

4 LV1 ANALYSES

With the aim to evaluate the seismic risk at territorial level, the expeditious model proposed by the DPCM2011 [7] schematizes the tower as a cantilever beam, subject to a system of horizontal forces, assuming that the collapse can occurs according to a combined compressive and bending stress mode. The simplified LV1 model allows to evaluate the collapse acceleration of the structure based on a limited number of geometrical and mechanical parameters (or qualitative tools such as visual test, construction features, and stratigraphic survey). It is hence mainly aimed to evaluate a "comparative ranking risk" between similar structures in order to highlight the need for subsequent in-depth investigations (or to program actions to mitigate the seismic risk).

Results of seismic vulnerability at territorial level should be a useful tool for the public administration for highlighting the most critical situations in the territory and to establish priorities for future interventions. It is hence implicitly assumed that lower LV1 safety indexes actually correspond to lower safety indexes in case of refined LV3 analyses.

In case of masonry tower, from the operative point of view, the LV1 model foresees to divide the structure into *n* sectors (blocks) having uniform characteristics. This step should be performed taking into account several aspects, among them: i) beginning and ending of the openings; ii) level of detachment of the tower from the neighbouring buildings (if the tower is not isolated); iii) levels in which there is a reduction in the thickness of the masonry walls; iv) levels where there are changes of materials and / or changes in the construction phases. To identify the sectors into which the tower must be divided responds to the need to obtain structural portions with geometrical and mechanical uniform characteristics where safety checks are to be performed. Afterwards, the safety checks are carried out by comparing, at the base of each sector and for each load direction, the seismic demand (the acting bending moments) with the seismic capacity (the correspondent ultimate resistant moment).

Since the towers (Figure 1) are largely incorporated into the neighbouring buildings, to apply the LV1 model following schemas were considered:

- Model A: the towers are analysed as an isolated construction, i.e. without considering the presence of the neighbouring buildings (it is implicitly assumed that the action offered by the neighbouring structures is ineffective);
- Models B and C: these models still considers the towers as isolated constructions, but assume as tower height the portion of the structure that emerges from the surrounding buildings.

The above models are aimed to introduce lower and upper bound within approximate the actual behaviour of the towers. The adjacency of the towers with the lower constructions can, in fact, significantly alter their structural behaviour: on the one hand, it reduces the effective slenderness (thus reducing the period); on the other hand these constructions constitute stiffeners which may produces localized areas of possible stress concentration (and pounding).

The evaluation of the acting bending moment requires the estimation of the ordinate of the elastic response spectrum $S_e(T_1)$ which is a function of the main period T_1 of the tower. It was shown ([10]) that the empirical correlation (3) provided by the NTC2008 [6], in case of slender masonry towers, tends to overestimate the natural period for values less than 1 s, while tends to underestimate the actual period for values greater than 1 s.

$$T_1 = 0.050 \cdot H^{0.75} \tag{3}$$

On the basis of experimental results concerning the main periods of historic masonry towers Ranieri and Fabbrocino [10] proposed the following empirical correlation, here also used for the estimation of the fundamental period:

$$\mathrm{T_1} = 0.013 \cdot \mathrm{H}^{1.10} \tag{4}$$

The Eq. (4), like the empirical correlation provided by the Italian building code, provides the main period of the structure as only function of the height H of the tower. For comparative purpose the main period of the towers were also estimated by employing the classical formula of the linear elasticity:

$$\mathrm{T_1} = 1.787 \cdot \mathrm{H}^2 \cdot \sqrt{\frac{\gamma \cdot \mathrm{A}}{\mathrm{E} \cdot \mathrm{J} \cdot \mathrm{g}}} \tag{5}$$

where A is the cross sectional area of the *i*-th sector, γ is the specific weight, E is the modulus of elasticity and J denotes the area moments of inertia (to be evaluated in the analysed load direction).

The Italian guidelines require, in order to account for the behaviour of the structure at the ultimate limit state (i.e. to consider the non-linear phenomena that occur as a result of the increasing levels of damage induced by the seismic loads) to amplify the linear elastic period T_1 by a coefficient which varies between 1.40 and 1.75.

The main periods T_1 evaluated by Eqs. (3)-(5) were thus amplified with a factor equal to 1.40 to obtain a period T_1^* representative of the damage phenomena induced by seismic load at the ultimate limit state. The estimated main periods of the three towers for the three schemas A, B and C are reported in Table 3.

Model	Eqs.	Chigi			Coppi-Campatelli			Becci		
		H [m]	T_1 [s]	T_1* [s]	H [m]	T_1 [s]	T_1* [s]	H [m]	T_1 [s]	T_1* [s]
	(3)		0.59	0.83		0.69	0.97		0.79	1.10
A	(4)	26.9	0.49	0.68	33.1	0.61	0.85	39.4	0.74	1.04
	(5)		0.63	0.88		1.09	1.52		1.47	2.06
	(3)		0.35	0.48		0.60	0.84		0.43	0.60
B	(4)	13.4	0.22	0.31	27.6	0.49	0.69	17.4	0.31	0.47
	(5)		0.16	0.22		0.89	1.25		0.30	0.42
	(3)		0.28	0.40		0.35	0.49		0.39	0.55
C	(4)	10.5	0.17	0.23	13.4	0.23	0.32	15.5	0.27	0.38
	(5)		0.08	0.11		0.75	1.05		0.24	0.34

Table 3: Main periods of the towers (empirical correlations and analytical expression).

Chigi	direction	T_1 [s]	$f_{a,SLV}$ [-]	$I_{S,SLV}$ [-]	V_N [years]	T_R [years]
Model A	N-S (X)	0.49	0.97	0.91	46	434
		0.88	1.29	2.29	115	1089
	E-W (Y)	0.49	1.04	1.12	56	530
		0.85	1.38	2.95	147	1399
Model B	N-S (X)	0.16	1.60	5.21	261	2475
		0.48	1.60	5.21	261	2475
	E-W (Y)	0.15	1.60	5.21	261	2475
		0.48	1.60	5.21	261	2475
Model C	N-S (X)	0.08	1.60	5.21	261	2475
		0.28	1.60	5.21	261	2475
	E-W (Y)	0.08	1.60	5.21	261	2475
		0.28	1.60	5.21	261	2475

Table 4: Chigi LV1 safety indexes.

Campatelli	direction	T_1 [s]	$f_{a,SLV}$ [-]	$I_{S,SLV}$ [-]	V_N [years]	T_R [years]
Model A	N-S (X)	0.85	1.39	1.62	81	771
		1.52	1.61	5.21	261	1529
	E-W (Y)	0.85	1.43	1.78	89	846
		1.52	1.71	3.37	169	1601
Model B	E-W (Y)	0.69	1.31	1.34	67	637
		1.25	1.58	2.51	126	1195
Model C	N-S (X)	0.87	1.87	4.74	238	2255
		1.05	1.87	4.75	238	2259
	E-W(Y)	0.87	2.34	5.21	261	2475
		1.05	2.34	5.21	234	2475

Table 5: Coppi-Campatelli LV1 safety indexes.

Tower	T_1 [s]	$f_{a,SLV}$ [-]	$I_{S,SLV}$ [-]	V_N [years]	T_R [years]
Chigi	0.49	0.97	0.91	46	434
	0.85	1.38	2.95	147	1399
Coppi-Campatelli	0.85	1.39	1.62	81	771
	1.52	1.71	3.37	169	1601
Becci	0.73	1.12	1.47	105	696
	0.88	1.34	2.67	191	1270

Table 6: LV1 safety indexes: acceleration factor ($f_{a,SLV}$), seismic safety index ($I_{S,SLV}$), nominal life (V_N) and return time (T_R).

Results of the analyses are summarized in Table 4 (Chigi tower) and Table 5 (Coppi-Campatelli tower) in terms of acceleration factor $f_{a,SLV}$, seismic safety index $I_{S,SLV}$, nominal life V_N and return period T_R. For all the analyzed cases, the minimum spectral acceleration is obtained in correspondence of the base section of each considered model.

The LV1 results show that no critical situations are detected (although, in the case of the Chigi tower, the A model with main period evaluated accordin to Eq. (4) without the amplification factor 1.40 provides an acceleration factor slightly less than one). Even the values of the nominal life V_N, representing the time period in which the constructions can be used with the same level of safety, do not highlight critical scenarios being the values of V_N always greater than V_R. It is possible to observe a general consistency of the results in terms of safety indexes. In addition, it also possible to observe, with respect to both $f_{a,SLV}$ and $I_{S,SLV}$, that the smaller values are obtained with the A models (isolated towers). Lower and upper bounds are summarized in Table 6.

5 LV3 ANALYSES

The third level of analysis is based on the use of numerical models able to simulate the global structural behaviour in order to evaluate the accelerations leading the structure to each analysed limit state. This level, compared with the previous one, is more demanding since it requires a deepen knowledge of the constructive techniques and the structural details, together with the material properties (tensile and compressive strength of the materials), to perform a reliable evaluation of the seismic capacity of the building. The reliability of the model, and consequently the provided results, is closely connected with the level of investigation and the available experimental data. In addition, when the construction is inserted into a context of aggregated buildings, as in the case of the towers of San Gimignano, the identifying between construction and transformation phases (edification of new buildings, raising, internal changes with partial demolition and/or reconstructions) is a fundamental element of knowledge required to assess the structural continuity of the construction with the surrounding. These, and other aspects not expressly called up, were addressed in this level of investigation, and analogously to what was done in the previous one, through a parametric investigation in order to identify lower and upper bound of behaviour.

To investigate this level, linear and nonlinear analyses were performed by means of finite element (FE) models of the towers. In particular, the FE models of the Chigi and Coppi-Campatelli towers were employed to perform nonlinear static analyses (pushover) analysing the directions +/- X and +/- Y (as reported in Figure 1) while the FE model of the Becci tower was employed to perform linear time-history analyses through a simplified approach. Hereinafter, main results and the employed methodology are discussed.

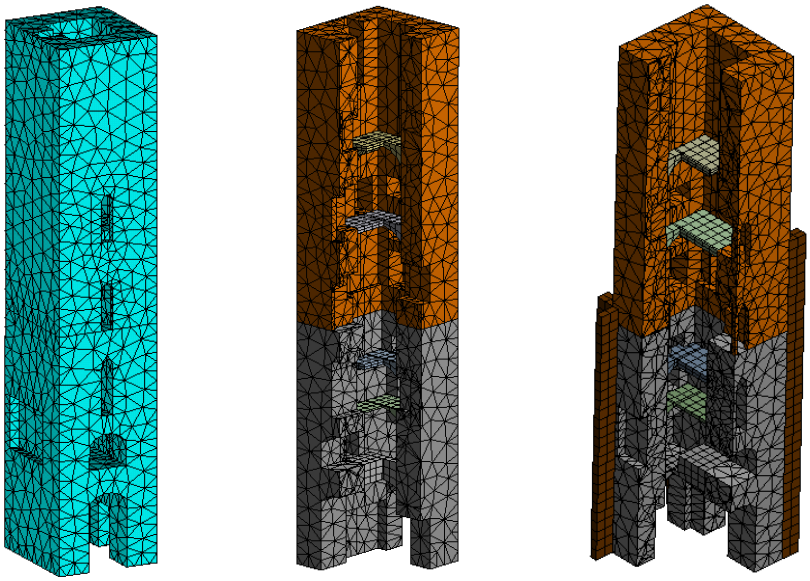


Figure 2: FE model of the Chigi tower (ANSYS).

5.1 The Chigi tower

The FE model of the Chigi tower (Figure 2) was built by using the commercial code ANSYS [11] accurately reproducing the geometry of the structure. The numerical model included the masonry vaults, while internal wooden slabs were not modelled. The major openings of the wall of the tower (doors, windows, recesses, etc.) were reproduced, and the nonlinear analyses were performed assuming a rigid ground foundation (fixed base model).

The strength parameters of the material were evaluated taking account the provision of the Italian Recommendation [8] but, in addition, due to the lack of experimental data, and within the aim of the project, an extensive parametric investigation was developed taking into account the variability of the strength parameters. The analysed configurations are reported in Table 7.

	Stone (lower part)				Brick (upper part)			
#	f_t [MPa]	f_c [MPa]	E [MPa]	γ [kg/m^3]	f_t [MPa]	f_c [MPa]	E [MPa]	γ [kg/m^3]
A11	0.106	0.493	1458	1600	0.195	0.901	2363	1800
A12	0.106	0.493	2916	1600	0.195	0.901	4726	1800
A21	0.106	0.986	1458	1600	0.195	1.801	2363	1800
A22	0.106	0.986	2916	1600	0.195	1.801	4726	1800
B11	0.212	0.986	1458	1600	0.390	1.801	2363	1800
B12	0.212	0.986	2916	1600	0.390	1.801	4726	1800
B21	0.212	1.973	1458	1600	0.390	3.603	2363	1800
B22	0.212	1.973	2916	1600	0.390	3.603	4726	1800

Table 7: Parametric values of strength parameters (f_t – tensile strength, f_c – compressive strength, E - modulus of elasticity, γ - own weight).

The seismic behaviour of the tower was analysed employing a pushover approach: the static nonlinear analyses were developed increasing monotonically the horizontal loads that were applied under conditions of constant gravity loads. The analyses were performed considering all the seismic directions (+/-X and +/-Y). Pushover curves were evaluated assuming as control point the displacement of the centre of mass of the upper section.

In addition to account for the confining effects provided by the lower buildings, the following two limit cases were considered to identify lower and upper bound of behaviour:

- model of isolated tower (IT): the first limit case considers the tower alone, without taking into account the interaction with the confining buildings (model IT);
- model of confined tower (CT): the second limit case considers the presence of the adjacent buildings (in all the directions) assuming their effects as a rigid constraint (model CT1 and model CT2).

The interactions of the tower with the lower buildings were considered as constraints for both the load directions, while the model of isolated tower takes into account the configuration where the connections with the confining buildings are not effective (i.e. ideally the situation where the tower, in case of earthquake, starts to oscillate detaching them from neighbouring structures).

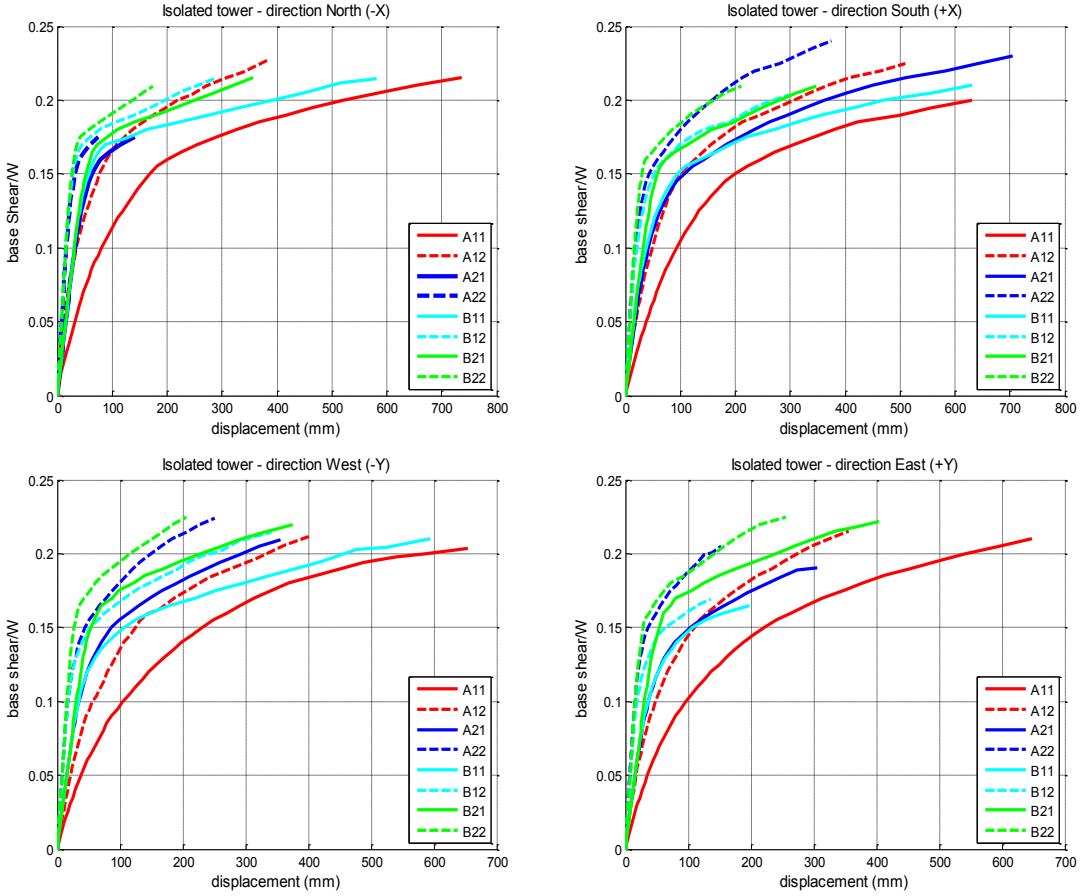


Figure 3: Pushover curves for +/-X (Up) and +/-Y directions (Down).
FE model of isolated Chigi tower.

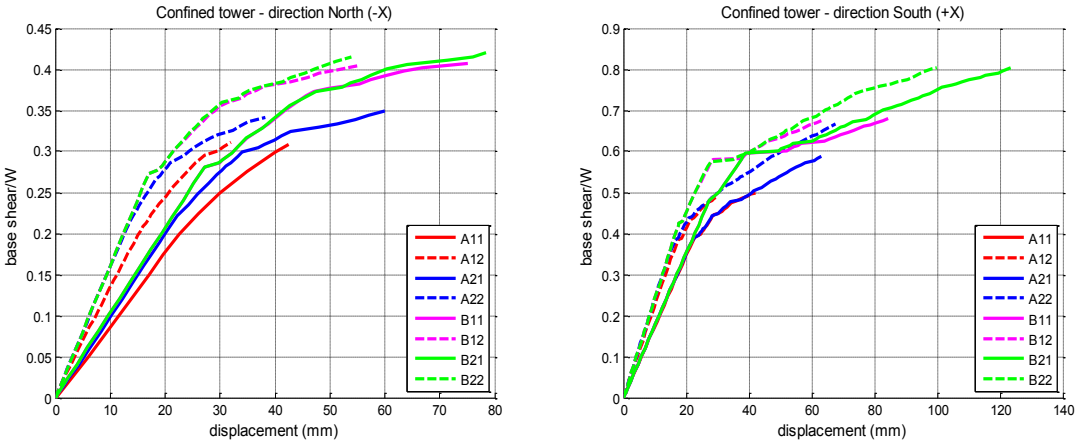


Figure 4: Pushover curves for +/-X directions.
FE model of confined Chigi tower.

The equivalent stiffness of the lower buildings was calculated by equating the displacements of the upper end of the confining wall, subjected to a unitary force, with the corresponding displacement of the elastic boundary constraints (taking into account both the flexural and shear deformation). The equivalent elastic modulus thus obtained, E_1, was employed to model the boundary elements (model CT1). As a further case, and for comparative purposes, was also analysed a value E_2 equal to 10 times the first (model CT2). This investigation can be quite significant since the presence of confining structures can be an effective constraint for the tower and the tower seismic vulnerability can be strongly influenced by the dynamic interaction with them (the confining structures reduce the slenderness of the tower and, at the same time originate, points of stresses concentrations and pounding).

The pushover curves (generalized force–displacement relationship) with respect to the case of loading acting in +/-X (the North-South) and +/-Y (the East-West) directions are reported in Figure 3 for the case of isolated tower. As control node to build the capacity curves, the horizontal displacements of the corner nodes of the top section of the tower were considered (their average value). The capacity curves of the isolated tower with the confined tower are reported in Figure 4.

Chigi	Model	T* [s]	$f_{a,\ SLV}$ [-]	T_R [years]	$I_{s,\ SLV}$ [-]
Direction South (+X)	IT	1.10	5.01	>2475	-
	CT1	0.39	2.60	>2475	-
	CT2	0.24	3.83	>2475	-
Direction North (-X)	IT	0.65	1.22	484	1.02
	CT1	0.42	1.38	979	2.04
	CT2	0.26	2.82	>2475	-
Direction East (+Y)	IT	0.79	2.82	>2475	-
	CT1	0.42	2.18	>2475	-
	CT2	0.27	4.19	>2475	-
Direction West (-Y)	IT	0.98	3.69	>2475	-

Table 8: Chigi LV3 safety indexes.

The obtained pushover curves were employed to build the curve of the equivalent bilinear single-degree-of-freedom (SDOF) oscillator employed to perform the seismic checks and to evaluate the acceleration factor, the seismic safety index and the return period T_R. Table 8 reports the safety indexes obtained for the material A22 (Table 7). Overall, the LV3 analyses have not highlighted critical situations: all the cases are verified and the results of the level of investigation LV3 are in agreement with the first level of evaluation (LV1).

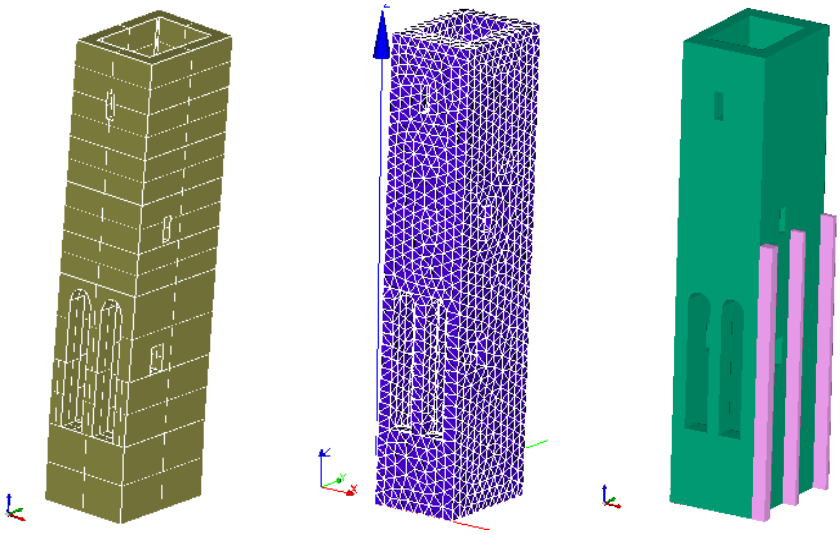


Figure 5: FE model of the Coppi-Campatelli tower (Code Aster).

5.2 The Coppi-Campatelli tower

The FE model of the Coppi-Campatelli tower (Figure 5) was built by using Code Aster, an Open Source finite element code. The code has a wide library of nonlinear material models and to reproduce the masonry nonlinear behaviour the continuum damage model of Mazars [12] was adopted. The numerical model was employed to perform pushover analyses analysing the directions +/- X and +/- Y (Figure 1) assuming a rigid ground foundation (fixed base model). The parameters required by the damage model to reproduce the masonry nonlinear behaviour were selected in order to fit the limit scheme DRS (dressed rectangular stone masonry) and the cases of confined (CT) and isolated (IT) tower were, as for the Chigi tower, analysed.

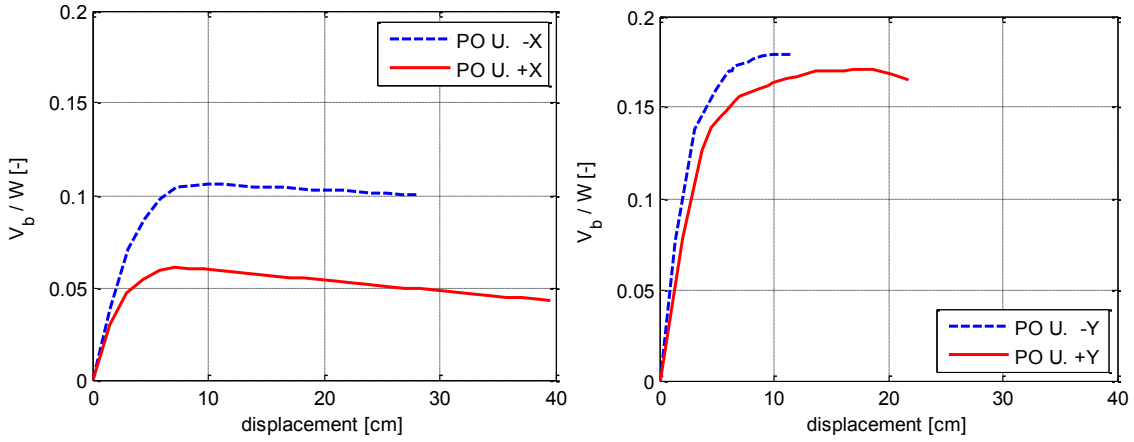


Figure 6: Pushover curves for +/-X and +/-Y directions. FE model of isolated Coppi-Campatelli tower.

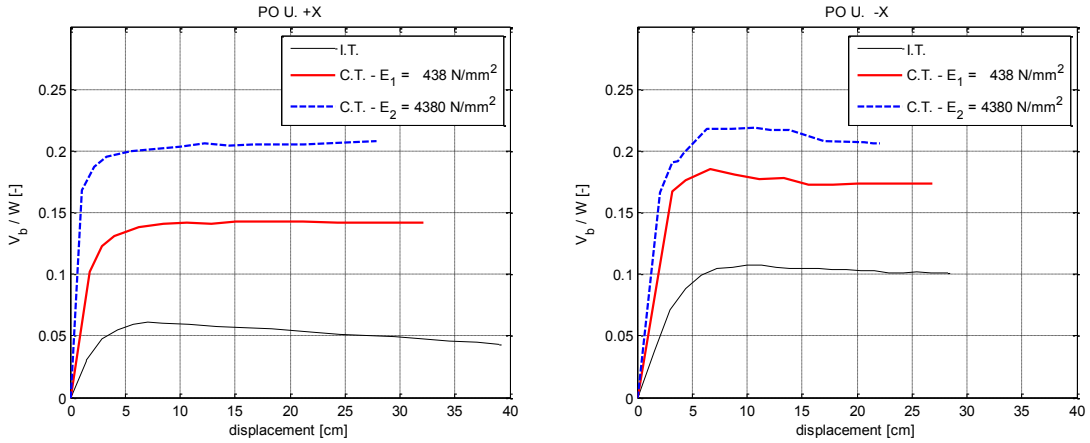


Figure 7: Pushover curves for +/-X and directions.
Comparison between capacity curves of isolated and confined Coppi-Campatelli tower.

The pushover curves with respect to the case of loading acting in +/-X (the North-South) and +/-Y (the East-West) directions are reported for the case of isolated tower in Figure 6. The comparison of the pushover curves of the isolated tower with the confined tower are reported in Figure 7 (load directions +/-X). In case of direction +X, for instance, it is possible to observe that the base shear, in the case of tower with constraint with equivalent elastic modulus E_1, shows an increase of about 135% if compared to the isolated tower case. This increase becomes about 240% if case E_2 is considered. In terms of ultimate displacement the two restrained cases show comparable values (25-35 cm), still lower than those obtained in the case of isolated tower (about 40 cm).

As in the previous case, the pushover curves were employed to characterize the equivalent bilinear single-degree-of-freedom (SDOF) oscillator employed to perform the seismic checks. Table 9 reports the safety indexes (acceleration factor, seismic safety index and return period T_R). Also for the Coppi-Campatelli tower the LV3 analyses do not highlight critical situations providing safety indexes in agreement with the one obtained with the LV1 model. It is interesting to observe that the acceleration factor obtained with the LV3 model are always higher than those obtained with the LV1 model.

Coppi-Campatelli	Model	T* [s]	$f_{a,\,SLV}$ [-]	T_R [years]	$I_{s,\,SLV}$ [-]
Direction South (+X)	IT	1.54	2.21	>2475	-
	CT1	0.84	4.40	>2475	-
	CT2	0.51	7.63	>2475	-
Direction North (-X)	IT	1.34	3.08	>2475	-
	CT1	0.89	4.33	>2475	-
	CT2	0.72	4.38	>2475	-
Direction East (+Y)	IT	1.07	2.87	>2475	-
	CT1	0.84	1.33	625	1.32
	CT2	0.47	1.57	992	2.09
Direction West (-Y)	IT	0.91	1.79	1519	3.20

Table 9: Coppi-Campatelli LV3 safety indexes.

5.3 The Becci tower

The seismic risk of the Becci tower was analysed through the simplified approach proposed by Bartoli et al. [13] performing time-history analysis. The approach, unlike the previous nonlinear one, requires only a reduced number of data (employed for the tuning of a linear numerical model). After the identification of a linear FE model of the whole structure, the model is employed to evaluate the load acting at every section of the tower due to a specified earthquake (modelled by an appropriate accelerogram). Loads acting at every section [z] of the tower are identified in global terms like shear force [T(z; t)], normal force [N(z)] and bending moment [M(z; t)]. After the evaluation of the time-history of each internal action, for a certain section of the tower, the evaluation of the seismic reliability is carried out by analysing the following two limit states:

- I limit state: tower over-turning (it is verified when the own weight combined with the seismic loads causes a resultant load which eccentricity is internal with respect to the cross-sectional area);
- II limit state: mechanical collapse of an external panel in its plane (it is verified when the seismic load acting on the tower is not able to produce a local cracking/crushing on a panel of the tower).

The proposed methodology aims to connect, for each of the above limit state (LS), an appropriate ground acceleration a_g able to assure their respect. The first limit state is identified in the whole tower, while the second one is related to the behaviour of a single masonry panel (with its actual nonlinear properties). The respect of the two limit states results by the comparison between the resisting force *R* (evaluate upon geometrical aspects for the I LS.; estimate upon the collapse behaviour of a masonry panel for the II LS) and the acting force *S* (obtained by the seismic load applied as ground acceleration time history). Despite its simplifications, the approach has the advantage that the I LS requires substantially only to evaluate the experimental frequencies of the tower that are needed for the tuning of the model. Subsequently, few mechanical data are required for the II LS (it requires to evaluate the collapse surface of elementary panels).

The Becci tower was analysed in order to evaluate the ground acceleration a_g able to assure the respect of the I LS. The FE model of the tower was built with the code SAP2000 that was tuned in order to reproduce the experimental frequencies. The earthquake loads acting at the base of the tower were modelled by artificial accelerograms generated by using SIMQKE (synthetic accelerograms) and REXEL (natural accelerograms). Different class of subsoil were considered to develop parametric analyses. The PGA of the considered input are reported in Figure 8 (according to the [6], 7 accelerograms were generated for each input), and an example of an accelerogram of each input is reported in Figure 8.

Types of accelerograms	Ground type	PGA [m/s^2]
Natural accelerograms		
INPUT 1	A	2.45
INPUT 2	B	2.21
INPUT 3	Subsoil of San Gimignano	2.56
Synthetic accelerograms		
INPUT 4	B	1.99

Table 10: Types of accelerograms.

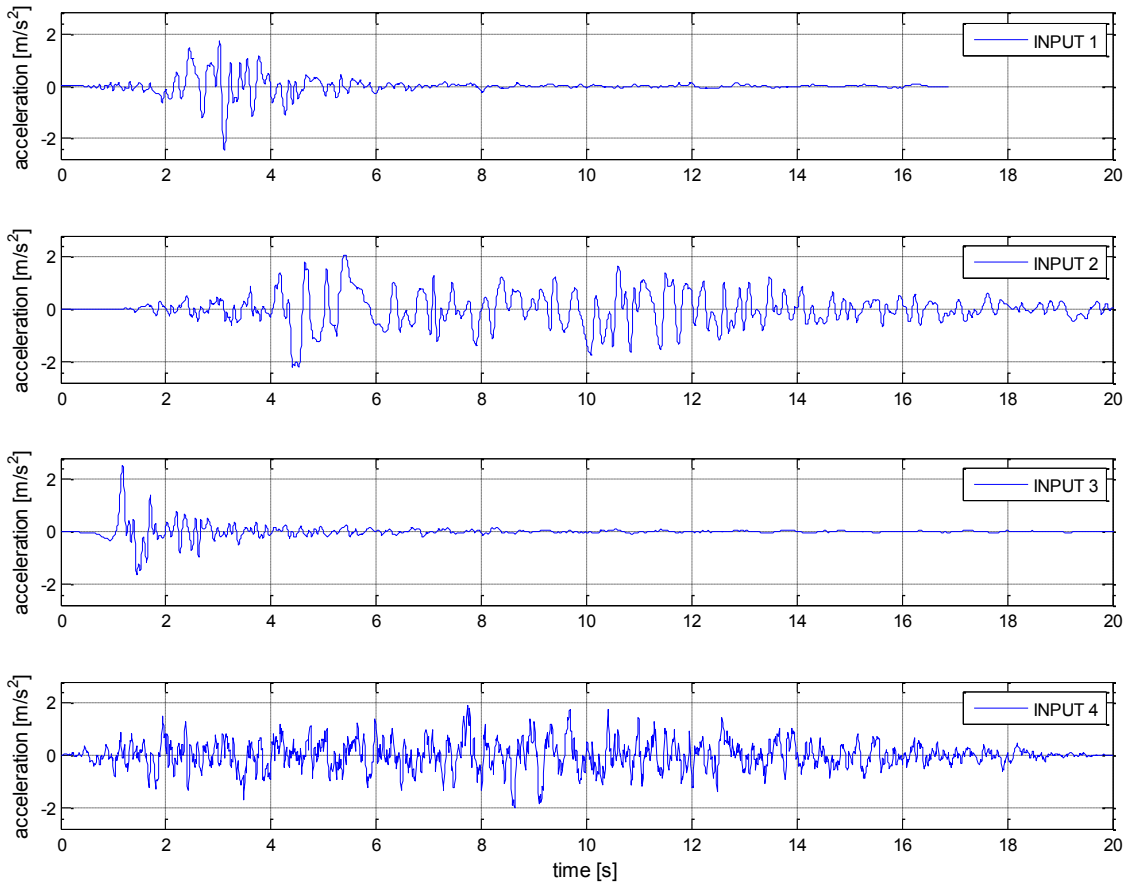


Figure 8: Time history of acceleration.

The accelerograms were applied on all restrained joints of the identified numerical model, and the time-history of the loads acting at every section [z] of the tower were evaluated: shear force [T(z; t)], normal force [N(z)] and bending moment [M(z; t)]. It is noteworthy to specify that due to the structural configuration of towers (which act structurally as cantilever beams), the internal forces acting at each level are statically determined and therefore they can be estimated by a simple dynamic linear model.

After the evaluation of the time-history of each internal action, the time history of the eccentricity was evaluated:

$$e(z,t) = \frac{M(z,t)}{N(z)} \tag{6}$$

Figure 9, as an example, reports the time-history of the eccentricity for one of the considered accelerogram. The verification of the I LS (tower over-turning) is ruled by following inequality:

$$|e_{max}| \leq |e_{lim}| \tag{7}$$

where e_{max} is the maximum value assumed by e(z,t) during the loading process, while e_{lim} is the value of the eccentricity of the normal force originating the over-turning (equal to the half-length of the tower section).

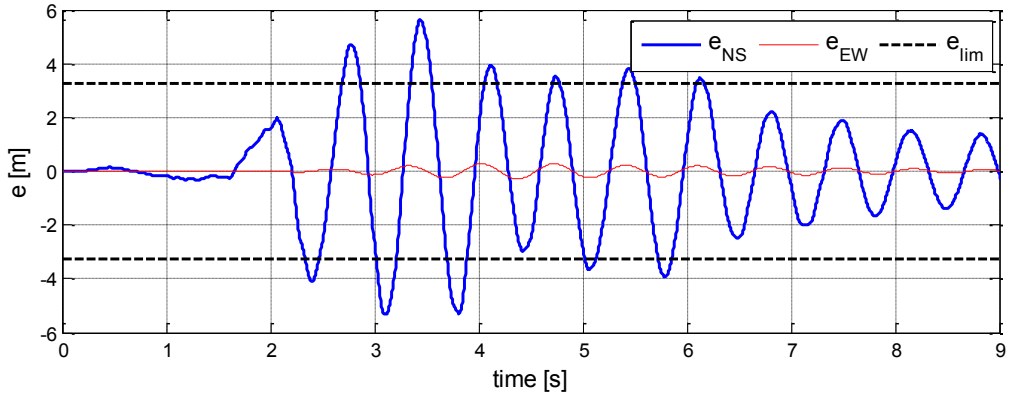


Figure 9 : Time-history of e(z,t) corresponding to a_g (INPUT 2)

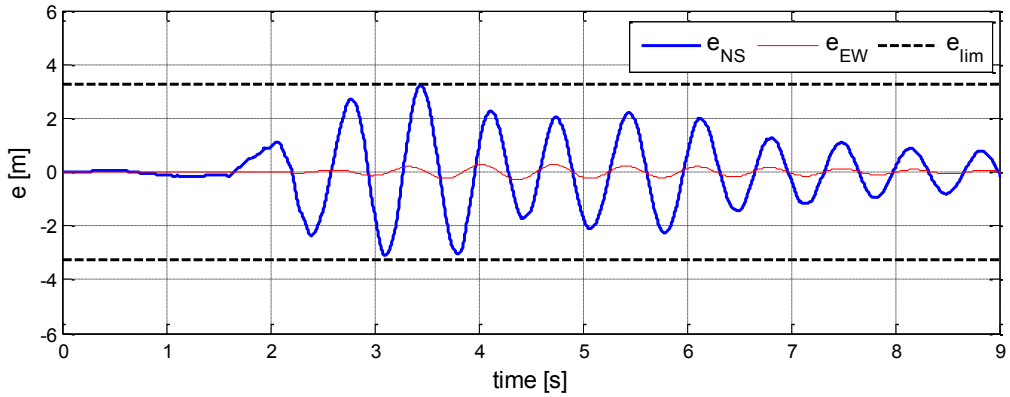


Figure 10 : Time-history of e(z,t) corresponding to reduced acceleration (INPUT 2)

The procedure leads to evaluate a coefficient of reduction of the seismic input able to assure the respect of the I LS:

$$\alpha = \frac{e_{max}}{e_{lim}} \tag{8}$$

The maximum acceleration that the tower can accept without over-turning is hence $a_{g1}=a_g/\alpha$. Figure 10 report the time-history of the eccentricity e(z,t) after the reduction of the seismic input.

The reduction coefficient was evaluated for each accelerogram of each group and the results in terms of α-factor (in both direction) are summarixed in Figure 11. Despite its semplification the index allows a synthetic and effective representation of the seismic behaviour of the tower. The value of the α-factor shows, for instance, a substantial structural simmetry of seismic response of the tower. In addition it is possibile to observe a strong dependence on the soil chacteristics. Highest α-factor are required when natural accelerograms with ground type A (INPUT 1) are considered. The α-factor obtained with the INPUT 2 (obtained assuming a ground type B) and INPUT 3 are similar. The INPUT 3 corresponds to the subsoil of San Gimignano and it is interesting to observe that the PGA of this class of input is greater than the PGA of the INPUT 1.

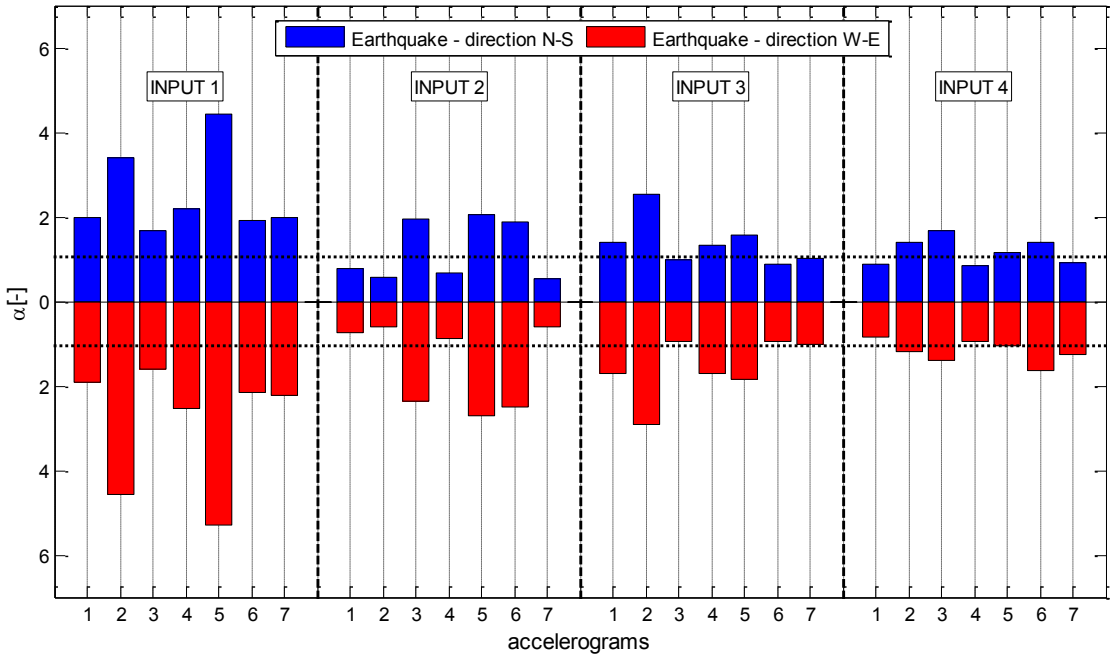


Figure 11 : α-factors.

CONCLUSION

The paper discussed about the methodology of analysis articulated on three levels of evaluation, according to an increasing knowledge of the structure, proposed by the Italian "Guidelines for the assessment and mitigation of the seismic risk of the Cultural Heritage". As a reference case, three of the masonry towers analysed within the research project RiSEM (Seismic Risk of Monumental Buildings) were discussed reporting the analyses performed to evaluate their seismic risk. The analyses were carried out by an articulated series of comparative assessments, aimed at investigating the effects of complementary and parametric hypothesis. The effects of the presence of the adjacent constructions at the lower lever, for instance, was assessed investigating the seismic response of the structures as a function of the degree of constraint provided by them.

The analysis at territorial scale (LV1) does not revealed critical situations. The last level of analysis, the LV3, was approached through global finite element models of the towers where proper damage models were employed to reproduce the masonry non-linear behaviour. The finite element models were employed to perform static nonlinear analyses and linear time-history analyses and the effects of the neighbouring buildings at the lower level of the towers were evaluated by analysing two limit cases: a) isolated tower and b) confined tower. The safety indexes (acceleration factor and seismic safety index) evaluated with the third level (LV3) confirm the results obtained with the first one and the LV3 safety indexes are always greater than those obtained with the LV1 model showing, despite the difference, a general coherence of the two models.

In addition, through a simplified approach, time-history analyses were performed in one of the case study and the results highlighted the strong dependence of the first safety index (the α-factor) on the energy content of the assumed accelerometer.

ACKNOWLEDGEMENTS

The authors kindly acknowledge the Region of Tuscany that financially supported the research (theme PAR FAS 2007-2013 - CIPE n°166/2007 - line 1.1.a.3: Science and Technology for the preservation and enhancement of cultural heritage).

REFERENCES

[1] M. Fioravanti, S. Mecca (eds), *The Safeguard of Cultural Heritage: A Challenge From the Past for the Europe of Tomorrow*. Firenze University Press, 2011.

[2] E. Bowitz, K. Ibenholt, Economic impacts of cultural heritage - Research and perspectives. *Journal of Cultural Heritage*, **10**(1), 1-8, 2009.

[3] G. Brandonisio, G. Lucibello, E. Mele, A. De Luca. Damage and performance evaluation of masonry churches in the 2009 L'Aquila earthquake. *Engineering Failure Analysis*, **34**, 693-714, 2013.

[4] D.F. D'Ayala, S. Paganoni, Assessment and analysis of damage in L'Aquila historic city centre after 6th April 2009. *Bulletin of Earthquake Engineering*, **9**(1), 81-104, 2011.

[5] D. Lo Presti, M. Sassu, L. Luzi, F. Pacor, D. Castaldini, G. Tosatti, C. Meisina, D. Zizioli, F. Zucca, G. Rossi, G. Saccarotti, D. Piccinini, A Report on the 2012 Seismic Sequence in Emilia (Northern Italy). *7th International Conference on Case Histories in Geotechnical Engineering*, Chicago, USA, 29 April - 4 May, 2013.

[6] NTC2008. D.M. del Ministero delle Infrastrutture e dei Trasporti del 14/01/2008. *Nuove Norme Tecniche per le Costruzioni*. G.U. n. 29 del 04.02.2008, S.O. n. 30 (in Italian).

[7] DPCM2011. *Direttiva del Presidente del Consiglio dei Ministri per la valutazione e riduzione del rischio sismico del patrimonio culturale con riferimento alle NTC 2008*. G. U. n. 47 del 26.02.2011 (in Italian).

[8] Circular2009. Circolare n. 617 del 2 febbraio 2009. *Istruzioni per l'Applicazione Nuove Norme Tecniche Costruzioni di cui al Decreto Ministeriale 14 gennaio 2008* (in Italian).

[9] G. Bartoli, M. Betti, S. Giordano, In situ static and dynamic investigations on the "Torre Grossa" masonry tower. *Engineering Structures*, **52**, 718-733, 2013.

[10] C. Rainieri, G. Fabbrocino, Il periodo elastico delle torri in muratura: correlazioni empiriche per la previsione. *XIV Congresso Nazionale L'Ingegneria Sismica in Italia*, Bari, Italia, 18-22 settembre 2011 (in Italian).

[11] Swanson Analysis System Inc. (1992). *ANSYS, Revision 5.0* (User's Manual, Theory Manual). Houston, Texas, USA.

[12] J.M. Mazars, G. Pijaudier-Cabot. Continuum Damage Theory. Application to Concrete. *Journal of Engineering Mechanics*, **115**(2), 345-365, 1989.

[13] G. Bartoli, M. Betti, P. Spinelli, B. Tordini, An 'innovative' procedure for assessing the seismic capacity of historical tall buildings: the 'Torre Grossa' masonry tower. *V International Conference on Structural Analysis of Historical Constructions (SAHC 2006)*, New Delhi, India, November 6-8, 2006, pp. 929-937.

COMPDYN 2015
5th ECCOMAS Thematic Conference on
Computational Methods in Structural Dynamics and Earthquake Engineering
M. Papadrakakis, V. Papadopoulos, V. Plevris (eds.)
Crete Island, Greece, 25–27 May 2015

SEISMIC VULNERABILITY OF THE PIERO DELLA FRANCESCA'S FRESCO CALLED "RESURRECTION"

Giulio Castori[1], Antonio Borri[1], Romina Sisti[1], Alessandro De Maria[2], Marco Corradi[3]

[1] Department of Engineering, University of Perugia
via Duranti 93, 06125 Perugia, Italy
giulio.castori@unipg.it, antonio.borri@unipg.it, rominasisti@hotmail.it

[2] Buildings Survey Office of Perugia
Via Palermo 106, 06129 Perugia, Italy
ale.dm2002@libero.it

[1] Department of Mechanical & Construction Engineering, Northumbria University
Wynne-Jones Building, NE18ST, Newcastle upon Tyne, United Kingdom
marco.corradi@northumbria.ac.uk

Keywords: Masonry modelling; Historical buildings; Finite-element analysis; Nonlinear static analysis; Kinematic analysis.

Abstract. *The structural analysis of monumental buildings requires to consider safety and conservation objectives, including also the possible presence of artistic assets. In order to face these issues, the paper presents an account of the results of diagnostic analyses conducted by the authors on a specific monumental masonry building: the Civic Museum of Sansepolcro, a small town near Arezzo; in fact, besides to be one of the most renowned civic structures built by Italian communes of Central Italy during the High Middle Ages to house their city governments, it is also characterized by the presence of Piero Della Francesca's fresco, known as "Resurrection", that is widely hailed as one of the masterpieces of late 15th-century Italian art. Within this context, the integrate use of three different modelling strategies of different complexity is discussed: the equivalent frame approach, the macro-block model and the finite element model. In the first part, a full 3D pushover analyses and a simplified approach based on the kinematic theorem of limit analysis are used in order to understand the large-scale structural performance of the building. Next, the results of the finite element method (FEM) tests conducted on a detailed 3D model of the wall containing the Piero Della Francesca's fresco are employed in order to investigate the origin of the surveyed crack pattern on this important artistic asset.*

1 INTRODUCTION

The preservation of cultural heritage assets must guarantee their capacity of lasting over time against decay, natural hazards and accidental events, without losing, as much as possible, their authenticity. Moreover, there is a need to ensure the safety of occupants, related to the use of the building (private or public). To this end it is necessary to make reference to the principle of "minimum intervention", under the constraint of an "acceptable safety level", a concept that still represents an open issue for monumental buildings. Furthermore, besides the preservation of the architectural value of the building, also immovable artistic assets should be considered in the assessment, such as: frescoes, stucco-works, pinnacles, battlements, banisters, balconies etc.

The seismic assessment of existing buildings, irrespective of whether they are historical, is a complex task, basically for two different reasons: a) the difficulty of interpreting and modeling the seismic response, because they have been designed without provisions for earthquake resistance and, in the case of ancient masonry structures, by an empirical approach; b) the difficulty of acquiring as-built information on material parameters and structural details, due to their spatial variability in the buildings and the need of avoiding invasive investigations [1]. To complicate the problem, every monumental building is characterized by its own history (the result of fusions, additions and replacements of structural elements that have led to its present configuration) so that each ancient building requires, though the typological similarities, a specific approach [2][3][4].

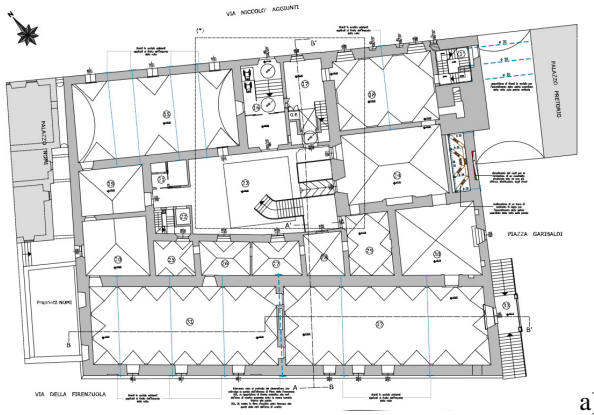
Within this context, a common denominator among the best known international guideline documents [5][6][7], on the assessment of cultural heritage assets, is the importance of the qualitative approach, based on historical analysis, the accurate investigation of structural details and the interpretation of seismic behavior, on the basis of observed damage in the building (due to previous events, if any) or on similar structures.

Within this field of research the present paper presents an account of the results of diagnostic analyses conducted by the authors on a illustrative case study: the Civic Museum of Sansepolcro. To analyze the structural behavior of the building and of its greatest artistic asset, the Piero Della Francesca's fresco, a performance based multi-scale approach is followed [1][8]. In such a context, according to the [9][10], a global analysis of the Museum is made by using the equivalent frame approach. In particular, a full 3D pushover analysis of the entire building is performed in order to predict the large-scale structural performance of the building. Afterwards, a macro-element approach based on the kinematic theorem of limit analysis is used to take into account the structure response at architectonic elements scale (damage in macroelements, usually related to out-of-plane displacements). After completing the knowledge phase at macro-scale level, it is crucial to have, at the meso-scale level, a precise evaluation of the seismic vulnerability of the wall containing the fresco. To this end the results of the finite element method (FEM) tests conducted on a detailed 3D model of the wall are employed in order to provide an interpretation of the manifested crack pattern on this important artistic asset.

2 STRUCTURAL ANALYSIS METHODOLOGY

As already discussed in the introduction, the analysis of the seismic behavior of historic masonry buildings is a difficult task due to several aspects: the difficult numerical modelling of the nonlinear behavior of masonry material, with almost no tensile strength; the incomplete experimental characterization of the mechanical properties of masonry structural elements; the complexity of the geometrical configuration [12]. The scientific literature has proposed mechanical models which accurately predict the behavior of masonry material and that adopt

different strategies to take into account the highly nonlinear behavior of the material both in tension (low tensile capacity and consequent cracking phenomena) and in compression. However, although these mathematical formulations can accurately describe the nonlinear phenomena that occur in the masonry, they are still hardly applicable to a complete 3D analysis of complex structural systems due to the large number of degrees of freedom required for meshing the structure. Within this context, the paper approaches the numerical problem using a performance based multi-scale analysis of structural system (Figure 1a) up to the masonry wall containing the most important artistic asset of the Museum: the Piero Della Francesca's fresco called "Resurrection" (Figure 1b).



a)



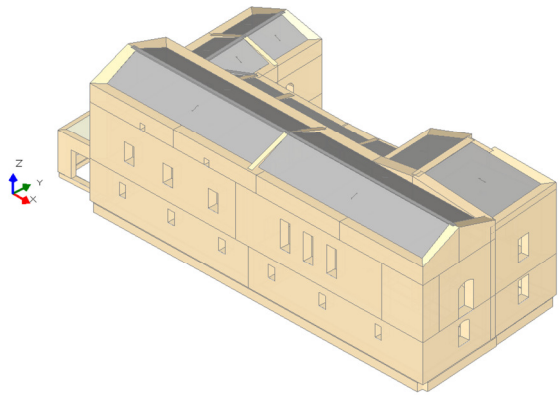
b)

Figure 1: a) plan layout of the Civic Museum; b) Piero Della Francesca's fresco known as "Resurrezione".

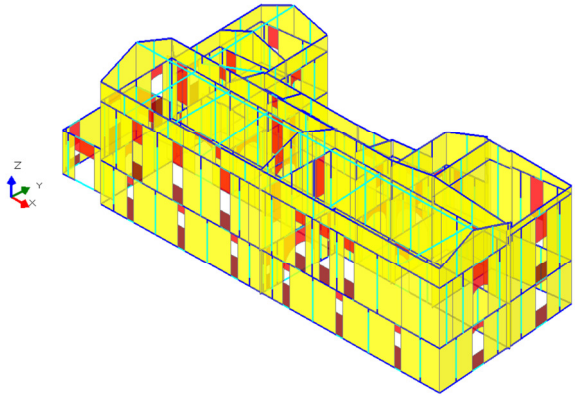
2.1 Global scale: pushover analysis

The analysis of the seismic behavior was analyzed by using a nonlinear static analysis method: under conditions of constant gravity loads a monotonically increasing horizontal load was applied using a pushover analysis [13].

An equivalent frame model (Figure 2) was set up by considering each wall pier as a beam element in which the in-plane behavior was modelled as elastic–perfectly plastic with a limited plastic strain at failure. Due to the presence of deformable floors, similar consideration were used for spandrel walls (the reader is referred to [10] for further details): i.e. the horizontal masonry elements of a wall were modelled in the same way as the piers. Finally, in agreement with Italian Code NTC 2008 [9] three possible failure mechanisms are taken into account for the elements, namely a sliding failure, a diagonal shear cracking and a rocking failure due to the bending moment. Obviously, rocking failure is active for slender elements.



a)



b)

Figure 2: a) Geometrical model; b) Equivalent frame model.

Based on this analysis method, the effects of the seismic loads were evaluated by applying of two systems of horizontal forces perpendicular to one another. These forces, not acting simultaneously, were evaluated taking into account two load distributions. The first load distribution was directly proportional to the building's masses (uniform); the second load distribution was proportional to the product of the masses for the displacements of the corresponding first modal shape. These two load distributions could be considered as two limit states for the building's capacity. The first distributions assume that the horizontal loads representative of inertia seismic forces are constant with respect to the building's height. This means that the displacements on the lower level of the building are overestimated, while the opposite happens on the displacement on the top level. On the contrary the second distributions overestimate the displacements on the top level.

It is noteworthy to point out that a conventional pushover was assumed in the study, i.e. loads applied on the building did not change with the progressive degradation of the building that occurs during loading. This means that the conventional pushover did not account for the progressive changes in modal frequencies due to yielding and cracking on the structure during loading. This is a critical point for the application of conventional pushover to the analysis of historic masonry buildings, because it is predictable that the progressive damage of the building may also lead to period elongation, and therefore to different spectral amplifications [14]. Hence the hypothesis of invariance of static loads could cause an overestimation in the analysis of the masonry building seismic capacity especially when a non-uniform damage on the buildings or a high level of cracking are expected. However, also in its conventional form, the pushover provides an efficient alternative to expensive computational inelastic dynamic analyses and can nevertheless offer useful and effective information on the damage state that the building can develop under seismic loads.

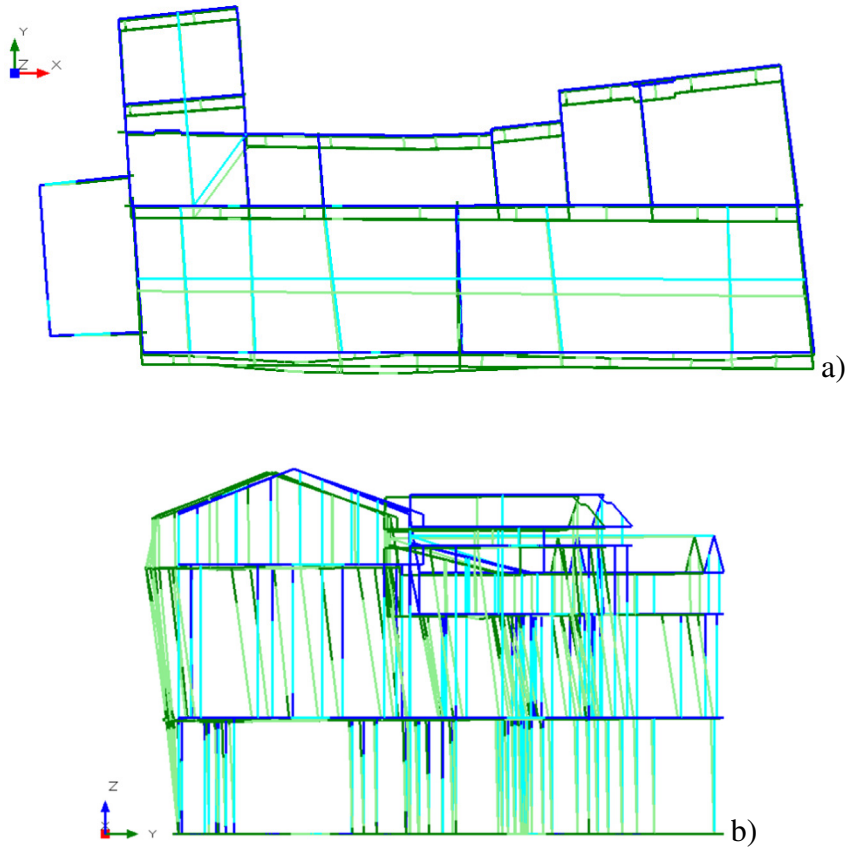


Figure 3: Deformed shape at collapse: a) plain view; b) front view.

The critical load distribution for the Museum was the case of load acting on the y-direction (direction perpendicular to main building direction) and results (obtained by using the commercial software Aedes Pcm 2014, Figure 3) were mainly detailed next with respect to this case. Figure 4 points out that the 3D strength of the building is insufficient and this lack of resistance is mainly related to out-of-plane collapses of orthogonal walls which are at the same time the longest and the most loaded ones.

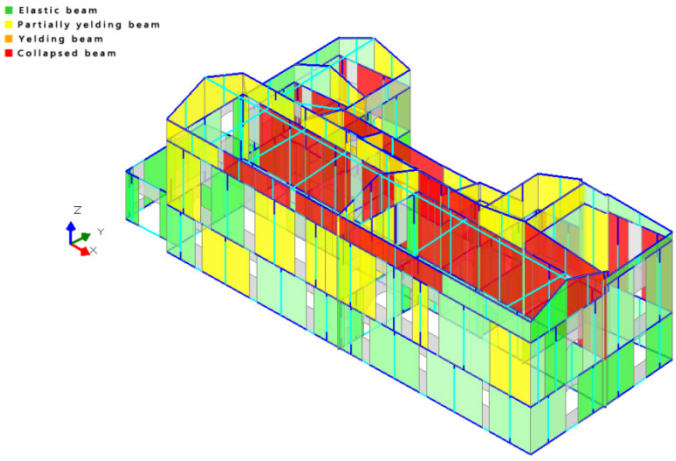


Figure 4: Damage pattern due to the rocking failure mechanism.

The displacement of a control point (center of mass of the roof level) versus the corresponding total shear is reported in Figure 5. Such a diagram can be named as the capacity curve of the palace in the y-direction as it furnishes, among other elements, the maximum seismic force which is borne by the structure, i.e. the level of the seismic action which activates the first local failure mechanism.

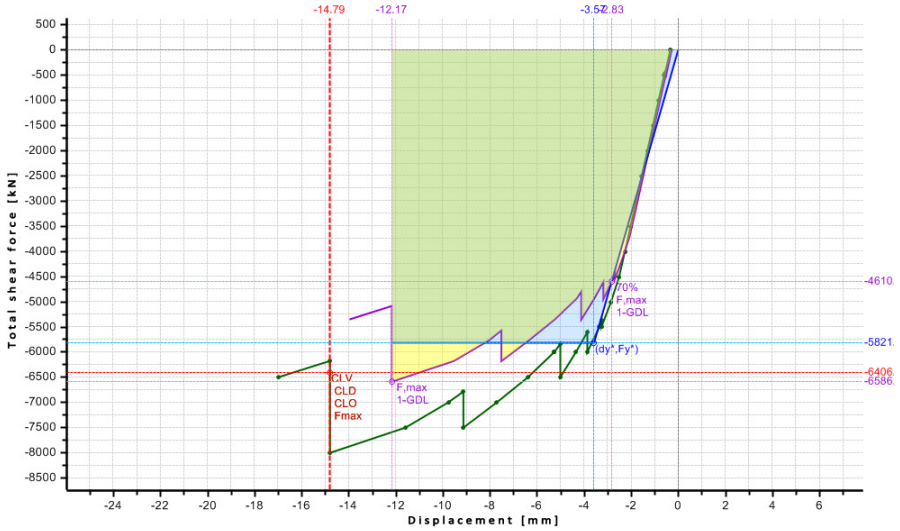


Figure 5: Structural response (maximum displacement vs total shear at the base) of the equivalent frame model: capacity curve of the actual structure (green line), the equivalent capacity curve (purple line) and the equivalent bilinear diagram (blue line).

The intensity measure (IM) adopted for the seismic assessment is the peak ground acceleration (PGA). On the basis of the computed values, seismic vulnerability is evaluated through a comparison between the maximum value of the PGA (obtained according to the procedure

illustrated in [1], IM_{kn} = 0.165g) compatible with the fulfillment of the assumed performance levels (Life Safety) and the reference target value ($\overline{IM_{kn}}$ = 0.260g) of the seismic demand (in terms of PGA) obtained by means of the Italian code [9]. Since the safety factor ratio IM_{kn} / $\overline{IM_{kn}}$ is equal to 0.478 and it is below the minimum level of safety proposed, for instance, by [15], the structure is clearly not verified.

2.2 Architectonic elements scale: limit analysis

Previous results obtained by the pushover analysis refer to the assessment of the building as a whole, the total seismic mass of the structure being involved. However, it is worth pointing out that an exhaustive seismic assessment would require also the verification of possible local mechanisms (mainly out-of-plane ones). The attribute "local" refers to mechanisms that involve only a portion of the building and may not be accurately analyzed by the global model; for this reason they were studied by a different specific local model, by considering only a fraction of the total mass.

The examination of the collapse and the damage consequent to past earthquakes allowed to predict the occurrence of recurrent modes and collapse mechanisms in historical masonry buildings [16][17]. The structure was so considered as the assemblage of a certain number of components depending on structural compound geometry and shape (e.g. the whole façade) and on the details (e.g. quality of existing connections) whose behavior is similar to the behavior of analogous macro-elements in other buildings, where the collapse mechanisms are identified. To this end, several elementary macro-elements were identified in the building and modelled as a system of rigid bodies, articulated by hinges, whose geometry and distribution were defined according to potential failure mechanism.

After the selection of the elementary macro-elements, the collapse multiplier (α_0) was evaluated by applying the Theorem of Virtual Work (TVW) on the rigid-body system, where the seismic load was assumed as an overturning force while the gravity load was assumed as a stabilization load [7]:

$$\alpha_0 \left(\sum_{i=1}^{n} P_i \delta_{x,i} + \sum_{j=n+1}^{n+m} P_j \delta_{x,j} \right) - \sum_{i=1}^{n} P_i \delta_{y,i} - \sum_{h=1}^{l} F_h \delta_h = W_{fe} \tag{1}$$

where P_i denotes the own weight of each element composing the kinematic chain; P_j (or F_h) is the weigh (or the load) transmitted at the selected macro-element by confining wall or roof; $\delta_{x,i}$ and $\delta_{x,j}$ are the virtual displacements of the elementary blocks centroids; $\delta_{y,i}$ and δ_h are the virtual displacements of the point of application of P_j and F_h respectively.

After the evaluation of the collapse multiplier (α_0), the corresponding seismic spectral acceleration α_0^* is evaluated by:

$$a_0^* = \frac{\alpha_0 \sum_{i=1}^{n+m} P_i}{M^* CF} \tag{2}$$

where M^* denotes the effective mass and CF is the confidence factor (assumed equal to 1.12 [7]). The respect of the analyzed limit state is assured by the respect of the following inequality:

$$a_0^* \geq \frac{a_g S}{q} \tag{3}$$

where a_gS is the design elastic acceleration spectral ordinate, q is the behavior factor (assumed equal to 2.0 [9]); Z is the height, with respect to the ground, of the centroid of all inertial masses involved in the mechanism and H is the total height of the building.

Several possible out-of-plane mechanisms (first type mechanisms) which best represent the surveyed damage patterns were taken into account. In particular the paper reports the results on the mechanisms that could be activated on the lateral bearing walls (Figure 6) and on the main façade (Figure 7).

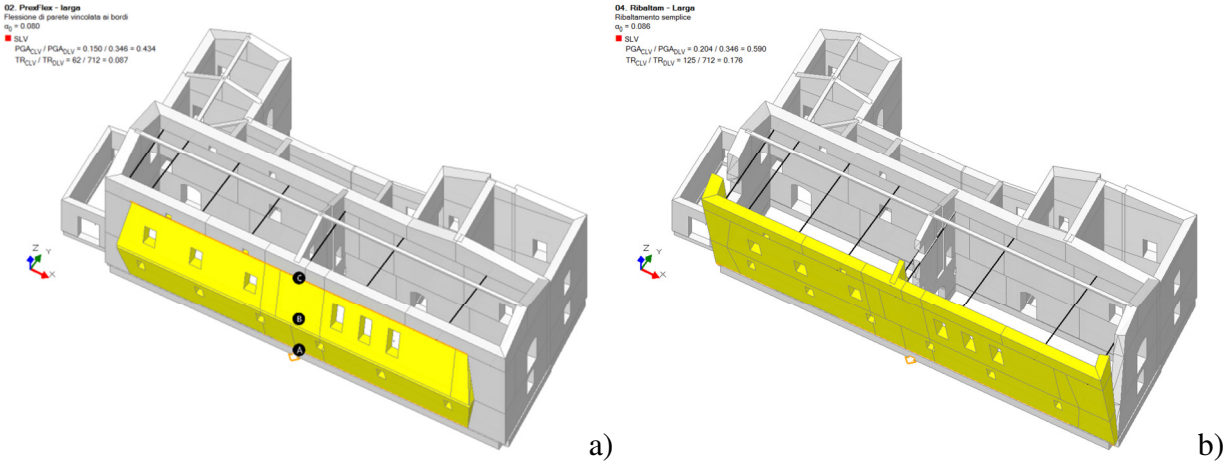


Figure 6: Lateral wall overturning: a) free-standing wall (Mechanism 01); b) wall restrained at the top (Mechanism 02).

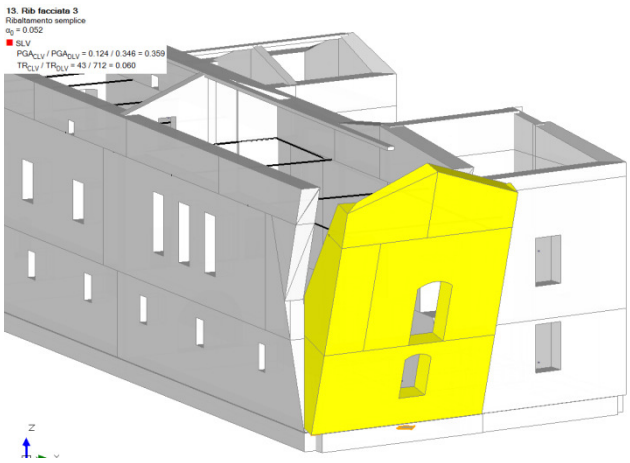


Figure 7: Main façade overturning: free-standing wall (Mechanism 03).

The evaluation of the vulnerability indexes upon Eq. (1)-(3) was been made by using an own code. Results from the macro-element approach, summarized in Table 1, agree with the results obtained with the pushover analysis via equivalent frame approach.

Title 1	Collapse multiplier (α_0)	Seismic spectral acceleration (a_0^*)	Seismic demand	Check
Mechanism 01 (lateral wall)	0.080	0.075g	0.173g	NO
Mechanism 02 (lateral wall)	0.086	0.102g	0.173g	NO
Mechanism 03 (main façade)	0.052	0.062g	0.173g	NO

Table 1: Vulnerability indexes, kinematic analysis results.

The critical behavior of the building is activated when the seismic load is acting on the transversal direction (y-direction) of the building. This is mainly due to the absence of a buttress capable to counteract the seismic action. Despite the good quality of the connection between the walls and the roof, this does not produce an effort in this direction. Other local collapses could arise in local areas of the Museum (main façade overturning) that however do not involve the entire structure.

2.3 Structural elements scale: FEM based analysis

A comprehensive reliable risk assessment for historical monuments should regard not only their architectural and structural components, but also movable (paintings, statues, libraries) and unmovable (frescos, stucco-works, pinnacles, battlements, banisters, balconies) artistic assets. This is an unexplored and critical issue, mainly owing to the evidence that the seismic damage of artistic assets is often related to small damage levels of the load bearing structure. The seismic protection of artistic assets thus requires the identification of the main damage mechanisms and, consequently, the development of suitable modelling strategies to evaluate their vulnerability and, if needed, design reliable and effective interventions.

Within this context, after completing the knowledge phase at macro-scale level, it was considered crucial to have, at the meso-scale level, a precise evaluation of the seismic vulnerability of the wall containing the most important artistic asset of the Museum: the Piero Della Francesca's fresco called "Resurrection". To this end the results of the finite element method (FEM) tests conducted on a detailed 3D model of the wall were employed in order to provide an interpretation of the manifested crack pattern on this important artistic asset.

A complete three-dimensional FE model of the wall was thus created using the commercial software ANSYS. The geometry of the wall was defined as accurately as possible, according to available drawings, photographs, and the photogrammetric and video-endoscopic survey. The numerical model has been built to accurately reproduce the geometry of the structure, focusing on the variations in the wall thickness, in the geometrical and structural irregularities and on the wall connections. In order to perform this operation the geometry of the wall was firstly reconstructed by means of CAD tools, next the volumes were imported and modelled by means of Solid65 elements (three-dimensional eight noded hexaedron isoparametric elements). The complete finite element model (FEM) is shown in Figure 8: it consists of 163952 nodes and 112128 elements, corresponding to 394992 degrees of freedom.

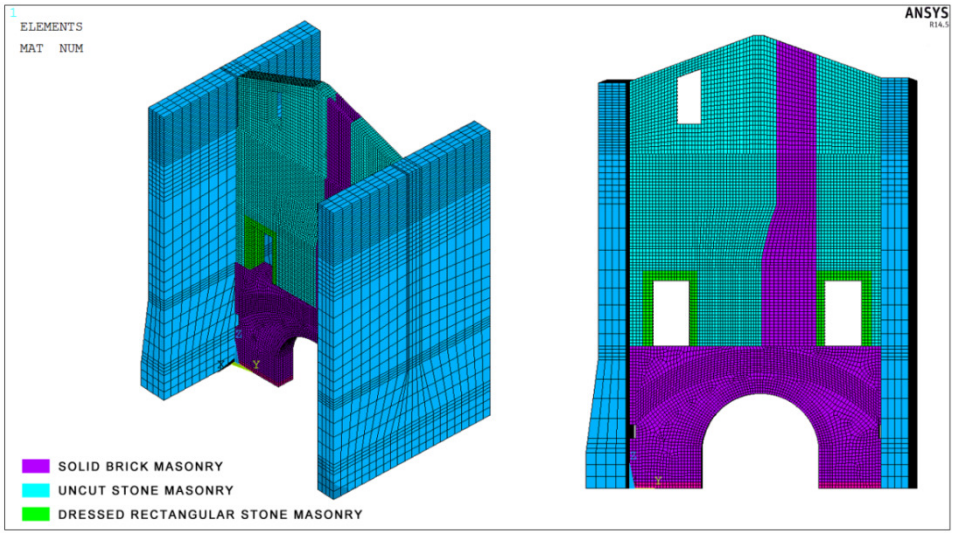


Figure 8: FEM model: mesh discretization and material map.

A physically non-linear model was adopted for masonry. For the sake of simplicity, both elastic and perfectly plastic behavior were adopted (a) with infinite ductility and (b) with isotropic behavior hypotheses for the material. It must be underlined that such assumptions do not take into account two important aspects of masonry at failure, the first related to the damaging behavior of joints, the latter related to the well-known higher masonry horizontal in-plane strength with respect to the vertical one, essentially due to brick staggering. Nevertheless, these aspects cannot be taken into account easily. On the other hand, the assumption of a zero tensile strength with frictional behavior is widely accepted [18] for the analysis of historical constructions. Within this approach a Mohr–Coulomb type failure criterion with tension cut-off type behavior was assumed for masonry. This failure criterion, initially adopted for concrete, accounts for both cracking and crushing failure modes through a smeared model. In particular, the masonry brittle behavior was here defined by means of only two constants: f_t (uniaxial tensile strength) and f_c (uniaxial compressive strength). Also, to increase the reliability of the proposed FEM, unilateral contact interfaces were used for the simulation of the joints between elements belonging to different periods in the history of the structure. The modeling of these joints necessitates the use of specific flexible/flexible contact elements. Specifically, for this application, an unilateral contact law was applied in the normal direction of each interface, indicating that no tension forces can be transmitted in this direction and a gap may appear if the stresses become zero. For the behavior in the tangential direction it was taken into account that sliding may or may not occur, by the usage of the Coulomb friction model with a friction coefficient equal to 0.5 [19].

Because of the artistic and historical value of the wall and in order to reduce the impact on conservation, in the present case in-situ tests could not be used in order to estimate the mechanical properties of the different types of brickwork forming the structure. Therefore, assumptions on the masonry material properties were made taking into account literature data for historic masonry (i.e. buildings with similar masonry texture [20]) and normative reference [10] deriving conservative values from these experiences. Table 2 report the selected values needed for the definition of the nonlinear model parameters with respect to the wall's masonry typologies.

Title 1	Solid brick masonry	Uncut stone masonry	Dressed rectangular stone masonry
Elastic modulus (N/mm^2)	1500	1230	2800
Poisson's ratio	0.25	0.25	0.25
Specific weight (kg/m^3)	1800	2000	2200
Uniaxial compressive strength (N/mm^2)	2.40	2.00	7.00
Uniaxial tensile strength (N/mm^2)	0.09	0.05	0.16

Table 2: Constitutive parameters of the materials adopted for nonlinear FEM analyses.

At this scale level, an equivalent static analysis was conducted, in which the structure was subjected to both vertical actions, i.e. self-weight and live loads, and seismic horizontal actions directly applied at the floor levels. More in details, the seismic action is modelled by a set of horizontal forces (acting along the x direction) which are applied with the distribution shown in Figure 9, where F_i represents the ultimate shear at the ith floor (with i = 1 to 3, being 3 the total number of floors) obtained from the pushover analyses at global scale. As for the boundary conditions, the FEM is perfectly constrained to the ground; no kinematic constraint is imposed between the wall and the surrounding structure.

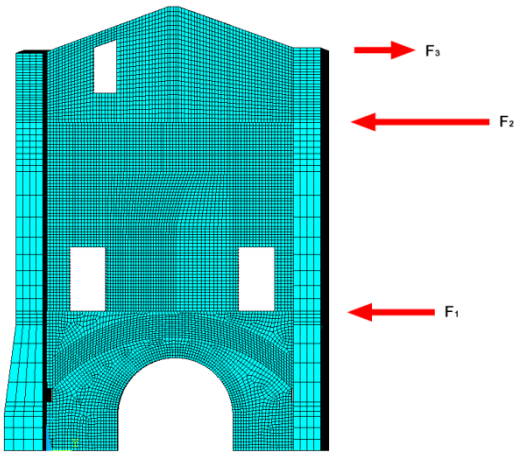


Figure 9: Application of the seismic action at every level.

Figure 10 shows the cracking pattern assessed at the end of the finite element analysis on the bearing wall. Cracking does not affect the structure as a whole, but mainly the southern (with diagonal and vertical cracks) and upper part of the wall close to the chimney (with vertical cracks between the inner and the outer leaf of the wall).

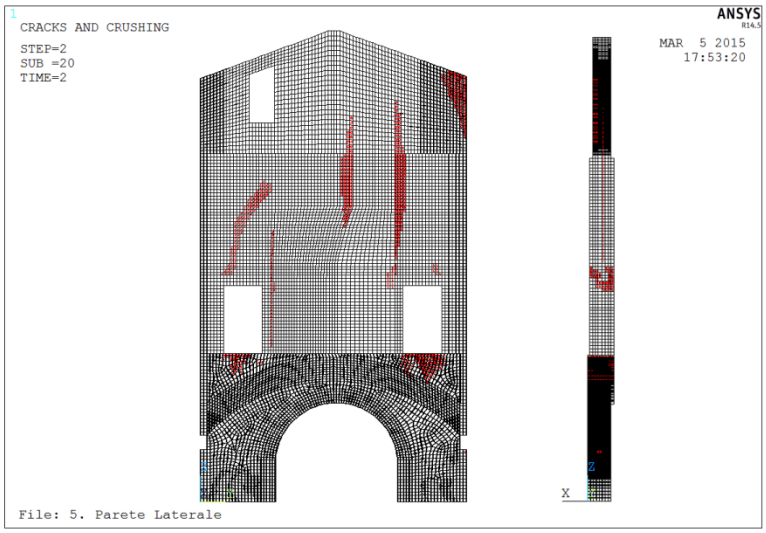


Figure 10: FEM model: cracking pattern.

As a general remark, it is possible to observe how the calculated cracking pattern matches the real crack distribution observed in the wall quite well. Cracks are in fact located in the neighborhood of the of the surveyed crack pattern, indicating that the performed analysis, at least from a qualitatively point of view, seems to explain most of the damage of the structure.

3 CONCLUSIONS

The paper approaches an account of the results of diagnostic analyses conducted by the authors on a specific monumental masonry building: the Civic Museum of Sansepolcro.

Assuming that preservation of monumental structures requires a detailed knowledge of the seismic behavior in order to minimize the interventions, for the sake of conservation, a performance based multi-scale approach has been adopted in the assessment procedure. In particular, the use of a 3D pushover analysis (equivalent frame approach) allowed, on the one hand, to improve the evaluation carried out through the nonlinear kinematic analysis (rigid

macro-block model) and, on the other one, to calibrate the use of a refined 3D detailed model (finite element analysis with nonlinear constitutive laws for masonry) for catching the response of the wall containing the most important artistic asset of the Museum: the Piero Della Francesca's fresco called "Resurrection".

Results highlight some deficiencies related to the capability of the structural complex to fulfill the performance levels related to the conservation of the fresco and the safety of people who daily use the Museum. As is possible to notice, the simplified scheme of limit analysis (macro-element approach), in agreement with the results obtained with the pushover analysis (equivalent frame approach), points out that the strength of the building under transversal direction (y-direction) is insufficient and this lack of resistance is related to out-of-plane collapses of single panels. Such partial collapses are supposed to coincide with the failure of the entire complex, even if the inner structure of the building remains standing, since the building will be left in an irrecoverable state. On the other hand, the finite element analysis allow to obtain a screening of the most vulnerable parts of the wall containing the fresco, at the maximum seismic force which is borne by the structure, i.e. at the level of the seismic action which activates the first local failure mechanism. However, to refine the model other aspects remain to be investigated. In this perspective, the answer to the question, "What strength earthquake should be assumed as a reference for the fresco?" should be defined. To this end, numerical analyses are scheduled, to suggest that measures should be taken sooner or later to provide adequate guarantees of protection and safety. Without interventions aimed at eliminating the causes, the cracking situation observed is, in fact, inevitably destined to worsen with the occurrence of future seismic events.

4 ACKNOWLEDGEMENTS

The Authors would like to express their gratitude to Dr. Agostino Bureca, Director of Soprintendenza dei Beni Architettonici (Monuments and Fine Arts Office) of Arezzo, for his invaluable contribution through the research program. The assistance in the research of Arch. Donatella Grifo of Soprintendenza dei Beni Architettonici of Arezzo is also acknowledged.

REFERENCES

[1] S. Lagomarsino, S. Cattari, PERPETUATE guidelines for seismic performance-based assessment of cultural heritage masonry structures. *Bullettin of Earthquake Engineering*, **13**, 13-47, 2015.

[2] M. Betti, A. Vignoli, Numerical assessment of the static and seismic behaviour of the basilica of Santa Maria all'Impruneta (Italy). *Construction and Building Materials*, **25**, 4308-4324, 2011.

[3] M. Betti, L. Galano, Seismic Analysis of Historic Masonry Buildings: The Vicarious Palace in Pescia (Italy). *Buildings*, **2**, 63-82, 2012.

[4] M. Rossi, S. Cattari, S. Lagomarsino, Performance-based assessment of the Great Mosque of Algiers. *Bullettin of Earthquake Engineering*, **13**, 369-388, 2015.

[5] ICOMOS, Recommendations for the analysis, conservation and structural restoration of architectural heritage. *International scientific committee for analysis and restoration of structures and architectural heritage (ISCARSAH)*, Barcelona, Spain, 2005.

[6] ISO 13822, *Bases for design of structures – assessment of existing structures, 2nd Edition.* ISO International Standard, 2010.

[7] DPCM 2011, *Assessment and mitigation of seismic risk of cultural heritage with reference to the Italian Building Code (NTC 2008).* Directive of the Prime Minister, G.U. no. 47, 2011 (in Italian).

[8] G. Manfredi, A. Prota, G.P. Lignola, Multiscale Nonlinear analysis of RC hollow piers wrapped with CFRP under shear-type load. *10th U.S. National Conference on Earthquake Engineering*, Anchorage, USA, July 21-25, 2014.

[9] NTC 2008. *Nuove Norme Tecniche per le Costruzioni.* Directive of the Prime Minister, G.U. no. 29, 2008 (in Italian).

[10] IMIT Circ. n. 617, *Istruzioni per l'applicazione delle Nuove Norme Tecniche per le Costruzioni di cui al decreto ministeriale 14 gennaio 2008.* Italian Ministry of Infrastructures and Transportation, Rome, Italy, 2011 (in Italian).

[11] A. Borri, G. Castori, Damage and seismic vulnerability of the portal of Palazzo dei Priori. *International Journal of Architectural Heritage*, **5**, 219-240, 2011.

[12] P.B. Lourenço, Computations of historical masonry constructions. *Prog. Struct. Eng. Mater*, **4**, 301–19, 2002.

[13] A. Falasco, S. Lagomarsino, A. Penna, On the use of pushover analysis for existing masonry buildings. *Proceeding first European conference on earthquake engineering and seismology.* Geneva, Switzerland, September 3-8, 2006.

[14] S. Antoniou, R. Pinho, Advantages and limitations of adaptive and non adaptive force-based pushover procedures. *Journal of Earthquake Engineering*, **8**, 497–522, 2004.

[15] R. Cardoso, M. Lopes, R. Bento, Seismic evaluation of old masonry buildings. Part I: Method description and application to a case-study. *Engineering Structures*, **27**, 2024–2035, 2005.

[16] L. Binda, A. Saisi, Research on historic structures in seismic areas in Italy. *Prog. Struct. Eng. Mater*, **7**, 71–85, 2005.

[17] D.F. D'Ayala, S. Paganoni, Assessment and analysis of damage in L'Aquila historic city centre after 6th April 2009. *Bullettin of Earthquake Engineering*, **9**, 81–104, 2011.

[18] V. Mallardo, R. Malvezzia, E. Milani, G. Milani, Seismic vulnerability of historical masonry buildings: A case study in Ferrara. *Engineering Structures*, **30**, 2223-2241, 2008.

[19] J. Heyman, *The masonry arch*. Ellis Harwood-Wiley, 1982.

[20] A. Borri, G. Castori, M. Corradi, E. Speranzini, Shear behavior of unreinforced and reinforced masonry panels subjected to in-situ diagonal compression tests. *Construction and Building Materials*, **25**, 4403–4414, 2011.

[21]

COMPDYN 2015
5th ECCOMAS Thematic Conference on
Computational Methods in Structural Dynamics and Earthquake Engineering
M. Papadrakakis, V. Papadopoulos, V. Plevris (eds.)
Crete Island, Greece, 25–27 May 2015

SENSITIVITY ANALYSIS OF THE SEISMIC RESPONSE OF BRITTLE STRUCTURAL ELEMENTS UNDER NEAR-FIELD SEISMIC INPUT EFFECTS

Paloma Pineda[1], Jorge D Navarro-Rubio[2], and Miguel Ángel Gil-Martí[1]

[1] Department of Building Structures and Geotechnical Engineering, University of Seville Avda Reina Mercedes, No2, ETS Arquitectura, 41012, Sevilla, Spain

palomapineda@us.es

[2] Abeinsa Engineering C/ Energía Solar no 1, Palmas Altas, Campus Palmas Altas - Sevilla

Keywords: Numerical Analyses, Brittle Materials, Structural Dynamics, Earthquake Engineering, Hazard analyses.

Abstract. *This research provides a sensitivity analysis, taking into account possible variations on the structural response of a specific type of brittle masonry vaults under near-field effects. Ground motions from the near- field contain distinct pulses in acceleration, velocity, and displacement histories, which can generate higher base shears and drifts, than signals from the far-field. Besides, under those inputs, the ductility demand could be increased. In a first step, the worst seismic scenario in the highest seismic area of the Iberian Peninsula under the premises of near-field loading is defined. The obtained seismic inputs are directly related to the structural properties of singular masonry vaults, which are representative of precious local constructions. In a second step, the sensitivity analysis, focused on the material properties, is carried out by means of non- linear transient analysis. A constitutive law for brittle materials able to capture collapse mechanism under dynamic loading via FEM is implemented. From those analyses, the influence of different control parameters on the structural response is identified, and deviations on the seismic response are analysed in terms of collapse mechanisms.*

1 INTRODUCTION

Brittle structures located in seismically active areas are especially prone to suffer structural damages, as they exhibit high vulnerability under horizontal actions, being critical for their preservation to assess seismic safety in order to evaluate their dynamic response and, if necessary, to improve their structural strength.

Strong ground motions from the near-field are the most severe earthquake loading that brittle structures undergo. The dynamic response of a structure is strongly affected by characteristics of the earthquake, such as intensity, duration and frequency content. The features of ground motion in the proximity of an active fault can be significantly different from those in the far-field.

With regards to the sensitivity and parametric analyses, it is worth noting that the sensitivity assessment of the seismic response parameters to the uncertain modelling variables is a recognized and validated method (e.g. [1, 2, 3, 4]). Uncertainties in the characteristics of the structural component (both mechanical and geometrical) are crucial and have a great impact on the response corresponding to the limit states of damage limitation and significant damage.

From the aforementioned, this research provides a structural safety analysis, taking into account possible variations on the structural response of a specific type of brittle masonry vaults (the medieval structures of the Axarquía, Spain) under near-field effects.

The present paper is arranged in two sections: the first section focuses on the analysis of the worst seismic scenario in the highest seismic area of the Iberian Peninsula under the premises of near-field loading. From that analysis, seismic inputs which are directly related to the structural properties of singular masonry vaults, are obtained. In the second section, sensitivity analyses are carried out by means of non-linear transient analysis. As far as the brittle behaviour is concerned, a constitutive law for brittle materials able to capture collapse mechanism under dynamic loading via FEM is implemented. From those analyses, the influence of different control parameters on the structural response is identified, and deviations on the seismic response are analysed in terms of collapse mechanisms.

2 THE NEAR FIELD SEISMIC INPUT

From a seismological perspective, the near field can be defined as all positions within a small fraction of a wavelength from the source [5]. From a structural perspective, the near-field is related with the potential for ground shaking of sufficient intensity to cause structural damage. In general, any distance less than 50 or 65 kilometres should be considered near for exposure to a major earthquake [6]. Near-fault ground motions are narrow-banded in nature and are characterized by a predominant period, and structures excited by them are severely affected [7]. Under those conditions, the motion may strongly depend on the complex coupling of the seismic source, rupture process, source-site travel path and local site conditions [8, 9]. Strong near-fault ground motion is usually characterized by a long period impulsive motion in the horizontal direction, with large amplitude both in displacement and incremental velocity [10]. Moreover, near-fault strong motions exhibit large incremental velocities which can give rise to large inelastic deformations of the structure regardless of the peak ground acceleration [10]. In addition, features of near-field ground motions such as directivity, can significantly enhance the destructive potential in small to moderate magnitude events [11]. The near-field directivity effects can result in high spectral ordinates at longer periods and their amplifying effects are not a monotonically increasing function with period but rather a narrow band effect at a period that increases with earthquake magnitude [12]. Furthermore, it has been demonstrated that near-field directivity effects not only need to be considered for earthquakes of moment magnitude 6.5 and greater [12]. Thus, near-field effects should be consid-

ered for all earthquakes at short distances from the sites of important or brittle structures, regardless of magnitude at least down to a lower limit that may be as small as 5 or even lower. Directivity effects in small to moderate magnitude events may be of more importance than in very large magnitude events for which the period of the near-field pulse will generally be beyond the range of most structures [12].

A main concern is that in spite of the availability of large digital input databases in many seismically active regions of the world, relatively few good quality strong motion records are available in near-field conditions [8]. Due to the lack of adequate data from close earthquakes, equations to estimate the motion are usually derived from intermediate and far-fields records. Ambraseys and Douglas presented strong-motion attenuation relationships for peak ground acceleration, spectral acceleration, energy density, maximum absolute input energy for near-field inputs [13]. That research highlights some of the singularities of those inputs (e.g. the ratio of the maximum peak ground acceleration to maximum horizontal, the significant distance dependence, …). Moreover, as the effects of near-fault motions can be variable depending on the ratio between the pulse period of the motion and the fundamental vibration period of the structure, peak ground acceleration can be inadequate to represent the structural damage potential of long-duration impulsive motions recorded near active faults [9]. The implication of possible near-field effects and destructive ground motions is related on how the hazard is evaluated. Therefore, inputs from hazard analyses are required.

As far as the Code framework is concerned, the design provisions provided by the Codes, take into account the effects of far-fault ground motions, but can be inadequate for near-fault motions [9]. Although the existing seismic codes consider near-fault shaking effects in the development of elastic response spectra, they do not currently consider the increased inelastic demands that may occur during near-fault ground motion [11]. At Present, Eurocode 8 [14] does not give specific guidelines to take into account the effects of near-fault ground motions in the design of brittle structures. According to that Code, only for base isolated buildings of importance class IV, located at less than 15 km from a known seismic source with a surface-wave magnitude M_s >6.5, the site-specific response spectra should be considered (under time-history analyses).

2.1 Hazard analysis and seismic input

The analysed structures are located at Salares and Árchez, Southern Spain, in the Betic Cordillera, the zone with the highest seismic hazard in the Iberian Peninsula. On a time scale, the seismicity is characterized by a high microseismic activity rate for magnitudes lesser than 4.5, and less frequent earthquakes of magnitudes between 4.5 and 6.5 which generated important damages in the past (e.g. the 1884 Earthquake) in the Granada basin and Málaga [15]. A seismic catalogue is constructed to define the historical seismicity of the area, considering a radius of 300 km, Table 1.

					Salares	
					latitude	longitude
					36,85	-4,0166667
Date	**Latitude**	**Longitude**	**Intensity**	**Location**	**distance** (km)	
01/01/1048	38,0833	-0,9167	**VIII**	**Orihuela.A**	306,31	
01/01/1169	38	-4	**VIII-IX**	**Andujar.J**	*128,01*	
01/01/1406	37,25	-1,8667	**VII-VIII**	**Vera.AL**	*196,1*	
24/04/1431	37,1333	-3,6333	**VIII-IX**	**S. Granada**	*46,43*	
10/10/1482	38,0833	-0,9167	**VIII**	**Orihuela.A**	*306,31*	
01/11/1487	36,8333	-2,4667	**VIII**	**Almería**	*138,07*	
26/01/1494	36,5833	-4,3333	**VIII**	**S. Málaga**	*40,98*	
05/04/1504	37,3833	-5,4667	**VIII-IX**	**Carmona.SE**	*141,72*	
09/11/1518	37,2333	-1,8667	**VIII-IX**	**Vera.AL**	*199,83*	
22/09/1522	36,9667	-2,6667	**VIII-IX**	**W.Alhama de Almería.AL**	*120,84*	
30/09/1531	37,5333	-2,7333	**VIII-IX**	**Baza.GR**	*136,86*	
21/10/1578	35,2667	-2,9333	**VIII**	**Melilla**	*201,38*	
31/12/1658	36,8333	-2,4667	**VIII**	**Almería**	*138,07*	
15/01/1673	38,0833	-0,9167	**VIII**	**Orihuela.A**	*306,31*	
28/08/1674	37,6833	-1,7	**VIII**	**Lorca.MU**	*225,18*	
09/10/1680	36,8	-4,6	**VIII-IX**	**NW. de Málaga**	*52,27*	
13/01/1804	36,0833	-3,5833	**VII-VIII**	**Mar de Alborán**	*93,74*	
25/08/1804	36,7667	-2,8333	**VIII-IX**	**Dalías.AL**	*105,86*	
27/10/1806	37,2333	-3,7333	**VIII**	**Pinos Puente.GR**	*49,54*	
25/12/1884	37	-3,9833	**IX-X**	**Arenas del Rey.GR**	***16,96***	
16/06/1910	36,6667	-3,3667	**VIII**	**ADRA.AL**	61,44	
21/03/1911	38,0167	-1,2167	**VIII**	**LAS TORRES DE COTILLAS.MU**	279,45	
03/04/1911	38,1	-1,2	**VIII**	**LORQUI.MU**	285,04	
31/05/1911	37,2	-3,7	**VIII**	**SANTA FE.GR**	48,06	
09/10/19	38,0833	-0,8333	**VIII**	**JACARILLA.A**	312,91	
05/07/1930	37,6167	-4,6333	**VIII**	**MONTILLA.CO**	101,33	
08/09/30	34,3	-5,4	**VIII**	**AIN DEFALI.MAC**	310,21	
03/05/32	37,4167	-2,45	**VIII**	**LUCAR.AL**	152,65	
23/06/1948	38,1417	-1,7583	**VIII**	**CEHEGIN.MU**	245,83	
03/10/51	38,1833	-3,8167	**VIII**	**LINARES.J**	149,45	
19/05/1951	37,5833	-3,9333	**VIII**	**ALCAUDETE.J**	81,95	
01/08/54	36,9333	-3,8833	**VIII**	**ARENAS DEL REY.GR**	15,06	
19/04/1956	37,1917	-3,6833	**VIII**	**NW PURCHIL.GR**	48,21	
09/06/1964	37,7367	-2,5667	**VIII**	**SW GALERA.GR**	161,93	

Table 1: Seismic catalogue.

From a literature review, the Ground Motion Prediction Equation proposed by Ambraseys and Douglas for the near-field [13] is selected as the most adequate for the area. The period range of interest includes all frequencies that are expected to significantly contribute to the non-linear response. Regarding attenuation of peak ground acceleration, PGA, a value of 0.21g is obtained.

A probabilistic seismic hazard analysis is performed. The applied theory is that of provided by Cornell [16] on the basis of the total probability theorem. The risk is calculated assuming that earthquakes occur as Poisson arrivals (Fig. 1). As the ground-motion intensity measure adopted is the acceleration, it is assumed that it is lognormally distributed. For a return period of 475 years, the obtained peak ground accelerations is 0.27g. According to EC8, this return period ascribes to a Limit State, LS, of Significant Damage, SD, corresponding to a probability of exceedance of 10% in 50 years. On the basis of these results, the relation between the structural performance criteria and the probability of exceedance related to significant LS may be provided.

As far as the procedure for input selection is concerned, an earthquake scenario-based selection is applied. The seismic hazard is disaggregated by: causative Moment Magnitude, M_w, Joyner-Boore distance, r_{jb}, and site class, at the determined probability level. Records that fall

in bins around central values of seismic those parameters are selected. Those parameters are strongly related to the structural response, and are correlated to important characteristics such us frequency content, spectral amplitude, shape and duration. It is worth noting that brittle masonry structures are particularly sensitive to the frequency content of the ground motion, so parameters which measure motions at similar periods to that of the structure are better correlated with damage. The adopted intervals are: [6, 6.6] for the M_w, [0 km, 30 km] for the r_{jb} and [360 m/s, 760 m/s] for the v_{s30}, following the magnitude bin width proposed by Bommer and co- workers [17]. Records are selected from a subset of 175 strong-motions of the Pacific Earthquake Engineering Research Center (PEER database). The selected real records are treated following a linear amplitude scaling. The geometric mean spectrum of the as-recorded components x and y is used (GM_{xy}). Pre- selected records are scaled in terms of spectral acceleration for the fundamental period, S_a (T_1,5%). After scaling of the records according to spectral matching, a screening aimed at obtaining seismic input with spectral shapes similar to the target spectrum is undertaken. A root-mean-square difference equation, D_{rms}, [18] between the spectrum of each real record and the reference spectrum is used. After performing a Coefficient of Variation comparison, COV, three records which exhibit the best goodness-of-fit are selected for the EC8 compatibility (Fig. 2).

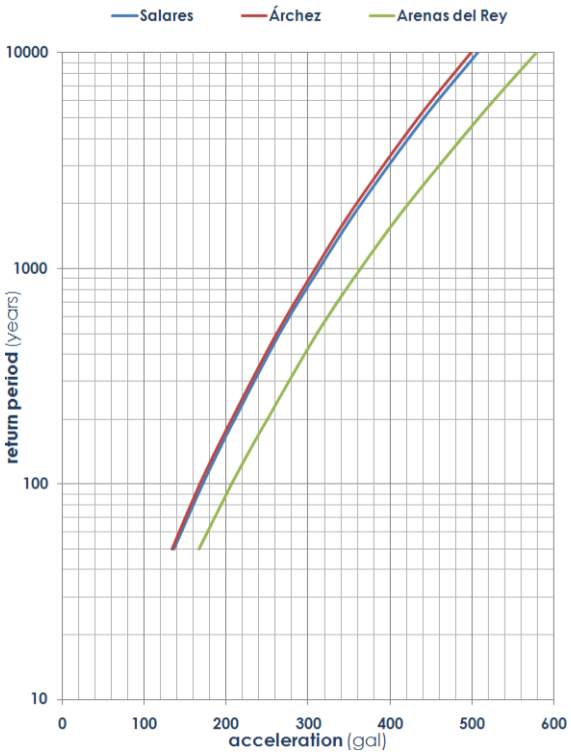


Figure 1: Probabilistic Seismic Hazard analysis.

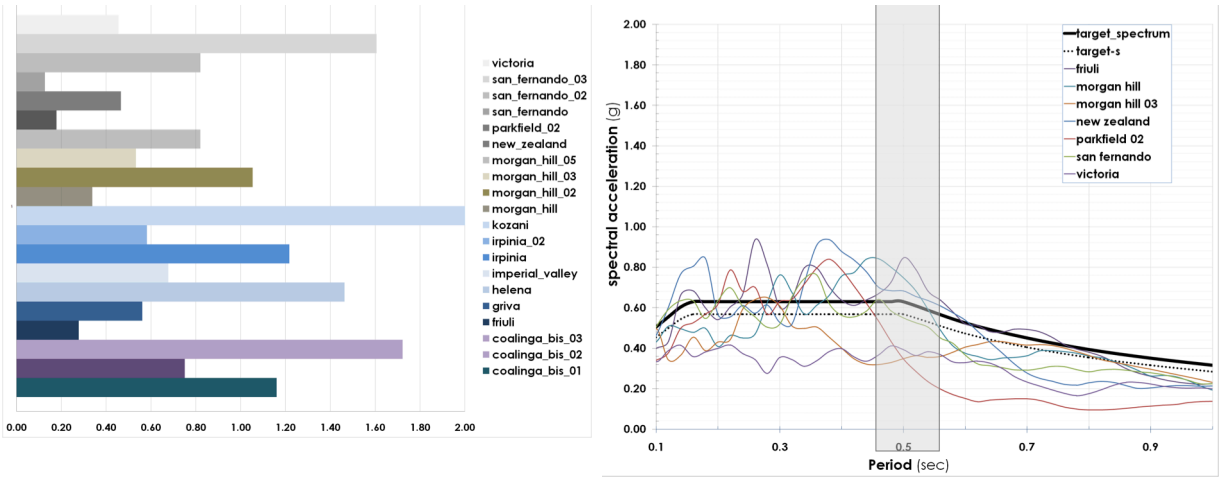


Figure 2: Record selection for the EC8 compatibility.

3 SENSITIVITY ANALYSIS OF THE SEISMIC RESPONSE

Transient analyses are performed on detailed three-dimensional finite element models, taking into account the material non-linear behaviour and the geometrical and structural properties. The ANSYS finite element software [19] is used to construct the model, and three-dimensional eight node solid elements, SOLID 65, are used for masonry material. A smeared model with homogenized properties is selected. The analysed vaults are structural elements of a medieval tower located in Salares, in the Axarquía (Fig. 3). The whole structure is built of clay bricks bonded with lime mortar. The Salares vaults are dramatically damaged (Fig. 4). Stiffness degradation as well as cracking and crushing evolution are taken into account. The Drucker- Prager, DP, perfectly plastic criterion [20] and the Willam-Warncke, WW, failure surface [21] are the selected theories. The stress-strain matrix has been adjusted by introducing a plane of weakness in a direction normal to the crack face. The expression that governs the failure of the material is:

$$\alpha\sigma + \sqrt{\frac{1}{3}\sigma^2 + \tau^2} - k = 0 \qquad (1)$$

where:

$$\alpha = \text{material constant} = \frac{2sin\phi}{(3 - sin\phi)\sqrt{3}}$$

σ = normal stress

τ = shear stress

$$k = \text{material constant} = \frac{6ccos\phi}{(3 - sin\phi)\sqrt{3}}$$

c = cohesion

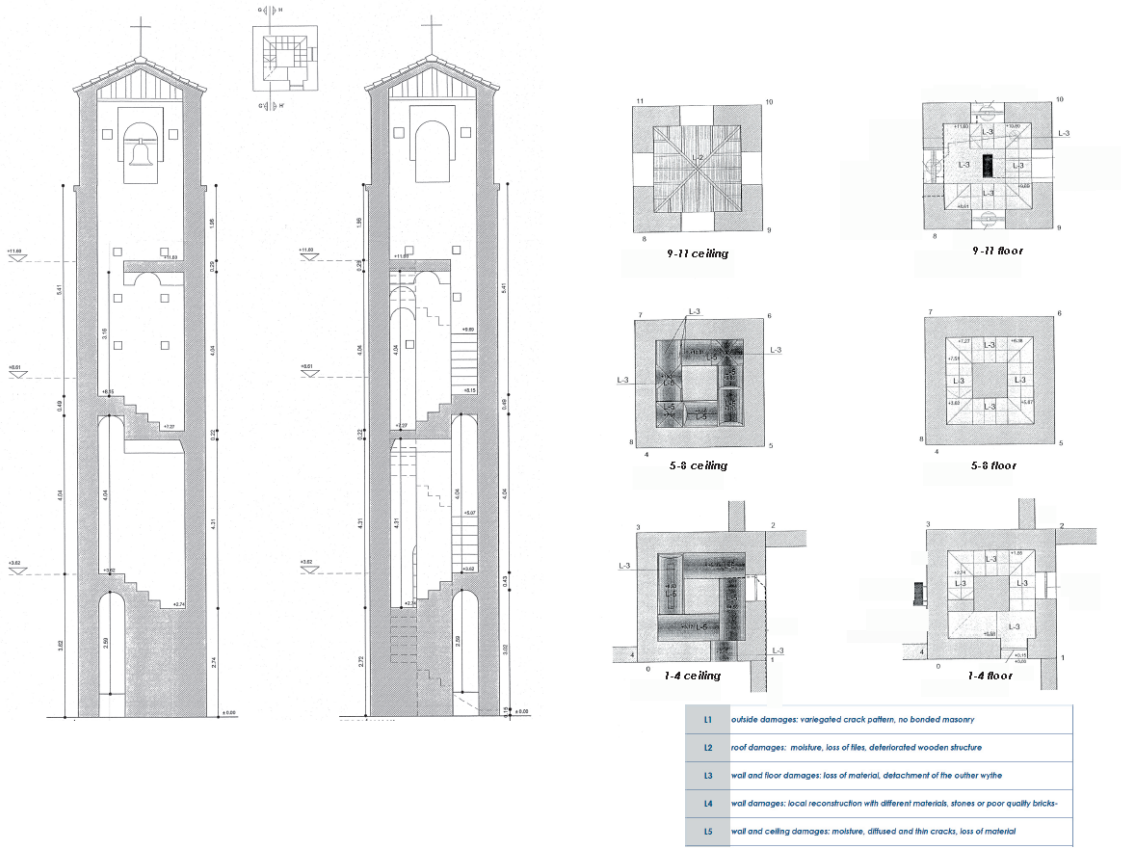


Figure 3: Geometrical and vault damage descriptions.

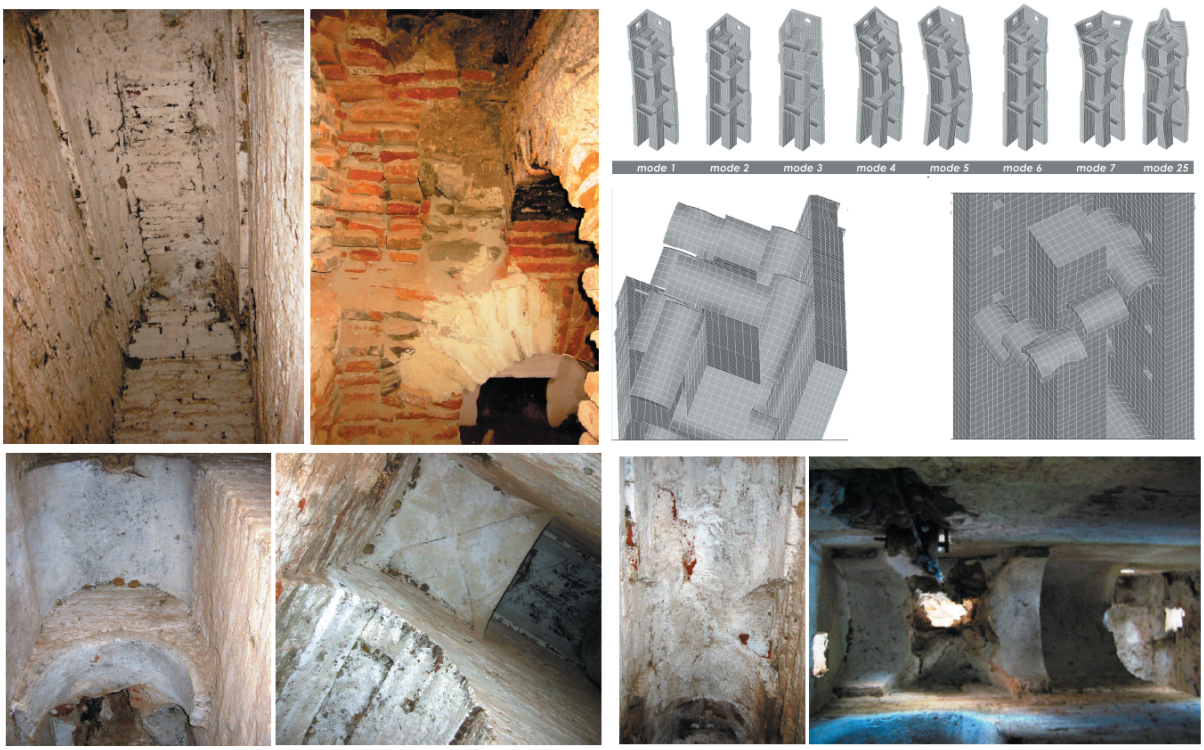


Figure 3: Vaults and FE model.

The time-dependent structural response is obtained from 3 nonlinear time-history analyses, following the component combinations proposed by EC8. The reference seismic scenario is that of previously obtained. A Rayleigh model for damping is applied. The effect of vertical loading in the near-field can be important for damaged masonry structures. Thus, in order to assess the inelastic dynamic response of these structures, the structural responses for bi and tri-directional inputs are compared.

A deterministic sensitivity analysis is used to measure the sensitivity of the seismic response to three performance levels: Near Collapse, NC, Significant Damage, SD, and Damage Limitation, DL. The return period associated to each LS, as well as the corresponding acceleration are those obtained from the probabilistic approach. In a first step, the seismic response parameters are computed for the base-case model on the basis of the best-estimate value. After this, a variation of the random variable to its 16^{th} or 84^{th} fractile is performed. The masonry compressive strength is determined by means of the equation provided by Eurocode 6, $f_{ck}=Kf_{cu}^{0.7}f_{cm}^{0.3}$, where $f_{c,k}$ is the masonry characteristic compressive strength and K, equal to 0.45 in this research, is a parameter that depends on the type of unit and on the type of masonry. The following input variables are considered: Young modulus, E, (median value 3E+09 Pa); masonry compressive strength, f_c (median value 3E+06 Pa); masonry tensile strength, f_t (median value 1E+05 Pa); the value of the friction angle (reference 54º) matches the uniaxial strengths in tension and compression at each step. Due to the low confined nature of the masonry, a reference value of 10º is adopted for the dilatancy. The value of the cohesion matches $1.5f_t$ at each step.

An extremely high cracking pattern is observed in the vaults. The analysis and comparison of the results from the bi and tri-dimensional inputs shows that the most significant gradient appears at the shear S_{xz}, with 85% growth in some time steps. The uncertainty in the mechanical parameters of the masonry, especially those of the mortar, has the greatest impact on the Limit State compliance. A comparison between the different steps reveals that stress field is influenced by sensible redistributions and high gradient values when the uniaxial strengths are varied. Shear stresses undergo dramatic decrease when the mortar compressive strength, f_{cm}, is increased (a maximum 60 % increase is observed) (Fig.5) and for the maximum f_{cm} a decrease of 55% is observed for the main period. From the dynamic response it may be concluded that the vaults do not act as rigid diaphragms and relative rotations are observed.

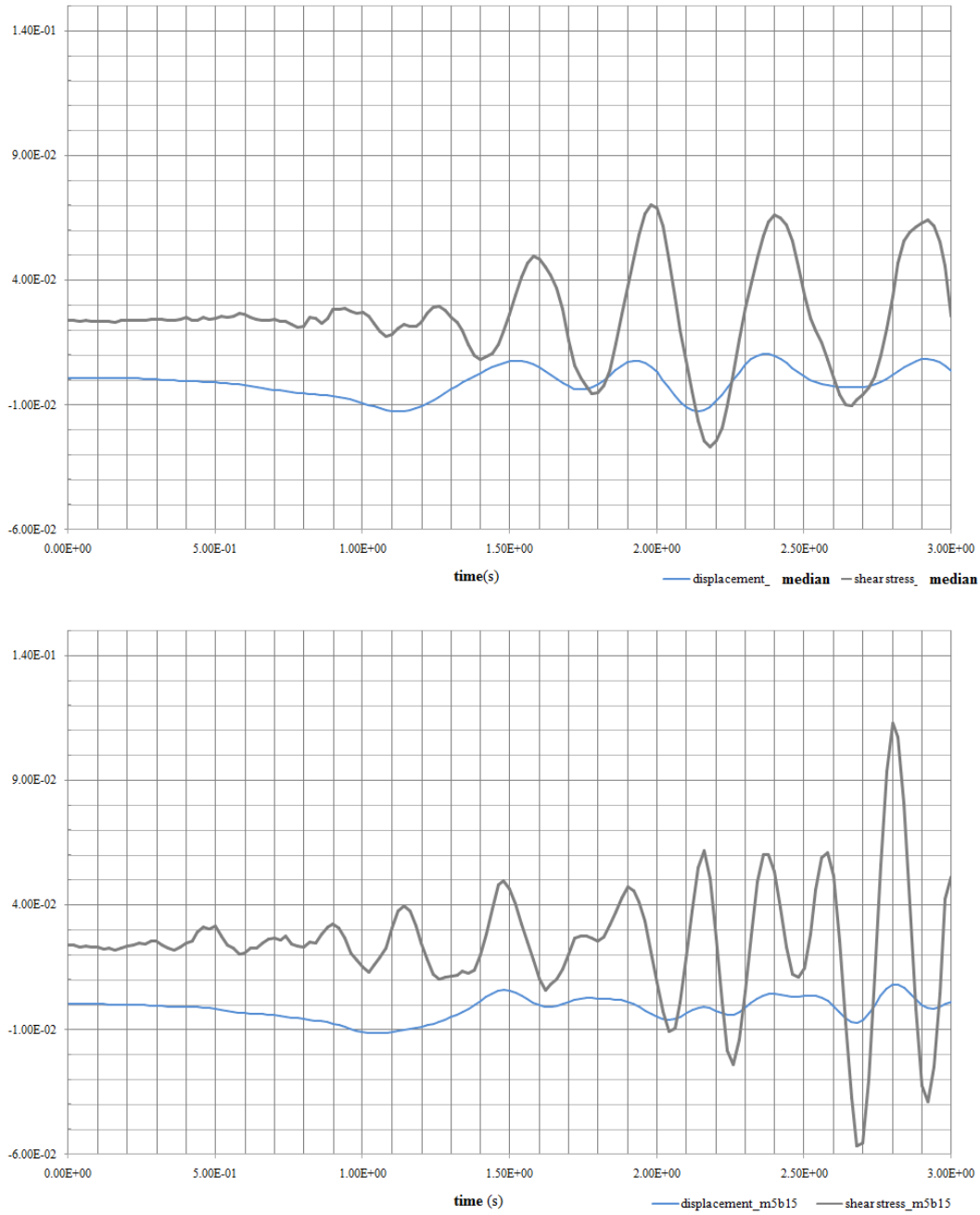


Figure 5: Transient analyses results.

4 CONCLUSIONS

- Ground motions from the near- field contain distinct pulses in acceleration, velocity, and displacement histories, which can generate higher base shear and drift than signals from the far-field.
- The worst seismic scenario in the highest seismic area of the Iberian Peninsula under the premises of near-field loading has been defined, focused on specific masonry vaults.
- The return periods ascribed to each LS are obtained from the probabilistic approach.

- A constitutive law for brittle materials able to capture collapse mechanism under dynamic loading via FEM is implemented.
- The uncertainty in the properties of the mortar has the greatest impact on the seismic response parameters.
- The analysis and comparison of the results from the bi and tri-dimensional inputs shows that the shear exhibits a significant gradient.
- Results for the expected PGA are higher than those of provided by the Codes, as near-field effects must be taken into account.

REFERENCES

[1] Rota, M., Penna, A., & Magenes, G. A methodology for deriving analytical fragility curves for masonry buildings based on stochastic nonlinear analyses. *Engineering Structures , **32*** (5), 1312-23, 2010.

[2] Vamvatsikos, D., & Fragiadakis, M. Incremental dynamic analysis for estimating seismic performance sensitivity and uncertainty. *Earthquake Engineering and Structural Dynamics , **39*** (2), 141-63, 2010.

[3] Dolsek , M. Incremental dynamic analysis with consideration of modeling uncertainties. *Earthquake Engineering and Structural Dynamics , **38*** (6), 805-25, 2009.

[4] Celarec, D., Ricci, P., & Dolsek, M. The sensitivity of seismic response parameters to the uncertain modelling variables of masonry-infilled reinforced concrete frames. *Engineering Structures, **35**,* 2012.

[5] Aki, K., & Richards, P. *Quantitative Seismology: Theory and Methods.* (W. H. Company, Ed., 1980.

[6] Blume, J. Earthquake ground motion and engineering procedures for important installations near active faults. *Proceedings of the Third World Conference on Earthq. Eng.*, *III*, págs. 53-71. Wellington. 1965.

[7] Rupakhety, R., Sigurdsson, S., Papageorgiou, A., & Sigbjornsson, R. Quantification of ground-motion parameters and response spectra in the near-fault region . *Bulletin of Eartquake Engineering , **9***, 893-930., 2011.

[8] Stupazzini, M., Paolucci, R., & Igel, H. Near-fault earthquake ground motion simulation in the Grenoble Valley by a high-performance spectral element code. *Bull Seismolog Soc Am , **99*** (1), 286-301, 2011.

[9] Mazza, F., & Vulcano, A. Nonlinear dynamic response of r.c. framed structures subjected to near-fault ground motions . *Bulletin of Earthquake Engineering , **8***, 1331-1350, 2010.

[10] Anderson, J., & Bertero, V. Uncertainties in establishing design earthquakes . *Journal of Structural Engineering , **113*** (8), 1709-1725, 1987.

[11] Bommer, J., Georgallides, G., & Tromans, I. (2001). Is therea near-field for smal to-moderate magnitude earthquakes? . *Journal of Earthquake Engineering , **5*** (3), 395-423, 2001.

[12] Somerville, P. New developments in seismic hazard estimation. *Sixth International Conference on Seismic Zonation.* Palm Spring, California, 2000.

[13] Ambraseys, N., & Douglas, J. Near-field horizontal and vertical earthquake ground motions . *Soil Dynamics and Earthquake Engineering , **23***, 1-18, 2003.

[14] EC8. (2003). Design of structures for earthquake resistance–part 1: General Rules, seismic actions and rules for buildings. *C.E.N., European Committee for Standardisation, Final Draft* .

[15] Morales, J, B Benito, and M Luján. "Expected ground motion in the south-east of Spain due to an earthquake in the epicentral area of the 1910 Adra earthquake. *Journal of Seismology* **7**, 175–192, 2003.

[16] Cornell, C A. "Engineering seismic risk analysis." *Bulletin of the Seismological Society of America*, 1583–1606, 1968.

[17] Bommer, J J, and A Acevedo. "The use of real earthquake accelerograms as input to dynamic analysis." *Journal of Earthquake Engineering* **8**, no. 1 43–91, 2004.

[18] Ambraseys, N N, et al. *Dissemination of European strong-motion data.* Vol. 2. CD-ROM collection. Engineering and Physical Sciences Research Council, 2004.

[19] ANSYS. *ANSYS Manual SET.* Southpoint, 1998.

[20] Drucker, D C, and W Prager. "Soil mechanics and plastic analysis or limit design." *Quarterly of Applied Mathematics* **10**, 157-173, 1952.

[21] Willam, K J, and E D Warnke. "Constitutive model for the triaxial behaviour of concrete." *Proceedings of the International Association for Bridge and Structural Engineering.* Bergamo, Italy, **174**, 1975.

COMPDYN 2015
5th ECCOMAS Thematic Conference on
Computational Methods in Structural Dynamics and Earthquake Engineering
M. Papadrakakis, V. Papadopoulos, V. Plevris (eds.)
Crete Island, Greece, 25–27 May 2015

ANISOTROPIC FAILURE CRITERION FOR BRITTLE MATERIALS USING ARTIFICIAL NEURAL NETWORKS

Vagelis Plevris[1] **and Panagiotis Asteris**[1]

[1] Computational Mechanics Laboratory, Department of Civil Engineering
School of Pedagogical & Technological Education
ASPETE Campus, Heraklion, GR 141 21, Athens, Greece
email: vplevris@aspete.gr, panagiotisasteris@gmail.com

Keywords: Anisotropy, brittle material, failure criterion, Artificial Neural Network.

Abstract. *Brittle materials are complex composite materials and a model is necessitated to realistically predict their load carrying capacity under any stress-state. During the last decades, a lot of failure criteria have been proposed for these materials in the literature. However, the majority of these models may substantially over-estimate the strength of the failure surface envelope. To overcome this problem a new approach is proposed which is based on Artificial Neural Networks (ANNs) techniques. The proposed approach is applied to a characteristic brittle anisotropic material such as the masonry material. The Neural Network managed to produce closed failure curves extending in all four quadrants of principal stresses, thus fully covering the compression and the tension stress areas. The comparison of the derived results with experimental findings demonstrates the promising potential of using ANNs for the reliable and robust approximation of the failure surface under biaxial stress state.*

1 INTRODUCTION

Despite the fact that masonry is one of the oldest structural materials and, actually, the main material of monumental structures such as churches, castles, mosques etc., our knowledge regarding its mechanical behavior is not as thorough as it should be and many aspects of its behavior remain to be investigated. Masonry exhibits distinct directional properties due to the influence of the mortar joints. Depending on the orientation of the joints to the stress directions, failure can occur in the joints alone or simultaneously in the joints and the blocks.

Nowadays, in developed societies, there is an increased interest about reliable and robust computational models for the modeling of masonry structures. This is primarily due to the growing interest of protecting heritage structures. The main characteristic of the majority of these structures is that they are mostly made of masonry. Taking into account the numerous uncertainties of the problem, a computational model, describing the masonry failure surface in a simple manner should be an efficient and useful tool for the investigation of the behavior of masonry structures.

To fulfill this need, in the last decades a large number of macro and micro computational models have been proposed for both the linear and the non-linear analysis of such structures [1-5]. Detailed and in-depth state-of-the-art reports can be found in [6-11]. The successful implementation of these advanced models requires reliable analytical constitutive rules such as constitutive equation models of masonry material failure. To date, research work has been focused on isotropic masonry models, which are based, primarily, on models applied for concrete. Regarding non-isotropic masonry, there are few research works in which failure criteria approximate the failure surface by employing different forms of quadratic polynomials. Many variations of such models have been published to date, including those defining the failure surface through the use of different functions for each quadrant [12-15]. However, for certain load cases, such models overestimate strength [16].

The present study applies Neural Networks in order to approximate the experimental failure curves of a brittle anisotropic material such as masonry. The aim of the study is to introduce an anisotropic (orthotropic) Neural Network – generated 3D failure surface under biaxial stress for masonry for any angle of the joints to the vertical compressive load, as described in detail in the following sections.

2 METHODOLOGY

The methodology of the present work is similar to another study by the authors [11], that focused only on the compression-compression area, where both principal stresses were compressive, i.e. it focused on the third quadrant of the σ_I-σ_{II} plane (compression-compression), without having to do with the other three quadrants. The present work continuous and extends that previous investigation to all four quadrants, namely the (A) tension-tension, (B) compression-tension, (C) compression-compression, and (D) tension-compression quadrant. This work utilizes the experimental data reported by Page [17-19], which have been also used by many other researchers [20, 21].

For all panels that were tested by Page [17-19], ratios of vertical compressive stress σ_I to horizontal compressive stress σ_{II} of 1, 2, 4, 10 and infinity (i.e. uniaxial σ_I) were used in conjunction with bed joint angle θ (with respect to σ_I) in directions of 0°, 22.5°, 45°, 67.5° and 90°. The pair cases (0°, 90°), (22.5°, 67.5°) are symmetric to each other. Principal stress ratios of 0 (i.e. uniaxial σ_{II}), 0.1, 0.25, 0.5 and 1 were obtained from the results using the symmetry of the panels and the loading. The failure envelopes that Page obtained by plotting mean curves for each bed joint angle can be found in Page [17-19] and [11]. These failure envelopes

are based on the peak strength values obtained from running bond masonry panel tests in which a uniform loading was applied proportionally. It should be emphasized that there are no real experimental data for the cases θ=67.5° and θ=90.0°, because these cases are equivalent to the cases θ=22.5° and θ=0.0°, respectively, if we reverse σ_I and σ_{II} stresses.

First, for each angle θ (0º, 22.5º, 45º, 67.5º, 90º) of the joints to the vertical compressive load, a Neural Network was trained with the experimental data of Page [17-19] as inputs (five NNs in total). Then each one of the five NNs was asked to produce the whole 2D failure curve (for each angle θ) as its output, filling also the gaps between the experimental points, thus "enriching" the experimental data with appropriate approximations. Then another, "global" NN was trained using the results of the five NNs as inputs with the angle θ as another input, also. The new NN was then asked to fill also the gaps between the angles θ, providing the whole 3D failure surface (a tube) for any angle θ (0º to 90º) and any ratio of σ_I/σ_{II}, for all four quadrants of stress.

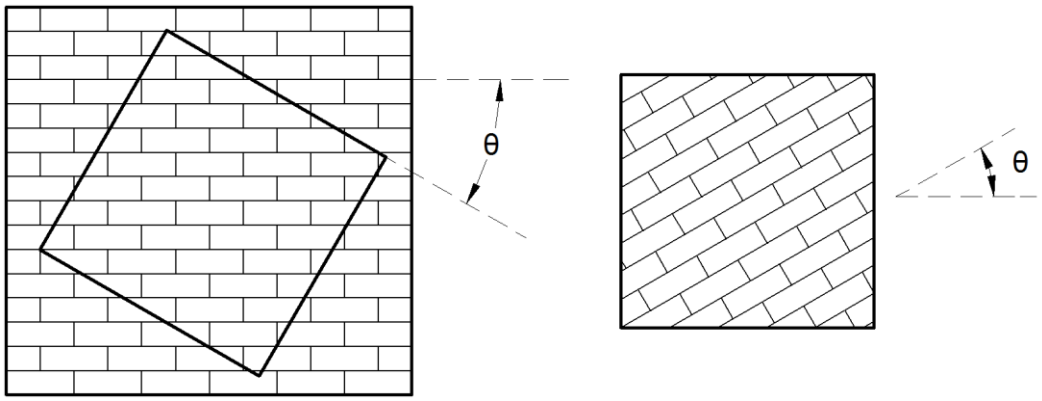
3 BIAXIAL TESTING PROCEDURE

Masonry is a composite, multi-phase material that exhibits distinct brittle and strongly anisotropic behavior. The highly anisotropic brittle nature of masonry, renders complicated, difficult and expensive the realization of reliable experimental tests under conditions of biaxial stress, and, even more, under conditions of biaxial tension or heterogeneous stress. The angle of the applied loading to the bed joint plays a significant role in the behavior of the brick masonry discs. In general, the highest strength of masonry is observed when the compressive load is perpendicular to the bed joints or in other words when the principal tensile stress at the center of the disc is parallel to the bed joints. In this case, failure occurs through bricks and perpendicular joints. On the other hand, the lowest strength is observed when the compressive load is parallel to the bed joints or in other words when the principal tensile stress at the center of the disc is perpendicular to the bed joints. In this case failure occurs along the interface of brick and mortar joint.

In our study, in order to obtain the experimental results, a biaxial stress state is induced in the panel by loading with hydraulic jacks in two orthogonal directions. A constant load ratio is maintained during each test by means of the spreader beam. The load in each direction is monitored by load cells immediately adjacent to the specimen. Two main methodologies are used in the literature in order to obtain the final test specimens with the correct shape and size, presented in [22, 17-19, 23].

3.1 First methodology

Specimens with horizontal and vertical joints (Figure 1a) are constructed with dimensions greater than those of the final specimen, and then a square with the desired dimensions is drawn on the surface of the wall by a pencil at the appropriate orientation to achieve the correct lay-up angle as shown in Figure 1b, where the angle θ is the bed joint angle with respect to the horizontal direction.



(a) (b)

Figure 1: Preparation of the masonry specimens.
(a) Wall panel before saw cut, (b) Saw cut specimen.

The lay-up angle is defined as the angle between the direction of the bed joints and one of the edges of the finished test specimen. Therefore, bed joints run at oblique incidence to the edges of the finished saw-cat specimen. After a time-span of 14 days the larger wall panels were cut to the required size and shape by a 'Clipper' saw. The 'Clipper' saw has the capacity to hold impregnated diamond edge circular blades of varying thickness and diameters. Two days prior to the date of testing, the 'compressive edge' of the panel (the side on which the compressive loads was to be applied) was capped with 1:1 (cement:sand) mortar [11].

3.2 Second methodology

According to Page [17-19] all specimens are constructed directly to their final shape and size as follows: All brickwork is constructed horizontally on a rigid form with bricks glued to a Perspex backing sheet to ensure a constant joint thickness. Panels are made with varying bed joint angles by cutting individual bricks to the required shape before casting. In the present study, five lay-up angles were selected for biaxial tests, namely 0°, 22.5°, 45°, 67.5° and 90°.

4 FIVE ARTIFICIAL NEURAL NETWORKS

In the present study, *Back-Propagation Neural Networks* (BPNNs) are used, in which the output values are compared with the correct answer to compute the value of a predefined error-function. The error is then fed back through the network. Using this information, the algorithm adjusts the weights of each connection in order to reduce the value of the error function by some small amount. The procedure is similar to the one used in a previous work by the authors [11], where more details can be found. The transfer function used in the present study is the hyperbolic tangent function, the same for all the hidden and the input layer, which yields output values in the interval [-1, 1], while its derivative yields output values in the interval [0, 1]. The transfer function for the output layer is a linear function. This scheme has been used for all the NNs of the study.

There are five NN models, one for each θ angle. For all five NNs, we used a BPNN with one hidden layer, one input layer and one output layer. The input layer had one node (neuron) which corresponds to the angle φ (in the range $[0, 2\pi]$), which defines the ratio σ_{II}/σ_{I}, while the output layer had also one node which corresponds to the distance (radius) r of the point on the failure curve to the origin of the axes. These two parameters (φ and r) will be described in detail in the next paragraphs. The hidden layer of each NN had 4 nodes for all θ (θ=0°, 22.5°,

45°, 67.5°, 90°), resulting in a 1-4-1 BPNN architecture for all five cases. These values have been chosen after some trial tests on various network architectures. The input and output values are normalized before the NN training and the inverse normalization is performed in order to obtain the NN results for other data, afterwards.

4.1 Preparation of the NN Input data

The experimental data of Page [17-19] have been used as inputs for the first five NN models of the present study.

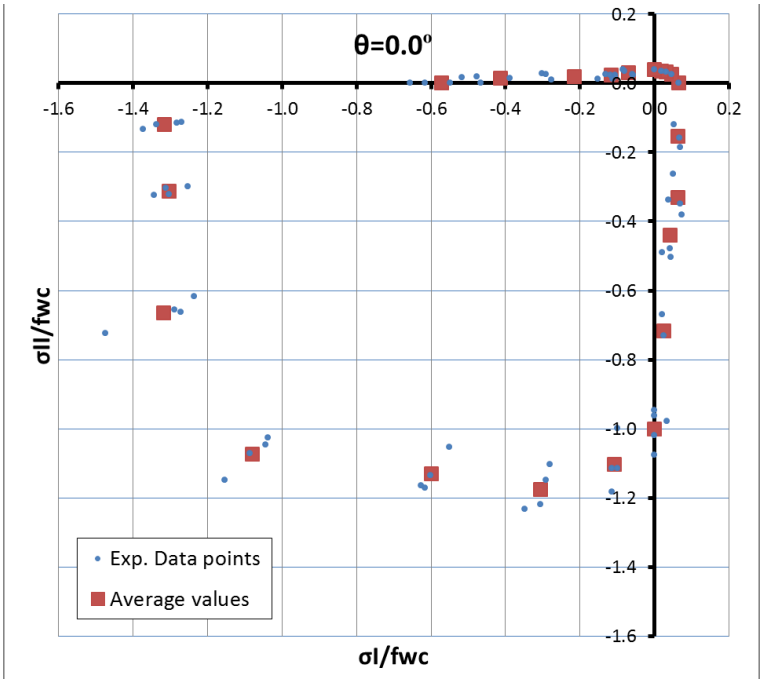


Figure 2: Normalized experimental data and average values for θ=0.0°.

The figure above shows the original data for the θ=0° case (in a normalized form, shown as blue points in the figure) together with the average values for each σ_I/σ_{II} ratio (shown as red squares). Table 1 shows the corresponding analytical data for the θ=0° case (average values for each test are shown only). The analytical data for the other θ cases are not reported in the present study.

The table consists of four parts, which correspond to four different types of tests, published in three different papers, as shown below:

A. 1st Quadrant: Biaxial Tension ($\sigma_I \geq 0$, $\sigma_{II} \geq 0$) [17]
B. 2nd Quadrant: Biaxial heterossemous Stresses (Compression – Tension) ($\sigma_I \leq 0$, $\sigma_{II} \geq 0$) [19]
C. 3rd Quadrant: Biaxial Compression ($\sigma_I \leq 0$, $\sigma_{II} \leq 0$) [18]
D. 4th Quadrant: Biaxial heterossemous Stresses (Tension – Compression) ($\sigma_I \geq 0$, $\sigma_{II} \leq 0$) [19]

Average σ_I/f_{wc}	Average σ_{II}/f_{wc}	Angle φ	Radius r	Region, Source
0.066	0.000	0.000	0.066	**A** Tension – Tension [17]
0.046	0.026	0.514	0.053	
0.032	0.032	0.784	0.045	
0.020	0.035	1.050	0.040	
0.000	0.038	1.571	0.038	
-0.070	0.031	2.731	0.077	**B** Compression – Tension [19]
-0.115	0.023	2.947	0.118	
-0.214	0.019	3.051	0.215	
-0.414	0.015	3.106	0.415	
-0.572	0.000	3.142	0.572	**C** Compression – Compression [18]
-1.316	-0.120	3.233	1.321	
-1.303	-0.312	3.377	1.340	
-1.318	-0.665	3.609	1.476	
-1.080	-1.073	3.924	1.522	
-0.599	-1.130	4.225	1.279	
-0.307	-1.175	4.457	1.215	
-0.107	-1.102	4.615	1.107	
0.000	-1.000	4.712	1.000	
0.025	-0.717	4.748	0.717	**D** Tension – Compression [19]
0.041	-0.440	4.806	0.442	
0.064	-0.331	4.904	0.337	
0.062	-0.154	5.097	0.166	

Table 1. Failure of Brickwork under Biaxial Compression, θ=0°.

The first two columns of the table contain the averages of the tests for each loading case, i.e. for each σ_{II}/σ_I ratio. The tension-tension experimental test (A) is the most difficult to perform and also the values are small and the data points more dense, so there is only one test for every σ_{II}/σ_I ratio, while for Parts B, C, D we have 2, 3 or 4 tests for each case. As a result, for Part A, the average values coincide with the values themselves, as there is only one test performed for each σ_{II}/σ_I ratio. The data are in a dimensionless form where the stresses have been divided with the stress f_{wc} which is the masonry strength for the case σ_I=0 for Case C (Compression – Compression case). The value of f_{wc} has been calculated as the average of the four values corresponding to four tests (7.15, 7.27, 7.69, 8.12) as 7.56 MPa.

For the data to be suitable for the Neural Network training, a conversion to polar coordinates (r, φ) is needed, where the distance (or radius, Column 4 of the table) r is given by

$$r = \sqrt{{\sigma_{I,aver}}^2 + {\sigma_{II,aver}}^2} \tag{1}$$

where $\sigma_{I,aver}$ and $\sigma_{II,aver}$ are the average stresses for each loading case (columns 1, 2). Since we are trying to describe a full circle, the polar angle value φ has to be within [0, 2π) range. Based on the values of σ_I and σ_{II}, we need to calculate the value of the polar angle φ. For Part A (Tension-Tension), this can be done easily using the Inverse Tangent function (Arctan) as follows:

$$\varphi_A = \mathrm{Arc}\tan\left(\frac{\sigma_{II}}{\sigma_I}\right) \tag{2}$$

The Arctan function always returns values within the (-π, π) range. In the last case of Part A, it is $\sigma_I=0$ and as a result Eq. (2) cannot be defined. In this case it is obviously $\varphi=\pi/2$. The range of φ_A is [0, π/2].

For Part B (2nd quadrant) it is $\sigma_I\leq 0$, $\sigma_{II}\geq 0$, while for Part C (3rd quadrant) it is $\sigma_I\leq 0$, $\sigma_{II}\leq 0$. In these two cases, in order to get the value of φ, the following formula hat to be used:

$$\varphi_B = \varphi_C = \pi + \text{Arc tan}\left(\frac{\sigma_{II}}{\sigma_I}\right) \tag{3}$$

In the last case of Part C, it is $\sigma_I=0$ and as a result Eq. (2) cannot be defined. In this case it is obviously $\varphi=3\pi/2$. The range of φ_B is [π/2, π] and the range of φ_C is [π, 3π/2].

For Part D (4th quadrant) it is $\sigma_I\geq 0$, $\sigma_{II}\leq 0$. In this case, the following formula is applicable:

$$\varphi_D = 2\pi + \text{Arc tan}\left(\frac{\sigma_{II}}{\sigma_I}\right) \tag{4}$$

Angle φ is given in Column 3 of the table. The figures below show the corresponding diagrams for the other two main θ cases (θ=22.5°, θ=45°). The other two cases, θ=67.5° and θ=90° are omitted here, as they are symmetric to the cases θ=22.5°, θ=45°), respectively. The symmetry is about the line $\sigma_I=\sigma_{II}$.

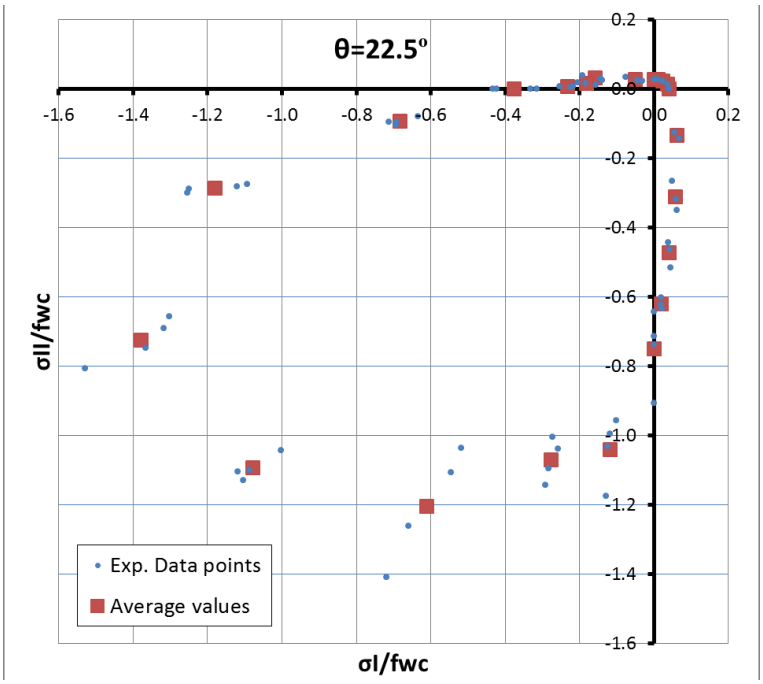


Figure 3: Normalized experimental data and average values for θ=22.5°.

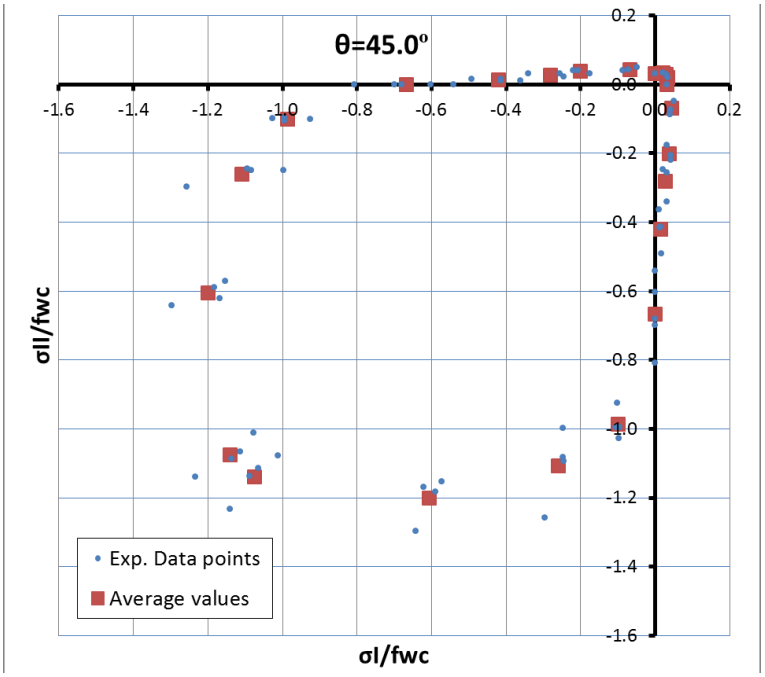


Figure 4: Normalized experimental data and average values for θ=45.0°.

The data (and also the failure curve itself) for θ=45° are symmetric with respect to the 45° diagonal line (σ_I=σ_{II}), due to not only the nature of the loading but also to the geometry of the masonry panel where for this special case the bed joint orientation is equal to angle θ=45°. The data for θ=0° and θ=90° that correspond to complementary angles are also mutually symmetric to the line σ_I=σ_{II}. The same also applies for the data for θ=22.5° and θ=67.5. These special conditions will be studied in detail in the next paragraphs.

For each of the five angles θ (θ=0°, 22.5°, 45°, 67.5°, 90°), a separate Neural Network is trained with the angle φ as its input and the radius r as its output. It should be noted that only the average values of each test (denoted as "square" points in the above figures) are used as training data for the Neural Networks.

4.2 Properties of the curves - NN Corrections

The failure curves have some distinct characteristics and the NN results need to be in some cases corrected in order to comply and exactly follow the rules. These characteristics are mentioned below.

1. *Consistency for φ=0 and φ=2π.* The case φ=0 (start of circle) is in fact the same case as φ=2π (end of circle) and the results in these two points (start and end of circle) should coincide.
2. *Symmetry for θ=45°.* For the special case of masonry with bed joint angle θ=45°, the masonry panel exhibits a symmetry which leads to a symmetric failure curve (to the line σ_I=σ_{II}).
3. *Symmetry for any complementary angles (θ and 90°-θ).* The failure curves that correspond to complementary angles (θ and 90°-θ), such as θ=0° and θ=90° as well as θ=22.5° and θ=67.5°, are mutually symmetric to the line σ_I=σ_{II}.

Although the results obtained by the NNs are in most cases very satisfactory in their original form, we apply some special corrections in order to ensure that the above rules are satisfied with 100% accuracy.

For point (1) of the above, we take into account two full identical cycles of data when training the NN. This means that instead of stopping at $\varphi=2\pi$, the NN is trained for two cycles of data, until $\varphi=4\pi$. Also, a correction is applied in order to ensure that the result (radius r) will be exactly the same for $\varphi=0$ and $\varphi=2\pi$.

For points (2) and (3), when a symmetric result is expected, we take into account the average values between the two symmetric cases and this way we apply the correction. This technique is applied in the $\theta=45°$ case itself and also for the mutually symmetric cases ($\theta=0°$, $\theta=90°$) as well as ($\theta=22.5°$, $\theta=67.5°$). In particular, the results of the two equivalent cases are both taken into account and the average is finally considered, ensuring that the result would be perfectly symmetric between the two cases. The symmetry is to the line $\sigma_I=\sigma_{II}$ for all cases.

4.3 Final approximation results of the five NNs

The five NNs were trained with the input and output data and then each NN was asked to produce the full curves for each bed joint angle, for a set of 80 segments (81 points). Although each NN was trained for two circles of data, it was asked to report results only for the first circle (in th

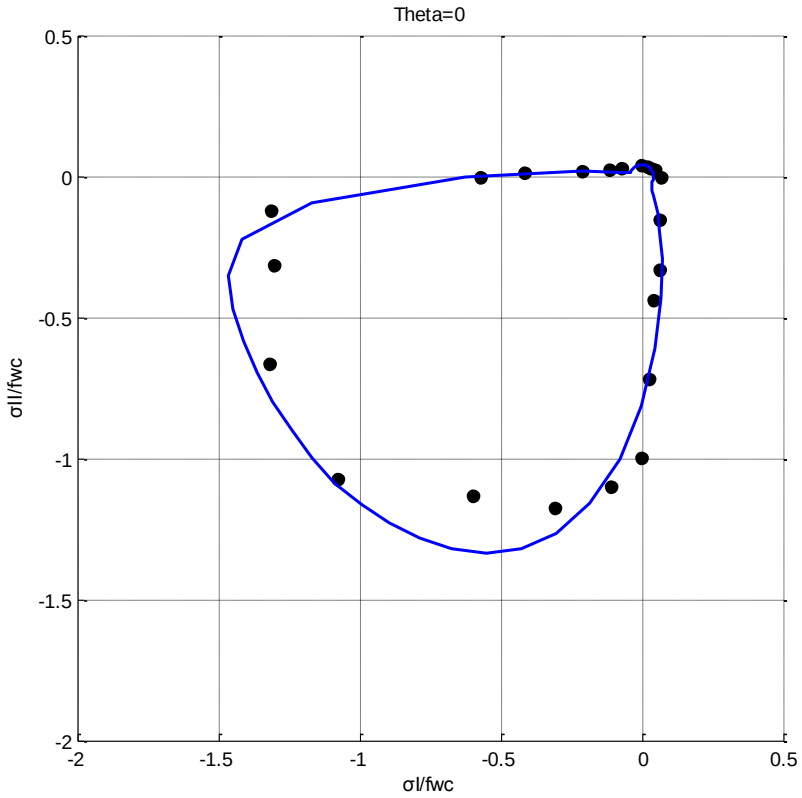


Figure 5: NN approximation result for θ=0°.

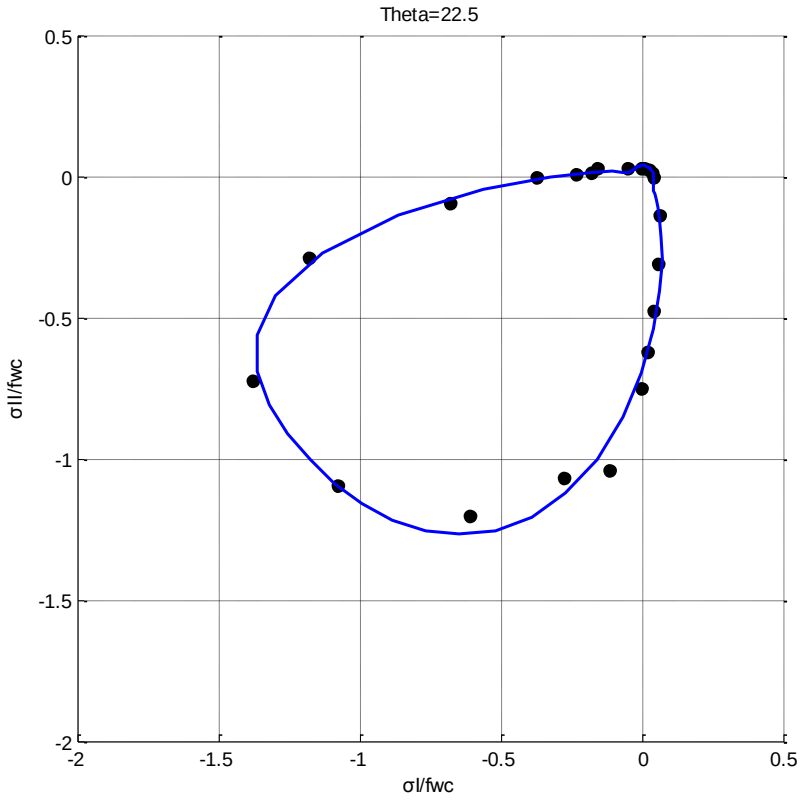


Figure 6: NN approximation result for θ=22.5°

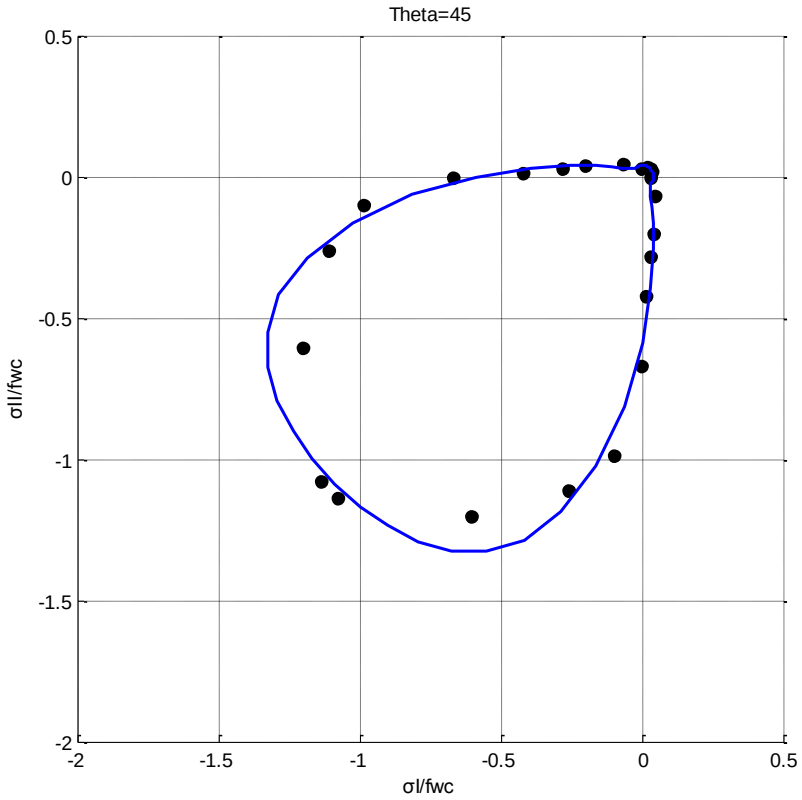


Figure 7: NN approximation result for θ=45°.

In all the above figures, the black dots denote the input data, i.e. the data corresponding to columns 3, 4 of the table. The blue curve denotes the NN prediction of the failure curve. It can be seen that the NN managed to fit all the training data with very good accuracy, providing smooth curves in all cases. For the θ=45° case, it can be seen that the curve is perfectly symmetric to the σ_I=σ_{II} line, due to the extra measures that have been taken.

5 "GLOBAL" NN MODEL AND RESULTS

Five NN Models were trained, each for one angle θ (0°, 22.5°, 45°, 67.5° and 90°). The final purpose of the study is to add also the angle θ as a parameter of the problem, thus create a model that will be able to predict the entire failure curve not only for the predefined angles, but for any angle θ, from 0° to 90°. In order to achieve this, after the five NNs were trained and they had provided their results, another "Global" NN was also trained which took the results of the five NNs as inputs with the angle θ as an additional input, also. The new NN was then asked to fill the gaps between the angles θ, providing the whole 3D failure "tube" for any angle θ and any angle φ (i.e. ratio of σ_{II}/σ_I), for all four stress quadrants.

The Global NN is a BPNN with one hidden layer containing 10 nodes (2-10-1 architecture). The two inputs are the angles φ (0 to 4π - two full circles) and θ (0° to 90°), while the output is the distance (radius) r. The transfer function of the global NN is the hyperbolic tangent function. For the global NN, we use all the results of the previous five NNs as training patterns. This means that we have 161*5 = 805 training patterns, as we use 161 points (80*2+1) for every angle θ (0°, 22.5°, 45°, 67.5° and 90°).

The global NN was trained and then asked to produce the whole 3D failure surface. Although the global NN was trained in two full circles ([0, 4π]), in order to achieve better performance and to manage to "close" the curve for the first circle, it was asked to produce results only for the first circle ([0, 2π]). Specifically, the NN was asked to produce points where the angle φ was divided again in 160 (80*2) segments (161 points, each segment is equivalent to 360°/80=4.5°), while angle θ is divided in 40 segments (41 points, each segment is equivalent to 90°/40=2.25°). The figure below shows the result of the NN approximation in 3D (two different views of the tube). The red points (dots) denote the initial training set of the first five NNs, i.e. the average values gathered from the experimental results and used for the training of the NNs.

6 CONCLUSIONS

In the last decades, there have been many attempts on modeling the materials' constitutive rules by means of Neural Networks. However there have not been many attempts to apply a Neural Network (NN) for the prediction of masonry behavior in general. In the present paper, following and expanding a previous work by the authors [10] which focused on biaxial compressive stress only, the use of Neural Networks is proposed to approximate the failure surface of masonry materials in a dimensionless form for any quadrant of stress state.

A novel procedure based on Neural Networks techniques has been introduced in order to model the failure/yield surface of masonry material in dimensionless form. Available classical experimental results from the literature are used as inputs for the training of the NN. The proposed NN procedure is demonstrated and has been shown to be reliable and robust.

The derived failure surface fits the experimental data with excellent accuracy, while it is in dimensionless form which is very important in order to be able to be applied for every masonry material. Furthermore, the derived surface can provide valuable information about areas of the masonry failure that have not been investigated until now (failure under heterosemous

stresses or failure under biaxial tension for any tilt angle of the bed joints) helping us better understand the phenomena involved in fracture mechanics.

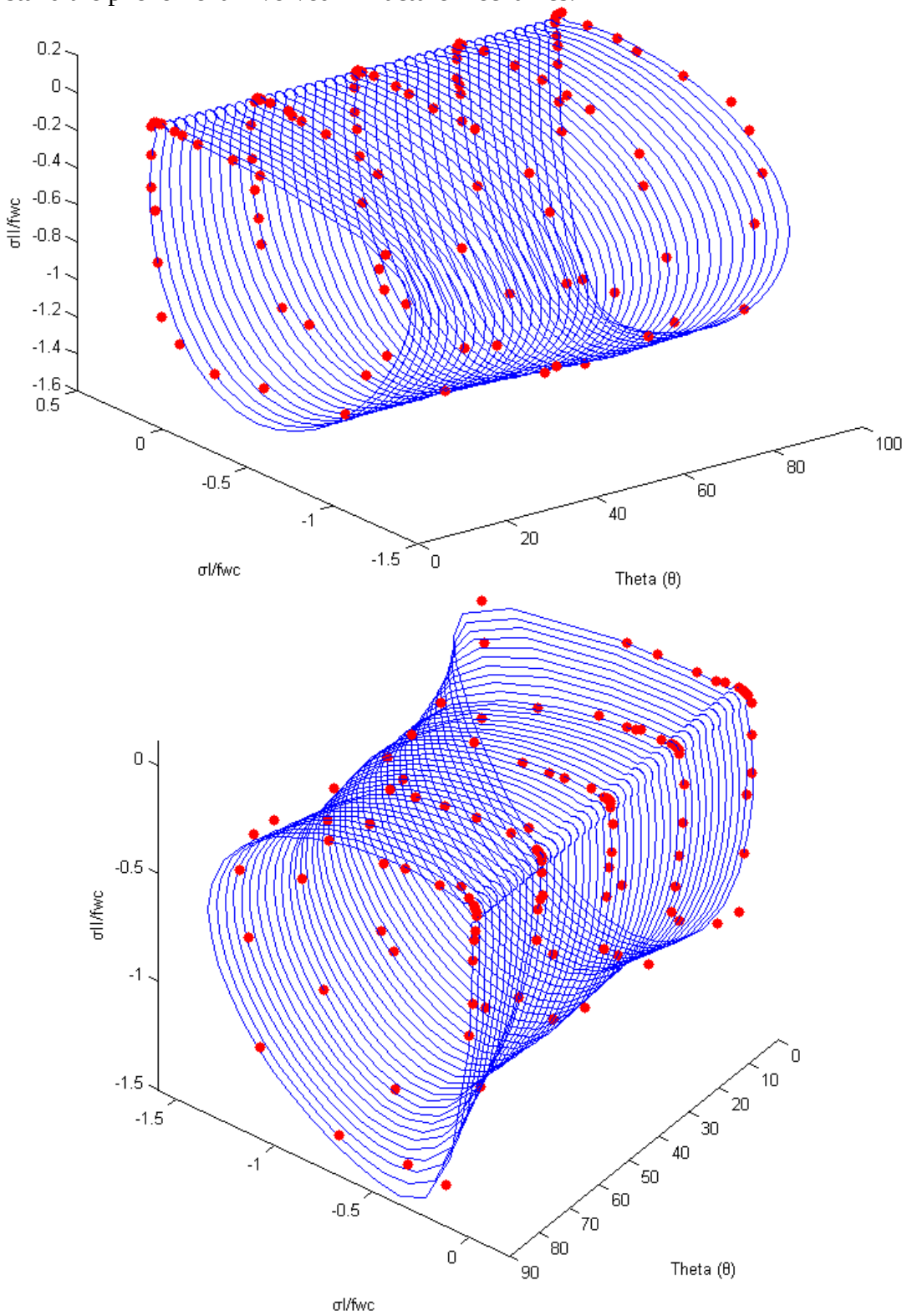


Figure 8: Global NN approximation result of the 3D failure surface in terms of principal stresses

(two different views of the failure tube.

REFERENCES

[1] Lourenço, P.B., Rots, J.G. and Blaauwendraad, J. (1998). Continuum model for masonry: parameter estimation and validation, Journal of Structural Engineering, 124(6), pp.642-652.

[2] Caliò I., Marletta M. and Pantò B. (2012). A new discrete element model for the evaluation of the seismic behavior of unreinforced masonry buildings, Engineering Structures, 40, pp. 327-338.

[3] Penna, A., Lagomarsino, S., Galasco, A. (2014). A nonlinear macroelement model for the seismic analysis of masonry buildings, Earthquake Engineering and Structural Dynamics, 43(2), pp. 159-179.

[4] Asteris, P.G., Chronopoulos, M.P., Chrysostomou, C.Z., Varum, H., Plevris, V., Kyriakides, N., Silva, V. (2014). Seismic vulnerability assessment of historical masonry structural systems, Engineering Structures, Volume 62-63, 15 March 2014, Pages 118-134

[5] Reccia, E., Milani, G., Cecchi, A., Tralli, A. (2014). Full 3D homogenization approach to investigate the behavior of masonry arch bridges: The Venice trans-lagoon railway bridge, Construction and Building Materials, 66, 567-586.

[6] Lourenço, P.B. (2002). Computations on historic masonry structures, Progress in Structural Engineering and Materials, 4(3), pp. 301-319.

[7] Roca, P., Cervera, M., Gariup, G. and Pela, L. (2010). Structural analysis of masonry historical constructions. Classical and advanced approaches, Archives of Computational Methods in Engineering, 17(3), pp. 299-325.

[8] Asteris, P.G., Antoniou, S.T., Sophianopoulos, D.S., Chrysostomou, C.Z. (2011). Mathematical macromodeling of infilled frames: State of the art, Journal of Structural Engineering, 137 (12), pp. 1508-1517

[9] Sarhosis V. (2012). Computational modelling of low bond strength masonry. Phd thesis. University of Leeds, UK

[10] Asteris, P.G., Cotsovos, D.M., Chrysostomou, C.Z.,Mohebkhah, A., Al-Chaar, G.K. (2013). Mathematical micromodeling of infilled frames: State of the art, Engineering Structures, 56, pp. 1905-1921

[11] Plevris, V., Asteris, P.G. (2014). Modeling of masonry failure surface under biaxial compressive stress using Neural Networks, Construction and Building Materials, 55, pp. 447-461

[12] Ganz, H.R. (1989). Failure criteria for masonry, Proc. of the 5th Canadian Masonry Symposium, pp. 65-77

[13] Lourenço, P.B., De Borst, R., Rots, J.G. (1997). Plane stress softening plasticity model for orthotropic materials. Int J Numer Methods Eng, 40:4033–57.

[14] Massart, T.J., Peerlings, R.H.J., Geers, M.G.D., Gottcheiner, S. (2005). Mesoscopic modeling of failure in brick masonry accounting for three-dimensional effects, Engineering Fracture Mechanics, 72 (8), pp. 1238-1253

[15] Pelà, L., Cervera, M., Roca, P. (2013). An orthotropic damage model for the analysis of masonry structures, Construction and Building Materials, 41, pp. 957-967

[16] Tsai, S.W., Wu, E.M. (1971). A general failure criterion for anisotropic materials. Journal of Composite Materials 1971; 5: 58-80

[17] Page, A. W. (1980), "A biaxial failure criterion for brick masonry in the tension-tension range." The International journal of Masonry Construction, Vol. 1, No. 1.

[18] Page, A. W. (1981), "The biaxial compressive strength of brick masonry", Proc. Instn Civ. Engrs, Part 2, Vol. 71, Sept., 893-906, 1981.

[19] Page, A. W. (1983). The strength of brick masonry under biaxial tension-compression, International Journal of Masonry Construction, 3(1), 26-31.

[20] Duan, Z.H., S.C. Kou, C.S. Poon, Using artificial neural networks for predicting the elastic modulus of recycled aggregate concrete, Construction and Building Materials 44 (2013) 524–532

[21] Naraine, K., and Sinha, S., "Cyclic Behavior of Brick Masonry under Biaxial Compression." Journal of Structural Engineering, ASCE, Vol. 117, No. 5, 1336-1355, 1991.

[22] Samarasinghe, W., "The in-plane failure of brickwork," PhD thesis, University of Edinburgh, 1980.

[23] Tassios, Th. P., and Vachliotis, Ch. (1989). ''Failure of masonry under heterosemous biaxial stresses.'' Proc., Int. Conf. Conservation of Stone, Masonry—Diagnosis, Repair and Strengthening, Athens.

COMPDYN 2015
5th ECCOMAS Thematic Conference on
Computational Methods in Structural Dynamics and Earthquake Engineering
M. Papadrakakis, V. Papadopoulos, V. Plevris (eds.)
Crete Island, Greece, 25–27 May 2015

EVALUATION OF THE SEISMIC VULNERABILITY OF THE "ANCIEN HÔPITAL DE SION" USING APPLIED ELEMENT MODELLING (AEM) AND LOCAL MECHANISM ANALYSIS

Angelo Garofano and Pierino Lestuzzi

École Polytechnique Fédérale de Lausanne (EPFL), Applied Computing and Mechanics Laboratory (IMAC), EPFL ENAC IIC IMAC, Station 18, CH-1015 Lausanne, Switzerland
e-mail: angelo.garofano@epfl.ch; pierino.lestuzzi@epfl.ch

Keywords: Seismic Behaviour, Historical Constructions, Applied Element Method (AEM), Non-linear Dynamic Analysis, Macro-element Analysis.

Abstract. *The evaluation of the seismic vulnerability of monumental buildings is a difficult task and presents significantly higher level of complexity if compared to the case of new or current existing structures. This is due to the inherent uncertainty characterizing ancient buildings, regarding structural characteristics and constructive techniques, material properties, damages due to past actions, which should be properly handled in their seismic assessment. For this reason, the approach to the study of such buildings unavoidably involves the completion of different assessment methods and their comparison, in order to represent the characteristics of a complex structure, its local and global behaviour. This paper describes the first results of the evaluation of the seismic safety of the "Ancien Hôpital de Sion", an important building belonging to the Swiss architectural heritage, sited in the Canton of Valais, the region with the highest seismic hazard in Switzerland. For the analysis of the building, three-dimensional Applied Element (AEM) modelling of the whole structure has been achieved and validated. The proposed modelling strategy, together with non-linear dynamic analysis, has been adopted on the basis of its capability to represent the actual behaviour and failure mechanisms of complex masonry structures, in addition to a good computational efficiency compared to other available numerical approaches. The local seismic collapse mechanisms have been also analysed through a kinematic limit analysis based on rigid block rotation. Both linear and non-linear approaches have been followed together with the capacity spectrum method. The results provided by the different methodologies have been compared with the aim to provide possible insights concerning a general procedure for the assessment of the safety of such type of structures.*

1 INTRODUCTION

The study of historical constructions presents many challenging aspects and often requires the application of different analysis methods and modelling techniques in order to satisfactorily describe their actual behaviour. A comprehensive and multidisciplinary procedure should be followed when approaching the assessment of the seismic vulnerability of heritage masonry buildings with the possibility to adapt different techniques to their particular charachteristics [1]. It is necessary, therefore, to combine both traditional and innovative investigation techniques with different level of complexity and detail of analysis. Simplified methods must be representative of particular aspects of the structural behaviour, yet support and validate the reliability of the results provided by more refined analysis procedures [2].

The present paper focuses on the study of a historical masonry building, the *Ancien Hôpital de Sion*, belonging to the Swiss architectural heritage and listed in the ISOS inventory (Federal Inventory of Swiss Heritage Sites). The building is located in the Canton of Valais, the region with the highest seismic hazard in Switzerland, therefore the assessment of its seismic vulnerability represents a crucial aspect within the phases of protection and safeguard of this important structure. The building represents a complex masonry structure, therefore different assessment methods have been considered for its study.

A three-dimensional Applied Element (AEM) model of the whole structure has been developed for non-linear dynamic analyses. Compared to the Finite Element Method (FEM), in the AEM the structure is discretized through an assemblage of relatively small elements connected by a set of non-linear springs located at contact points distributed along the element faces. Normal and shear springs transfer the normal and shear stresses between the elements. Through the springs it is possible to represent the non-linear material behaviour, the element separation or contact, and eventual collision [3, 4].

The possibilities of the AEM to overcome the drawbacks of FEM have been explored in the present work in the case of a masonry building subjected to a seismic excitation. The adopted modelling strategy has been employed to simulate the actual behaviour of the building and the possible failure mechanisms of a complex masonry structure.

In addition, the possible local collapse mechanisms of the building have been studied by means of a kinematic limit analysis, based on the decomposition into rigid macro-elements which can be individuated after the observation of typical seismic failure modes of existing masonry structures [5]. This is a useful method particularly for the study of buildings which do not feature a box behaviour under seismic actions due to the lack of stiff floors or weakening of connections between walls due to pre-existing damages. In the present case, both linear and non-linear static approaches have been followed in combination with the capacity spectrum method [6, 7].

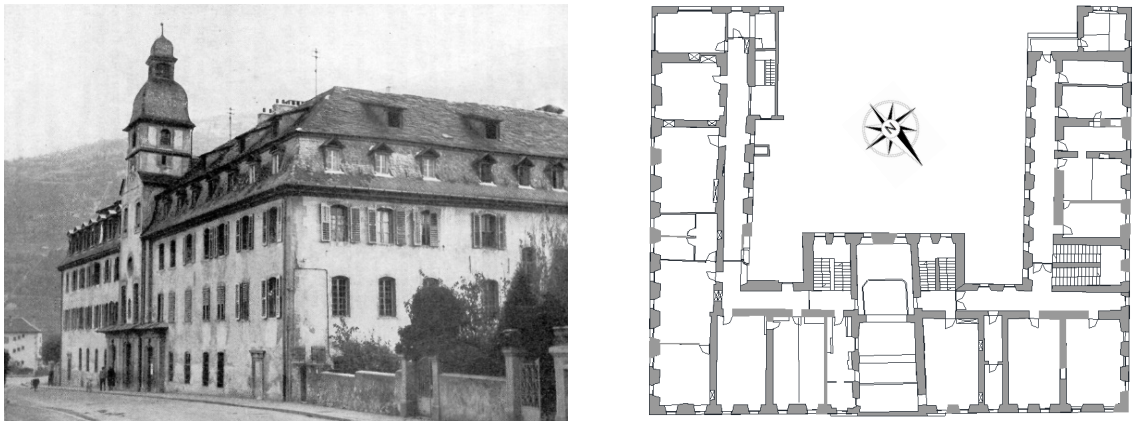
2 DESCRIPTION OF THE BUILDING

The construction of the *Ancien Hôpital de Sion* took place between 1763 and 1781 (Figure 1a) and it served as a hospital until 1937 [8, 9]. Presently, the Ancien Hôpital constitutes a representative and distinctive building of the city of Sion and it is placed under the protection of the Swiss Confederation. Due to its important role within the city and for its architectural quality, the building is listed in the ISOS inventory (Federal Inventory of Swiss Heritage Sites).

The building is an isolated structure, without any connection with surrounding buildings, as it can be seen from the general view in Figure 2a. A view of the building's main façade is shown in Figure 2b.

The Ancien Hôpital is a masonry building with timber slabs composed by a central body and two external wings (the Aile Nord and the Aile Sud) connected at its extreme sides forming a C-shaped floor plan (see Figure 1b). The building has three storeys over the ground floor, with a basement level under the central and southern areas of the structure. The overall in-plane dimensions of the building are 50 m x 42 m. The height of the ground and first level is 3.60 m, while the height of the second level is 3.30 m.

The structure's roof is a timber truss assembly [10, 11], reaching a total height of 17 m. The central part of the main body of the Ancien Hôpital is occupied by a chapel with a vaulted timber structure, surmounted by a tower with a total height of 26 m. The thickness of the masonry walls varies from about 1 m at the lower level to about 0.8 m at the higher levels.



(a) (b)

Figure 1: Historical image of the Ancien Hôpital [8] (a) and ground level floor plan [10] (b).



(a) (b)

Figure 2: Top view of the building in the historical center of the city of Sion (a) and view of the building's façade (b) *(Source: Map data ©2015 Google)*.

On the occasion of some restoration works completed in 2012 on the Northern wing, visual inspection and hole drilling were performed with the aim to define the masonry typology. The original stones used for the masonry are irregularly shaped, but they are optimally arranged and the overall conservation status of mortar joints was good (see Figure 3a).

The slabs found in the structure are made with timber beams having approximatively squared cross-section, with a timber layer, a mortar layer and the pavement. An example is

shown in Figure 3b. The slabs have been subjected to a survey and non-destructive testing for characterization of materials and for the evaluation of their bearing capacity in 2012 [12, 13]. Three classes were identified through ultrasonic in-situ testing, C18, C24 and C30, according to the European Norm EN338 [14]. In general, the beams were mainly belonging to the class of strength C30, while some C24 class beams were also found in the Southern wing and few C18 class in the Northern wing. The surveyed beams presented squared cross-sections of about 20 cm x 20 cm, with interspacing of 45-50 cm and supported length of about 30 cm.

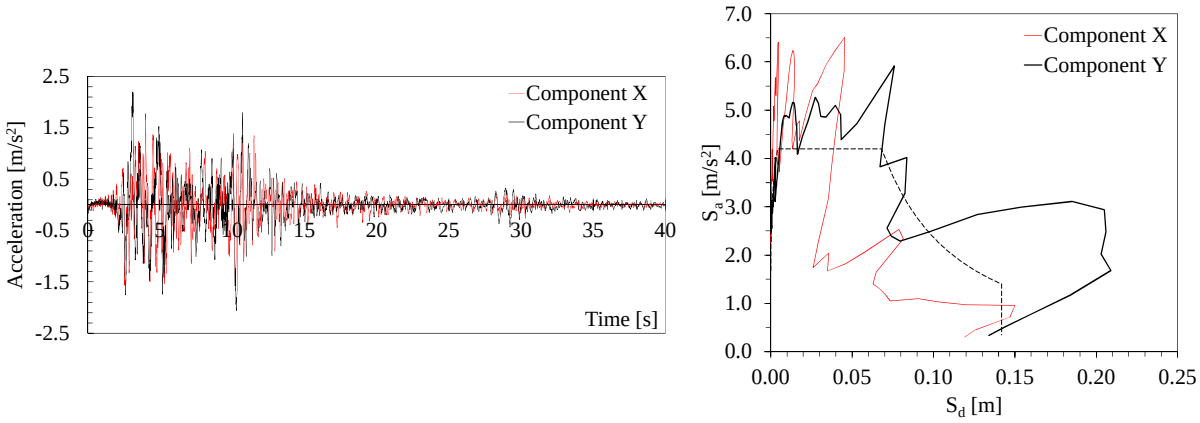


(a) (b)

Figure 3: Example of masonry (a) and bottom view of a slab typology (b) found in the structure [12].

3 SEISMIC HAZARD AT THE BUILDING SITE

The city of Sion is provided with a microzonation study for the distribution of the seismic hazard over the territory, identifying three seismic zones [15]. The Ancien Hôpital lies along the dividing line between two different zones; therefore, given the importance of the structure, a specific evaluation of the response spectrum was carried at the building site (dashed line in Figure 4b).



(a) (b)

Figure 4: Record ESD 198 (European Strong Motion Database, Montenegro Earthquake, M_S = 7.1, PGA = 0.224g): recorded ground accelerations in X and Y directions (a) and elastic response spectra (ADRS format) of the corresponding earthquake components for 5% damping (b).

In order to perform time-history dynamic analyses of the building, some records of seismic events respectful of the best fitting with the response spectrum provided for the Ancien

Hôpital were selected from international databases. One of these was represented by the Component Y of the Record ESD 198, with associated PGA = 0.224g. In particular, the model was subjected to the seismic registration reported in Figure 4a, illustrating the X (N-S) and Y (E-W) components of the recorded ground accelerations. The corresponding elastic response spectra for 5% damping are illustrated in Figure 4b, together with the response spectrum (dashed line) proposed for the site of the Ancien Hôpital for a comparison.

4 NUMERICAL MODELLING

4.1 Adopted modelling strategy

The methodology followed for the numerical modelling of the studied building is based on the Applied Element Method (AEM). This method represents an alternative modelling technique to the Finite Element Method and has been used in combination with non-linear dynamic analysis [4, 16, 17].

Considering the mechanical behaviour of a masonry building and the interaction between the structural elements, the Applied Element Method (AEM) gives the advantage to allow to consider all the possible failure mechanisms. The AEM method is based on dividing the masonry elements in small elements connected through springs (see Figure 5a). According to this strategy, there are no common nodes between elements and, therefore, it is possible to easily describe large displacements and elements progressive separation through successive failure of these springs [3]. Normal and shear springs located at the element contact points, distributed around the edges, as shown in Figure 5b, represent stresses, strains, and deformations of certain portions of the structure. Figure 5c illustrates an example of the configuration of springs between two elements, extended from the centreline of one element to the centreline of the adjacent one.

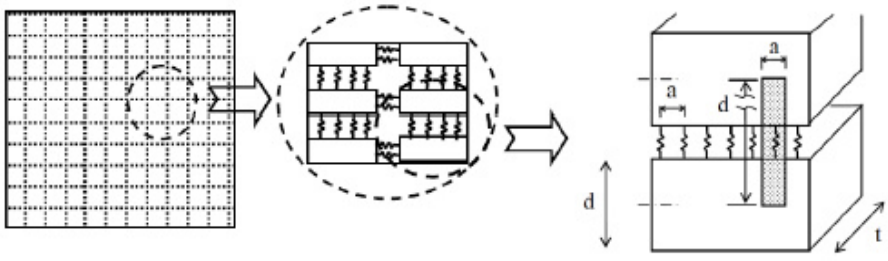
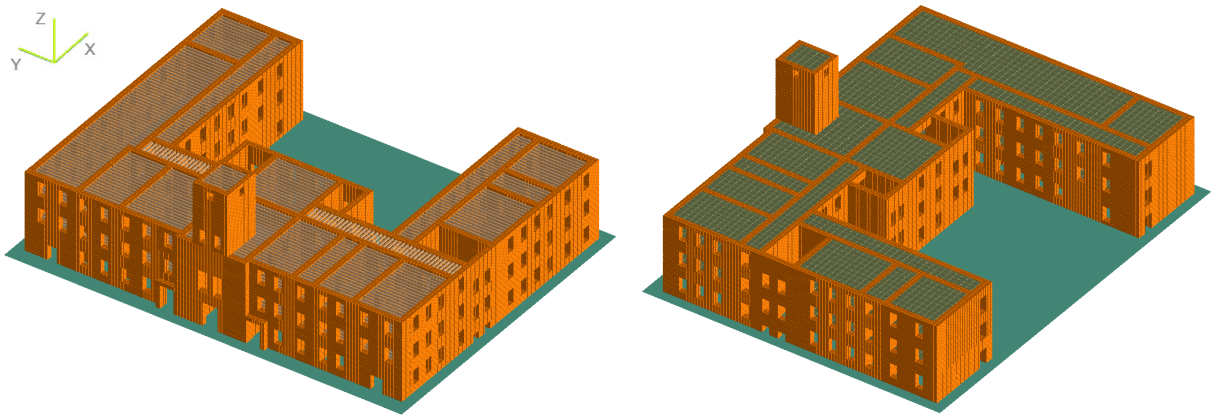


Figure 5: Masonry element modelling with AEM: element generation (a); spring distribution (b); area of influence of each springs pair (c) (Adapted from [16]).

For the studied masonry building, a total number of five springs was used on each face of the elements. The size of the meshing was selected and opportunely validated to avoid creating elements with large aspect ratios. In Figure 6 different views of the AEM model of the building are reported. The timber slabs have been modelled too according to the actual disposition in the structure.

Two models have been prepared, considering two different element sizes for masonry walls: a refined mesh (element dimensions $\leq$ 0.4 m) with two elements in the wall thickness and a large mesh division (element dimensions $\leq$ 0.8 m), with only one element in the wall thickness. This two cases were analysed with respect to the accuracy of the provided results and computational time requirements.



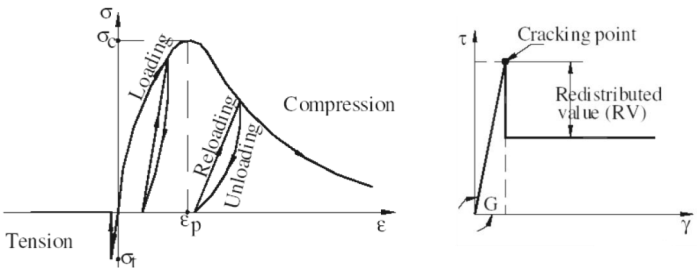
(a) (b)

Figure 6: Three-dimensional numerical model of the building with view of timber beams and slab (Refined mesh).

4.2 Failure criterion for masonry

Specific material models are assigned to the springs connecting the different applied elements in the AEM. Therefore, different material properties are described through the springs' characteristics, which are used to calculate strains, stresses and failure criteria [18]. Masonry is modelled similarly to concrete, adopting the Maekawa compression model including unloading and reloading [19], shown in Figure 7a. In this model, the envelope of compressive stress-strain diagram is defined using three values: the initial Young's modulus, the fracture parameter, representing the extent of the internal damage, and the compressive plastic strain. For the tensile behaviour, the relationship is linear until the cracking point. After cracking, stiffness of springs subjected to tension is set to zero. The residual stresses are then redistributed in the next loading step by applying the redistributed force values in the reverse direction. The material is assumed to crack when the major principal stress reaches the tensile strength.

Regarding the shear behaviour, the tangent modulus is calculated according to the strain at the spring location. After peak stresses, spring stiffness is assumed as a minimum value to avoid negative stiffness. This results in a difference between the calculated the stress and stress corresponding to the spring strain. These residual stresses are redistributed by applying the redistributed force values in the reverse direction in the next loading step. The relationship between shear stress and shear strain is assumed to remain linear till the cracking. Then, the shear stresses drop down as shown in Figure 7b. The level of drop of shear stresses depends on the aggregate interlock and friction at the crack surface.



(a) (b)

Figure 7: Constitutive models adopted for masonry under axial (a) and shear (b) stresses.

When the separation strain is reached, the adjacent elements are totally separated at the connecting face. In this case, all the springs are cut and, if the elements meet again during the analysis, they behave as two different rigid bodies in contact. When contact occurs between elements, linear springs are generated at contact points, governed by parameters such as the normal and shear contact stiffness factors and the contact spring unloading stiffness factor. During new contact friction between masonry portions is possible and depends on the friction coefficient value. There is no internal friction inside structural components which are already connected by normal and shear springs, and the friction coefficient has effect only after element separation when elements meet as rigid bodies. Mechanical parameters assumed in the analysis are reported in Table 1.

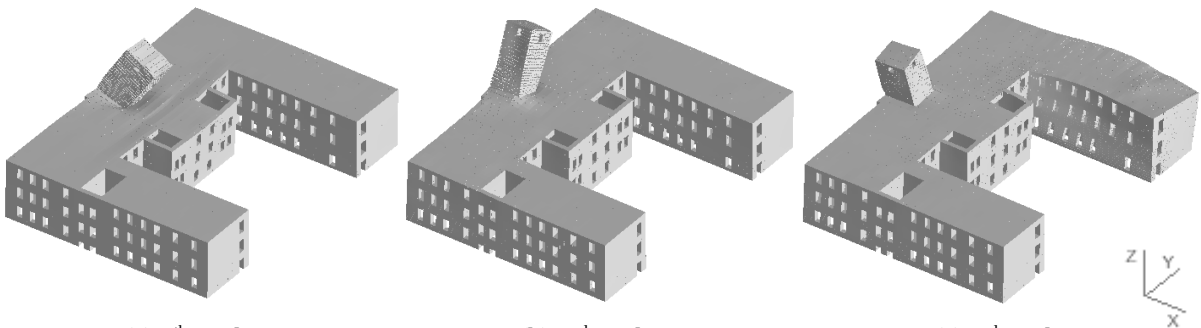
Unit weight [kN/m^3]	21
Young's modulus [N/mm^2]	1500
Shear modulus [N/mm^2]	700
Tensile strength [N/mm^2]	0.25
Compressive strength [N/mm^2]	3
Separation strain [−]	0.1
Friction coefficient [−]	0.8
External damping ratio [−]	0
Normal contact stiffness factor [−]	$1 \cdot 10^{-4}$
Shear contact stiffness factor [−]	$1 \cdot 10^{-5}$
Contact spring unloading stiffness factor [−]	2

Table 1: Mechanical parameters for masonry.

4.3 Modal analysis

From the analysis of the modal shapes of the building, the first two modes involve the vibration in the two principal directions of the central tower (see Figure 8a and 8b), which is also expected to be the most vulnerable part of the structure. The following modes involve mainly one or both lateral wings of the building. The vibration modes are the same in the case of the refined and large mesh division.

For both mesh divisions, the values of the periods for the first six modes are reported in Table 2. The differences in the periods when considering the refined mesh instead of the large mesh are negligible (lower than 3% for the first three modes), thus confirming the reliability of the model with large mesh from the dynamical point of view.



(a) 1th mode (b) 2nd mode (c) 3rd mode

Figure 8: Modal shapes of the building.

For the first three modes, the variation of the values of the periods is reported in Figure 9 in order to have an indication on the damage progression during the acceleration time-history. In particular, the irregular path in the variation of the first mode's period reveals the damage of the tower with out-of-plane collapse in the X direction. The comparison of the two mesh divisions showed, in this case, the tendency of the values of periods associated to the refined mesh to reduce more than in the case of the normal mesh for higher time steps of the analysis. Therefore, a higher susceptibility of the model with refined mesh to present higher damage was found.

During the study of the building, the modal shapes have been also compared to the case of the structure without the timber slabs in order to simulate an extreme case of completely ineffective connection at the floor level between the masonry walls. As expected, in this case the modal shapes involved firstly single walls of the structure before the central tower.

Mode	Refined mesh	Large mesh	Δ [%]
	T [s]	T [s]	
1	0.222	0.219	+1.4
2	0.215	0.218	+1.5
3	0.175	0.170	+2.7
4	0.155	0.151	+2.6
5	0.143	0.140	+2.7
6	0.131	0.126	+3.4

Table 2: Periods and frequencies.

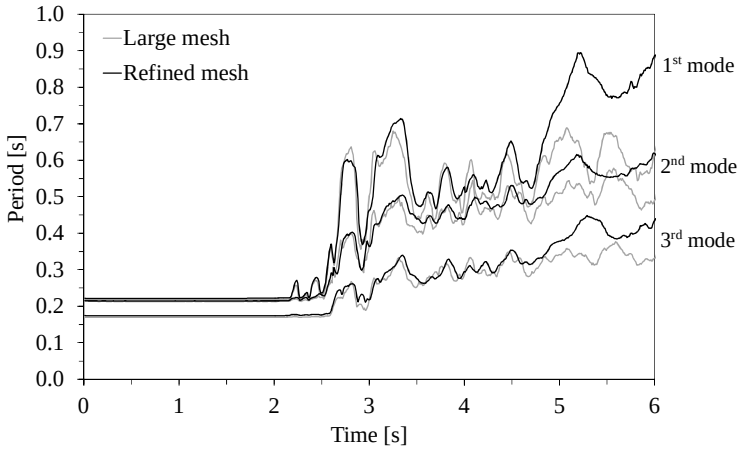


Figure 9: Period variation for the first three modes and comparison between large and refined mesh.

4.4 Time-history dynamic analysis

The dynamic analysis carried out considering the recorded time-history reported in Figure 4 allowed to confirm that the most vulnerable part of the structure is the central tower, which presented out-of-plane damages. However, the rest of the building did not suffer high damage due to the application of this seismic registration. The most evident crack is located in the middle of the back wall of the Southern wing.

In a second phase, time-history analysis have been repeated in order to evaluate the level of ground acceleration responsible of damage in the structure of the hospital. The record considered in the previous case was therefore amplified through the application of a factor of 2 to

the acceleration ordinates. In this case the seismic action is characterized by a double value of PGA and the corresponding spectrum can be representative of seismic demand with a higher return period.

The resulting damage distribution can be seen from Figure 10, where it can be noted that the considered ground acceleration record was responsible of the opening of several cracks. In particular, higher damage is located at the back corner of the Southern wing, where the connection of between the two converging walls is lost (see also Figure 12a and 12b). Severe damage was also obtained at the back of the central body of the building, involving the walls enclosing the staircases. In these areas, cracks opened at the intersection of the corner walls with the central body of the building, initiating the overturning of the whole corner or possibly of the single walls separately (see Figure 10 and 12a). The Northern wing of the building suffered more distributed damage, with cracks mainly located in the piers and starting from the openings. Again, the masonry walls in the area of the staircase suffered higher damage (see Figure 12c).

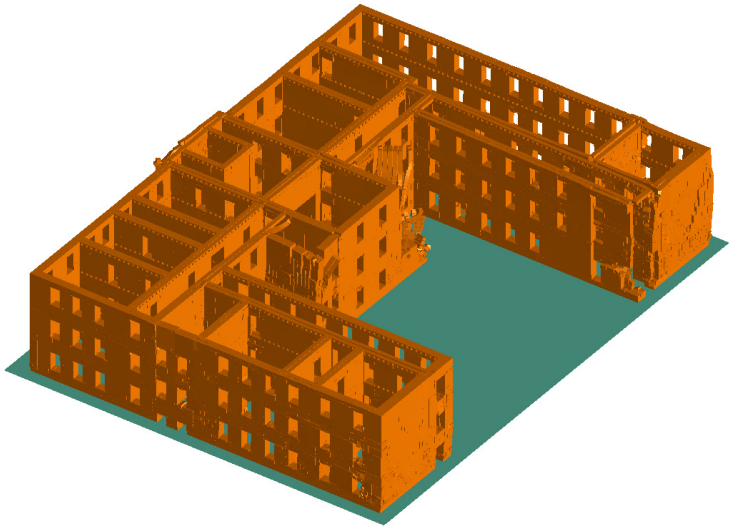


Figure 10: Damage distribution (X20) at the last time step (t = 40 s).

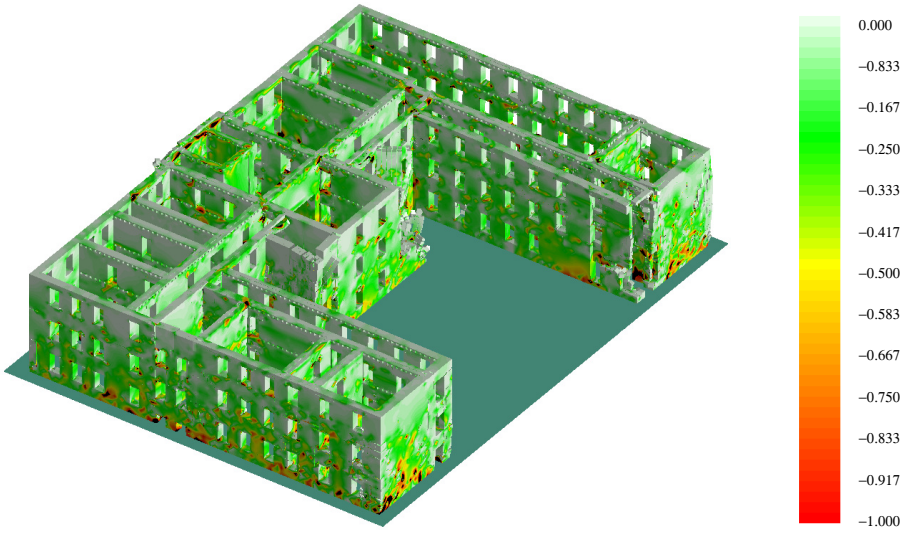


Figure 11: Compressive principal stress distribution (N/mm^2) at last time step (t = 40 s).

In Figure 11, the principal compressive stress distribution is illustrated over the damaged structure at the last time step of the analysis. The areas in dark red are characterized by a compressive stress higher than 1 N/mm^2 (it is reminded that the compressive strength of the masonry is 3 N/mm^2). The compressive damage involves only quite limited portions of masonry mainly localized at the lower zones of the ground level's masonry walls.

In Figure 12, the damage distribution obtained from the model with large mesh division and the model with refined mesh division is reported for the same walls of the building. From the comparison, it can be noted that the refined model is able to provide a more precise cracking distribution and a higher damage level (full overturning of some portions of masonry). However, the computational cost associated to the model with large mesh division is sensibly lower and represent an advantage in terms of time saving.

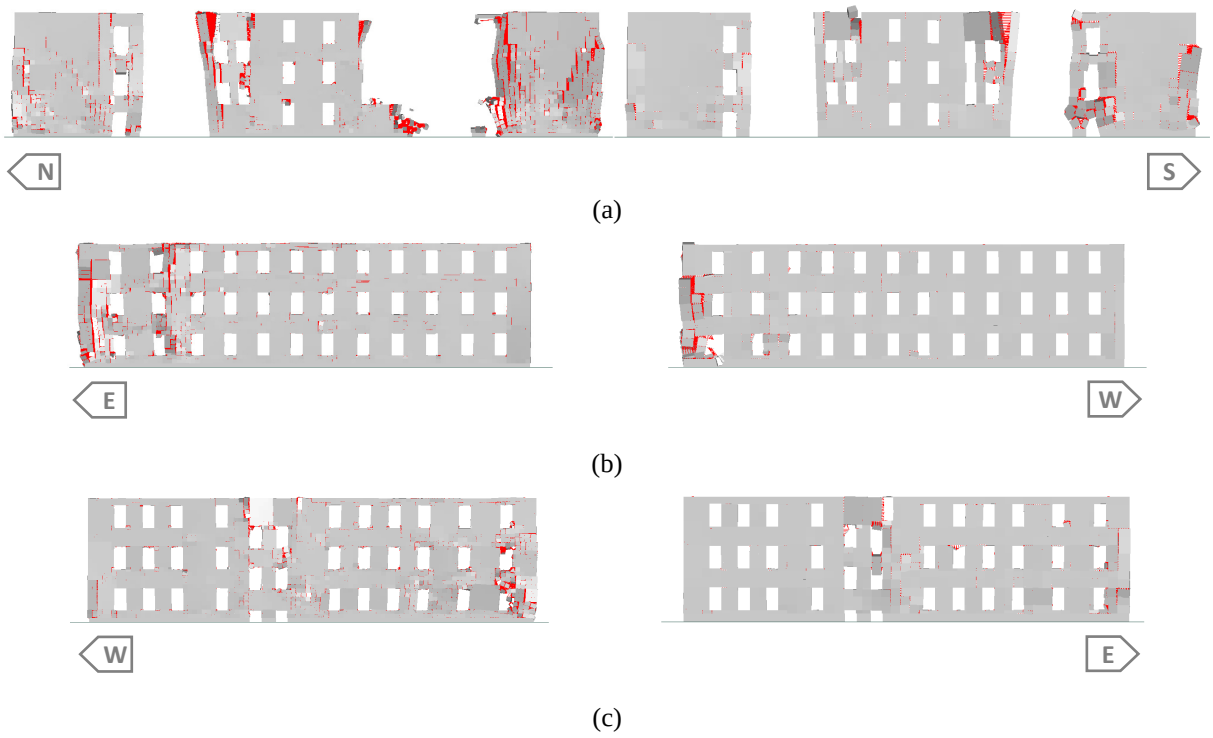


Figure 12: Damage distribution (X20) and cracking pattern at last time step (t = 40 s) for: (a) Eastern walls; (b) Southern walls; (c) Northern walls. (Elements dimensions ≤ 0.4 m (left) and ≤ 0.8 m (right)).

The influence of the horizontal elements plays a fundamental role in the response of an existing masonry building to the seismic action. However, the correct modelling of the slabs and representation of the actual connection conditions with the vertical masonry elements is a questionable point and sometimes can be carried out only thought very refined and time consuming models.

In order to compare the behaviour of the building in the case of very poor connection between the timber slabs and the masonry walls, a model without slabs was also employed in the analyses, representing an extreme condition for the stiffness of the horizontal elements and for the connection between the vertical elements.

The analysis was carried out considering the ground acceleration record amplified by 2, obtaining the damage distribution illustrated in Figure 13. The comparison of the damage distribution (Figure 10) with the one obtained in the case with slabs showed the higher damage suffered by the structure and a higher number of involved walls in the case without slabs, evidencing the important role of the slab stiffness in the seismic response of the structure.

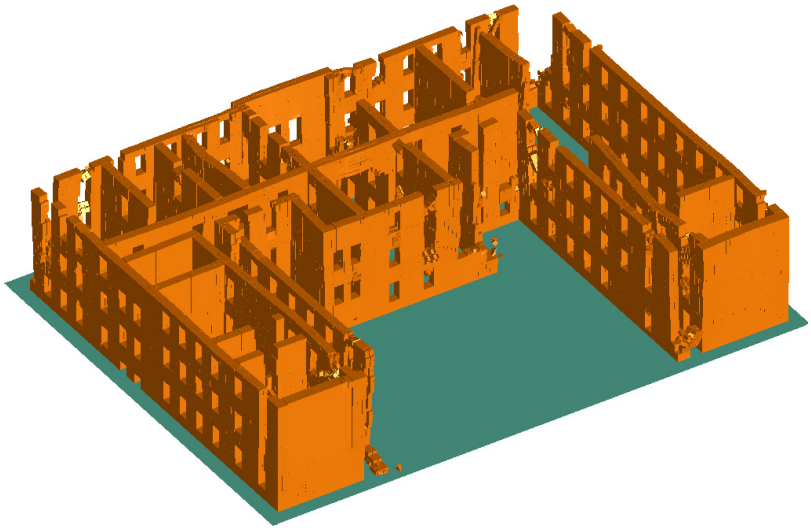


Figure 13: Damage distribution in the model without slabs at the last time step (t = 40 s).

5 ANALYSIS OF THE LOCAL COLLAPSE MECHANISMS

The safety of the structure was assessed through the analysis of different possible local collapse mechanisms following the linear and non-linear approaches [5, 20, 21]. The zones of the structure considered more likely vulnerable to overturning effects were identified for the calculations.

The kinematic linear approach allows to define the value of the load multiplier, α_0, connected to the horizontal force that the element is able to withstand. In terms of acceleration, the safety of the structure against the considered collapse mechanism is satisfied if:

$$a^*_0 \geq a_{g(SLU)} \tag{1}$$

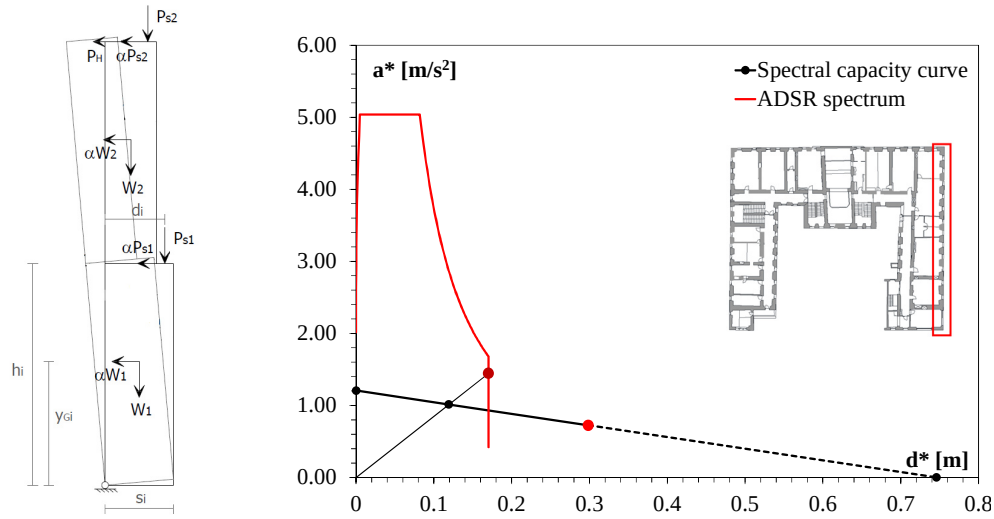
where $a_{g(SLU)}$ is the acceleration demand imposed by the earthquake calculated assuming a strength reduction factor equal to 2 [22].

Following the non-linear approach, the safety of the structure is carried out through the comparison between the ultimate displacement capacity, represented by d^*_u (assumed as 40% of the spectral displacement, d^*_0, corresponding to a null value of a^* [22]), and the displacement demand, $\Delta_d = S_{De}(T_s)$, obtained from the displacement spectrum for the secant period, T_s:

$$d^*_u \geq \Delta_d \tag{2}$$

As an example, the analysis of the mechanisms involving the Southern façade of the building is shown in Figure 14, considering an importance factor, $\gamma_I = 1.2$. The comparison between seismic demand and capacity is graphically reported in ADSR format.

The results of the analysis for some of the mechanisms are summarized in Table 3, reporting the safety coefficients, α_{eff}, obtained both from the linear and the non-linear kinematic approaches and for importance factors, γ_I, equal to 1.2 and 1.



(a) (b)

Figure 14: Example of overturning mechanism for masonry wall (two levels) (a) and spectral capacity curve and safety verification of the overturning of the Southern façade (b).

Mechanism	Importance factor $\gamma_I = 1.2$		Importance factor $\gamma_I = 1$	
	α_{eff} [−]		α_{eff} [−]	
	Linear analysis	Non-linear analysis	Linear analysis	Non-linear analysis
Southern façade	1.20	1.75	1.44	2.10
South-Eastern corner	1.72	2.97	2.06	3.56
Central staircase corner	2.23	3.26	2.68	3.92
Central staircase wall	0.75	0.94	0.90	1.13

Table 3: Summary of safety factors from the analysis of local mechanisms.

6 CONCLUSIONS AND FUTURE DEVELOPMENTS

The *Ancien Hôpital de Sion* is an important heritage structure located in the Canton of Valais, the region with the highest seismic hazard in Switzerland. The present paper aimed at the assessment of the seismic safety of such historical building through different approaches.

For the numerical modelling of the structure, the Applied Element Method (AEM) was followed and allowed to account for all possible failure modes of masonry.

The non-linear dynamic analysis carried out with an acceleration time history compatible with the site response spectrum evidenced that the building is able to stand the seismic action expected at the site suffering minor damaging.

When the acceleration is amplified by a factor of two (higher return period), the structure suffered cracking of several masonry walls, loss of connection at some corners and overturning of portions of masonry. The damage was more significant in the area of the Southern wing and in the walls enclosing the staircases. Higher cracks concentration at the connecting areas of the lateral wings with the central body was observed.

The building features a masonry tower in the central part of the main body, where a vaulted chapel is also located. This constitutes the most vulnerable element of the building and it is characterized by high damage even when the lower seismic action was considered. The struc-

ture and the behaviour of the central tower require deeper investigation and characterization in terms of construction technique and materials and to be studied with more detailed analyses.

Another point of interest evidenced by the numerical analysis concerns the level of connection between the slabs, through the timber beams, and the bearing masonry walls. The comparison between the model including the timber slabs according to the actual geometry and direction of beams, and a model with free walls showed the importance of the presence of the slabs in case the structure is subjected to a seismic action.

The study of possible local collapse mechanisms allowed to identify the most vulnerable parts of the structure. The safety factors are higher than one except for the case of the central staircase wall at the back of the building. The safety coefficients associated to a single wall are 0.9 from the linear approach and 1.13 from the non-linear approach, indicating the possible overturning of the wall for an action slightly higher than 1 (non-amplified registration). In comparison, the model subjected to the non-amplified seismic registration, showed a diffuse cracking in the area of this wall, but without reaching its out-of-plane failure. Therefore, in this case the application of the mechanisms analysis is more conservative, particularly in the linear approach.

Safety factors higher than 2 are obtained for the central staircase corner. In fact, the model subjected to an acceleration amplified by two showed that vertical cracks form at this corner with subsequent overturning of the two converging walls separetely, instead of the whole corner. For the Southern façade and the South-Eastern corner, the results of the numerical analysis are intermediate between the results given by the linear and the non-linear approaches. The model showed severe cracking and disconnection of masonry at the corners, but without complete overturning of the walls. Therefore, also in this case the application of the linear approach resulted to be more conservative than the non-linear approach which was found more realistic.

ACKNOWLEDGEMENTS

The present research was conducted with the support of the Office Fédéral de l'Environnement (OFEV) which is fully acknowledged.

REFERENCES

[1] F. Ceroni, M. Pecce, S. Sica, A. Garofano, Assessment of seismic vulnerability of a historical masonry building. *Buildings, MDPI, Special Issue: Earthquake Resistant Buildings*, 2012; 2(3):332-358. DOI: 10.3390/buildings2030332.

[2] F. Ceroni, A. Garofano, M. Pecce, Seismic behaviour of masonry buildings: application of different approaches to a case study. *14th European Conference of Earthquake Engineering*, 30.08-03.09.2010 Ohrid, Macedonia, CD Rom.

[3] K. Meguro, H.R. Tagel-Din, Applied element simulation of RC structures under cyclic loading. *Journal of Structural Engineering*, Vol. 127, No. 11, November, 2001.

[4] H.R. Tagel-Din, K. Meguro, Analysis of a small scale RC building subjected to shaking table tests using applied element method. *Proceedings of the 12th World Conference on Earthquake Engineering,* New Zealand, pp. 25–34, January 30 – February, 2000.

[5] C.F. Carocci, Guidelines for the safety and preservation of historical centres in seismic areas. In: *Historical constructions*. University of Minho, Guimaraes, pp 145–165, 2001.

[6] P. Fajfar, Capacity spectrum method based on inelastic demand spectra. *Earthquake Engineering and Structural Dynamics*, 28:979–993, 1999.

[7] S. Lagomarsino, On the vulnerability assessment of monumental buildings. *Bulletin of Earthquake Engineering*, 4:445–463. European Comission, Brussels, 2006.

[8] S. Crettaz, Hôpital de Sion (XII^{e} au XX^{e} siècle). In: *Annales Valaisannes, Société d'Histoire du Valais Romand*, 1949, 145-180, fig. (dont 1 portr.). (In French).

[9] P. de Rivaz, Les hôpitaux de Sion. In: *Annales Valaisannes, Société d'Histoire du Valais Romand*, 1940, 44-48. (In French).

[10] CERT Ingénierie SA, *Ville de Sion. Rénovation de l'Ancien Hôpital. Étude de faisabilité: toiture, plancher et colombage.* 20 Novembre 2009. (In French).

[11] Lignum-Cedotec, *Rapport "Ancien Hôpital de Sion" - Charpente et planchers en bois*. 2 June 2009. (In French).

[12] CERT Ingénierie SA, *Ville de Sion. Rénovation de l'Ancien Hôpital. Rapport d'évaluation de la capacité portante des planchers en bois.* Rapport AVP101, 5 June 2012. (In French).

[13] Concept Bois Technologie, *Evaluation de la résistance résiduelle de poutres en bois constituant le plancher de l'Ancien Hôpital de Sion (VS). Mesures sur échantillonnage.* Rapport d'expertise, 12 May 2012. (In French).

[14] European Commitee for Standardization (CEN), *EN 338 - Structural timber. Strength classes*. 2009.

[15] Centre de recherche sur l'environnement alpin (CREALP): www.crealp.ch

[16] A. Karbassi, P. Lestuzzi, Fragility analysis of existing unreinforced masonry buildings through a numerical-based methodology. *The Open Civil Engineering Journal*, vol. 6, (Suppl 1-M2) 121-130, 2012.

[17] A. Karbassi, M.-J. Nollet, Performance based seismic vulnerability evaluation of masonry buildings using Applied Element Method in a nonlinear dynamic-based analytical procedure. *Earthquake Spectra*, Vol. 29, No. 2, 399-426, 2013.

[18] Applied Science International. *Extreme Loading® for Structures (Version 3.1), Theoretical Manual; Modelling Manual*, Durham, NC, 2013.

[19] H. Okamura, K. Maekawa, *Nonlinear analysis constitutive models of reinforced concrete*. Gihodo Co. Ltd., Tokyo, 1991.

[20] F. Papa, G. Zuccaro, Un modello di valutazione dell'agibilità post-sismica attraverso la stima dei meccanismi di collasso. *XI Congresso Nazionale ANIDIS "L'Ingegneria Sismica in Italia"*, Genova, 2004.

[21] M.C. Griffith, G. Magenes, G. Melis, L. Picchi, Evaluation of out-of-plane stability of unreinforced masonry walls subjected to seismic excitation. *Journal of Earthquake Engineering*, Vol. 7, Special Issue 1, 141-169, 2003.

[22] Circolare 617. *Istruzioni per l'applicazione delle "Nuove norme tecniche per le costruzioni di cui al D.M. 14 gennaio 2008.* Ministero dei Lavori Pubblici, Roma, 02/02/2009. (In Italian).

COMPDYN 2015
5th ECCOMAS Thematic Conference on
Computational Methods in Structural Dynamics and Earthquake Engineering
M. Papadrakakis, V. Papadopoulos, V. Plevris (eds.)
Crete Island, Greece, 25–27 May 2015

NONLINEAR ANALYSIS AND SEISMIC STRENGTHENING OF MASONRY ARCHES: THE BLOCK-JOINT AND BLOCK-BLOCK FEM MODELS

Francesco Pugi[1], Alessio Francioso[2]

[1] AEDES Software
56028 San Miniato Basso, Pisa, Italy
info@aedes.it

[2] National Technical University of Athens
15780 Zografou, Athens, Greece
alessiofrancioso@gmail.com

Keywords: masonry arches, nonlinear analysis, block-joint, block-block, seismic strengthening.

Abstract. *The stability of masonry arches plays a crucial role in the seismic assessment of historic and monumental buildings. The block-joint FEM model represents a major step forward with respect to the traditional rigid-brittle approach, allowing the assessment of the in-plane and out-of-plane arch behaviour and modelling of spatial systems such as cross vaults. Recent improvements of the method, among which the blocks modelled as curved frame elements and the pursuit of a static admissible configuration at the first step of the pushover analysis, are introduced. Moreover, the simpler block-block model that captures the behaviour of the arch through a lower number of finite elements is presented. The effects of passive and active strengthening measures such as CFRP sheets or prestress state are also considered in the models.*

1 INTRODUCTION

The structural analysis of masonry arches can be performed following several methodologies, essentially aimed at assessing the stability of the structure under static and seismic loads.

Algorithms able to define the collapse mechanism of arches and vaults were developed following the Heyman's theory and an approach based on rigid-brittle elements [1-3]. However, the definition of the collapse mechanism and the collapse multiplier can also be pursued with traditional finite element methods, according to nonlinear procedures that take into account the progressive damage of the structures. In case of seismic actions, this type of incremental analysis, proposed as an alternative to limit analysis in recent standards [4], is referred to as "static nonlinear analysis" or "pushover analysis".

Among all the methodologies that can be used for the analysis of arches, modelling through spatial one-dimensional finite elements (frame elements) is particularly interesting. It allows to assess the arch static and seismic behaviour with low computational effort and ease of use. Frame elements allow for complete control over the analysis results and accurate vulnerability asassessments.

A previous work [5] introduced the "block-joint" model, where both blocks and joints are frame elements. The blocks have the mechanical properties of the stone and their cross section is the effective cross section of the arch, while the joints represent the mortar between the blocks and their cross section is ¼ of the one of the blocks. Each block interface is modelled through four joints placed at each vertex and connected to the block through rigid links. As shown in Figure 1, the joints are pin-fixed frame elements, the fixed-end provides continuity with the previous block, the pin-end transfers shear and axial force to the next block, in this manner the system transfers moment, shear and axial force from one block to another.

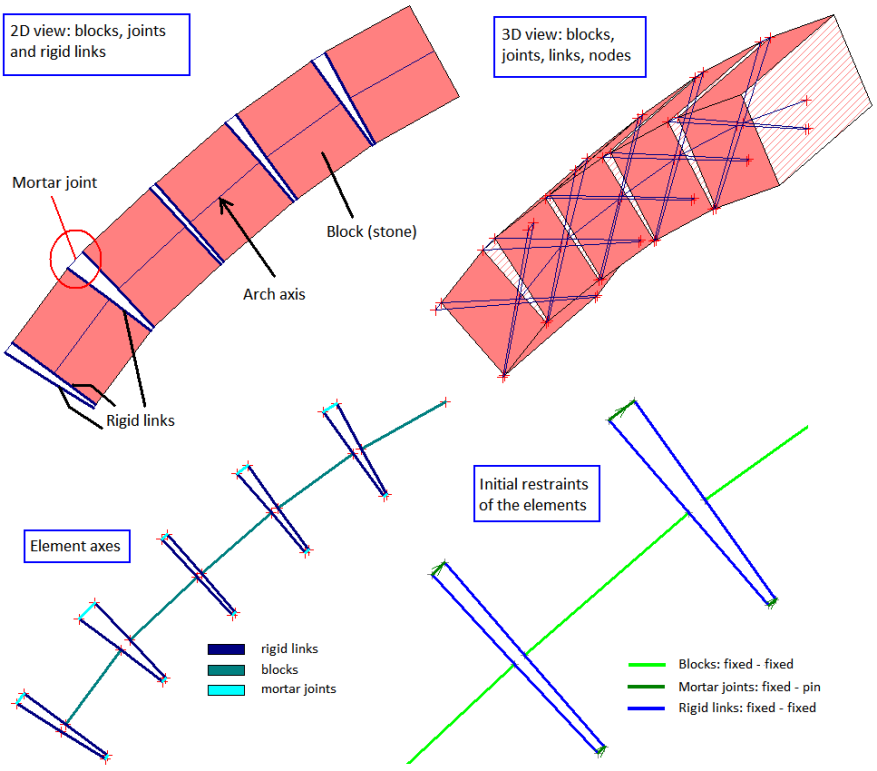


Figure 1. The finite element model block-joint

The “block-joint” model catches the arch in-plane and out-of-plane behaviour detecting the formation of plastic hinges where the tensile stresses overcome the resistance of the material.

Particularly interesting is the behaviour of the structure under horizontal inertial loads, especially when assessing monumental buildings in seismic prone areas. In these cases the structure is studied through static nonlinear analysis. An increasing horizontal force is applied to the system recording at each step the value of the control displacement, this leads to a force-displacement diagram that represents the capacity curve of the structure.

Performing a pushover analysis, increasing horizontal forces are applied to the system. At each step axial force verification is applied to the joints: if tensile stresses occur, the internal axial force is released and the fixed-end is turned to pin so that the element loses any stiffness and the internal actions remain constant at the value reached so far. As the analysis continues, the progressive deterioration of the joints leads to an unstable configuration that defines the end of the pushover curve.

Assuming that the internal actions remain constant after deterioration of the joints, this procedure is capable to easily find a balanced solution compatible with the mechanical characteristics of the materials. The procedure can be applied considering or not a limited tensile strength of the material: if the tensile strength is assumed to be null a comparison with the rigid-brittle limit analysis is feasible. However, accounting for the tensile strength of the joints surely leads to an increase of the collapse multiplier and allows not to underestimate the seismic capacity of the structure.

Besides the axial force verification, at each step of the pushover analysis compression and shear verifications can be applied to the blocks. As regards the compression verification, if the action overcomes the resistance of the material, the axial force is released. As regards the shear, if the axial force to shear ratio exceeds the friction coefficient of the material, the relevant frame turns into pin-pin and reacts only to axial force.

If the object of the analysis is a building that features arches and/or vaults, once the capacity curve has been calculated, the safety verification can be performed with the classic methodologies provided by the standards for pushover analysis.

Whereas if the object of the analysis is a macroelement, that is a portion of the building, the safety verification should follow the method provided by the standards for the kinematic analysis of collapse mechanisms [6]. In this case the collapse multiplier is pursued as the maximum static multiplier instead of the minimum kinematic multiplier.

Recent improvements of the method introduced: (a) the blocks modelled as curved beam elements, (b) a self-correcting procedure at the beginning of the pushover analysis in order to pursuit a stable configuration under static loads, (c) a solution for the automatic distribution of the vertical loads, (d) the possibility to account for passive and active strengthening techniques.

Moreover, the research for the development of the block-joint method led to the introduction of a simplified model that captures the behaviour of the arch with a lower number of finite elements: the “block-block” model. In fact, the arches modelled with the block-joint method may feature a high number of frame elements (blocks, joints, rigid links) depending on the discretization adopted, therefore this method is recommended for advanced analysis of macroelements, whereas the simpler block-block method can be used for the modelling of arches within complex buildings.

2 BLOCKS MODELLED AS SPATIAL CURVED BEAM

Modelling the blocks with curved elements, instead of straight frame elements, leads to certain advantages: (a) arches discretized in few blocks can be modelled adequately, (b) the

mortar joints between the blocks can be short enough both at the intrados and at the extrados of the arch, (c) the self-weight of the blocks is better approximated.

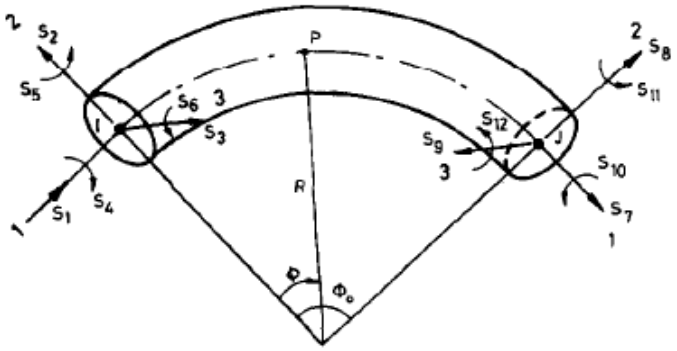


Figure 2. A curved beam element with coordinates and forces

As shown in Figure 2, formulation of the stiffness matrix of a spatial beam element with circular axis [7], validated through analytical formulas [8], was adopted for the blocks. The circular axis allows for a better modelling of several arch typologies such as semicircular arch, segmental arch, pointed arch, three-centered arch.

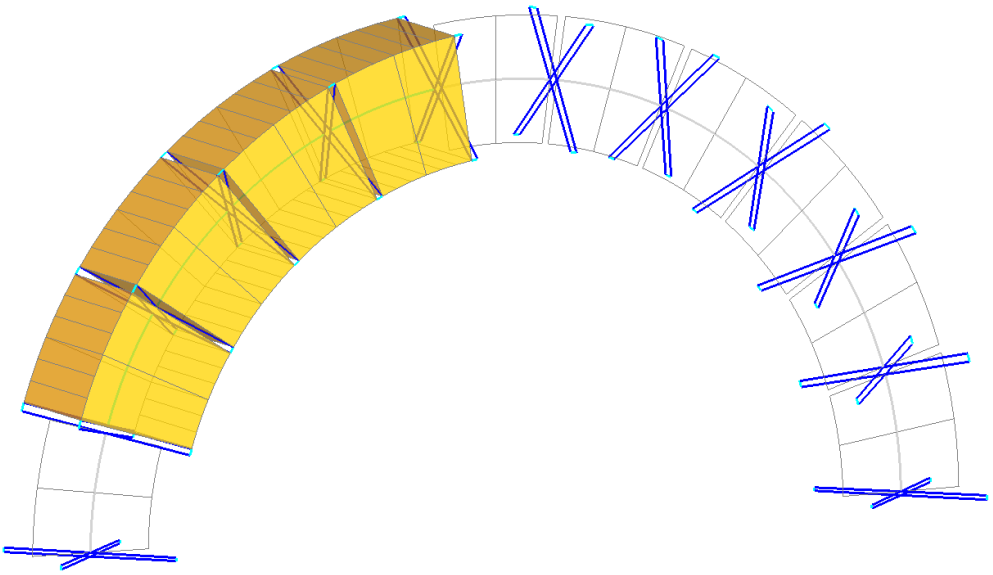


Figure 3. Block-joint modelling with curved beams

3 BLOCK-BLOCK MODELLING

Modelling of masonry buildings is frequently rather complex, a building that features many arches may need a large computational effort. Let us call “module” the portion of the arch between two consecutive mortar joints derived from arch discretization. The block-joint model consists of 14 frame elements per module (2 blocks + 4 joints + 8 rigid links), whereas the simplified block-block method allows modelling of the arch with only 2 blocks per

module. Each module consists at least of two blocks because the self-weight is applied as point load in the central node of each module.

Figure 4 shows the case an arch discretized in 11 modules. The block-joint model of the arch consists of 200 frames and 155 nodes, while the block-block model of the same arch consists of 56 frames and 47 nodes. Therefore, the block-block model leads to a number of elements 3 times smaller than the block-joint model, with clear advantages with respect to the computational effort. For this reasons the block-block method is recommended for the modelling of arches within complex buildings.

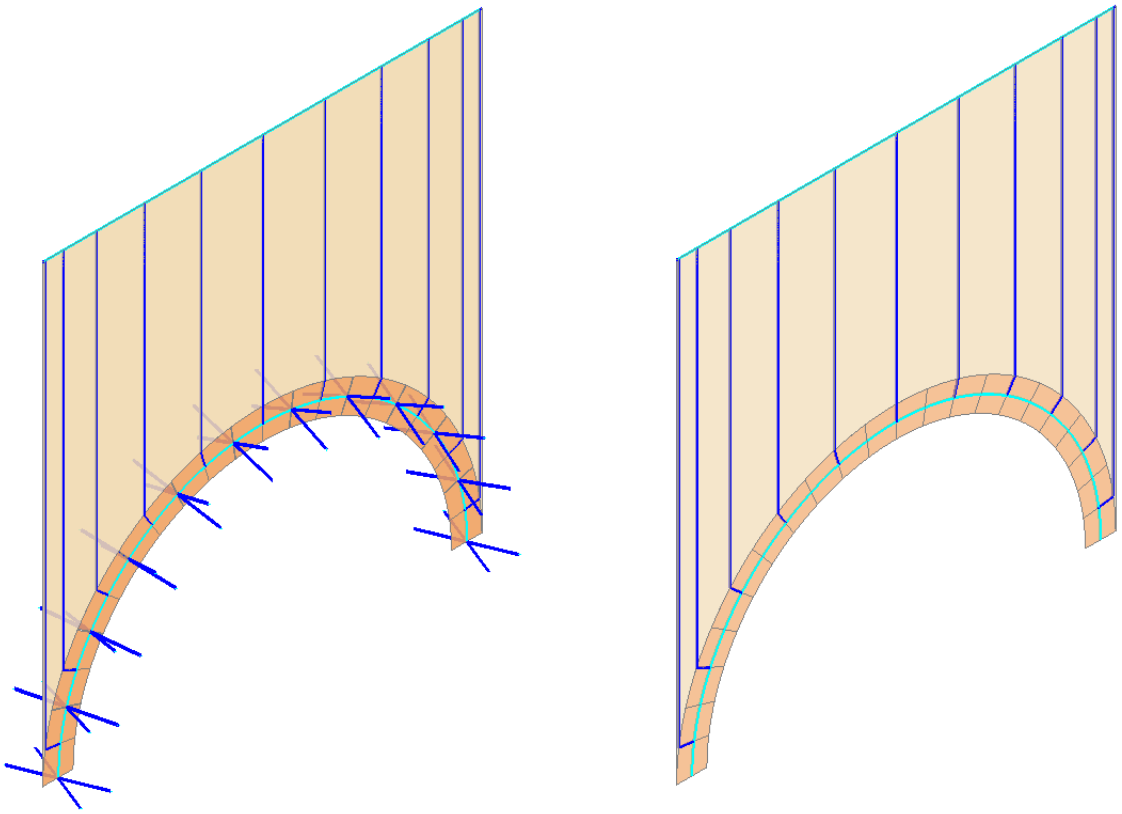


Figure 4. (a) block-joint model. (b) block-block model

The block-block method provides adequate verification procedures in order to achieve solutions compatible with the ones obtained with more advanced modelling. The blocks are spatial curved beam elements with fixed-fixed ends. The compressive strength of the blocks is the one of the stone while the tensile strength is the one of the mortar.

Performing pushover analysis, at each step a thrust-line verification is applied to the blocks. If the thrust-line comes out of the block cross section and the tensile stress exceeds the material tensile strength (and/or the reinforcement resistance) the verification is not satisfied, thus the bending moment is released by introducing a hinge in the relevant end of the block. In this way at the next steps of the analysis the position of the thrust-line remains practically the same: small variation may occur due to the variation of the axial force.

In a manner similar to the block-joint method, the compression and shear verification can be applied to complete the arch safety assessment.

4 SELF-CORRECTING GRAVITY ANALYSIS AT THE BEGINNING OF THE PUSHOVER ANALYSIS

Whatever the modelling method, the static asset, that is the resistant configuration under vertical static loads, is very important for the structural analysis of the arches. This asset matches the one at the beginning of the pushover analysis. It should be noted that the arch may develop hinges even if the only applied loads are the static ones. This simply means that the structure bears the static loads with a reduced degree of hiperstaticity. Therefore, a correct static nonlinear analysis must initially perform a self-correcting gravity analysis that pursuit a stable configuration of the arch under static loads .

The self-correcting procedure performs iteratively a static analysis and, at each iteration, it applies verification to the joints (or the blocks in the block-block model) and corrects the one in the most severe condition acting on its internal releases. In this way, at each step the arch loses one degree of hiperstaticity. The procedure continues until all the elements satisfy the verifications, then the pushover analysis can be performed on the resulting structure.

As regards the block-joint model, the corrections applied to the relevant joint during the gravity analysis consist in releasing the axial force and the bending moment at the two ends. Instead, as regards the block-block model, the bending moment is released in the section under the most sever conditions and two moments are applied at the adjacent blocks in order to fix the thrust-line in a position compatible with the geometry of the arch, the resistance of the material and eventually the presence of reinforcements.

During the iterative procedure and the application of several releases the structure may become unstable, that means that the structure cannot bear the static loads, thus the pushover analysis cannot be performed. For the examples described at section 7 of this work, the pushover analysis has been performed applying the self-correcting gravity analysis.

5 VERTICAL LOADS DISTRIBUTION

Frequently, arches are located within buildings and the modelling should account for the interaction with the adjacent structures such as masonry piers, columns, spandrels and beams. In the “Equivalent Frame” models the connections between different typologies can be set in order to achieve the correct distribution of the vertical loads.

Generally, the vertical loads acting on the structure above the arch are transferred to the arch through the spandrels. The solution proposed in this work (compatible with the equivalent frame model) consist of a series of rigid vertical struts that link arch and the beam above the arch providing the correct distribution of the vertical loads. The method has been validated through comparison between the loads directly applied to the blocks and the ones transferred by the struts through axial force [9, 10].

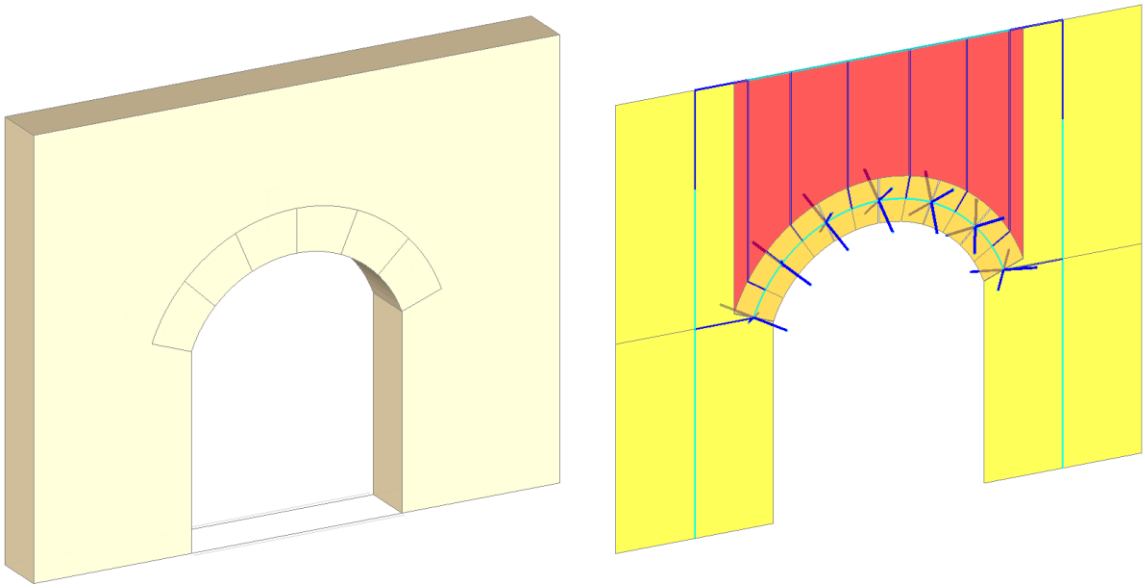


Figure 5. Rigid vertical struts for load distribution

More in details, the vertical struts connect the central node of each arch module to the above beam and feature a hinge at the interface with the arch, while the frame elements of the beam are pin-pin and carry a uniform load that represent the self-weight of the structure between consecutive struts. This system transfers to the arch the entire load of the above structure.

However, in real cases, a part of the load tends to migrate towards the adjacent masonry piers. In order to account for this behaviour the original configuration of the struts and the beam can be modified as follows: (a) exclude from the model some of the struts at the sides of the arch, (b) set as fixed-fixed the relevant frame elements of the beam.

Figure 6 shows the position of the nodal masses (red spheres) and highlights the portion of the structure that transfers load to the arch.

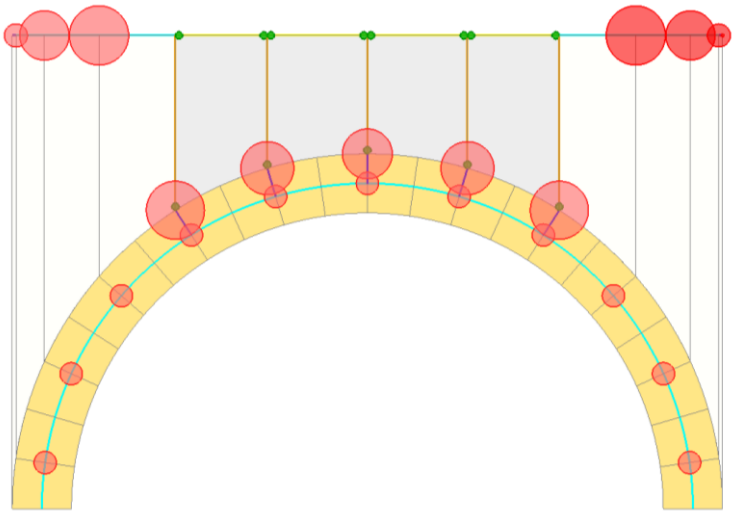


Figure 6. Partial load distribution

6 ACTIVE AND PASSIVE STRENGTHENING MEASURES

As mentioned before, the block-joint and the block-block method can account for a tensile strength of the mortar joints improving the stability of the arch. Moreover, besides the resistance of the material, the method can account for the benefic effects of passive and active strengthening measure.

The passive interventions such as FRP sheets applied at the intrados or at extrados of the arch provide an additional tensile resistance to blocks and joints, whereas the active interventions such as the "reinforced arch" technique, apply a prestress state in the arch aimed to bring the thrust-line closer to the central axis and to the formation of the plastic hinges [11].

An application of these strengthening typologies is provided in the next section.

7 APPLICATION EXAMPLES

The following examples, developed using Aedes Software PCM and SAV, apply the proposed methods [9, 10].

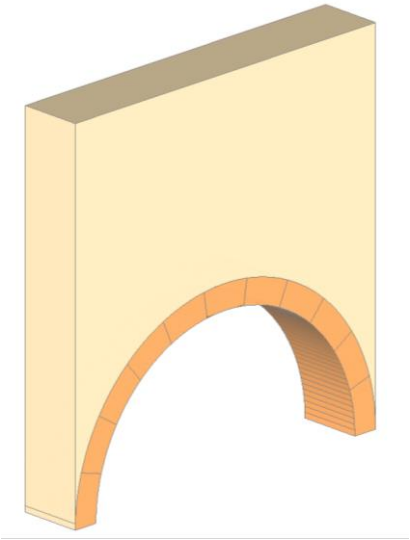


Figure 7. Reference arch

The reference arch shown in Figure 7 is semi-circular with the following characteristics: span 5.00 m, rise 2.50 m, depth 1.00 m, thickness 0.40 m. The height of the structure above the extrados of the arch is 3.10 m. The mechanical characteristics of the materials are shown in Table 1.

Masonry	Specific weight	19	kN/m^3
Blocks	Specific weight	20	kN/m^3
	Elastic modulus	50000	N/mm^2
	Shear modulus	20000	N/mm^2
	Compressive strength	35	N/mm^2
Joints	Elastic modulus	660	N/mm^2
	Shear modulus	264	N/mm^2
	Tensile strength	0.05	N/mm^2

Table 1. Mechanical properties of the materials

7.1 Vertical load distribution

This example aims to validate the distribution of the vertical load used in the block-joint and block-block methods through a comparison with the rigid-brittle method. Aedes SAV was used to model the arch according to the rigid-brittle method, the load arising from the structure above the arch is directly applied to the blocks as vertical point loads following the scheme shown in Figure 8a. The point loads applied to the blocks range from 15.98 kN at the imposts to 50.33 kN at the keystones.

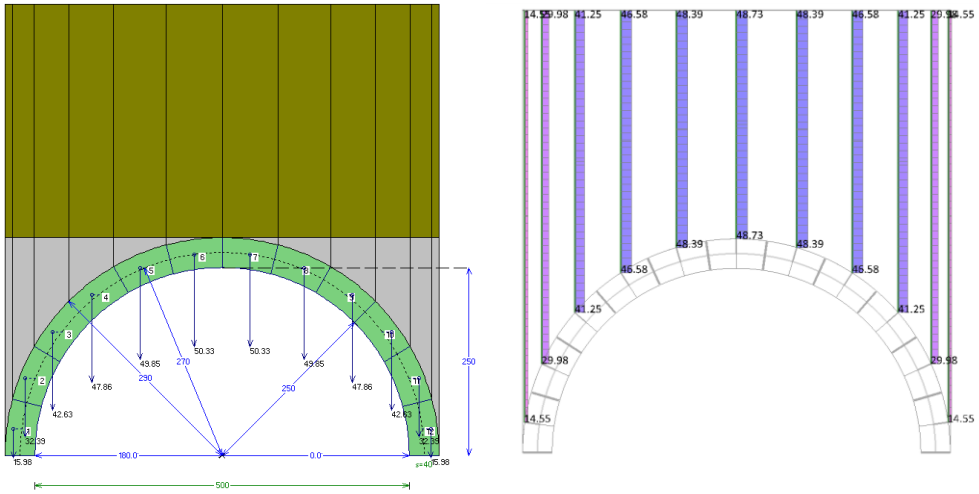


Figure 8. Vertical load distribution: (a) rigid-brittle model, (b) block-joint model

On the other hand, in the proposed methods (block-joint or block-block), the load is transferred to the arch through vertical rigid struts. Aedes PCM was used to model the arch according to the block-joint method. A static analysis was performed and, as shown in Figure 8b, the axial force in the vertical struts range from 14.55 kN at the imposts to 48.73 at the keystone. The values are very similar to the loads applied in the rigid-brittle method; therefore the use of vertical struts for load distribution is appropriate.

The rigid-brittle approach based on the Heyman's theory [2, 3] has been widely used for the structural analysis of arches [1], thus it represents a good reference for the calibration of alternative methodologies. Figure 9 shows the static analysis results (axial force diagram and thrust-line) obtained with the rigid-brittle approach and with the block-joint method.

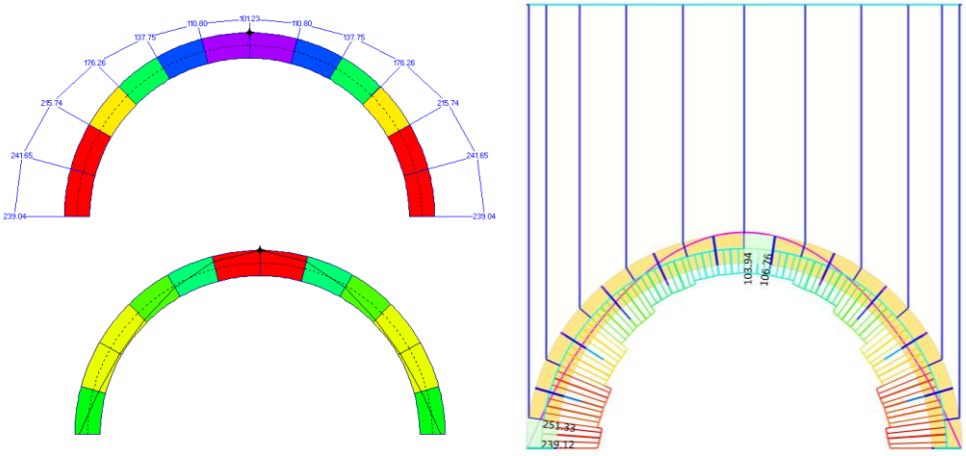


Figure 9. Static analysis: axial force diagram and thrust-line. (a) rigid-brittle approach. (b) block-joint method

Model	Vertical reaction	Horizontal reaction
Rigid-Brittle	239.04 kN	101.23 kN
Block-Joint	239.06 kN	103.92 kN

Table 2. External reactions at the imposts

Table 2 lists the vertical and horizontal external reactions at the fixed imposts. The analyses performed with the two approaches led to similar results and this validates the use of the block-joint method.

7.2 Comparison between block-joint and block-block methods

The reference arch is now modelled according to the two proposed methods (block-joint and block-block) performing modal, static and pushover FEM analyses. The following figures and tables show the results of the analyses performed.

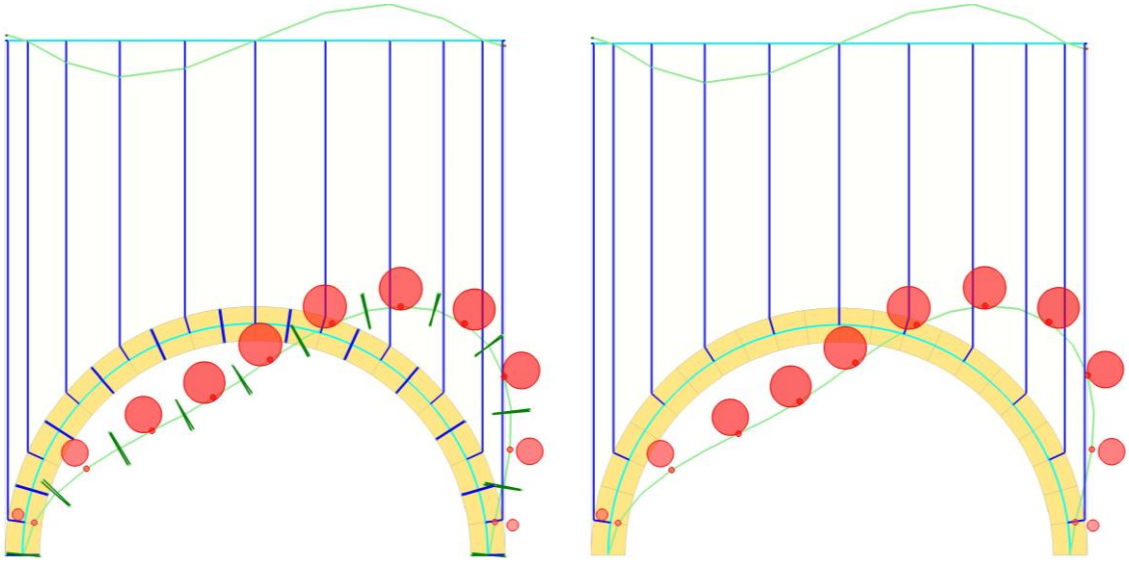


Figure 10. Modal analysis. (a) block-joint model, T = 0.060s. (b) block-block model, T = 0.050s

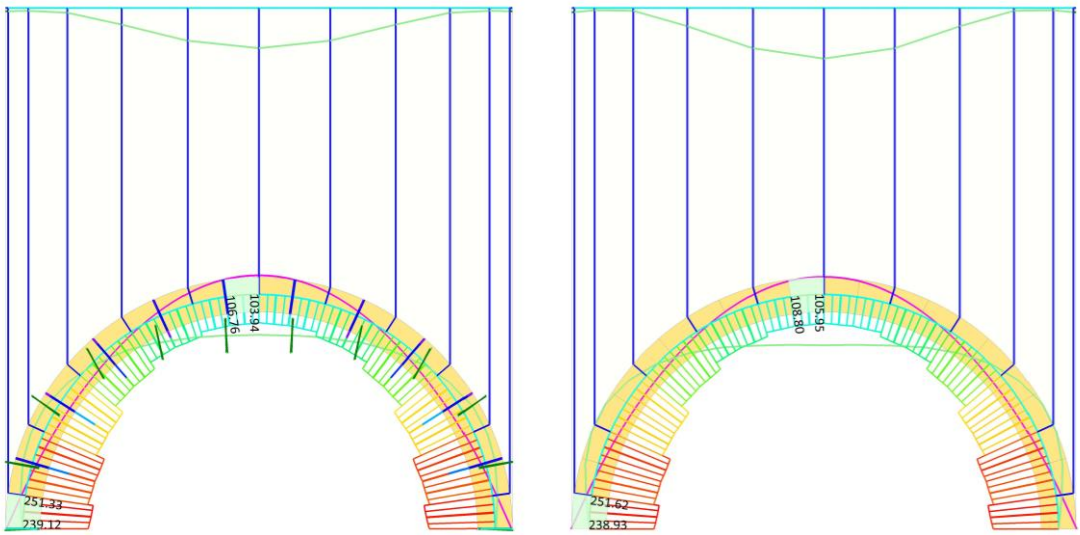


Figure 11. Static analysis. (a) block-joint model. (b) block-block model

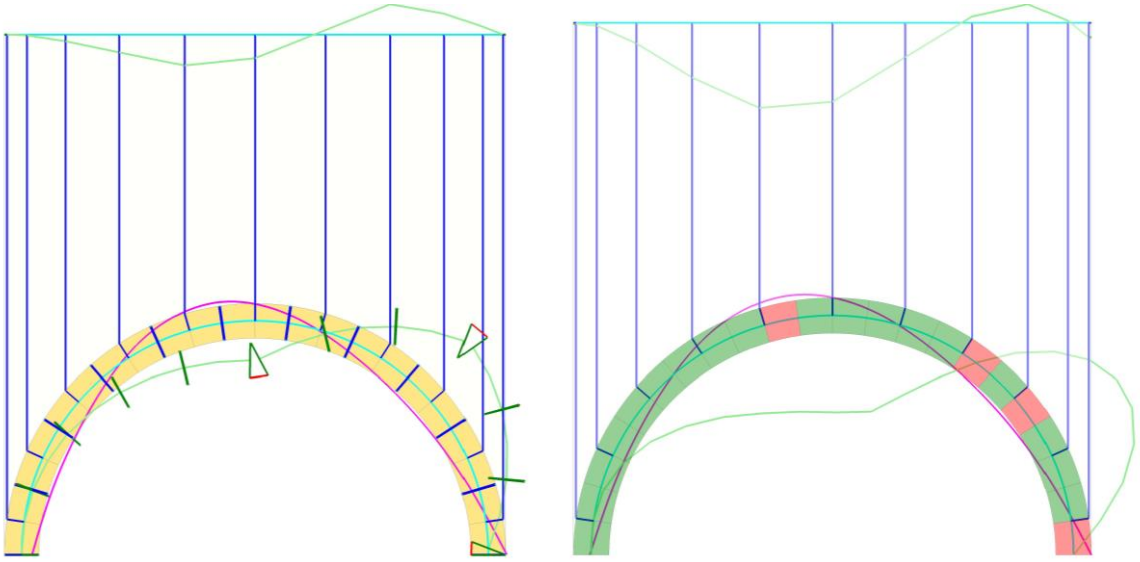


Figure 12. Pushover analysis. (a) block-joint model. (b) block-block model

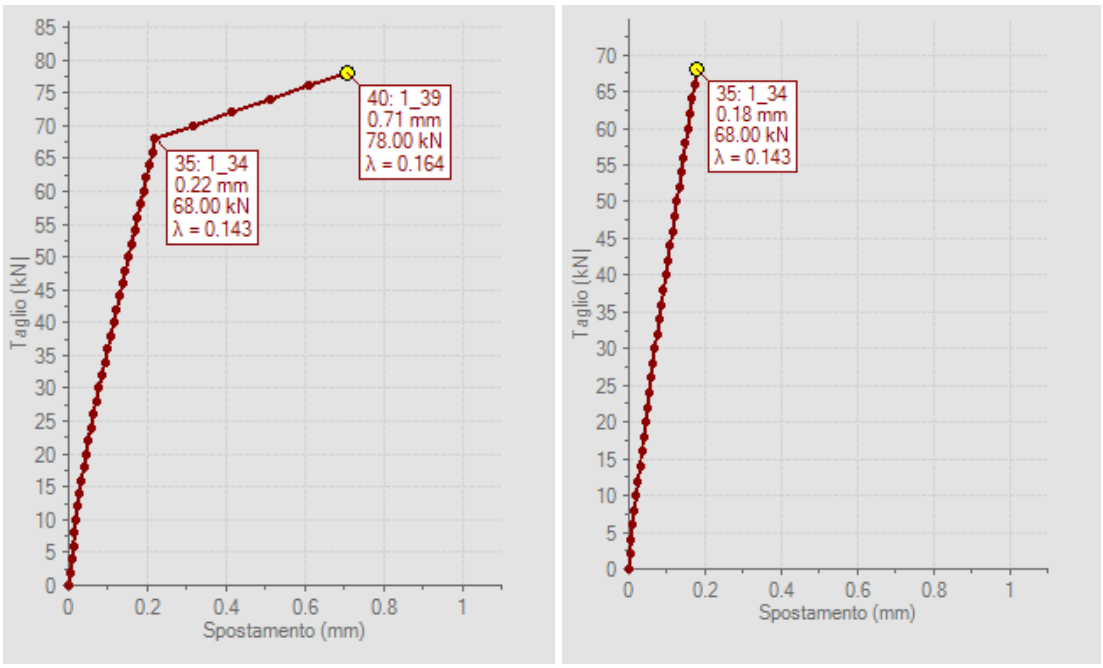


Figure 13. Pushover analysis, capacity curve. (a) block-joint model. (b) block-block model

The capacity curve obtained with the block-joint model features a plastic phase that lacks in the block-block model. The difference is certainly due to the higher accuracy of the block-joint with respect to the block-block modelling but it is not quite relevant for the seismic assessment of the arch, being the total force resistance and the position of the plastic hinges highly comparable.

7.3 Strengthening interventions

In this example passive and active strengthening interventions are applied to te reference arch and their efficiency is assessed through pushover analysis performed on the block-joint model.

As regards the passive interventions, we consider the application of FRP sheets at the intrados of the arch by increasing the tensile strength of the relevant joints according to the capacity of the intervention.

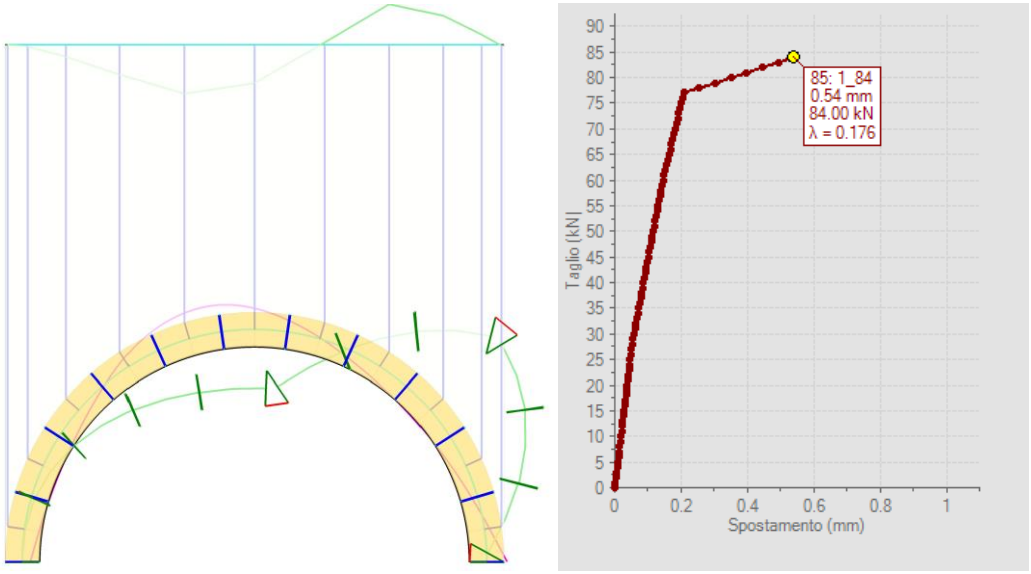


Figure 14. Pushover analysis, passive interventions (a) Thrust-line and displacement (b) capacity curve

As regards the active interventions, a prestress state is applied by means of ties placed along the intrados of the arch. The effect of the intervention is modelled with the application of radial point loads in the centroid of each block as shown in the following figure. This brings the thrust-lone closer to the central axis of the arch, thus it delays the formation of plastic hinges.

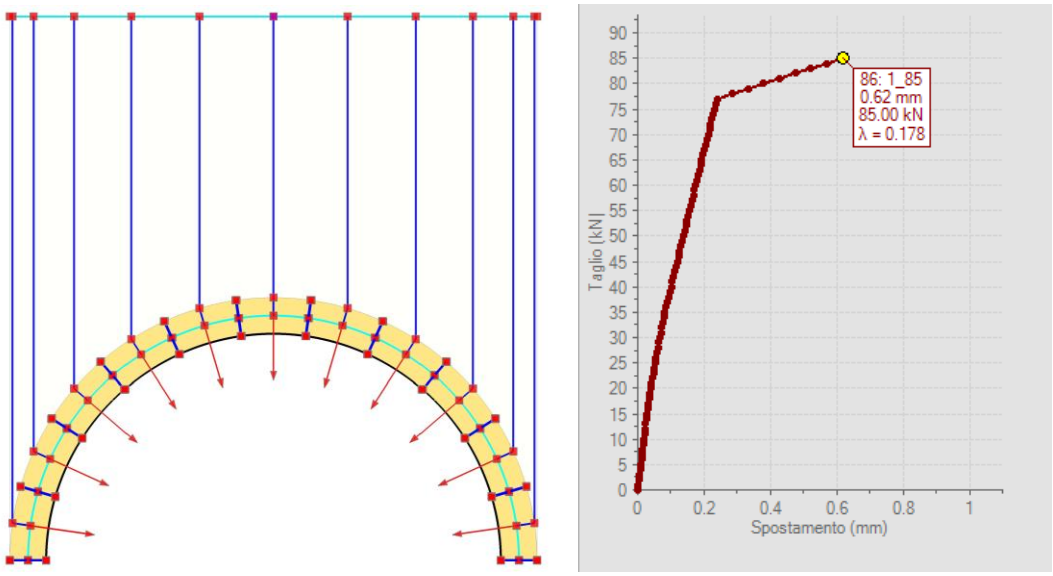


Figure 15. Active interventions (a) Radial point loads (b) Pushover analysis, capacity curve

Both the interventions considered led to a substantial improvement of the structural capacity of the arch.

8 CONCLUSIONS

This paper introduced the block-block model, a new method for the structural analysis of arches and vaults. The technique has been developed on the base of the block-joint method and aims to analyse arches located within macroelements or complex building through a simplified model. Both block-block and block-joint models allow for the correct assessment of the structural behaviour of the arch. The pushover analysis performed with the two methods leads to similar results.

Moreover the following aspects have been introduced and validated: (a) the blocks are now modelled with spatial curved beam elements, (b) at the beginning of the pushover analysis a self-correcting gravity analysis pursuits a stable configuration of the arch under static loads acting on the internal releases of the elements, (c) the vertical loads arising from the structure above the arch are transferred to the arch through vertical rigid struts, (d) the effect of passive and active strengthening interventions is accounted for in the methods proposed.

Several application examples have been presented to describe the proposed methodology.

REFERENCES

[1] M. Paradiso, G. Tempesta, S. Galassi, F. Pugi, *Sistemi voltati in muratura. Teoria e applicazioni.* DEI Tipografia del genio civile, 2007.

[2] J. Heyman, *The Masonry Arch*. Hellis Horwood Ltd., 1982.

[3] J. Heyman, *The Stone Skeleton*. Cambridge University Press, 1995.

[4] Direttiva del Presidente del Consiglio dei Ministri, 9 febbraio 2011: "*Valutazione e riduzione del rischio sismico del patrimonio culturale con riferimento alle Norme tecniche per le costruzioni di cui al decreto del Ministero delle infrastrutture e dei trasporti del 14 gennaio 2008*". Gazzetta Ufficiale della Repubblica Italiana n. 47 del 26 febbraio 2011, Supplemento ordinario n.54. (in Italian)

[5] F. Pugi, Seismic analysis of masonry arch structures through the finite element model "block-joint", *4th ECCOMAS Thematic Conference on Computational Methods in Structural Dynamics and Earthquake Engineering (COMPDYN 2013)*, Kos Island, Greece, June 12-14, 2013

[6] Ministero delle Infrastrutture e dei Trasporti, *Circolare. n. 617 del 02 febbraio 2009. Istruzioni per l'applicazione delle Nuove Norme Tecniche per le costruzioni, §C8A.4*, Gazzetta Ufficiale della Repubblica Italiana n. 47 del 26 febbraio 2009, Supplemento ordinario n.27. (in Italian)

[7] R. Palaninathan, P.S. Chandrasekharan, Curved beam element stiffness matrix formulation, *Computers & Structures*, **21**:**4**, 663-669, 1985.

[8] W.C. Young, R.C. Budynas, *Roark's Formulas for Stress and Strain*, McGraw-Hill, 2002.

[9] Aedes Sofware. SAV: Stabilità di Archi e Volte, www.aedes.it

[10] Aedes Software. PCM: Progettazione di costruzioni in muratura, www.aedes.it

[11] L. Jurina, Una tecnica di consolidamento attivo per archi e volte in muratura, Convegno: Seismic performance of built heritage in small historic centers, Assisi, Italia, April, 1999

COMPDYN 2015
5th ECCOMAS Thematic Conference on
Computational Methods in Structural Dynamics and Earthquake Engineering
M. Papadrakakis, V. Papadopoulos, V. Plevris (eds.)
Crete Island, Greece, 25–27 May 2015

SEISMIC PROTECTION OF HEAVY NON-STRUCTURAL MONOLITHIC OBJECTS AT THE TOP OF A HISTORICAL MASONRY CONSTRUCTION THROUGH BASE ISOLATION

A. Chiozzi[1], M. Simoni[1], and A. Tralli[1]

[1] University of Ferrara
Department of Engineering
I44122 – 1, Via Saragat – Ferrara (ITALY)
e-mail: {andrea.chiozzi, michele.simoni, tra}@unife.it

Keywords: Seismic Protection, Non-structural objects, Base Isolation, Masonry.

Abstract. *This contribution addresses the problem of earthquake protection of heavy non-structural monolithic objects, which are usually placed at the top of historical masonry constructions for mainly decorative purposes like pinnacles, merlons, sculptures and heavy artwork. Such objects, when subjected to base accelerations due to seismic actions, may undergo rocking phenomena, which may eventually lead to the overturning of the whole body. In particular, the specific case of the seismic protection of ancient marble pinnacles placed at the top of a three-arched masonry city gate in Ferrara (ITALY) is illustrated. In a preliminary rocking analysis, the pinnacles have been idealized as rigid bodies in unilateral contact with the underlying moving base and the resulting rocking motion have been analyzed. The structural safety level of the pinnacles have thus been assessed. As a consequence of these considerations, a base isolation system designed around multiple double concave curved-surface steel sliders have been devised. The effectiveness of the proposed isolation system has been assessed through numerical simulations. The amplification effect of the ground acceleration due to the underlying three-arched structure has been established through time-history dynamic analyses, where masonry has been considered as a viscoelastic material. To this aim, an equivalent viscous damping coefficient has been calculated for masonry following an iterative procedure involving the computation of capacity curves for both in- and out-of-plane load directions and the definition of simplified bi- and tri-linear inelastic load-displacement capacity curves for masonry panels.*

1 INTRODUCTION

Many research efforts have been devoted, in the past, to the prevention of seismic damage of civil and industrial constructions, both modern and historical. Among the many aspects that are targeted in these studies, an increasing attention is being addressed towards the understanding of the seismic behavior of non-structural elements belonging to such constructions. The ultimate goal is to devise effective seismic protection systems for heavy artwork, sculptures, pinnacles, and similar objects which do not have a structural function but belong to world heritage and, in many cases, have an inestimable value; for an introduction to this subject the reader is addressed to [1], [2], [3], [4], [5], [6], [7].

The aim of the present contribution is to illustrate the case study of the seismic protection through base isolation of eleven ancient marble pinnacles placed at the top of the three-arched masonry city gate in Ferrara, Italy, portrayed in Fig.1a, which underwent the 2012 Emilia seismic swarm.



(a) (b)

Figure 1: (a) Three-arched masonry city gate, Corso Giovecca, Ferrara, Italy; (b) damages from overturning of monolithic decorative elements during 2012 Emilia earthquake (Corso Giovecca, Ferrara, Italy).

From a mechanical point of view, in many cases, non-structural objects belonging to constructions are monolithic and therefore, they may be regarded as rigid bodies. The main phenomenon a rigid body undergoes when subject to earthquake excitations is an oscillating motion around different instantaneous rotation centers belonging to its base known as *rocking*, which may eventually lead to collapse due to the final toppling of the whole body.

In the study of pure rocking, a number of investigations have adopted a simple two-dimensional model, which was first proposed in [8], later derived independently in a seminal paper by Housner [9] and revised in [10]. The model is based on the assumption of no bouncing and sufficient friction to prevent sliding during impact.

Recently, new interest has been devoted to the study of seismic protection of the artistic heritage and several authors addressed the problem of the rocking motion of rigid bodies provided with base isolation systems ([12], [13], [14]) where the effectiveness of base isolation in increasing the safety level of art objects in case of earthquake has been assessed.

Finally, some three-dimensional models describing the dynamics of rigid bodies with impacts has been proposed in literature. In particular, the difficult problem of the three-dimensional motion of a an axisymmetric body rocking and rolling on a planar surface was addressed by [15], [16], [17].

The development of effective techniques for seismic risk mitigation of monolithic non-structural elements is a fundamental issue. A first approach [18] consists in anchoring objects

using different support mounts that essentially makes the object itself part of the structure. However, such a solution is not satisfying for it allows the transmission of large impulsive seismic forces which the object, being too brittle, cannot withstand. Furthermore, in this case the effects of the earthquake are usually not reversible.

An alternative approach consists in adopting base isolation systems which has been demonstrated to be an excellent solution in limiting the transferred seismic actions thus effectively mitigating the seismic risk on different types of structures [19]. Nevertheless, while base isolation for bridges or buildings has been largely developed in the last decades, base isolation for the comparatively much lighter art-objects and other kind of non-structural elements has not experienced the same level of development and it is still an open topic. As clearly pointed out in [20], even though the basic concepts which stand at the basis of base isolation systems are the same, the application of isolation techniques developed for civil structures to small objects requires more than a simple extension, and specific considerations are mandatory since the parameters governing the behavior of the seismic isolators need to be specifically calibrated.

As initially stated, the present paper addresses the problem of the structural safety assessment and seismic protection of heavy monolithic objects placed at the top of a monumental construction through the illustration of a specific case study which concerns the seismic risk mitigation for eleven marble pinnacles placed at the top of a three-arched masonry city gate built in Ferrara (Fig.1a), Italy, at the end of Corso della Giovecca, between 1703 and 1704 a.C. The marble pinnacles placed at the top of the gate have mainly a decorative purpose and their slenderness, coupled with their considerable mass, makes them highly vulnerable to seismic actions so that they cannot be considered safe. After the strong seismic events which struck Emilia in May 2012 and caused severe damage to the city's historical constructions, the pinnacles have been removed for safety reasons. In Fig.1b damages produced by a monolithic decorative non-structural element collapsed in Ferrara during 2012 Emilia earthquake is shown.

In order to protect the pinnacles from seismic actions, a specific base isolation system, based on the use of multiple double concave curved surface steel sliders. The proposed application, at the best of the authors' knowledge, is very peculiar and it is the first example in Italy of base isolation of heavy marble pinnacles at the top of a monumental construction.

The paper is organized as follows. In Section 2 the underlying three-arched masonry city gate structure is characterized from a dynamical point of view, a natural frequency analysis have been conducted and capacity curves for the masonry structure have been computed. In Section 3 the rocking behavior of the single pinnacle subject to ground accelerations is assessed. In Section 4 the proposed base isolation systems is described and in Section 5 its effectiveness is established through numerical simulations, which involves the evaluation of the amplification effect of the underlying masonry structure and the definition of equivalent viscous damping coefficients. In Section 6 conclusions and future research direction are given.

2 THE FERRARA MASONRY CITY GATE

The case study considered in the present work is a three-arched masonry construction whose geometry is shown in Fig.2a. The structure is in good general conditions and is made of clay artificial bricks and mortar. Eleven decorative marble pinnacles stand at the top of the gate.

Each pinnacle, whose geometry is portrayed in Fig.2b, is made of different axisymmetric marble blocks piled and bonded together by a central iron rod. A pinnacle may be regarded as an axisymmetric rigid body, which may undergo rocking motion when subjected to base excitations. As shown in Fig.2b, the pinnacle is 2.37 m tall and its circular base has a diameter B

of 0.60 m. Marble is assumed to have a density ρ of 2700 kg/m^3 and the resulting mass M of the pinnacle is 980 kg. Pinnacles are placed on two different orders; more precisely eight pinnacles are placed at an intermediate height of 9.80 m (hereinafter referred to as *lateral pinnacles*) and three pinnacles are placed on the top of the gate at a height of 18.50m (hereinafter referred to as *central pinnacles*).

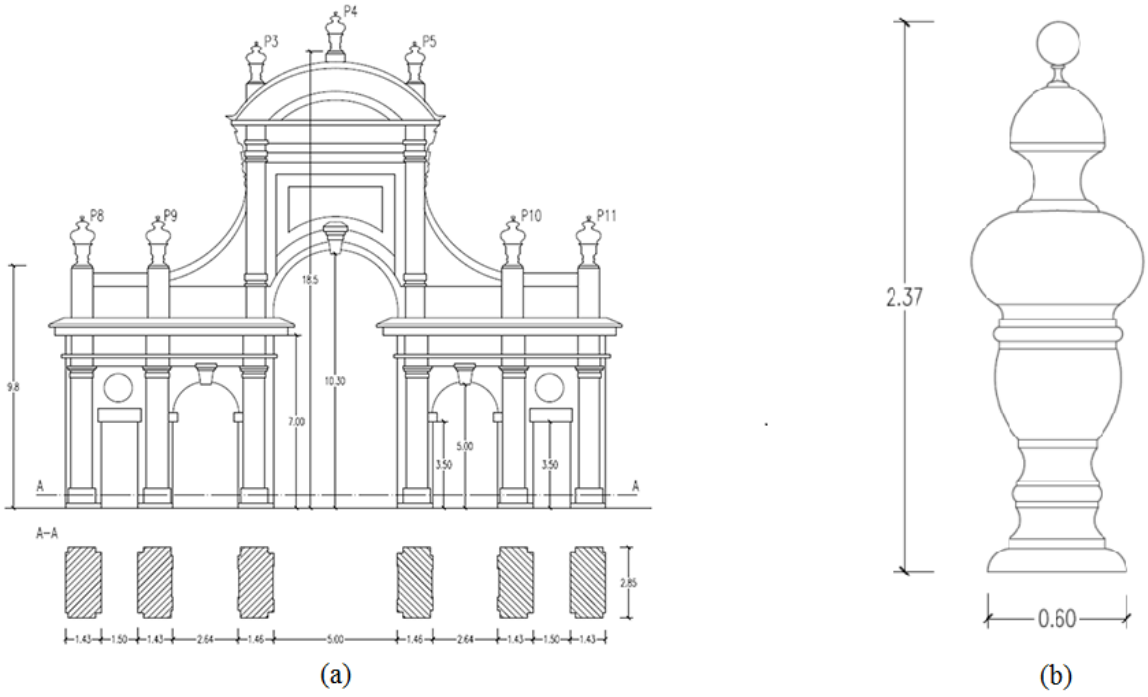


Figure 2: (a) Geometric representation of the three-arched masonry city gate; (b) Geometric representation of the pinnacle.

2.1 The design seismic action

Given the WGS84 coordinates for the city-gate location (44.832 N, 11.632 E), assuming a return period for the design seismic event of 712 years (i.e. corresponding to the ultimate limit

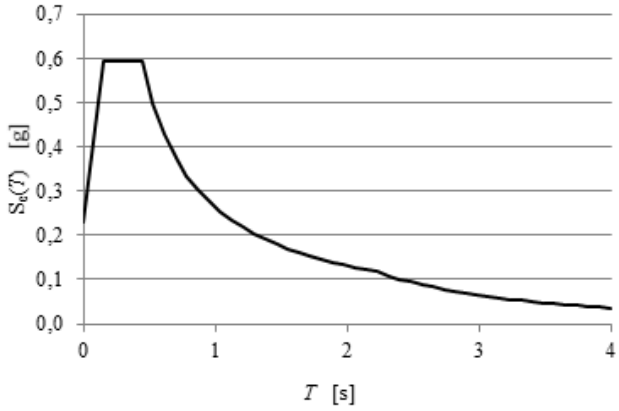


Figure 3: Design earthquake spectra for the three-arched masonry city gate according to NTC2008.

state in terms of life safety for a Class III structure and soil category C, in agreement with the Italian Building Code [20] the resulting design seismic action on the construction is determined. The corresponding design earthquake spectra is reported in Fig.3.

2.2 Natural frequency analysis of the masonry structure

In order to evaluate the fundamental period T_1 of the three-arched masonry structure and to establish its main vibration modes a linear finite element natural frequency analysis has been carried out using the finite element analysis software Straus7 [21]. The FEM model has been discretized with eight node brick-type finite elements and is shown in Fig.4a. The mechanical properties of the masonry material are reported in Tab.1 and are determined according to prescriptions contained in [22] for existing constructions.

Compressive strength f_m [MPa]	Shear strength τ_0 [MPa]	Elastic modulus E [MPa]	Tangential modulus G [MPa]	Specific weight w [kN/m^3]
2.4	6.0	1200	400	18

Table 1 Material parameters for masonry.

Mode	Frequency [Hz]	Participating mass in the in-plane direction [%]	Participating mass in the out-of-plane direction [%]
1	2.0131	0.00	54.54
2	6.0679	0.01	0.00
3	6.4394	87.96	0.00
4	7.5946	0.00	26.44

Table 2 Frequency and participating mass for the four vibration modes.

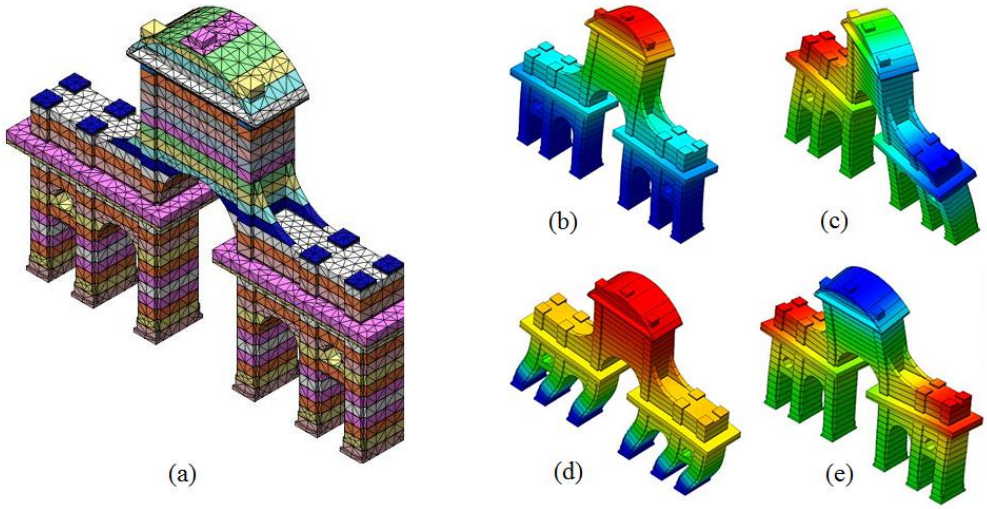


Figure 4: (a) Finite element model of the three-arched masonry city gate for natural frequency analysis; the first four vibration modes: (b) translational mode in the out-of-plane direction, (c) torsional mode, (d) translational mode in the in-plane direction, (e) partial translational model in the out-of-plane direction.

From the analysis, three pure translational and a torsional mode have been obtained as the main four vibration modes which are represented in Fig.4b. Tab.2 contains frequency and participating mass in the in-plane and out-of-plane directions for the four modes.

2.3 In- and out-of-plane capacity curves for the masonry structure

Using the commercial finite-element analysis software DIANA [23], in- and out-of-plane capacity curves for the masonry structure have been determined. The finite element model used is shown Fig. 4a. The masonry material has been assigned a *total strain crack model* constitutive law [23]. As shown in the previous paragraph the principal vibration mode in the in-plane direction is the third mode with a participating mass of 87.6%. Thus, a distribution of forces proportional to the third mode has been applied and the capacity curve have been computed through a finite-element non-linear incremental analysis. The same analysis has been conducted for the out-of-plane direction with a distribution of forces proportional to the first vibration mode, which is the principal mode in the out-of-plane direction with a participating mass of 54.54. The obtained in- and out-of-plane capacity curves, shown in Fig. 5, relates the total shear force F_b applied at the base of the structure with the in- and out-of-plane displacements d_c of a control point, which has been chosen as the medial point placed on one of the short sides of the construction, at a height of 3.00 m.

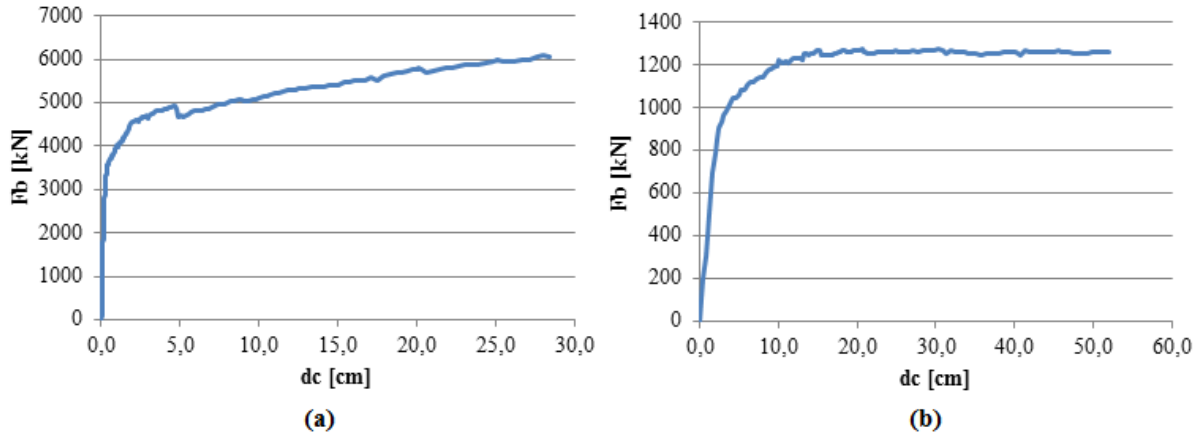


Figure 5: Capacity curves of the masonry structure for both in-plane (a) and out-of-plane (b) directions (third and first vibration mode respectively).

3 ROCKING BEHAVIOR OF THE PINNACLES

In this section, the dynamic behavior of the marble pinnacles regarded as rigid bodies is assessed. In particular, their rocking behavior under base excitations is analyzed, in order to assess their structural safety with regard to collapse by toppling.

3.1 Design seismic impulse at the base of the pinnacle

In the following analysis an impulsive seismic excitation acting on the pinnacle is considered. In order to obtain the design earthquake impulse, it is necessary to evaluate, at least in a conventional way, the amplification effect of the underlying masonry construction (a more sophisticated analysis for the evaluation of the amplification effect will be presented in Section 4).

As shown in Tab. 2, the fundamental period of the structure T_1 results equal to 0.49 s. As suggested in paragraph C8A.4.2.3 of [22], the design seismic acceleration acting on an object placed at a height Z on a construction may be evaluated with the approximated formula:

$$a_d = S_e(T_1) \cdot \Psi(Z) \cdot \gamma \tag{1}$$

where $S_e(T_1)$ is the design earthquake spectra evaluated in T_1, $\Psi(Z)$ is the first normalized vibration mode of the structure and γ is the corresponding participation factor. For an inverted triangular shape of the first mode, $\Psi(Z)$ can be evaluated with the formula $\Psi(Z) = Z/H$ where H is the maximum height of the construction.

For the case under study $S_e(T_1)$ is equal to 0.600 g. When considering central pinnacles, Z is equal to 18.25 m and $\Psi(Z)$ is equal to 1 whereas for lateral pinnacles Z is equal to 9.80 m and $\Psi(Z)$ is equal to 0.537. Finally, from the natural frequency analysis γ is equal to 1.2 for central pinnacles and equal to 1 for lateral pinnacles.

From equation (1) the design seismic acceleration a_d on central pinnacles results equal to 0.720 g whereas on lateral pinnacles of pinnacles is equal to 0.322 g.

3.2 Rocking motion of the pinnacles without isolation

In the present paper the rocking motion of the pinnacle is analyzed as a two-dimensional planar problem where the pinnacle is represented by one of its diametral sections [9], [10].

Let us assume that sliding between the pinnacle and its rigid base is prevented. In this case, in order to describe the two-dimensional rocking motion of the pinnacle under base excitations, a single Lagrangian parameter θ is needed. A possible choice for θ is the angle from the vertical as shown in Fig.6 where G indicates the center of mass of the rigid body which is lying on the symmetry axis, at a height z_G equal to 1.042 m above the base. Depending on the ground acceleration, the pinnacle may move rigidly with the ground or be set into rocking; in the letter case it will oscillate around the centers of rotation O and O'. Therefore, the problem is governed by two equation of motion. R represents the length of the segment connecting the center of mass G to one of the rotation centers.

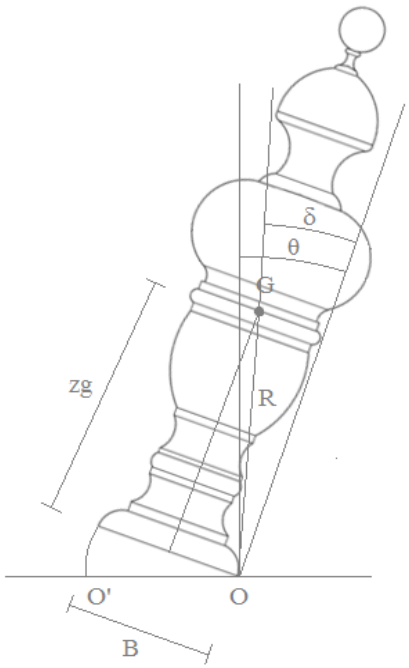


Figure 6: Rocking pinnacle.

When subjected to base acceleration $\bar{a}_g$ in the horizontal direction the pinnacle will be set into a rocking motion when the overturning moment of the horizontal inertia force about one of the centers of rotation exceeds the stabilizing moment due to the weight of the body:

$$\begin{aligned} M\,\bar{a}_g z_G &> M\,g\,\frac{B}{2} \\ \bar{a}_g &> \frac{B}{2z_g}\,g = 0.208g \end{aligned} \tag{2}$$

where M is the mass of the pinnacle and g is the acceleration of gravity. Equation (2) represents a necessary condition for the initiation of a rocking motion and is equivalent to a standard linear kinematic analysis as defined in [22]. For the present case-study, assuming $\bar{a}_g$ equal to the design seismic acceleration a_d calculated in Subsection 3.1, condition (2) is satisfied for both central and lateral pinnacles. Nevertheless, this condition does not guarantee the continuation of the rocking motion. In order to assess if, after initiation, a rocking motion of the pinnacles is established, it is necessary to look more in depth into the phenomenon.

The equations of motion of the pinnacle subjected to horizontal ground accelerations $a_g(t)$, governing the angle θ are derived by considering the equilibrium of moments about the centers of rotation. These equations can be expressed as

$$I_0\ddot{\theta} + MgR\sin(\delta-\theta) = -MR\cos(\delta-\theta)\,a_g(t) \tag{3}$$

when the pinnacle rocks about O and

$$I_0\ddot{\theta} - MgR\sin(\delta+\theta) = -MR\cos(\delta+\theta)\,a_g(t) \tag{4}$$

when it rocks about O'. In addition to the quantities defined earlier in Fig.6, I_0 represents the mass moment of inertia about O or O' and $\delta = \tan^{-1}\left(\mathrm{B}/2\,\mathrm{z}_G\right)$.

In particular for the present case study, $I_0 = 1434\,\mathrm{kg}\cdot\mathrm{m}^2$. Let us incidentally observe that the switching of equations back and forth between equations (3) and (4) during rocking motion, and the trigonometric functions of θ make equations (3) and (4) highly nonlinear.

At this point it is necessary to examine more closely the impact phase of the rocking motion. When the pinnacle is rotated through an angle θ and then released from rest with initial displacement, it will rotate about the center O and it will fall back into the vertical position. If the impact is assumed to be inelastic, the rotation continues smoothly about the center O' and the moment of the momentum about O' is conserved. Thus:

$$I_0\dot{\theta}_1 - MRB\dot{\theta}_1\sin\delta = I_0\dot{\theta}_2 \tag{5}$$

Dividing by $I_0\dot{\theta}_1$ Eqn. (5) gives the ratio between angular velocities after and before impact:

$$\frac{\dot{\theta}_2}{\dot{\theta}_1} = 1 - \frac{M}{I_0}RB\sin\delta. \tag{6}$$

If the ratio between angular velocities after and before impact is positive, then after impact the rotation of the pinnacle continues about the opposite center. If, conversely, angular velocity changes sign after impact the pinnacle bounces about the point of rotation prior to impact. Therefore, relationship (6) gives the following condition for the onset of a rocking motion:

$$\frac{MRB\sin\delta}{I_0}<1 \tag{7}$$

which is satisfied for the pinnacle in our case study. Let us observe that condition (7) depends only on geometric and mass properties of the rigid body. This means that, whenever a rigid body, for which condition (7) holds, gets tilted by an initial angle (e.g. in case of an external seismic excitation satisfying condition (2) like in our case) then a rocking motion will be established. Conversely, if condition (7) does not hold, the block will bounce about the same corner and a proper rocking motion will not be established.

3.3 Overturning by single-pulse excitations

Dynamic behavior of rigid bodies under seismic actions is very complex and requires a time step integration of equations of motion in order to be fully described. Nevertheless, in order to assess the safety of pinnacles under dynamical conditions, useful information may be obtained from an analytical investigation of the collapse by overturning under single-pulse earthquake excitations.

In this subsection a simple overturning analysis for the pinnacles under single-pulse excitations is presented. The excitation may be a rectangular pulse with constant acceleration a_{g0} lasting for a time t_1 or acceleration varying as a half-cycle sine-wave pulse of amplitude a_{g0} and duration t_1. In the present case-study, as seen in the previous section, the motion of central pinnacles is initiated by the base acceleration $a_{g0}=a_d=0.720\,\mathrm{g}$. Even if the motion is initiated (i.e. condition (2) satisfied) and the body is subjected to rocking motion (i.e. condition (7) satisfied) the body may or may not overturn depending on the magnitude of a_{g0} and the duration t_1. Housner [9] determined the duration t_1 of a rectangular pulse with acceleration a_{g0} required to overturn the block through the following equation:

$$\cosh\sqrt{\frac{MgR}{I_o}}t_1=1+\left[1/\left(2\frac{a_{g0}}{g\delta}\left(\frac{a_{g0}}{g\delta}-1\right)\right)\right]. \tag{8}$$

Analogously, for the half-cycle sine-wave pulse he derived the following equation relating the duration t_1 to the amplitude a_{g0} of the excitation:

$$\frac{a_{g0}}{g\delta}=\sqrt{\left[1+\frac{I_0}{MgR}\left(\frac{\pi}{t_1}\right)^2\right]} \tag{9}$$

This equations were determined in [9] starting from the linearized version of equations (3) and (4); therefore, they are valid only for slender blocks (like the ones in our case-study).

Let us study the case of central pinnacles. Considering the geometrical and mass properties of the pinnacles and assuming $a_{g0}=a_d=0.720\,\mathrm{g}$ equation (8) gives an overturning duration for the rectangular pulse excitation of $t_1=0.15\,\mathrm{s}$, while equation (9) gives an overturning duration for the sine-wave pulse excitation of $t_1=0.48\,\mathrm{s}$.

As shown in [24] typical pulse duration for earthquakes of low to medium intensity is between 0.10 s and 0.50 s. This means that the pulse-type excitations considered in this Section, with the computed duration t_1 that brings to collapse the pinnacles by overturning, are typical

of earthquakes that may occur in the Ferrara area. This corroborates the conclusion that pinnacles in our case-study are not safe under design seismic actions.
For these reasons, a base isolation system has been designed in order to protect pinnacles from potential earthquake excitations.

4 THE ISOLATION SYSTEM

This section contains a description of the base isolation system, which has been specifically devised for the protection of the pinnacles of the Ferrara city-gate.

4.1 The isolation system

Both lateral and central pinnacles are isolated through the use of double concave curved surface steel sliders. A schematic representation of the single isolator is depicted in Fig.7a. Two different isolating systems have been devised respectively for central pinnacles and lateral pinnacles.

For the three central pinnacles the isolating system for each pinnacle is made of three isolators placed at the vertex of a equilateral triangle and rigidly connected together by an upper steel plate on which the pinnacle lies. The system is schematically depicted in Fig.8a.

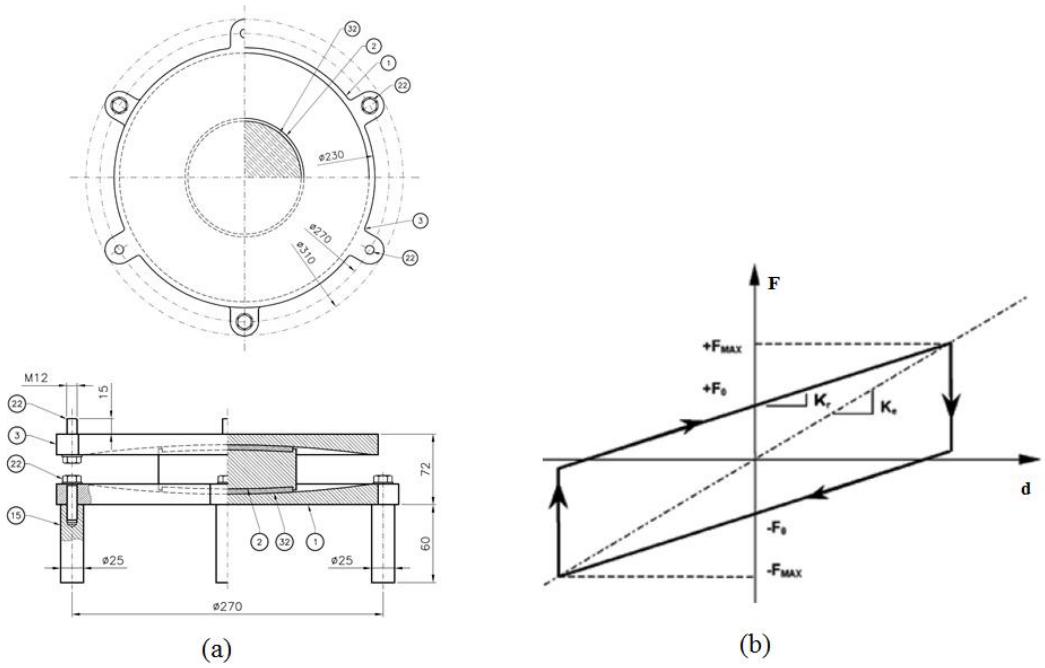


Figure 7: (a) Schematic view of the seismic isolator: a double concave curved surface steel slider developed and produced by the Research and Development Department of FIP Industriale Group; (b) force-displacement response of the isolator.

For each of the two groups of four lateral pinnacles the isolating system is made of four isolators (one beneath each pinnacle) connected together by a system of steel rods and plates which guarantees an approximatively zero relative displacement between isolators. In fact, the system may be regarded as a wide isolated base on which the four pinnacles lie. The system is schematically depicted in Fig.8b.

Thus, for the isolation of all the eleven pinnacles seventeen isolators will be employed.

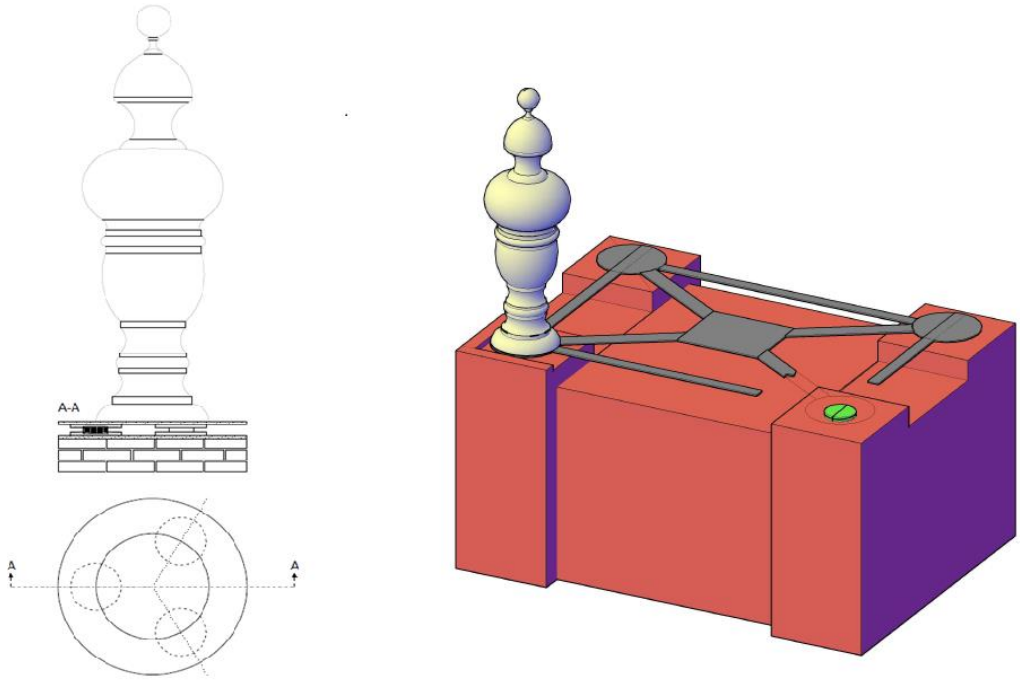


Figure 8: Isolating system devised for central pinnacles (a), and lateral pinnacles (b).

4.2 Mechanical properties of the steel sliders

According to producer specifications isolators force-displacement response is represented by a rigid-plastic with hardening and friction like behavior of the kind depicted in Fig.7b where F_0 is the maximum friction force which the isolator can develop, K_r is the stiffness of the hardening-like branch, $F_{\max}$ is the maximum force can develop at the end of the hardening-like branch. These quantities are defined by the following relations [19], [25]:

$$\begin{cases} F_0 = \mu N_{Sd}\,; \\ K_r = \dfrac{N_{Sd}}{R}; \\ F_{\max} = F_0 + K_r d\,; \end{cases} \tag{10}$$

where μ is the friction coefficient along the sliding surface, N_{Sd} is the vertical load acting upon the isolator, R is the equivalent curvature radius of the sliding surface and d is the maximum allowed displacement. Furthermore, an equivalent damping coefficient ξ_e can be defined through the following formula

$$\xi_e = \frac{2}{\pi}\left(\frac{d}{\mu R}+1\right)^{-1}. \tag{11}$$

Friction coefficient μ is a function of the vertical load N_{Sd} and temperature. Therefore, the producer has not provided this value for the isolators used, but a range of values varying between 0.5% and 2.5%. In the following analysis both these two values of μ have been taken into consideration.

Tab.3 summarize the mechanical properties for isolators used in the two isolation systems for the two different values of the friction coefficient.

	N_{Sd}	d	R	ξ_e	F_0	K_r	$F_{\max}$
	[kN]	[mm]	[mm]	[-]	[kN]	[N/mm]	[kN]
$\mu = 2.5\%$	3.33	150	2000	0.16	0.083	1.665	0.333
$\mu = 0.5\%$	3.33	150	2000	0.04	0.016	1.665	0.266

Table 3 Mechanical properties of the steel sliders isolation devices used.

5 NUMERICAL SIMULATIONS

In order to assess the effectiveness of the isolation system in preventing rocking and overturning of the pinnacles, time-history dynamic analyses with a seismic accelerogram applied to the base of the isolated pinnacle have been carried out and are described in this Section.

5.1 Design accelerograms and amplification effect

In order to evaluate the dynamic response of the pinnacle, the definition of a design accelerogram is necessary.

As required by Italian Building Code [20] and Eurocode 8 [26], a set of seven accelerograms compatible with the earthquake design spectrum of the site, defined in [20] for a ultimate limit state in terms of collapse, has been generated with the software Rexel 3.5.

For each accelerogram the corresponding spectrum (reported in Fig.9) can be generated.

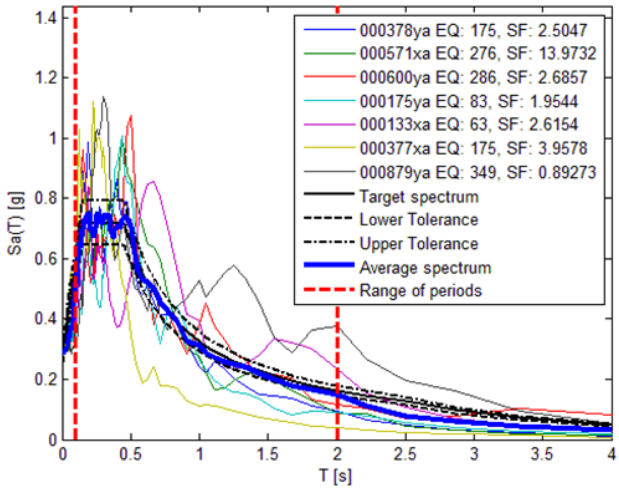


Figure 9: Earthquake spectra compatible with the design spectra defined by NTC2008 generated with Rexel 3.5.

In order to define the correct seismic action on the pinnacles, it is necessary to take into account the amplification effect due to the underlying masonry structure. Thus, for each spectrum compatible accelerogram, applied at the base of the structure as a forcing action, two different time-history dynamic analyses of the three-arched masonry city gate have been carried out using the finite element analysis software Straus7, one with the ground accelerations applied in the in-plane direction and one with the ground accelerations applied in the out-of-plane direction. Therefore, a total of fourteen analyses have been conducted.

The finite element model used is the same described in paragraph 2.3. Masonry has been modeled as a linear visco-elastic material with a Raleigh damping model. Rayleigh damping,

also known as proportional damping, assumes that the global damping matrix $\mathbf{C}$ is a linear combination of the global stiffness $\mathbf{K}$ and mass $\mathbf{M}$ matrices:

$$\mathbf{C} = \alpha\mathbf{M} + \beta\mathbf{K} \qquad (12)$$

where α and β are constants of proportionality. The two constants α and β are normally determined by using the following relationship

$$\xi = \frac{1}{2}\left(\frac{\alpha}{\beta} + \beta\omega\right) \qquad (13)$$

for two values of the damping ratio ξ_1 and ξ_2 at two chosen frequencies ω_1 and ω_2. Substituting the two sets of ξ and ω values into (13) the following two equations for α and β are obtained:

$$\alpha = \frac{2\omega_1\omega_2\left(\xi_2\omega_1 - \xi_1\omega_2\right)}{\omega_1^2 - \omega_2^2};\ \beta = \frac{2\left(\xi_1\omega_1 - \xi_2\omega_2\right)}{\omega_1^2 - \omega_2^2}. \qquad (14)$$

In the non-linear dynamic finite element analysis related to our case-study the values of α and β for the Raleigh damping model where determined through equation (14) assuming for ω_1 and ω_2 the frequencies of the two principal modes (respectively the out-of-plane and in-plane translational modes which were obtained through the natural frequency analysis) and for ξ_1 and ξ_2 the values 10% and 5% respectively as suggested in [27]. The choice of such equivalent viscous damping coefficient is justified in the subsequent paragraph through an ad-hoc numerical procedure.

At the end of each time-history dynamic analysis the response of the structure in terms of acceleration at the base of both lateral and central pinnacles have been recorded. This response represents the design seismic accelerogram to be applied at base of the isolated pinnacles in order to assess the effectiveness of the isolation system.

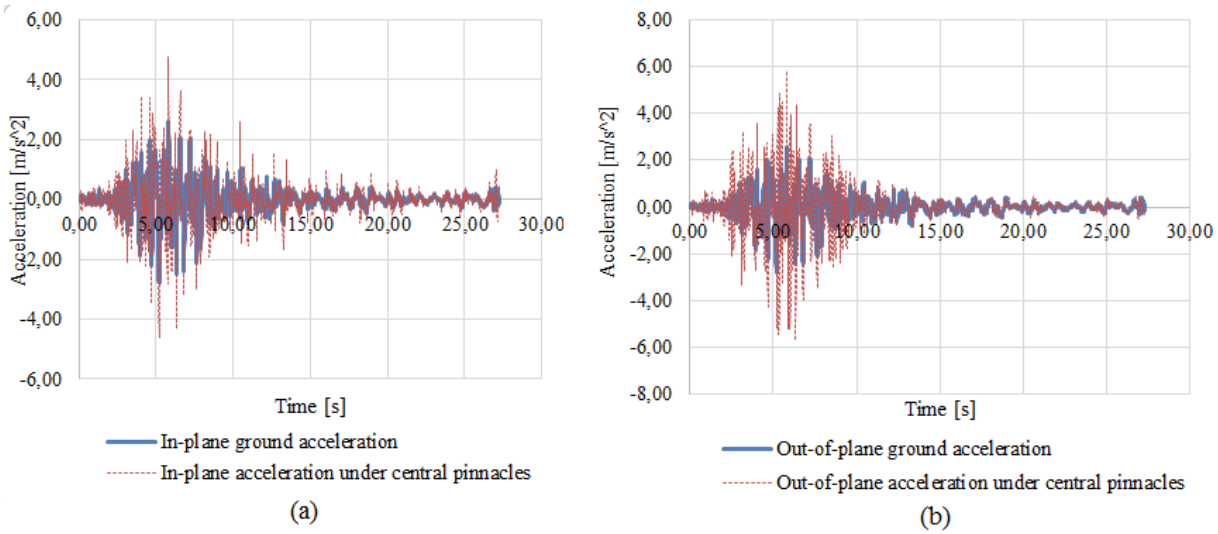


Figure 10: Amplification of the base seismic action 378ya due to the masonry structure on central pinnacles in the in-plane (a) and out-of-plane (b) directions.

Fig.10a-b depict a comparison between the accelerogram 378ya applied at the ground level in the two main directions respectively and the corresponding accelerogram computed at the

level of central pinnacles. Analogous results are obtained for lateral pinnacles and are here omitted for the sake of brevity.

5.2 Numerical evaluation of masonry equivalent viscous damping coefficients ξ_1 and ξ_2

In this paragraph the numerical procedure used to estimate the equivalent viscous damping coefficients ξ_1 and ξ_2 for masonry is outlined. The procedure is similar to the one described in [28] and is aimed to obtain a consistent value of the viscous damping coefficients that can be used within standard finite-element time-history dynamic analyses with the Rayleigh damping model described in the previous paragraph. More precisely, the equivalent viscous damping coefficient is assumed varying with the maximum displacement level reached by the structure during earthquake solicitation. Thus, the goal is to determine the relation between the equivalent viscous damping coefficient and the maximum displacement that the structure can reach under seismic actions. The algorithm, for each loading direction (in- and out-of-plane), can be summarized in the following steps:

1. A capacity curve of the masonry structure in a given loading direction is computed as explained in paragraph 2.3. This curve allows to determine the maximum displacement which the structure may undergo before collapse occurs.
2. The capacity curve obtained in Step 1 is reduced to the capacity curve of an equivalent single degree-of-freedom (d.o.f.) system following prescriptions contained in §C7.3.4.1 of [22]. Then, the new single d.o.f. capacity curve is further simplified to a bi- or tri-linear curve.
3. A hysteretic force-displacement law is assigned to the equivalent single d.o.f. structure which allows to evaluate the response of the structure under cyclic loading. In what follows, two hysteretic models will be used: a classical elastic-perfectly plastic law, which has the bi-linear curve determined in Step 2 as skeleton curve, and a newer inelastic model similar to the one described in [28] which uses the tri-linear curve determined in Step 2 as skeleton curve.
4. Since the aim is to determine a curve which relates the maximum displacement reached by the structure during seismic action and the equivalent viscous damping coefficient, it is necessary to fix several reference displacement values which subdivide the nonlinear part of the fixed skeleton curve. Furthermore, for each reference displacement value, the secant stiffness on the skeleton curve can be computed and stored.
5. For each reference displacement value nonlinear time-history dynamic analyses on the equivalent single d.o.f. structure with the chosen hysteresis constitutive model is carried out. Each analysis is performed with an external base acceleration history obtained from each of the seven spectrum-compatible accelerograms defined in paragraph 5.1 multiplied by a multiplication factor chosen so that the maximum displacement reached during the analysis is equal to the considered reference displacement value. The corresponding multiplication factor is saved as the value which gives the accelerogram which, acting on the structure, produces a maximum displacement equal to the reference displacement value considered.
6. A reference displacement value is fixed. A linear elastic single d.o.f. system equivalent to the non-linear single d.o.f. system is defined by assigning the secant stiffness computed in Step 4 for the assigned reference displacement value and an equivalent viscous coefficient determined though an iterative procedure: given the reference displacement value, a trial equivalent viscous coefficient is assigned to the system and a linear time-history analysis under the action of the design accelerogram multiplied by

the factor corresponding to the reference displacement value determined in Step 5 is carried out. The maximum displacement obtained through the linear time-history analysis is compared with the expected maximum displacement from the non-linear time-history analysis carried in Step 5. Then, the trial equivalent viscous coefficient is suitably changed and the linear analysis performed again until the maximum displacements obtained from linear and non-linear time-history analyses coincide. The corresponding value of the equivalent viscous damping coefficient is the value which corresponds to the assigned displacement reference value.

By going through Step 6 for each reference displacement value it is possible to obtain the curve relating the equivalent viscous damping coefficient to the corresponding value of the maximum displacement the structure undergoes. The described algorithm has been implemented within a MATLAB script and single d.o.f. time history dynamic analyses have been carried out using a Newmark type integration algorithm.

5.2.1 Out-of-plane equivalent viscous damping coefficient ξ_1

Both bilinear and trilinear approximations of the single d.o.f. out-of-plane capacity curve for the masonry structure, depicted in Fig. 11, are considered and ten reference displacement values are marked on each curve.

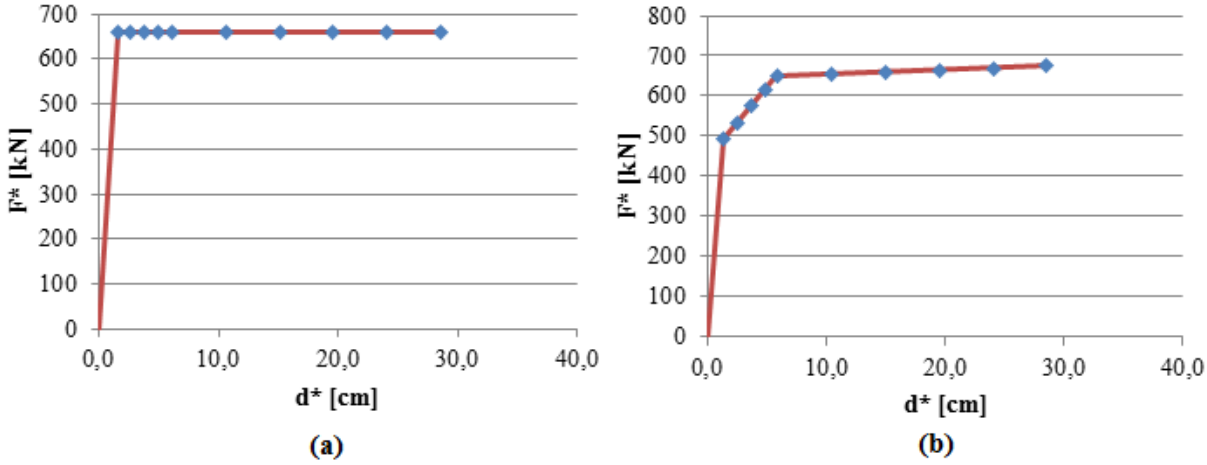


Figure 11: Bilinear (a) and trilinear (b) approximations of the single d.o.f. out-of-plane capacity curve for the masonry structure. Solid squares indicate reference displacements values.

The procedure described in the previous paragraph has been carried out for each of the seven spectrum compatible design accelerograms and for both the bilinear elastic-perfectly plastic and the trilinear Nicolini-type constitutive laws. In Fig. 12 a comparison between the single d.o.f. non-linear time-history analysis with both bilinear and trilinear inelastic laws and the final linear time-history analysis in Step 6 for a reference displacement equal to respectively 5.0 and 5.9 cm is shown for one of the seven spectrum-compatible accelerograms.

Fig. 13 depicts the final relation obtained at the end of the procedure, for each assigned reference displacement value, between equivalent viscous damping coefficient and the maximum out-of-plane displacement value the structure undergoes when it is subjected to seismic actions. In particular, the portrayed diagram is the average result obtained by repeating the numerical procedure described for each of the seven spectrum-compatible accelerograms.

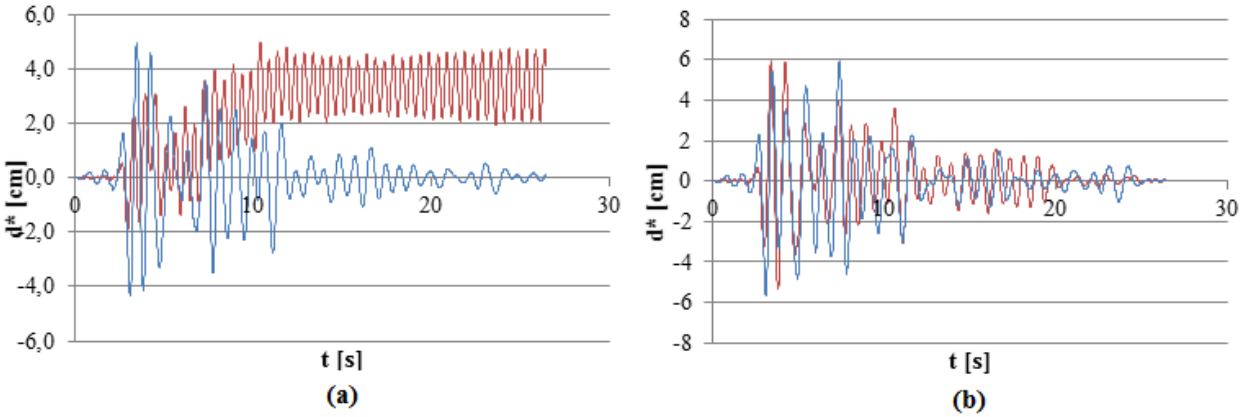


Figure 12: Comparison between inelastic time history analysis (red) and equivalent linear time history analysis (blue) for bilinear constitutive law and reference displacement value d = 5.0 cm (a) and trilinear constitutive law and reference displacement value d = 5.9 cm (b). Analyses conducted for accelerogram 378ya.

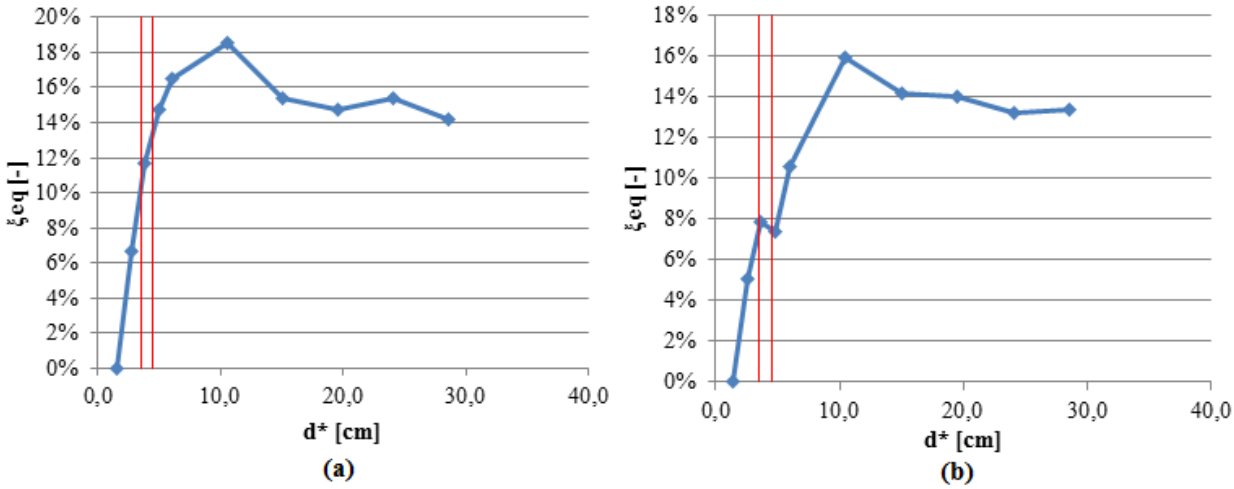


Figure 13: Final relation between equivalent viscous damping coefficient and the maximum out-of-plane displacement the structures may undergo for both bilinear constitutive law (a) trilinear constitutive law (b).

From an out-of-plane pushover analysis carried out according to [20] it is possible to infer that for the design earthquake, the maximum displacement the structure undergoes is 4.1cm. It is therefore reasonable to assume, for the evaluation of the equivalent viscous damping coefficient to be used in subsequent analyses, a displacement range of 3.5-4.5cm. In this range equivalent viscous damping coefficient varies between 10.25% and 13.52% when considering the bilinear constitutive law and of 7.5% when considering the trilinear constitutive law. It is then justified the use of the value $\xi_1 = 10\%$ as largely suggested in literature for masonry constructions (see, e.g. [27]).

5.2.1 In-plane equivalent viscous damping coefficient ξ_2

In analogy with the case discussed in the previous paragraph, both bilinear and trilinear approximations of the single d.o.f. in-of-plane capacity curve for the masonry structure, depicted in Fig. 14, are considered and ten reference displacement values are fixed on each curve.

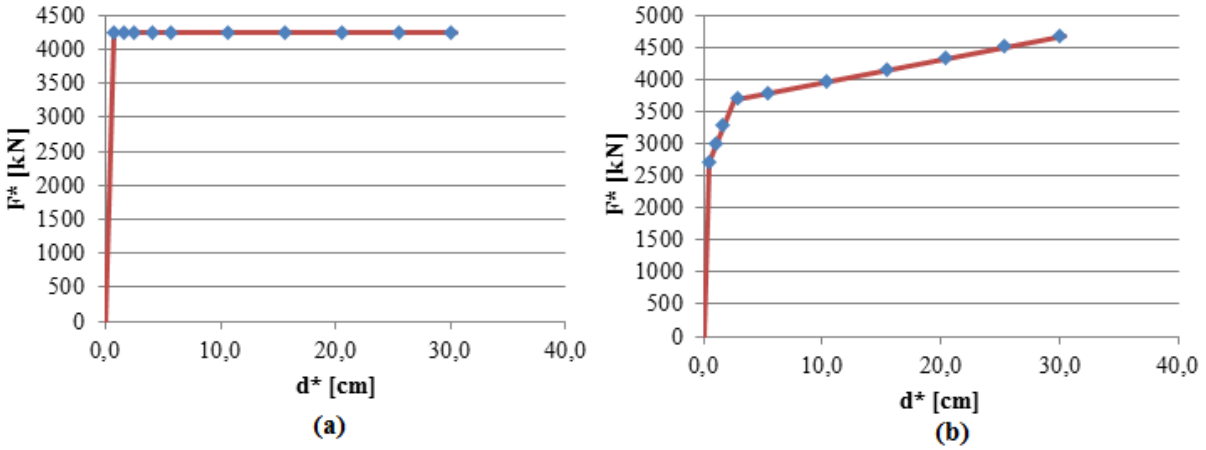


Figure 14: Bilinear (a) and trilinear (b) approximations of the single d.o.f. in-plane capacity curve for the masonry structure. Solid squares indicate reference displacements values.

Again, in Fig. 15 a comparison between the single d.o.f. in-plane non-linear time-history analysis with both bilinear and trilinear inelastic laws and the final linear time history analysis in Step 6 for a reference displacement equal to respectively 5.7 and 5.4 cm is shown for one of the seven spectrum-compatible accelerograms.

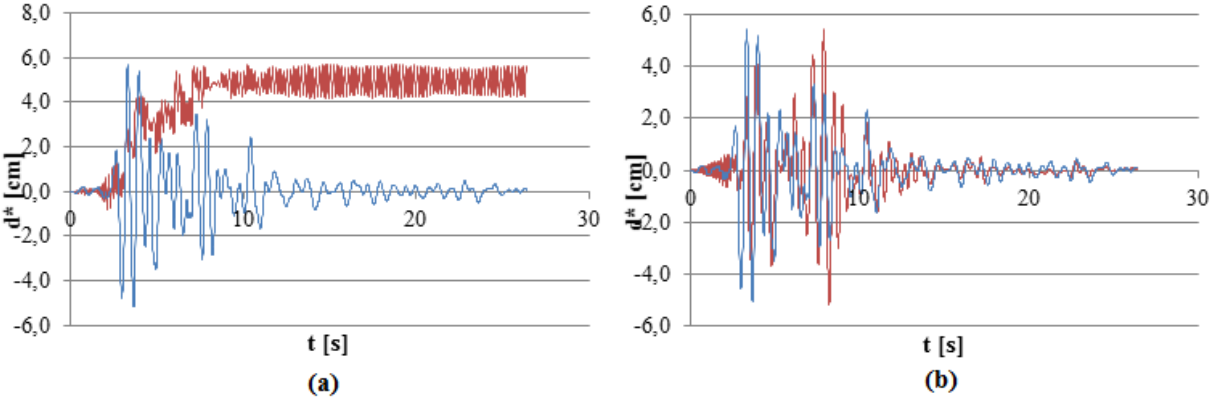


Figure 15: Comparison between inelastic time history analysis (red) and equivalent linear time history analyses (blue) for bilinear constitutive law and reference displacement value d = 5.7 cm (a) and trilinear constitutive law and reference displacement value d = 5.4 cm (b). Analysis conducted for accelerogram 378ya.

Fig. 16 depicts the final relation obtained at the end of the procedure, for each assigned reference displacement value, between equivalent viscous damping coefficient and the maximum in-plane displacement value the structure undergoes when it is subjected to seismic actions. In particular, the portrayed diagram, is the average result obtained by repeating the numerical procedure described for each of the seven spectrum-compatible accelerograms.

From an in-plane pushover analysis carried out according to [20] it is possible to infer that for the design earthquake, the maximum displacement the structure undergoes is 1.1cm. It is therefore reasonable to assume, for the evaluation of the equivalent viscous damping coefficient to be used in subsequent analyses, a displacement range of 0.5-1.5cm. In this range equivalent viscous damping coefficient varies between 0.0% and 8.0% when considering the bilinear constitutive law and between 1.35% and 12.70% when considering the trilinear constitutive law.

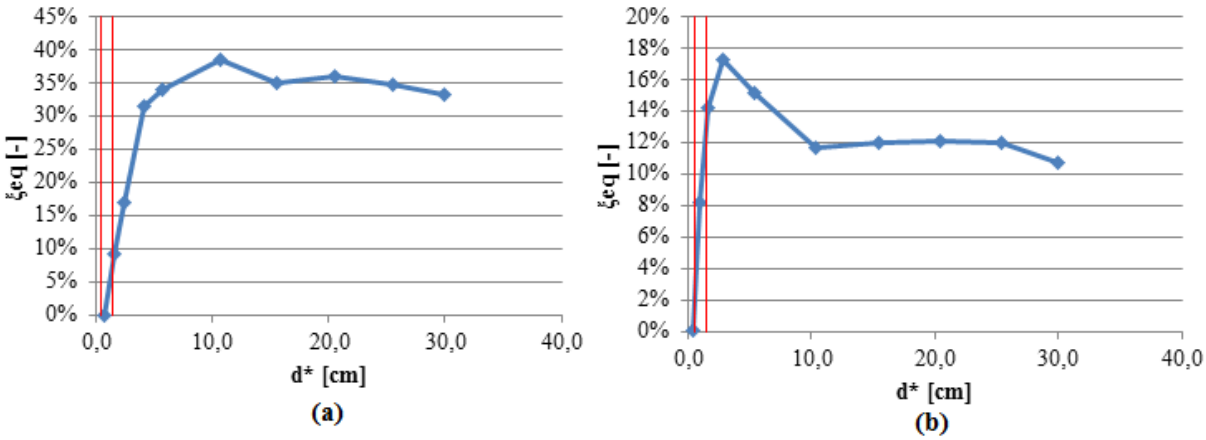


Figure 16: Final relation between equivalent viscous damping coefficient and the maximum in-plane displacement the structures may undergo for both bilinear constitutive law (a) trilinear constitutive law (b).

The value of $\xi_2 = 5\%$ largely suggested in literature for masonry constructions (see, e.g. [27]) is well within these ranges and thus, its use in the subsequent analyses is justified.

5.3 Non-linear dynamic analysis of the isolated pinnacles

In order to establish the seismic response of the isolated pinnacles and the effectiveness of the isolation system, time-history non-linear dynamic analyses with the amplified base accelerograms previously determined, have been conducted using the finite element software Straus7. Isolation system has been modeled as a parallel system of a spring and a damper, whereas the pinnacle has been modeled as a non-structural mass. Spring stiffness and damping coefficient for the damper are respectively K_r and ξ_e as defined in Tab. 3, considering both friction coefficients of 2.5% and 0.5%.

Results in terms of acceleration response to the amplified ground accelerogram 378ya for central pinnacles in both in-plane and out-of-plane directions are reported in Fig.17a-b respectively, for both friction coefficients, whereas results in terms of displacement response to the amplified ground accelerogram 378ya for central pinnacles are reported in Fig.17c-d respectively, for both friction coefficients.

As can be observed, the maximum acceleration transferred to the pinnacles is, in every case, smaller than the minimum value required to initiate rocking motion defined by equation (2).

Finally, it is to be noticed that the maximum displacement which the pinnacle undergoes is, in every case, smaller than the maximum displacement allowed by the isolators, which is equal to 0.15 m (see Tab.3).

Results in terms of acceleration response to the amplified ground accelerogram 378ya for lateral pinnacles in both in-plane and out-of-plane directions are analogous and for the sake of brevity are not reported in the following. Therefore, the effectiveness of the isolation system devised for the protection of the marble pinnacles from seismic excitations has been assessed for each pinnacle.

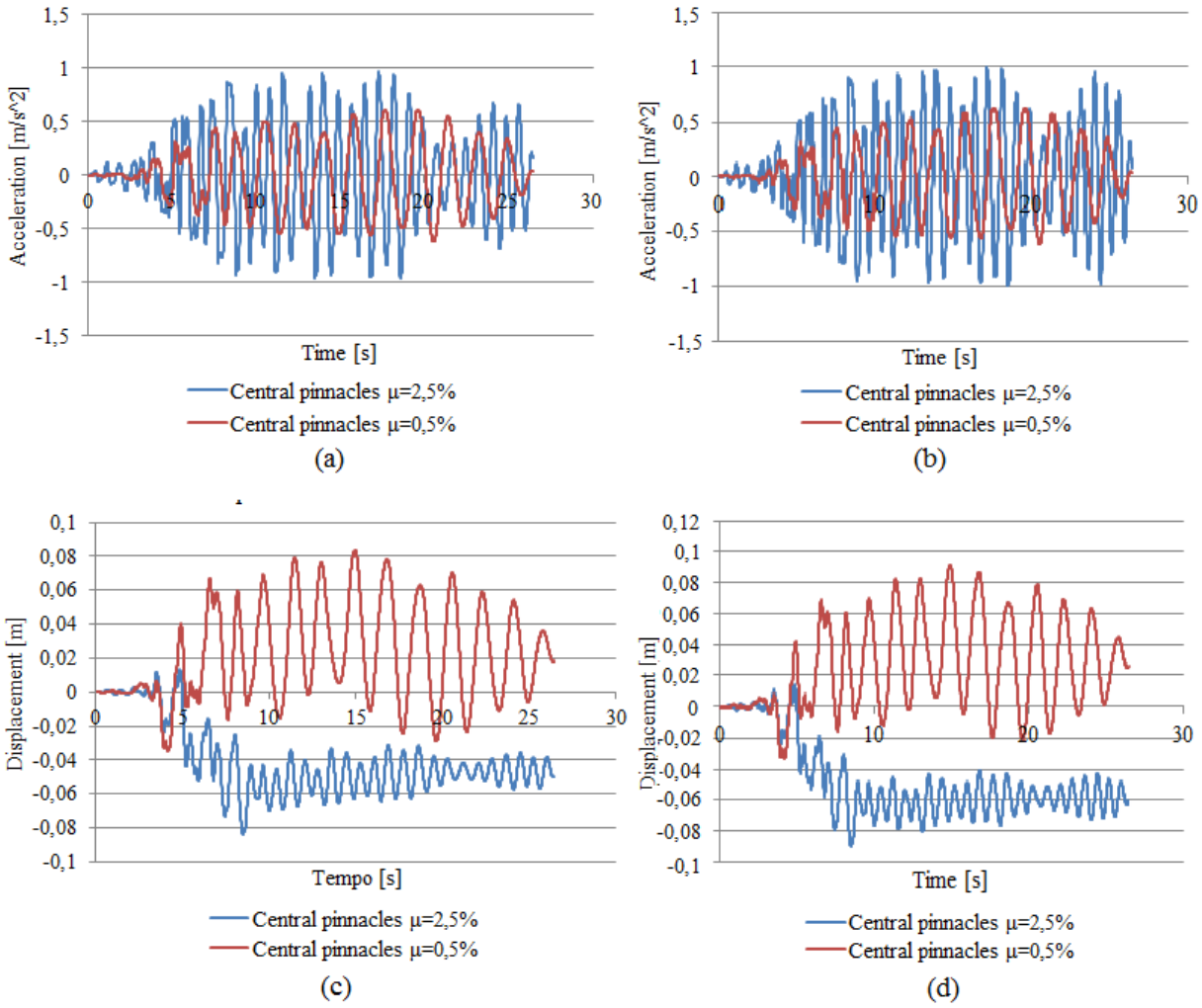


Figure 17: Response of central pinnacles to the seismic action defined by (amplified) accelerogram 378ya in terms of in-plane (a) and out-of-plane (b) acceleration, in-plane (c) and out-of-plane (d) displacements.

6 CONCLUSIONS

This contribution addressed the problem of seismic protection of heavy non-structural objects placed at the top of monumental masonry constructions through the illustration of the case study of the eleven marble monolithic pinnacles placed at the top of the three-arched masonry city gate in Ferrara.

The underlying masonry structure has been characterized with a natural frequency finite element analysis and through the computation of capacity curves with finite-element non-linear incremental analyses. Rocking motion and the safety against toppling of the pinnacles, regarded as rigid bodies under pulse-type earthquake excitations, have been discussed, showing that they are not safe under the design seismic action as defined by [20].

A seismic isolation system for the prevention of rocking and overturning phenomena has been devised and its effectiveness has been established through non-linear time-history dynamic analyses of the pinnacles under earthquake action expressed through base accelerograms, which are spectrum compatible with the design seismic action.

The amplification effect on the ground accelerations due to the underlying structure has been taken into account through time history dynamic analyses in which a Rayleigh damping model was adopted. A procedure for the estimation of the equivalent viscous damping coeffi-

cient for masonry has been outlined and the obtained values have been proven to be in agreement with the ones suggested in literature.

Non-linear time history dynamic analyses showed that the isolation system is effective in reducing seismic action transmitted to the pinnacles through the main structure, enough to prevent any rocking motion or overturning phenomena.

REFERENCES

[1] G.L. McGavin, *Earthquake protection of essential building equipment*, John Wiley and Sons, 1981.

[2] M.S. Agbabian, S.F. Masri, R.L. Nigbor, W.S. Ginell, Seismic damage mitigation concepts for art objects in museums, In: *Proceedings of 9th world conference on earthquake engineering*, Tokyo-Kyoto, Japan, August 1988.

[3] G. Augusti, M. Ciampoli, Guidelines for protection of museum contents, In: *Proceedings of 11th world conference on earthquake engineering*, Acapulco, Mexico, June 1996.

[4] F. Vestroni, S. Di Cintio, Base isolation for seismic protection of statues, In: *Proceedings of 12th world conference on earthquake engineering*, Auckland, New Zealand, June 2000.

[5] P.C. Roussis, E.A. Pavlou, E.C. Pisiara, Base-isolation technology for earthquake protection of art objects, In: *Proceedings of 14th world conference on earthquake engineering*, Beijing, China, October 2008.

[6] I. Caliò, M. Marletta, Passive control of the seismic rocking response of art objects, *Engineering Structures*, Vol. 25, 2003, pp. 1009-1018.

[7] A. Contento, A. Di Egidio, Seismic protection of monolithic objects of art using a constrained oscillating base, In. *Advances in Geotechnical Earthquake Engineering - Soil Liquefaction and Seismic Safety of Dams and Monuments*, Edited by Abbas Moustafa, InTech, 2012.

[8] H. Kimura, K. Iida, On rocking of rectangular columns, *Journal of the Seismological Society of Japan*, Vol 6., No. 3, 1934, pp. 125-149.

[9] G.W. Housner, The behavior of inverted pendulum structures during earthquakes, *Bulletin of the Seismological Society of America*, Vol. 53, No. 2, 1963, pp. 403-417.

[10] W.K. Yim, A.K. Chopra, J. Penzien, Rocking response of rigid blocks to earthquakes, *Earthquake Engineering and Structural Dynamics*, Vol. 8, No. 6, 1980, pp. 565-587.

[11] A. Di Egidio, A. Contento, Base isolation of sliding-rocking non-symmetric rigid blocks subjected to impulsive and seismic excitations, *Engineering Structures*, Vol. 31, 2009, pp. 2723-2734.

[12] A. Di Egidio, A. Contento, Seismic response of a non-symmetric rigid block on a constrained oscillating base, *Engineering Structures*, Vol. 32, 2010, pp. 3028-3039.

[13] M.F. Vassiliou, N. Makris, Analysis of the rocking response of rigid blocks standing free on a seismically isolated base, *Engineering Structures*, Vol. 41, No. 2, 2011, pp. 177-196.

[14] A.S. Koh, G. Mustafa, Free rocking of cylindrical structures, *Journal of Engineering Mechanics*, Vol. 116, 1990, pp. 34-54.

[15] A. Magravanis, I. Stefanou, I. Vardoulakis, Dynamic motion of a conical frustum over a rough horizontal surface, International Journal of Non-Linear Dynamics, Vol. 46, No. 1, 2011, pp. 114-124.

[16] Y. Li, B. Shi, Response of 3D free axisymmetric rigid objects under seismic excitations, *New Journal of Physics*, 2010.

[17] M. Lowry, D. Armendariz, B.J. Farra, J. Podany, Seismic mount making: a review of protection of objects in the J. Paul Getty museum from earthquake damage, In: *Advances in the protection of museum collections from earthquake damage*, symposium held at the J. Paul Getty museum at the Villa on May 3-4, 2006.

[18] L. Berto, T. Favaretto, A. Saetta, Seismic risk mitigation technique for art objects: experimental evaluation and numerical modelling of double concave curved surface sliders, *Bulletin of Earthquake Engineering*, Vol. 11, 2013, pp. 1817-1840.

[19] L. Berto, T. Favaretto, A. Saetta, F. Antonelli, F. Lazzarini, Assessment of seismic vulnerability of art objects: the "Galleria dei prigioni" sculptures at the Accademia Gallery in Florence, *Journal of Cultural Heritage*, Vol. 13, No. 1, 2012, pp. 7-21.

[20] NTC2008, Norme Tecniche per le Costruzioni, D.M. 14/01/2008, S.O. n. 30 G.U. n. 29, 4/2/2008.

[21] HSH, "Straus7, Finite Element Analysis System", hsh.info, 2014.

[22] CIRC2009, Circolare sulle "Nuove Norme tecniche per le costruzioni" di cui al DM 14/01/2008, S.O. n. 27, G.U. n. 47, 26/02/2009.

[23] TNO-DIANA, "DIANA, Finite Element Analysis", www.tnodiana.com, 2015

[24] V. Gioncu, F. Mazzolani, *Earthquake engineering for structural design*, CRC Press, 2010.

[25] J.M. Kelly, *Earthquake resistant design with rubber*, Springer-Verlag, 1993.

[26] EN1998, "Eurocode 8: Design of structures for earthquake resistance", 2004.

[27] F. Peña, P.B. Lourenço, N. Mendes, D. Oliveira, Numerical models for the seismic assessment of an old masonry tower, *Engineering Structures*, Vol. 32, 2010, pp. 1466-1478.

[28] Nicolini L., 2012. Equivalent viscous damping and inelastic displacement for strengthened and reinforced masonry walls. Ph. D. Thesis, University of Trento.

COMPDYN 2015
5th ECCOMAS Thematic Conference on
Computational Methods in Structural Dynamics and Earthquake Engineering
M. Papadrakakis, V. Papadopoulos, V. Plevris (eds.)
Crete Island, Greece, 25–27 May 2015

THE COMBINATION OF NDTS FOR THE DIAGNOSTIC STUDY OF HISTORICAL BUILDINGS: THE CASE OF KAISARIANI MONASTERY

Antonia Moropoulou[1], Maria Apostolopoulou[1], Petros Moundoulas[1], Maria Karoglou[1], Ekaterini Delegou[1], Kyriakos Lampropoulos[1], Margarita Gritsopoulou[1], Asterios Bakolas[1]

[1] Faculty of Chemical Engineering of the National Technical University of Athens
Iroon Polytexneiou 9, 15780, Athens, Greece
e-mail: amoropul@central.ntua.gr

Keywords: NDTs, Kaisariani Monastery, Historical Building Diagnosis, Ground-penetrating Radar(GRP), Infrared Thermography (IR), Fiber Optics Microscopy (FOM)

Abstract. *Diagnosis is the first and most crucial step in the process of monument protection. Diagnosis demands a variety of information and can be a complicated procedure especially when dealing with historical buildings and the limitations that these induce; nevertheless when the correct methodology is followed, diagnosis can be carried out whilst minimizing the amount of samples needed, as important features are already revealed and representative samples can be located. This is achieved through a thorough and organized survey of the historical building and the implementation of various non-destructive techniques (NDTs).*

The in-situ optical inspection of a historical building can offer valuable information regarding the preservation state of the building as well as utility problems which might create problems for the masonry, such as humidity problems due to the movement of rainwater. Following the optical inspection, the researchers can apply NDTs on the structure as a whole, focusing however on problematic areas or areas of interest. In this study NDTs were employed in order to investigate the type of masonry structure followed by the original masonry workers, the original building materials, the different construction phases and materials, as well as non-documented conservation interventions.

However, the use of one NDT alone cannot offer the required information; a combination of various NDTs is necessary in order to extract meaningful and useful results. In the case of Kaisariani monastery, presented here, after a thorough in-situ optical inspection, a variety of NDTs were applied: Ground-penetrating Radar (GRP), Infrared Thermography (IR), Fiber Optics Microscopy (FOM) and Schmidt rebound hammer. The results were analyzed and combined in order to extract results regarding the original building materials, the type of masonry construction, the preservation state of the building materials, as well as information regarding non-documented different construction phases and conservation interventions.

1 INTRODUCTION

An integrated diagnostic study includes historic documentation, characterization of the historic materials and study of their provenance, evaluation of previous interventions and assessment of the environmental impact [1].

When dealing with ancient masonry structures certain factors are important and require special attention. The masonries are generally not continuous, homogeneous or isotropic regarding their static and dynamic behavior and the properties of their building materials; in some cases, the wall texture strongly influences the stress distribution [2]. Therefore, an extensive understanding of the historic masonry structure is an essential prerequisite that must precede any intervention, especially when the ultimate aim is the reinstatement of the masonry's seismic response.

Non-Destructive Techniques (NDTs) are a useful tool in assessing the above factors, especially on monument level. Since sampling is restricted and in some cases even prohibited, a combination of NDTs can provide the researcher with valuable information regarding the materials, the structure and the decay mechanisms, thus unveiling the impact of the environment. In this current study, Infrared Thermography (IRT), Ground Penetrating Radar (GPR) and Fiber Optic Microscopy (FOM) were applied. Furthermore, Schmidt hammer test was also applied, in order to evaluate the compressive strength of the building materials [3].

Kaisariani Monastery

The Catholicon of Kaisariani Monastery is a typical mid-byzantine Athenian church structure, its main building elements consisting of carved stones, bricks and mortars. It is a 11th or 12th century monastery, built on the foothills of Hymettus and dedicated to the Presentation of the Virgin to the Temple; the exact date of construction is not known.

The monastery has a rich history, and subsequently many construction phases throughout the centuries. The original building was a complex cross-in-square four-column domed church, without a narthex. The domed narthex was added in the 17th century, and the barrel-vaulted chapel dedicated to Aghios Antonios positioned at the southwest of the Catholicon was an even later addition (Image 1) of the 17th century.

The monastery complex, including the church, has undergone many conservation treatments, which are not fully documented; however two important reconstruction projects took place in the complex in the beginning and the middle of the 20th century. The interventions mostly regarded buildings surrounding the Catholicon, such as the bath installations and the complex containing the kitchen and the refectory [4-6]. The chapel of Agios Antonios was repointed in 2011, using a lime-pozzolan mortar.

2 METHODS AND TECHNIQUES

The exact environmental conditions during the non-destructive testing, as well as the location they were measured at (church interior or exterior), are stated in Table 1.

DATE	Interior/Exterior	Temperature (^{o}C)	(RH%)
05.02.2014	Exterior	11^{o}C	65%
17.02.2014	Exterior	12^{o}C	52%
19.03.2014	Exterior	19^{o}C	50%
27.03.2014	Exterior	21^{o}C	50%
	Interior	14^{o}C	70%

Table 1: Environmental conditions during NDTs

In this current study Infrared Thermography (IRT), Ground Penetrating Radar (GPR) and Fiber Optic Microscopy (FOM) were applied. Furthermore, Schmidt hammer test was also applied, in order to evaluate the compressive strength of the building materials. All NDT results were combined in order to extract information regarding the monument's state of preservation, detect restoration materials and differentiate them from the original building materials and examine the structural techniques of the monument.

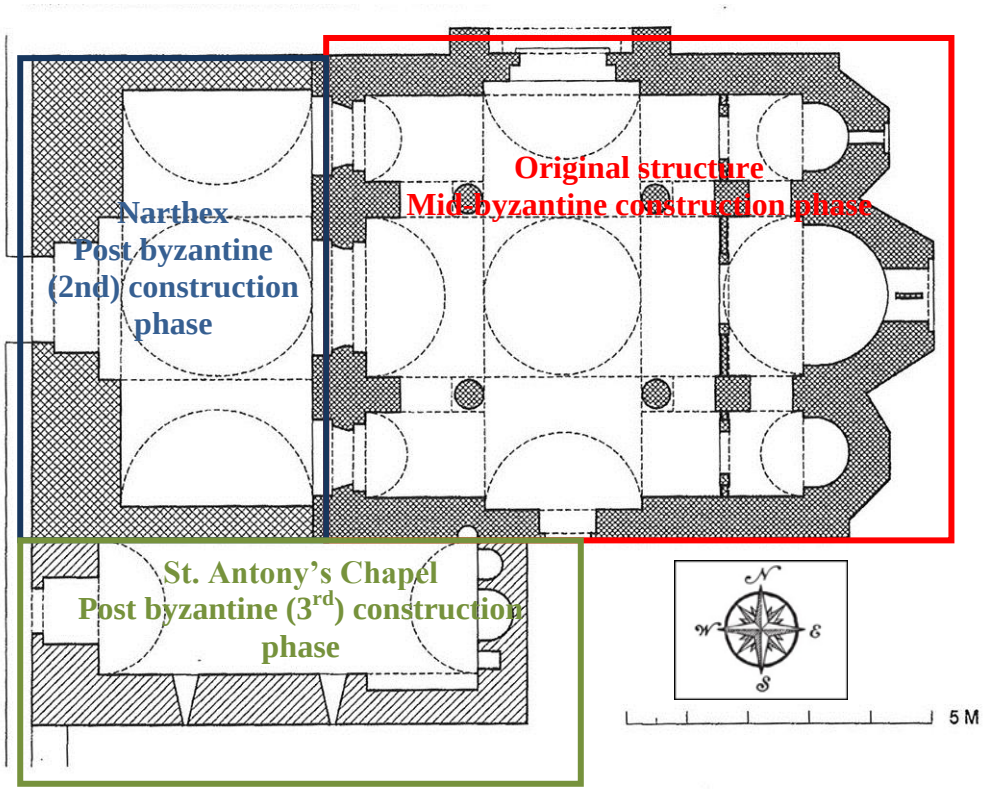


Image 1: Ground plan of the church [7], with probable construction phases

2.1 Fiber Optics Microscopy (FOM)

A Fiber Optics Microscope is a non-destructive microscope that can be utilized in-situ to acquire magnified, visual spectrum images [3]. With FOM, no sampling is required, as the image can be acquired in situ. In this survey a fiber optics microscopy (FOM) i-scope – Moritex was applied in several magnifications (x30, x50 and x120). FOM was employed for an initial material characterization, the assessment of the monuments building materials' decay and the comparison of building materials belonging to different construction phases.

2.2 Infrared Thermography (IRT)

Infrared Thermography is a very useful non-destructive technique, used extensively in the field of monument protection. In the current study, the passive approach was employed, as the area of interest was the masonries of the Catholicon and the materials under investigation are examined in terms of qualitative means [3].

IRT results in the current paper involve the detection of non-documented intervention materials, the examination of masonry interfaces at the interconnection of different construction phases and the comparison of the materials employed for each construction phase. Furthermore moisture transfer phenomena on monumental scale were made evident.

The infrared camera used in the survey was a FLIR Systems Therma Cam B200, with a detector of focal plane array microbolometer in the spectral range of 7.5-12 μm, with thermal sensitivity of 0.08 ^{o}C. All environmental conditions during the conduction of the survey, were measured and are stated in Table 1. During testing, the camera was positioned vertically to the surface under examination. The distance of the camera to the surface (d) was recorder at all measurements. Masonries are complex and non-homogenous materials; the result of a variety of materials with different values of emissivity. In this survey, an average value of 0.86 was selected for the masonry as a whole.

2.3 Ground Penetrating Radar (GPR)

Ground Penetrating Radar (GPR) is an established non-destructive technique [8, 9] that uses radar pulses to image the examined sub-surface. In the field of cultural heritage protection, GPR is used in the assessment of the preservation state of monuments and historic structures. GPR is utilized to locate the position of large voids and inclusions of different materials, to qualify the state of preservation of the structural system, to define the presence and the level of moisture, to control the effectiveness of repair interventions, and to reveal the morphology/geometry of wall sections in multiple-leaf stone and brick masonry structures [3, 10-13].

The ground penetrating radar system used in this survey was a MALÅ Geoscience ProEx system with 1.6GHz and 2.3GHz antennae. The MALÅ Geoscience Groundvision 2 software was used for data acquisition. The MALÅ Geoscience RadExplorer v.1.41 software was used for data processing. Processing of raw files included DC removal, Time-Zero Adjustment, Amplitude Correction, Bandpass filtering and Background removal.

Instead of applying the same mean velocity for the masonry as a whole, the velocity was calculated for each building material of the monument, where the dimensions of each material layer was measurable. The velocity through the stone was calculated at V_{stone} = 11,60 cm.ns^{-1}, the velocity through the mortar was calculated at V_{mortar} = 2,95 cm.ns^{-1}, and the velocity through the bricks is calculated at V_{brick} = 9,28 cm.ns^{-1}.

2.4 Schmidt Hammer Rebound Test

The Schmidt hammer test was initially developed in the late 1940s as an index apparatus for non-destructive testing of concrete in situ. Today it is also used for estimating the uniaxial compressive strength of building stones and bricks [14]. The Schmidt hammer provides a quick and inexpensive measure of surface hardness that is widely used for estimating the mechanical properties of rock material. However, a number of issues such as hammer type, normalization of rebound values, specimen dimensions, surface smoothness, weathering and moisture content, and testing, data reduction and analysis procedures continue to influence the consistency and reliability of the Schmidt hammer test results [15]. Many researchers attempt to uncover correlations for different case scenarios; however in the current study the instrument conversion curve was utilized.

In this survey an N-type Schmidt hammer, manufactured by Proceq, was employed. The impact direction was vertical to the examined surface. The rebound number (R) was utilized in order to estimate the compressive strength of different building materials, through the use of the instrument's conversion curves and in accordance to ASTM C 805. The results can serve as a first indication regarding the type of material tested, the quality of the technology production employed for the production of the brick, as well as limitations regarding the mechanical properties of any future intervention materials that could be utilized without exerting compatibility criteria.

3 RESULTS

The results deriving from all methods were analyzed and combined in order to extract information regarding the original building materials, the type of masonry construction, as well as non-documented construction phases and problematic areas. In this current paper, selected results regarding certain areas of interest will be presented to demonstrate the ability of NDTs to characterize the building materials, to assess the current state of the structure and to identify the construction phases of the building.

3.1 In situ optical inspection – Selection of Areas of Interest

Kaisariani Monastery is a typical mid-byzantine Athenian church structure, its main building elements consisting of carved stones and bricks. Each façade is evidently constructed with a different building technique, depending on the construction phase, as well as the projection of the façade upon entering the monastery complex. The mortars and bricks of each construction phase seem to be of a different technology, and the carved stones are of different origin. The east façade is the only one built in the typical byzantine cloisonné manner, with the carved stones, bricks and mortars presenting perfect symmetry (Image 2). The north and south façade of the Catholicon, attributed to the first construction phase, are also built in the byzantine cloisonné style, however perfect symmetry of form was not followed on these facades to the same extent (Images 3, 4). The walls constructed during the post-byzantine era, are not built in the byzantine construction style, but were constructed as rubble masonry, with asymmetric stones and bricks (Image 3). The in situ optical inspection revealed that the main issues the church is facing are due to humidity problems, intensified by past non-compatible interventions.

After a thorough in situ optical inspection, areas of interest were selected in order to perform non-destructive testing (Images 2-4).

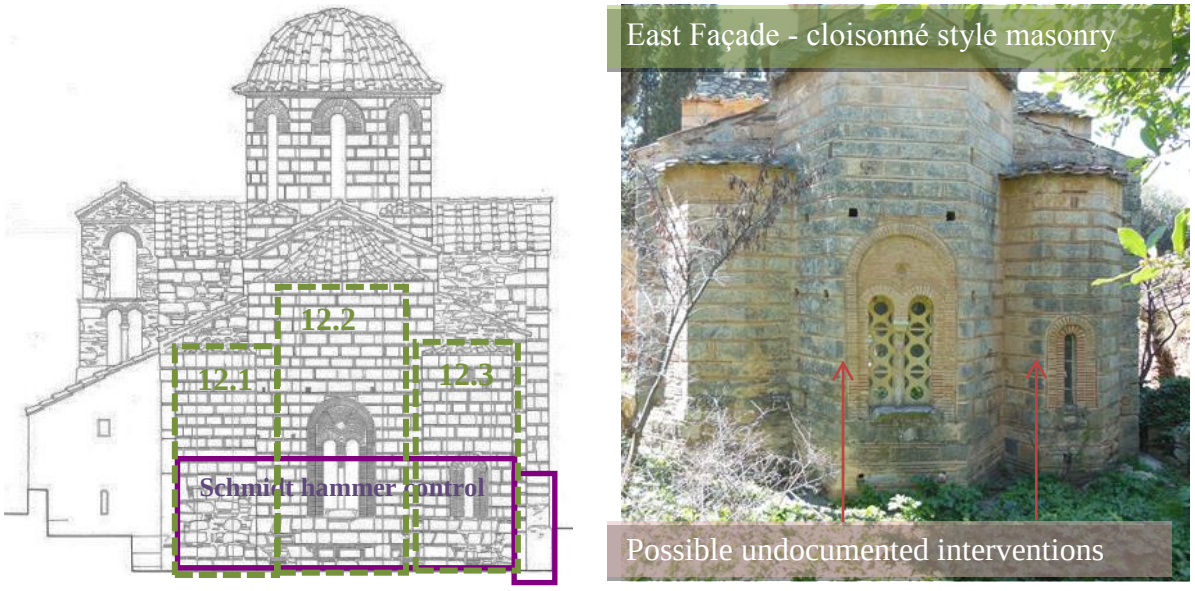


Image 2: East Façade [16] and control areas – Picture of cloisonné style construction and Areas 12.2&12.3

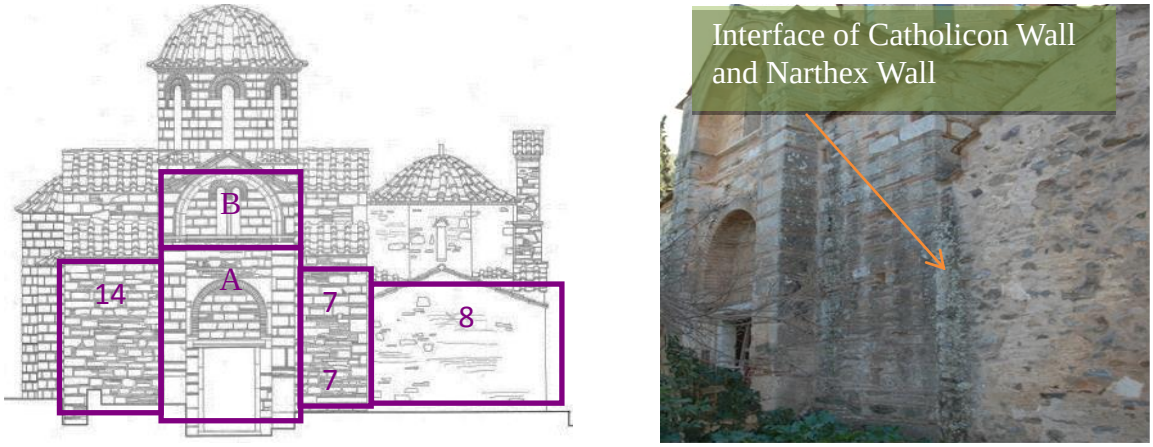


Image 3: North façade [16] and control areas – Picture of Areas 7&8 with distinct construction phases

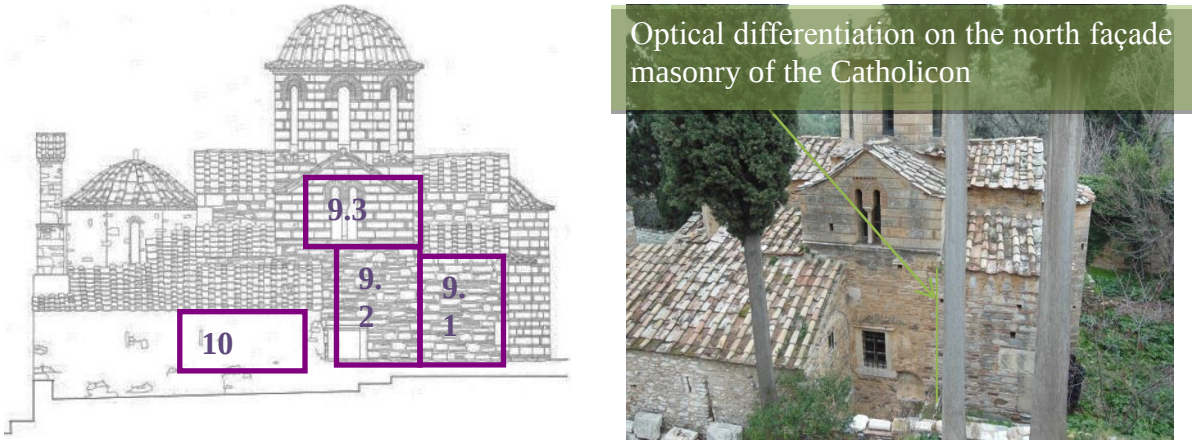


Image 4: South façade [16] and control areas – Picture of Areas 9.1&9.2 with evident differentiation

3.2 East façade – Areas 12.2 &12.3

Areas 12.2 and 12.3 (Image 2) were selected as areas of interest to demonstrate the use of NDTs for the detection of non-documented past interventions, as well as for the examination and characterization of building materials in historic structures. Schmidt hammer rebound testing was implemented to estimate compressive strength the building materials.

The porous stone of the east façade is a fossiliferous stone (Image 5). The original mortar of the east façade, although attributed to the first construction phase, and therefore subjected to environmental factors for a much longer period compared to the subsequent phase materials, is in a good preservation state (Image 6). A different type of mortar was encountered in areas around the windows of areas 12.2 and 12.3 (Image 7), which is most likely a restoration mortar applied during a past, undocumented restoration intervention. Microscopically these mortars seem to exhibit a certain extent of compatibility, although the restoration mortar seems to exhibit better coherence.



Image 5: Area 12.1 (x30)
Typical stone of the east façade



Image 6: Area 12.1 (x50)
Mortars

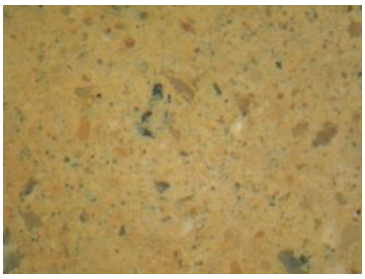


Image 7: Area 12.2 (x50)
Restoration mortar

The authentic bricks of the east façade showed relative homogeneity and appear in two different colors, due to a different production technology (Image 8 and 9). Another type of brick was detected, exhibiting a different microstructure (Image 10), which seems to correspond to a newer restoration brick; however, a corresponding intervention using this newer restoration brick was not documented. This type was encountered throughout the east façade around the window of area 12.2 and the window of area 12.3 in accordance to the presence of the restoration mortar described above. The restoration brick seems less porous than the original authentic byzantine brick.

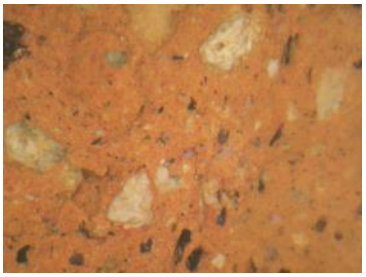


Image 8: Area 12.2 (x50) – Red brick

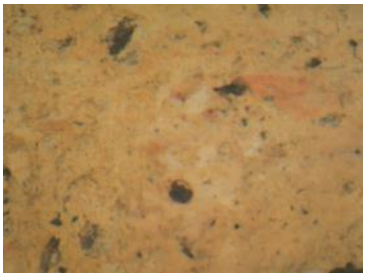


Image 9: Area 12.2 (x50) - Yellow Brick

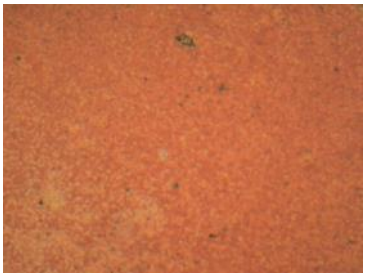


Image 10: Area 12.2 (x50) - New Restoration Brick

Schmidt hammer test was applied only on the carved stones and bricks of the east façade, due to the better conservation state of the materials on this side. A total of 22 bricks were examined. The bricks belonging to the intervention described with the previous methods were excluded, as the original materials of the masonry are of interest. Schmidt hammer test results revealed that the original byzantine bricks are of excellent quality, exhibiting relatively high compressive strength values, varying from 21,8 MPa to 44,6 MPa with an average value of 32,64 MPa and standard deviation of 6,75. The high standard deviation of the measurements, ranging up to 3 for each individual brick, is anticipated, as byzantine bricks were handmade; thus each brick is individual and homogeneity is not complete.

Furthermore, Schmidt hammer test results, deriving from 8 carved stones tested, revealed that the carved stone of the east facade exhibits relatively low values of compressive strength. The stones' compressive strength values, present values from 4,71 MPa to 9,80 MPa, exhibiting an average value of 8,2 MPa and a standard deviation of 1,72. This is anticipated and may be partly due to the roughness of the porous stone surface. Furthermore, as revealed by the FOM images taken during the microscopic examination of the east façade materials (Image 5), the carved stone is quite porous; therefore the Schmidt hammer results are in cohesion. The low compressive strength of the carved stones, imposes limitations regarding the compressive

strength that any restoration mortar should have in order to still be deemed compatible with the masonry in any future intervention.

The results from FOM indicated an undocumented intervention evident on the east façade; on the arch of the window of area 12.2 (Image 11), as well as around the window of area 12.3. When examined by Infrared Thermography (Image 12), the majority of the bricks of the east façade, corresponding to authentic bricks, exhibited temperatures well above 20 ^{o}C and up to 23 ^{o}C, compared to the bricks of different color above the window in area 12.2, which exhibit much lower temperatures, in the range 18-19 ^{o}C. The authentic joint mortar between the bricks surrounding the double arched window in area 12.2 exhibits temperatures between 17,3 ^{o}C and 18,1 ^{o}C. Again, the joint mortar with a different color exhibits lower temperatures, between 16,5 ^{o}C and 16,8 ^{o}C. This was also observed in area 12.3; the temperature differences are due to the different materials used in this undocumented intervention.



Image 11: Detail of area 12.2 - Thermogram area

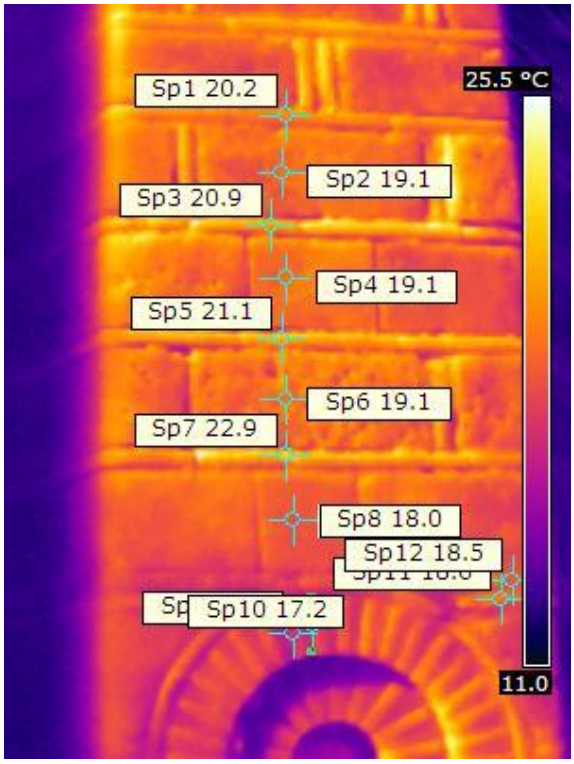


Image 12: IR image [6440], Date: 17/2/2014

3.3 North façade - Areas 7 & 8

Areas 7 and 8 were selected in order to examination the masonry structure and investigate possible construction phases. Areas 7 and 8 of the north wall belong to different construction periods, as area 7 is part of the original Catholicon and area 8 belongs to the Narthex (Image 3). The materials of area 7 appear in a much worse preservation state than the materials of area 8; this is highly evident in the comparison of slate stones in the two areas (Images 13-15) as well as in the comparison of bricks from the two areas (Images 16-18). However, it seems that a similar slate stone was used for the construction of both walls; furthermore, microscopically the bricks of area 7 seem to appear similar to those of area 8.

The worse preservation state of area 7 is also evident during the examination of mortars (Images 19-23); however it must be emphasized that area 8 has undergone many interventions, as the use of many different non-documented restoration mortars evidence. The different mor-

tars used in area 8 seem to exhibit different coherence and microstructure and may not be compatible to the original masonry materials.

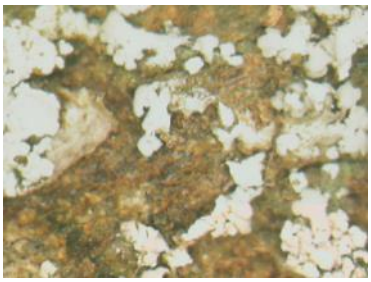


Image 13: Area 7 (x50) - Slate stone with evident decay

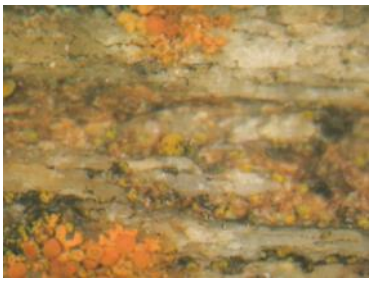


Image 14: Area 7 (x50) - Slate stone with evident decay



Image 15: Area 8 (x50) - Slate stone

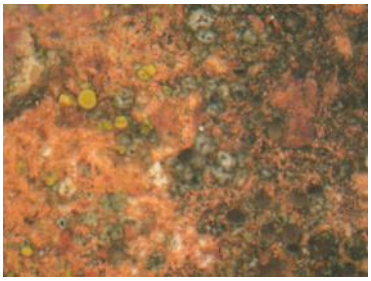


Image 16: Area 7 (x50) - Brick

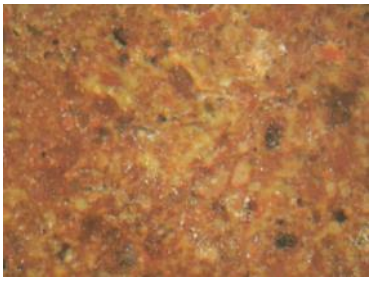


Image 17: Area 8 (x50) - Brick

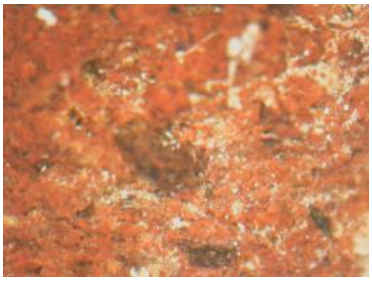


Image 18: Area 8 (x50) – Brick

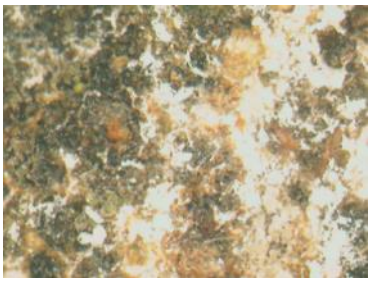


Image 19: Area 7 (x50) - Mortar

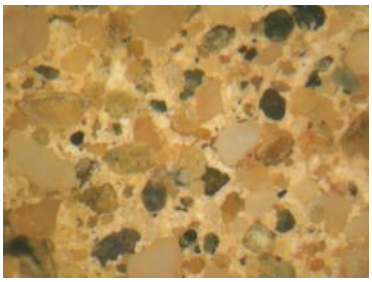


Image 20: Area 8 (x50) - Grey mortar



Image 21: Area 8 (x50) - Grey cementicious mortar

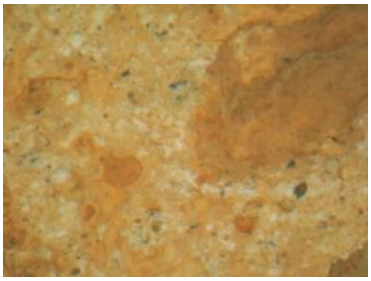


Image 22: Area 8 (x50) - Orange cementicious mortar

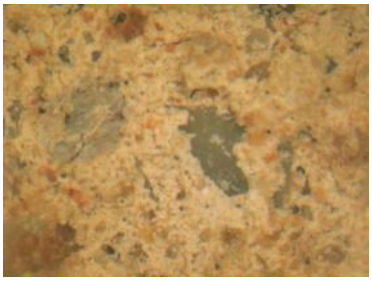


Image 23: Area 8 (x50) – Pink mortar

In order to better examine this area, a IR image was taken (Image 24) depicting the north wall of the Catholicon (area 7) and of the Narthex (area 8) simultaneously. The different construction phases are evident, even by macroscopic observation (Images 25-26), due to the different construction technique of the masonry during the mid-byzantine and post byzantine era. The difference between the two different phases is evident also in the thermogram, through

the intense surface temperature difference that the two areas exhibit. The wall of the Catholicon exhibits temperatures ranging from 11,2 ^{o}C to 13,2 ^{o}C, whilst the Narthex wall exhibits lower temperatures, ranging from 10,7 ^{o}C to 12,3 ^{o}C. This is due to the different type of construction and the use of different construction materials; however it is unclear through thermography alone whether this is the result of the higher humidity content of the Narthex.

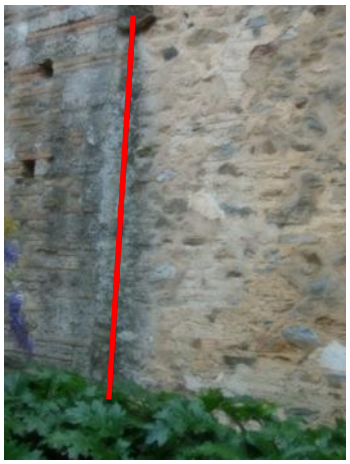


Image 24: The north wall - different construction phases



Image 25: Detail of the thermo gram area

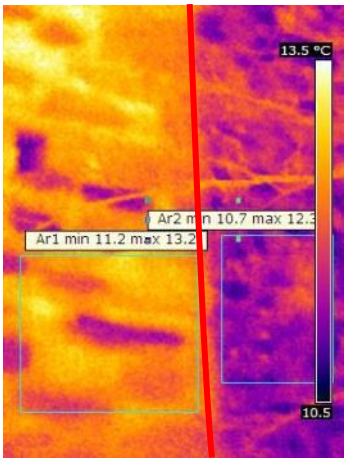


Image 26: Thermo gram [6357], Date: 5/2/2014

The ground penetrating radar was used at different areas of the north wall (Image 27), in order to better investigate areas 7 & 8 and to investigate the structural continuity of the wall between the two construction phases. The horizontal scans 581H and 582H (Image 28) were performed at the exterior of the north masonry, at a height of 100 cm and 150 cm above the ground level respectively, whereas scans 583 and 586 were performed at the interior of the building, to aid in the identification of the masonry features.

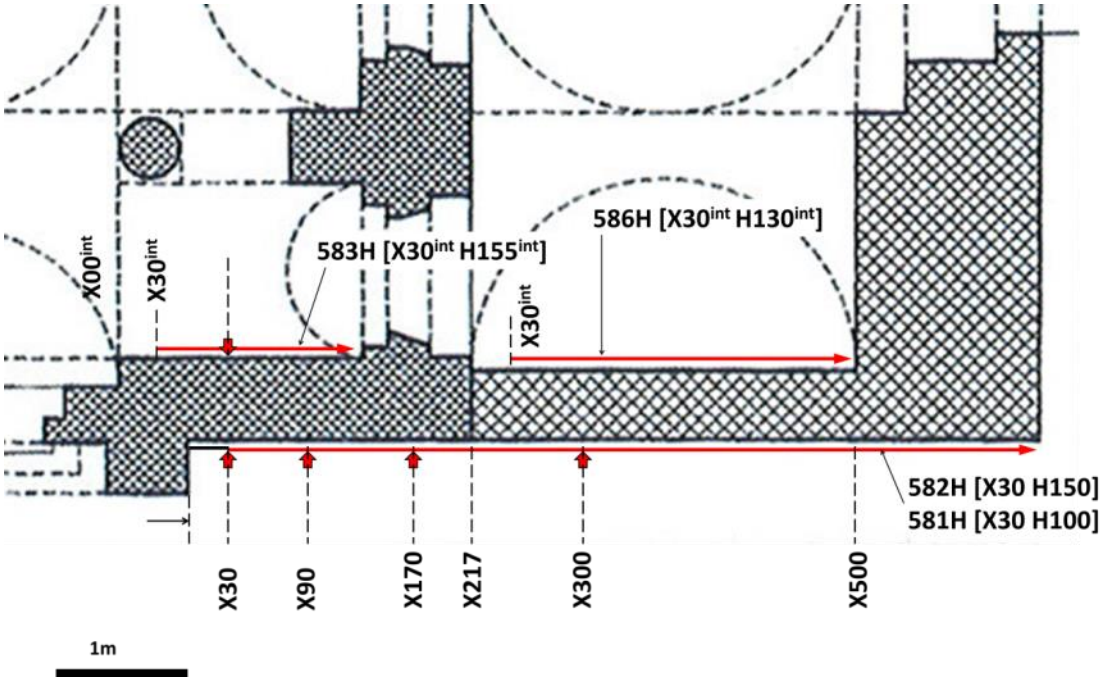


Image 27: Ground plan and GPR scan positions

The scans run across both the Catholicon and the Narthex wall, as well as across both sides of the north wall; therefore it is deemed possible to perceive discontinuities in the structure, even in the core of the masonry.

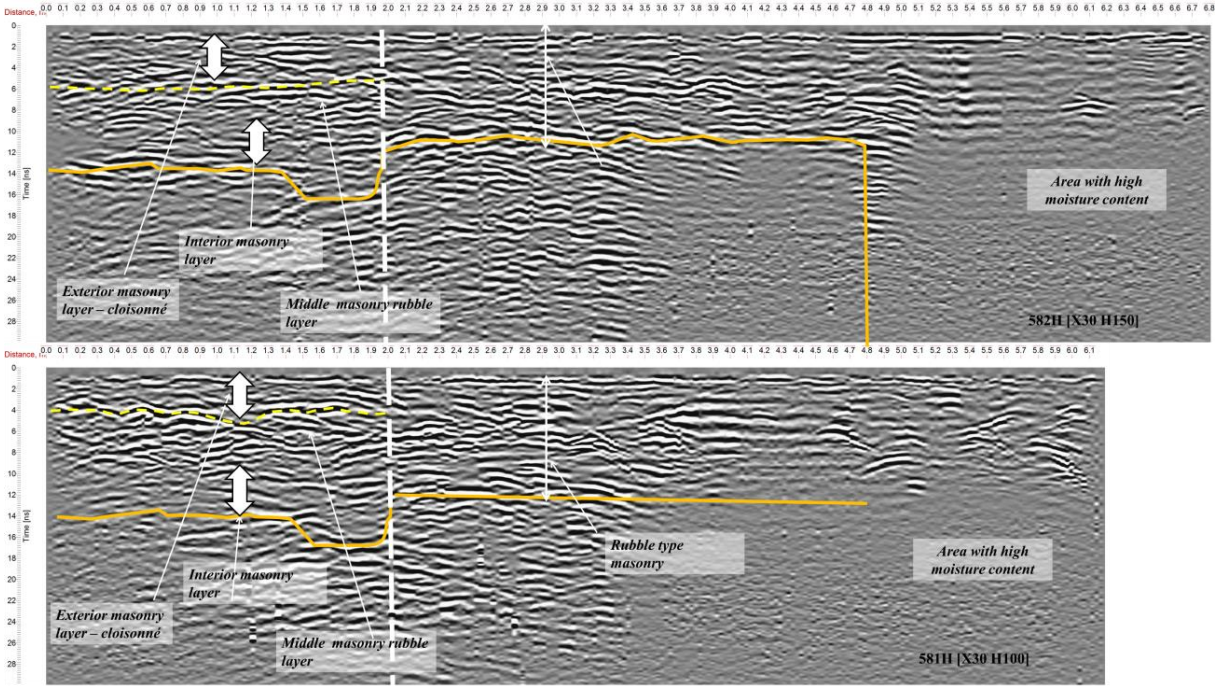


Image 28: Horizontal GPR scans H581 and H582 respectively

The GPR scans reveal interesting information. A discontinuity at the interface of the Catholicon wall and the Narthex wall is evident, at exactly 2 m from the beginning of the scan, confirming the IR results; furthermore, it is evident that the wall corresponding to the original mid-byzantine structure corresponds to a three leaf cloisonné masonry, whereas the wall corresponding to the Narthex clearly corresponds to rubble masonry extending to the core of the structure. Another interesting aspect that the GPR revealed is the presence of a high content of moisture in the Narthex wall; this explains the presence of several restoration mortars on the Narthex wall. It is also possible, that due to the incompatibility of the restoration mortars with the original masonry materials, transpiration of the masonry is difficult and humidity is trapped in the core of the Narthex wall, intensifying the problem.

3.4 South façade – Areas 9.1 & 9.2

On the south façade, Areas 9.1 and 9.2 were selected as areas of interest, in order to investigate the masonry structural continuity and possibly document a lost construction phase. The south façade of the Catholicon is optically divided into two areas, 9.1 and 9.2. Area 9.2 is characterized by its orange hue and spattered appearance. Areas 9.1. and 9.2 of the north wall, seem to be distinctly different (Image 4). The microscopic examination of the bricks, mortars and stones however does not offer a clear image, as all building materials of area 9.2 seem to be covered by an orange plaster residue (Images 31, 34, 36-37).

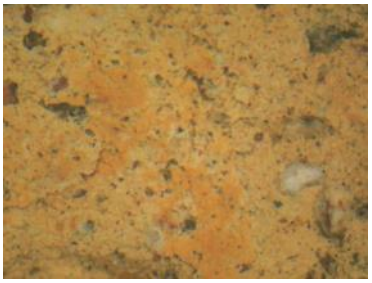


Image 29: Area 9.1 (x50) - Brick

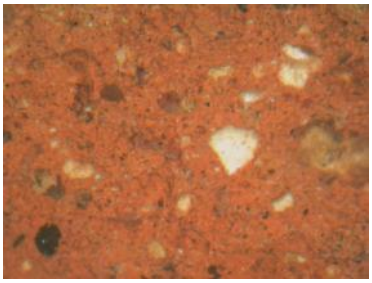


Image 30: Area 9.1 (x50) – Brick



Image 31: Area 9.2 (x50) – Brick



Image 32: Area 9.1 (x50) – Mortar

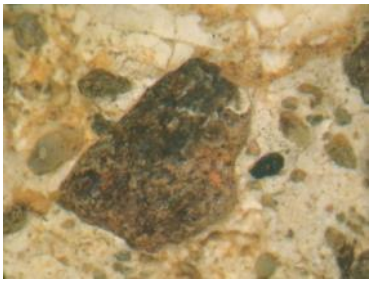


Image 33: Area 9.1 (x50) – Mortar

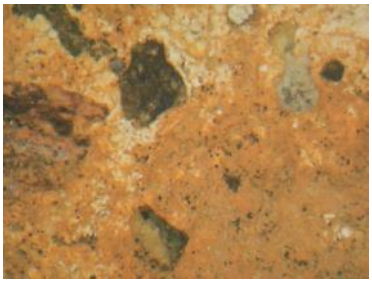


Image 34: Area 9.2 (x50) - Mortar



Image 35: Area 9.1 (x30) – Porous stone



Image 36: Area 9.2 (x50) - Porous stone



Image 37: Area 9.2 (x50) - Mortar

An IR image (Image 39) was taken in order to include both areas 9.1 and 9.2, simultaneously (Image 38). The surface temperature of the stones of both areas exhibit similar values, indicating that the same type of stone was used. The same applies in the case of the brick elements. However, in the case of the joint mortars, this is not the case; the temperature of the mortar in area 9.1 ranges from 29,1 ^{o}C to 29,5 ^{o}C, whereas in area 9.2 the temperature of the joint mortar ranges from 31,4 ^{o}C to 34,1 ^{o}C. This is an indication that a different mortar was used in the two areas. An explanation of this would be that the chapel used to extend further to the east, and therefore area 9.2 was at some point the interior of the chapel. In addition, the remains of a tile roof, which is observed by optical observation on the upper limit of area 9.2, exhibits the same temperature as the bricks, indicating that this is part of the older structure; perhaps it was the roof of the chapel when it extended further to the east. However, with IR thermography, the surface of the structure is examined; the masonry structure must be examined as to assess whether the different mortar is only on the surface or whether the use of the different material extends to the masonry core.



Image 38: South wall - Areas 9.1 and 9.2

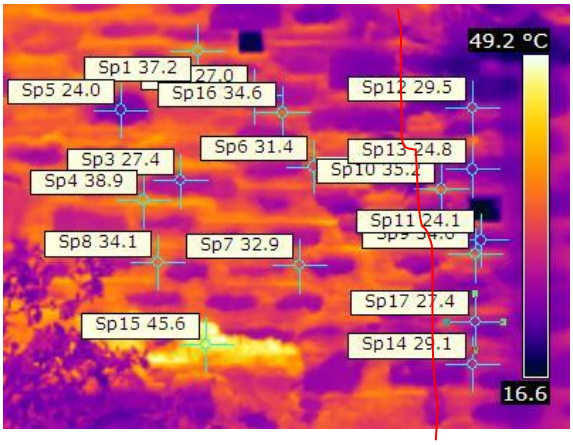


Image 39: Thermogram [7182], Date: 27/3/2014

Ground penetrating radar was employed in order to assess whether the differentiation of the masonry between these two areas is structural or only at the surface. Specifically, horizontal scans were carried out on the exterior of the south wall of the Catholicon, across area 9.2 and area 9.1., in order to assess whether the optical differentiation corresponds to a structural differentiation. Furthermore at the interface of area 9.1 and 9.2 it seems as though a crack is present; however this is not confirmed during a close optical investigation. This area of the south wall is where the pillars receiving the compressive forces from the dome are; through GPR scanning, it will be possible to examine whether these elements are constructed in a different manner than the rest of the masonry. Scans were conducted from the east side of the window to the corner of the east façade (Image 40).



Image 40: Exact positions of GPR scans on the south wall – depiction of the differentiation

The result (Image 41) shows that the differentiation of area 9.1 and 9.2 is due to the use of different materials in area 9.2 and area 9.1. This is obvious in the scan, as a diversification of the signal is evident at 1 m from the beginning of the scan; this is also where the optical differentiation occurs. However, this differentiation is at the surface; from 10 cm from the surface and below, the materials and the structure are continuous throughout the scan and therefore throughout the two areas. The end of the scan corresponds to a large carved stone at the southeast corner. Again the structure of the wall corresponds to the byzantine type of building, where three layers are evident; the outer layer, the middle rubble layer and the inner layer of the wall, thus indicating a three leaf masonry. Therefore, in the case of the south wall the middle layer and the interior layer are homogenous and continuous, whereas the joint mortar of area 9.2 is different, but only on the exterior layer, which is 10 cm deep.

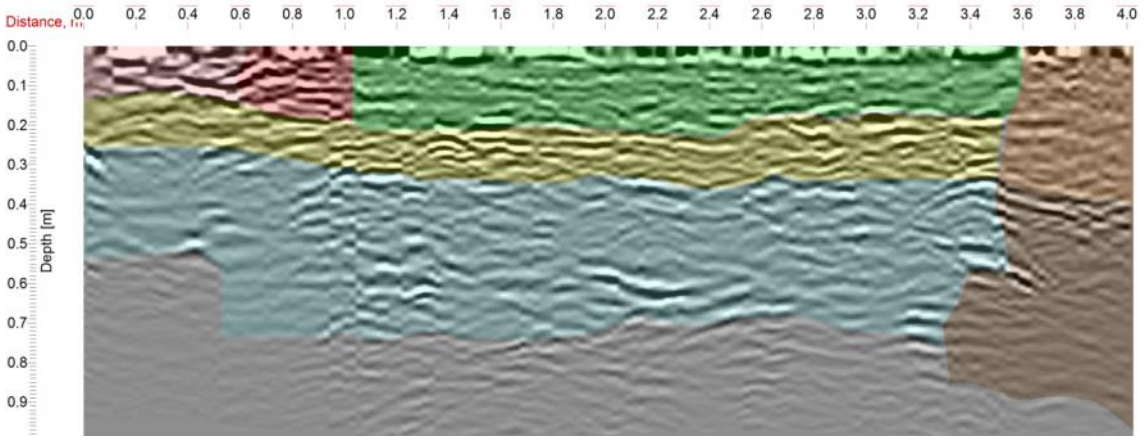


Image 41: GPR scan of south wall

4 CONCLUSIONS

- The carved stone of the first byzantine construction phase is a porous fossiliferous stone, with low values of compressive strength
- The building bricks of the east façade are of excellent quality and exhibit relatively high values compressive strength
- In the case of the Kaisariani Catholicon, the low compressive strength of the carved stones, imposes limitations regarding the compressive strength that any restoration mortar should have and still be deemed compatible with the masonry in any future intervention
- An undocumented intervention was revealed around the windows of the east façade
- The north wall of the Catholicon is a typical byzantine three leaf cloisonné masonry, whereas the north wall of the Narthex is obviously a rubble masonry. The temperature differentiation between the two areas is due to the different construction techniques of the two parts, as well as the high humidity of the Narthex wall
- The undocumented restoration mortars present on the north wall of the Narthex seem to enhance humidity problems, due to incompatibility with the original materials of the masonry
- The optical differentiation of the two areas of the south wall of the Catholicon is due to the different joint mortar of area 9.1 and area 9.2; the building stones and bricks are the same in both areas

- This differentiation does not extend to the core of the masonry; the middle layer and the interior layer are homogenous and continuous, whereas the joint mortar of area 9.2 is different than the mortar of area 9.2, but only on the exterior layer of the three leaf masonry, which in the case of the Catholicon of Kaisariani Monastery is 10 cm deep
- It is possible that the chapel extended further to the east, and therefore the difference of area 9.2 is due to the fact that it was once the interior of the chapel; this is further suggested due to the remain of a brick roof, the remains of which are evident in area 9.2
- The combination of different NDTs can reveal important information that would have been otherwise disregarded; furthermore it can confirm or disregard scenarios regarding non-documented construction phases
- NDTs can detect non-documented past interventions, as well as examine and characterize building materials in historic structures, as demonstrated on the east façade of the Catholicon; furthermore they can assist in the examination of the masonry structure as in the case of the north and south façade
- Schmidt hammer test results can be utilized as a first approximate limitation regarding the compressive strength that any restoration mortar should have in compatibility terms

ACKNOWLEDGEMENTS

The investigation was performed within the research project “Seismic Protection of Monuments and Historic Structures - SEISMO” which is co-financed by the Greek Ministry of Education and Religions and the European Union under the action “Thales” within the context of the Operational Programme - Education and Lifelong Learning, NSRF 2007-2013. The authors would like to thank the employees of the 1st Ephorate of Byzantine Antiquities for their cooperation.

REFERENCES

[1] Moropoulou A., Delegou ET, Avdelidis NP, Athanasiadou A. Integrated diagnostics using advanced in situ measuring technology. In: Proceedings of the 10th international conference on durability of building materials and components, Lyon, France; 2005, pp.1116-23

[2] L. Binda, A. Anzani, A. Saisi, G. Mirabella Roberti, 1.02 - Historic Masonry Structures, Comprehensive Structural Integrity, Volume 1, 2003, pp. 25-47

[3] Moropoulou, A., Labropoulos, K.C., Delegou, E.T., Karoglou, M., Bakolas, A. "Non-Destructive Techniques as a tool for the protection of Built Cultural Heritage", Construction and Building Materials 48 (2013), pp.1222-1239

[4] Nikolaos Charkiolakis, “The monasteries of mount Hymettus”, 7days Kathimerini newspaper, 28/9/1997

[5] Charalambos Bouras – Laskarina Boura, “Greek religious architecture in the 12th centrury” Commersial Bank of Greece, 2002

[6] Giorgos Pallis, “Topography of the Athenian field during the post-Byzantine period”, Post-Byzantine Mon-ments I, Thessalonica 2009

[7] Charalambos Bouras, "Byzantine Athens: 10th-12th c.", Benaki Museum 6th Supplement, Athens 2010

[8] Jol HJ, editor. Ground Penetrating Radar Theory and Applications. 1st ed: Elsevier; 2008

[9] Owen TE, editor. Special Issue on Ground Penetrating Radar. J of Applied Geophysics. 1995; 33: 1-255

[10] Binda L, Lenzi G, Saisi A. NDE of masonry structures: use of radar tests for the characterization of stone masonries. NDT & E International. 1998; 31(6), pp. 411-19

[11] Binda L, Zanzi L, Lualdi M, Condoleo P. The use of georadar to assess damage to a masonry Bell Tower in Cremona, Italy. NDT & E International. 2005; 38(3), pp. 171-79.

[12] Arias P, Armesto J, Di-Capua D, González-Drigo R, Lorenzo H, Pérez-Gracia V. Digital photogrammetry, GPR and computational analysis of structural damages in a medieval bridge. Engineering Failure Analysis. 2007; 14(8), pp. 1444-57

[13] Binda L, Saisi A, Tiraboschi C. Investigation procedures for the diagnosis of historic masonries, Construction and Building Materials, 2000; 14(4), pp. 199-233

[14] Ali Adb Elhakam Aliabdo, Abd Elmoaty Mohamed Abd Elmoaty, Reliability of using nondestructive tests to estimate compressive strength of building stones and bricks, Alexandria Engineering Journal, 51, 2012, pp.193-203

[15] A.Aydin, A.Basu, The Schmidt hammer in rock material characterization, Engineering Geology, 81, 2005, pp.1-14

[16] Chair of Architecture, Morphology and Rythmology E.P.P., "Byzantine monuments – Churches in the Attica region,", NTUA Editions, Athens, June 1970

COMPDYN 2015
5th ECCOMAS Thematic Conference on
Computational Methods in Structural Dynamics and Earthquake Engineering
M. Papadrakakis, V. Papadopoulos, V. Plevris (eds.)
Crete Island, Greece, 25–27 May 2015

EXPERIMENTAL AND NUMERICAL INVESTIGATIONS FOR THE STRUCTURAL CHARACTERIZATION OF A HISTORIC RC ARCH BRIDGE

R. Ferrari[1*], D. Froio[1], E. Chatzi[2], C. Gentile[3], F. Pioldi[1], E. Rizzi[1]

[1] Università di Bergamo, I-24044 Dalmine (BG), Italy
[*] Corresponding Author, rosalba.ferrari@unibg.it

[2] ETH Zürich, CH-8093 Zürich, Switzerland

[3] Politecnico di Milano, I-20133 Milano, Italy

Keywords: Reinforced Concrete (RC) arch bridge, Operational Modal Analysis (OMA), Structural identification, Finite Element (FE) modeling and updating, Structural Health Monitoring (SMH).

Abstract. *A comprehensive rational methodology for the structural assessment of existing bridges is presented and specifically applied to a historic reinforced concrete arch bridge. The methodology is based on the use of non-destructive testing tools and structural model updating procedures and involves: (a) preliminary documented research and on-site geometric surveys (aimed at collecting information on the "as built'' geometry); (b) ambient vibration testing performed by using a grid of conventional high-sensitivity accelerometers, aimed specifically at investigating the vertical dynamic characteristics of the bridge and c) development of an updated Finite Element (FE) model of the structure.*

The investigated bridge, completed in May 1917, crosses the Adda river between Brivio (province of Lecco) and Cisano Bergamasco (province of Bergamo), about 50 km North-East from Milano, Northern Italy. Given the still strategic position of the bridge in the current road transportation network and within a systematic surveillance program of main infrastructures by the Province of Lecco, dynamic tests were performed under operational conditions.

Main results in terms of Operational Modal Analysis and FE modelling and updating are presented and discussed. A hierarchy of FE models with different levels of refinement is developed, with the purpose of a future selection of the model that better reproduces the current structural properties of the bridge. In this paper an automated system identification procedure has been developed and applied to the simplest of the assembled (consistent) FE models, whose results will constitute a benchmark for further studies upon the other most refined models. The aim is to perform a final baseline reference model to be used for reliability assessment within Structural Health Monitoring (SHM) purposes.

1 INTRODUCTION

Nowadays the development of methodologies for accurate and reliable condition assessment of bridges, or other typologies of civil infrastructures, is becoming increasingly important. The process of developing or improving methodologies for determining and tracking the structural integrity of infrastructures based on automated monitoring systems is a main scope of SHM [1].

FE models play a key-role in the ordinary design process of new structures and in the assessment of existing ones [2]. With the current advances in numerical modeling and computational capabilities, it is generally expected that a FE model consistently based on original technical design drawings, on-site geometric surveys, engineering judgment and assessment processes, shall reliably reproduce both static and dynamic behaviors of a structure.

However, acquired experience shows that the process of developing a FE model of a structure involves assumptions and simplifications that may induce considerable errors, which are a consequence of the underlying complexity of the structural modeling, of the uncertainty of the boundary conditions and of the real mechanical behavior of materials and structural elements [3]. Moreover, variations in these features during the lifespan of a structure may occur due to the appearance of smeared or localized damage, causing final discrepancies between the characteristics of the structure at design stage and at the current state of duty and conservation.

Structural identification via modal dynamic analysis [4] and subsequent Finite Element Model Updating [5,6] represent consistent and widespread tools towards condition assessment of existing civil constructions, like bridges or structures endowed with historical values. In fact, it is well known that changes in the physical properties of a structure correspond to changes in the modal parameters (notably frequencies, mode shapes, and modal damping ratios) [7]. In most of Model Updating techniques the stiffness, mass and damping distributions of a numerical model chosen as reference configuration, are iteratively updated, so that the differences between the measured and the analytical values of the modal parameters are minimized [2]. There appear several works in the dedicated literature in which the results obtained from modal identification have revealed useful for performing model updating of a numerical model of existing bridges [2-3,8-14]. Within such a field, this paper presents the results obtained from a research study that involved both experimental and analytical modal analysis as well as subsequent finite element model updating of a reinforced concrete bridge with parabolic arches, namely the Brivio bridge (1917), Italy, as described below.

The investigation dealt within this paper involves: (a) exploiting OMA techniques to Ambient Vibration Testing (AVT) [3]; (b) establishing three FE models of the bridge with increasing levels of detail, based on the available design drawings and on surveys performed in situ; (c) exploring the sensitivity of the natural frequencies of a 2D FE model of the bridge to changes in some uncertain structural parameters; (d) setting the parameters of such 2D FE model, that appear good candidates for the updating procedure and (e) identifying such parameters, in order to enhance the fitting between experimental and theoretical natural frequencies and mode shapes. The aim is to create an improved FE model which can be adopted as a benchmark for further scheduled analyses on more complex and detailed numerical models.

Report on this present research investigation is organized in two companion papers. Companion work [15] focuses on the analysis of the various data coming from the different adopted instrumentation, accounting also for data fusion and for reliability and uncertainty assessment of the acquired data, while the present note exposes the detailed AVT performed

with conventional high-sensitivity accelerometers and the development of an updated FE models of the bridge, specifically in terms of prediction of modal properties.

The present paper is structured as follows. Section 2 describes the main characteristics of the Brivio bridge, which is the benchmark structural object taken for this study. In Section 3 the results of the output-only model identification performed on the bridge are presented. In Section 4 the three performed FE models are described in detail. Section 5 concerns the sensitivity analysis for the selection of the parameters to be considered within the model updating procedure, which is explained in Section 6. Finally, main conclusions are outlined in closing Section 7.

2 SALIENT FEATURES OF THE BRIVIO BRIDGE

The Brivio bridge (Figs. 1, 2), designed by Italian engineer Giuseppe Banfi on June 1912 and completed on May 1917, is a three-span historical reinforced concrete bridge with parabolic arches located in Lombardia, Northern Italy, about 50 km North-East away from Milano [16]. It crosses the Adda river at about 8 m from water, between the municipalities of Brivio and Cisano Bergamasco, linking the two provinces of Lecco and Bergamo. The spans of the bridge are 43.40 m, 44.00 m and 43.40 m long respectively, and consist of a deck joined on each of their sides to two lateral parabolic arches. The suspension is performed by means of sixteen hangers, per each side of each span, with rectangular cross-section that is 32 cm wide and 60 cm high. All structural elements are made of reinforced concrete.

The total width of the deck is 9.20 m, hosting a double-lane road and two pedestrian walkways, each 0.80 m wide. The deck cross section (Fig. 2) is constituted by two outer longitudinal girders framed by floor beams; girders, spaced 8.60 m center to center, display approximately rectangular cross sections with width of 45 cm and height of 100 cm, and floor beams, provided every 2.30 m, also show rectangular cross sections with width of 28 cm, but variable height along the beam axis. The floor beams are further connected to other two longitudinal ribs of width of 20 cm, placed symmetrically at a distance of 1 m with respect to the vertical longitudinal middle plane of the bridge. The resulting frame is covered by a reinforced concrete slab of 15 cm of high, which constitutes the support of the road.



Figure 1: Contemporary views of Brivio bridge seen from Brivio's riverside (right bank).

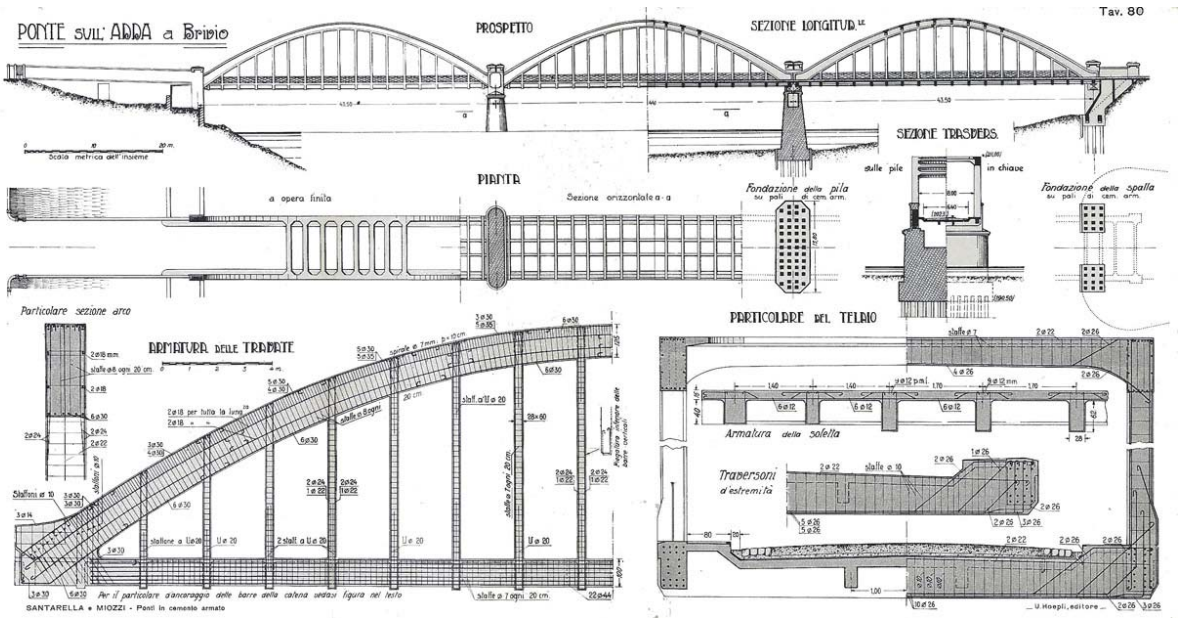


Figure 2: Historical representation of the technical drawings of the bridge [17].

The arches of the bridge show a span of about 42.80 m between the two ends and a rise of 8.00 m at the keystone. They display a rectangular cross section characterized by a constant width, equal to 60 cm, and a variable tapered height starting from around 1.50 m at the extrema to 1.25 m at the middle. To achieve higher structural stability, the arches are linked in the upper part by eight transverse girders, tapered from the end to the center.

Each span rests on either a pier or an abutment, where outer longitudinal girders end, through a mechanical system made of trusses, in order to allow little axial elongations, due e.g. to changes of temperature.

3 MODAL DYNAMIC IDENTIFICATION OF THE BRIDGE

This Section reports the modal estimates that have been obtained from output-only identification techniques based on the operational response data acquired on the bridge by using conventional high-sensitivity accelerometers.

The response of the bridge was measured at eighteen selected points, as shown in Fig. 3. Since it was decided to simultaneously use ten wired accelerometers during the tests, two set-ups were performed to measure the acceleration at opposite sides of eight cross-sections of the deck, considering two sensors as reference transducers, which were kept at the same locations in all the set-ups.

Two time windows of 3600 s were collected for each sensor layout, with a sampling rate of 200 Hz, which is higher than that required for this bridge, as the natural frequencies of the dominant modes are below 20 Hz. Hence, low pass filtering and decimation were applied to the data before the use of the identification tools, reducing the sampling rate from 200 Hz to 25 Hz.

The output-only modal identification was carried out by using both the Frequency Domain Decomposition (FDD) [18] and the data-driven Stochastic Subspace Identification (SSI-data) methods [19] available in the commercial software ARTeMIS [20].

The results of modal identification are summarized in Figs. 4-5 and in Table 1. The natural frequencies of the identified modes can be easily identified in Fig. 4 from the local maxima of the first Singular Value (SV) line resulting from the application of the FDD method; the corresponding mode shapes are shown in Fig. 5.

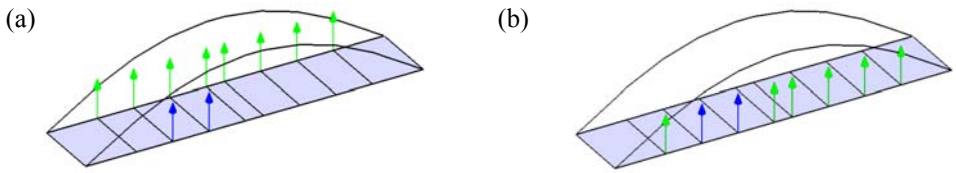


Figure 3: Points instrumented using wired accelerometers: (a) Set-up 1; (b) Set-up 2.

The inspection of Fig. 5 highlights that: (a) almost all mode shapes exhibit regular and smooth shape with dominant bending or torsion, with the exception of the 7th mode, which is characterized by coupled bending and torsion; (b) the first two modes exhibit different frequencies but practically the same mode shape. In addition, the 7th vibration mode also exhibits complex behaviour (i.e. the modal deflection phases significantly deviate from 0 or π).

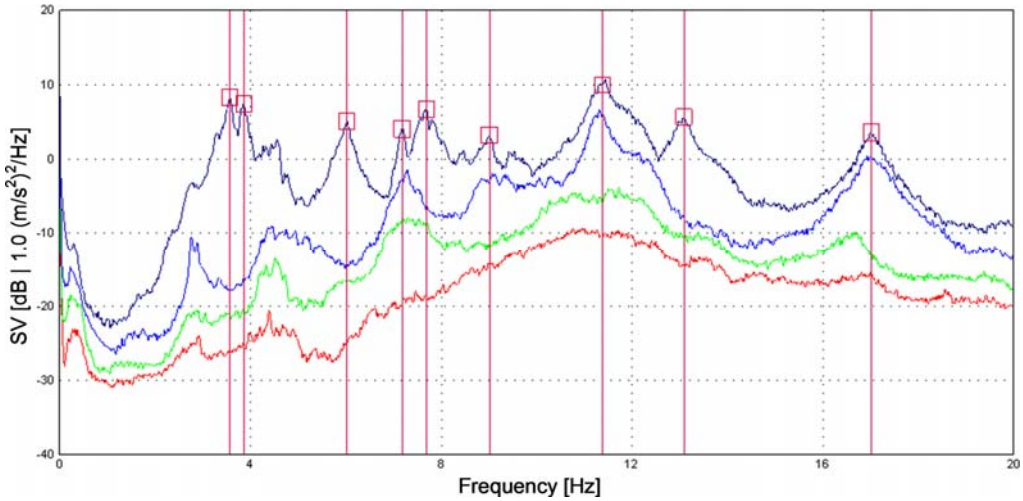


Figure 4: Singular value (SV) lines and identification of natural frequencies from the wired accelerometers data (FDD).

Mode N.	f_{FDD} *(Hz)*	f_{SSI} *(Hz)*	ζ_{SSI} *(%)*	*MAC*
1	3.564	3.449	4.60	0.997
2	3.857	3.887	4.09	0.991
3	6.018	5.968	3.17	0.998
4	7.178	7.146	1.51	0.989
5	7.690	7.592	2.82	0.991
6	9.009	8.928	1.67	0.990
7	11.377	11.390	1.28	0.938
8	13.086	13.040	2.01	0.987
9	17.017	16.990	1.44	0.935

Table 1: Identified frequencies f_i [Hz], first span, wired accelerometers.

Very close results, in terms of natural frequencies and mode shapes, are obtained by applying the SSI-data method, as it is summarized in Table 1. Furthermore, Table 1 reveals that the damping ratios of the first two modes are larger than 4%.

It should be noticed that the "splitting" of 1st mode (with quite high damping ratios) and the complex behaviour of the 7th mode deserves further investigation since both the observed phenomena might be related to the poor state of preservation and cracking of some vertical

hangers. In more details, the co-existence of two close spectral peaks with similar mode shapes in place of one single mode is sometimes referred to as “dispersive phenomenon” [21] and was mainly observed in the response of cracked reinforced concrete structures. The same physical behaviour has been recently detected in ambient vibration testing of two different arch bridges [22].

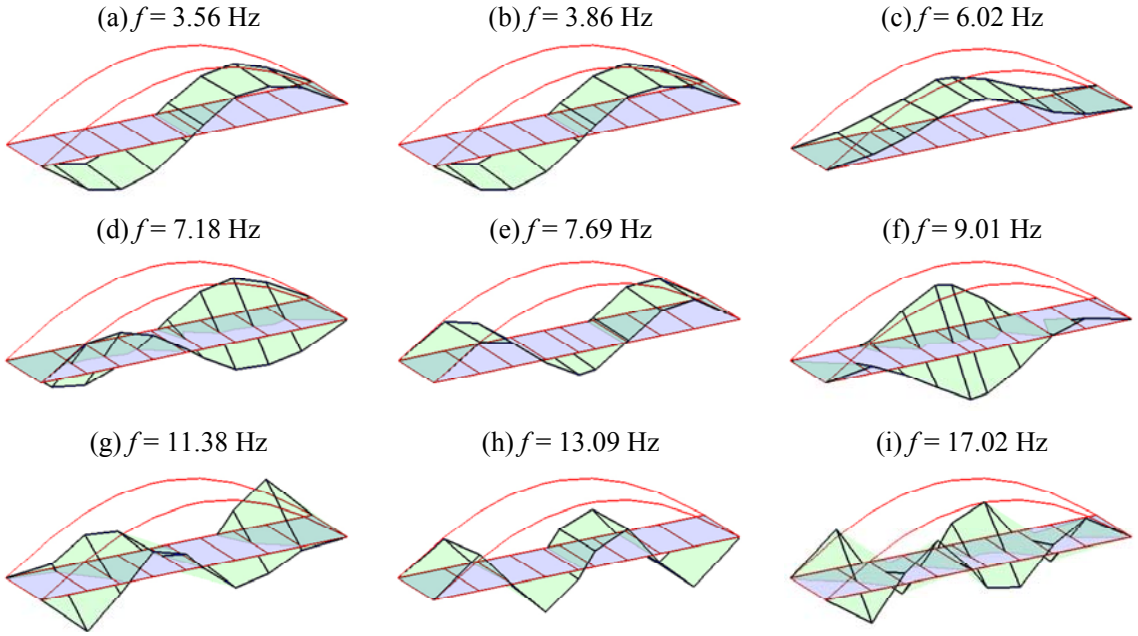


Figure 5: Vibration modes identified from the wired accelerometers data (FDD).

4 FE MODELING OF THE BRIDGE

Three Finite Element models of the Brivio Bridge with different levels of refinement have been assembled [16]. In particular, one two-dimensional model and two three-dimensional models have been implemented within the commercial FE code ABAQUS [23].

The main assumptions considered in the present FE models of the bridge are the following:

- Euler-Bernoulli beam finite elements have been used to model all the elements of the bridge, except for one of the two 3D models in which four-nodes shell elements have been employed to model the deck;
- uniform cross sections, homogeneous material properties and linear elastic mechanical behavior have been assumed; Poisson’s ratio of reinforced concrete has been held constant and set equal to 0.20;
- an additional weight per unit volume of 10 kN/m^3 has been considered on the deck slab, to account for the effects of the asphalt pavement and of the walkways;
- rigid links between the concrete slab and the grid of hangers and between the latter and the arches have been applied, for taking into account the real lengths of the structural elements; each of these links provides a rigid constraint for translation and rotation of one node with respect to the degrees of freedom of the other one;
- the deck has been assumed to be able to rotate only on one side, while on the opposite side boundary conditions have been modeled according to the design characteristics of

the bearing supports (which shall allow for longitudinal displacement); hence, a hinge-roller scheme has been assumed for the boundary conditions of each span;

- a single representative span of 42.80 m has been considered and no continuous beam effects are investigated so far.

In the following Sections 4.1-4.3 a brief description of each FE model is reported.

4.1 2D FE Beam model

The assembled 2D FE model of the bridge is depicted in Fig. 6. The *x* and *y* axes represent the longitudinal axis and the vertical axis of the bridge, respectively. The model is composed of 224 elements and 178 nodes, for a total of 986 free variables in the internal code representation [23].

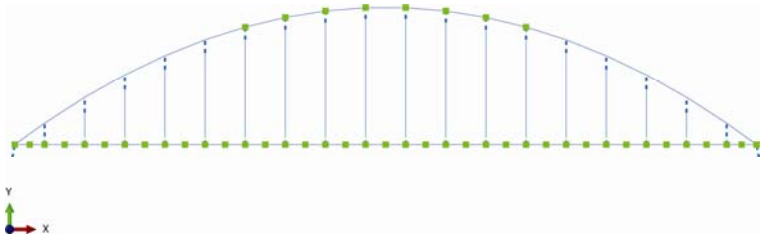


Figure 6: Assembled 2D FE Beam model (green markers specify where lumped masses have been placed).

According to the original design (see Fig. 2), the arches are composed of nineteen chunks with different heights; then, ten types of different double rectangular cross sections with height decreasing from the ends towards the top have been modeled. The hangers have been also represented by elements with a double rectangular cross section. The masses of the elements whose axes lie out of the plane of the model have been lumped at the corresponding nodal positions; the values of the lumped masses are reported in Table 2. Rotational inertia values are considered to be negligible.

Element	***Mass [kg]***
Transverse deck beam	5193
Transverse deck beam at the ends	7419
Transverse beam of the arches	3080

Table 2: Lumped masses added to the 2D FE Beam model.

The global geometrical parameters which characterize the 2D Beam model of the bridge are reported in Table 3. As a first step, the total mass has been evaluated by assuming a reinforced concrete density of 2500 kg/m^3. Further data on the geometrical characteristics are reported in [16].

Parameter	***FE model value***
Total mass	754.8 t
Component x of the center of mass	21.40 m
Component y of the center of mass	1.93 m
Moment of inertia about axis z on the center of mass	1.18 10^8 kg m^2

Table 3: Global geometric parameters of the 2D FE Beam model (concrete density = 2500 kg/m^3).

4.2 3D FE Beam model

The 3D FE beam model of the bridge is shown in Fig. 7. It has been assembled via exclusive use of only 3D beam elements. The *x*, *y* and *z* axes represent the longitudinal axis, the vertical axis and the horizontal transverse axis of the bridge, respectively. The FE model counts for 808 elements and 668 nodes, with a total number of free variables equal to 5900.

According to the original design drawings, each arch has been modeled as in the 2D FE model. Eight superior beam elements with T cross section have been added to the model, setting the two arches at a relative distance of 8.60 m. The deck has been modeled as a framework of beams. In the longitudinal direction, six beam elements have been placed, playing the role of longitudinal girders, included the reinforced concrete slab above. The cross sections of these elements have been modeled for best fitting the shape of the deck cross section, depicted in Fig. 2. In the transverse direction, beams with variable rectangular cross section have been placed.

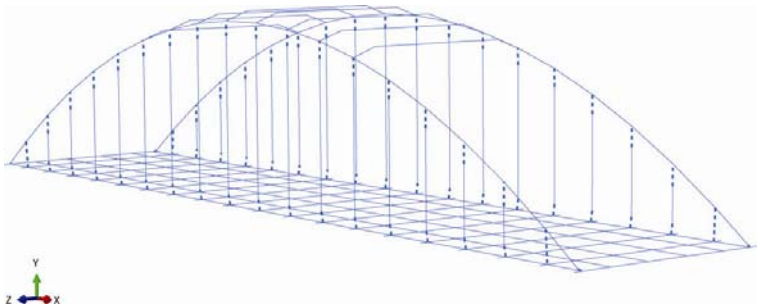


Figure 7: Assembled 3D FE Beam model.

The global geometrical characteristics of the 3D Beam model are reported in Table 4. Further data are available in [16].

Parameter	***FE model value***
Total mass	762.6 t
Component x of the center of mass	21.40 m
Component y of the center of mass	1.92 m
Component z of the center of mass	4.30 m
Moment of inertia about axis x on the center of mass	$1.53\ 10^8$ kg m^8
Moment of inertia about axis y on the center of mass	$1.23\ 10^8$ kg m^2
Moment of inertia about axis z on the center of mass	$1.20\ 10^8$ kg m^2

Table 4: Global geometric parameters of the 3D FE Beam model (concrete density = 2500 kg/m3).

4.3 3D FE Beam & Shell model

A further improvement in the FE description of the bridge has been performed by considering shell elements, instead of beam elements, in the modelization of the deck, as represented in Fig. 8. The use of shell elements allows to describe the mean line of the deck cross section, by providing a more accurate reproduction of its peculiar shape. Twelve shell elements with six different thicknesses have been employed in the model. The final assembly of the FE model counts for 3678 elements and 4188 nodes, with a total number of 22660 free variables.

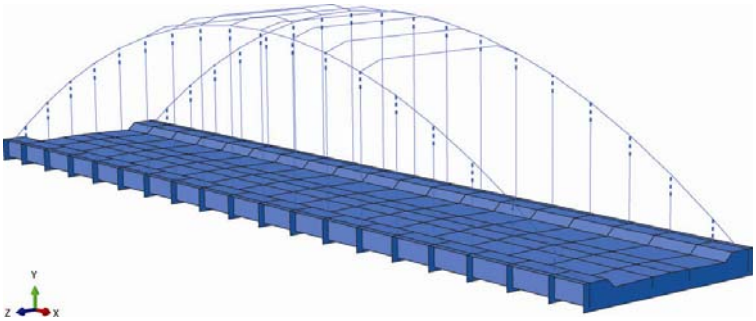


Figure 8: Assembled 3D FE Beam & Shell model.

The global geometrical parameters of the 3D Beam & Shell model of the bridge are reported in Table 5.

Parameter	***FE model value***
Total mass	767.0 t
Component x of the center of mass	21.40 m
Component y of the center of mass	1.90 m
Component z of the center of mass	4.30 m
Moment of inertia about axis x on the center of mass	$1.55\ 10^8$ kg m^2
Moment of inertia about axis y on the center of mass	$1.23\ 10^8$ kg m^2
Moment of inertia about axis z on the center of mass	$1.19\ 10^8$ kg m^2

Table 5: Global geometric parameters of the 3D FE Beam & Shell model (concrete density = 2500 kg/m^3).

As Tables 3-5 show, the FE models appear with a good level of similarity referring to the geometrical characteristics, demonstrating the consistency of the models themselves.

5 SENSITIVITY ANALYSIS

As mentioned in Introduction, the sensitivity analysis and the optimization procedure have been based on the simplest of the assembled FE models, that is, the 2D Beam model.

It is well known that the selection of the parameters to be updated is crucial, and that sensitivity analysis constitutes an efficient tool which allows for the selection of the parameters that most influence the structural responses. The sensitivity coefficients can be computed as the rate of change of a particular response of the model with respect to a change of the structural parameters [3]. Then, the sensitivity matrix **S** can be calculated as follows:

$$S_{ij} = \frac{\partial R_i}{\partial P_j} \tag{1}$$

where R_i and P_j represent a structural response index and a structural parameter, respectively, with $i=1,\ldots,N$, for N response indexes and $j=1,\ldots,M$, for M structural parameters. The sensitivity matrix can be computed for all physical element properties (material, geometrical, boundary, etc.), by using direct derivation or approximation techniques [2].

Eq. (1) evaluates the absolute sensitivities, which are characterized by the dimensions of responses and parameter values. If sensitivities for different types of parameters have to be compared, a normalized relative sensitivity matrix $\mathbf{S}_n$ should be better used:

$$S_{nij} = \frac{\partial R_i}{\partial P_j}\frac{P_j}{R_i} \tag{2}$$

Hence, the problem may be determined, over-determined or under-determined, depending on whether matrix $\mathbf{S}_n$ is square ($N=M$), tall-rectangular ($N>M$) or wide-rectangular ($N<M$), respectively. If the estimation of too many parameters is attempted, then the problem may appear ill-conditioned, in particular when observations are limited, as it usually occurs in vibration testing. Therefore, to achieve a well-conditioned updating problem it is necessary to select a smaller as possible number of updating parameters, which will be the most effective ones in producing a genuine improvement in the modeling of the structure [2].

In light of this, also concerning their influence in the overall dynamic behavior of the bridge, the following structural parameters have been selected to be used in the updating procedure:

- Young's modulus of reinforced concrete deck (E_{deck});
- Young's modulus of reinforced concrete arches and hangers ($E_{arch\&hang}$);
- mass per unit volume of reinforced concrete (ρ_{conc}).

As mentioned in the work of Brownjohn et al. [2], when performing a model updating procedure, it is very important to determine a suitable initial value of a selected parameter, i.e. a reasonable starting point for the optimization process; this is because if the initial value is too far away from its real value and large discrepancies exist between the experimental and the numerical model, the iterative process may result in convergence to another (local) minimum, or even in divergence. It is usually recommended to carry out a prior manual tuning, by engineering judgment or relevant preliminarily estimations, towards obtaining a reasonable approximation of the start point and of the parameter bounds before starting the optimization procedure.

To accomplish such manual tuning, a set of preliminary modal analyses have been performed on the 2D FE model of the bridge by varying the three parameters listed above. At this first stage, the goal was that of assuring that the chosen parameters truly affected the modal response of the structure and to roughly match experimental and numerical modal results. Considering 3.564 Hz as the first modal frequency of the bridge, the manual tuning of the parameters of the FE model has provided a significant matching with respect to the experimental outcomes. In particular, very good results have been obtained using the values of 33.0 GPa, 36.5 GPa and 2400 kg/m^3, for the Young's modulus of deck (E_{deck}), the Young's modulus of arches/hangers ($E_{arch\&hang}$) and the concrete mass density (ρ_{conc}), respectively. The FE model characterized by this particular set of parameters will be referred to as "base model" in the following. Fig. 9 shows the results of the modal analysis performed through the 2D FE base model.

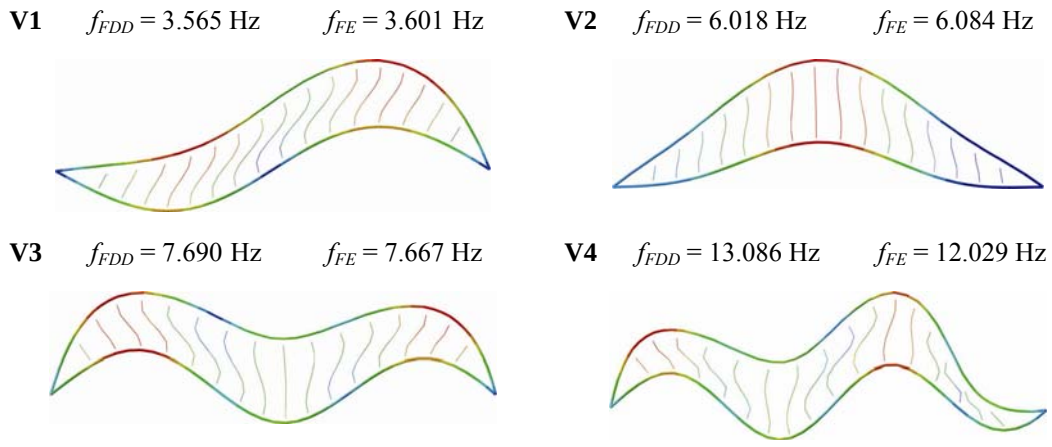


Figure 9: First four vibration modes of the 2D FE base model of the bridge (not updated).

The correlation between the dynamic characteristics of the FE base model and those coming from the experimental results is shown in Table 6, for the first four vibration modes, via the absolute frequency discrepancy and the modal assurance criterion (MAC) [24], to check correspondences of the mode shapes. The latter is defined as follows (MAC matrix):

$$MAC_{ij}(\boldsymbol{\varphi}_i^{exp}, \boldsymbol{\varphi}_j^{num}) = \frac{\boldsymbol{\varphi}_i^{expT} \cdot \boldsymbol{\varphi}_j^{num}}{(\boldsymbol{\varphi}_i^{expT} \cdot \boldsymbol{\varphi}_i^{exp})^{1/2} \cdot (\boldsymbol{\varphi}_j^{numT} \cdot \boldsymbol{\varphi}_j^{num})^{1/2}} \qquad (3)$$

where $\boldsymbol{\varphi}_i^{exp}$ and $\boldsymbol{\varphi}_j^{num}$ are the *i-th* experimental and *j-th* numerical mode shape vectors, respectively. Each value of the MAC matrix defined in Eq. (3) effectively represents a correlation coefficient ranging from 0 to 1, where a value of 1 represents a perfect correlation of the two mode shape vectors (i.e. a linear dependence), while a value close to 0 indicates uncorrelated vectors (i.e. linear independence or orthogonality condition). In general, a MAC value larger than 0.85÷0.90 is considered as a good match, while a MAC value less than 0.50 is considered to be a poor match [3].

Experimental			***2D Beam FE base model***		
Mode identifier	*Mode N*	f_{FDD} *(Hz)*	f_{FE} *(Hz)*	Δ_f *(%)*	*MAC*
V1	1	3.564	3.601	1.02	1.000
V2	3	6.018	6.084	1.10	0.991
V3	5	7.690	7.667	-0.31	0.993
V4	8	13.086	12.029	-8.08	0.889

Table 6: Correlation between experimental and 2D Beam FE base model dynamic characteristics for the first four vertical bending modes.

Some attempts have been also performed considering the value of 3.857 Hz as the frequency of the first vertical mode of the bridge, but the outcomes of the manual tuning have turned out unsatisfactory.

The normalized sensitivities (Eq. (2)) of the first six modal frequencies of the vertical bending modes with respect to the parameters above are represented in Fig. 10. The sensitivities have been evaluated by varying each time one of the parameters and keeping fixed the others to those of the base model. The plots in Fig. 10 have been obtained by linear interpolation of the point-wise values of partial derivatives of Eq. (2), which have been calculated by using a central difference evaluation.

The normalized relative sensitivities in Fig. 10 show that the chosen parameters truly affect the modal response of the structure. In particular, the plots show that: (a) the parameter that most influences the variations of the lower frequencies is the concrete mass density, with all sensitivity coefficients over 45% and almost constant for the considered frequencies; (b) concerning Young's moduli of deck and arches/hangers, the corresponding sensitivities range from 10% to 20% and from 30% to 40%, respectively; (c) the fundamental frequency f_1 of the first mode, which displays the typical antisymmetric mode shape of a vibrating arch, is indeed influenced mainly by Young's modulus of arches/hangers and, if compared to the other modes, is less influenced by the elastic modulus of deck.

Based on the obtained results, the parameters above have been set as the starting point for the optimization procedure of the 2D FE model of the bridge, as described in the following. Table 6 shows a fairly good correlation between experimental outcomes and numerical results from the base model for the first three flexural vertical modes: the higher frequency discrepancy ranges up to about 1% and the MAC index is never below 0.99. The forth vertical mode

shapes displays large deviations, in particular for the frequency discrepancy which is about the 8%. Then, it has not been considered in the optimization procedure.

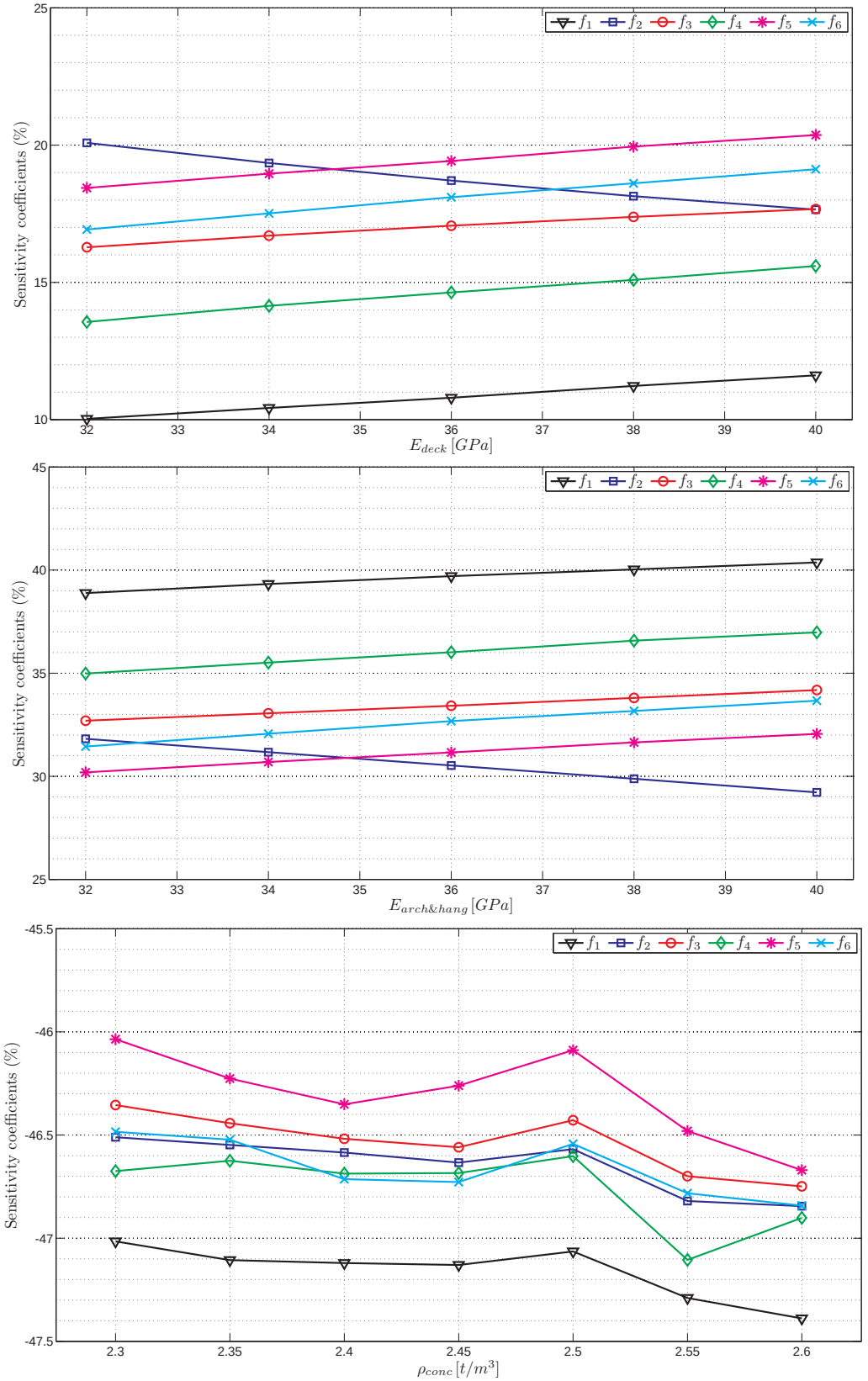


Figure 10: Sensitivity coefficients for the first six modal frequencies of the 2D Beam FE model.

6 OPTIMIZATION PROCEDURE FOR MODEL UPDATING

The optimization phase allows for obtaining the parameter values that minimize the differences between the experimental and numerical modal estimates. Then, this phase involves the definition of an appropriate objective function and the application of an optimization technique based on a non-linear least square algorithm. The algorithm of inverse analysis herein adopted is described in the following Section 6.1. It takes largely inspiration from the identification work performed in [25], in quite a different context (material indentation tests). In Section 6.2 the results obtained from the optimization procedure are reported.

6.1 Formulation

The algorithm makes use of two sources of information: experimental recorded dynamic results available before running, from which frequencies and mode shapes have been estimated through Operational Modal Analysis (FDD); numerical data that, depending on a number of modeling parameters to be identified (here three material parameters: E_{deck}, $E_{arch\&hang}$ and ρ_{conc}), arise from numerical simulations of modal analysis (Lanczos' method [23]) from the FE model.

The discrepancies among target data and simulated data are minimized, towards the identification of the material parameters allowing for most effective calibration. Such discrepancy minimization is measured in terms of an appropriate objective function, which quantifies, through a vector measure, the difference between target and predicted data. In the present case, the assumed objective function, $\boldsymbol{\omega(x)}$, corresponds to a discrete non-negative, non-dimensional, vector least-square discrepancy measure, and two types of terms, one related to the relative discrepancy of natural frequencies and another related to the MAC values [11] are considered:

$$\boldsymbol{\omega(x)} = \left[\alpha \left(\frac{f_i^{exp} - f_i^{comp}}{f_i^{exp}} \right)^2 , \; (1-\alpha)(1-MAC\,(\boldsymbol{\varphi}_i^{exp}, \boldsymbol{\varphi}_i^{num}))^2 \right]^T , \quad i = 1, 2, 3 \tag{4}$$

where f_i^{exp} and f_i^{num} are the experimental and numerical frequencies of mode i, $\boldsymbol{\varphi}_i^{exp}$ and $\boldsymbol{\varphi}_i^{num}$ are the eigenvectors containing the experimental and numerical modal information regarding mode i and $\boldsymbol{x}$ is the (3×1) vector including the parameters to be optimized with respect to the first three flexural vertical modes. If the MAC values between measured and updated models are near to one and the frequency differences between measured and updated estimates are near to zero, the model updating is deemed to be successful.

In Eq. (4) α represents a weight coefficient [25], bounded between zero and one ($0 \le \alpha \le 1$), allowing to shift the importance of information from frequencies and mode shapes (possibly based also on their availability or estimated accuracy), towards the identification process. Fundamental choices are (a) α=0 (information from MAC matrix only, that is from mode shapes only); (b) α=0.5 (equal information from natural frequencies and MAC matrix); (c) α=1 (information from natural frequencies only). For other values of α ranging between 0 and 1, both test profiles could be taken into account, with variable importance, depending on the specific reliability of estimated frequencies and mode shapes.

Fig. 11 presents a synoptic flowchart that illustrates the iterative process of calibration of the numerical model. The process involves the concatenated use of two software packages: ABAQUS [23] as structural solver and MATLAB optimization toolbox [26] as optimization routine. In the ABAQUS environment the numerical algorithm for the eigenvalues and eigenvectors problem of the FE models is run based on a set of initial parameter values. In the MATLAB routine, based on the experimental modal information, the mode pairing between

experimental and numerical modes is performed through the application of a least square optimization procedure. The minimization of the residuals in the objective function is achieved, by using a Trust Region method through the *"lsqnonlin"* function of the Optimization Toolbox [21].

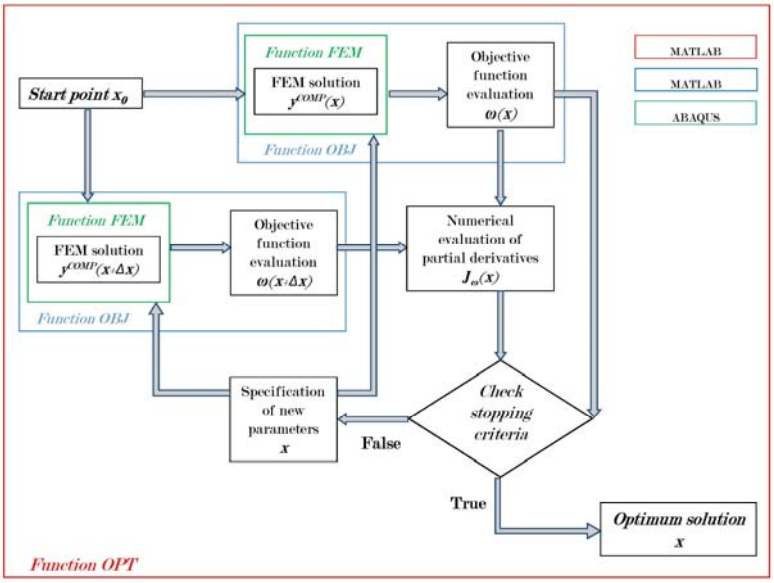


Figure 11: Flowchart of the optimization process for FE model updating (adapted from [25]).

The *"lsqnonlin"* function in MATLAB requires the following entries: the evaluation of the objective function; a start point $\boldsymbol{x}_0$ from which the search of the absolute minimum departs; lower and upper bounds for the optimization variables, which are applied to the procedure to assure that the variations of the parameters do not lay outside some reasonable limits. Then, the function proceeds to an iterative search towards the absolute minimum, by varying the optimization variables (material parameters), evaluating through them the objective function and its jacobian at each iteration, and checking convergence/stopping criteria, as reported in [25].

6.2 Optimization results

The updated value of Young's modulus of the deck is 34.9 GPa, of Young's modulus of arches/hangers is 35.7 GPa and of concrete density is 2437 kg/m^3, with a percentage variation of 5.76%, -2.19%, and 1.54%, respectively, if compared to the initially-assumed values in the base model.

The updated frequencies f_i are listed in the fourth column of Table 7. The frequency percentage discrepancies and mode-shape correlation MAC values between the measured and updated modes are reported in the fifth and sixth column in Table 7, respectively.

Experimental			***2D updated model***		
Mode identifier	*Mode N*	f_{FDD} *(Hz)*	f_{FE} *(Hz)*	Δ_f *(%)*	*MAC*
V1	1	3.564	3.564	-0.02	1.000
V2	3	6.018	6.065	0.78	0.992
V3	5	7.690	7.627	-0.81	0.993
V4	8	13.086	11.942	-8.74	0.889

Table 7: Correlation between experimental and FE updated model dynamic characteristics of the first four vertical bending modes.

The optimization procedure has resulted quite successful. The results show maximum frequency difference of lower than 1% and very high MAC values larger than 99% for the modes within the frequency range 0-10 Hz (first three modes).

7 CONCLUSIONS

Ambient vibration testing with conventional high-sensitivity accelerometers, the assembly of three FE models with different levels of refinement and the calibration of a simplified numerical FE model (2D) of a historic reinforced concrete arch bridge have been presented in this paper.

From the results of the identification analysis based on the operational response data collected on the bridge it is possible to observe that: (a) almost all identified mode shapes exhibit regular and smooth shape with dominant bending or torsion, with the exception of the 7th mode, which is characterized by coupled bending and torsion and exhibits complex behaviour; (b) the "splitting" of first mode and the complex behaviour of the 7th mode deserves further investigation since both the observed phenomena might be related to the poor state of preservation and cracking of some vertical hangers ("dispersive phenomenon").

The calibration of the 2D FE model of the bridge has been based on the estimated dynamic characteristics of the structure determined through an operational modal analysis and it has involved a prior manual tuning of structural parameters selected by engineering judgments. Then, a sensitivity analysis and a subsequent optimization process have been performed. The sensitivity analysis has confirmed as a good choice the structural parameters selected for model updating. The application of the updating procedure has provided a 2D linear elastic model of the bridge, adequately representing the modal behavior of the structure in its present condition. In fact, good correlations with the experimental results (natural frequencies and mode shapes) have been obtained in the frequency range 0-10 Hz.

The structural parameters determined for the 2D FE model will be set as the starting point in the updating procedures of the more refined 3D FE models, in order to finally constitute a FE model as a baseline reference within a possible long-term monitoring framework of the bridge.

ACKNOWLEDGMENTS

The authors thank very much the Province of Lecco, owner of the bridge, from allowing to perform the experimental tests; the cooperation of MSc A. Valsecchi (Director of the Bridge and Road Division, Province of Lecco) is gratefully acknowledged. The financial support by the University of Bergamo and by the Institute of Structural Engineering (IBK), ETH Zürich, within project ITALYR (Italian TALented Young Researchers) 2014, is also gratefully acknowledged.

REFERENCES

[1] K. Worden, C.R. Farrar, G. Manson, G. Park, The fundamental axioms of structural health monitoring. *Proceedings of the Royal Society A: Mathematical, Physical and Engineering Sciences*, **463(2082)**, 1639-64, 2007.

[2] J.M.W. Brownjohn, P.Q. Xia, H. Hao, Y. Xia, Civil structure condition assessment by FE model updating: methodology and case studies. *Finite Elements in Analysis and Design*, **37(10)**, 761-775, 2001.

[3] F. Benedettini, C. Gentile, Operational modal testing and FE model tuning of a cable-stayed bridge. *Engineering Structures*, **33(6)**, 2063-2073, 2011.

[4] F. Magalhães, A. Cunha, Explaining operational modal analysis with data from an arch bridge. *Mechanical Systems and Signal Processing*, **25(5)**, 1431-1450, 2010.

[5] J.E. Mottershead, M.I. Friswell, Modal updating in structural dynamics: a survey. *Journal of Sound and Vibration*, **167(2)**, 347-375, 1993.

[6] M.I. Friswell, J.E. Mottershead, *Finite Element Model Updating in Structural Dynamics*, Kluwer Academic Publishers, Dordrecht, 1995.

[7] O.S. Salawu, Detection of structural damage through changes in frequency: a review. *Engineering Structures*, **19(9)**, 718-723, 1997.

[8] G. de Roeck, B. Peeters, J. Maeck, Dynamic monitoring of civil engineering structures. *Proceedings of the 4th International Colloquium on Computation of Shells and Spatial Structures (IASS-IACM 2000)*, Chania, Crete, Greece, 4-7 June, 824-848, 2000.

[9] F. Magalhães, A. Cunha, E. Caetano, Vibration based structural health monitoring of an arch bridge: from automated OMA to damage detection. *Mechanical Systems and Signal Processing*, **28(4)**, 212-228, 2012.

[10] F. Magalhães, A. Cunha, E. Caetano, Dynamic monitoring of a long span arch bridge. *Engineering Structures*, **30(11)**, 3034-3044, 2008.

[11] D. Ribeiro, R. Calçada, R. Delgado, M. Brehm, V. Zabel, Finite element model updating of a bowstring-arch railway bridge based on experimental modal parameters. *Engineering Structures*, **40**, 413-435, 2012.

[12] H. Schlune, M. Plos, K. Gylltoft, Improved bridge evaluation through finite element model updating using static and dynamic measurements. *Engineering Structures*, **31(7)**, 1477-1485, 2009.

[13] B.A. Zárate, J.M. Caicedo, Finite element model updating: Multiple alternatives. *Engineering Structures*, **30(12)**, 3724-3730, 2008.

[14] Z.H. Zong, B. Jaishi, J.P. Ge, W.X. Ren, Dynamic analysis of a half-through concrete-filled steel tubular arch bridge, *Engineering Structures*, **27(1)**, 3-15, 2004.

[15] R. Ferrari, F. Pioldi, E. Rizzi, C. Gentile, E. Chatzi, R. Klis, E. Serantoni, A. Wieser, Heterogeneous sensor fusion for reducing uncertainty in Structural Health Monitoring, *1st ECCOMAS Thematic Conference on International Conference on Uncertainty Quantification in Computational Sciences and (UNCECOMP 2015)*, Crete Island, Greece, May 25-27, 2015.

[16] D. Froio, R. Zanchi, *Finite element modelization and modal dynamic analyses of an historical reinforced concrete bridge with parabolic arches*, M.Sc. Thesis in Building Engineering, Advisor E. Rizzi, Co-Advisor R. Ferrari, Università di Bergamo, Scuola di Ingegneria, 228 pages, 2014.

[17] L. Santarella, E. Miozzi, *Ponti Italiani in Cemento Armato*, Hoepli, Milano, 1948.

[18] R. Brincker, L. Zhang, P. Andersen, Modal identification of output-only systems using frequency domain decomposition. *Smart Materials and Structures*, **10(3)**, 441-445, 2001.

[19] B. Peeters, G. De Roeck, Reference-based stochastic subspace identification for output-only modal analysis. *Mechanical Systems and Signal Processing,* **13(6)**, 855-78, 1999.

[20] D. Zonta, C. Modena, Observations on the appearance of dispersive phenomena in damaged structures. *Journal of Sound and Vibration,* **241(5)**, 925-933, 2001.

[21] SVS, *ARTeMIS Extractor 2011*, http://www.svibs.com/, 2012.

[22] F. Ubertini, C. Gentile, A.L. Materazzi, Dispersive phenomena in bridges by time-frequency analysis. *Proceedings of the 5th International Operational Modal Analysis Conference (IOMAC 2013)*, Guimaraes, Portugal, 2013.

[23] Hibbit, Karlsson and Soresen, Inc, A.A.V.V., *Abaqus, Theory Manual*, Version 6.7-1, 2004.

[24] R.J. Allemang, The modal assurance criterion - twenty years of use and abuse. *Journal of Sound and Vibration*, **37(8)**, 14-21, 2003.

[25] F. Arizzi, E. Rizzi, Elastoplastic parameter identification by simulation of static and dynamic indentation tests. *Modelling and Simulation in Materials Science and Engineering*, **22(3)**, 1-22, 2014.

[26] The MathWorks Inc. *User's Guide and Optimization Toolbox*, Release 7.5, Matlab. 2007.

COMPDYN 2015
5th ECCOMAS Thematic Conference on
Computational Methods in Structural Dynamics and Earthquake Engineering
M. Papadrakakis, V. Papadopoulos, V. Plevris (eds.)
Crete Island, Greece, 25–27May 2015

EVALUATION OF THE DYNAMIC RESPONSE FOR A HISTORIC BYZANTINE CROSSED-DOME CHURCH THROUGH BLOCK-JOINT AND KINEMATIC ANALYSIS

Constantine C. Spyrakos[1], Francesco Pugi[2], Charilaos A. Maniatakis[1], and Alessio Francioso[1]

[1]Laboratory for Earthquake Engineering, National Technical University of Athens
HeroonPolytechniou 9, 15780 Zografou, Athens, Greece
{cspyrakos@central.ntua.gr; chamaniatakis@gmail.com; alessiofrancioso@gmail.com}

[2]Aedes Software
56028 San Miniato Basso, Pisa, Italy
info@aedes.it

Keywords: Historic Masonry Structures, Crossed-dome Byzantine Church, Seismic Response, Pushover Analysis, Kinematic Analysis.

Abstract. *The protection of historic masonry structures against earthquakes constitutes a rather complex problem. The calculation of their anticipated response involves significant difficulties, such as the selection of the proper simulation in conjunction with the measurement of the materials mechanical properties. In the present research the central church (Catholicon or Katholikó) of the Monastery of Kaisariani located on a hillside at the foot of Mount Hymettus on the east of Athens, Greece, is selected as a case study of a historic structure to study its seismic response. The Catholicon is a Byzantine crossed-dome church constructed during the 11th/12th centuries. Full survey and detailed in-situ and laboratory tests were carried out by the multidisciplinary team of an on-going research program in order to document its geometry, the construction details and the mechanical properties of the constituent materials. The current condition of the structure and its seismic behavior were assessed by means of a block-joint and kinematic analysis. Specifically, the stability of selected macroelements was evaluated through (a) pushover analysis applied to block-joint models of arches and vaults and (b) kinematic analysis of rigid bodies.*

The investigation was performed within the research project "Seismic Protection of Monuments and Historic Structures - SEISMO" which is co-financed by the Greek Ministry of Education and Religions and the European Union under the action "Thales" within the context of the Operational Programme - Education and Lifelong Learning, NSRF 2007-2013.

1 INTRODUCTION

The protection of monuments under seismic excitations is an issue of critical importance for countries that present significant seismic activity [1, 2]. In the Mediterranean basin, a region of intense seismic activity, there is a significant number of monuments of world cultural heritage representative of a wide range of historical periods: Minoan, Mycenaean, Archaic and Classical, Hellenistic, Roman, Medieval, Byzantine, Ottoman and modern. Between those countries that combine rich cultural heritage and considerable seismicity, Greece presents the most significant seismic activity in Europe while ranks among the most seismically active regions on global scale [3]. The same time Greece is a country well celebrated for its cultural heritage with monuments belonging to the classical era like the Acropolis in Athens (5^{th} century BC) and monuments of the byzantine era like the Monasteries of Daphni, Hosios Loukas and Nea Moni of Chios (11^{th} – 12^{th} centuries AC) all inscribed in the World Heritage List of UNESCO [4]. Seismic activity is also important for other countries located within the Mediterranean basin well known for their cultural heritage such as Italy, the Balkan counties, Cyprus, Turkey and the north coast of Africa [5].

The need for the reservation of monuments led to the adoption of “The Athens Charter” for the Restoration of Historic Monuments in 1931 [6] and later with the contribution of international organization like UNESCO, ICOMOS and the European Council “The Charter of Venice” was adopted in 1964 for the Conservation and Restoration of Monuments and Sites [7]. Nowadays, the use of contemporary computational tools, the application of instrumentation and non-destructive evaluation and the use of new materials, allow for a more thorough confrontation of the reservation problem. However, seismic activity still represents an important parameter of vulnerability for monuments and historic structures. For that reason significant efforts have been made towards the establishment of provisions for the seismic strengthening of monuments [8-10].

The ongoing research project entitled “Seismic Protection of Monuments and Historic Structures - SEISMO” which is conducted under the coordination of the Laboratory for Earthquake Engineering of the National Technical University of Athens, LEE-NTUA [11], aims at the development of an integrated, interdisciplinary and innovative methodology for the evaluation of the seismic behavior of monuments and historic structures.

Two monuments of major historical and architectural significance were selected as case studies in the context of the SEISMO Project both located in Athens, Greece: a) the temple of Hephaestus or "Hephaisteion" (449-444 BC) dedicated to Hephaestus and Athena, in the Ancient Agora and b) the Catholicon of the Kaisariani Monastery (11^{th}-12^{th} century AC) dedicated to the Presentation of the Virgin, at the foot of Mount Hymettus. This work focuses on the second monument, the central church of the Kaisariani Monastery constructed during the byzantine period and presents only a part of the analyses carried out in order to study its seismic behavior.

The vulnerability of church-type structures under earthquake loadings was confirmed during major recent earthquake events, i.e., the M=7.1 Christchurch 2011 earthquake in New Zealand [12] and the two earthquakes with magnitudes of M=6.0 and M=6.1 Cephalonia, Greece 2014, earthquakes that provoked extensive damages to churches made of unreinforced masonry [13]. The topic has been extensively studied in the literature, e.g. [14-18].

2 THE CATHOLICON OF KAISARIANI MONASTERY

2.1 History, Architectural Perspectives and Structural Characteristics

Several different names were used in the literature for the Monastery during its long life including “Kaisariani”, a name of unconfirmed origin, “Kyriani”, “Sancta Siriani” during the period of Frankish rule, and the Monastery of “Koç basi” (“Ram’s Head”) during the Ottoman period. The first Christian center had been founded southwest of the Monastery on the hill of the Cemetery of the Fathers where ruins of a 10th century Byzantine church built on the foundations of a 5th-6th c. three-aisled basilica are preserved. The Monastery was moved to its present location during the late 11th century [19].

The central church, Catholicon, of the Kaisariani Monastery is considered to be one of the finest byzantine monuments of Attica. It is dating back to the end of the 11th– beginning of the 12th century and has been preserved from the Byzantine era. It is constructed according to the cross-in-square or crossed-dome architectural type and is dedicated to the Presentation of the Virgin [19, 20], probably firstly introduced in Constantinople in the 9th century during the reign of Vasileios A (867-886 AD) and spread quickly all over the Byzantine Empire. It is considered to be the most representative byzantine architectural type. The main feature of this rhythm is the formation of a cross inside and outside the nave, which is almost square, with one or five domes [21-23].

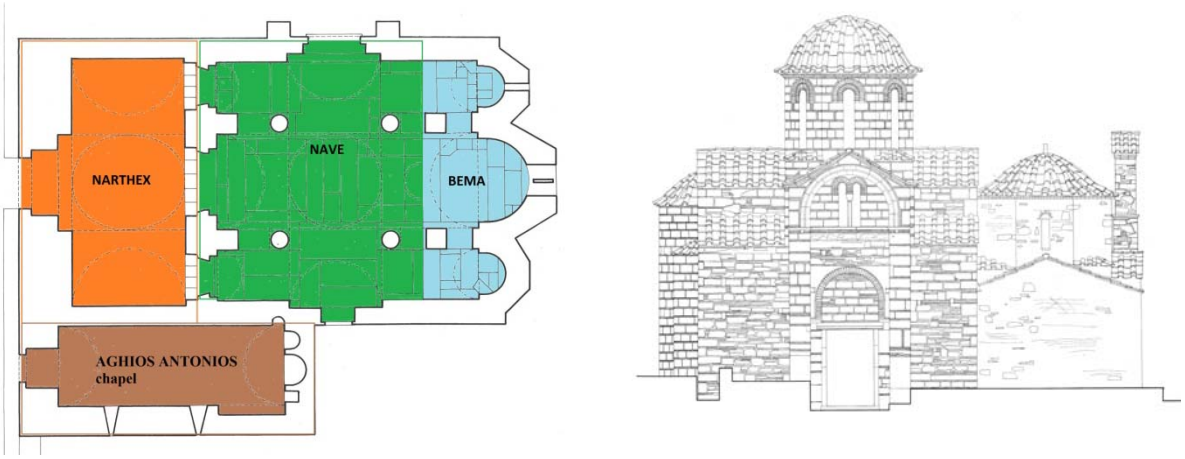
In a typical cross-in-square church the nave is divided into nine bays by four columns (or piers). The central bay is roofed by a central dome which is supported on the four columns. The inner five divisions form the shape of a cross. Barrel vaults usually cover the four rectangular bays that directly adjoin the central bay while groin-vaults usually cover the four remaining bays in the corners. The spatial hierarchy of the three types of bay, from the largest central bay to the smallest corner bays, is mirrored in the elevation of the building with the domed central bay being the taller [21-23].

The so-called “Athenian dome” is constructed in the Catholicon that may be found in many other Byzantine churches of Athens and Greece. This type of dome consists of eight sides with its corners decorated by small upright marble columns; a semi-circular eave forms at the top of each hexagon. As a rule, there is one simple window on each side of the octagon.

In the case of the Kaisariani Catholicon the octagonal dome has a straight horizontal dentil cornice on its roof, as an exception to the usual corrugated cornice of the "Athenian type" domes. Also the four central pillars that support the dome are made of marble while in this architectural rhythm it was also common the construction of brick piers [19, 23].

At the western wall of the nave usually a narthex is placed that is practically an entrance hall. A narthex and a single-room, vaulted chapel of Aghios Antonios were added to the western and southern side of Catholicon, respectively, in the 16th or 17th century as depicted in Figure 1. The narthex is consisted by three bays with the central one crowned by a lower dome [19].

To the eastern part of the nave stands the bema, or sanctuary, separated from nave by a templon made also by marble. Three additional bays form the sanctuary adjoining the easternmost bays of the nave, each of which terminates in an apse crowned by a conch (half-dome). The central apse is larger than those to the north and south. The plan view of the nave is nearly quadrangle with length and width approximately equal to 8.5 meters. The height up to the base of the dome is 7.4 m and the internal height of the dome is approximately 4.2 m.



(a) (b)

Figure 1: Catholicon of Kaisariani monastery in Athens: (a) Plan view; (b) North façade [24].

The masonry construction is mixed including rubble masonry and carved stones. The external walls of the Catholicon are constructed in the cloisonné system that is made by shelly limestone surrounded in many places by bricks.

The north side placed at the initial entrance of the monastery was sculpturally rendered carrying arches of well-hewn limestone, as shown in Figure 1b, while the south side presents parts of rubble masonry. The Catholicon is partly covered by frescoes dating back to the early 18th century while the oldest one is a mural of the Theotokos Praying of the 14th century located on a wall initially exterior and today incorporated into the Aghios Antonios chapel. Of particular interest are also the brick decorative frames of the arched openings.

In 1921, the Kaisariani Monastery was declared an archaeological monument and came under the jurisdiction of the State Archaeological Service [19].

2.2 Research Outline

As already mentioned the Catholicon of the Kaisariani Monastery was selected as a representative monument of the byzantine period to be studied in the context of the SEISMO Research Project.

A thorough methodology is currently in progress in order to assess the current condition of the monument and evaluate its vulnerability under seismic loading. The implementation of the proposed methodology includes: (a) documentation of the existing state through surveys and architectural studies; (b) recording of the pathology of the structure; (c) identification of the construction materials with non-destructive and laboratory testing; (d) assessment of the seismic hazard based on regional seismicity and soil conditions; (e) proposal for a monitoring scheme; (f) development of mathematical models in order to analytically assess its seismic response.

Given the importance and complexity of monuments and historic structures in terms of design, construction techniques and materials, advanced computational tools and methods are utilized to meet the needs of the proposed research. Several types of analysis, failure criteria and innovative applications, such as base isolation will be utilized to study the dynamic behavior. Moreover, the methodologies established for the study of the monument, will be assessed in terms of their reliability, accuracy and effectiveness by comparing analysis results with experimental data. In the following the dynamic behavior of the Catholicon is studied applying local analysis with macroelements [17, 18, 25, 26]. Macroelements are local parts of the structure that may deform almost independently from the whole bearing body. These parts

may be determined with acceptable reliability based on a survey of the damaged structure [18, 27]. The macroelement approach is followed herein by a kinematic limit analysis with different collapse mechanisms and a non-linear static analysis with a "blocks and joints" finite element model that includes arches and pillars of the central nave [17, 18, 25, 26].

3 LOCAL ANALYSIS

The importance of studying the dynamic behavior of the Catholicon of Kaisariani Monastery is justified by the fact that it regards a monument of well known historic and aesthetic value. Furthermore, this significance is enforced by the fact that its structural type is typical for a series of byzantine monuments constructed according to the cross-in-square rhythm located in seismically active regions. Thus, the results may be applicable to other cases given that the basic assumptions made for the analysis conducted herein are met.

The inspection of the damages suffered by the churches after major earthquakes revealed that the seismic behavior of this kind of structures can be assessed by local analysis of several architectonic portions whose seismic response is actually independent from the church as a whole. Such portions referred to as macroelements, can be identified for example as the façade, the apse, the bell tower or the triumphal arch. The selection of the significant macroelements should take into account the architecture of the church, the knowledge of its constituent materials and construction details, the presence of any earthquake-resistant presidium and the visual inspection of existing cracks and damages.

The local analysis of each macroelement consists in the definition of its collapse mechanism and the relevant collapse multiplier by means of kinematic analysis and/or pushover analysis.

Through kinematic analysis the collapse multiplier α_0 may be calculated using the principle of virtual work given in the following form [8, 9]:

$$\alpha_o \left(\sum_{i=1}^{n} P_i \cdot \delta_{x,i} + \sum_{j=n+1}^{n+m} P_j \cdot \delta_{x,j} \right) - \sum_{i=1}^{n} P_i \cdot \delta_{y,i} + \sum_{h=1}^{o} F_h \cdot \delta_h = L_{fi} \tag{1}$$

where: n is the number of the weights applied to the different blocks of the kinematic system; m is the number of the weights non-directly applied to the blocks, which because of the seismic action transfer a horizontal force to the blocks; o is the number of the non-related to masses external forces applied to the blocks; P_i is the generic weight applied to the block (self-weight applied to the centroid or any other carried weight); P_j is the generic weight (non-directly applied to the blocks) which, because of the seismic action, transfers horizontal forces to the blocks; $\delta_{x,i}$ is the virtual horizontal displacement of the weight application point; $\delta_{y,i}$ is the virtual vertical displacement of the weight application point; F_h is the absolute value of generic external force applied to the blocks; δ_h is the virtual displacement of the force application point in its direction and L_{fi} is the work of internal forces. In eq (1) the x direction is the direction of the collapse of each mechanism that is normal to the direction of the axes of rotation in case of overturning.

Through pushover analysis the collapse multiplier α_0 is pursued as the maximum static multiplier instead of the minimum kinematic multiplier and it is calculated with the following formula:

$$a_0 = \frac{F_{\max}}{W} \tag{2}$$

where: F_{max} is the maximum lateral force that the structure can sustain; W is the total weight of the structure.

Once the collapse multiplier is calculated, according to the Italian Structural Standards [8, 9] the verification in terms of Ultimate Limit State can be applied with the following procedure. The spectral acceleration a_0^* that causes the collapse mechanism is given by:

$$\alpha_0^* = \frac{\alpha_o \cdot g}{e^* \cdot FC} \tag{3}$$

where: e^* is the participating mass ratio (it can be taken equal to 1) and FC is the confidence factor (taken equal to 1.35 for kinematic analysis).

The macroelement response fulfils the Ultimate Limit State when

$$a_0^* \geq Max\left(\alpha_{Rig}^*, \alpha_{Def}^*\right) \tag{4}$$

where: α_{Rig}^* and α_{Def}^* are the accelerations that the structure should sustain. Assuming that the structure is either rigid or deformable the α_{Rig}^* and α_{Def}^* are given by the following expressions:

$$\alpha_{Rig}^* = \frac{a_g \cdot S}{q} \qquad \alpha_{Def}^* = \frac{S_e\left(T_1\right) \cdot \Psi\left(Z\right) \cdot \gamma}{q} \tag{5}$$

where: $a_g = \gamma_I \cdot a_{gR}$ is the ground acceleration, S is the soil factor, q is the behavior factor, $S_e(T_1)$ is the elastic spectrum calculated for the first period of vibration of the structure T_1 in the considered direction, $\Psi(Z)$ is the first mode of vibration in the considered direction normalized in order to be equal to 1 at the top of the structure, Z is the height of the rotation axis with respect to the building foundations and γ is the correspondent modal participation coefficient.

The following Figures 3-5 show the macroelements for which a kinematic analysis was performed with the aid of [25]. The values of the collapse multipliers are given in Table 1. The specific weight of the masonry rigid bodies was taken equal to 18 kN/m^3.

The transversal behavior of the church was assessed through pushover analysis applied to the "block-joint" model [26] of the three arches and relevant pillars shown in Figure 6.

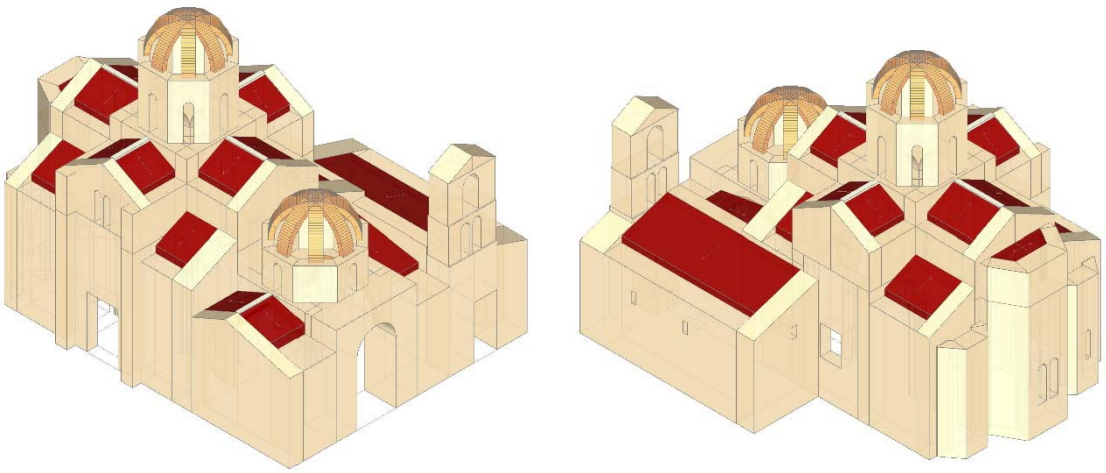
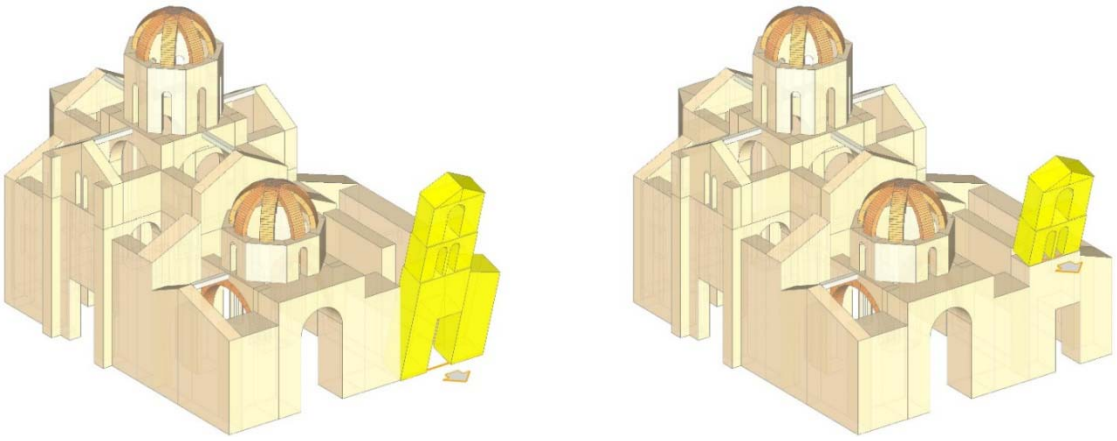
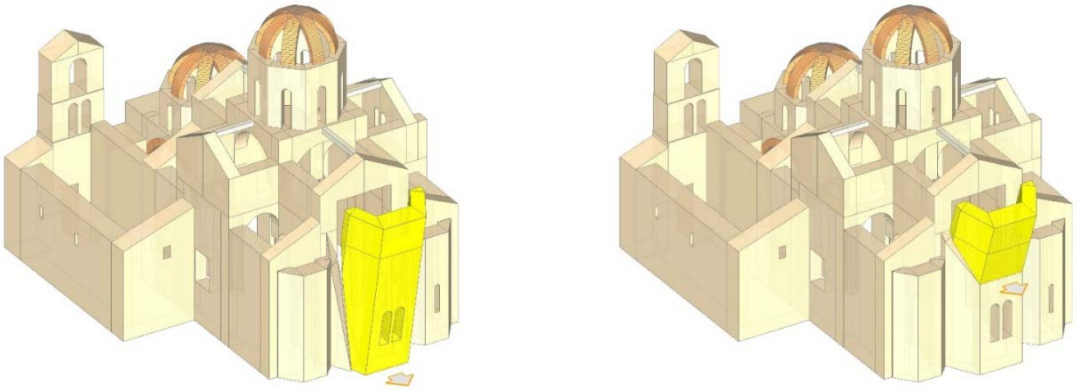


Figure 2: 3D model of the church.



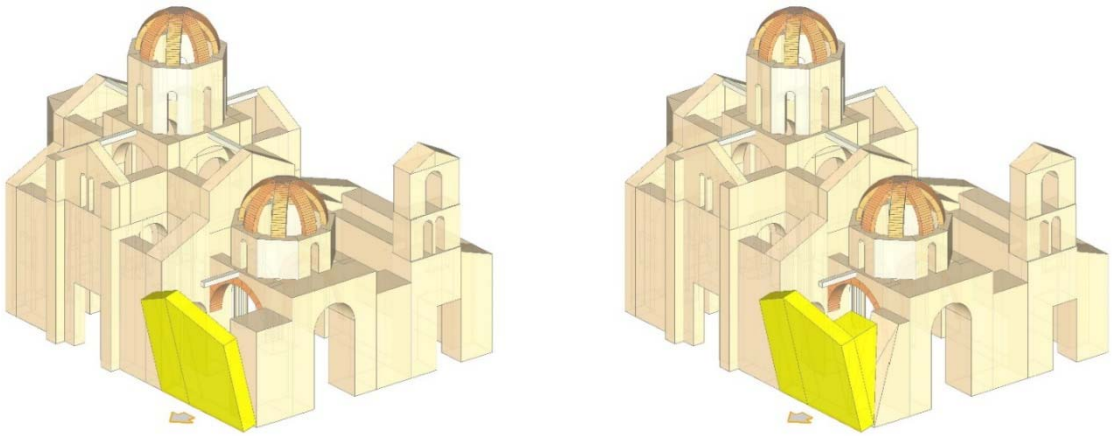
(a) (b)

Figure 3: a) M01 - Overturning of the belfry façade; b) M02 - Overturning of the belfry.



(a) (b)

Figure 4: a) M03 - Overturning of the central apse; b) M04 - Partial overturning of the central apse

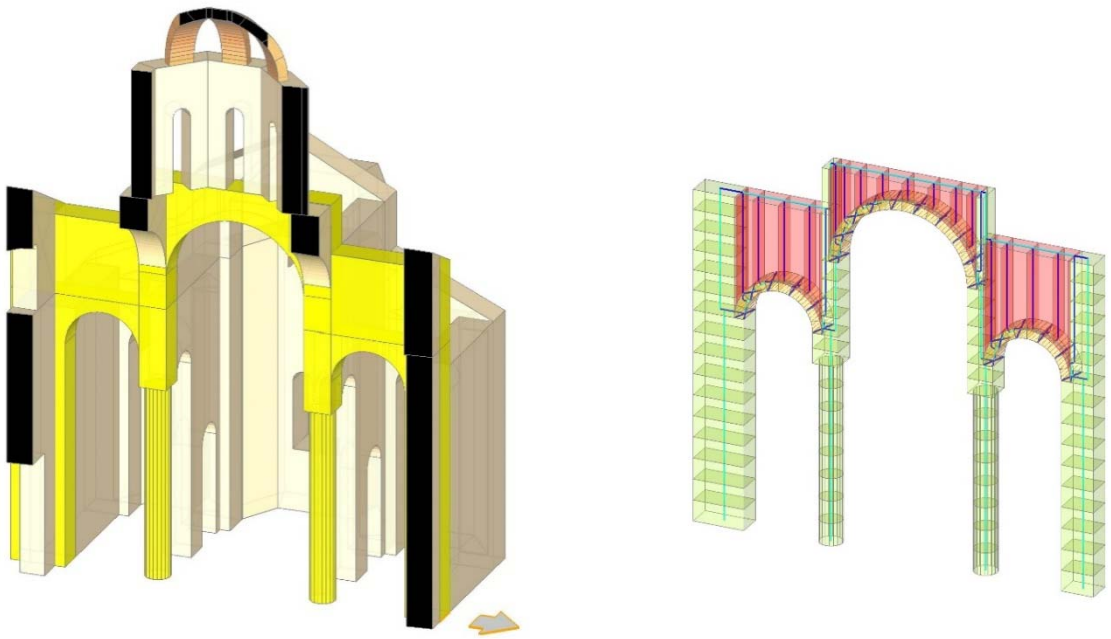


(a) (b)

Figure 5: a) M05 - Overturning of a north wall; b) M06 – Overturning of a north wall wide one side wing.

Macroelement	Collapse multiplier
M01 - Overturning of the belfry façade	0.128
M02 - Overturning of the belfry	0.234
M03 - Overturning of the central apse	0.111
M04 - Partial overturning of the central apse	0.307
M05 - Overturning of a north wall	0.120
M06 – Overturning of a north wall wide one side wing	0.173

Table 1: Collapse multiplier for the different mechanisms considered.



(a) (b)

Figure 6: a) Transversal behavior of the church; b) Block-joint model of the macroelement.

The mechanical properties of the constituent materials are shown in Table 2.

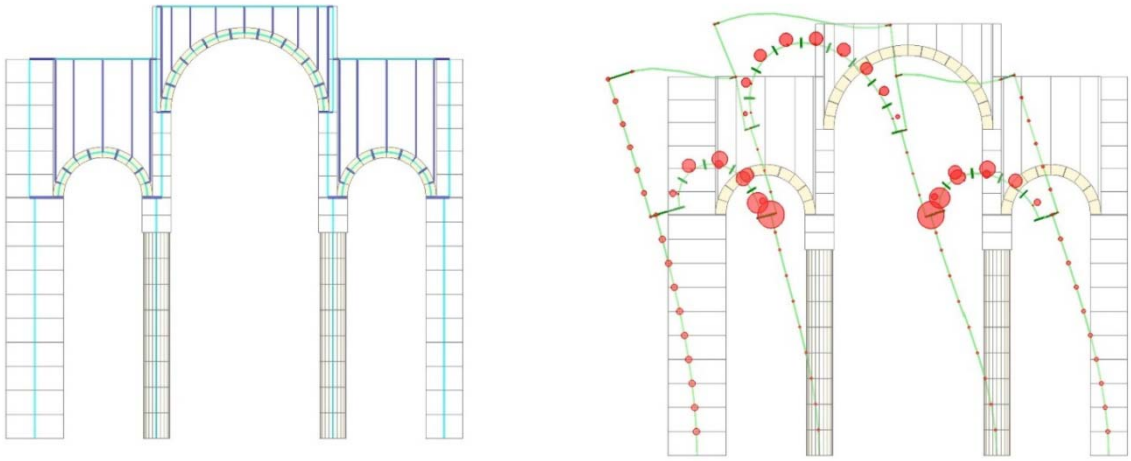
Masonry	Specific weight	18	kN/m^3
	Elastic modulus	1300	N/mm^2
	Shear modulus	500	N/mm^2
Blocks	Specific weight	20	kN/m^3
	Elastic modulus	1800	N/mm^2
	Shear modulus	720	N/mm^2
Joints	Elastic modulus	500	N/mm^2
	Shear modulus	200	N/mm^2
	Tensile strength	0.30	N/mm^2

Table 2: Mechanical properties of the materials.

The characteristics of the masonry constituting the walls and the pillars were based on the literature [28], while the mechanical properties of blocks and joints were chosen as the ones that led to a balance configuration at the beginning of the pushover analysis. A more accurate evaluation of the structural behaviour of this macroelement will be feasible when the actual values of the material properties will be available from the SEISMO Project.

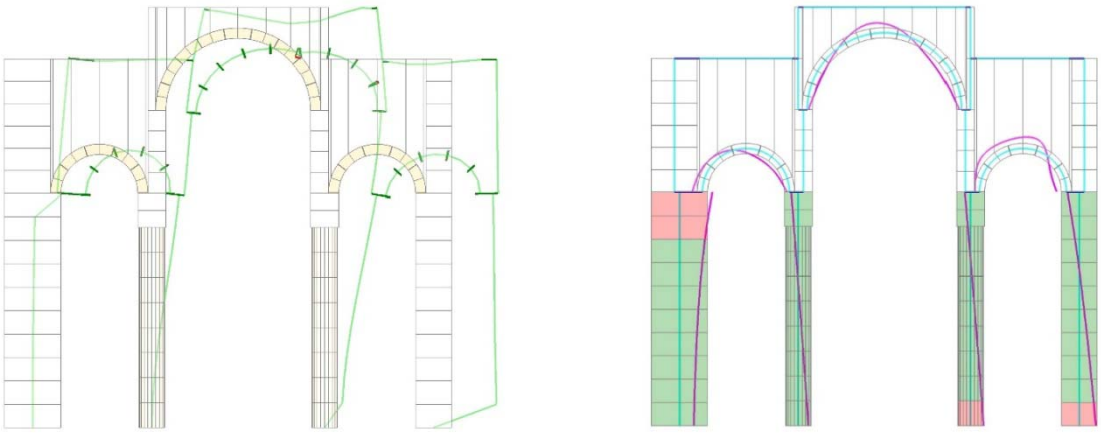
Figure 7 shows a front view of the block-joint model and the modal shape of the first mode of vibration. Moreover, the red spheres symbolize the mass applied at each node and highlight how the loads were distributed in the model.

The pushover analysis was performed in the direction shown in Figure 6, considering a lateral force distribution proportional to the nodal masses and a base shear increment equal to 1 kN. Figure 8a shows the displacements registered at the last step of the analysis when the base shear is equal to 32 kN, while Figure 8b shows the position of the thrust-line for arches and pillars as well as the state of the verification applied to the pillars. The red drums are the ones where the thrust-line has come out of the cross section and therefore feature a plastic hinge.



(a) (b)

Figure 7: a) Block-joint model. b) First mode modal shape.



(a) (b)

Figure 8: Pushover analysis, last step: a) displacements; b) Thrust-lines and verifications.

Blocks Elastic Modulus	Collapse multiplier
1200 N/mm^2	0.069
1500 N/mm^2	0.066
1800 N/mm^2	0.071
2100 N/mm^2	0.038

Table 3: Relation between blocks elastic modulus and collapse multiplier.

The value of the collapse multiplier was proved to be quite sensitive to the value of the modulus of elasticity of the arch blocks. Table 3 shows the relation between these two values.

4 CONCLUSIONS

This work presents preliminary analytical results of the central church (Catholicon) of the Kaisariani Monastery in Athens. The church is constructed during the 11th and 12th centuries according to the crossed-dome architectural rhythm and is considered to be one of the finest byzantine monuments of Greece. This monument was selected as a case-study of a historic structure located in an earthquake active region to be studied in the context of the ongoing research program entitled “Seismic Protection of Monuments and Historic Structures - SEISMO”.

The preliminary analysis includes the study of selected macroelements, i.e., parts of the structure that are susceptible to behave independently from the whole structure. Six different macroelements were considered to perform kinematic limit analyses: M01 - Overturning of the belfry façade; M02 - Overturning of the belfry; M03 - Overturning of the central apse; M04 - Partial overturning of the central apse; M05 - Overturning of a north wall; M06 – Overturning of a north wall wide one side wing. Also, pushover analysis was conducted to assess the transversal behavior of the church by means of a macroelement that isolates three arches and the supporting pillars of the central nave with the “block-joint” approach.

In summary the results show that the collapse mechanism that is more hazardous for the overall stability of the monument is the mechanism M03 that presents the smaller collapse multiplier and suggests out-of-plane overturning of the central apse. The second most likely to occur mechanism is the mechanism M05 that suggests overturning of a wall in the north facade of the outer narthex. The collapse multiplier for the block-joint model is even smaller and presents considerable sensitivity in the assumptions made regarding the material properties.

The assessment of the current condition of the monument is made by the application of detailed surveying, in-situ and laboratory testing which are currently in progress and will allow for a more thorough assessment of seismic behavior of the monument in the near future.

ACKNOWLEDGEMENTS

The financial support of the research project “Seismic Protection of Monuments and Historic Structures - SEISMO” which is co-financed by the Greek Ministry of Education and Religions and the European Union under the action “Thales” within the context of the Operational Programme - Education and Lifelong Learning, NSRF 2007-2013 is gratefully acknowledged. Also the assistance of the technical and administrative personnel of the Archaeological Service of Athens is acknowledged.

REFERENCES

[1] T.P. Tassios, Seismic Engineering of Monuments. M. Garevski, A. Ansal. Editors, *Earthquake engineering in Europe*, Springer Netherlands, 1-42, 2010.

[2] C.C. Spyrakos, Seismic Risk of Historic Structures and Monuments: A need for a unified policy. *In proceedings of COMPDYN 2015, 5th ECCOMAS Thematic Conference on Computational Methods in Structural Dynamics and Earthquake Engineering,* Crete, 2015.

[3] T.M. Tsapanos, P.W. Burton, Seismic hazard evaluation for specific seismic regions of the world. *Tectonophysics*, **194**, 153–169, 1991.

[4] UNESCO. Greece: Properties inscribed on the World Heritage List. (http://whc.unesco.org/en/statesparties/gr) retrieved 2015-03-15.

[5] A. Udías, Seismicity of the Mediterranean Basin. In: Geological Evolution of the Mediterranean Basin, Raimondo Selli Commemorative Volume, D. J. Stanley, F.-C. Wezel Editors, 55-63, 1985.

[6] *The Athens Charter for the Restoration of Historic Monuments*. First International Congress of Architects and Technicians of Historic Monuments, Athens, 1931.

[7] International Council on Monuments and Sites – ICOMOS. *International Charter for the Conservation and Restoration of Monuments and Sites* (The Venice Charter 1964). Second International Congress of Architects and Technicians of Historic Monuments, Venice, 1964.

[8] Ministero delle Infrastrutture e dei Trasporti, *Circolare. n. 617 del 02 febbraio 2009. Istruzioni per l'applicazione delle Nuove Norme Tecniche per le costruzioni, §C8A.4*, Gazzetta Ufficiale della Repubblica Italiana n. 47 del 26 febbraio 2009, Supplemento ordinario n.27. (in Italian)

[9] Decreto del Presidente del Consiglio dei Ministri (D.P.C.M.). Linee guida per la valutazione e la riduzione del rischio sismico del patrimonio culturale con riferimento alle Norme tecniche per le costruzioni di cui al D.M. 14/01/2008, 2011. (in Italian)

[10] Earthquake Planning Protection Organization (EPPO) and European Centre on Prevention and Forecasting of Earthquakes (ECPFE). Draft framework regulatory document for structural interventions to and seismic protection of monuments, 2011.

[11] Laboratory for Earthquake Engineering, Structural Engineering Department, School of Civil Engineering, National Technical University of Athens. (http://lee.civil.ntua.gr/index_en.html)

[12] D. Dizhur, J. Ingham, L. Moon, M. Griffith, A. Schultz, I. Senaldi, G. Magenes, J. Dickie, S. Lissel, J. Centeno, C. Ventura, J. Leite, P. Lourenco, Performance of masonry buildings and churches in the 22 February 2011 Christchurch earthquake. *Bulletin of the New Zealand Society for Earthquake Engineering*, **44**(4), 279-296, 2011.

[13] GEER-EERI-ATC. (2014). Earthquake Reconnaissance January 26th/ February 2nd 2014 Cephalonia, Greece events. GEER Association Report No. GEER-034 in collaboration with EERI and ATC, Version 1: June 6, 2014.

[14] E. Mele, A. De Luca, A. Giordano, Modeling and analysis of a basilica under earthquake loading. *Journal of Cultural Heritage*, **4**, 355–367, 2003.

[15] I.N. Psycharis, H.P. Mouzakis, A. Miltiadou, E.P. Pavlopoulou, I.M. Taflampas, Investigation of the seismic response of a Byzantine church and evaluation of the effectiveness of proposed interventions. *Earthquake Spectra*, **26**(2), 473-497, 2010.

[16] C.C. Spyrakos, P.D. Kiriakopoulos, E. Smyrou, Seismic Strengthening of the Historic Church of Sts Helen and Constantine in Piraeus. In Proceedings of the 3rd International Conference on Computational Methods in Structural Dynamics and Earthquake Engineering COMPDYN 2011. Corfu, Greece; ECCOMAS, 2011.

[17] C.C. Spyrakos, A. Francioso, P.D. Kiriakopoulos, S. Papoutsellis, Seismic evaluation of the historic church of St. Nicholas in Piraeus before and after interventions. M. Papadrakakis, V. Papadopoulos, V. Plevris eds. *COMPDYN 2013, 4th ECCOMAS Thematic Conference on Computational Methods in Structural Dynamics and Earthquake Engineering*, Kos Island, Greece, 12–14 (pp. 3015-3029), June 2013.

[18] C.C. Spyrakos, C.A. Maniatakis, P. Kiriakopoulos, A. Francioso, I.M. Taflampas, Performance of a post-Byzantine Triple-domed Basilica under Near and Far Fault Seismic Loads: Analysis and Intervention. In *Seismic Assessment and Rehabilitation of Historic Structures*, P.G. Asteris, V. Plevris Editors, 2015.

[19] A. Pantelidou-Alexiadou, *Kaisariani Monastery*, Archaeological Receipts Fund, Ministry of Tourism and Culture, 2011.

[20] N. Gkioles, *Byzantine Church Architecture* (600-1204 AD), Kardamitsa Editions, 1987. (in Greek)

[21] C. Mango, *Byzantine Architecture* (History of World Architecture), Electa / Rizzoli Publisher, 1985.

[22] R. Krautheimer, *Early Christian and Byzantine Architecture*, The Yale University Press, 1984.

[23] C. Bouras, *History of Architecture*, Melissa Editions, 1994. (in Greek)

[24] A. Barzoukas, *Monastère de Kaisariani, Le Catholicon*. Drawings from the Collection and Archive of Architectural Research, Institute of Architectural Morphology, National Technical University of Athens, 1957.

[25] Aedes Software. PCM: Progettazione di costruzioni in muratura, www.aedes.it

[26] F. Pugi, Seismic analysis of masonry arch structures through the finite element model "block-joint". M. Papadrakakis, V. Papadopoulos, V. Plevris eds. *COMPDYN 2013, 4th ECCOMAS Thematic Conference on Computational Methods in Structural Dynamics and Earthquake Engineering*, Kos Island, Greece, 12–14 (pp. 2997-3014), June 2013.

[27] D. D'Ayala, E. Speranza, Definition of collapse mechanisms and seismic vulnerability of historic masonry buildings. *Earthquake Spectra*, **19**(3), 479–509, 2003.

[28] K. Syrmakezis, O. Mavrouli, P. Papaevaggeliou, E. Aggelakopoulou, A. Bakolas, A. Moropoulou, Finite element analysis and fragility curves for the evaluation of restoration mortars behavior regarding the earthquake protection of historic structures. *Soil Dynamics and Earthquake Engineering*, **54**, 61-65, 2013.

COMPDYN 2015
5th ECCOMAS Thematic Conference on
Computational Methods in Structural Dynamics and Earthquake Engineering
M. Papadrakakis, V. Papadopoulos, V. Plevris (eds.)
Crete Island, Greece, 25–27 May 2015

NUMERICAL INVESTIGATION OF THE SEISMIC RESPONSE OF HEPHAESTUS TEMPLE IN ATHENS, GREECE

Maria-Eleni Dasiou[1], **Ioannis N. Psycharis**[2]

[1] Ph.D. Student
School of Civil Engineering, National Technical University of Athens
9, Heroon Polytechneiou Str., Zografos, 15780, Greece
email: medasiou@yahoo.com

[2] Professor
[2]School of Civil Engineering, National Technical University of Athens
9, Heroon Polytechneiou Str., Zografos, 15780, Greece
email: ipsych@central.ntua.gr

Keywords: Temple of Hephasteus; discrete element method; earthquake response

Abstract. *In this paper, the seismic response of the Temple of Hephasteus in Athens, Greece is investigated numerically. The temple of Hephaestus was probably erected between 460 and 420 BC by a yet unknown architect on top of Agoraios Kolonos hill, which is delimiting the Ancient Agora of Athens to the west. It is one of the best preserved ancient temples, partly because it was transformed into a Christian church. The analyses were performed using the general purpose code 3DEC, which is based on the distinct element method, and can capture well the dynamics of multi-block systems, which respond to strong earthquakes with intense rocking and sliding of the individual blocks. The ground motions that were used as base excitations were selected to be compatible with the seismotectonic environment of the ancient center of Athens and within the range of the maximum expected earthquakes. In the numerical model, the full monument was implemented, but an investigation of the accuracy obtained with sub-models concerning small parts of the temple was also performed. The structural members were simulated quite accurately, but the columns and the walls were modeled intact, without the imperfections and the damage observed in the current state of the monument. However, the computer codes that were used were producing damage to the structure after each earthquake. In this way, it was possible to evaluate the effectiveness of the used software by comparing the predicted damage with the existing one.*

1 INTRODUCTION

1.1 Description of the structure

The Temple of Hephaestus, mostly known as Thision, dedicated to god Hephaestus, protector of blacksmiths and metallurgy, and to goddess Athena Ergane, is one of the most well preserved Doric peripteral temples [Figure 1]. Built between 460 and 420 BC by a yet unknown architect, to whom, however, are attributed other temples of similar structure in the Attica region, the temple is located on top of the Agoraios Kolonos hill, on the west side of the Athenian Agora in the historical center of Athens.

During the raid of the Heruli and later of the Goth the temple was left intact, and it was around 700 CE that the temple was converted to a Christian church, dedicated to Saint George. During that period, some alterations were conducted, including the shifting of the main entrance to the opisthodomos, the removing of the marble floor, the opening of two new entrances at the long side of the walls of the cella, and a cupola that was constructed over the cella. The last divine liturgy in the temple took place in 1833 during the celebrations for the arrival of Otto in Greece. After that, the temple was used as an archaeological museum, until 1930 when excavations were conducted in its interior by the American School for Classical Studies.



Figure 1. East view of Temple Hephaestus.

Figure 2 shows the temple in plan view. The structure, a peripteral temple of Doric order, consists of the Opisthodomos, the Cella, the Pronaos and the external colonnade. It is made of marble that was quarried at the Penteli Mountain from where the marble of the Parthenon also originates. The dimensions of the base are 31.80 m × 13.80 m. The Cella is 22.50 m long and 7.85 m wide. The external colonnade has six columns at the east and the west facades and thirteen columns at the north and the south facades. Each column consists of seven (7) drums of different height. The total height (drums and capital) of the columns is 5.70 m and the diameter at the base is 0.95 m.

Vertically, the temple can be divided in three parts (Figure 2): the crepidoma, the columns and the entablature. The crepidoma provides the surface on which the columns and the walls are placed and is comprised with several layers of squared stone blocks. The capital of the columns is made of a circular torus bulge, the echinus and a square slab called the abacus. The capitals support the entablature, which consists of two parts: the architraves (lowest part) and the frieze. The architraves consist of two beams at each span between adjacent columns.

The origin of the imperfections and damages observed in the current state of the monument differs. Some have been attributed to human intervention, such as the undercutting of the col-

umns (Figure 3a) that took place for the placement of the sarcophagi in the peristyle [1, 2]. Others, such as the opening of the joints between the architrave beams at the corners of the temple (Figure 3b), are probably the result of several earthquake events that have hit Athens.

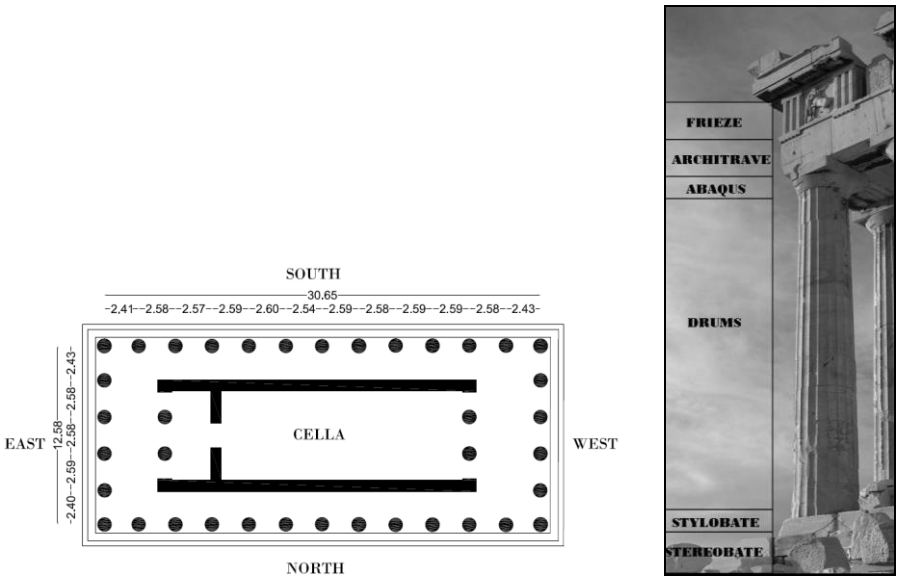


Figure 2. Plan view and elevation of Temple Hephaestus.



Figure 3. (a) Cutoffs of the lower drums of the columns at the north side of the temple; (b) opening of the joints of the architraves at the corners of the temple.

1.2 Numerical Simulation

Due to their spinal construction, the dynamic behaviour of ancient monuments is highly nonlinear and very sensitive to even trivial changes in the geometry or the base motion characteristics. During a seismic event, rocking and/or sliding of blocks (drums in case of columns), individually or in a group, can occur, leading to large displacements and rotations. For the numerical analyses presented in this paper, the code 3DEC by Itasca Consulting Group, Inc. [4] was employed, which is based on the discrete element method. The code was initially designed for the analysis of the behaviour of rock masses, which are modeled as assemblies of discrete rigid bodies and discontinuities are considered as boundary conditions. Large displacements and rotations and even complete detachment of the blocks is permitted, while the

code automatically detects new contacts during the response. For rigid block problems, the code gives an accurate contact formulation, in which the interaction takes place at a number of contact points–. The contact between two blocks is represented by several sub-contacts where various types of contact are considered (apex to apex, apex to edge etc.) and interaction forces are applied. Each contact is assigned a contact area, which is used to calculate the local point stiffness, in terms of the user-defined normal and shear stiffness of the discontinuity surface. In addition a damping coefficient is introduced. The values of the joint stiffness used in the model were 5×10^9 Pa/m in the normal direction and 1×10^9 Pa/m in the tangential direction, based on values that were derived by comparing numerical results with corresponding experimental data obtained from shaking table tests performed at the Laboratory for Earthquake Engineering of the National Technical University of Athens [5-8].

In Figures 4 and 5, the numerical model of the temple of Hephaestus is shown. To simplify the simulation, without influencing the dynamic characteristics of the structure, the architectural details of the architraves and frieze, the flutes of the columns and the curvature of the stylobate were omitted. In addition all the drums of the external colonnade were considered with equal height. The cella was included in the model without taking into account any discontinuities. As in reality, it is connected to the exterior colonnade through beams located above the level of the entablature.

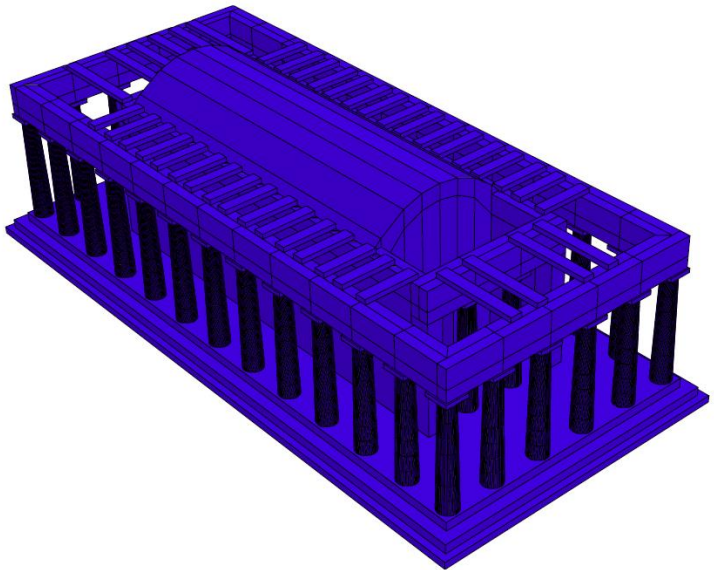


Figure 4. 3d view of the numerical model used in the analyses with 3DEC.

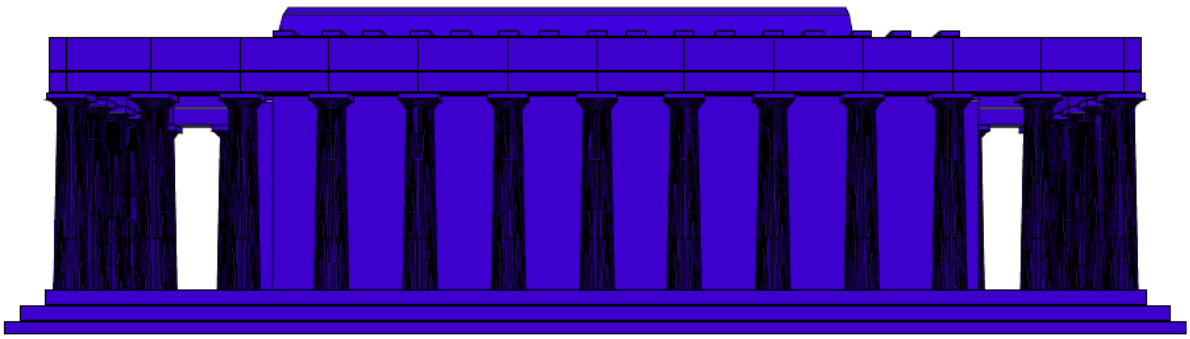


Figure 5. Side view of the numerical model used in the analyses with 3DEC.

2 SELECTION OF BASE MOTIONS

For the selection of the earthquake records to be used in the analyses, the records considered in [9], which are compatible with the seismotectonic environment and the ground profile of the historical center of Athens were selected. According to the results presented in [9], where back analyses on a free standing column of Thrasyllos, which is located nearby the Temple of Hephaestus, were performed, the maximum earthquake that could have happened in Athens during the last 2,300 years is unlikely it had peak ground velocity (*pgv*) larger than 35 cm/s and predominant period in the range 0.5–1.2 s which is consistent with the results of seismotectonic analyses. Within this range of the maximum expected earthquakes, the model was subjected to the ground motion of four earthquakes amplified accordingly [9]. The main parameters of the seismic input motions are shown in Table 1. Both horizontal components and the vertical one of the considered records were applied simultaneously as the base motion to the numerical model.

Earthquake record	Magnitude M_w	Fault dist. [km]	Amplification factor	Long		Trans	
				pga (m/s^2)	*pgv* (m/s)	*pga* (m/s^2)	*pgv* (m/s)
Syntagma-B (1999)	5.97	10	3.5	1.07	10	0.84	11
Assisi-Stallone (1997)	6.04	14	2.0	1.84	10	1.64	8
Cascia (1979)	5.89	1	2.5	1.42	8	1.99	11
Kozani (1995)	6.61	14	2.5	2.13	9	1.38	7

Table 1: Earthquake records considered in the numerical analyses.

3 RESULTS

Indicative results are presented in Figure 6 which shows the time-histories of the displacements at the capital of three columns (the two corner column and one middle column) located at the north façade. With the exception of the response for the Assisi-Stallone earthquake, the three columns exhibited somehow different displacements and rotations despite the symmetry in the external collonade itself. It is noted, though, that there is a small asymmetry in the connections of the collonade to the cella. The maximum displacement of the capital was observed during the Syntagma-B excitation (amplified 3.5 times) and had a value of 8 cm. The maximum permanent dislocation at the capital was 2.4 cm, whilst, for all excitations, larger values were observed at the middle drums of the columns, a fact that conforms with the current state of the temple (see Figure 7).

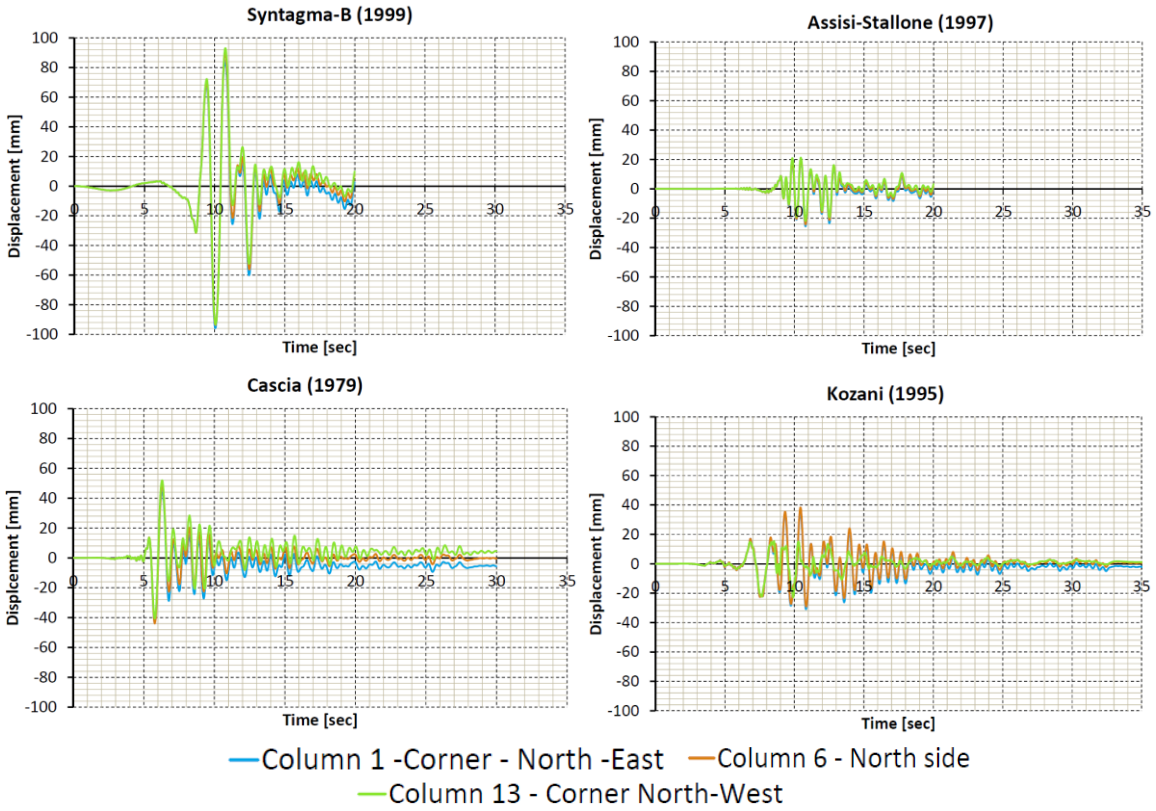


Figure 6. Capital displacements of three columns (the two corner column and one middle column), located at the north façade.

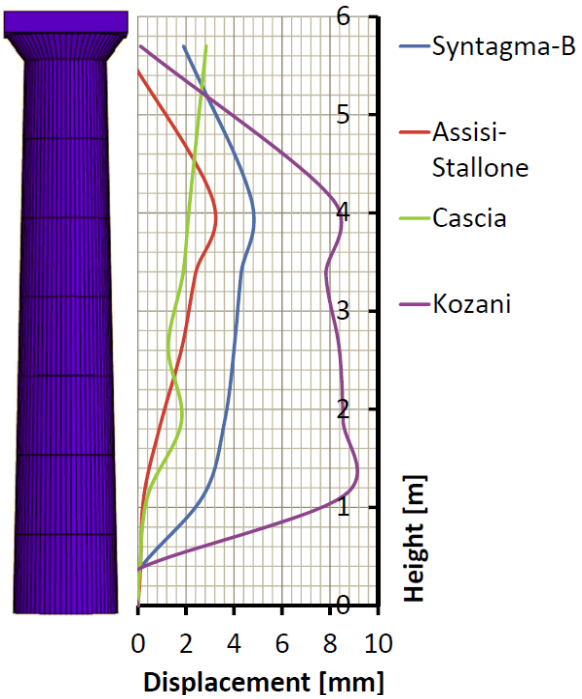


Figure 7. Residual displacements along the height of the corner column.

Figure 8 shows the time-history of the displacement of the outer architrave at the corner of the temple. It can be seen that, for all excitations, significant permanent displacement is evident, which led to the opening of the joint between the architrave beams. It should be noted

that experiments performed in a 1:3 scale model of three columns with architraves [8] indicated that existing dislocations from previous earthquakes may enlarge the displacements during future seismic events compared to the intact structure.

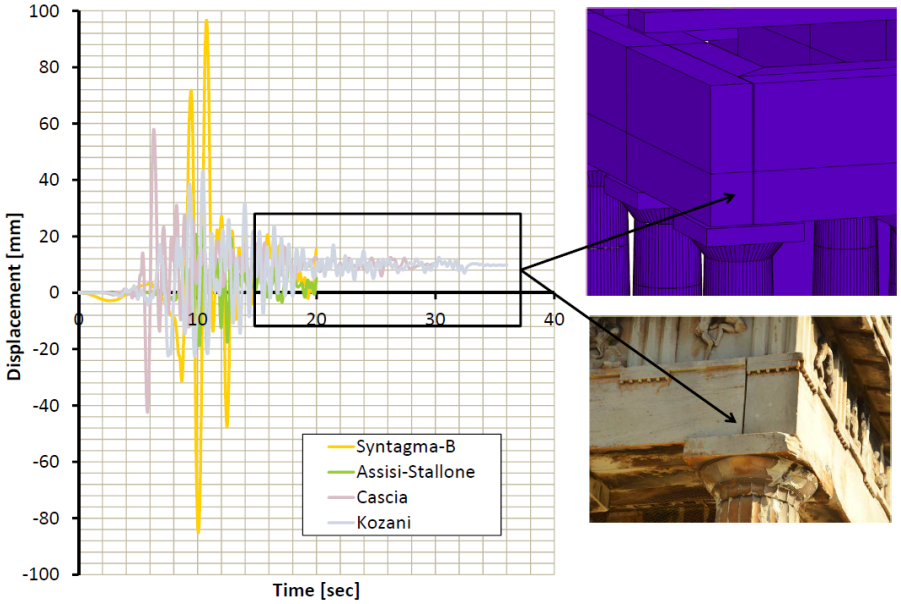


Figure 8. Time-history of the displacement of the outer architrave at the corner of the temple.

4 SUB-MODELS

4.1 Numerical Model

The dynamic analysis of the complete structure of a monument is difficult and very time-consuming, which leads to the necessity to create sub-assemblies in order to make their study more efficient without compromising with the accuracy of the results. In order to check whether such an approach is acceptable, a sub-assembly of the corner of the temple was created and compared to the full model presented above. In the sub-model, four columns of the long side and two columns of the short side were considered, keeping the same ratio of the number of columns on these sides as in the actual structure (13:6).

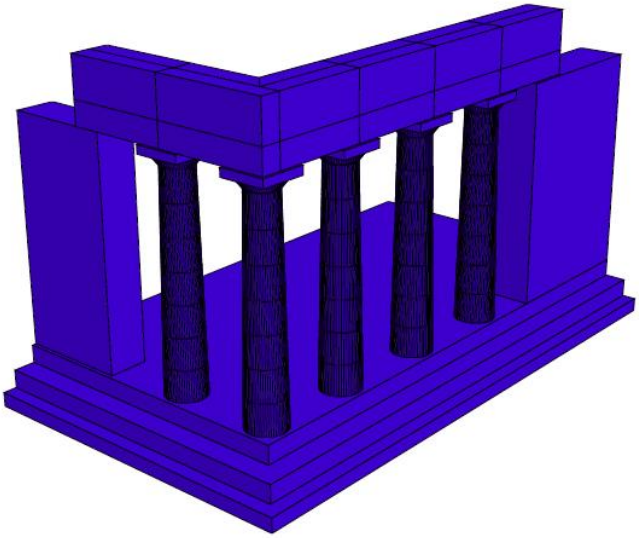


Figure 9. 3d view of the sub-model considered.

4.2 Results

In Figure 10, the residual displacements along the height of the corner column obtained from the complete model and the sub-model are depicted. In the case of the Assisi-Stallone and the Cascia excitations, the results are similar, but in the case of the Syntagma-B and the Kozani earthquakes, larger displacements occurred full model and the form of the dislocations of the drums along the height of the column was different. Evidently, further investigation is needed regarding this important issue.

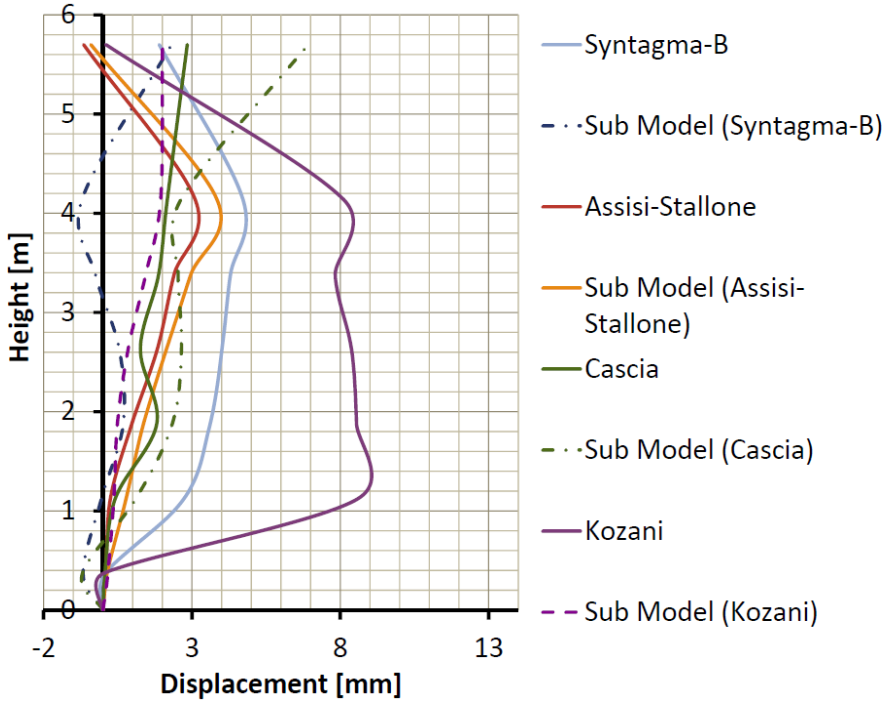


Figure 10. Comparison of the residual displacements along the height of the corner column

AKNOWLEDGEMENTS

The investigation was performed within the research project "Seismic Protection of Monuments and Historic Structures - SEISMO" funded by the Greek Ministry of Education and Religions under the action "Thalis" of the program "Education and lifelong learning".

REFERENCES

[1] W. B. Dinsmoor, *Observations on the Hephaiston, Vol. I, 4th Edition*. Swets & Zeitlinger B.V., Amsterdam, 1975.

[2] W. B. Dinsmoor, *The Architecture of Ancient Greece,*. W.W. Norton, 1975.

[3] A.W. Lawrence, *Greek Architecture*, *Fifth Edition*, The Yale University Press Pelican History of Art

[4] Itasca Consulting Group, Inc. *3DEC: 3-Dimensional Distinct Element Code, Theory and Background.*

[5] Psycharis I.N., Lemos J.V., Papastamatiou D.Y., Zambas C., Papantonopoulos C., Numerical study of the seismic behaviour of a part of the Parthenon Pronaos, *Earthquake Engineering and Structural Dynamics*, **32**: 2063-2084, 2003.

[6] Dasiou M.-E., *Report in Work package 7 and Work package 8, Research Project Earthquake Protection of Historical Buildings by reversible mixed technologies* (PROHITECH), 2007.

[7] Dasiou M.-E., Psycharis I. N., Vayas I., *Verification of numerical models used for the analysis of ancient temples,* Proceedings of PROHITECH Conference, Rome, 2009.

[8] Dasiou M.-E., Psycharis I., Vayas I., *Seismic behaviour of ancient temples' columns and collonades analysis,* Proceedings of 3rd Panehellenic Conference on Earthquake Engineering and Engineering Seismology, Athens, 5-7 November 2008 (in Greek).

[9] Ambraseys, N. and Psycharis, I. N., *Assessment of the long-term seismicity of Athens from two classical columns*, Vol. 10, Bulletin of Earthquake Engineering, , pp. 1635–1666, 2012

COMPDYN 2015
5th ECCOMAS Thematic Conference on
Computational Methods in Structural Dynamics and Earthquake Engineering
M. Papadrakakis, V. Papadopoulos, V. Plevris (eds.)
Crete Island, Greece, 25–27 May 2015

LASER SCANNING, MODELING, AND ANALYSIS FOR DAMAGE ASSESSMENT AND RESTORATION OF HISTORICAL STRUCTURES

Shakhzod Takhirov[1], Khalid M. Mosalam[1], Mohamed A. Moustafa[1], Liliya Myagkova[2], and Brian Quigley[3]

[1] University of California, Berkeley, Berkeley, CA, USA
{takhirov, mosalam, mmoustafa}@berkeley.edu

[2] Smart Scanning Solutions, Tashkent, Uzbekistan
myagkova_liliya@mail.ru

[3] BNZ, Tashkent, Uzbekistan
hitg.eurasia@gmail.com

Keywords: Earthquakes, finite elements, historic buildings, laser scanning, structural assessment, seismic analysis and retrofit.

Abstract. *High-definition laser scanning is rapidly becoming an essential tool for accurate non-destructive three-dimensional measurements of structures. This technology provides valuable information about an object which is discretized in space as "point clouds". Two representative examples of current research activities on use of laser scanning in historic buildings in Uzbekistan and California are discussed. The first example is the Registan Square ensemble in Samarkand, Uzbekistan. The ensemble includes several heritage structures. Earthquakes, extreme seasonal temperatures, etc. have left the ensemble in a ruined condition. Domes and portals were partially or totally destroyed. The minarets were dangerously inclined, and some façades lost 70-80% of their ceramic tile coverings. Structural repairs and straightening of the minarets had been conducted over the years. In this study, the ensemble was scanned from about 70 positions to capture the current condition of the historic structures and to conduct structural assessment of the ensemble and its components. The scan data are expected to be used for monitoring of the ensemble's structural condition. In addition to visual scan data inspection, detailed finite element model of the ensemble was generated from the as-found geometry captured by laser scans. This model allows detailed seismic analysis of the monuments and its components. The model developed for the Sher-Dor Madrasah, part of the ensemble, using the scan data and sample preliminary analysis results are presented in this paper. The research team also investigated several historic buildings damaged during the 2014 South Napa Earthquake, California, USA, as the second example. In that regard, structural damage assessment using laser scanning for several historic buildings, including three churches, were conducted. The results of one of the damaged churches are discussed herein.*

1 INTRODUCTION

Laser scanning technology is rapidly expanding into many fields and becoming an essential tool for accurate non-destructive three-dimensional (3D) measurements of structures. This technology enables users to capture many points from the subject structure with high accuracy. In particular, high-definition laser scanning (HDS) technology provides both qualitative and quantitative information about a complex object which is discretized as a cloud of millions or billions of points in space. Nowadays, the HDS technology is going beyond the limits of its traditional usage, namely topographical surveying, reverse engineering, etc., and is finding excellent applications in several fields, e.g. scanning surfaces of visible faults in earthquake-prone regions and analysis of their roughness led to new developments in seismology [1]. Extensive studies of heritage buildings are being conducted for historic places throughout the world, e.g. [2]. The HDS has been extensively used for documentation and damage assessment of test structures subjected to earthquake loads at the University of California, Berkeley (UCB) [3]. In that regard, a unique study of the accuracy of laser scans compared to conventional measurements on a shaking table test of a seismically vulnerable two-story wood house over garage due to soft story and torsional effects was conducted [4].

This paper extends the ideas presented earlier [3-5] and uses laser scans as a tool to capture as-found geometry of historic structures. The geometry is used in generation of accurate finite element (FE) models to be used for detailed structural assessment, seismic analysis, and development of retrofit strategies.

2 LASER SCANNING OF HISTORIC BUILDINGS IN UZBEKISTAN

An extensive program of laser scanning of historic monuments in Uzbekistan was conducted in October 2013. As a representative example of many heritage monuments, the Registan Square ensemble in Samarkand, Uzbekistan was selected. The ensemble includes the Ulugh Beg Madrasah, 1417-1420, the Sher-Dor Madrasah, 1619-1636, the Tilya-Kori Madrasah and Mosque, 1646-1660, and the 18th century Chorsu domed market as shown in the Google map presented in Fig. 1. Earthquakes, extreme seasonal temperatures, normal depreciation of the buildings and the economic crises of the 18th and 19th centuries had left the ensemble in a ruined condition. Domes and portals were partially or, in some cases, totally destroyed. The minarets were dangerously inclined, and façades in some places had lost 70-80% of their ceramic tile coverings. Structural repairs and straightening of the minarets had been conducted in 1923 and 1932. However, the major restoration works were undertaken in recent years. The ensemble is in its best condition since late 19th century, although some inclination and cracks can be observed in the portals, minarets, and the domes of the monuments. In the course of this study, the ensemble was scanned from about seventy positions (scan stations). The main objective of this scanning program was to capture the current conditions of the historic monuments and conduct structural assessment of the ensemble and its components. A detailed FE model of the ensemble was generated from the as-found geometry captured by laser scans. The model was utilized for detailed seismic analysis of the monuments and its components. The scan data produced extremely valuable results that could be used in determining further restoration strategies of the monument located in this earthquake-prone area of Central Asia. The scan data are expected to be regularly used for monitoring of the ensemble's structural condition. This paper presents some representative examples of this extensive program.



Fig. 1. Google map of the Registan Square ensemble

3 VISUAL ASSESSMENT OF CURRENT CONDITION

The Registan Square ensemble has a long and rich history of being one of the major centers of ancient culture. It is one of the major historic ensembles of Samarkand. The city is most noted for its central position on the Great Silk Road, the trade route between China and the West, and for being an Islamic center for scholarly study. In the 14th century, Samarkand became the capital of the Timurid Empire. The Registan was the center of the ancient city. The economic crises of the 18th and 19th centuries had left the ensemble in a ruined condition. Typical images of the Ulugh Beg Madrasah, the Tilya-Kori Madrasah, and the Sher-Dor Madrasah dated to the late 19th century are presented in Figs. 2(a), 3(a), and 4(a), respectively. These photographs are taken by G. A. Pankratiev [6], a Russian army captain and amateur photographer. He produced a unique series of photographs of the architectural monuments and images of the city of Samarkand between 1894 and 1904. As shown in the images, the domes and portals of the monuments remained in extremely poor shape from a structural and an esthetics' point of view. Moreover, the minarets and portals were dangerously inclined. A large number of the ceramic tile coverings were lost from the façades due to deterioration. Structural repairs and straightening of the minarets had been conducted in 1923 and 1932. Several other restoration efforts have taken place in recent years.

As a result of all restoration efforts (shown in Figs. 2(b), 3(b), and 4(b)), the current condition of the ensemble is significantly better than it used to be in the late 19th century. Nevertheless, there are evidences of structural anomalies in the ensemble's monuments. For example, a visual observation reveals the following: 1) A large crack in the dome of Tilya-Kori Mosque, 2) An inclined minaret on North-West side of the Ulugh Beg Madrasah, and 3) A visible misalignment in the Ulugh Beg Madrasah's portal. The current view of the whole ensemble is presented in Fig. 5. The Ulugh Beg Madrasah is on the left side, the Tilya-Kori Madrasah and Mosque are in the center, and the Sher-Dor Madrasah is on right side of the image.



(a) View in 1890 (after [6])



(b) Current view

Fig. 2. Main entrance of the Ulugh Beg Madrasah



(a) View in 1890 (after [6])



(b) Current view

Fig. 3. Main entrance of the Tilya-Kori Madrasah and Mosque (Note that the mosque dome is not present in the old photo (a))



(a) View in 1890 (after [6])



(b) Current view

Fig. 4. Main entrance of the Sher-Dor Madrasah



Fig. 5. Current view of the Registan Square ensemble.

4 CURRENT CONDITION BY LASER SCANS AND FE MODELING

All three monuments were scanned by means of P20, a high-definition laser scanner manufactured by Leica Geosystems, Inc. The scans were conducted from about seventy positions (stations). The individual scans were stitched (registered) together in Cyclone application [7]. As a result, a fully stitched point cloud (registration) contains the geometric details of all three monuments. A typical result is presented in Fig. 6 that shows registration of the Tilya-Kori Madrasah and Mosque. The scans were conducted from all positions, including: inside of the monument, in the courtyard, around the exterior wall, and on the roof. Therefore, the registration documented the spatial locations of all surfaces.

In addition to the global dimensions of all monuments located within the ensemble, the scans captured all details of the monuments, namely tile shape, dimensions, and their locations in the monuments, any imperfections, and the overall geometric shapes of the portals and facades. To achieve this level of detail in point density, all scans were conducted with a density of 2 mm by 2 mm. One of the typical results for a portal is shown in Fig. 7. In addition to spatial locations of the details, the colors from the built-in camera and intensity colors of the reflected light (closely correlated to an object's color) were also documented.

In addition to the global dimensions of all monuments located within the ensemble, the scans captured all details of the monuments, namely tile shape, dimensions, and their locations in the monuments, any imperfections, and the overall geometric shapes of the portals and facades. To achieve this level of detail in point density, all scans were conducted with a density of 2 mm by 2 mm. One of the typical results for a portal is shown in Fig. 7. In addition to spatial locations of the details, the colors from the built-in camera and intensity colors of the reflected light (closely correlated to an object's color) were also documented.

One of the main objectives of the project was the development of finite element models based on the as-found geometry of the monuments and subsequent detailed structural analysis of their vulnerability to the seismic effects. Examples of how this objective was achieved are presented in this section of the paper.

The Cyclone application [7] is capable of reducing a point cloud into a mesh. This option was utilized for surfaces with complex geometry, approximation of which by a regular mesh is not practical. A typical example of a ceiling in one of the two main entrances into the Sher-Dor Madrasah is presented here. A small portion of the point cloud extracted from the full registration is presented in Fig. 8.

The point cloud of the ceiling surface reveals its irregular and complex geometry as shown in the top view of the point cloud in Fig. 9a. This complex surface is approximated in Cyclone [7] by a mesh as presented in Fig. 9b. The vaults supporting the ceiling are removed from the mesh to simplify the presentation.

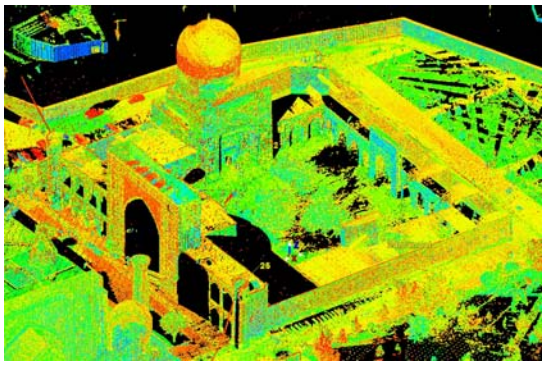


Fig. 6. Registration of the Tilya-Kori Madrasah and Mosque.

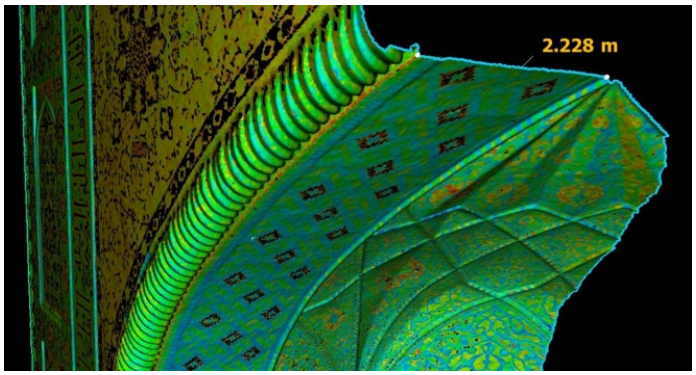
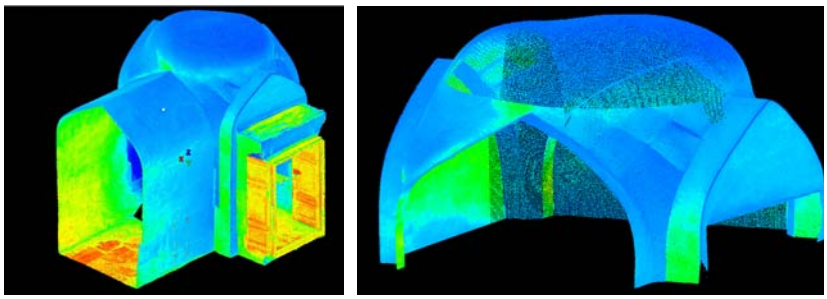
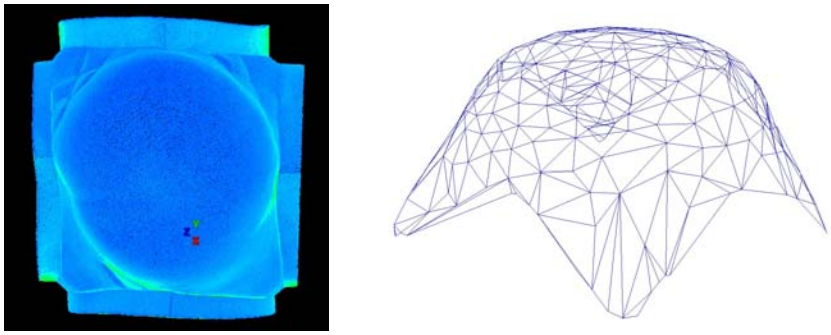


Fig. 7. Tile details captured by laser scans.



(a) Part of full registration (b) Global view of the ceiling

Fig. 8. Point cloud of north side entrance to the Sher-Dor Madrasah.



(a) Top view of the ceiling (b) Mesh capturing irregular ceiling surface

Fig. 9. Irregular surface of the ceiling in the Sher-Dor Madrasah's entrance.

To simplify the presentation of the point cloud, the main part of the Tilya-Kori Mosque was extracted from the full registration. Horizontal slices of the point cloud were introduced at several elevations. The slices contain a massive amount of information about the global geometry, dimensions, and structural anomalies. Some representative results are discussed here. The first horizontal slice was introduced at the highest point of the floor. Fig. 10 presents a horizontal slice at 0.20 m above the floor. Detailed analysis of the plan view revealed that there is an opening between the tiles on the West side of the mosque. This opening is about 11 cm deep as shown in this figure.

The identified opening, discussed above and shown in Fig. 10, can be related to a crack in wall that was observed earlier [8]. During this review, it was observed that there was a crack in one of the vaults in the Tilya-Kori Mosque. It was concluded that this can be the result of a low load bearing capacity of the underlying soil that can compromise the structural integrity

of the monument in the long run or during an earthquake. It is to be noted that the vaults represent the major load-bearing structural elements in all monuments of the ensemble.

The horizontal slice provided an estimate of an overall thickness of the west side wall as shown in Fig. 11. This estimate includes the thickness values of the tiles on both sides of the wall, the mortar attaching the tiles to brick walls, and the brick wall itself.

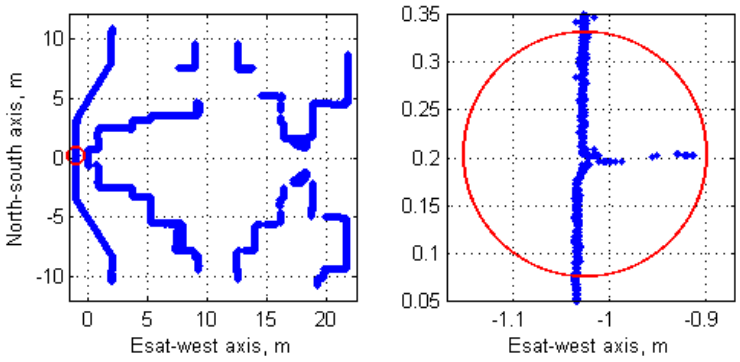


Fig. 10. Opening in west side wall of Tilya-Kori Mosque (about 11 cm deep)

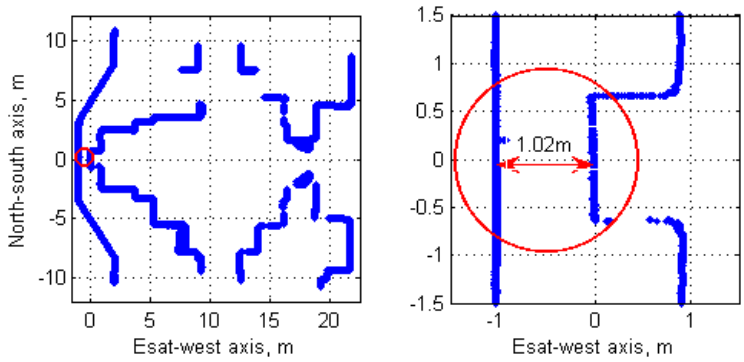


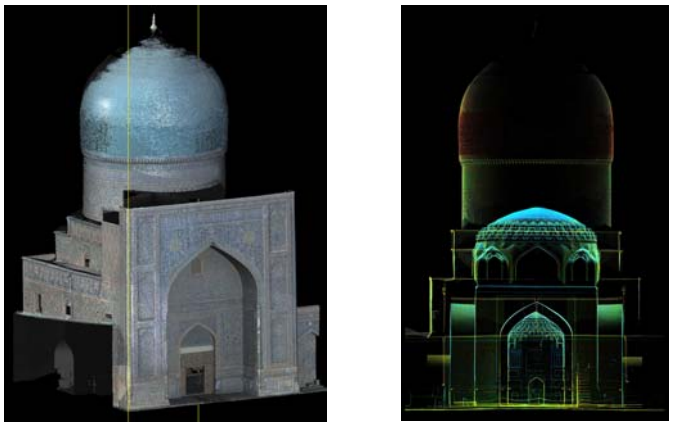
Fig. 11. Thickness of west wall of Tilya-Kori Mosque with tiles on both sides

The left images of Figs. 12 and 13 show the isometric view of the Tilya-Kori Mosque in colors obtained from the scanners' still imaging camera and point cloud. The right image of Fig. 13 presents the half-space view of the west half of the mosque. The details required for structural modeling and analysis (wall thickness and its dimensions for example) are obtained from the half-space and thin slices as presented in Fig. 13.

Since the majority of the scan stations were conducted from ground level, the dome of the Tilya-Kori Mosque was not captured completely. This shortcoming was anticipated and is attributed to the limited duration of the field work. This problem was addressed by making sure that the scan positions are providing a view of the observed crack in the dome from as many positions as possible. To cover this surface with maximum efficiency, two stations from the roof and more than 20 stations from the ground level of the courtyard and outside of the exterior wall area were utilized. This approach was successful in capturing the majority of the dome surface. The resulting stitched point cloud of the Tilya-Kori Mosque extracted from the full registration of the whole ensemble is shown in Fig. 14.

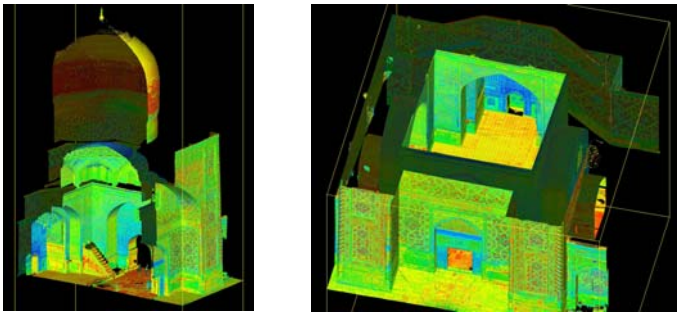
Modeling of the dome, shown in Fig. 14, was one of the main objectives of the study since there was a visible crack on the east side of the dome. The mesh generation option provided by Cyclone [7] was not utilized in this case because a mesh with a regular size was preferred

for this monument. The regularly spaced meshing was based on utilization of 5 mm thick horizontal slices as shown in Fig. 15 showing two vertical cross sections perpendicular to each other and located at the North-South and East-West planes. They are plotted on top of each other to demonstrate the differences in the geometry of the dome, refer to the bottom left portion of the image where arrows point at the region with inconsistent geometry.



Isometric view in camera colors Elevation showing west half

Fig. 12. Point cloud of the Tilya-Kori Mosque.



Isometric view Half-space view showing west half

Fig. 13. Slice views of the Tilya-Kori Mosque.

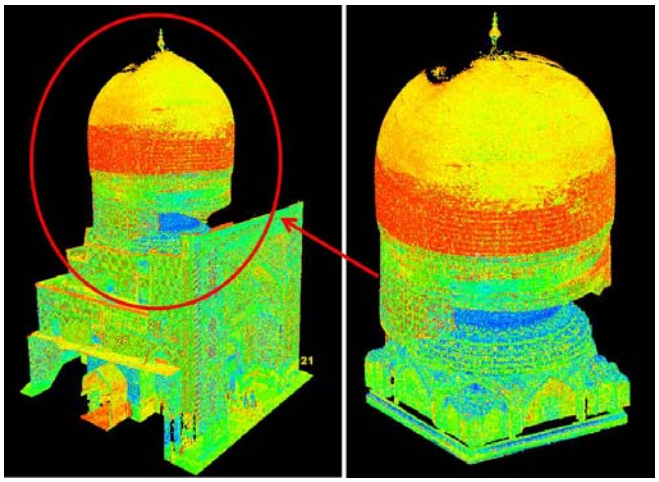


Fig. 14. Point cloud of dome.

At all other locations, the sections perfectly match each other, which demonstrates the accuracy of the dome's design and construction. It is worthy to note that the dome was constructed after 1976 [9] and as such represents a large and heavy addition to the monument that can challenge the load-bearing capacity of the vaults.

The mesh of the dome was generated at the elevations identified by the green dashed lines in Fig. 15. To have strong control over the meshing procedure while maximizing usage of the point cloud, a special set of programs was prepared in Matlab [10]. The mesh was generated by using the points of the cloud that were present in the vicinity of a regularly spaced mesh. In the shadow zones, where points were missing in the point cloud, the following procedure was used. The horizontal slice of a point cloud was approximated by a circle using a best fit procedure applied to the scanned points of the surface. The mesh in the shadow zones were selected based on these circles. A resulting mesh is presented in Fig. 16.

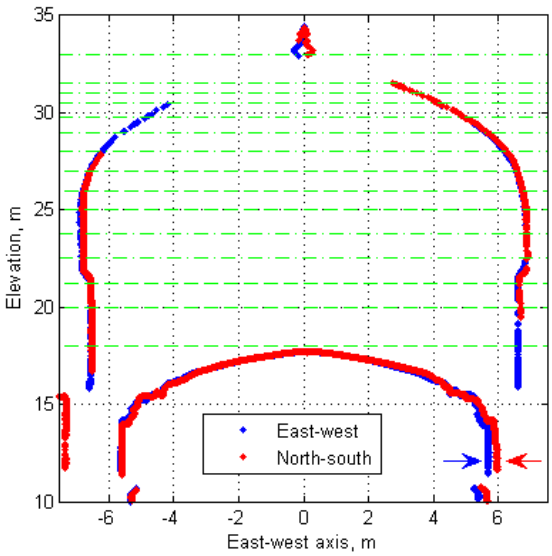


Fig. 15. Vertical slices of the Tilya-Kori Mosque where elevations of horizontal slices are shown by dashed green lines.



(a) Current photograph (b) Regularly spaced mesh

Fig. 16. Regularly spaced mesh of the Tilya-Kori Mosque's dome.

A visual observation of the minarets of Ulugh Beg Madrasah revealed that one of the minarets, namely the one on the North-West side of the monument, is inclined. The visual obser-

vation failed to estimate the overall direction of the inclination and its dependency on the minaret's elevation. The point cloud of the minaret provided answers to these questions based on detailed information on the surface points captured by a laser scanner. A small portion of the full registration of the monument was analyzed for this purpose which consisted of the point cloud of the minaret and two outside walls. The total number of points was close to 20 million. This allowed us to capture the surface with much more detail. Several horizontal slices of this portion of the point cloud revealed the following results. First, the angle between the walls is very close to 90 degrees, as presented in Fig. 17 by red arrows.

Second, the minaret is mainly inclined away from both walls. Therefore, the overall direction of inclination from the walls is close to 45 degrees, as shown in Fig. 18 (horizontal direction in the plot). The inclination of the minaret was noticed earlier [9] and it is mostly related to the uneven settlement of the underlying soil.

Third, a large portion of the tiles are bulging out at the bottom of the minaret in the direction of the inclination as shown in Fig. 19. The bulging portion of the tile covering represents large compression forces in this part of the minaret. As a result, the tile covering is buckling away from the minaret's wall at this location. This is most likely associated with the fact that the center of gravity of the minaret is shifted towards the bulging region. Therefore, the mass distribution in the cross-section is mainly concentrated next to this region. The dense point cloud displaying many details of the minaret's tile covering is presented in Fig. 20a. A zoomed view of the bulged region where the tile cover has buckled away from the wall is presented in Fig. 20b.

The mesh of the minaret was generated by utilizing the approach described above and it was based on a best fit of the sections of the point cloud using circles. The resulting regular mesh has fine spacing at the elevations where the bulging has occurred and coarse spacing elsewhere. The mesh was generated for two conditions of the minaret, namely the current inclined condition and the so-called "original", where the axis of the conic surface of the minaret is vertical. The latter assumes that the minaret was plumbed during its original construction. The meshes were generated at the elevations shown with dashed green lines in Fig. 19. The meshes generated from the point cloud and representing the current inclined and the 'original' conditions are shown in Fig. 21.

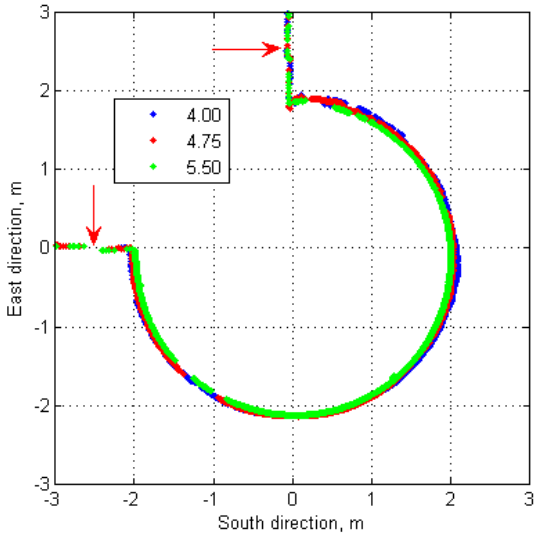


Fig. 17. Horizontal slices at bottom of one of the minarets of the Ulugh Beg Madrasah.

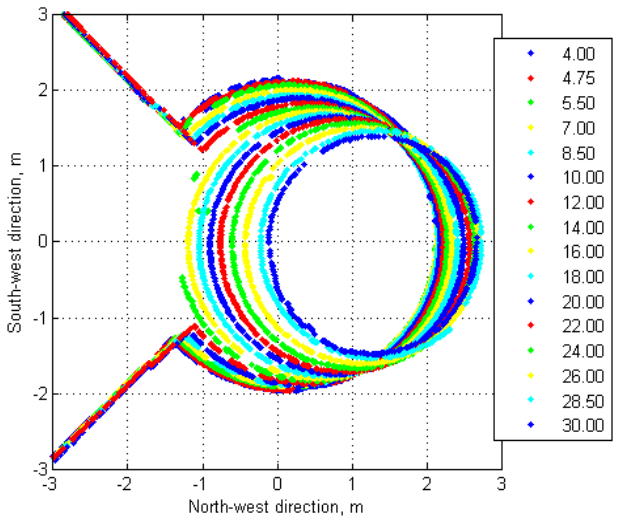


Fig. 18. Horizontal slices along the elevation of one of the minarets of the Ulugh Beg Madrasah.

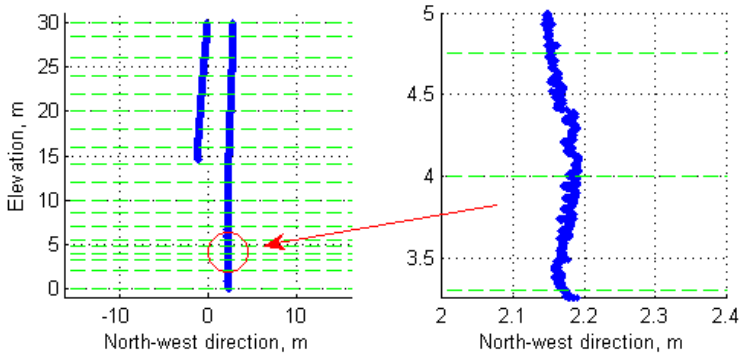


Fig. 19. Vertical slice of one of the minarets of the Ulugh Beg Madrasah at 45 degrees to the walls (bulged section is shown on right).

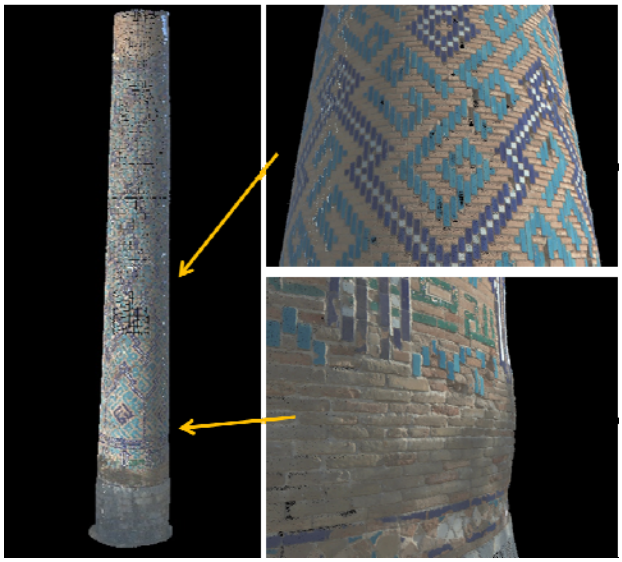
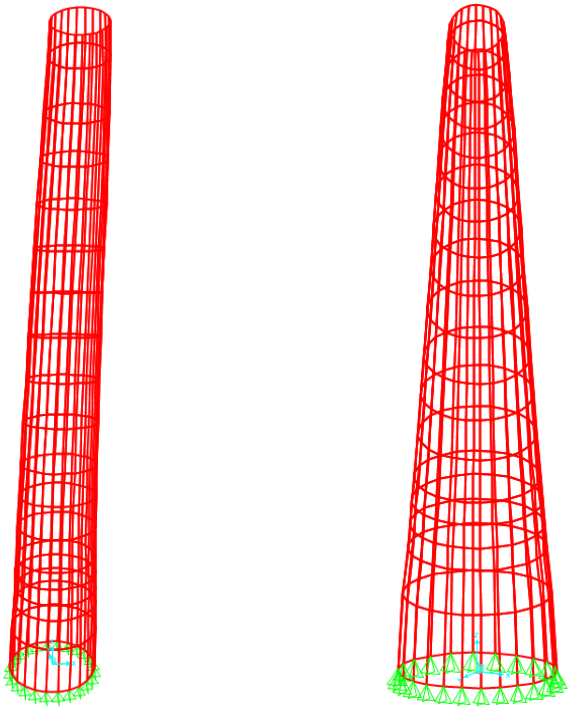


Fig. 20. Point cloud displaying the details and the bulged region of one of the minarets of the Ulugh Beg Madrasah.

From a geometric point of view, the minaret represents a tapered cone without a tip. Therefore, it is not simple to estimate its inclination since the surface of the cone is tapered. To estimate the inclination of the minaret, the special procedure was devised as discussed in this paragraph. Analysis of shapes of the horizontal slices from the point cloud of the minaret revealed that all sections can be closely fitted by circles. The radii of these circles were used for the estimates of the original taper and the circle's origin locations were used to estimate the global direction of inclination. The results of this procedure are presented in Fig. 22 where the green straight lines represent linear best fits of the radii of the circular cross-sections and the corresponding inclinations. Based on these linear approximations, an estimate of 4.6% inclination was obtained. It is to be noted that the original taper of the minaret is estimated as 2.3%.

It is worth noting that the inclination of the minaret's axis is very close to being linear. This observation can serve as evidence for the following two important remarks: (1) The structural connection between the walls and the minaret is most likely compromised and (2) The residual deformation (inclination) is most likely related to soft soil conditions (concentrated rotation at the base leading to the observed almost rigid body rotation of the minaret from the point cloud of the laser scanning) under the minaret. It is also noted that the adjacent walls of the monument end at about 12 meters of elevation and they have negligible effect on the inclination shape of the minaret, refer to Fig. 17. Hence, as a starting point for the planned detailed seismic analysis, the minaret can be analyzed independently from the walls and the rest of the monument. Subsequently, the next step is to take into account the evident soil-structure-interaction in the seismic analysis of the structure. It is to be stressed that the consideration of the soil-structure-interaction can be significant for this monument where its structural integrity is compromised by a soft underlying soil.



(a) Mesh generated from point cloud for current - inclined condition

(b) Mesh generated from point cloud for "original" condition

Fig. 21. Generated mesh of the inclined minaret of the Ulugh Beg Madrasah.

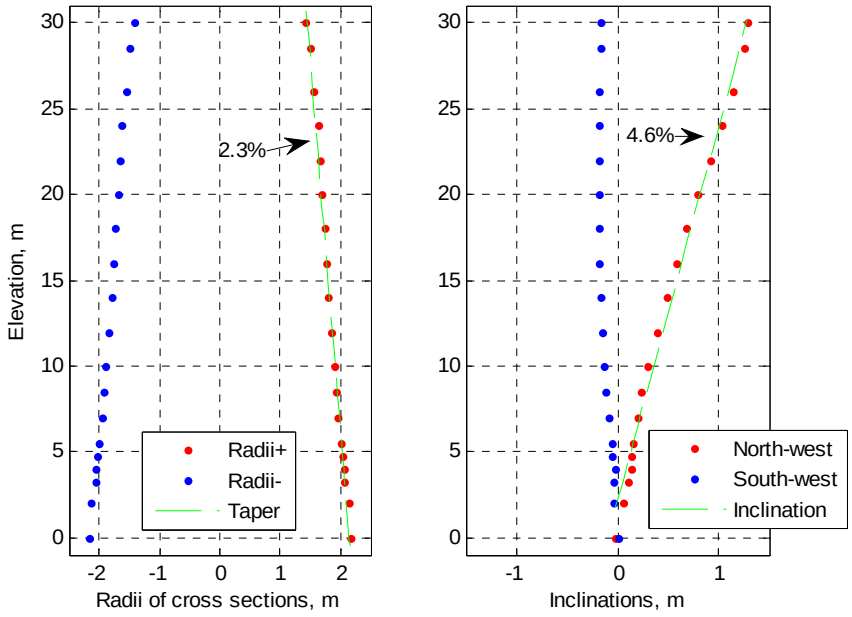


Fig. 22. Taper and inclination estimates of the inclined minaret of the Ulugh Beg Madrasah.

5 DETAILED FE MODELING USING LASER SCANNER POINT CLOUDS

The previous section presented in details some of the different applications for utilizing and manipulating scan data and point clouds generated from the HDS. The presented applications relied primarily on best fitting well-defined geometric shapes and/or solids for different components or parts of scanned structures for possible use in FE modeling or generating accurate geometric surface mesh to capture deformations of the cross sections and construction defects. In this section, scan data is further utilized for a different application or extension to previous applications. This application focuses on generating accurate and detailed 3D structural FE models that can be used for structural and seismic analysis and assessment of historical buildings. Currently, the FE method is extensively used for analyzing new or existing structures for which geometric models can be reproduced from available structural information (geometrical properties, material properties, boundary conditions, and loading conditions). However, due to the complexity and uniqueness of historical monuments, accurate FE models are challenging to be produced based on data collected from regular measurements techniques or seldom available as-built construction drawings. Therefore, possible use of datasets in the form of 3D point clouds acquired from HDS using laser scanners for FE modeling can be extremely useful for historical monuments condition and structural assessment.

An application for using the collected Registan Square ensemble laser scanning data is one of the first attempts to generate detailed 3D FE models and is presented here. The process of developing the FE model for the north side entrance of the Sher-Dor Madrasah, which is the point cloud shown in Fig. 8, is discussed in this section of the paper. Several software packages are required to start with a point cloud and end up with detailed FE analysis results. In this study, two graphics packages were utilized, namely Cyclone [7] and Rhino 3D [11], along with the general-purpose FE package TNO DIANA [12].

The framework and relevant software used for conducting the FE analysis of historical structures is summarized in Fig. 23. First, the scan data is registered and point cloud is generated using the Leica laser scanner software. The point cloud is then exported to specialized graphics software to connect the point cloud nodes and create a polygon (triangular or quadri-

lateral) surface mesh. For this purpose, the software Rhino3D [11] was utilized not only to create the surface mesh, but also to create additional meshes of reduced sizes for more computationally efficient FE simulations. Typically, the point cloud is a result of a detailed HDS of a 1 mm resolution, which generates millions of nodes and becomes unsuitable for FE meshes at the structure macro-level. Therefore, a much reduced-size mesh is required to make it possible for the available FE packages and available computing resources to handle the model. It is to be noted that the 1 mm resolution for FE models is not suitable only because it is computationally expensive and the current FE packages cannot usually handle models of millions of nodes yet.

The approximately 310,000 element polygon mesh created for the north side entrance of the Sher-Dor Madrasah from the original point cloud as viewed in Rhino3D is shown in Fig. 24. A reduced size mesh that comprises roughly of 45,000 polygon faces was developed using Rhino3D as shown in Fig. 25. The reduced mesh was exported in an advanced geometry and CAD file type, namely a *.STEP file format for the FE pre-processor software to be able to load the model. The FX+ is a pre- and post-processor that comes with the DIANA FE package and is a powerful tool used to generate FE models and output analysis results. The reduced surface mesh was imported in FX+ for the purpose of developing a detailed FE model using 2D shell elements. A linear elastic material model was used to define the masonry material of the structure and uniform thickness shell elements were used for FE mesh. These approximations of linearity, elasticity, and geometric uniformity are for the purpose of preliminary analyses. Future analyses will include more refined modeling assumptions. The detailed FE created in FX+ and defined boundary conditions for the Sher-Dor Madrasah entrance are shown in Fig. 26. Once the FE model is created, the analysis files are defined through another part of the DIANA package, which is MeshEDIT, and the analysis is run through DIANA as described in steps 4 and 5 in Fig. 23. Finally, the results of the analysis can be viewed through FX+ and different response quantities can be observed according to the conducted analysis type.

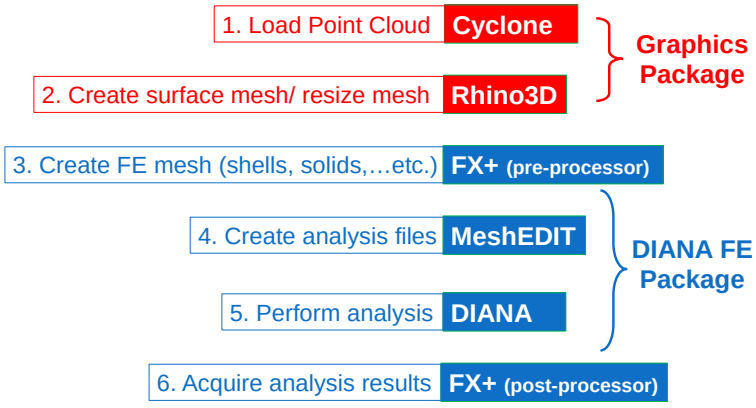


Fig. 23. Summary of the framework to develop FE model and conduct FE analysis from HDS point clouds.

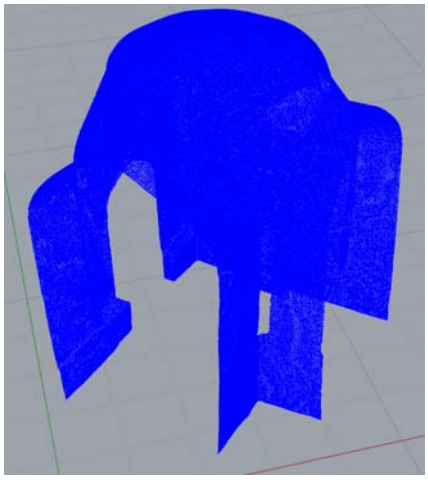


Fig. 24. A dense 310,000 polygon mesh obtained from the original point cloud for the north side entrance to the Sher-Dor Madrasah as viewed in Rhino3D.

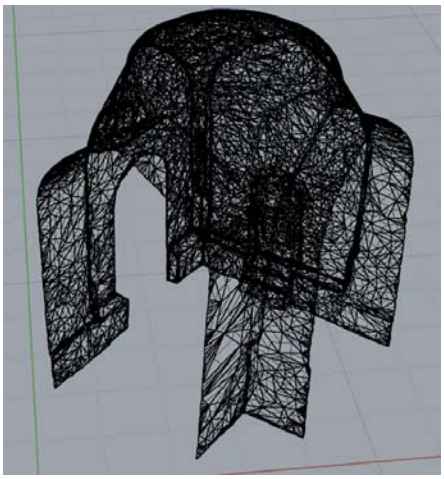


Fig. 25. View of a less dense mesh generated using Rhino3D for the north side entrance to the Sher-Dor Madrasah.

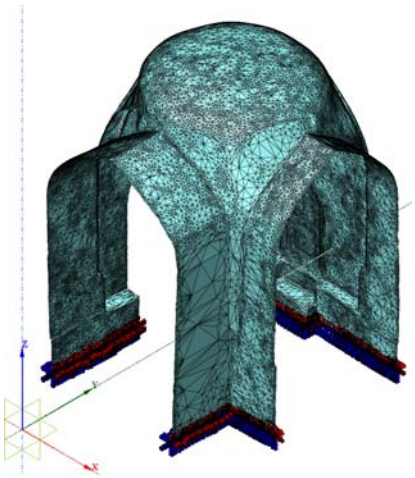


Fig. 26. View of the FE mesh using 2D shell triangular elements generated using FX+ for the north side entrance to the Sher-Dor Madrasah.

Two analyses that utilized the north entrance to the Sher-Dor Madrasah FE model were conducted. Both are linear static analyses under (1) The structure's own weight and (2) Lateral load to identify the lateral stiffness and deformations of this particular part of the structure. The deformed shapes of the structure under gravity load and a lateral load of 2000 kN are shown in Figs. 28 and 29, respectively. A third analysis using the same FE model was conducted for the purpose of obtaining the eigen-solution to find the modes of vibration and natural frequencies of this part of the Sher-Dor Madrasah entrance. The eigenvalue analysis is necessary before a meaningful dynamic analysis or seismic assessment because of the indispensable insight it provides about the dynamic properties of the vibrating system. Two of the vibration modes for the developed FE model are shown in Fig. 29. A larger model for the entrance along with the adjacent and connected structures is required for proper representation of the dynamic interaction and properties. However, as mentioned above, this part of the entrance model is an illustrative example.

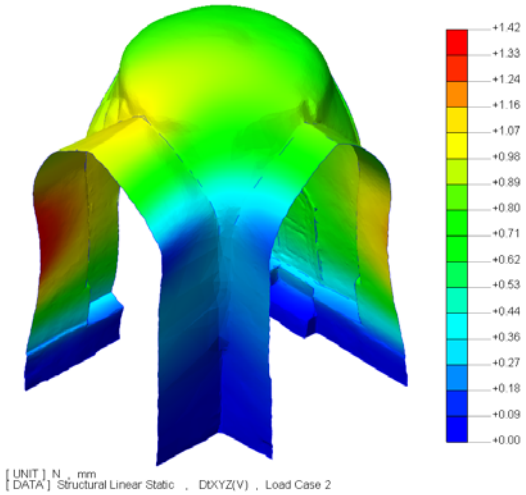


Fig. 27. Deformed shape of FE model for the north entrance of the Sher-Dor Madrasah from DIANA under gravity load [units: mm].

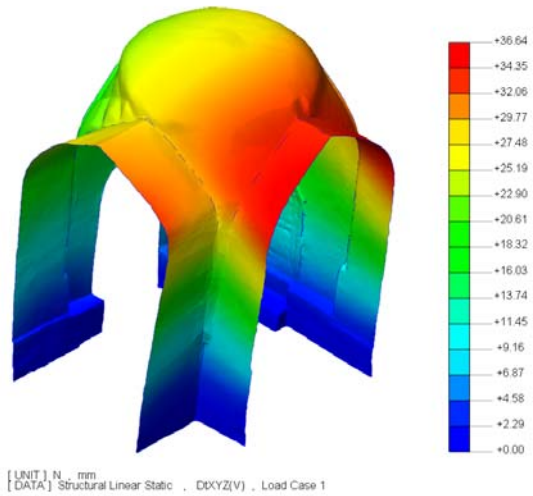


Fig. 28. Deformed shape of the FE model for the north entrance of the Sher-Dor Madrasah from DIANA under lateral load [units: mm].

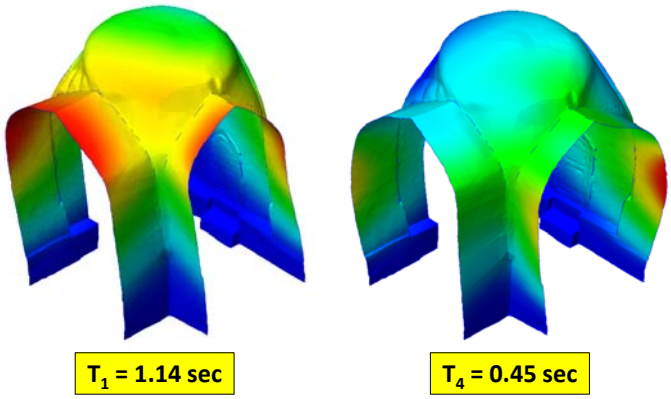


Fig. 29. Two mode shapes from the DIANA eigen-solution of the FE model using 2D shell triangular elements post-processed using FX+ for the north entrance to the Sher-Dor Madrasah.

Although simple linear elastic model and shell elements were used in the previously discussed FE analysis, yet a powerful general-purpose FE package, e.g. DIANA, can be utilized to define a variety of nonlinear material and geometrical models and more accurate solid element types. Defining accurate material properties, especially for nonlinear constitutive models, for historical masonry buildings and monuments is still a challenging task. However, the accurate geometric modeling and FE meshing of irregular shapes and unique geometries of historical structures is a bigger challenge. The examples shown in this study demonstrate that using point clouds can be an excellent way to generate very detailed models for better structural and seismic assessment of historical buildings. There is a great potential in extending the preliminary framework proposed in this study for using point clouds for FE mesh generation to more advanced nonlinear and dynamic FE analyses.

6 FIELD INVESTIGATIONS OF HISTORICAL BUILDINGS IN THE AFTERMATH OF 2014 SOUTH NAPA EARTHQUAKE

A number of churches were damaged during the 2014 South Napa earthquake. Three churches were studied by means of laser scanning. As a representative example, an ensemble of First United Methodist Church in downtown Napa, California, USA, was studied and presented in this paper. The ensemble consists of three adjacent buildings: A) Church's main sanctuary building (1917), B) Centennial hall (1952), and C) Educational building (1955) as identified in Fig. 30.

The research team arrived at the site within several hours after the main shock and scanned the ensemble from 4 positions (stations). It was discovered that the east wall of the church's main sanctuary building (building A) separated from the roof on top and bowed out towards the nearby street as presented in Fig. 31. Since no damages were observed in other buildings of the ensemble, the research team focused their investigation on this unreinforced masonry building only. The views of the wall before and after the earthquake are presented in Fig. 32.

To assess the residual deformations of the east wall and monitor its condition after the aftershocks, several scans of the church were conducted. On the day of the earthquake, the church was scanned from 4 corners to obtain a complete geometry of the structure. On the following day, in about 24 hours after the main shock, two more scans of the church were conducted from the street on the east side of the building. Fig. 33 shows the residual deformation of the east wall where the color of a point in the point cloud depends on the distance from a vertical plane. The arrows show the locations of visible cracks observed in the wall. Fig. 34

shows the vertical slice of the east wall right after the main shock of the earthquake and that after several aftershocks that took place within 24 hours.



Fig. 30. Google Earth view of First United Methodist church ensemble, Napa.



Fig. 31. Ground elevation views of the separation of the east wall of First United Methodist church ensemble, Napa.



Fig. 32. East side wall before (left) and after (right) of First United Methodist church ensemble, Napa.

The comparison of the vertical slices before and after the aftershocks leads to a conclusion that the aftershocks were not strong enough to change the wall's residual deformation caused by the main shock. Depending on future shaking, the situation can change dramatically where the wall can fall on the east side street. Nevertheless, due to the high hazard for passing by traffic and pedestrians, the building was fenced out by a tape right after the earthquake and it was red tagged on the following day.

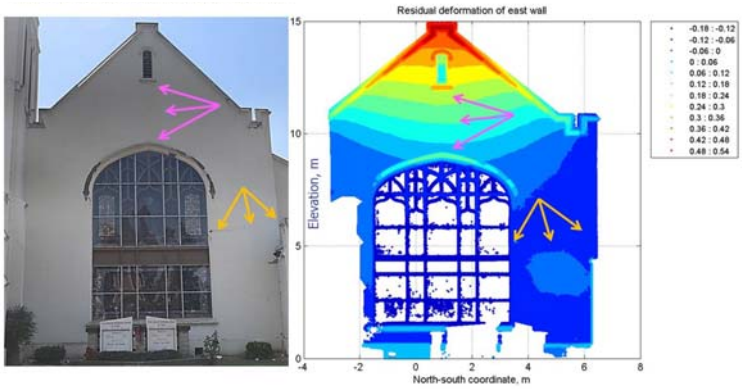


Fig. 33. Residual deformations and cracks of east wall of First United Methodist church main building, Napa: photograph (left); point cloud (right).

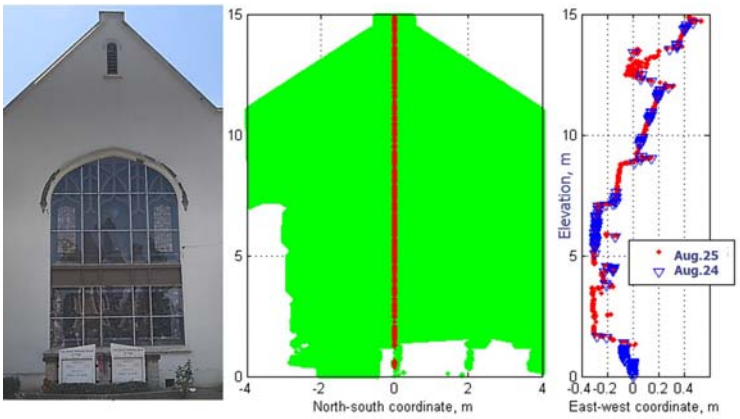


Fig. 34. Laser scans of First United Methodist church main building, Napa, after the main shock and the aftershocks indicating no failure progression.

7 CONCLUSIONS

The paper presents a comprehensive approach to the structural assessment of historic buildings and monuments through the means of laser scanning. The choices of mesh generation techniques have been enriched by a Matlab-based package that uses a point cloud for a regular meshing. The approximate best-fit geometry used in preliminary finite element (FE) models closely represents the as-found geometry of the historic monuments. A new framework was proposed and used in this study to generate detailed 3D FE meshes and models from 3D laser scanning point clouds. It was shown that FE models generated directly from point clouds can be used for better structural and seismic assessment of historical buildings. More detailed future nonlinear and dynamic analyses to be conducted in the next phase of this study are expected to reveal the shortcomings of structural and seismic performances of the historical buildings and monuments.

ACKNOWLEDGEMNT

Special thanks are due to Metrafor and BNZ companies from Uzbekistan for funding the pilot program of heritage scanning in Samarkand and providing access to the laser scan data and high-resolution still images. The authors would like to express their great appreciation to each restless member of the field work team: Mr. Anvar Ishankhodjaev (BNZ), Mr. Roman Kevkhayants (BNZ), Mr. Ruslan Islamgaraev (Metrafor), and Mr. Ilkom Kholov (Metrafor). Special thanks are due to Mr. Ruslan Islamgaraev (Smart Scanning Solutions) and Mr. Evgeniy Melekov (BNZ) for their invaluable help with the data reduction. Strong participation of Miyamoto International in data reduction of Samarkand's laser scans and subsequent finite element analysis is greatly appreciated. The authors would like to acknowledge National Science Foundation which provided financial support for development and operations of nees@berkeley experimental site. The authors would like to acknowledge the Research Institute of Mathematical Physics and Seismodynamics Grozny, Russia for sponsoring some data reduction of the point clouds obtained during the Samarkand project.

REFERENCES

[1] Sagy, A., Brodsky, E.E., and Axen, G.J., 2007. Evolution of Fault-Surface Roughness with Slip, Geology, 35, 283-286.

[2] Spring, A.P. and Wetherelt, A., 2007. Virtually Butrint: Digitally Capturing a World Heritage Site in 3D Using a Mid-Range Laser Scanner, 21st CIPA UNESCO Symposium.

[3] Mosalam, K.M., Takhirov, S.M., and Park, S., 2014. Damage Assessment Using Laser Scanning after the January, 12, 2010 Haiti Earthquake, Structural Control and Health Monitoring, 21(1), 115-134.

[4] Mosalam, K.M., Takhirov, S., and Hashemi, A., 2009. Seismic Evaluation of 1940s Asymmetric Wood-Frame Building Using Conventional Measurements and High-Definition Laser Scanning, Earthquake Engineering and Structural Dynamics, 38(10), 1175–1197.

[5] Takhirov, S.M., 2010. Laser Scanners in Structural Assessment and FE modeling, Proc. 2010 Structures Congress, Orlando, Florida, May.

[6] Pankratyev, G.A. 1890. Album of historical monuments of the city of Samarkand by the amateur photographer G. A. Pankratyev (copyright: in public domain).

[7] Leica Geosystems, 2006. HDS Training Manual: Scanning & Cyclone 5.4.1, San Ramon, CA.

[8] Schroeder, H., Schwarz, J. (1996): Uzbek-German Workshop on the "Seismic-resistant Strengthening of Tilakari Madrasah at Registan Square, Samarkand"- Review by the Organizers. In: Historic Monuments in Seismic Regions (compiled by Schroeder, H. and J. Schwarz), Wiss. Zeitschrift der Bauhaus-Universität Weimar 42, 1, 9-16.

[9] Sourdel-Thomine, J; Spuler, B. (1990) Die Kunst des Islam. Propyliien Kunstgeschichte. Berlin: Propylaen-Verlag.

[10] MathWorks, Inc., 2007. Getting Started with Matlab 7, Natick, MA.

[11] Robert McNeel & Associates, 2014. Rhinoceros 3D User's Guide, Seattle, WA.

[12] TNO Diana, 2014. User's Manual - Release 9.5, Delft, Netherlands.

COMPDYN 2015
5th ECCOMAS Thematic Conference on
Computational Methods in Structural Dynamics and Earthquake Engineering
M. Papadrakakis, V. Papadopoulos, V. Plevris (eds.)
Crete Island, Greece, 25–27 May 2015

STRUCTURAL HEALTH MONITORING AND DIAGNOSTIC INVESTIGATIONS OF THE SCROVEGNI CHAPEL, ITALY

C. Modena[1], F. Lorenzoni[2], M. Caldon[2] and M.R. Valluzzi[2]

[1] Dpt. of Civil, Architectural and Environmental Engineering, University of Padova
via Marzolo, 9 35131- Padova (Italy)
e-mail: claudio.modena@dicea.unipd.it

[2] Dpt. of Civil, Architectural and Environmental Engineering, University of Padova
via Marzolo, 9 35131 - Padova (Italy)
{filippo.lorenzoni, mauro.caldon, mariarosa.valluzzi}@dicea.unipd.it

Keywords: Structural health monitoring, diagnostic investigations, damage detection.

Abstract. *The Scrovegni Chapel represents without doubt a masterpiece in the history of painting in Italy and Europe in the 14th century and it is considered the most complete series of frescos executed by Giotto in his mature age. Given the crucial importance of the building from a cultural point of view, in 1995 a systematic research campaign started, including the execution of studies on the structural health state of the Chapel. The final aim is to guarantee optimal preservation conditions on the occasion, and in direct continuation, of the restoration of the Giotto's frescoes performed in 2001-2002. The investigation plan, based on non-destructive techniques, includes punctual tests, periodically repeated, and continuous monitoring, direct measurements and indirect identifications (back-analysis) of relevant structural parameters. Although the structural layout of the chapel is apparently simple, the protection of the monument is strongly connected to the fact that its historic and artistic value cannot be separated from the structure itself and the effects of strengthening interventions carried out in the last 150 years need to be carefully evaluated. In this framework a structural health monitoring system has been recently installed by the authors. A network of static and dynamic sensors controls the relevant parameters related to the structural safety of the monument and the protection of the artistic content. The paper describes the diagnostic investigations carried out, including ambient vibration tests, crack pattern survey and identification of possible ongoing degradation phenomena. Then the installed monitoring equipment is presented focusing on the algorithms developed and implemented into a processing software to perform the online automatic analysis of static data and the identification of modal parameters. Relevant features extracted from monitoring data are then used as inputs for the application of damage detection algorithms and the numerical calibration of a finite element model of the structure.*

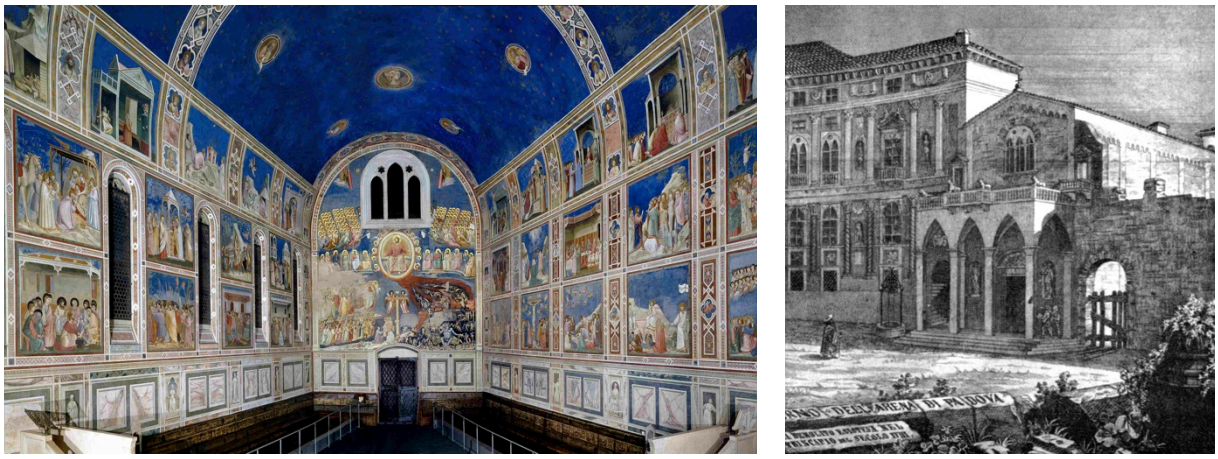
1 INTRODUCTION

1.1 Historical background

The Scrovegni Chapel, dedicated to St. Mary of the Charity and frescoed by Giotto between 1303 and 1305, is located in the hearth of the historical city center of Padua and it is one of the most important masterpieces of Italy (Figure 1a). In 1300 Enrico Scrovegni of Padova purchased a piece of land from Dalesmanini family. The property included an oval area where a Roman Arena was originally present and he decided to build in this perimeter a family palace with a private chapel. Giotto's Last Judgment covers the entire wall above the chapel's entrance. Opposite it, on the chancel arch above the altar, there is an unusual scene of God in Heaven. The longitudinals walls are arranged in three tiers of narrative frescoes, each with four two-meter-square scenes, representing the Nativity, the Passion of Jesus, the Resurrection, and the Pentecost [1] [2].

The building was subjected to several transformation and interventions over centuries. During the 16th c. mainly modifications were introduced on the palace. The last heirs, the Gradenigo family, occupied the arena since 18th c. and by the time the lack of maintenance was evident showing several damages on the buildings. In 1817 the portico of the chapel collapsed and was demolished. Even after this event the family took no interest and instead of looking for bills for urgent repairs, the palace was demolished in 1827 (Figure 1b). Without the protection of the palace, the north wall of the chapel began to deteriorate, allowing rainwater to seep through and causing serious damage to the frescos inside.

Since then several damages and deteriorations are progressively reported: cracks on the triumphal arch, propped in 1871, cracks in the barrel vault, walls, break of iron ties, etc. In 1901 a long series of works repair began. In 1937 the foundations at the south-east corner of the chapel were strengthen and in 1957 huge interventions were performed on the facade, with insertion of iron ties in the wall thickness. Finally in 1963 the original timber structure of the roof was substituted with steel trusses and the iron ties of the main vault replaced.



a) b)

Figure 1: a) Interior view of the chapel with the Giotto's frescos; b) Drawing of 1842 referring to a scene from 1817, before the demolition of the Scrovegni palace

1.2 Geometrical and structural description

The general floor plan has a rectangular shape of 10.40 m by 20.89 m composed by a nave, a square chancel of about 4 m and a polygonal apse (Figure 2). The perimeter walls of the nave (about 12 m high) are the lowest volume of the building. The height increases gradu-

ally up to 13,5 m in the chancel and vestry, until reaching 15 m in the small octagonal tower of the apse. A crypt extends beneath the whole nave, having a height of about 2.66 m from the crypt floor level to the sides of the vaults, and a maximum height of 4.15 m from the crypt floor to the top vault.

The building maintains the homogeneity of materials originally used, even if several interventions were executed during its history. Brick masonry is the principal constitutive material used for the side walls, the pillars, the barrel vaults over the nave and crypt, the cross vault of the vestry and over the apse ceiling vaults. The side walls of the nave chapel are 0.67 m thick, increasing their thickness up to 0.88 m to contain five pillars in the north and south façade respectively. The external brickwork was originally plastered. The reddish-brown color clay bricks of 25x12 x2,5 cm used for its construction were placed according to the Flemish type. The mortar joints between the brick courses of a pinkish-white color are about 2-2,5 cm height.

The horizontal structure of the main body consists of two masonry vaults and the roofing. The brick barrel vault over the nave is a typical stilted semicircular arch structure, about 0.24 m thick, with a span of 180 degrees and a radius of 4m. The vault over the crypt is a flat arch of solid brickwork, 0.27 m thick.

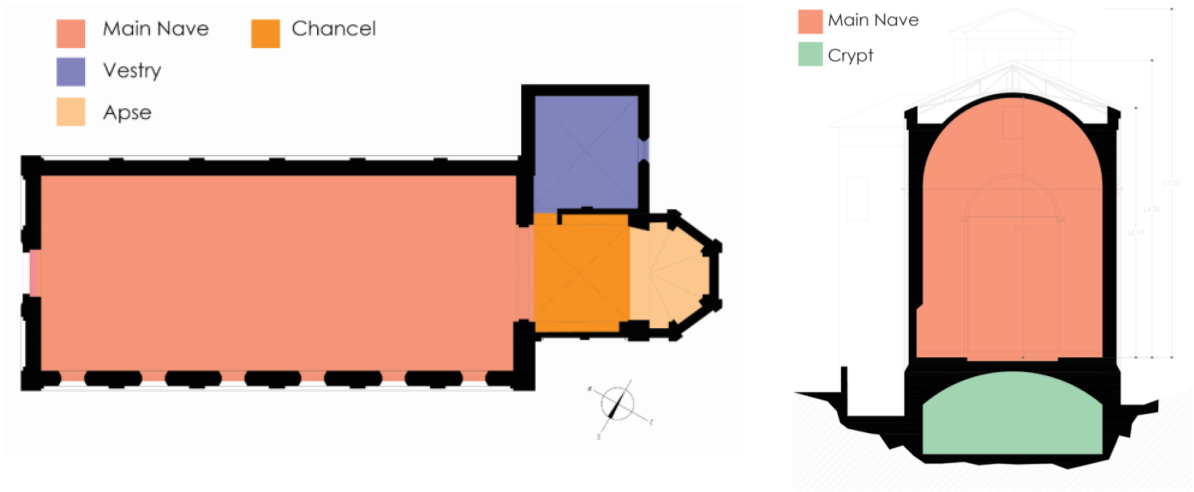


Figure 2 - Floor plan and section of the chapel

1.3 Past strengthening interventions

Unfortunately nothing is known about the work that took place before 1817, when the portico of the Chapel collapsed. The main structural interventions performed on the chapel date back to the 20th c. (Figure 3). In the period 1936-1946 some consolidation works on the foundations were carried out; the crypt vault was strengthened through the insertion of three tie beams besides the side walls; during the Second World War in the crypt 8 equidistant buttresses were built, at right angles to the side walls, up to the height of the ceiling vaulting in order to prevent possible collapse due to bombing.

During the early Sixties the original wooden truss beams of the roof were replaced with eight steel trusses. The weight of the roof was taken by the side walls where a RC beam was constructed. Five tie-rods of the nave were replaced and anchored through external steel plates on the side walls. The ceiling vaults of the vestry and loggia were strengthening by constructing reinforced concrete sections and the original roofing over the loggia was replaced by concrete V beams and tie rods. The original floor over the vestry vaulting was

probably strengthening at the same time, during the 1960 intervention, applying the same technique.

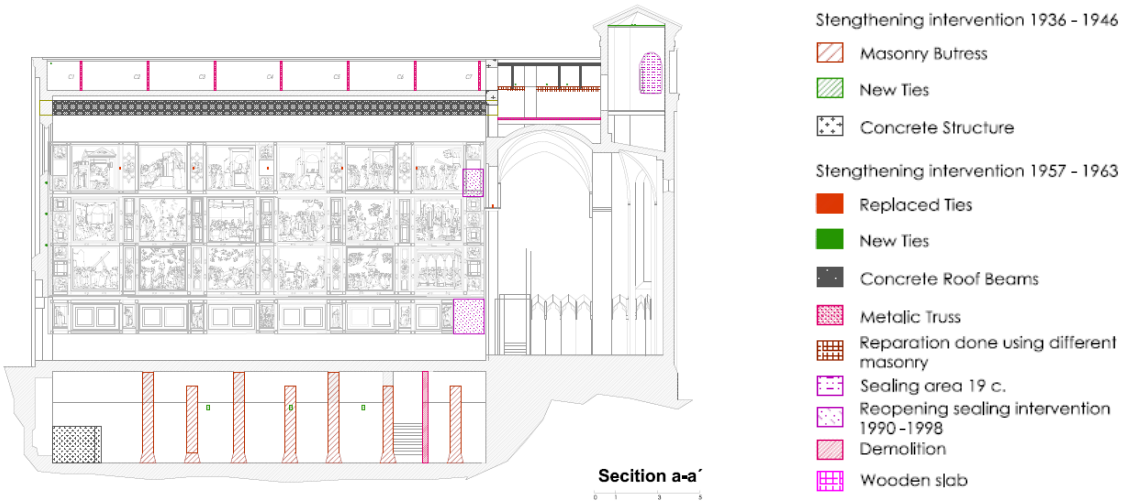


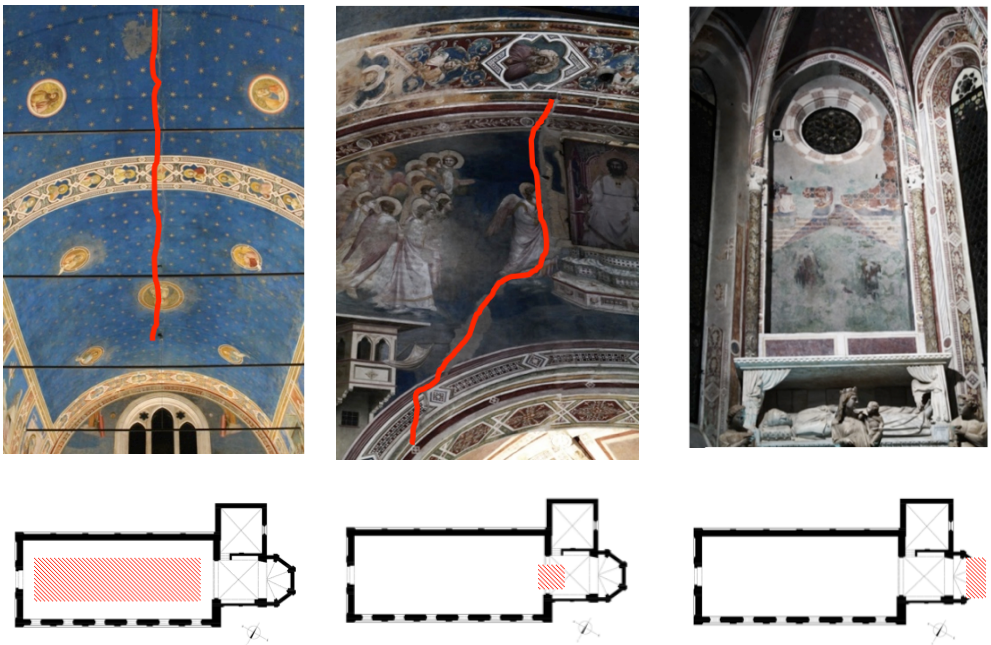
Figure 3: Strengthening interventions performed in the 20th c. on the chapel

2 ON SITE INSPECTIONS

2.1 Damage survey

In order to define the current state of the building and design the optimum layout of the monitoring system detailed visual inspections were carried out to correct and refine the available geometrical surveys and perform a precise survey of the structural, physical and chemical deterioration factors affecting the chapel.

Most of the interior cracks surveyed within this work were already reported during the 19th century. The geometrical survey of 1871 showed several cracks still present at that time in the south wall, in the triumphal arch, in the main façade (below the window) and on the vault.



a) b) c)

Figure 4: Damage survey: cracks on the intrados of the frescoed vault of the main nave (a) and on the triumphal arch (b); damages due to salt crystallization on the wall of the apse (c)

Without any doubt, the most critical crack is placed on the main triumphal arch mentioned in several reports and subjected to subsequent reparations that included a partial reconstruction of the upper part of the wall (Figure 4b).

Three main longitudinal cracks are visible along the development of the nave barrel vault: two at the thirds of the vault on the extrados and one at the top on the intrados (Figure 4a), showing a clear three-hinges behavior of the arch. These cracks were probably induced by the structural configuration of the previous roof and the geometry of the vault. Moreover horizontal cracks at the impost of the vault were observed at the end of the 19th Century, probably due to the ineffectiveness of the ties that counteract the thrust of the vault.

Comparing the current condition to previous reports, it is possible to observe that the chancel was severely damage with vertical cracks and repaired afterwards. Today is only possible to recognize some detached area, without any evidence of serious stability risk.

Rising damp has severely affected the frescos and also contributed to cause damage on the masonry surface. Salts crystallization were manifested in different areas due to different mechanism of deterioration: efflorescence, spoiling, spalling and splitting (Figure 4c). Even if several structural problems were solved in the middle of the 19th century, the cracked areas of lunette and triumphal arch were still subjected to serious detachments at the end of the 90s, clearly caused by water infiltration from the roof. The roof was repaired in 1999 to solve the water infiltration problems. However, still now soluble salts are detected in the façade as efflorescence, what reveals the presence of moisture at different location of the walls.

At the base of the exterior walls the mechanism of deterioration is manifested mostly due to spoling, splitting and biological attacks, related to the groundwater absorption and the atmospheric dry/wet deposition that lead to fluctuations of the moisture content.

2.2 Ambient vibration tests

Before the installation of the Structural Health Monitoring (SHM) system, dynamic identification tests were performed on the main nave of the chapel. The objective is to understand the dynamic response of the structure subjected to ambient vibrations and to extract the fundamental modal parameters (natural frequencies, damping ratios and mode shapes), later used to calibrate numerical models. It was decided to use 5 single-axial acceleration transducers, which later were kept in the same positions for continuous dynamic monitoring. Two accelerometers were placed along the two orthogonal horizontal directions at the NW corner between the façade and the longitudinal wall (A4, A5); one in the middle of the nave, on the NW wall (A6); at the same section of the vault two other sensors were installed perpendicular to the vault, one in the haunch (A7) and the last at the key (A8) (Figure 5).

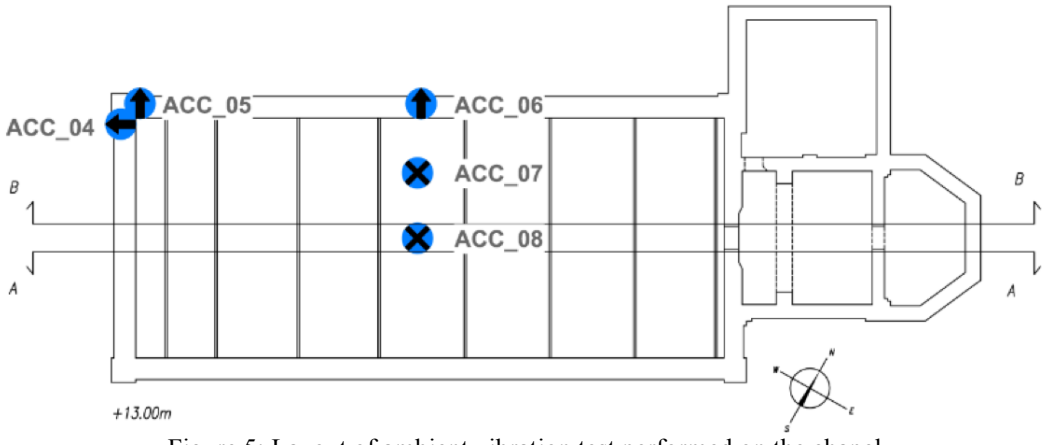


Figure 5: Layout of ambient vibration test performed on the chapel

Once fixed the transducers to the structure in the selected positions, tests consisted in acquiring data in 5 different registrations over a predetermined period, at a specific sampling rate. A typical acquisition consisted in a record length of 131'072 samples, resulting in an acquisition time of approximately 20 minutes at a sampling frequency of 100 Hz. For the identification of the modal parameters (natural frequencies and corresponding mode shapes), output only identification techniques were used (Operational Modal Analysis).

The signal-processing phase consisted in the elaboration of the measured data using dedicated software for OMA: SVS ARTeMIS Extractor 4.0, 2007 [3]. It was decided to use different frequency-domain modal parameter extraction techniques and compare the results: FDD (Frequency Domain Decomposition) and EFDD (Enhanced Frequency Domain Decomposition) [4]. Both methods are based on the evaluation of the spectral matrix (i.e. the matrix of cross-spectral densities) in the frequency domain:

$$\boldsymbol{G}(f) = E[\boldsymbol{A}(f)\boldsymbol{A}^H(f)] \tag{1}$$

where the vector A(f) collects the acceleration responses in the frequency domain, superscript H denotes complex conjugate transpose matrix and E denotes expected value. The diagonal terms of the matrix G(f) are the (real valued) auto-spectral densities (ASD) while the other terms are the (complex) cross-spectral densities (CSD). The ASDs and CSDs were estimated from the recorded time-histories using the Welch's averaged periodogram method.

Peaks in the frequency domain related to structural frequencies were selected through the peak peaking method and the corresponding mode shapes defined (Figure 6).

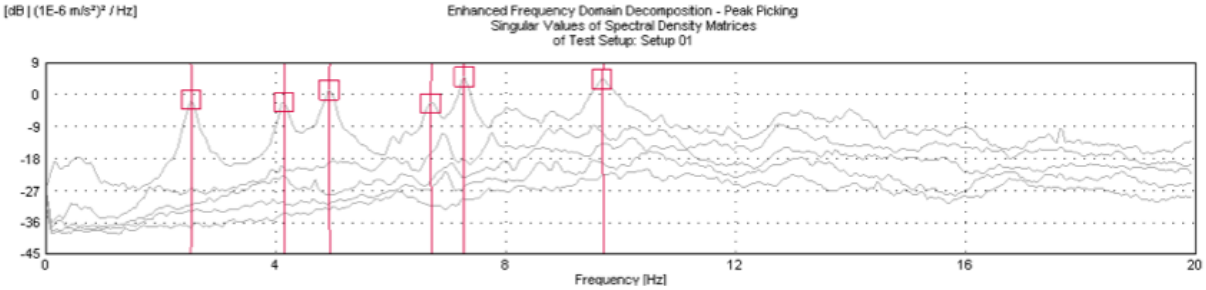


Figure 6: Singular values decomposition of the spectral density matrices: peaks related to structural frequencies are identified on the first singular value through the peak peaking method

Since the number of sensors used in the test is limited it was decided to exploit all the records, comparing the outcomes derived from different OMA algorithms. Once the modal identification phase was completed, the two sets of mode shapes resulting from the application of FDD and EFDD were compared by using the well-known Modal Assurance Criterion (MAC) [5]. The MAC is probably the most commonly used procedure to correlate two sets of mode shape vectors and is defined as follows:

$$MAC\left(\Phi_{A,k}, \Phi_{B,j}\right) = \frac{(\Phi_{A,k}^T \Phi_{B,j})^2}{(\Phi_{A,k}^T \Phi_{A,k})(\Phi_{B,j}^T \Phi_{B,j})} \tag{2}$$

where $\Phi_{A,k}$ is the k-th mode of data set A and $\Phi_{B,j}$ the j-th mode of the data set B. The MAC is a coefficient analogous to the correlation coefficient in statistics and ranges from 0 to 1; a value of 1 implies perfect correlation of the two mode shape vectors while a value close to 0 indicates uncorrelated (orthogonal) vectors. In general, a MAC value greater than 0.80 is

considered a good match while a MAC value less than 0.40 is considered a poor match. The MAC was also later on used to correlate the results of FE models and OMA.

Table 1 reports the six main natural frequencies and corresponding damping ratios of the chapel, identified through ambient vibration tests. The comparison between different OMA techniques (FDD and EFDD) is also reported in terms of percentage errors of the frequency variations and MAC coefficients calculated on the mode shapes extracted with the two methods. It is possible to state that both techniques prove to be reliable and provided consistent results.

Mode no.	f_{FDD} [Hz]	f_{EFDD} [Hz]	ξ [%]	Error [%]	MAC (Φ_{FDD}, Φ_{EFDD})
1	2.539	2.535	2.356	0.16	0.99
2	4.15	4.147	2.268	0.07	0.98
3	4.932	4.939	2.087	0.14	0.96
4	6.738	6.715	1.338	0.34	0.99
5	7.227	7.241	1.549	0.19	0.98
6	9.668	9.666	1.973	0.02	0.95

Table 1: Results of dynamic identification tests in terms of natural frequencies and damping. A comparison between different OMA techniques is also reported as percentage error of frequency variations and MAC coefficients between mode shapes

Figure 7 shows the mode shapes related to the structural frequencies of the chapel identified through ambient vibration tests.

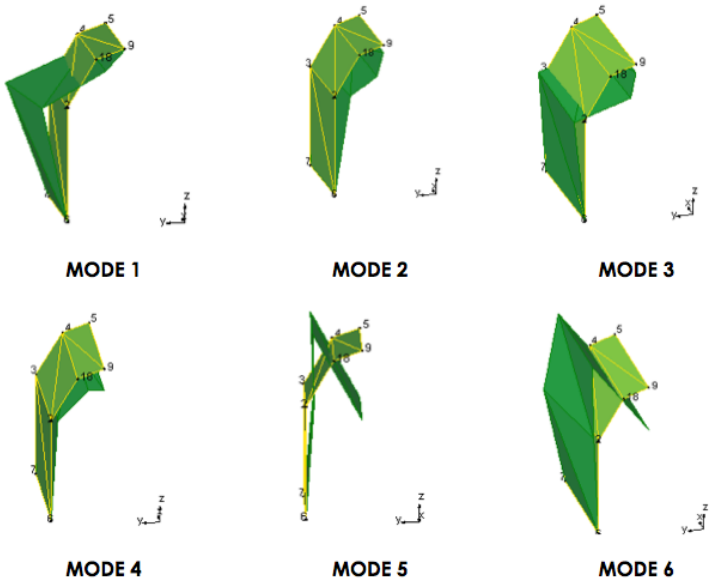


Figure 7: Mode shapes of the chapel identified through ambient vibration tests

3 STRUCTURAL HEALTH MONITORING

Once the on site investigations were concluded, a static and dynamic monitoring system was installed on the Chapel in August 2013 to assess continuously its structural health state. It acquires vibration characteristics, evaluates the opening or reclosing of the main cracks and controls the inclination of the lateral main walls. The system gives interesting information on the progression or stability of the assessed damage pattern. These readings are constantly related to environmental parameters (temperature and relative humidity). The evaluation of the measured quantities, and in particular their changes over time, gives a strong indication in assessing the structural behaviour of the building.

3.1 Equipment and layout

The monitoring system installed is composed by: (i) static sensors to control the damage and crack pattern of the structure and (ii) accelerometers to measure ambient vibrations and capture possible seismic events (Figure 8).

The static system includes devices to measure displacements of the surveyed cracks and inclinations of the lateral walls. It is composed by 12 static channels: 7 displacements transducers installed on representative cracks on the vault and 1 on triumphal arch; 2 inclinometers to control the overturning of the two lateral walls; 2 integrated sensors of temperature and relative humidity to control both internal and external environmental conditions. Data from the static system are registered every 2 hours.

The dynamic monitoring system is composed by 8 high sensitivity piezoelectric accelerometers connected to the acquisition unit. 3 reference sensors are fixed at the base of the structure to record the ground acceleration both in operational conditions and during seismic events. The other acceleration sensors are placed in the same positions of ambient vibration tests. High-density (100 samples per second) dynamic information is continuously recorded every 12 hours.

The continuous dynamic monitoring has several connected purposes: (i) characterize the dynamic response from ambient vibrations along with its dependence with environmental parameters; (ii) capture the dynamic response in the occasion of possible seismic events; (iii) calibrate reference Finite Element models based on the daily extraction of modal parameters from recorded vibrations.

The system is equipped with an internet router for remote data transmission.

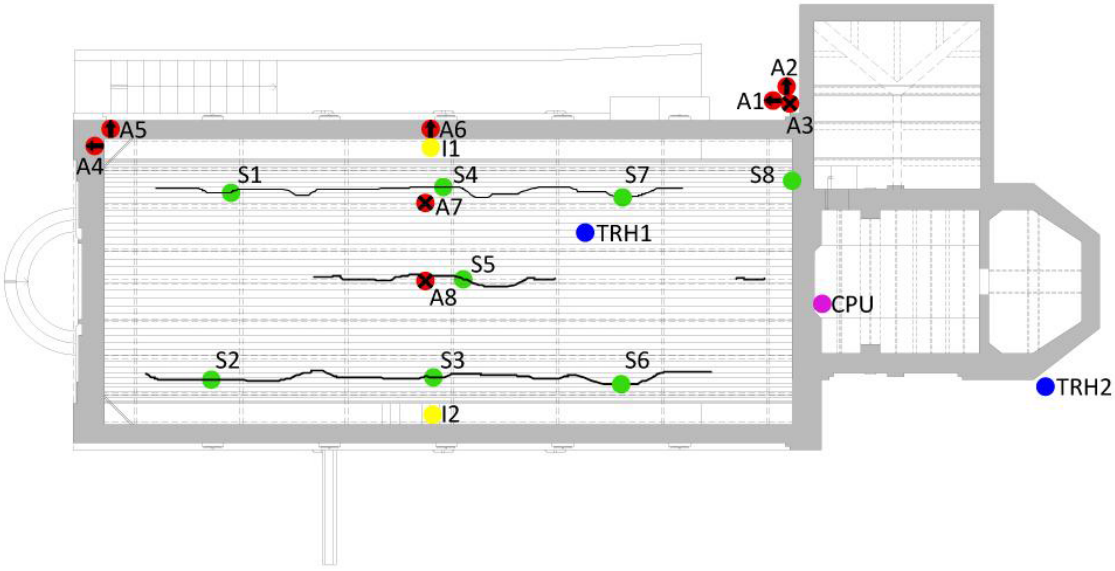


Figure 8: Layout of the monitoring system: S1 to S8 are displacement transducers, I1 and I2 inclinometers, TRH1 and TRH2 temperature and relative humidity sensors, A1 to A8 accelerometers, CPU the acquisition unit.

With regard to the dynamic measurements, two strategies have been set: "long" acquisition, (corresponding to 131'072 points), on regular intervals to allow subsequent identification by means of structural vibration in different environmental conditions (seasonal cycle), and "short" acquisition which is done automatically when the vibrations exceed the trigger (significant event).

3.2 Automatic data analysis

The installed monitoring system stores a huge amount of static and dynamic data every day and thus significant effort is devoted to the analysis of recorded data. For this reasons, it has been implemented automatic procedures for both static and dynamic data processing in Matlab environment.

The automatic procedure applied to static data elaborates a standard .txt file acquired by the static system and create automatically a series of graphs, representing the variation over time of the monitored parameters (displacements and inclination) and correlating them with temperature variations. The algorithm is also equipped by an early warning system that automatically send a message if a sensor exceed a predefined threshold.

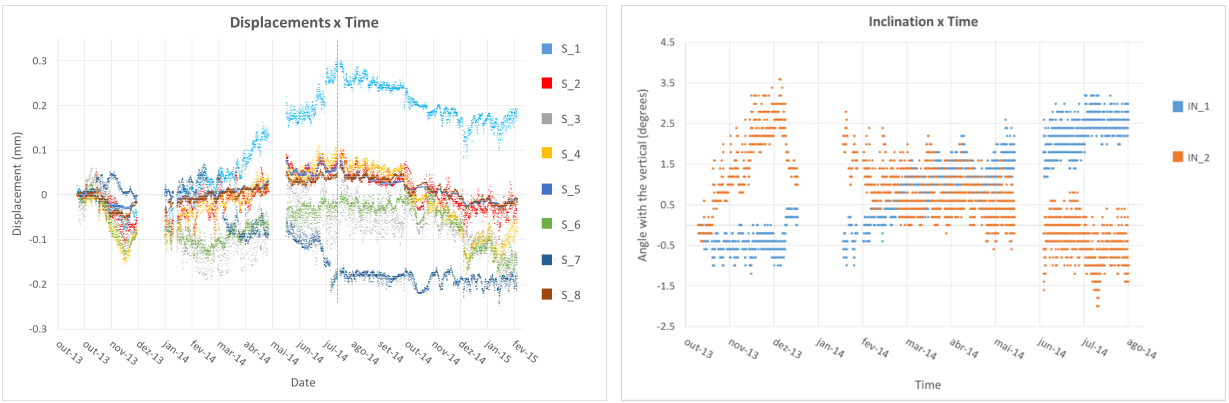
The automatic procedure applied to dynamic data elaborates the acquisition files and automatically estimate modal parameters from measured vibrations. Usually this process involves a large amount of user interaction, especially when lots of data need to be processed in a short amount of time. The developed algorithm, based on a Matlab toolbox (MACEC 3.2, 2011) [6], implements several frequency-domain OMA techniques in order to extract automatically model parameters (frequency and damping ratio development over time, MAC indexes variation between the starting reference identification and the daily identification).

3.3 Monitoring results

Both static and dynamic data are transmitted from the acquisition unit to the central server of the University of Padova and processed on arrivals by the automated algorithms. In this section the development of static (Figure 9a) and dynamic (Figure 9b) measurements are reported and correlated with the variations of the environmental parameters.

Based on the initial dynamic identification, the variations of the fundamental natural frequencies, mode shapes and damping ratios of the Chapel, especially of the vault, are constantly extracted from the measured vibrations. The frequency development over time (Figure 10) gives a strong indication on the dynamic characteristics of the structure and it is directly related to the environmental parameters. The evolution of the 11 possible natural frequencies are investigate in the period from 22/10/2013 to 02/10/2014.

Unfortunately, a thunder hit the Chapel in August 2014, 09. As a consequence, accelerometers 4 and 5 were severe damaged and was not possible to obtained the values of some natural frequencies anymore.



a) b)

Figure 9: Variation of the crack opening (a) and of the two sidewalls inclination (b) during the monitoring period

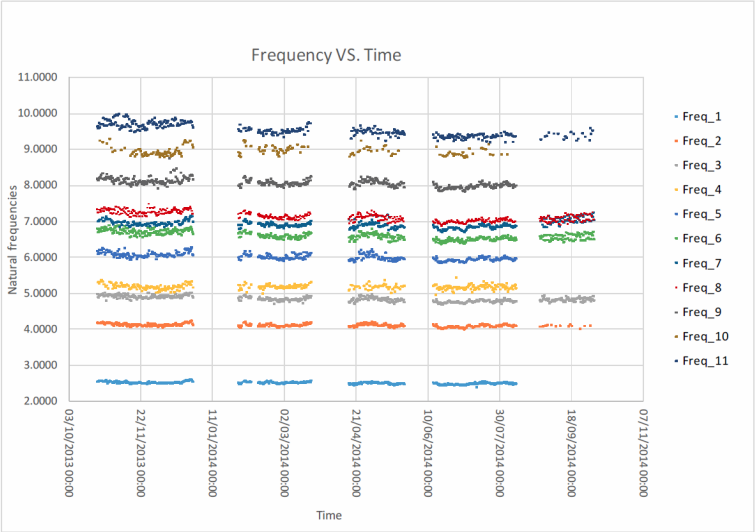


Figure 10: Natural frequencies variation during the monitoring period

3.4 Modeling of environmental effects and amage detection

Analysing the structural behaviour of the monitored cracks or the frequencies trend it is possible to confirm a strong dependence of the these results from environmental parameters, whose control and quantification become essential before any attempt to identify the presence of damage. In fact once the environmental effects are filtered out from recorded data, it is possible to accurately decompose the measurements into their reversible and irreversible components, the latter being associated to active deteriorating processes. Different methods can be applied to remove the effects of environmental or operational factors on the extracted parameters and thus increase the structural reliability.

Within the present research regression analysis and black box models are tested and applied, exploiting a large number of observations to establish relations between the recorded parameters (e.g. crack opening) and the factors that may influence them. Statistical models can be exploited, in an initial phase, to understand the influence of each predictor (input of the model) on the dependent variable (output of the model) and then, to predict future values of the response when only predictors are known. In this case ARX models [7] that comprehends an Auto-Regressive output and an eXogeneous input part are used. This is ideal for representing monitored parameters when they depend (linearly) on the rate of change or trend in temperature as well as the present temperature. The multivariable ARX model with n inputs x and one output y is presented by:

$$\hat{y}_k + a_1 y_{k-1} + \cdots + a_{na} y_{k-na} = b_1 x_k^{env} + b_2 x_{k-nk-1}^{env} + \cdots + b_{nb} x_{k-nk-nb+1}^{env} + e_k \qquad (3)$$

where a_i and b_i are coefficients for the autoregressive and exogenous part, respectively, na is the autoregressive order, nb the exogenous order, nk is the number of delays from input to output, and $e_k = y_k - \hat{y}_k$ is the unknown residual that can be assumed Gaussian. y_k and $\hat{y}_k$ are the actual (real) and the estimated (model) responses respectively.

Preliminarily a correlation analysis is performed with the objective of identifying the time series of environmental parameters x_k presenting higher correlation coefficients with the time series containing the measured output y_k (i.e. crack opening).

The correlation coefficient r_{xy}, which represents the normalized measure of the strength of linear relationship between the two variables, is given by:

$$\hat{r}_{xy} = \frac{cov(x_k, y_k)}{\sigma_x \sigma_y} \qquad (4)$$

The value of the correlation coefficient varies between -1 and +1: the closer to unity, the more the two variables are correlated.

The parameters of the model, equal to na+nb, were calculated using a least-squares procedure, minimizing the residuals e_k. y_k is the measured output and $\hat{y}_k$ is the output predicted by the model at the same time step. Once the best ARX model is obtained from the first half of the time history of monitoring (estimation phase), new measured environmental parameters (fresh data), collected during the second half (validation period), are used to simulate the response of the studied crack.

From the comparison between the simulated measures behaviour and its recorded counterparts (Figure 11), changes caused by structural damage can be distinguished from those caused by varying environmental conditions. The standard deviations can be used to establish confidence intervals around the predicted values. For instance, if $\hat{y}$ is the predicted output and $\hat{\sigma}_y$ the estimated standard deviation on a new observation, the $(100-\alpha)\%$ confidence interval on $\hat{y}$ is given by:

$$\left[\hat{y} - t_{\alpha/2,\nu}\hat{\sigma}_y \quad , \quad \hat{y} - t_{\alpha/2,\nu}\hat{\sigma}_y\right] \tag{5}$$

where the value $t_{\alpha/2,\nu}$ is found from a statistical table of the t-Student distribution and for a large number of data (as in this case) and $\alpha = 0{,}05\%$ (leading to 95% confidence intervals), we have $t_{\alpha/2,\nu} = 1{,}96$. The confidence intervals defined can be used as an objective criterion to detect damage.

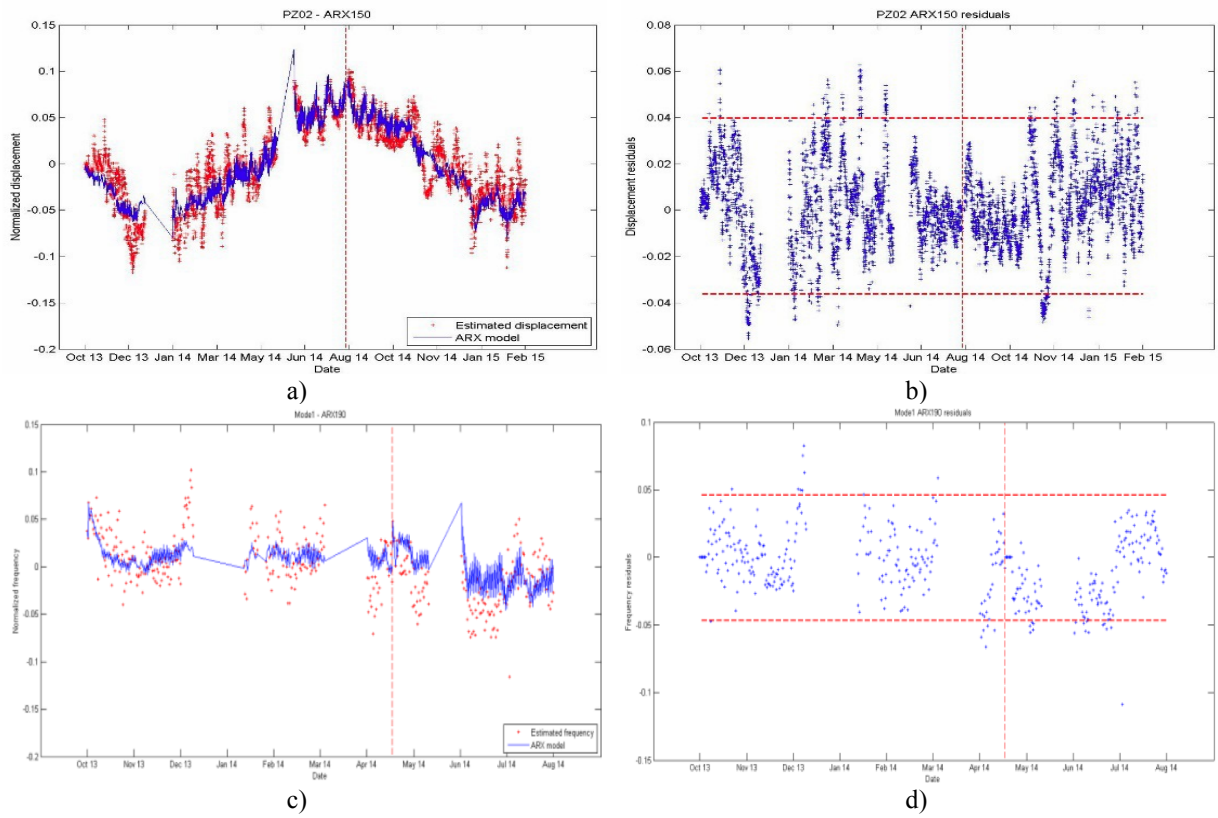
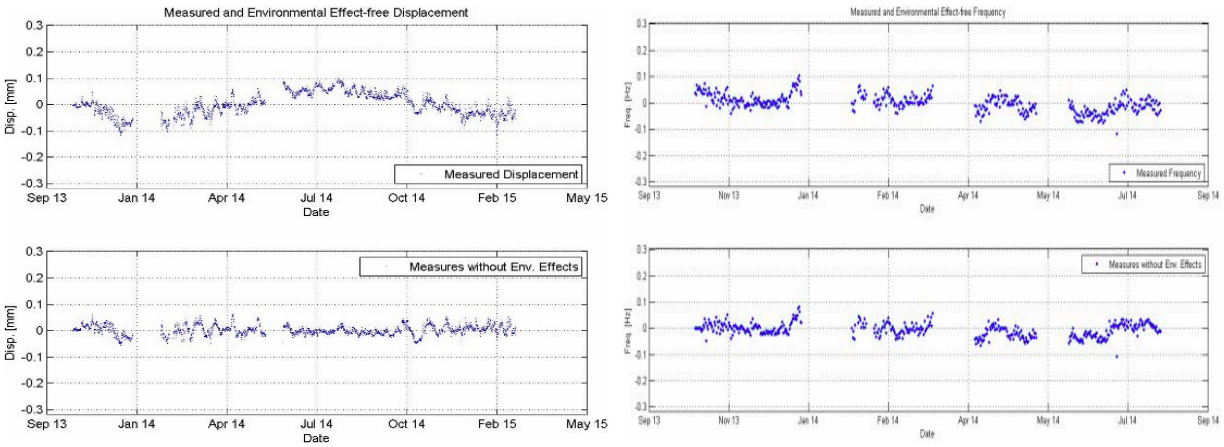


Figure 11: Comparison between measured (red) and simulated outputs of the crack controlled by sensor S2 (a) and first natural frequency variation (c). Residual analysis (blue dots) between measured and predicted values of the same parameters with 95% confidence intervals (b) (d).

Figure 12 shows the temporal evolution of the displacement of a vault crack (a) and of the frequency trend (b) during a period of 18 months before and after the elimination of the envi-

ronmental effects performed through the described dynamic regression models. It can be observed that the variation of filtered value is reduced to a small range, which proves that the selected ARX model properly describes the factors with greater influence on the output. Any other event, besides temperature, would represent a potential damage.



a) b)

Figure 12: Time evolution of crack displacement (a) and natural frequency variation (b) before and after the elimination of the environmental effects (regression model).

The application of regression analysis and black box models gives the possibility to model and remove the environmental effects from monitoring results. It is possible to state that the controlled crack pattern is stable and that the displacement variations are related only to the seasonal thermal cycles.

Regarding the natural frequency variation it is noted that these parameters are slightly influenced by environmental parameters and poor correlation was calculated with the changes of both internal and external temperature and relative humidity. The applied algorithm form damage detection do not show a variation of frequency related to structural damages.

4 FE MODELING AND CALIBRATION

A detailed FE numerical model of the Scrovegni chapel was implemented in DIANA 9.6 [8] order to evaluate the static and dynamic behaviour of the building. The FE model was calibrated on the basis of the results of the experimental activities, in order to be subsequently used to simulate the response of the structure to different external actions.

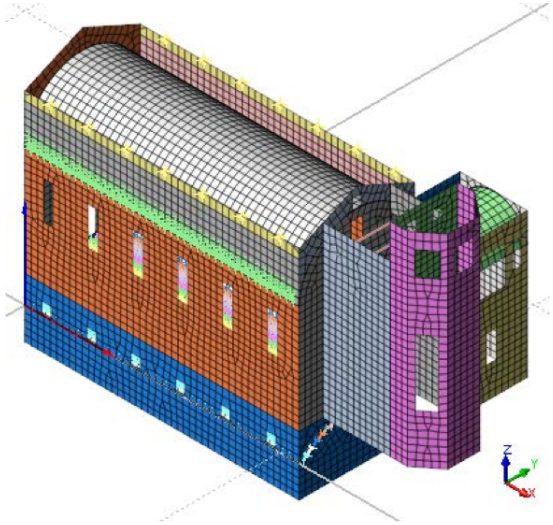


Figure 13: FE model of the Scrovegni chapel

The structure has been modeled with plate elements to schematize walls and vaults and truss elements for iron ties. The weight of the roof and the filling of the vaults are represented in the form of translational masses applied to the nodes (Figure 13).

4.1 Calibration strategy and model updating

The construction and calibration of the FE model was performed as follows:

- Execution of dynamic identification test and extraction of the experimental modal parameters used as reference values
- Construction of the FEM model assigning the most reliable material parameter based on visual inspections and masonry quality identification
- Sensitivity analysis of the elastic parameters that influence more the dynamic response
- Calibration of the parameters
- Quality analysis through MAC comparison of mode shapes

The calibration process is an iterative procedure in which the parameters are changed one by one to achieve an optimal match between experimental and numerical modal parameters.

Model updating results are reported in Table 2 and Figure 14.

Mode no.	f_{EXP} [Hz]	f_{FEM} [Hz]	Error [%]	MAC (Φ_{EXP}, Φ_{FEM})
1	2.539	2.49	1.97	0.81
2	4.15	4.14	0.24	0.56
3	4.932	4.96	0.56	0.65
4	6.738	6.43	4.79	0.72
5	7.227	6.97	3.69	0.90
6	9.668	9.46	2.20	0.63

Table 2: Calibration results of the FE model: comparison between experimental and numerical modal parameters

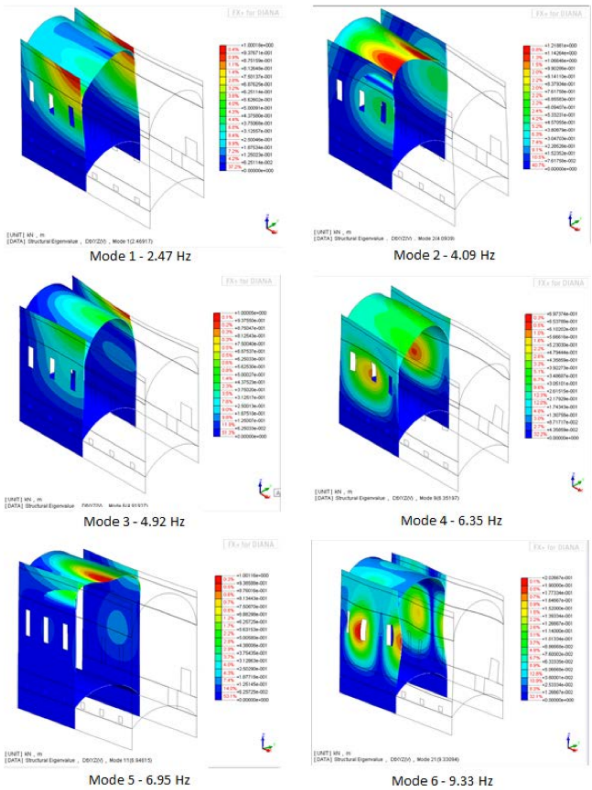


Figure 14: Numerical mode shape of the chapel after the calibration

The model updating leads to excellent results in terms of natural frequency and rather good matching in terms of mode shapes calculated through the MAC coefficient. The absolute frequency errors are less than 5% and on average equal to 2.05%.

5 CONCLUSIONS

A methodology for the study and assessment of an important Cultural Heritage structure based on diagnostic investigations and structural health monitoring is reported in this paper.

The first step was the execution of visual inspections and ambient vibration tests to define the current state of the building and design the optimum layout of the monitoring system, composed by static and dynamic sensors. The aim of monitoring is to control permanently the structural response of the chapel subjected to both operational and exceptional actions (such as earthquakes). It can be used also to assess possible vulnerabilities and avoid the execution of intrusive interventions, unless critical structural problems are detected.

Features automatically extracted from the monitoring data have been statistically analyzed through regression analysis and ARX models. The proposed data driven approach proved to be very effective to remove environmental effects and identify possible damages.

Finally modal parameters extracted from dynamic testing and monitoring were used to calibrate reference FE models of the chapel.

REFERENCES

[1] Fabbri, Colabich, Giorgio**,** *I recenti lavori di restauro alla Cappella degli Scrovegni e le indagi esperite per la sua conservazione*, 1961-63

[2] VV.AA., *La Cappella degli Scrovegni a dieci anni dal resturo*, Atti del convegno svolto il 25 giugno 2012

[3] SVS, ARTeMIS Extractor, Release 4.0, Structural Vibration Solutions A/S, Aalborg East, Denmark

[4] Brincker R., Zhang L., Andersen P. (2000), Modal identification from ambient responses using frequency domain decomposition, in Proceedings of the IMAC 18, International Modal Analysis Conference, San Antonio, USA.

[5] Allemang R.J., Brown D.L. (1982) A correlation coefficient for modal vector analysis, in: Proceedings of the IMAC 1, International Modal Analysis Conference, Orlando, FL, USA, 1982.

[6] MACEC 3.2 Released, a MATLAB Toolbox for Experimental and Operational Modal Analysis, developed by Edwin Reynders, Mattias Schevenels, and Guido De Roeck. Copyright © KU Leuven

[7] Ljung L. (1999) System Identification: Theory for the User, Second edition, Prentice Hall, Upper Saddle River, NJ, USA.

[8] DIANA 9.6 Finite Element Analysis, User's Manual-Release 9, TNO, Netherlands, 2014.

COMPDYN 2015
5th ECCOMAS Thematic Conference on
Computational Methods in Structural Dynamics and Earthquake Engineering
M. Papadrakakis, V. Papadopoulos, V. Plevris (eds.)
Crete Island, Greece, 25–27 May 2015

STRUCTURAL MONITORING OF MONUMENTAL BUILDINGS: THE BASILICA OF SANTA MARIA DEGLI ANGELI IN ASSISI (ITALY)

Nicola Cavalagli, Massimiliano Gioffrè and Vittorio Gusella

Department of Civil and Environmental Engineering, University of Perugia
via G. Duranti 93, 06125, Perugia, Italy
e-mail: {nicola.cavalagli,massimiliano.gioffre,vittorio.gusella}@unipg.it

Keywords: Structural Health Monitoring, Architectural Heritage Preservation, Masonry dome, Monumental Buildings.

Abstract. *The preservation of architectural heritage and monumental structures is an important challenge of the scientific research, especially for the countries where cultural heritage is of primary concern and, at the same time, there are significant risk factors due to natural hazards as earthquakes. In this perspective, structural health monitoring systems can improve the protection of structures by providing real-time diagnostic data together with suitable procedures, which are able to identify possible occurring problems. In this work the first results given by a monitoring system placed in the Basilica of Santa Maria degli Angeli in Assisi will be presented. Data recorded by nine linear variable displacement transducers (LVDTs) are shown together with power spectral densities of acceleration time histories measured during ambient vibration tests. The spectral analysis results are compared with the natural frequencies given by a numerical model of the Basilica structural system.*



Figure 1: Basilica of Santa Maria degli Angeli in Assisi.

1 INTRODUCTION

Structural health monitoring can give crucial information on the variation in space and time of the main mechanical features of existing buildings. These information assume significant meaning especially when dealing with historical and monumental constructions where it is important to preserve architectural and cultural heritage [1],[2].

Within this context, monitoring systems can be used to provide real-time diagnostic data together with all the relevant information that can be useful to detect changes is structural parameters, often associated with some kind of structural damage.

In order to obtain such information a research program has been recently started to monitor two relevant historical constructions in the center of Italy: the bell-tower of the Basilica of San Pietro in Perugia [3] and the dome of the Basilica of Santa Maria degli Angeli in Assisi.

In this paper the first results obtained by the monitoring system placed in the Basilica of Santa Maria degli Angeli in Assisi are presented.

The Basilica of Santa Maria degli Angeli (Fig. 1) is located in the center of Italy. Over the years the structural system has been affected by significant seismic events, among which the earthquakes in 1832 and in 1997 were the most severe. In particular, the event in 1832 caused the collapse of the nave and the left aisle, together with a wide spread damage scenario, which also involved the drum-dome system.

The seismic event of 1997 induced damages only in a few parts of the structural system, nevertheless, after a set of strengthening and rehabilitation works, a ”static” monitoring system consisting of nine linear variable displacement transducers (LVDTs) has been installed.

In the first part of the paper, after recalling the main historical and geometrical features of the Basilica, the data of the LVDTs recorded in the years 2001-2003 are presented. This system

(a)  (b) 

Figure 2: (a) Image of the drum-dome structural system. Three orders of steel rings can be easily seen. (b) Line-engraving of the damage conditions after the 1832 earthquake. *Prospetto delle ruine del famoso Tempio di Santa Maria degli Angioli di Asisi*, by Cilleni Nepis.

failed after a severe thunderstorm and it was possible to restart it only at the beginning of 2015.

The research program has started in 2014 with a preliminary investigation using two accelerometers installed at the base of the dome to detect the first modal frequencies. The acceleration time histories together with their spectral representation are shown in the second part of the paper and compared with the modal analysis of a preliminary numerical structural system.

These results will be used to design a permanent ”dynamic” monitoring system and to calibrate a numerical finite element model (FEM) that can be used to assess the spatial and time variation of the main mechanical features of the Basilica of Santa Maria degli Angeli in Assisi.

2 THE BASILICA OF SANTA MARIA DEGLI ANGELI IN ASSISI

The Basilica of Santa Maria degli Angeli in Assisi was built between 1569 and 1679. Its original drawing is attributed to the architect Galeazzo Alessi, even if the philological respect of the design is controversial, since the structure was completed many years after the Architect's death. The basilica has a latin cross plan, with 126m and 65m dimensions, with a nave and two aisles and a semicircular apse. The central core, at the intersection between the transept and nave, consists of the four pillars which bear the triumphal arches, the drum and the dome. At the vertical axis of the dome's lantern is located the Porziuncola, a little ancient chapel, heart of the basilica and symbol of Franciscan spirituality.

The current architectural configuration of the façade is quite recent. It was designed by Cesare Bazzani with the aim to confer just the right monumental dignity to the Basilica. It was built at the beginning of the 20th Century and inaugurated in 1930. The actual configuration hides the original façade, more simple and poor, and seems to balance the visual attraction, which was previously dominated only by the drum-dome system.

The dome of the Basilica is majestic and impressive, and is characterized by a singular slenderness due to the lightness of the drum (Fig. 2 (a)) [4]. The inner diameter is of about 20m and the variable thickness of the unique shell starts from 1.60m to 0.70m. The inner perimeter of the drum is circular, while the outer is octagonal; the coupled pilasters at the angles of the

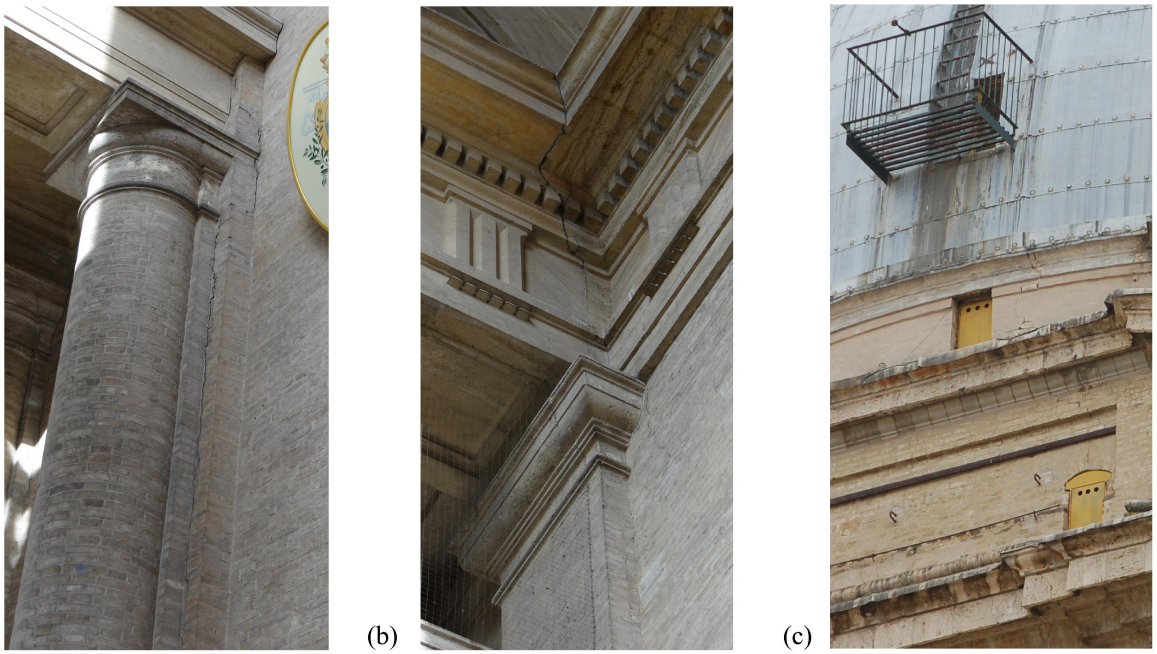


Figure 3: (a)-(b) Vertical cracks between the new and the old façades. (c) Major through crack of the drum-dome system.

octagon become stiffening ribs which join at the *oculus*, the base of the lantern, that gives a total height of about 75m to the structure.

Throughout its history the structure has been subjected to significant seismic events that have compromised also the structural integrity of the Porziuncola. Historical documents describe the damages due to the earthquake of 1832, that caused the collapse of the nave and of a portion of the left aisle (Fig. 2 (b)). The drum-dome system did not collapse, but was severely damaged. Date back to this event the strengthening measures of the drum with three orders of steel rings (Fig. 2 (a)). After the Umbria-Marche earthquake of 1997 the basilica has been subjected to several rehabilitation and strengthening measures [5]. The works have mainly concerned the façade stability, the strengthening of the transepts and aisle vaults and the reinforcement of the drum. The kinematic mechanisms related to these crucial aspects can be detected by the evident cracks, especially for the façade and the drum (Fig. 3).

The cracks and micro-cracks pattern which affects the drum-dome system has been recently surveyed (Fig. 4) [7]. The widespread cracks type and configuration suggest that they are imputable both to seismic and static loads acting over the years. The most significant cracks are located above the north-east wall, due to the presence of internal staircases and a door on extrados of the dome (Fig. 4(a)-(c)), and the west wall of the drum (Fig. 4(b)-(d)).

3 STATIC MONITORING SYSTEM

In 2001 a continuous static monitoring system, consisting of nine linear variable displacement transducers (LVDTs), was installed in order to record displacement time histories as follows (Fig. 5):

- LVDT 1. Installed across the joint between the old façade and the vault of the nave. The sensor monitors the overturning of the façade after consolidation, which has consisted of the foundation's strengthening by means of a series of micro-poles, in addition to the

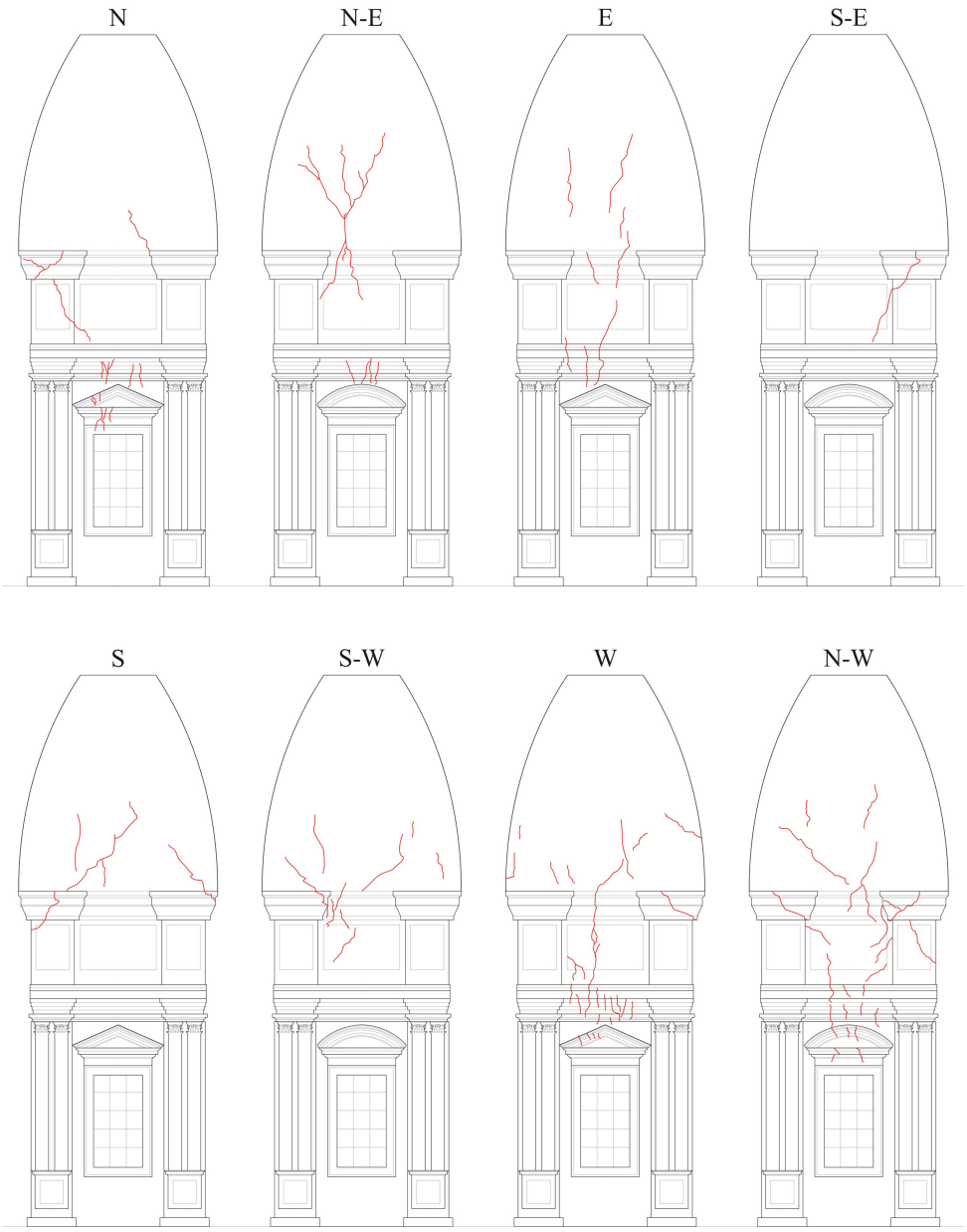


Figure 4: Survey of the cracks pattern at the dome intrados [7].

installation of four orders of couple tie rods to anchor the façade to the lateral walls of the nave.

- LVDT 2-4. In the following they will be identified as “wire-sensor”. The wires are fixed at the nave vault imposts. The LVDT 2 is located at the beginning of the nave, near to the entrance, and LVDT 3 at the end, near to the drum. The wire-sensor LVDT 4 is fixed at the triumphal arch imposts, in the intersection between the nave and the transept. The LVDT 4 has recorded very few good data, so it will not be shown in the following.

- LVDT 5. Installed at the base of the drum, across a crack over the triumphal arch at the

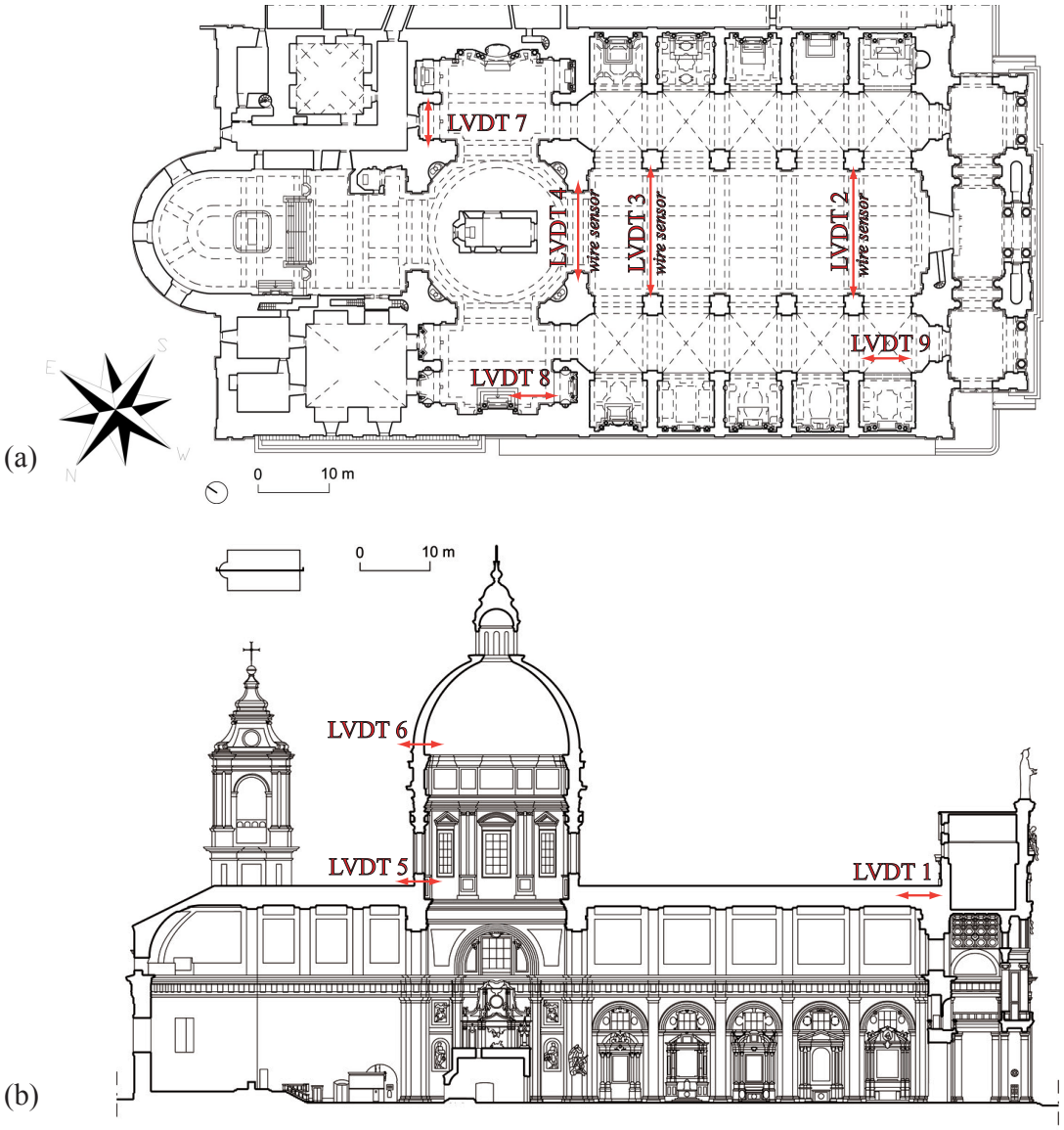


Figure 5: LVDTs' installation layout. (a) Plan. (b) Longitudinal section.

intersection between the nave and the right transept.

- LVDT 6. Installed across the major dome's crack. This critical point is evident both from inside and outside the structure. The importance of this crack is related to a weak section of the wall due to the presence of inner spiral staircases.

- LVDT 7. Installed over the sacristy arch. The monitored crack is linked to an important structural settlement which involves all the right transept.

- LVDT 8. Installed on the vault crown of the left transept.

- LVDT 9. Installed across a significant crack on the vault of S.Diego chapel. Owing to its position, the crack behaviour can be related to the overturning of the façade, and then to the LVDT 1.

The recorded data are continuously available from April 13th 2001 to September 28th 2003. On that day the system was shut down. After three years, in 2006, it was started again, but crashed after only a few months, maybe because a severe thunderstorm. The system has been repaired and restarted in March 2015.

Figures 6 and 7 show the time evolution of the data recorded by the LVDTs in the period 2001/04/13-2003/09/28. All the data highlight the classic seasonal trend, given by ambient conditions, such as temperature and moisture.

Moreover, some aspects are noteworthy. In particular, LVDT 1-2-3-5-9 seem to show an increasing or decreasing trend, which could be related to ongoing motions. As said before, LVDT 1 and 9 are consistent, since S.Diego chapel is the near to the façade. At the same time, LVDT 2 and 3 describe the same phenomenon viewed by two different points, as the realtive motion between the walls of the nave.

Specific attention must be given to the LVDT 6, which path is related to the lateral thrust of the dome. The occurrence and the slow opening of the meridian cracks at the base of a dome describe a physiological static response of such structures [7]. Nevertheless, more investigations are needed to give proper interpretation of the data.

4 DYNAMIC INVESTIGATIONS AND NUMERICAL MODEL

4.1 Ambient vibration test

Ambient vibration testing is considered a reliable method for assessing modal parameters also for historical constructions. In this chapter, the results of a first dynamic investigation are shown. In particular two accelerometer sensors have been installed at the highest reachable level (about 50m high), at the base of the dome (Fig. 8).

Two ambient vibration tests have been carried out by using different types of sensors: form January 29th to February 5th 2015 by using piezoelectric uni-axial accelerometers model PCB 393C (1 V/g sensitivity); form February 17th to 24th 2015 by using high sensitivity piezoelectric uni-axial accelerometers model PCB 393B12 (10 V/g sensitivity). Data have been recorded continuously with a sampling rate of 100 Hz and stored with a time length of 30 minutes. Moreover a weather station is installed nearby the Basilica and the main wind and temperature data are also available.

Both the tests have been characterized by a quite fast wind speed. In particular, wind gusts of 66.6 km/h and 57.4 km/h have been recorded on January 30th and February 18th, respectively. In these days the data recorded by the different sensors are similar. Figure 9 shows the acceleration time histories (Fig. 9(a)) and related frequency spectra (Fig. 9(b)) of the latter event. Form the frequency analysis the first natural frequencies of the structure can be estimated: it should be noted resonant peaks for both Acc1 and Acc2 sensors for $1.7 \div 1.8$ Hz, a peak at a frequency of about 3.0 Hz only for Acc2 and for both the sensors in the ranges of $3.5 \div 4.0$ Hz, $4.0 \div 4.5$ Hz and $6.0 \div 6.5$ Hz. However, an in-depth dynamic identification analysis is necessary to better understand the complex dynamic behaviour and the modal structural properties.

In both the tests has been also observed a significant contribution of vibration, in the range of $10 \div 15$ Hz, due to the traffic during daytime. Moreover, another interesting phenomenon is

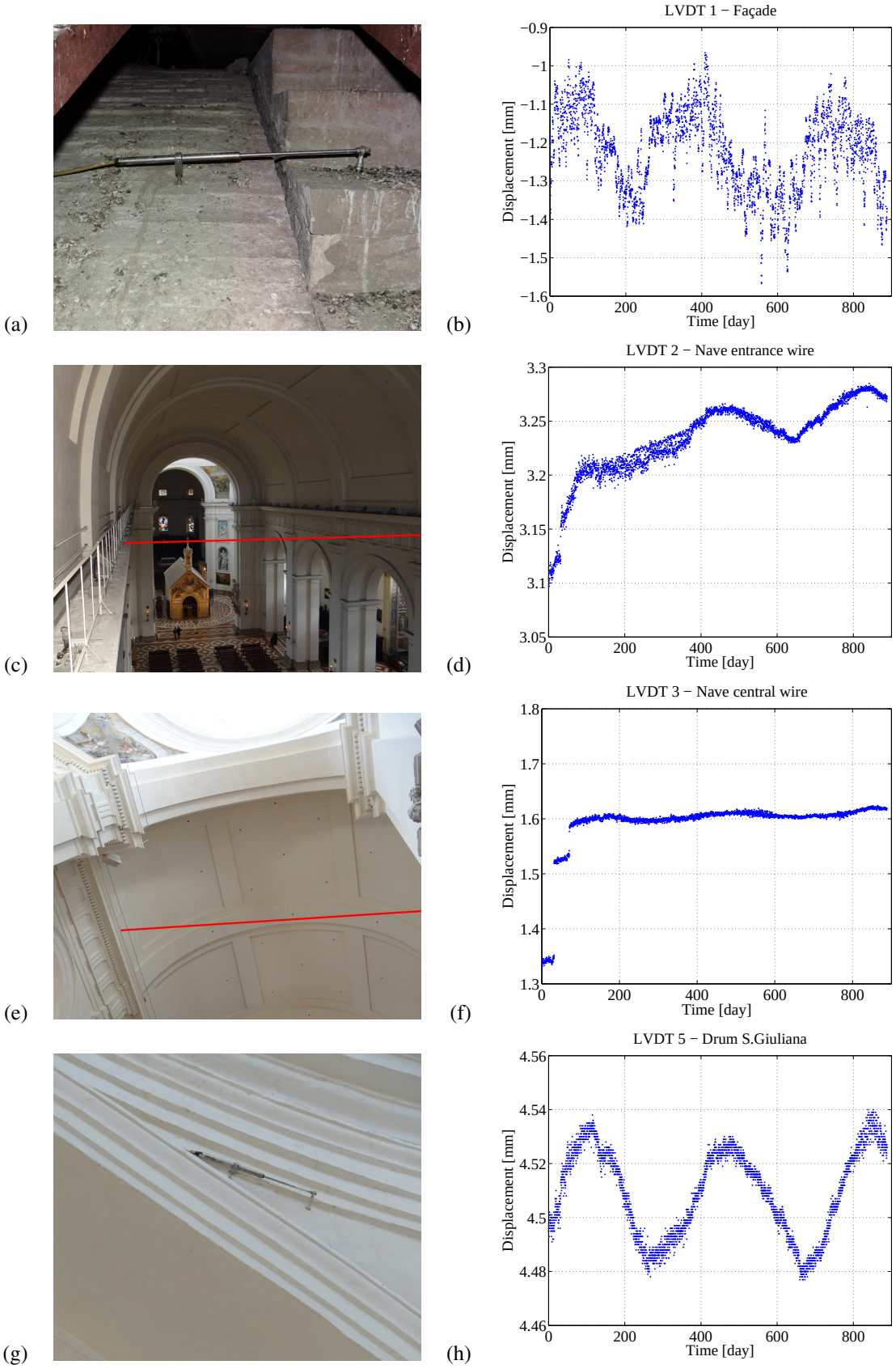


Figure 6: Images (a-c-e-g) and timeline (b-d-f-h) of the displacement transducers n. 1, 2, 3 and 5.

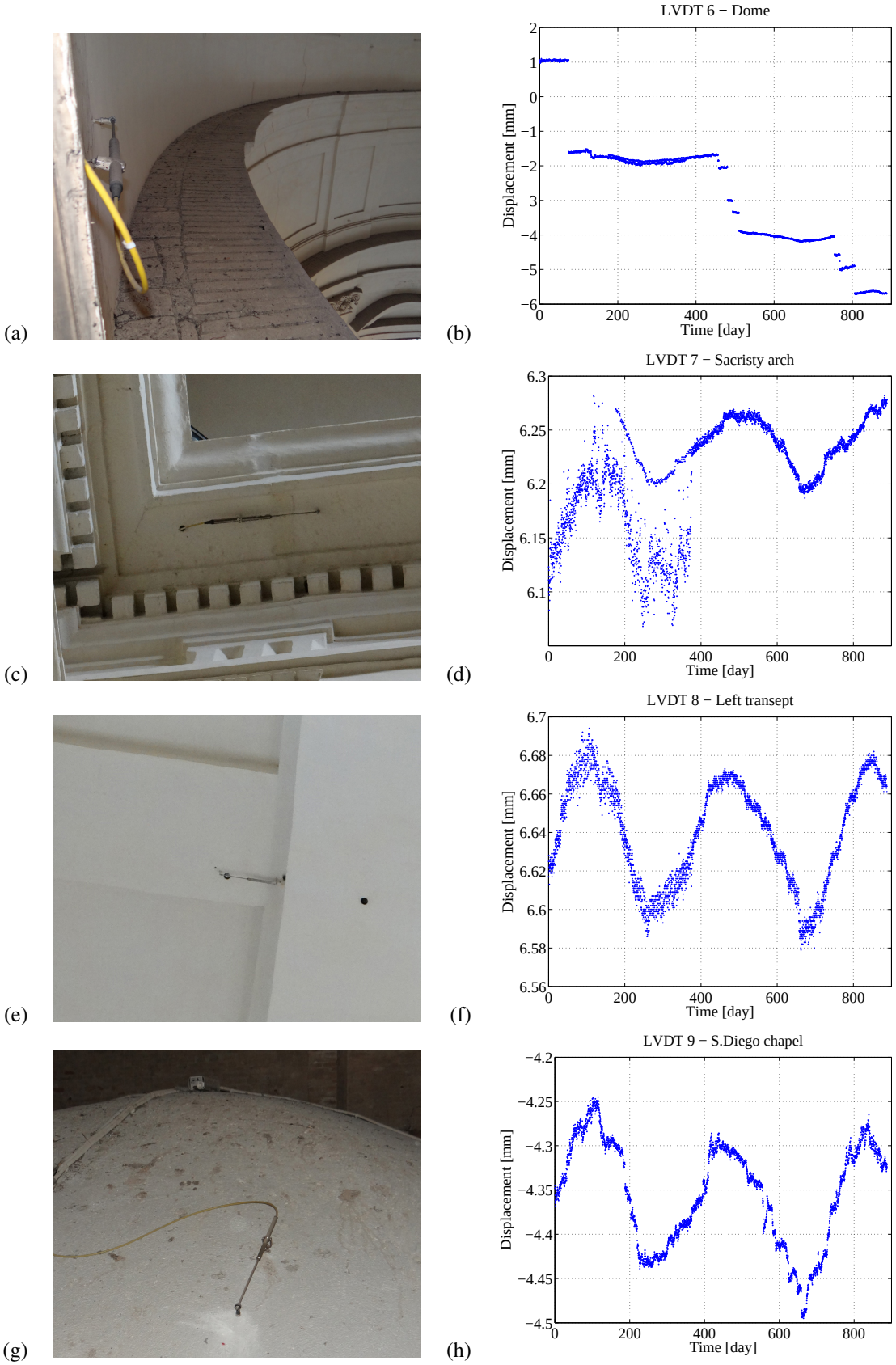


Figure 7: Images (a-c-e-g) and timeline (b-d-f-h) of the displacement transducers n. 6, 7, 8 and 9.

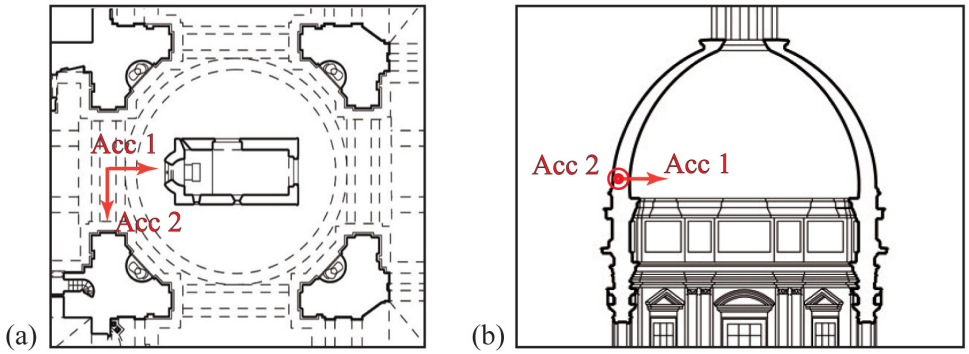


Figure 8: Instrumentation layout used in the ambient vibration tests.

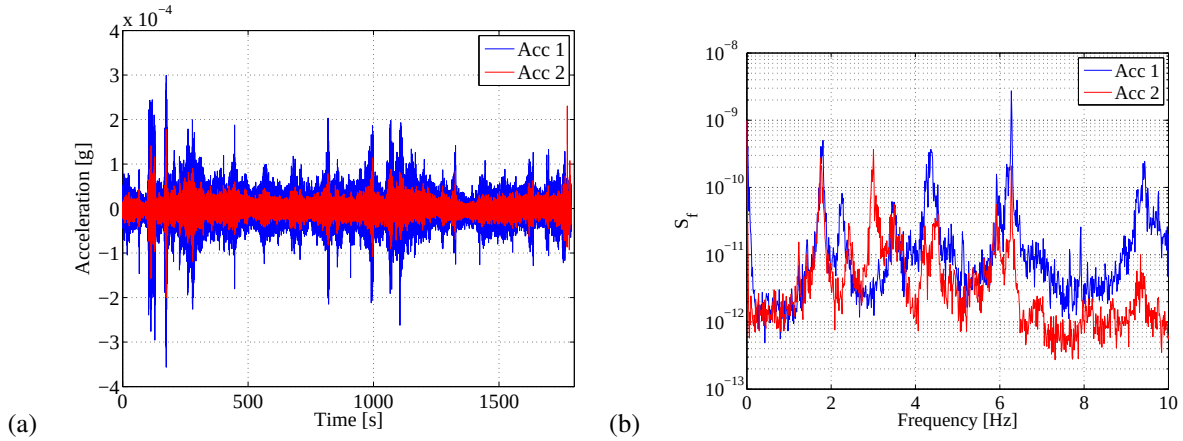


Figure 9: Output signals (a) and frequency analysis (b) of acceleration sensor recorded on February 18th under wind excitation.

related to the driven oscillations due to the bell-tower motion, which can be reached whenever the bells sound.

4.2 Numerical model

A numerical FE model has been performed by means of a commercial code. The model has been focused on the central core of the basilica, i.e. the triumphal arches, the drum and the dome. However, sketch models of the nave, the transepts and the apse have been introduced to attain a better modeling of the lateral restraints. Due to the lack of knowledge concerning the mechanical parameters of the materials, a probabilistic approach has been used in the estimation of the natural frequencies in function of the variability of the elastic moduli of the materials [7].

The constituent material is brickwork everywhere, excepting for the stone pillars of the nave. An homogeneous material with orthotropic elastic behaviour has been considered. The values of stiffness, and their lognormal distribution parameters, proposed by the recent Italian instructions [8] have been used (Tab. 1). A set of 1000 samples have been generated for both the Young's modulus (E) and shear modulus (G) of the brickwork (Fig. 10), and then multiplied by a coefficient α=1.5 which takes into account the good condition of the mortar.

Figure 11 shows the first seven modal shapes obtained by the eigenproblem solutions with the respective range and distribution of frequencies related to the variability of the elastic properties.

	ρ [ton/m^3]	μ_E [MPa]	$\sigma_{ln,E}$	μ_G [MPa]	$\sigma_{ln,G}$
Brickwork	1.8	1500	0.2	500	0.2
Stone masonry	2.2	2800	-	860	-

Table 1: Mechanical material properties: mass density (ρ); mean value ($|mu_E$) and standard deviation of the logarithm ($\sigma_{ln,E}$) for the elastic modulus; mean value (μ_G) and standard deviation of the logarithm ($\sigma_{ln,G}$) for the shear modulus

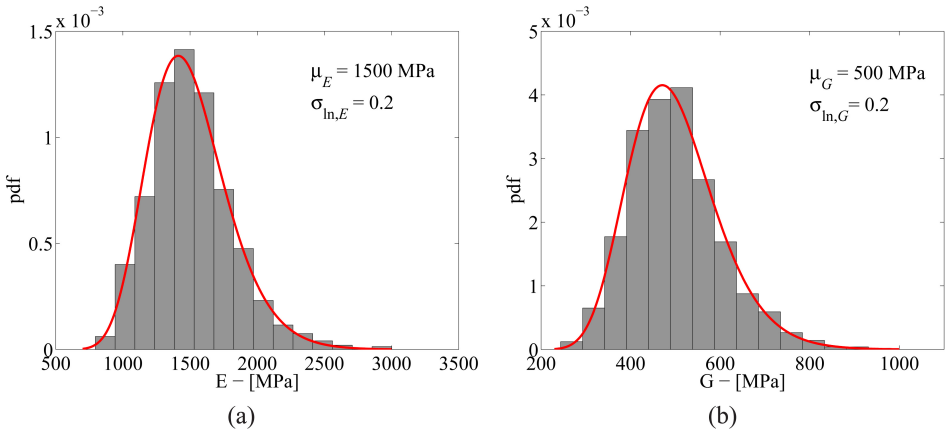


Figure 10: Generated values of Young's modulus (a) and shear modulus (b) from the statistical moments of the related distributions [7].

It can be observed a link with the resonant peak ranges reached by experimental tests (Fig. 9(b)). Further dynamic investigation will allow to identify the actual modal parameters of the structure and to obtain a tuned numerical model.

5 CONCLUSIONS

In this paper the first results obtained by the monitoring system placed in the Basilica of Santa Maria degli Angeli in Assisi have been presented.

A static monitoring system, consisting of 9 LVDTs, was installed during the rehabilitation works after the seismic events of 1997. The available data, recorded in the years 2001-2003, have been presented and discussed, even if more investigations are needed to give proper interpretation of them.

Moreover, some preliminary dynamic investigations have been performed by using two accelerometers installed at the base of the dome to detect the first modal frequencies. The spectral representation of the acceleration time histories has been compared with the modal analysis of a numerical FE model. The modal analysis has been applied to a series of FEM samples, by varying the mechanical characteristics of the constituent materials. The comparison between the experimental data and the numerical results is of interest to calibrate the FE model.

These results will be used to design a permanent dynamic monitoring system of the Basilica of Santa Maria degli Angeli in Assisi.

ACKNOWLEDGEMENTS

The Authors gratefully acknowledge the financial support of the "Cassa di Risparmio di Perugia" Foundation that funded this study through the project "Structural Monitoring for the

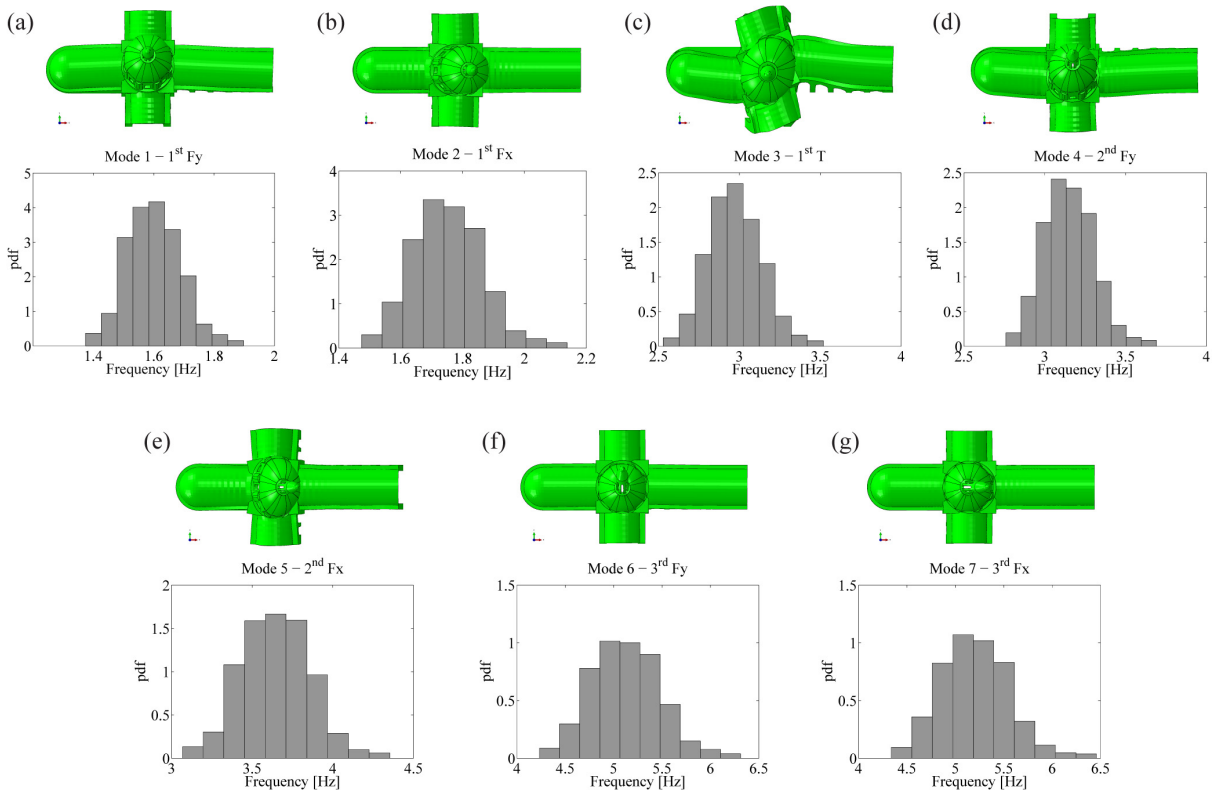


Figure 11: Modal shape and distribution of the related frequencies of the first seven modes derived by FE model by varying material stiffness.

protection of the Cultural Heritage: the bell-tower of the Basilica of San Pietro in Perugia and the dome of the Basilica of Santa Maria degli Angeli in Assisi" (Project Code 2014.0266.021).

The authors are also grateful to the Seraphic Province of St. Francis of Umbria for the availability and the interest demonstrated to the research.

REFERENCES

[1] G. Bartoli, A. Chiarugi, V. Gusella, Monitoring systems on historic buildings: the Brunelleschi Dome. *Journal of Structural Engineering, ASCE*, **122**(6), 663?-673, 1996.

[2] M. Gioffrè, V. Gusella, F. Cluni, Performance evaluation of monumental bridges: testing and monitoring 'Ponte delle Torri' in Spoleto. *Structure and Infrastructure Engineering: Maintenance, Management, Life-Cycle Design and Performance*, **4**(2), 95–106, 2008.

[3] F. Ubertini, N. Cavalagli, G. Comanducci, Sensing hardware optimization and automated condition assessment of a monumental masonry bell-tower. *Proceedings of the 1st International Conference on Uncertainty Quantification in Computational Sciences and Engineering, UNCECOMP 2015*, Crete Island, Greece, 25-27 May, 2015.

[4] V. Gusella, P. Belardi, F. Bianconi, M. Armeni, N. Cavalagli, L. Martini, The domed skyscraper of Galeazzo Alessi. The geometric and structural ambiguities of dome of the Saint Mary of the Angels Basilica. *Proceedings of the International Conference DOMES IN THE WORLD*, Florence, Italy, 19-23 March, 2012.

[5] P. Capaldini, D. Ripa di Meana, B. Salvatici, Basilica patriarcale della Porziuncola: progetto di ripristino statico e funzionale a seguito degli eventi sismici del 26.09.1997 e successivi. *Ingegneria Sismica*, **2**, 5-16, 1999.

[6] N. Cavalagli, V. Gusella, Dome of the Basilica of Santa Maria degli Angeli in Assisi: Static and Dynamic Assessment. *International Journal of Architectural Heritage*, **9**(2), 157–175, 2015.

[7] N. Cavalagli, V. Gusella, Structural Investigation of 18th-Century Ogival Masonry Domes: From Carlo Fontana to Bernardo Vittone. *International Journal of Architectural Heritage*, **9**(3), 265–276, 2015.

[8] Consiglio Nazionale delle Ricerche, CNR-DT 212/2013. Istruzioni per la Valutazione Affidabilistica della Sicurezza Sismica di Edifici Esistenti. CNR, Rome, Italy, 2013.

COMPDYN 2015
5th ECCOMAS Thematic Conference on
Computational Methods in Structural Dynamics and Earthquake Engineering
M. Papadrakakis, V. Papadopoulos, V. Plevris (eds.)
Crete Island, Greece, 25–27 May 2015

SEISMIC RISK OF HISTORIC STRUCTURES AND MONUMENTS: A NEED FOR A UNIFIED POLICY.

Constantine C. Spyrakos

Laboratory for Earthquake Engineering, National Technical University of Athens
HeroonPolytechniou 9, 15780 Zografou, Athens, Greece
cspyrakos@central.ntua.gr

Keywords: Historic structures, Monuments, Seismic Risk, Interventions, Safety levels, Nominal life, Near-source phenomena.

Abstract. *There is lack for a common approach on the assessment of seismic risk for historic structures and monuments. Performance of interventions for a partial mitigation of seismic risk is yet a challenge. In most cases limitations stemming from the implementation of interventions on historic structures and monuments that are contrary to internationally accepted guidelines, e.g., Carta di Venezia, do not allow fulfilling the safety level of new constructions.*

The challenge of balancing safety versus maintenance of the architectural and artistic features of historic structures remains a pressing issue to address. In addition, new developments on the seismic hazard and proper interventions related to near-source phenomena are scarcely considered in the literature.

Through representative examples, this work attempts to provide a framework that: (i) quantifies the "safe" duration (nominal life) of an intervention on a monument; (ii) considers the effects of near-source phenomena and; (iii) elaborates on the integration of experimental/ analytical methods in view of recent developments in the field.

1 SEISMIC REHABILITATION OBJECTIVES AND PERFORMANCE LEVELS

A seismic *Rehabilitation Objective* consists of one or more rehabilitation goals. Each goal consists of the verification of a target *Building Performance Level* with an associated *Earthquake Hazard Level*. By considering not only the structural damage but also the response of non structural elements and artistic assets, performance levels may be defined in relation to different performance targets of the construction, associated to the functionality and the cultural properties of buildings.

The modern seismic codes for the design of new buildings, as well as pertinent recommendations for the evaluation and rehabilitation of existing ones, are based on the performance based assessment (PBA), that is the fulfillment of some target performance levels (limit states) in correspondence to predefined seismic actions [1,2,3,4].

The EC8-3 specifies as T_L=50 years the duration of "nominal life" of a structure and defines three building performance levels (Limit States) considered as appropriate for the seismic protection of ordinary new buildings: (a) Near Collapse (NC); b) Significant Damage (SD); and (c) Damage Limitation (DL). Each one of the limit states is associated to a seismic action defined by the return period (T_{RL}) and a probability of exceedance (p) for T_L=50 years. Specifically for the (a) NC, the T_{RL} is 2475 years and p= 2%; (b) SD, the T_{RL} is 475 years and p=10% and (c) DL, the T_{RL} is 225 years and p=20%.

The Italian code for the monuments (DR14/01/2008)-[5] specifies five limit states: the SLC, SLV, SLD, SLO and SLA. The first three correspond to the (NC), (SD) and the (DL) of the EC8-3, respectively, and the fourth one specifies "almost" no damage conditions. The SLA defines the limit state for structural members/parts and even contents of artistic value. For the first four limit states the probabilities of exceedance are 5%, 10%, 63%, 81%, respectively, which are related to the *reference duration* (V_R). The V_R can be calculated from the *nominal life* of the structure (V_N), which for an ordinary structure is considered to be V_N=50 years, and the importance factor (C_U), that is ($V_{R=}$ V_N x C_U).The code specifies four important classes, assigning to each one a value for the importance factor (C_U).

Currently in Greece there is not yet a code for the seismic protection of monuments. Worth noting are two recent attempts that set the basis to address the pressing issues on the seismic protection of masonry structures and monuments [6,7]. From Ref [7] on monuments, presenting many similarities with the Italian code, it is worth mentioning the proposal to select the design seismic actions as well as the acceptable damage levels on the basis of the importance of a monument, proposing three levels (l_i i=1,,2,3): monuments of universal importance (I_1), monuments of national importance (I_2), and monuments of local interest(I_3).

Also, depending on the exposure to visitors, it proposes that the monuments are classified into three categories (C_i i=1,2,3) assigning a proper $C_{u,}$ that is: C_1: almost continuous presence of public or frequent presence of large groups: (i) inhabited buildings in historical city centers, (ii) monuments used as museums, and (iii) monuments continuously used for worshipping; C_2: occasional habitation or intermittent presence of small groups: (i) monuments visited only under specific conditions, and (ii) remote and rarely visited monuments; C_3: entrance allowed only to service-personnel with visitors standing only outside the monument.

Thus, the earthquake protection of cultural heritage assets can be realized through a preventive knowledge of the seismic risk, in order to plan mitigation strategies and schedule the necessary strengthening interventions for the reduction of vulnerability. Seismic risk is the outcome of three different factors: the seismic hazard (probability of occurrence of an earthquake of a given intensity at a certain site); the vulnerability (predisposition of the building to be damaged by an earthquake); the exposure (related to the conditions of use and presence of the public, but also to the value of the building and the artistic assets that contains). Clearly,

the earthquake protection of cultural heritage assets is a task that involves not only the safety and economic impact, but also the conservation of the cultural properties of the assets.

1.1 Seismic Hazard

Seismic hazard requires the selection of the proper ground excitation. It is recommended that the site ground excitation is determined by taking into consideration the following: 1. The response of the monument to past earthquakes, so that, in case of a damaged structure from an earthquake, the action that caused the damages may be the first choice, 2. The soil stratification and the foundation and 3. Topographic amplification effects. For important monuments, the seismic action may be modified by taking into account local soil dynamic conditions, geomorphology, an estimation of the duration of the earthquake and especially the effects of neighboring active faults that could create near-fault phenomena.

For the last parameter it should be stated that, even though there is considerable literature on reinforced concrete and steel structures considering near-fault phenomena, the study of masonry structures and monuments under near-fault seismic excitations is scarce compared to their significance in seismic design [8,9]**.** For this reason a relatively extensive introduction on this issue is presented, followed by an example that demonstrates the significance of near-fault phenomena associated with the presence of an active fault in the vicinity of a monument.

1.2 Near-Fault Strong Ground Motion Characteristics

The increased density of recording stations in the near fault areas has permitted the collection of near-fault ground motion recordings that present characteristics quite different from those of the usual far-field ground motions. These near-fault characteristics are mainly present in the form of large pulses in the ground velocity time history records at sites towards which the fault ruptures, a phenomenon called directivity. The directivity characteristics and effects are briefly presented and explained in the following.

Rupture generally progresses across a fault as a series of individual cracks or sub-events. Each crack produces a dislocation or slip which has a duration called the rise time and a slip velocity or slip rate amounting to 50-150 cm/sec. Each crack creates a velocity pulse with duration equal to the rise time and amplitude equal to the slip rate. These pulses travel along the fault with the velocity of shear waves. At the same time the rupture spreads towards a certain direction with a rupture velocity similar to that of the shear waves. In the rupture direction, rupture cracks and crack velocity pulses travel with the same velocity. Accordingly, in the rupture direction, a phenomenon similar to the Doppler phenomenon takes place. The generated pulses overlap and the waves arrive at a site in the direction of rupture as a large pulse of motion creating a shock wave effect that occurs at the beginning of the record. The phenomenon is called *forward directivity* and the pulse of the ground motion is typically characterized by large amplitude and short duration. At a site located near the epicenter, where rupture propagates away from the site, the arrival of the pulses is distributed in time. This condition, referred to as *backward directivity*, is characterized by motions with relatively long duration and low amplitude.

Research has shown that simplified representations of the velocity pulse can capture the salient characteristics of the response of structures to near-fault ground motions. The simplified pulse representations of velocity time histories are defined by the number of equivalent half cycles, the period of each half cycle and the corresponding amplitudes [11]. The amplitude of the velocity pulse is significantly affected by magnitude, distance and site conditions. The number of half cycles in a velocity pulse affects the spectral amplification, that is, as the number of cycles increases the spectral amplification increases as well [12, 13, 14, 15].

Rupture directivity effects can be present both for strike-slip and dip-slip events. Because of its polarization, the pulse of motion is predominant in the orientation perpendicular to the fault plane. The same phenomenon is present for a dip-slip fault, where forward directivity conditions occur for sites located near the up-dip projection of the fault plane. In this case, also, the pulse of motion is oriented perpendicularly to the dip of the fault plane. Thus, fault parallel spectra are in most cases comparable with design code spectra. Procedures that incorporate amplification of the standard response spectrum to account for near-fault phenomena are available in the literature and are recently incorporated in the Next Generation of Ground Motion Attenuation (NGA) Project [16, 17].

2 INTERVENTION STRATEGIES

Historical buildings may be considered to belong to importance class III or IV leading to large seismic requirements and seismic actions that are characterized by a high return period [4,5]. Thus, their preservation could most likely require invasive interventions in order to meet the "safety standards" for new construction. According to the principles of interventions on historic buildings and monuments less intrusive interventions are imposed, which, nevertheless, would continue to ensure to a certain degree the safety of the monument, e.g.,[18, 19]. In general, interventions on monuments should satisfy the following three principles: (i) Reversibility, (ii) Durability (in-time), and (iii) Feasibility of the proposed solution.

The basic philosophy of codes and comprehensive research efforts, e.g. [5,41], promotes three intervention alternatives: (i) Basic Safety, with a Rehabilitation Objective that practically achieves the dual rehabilitation goals of Near Collapse (NC) and Significant Damage (SD) of [4]; (ii) Limited Rehabilitation, which attempts to improve the seismic safety of the whole structure by means of non intrusive, yet, extensive interventions that are inferior to the Basic Safety objectives and (iii) Local Rehabilitation, which improves the response of the structure through local interventions not affecting the overall behavior of the structure. The last two alternatives appear to be the most appropriate and in fact the most widely used (in many cases "silently adopted") for the preservation of historic structures and monuments.

2.1 SD Performance through Limited Duration Rehabilitation Measures

This section proposes an alternative approach that handles the Limited Rehabilitation Objective (LRO) in a totally different way. The basic idea is to consider the rehabilitation measures as fulfilling a predefined limit state for a certain time duration, after which the structure with its interventions should be re-evaluated and, if necessary, appropriate measures will be taken at this later time.

The methodology is demonstrated through the following example, applied in order to achieve the SD performance level, as specified in EC8-3, through Limited Rehabilitation measures valid for a certain period of time.

The methodology also requires the introduction of the term "nominal life of an intervention T_{Δ}", defined as the time for which the intervention ensures a selected performance level, e.g., SD or DL for the probability of exceedance being P_R = 10% or 20%, respectively [4].

The methodology requires the use of either an attenuation relationship or side specific spectra. In this example the following attenuation relations are selected, as forming the basis for the calculation of the a_{gR} of the current EC8-1 design spectra for Greece. As Greece is divided in three seismic hazard zones, Z_i, (i=1,2,3), each equation specifies the corresponding a_{gR} (design ground acceleration) in terms of the return period T_{RL} [20]:

$$\text{Zone Z1: } \log a_{gR} \approx 0.277 \log T_{RL} + 1.579 \tag{1}$$

$$\text{Zone Z2: } \log a_{gR} \approx 0.264 \log T_{RL} + 1.739 \tag{2}$$

$$\text{Zone Z3: } \log a_{gR} \approx 0.240 \log T_{RL} + 2.015 \tag{3}$$

Adapting a Poissonian distribution for the seismic events, that is the seismic events are statistically independent from each other, the T_{Δ} is related to the return period T_{RL} and to the probability of occurrence as given by

$$T_{RL} = -\frac{T_{\Delta}}{\ln(1-P_R)} \approx \frac{T_{\Delta}}{P_R} \tag{4}$$

It should be noted that the a_{gR} resulting from equations (1) – (3) is decreased by 20% prior to being used in the code spectra [20].

Also, if the seismic action is defined in terms of the reference peak ground acceleration a_{gR}, the value of the importance factor γ_I multiplying the reference seismic action to achieve the same probability of exceedance in T_{Δ} years as in the $T_{\Delta R}$ years for which the reference seismic action is defined, may be computed from

$$\gamma_1 \approx (T_{\Delta R} / T_{\Delta})^{-1/k} \tag{5}$$

where k is in the order of 3 (EC8-1).

The example considers a historic building located in the seismic zone Z_1 founded on a soil class A.

By implementing the maximum of the interventions that comply with the archeological /architectural restrictions to the monument [18, 19] and after performing the analysis, evaluation of the results indicate that the structure reaches the SD performance level for a_{gRL} = 0.155g.

In order to use equation (1), the a_{gRL} should be divided by 0.8 leading to a_{gRL} = 0.194g. Substituting a_{gRL} in eq. (1) leads to

$$\log 194 \approx 0.277 \log T_{RL} + 1.579 \tag{6}$$

providing the return period T_{RL} = 360.5 years. Consequently, substituting in eq. (4) the T_{RL} = 360.5 years for P_R = 0.1 yields T_{Δ} = 38 years.

At this point one could consider two possibilities regarding the importance class of the historic structure, that is class III or IV corresponding to γ_I = 1.2 or 1.4, respectively.
Equation (5) results in: $T_{\Delta R}$ = 22 years for γ_I = 1.2 and $T_{\Delta R}$ = 14 years for γ_I = 1.4.

Thus, the implemented interventions can be considered as fulfilling the SD state for the duration of either 22 or 14 years depending on the importance classification of the structure. If the classification of the structure can be considered that it is exclusively related to the "exposure to visitors", then the nominal duration of the interventions could be further extended by setting γ_I = 1.0 leading to a $T_{\Delta R}$ = 38 years.

The Damage Limitation Level can be treated in exactly the same way considering as the probability of exceedance in 50 years to be 20%. In this case for T_{RL} = 360.5 years, use of equations (1), (4) and (5) results in: $T_{\Delta R}$ = 46.5 years for γ_I = 1.2, $T_{\Delta R}$ = 29 years for γ_I = 1.4, and T_{Δ} = 80 years for γ_I = 1.0.

Therefore, the implemented interventions can be considered as fulfilling the DL state for the duration of 80, 46.5 or 29 years depending on the importance classification of the structure.

It can be concluded that for either the SD or the DL limit states, additional and more invasive interventions can be postponed in time. At the end of the nominal duration of the interventions, a new evaluation of the structure should be performed. At that later time any

necessary measures might be implemented making use of a more accurate knowledge of the seismic hazard, the ability to assess more reliably the vulnerability of the monument and the availability of less invasive intervention techniques.

3 METHODS OF ANALYSIS

This section attempts to clarify several important issues related to limitations of [3, 4] specified solution methods as well as the selection of the most appropriate solution method(s) for historic masonry structures and monuments.

In section 4.4.3, EN 1998-3 reports that the seismic action effects may be evaluated using one of the following methods: a) lateral force analysis (static linear), b) modal response spectrum analysis (linear), c) q- factor approach, d) non-linear static (pushover) analysis and, e) non-linear time history dynamic analysis.

Options (a) and (b), are applied with the un-reduced elastic spectrum to a structure that behaves elastically. In addition, according to Annex C of [4] both methods assume conditions of rigid diaphragm and a clear distinction between ductile and failure mechanisms, both requirements are not met in a great majority of masonry structures.

Also, classifying such mechanisms as strictly "brittle" without whatsoever nonlinear deformation capacity would lead to a significant underestimation of the seismic capacity of a masonry structure, and, therefore, to unusable results. It is well documented that a moderate "ductility" has to be recognized also for shear failures. Thus, one may conclude that for masonry structures, both options are impractical, e.g., [28, 29].

According to EC8-3 (4.4.1 (5)) and the informative Annex C, the *q*-factor approach is practically applicable to masonry structures with rigid diaphragm behavior. The approach proposes either a reduced response spectrum or its equivalent alternative representations, given in [3], that use properly developed time histories of ground motion. Of the two alternatives of linear elastic analysis, clearly the option of time history analysis of modal response and real time superposition of modal contributions is the only accurate option. Despite this, most commercial software for the analysis of masonry structures offer only the possibility of combining the Modal Maxima either through the Complete Quadratic Combination (CQC) or the Square - Root - of the - Sum- of the - Squares (SRSS) option. Both approaches combine maximum responses of different modal contributions which, in time history records, are not concurrent. The danger from these approaches is that they may lead to overly conservative estimates, in light of the fact that several modes need be accounted for before 70% of the total masonry structural mass may be engaged in elastic finite element (F.E.) modal analysis, since, in the absence of diaphragms numerous subordinate modes could be excited in such F.E. models. These modes are occasionally spurious and are not related to the actual behavior of the structure. Overly conservative estimates of response emanating from SRSS may lead to excessively invasive (nonreversible) interventions in masonry structures, and as such, they should be always treated with particular caution.

The EC8-3 specifies the use of the last two alternatives (d) and (e) when the conditions of its section C.3.2 are not met, simply stated: for "irregular" structures with or without rigid diaphragms. First we elaborate on the method (d), i.e., the pushover analysis. We distinguish the combination of two cases: "regularity", as defined in 4.4.2(1)P and in C.3.2, as well as presence of rigid diaphragm behavior. In the case of rigid diaphragms and regular structures, pushover can be used with two fixed force pattern distributions: modal (mass-proportional) with a force distribution proportional to the first modal shape of the structure; being able to represent the structural dynamic amplification which increases the action on higher stories and, a constant distribution that is consistent with a soft ground storey response. These two distributions may be assumed as bounds for seismic analysis of regular buildings: the actual

result, resulting from dynamic analysis can be usually assumed to be within these two solutions. For irregular structures with rigid diaphragms, an adaptive pushover analysis is considered a better approach. In that case the analysis is progressively updated to account for the structural response evolution in terms of stiffness degradation.

The presence of in-plane flexible diaphragms, such as typical wooden floors or thin masonry vaults, is very common in historic masonry structures. Even though connections between walls and floors could prevent to a certain extent local first mode mechanisms, the presence of flexible floors results in a quite complex global seismic response, demonstrating little coupling between the vertical walls that tend to behave independently.

In the presence of plane deformable diaphragms use of pushover presents several issues and difficulties which have not yet been taken into consideration in codes, the choice of the control node being a characteristic example. An acceptable approach in practice could be to analyze separately the in-plane seismic response of each masonry wall, as extracted from the global structure with its supporting loads and inertial masses [21].

For mixed structural systems that are commonly encountered in strengthened existing structures with either steel or concrete members the [22] favors the use of pushover analysis.

Certainly, the most general but complicated option is the option (e), in which case the solution algorithm marches in time satisfying at each time step the conditions of dynamic equilibrium. Clearly, nonlinear F.E. solutions are still hampered today by the convergence and numerical stability problems attributed to cracking in masonry, combined with the absence of the stabilizing effect of steel reinforcement that is available in concrete structures.

Alternative methods that reproduce the nonlinear characteristics of the response, while taking advantage of the stability of the elastic approaches have been developed. An effective option is re-meshing of the structure, while allowing the creation of new boundaries of discontinuity in the structure along the paths of crack formation. By the incremental propagation of a crack, each time a new boundary is created, followed by remeshing and restructuring of the elastic stiffness matrix of the structure, which however, becomes more compliant as the connectivity between adjacent nodes is lost caused by the opening of a crack.

In conclusion nonlinear static analysis and the q-factor approach seem the real options for designers at the present.

4 EVALUATION OF SEISMIC RISK CONSIDERING NEAR FAULT EFFECTS

The church of St. Demetrios, located on the island of Lemnos in the North Aegean sea, has been selected as a case study of a historic structure constructed without seismic regulations in a highly seismically active region. It is a post-Byzantine triple-domed basilica with a timber roof constructed in 1892 [23]. The plan view is nearly quadrangle with three polygonal apses on the eastern façade. The length and width of the church are 25 and 21 meters, respectively. The central aisle has a vaulted ceiling, where a 5.6 m high dome and a Π-shaped outer narthex are incorporated. The height, up to the base of the dome, is 12m. The masonry construction is mixed including rubble masonry with carved corner-stones and is coated with plaster at the exterior facade of the church, while inside it is partly covered with coating and partly with frescoes.

The evaluation of seismic risk involves a thorough condition investigation of the monument as well as the selection of the seismic hazard followed by several analysis in order to specify the type and the extent of the interventions. All steps of the process are briefly presented in the following.

4.1 Condition assessment

Visual inspection as well as a series of in-situ and laboratory tests has been conducted for condition assessment of the church. Main objectives of the testing program were the collection of information regarding the mechanical and chemical properties of the materials as well as the construction details [25, 26, 31].

Geotechnical investigation and soil amplification: At first a geotechnical study was performed in order to investigate the stratigraphy of the soil and the level of groundwater table, followed by a soil dynamic amplification study. The geotechnical study provided the soil parameters needed to estimate the bearing capacity of the soil, the expected subsidence, the modulus of subgrade reaction and the soil category according to [24]. The study of the dynamic soil response aimed at calculating a design spectrum that accounted for the amplification of seismic excitation through the local soil strata.

Three accelerograms from representative Greek seismic events were selected in order to evaluate soil amplification: (a) the 1986 Kalamata earthquake with magnitude M=6; (b) the 1981 Korinthos (Alkyonides) aftershock earthquake at the Corinthian gulf with magnitude M=6.4; and the Athens 1999 earthquake with magnitude M=5.9 recorded at the Sepolia station. All three accelerograms were scaled in order to be compatible with the seismic zone according to [3]. The scaled accelerograms excited the base of the soil column and the amplified spectra were obtained at the soil surface, as depicted in Figure 1.

Visual Inspection: A preliminary assessment of the condition was performed with visual inspection and surveying in order to record damage, i.e., cracking, peeling or other imperfections of the structure. Noticeable cracking, observed almost everywhere on the internal and external facades of the church, was recorded in detail and classified according to its type and size. In Figure 2 the location and the shape of the crack pattern is depicted in all views of the structure. it should also be noted that significant cracking was also recorded at the vaults and the pillars.

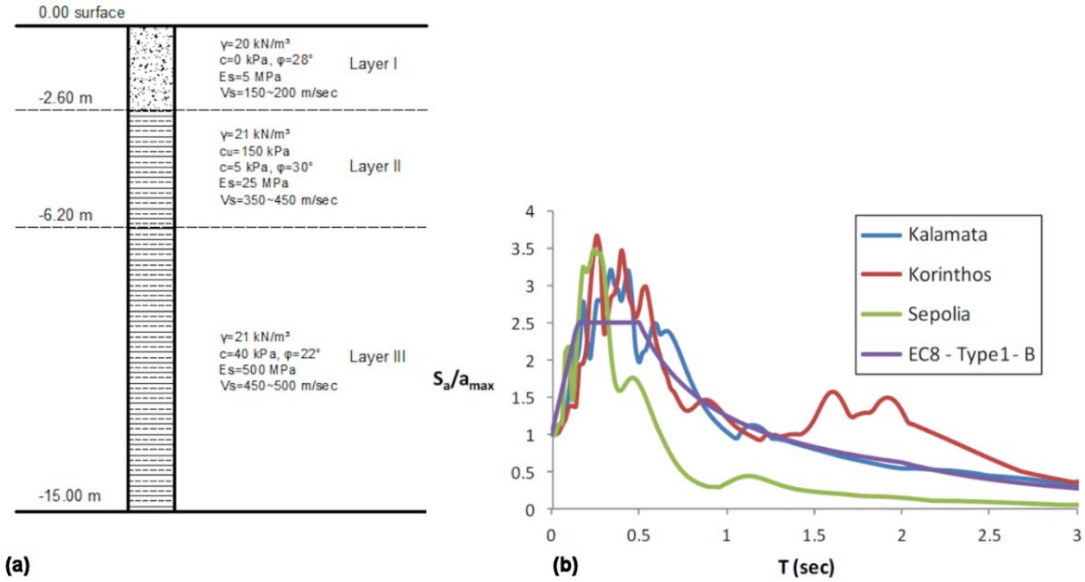


Figure 1: Geotechnical investigation: (a); soil profile; (b) amplified spectra at soil surface.

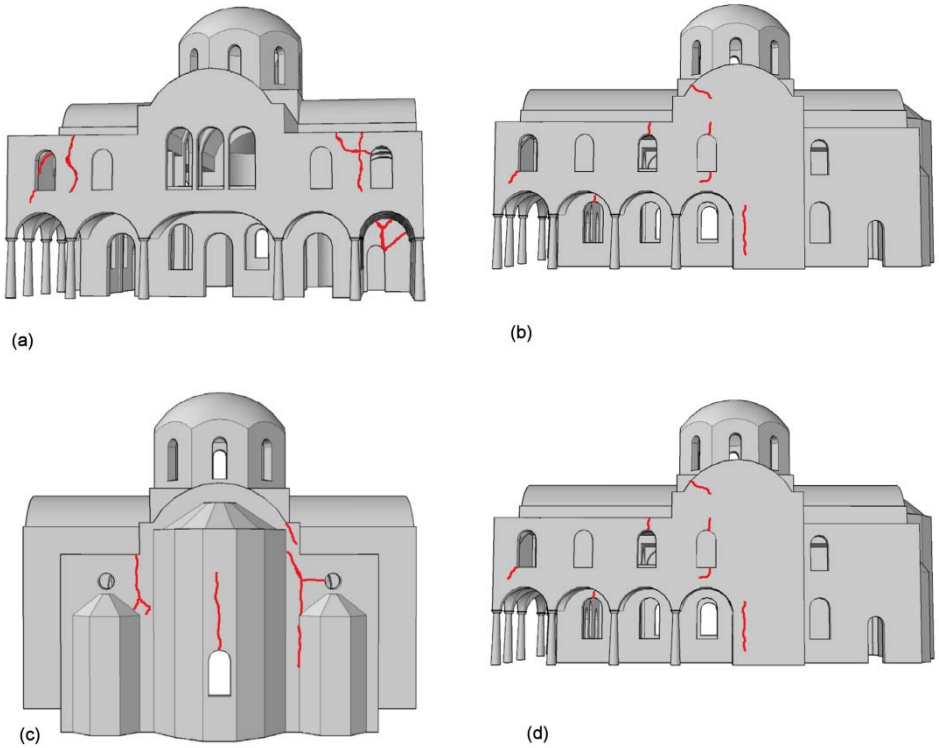


Figure 2: Major cracks in the masonry structure: (a) frontage (west façade); (b) south façade; (c) east façade; (d) north façade.

Measurement of Mechanical and Chemical Properties of Masonry: In order to measure the compressive strength of the stones and the bricks, both laboratory and in-situ tests were performed. Application of rebound hammer tests at selected positions, in conjunction with the laboratory tests provided the compressive strength of the stones (lime stones): f_{bc}=45.8 MPa.

Mortar samples were taken from various positions and their composition was examined in the laboratory. The laboratory work focused on the following issues: (i) nature of mortar (e.g., hydraulic, mixed, etc.), (ii) composition of binder, (iii) type and gradation of the aggregates, and (iv) ratio of raw materials. The following techniques were applied for the characterization of the mortar: (i) optical microscopy, (ii) study of the gradation of the aggregates, and (iii) x-ray diffractometry (xrd).

Infrared thermography: Application of the method revealed areas of humidity in the walls and confirmed testimonies and historic data about the absence of either partial or full closure of openings [27].

Endoscopy: Endoscopy was applied to a total of five positions of the walls of the church. In addition a number of endoscopies were applied at selected positions in order to examine the construction system of the central pillars and the anchorage length of the tie-rods in the masonry walls. It was found that (i) the bearing walls were composed by three-leaf masonry, (ii) there is no uniformity in the layout, since stones of different sizes have been used at several locations and (iii) the tie rods were improperly connected to the walls

Ambient Vibration Measurements: The modes of vibration and the natural frequencies of the church were measured applying ambient vibration testing. In total eight measurements were performed with direction either western-eastern or north-south. The positions included the center of the church beneath the dome at the ground floor and at the roof of the mezzanine

as shown in Figure 3 appropriate software was used to calculate the transfer functions and the Fourier spectra at different positions.



(a) (b)

Figure 3: Ambient Vibration testing at indicative positions: (a) ground floor beneath the central dome; (b) roof of the mezzanine.

4.2 Types of Analysis

The mechanical characteristics of the masonry, based on the testing procedures, were applied in subsequent analysis. Two types of analysis were performed: (i) Global analysis considering the structure as a continuum where all the inter-connected individual parts act and deform together during excitations and (ii) local analysis studying parts of the structure that may deform almost independently from the whole bearing body. These parts, also referred as macroelements, were determined with acceptable reliability based on a survey of the structure. At this point it should be emphasized that structures with no diaphragms are mostly vulnerable to local failure mechanisms. The selection and evaluation of different possible collapse mechanisms is an issue of critical importance in order to assess the behavior of a masonry structure [28, 29, 30].

The macroelement approach may be usually followed by either a kinematic limit analysis or a non linear static analysis. The first alternative, which has been selected in this article, involves the proper selection of a collapse mechanism, while the second one uses a finite element model as well as a "blocks and joints" analysis [31, 32, 33].

4.3 Seismic Loads

Greece is the most seismically active region in Europe and among the most seismically active regions on a global scale [34]. The island of Lemnos is located in a seismic zone II that is characterized by a reference peak ground acceleration a_{gR}=0.24 g according to the seismic zone map of Greece [35]. The North Aegean is a well known area for its high seismicity with strong earthquakes reported even from ancient historical era up to as recently as 2014 [36]: M=7.0 in 197 BC; M=7.0 in 1471; M=7.0 on May 14, 1887; and M=6.8 on August 6, 1983. Most recently on May 24, 2014, a M=6.3 earthquake occurred with an epicenter between the islands of Lemnos and Samothraki, as the result of strike-slip faulting at shallow depths beneath the northern Aegean Sea. Faults within the North Aegean trough represent the northern branch of the North Anatolian fault system, the major transform faulting structure in northern Turkey (USGS webpage). In the analysis the seismic loads were determined according to: (i) the current version of [3, 4]; (ii) the first Greek seismic code adopted in 1959 [37]; (iii) spectra accounting for near-fault effects.

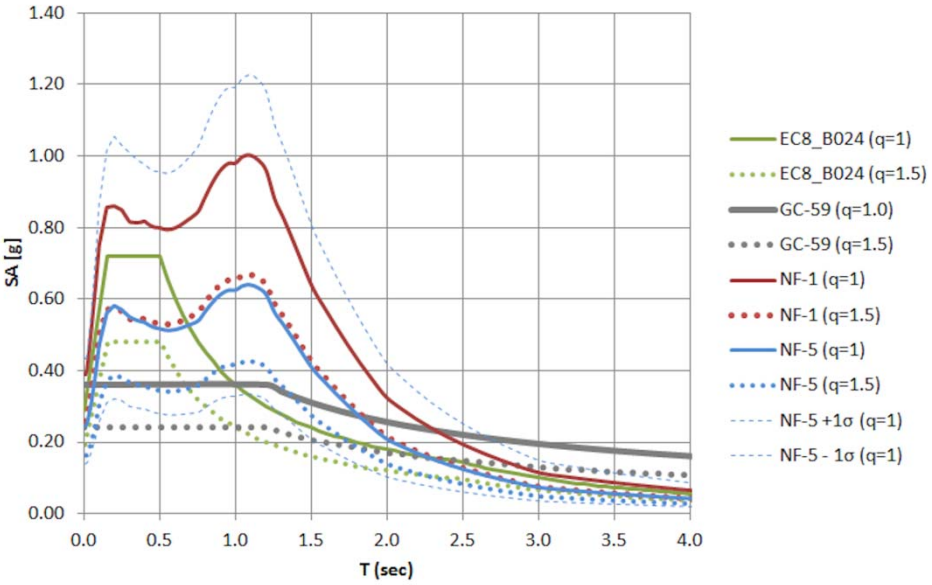


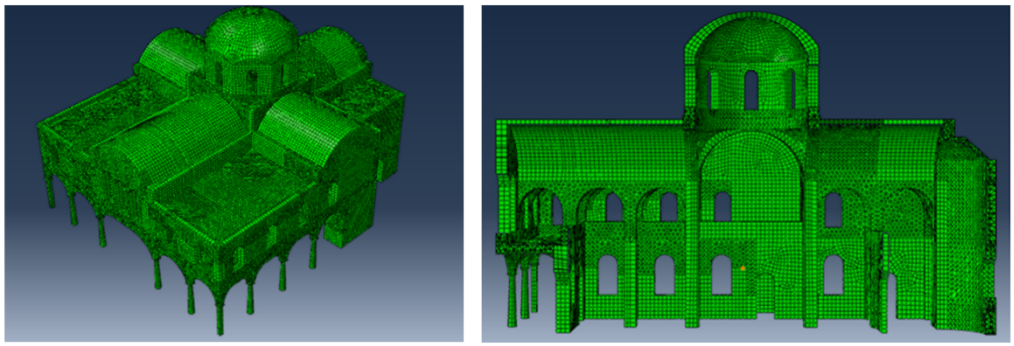
Figure 4: Comparison of different spectra applied in the analyses.

In Figure 4 the different spectra applied in the analyses are shown. The [4] spectra were considered with the following characteristics: reference ground acceleration for seismic zone II; a_{gR}=0.24 g; importance factor γ_I=1.2, characteristic periods T_B=0.15 sec, T_C=0.50 sec and T_D=2.00 sec and soil factor S=1.2. The near-fault spectra determined by applying the procedure proposed in [16] are representative of an M=6.5 seismic event at distance from the surface projection of the fault R=1 km and R=5 km, denoted as NF-1 and NF-5, respectively. The R denotes the minimum distance from the site to the projection of the fault to the surface. For clarification, it is mentioned that R=1 km or R=5 km indicate epicenter distances that could be in the range of 15 to 25 km from the epicenter. The elastic spectra are depicted with a continuous line, dotted lines correspond to inelastic spectra and dashed lines correspond to mean spectral acceleration (±) one standard deviation for the NF-5 scenario. A behavior factor q=1.5 was considered for all cases indicating a structure with small ductility [38]. The results from spectral analysis for the NF-5 scenario are not presented in detail, since as shown in Figure 4, they correspond to spectral values lower than the spectrum [4] for the range of periods considered; thus, it could provoke less damages than the spectra [4].
However, this overall conclusion is valid in average sense only, since consideration of the mean spectrum plus one standard deviation (NF-5 + 1σ) might be more damaging even from the NF-1 scenario, as also depicted in Figure 4.

4.4 Global Analyses and Results

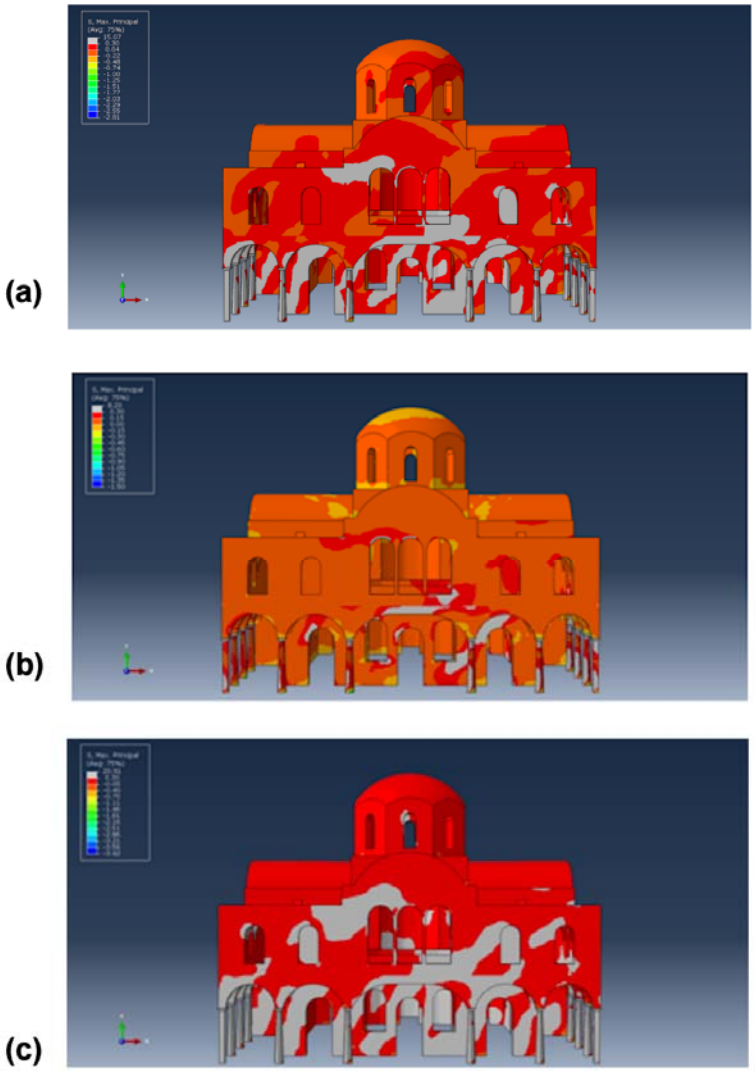
The finite element model, shown in Figure 5, consists of 317929 six and eight-node solid elements. Prior to the response spectrum analysis, an eigenvalue analysis of the model was performed and the results were validated based on the results of the ambient vibration testing [31].

The distribution of maximum stresses, for all the different spectra, is depicted in Figure 6 for the representative west façade. It should be noted that grey colors in the contour diagrams indicate exceedance of the tensile strength. The grey color denotes failures that occurred nearly at all facades and for all cases prior to the interventions on the structure.



(a) (b)

Figure 5: General views of the finite element model: (a) three dimensional view; (b) sectional view along the west-east direction.



(a)

(b)

(c)

Figure 6: West façade - Distribution of maximum stresses in the original model without interventions for the G+0.5Q+Ex+0.3Ey combination: (a) Eurocode 8 spectrum; (b) 1959-Greek Seismic Code spectrum; (c) Near-fault spectrum with R=1 km.

As depicted in Figure 4 the maximum demand is imposed from the near-fault spectrum at R=1 km (NS-1), while the second most damaging loading should be expected for the other spectrum in the near-fault area at R=5 km (NS-5). Indeed the maximum stresses for seismic combinations are noticed for the NS-1 spectrum, as shown in Figure 6, while the NS-5 seismic scenario also results in extended damage as also shown in Figure 6. The capacity checks included: in plane flexural resistance, shear resistance and out of plane flexural resistance parallel to the joints.

4.5 Local Analyses and Results

The determination of possible out-of-plane collapse mechanisms was obtained through a kinematic limit analysis [39]. Given the pattern of the cracks existing on the structure, two collapse mechanisms were examined, that is, the overturning of a part of the left façade and the overturning of the central apse, as shown in Figure 7.

Table 1 shows the results of the kinematic limit analysis performed for the two macroelements as well as the results of the verification with respect to the ultimate limit state according to Eurocode 8 and the NF-1 and NF-5 near-fault spectra. The verification was performed with the spectra shown in Figure 4 considering an importance factor γ_I=1.2. The verifications performed for the collapse mechanisms of the left façade and the central apse yielded different results depending on the spectra. The red color in Table 1 denotes collapse, while the green color denotes fulfillment of the ultimate limit state [3, 4].

4.6 Intervention Scheme and Performance of the Strengthened Structure

The assessment of the current condition of the structure revealed significant problems that may affect the structural behavior including extensive cracking of the masonry walls at all façades.

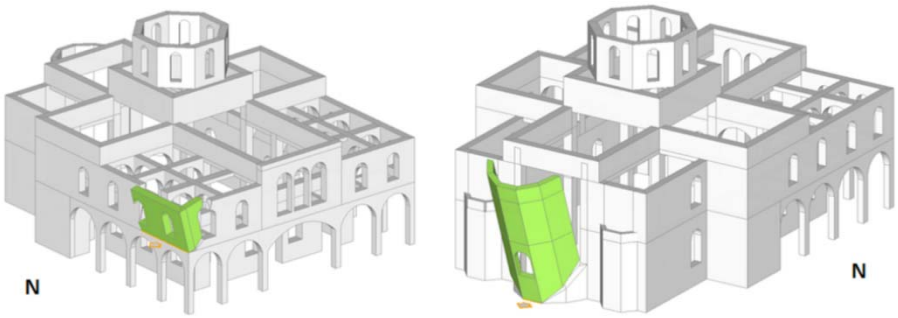


Figure 7: Selection of different local collapse mechanisms: (a) overturning of a structural part in the north façade; (b) overturning of the central apse in the east façade.

Collapse mechanism	a_0	a_0^* (g)	EC8		NF-1		NF-5	
			α_{Rig}^* (g)	α_{Def}^* (g)	α_{Rig}^* (g)	α_{Def}^* (g)	α_{Rig}^* (g)	α_{Def}^* (g)
North façade (mezzanine wall)	0.243	0.185	0.173	0.203	0.233	0.242	0.147	0.163
Central apse	0.162	0.142	0.173	-	0.233	-	0.147	-

Table 1: Results of kinematic limit analyses.

The existence of damage, nearly from the construction period, can be attributed to the limited strengthening measures that have been taken. The analysis of the structure "as is", revealed that there is a number of significant exceedances in capacity at many positions. Failure is expected for seismic loads according to [4], while more extensive damage should be expected for seismic loads corresponding to near-fault phenomena. Moreover the results of kinematic analyses imply an out-of-plane failure for a wall of the mezzanine at the north façade for the NF-5 spectra and an overturning of the central apse for both the EC-8 and the NF-5 spectra.

In order to overcome these structural weaknesses, a retrofit and strengthening scheme was suggested that included the following measures: (i) replacement of tie-rods with steel bars of a 20mm diameter, and (ii) consolidation of the masonry through grout injections.

At this stage, the analysis demonstrated that SD level was attained for a_{gr}=0.20g. Following the procedure presented in Section 2.1, resulted that the nominal life of the interventions is: $t_{\delta r}$ = 19 years for γ_i = 1.2, $t_{\delta r}$ = 12 years for γ_i = 1.4 and $t_{\delta r}$ = 33 years for γ_i = 1.0.

At this point, given the possibility to perform further " interventions" it was decided to either use carbon fiber sheets (CFRP) placed at selected locations of the structure in order to increase the tensile strength of the masonry walls or a stainless steel grid of a particular form and size [40]. Further analysis demonstrated that application of the additional interventions increased the strength of the church to meet the SD limit state as specified for a newly constructed structure.

5 CONCLUSIONS

The study: (i) demonstrates the pressing need to develop a common approach for the assessment of seismic risk of historic structures and monuments. It acknowledges the presence of several national codes and attempts for code development and comments on their approaches; (ii) by introducing the notion of "nominal life of interventions" it proposes and demonstrates through an example, a framework that quantifies the duration of an intervention in order to achieve a predefined limit state; (iii) presents fundamental concepts on "near-field" phenomena that should be included in the analysis of monuments; (iv) clarifies numerous issues related to the use and limitations of the most widely used numerical solution methods and, finally; (v) presents a comprehensive evaluation and retrofit study of a historic structure that: (a) combines in-situ and laboratory testing with structural analysis using the notion of "nominal life of intervention", (b) demonstrates the significance of near-fault effects and, (c) leads to the selection of appropriate intervention measures that use both traditional and modern state-of-the art techniques that respects the historic and architectural characteristics of the monument.

ACKNOWLEDGEMENTS

The financial assistance of the research project "SEISMO" [41], that made this work possible, is gratefully acknowledged.

REFERENCES

[1] ASCE/SEI 41/06: *Seismic Rehabilitation of Existing Buildings*.

[2] FEMA 356, 2000: *Prestandard and Commentary for the Seismic Rehabilitation of Buildings*, prepared by American Society of Civil Engineers for the Federal Emergency Management Agency, Washington, DC.

[3] Eurocode 8 (EC8-1), 2005: Design of structures for earthquake resistance *Part 1: General rules, seismic actions and rules for buildings*.

[4] Eurocode 8 (EC8-3), 2005: Design of structures for earthquake resistance *Part 3: Assessment and retrofitting of buildings*.

[5] DR (226/02/2011): Valutazione e riduzione del riscio sismico del patrimonio culturale con riferimento alle Norme Tecniche per le costruzioni di cui al D.M. 14/01/2008.

[6] Earthquake Planning Protection Organization (EPPO) and European Centre on Prevention and Forecasting of Earthquakes (ECPFE): *Draft Regulations for the Assessment and Intervention on Masonry Structures*, (1st Draft).

[7] Earthquake Planning Protection Organization (EPPO) and European Centre on Prevention and Forecasting of Earthquakes (ECPFE): *Draft Framework regulatory document for structural interventions and seismic protection of monuments*.

[8] C.C. Spyrakos, C.A. Maniatakis, Retrofitting of a Historic Masonry Building. In *Proceedings of the 10th National and 4th International scientific meeting on Planning, Design, Construction and Renewal in the construction industry iNDiS 2006*, (535-544). Novi Sad-Serbia, 2006.

[9] C.C. Spyrakos, P. Touliatos, D. Patsilivas, G. Pelekis, A. Xampesis, C.A. Maniatakis, Seismic analysis and retrofit of a historic masonry building, In S. Syngellakis Editor, *Retrofitting of Heritage Structures - Design and evaluation of strengthening techniques* (pp. 65-74). Southampton, UK: Wessex Institute of Technology Press, 2013.

[10] J.P. Stewart, S.J. Chiou, J.D. Bray, R.W. Graves, P.G. Somerville, N.A. Abrahamson, *Ground Motion Evaluation Procedures for Performance-Based Design*. Pacific Earthquake Engineering Research Center, PEER-2001/09; 2001.

[11] G.P. Mavroeidis, G. Dong, A.S. Papageorgiou, Near-fault ground motions, and the response of elastic and inelastic single-degree-of-freedom (SDOF) systems. *Earthquake Engineering and Structural Dynamics*, **33**, 1023-1049, 2004.

[12] C.C. Spyrakos, C.A. Maniatakis, J. Taflambas, Evaluation of near source seismic records based on damage potential parameters: Case study: Greece. *Soil Dynamics and Earthquake Engineering*, **28**, 738-753, 2008.

[13] I.M. Taflampas, C.C. Spyrakos, C.A. Maniatakis, A new definition of strong motion duration and related parameters affecting the response of medium-long period structures. In *Proceedings of the 14th World Conference in Earthquake Engineering* (No. 03-01-0057). Beijing, China: International Association for Earthquake Engineering, 2008.

[14] I.M. Taflampas, C.C. Spyrakos, I.A. Koutromanos, A new definition of strong motion duration and related parameters affecting the response of medium-long period structures. *Soil Dynamics and Earthquake Engineering*, **29**, 752–763, 2009.

[15] C.A. Maniatakis, C.C. Spyrakos, A new methodology to determine elastic displacement spectra in the near-fault region. *Soil Dynamics and Earthquake Engineering*, **35**, 41-58, 2012.

[16] S.K. Shahi, J.W. Baker, An empirically calibrated framework for including the effects of near-fault directivity in Probabilistic seismic hazard analysis. *Bulletin of the Seismological Society of America*, **101**(2), 742-755, 2011.

[17] D.M. Boore, G.M. Atkinson, Ground-motion prediction equations for the average horizontal component of PGA, PGV, and 5%-damped PSA at spectral periods between 0.01s and 10.0s. *Earthquake Spectra*, **24**(1), 99–138, 2008.

[18] International Council on Monuments and Sites – ICOMOS. *International Charter for the Conservation and Restoration of Monuments and Sites* (The Venice Charter 1964). Second International Congress of Architects and Technicians of Historic Monuments, Venice, 1964.

[19] Congress on the European Architectural Heritage, 21 - 25 October 1975: The Declaration of Amsterdam.

[20] B.C. Papazachos, Ch.A. Papaioannou, B.N. Margaris, N.P. Theodulidis, Regionalization of Seismic Hazard in Greece Based on Seismic Sources. *Natural Hazards,* **8**, 1-13, 1993.

[21] C.C. Spyrakos, F. Pugi, C.A. Maniatakis, A. Francioso, Evaluation of the Dynamic Response for a Historic Byzantine crossed-dome church through Block joint and Kinematic analysis. M. Papadrakakis, V. Papadopoulos, V. Plevris eds. *COMPDYN 2015, 5th ECCOMAS Thematic Conference on Computational Methods in Structural Dynamics and Earthquake Engineering*, Crete island, Greece, 25-27 May 2015.

[22] Ministero delle Infrastrutture e dei Trasporti, Circolare. n. 617 del 02 febbraio 2009. Istruzioni per l'applicazione delle Nuove Norme Tecniche per le costruzioni, §C8A.4, Gazzetta Ufficiale della Repubblica Italiana n. 47 del 26 febbraio 2009, Supplemento ordinario n.27. (in Italian)

[23] T. Palamida-Efthymiadou, *The Metropolis of Lemnos during the last century of Ottoman rule (1800-1912), according to the Bishopric Codes of Lemnos*. Alexandroupolis; Melissa Press, 2007. (in Greek)

[24] Comité Européen de Normalisation (CEN). *Eurocode 7 (EC7)-2007: Geotechnical Design*. Brussels: CEN, 2007.

[25] American Society for Testing and Material (ASTM). *Standard C 805/C 805M – 08. Standard Test Method for Rebound Number of Hardened Concrete*, 2008.

[26] L. Binda, A. Saisi, Knowledge of the building, on site investigation and connected problems. *Eurocode 8 Perspectives from the Italan Standpoint Workshop*, 213-224, Doppiavoce, Napoli, Italy, 2009.

[27] D.J. Titman, Applications of thermography in non-destructive testing of structures. *NDT & E International*, **34**(2), 149-154, 2001.

[28] D. D'Ayala, E. Speranza, Definition of collapse mechanisms and seismic vulnerability of historic masonry buildings. *Earthquake Spectra*, **19**(3), 479–509, 2003.

[29] S. Lagomarsino, A. Penna, A. Galasco, S. Cattari, TREMURI program: An equivalent frame model for the nonlinear seismic analysis of masonry buildings. *Engineering Structures*, **56**, 1787–1799, 2013.

[30] S. Pantazopoulou, *State of the art report for the analysis methods for unreinforced masonry heritage structures and monuments*. European Centre on Prevention and Forecasting of Earthquakes (ECPFE) Report, 2013.

[31] C.C. Spyrakos, A. Francioso, P.D. Kiriakopoulos, S. Papoutsellis, Seismic evaluation of the historic church of St. Nicholas in Piraeus before and after interventions. M. Papadrakakis, V. Papadopoulos, V. Plevris eds. *COMPDYN 2013, 4th ECCOMAS Thematic Conference on Computational Methods in Structural Dynamics and Earthquake Engineering*, Kos Island, Greece, 12–14 (pp. 3015-3029), June 2013.

[32] Aedes Software. PCM: Progettazione di costruzioni in muratura, www.aedes.it.

[33] F. Pugi, Seismic analysis of masonry arch structures through the finite element model "block-joint". M. Papadrakakis, V. Papadopoulos, V. Plevris eds. *COMPDYN 2013, 4th ECCOMAS Thematic Conference on Computational Methods in Structural Dynamics and Earthquake Engineering*, Kos Island, Greece, 12–14 (pp. 2997-3014), June 2013.

[34] T.M. Tsapanos, P.W. Burton, Seismic hazard evaluation for specific seismic regions of the world. *Tectonophysics*, **194**, 153–169, 1991.

[35] Hellenic Organization for Standardization (ELOT). EN 1998-1:2005. *Greek National Annex to Eurocode 8: Design of structures for earthquake resistance - Part 1: General rules, seismic actions and rules for buildings*. Athens: ELOT, 2005.

[36] B.C. Papazachos, C.B. Papazachou, *The earthquakes of Greece*, Thessaloniki: Ziti Publications, 2003.

[37] Royal Decree 26/19 - 2 -1959: *On the seismic design of structures*, 1959. (in Greek)

[38] Comité Européen de Normalisation (CEN). EN 1996-1-1: 2005. Eurocode 6: Design of Masonry Structures. Brussels: CEN, 2005.

[39] Ministero delle Infrastrutture e dei Trasporti, *Circolare. n. 617 del 02 febbraio 2009. Istruzioni per l'applicazione delle Nuove Norme Tecniche per le costruzioni, §C8A.4*, Gazzetta Ufficiale della Repubblica Italiana n. 47 del 26 febbraio 2009, Supplemento ordinario n.27, 2009. (in Italian)

[40] CNR-dt 200 R1/2013: *Guide for the Design and Constuction of Externally Bonded FRO Systems for strengthening Existing Structures. Materials, RC and PC structures, masonry structures*, 2013.

[41] Seismic Protection of Monuments and Historic Structures - SEISMO. Thales Context - Greek Ministry of Education and Religions - The European Union, Operational Programme - Education and Lifelong Learning, NSRF 2007-2013.

COMPDYN 2015
5th ECCOMAS Thematic Conference on
Computational Methods in Structural Dynamics and Earthquake Engineering
M. Papadrakakis, V. Papadopoulos, V. Plevris (eds.)
Crete Island, Greece, 25–27 May 2015

THE IMPACT OF VERTICAL HUMAN-STRUCTURE INTERACTION FOR FOOTBRIDGES

Katrien Van Nimmen[1,2], Kristof Maes[1], Geert Lombaert[1], Guido De Roeck[1] and Peter Van den Broeck[1,2]

[1] KU Leuven, Department of Civil Engineering, Structural Mechanics
B-3001 Leuven, Belgium
e-mail: katrien.vannimmen@kuleuven.be

[2] KU Leuven, Department of Civil Engineering, Technology Cluster Construction
B-9000 Ghent, Belgium
e-mail: peter.vandenbroeck@kuleuven.be

Keywords: human-structure interaction, footbridge, human-induced vibrations, vibration serviceability, full-scale testing.

Abstract. *To allow for a more accurate description of crowd-induced loading, the present study aims to provide the necessary insights into vertical human-structure interaction (HSI) phenomena, to date ignored in current load models. A parametric study is performed to investigate the effects of the mechanical interaction between pedestrians, represented by simple lumped parameter models, and the supporting footbridge. The most significant HSI-effect for the low-frequency modes of a footbridge, is in the effective damping ratio of the coupled system which is much higher than the inherent structural damping. The effective damping ratio increases monotonically with the pedestrian density but is highly dependent on the natural frequency of the footbridge. In order to verify the findings, a comprehensive full-scale experimental study is performed on two footbridges. It is shown that the crowd-structure model is able to reproduce the experimentally identified dynamic characteristics of the coupled system.*

1 INTRODUCTION

The relatively small service loads allows for very slender and lightweight footbridge designs. Characterised by a low stiffness to mass ratio, footbridges often have one or more natural frequencies below 6 Hz. Given the force spectrum of pedestrian excitation which is dominated by contributions around the fundamental ($1.25 - 2.50$ Hz) and the second ($2.50 - 5.00$ Hz) harmonic of the walking load, the vibration serviceability of footbridges is mostly governed by (near-)resonant loading [1, 2].

In the prediction of crowd-induced vibrations, persons crossing a footbridge are often simplified to (moving) forces [3]. However, this approach does not consider that people are mechanical systems which interact with the structure that is supporting them [4]. In some cases, the modal characteristics of the coupled crowd-structure system significantly differ from those of the empty footbridge [5, 6, 7]. The degree to which the dynamic behaviour is modified is expected to increase with an increasing crowd to structural mass ratio. Hence, these effects are expected to be non-negligible for lightweight footbridges [8, 9].

To characterise HSI-effects for slender footbridges, the low-frequency behaviour of the human body ($<$ 10 Hz) is of interest in this paper. As the human dynamics in the vertical direction largely depends on the body posture [10], a distinction is made between *active* and *passive* postures as assumed by active (e.g. walking, jogging, ...) and passive (e.g. standing still) persons, respectively. Passive persons are most likely to assume a standing posture characterised by legs being straight. On the other hand, the posture of an active individual is changing continuously during the gait cycle and it involves either one or two legs slightly bent.

In the present work, the effects of the mechanical interaction between pedestrians and the supporting footbridge are investigated by means of a parametric study. The latter considers a realistic crowd model, composed of active and passive individuals and subject to inter-person variability.

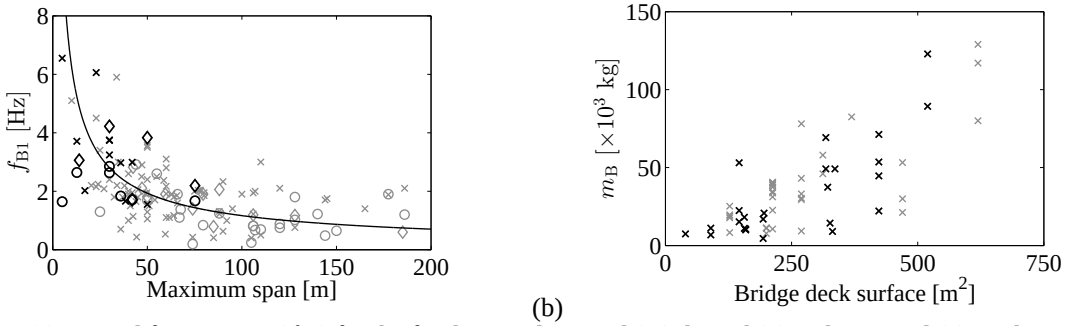
The outline of this paper is as follows. First, the low-frequency dynamic properties of the footbridge and the human body are discussed and the coupled human-structure model is presented. Second, the implications for the practical design of footbridges are evaluated based on a realistic crowd model representative of the inter-person variability. Finally, the predicted dynamic behaviour of the coupled human-structure system is verified by means of field-tests on two footbridges.

2 FRAMEWORK

This section aims at providing a concise and structured overview of the relevant dynamic properties of footbridges and the human body with the prime purpose to determine realistic parameter ranges for the parametric study.

2.1 Dynamic behaviour of footbridges

The low-frequency dynamic behaviour of footbridges is characterised by the modal properties [1], i.e. the natural frequencies $f_{\mathrm{B}j}$, modal damping ratios $\xi_{\mathrm{B}j}$ and modal masses $m_{\mathrm{B}j}$, of the low-frequency vibration modes. During the last decade, numerous experimental studies of the dynamic behaviour of footbridges have been performed. The following paragraphs present a synopsis of the relevant modal properties reported in literature. The collected footbridge data are composed of 11 structures investigated by the authors and over 100 footbridges discussed in other reports and publications. The main sources of information used are the SYNPEX report [2], the French Sétra guideline [11], the JRC document for the design of lightweight footbridges



(a) (b)

Figure 1: (a) Natural frequencies (f_{B1}) for the fundamental vertical ($\times$), lateral ($\circ$) and torsional ($\diamond$) modes in terms of the maximum span length of the footbridge, (b) modal mass (m_B) in terms of the total bridge deck surface: as reported in literature (grey), for the 11 cases investigated by the authors (black) and the relationship defined in [15] (line).

[12] and the reference lists of GERB [13] and MAURER-SÖHNE [14].

Figure 1-a presents the identified natural frequencies in relation to the maximum span length, including only the first (fundamental) lateral, vertical and/or torsional mode. As expected, the natural frequencies tend to decrease with increasing span length. However, even bridges with short spans can exhibit low natural frequencies (< 6 Hz) which is due to the distinct slender designs. The collected data qualitatively agree with the natural frequency to span relationship as proposed by Bachmann et al. [15] based on data for 67 footbridges with spans between 15 and 50 metres:

$$f_{B1} = 33.6\, l^{-0.73} \tag{1}$$

where f_{B1} [Hz] denotes the fundamental natural frequency and l [m] the span of the footbridge (figure 1).

The second modal property of interest is the modal mass. When obtained via the unity-scaled mode shapes, the modal mass is a measure of the physical mass of the system that is engaged in a particular mode [16]. The modal masses reported in literature include both experimentally identified and numerically calculated values. Figure 1-b presents the reported modal masses in relation to the total bridge deck surface. As expected, the modal masses increase with increasing functional area.

The third relevant modal property is the modal damping ratio. Design guides for the vibration serviceability assessment of footbridges propose numerical values for the modal damping ratios based on experience obtained from similar construction types (table 1). Figure 2 presents the identified modal damping ratios for different construction types in relation to the corresponding natural frequency. This figure illustrates that the lowest modal damping ratios are retrieved for steel and composite bridges with minimum and mean values that agree with the provisional values reported by the guidelines (see table 1).

2.2 Dynamic behaviour of the human body

The low-frequency (0-10 Hz) dynamic behaviour of the human body in the vertical direction can be represented by a highly damped single degree of freedom (SDOF) system [21, 22, 23]. The mass $m_{H,k}$, being equal the total mass of the corresponding individual k, is divided into two lumped masses, i.e. a sprung mass $m_{H1,k}$ [21, 22, 24] and a rigid mass $m_{H0,k}$ at the support ($m_{H,k} = m_{H0,k} + m_{H1,k}$). The corresponding mechanical properties ($f_{H1,k}$ and $\xi_{H1,k}$) largely depend on the body posture [10]. On a footbridge, usually both active and passive persons are

Type	Bachmann [15]		Sétra [11]		HiVoSS [17]		ISO 10137 [18]	EC 1 EC 5 [19, 20]
	min	max	min	mean	min	mean		
RC	0.8	2.0	0.8	1.3	0.8	1.3	0.8	1.5
PC	0.5	1.7	0.5	1.0	0.5	1.0	0.8	1.0
S	0.2	0.4	0.2	0.4	0.2	0.4	0.5	0.5
C	0.3	0.6	0.3	0.6	0.3	0.6	0.6	0.5
T	1.5	3.0	1.5	3.0	1.0	1.5	-	1.0-1.5
S-R	-	-	-	-	0.7	1.0	-	-

Table 1: Provisional modal damping ratios ξ_{B} [%] as suggested by the current codes of practice for different construction types: reinforced concrete (RC), prestressed concrete (PC), steel (S), composite (C), timber (T) and stress-ribbon (S-R).

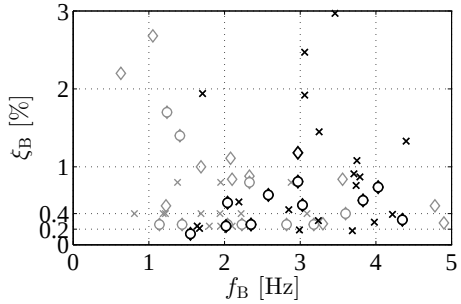


Figure 2: Identified modal damping ratios (ξ_{B}) for steel ($\times$), composite ($\circ$) and concrete ($\diamond$) footbridges in terms of the corresponding natural frequencies (f_{B}): as reported in literature (grey) and for the 11 cases investigated by the authors (black).

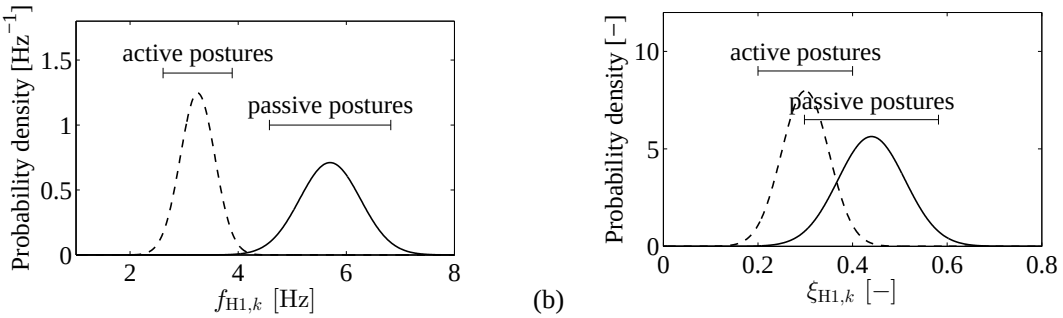


Figure 3: The adopted truncated Gaussian distributions for active (dashed) and passive (solid) postures: (a) the natural frequency $f_{\text{H1},k}$ and (b) modal damping ratio $\xi_{\text{H1},k}$.

present. Passive individuals most often assume a standing posture whereas the posture of active individuals is changing continuously during the walking cycle. In the following, active persons are represented by (stationary) human body models representative of a body posture with one or two legs, i.e. considered in this paper as an approximation of the postures assumed during the walking cycle.

The fundamental natural frequency of an active person is situated between 2.5 Hz and 4 Hz with a corresponding modal damping ratio between 20% and 40% [22, 25]. For passive persons, the natural frequency and damping ratio are generally situated between 5.0-6.5 Hz and 35%-50%, respectively [22, 26]. In both cases, the mass $m_{\text{H1},k}$ is found between 85% and 99% of the total mass $m_{\text{H},k}$ with the remaining mass $m_{\text{H0},k}$ lumped at the support.

In the following, inter-subject variability is accounted for by assuming a Gaussian distribution of the natural frequency and modal damping ratio of the human body model. The mean values and coefficient of variation are based on the results reported by Matsumoto and Griffin

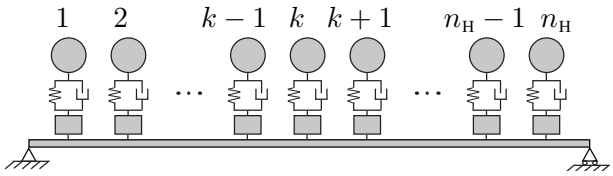


Figure 4: The coupled system composed of n_{H} persons and the supporting footbridge.

[22] and the results from an experimental study performed by the authors [25] (see figure 3):

$$\text{Passive persons:} \tag{2}$$

$$f_{\mathrm{H}1,k} \sim \mathcal{N}(\mu_{f_{\mathrm{H}1,k}}, \sigma_{f_{\mathrm{H}1,k}}) = \mathcal{N}(5.7, 0.56) \quad [\mathrm{Hz}] \tag{3}$$

$$\xi_{\mathrm{H}1,k} \sim \mathcal{N}(\mu_{\xi_{\mathrm{H}1,k}}, \sigma_{\xi_{\mathrm{H}1,k}}) = \mathcal{N}(0.44, 0.07) \quad [-] \tag{4}$$

$$\text{Active persons:} \tag{5}$$

$$f_{\mathrm{H}1,k} \sim \mathcal{N}(\mu_{f_{\mathrm{H}1,k}}, \sigma_{f_{\mathrm{H}1,k}}) = \mathcal{N}(3.25, 0.32) \quad [\mathrm{Hz}] \tag{6}$$

$$\xi_{\mathrm{H}1,k} \sim \mathcal{N}(\mu_{\xi_{\mathrm{H}1,k}}, \sigma_{\xi_{\mathrm{H}1,k}}) = \mathcal{N}(0.30, 0.05) \quad [-] \tag{7}$$

2.3 Coupled human-structure model

When a person is present on a footbridge, interaction occurs between his body and the structure. The two subsystems interact with each other through contact forces induced at the contact points between the person and the bridge deck, i.e. at the feet-bridge deck interface. In the following, both active and passive persons are modelled as stationary. The governing equations of motion can be written for two linear dynamic subsystems separately. In order to ensure coupling, compatibility and equilibrium conditions at the contact points need to be satisfied (analogous to the problem of vehicle-bridge interaction [27]). As the persons are assumed to be stationary, the coupled system is time-invariant. The reader is referred to [25] for a detailed description of the coupled system and corresponding system matrices.

3 PARAMETRIC STUDY

The HSI-effects are investigated for a realistic crowd model consisting of n_{H} individuals (n_{H} human body models), with a distribution of human body model parameters representative of inter-subject variability (see section 2.2). The observed quantities are evaluated using Monte Carlo simulations. Since the dynamic characteristics of the human body are quite different for active and passive body postures, the *activity ratio* is considered as an additional parameter here. A unit value of the activity ratio corresponds to the case where all the persons on the bridge are active. As it is expected that most people present on a footbridge are active, an activity ratio of 0.5 up to 1.0 is considered.

Natural frequencies between 0.5 Hz and 6.0 Hz are considered for the empty footbridge. In addition, the implications of HSI for practical design of footbridges are investigated assuming a range of: (i) the mass ratio ($0.02 \leq \mu_{\mathrm{HB}} \leq 0.50$ [-]) and (ii) the structural modal damping ratio ($\xi_{\mathrm{B}} = \{0.2, 0.5, 2.0\}$ [%]). To facilitate the practical interpretation, the results are expressed in terms of the natural frequency of the footbridge f_{B} [Hz].

First, the output quantities of interest are selected. Second, the Monte Carlo simulation of the crowd composition is discussed. Subsequently, the influence of the activity ratio and the structural modal damping ratio are investigated.

3.1 Output quantities of interest

The parametric study aims to determine when the interaction effects with the crowd are significant and whether or not they are beneficial. An interaction effect is here understood as beneficial if it reduces the maximum acceleration response of the footbridge. The vibration serviceability of footbridges is mostly governed by (near-)resonant loading [1]. For the empty footbridge, the maximum steady-state amplitude $\ddot{u}_{\mathrm{B,max}}$ to harmonic excitation is found as:

$$\ddot{u}_{\mathrm{B,max}} \sim \frac{1}{2\xi_{\mathrm{B}} m_{\mathrm{B}}} = |\mathrm{H}_{\mathrm{B}}(\omega_{\mathrm{B}})| \tag{8}$$

with $\mathrm{H}_{\mathrm{B}}(\omega)$ the frequency response function (FRF) of the footbridge and ω_{B} the natural frequency of the footbridge in rad/s. In this case, the natural frequency f_{B}, modal damping ratio ξ_{B} and modal mass m_{B} are the key parameters that determine the structural dynamic response.

Similarly, the FRF of the coupled system relating the harmonic input excitation to the acceleration response (in the following referred to as $\mathrm{H}_{\mathrm{HB}}(\omega)$), both taken at the footbridge DOF, is examined and its key parameters are identified. First, a reference case is defined for the coupled crowd-structure system. For this reference case, the HSI-effects are evaluated for a selection of frequency ($f_{\mathrm{H1}}/f_{\mathrm{B}}$) and mass ($\mu_{\mathrm{HB}}$) ratios. The selected case corresponds to a footbridge with a modal damping ratio of $\xi_{\mathrm{B}} = 0.5\%$, occupied by a crowd that is represented by the human body model with modal damping ratio $\xi_{\mathrm{H1}} = 40\%$ and mass ratio $\mu_{\mathrm{H1}} = 0.95$.

Figure 5-a presents the FRF of the coupled system $\mathrm{H}_{\mathrm{HB}}(\omega)$ for a fixed mass ratio ($\mu_{\mathrm{HB}} = 0.3$) and for ten different frequency ratios $f_{\mathrm{H1}}/f_{\mathrm{B}}$, uniformly spaced between 0.2 and 2. This figure illustrates that the FRF $\mathrm{H}_{\mathrm{HB}}(\omega)$, relating the harmonic input excitation to the acceleration response of the footbridge, is characterised by a single peak. Furthermore, figure 5-a shows that the peak value of $\mathrm{H}_{\mathrm{HB}}(\omega)$ highly depends on the frequency ratio $f_{\mathrm{H1}}/f_{\mathrm{B}}$, and, is at its lowest for frequency ratios $f_{\mathrm{H1}}/f_{\mathrm{B}}$ slightly lower than unity.

Figures 5-b and 5-c compare the FRF of the empty footbridge with the FRF of the coupled system for a mass ratio μ_{HB} of 0.1 and 0.4, respectively. Both figures present the FRF $\mathrm{H}_{\mathrm{HB}}(\omega)$ for five different frequency ratios $f_{\mathrm{H1}}/f_{\mathrm{B}} = \{0.4, 0.6, 0.8, 1.0, 1.2\}$. The peak value of the FRF of the coupled system is in all cases lower than the one of the empty footbridge. Comparing figure 5-b with figure 5-c shows that the interaction effects, i.e. the change of the peak value and corresponding frequency (abscissa), increase with the mass ratio, as expected. Furthermore, the frequency at which the corresponding peak value of $\mathrm{H}_{\mathrm{HB}}(\omega)$ is reached, also depends on the frequency ratio $f_{\mathrm{H1}}/f_{\mathrm{B}}$. For frequency ratios lower and higher than unity, this frequency is found above and below the natural frequency of the empty footbridge, respectively.

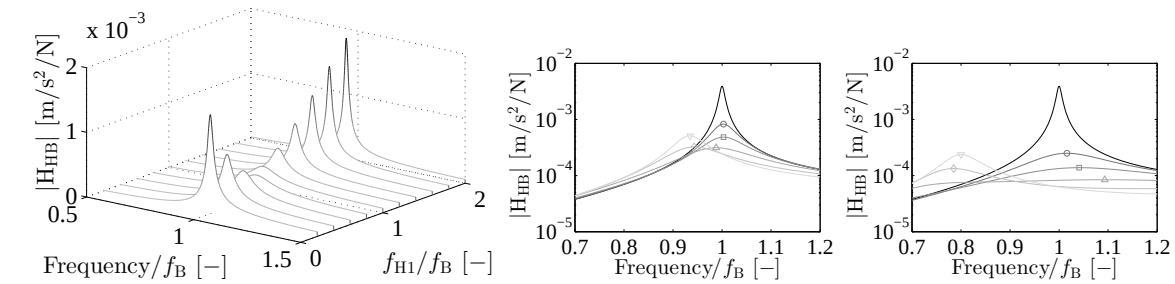
The peak value of the FRF $\mathrm{H}_{\mathrm{HB}}(\omega)$ determines the maximum amplitude of the steady-state acceleration response of the footbridge $\ddot{u}_{\mathrm{HB,max}}$ when subjected to harmonic excitation:

$$\begin{aligned} &\ddot{u}_{\mathrm{HB,max}} \sim |\mathrm{H}_{\mathrm{HB}}(\omega_{\mathrm{HB}})|\,, \\ &\text{with} \quad \omega_{\mathrm{HB}} = \underset{\omega}{\operatorname{argmax}} |\mathrm{H}_{\mathrm{HB}}(\omega)| \end{aligned} \tag{9}$$

The effective natural frequency of the coupled system f_{eff} [Hz] is now defined as:

$$f_{\mathrm{eff}} = \frac{\omega_{\mathrm{HB}}}{2\pi} \tag{10}$$

Accordingly, the effective damping ratio ξ_{eff} [-] is defined as a measure for the change in maxi-



(a) (b) (c)

Figure 5: The FRF $\mathrm{H}_{\mathrm{HB}}(\omega)$ for a footbridge with $\xi_{\mathrm{B}} = 0.5\%$ coupled to the human body model with $\mu_{\mathrm{H1}} = 0.95$, $\xi_{\mathrm{H1}} = 40\%$ for a mass ratio of (a) $\mu_{\mathrm{HB}} = 0.3$, (b) $\mu_{\mathrm{HB}} = 0.1$ and (c) $\mu_{\mathrm{HB}} = 0.4$ for frequency ratio $f_{\mathrm{H1}}/f_{\mathrm{B}}$: 0.4 (○), 0.6 (□), 0.8 (△), 1.0 (◇) and 1.2 (▽), in terms of the frequency ratio ($f_{\mathrm{H1}}/f_{\mathrm{B}}$).

mum steady-state acceleration response in relation to that of the empty footbridge:

$$\begin{aligned} \ddot{u}_{\mathrm{HB,max}} &\sim \frac{1}{2\xi_{\mathrm{eff}} m_{\mathrm{B}}} \\ \Rightarrow \xi_{\mathrm{eff}} &= \frac{\ddot{u}_{\mathrm{B,max}}}{\ddot{u}_{\mathrm{HB,max}}}\,\xi_{\mathrm{B}} = \frac{|\mathrm{H}_{\mathrm{B}}(\omega_{\mathrm{B}})|}{|\mathrm{H}_{\mathrm{HB}}(\omega_{\mathrm{HB}})|}\,\xi_{\mathrm{B}} \end{aligned} \tag{11}$$

Finally, the reduction of the bridge acceleration due to human-structure interaction is described by the factor R_{HB} [-]:

$$R_{\mathrm{HB}} = \frac{\ddot{u}_{\mathrm{B,max}}}{\ddot{u}_{\mathrm{HB,max}}} = \frac{|\mathrm{H}_{\mathrm{B}}(\omega_{\mathrm{B}})|}{|\mathrm{H}_{\mathrm{HB}}(\omega_{\mathrm{HB}})|} \tag{12}$$

The interaction effect is beneficial when the reduction factor is larger than unity ($R_{\mathrm{HB}} > 1$) whereas it is disadvantageous when lower than unity ($R_{\mathrm{HB}} < 1$).

3.2 Monte Carlo Simulation of the crowd configuration

The crowd consists of an integer number of persons n_{H} (see figure 4 and section 2.3). Each individual is represented by a human body model with a mass $m_{\mathrm{H}} = 70$ kg. The number of persons n_{H} corresponding to a mass ratio μ_{HB} is calculated by assuming the previously introduced simply supported reference structure, with a total mass of 50 $\times 10^3$ kg (see section 3). This results in a number of 15 and 360 persons for the lower (0.02) and upper (0.50) limit of the considered mass ratios, respectively.

The human body model parameters (f_{H1} and ξ_{H1}) are sampled from the truncated distributions suggested in section 2.2. Since the influence of the mass ratio (μ_{H1}) was found to be insignificant, the corresponding parameter value is fixed at 0.95 [-]. The selected activity ratio defines the number of active and passive persons. The location of each individual is chosen randomly along the bridge deck assuming a uniform distribution (see figure 4).

For each crowd configuration, the normalised effective natural frequency $f_{\mathrm{eff}}/f_{\mathrm{B}}$ and effective damping ratio ξ_{eff} are calculated. In order to obtain a conservative (or *lower bound*) estimate of the interaction benefit, the 95%-percentile of the minimum effective damping ratio is evaluated [28]. For the normalised effective natural frequency, both the 5%-percentile and 95%-percentile value are equally relevant. For reasons of conciseness, only the percentile value corresponding to the largest modification in comparison to f_{B} is presented.

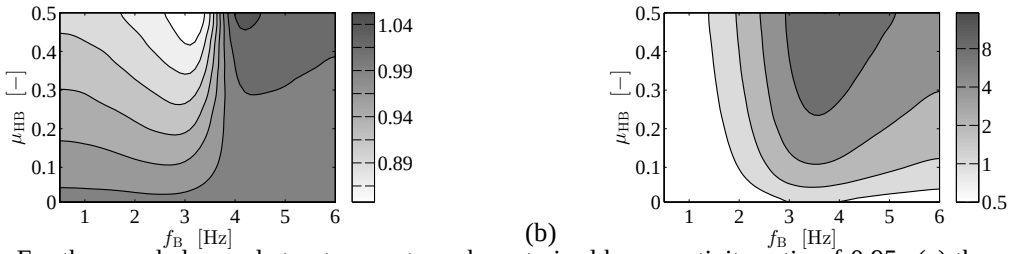


Figure 6: For the coupled crowd-structure system characterised by an activity ratio of 0.95: (a) the normalised effective natural frequency $f_{\text{eff}}/f_{\text{B}}$ and (b) effective damping ratio ξ_{eff} in terms of the natural frequency of the footbridge (f_{B}) and the considered mass ratios (μ_{HB}), for a footbridge with a modal damping ratio ξ_{B} of 0.5%.

3.3 HSI-effects for a reference case

As a starting point, the influence of HSI is discussed for a reference case. In this reference case, a structural modal damping ratio of $\xi_{\text{B}} = 0.5\%$ is considered and the activity ratio of the crowd is set to 0.95. The HSI-effects are analysed for a natural frequency of the footbridge f_{B} between 0.5 Hz and 6.0 Hz and mass ratios μ_{HB} up to 0.5. Figure 6 presents the normalised effective natural frequency $f_{\text{eff}}/f_{\text{B}}$ and effective damping ratio ξ_{eff} in terms of the mass ratio and the natural frequency of the empty footbridge.

For low natural frequencies of the empty footbridge ($f_{\text{B}} < 2.5$ Hz), the human body models are stiffer than the supporting structure and the HSI-effect is limited to that of an equivalent added mass: the natural frequencies reduce in relation to the considered mass ratio and the effective damping ratio approximately equals the modal damping ratio of the empty footbridge ($\xi_{\text{eff}} \approx \xi_{\text{B}}$).

For intermediate natural frequencies of the empty footbridge ($2.5 < f_{\text{B}} < 4.5$ Hz), the effective natural frequency of the coupled system is slightly lower (for $f_{\text{B}} < 3.25$ Hz) or higher (for $f_{\text{B}} > 3.25$ Hz) than the natural frequency of the empty footbridge. More striking is the significant increase in the effective damping ratio. For low mass ratios, the effective damping ratio increases up to 1%-2% while for high mass ratios, the effective damping ratio easily exceeds 8%. This is due to the fact that the crowd is mainly composed of pedestrians with natural frequencies around 3.25 Hz for the considered high activity ratio. As a result, the frequency ratios are close to unity ($f_{\text{H1}}/f_{\text{B}} \approx 1$) and the corresponding HSI-effects are significant. In this case, the crowd behaves in a similar way as a tuned mass damper (TMD).

For high natural frequencies of the empty footbridge ($4.5 < f_{\text{B}} < 6$ Hz), the effective damping ratio again increases with the mass ratio, but less strongly than for intermediate natural frequencies. For these frequency ratios, the crowd is more flexible than the footbridge and the two subsystems remain largely decoupled. For high mass ratios, the effective natural frequency is also slightly higher than the natural frequency of the empty footbridge while for low mass ratios, the HSI-effects are insignificant.

3.4 Influence of activity ratio

Figure 7 presents the normalised effective natural frequency ($f_{\text{eff}}/f_{\text{B}}$) and effective damping ratio (ξ_{eff}) in terms of the activity ratio and the natural frequency of the empty footbridge. The influence of the activity ratio on the HSI-effects is evaluated for four mass ratios μ_{HB}: 0.05, 0.10, 0.20 and 0.5. For the reference case, these mass ratios roughly correspond to pedestrian densities of 0.25, 0.5, 1.0 and 2.5 $\text{persons}/\text{m}^2$, respectively. A fixed value is assumed for the modal damping ratio of the footbridge ($\xi_{\text{B}} = 0.5\%$).

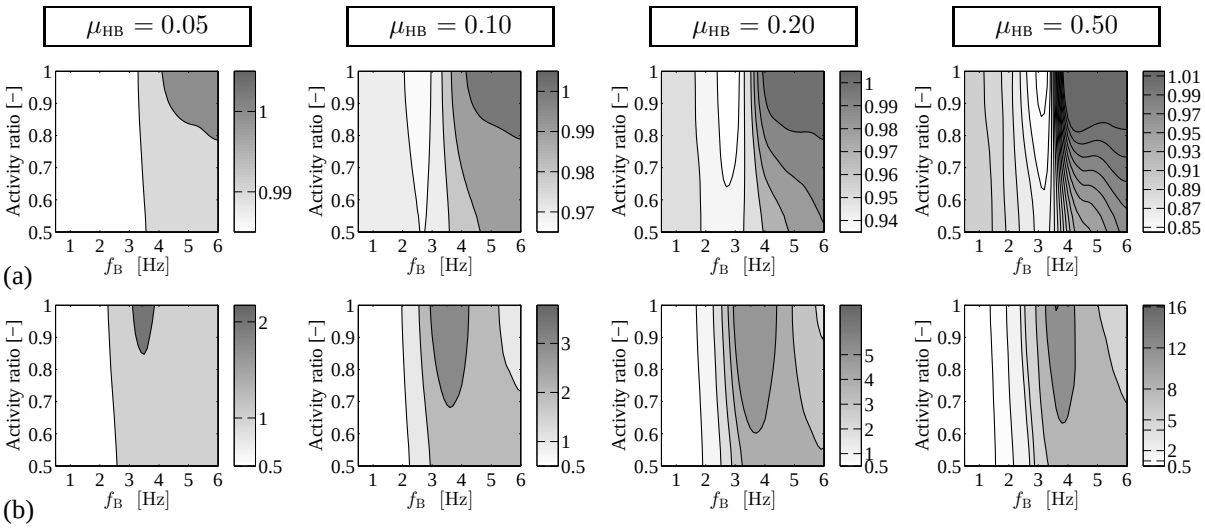


Figure 7: For the coupled crowd-structure system consisting of a footbridge with modal damping ratio $\xi_B = 0.5\%$: (a) the normalised effective natural frequency f_{eff}/f_B and (b) effective damping ratio ξ_{eff} for a mass ratio μ_{HB} of 0.05, 0.1, 0.2 and 0.5 in terms of the activity ratio and the natural frequency of the footbridge (f_B).

For low natural frequencies of the empty footbridge ($f_B < 2.5$ Hz), the HSI-effects are independent of the activity ratio. As the crowd is composed of pedestrians with a natural frequency around 5.70 Hz or 3.25 Hz, the frequency ratios are, in both cases, relatively high ($f_{H1}/f_B > 1.5$). Hence, the pedestrians act as an equivalent added mass, regardless of their activity.

For intermediate natural frequencies of the empty footbridge ($2.5 < f_B < 4.5$ Hz), the HSI-effects slightly decrease with a reducing activity ratio. A reduction of the activity ratio leads to a higher number of passive persons with corresponding frequency ratios (f_{H1}/f_B) that increase from approximately unity up to 1.75 and, therefore, leads to smaller HSI-effects.

Accordingly, *for high natural frequencies of the empty footbridge* ($f_B > 4.5$ Hz), the HSI-effects are higher for lower activity ratios as this increases the number of individuals with a frequency ratio (f_{H1}/f_B) close to unity.

3.5 Influence of structural damping

Figure 7 presents the normalised effective natural frequency (f_{eff}/f_B) and effective damping ratio (ξ_{eff}) in terms of the mass ratio (μ_{HB}) and the natural frequency of the empty footbridge, for a fixed activity ratio of 0.95. The influence of the structural damping on the HSI-effects is investigated by considering three different modal damping ratios of the empty footbridge: $\xi_B = \{0.2, 0.5, 2.0\}\,\%$.

Figure 7 shows that the effect of the structural damping ratio on the effective natural frequency of the coupled system, is insignificant.

For low natural frequencies of the empty footbridge ($f_B < 2.5$ Hz), the effective damping ratio increases with the mass ratio and the natural frequency of the empty footbridge. For natural frequencies below 1.5 Hz, the effective damping ratio is close to the inherent structural damping. As the natural frequencies increase towards 2.5 Hz, the increase in effective damping ratio becomes significant. The lower the inherent structural damping, the stronger the increase in the effective damping ratio.

For intermediate natural frequencies of the empty footbridge ($2.5 < f_B < 4.5$ Hz), the effec-

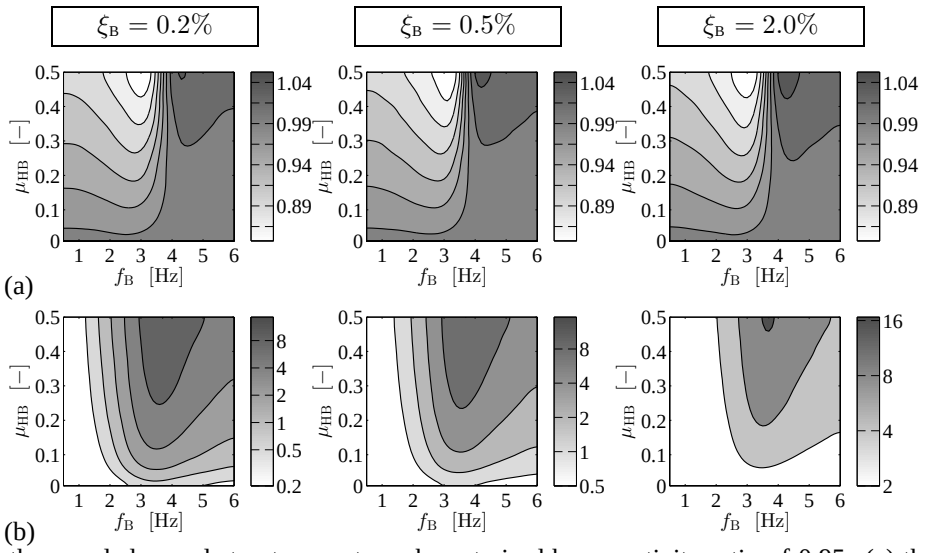


Figure 8: For the coupled crowd-structure system characterised by an activity ratio of 0.95: (a) the normalised effective natural frequency $f_{\text{eff}}/f_{\text{B}}$ and (b) effective damping ratio ξ_{eff} (right) in terms of the natural frequency of the footbridge (f_{B}) and the considered mass ratios (μ_{HB}), for a footbridge with a modal damping ratio ξ_{B} of 0.2%, 0.5% and 2.0%.

tive damping ratio increases significantly with the mass ratio as the frequency ratios ($f_{\text{H1}}/f_{\text{B}}$) are close to unity. For low mass ratios, this HSI-effect is insignificant for structures with a relatively high inherent damping ($\xi_{\text{B}} \geq 2\%$). For very lowly-damped structures ($\xi_{\text{B}} \leq 0.5\%$) on the other hand, the increase in effective damping ratio is considerable, even for very low mass ratios. Note that for high mass ratios ($\mu_{\text{HB}} > 0.25$), the effective damping ratio reaches extremely high values ($\xi_{\text{eff}} > 8\%$), independently of the inherent structural damping.

For high natural frequencies of the empty footbridge ($4.5 < f_{\text{B}} < 6.0$ Hz), the effective damping ratio again increases significantly with the mass ratio, but less strong than for intermediate natural frequencies.

4 FULL-SCALE EXPERIMENTAL VERIFICATION

This section examines the effect of HSI based on in situ tests on two lightweight steel footbridges. By comparing the measured and predicted effective natural frequencies and modal damping ratios, it is verified if the coupled human-structure model allows reproducing the experimentally identified dynamic behaviour of the coupled system.

On the Eeklo footbridge, tests with both passive and active persons are performed. In addition, small-scale tests are performed on the Charleroi footbridge involving a limited number of pedestrians.

4.1 Eeklo footbridge

The experimental identification of the modal characteristics and the calibration of the numerical model of the Eeklo footbridge, was previously discussed in [29]. The two modes of interest in the present analysis are the fundamental lateral-torsional mode ($f_1 = 1.71$ Hz, $\xi_1 = 2.3\%$, $m_1 = 34 \times 10^3$ kg) and the first vertical bending mode ($f_2 = 2.99$ Hz, $\xi_2 = 0.2\%$, $m_2 = 22 \times 10^3$ kg). From the previous analyses, it is expected that the second mode will be strongly affected by the presence of persons on the bridge deck.

The structural response is registered during free vibration tests as well as trials involving

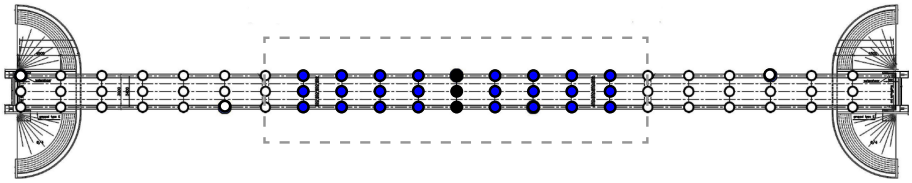


Figure 9: Top view of the Eeklo footbridge with walking area (box) and stationary subject locations (solid).

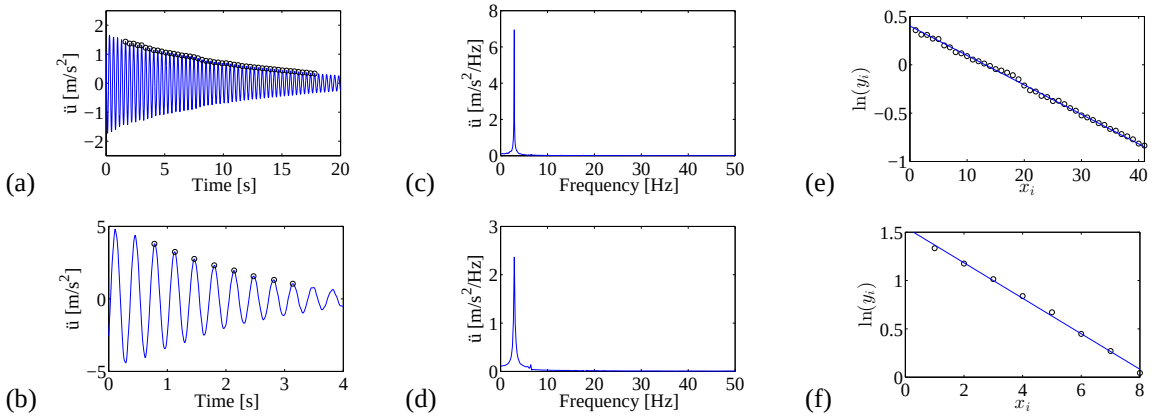


Figure 10: Measured vertical free vibration response of the footbridge at midspan with 15 human persons adopting the posture (a, c, e) with straight legs and (b, d, f) slightly bent legs: (a, b) time series with selected peak values, (c, d) corresponding amplitude spectrum and (e, f) natural logarithm and best-fit line of peak amplitudes (y_i) and abscissa (x_i).

ambient and random walking excitation. In order to obtain a free vibration dominated by the contribution of a single mode, the bridge is first brought into motion by rhythmical human activities (bobbing) tuned at the selected natural frequency using a metronome. Once the desired level of vibration is reached, the persons cease bobbing and get into the selected body posture, thereby initiating the free vibration phase. The natural frequency and damping ratio of the considered mode of the coupled system are subsequently identified from a free decay analysis. For the trials involving ambient and random walking excitation, the natural frequency and modal damping ratio of the first and the second mode of the coupled system are identified from an operational modal analysis.

Free decay analysis

The experiments include trials with a different number of persons on the bridge deck. Every individual is positioned at a point where a stringer crosses a cross girder. In the first setup, only three persons are positioned at midspan (figure 9). For each of the following setups, the number of persons is increased by six, three on the left and three on the right adjacent cross girder, respectively. For the setups involving the free vibration of the fundamental torsional mode, the persons on the central stringer are not included. In addition, the influence of the body posture on the dynamic behaviour of the coupled system is examined. The experiments therefore consider the human body in the normal standing posture with (1) straight legs and (2) slightly bent legs.

In order to estimate the effective damping ratio, an exponential function is fitted to the peak values of the recorded decay with amplitudes between 90% and 20% of the maximum peak value of the acceleration levels [30]. Figures 10-c and 10-d confirm that the applied excita-

tion indeed leads to free vibration dominated by a single mode as assumed for the derivation of the effective damping ratio and natural frequency. Figures 10-e and 10-f present the natural logarithm and the least-squares approximation of peak amplitudes (y_i) with abscissa (x_i). The excellent fit that is obtained by the linear function with slope $-\delta$ (where δ represents the logarithmic decrement [31]), illustrates that the damping characteristics hardly depend on the vibration amplitudes.

Operational modal analysis

For the setups with ambient excitation, 9 or 21 persons were requested to stand still during 3 minutes, all adopting either an active or a passive posture. In addition, the persons were asked to walk at a slow, normal (self-selected) or fast speed along the main span of the bridge during 3 minutes (figure 9). The output-only data have been processed using the reference-based data-driven stochastic subspace identification (SSI-data/ref) algorithm [32, 33].

Characteristics of the coupled human-structure model

The dynamic behaviour of the footbridge is simulated with the experimentally identified natural frequencies and modal damping ratios and the mode shapes of the calibrated FE model of the empty structure. All individuals involved were weighted in the laboratory to determine their nominal mass. For each trial involving stationary persons, the location of every individual was determined. To account for inter-subject variability, the natural frequency f_{H1} and damping ratio ξ_{H1} of the human body models are sampled from the truncated Gaussian distributions defined for passive and active postures (in Eq. (7)). The mass ratios of the human body models are fixed to values of $\mu_{\text{H1}} = 0.95$ [-] and $\mu_{\text{H0}} = 0.05$ [-] for both postures. From the Monte Carlo simulations, the 5% and 95% percentile value of the effective natural frequency and damping ratio of the coupled crowd-structure model are retained.

Results

Figure 11 shows the effective natural frequency and modal damping ratio of the vertical bending mode for individuals in the passive posture, an active posture and walking at midspan.

For the passive posture (figures 11-a and 11-b), the frequency ratio is relatively high ($f_{\text{H1}}/f_{\text{B}} \approx [1.5, 2]$). As a result, the natural frequency of the footbridge decreases with the added (modal) mass. Despite the low mass ratio, the effective damping increases substantially which is owed to the very low inherent damping of the empty structure. Both effects are accurately predicted by the coupled model.

For figures 11-b and 11-e) that involve active postures, the frequency ratio is close to unity. As expected, this results in a small modification of the natural frequency and a very large value of the effective damping ratio, e.g. $\xi_{\text{eff}} > 3.5\% \lll \xi_{\text{B}} = 0.2\%$ when 26 persons are involved. Although small variations of the natural frequencies of the human body models cause a large scatter in the predicted effective damping ratio, the trend is clear and corresponds well with the observations. The attained effective damping ratio is more than five times higher than for the passive posture.

Comparing the results in figures 11-e and 11-f with those in figures 11-c and 11-d, shows that the natural frequency and damping ratio obtained from the OMA involving walking persons, are in good agreement with the predictions which consider human body models with parameters corresponding to the active postures. This confirms that the presence of moving persons affects

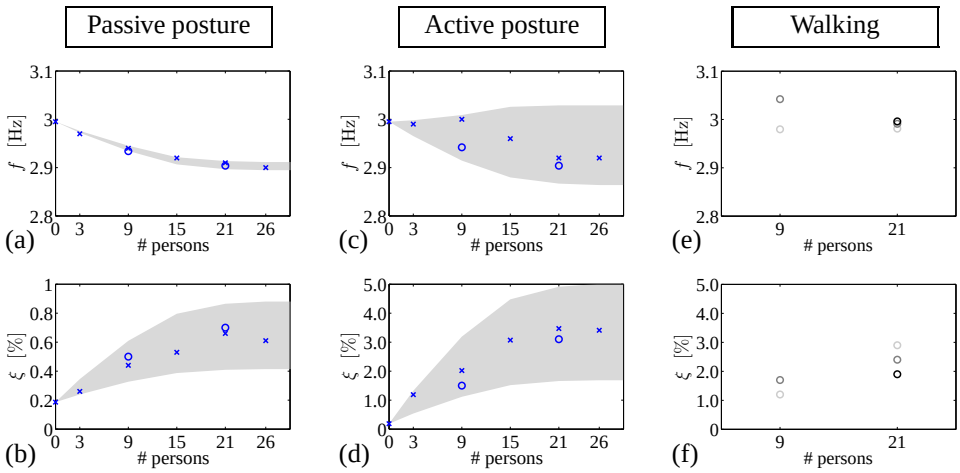


Figure 11: The effective natural frequency (a,c,e) and damping ratio (b,d,f) of the vertical bending mode: the 90% confidence region computed by the coupled human-structure model (grey area), identified from the free decay analysis ($\times$) and identified from the OMA ($\circ$), for the human body in a (a,b) passive, or (c,d) active posture and for persons walking (e,f) at a low (light), normal (dark) and fast (black) speed.

the dynamic characteristics of the coupled system in a way which appears similar as in the case of stationary persons with two legs bent. The amount of added damping seems to decrease with the walking speed.

Figure 12 shows the effective natural frequency and modal damping ratio of the fundamental lateral-torsional mode, involving individuals in the passive posture, an active posture and walking. For both postures, the persons act as an additional mass, resulting in a small reduction in natural frequency. The latter can be explained by the fact that in both cases, the natural frequency of the persons is relatively high compared to the natural frequency of the considered mode ($f_{\text{H1}}/f_{\text{B}} > 1.5$).

However, figures 12-d and 12-e show that experimentally, an increase of the effective damping ratio is identified as well. It is believed that this mode, which is dominated by lateral motion, is also affected by HSI in the lateral direction. In order to verify this conjecture, the coupled model considered in addition a lateral SDOF system for each person with a fundamental natural frequency between 0.5 Hz and 1.0 Hz, i.e. in agreement with the preliminary results as reported by Matsumoto et al. [34]. Figures 12-d and 12-e show that the considered lateral HSI allows to explain the observed increase in effective damping.

Comparing the results in figures 12-e and 12-f with those in figures 12-c and 12-d, shows that the results from the OMA involving walking persons, are in good agreement with the predictions which consider both the vertical and horizontal body motion.

4.2 Charleroi footbridge

The second set of full-scale observations involves the Charleroi footbridge (see figure 13). The tests include ambient and pedestrian excitation. The latter consider 8 or 18 persons walking at a self-selected speed during 4 minutes. The output-only data have been processed using the reference-based data-driven stochastic subspace identification (SSI-data/ref) algorithm [32, 33]. The first three modes are the fundamental vertical bending mode ($\tilde{f}_1 = 1.66$ Hz, $\tilde{\xi}_1 = 0.13\%$, $m_1 = 122 \times 10^3$ kg), the second vertical bending mode ($\tilde{f}_2 = 5.16$ Hz, $\tilde{\xi}_2 = 0.29\%$, $m_2 = 122 \times 10^3$ kg) and the torsional mode ($\tilde{f}_3 = 5.56$ Hz, $\tilde{\xi}_3 = 0.48\%$, $m_3 = 88 \times 10^3$ kg),

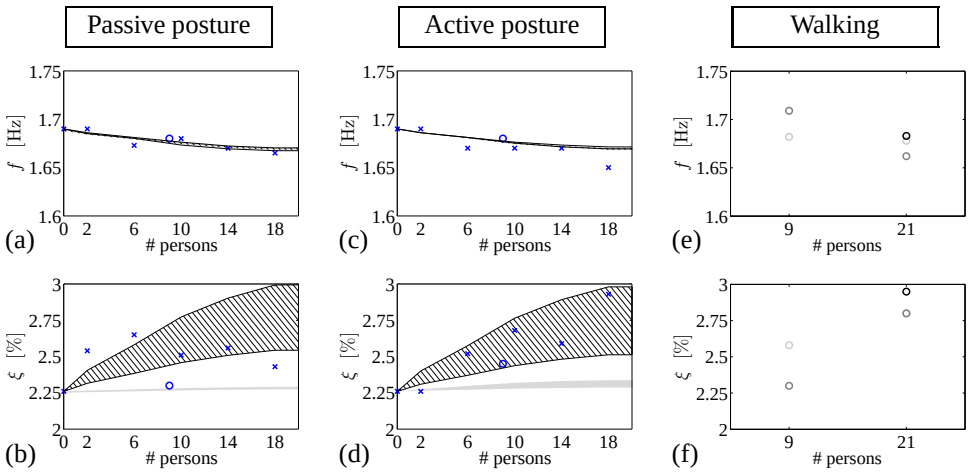


Figure 12: The effective natural frequency (a,c,e) and damping ratio (b,d,f) of the fundamental mode: the 90% confidence region computed by the coupled human-structure model (grey area), including in addition the horizontal human body models (hatched), identified from the free decay analysis ($\times$) and identified from the OMA ($\circ$), for the human body in a (a,b) passive, or (c,d) active posture and for persons walking (e,f) at a low (light), normal (dark) and fast (black) speed.

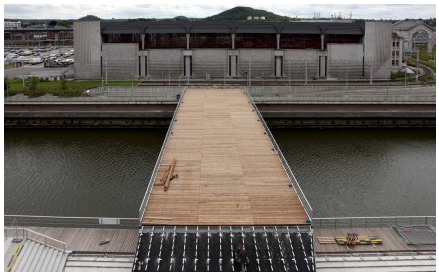


Figure 13: The Charleroi footbridge.

n_{H} [-]	$\tilde{f}_1$ [Hz]	$\tilde{\xi}_1$ [%]	$\tilde{f}_2$ [Hz]	$\tilde{\xi}_2$ [%]	$\tilde{f}_3$ [Hz]	$\tilde{\xi}_3$ [%]
-	1.66	0.13	5.16	0.29	5.56	0.48
8	1.65	0.16	5.15	0.46	5.54	0.56
18	1.65	0.19	5.15	0.83	5.53	0.93

Table 2: The identified natural frequencies and damping ratios of the first three modes of the Charleroi footbridge occupied with n_{ped} walking persons.

respectively. Due to the high modal masses and the high (≈ 2) and low (≈ 0.6) frequency ratios for the case of the first and the second and third mode, respectively, the effect of only 18 persons present on the bridge is expected to be limited. However, table 2 shows that as a result of the distinctly low inherent structural damping, even these low mass ratios lead to a non-negligible increase of the effective damping.

5 CONCLUSIONS

A parametric study is performed to investigate the interaction between the crowd and the low-frequency modes of the footbridge. The results show that taking into account HSI reduces the structural response. The most significant HSI-effect for vertical modes with a natural frequency up to 6 Hz, is in the effective damping ratio of the coupled system which is much higher than the inherent damping of the footbridge. The effective damping ratio increases monotonically with the mass ratio but is highly dependent on the natural frequency of the footbridge.

For practical design, the increase in effective damping can be considered relevant for modes with a natural frequency above 1.5 Hz. The most substantial increase is identified for modes with a natural frequency between 2.75 Hz and 5.0 Hz, as these are close to the natural frequency of active persons. In the case of (near-)resonant excitation at the second harmonic of the walking load (between 2.5 Hz and 5.0 Hz), the structural response reduces when HSI is taken into

account, even for low mass ratios. For the case where (near-)resonant excitation is considered at the fundamental harmonic of the walking load (between 1.5 Hz and 2.5 Hz), the HSI-benefit is far less important and only relevant for high mass ratios or for structures with very low inherent damping ratios. For the considered range of footbridge parameters, the maximum attained effective damping is limited to 2%, 3.5%, 7% and 16% for pedestrian densities of 0.25, 0.5, 1.0 and 2.5 $\mathrm{persons}/\mathrm{m}^2$, respectively.

The findings from the parametric study were verified by means of a comprehensive full-scale experimental study. It is shown that the coupled human-structure model is able to reproduce the experimentally identified modal characteristics of the coupled system. From these tests it is furthermore found that the interaction with the human body in the horizontal direction is of similar importance for structural modes with considerable lateral components.

6 ACKNOWLEDGEMENTS

This research is funded by the Agency for Innovation by Science and Technology in Flanders (IWT). Their financial support is gratefully acknowledged. The authors affiliated to KU Leuven are members of the KU Leuven - BOF PFV/10/002 OPTEC - Optimization in Engineering Center.

REFERENCES

[1] S. Živanović, A. Pavić, and P. Reynolds, "Vibration serviceability of footbridges under human-induced excitation: a literature review," *Journal of Sound and Vibration*, vol. 279, no. 1-2, pp. 1–74, 2005.

[2] C. Butz, M. Feldmann, C. Heinemeyer, and G. Sedlacek, "SYNPEX: Advanced load models for synchronous pedestrian excitation and optimised design guidelines for steel footbridges," Technical Report, Research Fund for Coal and Steel, 2008.

[3] V. Racić, A. Pavić, and P. Reynolds, "Experimental identification and analytical modelling of walking forces: a literature review," *Journal of Sound and Vibration*, vol. 326, pp. 1–49, 2009.

[4] R. Sachse, A. Pavić, and P. Reynolds, "Parametric study of modal properties of damped two-degree-of-freedom crowd-structure dynamic systems," *Journal of Sound and Vibration*, vol. 274, pp. 461–480, 2004.

[5] G. Busca, A. Cappellini, S. Manzoni, M. Tarabini, and M. Vanali, "Quantification of chances in modal parameters due to the presence of passive people on a slender structure," *Journal of Sound and Vibration*, vol. 333, pp. 5641–5652, 2014.

[6] M. Bocian, J. Macdonald, and J. Burn, "Biomechanically-Inspired Modelling of Pedestrian-Induced Vertical Self-Excited Forces," *Journal of Bridge Engineering*, vol. 18, pp. 1336–1346, 2013.

[7] L. Pedersen, "Implications of interaction between humans and structures," in *Proceedings of IMAC 33, the International Modal Analysis Conference*, 2015.

[8] C. Jones, P. Reynods, and A. Pavić, "Vibration serviceability of stadia structures subjected to dynamic crowd loads: a literature review," *Journal of Sound and Vibration*, vol. 330, pp. 1531–1566, 2011.

[9] J. Dougil, J. Wright, J. Parkhouse, and R. Harrison, "Human structure interaction during rhytmic bobbing," *The Structural Engineer*, pp. 32–39, 2006.

[10] G. Subashi, Y. Matsumoto, and G. M.J., "Modelling resonances of the standing body exposed to vertical whole-body vibration: Effects of posture," *Journal of Sound and Vibration*, vol. 317, pp. 400–418, 2008.

[11] Association Française de Génie Civil, Sétra/AFGC, *Sétra: Evaluation du comportement vibratoire des passerelles piétonnes sous l'action des piétons*, 2006.

[12] C. Heinemeyer, C. Butz, A. Keil, M. Schlaich, A. Goldack, S. Trometer, M. Lukic, B. Chabrolin, A. Lemaire, P. Martin, A. Cunha, and E. Caetano, "Design of lightweight Footbridges for Human Induced Vibrations - background document in support to the implementation, harmonization and further development of the eurocodes," Technical Report, JRC-ECCS Scientific and Technical Reports - European Comission, 2009.

[13] GERB, "Tuned mass dampers," reference list, GERB Engineering, March 2014.

[14] Maurer-Sohne, "Extract of reference list for tuned mass dampers," reference list, Maurer-Sohne, February 2013.

[15] H. Bachmann, W. Ammann, and F. Deischl, *Vibration problems in structures: practical guidelines*. Springer, 1995.

[16] J. Brownjohn and A. Pavić, "Experimental methods for estimating modal mass in footbridges using human-induced dynamic excitation," *Engineering Structures*, vol. 29, pp. 2833–2843, 2007.

[17] Research Fund for Coal and Steel, *Hivoss: Design of footbridges*, 2008.

[18] International organization for Standardization (ISO 10137), *Bases for design of structures - Serviceability of buildings and walkways against vibrations*, 2007.

[19] NBN EN 1991-2 NL, *Eurocode 1: Actions on structures - Part 2: Traffic loads on bridges*, 2013.

[20] NBN EN 1995-2, *Eurocode 5: Design of timber structures - Part 2: Bridges*, 2005.

[21] Y. Matsumoto and M. Griffin, "Dynamic response of the standing human body exposed to vertical vibration: influence of posture and vibration magnitude," *Journal of Sound and Vibration*, vol. 212, no. 1, pp. 85–107, 1998.

[22] Y. Matsumoto and M. Griffin, "Mathematical models for the apparent masses of standing subjects exposed to vertical whole-body vibration," *Journal of Sound and Vibration*, vol. 260, pp. 431–451, 2003.

[23] J. Brownjohn, P. Fok, M. Roche, and P. Omenzetter, "Long span steel pedestrian bridge at Singapore Changi Airport - part 2: Crowd loading tests and vibration mitigation measures," *The Structural Engineer*, vol. 82, no. 16, pp. 28–34, 2004.

[24] J. Brownjohn, "Energy dissipation from vibration floor slabs due to human-structure interaction," *Journal of Shock and Vibration*, vol. 8, pp. 315–323, 2001.

[25] K. Van Nimmen, K. Maes, S. Živanocić, G. Lombaert, G. De Roeck, and P. Van den Broeck, "Identification and modelling of vertical human-structure interaction," in *Proceedings of IMAC 33, the International Modal Analysis Conference*, 2015.

[26] International Organisation for Standardization, *ISO 5982:1981 Vibration and shock - Mechanical driving point impedance of the human body*, 1981.

[27] Y. Yang, J. Yau, and Y. Wu, *Vehicle-bridge interaction dynamics: With applications to high-speed railways*. World Scientific Publishing Co. Pte. Ltd., 2004.

[28] A. Doménech, P. Museros, and M. Martínez-Rodrigo, "Influence of the vehicle model on the prediction of the maximum bending response of simply supported bridges under high-speed railway traffic," *Engineering Structures*, vol. 72, pp. 123–139, 2014.

[29] K. Van Nimmen, G. Lombaert, I. Jonkers, G. De Roeck, and P. Van den Broeck, "Characterisation of walking loads by 3D inertial motion tracking," *Journal of Sound and Vibration*, vol. 333, pp. 5212–5226, 2014.

[30] F. Magalhães, A. Cunha, E. Caetano, and R. Brincker, "Damping estimation using free decays and ambient vibration tests," *Mechanical Systems and Signal Processing*, vol. 24, pp. 1274–1290, 2010.

[31] A. Chopra, *Dynamics of structures*. Prentice Hall, 1995.

[32] B. Peeters and G. De Roeck, "Reference-based stochastic subspace identification for output-only modal analysis," *Mechanical Systems and Signal Processing*, vol. 13, no. 6, pp. 855–878, 1999.

[33] E. Reynders, R. Pintelon, and G. De Roeck, "Uncertainty bounds on modal parameters obtained from Stochastic Subspace Identification," vol. 22, no. 4, pp. 948–969, 2008.

[34] Y. Matsumoto and G. M.J., "The horizontal apparent mass of the standing human body," *Journal of Sound and Vibration*, vol. 330, pp. 3284–3297, 2011.

COMPDYN 2015
5th ECCOMAS Thematic Conference on
Computational Methods in Structural Dynamics and Earthquake Engineering
M. Papadrakakis, V. Papadopoulos, V. Plevris (eds.)
Crete Island, Greece, 25–27 May 2015

INFLUENCE OF HUMAN INDUCED FLOOR VIBRATIONS ON THE MEASUREMENT PRECISION OF FORCE PLATES IN A BIOMECHANICS LABORATORY

Horst Werkle[1], Wolfgang Francke[2] and Andrei Firus[3]

[1] Prof. Dr.-Ing., Department of Civil Engineering, University of Applied Sciences Konstanz (HTWG),
Brauneggerstr. 55, D-78462 Konstanz, Germany
e-mail: werkle@htwg-konstanz.de

[2] Prof. Dr.-Ing., Department of Civil Engineering, University of Applied Sciences Konstanz (HTWG),
Brauneggerstr. 55, D-78462 Konstanz, Germany
e-mail: francke@htwg-konstanz.de

[3] M.Eng., Technische Universität Darmstadt, Institute of Structural Mechanics and Design
Franziska-Braun-Straße 3, D-64287 Darmstadt, Germany
e-mail: firus@ismd.tu-darmstadt.de

Keywords: Biomechanics Laboratory, Countermovement Jump, Floor Vibrations, Force Plate, Gait Analysis Laboratory, Human Induced Vibrations.

Abstract. *In biomechanics laboratories the ground reaction force time histories of the footfall of persons are usually measured using a force plate. The accelerations of the floor, in which the force plate is embedded, have to be limited, as they may influence the accuracy of the force measurements. For the numerical simulation of vibrations induced by humans in biomechanical laboratories, loading scenarios are defined. They include continuous motions of persons (walking, running) as well as jumps, typical for biomechanical investigations on athletes. The modeling of floors has to take into account the influence of floor screed in case of portable force plates. Criteria for the assessment of the measuring error provoked by floor vibrations are given. As an example a floor designed to accommodate a force platform in a biomechanical laboratory of the University Hospital in Tübingen, Germany, has been investigated for footfall induced vibrations. The numerical simulation by a finite element analysis has been validated by field measurements. As a result, the measuring error of the force plate installed in the laboratory is obtained for diverse scenarios.*

1 INTRODUCTION

Biomechanics laboratories allow the study and analysis of human motion, especially human gait, by means of the methods of mechanics. They are used in sports science to help athletes to evaluate and improve their performance. Biomechanics or gait analysis laboratories are also used in medicine for orthopaedic purposes such as the analysis of motion restrictions in diagnosis or the verification of orthopaedic rehabilitation measures by means of objective criteria [1] .

The measurements in gait analysis laboratories can be performed by employing different, complementary systems, such as video recordings with subsequent computer analysis, force measurements using force plates, or neurological methods of the electromyography (measurement of the electrical muscle activity). The measurements of the time dependent ground reaction forces of the human footfall are carried out using force plates embedded in the laboratory floor.

Force plates are sensitive to environmental vibrations of the floor which may influence the accuracy of the measurements. The paper investigates human induced vibrations in the laboratory and their influence on the measurement accuracy of a force plate.

2 FORCE PLATES IN GAIT LABORATORIES

The measurement of the force can be done using piezoelectric elements or by the use of strain gauges. In the case of the piezoelectric measuring technique, the piezoelectric effect, i.e. the electrical charge of crystals due to mechanical loads, is used for force measurements. Piezoelectric force plates possess a very high measuring accuracy within an extremely wide measuring range. They will be considered in the following. The reaction force of a multicomponent force plate caused by the footfall load is measured as three-dimensional vector with the vertical and the two horizontal components parallel to the plate edges. Usually a walking and running path parallel to the plate edges is adopted, so that the force components are parallel and perpendicular to the direction of movement, respectively. Fig. 1 shows an example of a measured force time history for a single gait of a walking person with a weight of $G = 0.87$ kN and a step frequency of $f_s = 2$ Hz. Herein F_z denotes the vertical force component and F_y, F_x are the horizontal components in the walking direction and perpendicular to it, respectively.

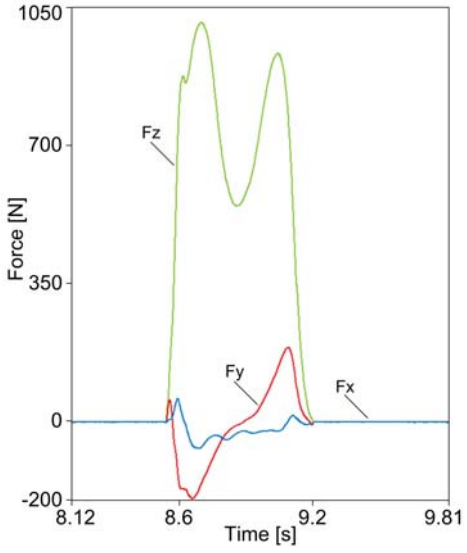


Figure 1: Force time history measured with a force plate ($G = 0.87$ kN, $f_s = 2$ Hz).

Force plates consist of a cover plate made of steel, aluminum or glass and the underlying support construction with the piezoelectric sensors (Fig. 2). For a fixed installation in a laboratory, force plates are usually embedded in a planned indentation of the floor, using an installation frame. In addition to stationary force plates, portable force plates are also available. They are mobile and can be used on any flat surface (Fig. 3). Portable force plates allow force measurements in various locations as e.g. in field situations where no mounted force plates are available.

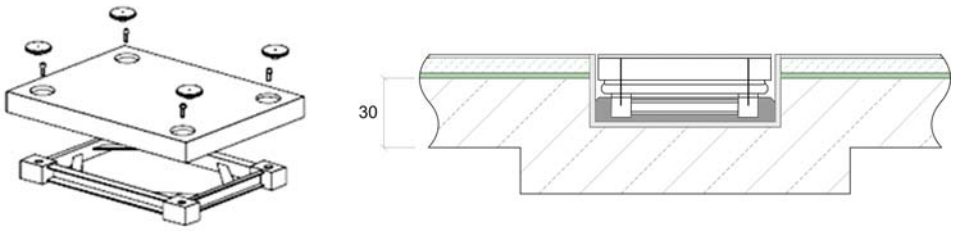


Figure 2: Force plate and installation frame in a floor indentation

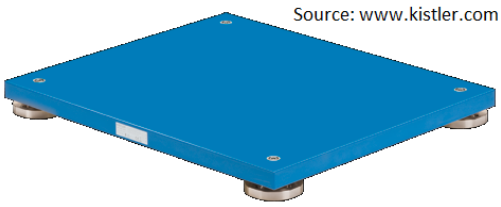


Figure 3: Portable force plate

3 MEASURING ACCURACY OF FORCE PLATES

Floor vibrations can be induced by the person being subject of the force measurement or by other persons moving around in the laboratory [2, 3]. Other external sources of vibration may be machinery vibrations, traffic induced vibrations or construction-related vibrations. Accelerations of the floor, in which a force plate is embedded or on which a portable plate is deployed may alter the measuring signal. Especially piezoelectric force plates are able to monitor extremely small forces indicating floor accelerations without any loading. In order to limit the resulting measuring error, the floor accelerations have to be limited. In the following the measuring error allowed is assumed to be 1% of the maximal force measured.

The vertical eigenfrequency of the force plates is usually very high (> 500 Hz) due to the very stiff bearing elements. Therefore internal vibrations of the plate device as well as vibrations of the plate relative to the floor can be excluded, presuming that the plate was installed properly. Hence, the relative measuring error p can be determined as a ratio of the mass force of the cover plate and the maximum force measured as

$$p = \frac{m_{Pl} \cdot a_g}{F_{\max}} \tag{1}$$

where m_{Pl} is the mass of the cover plate, a_g is the acceleration of the floor and $F_{\max}$ is the maximum force measured [4]. The limit value of the floor acceleration for a given measuring accuracy is determined to be

$$a_g = \frac{F_{\max} \cdot p}{m_{Pl}} \tag{2}$$

Assuming a tolerable measuring error of 1% and a static load due to a subject with a weight force of 0.4 kN and mass of the cover plate of 40 kg, a threshold value of the acceleration of 0.1 m/s² is obtained. This value is given in some specifications of force plates [4]. However, it should be noted that this simple threshold value of 0.1 m/s² neglects the influence of the weight of the individual, dynamic effects of the force time history and the weight of cover plate of the specific force plate device.

The force to be measured is proportional to the weight of the subject i.e. $F_{\max} = \overline{\alpha} \cdot G$. If the coefficient $\overline{\alpha}$ is not determined by force time history measurements, lower limits are to be chosen. The following values for $\overline{\alpha}$ are adopted: 1.0 for static load (standing), 1.1-1.2 for walking [5], 1.8-2.2 for running and 3.0 for jumping [6]. Hence the relative measuring error for an external excitation inducing the floor acceleration a_{g0} is

$$p = \frac{m_{Pl} \cdot a_{g0}}{\overline{\alpha} \cdot G} \tag{3}$$

In the case of vibrations induced by the person being subject to the measurement, the maximum acceleration of the floor is proportional to the weight G of the subject. Employing the acceleration normalized to the subject weight, $\overline{a} = a_g / G$, the relative error of the measurement is determined to be

$$p = \frac{m_{Pl} \cdot \overline{a}}{\overline{\alpha}} \tag{4}$$

Both types of excitations are to be superposed [7]. Assuming a random distribution of the time instants at which the maxima of both time histories occur, the measuring error is determined to be

$$p = \frac{m_{Pl}}{\overline{\alpha}} \cdot \sqrt{\left(\frac{a_{g0}}{G}\right)^2 + \overline{a}^2} \tag{5}$$

4 LOADING SCENARIOS

The loading scenarios are intended to describe typical situations during force measurements in orthopedic and sport biomechanics laboratories. In the following, only human induced vibrations are considered. If external sources of vibrations are existent, they must be examined in addition.

In either case the vibrations induced by the person being subject to the force measurement must be investigated. The subject may be walking or running on a runway in the gait laboratory. In sport science different types of jumps are typical for tests on a force plate [8]. In addition vibrations may be induced by persons moving around in the laboratory during the tests. The following typical scenarios can be assumed:

- Walking: The subject is walking on a predefined path (runway), including the force plate.
- Running: The subject is running on a predefined path (runway), including the force plate.
- Counter movement jump: The subject stands on the force plate with straight legs, and performs a jump starting with bending the knees in a quick counter movement.
- Squat jump: The subject stands on the force plate, squats down until the knees are bent about 90 degrees and then performs a jump.

- Drop jump: The subject jumps from an elevated platform and performs a jump similar to the counter movement jump after landing.
- Repetitive hops: The subject stands on the force plate and performs a series of jumps.
- Persons moving around in the laboratory: 5 people with a weight of 80 kg each are walking around in the room. The walking path is random.

Depending on the function of the laboratory, the scenarios relevant for the analysis are to be defined in the individual case.

5 STRUCTURAL ANALYSIS

Footfall induced vibrations can be computed with a time history analysis of a finite element model. As reinforced concrete floors typically possess eigenfrequencies above 7-10 Hz, simplified approaches for "high-frequency floors" representing the load by equivalent impulses may be applied. Both methods are addressed in the following.

5.1 Load Models

The load generated by a single walking or running subject can be described by load functions for every step or simplified, using a continuous, time dependent, single load. Zivanovic [9], Butz [10], Werkle [11] and Racic [12] give overviews over various approaches for human-induced walking and running loads.

In the following, the time dependent load is represented as a Fourier series:

$$F(t) = G \cdot \left(1 + \sum \alpha_j \cdot \sin\left(2 \cdot \pi \cdot j \cdot t \cdot f_s - \varphi_j\right)\right) \tag{6}$$

Here f_s is the step frequency. The subject weight was assumed to be 0.8 kN. The Fourier-coefficients α and φ have been determined by different authors. Table 1 shows the values for walking and running according to Bachmann [13] and higher frequency terms estimated based on tentative tests in [14]. These higher Fourier coefficients include the heel-strike effect and are important for the vibration response of high-frequency floors [15, 16].

The load is moving along a predefined path on the floor with the speed

$$v = f_S \cdot L_S \tag{6a}$$

where f_s denotes the step frequency which is to be chosen conservatively and L_S represents the step length. Typical values are given by [9-11].

		Walking	**Running**
j	**f_s**	1.5 – 2.5 [Hz] (Average value 2 Hz)	2.0 –3.0 [Hz]
1	**α_1**	0.4 for $f_s \le 2$ *Hz* $0.4 + 0.1 \cdot (f_s - 2) / 0.4$ for 2.0 *Hz* $\le f_s \le$ 2.4 *Hz* 0.5 for $f_s \ge$ 2.4 *Hz*	1.6
2	**α_2**	0.1	0.7
3	**α_3**	0.1	0.2
4	**α_4**	0.07*	0.15*
5	**α_5**	0.06*	0.12*
6	**α_6**	0.06*	0.12*
1	**φ_1**	0	0
2	**φ_2**	$\pi / 2$	$\pi / 2$
3	**φ_3**	$\pi / 2$	$\pi / 2$

Table 1: Coefficients α and φ for walking and running ([13] and * acc. to [14])

Eq. 6 is valid for a single person. For an excitation induced by several persons, the acceleration obtained for "walking" of a single person is multiplied by the factor $m = \sqrt{n}$, where n is the number of the persons.

High-frequency floors may also be analyzed by an effective impulse approach as given in [16, 17]. The method is based on the assumption that due to the high frequency response and the damping, the transient vibration generated by an individual footfall practically has vanished before the next footfall begins.

Equivalent impulses for a countermovement jump and a drop jump have been developed by Firus et. al [18] based on force time history measurements of more than 200 jumps. For a countermovement jump the equivalent impulses in kNs are given by

$$I_{50\%} = G \cdot 0{,}4028 \cdot f^{-0{,}810} \quad (p = 50\%), \tag{7a}$$

$$I_{25\%} = G \cdot 0{,}3471 \cdot f^{-0{,}642} \quad (p = 25\%), \tag{7b}$$

where f denotes the corresponding eigenfrequency of the structure in [Hz], G represents the subject weight in [kN] and p = 50% and p = 25% are the exceedance probabilities, respectively. The paper also gives a procedure for the analysis of drop jumps using equivalent impulses [18].

5.2 Structural Model

The structural finite element model must be detailed with care in order to represent the response of the structure adequately. For continuous slabs the number of floor panels considered in the structural model must be large enough to include all mode shapes relevant for the vibration response. For a stationary force plate (Fig. 2) the modelling of the raw concrete floor is appropriate. However, if a portable force plate (Fig. 3) is used, the structural model should include a floating floor screed which may affect the local acceleration significantly.

5.3 Time history analyses

Time history analyses can be performed by direct integration or by modal superposition. In a modal superposition approach, the number of mode shapes to be considered in the analysis must be chosen carefully. It should not only reflect the frequency content of the load time history but also enable all relevant static deformations of the model. In order to describe local deformations on the top of a floating floor screed and the corresponding accelerations, higher mode shapes must necessarily be included in the analysis. This applies for modal superposition but it is not relevant for direct integration.

5.4 Equivalent impulse analyses

The structural response caused by an impulse can be easily computed analytically by modal superposition. The acceleration *a(t)* is obtained as:

$$a(t) = \mu_i \cdot \mu_j \cdot \frac{I}{m_{\mathrm{mod}}} \cdot e^{-\xi \cdot \omega \cdot t} \cdot \left(-\omega_d \cdot \sin(\omega_d \cdot t) - \xi \cdot \omega \cdot \cos(\omega_d \cdot t)\right) \tag{8}$$

where I $[kN \cdot s]$ is the impulse, μ_j the mode shape at the point where the impulse is applied, μ_i the mode shape at the point where the response is measured (i.e. where the force plate is situated), m_{mod} $[to]$ the modal mass (using the same scaling of the mode shapes as for μ_i and μ_j), ξ the damping ratio and $\omega = 2 \cdot \pi \cdot f$ $[Hz]$ and $\omega_d = \omega \cdot \sqrt{1 - \xi^2}$ the undamped and damped

angular eigenfrequency of the floor, respectively. In order to consider several modes, the responses of the individual mode shapes have to be superposed.



Figure 4: Health Center Tübingen: Building and biomechanics laboratory

6 EXAMPLE

6.1 Building

The influence of floor vibrations on the measurement accuracy of a force plate has been investigated for a biomechanics laboratory in Tübingen, Germany. The laboratory is located in the new building of the Health Center at the University Hospital in Tübingen, which was built between 2011 and 2012 (Fig. 4). The gait analysis facilities are situated in an open space area, used for office as well as for therapeutic purposes. The paper describes the investigation of the influence of floor vibrations, induced by footfall in the office section, on the accuracy of the simultaneous measurements with the force plate. For this, vibration field measurements and finite element analyses were made.

6.2 Structural model

The floor where the biomechanics laboratory is situated consists of a reinforced concrete slab with a thickness of 30 cm and span widths of the floor panels between 8 and 11 m. The entire floor is represented by a detailed finite element model which consists of 6615 quadrangular plate-elements, containing 40725 degrees of freedom. The reinforced concrete floor is assumed to be elastically clamped by the outer walls. A damping ratio of 1% was determined by measurements. The eigenfrequencies of the floor are given in Table 2, some relevant mode shapes are shown in Figure 5.

Eigenmode	FE-Analysis [Hz]	Measured [Hz]	Eigenmode	FE-Analysis [Hz]	Measured [Hz]
1	7.32	7.27	6	13.52	13.68
2	7.68	7.63	7	13.96	13.93
3	8.21	8.07	8	16.19	16.30
4	11.62	11.55	9	17.17	17.32
5	12.87	12.78	10	18.58	18.90

Table 2: Eigenfrequencies of the floor

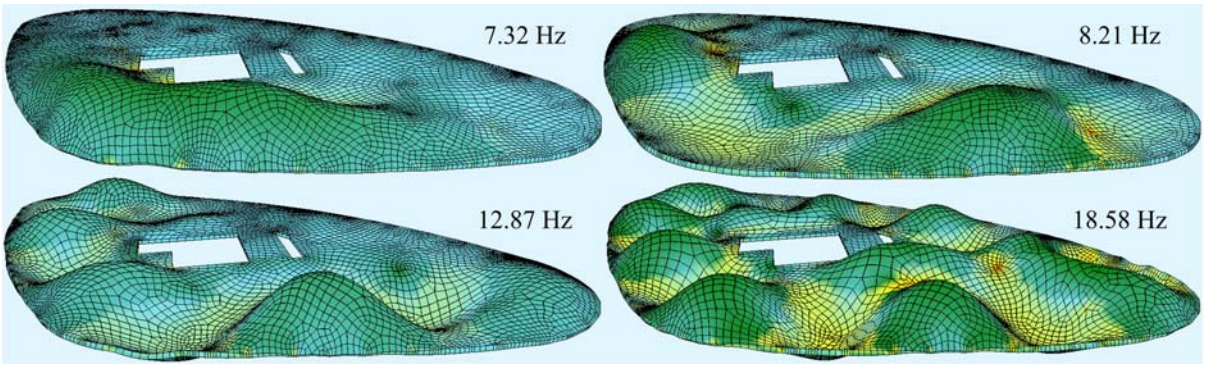


Figure 5: Mode shapes

6.3 Numerical computation of the human-induced vibrations

The time history for a propagating load acc. to eq. (6) was computed by modal analysis. Figure 6 shows typical acceleration time histories of the raw floor at the location point of the force plate. They are shown for the scenarios walking and running on a runway in the laboratory as well as for a countermovement jump acc. to eq. (8). The maximum accelerations for various walking and running frequencies are shown in Figure 9. Eigenfrequencies up to 30 Hz were considered for the computations as well as for the experimental investigations.

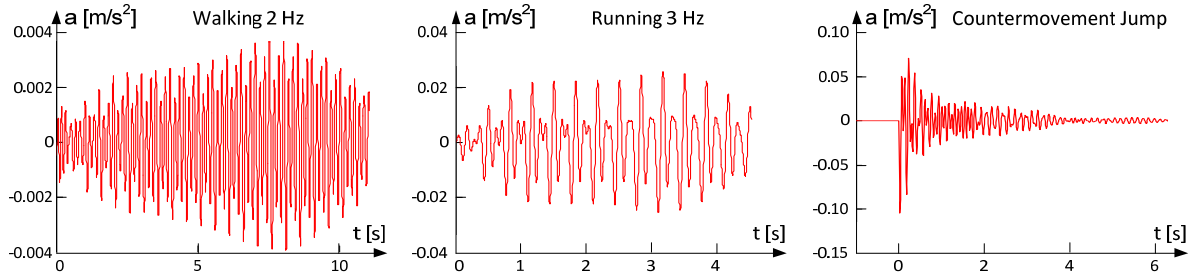


Figure 6: Time histories for walking, running and vertical jumping of a subject (FEM)

6.4 Experimental investigations

The eigenfrequencies of the raw floor were determined through measurements of ambient vibrations and subsequent Fourier analyses. They show a good correlation with the eigenfrequencies obtained by the FE analysis (Table 2).

The vibrations caused by walking, running and jumping of a person were measured using extremely sensitive seismic accelerometers. The subjects wore sports shoes, which are typical for the activities in the biomechanics laboratory. For each scenario, acceleration time histories at different relevant points were recorded. The results were normalized to a subject weight of 0.8 kN.

These tests were done for two stages of the construction, namely the raw concrete floor and the final state of the finished floor, including a layer of sound insulation and a floating floor screed. Figures 7 and 8 show the measured time histories for walking and running on the raw concrete floor and on the finished floor, respectively.

On the raw concrete floor, the maximum accelerations agree well with those of the finite element analysis. Additional investigations showed that walking and running on the finished floor did not significantly affect the accelerations on the raw floor. However the accelerations measured on top of the finished floor are significantly larger than those on the raw floor. It can be noted that the maximum acceleration of the floor in the final construction stage is rep-

resented by a single peak at the moment when the subject is stepping close to the acceleration sensor. This indicates that the local deformation of the soft sound insulation layer of the finished floor and the accelerations resulting thereof are the cause of the local augmentation of the structural response.

Hence, for a stationary force plate embedded in the concrete slab, computations can be made for a raw floor neglecting the finishing of the floor. However, for portable force plates which are placed on the finished floor, the additional accelerations caused by the finishing of the floor should be taken into account.

Figure 9 shows the maximum accelerations for walking and running at different step frequencies measured in both construction stages, as well as for the finite element analysis of the raw floor.

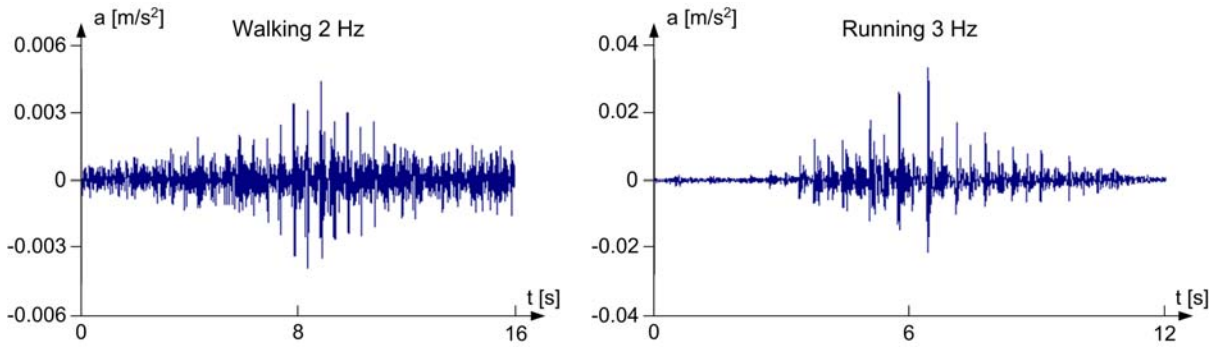


Figure 7: Measured time histories for walking and running (raw concrete floor)

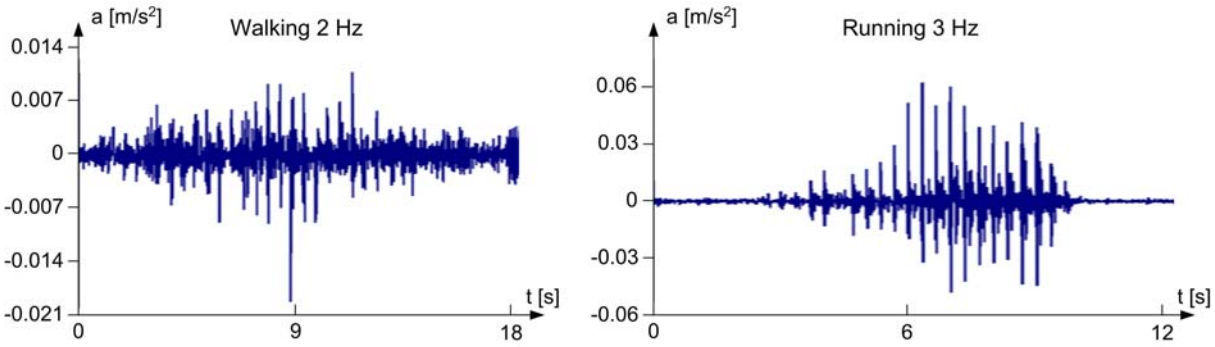


Figure 8: Measured time histories for walking and running (finished floor)

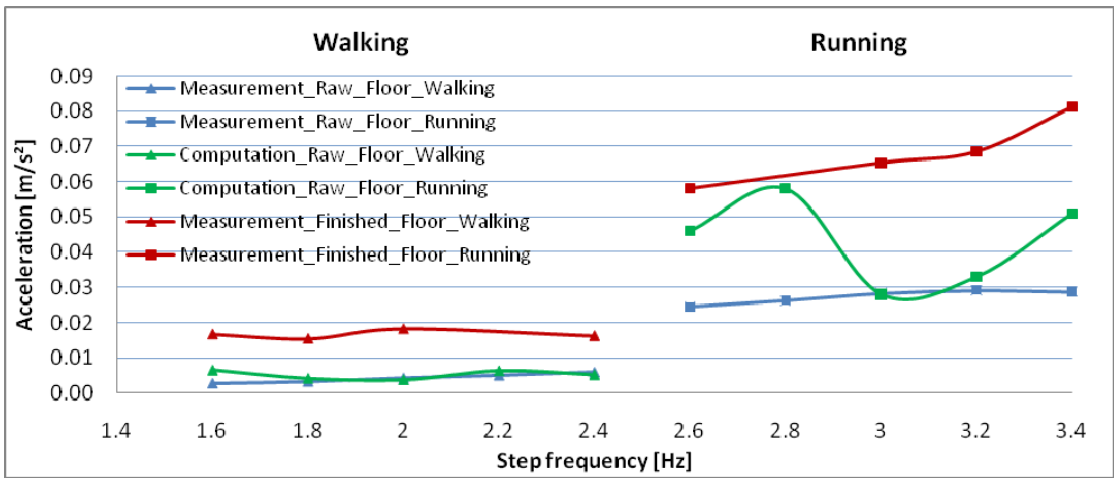


Figure 9: Maximum accelerations of the force plate – computation and measurements

A good correlation between the measurements performed on the raw concrete floor and the corresponding computations can be observed if some resonance effects computationally obtained for running are neglected. However it should be noted that the accelerations of 0.005 m/s^2 for walking and 0.03-0.06 m/s^2 for running are quite low. The highest accelerations in this stage of construction, of about 0.1 m/s^2, occur as a response to the countermovement jump.

The measurements in the final stage of the finished floor, however, revealed much higher accelerations than the ones of the raw concrete floor for the same scenarios investigated. The maximum accelerations in this case are about 2 to 4 times higher than the accelerations of the raw floor. The maximum value of 0.25 m/s^2 was obtained again for jumping.

6.5 Measurement accuracy of the force plate

The measurement accuracy has been evaluated for a stationary plate of the type Kistler 9287 CA. Its total mass is 25 kg, the cover plate has a mass of 20,7 kg [4]. The weight of the subject was assumed to be 0.8 kN, while the values of the coefficient $\overline{\alpha}$ are taken to 1 for walking, 2 for running and 3 for vertical jumping. Furthermore it is assumed that during the measurement 5 persons are walking in the laboratory room. The excitation by the person being subject to the force measurement as well as the excitation by the persons walking in the room is considered to act simultaneously.

The measuring error of the force plate was determined according to Eq. 5 employing the measured floor accelerations. For all scenarios considered, the measuring error was calculated to be less than 0.1% (see Table 3). Even when parameter variations due to model uncertainties (induced, for instance, by the shoe type) are considered, the measuring error remains in the per mille domain and thereby very low.

If a portable force measuring plate with the same mass will be used in the laboratory, it will be placed on the finished floor, which possesses higher floor accelerations than the raw concrete floor. Therefore the measuring error increases significantly, up to 0.2% for the worst case scenario of a subject performing a jump with simultaneous external excitation by persons walking in the laboratory (see Table 4).

It should be noted that the measuring error of the force plate would be slightly higher for a more conservative assumption of the subject weight, e.g. 0.5 kN.

Scenario	Floor acceleration (1 person) [m/s²]	Absolute error [N]	Maximal force assumed [kN]	Relative error induced by subject (Eq. 4)	Total error including external excitation (Eq. 5)
Walking	0.007 (0.016*)	0.1	0.8	0.02 %	0.03 %
Running	0.058**	1.0	1.6	0.07 %	0.07 %
Countermovement Jump	0.115**	2.4	2.4	0.10 %	0.10 %

Table 3: Measuring error – stationary force plate (* for 5 persons; **computed values)

Scenario	Floor acceleration (1 person) [m/s²]	Absolute error [N]	Maximal force assumed [kN]	Relative error induced by subject (Eq. 4)	Total error including external excitation (Eq. 5)
Walking	0.02 (0.045*)	0.4	0.8	0.05 %	0.13 %
Running	0.081	1.7	1.6	0.11 %	0.12 %
Countermovement Jump	0.25	5.2	2.4	0.22 %	0.22 %

Table 4: Measuring error – portable force plate (* for 5 persons)

7 CONCLUSIONS

The measuring error of force plates in biomechanics laboratories can be evaluated based on experimental and numerical investigations. Scenarios and formulas for determining the measuring error were proposed. The largest accelerations are obtained for jumps being part of typical investigations in sports gait analysis laboratories. Portable force plates are subjected to larger floor accelerations than stationary ones due to the augmentation of vibrations by the floor screed and sound insulation.

It was shown that the measuring accuracy of the force plate from the biomechanics laboratory at the University Hospital in Tübingen, Germany, is not significantly influenced by the human induced vibrations of the floor. This may be typical for similar floors consisting of a thick reinforced concrete slab. In cases of steel constructions or composite slabs, larger accelerations which may influence the measuring accuracy of the force plate noticeably are to be expected.

ACKNOWLEDGEMENTS

The authors would like to thank Prof. Dr. Stefan Grau for supporting the experimental investigations as well as for providing measurement data of the force plate.

REFERENCES

[1] J. Perry, *Ganganalyse (Gait analysis).* Urban&Fischer/Elsevier, 2003

[2] S.J. Hicks, P.J. Devine, *Design Guide on the Vibration of Floors in Hospitals*. The Steel Construction Institute. Silwood Park, Ascot Berkshire, 2004

[3] HIVOSS: *Schwingungsbemessung von Decken (Design of floor vibration)*, Research Fund for Coal and Steel, 2007

[4] Kistler - Company: *Betriebsanleitung - Installation und Wartung aller Typen von Messplattformen (operating manual - installation and maintenance for all types of force measuring plates)*. Kistler Instrumente AG Winterthur. Winterthur, Switzerland, 2012

[5] S.C. Kerr, *Human Induced Loading on Staircases*. PhD Thesis. Mechanical Engineering Department. University College London, UK, 2008

[6] A. Richter, *Aspekte der Sprungkraft und Sprungdiagnostik unter besonderer Berücksichtigung der Entwicklung im Kindes- und Jugendalter (Aspects of the jumping force and the jumping diagnostics under the consideration of the progress in childhood and adolescence)*. PhD Thesis. Karlsruhe Institute of Technology (KIT), 2011

[7] H. Werkle, W. Francke, A. Firus, C. Clausner, *Einfluss von Deckenschwingungen auf die Messgenauigkeit in Ganglaboren. Proceedings of the 13. D-A-CH Conference for Earthquake engineering and Structural Dynamics,* Adam, C.; Heuer, R.; Lenhardt, W.; Schranz, C. (ed.), Vienna, Austria, 2013

[8] W.P. Ebben, M.L. Fauth, C.E. Kaufmann, E.J. Petushek, Magnitude and rate of mechanical loading of a variety of exercise modes. The Journal of Strength & Conditioning Research 24, 213–217, 2010.

[9] Zivanovic, S.; Pavic, A.; Reynolds, P.: *Vibration Serviceability of footbridges under human-induced excitation: a literature review.* Journal of Sound and Vibration **279**, 1–74, 2005

[10] C. Butz, J. Distl, *Personen-induzierte Schwingungen von Fußgängerbrücken* In: *Stahlbau Kalender 2008*. Ernst&Sohn, Berlin, 2008.

[11] H. Werkle, *Human induced vibrations of steel and aluminium bridges* In: *Traffic induced environmental vibrations and controls: Theory and application,* Xia, H.; Calçada, R. (ed.). Nova Science Publishers, Inc. New York, United States of America, 187–216, 2013

[12] V. Racic, A Racic, J.M.W. Brownjohn, *Experimental Identification and Analytical Modelling of Human Walking Forces: Literature Review*, Journal of Sound and Vibration 326, Elsevier, 1-49, 2009

[13] H. Bachmann, *Schwingungsprobleme bei Fußgängerbrücken.* Bauingenieur **63**, 67–75, 1988.

[14] A. Firus, Einflussfaktoren der Belastung und Strukturmodellierung bei der Berechnung personeninduzierter Schwingungen von Decken, Master Thesis, HTWG Konstanz, 2014

[15] A. Pavic, Prichard, S.; Reynolds, P.; Lovell, M.: *Evaluation of Mathematical Models for Predicting Walking-Induced Vibrations of High-Frequency Floors.* International Journal of Structural Stability and Dynamics 03, 107, 2003

[16] J.M.W. Brownjohn C.J. Middleton, Procedures for vibration serviceability assessment of high-frequency floors, Engineering Structures 30, 2008

[17] A. Pavic, M. Willford, Appendix G – Vibration serviceability of post-tensioned concrete floors. In CST43. The Concrete Society, 2005

[18] A. Firus, A. Kramer, H. Werkle, W. Francke, Schwingungsantwort einer Decke infolge von vertikalen beidbeinigen Sprüngen in der Sprungkraftdiagnostik, VDI-Tagung Baudynamik, Kassel, 2015

COMPDYN 2015
5th ECCOMAS Thematic Conference on
Computational Methods in Structural Dynamics and Earthquake Engineering
M. Papadrakakis, V. Papadopoulos, V. Plevris (eds.)
Crete Island, Greece, 25–27 May 2015

EQUIVALENT SPECTRAL MODEL FOR PEDESTRIAN-INDUCED FORCES ON FOOTBRIDGES: A GENERALIZED FORMULATION

Alberto Ferrarotti[1] **and Federica Tubino**[1]

[1] DICCA, University of Genoa
Via Montallegro 1, 16145, Genova, Italy
alberto.ferrarotti@edu.unige.it; federica.tubino@unige.it

Keywords: Coherence Function, Dynamic Response, Footbridges, Pedestrian Dynamics, Serviceability Analysis, Spectral Model.

Abstract. *This paper proposes a generalized equivalent spectral model of pedestrian-induced forces. The model can be applied for the serviceability analysis of footbridges subjected to unrestricted pedestrian traffic, but also in crowded conditions, in absence of pedestrian-structure interaction. It is based on the introduction of a suitable physically-based expression for the coherence function and a pedestrian density – velocity law. The proposed coherence model is a function of both pedestrian density and distance among pedestrians: it reduces to perfect uncorrelation for low pedestrian density (i.e. spatially unrestricted traffic), and to perfect correlation for high pedestrian density (i.e. crowded condition). Since the step frequency, the pedestrian speed and the pedestrian density are strictly correlated, the harmonic content of pedestrian-induced forces depends on pedestrian density. Based on the proposed equivalent spectral model of the loading, vibration serviceability analysis of footbridges subjected to any traffic conditions can be dealt with the classic methods of linear random dynamics. Similarly to classical procedures adopted in the wind engineering field, simple closed-form expressions for the evaluation of the maximum dynamic response are provided.*

1 INTRODUCTION

Modern footbridges are very slender structures, often characterized by natural frequencies within the range of the dominant walking harmonics. As a consequence, they can be very sensitive to walking-induced vibration.

During its lifetime, a footbridge could be exposed to different loading scenarios, including a single crossing pedestrian, spatially unrestricted traffic, crowd traffic, joggers and runners and vandal loading; an exhaustive description can be found in [1]. The case of single crossing pedestrian can be modeled as a harmonic resonant moving load. The maximum structural response in such a case can be obtained in closed form [2]. Of course, the most common loading scenario is spatially unrestricted traffic. However, crowd loading can occur for footbridges placed in strategic areas or in particular conditions, such as during opening days.

In these last years, the vibration serviceability analysis of footbridges subjected to unrestricted pedestrian traffic has become a very topical subject in the international research panorama. A critical review of the different approaches for the estimate of the dynamic response in such a loading condition can be found in [3]. They may be classified into three categories: Monte Carlo simulations, simplified procedures ([4]-[7]) and spectral approach ([8], [9]). Monte Carlo simulations may be very time consuming and not practical from the usual design of footbridges. Simplified procedures have been proposed with the aim of simulating, in an approximate way, groups of pedestrians walking in a natural (i.e. random) way on a footbridge. The more widespread approach is based on the definition of equivalent uniform resonant loads producing the maximum dynamic response; this approach is usually very conservative, in particular for group loading. The spectral approach [9] is an interesting alternative: it consists in modelling the pedestrian-induced loading in unrestricted traffic conditions as a stationary random process through the analytical definition of a suitable spectral model.

On increasing pedestrian density, pedestrian traffic cannot be considered as unrestricted. The walking velocity monotonically decreases with growing density ([10]-[14]); furthermore, when pedestrian density is high enough, pedestrians are inclined to walk with the same step length [12]. Since walking velocity is directly proportional to step frequency and step length [15] , the increase in pedestrian density produces a shift of the harmonic content of pedestrian-induced load towards lower values of frequency. It follows that some structures, with natural frequencies lower than those typical of unrestricted pedestrian traffic, may be affected by heavy vibrations if crowded conditions occur.

At the state of the art, to the authors' knowledge, the only attempt to estimate footbridges' dynamic response in crowded conditions relies on numerical simulations. The simulations are based on suitable models of pedestrian dynamics (e.g., [16]-[18]), representing the correlation among the forces exerted by each single pedestrian (e.g. [19]). These methods are very time consuming and are not appropriate for design purposes.

In this paper, a generalized equivalent spectral model is proposed, which can be applied for the serviceability analysis of footbridges also in crowded conditions in absence of pedestrian-structure interaction. Starting from the spectral model of the modal force proposed by Piccardo & Tubino [9] and from the main rules and relationships of pedestrian dynamics, the generalized spectral model of pedestrian-induced forces is defined by introducing a suitable physically-based expression for the coherence function of the equivalent stationary random process and a pedestrian density – velocity law. The proposed coherence model is defined as a function of both pedestrian density and distance among pedestrians. It reduces to perfect uncorrelation for low pedestrian density (i.e. spatially unrestricted traffic), and to perfect correlation for high pedestrian density (i.e. crowded condition). Because of the fact that the step

frequency, the walking speed and the pedestrian density are strictly correlated ([10]-[15]), a dependency of the harmonic content of the force on the pedestrian density is introduced. Based on the proposed analytical generalized spectral model of the loading, simple expressions for the evaluation of the maximum dynamic response are sought for performing the vibration serviceability analysis of footbridges in a closed-form, similarly to classical procedures adopted in the wind engineering field. A numerical application to a real footbridge is finally proposed.

2 EQUIVALENT SPECTRAL MODEL FOR SPATIALLY UNRESTRICTED TRAFFIC

Unrestricted pedestrian traffic (i.e. pedestrians arriving in a random way and able to move undisturbed, each of them with his own characteristics in terms of loading amplitude, frequency, velocity and phase) was recently analyzed by Piccardo & Tubino [9]. The authors proposed an equivalent spectral model of pedestrian-induced load, which allows to evaluate very easily the maximum structural response.

The force per unit length exerted by N_p uncorrelated pedestrians can be expressed as the sum of the forces exerted by each single pedestrian, modeled as harmonic moving loads. Taking into account only the main harmonic for each pedestrian, the force per unit length can be written as follows [9]:

$$f(x,t)=\sum_{i=1}^{N_p}\alpha_i G_i \sin\left(\Omega_i\left(t-\tau_i\right)+\Psi_i\right)\delta\left[x-c_i\left(t-\tau_i\right)\right]\left[H\left(t-\tau_i\right)-H\left(t-\tau_i-\frac{L}{c_i}\right)\right] \quad (1)$$

where $\delta(\bullet)$ and $H(\bullet)$ are, respectively, the Dirac Delta function and the Heaviside step function, t, x, L are, respectively, the time, the abscissa along the structure and the length of the structure. Furthermore α_i, G_i, Ω_i, c_i, τ_i are the dynamic load factor (DLF), the weight, the walking circular frequency, the walking velocity and the arrival time of the i-th pedestrian. All these quantities have to be probabilistically modeled. In particular, the step circular frequency Ω, the pedestrian weight G, the DLF α and the walking velocity c can be considered as Gaussian random variables. The phase-angle Ψ among different pedestrians may be assumed as uniformly-distributed in the interval $[0,2\pi]$. Considering pedestrian arrivals as Poisson events, then the time-lags between their arrivals are represented by an exponentially-distributed random variable with an average return period $T= T_{pm}/N_p$, where $T_{pm} =L/c_m$ is the footbridge mean crossing time for a single pedestrian (c_m being the mean value of the walking speed).

By assuming linear behavior and classical damping, the equation of motion of the j-th principal coordinate p_j can be expressed as:

$$\ddot{p}_j(t)+2\xi_j\omega_j\dot{p}_j(t)+\omega_j^2 p_j(t)=\frac{1}{M_j}\int_0^L f(x,t)\varphi_j(x)dx \quad (2)$$

where ξ_j ω_j and M_j are, respectively, the j-th modal damping ratio, natural circular frequency and modal mass, and φ_j the j-th mode shape.

Eq. (2) can be rewritten in non-dimensional form:

$$\ddot{\tilde{p}}_j(\tilde{t})+2\xi_j\dot{\tilde{p}}_j(\tilde{t})+\tilde{p}_j(\tilde{t})=\tilde{F}_j(\tilde{t}) \quad (3)$$

where the following non-dimensional quantities have been introduced:

$$\tilde{t} = \omega_j t \quad \tilde{p}_j = \frac{p_j M_j \omega_j^2}{\alpha_m G_m} \quad \tilde{f}(\tilde{x},\tilde{t}) = \frac{f(x,t)L}{\alpha_m G_m} \quad \tilde{x} = \frac{x}{L} \quad \tilde{F}_j(\tilde{t}) = \int_0^1 \tilde{f}(\tilde{x},\tilde{t})\varphi_j(\tilde{x})\, d\tilde{x} \tag{4}$$

being α_m the mean DLF, G_m the mean pedestrian weight.

Furthermore, considering Eqs.(1), (2), (4), the non-dimensional modal force $\tilde{F}_j(\tilde{t})$ is given by:

$$\tilde{F}_j(\tilde{t}) = \sum_{i=1}^{N_p} \tilde{\alpha}_i \tilde{G}_i \sin\left(\tilde{\Omega}_i\left(\tilde{t}-\tilde{\tau}_i\right)+\Psi_i\right)\varphi_j\left(\tilde{\Omega}_{ci}\left(\tilde{t}-\tilde{\tau}_i\right)\right)\left[H\left(\tilde{t}-\tilde{\tau}_i\right)-H\left(\tilde{t}-\tilde{\tau}_i-\frac{1}{\tilde{\Omega}_{ci}}\right)\right] \tag{5}$$

where the non-dimensional parameters are defined as:

$$\tilde{\alpha}_i = \frac{\alpha_i}{\alpha_m} \quad \tilde{G}_i = \frac{G_i}{G_m} \quad \tilde{\Omega}_i = \frac{\Omega_i}{\omega_j} \quad \tilde{\Omega}_{ci} = \frac{c_i}{\omega_j L} \quad \tilde{\tau}_i = \omega_j \tau_i \tag{6}$$

Let us define the mean non-dimensional walking speed $\tilde{\Omega}_{cm}$ analogously to $\tilde{\Omega}_{ci}$ in Eq. (6) with c_i=c_m. Assuming that the structural mode shape is sinusoidal, $\varphi_j(\tilde{x}) = \sin(\pi\tilde{x})$, considering $\tilde{\alpha}_i = 1$, $\tilde{G}_i = 1$, $\tilde{\Omega}_{ci} = \tilde{\Omega}_{cm}$, $\tilde{\tau}_i = i/\tilde{\Omega}_{cm}N_p$ (i.e. focusing attention only on the randomness of the step frequency), and under the hypothesis that $\tilde{\Omega}_{cm}$ is very small compared with $\tilde{\Omega}_i$, the following expression for the power spectral density function (psfd) of the non-dimensional modal force is obtained [9]:

$$S_{\tilde{F}_j}(\tilde{\Omega}) = \frac{N_p}{4}\, p_{\tilde{\Omega}}(\tilde{\Omega}) \tag{7}$$

where $p_{\tilde{\Omega}}(\tilde{\Omega})$ is the probability density function of the non-dimensional circular step frequency $\tilde{\Omega}$.

By considering Eqs. (4), (6) and (7), the psdf of the *j*-th modal force can be rewritten in dimensional form as follows:

$$S_{F_j}(\Omega) = \frac{N_p}{4} \cdot \frac{\left(\alpha_m G_m\right)^2}{\omega_j}\, p_{\Omega}(\Omega) \tag{8}$$

The mean values of the DLFs and statistical moments of the step frequency can be found e.g. in Ref. [1], [9].

3 PEDESTRIAN DYNAMICS

When pedestrian density reaches values high enough, pedestrian traffic cannot be considered as unrestricted because pedestrians are inclined to synchronize their step length [12]. Furthermore, the harmonic content of the pedestrian-induced force may change because of the variation of both step frequency and velocity with pedestrian density ([10]-[15]). In order to model accurately these phenomena, it is necessary to study pedestrian dynamics.

To this day, a central problem in pedestrian dynamics is the relation between density and flow or velocity (fundamental diagram), which in general depends on the directionality of the flow (mono-directional, Section 3.1 or bi-directional, Section 3.2).

3.1 Mono-directional stream

The mono-directional movement of pedestrians is the most widely studied scenario. All the proposed speed-density relations have some common features, concerning monotonic decreasing trend of the mean velocity c_m with increasing density ρ and the identification of some critical points [11]: the unrestricted flow speed c_u (i.e. the mean maximum velocity), the critical density ρ_u (i.e. the lower bound for unconstrained free walking), the jam density ρ_{max} (i.e. the maximum admissible density corresponding to null speed and flow). The free speed varies between about 1.1 m/s and 1.5 m/s [10], while the jam density may assume values up to 7 Ped/m^2 [10].

In the context of mono-directional flow, one of the most important laws is the fundamental diagram of Weidmann [13], a part of a review work in which the author summarized 25 different investigations. The author found a jam density ρ_{max} =5.4 Ped/m^{2}and a free flow speed probabilistically characterized as a Gaussian random variable with a mean value c_{um}=1.34 m/s and σ_{cu}=0.26 m/s standard deviation. The mean velocity-density relation proposed by Weidmann, named "Kladek formula"[13], can be written in a generic form, as proposed by Venuti & Bruno [11]:

$$c_m(\rho) = c_u \left\{ 1 - \exp\left[-\gamma \rho_{\max} \left(\frac{1}{\rho} - \frac{1}{\rho_{\max}} \right) \right] \right\} \tag{9}$$

in which γ depends on the travel purpose. By assuming ρ_{max} =5.4 Ped/m^2, c_u =c_{um}=1.34 m/s and γ=0.354, Eq. (9) matches with the original one proposed by Weidmann.

A significant explanation of the microscopic phenomena of the pedestrian traffic (i.e. inter-pedestrians relations) hidden behind the Kladek formula has been provided by [12]. The authors focused their attention on the changing in slope of the fundamental density – velocity law, and they identified different density domains in which the fundamental law can be considered about linear. The authors imputed these differences as a consequence of different effects due to microscopic characteristics of pedestrian traffic [12]. To support this claim, they performed an experimental campaign, in which flow characteristics were measured using both manual and automatic video procedures.

Starting from experimental results available in [12] and [15], Venuti et al. [11] proposed an interpretative model for the fundamental pedestrian diagram. The authors focused their attention on the Pedestrian Area Module (PAM), i.e. the surface required by a pedestrian during his motion. It should be noted that the PAM is the reciprocal of the pedestrian density. The PAM required by a pedestrian, with the hypothesis of rectangular surface, is S=wd [11], being w the lateral space and d the forward distance. Both the quantities, in terms of mean values, can be considered as the sum of the dimension of a motionless pedestrian, and a dimension defined as function of the mean walking velocity thanks to the experimental results [11]:

$$\begin{cases} w_m(c_m) = w_0 \left(1 + 0.62 \dfrac{c_m}{c_u} \right) \\ d_m(c_m) = d_0 + 1.06 c_m + b c_m^{10} \end{cases} \tag{10}$$

where $b = (2.08 c_u - d_0) / c_u^{10}$, w_0 and d_0 are the average lateral width and depth of the human body, which can be respectively assumed equal to 0.45 m and 0.36 m [11].

Moreover, the step frequency– speed relation, in terms of mean values, can be derived from a cubic fitting to the experimental data [11]:

$$n_m = 0.35c_m^3 - 1.59c_m^2 + 2.93c_m \quad (11)$$

The mean value of the critical density ρ_{um} below which pedestrian traffic is unrestricted can be deduced from the definition of PAM, that could be intended as the reciprocal of the pedestrian density. By substituting $c_m = c_u = c_{um}$ in Eq. (10), $\rho_{um}=[d_m w_m]^{-1}$ =0.33 Ped/m^2 is obtained. The value is very similar to the one suggested by Grundmann et al [27]. Then, by substituting $c_m = c_u$ into Eq. (11), the unconstrained step frequency n_u can be obtained. It appears as Gaussian random variable with mean value n_{um}=1.91 Hz and σ_{nu}=0.144Hz.

Figure 1 (a) shows the trend of the forward distance d_m with the pedestrian mean speed. It should be noted that d_m has linear trend with pedestrian velocity for speed values smaller than about 0.9 m/s. Let us indicate this value as lock-step speed, c_{LS}. Corresponding values in terms of pedestrian density and step frequency are, respectively, ρ_{LS} = 1.3 Ped/m^2 (from Eq. (9)) and n_{LS} = 1.6 Hz (from Eq. (11)). According to Seyfried et al. [12], the marching in lock-steps, which compensate the slower step frequency, are possible explanation for the linearity between the required length and the velocity.

Figure 1(b) shows the trend of the total outward distance with the pedestrian density. According to the same criteria used by Seyfried et al. [12], it is possible to individuate three domains in which the law d_m-ρ_m is almost linear. In particular:

Domain I (unconstrained traffic). $\rho \leq \rho_{um}$. The forward distance between pedestrians is constant and equal to its maximum value. Pedestrians' movement is completely free.

Domain II (correlated traffic). $\rho_{um} < \rho \leq \rho_{LS}$. The forward distance between pedestrians quickly decreases with increasing in pedestrian density. In this domain, pedestrians' movement are not completely free.

Domain III (constrained traffic). $\rho > \rho_{LS}$. The forward distance between pedestrians is almost linear with pedestrian density, it is small and it slowly decreases with increasing in density. Marching in lock-steps totally occurred. Pedestrians' movements are completely constrained by the presence of other pedestrians.

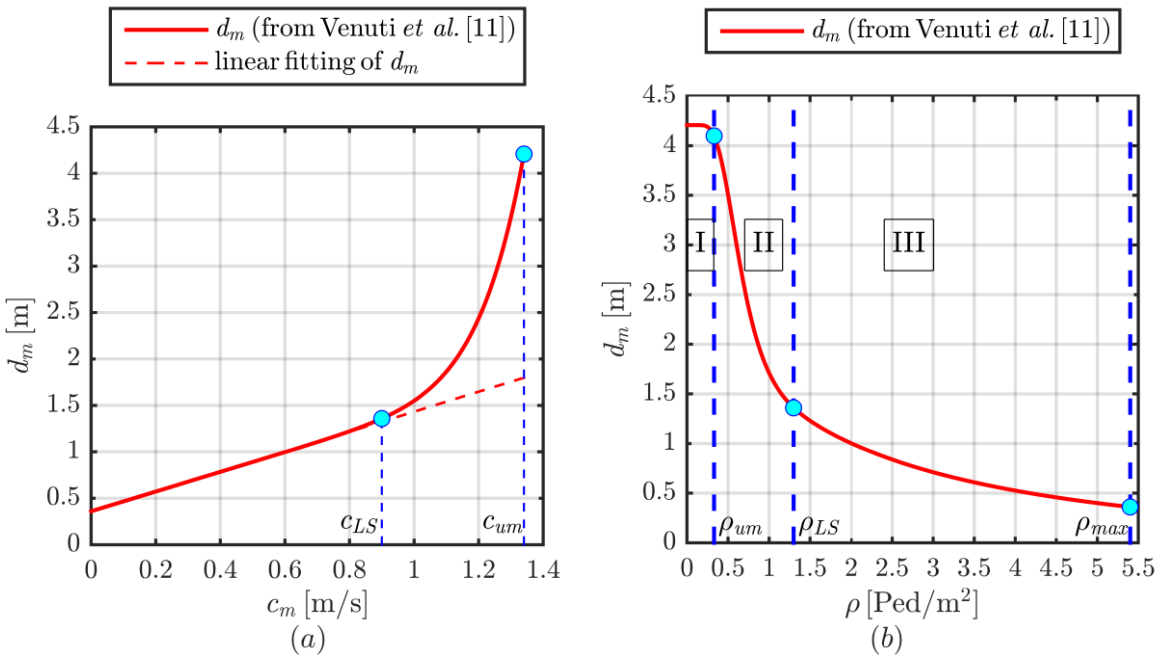


Figure 1: Trend of the mean forward distance with mean pedestrian velocity (a) and with pedestrian density (b)

3.2 Bi-directional stream

In the last decades, problems related to bidirectional flows and its effects on pedestrian dynamics have gained increasing attention. First experimental studies about bi-directional streams were carried out by Older in 1968 [20] on footways in shopping streets. Several other experimental campaigns were carried out in transportation field [10]. At the same time, different microstructure methods for numerical simulation of pedestrian dynamics became an increasingly used instrument in order to study bi-directional streams (e.g. [16]-[18]).

Despite many experimental works in the transportation field and numerical works available in literature, a univocal proposal of a suitable fundamental law for bi-directional streams does not exist, to the authors' knowledge. Furthermore, at the state of art there is still no consensus whether the fundamental diagrams of mono- and bi-directional flows are different or not.

Fruin [22] states that the fundamental diagrams of mono- and bi-directional flow differ only slightly. Weidmann [13] neglected the differences in accordance with [22], but Navin and Wheeler [14] found a reduction of the flow in dependence of directional imbalances. Older [20] highlighted the phenomenon of lane formation as a natural system of limiting obstructions. Thanks to lanes, no differences occur between mono- and bi-directional streams, at least at low and medium densities [20].

A comprehensive description of the main phenomena that occur in bi-directional flows can be found Blue et al. [18]. They performed a large number of numerical simulations using CA Models, with the aim to study the fundamental diagram for the different types of bi-directional flows, over a range of directional splits in 10% increments from 100-0 (i.e. mono-directional flow) to 50-50 (i.e. balanced bi-directional flow). No significant differences among the mono-directional stream (i.e. 100-0) and bi-directional ones could be pointed out for stationary conditions.

Recently, Zhang et al. [21] carried out an experimental campaign with the aim to compare the fundamental diagrams of mono-directional flow with bi-directional one. They investigated bi-directional flows with balanced (50-50) and unbalanced (about 60-40) flow conditions. In 2015, Flötteröd and Lämmel [23], starting from experimental works of Zhang et al. [21], finally proposed a bi-directional pedestrian fundamental diagram, drawing inspiration from the cellular automata (CA) approach. At least until $\rho<2$ Ped/m^2, no meaningful mismatches can be found between the fundamental law proposed by Flötteröd and Lämmel [23] and the fundamental diagram for mono-directional streams (Eq. (9)).

4 A PHISICALLY-BASED COHERENCE FUNCTION

The coherence function of pedestrian-induced forces is a sparsely studied topic in the research panorama. Some studies on coherency, which concern relative phase angles among pedestrians, were done by Ebrahimpour et al. ([25], [26]). Piccardo & Tubino [9], dealing with unrestricted pedestrian traffic, assumed as a coherence function the Dirac delta function in order to model perfect uncorrelation. At the state of art, a proper model of coherence function suitable for any pedestrian traffic conditions does not exist, to the authors' knowledge.

Some guidelines for a convenient definition of the coherence function were provided by Brownjohn et al. [8]. The spatial correlation in the pedestrian loading may be analogous to turbulent buffeting wind loads on a linear structure where cross-spectral density at two spatially separated points is assumed to diminish exponentially with increasing separation and frequency. For pedestrians, coherence depends on being able to see and keep up with others, and it is likely that it would drop to zero beyond a short separation distance [8].

A physically-based expression for the coherence function of the equivalent stationary random process is here introduced. It is composed by a unitary step function for small distance and an exponentially decreasing function for greater distance:

$$Coh_{ff}(x,x',\varepsilon,C)=\begin{cases} H\left(\frac{|x-x'|}{\varepsilon}\right)-H\left(\frac{|x-x'|}{\varepsilon}-1\right) & \text{if } |x-x'|\le\varepsilon \\ \exp\left[-C\left(\frac{|x-x'|}{\varepsilon}-1\right)\right] & \text{otherwise} \end{cases} \tag{12}$$

where x and x' are the current abscissa, ε is the width of the initial unitary step function and C is the exponential decay coefficient. The main issue is the definition of the exponential decay coefficient C and of the width of the initial step ε.

The width of the initial unitary step function ε should be intended as a separation distance that each pedestrian interposes with others, in order to avoid contacts. The assumption of unitary step function is equivalent to assume that, on this distance, the single pedestrian has perfect synchronization with himself. It is possible to identify the separation distance between two pedestrians moving on a linear domain as strictly connected with the forward distance d_m. Moreover, by taking into account that, in the spectral model proposed at Section 2, each pedestrian is modeled as a moving harmonic punctual load (Eq. (1)), the separation distance between two pedestrians becomes of course d_m-d_0/2.

The trend of d_m with the pedestrian density is shown in Figure 1 (b). Considering Domain I, ε should be identified as the forward distance corresponding to the mean free flow velocity c_{um}. By substituting c_m= c_{um} in Eq. (10), ε=d_m(c_{um})-d_0/2 ≅ 4 m is obtained.

The exponential part of the coherence function has the purpose to model the increase in synchronization between pedestrians that occurs when pedestrian density grows up (in Domains II and III). To do that, some limit behavior may be considered. For low pedestrian density (i.e. Domain I), pedestrians' walking is completely free [12] and the pedestrian-induced loading is uncorrelated. As a consequence, the coherence function may drop to zero very quickly, so the exponent must reach values high enough. On the contrary, for high pedestrian density (i.e. Domain III), marching in lock-step totally occurs [12]. Pedestrians' movements are completely constrained by others all around, and each of them is marching with the same step length and the same velocity [12]. Since the step length $l_s = c/n$ [11], then pedestrians are walking with the same step frequency. It follows that the pedestrian-induced loading is perfectly correlated. The coherence function may reach unitary values, so the exponent must drop to zero.

In order to satisfy all the conditions outlined above, it is reasonable to express the exponential decay coefficient as function of the mean step frequency. A suitable expression for the exponent can be identified through the following exponential function:

$$C = C(n_m) = \exp(C_1 n_m + C_2) \tag{13}$$

where the two coefficients C_1 and C_2 can been obtained by enforcing the conditions $C(n_u)$=C_{max}=10, $C(n_{LS})$=C_{min}=0.1. The limit values for the coefficient have been assumed based on numerical simulations: the exponential portion of the coherence function becomes negligible for values of the exponent greater than 10, and it becomes almost unitary for exponents lower than 0.1. Under the hypothesis of n_u=n_{um}, the values C_1=22 s^{-1} and C_2=-38 are obtained.

The exponent C proposed in Eq. (13) could be rewritten as a function of the pedestrian density. In fact, the step frequency can be expressed as a function of the pedestrian density by substituting Eq. (9) into Eq.(11).

Figure 2 shows the trend of the exponential decay coefficient with respect to the step frequency (Figure 2 (a)) and pedestrian density (Figure 2 (b)).

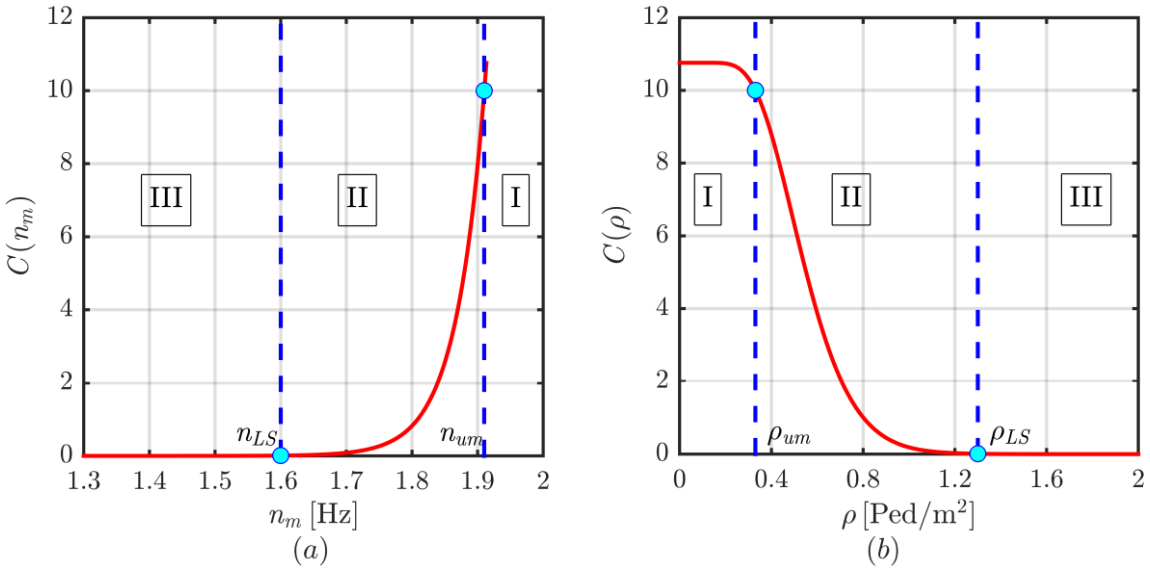


Figure 2: Exponential decay coefficient of the coherence function as a function of (a) mean step frequency and (b) pedestrian density

The proposed coherence function can be rewritten in the following non-dimensional form:

$$Coh_{\tilde{f}\tilde{f}}(\tilde{x},\tilde{x}',\tilde{\varepsilon},C)=\begin{cases} H\left(\frac{|\tilde{x}-\tilde{x}'|}{\tilde{\varepsilon}}\right)-H\left(\frac{|\tilde{x}-\tilde{x}'|}{\tilde{\varepsilon}}-1\right) & \text{if } |\tilde{x}-\tilde{x}'|\le\tilde{\varepsilon} \\ \exp\left[-C\left(\frac{|\tilde{x}-\tilde{x}'|}{\tilde{\varepsilon}}-1\right)\right] & \text{otherwise} \end{cases} \tag{14}$$

where $\tilde{\varepsilon}$ is the non-dimensional width of the initial unitary step function $\tilde{\varepsilon}=\varepsilon/L$. Figure 3 plots the resulting non-dimensional coherence function (Eq.(14)) as a function of the non-dimensional distance, for fixed values of pedestrian density, assuming $\tilde{\varepsilon}=0.1$. As expected, the exponential portion is negligible for low values of the pedestrian density (i.e. $\rho<\rho_{um}$). Then, it monotonically increases with the pedestrian density and, finally, it reaches unitary value for $\rho > \rho_{LS}$.

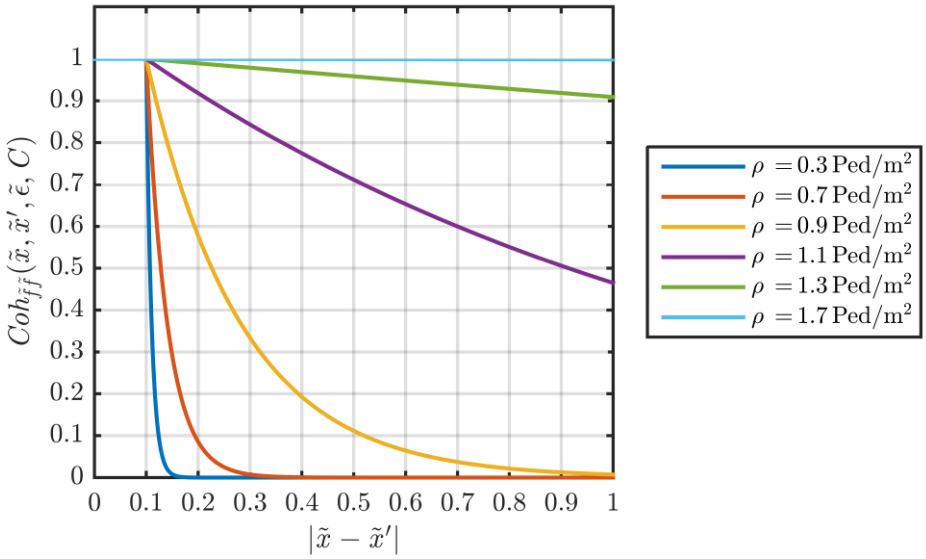


Figure 3: Proposed coherence function for different values of pedestrian density.

5 THE GENERALIZED EQUIVALENT SPECTRAL MODEL OF THE HUMAN-INDUCED LOADING

The power spectral density function of the non-dimensional modal force is given by:

$$S_{F_j}(\tilde{\Omega}) = \int_0^1 \int_0^1 S_{\tilde{f}\tilde{f}}\left(\tilde{x},\tilde{x}',\tilde{\Omega}\right)\varphi_j(\tilde{x})\varphi_j(\tilde{x}')\mathrm{d}\tilde{x}\mathrm{d}\tilde{x}' \tag{15}$$

where $S_{\tilde{f}\tilde{f}}\left(\tilde{x},\tilde{x}';\tilde{\Omega}\right)$ is the cross-psdf of the non-dimensional force $\tilde{f}(\tilde{x},\tilde{t})$. It's given by:

$$S_{\tilde{f}\tilde{f}}\left(\tilde{x},\tilde{x}',\tilde{\Omega}\right) = \sqrt{S_{\tilde{f}}\left(\tilde{x},\tilde{\Omega}\right)S_{\tilde{f}}\left(\tilde{x}',\tilde{\Omega}\right)}\cdot Coh_{\tilde{f}\tilde{f}}(\tilde{x},\tilde{x}',\tilde{\varepsilon},C) \tag{16}$$

In Eq. (16) $S_{\tilde{f}}\left(\tilde{x},\tilde{\Omega}\right)$ is the psdf of the non-dimensional force and $Coh_{\tilde{f}\tilde{f}}(\tilde{x},\tilde{x}',\tilde{\varepsilon},C)$ is the coherence function described in Section 4. Under the assumption that the non-dimensional force has uniform psdf [9], $S_{\tilde{f}}\left(\tilde{x},\tilde{\Omega}\right) = S_{\tilde{f}}\left(\tilde{x}',\tilde{\Omega}\right) = S_{\tilde{f}}\left(\tilde{\Omega}\right)$, considering Eqs. (15) and (16), the psdf of the non-dimensional force can be rewritten as follows:

$$S_{F_j}(\tilde{\Omega}) = S_{\tilde{f}}\left(\tilde{\Omega}\right)\cdot\chi_j\left(\tilde{\varepsilon},C\right) \tag{17}$$

where the admittance function $\chi_j\left(\tilde{\varepsilon},C\right)$ has been introduced:

$$\chi_j\left(\tilde{\varepsilon},C\right) = \int_0^1 \int_0^1 Coh_{\tilde{f}\tilde{f}}(\tilde{x},\tilde{x}';\tilde{\varepsilon};C)\varphi_j(\tilde{x})\varphi_j(\tilde{x}')\mathrm{d}\tilde{x}\mathrm{d}\tilde{x}' \tag{18}$$

As outlined in Section 4, the exponential part of the coherence function is almost null under the hypothesis of unconstrained pedestrian traffic (i.e. $\rho<\rho_{um}$). Moreover, it should be noted that the Eq. (14a) can be interpreted, from a perturbative point of view, as the incremental ratio of the Dirac delta function (i.e. the first derivative of the unitary step function), being the non-dimensional width of the initial unitary step function a small parameter. Thus, for $\rho<\rho_{um}$ (i.e. in unrestricted traffic condition) the admittance function (Eq. (18)) assumes the following simplified expression:

$$\chi_j\left(\tilde{\varepsilon},C\right)\cong\chi_{uj}\left(\tilde{\varepsilon}\right)\cong 2\tilde{\varepsilon}\int_0^1\varphi_j(\tilde{x})^2\,\mathrm{d}\tilde{x} \tag{19}$$

Finally, assuming that the structural mode shape is sinusoidal [9], Eq. (19) becomes $\chi_{uj}\left(\tilde{\varepsilon}\right)\cong\tilde{\varepsilon}$ .Considering Eqs. (7) and (17), the psdf of the non-dimensional equivalent distributed pedestrian-induced loading can be obtained:

$$S_{\tilde{f}}\left(\tilde{\Omega}\right)=\frac{N_p}{4\tilde{\varepsilon}}\,p_{\tilde{\Omega}}(\tilde{\Omega}) \tag{20}$$

Eq. (20) can be rewritten in the dimensional form as follows:

$$S_f(\Omega)=\frac{N_p}{4}\cdot\frac{\left(\alpha_m G_m\right)^2}{\omega_j}\cdot\frac{1}{\varepsilon L}\cdot p_{\Omega}(\Omega) \tag{21}$$

The psdf of the modal force for a generic footbridge, with any mode shape and pedestrian density, can be evaluated through following steps: (i) assumption of the value of the free flow speed c_u in the range $[c_{um}\pm\sigma_{cu}]$, (ii) evaluation of the mean step frequency n_m (Eqs. (9) and (11)) and of the exponential decay coefficient C (Eq. (13)), (iii) computation of the admittance function $\chi_j\left(\tilde{\varepsilon},C\right)$ (Eq. (18)) and (iv) application of Eq. (17) taking as mean value of the non-dimensional step frequency the one corresponding to the calculated mean step frequency $n_m\,(\tilde{\Omega}_m=2\pi n_m/\omega_j)$.

6 MAXIMUM STRUCTURAL RESPONSE

Starting from the spectral model of the pedestrian-induced loading (Eq. (17)), the maximum dynamic response can be estimated through the classical methods of linear random dynamics [9]. The mean value of the maximum non-dimensional principal component $\ddot{\tilde{p}}_{j_{\max}}$ can be evaluated as follows [9]:

$$\ddot{\tilde{p}}_{j_{\max}}=g_{\ddot{\tilde{p}}_j}\sigma_{\ddot{\tilde{p}}_j} \tag{22}$$

where $\sigma_{\ddot{\tilde{p}}_j}$ is the standard deviation of $\ddot{\tilde{p}}_j$ and $g_{\ddot{\tilde{p}}_j}$ is the peak coefficient.

By assuming that the pedestrian-induced response is mainly resonant [9], the variance of $\ddot{\tilde{p}}_j$ can be estimated as [9]:

$$\sigma^2_{\ddot{\tilde{p}}_j}\cong\frac{\pi}{4\xi}S_{\tilde{F}_j}\left(1\right) \tag{23}$$

being $S_{\tilde{F}_j}\left(1\right)$ the psfd of the non dimensional modal force, Eq. (17), calculated for $\tilde{\Omega}=1$.

The peak coefficient assumes the following expression [9]:

$$g_{\ddot{\tilde{p}}_j}=\sqrt{2\ln\left(2\nu^e_{\ddot{\tilde{p}}_j}\tilde{T}\right)}+\frac{0.5772}{\sqrt{2\ln\left(2\nu^e_{\ddot{\tilde{p}}_j}\tilde{T}\right)}} \tag{24}$$

in which the following non-dimensional parameters appear [9]:

$$\tilde{T} = \frac{N}{\tilde{\Omega}_{cm}} \quad v_{\ddot{\tilde{p}}_j}^{e} = \left(1.63 q_{\ddot{\tilde{p}}_j}^{0.45} - 0.38\right) v_{\ddot{\tilde{p}}_j} \quad v_{\ddot{\tilde{p}}_j} \cong \tilde{n}_j = \frac{1}{2\pi} \quad q_{\ddot{\tilde{p}}_j} \cong 2\sqrt{\frac{\xi_j}{\pi}} \tag{25}$$

being N the number of consecutive pedestrian groups to be considered in order to satisfy the stationarity hypothesis. It should be noted that $\tilde{\Omega}_{cm}$ is the non-dimensional walking speed obtained by substituting in Eq. (6) the value $c_i = c_m(\rho)$ (Eq. (9)).

Starting from Eq. (22), the maximum acceleration of the principal coordinate $\ddot{p}_{j_{\max}}$ can be estimated as follows [9]:

$$\ddot{p}_{j_{\max}} = \frac{\alpha_m G_m}{M_j} \ddot{\tilde{p}}_{j_{\max}} \tag{26}$$

Then, assuming that the structural response is dominated by the jth natural mode, the maximum acceleration in physical coordinates may be finally estimated as follows [9]:

$$\ddot{q}_{\max}(x) = \varphi_j(x) \ddot{p}_{j_{\max}} \tag{27}$$

7 NUMERICAL APPLICATION.

The proposed procedure is applied in order to estimate the maximum dynamic response of a real footbridge to various pedestrian traffic conditions, from completely unrestricted to fully-restricted pedestrian traffic. The structure is a slender footbridge in Milan, that was recently investigated through full-scale measurements [28]. The footbridge has a main span length L = 60 m. It's characterized by a first vertical flexural mode shape similar to the first mode of a double-hinge beam, with an identified natural frequency n_1 = 2.17 Hz, modal damping ξ_1 = 0.005 and modal mass M_1 = 51 000 kg [28].

The structural response can be estimated by the proposed formulation. It's assumed G_m = 700 N and α_m = 0.40. According to [9], the standard deviation of the step frequency may be chosen 0.17 Hz. In order to ensure stationarity N=10 is set.

By remembering that the free flow speed appearing in Eq. (9) is indeed a Gaussian random variable with mean value c_{um}=1.34 m/s and standard deviation σ_{cu} =0.26 m/s [13] (i.e. mean unconstrained step frequency n_{um}=1.91 Hz and standard deviation σ_{nu}=0.144 Hz), the dynamic response of the footbridge may be evaluated by adopting a free flow speed in the range $[c_{um} \pm \sigma_{cu}]$. Therefore different equivalent modal psdf may be obtained, and variable results may be found in terms of maximum structural response.

Figure 4 shows the maximum dynamic response of the bridge (Eq. (27) as a function of pedestrian density. The different curves correspond to different values of free-flow speed.

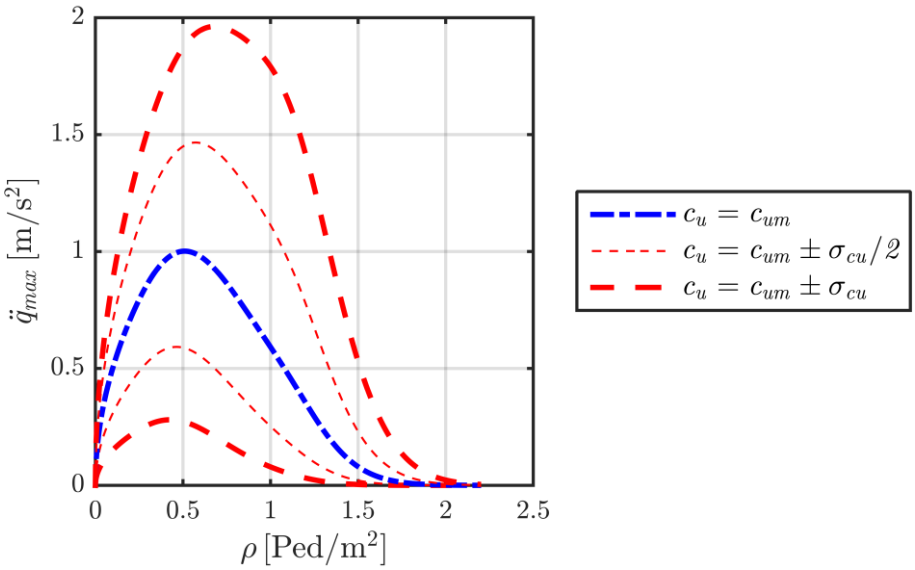


Figure 4: Maximum mid-span acceleration for a real footbridge for different values of free-flow speed

For low values of pedestrian density, the dynamic response tends to increase on increasing pedestrian density due to the growth of the number of pedestrians exciting the footbridge. Then, for high values of pedestrian density, the mean speed and mean step frequency progressively decrease; thus, the mean step frequency moves away from the structural frequency, and the structural response starts to decrease and progressively drops to zero, despite N_p is still growing.

The analysis of the structural response shows that this real footbridge has a high sensitivity to human-induced vibrations. As a matter of fact, the structural response may reach values much higher than 1 m/s (i.e. corresponding to minimum comfort, see [6] and [7]). Moreover, it demonstrates that small variations in terms of pedestrian velocity correspond to huge variations in terms of structural acceleration. This fact is due to the closeness between the first structural frequency and the mean step frequency. In order to avoid problems in terms of pedestrian comfort, the footbridge was recently equipped with tuned-mass dampers [29] .

8 CONCLUSIONS AND PROSPECTS

In this paper, the equivalent spectral model, originally introduced for unrestricted pedestrian traffic, has been generalized in order to account for correlation among pedestrians that can occur in crowded conditions. The generalization relies on the analysis of pedestrian dynamics and it is based on the introduction of a physically-based coherence function. The proposed spectral model allows to model both the change in the harmonic content of pedestrian-induced loading and the synchronization phenomenon on increasing pedestrian density.

A preliminary application to a real footbridge shows the potentiality of the model for the serviceability evaluation of footbridges in any traffic condition.

A validation (experimental and/or numerical) of the proposed model is necessary. The experimental validation could be provided by the comparison of the estimated maximum dynamic response with full-scale measurements in crowded conditions. The numerical validation may be carried out through numerical simulation of pedestrian flows based on suitable models of pedestrian dynamics.

REFERENCES

[1] S. Zivanovic, A. Pavic, P. Reynolds. Vibration serviceability of footbridges under human-induced excitation: a literature review. *Journal of Sound and Vibration*, **279**, 1-74, 2005.

[2] G. Piccardo, F. Tubino, Dynamic response of Euler-Bernoulli beams to resonant harmonic moving loads. *Structural Engineering and Mechanics*, **44(5)**, 681-704, 2012.

[3] S. Zivanovic, A. Pavic, E.T. Ingolfsson. Modelling spatially unrestricted pedestrian traffic on footbridges. *Journal or Structural Engineering ASCE*, **136(10)**, 1296-1308, 2010.

[4] G. Piccardo, F. Tubino. Simplified procedures for the vibration serviceability analysis of footbridges subjected to realistic walking loads. *Computers and Structures*, **87**, 890-903, 2009.

[5] FIB, *Guidelines for the Design of Footbridges*, *Bulletin 32*. International Federation for Structural Concrete, Lauzanne, Switzerland, 2005

[6] SETRA, *Footbridges – assessment of vibrational behaviour of footbridges under pedestrian loading.* Technical Department for Transport, Roads and Bridges Engineering and Road Safety, Ministry of Transport and Infrastructures, Paris, France, 2006

[7] HIVOSS, *Design of footbridges guidelines, Human induced vibrations of steel structures*. http://www.stb.rwthaachen.de/projecte/2007/HIVOSS/download.phpRFS2-CT-2007-00033 [22.04.09], 2008.

[8] J.M.W. Brownjohn, A. Pavic, P.A. Omentzetter. Spectral density approach for modelling continuous vertical forces on pedestrian structures due to walking. *Canadian Journal of Civil Engineering*, **31(1)**, 65–77, 2004.

[9] G. Piccardo, F. Tubino. Equivalent spectral model and maximum dynamic response for the serviceability analysis of footbridges. *Engineering Structures*, **40**, 445-456, 2012.

[10] W. Daamen. *Modelling passenger flows in public transportat facilities.* PhD thesis, Delft University of technology, Department transport and planning, 2004

[11] F. Venuti, L. Bruno. An interpretative model of the pedestrian fundamental relation. *C.R. Mecanique*, **335**, 194-200, 2007

[12] A. Seyfried, B. Steffen, W. Klingsch, M. Boltes. The fundamental Dyagram of Pedestrian Movement Revisite. *Journal of Statistical Mechanics*, **10**, 2005

[13] U. Weidmann. *Transporttechnik der Fußgänger.* ETC Zürich, Ivt. Report no. 90, March 1993.

[14] P.D. Navin, R.J. Wheeler. Pedestrian Flow Characteristics. *Traffic Engineering*, **39(9)**, 30-33, 1969

[15] J.E. Bertram, A. Ruina. Multiple walking speed-frequency relations are predicted by constrained optimization. *Journal of Theoretical Biology*, **209**, 445-453, 2001

[16] D. Helbing, P. Molnár. Social force model for pedestrian dynamics. *Phisical Review E*, **51(5)**, 4282-4286, 1995

[17] F. Dietrich, G. Köster. Gradient navigation model for pedestrian dynamics. *Phisical Review E*, **89(6)**, 2801-1-8, 2014

[18] V.J. Blue, J.L. Adler. Cellular automata microsimulation for modeling bi-directional pedestrian walkway. *Transportation Research Part B*, **35**, 293-312, 2001

[19] C.C. Caprani, J. Keogh, P. Archbold, P. Fanning. Characteristic Vertical Response of a Footbridge Due to Crowd Loading. *8th. International Conference on Structural Dynamics (EURODYN 2011)*, Leuven, Belgium, 2011

[20] S. Older. Movement of pedestrians on footways in shopping streets. *Traffic Engineering and Control*, **10(4)**, 160-163, 1968

[21] J. Zhang, W. Klingsch, A. Schadschneider, A. Seyfried. Ordering in bidirectional pedestrian flows and its influence on the fundamental diagram. *Journal of Statistical Mechanics*, **2**, P02002, 2012

[22] J.J. Fruin. *Pedestrian planning and design.* Elevator World Inc., 1987.

[23] G. Flötteröd, G. Lämmel. Bidirectional pedestrian fundamental diagram. *Transportation research Part B*, **71**, 194-212, 2015

[24] Transportation Research Board, Special Report 209, *Highway Capacity Manual*. National Research Council, Washington, DC, 1994.

[25] A. Ebrahimpour, L.L. Fitts. Measuring coherency of uman-induced rhythmic loads using force plates. *ASCE Journal of Structural Engineering*, **122**, 829-831, 1996.

[26] A. Ebrahimpour, A. Hamam, R.L. Sack, W.N. Patten. Measuring and modeling dynamic loads imposed by moving crowds. *ASCE Journal of Structural Engineering* **122**, 1468-1474, 1996

[27] H. Grundmann, M. Kreuzinger, M. Schneider. Dynamic Calculations of footbridges. *Bauingenieur*, **68**, 215-225, 1993

[28] F. Tubino, L.Carassale, G. Piccardo, Human-induced vibrations on two lively footbridges in Milan, *Journal of Bridge Engineering* ASCE, tentatively accepted, 2015.

[29] F. Tubino, G. Piccardo, Tuned-Mass-Damper optimization for the mitigation of human-induced vibrations of footbridges, *Meccanica*, **50(3)**, 809-824, 2015.

COMPDYN 2015
5th ECCOMAS Thematic Conference on
Computational Methods in Structural Dynamics and Earthquake Engineering
M. Papadrakakis, V. Papadopoulos, V. Plevris (eds.)
Crete Island, Greece, 25–27 May 2015

EXPERIMENTAL INVESTIGATINO ON COHERENCE FACTOR OF RHYTHMIC JUNMPING AND ITS APPLICATION FOR SIMULATION OF CROWD JUMPING LOAD

Ziye Pan[1], Yonglei Zhao[2],Jun Chen[3*]

[1] Master candidate, Department of Structural Engineering
A422, Tumu Building, Shanghai, 200092, PR China
987734852@qq.com

[2] Master, Tongji Architectural Design (Group), Co., Ltd
1230# Siping Rd., Shanghai, 200092, PR China
ylzhao.666@163.com

[3] Professor, State Key Laboratory of Disaster Reduction in Civil Engineering, Tongji University
A409, Tumu Building, Shanghai, 200092, PR China
cejchen@tongji.edu.cn

Keywords: Coherence Factor, Three-dimensional Motion Capture Technique, Individual Jumping, Simulation of Crowd Jumping Load.

Abstract. *This paper investigates the coherence factor of rhythmic jumping and its application for simulation of crowd jumping load. Experiments were conducted using three-dimensional motion capture technique on single person jumping. Seventy three test subjects participated in the experiments and each of them conducted four test cases of different frequencies. Thirty nine markers were attached to each test subject during the test. The jumping frequency was simulated by a metronome. The time lag between metronome time and landing time was proposed as the coherence factor of rhythmic jumping. The statistical analysis of experimental data shows that probability distribution characteristics of coherence factor can be described as the combination of uniform distribution and Beta distribution, which are corresponding to individual random jumping and coherent jumping in crowd respectively. The parameters of factor model functions are determined by experimental results. Simulation of crowd jumping load is carried out by combining the coherence factor with single random jumping load model. The simulating method is proved to be reasonable by application examples.*

* Correspondence author, email:cejchen@tongji.edu.cn

1 INTRODUCTION

With the application of high-strength and light-weight building materials and building owner's demands for large column-free open space, large-span floor structures have became more and more popular in assembly buildings, cantilever grandstands, waiting halls, dance halls and so on. For example, the Qingdao Training Center adopt 72m×42m prestressed concrete floor [1] and the Chongqing University Sports Center had a 10m cantilever grandstand[2]. Although these structures are designed for different functions, they share common structural features as low fundamental frequency and small damping. Therefore, these structures are prone to human-induced vibrations which may, when larger than certain threshold value, cause vibration serviceability issue.

There are typical two ways to address the vibration serviceability problem. One is to limit the structure's fundamental frequency to be higher than a given threshold value, the other is to limit the structure's maximum vibration amplitude (typically acceleration) to be lower than a given threshold value. The second way is more reliable since the vibration amplitude is the key parameter for judging vibration level. It is acknowledged that an accurate load model is an important premise for the engineering design. For human-induced load especially for group (crowd) -induced load, such a model is still absent. Experimental investigations have been conducted on human jumping load [2-6]. In China, little research has been done so far on the crowd-jumping load. Due to the difference of body features like average heights, body weights and even culture background, studies in biomechanical fields already prove that different population can have different gait leading to different GRF. Therefore, it is not suitable to use overseas human-induced load directly. Among all human-induced loads such as running, walking, jumping, bobbing, marching on the spot and so on, jumping load has maximum dynamic load factor. Moreover, jumping load is frequently encountered in the design of structures of gymnasium, dancing halls, and music halls.

In this paper, experiments were conducted on human jumping load using three dimensional motion capture system in conjunction with force plates. Seventy-three volunteers participated in the experiments. Based on the experimental data, a new synchronization factor has been introduced to represent the coherence of the crowed jumping load. Group-induced jumping load can then be simulated by combining the synchronization factor with the single person's jumping load model.

2 EXPERIMENT ON INDIVIDUAL JUMPING LOAD

2.1 Experimental arrangement

A series of experiments were conducted to collect individual jumping load records. The experiments were conducted in Gait lab of Ruijin Hospital, Shanghai, China. Vicon 3D motion capture system consisting of 10 T40 infrared cameras was used in the experiments. Moreover, two AMTI OR6-7 force plates were employed to record test subject's jumping load. The forces were sampled at 1000Hz. Thirty-nine reflective markers were attached to every test subject according to a standard template for gait experiment. The trajectories of all the markers were captured by the Vicon system at a sampling frequency of 200 frames per second (i.e. 200 Hz). The whole experiments were monitored by a DV recorder. More details about the jumping experiments can be found in Zhao (2013) [1].

2.2 Test cases

Ginty[3] has analyzed the frequency contents of 210 pop songs and found that 96.2% frequencies of those songs range from 1.0Hz to 2.8Hz, which indicates that persons rhythmic

jumping frequencies also belong to this range when they jumped to music beat. However, it has been considered when the music frequency is lower than1.5Hz, most people can't jump constantly and consistently. For example, The British Standard BS6399:Part 1(1996) indicates the frequency of the crowd consistent jumping ranges from 1.5Hz to 2.8Hz, when beyond this range, it's difficult for people to jump normally. On the other hand, Littler[4] proposed the maximum of the jumping frequency should exceed 2.8Hz, and can be as high as 3.0Hz to 3.5Hz. Consequently, on the basis of those achievements above and the feedback of the volunteers in the preliminary experiment, it is decided to set the jumping test frequency as 1.5Hz, 2.0Hz, 2.67Hz, and 3.5Hz in our experiment. Therefore, each test subjected performed seven test cases: four cases at the above four frequencies which were instructed by a metronome, and three cases at self-chosen slow, normal and fast jumping frequency. 73 volunteers from Tongji University participated in this experiment.

2.3 Statistics of test subjects

After data quality check on the original experimental data, 37 groups jumping load with complete records were selected for further analysis, in which contain 27 man groups and 10 woman groups. The genders, ages, weights, and heights of volunteers are showed as table 1 as below.

Gender	Number	Age (20-29)		Weight (39-88kg)		Height (1550-1850mm)	
		Average	Standard deviation	Average	Standard deviation	Average	Standard deviation
Man	27	23.4	1.7	68.4	10.4	1759	57
Woman	10	22.8	1.5	51.6	7.9	1633	24

Table 1: The basic information statistics of the volunteers.

3 THE COHERENCE ANALYSIS OF THE CROWD JUMPING EXCITATION

The synchronization of crowd jumping is the foundation of modeling the crowd jumping load proposing a reasonable coherence factor (or coherence index) based on experimental records, and studying on its statistical property is a core work and also an essential part where the difficulty lies.

3.1 The definition of coherence factor

Coherence factor is a parameter for analyzing the synchronization of individuals in a jumping crowd. Sim and Blakeborough[5], Fitts[6] and Parkhouse and Ewing [7] introduced different coherence factors based on their experiments. Sim and Blakeborough's suggestion doesn't have clear physical meanings. Ebrahimpour and Fitts's suggestion is only suitable for the condition of two persons, which isn't available for the crowd jumping cases. Parkhous and Ewins's suggestion actually utilizes the first order phase of Fourier series to replace the time history of the jumping load, however, this method will introduce new truncation error.

This paper defines a new coherence factor that is taken as the time difference between time instant of metronome's sound and the time instant of test subject's tiptoe touching the ground. The new coherence factor is illustrated in Figure 1, where Tb is the metronome period. $t_{b,i}$ is the moment of the number i beat. $t_{d,i}$ is lag time difference of the number i jumping, and $t_{t,i}$ is the moment of the number i tiptoe touching ground.

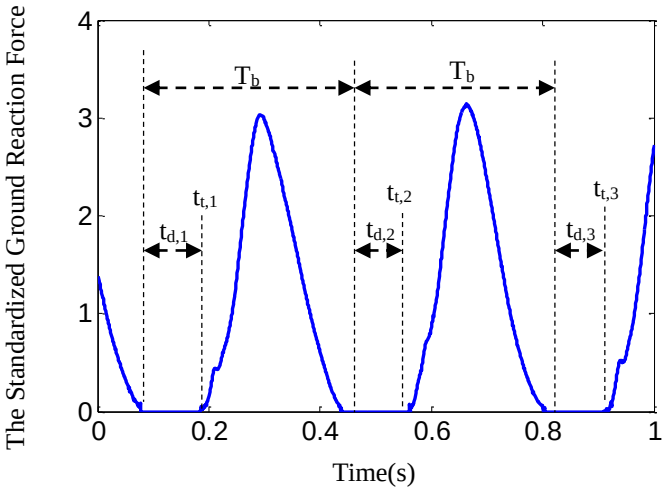


Figure 1: Definition of coherence factor.

3.2 Statistical property of the coherence factor

First of all, split every actually measured reaction force time history into several intervals due to the metronome' sound time instant (shown as the middle part between the two dotted lines in Figure 1. In other words, every interval is equal to the metronome period, and every interval can be treated as an independent jumping case. In this way, *n* reaction force impulses can be treated as *n* persons jumping one time.

Take the 2.0Hz jumping case for instance, a 30s reaction force time history usually contains 60 jumping periods, which we can regard as 60 persons jumping one time. This experiment has totally measured 37 reliable reaction force time history curves, so we can regard these 37×60 reaction force impulses as 37×60 persons jumping one time. Finally, diversity of jumping coherence can be obtained by statistically analyzing every time lag of those reaction force impulses.

Every time lag of reaction force impulse has been given as the following Equation:

$$t_{d,i} = t_{t,i} - t_{b,i} \qquad (0 < t_{d,i} < T_b) \tag{1}$$

In order to compare the frequencies under different test cases, the time lag $t_{d,i}$ should be standardized by the metronome period T_b, like the following Equation:

$$\delta_{d,i} = t_{d,i}/T_b \qquad (0 < \delta_{d,i} < 1) \tag{2}$$

Where, $t_{t,i}$ is the number i moment when tiptoe touching the ground, and $t_{b,i}$ is the number i metronome corresponding moment. After standardization, the range of the time lag changes from $0 < t_{d,i} < T_b$ to $0 < \delta_{d,i} < 1$.

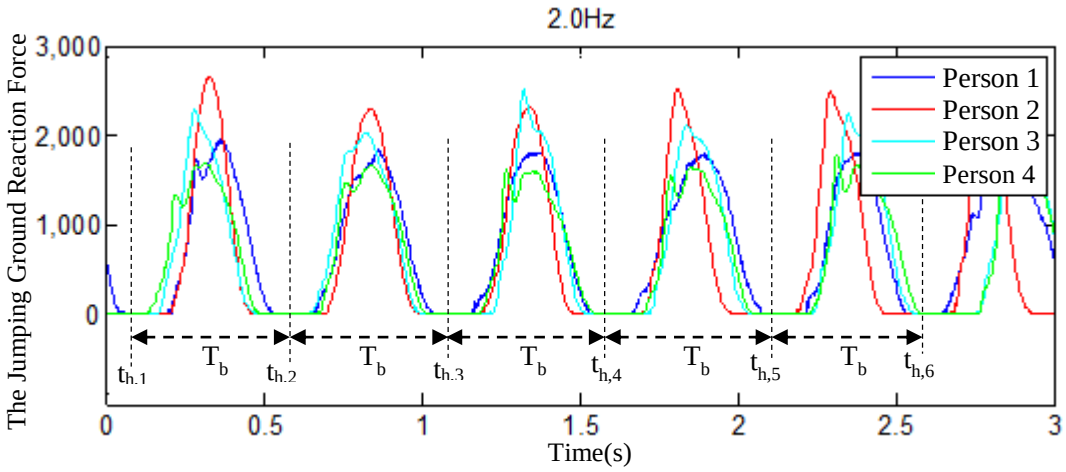


Figure 2:The crowd jumping load coherence diagram

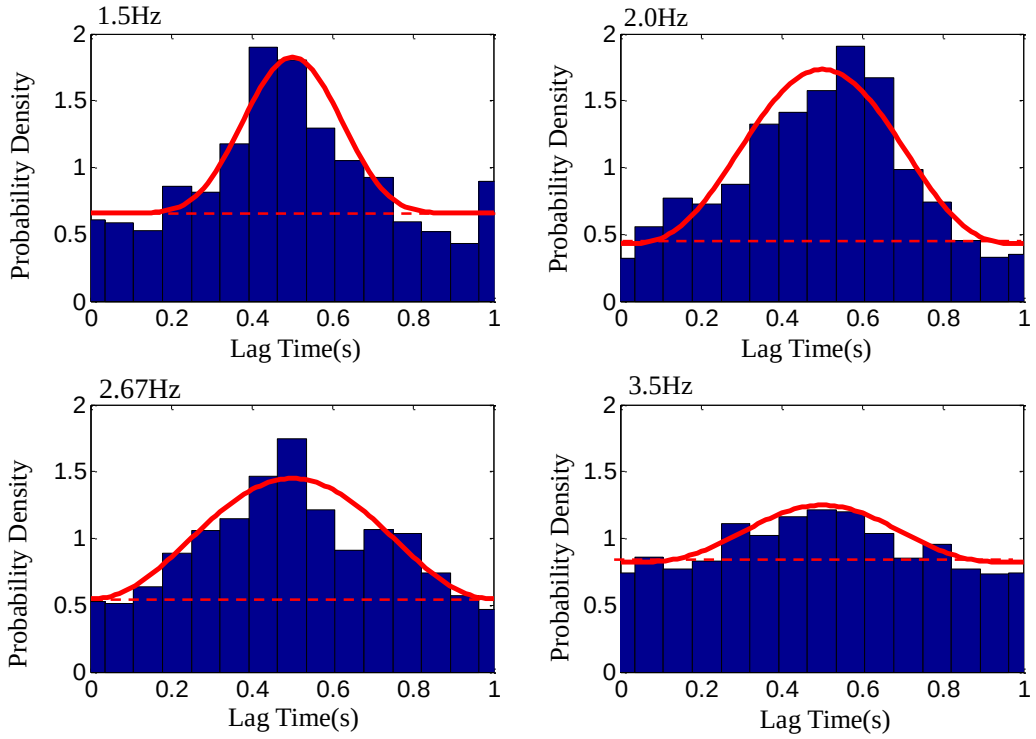


Figure 3: Standardized lag time probability density diagram.

Figure 3 presents the standardized probability density diagram of the time lag under four different frequency cases. Furthermore, every diagram can be approximately treated as a symmetric figure superposed by two parts, namely the rectangle under the red dotted line and the convex above the dotted line. In conclusion, this probability density function can be

modeled by adding up the two functions which represent each part respectively, and the Equation has been provided below.

$$f(x) = p_1 f_1(x) + p_2 \tag{3}$$

Where, $f_1(x)$ is standard Beta probability density distribution function, as shown in Equation (4), and p_1, p_2 are real numbers with the range of [0,1] and $p_1 + p_2 = 1$.

$$f_1(x, \gamma, \eta) = \frac{1}{B(\gamma,\eta)} x^{\gamma-1}(1-x)^{\eta-1} \tag{4}$$

Where, $B(\gamma, \eta) = \int_0^1 x^{\gamma-1}(1-x)^{\eta-1}dx, \gamma > 0, \eta > 0, 0 \le x \le 1$.

In Equation (3), p_2 stands for the position of the dotted line on the vertical coordinate, namely the height of the rectangle under that red dotted line, and the height value reflects the random part of this rhythmic jumping excitation. Moreover, it also means the bigger p_2 is, the greater proportion of random will be, namely, the worse coherence will be shown.

The shape of the Beta probability density distribution function depends on two parameters γ and η, which can change from uniform distribution to approximately normal distribution and from symmetry to asymmetry with the domain of 0 to 1. When $\gamma = \eta$, the shape of this function is symmetry.

When $\gamma \neq \eta$, the shape of the function is asymmetry. It has been discovered in Figure 3 that lag time has a symmetry distribution, so it is reasonable to utilize symmetry fitting function to approach it, namely let $\gamma = \eta$ in Equation (4). Thus, the number of unknown parameters are reduced from 3 to 2. At last, utilize the least square method to evaluate unknown parameters, and the result are shown in Table 2.

Frequency（Hz）	P_2	γ
1.50	0.66	9.46
2.00	0.43	4.36
2.67	0.55	3.37
3.50	0.82	4.71

Table 2: The result of fitting parameter.

Note from Table 2 that when the jumping frequency is 2.0Hz, or 2.67Hz, p_2 is relatively smaller, which also means the jumping action has a relatively better coherence. However, when the jumping frequency is relatively lower, like 1.5Hz, a long time interval exists between the tiptoe touching the ground and the begin of the next jumping, which make the jumping become a discontinuous action, thus causing a worse coherence. In contrast, when the jumping frequency is 3.5Hz, this case has already approached the upper boundary of the crowd jumping action, as a results, it's hard to keep jumping by such high frequency, thus causing the coherence worse as well.

3.3 The relation between coherence and jumping frequency

Jumping frequencies other than the above four jumping frequencies will be considered for practical application. Therefore, it's necessary to investigate the relation between the jumping frequency and coherence factor. Based on the existing research achievements for the range of jumping frequency and the knowledge of the parameter variation tendency in Table 2, this

paper assumes that when metronome frequency is under 1.0Hz or above 4.0Hz, because of the restriction of physiological condition, it is impossible for people to follow the rhythm of metronome to complete random jumping action. In conclusion, it is assumed that when the metronome frequency changes in the range of $f \leq 1.0$ or $f \geq 4.0$, $p_2 = 1$.

As shown in Figure 4, the red circles stand for actual measurement in Table 2, and the red boxes stand for the assumed values when the jumping frequency is 1.0Hz or 4.0Hz. By utilizing polynomial fitting, it has been found that cubic polynomial fitting is able to reflect the parameter variation tendency very well, and also has a better fitting goodness. Therefore, the relation between coherence factor p_2 and the jumping frequency can be fitted by cubic polynomial well, which is given in Equation (5). Additionally, what can be presented from Figure 4 is when the jumping frequency is changing around 2Hz, the jumping action has the best coherence, or the jumping coherence will become worse.

$$p_2 = \begin{cases} -0.0821f^3 + 0.8425f^2 - 2.4920f + 2.7420 & 1.0 < f < 4.0 \\ 1 & f \leq 1.0 \; or \; f \geq 4.0 \end{cases} \tag{5}$$

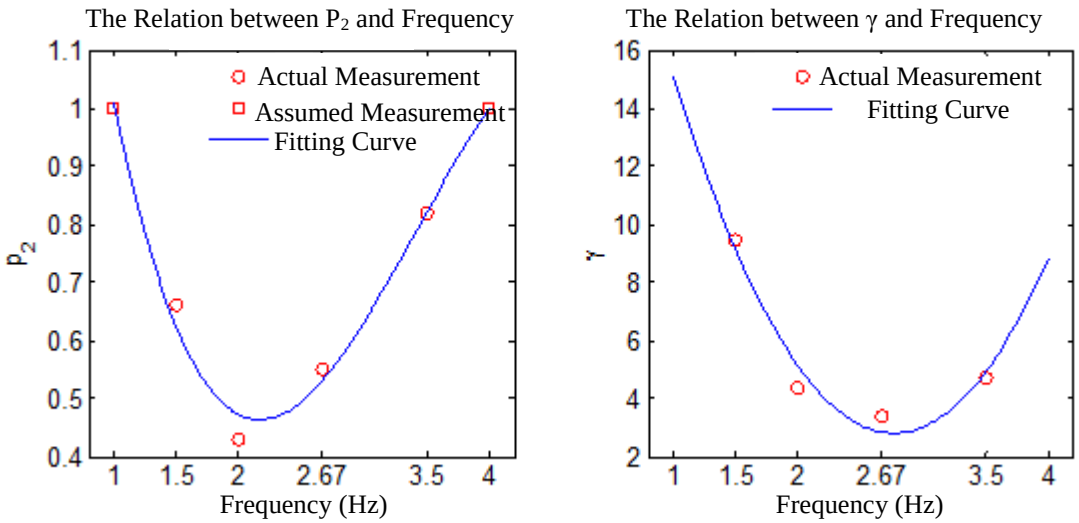


Figure 4: The relation between jumping coherence and jumping frequency.

As for the second parameter γ, utilize quadratic polynomial to fit the actually measured points, as shown in Figure 4. The red circles stand for the measured points, and the blue lines stand for quadratic polynomial fitting curve. In Equation(3), the constrain condition is $p_1 + p_2 = 1$, and when f≤1.5 or f≥3.5， parameter $p_1$is relatively small, which also means the function $f_1(x)$has less influence on f(x). In other words, the value of parameter γ in $f_1(x)$has less effect on the whole function f(x), so we won't discuss the details of γ.

$$\gamma = 3.9550f^2 - 21.9200f + 33.1200 \qquad 1.0 < f < 4.0 \tag{6}$$

4 MODELING OF THE CROWD JUMPING LOAD

Based on the above jumping coherence factor and single person's jumping load model, the crowd jumping load model can be simulated.

4.1 The single jumping load model

A complete jumping process can be divided into three parts, namely touching the ground, the beginning of jumping and soaring in the air. These three parts are demonstrated in Figure 5. In order to precisely describe these three actions, this paper defines three parameters, namely jumping period, contacting time and impulse factor. In Figure 5, the blue full line stands for the ground reaction force normalized by body weight, and T_p is the jumping period, namely the time difference between two adjacent moments when people touching ground, and t_p is the contacting time, namely the time between the moment of touching and leaving in one period. K_p is the peak factor that defines the maximum value of the ground reaction force.

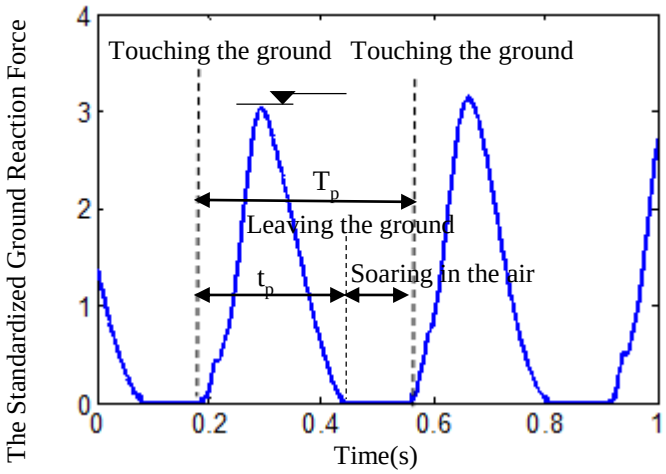


Figure 5: Parameter definitions.

Wang [8] has studied on the dynamic properties of the jumping load and proposed a mathematical model for single person jumping load. The model assumed that the jumping period T_p is a constant value, so only the contact time and the pulse factor are required to model the ground reaction force curve. Contact ratio, which is defined as the ratio between contact time over jumping period, follows approximately normal distribution. The mean and standard deviations of contact ratios for different jumping frequencies are summarized in Table 3.

Frequency of Test cases	1.5Hz	2.0Hz	2.67Hz	3.5Hz
Mean	0.7023	0.6660	0.6734	0.6692
Standard deviation	0.0913	0.0823	0.0685	0.0686

Table 3: The statistical property of the contact rate [8]

We also found that the peak factor could be expressed by the contact ratio as given in Equation (7). Finally the jumping load curve of each jumping event can be represented by piece-wise function as given in Equation (8).

$$K_p = \begin{matrix} 1.554/\alpha & (1.5\text{Hz}) \\ 1.913/\alpha & (2.0Hz) \\ 2.145/\alpha & (2.5Hz) \\ 2.097/\alpha & (3.5Hz) \end{matrix} \tag{7}$$

Where, contact rate α can be represented by $\alpha = t_p/T_p$.

$$\mathrm{F(t)} = \begin{cases} K_P G \sin(\pi t/t_p), & 0 \le t \le t_p, f_p = 1. \\ K_P G \sin^2(\pi t/t_p), & 0 \le t \le t_p, f_p = 2.0 - 3.5Hz. \\ 0 & t_p \le t \le T_p. \end{cases} \tag{8}$$

4.2 The application steps of the crowd jumping load model

Based on proposed coherence index and single person's jumping load model, the simulation of the crowd jumping load can performed by the following steps:

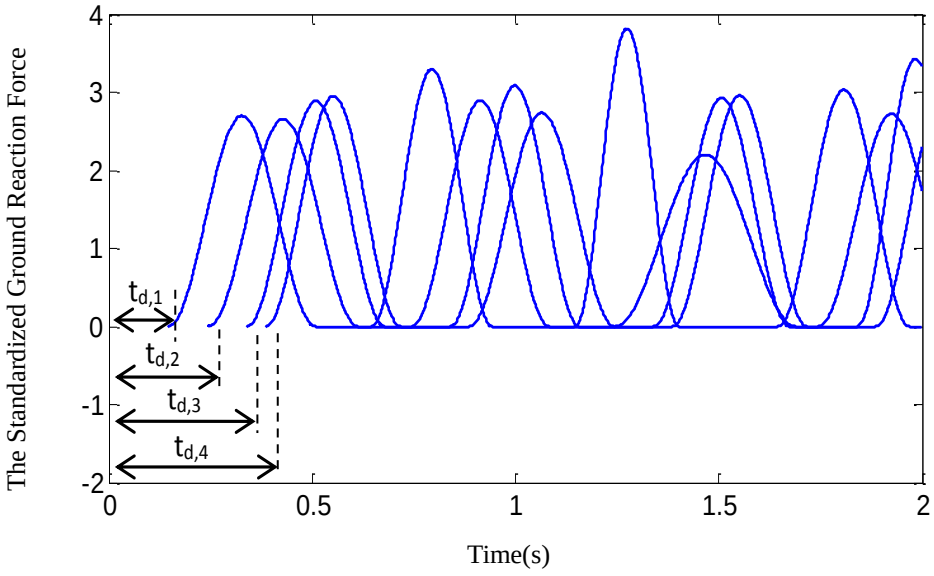


Figure 6: The start points of the crowd jumping load time history curve

(1) Determine the number of persons N in the crowd. Determine the number of impulses M in every jumping time history curve. That's to say we have a crowd of N persons each of them jumps M times.

(2) Determine the jumping frequency f_p, and accordingly determine the mean value and standard deviation of contact ratio from Table 3.

(3) Under normal distribution assumptions, randomly generate M contact ratios α_i in one jumping load time history curve.（i=1~M）

(4) Calculate M impulse factor K_p^i, the jumping period $T_p = 1/f_p$, and the touching time $t_p^i = T_p \alpha_i$ by Equation (8).

(5) Put K_p^i,T_p and t_p^i into Equation (9) to get M single jumping load curves, and integrate M curves into one jumping load time history curve.

(6) Repeat step (2) to step (5) N times. N time history curves can be generated for N persons. Then based on the probability density distribution function (4) of the time lag to randomly generate N the start points of the time history curve, and finally ensure the time differences between each curve (Figure 6).

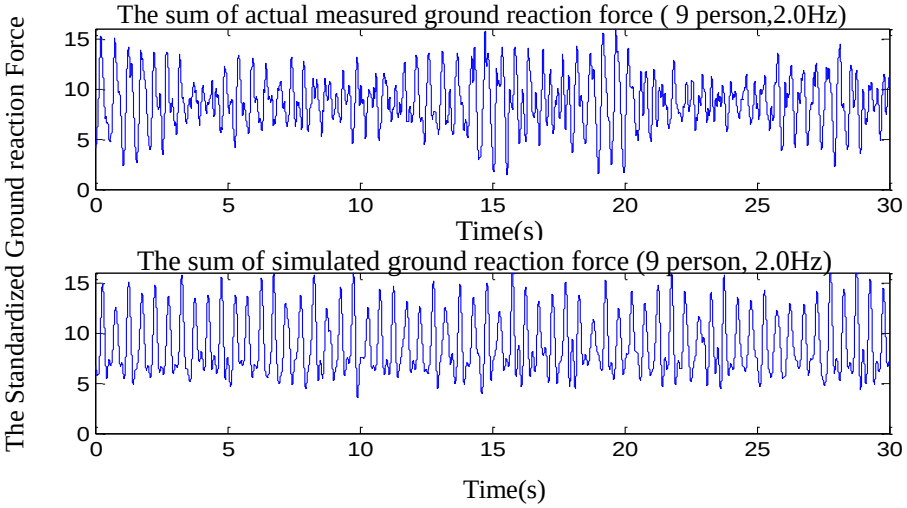


Figure 7: Actual measured load versus simulated load.

Figure 7 presents the comparison diagram between the actual measurement and simulation of the crowd jumping load, where horizontal coordinate stands for time, and vertical coordinate stands for the total reaction force of the nine-people jumping loads, in addition, metronome frequency has been set as 2.0Hz.

5 CONCLUDING REMARKS

Based on single person's jumping load experiments, this paper has suggested a new coherence factor that is defined as the difference between the time instant of the feet touching the ground and metronome beat. The new factor has clear physical meaning and easy-to-use in simulating the crowd load. Statistical properties of the factor have been investigated using measurements from jumping tests at four fixed frequencies as 1.5, 2.0, 2.67 and 3.0Hz. Crowd-induced loads can be simulated by combing coherence factor with single persons jumping load. Application examples show that the suggested simulation procedure gives reasonable results.

REFERENCES

[1] Yonglei Zhao, Modeling and application research of the crowd jumping load experiment, Shanghai: Tongji University, 2013.

[2] Bin Jian, Shanghong Qin, Pingyou Chen et al, The design for the prestressed frame structural of the cantilever bleacher in Chongqing University Gymnasium, *Building Structure*, 2003, 33(2).

[3] Ginty D, Derwent J M, Ji T. The frequency rangs of dance-type loads, *The Structural Engineer*, 2001, 79(6): 27-31.

[4] Littler J D, Frequencies of synchronized human loading from jumping and stamping, *The Structural Engineer*, 2003.

[5] Sim J, Blakeborough A, Williams M S et al, Statistical model of crowd jumping loads, *Journal of Structural Engineering*, 2008, 134(12): 1852-1861.

[6] Ebrahimpour A, Fitts L L, Measuring Coherence OF Human-induced Rhythmic Loads Using Force Plates, *Journal of Structural Engineering*, 1996.

[7] Parkhouse J G, Ewins D J. Vertical dynamic loading produced by people moving to a beat, *Proceedings of ISMA2004*, 2004.

[8] Ling Wang, The research for dynamic property of jumping excitation experiment and load model, Shanghai: Tongji University, 2012.

[9] Racic V, Pavic A and Brownjohn JMW (2013), Modern facilities for experimental measurement of dynamic loads induced by humans: a literature review, Shock and Vibration, 20(1), 53-67

COMPDYN 2015
5th ECCOMAS Thematic Conference on
Computational Methods in Structural Dynamics and Earthquake Engineering
M. Papadrakakis, V. Papadopoulos, V. Plevris (eds.)
Crete Island, Greece, 25–27 May 2015

DYNAMIC ANALYSES OF A CURVED CABLE-STAYED FOOTBRIDGE UNDER HUMAN INDUCED VIBRATIONS: NUMERICAL MODELS AND EXPERIMENTAL TESTS

Elisa Bassoli[1], Paola Gambarelli[1], Laura Simonini[1] and Loris Vincenzi[1]

[1] DIEF – University of Modena and Reggio Emilia
via Pietro Vivarelli, 10 – 41125 Modena
e-mail: elisa.bassoli@unimore.it; paola.gambarelli@unimore.it; laura.simonini@unimore.it; loris.vincenzi@unimore.it

Keywords: Footbridge, human-induced vibrations, dynamic identification, model updating, experimental tests.

Abstract. *Nowadays, pedestrian bridges are increasingly lively and slender structures due to the development of improved structural materials and aesthetic requirements. As a result of this trend, contemporary footbridges are more and more prone to human-induced vertical and lateral vibrations that can compromise the comfort serviceability conditions. The goal of this paper is to characterize the dynamic behaviour of a curved cable-stayed footbridge subjected to pedestrian loads starting from experimental tests and numerical dynamic analyses. The dynamic behaviour of the footbridge is investigated thanks to an experimental campaign performed by means of an advanced MEMS-based SHM system. Accelerations due to ambient vibrations are recorded and the modal parameters of the structure are identified by means of a classic identification method. Then, to investigate the dynamic response of the footbridge subjected to pedestrian actions, a wide number of experimental tests were performed with different-sized groups of pedestrians crossing the footbridge, running, free or synchronized walking with different pacing frequencies. Then, a finite element model of the footbridge is developed and calibrated so that the numerical dynamic predictions agree with the experimental modal properties. Then, to simulate dynamic loading conditions due to a single pedestrian or a crowd of people crossing the footbridge, two mathematical models are examined. In the first approach both the non-calibrated and the updated FE model are adopted to evaluate the vertical dynamic response of the footbridge when subjected to pedestrian loads. Dynamic analyses are performed by simulating the pedestrian walking through a periodic load model representing the human-induced force as a deterministic force. The second approach is based on the solution of the equation of motion via modal decomposition, considering multi-harmonic forces and experimental mode shapes and frequencies. Finally, the accelerations obtained through the mathematical approaches are compared with the experimental results.*

1 INTRODUCTION

Over the last decades, cable-stayed bridges and footbridges have reached great importance and popularity thanks to the ease of construction, the economical convenience and the reduction of the deck bending moments due to the benefit of cables. Nevertheless, footbridges are generally slender structures due to the structural solutions adopted even for aesthetic requirements and the using of deformable elements, and so they are increasingly sensitive to dynamic vibrations induced by pedestrian actions [1, 2] that can compromise the comfort serviceability conditions. Hence, the full assessment of footbridge dynamic behaviour with reference to pedestrian dynamic amplifications is a topical issue in the vibration serviceability analyses [3-5].

Accurate FE models are often needed to investigate the dynamic behaviour of these kinds of structures and to reproduce the pedestrian effects through dynamic analyses considering adequate human-induced load models. However, the complex shapes of these structures usually involve difficulties in accurate structural modelling and simulation. Therefore, model updating procedures are required to develop reliable models starting from the comparison between the structural dynamic behaviour investigated through dynamic tests and its numerical model response [6].

This paper is a part of a research that aims to characterize the dynamic behaviour of a curved cable-stayed footbridge subjected to pedestrian loads starting from experimental tests and numerical dynamic analyses. The case study is the Pasternak footbridge that is about 270 meters long and 3 meters wide and it crosses an important freeway in Modena (Italy). It is composed of two steel towers 18 meters high that support the steel-concrete deck by means of 6 pairs of cables.

First of all, the dynamic behaviour of the footbridge is investigated thanks to an experimental campaign performed by means of an advanced MEMS-based SHM system [7]. Through the dynamic tests the accelerations due to ambient vibrations (wind) are recorded and the modal parameters (frequencies, mode shapes and damping ratios) are identified [8]. To study the dynamic behaviour of the footbridge subjected to pedestrian loads, several experimental tests were performed with different-sized groups crossing the footbridge running, free or synchronized walking with different pacing frequencies. To simulate dynamic loading conditions due to a single pedestrian or a crowd of people crossing the structure, two mathematical models are examined. In these models, vertical dynamic actions depend on the pacing frequency, the walking (or running) speed, the step length, the number of people involved and the synchronous action modelling. To apply the first approach, a finite element model is developed and calibrated so that the numerical dynamic predictions agree with the experimental modal properties [9, 10]. Both the updated and the non-calibrated models are used to evaluate the dynamic response of the footbridge when subjected to pedestrian loads. In the second approach, the equation of motion is solved via modal decomposition, considering a multi-harmonic force model and experimental mode shapes and frequencies. The numerical accelerations obtained through dynamic analyses are finally compared with the experimental results.

2 THE PASTERNAK FOOTBRIDGE

The dynamic tests were performed on a steel curved cable-stayed footbridge, the Pasternak footbridge (see Figure 1*a*), by means of the SHM602 system. The structure was built in 2008 and it overpasses an important freeway crossroad in Modena (Italy). The footbridge is about 270 meters long and it is composed of a curved central span 60 meters long and two access ramps with bent layout. The main span is sustained by cables linked with two V-shaped steel towers each of them composed of inclined masts connected with each other by X-bracings

(Figure 1*b,c*). Each mast is approximately 18 meters high with an inclination of about 15 degrees with respect to the vertical. The lateral access ramps are composed of several spans supported by V-shaped precast concrete piers. The structure is about 3 meters wide and it has a constant radius of approximately 32 meters. The deck is composed of steel trusses that support a concrete slab. The main span stiffening spatial truss girder (see Figure 1*d*) is composed of circular hollow profiles, connected with the steel-concrete deck. At the deck level trusses are made up of two open-shaped concrete-filled chords connected in plane with H- and L-shaped profiles. The masts are constituted by prismatic hollow profiles with variable sections linked with each other with H-shaped bracings by means of bolted connections. Each cable is composed of two or three elements connected with each other and anchored to the towers with plates and bolts. Finally, the footbridge is provided with steel parapets along the entire length.

3 DYNAMIC IDENTIFICATION

Dynamic tests were performed to investigate the dynamic behavior of the footbridge subjected to ambient vibrations. Then, the modal properties of the footbridge are identified by applying identification techniques to the experimental measurements [8].

The experimental campaign was carried out by means of an advanced MEMS-based SHM system. The main components of the SHM602 system consist in a controller and storage unit and in several intelligent bus-connected sensing units. Each sensing unit can record the accelerations along two orthogonal axes and the temperature. Thanks to local digital filtering techniques and oversampling rates implemented, these units relied on MEMS sensors can exhibit



Figure 1: (*a*, *b*) General view of the Pasternak footbridge; (*c*) detail of the V-shaped steel towers and (*d*) the spatial truss girder.

a noise level of about 0.3÷0.5 mg [7] and thus lower than those measured by other MEMS-based systems [11].

3.1 The dynamic tests

To estimate as many natural modes as possible, several setups were arranged. For each set-up, 12 sensors were installed on the vertical elements of the steel parapets at the deck level by means of magnets. The sensors were mainly placed in the curved central span to acquire accelerations along two orthogonal axes, in the vertical and horizontal directions. The sensors located at the towers measured accelerations in the radial (transverse) and longitudinal directions, and some sensors in the main span were installed to record vertical and longitudinal accelerations. In the first setup, sensors were arranged quite equally spread on both deck sides along the whole central span. In the second and third setups, sensors were mainly arranged on the north or the south side of the central span to cover the maximum possible length of the footbridge and to better identify the greater number of modes. For all test arrangements, some sensors were placed at the same locations to combine data obtained from different setups. Setups no. 2 and 3 are reported in Figure 2*a*,*b* respectively.

3.2 Results of dynamic identification

To identify the footbridge dynamic parameters, the Power Spectral Density (PSD) [12] matrix of the acquired accelerations is calculated and the Enhance Frequency Domain Decomposition method is applied [13].

Examples of PSDs achieved from vertical accelerations are reported in Figure 3. Ten modes (6 vertical modes and 4 torsional ones) involving the central span with frequencies in the range 1.462÷12.061 Hz are clearly identified. Values of identified damping ratios are in the range 0.12÷0.67%. The identified natural frequencies and damping ratios are reported in

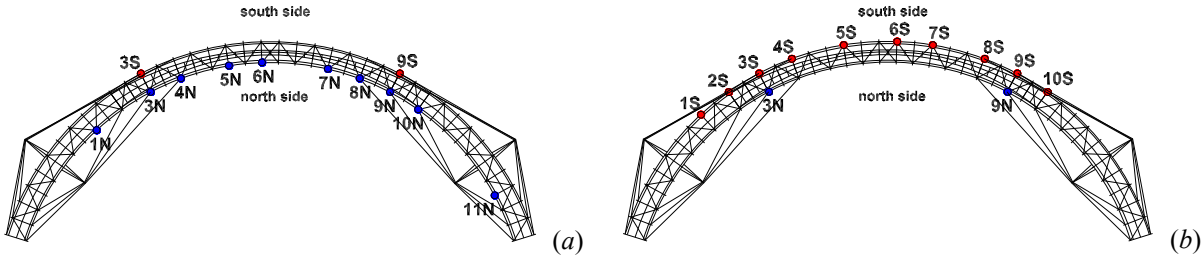


Figure 2: The second (*a*) and the third (*b*) experimental setups

Mode Type	Experimental Frequency [Hz]	Damping Ratio [%]
1st Vertical	1.462	0.67
2nd Vertical	2.274	0.56
3rd Vertical	3.210	0.39
4th Vertical	4.949	0.40
1st Torsional	6.551	0.30
2nd Torsional	7.605	0.15
6th Vertical	8.772	0.22
3rd Torsional	9.409	0.24
7th Vertical	11.453	0.18
4th Torsional	12.061	0.12

Table 1: Experimental modes

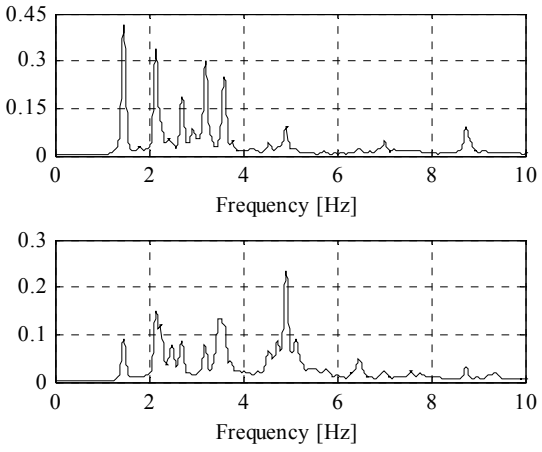


Figure 3: Examples of PSDs obtained from vertical accelerations

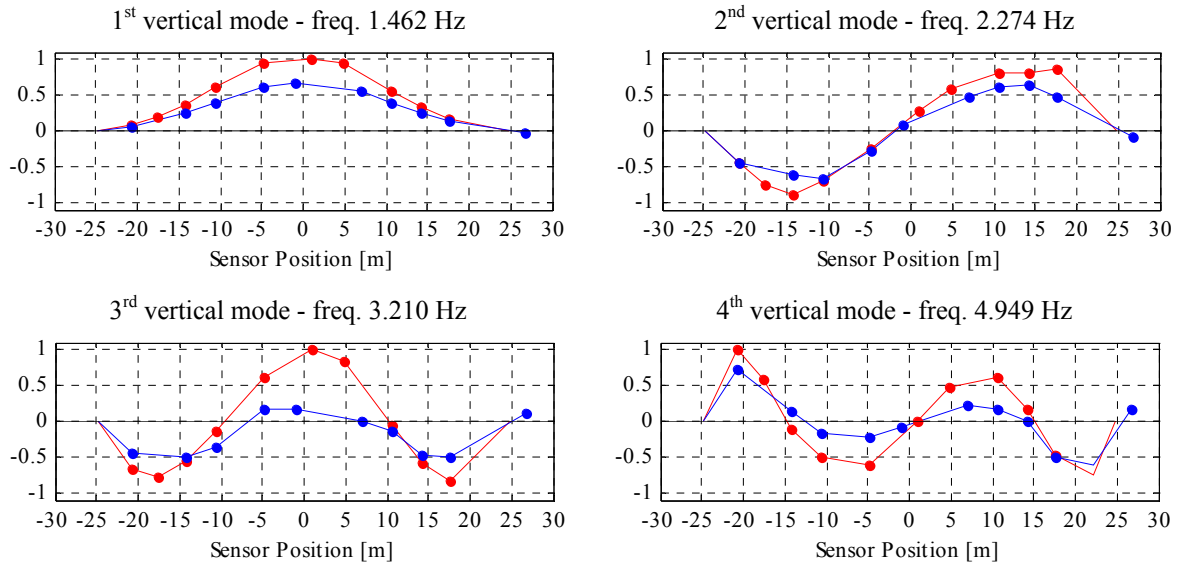


Figure 4: Vertical components of some of the more relevant experimental modes

Table 1 while Figure 4 shows the vertical components of the first 4 mode shapes. The blue and the red colour represent the north and the south side of the footbridge respectively.

4 FINITE ELEMENT MODEL AND MODEL UPDATING

A FE model of the footbridge is developed representing the curved main span and portions of the lateral spans. To accurately model the steel-concrete deck and the towers, beam and shell elements are used; particularly, steel members and cables are modeled adopting 1D elements while the concrete slabs and the towers with 2D elements. Constraints are applied at the base of towers and piers. The equivalent density of longitudinal chords is defined by considering the weight increment due to the parapets and the concrete fillings.

The modal analysis provides for frequencies and mode shapes. The first four mode shapes are shown in Figure 5. Referring to the developed model (called FE Model A in the following) numerical frequencies are reported and compared with the experimental ones in Table 2. Numerical results match quite well all the experimental modes, with errors in frequencies in the range 2÷4% and MAC values greater than 94%. All the identified modes are characterized by prevailing vertical displacements, thus the MAC values are calculated considering only the vertical components of the mode shapes.

Then, the FE model is adjusted by means of a model updating procedure so that the numerical frequencies and mode shapes match as better as possible the experimental ones; the updated model is identified as FE Model B in the following. The optimization process is carried out through an improved surrogate-assisted evolutionary algorithm. Surrogate-assisted evolutionary strategies use efficient computational models, as response surface or high polynomial functions, to approximate the objective function. Recently, they received considerably increasing interest in reducing the computational effort in optimization problems, mainly when the evaluation of the objective function is highly time consuming [14]. In this work, the so-called DE-Q algorithm is adopted [9, 10]; it combines the robustness of the DE algorithm with the computational efficiency due to a second-order surrogate approximation of the objective function. The optimal parameters are obtained through the minimization of an objective function defined as the relative error between numerical and experimental modal frequencies and mode shapes. To obtain a reliable comparison, the numerical and the experimental mode shapes are coupled by using the MAC. In the dynamic analyses described in Section 6, the

human-induced walking forces are simulated by using harmonics with frequencies not greater than 4.5 Hz. Therefore, the first four vertical modes (modes no. 1÷4 in Table 1) with frequencies in the range 1.462÷4.949 Hz are selected for the optimization process. Moreover, only the vertical components of mode shapes are considered as the purpose of the presented work is to evaluate the vertical effects of pedestrians on the footbridge.

In Table 2, frequencies of the updated model (FE Model B) are reported and compared with the experimental results. The numerical frequencies match very well the experimental ones, with error values smaller than 1% for the first 2 modes and about 1% for the 3rd and the 4th modes; MAC reaches values greater than 95% for all modes.

It is worth noting that after the updating procedure the correlation between numerical and experimental mode shapes is almost perfect as regards the vertical components (high MAC values that are computed considering only the vertical components of the mode shapes). Instead, the transverse mode shape components are not accurately appreciated by the numerical model; as a matter of fact the model exhibits transverse deformations considerably higher than those obtained experimentally particularly referring to the first mode.

5 PEDESTRIAN-INDUCED ACCELERATIONS

To study the dynamic behaviour of the footbridge subjected to pedestrian loads, several experimental tests were performed with pedestrians crossing the footbridge running and free or synchronized walking with different pacing frequencies.

A number of crowd tests were carried out with different-sized groups of pedestrian walking on the footbridge. In some tests, the crowd was asked to cross the footbridge at their own normal walking pace. Afterwards, 12 pedestrians were asked to walk in single file starting from one end of the footbridge. Tests with pedestrians on the north (see Figure 6*a*) or the south side of the deck were performed considering different pacing frequencies. In addition, several tests were carried out arranging a stream of 44 walking pedestrians that completely filled the deck. To achieve a better synchronisation between pedestrians a megaphone and a

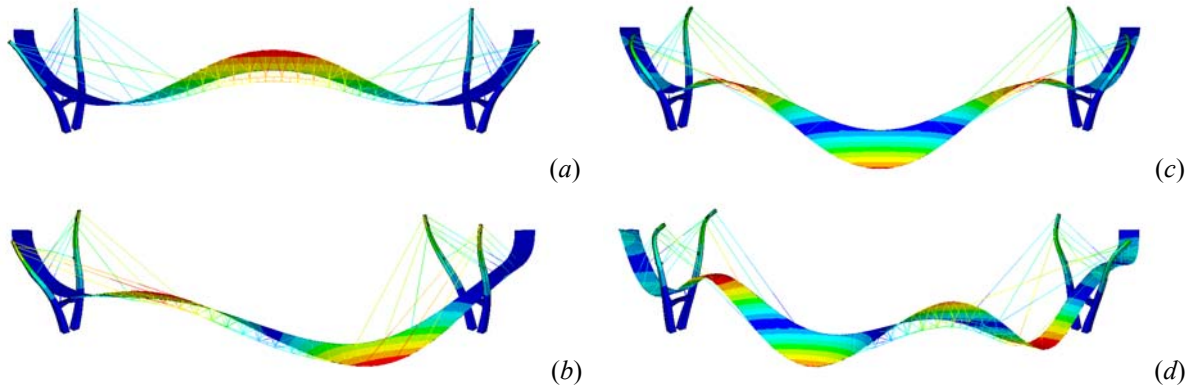


Figure 5: Numerical mode shapes: 1st (*a*), 2nd (*b*), 3rd (*c*) and 4th (*d*) vertical modes

Mode Type	Experimental Frequency [Hz]	FE Model A			FE Model B		
		Freq. [Hz]	Error [%]	MAC [%]	Freq. [Hz]	Error [%]	MAC [%]
1st Vertical	1.462	1.419	-2.94	99.7	1.455	-0.51	97.7
2nd Vertical	2.274	2.365	+4.00	97.4	2.269	-0.23	97.1
3rd Vertical	3.210	3.249	+1.21	94.4	3.256	+1.42	95.9
4th Vertical	4.949	4.837	-2.25	97.9	4.904	-0.91	97.6

Table 2: Experimental and numerical modes

metronome were always used to control the step frequency that generally ranged between 1.2 Hz to 2.2 Hz. Several tests were performed with a step frequency close to the first vertical frequency of the footbridge (i.e. f_s = 1.45 Hz) with an increasing number of pedestrians. Moreover, some tests were also carried out with few people (from 1 up to 4) running at about 2.2 Hz, with the purpose to excite the second vertical mode of the structure. Finally, tests with 44 pedestrians walking in a closed loop on the main span were also performed to excite the first torsional mode of the structure (see Figure 6*b*).

5.1 Recorded accelerations and comfort criteria

In Figure 7 vertical accelerations induced by pedestrians are reported. In each graph, the black line represents the measured accelerations while the red line denotes the root-mean-squared (RMS) accelerations. The experimental measurements show that vertical accelerations caused by pedestrians in unsynchronized tests are about 15÷18 mg (where g indicates the gravity acceleration) corresponding to 0.15÷0.18 m/s^2. The accelerations measured in a test with 44 pedestrians walking at a pacing frequency of 1.2 Hz are reported in Figure 7*a*. In this scenario, vertical acceleration amplitudes between 20÷25 mg were recorded without any evidence of excessive vibration amplitudes. High dynamic amplifications are obtained for a pacing frequency close to the first vertical frequency of the structure. Figure 7*b* shows accelerations induced by 12 pedestrians crossing the footbridge in single file on the north side of the deck with a step frequency of 1.45 Hz (close to the frequency of the first vertical mode). The RMS accelerations reach maximum values of about 80 mg.

Then, accelerations induced by 44 pedestrians walking in a closed loop on the main span with a step frequency of 1.45 Hz are reported in Figure 7*c*. It can be noticed that acceleration values greater than 120 mg are reached only about 25 seconds after the test start; these high accelerations produced feelings of discomfort for pedestrians and then, the test was immediately suspended. After that, accelerations gradually decreased up to 20 mg in about 30 seconds. The long period spent to reach low accelerations confirms the small values of damping ratio obtained by the identification procedure. Even larger vibration amplitudes may have been measured if people had been allowed to continue walking.

Finally, RMS accelerations reached maximum values of about 4 mg when a single person run with a step frequency of 2.2 Hz (Figure 7*d*).

Peaks and maximum RMS values of the vertical accelerations recorded by the monitoring system during the dynamic tests are compared with the comfort criteria given by Eurocode, ISO 10137, Sétra and HiVoSS guidelines, for each different pacing frequency.

Eurocode [15] recommends maximum acceptable acceleration values for the deck of 71 mg (0.7 m/s^2) for vertical vibrations and 20 and 41 mg for horizontal vibrations in normal use and for exceptional crowd conditions, respectively. These recommendations mainly neglect


(*a*)


(*b*)

Figure 6: Dynamic tests: 12 pedestrians in single file on the north side of the deck (*a*) and 44 pedestrians walking in a closed loop on the main span (*b*)

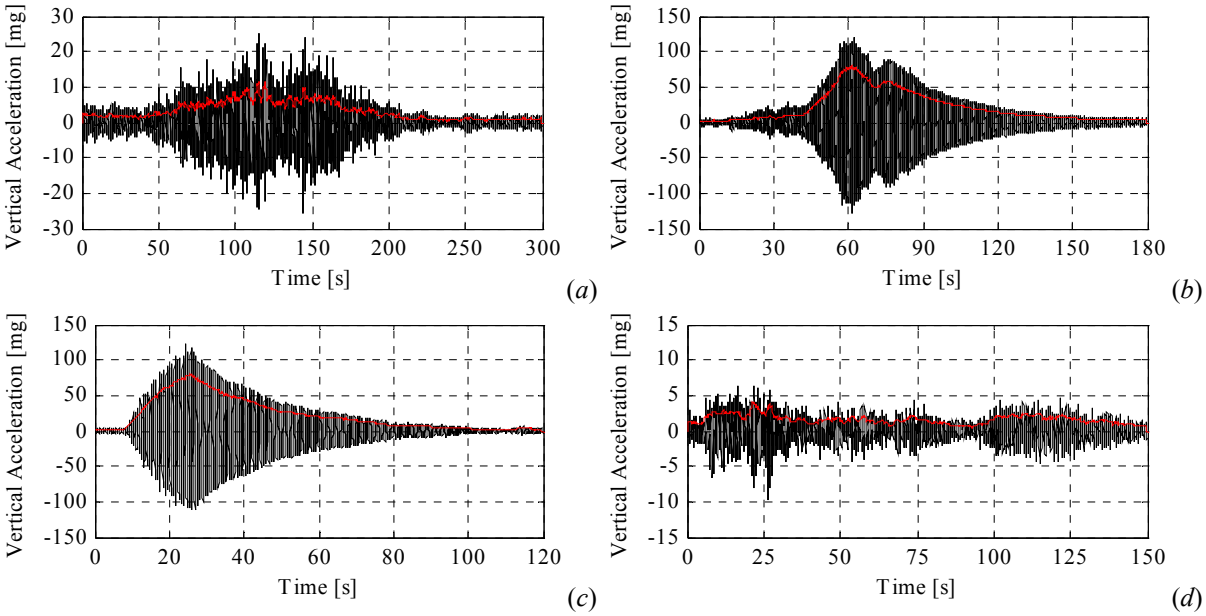


Figure 7: Measured vertical accelerations and RMS acceleration traces due to different loading conditions: a stream of 44 pedestrians walking at a pacing frequency of 1.2 Hz (*a*), 12 pedestrians at 1.45 Hz in single file (*b*), 44 pedestrians at 1.45 Hz in a closed loop (*c*) and a single individual running at 2.2 Hz (*d*)

the vibration frequencies of the structure, the kind and the duration of the human activity. ISO 10137:2007 [16] gives recommendations for the evaluation of serviceability against vibrations of buildings and walkways. Different scenarios are defined considering different crowd concentrations. Threshold acceleration is provided, depending on the natural frequency of the structure and on the traffic condition. Sétra [17] and HiVoSS [18] guidelines present four intervals of acceleration levels with corresponding comfort levels, defined for vertical and horizontal vibrations. Levels are maximum, mean, minimum comfort and uncomfortable.

Results obtained for vertical accelerations are shown in Figure 8. Peak acceleration values measured in the case of 12 pedestrians crossing the footbridge are reported. Eurocode considers acceptable all induced vertical accelerations except for the peak acceleration of 129 mg caused by 12 pedestrians crossing the footbridge at a pacing frequency of 1.45 Hz. This peak exceeds also comfort standards prescribed in ISO 10137. For Sétra and HiVoSS, the peak acceleration of 129 mg satisfies a minimum comfort level; however, for these guidelines, the reached accelerations are only allowed in very dense traffic situation. Accelerations reached for other step frequencies are included in the so-called “mean comfort level”.

6 PEDESTRIAN DYNAMIC LOADS

Dynamic analyses are performed to reproduce pedestrian dynamic effects on the footbridge and, consequently, to compare experimental and numerical maximum accelerations. To carry

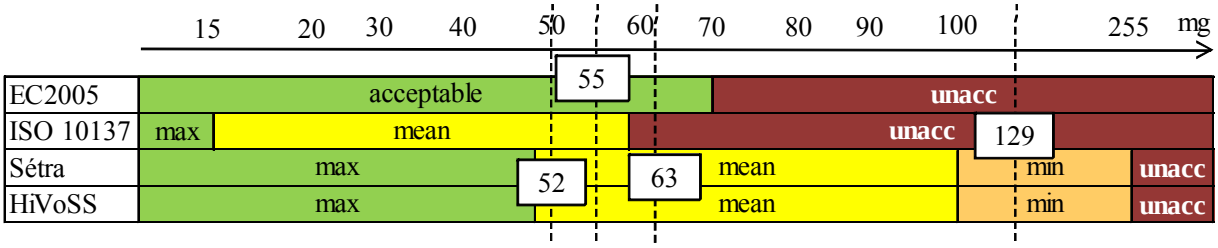


Figure 8: Comparison between comfort criteria and recorded accelerations

out dynamic analyses, mathematical models representing the dynamic forces due to a single pedestrian or a crowd of people crossing the structure are needed.

Pedestrian walking on a structure produces a dynamic force that has components in all three directions. Most of the studies performed to characterize pedestrian-induced force [19-23] show that it depends on the pacing frequency, the walking (or running) speed and the step length. The present work is focused on the simulation of the human-induced force in the vertical direction, adopting the numerical models described in the following. The dynamic walking excitation is commonly modelled as a series of moving single footsteps, for which the time-history of the vertical component is described by a Fourier series. In this study two models to simulate the pedestrian action are adopted. The first model (Model I) is proposed by Li [24] and it represents the human-induced force as a deterministic periodic force, while the second one (Model II), developed by Živanović [25], allows to take into account the inter- and intra-subject variability during walking.

The first model is adopted to perform numerical dynamic analyses with the FE models of the structure. It provides the single step force that is applied to consecutive nodes of the footbridge to simulate the pedestrian crossing. Besides the numerical dynamic analyses performed with the FE models, the dynamic behaviour of the footbridge under pedestrian loads is also investigated solving the differential equations of motion for the decoupled vibration modes. The modal force acting on each SDOF system is characterized through the pedestrian load model developed by [25].

To take into account the effect of pedestrian groups, the load induced by a single pedestrian has to be increased considering the pedestrian number N. In [19, 21] an amplification factor equal to N in the case of pedestrian synchronization or $\sqrt{N}$ otherwise is suggested.

6.1 Simulation Model I

According to the model proposed by [24], the walking force induced by a single pedestrian is simulated using the step-by-step load model described in the following. The step frequency f_s, along with the static weight of the pedestrian G, determines the vertical single foot force $F_v(t)$ as

$$F_v(t) = G\sum_{n=1}^{5} A_n \sin\left(\frac{\pi n}{T_C}t\right), \qquad 0 \le t \le T_C \tag{1}$$

where A_n are the Fourier coefficients, normalized to the weight of the pedestrian, and T_C is the duration of the contact between the foot and the ground, both defined as functions of the step frequency. Values of the Fourier coefficients for the first five harmonics, depending on the pacing frequency, are shown in Table 3. According to the statistical results reported in [26], the ratio of the one foot contact duration (T_C) to the period during which both feet have contact with ground (Δt) is relatively insensitive to the different walking speeds [24] and it is equal to

$$\frac{T_C}{\Delta t} = 4.165 \tag{2}$$

With reference to the Figure 9 the one foot contact duration T_C can be expressed as the sum between Δt and the cycle of the continuous walking force T_S (i.e. the inverse of the step frequency f_s), leading to a constant relation between the step frequency and the contact duration

$$T_C = \frac{1}{0.76 f_S} \tag{3}$$

An example of the single foot force obtained for a step frequency of 1.8 Hz is presented in Figure 9, while Figure 10 shows the continuous foot force. Both forces are normalized to the average weight of the pedestrian *G*.

The described pedestrian load model is adopted to perform dynamic analyses considering the vertical forces due to a single step applied to consecutive nodes of the footbridge model, to simulate the pedestrian walking. For each node, forces are defined by the Eq. 1 for values of time *t* between t_i and t_i+T_C and equal to zero otherwise.

6.2 Simulation Model II

Besides the finite element solution, the dynamic behaviour of the footbridge under pedestrian loads can be investigated solving the decoupled equations of motion. At first, the well-known equation of motion of the MDOF system is defined, where the external force represents the pedestrian moving across the structure. The moving load *P* is expressed as

$$P(t,x) = F(t)\,\delta(x - v_p t) \tag{4}$$

where v_p is the pedestrian velocity, $\delta(x\text{-}v_p t)$ is the Dirac delta function and $F(t)$ is the pedestrian-induced force, defined through the analytical model described in the following.

Based on the principle of modal superposition, the equation of motion is transformed into modal coordinates. Then, integrating over the structure length *x* and using the modal orthogonality conditions, the equation of motion for the *n*-th decoupled mode is obtained:

$$\ddot{y}(t) + 2\xi_n(2\pi f_n)\dot{y}(t) + (2\pi f_n)^2 y(t) = \frac{F(t)}{M_n}\phi_n(t) \tag{5}$$

where $\ddot{y}(t)$, $\dot{y}(t)$ and $y(t)$ are the modal acceleration, velocity and displacement respectively, while ξ_n, M_n, f_n are the modal damping, mass and frequency, respectively. The right hand side of the equation represents the modal force acting on the SDOF system, expressed as the product of the walking force $F(t)$ and the mode shape $\phi_n(t)$ transformed from the space- to the time-domain. As such, the human-induced force is weighted by the mode shape ϕ_n in order to take into account that the force moves across the footbridge and it has a limited duration. The

Fourier coefficients	1.6 Hz ≤ f_s ≤ 2.32 Hz	2.32 Hz < f_s ≤ 2.4 Hz
A_1	-0.0698 f_s + 1.211	-0.1784 f_s + 1.463
A_2	0.1052 f_s - 0.1284	-0.4716 f_s + 1.210
A_3	0.3002 f_s - 0.1534	-0.0118 f_s + 0.5703
A_4	0.0416 f_s - 0.0288	-0.2600 f_s + 0.6711
A_5	-0.0275 f_s + 0.0608	0.0906 f_s - 0.2132

Table 3: Fourier coefficients for the first five harmonics – Model I

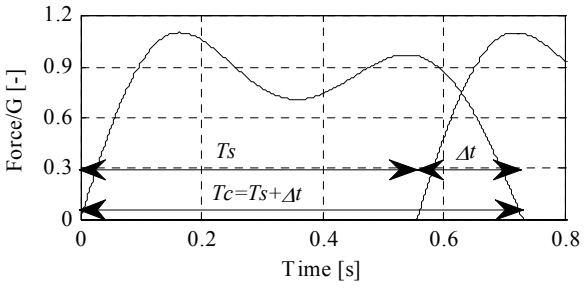


Figure 9: Normalized single foot force obtained for f_s=1.8 Hz – Model I

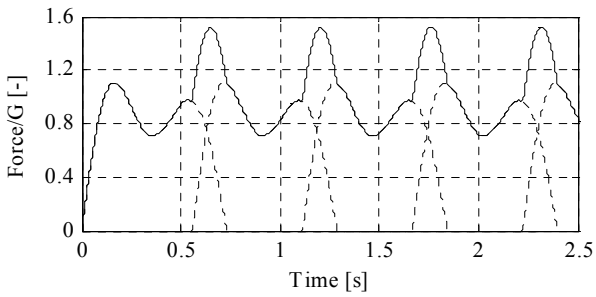


Figure 10: Normalized continuous foot force obtained for f_s=1.8 Hz – Model I

weighted modal force is used to calculate the footbridge modal response based on the time integration of the equation formulated for the modal coordinates. Then, the modal responses obtained for individual vibration modes have to be summed according to the mode superposition principle.

The walking force $F(t)$ is represented through the pedestrian load model proposed by [25] and based on the results obtained from [27]. By analyzing walking force time-histories measured on a treadmill, [27] found that human-induced walking force is not periodic, but rather it is a narrow band random process, meaning that there is a leaking of energy around the main harmonics in the force spectrum. Based on the results provided from Brownjohn [27], Živanović [25] developed a multi-harmonic force model for the calculation of the multi-mode structural response to a single person walking across a footbridge. The proposed model takes into account the inter- and intra-subject variability in the induced walking force. The former term implies that different pedestrians generate different dynamic forces, and the latter means that even a single pedestrian induces a walking force that differs with each step. Variability in the walking force is considered via probability-based modeling, defining the variables that describe the human-induced force through their probability density function. Parameters that describe the variability in walking forces induced by different pedestrians (inter-subject variability) are the walking frequency, the step length and the magnitude of the walking force. As regards the intra-subject variability, imperfections in the human walking can be described through slight changes in the walking frequency and, consequently, in the spectrum of the walking force, resulting in a narrow band spectrum. Using walking force time-histories measured on the treadmill, [27] investigated the frequency content of the force and observed that main harmonics appear at frequencies equal to the pacing frequency and its integer multiples but some sub-harmonics appear at frequencies between the main harmonics. Starting from the frequency content of the walking force, a model representation of the spectrum amplitudes and phases was achieved and the multi-harmonic force model was formulated. For all details about the model see [25].

For the i-th harmonic, occurring at frequency $i\,f_s$, the force in the time domain has the following expression:

$$F_i(t) = G \cdot DLF_i \cdot \sum_{\hat{f}_j = i-0.25}^{i+0.25} \overline{DLF}_i\left(\hat{f}_j\right) \cos\left(2\pi \hat{f}_j f_s t + \theta\left(\hat{f}_j\right)\right) \tag{6}$$

while for the i-th sub-harmonics it is

$$F_i^s(t) = G \cdot DLF_i^s \cdot \sum_{\hat{f}_j^s = i-0.75}^{i-0.25} \overline{DLF}_i^{\,s}\left(\hat{f}_j^s\right) \cos\left(2\pi \hat{f}_j^s f_s t + \theta\left(\hat{f}_j^s\right)\right) \tag{7}$$

where f_s is the step frequency, the product $\hat{f}_j\, f_s$ is a frequency line within the energy range of the (sub-) harmonic analysed and θ is the phase assigned to the current line in the spectrum. This assignment is based on a uniform distribution of phases in the interval $[-\pi,+\pi]$. The dynamic load factors for the harmonics DLF_i and sub-harmonics DLF_i^s analysed are reported in Table 4, while the normalized amplitudes for the same harmonics $\overline{DLF}_i$ and sub-harmonics $\overline{DLF}_i^{\,s}$ for each spectrum line can be found in [25]. Finally, G is the average weight of a pedestrian. The total force induced by a single pedestrian can be obtained as

$$F(t) = \sum_{i=1}^{2} F_i(t) + \sum_{i=1}^{2} F_i^s(t) \tag{8}$$

The force should be reconstructing for time equal to the crossing time T_T that is obtained as

$$T_T = \frac{L}{l_s f_s} \tag{9}$$

where L is the length of the footbridge and l_s is the step length. Note that the model proposed by [25] covers the frequency range of the walking force related to the first five harmonics and sub-harmonics while in the present study only the first two harmonics and sub-harmonics are considered.

In the present study the simulations are performed considering pedestrians crossing the footbridge at defined pacing frequencies, to reproduce the in-situ test conditions. Thus, the variability in the walking frequency is neglected and the step length l_s is deterministically imposed proportional to the step frequency and the pedestrian height h:

$$l_s = 0.24 h f_s \tag{10}$$

As regards the magnitude of the walking force, the mean values of the *DLFs* are considered instead of their probability distributions. Thus, in this study the inter-subject variability is neglected.

An example of the walking force normalized to the weight of the pedestrian G is reported in Figure 11. Note that, differently from the Model I, the continuous foot force is not perfectly periodic, as the intra-subject variability during walking is taken into account.

7 COMPARISON BETWEEN EXPERIMENTAL AND SIMULATED ACCELERATIONS INDUCED BY PEDESTRIANS

Numerical simulations are performed to predict the dynamic behaviour of the Pasternak footbridge under pedestrian load actions. The essential components of the simulation model are the dynamic behaviour of the footbridge, the characterization of the dynamic footfall load and the response calculation.

Two types of simulation analyses are performed: the first type is based on a finite element resolution with the numerical model of the footbridge described in Section 4 and with the step-by-step load model (Model I), where the walking forces are simulated as a series of moving single foot forces as proposed by [24]. The numerical dynamic analyses are performed considering both the un-calibrated FE model (Model A) and the updated FE model (Model B). In the following, results obtained from the un-calibrated model are referred as "Model I-A", while "Model I-B" is used to indicate the results obtained from the updated FE model. The second type of simulation is based on the resolution of the equation of motion in the modal coordinates. In this case, the dynamic properties of the footbridge are those determined experimentally and the walking forces are represented through the model proposed by [25] (Model II). For the presented simulation, the first three natural modes are taken into account.

DLF_1	$-0.2649 f_s^3 + 1.3206 f_s^2 - 1.7597 f_s + 0.7613$
DLF_2	0.07
DLF_1^s	$0.026\ DLF_1 + 0.0031$
DLF_1^s	$0.074\ DLF_1 + 0.01$

Table 4: Dynamic load factors for the first 2 harmonics and sub-harmonics – Model II

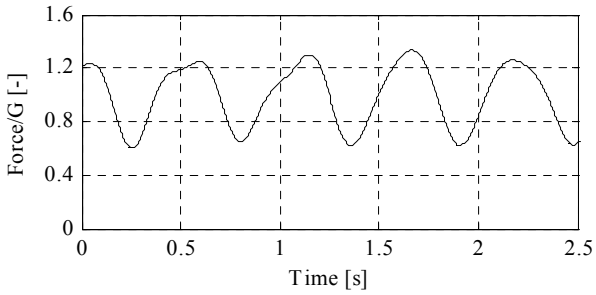


Figure 11: Normalized walking force obtained for f_s=1.8 Hz – Model II

Accelerations obtained from the Model I and II are first compared with each other by means of the amplification factors of the vertical accelerations, considering a single pedestrian crossing the footbridge with different pacing frequencies. Particularly, the pacing frequency is varied from 1 Hz up to 2.5 Hz for the Model I and from 1 Hz to 3.5 Hz for the Model II. Note that the Fourier coefficients for Model I are defined for a pacing frequency from 1.6 Hz up to 2.4 Hz while in the numerical simulations the frequency is varied in the range 1÷2.5 Hz. In the opinion of the authors, this assumption is necessary to investigate also the dynamic behaviour of the footbridge close to the first natural frequency but it may cause inaccuracies in the amplitude response at upper and lower frequencies.

In Figure 12 the response amplification factors obtained from the Model I-A and the Model II are compared with reference to a position at midspan (Figure 12*a*) and at one quarter (Figure 12*b*). Simulation results illustrate the strong dependency of the footbridge acceleration levels on the step frequency of the pedestrian. Regarding results obtained from Model II (blue line), three peaks are clearly present, corresponding to the first three natural modes of the structure. Moreover, two other peaks are obtained for a pacing frequency of 1.14 Hz and 1.60 Hz due to the contribution of higher order harmonics of the walking forces. Particularly, at a step frequency of about 1.14 Hz the fourth harmonic component generates near resonance conditions with the second natural mode, while at a step frequency of about 1.60 Hz the fourth harmonic component generates near resonance conditions with the third natural mode.

Regarding the Model I-A, dynamic amplifications are obtained for pacing frequencies rather different from the experimental ones, as the FE Model A is not calibrated with respect to the experimental modal quantities. It is worth noting the difference in the response amplitude of the two models, especially for frequencies corresponding to the first and the second natural modes (i.e. at about 1.4 and 2.2 Hz).

Then, the acceleration levels recorded at the different measuring positions and for the dif-

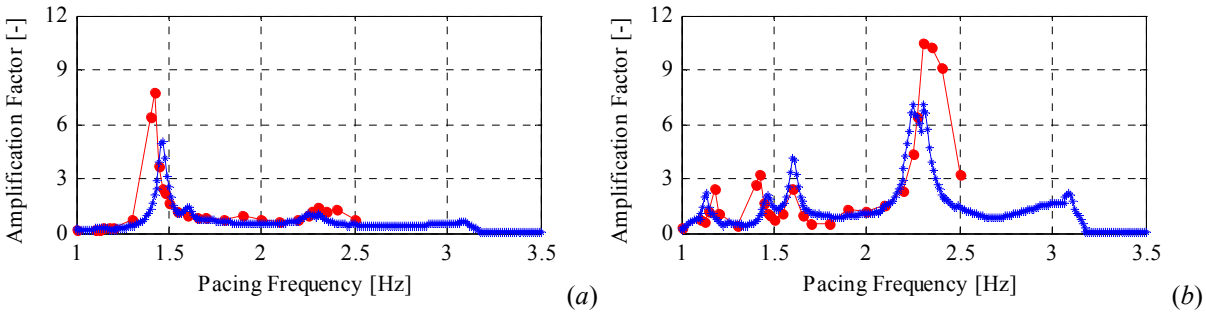


Figure 12: Response amplification factors vs. pacing frequency obtained from the Model I-A (red line) and the Model II (blue line) at midspan (*a*) and at one quarter (*b*)

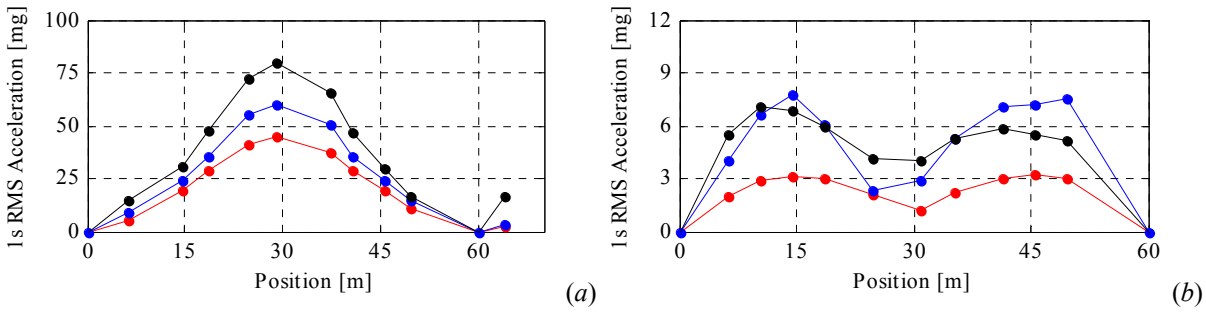


Figure 13: Acceleration levels recorded at the different measuring positions and for different test conditions: 12 pedestrians walking at a step frequency of 1.45 Hz (*a*) and a single pedestrian running at a step frequency of 2.2 Hz (*b*). Black line: experimental RMS accelerations; red line: RMS accelerations from Model I-A; blue line: RMS accelerations from Model II

ferent test conditions (described in Section 5) are compared with those obtained from the Model I-A and II. Results are compared in terms of maximum root-mean-square values of the vertical acceleration, with an averaging period of 1 s. Maximum RMS values of the vertical accelerations caused by 12 pedestrians walking at a step frequency of 1.45 Hz are presented in Figure 13*a*. Blue line represents accelerations simulated through the Model II, the red line indicates values obtained from Model I-A and the recorded response is the black line. It can be clearly seen how the pedestrian action mainly excites the first natural mode of the structure. In the same way, the maximum RMS accelerations caused by one pedestrian walking at a step frequency of 2.2 Hz, close to the second natural mode of the structure, is shown in Figure 13*b*. As regards the Model II, good agreement between the simulated and measured response can be noted, while smaller response amplitudes are obtained from the Model I-A. These inaccuracies are mainly related to the fact that the FE Model A is not calibrated, and so its natural frequencies do not match properly the experimental ones.

This is further demonstrated by the fact that results obtained from the updated FE model match very well the experimental ones, as show in Figure 14,15. At first, the response amplification factors obtained with the updated FE model (Model I-B) and with the Model II are

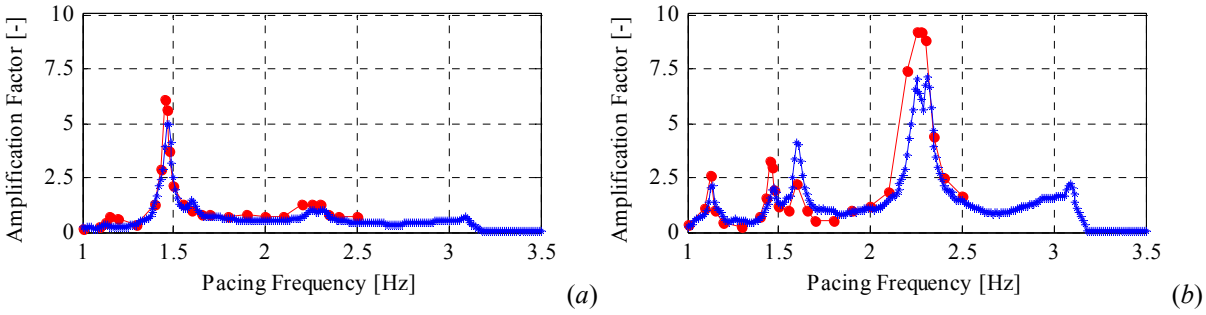


Figure 14: Response amplification factors vs. pacing frequency obtained from the Model I-B (red line) and the Model II (blue line) at midspan (*a*) and at one quarter (*b*)

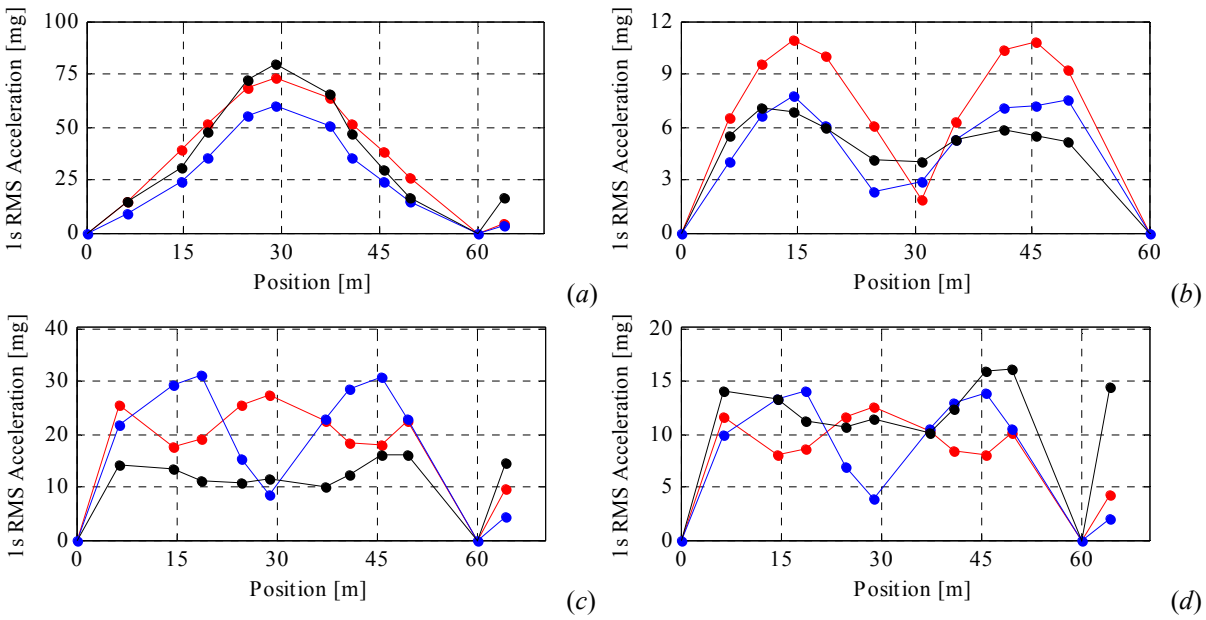


Figure 15: Acceleration levels recorded at the different measuring positions and for different test conditions: 12 pedestrians walking at a step frequency of 1.45 Hz (*a*); a single pedestrian running at a pacing frequency of 2.2 Hz (*b*); 44 pedestrians walking at a pacing frequency of 1.2 Hz, with a synchronization factor equal to *N* (*c*) or 0.5*N* (*d*). Black line: experimental RMS accelerations; red line: RMS accelerations from Model I-B; blue line: RMS accelerations from Model II

compared in Figure 14. The amplification factors are in good agreements and both models well represent the dynamic behaviour of the footbridge. The experimental results are accurately reproduced also with reference to acceleration levels recorded at the different measuring positions. Similar to Figure 13, Figure 15 shows the RMS acceleration values caused by 12 pedestrians walking at a step frequency of 1.45 Hz (Figure 15*a*) and by a single runner crossing the footbridge with a pacing frequency of 2.2 Hz (Figure 15*b*). Simulated results match the experimental ones in both cases; only the response amplitude obtained from the Model I-B is slightly overestimated.

Finally, the recorded accelerations caused by 44 pedestrians walking at a pacing frequency of 1.2 Hz are compared with the simulated ones (Figure 15*c,d*). The frequency of 1.2 Hz indicates a very slow velocity of pedestrian, typical of a crowded situation. If a perfect synchronization between the pedestrians is considered (i.e. by multiplying the accelerations caused by one pedestrian by 44), the simulated accelerations become higher than the measured ones (Figure 15*c*). In fact, even if pedestrians were guided by the metronome signal, the synchronization was not perfectly obtained because of the slow velocity imposed. On the other end, the assumption of total absence of synchronization leads to an underestimation of the induced accelerations, causing maximum values of about 5 mg. It is reasonable to assume that the effective synchronization was intermediate between the perfect and the unsynchronized case; a synchronization factor equal to $0.50\sqrt{N}$ gives the results reported in Figure 15*d*.

8 CONCLUSION

In this paper the dynamic behaviour of the Pasternak footbridge subjected to pedestrian loads is investigated. First of all, an experimental campaign is carried out to characterize the dynamic behaviour of the footbridge subjected to ambient vibrations. Starting from the acquired accelerations, 10 modes (6 vertical and 4 torsional) with frequencies in the range 1.462÷12.061 Hz are clearly identified. Then, several dynamic tests with different-sized groups of pedestrians crossing the footbridge at different step frequencies were performed to investigate the dynamic response of the structure subjected to pedestrian loads. High dynamic amplifications are obtained for a pacing frequency close to the first vertical frequency of the structure; RMS accelerations reach maximum values of about 80 mg considering a group of pedestrians crossing the footbridge with a step frequency of 1.45 Hz. After, a FE model is developed and calibrated, so that numerical frequencies and mode shapes match as well as possible the experimental ones. Then, two mathematical models to simulate the dynamic walking excitations due to a single pedestrian or a crowd of people crossing the footbridge are tested. The first method, based on a periodic load model, is adopted to perform dynamic analyses on both the updated and non-calibrated FE models. In the second approach, the equation of motion is solved via modal decomposition, considering experimental mode shapes and frequencies and the multi-harmonic force model.

Simulation results illustrate the strong dependency of the footbridge acceleration levels on the step frequency of the pedestrian. Accelerations obtained through the mathematical approaches and the experimental tests are generally in good agreements and both simulation models well represent the dynamic behaviour of the footbridge.

As regards the Model II, good agreement between the simulated and the measured response can be noted, mainly due to the direct use of experimental natural frequencies and mode shapes. Moreover, the possibility to take into account the uncertainties in the step frequencies and the walking force (i.e. the inter- and intra-subject variability during walking) is appreciable. As for Model I, the need to develop a proper FE model to obtain numerical accelerations in good agreement with the experimental results is confirmed.

REFERENCES

[1] P. Dallard, T. Fitzpatrick, A. Flint, S. Le Boutva, A. Low, R. Ridsdill Smith, M. Willford, The London Millennium Footbridge. *The Structural Engineering*, **79**, 17–33, 2001.

[2] F. Danbon, F. Grillaud, Dynamic Behaviour of a Steel Footbridge. Characterization and Modeling of the Dynamic Loading Induced by a Moving Crowd on the Solferino Footbridge in Paris. *Footbridge 2005*, Venice, Italy, December 6-8, 2005.

[3] E. Caetano, Á. Cunha, F. Magalhães, C. Moutinho, Studies for controlling human-induced vibration of the Pedro e Inês footbridge, Portugal. Part 1: Assessment of dynamic behaviour. *Engineering Structures*, **32**(4), 1069–1081, 2010.

[4] E. T. Ingólfsson, C. T. Georgakis, J. Jönsson, Pedestrian-induced lateral vibrations of footbridges: A literature review. *Engineering Structures*, **45**, 21–52, 2012.

[5] K. Van Nimmen, G. Lombaert, G. De Roeck, P. Van den Broeck, Vibration serviceability of footbridges: Evaluation of the current codes of practice. *Engineering Structures*, **59**, 448–461, 2014.

[6] O. S. Bursi, A. Kumar, G. Abbiati, R. Ceravolo, Identification, Model Updating, and Validation of a Steel Twin Deck Curved Cable-Stayed Footbridge. *Computer-Aided Civil and Infrastructure Engineering*, **29**(9), 703–722, 2014.

[7] R. Guidorzi, R. Diversi, L. Vincenzi, C. Mazzotti, V. Simioli, Structural monitoring of a tower by means of MEMS-based sensing and enhanced autoregressive models. *European Journal of Control*, **20**(1), 4–13, 2014.

[8] E. Bassoli, P. Gambarelli, L. Simonini, L. Vincenzi, M. Savoia, Dynamic monitoring of the Pasternak footbridge using MEMS-based sensing system. *7th International Conference on Structural Health Monitoring of Intelligent Infrastructure*, Turin, Italy, July 1-3, 2015. [in press]

[9] P. Gambarelli, L. Vincenzi, A surrogate-assisted evolutionary algorithm for dynamic structural identification. *4th International Conference on Engineering Optimization (ENGOPT 2014)*, Lisbon, Portugal, September 8-11, 2014.

[10] L. Vincenzi, M. Savoia, Coupling Response Surface and Differential Evolution for Parameter Identification Problems. *Computer-Aided Civil and Infrastructure Engineering*, 2015. DOI:10.1111/MICE12124

[11] J. Santana, R. van den Hoven, C. van Liempd, M. Colin, N. Saillen, D. Zonta, D. Trapani, T. Torfs, C. Van Hoof, A 3-axis accelerometer and strain sensor system for building integrity monitoring. *Sensors and Actuators A: Physical*, **188**, 141–147, 2012.

[12] J. S. Bendat, A. G. Piersol, *Engineering applications of correlation and spectral analysis, 2nd Edition.* John Wiley & Sons, Inc., 1993.

[13] R. Brincker, L. Zhang, P. Andersen, Modal identification of output-only systems using frequency domain decomposition. *Smart Material Structures*, **10**(3), 441, 2001.

[14] Y. Jin, M. Olhofer, B. Sendhoff, A framework for evolutionary optimization with approximate fitness functions. *IEEE Transactions on Evolutionary Computation*, **6**(5), 481–494, 2002.

[15] EN 1990:2002/A1:2005, *Eurocode - Basis of structural design. Application for bridges*.

[16] ISO 10137:2007*, Bases for design of structures - Serviceability of buildings and walkways against vibrations*.

[17] Sétra, *Footbridges - Assessment of vibrational behaviour of footbridges under pedestrian loading. Technical guide*.

[18] HiVoSS 2008, *Design of Footbridges*.

[19] Y. Matsumoto, T. Nishioka, H. Shiojiri, K. Matsuzay, Dynamic design of footbridges. *Proceedings of IABSE Conference*, Bergamo, Italy, May, 1978.

[20] P. Young, Improved floor vibration prediction methodologies, *Proceedings of ARUP Vibration Seminar,* London, United Kingdom, October 4, 2001.

[21] H. Bachmann, "Lively" footbridges - A real challenge. *Proceedings of the International Conference on the Design and Dynamic Behavior of Footbridges*, Paris, France, November 20-22, 2002.

[22] S. Živanović, A. Pavic, P. Reynolds, Vibration serviceability of footbridges under human-induced excitation: a literature review. *Journal of Sound and Vibration*, **279**(1–2), 1–74, 2005.

[23] S. Nakamura, Model for Lateral Excitation of Footbridges by Synchronous Walking. *ASCE Journal of Structural Engineering*, **130**(1), 32–37, 2004.

[24] Q. Li, J. Fan, J. Nie, Q. Li, Y. Chen, Crowd-induced random vibration of footbridge and vibration control using multiple tuned mass dampers. *Journal of Sound and Vibration*, **329**(19), 4068–4092, 2010.

[25] S. Živanović, A. Pavić, P. Reynolds, Probability-based prediction of multi-mode vibration response to walking excitation. *Engineering Structures*, **29**(6), 942–954, 2007.

[26] A. Ebrahimpour, A. Hamam, R. L. Sack, W. N. Patten, Measuring and modeling dynamic loads imposed by moving crowds. *Journal of Structural Engineering*, **122**(12), 1468–1474, 1996.

[27] J. M. Brownjohn, A. Pavic, P. Omenzetter, A spectral density approach for modelling continuous vertical forces on pedestrian structures due to walking. *Canadian Journal of Civil Engineering*, **31**(1), 65–77, 2004.

COMPDYN 2015
5th ECCOMAS Thematic Conference on
Computational Methods in Structural Dynamics and Earthquake Engineering
M. Papadrakakis, V. Papadopoulos, V. Plevris (eds.)
Crete Island, Greece, 25–27 May 2015

ROBUST VIBRATION SERVICEABILITY DESIGN OF A TUNED MASS DAMPER FOR THE PHÉNIX FOOTBRIDGE

Klaus Lievens[1], Peter Van den Broeck[1], Guido De Roeck[2] and Geert Lombaert[2]

[1] KU Leuven, Department of Civil Engineering, Technology Cluster Construction
B-9000 Ghent, Belgium
e-mail: Klaus.Lievens@kuleuven.be, Peter.VandenBroeck@kuleuven.be

[2] KU Leuven, Department of Civil Engineering, Structural Mechanics
B-3001 Leuven, Belgium
e-mail: Guido.DeRoeck@bwk.kuleuven.be, Geert.Lombaert@bwk.kuleuven.be

Keywords: Vibration Serviceability Assessment, Response Reduction, Tuned Mass Damper, Robust Design, Worst Case

Abstract. *Slender structures such as footbridges may be prone to human induced vibrations such that vibration mitigation devices as TMD's are adopted to increase the structural damping. Both the prediction of the structural response and the tuning of the TMD parameters rely on the modal parameters of the footbridge. These parameters are subjected to uncertainty in design stage, when only an estimation can be made for example using finite element models. After construction, the natural frequency and damping ratio can be measured but variations due to environmental effects such as temperature can result in parameter variations.*

Therefore it is important to take into account these uncertainties for the vibration serviceability assessment and the design of the TMD.

The present paper proposes a robust TMD design which adopts a worst case approach to take into account uncertainties in design stage. The proposed approach is illustrated for the Phénix footbridge. Considering an uncertain natural frequency and damping value for the case study, a worst case approach is adopted to determine the optimal values of the TMD mass, stiffness and damping.

A significant difference is found between the optimal TMD parameters of a nominal and robust tuned TMD. The mass and damping ratio of the robust TMD are found to be much higher than for the TMD tuned at nominal values of the natural frequency and damping ratio. This ensures that the comfort constraints are satisfied in all possible cases.

1 INTRODUCTION

The upcoming of advanced design methods and high strength materials enables the design of slender footbridges characterised by low natural frequencies, possibly in the range of loading frequencies induced by human walking. Recently, several vibration serviceability problems were reported [1, 2].

Currently, the Sétra [3] and HiVoSS [4] guidelines are often used to evaluate the dynamic behaviour of footbridges in design stage. The acceleration levels of the footbridge are evaluated based on calculations with assumptions for both the dynamic behaviour of the construction and the dynamic load.

If the calculated vibration levels exceed the required comfort threshold, a Tuned Mass Damper (TMD) can be included as a passive vibration control device. The TMD serves as an energy absorber and is characterised by its mass, stiffness and damping parameter. The tuning of the TMD parameters is based on the modal parameters of the main structure.

Uncertainties in the modal parameters of the bridge strongly influence the predicted response. Moreover, a TMD tuned for the nominal values of the modal parameters may result in an ineffective response reduction. Therefore, the authors suggest to take into account uncertainties in the modal parameters for the TMD tuning.

In the last decades, two types of optimisation methods were developed to deal with uncertainties in design. A first one is the reliability-based optimisation method (RBO) which optimises the design variables under uncertain conditions to reach a predefined target reliability. A second approach is a robust design optimisation (RDO) resulting in a design less sensitive to the effect of uncertainties [5, 6, 7]. A reliability-based robust design optimisation problem (RBRDO) combines the two aforementioned methods [8].

To obtain a robust design of the TMD that guarantees a prescribed response level despite of the considered uncertainties, a worst case approach is here adopted. This approach is illustrated for the Phénix footbridge in Charleroi. The present contribution compares a TMD tuned at nominal values of the modal parameters with the robust TMD. The paper focuses on the TMD optimisation in design stage. After construction, the uncertainty interval on the modal parameters can be reduced with measurements. A TMD designed in post-construction stage thus may differ from the presented. Also here variations due to environmental effects such as temperature may be expected.

The structure of the paper is as follows. The Phénix footbridge is presented and its vibration serviceability is assessed following the Sétra and HiVoSS guidelines. Subsequently, a deterministic optimisation problem is formulated to determine the parameters of the TMD. The effect of uncertainties on the modal parameters of the footbridge is studied by considering a variation of the natural frequency and damping ratio within a range reasonably expected in design stage. The next section proposes a robust design optimisation of the TMD to deal with these uncertainties. Finally the optimal TMD parameters and the response reduction obtained for the different designs are compared.

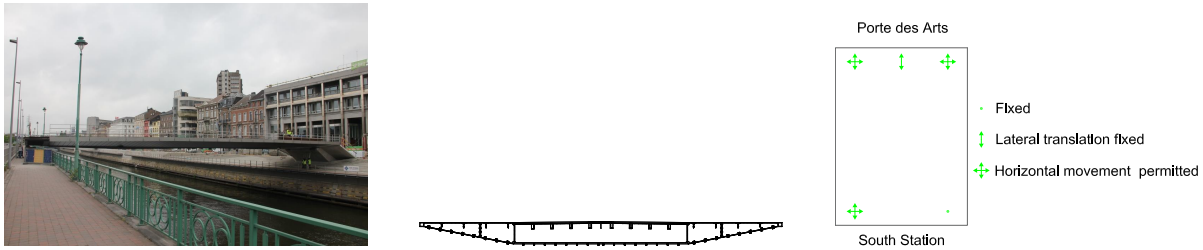
2 THE PHÉNIX FOOTBRIDGE - CHARLEROI

2.1 Description of the footbridge

The Phénix footbridge is a slender construction with a single span of 38.25 m and a width of 13.35 m and is situated nearby the railway station of Charleroi (Belgium). The cross section of the bridge consists of three parts. The midspan is a main box of 6.5 m by 1 m with on both sides, cantilevered tapering I-profiles that are mounted on fixed distances. Figures 1(a) and 1(b)

show a global view of the footbridge and the cross section of the structure respectively.

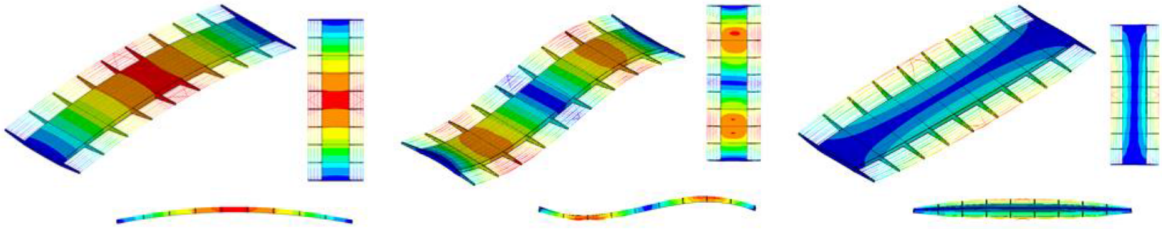
The bridge is supported by four neoprene bearings. Vertical translations are fixed at all corners but horizontal translations are fixed at one. An additional support is added in the middle of one side of the bridge to avoid lateral movements. An overview of the support conditions is given schematically in figure 1(c).



(a) (b) (c)

Figure 1: (a) The Phénix footbridge in Charleroi, (b) Cross section, (c) Support conditions.

The dynamic behaviour of the construction is defined by its modal parameters. The mode shapes as calculated by an initial finite element model (FE-model) are given in figure 2. The first mode has a natural frequency of 1.65 Hz which is in the range of the loading frequencies of the walking load because its natural frequency is lower than 5 Hz.



(a) (b) (c)

Figure 2: Modal parameters of the Phénix footbridge based on the initial FE-model: (a) 1st bending mode ($f_1 = 1.65$ Hz), (b) 2nd bending mode ($f_2 = 5.22$ Hz), (c) 1st torsional mode ($f_3 = 6.15$ Hz)

2.2 Vibration serviceability assessment

For lively footbridges, a vibration serviceability assessment is often performed following the guidelines [3, 4]. The maximal acceleration response is predicted for all sensitive modes assuming resonance conditions disregarding contributions from other modes. A human induced loading for different pedestrian densities is therefore considered. Both the dynamic load and the dynamic behaviour of the structure are discussed next.

2.2.1 Dynamic load

The walking force is considered as a periodic load and thus written as a Fourier series:

$$F_e(t) = G + \sum_{h=1}^{n_h} G\alpha_{eh} \sin\left(2\pi h f_s t - \theta_h\right) \tag{1}$$

with $F_e(t)$ the walking force in direction e (vertical, lateral or longitudinal) in the time domain, G the weight of the pedestrian, h the number of the harmonic load component, α_{eh} the dynamic load factor in direction e for the h^{th} harmonic, f_s the step frequency and θ_h the phase shift for harmonic h. Only the first two harmonic components ($n_h = 2$) are taken into account in the evaluation by the guidelines.

Sétra and HiVoSS simplify the forces due to a group of N random pedestrians into an equivalent load which is uniformly distributed on the bridge deck. Therefore, different traffic classes were introduced representing different pedestrian densities. In table 1, an overview is given of the classes for Sétra and HiVoSS for different pedestrian densities.

	Pedestrian density $d\,[\#\mathrm{pers.}/\mathrm{m}^2]$					
	15 pers.	0.2	0.5	0.8	1.0	1.5
Sétra			Class III	Class II	Class I	
HiVoSS	TC1	TC2	TC3		TC4	TC5

Table 1: Sétra and HiVoSS traffic classes and corresponding pedestrian densities.

The proposed load model consists of an equivalent number of perfectly synchronised pedestrians N_{eq}. A distinction is made between sparse and dense pedestrian densities. For low pedestrian densities, free movements of the pedestrians are possible and the equivalent number depends on the structural damping ξ_j. For higher densities, the walking behaviour of the pedestrians is obstructed and the levels of synchronisation increase. The higher level of synchronisation results in an increased number of equivalent pedestrians. N_{eq} can be found as follows:

$$N_{eq} = 10.8\sqrt{\xi_j N} \qquad \text{for } d < 1\,\mathrm{pers.}/\mathrm{m}^2 \tag{2}$$

$$N_{eq} = 1.85\sqrt{N} \qquad \text{for } d \geq 1\,\mathrm{pers.}/\mathrm{m}^2 \tag{3}$$

The amplitude of the equivalent uniformly distributed load $q_{eq,e}\ [\mathrm{N}/\mathrm{m}^2]$ in direction e is calculated as:

$$q_{eq,e} = \frac{N_{eq}}{S}\alpha_{eh} G \psi_{eh}(f_j) \tag{4}$$

with S the surface of the bridge deck and ψ_{eh} a reduction factor that brings into account the possibility of resonance as a function of the natural frequency f_j of the bridge. The reduction factor depends on the direction of the force (longitudinal, lateral or vertical). Figure 3 shows ψ_{eh} for vertical vibrations as a function of the natural frequency of the system.

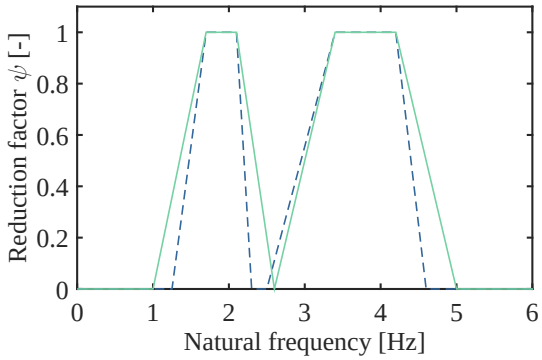


Figure 3: Reduction factor $\psi(f_j)$ for vertical vibrations according to the guidelines Sétra (–) and HiVoSS (- -).

2.2.2 Dynamic behaviour of the construction

The dynamic behaviour of the construction is determined by its modal parameters (natural frequency, mode shape and damping ratio). In design stage, the natural frequencies and mode shapes can be calculated by a FE-model but the damping ratio must be estimated based on prior experience with similar structures. Suggested values for the damping ratio are given by the guidelines. After construction, the modal parameters can be estimated from measurements.

For different pedestrian densities, the natural frequencies of the structure change due to the additional mass of the pedestrians. The guidelines prescribe that, for each traffic class, the natural frequencies and mode shapes must be extracted from a modified FE-model which takes into account the additional mass. For each of these calculated frequencies, the possibility of resonance with the pedestrian's step frequency is evaluated.

If resonance with the first or second harmonic of the load is likely to occur, a response calculation is required. Higher harmonic components of the walking force are not considered in the guidelines.

2.2.3 Response calculation and evaluation

The maximum acceleration $\ddot{u}_{j,e,max}$ for mode j in direction e is calculated as follows:

$$\ddot{u}_{j,e,max} = \frac{q_{eq,e} \sum_i S_i \left|\phi_{j,p(i)e}\right|}{2\xi_j} \max_{p(i)} \left|\phi_{j,p(i)e}\right| \tag{5}$$

with S_i the discretisation of the bridge deck, $p(i)$ the position on the bridge, $\phi_{j,pe}$ the modal displacement on position p in direction e of the j-th mode shape. The latter formula is equivalent to the response calculation assuming resonance for an SDOF-system as follows:

$$\ddot{u}_{max} = \frac{F_{ext}}{2\xi_j m_j} \tag{6}$$

with the following parameters describing mode shape j as an equivalent SDOF-system,

$$m_j = \frac{1}{(\max_{p(i)} \left|\phi_{j,p(i)e}\right|)^2}, k_j = (2\pi f_j)^2 m_j, c_j = 2\xi_j m_j (2\pi f_j) \tag{7}$$

and F_{ext} the amplitude of the external force assumed by the guidelines. Combining equation (5) and (6) allows to calculate F_{ext} as next:

$$F_{ext} = \frac{q_{eq,e} \sum_i S_i |\phi_{j,p(i),e}|}{\max_{p(i)} |\phi_{j,p(i)e}|} \tag{8}$$

Afterwards, the predicted vibration levels are evaluated by means of a comfort scale (maximal, mean, minimal comfort or unacceptable). Note that the vibration serviceability assessment must be performed for the different pedestrian densities considering all excited modes.

2.3 Vibration serviceability assessment for the Phénix footbridge

Because of the low natural frequency of the first mode (f_1 <5 Hz), resonance with the first or second harmonic of the walking force must be considered. For higher natural frequencies, the guidelines assume no risk for resonance with the walking force. Since the Phénix footbridge is a steel structure, the assumed damping ratio is 0.4% as proposed for steel structures [3, 4].

The results of the vibration serviceability assessment for the first mode are given in figure 4. For low pedestrian densities, minimal comfort is guaranteed. In table 2, the acceleration levels are summarised for the different traffic classes of both guidelines. The highest accelerations are predicted for a pedestrian density of $1\,\mathrm{pers./m^2}$ corresponding to Sétra class I.

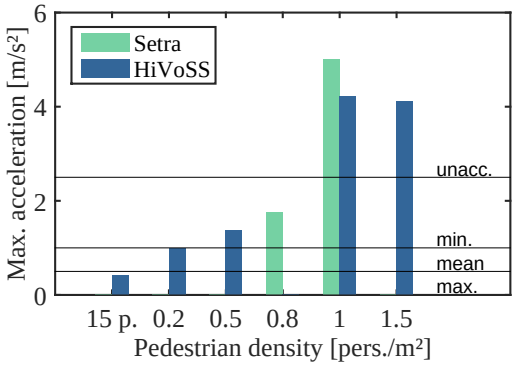


Figure 4: Vibration serviceability assessment of the first bending mode of the Phénix footbridge according to Sétra and HiVoSS (based on initial FE-model).

$d\,[\#\mathrm{pers./m^2}]$	15 pers.	0.2	0.5	0.8	1	1.5
Sétra	/	/	0	1.75	5.00	/
HiVoSS	0.41	0.99	1.37	/	4.22	4.12

Table 2: Predicted acceleration levels $\ddot{u}_{\max}[\mathrm{m/s^2}]$ for the different pedestrian densities.

2.4 Effect of uncertainties on the predicted response

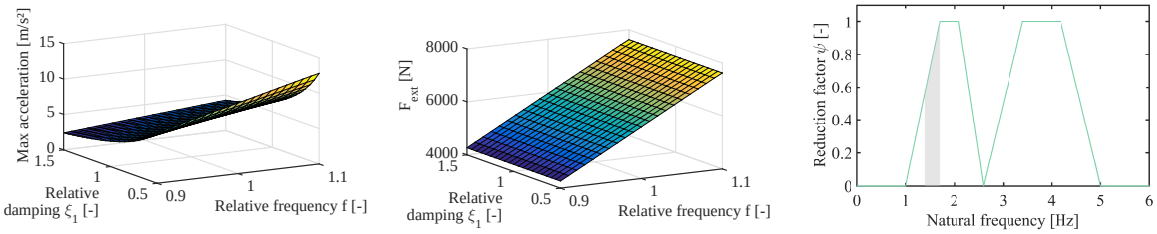
The accuracy of the vibration serviceability assessment strongly depends on the knowledge of the structure's modal parameters. The predictions are however highly sensitive to changes in the natural frequencies and damping ratios.

The influence of deviations in the values of the natural frequency and structural damping is illustrated for the Phénix footbridge. For the natural frequencies, a range of 0.9 to 1.1 times the

nominal value is considered in line with deviations recently observed in a large number of case studies [9]. For the damping ratio, a larger interval of 0.5 to 1.5 times the proposed value of 0.4% is adopted. The same uncertainty range will be assumed in all analyses next:

$$\begin{aligned} 0.9\, f_{j,\text{nom}} \leq f_j \leq 1.1\, f_{j,\text{nom}} \\ 0.5\, \xi_{j,\text{nom}} \leq \xi_j \leq 1.5\, \xi_{j,\text{nom}} \end{aligned} \tag{9}$$

The influence of the assumed uncertainty is investigated for the Phénix footbridge considering Sétra Class I. Figure 5(a) shows that the maximal acceleration predicted by the guidelines is very sensitive to the deviations in the natural frequency. The influence of the uncertain frequency on the external load F_{ext} is given in figure 5(b). The load F_{ext} does not depend on the structural damping because of the calculation of N_{eq} for $d \geq 1\,\text{pers.}/\text{m}^2$ (see equation (3)). The load F_{ext} depends on the natural frequency mainly through the reduction factor ψ_{eh} for the considered frequency range (figure 5(c)) since all other terms are frequency independent in this case.



(a) (b) (c)

Figure 5: Sétra - Class I $(1\text{p.}/\text{m}^2)$: (a) Maximal response for structure without TMD as a function of uncertain natural frequency and damping ratio. (b) Maximal equivalent force F_{ext} as a function of uncertain natural frequency and damping ratio. (c) Frequency dependent load reduction factor for Sétra class I with considered uncertainty range in filled area.

3 DETERMINISTIC DESIGN OPTIMISATION OF TMD

In order to reduce the vibration levels and to satisfy the threshold for pedestrian comfort as described in section 2.2, a TMD is added for the Phénix footbridge. The present section discusses a design of the TMD tuned at nominal values disregarding uncertainties on the modal parameters of the footbridge.

3.1 Deterministic problem formulation

In designs, a trade off must be made between performance and cost-efficiency. The design of the TMD can be described as an optimisation problem where a cost function is to be minimised satisfying a set of constraints. A linear relation between the total cost and the TMD mass m_{TMD} is assumed. The objective function is therefore given by the TMD mass. A limit value of $1\,\text{m}/\text{s}^2$ is chosen as the maximal allowed vertical acceleration $\ddot{u}_{\text{comfort}}$ and is implemented as a constraint. The response is calculated according to equation (5). Second, a constraint is added to limit the relative displacement of the TMD to a tolerable value Δ_{tol} for which a value of $0.05\,\text{m}$ is assumed. An upper and lower limit for the stiffness k_{TMD} and damping c_{TMD} of the TMD is included to ensure buildability. This leads to the following formulation of the optimisation

problem:

$$\begin{aligned} &\underset{m_{\text{TMD}},k_{\text{TMD}},c_{\text{TMD}}}{\text{minimise}} \; m_{\text{TMD}} \\ &\text{subject to} \qquad \ddot{u}_{\text{max}} < \ddot{u}_{\text{comfort}} \text{ (nominal)} \\ &\qquad\qquad\qquad \Delta_{\text{rel}} < \Delta_{\text{tol}} \text{ (nominal)} \\ &\qquad\qquad\qquad k_{\text{min}} \leq k_{\text{TMD}} \leq k_{\text{max}} \\ &\qquad\qquad\qquad c_{\text{min}} \leq c_{\text{TMD}} \leq c_{\text{max}} \end{aligned} \tag{10}$$

with the limit values of the constraints summarised in following table 3. The stiffness and damping constraints are determined in a realistic range so they do not affect the optimal mass.

$\ddot{u}_{\text{comfort}}[\text{m/s}^2]$	1.00
$\Delta_{\text{tol}}[\text{m}]$	0.05
$k_{\text{TMD}}[\text{N/m}]$	[0 - 10^6]
$c_{\text{TMD}}[\text{Ns/m}]$	[0 -10^5]

Table 3: Constraints TMD optimisation problem

3.2 Results nominal TMD design for the Phénix footbridge

Solving the deterministic optimisation problem (10) with the *fmincon* function in Matlab, the TMD parameters are summarised in table 4. The TMD is located at the midpoint of the footbridge, assuming a maximal modal displacement for the damped mode shape on that location. Both the absolute values and the dimensionless TMD parameters are given: mass ratio μ_{TMD} ($= m_{\text{TMD}}/m_1$), frequency ratio ρ_{TMD} ($= f_{\text{TMD}}/f_1$) and damping ratio ξ_{TMD} ($= c_{\text{TMD}}/(2\sqrt{m_{\text{TMD}}k_{\text{TMD}}})$).

μ_{TMD} [%]	ρ_{TMD} [-]	ξ_{TMD} [%]
0.56	0.98	8.56
m_{TMD} [kg]	k_{TMD} [N/m]	c_{TMD} [Ns/m]
835	76239	1364

Table 4: Optimal TMD parameters - nominal design.

A vibration serviceability assessment for the footbridge equipped with the nominal tuned TMD is given in figure 6(a). The acceleration comfort constraint is satisfied for all traffic classes disregarding an uncertain natural frequency and damping ratio of the footbridge. The effect of uncertainties in modal parameters on the response is given in figure 6(b) for Sétra Class I. The maximal acceleration value is very sensitive to deviations in the natural frequency and damping ratio of the footbridge and the worst case scenario is found for a combination of the lowest damping ratio and highest frequency. This can be explained on the basis of figure 5(c).

In order to verify the design constraints, the acceleration response is plotted in figure 6(c). For the nominal set of modal parameters, the response reaches the limit value of $1\,\text{m/s}^2$, which implies that the acceleration constraint is active. An evaluation of the displacements is given in figure 6(d). The relative displacement of the TMD also reaches its upper value of $0.05\,\text{m}$ so this constraint is active as well.

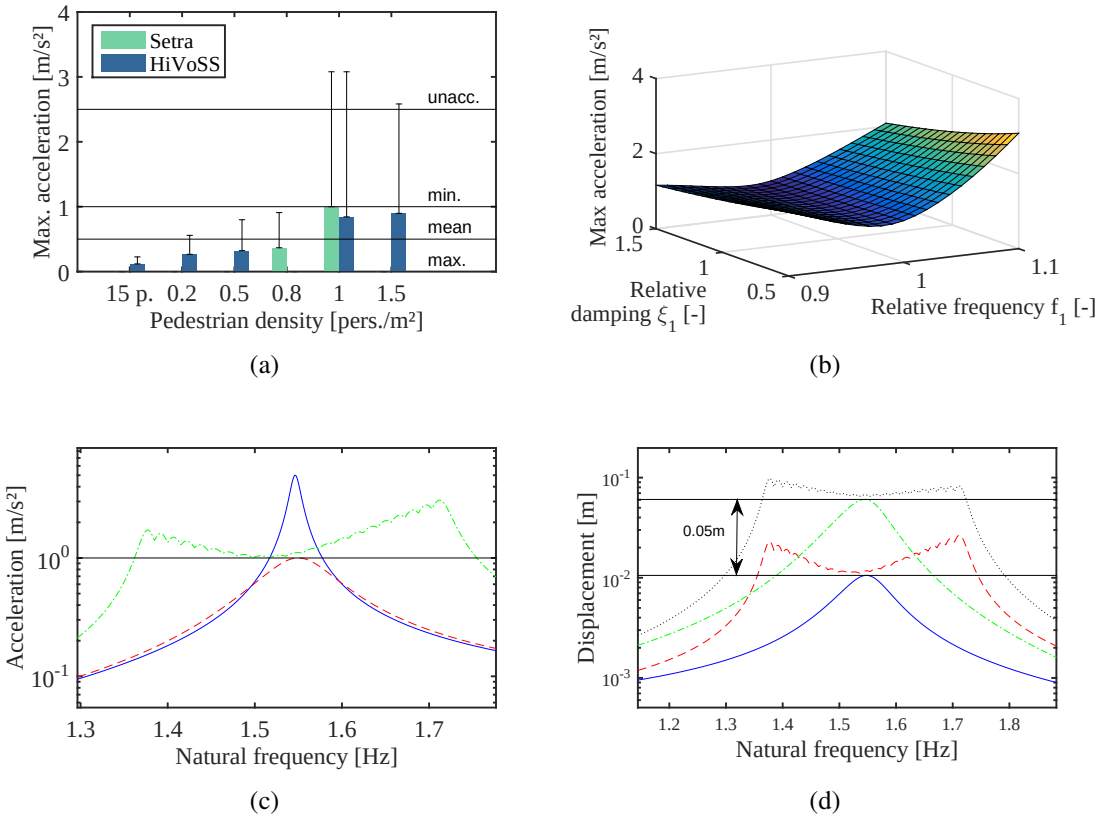


Figure 6: (a) Vibration serviceability assessment for structure with TMD tuned for nominal values of natural frequency and damping ratio. (b) Maximal acceleration response for Sétra Class I under uncertain natural frequency and damping with nominal tuned TMD. (c) Maximal acceleration as a function of frequency for structure without TMD (–), with nominal tuned TMD (- -) and with nominal tuned TMD under uncertain natural frequency and structural damping (enveloping curve of all possible combinations) (-.). In black the $\ddot{u}_{\text{comfort}}$ value. (d) Maximal displacement as a function of frequency: bridge deck (– and - -) and TMD (-. and $\cdots$) displacements respectively with and without uncertainties for nominal tuned TMD.

4 ROBUST DESIGN OPTIMISATION OF A TMD

Both subsections 2.4 and 3.2 show that uncertainties in the natural frequency and damping ratio have a considerable influence on the response evaluation and TMD behaviour. Robust approaches consider the effects of uncertainties in their designs.

In robust design optimisation, Jung and Lee [10] define robustness in a dual way. Sensitivity robustness on the one hand guarantees the insensitivity of the objective function to variations in the design parameters. Feasibility robustness on the other hand, ensures that the final design is situated in a feasible region, in spite of the uncertainties. A good literature review about robust optimisation is given by Beyer and Sendhoff [11]. The authors discuss several techniques including a robust multi-objective optimisation to minimise both the expected value and the standard deviation of the objective function. This formulation is also used by Doltsinis and Kang [7]. Constraints here ensure a specific level of reliability. Very often, a distinction is made between robustness in objective function and robustness in constraints. A frequently used type in the latter class is the worst case approach where the objective function still satisfies the constraints in the worst case [10, 12].

In the present section, a robust optimisation of a TMD is proposed to deal with uncertainties

in the natural frequencies and damping ratios of the bridge.

4.1 Robust TMD design

Uncertainties in loading or in the main system modal parameters are usually disregarded in conventional approaches. Several studies were performed to optimise the parameters of the TMD under uncertain conditions. In [13] a conventional TMD design and two robust optimisations (single and multi-objective) are compared. The analysis showed that the TMD parameters of the conventional and the robust solution considerably differ from each other. Zang et al. [14] propose to determine the TMD mass, stiffness and damping by minimising a linear combination of the mean value and the standard deviation of the peak response solving a multi-objective optimisation problem. It is frequently assumed that the loads are the only uncertain parameter [5]. However, the uncertainty of the main system parameters often has a larger influence on the response than uncertainty on the load [15].

This paper suggests to take into account uncertainties in modal parameters to obtain a robust design.

4.2 Robust problem formulation

The response for the nominal designed TMD satisfies the constraints only for the design point. In order to obtain a robust design, it is necessary to account for the influence of an uncertain natural frequency and damping ratio of the bridge in design stage. A *worst case* approach is adopted here to ensure that the TMD performs well for the entire uncertainty intervals. By minimising the TMD mass, the acceleration comfort constraint ($1\,\mathrm{m/s^2}$) must be satisfied for the worst case scenario considering the uncertain natural frequency and damping ratio. The maximal relative displacement in the worst case scenario is limited to $0.05\,\mathrm{m}$. The robust optimisation problem thus is formulated as in (11). The constraints are summarised in table 3.

$$\begin{aligned} &\underset{m_{\text{TMD}},k_{\text{TMD}},c_{\text{TMD}}}{\text{minimise}} \; m_{\text{TMD}} \\ &\text{subject to} \qquad \ddot{u}_{\max} < \ddot{u}_{\text{comfort}} \text{ (worst case)} \\ &\qquad\qquad\qquad \Delta_{\text{rel}} < \Delta_{\text{tol}} \text{ (worst case)} \\ &\qquad\qquad\qquad k_{\min} \leq k_{\text{TMD}} \leq k_{\max} \\ &\qquad\qquad\qquad c_{\min} \leq c_{\text{TMD}} \leq c_{\max} \end{aligned} \tag{11}$$

4.3 Results Robust TMD design for the Phénix footbridge

The optimal parameters of the robust optimisation problem are summarised in table 5. The robust TMD design is characterised by a much higher mass ratio than for the nominal design in table 4. To satisfy the constraints in the worst case approach, a strongly increased damping is found. Note that for the TMD frequency ratio ρ_{TMD} an interval is given due to the uncertain natural frequency.

μ_{TMD} [%]	ρ_{TMD} [-]	ξ_{TMD} [%]
1.65	0.92-1.13	12.94
m_{TMD} [kg]	k_{TMD} [N/m]	c_{TMD} [Ns/m]
2458	239792	6285

Table 5: Optimal TMD parameters - robust design.

The pedestrian comfort is guaranteed for all traffic classes considering an uncertain natural frequency and damping ratio of the footbridge. Figure 7(a) shows the vibration serviceability assessment for the Phénix footbridge equipped with the robust tuned TMD. Variations in maximal response are rather small as illustrated in figure 7(b) for Sétra Class I. The limit value is reached only in the worst case scenario (combination of lowest damping and highest natural frequency).

Figure 7(c) compares the acceleration response for the bridge with and without TMD. The nominal response with TMD satisfies clearly the constraints and for the worst case response, the maximal allowable acceleration is reached. The constraint for relative TMD displacement is not active for the robust solution (figure 7(d)).

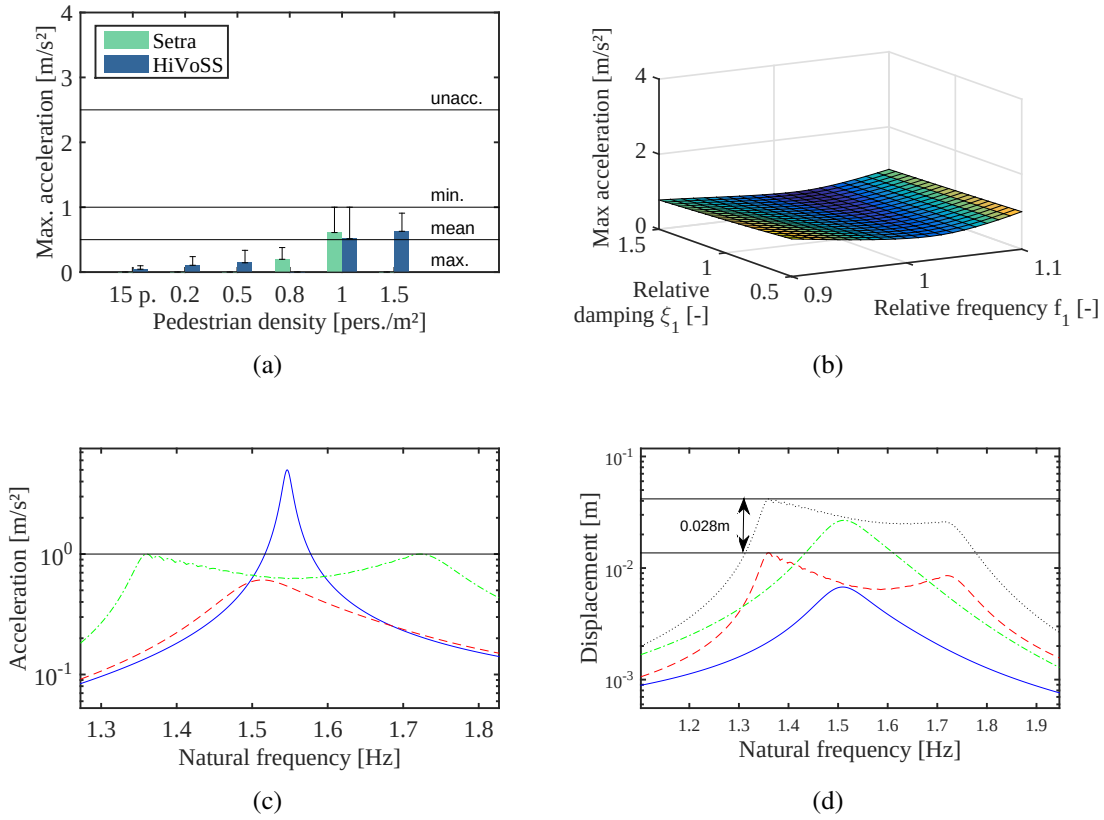


Figure 7: (a) Vibration serviceability assessment for structure with TMD tuned accounting for uncertain natural frequency and damping ratio. (b) Maximal acceleration response for Sétra Class I under uncertain natural frequency and damping with robust tuned TMD. (c) Maximal acceleration as a function of frequency for structure without TMD (–), with robust tuned TMD (- -) and with robust tuned TMD under uncertain natural frequency and structural damping (enveloping curve of all possible combinations) (-.). In black the $\ddot{u}_{\text{comfort}}$ value. (d) Maximal displacement as a function of frequency: bridge deck (– and - -) and TMD (-. and $\cdots$) displacements respectively with and without uncertainties for robust tuned TMD.

5 CONCLUSIONS

Changes in the natural frequency and damping ratio of the footbridge have a significant influence on both the response with and without TMD.

For a TMD tuned at nominal values, the response constraints are satisfied for nominal values of the modal parameters of the footbridge. Considering the proposed uncertainties, the response

reduction is not sufficient. In order to make the performance of the TMD robust with respect to uncertainties, a robust TMD optimisation is characterised by a strongly increased TMD mass and damping ratio. The required constraints are guaranteed in the worst case approach.

The proposed method in this paper allows for a robust design of a TMD based on the simplified load model used by the Sétra and HiVoSS design guidelines. Future research may consider more advanced load models for the pedestrian excitation.

6 ACKNOWLEDGEMENTS

This research is funded by the Agency for Innovation by Science and Technology in Flanders (IWT). Their financial support is gratefully acknowledged.

REFERENCES

[1] P. Van den Broeck, K. Van Nimmen, B. Gezels, E. Reynders, and G. De Roeck, "Measurement and simulation of the human-induced vibrations of a footbridge," in *Proceedings of the 8th International Conference on Structural Dynamics of EURODYN*, (Leuven, Belgium), pp. 941–948, July 2011.

[2] S. Živanović, A. Pavic, and P. Reynolds, "Vibration serviceability of footbridges under human-induced excitation: a literature review," *Journal of Sound and Vibration*, vol. 279, no. 1-2, pp. 1–74, 2005.

[3] Association Française de Génie Civil, Sétra/AFGC, *Sétra: Evaluation du comportement vibratoire des passerelles piétonnes sous l'action des piétons*, 2006.

[4] Research Fund for Coal and Steel, *HiVoSS: Design of footbridges*, 2008.

[5] G. C. Marano and R. Greco, "Robust optimization for tmd with uncertain bounded system parameters and stochastic excitation," *Asian Journal of Civil Engineering (Building and Housing)*, vol. 9, no. 5, pp. 433–455, 2008.

[6] G. I. Schuëller and H. A. Jensen, "Computational methods in optimization considering uncertainties–an overview," *Computer Methods in Applied Mechanics and Engineering*, vol. 198, no. 1, pp. 2–13, 2008.

[7] I. Doltsinis and Z. Kang, "Robust design of structures using optimization methods," *Computer Methods in Applied Mechanics and Engineering*, vol. 193, no. 23, pp. 2221–2237, 2004.

[8] H. Yu, F. Gillot, and M. Ichchou, "Reliability based robust design optimization for tuned mass damper in passive vibration control of deterministic/uncertain structures," *Journal of Sound and Vibration*, vol. 332, no. 9, pp. 2222–2238, 2013.

[9] K. Van Nimmen, G. Lombaert, G. De Roeck, and P. Van den Broeck, "Vibration serviceability of footbridges: Evaluation of the current codes of practice," *Engineering Structures*, vol. 59, pp. 448–461, 2014.

[10] D. H. Jung and B. C. Lee, "Development of a simple and efficient method for robust optimization," *International Journal for Numerical Methods in Engineering*, vol. 53, no. 9, pp. 2201–2215, 2002.

[11] H.-G. Beyer and B. Sendhoff, "Robust optimization–a comprehensive survey," *Computer methods in applied mechanics and engineering*, vol. 196, no. 33, pp. 3190–3218, 2007.

[12] S. Jeong and G. Park, "Reliability-based robust design optimization using the probabilistic robustness index and the enhanced single loop single vector approach," in *10th World Congress on Structural and Multidisciplinary Optimization*, pp. 19–24.

[13] G. C. Marano, R. Greco, and S. Sgobba, "A comparison between different robust optimum design approaches: application to tuned mass dampers," *Probabilistic Engineering Mechanics*, vol. 25, no. 1, pp. 108–118, 2010.

[14] C. Zang, M. Friswell, and J. Mottershead, "A review of robust optimal design and its application in dynamics," *Computers & structures*, vol. 83, no. 4, pp. 315–326, 2005.

[15] T. Igusa and A. Der Kiureghian, "Response of uncertain systems to stochastic excitation," *Journal of engineering mechanics*, vol. 114, no. 5, pp. 812–832, 1988.

COMPDYN 2015
5th ECCOMAS Thematic Conference on
Computational Methods in Structural Dynamics and Earthquake Engineering
M. Papadrakakis, V. Papadopoulos, V. Plevris (eds.)
Crete Island, Greece, 25–27 May 2015

WALKING-INDUCED VIBRATION OF A FOOTBRIDGE

Eleonora Lai[1], **Maria Gabriella Mulas**[2]**,**

[1]Ph.D Student, DICA, Politecnico di Milano
e-mail: eleonora.lai@polimi.it

[2]Associate Professor, DICA, Politecnico di Milano
e-mail: mariagabriella.mulas@polimi.it

Keywords: Structural Dynamics, Footbridges, Dynamic loads, Pedestrian-Structure Interaction, Vibration, Design-Criteria, FE-model.

Abstract. *In the last years, the need for structures able to link the functional and aesthetic role has led engineers and architects to design footbridges characterized by long span, light materials and increasing slenderness. The low ratio between permanent and variable loads makes recent footbridges more sensitive to the dynamic loads, such as the forces transmitted by pedestrian. Excessive vibrations may arise when the bridge natural frequencies are very close to those characterizing the human activities: walking, jogging and running. This issue became relevant after the Millenium Bridge inauguration, when an excessive lateral sway motion was triggered by the synchronization between bridge and pedestrian movements.*

The dynamic behavior of a lively footbridge over-passing the Serio river near Seriate (about 50 km far from Milan), Italy, is investigated in this paper. The suspension bridge, 63.75 m long, is composed of a timber deck on a steel grid. The footbridge model, based on the as-built design data, is implemented in the ANSYS framework. The numerical frequencies computed through the FE model match those identified from the results of the experimental campaign of ambient vibration measurements in a fully satisfactory way. Since the bridge displays several frequencies in the range excited by human activities, its response to crossing pedestrians is investigated. The dynamic interaction pedestrians-footbridge is analyzed for different classes of traffic with two approaches. First, the FE model developed in ANSYS is excited by the distributed harmonic load model for a pedestrian stream, applied on the bridge coherently with the corresponding mode shape, as suggested by the Hivoss Guideline. Second, an ad-hoc developed numerical code is adopted to compute the bridge dynamic response to moving forces. This code reads as input data the structural matrices computed in ANSYS and integrates the equations of motion of a system in which the pedestrian is modeled as a constant vertical travelling force along the footbridge deck. The vibration serviceability under the vertical component of pedestrian load is assessed by comparison to comfort criteria. The results of the Hivoss guideline show accelerations exceeding the value of comfort. The transient analysis predicts lower values within the limits. The two sets of values can be interpreted as an upper and lower bound of the actual response.

1 INTRODUCTION

The Seriate footbridge at study (Figure 1), about 64.0 m long, follows the recent aesthetic trend of light and slender footbridges. The structural solution includes a slender deck supported by a main spatial system of suspension cables and equipped by two lateral stabilizing cables with opposed curvatures, one on each side. At the bridge ends, two steel frames support the suspension cables and the backstays. Before the opening, the footbridge was subjected to dynamic tests, performed by the Laboratory of Vibration and Dynamic Monitoring of Structures (VibLab), Politecnico di Milano [1]. The tests included both operational modal testing and human-induced vibration due to the crossing of different groups of pedestrians, moving at several step frequencies. The dynamic behaviour of the structure turned out to be characterized by frequencies within the range of values perceived by human beings.

In a previous work [2] a numerical Finite Element (FE) model was developed within the ANSYS framework, to reproduce the experimental dynamic properties. In this work the FE model, capable to match the experimental frequencies, is adopted to simulate the pedestrians-structure dynamic interaction. In a first study on the vibration serviceability performance due to human-walking activity, a harmonic analysis is carried out with ANSYS, according to the Hivoss guidelines. Two different traffic classes are considered, coherently with the role of the bridge, connecting two cycle routes located in the "Serio Park". Subsequently, the pedestrians-footbridge dynamic interaction is investigated in more detail with an ad-hoc developed numerical Fortran code, named INTER: the structural matrices computed by ANSYS are read in input and the bridge equations of motion are integrated. Forcing terms are given by the pedestrians' weight travelling at a constant speed v on the deck, along straight trajectories parallel to the bridge longitudinal axis. The moving forces, simulating groups of pedestrians, can act with different spatial configurations, entering and exiting the bridge at different time instants.

The accelerations due to walking, predicted by the two numerical codes, have been compared to the comfort criteria prescribed by Hivoss guideline in order to estimate the vibration serviceability assessment under the vertical component of pedestrian load.

2 THE SUSPENSION FOOTBRIDGE

2.1 Bridge description

The "Seriate footbridge" (shown in Figure 1a), 63.75 m long, connects two cycle routes in the "Serio Park" (close to Milan, Italy). The timber deck on a steel grid (Figure 1b) has a width ranging between 2.5 m at the entrance and 5 m at midspan; the longitudinal steel girders are slightly curved with a rise of 1.3 m. The transverse beams of the steel grid (Figure 1b), spaced 1 m apart, fall into two categories: the main girders, connected to the hangers, with a tapered section and the secondary ones, with an IPE 120 cross-section. The stringers are a pair of IPE 330 beams at the edges, and a central beam with a circular section (ϕ=298.5 mm), deemed to stabilize the deck on the horizontal plane. A series of X-braces, shown in Figure 1b and connecting the main transverse girders, provides stiffness in the horizontal plane. The timber deck (shown in Figure 1b) has only a minor structural role, providing the walking surface and support for the pedestrian. The ends of the transverse main girders are crossed by stabilizing cables, whose sliding in the longitudinal direction is allowed by the interposition of a polymeric layer between the two contact surfaces.

The suspension system supporting the deck is composed of:

- steel main pylons, slightly inclined with respect to the vertical plane, and arranged in pairs creating an A-shaped portal. The portals support the suspension system and the

backstays cables as shown in Figure 1a;

- 2 main suspension cables, ϕ = 60 mm, supporting the longitudinal girders through 42 vertical hangers, of diameter 16 mm;
- backstays cables, ϕ = 60 mm, connecting the pylons top to the ground;
- 2 stabilizing cables of opposed curvatures ϕ = 40 mm.

The suspension system is not symmetric about the vertical plane crossing the longitudinal bridge axis: the two hangers connected to the same main transverse girder have different length and the main cables do not follow the same parabolic function. All the cables were pretensioned during construction.

(a)   (b)

Figure 1. Seriate Footbridge: (a) overall view; (b) footbridge deck, detail of longitudinal and transverse beam.

2.2 FE model

The bridge model, shown in Figure 2, is based on the as-built design data and has been implemented within the ANSYS framework. The girders of the steel grid, the pylons and the hangers are modeled with "BEAM 188". This beam element, with 6 degrees of freedom (DOFs) at each node, includes shear-deformation effects according to Timoshenko beam theory. Cables and braces are modeled with "LINK 180", a spar element transmitting axial force only, with 3 DOFs at each node [3]. The timber planks and the handrails are modeled as lumped masses applied on steel grid without any contribution to the overall stiffness; their weight is included in the dead load. The boundary conditions of the footbridge model, as the constraint conditions between adjacent elements, are inferred from the technical drawings.

The cables geometric stiffness and the variation of configuration associated to dead loads have been accounted for in a preliminary non-linear static analysis. Once the model correctly reproduces the design value of tension in cables and the deformed geometry, the modal analysis has been performed. Further details on the derivation of the FE model are found in [2].

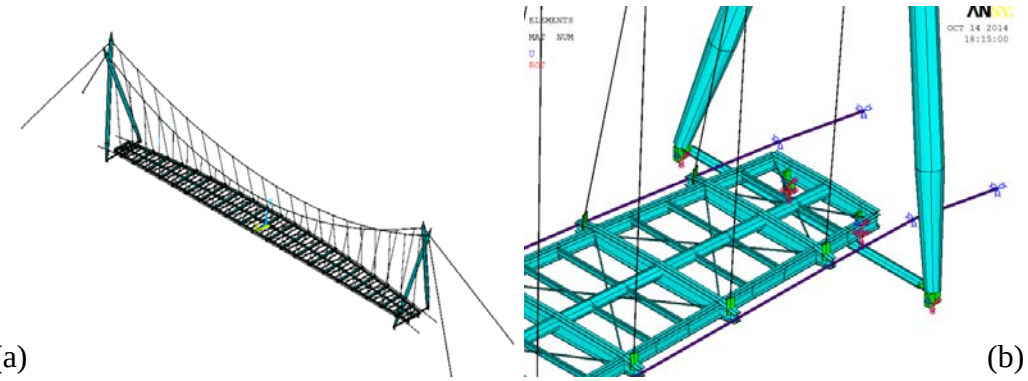
(a)  (b)

Figure 2. Finite element model of "Seriate Footbridge": (a) overall view; (b) detail of steel grid.

The results of modal analysis, in terms of frequencies and mode shapes, are compared with those obtained through the experimental campaign [1] in Table 1, also listing the percentage errors on the frequencies and the MAC (Modal Assurance Criterion, [4]) values computed on the mode shapes. The good correlation between the numerical and experimental dynamic properties makes the FE model a solid base for further numerical calculations.

Mode	Mode Type	Frequency			MAC
		Experimental (Hz)	Numerical (Hz)	ε (%)	
1	Vertical-flexural	1.025	1.079	5.22	0.995
2	Vertical-flexural	1.475	1.565	6.07	0.994
3	Vertical-torsional	1.924	1.997	3.77	0.908
4	Vertical-transversal	1.953	2.109	7.99	0.842
5	Vertical-flexural	2.168	2.311	6.58	0.984
6	Vertical-torsional	2.754	2.635	-4.33	0.975
7	Vertical-flexural	2.861	2.827	-1.17	0.996
8	Vertical-torsional	3.691	3.645	-1.24	0.957
9	Vertical-flexural	4.121	4.076	-1.10	0.988
10	Vertical-torsional	4.385	4.409	0.55	0.982
11	Vertical-flexural	5.645	5.512	-2.36	0.958
12	Vertical-torsional	6.006	5.875	-2.18	0.982
13	Vertical-flexural	7.217	7.255	0.52	0.976
14	Vertical-torsional	7.490	7.394	-1.28	0.983

Table 1. Comparison between experimental and numerical results

3 VIBRATION SERVICEABILITY DUE TO WALKING: HIVOSS GUIDELINE

The first assessment of the serviceability conditions of the footbridge has been carried out following the Hivoss guideline (HG). For the sake of completeness, the main features of the HG of interest in this work will be summarized in the following. The guideline indicates the critical ranges for the natural frequencies f of the footbridges subjected to pedestrian walking as it follows [5]:

- for vertical and longitudinal vibrations: $1.25\ Hz \leq f \leq 2.3\ Hz$
- for lateral vibration: $0.5\ Hz \leq f \leq 1.2\ Hz$

Moreover, footbridges with natural frequencies in the range $2.5\ \text{Hz} \leq f \leq 4.6\ \text{Hz}$ might be excited to resonance by the second harmonic of pedestrian loads [4]. In this case, the critical frequency range for vertical and longitudinal vibration expands to $1.25\ \text{Hz} \leq f \leq 4.6\ \text{Hz}$ [4]. Lateral vibrations are not affected by the second harmonic of pedestrian loads. The "Seriate footbridge" shows 10 natural frequencies in the critical range. In particular, the first frequency is in the range characterizing the lateral vibration, while the remaining ones might produce vertical and longitudinal vibrations. It must be specified that, starting from the fifth mode, the 2^{nd} harmonic of pedestrians load has to be considered.

The HG [5] proposes a load model to simulate the walking activity induced by a group of pedestrians. A uniformly distributed harmonic load $p(t)$ [N/m^2] represents the equivalent pedestrian stream:

$$p(t) = P * \cos(2\pi f_s t) * n' * \psi \tag{1}$$

In eqn. (1), $P * \cos(2\pi f_s t)$ is the harmonic load due to a single pedestrian. P is the component of the force due to a single pedestrian ($P = 280\ N$ for vertical load, $P = 140\ N$ for longitudinal load and $P = 35\ N$ for lateral load) with a walking step frequency f_s. The step frequency f_s is assumed equal to the footbridge natural frequency under consideration; n' is the equivalent number of pedestrians on the loaded surface S. The reduction coefficient ψ takes into account the probability that the footfall frequency approaches the critical range of natural frequencies under consideration. HG adopts two load models to calculate the response of the footbridge depending on pedestrian density and traffic class (Table 2) [5]:

- load model for TC1 to TC3 (density $d < 1.0\ P/m^2$)
- load model for TC4 to TC5 (density $d \geq 1.0\ P/m^2$)

Traffic class	Density (pedestrian/m^2)	Description
TC1	15P/(B×L)	Very weak
TC2	0.2 P/m^2	Weak
TC3	0.5 P/m^2	Dense
TC4	1.0 P/m^2	Very dense
TC5	1.5 P/m^2	Exceptionally dense

Table 2. Pedestrian traffic classes and density (from [5])

In the first class TC1 only 15 pedestrians are moving on the whole area B×L of the footbridge. The equivalent number of pedestrians n' depends on the structural damping ratio ξ, on the loaded surface S and on the number of pedestrians n on the surface($n = S * d$):

TC1 to TC3
$$n' = \frac{10.8\sqrt{\xi * n}}{S} \quad \left[\frac{1}{m^2}\right] \tag{2}$$

TC4 to TC5
$$n' = \frac{1.85\sqrt{n}}{S} \quad \left[\frac{1}{m^2}\right] \tag{3}$$

The value of the reduction coefficient ψ is depicted in Figure 3, for the two situations in which the excitation frequency is in the first or second harmonic of the pedestrian load.

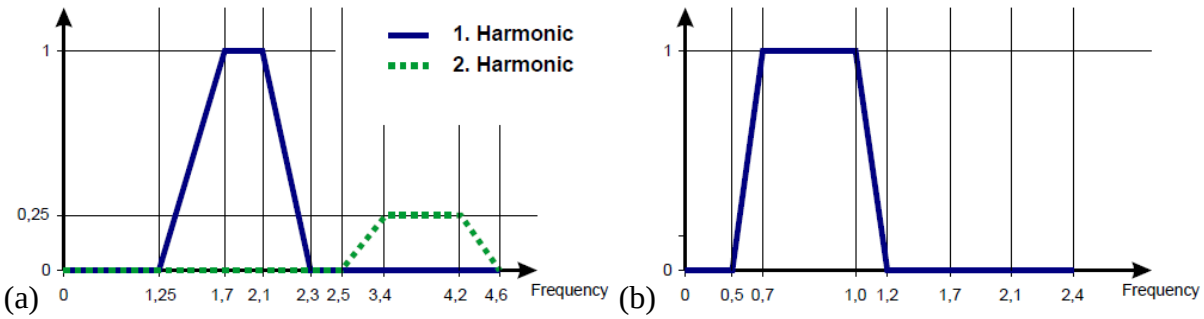


Figure 3. Reduction factor: (a) vertical and longitudinal load, (b) lateral load (from [5])

The direction of the harmonic load is the same of the half-waves characterizing the mode shapes associated to the natural frequency considered in the dynamic analysis (Figure 4).

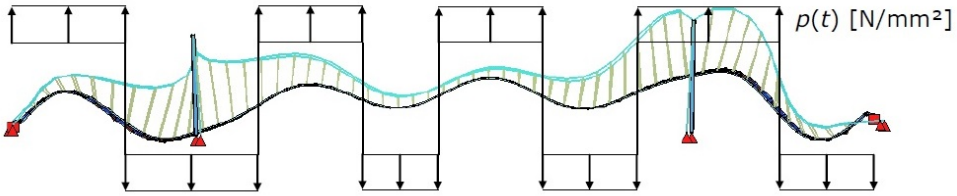


Figure 4. Application of a harmonic load according to mode shape (from [5])

The fulfillment of vibration serviceability conditions requires that the computed values of acceleration stay within the acceleration limits corresponding to four classes with a decreasing degree of comfort (Table 3). Two different traffic classes are here considered: TC1 (very weak traffic), associated to a comfort class CL1, and TC2 (weak traffic), associated to a comfort class CL2. Since the footbridge is located in a country park, the probability to find a "dense traffic" is very small and higher traffic classes are not taken into account.

Comfort classes			
Comfort class	Degree of comfort	Vertical a_{lim}	Lateral a_{lim}
CL1	Maximum	< 0.5 m/s^2	< 0.1 m/s^2
CL2	Medium	0.5 – 1.0 m/s^2	0.1 – 0.3 m/s^2
CL3	Minimum	1.0 – 2.5 m/s^2	0.3 – 0.8 m/s^2
CL4	Unacceptable discomfort	> 2.5 m/s^2	> 0.8 m/s^2

Table 3. Comfort classes with common acceleration ranges (from [5])

As shown in Table 1, there are 10 natural frequencies in the critical bandwidth. For each frequency, and for each traffic class considered, a dynamic analysis is performed. Each analysis is characterized by a harmonic load acting up and down coherently with the corresponding mode shape directions and by an excitation frequency equal to one of the natural frequency of the bridge. The maximum accelerations have been computed with a harmonic analysis in ANSYS. The numerical results are evaluated, in three cross sections of the deck (at half-span and at a 1/4 of span, both sides) for three points: two are placed at the base of handrails and the third one is on the longitudinal axis of the footbridge deck (Figure 5).

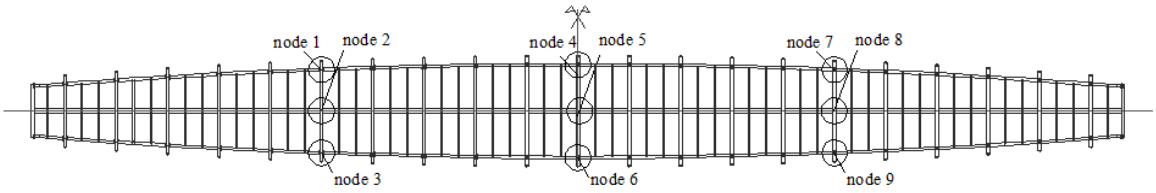


Figure 5. Cross sections and corresponding points considered in the analysis

The "Seriate footbridge" exhibits natural mode shapes with a flexural or torsional-flexural behavior, except for the 4th mode (*f = 1.95 Hz*), characterized by a displacement field in the transverse horizontal plane. For each flexural mode, the significant output response parameter is the amplitude of the vertical acceleration due to the related harmonic load; lateral accelerations are considered, due to the harmonic load tuned to the 4th mode. Figure 6 and Figure 7 depict the results for the traffic classes TC1and TC2, respectively. The maximum values of footbridge acceleration, at the selected nodes and for each mode, are depicted in Figures 6a, 7a and 6b, 7b for vertical vibration and lateral vibration respectively. Horizontal lines denote the limit values proposed by Hivoss guideline.

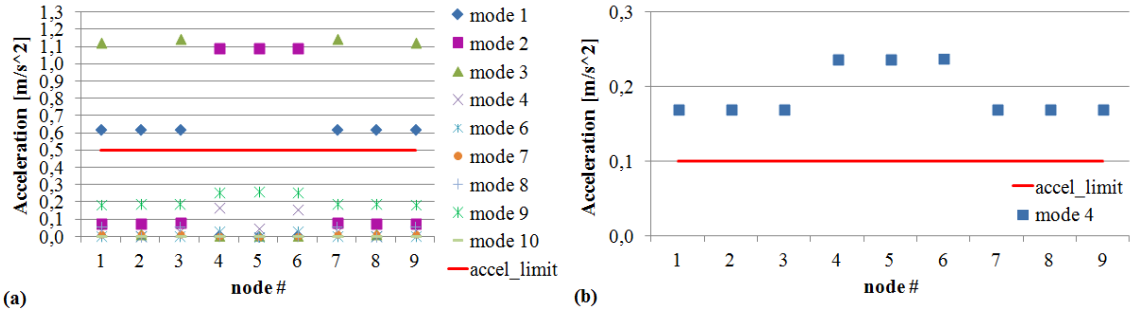


Figure 6. Vibration serviceability assessment, traffic class TC1: (a) vertical vibration, (b) lateral vibration.

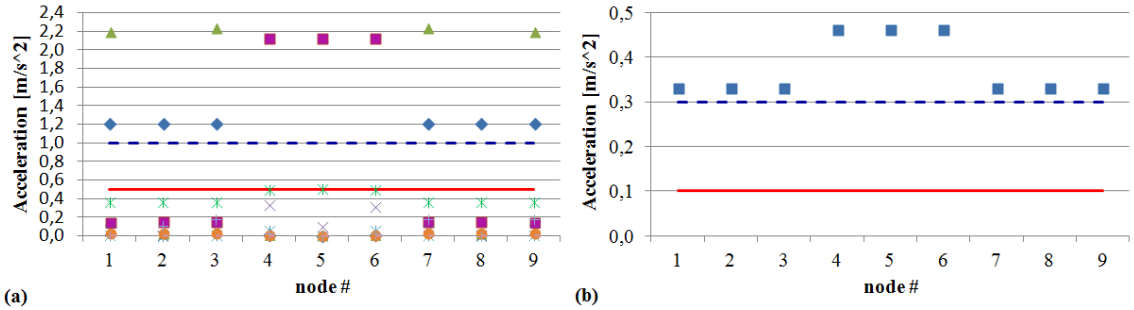


Figure 7. Vibration serviceability assessment, traffic class TC2, (a) vertical vibration, (b) lateral vibration.

In Figure 7, having the same legend as in Figure 6, the dashed and the solid line represent the upper and the lower bound of the limit acceleration value, respectively, for the comfort class CL2. The results show that the accelerations due to the harmonic loads tuned with the first 4 mode shapes exceed the comfort limits in both traffic classes considered. Conversely, starting from the 6th mode shape, the maximum acceleration are lower than those prescribed by HG. The 5th mode doesn't appear in the Figures 6-7 since its reduction factor ψ is equal to zero, making the load amplitude null. When the excitation frequency exceeds the value of the 4th mode, the second harmonic of pedestrians loads comes into play. Until now, there is no hint in the literature that significant vibrations have occurred due to the second harmonic of pedestrians [5] and the numerical results confirm this finding.

4 VIBRATION SERVICEABILITY DUE TO WALKING: TRANSIENT ANALYSIS

The HG provides an engineering approach to the prediction of dynamic effects due to walking pedestrians. The bridge modal properties must be determined, and the dynamic load-induced model is applied in a harmonic analysis. However, the need arises of a more sophisticated approach to compute the bridge response, able to account in a more realistic way the human walking activity. Different models for the time variation of the vertical force induced by walking derived from experimental tests can be found in the literature. The bridge response to a moving variable force can only be computed with a numerical transient analysis, able to account for the force variation both in time and in space. To this aim, in this work a numerical code named INTER, written in Fortran language and originally developed to study the bridge-vehicle dynamic interaction [7], has been modified to analyze the interaction between pedestrians and bridge. Modifications have also affected the routines related to the bridge geometry. The updated INTER 2.0 version of INTER is able to consider bridges with different geometry, such as suspension bridges with an arch deck.

INTER 2.0 performs the transient analysis of a footbridge subjected to moving forces (pedestrians) in the time domain, by integrating the equations of motion with the Newmark's

method of constant acceleration. The structural matrices (stiffness and mass) of the footbridge, extracted from ANSYS at the end of the non-linear analysis, are read as input data. Thus, the stiffness matrix takes into account the stress stiffening, i.e. the stiffening of the structure due to its stress state (pre-tension applied in each cables). The relevant information about the bridge geometry and the characteristics of pedestrian stream are also input data.

As a first approximation, each pedestrian is modeled as a moving force travelling along the bridge deck with a constant velocity v and along a rectilinear trajectory parallel to the bridge axis. The pedestrian's position on the bridge deck is identified by the transverse and longitudinal coordinates x_p, y_p. Under the above assumptions, the former remains constant during motion, the latter varies linearly in time. The moving force is vertical and no horizontal force is transmitted from pedestrian to bridge. In the first implementation of the algorithm, the force amplitude is constant, and only its position on the bridge changes at each time step. Given the time step Δt of the numerical integration, at the generic instant $k\Delta t$, the pedestrian's position y_k along the longitudinal axis is computed from the pedestrian's position y_{k-1} at the previous *k-1* step as:

$$y_k = y_{k-1} + v * \Delta t \tag{4}$$

The equations of motion of the footbridge are:

$$\boldsymbol{M\ddot{q}} + \boldsymbol{C\dot{q}} + \boldsymbol{Kq} = \boldsymbol{N}(x_p, y_p(t))^T * F_P \tag{5}$$

where $\boldsymbol{q}$ is the vector listing the lagrangian coordinates of the footbridge FE model, $\boldsymbol{M}$ and $\boldsymbol{K}$ are the ANSYS mass and stiffness matrices respectively, $\boldsymbol{C}$ is the Rayleigh damping matrix, computed by INTER 2.0, and $\boldsymbol{N}(\boldsymbol{x_p}, \boldsymbol{y_p}(\boldsymbol{t}))^{\boldsymbol{T}} * F_P$ is the pedestrian forcing term. Since F_P is a constant term equal to the pedestrian's weight, the time variation is all included in the term, $\boldsymbol{N}(\boldsymbol{x_p}, \boldsymbol{y_p}(\boldsymbol{t}))^{\boldsymbol{T}}$, a vector of interpolating shape functions that transfers each load from its point of application to the proper nodes of the FE mesh.

The need for a shape functions vector arises from the following rationale. At a generic time instant, the pedestrian does not stay on a mesh node. In fact, he can follow a *quasi-random* rectilinear trajectory, only constrained to move parallel to the bridge axis and with a x_p coordinate inside the deck grid. At each time step, the shape functions transform the moving force into equivalent nodal loads on properly selected nodes. As shown in Figure 8, if the pedestrian trajectory coincides with a line of nodes, the loaded nodes will be those placed immediately before and after the force position. In the opposite case, the loaded nodes will be the four nodes of the mesh surrounding the pedestrian's position. The shape functions values, depending on the pedestrian's position $(x_p, y_p(t))$, change at each time step and their implementation takes care of unloading the nodes left behind and loading the approaching nodes. At each time step the terms of $\boldsymbol{N}(x_p, y_p(t))^T$ are all zero, except for the rows corresponding to the DOFs related to the nodes directly or indirectly loaded by the pedestrian.

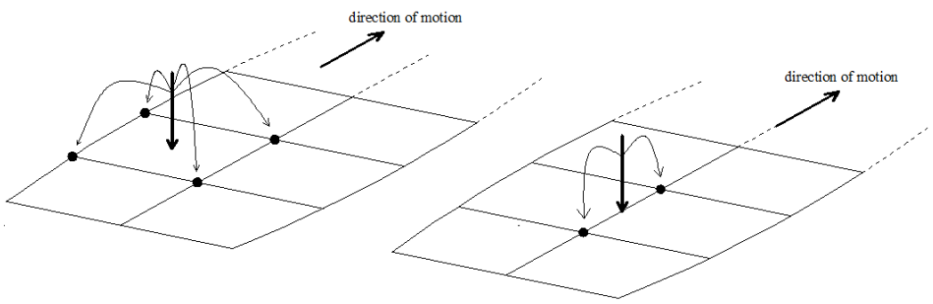


Figure 8. Loaded nodes: (a) pedestrian outside a line of nodes, (b) pedestrian on a line of nodes.

The FE model of the bridge deck contains only beam elements. Nevertheless, the shape functions are those of a 4-node shell element with 12 DOFs, based on Kirchhoff theory, already implemented in the code. This choice is acceptable if we consider the real situation of the timber deck and has proven to be able to minimize numerical problems tied to high frequency oscillation in the response. Since loads on the bridge are only vertical, the "virtual mesh" simulates a bending plate element and the selected shape functions produce, in each node, nodal forces on the vertical DOF and on the two out-of-plane rotational DOFs.

4.1 Numerical results

Either a single pedestrian or a group of pedestrians can move on the deck. Different spatial configurations of pedestrians have been implemented in INTER 2.0 to represent both a regular stream, with positions placed into a "uniform grid", and a random group of pedestrians in a "chess grid" with variable distance between them. This work considers a group of 15 pedestrians, as in the traffic class TC1, placed with a *random-like* distribution (Figure 10). The center of gravity of the group is eccentric with respect to the bridge axis. The distance between the first and last pedestrian is 17 m; the position of the resultant force in longitudinal direction is 9.6 m behind the first pedestrian row. A velocity of 1.3 m/s is considered [8]. Each pedestrian crosses the bridge in 49 s and the last pedestrian exits the bridge 13,7 s after the first.

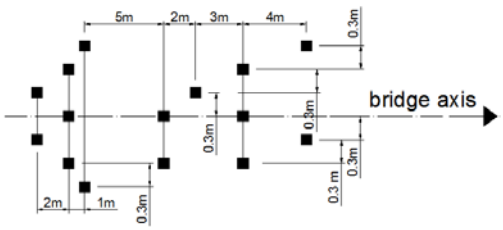


Figure 9. Distribution of pedestrians associated to traffic class TC1; the arrow defines the direction of motion.

The integration time step Δt is 0.001s, quite smaller than 1/10 of the period of the 14th mode. At time $t=0$ the first pedestrian enters the bridge; the analysis goes on for 25 s after the last pedestrians exit the bridge. The Rayleigh damping matrix is computed for a 1% damping, a value experimentally identified, on the first and fourth mode. The time history of displacements and accelerations at the nodes considered in the harmonic analysis (Figure 5) are the relevant response parameters. Figure 10 depicts the accelerations of the nodes 2-5-8 along the bridge axis. Figure 11 shows the same quantity for the lateral nodes 3-6-9. A different pattern is detected, with largest values in the lateral nodes, due to the torsional effect induced by the load scheme. The acceleration at midspan (nodes 5-6) when the resultant force reaches the cross section (t≅30 s), is coherent with the mode shape of the 6th torsional mode.

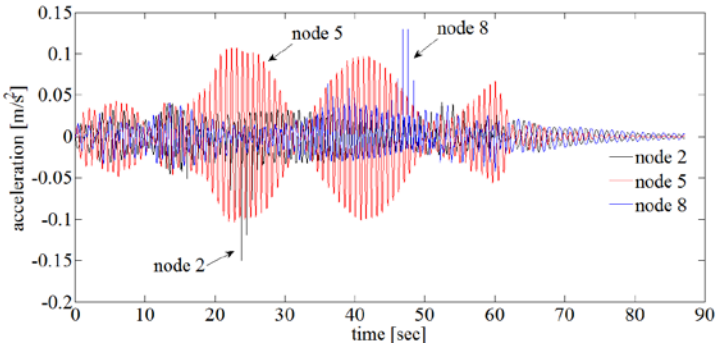


Figure 10. “Random” pedestrian stream: time history of acceleration, nodes 2-5-8.

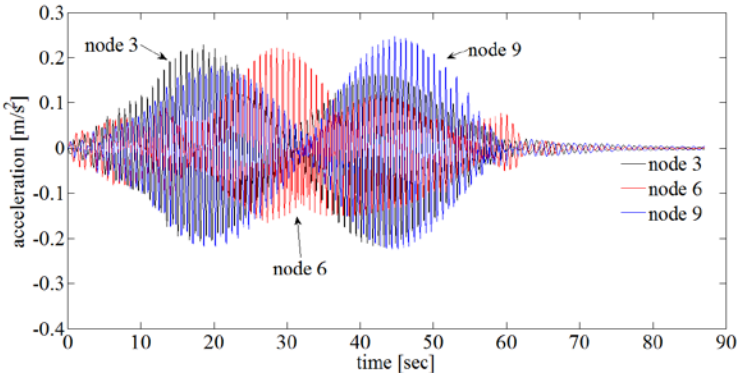


Figure 11. “Random” pedestrian stream: time history of acceleration for nodes 3-6-9.

Figure 12 shows the displacement responses of the nodes along the bridge axis (2-5-8). The nodes 2 and 8, at the ¼ of the span, show quasi-specular results; each node attains the maximum displacement in the time interval when is reached by the center of the parallel forces. In Figure 13 the displacement responses of the nodes at midspan (4-5-6) have a similar pattern but different magnitude due to the eccentricity of the load pattern. Node 6 experiences the maximum value of displacement.

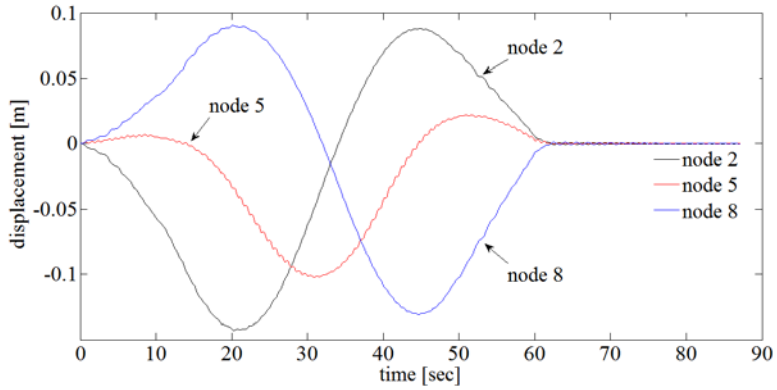


Figure 12. “Random” pedestrian stream: time history of displacement for nodes 2-5-8.

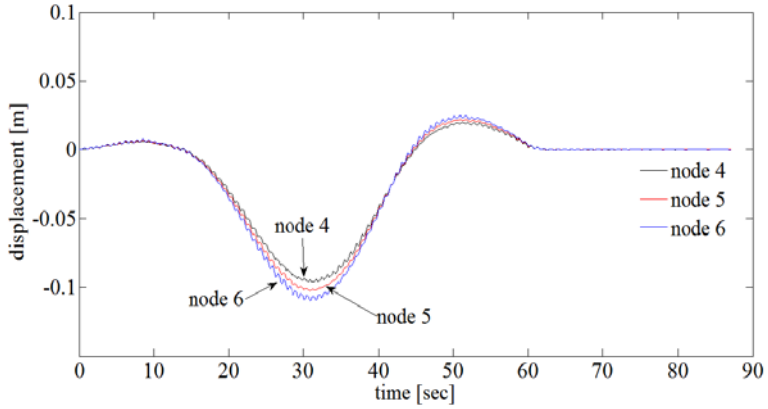


Figure 13. “Random” pedestrian stream: time history of displacement for nodes 4-5-6.

5 CONCLUSIONS

The results of serviceability assessment of a lively footbridge have been obtained with a harmonic analysis in ANSYS, as suggested by the HG, and with a transient step-by-step anal-

ysis performed with an *ad-hoc* numerical code named INTER. Two traffic classes are considered, very weak and weak (TC1, TC2), respectively associated to maximum CL1 and medium CL2 comfort classes. Ten natural frequencies of the footbridge are in the critical range characterizing the walking activity. Even though the pedestrian-induced loads are different in the two approaches, a comparison between the predicted acceleration values appears significant.

In the HG implementation, the 2^{nd} harmonic of pedestrian load has to be considered starting from the 5^{th} mode. The accelerations due to the harmonic loads tuned to the first 4 modes exceed the comfort limits in both traffic classes considered. Moreover, no significant vibrations have been detected due to the second harmonic of pedestrians load. The transient analysis is performed with the code INTER 2.0 under a stream of 15 pedestrian aimed to represent the TC1 condition. The peaks of the acceleration value are lower, but of the same order of magnitude of those induced by the harmonic loads for the higher modes. The results provided by HG and INTER 2.0 can represent an upper and lower bound of the expected acceleration. On one side, a very low value of damping ratio is related to a high value of the amplification factor in the harmonic analysis of HG. On the other side, the dynamic effect induced by the moving pedestrian, as computed by INTER 2.0, is underestimated by the approximations of constant force moving in a continuous way on the deck.

The numerical results hint that the vibration serviceability conditions of the footbridge may not be fulfilled. Further studies will address the issues tied to the transient analysis, namely the efficiency of the numerical integration, the modeling – in space and time - of the pedestrian-induced force and the effect of the space distribution of pedestrians. Final aim of the research work is the study of the dynamic interaction based on the adoption of a mechanical system for each pedestrian.

REFERENCES

[1] E. Lai, C. Gentile, Mulas M.G., Vibration testing and FE modelling of a lively footbridge. *6th International Operational Modal Analysis Conference (IOMAC'15)*, Gijón, Spain, May 12-14, 2015, submitted for possible publication.

[2] E. Lai, M.G. Mulas, C. Gentile, Numerical modeling of a suspension footbridge. *30th International CAE Conference*, Pacengo del Garda, Italy, October 27-28, 2014.

[3] ANSYS (2015). Online Manuals Release 5.5. http://mostreal.sk/html/guide_55/GBooktoc.htm.

[4] R.J. Allemang, D.L. Brown,. Correlation coefficient for modal vector analysis. In *Proceedings of the 1st Int. Modal Analysis Conf. (IMAC-I)*, Orlando, FL, USA(1983).

[5] *Human induced vibration of steel structures guidelines*, 2007 (http://www.stb.rwth-aachen.de/projekte/2007/HIVOSS/download.php).

[6] C. Heinemeyer, C. Butz, A. Keil, M. Schalaich, A. Goldack, S. Trometer, M. Lukic, B. Chabrolin, A. Lemaire, P. O. Martin, A. Cunha, E. Caetano, *Design of lightweight footbridges for human induced vibrations – Joint Report*, JRC First Edition, May 2009.

[7] A. Feriani, M.G. Mulas, E. Poli, An uncoupled iterative approach for bridge-vehicle coupled systems. *8th International Conference on Structural Dynamics (EURODYN 2011)*, Leuven, Belgium, July 4-6, 2011.

[8] A. Pachi, T. Ji, Frequency and velocity of people walking. *Journal of Structural Engineering*, **83(3)**, 36-40, 2005.

COMPDYN 2015

Proceedings of the
5th International Conference on
Computational Methods in Structural Dynamics and Earthquake Engineering

M. Papadrakakis, V. Papadopoulos, V. Plevris (Eds)

First Edition, September 2015

ISBN: 978-960-99994-7-2



Institute of Structural Analysis and Antiseismic Research
National Technical University of Athens, Greece